



**CHL
LIBRARY**

VOLUME 1
Edited by Billy L. Edge

Coastal Engineering

1990 PROCEEDINGS

Twenty-Second Coastal Engineering Conference

Proceedings of the International Conference
VOLUME 1

July 2–6, 1990
Delft, The Netherlands

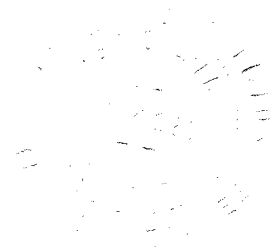
Conference held under the auspices of the
Coastal Engineering Research Council of the
American Society of Civil Engineers

Organized by the Royal Institution of Engineers in the
Netherlands (KIVI), Division for Civil Engineering and
co-sponsored by the Permanent International Association of
Navigation Congresses and the International Association for
Hydraulic Research.

Edited by Billy L. Edge



Published by the
American Society of Civil Engineers
345 East 47th Street
New York, New York 10017-2398



ABSTRACT

This proceedings contains over 250 papers presented at the 22nd International Conference on Coastal Engineering which was held in Delft, The Netherlands, July 2-6, 1990. The book is divided into eight parts: 1) Characteristics of coastal waves and currents; 2) long waves and storm surges; 3) coastal structures; 4) the Dutch coast 5) coastal processes and sediment transport; 6) coastal, estuarine and environmental problems; 7) ship motions; and 8) case studies. The individual papers include such topics as the sedimentation and beach nourishment. Special emphasis is given to case studies of completed engineering projects. With the inclusion of both theoretical and practical information, these papers provide the civil engineer and related fields with a broad range of information on coastal engineering.

Library of Congress Cataloging-in-Publication Data

Coastal Engineering Conference (22nd: 1990: Delft, Netherlands)

Coastal engineering 1990 proceedings: proceedings of the international conference. July 2-6, 1990, Delft, The Netherlands/Twenty-second Coastal Engineering Conference; edited by Billy L. Edge: organized by the Royal Institution of Engineers in the Netherlands (KIVI), Division for Civil Engineering and co-sponsored by the Permanent International Association of Navigation Congresses and the International Association for Hydraulic Research.

p. cm.

“Conference held under the auspices of the Coastal Engineering Research Council of the American Society of Civil Engineers.”

Includes index.

ISBN 0-87262-776-4

1. Coastal engineering—Congresses. I. Edge, Billy L. II. Koninklijk Instituut van Ingenieurs (Netherlands). Division for Civil Engineering. III. Permanent International Association of Navigation Congresses. IV. International Association for Hydraulic Research. V. Title.

TC203.5.C62 1990

627—dc20

91-9069

CIP

The Society is not responsible for any statements made or opinions expressed in its publications.

Authorization to photocopy material for internal or personal use under circumstances not falling within the fair use provisions of the Copyright Act is granted by ASCE to libraries and other users registered with the Copyright Clearance Center (CCC) Transactional Reporting Service, provided that the base fee of \$1.00 per article plus \$.15 per page is paid directly to CCC, 27 Congress Street, Salem, MA 01970. The identification for ASCE Books is 0-87262/88. \$1 + .15. Requests for special permission or bulk copying should be addressed to Reprints/Permissions Department.

Copyright © 1991 by the American Society of Civil Engineers, All Rights Reserved.

Library of Congress Catalog Card No: 91-9069

ISBN 0-87262-776-4

ISSN 0893-8717

Manufactured in the United States of America.

Foreword

The 22nd International Conference on Coastal Engineering was held in Delft, The Netherlands. The 22nd ICCE, like the ones before it, was organized and managed by volunteers from within The Netherlands representing private, industrial and governmental contributors. This Conference represented an opportunity to share scientific and engineering information and provided a forum for interaction with other engineers and scientists working on similar coastal problems. The time and effort contributed to the development and organization of each conference becomes more complex and difficult as they continue to grow in size and content. The Local Organizing Committee worked on the planning for this Conference for nearly four years. All who attended the 22nd ICCE will agree that it was a tremendous success. The **Proceedings** of this Conference will represent a major step forward in the field of coastal engineering.

The chapters in this **Proceedings** have been prepared by the authors who were selected to make presentations at the 22nd International Conference on Coastal Engineering. The authors were asked to make the presentations and submit the final papers based upon review of the abstracts which were submitted well in advance of the Conference. The Technical Review Committee included four professionals who are active in the field of coastal engineering. One of the members is a representative of the Local Organizing Committee, a second member was part of the technical program committee for a previous conference in his country and the other two review members were selected for their broad understanding and recognition in the field. The papers included in this volume are eligible for discussion in the **Journal of the Waterways, Port, Coastal and Ocean Division** of the ASCE. All papers are eligible for ASCE awards.

Venues for the upcoming conferences are listed below:

23rd ICCE - Venice, Italy	1992
24th ICCE - Kobe, Japan	1994
25th ICCE - Orlando, FL, USA	1996
26th ICCE - Copenhagen, Denmark	1998

Coastal engineers who would desire to host a future conference in their country should contact the Secretary of the Coastal Engineering Research Council to receive information about submitting a proposal.

The continuing coordination of the International Conferences on Coastal Engineering is through the Coastal Engineering Research Council of the ASCE. The Research Council began at the instigation of Professor Boris Bakhmeteff who as chairman of the Research Committee of the Engineering Foundation suggested the formation of the Council on Wave Research. The Council was established in June 1950 under the Engineering Foundation.

Subsequently in 1963 the Council was transferred from the Foundation to the ASCE

and was renamed the Coastal Engineering Research Council which better described its expanded function.

Members of the Foundation and subsequently members of the Council recognized that coastal engineering problems required broad based research to better define the coastal and ocean phenomena with which they dealt. The Foundation felt that it was important that all disciplines working in the coastal area should have an opportunity and be encouraged to communicate with one another through the mechanism of interdisciplinary conferences.

The first conference was held in Long Beach, CA in 1950. The papers which were delivered at that conference were published and became the first coastal engineering conference **Proceedings**. Although the conferences began with a national focus they quickly became international in scope. After planning and conducting 22 conferences on coastal engineering the Series has been established as the principal conference on coastal engineering in the world. Contributors to the conference represent nearly all coastal nations and the numbers of abstracts which are submitted for consideration are generally twice as large as the available opportunity for presentations. The **Proceedings** of the conferences are all available from the ASCE.

Billy L. Edge, Secretary
Coastal Engineering Research Council, ASCE

ACKNOWLEDGMENTS

ORGANIZING COMMITTEE

Chairman:
E.W. Bijker - formerly Delft University of Technology

Secretary:
J. van der Weide - Delft Hydraulics
A.P.H. van Baardewijk - International Contracting
J.A. Battjes - Delft University of Technology
P.H.A. Hoogweg - Rijkswaterstaat
J.M. van der Kamp - Congress Office KIVI

SCIENTIFIC COMMITTEE

Chairman:
J.A. Battjes - Delft University of Technology
W.T. Bakker - Rijkswaterstaat
J. van de Graaff - Delft University of Technology
K.W. Pilarczyk - Rijkswaterstaat
P.J. Visser - Delft University of Technology
J.J. de Vriend - Delft Hydraulics

ACCOMPANYING PERSONS' COMMITTEE

Mrs. Fenneke d'Angremond-Pols
Mrs. Lenie Bakker-Walter
Mrs. Gerie Battjes-Hollander
Mrs. Greta Bijker-Jellerna
Mrs. Connie van de Graaff-Goedendorp

COASTAL ENGINEERING RESEARCH COUNCIL (ASCE)

Chairman:
Robert L. Wiegel

Vice-Chairman:
Orville T. Magoon

Secretary:
Billy L. Edge

Members:
Eco W. Bijker
Robert G. Dean
Kyoshi Horikawa
Ronald M. Noble
Thorndike Saville, Jr.
Leonardo Zeevaert

FINANCIAL SUPPORT

Financial Support has been given by:

Ministry of Transport and Public Works, Dept. Rijkswaterstaat
Ministry of Economic Affairs, Netherlands Foreign Trade Agency

C.B. Association of Dutch Dredging Contractors
D.H. Delft Hydraulics
K & O Netherlands Coastal Works Association
NABU Netherlands Association of International Contractors
NEDECO Netherlands Engineering Consultants
VGB Dutch Association of Major Contractors

CONTENTS

OPENING ADDRESS

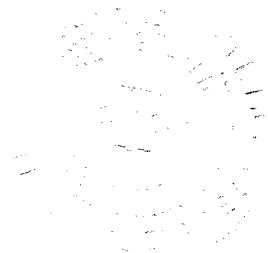
His Royal Highness Prince Claus of The Netherlands

KEYNOTE ADDRESS

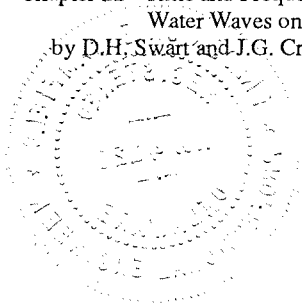
Rethinking Our Role in Coastal Zone Development
by J.E. Prins

Part I: CHARACTERISTICS OF COASTAL WAVES AND CURRENTS

Chapter 1 - Distribution Function Fitting for Storm Wave Data by Y. Goda and K. Kobune	18
Chapter 2 - A Model for Surf Beat by P.J. van Lecuwen and J.A. Battjes	32
Chapter 3 - Evaluation of Empirical Model for Wave Runup Elevations by R. Hallermeier, K.B. Nosek and C.J. Andrassy	41
Chapter 4 - Model Predictions of Nonbreaking Shoaling Waves by S. Elgar, M.H. Freilich and R.T. Guza	55
Chapter 5 - Transition Zone Width and Implications for Modelling Surfzone Hydrodynamics by R.B. Nairn, J.A. Roelvink and H.N. Southgate	68
Chapter 6 - The Group Characteristics of Sea Waves by Y.-X. Yu and S.-X. Liu	82
Chapter 7 - Field Observation on Wave Set-Up Near the Shoreline by S.-i. Yanagishima and K. Katoh	95
Chapter 8 - Modelling Shoaling Directional Wave Spectra in Shallow Water by J.T. Kirby	109
Chapter 9 - Modeling of Energy Transfer and Undertow in the Surf Zone by A. Okayasu, A. Watanabe and M. Isobe	123



Chapter 10 - Numerical Simulation of Nonlinear Wave Transformation Over a Submerged Plate by X. Yu, M. Isobe and A. Watanabe	136
Chapter 11 - Vertically 2-D Nearshore Circulation Model by T. Yamashita, Y. Tsuchiya and D.A. Suriamihardja	150
Chapter 12 - Violent Water Motion at Breaking-Wave Impact by M.J. Cooker and D.H. Peregrine	164
Chapter 13 - Wave Group Properties of Coastal Waves by H. Mase, T. Yamashita and K. Hayashi	177
Chapter 14 - Measurement and Computation of Wave Induced Velocities on a Smooth Slope by J.W. van der Meer and M.K. Breteler	191
Chapter 15 - A Numerical Model for Refraction Computation of Irregular Waves Due to Time-Varying Currents and Water Depth by M. Yamaguchi and Y. Hatada	205
Chapter 16 - Extreme Storms in the Adriatic Sea by L. Cavaleri, L. Bertotti, P. Canestrelli and P. Lionello	218
Chapter 17 - Set-Up Driven Undertows on a Barred Beach by P.D. Osborne and B. Greenwood	227
Chapter 18 - Nearshore Circulation with 3-D Profiles by I.A. Svendsen and U. Putrevu	241
Chapter 19 - Conditional Simulations in Laboratory Flumes by M.H. Gimenez, L.E. Borgman, R.T. Hudspeth, J.R. Medina, C. Sanchez-Carratala and H. Tuah	255
Chapter 20 - The Effect of Wave Directionality on Nearshore Waves by M.J. Briggs and J.M. Smith	267
Chapter 21 - Similarity of Velocity Profiles in Non-Uniform Longshore Currents by H. El A.A. Refaat, Y. Tsuchiya and Y. Kawata	281
Chapter 22 - Time and Frequency Domain Analyses of Shallow Water Waves on a Slope by D.H. Swart and J.G. Crowley	293



Chapter 23 - Extension of Mild Slope Equation for Waves Propagating Over a Permeable Submerged Breakwater by T. Izumiya	306
Chapter 24 - Another Quasi-3D Model for Surf-Zone Flows by A. Sanchez-Arcilla, F. Collado, M. Lemos and F. Rivero	316
Chapter 25 - Wave Attenuation on an Offshore Coral Reef by T.A. Hardy, I.R. Young, R.C. Nelson and M.R. Gourlay	330
Chapter 26 - Application of Lognormal Truncated Distribution to Prediction of Long Term Sea State Using Visual Wave Height Data by A. Gonzalez, J. Martinez and R. Blazquez	345
Chapter 27 - Extreme Waves and Wave Counts in a Hurricane by R.J. Sobey, B.A. Harper and B.D. Chandler	358
Chapter 28 - A Prediction Model of Irregular Wave Run-Up Height on Coastal Structures by C.-R. Ryu and H.-Y. Kang	371
Chapter 29 - Effects of the Gulf Stream on Nearby Coastal Waves by L.H. Holthuijsen and H.L. Tolman	384
Chapter 30 - Improved Calculation of the Shoaling Wave Field by M. Hattori and T. Katsuragawa	396
Chapter 31 - A Model for Long Waves at Grazing Angle to a Rubble-Mound Jetty by E. Melo and R.T. Guza	410
Chapter 32 - Movable Bed Friction Factors for Spectral Waves by O.S. Madsen, P.P. Mathisen and M.M. Rosengaus	420
Chapter 33 - Second Order Wave Generation and Application to Shoaling Investigations by A. Gotschenberg and K.F. Daemrich	430
Chapter 34 - Computation of 3-D Wind-Driven Currents by Response Function Method by S.-K. Liu and J.J. Leendertse	444
Chapter 35 - Velocities and Bed Friction in Combined Flows by J.F.A. Sleath	450
Chapter 36 - On the Fitting of Jonswap Spectra to Measured Sea States by E.P.D. Mansard and E.R. Funke	464

Chapter 37 - An Efficient Method for the Reproduction of Non-Linear Random Waves by G. Klopman and P.J. van Leeuwen	478
Chapter 38 - An Experimental Study of Waves on a Strongly Sheared Current Profile by C. Swan	489
Chapter 39 - Wave Kinematics in the Surface Zone by J.E. Skjelbreia and A. Torum	503
Chapter 40 - Stochastic Modeling of Surfing Climate by W.R. Dally	516
Chapter 41 - Wave Model Application in a Wadden Sea Area by J.D. den Adel, H.D. Niemeyer, A.F. Franken N. Booij, J. Dekker and J.A. Vogel	530
Chapter 42 - The Mass Transport of Waves Propagating on a Sloping Bottom by H.H. Hwung and C. Lin	544
Chapter 43 - Turbulence Scales in the Surf and Swash by R.E. Flick and R.A. George	557
Chapter 44 - Reflection From Swash Zone on Natural Beaches by S. Kubota, M. Mizuguchi and M. Takezawa	570
Chapter 45 - Instabilities in the Longshore Current by N. Dodd, J. Oltman-Shay and E.B. Thornton	584
Chapter 46 - A Comparison of the Performance of Three Mathematical Models of Wave Disturbance in Harbour Approaches by J.V. Smallman and N.P. Tozer	597
Chapter 47 - Observations of Wind Wave Nonlinearity by T.H.C. Herbers and R.T. Guza	611
Chapter 48 - Applicability of a New Hybrid Parametric Wave Prediction Model by Y. Hatada and M. Yamaguchi	623
Chapter 49 - Bottom Shear Stress and Friction Factor Due to the Asymmetric Wave Action by C.-T. Kuo and W.-J. Chen	637
Chapter 50 - Estimation of Directional Spectrum Expressed in Standard Form by M. Isobe	647

Chapter 51 - Characteristics of Oscillatory Flow Over Ripple Models by K. Horikawa and S. Ikeda	661
Chapter 52 - Sensitivity Analysis for Multi-Element Wavemakers by G.S. Harkins, R.A. Dalrymple and M.A. Losada	675
Chapter 53 - A Model to Propagate Nonlinear Water Waves by J.M.C. Leitao and J.L.M. Fernandes	689
Chapter 54 - Wave Direction Measurement Using Marine X Band Radar by H. Hirakuchi and M. Ikeno	703
Chapter 55 - Variation of Surf Zone Turbulence In a Wave Period by Y. Tada, T. Sakai and E. Obana	716
Chapter 56 - Wave Group Forced Nearshore Circulation by R.E. Fowler and R.A. Dalrymple	729
Chapter 57 - Bore-Like Surf Beat on Reef Coasts by E. Nakaza, S. Tsukayama and M. Hino	743
Chapter 58 - Bragg Reflection of Waves by Artificial Bars by J.T. Kirby and J. Anton	757
Chapter 59 - Generation Mechanism of Abnormal Waves Along the Japan Coast by T. Komaguchi, Y. Tsuchiya and N. Shiraishi	769
Chapter 60 - Field Measurements and Analysis of Wave Induced Nearshore Currents by H. Niemeier	783
Chapter 61 - Directional Random Wave Propagation on Beaches by J.M. Grassa	798
Chapter 62 - Spatial Variation of Wave Group Statistics and Representative Wave-Heights of Swell by A. Ukai, T. Yasuda and K. Ito	812
Chapter 63 - Sea-Air Interactions in the Coastal Circulation Around Gran Canaria Island (Spain) by B. Tejedor, M. Alejo and L. Tejedor	826
Chapter 64 - A Numerical Method of Solitary Wave Forces Acting on a Large Vertical Cylinder by T. Ohyama	840

Chapter 65 - A Numerical Model of the Rough Turbulent Boundary Layer in Combined Wave and Current Interaction by H.-T. Son and A. Temperville	853
Chapter 66 - Runup, Setup and the Coastal Watertable by P. Nielsen	867
Chapter 67 - Application of the Second-Order Mode Coupling Equation to Coastal Engineering Problems by M. Tanaka	881
Chapter 68 - Full-Scale Measurements of Wave Run-up at Sea Dykes by U. Sparboom, J. Grune, S. Grosche and M. Haidekker	895
Chapter 69 - Statistical Characteristics of Offshore Currents by M. Ochi	909
Chapter 70 - Breaking and Reflection of a Steep Solitary Wave Caused by a Submerged Obstacle by T. Yasuda and M. Hara	923
Chapter 71 - Report from the NATO ARW on Water Wave Kinematics, May 1989 by A. Torum and O. T. Gudmestad	935
Chapter 72 - Prediction of the Dimensions of a Rip Current System on a Coast With Bars by J. Zyserman, J. Fredsoe and R. Deigaard	959
Chapter 73 - Scale Effects in Breaking Waves by A.D. Toumazis and K. Anastasiou	973
Chapter 74 - Comparison of Wave Hindcast Methods for Lower Gulf of Thailand by S. Weesakul and S. Charulakana	986
Chapter 75 - Developing Wave-Current Boundary Layers by R. Simons and A.G. Kyriacou	993
Chapter 76 - Incorporation of Wave Effects in a 3D Hydrostatic Mean Current Model by H. de Vriend and N. Kitou	1005
Chapter 77 - Nonsteady Computations of Undular and Breaking Bores by A.F.T. da Silva and D.H. Peregrine	1019
Chapter 78 - Experimental and Numerical Study on Solitary Wave Breaking by H. Nishimura and S. Takewaka	1033

Chapter 79 - Wave Reflection by a Number of Thin Porous Plates Fixed in a Semi-Infinitely Long Flume by S. Twu and D.T. Lin	1046
Chapter 80 - Modeling of Wave Transformation on Submerged Breakwater by S. Rojanakamthorn, M. Isobe and A. Watanabe	1060
Chapter 81 - Wind-Induced Cross-Shore Water Flows by J.B. Crowley and D.H. Swart	1074
Chapter 82 - Irregular Waves on a Current by H.-H. Pruser and W. Zielke	1088
Chapter 83 - Wave Spectra Transformations by G. Chiaia, L. Damiani and A. Petrillo	1102

Part II: LONG WAVES AND STORM SURGES

Chapter 84 - Evolution of Infragravity Variance During a Storm by P.A. Howd, J. Oltman-Shay, R. Holman and P.D. Komar	1118
Chapter 85 - Theory Versus Experiments in Two-Dimensional Surf Beats by H.A. Schaffer, I.G. Jonsson	1131
Chapter 86 - Bottom Pressures Due to Long Waves: Laboratory & Field Measurements by F. Raichlen, J.D. Ramsden and J.R. Walker	1144
Chapter 87 - Sea Level Rise: A Probabilistic Design Problem by J.K. Vrijling and I.J.C.A. van Beurden	1160
Chapter 88 - Nearfield Tsunamis Generated by Three Dimensional Bed Motions by J.-J. Lee and J.J. Chang	1172
Chapter 89 - Numerical 3-D Current Modelling of Stratified Seas by E.B. Rasmussen, H.J. Vested and L.C. Ekebjerg	1186
Chapter 90 - Long Wave Interaction with Steeply Sloping Structures by S.T. Grilli and I.A. Svendsen	1200
Chapter 91 - North Sea Winds on Tides and Storm Surges by H.L. Tolman	1214
Chapter 92 - Decomposition and Interception of Long Waves by a Submerged Horizontal Plate by H. Kojima, T. Ijima and A. Yoshida	1228

Chapter 93 - Observations of the Swash Expression of Far Infragravity Wave Motions by R.A. Holman, P.A. Howd, J.M. Oltman-Shay and P.D. Komar	1242
Chapter 94 - Safety Philosophy for Dike Design in The Netherlands by A.W.C.M. Vrouwenvelder and P. Struik	1254

Part III: COASTAL STRUCTURES

Chapter 95 - Dynamic Stability of Armor Units - A BEM Approach by C. Chian and F. Gerritsen	1270
Chapter 96 - Wave Forces on Cylindrical Members at Offshore Structure by Y. Mizuno, K. Tokikawa, M. Hirasawa, Y. Nagai and T. Kadono	1280
Chapter 97 - The Effect of Seawalls on Long-Term Shoreline Change Rates for the Southern Virginia Ocean Coastline by D.R. Basco	1292
Chapter 98 - Rock Slopes Under Irregular Wave Attack by N. Kobayashi, A. Wurjanto and D.T. Cox	1306
Chapter 99 - Dynamic Analysis of Floating Breakwater Mooring Systems by J.R. Headland and Vallianos	1320
Chapter 100 - Wave Induced Pore Pressure In Rubble Mound Breakwaters by H. Oumeraci and H.W. Partenscky	1324
Chapter 101 - Reduction of Wave Forces and Overtopping by Submerged Structures in Front of a Vertical Breakwater by B. Gonzales-Madrugal and J. Olwares Prud'Homme	1348
Chapter 102 - Stability of Breakwaters Constructed on Dredged Sand Mound by K. Yano, Y. Mizuno, N. Umezawa and T. Yanase	1362
Chapter 103 - Stability of Low-Crested and Reef Breakwaters by J.W. van der Meer and K.W. Pilarczyk	1375
Chapter 104 - Forces on and Particle Motions Around Submerged Structures in Steep Waves by J. Skourup and I.G. Jonsson	1389
Chapter 105 - Reliability Analysis of Composite Breakwaters Protected with Armor Blocks by M. Yamamoto, K. Mizumura, T. Endo and N. Shiraishi	1403

Chapter 106 - Stresses in Dolosse by H.F. Burcharth, L. Zhou, G.L. Howell and W.G. McDougal	1417
Chapter 107 - Verification and Practical Use of Block Revetment Design Method by A. Burger, A. Bezuijen, K.W. Pilarczyk and M.K. Breteler	1431
Chapter 108 - Rock Armour Stability Formulae - Influence of Stone Shape and Layer Thickness by A.P. Bradbury, J-P Latham and N.W.H. Allsop	1446
Chapter 109 - Reflection Performance of Rock Armoured Slopes in Random Waves by N.W.H. Allsop	1460
Chapter 110 - A Model for Breaking Wave Impact Pressures by M.J. Cooker and D.H. Peregrine	1473
Chapter 111 - Overtopping of Solitary Waves at Model Sea Dikes by E. Ozhan and A.C. Yalciner	1487
Chapter 112 - Permeability Characteristics of Rubble Material - New Formulae by R.W.K. Shih	1499
Chapter 113 - Morison Equation Coefficients and Data Condition by R.T. Hudspeth	1513
Chapter 114 - New Criteria for Granular Filters and Geotextile Filters Under Revetments by K.J. Bakker, M.K. Breteler and H. den Adel	1524
Chapter 115 - Wave Forces on Breakwater Armour Units by J. Juhl and O.J. Jensen	1538
Chapter 116 - Effects of Wave Groups on the Stability of Rubble Mound Breakwaters by J.R. Medina, C. Fassardi and R.T. Hudspeth	1552
Chapter 117 - Monitoring Hydraulic Loads on the Eastern Scheldt Storm Surge Barrier by L. Klatter, J. Konter and T. Jongeling	1564
Chapter 118 - Stresses in Tetrapods: Results of Large Scale Model Tests by W.W. Burger, H. Oumeraci and H.W. Partenscky	1578

Chapter 119 - Experiments on Coastal Protection Submerged Breakwaters: A Way to Look at the Results by G. Gomez-Pina and J.M. Valdes Fernandez	1592
Chapter 120 - Numerical Simulation of the Motion of a Loose Revetment Block by A. Bezuijen, J. Wouters and H. den Adel	1606
Chapter 121 - Wave Pressure Attenuation in Breakwater Armour Layers by K.R. Hall	1620
Chapter 122 - Concrete Armor Unit Structural Design Criteria by C.D. Anglin, R.D. Scott and D.J. Turcke	1634
Chapter 123 - A Fundamental Study on Construction Scheme for Rubble Foundation of Deep Water Breakwater from Hopper Barges by Y. Matsumi	1648
Chapter 124 - Resistance of Grassmat to Wave Attack by J.W. Seiffert and L. Philipse	1662
Chapter 125 - Practical Study on Larger-Scale Cylindrical Caisson Breakwater in Port of Kaohsiung by S.-D. Kuo	1675
Chapter 126 - Arctic Slope Protection Methods by C.B. Leidersdorf, P.E. Gadd and W.G. McDougal	1687
Chapter 127 - Bragg Reflection Breakwater: A New Shore Protection Method? by J. Bailard, J. DeVries, J.T. Kirby and R.T. Guza	1702
Chapter 128 - Scale Effect of Wave Force on Armor Units by T. Sakakiyama and R. Kajima	1716
Chapter 129 - Trends in Stability of Dynamically Stable Breakwaters by J.S. Kao and K.R. Hall	1730
Chapter 130 - Forces on Vertical Walls Due to Obliquely-Incident Waves by C.-P. Tsai and D.-S. Jeng	1742
Chapter 131 - Static and Dynamic Loading Tests on the Haro Armor Unit by L. Van Damme, J. de Rouck, L. Taerwe R. Dedeyne and J. Degriek	1755

Chapter 132 - Determination of Coefficients in Morison Formula by a Kalman Filter by P. Wilde, E. Sobierajski and W. Romanczyk	1769
Chapter 133 - Wave Forces on Vertical Breakwater on Reef Coasts by E. Nakaza, S. Tsukayama and M. Hino	1781
Chapter 134 - Local Scour Around a Large Circular Cylinder Due to Wave Action by E. Saito, S. Sato and T. Shibayama	1795
Chapter 135 - Stability of Dolosse with Different Waist Thicknesses for Irregular Waves by A.H. Holtzhausen and J.A. Zwamborn	1805
Chapter 136 - Estimation of Peak Wave Stresses in Slender Complex Concrete Armor Units by G.L. Howell, H.F. Burcharth and J.P. Rhee	1819
Chapter 137 - Research of Wave Forces of Breakwater in Deep Water Area by H.-S. Hou	1827
Chapter 138 - Dynamic Revetments by J. Ahrens	1837
Chapter 139 - Statistical Approach of Duration of Extreme Storms: Consequences on Breakwater Damages by C. Teisson	1851

Part IV: THE DUTCH COAST

Chapter 140 - Coastal Defence Alternative in the Netherlands by C.J. Louisse and T.J. Kuik	1862
Chapter 141 - Reconstruction of the Holocene Evolution of the Dutch Coast by T.J. Zitman, M.J.F. Stive and H.J. Wiersma	1876
Chapter 142 - Long Term Changes in Wind and Wave Climate on the North Sea by F.M. Hoozemans	1888
Chapter 143 - Sand Budget of the Dutch Coast by P. van Vessem and A. Stolk	1895
Chapter 144 - Sand Transport on the Shoreface of the Holland Coast by J.A. Roelvink and M.J.F. Stive	1909

Chapter 145 - Cross-Shore Transport During Storm Surges by H.J. Steetzel	1922
Chapter 146 - Prediction of Coastline Evolution for the Holland Coast by M.J. Dijkman, W.T. Bakker and J.H. de Vroeg	1935
Chapter 147 - Morphologic Response of Tidal Basins to Changes by W.D. Eysink	1948
Chapter 148 - Large-Scale Coastal Evolution Concept by M.J.F. Stive, J.A. Roelvink and H.J. de Vriend	1962
Chapter 149 - Research on Large-Scale Coastal Behaviour by J.H.J. Terwindt and J.A. Battjes	1975
Chapter 150 - Beach and Dune Nourishment in the Netherlands by P. Roelse	1984
Chapter 151 - Offshore Sand Extraction and Nearshore Profile Nourishment by J.S.L.J. van Alphen, F.P. Hallie, J.S. Ribberink J.A. Roelvink and C.J. Louisse	1998
Chapter 152 - Seaward Coastal Defence for the Dutch Coast by M.Pluijm	2010

PartV: COASTAL PROCESSES AND SEDIMENT TRANSPORT

Chapter 153 - The Effect of Shore-Parallel Offshore Breakwater on the Beaches at Ocean City, New Jersey by J.R. Weggel and S.C. Farrell	2020
Chapter 154 - Shoreline Response to a Single Transmissive Detached Breakwater by H. Hanson and N.C. Kraus	2034
Chapter 155 - Flow-Fine Sediment Hysteresis in Sediment-Stratified Coastal Waters by R.G. Costa and A.J. Mehta	2047
Chapter 156 - Nearshore Current Patterns on Barred Beaches by D.G. Hazen, B. Greenwood and A.J. Bowen	2061
Chapter 157 - Berm Erosion Due to Long Period Waves by K. Katoh and S.-i. Yanagishima	2073

Chapter 158 - A Field Experiment on Breach Growth in Sand-Dikes by P.J. Visser, J.K. Vrijling and H.J. Verhagen	2087
Chapter 159 - Multi-Scale Nearshore and Beach Changes by R. Ostrowski, Z. Pruszek and R.B. Zeidler	2101
Chapter 160 - Laboratory Study on Beach Processes Due to Random Waves by R. Nishi, M. Sato and K. Nakamura	2117
Chapter 161 - A Quasi-3D Model for Suspended Sediment Transport by Currents and Waves by I. Katopodi and J.S. Ribberink	2131
Chapter 162 - Method of Prediction of Bar Formation & Migration by S.H. Houston and R.G. Dean	2145
Chapter 163 - A Micro-Computer Based QUASI 3-D Sediment Transport Model by M.H.G. Briand and J.W. Kamphuis	2159
Chapter 164 - Decoupled Numerical Model of Three-Dimensional Beach Change by M. Larson, N.C. Kraus and H. Hanson	2173
Chapter 165 - Oscillatory Flow and Sediment Motion Over a Rippled Bed by P. Blondeaux and G. Vittori	2186
Chapter 166 - Wave Entrainment of Sand from a Rippled Bed by M.O. Green and C.E. Vincent	2200
Chapter 167 - Modelling of Multicomponent Sandy Beds Evolution Under Shallow Water Waves by G. Chapalain and B. Boczar-Karakiewicz	2213
Chapter 168 - Nearshore Sediment Flux and Bottom Boundary Dynamics: The Canadian Coastal Sediment Transport Programme (C-Coast) by B. Greenwood, P.D. Osborne, A.J. Bowen, D.G. Hazen and A.E. Hay	2227
Chapter 169 - Nearshore Nourishment Implementation, Monitoring and Model Studies of the 1.5 M m ³ at Kirra Beach by L.A. Jackson and R.B. Tomlinson	2241
Chapter 170 - A New Approach to 3D Flow and Transport-Modeling by J.C.M. Dijkzeul and J.J. Leendertse	2255

Chapter 171 - The Analysis and Role of Bars on the Protection of a Beach System, Gold Coast, Queensland, Australia by B. Boczar-Karakiewicz and L.A. Jackson	2265
Chapter 172 - Sea Bottom Topography with Imaging Radar by J. Vogelzang, G.J. Wensink, D. van Halsema and G. van der Burg	2279
Chapter 173 - Application of Equilibrium Beach Concepts to Sandy Great Lakes Profiles by M. Stockberger and W.L. Wood	2291
Chapter 174 - Advances in Numerical Modeling of Dune Erosion by D.L. Kriebel	2304
Chapter 175 - Bedforms, Sediment Concentrations and Sediment Transport in Simulated Wave Conditions by J.S. Ribberink and A. Al-Salem	2318
Chapter 176 - The In Situ Measurements of Sediment Transport and Bottom Topography Changes by Y. Kawata, H. Yoshioka and Y. Tsuchiya	2332
Chapter 177 - Single-Phase Fluid Modelling of Sheet-Flow Toward the Development of "Numerical Mobile Bed" by K. Nadaoka and H. Yagi	2346
Chapter 178 - Site Investigation on Sand Concentration in the Sheet-Flow Layer by Z. Yu, H.D. Niemeyer and W.T. Bakker	2360
Chapter 179 - Two-Phase Flow Model on Oscillatory Sheet-Flow by T. Asano	2372
Chapter 180 - Abrasion at the Tanah Lot Temple - Bali - Indonesia, and Its Counter Measures by Syamsudin and Kardana	2385
Chapter 181 - Man-Made Beaches: More Than 20 Years On by F. Rouch and B. Bellessort	2394
Chapter 182 - Littoral Transport Rate by J.W. Kamphuis	2402
Chapter 183 - Causes of Damage to Saldanha Sand Breakwater by J.S. Schoonees, J.W.J. Kluger and J.A. Zwamborn	2416

Chapter 184 - Numerical Modelling of the Dredged Spoil Disposal by C. Zude and W. Guifen	2430
Chapter 185 - Modeling of Wave-Current Interaction and Beach Change by S. Ohnaka and A. Watanabe	2443
Chapter 186 - Validation of Movable-Bed Modeling Guidance by S.A. Hughes and J.E. Fowler	2457
Chapter 187 - Large Scale Laboratory Tests of Dune Erosion by M.F. Overton, J.S. Fishcr and A.L. Stone	2471
Chapter 188 - Practical Application of the Three-Dimensional Beach Evolution Model by T. Shimizu, H. Nodani and K. Kondo	2481
Chapter 189 - Sand Transport Rate Under Wave-Current Action by A. Watanabe and M. Isobe	2495
Chapter 190 - Dynamic Numerical Models for Sand Waves and Pipeline Self-Burial by C. Staub and R. Bijker	2508
Chapter 191 - Even/Odd Analysis of Shoreline Changes Adjacent to Florida's Tidal Inlets by P.A. Work and R.G. Dean	2522
Chapter 192 - Behaviour of Mobile Beds at High Shear Stress By K.C. Wilson and F.N. Nnadi	2536
Chapter 193 - To Retreat in Order to Better Fight: Littoral Protection of Shingle Beaches in the North of France by B. Manoha and C. Teisson	2542
Chapter194 - Experimental Results on the Sediment Grain Threshold Under Short-Wave Action by C. Moutzouris	2552
Chapter 195 - Movable Bed Modeling Criteria for Beach Profile Response by H. Wang, T. Toue and H. Dette	2566
Chapter 196 - Storm Erosion on the Sandy Beach by M. Martinez, R. Alvarcz and I. Alonso	2580
Chapter 197 - A Regional Study of Coastal Morphology by I.H. Townend, C.A. Fleming, P. McLaren and A. Hunter-Blair	2589

Chapter 198 - Function of Detached Breakwater to Control Longshore Sediment Transport by T. Sawaragi, I. Deguchi and G.-Y. Kim	2603
Chapter 199 - Oscillatory Flow Investigations in Porous Media by G.M. Smith and K.R. Hall	2616
Chapter 200 - Instantaneous Sediment Concentration Due to Wave Action at Prototype Scale by K. Uliczka	2630
Chapter 201 - Underground Water Table and Beach Face Erosion by M. Sato	2644
Chapter 202 - A Numerical Model for Sand Transport Under Compound Waves by S. Sato and N. Mitsunobu	2658
Chapter 203 - Dike Failure Calculation Model Based on in Situ Tests by C. Laustrup, H.T. Madsen, J. Jensen and L. Poulsen	2671
Chapter 204 - How To Analyse Beach Profile Measurements? by J. van de Graaff	2682
Chapter 205 - Grain-Grain Interaction in Oscillating Sheetflow by W.T. Bakker, W.G.M. van Kesteren and W.H.G. Klomp	2696
Chapter 206 - Evaluation of Radioactive Sand Tracers to Measure Longshore Sediment Transport Rates by G. Drapeau, B. Long and J.W. Kamphuis	2710

Part VI: COASTAL, ESTUARINE AND ENVIRONMENTAL PROBLEMS

Chapter 207 - Beach Erosion Due to Large Coastal Structure and Its Control by Y. Tsuchiya, T. Yamashita and R. Silvester	2726
Chapter 208 - Beach Erosion Control by Submerged Floating Structure by N. Shimoda, N. Murakami and K. Iwata	2740
Chapter 209 - Function of Sand Fence Placed in Front of Embankment by S. Hotta and K. Horikawa	2754
Chapter 210 - Recent Performance of Linked Concrete Mat Armor Under Wave and Ice Impact by P.E. Gadd and C.B. Leidersdorf	2768

Chapter 211 - Three Dimensional Effects of Seawall on the Adjacent Beach by T. Toue and H. Wang	2782
Chapter 212 - Predicting Damage Benefits of Shore Protection Projects by K.R. Bodge	2796
Chapter 213 - The Impacts of Shoreline Protection Structures on Beaches Along Monterey Bay, California by G.B. Griggs, J.F. Tait and K. Scott	2810
Chapter 214 - Fate of Dredged Material Dumped Off the Dutch Shore by R. Spanhoff, Tj. van Heuvel and J.M. de Kok	2824
Chapter 215 - Development of Water Level Changes in the German Bight, An Analysis Based on Single Value Time Series by J. Jensen, H.-E. Mugge and W. Schonfeld	2838
Chapter 216 - Day Visitor Pontoon - Great Barrier Reef, Australia by A.A.C. Grummitt	2852
Chapter 217 - Salt Intrusion in Tideless Estuaries by E. Jasinska	2866
Chapter 218 - Coastal Lagoon Entrance Dynamics by A.D. Gordon	2880
Chapter 219 - Extent of Contaminated Marine Sediments and Cleanup Methodology by J.B. Herbich	2894
Chapter 220 - Designing for Storm and Wave Damage in Coastal Buildings by S.M. Rogers, Jr.	2908
Chapter 221 - Cross-Sectional Stability of Estuary Channels in the Netherlands by F. Gerritsen, H. de Jong and A. Langerak	2922
Chapter 222 - Variations in Rheological Properties of Muds in the Gironde Estuary by P. Galichon, A. Feral, J. Granboulan and J. Viguiet	2936
Chapter 223 - Hydraulic Aspects of the Construction of the Eastern Scheldt Storm Surge Barrier by J. Konter and L. Klatter	2950

Chapter 224 - Investigation on Improvement of Yangtze Estuary by Y. Kai and Y. Yixin	2964
Chapter 225 - Consolidation and Rheological Properties of Mud Deposits by C. Migniot and L. Hamm	2975
Chapter 226 - Integrated Coastal Research in the SW Netherlands by J.P.M. Mulder, T. Louters, F.P. Hallie, R. Postma J.A. Craeymeersch and O. Hamerlynck	2984
Chapter 227 - Numerical Simulations of Mud Transport by a Multi- Layered Nested Grid Model by H. Tsuruya, K. Murakami and I. Irie	2998
Chapter 228 - Modelling of Cohesive Sediment Transport. A Case Study: The Western Scheldt Estuary by H.P.J. Mulder and C. Udink	3012
Chapter 229 - The Great Belt Link - How to Achieve Zero Environmental Impact on the Baltic Sea by J.S. Moller and N.-E.O. Hansen	3024
Chapter 230 - Mud Transport Rate In Mud Layer Due to Wave Action by T. Shibayama, M. Okuno and S. Sato	3037
Chapter 231 - Estuary Geometry as a Function of Tidal Range by B. O'Connor, J. Nicholson and R. Rayner	3050
Chapter 232 - Flow Area Prediction of Tidal Inlets After Sea Level Rise by H. Kondo	3063
Part VII: SHIP MOTIONS	
Chapter 233 Criteria for Ship Movements in Harbours by O.J. Jensen, G. Viggosson, J. Thomsen, S. Bjordal and J. Lundgren	3074
Chapter 234 - Navigability in Channels Subject to Siltation - Physical Scale Model Experiments by C. Brossard, A. Delouis, P. Galichon, J. Granboulan and P. Monadier	3088
Chapter 235 - Integration of Marine Simulation in Harbour Design by S.E. Sand and O.J. Jensen	3102

Chapter 236 - Extension of the Boussinesq Equations to Include Wave Propagation in Deeper Water and Wave-Ship Interaction in Shallow Water by P.A. Madsen and O.R. Sorensen	3112
Chapter 237 - Safe Underkeel Allowances for Vessels in Navigation Channels by J.M.A. Spencer, E.C. Bowers and G.H. Lean	3126
Chapter 238 - Numerical Model of the Nonlinear Interaction of Waves and Floating Bodies by M. Brorsen and H.I. Bundgaard	3140

Part VIII: CASE STUDIES

Chapter 239 - Ria De Foz: Works Behaviour by J. Diez Gonzalez and V. Escobar	3154
Chapter 240 - Emergency Situation in the Shoreline Reach of an Offshore Oilfield Pipeline and Remedial Measures by J.V. Bandeira, L.C. Araujo and A.B. do Valle	3171
Chapter 241 - Sand Bypassing to "Playa de Castilla" (Huelva-Spain) by J. Fernandez, G. Gomez Pina and A. Munoz	3183
Chapter 242 - Berm Breakwater Contamination Study Sergipe Marine Terminal, Brazil by C.P. Fournier, O.J. Sayao and J.F. Caldas	3194
Chapter 243 - Offshore Breakwater for the Sergipe Marine Terminal, Brazil by M. Malcolm and O.J. Sayao	3207
Chapter 244 - St. Paul Breakwater, Phase I (The Project, the Failure and the Subsequent Investigations) by T. Sorensen and O.J. Jensen	3222
Chapter 245 - The Durban Beach Restoration Scheme After 30 Years by W. Laubscher, D.H. Swart, J.S. Schoonees, W.M. Pfaff and A.B. Davis	3227
Chapter 246 - Design and Construction of Pleasure Craft Harbour - Club Mykonos Langebaan by D.E. Bosman, G. de F. Retief, J.F. Kapp, M. Kloos and A. B. Ridge	3239
Chapter 247 - Artificial Beach Nourishment on Norderney, A Case Study by H. Kunz	3254

Chapter 248 - Design and Installation of Scour Protection for the Acosta
Bridge to Protect Against Hurricane Conditions
by B.L. Edge, D.K. Crapps, S. Jones and W. Dean 3268

Chapter 249 - Influence Functions
by H.G. Wind 3281

Subject Index 3295

Author Index 3301

OPENING ADDRESS

His Royal Highness Prince Claus of the Netherlands

Mr. Chairman, Ladies and Gentlemen,

It is a great pleasure for me, to be able to speak to you this morning on the occasion of your 22nd International Conference on Coastal Engineering.

You have chosen to hold your conference in a place where the important and fascinating field of Coastal Engineering, in which you are all involved, is particularly significant. Not only would the land we are now standing on still be under water were it not for coastal engineering, but the Faculty of Civil Engineering here at Delft University of Technology is an important centre of education and research in this field.

In Roman times, this area was described as an inhospitable land, lying just above sea level, subject to flooding during storms and sparsely inhabited by a few miserable folk. In the centuries that followed, however, these miserable folk succeeded in forcing back the sea and turning the low-lying land into an area suitable for long-term habitation.

This enormous task could not have been achieved without a joint effort. The awareness of this need to work together grew naturally among the people, and they chose leaders from amongst themselves to coordinate and direct their activities. This was possible, because the members of the community were directly involved, were aware that they had a personal interest in good communal water management in the area in which they lived, and were prepared to contribute to it in any way they could.

These principles of a personal *interest*, an individual *contribution* (both financially and in terms of labour), and an *involvement* in the decision-making process, formed the basis of the structures of cooperation which arose. The water authority which, as a result, was established on a formal basis in the Delft area more than 700 years ago, was actually the first democratic institution in the Netherlands. Some people even claim that this foundation of our first administrative institutions on democratic principles, was an absolute precondition for the establishment and survival of our country. Democracy, as it were, flowed into the Netherlands along with the water.

Although solutions developed in the Netherlands, cannot necessarily be applied wholesale in other countries, it is true that similar organisations for good coastal management, are required in other low-lying areas which are threatened by the sea. In the giving of aid to coastal defence programmes, this institutional aspect, which provides a solid base for coastal defence in society, should receive sufficient attention.

Unfortunately, this is not always the case. On the other hand, one example of this approach being used successfully, is the Beach Protection Authority Queensland in Australia, which was set up along the lines of the Schieland Water Authority in the Province of South Holland.

Ladies and Gentlemen,

It may seem strange that people should choose to live in such a low-lying and vulnerable area, but this is by no means a purely Dutch phenomenon. People have settled in low-lying areas all over the world, since these generally have very fertile soil, and the water facilitates transport and communications, which in turn promote trade and industry. And of course, fish are readily available as a welcome supplement to the daily diet. This then is the reason why your field of interest is so important for these coastal areas, and has always received a great deal of well-earned interest.

Of course, the fight against the sea has always been a process of trial and error, but one in which a considerable pool of knowledge has slowly but surely been built up concerning the relationship between those factors which present a threat - such as waves and currents - and the behaviour of the coast itself. Throughout the world, this knowledge acquired from centuries of practice represented the first humble beginnings of the science of coastal engineering.

This process, of course, went hand in hand with all kinds of other technical developments. A good example of this, was the use of windmills here in the Netherlands to control the water level in the polders. Windmills had already been in use for some time, particularly around the Mediterranean Sea, but the most important innovation in the Netherlands was the development of the mill with the revolving cap. The wind blows in all directions in this country, so this innovation increased the productivity of the mills considerably. The oldest surviving record of mills of this type being built dates from 1408, and refers to mills in Gouda and Alkmaar. These mills, many examples of which can still be seen in the Netherlands, also played another important role, namely in the development of our crafts and industry. Windmills were used not only, for example, for the grinding of grain and spices, but also to provide power for the mechanical sawing of the wood used to build ships. This enabled the Netherlands to strengthen its position as a shipbuilding nation and to establish itself as a prosperous seafaring and trading power in the seventeenth century. Clearly, the Netherlands and other similar areas have much reason to be grateful to the sea and the wind. We have an expression here in the Netherlands, "van de wind kun je niet leven", which literally means "you cannot live from the wind". I have no idea where it comes from, but it certainly does not apply to the mill operators.

Ladies and Gentlemen,

The first time science really took a hand in your branch of hydraulic engineering in the Netherlands, was in the enclosure of the Zuider Zee. The decision to undertake this ambitious project was prompted by the great floods of 1916, during which large areas around the Zuider Zee were under water. One of the civil engineers who devoted himself to the project and drew up carefully considered plans for the dam, was Dr. Cornelis Lely. As Minister of Transport and Public Works at the time, he introduced the Bill proposing the project into Parliament and successfully defended it.

In order to investigate the possible effects of the enclosure on the water levels and currents in the Waddenzee and the adjoining part of the North Sea, the Netherlands Department of Public Works called in Dr. Hendrik Antoon Lorentz, theoretical physicist, Nobel Prize winner and professor at the University of Leiden. Professor Lorentz had not previously worked in this field of applied fluid mechanics, but he was a brilliant fundamental scientist with a great interest in technology, making him the perfect man to solve the problem - an excellent example of the symbiosis of science and technology. He also had the young engineer Johannes Thijssse, assisting him, who combined intuition and technical insight with a fine scientific mind. It can be said that Professor Thijssse took over from Professor Lorentz as the torchbearer, promoting this scientific approach to hydraulic engineering. He was in a position to do this as director of the Delft Hydraulics Laboratory and as a Professor at Delft University of Technology, training a whole generation of engineers to pave the way for the second great challenge for the science of coastal engineering in the Netherlands, the development and implementation of the Delta Project.

This project - a reaction to the disastrous floods in Zeeland in 1953 - entailed the building of a series of dams in the delta area in the southwest of the Netherlands, rendering the coastline continuous, and in particular, the construction of the storm surge barrier in the Eastern Scheldt. The Delta Project practically guarantees this previously vulnerable area against flooding. I was pleased to see that your programme for the conference includes a visit to the storm surge barrier. This barrier across the Eastern Scheldt, which can be opened and closed as the situation demands, was the perfect solution to the conflict which arose between the need for a permanent dam to protect this coast, and the desire to preserve the natural environment behind the dam. The movable barrier represents the successful reconciliation of the technological requirements with other interests, for example, those of the biological environment. This remarkable construction could never have been completed, without the contributions of many other scientific disciplines.

The latest product of this line of development in coastal protection in the Netherlands, is the Coastal Genesis Project, which was set up to study the origins and evolution of our sandy coastline, with the aim of making reliable predictions for the future. The results of this study will be presented in detail at this conference.

Coastal management in the Netherlands, like that of many other plans and policy proposals, is set within the now well-known framework of "sustainable development". The findings of the Genesis Project, prompted the Netherlands Government to decide on a coastal policy for the future based on preserving the present coastline, but doing so in a responsible and intelligent way. Not, therefore, a policy of large-scale intervention with grand projects and no expense spared, but more what might be considered a typically Dutch approach, allowing the sea - or nature, if you like - to work for us where it is necessary to defend ourselves against her power. Or, as Andries Vierlingh, the first engineer to build coastal and dyke defences systematically in the Netherlands, put it as long ago as 1560, to entice the water to follow the desired course by using "gentle persuasion".

Nature, the earth on which we live, is our host. If we treat her with care and respect, we shall achieve our aims more often and with better results.

Ladies and Gentlemen,

I remember once, years ago when I was living and working in Ivory Coast, being taken to the Canal du Vridi, the approach channel to the port of Abidjan. A relatively short mole had been built there, together with a specially shaped approach channel. I was told that this design directed the sand, which was driven along the coast by the strong current generated by the waves, in such a way as to deposit it with great precision in a canyon in the seabed, the "trou sans fond". "Ah, ce sont les Hollandais qui ont trouvé la solution" said my African friend. As I discovered later, upon my first visit to Delft, it had been devised by Professor Thijsse and by Chief Engineer Jan Schijf of the Delft Hydraulics Laboratory. This was, of course, an intervention in nature, but one which took as great advantage as possible of the natural forces present, rather than tackling them head on. We have another saying in the Netherlands "Wie tegen de wind spuwt, krijgt een vuile baard", which means "If you spit into the wind, you will get a dirty beard".

With both small and large scale projects, it is often possible to fall back on more traditional or locally developed techniques, if the circumstances call for this. For example, in 1985, when the Feni river in Bangladesh had to be dammed as part of the large Muhuri irrigation project, (a joint Bangladeshi, Canadian, World Bank and Dutch endeavour), the decision was made by the project managers, to use traditional - age old - highly labour intensive techniques of dyke building, using fascine mattresses and bags of clay. One million bags, put into place by fifteen thousand workers, were required to complete the dam. This great mobilisation of people and materials, was excellently organised by local Bangladeshi contractors. With the exception of modern geo-textiles, the fascine mattresses which were used to protect the river bed, were made entirely according to traditional methods.

The Dutch are, of course, not the only ones who are involved in the field of coastal defence. It is no coincidence that these conferences were originally organised by the United States, with their long

tradition of coastal defence projects on both the Atlantic and Pacific coasts. And a number of other countries, whose representatives are present here, have also won their spurs in this field.

All of you here have one thing in common, you devote yourselves to defending the land against the sea. Often our friend and ally, the sea is a formidable enemy when she is seen as a threat to the land or to man. This tends to lead a belief in the maxim "safety first". Yet, as you are all aware, the concepts of safety and protection must be applied in a sensible and responsible way. We should not only protect densely populated areas, but also the environment - for example, the wetlands and the tidal forests which are so important for our animal and plant life. And when we inevitably have to sacrifice a valuable natural area for reasons of safety, or indeed for economic development, we should only do it after very careful consideration and see to it that the lost area is replaced somewhere else. If this is not possible, then let us strive to leave irreplaceable natural areas alone.

Just how much attention can and should be given to the protection of the environment is a difficult question to answer. The Netherlands gives a great deal of attention to the protection of both the population and the environment behind the Eastern Scheldt Barrier. Under normal circumstances, the storm surge barrier is open, allowing the water to flow freely and thereby maintaining the natural tidal environment. It is only closed when there is threat of a storm surge, to protect the hinterland. By taking into account the requirements of the environment, as well as the safety aspects, the costs of the project more or less doubled. The results were, however, that the technology applied enabled a particularly valuable ecosystem to be preserved, and new methods to be developed which can be employed in other parts of the world. As a matter of fact, the costs involved in coastal defence in general in the Netherlands are not high, relatively speaking, and can fortunately be borne by the community without causing undue problems.

However, the message which should be accepted by all coastal engineers at this time, is that they are the guardians of our extremely precious and vulnerable coastal areas. In fulfilling this task, they will often have to let the sea have its way to some extent, as in the case of the dune coast in the Netherlands. Dune erosion due to storms, such as we have experienced in the Netherlands in the past few months, need not be a cause for alarm, as long as it remains within the predicted and tolerable limits.

Ladies and Gentlemen,

The question of rising sea levels as a result of global warming also inevitably comes to mind here. Although it is by no means certain, let alone proven, that sea levels are actually rising, we cannot afford to ignore the possibility. The precautionary principle also applies here. It would be foolish to wait until we know exactly how much of a threat exists, because by then it may already be too late to do anything about it. Uncertainty is no reason for complacency. The costs of doing nothing could prove in the long run to be far higher than the costs of taking adequate action immediately. We should therefore not only be alert, but should also make immediate

plans for the taking of countermeasures. The area around here would of course be directly affected by any rise in sea level. The Public Works Department has already carried out a preliminary study, which indicates that the most probable expected rise, of between sixty and eighty centimetres in the next one hundred years, would present the Netherlands with no insurmountable problems. A rise of these proportions could, however, have disastrous consequences in other areas of the world. Thorough investigation should therefore be carried out in these areas into possible solutions. I am thinking here in particular of the Maldivé Islands and the great river deltas, such as those of the Nile in Egypt and the Ganges and Brahmaputra in Bangladesh. It is quite possible that traditional Dutch methods could be applied in some of these areas. Relatively simple constructions, such as training moles, could be used to try and change current and wave patterns in such a way, that sand and silt would be deposited in the threatened areas. As I mentioned before, the secret is to use the gentle touch to influence nature and encourage her to work together with man.

Simply thinking about countermeasures is not enough, however. The causes of the problem have to be identified and tackled. Growing trees that are resistant to acid rain is not a solution, any more than it is desirable that people should eventually be born with webbed feet as a solution to rising sea levels.

"State of the art" technology and the current possibilities it offers in coastal engineering, are undoubtedly impressive, but a great deal of research and study is still necessary if we are to tackle the challenges we are now faced with. That is why I believe that it is important for the latest developments in your field to be discussed regularly. These biennial International Coastal Engineering Conferences have proved to be an excellent forum for such discussions over the past forty years.

I wish you all a good reference, with searching and fruitful discussions, and it is with pleasure that I hereby declare the twenty-second International Coastal Engineering Conference open.

Thank you.

RETHINKING OUR ROLE IN COASTAL ZONE DEVELOPMENT

J.E. Prins^{*}

Your Royal Highness, Mr. Chairman, Ladies and Gentlemen,

For the twenty-second time the International Conference on Coastal Engineering is ready to start. The first Conference was the one in Long Beach, 40 years ago! I hope you noticed that it is your 8th Lustrum today! Congratulations!

There is something special in consistency. Those things in life that for sure are there and give anchorage. The regular participants share the same past experiences and have the same anticipations of seeing each other back next time. The world events pass by, but there is something to hang on to: ICCE, the International Conference on Coastal Engineering. And, for sure, at the Conferences we do meet many of our friends in the profession and beyond that, between many families personal friendships for life have grown.

40 years of Coastal Engineering Conferences is quite a considerable time, but there are institutions that go back in time much further. Take for instance ICES, the International Council for the Exploration of the Sea, dating from July 22, 1902. Once an older colleague told me how back in the thirties delegates of ICES went to Reykjavik on Iceland by ship to attend their meeting. And even in 1955 I went to the United States sailing by the flagship of the Holland-America line, the New Amsterdam, to enjoy a Fulbright scholarship. But shortly after, in 1957, I crossed the Atlantic by plane to be at the 6th ICCE in Miami, Florida.

Today we fly Amsterdam-Los Angeles and back for a day's meeting with cabin luggage only, in order not to let our break cost too much time.

Why am I telling this to you? Well, *I wanted to illustrate that society changes with time, not only because of technological development, but also because of change of mentality. Those changes can go rather fast and obviously are rather unpredictable in view of the time frame.* Extending the example with reference to shipping: the Queen Elisabeth II was ordered in 1965 to become a liner for regular services between the UK and the USA. After completion in 1969, four years later, it rather immediately was engaged in tourist cruises. The big liners were history.

* Former General Director DELFT HYDRAULICS, The Netherlands
Secretary General International Association for Hydraulic Research

Apart from gradual or obvious changes we may encounter surprises of physical, ecological, social, economic or political nature, such as the cyclone that hit Bangladesh in 1970 and caused the death of 300,000 people; recently the death, due to a virus infection, of 60% of the seals in the North Sea within a year's time; the illness AIDS, for which there is no remedy yet; the oil crisis in 1973 and the political landslides of today. *Such changes call for fundamental adaptations, heavily bearing upon the societal structure.*

It is about the changes with time and how these effect our coastal engineering profession, that I wanted to dwell on with you for a while, **rethinking our role in coastal zone development.** In fact His Royal Highness did so already and gave us a bird's-eye view of the developments from Roman times to the present. I will in addition to that cover more explicitly our individual position as it stands today and has to develop.

As I mentioned before, the ICCE is a constant factor in life. It rather strictly maintains its character as a meeting place for discussing sciences and technologies related to engineering aspects. But it is quite clear, as was pointedly indicated by His Royal Highness, that the context within which coastal engineering performs, shows changes over the years and will change in the future. Thus thrusting continuously upon the coastal engineer different demands of positioning himself in the creative processes in which coastal engineering is incorporated.

Saying this I express that coastal engineering cannot be exercised in isolation and it is necessary that the coastal engineer should be aware of that and plan accordingly. How can we anticipate on this?

In the course of the second half of this century, which means for the last 40 years, the structure of thinking has changed tremendously and with it the range of our responsibility for the deeds we perform; that is to say, today we are held responsible for the overall impact of our deeds even when the deeds in themselves are legal. I would call this moral engagement our "extended responsibility". In coastal engineering we are dealing with projects and processes with very large time scales - from decades to centuries - and we really saddle our descendants with our produce. So it is a must to incorporate the appreciation that future generations will have for our coastal works. For that reason it is of interest to try to analyse how thinking developed over time and to see what that means for the future.

One observation before starting this exercise. Of course, I was much interested which audience I was going to address. From the list of presentations it is evident that you, my audience, predominantly consist of scientists, researchers and engineers dealing with the physical environment, primarily with the aim to understand processes in order to control, to reshape or to maintain a physical condition, either related to nature itself or related to man-made works. I found only a few contributions that link up with conceptual thinking at large. Say, with a very liberal interpretation, some 8%. Moreover, the nature of this type of congresses is such that there is not much of a formal synthesis on the ten subjects you are going to deal with, although there will be in-depth discussions, particularly in the social hours. This makes the congress result in quite an individual experience. And regardless of the huge capital of

brains united here in this auditorium the follow-up action due to a joint effort will be absent. This - to my view - "lost opportunity" much engages me as it is an imperfection of many congresses, but difficult to overcome. I will return to this later.

Coming back to the analysis of developments in thinking, I want to explore with you in what kind of framework our thinking operates. As I noted already, since the middle of this century, the framework has changed considerably and logically will change in the future. Of course, we can do much to that change and guide it towards a desirable direction.

There is the big question on how far we can and should relate our specific task as coastal engineer to the broad context in which we work. And how broad do we go?

Generally speaking, at the beginning of this century technical matters got a very direct approach. Once the decision makers had decided to go for a project, the engineers performed their job straightforwardly in producing a technically sound solution within the boundaries of their available know-how. Today there is a definite interplay between the various actors in a project.

For thinking in a broad context I will distinguish four important components in the structure of thinking. They are:

- the scale of time,
- the scale of space,
- the extended responsibility and
- the knowledge base.

I had better give you an example of what I mean and you can assimilate your own examples with it.

I will use the sealing off of the Zuider Zee from the North Sea (Figure 1 and 2). This project is known to you in the meantime through the reference His Royal Highness made to it, because of the pronounced role science played there. This undertaking has a long history through which I can illustrate the gradual growth of the time and space dimensions in the project induced by technological and scientific development, the knowledge base.

The long coastline of the Zuider Zee encountered many threats from storm surges. When a storm surge occurred in the North Sea the inflowing water was swept up anew in the shallow Zuider Zee. In 1667 already, Hendric Stevin suggested to separate the Zuider Zee from the North Sea and reclaim land. He was inspired by the many polders that were created at that time as investment projects of the rich merchants of the 17th century. It is obvious that the scientific level and the technical means at that time were insufficient to execute such a huge work that even today would need mobilization of advanced design capabilities, equipment and organization.

Only after the stormsurge of 1825 a well thought-out plan was launched in 1849. It proved to be too ambitious and was followed by a more modest approach (Figure 3), which got a legal status in 1877, but was abandoned again. Fortunately, as the plan - by ignorance - did not consider the effects of change in resonance characteristics of the remaining basin - becoming in length about one quarter wavelength! - which would have augmented the stormsurge levels along the new dikes and remaining coastlines by 1 to 2 meters! The 1891 plans of Lely (figure 4) did incorporate increase of the tidal amplitude,

but they could not be calculated and were mere guesses. Only in the nineteen-twenties the physicist and Nobel Prize winner, Lorentz, managed to perform sufficiently accurate calculations. However, we may note that in 1891 the relative upward movement of the mean sea level due to tectonic movement of the earth crust was taken care of. So, we see *the space and time dimensions gradually entering the concept of thinking thanks to a growing knowledge base.*

After the severe storm surge of 1916, the Law of 1918 officially settles the closing off and reclamation of the Zuider Zee. The Law also allows for the execution of technical works in the interest of safety, water management and navigation, in those cases where there would be adverse effects due to the closing. Aggrieved parties can call on the government.

It should be noted that the drastic change of the ecological system of this 4000 km² large sea, that would turn into a freshwater lake and reclaimed land, and a possible impact on the Wadden Sea area due to the changed flow regime and tidal range, was not referred to at all. The disappearance of herring and anchovy was incorporated in the project as a matter of course and only the loss of economic value was compensated financially to the fishermen. I could not trace whether at that time there was something present in the sense of a feeling of extended responsibility in the minds of the scientists and coastal engineers. The historical words spoken by the president of the combined contractors on the very site just after closing to the Minister of Public Works, expressed only pride: "Excellency, we have completed your order. The Zuider Zee is closed off".

Today it is out of the question that the Wadden Sea would be closed off from the North Sea, although it is technically logic and practically possible.....**Why?**

Well, in the second half of this century many factors did change our way of thinking:

- I remember that in the fifties, in the Royal Institution of Engineers, we were formulating a code of ethics - like medical doctors have their Hippocratic oath. This committed the engineer to a broader responsibility than the mere technical features.
- In the seventies we enter global thinking initiated by the Report for the Club of Rome by Dennis L. Meadows (1972), who at that time presented his views on the **Limits to Growth** in this same auditorium.
- Writing scenarios becomes "en vogue".
- At the same time we enter the era of thinking in systems, recognizing interrelations. As a consequence systems approach and policy analysis emerge. The computer makes interrelations manageable and provides easy generation of alternative solutions, optimization, sensitivity analysis, etc.
- Also, technological development brings us informatics and extremely accurate detection methods revealing ruthlessly the presence of toxics in our environment.
- Public opinion becomes an ingredient in decision making.
- In the design of large coastal engineering works a new formula is applied by introducing probabilistics as a philosophy for safety.
- In 1987 the Brundtland Report was issued under the stirring title "Our Common Future".

*In the nineties the keyword will be **sustainable development**, defined as development that meets the needs of the present without compromising the ability of future generations to meet their own needs (Our Common Future, 1987, page 43).*

For us, coastal engineers, this mission was nicely framed by His Royal Highness by calling on us to act as prudent guardians of the precious and vulnerable coastal zone.

Our framework of thinking has been shaken up:

- Our **time dimension** changed from short term to long term
- Our **space dimension** went beyond that of the locality into the global sphere
- The **extended responsibility** forces us to integrate our own expertise in the multidisciplinary system of which our project is part
- The **knowledge base** seems to set the limitations on this "liberation" of mind.

It is interesting how much this - somewhat abstracted - picture fits activities in coastal engineering. It is a fact that the coastal zone, including the deltas, is the most intensively used area of our planet, providing many vital functions for our society. It is expected that in 2000 about 80% of mankind is living in this area. With this in mind sea level rise is more catastrophic than at first sight. It will be a real global threat. And we might add to this that the following hypothesis considerably contributes to the importance of the coastal zone:

When climate change develops, most likely the coastal zones are less affected than the central areas of the continents and act as a basis for continuity. This poses a great value on the coastal zones and the coastal zone resources derived from it - on land and water. This throws a new light on coastal zone development in view of taking note of scale of time, extended responsibility and knowledge base.

Here the keyword **sustainable development** is particularly on its place; seen in the light of both physical and ecological processes.

In the context of thinking given above, we have to try to find ourselves back as the individual, or the alliance of individuals, that is held responsible for his produce.

The reality is that we, as scientists, researchers and engineers in coastal engineering have - because of our specialization - a specific task that demands priority. At the same time we have to acknowledge that our produce is part of a system in which it has to function - in coastal engineering for decades or centuries - and has to match the environment at large.

To indicate an individual position we might use the STEM diagram (Figure 5).

Some 15 years ago MIT applied this kind of approach for the different kind of engineers they wanted to deliver. Also, for continuing education it is helpful. But above all we might check our own place in the diagram and that of the counterparts with whom we communicate. Science, technology, engineering and management are related to their orientations, which are subject, product and control orientation. The shaded areas show the main position of the respective actions. In a career a person might even cross the complete matrix along the diagonal.

orientation action	subject orientated	product orientated	control orientated
science (knowledge)			
technology (tools)			
engineering (workplan)			
management (master plan)			

Figure 5 STEM diagram

Knowledge generation is very essential as the knowledge base is determinative for the quality of decisions. This does not mean that created knowledge automatically is implemented. Communication along the diagonal to adjust to application is required.

This brings me back to congresses where, as I said some minutes ago, a capital of brains is united. Communication is the major agent for effectiveness. A congress with only scientists and researchers asks for presentations directed towards what I call: **horizontal exchange** - one is speaking essentially the same language, but there may be use of different jargon, considering the various disciplines (we stay within the top left boxes).

A congress where scientists want to communicate with managers, c.g. decision makers, asks for a different type of presentations directed towards what I call: **vertical exchange** - application oriented and users friendly language (we go from top left to bottom right). Awareness for this aspect is important for congress organizers and participants, and would facilitate to conclude congresses with pertinent conclusions and recommendations. This is as you know my great wish.

The above might also lead to a review of what is going on in the related congress world. The ICCE, the IAHR (International Association for Hydraulic Research), the PIANC (Permanent International Association of Navigation Congresses), the COPEDEC (Int. Conference on Coastal and Port Engineering in Developing Countries), the ECOR (Engineering Committee on Oceanic Resources) and SCOR (Scientific Committee on Oceanic Research), all have their own identity but they definitely show overlap too.

When I am going to summarize I like to do that with another example, that of integrated coastal zone policy.

You will appreciate that from the "solo"-conception from a century ago we have entered the era of the "long-term thinking in interrelations" - conception. We are looking at the system at large with its physical, ecological, social, economic, and political components.

You could visualize the structure by considering a successive support system (Figure 6). The physical foundation supports the ecological system that provides living conditions for the social system - nature, habitat and food. The social system creates the cultural values. The economic system secures the distribution of resources and the political system provides the forum for decisions.

For an integrated coastal zone policy the coastal engineering fits in at the physical basis of the system at large and its knowledge base is fundamental for the result a coastal zone policy can produce.

Integrated coastal zone resources management has got intensive attention in the Netherlands and progressed into a scientifically based action thanks to the joint effort of the Public Works Department, Delft Hydraulics and the International Federation of Institutes for Advanced Study - IFIAS. Through the channels of IFIAS and Delft Hydraulics the principles could be and are disseminated to various places in the world.

In the Netherlands the politician Ronald Waterman has presented proposals for integrated projects along the Dutch coast, extending into the sea and serving various functions. For instance a considerable extension of the coastal area between Hook of Holland and Scheveningen has been proposed by him (Figure 7). By considering all functions, including "nature", that are performed in society he adapts the extended area to the relevant functions of the area by optimizing them in relation to the existing coastal zone. He eventually ends up with an economically feasible project.

Of interest to the coastal engineers is that the extended coastal area would maintain itself at long term, predominantly by natural morphological processes. Hence Waterman's expressive catchword: Building with nature. For smaller projects intelligent use of the forces and materials of nature has proved profitable. In the large scale projects, however, the long term prediction of the topography due to currents, waves, wind and vegetation is a real challenge for the coastal engineering profession. The Kansai international airport and the Aeropolis coastal development project in Osaka Prefecture is another product of an integrated coastal policy.

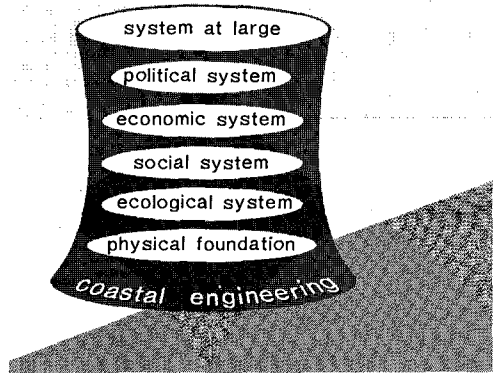


Figure 6 Successive support system as base for integrated coastal zone policy

For this type of multi-functional coastal extensions we are discussing here, the advice given by the coastal engineers are determinative for the economics of the project. *The responsibility going together with the advice is extremely large, as such an advice should incorporate long term considerations, such as sustainable development, sensitivity to climate change and sea level rise. Large size projects of this kind tend to "technology venturing" where the risk-taking has to be defined beforehand. They are, in particular, apt for a probabilistic approach.*

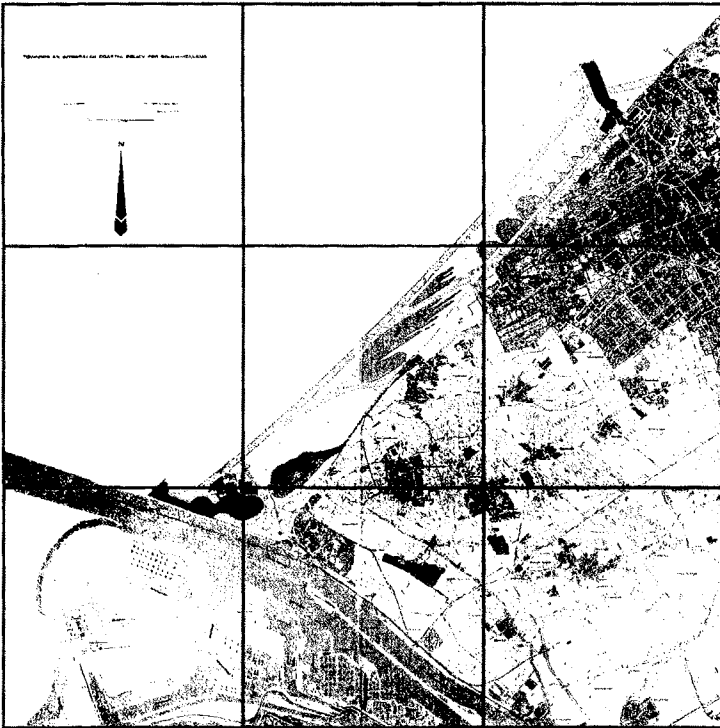


Figure 7 Plan for integrated coastal zone development by Ronald Waterman

Research projects such as the **Coastal Genesis Project** are a fundamental need for long-term extrapolations. You will certainly hear about it this week.

And let me also mention here with much joy the **Marine Science & Technology Programme** of the European Commission. This MAST programme shortly starts its first phase with a budget of 50 M\$, whereof about 10 M\$ is allocated for the coastal engineering component.

The importance of the coastal zone for the -rapidly increasing- world population is evident and it is crucial to safeguard its optimum outturn at long-term through sound coastal zone management. *As coastal engineering is absolutely determinative for sound management*

the coastal engineers might internationally intensify the coordination of education, research and transfer in the domain of coastal engineering. There is a need for creating worldwide awareness and giving directives. The ingredients are there! You only have to unite them. The coastal engineers should be the promoters, they are the people having the ability to control the physical system and bring into effect sustainable development, including terrestrial and water quality aspects.

Overlooking the position of the coastal engineer, including his colleagues in science and research, *I conclude that for the coastal engineer thinking in large time and space scales is a necessity. Extending his knowledge base is fundamental in view of the determinative role coastal engineering plays and increasingly has to play. Exercising a fair deal of extended responsibility will be needed to assure that the coastal engineer is a good, and above all, wanted partner in integrated coastal zone management.*

Let me close my lecture with this little story:
Ten years ago I had a serious discussion with the Public Works Department to finance research projects to deepen the understanding of the processes in and along the North Sea. They told me that for their policy decisions the available knowledge base was sufficient. I asked them whether they would be able to do their job with the knowledge of ten years ago. The answer was no. I am convinced that also today the answer is no when we refer to 1980 and ten years from now, in 2000, the answer will be no again referring to 1990. And that gives the meaning to this conference where we check the state-of-the-art and try to find the deficiencies to get them compensated - to ensure progress.

I wish you a fruitful Conference.

PART I

Characteristics of Coastal Waves and Currents



CHAPTER 1

Distribution Function Fitting for Storm Wave Data

Yoshimi Goda¹ and Koji Kobune²

Abstract

New objective criteria are established for rejecting unfitting distribution functions to a sample of extreme wave data. Another criterion is also introduced to select the best fitting function among the eligible ones. Application of these criteria to storm wave data around Japan indicates a possibility of identifying the parent distributions for the regional population of storm wave data.

Introduction

Selection of design wave height is generally made on the basis of storm wave data fitting to some model distribution function. Methodology of distribution fitting has been discussed by many people including Goda [1988], and various techniques are used in design processes. However, selection of the distribution function for a given set of wave data among several candidates is still left to subjective judgment of a wave analyst or design engineer. Although the correlation coefficient between the extremal wave height and its reduced variate provides a measure of the degree of fitting, there is no guarantee that the best fitting distribution represents the true distribution of storm waves. The bootstrap technique as applied for storm wave data by Rossouw [1988] and Andrew and Hemsley [1990] provides an alternative means for distribution function selection, but it is not effective enough for distinguishing the true distribution from other candidate functions.

The first step to find the true distribution is to establish sound criteria by which inappropriate candidate functions can be rejected from distribution fitting to a given set of wave data. Application of such rejection criteria to a number

¹ Prof., Yokohama National Univ., Dept. Civil Engg., Hodogaya-Ku, Yokohama 240, Japan, M. ASCE.

² Dr. Eng., Chief, Marine Obs. Lab., Marine Hydrodyn. Div., Port and Harbour Res. Inst., Nagase, Yokosuka 239, Japan.

of storm wave data sets within a particular region would yield an indication of the parent distribution pertinent to that region. The present paper describes the derivation of such rejection criteria based on the Monte Carlo simulation as well as a best-fitting criterion for the case of the least square method application. Examination of storm wave data around Japan with the newly derived rejection criteria indicates existence of regional parent distributions as discussed in the last part of this paper.

Candidate Distribution Functions and Plotting Position Formulas

The distribution functions examined herein are the Fisher-Tippett type I and II (hereafter denoted as FT-I and FT-II) and the Weibull distribution of the following form:

$$\text{FT-I : } F(x) = \exp\{-\exp[-(x - B)/A]\} \quad (1)$$

$$\begin{aligned} \text{FT-II : } F(x) &= \exp\{-[1 + (x - B)/kA]^{-k}\} \\ &: k = 2.5, 3.33, 5.0, \text{ and } 10.0 \quad (2) \end{aligned}$$

$$\begin{aligned} \text{Weibull : } F(x) &= 1 - \exp\{-[(x - B)/A]^k\} \\ &: k = 0.75, 1.0, 1.4, \text{ and } 2.0 \quad (3) \end{aligned}$$

where $F(x)$ denotes the distribution function of extreme data x , and A , B , and k are the scale, location, and shape parameters, respectively. The fixing of the shape parameter k of the Weibull distribution at the four values above is due to Goda [1988]. The functional form of the FT-II distribution is so selected to make it asymptotically approach to FT-I as $k \rightarrow \infty$. It is essentially same as the generalized extremal distribution by Jenkinson [1955]. The shape parameter k for FT-II is so set that $1/k$ would linearly increase from 0.1 to 0.4. In addition to the above distributions, the two-parameter log-normal distribution is also examined.

The present paper employs the least square method for parameter estimation for a sample of storm wave data, because of its simple algorithms, adaptability to censored data, and well-established information on confidence intervals of return wave heights based on a Monte Carlo simulation study (Goda 1988). The choice of the plotting position then becomes crucial to yield unbiased estimates of return wave heights. The unbiased plotting position formulas for the FT-I, Weibull, and log-normal distributions have been recommended by Goda [1988]. Another Monte Carlo simulation was carried out by Goda and Onozawa [1990] for the FT-II distribution with the sample size ranging from 10 to 200. For each condition, 10,000 samples were simulated and analyzed. Based on this simulation, the following plotting position formula has been derived:

$$\widehat{F}_m = 1 - \frac{m - 0.11 - 0.52/k}{N_T + 0.12 - 0.11/k} \quad (4)$$

where \widehat{F}_m is an estimate of the non-exceedance probability for the m -th largest variate, and N_T denotes the total number of storm wave events occurring during the period of data analysis.

The extremal analysis of storm wave data is usually made for the peak values of individual storms which exceed a certain threshold value. The number of storm wave data thus collected, N , is less than N_T . The ratio of N to N_T is called the censoring parameter (Goda 1988) and denoted by ν .

Equation (4) becomes same as the Gringorten formula for the FT-I distribution as $k \rightarrow \infty$. According to the simulation study with the above plotting position formula, the mean value of return wave height (averaged over 10,000 samples) estimated at the return period 10 times the sample duration showed a difference of $-2.7\% \sim +0.3\%$ from the true value, depending on the sample size and shape parameter. For the shape parameter $k = 5$ and 10, the difference was $-0.6\% \sim +0.3\%$.

Confidence Interval of FT-II Distribution

Another simulation study was carried out to examine the sample variation of the return value of the FT-II distribution. Two sets of 10,000 sample runs were analyzed and their results were averaged. An empirical formula for the standard deviation of the estimated return value \widehat{x}_R at the return period R has been given as (Goda and Onozawa 1990)

$$\sigma(\widehat{x}_R) = [1 + a(y_R - c + \alpha \ln \nu)^2]^{1/2} \sigma_x / N^{1/2} \quad (5)$$

where ν is the censoring parameter defined as N/N_T , σ_x is the unbiased standard deviation of sample data, a , c , and α are empirical coefficients given by Eq.(6) and Table 1, and y_R is the reduced variate for the return period R expressed by Eq.(7) below:

$$a = a_1 \exp\{a_2[\ln(N \nu^{0.5}/N_0)]^2 - \kappa [\ln(\nu/\nu_0)]^2\} \quad (6)$$

$$y_R = k \{-\ln[1 - 1/(\lambda R)]\}^{-1/k} - 1 \quad (7)$$

in which λ denotes the mean rate, or the average number of storm events per year.

The senior author (Goda 1988) proposed empirical formulas for the correction of possible bias in the estimate of return wave height when the true distribution is unknown. He also presented other formulas to estimate standard errors under the

Table 1 Empirical Coefficients for The Standard Deviation of The FT-II Return Value

Shape Par.	a_1	a_2	N_0	κ	ν_0	c	α
$k = 2.5$	1.27	0.12	23	0.24	1.34	0.3	2.3
$k = 3.33$	1.23	0.09	25	0.36	0.66	0.2	1.9
$k = 5.0$	1.34	0.07	35	0.41	0.45	0.1	1.6
$k = 10.0$	1.48	0.06	60	0.47	0.34	0	1.4

same situation. In the present paper no proposal is made however, because it is hoped that the use of new rejection criteria to be discussed below will diminish the possibility of choosing a distribution other than the true one.

Rejection Criterion Based on Outlier (DOL Criterion)

Another series of Monte Carlo simulations were carried out to explore the possibilities of establishing new criteria for distribution fitting. The sample size was from 10 to 400, the censoring parameter was set at 0.25, 0.50, and 1.0, and 10,000 sets of simulated data were produced and analyzed for each combination of the distribution function, sample size, and censoring parameter.

In the extremal analysis of wave data, presence of an outlier or an abnormally large data often causes a trouble for analysts in data interpretation and distribution fitting. However, the outlier can provide a good measure of sample deviation from its population. Let x_1 be the value of largest data among a sample. Then its magnitude is measured with the following dimensionless deviation ξ :

$$\xi = (x_1 - \bar{x})/s \quad (8)$$

where \bar{x} and s are the mean and the standard deviation of sample data.

In the statistical test of the normality of a sample, Thompson's test is sometimes used against its mean value in comparison with the overall means of many samples. By dividing the data set into a sample composed of the largest data only and that of remaining data, Thompson's test can be applied to the dimensionless deviation ξ . Then, the ξ value having the non-exceedance probability P is approximately given by

$$\xi_P = \left[\frac{(N-1)F(1, N-2; \alpha)}{N-2 + F(1, N-2; \alpha)} \right]^{1/2} \quad (9)$$

where $F(1, N-2; \alpha)$ denotes the F distribution with the $(1, N-2)$ degrees of freedom at the exceedance probability α . For the largest data x_1 in a sample with the size N , α is given as $2(1-P^{1/N})$.

Analysis of simulated samples from the Normal distribution has yielded the cumulative distribution of ξ as shown in Fig. 1. Simulated data are in agreement with the theory by Eq.(9) except for the range of low ξ value. Difference is

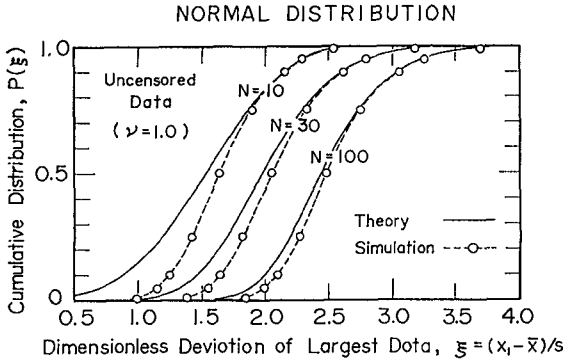


Fig.1 Cumulative distribution of ξ value.

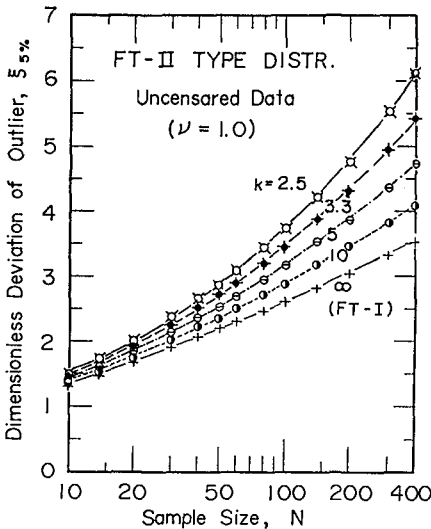


Fig.2 Examples of $\xi_{5\%}$ value.

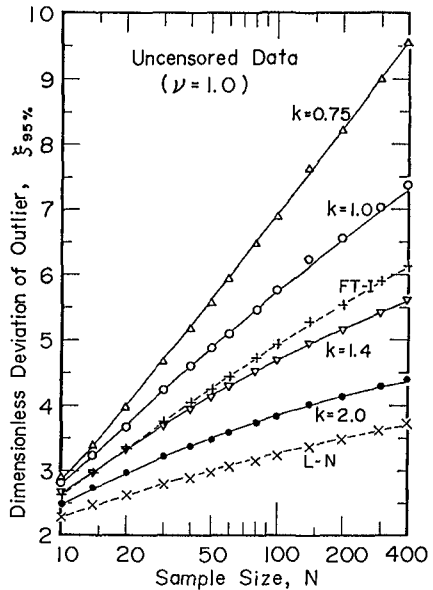


Fig.3 Examples of $\xi_{95\%}$ value.

attributed to the fact that use of Thompson's test for a single sample with the constraint of the largest data among the whole sample is beyond its range of applicability. Thus, the simulation data rather than theory were used in the following analysis of cumulative distribution of ξ value.

If the ξ value of a sample occupies a location at either the upper or lower tail of the cumulative ξ -curve of the distribution function being tested for fitting, the chance that the sample belongs to that population is slim and the fitting of that distribution could be rejected. The 5% and 95% cumulative ξ values were tentatively chosen as the threshold values for rejection. These threshold values were obtained from the simulation data for various sample sizes. Figures 2 and 3 shows examples of such ξ values for the case of uncensored samples. These results were formulated into the following expression:

$$\xi_{5\%}, \xi_{95\%} = a + b \ln N + c (\ln N)^2 \quad (10)$$

The coefficients a , b , and c have been expressed as the functions of the censoring parameter ν for each distribution function as listed in Tables 2 and 3. The difference between the estimates of $\xi_{5\%}$ and $\xi_{95\%}$ by Eq. (10) and the simulation data was less than 2%.

Fitting of a distribution function to a given sample could be rejected, if the ξ value of the sample is either greater than the $\xi_{95\%}$ value or less than the $\xi_{5\%}$ value of that distribution. This rejection criterion is hereby called the DOL (Deviation of OutLier) criterion. Note that the DOL criterion is applicable to any sample regardless of data fitting methods.

Table 2 Empirical Coefficients for The Lower DOL Criterion $\xi_{5\%}$

Distribution	Coefficient a	Coefficient b	Coef. c
FT-II ($k = 2.5$)	$1.481 - 0.126 \nu^{1/4}$	$-0.331 - 0.031 \nu^2$	0.192
FT-II ($k = 3.3$)	1.025	$-0.077 - 0.050 \nu^2$	0.143
FT-II ($k = 5.0$)	$0.700 + 0.060 \nu^2$	$0.139 - 0.076 \nu^2$	0.100
FT-II ($k = 10.0$)	$0.424 + 0.088 \nu^2$	$0.329 - 0.094 \nu^2$	0.061
FT-I	$0.257 + 0.133 \nu^2$	$0.452 - 0.118 \nu^2$	0.032
Weibull ($k=0.75$)	$0.534 - 0.162 \nu$	$0.277 + 0.095 \nu$	0.065
Weibull ($k=1.0$)	0.308	0.423	0.037
Weibull ($k=1.4$)	$0.192 + 0.126 \nu^{3/2}$	$0.501 - 0.081 \nu^{3/2}$	0.018
Weibull ($k=2.0$)	$0.050 + 0.182 \nu^{3/2}$	$0.592 - 0.139 \nu^{3/2}$	0
Log-normal	$0.042 + 0.270 \nu$	$0.581 - 0.217 \nu^{3/2}$	0

Table 3 Empirical Coefficients for The Upper DOL Criterion $\xi_{95\%}$

Distribution	Coefficient a	Coefficient b	Coef. c
FT-II ($k = 2.5$)	$4.653 - 1.076\nu^{1/2}$	$-2.047 + 0.307\nu^{1/2}$	0.635
FT-II ($k = 3.3$)	$3.217 - 1.216\nu^{1/4}$	$-0.903 + 0.294\nu^{1/4}$	0.427
FT-II ($k = 5.0$)	$0.599 - 0.038\nu^2$	$0.518 - 0.045\nu^2$	0.210
FT-II ($k = 10.0$)	$-0.371 + 0.171\nu^2$	$1.283 - 0.133\nu^2$	0.045
FT-I	$-0.579 + 0.468\nu$	$1.496 - 0.227\nu^2$	-0.038
Weibull ($k=0.75$)	$-0.256 - 0.632\nu^2$	$1.269 + 0.254\nu^2$	0.037
Weibull ($k=1.0$)	-0.682	1.600	-0.045
Weibull ($k=1.4$)	$-0.548 + 0.452\nu^{1/2}$	$1.521 - 0.184\nu$	-0.065
Weibull ($k=2.0$)	$-0.322 + 0.641\nu^{1/2}$	$1.414 - 0.326\nu$	-0.069
Log-normal	$0.178 + 0.740\nu$	$1.148 - 0.480\nu^{3/2}$	-0.035

Rejection Criterion Based on Correlation Coefficient (REC Criterion)

Rejection of distribution fitting can also be made by using the absolute value of the correlation coefficient r between the extremal wave height x_m and its reduced variate y_m . Figure 4 shows examples of the cumulative distribution of the residue of r from 1, i.e., $\Delta r = 1 - r$ for the case of the uncensored Weibull distribution with $k = 1.0$. If a sample is fitted to this distribution and the residue of correlation coefficient shows a value located at the upper tail of cumulative curve corresponding to the size of the sample, then the fitting of this distribution to that sample should be rejected. For quantitative analysis, the 95% exceedance value was taken as the threshold value and analyzed from the simulation data. Figure 5 shows examples of the variation of $\Delta r_{95\%}$ with respect to the sample size N . An empirical formulation has been made for $\Delta r_{95\%}$ as

$$\Delta r_{95\%} = \exp[a + b \ln N + c (\ln N)^2] \quad (11)$$

The coefficients a , b , and c are expressed as the functions of censoring parameter for each distribution as listed in Table 4. The difference between the estimates of $\Delta r_{95\%}$ by Eq.(11) and the simulation data was mostly within $\pm 3\%$.

The 95% exceedance value of the residue of correlation coefficient can be utilized as a reference for the rejection of distribution fitting. This is hereby called the REC (Residue of Correlation coefficient) criterion. This rejection criterion is introduced primarily for the case of parameter esti-

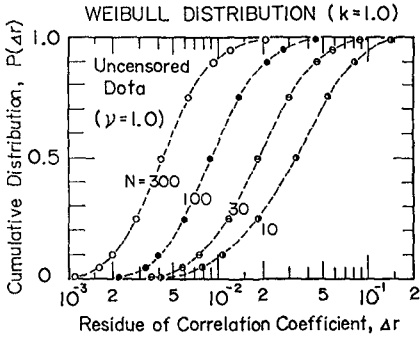


Fig. 4 Cumulative distribution of Δr .

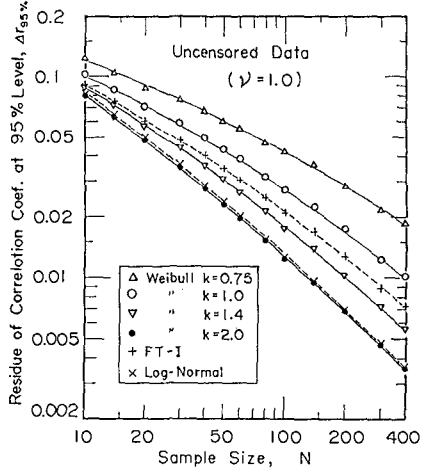


Fig. 5 Examples of $\Delta r_{95\%}$ versus N .

Table 4 Empirical Coefficients for $\Delta r_{95\%}$ in The REC Criterion

Distribution	Coefficient a	Coefficient b	Coef. c
FT-II ($k = 2.5$)	$-1.122 - 0.037\nu$	$-0.3298 + 0.0105\nu^{1/4}$	0.016
FT-II ($k = 3.3$)	$-1.306 - 0.105\nu^{3/2}$	$-0.3001 + 0.0404\nu^{1/2}$	0
FT-II ($k = 5.0$)	$-1.463 - 0.107\nu^{3/2}$	$-0.2716 + 0.0517\nu^{1/4}$	-0.018
FT-II ($k = 10.0$)	$-1.490 - 0.073\nu$	$-0.2299 - 0.0099\nu^{5/2}$	-0.034
FT-I	-1.444	$-0.2733 - 0.0414\nu^{5/2}$	-0.045
Weibull ($k=0.75$)	$-1.473 - 0.049\nu^2$	$-0.2181 + 0.0505\nu^2$	-0.041
Weibull ($k = 1.0$)	-1.433	-0.2679	-0.044
Weibull ($k = 1.4$)	-1.312	$-0.3356 - 0.0449\nu$	-0.045
Weibull ($k = 2.0$)	$-1.188 + 0.073\nu^{1/2}$	$-0.4401 - 0.0846\nu^{3/2}$	-0.039
Log-normal	$-1.362 + 0.360\nu^{1/2}$	$-0.3439 - 0.2185\nu^{1/2}$	-0.035

mation by the least square method, but it can also be applied to the case of other distribution fitting method after the parameters have been estimated.

Best Fitting Criterion Based on Correlation Coefficient (MIR Criterion)

After rejection of unfitting distribution functions, there arises the question of choosing the distribution closest to the true one. However, the parent distribution of the population of storm wave heights is unknown at present. When one

set of extremal wave data at a particular location is analyzed for design purposes, a distribution function which seems best fitting to the sample is chosen as representative of the unknown true distribution. The senior author (Goda 1988) proposed to use the absolute value of the correlation coefficient between the extremal height x_m and its reduced variate y_m as the measure of best fitting: *i. e.*, to choose the distribution exhibiting the largest value of correlation coefficient.

Examination of the nature of the correlation coefficient, however, has indicated the fact that its mean value varies from one distribution to another. Figure 6 shows examples of the mean residual values of correlation coefficient Δr_{mean} of various distribution functions against the sample size N . The distribution with a long tail such as the Weibull with $k = 0.75$ yields a relatively low value or a large residual value of the correlation coefficient. It is therefore not fair to compare the degree of fitting of various distributions to a sample by means of the absolute value of correlation coefficient alone.

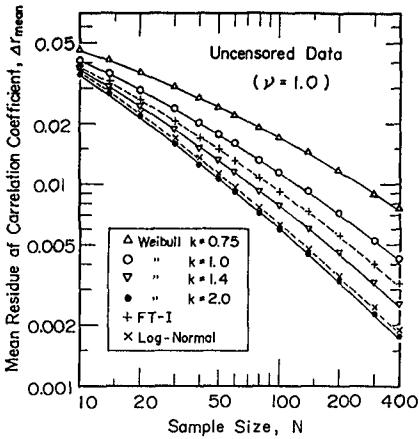


Fig. 6 Examples of Δr_{mean} versus N .

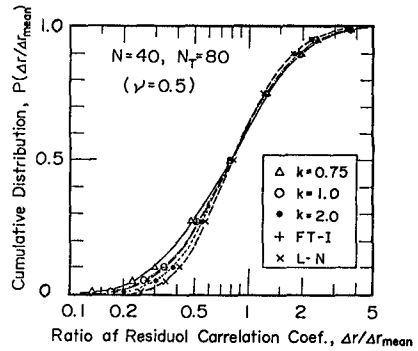


Fig. 7 Cumulative distribution of $\Delta r/\Delta r_{mean}$.

Differences in the absolute magnitudes of Δr among various distributions become insignificant, however, when their ratio to the respective mean values are compared. Figure 7 gives such an example, showing the cumulative distribution of $\Delta r/\Delta r_{mean}$ for the case of censored data with the sample size $N = 40$. Thus it is hereby proposed to employ the ratio $\Delta r/\Delta r_{mean}$ as the measure of best fitting and adopt the distribution which shows the minimum value of this ratio. This is called the MIR (Minimum Ratio of residual correlation coefficient) criterion for best fitting. It will be found in actual data analysis however that the MIR criterion is satisfied by most of distributions which show the largest correlation coefficient among various candidate functions.

The MIR criterion requires the formulation of Δr_{mean} for various distribution functions, sample sizes and the value of censoring parameter. An empirical expression same as Eq.(11) has been applied to the simulation data, *i.e.*,

$$\Delta r_{mean} = \exp[a + b \ln N + c (\ln N)^2] \quad (12)$$

and the coefficients a , b , and c have been formulated as listed in Table 5. The difference between the estimate of Δr_{mean} by Eq.(12) and the simulation data was mostly within $\pm 3\%$.

Table 5 Empirical Coefficients for Δr_{mean} in The MIR Criterion

Distribution	Coefficient a	Coefficient b	Coef. c
FT-II ($k = 2.5$)	$-2.470 + 0.015 \nu^{3/2}$	$-0.1530 - 0.0052 \nu^{5/2}$	0
FT-II ($k = 3.3$)	$-2.462 - 0.009 \nu^2$	$-0.1933 - 0.0037 \nu^{5/2}$	-0.007
FT-II ($k = 5.0$)	-2.463	$-0.2110 - 0.0131 \nu^{5/2}$	-0.019
FT-II ($k = 10.0$)	$-2.437 + 0.028 \nu^{5/2}$	$-0.2280 - 0.0300 \nu^{5/2}$	-0.033
FT-I	$-2.364 + 0.054 \nu^{5/2}$	$-0.2665 - 0.0457 \nu^{5/2}$	-0.044
Weibull ($k = 0.75$)	$-2.435 - 0.168 \nu^{1/2}$	$-0.2083 + 0.1074 \nu^{1/2}$	-0.047
Weibull ($k = 1.0$)	-2.355	-0.2612	-0.043
Weibull ($k = 1.4$)	$-2.277 + 0.056 \nu^{1/2}$	$-0.3169 - 0.0499 \nu$	-0.044
Weibull ($k = 2.0$)	$-2.160 + 0.113 \nu$	$-0.3788 - 0.0979 \nu$	-0.041
Log-normal	$-2.153 + 0.059 \nu^2$	$-0.2627 - 0.1716 \nu^{1/4}$	-0.045

Application of New Criteria to Wave Data around Japan

Japanese islands have various wave climates along their coasts owing to their topography. As seen in Fig. 8, one side of the long stretched islands faces the Sea of Japan, the other side faces the Pacific, and the southwestern side is in the East China Sea. Waves in the Sea of Japan are fetch-limited wind waves, while waves from the Pacific are typhoon-generated seas and swell. Several dozens of nearshore wave stations at the depth 20 to 50 m have been operating with cable-connected acoustic wave recorders. Every 2 hours these wave sensors register surface wave records for 20 minutes. Most of the wave data which are under control of the Ministry of Transport are collected at the Port and Harbour Research Institute, analyzed and filed in a database. From this archives of wave records, extremal data of storm waves up to 1984 were selected and analyzed. (Further analysis with addition of recent data will be made in near future.)

Table 6 Distribution Fitting to Storm Wave Data around Japan

No.	Location	(1) <i>K</i>	(2) <i>N</i>	(3) ν	(4) ξ	Rejection Test of Dist.												
						I	II	III	IV	V	VI	VII	VIII	IX				
A	Monbetsu	7.4	75	0.42	3.62	×	○	○	○	○	○	○	○	○	○	○	○	○
B	Rumoi	13.1	284	0.44	3.70	▼	▼	▼	▼	▼	▽	▼	▼	○	○	○	○	
C	Setana	4.3	153	0.73	3.07	▼	▼	▼	▼	▽	▼	▼	○	○	○	○	○	
D	Fukaura	4.2	156	0.78	3.58	▼	▼	▼	○	○	▼	▼	○	○	○	○	○	
E	Sakata	10.1	361	0.72	3.19	▼	▼	▼	▼	▼	▼	▼	○	○	○	○	○	
F	Hajiki-zaki	5.7	173	0.62	2.69	▼	▼	▼	▼	▼	▼	▼	○	○	○	○	○	
G	Wajima	5.9	196	0.68	3.13	▼	▼	▼	▼	▽	▼	▼	▼	○	○	○	○	
H	Kanazawa	12.0	263	0.44	3.02	▼	▼	▼	▼	▼	▼	▼	○	○	○	○	○	
I	Fukui	3.6	94	0.52	3.18	▼	▼	▼	○	○	○	○	○	○	○	○	○	
J	Tottori	4.9	143	0.60	4.75	×	○	○	○	○	○	○	○	○	○	○	△	
K	Hamada	8.0	194	0.49	4.22	▼	▼	▼	▼	○	○	×	○	○	○	○	○	
L	Genkai-nada	3.0	78	0.52	3.00	▼	▼	▼	○	○	○	○	○	○	○	○	○	
M	Naze	7.6	166	0.44	3.16	▼	▼	▼	▼	▼	▼	○	○	○	○	○	○	
N	Naha	9.9	283	0.59	5.11	▼	×	×	○	○	○	○	○	○	○	○	△	
a	Tomakomai	13.9	213	0.47	4.78	▼	○	○	○	○	○	○	○	○	○	○	×	
b	Mutsu-Ogawara	10.4	250	0.50	3.07	▼	▼	▼	▼	▼	▼	○	○	○	○	○	×	
c	Hachinohe	10.6	368	0.61	4.14	▼	▼	▼	○	○	○	○	○	○	○	○	×	
d	Miyako	3.0	138	0.77	4.05	▼	○	○	○	○	×	○	○	○	○	○	×	
e	Kamaishi	3.3	81	0.43	2.91	▼	▼	▼	○	○	○	○	○	○	○	○	○	
f	Sendai	5.3	176	0.57	3.94	▼	▼	○	○	○	○	○	○	○	○	○	×	
g	Onahama	3.7	102	0.49	3.48	▼	▼	○	○	○	○	○	○	○	○	○	×	
h	Hitachi-Naka	4.8	121	0.43	3.22	▼	▼	○	○	○	○	○	○	○	○	○	×	
i	Kashima	9.4	407	0.73	4.71	▼	▼	○	○	○	○	○	○	○	○	○	×	
j	Habu (Ohshima)	9.9	401	0.60	5.37	▼	▼	○	○	○	○	○	○	○	○	×	▲	
k	Shiono-misaki	11.8	365	0.56	4.94	▼	▼	○	○	○	○	○	○	○	○	○	×	
l	Kochi-offshore	3.6	149	0.75	5.08	○	○	○	○	○	×	○	○	×	×	×	▲	
m	Aburatsu	7.5	71	0.18	4.94	○	○	○	○	○	○	○	○	○	×	△	▲	
n	Shibushi	4.5	91	0.41	5.22	○	○	○	○	○	×	○	○	×	×	▲	▲	
p	Nakagusuku	8.9	270	0.68	4.74	▼	▼	○	○	○	×	○	○	○	○	×	▲	

REMARKS:

- Column (1) : Effective duration of observation in years.
 (2) : Number of storm wave events above a threshold value.
 (3) : Censoring parameter ($=N/N_T$).
 (4) : ξ value of storm wave data.

Distribution Functions :

- I = FT-II ($k = 2.5$), VI = Weibull ($k = 0.75$),
 II = FT-II ($k = 3.3$), VII = Weibull ($k = 1.0$),
 III = FT-II ($k = 5.0$), VIII = Weibull ($k = 1.4$),
 IV = FT-II ($k = 10.0$), IX = Weibull ($k = 2.0$).
 V = FT-I,

Distribution Fitting :

- = Fitting acceptable,
 △ = Rejected by the upper DOL but not by the REC criteria,
 ▲ = Rejected by both the upper DOL and the REC criteria,
 ▼ = Rejected by the lower DOL but not by the REC criteria,
 ▼ = Rejected by both the lower DOL and the REC criteria,
 × = Rejected by the REC but not by DOL criteria.

Table 6 lists the location names of wave stations, the effective durations of wave observations in years excluding the periods of downtime, the number of storm wave data analyzed, and so on. The locations of these stations are shown in Fig. 8 with the alphabet. The average number of storm wave events at these stations was about 50 to 60 per year, and the threshold wave height for censoring varied from station to station; thus the censoring parameter ranged from 0.18 to 0.78. In total, wave data at 29 stations were analyzed, and the duration of wave observation ranged from 3.0 to 13.9 years.

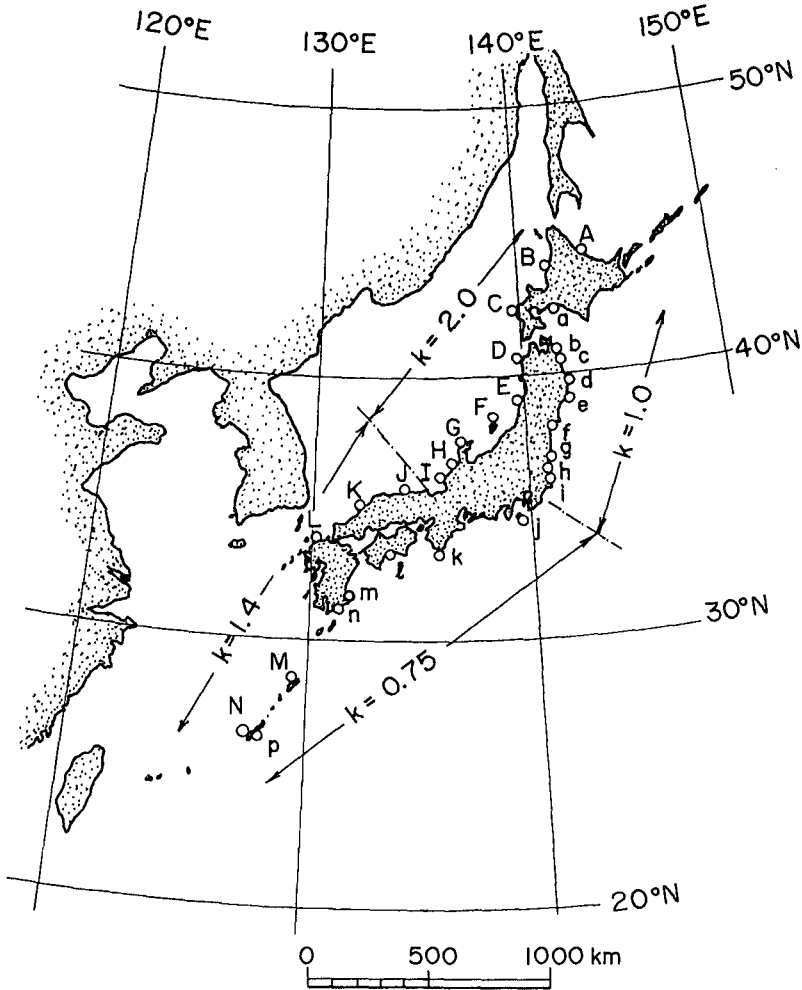


Fig. 8 Location map of wave stations used in the analysis.

The dimensionless deviation ξ of the largest data at each station is listed in the column (4) of Table 6, and the rejection test of the distribution functions of Eqs.(1) to (3) has been made with this ξ value and the residue of correlation coefficient Δr . The result of rejection test is marked with various symbols for each distribution. The upper DOL criterion is applied when the sample ξ value exceeds the $\xi_{95\%}$ value of the distribution being fitted, while the lower DOL criterion is for the case of $\xi < \xi_{5\%}$. The marks except for the open circle indicate that the distribution fitting should be rejected with the probability of misjudgment being less than 5%. In other words, one sample out of 20 samples would be rejected even if all the 20 samples are drawn from the same population.

Although the rejection test for the storm wave data of individual stations yields versatile answers, the results point out the presence of a characteristic distribution which is unrejectable in a group of stations located in the same region. For example, the stations 'A' to 'I' along the Sea of Okhotsk and the upper part of Japan Sea seems to support the Weibull distribution with $k = 2.0$ as the common distribution. For the stations 'J' to 'N', the Weibull with $k = 1.4$ seems more appropriate, probably because of occasional high waves generated by typhoons. In the region covering the stations from 'a' to 'i', the Weibull distribution with $k = 1.0$ has the least frequency of rejection. This area is exposed to swell from typhoons, but direct attack of typhoon waves is infrequent. The region for the station 'j' to 'p' where typhoon-generated waves dominate extreme wave climate seems to accept three distributions of the Weibull with $k = 0.75$ and the FT-II with $k = 5.0$ and 10.0 as the candidates for the population distributions.

The analysis of Table 6 will require further examination with additional data after 1985, especially from the viewpoint of the data homogeneity. Analysis of seasonal or monthly extremal wave data will be the easiest way to separate storm waves generated by different types of meteorological disturbances. Nevertheless, the result of Table 6 indicates the possibility of identifying the parent distribution for the regional population of storm wave data by filtering out various candidate functions with the new rejection criteria.

Concluding Remarks

Choosing a distribution function for a sample of extremal data sample is always a troublesome task, because no steadfast guidelines exist. It will be very difficult and almost impossible to establish such guidelines for affirmative recommendation. The present paper is intended to enable to issue negative recommendations for distribution fitting by establishing

objective rejection criteria for extreme statistics. Two empirical criteria introduced herein well function in identifying possible regional population distributions of storm waves around Japan.

A question often asked is the minimum size of extremal sample at which an analyst can answer with confidence which one of candidate distributions is the true distribution of the population for that sample. An answer can be obtained by examining the sample size at which the lower DOL criterion $\xi_{5\%}$ of a longer-tailed distribution becomes equal to or greater than the upper DOL criterion $\xi_{95\%}$ of a shorter-tailed distribution. Beyond that sample size, the two distributions could be safely discerned. However, this sample size turns out to be quite large. For example, the FT-I and FT-II with $k = 3.3$ are only discernible at the sample size greater than 900 for an uncensored sample and greater than 1900 for a censored sample with $\nu = 0.25$. The FT-I and the Weibull with $k = 1.4$ are very difficult to distinguish each other by means of the DOL criterion alone.

In the extremal analysis of storm wave data, emphasis should be placed on the effort of collecting as many data as possible over a period as long as feasible, so that the danger of choosing a distribution not belonging to the population will be minimized and the range of confidence interval of the return wave height will be lowered.

References

- Andrew, M.E. and Hemsley, J.M. [1990]: Resampling approach to extreme wave-height analysis, *J. Waterway, Port, Coastal, and Ocean Engg.*, ASCE, Vol.116, No.4, pp.444-458.
- Goda, Y. [1988]: On the methodology of selecting design wave height, *Proc. 21st Int. Conf. Coastal Engg.*, Malaga, pp. 899-913.
- Goda, Y. [1990]: Rejection criteria for outliers and their applications in extreme statistics, *Proc. Japan Soc. Civil Engrs.*, No.417/II-13, pp.245-254 (*in Japanese*).
- Goda, Y. and Onozawa, M. [1990]: Characteristics of the Fisher-Tippett type II distribution and their confidence intervals, *Proc. Japan Soc. Civil Engrs.*, No.417/II-13, pp.289-289 (*in Japanese*).
- Jenkinson, A.F. [1955]: The frequency distribution of the annual maximum (or minimum) values of meteorological elements, *Quart. J. Roy. Meteor. Soc.*, Vol.81, pp.158-171.
- Rossouw, J. [1988]: Design waves and their probability density functions, *Proc. 21st Int. Coastal Engg.*, Malaga, pp.822-834.

CHAPTER 2

A MODEL FOR SURF BEAT

P.J. van Leeuwen¹ and J.A. Battjes¹

Abstract

A model is presented for the generation of low-frequency waves propagating normal to the beach. The input parameters are the bottom profile and the variance spectrum of the incoming wind waves. The model predicts the variance spectrum of the low-frequency waves. Also correlations between e.g. wind wave envelope and low-frequency surface elevation can be calculated. Results of the model are compared to field data.

1 Introduction

When wind waves approach mildly sloping beaches, a significant amount of energy can be found at frequencies an order of magnitude lower than those of the incoming wind waves. Part of this low-frequency energy can be ascribed to edge waves, whose phase variation is alongshore. An important part however can be assigned to two-dimensional shorenormal waves, which are here called surf beat.

The first observations of surf beat were made 40 years ago by Munk (1949). He found a linear relation between the amplitudes of the low-frequency waves and those of the wind waves. Looking at the time records of both types of waves he found that the low-frequency waves lagged behind the wind wave envelope with about 140 seconds, which he attributed to the time needed for the wind wave envelope to travel to the surf zone and for the low-frequency waves to travel back to the wave recorder. Tucker (1950) reported the same kind of measurements, but he used correlograms to analyze his data. He also found that the low-frequency waves are lagging behind the wind wave envelope, and that the largest absolute value of the correlation coefficient occurs when this coefficient is negative. This means that the wind wave envelope and the low-frequency waves are 180 degrees out of phase, apart from travel considerations.

Biésel (1952) proved theoretically that groups of short waves are accompanied by nonlinear long waves, bound to these groups. Longuet-Higgins and Stewart (1964) clarified this theoretical result with the concept of radiation stress. Due to this nonlinear effect, water is pushed away from areas with high waves and accumulated

¹ Delft tech. Univ., Dept. of Civil Engineering, Delft, The Netherlands.

under low waves. This results in long waves, bound to the wind wave groups. An important feature is that the bound long waves are 180 degrees out of phase with the wind wave envelope. A way to explain the observations by Munk (1949) and Tucker (1950) qualitatively is to suppose that the bound long waves are reflected in the surf zone, and propagate seaward as free long waves. Since the paper pays no attention to the mechanism of reflection, it is difficult to compare the theoretical results with experiments.

Quantitative models were lacking until 1981. The relatively simple case of bichromatic wind waves is here addressed first. Lo (1981) presented a bichromatic model which calculates in the time domain and in which he could explain the linear relation between the low-frequency wave amplitude and the wind wave envelope height by taking the generation of low-frequency waves due to the breaking of the regular wave groups into account. He found that the surf zone region was very important for low-frequency wave generation, and that the smaller the beach slope, the higher the surf beat wave heights. The reason for this is that more time is available for the energy transfer from the wave groups to the low-frequency waves. Lo (1981) did not mention how the forcing of the low-frequency waves due to wave breaking was modelled.

Symonds et al. (1982) investigated the forcing of low-frequency waves by the time variation of the location of the break point. This variation gives rise to a time-varying set up and hence produces low-frequency waves. The analysis was performed for bichromatic short waves with periodic wave groups. The difference between this model and that of Lo (1981) is that the calculations are done in the frequency domain and that the bound long waves are ignored. Kostense (1984) verified this model in a wave flume and found good qualitative agreement.

Schäffer and Svendsen (1988) presented a spectral bichromatic model in which they allow for wave height modulations after the waves are broken by taking a fixed (in space) break point. The model uses both the bound long waves and the long wave generation due to wave breaking, but because of the wave modulations inside the breakpoint bound long waves are generated in this region too. In a later paper by Schäffer and Jonsson (1990) the model is compared with the Kostense (1984) data. An overestimation of the outgoing low-frequency wave amplitude was attributed to bottom friction, which is not included in the model. This is the only model which allows for wave height modulations inside the surfzone and the consequent generation of low-frequency waves in this region.

The calculation of surf beat using random wind waves was first addressed by Lo (1981). He uses both types of forcing of low-frequency waves and calculates in the time domain. A comparison of his model with field data by Goda (1975), using a full wind wave spectrum as input, showed the right order of magnitudes for the low-frequency spectral components.

List (1990) also proposed a model for random wind waves in which both generating mechanisms are present and in which the calculations are done in the time domain. The model uses as input measured wind wave envelope time series, from which low-frequency wave time series are calculated. A comparison with field data showed results for the low-frequency wave energy levels which are 5 to 50% off, and good qualitative results for the correlation between wind wave envelope and low-frequency surface elevation.

The present paper also deals with low-frequency wave generation by random wind waves. The main difference with the models of Lo (1981) and List (1990) is that the calculations are here performed in the frequency domain. The input of the model is the energy spectrum of the wind waves, the idea being that the low-frequency energy spectrum is not dependent on one specific realisation of the process described by the energy spectrum of the wind waves.

In the present paper the theoretical model is developed first. Then a few remarks are made about the collection and the processing of the field data, used for comparison with model results. The next section deals with the comparison and a discussion of the results. Some concluding remarks close the paper.

2 The model

The basic philosophy behind the model is to combine the ideas of Longuet-Higgins and Stewart (1962) and Symonds e.a. (1982), and to extend them to the case of wind waves with a continuous spectrum. A spectral approach will be followed, because usually input information is in that form, and not in the form of time series. The basic equations are the linearized shallow water equations. After elimination of the velocity a second order partial differential equation results for the low-frequency surface elevation (see e.g. Symonds e.a. 1982):

$$\frac{1}{g} \zeta_{tt} - h_x \zeta_x - h \zeta_{xx} = -\frac{1}{g\rho} S_{xx} \quad (1)$$

in which ζ is the low-frequency surface elevation, h the mean water depth, ρ the water mass density, g the acceleration of gravity and S the radiation stress. The subscripts denote partial differentiation. The driving term for the low-frequency waves is the second space derivative of the radiation stress. Because the wind waves have a continuous spectrum the radiation stress is randomly varying.

The idea is now to expand the variables in a Fourier-Stieltjes (FS) integral according to

$$\alpha = \int_0^{\infty} e^{i\omega t} dA$$

in which dA is a random increment function for an interval $d\omega$. It can be seen as the complex amplitude of the waves in a frequency interval $d\omega$ and is related to the variance spectrum $G_{\alpha\alpha}$ of α by

$$G_{\alpha\alpha} d\omega = \frac{1}{2} \langle dA dA^* \rangle \quad (2)$$

where $\langle \dots \rangle$ indicates ensemble averaging, and the asterisk denotes the complex conjugate.

For the FS transformed long wave equation one now finds

$$\frac{\omega^2}{g} dZ(x, \omega) + h_x dZ_x(x, \omega) + h dZ_{xx}(x, \omega) = -d\phi_{xx}(x, \omega) \quad (3)$$

in which dZ is the FS transform of the low-frequency surface elevation ζ , and $d\phi$ the FS transform of the forcing. First note that equation (3) is a second order ordinary differential equation, which is much easier to solve than its partial counterpart. For instance in the case of a plane sloping bottom, the solution of (3) is found as a combination of integrals over Bessel functions of first and second kind.

The calculation of the forcing term in equation (3) needs extra attention. Because it is a complex quantity its absolute value as well as its phase has to be calculated.

The phase will be space and frequency dependent. The frequency dependence of the phase cannot be determined because only the wind wave variance spectrum is given. However, we want to calculate the variance spectrum of the low-frequency waves so this frequency dependence is of no importance. The space dependence of the phase of the forcing will be important. The forcing will have a phase shift along the spatial coordinate due to the fact that the forcing is related to the wind wave envelope squared via the radiation stress. Because it takes the wind wave envelope some time to pass through the surf zone, a certain distance Δx corresponds to a phase shift $\Delta\psi$ in the forcing. A way to calculate this phase shift is to assume that the wind wave envelope travels with group velocity C_g of the peak frequency. The phase shift due to the finite travel time of the wind wave envelope now becomes

$$\Delta\psi(x - x_0) = \arg\{d\phi(x, \omega)\} = \int_{x_0}^x \frac{\omega}{C_g} dx \quad (4)$$

The absolute value of the forcing term in equation (3) will be calculated from the variance spectrum of the forcing which in turn will be determined from the variance spectrum of the wind waves. As mentioned above, the forcing term is proportional to the second space derivative of the radiation stress, which in turn is proportional to the wave envelope R squared. Consequently, the variance spectrum of the envelope squared has to be determined to obtain the variance spectrum of the forcing. A way to calculate the variance spectrum of the wind wave envelope squared is to start from the covariance of two squared envelopes:

$$C[R^2(t), R^2(t + \tau)] = E[R^2(t)R^2(t + \tau)] - E^2[R^2(t)] \quad (5)$$

in which $C \dots$ is the covariance, and $E \dots$ is the expected value operator. The Fourier transformation of the covariance gives the required variance spectrum.

The expected values in equation (5) can be found from the joint probability density $p(R_1, R_2)$ of two envelopes at a time lag τ . For a narrow-band Gaussian process, this probability density has been derived by Rice (1944, 1945). It has since been called the 2-D Rayleigh distribution. This density has been used successfully by Kimura (1980) in his description of wave groups. In the case of breaking waves

the probability density $p(R_1, R_2)$ has to be modified because the wave height is limited to a critical value, mainly determined by the local depth. A truncated 1-D Rayleigh distribution developed and used successfully by Battjes and Jansen (1978) to determine the mean energy dissipation in breaking waves is adopted here, extended in a straightforward manner to the two-dimensional case.

Now that the variance spectrum of the forcing has been found in which both breaking and nonbreaking waves are incorporated, the variance spectrum of the low-frequency waves can be obtained by solving the ordinary differential equation (3) and using (2).

The method outlined above also gives one the opportunity to calculate correlation coefficients, for instance for the correlation between low-frequency surface elevation and wind wave envelope. At first sight this may seem impossible because the frequency dependence of the phases of the spectral components of e.g. low-frequency surface elevation is not known. To solve this problem it is noted that only the phase difference between the FS transform of the low-frequency surface elevation and the FS transform of the wind wave envelope at each frequency has to be known, not the phase difference between different spectral components. The required phase differences at each frequency follow directly from differential equation (3).

3 Data collection and processing

The data used are from a field experiment conducted at the U.S. Army Corps of Engineers Field Research facility in Duck, North Carolina, U.S.A., on September 9, 1500 EST 1985. The beach was approximately two-dimensional. A cross-shore array of eight pressure sensors and bi-axial horizontal current meters provided time series with a sample rate of 2 Hz. Figure 1 shows the bottom profile with the positions of the sensors. The pressure sensors were of the diaphragm type and the current meters were Marsh McBirney electromagnetic meters.

The data describe swell with highly grouped waves and a narrow spectral peak near 0.08 Hz. The root mean square wave height was 0.4 m. This data set was chosen because of the profound group structures present during the measurements and the nearly shorenormal incidence.

The low-frequency wave band is defined as $0.007\text{Hz} < f < 0.03\text{Hz}$, because outside this region the waves were found to be uncorrelated with the wave groups. Low-frequency standard deviations were calculated from the pressure sensors at each of the sensor locations. The cross-correlation coefficient between wind wave envelope and incoming and outgoing low-frequency waves at a sensor location outside the surfzone ($x=222\text{m}$) was calculated. The wind wave envelope was found by calculating the Hilbert transform of the time series, using an approximate temporal Hilbert filter given by McClellan et al. (1979), with 95 points (Pierce, 1985). The low-frequency waves were obtained by lowpass filtering the time series and separated into incoming and outgoing waves using the method proposed by Guza et al. (1985):

$$\zeta_{\text{in}} = \frac{\xi + \sqrt{\frac{h}{g}}U}{2}, \quad \zeta_{\text{out}} = \frac{\xi - \sqrt{\frac{h}{g}}U}{2} \quad (6)$$

in which ξ is the low-frequency surface elevation and U is the low-frequency orbital velocity defined positive offshore.

As mentioned before, the model needs as input the variance spectrum of the wind waves. This was obtained by a Fourier transform of the time series from the seawardmost sensor.

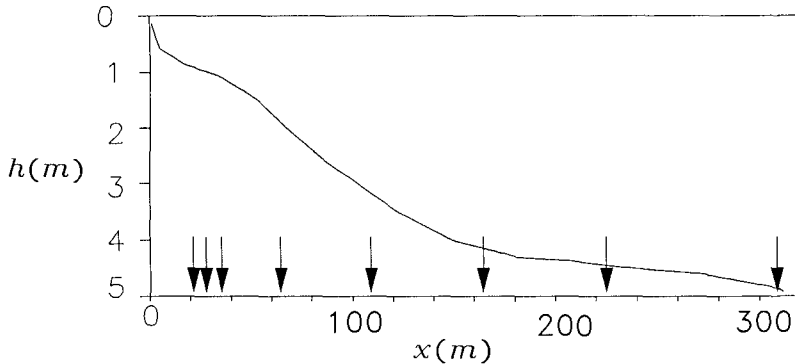


Figure 1 Bottom profile, arrows indicate sensor locations.

4 Comparison and discussion

To verify the model, both field data and laboratory data will be used. In this paper only field data are used to test the model. The first test uses the standard deviation of the outgoing low-frequency waves $\sigma_{\xi_{out}}$. The second uses the correlation between wind wave envelope and surface elevation of the incoming and outgoing low-frequency waves.

The ratio of breaker height to local depth, γ , is a free parameter in the model. It has been set equal to 0.4. However, a change in γ does not give a strong change in the results presented here.

The reason for the test using the standard deviation of the outgoing low-frequency waves is the following. The outgoing low-frequency waves are a combination of low-frequency waves of three different origins: waves, which were first incoming and bound to the wave groups, and then reflected on the beach to become outgoing; waves which are produced by the time-varying breakpoint mechanism as outgoing waves, and finally waves which are produced by the time-varying breakpoint mechanism as incoming waves, and which then are reflected by the beach to become outgoing. If a model can reproduce the energy level of this complicated mixture within the error margins (5% in this case) without tuning parameters (except maybe γ), the physics in that model can be close to the real physics involved. Of course, more situations have to be used as test cases for the 'can' to be a 'must'.

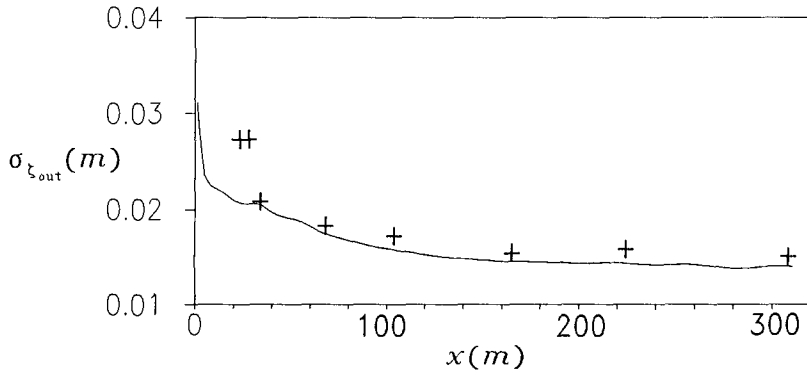


Figure 2 Standard deviation of surface elevation of outgoing low-frequency waves as function of distance from the water line. (+) data, (-) theory.

In figure 2 the standard deviation of the outgoing low-frequency surface elevation is given as function of the distance from the shore line. The surfzone extends to about 60 m from the water line. The model shows good agreement with the data from six sensors. Unfortunately the two innermost pressure sensors have spurious energy in the low-frequency band, so that the comparison in this region is not conclusive. The reason that some energy must be spurious is that these sensors both show a large peak at a different frequency, with a spectral energy density as high as that of the wind waves, while outside the surfzone these peaks are not observed. In principle it could be possible that some unknown forcing mechanism for low-frequency waves is active inside the surfzone, the waves of which are cancelling each other somehow when they try to leave the surfzone. It is noted however that the beach does not have a certain length scale, like a bar, so this might be unlikely to happen on this beach.

Figure 3a shows the correlation coefficient for the wind wave envelope and the surface elevation of the incoming low-frequency waves. The 95% confidence interval on zero correlation was found to be below 0.09 for the data. A strong negative peak can be observed at zero lag, which must be attributed to the bound low-frequency waves. The fact that the peak from the field data is not that pronounced shows that the bound low-frequency waves are not the only low-frequency waves with a shorenormal particle velocity component. Probably edge waves and shore-oblique leaky mode waves are present.

Figure 3b shows the correlation coefficient for the wind wave envelope and the surface elevation of the outgoing low-frequency waves. Again the 95% confidence interval on zero correlation was found to be below 0.09 for the data. A strong negative peak can be seen in the theoretical curve at a time lag of about 100 s, which is precisely the time needed for the bound long waves to travel to the beach (at the still-water line), reflect from the beach, and travel back as free waves to the pressure sensor again. The data also show a peak at this time lag. The theory additionally shows significant oscillations at smaller and larger time lags. The reason for this is not entirely clear yet. The negative peak at about 62 s time lag may be associated with the outgoing waves produced by the time-varying breakpoint mechanism. This time lag corresponds to the time needed for the wave

envelope to travel to the 'mean' breakpoint and for the generated low-frequency waves to travel back to the sensor. The 'mean' breakpoint is here defined as the point in which the rms wave height is maximum. The data do not show significant correlations at this time lag.

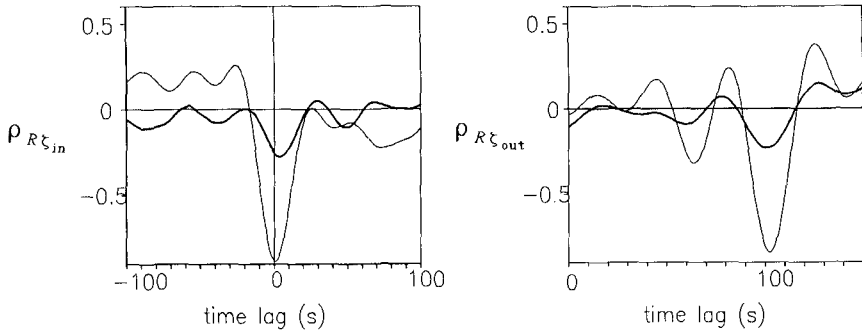


Figure 3 Cross correlations between wind wave envelope and low-frequency surface elevation at $x=222$ m. a) incoming low-frequency waves, b) outgoing low-frequency waves. The thick line represents the data, the thin line represents the theoretical results.

5 Conclusions

A model has been developed for the generation of shorenormal low-frequency waves by random wind waves. The model needs as input the energy spectrum of the wind waves, and calculates in the frequency domain. The results of the model are compared to field data.

The comparison showed that the measured low-frequency standard deviations at a range of distances from the water line are predicted within their error margins. However the innermost pressure sensors are believed to contain spurious low-frequency energy, so the comparison was not conclusive in this region.

The time lag of strongest cross-correlation between wind wave envelope and incoming and outgoing low-frequency waves is predicted correctly, although the magnitude of the correlation coefficient is overestimated. The remaining structure of the theoretical cross-correlation function requires further investigation.

Acknowledgements

The investigations were supported by the Working Group on Meteorology and Physical Oceanography (MFO) with financial aid from the Netherlands Organization for the Advancement of Research (N.W.O.). The U.S. Army Corps of Engineers is thanked for the DUCK85 field data from their Field Research Facility in Duck, North Carolina, U.S.A..

References

- Battjes J.A. and J.P.F.M.Jansen (1978), Energy loss and set up due to breaking of random waves. *Proc. 16th Coastal Eng. Conf. ASCE*, 569-587, Hamburg.
- Biésel F. (1952), Equations générales au second ordre de la houle irrégulière. *La Houille Blanche*, 7, 372-376
- Kimura A. (1980), Statistical properties of random wave groups. *Proc. 17th Coastal Eng. Conf. ASCE*, 2955-2973, Sydney.
- Kostense J.K. (1984) Measurements of surf beat and set down beneath wave groups. *Proc. 19th Coastal Eng. Conf. ASCE*, 724-740, Houston.
- List J.H. (1990) A model for two-dimensional surf beat. *Submitted for publication*.
- Lo J-M. (1981) Surf beat: numerical and theoretical analysis. *Ph.D. Dissertation*, University of Delaware.
- Longuet-Higgins M.S. and R.W. Stewart (1964), Radiation stresses in water waves; a physical discussion, with applications. *Deep Sea Res.*, 11, 529-562.
- Munk W.H. (1949), Surf beat, *EOS Trans. AGU.*, 30, 849-854.
- Rice S.O. (1944, 1945) Mathematical analysis of random noise. *Bell System Technical Journal*, 23, 24.
- Schäffer H.A. and I.A.Svendsen (1988) Surf beat generation on a mild-slope beach. *Proc. 21st Coastal Eng. Conf. ASCE*, 1058-1072, Malaga.
- Schäffer H.A. and I.G. Jonsson (1990) Theory versus experiments in two-dimensional surf beat. *Presented at the 22nd International Coastal Eng. Conf. ASCE*, Delft.
- Symonds G., B.A. Huntley and A.J. Bowen (1982), Two-dimensional surf beat: Long wave generation by a time-varying breakpoint, *J. Geophys. Res.*, 87, 492-498.
- Tucker M.J. (1950), Surf beats: Sea waves of 1 to 5 minutes' period, *Proc. Roy. Soc., Ser A*, 202, 565-573.

CHAPTER 3

EVALUATION OF EMPIRICAL MODEL FOR WAVE RUNUP ELEVATIONS

Robert J. Hallermeier*, Kevin B. Nosek*,
Christopher J. Andrassy*

Abstract

Predicted runup elevations for given waves and nearshore profile are confirmed as accurate by large tank and field studies with over 400 published measurements, the majority exceeding 1 m above static water level. Predictions are provided by a public-domain computer code incorporating detailed empirical guidance for smooth slopes developed by Stoa (1978). This model examines the geometrical match with specified situations, applies the composite-slope method of Saville (1958) where necessary, treats barrier texture using standard runup-reduction coefficients, and executes suitable interpolation and iteration for a fully consistent runup estimate. With irregular wave action, basic empirical guidance for uniform waves gives the mean runup elevation from the mean wave description. There is definite agreement between predictions and measurements for smooth or rough barriers with uniform waves, for controlled irregular waves, and for field situations.

INTRODUCTION

Runup may define the landward limit to wave effects, defined as a vertical distance above static water level on the shore barrier. Expected runup elevations can be important in forecasts of flooding hazards due to storms and in designs of coastal structures meant to halt wave action. The improved prediction of wave runup has been

*Dewberry & Davis, METS Division, 8401 Arlington Blvd.,
Fairfax, Virginia 22031-4666

*Now with: Los Angeles District, U.S. Army Corps of
Engineers, P.O. Box 2711, Los Angeles, CA 90053-2325

a continuing engineering concern, with progress assisted by data collection programs, analytical approaches, and developments in numerical modeling. This paper describes evaluation of a convenient prediction model implementing long-available guidance with an extremely detailed basis in laboratory runup elevations.

Measurements with breaking waves indicate that runup elevation normalized by wave height is primarily related to the value of the surf similarity parameter (ratio of the barrier slope to the square root of wave steepness). With reflecting waves, peak water elevation at the barrier is more susceptible to theoretical treatment but still has an empirically defined dependence on the type of barrier surface. Within an individual study of certain shore geometries, runup effects for a range of wave action may often be summarized by some relatively simple expression spanning the two regimes of behavior. However, runup exhibits appreciable dependences on detailed wave characteristics such as nonlinearity, and on geometrical particulars such as the seaward extent to the shore barrier and its approach slope. Thus, the most accurate runup guidance consists of empirical curves pertaining to a specific range of situations. Examples include the curve sets provided by Horikawa (1978), the U.S. Navy (1982) *Coastal Protection Design Manual*, and the U.S. Army (1984) *Shore Protection Manual*.

The detailed guidance utilized here is that originally documented by Stoa (1978), where each set of runup curves pertains to a precisely specified two-dimensional geometry at small scale. Ten distinct configurations of smooth shore barrier and approach have been addressed for wide ranges of barrier slope and wave steepness, with mean runup elevation indicated for uniform incident waves described in deep water. A computer code provides automated application of the Stoa guidance to a given situation, for an estimate of runup elevation with a definitive empirical basis.

COMPUTER CODE

In 1979, the Federal Emergency Management Agency contracted Stone & Webster Engineering Corporation to develop a consistent method for determining wave runup elevations associated with extreme storms. Such methodology was required within the National Flood Insurance Program to assess coastal wave hazards additional to stillwater inundation during the 100-year flood. The product was a computer code giving an empirically based estimate of representative runup elevation for a profile of linear segments with specified incident waves (Stone & Webster,

1981). Later tests demonstrated that the original code was liable to provide inaccurate results because of oversimplifications in following the basic guidance given by Stoa (1978). The effort reported here has consisted of an extensive upgrade to the code details, along with verification of computed results using the large data base now available.

Automated implementation of detailed runup guidance meant for manual application informed by engineering judgment has entailed the development of several objective analyses to summarize basic shore geometry. The code is fully documented in a comprehensive report on the present study (Dewberry & Davis, 1990), but Figure 1 shows a flowchart indicating the level of detail in these analyses. Each decision block relates to a separate consideration affecting runup estimation, according to basic guidance given by Stoa (1978). This suite of decision-making has required several quantitative distinctions in characterizing shape, and these choices treated shore geometries in documented runup investigations as typical. Results generally show smooth variations of runup for changed input, but the automatic analyses are not foolproof; runup estimates will be most appropriate if engineering judgment is applied in idealizing the actual profile, by taking into account the code's operations.

Initial analysis within the code effects a separation of the specified profile into a steep shore barrier, an appreciably inclined approach, and a seaward portion; for example, the designated barrier sequentially incorporates additional profile segments which do not lower the overall slope appreciably (cotangent increases less than 20%). A major distinction is whether the approach is effectively horizontal or sloped, since there are separate curve sets for these cases; an overall approach slope steeper than 1 on 15 is regarded as equivalent to the 1 on 10 specified by Stoa (1978). Other factors considered in detail are the length of the approach slope, since Stoa specified a minimum extent, and the expected breaker location, to check congruence with basic laboratory situations where waves do not break seaward of the approach.

The strategy implemented in the code is full reliance on Stoa's runup guidance where it is fully appropriate, i.e., where the situation of interest falls within the range covered by that specific guidance. In such cases, runup elevation is defined by wave dimensions along with the overall slope from barrier toe to runup limit, the water depth at the barrier toe, and the approach geometry. Where the geometrical match to tested situations is found to be inexact, some reliance is placed on the original composite-slope method of Saville (1958) with the entire

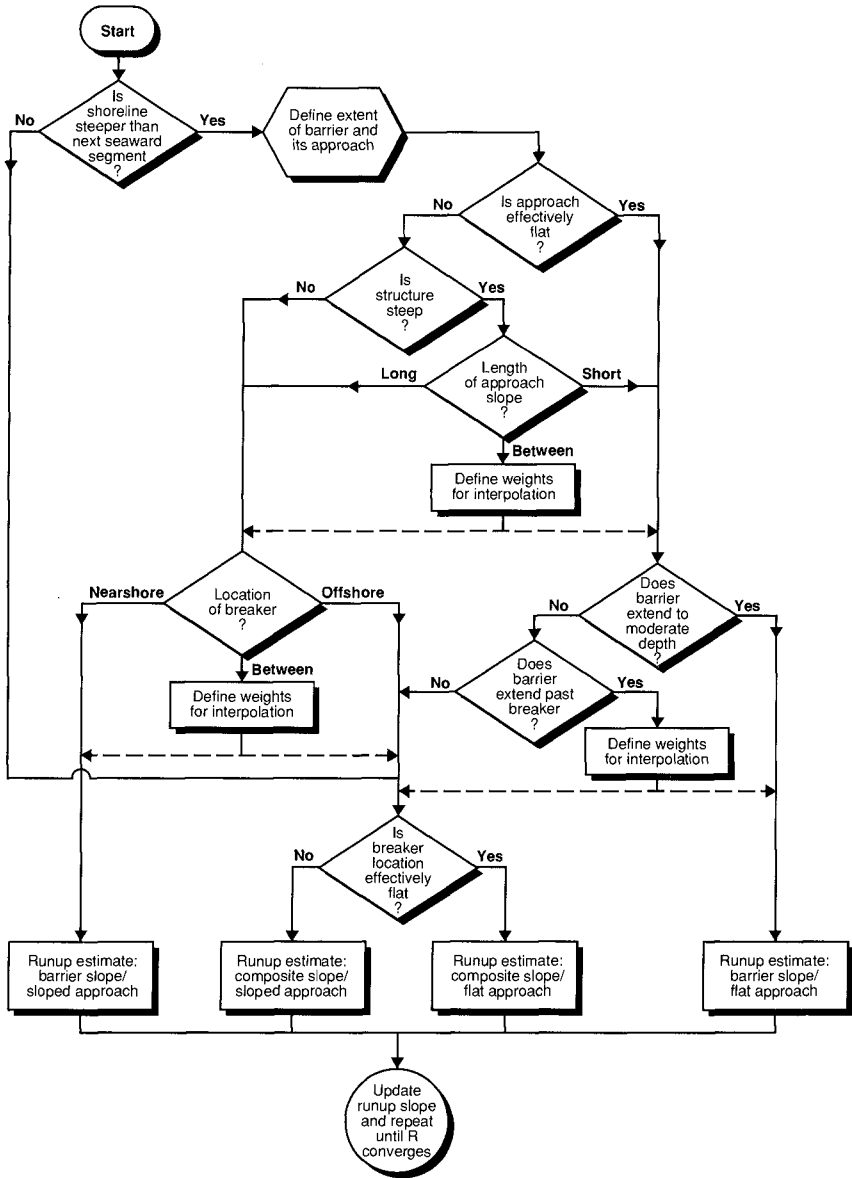


FIGURE 1. FLOWCHART OF ANALYSES WITHIN THE COMPUTER CODE.

breaker zone considered in estimating runup. Then the geometrical parameters are the overall slope from break point to runup limit, along with water depth and approach slope at the break point. The code incorporates Goda's guidance on uniform wave breaking, presented in Horikawa (1978) as normalized water depth versus wave steepness and bottom slope. An allowance for a runup scale effect on smooth slopes is applied using the multipliers proposed by Stoa (1978). Roughness and permeability of the runup surface is treated by means of usual values for a reduction coefficient (r) shown useful in considering barrier texture for wave runup and overtopping computations.

Although all might be utilized, four basic alternatives arise in runup determination: applying a barrier slope or a breaker-zone slope, and treating the approach as horizontal or inclined. The runup curves in Stoa (1978) are used in each case, but with different entry points. Transitions between these distinct computation bases provide finite ranges where runup elevation is determined by more than one viewpoint; Figure 1 indicates the various possibilities in blends of empirical results. Each contribution to the runup estimate is defined where possible by interpolation between separate curve sets bracketing the given situation. In addition, a runup elevation is extracted from an individual curve set by suitable interpolation between results originally provided in logarithmic format. The controlling slope can depend on runup limit, so the computation procedure is repeated until it converges to a self-consistent runup estimate.

For a specified profile and water level, along with wave height and period, the automatic procedure gives a runup prediction firmly based on detailed empirical guidance. Simple geometrical approximations are applied in treating the profile, and results generally reflect a blend of pertinent viewpoints in runup estimation. Computed runups are confirmed to be accurate by the following comparisons with large runup elevations measured in many studies. Data are considered in order of increasing complexity of the situations investigated.

VERIFICATION FOR UNIFORM WAVES

Figure 2 displays measurements versus computations for large tank tests with (a) smooth barriers and (b) rough structures in uniform or monochromatic wave action. These results exhibit extremely strong correlation for runup elevations typically on the order of 1 to 3 m, i.e., of common prototype magnitudes.

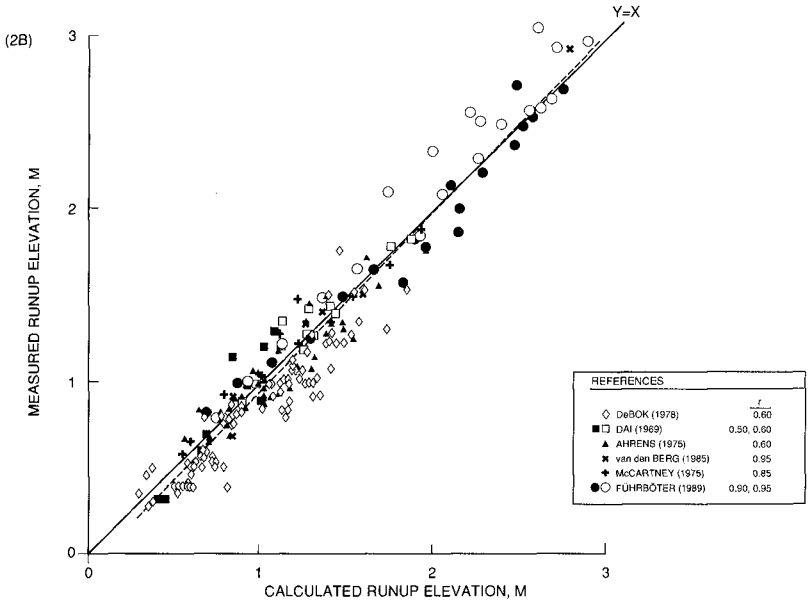
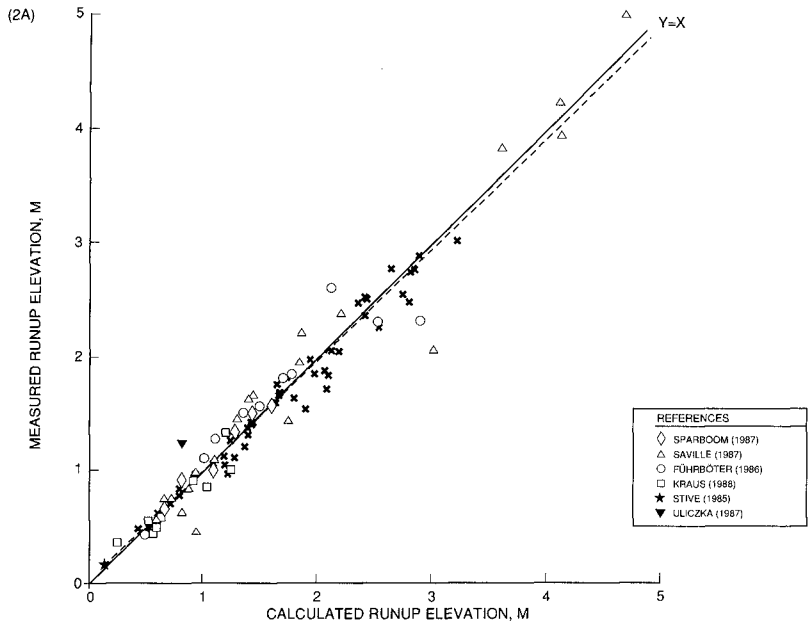


FIGURE 2. RUNUP MEASUREMENTS VERSUS PREDICTIONS FOR LARGE, UNIFORM WAVES.

For the hydraulically smooth surfaces of plywood, sand, or asphalt, almost all these 96 test situations are fully congruent with the shore configurations treated in the Stoa guidance: either a horizontal or a 1 on 10 approach to a plane barrier. Thus, the nearly ideal agreement in Figure 2a isolates the appropriateness of interpolation procedures for runup curves, along with the accuracy of scale-effect allowances up to 12% used for these barrier slopes of 1 on 3, 4, 6, 15, or 40. Differences between measurements and computations may be summarized best as random and about ± 0.1 m, rather than as some percentage error. These results are for fairly simple geometries with no very steep barriers.

The results for rough structures in Figure 2b reflect more comprehensive tests of computations. Barrier cotangents are 1.5, 2, 2.5, 3, 3.5, 5, and 6, with surfaces of loose or fitted stones, quadripods, various concrete blocks, or artificial grass. Approach geometries include a notable range in tests by DeBok and Sollitt (1976). The stated r values of runup reduction relative to a smooth barrier conform to standard guidance for these roughness types. There is marked correlation between the 199 measurements and computations, but differences amount to about ± 0.15 m; this is appreciable in view of the reduced runups.

Along with the greater uncertainty in runup measurements for rough, permeable structures, some of the increased error in Figure 2b is due to the often noted inaccuracy in assuming a constant r value for each given surface. Runup elevations on rough barriers are not linearly related to those on smooth slopes of similar geometry. The large data set of Ahrens (1975) clearly indicates greatest runup reductions relative to smooth slopes for collapsing breakers, with surf similarity parameter near 3 and minimum stone stability. However, other data sets do not show such notable error introduced by taking r as a constant for uniform waves and more stable structures. In addition, constant r may improve as an approximation in irregular waves, where an appreciable variation of surf similarity parameter must arise for a given case.

Addressing the actual variations in r would appear to require detailed empirical investigations, rather than use of a general expression. Since runup elevations are well defined over a broad range of smooth geometries, for some applications the convenience of taking r as constant can outweigh inaccuracies typically introduced. The evidence of Figure 2 manifests notable predictive capability for runup elevation in independent tests similar to those providing the basic guidance.

APPLICATION TO IRREGULAR WAVES

There is modest variability in runup elevations with uniform waves on a given barrier, but a greatly enlarged runup range occurs for irregular waves. The probability distributions of runup elevation must have some common value for comparable uniform and irregular wave action with a similar shore geometry. In fact, the mean runup elevation for irregular waves is predictable if mean wave condition is taken as the appropriate description to use with empirical guidance for uniform waves. This finding contradicts a runup treatment in terms of significant conditions presented in the *Shore Protection Manual*, but a recent publication (Walton et al., 1989) has described that methodology as "untested." Actually, measurements from small tests with smooth slopes of 1 on 1 through 10 (Kamphuis and Mohamed, 1978; Mase, 1989) demonstrate clearly that mean conditions provide the correct link between runup curves for uniform waves and effects in irregular wave action.

To date, only limited data have been openly published on irregular wave runups measured in large tank situations. Figure 3a compares the documented mean or median runup elevations to computed results using the mean wave description. The major data set here is that presented by Führböter et al. (1989) for 1 on 6 slope and moderate wave steepnesses with a Pierson-Moskowitz spectrum; only periods for peak wave energy were reported, and they are converted into mean wave periods using measured results for the same spectrum and steepnesses provided by Mase and Iwagaki (1984).

There is close agreement in trend here, but an apparent tendency for the 41 measurements to exceed computations. Other runup data from proprietary Delft Hydraulics tests have also been examined (Dewberry & Davis, 1990), with similar agreement between measurements and computations for additional wave conditions and barriers. All this evidence might be taken to indicate that the steady-wave setup on steep slopes is not fully represented in runup guidance for uniform waves. However, empirical results on wave runup and setup do not appear to permit a definitive judgment in view of the limited ranges of test geometries and wave conditions, and Figure 3a does not demonstrate a significant deficiency in the present runup computations.

Field data on wave runup provide the final level of complexity in variables and processes. Three sets of field measurements serve as useful examples covering a range of situations: Battjes (1971) for a 1 on 3.6 dike,

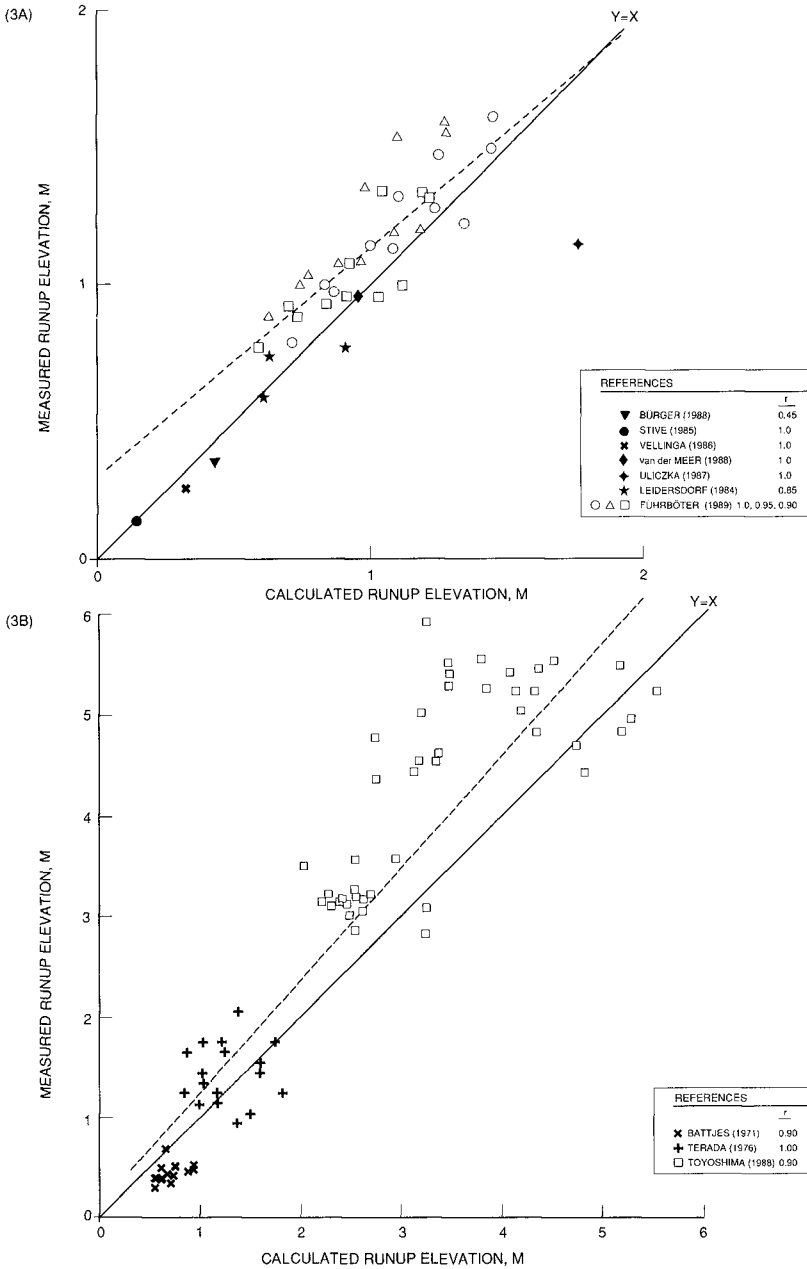


FIGURE 3. RUNUP MEASUREMENTS VERSUS PREDICTIONS FOR LARGE, IRREGULAR WAVES.

Terada (1976) for a 1 on 10 sand foreshore, and Toyoshima (1988) for a 1 on 5 seawall. Runup computations have proceeded using documented conditions in a straightforward way (Dewberry & Davis, 1990), and Figure 3b compares results to the representative elevations as reported for 76 situations. There is notable agreement in magnitudes and trend, but also sizable scatter and a marked tendency to underpredict the large runup elevations of Toyoshima (1988). Those results might be taken to corroborate the finding (Grüne, 1982) that runup elevations are increased as a direct effect of onshore storm winds. However, each of these field data sets has important shortcomings in regard to documentation.

Battjes (1971) reported winds but not waves for 7 days of measurements at two tideless lake sites. Published runup elevations are apparently with respect to mean water level at the shore, thus excluding the wave setup contribution. Presuming a moderate fetch, wave characteristics can be estimated following procedures in the *Shore Protection Manual*, and then converted to a mean wave condition in deep water; this yields a narrow range in wave steepnesses and a typical mean period of 3.5 sec, in agreement with other reported information. Terada (1976) documented deep-water wave conditions, without directions, and runup elevations relative to mean sea level, for 7 days on a Pacific Ocean beach. It is not clear what statistics were used in reported measurements. Toyoshima (1988) provided offshore wave conditions, water levels, and runup heights for 8 days of measurements at a Sea of Japan site. Wave directions are omitted, and statistical measures employed are non-standard, mixed, and somewhat extreme (beyond the significant conditions). Other information pertains to infragravity wave effects, indicated by the numbers of incident waves versus runups; however, basic variations in the numerical ratios with wave steepness are opposite findings from other field data (Holman, 1986). Finally, the total range in reported water level is 0.35 m, much less than the tidal range at the shore, so it appears that runup elevations refer to offshore not local water level.

Given these perplexing aspects in documentation, perhaps only simplified analyses are warranted for these data sets. Note that runup variations in the data of Terada (1976) and Toyoshima (1988) show definite agreement with the dependence on wave steepness given by Hunt's equation for breaking waves, although runup elevations appear magnified by about 20% above that equation in each field situation. Nevertheless, Figure 3b confirms that computed runup elevations over a very wide range are appropriate in some quantitative sense.

ADDITIONAL DISCUSSION ON APPLICATIONS

Usual applications may require a more extreme measure than the mean runup elevation predictable from the mean wave conditions. The Rayleigh distribution seems to provide an appropriate, generally conservative formulation for relating common runup elevations to those occurring only rarely in a given situation. Battjes (1971) documented field runup measurements conforming to the Rayleigh distribution at least for 0.95 to 0.05 exceedance probabilities; he concluded that a submerged berm contributed to this agreement, and expressed the expectation that runup elevations with a plane slope would extend over a narrower range than given by the Rayleigh distribution. Measured runup distributions now documented for a variety of situations all support such an effect of barrier geometry, although other factors may merit consideration in regard to conformance with the Rayleigh distribution. For example, a narrow wave energy spectrum or a sizable contribution from wave setup might act to decrease the runup range relative to the mean elevation.

The Rayleigh distribution must be expected to become inaccurate for truly extreme runup values, perhaps on the order of 0.01 exceedance probability. In addition, extrapolation from the mean elevation can require multiplication by appreciable factors, for example, 2.23 for the exceedance probability of 0.02 commonly considered. This may introduce significant magnification of usual uncertainty associated with a mean elevation prediction. Where possible, direct empirical investigation at large scale must be preferred in defining actual extreme runup elevations for a given situation. Of course, such data need not be organized using the mean wave description.

Some complications clearly require further consideration in predicting wave runup elevations for extreme storms. Several factors ignored in the present treatment seem unlikely to make an appreciable difference, viewed here as a 10% change in runup elevations; oblique incidence of waves is one such factor (Tautenhain et al., 1982), and one more is the runup scale effect on rough barriers (subsumed into chosen r values). Notable difficulties may be involved in the specification of deep-water wave conditions as input to predictions, since runup guidance is fundamentally based on incident wave characteristics at the approach to the shore barrier. Determining those waves and converting to offshore conditions may involve appreciable uncertainties in some situations. However, the most significant questions appear to require further measurements for storm conditions, to clarify effects of winds, wave setup, and infragravity motions.

CONCLUSIONS

The present computer code provides mean runup elevations based on detailed empirical guidance for uniform waves on smooth slopes (Stoa, 1978). The specified situation is analyzed to identify suitable prediction procedures, with interpolation and iteration automatically executed for a consistent runup elevation. Published data sets confirm computations of runup elevations to be usefully accurate for wide ranges of wave action and geometry. Despite the notably larger errors to be expected for increasing complex situations, appropriate magnitudes and trends demonstrate that there is no definite defect in present runup predictions.

This verification of automated computation procedures supports the model's applicability for the full coverage of incorporated runup guidance. Appreciable refinement in empirical runup predictions for steep barriers and storm waves appears to require additional data sets from large tank investigations of realistic situations and from field studies with complete documentation.

Acknowledgments. The present investigation relates to the development of upgraded methodology for predicting wave runup elevations associated with a 100-year flood, a task undertaken by Dewberry & Davis as technical evaluation contractor for the National Flood Insurance Program, Federal Insurance Administration, Federal Emergency Management Agency. However, analyses and determinations reported here represent the views of the authors alone. We wish to thank Chuck Wood of Dewberry & Davis for assistance in the code development. We also are indebted to the following individuals for help in obtaining wave runup data: J. P. Ahrens, J. H. Balsillie, H. H. Dette, S. Kielsingard, M. Klein Breteler, C. B. Leidersdorf, K. W. Pilarczyk, U. Sparboom, O. Toyoshima, and K. Uliczka.

APPENDIX - REFERENCES

- Ahrens, J. P. (1975). "Large Wave Tank Tests of Riprap Stability," Technical Memorandum 51, Coastal Engineering Research Center, Fort Belvoir, VA.
- Battjes, J. A. (1971). "Runup Distributions of Waves Breaking on Slopes," Journal of the Waterways, Harbors and Coastal Engineering Division, ASCE, Vol. 97, No. WW1, pp. 91-114.
- van den Berg, C., and Lindenberg, J. (1985). "Stability of Armorflex Revetment System Under Wave Attack," in *Flexible Armoured Revetments Incorporating Geotextiles*, Thomas Telford, London, pp. 143-156.

- Bürger, W., Oumeraci, H., and Partenscky, H. W. (1988). "Geohydraulic Investigations of Rubble Mound Breakwaters," Proceedings of the 21st Coastal Engineering Conference, pp. 2242-2256.
- Dai, Y. B., and Kamel, A. M. (1969). "Scale Effect Tests for Rubble-Mound Breakwaters," Research Report H-69-2, Waterways Experiment Station, Vicksburg, MS.
- DeBok, D. H., and Sollitt, C. K. (1978). "A Large Scale Model Study of Placed Stone Breakwaters," Ocean Engineering, Oregon State University, Corvallis, OR.
- Dewberry & Davis (1990). "Investigation and Improvement of Capabilities of the FEMA Wave Runup Model," draft report for Federal Insurance Administration, Federal Emergency Management Agency, Fairfax, VA.
- Führböter, A. (1986). "Model and Prototype Tests for Wave Impact and Runup on a Uniform 1:4 Slope," Coastal Engineering, Vol. 10, pp. 49-84.
- Führböter, A., Sparboom, U., and Witte, H. H. (1989). "Hannover Large Wave Flume: Experimental Results Regarding Wave Runup on Smooth and Rough Dike Banks with 1:6 Slope," Die Küste, Heft 50, pp. 155-195.
- Grüne, J. (1982). "Wave Runup Caused by Natural Storm Surge Waves," Proceedings of the 18th Coastal Engineering Conference, pp. 785-803.
- Holman, R. A. (1986). "Extreme Value Statistics for Wave Runup on a Natural Beach," Coastal Engineering, Vol. 9, pp. 527-544.
- Horikawa, K. (1978). *Coastal Engineering, An Introduction to Ocean Engineering*, Wiley, New York.
- Kamphuis, J. W., and Mohamed, N. (1978). "Runup of Irregular Waves on Plane Smooth Slopes," Journal of the Waterway, Port, Coastal and Ocean Division, ASCE, Vol. 104, pp. 135-146.
- Kraus, N. C., and Larson, M. (1988). "Beach Profile Change Measured in the Tank for Large Waves, 1956-1957 and 1962," Technical Report CERC-88-6, U.S. Army Corps of Engineers, Coastal Engineering Research Center, Vicksburg, MS, p. A15.
- Leidersdorf, C. B., Potter, R. E., and Sonu, C. J. (1984). "Study of Slope Protection Works for Arctic Ocean," Proceedings of the 31st Annual Conference, Japanese Society of Civil Engineers, pp. 552-556.
- Mase, H. (1989). "Random Wave Runup Height on Gentle Slope," Journal of Waterway, Port, Coastal, and Ocean Engineering, Vol. 115, pp. 649-661.
- Mase, H., and Iwagaki, Y. (1984). "Runup of Random Waves on Gentle Slopes," Proceedings of the 19th Coastal Engineering Conference, pp. 593-609.
- McCartney, B. L., and Ahrens, J. P. (1975). "Stability of Gobi Block Revetment to Wave Attack," Technical Memorandum 55, Coastal Engineering Research Center, Fort Belvoir, VA.

- van der Meer, J. W. (1988). "Rock Slopes and Gravel Beaches Under Wave Attack," Delft Hydraulics Communication No. 396, Delft, The Netherlands.
- Saville, T., Jr. (1958). "Wave Runup on Composite Slopes," Proceedings of the 6th Coastal Engineering Conference, pp. 691-699.
- Saville, T., Jr. (1987). "Early Large-Scale Experiments on Wave Runup," *Shore and Beach*, Vol. 55, No. 3-4, pp. 101-108.
- Sparboom, U., and Grosche, S. (1987). "Measurement of Wave Runup on a 1:6 Sloped Asphalt Dike in the Large Wave Channel," Technical Report, University of Hannover, West Germany.
- Stive, M. J. F. (1985). "A Scale Comparison of Waves Breaking on a Beach," *Coastal Engineering*, Vol. 9, pp. 151-158.
- Stoa, P. N. (1978). "Reanalysis of Wave Runup on Structures and Beaches," Technical Paper 78-2, Coastal Engineering Research Center, Fort Belvoir, VA.
- Stone & Webster Engineering Corporation (1981). "Manual for Wave Runup Analysis, Coastal Flood Insurance Studies," Boston, MA.
- Tautenhain, E., Kohlhase, S., and Partenscky, H. W. (1982). "Wave Run-Up at Sea Dikes Under Oblique Wave Approach," Proceedings of the 18th Coastal Engineering Conference, pp. 804-810.
- Terada, M. (1976). "On the Wave Runup After Breaking on the Beach at Hiratsuka, Kanagawa Prefecture," *Geographical Review of Japan*, Vol. 49, pp. 550-561.
- Toyoshima, O. (1988). "Gentle Slope Seawalls Covered with Armour Units," Proceedings of the 21st Coastal Engineering Conference, pp. 1983-1996.
- Uliczka, K., and Dette, H. H. (1987). "Development of Wave Runup at Dune With and Without Foreshore - Prototype Scale," *Mitteilungen Leichtweiss-Institute*, Heft 94, 12 pp.
- U.S. Army Corps of Engineers, Coastal Engineering Research Center (1984). *Shore Protection Manual*, Fourth Edition, 2 volumes, Washington, D.C.
- U.S. Navy, Facilities Engineering Command (1982). *Coastal Protection*, Design Manual 26.2, Washington, D.C.
- Vellinga, P. (1986). "Beach and Dune Erosion During Storm Surges," Delft Hydraulics Communications No. 372, Delft, The Netherlands.
- Walton, T. L., Jr., Ahrens, J. P., Truitt, C. L., and Dean, R. G. (1989). "Criteria for Evaluating Coastal Flood-Protection Structures," Technical Report CERC 89-15, U.S. Army Corps of Engineers, Coastal Engineering Research Center, Vicksburg, MS.

CHAPTER 4

MODEL PREDICTIONS OF NONBREAKING SHOALING WAVES

Steve Elgar; Electrical and Computer Engineering; Washington State University; Pullman, WA 99164-2752

M.H. Freilich; Jet Propulsion Laboratory 300-323; California Institute of Technology; Pasadena, CA 91109

R.T. Guza; Center for Coastal Studies; Scripps Institution of Oceanography A-009; La Jolla, CA 92093

ABSTRACT

The predictions of linear and nonlinear (Boussinesq) shoaling wave models for nonbreaking unidirectional surface gravity waves are compared to field observations, with particular emphasis on quantities that may be important for cross-shore sediment transport. The extensive data sets were obtained on two natural beaches, span water depths between 1-10 m, and include incident wave power spectra with narrow, broad, and bimodal shapes. Significant wave heights varied between approximately 30 and 100 cm and peak periods between approximately 8 and 18 seconds. Only the nonlinear theory predicts the increasingly asymmetric sea-surface elevations and horizontal velocities (pitched-forward wave shape) and the weaker variation of skewness (difference between crest and trough profiles) which are observed to occur during shoaling. The nonlinear theory also models qualitatively well the large skewed accelerations which occur during the passage of asymmetric waves.

INTRODUCTION

Because nonbreaking shoaling waves are both weakly nonlinear and weakly dispersive they are frequently described by models based on the nonlinear Boussinesq equations (Peregrine 1967). In general, the Boussinesq equations

include the effects of shoaling, refraction, reflection, and diffraction for arbitrary wave fields (i.e. directionally spread and broad banded in frequency). Most implementations of Boussinesq shoaling models include a subset of these phenomena, and have been successfully tested against a variety of laboratory data and analytical results. Freilich & Guza (1984, FG) and Liu et al. (1985) have respectively derived one- and two-dimensional nonlinear shoaling models based on perturbation solutions to the Fourier transformed Boussinesq equations. The models clearly identify nonlinear near-resonant triad interactions as the primary cause for evolution of third moments of the wave field. The one-dimensional, many mode (i.e. broad banded in frequency) Boussinesq model has been compared to a limited set of ocean field data (FG, Elgar and Guza 1985 (EG), 1986, Elgar et al. 1990).

The Boussinesq equations require both shallow water depths ($(kh)^2 \ll 1$, where k is the wavenumber and h is the water depth) and small wave amplitudes ($a/h \ll 1$, where a is the wave amplitude) such that the Ursell number, $U = (a/h)/(kh)^2$ is approximately unity. The one-dimensional shoaling model assumes that the waves are normally incident to a beach with plane-parallel contours, and neglects dissipation and reflection.

The one-dimensional model is cast in terms of coupled, nonlinear, ordinary differential equations with the (temporal) Fourier coefficients of the wave field as the dependent variables. Since the model describes the spatial evolution of the Fourier coefficients (i.e. both the amplitudes and phases), it contains information relating to wave shapes and instantaneous oscillatory velocities.

Freilich and Guza (1984) give details of numerically implementing the nonlinear model. Fourier coefficients used as initial conditions for nonlinear model predictions are provided by measurements at the seaward edge of the region of interest. The model equations are then integrated numerically, yielding predicted values of Fourier coefficients of sea-surface elevation in shallower water. The predicted and observed Fourier coefficients can then be manipulated and compared in various ways. Alternatively, after inverse Fourier transforming the predicted coefficients, comparisons can be made between predicted and observed time series.

The present study evaluates the performance of the 1-D shoaling model for nonbreaking waves in 18 data sets obtained from month-long field experiments at two beaches. A variety of incident wave conditions were observed, including swell from a distant storm, locally generated sea, and combinations of swell and sea. The model performance is good. The spatial evolution of sea surface elevation (SSE), velocity, and acceleration statistics are at least qualitatively well predicted for a wide range of ocean conditions.

FIELD EXPERIMENTS AND DATA REDUCTION

Two field experiments conducted in 1980 (Torrey Pines and Santa Barbara, California) provide the data used for model verification. The bottom contours were relatively straight and parallel at both experimental sites, and the mean beach slopes through the shoaling region were 0.022 and 0.050 at Torrey Pines and Santa Barbara, respectively. Data were obtained from wave staffs and bottom-mounted pressure and electromagnetic current meters. The field experiments, including representative beach profiles and descriptions of the sensors and data reduction are presented in FG, EG, and Thornton & Guza (1986). Measurements from cross-shore arrays extending for approximately 267 m (Torrey Pines) and 56 m (Santa Barbara) are used in the model-data comparisons presented below.

Initial conditions for the nonlinear Boussinesq shoaling model were generated with data from a bottom-mounted pressure sensor in 10 m depth at Torrey Pines and in 4 m depth at Santa Barbara. Short sections of data were Fourier transformed and converted to Fourier coefficients of sea-surface elevation using linear finite depth theory. Results of integrations of the Boussinesq shoaling wave model for consecutive short sections were averaged together for statistical comparisons. The maximum frequency considered is 0.234 and 0.4 Hz at Torrey Pines and Santa Barbara, respectively. The different cutoff frequencies reflect the requirement that the waves be relatively long compared to the depth, and the relatively deeper water at Torrey Pines.

All pressure and current meters were positioned within 80 cm of the sea bed, and the pressure data were converted to sea-surface elevation using linear theory. Because linear theory accurately relates local values of near-bottom pressure and elevation in nonbreaking waves (Guza & Thornton 1980 and references therein), hereafter no differentiation will be made between direct measurements of sea-surface elevation and sea-surface elevation inferred from pressure data. Comparisons between model predictions and current meter data are made at the known depth of the current meter sensing element (i.e. no theory is applied to the current meter data).

Energy dissipation was not important in the model-data comparisons discussed here because the evolution distances were relatively short, white-capping was not pronounced, and the comparisons were terminated when measured energy losses owing to wave breaking were significant. The Torrey Pines experiment was designed to study nonbreaking waves, and thus all sensors were seawards of the breaking zone and dissipation was found to be negligible. Many of the Santa Barbara sensors were sometimes within the surf zone, and the estimated dissipation was sometimes significant in depths less than 1.6 m. Model-data comparisons are presented only for sensors where the total shoreward energy flux (integrated over all frequencies) was at least 85% of the value measured at the most seaward instrument.

The effects of directional spread and/or non-normal incidence in the incoming wave field on the nonlinear evolution of shoaling waves are not yet well understood. Boussinesq models appropriate for this case (e.g. Liu et al. 1985) have not been applied to random ocean waves. The data sets discussed here include locally generated wind-driven seas having broad directional spread, as well as wave fields composed of swell and sea arriving from different directional quadrants. Although the incident wave field was neither unidirectional nor normally incident, 1-D Boussinesq model predictions are possible because fundamentally nondirectional statistics are considered here. Moreover, as refracting surface waves propagate into shallower water they are strongly polarized in the cross-shore direction and thus the approximation of normal incidence often is not grossly violated. A longshore array of sensors in 10 m depth at Torrey Pines and a colocated pressure sensor-bidirectional current meter pair in 4 m depth at Santa Barbara showed that the principal wave directions at the offshore, initial conditions for the model predictions are less than 20° relative to normal incidence (FG, EG, Thornton & Guza 1986, Freilich et al. 1990)

MODEL-DATA COMPARISONS

As a primarily swell wave field (S11 and F2 in fig 1) shoals, the power spectrum undergoes significant evolution, with harmonics of the spectral peak increasing in power with decreasing water depth (fig 2). Linear finite depth theory (LFDT) does not predict the growth of harmonics, but the Boussinesq model accurately predicts the observed spectral evolution, except for high frequencies (e.g. $f \geq 0.3$ Hz for the data considered here). Along with cross-spectral transfers of energy (e.g. harmonic growth) owing to nonlinear interactions as the waves shoal, there is also substantial nonlinear phase evolution of the individual Fourier components (equivalent to a nonlinear effect on the phase speed). In shallow water where nonlinear effects are largest, phase differences between the nonlinear model and the data are small, while the phase differences between data and LFDT are large (fig 2). The coherence between the nonlinear model predictions and data is high (fig 2), except for a decreasing coherence with increasing frequency, which can be explained by directional spreading of the wave field (FG). Boussinesq model predictions for wave fields with broad band and bimodal spectra are also more accurate than LFDT predictions (not shown). LFDT predictions that include the effects of the directional distribution of energy (EG) are not substantially better than the unidirectional LFDT predictions shown in fig 2.

As waves shoal, their profiles evolve from nearly sinusoidal shapes in deep water to positively skewed (sharp peaks and broad troughs) shapes to vertically asymmetrical, sawtooth shapes just prior to breaking. The change in wave form during shoaling is statistically described by the skewness, S and

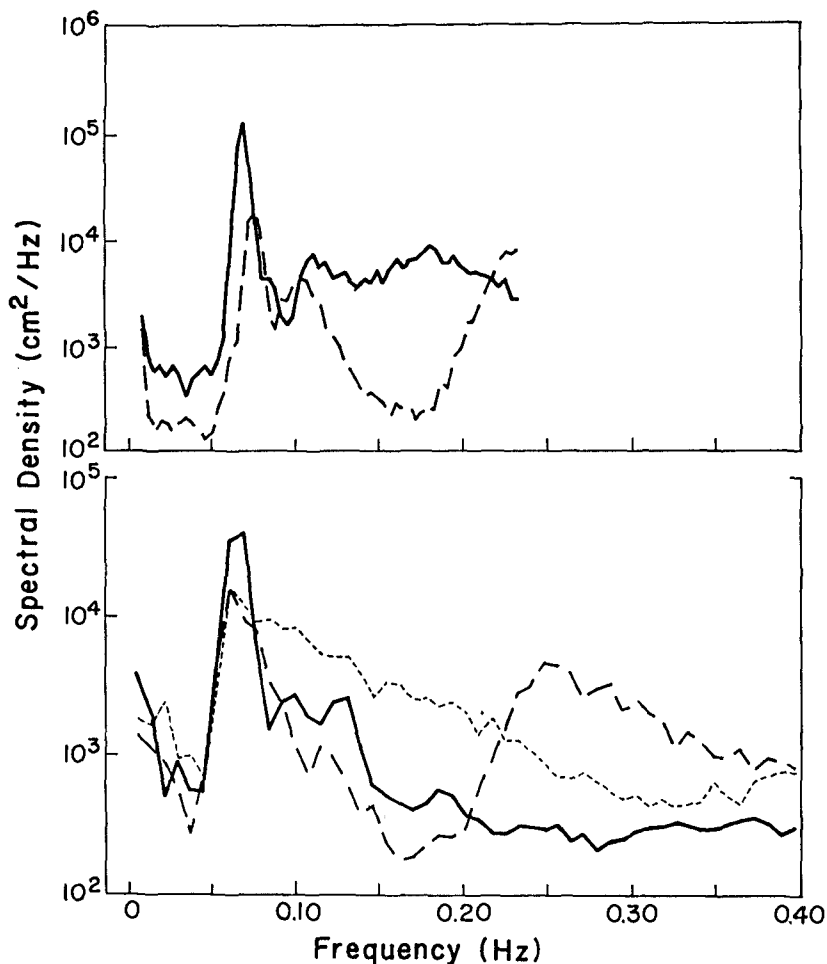


Figure 1. Initial power spectra of sea surface elevation for the model predictions. Top, Torrey Pines, $h \sim 10$ m (solid line, S11, $H_{sig} = 90$ cm; dashed line, S16, $H_{sig} = 56$ cm); bottom, Santa Barbara, $h \sim 4$ m (solid line, F2, $H_{sig} = 63$ cm; dashed line, F12, $H_{sig} = 57$ cm; dotted line, F15, $H_{sig} = 66$ cm), where H_{sig} is the significant wave height at the depth indicated.

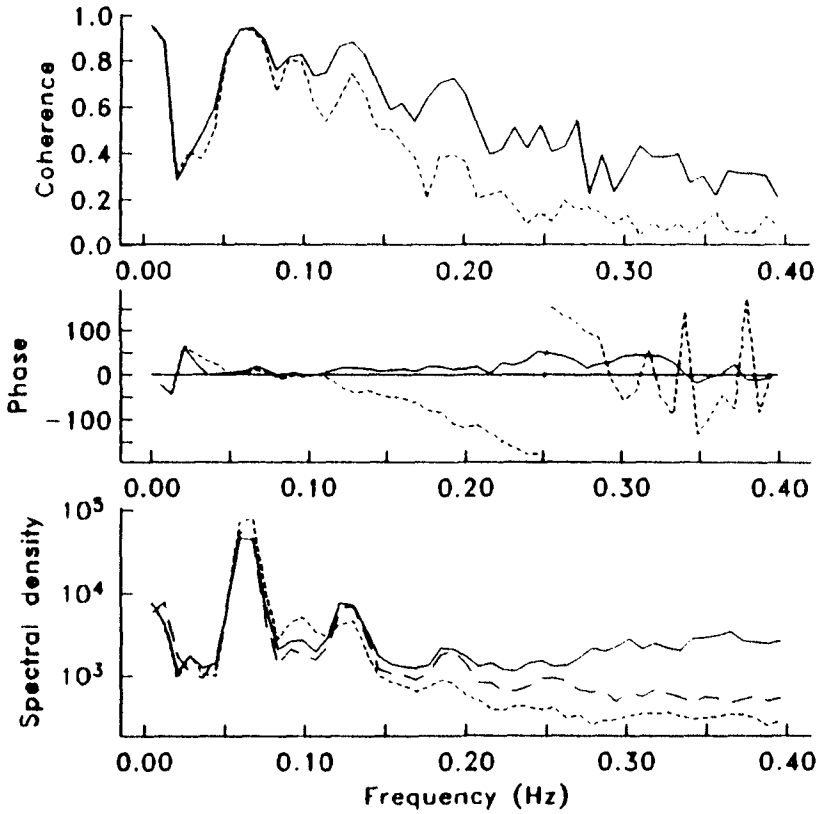


Figure 2. Comparison of model predictions (based on initial conditions in 4.5 m depth, F2 in fig 1) to swell data in 1 m depth. Coherence and phase differences between Boussinesq (solid line) and LFDT (dotted line) model predictions and observations are shown in the upper and center panels, respectively. The power spectra predicted by the Boussinesq (solid line) and LFDT (dotted line) models are compared to observed values (dashed line) in the lower panel.

asymmetry, A (third moments of the wave field, which measure deviations from symmetry about the horizontal and vertical axis, respectively (Masuda & Kuo 1981)). A sawtooth shape has $S = 0$ and $A \neq 0$, while a "Stokes wave" shape (broad, low troughs and narrow, tall crests) has $S \neq 0$ and $A = 0$.

The observed and predicted evolution of skewness and asymmetry for swell is displayed in fig 3. Third moments are small in deep water ($A = S = 0$ for linear waves), and increase owing to nonlinear interactions as the waves shoal. In both the observations and the model predictions, skewness of SSE and velocity attains a maximum and starts to decrease before the waves break (wave breaking is significant only for the shallowest sensor shown in fig 3). Asymmetry increases approximately monotonically, consistent with the steepening shape of shoaling waves. The random phase assumption underlying linear theory results in sinusoidal waves, and thus LFDT cannot predict the changes in wave shape as the wave field shoals. On the other hand, the Boussinesq model accurately predicts the observed evolution of third moments of the wave field, as shown in fig 3.

Observed and predicted third moments for a broad band wave field (i.e. locally generated sea, F15 in fig 1) are shown in fig 4. Although the shape of the power spectrum at the seaward edge of the shoaling region differs from the narrow band wave field discussed above, many aspects of the evolution during shoaling are similar. In particular, the wave shapes undergo similar shoaling evolution from sinusoidal to sawtooth profiles.

For broad band wave fields, the total skewness and asymmetry are not dominated by contributions from a few isolated harmonic triads, as is the case with narrow band wave fields. Rather, nonlinear interactions significantly couple many frequencies within the wind wave band, with each triad of coupled waves contributing to the overall third moments. The assumptions underlying the Boussinesq model become invalid at high frequencies where the lowest order Boussinesq dispersion relation deviates significantly from the exact finite-depth solution. Thus, it is not surprising that nonlinear model predictions of third moments for broad banded conditions (fig 4) are not as accurate as those for swell-dominated spectra (fig 3). This is especially true for acceleration statistics (fig 4c), where high frequency motions are even more important (Elgar et al. 1988). Nonetheless, the nonlinear model correctly predicts the depth-dependent trends in the third moments of sea-surface elevation, horizontal velocity, and acceleration.

Observed and predicted third moments for a wave field consisting of both sea and swell, S16 and F12 in fig 1) are shown in fig 5. The sea and swell arrived at the outer edge of the shoaling region from different directions, separated by about 45° at Santa Barbara and about 25° at Torrey Pines. As in the narrow- and broad-band cases discussed above, the steepening of the wave profile during shoaling is fairly well predicted by the Boussinesq model, as shown in fig 5a. The predictions of near-bottom velocity third moments (figs

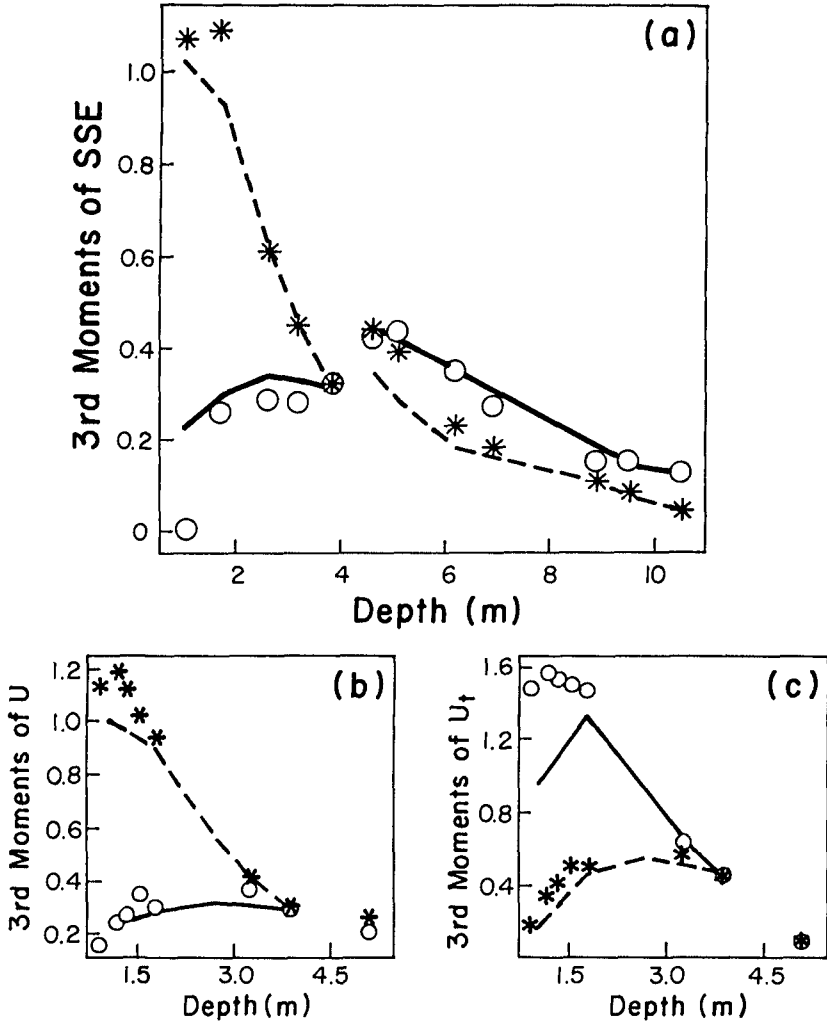


Figure 3. Predicted and observed normalized third moments versus depth for the narrow band swell data ($h > 4$ m, Torrey Pines (S11); $h \leq 4$ m, Santa Barbara (F2)). a) sea-surface elevation; b) near-bottom horizontal (e.g. cross-shore) velocity; c) near-bottom horizontal acceleration. Solid and dashed lines are model predictions of skewness and -asymmetry, respectively. Circles and asterisks are observed values of skewness and -asymmetry, respectively.

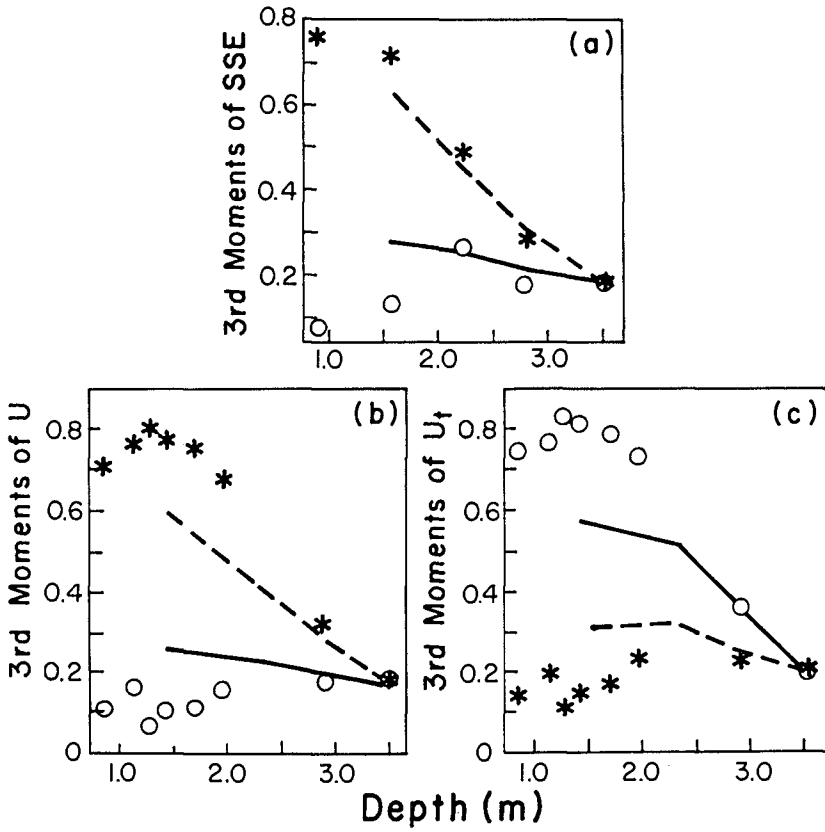


Figure 4. Predicted and observed normalized third moments versus depth for the broad band data, Santa Barbara (F15). a) sea-surface elevation; b) near-bottom horizontal velocity; c) near-bottom horizontal acceleration. Format is the same as Figure 3.

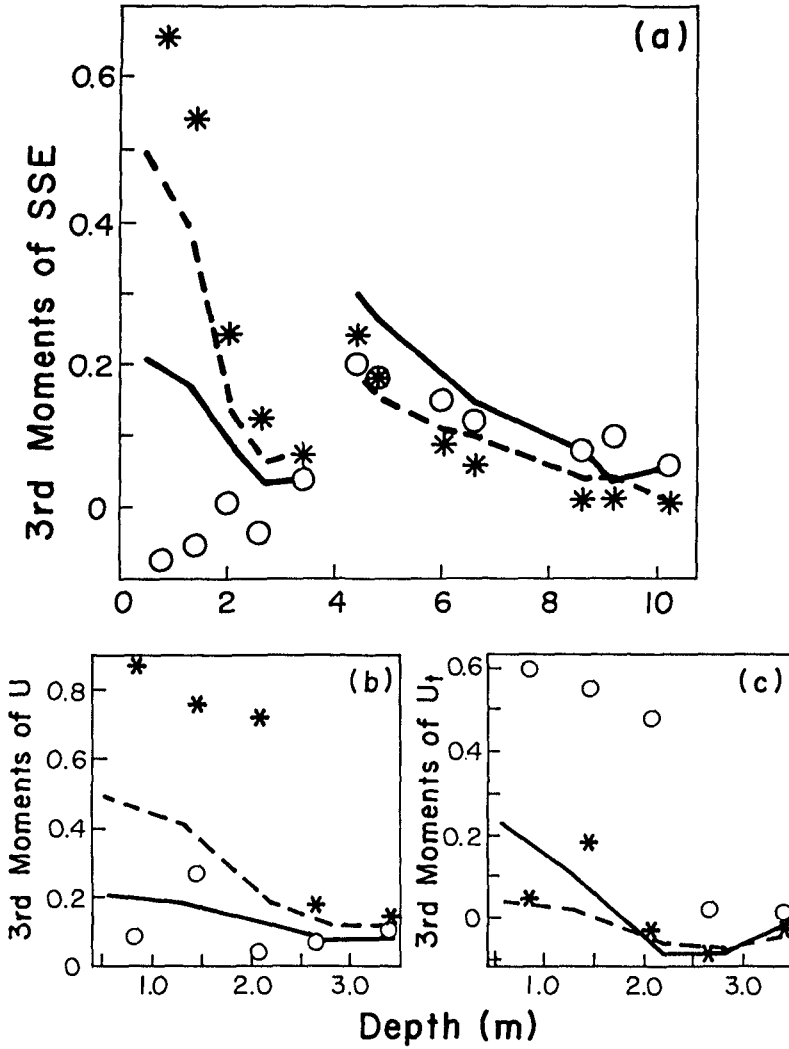


Figure 5. Predicted and observed normalized third moments versus depth for the bimodal data ($h > 4$ m, Torrey Pines (S11); $h \leq 4$ m, Santa Barbara (F2)). a) sea-surface elevation; b) near-bottom horizontal velocity; c) near-bottom horizontal acceleration. Format is the same as Figure 2.

5b,c) are considerably less accurate, perhaps owing to directional effects.

From the model-data comparisons discussed above it is clear that the one-dimensional Boussinesq model predicts the evolution of shoaling waves for the conditions considered at least qualitatively well. In addition, model-data comparisons for many more data sets are displayed in fig 6, where predictions of SSE and near-bottom horizontal velocity third moments are compared to observed values. The Boussinesq model predictions of SSE skewness are accurate for both field sites. The predictions of SSE asymmetry for the Torrey Pines data are qualitatively correct, but somewhat less than observed values, while the predictions of SSE asymmetry for the Santa Barbara data are accurate (fig 6a). Model predictions of third moments of near-bottom velocity in 4.5 m depth, 250 m from the initial conditions ($h \approx 10$ m) at Torrey Pines and for 12 and 56 m from the initial conditions at Santa Barbara are compared to observations in fig 6b. Overall the predictions are good. The Boussinesq model also provides accurate predictions of acceleration skewness and asymmetry (fig 6c).

CONCLUSIONS

Given measurements of the incident wave field, low-order statistics of the shoaling wave field seawards of the surf zone can be accurately predicted by the Boussinesq equations, as demonstrated by the model-data comparisons presented above. The Boussinesq model has no free or adjustable parameters, is not limited to any particular spectral shape, and accurately predicts the evolution of the wave field for swell, locally generated sea, combinations of swell and sea, and other typical field conditions. The nonlinear model also is not dependent on the particular field location, as long as dissipation outside the surf zone and reflection from the beach face are negligible. Although the two beaches discussed here were nearly planar, more complex bathymetry can, in principle, be incorporated into the nonlinear model.

Acknowledgements

This research was supported by NSF, ONR, NASA, and SDSC. Permission to publish figures 2-6 has been granted by the American Geophysical Union

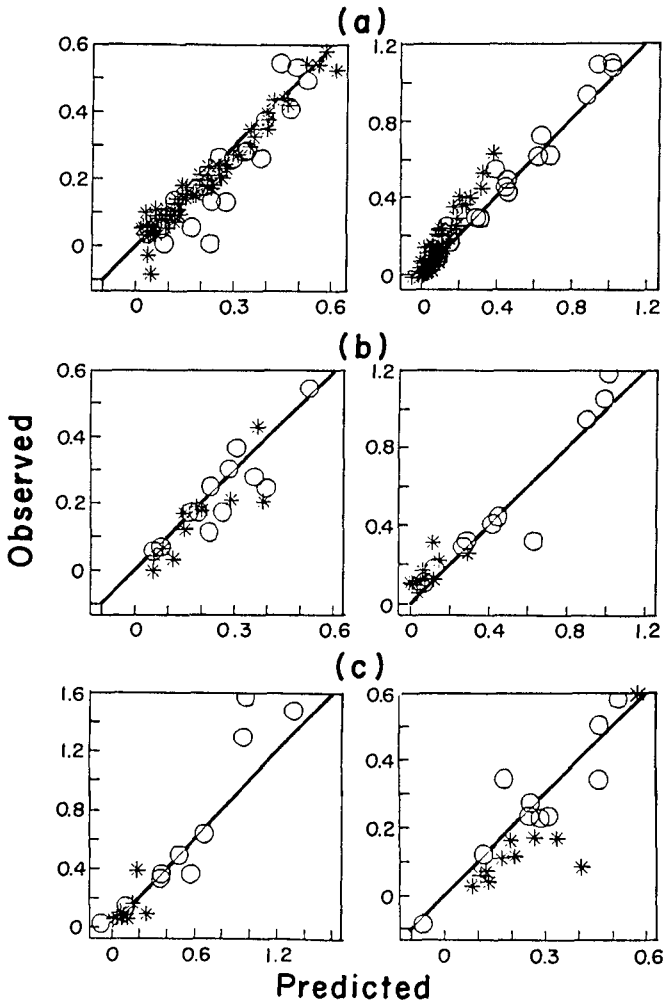


Figure 6. Observed third moments versus Boussinesq model predictions of third moments. Left hand panels, skewness; right hand panels, -asymmetry. a) SSE; b) near-bottom horizontal velocity; c) near-bottom horizontal acceleration. Asterisks are Torrey Pines beach and circles are Santa Barbara. Values falling on the 45° solid lines correspond to agreement between data and model predictions.

REFERENCES

- Elgar, Steve and Guza, R.T., Shoaling gravity waves: comparisons between field observations, linear theory, and a nonlinear model, *J. Fluid Mech.* 158, 47-70, 1985.
- Elgar, Steve and Guza, R.T., Nonlinear model predictions of bispectra of shoaling surface gravity waves, *J. Fluid Mech.* 167, 1-18, 1986.
- Elgar, Steve, Guza, R.T., and Freilich, M.H., Eulerian measurements of horizontal accelerations in shoaling gravity waves, *Journal of Geophysical Research* 93, 9261-9269, 1988.
- Elgar, Steve, Freilich, M.H., and Guza, R.T., Model-data comparisons of moments of nonbreaking shoaling surface gravity waves, *Journal of Geophysical Research*, 1990, in press.
- Freilich, M.H. and Guza, R.T., Nonlinear effects on shoaling surface gravity waves, *Philos. Trans. R. Soc. London, Ser. A* 311, 1-41, 1984.
- Freilich, M.H., Guza, R.T., and Elgar, Steve, Observations of nonlinear effects in directional spectra of shoaling surface gravity waves, *J. Geophys. Research* 95, 9645-9656, 1990.
- Guza, R.T. and Thornton, E.B., Velocity moments in nearshore, *ASCE J. Waterway, Port, Coastal and Ocean Engineering* 111, 235-256, 1985.
- Liu, P.L.-F., Yoon, S.B., and Kirby, J.T., Nonlinear refraction-diffraction of waves in shallow water, *J. Fluid Mech.* 153, 185-201, 1985.
- Masuda, A. and Kuo, Y., A note on the imaginary part of bispectra, *Deep Sea Res. Part A*, 28, 213-222, 1981.
- Peregrine, D.H., Long waves on a beach, *J. Fluid Mech.* 27, 815-827, 1967.
- Thornton, E.B. and Guza, R.T., Surf zone longshore currents and random waves: field data and models, *J. Physical Oceanography* 16, 1165-1178, 1986.

CHAPTER 5

Transition Zone Width and Implications for Modelling Surfzone Hydrodynamics

Robert B. Nalrn¹, J.A. (Dano) Roelvink² and Howard N. Southgate³

INTRODUCTION

The surfzone associated with a wave breaking on a plane slope may be subdivided into three regions: the transition zone, the inner zone and the swash zone. The transition zone is the region just shoreward of the point of wave breaking and is characterised by rapid wave decay and also by constant wave setdown (and thus constant radiation stress). In this paper, an empirical expression for the width of this zone is developed from monochromatic wave data. Two techniques are proposed for the consideration of this phenomenon in the numerical modelling of surfzone hydrodynamics for random waves. The implications of a zone of nearly constant radiation stress inside the breakpoint are examined with respect to wave-induced current generation - both cross-shore and longshore - and sediment transport prediction. Comparisons are made to both field and laboratory data from plane and undulating profiles.

BACKGROUND

The existence of a zone of transition between the unbroken wave shape and the turbulent bore form of the broken wave was first reported by Svendsen et al (1978) based on visual observations of wave breaking. Svendsen (1984) proposed a definition of the transition zone as the region of nearly horizontal or very weakly sloping water level inside the breakpoint before the beginning of a steep gradient in the water level due to wave setup.

Both Svendsen (1984) and subsequently Basco and Yamashita (1986), were concerned with the influence of the transition zone on the description of wave height decay and mean water level variation in the surfzone through the solution of the energy and momentum balance equations. The transition zone features rapid wave decay without an associated increase in energy dissipation. Svendsen (1984) suggested that the large amount of potential energy lost in this region is converted to forward

¹Department of Civil Engineering, Imperial College of Science, Technology and Medicine, London, England. SW7 2BU.

²Delft Hydraulics. P.O. Box 152, 8300 Emmeloord, The Netherlands.

³Hydraulics Research Limited. Wallingford, Oxon., England. OX10 8BA.

momentum flux, specifically in the surface roller. Basco and Yamashita (1986) viewed the process in the transition zone as a transformation from oscillatory wave motion to highly rotational (turbulent) motion. Thus, the region is essentially a development zone where the just broken wave is transformed into a turbulent bore. Basco (1985) notes that both plunging and spilling breakers feature this same development process, albeit at much different scales. Two approaches for considering the role of the transition zone processes in the prediction of wave height decay are presented in the above-noted papers.

A zone of nearly constant mean water level, through consideration of the momentum balance equation, implies that the radiation stress is also constant. Consequently, the generation of wave-induced cross-shore and longshore currents by the reduction in radiation stress due to energy dissipation does not commence until the inner limit of the transition zone is reached. In a comparison of numerical model estimates to laboratory measurements of the distribution of longshore currents across a profile for plunging waves, Visser (1984) found that it was critically important to delay the initiation of the influence of energy dissipation on the generation of longshore currents until the plunge point. As noted by Basco and Yamashita (1986), the distance from the breakpoint to the plunge point is a significant fraction of the transition zone width. A similar influence of the transition zone has been observed in the prediction of wave-induced return flow in the surfzone (or undertow) by Roelvink and Stive (1989), Nairn (1990a) and Okayasu et al (1990).

TRANSITION ZONE WIDTH

Basco and Yamashita (1986) proposed that the width of the transition zone would vary with the surf similarity parameter; the zone would be wider for spilling breakers than for plunging breakers. Whilst this may be so in an absolute sense, considering that the plunging breaker must undergo a much greater change in wave shape, it is more likely that the dimensionless width of the transition zone (normalised by the depth at breaking) will be larger for plunging breakers. An empirical expression can be developed for the dimensionless transition zone width using dimensional analysis techniques. The ratio of the depth at the inner limit of the transition zone, d_t , to the depth at breaking, d_b , is found to be a function of two parameters as follows,

$$\frac{d_t}{d_b} = f \left(\frac{m_b}{(H_b/L_o)^{0.5}}, \frac{d_b}{L_b} \right) \tag{1}$$

The first variable is the surf similarity parameter, where m_b is the bottom slope in the vicinity of the breakpoint, H_b is the wave height at breaking and L_o is the deepwater wavelength; the second variable is the ratio of the depth at breaking to the wavelength at breaking and provides an indication of the scale of the wave with respect to the width of the surfzone. A data set on the width of the transition zone was gathered from laboratory experiments with monochromatic waves - the width was defined as the distance from the breakpoint to the abrupt change in slope of the mean water level (an example of one of these laboratory experiments is given in Figure 1). By combining the two variables of Equation 1 into a single parameter and performing a regression analysis on the data set, the following relationship was derived,

$$d_v/d_b = 0.47 \xi_{bb}^{-0.275}, \text{ for } \xi_{bb} \geq 0.05$$

$$d_v/d_b \sim 1, \text{ for } \xi_{bb} \leq 0.05$$

$$\xi_{bb} = m_b / (H_b/L_b)^{0.5} \quad (2)$$

Note that the dimensionless transition zone depth is given as a function of the surf similarity parameter evaluated entirely with breakpoint values. This differs from the conventional surf similarity parameter in that the local wavelength at breaking is used in the definition of wave steepness instead of the deepwater value (thus accounting for the second variable in Equation 1). A comparison of this relationship to the data set is given in Figure 2, the correlation coefficient for the regression analysis was 0.85. As anticipated, the dimensionless width (which varies from 5 to 50 % of a plane sloping surfzone) increases with the surf similarity parameter and consequently is greater for plunging breakers than for spilling breakers. In a random wave climate, the transition zone width will vary according to the surf similarity parameter of each individual wave at breaking.

MODELLING THE INFLUENCE ON WAVE-INDUCED CURRENTS

1) Empirical Approach

A numerical model has been developed for the prediction of cross-shore and alongshore sediment transport on a beach profile. The principal components of the model include: 1) wave transformation based on the technique of Battjes and Janssen (1978) for random waves; 2) a description of the mean cross-shore flows under random waves using an adaptation of the method presented by DeVriend and Stive (1987); 3) prediction of the longshore current variation across the profile employing the technique of Southgate (1989); 4) calculation of the central velocity moments based on the non-linear Vocoldal theory (after Swart, 1978) for time-varying orbital velocities; and 5) prediction of the cross-shore and alongshore sediment transport rates across the profile using a modified version of the Energetics approach which was originally developed for coastal applications by Bailard (1981) and Bowen (1980). The influence of the transition zone primarily affects the calculation of the mean wave-induced cross-shore and longshore currents of steps 2 and 3 above. Of course, this influence will also be transmitted to the calculation of sediment transport rates based on the modified currents.

The Battjes and Janssen (1978) description of random wave transformation at each point across a profile consists of two parameters, the root mean square wave height, H_{rms} , and the fraction of broken waves, Q_b . In this time-averaged approach to modelling random waves, the fraction of broken waves represents the proportion of time that waves are breaking at a given point on the profile over a model time step. Both the techniques of DeVriend and Stive (1987) and Southgate (1989) for wave-induced cross-shore and longshore currents respectively are based on a similar approach to random waves. The principal driving force for currents under breaking waves is represented by the reduction in radiation stress, which in turn may be related to the dissipation of wave energy. Therefore, in a time-averaged sense, a driving force for the currents between any two points on a profile is derived from the local decay in the rms

wave height multiplied by the fraction of broken waves. However, the stipulation of the transition zone influence suggests that the incremental increase in the driving force due to the local initiation of wave breaking - represented by the increase in the fraction of broken waves between the two points - should be delayed by a distance equivalent to the transition zone width. Therefore, at each point across the profile a revised value of the fraction of broken waves is determined by delaying the incremental increase in Q_b for a distance equivalent to the local transition zone width (i.e. using the local wave height, wavelength and beach slope in Equation 2). The revised Q_b is treated as a new variable and is used in the calculation of energy dissipation for the driving force of radiation stress related quantities such as mean currents and wave setup. A comparison of the revised Q_b to the actual Q_b is presented in Figure 3 which shows the details of the prediction of wave transformation across a profile corresponding to Case 5 of the DUCK85 sediment transport field experiments (this experiment is discussed in more detail later). The revised Q_b distribution is shifted onshore approximately 10 m for this example.

2) Analytical Approach

The mean wave energy balance equation:

$$\frac{\partial}{\partial x} EC_g = S \tag{3}$$

where E is the mean wave energy, C_g the group velocity and S a (negative) source term, has been used successfully to describe the decay of organised wave energy by means of a bore model. Battjes and Janssen (1978) extended the formulation to the case of random waves by assuming a parametric shape for the wave height distribution. If it is assumed that the organised wave energy is instantly converted to isotropic turbulence energy, the horizontal cross-shore momentum balance reads:

$$\frac{\partial}{\partial x} \tilde{S}_{xx} + \rho gh \frac{\partial \eta}{\partial x} + \tau_b = 0 \tag{4}$$

where \tilde{S}_{xx} with a tilde is the radiation stress related to the organised wave motion, ρ is the density of water, g the acceleration of gravity, h the water depth, η the mean water level and τ_b the bottom shear stress. Since the term τ_b is generally small, the setup should respond directly to the radiation stress gradients. As has been noted previously, this is not the case; this means that an additional term should exist in the momentum balance equation.

Svendsen (1984) suggested that part of the organised wave energy is first converted into forward momentum flux in the roller, and accounted for this roller influence both in the energy balance, by means of a term:

$$E_r = \rho AC^2/2L = \rho AC/2T \tag{5}$$

where A is the roller area, C is the phase velocity and T the wave period, and in the momentum balance by means of a term:

$$S_{xx, roller} = \rho AC^2/L = \rho AC/T = 2E_r \quad (6)$$

The equations for the energy balance and the momentum balance can then be written respectively as:

$$\frac{\partial}{\partial x} EC_g + \frac{\partial}{\partial x} E_r C = -D \quad (7)$$

where D is the dissipation per unit area, and:

$$\frac{\partial}{\partial x} \tilde{S}_{xx} + \frac{\partial}{\partial x} 2E_r + \rho gh \frac{\partial \eta}{\partial x} + \tau_b = 0 \quad (8)$$

Svendsen (1984) then relates the roller area directly to the local wave height H by using the empirical finding:

$$A = 0.9 H^2 \quad (9)$$

When this formulation is used, the absolute magnitude of the setup changes, but the spatial distribution of the setup remains directly linked to the wave energy decay, and no transition zone lag effect is found.

On the other hand, Roelvink and Stive (1989) suggested that the organised wave energy is first converted to turbulent kinetic energy which is not dissipated immediately. They proposed to use a k -equation in which the production of turbulent kinetic energy is equal to the decay of organised wave energy:

$$\frac{\partial}{\partial x} EC_g + \frac{\partial}{\partial x} \beta_f khC = -\rho \beta_d k^{3/2} \quad (10)$$

where k is the depth- and time-mean turbulence intensity and β_f and β_d are coefficients of order one. The second term in this equation represents a storage term, whereas the term on the right is the actual dissipation. Due to the storage term, which is positive in the area of initial decay of wave energy, the dissipation lags behind the production of turbulence energy. The influence of the turbulence on the momentum balance was estimated as:

$$S_{xx, turbulence} = \int_{-d}^{\eta} (\rho u'^2 - \rho w'^2) dz \sim \beta_s \rho kh \quad (11)$$

so the momentum balance in this case reads:

$$\frac{\partial}{\partial x} \tilde{S}_{xx} + \frac{\partial}{\partial x} \beta_s \rho kh + \rho gh \frac{\partial \eta}{\partial x} + \tau_b = 0 \quad (12)$$

The value of β_s depends on the ratio between the turbulence intensities in the x , y and z -directions; based on the analogy of a wake, a value of 0.22 was suggested. The result

was that hardly any influence on the setup distribution was found, although there was a significant lag between the production and dissipation of turbulence energy. This leads to the conclusion that either the turbulence which is generated is much more anisotropic than assumed, or that the wave motion is converted into a different form of motion.

A synthesis of these two approaches can be developed using Svendsen's concept of a roller as a 'block' of water moving at the phase velocity, dropping the empirical Equation 9, and assuming the sink term S of the organised wave energy to be a known function of the local wave parameters, as for instance in the Battjes and Janssen model. The roller energy, E_r , in this case becomes the unknown parameter; if the dissipation can be related to this parameter, E_r can be solved from Equation 7. In this way the roller will serve as a storage of kinetic energy, leading to a lag effect similar to that modelled by Equation 10.

The dissipation in this case can be modelled according to Delgaard and Fredsoe (1989) as the work performed by the shear stress, τ_r , between the roller and the organised wave motion:

$$D = \overline{\tau_r} C \quad (13)$$

The shear stress can be deduced by considering the vertical force balance equation on the roller, which leads to:

$$\overline{\tau_r} = \beta \rho g A / L \quad (14)$$

where β is the mean slope under the roller. Combining Equations 13 and 14,

$$D = \beta \rho g A / T = 2\beta g E_r / h \quad (15)$$

so Equation 7 can be written as:

$$\frac{\partial}{\partial x} EC_g + \frac{\partial}{\partial x} E_r C = -2\beta g E_r / C \quad (16)$$

This equation is quite similar to Equation 10; if it is assumed that $E_r = \rho kh$, $C = \sqrt{gh}$ and the order of magnitude estimate $k \sim 1/2 \beta_1 C^2$ is taken, the result is:

$$\frac{\partial}{\partial x} EC_g + \frac{\partial}{\partial x} \rho kh C = - (2\sqrt{2} \beta / \sqrt{\beta_1}) \rho k^{3/2} \quad (17)$$

The above expression, with $\beta \sim \beta_1 \sim 0.10$, leads to Equation 10 with $\beta_d \sim 1$.

Comparison of Equations 6 and 11 now shows that the roller contribution to the radiation stress is $0.22 E_r$ in the turbulence model, against $2 E_r$ according to the Svendsen concept. In view of the fact that for the first estimate no significant transition zone lag effect in the setup was found, the second estimate seems more realistic. In order to check this, two tests documented in Battjes and Janssen (1978) were hindcast with respect to wave energy decay and setup, specifically, Test HJ2, with a plane beach, and HJ12, with a schematised bar-trough profile. A Battjes type model was used to predict the sink term S ; the roller energy E_r was solved both from Equation 10 and from

Equation 16 and the setup was computed from Equation 8. A value for the roller slope of 0.10 was applied in Equation 14. In Figures 4 and 5, the results are presented for the wave energy, represented by $H_{rms} = \sqrt{3E/\rho g}$, and for the setup, without the transition zone lag effect and with the lag effect according to both formulations. There is a considerable improvement in the setup prediction in the area of incipient breaking; also, Equations 10 and 16 produce very similar results. With respect to wave-driven currents it is likely that the dissipation rate should be the term D in Equation 7, rather than the sink term S in Equation 1, however formal proof of this has not yet been derived and should be the subject of further study.

The analytical approach described above can be applied to predict the general behaviour of the transition zone width as a function of beach slope and wave steepness. The model was tested for a plane beach with slopes in the range of 0.005 to 0.05 and incident wave steepnesses - defined as H_{rms}/L_o - in the range 0.01 to 0.04. The transition zone width was defined as the distance between the peak of the sink term S and the peak of the dissipation term D , as the peak in S defines the location of maximum gradient in H_{rms} , and the peak in D a location of rapid water level increase. Though this definition differs slightly from that used for the empirical approach, the general behaviour can be expected to be quite similar. The analytical approach may also be applied to either monochromatic or random waves.

The dimensionless transition zone width (i.e. the ratio of the depths at the dissipation peak and the sink term peak) is plotted against the deepwater surf similarity parameter, ξ_o , the similarity parameter at breakpoint values, ξ_{bb} , and against the bottom slope in Figures 6a, b and c respectively. The empirical approach is also plotted in Figure 6b and reasonable agreement with the analytical approach is apparent. Figure 6c demonstrates that the analytical approach is almost entirely dependent on beach slope (there is very little dependence on wave steepness). In contrast, the empirical approach does have a significant dependency on wave steepness based on the monochromatic wave data. The existence of a steepness influence in random waves is indirectly shown in the next section; however, a direct proof of this should be the topic of further study.

COMPARISON TO DATA ON WAVE CURRENT PREDICTION

In this section, examples of the influence of the transition zone width on the prediction of undertow and longshore currents under random waves using the empirical approach are presented. However, the first example relates to the measurement of mean cross-shore flows generated by monochromatic waves. The vertical distributions of mean flow for five locations across a laboratory profile (Case 5 of Nadoaka and Kondoh, 1982) are shown in Figure 7 along with the predicted extent of the transition zone width. Clearly, the measured distribution located between 2 and 3 m on the baseline - which is shoreward of the breakpoint and in the transition zone - bears more similarity to the seawardmost distribution (which relates to the mean flow under an unbroken wave) than to the shoreward breaking wave undertow distributions. This apparent lag between wave breaking and the generation of undertow has been noted on several occasions in the literature (i.e. Nadoaka and Kondoh, 1982 and Longuet-Higgins, 1983 among others). Within the transition zone, the forcing of the undertow due to the reduction in radiation stress is not yet realised; this demonstrates the importance of considering the influence of the transition zone shift on the prediction of mean return flow.

The predictions of undertow under random waves for two laboratory tests with and without the use of a revised Q_o are shown in Figures 8 and 9 (the data for these two

tests were given by Roelvink and Stive, 1989 and Sato et al, 1988 respectively). In both cases, the influence of the transition zone has a considerable effect on the predictions; the results with a revised Q_b provide a much better match to the measured data. Field measurements of the cross-shore distributions of undertow (along with the important recordings of profile shape and inshore wave climate) are generally unavailable, however, as a demonstration of a field case, the predicted undertow for the DUCK85 Case 5 example (corresponding to Figure 3) is compared to the measurements from two electromagnetic current meters in Figure 10. It is difficult to assess the validity of the predictions from this data, however, the exercise does reveal the importance of accounting for the transition zone shift in the predictions.

It has become abundantly clear that the distribution of undertow across the profile is a primary factor in the reshaping of beach profiles during erosion events (see Nairn, 1990a and Roelvink and Stive, 1989). A brief example of the influence of the transition zone shift on profile development is shown in Figure 11. This laboratory test corresponds to the undertow prediction given in Figure 8, the test duration was 12 hours. Again, the importance of considering the transition zone effect is revealed by a comparison of the predictions with and without the shift to the measured profile change. Specifically, the bar position is shifted too far seaward in the numerical model test without the transition zone influence (i.e. using the unrevised value for the fraction of broken waves, Q_b).

A field experiment to measure alongshore sand transport in the surfzone was conducted at the Field Research Facility of the Coastal Engineering Research Centre, U.S. Army Corps of Engineers at Duck, North Carolina (see Kraus et al, 1989). Eight tests were performed in September of 1985 as part of the DUCK85 programme using a series of portable sand traps deployed across the surfzone (the traps consisted of polyester sieve cloth streamers suspended on a rack). Two electromagnetic current meters were also deployed to monitor the cross-shore and longshore flow velocities in the surfzone. For a selected test, the cross-shore flows were presented in Figure 10 and the wave transformation prediction including the revised fraction of broken waves accounting for the transition zone influence were given in Figure 3. A demonstration of the effect of using the revised fraction of broken waves in the prediction of longshore currents for the same DUCK85 test is shown in Figure 12. The peak longshore current is reduced and predicted velocities in the outer part of the surfzone have been considerably diminished. The influence is large due to the low steepness of the incident wave ($H_{rms} = 0.31$ m, $T = 9.7$ s), indicating that a plunging breaker and a correspondingly large transition zone width would have existed. The predicted velocities compare well with the field measurements, however, the two isolated recordings are not sufficient to verify the transition zone phenomenon.

In the numerical model used for these investigations, both the longshore and cross-shore sediment transport rates are calculated using a modified version of the Energetics approach adapted for coastal sediment transport by Bowen (1980) and Ballard (1981) from the original formulation of Bagnold (1963) for sediment transport in rivers. Modifications to the cross-shore and alongshore components of this approach are given in Nairn (1990a) and Nairn (1990b) respectively. Simply stated, the Energetics approach is based on the concept that the wave action acts to support the sediment in bed and suspended load which is then advected by mean currents, orbital velocity asymmetry and gravity. Therefore, the distribution of the longshore current across the profile is a critically important element of the alongshore transport estimate. This is reflected in a comparison of the predicted (with and without the transition zone influence) and measured alongshore transport rates given for the selected test of the DUCK85 field

experiment in Figure 13. Clearly, this figure serves indirectly to confirm the extent of the transition zone influence on the generation of longshore currents.

DISCUSSION

The existence of a transition zone where wave decay and turbulent energy production occur unaccompanied by energy dissipation is clearly evident for monochromatic waves. The processes which are associated with the reduction in radiation stress (caused by the dissipation of wave energy) - including wave setup, undertow and longshore current - are initiated at the inner limit of the transition zone instead of at the breakpoint due to the lag between the production and the dissipation of wave energy from wave decay after breaking. The transparency of the problem in monochromatic wave situations allows for an empirical expression to be developed relating the dimensionless transition zone width (i.e. the depth at the inner limit of the transition zone divided by the depth at breaking) to the surf similarity parameter evaluated entirely with breakpoint parameters (see Equation 2). The dimensionless width is found to be greater for plunging breakers than for spilling breakers.

The clarity of this phenomenon is obscured for random waves since the width of the surfzone and the transition zone varies with each individual wave in the incident climate. However, if wave-wave interaction is ignored in the surfzone, it may be assumed that each individual wave behaves as a wave from a monochromatic wave train and the expression derived for transition zone width should be equally applicable to this situation. Neglecting wave-wave interaction is probably an acceptable assumption since the larger waves will have a celerity proportional to the depth based on the shallow water assumption and thus the possibility of one wave overtaking another is limited. Therefore, whilst the influence of the transition zone shift is less transparent in random wave surfzones, it is nonetheless very important to consider in the numerical prediction of the time-averaged values of wave setup, undertow and longshore current. With the aid of field and laboratory experiments it has been demonstrated that transition zone influence has a significant effect on the generation of time-averaged currents and the associated sediment transport (i.e. both alongshore and cross-shore).

Two techniques are presented for the description of the transition zone influence on random wave processes. The empirical approach has the benefit of responding to different incident wave conditions. However, the development of the analytical technique will ultimately allow for a better understanding of the physical phenomena.

Caution is advised in applying Equation 2 to situations of waves with very low steepness breaking on steep slopes - especially for surging and collapsing breakers (i.e. high values of the surf similarity parameter at breaking) - as there are indications that the transition zone width is over-estimated for these cases. More data on the monochromatic transition zone width is required to improve the reliability of Equation 2 in these instances. There is also a need to verify directly the transition zone influence in random waves through the analysis of a time series of simultaneous measurements of velocity, turbulence and water surface elevation.

REFERENCES

Bagnold, R.A. (1963). Beach and Nearshore Processes. In *The Sea*. Vol. 3. ed., M.N. Hill. Interscience, N.Y.

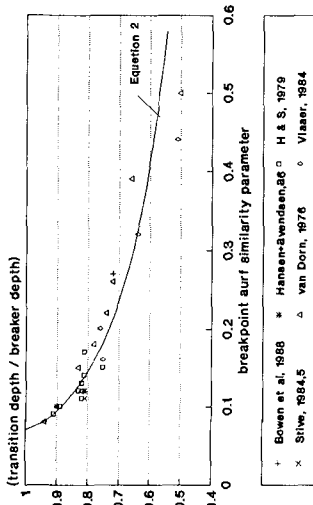
- Ballard, J.A. (1981). An Energetics Total Load Transport Model for a Plane Sloping Beach. *J. of Geophys. Res.* Vol. 86, No. C11. pp. 10938-10954.
- Basco, D.R. and Yamashita, T. (1986). Toward a Simple Model of the Wave Breaking Transition Region in Surfzones. *Proc. of the 20th Conf. on Coastal Eng., ASCE.* pp. 955-970.
- Basco, D.R. (1985). A Qualitative Description of Wave Breaking. *J. of Waterway, Port, Coastal and Ocean Eng., ASCE.* Vol. 111, No. 2. pp. 171-188.
- Battjes, J.A. and Janssen, J.P. (1978). Energy Loss and Setup Due to Breaking of Random Waves. *Proc. of the 16th Conf. on Coastal Eng., ASCE.* pp. 569-588.
- Bowen, A.J. (1980). Simple Models of Nearshore Sedimentation: Beach Profiles and Longshore Bars. In *The Coastline of Canada.* ed., S.B. McCann. pp. 1-11.
- Delgaard R. and Fredsoe J. (1989). Shear Stress Distributions in Dissipative Water Waves. *Coastal Engineering.* Vol. 13. pp. 357-378.
- DeVriend, H.J. and Stive, M.J.F. (1987). Quasi-3D Modelling of Nearshore Currents. *Coastal Engineering.* Vol. 11. pp. 565-601.
- Kraus, N.C., Gingerich, K.J. and Dean Rosati, J. (1989). DUCK85 Surf Zone Sand Transport Experiment. *CERC Rept. No. 89-5.* 48 pp.
- Longuet-Higgins, M.S. (1983). Wave Setup, Percolation and Undertow in the Surfzone. *Proc. of the Royal Society of London.* A390. pp. 283-291.
- Nadoaka, K. and Kondoh, T. (1982). Laboratory Measurements of Velocity Field Structure in the Surf Zone by LDV. *Coastal Eng. in Japan.* Vol. 25. pp. 125-145.
- Nairn, R.B. (1990a). Prediction of Cross-Shore Sediment Transport and Beach Profile Evolution. Ph.D. Thesis. Imperial College, University of London. 391 pp.
- Nairn, R.B. (1990b). Validation of a Detailed Alongshore Transport Model. *Proc. Euromech 262, Sand Transport in Rivers, Estuaries and the Sea.* Wallingford.
- Okayasu, A., Watanabe, A. and Isobe, M. (1990). Modeling of Energy Transfer and Undertow in the Surf Zone. *Proc. of the 22nd Conf. on Coastal Eng., ASCE.*
- Roelvink, J.A. and Stive, M.J.F. (1989). Bar Generating Cross-Shore Flow Mechanisms on a Beach. *J. of Geophys. Res.* Vol. 94, No. C4. pp. 4785-4800.
- Sato, S., Fukuhamma, M. and Horikawa, K. (1988). Measurements of Near-Bottom Velocities in Random Waves on a Constant Slope. *Coastal Eng. in Japan.* Vol. 31, No. 2. pp. 219-229.
- Southgate, H.N. (1989). A Nearshore Profile Model of Wave and Tidal Current Interaction. *Coastal Eng., Vol. 13.* pp. 219-245.
- Svendsen, I.A. (1984). Wave Heights and Setup in a Surfzone. *Coastal Eng., Vol. 8.* pp. 303-329.

Svendsen, I.A., Madsen, P.A. and Hansen J.B. (1978). Wave Characteristics In the Surfzone. Proc. of the 16th Conf. on Coastal Eng., ASCE. pp. 520-539.

Swart, D.H. (1978). Vocoidal Water Wave Theory, Volume 1: Derivation. National Research Institute for Oceanology, South Africa. CSIR Rept. No. 357. 137 pp.

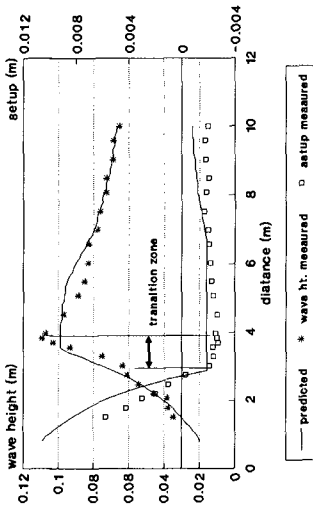
Visser, P.J. (1984). Uniform Longshore Current Measurements and Calculations. Proc. of the 19th Conf. on Coastal Eng., ASCE. pp. 2192-2207.

Figure 2 - Transition Zone Width Empirical Approach



The correlation coefficient for the regression fit of Equation 2 is 0.85.

Fig.1 - Regular Wave Height and Setup Hansen and Svendsen (1979) Case N



With the Dally et al (1985) wave decay and the Moore (1982) breaker criterion.

Figure 3 - Wave Transformation DUCK85 Case 5 - Hrms = 0.31 m, T = 9.7 s

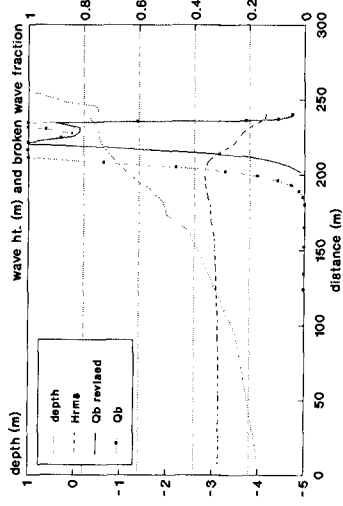


Fig. 4 - Random Wave Height and Setup Battjes and Janssen (1978) Test HJ2

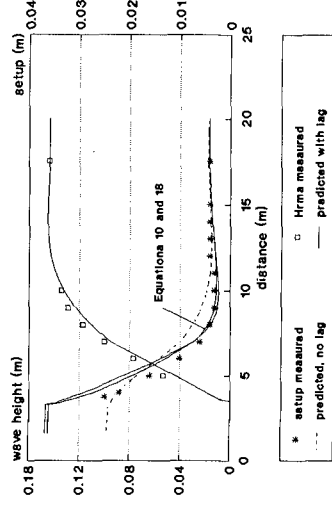


Fig. 5 - Random Wave Height and Setup
Battjes and Janssen (1978) Test HJ12

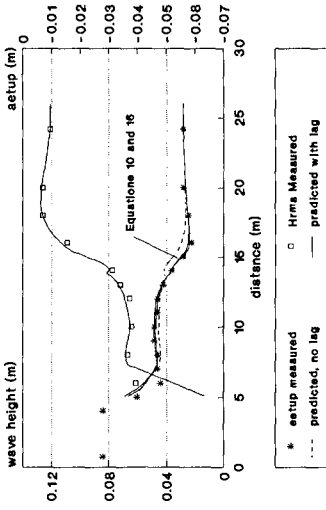


Figure 6a - Transition Zone Width
Analytical Approach
vs. Deepwater Surf Similarity Parameter

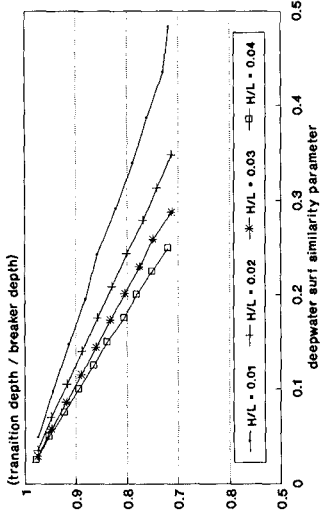


Figure 6b - Transition Zone Width
Analytical Approach
vs. Breakpoint Surf Similarity Parameter

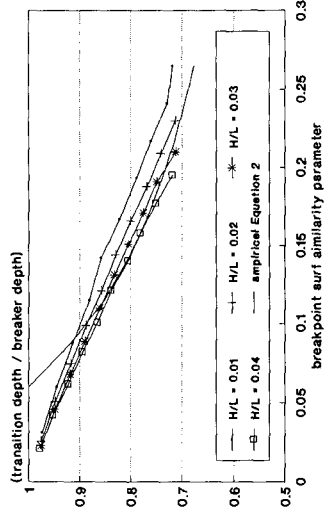


Figure 6c - Transition Zone Width
Analytical Approach vs. Beach Slope

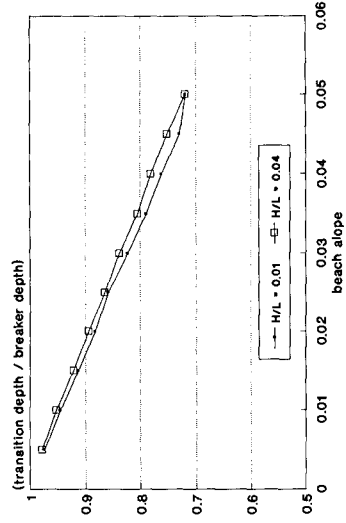


Figure 7 - Regular Wave Undertow
Nadoaka and Kondoh (1982) data

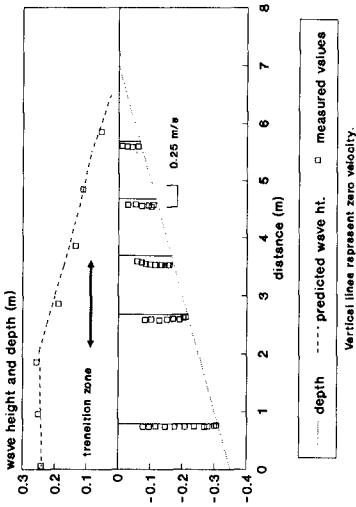


Figure 8 - Random Wave Undertow
Delft Case 1 - H = 0.123 m, T = 2 s

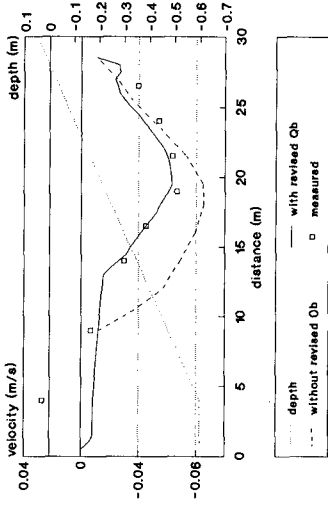


Figure 9 - Random Wave Undertow
Sato Case 3 - Hrms = 0.036 m, T = 0.92 s

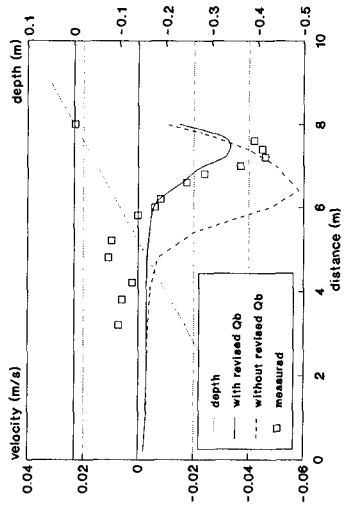


Figure 10 - Random Wave Undertow
DUCK85 Case 5 - H = 0.31 m, T = 9.7 s

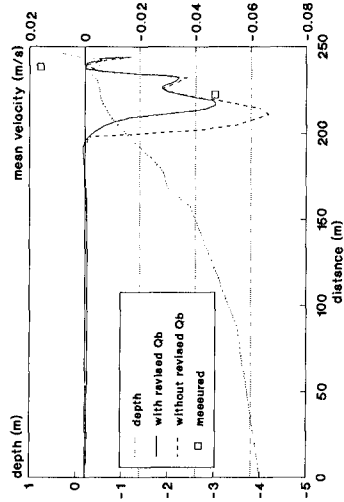


Figure 12 - Longshore Current
DUCK85 Case 5 - H = 0.31 m, T = 9.7 s

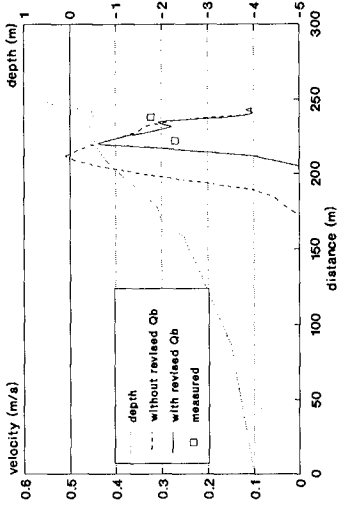


Figure 13 - Alongshore Transport
DUCK85 Case 5 - Energetics Approach

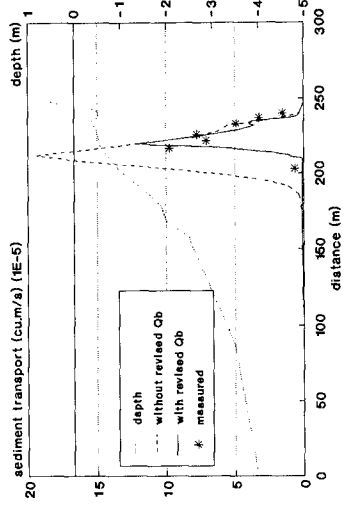
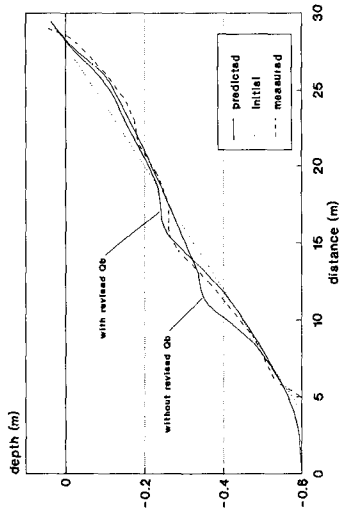


Figure 11 - Profile Change
Deft Case 1 after 12 hrs.



CHAPTER 6

THE GROUP CHARACTERISTICS OF SEA WAVES

Yu-xiu Yu¹ and Shu-xue Liu²

Abstract -- A review concerning the methods of studying and describing wave groups is presented in this paper. After analysing 73 field records collected in Shijiu Port, China, the measured parameters of wave groups and some factors describing wave groupiness and their variations are given. Moreover, these results are compared with that of theory.

1. INTRODUCTION

It is found that the higher waves often appear in group in a continuous record. The existence of wave groups has been known to sailors for a long time, but the phenomena had not been studied systematically until the first year of 1970's. Many experiments have shown that the wave groups are not only more disastrous to the rubble mound breakwaters, the moored floating bodies and capsizing of ships, but also important for harbour resonance. Therefore wave groups received more attentions and they are studied by field experiments, simulation (physioal and numerioal) tests and theoretical analyses. In this paper, the existing methods for studying wave groups and some factors describing wave groupiness are summarized. Then, the 73 field records collected in Shijiu Port are analysed. Based on these analyses, the wave group parameters and the factors describing wave groupiness and their variations are investigated, and their results are used to examine the existing theoretical methods. It may be a good reference for theoretical study and engineering practice.

2. METHODS OF STUDYING WAVE GROUPS

2.1 Theory of wave envelope

The concept of wave group has been proposed in classical hydrodynamics. Wave groups can be formed by two trains of waves of the same height propagating in the

1. Prof., Department of Civil Engineering

Dalian University of Technology, Dalian, 116024, CHINA

2. Assistant Researcher, Department of Civil Engineering

Dalian University of Technology, Dalian, 116024, CHINA

same direction with slightly different frequencies. But the sea waves are considerably more complicated. Nolte (1972) and Ewing (1973) used the envelope theory proposed by Rice and Longuet-Higgins to study the sea wave groups and obtained many results. In Fig.1, the crest and trough envelope can be obtained by linking the top and bottom points respectively. Making a horizontal line at the specified level to cross the crest envelope, t_1 , t_2 etc. are obtained which are

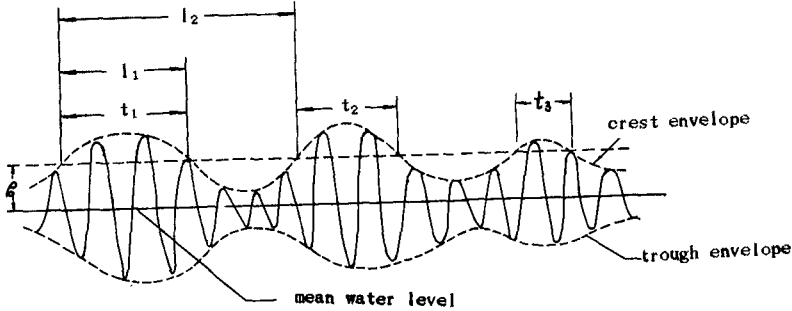


Fig.1 Sketch of wave envelope

called the time durations of wave groups at ρ_0 level. One can also use the wave number Ω_1 included in a wave group to describe the time duration. In the case of narrow-band spectrum, the mean wave number of wave group expressed by the spectral moment can be derived using the envelope theory, i.e.,

$$\bar{\Omega}_1 = [\bar{m}_2 / (2\pi \bar{\mu}_2)]^{1/2} m_0^{1/2} / \rho_0 \quad (1)$$

where m_r is the r th moment of wave spectrum and μ_r is the r th central spectral moment.

$$\mu_r = \int_0^{\infty} (\omega - \bar{\omega})^r S(\omega) d\omega \quad (2)$$

where $\bar{\omega} = m_1 / m_0$

The mean wave number between two successive wave groups is defined as

$$\bar{\Omega}_2 = [\bar{m}_2 / (2\pi \bar{\mu}_2)]^{1/2} m_0^{1/2} / \rho_0 \cdot \exp[\rho_0^2 / (2m_0)] \quad (3)$$

2.2 Statistical theory of runs

Goda (1978) determined the wave heights by means of the zero-up-crossing method and defined successive waves whose heights exceed a specified threshold H_0 as a run. As shown in Fig.2, the threshold $H_0 = H_{1/3}$ and the first run contains 3 waves in a group ($j_1 = 3$). He also defined the wave number between two successive wave groups exceeding H_0 as the total run length j_2 . For example, $j_2 = 8$ in Fig.2. Assuming the change of successive wave height is stochastic and independent, and letting the occurrence probability of $H > H_0$ be denoted as p_0

and non-occurrence probability by $q_0 = 1 - p_0$, the mean run length and its standard

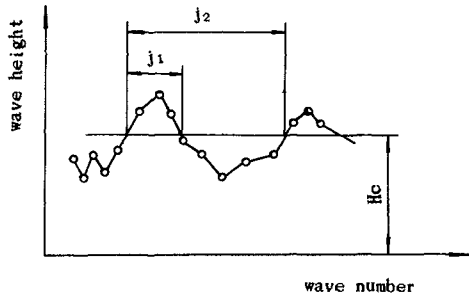


Fig. 2 Sketch of run

deviation can be obtained by the probability distribution method as

$$\bar{j}_1 = 1/q_0 \quad \sigma(j_1) = \sqrt{p_0/q_0} \quad (4)$$

$$\bar{j}_2 = 1/p_0 + 1/q_0 \quad \sigma(j_2) = \sqrt{p_0/q_0^2 + q_0/p_0^2} \quad (5)$$

In the case of $H_0 = H_{1/3}$, according to the Rayleigh distribution $p_0 = 0.1348$, $q_0 = 0.8652$, one can obtain that $\bar{j}_1 = 1.16$, $\sigma(j_1) = 0.42$ and $\bar{j}_2 = 8.57$, $\sigma(j_2) = 8.91$.

Goda pointed out that in the case of wide-band spectrum, the run length got by Eq. (1) is probably less than 1, which is irrationable. He tried to modify it and derived the relationship between the average number of wave in a wave group \bar{j}_1 and the mean length of the group \bar{L}_1 as follows

$$\bar{j}_1 = 1 / (1 - \exp(-1/\bar{L}_1)) \quad (6)$$

Goda used the spectral peakedness parameter Q_p to describe the spectral width, i.e.,

$$Q_p = 2/m\sigma^2 \int_0^{\infty} f \cdot s^2(f) \cdot df \quad (7)$$

He obtained that \bar{j}_1 increases with increasing Q_p from field data and numerical simulation. But the values of \bar{j}_1 from field data are very scattered and they are greater than that from Eq. (6) generally. It is because the successive wave heights in field are not independent. The average value of the correlation coefficients between successive waves heights is 0.324 (see Table 2) from our data.

Kimura (1980) gave the probability theory of wave run length by considering the correlation of wave heights. Assuming the distribution of wave height obey Rayleigh distribution, he derived the joint probability function, $p(H_1, H_2)$ of two successive wave heights (H_1 and H_2) as

$$p(H_1, H_2) = \frac{4H_1H_2 / [(1-4\rho^2)H_{rms}^4] \exp\{-(H_1^2+H_2^2)/[(1-4\rho^2)H_{rms}^2]\}}{I_0(4H_1H_2 / [(1-4\rho^2)H_{rms}^2])} \quad (8)$$

where H_{rms} is the root-mean-square value of wave heights, I_0 denotes the

modified Bessel function of zeroth order and ρ is a correlation parameter and can be defined as a function of the correlation coefficient $\gamma_{HH}(1)$ between H_1 and H_2 , i.e.,

$$\gamma_{HH}(1) = [E(2\rho) - (1-4\rho^2)K(2\rho)/2 - \pi/4] / (1-\pi/4) \quad (9)$$

where K and E are the complete elliptic integrals of first and second kinds respectively. $\gamma_{HH}(1)$ will be defined by the following Eq. (21).

Let the probability that neither H_1 nor H_2 exceeds the threshold H^* be denoted as p_{11} and that of H_1 and H_2 simultaneously exceed as p_{22} , i.e.,

$$\left. \begin{aligned} p_{11} &= \int_0^{H^*} \int_0^{H^*} p(H_1, H_2) dH_1 dH_2 / \int_0^{H^*} q(H_1) dH_1 \\ p_{22} &= \int_{H^*}^{\infty} \int_{H^*}^{\infty} p(H_1, H_2) dH_1 dH_2 / \int_{H^*}^{\infty} q(H_1) dH_1 \end{aligned} \right\} \quad (10)$$

where $q(H_1)$ is the wave height distribution which Rayleigh distribution can be used, i.e.,

$$q(H_1) = 2 \times H_1 / H_{rms}^2 \exp(-H_1^2 / H_{rms}^2) \quad (11)$$

Then the probability of the run with the length of j_1 can be given by

$$p(j_1) = p_{22}^{j_1 - 1} (1 - p_{22}) \quad (12)$$

The mean and the standard deviation of run length are

$$\bar{j}_1 = 1 / (1 - p_{22}) \quad \sigma(j_1) = \sqrt{p_{22} / (1 - p_{22})} \quad (13)$$

The probability of the total run length is

$$p(j_2) = \frac{(1 - p_{11})(1 - p_{22})}{(p_{11} - p_{22})} (p_1^{j_2 - 1} - p_{22}^{j_2 - 1}) \quad (14)$$

The mean and the standard deviation of total run length are

$$\left. \begin{aligned} \bar{j}_2 &= 1 / (1 - p_{11}) + 1 / (1 - p_{22}) \\ \sigma(j_2) &= [1 / (1 - p_{11})^2 + 1 / (1 - p_{22})^2 + 1 / (1 - p_{11}) + 1 / (1 - p_{22})]^{1/2} \end{aligned} \right\} \quad (15)$$

The agreement between Kimura's theoretical results and \bar{j}_1, \bar{j}_2 obtained from field swell record ($\gamma_{HH}(1) = 0.881$) is quite good.

2.3 Wave energy history method

Because the wave energy is directly proportional to the variance of the wave record, the energy at the crest of a crest envelope is greater than that at its trough (Fig. 1). The wave groups can be described effectively by the wave energy history. Funke and Mansard (1979) and Nelson (1980) proposed some similar methods. Here, Funke's method is illustrated.

Calculate the mean square of the wave surface elevation within a time duration (time window) T_p and define it as the instantaneous wave energy $E(t)$ at

the middle time t of T_p .

$$E(t) = 1/T_p \int_{\tau = -T_p/2}^{T_p/2} \eta^2(t+\tau) d\tau$$

It can be rewritten as follows after smoothing above $E(t)$.

$$E(t) = 1/T_p \int_{\tau = -T_p}^{T_p} \eta^2(t+\tau) Q_1(\tau) d\tau \quad (16)$$

$T_p \ll t \ll T_n - T_p$

where T_p is the wave period at the spectral peak, T_n the total length of wave record and $Q_1(\tau)$ the smoothing function. A superior smoothing function is the Bartlett window which is given as

$$Q_1(\tau) = 1 - |\tau|/T_p \quad -T_p \leq \tau \leq T_p \quad (17)$$

$= 0 \quad \text{others}$

$E(t)$ defined by Eq.(16) is called smoothed instantaneous wave energy history (SIWEH) and can describe the extent of wave groupiness (Funke and Mansard, 1980, Yu, 1986) effectively (Fig.3). Let $\xi(f)$ denotes the spectral density of SIWEH, i.e.,

$$\xi(f) = 2/T_n \left| \int_0^{T_n} [E(t) - \bar{E}] \exp(i\omega t) dt \right|^2 \quad (18)$$

$$\bar{E} = 1/T_n \int_0^{T_n} E(t) dt = \int_0^{\infty} S_{\eta\eta}(\omega) d\omega = m_0 \quad (19)$$

Funke and Mansard used the groupiness factor GF to describe the extent of wave groupiness, i.e.,

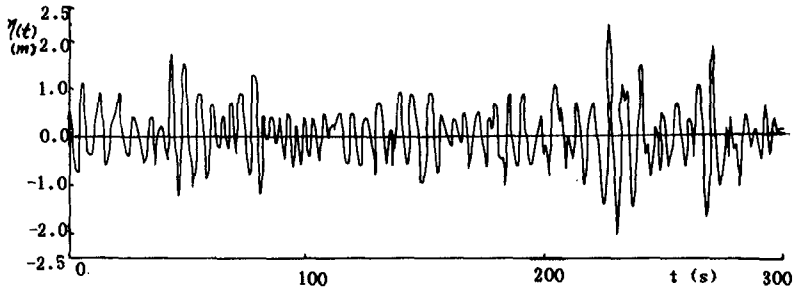
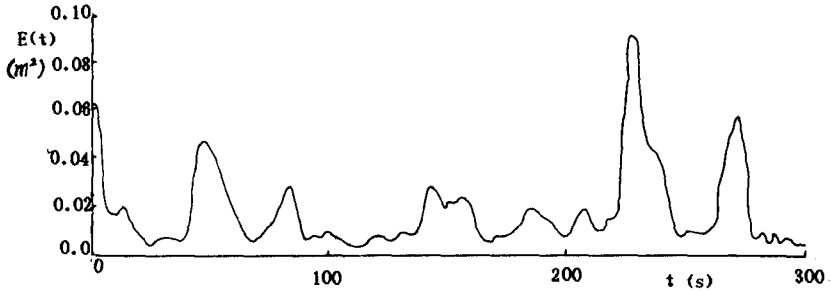
$$GF = \sqrt{1/T_n \int_0^{T_n} [E(t) - \bar{E}]^2 dt} / \bar{E} = \sqrt{m_{E,0}} / m_0 \quad (20)$$

where $m_{E,0}$ and m_0 are the zeroth order moments of SIWEH spectrum and the wave spectrum respectively. The field data of wind waves from the Sea of Japan during a period of six months gave the value of GF in the range of 0.48 and 0.94. From our data, GF changes from 0.38 to 0.93.

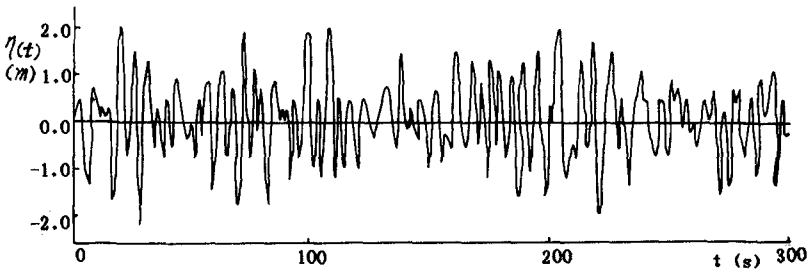
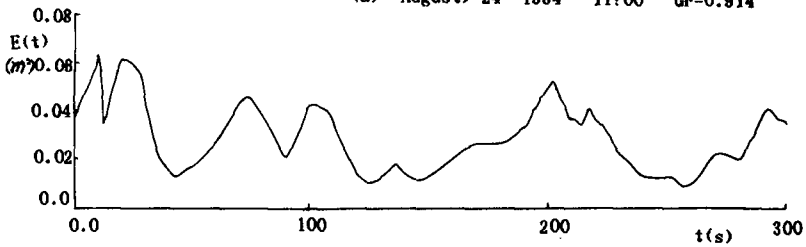
Rye (1982) also studied the wave groups by the correlation function.

3. WAVE GROUPINESS FACTORS

The parameters mentioned above such as the number of wave l_1 in a wave group whose heights exceed the specified threshold H_c (or run length j_1) and the number of waves l_2 between two wave groups in succession (or total run length j_2) and so on., are insufficient to represent the wave groupiness. So some factors have been proposed to describe the wave groupiness. In this paper, the following five factors will be studied.



(a) August, 24 1984 11:00 GF=0.914



(b) August, 19 1984 20:00 GF=0.482

Fig.3 Examples of measured SIWEH

(1). Correlation coefficient between succeeding wave heights $\gamma_{HH}(1)$

$$\gamma_{HH}(1) = \frac{1}{\gamma_{HH}(0)(N-1)} \sum_{i=1}^{N-1} (H_i - \bar{H})(H_{i+1} - \bar{H}) \quad (21)$$

$$\gamma_{HH}(0) = \frac{1}{N} \sum_{i=1}^N (H_i - \bar{H})^2$$

where \bar{H} is the average wave height determined by zero-up-crossing method. Larger $\gamma_{HH}(1)$ means that high wave follows high wave. Rye computed $\gamma_{HH}(1)$ for 60 wave records from the North Sea and the average value of $\gamma_{HH}(1)$ was 0.24. Su reported that it was 0.329 for 6 records of wind waves from the Mexico Bay. For swell, $\gamma_{HH}(1)$ is up to 0.68.

(2). Correlation coefficient between succeeding wave periods $\gamma_{TT}(1)$.

$\gamma_{TT}(1)$ is defined in the same way as $\gamma_{HH}(1)$ by replacing H_i and \bar{H} with T_i and \bar{T} respectively. Existing observed results show that $\gamma_{TT}(1)$ varied between 0 and 0.5.

(3). Correlation coefficient γ_{HT} between the wave height and the period.

$$\gamma_{HT} = \frac{1}{N\sigma_H\sigma_T} \sum_{i=1}^N (H_i - \bar{H})(T_i - \bar{T}) \quad (22)$$

where σ_H and σ_T are the standard deviations of wave height and wave periods respectively. γ_{HT} is generally greater than zero.

(4). Wave groupiness factor GF

It has been defined by equatin (20).

(5). Another parameter representing wave groupiness \bar{T}_{SIVEH}

$$\bar{T}_{SIVEH} = \frac{1}{T_p N_g} \sum_{j=1}^{N_g} (T_{SIVEH})_j \quad (23)$$

where \bar{T}_{SIVEH} is the zero-up-crossing period of the time trace of $[E(t) - \bar{E}]$. \bar{T}_{SIVEH} is the average of T_{SIVEH} normalized to peak period of wave spectrum and can represent the wave number in one group approximately.

4. THE CHARACTERISTICS OF THE WAVE GROUPS IN SHIJIU PORT

4.1 General description of field data

During September to November, 1984, a ENDECO 949 recording buoy made in U.S.A. was installed in Shijiu Port, Shandong Province, China, at 14.8m of water depth (d) by the First Design Institute of Navigation Engineering, Ministry of Communications. Wave data were collected for about 17 minutes every three hours. The sampling of record was done at the interval of 0.5 second and the data length was 2048 points in every record. In this paper, only 73 records whose signifoant wave heights are greater than 0.6m are analysed. The average wave heights are in the range of 0.42 and 1.34m, the maximum wave heights of 1.10 and 3.99m, and the average wave periods of 3.444 and 6.04 second. The wave number in one train varies from 167 to 296. \bar{H}/d is equal to 0.03~0.09. So the field situation is basically close to deep water. The wave spectra showed that

some records are of mixed wave with wind wave and swell, but most are wind waves only.

4.2 Parameters of sea wave groups

Letting the threshold height H_c equal to $H_{1/3}$, the statistical analyses are conducted for every record and the average number of waves \bar{N}_1 in a group (i.e., the mean run length \bar{J}_1) and the average number of waves \bar{N}_2 (i.e., the mean total run length \bar{J}_2) between two successive wave groups are listed in Table.1. The results obtained from the theoretical methods are also given in the Table. It is shown by comparing these results that the values from the wave envelope theory, Eq.(1) and Eq.(3), are evidently smaller than measured results, the values calculated by the statistical theory, Eq.(4) and Eq.(5), are also on the small side and \bar{J}_1 obtained from Eq.(6) is smaller yet. The average values of the Kimura's results \bar{J}_1 , \bar{J}_2 are quite close to the observed values, but the calculated distribution are more concentrated.

Table.1 Observed and theoretical parameters of wave group

Theory	Parameter	the ranges	means	deviations
observed	\bar{J}_1	1.15~2.07	1.47	0.18
	\bar{J}_2	7.25~14.90	10.77	1.75
wave envelope theory	\bar{N}_1	0.40~0.52	0.45	0.03
	\bar{N}_2	1.44~3.05	2.33	0.37
theory of runs	\bar{J}_1	-----	1.16	0.42
	\bar{J}_2	-----	8.57	6.91
Eq.(6)	\bar{J}_1	1.09~1.17	1.12	0.02
Kimura's theory	\bar{J}_1	1.26~1.73	1.51	0.12
	\bar{J}_2	8.47~12.69	10.22	0.92

The relationships between \bar{J}_1 , \bar{J}_2 and Q_p are more scattered than that between \bar{J}_1 , \bar{J}_2 and GF (Fig.4), \bar{J}_1 and \bar{J}_2 increase with the increase of GF generally.

4.3 Factors of wave groupiness

The factors of wave groupiness are analysed by above equations for 73 records, and their results are listed in Table.2. The spectral peakednesses Q_p determined by equation (7) are also given in Table.2. The Table shows that some values of $\mathcal{Y}_{TT}(1)$ are negative, but are positive mostly. It means that there are "memory" effect between successive wave heights and periods, which causes the wave grouping phenomena.

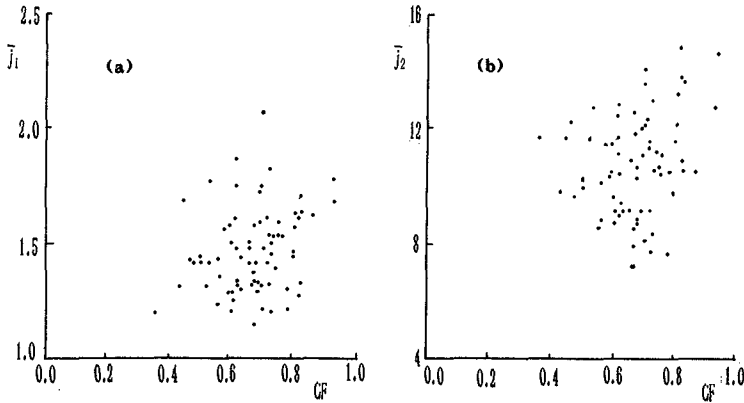


Fig.4 Relationships between \bar{J}_1 , \bar{J}_2 and GF

Table.2 Observed wave groupiness factors and the spectral peakedness

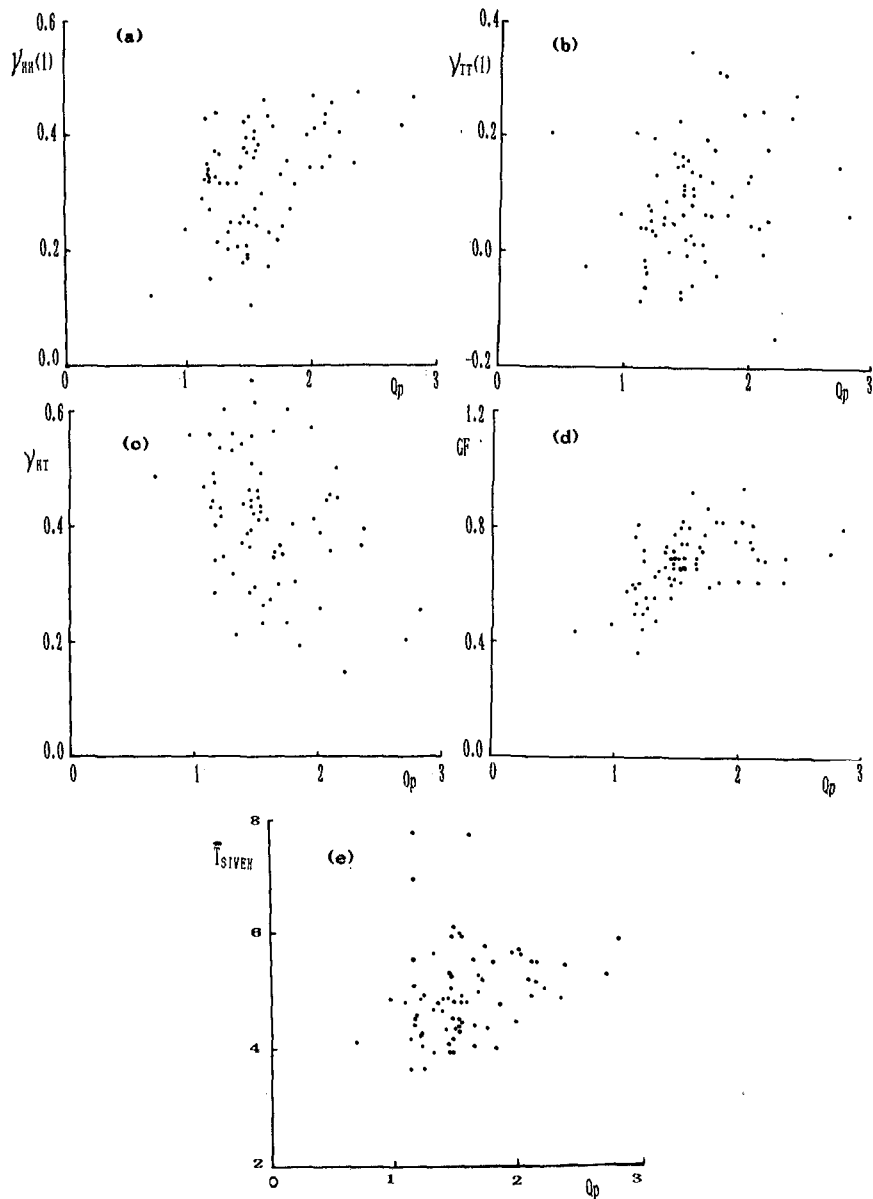
factors	$\gamma_{HH}(1)$	$\gamma_{TT}(1)$	γ_{HT}	GF	\bar{T}_{SIVEH}	Q_p
ranges	0.103~ 0.472	-0.149~ 0.348	0.147~ 0.652	0.360~ 0.932	3.661~ 7.778	0.704~ 2.821
average	0.324	0.085	0.413	0.673	4.953	1.597
deviations	0.093	0.100	0.110	0.113	0.801	0.393

4.4 Relationships between the wave groupiness factors and the spectral width parameter

Many scientists pointed out that the wave groupiness is directly correlated to the width of its spectrum, i.e., the narrower the spectrum is, the more strong of groupiness the wave is. Scientists used to judge the width of the spectrum by the width parameter ϵ . But Rye's work showed that the parameter ϵ is not able to express the spectral width definitely and it also varies significantly with the choice of the high cut-off frequency. However, Q_p defined by Eq.(7) is more stable and reliable than ϵ . So the relationships between the five previously defined wave groupiness factors and the spectral peakedness parameter Q_p are given in Fig.5 according to the field data. In general, $\gamma_{HH}(1)$, GF and \bar{T}_{SIVEH} increase while γ_{HT} decreases as Q_p increases although the points are scattering. But $\gamma_{TT}(1)$ is not evidently correlated to Q_p . It proves that the wave groupiness is strengthened as the spectrum becomes narrower. But the effect of Q_p on the wave groupiness gradually becomes weaker as Q_p increases.

However, Van Vliedder and Battjes (1990) pointed out that Q_p can be affected by the smoothing method and the number of smoothing when estimating the spectrum and suggested a parameter K to express the spectral width, i.e.,

$$K = \int_0^{\infty} s(f) \exp(2\pi ifT_{02}) df / m_0 \tag{24}$$

Fig.5 Relationships between wave groupiness factors and Q_p

where T_{02} is the mean period calculated using the spectral moments. But the correlation function method is used to estimate the spectrum and the spectrum was smoothed by Hamming window once in this paper. The relationships between Q_p , GF and K are given in Fig.6. It is shown that Q_p and K can give similar results in our case and both Q_p and K can be the spectral width parameters for wave group characteristics.

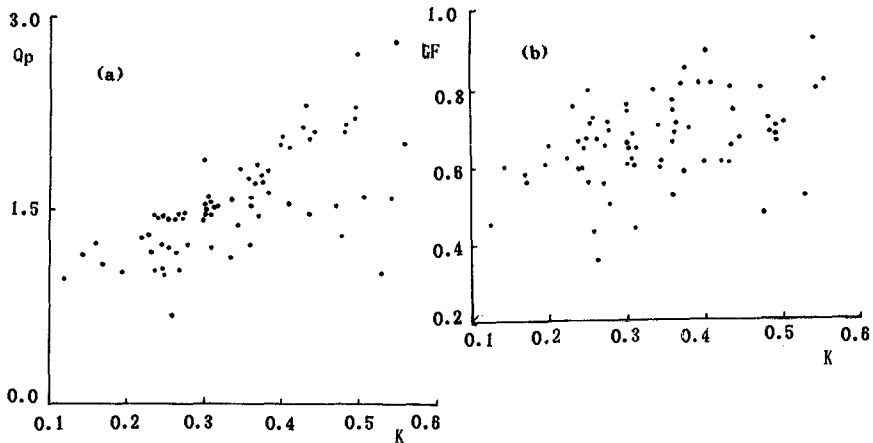


Fig.6 Relationships between Q_p , GF and K

4.5 Relationships between wave groupiness factors and GF

The relationships between $\gamma_{HH}(1)$, $\gamma_{TT}(1)$, γ_{HT} , \bar{T}_{SIVEH} and GF are given in Fig.7. All factors are evidently correlated to GF except $\gamma_{TT}(1)$. It means that GF is the main factor for representing the wave groupiness.

5. CONCLUSIONS

(1). At present, there are several methods for studying the wave group phenomenon. The results of analysis from the field data in this paper indicate once again that the wave envelope theory is not available because its results are far less than the field values. The results obtained from the statistical theory of runs are also smaller. Kimura's probability theory of run length based on the correlated wave heights can give the average values of the wave group parameters which agree with the field values quite well, but the distribution of calculated values are more concentrated than that in field.

(2). There are close relationships between the wave groupiness and the spectral peakedness (or width), i.e., the groupiness is strengthened as the spectrum becomes narrower. Most of the factors representing the wave groupiness are correlated to the spectral peakedness Q_p to some extent, $\gamma_{HH}(1)$, GF , and \bar{T}_{SIVEH} increase and γ_{HT} decreases with the increase of Q_p . K is also a spectral width parameter for wave group characteristics.

(3). Among the factors describing the wave groupiness, the wave groupiness

factor GF defined by Eq.(20) is the principal parameter. The other factors are correlated to GF to some extent except $\gamma_{TT}(1)$ which is not available. The

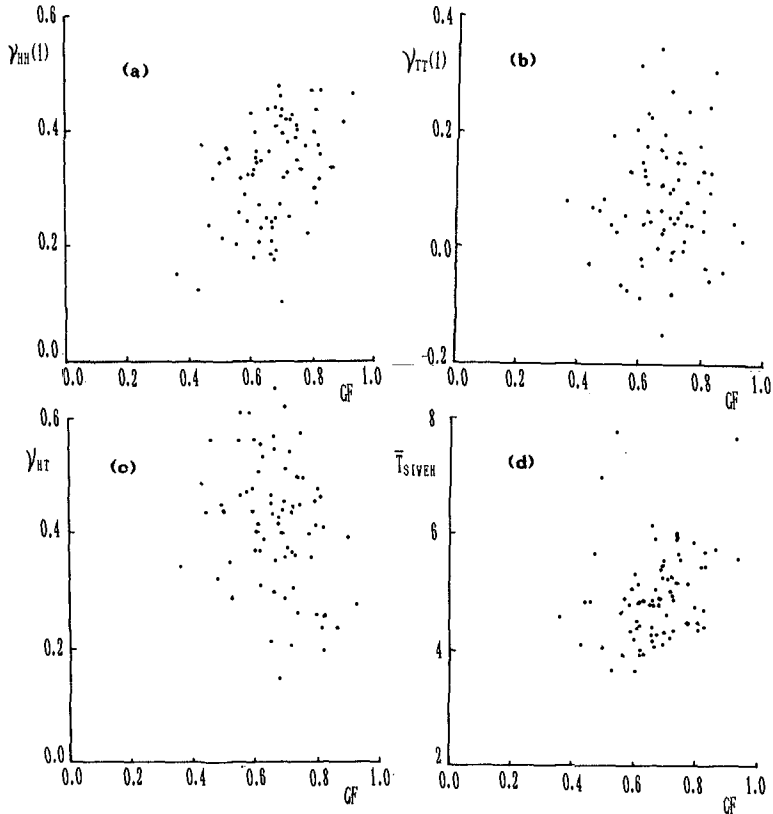


Fig.7 Relationships between wave groupiness factors and GF

mean length of runs (the mean length of wave group) and the mean total length of run (the average number of waves between successive groups) also increases with the increase of GF .

ACKNOWLEDGMENT

The authors wish to express their heartfelt gratitude to the First Design Institute of Navigation Engineering, Ministry of Communications, for offering gratis the field wave records in Shijiu Port and Mr. Minquan Gu, Chief Engineer of the Institute for his valuable suggestions. Also, the gratitude is owed to prof. Dacuo Zhang and Mr. Weitao Tai, both of Qingdao Oceanographic University and Mr. Muguo Li and Mr. Ningchuan Zhang, both of Dalian University of Technology for their great help during data processing.

REFERENCE

- Ewing, J.A., 1973, Mean length of runs of high waves, *J. Geophys. Res.*, Vol.78, No.12, 1933-1938.
- Funke, E.R., and E.P.E. Mansard, 1980, On the synthesis of realistic sea state in a laboratory flume, 17th Int.Conf. Coastal Eng., Sydney, 2974-2991.
- Goda, Y., 1976, On ocean wave groups, *Proc. BOSS*, Vol.1., pp.115-128.
- Kimura, A., 1980, Statistical properties of random wave groups, *Proc. 17th Int. Conf. Coastal Eng.*, Sydney, 2955-2973.
- Nelson, A. R., 1980, Statistical properties of ocean wave groups, Thesis, M. SC. Naval postgraduate school, Monterey, California, U.S.A.
- Noite, K. C. and F. H. Hsu, 1972, Statistics of ocean wave groups, *Proc. of OTC Conf.*, OTC-1688.
- Rye, H., 1982, Ocean wave groups, Report UR-82-18, Department of Marine Technology, University of Trondheim.
- Van Vledder, G. R. and J. A. Battjes, 1990, Discussion on paper " List of sea-state parameter (will be published in *Journal of Waterway, Port, Coastal and Ocean Engineering*)
- Yu, Y. X., 1988, The modelling of the sea wave groups, *Coastal Eng.*, Vol.5, No.1, P1-9.(in Chinese).
- Yu, Y. X. and S. X. Liu, 1988, Statistical properties and spectrum of sea waves in Shijiu Port, *Port Engineering Technology*, No.4.(in Chinese).

CHAPTER 7

Field Observation on Wave Set-up near the Shoreline

Shin-ichi YANAGISHIMA¹ and Kazumasa KATOH²

Abstract

To understand the actual condition of the abnormal rise of sea water on the beach in a storm, the field observation has been carried out at Hazaki Oceanographical Research Facility for about one year under the comprehensive conditions. The relation between the sea level rising and the external forces such as waves, deviations of atmospheric pressure and the winds are examined. The contribution of the wave set-up on the sea level rising is large, while those of the atmospheric pressure and the wind are small. The observed wave set-up near the shoreline agrees well with the predicted value by the Goda's theory. There are other factors which slightly affect the sea level changing, that is to say, a time lag behind the storm, the ocean currents, and the wave steepness.

1. Introduction

Since the sea level rising near the shoreline is considered to be strongly related to the beach erosion in a storm, it is important for predicting the changes of beach and for developing more reliable shore protection technique to estimate the precise result of sea level rising in the field.

The incident wave raises the sea level in the surf zone, that is the wave set-up. The mechanism of wave set-up has been already theoretically explained by introducing the concept of radiation stress (Longuet-Higgins and Stewart, 1962). It has been experimentally proved in the laboratory, for example by Bowen, Inman and Simmons(1968). The wave set-up on the complicated beach topography could

¹Littoral Drift Lab., Port and Harbour Research Institute, Nagase 3-1-1, Yokosuka, Kanagawa, Japan

²Chief of Littoral Drift Lab., Port and Harbour Research Institute

be also calculated by using a electric computer. So far, several fields observation on the wave set-up have been done (eg., Hansen, 1978; Holman, 1986). They were, however, not sufficient to verify the predicted wave set-up by these method.

On the actual beach, in addition to the wave set-up, the wind and the depression of atmospheric pressure have also the effects on sea level rising in a storm.

In this study, the field observation has been carried out at Hazaki Oceanographical Research Facility (HORF) for about one year to understand the actual sea level rising near the shoreline and to examine the theory of wave set-up by using the field data.

2. Field Observation

The site of the field observation is a entirely natural sandy beach, being exposed to the full wave energy of the Pacific Ocean, and is classified as micro tidal beach with the tide range of about 1.4 meters (see Figure 1). On this beach, Port and Harbour Research Institute, Ministry of Transport, has constructed the Hazaki Oceanographical Research Facility (HORF) in 1986 for carrying out the field observation in the surf zone even under sever sea conditions. The research pier is a 427 meters long concrete structure. It is supported by 0.8 meter diameter concrete-filled steel piles in a single line, at 15 meters interval. The pier deck is 2.5 meters wide and 7 meters above L.W.L. In this facility, the field observation on the wave set-up had been carried out near the shoreline for about one year from 14 January to 2 December in 1987.

In Figure 2, although many instruments are permanently installed along the research pier, only the locations of

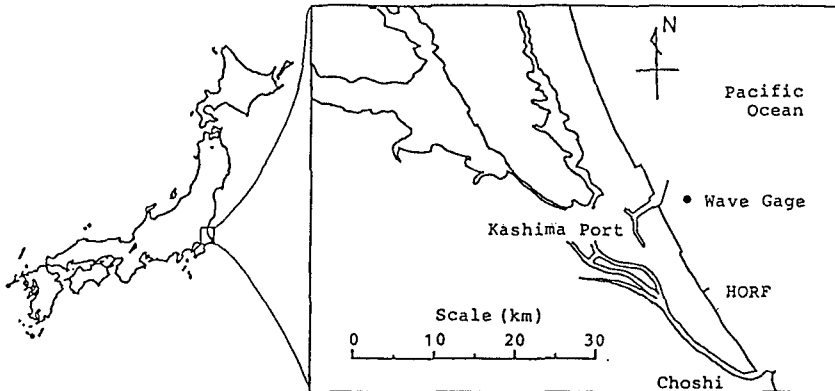


Figure 1 Site of field observation

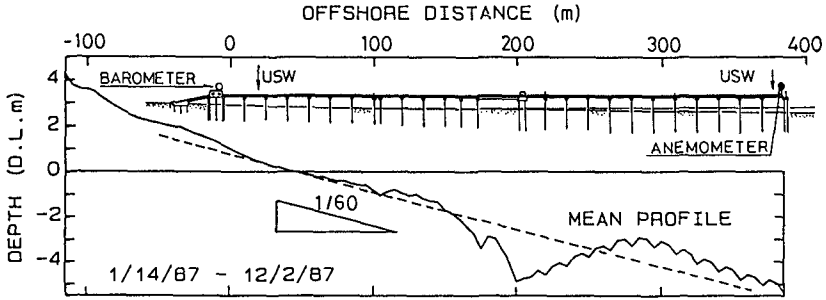


Figure 2 Locations of instruments

instruments used in this study are shown.

In order to measure the mean sea level at the shoreline with a good precision, it is necessary to measure the wave run-up and down on the beach by the tedious technique such as taking pictures by using 16 mm motion-picture camera (Holman, 1986). It is, however, very difficult to measure the mean sea level by this method for a long time, which will be the main cause of losing the chance to measure the most desirable situation in a storm. Furthermore, this method will take much time to analyze the many films. Then, an ultrasonic wave gauge was installed to the pier deck at the reference point +22m (see Figure 2 and 3). The latitude of installation was 6 meters above the mean water level. The mean grand level at the observation point was 0.3 meter above the datum line. The mean water depth was about 0.4 meter in M.W.L. Since the observation point was fixed, its relative position from the shoreline changed with time due to the change of tide level. The measurement had been done during 20 minutes of every two hours with the sampling interval of 0.3 second.

The wind direction and velocity was measured at the tip of research pier by using the two-component type ultrasonic anemometer. The installed latitude of anemometer was 10 meters above the mean water level. The atmospheric pressure was measured in the laboratory by using a barometer. These measurements had been also carried out every two hours.

The measurements described above were automatically controlled by using a mini-computer in the laboratory at the base of research pier.

The offshore waves have been measured at the mean water depth of 23.4 meters near the Kashima Port (see Figure 1). This measurement

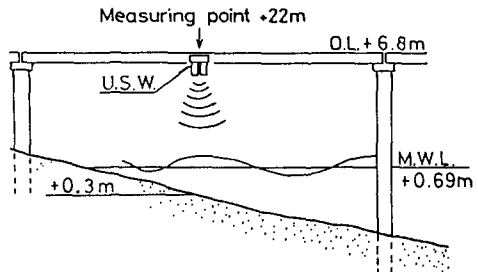


Figure 3 Ultrasonic wave gauge

has been also done during 20 minutes of every two hours.

The beach profile along the research pier was surveyed with a lead from the pier deck. The profile of the backshore and the foreshore was surveyed by using a surveyor's staff and a transit. The cross-shore interval of these measurements was 5 meters. The measurements had been done, once a day except on Sunday and on the national holiday, by the researchers stayed in the HORF. The mean profile during the observation which is calculated with these data is shown in Figure 2.

3. General conditions during Observation

Photo. 1 is the side view of HORF which was taken under a calm condition when we could easily come out from the HORF on foot on the beach. On the other hand, Photo. 2 was taken in a storm wave condition. The facility was isolated since the sea level rose and also the long period wave became larger near the shoreline. In connection with the long period waves in this area, Katoh and Yanagishima(1990) examined the berm erosion in the storm.

Data set of 1305 obtained in these measurements are utilized in analyses. In this chapter, based on these data, the general conditions of sea and whether during the observation are described.

Figure 4 shows the frequency distribution of offshore wave heights which distribute in the range from 0.4 meter to 6.4 meters. The highest frequency is in the rank of 1 to 1.5 meters. There are 91 sets of data containing the storm waves, in which the wave heights are greater than 3.0 meters. Figure 5 is the frequency distribution of the



Photo. 1 HORF (Calm condition)



Photo.2 Isolated HORF (in a storm)

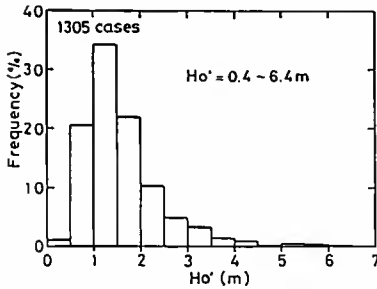


Figure 4 Frequency of off-shore wave height

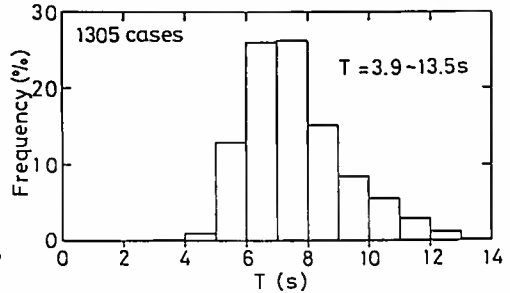


Figure 5 Frequency of period

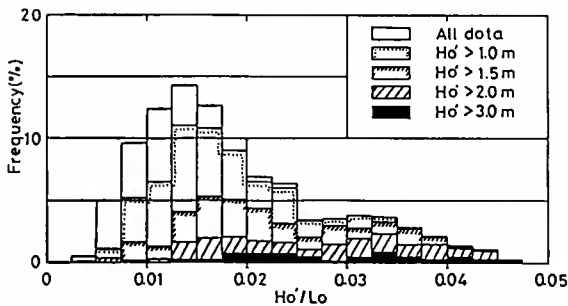


Figure 6 Frequency of steepness

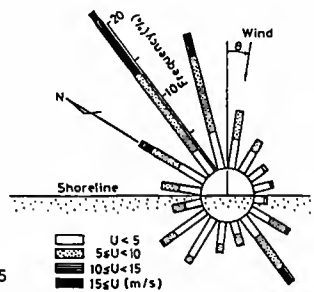


Figure 7 Frequency of wind

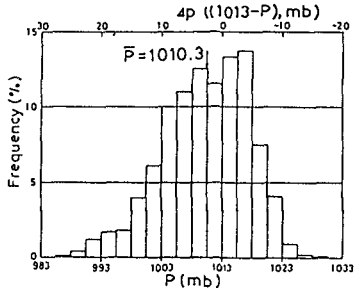


Figure 8 Frequency of atmospheric pressure

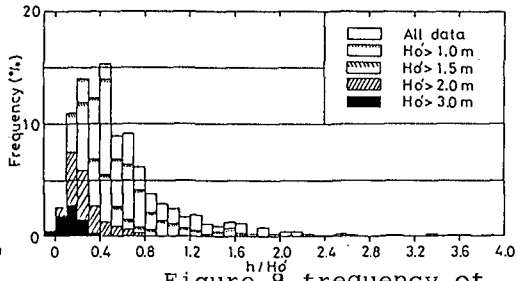


Figure 9 frequency of water depth

offshore significant wave periods during about one year observation. The periods distribute in the wide range from 3.9 seconds to 13.5 seconds, being about 7.6 seconds in average.

Figure 6 shows the combined distribution of significant wave heights and periods, that is, the wave steepness. The high waves greater than 2 meters have two modes at about 0.015 and 0.032 in the steepness. The former is corresponding to the swells, and the latter is to the wind waves.

Figure 7 shows the wind rose by distinguishing the rank of wind velocities which range from 0.6 to 19.8 m/s. The symbol θ in this figure is a wind direction defined in the later analysis.

Figure 8 is a frequency distribution of atmospheric pressures which range from 987 to 1030 mb, being about 1010 mb in average. On the upper abscissa, the deviation of atmospheric pressures from 1013 mb is also shown.

Figure 9 is the frequency distribution of non-dimensional water depth at the observation point. The mode for all data is at about 0.2 to 0.5, while it is at about 0.1 to 0.2 for the offshore waves greater than 2 meters.

As we have seen so far, the field observation of sea level rising near the shoreline had been carried out under the comprehensive sea and whether conditions.

4. Data Analyses on Wave Set-up

The mean sea water level near the shoreline was estimated by calculating the mean value of the wave profile data measured at the reference point +22m. The mean water depth during the each measurement period of 20 minutes can be estimated with the daily beach profile data. The case that the mean water depth is less than 50 cm has never been included in the total number of available data sets of 1305, since the bottom at the observation point occasionally emerged when the swash run down in this situation.

In order to evaluate the rate of sea level rising, it is

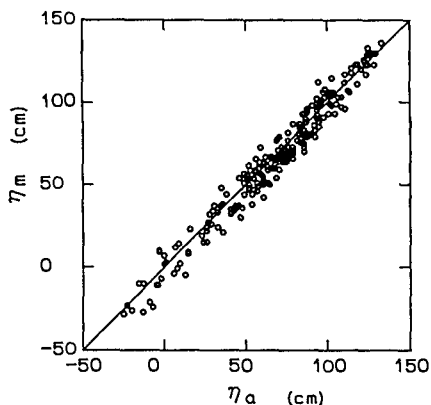


Figure 10 Comparison of astronomical tide level with mean sea level at a tip of pier

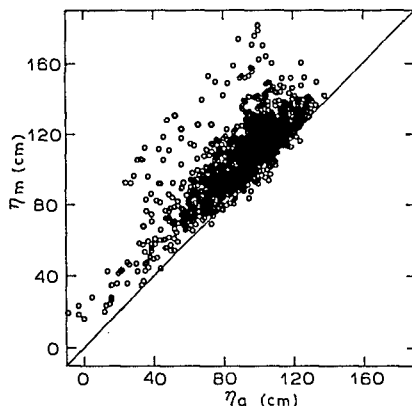


Figure 11 Relation between still water level and measured water level

necessary to know the still water level. In the laboratory, it is easy to measure it by stopping the wave generator. It is, however, impossible to control the wave characteristics in the field. One method to estimate the still water level is to measure the offshore sea level where there is no wave set-up due to the waves. There was, however, no facility to measure it in the offshore. The mean water level measured at the tip of research pier is not considered as the still water level, because the research pier is located entirely inside the surf zone when the large waves came to the site. Then, the astronomical tide levels at the site were calculated by composing 40 tidal constituents which is the result of harmonic analysis with the tide data obtained in the Kashima Port, to consider it as the still water level.

Figure 10 is the comparison of the predicted astronomical tide level on an abscissa with the mean sea level measured at the tip of research pier on an ordinate. In this comparison, only the cases which satisfy the following conditions simultaneously are plotted, that is to say; the significant wave height was less than 1 meter, under which the tip of pier was located far offshore from the surf zone; the absolute deviation of atmospheric pressure was less than 5 mb; the wind velocity was less than 3 m/s. There is a good agreement between them in Figure 10 which encourage us to consider the predicted tide level as the still water level.

In Figure 11, the measured mean sea levels near the shoreline are plotted on an ordinate against the predicted still water level on an abscissa for 1305 cases. Almost all of the measured sea levels are higher than the still

levels. In short, there were usually some amount of sea level rising.

Figure 12 shows the changes of offshore wave heights, atmospheric pressures, wind velocities and the sea levels in the storm due to the typhoon in september, 1987. In the lowest figure, the solid line is the predicted still water level and the plotted data are the measured mean sea levels. When the measured sea level was maximum, being about 80 cm higher than the still water level, the offshore wave height was maximum; the atmospheric pressure was minimum; and the wind velocity was maximum. That is to say, the sea level rising depends on not only the incident waves but also the deviation of atmospheric pressure and the wind velocity. Therefore, to examine the wave set-up with the field data, we must take these factors into account at the same time in the analysis as follow;

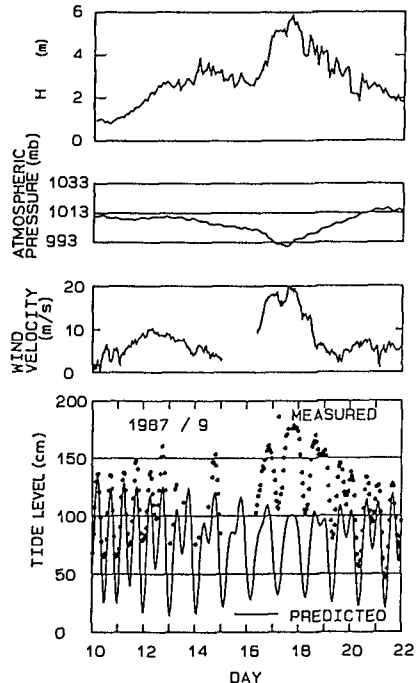


Figure 12 Sea level rising due to typhoon in 1987

$$\eta = f_1(\text{wave}) + f_2(\text{atmo. pressure}) + f_3(\text{wind}). \quad (1)$$

Concerning to the wave set-up due to the incident waves, the theoretical treatments had been developed since Longuet-Higgins and Stewart (1962) introduced the concept of radiation stress. In the early stage, the rate of wave set-up was expressed by only the wave height. In contrast to this, Goda(1975) theoretically investigated the effects of the beach slope and the offshore wave steepness on the wave set-up, based on his model of the random wave deformation in the surf zone.

Figure 13 shows the Goda's theory on the wave set-up for the sea bottom slopes of 1/50 and 1/100, by taking the non-dimensional wave set-up at the shoreline normalized by the offshore wave height on an ordinate and the offshore wave steepness on an abscissa. To introduce his theory into the

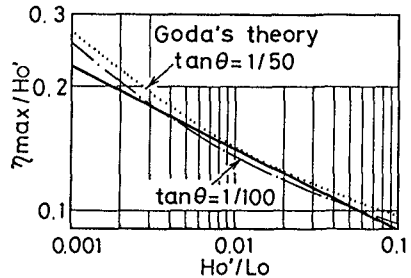


Figure 13 Goda's theory on wave set-up

analyses, let's inspect the natural conditions. The mean sea bottom slope at the observation site is about 1/60 as shown in Figure 2. The value of wave steepness distributes in the range from 0.005 to 0.047 for all wave data, and in the range from 0.01 to 0.047 for the waves greater than 2 meters in height as shown in Figure 6. Therefore, in this scope of conditions, the Goda's theory can be approximated by the straight line in the Figure 13. Taking only the inclination of this line into account, we have

$$f_1(\text{wave})/Ho' = a (Ho'/Lo)^{-0.2}, \quad (2)$$

where a is a coefficient, Ho' and Lo are the offshore wave height and wave length respectively.

As the deviation of atmospheric pressure, ΔP , induces the statistical rising of sea level, let's assume the following proportional relation between them;

$$f_2(\text{atmo. pressure}) = b \Delta P, \quad (3)$$

where b is a coefficient.

Since the shear stress exerted by wind on sea surface is proportional to the square of wind velocity, the relation

$$f_3(\text{wind}) = c U^2 \cos \theta \quad (4)$$

is usually assumed, where c is a coefficient, U is the wind velocity at the altitude of 10 meters above the sea surface, and θ is the wind direction (see Figure 7).

By substituting Eqs.(2), (3), and (4) into Eq.(1) and adding one more coefficient C , we have

$$\eta = a(Ho'^2 Lo^{1/2})^{0.4} + b \Delta P + c U^2 \cos \theta + C. \quad (5)$$

The physical units of the term in Eq.(5) follow the general customs, that is, cm for η , mb for ΔP , m/s for U , and m for Ho' and Lo .

Using the multiple regression analysis with 1305 sets of data, we decided the values of four coefficients as follows;

$$a=5.20(\text{cm/m}), b=0.69(\text{cm/mb}), c=0.04(\text{cm/m}^2/\text{s}^2), C=-4.85(\text{cm}). \quad (6)$$

By using Eq.(5) with the coefficients in Eq.(6), the total sea level risings have been calculated for 1305 cases. Furthermore, to have mean sea level, the predicted still water level (astronomical tide level) has been added to every total sea level rising. Figure 14 is a comparison of the measured sea level with the calculated one, by taking the abscissa for the calculated values. There is a close agreement between measured and calculated values, excepting that the measured sea levels are slightly higher than calculated one when the sea levels are low.

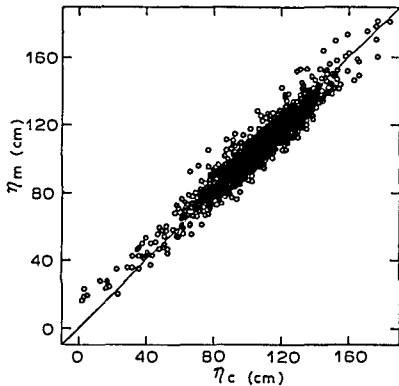


Figure 14 Comparison of measured sea level with calculated one

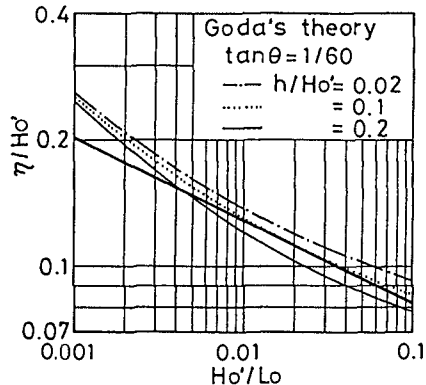


Figure 15 Comparison of Eq.(8) with Goda's theory

The exception is due to the reason that the observation point was shifted relatively to the onshore-side when the sea level was low, which induced the higher rate of wave set-up.

Now we have the empirical relation between the wave set-up and the wave characteristics, that is,

$$\eta_{\text{wave}} = 0.052(Ho'^2Lo^{1/2})^{0.4}, \tag{7}$$

or

$$\eta_{\text{wave}}/Ho' = 0.052(Ho'/Lo)^{-0.2}, \tag{8}$$

where η_{wave} is the rate of wave set-up near the shoreline. Please pay attention to the physical unit in these expression, that is to say, in meter.

Let's compare Eq.(8) with the Goda's theory in Figure 15. The solid straight line is Eq.(8). The three curved lines are the Goda's theory for the wave set-up rate at the non-dimensional water depth of 0.02, 0.1 and 0.2 respectively on the beach sloping of 1/60. In the storm, the range of non-dimensional water depth at the observation point was from 0.1 to 0.2 as shown in Figure 10, and the wave steepness distributes in the range from 0.01 to 0.047 as shown in Figure 6. Considering these conditions, there is a well agreement between Eq.(8) and the Goda's theory.

The interesting modification can be done by substituting the energy flux of incident wave in the offshore,

$$E_i = (\omega\rho)(g/2\pi)^{1/2}Ho'^2Lo^{1/2}, \tag{9}$$

into Eq.(7), where E_i is the wave energy flux and ω is the density of sea water. In short, the rate of wave set-up near the shoreline can be expressed with the incident

wave energy flux,

$$\eta_{\text{wave}} = 0.14 E_f. \quad (10)$$

Based on the empirical relation obtained, the contribution of each factor on the sea level rising has been estimated for 1305 cases and shown in Figure 16. For example, the level rising of about 80 cm occurred in eleven cases, in which the averaged wave set-up rate is 57 cm, the level rising due to the wind is about 9 cm, and that due to the atmospheric pressure is about 14 cm. According to this figure, the contribution of the wave set-up is predominant, which occupies about 75% portion of the total sea level rising.

5. Contribution of Other Factors on Sea Level Rising

So far, to explain the sea level rising, the waves, the atmospheric pressures, and the winds have been considered as the external forces in the regression analysis. As the result, the real sea level rising have been practically explained by these three factors as shown in Figure 14. There are, however, a little scatter in the plotted data in Figure 14, which may be due to not only the errors in measurements but also the other factors we did not considered. Figure 17 shows the difference between the measured sea levels and the calculated ones in a time series. If the measured and the calculated ones agree precisely, the data should lie in a zero line. The plotted

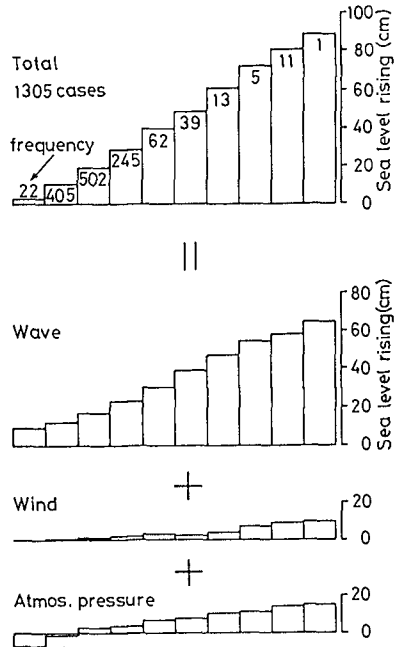


Figure 16 Contribution of wave on wave set-up

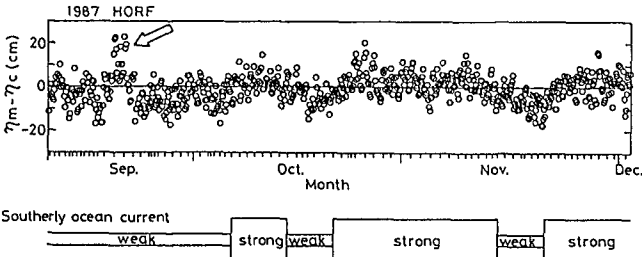


Figure 17 Difference between the mesured sea levels and calculated ones in a time series

data, however, scatter around the line. According to this figure, three items can be pointed out.

First, the data are scattered in a belt of about 15 cm in width. Although the observation point was fixed, the distance from the shoreline to the observation point changed with time since the shoreline position changed with the tide level, yielding the change of wave set-up rate. The tidal range in the site is about 1.4 meters, which introduces the fluctuation of about 13 cm in the wave set-up rate, according to the Goda's theory (see, Katoh et al., 1989). Therefore, it is considered that the data scattering in the belt is mainly due to the change of tide level.

Secondly, there is a large difference between the measured sea levels and the calculated ones, which is denoted by an arrow in Figure 17. In order to investigate the cause of it, it is necessary to inspect more precise data during these days. Figure 18 shows the changes of offshore wave height, wave period, and the measured and the calculated sea level rising during the corresponding days. The measured and the calculated rising change in the similar manner. There is, however, the time lag between them. That is to say, the change of actual sea level rising is 2 to 3 hours behind the calculated one in both the development and decrement of incident waves during the storm, which introduces the large difference on the day denoted by the arrow in Figure 17.

Thirdly, the belt, in which the plotted data are scattered, fluctuates with a period of about one month. To investigate this cause, the ocean currents must be considered since two ocean currents from the north (Oyashio) and from the south (Kuroshio) come across in the offshore area just in front of the observation site. When the Oyashio, the southerly ocean current, is relatively stronger as shown in Figure 19, the Corioli's force due to this current should raise the sea level near the coast. Then, we have inspected the weekly averaged patterns of these currents which are issued by Ibaraki Prefectural Fisheries Experimental Station every week (Figure 19 is an example). The strength of southerly ocean currents have been decided and shown in the lower in Figure

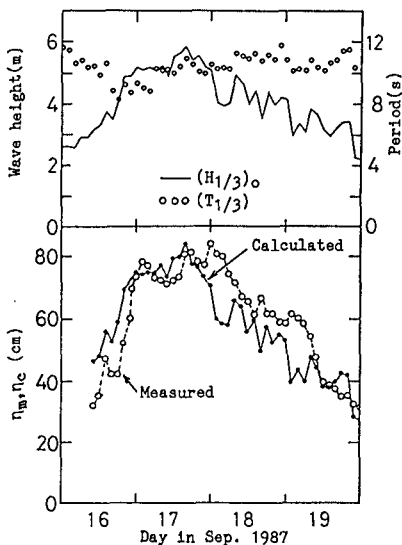


Figure 18 Time lag between measured set-up and calculated one

17. During the period when the southerly ocean current was strong, the measured sea levels were higher than the predicted ones, and vice versa. Then, it can be said that the long period fluctuation of the difference between the measured sea levels and the predicted ones are due to the changes of the Corioli's force which depends on the strength of southerly ocean current.

Next, the dependency of wave set-up on the offshore wave steepness will be examined. According to the Goda's theory, the wave set-up depends also on the offshore wave steepness. In order to confirm this dependency, we had selected the data which satisfy the following three criteria at the same time.

- (a) The offshore significant wave height is greater than 2 meters.
- (b) The non-dimensional water depth, h/H_0' , is less than 0.2, which is a condition to select the data measured close to the shoreline.
- (c) The absolute difference between the measured sea level and the predicted one is less than 5 cm, which is a condition to omit the data containing the unknown effects in it.

Figure 20 shows the comparison of the selected data with

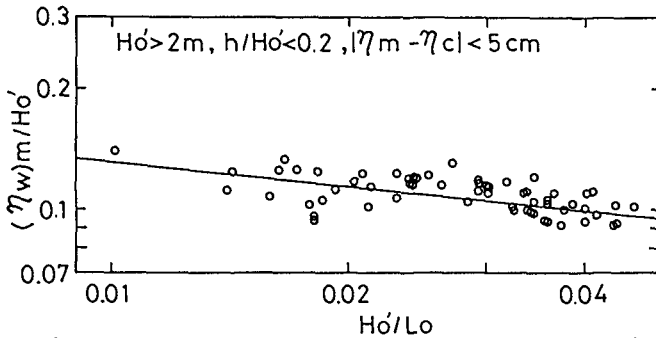


Figure 20 Effect of wave steepness on wave set-up

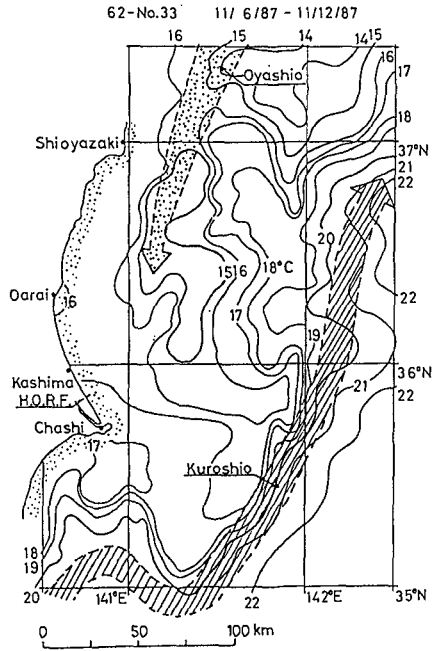


Figure 19 Pattern of ocean currents

the Goda's theory which is the straight line in the figure. The rate of wave set-up weakly depends on the offshore wave steepness. The non-dimensional wave set-up becomes to be slightly larger with decreasing of the wave steepness.

The dependency of wave set-up on the incident wave angle to the beach have not been examined, since the wave direction had not been measured.

6. Conclusions

The conclusions obtained in this study are as follows:

- (1) The wave set-up measured near the shoreline in the field strongly supports the Goda's theory.
- (2) The rate of wave set-up, which becomes to be larger with decreasing of the wave steepness, can be expressed with the incident wave energy in stead of wave height.
- (3) In total sea level rising, the contribution of the wave set-up is large, which occupies about 75% portion, while those of depression of atmospheric pressure and the winds are small.
- (4) There are other factors which slightly affect the sea level changing as follows:
 - a. The actual sea level rising (or changing) is 2 to 3 hours behind the development and decrement of incident waves during the storm.
 - b. The strength of ocean current velocity in Oyashio in the offshore area induces the sea level changing with the period of about one month.

References

- Bowen, A.J., D.L. Inman and V.P. Simmons (1968): Wave 'set-down' and set-up, Jour. of Geoph. Res., Vol.73, No.8, pp.2569-2577.
- Goda, Y. (1975): Deformation of irregular waves due to depth-controlled wave breaking, Rep. of PHRI, Vol.14, No.3, pp.59-106 (in Japanese, see Goda, 1985).
- Goda, Y. (1985): Random seas and design of maritime structures, University of Tokyo Press, 323p.
- Hansen, U.A. (1978): Wave setup and design water level, Jour. of Waterway Port and Ocean Div., ASCE, Vol.104, WW2, pp.227-240.
- Holman, R.A. (1986): Extreme value statistics for wave run-up on a natural beach, Coastal Engineering, Vol.9, pp.527-544.
- Katoh, K. et al. (1989): Wave set-up near the shoreline, Rep. of PHRI, Vol.28, No.1, pp.3-41 (in Japanese).
- Katoh, K. and S. Yanagishima (1990): Berm erosion due to long period waves, Proc. of 22nd ICCE.
- Longuet-Higgins, M.S. and R.W. Stewart (1962): Radiation stress and mass transport in gravity waves, with application to 'surf beat', Jour. of Fluid Mech., 13, pp.481-504.

CHAPTER 8

Modelling Shoaling Directional Wave Spectra in Shallow Water

James T. Kirby¹

Abstract

This paper describes the development of a model for the shoaling and refraction of an incident directional spectrum over beach topography. The present model is limited to topography which varies only in the on- offshore direction, but no restriction is made on allowed angles of incidence with respect to the shore-normal direction. The model is verified in comparison to laboratory data for Mach reflection of cnoidal waves from a vertical plane wall. It is shown that the model provides a more accurate representation of the evolving wave field than does an earlier parabolic approximation, using the same laboratory data.

Introduction

As ocean surface waves propagate towards shore, they pass through a shoaling zone prior to breaking in which nonlinear interactions become strong and can significantly modify the wave train. This zone is characterized by weak frequency dispersion, since waves become relatively long compared to local water depth. In addition, the weak dependence on wavelength in the wave phase speed leads to the occurrence of strong nonlinear interactions at second-order in wave height. The combined effects of weak dispersion and nonlinearity may be modelled by the Boussinesq equations, which serve as a reasonably accurate general purpose model for the domain in question as long as waves do not become too high.

Since the area being studied here can be quite extensive in comparison to the characteristic wavelength of the waves being modelled, the choice of an efficient numerical solution technique is crucial. The Boussinesq equations may be successfully solved by time-stepping techniques, but these methods are too inefficient for the spatial and temporal spans being considered in applications to an open coastal zone. Instead, various prior studies have found that it is efficient to decompose the time-dependent wave train into a stack of frequency components by Fourier decomposition, and then solve for the spatial evolution of each frequency mode. This is exactly the same kind of manipulation that is done in Fourier analysis of data, and is valid as long as the wave train satisfies the requirements for the transform to exist. In field applications, the Fourier decomposition into a finite set of discrete frequencies under the assumption of periodicity is exactly the same as applying an FFT to data. Assumptions about stationarity of the

¹Center for Applied Coastal Research, Department of Civil Engineering, University of Delaware, Newark, Delaware 19716

process are implicit and should be kept in mind when determining if the present approach is useful.

The solution for the spatial behavior of each frequency component is itself involved. A number of studies (Freilich and Guza, 1984; Elgar and Guza, 1985 and 1986 and subsequent contributions) have considered only the shoreward propagation in one space dimension, and have shown that the resulting one-dimensional, first-order coupled mode equations are capable of modelling the evolution of the spectrum and bispectrum of shoaling waves, as verified by comparison with field measurements. Liu, Yoon and Kirby (1985; referred to here as LYK) alternately proposed a parabolic model for the shoreward propagation of each frequency component over two-dimensional topography, and verified the method in comparison to a laboratory experiment on the focussing of periodic long waves by topography. The parabolic model approach has also been used to study a field application (Freilich et al, 1990), with successful results.

In this study, we derive a model for the evolution of each frequency mode in two dimensions, based on the angular spectrum approach. This approach has been applied to the study of intermediate depth waves by Dalrymple and Kirby (1988) and Dalrymple et al (1989). For the case of linear theory, the angular spectrum is usually posed as the continuous Fourier transform of the wave field in the longshore direction. Here, in keeping with the mental framework associated with the discrete transforms being employed in time, we impose longshore periodicity as well and obtain a discrete spectrum in longshore wavenumber. This frequency - longshore wavenumber spectrum is subsequently referred to as the *discrete angular spectrum*.

The model developed here is applicable both to simple periodic waves generated in the laboratory environment and to irregular, "random" waves in the field environment. In this paper, we concentrate on a model verification conducted from the first viewpoint. The model is tested against laboratory data obtained by Hammack, Scheffner and Segur (1990), who investigated the development of a Mach stem arising during the glancing-angle reflection of a cnoidal wave by a vertical wall. Results obtained using the parabolic equation model described in LYK are also compared to data. (The case of Mach reflection of a cnoidal wave has been studied using the parabolic approximation by Yoon and Liu (1989); however, no comparison to data was provided in that study.) The spectral model is shown to give a more accurate representation of the data than the parabolic model over the entire range of angles of incidence considered.

The Boussinesq Equation Model

We first establish the form of a model for waves in a laterally unrestricted domain. A Cartesian coordinate system is adopted which has x pointed in the onshore direction and y pointing alongshore. Depth is assumed to vary as $h(x)$ only. We take as a starting point the variable depth Boussinesq equations as given by Peregrine (1967):

$$\eta_t + \nabla \cdot (h\mathbf{u}) + (\epsilon)\nabla \cdot (\eta\mathbf{u}) = 0 \quad (1)$$

$$\mathbf{u}_t + (\epsilon)\mathbf{u} \cdot \nabla \mathbf{u} + g\nabla\eta = (\mu^2)\left\{\frac{h}{2}\nabla(\nabla \cdot (h\mathbf{u}_t)) - \frac{h^2}{6}\nabla(\nabla \cdot \mathbf{u}_t)\right\} \quad (2)$$

Here, η is the surface displacement and \mathbf{u} is the horizontal wave-induced velocity. The equations are kept in dimensional form; the scaling parameters $\epsilon = \max(\eta)/h$ for nonlinearity and $\mu^2 = \omega^2 h/g$ for weak dispersion are present only schematically and will be subsequently dropped. We will assume that either bottom slope

or the amplitude of bottom features (as scaled by water depth) are also small and hence the model will be developed to leading order in nonlinearity, dispersion, and domain inhomogeneity. This leads to immediate neglect of bottom slope effects in the dispersive terms of (2). Using the linear portion of (1), we may then write (2) in the reduced form

$$\mathbf{u}_t + \mathbf{u} \cdot \nabla \mathbf{u} + g \nabla \eta + \frac{h}{3} \nabla \eta_{tt} = 0. \quad (3)$$

We now make the following assumptions. First, the model will be applied to time-periodic wave trains, where periodicity is in the sense of either a regular wave train, or of a discrete FFT over a finite length of sampled data. Secondly, the wave field will be assumed to be periodic in the transverse y direction. This corresponds again to a fixed longshore wavelength in the regular wave case, or to periodicity over a long spatial interval in the spectral sense.

The governing equations are first split into coupled elliptic models for separate harmonic components. Following LYK, we write the surface displacement and velocity as

$$\eta = \sum_{n=0}^N \frac{\eta_n(x, y)}{2} e^{-in\omega t} + c.c. \quad (4)$$

$$\mathbf{u} = \sum_{n=0}^N \frac{\mathbf{u}_n(x, y)}{2} e^{-in\omega t} + c.c. \quad (5)$$

Substitution of (4) and (5) in (1) and (3) and subsequent elimination of the velocity leads to the following model equation for the η_n in the horizontal plane:

$$n^2 \omega^2 \eta_n + \nabla \cdot (G_n \nabla \eta_n) + [n.l.t.]_n = 0; \quad n = 1, \dots, N \quad (6)$$

Here, $[n.l.t.]_n$ denotes the nonlinear interactions with other discrete frequency components which are sorted by means of the rules for triad interactions applied to the time dependence. (Omitted details may be found in the more complete paper; Kirby (1990).) The mode $n = 0$ corresponding to the steady, wave-induced setdown is neglected since it is at most second order in the largest wave amplitudes present (see LYK). Also,

$$G_n(x) = gh(x) - \frac{1}{3} n^2 \omega^2 h^2(x). \quad (7)$$

We now apply a spectral transform to the y dependence of the wavefield, assuming propagation is to be considered in the on-offshore ($\pm x$) direction. We consider here the case of an unbounded lateral domain and a wavefield which is periodic over the basic interval L . We then represent $\eta_n(x, y)$ as

$$\eta_n(x, y) = \sum_{m=-M}^M \eta_n^m(x) e^{im\lambda_0 y} \quad (8)$$

where

$$\lambda_0 = \frac{2\pi}{L}. \quad (9)$$

Substituting (8) in (6) and neglecting x - derivatives of small terms in G_n then leads to a set of coupled second-order ODE's for the η_n^m , given by

$$\frac{G_n}{gh} \eta_{n,xx}^m + \frac{h_x}{h} \eta_{n,x}^m + (\gamma_n^m)^2 \eta_n^m + \frac{1}{3} m^2 n^2 \lambda_0^2 k^2 h^2 \eta_n^m + \frac{1}{gh} [n.l.t.]_n^m = 0; \quad (10)$$

$$n = 1, \dots, N; \quad m = -M, \dots, M.$$

where $[n.l.t.]_n^m$ now represents triad interactions satisfying resonance conditions in t and y . Here, k is the wavenumber determined by the lowest order dispersion relation

$$\omega^2 = gk^2 h. \quad (11)$$

Also,

$$(\gamma_n^m)^2 = n^2 k^2 - m^2 \lambda_0^2 \quad (12)$$

For fixed n, k, λ_0 , large values of m will make γ_n^m imaginary, which corresponds to modes which are exponential rather than oscillatory in x in the linear approximation. In the linear case, the presence of these modes in the initial conditions would be interpreted in the same light as the presence of evanescent modes in the general wavemaker problem (see Dalrymple and Kirby, 1988). However, the interpretation in the case of possible nonlinear forcing of the offshore portion of trapped modes in the nearshore region is non-trivial and will need to be considered carefully in applications where the inclusion of this effect is desired. In addition, nonlinearity could force the propagation of modes that would not be present in a linearized wave field, and which could affect a detailed representation of an individual wave. At present, the range of M at each value of n may be restricted to $M_n \leq nk/\lambda_0$ in order to eliminate forcing of these modes arbitrarily.

Shoaling Waves

Based on the linear, nondispersive portion of the model (10), we assume that the incident wave may be written in the form

$$\eta_n^m(x) = A_n^m(x) e^{in \int k \tilde{\gamma}_n^m dx} \quad (13)$$

where it is assumed that the x dependence of A , k and $\tilde{\gamma}$ is on a slow scale of $O(\epsilon)$, and where

$$\tilde{\gamma}_n^m = \left(1 - \left(\frac{m}{n}\right)^2 \left(\frac{\lambda_0}{k}\right)^2\right)^{1/2} = \frac{\gamma_n^m}{nk} \quad (14)$$

(where the positive root is taken). The amplitudes A represent the discrete angular spectrum being considered here, and are allowed to vary owing to refraction, shoaling, dispersion and nonlinear interaction. (It would be possible to absorb shoaling and refraction effects by the use of the usual linear refraction formulae; this step is not taken here.) Substitution of (13) in (10) leads to the spectral model for incident waves, given by

$$\tilde{\gamma}_n^m A_{n,x}^m + \frac{(kh\tilde{\gamma}_n^m)_x}{2kh} A_n^m - \frac{1}{6} in^3 k^3 h^2 A_n^m + \frac{ink}{8h} \left\{ \sum_{l=1}^{n-1} \sum_{p=P_1}^{P_2} \Gamma_{n,l}^{m,p} A_l^p A_{n-l}^{m-p} e^i \int \Theta_{n,l}^{m,p} dx \right. \\ \left. + 2 \sum_{l=1}^{N-n} \sum_{p=P_3}^{P_4} \Gamma_{n,l}^{m,p} A_l^{p*} A_{n+l}^{m+p} e^i \int \Upsilon_{n,l}^{m,p} dx \right\} = 0; \quad (15)$$

$$n = 1, \dots, N; \quad m = -M_n, \dots, M_n.$$

Here, $(\cdot)^*$ denotes the complex conjugate. The limits of summation $P_1 - P_4$ are determined by the range of allowed modes taking part in each interaction. The interaction coefficients I and J are given by

$$I_{n,l}^{m,p} = 1 + [\tilde{\gamma}_l^p \tilde{\gamma}_{n-l}^{m-p} + \frac{p}{l} \frac{m-p}{n-l} (\frac{\lambda_0}{k})^2] \cdot [1 + (\frac{m}{n})^2 (\frac{\lambda_0}{k})^2 + \frac{(l\tilde{\gamma}_l^p + (n-l)\tilde{\gamma}_{n-l}^{m-p})^2}{n^2}] \quad (16)$$

$$J_{n,l}^{m,p} = I_{n,-l}^{m,-p}. \quad (17)$$

The phase arguments Θ and Υ represent the basic mismatch in the x direction of the triads chosen based on perfect matching in y and t . Generally, the only components which experience complete resonance in the long wave limit must have parallel propagation directions; all obliquely interacting components are somewhat detuned. The phase arguments are given by

$$\Theta_{n,l}^{m,p} = lk\tilde{\gamma}_l^p + (n-l)k\tilde{\gamma}_{n-l}^{m-p} - nk\tilde{\gamma}_n^m \quad (18)$$

$$\Upsilon_{n,l}^{m,p} = \Theta_{n,-l}^{m,-p} \quad (19)$$

The spectral model (15) is a set of coupled first order ODE's which are solvable by standard techniques. Results presented in sections 4 and 5 were obtained using a standard 4th-order Runge-Kutta scheme with fixed step size and no error checking. Presently, extensions of the model using error control and adaptive step size are being tested and will likely be the vehicle for further field testing of the model beyond the scope of the present study.

Comparison with Data and a Parabolic Model Approximation

In order to verify the basic computational model provided by (15) and to test whether the present angular spectrum provides a more accurate representation of the wave field relative to earlier parabolic models (LYK; Yoon and Liu, 1989), we have compared model predictions to laboratory data obtained by Hammack et al (1990) for the case of glancing, or Mach, reflection of a cnoidal wave by a vertical wall. The experimental tests were conducted using the directional wave maker at the Coastal Engineering Research Center, Vicksburg, MS. A prior use of this facility to study the properties of intersecting cnoidal waves is described in Hammack et al (1989), referred to here as HSS.

Layout of Experimental Facility

For the tests considered here, the wave basin was operated with a water depth of 20cm in a constant depth region extending 12.55m in front of the wavemaker, after which a beach with 1:30 slope provided an efficient wave absorber giving little reflection. The basin floor was leveled to a tolerance of 0.01ft in order to remove some of the spatial irregularity of the waves reported in HSS resulting from local refraction effects. For the Mach stem tests, two parallel false walls were installed perpendicular to the wavemaker axis in order to provide a closed channel. The channel walls were situated 13.26m apart, which fixes the width of the numerical domain to be considered.

Instrumentation and data acquisition are described in HSS, and readers are referred there for greater detail. In the present tests, an array of 18 wave gages

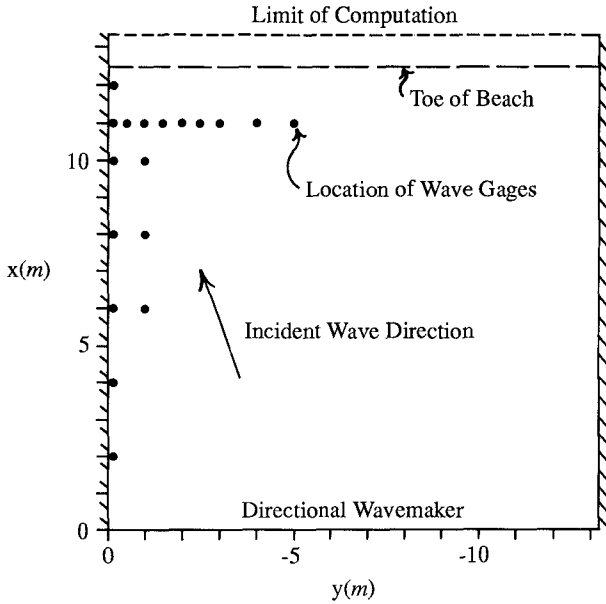


Figure 1: Basin configuration, Mach reflection experiments

were installed in the basin as shown in Figure 1. In this figure, the directional wavemaker occupies the y -axis, and the channel sidewalls lie along the x -axis and the line $y = -13.26m$. The positions of the gages are given in Table 1. The linear gage array 13-9-8-7-6-4-3-2-1 provides a transect perpendicular to the reflecting sidewall which allows a determination of the width and structure of the Mach stem and additional crests in the reflection pattern. This array is used to provide most of the information described below. An additional array 18-17-16-15-14-13-5 provides measurements of the evolution of the reflected stem wave along the wall. For each gage, data consists of a time series of 1250 points with a sampling rate of $25Hz$.

gage	$x(m)$	$y(m)$	gage	$x(m)$	$y(m)$	gage	$x(m)$	$y(m)$
1	11	-5	7	11	-1.5	13	11	-0.07
2	11	-4	8	11	-1	14	10	-0.07
3	11	-3	9	11	-0.5	15	8	-0.07
4	11	-2.5	10	8	-1	16	6	-0.07
5	12	-0.07	11	6	-1	17	4	-0.07
6	11	-2	12	10	-1	18	2	-0.07

Table 1: Wave gage positions in Mach reflection experiments

test	CR15	CR22	CR30	CR38	CR48	CR58
α	14.5	22.0	30.0	38.5	47.5	57.6
β	10.13	15.48	21.34	27.84	35.18	44.32

Table 2: Paddle phase angles and directed wave angles; Mach reflection experiments

Specification of the Incident Wave

The generation of oblique cnoidal waves using the directional wavemaker has been described in HSS. In the present laboratory tests, waves were initially specified as having a wavelength of $2m$ and a crest elevation $4cm$ above mean water level. The algorithms given by Goring and Raichlen (1980) were used to generate a time series of paddle displacement corresponding to one-dimensional generation. Oblique waves were then generated by phase lagging adjacent paddles. The relation between paddle phase shift angle β and directed wave angle α is given by

$$\beta = \arcsin(\alpha L/360W) \quad (20)$$

where L is the wave length and $W = 45cm$ is the individual paddle width. Tests were conducted for six paddle phase lags, and are denoted $CRxx0204$, where xx denotes paddle phase lag. Note that (48) corrects a typographic error appearing in HSS. Table 2 gives a list of α and β values for the six tests.

Prior to running the Mach reflection experiments, the nominally $4cm$ high wave was generated in the normally incident direction (traveling parallel to sidewalls) in order to study its characteristics. It was found that the wave actually had a crest elevation close to $3.3cm$ above mean water level. This value was used to specify incident waves in the numerical computation, along with a wave period of $1.478s$ as specified by KdV cnoidal wave theory. We note that it is uncertain whether the value of $3.3cm$ was invariant under changes of angle of incidence in the laboratory experiment. Variation of this quantity would add an untraceable source of error in model-data comparison.

The computed wave angle and the Fourier coefficients for the input cnoidal wave were used to compute the surface displacement for oblique cnoidal waves along the boundary $x = 0m$ corresponding to the wavemaker. For parabolic model calculations, information in the range $-13.26m \leq y \leq 0m$ was used to start the computation. The model was run with reflective sidewalls at $y = 0, -13.26m$. For the spectral model, a periodic interval was constructed by using a mirror image about $y = 0m$; the computational domain thus corresponds to the region $-13.26m \leq y \leq 13.26m$. The computed waveform was then Fourier transformed over this interval and the resulting frequency-wavenumber spectrum was fed into the spectral model. (It is noted that the problem as stated could be handled directly by means of a cosine transform over the true model domain; this was not done because of the reprogramming of the basic model that would have been required.)

For the examples shown here, the parabolic model was run with a grid spacing $\Delta x = \Delta y = 0.0625m$, and $N = 9$ frequency components were used. Tests were performed for two cases for both half the grid spacing and twice the number of harmonics to insure that convergence was adequate for the parameters finally used. In the spectral model, we used $N = 9$ and $M = 64$. The large value of M insures that all freely propagating modes of the solution are retained for the highest harmonic considered. The forward grid space step was also $\Delta x = 0.0625m$. Again, these parameters were found to give sufficient convergence of solutions

when compared to runs with smaller grid steps and more retained frequency components.

Results

Results of model calculations are presented here in two forms: gray level contour plots of instantaneous surface over the model basin, and time series computed from model output and compared to experimental data. The gray level plots are actually of the quantity $-\partial\eta/\partial x$, and the pictures thus mimic the visual image that would be obtained in an overhead photograph resulting from lighting at a low angle from the direction of the wavemaker. (This is similar to the photographic arrangement in HSS). In all cases, the gray level plots from parabolic model computations are similar to those from spectral model computations, and only spectral model results are shown. Figure 2 presents results for the test CR150204, which clearly shows the evolution of a wide Mach stem wave along the reflecting boundary. In contrast, the wave field for test CR580204, where the angle of incidence is about 45° , exhibits almost a regular (i.e., linear) reflection pattern consisting of superposed waves (Figure 3).

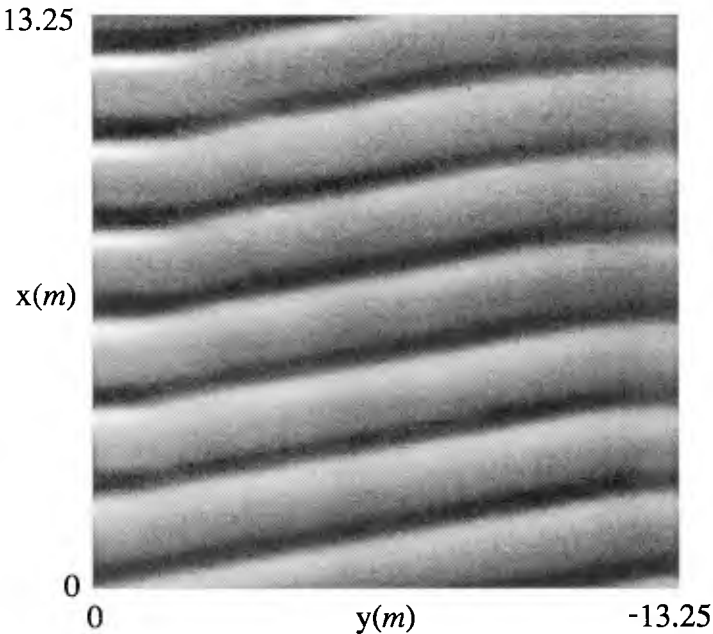


Figure 2: Predicted wave field, test CR150204. Spectral model

In order to compare time series from experiment and model calculations, the

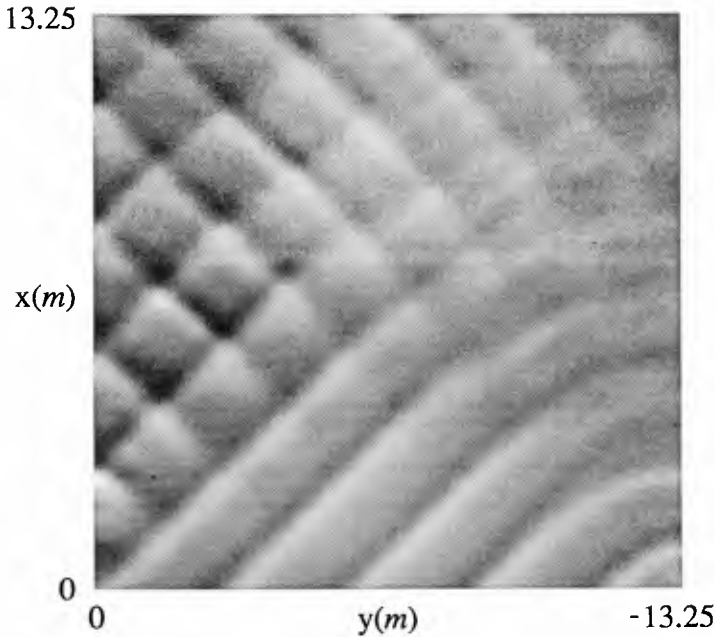


Figure 3: Predicted wave field, test CR580204. Spectral model

following procedure is used. First, after allowing some time for nearly periodic motion to be established in the experiment, a reference time t_0 is established at the position of a wave crest at gage 13 ($x = 11m, y = -0.07m$). This start time is used for all other gages as well, in order to maintain synchronization. Then, a start time is also established for the model- predicted time series by identifying a crest at model gage 13. Synchronization between model and data time series is thus based on correlating the series at a gage location, rather than (more correctly) correlating at the wavemaker. This step is necessary since the wavemaker control is not available and since absolute time in the model-constructed time series is arbitrary.

After determining the synchronous start times for model and data at gage 13, time series were plotted for the transect along the wall (gages 18-17-16-15-14-13-5) and perpendicular to the wall (gages 13-9-8-7-6-4-3-2-1). Aside from the presence of experimental errors, a correct model result would be indicated by complete agreement between model and data time series at each gage. As examples, two periods of time series for the perpendicular transect are shown in Figure 4 for the spectral model predictions for CR150204. The plot shows a stem developed near the wall in the area spanned by gages 13-9-8-7, beyond which there is a clear phase lead at each subsequent gage, indicating the approach of

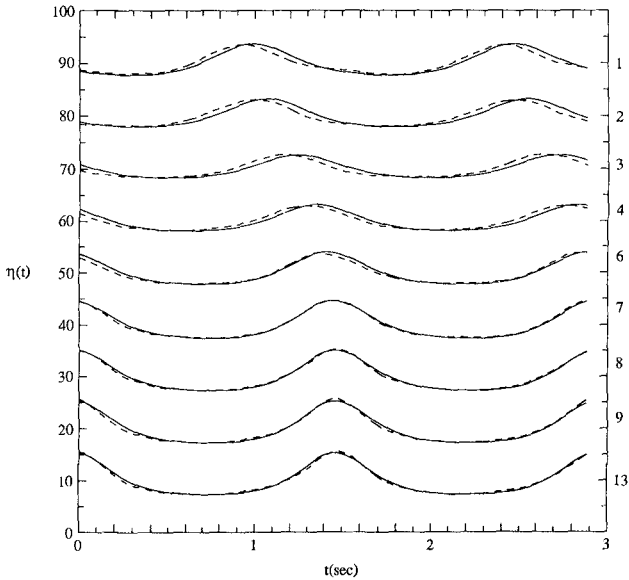


Figure 4: Measured and predicted time series for test CR150204, perpendicular transect. —, model; ---, data. Spectral model

the incident wave at a small angle of incidence. In this plot, model predictions are indicated by solid lines and experimental data by dashed lines. At the opposite extreme, Figure 5 shows spectral model predictions and data for the case CR580204. This figure indicates the structure of a short crested wave field, with one complete diamond over the range of gages 13-9-8-7-6-4-3, whereas the signal in gages 3-2-1 indicating a strong progressive phase lag, corresponding to a wave travelling *away from* the wall at close to 45° . The structure of the plots in Figures 4 and 5 may be further clarified by comparison with the surface plots in Figures 2 and 3, respectively.

In order to quantify the comparison between model predictions and measurements, an rms error measure was constructed. This measure e is given by

$$e_j = \sqrt{\frac{\frac{1}{j} \sum_{i=1}^j (\eta_{2,j}(i) - \eta_{1,j}(i))^2}{\frac{1}{j} \sum_{i=1}^j (\eta_{1,j}(i))^2}} \quad (21)$$

for each gage, where the normalization of the mean square error is with respect to the true (data) standard deviation. A composite value \bar{e} for each angle or test is constructed from the ratio of the rms error for all points divided by the total

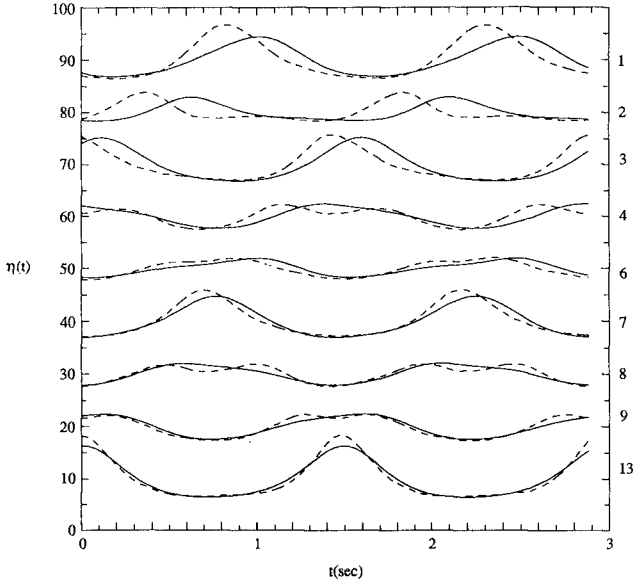


Figure 5: Measured and predicted time series for test CR580204, perpendicular transect. —, model; ---, data. Spectral model

standard deviation for all points. Table 3 gives the computed error estimates for all tests, and Figure 6 shows the composite error as a function of incidence angle for the two models. In this case, the trend towards increasing error with increasing angle is clear in the parabolic model results. The spectral model also shows an increasing trend in this case, which would not necessarily be expected.

One possible reason for an increase in error in the spectral model as wave angle becomes large rests in the fact that the reflected wave crests at the wall and in the short-crested wave pattern away from the wall result from the interaction between waves that are colliding head on to the same extent as they are interacting colinearly. Tests and analysis of head on collision and vertical wall reflection of solitary waves have indicated that the leading order theory (as in the Boussinesq model employed here) is not capable of predicting the height of the runup or maximum elevation, or the phase lag associated with the opposite-going interaction. See Su and Mirie (1980) for an example of this type of analysis. Effects of this nature may be present in the experiments being considered here. It is also possible that the increase in error with incidence angle in the spectral model is due to a change in the incident wave height with angle, as mentioned above. This error, if present, would tend to increase the wave height with angle,

spectral model										
gage	13	9	8	7	6	4	3	2	1	average
CR15	.089	.109	.078	.076	.177	.296	.386	.349	.285	.193
CR22	.228	.292	.281	.305	.326	.496	.346	.148	.526	.296
CR30	.208	.234	.168	.214	1.250	.306	.317	.124	.196	.250
CR38	.276	.535	.578	1.060	.206	.275	.442	.520	.190	.383
CR48	.128	.137	.636	.206	.216	.524	.953	.162	.124	.273
CR58	.194	.277	.479	.293	.540	.717	.631	1.280	.612	.540
parabolic model										
gage	13	9	8	7	6	4	3	2	1	average
CR15	.113	.132	.093	.103	.327	.600	.713	.503	.422	.319
CR22	.191	.326	.407	.556	.916	1.240	.678	.370	1.020	.509
CR30	.242	.225	.418	.597	1.975	.386	.231	.690	.333	.365
CR38	.211	.324	.706	1.936	.430	.550	.612	.713	.489	.494
CR48	.513	.743	1.911	.473	.398	.799	1.425	.476	.598	.599
CR58	.261	.534	1.099	.969	1.611	.630	.672	.697	.515	.689

Table 3: RMS error coefficients $\bar{\epsilon}$ for spectral and parabolic model runs

contributing to the deviation between model results and data in the expected way.

Discussion

We have described the development of a solution technique for the Boussinesq model of long waves, based on a discrete representation of the angular spectrum for waves incident towards shore from the ocean. The model is similar in intent to the parabolic model developed earlier by LYK, with the exception that the present model does not impose a restriction on the range of directions that can be accurately modelled. This advantage is counterbalanced (at this stage of development) by the need to impose periodic boundary conditions on the modelled problem. This restriction must be alleviated before the various representations of angular spectrum models (present model; Dalrymple and Kirby, 1988; Dalrymple et al, 1989) become generally applicable as coastal wave models.

Comparison of the present model, a parabolic model and laboratory data indicates that differences do occur between predictions of a small-angle approximation and the fully directional expansion employed here, and that the deviation is apparent even at small angles of incidence. This result indicates that the further development of the angular spectrum model is worth pursuing as a means of providing accurate prediction of coastal wave fields. The first extension of the present model to include weak longshore topographic variation and on-offshore reflection is presently underway and will be described shortly.

Acknowledgements

The author would like to thank the Office of Naval Research for support for this study through grants N00014-89-J-1717 and N00014-90-J-1678, and Joe Hammack, Norm Scheffner and Harvey Segur for their very generous donation of experimental data prior to their own analysis or publication of it. James Kai-

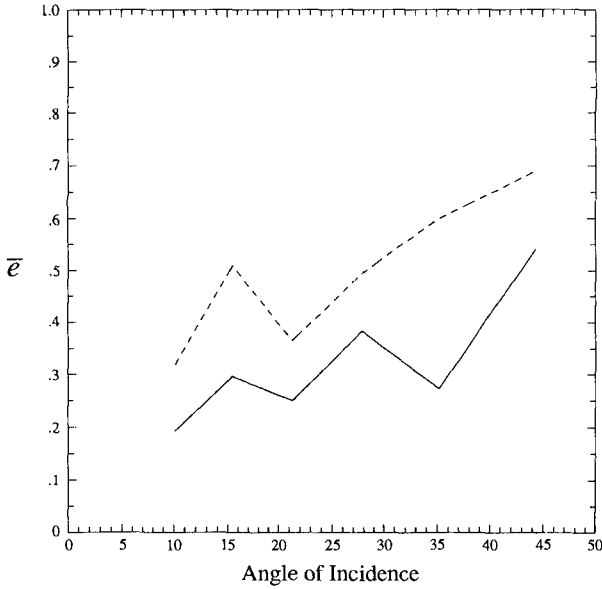


Figure 6: Variation of overall normalized error \bar{e} with angle of incidence β . —, spectral model; - - -, parabolic model.

hatu performed the parabolic model computations and the parabolic model - data comparisons.

Appendix A: References

- Dalrymple, R.A. and Kirby, J.T., 1988, "Models for very wide-angle water waves and wave diffraction", *J. Fluid Mech.*, 192, 33-50.
- Dalrymple, R.A., Suh, K. D., Kirby, J.T. and Chae, J. W., 1989, "Models for very wide-angle water waves and wave diffraction. Part 2. Irregular bathymetry", *J. Fluid Mech.*, 201, 299-322.
- Elgar, S. and Guza, R.T., 1985, "Shoaling gravity waves: comparisons between field observations, linear theory, and a nonlinear model", *J. Fluid Mech.*, 158, 47-70.
- Elgar, S. and Guza, R.T., 1986, "Nonlinear model predictions of bispectra of shoaling surface gravity waves", *J. Fluid Mech.*, 167, 1-18.

- Freilich, M.H. and Guza, R.T., 1984, "Nonlinear effects on shoaling surface gravity waves", *Phil. Trans. Roy. Soc. Lond.*, A 31, 1-41.
- Freilich, M.H., Guza, R.T. and Elgar, S., 1990b, personal communication.
- Goring, D.G. and Raichlen, F., 1980, "The generation of long waves in the laboratory", *Proc. 17th Intl. Conf. Coastal Engrng.*, Sydney.
- Hammack, J., Scheffner, N. and Segur, H., 1989, "Two-dimensional periodic waves in shallow water", *J. Fluid Mech.* 209, 567-589. (referred to in the text as HSS).
- Hammack, J., Scheffner, N. and Segur, H., 1990, personal communication.
- Kirby, J. T., "A discrete angular spectrum model for nonlinear shallow water waves. Part 1. Waves in laterally uniform domains," submitted to *Journal of Fluid Mechanics*.
- Kirby, J. T., 1990, "Intercomparison of truncated series solutions for shallow water waves", submitted to *J. Waterway, Port, Coastal and Ocean Engrng.*
- Liu, P.L-F., Yoon, S.B. and Kirby, J.T., 1985, "Nonlinear refraction- diffraction of waves in shallow water", *J. Fluid Mech.*, 153, 185-201. (referred to in the text as LYK)
- Peregrine, D.H., 1967, "Long waves on a beach", *J. Fluid Mech.*, 27, 815-827.
- Su, C. H. and Mirie, R. M., 1980, "On head-on collisions between two solitary waves", *J. Fluid Mech.*, 98, 509-525.
- Yoon, S. B. and Liu, P. L.-F., 1989, "Stem waves along a breakwater", *J. Waterway, Port, Coast. and Ocean Engrng.*, 115, 635-648.

CHAPTER 9

MODELING OF ENERGY TRANSFER AND UNDERTOW IN THE SURF ZONE

Akio Okayasu¹, Akira Watanabe² and Masahiko Isobe³

Abstract

A model is presented to describe accurately the energy transfer under breaking waves. In the model, the energy of organized large vortexes as well as those of wave-induced motion and turbulence is taken into account. The model allows to estimate the dissipation rate and distribution of energy, and then the cross-shore two-dimensional distribution of an undertow. The applicability of the model is confirmed by laboratory experiments.

1. Introduction

In order to predict the sediment transport and the material diffusion in the surf zone, it is necessary to estimate the distribution of an undertow. Since the undertow distribution has been evaluated from local properties of waves and turbulence in most of previous models, additional models are needed to evaluate the local properties from incident wave conditions. These undertow models have another disadvantage that they are applicable only to wave breaking in the inner region of the surf zone. Hence, to complete an undertow model which is valid through the whole surf zone, it is necessary to combine it with an accurate description of wave attenuation, energy distributions or generation of turbulence based on the actual breaking mechanism. However, energy of the organized vortexes which were pointed out to be formed around crests of breaking waves was not taken into account in the previous models for wave deformation in the surf zone.

The first objective of the present study is to describe accurately the energy transfer process in the surf zone by taking the energy of the organized

¹ Research Associate, Department of Civil Engineering, Yokohama National University, Hodogaya-ku, Yokohama 240, Japan

² Professor, Department of Civil Engineering, University of Tokyo, Bunkyo-ku, Tokyo 113, Japan

³ Associate Professor, ditto

large vortexes into account. The second objective is to formulate a model to estimate cross-shore vertically two-dimensional distribution of the undertow on arbitrary beach topographies from the energy distributions obtained by the energy transfer model.

2. Energy Transfer Model

2.1 Energy balance in the surf zone

In order to describe the transfer of energy by wave breaking, a model is presented in which the organized large vortexes are taken into account as a transmitter of energy in the energy transfer process from wave motion to turbulence. The total energy in the surf zone is described as

$$E_t = E_w + E_v \quad (1)$$

where E_t is the total energy of wave per unit area, E_w the energy of wave motion and E_v the energy of organized large vortexes.

The energy of the organized vortexes converted from wave energy is transferred to smaller size eddies, and then dissipates. It is assumed that the converted energy from wave motion to the large vortexes never transferred back to the wave motion and the energy which dissipates directly from the wave motion to heat by wave breaking is negligible. By using the energy flux by wave motion $E_w c_g$ and energy dissipation rate by bottom and wall friction D_{b+w} , the transfer rate T_B from the wave energy to the energy of the vortexes per unit length and unit width is expressed as

$$T_B = -\frac{d(E_w c_g)}{dx} - D_{b+w} \quad (2)$$

where x is the horizontal coordinate in the shoreward direction and c_g is the group velocity of waves. It is considered that D_{b+w} directly dissipates without conversion through the large vortexes and is not negligible for wave propagation in wave flumes.

The organized large vortexes propagate with the wave crests. Since the phase velocity c is nearly equals to the group velocity c_g in the surf zone, the energy flux by the large vortexes can be approximated by $E_v c_g$, which satisfies the following equation:

$$\frac{d(E_v c_g)}{dx} = T_B - D_B \quad (3)$$

where D_B is the dissipation rate per unit area through turbulence by wave breaking. Since the energy once transferred from wave motion to the organized vortexes is kept by the vortexes for a while, difference appears in the spatial distributions between the attenuation of wave energy E_w and the generation of turbulence energy.

2.2 Mass and momentum fluxes by breaking waves

The mass transport by breaking waves consists of those by the wave motion M_w and by the organized vortexes M_v [Okayasu *et al.* (1988)]. By using the linear long wave theory, the mass flux by the wave motion M_w is described as

$$M_w = \rho \frac{c}{h} \overline{(\zeta - \bar{\zeta})^2} = \frac{2c}{gh} E_p \quad (4)$$

where h is the mean water depth, ζ the water surface elevation and E_p the potential energy of waves.

If the length and velocity scales of the organized vortexes can be represented by the wave height H and the wave celerity c , respectively, the mass flux by organized vortexes M_v satisfies

$$M_v \propto \frac{E_v}{c} \quad (5)$$

The total mass flux due to breaking waves can be described in terms of the potential energy and the energy of organized large vortexes as

$$M_t = 1.6 \frac{c}{gh} E_p + \frac{2}{c} E_v \quad (6)$$

in which the coefficients were determined so as to fit the measured values.

As for the radiation stress, the total radiation stress S_t can also be divided into two parts which are the excess momentum flux by wave motion S_w and that by the organized large vortexes S_v . The small amplitude wave theory is adopted for convenience to calculate S_w in this study. The radiation stress by the organized large vortexes S_v is evaluated as

$$S_v = \frac{5}{3} E_v \quad (7)$$

3. Estimation of Energy Distribution

In the present model, the one dimensional time-dependent mild slope equation is adopted to calculate the distribution of the energy of wave motion E_w . The energy of organized large vortexes E_v supplied from E_w at a certain point is assumed to be transferred to the turbulence energy within some distance determined in terms of the local water depth. The energy dissipation rate D_B is obtained by integrating the transferred energy.

3.1 Estimation of energy of wave motion

The time-dependent mild slope equation was originally derived by using the small amplitude wave theory. However, waves in the surf zone can no more be regarded as small amplitude waves. In that sense, the time-dependent mild

slope equation may not be appropriate for waves in the surf zone, but it is also a fact that there is no wave theory which can express the waves in the surf zone adequately. It has been reported that the wave energy calculated by the time-dependent mild slope equation fits well with the measured wave energy [see e.g. Watanabe and Dibajnia (1988)]. Hence, in this study, the time-dependent mild slope equation is adopted as the governing equations to estimate the wave energy variation in the surf zone.

The following time-dependent mild slope equation with the dissipation term is used after Watanabe and Dibajnia (1988):

$$\frac{\partial Q}{\partial t} + c^2 \frac{\partial \zeta}{\partial x} + f_A Q = 0 \quad (8)$$

$$\frac{\partial \zeta}{\partial t} + \frac{1}{n} \frac{\partial(nQ)}{\partial x} = 0 \quad (9)$$

in which t is the time, Q the flow rate, $n = c_g/c$. The attenuation factor f_A by wave breaking is the sum of f_T and f_{b+w} , where f_T is the energy transfer factor from wave motion to large vortexes and f_{b+w} the energy dissipation factor due to energy loss by bottom and wall friction. f_T is expressed as

$$f_T = \alpha_T \tan \beta \sqrt{\frac{g}{h} \left(\frac{\gamma - \gamma_r}{\gamma_s - \gamma_r} \right)} \quad (10)$$

which was given by Watanabe and Dibajnia. In Eq. (10), α_T is a parameter which linearly increases from 0 to 2.5 around the breaking point, then takes a constant value 2.5 in the inner region. The bottom slope $\tan \beta$ is the average value of the bottom slope near the breaking point, g the acceleration of gravity, γ the ratio of water particle velocity to wave celerity. The symbols γ_s and γ_r are γ on constant slope and for wave recovery zone, respectively. The energy dissipation factor f_{b+w} is obtained from the laminar solution by Iwagaki and Tsuchiya (1966) as

$$f_{b+w} = \frac{1}{n} \sqrt{2\nu\sigma} \left(\frac{1}{B} + \frac{k}{\sinh 2kh} \right) \quad (11)$$

where ν is the kinematic viscosity, σ angular frequency of wave, k the wave number, B the width of wave flume. In the surf zone, the bottom and wall boundary layers may not be laminar flow, but the dissipation by wave breaking is so large that the damping due to the bottom and wall friction is negligible.

The breaking point x_b is determined as the point where the wave height takes its maximum value. Isobe (1987) approximated it by the following formula:

$$\begin{aligned} \gamma_b = & 0.53 - 0.3 \exp(-3\sqrt{h_b/L_0}) \\ & + 5(\tan \beta)^{3/2} \exp\{-45(\sqrt{h_b/L_0} - 0.1)^2\} \end{aligned} \quad (12)$$

where L_0 is the deep-water wavelength and subscript b denotes the quantity at the breaking point.

The breaking points slightly differ depending on its definition. Since the energy transfer from the wave motion to the organized large vortexes and also the energy dissipation should occur from the point where the wave crests begin to break, the coefficient α_T in Eq. (10) is set to be 0 at the crest breaking point x'_b and to be the maximum value 2.5 at the transition point x_t . Considering the results by Seyama and Kimura (1988), the crest breaking point is given as

$$x'_b = x_b - 2h_b \quad (13)$$

in this model.

According to the small amplitude wave theory, the value of the potential energy E_p is equal to that of the kinetic energy E_k . However, E_k is larger than E_p for non-linear waves in general. Dibajnia *et al.* (1988) obtained the result that the maximum ratio of E_k to E_p calculated by the finite amplitude wave theory is up to 1.2 as far as the calculation converged. Since the breaking waves in the surf zone can be considered as non-linear, the ratio $R_p \equiv E_p/E_k$ is made to change linearly from 1 at x'_b to its minimum value at the wave plunging point x_p in this model. E_p is reduced to about 90% of $E_w/2$ in the inner region of the surf zone.

The values γ_s and γ_r in Eq. (10) have been determined so that the potential energy agreed well with the measured value. They should be reduced in proportion to the decrease of E_p , because the variation of R_p accelerates the decrease of E_p apparently. Hence, in this study, they are determined as

$$\gamma_s = 0.35(0.57 + 5.3 \tan \beta) \quad (14)$$

$$\gamma_r = 0.45 \left(\frac{a}{h} \right)_b \quad (15)$$

where a is the wave amplitude.

The time-dependent mild slope equation can deal with wave reflection, however, a rapid change of the energy transfer factor f_A generates considerable numerical reflection in the offshore side of the breaking point. Since the energy dissipation by wave breaking occurs with little wave reflection, it is necessary to keep it small for the accurate description of the wave field. It is possible to decrease the energy of the reflected waves by changing the wave number in the onshore region according to the value of f_T . The modified wave number k' is given as

$$k' = \frac{a_k}{2(a_k^2 + b_k^2)} k \quad (16)$$

$$a_k = \frac{\sqrt{1 + \sqrt{1 + \frac{f_T^2}{\sigma^2}}}}{2\sqrt{2}}, \quad b_k = \frac{f_T}{2\sqrt{2}\sigma\sqrt{1 + \sqrt{1 + \frac{f_T^2}{\sigma^2}}}} \quad (17)$$

If $f_T = 0$, k' is equal to k which is calculated by the small amplitude wave theory. In the surf zone, k' is smaller than k in general. The smaller wave number results larger wave celerity. Horikawa and Isobe (1980) found that the wave celerity in the surf zone can be predicted fairly well by the solitary wave theory. It means that the modification agree with the reality. However, k/k' is kept to be less than 1.2 to prevent the wave celerity from increasing too much due to the extremely large value of f_T close to the shoreline.

The offshore and shoreline boundary conditions, the method of numerical computation and the adopted mesh scheme are the same as those employed by Watanabe and Dibajnia (1989). The solution is assumed to be converged when the absolute errors between the values obtained from two successive cycles of the calculation at every point are less than a tolerance error throughout the field. In the present study, the required absolute error is equal to 1% of the incident wave height for both the wave amplitudes and the setup calculation.

3.2 Estimation of energy dissipation rate

In order to evaluate the dissipation rate D_B , the vortex energy supplied from wave energy by wave breaking is assumed to be equally transferred to the turbulence energy in a distance l_d given in terms of the local water depth h . The distance l_d is determined as

$$l_d = \begin{cases} 4 \left(\frac{x_t - x}{x_t - x'_b} + 1 \right) h & (x \leq x_t) \\ 4h & (x > x_t) \end{cases} \quad (18)$$

where x_t is the wave transition point which is the boundary between the outer and inner regions in the surf zone. By using l_d , D_B is calculated as

$$D_B(x) = \int_{-\infty}^x t_d(x; x') dx' \quad (19)$$

where

$$t_d(x, x') = \begin{cases} 0 & (x \leq x') \\ \frac{T_B(x')}{l_d(x')} & (x' \leq x < x' + l_d(x')) \\ 0 & (x' + l_d(x') \leq x) \end{cases} \quad (20)$$

3.3 Determination of transition and plunging points

The determination of the transition and plunging points is necessary for evaluating the energy distribution in the present model. For that sake, the transition and plunging points were measured for various incident waves on different bottom slopes.

Figure 1 shows the relation between the averaged value of l_t/h_{0b} and the bottom slope $\tan \beta$, where l_t is the distance from the breaking point to the transition point and h_{0b} the still water depth at the breaking point. The marks

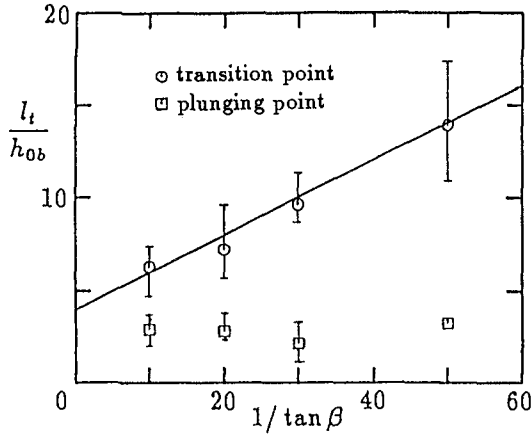


Fig. 1 Relationships between bottom slope and transition and plunging distance.

in the figure express the averages and the vertical lines express the fluctuations. The solid line expresses

$$l_t = \left(\frac{1}{5 \tan \beta} + 4 \right) h_{ob} \quad (21)$$

by which the transition point can roughly be estimated.

As for the plunging points, the averages are nearly constant and do not depend on the bottom slope. The distance l_p from the breaking point to the plunging point is expressed roughly as

$$l_p = 2.5 h_{ob} \quad (22)$$

4. Undertow Model

4.1 Vertical variation of mean shear stress and eddy viscosity

The Reynolds stress and the eddy viscosity coefficient are quantitatively evaluated from the energy dissipation rate by means of dimensional analysis in the model. By using dimensional analysis, Battjes (1975) obtained the representative velocity of turbulence q as

$$q \approx \left(\frac{D_B}{\rho} \right)^{1/3} \quad (23)$$

The vertically averaged mean shear stress τ_m in the horizontal plane and the vertically averaged mean eddy viscosity ν_m are expressed as

$$\tau_m = C_\tau \rho^{1/3} D_B^{2/3} \quad (24)$$

$$\nu_m = C_\nu \rho^{-1/3} h D_B^{1/3} \quad (25)$$

respectively. C_τ and C_ν are constant and taken to be 0.02 and 0.03, respectively, in this model.

The mean shear stress τ and the eddy viscosity ν_e are assumed to be linear functions of the vertical elevation z' from the bottom [Okayasu *et al.* (1988)] and are expressed as

$$\tau = a_\tau z' + b_\tau = \frac{0.04}{3} \rho^{1/3} D_B^{2/3} \left(\frac{5}{d_t} z' - 1 \right) \quad (26)$$

$$\nu_e = a_\nu z' = 0.06 \rho^{-1/3} D_B^{1/3} \frac{h}{d_t} z' \quad (27)$$

where d_t is water depth at wave troughs.

4.2 Vertical variation of undertow

Though the molecular viscosity ν is far smaller than the eddy viscosity ν_e in the surf zone in general, it cannot be neglected near the bottom or in the offshore region. The total viscosity is therefore defined as follows:

$$\nu_t = \nu_e + \nu \quad (28)$$

By using the eddy viscosity model, the relation between the mean shear stress τ acting on the horizontal plane and the steady current U in x -direction is expressed as

$$\tau = \rho \nu_t \frac{\partial U}{\partial z} \quad (29)$$

Substituting Eqs. (26), (27) and (28) into Eq. (29), the steady current U can be expressed as

$$U = \frac{a_\tau}{a_\nu} z' + \frac{a_\nu b_\tau - a_\tau \nu}{a_\nu^2} \log(a_\nu z' + \nu) + C_1 \quad (30)$$

where C_1 is an integral constant which is obtained in terms of the mass transport by waves M_t as

$$C_1 = -\frac{1}{2} \frac{a_\tau}{a_\nu} d_t - \frac{a_\nu b_\tau - a_\tau \nu}{a_\nu^3 d_t} (a_\nu d_t + \nu) \log(a_\nu d_t + \nu) - \nu \log \nu - a_\nu d_t - \frac{1}{h} M_t \quad (31)$$

In order to obtain the same vertical distribution as what was proposed by Longuet-Higgins (1953) when $D_B = 0$, and to give a continuous solution in and out the surf zone, Eq. (30) is modified as

$$U = \frac{a'_r}{a_\nu} \left(z' - \frac{d_t}{2} \right) + \frac{a_\nu b'_r - a'_r \nu}{a_\nu^2} \left(1 + \log \frac{a_\nu z' + \nu}{a_\nu d_t + \nu} - \frac{\nu}{a_\nu d_t} \log \frac{a_\nu d_t + \nu}{\nu} \right) - \frac{1}{h} M_t \quad (32)$$

$$\left. \begin{aligned} a'_r &= a_r + \frac{\nu a^2 \sigma k}{2h^2 \sinh^2 kh} \left(3kh \sinh 2kh + \frac{3 \sinh 2kh}{2kh} + \frac{9}{2} \right) \\ b'_r &= b_r - \frac{\nu a^2 \sigma k}{4h \sinh^2 kh} \left(2kh \sinh 2kh + \frac{6 \sinh 2kh}{2kh} + 9 \right) \end{aligned} \right\} \quad (33)$$

The values of the second terms in Eq. (33) are far smaller than those of the first terms in the inner region of the surf zone.

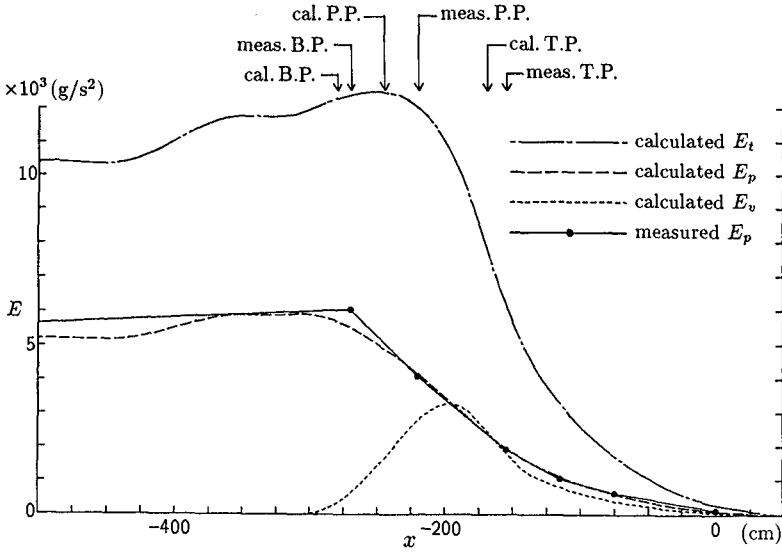


Fig. 2 Calculated and measured energy variations (1/20 slope).

5. Results

Figure 2 shows variations of the calculated values of the potential energy of wave motion E_p , the energy of the organized large vortexes E_v and the total energy of wave E_t for wave breaking on 1/20 constant slope. Measured potential energy is also shown in the figure. The period and height of the incident waves are 2.00 s and 8.50 cm, respectively. The calculated and measured value of E_p agree well. E_v takes almost the same value as E_p at the transition point (indicated by T.P.). E_p does not attenuate so much up to the plunging point (P.P.). The calculated values of the energy transfer rate T_B and the energy dissipation rate D_B are shown in Fig. 3. The hatched area corresponds to the rate of change of the vortex energy. The small value of D_B near the plunging point is consistent with the reality.

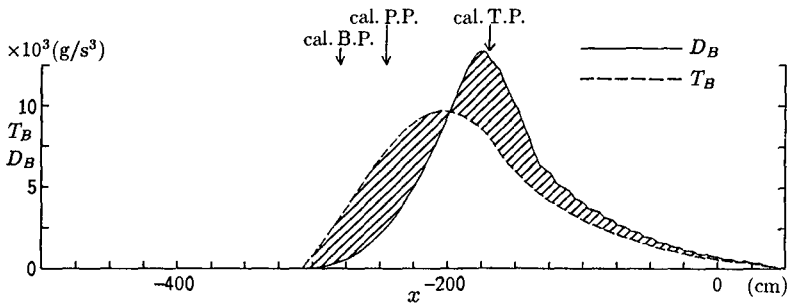


Fig. 3 Rate of energy transfer and dissipation.

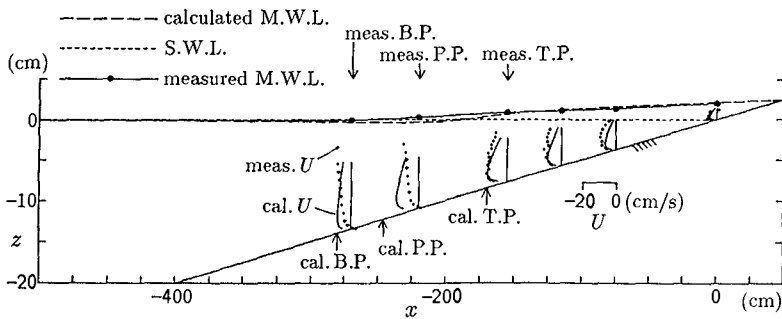


Fig. 4 Calculated and measured undertow distributions (1/20 slope).

Figure 4 shows a comparison of the calculated and the measured distribution of an undertow together with the bottom profile. The variation of the mean water level is also given in the figure. The undertow profiles are well evaluated except near the plunging point. The discrepancy near the plunging point may be caused by the insufficient accuracy of the evaluation of the energy dissipation rate or the energy and mass flux by the organized large vortexes in the outer region. Discrepancy is also found in the variation of setup around the plunging point, but the accuracy is good near the shoreline.

Figure 5 shows a result on a step-type beach. Period and height of the incident waves are 1.20 s and 9.24 cm in this case. The agreement between the calculated and measured values is good, although the calculated energy oscillates in the wave recovery zone. Comparisons of the distributions of undertow and variations of the mean water level are shown in Fig. 6. They agree well in the whole surf zone except around the plunging point, although the calculations were carried out only from the incident wave conditions. It can be concluded that the present model can compute the steady current distributions on various beach topographies with a good accuracy.

5. Concluding Remarks

In order to describe accurately the mechanism of the energy transfer during wave breaking, a model was presented in which the organized large vortexes were taken into account as a transmitter of energy in the energy transfer process from wave motion to turbulence. The mass and momentum fluxes by the organized large vortexes were also discussed.

By using the models of the energy distribution and the mass transport, a model was presented for the two-dimensional distribution of the undertow. The Reynolds stress and the eddy viscosity coefficient were quantitatively evaluated from the energy dissipation rate on the basis of the dimensional analysis. The variation of the mean water level in the surf zone was also predicted with a good accuracy by considering the momentum flux by the organized vortexes. The model can evaluate the distribution of the undertow on an arbitrary beach topography from the incident wave condition.

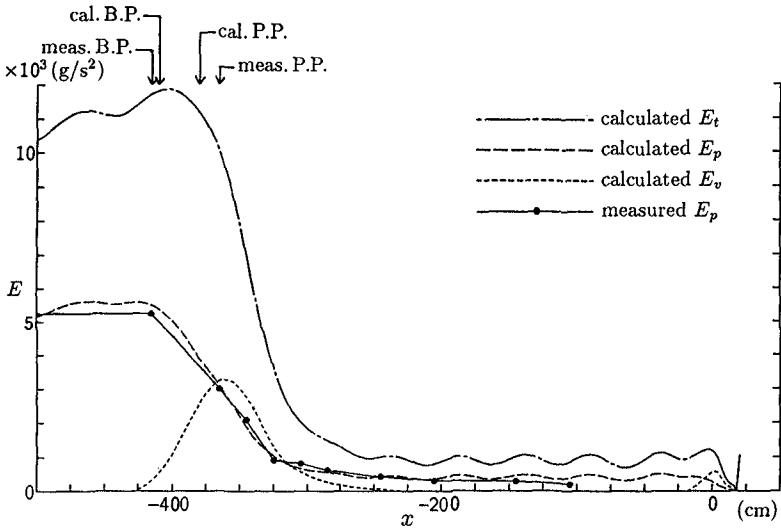


Fig. 5 Calculated and measured energy variations (step type).

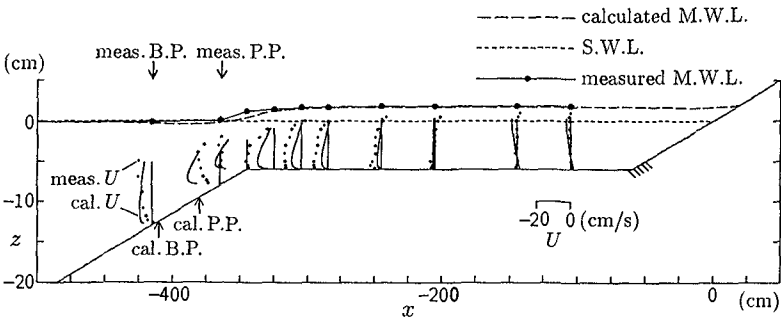


Fig. 6 Calculated and measured undertow distributions (step type).

References

- Battjes, J.A. 1975: A note on modeling of turbulence in the surf zone, *Symp. Model. Techniques, ASCE, San Francisco*, pp.1050-1061.
- Dibajnia, M., M. Isobe and A. Watanabe 1988: A comparison between finite amplitude and small amplitude waves in shoaling process, *Proc. 43rd Ann. Conf., JSCE, No.2*, pp.580-581 (in Japanese).
- Horikawa K., M. Isobe 1980: Dynamic character in the near shore area, *Proc. 17th Int. Conf. Coastal Eng.*, pp.480-498.
- Isobe, M. 1987: Parabolic equation model for transformation of irregular waves due to refraction, diffraction and breaking, *Coastal Eng. Japan*, Vol.30, No.1, pp.33-47.
- Iwagaki, Y., Y. Tsuchiya 1966: Laminar damping of oscillatory waves due to bottom friction, *Proc. 10th Int. Conf. Coastal Eng.*, pp.149-174.
- Longuet-Higgins, M.S. 1953: Mass transport in water waves, *Phil. Trans. Roy. Soc. London, Ser.A, Vol.245*, pp.535-581.
- Okayasu, A., T. Shibayama and K. Horikawa 1988: Vertical variation of undertow in the surf zone, *Proc. 21st Int. Conf. Coastal Eng.*, pp. 478-491.
- Seyama, A. and A. Kimura 1988: The measured properties of irregular wave breaking and wave height change after breaking on the slope, *Proc. 21st Int. Conf. Coastal Eng.*, pp.419-432.
- Watanabe, A. and M. Dibajnia 1988: A numerical model of wave deformation in surf zone, *Proc. 21st Int. Conf. Coastal Eng.*, pp.578-587.

CHAPTER 10

NUMERICAL SIMULATION OF NONLINEAR WAVE TRANSFORMATION OVER A SUBMERGED PLATE

Xiping Yu * Masahiko Isobe † Akira Watanabe ‡

Abstract

The Euler equation of fluid motion is integrated in the vertical direction by assuming a hyperbolic cosine distribution of pressure. As a result, quasi-linear hyperbolic equations governing the wave motion above a solid bed are obtained. The equations are then applied to describing the wave transformation over a submerged plate.

An algorithm based on the method of characteristics is developed in the numerical computation. The wave reflection and transmission coefficients computed under various conditions are compared with the experimental data, and the overall agreement is found to be fairly satisfactory.

1 INTRODUCTION

Persistent efforts have been devoted to developing efficient and economical breakwaters. The efforts are still needed since new requirements are constantly brought up in the course of further developing coastal zones. As construction sites advanced offshore further and further and the water depth to be dealt with becomes larger and larger, fundamental changes take place even in the design concept of breakwaters. Among many initiatives, it is found that some simple structures are very promising to lower the design wave height for main structures and thus to achieve an overall optimum of the project concerned, or even to stand alone to create a relatively calm area. A submerged horizontal or slightly inclined plate represents one example of such new simple types of breakwaters.

*Graduate student, Dept. of Civil Eng., Univ. of Tokyo, Bunkyo-ku, Tokyo 113, Japan.

†Dr. Eng., Assoc. Prof., ditto.

‡Dr. Eng., Prof., ditto.

When incident waves propagate over a submerged plate, part of the wave energy is reflected because of the interaction between the flows above and below the plate. Under certain conditions waves even break above the plate and the energy is thus considerably dissipated. It is by virtue of the reflection and dissipation that a submerged plate functions as a breakwater. However, unlike conventional breakwater, the effectiveness of the submerged plate is very sensitive to the incident wave conditions as well as the dimensions and the placement of the plate. Proper design of the submerged plate breakwaters requires reliable evaluation of the wave reflection and energy dissipation as well as the associated wave transmission under various conditions.

The wave deformation due to a plate has been treated in several previous studies. For example, analytical solution has been obtained for horizontal plate under long wave condition (Hattori and Matsumoto, 1977), and a numerical model based on the time-dependent mild slope equation is also available (Aoyama et al., 1988).

Most of the previous studies are based on the linear wave theory. To ensure the effectiveness, however, the submerged depth of the plate should not be too large, and then the wave nonlinearity becomes significant over the plate. Furthermore, wave breaking, a typical nonlinear phenomenon, is necessary to serve as an energy dissipator to minimize the wave transmission and reflection. Simulation of nonlinear waves is thus needed. In the present study a set of wave equations including nonlinear terms is derived to describe the wave deformation over a submerged plate. The nonlinear equations are solved numerically by the method of finite characteristics. Numerical results are compared with experimental data.

2 GOVERNING EQUATION OF WAVE MOTION

Wave motion is fundamentally governed by the following continuity equation and Euler equations.

$$\frac{\partial u_j}{\partial x_j} + \frac{\partial w}{\partial z} = 0 \quad (1)$$

$$\frac{\partial u_i}{\partial t} + \frac{\partial}{\partial x_j}(u_i u_j) + \frac{\partial}{\partial z}(u_i w) + \frac{\partial}{\partial x_i}\left(\frac{p}{\rho}\right) = 0 \quad (2)$$

$$\frac{\partial w}{\partial t} + \frac{\partial}{\partial x_j}(w u_j) + \frac{\partial}{\partial z}(w w) + \frac{\partial}{\partial z}\left(\frac{p}{\rho}\right) + g = 0 \quad (3)$$

where, u_j ($j = 1, 2$) and w are, respectively, the horizontal and vertical components of the velocity, p the pressure, ρ the fluid density, g the gravitational acceleration, x_j and z the horizontal and vertical coordinates, and t the time. Through denoting the

water surface elevation by η and the still water depth by h , the kinematic boundary conditions on the free surface as well as at the solid bottom are expressed by

$$\frac{\partial \eta}{\partial t} + u_j^f \frac{\partial \eta}{\partial x_j} - w^f = 0 \quad (4)$$

$$u_j^b \frac{\partial h}{\partial x_j} + w^b = 0 \quad (5)$$

in which the superscript f and b represent the values at free surface and bottom, respectively.

It is known that the small amplitude wave theory gives the pressure as

$$\frac{p}{\rho} = -gz + g\eta \frac{\cosh k_M(h+z)}{\cosh k_M(h+\eta)} \quad (6)$$

where a modification has been made to assure that the pressure becomes exactly zero on the free surface, which does not violate the small amplitude assumption. The quantity k_M in Eq. (6) is the modified wave number determined by the following modified dispersion relation:

$$C_M^2 = \frac{g}{k_M} \tanh k_M(h+\eta) \quad (7)$$

in which $C_M = \sigma/k_M$ is the modified wave celerity, and σ the angular frequency.

It has been shown that the small amplitude wave theory is adequate up to the location near the breaking point (e.g., Isobe, 1985). Hence Eq. (6) is regarded as valid in the shoaling zone. In the surf zone, while the small amplitude wave theory is no longer valid, the assumption of hydrostatic pressure distribution may be acceptable. Since Eq. (6) yields the hydrostatic pressure distribution when the water depth becomes small, it may still be a rather good approximation at this situation. Thus Eq. (6) is not erroneous except for a narrow region around the breaking point.

With the assumption of the pressure distribution expressed by Eq. (6), Eqs. (1) and (2) can be integrated with respect to z from the bottom ($z = -h$) to the free surface ($z = \eta$). By recognizing that η is a function of x_j and t , and h a function of x_j only, and introducing the boundary conditions (4) and (5), the continuity equation (1) is integrated as

$$\frac{\partial \eta}{\partial t} + \frac{\partial q_j}{\partial x_j} = 0 \quad (8)$$

where, $q_j = \int_{-h}^{\eta} u_j dz$ is defined as the component of fluid discharge in x_j direction. In a similar way, the integrated momentum equation (9) can be obtained by further considering that the pressure on the free surface vanishes.

$$\frac{\partial q_i}{\partial t} + \frac{\partial}{\partial x_j} \left(\beta \frac{q_i q_j}{h+\eta} \right) + \frac{\partial}{\partial x_i} (C_M^2 \eta) - g\eta \frac{\partial \eta}{\partial x_i} - \frac{g\eta}{\cosh k_M(h+\eta)} \frac{\partial h}{\partial x_i} = 0 \quad (9)$$

where β is the momentum factor. By assuming the vertical distribution of u_i as:

$$u_i = u_i^b(x_j, t) \cosh k_M(h + z) \quad (10)$$

β can be derived as

$$\beta = n_M \alpha \quad (11)$$

with

$$\alpha = \frac{g(h + \eta)}{C_M^2} \quad (12)$$

$$n_M = \frac{1}{2} \left[1 + \frac{2k_M(h + \eta)}{\sinh 2k_M(h + \eta)} \right] \quad (13)$$

Equations (8) and (9) govern the wave motion over a solid bottom. The equations are mathematically termed as quasi-linear hyperbolic differential equations, which have been extensively studied (Courant and Hilbert, 1962). Among many of the properties discovered, it is recognized that discontinuities are included in the solutions under certain conditions even if the initial and boundary conditions are continuous functions. The discontinuity is related to the breaking in wave dynamics (Stoker, 1957).

Since Eq. (9) is derived from the basic equations of ideal fluid flow, the momentum loss is neglected. When waves propagate into the surf zone, the energy loss due to nonlinearity may become remarkable. However, the mechanical energy loss does not always mean a noticeable momentum loss. In some cases, the energy loss is significant but the momentum loss may be negligible, as stated in many textbooks about hydraulic jump (e.g., Rouse, 1946). In the present study we use Eq. (9) and neglect the momentum loss.

Since the pressure distribution given by Eq. (6) is assumed, only progressive waves are considered. Complete or partial standing waves, which are the superposition of two wave trains propagating in the opposite directions, can also be dealt with. However, if there are some rapid changes in boundary conditions, which may cause scattering waves, the validity of Eq. (9) should be reexamined.

3 FORMULATION OF WAVE MOTION OVER SUBMERGED PLATE

3.1 Basic equations

In the following we deal with a vertically two-dimensional wave field in the x - z plane. As shown in Figure 1, the flow field is divided into the four regions: (i) the offshore

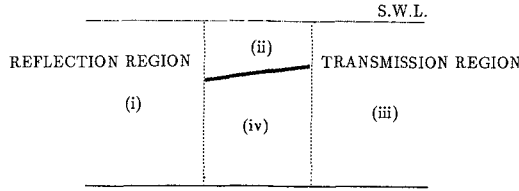


Figure 1: Definition sketch of submerged plate

or reflection region, (ii) the region above the plate, (iii) the onshore or transmission region, and (iv) the region under the plate. The flow in the regions (i), (ii) and (iii) can be described by the one-dimensional form of Eqs. (8) and (9).

In order to simplify the equations, we assume that the bottom slope is mild as

$$\left| \frac{\partial h}{\partial x} \right| \ll \left| \frac{\partial \eta}{\partial x} \right| \tag{14}$$

Furthermore, we neglect the terms originating from the nonlinearity but vanishing when the water depth becomes small, because the nonlinearity is considered to become significant only when the water depth is small. Then Eqs. (8) and (9) reduce to

$$\frac{\partial \eta}{\partial t} + \frac{\partial q}{\partial x} = 0 \tag{15}$$

$$\frac{\partial q}{\partial t} + 2\beta v \frac{\partial q}{\partial x} + (C_M^2 - \beta v^2) \frac{\partial \eta}{\partial x} = 0 \tag{16}$$

where $v = q/(h + \eta)$ is the sectional mean velocity.

To derive the equation governing the flow under the plate, the procedure for deriving Eqs. (8) and (9) is followed. If the slope of the plate is small enough, it is expected that the hydrostatic pressure distribution may be assumed in the region (iv) because the flow can reasonably be treated as nearly parallel. Hence,

$$\frac{p}{\rho} = \frac{P_d}{\rho(h - d)} - gz \tag{17}$$

where P_d is the total dynamic pressure force on a vertical cross section below the plate, h and d are the total water depth and the depth above the plate, respectively. Eqs. (1), (2) and (5) are still valid, whereas the boundary condition on the plate becomes

$$w^p \frac{\partial d}{\partial x} + w^p = 0 \tag{18}$$

where the superscript p denotes the values on the surface of the plate. Substituting Eq. (17) into Eq. (2) and then integrating Eqs. (1) and (2) from $z = -h$ to $z = -d$ under the boundary conditions (5) and (18), we have

$$q = \text{const.} \quad (19)$$

$$\frac{\partial q}{\partial t} + \frac{\partial}{\partial x} \left(\frac{q^2}{h-d} \right) + \frac{\partial P_d}{\partial x} = 0 \quad (20)$$

Since q is only a function of t , Eq. (20) can be integrated with respect to x from one end of the plate to the other. Therefore, the differential equation for the fluid discharge under the plate is finally given as:

$$\frac{\partial q}{\partial t} + q^2 \frac{\tan \theta}{(h-d)(h-d_u)} + \frac{P_{dd} - P_{du}}{l \cos \theta} = 0 \quad (21)$$

where l and θ are the length and slope angle of the plate and the subscript u and d represent the values at the upstream and downstream ends of the plate, respectively.

3.2 Boundary Conditions

At the offshore lateral boundary of the reflection region (i), waves are assumed to be described by the superposition of the incident and reflected waves as

$$\eta = \eta_I(x - C_h t) + \eta_R(x + C_h t) \quad (22)$$

where the subscripts I and R represent, respectively, the incident and reflected waves; C_h is the wave celerity in the region of constant water depth h . By differentiating η with respect to t and x , it is found that

$$\frac{\partial \eta}{\partial t} - C_h \frac{\partial \eta}{\partial x} = 2 \frac{\partial \eta_I}{\partial t} \quad (23)$$

Equation (23) gives the offshore lateral boundary condition. In a similar way, at the onshore lateral boundary of the region (iii), it can be assumed that

$$\eta = \eta_T(x - C_h t) \quad (24)$$

where the subscript T represents the transmitted waves. The onshore lateral boundary condition can thus be obtained as:

$$\frac{\partial \eta}{\partial t} + C_h \frac{\partial \eta}{\partial x} = 0 \quad (25)$$

Generally, under the boundary conditions periodic in time, a solution of hyperbolic differential equation consists of two parts: one is the contribution of the boundary

conditions and thus also periodic; the other is the contribution of the initial condition which decays rapidly with time if any damping factor is included. In many practical problems of coastal engineering, only the periodic solution is important. As a result, it allows the initial conditions to be arbitrarily specified so far as they will become trivial after several wave period. In the present case, however, the boundary conditions are given in terms of differential equations. Hence, arbitrary constants involved should be determined so as to make the solution unique. Since the constants may implicitly be specified in the initial conditions of q and η , there should be certain restriction on the specification of q and η at the initial step. However, the state of still water can be utilized as reasonable initial conditions if we do not consider any steady current.

The matching boundary conditions at both ends of the plate are

$$\eta_h = \eta_a \quad (26)$$

$$q_h = q_a + q_b \quad (27)$$

$$\frac{P_{db}}{\rho} = \frac{P_{dh} - P_{da}}{\rho} \quad (28)$$

where the subscripts h , a and b represent, respectively, the values at the region of constant water depth, above and below the plate. It is obvious that Eqs. (26), (27) and (28) physically imply the continuity of the free surface, the conservation of mass and the balance of the pressure force. The substitution of Eq. (6) into Eq. (28) gives

$$\frac{P_{db}}{\rho} = (C_{Mh}^2 - C_{Ma}^2)\eta_h \quad (29)$$

4 METHOD OF FINITE CHARACTERISTICS

The method of characteristics has been developed as an effective technique to solve quasi-linear hyperbolic differential equations. By introducing two families of characteristic curves in the x - t plane, partial differential equations are replaced by the characteristic equations including only ordinary derivatives along the characteristic curves.

Equations (15) and (16) can be rewritten in a matrix form as:

$$\frac{\partial}{\partial t} \begin{pmatrix} \eta \\ q \end{pmatrix} + \begin{bmatrix} 0 & 1 \\ C_M^2 - \beta v^2 & 2\beta v \end{bmatrix} \frac{\partial}{\partial x} \begin{pmatrix} \eta \\ q \end{pmatrix} = 0 \quad (30)$$

It has been shown that the slopes of the characteristic curves are equal to the two eigenvalues of the coefficient matrix (Abbott, 1979). Thus,

$$\begin{aligned} \frac{dx}{dt} &= \beta v \pm \sqrt{\beta(\beta - 1)v^2 + C_M^2} \\ &\equiv \xi_{\pm} \end{aligned} \tag{31}$$

The characteristic equations are, then

$$\frac{dq}{dt} - \xi_{\mp} \frac{d\eta}{dt} = 0 \tag{32}$$

Several numerical techniques for solving the characteristic equations are available (Lin, 1952; Freemman and LeMehaute, 1964; Abbott and Verwey, 1970). Here a scheme, called the method of finite characteristics, is introduced through the improvement of Lin's method. The improvement, which is to include some higher order terms in the computation, has been found necessary because the ratio of the grid size to the wavelength in the computation of sea waves can not be as small as that for flood waves, owing to the restriction of the computational time.

The method of finite characteristics can be explained by Figure 2. Two finite charac-

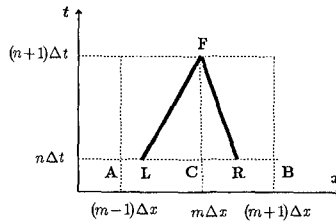


Figure 2: Definition sketch for FCM

teristic curves are issued backward from the computation point F toward the previous time step. The finite characteristic curves are approximated by straight lines with the slope determined through the algorithmic form of Eq. (31)

$$x_F - x_L = \xi_{+,L} \Delta t \tag{33}$$

$$x_F - x_R = \xi_{-,R} \Delta t \tag{34}$$

where the subscripts F , L and R express the values at the points F, L and R. $\xi_{+,L}$ and $\xi_{-,R}$ are computed through linear interpolation of the values at the grid points A, B and C as follows:

$$\xi_{+,L} = \xi_{+,C} - \frac{x_L - x_C}{\Delta x} (\xi_{+,A} - \xi_{+,C}) \tag{35}$$

$$\xi_{-,R} = \xi_{-,C} + \frac{x_R - x_C}{\Delta x} (\xi_{-,B} - \xi_{-,C}) \quad (36)$$

By substituting Eqs. (35) and (36) into Eqs. (33) and (34), the positions x_L and x_R are explicitly expressed as:

$$x_L = x_F - \frac{\xi_{+,C} \Delta t}{1 + \frac{\Delta t}{\Delta x} (\xi_{+,C} - \xi_{+,A})} \quad (37)$$

$$x_R = x_F - \frac{\xi_{-,C} \Delta t}{1 + \frac{\Delta t}{\Delta x} (\xi_{-,B} - \xi_{-,C})} \quad (38)$$

Provided that the positions of the points L and R are determined, the values of η and q at these points are computed through the following second order interpolation.

$$\begin{aligned} \begin{pmatrix} \eta \\ q \\ \xi_{\pm} \end{pmatrix}_{L,R} &= \begin{pmatrix} \eta \\ q \\ \xi_{\pm} \end{pmatrix}_A \frac{(x_{L,R} - x_C)(x_{L,R} - x_B)}{2\Delta x^2} \\ &- \begin{pmatrix} \eta \\ q \\ \xi_{\pm} \end{pmatrix}_B \frac{(x_{L,R} - x_A)(x_{L,R} - x_B)}{\Delta x^2} \\ &+ \begin{pmatrix} \eta \\ q \\ \xi_{\pm} \end{pmatrix}_C \frac{(x_{L,R} - x_A)(x_{L,R} - x_C)}{2\Delta x^2} \end{aligned} \quad (39)$$

On the other hand, Eq. (32) is discretized along the finite characteristic curves as

$$q_F - q_L = \xi_{-,L} (\eta_F - \eta_L) \quad (40)$$

$$q_F - q_R = \xi_{+,R} (\eta_F - \eta_R) \quad (41)$$

Hence, η_F and q_F can be expressed in terms of η_L , η_R , q_L , q_R , $\xi_{-,L}$ and $\xi_{+,R}$ as:

$$\eta_F = \frac{\xi_{-,L} \eta_L - \xi_{+,R} \eta_R - (q_L - q_R)}{\xi_{-,L} - \xi_{+,R}} \quad (42)$$

$$q_F = \frac{\xi_{-,L} q_R - \xi_{+,R} q_L + \xi_{-,L} \xi_{+,R} (\eta_L - \eta_R)}{\xi_{-,L} - \xi_{+,R}} \quad (43)$$

When the computational point is located at the matching boundaries, the discontinuity of q should be considered. The jump of the value of q is determined through the matching boundary condition (27) as well as the algorithmic form of Eq. (21), that is

$$q^{n+1} = q^n - [q^{n+1} q^n \frac{\tan \theta}{(h - d_d)(h - d_u)} + \frac{P_{dd}^n - P_{du}^n}{l \cos \theta}] \Delta t \quad (44)$$

The offshore and onshore boundary conditions are discretized as:

$$\eta_{\text{off}}^{n+1} = \eta_{\text{off}}^n + \left[C_h \frac{\partial \eta}{\partial x} \Big|_{\text{off}}^n + 2 \frac{\partial \eta}{\partial t} \Big|_{\text{off}}^n \right] \Delta t \quad (45)$$

$$\eta_{\text{on}}^{n+1} = \eta_{\text{on}}^n - C_h \frac{\partial \eta}{\partial x} \Big|_{\text{on}}^n \Delta t \quad (46)$$

in which $\frac{\partial \eta}{\partial x} \Big|_{\text{off}}^n$ and $\frac{\partial \eta}{\partial x} \Big|_{\text{on}}^n$ are calculated through the numerical differentiation method based on Lagrangian interpolation formula (Hildebrand, 1987).

Lin's method was initially developed for the computation of continuous flow, but its further application have shown that it can also simulate discontinuities (Lin et al., 1982).

As long as the water surface elevation near the lateral boundaries is obtained, the reflection coefficient K_R and the transmission coefficient K_T can easily be calculated.

5 SOME COMPUTATIONAL RESULTS

Wave reflection and transmission coefficients are dependent on the incident wave conditions as well as the placement of the plate. The incident wave steepness H_1/L_0 , the relative water depth h/L_0 , the relative submerged depth d/h , the slope of the plate $\tan \theta$ and the relative length of the plate l/L_0 can be chosen as independent dimensionless parameters. To investigate the relationships, the variation of K_R and K_T against l/L_0 is computed for various values of the other parameters. The results are shown in Figs. 3 to 6 along with the experimental data. Table 1 summarizes the conditions.

Figure 3 shows the comparison of reflection and transmission coefficients among linear waves and waves with different incident steepness. It can be found that the influence of the incident wave steepness becomes remarkable when the wave nonlinearity is considered; the transmission coefficient decreases with the increase of the incident wave steepness.

Figure 4 shows the change in the wave reflection and transmission coefficients against the submerged depth of the plate. Since wave motion decays downwards from the free surface, too large a submerged depth of the plate makes little contribution to the wave deformation.

Figure 5 shows the variation of the reflection and transmission coefficients of waves with different relative water depth. It is found that for a given relative length of the plate, the reflection and transmission coefficients does not show very large difference for the wide change of the relative water depth. This indicates, as naturally expected,

Table 1: Conditions for computation and experiment

CASE	$h(\text{cm})$	$T(\text{s})$	$H_I(\text{cm})$	d/h	$\tan \theta$	
STP	1	20.0	0.80	SMALL	0.2	0.0
	2	20.0	0.80	1.5	0.2	0.0
	3	20.0	0.80	3.6	0.2	0.0
SMD	1	20.0	0.80	2.0	0.2	0.0
	2	20.0	0.80	2.0	0.5	0.0
RWD	1	20.0	0.88	1.5	0.2	0.0
	2	20.0	0.62	2.0	0.2	0.0
SLP	1	20.0	0.80	1.8	0.3	0.2
	2	20.0	0.80	1.8	0.3	0.4

that for a given absolute length of the plate, longer waves are easier to transmit over the plate. For very long waves, like tsunami, a plate can not function at all as a breakwater.

Figures 6 indicates that there is no significant change in the reflection and transmission coefficients with the slope of the plate if the mean submerged depth is kept constant. The computation for the inclined plate is available only for l/L_0 less than a certain value, because a longer plate would emerge from the free surface, for which the present model is not valid.

6 CONCLUDING REMARKS

A mathematical model of nonlinear wave motion has been developed and applied to simulating the wave transformation over a submerged plate. Numerical computation based on the method of finite characteristics for general conditions have been proposed. The computed wave reflection and transmission coefficients have been compared with the experimental data under various conditions. The overall agreement is satisfactory.

References

- [1] Abbott, M. B., 1979: *Computational Hydraulics*, The Pitman Press, 324p.

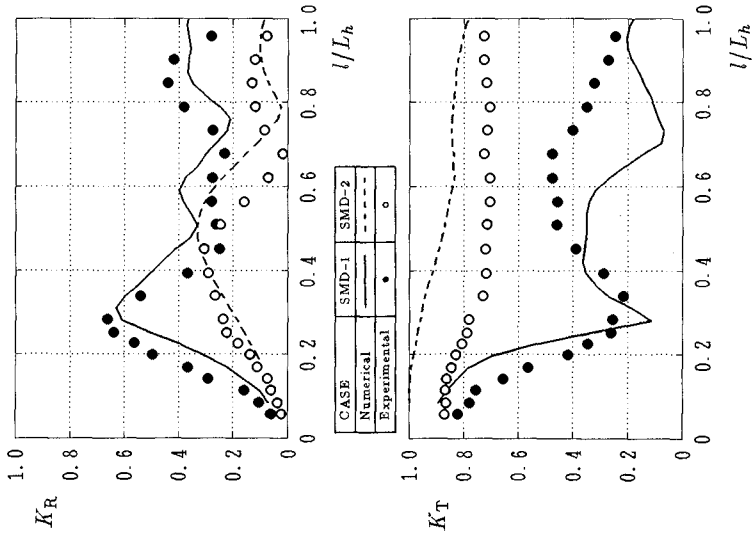


Figure 4 Computed and measured K_R and K_T (case SMD)

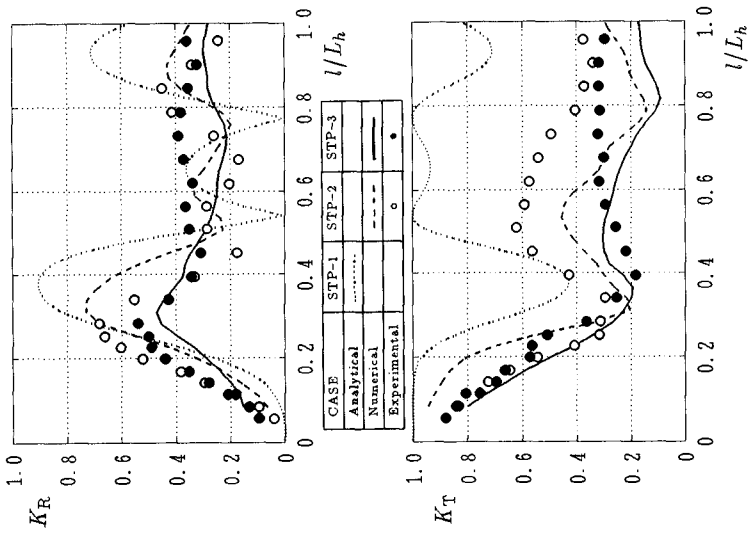


Figure 3 Computed and measured K_R and K_T (case STP)

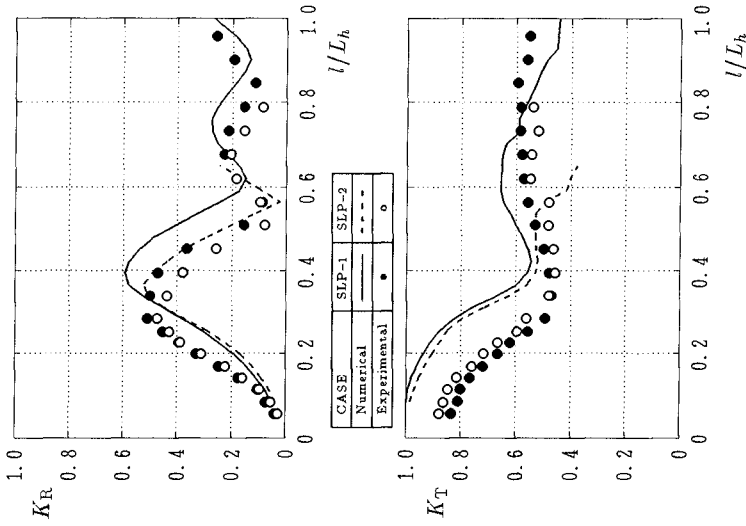


Figure 5 Computed and measured K_R and K_T (case RWD)

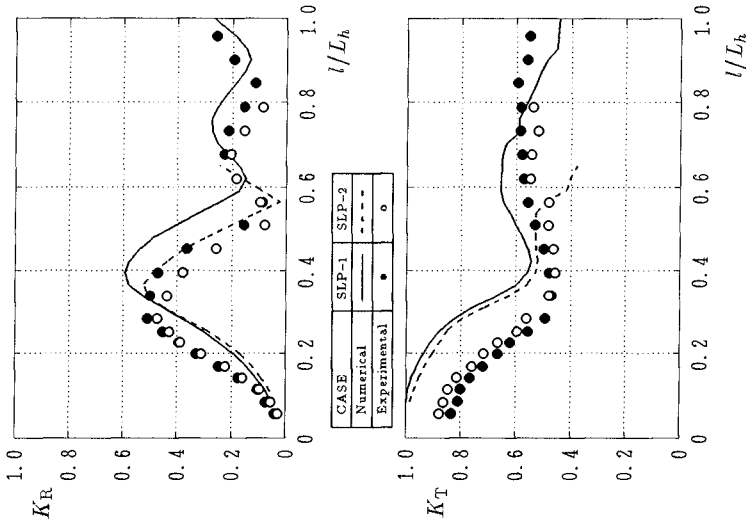


Figure 6 Computed and measured K_R and K_T (case SLP)

- [2] Abbott, M. B. and A. Verwey, 1970: Four-point method of characteristics, *J. of the hydraulics division*, ASCE, Vol. 96, No. HY12, pp. 2549–2564.
- [3] Aoyama, T., M. Isobe, T. Izumiya and A. Watanabe, 1988: Study on wave control in offshore region using a submerged plate, *35th Japanese Conf. on Coastal Eng.*, pp. 507–511 (in Japanese).
- [4] Courant, R. and D. Hilbert, 1962: *Method of Mathematical Physics*, Vol.2, Interscience Publisher, 839p.
- [5] Freeman, J. C. and B. LeMehaute, 1964: Wave breaks on a beach slope and surges on a dry bed, *J. of the Hydraulics division*, ASCE, Vol. 90, No. HY2, pp. 187–216.
- [6] Hattori, M. and H. Matsumoto, 1977: Hydraulic performances of a submerged horizontal plate breakwater, *24th Japanese Conf. on Coastal Eng.*, pp. 266–270 (in Japanese).
- [7] Hildebrand, F. B., 1974: *Introduction to Numerical Analysis*, Dover publications, 669p.
- [8] Isobe, M., 1985: Calculation and application of first order cnoidal wave theory, *Coastal Eng.*, Vol. 9, pp. 309–325.
- [9] Lin, P. N., 1952: Numerical analysis of continuous unsteady flow in open channel, *Trans. Amer. Geophys. Union*, Vol. 33, No. 2, pp. 226–234.
- [10] Lin, B., Z. Dai and K. Li, 1982: Unsteady flow studies in China, *J. Waterway Port Coastal and Ocean Division.*, ASCE, Vol. 108, No. WW3, pp. 343–360.
- [11] Rouse, H., 1964: *Elementary Mechanics of Fluids*, Dover Publication, 376p.
- [12] Stoker, J. J., 1957: *Water Waves*, Interscience, 567p.

CHAPTER 11

Vertically 2-D Nearshore Circulation Model

Takao Yamashita¹, Yoshito Tsuchiya²
and
Dadang Ahmad Suriamihardja³

Abstract

A two layer undertow model is developed which consists of surface and inner layer. The surface layer defines breaking wave dynamics and the inner layer defines the mean flow(circulation) and turbulence fields. The interface between two layers is determined by time and depth averaging of the mean water level and wave height in the surf zone (interface model), in which Reynolds stresses are taken into consideration as well as radiation stresses. The system of equations in the inner layer is derived by time averaging the mass and momentum equations over one wave period. Time and space averaging of these equations in the surface layer defines the surface boundary conditions of the mean flow field in the inner layer. Turbulence in the inner layer is described by the standard $k - \epsilon$ model.

The numerical calculation method is also discussed and model calibration is performed by comparing with the experiments by Stive and Wind (1985).

1. Introduction

The vertical circulation occurring in the surf zone consists of both the shoreward mass transport due to breaking wave and the offshore-directed bottom current (undertow). Combining the 2-D vertical and horizontal models, it may be possible to construct a 3-D model of the nearshore circulation system.

Svendsen (1984)[6] developed a theoretical model using the first order approximation technique in describing breaking waves. Hansen and Svendsen (1984) [2] considered the effect of the bottom boundary layer in the undertow. This model was examined by using Stive and Wind's experimental data (1985)[4]. It was shown that the undertow is suppressed by the shear stress at the trough level, the static pressure induced by set-up, and the constraint of zero net flow.

Madsen and Svendsen (1979) [3] developed a theory of vertically integrated conservation equations for breaking waves in the surf zone by introducing the concept of time and depth averaging of mass, momentum and energy between the bottom and mean water level (M.W.L.). From their treatment an idea came

¹Instructor, Disaster Prevention Research Institute (DPRI), Kyoto University, Gokasho, Uji, Kyoto 611, Japan

²Professor, DPRI, Kyoto University, Gokasho, Uji, Kyoto 611, Japan

³Lecturer, Faculty of Mathematics and Natural Sciences, Hasanuddin University, Ujung Pandang, Indonesia

to mind to define the total depth by the surface and inner layers, thus allowing a theoretical treatment of the breaking waves in the surface layer.

In this study, a simplified two layer model is proposed, in which the surface layer is introduced to describe breaking wave dynamics and to obtain the time-averaged boundary conditions for dynamics in the inner layer. The interface between these two layers is set by M.W.L. The breaking waves generate turbulence and the turbulent kinetic energy conservation is considered in the model for the inner layer. Therefore, the boundary conditions for the $k - \epsilon$ equations in the inner layer are defined by modelling the dynamics of surface layer. Mass, momentum, and energy conservation laws are formulated by employing Madsen and Svendsen's model. The motion in the inner layer is decomposed into time-averaged mean flow and turbulence. The governing equations of mean flow motion are expressed in terms of the vorticity and stream function, which are derived from the mass and momentum conservation equations. The standard $k - \epsilon$ model is employed as the governing equation for turbulent motion. The coordinate transformation (conformal mapping) method developed by Wanstrath, Whitaker and Reid (1976)[7], is used to numerically calculate the 2-D vertical circulation pattern in arbitrary depth. Calibration of the numerical model is performed by a comparison with the experimental data of Stive and Wind (1985) [4].

2. Model Outline and Basic Equations

Using the coordinates and variables shown in Fig.1, the governing equations are derived. The inner layer is defined as the region extending from the bottom to the mean water level (wave set-up) $\bar{\zeta}$. While the surface layer extends from the trough of the breaking wave to its crest.

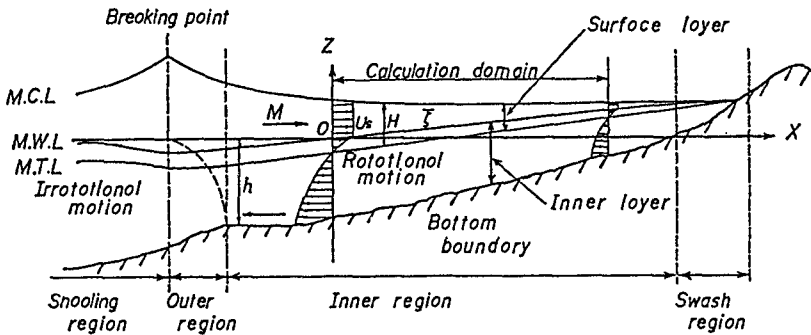


Fig.1 Schematic explanation of the model and coordinate system

The velocities u_i are decomposed into three modes, i.e. the mean flow \bar{u}_i , waves u_{wi} and fluctuations u'_i . Other quantities, σ_{ij} , p , s_{ij} are also decomposed in the

same manner, as:

$$\begin{aligned} u_i &= \bar{u}_i + u_{wi} + u'_i, & \sigma_{ij} &= \bar{\sigma}_{ij} + \sigma_{wij} + \sigma'_{ij}, \\ p_{ij} &= \bar{p}_{ij} + p_{wij} + p'_{ij}, & s_{ij} &= \bar{s}_{ij} + s_{wij} + s'_{ij} \end{aligned} \quad (1)$$

The characteristic time-scales of the three components are assumed to be quite different, therefore no correlation between them is considered. Applying these operations to the mass and momentum equations, the basic equations for the mean flow are obtained. When the Boussinesq's eddy-viscosity assumption is used to describe the Reynolds stresses $\overline{u'_i u'_j}$ by means of velocity gradients, the closure problem becomes a matter of how to determine the eddy viscosity ν_t , which is defined by:

$$\overline{u'_i u'_j} = -\nu_t \left(\frac{\partial \bar{u}_i}{\partial x_j} + \frac{\partial \bar{u}_j}{\partial x_i} \right) + \frac{2}{3} k \delta_{ij}, \quad \nu_t = C_\mu \frac{k^2}{\varepsilon}, \quad k = \frac{1}{2} \overline{u'_i u'_i} \quad (2)$$

(a) Inner layer: mean-flow equations

By differentiating x and z momentum equations and eliminating the pressure term \bar{p} , we get

$$\begin{aligned} \frac{\partial^2}{\partial x \partial z} (\bar{u}\bar{u} + \overline{u_w u_w} + \overline{u' u'}) + \left(\frac{\partial^2}{\partial z^2} - \frac{\partial^2}{\partial x^2} \right) (\bar{u}\bar{w} + \overline{u_w w_w} + \overline{u' w'}) \\ - \frac{\partial^2}{\partial x \partial z} (\bar{w}\bar{w} + \overline{w_w w_w} + \overline{w' w'}) = \nu \nabla^2 \left(\frac{\partial \bar{u}}{\partial z} - \frac{\partial \bar{w}}{\partial x} \right) \end{aligned} \quad (3)$$

When small amplitude wave theory is assumed the momentum fluxes of the total wave component, $\overline{u_w u_w}$, $\overline{u_w w_w}$ and $\overline{w_w w_w}$, become zero in Eq.(3).

The stream function ψ and vorticity Ω are now defined as

$$\frac{\partial \psi}{\partial z} = \bar{u}, \quad \frac{\partial \psi}{\partial x} = -\bar{w} \quad \text{and} \quad \Omega = \frac{\partial \bar{u}}{\partial z} - \frac{\partial \bar{w}}{\partial x} \quad (4)$$

In terms of the stream function and vorticity defined above, the basic equations are rewritten as:

$$\nabla^2 \psi = \Omega \quad (5)$$

and

$$\begin{aligned} \left(\frac{\partial \psi}{\partial z} \right) \left(\frac{\partial \Omega}{\partial x} \right) - \left(\frac{\partial \psi}{\partial x} \right) \left(\frac{\partial \Omega}{\partial z} \right) - \frac{\partial^2}{\partial x \partial z} \left(4\nu_t \frac{\partial^2 \psi}{\partial x \partial z} \right) \\ + \left(\frac{\partial^2}{\partial x^2} - \frac{\partial^2}{\partial z^2} \right) \left\{ \nu_t \left(\frac{\partial^2 \psi}{\partial z^2} - \frac{\partial^2 \psi}{\partial x^2} \right) \right\} = \nu \nabla^2 \Omega \end{aligned} \quad (6)$$

(b) Inner layer: standard $k - \varepsilon$ model

The k -equation is rewritten in the $x - z$ plane as:

$$\bar{u} \frac{\partial k}{\partial x} + \bar{w} \frac{\partial k}{\partial z} = \frac{\partial}{\partial x} \left\{ \left(\frac{\nu_t}{\sigma_k} + \nu \right) \frac{\partial k}{\partial x} \right\} + \frac{\partial}{\partial z} \left\{ \left(\frac{\nu_t}{\sigma_k} + \nu \right) \frac{\partial k}{\partial z} \right\} + \text{Prod} - \varepsilon \quad (7)$$

where

$$\text{Prod} = \nu_t \left\{ 2 \left(\frac{\partial \bar{u}}{\partial x} \right)^2 + 2 \left(\frac{\partial \bar{w}}{\partial z} \right)^2 + \left(\frac{\partial \bar{u}}{\partial z} + \frac{\partial \bar{w}}{\partial x} \right)^2 \right\} \quad (8)$$

The ε -equation is also rewritten as

$$\bar{u} \frac{\partial \varepsilon}{\partial x} + \bar{w} \frac{\partial \varepsilon}{\partial z} = \frac{\partial}{\partial x} \left\{ \left(\frac{\nu_t}{\sigma_\varepsilon} + \nu \right) \frac{\partial \varepsilon}{\partial x} \right\} + \frac{\partial}{\partial z} \left\{ \left(\frac{\nu_t}{\sigma_\varepsilon} + \nu \right) \frac{\partial \varepsilon}{\partial z} \right\} + \frac{\varepsilon}{k} (C_{1\varepsilon} \text{Prod} - C_{2\varepsilon} \varepsilon) \quad (9)$$

(c) Interface model

The boundary conditions for the governing equations in the inner layer are discussed here. The surface boundary is the mean water level $\bar{\zeta}$ which is an unknown value in the two layer system. Previous investigations of surf zone wave height and set-up show fairly good predictability of both quantities. Therefore, Svendsen's (1984)[6] model is employed to determine the wave set-up $\bar{\zeta}$ and breaking wave height variation. Svendsen also presented the mass, momentum, and energy dissipation due to breaking waves in his model by employing the first order approximation of motion, the effect of the surface roller and the wave shape parameter B_o . Consequently, Svendsen's model is needed to determine the wave energy dissipation (production in the k equation), mass flux and shear stress acting on the interface (surface) boundary.

On the other hand, the boundary condition for the stream function ψ , the vorticity Ω , the turbulent kinetic energy k , and its dissipation ε must be determined. For this problem, Madsen and Svendsen's (1979)[3] formulation of the mass and momentum conservation equations are employed.

The momentum equation in the x -direction is integrated over depth and then averaged over the wave period T_w as

$$\frac{\partial}{\partial x} \int_{-h}^{\bar{\zeta}} \rho \bar{u} \bar{u} dz + \frac{\partial}{\partial x} (S' + S_w) = -\rho g (h + \bar{\zeta}) \frac{\partial \bar{\zeta}}{\partial x} \quad (10)$$

where S' is the depth-integrated Reynolds stress and S_w the radiation stress defined by respectively

$$S' = \int_{-h}^{\bar{\zeta}} \rho \left(2\nu_t \frac{\partial \bar{u}}{\partial x} - \frac{2}{3} k \right) dz \quad (11)$$

$$S_w = \int_{-h}^{\bar{\zeta}} \rho \bar{u}_w \bar{u}_w dz + \int_{-h}^{\bar{\zeta}} \bar{p}_o dz - \frac{1}{2} \rho g \bar{\zeta}_w \bar{\zeta}_w \quad (12)$$

where p_o is the dynamic pressure given by

$$p_o = \rho g (z - \bar{\zeta}) + p \quad (13)$$

In Eq.(10), the inertia term, and the depth-integrated Reynolds stress term are added to the usual momentum balance equation. The latter term described by Eq.(11) is the interaction term between a mean flow distribution and k -equation in the inner layer.

The energy equation is given by

$$\frac{\partial B_*}{\partial x} = D_* \quad (14)$$

where B_* is the mean wave energy flux and D_* the wave energy dissipation. The non-dimensional wave energy flux B and energy dissipation D are introduced respectively, as:

$$B = \frac{B_*}{\rho g C H^2} \quad \text{and} \quad D = D_* \frac{4hT_w}{\rho g C H^3} \quad (15)$$

where C is the propagation speed of the breaker. In the surf zone, C is approximated by $C \sim \sqrt{g(h + \bar{\zeta})}$. Using Eqs.(14) and (15), the equation for the wave height variation is finally botained as

$$\frac{H}{H_r} = K_S / \left(1 - \frac{H_r}{8C_r B_r T_w} \int_{x_r}^x \frac{DK_S^3}{h + \bar{\zeta}} dx \right) \quad (16)$$

where the subscript r refers to some chosen reference points, and K_S is the shoaling coefficient.

Solving Eqs.(10) and (16) simultaneously, the wave set-up and breaker wave height variation are obtained. However, in these equations, three parameters must be estimated, B , S_w and D . Svendsen (1984) [5] evaluated these parameters assuming that (i) the mean velocity in the roller is equal to the propagation speed C , (ii) the cross sectional area A of the roller is equal to $0.9H^2$, and (iii) wave energy dissipation is analogous to that of hydraulic jump, these are respectively given as:

$$S_w \simeq \rho g \left(\frac{3}{2} B_o + 0.9 \frac{h + \bar{\zeta}}{L} \right) H^2 \quad (17)$$

$$B = B_o + 0.45 \frac{h + \bar{\zeta}}{L} \quad (18)$$

$$D = - \left[\left(1 + \frac{\zeta_c}{H} \frac{H}{h + \bar{\zeta}} \right) \left\{ 1 + \frac{H}{h + \bar{\zeta}} \left(\frac{\zeta_c}{H} - 1 \right) \right\} \right]^{-1} \quad (19)$$

where L is the wave length, ζ_c :the crest elevation and B_o : wave shape parameter defined by

$$B_o = \frac{1}{T_w} \int_0^{T_w} \left(\frac{\zeta}{H} \right)^2 dt \quad (20)$$

(d) Surface layer model

The boundary conditions for the stream function ψ and the vorticity Ω equations are considered here. To determine the boundary conditions at the surface $\bar{\zeta}$ of the inner layer, the equations of mass and momentum are derived in the

surface layer. The kinematic boundary condition at $z = \bar{\zeta}$ is derived from the conservation of mass in the surface layer as

$$\bar{u}(\bar{\zeta}) \frac{\partial \bar{\zeta}}{\partial x} - \bar{w}(\bar{\zeta}) = -\frac{\partial}{\partial x} \int_{\zeta}^{\bar{\zeta}} u dz \quad (21)$$

The dynamic boundary condition at $z = \bar{\zeta}$ is derived from the conservation of momentum in the surface layer. The pressure at $z = \bar{\zeta}$ is obtained by integrating the vertical momentum equation between ζ and $\bar{\zeta}$ and time-averaging over the wave period T_w , as

$$\frac{\bar{p}(\bar{\zeta})}{\rho} = -\overline{w'(\zeta)w'(\bar{\zeta})} + \overline{u'(\zeta)w'(\bar{\zeta})} \frac{\partial \bar{\zeta}}{\partial x} - \overline{w(\bar{\zeta})} \frac{\partial}{\partial x} \int_{\zeta}^{\bar{\zeta}} u dz \quad (22)$$

where the viscous term is neglected. The time-averaged horizontal momentum conservation in the surface layer is derived from the following definition.

$$\overline{\int_{\zeta}^{\bar{\zeta}} \text{momentum} dz} = \overline{\int_{-h}^{\zeta} \text{momentum} dz} - \overline{\int_{-h}^{\zeta} \text{momentum} dz} \quad (23)$$

The horizontal momentum equation is given by

$$\frac{\partial}{\partial x} \overline{\int_{\zeta}^{\bar{\zeta}} \left(u^2 + \frac{p}{\rho} \right) dz} = -\frac{\bar{p}(\bar{\zeta})}{\rho} \frac{\partial \bar{\zeta}}{\partial x} - \overline{u'(\zeta)u'(\bar{\zeta})} \frac{\partial \bar{\zeta}}{\partial x} + \overline{u'(\zeta)w'(\bar{\zeta})} - \bar{u}(\bar{\zeta}) \frac{\partial}{\partial x} \overline{\int_{\zeta}^{\bar{\zeta}} u dz} \quad (24)$$

Substituting the pressure Eq.(22) into Eq.(24), the right-hand side of the equation becomes:

$$\begin{aligned} \text{RHS} = & \left\{ \overline{w'(\zeta)w'(\bar{\zeta})} - \overline{u'(\zeta)w'(\bar{\zeta})} \right\} \frac{\partial \bar{\zeta}}{\partial x} + \left\{ \bar{u}(\bar{\zeta}) + \bar{w}(\bar{\zeta}) \frac{\partial \bar{\zeta}}{\partial x} \right\} \frac{\partial M_S}{\partial x} \\ & - \overline{u'(\zeta)w'(\bar{\zeta})} \left(\frac{\partial \bar{\zeta}}{\partial x} \right)^2 + \overline{u'(\zeta)w'(\bar{\zeta})} \end{aligned} \quad (26)$$

where

$$M_S = \overline{\int_{\zeta}^{\bar{\zeta}} u dz} \quad (27)$$

When the orders of $\bar{u}(\bar{\zeta})$ and $\partial \bar{\zeta} / \partial x$ are $O(1)$ and $O(\delta)$, the orders of the following terms can be estimated by the kinematic boundary condition, Eq.(21).

$$\bar{w}(\bar{\zeta}) \sim O(\delta), \quad \frac{\partial M_S}{\partial x} \sim O(\delta) \quad (28)$$

In the surface layer, strong shear flow is generated by the mass transport shoreward due to the breaker. Then the following order estimation may be reasonable.

$$\overline{u'(\zeta)w'(\bar{\zeta})} \sim \frac{\partial \bar{u}}{\partial z} \sim O(1) \quad (29)$$

This order estimation leads to the brief expression of Eq.(26), as

$$\text{RHS} = \overline{u'(\zeta)w'(\zeta)} + O(\delta) \quad (30)$$

On the other hand, LHS of Eq.(24) can be estimated as follows. The local pressure is given by integrating the vertical momentum equation between z and ζ as

$$\frac{p(z)}{\rho} = g(\zeta - z) + \frac{\partial}{\partial x} \int_z^\zeta u w dz - \rho w^2(z) \quad (31)$$

Assuming that u^2 is decomposed as

$$u^2(z) = \bar{u}^2(z) + u_w^2(z) + u'^2(z) \quad (32)$$

then, substituting these equations into the left-hand side of Eq.(24) yields

$$\begin{aligned} \text{LHS} = \frac{\partial}{\partial x} \left\{ \frac{g}{2} \overline{(\zeta - \bar{\zeta})^2} + \overline{(\zeta - \bar{\zeta}) \int_z^\zeta u w dz} - \overline{\int_z^\zeta w w dz} \right. \\ \left. + \overline{(\zeta - \bar{\zeta}) (\bar{u}^2(\bar{\zeta}) + u_w^2(\bar{\zeta}) + u'^2(\bar{\zeta}))} \right\} \quad (33) \end{aligned}$$

It is then assumed that in the surface layer, the large scale turbulence exists whose velocity and surface fluctuation have dominant frequency in the spectral domain. If this dominant frequency is a harmonics of the wave, and other spectral components are negligibly small, the turbulence components can be treated in the same manner as wave components. However, this assumption may be too bold to apply at this time since turbulence is usually characterized by multi-phase motion. However, eddies generated by breaking waves seem to have the same dominant frequency which is strongly related to the wave motion. If the above assumption is allowed, the brief expression of Eq.(33) can be obtained, as

$$\text{LHS} = \frac{\partial}{\partial x} \left\{ \frac{g}{2} (\overline{\zeta_w \zeta_w} + \overline{\zeta' \zeta'}) \right\} \quad (34)$$

Finally the dynamic boundary condition at the surface of the inner layer is

$$\overline{u'(\zeta)w'(\zeta)} = \frac{\partial}{\partial x} \left\{ \frac{g}{2} (\overline{\zeta_w \zeta_w} + \overline{\zeta' \zeta'}) \right\} \quad (35)$$

In the equation, the first term on the right-hand side is approximated by Eq.(20) and, for the second term, the following assumption is made.

$$\overline{\zeta' \zeta'} \simeq \left(\frac{A}{L} \right)^2 \quad (36)$$

Furthermore, the shear stress due to turbulence is described by

$$\overline{u'(\zeta)w'(\zeta)} = -\frac{\tau_s}{\rho} \simeq -\nu_t \left. \frac{\partial \bar{u}}{\partial z} \right|_{z=\zeta} \quad (37)$$

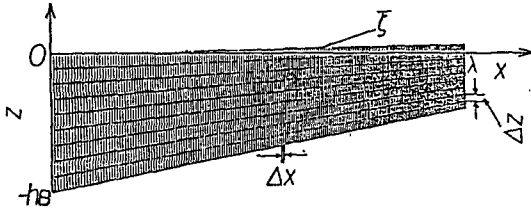
Consequently, the dynamic surface boundary condition, which is expressed by breaking wave quantities, is given as

$$\nu_t \left. \frac{\partial \bar{u}}{\partial z} \right|_{z=\bar{\zeta}} = -\frac{\partial}{\partial x} \left\{ \frac{g}{2} \left(H^2 B_0 + \frac{A^2}{L^2} \right) \right\} \quad (38)$$

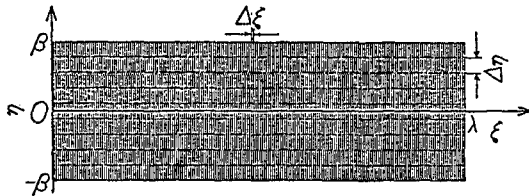
3. Numerical Model

a. Coordinate transformation

In the numerical model the conformal mapping method (Wanstrath, Whitaker and Reid (1976)[7]) is employed to make the model applicable over a wider range of surf zone topography. The governing equations derived in the Z -plane are transformed to the ζ^* -plane(Fig.2). The arbitrary surface and bottom boundaries in Z -plane are transformed into straightline ($\eta = \pm\beta$) in the ζ^* -plane.



(a) Z -plain



(b) ζ^* -plane

Fig.2 Z and ζ^* -plane in the coordinate transformation

$$x(\xi, \eta) = \xi + \sum_{n=1}^N (b_n \sinh nk_c \eta + c_n \cosh nk_c \eta) \sin nk_c \xi \quad (39)$$

$$z(\xi, \eta) = b_0 + \eta + \sum_{n=1}^N (b_n \cosh nk_c \eta + c_n \sinh nk_c \eta) \cos nk_c \xi. \quad (40)$$

The Fourier coefficients b_n ($n = 0, 1, 2, \dots, N$), and c_n ($n = 1, 2, 3, \dots, N$) are determined by matching the surface and bottom boundaries at $\eta = \pm\beta$, using the least square error. The transformation function J^2 is:

$$\frac{\partial(x, z)}{\partial(\xi, \eta)} = \left(\frac{\partial x}{\partial \xi}\right)^2 + \left(\frac{\partial z}{\partial \xi}\right)^2 \equiv J^2. \quad (41)$$

Using these definitions, the relations of partial differentiations of function ϕ with respect to (x, z) and (ξ, η) are

$$\frac{\partial \phi}{\partial x} = -\frac{1}{J^2} \left(\frac{\partial z}{\partial \xi} \frac{\partial \phi}{\partial \eta} - \frac{\partial x}{\partial \xi} \frac{\partial \phi}{\partial \xi} \right) = a \frac{\partial \phi}{\partial \xi} - b \frac{\partial \phi}{\partial \eta} \quad (42)$$

$$\frac{\partial \phi}{\partial z} = -\frac{1}{J^2} \left(-\frac{\partial z}{\partial \xi} \frac{\partial \phi}{\partial \xi} - \frac{\partial x}{\partial \xi} \frac{\partial \phi}{\partial \eta} \right) = a \frac{\partial \phi}{\partial \eta} + b \frac{\partial \phi}{\partial \xi} \quad (43)$$

where

$$a \equiv \frac{1}{J^2} \left(\frac{\partial x}{\partial \xi} \right), \quad b \equiv \frac{1}{J^2} \left(\frac{\partial z}{\partial \xi} \right). \quad (44)$$

Finally, operators of the first order partial differentiation are given by

$$\frac{\partial}{\partial x} = a \frac{\partial}{\partial \xi} - b \frac{\partial}{\partial \eta} \equiv D_x, \quad \frac{\partial}{\partial z} = a \frac{\partial}{\partial \eta} + b \frac{\partial}{\partial \xi} \equiv D_z. \quad (45)$$

The second order partial differentiations are

$$D_{xx}(\) = aD_{\xi\xi}(a, \) + bD_{\eta\eta}(b, \) - aD_{\xi\eta}(b, \) - bD_{\eta\xi}(a, \) \quad (46)$$

$$D_{zz}(\) = aD_{\eta\eta}(a, \) + bD_{\xi\xi}(b, \) + aD_{\eta\xi}(b, \) + bD_{\xi\eta}(a, \) \quad (47)$$

$$D_{xz}(\) = D_{zx}(\) = aD_{\xi\xi}(b, \) - bD_{\eta\eta}(a, \) + aD_{\xi\eta}(a, \) - bD_{\eta\xi}(b, \) \quad (48)$$

where

$$\begin{aligned} D_{\xi\xi}(a, \) &= \frac{\partial}{\partial \xi} \left(a \frac{\partial}{\partial \xi} \right), & D_{\xi\eta}(a, \) &= \frac{\partial}{\partial \xi} \left(a \frac{\partial}{\partial \eta} \right), \\ D_{\eta\xi}(a, \) &= \frac{\partial}{\partial \eta} \left(a \frac{\partial}{\partial \xi} \right), & D_{\eta\eta}(a, \) &= \frac{\partial}{\partial \eta} \left(a \frac{\partial}{\partial \eta} \right). \end{aligned} \quad (49)$$

The governing equations derived in the Z -plane are transformed to the ζ^* -plane by applying the above mentioned operators. The stream function and vorticity equations are rewritten as:

$$\nabla_{(\xi, \eta)}^2 \psi = J^2 \Omega \quad (50)$$

$$D_z(\psi) \left(a \frac{\partial \Omega}{\partial \xi} - b \frac{\partial \Omega}{\partial \eta} \right) - D_x(\psi) \left(a \frac{\partial \Omega}{\partial \eta} + b \frac{\partial \Omega}{\partial \xi} \right) + F^*(\Omega, \nu_t) = \frac{\nu_t}{J^2} \nabla_{(\xi, \eta)}^2 \Omega \quad (51)$$

where

$$F^*(\Omega, \nu_t) = -4D_{xz}\psi D_{xz}\nu_t + \{D_{zz}(\nu_t) - D_{xx}(\nu_t)\} \{\Omega - 2D_{xx}(\psi)\} \quad (52)$$

Similarly, the k and ε -equations are transformed to the ζ^* -plane as, respectively:

$$\begin{aligned}
 & a \frac{\partial}{\partial \xi} (\bar{u}k) - b \frac{\partial}{\partial \eta} (\bar{u}k) + a \frac{\partial}{\partial \eta} (\bar{w}k) + b \frac{\partial}{\partial \xi} (\bar{w}k) - \left\{ a \frac{\partial}{\partial \xi} \left(\frac{\nu_t}{\sigma_k} \right) - b \frac{\partial}{\partial \eta} \left(\frac{\nu_t}{\sigma_k} \right) \right\} \left(a \frac{\partial k}{\partial \xi} - b \frac{\partial k}{\partial \eta} \right) \\
 & - \left\{ a \frac{\partial}{\partial \eta} \left(\frac{\nu_t}{\sigma_k} \right) + b \frac{\partial}{\partial \xi} \left(\frac{\nu_t}{\sigma_k} \right) \right\} \left(a \frac{\partial k}{\partial \eta} + b \frac{\partial k}{\partial \xi} \right) - \frac{\nu_t}{\sigma_k J^2} \nabla^2_{(\xi, \eta)} k = \text{Prod} - \varepsilon \quad (53) \\
 & a \frac{\partial}{\partial \xi} (\bar{u}\varepsilon) - b \frac{\partial}{\partial \eta} (\bar{u}\varepsilon) + a \frac{\partial}{\partial \eta} (\bar{w}\varepsilon) + b \frac{\partial}{\partial \xi} (\bar{w}\varepsilon) - \left\{ a \frac{\partial}{\partial \xi} \left(\frac{\nu_t}{\sigma_\varepsilon} \right) - b \frac{\partial}{\partial \eta} \left(\frac{\nu_t}{\sigma_\varepsilon} \right) \right\} \left(a \frac{\partial \varepsilon}{\partial \xi} - b \frac{\partial \varepsilon}{\partial \eta} \right) \\
 & - \left\{ a \frac{\partial}{\partial \eta} \left(\frac{\nu_t}{\sigma_\varepsilon} \right) + b \frac{\partial}{\partial \xi} \left(\frac{\nu_t}{\sigma_\varepsilon} \right) \right\} \left(a \frac{\partial \varepsilon}{\partial \eta} - b \frac{\partial \varepsilon}{\partial \xi} \right) - \frac{\nu_t}{\sigma_\varepsilon J^2} \nabla^2_{(\xi, \eta)} \varepsilon = \frac{\varepsilon}{k} (C_{1\varepsilon} \text{Prod} - C_{2\varepsilon} \varepsilon) \quad (54)
 \end{aligned}$$

where

$$\text{Prod} = \nu_t \left[2D_x(\bar{u})^2 + 2D_z(\bar{w})^2 + \{D_z(\bar{u}) + D_x(\bar{w})\}^2 \right] \quad (55)$$

b. Numerical scheme

Numerical solution to an advection and diffusion (A/D) equation such as the vorticity equation, suffers from the numerical (artificial) diffusion as well as wiggles. The Dennis-Chang method is known as one of methods which can reduce these numerical problems in the A/D equation with the second order accuracy. An iteration form is discretized by this scheme and calculated till the solution converges. Using the operator notations, $A(\)$ and $D(\)$, for advection and diffusion terms, finite difference equation are represented as:

$$A_{UD}(\Omega^{n+1}) - D(\Omega) = A_{UD}(\Omega^n) - A_{CD}(\Omega^n) \quad (56)$$

where $A_{UD}(\)$ and $A_{CD}(\)$ are the upwind and centered difference operators, respectively, which given by:

$$\begin{aligned}
 A_{UD}(\Omega) &= \frac{U+|U|}{2\Delta x} (\Omega_{i,j} - \Omega_{i-1,j}) + \frac{U-|U|}{2\Delta x} (\Omega_{i+1,j} - \Omega_{i,j}) \\
 &+ \frac{V+|V|}{2\Delta z} (\Omega_{i,j} - \Omega_{i,j-1}) + \frac{V-|V|}{2\Delta z} (\Omega_{i,j+1} - \Omega_{i,j}) \quad (57)
 \end{aligned}$$

$$A_{CD}(\Omega) = \frac{1}{2\Delta x} \{ (U\Omega)_{i+1,j} - (U\Omega)_{i-1,j} \} + \frac{1}{2\Delta z} \{ (V\Omega)_{i,j+1} - (V\Omega)_{i,j-1} \} \quad (58)$$

and for the diffusion term :

$$\begin{aligned}
 D(\Omega) &= \frac{1}{\Delta x^2} \{ (\nu_t \Omega)_{i+1,j} - 2(\nu_t \Omega)_{i,j} + (\nu_t \Omega)_{i-1,j} \} \\
 &+ \frac{1}{\Delta z^2} \{ (\nu_t \Omega)_{i,j+1} - 2(\nu_t \Omega)_{i,j} + (\nu_t \Omega)_{i,j-1} \} \quad (59)
 \end{aligned}$$

where the advection velocity U and V are written as:

$$U = aD_x(\psi) - bD_z(\psi), \quad V = -\{aD_x(\psi) + bD_z(\psi)\} \quad (60)$$

For stable calculation, the dumping coefficient α_* is used at each iteration as

$$\Omega^{n+1} = \alpha_* \Omega^n \quad (61)$$

In the cases of Dirichlet boundary problem, Woods boundary condition is applicable as

$$\Omega_0 = -\frac{1}{2}\Omega_1 - \frac{3}{\Delta x^2}(\Omega_1 - \Omega_0) + O(\Delta x^3) \quad (62)$$

where the suffix 0 indicates the value at the boundary, and 1 indicates the value just inside the boundary.

c. Interface boundary conditions

At the surface, both the kinematic and dynamic boundary conditions for mean flow variables, ψ and Ω , are determined by the approximate expressions of the momentum and mass conservation equations in the surface layer.

The kinematic boundary condition in the Z -plane determines the stream function in the transformed coordinates. One possible example can be given as follows.

The velocity components \bar{u}^* , \bar{w}^* in the ζ^* -plane can be transformed to

$$\bar{u}^* = -\frac{\partial x}{\partial \eta}(\bar{w}_s - \bar{u}_s \frac{\partial \bar{\zeta}}{\partial x}) = -\frac{\partial M_S}{\partial \eta}, \quad \bar{w}^* = \frac{\partial x}{\partial \xi}(\bar{w}_s - \bar{u}_s \frac{\partial \bar{\zeta}}{\partial x}) = \frac{\partial M_S}{\partial \xi} \quad (63)$$

In these equations $-M_S$ is the stream function in the transformed coordinates system, which gives the surface boundary condition for the ψ -equation.

The boundary condition for the vorticity equation is

$$\Omega_s^* = \frac{\partial \bar{u}^*}{\partial \eta} \Big|_s - \frac{\partial \bar{w}^*}{\partial \xi} \Big|_s = \frac{\tau_s}{\rho \nu_t} \Big|_s - \frac{\partial^2 M}{\partial \xi^2} \Big|_s \quad (64)$$

The boundary condition for the k -equation at the surface can be given by

$$k|_s = \sqrt{\frac{\gamma_s}{C_\mu}} \left| \frac{\tau_s}{\rho} \right| \quad (65)$$

where τ_s is shear stress at the surface. The boundary condition for ε is

$$\varepsilon = \gamma_s \text{Prod}|_s \quad (66)$$

where

$$\text{Prod}|_s = \frac{gH^3D}{4h^2T_w} + \nu_t \left\{ 2 \left(\frac{\partial \bar{u}}{\partial x} \right)^2 + 2 \left(\frac{\partial \bar{w}}{\partial z} \right)^2 + \left(\frac{\partial \bar{u}}{\partial z} + \frac{\partial \bar{w}}{\partial x} \right)^2 \right\} \Big|_s \quad (67)$$

where γ_s is the coefficient to be determined by turbulence properties.

For both side boundary conditions, a third order polynomial stream function may be assumed and for the bottom boundary conditions, usual boundary conditions can be employed.

4. Model tests and conclusions

In order to verify the applicability of the model, test calculations were performed in the inner layer, using the following assumptions; uniform distribution of ν_t , third order polynomial of stream function distribution at both side-boundaries, and the slip condition on the bottom.

Fig.3 shows the changes in the relative values of wave celerity C/C_B , wave heights H/H_B and mean water level ζ/h_B with the relative water depth h/h_B to compare with the experiments by Hansen and Svendsen (1979) [1]. Their experimental conditions are; the beach slope $s = 1/40$, wave period $T = 1.79s$, deep water steepness $H_o/L_o = 0.032$. The figure shows that the calculations of breaking waves and mean water level are in reasonable agreement with the experiments. Furthermore, the test calculation of undertow velocity profile corresponding to Hansen and Svendsen's experimental condition is shown in Fig.4.

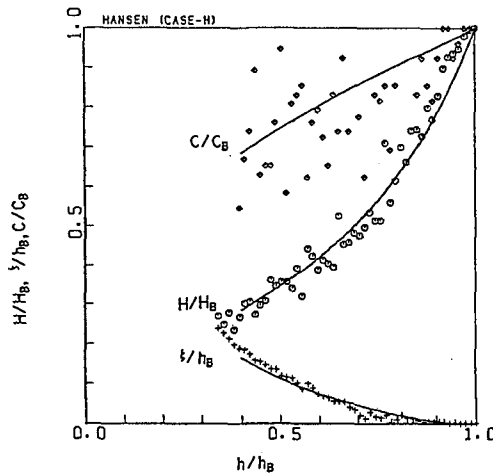


Fig.3 Changes in the calculated wave celerity C/C_B , height H/H_B and mean water level ζ/h_B in comparison with Hansen and Svendsen's experiments [1].

The vertical velocity distribution of undertow in the inner layer region is compared with experiments by Stive and Wind (1985) [4] in the relative water depth range of $h/h_B = 0.88, 0.765, 0.647$ and 0.53 . Comparisons between the calculated velocity vectors and the experiments are shown in Fig.5, where solid circles indicate the experimental data of Stive and Wind. The vertical circulation pattern calculated by the 2-D vertical circulation model under their experimental condition is shown in Fig.6.

Because of an insufficient quantity of experimental data verification is not possible, however, the theoretical curves agree reasonably well with experiments. From the comparison between Stive and Wind's laboratory experiment of undertow and our test calculations, where a uniform distribution of eddy viscosity ν_t is assumed,

it could be concluded that the undertow velocity field in the inner surf zone can be calculated by the 2-DV model developed in this study. For the cases of arbitrary bathymetry, this model is more applicable than the previous 1-DV model.

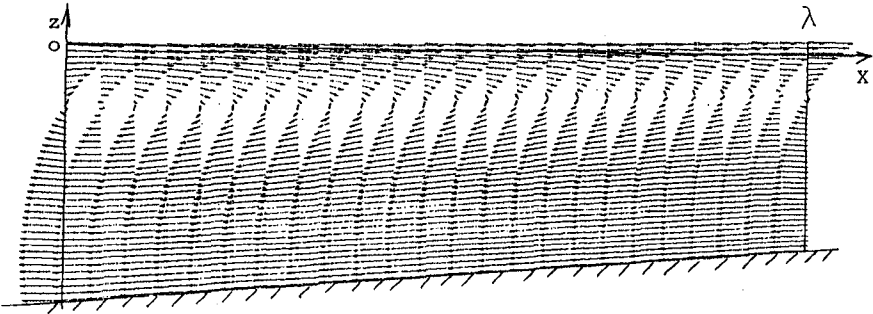


Fig.4 Test calculation of undertow velocity profile

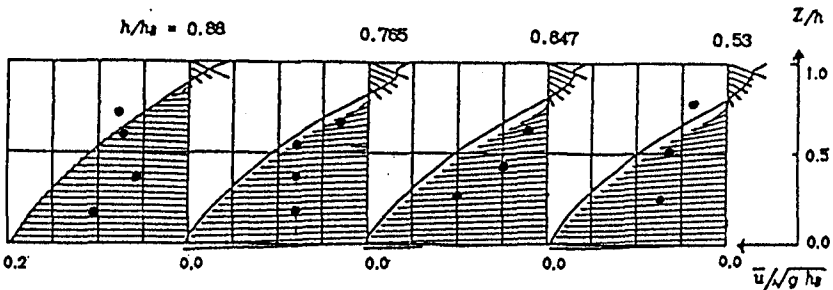


Fig.5 The vertical distributions of undertow velocity vectors and horizontal velocity profiles (solid curves) by Stive and Wind's experiment [4], at the points of $h/h_B = 0.88, 0.765, 0.647, 0.53$.

Difficulties, however, still exist in improving the side boundary conditions which are in consistency with both mean and turbulent flow fields including bottom and surface boundary conditions. In other words, further extension of the proposed 2-DV model is required to clarify the treatment of the bottom boundary conditions which can satisfy the no-slip condition of mean flow and wall boundary condition of the $k - \epsilon$ equations. It is emphasized that development of the 2-DV undertow model, which includes turbulent properties, contributes to the progress of surf zone investigations, such as sand transport mechanism, numerical calculation of the equilibrium beach profile, 3-D nearshore circulation model.

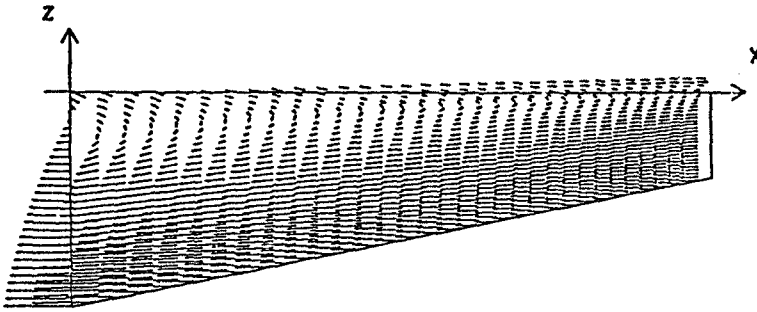


Fig.6 The vertical circulation field calculated by the model under the experimental condition of Stive and Wind [4].

References

- [1] J. Hansen and I.A. Svendsen. Regular waves in shoaling water –experimental data. *Ins. Hydrodyn. Hydraulic Eng., Series paper 21, Tech. University of Denmark, Lyngby*, 1979.
- [2] J. Hansen and I.A. Svendsen. A thoretical and experimental study of undertow. *Proc. 19th Inter. Conf. on Coastal Eng., pp.2246-2262*, 1984.
- [3] P.A. Madsen and I.A. Svendsen. On the form of the integrated conservation equations for waves in the surf zone. *Inst. Hydrodyn. and Hydraulic Engrg., Tech. Univ. Denmark, Prog. Rep.48, pp.31-39*, 1979.
- [4] M.J.F. Stive and H.G. Wind. Cross-shore mean flow in the surf zone. *Delft Hydraulics Laboratory-Report R1351, 15p.*, 1985.
- [5] I.A. Svendsen. Mass flux and undertow in a surf zone. *Coastal Engineering, Vol.8, pp.347-365*, 1984.
- [6] I.A. Svendsen. Wave heights and set-up in a surf zone. *Coastal Engineering, Vol.8, pp.303-329*, 1984.
- [7] J.J. Wanstrath, R.E. Whitaker, R.O. Reid, and A.C. Vastano. Storm surge simulation in transformed coordinates, volume i. *Technical Report No.76-3, U.S. Coastal Engineering Research Center, 166p.*, 1976.

CHAPTER 12

Violent Water Motion at Breaking-Wave Impact

M.J. Cooker* and D.H. Peregrine†

Abstract

A numerical study of water waves breaking against a vertical wall is described. The exact equations for free-surface potential flow are solved. Solutions for a simple overturning wave meeting a vertical wall placed at several positions give unexpectedly violent water motion. The face of the incident wave can converge towards a point on the wall causing very high pressure, acceleration and velocity. It seems likely that this particular type of flow corresponds to the most extreme conditions encountered in laboratories and on coasts despite the lack of any direct water impact. Details of the flow reveal that compressibility of the water is unlikely to be relevant for wave forces, but that scaling from laboratory to prototype should allow for wall roughness and for small waves riding on the incident wave.

1. Introduction

We describe results from a computational study of waves which are breaking or near breaking as they strike a vertical wall. Our aim has been to see how much information can be obtained about violent wave impacts, from a two-dimensional numerical model of irrotational inviscid flow. The model accurately deals with the overturning motion of a breaking wave and provides full information on velocities, pressures etc. up to the instant of impact.

A prototype example of the type of wave impact we envisage is sketched in figure 1. Shoaling water in front of a sea wall or breakwater causes an incident wave to break. Since such waves can cause appreciable damage many model experiments have been performed, e.g. Bagnold (1939), Nagai (1960), Mitsuyasu (1966), Richert (1968), Kirkgöz (1982), Chan & Melville (1988) and Partenscky (1988).

*Research Assistant. †Professor.
School of Mathematics, University of Bristol, University Walk,
Bristol, BS8 1TW, England.

The underwater shape of the structure, or bed profile may cause the height/depth ratio of breaking waves to be much greater than that for a typical wave on a gently sloping beach. For example in some of Nagai's experiments the base of the vertical wall was exposed in front of some incident waves. This large height/depth ratio indicates that either the particular topography of an experimental or prototype structure should be modelled or an unconventional incident wave, much higher than the depth, should be used. We make the latter choice.

In addition we wish to study the effect of varying the distance between the wall and the breaking point of the wave. We do this by forming a wave which propagates over a flat horizontal bed. The initial wave has a gradual, monotonic increase in surface elevation. Hence, when it propagates, it steepens as the higher parts tend to catch up the lower portion of the wave. By choosing wave heights larger than 0.3 times the depth, the wave continues to steepen until it breaks. There is zero flow in front of this wave so that a vertical wall can be placed at any chosen spot in the path of the wave. This gives two primary parameters that may be varied:

- (i) the wave height
- (ii) the position of the wall relative to the position at which the wave would break in the absence of a wall.

In this paper, we consider a single wave height and look at variations of the wall position. Comparisons can be made with other types of wave by noting that our initial depth of water, h , corresponds to the depth of water in the *trough* of oscillatory waves, and not to the mean water level.

2. The mathematical and numerical model

The flow is assumed to be inviscid, two-dimensional and incompressible with irrotational flow so that a velocity potential satisfying Laplace's equation can be used. The effect of the air above the water is neglected, so that the free surface is at constant pressure. No further approximations are made in the mathematical formulation.

The numerical modelling is carried out with a program developed from the accurate and efficient, high-order, boundary-integral method of Dold and Peregrine (1986). Recent examples of work with closely related programs are Tanaka, Dold, Lewy and Peregrine (1987) and Cooker, Peregrine, Vidal and Dold (1990).

The initial wave, we have chosen, has a horizontal velocity

$$u(x,0) = -\frac{1}{2}u_0(gh)^{\frac{1}{2}}[1+\tanh \lambda(x-x_0)]$$

and elevation $\zeta(x_0) = (|u_0| + \frac{1}{2}u_0^2)h$.

This corresponds to a "simple-wave" solution of shallow-water theory for a wave propagating in the $-x$ direction if the initial surface slope is gentle enough. Using units in which g and h are both unity, we illustrate results for the wave of height

$$\Delta h = \zeta(\infty, 0) - \zeta(-\infty, 0) = 1.5$$

(i.e. $u_0 = 1.1623$). With $\lambda = 0.5$, there was no significant wave in the $+x$ direction and the wave soon develops into a plunging breaker as shown in figure 2 where $x_0 = 0$. Although shallow-water theory guides our choice of initial conditions, the computations make no such simplifying assumptions.

A vertical wall can be inserted in this flow at any chosen place. In fact, the wall is modelled by using symmetry: two equal and oppositely-directed waves travel towards each other starting a distance x_0 from the line of symmetry ($x=0$). For example $x_0 = 9$ gives a wall positioned at $x = -9$ in figure 2, directly in the path of the overturning jet. On the other hand $x_0 = 7.5$ places a wall close to the point where the wave first has a vertical tangent to its free surface.

For purposes of illustration just the one initial wave, $\Delta h = 1.5$, $\lambda = 0.5$, is used with different values of x_0 . This wave can be compared with other more realistic waves by noting that at the initial time there is no motion at the wall and water is moving towards the wall. Thus, our initial condition resembles an oscillatory or irregular wave at the moment its trough is adjacent to the wall. That means our depth h , corresponds to *minimum* water depth at the wall.

3. Examples of wave motion against a wall

First we consider the case $x_0 = 9$ where an overturning wave meets the wall. This is illustrated in figure 3. As may be seen, the profile of the overturning part of the wave appears to be unaffected by the wall. Examination of the computed velocities and accelerations shows that the velocity of the jet is unchanged at $2.6 (gh)^{\frac{1}{2}}$ and the horizontal acceleration under the jet, which is $3.4g$ in the undisturbed wave, changes little. On the other hand, the part of the wave near the water-line cannot pass through the wall and *rises quickly up the wall*. For the last profile calculated the vertical velocity and acceleration at the wall are $18.5 (gh)^{\frac{1}{2}}$ and $17.5 g$, respectively.

The current program is unable to model the direct impact of the jet on the wall (though see Cooker and Peregrine, 1990). However, experiments from those of Bagnold (1939) onwards, clearly show that maximum pressures occur if the wave has a vertical face when it meets the wall. Hence we could expect from figure 2 a value of $x_0 = 7.5$ to give us a more severe impact.

As may be seen in the illustrations of figure 4(a) and (b) the wave with $x_0 = 7.5$ fails to develop a vertical face, because of the proximity of the wall. The water surface rises smoothly and then forms a thin vertical jet at the wall, so no actual impact occurs. Except for the region near its base the jet is in free fall. Its velocity of $14 (gh)^{\frac{1}{2}}$ indicates it could rise to a height of about $100h$. In practice its motion is likely to be disrupted by the air.

The flow at the base of the jet is interesting, especially at its inception. Here a maximum water acceleration of nearly $2000g$ is computed and the correspondingly high pressure gradients lead to a brief high pressure on the wall, as the jet forms. The distribution of pressure on the wall at the time of maximum pressure is given in figure 5. Note how the pressure is significantly greater than instantaneous hydrostatic pressure all the way down to the bed. In figure 6 contours of pressure field throughout the water are shown. It can be seen that substantial pressures extend some distance from the wall.

From an engineering point of view it is the pressure distribution on the wall which is usually most relevant. This is plotted as a function of time in figure 7. Only a brief interval $(-0.7 \text{ to } +0.045)(h/g)^{\frac{1}{2}}$ each side of the maximum is shown, but as may be seen this covers all the pressure greater than $8\rho gh$. The values that would be read by a fixed pressure gauge on the wall are easily deduced by looking along a horizontal line in the diagram.

As already noted the incident wave does not become vertical for $x_0 = 7.5$; computations with $x_0 = 8$ do give a vertical face. As shown in figure 8 this wave only briefly has a vertical face. The free surface flow is dominated by a convergence toward the wall. Again a jet forms. This example gives the most severe conditions we have computed so far. Compared with the case of $x_0 = 7.5$ the greater convergence of the flow gives a smaller, more violent jet. Its velocity is $20 (gh)^{\frac{1}{2}}$, corresponding to a height of $200h$ in free fall. The small jet size leads to greater computational effort being needed to resolve the motion. At the last reliably resolved time, pressure and acceleration are still increasing at levels in excess of $50\rho gh$ and $6000g$, respectively. Maxima of over $60\rho gh$ and $8000g$ are expected. The maximum value of $\partial p/\partial t$ has been calculated and is $3000\rho g^{\frac{3}{2}}h^{\frac{1}{2}}$, which gives a typical time scale for the pressure rise of about $0.005(h/g)^{\frac{1}{2}}$.

4. Discussion

It has been a surprise that high "impact-type" pressures are found in a smooth potential flow. These pressures are of the same order of magnitude as the maximum pressures found experimentally for laboratory waves. As is well known these do not agree well with large-scale measurements when Froude scaling is used. Nevertheless we show in table 1, how our estimated maximum results scale for different heights of wave from laboratory to full-scale.

Table 1: Scaling of extreme conditions

Initial water depth	h	<u>50mm</u>	<u>100mm</u>	<u>1m</u>	<u>5m</u>
Total initial wave height	1.5h	75mm	150mm	1.5m	7.5m
Maximum velocity	$20(g/h)^{\frac{1}{2}}$	$14m\ s^{-1}$	$20m\ s^{-1}$	$60m\ s^{-1}$	$140m\ s^{-1}$
Maximum acceleration	8000g				
Maximum pressure (as a head of water)	$60\rho gh$	3m	6m	60m	300m
Time scale of pressure rise	$0.005(h/g)^{\frac{1}{2}}$	0.35ms	0.5ms	1.6ms	3.5ms

The maximum pressures occur while a jet forms from a flow which has converged towards a point on the wall. Experimental descriptions mention an impact of the vertical wave face, yet this does not occur, the water surface violently "flips through" from a contracting half-cavity to a high speed vertical jet. In a recent paper Chan and Melville (1988) observe from high-speed photography "that wave impact occurred through the focussing of the incident wavefront onto the wall; that is through a convergence of the wave crest and the surface intersection point at the wall"; a description which fits our results.

Hattori (private communication 1990) measures high impact pressures of $120\rho gh$ in an experiment which looks similar to our computation. There is a trace of a jet in one of his video frames. However we expect the jet to be only 0.3mm thick and to form on a time scale of 0.3ms so it is not surprising that it is difficult to observe, for example Chan and Melville use film at 1100 frames per second, and Hattori's video is at 200 frames per second. Both these recent experiments were made on a scale where the incident wave was only a few centimetres high, and both measured highest peak pressures at the "flip through" condition.

Our results lead us to speculate that if the filling "cavity" contracts to a small enough size then there is no upper limit on pressure and jet velocity within our model. Clearly, neglected physical properties such as viscosity and compressibility might change this picture. Since we have full details of the potential flow it is easy to assess the relevance of these effects.

We have considered incident waves as low as 10mm high and estimate that the effects of surface tension and viscosity are unimportant until after the formation of the jet. Even then it is only in the jet that surface tension can be relevant. The major physical effects in this "flip through" motion are the fluid inertia and the pressures it generates. Once water is in the jet these hydrodynamic pressures become negligible so that we expect surface tension and aerodynamic effects to become important, e.g. thin jets rapidly break up into spray.

The role of compressibility has often been discussed in the context of water wave impact. In the most violent impact we have calculated, where no air is trapped, we have a maximum value of $\partial p / \partial t = 3000 \rho g^{\frac{2}{3}} h^{\frac{1}{3}}$. This can be used to compare terms in the continuity equation for a *compressible* fluid. We find the ratio

$$\frac{\partial p}{\partial t} / \rho \frac{\partial v}{\partial y} \approx 15 \frac{gh}{a^2}$$

where a^2 is the velocity of sound.

A low value of $a = 100 \text{ m sec}^{-1}$, corresponds to water aerated with 1% by volume of small bubbles. Even then for $h = 1 \text{ m}$ this ratio is 0.015. Hence compressibility has little effect on the fluid dynamics. However a loud noise only requires a small amount of energy compared with that in the water motion.

Although it is hard to compare prototype conditions with experiments it is generally considered that the Froude scaling, which is natural for relating our computations to physical reality, generally overestimates prototype pressures. Since compressibility and viscosity appear to be irrelevant for this scaling we consider a different possibility.

From our computations it appears that high pressures are obtained when the wave surface focusses toward a point before a vertical jet is formed. Superficially, there seems to be no limit to this focussing and hence to the maximum pressure. On the other hand finer focussing implies a smaller and more violent jet. The minimum size of coherent jet that can be created depends on the roughness of the wall and liquid surfaces involved, e.g. if a wall has a roughness of about 10mm amplitude then pressures computed for the generation of a jet of width 10mm at a smooth wall are likely to be gross over-estimates. Large waves almost always have smaller waves upon them, and this free surface "roughness" is also likely to influence the maximum pressures at a wall, by either disrupting the surface focussing or inducing premature jet formation.

One further unexpected feature is the large extent of short-lived pressures which are several times higher than the hydrostatic value. The bed experiences this pressure pulse and it is interesting to speculate on the response of sediments to such a loading.

5. Conclusion

Potential flow computations reveal that there is violent water motion and very high pressures when near-breaking waves meet a vertical wall. The highest pressure occurs when a high-speed vertical jet forms at the wall. It seems likely that this "flip-through" type of interaction between wave and wall can give higher pressures than a direct impact by the jet from an overturning wave. The computed results indicate that the compressibility of water is unlikely to be of any importance, but that roughness of the wall or water surface may be significant in limiting extreme pressures for coastal waves.

References

- Bagnold, R.A. (1939) "Interim report on wave-pressure research". J.Inst. of Civil Engineers (1938-39), 12, p201-226.
- Blackmore, P.A. and Hewson, P.J. (1984) "Experiments on full-scale wave impact pressures". Coastal Engineering, 8, pp 331-346.
- Chan, E.S. and Melville, W.K. (1988) "Deep water plunging wave pressures on a vertical plane wall". Proc.R.Soc.Lond A417, 95-131.
- Cooker, M.J. and Peregrine, D.H. (1990) "A model for breaking wave impact pressures". Proc.22nd Intl.Conf.Coastal Eng. The Netherlands, June 1990.
- Cooker, M.J., Peregrine, D.H., Vidal, C. and Dold, J.W. (1990) "The interaction between a solitary wave and a submerged semi-circular cylinder". J.Fluid.Mech., 215, 1-22, Apr. 1990.
- Dold, J.W. and Peregrine, D.H. (1986) "An efficient boundary-integral method for steep unsteady water waves" in "Numerical methods for fluid dynamics II". Eds.K.W. Morton and M.J. Baines. Oxford.Univ.Press, 671-679.
- Kirkgöz, M.S. (1982) "Shock pressure of breaking waves on vertical walls". Eng.Div., Proc.ASCE, 108, Feb. 1982.
- Mitsuyasu, H. (1966) "Shock pressure of breaking waves I". Coastal Eng.Japan, 9, 83-96.

Nagai, S. (1960) "Shock pressures exerted by breaking waves on breakwaters". J. Waterways and Harbours Div. Proc., ASCE, WW2, 86, 1-38.

Partensky, H.W. (1988) "Dynamic forces due to breaking waves at vertical coastal structures". Proc. 21st Coastal Eng. Conf. June 1988, 2504-2518.

Richert, G. (1968) "Experimental investigation of shock pressures against breakwaters". Proc. 11th Conf. Coastal Eng. ASCE, 1, 954-973.

Tanaka, M, Dold, J.W., Lewy, M. and Peregrine, D.H.(1987) "Instability and breaking of a solitary wave". J.Fluid Mech.,185, 235-248.

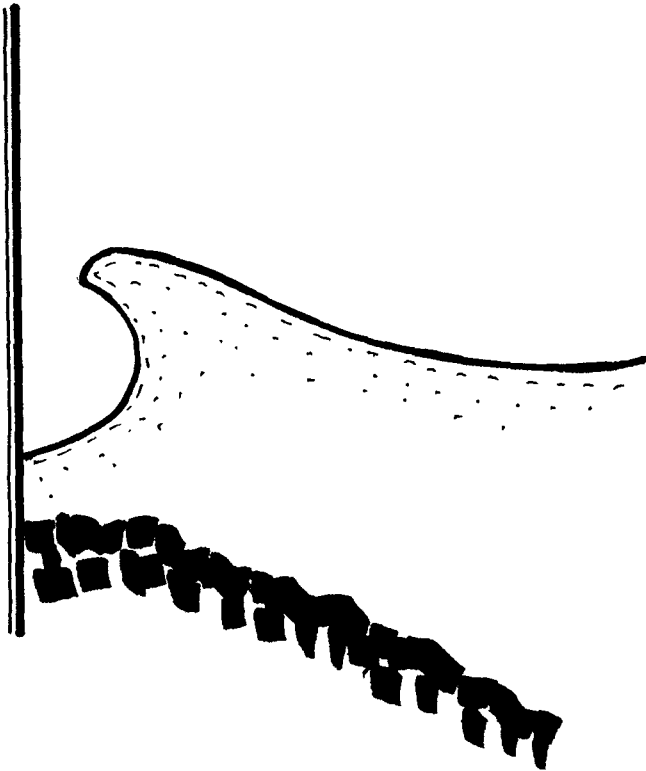


Figure 1: Sketch of a wave hitting a wall.

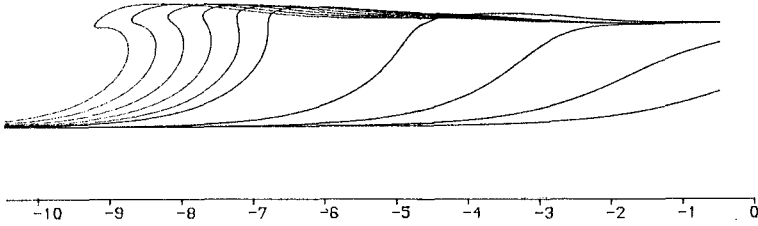


Figure 2: A wave of height $1.5h$ advancing into still water of depth h *without any wall*. The free-surface profiles are at times $t = 0$ (1) 4 (0.2) 5 $\sqrt{(h/g)}$. The maximum velocity in the jet is $2.6 \sqrt{(gh)}$. The steady flow at $x = +\infty$ has speed 1.162, and is directed to the left.

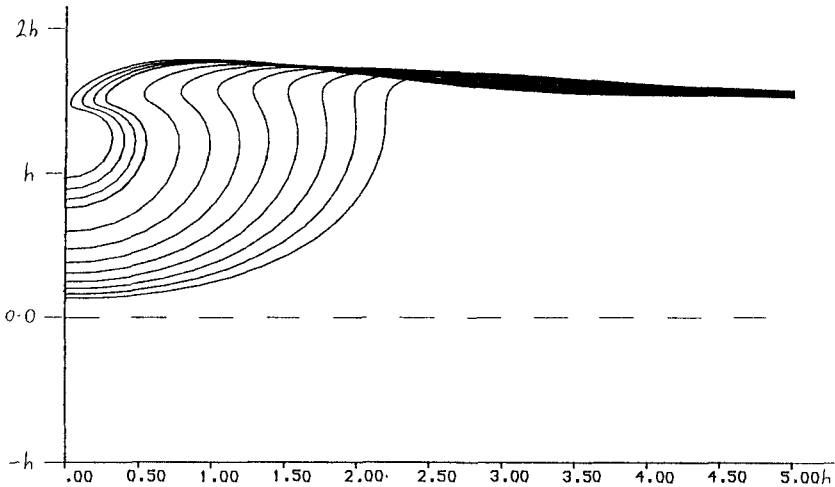


Figure 3: The wave of figure 2 meeting a wall as it overturns. The initial wall-wave distance, $x_0 = 9$. Surface profiles at $t = 4$ (0.1) 4.8 (0.03) 4.89

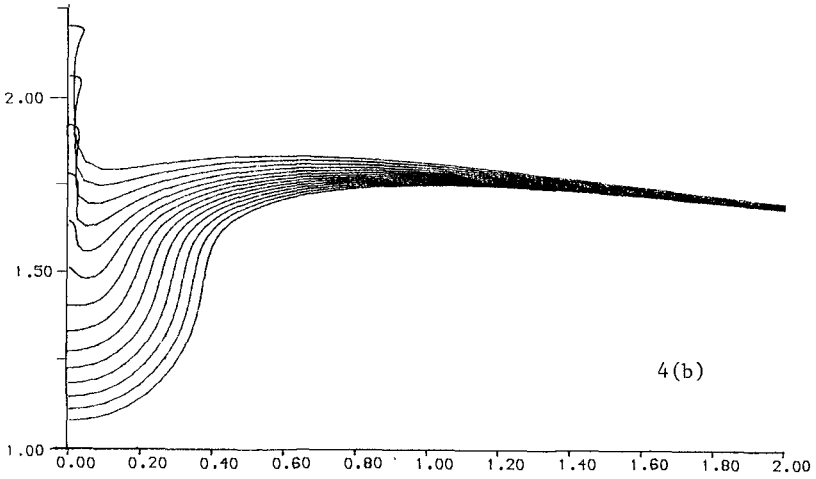
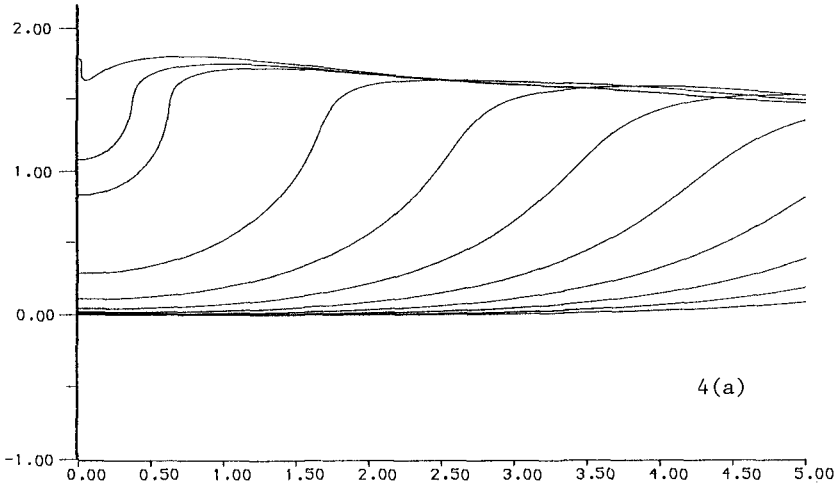


Figure 4:

The wave of figure 2 meeting a wall *before* it overturns ($x_0=7.5$).

(a) Surface profiles at times $t = 0$ (0.5) 4.0, 4.1, 4.2 .

(b) Close-up view near the water-line at times $t = 4.10$ (0.01) 4.23

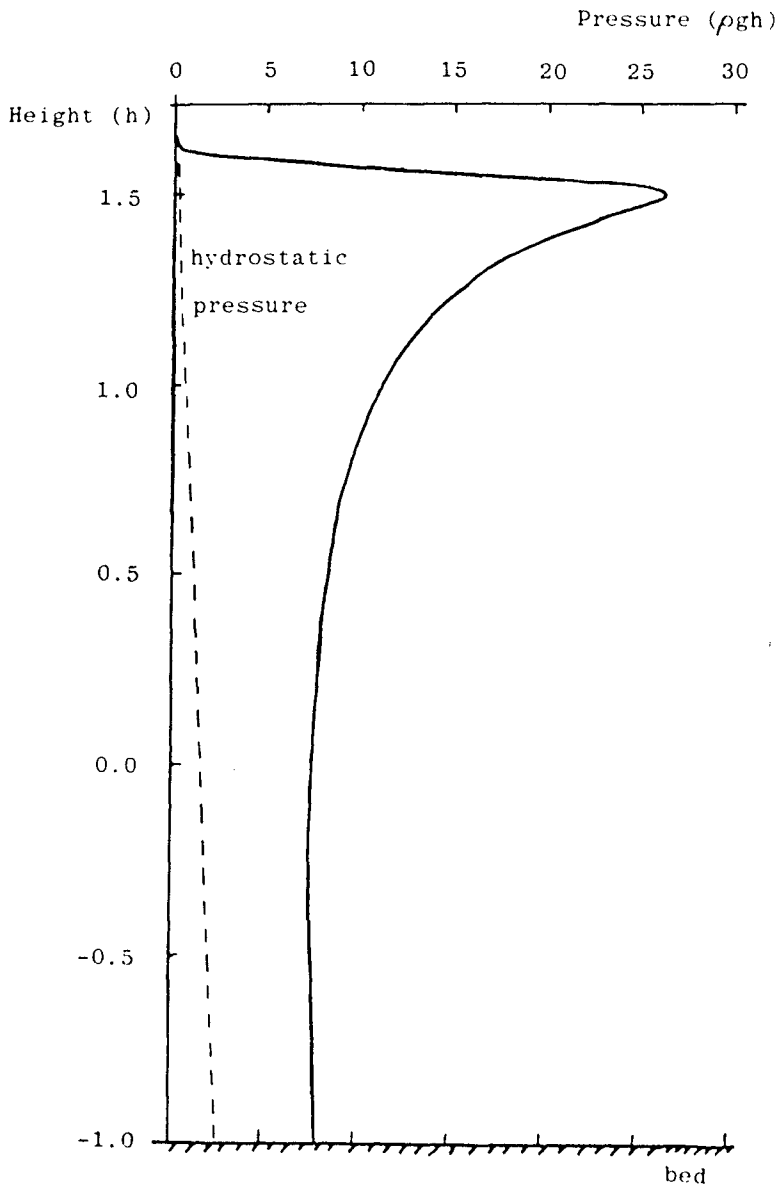


Figure 5: Pressure on the wall at time $t = 4.19$, for the wave in figure 4. This is the time of maximum pressure. The broken line shows the relatively small component of hydrostatic pressure.

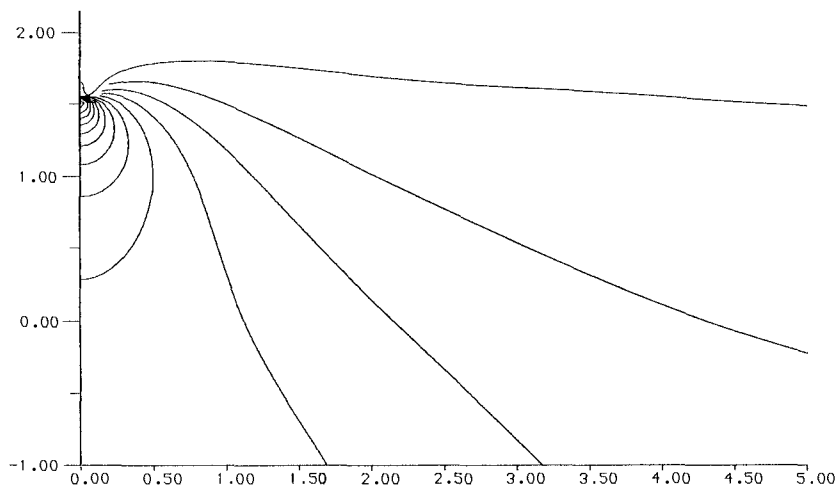


Figure 6: Pressure contours for the wave in figure 4 at time 4.19. The free surface has pressure zero. The pressure contour increment is $2 \rho gh$. The peak pressure is $26 \rho gh$, and lies just below the water-line.

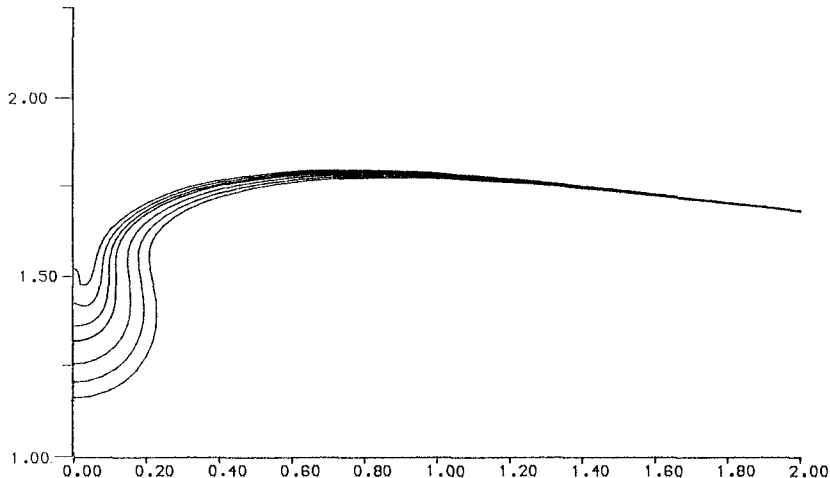


Figure 8: The wave of figure 2 meeting the wall, with $x_0 = 8$. Note that this is a close-up view near the water-line. Surface profiles at times $t = 4.400 (0.01) 4.430 (0.005) 4.445$.

Note this is drawn on the same spatial scale as figure 4(b).

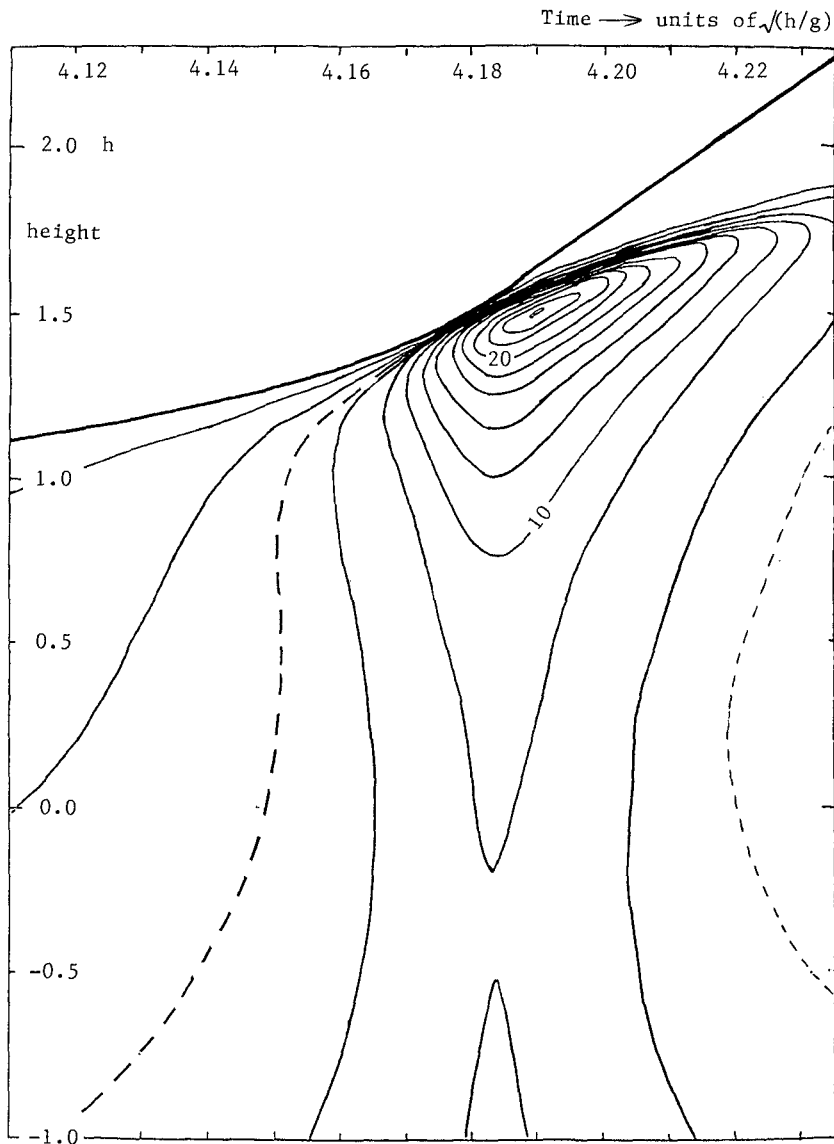


Figure 7: Pressure on the wall for the wave in figure 4. The pressure contours are drawn here as a function of *distance up the wall* (vertical axis) and *time* (horizontal axis). The solid upper curve is the position of the water-line. The contour interval is 2 pgh, except for the broken-line contour at 5 pgh.

Wave Group Properties of Coastal Waves

Hajime Mase¹, M. ASCE, Takao Yamashita² and Katsuyuki Hayashi³

ABSTRACT

This paper examines the following properties of observed wave groups: (1) the change of wave grouping from offshore to shallow water region including the surf zone; (2) the relation between wave groupiness and wave height distributions; and (3) the distribution of run lengths and time series of wave heights of extreme wave groups which contain the maximum wave height in each wave record. Main results are summarized as follows: (1) wave groups become flattened as they propagate landward; (2) no clear maximum in mean length of runs is seen around the position where the significant wave height is the maximum, in contrast to the laboratory data, while the tendency of the change of GF is the same as the experimental data; (3) when wave grouping becomes pronounced, the distribution of wave heights becomes wider; (4) extreme wave groups accompany more large waves than ordinary wave groups; (5) for the case of narrow spectra, the time series of wave heights of extreme wave groups is represented fairly well by that of the wave group formed by the side-band instability, and the distribution of three high waves is also in qualitative agreement with that of envelope soliton, and (6) for wide spectra, which may occur during the peak of storms, wave heights in front and rear of the maximum wave are half as large as the maximum wave height, implying that a maximum wave tends to appear without accompanying other large waves.

INTRODUCTION

Certain sequences of large waves or wave groups are important not only in engineering problems, such as the stability of rubble mound breakwaters, the fluctuation of wave overtopping, and the slow drift oscillation of moored and floating structures, but also in hydrodynamical problems, such as the surf beat, the modulational instability, and the evolution of finite amplitude waves.

The degree of wave grouping is described by run lengths of large waves, groupiness factors, correlation coefficients of successive wave heights, and parameters related to the wave spectra. Elgar et al. (1984) showed that the observed mean lengths

¹ Research Assoc., Department of Civil Engrg., Kyoto University, Kyoto, 606, Japan.

² Research Assoc., Disaster Prevention Research Institute, Kyoto University, Uji, 611, Japan.

³ Engineer, Aichi Prefectural Government, Nagoya, 460, Japan.

of runs and occurrence probabilities of run lengths in relatively deep water were statistically consistent with the numerical simulations based on linear wave theory using the measured spectra with assumed random phases. However, the observations in shallow water deviated from the linear simulations and the observed mean lengths of runs were larger than the simulated mean lengths. Lake and Yuen (1978) explained amplitude-modulation periods of laboratory wind waves from a hydrodynamical viewpoint such as the side-band instability. Su (1986) examined the time series of wave heights of extreme wave groups which contained the maximum wave height in each wave record and showed that the observed time series of wave heights was described by the wave height sequence of the wave group formed by the side-band instability. The fact that wave group properties can be explained in different ways may show that various phenomena or mechanisms exist in random sea waves. Therefore, further examinations of wave group properties from various aspects or by different methods are necessary so that the wave group properties may eventually become predictable.

This study is a part of large field observations to investigate wave transformations, directional spectra, nearshore currents, and sediment transports. This paper examines the following aspects of wave groups by analyzing the observed wave data: (1) the change of wave grouping from offshore to shallow water region as well as in constant shallow water region; (2) the relation between wave groupiness and wave height distributions; and (3) the distribution of run lengths and time series of wave heights of extreme wave groups. These properties are compared with theoretical and experimental results.

FIELD OBSERVATION

Wave observations were carried out at the Ogata Wave Observatory, Disaster Prevention Research Institute, Kyoto University, located at the Ogata Coast facing the Japan Sea. A T-shaped observation pier, which is 256 m long in the cross-shore direction and 107 m long in the alongshore direction, was constructed with truss girders of five spans of 50 m supported by piers composed of three steel piles to minimize its effects on the nearshore hydrodynamics and sediment transport. The location of the Ogata Wave Observatory and the bottom topography in the vicinity of the T-shaped pier are shown in Fig.1.

The field data were collected from November 27 to December 8, 1987, and from January 11 to 18, 1989. Fig.2 shows the arrangement of sensors used in the observations. Nine capacitance-type and seven ultrasonic-type wave gauges were mounted on the pier, as indicated by the letter 'C' and 'US' in Fig.2 (a). Three ultrasonic current meters, indicated by the letter 'CM', were installed at the elevation of approximately 1 m above the seabed under the ultrasonic wave gauges. On the extension of the line of the pier (along the straight line normal to the shoreline), a waverider buoy ('WR' in short) was installed at the water depth of 30 m (in the first observation) or 20 m (in the second observation), and three sets of an ultrasonic wave

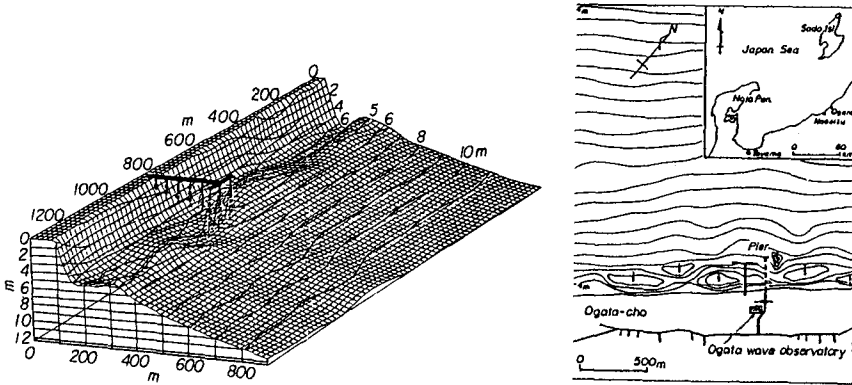


Figure 1 Location of Ogata Wave Observatory and bottom topography around T-shaped pier (from the pamphlet of Ogata Wave Observatory, Kyoto University).

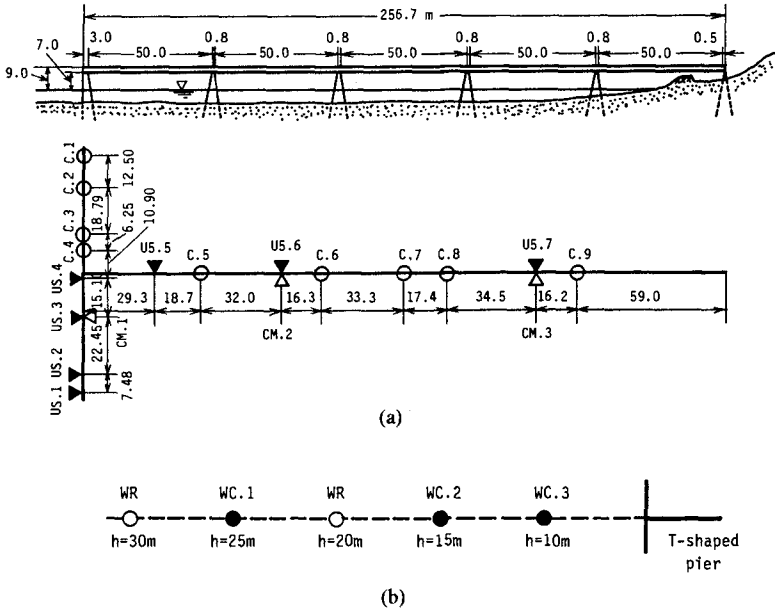


Figure 2 Arrangement of sensors at T-shaped pier in (a) and seaward of T-shaped pier in (b).

gauge and a two-components electromagnetic current meter ('WC' in short) were set on the seabed at the water depths of 25, 15 and 10 m, which are indicated by 'WC.1', 'WC.2' and 'WC.3' in Fig.2 (b). The water depth at the locations of 'C.1'~'C.8' is approximately constant and 5.1 m. The bottom slope seaward of the tip of the pier is about 1/100. For the first field data from November 27 to December 8, 1987, the time series from all sensors were recorded by two analog data recorders for 90 minutes every three hours. The recorded time series were digitized at a sampling interval $\Delta t=0.256$ sec. For the second field data from January 11 to 18, the time series from the sensors 'C', 'US', 'WR' and 'CM' were recorded directly on digital magnetic tapes as follows: for 40 minutes every hour at $\Delta t=0.1$ sec from 11th 19:00 to 15th 7:40; for 20 minutes every hour at $\Delta t=0.2$ sec until 16th 8:20; and hereafter for 20 minutes every two hours at $\Delta t=0.2$ sec. The data of 90 and 40 minutes long were divided into segments of 20 minutes. The time series of 'WC' were stored on an internal digital magnetic tape for 17 minutes every hour at $\Delta t=0.5$ sec.

In order to remove low and high frequency motions from each wave record and limit the following analyses to incident wind waves only, the Fourier components with frequencies smaller than half the peak frequency and larger than six times of the peak frequency were set zero. The modified Fourier components were then transformed into the time domain variations by a inverse FFT technique. The observed data included a wide range of incident wave conditions from narrow-banded to broad-banded spectra. The significant wave heights measured by 'WR' ranged from 0.5 m to 4.5 m, and the significant wave periods ranged from 4.0 sec to 10.0 sec. Dominant wave directions were normal to the shoreline.

RESULTS AND DISCUSSION

Change of Wave Grouping from Offshore to Shallow Water Region

In order to describe the magnitude of wave grouping, at least two parameters are needed (Mase and Iwagaki, 1986): One parameter for representing the length of sequence of high waves in a time series such as the mean length of runs, $\overline{\lambda(H)}$, exceeding the mean wave height, \bar{H} ; and the other for representing the magnitude of the variation of wave energy such as the groupiness factor, GF . The measured changes of the two parameters $\overline{\lambda(H)}$ and GF will indicate whether wave grouping becomes pronounced or not. When wave grouping pronounced, GF increases but $\overline{\lambda(H)}$ may not decrease. When wave grouping becomes weakened, GF decreases but $\overline{\lambda(H)}$ may increase or decrease. Fig.3 shows the changes of $\overline{\lambda(H)}$ and GF against the nondimensional water depth, $k_m h$ with k_m being the wavenumber based on the mean wave period in the water depth h , where the data of 'WR', 'WC.3', 'C.4', and 'US.4' were plotted. It is noted that the classification by wave steepness did not show any clear tendency. The linear regression lines plotted in Fig.3 show that GF decreases and

$\overline{J(H)}$ increases as $k_m h$ is decreased. This implies that wave groups of shoaling random waves tend to become flattened.

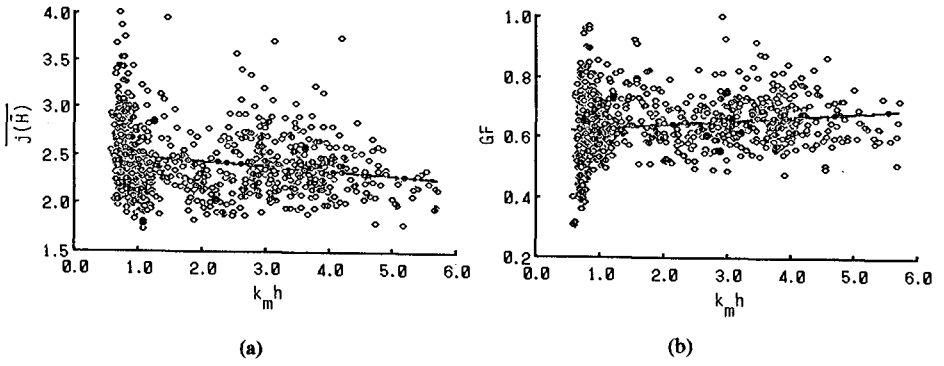


Figure 3 Change of wave grouping from offshore to shallow water region: (a) mean length of runs; (b) groupiness factor.

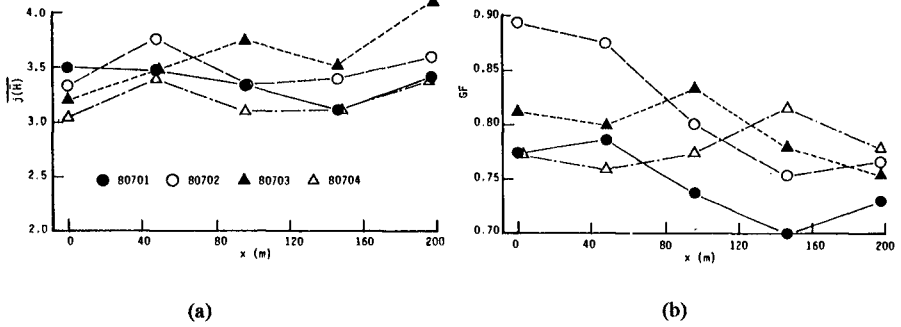


Figure 4 Change of grouping of non-breaking waves in shallow water of constant depth: (a) mean length of runs; (b) groupiness factor.

Change of Grouping of Non-Breaking Coastal Waves in Shallow Water of Constant Depth

Fig.4 shows the values of $\overline{\lambda(H)}$ and GF at the locations of 'C.4', 'C.5', 'C.6', 'C.8' and 'C.9' (the horizontal coordinate x is positive landward with $x=0$ at the location of 'C.4') under the condition of $k_m h < 1.0$, narrow-banded wave spectra, and no wave breaking. For the cases of B0701 (20:30 of November 30, 1987) and B0702 (23:30 of November 30, 1987), $\overline{\lambda(H)}$ is nearly constant and GF decreases in the shoreward direction. For the case of B0703 (2:30 of December 1, 1987), GF decreases and $\overline{\lambda(H)}$ increases. These tendencies mean that wave groups of random waves become flattened with the propagating distance as was the case with the experimental results of Mase and Iwagaki (1987) in which the flattening of a single wave group was verified in laboratory experiment and by numerical simulations using the nonlinear Schrödinger equation.

Change of Wave Grouping in Shallow Water Including Surf Zone

Fig.5 shows the changes of $\overline{\lambda(H)}$ and GF against the normalized water depth h/H_0' (H_0' is the deep water significant wave height estimated from the significant wave at 'WR' using linear wave theory). The curves in Fig.5 (a) and (b) are the fifth and fourth polynomial regression curves, respectively, which are found to give the best fit among the first to fifth polynomial equations. The change of the significant wave height $H_{1/3}/H_0'$ against h/H_0' is shown in Fig.6, where the curves are the results calculated by the random wave model of Mase et al. (1986) for wave steepness of 0.01 and 0.04, approximately corresponding to the observed maximum and minimum wave steepness. The experimental data on $\overline{\lambda(H)}$ by Mase (1989) became the maximum around the point where $H_{1/3}/H_0'$ was the maximum. This point for the present field data is roughly at $h/H_0'=2.5$; however, no clear maximum in $\overline{\lambda(H)}$ is seen around $h/H_0'=2.5$ in Fig.5 (a). It is seen in Fig.5 (a) that the range of $\overline{\lambda(H)}$ in the region of $h/H_0' > 2.5$ is larger than that in the region of $h/H_0' < 2.5$. GF is almost constant in the region of $h/H_0' > 3.0$, and decreases with the decrease of the water depth for $h/H_0' < 3.0$. This is the same tendency as the experimental data by Mase (1989). The mean length of runs seems to be more unstable statistically than the groupiness factor, since the number of runs is small for twenty-minute-long records.

Wave Grouping and Wave Height Distribution

The observed wave height distributions were presented by the Weibull distribution whose the shape factor, m , was estimated by the maximum likelihood method (Cohen, 1965). The Rayleigh distribution is a special case with $m=2$ of the Weibull distribu-

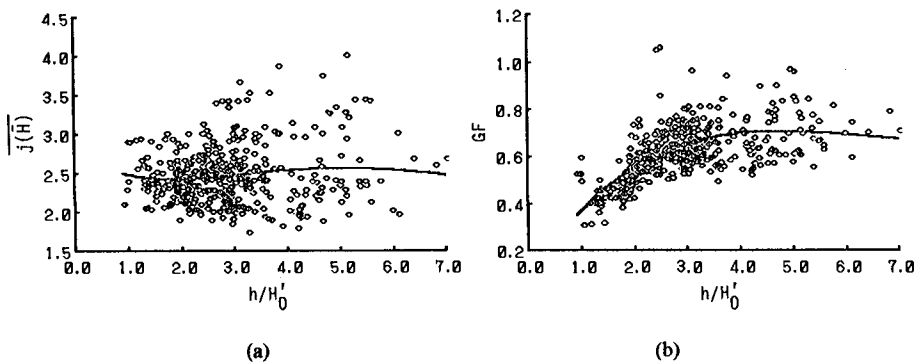


Figure 5 Change of wave grouping in shallow water including surf zone: (a) mean length of runs; (b) groupiness factor.

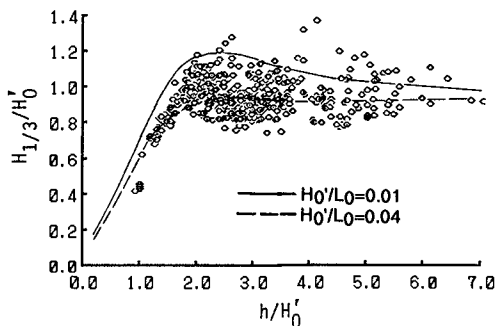


Figure 6 Transformation of significant wave heights in shallow water.

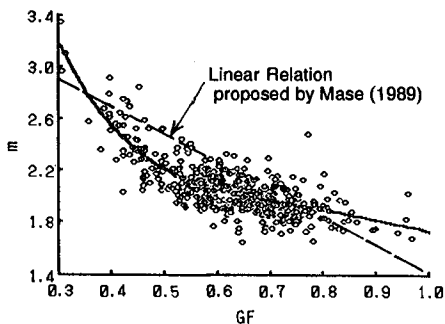


Figure 7 Relation between groupiness factor GF and shape factor m of wave height distribution.

tion. Fig.7 shows the relationship between GF and m . The tendency of the data points may be represented simply by the broken line proposed by Mase (1989), whereas the solid line is the following fifth polynomial equation fitted to the data points:

$$m = 9.45 - 37.83 GF + 76.33 GF^2 - 75.34 GF^3 + 35.30 GF^4 - 6.17 GF^5 \quad (1)$$

Fig.7 shows that as wave grouping increases (GF becomes larger), the distribution of wave height becomes wider (m becomes smaller). The Rayleigh distribution would underestimate the occurrence probability of extreme wave heights. The scatter in the data suggests that the relationship between the two parameters is not simple because of neglected effects of other wave characteristics.

Distribution of Run Lengths of Extreme Wave Groups

A phenomenon that the maximum wave in a wave record seldom appears alone but usually accompanies with several large waves was reported by Goda (1976). Fig.8 (a) shows that the occurrence probability of $j(\bar{H})=1$ is the largest for the case of ordinary runs of wave heights, as indicated by the symbols of \circ and \square corresponding to the data of 'WR' and 'C.4', respectively, while the occurrence probability of $j(\bar{H})=4$ is the

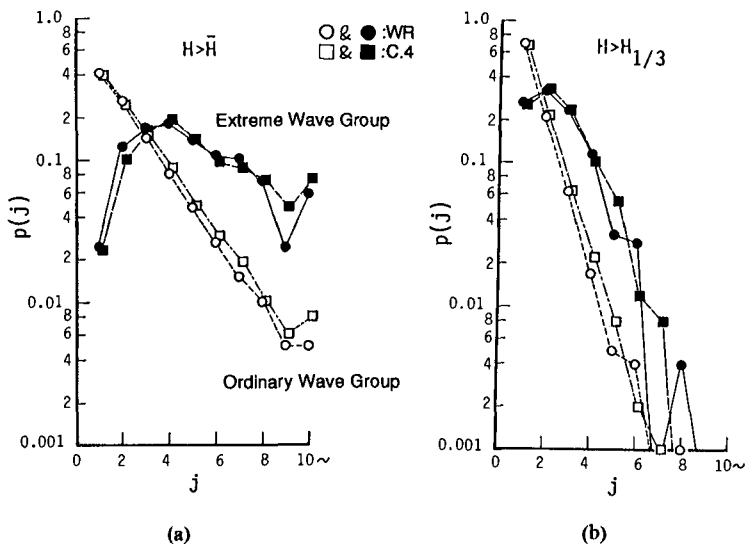


Figure 8 Occurrence probabilities of run lengths of ordinary and extreme wave groups where the threshold is the mean wave height in (a) and the significant wave height in (b).

largest for the conditional runs containing the maximum wave height in each wave record (extreme wave groups), as indicated by the symbols of ● and ■. The occurrence probabilities of run lengths with the threshold of $H_{1/3}$ are shown in Fig.8 (b), which also shows that extreme wave groups contain more large waves than ordinary wave groups. However, this analysis of runs is based on the number of large waves exceeding a threshold and does not account for the relative magnitude of the waves around the maximum wave.

Time Series of Wave Heights in Extreme Wave Groups

Following the analysis of Su (1986), we describe the time series of wave heights in a extreme wave groups as $H_{-3}, H_{-2}, H_{-1}, H_0, H_1, H_2, H_3$, where H_0 is the maximum wave height. Su (1986) found that the extreme wave group consisted of three high waves whose heights were greater than the significant wave height. On the basis of the experimental observations of the nonlinear side-band instability of finite amplitude waves, Su (1986) showed that the extreme wave group could be explained as the manifestation of the maximum modulation of waves. Time series of the surface displacement, $\eta(t)$, under the maximum modulation due to the side-band instability, was expressed as:

$$\eta(t) = a_0 \sin 2\pi f_0 t + \frac{a_0}{\sqrt{2}} \left[\sin\{2\pi(1-a_0k_0)f_0t\} + \sin\{2\pi(1+a_0k_0)f_0t\} \right] \tag{2}$$

which can be simplified as

$$\eta(t) = a_0 \left\{ 1 + \sqrt{2} \cos(2\pi a_0 k_0 f_0 t) \sin(2\pi f_0 t) \right\} \tag{3}$$

where a_0, k_0 and f_0 are the amplitude, wavenumber and frequency of a carrier wave. Under the maximum modulation, the amplitudes of disturbances were equal to $a_0/\sqrt{2}$ and the frequency differences from a carrier wave were $\pm a_0 k_0 f_0$. For $a_0 k_0 = 0.1$ as a typical value, the phase of wave envelope changes 36° during one cycle of the carrier wave. If the maximum wave height is taken as

$$H_0 = 2a_0(1 + \sqrt{2} \cos 0^\circ) = 4.828a_0 \tag{4}$$

the wave heights around the H_0 are expressed by

$$\left. \begin{aligned} H_{-1}, H_1 &= 2a_0(1 + \sqrt{2} \cos 36^\circ) = 0.888H_0 \\ H_{-2}, H_2 &= 2a_0(1 + \sqrt{2} \cos 72^\circ) = 0.595H_0 \\ H_{-3}, H_3 &= 2a_0(1 + \sqrt{2} \cos 108^\circ) = 0.233H_0 \end{aligned} \right\} \tag{5}$$

Zakharov and Shabat (1972) showed that finite disturbances could evolve into a number of envelope solitons. Extreme wave group may be attributed to envelope solitons formed by some mechanism even in usual wind wave fields. As an attempt, time series of wave heights of extreme wave groups are analyzed using the envelope soliton model as well as the instability model by Su (1986), although these models may not be really applicable to the field data.

The temporal variation of amplitude of the envelope soliton in deep water region was described by

$$A = a_0 \operatorname{sech}\{(a_0^2 \beta / 2\alpha)^{1/2} C_g t\} \quad (6)$$

$$\text{with } \left. \begin{aligned} \alpha &= \omega_0 / 8k_0^2 \\ \beta &= \omega_0 k_0^2 / 2 \\ C_g &= \omega_0 / 2k_0 \end{aligned} \right\} \quad (7)$$

Substitution of Eq.(7) into Eq.(6) yields

$$A = a_0 \operatorname{sech}(a_0 k_0 \omega_0 t) \quad (8)$$

For $a_0 k_0 = 0.1$ as a typical value, the maximum wave height may be taken as

$$H_0 = 2a_0 \operatorname{sech}(0) = 2a_0 \quad (9)$$

The wave heights around H_0 may be estimated by

$$\left. \begin{aligned} H_{-1}, H_1 &= 2a_0 \operatorname{sech}(0.2\pi) = 0.831H_0 \\ H_{-2}, H_2 &= 2a_0 \operatorname{sech}(0.4\pi) = 0.527H_0 \\ H_{-3}, H_3 &= 2a_0 \operatorname{sech}(0.6\pi) = 0.297H_0 \end{aligned} \right\} \quad (10)$$

The observed time series of wave heights of extreme wave groups normalized by the square root of the zero moment m_0 of the spectral density $S(f)$ were analyzed statistically according to the classification of spectral width based the following parameter:

$$\kappa(T_p) = \left[\left\{ \int_0^\infty S(f) \cos(2\pi f T_p) df \right\}^2 + \left\{ \int_0^\infty S(f) \sin(2\pi f T_p) df \right\}^2 \right]^{1/2} / \left[\int_0^\infty S(f) df \right] \quad (11)$$

where T_p is the peak period and f is the frequency. The parameter κ represents the correlation between two points of wave envelope separated by the time lag T_p and is more stable than the spectral peakedness parameter Q_p in terms of the degree of

freedom and resolution frequency of wave spectrum. In the calculation of $S(f)$, the number of data points was 4096, the Nyquist frequency 0.014Hz, and the degree of freedom was 30. The range of integration in Eq.(10) was taken to be $0.5f_p$ to $1.8f_p$ with f_p being the peak frequency instead of 0 to ∞ . As a whole, κ was found to be linearly correlated to Q_p , seen in Fig.9.

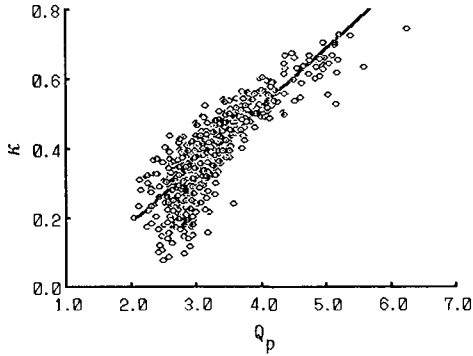


Figure 9 Relation between correlation coefficient κ and spectral peakedness parameter Q_p .

Fig.10 shows the time series of wave heights, in which the data of 'WR', 'C.4' and of Su (1986) are denoted by \circ , \bullet , and Δ , respectively. The solid line and dotted line bars denote the ranges of wave heights when a_0k_0 is taken as 0.1 and 0.2 in Eqs.(3) and (8), respectively. For the case of narrow spectra shown in Fig.10 (a), the wave height sequence is represented fairly well by that of wave groups formed by the nonlinear side-band instability as well as by the envelope soliton, although the agreement depends on the selected value of a_0k_0 . Even in shallow water (the data of 'C.4') where wave breaking may have occurred and the side-band instability cannot occur theoretically, the distribution of wave heights of extreme wave group is almost the same as that in deep water.

For the case of wide spectra of Fig.10 (b), usually observed during the peak of a storm, the wave heights in front and rear of the maximum wave are half as large as the maximum wave height. This implies that the maximum wave tends to appear without accompanying other large waves comparable to the maximum wave.

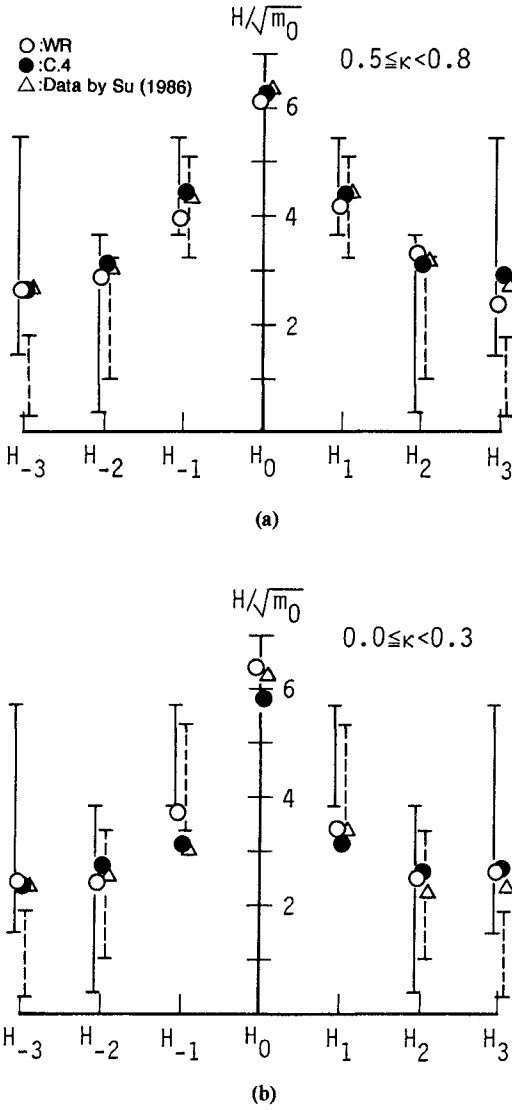


Figure 10 Time series of wave heights of extreme wave groups: (a) narrow band spectra; (b) wide band spectra.

CONCLUSIONS

The wave group properties observed in the field and analyzed in this paper are summarized as follows:

1. The observed tendencies of increase in $\overline{H(H)}$ and decrease in GF with the decrease of $k_m h$ from offshore to shallow water as well as with the increase of propagating distance in shallow water of constant depth imply that wave groups become flattened as they propagate landward.

2. No clear maximum in $\overline{H(H)}$ was seen around the position where the significant wave height was the maximum, in contrast to the laboratory data, while the tendency of the change of GF is the same as the experimental data. The mean length of runs was more unstable statistically than the groupiness factor, since the number of runs was small for the twenty minutes records.

3. When wave grouping became pronounced, the distribution of wave heights became wider. The Rayleigh distribution would underestimate the occurrence probabilities of higher waves.

4. Extreme wave groups accompanied more large waves than ordinary wave groups. However, the analysis of runs yields the number of waves only and does not account for the relative magnitude of the waves around the maximum wave.

5. For the case of narrow spectra, the time series of wave heights of extreme wave groups was represented fairly well by that of the wave group formed by the side-band instability (Su, 1986). The distribution of three high waves was also in qualitative agreement with that of envelope soliton. For wide spectra, which may occur during the peak of storms, wave heights in front and rear of the maximum wave were half as large as the maximum wave height, implying that a maximum wave tends to appear without accompanying other large waves.

ACKNOWLEDGEMENTS

Field observations were performed by the staff of Coastal Disaster Research Section, Disaster Prevention Research Institute, Kyoto University, and the authors would like to acknowledge their efforts. The authors would like to thank N. Kobayashi, University of Delaware, for his review and critical comments on the initial manuscript. This work is a result of research supported by The Ministry of Education, Science and Culture, under Grant-in-Aid for Co-operative Research (No.62302045, Representative Y. Tsuchiya, Disaster Prevention Research Institute, Kyoto University).

REFERENCES

- Cohen, A. C., Jr. (1965): Maximum likelihood estimation in Weibull distribution based on complete and on censored samples, *Technometrics*, Vol.7, No.4, pp.579-588.
- Elgar, S., Guza, R. T. and Seymour, R. J. (1984): Groups of waves in shallow water, *J. Geophys. Res.*, Vol.89, No.C3, pp.3623-3634.
- Goda, Y. (1976): On wave groups, *Proc. Int. Conf. on Behavior of Offshore Structures*, pp.115-128.
- Lake, B. M. and Yuen, H. C. (1978): A new model for nonlinear wind waves, *J. Fluid Mech.*, Vol.88, pp.33-62.
- Mase, H. (1989): Groupiness factor and wave height distribution, *J. Waterway, Port, Coastal and Ocean Eng.*, Vol.115, No.1, pp.105-121.
- Mase, H. and Iwagaki, Y. (1986): Wave group analysis from statistical viewpoint, *Proc. Ocean Structural Dynamics Symp. '86*, ASCE, Oregon State Univ., pp.145-157.
- Mase, H. and Iwagaki, Y. (1987): Evolution of wave groups in shallow water and wave group properties of random waves, *Coastal Engrg. in Japan*, JSCE, Vol.30, No.1, pp.19-32.
- Mase, H., Matsumoto, A. and Iwagaki, Y. (1986): Calculation model of random wave transformation in shallow water, *Proc. JSCE*, Vol.375, No.11-6, pp.221-230 (in Japanese).
- Su, M. Y. (1986): Extreme wave group in storm seas near coastal water, *Proc. 20th Int. Conf. on Coastal Engrg.*, ASCE, pp.767-779.
- Zakharov, V. E. and Shabat A. B. (1972): Exact theory of two-dimensional self-focusing and one-dimensional self-modulating waves in nonlinear media, *Sov. Phys. -JETP (Engl. Transl.)* 65, pp.997-1011.

CHAPTER 14

MEASUREMENT AND COMPUTATION OF WAVE INDUCED VELOCITIES ON A SMOOTH SLOPE

Jentsje W. van der Meer¹⁾ and Mark Klein Breteler¹⁾

Abstract

Two main items are treated in this paper. The first item is measurement of wave induced velocities in a large scale model and the second one is a verification of the 1-D numerical model, developed by Kobayashi and Wurjanto (1989).

Wave induced velocities on a smooth slope were measured in Delft Hydraulics large Delta flume. The run-up and run-down velocities were compared with theoretically derived upper bounds and formulas for these velocities were derived on the basis of these upper bounds.

Computations were performed with the numerical model of Kobayashi and the results (velocities, pressures and run-up and run-down levels) were compared with measurements, partly from the investigation mentioned above. The results for run-down velocities and run-up levels were acceptable, the results for run-up velocities were a little worse and the results for pressures and run-down levels were bad.

Introduction

Knowledge of wave induced velocities on a slope is an important step towards a better understanding of the behaviour of coastal structures under wave attack. These velocities are important to calculate wave forces on rubble mound structures and on placed block revetments and to calculate run-up or overtopping.

Therefore, large scale physical model tests were performed in the Delta flume of Delft Hydraulics with regular waves on a smooth slope. Velocities were measured at various locations and for various wave conditions. Furthermore, the numerical model of Kobayashi and Wurjanto (1989) was used to calculate wave induced velocities and these results were compared with the measurements.

The numerical model is a 1-D model and is based on solving the non-linear equations for long waves on a slope. The model was a ver-

1) Delft Hydraulics, PO Box 152, 8300 AD Emmeloord, The Netherlands

sion, specially developed for CERC, USA and Prof. N. Kobayashi of the University of Delaware and Mr. J.P. Ahrens of CERC are gratefully acknowledged for the permission of using this model.

Tests in the Delta flume

Large scale model tests have been performed which were aimed on measuring the water velocities just above (about 3-5 cm) the slope surface. The dimensions of the Delta flume are 230 m long, 5 m wide and 7 m deep. All tests were performed with regular waves and on a smooth slope of 1:3. The slope consisted of a placed block revetment with block dimensions 0.5 m x 0.5 m and thick 0.15 m. Some blocks had circular holes in the center of the block, but these were filled with shingle during the tests.

The velocities were measured with four-quadrant electro-magnetic velocity meters (EMS) mounted on a horizontal rod just above the slope. The EMS was developed and constructed by the Instrumentation Section of Delft Hydraulics. The disc of the EMS has a diameter of 0.035 m and the range is +/- 5 m/s. The accuracy is 2% of the recorded value or 0.02 m/s for small velocities. The velocities were measured at seven locations around the still water level. The water depth was 5 m during all tests.

The test program is shown in Table 1. Four wave periods were generated and for each wave period 3-4 wave heights. The Table gives the wave periods, T, wave heights, H, wave steepnesses, s_{op} , defined as $s_{op} = 2\pi H/gT^2$ and the surf similarity parameter, ξ_o , defined as $\xi_o = \frac{op}{\tan\alpha\sqrt{s}}$, where α is the slope angle of the structure.

T (s)	H (m)	s_{op}	ξ_o	T (s)	H (m)	s_{op}	ξ_o
2.25	0.20	0.025	2.09	4.0	0.65	0.026	2.07
2.25	0.29	0.037	1.74	4.0	0.84	0.034	1.82
2.25	0.38	0.048	1.51	4.0	1.11	0.045	1.58
3.0	0.37	0.026	2.05	5.0	0.30	0.008	3.78
3.0	0.50	0.036	1.77	5.0	0.51	0.013	2.92
3.0	0.62	0.044	1.58	5.0	0.70	0.018	2.48

Table 1 Tests for measurement of velocities on a smooth 1:3 slope

The time signals of the velocity meters were analysed. The maximum run-up and run-down velocity for each wave in a record of 30 s was established. The maximum run-up and run-down velocities in this paper are defined as the average of the highest three recorded values.

Theoretical considerations on velocities

A simple theory was developed to support the analysis of the measurements. The water velocity on a slope due to breaking waves depends largely on the process of wave run-up, run-down and wave impact. With respect to the run-down velocity, v_d , the theory is based on the fall velocity of a particle, falling without friction.

$$E_{kin} = 0.5 m v_d^2 = mg(R_u - z) = E_{pot} \quad (1)$$

where:

E_{kin} = kinetic energy

E_{pot} = potential energy

m = mass of water particle

g = gravity acceleration

R_u = level of maximum run-up relative to swl

z = location on slope, measured vertically relative to swl

Elaboration of Eq. 1 gives:

$$v_d = \sqrt{2g(R_u - z)} \quad (2)$$

This means that the run-down velocity is independent on the wave height and period, but only on the run-up level and the location on the slope. In order to use a dimensionless velocity both parts can be divided by \sqrt{gH} . But again, strictly speaking, this is not required. The final formula for the run-down velocity becomes then:

$$v_d/\sqrt{gH} = \sqrt{2R_u/H} \sqrt{(1-z/R_u)} \quad (3)$$

Eq. 3 shows that the dimensionless run-down velocity is a function of the dimensionless run-up level and the dimensionless location on the slope. This equation is an upper bound for the run-down velocity, since the friction influence is neglected.

With respect to the run-up velocity, v_{up} an upper bound can be derived from the wave celerity, c , defined for deep water by $c = \sqrt{gL/2\pi}$. If this wave celerity is assumed to be the run-up velocity at swl and if again \sqrt{gH} is used to make the velocity dimensionless (again strictly speaking not required), the run-up velocity becomes:

$$v_{up}/\sqrt{gH} = \sqrt{1/2\pi s} \quad (4)$$

where s = wave steepness, H/L . The run-up velocity will become zero at the maximum run-up level R_u . A similar term as used in Eq. 3 gives this effect. The final formula for the run-up velocity becomes then:

$$v_{up}/\sqrt{gH} = \sqrt{1/2\pi s} \sqrt{(1-z/R_u)} \quad (5)$$

The dimensionless run-up velocity is a function of the (dimensionless) wave steepness and the dimensionless location on the slope. As quite a lot of energy is dissipated by the wave breaking process, Eq. 5 can be regarded as a high upper bound.

Analysis of measurements

Run-down velocity

The measured run-down velocities are plotted versus the location on the slope, z/R_u , in Fig. 1. The maximum run-up level, the still water level and the maximum run-down level are shown in the Figure. The maximum upper bounds given by Eq. 3, are shown for $\xi_0 = 1.5$ and 2.5, giving more or less the measured range. As the run-up level R_u/H depends on ξ_0 , the upper bound depends on this parameter too.

The relationship between R_u/H and ξ_0 is shown in Fig. 5 and will be treated there.

Fig. 1 shows that all points are below the upper bound and that for $z/R_u > -0.4$ the same trend is found as for the theoretical upper bound. For smaller values of z/R_u (below the run-down point), the velocities decrease rapidly. In order to analyse the trend for the higher values of z/R_u , Fig. 2 was composed with on the horizontal axis the parameter $\sqrt{R_u/H} \sqrt{1-z/R_u}$, according to Eq. 3.

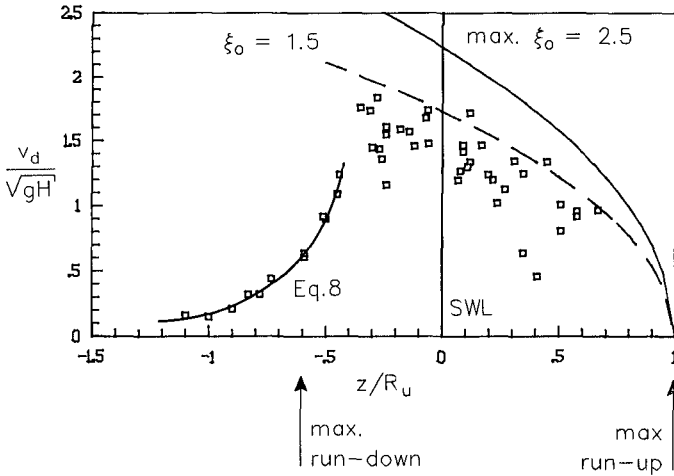


Figure 1 Run-down velocity as function of the location on the slope

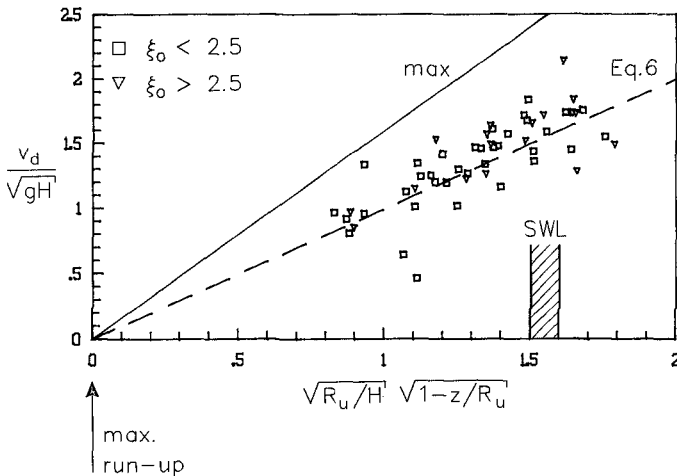


Figure 2 Run-down velocity for $z/R_u > -0.4$

This Fig. 2 gives the maximum upper bound for $\xi_o < 2.5$ and makes also a distinction between the plunging waves ($\xi_o < 2.5$, see Fig. 5) and surging waves ($\xi_o > 2.5$). Although there is some scatter, a linear expression between the parameters on respectively the horizontal and vertical-axis is acceptable, which means that the trend of Eq. 3 can be maintained. An expression for the run-down velocity on a smooth slope for $z/R_u > -0.4$ becomes then:

$$v_d/\sqrt{gH} = 1.1 \sqrt{R_u/H} \sqrt{(1-z/R_u)} \tag{6}$$

This equation is also shown in Fig. 2. As the run-down velocity is in fact not dependent on the wave height, a better expression is:

$$v_d/\sqrt{gR_u} = 1.1 \sqrt{(1-z/R_u)} \tag{7}$$

For the run-down velocity below the point $z/R_u = -0.4$, an expression can be found based on Fig. 1. The velocity decreases rapidly with decreasing z/R_u and the relationship can therefore be given by a power curve:

$$v_d/\sqrt{gH} = 0.18 z/R_u^{-2.3} \quad \text{for} \quad z/R_u < -0.4 \tag{8}$$

Run-up velocity

The measured run-up velocities are shown in Fig. 3 as a function of z/R_u . Fig. 3 is similar to in Fig. 1. Both upper bounds for $\xi_o = 1.5$ and 2.5 are shown. The measured velocities are well below these upper bounds which means that quite some energy is dissipated by the wave breaking process. As the influence of the surf similarity parameter is large, see the difference between the two upper bounds, it can not be concluded on the basis of Fig. 3 that the velocities for $z/R_u > 0$ follow the same trend as the upper bounds. Therefore, another figure was composed based on Eq. 5.

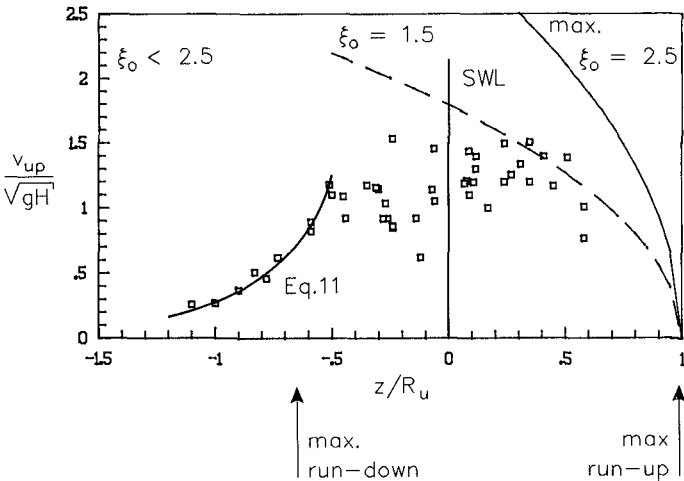


Figure 3 Run-up velocity as function of the location on the slope

Fig. 4 gives the run-up velocity as a function of $1/\sqrt{s} \sqrt{(1-z/R_u)}$, including the upper bound. Again a linear expression fits the data and the following equation for the run-up velocity for $z/R_u > 0$ can be derived:

$$v_{up}/\sqrt{gH} = 0.27 \frac{1}{\sqrt{s}} \sqrt{(1-z/R_u)} \quad (9)$$

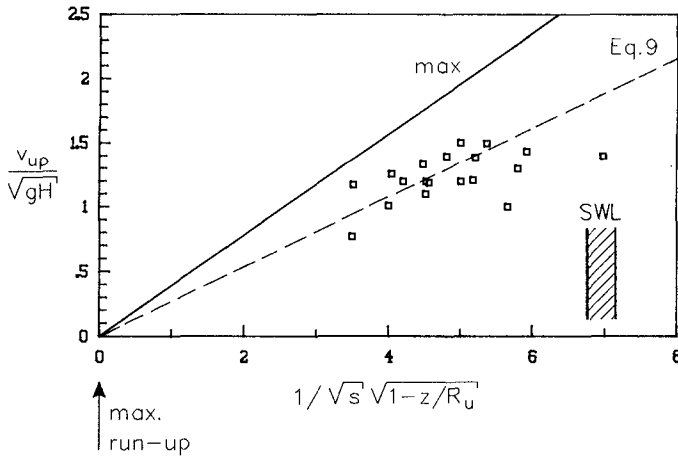


Figure 4 Run-up velocity for $z/R_u > 0$

This equation is shown in Fig. 4. Fig. 3 shows furthermore that the run-up velocity in the area $-0.4 < z/R_u < 0$ is not really dependent on the location. Analysis showed that it is only a function of the wave steepness:

$$v_{up}/\sqrt{gH} = 0.2/\sqrt{s} \quad \text{for} \quad -0.4 < z/R_u < 0 \quad (10)$$

Finally the run-up velocity decreases rapidly for decreasing z/R_u and for $z/R_u < -0.4$, see Fig. 3. A relationship similar to Eq. 8 which gives a good fit is:

$$v_{up}/\sqrt{gH} = 0.30 \frac{z/R_u}{z/R_u^2} \quad \text{for} \quad z/R_u < -0.4 \quad (11)$$

Eqs. 6 - 11 give empirical relationships for the run-down and run-up velocities on a smooth slope. The relationships are based on large scale experiments for a slope of 1:3. A limit for application of the formulas is therefore a slope close to 1:3.

The model IBREAK

Kobayashi and Wurjanto (1989) describe the model IBREAK that can simulate the wave motion on an arbitrary rough or smooth slope. The model IBREAK is a second and more user's friendly version than the original model and runs on a main frame computer. Broekens (1988) developed the same model, based on Kobayashi's papers and reports, but now for a personal computer and more user's friendly. This was done at the time that IBREAK was not yet available. As IBREAK is the

original work of Kobayashi it was decided to verify this model and not the version of Broekens (although the results would be similar).

The model is based on the non-linear long wave equations and is a 1-dimensional model, i.e. only a depth averaged water velocity is assumed. This means that breaking (plunging) waves are simulated by a "bore-type" wave. The wave front can become almost vertically as a limit. Furthermore, pressures are assumed to be hydrostatic. A rough slope is simulated as a "smooth" slope with a large friction coefficient.

Applications of the model to stability of rock slopes were described by Kobayashi and Otta (1987) and applications to run-up and reflections on rough slopes by Kobayashi et al. (1987). The model of Broekens (1988) was used to describe the stability of rock slopes (De Graaf (1988)).

Most applications described by Kobayashi are for rough impermeable slopes. Only Kobayashi and Watson (1987) describe the application and verification of the model for a smooth slope. There conclusions were:

- Water velocities were not verified.
- Water pressures were verified with 3 model tests for one location on the slope. Large deviations were found for the maximum and minimum pressures.
- Run-up and run-down were verified with formulas described by Ahrens and Titus (1985). Run-up was a little smaller for the calculations and run-down was not accurate.
- The general conclusion was that the model is applicable for smooth slopes, although the friction coefficient should have a small value, greater than zero. A value of 0.05 was recommended.

The model IBREAK was used by permission of CERC and prof. Kobayashi. Calculations were performed in order to verify the model more in depth for a smooth slope. The large scale measurements in the Delta flume described in the first part of the paper, form the main basis for this verification. The following parameters were taken into account: the maximum run-up and run-down levels, the water velocities and the water pressures.

Verification of run-up and run-down

Fig. 5 shows the results of calculations and measurements on run-up and run-down levels on a 1:3 smooth slope with waves roughly between 0.2 and 1.1 m. On the basis of the measurements the following relationships for run-up and run-down levels were established:

$$R_u/H = \xi_0 \quad \text{for } \xi_0 < 2.6 \quad (\text{plunging waves}) \quad (12)$$

$$R_u/H = -1.5\xi_0 + 6.5 \quad \text{for } 2.6 < \xi_0 < 3.0 \quad (\text{collapsing waves}) \quad (13)$$

$$R_u/H = 2.0 \quad \text{for } \xi_0 > 3.0 \quad (\text{surging waves}) \quad (14)$$

$$R_d/H = -0.1\xi_0^2 + \xi_0 - 0.5 \quad (15)$$

Eqs. 12-15 are shown in Fig. 5. From this figure it can be concluded that:

- IBREAK gives a constantly increasing curve for the run-up and does not give a maximum for the transition from plunging to surging waves ($\xi_0 = 2.6 - 3.0$). This is probably caused by the fact that the model simulates a bore-type wave. The run-up is a little too small for plunging waves and a little too large for surging waves.
- The average deviation between calculated and measured run-up is 12% which is reasonable. The general conclusion is that the run-up is predicted within acceptable limits.
- The calculated run-down is much smaller than the measured one, especially for the smallest ξ_0 values. The deviation is very large there and not acceptable for practical use.

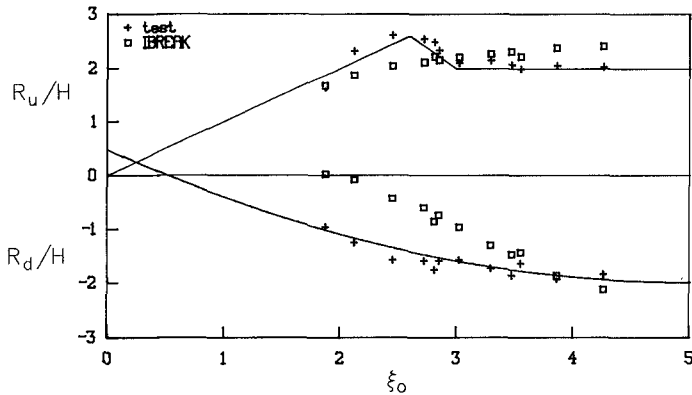


Figure 5 Measured and calculated run-up and run-down on a 1:3 smooth slope

Verification of velocities

A few tests from the series described in the first part of this paper were also calculated with the model IBREAK. Fig. 6 shows a part of the time signal of one of the tests with a surging wave of $H = 0.3$ m and $T = 5$ s. The location was -0.42 m which means about $1.5H$ below the still water level. The qualitative agreement between the measured and calculated signal is good. The quantitative results will be described below.

The maximum value (run-up velocity) and the minimum value (run-down velocity) of the time signal were used for comparison. First the influence of the friction factor f on the run-up and run-down velocities was studied. Friction factors of 0.0, 0.02 and 0.05 were used. Fig. 7 gives the results together with the measured values.

From Fig. 7 it can be concluded that a lower friction factor leads to higher velocities. A decrease of the friction factor from 0.05 to 0.02 leads to an increase in velocities of about 20%. A decrease of f from 0.05 to 0.0 leads to an increase of the velocities of about 40%. This means that even for a smooth slope the friction factor plays an important role with regard to velocities.

During run-down the energy dissipation is only due to friction, where for run-up the wave breaking process is important too. There

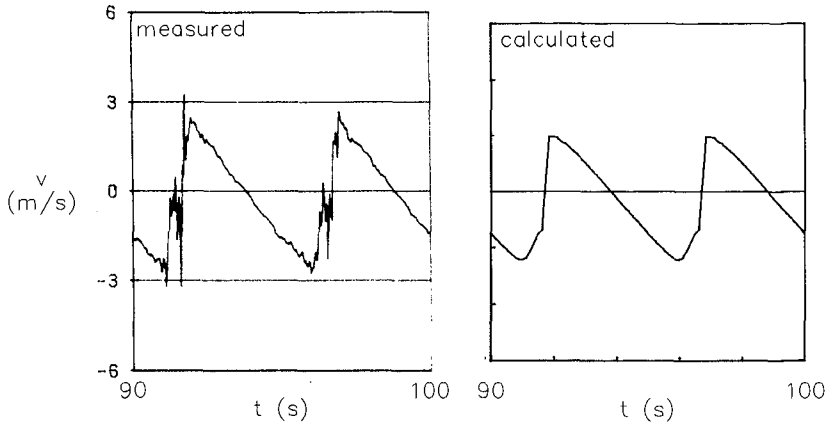


Figure 6 Time series for measured and calculated velocities on a 1:3 smooth slope

fore, the "calibration" of the friction factor for the model should be based on the run-down velocities. For the run-down values a friction factor of $f = 0.02$ gives the best results and this factor of 0.02 was used for the further calculations.

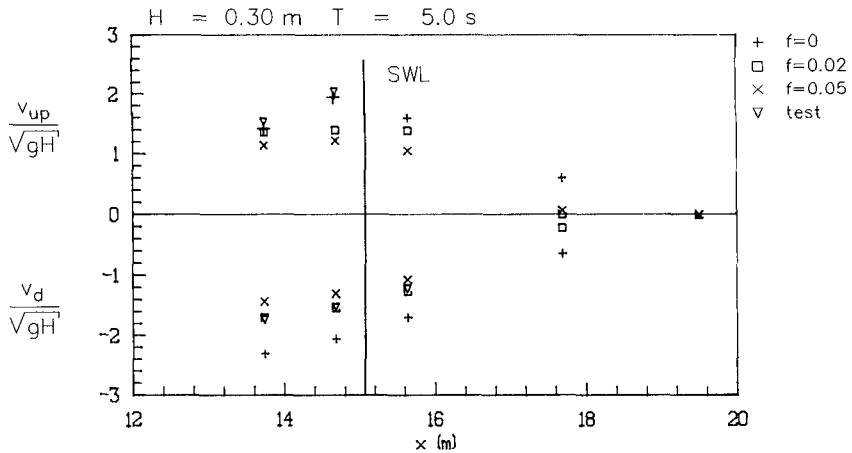


Figure 7 Influence of friction factor on run-up and run-down velocities

It should be noted again that the model gives a depth-averaged horizontal velocity and that the model tests give the velocity a few centimeters above and along the slope.

Fig. 8 gives the results on velocities for 3 tests, ranging from plunging to surging waves (ξ_0 values of 1.51, 2.07 and 2.92 respectively). The average deviation of the calculated run-up velocities from the measured ones was 16%. This average deviation amounted to

10% for the run-down velocities. Values smaller than 40% of the maximum velocities on the slope were not taken into account for the calculation of the deviations. Fig. 8 shows furthermore that the calculated velocities were consequently smaller than the measured velocities. A smaller friction factor than 0.02 would therefore increase the agreement.

Fig. 8 shows no influence of the surf similarity parameter on the results. The deviations of the calculated velocities from the measured ones is similar for plunging, collapsing or surging waves.

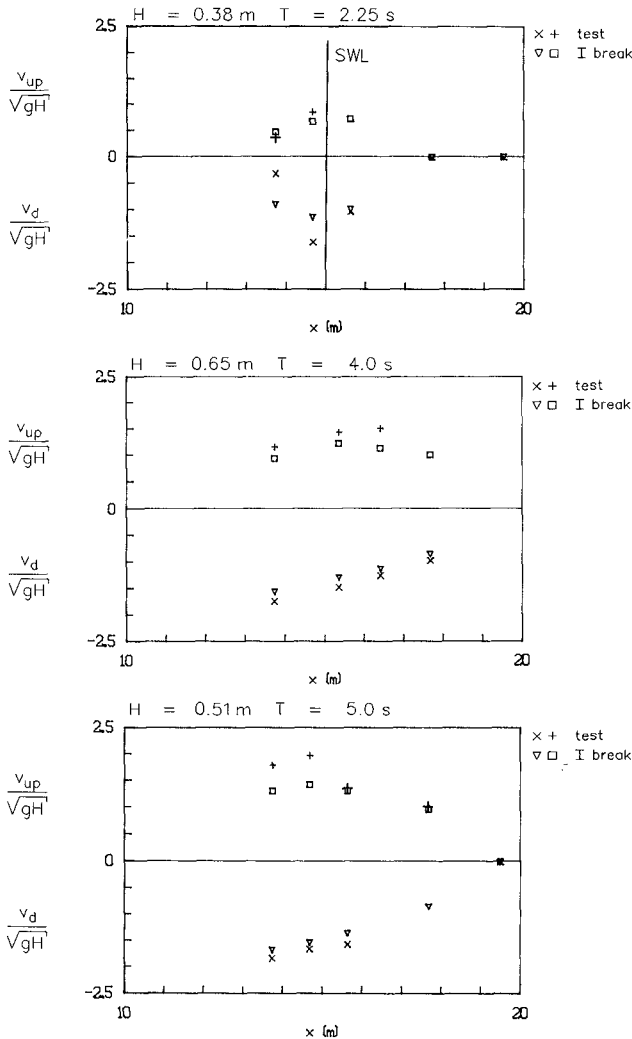


Figure 8 Measured and calculated maximum velocities on a 1:3 smooth slope

The general conclusion is that IBREAK gives a reasonable prediction of the velocities on a smooth slope.

Verification of wave pressures

A part of the time signal for the wave pressure on a location below the still water level is shown in Fig. 9 for one of the large scale tests on a slope of 1:3. The qualitative agreement is good. Fig. 10 shows again a part of a time signal for the wave pressure, but now for a small scale test on a slope of 1:2. Here the agreement is very poor. The only agreement is the irregularity of the signal.

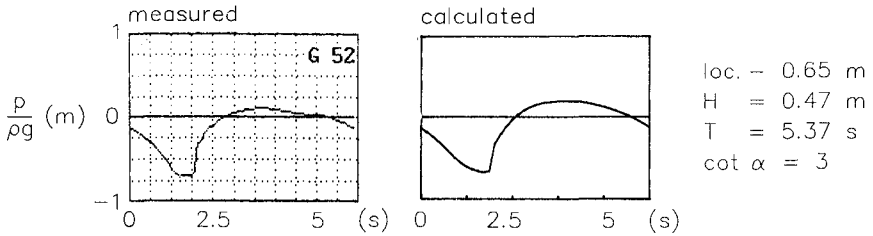


Figure 9 Measured and calculated wave pressures on a 1:3 smooth slope

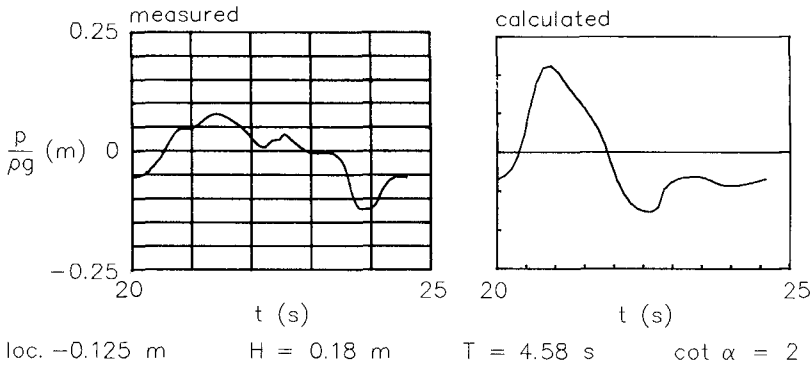


Figure 10 Measured and calculated wave pressures for a 1:2 smooth slope (small scale tests)

The influence of the friction factor on the calculated wave pressures was investigated for the same test as shown in Fig. 9. Fig. 11 gives the results for $f = 0.02, 0.05$ and 0.10 . A value of 0.0 led to numerical instability. This figure shows that the influence of the friction factor on the wave pressures is small and not consistent. Sometimes the lowest value of the friction factor gives the highest wave pressures, sometimes the highest value, depending on the location of the slope.

Fig. 12 gives the results on wave pressures of three tests. The upper graph gives the results of a large scale test on a slope 1:3 with a wave height of 1.38 m and a wave period of 5.37 s. The other

graphs give small scale tests on a slope 1:4. The middle graph that of a plunging wave and the lowest graph that of a surging wave.

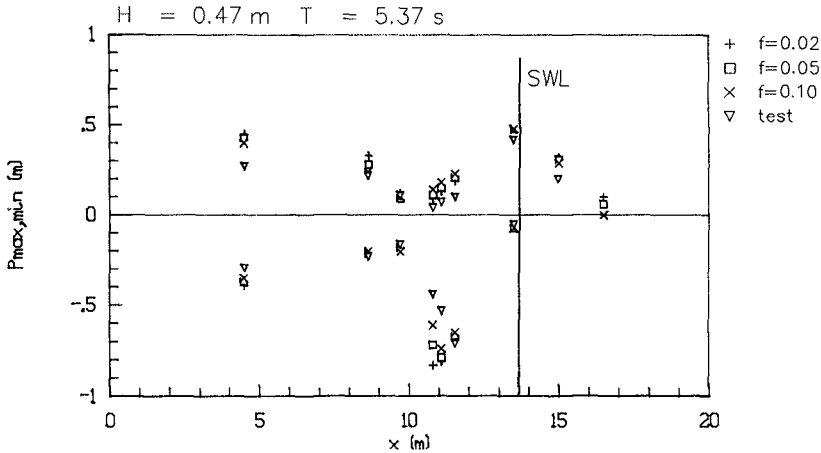


Figure 11 Influence of the friction factor on wave pressures

Calculations were performed for three large scale tests and for five small scale tests (two on a slope 1:2, one on a slope 1:3 and two on a slope 1:4). In all tests the pressures were measured on nine locations as shown in Fig. 12. From the comparison of measured and calculated pressures it could be concluded that the average deviation for the large scale tests was 37% for the minimum pressure and 44% for the maximum pressure. For the small scale tests this was respectively 55% and 113%. Values smaller than 40% of the maximum pressure on the slope were not taken into account for calculation of the deviation of the pressures.

The deviations between measurements and calculations are larger than for the velocities described in the previous section. Furthermore, the deviations for the small scale tests are larger than for the large scale tests. Although the deviations between measurements and calculations are large, the trend along the slope is similar. The location where the maximum pressure occurs on the slope is calculated fairly accurate. In most cases the calculated pressure is (much) higher than the measured one. A smaller friction coefficient than used, however, has almost no influence, see Fig. 11.

The general conclusion on pressures is that IBREAK can not accurately simulate wave pressures on a smooth slope. It can simulate the location where the maximum wave pressure occurs.

Conclusions

Eqs. 6 - 11 give empirical relationships for the run-down and run-up velocities on a smooth slope, based on theoretically derived upper bounds. The relationships are based on large scale experiments for a slope of 1:3. A limit for application of the formulas is therefore a slope close to 1:3.

Eqs. 12 - 15 give empirical relationships for maximum run-up and run-down levels on a smooth slope, based on large scale experiments on a slope of 1:3.

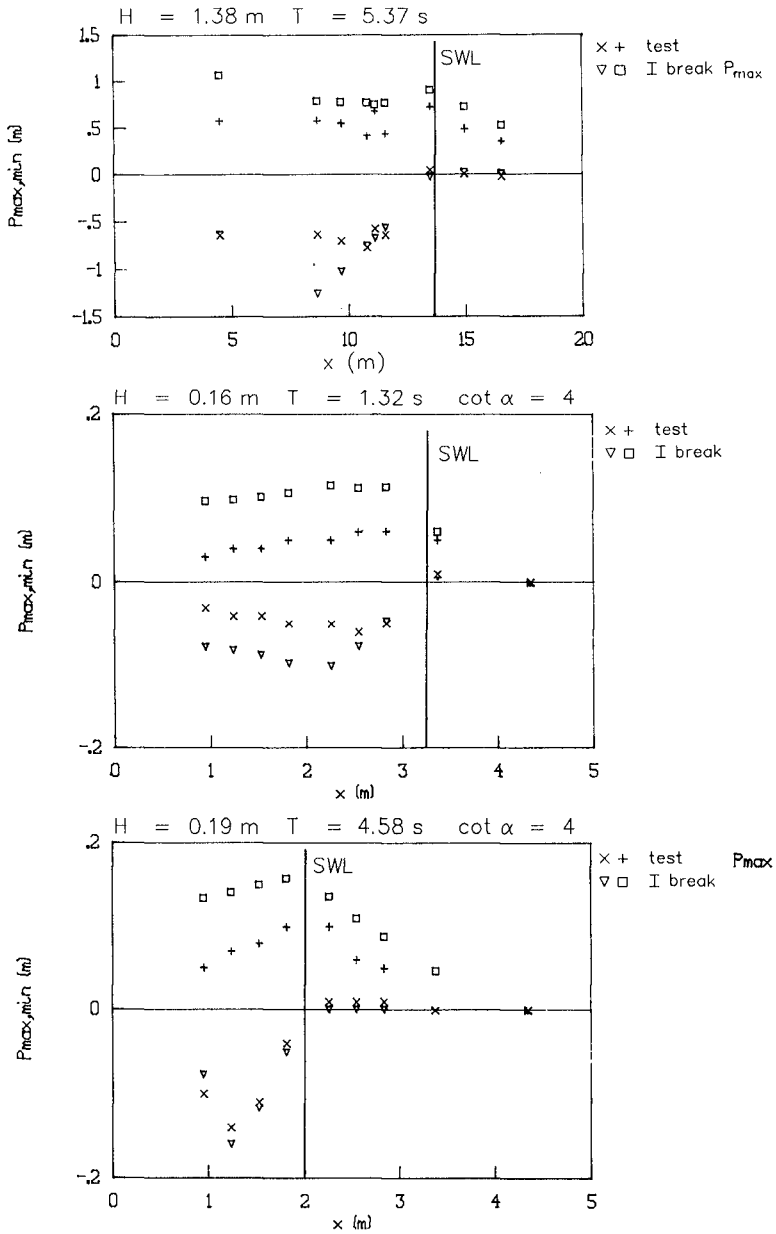


Figure 12 Measured and calculated maximum and minimum pressures

The model IBREAK was verified on maximum run-up and run-down levels, and velocities and water pressures along and on a smooth slope.

The average deviation between calculated and measured run-up is 12% which is reasonable. The general conclusion is that the run-up is predicted within acceptable limits. The calculated run-down is much smaller than the measured one, especially for the smallest ξ_0 values. The deviation is very large there and not acceptable for practical use.

The friction factor plays an important role with regard to velocities, even for a smooth slope. The general conclusion is that IBREAK gives a reasonable prediction of the velocities on a smooth slope.

The friction factor has no influence on wave pressures when this factor is in the range of $f = 0.02 - 0.10$. The general conclusion on pressures is that IBREAK can not accurately simulate wave pressures on a smooth slope. It can simulate the location where the maximum wave pressure occurs.

References

- Ahrens, J.P. and Titus, M.F., 1985.
Wave run-up formulas for smooth slopes.
Proc. ASCE, Journal of WPC and OE, Vol. 111, No. 1.
- Broekens, R.D., 1988.
De berekening van de waterbeweging op een talud onder golfaanval met een numeriek model (The computation of the water motion on a slope under wave attack with a numerical model).
MSc thesis, Delft University of Technology, (in Dutch).
- De Graaf, M.A., 1988.
De beschrijving van de stabiliteit van een stortsteen talud onder regelmatige golfaanval met een numeriek model (The description of the stability of a rock slope under regular wave attack with a numerical model).
MSc thesis, Delft University of Technology, (in Dutch).
- Kobayashi, N. and Otta, A.K., 1987.
Hydraulic stability of armor units.
Proc. ASCE, Journal of WPC and OE, Vol. 113, No. 2.
- Kobayashi, N., Otta, A.K. and Roy, I., 1987.
Wave reflection and run-up on rough slopes.
Proc. ASCE, Journal of WPC and OE, Vol. 113, No. 3.
- Kobayashi, N. and Watson, K.D., 1987.
Wave reflection and runup on smooth slopes.
Proc. Coastal Hydrodynamics.
- Kobayashi, N. and Wurjanto, A., 1989.
Numerical model for design of impermeable coastal structures.
Research Report No. CE-89-75. University of Delaware.

CHAPTER 15

A NUMERICAL MODEL FOR REFRACTION COMPUTATION OF IRREGULAR WAVES DUE TO TIME-VARYING CURRENTS AND WATER DEPTH

Masataka Yamaguchi¹ and Yoshio Hatada²

ABSTRACT

This paper presents two models for current-depth refraction of directional spectra due to time-varying currents and water depth, in which a piecewise ray method and a full ray method are used for numerical computations respectively. The results computed by the piecewise ray model in the cases of time-varying one-dimensional and two-dimensional currents are in reasonable agreement with those by the full ray model, which gives the almost exact solution in the case of linear current and water depth variations, except for a slight difference during the phase of strong opposing currents. The computations indicate that time-dependency of currents gives rise to a phase difference between wave height and current variations, and reduction in the amplification effect of directional spectrum due to opposing currents in comparison with steady current case.

1. INTRODUCTION

It is empirically known that waves are greatly amplified by the presence of strong opposing currents and that waves affected by tidal currents vary regularly with a pseudo-period of tidal currents (Vincent, 1979). As an example, Fig. 1 describes the time variation of significant waves observed at Naruto Strait which is located between Shikoku Island and Awaji Island. Naruto Strait is very famous for strong tidal currents and tide-induced large scale vortices. The investigation of such a phenomenon which might be caused by wave-current interac-

1 Prof., Dept. of Ocean Eng., Ehime Univ., Bunkyocho 3, Matsuyama 790, Ehime Pref., Japan

2 Research Assistant, Dept. of Ocean Eng., Ehime Univ., Bunkyocho 3, Matsuyama 790, Ehime Pref., Japan

tion, and the establishment of the evaluation method are of great importance for mitigation of coastal hazard, design of maritime structures, ship operation and so on.

Fig. 2 is a classification of the existing current-depth refraction models for irregular waves. The previous models assume time-independent fields for currents and water depth. Recently, Yamaguchi et al.(1988) and Tolman(1988) proposed numerical models applicable to the refraction computation of irregular waves with time-varying currents and water depth. The former model is a generalization of the time-independent model by Mathiesen (1984) and

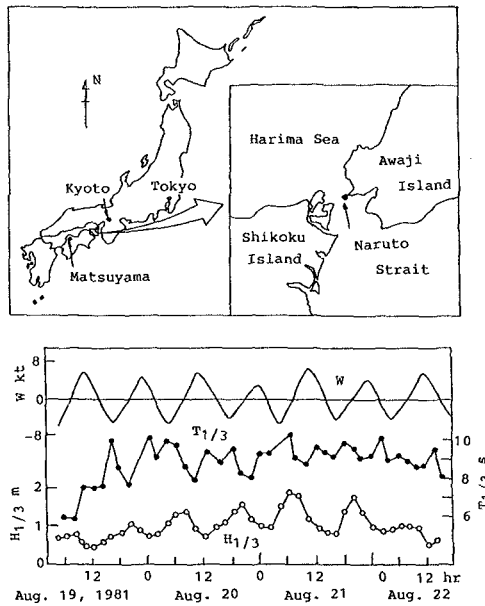


Fig. 1 Naruto Strait, and observed tidal currents and significant waves.

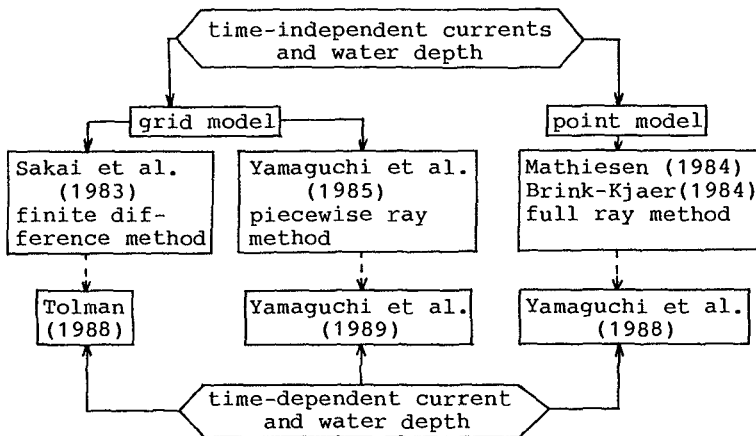


Fig. 2 A classification of current-depth refraction models for irregular waves.

Brink-Kjaer(1984) using a full ray method hereafter referred to as point model or full ray model, and the latter model is an extension of the time-independent model by Sakai et al.(1983) based on a finite difference method to a time-dependent model. Yamaguchi et al.(1989) also developed another numerical model for the refraction computation of directional spectra due to time-varying currents and water depth, which is a generalization of the authors' model(1985) based on a piecewise ray method hereafter referred to as grid model or piecewise ray model.

The aim of this study is to present two models for the time-dependent current-depth refraction of irregular waves developed by the authors and some examples of the numerical computation based on both models. First, the computation methods used in the models are explained in detail. Next, the models are applied to the computation of wave refraction caused by time-varying one-dimensional and two-dimensional model currents on a uniformly sloping beach. The accuracy of the piecewise ray model is investigated in comparison with the results based on the full ray model. The effect of time-dependency of currents and water depth on wave transformation is also examined from the comparison with the results for steady current case.

2. MODEL DESCRIPTIONS

(1) Basic Equations

The basic equations used in the model are the conservation equation for wave action density spectrum $N(\mathbf{k})$ defined by the ratio of wave number spectrum $E(\mathbf{k})$ to intrinsic angular frequency σ_m ,

$$\begin{aligned} \frac{\partial N(\mathbf{k})}{\partial t} + (C_\theta \cos \theta + U) \frac{\partial N(\mathbf{k})}{\partial x} + (C_\theta \sin \theta + V) \frac{\partial N(\mathbf{k})}{\partial y} \\ + \frac{dk_x}{dt} \frac{\partial N(\mathbf{k})}{\partial k_x} + \frac{dk_y}{dt} \frac{\partial N(\mathbf{k})}{\partial k_y} = 0 \end{aligned} \quad (1)$$

a set of equations for wave number vector components k_x and k_y ,

$$\begin{aligned} \frac{\partial k_x}{\partial t} + (C_\theta \cos \theta + U) \frac{\partial k_x}{\partial x} + (C_\theta \sin \theta + V) \frac{\partial k_x}{\partial y} \\ = - \frac{gk^2 \operatorname{sech}^2 kh}{2 \sigma_m} \frac{\partial h}{\partial x} - k_x \frac{\partial U}{\partial x} - k_y \frac{\partial V}{\partial x} \end{aligned} \quad (2)$$

$$\begin{aligned} \frac{\partial k_y}{\partial t} + (C_\theta \cos \theta + U) \frac{\partial k_y}{\partial x} + (C_\theta \sin \theta + V) \frac{\partial k_y}{\partial y} \\ = - \frac{gk^2 \operatorname{sech}^2 kh}{2 \sigma_m} \frac{\partial h}{\partial y} - k_x \frac{\partial U}{\partial y} - k_y \frac{\partial V}{\partial y} \end{aligned} \quad (3)$$

the Doppler relation,

$$\sigma = \sigma_m + k_x U + k_y V, \quad \sigma_m = \sqrt{gk \tanh kh} \quad (4)$$

and the equation of absolute angular frequency σ

$$\begin{aligned} \frac{\partial \sigma}{\partial t} + (C_g \cos \theta + U) \frac{\partial \sigma}{\partial x} + (C_g \sin \theta + V) \frac{\partial \sigma}{\partial y} \\ = \frac{gk^2 \operatorname{sech}^2 kh}{2 \sigma_m} \frac{\partial h}{\partial t} + k_x \frac{\partial U}{\partial t} + k_y \frac{\partial V}{\partial t} \end{aligned} \quad (5)$$

where C_g is the group velocity of a component wave, θ the wave direction, k the wave number, $k_x = k \cos \theta$, $k_y = k \sin \theta$, h the water depth, g the acceleration of gravity and (U, V) are the current components. Eq. (2) to Eq. (5) are not mutually independent, as is clear from their derivation. We choose the three equations, Eq. (2) to Eq. (4) for their relative simplicity of computation.

Eq. (1) means that even in the case of time-varying currents and water depth, the action spectrum for each wave component is conserved along the wave ray defined by

$$\frac{dx}{dt} = C_g \cos \theta + U, \quad \frac{dy}{dt} = C_g \sin \theta + V \quad (6)$$

where the wave number components are computed from

$$\frac{dk_x}{dt} = -\frac{gk^2 \operatorname{sech}^2 kh}{2 \sigma_m} \frac{\partial h}{\partial x} - k_x \frac{\partial U}{\partial x} - k_y \frac{\partial V}{\partial x} \quad (7)$$

$$\frac{dk_y}{dt} = -\frac{gk^2 \operatorname{sech}^2 kh}{2 \sigma_m} \frac{\partial h}{\partial y} - k_x \frac{\partial U}{\partial y} - k_y \frac{\partial V}{\partial y} \quad (8)$$

Thus, the conservation of the action spectrum $\psi(f, \theta)$ in frequency-direction space (f, θ) is written as

$$\begin{aligned} \psi(f, \theta) &= |(C_{g1} + U_1 \cos \theta_1 + V_1 \sin \theta_1) / 2 \pi k_1 \sigma_{m1}| E(f_1, \theta_1) \\ &= |(C_{g2} + U_2 \cos \theta_2 + V_2 \sin \theta_2) / 2 \pi k_2 \sigma_{m2}| E(f_2, \theta_2) \\ &= |(C_g + U \cos \theta + V \sin \theta) / 2 \pi k \sigma_m| E(f, \theta) \\ &= \Phi(f, \theta) E(f, \theta) = \text{const.} \end{aligned} \quad (9)$$

where f is the absolute frequency, $\Phi(f, \theta)$ the amplification factor due to current-depth refraction, $E(f, \theta)$ is the directional spectrum, and subscripts '1' and '2' are used for denoting different time as well as different place. This is the basic relationship used to compute current-depth refraction of directional spectrum.

Wave statistics are obtained by the numerical integration over wave direction and frequency using

$$\begin{aligned} E(f) &= \int_0^\pi E(f, \theta) d\theta, \quad \epsilon = \int_0^\infty E(f) df, \quad H_{1/3} = 4\sqrt{\epsilon}, \\ T_{1/3} &= 1.22 \sqrt{\epsilon / \int_0^\infty f^2 E(f) df}, \quad \bar{\theta} = \tan^{-1} \left\{ \frac{\int_0^\pi \int_0^\infty E(f, \theta) \sin \theta d\theta df}{\int_0^\pi \int_0^\infty E(f, \theta) \cos \theta d\theta df} \right\} \end{aligned} \quad (10)$$

where $E(f)$ is the frequency spectrum, ϵ the total wave energy, $H_{1/3}$ the significant wave height, $T_{1/3}$ the significant wave period and $\bar{\theta}$ the mean wave direction.

The input directional spectrum is given as

$$E_0(f, \theta) = E_0(f) \cdot D_0(f, \theta) \tag{11}$$

where $D(f, \theta)$ is the angular spreading function and subscript '0' indicates the offshore boundary. The frequency spectrum and angular spreading function rely on the Bretschneider-Mitsuyasu type spectrum and the Mitsuyasu type function respectively. They are expressed as

$$E_0(f) = 0.257 H_{1/3}^{(0)2} T_{1/3}^{(0)} (T_{1/3}^{(0)} f)^{-5} \exp \{-1.03 (T_{1/3}^{(0)} f)^{-4}\} \tag{12}$$

$$D_0(f, \theta) = \frac{1}{\pi} 2^{2s-1} \frac{\Gamma^2(s+1)}{\Gamma(2s+1)} \cos^{2s} \frac{(\theta - \theta_w)}{2}, \quad S = \begin{cases} S_{\max}(f/f_{op})^5 & ; f < f_{op} \\ S_{\max}(f/f_{op})^{-2.5} & ; f \geq f_{op} \end{cases} \tag{13}$$

where S and S_{\max} are the energy concentration factor and its maximum value, θ_w the principal wave direction, Γ the gamma function, $f_{op} (= 1/1.05 T_{1/3})$ the peak frequency, and superscript '(0)' denotes the offshore boundary as well as the above-mentioned subscript '0'.

(2) Numerical Methods

a. Piecewise ray model: The basic idea in the numerical computation is to assume that the action spectrum of a component wave of interest at an inner point (x, y) at $t - \Delta t$ -time, $\psi(f_r^{t-\Delta t}, \theta_s^{t-\Delta t}; x, y, t - \Delta t)$ becomes the one at a grid point (i, j) at t -time, $\psi(f_p, \theta_q; i, j, t)$ after propagation along a ray over time increment Δt , where subscripts ('r', 'p') and ('s', 'q') denote the frequency and direction at different positions and times respectively, and the directional spectrum at a grid point (i, j) at t -time, $E(f_p, \theta_q; i, j, t)$ can be evaluated using the action spectrum $\psi(f_p, \theta_q; i, j, t)$ and the characteristics of a component wave, water depth and current components at the same grid point and time, $(C_s^t, k^t, \sigma_m^t, h^t, U^t, V^t)$. Time-variability and inhomogeneity of current and water depth fields induce changes of not only wave direction but also absolute frequency of a component wave with its propagation.

A piecewise ray method is used to obtain the horizontal distribution of wave characteristics. The method consists of two steps. The first step is to trace all wave ray components from the grid points backward by one time step Δt , as shown in Fig. 3. Each wave ray is followed by solving the equations of wave number vector components, Eqs. (2) and (3) with the Runge-Kutta method under initial values of wave number components at a starting grid point. The initial values are estimated from iterative numerical solution of the Doppler relation, Eq. (5) under the given conditions of absolute frequency,

wave direction, water depth and current components. It should be noted that there exist sets of cut-off direction and frequency where propagation of directional spectrum is blocked. In the ray computation, input wave direction and current direction are reversed, and current components and water depth at the ray tip are interpolated not only in space but also in time owing to their time-dependency.

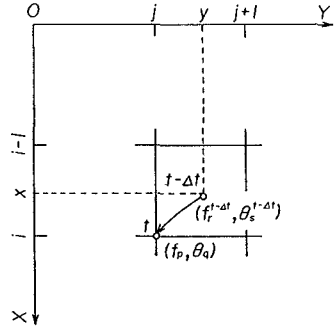


Fig. 3 Backward piecewise ray tracing.

The second step is to interpolate the action spectrum at the ray tip for the wave direction and absolute frequency shifted due to refraction. First, the Lagrange interpolation formula with third order accuracy is applied to the action spectra at the grid points surrounding the ray tip in order to estimate the action spectra for six sets of the prescribed input wave directions and absolute frequencies, namely two input wave directions (θ_n, θ_{n+1}) putting the refracted wave direction at the ray tip $\theta_s^{t-\Delta t}$ between them, and three input frequencies (f_{m-1}, f_m, f_{m+1}) putting the shifted absolute frequency at the ray tip $f_r^{t-\Delta t}$ among them. The formula is given as

$$\psi_{i+r, j+s} = \sum_{i=1}^{i+2} \sum_{j=1}^{j+2} \left(\prod_{k=1}^i \frac{x - x_k}{x_i - x_k} \right) \left(\prod_{l=1}^j \frac{y - y_l}{y_j - y_l} \right) \psi_{ij}$$

$$r = (x - [x]) / \Delta x, \quad s = (y - [y]) / \Delta y \tag{14}$$

Second, the action spectrum at the ray tip for the refracted wave direction and the input frequency is obtained by a linear interpolation over wave direction of the action spectra for the input wave directions estimated every input frequency as

$$\begin{aligned} \psi(f_k, \theta_s^{t-\Delta t}; x, y, t - \Delta t) = & \psi(f_k, \theta_n; x, y, t - \Delta t) + |\psi(f_k, \theta_{n+1}; x, y, t - \Delta t) \\ & - \psi(f_k, \theta_n; x, y, t - \Delta t)| \cdot (\theta_s^{t-\Delta t} - \theta_n) / (\theta_{n+1} - \theta_n) \end{aligned} \tag{15}$$

where k ($=m-1, m, m+1$) means the index of input frequency. Third, the action spectrum at the ray tip for refracted wave direction and frequency is estimated by use of parabolic interpolation of the log-transformed action spectra with respect to frequency as

$$\log \psi(f_r^{t-\Delta t}, \theta_s^{t-\Delta t}; x, y, t - \Delta t) = a(\log f_r^{t-\Delta t})^2 + b(\log f_r^{t-\Delta t}) + c \tag{16}$$

where a, b and c are the coefficients in a parabola curve determined from three sets of $\{ f_k, \psi(f_k, \theta_s^{t-\Delta t}; x, y, t - \Delta t) \}$, $k = m-1, m, m+1$. This procedure is required because the frequency of each wave component changes due to time-variation of currents and water depth.

b. Full ray model: The basic idea used in the model is the same as the one in the piecewise ray model. The computation in the full ray model consists of two steps.

The first step is to trace the wave ray of a component wave backward from a selected computation point to the grid boundary by the numerical integration of Eqs. (2) and (3) with the Runge-Kutta method, as illustrated in Fig. 4. In the ray tracing, currents and water depth at the ray tip are interpolated from those at the grid points, taking into account their space and time dependency.

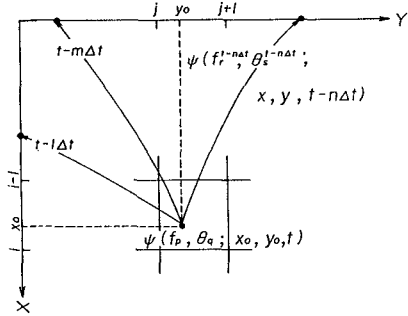


Fig. 4 Backward full ray tracing.

The second step is to estimate the action spectrum at grid boundary for frequency and direction shifted due to refraction at an arrival time of the ray, using input data for directional spectra. It should be emphasized that the arrival time of each ray is different. By iterating these procedures every direction and frequency, directional spectra at a certain time at the prescribed position can be computed.

The full ray model can give the almost exact solution in a simple case of linear currents and uniformly sloping bottom, because errors associated with interpolation are negligibly small, but it is less advantageous for the evaluation of horizontal distribution of wave characteristics when compared to the piecewise ray model, as the computation is conducted separately and independently at each position.

3. COMPUTATIONAL RESULTS AND CONSIDERATIONS

(1) One-dimensional current case

Fig. 5 shows the computation region with a grid spacing of $\Delta x=4$ km and a spatial distribution of sinusoidally-varying unsteady one-dimensional linear currents with period of $\widehat{T}=12$ hours on a uniformly sloping beach of $i=1/1000$. The currents are given by

$$U=0, \quad V= \begin{cases} -0.2(j-4) \sin [(k-1)\pi/6]; & j \geq 4 \\ 0 & ; j < 4 \end{cases} \quad (17)$$

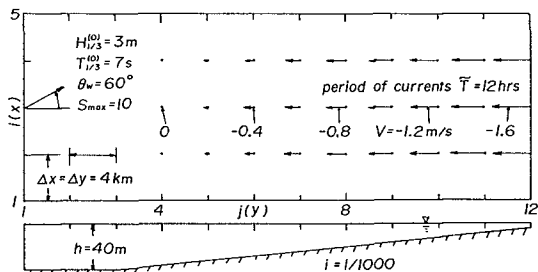


Fig. 5 Computation region and current distribution.

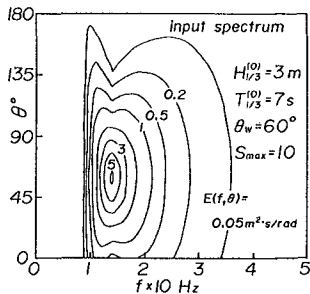


Fig. 6 Input directional spectra.

where k is the index denoting the time of the input currents given every 1 hour. The input wave conditions at the offshore boundary are also indicated in the figure. The 30 unevenly-spaced frequency data ranging from 0.09 to 0.571 Hz and the 37 evenly-spaced direction data from 0 to 180° are used with a time increment of 5 min. We focus our discussion on the wave characteristics at the grid point where water depth is 8 m deep and maximum current velocity is 1.4 m/s. Fig. 6 is the contour plot of input directional spectra.

Fig. 7 is the comparison between the time variations of wave height computed by both the full ray model and the piecewise ray model. The figure contains time variations of a current component V and wave height at the offshore boundary $\bar{H}_{1/3}^{(0)}$. This wave height is different from the input wave height given in the directional spectral model, Eqs. (11) to (13), defined on the entire circle ($\theta = 0 - 360^\circ$), because the computation is conducted on the half circle ($\theta = 0 - 180^\circ$). Both models are in close agreement except for a slight difference during the phase of opposing currents. The figure also shows that time-dependency of currents brings about a phase shift between the time variations of wave height and currents, and reduction in the amplification effect of wave height due to opposing currents in comparison with the steady current case.

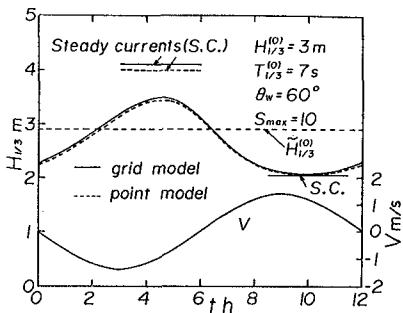


Fig. 7 Time-variation of wave heights with unsteady one-dimensional currents.

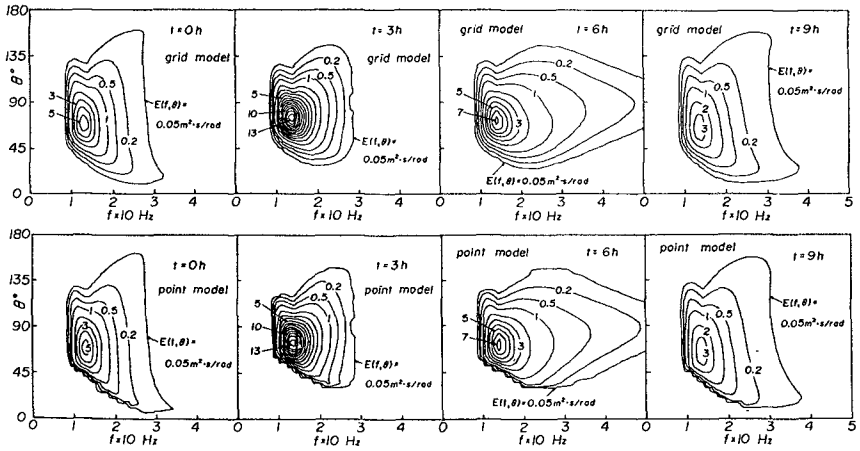


Fig. 8 Time variations of directional spectra with unsteady one-dimensional currents.

Fig. 8 describes the variations every 3 hours of the directional spectra at the before-mentioned point computed by both models. Shrinking and expanding of the distribution of directional spectra associated with temporal variation of currents are observed in the figure. Comparison between the results with the piecewise ray model and those with the full ray model suggests that both models give similar distributions of directional spectra at each time, although the piecewise ray model predicts smoother distribution in the vicinity of cut-off direction and frequency by use of interpolation formulas in the computation of action spectrum.

(2) Two-dimensional current case

Current-depth refraction of directional spectra induced by sinusoidally-varying unsteady two-dimensional model currents with period of $\bar{T}=6$ hours shown in Fig. 9 was computed on a uniformly sloping beach of $i=1/250$ divided into 17×10 with a grid spacing of 1 km. This current pattern is a modeling of tidal currents flowing in and out of a river mouth. The 18 unevenly-spaced frequency data from 0.09 to 0.351 Hz and the 37

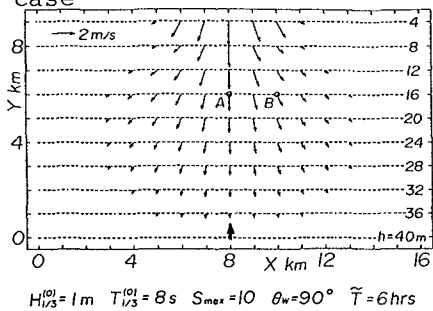


Fig. 9 An example of two dimensional current patterns given in the computation.

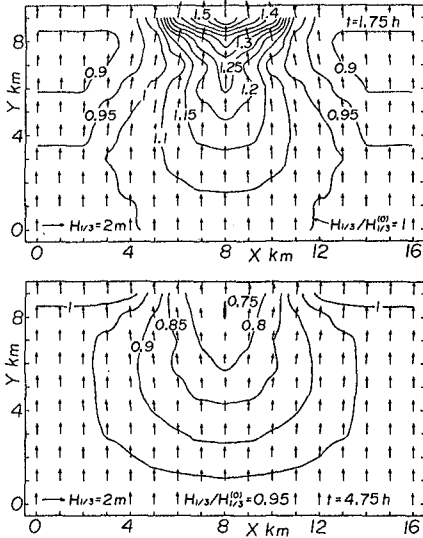


Fig. 10 Spatial distribution of wave heights and directions with unsteady two-dimensional currents.

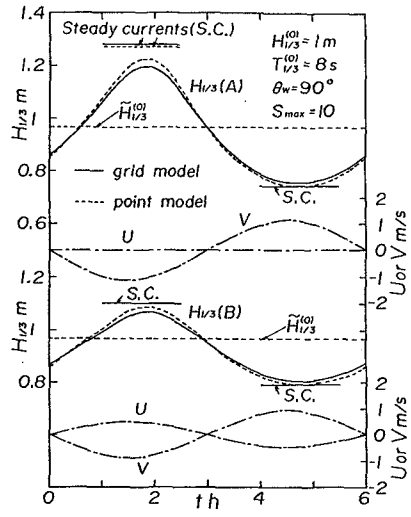


Fig. 11 Time variation of wave heights with unsteady two-dimensional currents.

evenly-spaced direction data are used with a time increment of 1.5 min. Input wave conditions are given in the figure. The computation making use of the symmetry of the solution was carried out to save computer processing time. We concentrate our concern on the change of wave characteristics at the points A and B except for wave height distribution.

Fig. 10 illustrates the horizontal distribution of wave height and wave direction at the phase of almost maximum opposing currents and the one at the phase of almost maximum following currents respectively, which are obtained by use of the piecewise ray model. At the phase of opposing currents, waves tend to converge toward the river mouth and wave height increases rapidly. But the amplification ratio is not so large as that in the case of steady opposing currents, as seen in the one-dimensional case. On the other hand, at the phase of following currents, waves tend to refract so as to be away from the river mouth and wave height reduces slowly compared to the opposing current case.

Fig. 11 shows the time variations of currents and wave height at the points A and B computed with both models.

The wave height variation follows the current variation behind about 1 hour. Due to energy leakage introduced through the repeated interpolation of action spectra, the piecewise ray model gives slightly smaller variation of wave height, when compared to the full ray model.

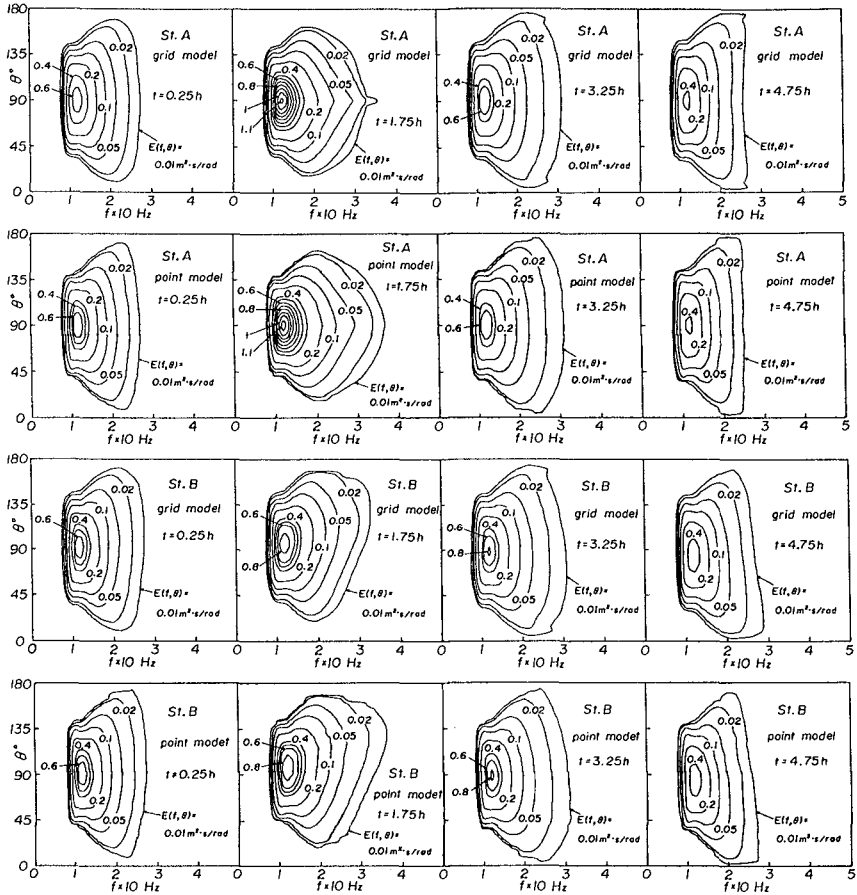


Fig. 12 Time variation of directional spectra with unsteady two-dimensional currents.

The time variations of directional spectra at the points A and B computed with both models are illustrated in Fig. 12. Both models produce close agreement in general patterns of directional spectra, but the distribution with the piecewise ray model are slightly smoother than those with the full ray model as well as the

case of one-dimensional currents. Convergence and divergence of the directional spectral distribution are alternately repeated with time-variation in direction and velocity of currents.

The directional spectra at the point A has a symmetrical distribution with respect to $\theta=90^\circ$ axis. Whereas at the point B of some distance from the center line of the region, component waves with directions of 90 to 180° receive stronger effect of currents than those with directions of 0 to 90° because of the current direction, and the resulting directional spectra at the phase of maximum opposing currents and those at the phase of maximum following currents have asymmetrical distribution relative to input wave direction. But, at the phase of zero currents, directional spectra have quasi-symmetrical distribution and the effect of currents is not clear.

4. CONCLUSIONS

The results obtained in this study are summarized as follows;

- 1) Two models for current-depth refraction of directional spectra due to time-varying currents and water depth are established, in which a piecewise ray method and a full ray method are used in numerical computation for propagation of directional spectra respectively.
- 2) The results computed with the piecewise ray model in the cases of time-varying one-dimensional and two-dimensional currents are in relatively close agreement with those by the full ray model except for a slight difference associated with the repeated interpolation of action spectra.
- 3) Time-dependency of currents gives rise to a time lag between wave height and current variations, and reduction in the amplification effect of directional spectrum due to opposing currents in comparison with steady current case.

5. ACKNOWLEDGEMENTS

Thanks are due to Mr. M. Ohfuku, Technical Officer, Department of Ocean Engineering, Ehime University, for his sincere help during the study. A part of this study was accomplished with the support of the Science Research Fund (No. 01550408) of the Ministry of Education, for which the authors express their appreciation.

REFERENCES

- Brink-Kjaer (1984): Depth-current refraction of wave spectra, Sympo. on Description and Modelling of Directional Seas, C-7-1-12.
- Mathiesen, M. (1984): Current-depth refraction of directional spectra, Sympo. on Description and Modelling of Directional Seas, C-6-1-8.
- Sakai, T. et al. (1983): Irregular wave refraction due to current, Jour. of Hydraul. Eng., ASCE, Vol. 109, pp. 1203-1215.
- Tolman, H. L. (1988): Propagation of wind waves on tide, Proc. of 21st ICCE, Vol. 1, pp. 512-523.
- Vincent, C. E. (1979): The interaction of wind-generated sea waves with tidal currents, Jour. of Phys. Oceanogr., Vol. 9, pp. 748-755.
- Yamaguchi, M. et al. (1985): Numerical models for wave transformation due to current-depth refraction, Proc. of JSCE, Vol. 357/II-3, pp. 187-195(in Japanese).
- Yamaguchi, M. et al. (1988): A numerical model for refraction computation due to time-varying currents, water depth and incident waves, Natural Disas. Science, Vol. 7-1, pp. 1-9(in Japanese).
- Yamaguchi, M. et al. (1989): A numerical model for refraction computation of irregular waves due to time-varying currents and water depth, Proc. of JSCE, Vol. 405/II-11, pp. 225-234(in Japanese).

CHAPTER 16

EXTREME STORMS IN THE ADRIATIC SEA

L. Cavaleri*, L. Bertotti*, P. Canestrelli** and P. Lionello*

* Istituto Studio Dinamica Grandi Masse-CNR, San Polo 1364,
30125 Venice, Italy

** Centro Previsione Maree, Comune di Venezia, San Marco 4299,
30124 Venice, Italy

Abstract

We discuss the application of the third generation WAM wave model to the Adriatic Sea. We focus in particular on one of the extreme storms that produced also heavy flooding in Venice. We discuss the problem of a correct description of the wind fields as a crucial input information to the wave model. After hindcasting the wave conditions during the storm, we use them as input for an estimate of the wave set-up towards the shore. We show that its consideration is essential for a proper evaluation of the flood level in the town.

Introduction

We discuss the application of the third generation WAM wave model to the Adriatic Sea. The recent tendency in wave modelling (see WAM-DI Group 1988, Tolman 1989) of neglecting, as far as possible, any empirical parametrization, and to numerically describe the field evolution only in terms of the physics of the phenomena involved, has allowed to properly model also storms with a complicated structure. The Adriatic Sea, enclosed between Italy and Yugoslavia, with a pronounced bordering orography, is characterized by strong gradients, both in space and time, of wind and wave fields. Provided the basin is represented with a sufficiently fine grid, a third generation wave model is likely to provide a very good overall description of the storm.

Three of us (see Cavaleri et al. 1989) have done extensive application of WAM to the Adriatic Sea, considering the various kind of storms acting in the basin, particularly in its northern part. We focus here on one of the heaviest storms, occurred in December 1979. The storm produced also a strong flood of the Venice Lagoon. The main task of this paper is to show how the evaluation of the wave set-up at the coast, obtained from the hindcasted wave conditions offshore, is an essential step for a correct estimate of the flood level in the town of Venice.

Wind and Wave Modelling

The WAM wave model is based on the numerical integration of the wave energy balance equation. This describes, point by point, time step by time step, the energy budget connected to advection, production and dissipation, and to the exchange among the various wave components. The model has been extensively described in the literature (e.g. WAM-DI Group 1988, Cavaleri et al. 1989) and we will limit here to the essential information. In the version used for this study the model runs with twenty-five frequencies in geometric progression ($f_1 = 0.0418$ hz, $f_{n+1} = 1.1 f_n$) and twelve directions at 12 degree intervals. The Adriatic Sea (Fig. 1) is represented on a 20 km step grid. The main axis of the basin, whose dimensions are approximately 750 x 200 km, is aligned from north-west to south-east; Venice is located at the upper left end. The last 200 km to the north are shallow, the depth of the continental platform decreasing with a more or less constant 1/1000 slope toward the northern end.

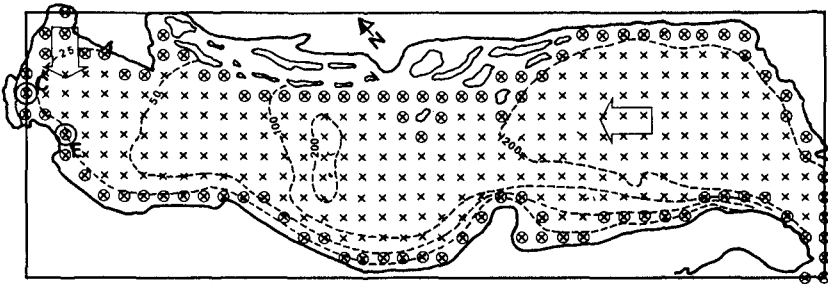


Fig. 1. Grid representation of the Adriatic Sea. The grid step is 20 km. C marks the position of the oceanographic platform off the Venetian coast. The wind model uses the same grid, but with one point out of two in each direction. Depths are in metres.

In general the most crucial aspect in the evaluation of a wave field is the accuracy of the wind field. It is obvious that, if a sophisticated wave model is to be used, the input wind field must have at least a comparable accuracy. This can be a problem when we are dealing with a relatively small basin with a complicated surrounding orography. In this case the large scale atmospheric models fail to correctly reproduce the relatively small details of the field that are nevertheless essential at the scale of the basin. The Adriatic Sea (Cavaleri et al., 1989) is almost completely bordered by high mountain ridges (Apennines to the west, Dinaric Alps to the east), and there is experimental evidence of wind space gradients up to 10 s in modulus and 10 deg m in direction. In these conditions the required grid resolution is of the order of 30-50 km, compared to the 100-150 km resolution of the present models, and to the 70 km one of the high resolution local models. Better examples do exist for specific areas, but they cannot be considered for generalized applications. Note anyhow that these figures should be halved with the next generation models, expected to come into operation in 1990-1991.

To satisfy the accuracy requirements we resorted therefore to a much simpler model (Cavaleri et al., 1990), where the accuracy is obtained by tuning the model to the local conditions. The model makes use of the one-layer balance equation whose solution provides the gradient wind. This is then transferred to the surface on the base of wind speed and air-sea stability conditions. The field modification, in modulus and direction, due to the constraintment of the bordering ridges is evaluated on the base of long-term experimental evidence. The input information is given by the atmospheric pressure recorded at the bordering meteorological stations. These are interpolated in space at the knots of a 40 km grid (Fig. 1) fitted to the wave model grid. A higher resolution would be only apparent because of the distance among the various stations. The above procedure provides one wind field for each synoptic time at the 3-hour interval.

The Storm of 21-23 December 1979

In these days strong wind over 20 ms , aligned all the way along the axis of the basin, produced very high waves in its central and northern part. Fig. 2 shows the wind and wave fields at 06 UI of 22 December. Note how the wave field is aligned along the axis of the basin till the northern coast (the left in the figure). No detailed comparison between model results and recorded data is possible as the oceanographic tower located offshore the Venetian

coast (point C in Fig. 1) suffered heavy damage during the storm. Our estimate of wave height at the tower is anyhow consistent with the damage reported on board.

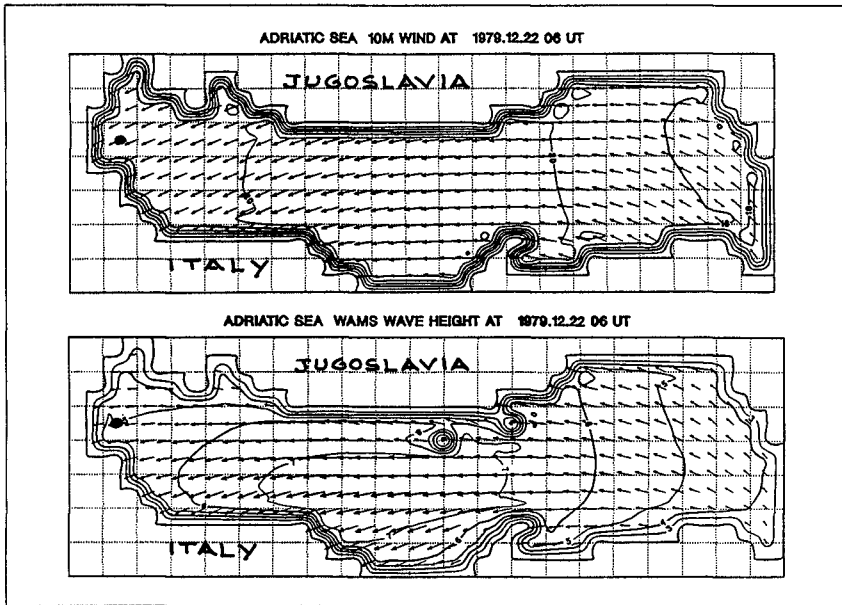


Fig. 2. Wind and wave fields at 06 UT of 22 December 1979. The wind has been interpolated from its 40 km resolution on the original grid. The dot to the left marks the position of the oceanographic platform.

The storm produced also one of the most severe floods ever recorded in Venice. The local geometry is shown in Fig. 3. At the town the peak sea level was measured at +1.66 metres above m.s.l., +1.85 metres at the Lido harbour entrance. Subtracting the expected +30 cm due to astronomical tide (Fig. 4a,b), we are left with +1.36 and +1.55 cm surge respectively. Fig. 4b shows also the predicted storm surge level, obtained by a statistical model fitted to data of the last decade (Canestrelli et al., 1986). There is an evident strong underestimate of the flood, particularly at and after the peak. This was not surprising. On the average the model works

rather well (r.m.s. error at the peak of the order of 10 cm), but it seems to fail, with a permanent underprediction, for the largest storms.

The only oceanographic instrument on the platform to survive the storm was the tide gauge, and we could therefore compare its record with the one at the Lido entrance (point B in Fig. 3). The two records showed up to 40 cm difference (Fig. 4c), the higher values being recorded at the coast. Notwithstanding our immediate doubts, a careful check confirmed the correct functioning of the gauge on board and the correctness of the data.

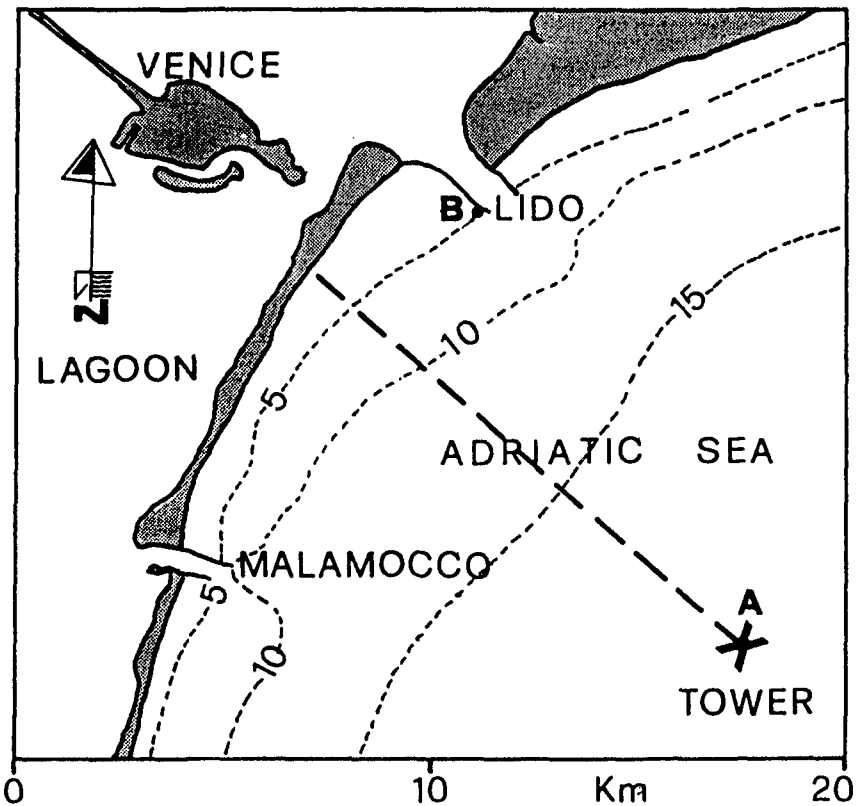


Fig. 3. Geometry of the Venetian coast. Lido and Malamocco are two of the three inlets connecting the lagoon to the sea. A and B show the position of the tide gauges. Depths are in metres.

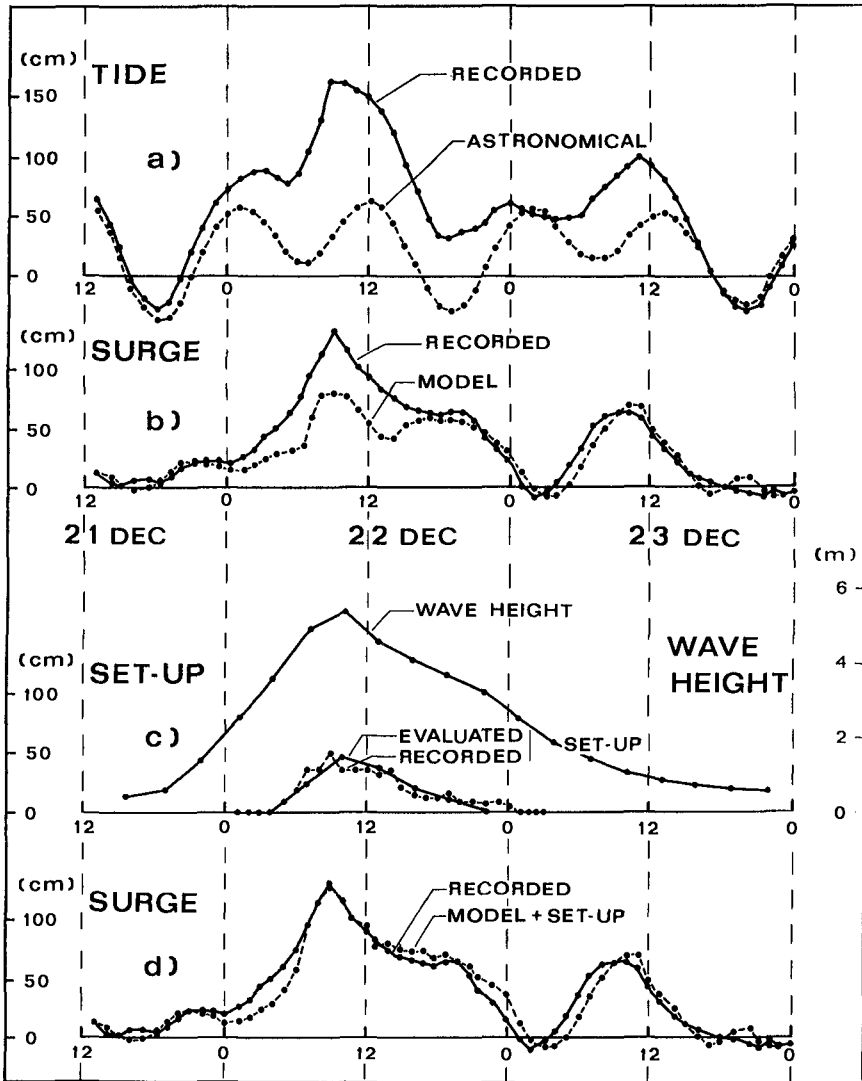


Fig. 4. a) Recorded and astronomical tide at Venice; b) recorded storm surge level (difference of the two graphs in a) and model prediction; c) wave height at the tower, evaluated and recorded set-up at the harbour entrance; d) recorded storm surge level (same as b) and corresponding model result (addition of prediction in b) and recorded set-up in c).

The explanation of this large difference is found in the wave fields. The entrance pier extends 3 km offshore till 6-metre depth. Both the reported damage on the platform and the hindcast (Fig. 4c) indicate that the waves were already breaking well before reaching the pier end. We must therefore expect that wave set-up was present at the pier end (and higher at the beach of course) and contributing to the local sea level. Starting from the hindcasted wave conditions at the platform we have evaluated the set-up at B (Fig. 3) making use of a one-dimensional set-up model (Bertotti and Cavaleri, 1985). The model assumes equilibrium conditions and evaluates the surface profile due to set-up from the platform till the shore. The one-dimensionality is justified by the strong concentration in direction of the wave field perpendicular to the shore, the equilibrium conditions by the limited distance (16 km) between the platform and the coast and the consequent fast response to any change in conditions.

The evaluated set-up, as sea level difference between the pier end and the platform, is shown in Fig. 4c. Its fit with the recorded difference is excellent (average difference at the estimate times + 1 cm), and we confidently conclude that the difference between the two gauges is effectively due to set-up.

We now make the hypothesis (discussed in the next section) that the storm surge model does not take set-up into consideration. Consequently we combine the predicted sea level and the set-up (Figs. 4b and 4c respectively) and compare again with the recorded sea level. The result is in Fig. 4d. The error has been drastically reduced (average error -1 cm, r.m.s. 9 cm), and the model evaluation is now good for all practical purposes.

Discussion

In the previous section we have stated that the statistical model of storm surge is actually evaluating the sea level off the coast, and, for the evaluation of the coastal sea level, we have to take into account the set-up due to waves. To be conclusive this statement must be made consistent with the general behaviour of the storm surge model, i.e. good results in most of the cases, with underestimate in the worst storms.

We first point out the structure of the storm surge model. Its estimate for the immediate future is based on the local sea level data during the last 15 hours and on the pressure values at some chosen station. Whatever the physics at the base of the phenomenon under study, it would be natural to assume that a statistical model should reproduce it, the degree of accuracy depending on the

complication of the phenomenon itself and on that of the model.

The second argument points to the structure of the wind fields during the storm surge events. These are basically due to the Sirocco wind, blowing from the southeast along the axis of the Adriatic Sea. Fig. 2 is a good example in this sense. But the Sirocco produces also heavy sea conditions in the northern part of the basin. Hence a surge in the Venice area is usually associated with high waves from the southeast, that produce also a coastal set-up. For our purpose, i.e. for the evaluation of the surge in Venice, we are not interested in the set-up at the shoreline, but at the end of the pier (point B in Fig. 3). A positive set-up at B is present only when breaking begins before B, which is true only for the heaviest sea conditions. Consequently the storm surge model statistically fitted to the data of the last decade, and implicitly to the main body of them, is unavoidably built with no set-up information into it. When this appears also at B, the model produces only the surge part, with a consequent underestimate of the sea level.

Our conclusion is therefore that the set-up plays an important role in determining the flood level in the Venice Lagoon during the worst event. As a correct estimate of the set-up requires the knowledge of the wave conditions off the Venice coast, their estimate becomes mandatory for a correct tidal forecast at the town.

References

Bertotti, L. and L. Cavaleri, "Coastal set-up and wave breaking", Oceanologica Acta, Vol 8, No. 2, 1985, pp. 237-242.

Canestrelli, P., F. Pastore and A. Tomasin, "Sviluppi di un modello operativo previsionale delle maree di Venezia e revisione di casi rilevanti", Comune di Venezia, 1986, 20 pp.

Cavaleri, L., L. Bertotti and P. Lionello, "Shallow water application of the third generation WAM wave model", Journal Geoph. Res., Vol 94, No. C6, 1989, pp. 8111-8124.

Cavaleri, L., L. Bertotti and P. Lionello, "Wind evaluation in the open sea and in coastal regions", accepted for presentation at the Primo Convegno Nazionale di Ingegneria del Vento, Firenze, 1990.

The WAM-DI Group, "The WAM model - a third generation ocean wave prediction model", Journal Phys. Ocean., 18, 1988, pp. 1775-1810.

Tolman, H.L., "Wind wave propagation in tidal seas", Communications on Hydraulic and Geotechnical Engineering, TU Delft, Report 90-1, 1990, 135 pp.

CHAPTER 17

SET-UP DRIVEN UNDERTOWS ON A BARRED BEACH

Philip D. Osborne¹ and Brian Greenwood¹

ABSTRACT

Field measurements of cross-shore velocity and water surface elevation from a natural barred surf zone during two storm events confirm the presence of undertow. The undertow is characterized by:

- i) mean cross-shore velocities reaching 0.20 m s^{-1} and directed offshore;
- ii) mean cross-shore velocity decreasing towards the surface with occasional reversals in the mean flow to a landward direction in the upper water column;
- iii) a strongly oscillatory velocity field with speeds increasing towards the surface and a distinct landward skewness superimposed.

The undertow is strongly correlated with set-up of the mean water surface. The set-up is characterized by:

- i) increasing values shoreward with perturbations closely following topography indicative of a primary forcing by waves;
- ii) maxima (0.35 m in the inner system) occurring over the bar troughs in association with decreasing wave height over the preceding bar crest as predicted by theory and laboratory experiments.

INTRODUCTION

Traditionally, undertow was thought to be a major control on shoreface erosion and the development and maintenance of nearshore bars (e.g. Johnson (1919), Keulegan (1948), Dally (1980), Roelvink and Stive (1988)). Although attention shifted towards horizontal circulation mechanisms rather than vertically stratified flows following work by Shepard and LaFond (1939) and Shepard et al. (1941), the theoretical basis for a two-dimensional

¹ Scarborough College Coastal Research Group, University of Toronto, Scarborough, Ontario, Canada, M1C 1A4.

circulation was firmly established by Longuet-Higgins (1953), Longuet-Higgins and Stewart (1962; 1963; 1964) and Lundgren (1963). A considerable effort has now been directed at modelling cross-shore mean flows which occur under shoaling and breaking waves (e.g. Stive and Wind, 1986, and Svendsen and Hansen, 1988) and the driving mechanism, the pressure gradient due to set-up (and set-down) of the mean water surface (e.g. Battjes and Janssen, 1978, and Dally et al., 1985). However, field observations which document the spatial and temporal structure of undertow and which demonstrate a direct relationship to water level set-up by wave breaking have been lacking.

Recently, Greenwood and Osborne (1990a, 1990b) carried out eulerian measurements of the horizontal velocity field and water surface elevation from a natural barred surf zone in order to:

- i) examine the spatial and temporal variability of cross-shore flow; especially its vertical structure;
- ii) examine cross-shore flow in relation to topography; especially its possible role in bar formation;
- iii) identify the mechanism(s) responsible for cross-shore flow; especially its relationship to wave-induced set-up.

Measurements were taken during two storm events in June 1986 at Wymbolwood Beach, Georgian Bay, Ontario, Canada. Measurements from the first storm event on June 16-18, 1986, clearly identified an undertow which was shown to respond in a coherent manner to measurements of wave-induced set-up of the mean water level. In this paper we illustrate that measurements from a second, smaller storm event on June 24-25, 1986, compare favourably with those from the previous event under similar surf zone conditions and confirm the existence of undertow on barred beaches.

LOCATION OF STUDY

Wymbolwood Beach is a lacustrine, barred shoreface composed of medium-to-fine sands situated on southern Georgian Bay, Ontario, Canada (Figure 1). The site is ideal for measuring set-up and cross-shore flows; periods of wave activity are restricted to discrete storm events associated with the passage of meteorological depressions and are separated by periods of flat calm. The beach is exposed to fetch-limited storm waves, which may reach 1.5 m at breaking. Water level shifts are restricted to seasonal hydrologic and climatic effects, higher frequency seiching and wind and wave set-up.

During the experiment two bars were present on a mean nearshore slope of 0.015 (Figure 2). The inner bar had relatively steep slopes (landward = 0.083; lakeward = 0.047 - 0.031). The outer bar consisted of a laterally extensive,

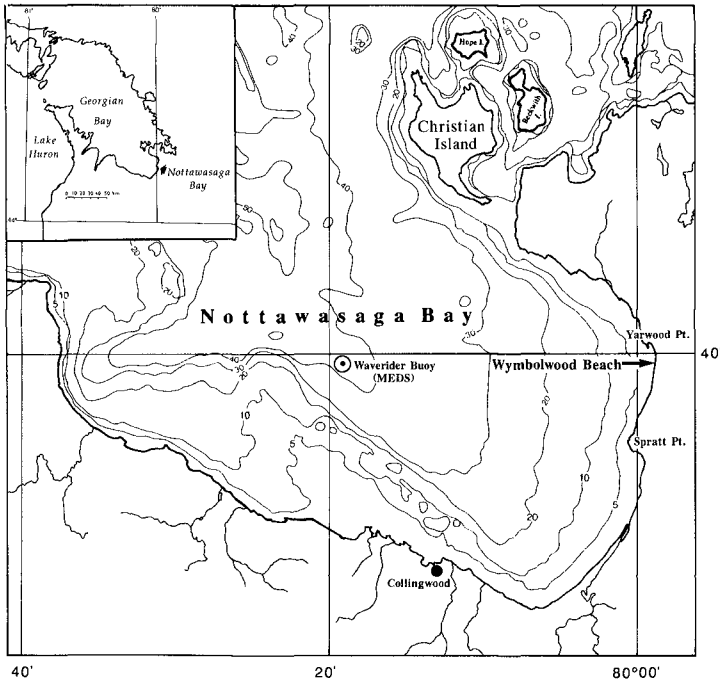


Figure 1. Location of study; bathymetric contours are in fathoms.

very gently sloping landward slope (0.005) and a lakeward slope approximately equal to that of the mean beach slope. Changes in the beach profile along the instrument transect during the two storm events were restricted essentially to the inner bar and beach face. The outer bar remained essentially two-dimensional and unchanged throughout the experimental period (Greenwood and Osborne, 1990a). No rip channels or other irregularities were present.

EXPERIMENTAL DESIGN

Sensor deployment was designed to satisfy two aims:
 i) to relate waves, mean water-surface elevation and cross-shore flows to varying topographic constraints, horizontal spatial coverage should be as complete as possible;
 ii) to relate cross-shore flows to elevation above the bed, a dense network of sensors in the vertical was necessary. However, deployment was constrained by the number of sensors available (15 continuous resistance wave staffs, 11 electromagnetic current meters). Figure 2 illustrates the final deployment of sensors along a shore-normal

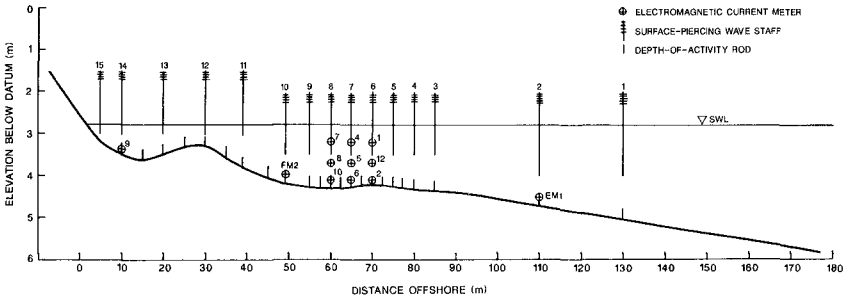


Figure 2. Nearshore profile and instrument deployment.

transect; note the fairly complete coverage of the nearshore by the wave sensors and the dense tri-level array of current meters on the landward slope of the outer bar. The latter might be expected to provide information on the character of any undertow that might occur and in a location where, according to theory, it might be expected to contribute to sediment transport causing bar growth. All sensors were scanned at 0.42 Hz for approximately 20 minutes. Wind speed and direction were measured at the beach face with a Beaufort anemometer and wind vane. Time-averaged statistics (such as the mean, standard deviation, and skewness) used to describe the wave and velocity fields, were computed over twenty minute sample periods (2925 points) as follows:

$$\bar{u} = 1/n \sum u_{(t)} \quad \text{or} \quad \bar{\eta} = 1/n \sum \eta_{(t)}$$

$$u_s = [1/n-1 \sum (u_{(t)} - \bar{u})^2]^{1/2} \quad \text{or} \quad \eta_s = [1/n-1 \sum (\eta_{(t)} - \bar{\eta})^2]^{1/2}$$

$$u_m = 2.8u_s \quad H_s = 4 s$$

$$u_{sk} = [1/n-1 \sum (u_{(t)} - \bar{u})^3] / u_s^3$$

Where n = sample size, $u_{(t)}$, $\eta_{(t)}$ = time-varying velocity, water-surface elevation, \bar{u} , $\bar{\eta}$ = mean, u_m = maximum orbital speed, H_s = significant wave height, u_{sk} = velocity skewness. Water level set-up and set-down were computed using the difference between mean water levels during the storm events and mean water levels under flat-calm conditions on June 19-20 between the storms.

TEMPORAL VARIABILITY OF WAVE AND VELOCITY FIELDS

Both storms studied were of a magnitude frequently encountered in this location (e.g. the recurrence interval of the June 16 storm was 0.2 years). Temporal variation in wind speed and direction, significant wave height and

peak wave period is presented in Figure 3. Incident wave heights reached 1.5 m with a peak period of 4 to 6 s in the June 16-18 storm. A relatively rapid reduction in wave height occurred following the storm peak due to a reduction in wind speed and a shift in wind direction away from maximum fetch. During the storm peak, a surf zone dominated by spilling breakers extended well beyond the outer bar crest for a period of at least 11 hours and breaking was present on the outer bar crest and area landward for a significantly longer period. Although wave activity lasted for 49 hours, the most intense activity was concentrated between 1600 h and 2330 h on June 16. In the June 24-25 storm, incident wave heights reached 1.1 m with a peak period of 4 s. Both wave height and period increased in response to wind from the WSW but decayed more gradually following the storm peak as wind direction shifted to the W and WNW (maximum fetch) and wind speeds were reduced. Spilling breakers dominated the outer bar crest and area landward for a period of approximately 6.5 hours between 1330 h and 2100 h.

Temporal variation in the near-bed velocity parameters: \bar{u} , u_s , and u_{sk} at 10 m, 65 m and 110 m offshore are shown in Figure 4. The first three moments of the cross-shore velocity field exhibit strong positive correlations with wave energy and a high degree of spatial coherence (Greenwood and Osborne, 1990b). Near identical values of wave-induced orbital currents (u_s) were recorded from the closely spaced flowmeters on the outer bar throughout the two storms.

On June 16, a distinct offshore mean flow was superimposed on the oscillatory motion at all measurement stations from 1300 h until 2330 h. The cross-shore mean-flow was not a local anomaly, but was coherent spatially and temporally. During the storm growth mean flows decreased across the landward slope of the outer bar; in contrast, a lakeward increase in mean flow speeds from 0.12 m s^{-1} to 0.18 m s^{-1} was observed during the storm peak.

On June 24, mean flows were again predominantly offshore, but of much smaller magnitude than in the previous event. In general, mean speeds increased lakeward across the landward slope of the outer bar from near zero ($< \pm 0.03 \text{ m s}^{-1}$) at 60 m to 0.09 m s^{-1} at 70 m. The reduction in mean flow on the lakeward slope of the outer bar (110 m) suggests that the cross-shore mean flow was confined to the surf zone and was being driven by local forcing.

Coincident in time with the offshore mean flows was a large onshore directed skewness in the cross-shore velocity field. There does not appear to be a clear spatial pattern in the skewness, but rather a marked uniformity for a third order statistic which is highly susceptible to sampling variability. The positive skewness coincides well with the period in time when spilling breakers were

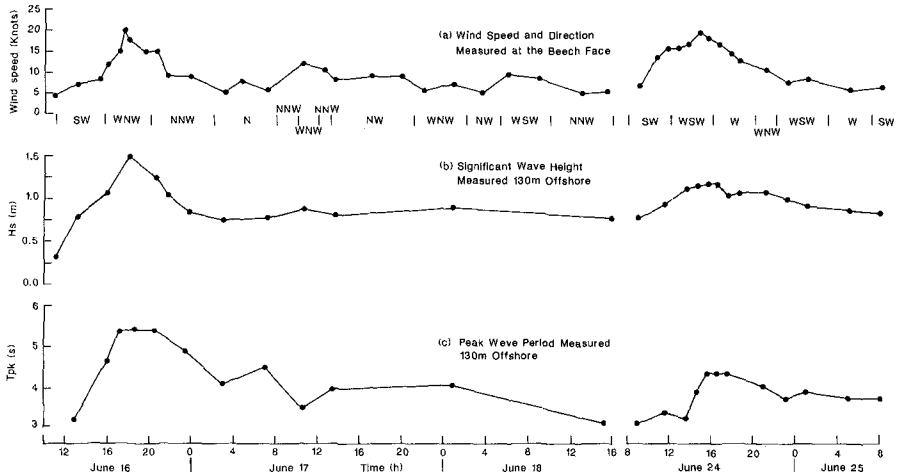


Figure 3. Wind and wave conditions, Wymbolwood Beach: June 16 to 18, 1986 (a); June 24 to 25, 1986 (b).

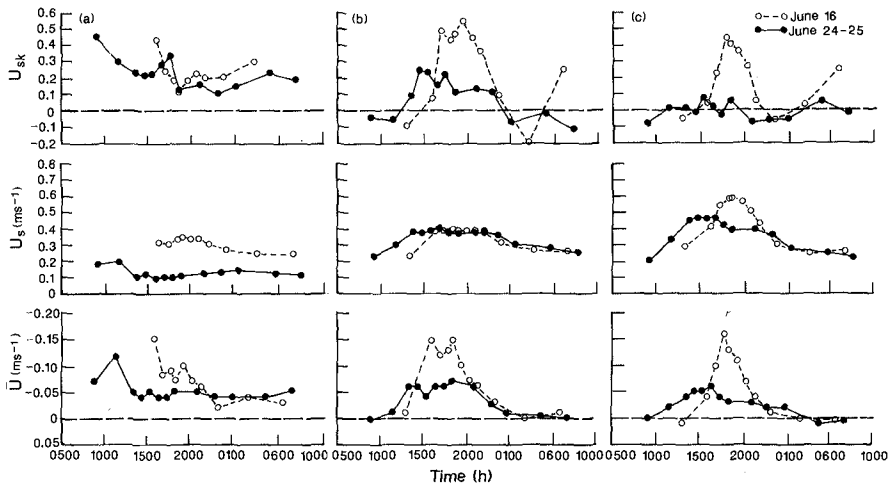


Figure 4. Temporal variation of near-bed (0.10 m) velocity parameters, \bar{u} , u_s , and u_{sk} , during the two storm events: 10 m offshore (a), 65 m offshore (b), and 110 m offshore (c). Note: positive values indicate onshore direction.

propagating through the tri-level sensor array, and this asymmetry was undoubtedly due to the non-linear nature of the surface waves. In the second storm, breaking waves were restricted landward of the outer bar crest, consistent with the near-zero skewness in velocity observed on the lakeward slope (Figure 4c).

CROSS-SHORE FLOW CHARACTERISTICS

Vertical variation in \bar{u} , u_s , and u_{sk} recorded on the landward slope of the outer bar (65 m) during both storms (1700 - 2030 h, June 16; 1500 -1730 h, June 24) is shown in Figure 5. The offshore mean flows exhibit a distinct vertical stratification; they were a maximum at the 0.1 m elevation and decreased in magnitude with elevation above the bed. At times, the mean flow exhibited a reversal, being directed onshore at the 1 m elevation, although these flows were small. In contrast, the wave-induced oscillatory motion was generally uniform in magnitude with elevation above the bed. Orbital speeds were similar during both storm events, indicative of the limiting velocity under wave breaking. Velocity skewness, on the other hand, exhibited more vertical variation, although it was almost always positive (directed onshore) at all elevations.

Figure 6 is an example of time-series of cross-shore velocities and water surface elevations under breaking waves during the storm peaks which illustrates that, even though a significant quasi-steady flow was present, the time-dependent, cross-shore flows were still dominated by oscillatory motion. The strongly non-linear nature of the water surface profile and the resulting velocity asymmetry associated with the spilling breakers is clearly displayed in these time-series; note also the "saw-toothed" water surface profile. Figure 7 illustrates a typical distribution of total velocity vector magnitude as a function of angle relative to the shore-normal during the storm peaks. It is evident that the vectors are distributed across all angles with the majority (greatest density of points) distributed about 200° , indicating that most flow vectors were associated with the offshore and alongshore currents. The distribution is also peaked at $0^\circ/360^\circ$ (the onshore direction); note that the magnitude of the relatively infrequent onshore directed vectors is similar to that of the offshore directed flows. This is in marked contrast with the signature of an active rip current recorded by Bowman et al. (1988).

In summary, the velocity field under spilling breakers was predominantly oscillatory, but with a well-defined offshore mean flow superimposed. The velocities exhibited a landward directed skewness, which was caused by the non-linear breaking waves. The spatial and temporal coherence

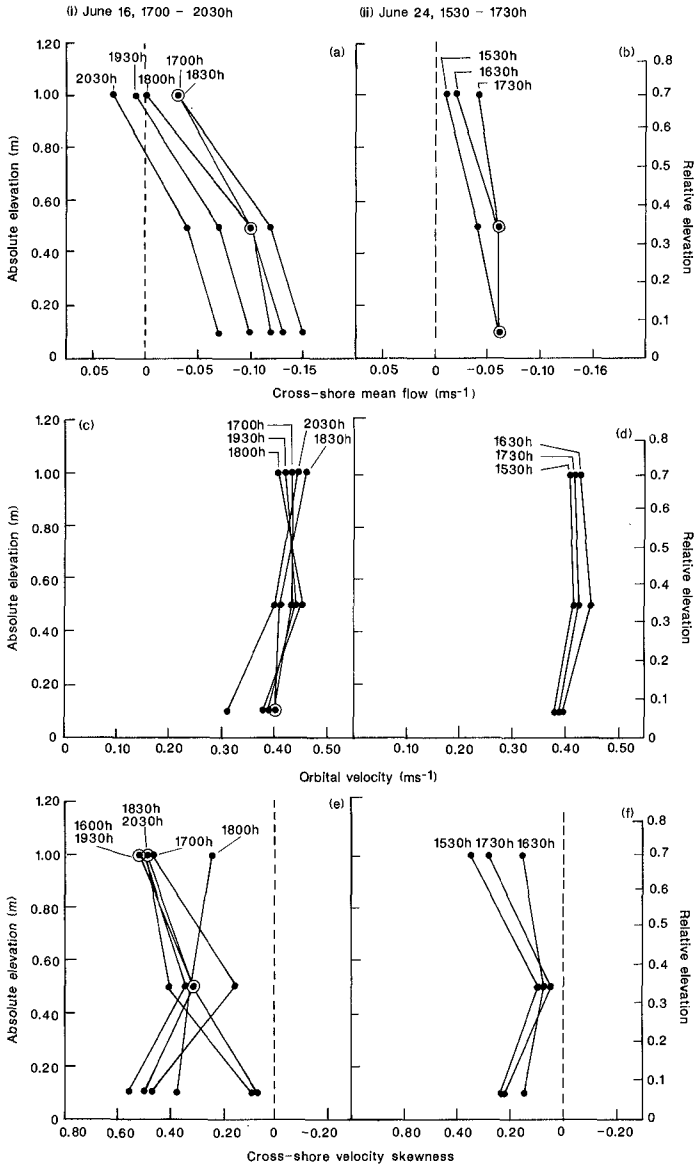


Figure 5. Vertical variation in the horizontal velocity field at 65 m offshore: i) 1700 - 2030 h on June 16; ii) 1500 - 1800 h on June 24; cross-shore mean velocity, \bar{u} , (a, b); cross-shore orbital velocity, u_s , (c, d); cross-shore velocity skewness, u_{sk} , (d, e). Note: positive values indicate onshore direction.

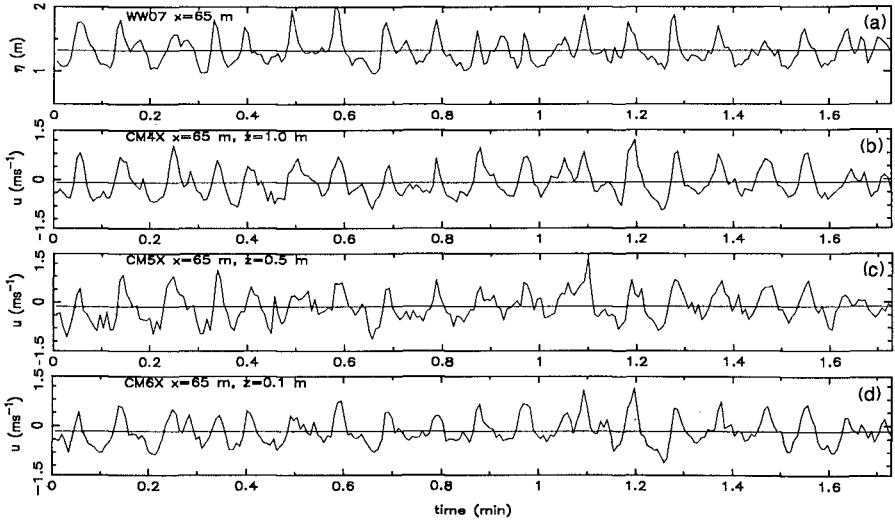


Figure 6. Time-series of: water surface elevation (a), and cross-shore velocities at 1.0 m (b), 0.5 m (c), and 0.1 m (d) elevation at 65 m offshore during the storm peak on June 16, 1800 h.

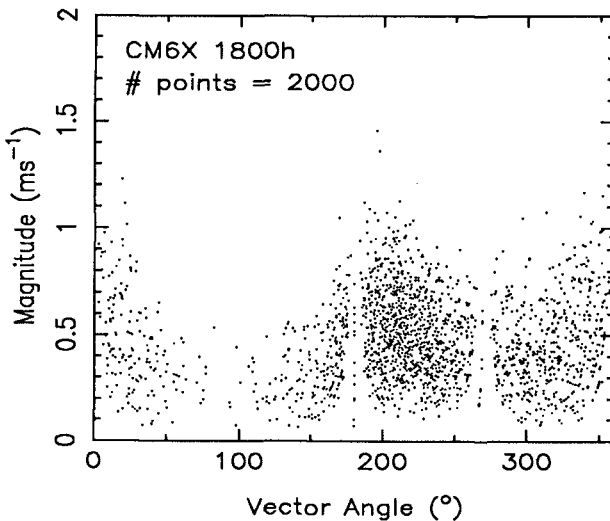


Figure 7. Velocity vector magnitude as a function of angle relative to shore normal (1800 h, June 16).

of the mean flow, with its maximum near the bed, has the characteristics of an undertow.

SPATIAL AND TEMPORAL VARIATION IN SET-UP AND WAVE HEIGHT

Temporal changes in the set-up of the mean water level in the inner part of the surf zone are shown in Figure 8. The set-up was well correlated with wave energy and also with the offshore mean flow. This is to be expected if the set-up is primarily wave-forced and the undertow is set-up driven.

In general, wave height decreased and set-up increased towards the shoreline during the storm peaks (1800 h, June 16; 1630 h June 24); however spatial variation in the wave height decay and elevation of the water level indicate a strong topographic influence induced by the bars (Figure 9). In both storms there was a rapid decay spatially in wave height across the upper lakeward slope and crest of the outer bar, the minimum height occurring just landward of the bar crest. The overall pattern for June 16 is consistent with the visual observation that breaking occurred by spilling across the whole experimental array and actually began well lakeward of the array. The wave height decay pattern also indicates that more intense breaking was associated with local decreases in water depth on the bar crests and at the shoreline. On June 24, the wave height decay across the lakeward slope of the outer bar (> 85 m) was less rapid than that observed during the June 16 storm owing to the smaller incident wave heights.

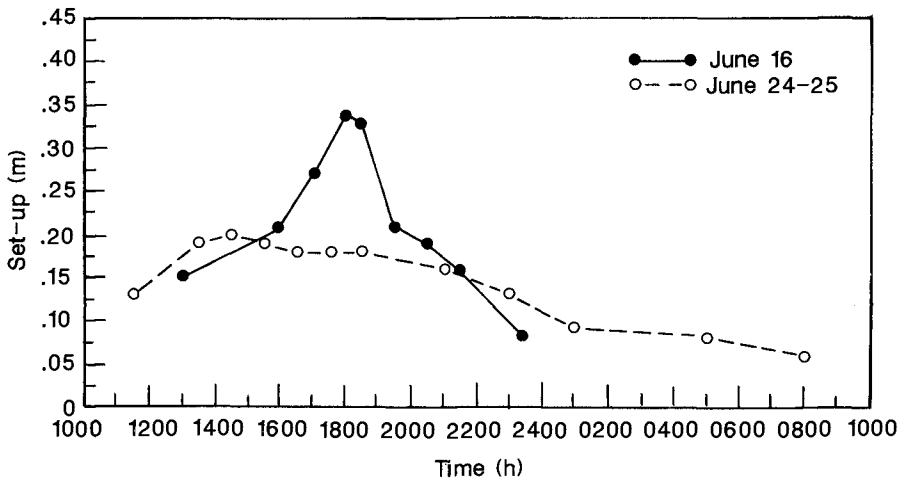


Figure 8. Temporal changes in the set-up of the mean water level measured at 10 m offshore.

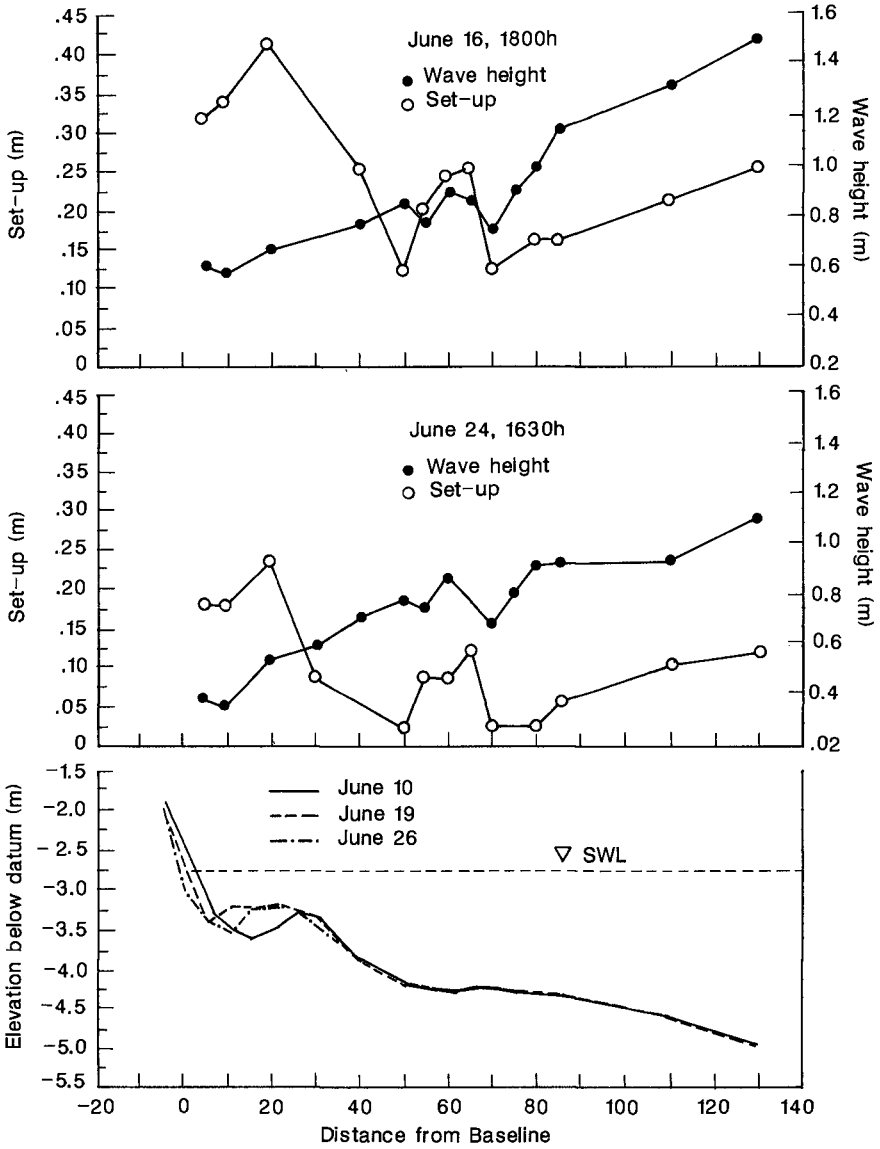


Figure 9. Shore-normal variations in the significant wave height and mean water surface set-up during the storm peaks: 1800 h June 16 (a); 1630 h June 24 (b).

The maximum local gradient in set-up occurred across the lakeward slope and crest of the inner bar, with maximum set-up in the trough and landward. There was a distinct decrease in the set-up landward of this local maximum. This pattern is consistent with the observed increase in local energy dissipation, often characterized by the presence of plunging breakers, which occurred over the crest and upper lakeward slope of the inner bar and again at the shoreline. No measurements of the water surface across the beach face were possible in this experiment to confirm the expected set-up due to the shoreline breakers, but visual observations confirmed an increase in the elevation of wave run-up during the storm peaks. A similar but less pronounced pattern in set-up is evident over the outer bar in association with the gradients in dissipation occurring in that region.

These observations provide strong evidence that topographic variations introduce spatial variability in both wave height and set-up, the former through enhanced shoaling, breaking and frictional effects as both theory and laboratory experiments suggest (Battjes and Janssen, 1978; Dally et al., 1985). However, the spatial gradients in set-up are significantly smaller than those expected for the measured wave height decay (Greenwood and Osborne, 1990b; Hazen et al., 1991).

DISCUSSION AND CONCLUSIONS

In this paper we illustrate the presence of an undertow on a natural barred beach which responds to both spatial and temporal variations in a wave-induced set-up. This distinctive two-dimensional cross-shore circulation pattern has been identified during two moderate storm events through detailed velocity and water surface elevation measurements.

During periods of breaking waves, the cross-shore velocity field was dominated by wave-induced flows with an average oscillatory speed of 0.40 m s^{-1} . A strong asymmetry in these oscillatory flows was evident in terms of large non-zero mean values (upto 0.20 m s^{-1}) directed offshore, and positive (onshore) directed skewness values. Vertical profiles of the wave-induced oscillatory velocity (u_s), the mean velocity (\bar{u}) and the velocity skewness (u_{sk}) indicate radically different structures. The oscillatory velocities were essentially uniform, perhaps increasing slightly with elevation above the bed, whereas the offshore mean flows generally decreased in speed with elevation, and in some cases flow reversals were present in the upper part of the water column. Velocity skewness was positive with considerable vertical variability, although a less distinct stratification than the mean and oscillatory components. These observations reveal a mean flow, which is separate and distinct, and imply the existence of a quasi-steady

current superimposed on highly non-linear oscillatory motion.

The large positive skewness values together with the vertical structure of the oscillatory and mean flow components suggest a shoreward directed, depth-dependent momentum and mass flux which is greater near the surface as suggested by theory. The mass and momentum balance is achieved by the large offshore mean currents in the lower water column. A large number of vertical profiles with this distinctive vertical structure from across the outer part of a surf zone saturated with spilling waves, suggest a well-developed and spatially coherent undertow.

The undertow responds to changes in the set-up of the mean water level, which in turn is strongly correlated with the growth and decay of the incident wave height. This is consistent with the hypothesis of a two-dimensional circulation driven by the vertical differences in the water column between the depth-dependent radiation stress and a depth-uniform pressure gradient force associated with a sloping water surface.

Local variations in the set-up, wave height and cross-shore mean flow are topographically controlled on a barred beach (see also Hazen et al., 1991). Large set-up gradients on the steepest part of the beach (lakesward slope of the inner bar) are associated with large gradients in wave height decay over the outer bar crest. These observations together with the presence of vertically stratified flows lend support to the notion a two-dimensional circulation system, undertow, driven by wave set-up.

ACKNOWLEDGEMENTS

This research was supported by operating and equipment grants from the Natural Sciences and Engineering Research Council Canada to Brian Greenwood, and an Ontario Graduate Scholarship to Philip Osborne. We would like to thank Drs. D.J. Sherman and B.O. Bauer, together with A. Hincenbergs and R. Blair for their invaluable assistance in the field.

REFERENCES

- Battjes, J.A. and Janssen, J.P.F.M. (1978) Energy loss and set-up due to breaking of random waves. Proc. 16th Coastal Eng. Conf., ASCE, p. 569-587.
- Bowman, D., Arad, D., Rosen, D.S., Kit, E., Goldberg, R., and Slavicz, A. (1988) Flow characteristics along the rip current system under low energy conditions. Marine Geol., 82: 149-167.
- Dally, W.R. (1980) A numerical model for beach profile evolution. Unpubl. M.Sc. Thesis, University of Delaware, 122 pp.

- Dally, W.R., Dean, R.G. and Dalrymple, R.A. (1985) Wave height variation across beaches of arbitrary profile. *J. Geophys. Res.*, 90: 11917-11927.
- Greenwood, B. and Osborne, P.D. (1990a) Equilibrium slopes and cross-shore velocity asymmetries in a storm-dominated barred nearshore system. *Marine Geol.*, 94: in press.
- Greenwood, B. and Osborne, P.D. (1990b) Vertical and horizontal structure in cross-shore flows: an example of undertow and wave set-up on a barred beach. *Coastal Engineering*, 14: in press.
- Hazen, D.G., Greenwood, B. and Bowen, A.J. (1991) Nearshore current patterns on barred beaches. *Proc. 22nd Coastal Eng. Conf., ASCE* (these proceedings).
- Johnson, D.W. (1919) Shore processes and shoreline development. John Wiley & Sons, New York, NY, 584p.
- Keulegan, G.H. (1948) An experimental study of submarine sand bars. U.S. Army Corps of Engineers, Beach Erosion Board Tech Rep., 3, 40 pp.
- Longuet-Higgins, M.S. (1953) Mass transport in water waves. *Phil. Trans., Roy. Soc. London*, (A) 245: 535-581.
- Longuet-Higgins, M.S. and Stewart, R.W. (1962) Radiation stress and mass transport in gravity waves. *J. Fluid Mechanics*, 13: 481-504.
- Longuet-Higgins, M.S. and Stewart, R.W. (1963) A note on wave set-up. *J. Marine Res.*, 21: 4-10.
- Longuet-Higgins, M.S. and Stewart, R.W. (1964) Radiation stresses in water waves; a physical discussion with applications. *Deep Sea Res.*, 11: 529-562.
- Lundgren, H. (1963) Wave thrust and energy level. *Proc. Congress Int. Assoc. Hydraulic Res.*, London, IAHR, Delft, The Netherlands, p. 147-152.
- Roelvink, J.A. and Stive, M.J.F. (1988) Bar-generating cross-shore flow mechanisms on a beach. *J. Geophys. Res.*, 90, p. 4785-4800.
- Shepard, F.P. and LaFond, E.C. (1939) Undertow. *Science*, 89: 1-2.
- Shepard, F.P., Emery, K.O. and LaFond, E.C. (1941) Rip currents: a process of geological importance. *J. Geol.*, 49: 337-369.
- Stive, M.J.F. and Wind, H.G. (1986) Cross-shore mean flow in the surf zone. *Coastal Engineering*, 10: 1-25.
- Svendsen, I.A. and Hansen, J.B. (1988) Cross-shore currents in surf zone modelling, *Coastal Engineering*, 12: 23-42.

CHAPTER 18

NEARSHORE CIRCULATION WITH 3-D PROFILES

Ib A. Svendsen,¹ Member, ASCE and Uday Putrevu,² Student Member, ASCE.

ABSTRACT

A model that predicts the depth variations of wave generated currents within the framework of a 2-D depth-integrated surf-zone model is described. The equations are formulated and solved for the case of a long, straight coast. The model is used to demonstrate that the effects of current refraction are weak and to determine the variation of the 3-D spiral shaped current profiles across the surf-zone. Finally, we show that the mixing coefficient required to get realistic variations of the longshore current is much larger than what the turbulence measurements can justify.

1. INTRODUCTION

The present paper describes a hydrodynamical model for 3-D wave generated currents in the nearshore region. The model is based on the idea of using a 2D-horizontal, depth integrated description to determine the integration constants in the analytical solutions for the vertical variation of the horizontal velocities. This idea was developed for the 2D cross-shore circulation by Svendsen & Hansen (1988). Independently, Davis (1987) pursued a similar idea for wind generated currents.

Quasi 3-D local solutions for current profiles were derived by deVriend & Stive (1987) based on dividing the flow into a primary and a secondary component. The more general approach used here was developed by Svendsen & Lorenz (1989) (S & L) who used a perturbation expansion to establish the equations. Concentrating on the longshore current profiles, they found that the equation normally used for the depth averaged longshore currents actually applies to the first approximation to the bottom velocity. The longshore velocity above bottom level increases uniformly, yielding somewhat (10-20%) larger depth averaged velocities at all locations than found by the classical depth integrated models.

In the present paper, the method of S & L is combined with the energy and cross-shore momentum equations to form a comprehensive computer model, the solution of which predicts wave heights, set-up, and, longshore and cross-shore currents and their variation over depth. For simplicity, the model equations are only established for a long cylindrical coast. This implies Snell's law is valid and it is possible to incorporate the wave-current refraction in the energy and

¹Professor, Center for Applied Coastal Research, Department of Civil Engineering, University of Delaware, Newark, DE 19716, USA

²Graduate Student, Center for Applied Coastal Research, Department of Civil Engineering, University of Delaware, Newark, DE 19716, USA

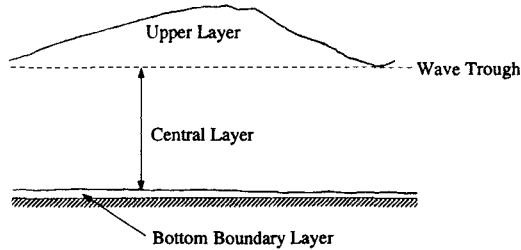


Figure 1: The three layer model concept

momentum equations in a simple manner. The basic equations of the model are described in Sections 2 and 3. This includes a description of how the bottom friction is incorporated as a boundary condition in the model.

On a long straight coast, the model equations become ordinary differential equations in x , the cross-shore coordinate. The energy and momentum equations represent initial value problems solved by specifying wave conditions at the seaward boundary. The longshore momentum equation is solved as a boundary value problem.

The system contains a number of features not previously included in such models though for reasons of limited space only a few of them can be analyzed and discussed here. In Section 4, we show that the wave-current interaction is really not modifying the wave motion or the current motion significantly even though the longshore current may be a substantial fraction of the wave speed. This is partly because the refractions due to the longshore and the cross-shore currents counteract each other, partly because the angle of incidence of the waves is usually small.

We also show the full cross-shore array of the 3-D spiral shaped current profiles corresponding to a given wave situation.

Finally, we confirm the logical conflict that still remains between which eddy viscosities are reasonable for the cross-shore circulation ($\nu_t \sim 0.01 h \sqrt{gh}$) and the many times larger coefficient for horizontal mixing required to achieve realistic variations of the longshore currents, particularly outside the surf zone for which we can find no justification in our knowledge about the turbulence characteristics. Though it has been suggested (Thornton & Guza, 1986) that on natural beaches this paradox may be accounted for by including the irregularity of wave breaking, that explanation does not cover experiments with regular waves where the effect seems equally strong (e.g., Visser 1982, 1984). Further examination of this problem would be desirable.

2. BASIC EQUATIONS FOR THE CURRENT VARIATION OVER DEPTH

The three layer model concept

The general approach is to utilize the concept of a 3 layer flow situation first suggested by Hansen & Svendsen (1984) and later used by Stive and Wind (1986) and Svendsen *et al.* (1987) (Fig. 1).

This approach assumes that there is a (mainly oscillatory) boundary layer at the bottom, within which the turbulence characteristics are dominated by the locally generated turbulence. In 2D cross-shore circulation, this assumption is

supported by the variation of current measurements and leads to very accurate results and there is no reason to expect the situation to be different in the general 3D case.

The method concentrates on the central or core layer, between the boundary layer and the wave trough. The third layer, between wave trough and wave crest, is considered separately from the middle layer because in that region there is water only part of the time, so we cannot separate the total particle velocity into an oscillatory and a mean (current) component.

In the central layer it is assumed that the turbulence is primarily produced by the breaking process. This means that it is both more intensive and has a larger length scale than the turbulence in the bottom boundary layer (Svendsen *et al.* 1987). This, in turn, justifies the assumption of a higher eddy viscosity ν_t in the central layer, based on the Prandtl-Kolmogorov assumption that

$$\nu_t \sim \ell \sqrt{q} \quad (1)$$

where q is the turbulent kinetic energy.

The basic equations

The general equations for the wave averaged (current) motion below trough level were derived by S & L. For a steady situation on a long straight coast, where $\partial/\partial y = 0$ (y being the shore parallel coordinate and x the shore normal coordinate pointing shorewards, see Fig. 2) those equations reduce to the following in the x and y directions, respectively:

$$\frac{\partial}{\partial z} \left(\nu_{tz} \frac{\partial U}{\partial z} \right) = \frac{\partial}{\partial x} \left(\overline{u_w^2} - \overline{w_w^2} + gb \right) + \frac{\partial \overline{u_w w_w}}{\partial z} + \frac{\partial U^2}{\partial x} \quad (2)$$

and

$$\frac{\partial}{\partial z} \left(\nu_{tz} \frac{\partial V}{\partial z} \right) = \frac{\partial \overline{u_w v_w}}{\partial x} + \frac{\partial \overline{v_w w_w}}{\partial z} + \frac{\partial UV}{\partial x} - \frac{\partial}{\partial x} \left(\nu_{tx} \frac{\partial V}{\partial x} \right) \quad (3)$$

Here $U(x, z)$, $V(x, z)$ are the cross and longshore current velocity components and u_w , v_w , w_w the oscillatory "wave" velocity components whose mean is zero below trough level. In (2) and (3) we have also modelled the turbulent shear stresses by introducing the eddy viscosity ν_t mentioned earlier. For later discussion we have distinguished between ν_{tx} and ν_{tz} . Reference is made to Fig. 2 for definitions of other variables.

It is inherent in the wave averaged approach that the wave particle velocities u_w , v_w and w_w are assumed known to the extent that the terms on the right hand side containing those parameters can be considered known.

Then (2) and (3) are actually two nonlinear equations for U and V . In classical models for nearshore circulation those terms are usually neglected because they are assumed small. To simplify the presentation, we will also neglect the nonlinear current terms. Furthermore, the findings from the perturbation solution by S & L justify that to the first approximation the horizontal mixing for the longshore current (last term in (3)) can be determined using the value V_b of V at the bottom.

Hence, as far as the depth variation of U, V is concerned, all terms on the right hand side of (2) and (3) are regarded as known forcing terms provided we can determine V_b . We define

$$\alpha_{1x}(x, z) = \frac{\partial}{\partial x} \left(\overline{u_w^2} - \overline{w_w^2} + gb \right) + \frac{\partial \overline{u_w w_w}}{\partial z} \quad (4)$$

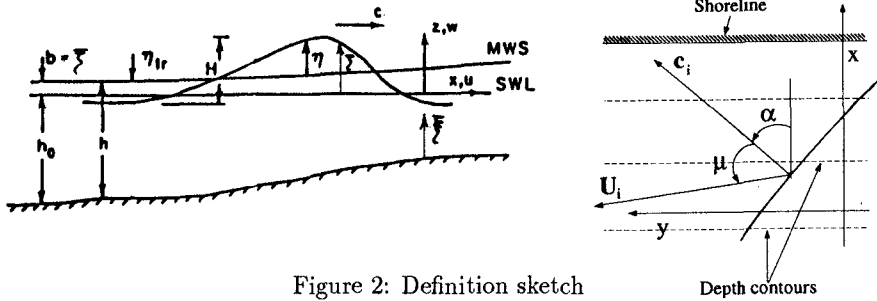


Figure 2: Definition sketch

$$\alpha_{1y}(x, z) = \frac{\partial \overline{u_w v_w}}{\partial x} + \frac{\partial \overline{u_w w_w}}{\partial z} - \frac{\partial}{\partial x} \left(\nu_{tx} \frac{\partial V_b}{\partial x} \right) \tag{5}$$

This means that (2) and (3) can be integrated directly, and the solutions written

$$U(x, z) = \int \frac{1}{\nu_{tz}} \int \alpha_{1x} d\xi d\xi + \int \frac{A_1}{\nu_{tz}} d\xi + A_2 \tag{6}$$

and the equivalent for V with α_{1y} instead of α_{1x} .

Thus (2) and (3) can be expressed in closed form for arbitrary α_1 and ν_{tz} . To simplify discussions, however, we will in the following assume $\nu_{tz}(x, z) = \nu_{tz}(x)$ and $\alpha_1(x, z) = \alpha_1(x)$. Hence, (6) simplifies to

$$U(x, z) = \frac{1}{2} \frac{\alpha_{1x}}{\nu_{tz}} \xi^2 + \frac{A_1}{\nu_{tz}} \xi + A_2 \tag{7}$$

$$V(x, z) = \frac{1}{2} \frac{\alpha_{1y}}{\nu_{tz}} \xi^2 + \frac{B_1}{\nu_{tz}} \xi + B_2 \tag{8}$$

where A_1, A_2, B_1 and B_2 are arbitrary functions of x to be determined from the boundary conditions discussed in the following and $\xi = z + h_o$ is the height above the bottom. To determine the four constants A_1, A_2, B_1 and B_2 we need two conditions for each of the two velocity components U and V .

The bottom boundary condition

The first condition used is related to the variation of U, V at the bottom. Strictly speaking, the bottom condition is $U, V = 0$. Due, however, to the assumption of a boundary layer with relatively low eddy viscosity a large value U_b, V_b of U, V exists at a short distance above the bottom (the “top” of the boundary layer). Hence, the mean bottom shear stress in the middle layer is related to U_b, V_b and to the oscillatory motion u_{wb}, v_{wb} at the bottom. We assume here that this relation is given by ($i = 1, 2$ corresponding to the x, y components)

$$\tau_{bi}(t) = \frac{1}{2} \rho f u_{bi}(t) | u_{bi}(t) | \tag{9}$$

where $u_{bi}(t)$ is the ensemble averaged bottom velocity, $| u_{bi} |$ the numerical value of u_{bi} and f is a (constant) friction factor (see, e.g., Jonsson 1966). For u_{bi} we have

$$u_{bi} = U_{bi} + u_{wbi} \tag{10}$$

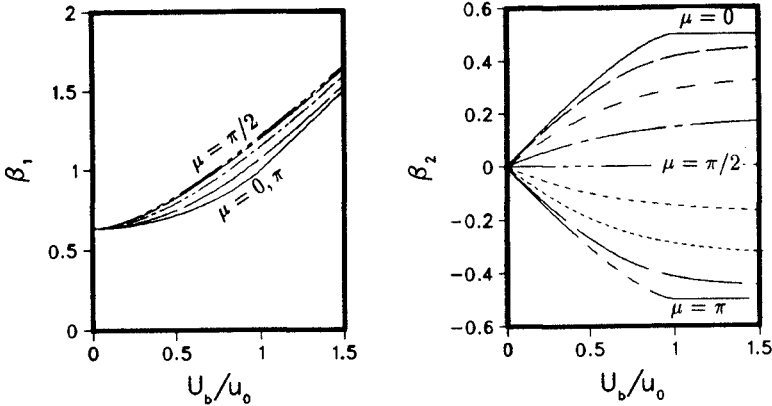


Figure 3: Variation of β_1 and β_2

where $U_{bi} = (U_b, V_b)$ and $u_{wbi} = (u_{wb}, v_{wb})$.

To determine the time mean of $\tau_{bi}(t)$, we also assume that

$$u_{wbi} = u_{oi} \cos \theta \quad (\theta = \omega t - kx) \tag{11}$$

and define, for short

$$u_o = |u_{oi}|, \quad U_b = |U_{bi}| \tag{12}$$

The mean shear stress $\tau_{bi} = \overline{\tau_{bi}(t)}$ is then determined by substituting (10), (11) and (12) into (9) and time averaging.

Liu and Dalrymple (1978) derived expressions for τ_{bi} for the special cases $U_b/u_o \gg 1$ (strong current) and $U_b/u_o \ll 1$ (weak current).

Here we present a more general formulation for arbitrary values of U_b/u_o and also arbitrary angles, μ , between the current direction and the wave direction. Performing the averaging operation we introduce the parameters

$$\beta_1 = \overline{\beta_1(t)} = \left[\left(\frac{U_b}{u_o} \right)^2 + 2 \frac{U_b}{u_o} \cos \theta \cos \mu + \cos^2 \theta \right]^{1/2} \tag{13}$$

$$\beta_2 = \overline{\beta_1(t) \cos \theta} \tag{14}$$

It then turns out that τ_{bi} can be written, without any further approximations, in the simple form

$$\tau_{bi} = \frac{1}{2} \rho f u_o [\beta_1 U_{bi} + \beta_2 u_{oi}] \tag{15}$$

which expresses τ_{bi} as the sum of two contributions, one in the direction of the current vector U_{bi} with weight β_1 , the other in the direction of the wave particle motion with weight β_2 . It is apparent from (13) and (14) that β_1 and β_2 are functions of two variables: U_b/u_o , the current strength relative to wave particle velocity amplitude and μ the angle between wave and current vectors. The variation of β_1 and β_2 with those parameters is shown in Fig. 3.

The expression (15) of course includes the cases of very weak and very strong currents. Though it is not apparent from (15), the case of $U_{bi} \rightarrow 0$ does yield $\tau_{bi} \rightarrow 0$: in purely sinusoidal motion there is no mean shear stress.

In the central layer the shear stress is given by

$$\tau_{zi} = \rho \nu_{tz} \frac{\partial U_i}{\partial z} \quad (16)$$

and for $z \rightarrow -h_o$ this shear stress must equal τ_{bi} determined from (15). Hence, combining (15) and (16) we get the mixed bottom boundary condition:

$$\frac{\partial U_i}{\partial z} - f(u_o, U_i) = 0 \quad z = -h_o \quad (17)$$

or, if we define

$$\begin{aligned} a &= \frac{1}{2} \frac{f}{\nu_{tz}} \beta_1 u_o \\ b_i &= \frac{1}{2} \frac{f}{\nu_{tz}} \beta_2 u_o u_{oi} \end{aligned} \quad (18)$$

and accept the slightly inconsistent nomenclature of $(\partial U_i / \partial z)_{-h_o} = \partial U_{bi} / \partial z$ then we can write (17) as the inhomogeneous mixed pseudo-linear condition for U_{bi}

$$\frac{\partial U_{bi}}{\partial z} - a U_{bi} = b_i \quad z = -h_o \quad (19)$$

This is the first of the boundary conditions used for the depth variation of U_i . Equation 19 is not quite linear because β_1 and β_2 depend on U_{bi} . It may also be noted that this implies that we can specify neither U_b nor τ_b at the bottom. It is the combination of U_b and τ_b imbedded in (19) that is controlled.

Applying (19) to the solutions (7) and (8) for U and V yields

$$U_i = \frac{1}{2} \frac{\alpha_{iz}}{\nu_{tz}} \xi^2 + (1 + a\xi) U_{bi} + b_i \xi \quad (20)$$

which expresses the vertical variation of the current velocity in terms of the unknown bottom velocity U_{bi} .

The second boundary condition

Hence, the function of the second boundary condition to be specified is essentially to determine the bottom velocity U_{bi} . The conditions used here are different in the longshore and in the cross-shore directions. In the longshore (y) direction, the second boundary condition is equivalent to specifying the shear stress τ_{sy} at wave trough level. τ_{sy} can be determined from the momentum balance for the flow above trough level (Stive and Wind 1986).

If the horizontal momentum flux above trough level is M_{ij} then we have

$$\tau_{sy} = \frac{\partial M_{xy}}{\partial x} \quad (21)$$

However, when combining the local depth variation of the flow given by (2) and (3) with a fully depth integrated model to give the horizontal variation it turns out to be more convenient not to impose (21) directly on the depth variation of the current. Instead, we apply the mixed condition (19) also to the fully depth integrated longshore momentum equation. This results, as shown in the next section, in an equation for the x variation of V_b , almost identical with the usual equation for the depth averaged longshore current. Solution of that equation therefore provides V_b and, hence, completely specifies the depth variation of the longshore component.

The question that naturally arises now is the following: Why is using the momentum equation integrated over the total depth to determine V_b completely equivalent to imposing (21) as a boundary condition for (20)? The explanation is the following: Determining the bottom velocity V_b from the total depth integrated momentum equation with (15) included means fixing the bottom shear stress so that depth integrated momentum is satisfied. At the same time, the solution (20) for V automatically accounts for the forcing that occurs below trough. Therefore, (20) with V_b determined as described will show a shear stress at trough level which corresponds exactly to (21) since τ_{sy} represents the difference between the total forcing and the forcing below trough level.

In the cross-shore direction, it is necessary to use a different approach. Because the cross-shore radiation stress is almost equal to the pressure gradient from the set-up, the method described above for V would lead to determining the bottom shear stress τ_{bx} as a (small) difference between these two large contributions (see Svendsen & Hansen, 1988). Instead we utilize that the net cross-shore flux Q_x is zero, so that

$$\int_{-h_o}^{\zeta_t} U dz = -Q_{sx}/(h_o + \zeta_t) \quad (22)$$

where Q_{sx} is the x -component of the mass flux in the wave, ζ_t is the trough elevation below SWL (Fig. 2).

Notice that this approach is only applicable for a straight coast where $\partial/\partial y$ and Q_x are zero. On a general coast we cannot distinguish between "cross-shore" and "longshore" and a different procedure is required.

3. THE DEPTH INTEGRATED EQUATIONS

The depth integrated equations are generalizations of the H-b model for calculation of the wave height H and set-up b in the surf zone first introduced by Svendsen (1984). That approach is based on dimensionless coefficients for radiation stress (P), energy flux (B), and energy dissipation (D). Using Phillips' (1977) equations the method was extended to 2D combination of waves and currents by Svendsen & Hansen (1986).

In most previous applications in the past the model has been applied using the special form of P , B and D found by incorporating experimental data for the real surface profile of the broken waves and including a roller contribution separately (Svendsen, 1984). The method as such, however, is general and by suitable choices of P , B and D can represent all H-b models. That was utilized by Hansen (1990) who specified empirical expressions for many of the surf-zone wave characteristics derived from actual measurements and found, not surprisingly, that they deviate substantially from sine-wave values. Here we use some of Hansen's results. The specific values of P , B and D used will be discussed further in connection with the applications (section 4).

We assume here that the waves are locally plane so that all wave properties can be described by 2-D wave theory. It is then convenient to define the momentum and pressure part of the radiation stress on a section perpendicular to the direction of wave propagation as the scalars

$$S_m = \overline{\int_{-h_o}^{\zeta} \rho u^2 dz} \quad (23)$$

$$S_p = -\overline{\int_{-h_o}^{\zeta} w_w^2 dz} + \frac{1}{2} \overline{\rho g (\zeta - \bar{\zeta})^2} \quad (24)$$

where $u^2 = u_w^2 + v_w^2$ is the horizontal wave particle velocity in the direction of wave propagation, ζ is the surface elevation above the horizontal axes.

We also define

$$e_{ij} = \begin{Bmatrix} \cos^2 \alpha & \sin \alpha \cos \alpha \\ \sin \alpha \cos \alpha & \sin^2 \alpha \end{Bmatrix} \quad (25)$$

where α is the direction of wave propagation relative to the x -axis (Fig. 2).

The radiation stress for a section with arbitrary normal vector then can be written

$$S_{ij} = e_{ij} S_m + \delta_{ij} S_p \quad (26)$$

where δ_{ij} is the Kroenecker δ . The generalized version of the dimensionless radiation stress P then is defined as

$$P_{ij} = \frac{S_{ij}}{\rho g H^2} = e_{ij} \frac{S_m}{\rho g H^2} + \delta_{ij} \frac{S_p}{\rho g H^2} \quad (27)$$

In particular, for our long straight coast we get

$$\begin{aligned} P_{xx} &= \frac{S_m}{\rho g H^2} \cos^2 \alpha + \frac{S_p}{\rho g H^2} \\ P_{xy} &= \frac{S_m}{\rho g H^2} \sin \alpha \cos \alpha \end{aligned} \quad (28)$$

Similarly, we define the dimensionless energy flux B by

$$E_{fi} = \rho g H^2 B c_i \quad (29)$$

where E_{fi} , the energy flux, is given by

$$E_{fi} = \overline{\int_{-h_o}^{\zeta} u_i \left[\rho g z + p + \frac{1}{2} \rho (u_w^2 + v_w^2 + w_w^2) \right] dz} \quad (30)$$

and

$$c_i = c \frac{k_i}{k} \quad (31)$$

k here represents the magnitude of the wavenumber vector, k_i .

Finally, we define the nondimensional energy dissipation D relative to the actual dissipation D by

$$D = D \cdot \frac{4hT}{\rho g H^3} \quad (32)$$

The three depth integrated equations solved are the cross-shore and the long-shore momentum equations, and the energy equation. We introduce the definitions above into the general equations of Phillips (1977) for waves and currents, simplifying to the conditions of a long straight coast including Snell's law. Finally, the dominating terms for H and b are isolated along the same lines as done by Svendsen & Hansen (1986) for the 2D cross-shore case. We then get, neglecting a few small terms, the depth integrated equations in the following form.

Cross-shore momentum equation

$$\frac{db}{dx} = - \left\{ \frac{P_{xx}}{h} [D' + g_1 + H^2 g_2] + \frac{\tau_{bx}}{\rho gh} \right\} \left(1 - \frac{1}{2} P_{xx} \cdot \left(\frac{H}{h} \right)^2 \right)^{-1} \quad (33)$$

where

$$g_1 = \left(\tau_{bi} U_{bi} - S_{xi} \frac{dU_i}{dx} - \frac{dUE}{dx} \right) / (\rho g c B \cos \alpha) \quad (34)$$

$$g_2 = \frac{1}{P_{xx}} \frac{dP_{xx}}{dx} - \frac{1}{2h} \frac{dh_o}{dx} - \frac{1}{B} \frac{dB}{dx} + \tan \alpha \frac{d\alpha}{dx} \quad (35)$$

$$D' = D / (\rho g c B \cos \alpha) \quad (36)$$

Energy equation

$$\frac{dH^2}{dx} = D' + g_1 - H^2 \left[\frac{1}{c} \frac{dc}{dx} + \frac{1}{B} \frac{dB}{dx} - \tan \alpha \frac{d\alpha}{dx} \right] \quad (37)$$

Longshore momentum equation

$$\frac{d}{dx} \int_{-h_o}^{\bar{n}} \nu_{tx} \frac{\partial V}{\partial x} dz - \frac{\tau_{by}}{\rho} = \frac{1}{\rho} \frac{dS_{xy}}{dx} \quad (38)$$

Solution of the equations

The desired equation for the bottom velocity V_b is found by substituting (15) and (20) into (38). Utilizing the findings of the perturbation solution developed by S & L, a first approximation to the resulting equation may be written

$$\frac{d}{dx} \left(\nu_{tx} h \frac{dV_b}{dx} \right) - a V_b = \frac{1}{\rho} \frac{dS_{xy}}{dx} + b_y \quad (39)$$

which is the differential equation we solve for V_b . The approximation made in (39) is that the turbulent mixing can be represented over the entire depth by using the bottom velocity V_b . The boundary conditions used for (39) are

$$V_b = 0 \quad \text{at} \quad x = x_{\text{shore}}, \rightarrow -\infty \quad (40)$$

Further, two matching conditions are used at the transition point x_t which is the point where the radiation stress starts to change. The matching conditions at x_t specify continuity in velocity and shear stress at x_t , that is:

$$V_{b+} = V_{b-}; \quad \nu_{tx+} \left(\frac{dV_b}{dx} \right)_+ = \nu_{tx-} \left(\frac{dV_b}{dx} \right)_- \quad \text{at} \quad x_t$$

where + and – refer to values immediately adjacent to x_i . Outside the surf-zone, dS_{xy}/dx is zero.

4. RESULTS

The 3D model system established above can be used to study a number of effects on a long straight coast which has not been analyzed previously in the literature. For reasons of limited space, the discussion is limited to a few mechanisms.

The numerical results will depend on the wave incidence angle α , the bottom slope h_{ox} (here assumed constant for simplicity, not necessity), and the way the wave properties are modelled, as a function of wave height, including the breaking criteria. Following Svendsen (1987), we have chosen to assume that the breaker height is given by $(H/h)_b = 1.11 \cdot (h_x L/h)_b^{1/4}$. An almost identical expression was suggested independently by Hansen (1990). The vertical eddy viscosity, ν_{tz} , was taken to be $\nu_{tz} = 0.01 h \sqrt{gh}$ (a discussion of the eddy viscosity is given later). The horizontal eddy viscosity, ν_{tx} , was taken to be $\nu_{tx} = 0.01 h \sqrt{gh}/h_x$.

The wave parameters—energy flux (B) and radiation stress (P)—depend on the shape of the surface profile and the area of the roller (Svendsen 1984). The shape of the surface profile is measured in terms of the dimensionless parameter B_o defined as $B_o = (\eta/H)^2$. In the present applications these parameters have been derived using the B_o suggested by Hansen (1990) and modified for waves with a current as in Svendsen & Hansen (1986), and the roller area found by Okayasu (1989). The dimensionless energy dissipation rate is taken to be the same as in a bore. The reason for choosing this set of parameters is that in this way we include the actual characteristics of broken waves. Usually, this model gives the best prediction of the set-up, which means of dS_{xx}/dx . Since S_{xy} through (25) and (26) is related to S_{xx} , it is evident that this also potentially implies a better prediction of the driving force for the longshore current. This point is important though it is usually disregarded in the discussions of surf zone wave theories and longshore currents.

Wave-current refraction

Many of the measurements of longshore currents both in the field and in the laboratory show very high velocities. The steeper the local bottom slope, the higher the velocity. For a coast with a slope of 1:30, velocities typically correspond to a Froude number of 0.2–0.4 or longshore velocities of 20–40% of the wave celerity. Visser in his experiments on 1:20 and 1:10 slope beaches obtained velocities corresponding to Froude numbers as large as 0.7–1.2; i.e., current velocities equal to or higher than the propagation speed of the waves. Wave current refraction is caused by the gradient in current velocity so one would expect a strong change in the wave pattern and hence on the current itself from this mechanism.

Dalrymple (1980) used a perturbation expansion to examine the simplified case of no turbulent mixing. The present model includes both turbulent mixing and the additional effect of the undertow. Based on Kirby & Chen (1989), this cross-shore current is represented by the mean value of the velocity below trough level.

Fig. 4a shows the changes in wave incident angle for a case with slope 1:30, deep water incident angle $\alpha_o = 15^\circ$. Four cases are shown: No current refraction, longshore current only, undertow only, and the full 3D case with both longshore and cross-shore flow. It is seen that the effects of the cross and the longshore

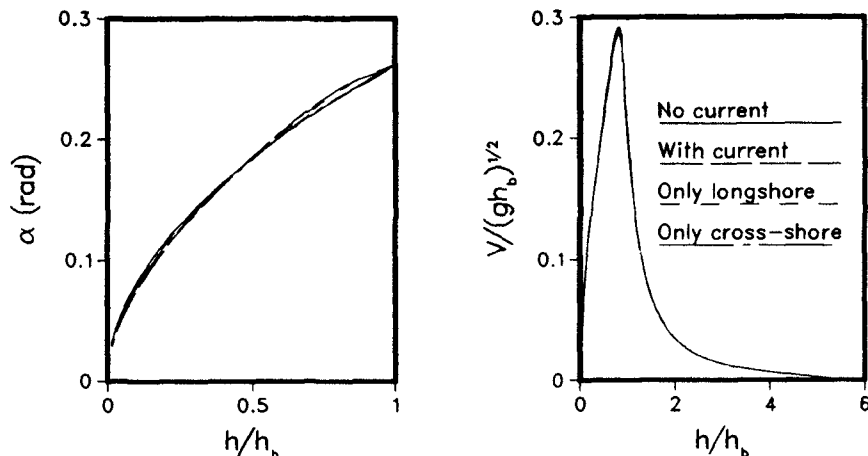


Figure 4: Effect of current refraction

currents counteract and almost cancel each other. Also, the effect of each of the two factors isolated is actually very modest. This is also clear from the resulting longshore current profiles shown in Fig. 4b. The effect of the current refraction is only just discernible at the peak of the velocity distribution even if the undertow is neglected.

Steeper slopes and larger angles of incidence will increase the effect and so will a 3D circulation pattern that locally creates a significant shoreward flow. Even then, however, our computations suggest that wave current refraction is not a very important mechanism for changing the current velocities.

Velocity profiles

Another feature of the present model is its capability of supplying the fully 3-dimensional velocity profiles from the 2-D horizontal, depth integrated solutions to equations (32)–(35).

The generic form of the velocity profiles was shown by S & L. As is apparent from the model, however, to obtain the profiles pertaining to each location it is necessary first to calculate the wave height and setup variation described by (32) and (33). In many previous nearshore models this part is eliminated by simply assuming that the wave height is a constant fraction γ of the waver depth.

Fig. 5 shows a set of consecutive 3D current profiles in the surf zone for a situation with slope $h_{ox} = 1/30$, and angle of incidence at the breakpoint of $\alpha_b = 5^\circ$. To obtain equal detailing, each profile has been scaled relative to the local depth under wave trough and the local wave celerity. We see that in the region where the longshore current is largest the bottom velocity is predominantly longshore, but in other regions the cross-shore motion is more prevailing.

If the angle of incidence increases, the longshore current velocity increases similarly and hence prevails more. Similarly, on a steeper slope, the cross-shore motion becomes stronger.

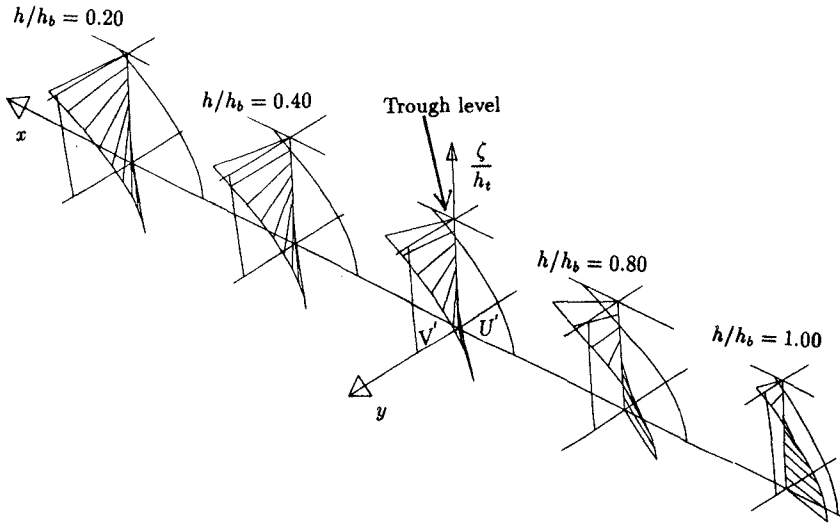


Figure 5: Variation of the velocity profiles across the surf-zone

Eddy viscosity

The eddy viscosity, ν_{tz} , in the surf-zone has been determined previously by fitting computed undertow profiles to measured data. Values reported range from $0.007h\sqrt{gh}$ through $0.03h\sqrt{gh}$ (Svendsen and Hansen 1988) to a linear variation between zero and $0.3h_x h\sqrt{gh}$ (Okayasu *et al.* 1988), the later yielding $0.01h\sqrt{gh}$ for $h_x = 1/30$.

In contrast, the eddy viscosity, ν_{tx} used by, e.g., Longuet-Higgins (1970) for longshore currents is equivalent to $0.01h\sqrt{gh}/h_x$, which on $1/30$ yields $0.3h\sqrt{gh}$ or about 30 times the value that can be justified for the undertow even inside the surf-zone. The large absolute value of $\nu_{tx} = 0.3h_b\sqrt{gh_b}$ at the breaker point is required to apply everywhere outside that point, and our comparison with Visser's (1982) measurements for regular waves confirm that such a large eddy viscosity is necessary to make the computations match with the measurements. Figure 6 shows that the difference obtained in the longshore current distribution using ν_{tx} equal to the ν_{tz} value found from undertow and ν_{tx} given by the Longuet-Higgins value mentioned above is very substantial.

On the other hand, if we combine the hypothesis described by (1) for the nature of the mechanism behind ν_t with the fact that outside the surf-zone the turbulence is rather weak, it becomes inconceivable that this mixing mechanism can be due to turbulence. In this context, it is interesting that Thornton and Guza (1986) find that the effect of the eddy viscosity in their NSTS data from Santa Barbara is negligible in comparison to the variability of the waves even during periods of narrow banded, almost unidirectional incident waves. In other words, a physically realistic eddy viscosity would still give correct results. However, this does not explain which mechanism causes a similar mixing in the regular wave experiments. It is beyond the space available to discuss possible explanations to

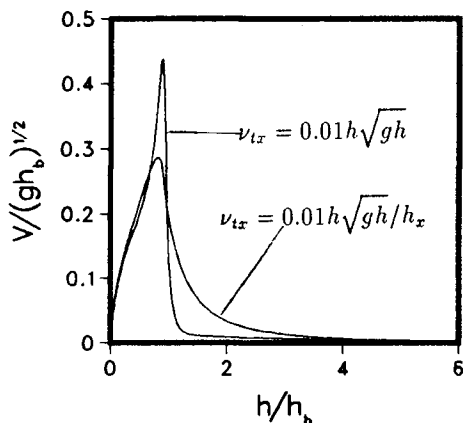


Figure 6: Effect of eddy viscosity

this paradox. What we seem to be able to conclude at this moment is that a very strong mixing process is controlling the longshore current distribution outside the breaker point both in regular and irregular waves.

ACKNOWLEDGEMENTS

This work is part of a project funded by the National Sea Grant Program. The authors wish to thank A. Wurjanto (University of Delaware) for his help with the graphics.

REFERENCES

- Davies, A. M., 1987. On extracting current profiles from vertically integrated numerical models. *Coastal Engineering*, 11, pp. 445-477.
- Dalrymple, R. A., 1980. Longshore currents with wave current interaction. *Journal of Waterway, Port, Coastal, and Ocean Engineering*. Vol. 106, No. WW3, pp. 414-420.
- deVriend, H. J. and M. J. F. Stive, 1987. Quasi-3D modelling of nearshore currents. *Coastal Engineering*, 11, pp. 565-601.
- Hansen, J. B., 1990. Periodic waves in the surf-zone: Analysis of experimental data. *Coastal Engineering*, 14, pp. 19-41.
- Hansen, J. B. and I. A. Svendsen, 1984. A theoretical and experimental study of the undertow. *Proc. 19th ICCE, Houston*. pp. 2246-2262.
- Jonsson, I. G., 1966. Wave boundary layers and friction factors. *Proc. 10th ICCE, Tokyo*. pp. 127-148.
- Kirby, J. T. and T.-M. Chen, 1989. Surface waves on vertically sheared flows: Approximate dispersion relations. *Journal of Geophysical Research*, 94 (C1), pp. 1013-1027.
- Liu, P. L.-F. and R. A. Dalrymple, 1978. Bottom frictional stresses and longshore currents due to waves with large angles of incidence. *Journal of Marine Research*, 36, pp. 357-375.
- Longuet-Higgins, M. S., 1970. Longshore currents generated by obliquely incident sea waves. Part 2. *Journal of Geophysical Research*, 75, pp. 6790-6801.

- Okayasu, A., 1989. Characteristics of turbulence structure and undertow in the surf-zone. Doctoral dissertation, University of Tokyo, 119 pp.
- Okayasu, A., T. Shibayama and K. Horikawa, 1988. Vertical variation of undertow in the surf-zone. Proc. 21st ICCE, Costa del Sol-Magala. pp. 478-491.
- Phillips, O. M., 1977. The dynamics of the upper ocean. Cambridge University Press, 336 pp.
- Stive, M. J. F. and H. G. Wind, 1986. Cross-shore mean flow in the surf-zone. Coastal Engineering, 6, pp. 325-340.
- Svendsen, I. A., 1984. Wave heights and set-up in a surf-zone. Coastal Engineering, 8, pp. 303-329.
- Svendsen, I. A., 1987. Analysis of surf-zone turbulence. Journal of Geophysical Research, 92 (C5), pp. 5115-5124.
- Svendsen, I. A. and J. B. Hansen, 1986. Interaction of waves and currents over a longshore bar. Proc. 20th ICCE, Taipei. pp. 1580-1594.
- Svendsen, I. A. and J. B. Hansen, 1988. Cross-shore currents in surf-zone modelling. Coastal Engineering, 12, pp. 23-42.
- Svendsen, I. A. and R. S. Lorenz, 1989. Velocities in combined undertow and longshore currents. Coastal Engineering, 13, pp. 55-79.
- Svendsen, I. A., H. A. Schaffer and J. B. Hansen, 1987. The interaction between the undertow and the boundary layer flow on a beach. Journal of Geophysical Research, 92 (C11), pp. 11845-11856.
- Thornton, E. B. and R. T. Guza, 1986. Surf-zone longshore currents and random waves: Field data and models. Journal of Physical Oceanography, 16, pp. 1165-1178.
- Visser, P. J., 1982. The proper longshore current in a wave basin. Communications on Hydraulics. Report 82-1, Dept. of Civil Engineering, Delft Univ. of Technology, 86 pp.
- Visser, P. J., 1984. A mathematical model of uniform longshore currents and comparison with laboratory data. Communications on Hydraulics. Report 84-2, Dept. of Civil Engineering, Delft Univ. of Technology, 151 pp.

CHAPTER 19

CONDITIONAL SIMULATIONS IN LABORATORY FLUMES

Marcos H. Giménez¹
Leon E. Borgman²
Robert T. Hudspeth³
Josep R. Medina⁴
Carlos R. Sánchez-Carratalá⁵
Hang Tuah⁶

ABSTRACT

A robust algorithm is presented which is capable of embedding a deterministic sequence of waves into a randomly generated wave train without changing the stochastic properties of the random waves.

¹Profesor Asociado, Dept. of Applied Physics, Univ. Politécnic de Valencia, Valencia 46071, SPAIN.

²Professor, Dept. of Geology, Univ. of Wyoming, Laramie, WY 82070, U.S.A.

³Professor, Ocean Engineering Program, Dept. of Civil Engineering, Oregon State University, Corvallis, OR 97331, U.S.A.

⁴Profesor Titular, Dept. of Transportation, Univ. Politécnic de Valencia, Valencia 46071, SPAIN.

⁵Research Asst., Dept. of Transportation, Univ. Politécnic de Valencia, Valencia 46071, SPAIN.

⁶Professor, Bandung Institute of Technology, Bandung, INDONESIA.

INTRODUCTION

A frequent request by sponsors of research projects in maritime laboratories is to analyze the behavior of a structure for a given design sea state. During the years, the testing of physical models in wave flumes has proven to be both cost-effective and reliable. Physical modelling of random waves requires generating random wave trains with a specified variance spectrum.

Funke and Mansard (1987) pointed out that present technology now makes it possible to treat the wave generator and the digital simulation technique as two essentially separate problems in wave generation. During the last decade, digital to analog numerical simulations have become extremely efficient. Several methods are available for generating these numerical simulations. Borgman (1969) identified two fundamental methods: 1) the superposition of sinusoidal waves; and 2) the filtering of white noise. Hudspeth and Borgman (1979) demonstrated the advantages of using FFT algorithms for numerical simulations. Tuah and Hudspeth (1982) introduced deterministic (DSA) and non-deterministic (NSA) spectral amplitude models for random wave simulations based on FFT algorithms. Medina and Sánchez-Carratalá (1988) compared the different methods available for the numerical simulation of random waves.

At the present, the physical simulation of random waves having a specified variance spectrum in a wave flume may be accomplished by using a variety of techniques. However, sometimes research sponsors want to include a deterministic sequence of waves in the random wave simulation used to test structures. For example, sponsors may want to know how a particular wave group that occurs in a random wave simulation that is defined by a specified variance spectrum affects the performance of a structure. This request usually requires a laborious wave by wave analysis of many random wave simulations searching for a sequence of waves that almost resembles the requested one. An alternative method to this searching technique is to use "conditional simulation". This alternative method generates a numerical random wave simulation that has a specified variance spectrum and also includes the deterministic sequence of waves requested by the sponsor. A robust algorithm is derived for this "conditional simulation".

CONDITIONAL SIMULATION

Conditional simulation is a technique for generating a numerical realization that includes a given deterministic sequence of waves and that has a specified variance spectrum. This technique simulates realizations for a stochastic process that is defined by a specified variance spectrum and that contain a deterministic sequence of waves which occur at a prescribed time in the realizations. The method presented here may be used either in the time domain or in the frequency domain. In either case, the method is a two-step procedure.

The first step requires that a random time sequence be simulated that has a specified variance spectrum, $S_u(f)$. This simulation is called an "unconditional time sequence" and is denoted by $\eta_u(t)$. Figure 1-a shows an example of an unconditional time sequence obtained using a DSA algorithm (cf., Tuah and Hudspeth, 1982) and a specified Goda-JONSWAP variance spectrum (cf., Goda, 1985) using: $\gamma=1$, $m_0=1 \text{ m}^2$ and $f_p=0.27 \text{ Hz}$. The total number of points in the time sequence is $N=2048$ and the time interval $\Delta t=0.1$ seconds.

The second step is to embed the deterministic sequence of waves into the unconditional time sequence at a prescribed point in time. These two steps may be done either in the time domain or in the frequency domain. The deterministic sequence of waves is called the "embedded sequence" and is denoted by $\eta_e(t)$. The realization that contains the "embedded sequence" is called the "conditional time sequence" and is denoted by $\eta_c(t)$.

Figure 1-b shows a deterministic wave group or the "embedded sequence" that is to be embedded into the unconditional time sequence shown in Fig. 1-a. The time interval Δt of the "embedded sequence" must be the same as the time interval of the unconditional time sequence (e.g., $\Delta t=0.1$ seconds in Fig. 1). In Fig. 1, the first and last values of the embedded sequence $\eta_e(t)$ are to be embedded at the prescribed times $n_1=961$ and $n_2=1088$, respectively, of the unconditional time sequence $\eta_u(t)$. The total difference between the two prescribed time values is $\nu=n_2-n_1=127$. Therefore, the total number of values of the embedded sequence is $\nu+1=128$.

Finally, Figure 1-c shows the conditional time sequence containing the deterministic wave sequence embedded in a random wave simulation having a specified variance spectrum. The total number of points ($N=2048$) and the time interval ($\Delta t=0.1$ seconds) are the same for both $\eta_u(t)$ and $\eta_c(t)$. Near the two ends of the embedded wave group, the conditional simulation algorithm modifies the unconditional time sequence $\eta_u(t)$ in order to maintain the correlation structure in the conditional time sequence $\eta_c(t)$ in accordance with the specified variance spectrum $S_u(f)$.

TIME DOMAIN ALGORITHM

In the time domain, the conditional simulation algorithm inserts the embedded sequence $\eta_e(t)$ into the unconditional time sequence $\eta_u(t)$ between the two points of time n_1 and n_2 . The remaining values of the unconditional time sequence are modified in order to maintain the correlation structure that is associated with the specified variance spectrum $S_u(f)$.

The conditional time sequence may be obtained from (cf., Hudspeth et al. 1990):

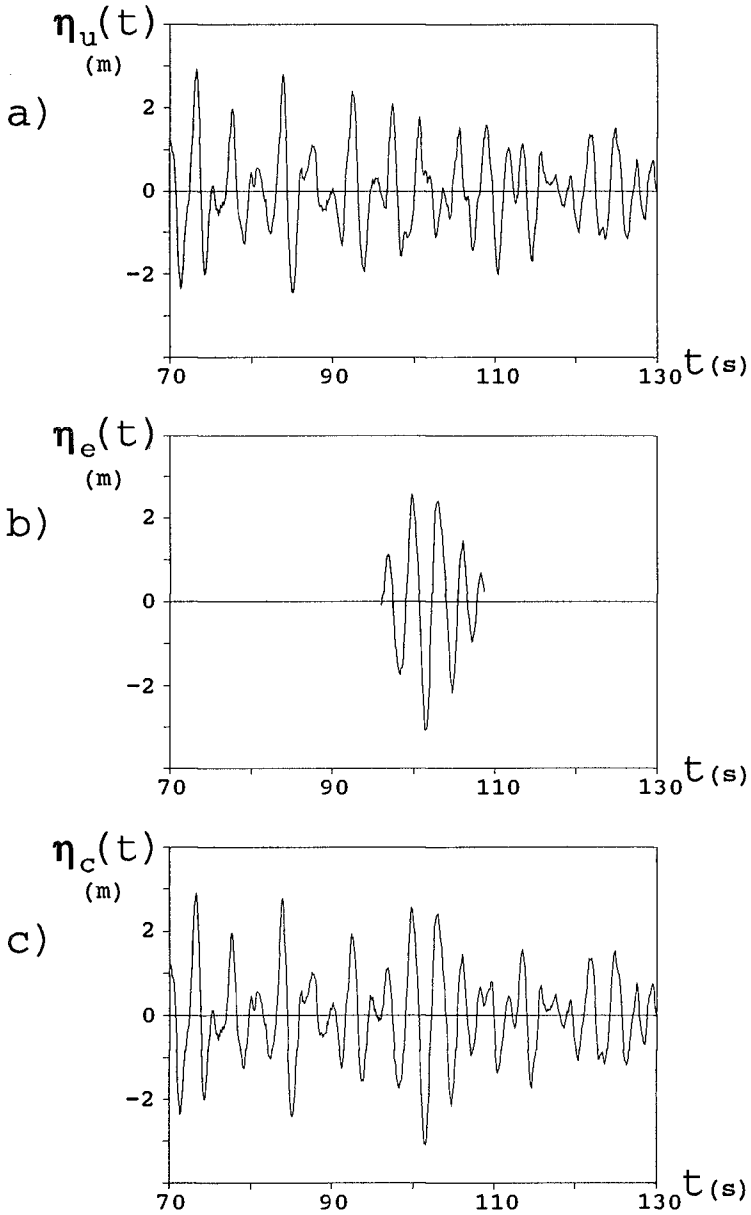


Figure 1. Example of a Conditional Simulation:
a) Unconditional Time Sequence; b) Embedded Sequence;
c) Conditional Time Sequence.

$$\mathbf{n} \in [n_1, n_2] \rightarrow \eta_c(\mathbf{n}\Delta t) = \eta_c(\mathbf{n}\Delta t) \tag{1}$$

$$\mathbf{n} \notin [n_1, n_2] \rightarrow \eta_c(\mathbf{n}\Delta t) = \eta_u(\mathbf{n}\Delta t) + C_{12}\mathbf{X} \tag{2}$$

where:

$$C_{12} = [c_{n-n_1}, c_{n-n_1+1}, \dots, c_{n-n_2}] \tag{3}$$

where c_k is the covariance at lag $|k|\Delta t$ associated with the specified variance spectrum $S_u(f)$; and \mathbf{X} is the solution of the following system of equations:

$$C_{11}\mathbf{X} = \mathbf{v}_e - \mathbf{v}_u \tag{4}$$

where:

$$C_{11} = \begin{bmatrix} c_0 & c_1 & \dots & c_v \\ c_1 & c_0 & \ddots & \vdots \\ \vdots & \ddots & \ddots & c_1 \\ c_v & \dots & c_1 & c_0 \end{bmatrix} \tag{5}$$

$$\mathbf{v}_e = [\eta_e(n_1\Delta t) \dots \eta_e(n_2\Delta t)]^T \tag{6}$$

$$\mathbf{v}_u = [\eta_u(n_1\Delta t) \dots \eta_u(n_2\Delta t)]^T \tag{7}$$

where C_{11} is the covariance matrix; \mathbf{v}_e is the vector of values of the embedded sequence; and \mathbf{v}_u is the vector of values of the unconditional time sequence at the prescribed time values where the embedded sequence is to be inserted.

The conditional simulation algorithm inserts the deterministic sequence of waves into the unconditional time sequence and modifies only those values of the unconditional time sequence that are near the two ends of the embedded sequence (vide Fig. 1). For the values of the unconditional time sequence that are located far from the interval of the embedded sequence, the values of the time lags $|n-n_1|$, $|n-n_1+1|, \dots, |n-n_2|$ are large and the values of the covariances in the matrix C_{12} associated with these large time lags are small. Consequently, at these large values of time from the embedded time interval Eq. 2 becomes, approximately:

$$\eta_c(\mathbf{n}\Delta t) = \eta_u(\mathbf{n}\Delta t) + C_{12}\mathbf{X} \sim \eta_u(\mathbf{n}\Delta t) + [0 \dots 0]\mathbf{X} = \eta_u(\mathbf{n}\Delta t) \tag{8}$$

and the differences are small between the unconditional and the conditional time sequences far from the time interval of the embedded sequence.

FREQUENCY DOMAIN ALGORITHM

In the frequency domain, the conditional simulation algorithm for inserting an embedded sequence $\eta_c(t)$ into an unconditional time sequence $\eta_u(t)$ may be shown to be equivalent to the time domain algorithm (cf., Hudspeth et al. 1990). The advantage the frequency domain algorithm is that FFT algorithms reduce substantially the computer time needed to obtain a long conditional time sequence.

The unconditional and the conditional time sequences may be expressed as a superposition of sinusoidal waves with frequencies which are multiple integers of the discrete frequency interval $\Delta f = 1/(N\Delta t)$ according to

$$\eta_u(n\Delta t) = \sum_{m=0}^{N-1} (a_m - i b_m) \exp(i2\pi mn/N) \quad (9)$$

$$\eta_c(n\Delta t) = \sum_{m=0}^{N-1} (\alpha_m - i \beta_m) \exp(i2\pi mn/N) \quad (10)$$

The FFT coefficients of the conditional time sequence $\{\alpha_m$ and $\beta_m\}$ may be obtained from the FFT coefficients of the unconditional time sequence $\{a_m$ and $b_m\}$. These coefficients are related by

$$\begin{bmatrix} \alpha_m \\ \beta_m \end{bmatrix} = \begin{bmatrix} a_m \\ b_m \end{bmatrix} + C'_{12} X \quad (11)$$

where X is the solution of the same system of equations given by Eq. 4 that were used for the time domain algorithm; and C'_{12} is given by:

$$C'_{12} = S_{\alpha}(m\Delta f) \Delta f \begin{bmatrix} \cos(2\pi mn_1/N) & \dots & \cos(2\pi mn_2/N) \\ \sin(2\pi mn_1/N) & \dots & \sin(2\pi mn_2/N) \end{bmatrix} \quad (12)$$

APPLICATIONS

The solution of Eq. 4 requires two constraints: 1) a goodness-of-fit constraint to the specified variance spectrum and 2) an ill-conditioned constraint for matrix C_{11} .

Firstly, the goodness-of-fit to the specified variance spectrum must be constrained by both the length and characteristics of both the embedded deterministic wave sequence and the unconditional time sequence.

Secondly, the covariance matrix may become ill-conditioned for typical ocean spectra because of the relatively low energy content of the specified variance spectrum at both low and high frequencies for relatively long simulations at relatively small time intervals of Δt . This combination of low energy levels and relatively long simulations at relatively small time intervals may produce numerical instabilities when inverting the ill-conditioned covariance matrix C_{11} in Eq.4. A similar numerical instability was described and solved by Medina and Sánchez-Carratalá (1988) using robust AR models for ocean spectra. Therefore, it is reasonable to use their solution in order to obtain a robust method for the conditional simulation of random ocean waves.

The robust method introduces into the specified variance spectrum a very low level of white noise that is acceptable for any practical application. If m_0 is the specified variance, satisfactory results were obtained by introducing a white noise level of $0.0025m_0$ which reduced the original specified variance spectrum, $S_u(f)$, by a factor of 0.9975. The modified specified variance spectrum which is satisfactory for practical engineering purposes is given by $S_u'(f) = 0.9975 m_0 + \text{white noise}$. Finally, the modified specified variance spectrum $S_u'(f)$ is used in Eqs.3,5 and 12 instead of the original specified variance spectrum $S_u(f)$. The relative advantages of the robust method is illustrated below for typical ocean spectra.

In order to illustrate the stability of the robust method, consider removing a short piece of record from an unconditional time sequence and then inserting the same short piece back into the same unconditional time sequence at the same place. In this case, the vectors v_e and v_u in Eq.4 are equivalent and the resulting conditional time sequence η_c is equal to the unconditional time sequence η_u .

If the values of the embedded sequence shown in Fig. 2-a are modified only by a small amount, then the conditional and the unconditional simulations should differ by only the same small amount. However, that is not always the case if the matrix C_{11} becomes ill-conditioned. For example, if the values of the short piece of record shown in Fig. 2-a between 80-85 seconds are truncated to centimeters (a reduction of about 1%) and then embedded back into the unconditional time sequence at the same position in time, the resulting conditional time sequence shown in Fig. 2-b, is unsatisfactory. However, by using the robust method with a level of white noise of only $0.0025m_0$, the resulting conditional time sequence shown in Fig. 2-c differs only slightly from the unconditional time sequence. We note that any wave record from a laboratory simulation or from the ocean may be contaminated by levels of noise equal to or larger than this amount. Therefore, $S_u(f)$ and $S_u'(f)$ are equally acceptable for representing the variance spectrum of ocean waves. Figure 1 illustrates an application of the robust method for embedding a wave group.

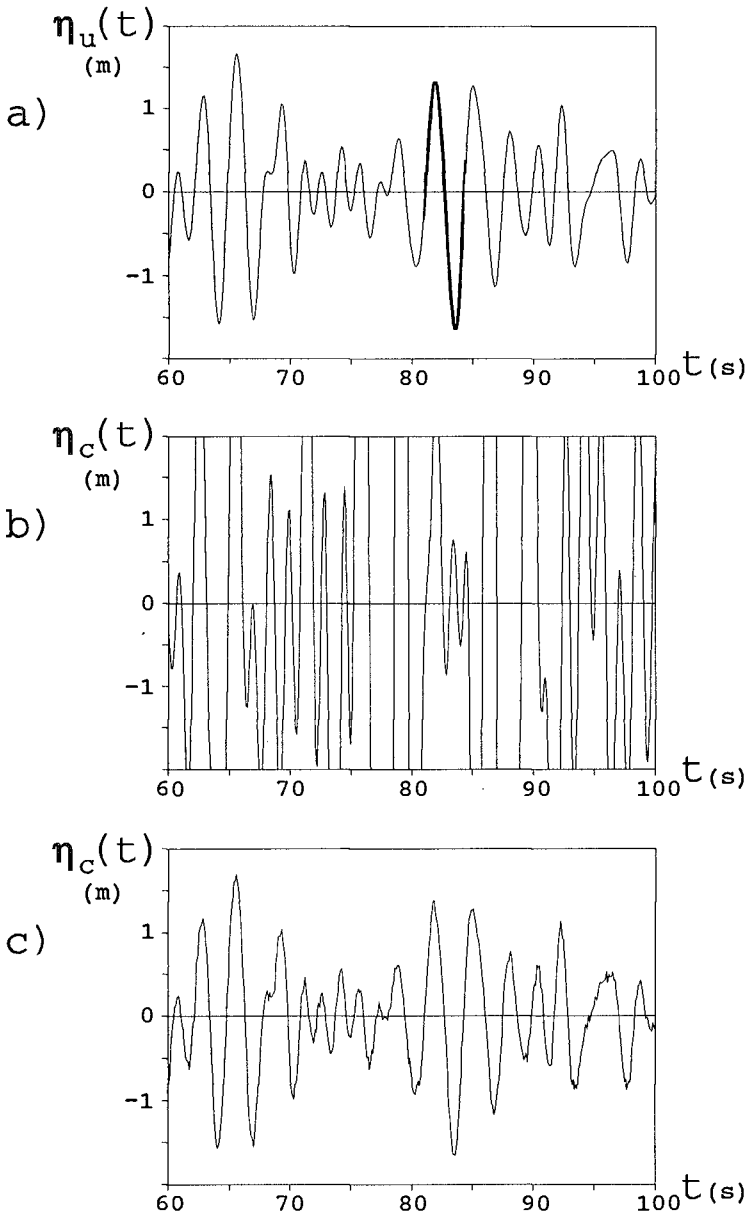


Figure 2. Comparisons of Conditional Simulation Methods: a) Unconditional Time Sequence; b) Example of Unstable Conditional Simulation; c) Example of Stable Robust Simulation.

The goodness-of-fit to the specified variance spectrum is influenced by several variables. First, the lengths of both the embedded sequence and the unconditional simulation must be considered. The wave group ($\nu+1=127$) shown in Fig. 1-b has been embedded into unconditional simulations having total lengths of $N = 512$, 1024 and 2048. These unconditional simulations are realizations from a specified Goda-JONSWAP variance spectrum having spectral parameters: $\gamma=1$, $m_0=1 \text{ m}^2$ and $f_p=0.27 \text{ Hz}$. The variance of the embedded wave group is $2m_0$. Table 1 compares the relative errors of the spectral moments computed from the conditional and from the unconditional time sequences as a function of the total length of the simulation with the length of the embedded sequence held constant ($\nu+1=127$).

TABLE 1. Effect of N on Errors in Spectral Moments Between η_c & η_u

Moments	N=512	N=1024	N=2048
m_0	17.6%	11.6%	4.8%
m_1	16.0%	10.1%	4.3%
m_2	13.9%	8.4%	3.5%

The goodness-of-fit to the specified variance spectrum improves as N increases relative to the length of ν . Figs. 3-a&-b compare the specified variance spectrum for the unconditional simulation with the variance spectrum for the conditional time sequence for $N=512$ and for $N=2048$, respectively.

The goodness-of-fit to the specified variance spectrum must also be constrained by the stochastic properties of the embedded sequence with respect to the specified variance spectrum. One of these stochastic properties is the contribution of the embedded sequence to the specified variance spectrum. Table 2 compares the relative errors of the spectral moments computed from the unconditional and from the conditional time sequences for the conditional simulation in Fig. 1 as a function of the contribution of the embedded sequence to the specified variance spectrum for an unconditional time sequence of length $N=2048$.

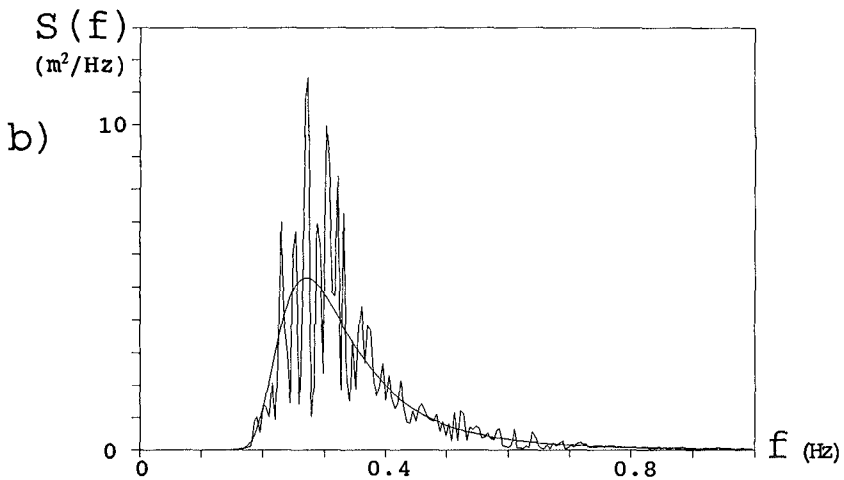
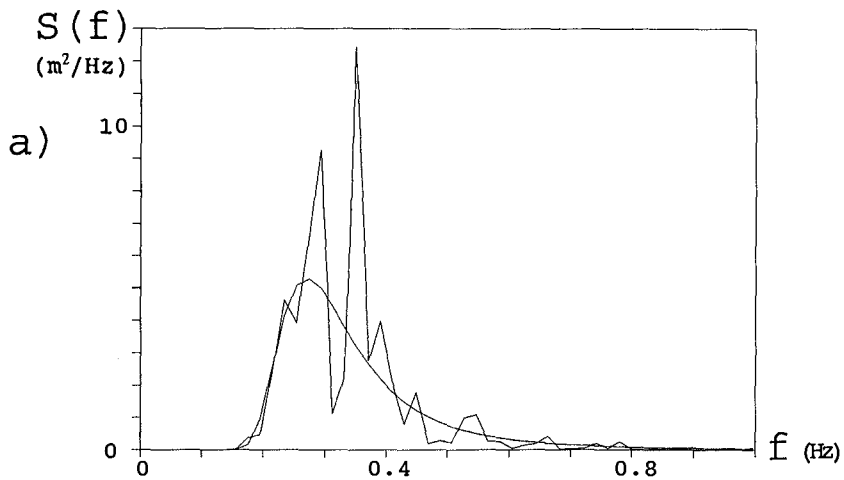


Figure 3. Specified Variance Spectrum and Conditional Time Sequence Spectrum for: a) $N=512$; b) $N=2048$.

TABLE 2. Effect of contribution of embedded sequence to specified variance spectrum on errors in spectral moments between η_s & η_e .

Moments	$m_0/2$	m_0	$2m_0$	$4m_0$
m_0	-5.6%	-2.1%	4.8%	18.5%
m_1	-5.1%	-1.9%	4.3%	16.8%
m_2	-4.8%	-2.0%	3.5%	14.5%

The goodness-of-fit improves as the contribution of the embedded sequence becomes more consistent with the specified variance spectrum.

SUMMARY AND CONCLUSIONS

A robust method is presented for the conditional simulation of random ocean waves having a specified variance spectrum and containing a deterministic sequence of waves at prescribed point in time. The addition of a low level of white noise (variance $0.0025m_0$) to the specified variance spectrum for the unconditional simulation avoids the instabilities that are due to inverting an ill-conditioned matrix. The effects of the length of the embedded wave sequence $\nu+1$ compared to the total length of the simulation N and of the contribution of the embedded wave sequence to the specified variance spectrum were illustrated for a Goda-JONSWAP spectrum.

ACKNOWLEDGEMENTS

We gratefully acknowledge the financial support provided by The Dirección General de Investigación Científica y Técnica, under Grant PB88-0353. RTH was funded by the Office of Naval Research under the University Research Initiative (ONR-URI) Contract No. N00014-86-K-0687 and by Oregon Sea Grant and the National Oceanic and Atmospheric Administration, Office of Sea Grant, Dept. of Commerce, under grant no. NA85AA-D-SG095 (project no. R/CE-21) and from appropriations made by the Oregon State Legislature.

REFERENCES

- Borgman, L.E. (1969): "Ocean Wave Simulation for Engineering Design", Journal of the Waterways and Harbors Division, ASCE, Vol. 95, No. WW4, Proc. Paper 6925, Nov., 1969, pp. 557-583.
- Funke, E.R. and Mansard, E.P.D. (1987): "A Rationale for the Use of the Deterministic Approach to Laboratory Wave Generation", IAHR Seminar on Wave Analysis and Generation in Laboratory Basins, 22nd IAHR Congress, Sept. 1-4, 1987, Lausanne, pp. 153-195.
- Goda, Y. (1985): "Random Seas and Design of Maritime Structures", University of Tokyo Press, 1985.
- Hudspeth, R.T. and Borgman, L.E. (1977): "Efficient FFT Simulation of Digital Time Sequences", Journal of the Engineering Mechanics Division, ASCE, Vol. 105, No. EM2, Proc. Paper 14517, Apr., 1979, pp. 67-85.
- Hudspeth, R.T., Borgman, L.E., Tuah, H. and Shields, D.A. (1990): "Conditional Simulation of Laboratory Waves", Engineering with Computers (in review).
- Medina, J.R. and Sánchez-Carratalá, C.R. (1988): "Comparisons of Numerical Random Wave Simulators", Proceedings, 21st ICCE, June 20-25, 1988, Torremolinos, Vol. 1, pp. 941-955.
- Tuah, H. and Hudspeth, R.T. (1982): "Comparisons of Numerical Random Sea Simulations", Journal of the Waterway, Port, Coastal and Ocean Division, ASCE, Vol. 108, No. WW4, Proc. Paper 17488, Nov. 1982, pp. 569-584.

CHAPTER 20

THE EFFECT OF WAVE DIRECTIONALITY ON NEARSHORE WAVES

Michael J. Briggs and Jane M. Smith¹
Member and Associate Member, ASCE

ABSTRACT

A three-dimensional, physical model study of the effects of nonlinearity and wave directionality (i.e. directional distribution of energy or the directional spread of energy about a peak wave direction) on wave transformation in the nearshore region is presented. The model consisted of a 1:30 fixed bed beach with plane-parallel contours. Fifty-four irregular wave conditions, typical of unimodal and bimodal directional spectra, were simulated. Twenty capacitance wave gages formed offshore and nearshore linear arrays to measure directional distributions and a cross-shore array to study transformation of the frequency spectra. Both linear and nonlinear processes were observed in the transformed directional spectra. The primary effect of wave directionality was reduction in the strength of the nonlinear phase coupling between modes. Directional spreading also reduced the formation of subharmonics (i.e. long period energy) in the transformed spectra.

1.0 INTRODUCTION

The transformation of waves in shallow water is dependent on irregularity of the wave field. The wave field is composed of a variety of periods, heights, and directions, but little guidance exists on combined effects of energy and directional distributions on wave shoaling, refraction, and breaking.

Accurate nearshore wave predictions are critical for estimating beach evolution and designing coastal structures. Site-specific wave conditions in the nearshore

¹Research Hydraulic Engineer, USAE Waterways Experiment Station, Coastal Engineering Research Center, 3909 Halls Ferry Rd., Vicksburg, MS 39180.

region are difficult and expensive to acquire, so designers of coastal structures often rely on measurements taken offshore. These measurements are then transformed to the desired shallow-water location using linear, numerical models which include the effects of shoaling, refraction, and bottom friction (Jensen, et. al. 1987). Unfortunately, these numerical models do not include the effects of nonlinear wave-wave interactions and wave directionality.

Although incident nearshore wave energy is usually concentrated in a narrow band of frequencies and directions, measured spectra seaward of the shoaling region are often multi-modal in frequency with broad directional spreading (Long 1989). Waves in the shoaling region are both weakly nonlinear and dispersive.

Elgar and Guza (1985) found that nonlinear coupling between frequencies was a significant mechanism in the transformation of ocean surface gravity waves. Freilich, et. al. (1990) showed that linear theory inaccurately predicts both the shapes and total variances of directional spectra in shallow water. They also found that the "vector resonance conditions" for frequency and wavenumber accurately predicted directions of harmonics due to energy transfers from nonlinear, near-resonant triad interactions in the shoaling wave field. Elgar, et. al. (1990) showed that nonlinear effects observed in nonbreaking waves at Torrey Pines, California, could be successfully reproduced in a laboratory experiment.

Smith and Vincent (1990) conducted a series of flume tests on the shoaling and breaking of bimodal unidirectional wave spectra. They found that during wave decay, wave energy is lost preferentially in the higher frequency mode. The flume results also showed that relative "closeness" and distribution of energy between modes were important. These results support nonlinear wave-wave interactions as a mechanism for wave evolution.

Sand, et. al. (1983) measured diffracted wave energy in the lee of a model entrance breakwater and found larger waves for the directional cases. However, in model tests of wave transformation in the lee of a submerged mound, Vincent and Briggs (1989) found the unidirectional waves higher than equivalent directional waves. Bowers (1987) found that directional spreading significantly reduced the long period energy associated with wave grouping in harbor modelling. Hasselman, et. al. (1963) found that directional spreading and uncoupled waves at harmonic frequencies decreased the measured nonlinearity.

Thus, inclusion of nonlinear transformation processes and wave directionality can have a significant effect on

coastal design by providing more realistic estimates of nearshore conditions. The results of these tests will be used to upgrade numerical wave transformation models for predicting nearshore wave properties from offshore measurements or hindcasts.

In this paper, the experimental setup is described in section 2. In section 3, the wave and test conditions for the 54 unimodal and bimodal, frequency and directional distributions are presented. Data collection and analysis procedures are described in section 4. Section 5 describes preliminary tests conducted to calibrate the model and control signals. Transformation of the directional spectra is discussed in section 6. Finally, conclusions are contained in section 7.

2.0 EXPERIMENTAL SETUP

A three-dimensional, physical model of a gently sloping beach with plane, parallel contours (Fig. 1) was constructed in CERC's 28 m by 40 m directional spectral wave basin. The model scale for the 1:30 slope fixed bed model was approximately 1:25. The toe of the slope was located 4.5 m in front of the directional spectral wave generator (DSWG), in a water depth of 50 cm. The rear of the basin was lined with wave absorber backed by a concrete wall. The basin sides were lined with absorber and open to adjacent basins. Thus, wave energy was able to propagate away from the test area into adjacent larger basins with minimal reflections from distant vertical walls and associated basin cross-seiching.

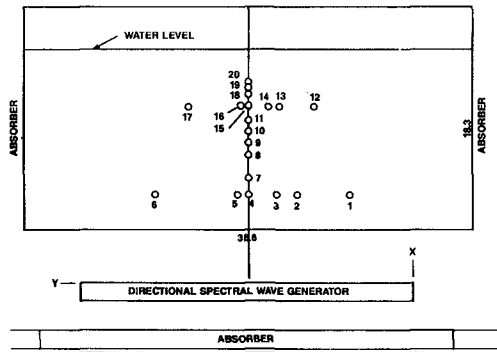


Fig. 1. Experimental Set-Up

Twenty capacitance wave gages were arranged in patterns and water depths similar to the prototype arrays used in 1978 and 1980 field experiments at Torrey Pines Beach, California (Pawka 1982). The gage pattern consisted of two 8-1-3-2-5 longshore linear arrays to measure changes in directional distributions and a cross-shore array to study frequency spectral evolution. The offshore (OGA) and near-shore (NGA) linear arrays were located in water depths of 40 cm and 16 cm, respectively. Lag spacings between gages for the OGA and NGA were 85 cm and 55 cm, respectively. The design of these arrays allowed measurements of waves with a directional resolution of approximately 8 deg (Pawka 1983). The cross-shore gage array (CSA) was nested within these two linear arrays, transverse to their axes and aligned with the physical model centerline. The spacing between the ten CGA gages was not uniform, varying between 0.5 to 2.0 m.

3.0 WAVE CONDITIONS

A total of 54 directional spectra were simulated as the product of the TMA shallow-water spectral form and a wrapped normal spreading function (Briggs, et. al. 1987). Both unimodal and bimodal frequency spectra with varying energy distributions were tested. The ratios of energy between modes in the bimodal spectra were 1/3:2/3, 1/2:1/2, and 2/3:1/3. Directional distributions were both narrow and broad and varied between modes. Target directional spectral parameters for individual modes were: $T_p = 1.25, 1.75, \text{ and } 2.50 \text{ sec}$ ($f_p = 0.40, 0.57, \text{ and } 0.80 \text{ Hz}$, respectively); $H_{m0} = 6.5, 7.6, 10.8, 12.2, 13.2, \text{ and } 15.2 \text{ cm}$; $\gamma = 3.3 \text{ or } 20.0$; $\theta = 0$ (shore-normal) and 20° ; and $\sigma_m = 0$ (unidirectional), 20 , and 40° . Wave direction is the angle towards which the waves travel, with positive angles measured clockwise from the normal to the DSWG.

These 54 wave conditions were converted into stroke control signals for each of the 61 paddles of the DSWG using a frequency domain, double summation, deterministic amplitude, random phase model. Typically, control signals were digitized at 20 Hz for 750 sec. After Fourier transformation in the frequency domain, this signal duration corresponded to an evenly-spaced frequency increment $\Delta f = 0.00133 \text{ Hz}$, or 1464 frequencies between the lower and upper cutoff frequencies $f_l = 0.05$ and $f_u = 2.00 \text{ Hz}$, respectively.

4.0 DATA COLLECTION & ANALYSIS

The wave gages were calibrated daily with a computer-controlled procedure incorporating a least square fit of measurements at 11-steps. After a waiting time of 20 sec to allow slower traveling high-frequency components to

reach the shallowest gages, surface elevation data were sampled at 10 Hz (i.e. $\Delta t = 0.10$ sec).

Data analyses consisted of single channel frequency spectral analysis for the CGA gages and directional spectral analysis for the OGA and NGA linear arrays. Data records of 500 sec were zero-meanded, tapered by a 10% cosine bell window, Fourier transformed, and band averaged, yielding a frequency resolution $B_e = 0.024$ Hz and $V = 24$ degrees of freedom. For the directional spectral analysis, the measured data again were zero-meanded, windowed, and Fourier transformed to the frequency domain. A Gaussian smoothing function then was used to smooth the cross-spectral matrix of auto- and cross-spectra with approximately $V = 56$. A high-resolution Maximum Likelihood Method (MLM) estimator was used to solve for the Fourier coefficients of the directional spreading function.

5.0 PRELIMINARY TESTS

Prior to wave transformation tests, three preliminary test phases were conducted: basin circulation, signal duration, and signal calibration. Based on current meter measurements and dye and visual observations, wave-induced circulation was not judged significant. In the second phase, measured spectral characteristics from test durations of 200 waves and 400 waves at the peak period were compared to determine proper sampling duration. Wave period, height, and spectral shape variations were within 95% confidence limits, so the shorter duration of 200 waves was selected for further tests. In the signal calibration phase, a frequency domain transfer function (Briggs and Jensen 1988) was used to iteratively correct the measured OGA spectra for variations in target peak period, wave height, and spectral shape.

The agreement between measured and target frequency spectra was very good to excellent. The peak of the measured spectra was often slightly smaller than the target spectra, but within 95% confidence limits. The maximum variation in peak frequency was ± 0.04 Hz (i.e. 2 frequency bands), occurring in only two cases. In most cases there was no significant difference between target values. Wave heights matched target values within 8% for all 54 cases. The agreement between measured and target directional distributions was good to excellent. The agreement for the unidirectional cases was excellent. The directionally spread cases, however, exhibited much more variability, with the measured results somewhat narrower than target distributions. Probable explanations are the resolving power of the arrays and MLM analysis technique and refractive-narrowing between the DSWG and OGA.

6.0 WAVE TRANSFORMATION RESULTS

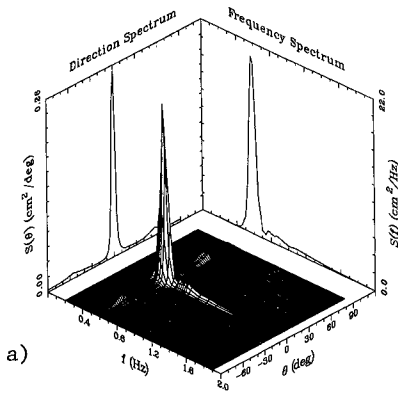
Since it is impractical to present the results from all 54 cases (Briggs, et. al. 1990), three representative cases will be discussed in detail. The first case is a unimodal, unidirectional spectrum, representative of narrow-banded swell. The second case is a bimodal case, composed of two crossing, narrow-banded (in both frequency and direction) wave trains. The third example is another bimodal case, narrow-banded in frequency and broad-banded in direction. This last case is typical of a sea and swell spectrum with greater energy in the swell peak.

In the paragraphs below, the OGA and NGA directional spectra are presented to illustrate the spectral evolution between linear gage arrays. Next, the frequency spectra from the CGA provide greater detail on the energy transfers closer to shore. Since linear theory does not predict the formation of harmonics, bicoherence spectra from bispectral analysis are used to confirm the presence of nonlinear wave-wave interactions in the shoaling waves. Finally, peak wave period and significant wave height are discussed.

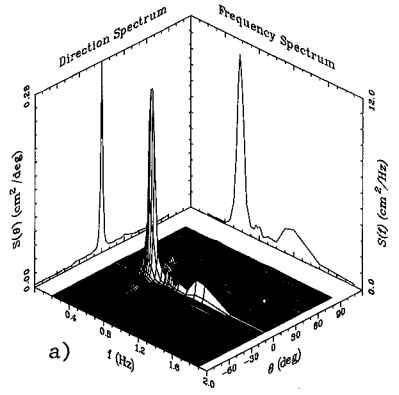
6.1 OGA Directional Spectra

MLM estimates of the directional spectra at the OGA for each of these three cases are shown in Fig. 2. The right vertical panel shows the frequency spectrum obtained by summing energy at each frequency over all directions. The left rear panel is the direction spectrum obtained in a similar manner, except that direction is held fixed and energy is summed over all frequencies. Frequency lines have variable spacing and are denser around the peaks and direction lines are spaced every 2° .

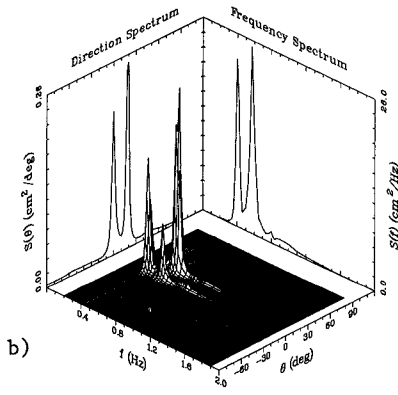
The first case (Fig. 2a) shows a single narrow peak, approaching the beach normally and centered at ($f_p = 0.40$ Hz, $\theta = 0^\circ$). Measured H_{m0} was 7.4 cm. The second example (Fig. 2b) shows a bimodal spectrum with crossing modes centered at ($f_{p,1} = 0.40$ Hz, $\theta_1 = 0^\circ$) and ($f_{p,2} = 0.57$ Hz, $\theta_2 = 20^\circ$), respectively. Measured H_{m0} was 8.4 cm, with a target distribution of 6.5 cm in each mode. A small secondary peak is observed centered at (0.57 Hz, 0°) which may be an artifact of the MLM estimation procedure or due to nonlinear effects on the spectra between the DSWG and the OGA. The third case (Fig. 2c) shows two shore-normal peaks centered at ($f_{p,1} = 0.40$ Hz, $\theta_1 = 0^\circ$) and ($f_{p,2} = 0.57$ Hz, $\theta_2 = 0^\circ$), with different amounts of full-width directional spreading ($\sigma_{m,1} = 20^\circ$, $\sigma_{m,2} = 40^\circ$). Measured H_{m0} was 13.1 cm. Wave refraction produced narrowing of the wider directional distributions by 6 to 10 deg between the DSWG and the OGA. Target wave heights were small enough to prevent wave breaking between the DSWG and the OGA.



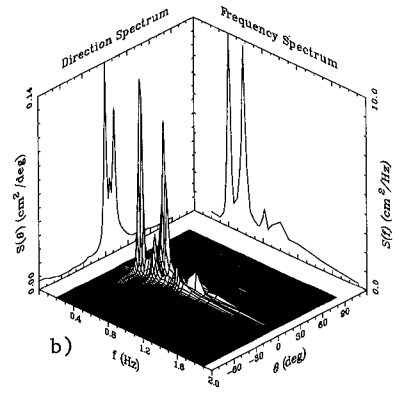
a)



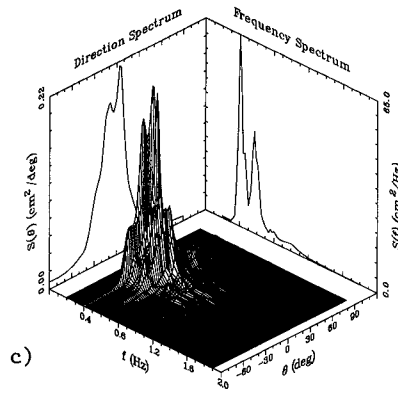
a)



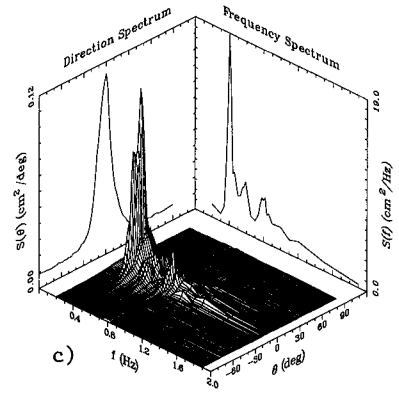
b)



b)



c)



c)

Fig 2. OGA Directional Spectra

Fig 3. NGA Directional Spectra

6.2 NGA Directional Spectra

Fig. 3 shows the NGA directional spectra for the three example cases. Fig. 3a for the first case indicates two distinct concentrations of energy: the narrow, unidirectional peak centered at (~ 0.57 Hz, 0°) and a broad, high frequency peak at (~ 1.14 Hz, 0°). Measured H_{m0} was 7.77 cm, indicating that the wave had not yet begun to decay. The transformed directional spectrum for the second case (Fig. 3b) shows five concentrations of energy: the low frequency peak centered at (~ 0.40 Hz, 0°); the high frequency peak at (~ 0.57 Hz, 10°); the "artifact" peak at (~ 0.57 Hz, 0°); a narrow harmonic peak at (~ 0.80 Hz, 0°); and a wider peak at (~ 0.97 Hz, 5°). The spectral energy is more shore-normal and the low-frequency, first mode appears to have gained energy at the expense of the high-frequency, second mode. This wave was still in the shoaling region because its measured H_{m0} was 8.74 cm. Finally, three concentrations of energy are evident (Fig. 3c) for the third case: the first mode centered at (~ 0.40 Hz, 0°); the remnant of the second mode at (~ 0.57 Hz, 0°); and a harmonic at (~ 0.80 Hz, 0°). The low-frequency peak has maintained its energy at the expense of the high-frequency peak, similar to observations in Smith and Vincent (1990). The measured H_{m0} for this last case was 11.68 cm, indicating that it was in the decay region of the surf zone.

The wave fields have transformed significantly between the two gage arrays. In general, the peaks are narrower and closer to shore-normal than the OGA spectra. Linear wave refraction accounts for approximately $10\text{--}14^\circ$ of the observed narrowing of the directional distributions. Wave breaking was observed between the OGA and NGA for all cases. The extent and initial location varied as a function of the target wave energy, being closer to shore for the initially smaller wave heights.

6.3 CSA Frequency Spectra

The NGA directional spectra suggested the formation of harmonics as the waves shoaled between deep and shallow arrays. Greater detail of this spectral evolution can be found by studying the frequency spectra from the CGA gages. Fig. 4 shows semi-log plots of the measured frequency spectra for two gages in the CGA: gage 4 (center of the OGA and incident conditions) and gage 20 (closest to shore). Corresponding water depths were 40.0 and 9.5 cm, respectively.

The first case (Fig. 4a) shows energy transfers from the peak frequency at (0.57 Hz) to second (~ 0.114 Hz) and third (~ 1.71 Hz) harmonics as the wave shoals. The fourth subharmonic (~ 0.14 Hz) experiences a fivefold increase in energy. The second case (Fig. 4b) supports the growth of

harmonics seen in the NGA directional spectrum (Fig. 3b), and suggests even higher harmonic growth at (~ 1.14 Hz, ~ 1.37 Hz, and ~ 1.71 Hz). Subharmonics at the difference frequency between modes (~ 0.17 Hz) and the second mode (~ 0.28 Hz) are indicated. The third case (Fig. 4c) becomes unimodal as it transforms; the "spectral valley" originally between first and second modes disappears. At a depth of 29.3 cm (not shown), energy is initially transferred to the harmonic frequency corresponding to the summation of mode frequencies (~ 0.97 Hz). By the time the wave travels to 9.5 cm depth, energy is transferred out of this harmonic and the second mode ($f_{p,2} = 0.57$ Hz) to the second and third harmonics of the first mode peak at (~ 0.80 Hz and ~ 1.20 Hz). The two subharmonic peaks present in the second case have coalesced into a single peak at the difference frequency at (~ 0.17 Hz).

6.4 Bispectral Analysis

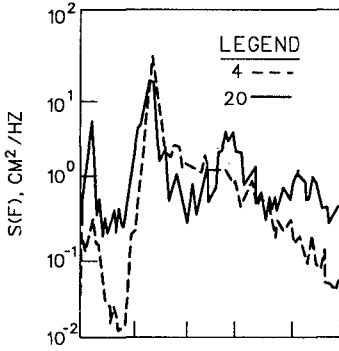
From the previous two sections, it is obvious that both linear and nonlinear processes are responsible for the observed changes in transformed wave spectra. Linear theory does not predict the growth of harmonics during wave shoaling. One method used to detect these nonlinear wave-wave interactions is bispectral analysis. The bispectrum (third-order spectrum) is a useful tool because only phase-coupled components appear. In the absence of this quadratic phase coupling (i.e. mode independence), the bispectrum is zero. Two wave components are harmonically related (i.e. dependent) if their interaction transfers energy at their sum and/or difference frequencies. A special case is harmonics at an integer multiple of a primary mode. The "vector resonance conditions" define this nonlinear, near-resonant triad interaction phenomenon. Both the frequencies f_i and vector wavenumbers k_i must sum to nearly zero and are given by

$$f_3 = f_1 \pm f_2 \quad (1a)$$

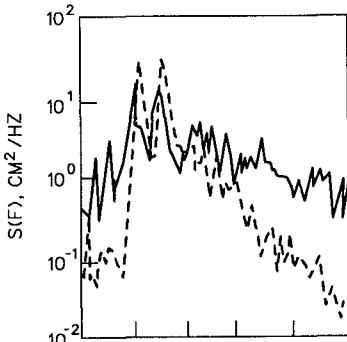
$$k_3 = k_1 \pm k_2 \quad (1b)$$

Freilich, et. al. (1990) showed that these conditions accurately predicted phase coupling between wave trains at Torrey Pines, California, approaching the beach at different directions, with energy transferred to a third mode corresponding to the sum frequency and vector sum direction.

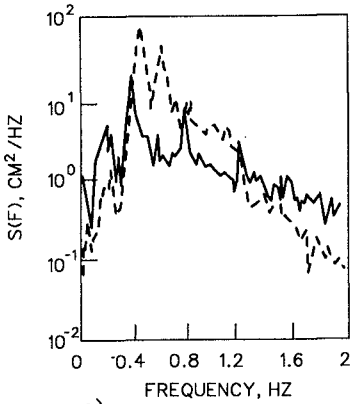
Fig. 5 shows the measured bicoherence spectra for our three example cases at gage 20 (9.4 cm). Because of the short durations of collected data, the number of degrees of free-



a)

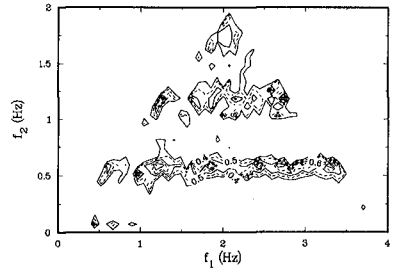


b)

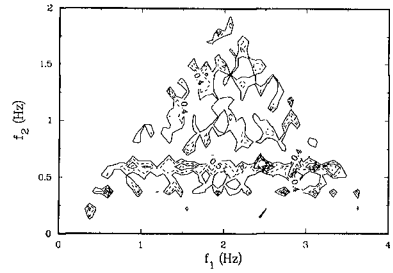


c)

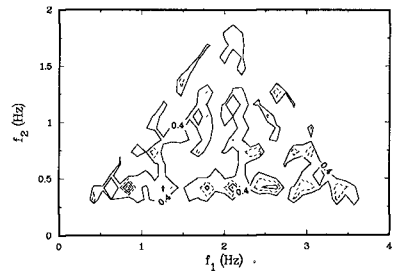
Fig 4. CGA Frequency Spectra



a)



b)



c)

Fig 5. Bicoherence Spectra

dom for the bispectral analysis is only 58 or 82. Elgar and Guza (1985) recommended $N = 150$ to 300 to improve statistical stability for field data. The minimum contour in the figures is at 0.4, with additional contours at 0.1. The first case (Fig. 5a) has bicoherence maxima (strong nonlinear interactions) between the first mode and its harmonics at $(f_2 = 0.57, f_1 = 0.57)$, $(0.57, 1.14)$, $(0.57, 1.71)$, $(0.57, 2.28)$, $(0.57, 2.85)$, and $(0.57, 3.42)$. Also, the second (1.14 Hz) and third (1.71 Hz) harmonics show similar strong nonlinear phase coupling among themselves and their harmonics. The third frequency f_3 of each triad is the sum of the two in parentheses. The bicoherence peak at $(0.57, 0.57)$ is the self-self-second harmonic triad observed in Figs. 3a and 4a at (1.14 Hz, 0°). It satisfies the "vector resonance condition" since $f_2 = f_1$, $f_3 = 2f_1 = 2(0.57) = 1.14$ Hz, and the wavenumber of the second harmonic is oriented in the same direction (0°) as the first mode.

Fig. 5b shows the bicoherence spectrum for the second example case. The phase coupling is more confused than the previous case due to the addition of the second mode and the non-aligned directions of the wave trains, although the horizontal trends at the two primary modes is similar to Fig. 5a. Bicoherence maxima are observed at $(0.17, 0.28)$, $(0.40, 0.57)$, $(0.40, 0.97)$, $(0.57, 0.57)$, $(0.57, 0.80)$, and $(0.57, 1.14)$. The first set corresponds to an apparent nonlinear interaction of the subharmonics of the difference frequency between primary modes and the second subharmonic of the second mode (Fig. 4b). This is indicative of the low-frequency phenomenon "surf beat" composed of infragravity modes. The second triad corresponds to the peak at $(0.97, 5^\circ)$ in Fig. 4b, at the sum frequency of the primary modes and the direction corresponding to the approximate vector sum of the wavenumbers. Peaks corresponding to the third frequency of the remaining triads can be seen in the high frequency portion of Fig. 4b. Lack of sufficient degrees of freedom in the bispectral analysis and non-alignment of wave directions in the primary modes might explain why the peak at $(0.80$ Hz, $0^\circ)$ does not show a strong nonlinear coupling in the bicoherence spectrum.

The bicoherence spectrum for the third case is shown in Fig. 5c. In this case, energy is narrow-banded in frequency but broad-banded in direction with aligned wave directions normal to the beach. Elgar and Guza (1985) found that directional spreading produced a weaker bicoherence spectrum. Bicoherence maxima are located at $(0.40, 0.40)$, $(0.40, 0.57)$, $(0.40, 0.80)$, and several higher harmonics. The first triad represents the self-self-second harmonic degenerate triad which produces the second harmonic at $(0.80$ Hz, $0^\circ)$ observed in Figs. 4c and 5c. The second triad is the harmonic at $(0.97$ Hz, $0^\circ)$ due to the sum of

the first and second modes. The nonlinear interaction of the primary (0.40 Hz, 0°) with the nonlinearly-generated second harmonic at (0.80 Hz, 0°) produces the third harmonic at (1.20 Hz, 0°). The "vector resonance conditions" are again satisfied since all components are collinear at 0° . Also, the growth of subharmonics seems to be suppressed relative to the first two cases without directional spreading.

6.5 Wave Period and Height Transformation

Peak wave periods in the CGA showed little change. Typically, they remained invariant or shifted slightly to a lower frequency. Since the resolution bandwidth is 0.024 Hz, some of this frequency variation is explained by statistical variability.

As the waves shoaled, wave height initially remained fairly flat or increased slightly. Inside the surf zone (decay region), wave height became locally depth controlled, no longer governed by outside (deep water) conditions, as the waves became saturated. Fig. 6 shows these trends for the CGA gages for 38 cases with target wave heights of 15.2 cm. The first two example cases have been omitted since the shoaling region extended throughout most of the model slope (i.e. closer to shore). A fourth degree polynomial, least square fit to the data is also shown for illustrative purposes. The fitted curve has been smoothed using locally weighted scatterplot smoothing (Cleveland 1979, 1981) which uses a weighted average of the nearby y values.

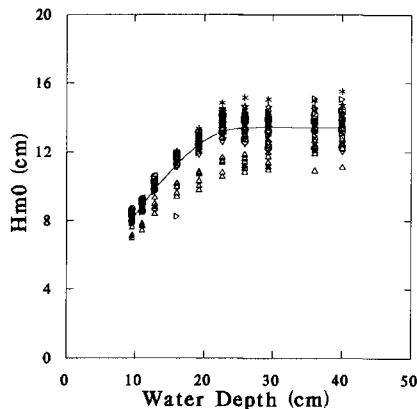


Fig 6. Wave Height vs. Depth

7.0 CONCLUSIONS

These tests have demonstrated that realistic ocean wave fields can be reproduced in a controlled laboratory experiment to study the mechanisms which effect transformation of nearshore waves. Both linear and nonlinear processes were observed in the shoaled directional spectra. The primary effect of wave directionality was reduction in the strength of the nonlinear phase coupling between modes, more so for directional spreading than wave direction. Directional spreading also reduced the formation of subharmonics (i.e. long period energy) in the transformed spectra.

ACKNOWLEDGEMENTS

The authors wish to acknowledge the Office, Chief of Engineers, U.S. Army Corps of Engineers, for authorizing publication of this paper. It was prepared under the Coastal Flooding and Storm Protection Program of the Civil Works Research and Development Program, managed by Dr. C. Linwood Vincent. We would like to thank Ms. Debra Green, Mr. David Daily, and Mr. Larry Barnes for their assistance. Dr. Charles Long made many helpful suggestions which were greatly appreciated. Dr. Steve Elgar, Washington State University, developed the bispectral analysis software.

REFERENCES

- Bowers, E.C. 1987. "Short Crested Seas in Harbor Modeling," Report No. SR 141, Hydraulics Research Limited, Wallingford, England, pp 24.
- Briggs, M.J., Borgman, L.E. and Outlaw, D.G. 1987. "Generation and Analysis of Directional Spectral Waves in a Laboratory Basin," Paper OTC 5416, Offshore Technology Conference, Houston, TX.
- Briggs, M.J. and Jensen, R. 1988. "Simulation of Extreme Storm Events in Coastal Structural Models," OSDS '88, Oregon State University, Corvallis, September, pp 119-133.
- Briggs, M.J., Smith, J.M., and Green, D.R. 1990. "Wave Transformation over a Generalized Beach," CERC Technical Report (in Press), USAE Waterways Experiment Station, Vicksburg, MS.
- Cleveland, W.S. 1979. "Robust Locally Weight Regression and Smoothing Scatterplots," J. ASA, 74, 829-836.
- Cleveland, W.S. 1981. "LOWESS: A Program for Smoothing Scatterplots by Robust Locally Weighted Regression," Am. Stat. 35, 54.

Elgar, S. and Guza, R.T. 1985. "Observations of Bispectra of Shoaling Surface Gravity Waves," JFM, Great Britain, 161, 425-448.

Elgar, S., Guza, R.T., Freilich, M.H., and Briggs, M.J. 1990 (Submitted). "Laboratory Simulations of Directionally Spread Shoaling Waves," J. WPCOE.

Freilich, M.H., Guza, R.T., and Elgar, S.E. 1990. "Observations of Nonlinear Effects in Directional Spectra of Shoaling Gravity Waves," JGR, 95(C6), June, 9645-9656.

Hasselmann, K., Munk, W., and MacDonald, G. 1963. "Bispectra of Ocean Waves," In Time Series Analysis (Ed. M. Rosenblatt), Wiley, pp 125-139.

Jensen, R.E., Vincent, C.L., and Abel, C.A. 1987. "A User's Guide to SHALWV: Numerical Model for Simulation of Shallow Water Wave Growth, Propagation, and Decay," Report 2, USAE Waterways Experiment Station, Vicksburg, MS.

Long, C.E. 1989. "Directional Characteristics of Waves in Shallow Water," Technical Report (In Publication), USAE Waterways Experiment Station, Vicksburg, MS.

Pawka, S.S. 1982. "Wave Directional Characteristics on a Partially Sheltered Coast," Ph.D. dissertation, UCSD, La Jolla, CA.

Pawka, S.S. 1983. "Island Shadows in Wave Directional Spectra," JGR, 88, 2579-2591.

Sand, S.E., Kirkegaard, J., Larsen, J., and Rodenhuis, G.S. 1983. "Numerical and Physical Modeling of Directional Diffraction of Waves," Coastal and Port Engineering in Developing Countries, Colombo, March.

Smith, J.M. and Vincent, C.L. 1990 (Submitted). "Shoaling and Decay of Two Wavetrains on a Beach," J. WPCOE.

Vincent, C.L. and Briggs, M.J. 1989. "Refraction-Diffraction of Irregular Waves Over a Mound," J. WPCOE, 115(2), March, 269-284.

CHAPTER 21
SIMILARITY OF VELOCITY PROFILES IN NON-UNIFORM
LONGSHORE CURRENTS

Hossam El-din A.A. Refaat¹, Yoshito Tsuchiya², M. ASCE
and
Yoshiaki Kawata³, M. ASCE

Abstract

In studying beach changes a law for non-uniform longshore sediment transport is generally needed, which concerns the non-uniform longshore currents. Therefore, experimental study on the similarity of velocity profiles in non-uniform longshore currents was carried out on a plane beach. It was concluded that, the velocity profiles are in similitude alongshore by comparing the nominal velocity at the breaker point. The boundary layer approximation can therefore be applied to the nearshore current equations to derive a single integral equation of non-uniform longshore currents. The theoretical solution of the equation is shown to compare with experimental results. The comparison between the theoretical and experimental non-uniform longshore current velocities are in satisfaction.

1. Introduction

In recent years, the coastal region has become an area of intense human activity for industry, transportation, recreation, as well as coastal protection works. The longshore current has a significant influence on beach changes. The prediction of the longshore current is of great importance for studying beach changes. Many investigators have studied uniform longshore currents, but only a few such as Eagleson(1965), Horikawa and Sasaki(1968), and Gourlay(1976) have concentrated on the phenomenon of non-uniform longshore currents. The phenomenon of

¹Research Fellow, Disaster Prevention Research Institute (DPRI), Kyoto University, Gokasho, Uji, Kyoto 611, Japan, on leave from Faculty of Engineering, Cairo University, Giza, Egypt.

²Professor, DPRI, Kyoto University, Gokasho, Uji, Kyoto 611, Japan.

³Associate Professor, DPRI, Kyoto University, Gokasho, Uji, Kyoto 611, Japan.

non-uniform longshore currents can be seen clearly in the vicinity of reefs and headlands, as well as coastal structures. The magnitude of the longshore current velocity increases from the upcoast initial current location and increases rapidly in the downcoast direction until a constant profile shape or uniform longshore current is established. Therefore, we may say that the non-uniform longshore currents are responsible for rapid erosion or accretion around coastal structures, where the non-uniform longshore current exist.

The shoreline is simply defined as the boundary between sea and land. Immediately seaward of the shoreline there exists a narrow band of fluid known as the surf zone. The surf zone is characteristic of extremely complex fluid motion induced by the rapid dissipation of the incoming wave energy. Moreover, in the field of hydraulics, particularly in the open channel flow, there exists a thin layer near the bed. Consequently, it may be possible to describe the longshore current motion in the surf zone using the boundary layer concept. Based on this analogy, the concept of boundary layer theory is introduced to the nearshore region. In order to verify this analogy, an experimental study on the velocity profiles in non-uniform longshore currents was performed. If the similarity in velocity profile can be obtained, the boundary layer approximation may lead to a single integral equation of non-uniform longshore currents from the nearshore current equations.

Applying this similarity of velocity profile in non-uniform longshore currents, we have derived the single integral equation of non-uniform longshore currents which is presented by the nominal longshore current velocity at the breaker point (Tsuchiya and Refaat, 1990). The solution of the equation is very briefly shown in the case of plane beaches, and compared with experimental results in good agreement.

2. Experiments

2.1 Experimental setup

The experiments were performed in the fan-shaped wave basin (semicircular part: $r=17.5$ m and rectangular part: 35×10 m) of Ujigawa Hydraulics Laboratory, Disaster Prevention Research Institute, Kyoto University. A smooth concrete beach was constructed with slope 1:10. Two smooth wave guide walls were installed in the normal direction to the wave board. The upstream guide wall was closed to the beach and the downstream one extended to the toe of the fixed bed, see Figure 1. The purpose for having an upstream guide wall closed to the beach is to keep the wave

height uniform along the beach. While, the opening at downstream guide walls helps to minimize the water circulation between the guide walls and to carry it away behind at the still water area.

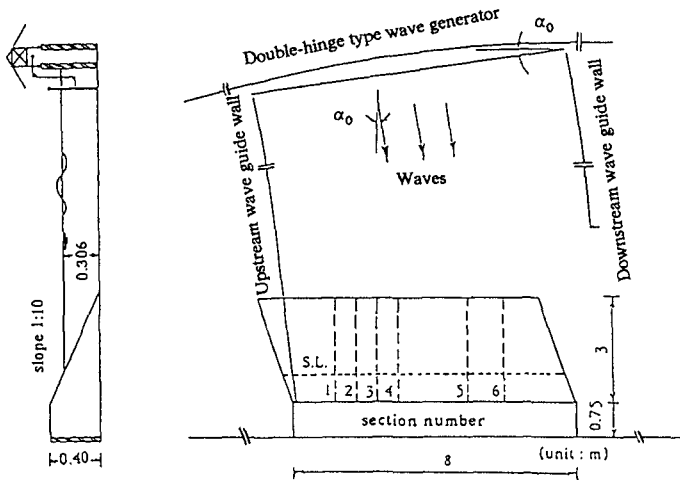


Figure 1. Schematic diagram of experimental arrangement of similarity of velocity profiles in non-uniform longshore currents.

2.2 Experimental procedure

The sloping part of the wave basin was marked by a 20 square cm grid. Measurements of current velocity were made at every grid line perpendicular to the shoreline. Two different types of colored tracers were used; 3 cm square shaped paper tracers and 2.5 cm ball tracers. The tracer trajectories within each grid was recorded by using a video camera system. Measurements of wave heights in the constant depth of the basin were made with capacitance type wave gauges. While on the sloping part, measurements of wave heights and mean water level were made over the entire grid area using capacitance type wave gauge and low frequency filter, respectively. The wave gauge and low frequency filter were installed on a vehicle mounted on rails controlled by personal computer. The angles of incoming wave incidence were measured at the constant depth part by measuring the angles of

inclination of the wave generator to the beach. The measurements of angles of incoming waves were done at the breaker line from the video tape record. Snell's law and linear wave theory were used to estimate and compute the measured angles of wave incidence at the breaker line.

2.3 Experimental results

In order to develop a more realistic model for non-uniform longshore currents, it is necessary to employ regular waves under various conditions. To carry out this investigation, eight experiments were performed under the conditions that the still water depth at the constant depth part is 30.6 cm, the wave period is 1.13 sec, the range of angle of incidence is 15° to 55° , and the wave height is varied from 3.8 cm to 8.5 cm, as shown in Table 1 where H is wave height, α is angle of wave incidence, h is still water depth, γ is breaker index, W is mean width of the surf zone, P is Longuet-Higgins parameter and the indices o and b refer to values on constant depth part of the wave basin and the breaker line, respectively.

Table 1. Experimental conditions of wave field

Ex. No.	H_o (cm)	α_o deg.	H_b (cm)	h_b (cm)	γ (H_b/h_b)	α_b deg.	W_b (cm)	P
R1	3.80	17.0	5.68	6.05	0.94	7.32	80	0.20
R2	5.10	17.0	6.73	7.87	0.86	8.36	100	0.09
R3	8.50	17.0	11.61	11.72	0.99	10.22	150	0.10
R4	4.50	35.0	7.98	8.80	0.91	17.56	90	0.05
R5	5.20	45.0	7.21	8.03	0.90	20.81	100	0.10
R6	7.75	45.0	9.63	11.80	0.82	25.51	130	0.10
R7	5.50	55.0	7.74	9.48	0.82	26.56	100	0.10
R8	6.65	55.0	8.60	10.03	0.86	27.38	120	0.08

The experimental results are classified mainly into two categories, they are:

(1) Similarity of velocity profiles

Figures 2 and 3 show the examples of the measured longshore velocities, for two incident wave angles 17° and 45° , compared with the theoretical curves of Longuet-Higgins (1972). The rate of agreement between measured and computed longshore current profiles is influenced by the choice of Longuet-Higgins parameter

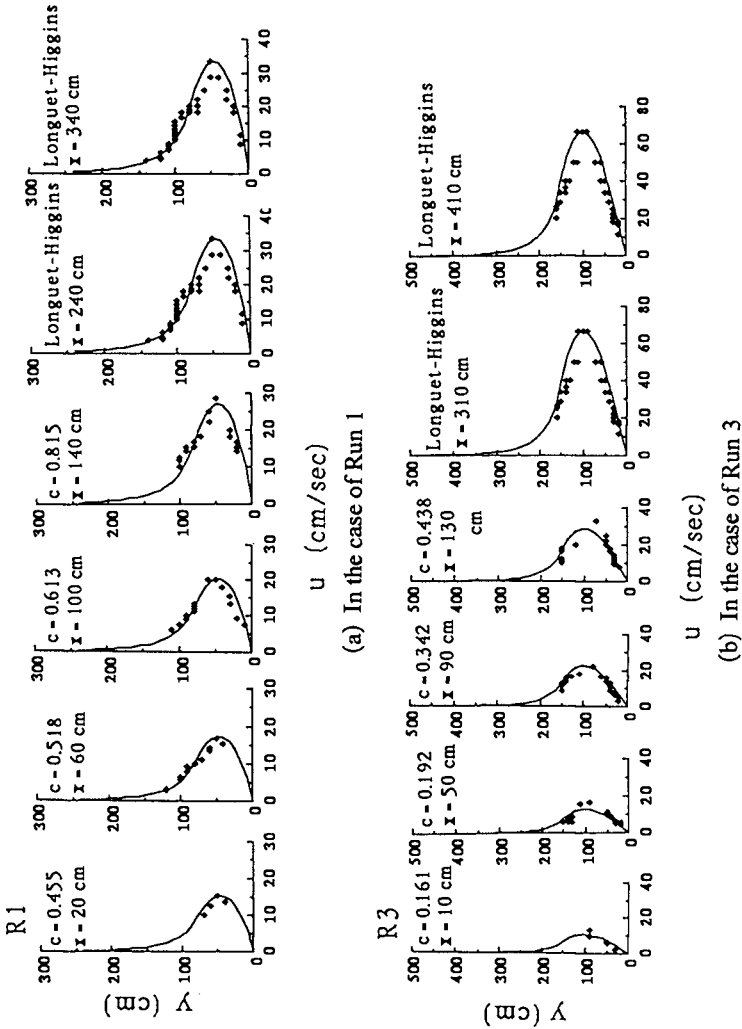


Figure 2. Examples of measured longshore velocity profiles compared with theoretical curves of Longuet-Higgins model in the case of incident wave angle $\alpha_0 = 17^\circ$.

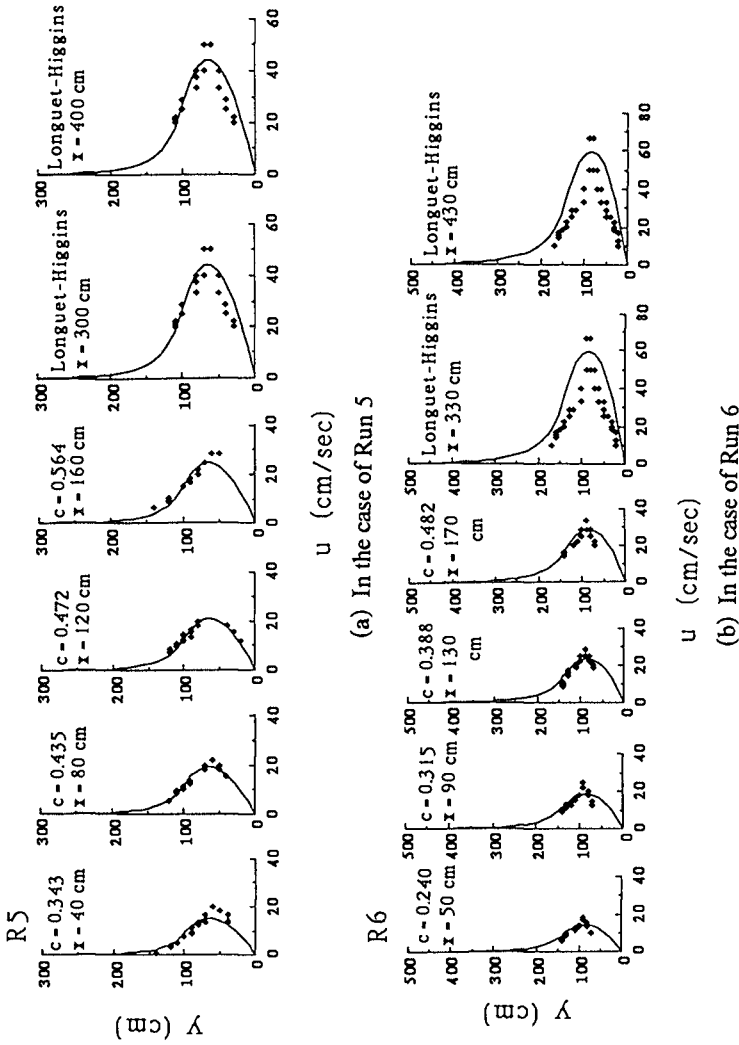


Figure 3. Examples of measured longshore velocity profiles compared with theoretical curves of Longuet-Higgins model in the case of incident wave angle $\alpha_0 = 45^\circ$.

P . The curves were fitted to the data using the method of least square. It is noted that for all experiments Longuet-Higgins parameter P is less than 0.2. From these figures it is obvious that:

a) The similarity of velocity profiles is quite satisfactory. The shape of the velocity distribution starts to grow from the initial boundary until reaching a constant shape, which represents uniform velocity profile. Therefore, the integration coefficients, which appeared in the equation of non-uniform longshore currents to be described in Eq. (1), are not functions of longshore direction nor time.

b) For a small angle of incidence, the agreement between the measured velocities and Longuet-Higgins curve is good. While in the case of large angle of incidence, the agreement is less.

The development of non-uniform longshore current velocity at the breaker line is shown in Figure 4, where the velocity is normalized by the one at breaker point and the longshore distance is normalized by the factor B to be described in Eq. (4). The longshore current velocity increases rapidly from zero, at the initial condition, to a constant value which corresponds to the uniform longshore current.

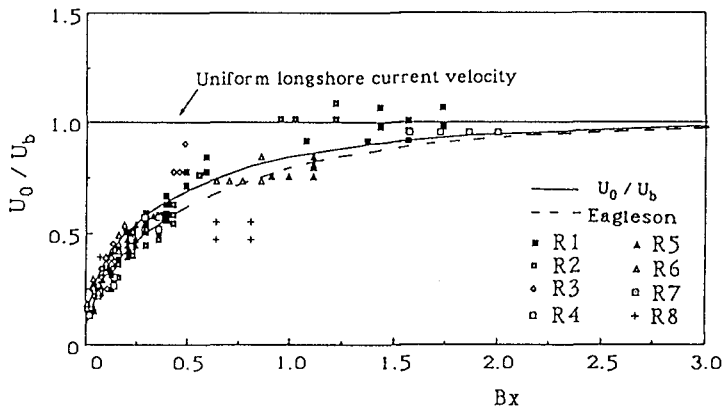
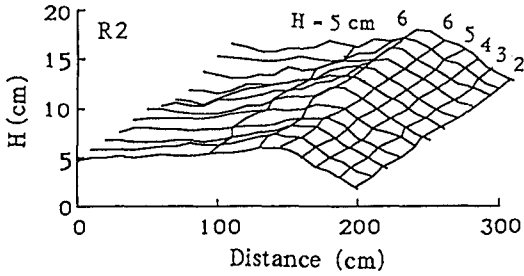


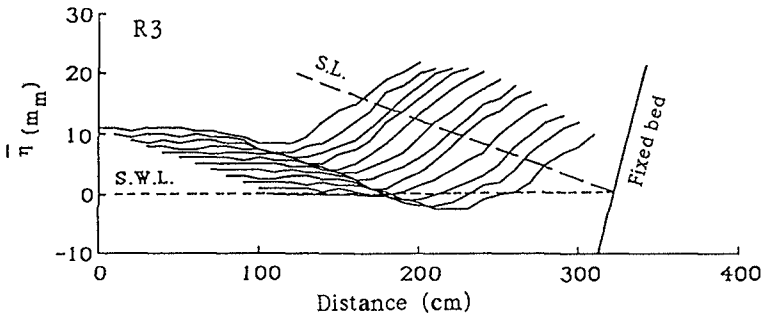
Figure 4. Comparison of measured and computed non-uniform longshore current velocity.

(2) Uniformity of wave set-up

Figure 5(a) and 5(b) illustrate the distribution of measured wave height for Run 2 and the mean water level for Run 3 over the entire sloping bed area. In these figures the horizontal axis represents the cross-shore direction, while the longshore direction is represented by the third axis. The uniformity of wave height and wave



(a) Distribution of measured wave height in the case of Run 2.



(b) Distribution of measured mean water level in the case of Run 3.

Figure 5. Distribution of measured wave height and mean water level over the entire sloping bed area.

set-up alongshore are clearly seen in these figures. Figure 6 shows the cross-shore measurements of the wave field for Run 2. The lower part of the figure shows the measured wave height computed with the calculated one by linear wave theory. In the experiments, the breaking wave is a plunging type, this means that the wave height continues to increase up to the breaker point. The effect of nonlinearity is so small that the measured values fit the calculated ones well. The upper part of the figure shows the changes in the mean water level presented by waves. Bowen, Inman and Simmons's (1968) formula for wave set-down was used to fit the measured data. It is clear from this figure that wave set-up increases linearly toward the shoreline. Therefore we can conclude from Figures 5 and 6, that wave set-up is uniform alongshore and increases linearly toward the shoreline.

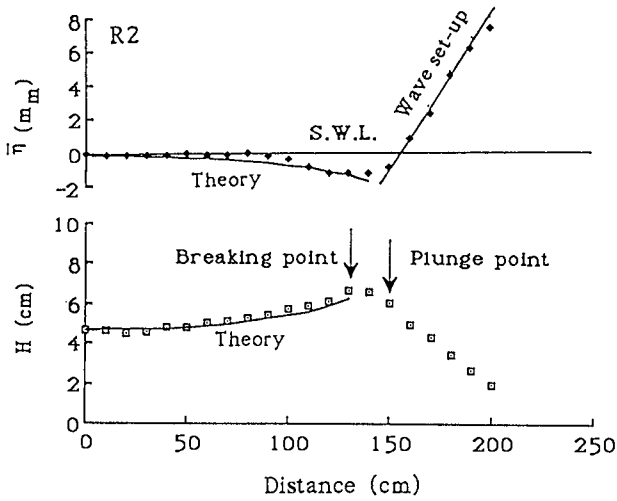


Figure 6. Cross-shore measurements of wave height and mean water level in the case of Run 2.

Figure 7 illustrates the variation of the measured wave set-up along the shoreline. The measured values used in this figure are 20 cm from the initial shoreline because the limitation of measurements at this region. But, fortunately, the wave set-up increases linearly, thus we can use this value instead of the maximum wave set-up value. In this figure Run 2 shows the maximum variation of wave set-up which is less than 7%, other cases are much smaller. Thus the wave set-up

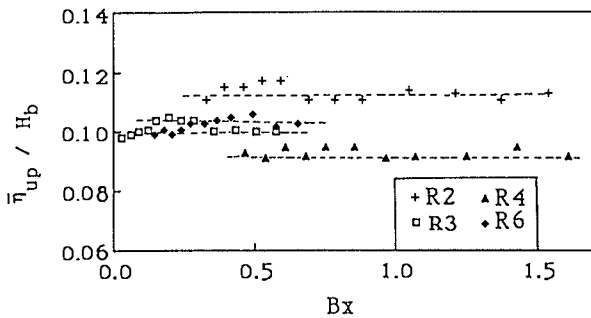


Figure 7. Longshore variation of measured wave set-up.

will be uniform alongshore. Furthermore, it is well known that wave set-up is a function of breaker index, H_b/h_b . Figure 8 demonstrates the uniformity of breaker index, H_b/h_b , along the shoreline. In this figure, the value of the breaker index, H_b/h_b , is laid between 0.8 and 1.0.

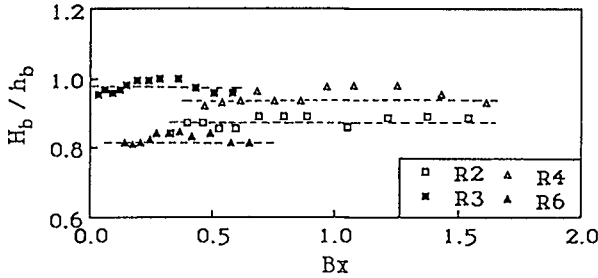


Figure 8. Longshore variation of measured breaker index, H_b/h_b .

3. The Theoretical Solution of Non-Uniform Longshore Current

Based on the similarity of velocity profiles in the non-uniform longshore currents, as previously discussed, a single equation of non-uniform longshore currents can be derived. Tsuchiya and Refaat (1990) have recently applied the so-called boundary layer approximation to the nearshore current equations to obtain the equation of non-uniform longshore currents. This equation can be written as:

$$\alpha_2 \frac{\partial}{\partial x} (U_0^2 h_b^2) + \alpha_3 \frac{\gamma C_f c_b}{\pi} U_0 h_b = f(x) \tag{1}$$

where

$$f(x) = \frac{\gamma^2}{16} g h_b^2 \left\{ \sin 2\alpha_b - 2 \cos^2 \alpha_b \frac{\partial y_b}{\partial x} - (5\beta_1 - 6\beta_2 + 6\beta_3 \sin^2 \alpha_b) \frac{\partial h_b}{\partial x} - 2\beta_3 h_b \sin 2\alpha_b \frac{\partial \alpha_b}{\partial x} \right\} \tag{2}$$

where U_0 is the non-uniform longshore current velocity at the breaker line, $\gamma = H_b/h_b$ is the breaker index where H_b and h_b are the breaker height and depth respectively, y_b is the position of the breaker line from the datum line, α_b is the breaking wave

angle, C_f is the bed shear stress coefficient, $c_b = \sqrt{gh_b}$ is the breaking wave celerity, g is the acceleration of gravity, and α_i, β_i ($i = 1, 2, 3$) are the integration coefficients. These integration coefficients depend only on the velocity profiles of longshore currents. Regarding the similarity of the velocity profiles of longshore currents, these integration coefficients are not functions of the longshore direction nor time.

This equation includes many parameters, but in the case of plane beach it is only one unknown U_0 , because the right hand side becomes constant. With the boundary condition that at $x = 0, U_0 = \bar{U}_0$ the solution of this equation is derived as:

$$\frac{(1 - \bar{U}_0/U_b) \exp(1 - U_0/U_b)}{(1 - U_0/U_b) \exp(1 - \bar{U}_0/U_b)} = \exp(Bx) \quad (3)$$

where

$$U_b = \frac{5\pi\gamma m}{16C_f} g h_b \left(\frac{\sin \alpha_b}{c_b} \right) \cos \alpha_b$$

$$B = \left(\frac{8C_f}{5\pi m} \right)^2 \frac{2}{\alpha_b h_b \sin 2\alpha_b} \quad (4)$$

In Figure 4, a solution to Eq. (3) for boundary condition at $x=0, U_0 = 0$, is shown and compared with the experimental values. Each point in the figure is identified by the plotting symbol corresponding to each run in the experimental measurements. It is shown that most of the points lie around the theoretical curve expressed by Eq. (3). The theoretical curve given by Eagleson (1965) is also shown in the figure for comparison. Based on the similarity of velocity profiles of longshore currents, the theoretical solution given by Eq. (3) describes not only the non-uniform longshore velocity at the breaker line but also at any given relative local depth ratio.

4. Conclusions

In this paper, an experimental study on the velocity profiles in non-uniform longshore currents was performed in order to investigate their similarity. From the comparison of the experimental measurements of longshore currents with the theoretical curves of Longuet-Higgins, it is observed that the degree of agreement between measured and computed longshore current profiles is influenced by the choice of Longuet-Higgins parameter P , and while the shape of the velocity

distribution starts to grow in a similar shape from the initial boundary until reaching a constant shape which represents uniform velocity profile, the similarity of velocity profiles is very satisfactory. The theoretical solution of non-uniform longshore currents on a plane beach was compared with the experimental result. The solution describes not only the non-uniform longshore velocity at the breaker line but also at any given relative local depth ratio.

References

Eagleson, P.S., 1965, "Theoretical Study of Longshore Currents on a Plane Beach," Report R65-28, Massachusetts Institute of Technology, Cambridge, Mass.

Gourlay, M.R., 1976, "Non-uniform Alongshore Currents," Proc. 15th ICCE, ASCE, Vol. 1, pp. 701-720.

Horikawa, S. and Sasaki, T., 1968, "Some Studies on Longshore Currents Velocity," Proc. 18th Japanese Conf. on Coastal Eng., JSCE, pp. 126-135 (in Japanese).

Longuet-Higgins, M.S., 1972, "Recent Progress in the Study of Longshore Currents," Waves on Beaches and Resulting Sediment Transport, ed. R.E. Meyer, Academic Press, Inc., pp. 203-248.

Longuet-Higgins, M.S., and Stewart, R.W., 1964, "Radiation Stress in Water Waves; a Physical Discussion with Applications," Deep-Sea Research, Vol. 11, No. 4, pp. 529-562.

Tsuchiya, Y. and Refaat, H., 1990, "Non-uniform Longshore Currents; Theory and Experiments," Jour. Waterway, Port, Coastal and Ocean Engineering, ASCE, 1990 (in review).

CHAPTER 22

Time and Frequency Domain Analyses of Shallow Water Waves on a Slope

D H Swart¹ and J B Crowley²

¹ CSIR, P O Box 395, Pretoria 0001, South Africa

² CSIR, P O Box 320, Stellenbosch 7600, South Africa

Abstract

Classical time and frequency domain analyses give results with limited physical meaning when applied to shallow water cases. Lower heights and periods than suggested by the actual data are obtained via these analyses. It appears that slope effects make waves less non-linear for steeper than for flatter slopes. One can obtain useful trends by making use of higher-order analyses, utilising higher-order, asymmetrical waves of the covocoidal type as an example.

Introduction

Most coastal engineering applications are done in water depths shallower than 20 m depth, either inside or outside the breaker zone and nearly invariably on a sloping sea bed.

Scientific and technological advances over the past decade have led to a substantially increased understanding of the physical processes taking place in the nearshore environment. This in turn has led to more sophisticated mathematical descriptions of these physical processes, which form the basis of the extensive numerical treatment of most of these processes.

In sediment transport research, rigorous advances have been made towards understanding the relationship between the driving forces and the resulting sediment movement. Nevertheless, it is still necessary to make, sometimes sweeping, simplifications in order to get workable numerical models of, e.g. cross-shore sediment transport. Baillard (1981) and Nairn (1988) have, amongst others, shown that, in order to correctly predict near-bottom sediment flows, it is essential to take cognisance of the higher, uneven moments of the orbital flow due to non-linear surface waves. The question that

now arises is to what extent the asymmetry of the surface waves in the nearshore region, which are clearly discernable on wave records and with the naked eye, would influence the cross-shore transport models. Similarly, we believe the time has come to critically analyse the saturation spectrum concept for nearshore situations, again with reference to asymmetrical, non-linear, nearshore surface waves.

With this understanding as a platform, we believe that the substantial body of research on nearshore waves and their related phenomena can serve as a bridge to take currently used predictive techniques for sediment transport and other wave-induced processes, such as wave forces, to new levels of sophistication with associated improved predictive skills. At all times, however, one has to be careful not to become more sophisticated just for the sake of it. The additional benefits have to be quantified.

3. Background

Nelson (1981) conducted a series of controlled laboratory experiments to establish the relationship, if any, between wave properties on a sloping bottom and the bed slope itself. His experiments were run on bed slopes ranging from horizontal to 1 in 10. He came to the following conclusions:

- (1) integral wave properties, such as wave length and wave energy, are for all practical intents and purposes *independent* of the bed slope; and
- (2) time-dependent wave properties, such as wave shape, orbital velocities and orbital accelerations, are very definitely dependent on bed slope.

Most traditionally used wave theories suffer from one of two problems, namely, it either predicts a linear wave shape or it is higher order, that is, non-linear, but symmetrical around the wave crest. Typically, as the wave non-linearity increases, the numerical complexity also increases. This led Swart (1978) to develop a wave theory with a fairly simple expansion in terms of a higher power of the cosine function, the so-called vocoidal wave theory, which was subsequently shown (Swart and Loubser, 1979) to be as accurate in predicting nearshore wave parameters as Dean's stream function theory (Dean, 1974).

The wave shape in the variable order cosine theory, or vocoidal theory, is defined by:

$$\eta/H = \text{voc}(P, X) - \eta_{st} \quad (1)$$

$$\begin{aligned} \text{and } \text{voc}(P, X) &= \text{the vocoidal function} \\ &= \{\cos^2(\pi x)\}^P \quad (2) \end{aligned}$$

where η/H = surface elevation, P is the order of the function, with $P \geq 1$, X is the location within the framework from wave crest to wave crest, non-dimensionalised by the wave length, and η_{*t} is the trough depth, relative to the still-water level and non-dimensionalised by the wave height.

On the basis of Nelson's results, referred to above, the thought occurred that it may be possible to, in a similar fashion as was done for vocoidal theory, obtain a function which is on the one hand simple and on the other hand closely resembles the actual behaviour of waves on a sloping sea bed.

As was the case for vocoidal theory, it was again intended to start from first principles, that is, the conformity equation and the equations of motion, with suitable kinetic and dynamic boundary conditions, and to then proceed to derive the wave properties, given the qualitative vocoidal (or in this case covocoidal) wave shape.

After some investigation, the following asymmetrical wave shape was defined (Swart and Crowley, 1989):

$$\eta/H = h_\alpha [\text{voc}(P, X) - \eta_{*t}] + 0.5r_\alpha [\text{cov}(P, X)(1 + \cos\pi X) - (1 - \eta_{*t})] \quad (3)$$

$$\text{and } \text{cov}(P, X) = 1 - \text{voc}(P, X) \quad (4)$$

where the first term in Equation (3) gives a symmetrical shape, basically the vocoidal wave shape, and the second term adds the asymmetry around the wave crest. Furthermore, the order P was assumed to be the same as for the similar case on a horizontal sea bottom, and h_α and r_α are functions of P and the bed slope $\tan \alpha$. These functions had to be determined in the derivation. Figure 1 contains spatial and temporal views of the wave shape.

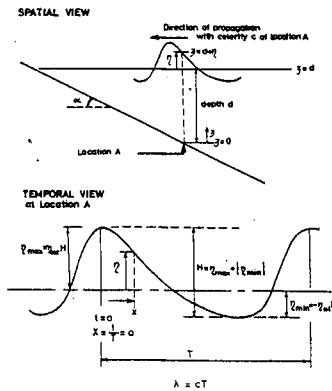


Figure 1. Axis-notation for development of generalised vocoidal theory on a sloping bottom.

A comparison to Nelson's laboratory data showed a very reasonable agreement (Swart and Crowley, 1989) and paved the way for further analyses with the covocoidal theory. It is not intended to submit that the vocoidal and covocoidal theories are the ultimate answers for nearshore, shallow water applications on a horizontal and sloping sea bed respectively, they are definitely not. However, these theories are very useful to investigate trends in data, specifically because of their good adherence to laboratory and field data. Using these theories allows the establishment of numerical techniques which would have been more difficult to construct with more complicated wave theories.

"Uncontrolled" field experiments of surface elevation variations in the nearshore environment in an exposed bay on the southwestern coastline of South Africa, are used in this paper to within the framework of covocoidal theory perform time and frequency domain analyses. These are then used to make some general deductions about the necessity for future research regarding waves on a slope.

4. Experimental set-up

The CSIR has over the past four years repeatedly performed extensive field measurement programmes in the shallow water in a flat bay, ca 20 km long and exposed to the dominant southwesterly swells off the southwestern coast of South Africa.

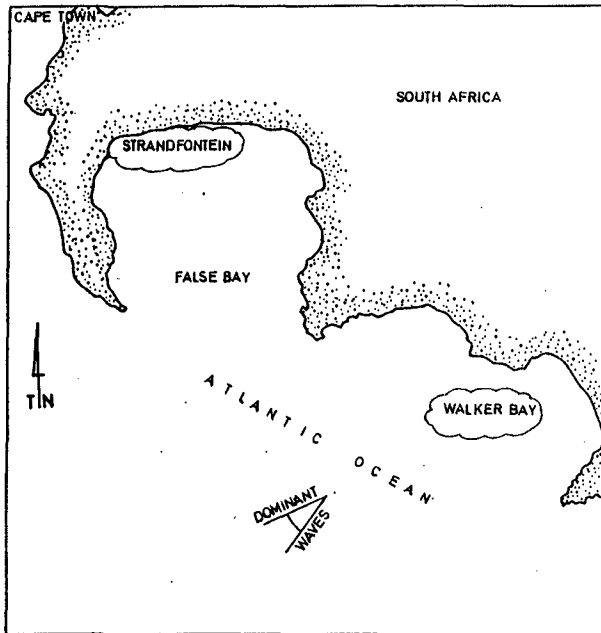


Figure 2. Location of field measurement site.

Four major field exercises have been performed to date, namely in March and September 1986, November 1987 and March 1990.

The September 1986 data had the best initial conditions to allow a comparison of depth effects and slope effects within the same data set. The three measurement sites that were used are characterised in the table below.

Site	Water depth	Slope	Type of instrument used
1	10-11 m	1 in 220	Pressure transducer
2	1- 2 m	Horizontal	Wave staff
3	1- 2 m	1 in 15	Wave staff

Some typical results obtained at each of these three sites are given below to familiarise the reader with the obvious differences between these sites.

Site 1

Figure 3 contains a few typical time records of wave profile and also a typical energy density spectrum. The wave trace shows a high degree of symmetry around the wave crest and also elements of wave grouping. This is supported by the energy density spectrum which contains two clear peaks, the dominant one at a frequency of 0.087 s^{-1} (11.45) and a secondary peak, more than one order of magnitude lower, but clearly discernable, at 0.014 s^{-1} (70s).

Site 2

Figures 4 and 5 show two sets of results which typify the range of variables found at this very nearshore location, where the bottom is for all practical intents and purposes horizontal in the area around it.

The time record of the wave profile in Figure 4 shows mostly a fair symmetry around the wave crest, as well as some clear indications of surf beat. The frequency domain analysis below shows three distinct peaks, now in descending importance with increasing frequency. The peak frequencies are at 0.011 s^{-1} , 0.045 s^{-1} and 0.07 s^{-1} . It is interesting to note that the tail of the frequency spectrum remains practically constant for frequencies greater than 0.08 s^{-1} at a value around 0.04 s^{-1} .

Figure 5, on the other hand, shows some clear signs of asymmetry around the wave crest, and furthermore a somewhat greater decomposition than in Figure 4, although the same three peaks can still be seen in the energy-density spectrum.

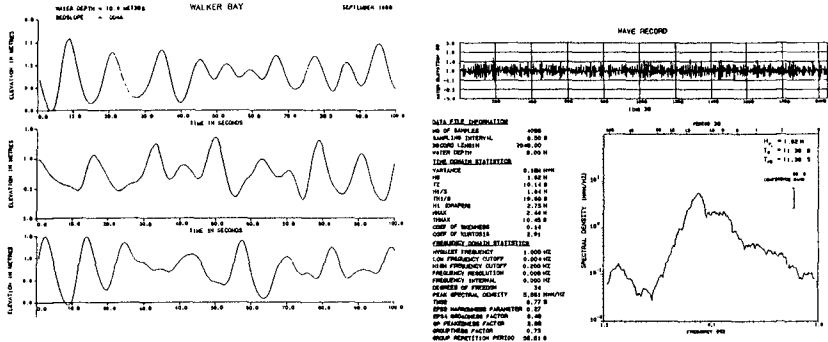


Figure 3. Typical time and frequency domain results for Site 1.

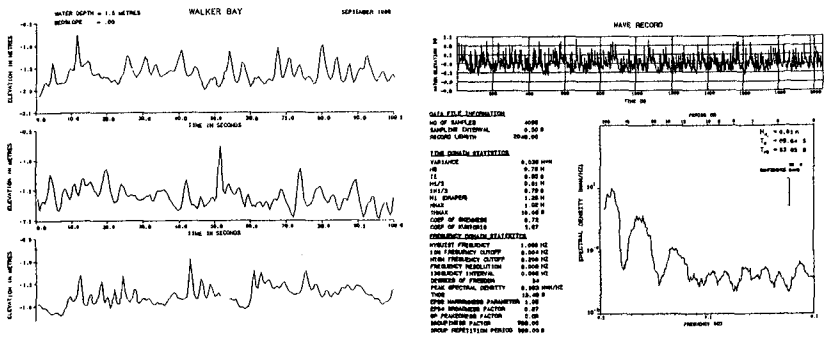


Figure 4. Typical time and frequency domain results for Site 2.

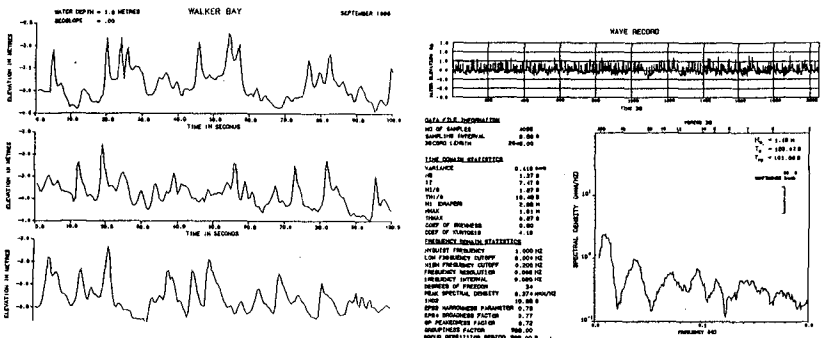


Figure 5. Typical time and frequency domain results for Site 2.

The wave groupiness exhibited in the time domain data is quite substantial.

Most of the data for this site are closer in resemblance to Figure 4 than to Figure 5.

Site 3

The data in Figure 6, for the same general water depth as for Figures 4 and 5, are in quite striking contrast to those for the earlier two figures. Whilst the time domain data also show signs of wave groupiness, the asymmetry of the waves around the wave crest is really very marked. This is general for all data collected at this site.

The energy density spectrum again has three distinct peaks, in order of importance at 0.005 s^{-1} , 0.023 s^{-1} and 0.048 s^{-1} . However, the spectrum now has a clearly saturated tail. Again, this is fairly common for all data collected at this site.

5. Time Domain Analyses

In this section, comparisons will be made of wave height calculated via time domain and frequency domain analysis techniques. The following two time-domain parameters are defined:

H_s ; which equals four times the square root of the variance

$H_{1/3}$; which is the average of the highest one-third waves, using the down-crossing method.

These two time-domain estimates of significant wave height are compared with the spectral estimate H_{m_0} of the significant wave height. All of these apply to the short wave component of the wave trace, defined by $f > 0.033$.

The results are shown in Figures 7 and 8. The results show that there is close correspondence between $H_{1/3}$, H_s and H_{m_0} at Site 1, at 10 m depth. However, at the two shallower sites, both $H_{1/3}$ and H_s are substantially higher than the spectral estimate H_{m_0} of the significant height.

The results are summarised in the table below.

Site	Median value of	
	H_{m_0}/H_s	$H_{m_0}/H_{1/3}$
1	0.99	0.96
2	0.80	0.90
3	0.80	0.65

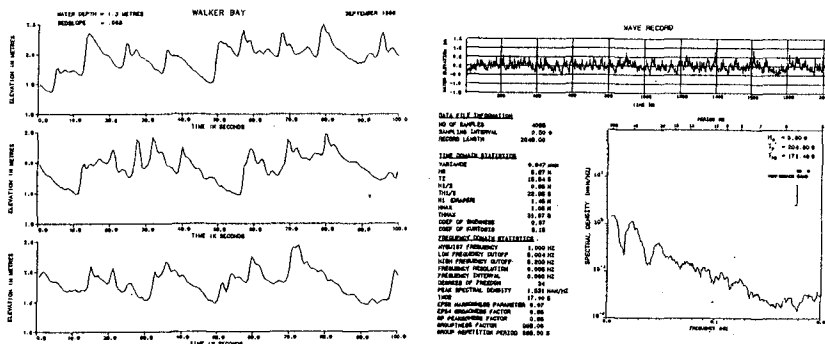


Figure 6. Typical time and frequency domain results for Site 3.

The reason for H_{m0} being less than H_s and $H_{1/3}$ for shallower water depths, is discussed in Section 6 below. It is noteworthy, however, that H_s is generally slightly higher than $H_{1/3}$.

Logically, because $H_{1/3}$ reflects the average of the highest one-third of the waves in the trace, it should be the reference value. Because of the non-linear nature of the waves in shallow water, the H_s value normally should deviate lower than $H_{1/3}$ progressively more as the non-linearity increases. The data seem to indicate the reverse. The reason for this is not clear.

5. Frequency Domain Analyses

Traditionally, spectral analysis of water waves has implied that a linear analysis was performed, whereby sinusoidally-shaped component waves are extracted. Over the years, various variations have been implemented, basically aimed at using bigger computing power to speed up the analysis. Various verification studies have been performed and it is generally accepted that this is a very sound procedure, yielding reliable, robust results, which can be replicated by any other researcher using standard techniques. However, in shallow water, this is not the case. Swart (1982) and Thompson and Vincent (1985), amongst others, have shown that, due to the fact that shallow water waves are non-linear, spectral estimates of wave height and period are too low in this area. This happens because a monochromatic non-linear wave train would, when analysed with a standard spectral technique, yield a spectrum of "apparent" wave heights rather than a single height at the appropriate frequency.

Thornton (1977) showed, by using both the kinematic and dynamic wave breaking criteria, that waves at higher frequencies in the wave energy spectrum are saturated with energy and that energy falls off in the region with a slope of f^{-2} , where f is the wave frequency. Banner and Phillips (1974) showed that, in

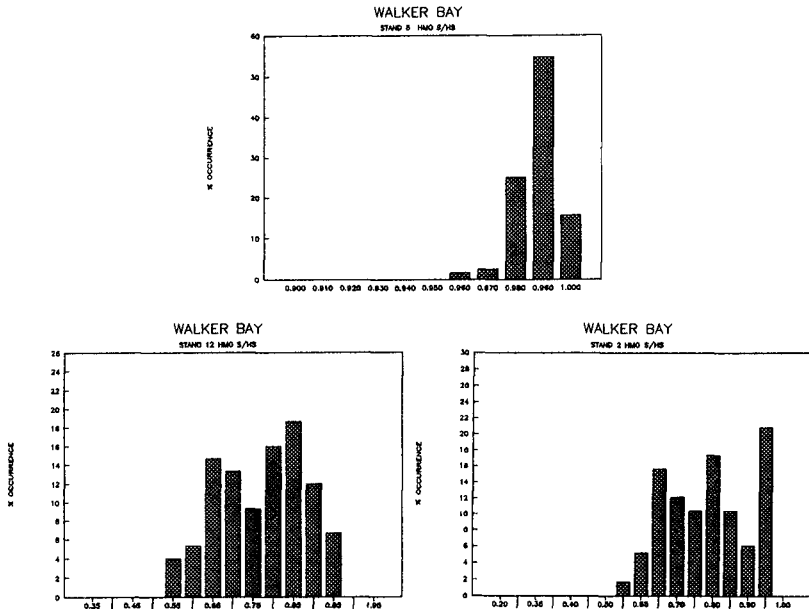


Figure 7. Histograms of H_{mo}/H_s values at Sites 1 to 3.

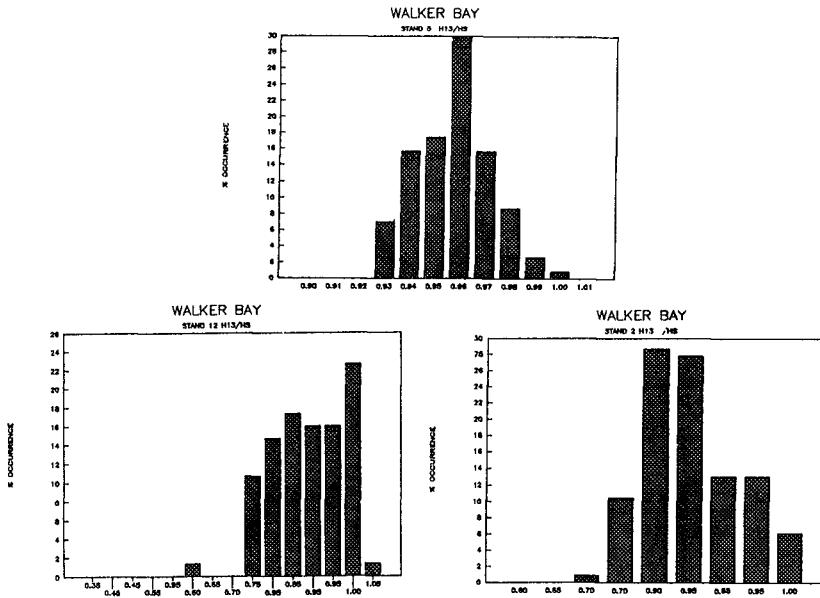


Figure 8. Histograms of $H_{1/3}/H_s$ values at Sites 1 to 3.

deepwater, the critical parameter associated with deepwater wave breaking is the wave celerity which leads to a saturation slope in this area of f^{-5} . Thornton (1977) presented data for 20 m and 1.5 m depth, respectively, and showed that the wave spectrum indeed exhibited saturation at f^{-5} and f^{-3} , respectively. However, vertical orbital velocity spectra at both depths had a saturation slope of f^{-3} . Thornton (1976) contains similar spectra for primarily breaking waves, which have a saturation slope of $f^{-7/3}$, which seems to tie in with theoretical work by Phillips (1966) for cases where surface tension is important. On the other hand, Huntley, Guza and Bowen (1977) present wave run up data which has saturation slopes of f^{-3} .

In all this work, the magnitude of the slope is basically explained in terms of the ease with which energy can be transferred from lower to higher frequencies, thus, by a physical constraint. Thornton (1977) remarks that all the spectra he observed for depths of 20 m and shallower contained some degree of saturation. He remarks that "it is not understood whether the apparent saturation region was the residual of an earlier saturated wave condition, or the transfer of energy by non-linear interaction of wave components".

In the present paper, it is shown that another explanation for the saturated tail in the energy spectrum can be sought in the decomposition of non-linear waves into sinusoidal components, thus, due to a numerical imposition, especially at the shallow water depths.

Swart (1982) came up with the concept of extracting, via a Fourier analysis, non-linear wave shapes instead of sinusoidal wave shapes. Using an iteration procedure, Swart extracted appropriately scaled vocoidal waves (Swart, 1977) from shallow water wave trains. Via numerical simulation, he showed the accuracy with which the original input non-linear wave height spectrum is returned via this method, as well as the corresponding drop in wave height due to spectral decomposition of the non-linear wave shapes when a traditional linear method was used. One could employ any wave shape in this method of analysis, provided that the shape can be described numerically in terms of the initial conditions, typically water depth, wave period (frequency) and wave height. It is due to the last parameter that an iteration is required, because the purpose of the analysis is to determine wave height.

In this paper, the non-linear spectral analysis was performed on sample data sets to establish whether the method yields meaningful results and whether this is an avenue of research worth pursuing for random waves on a slope. The analysis was done for both vocoidal and covocoidal waves.

Examples are given here for the two shallow water stands in Figures 9 and 10. It is immediately apparent that the normal Fourier analysis in the top graph of each figure yields a spectrum which is very flat with an appreciable portion of the energy resident at frequencies greater than 0.2. On the other hand, the lower two graphs,

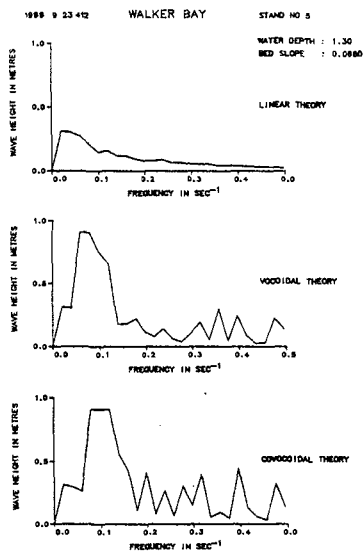


Figure 9. Linear and non-linear Fourier analysis in shallow water for Site 3.

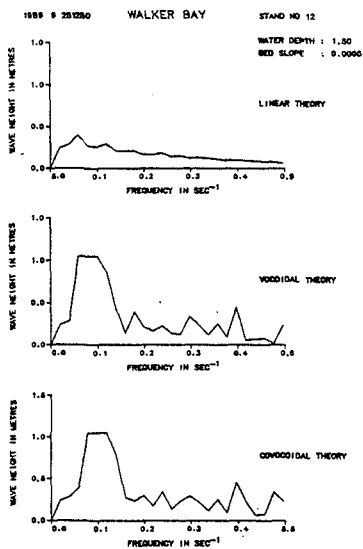


Figure 10. Linear and non-linear Fourier analysis in shallow water for Site 2.

which represent the higher order analysis, show spectra which are much more representative of deepwater spectra. At first sight, it would appear as if the energy associated with the lower two graphs is much higher than that for the upper graph. However, it should be borne in mind (Swart, 1978) that the total energy coefficient for these shallow water waves in a higher order theory is much lower than 0.125.

Furthermore, preliminary calculations show that the tail of a JONSWAP spectrum, of which the wave heights define shallow water wave shapes, falls off at a slope of between $f^{-2.5}$ and $f^{-3.5}$ when the resulting wave trace is subjected to a normal Fourier analysis. This supports the concept of the numerical method leading to the down position of the actual wave.

6. Conclusions

The following is a summary of the main conclusions reached during this study:

- Classical time and frequency domain analyses give results with limited physical meaning when applied to shallow water cases.
- Heights and periods are lower in these analyses than are suggested by actual data.
- Slope effects would appear to make waves less non-linear for the steepest slopes.
- Useful trends can be established by making use of simulations with higher-order, asymmetrical wave shape.
- Higher-order Fourier analysis "pulls" energy from higher frequencies towards lower frequencies, whereby the "saturation" shape disappears and the shallow water spectra then resemble deeper water spectra.
- Heights obtained from higher-order spectral analysis are more in tune with the wave trace than is the case for a linear analysis.

On the basis of these findings, we would suggest a critical review of the physical meaning of shallow water wave spectra and a more indepth analysis of the ramifications of using a non-linear spectral analysis technique.

References

BAILARD J A (1981). An energetics bedload model for a plane sloping beach: Local transport. *Journal of Geophysical Research*, Vol. 86 No. C3.

BANNER M L and PHILLIPS O M (1974). On the incipient breaking of small-scale waves. *J. Fluid Mech.*, Vol. 4, 647-656.

DEAN R G (1974). Evaluation and development of water wave theories for engineering application. Special Report No. 1, prepared for US Army, Corps of Engineers, Coastal Engineering Research Center, Vol. 1 and 2.

HUNTLEY D A, GUZA R T and BOWEN A J (1977). A universal form for shoreline run-up spectra. *J. of Geophysical Research*, Vol. 82 No. 18, 2577-2581.

NAIRN R B (1988). Prediction of wave height and mean return flow in cross-shore sediment transport modelling. *IAHR Symposium in Mathematical Modelling of Sediment Transport in the Coastal Zone*. Copenhagen.

NELSON R C (1981). The effect of bed slope on wave characteristics. CSIR Research Report 372.

SWART D H (1978). Vocoidal water wave theory. Vol. 1: Derivation. CSIR Research Report 357.

SWART D H and LOUBSER C C (1979). Vocoidal water wave theory Vol. 2: Verification. CSIR Research Report 360.

SWART D H (1982). The nature and analysis of random waves in shallow water. Part 1.

SWART D H and CROWLEY J B (1989). Approximate solution for waves on a sloping bottom. CSIR Research Report 641.

THOMPSON E F and VINCENT C L (1985). Significant wave height for shallow water design. *Journal of Waterway, Port, Coastal and Ocean Engineering*, Vol. 111 No. 5, September.

THORNTON E B (1977). Rederivation of the saturation range in the frequency spectrum of wind-generated gravity waves. *Journal of Physical Oceanography*, Vol. 7, 137-140.

CHAPTER 23

EXTENSION OF MILD SLOPE EQUATION FOR WAVES PROPAGATING OVER A PERMEABLE SUBMERGED BREAKWATER

Takashi Izumiya

ABSTRACT

A wave equation is presented for predicting reflected and transmitted waves for a permeable submerged breakwater. This equation includes the mild slope equation derived by Berkhoff(1972), which is a vertically integrated refraction-diffraction equation. Therefore, the equation derived can also predict the combined effects of refraction and diffraction. Numerical calculations with a dissipation term due to breaking are performed to obtain reflection and transmission coefficients as well as wave height distributions. Through the comparisons with the experimental results, the validity of the model is confirmed.

1. INTRODUCTION

Detached breakwaters and groins have been constructed on the coasts of Japan to prevent beach erosion. Recently, defense works against beach erosion, which is the combination of submerged breakwaters with wide crown width and large groins, has been planned on the Niigata west coast. It is very important for coastal engineers to estimate an effectiveness of the breakwaters. However, many of us are faced with a problem of how to estimate a distribution of wave height in the region existing such coastal structures.

Several analytical approaches have been done to predict the wave height of reflected and transmitted waves for permeable breakwaters (e.g., Ijima et. al,1971, Sollit and Cross,1972). Analytical solution obtained by them are valid only for rectangular permeable structures on a uniform bottom. These techniques cannot be applied to structures with arbitrary cross-section and require long algebraic operations to estimate the values of reflection and transmission coefficients. More recently, Sulisz(1985) has developed a numerical technique to predict wave reflection and transmission through a rubble mount breakwater of arbitrary cross section. The technique is, however, so complicated that it cannot be applied in the three dimensional problem. Therefore, a simple calculation method for wave transformation is required for coastal engineers.

Berkhoff(1972) has derived the mild slope equation which is a vertically integrated refraction-diffraction equation and is easy to be applied for a three dimensional problem. It should be noted that the mild slope equation can be applicable to waves propagating over bottom slopes as steep as $1/3$ and even to waves propagating across a

Assistant Professor, Department of Civil Engineering, Niigata University, Ikarashi 2-nocho, Niigata 950-21, Japan

step(Booij,1983). In this paper, a theoretical approach utilizes the linearized equation of motion in a permeable structure. A wave equation is derived by vertically integrating the equation of motion. The derivation of the wave equation is based on the assumptions that the slope of the permeable structure is adequately gentle, and that evanescent wave components of larger decay rate are negligible. The wave equation derived under the above assumptions is a two-dimensional elliptic type equation and includes the mild slope equation by Berkhoff.

2. DERIVATION OF EXTENDED MILD SLOPE EQUATION

2.1 Wave transformation within a porous medium

The analytical approach in this study begins with unsteady equations of motion for flow in a porous medium. After Madsen and White (1975), the linearized equations of mass and momentum in a porous medium are expressed as:

$$\frac{\partial u}{\partial x} + \frac{\partial v}{\partial y} + \frac{\partial w}{\partial z} = 0 \tag{1}$$

$$\frac{\tau}{\lambda} \frac{\partial u}{\partial t} = -\frac{1}{\rho} \frac{\partial p}{\partial x} - f \frac{\sigma}{\lambda} u \tag{2}$$

$$\frac{\tau}{\lambda} \frac{\partial v}{\partial t} = -\frac{1}{\rho} \frac{\partial p}{\partial y} - f \frac{\sigma}{\lambda} v \tag{3}$$

$$\frac{\tau}{\lambda} \frac{\partial w}{\partial t} = -\frac{1}{\rho} \frac{\partial p}{\partial z} - f \frac{\sigma}{\lambda} w - g \tag{4}$$

where (u,v,w) is the average discharge velocity components in the direction of x-, y- and z-axis, respectively. These are conceptual quantities which are averaged over finite and total volumes. The quantity p is the pressure averaged over finite pore volumes, λ is the porosity of the porous medium, f is the linearized friction factor, and τ is a inertia coefficient and expressed in terms of a virtual mass coefficient C_M as:

$$\tau = 1 + \kappa(1 - \lambda) = \lambda + C_M(1 - \lambda) \tag{5}$$

Hence, we assume that the flow in a porous medium is irrotational. Then the velocity potential φ for virtual discharge velocity is defined as:

$$(u, v, w) = \nabla \phi \tag{6}$$

Substituting Eq.(6) into the momentum equations (2)-(4) and integrating yields:

$$\frac{\tau}{\lambda} \phi_t + \frac{p}{\rho} + gz + f \frac{\sigma}{\lambda} \phi = C(t) \tag{7}$$

where C(t) is a integration constant. Equation (7) is the linearized unsteady Bernoulli equation. In order to remove the integration constant C(t), we introduce a new velocity potential defined by

$$\phi' = \phi - e^{-\frac{f\sigma}{\tau}t} \left[\frac{\lambda}{\tau} \int^t C(t) e^{\frac{f\sigma}{\tau}t} dt \right] \tag{8}$$

For simplicity, the prime will be omitted hereafter. The incompressible equations of motion can be expressed in terms of the velocity potential defined in Eq.(8)

$$\nabla^2 \phi + \frac{\partial^2 \phi}{\partial z^2} = 0 \tag{9}$$

$$\frac{\tau}{\lambda} \phi_t + \frac{p}{\rho} + gz + f \frac{\sigma}{\lambda} \phi = 0 \tag{10}$$

where ∇ is the gradient operator in the horizontal plane. The set of equations (9) and (10) govern the flow within a porous medium, should

be solved under appropriate boundary conditions. Boundaries of the domain are the bottom at a depth $z=-h$ and a free surface, $z=\zeta$. The dynamic free surface condition is obtained by setting $P=0$ at $z=\zeta$ in the above linearized Bernoulli equation.

$$\frac{\tau}{\lambda} \varphi_t + g\zeta + f \frac{\sigma}{\lambda} \varphi = 0 \quad : z=0 \quad (11)$$

where φ and its derivative with respect to t are evaluated at the still water level $z=0$. The linearized kinematic boundary condition at a free surface and a bottom are expressed by

$$\varphi_z = \lambda \zeta_t \quad : z=0 \quad (12)$$

$$\varphi_z = -f \varphi / h \quad : z=-h \quad (13)$$

Our task is to seek a solution to the Laplace equation (9) which satisfies the above boundary conditions Eqs.(11) to (13).

It is assumed that a velocity potential φ is expressed by:

$$\varphi = \hat{\phi} e^{-i\omega t} = f(z) \eta(x, y) e^{-i\omega t} \quad (14)$$

In case of constant water depth or very gentle slope, substitution of Eq.(14) into Eq.(9) yields

$$f = A \cosh k(h+z) \quad (15)$$

where k is the complex wave number satisfying a dispersion relation which will be described just later. Elimination of ζ in Eqs.(11) and (12) and substitution of Eq.(14) together with Eq.(15) into the boundary condition gives a dispersion relation as follows:

$$\sigma^2(\tau + if) = gk \tanh kh \quad (16)$$

Equation (16) has a countable infinite number of complex roots. Since evanescent wave components may decrease their magnitudes rapidly, we will neglect them. If $\tau=1$ and $f=0$, then we obtain the dispersion relation for linear free surface waves. In order to obtain a wave equation for the mild bottom slope, we apply the following Green's identity (see, Mei, 1983).

$$\int_{-h}^0 \left\{ \Psi_0 L(\Psi_1) - \Psi_1 L(\Psi_0) \right\} dz = \left[A(z) (\Psi_0 \Psi_1' - \Psi_1 \Psi_0') \right]_{-h}^0 \quad (17)$$

where L is the self-adjoint differential operator which is expressed as

$$L = \frac{d}{dz} \left[A(z) \frac{d}{dz} \right] + B(z) \quad (18)$$

Applying Green's formula for $\hat{\phi}$ and f and integrating from the bottom to the still water level yields

$$\nabla(C^* C^* \nabla \eta) + k^2 C^* C^* \eta = 0 \quad (19)$$

where

$$C^* C^* = \frac{g}{k} \tanh kh - \frac{1}{2} \left\{ 1 + \frac{2kh}{\sinh 2kh} \right\} \quad (20)$$

Equation (19) is the same as the expression as the mild slope equation derived by Berkhoff (1972). However, it is different that the wave number k in Eq.(19) is a complex number. If we put $\tau=1$ and $f=0$, Eq.(19) reduces to the mild slope equation by Berkhoff. In case of constant water depth, Eq.(19) reduces to the Helmholtz equation which has a solution with an exponential decay in the direction of incident wave propagation.

2.2 Wave transformation over a permeable submerged breakwater

Let us consider the wave transformation over a submerged permeable breakwater as shown in Fig.1. In this figure, h is the still

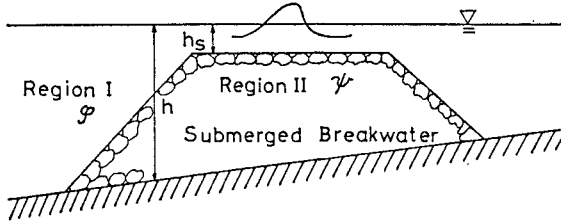


Fig. 1 Definition sketch.

water depth, and h_s is the depth above the interface of a submerged breakwater. The domain is divided into two regions, i.e., regions outside and inside the submerged breakwater, denoted as Region I and Region II, respectively. Irrotationality for the flow in pore of the breakwater permits to define the velocity potential ψ in Region II.

In Region I, governing equation and boundary conditions can be expressed in terms of the velocity potential φ as:

$$\nabla^2 \varphi + \varphi_{zz} = 0 \tag{21}$$

$$\varphi_{tt} + g\varphi_z = 0 \quad : z = 0 \tag{22}$$

$$\varphi_t + \frac{p}{\rho} - gh_s = 0 \quad : z = -h_s \tag{23}$$

$$\varphi_z = -\nabla \varphi \nabla h_s + w_s \quad : z = -h_s \tag{24}$$

where w_s is the average discharge velocity at $z = -h_s$. Equation (22) is the boundary condition arising from the kinematic and dynamic condition at the free surface, and Eq.(23) is the dynamic condition at the interface $z = -h_s$. Equation (24) is the modified kinematic condition including the discharge at the interface of the permeable bed.

In Region II, governing equation and boundary conditions are as follows:

$$\nabla^2 \psi + \psi_{zz} = 0 \tag{25}$$

$$\frac{\tau}{\lambda} \psi_t + \frac{p}{\rho} - gh_s + f \frac{\sigma}{\lambda} \psi = 0 \quad : z = -h_s \tag{26}$$

$$\psi_z = -\nabla \psi \nabla h_s + w_s \quad : z = -h_s \tag{27}$$

$$\psi_z = -\nabla \psi \nabla h \quad : z = -h \tag{28}$$

where Eqs.(26) and (27) are the dynamic and kinematic conditions at the interface $z = -h_s$, respectively, Eq.(28) is the kinematic condition for an impermeable bed. Since the pressure and the vertical discharge velocity at the interface must be continuous, the following continuity

conditions should be required.

$$p_1 = p_{11} \quad : \quad z = -h_s \quad (29)$$

$$\varphi_x = \varphi_x \quad : \quad z = -h_s \quad (30)$$

From Eqs.(23),(26) and (29), we have

$$\varphi_t = (\tau/\lambda)\psi_t + (f\sigma/\lambda)\psi \quad : \quad z = -h_s \quad (31)$$

The velocity potentials φ and ψ may be expressed as follows:

$$\varphi = -\frac{ig}{\sigma} F_1(z) \eta(x, y) e^{-i\sigma t} \quad (32)$$

$$\psi = -\frac{ig}{\sigma} F_2(z) \zeta(x, y) e^{-i\sigma t} \quad (33)$$

Substituting Eqs.(32) and (33) into Eqs.(21) and (25) respectively, and invoking the mild slope assumption, we obtain

$$F_1(z) = A \cosh k(h_s + z) + B \sinh k(h_s + z) \quad (34)$$

$$F_2(z) = D \cosh k(h + z) \quad (35)$$

where A, B and D are integration constants. The free surface boundary condition and the continuity condition for mass flux at the the interface together with Eqs.(32) to (35) give a dispersion relation by

$$\sigma^2 = gk \frac{\tanh kh_s + q \tanh k(h-h_s)}{1 + q \tanh k(h-h_s) \tanh kh_s} \quad (36)$$

where $q = \lambda/(\tau + if)$. When $\lambda=1$, $\tau=1$ and $f=0$, or $\lambda=0$, the dispersion relation Eq.(36) reduces to that for the linear wave over an impermeable bottom.

Applying Green's formula for F_1 and $\hat{\varphi}$, and for F_2 and $\hat{\psi}$,

$$\int_{-h_s}^{-h} \left\{ F_2 \frac{\partial^2 \hat{\psi}}{\partial z^2} - \frac{\partial^2 F_2}{\partial z^2} \hat{\psi} \right\} dz + \int_{-h_s}^0 \left\{ F_1 \frac{\partial^2 \hat{\varphi}}{\partial z^2} - \frac{\partial^2 F_1}{\partial z^2} \hat{\varphi} \right\} dz = \left[F_2 \frac{\partial \hat{\psi}}{\partial z} - \frac{\partial F_2}{\partial z} \hat{\psi} \right]_{-h_s}^{-h} + \left[F_1 \frac{\partial \hat{\varphi}}{\partial z} - \frac{\partial F_1}{\partial z} \hat{\varphi} \right]_{-h_s}^0 \quad (37)$$

and substituting Eqs.(32) to (35) into Eq.(37), we get the extended mild slope equation.

$$\nabla(a\nabla\eta) + k^2 a \eta = 0 \quad (38)$$

$$a = \frac{g}{k} \tanh kh_s \frac{1}{2} \left[1 + \frac{2kh_s}{\sinh 2kh_s} \right] + q \frac{g}{k} \tanh k(h-h_s) \tanh^2 kh_s \quad (39)$$

$$+ q \frac{g}{k} \frac{\tanh k(h-h_s)}{\cosh^2 kh_s} \frac{1}{2} \left[1 + \frac{2k(h-h_s)}{\sinh 2k(h-h_s)} \right] + q^2 \frac{g}{k} \tanh kh_s \cdot \tanh^2 k(h-h_s) \frac{1}{2} \left[1 - \frac{2kh_s}{\sinh 2kh_s} \right]$$

If we put $\lambda=0$, or $h=h_s$ in Eqs.(38) and (39), Eq.(38) reduces to the mild slope equation for an impermeable bed. So the wave equation (38) includes the mild slope equation derived by Berkhoff(1972). Furthermore, when $h_s=0$, we get a wave equation similar to that for wave transformation within a permeable media in previous section, but have a dispersion relation slightly different from Eq.(16).

2.3 Modeling of wave breaking over a submerged breakwater.

Wave breaking over a submerged breakwater is very important mechanism of wave energy dissipation. The wave equation (38) should be modified to include a energy dissipation due to breaking. To do this, we add the energy dissipation term in Eq.(38) to be expressed by

$$\nabla (a\nabla\eta) + k^2 a\eta = -i\sigma f_D \eta \tag{40}$$

where f_D is the energy dissipation factor, σ is the angular frequency and i is the imaginary unit. Since breaking waves over a wide submerged breakwater may recover, the value of f_D for recovered waves must be required to be equal to zero. Referring the studies by Watanabe and Dibajnia(1988) and Isobe et. al(1988), we will adopt the following expression for f_D .

$$f_D = \alpha_D \tanh\left[\beta_D \frac{\bar{h}_s}{L_0}\right] \sqrt{\frac{g}{h_s}} \sqrt{\frac{\gamma - \gamma_r}{\gamma_s - \gamma_r}} s_a \tag{41}$$

where \bar{h}_s and h_s are the water depth above the breakwater crown and the local water depth above the interface of the breakwater, respectively. The quantity γ is the ratio of the wave amplitude to the water depth h_s , γ_s and γ_r show the values of γ for breaking waves over a uniformly sloping beach and for recovered waves over a step type beach, respectively. The quantity s_a is the averaged bottom slope defined by Izumiya and Isobe(1986). The proportionality constants α_D and β_D will be determined from the results of experiment on wave transformation.

3. EXPERIMENTS ON WAVE TRANSFORMATION OVER A PERMEABLE SUBMERGED BREAKWATER

3.1 Experimental equipments and procedure

In order to confirm the validity of the model, the experiments on the wave transformation over a submerged permeable breakwater were conducted. A uniform slope of 1/15 made of wooden board was installed in a wave flume, and a submerged breakwater composed of three kinds of gravels was placed on the slope. The cross section of the model breakwater is shown in Fig.2. The average weight of gravels, W_1, W_2 and W_3 , is 86.3 gf, 10.4 gf and 0.89 gf respectively. The average porosity of the submerged breakwater is 0.433. The experiments with 24 cases were made for various wave heights and periods with the crown water depth of 3 cm.

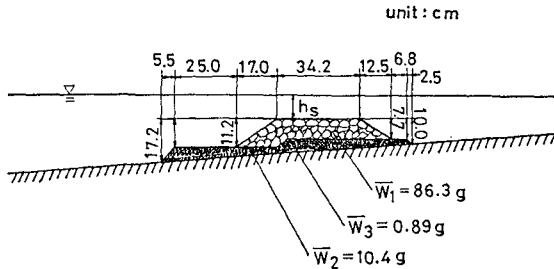


Fig. 2 Cross section of model submerged breakwater.

3.2 Wave breaking condition over a submerged breakwater

A few investigation on wave breaking over a submerged breakwater has been made. For this, a large number of experiments were carried out to obtain the empirical formula for the breaking condition. In case of wave breaking over a submerged breakwater, the breaking water

depth is defined as a depth from the interface of a submerged breakwater to the still water level. From the experimental data of the breaking water depth h_B , wave period and the local average slope s_a , the following expression for the non-dimensional breaking depth is obtained.

$$\frac{h_B}{H_0} = 0.43 + \frac{0.1}{-0.77 - \log_{10}(H_0/L_0)} + 0.22 \left\{ 1 - \frac{0.184 s_a^2}{s_a^2 - 0.107 s_a + 0.054} \right\} \cdot \left(\frac{H_0}{L_0} \right)^{-0.37} \quad (42)$$

where H_0 is the deepwater wave height and L_0 is the deepwater wavelength. When the local average slope steeper than 0.1, s_a takes a value of 0.1. The relation (42) is obtained to be slightly modified from the expression for steep slopes proposed by Isobe et. al(1988). Using Eq.(42), we can evaluate the breaking water depth as a function of the deepwater steepness and the average bottom slope.

4. METHOD OF NUMERICAL CALCULATION

A two-dimensional problem in the vertical plane is analyzed to examine the validity of the model equation. Equation (38) is discretized into a finite difference form and is solved by using two boundary conditions, i.e., the offshore boundary condition and the non-reflective boundary condition at a shoreward boundary to be expressed by

$$ik_i \varphi + \varphi_x = ik_i H_i e^{ik_i x_0} \quad (43)$$

$$ik_i \varphi - \varphi_x = 0 \quad (44)$$

where k_i is the wave number at the offshore boundary, H_i is the incident wave height and x_0 is the location of the offshore boundary. These boundary conditions are also discretized into finite difference schemes. The procedure of numerical calculation is summarized as follows:

- 1) Solve the dispersion equation, (36), for the first eigen value.
- 2) Assume $f_D = 0$, and solve Eq.(38) with the boundary conditions Eqs.(43) and (44).
- 3) Determine the breaking point using the breaking condition Eq.(42).
- 4) Calculate the wave heights with Eqs.(40), (41), (43) and (44).
- 5) Calculate the difference of wave heights for the successive iterations at each location.
- 6) Repeat 4) and 5) until the solution converges.

Through the above procedure, the converged solutions are obtained within 7 to 8 iterations.

5. COMPARISON OF THE MODEL RESULTS AGAINST THE EXPERIMENTAL DATA

The computed results with Eqs.(38) and (39) are compared with the experimental data to examine the applicability and the validity of the present model. In the calculation, The values of α_D , β_D , τ and f are determined by fitting experimental data for wave height. The results are $\alpha_D = 0.8$, $\beta_D = 90.0$, $\tau = 1.1$ and $f = 10.0$. Figure 3-(a) to (e) show the comparison between measured and calculated values of wave height. The solid lines indicate the wave height distributions calculated with the extended mild slope equation (38) including the dissipation term due to breaking. The closed circles show the experimental data. The agreement of wave heights outside the surf zone is very good. This means that the magnitude and the phase of reflected waves are well predicted by the present model. On the other hand, the

wave heights measured over a submerged breakwater are fairly smaller than the computed results. This is because that since the water depth above the breakwater crown, 3 cm, is shallow, the waves collapse on the breakwater with the strong nonlinearity of motion. So the difference between measured and computed wave heights occurred. Nevertheless, the transmitted wave heights calculated from this model are in good agreement with the experimental results.

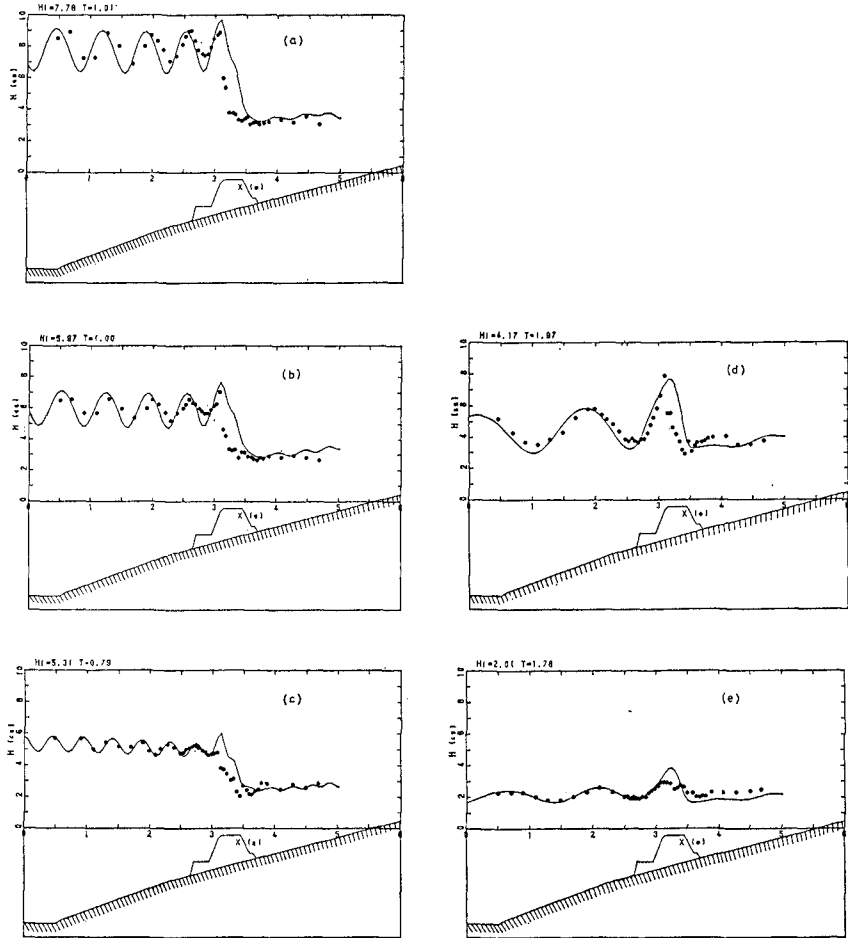


Fig. 3 Wave height transformations.

Figure 4 shows the comparison between measured and calculated values of reflection coefficient as a function of relative crown width B/L_0 . It is found that although the computed results in the range ($0.1 < B/L_0 < 0.2$) indicate values slightly larger than the experimental data, the agreement is fairly good. Figure 5 compares the the transmission coefficients with the measured and calculated results. From this figure, we can find that the estimated values of the transmission coefficient agree well with the experimental data, and also find that the coefficient decreases with decreasing relative crown depth h_s/H_0 . Figure 6 shows the comparison between measured and calculated values of energy loss coefficient as a function of the relative crown depth h_s/H_0 . It is seen from the figure that there is a scatter in the data in the range of $h_s/H_0 > 0.8$, however, the agreement is fairly good in the range of $h_s/H_0 < 0.8$.

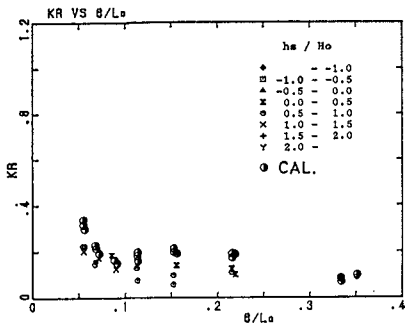


Fig. 4 Comparison between measured and calculated values of reflection coefficient.

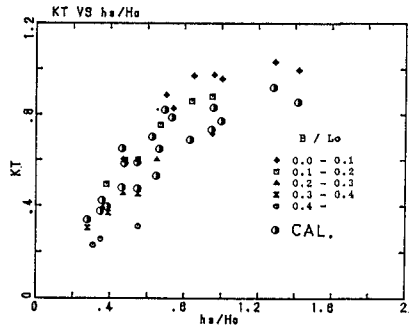


Fig. 5 Comparison between measured and calculated values of transmission coefficient.

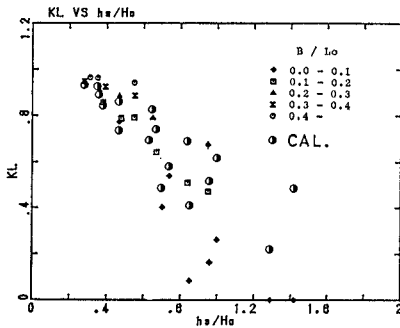


Fig. 6 Comparison between measured and calculated values of energy loss coefficient.

6. CONCLUDING REMARKS

A wave equation has been developed to evaluate the important characteristics of permeable breakwater. The wave equation obtained is applicable in and outside of a permeable structure, and has the advantage that the computation time is fairly shorter than those of existing methods. The validity of the model was confirmed through a comparison with the experimental data for a two-dimensional case. As the result, it was found that the present model can produce accurate results for practical purposes for the reflection, transmission and dissipation characteristics.

ACKNOWLEDGMENTS

This study was financially supported by the Science Research Fund of the Ministry of Education, Science and Culture, Japan, and by the Kajima Foundation's Research Grant.

REFERENCES

- 1) Berkhoff, J.C.W.(1972): Computation of combined refraction diffraction, Proc. 13th Coastal Eng. Conf., ASCE, pp.471-490.
- 2) Booij, N.(1983): A note on the accuracy of the mild-slope equation, Coastal Eng., Vol. 7, pp.191-203.
- 3) Dalrymple, R.A., J.T. Kirby and P.A. Hwang(1984): Wave diffraction due to areas of energy dissipation, J. Waterway, Port, Coastal and Ocean Eng., ASCE, Vol.110, pp.67-79.
- 4) Deguchi, I., T. Sawaragi, and H. Shiratani(1988): Applicability of non-linear Darcy law to the analysis of wave deformation on a permeable bed, Proc. 35th Japanese Conf. on Coastal Eng., pp.487-491. (in Japanese)
- 5) Ijima, T., Y. Eguchi, and A. Kobayashi(1971): Study on permeable breakwaters and quays, Proc. 18th Japanese Conf. on Coastal Eng., pp.121-130. (in Japanese)
- 6) Isobe, M., Y. Shibata, T. Izumiya, and A. Watanabe(1988): Set-up due to irregular waves on a reef, Proc. 35th Japanese Conf. on Coastal Eng., pp.192-196. (in Japanese)
- 7) Izumiya, T. and M. Endo(1989): Wave Reflection and Transmission due to a submerged breakwater, Proc. 36th Japanese Conf. on Coastal Eng. pp.638-642. (in Japanese)
- 8) Kondo, H.(1970): An analytical approach to wave transmission through permeable structures, Coastal Eng. in Japan, Vol. 13, pp.31-42.
- 9) Madsen, O.S. and White S.M.(1975): Reflection and transmission characteristics of porous rubble mount breakwaters, Rt. No.207, MIT, 183p.
- 10) Madsen, O.S.(1974): Wave transmission through porous structures, Proc. ASCE, WW3, Vol.100, pp.169-188.
- 11) Mei, C.C.(1983): Applied Dynamics of Ocean Surface Waves, John Wiley & Sons, New York, pp.86-88.
- 12) Sollit, C.W. and R.H. Cross(1972): Wave transmission through permeable breakwaters, Proc. 13th Coastal Eng. Conf., ASCE, pp.1827-1846.
- 13) Sulisz, W.(1985): Wave reflection and transmission at permeable breakwaters of arbitrary cross-section, Coastal Eng., Vol.9, pp.317- pp.371-386.
- 14) Watanabe, A. and M. Dibajnia(1988): A numerical model of wave deformation in surf zone, Proc. 21st Coastal Eng. Conf. ASCE, pp.578-587.

CHAPTER 24

ANOTHER QUASI-3D MODEL FOR SURF-ZONE FLOWS

A. Sánchez-Arcilla, F. Collado, M. Lemos, F. Rivero*.

Abstract

In this report, a quasi-3D model for nearshore circulation is presented. The aim of the model is an economic simulation of surf- zone flow features.

This model relies on the efficient integration of three main modules: i) Wave propagation, ii) Depth-uniform currents, and iii) 1DV model for current-profiles calculation.

The basic equations are vertically integrated up to the trough level (z_{tr}), assuming at this level the existence of a rigid-lid, which permits to replace the free surface elevation by an equivalent pressure.

This device allows a continuous description of the flux below z_{tr} , making possible the obtention of the flux components in the same vertical solution domain.

The model is still under development. The results obtained, although insufficient to validate the code, serve to explore its capabilities.

1.-Introduction

A new model for surf-zone flow analysis has been developed at the University of Catalonia U.P.C.. It's a versatile tool, valid for a wide range of coastal engineering problems, that maintains cost/accuracy in the range considered nowadays reasonable (for desk-top computers). This is mainly due to the use of a Quasi-3D scheme (3D codes are still too expensive). In the development of the code, it has been preferred to keep some degree of vertical resolution to make possible, for instance, sediment transport computations.

The code (ALF) is composed of:

- Wave propagation module.
- Rigid-lid 2DH module.
- 1DV module for the vertical profiles.

The last two modules will allow a reasonably accurate 3D resolution, with nearly the cost of a 2DH model.

* Lab. de Ingeniería Marítima, Univ. Politécnica de Cataluña, U.P.C., Barcelona, Spain.

In spite of the general formulation, herein we'll focus on the nearshore circulation, with emphasis on the internal consistency of the equations and associated simplifications.

The solution domain (vertical and horizontal) of the uniform (\bar{u}) and the depth-varying (\vec{u}) current components is the same. The water column is divided into three layers, coupled by mass/momentum transfers. The surface layer (above wave trough level) is not solved, and its effects are considered through boundary conditions identical for \bar{u} and \vec{u} . The middle layer goes from the top of the bottom boundary layer to z_{tr} for both variables. The third layer corresponds to the bottom boundary layer. To begin with and for simplicity, this layer will not be solved explicitly, its effects considered through continuity conditions for \bar{u} and $\frac{\partial \bar{u}}{\partial z}$ at the interphase. Alternatively, and depending on the fit obtained in the selected test cases, the bottom boundary layer could be included in the solution domain. In this case, the boundary conditions become even simpler (for instance, no-slip at the bottom), although some additional complications appear due to the need to make "closure" assumptions for waves and turbulence near the bottom.

The driving terms here considered are basically the incident wind waves, described in terms of frequency (f) and angle of incidence (θ). Although it has been shown that the inclusion of randomness is essential for a rigorous treatment of wind-wave phenomena, for now it has been preferred to run a model lumped in f and θ , assuming that the wave climate is well defined by these two parameters. An additional reason is that most available expressions for D (the rate of wave energy dissipation per unit area, closely related to surf-zone circulation features) have been derived for waves described in this lumped manner. The wave velocity field, \vec{u} , is obtained from linear theory.

With respect to the numerical discretization, suffice it to say that in this initial stage, the simplest possible technique has been selected to concentrate on the physics of the problem.

In what follows, the set of equations and simplifications involved in the model will be exposed, together with some preliminary results.

2.- Current Modelling

2.1- Assumptions

- Incompressible - newtonian fluid.
- z_{tr} , z_b and $\langle \eta \rangle$ are time-independent, ($\langle \rangle$ is the time-averaging operator at the wave-scale), see fig. 1.

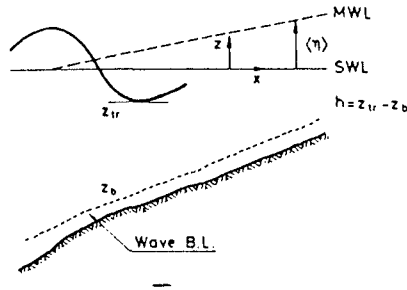


Figure 1.

- Horizontal gradients of z_{tr} and z_b are much smaller than the corresponding Reynolds stresses.
- Horizontal gradients of vertical velocities are much smaller than vertical gradients

of horizontal velocities.

- The current flow is quasi-horizontal (i.e. vertical accelerations are negligible). Thus, the pressure is given by:

$$p = p_{\text{hydrostatic}} - \rho \langle \tilde{w}^2 \rangle \quad (1)$$

- There is no mass flow through the z_b and η boundaries, but there certainly is through the z_{tr} level.

Once all these assumptions have been made, the operators $\int_{z_b}^{z_{tr}} () dz$ and $\langle \rangle$ will be applied to the mass and momentum equations. In order to avoid discontinuity problems of the variables describing the surface layer, the following decomposition will be used:

$$\vec{u} = \bar{u} + \tilde{u} \quad (2)$$

where:

\bar{u} : current velocity.

\tilde{u} : depth-invariant component.

\tilde{u} : z -dependent component.

The \tilde{u} component satisfies:

$$\int_{z_b}^{z_{tr}} \tilde{u} dz = 0 \quad (3)$$

From now on, the overbar symbol on a variable will be used to denote its mean value in the middle layer. The symbol " $\tilde{\quad}$ " on a variable has the effect of centering the variable around its mean. So, it will always be:

$$\int_{z_b}^{z_{tr}} \tilde{f} dz = \underline{0}, \text{ for every variable } \tilde{f} \quad (4)$$

2.2- Mass conservation Equation

The continuity equation, obtained after applying the depth-integration and time-averaging operators, is:

$$\frac{\partial(h\bar{u})}{\partial x} + \frac{\partial(h\bar{v})}{\partial y} = -G \quad (5)$$

where G is the net volume flux over z_{tr} , which reads:

$$\begin{aligned} G &= \frac{\partial}{\partial x} \langle \int_{z_{tr}}^{\eta} (u + \tilde{u}) dz \rangle + \frac{\partial}{\partial y} \langle \int_{z_{tr}}^{\eta} (v + \tilde{v}) dz \rangle \\ &= \nabla_h \cdot \langle \vec{Q}_s \rangle \end{aligned} \quad (6)$$

($h = z_{tr} - z_b$ is the thickness of the middle layer)

Invoking the starting assumptions, G is also seen to satisfy:

$$G = [w - u \frac{\partial z_{tr}}{\partial x} - v \frac{\partial z_{tr}}{\partial y}] (z_{tr}) \quad (7)$$

The wave contribution to the volume flux above z_{tr} is calculated with an expression deduced by Svendsen (1984b), which has been later used by other authors (e.g. Stive and De Vriend, 1987):

$$\langle \vec{Q}_s \rangle_w = \left(1 + \frac{7d}{L}\right) \frac{E}{\rho c} \tag{8}$$

d : Water depth.

L : Wavelength.

c : Wave celerity.

E : Wave energy density.

(The second term of the parenthesis is only considered inside the surf zone)

The current contribution to z_{tr} is more difficult to evaluate, due to the loss of physical meaning of this concept in a wave averaged time scale, because in this layer there are then "dry" and "wet" instants. Nevertheless, in the currents time-scale it looks reasonable to expect values of this contribution to be proportional to the values of the current in the middle layer (at $z = z_{tr}$) and the mean width of the surface layer. This term will be thus modelled by:

$$\langle \vec{Q}_s \rangle_c = \alpha \langle \eta \rangle - z_{tr} \vec{u} \tag{9}$$

Where α is a parameter to be evaluated.

2.3- Momentum Conservation equation for \vec{u}

The momentum equation obtained integrating between z_b and z_{tr} and applying the wave time-averaging operator is for the x-component (analogous for y):

$$\begin{aligned} & \frac{\partial(h\bar{u})}{\partial t} + \frac{\partial(h\bar{u}^2)}{\partial x} + \frac{\partial(h\bar{u}\bar{v})}{\partial y} - f(h\bar{v}) + (\bar{u} + \hat{u}(z_{tr}))G \\ &= -\frac{h}{\rho} \frac{\partial p_t}{\partial x} + \frac{\partial}{\partial x}(\bar{R}_{xx} + \hat{R}_{xx}) + \frac{\partial}{\partial y}(\bar{R}_{xy} + \hat{R}_{xy}) + \frac{\langle \hat{\tau}_{tr} - \hat{\tau}_b \rangle_x}{\rho} + \bar{W}_x \end{aligned} \tag{10}$$

Where:

$p_t = \rho g \langle \eta \rangle$, which shows the formal equivalence between pressure and set-up/down.

$\bar{R}_{ij} = h \bar{v}_t \left(\frac{\partial \bar{u}_i}{\partial x_j} + \frac{\partial \bar{u}_j}{\partial x_i} \right)$, stresses which take account of the horizontal momentum transfer due to \bar{v}_t .

$\hat{R}_{ij} = \int_{z_b}^{z_{tr}} [\hat{v}_t \left(\frac{\partial \hat{u}_i}{\partial x_j} + \frac{\partial \hat{u}_j}{\partial x_i} \right) - \hat{u}_i \hat{u}_j] dz$, term which takes account of the horizontal momentum transfer due \hat{v}_t and the interaction effects of the z-dependent flow in the uniform flow.

$\bar{W}_x = -\frac{h}{\rho} \int_{z_b}^{z_{tr}} \langle \bar{u}^2 - \bar{w}^2 \rangle dz - \frac{h}{\rho} \int_{z_b}^{z_{tr}} \langle \bar{u} \bar{v} \rangle dz$, which represents the horizontal gradient of driving terms due to the correlations of the wave-component velocities. This term doesn't exactly coincide with the usual definition of the radiation stress tensor S_{ij} (in our formulation vertical integration has been made up to z_{tr}).

Comparing (10) with the equation obtained integrating up to the free surface and disregarding time and space derivatives of the current over z_{tr} (and other terms that, according to the assumptions, are negligible), the following expression is obtained:

$$\bar{W}_i + \langle \tau_{tr} \rangle_i = -\frac{\partial \bar{S}_{ij}}{\partial x_j} + (\bar{u}_i + \hat{u}_i(z_{tr}))G \tag{11}$$

Replacing this expression in the momentum equations for \bar{u} and \bar{v} , the usual horizontal gradients of the radiation stress tensor are recovered. This approach requires however variables evaluated at the trough level which is, in the surf-zone, particularly difficult. An interesting alternative, at present under analysis, is the direct calculation of \bar{W} and G , with a suitable wave theory together with a semi-empirical model for $\langle \tau_{tr} \rangle$ as a function of D similar to the formulation used by De Vriend and Stive (1987). This D formulation has been already used for the description of the z-dependent flow.

With all this, the momentum equation can be written (similarly for the y-component):

$$\begin{aligned} & \frac{\partial(h\bar{u})}{\partial t} + \frac{\partial(h\bar{u}^2)}{\partial x} + \frac{\partial(h\bar{u}\bar{v})}{\partial y} - f(h\bar{v}) \\ &= -\frac{h}{\rho} \frac{\partial p_t}{\partial x} + \frac{\partial}{\partial x}(S_{xx} + \bar{R}_{xx} + \hat{R}_{xx}) + \frac{\partial}{\partial y}(S_{xy} + \bar{R}_{xy} + \hat{R}_{xy}) - \frac{\langle \hat{\tau}_b \rangle_x}{\rho} \end{aligned} \quad (12)$$

These equations, together with the continuity equation (5), become the usual ones for the calculation of free surfaces flows upon neglectation of the z-dependent component of the current and horizontal gradients of the volume flux over z_{tr} , and identifying h as the total depth.

2.4- Momentum conservation equation for \bar{u}

Considering that:

- Wave stresses are approximately uniform in the vertical (Stive and Wind, 1986)
- Horizontal gradients of turbulent stresses as well as interaction terms can be neglected (as suggested from an order-of-magnitude analysis)
- \bar{u}/\bar{u} interaction terms associated to convective accelerations do not appear to play an essential role. Thus it has been preferred to retain only the terms which make possible an efficient 1DV model. These terms which preserve the order of magnitude of convective terms, are for the x-component (similarly for y):

$$\hat{u} \frac{\partial \bar{u}}{\partial x} + \hat{v} \frac{\partial \bar{u}}{\partial y} \quad (13)$$

- The coriolis term is also neglected, since its effects (e.g. Ekman's layer) are usually masked by surf-zone turbulence.

Taking all this into account, the resulting equation for \hat{u} is:

$$\frac{\partial \hat{u}}{\partial t} + \hat{u} \frac{\partial \bar{u}}{\partial x} + \hat{v} \frac{\partial \bar{u}}{\partial y} - \hat{u}(z_{tr})G - \frac{\partial}{\partial z}(\nu_t \frac{\partial \hat{u}}{\partial z}) + \frac{\langle \hat{\tau}_{tr} - \hat{\tau}_b \rangle_x}{\rho h} = Res_x \quad (14)$$

The term $\frac{\partial \hat{u}}{\partial t}$ is retained to allow transient computations (in the future) and in order to use t as a marching variable for stationary cases (at present).

The \bar{u} equation, though parabolic in t-z, is of elliptic-type in z. Once it has been discretized in time, the resulting equation is of second-order in z. Thus, only 2 independent boundary conditions are needed to have a "well-posed" problem. Nevertheless, at least formally, there is a larger number of available boundary conditions, as pointed out by Battjes et al (1988). The choice is not obvious, and this remains a still open problem.

The term $\hat{u}(z_{tr})G$ is evaluated lagged backwards one time-step (error $O(\Delta t)$).

The term $Res_x(x, y, z)$ is a residual, which includes:

- All neglected terms (related or not to \hat{u}/\hat{v}).

- Errors (incompatibilities) due to closure submodels.
- Errors due to the discretization.

As for now, to simplify the computations, the term associated to G , will be included inside Res_x . With all this, the \vec{u} equations can be written in a compact manner as:

$$\frac{\partial \vec{u}}{\partial t} + A\vec{u} - \frac{\partial}{\partial x} \left(\nu_t \frac{\partial \vec{u}}{\partial x} \right) + \vec{T} = \vec{Res} \quad z_b \leq z \leq z_{tr} \quad (15)$$

Where:

$$A = \begin{pmatrix} \frac{\partial \bar{u}}{\partial x} & \frac{\partial \bar{u}}{\partial y} \\ \frac{\partial \bar{v}}{\partial x} & \frac{\partial \bar{v}}{\partial y} \end{pmatrix} ; \quad T = \frac{1}{\rho h} \begin{pmatrix} < \hat{\tau}_{tr} - \hat{\tau}_b >_x \\ < \hat{\tau}_{tr} - \hat{\tau}_b >_y \end{pmatrix}$$

These equations (after simplifying some terms) turn out to be similar to the usual ones. For instance, for waves normally incident to the coast, the expression obtained adding the \bar{u} and \bar{v} components is analogous to the one used by Svendsen (1987) in the calculation of undertow.

2.5- Boundary/Initial Conditions

i) Equations for \bar{u}/\bar{v}

- Any initial condition compatible with the continuity equation, as shown in figure 2.

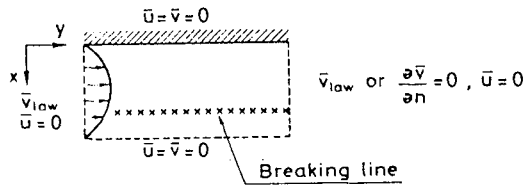


Figure 2.

- Boundary conditions are the same as those required by the 2D Navier-Stokes equations, i.e., Dirichlet or Neumann for \bar{u} and \bar{v} at each boundary point (compatible with the continuity equation).

ii) Equations for \hat{u}/\hat{v}

- Initial conditions: zero velocities.

$$\vec{\hat{u}} = 0, \quad \forall z \in [z_b, z_{tr}].$$

- As for boundary conditions, a summary of possible choices (some of them suggested in publications by authors such as Svendsen, De Vriend and Stive) is:

At $z = z_{tr}$:

$\nu_t \frac{\partial \hat{u}}{\partial x} = < \hat{\tau} >_x ; < \hat{\tau} >_y$, being related to the wave-height decay over z_{tr} , is also strongly related to the shape of $\vec{\hat{u}}(z)$. Furthermore, there is experimental evidence suggesting a non-negligible value of $\frac{\partial \hat{u}}{\partial x}$ at z_{tr} (Hansen et al, 1984; Nadaoka, 1986).

$\vec{\hat{u}}(z_{tr})$; is left free, since it doesn't exist any reliable information on this parameter in the state-of-art.

At $z = z_b$:

If z_b coincides with the upper limit of the bottom boundary layer, then $\bar{u}(z_b)$ and $\frac{\partial \bar{u}}{\partial x}(z_b)$ are obtained from a closure submodel for the bottom boundary layer imposing continuity at z_b .

If z_b coincides with the bottom (zero-intercept level), the no-slip condition $\bar{u}(z_b) = 0$ appears naturally, although its use requires an explicit specification, inside the boundary layer, of poorly-known variables such as the eddy viscosity profile and the correlation (product) of wave velocities.

For now, in order to simplify the numerical development attention will be focussed on the middle layer. The available boundary conditions are (according to what has just been presented) $\bar{u}(z_b)$, $\frac{\partial \bar{u}}{\partial x}(z_b)$ and $\frac{\partial \bar{u}}{\partial x}(z_{tr})$, all of them obtained with closure models. These condition plus an externally obtained $\bar{R}es$, give an over-determined problem. Assuming known values for \bar{u}/\bar{v} and ν_t there are 3 possible options to solve this problem:

- a) Choosing 2 boundary conditions and assuming $\bar{R}es = \bar{0}$
- b) Parameterizing $\bar{u}(z_b)$ and $\frac{\partial \bar{u}}{\partial x}(z_b)$ as a function of \bar{u} . (shear velocity) and using this free parameter to satisfy the third boundary condition (see Stive and De Vriend, 1987).
- c) Inserting in the definition of $\bar{R}es$ an extra degree of freedom in order to accomodate the third boundary condition.

Option c) has been initially selected, since it seems the cheapest way to apply the three boundary conditions. This choice requires $\bar{R}es$ to be kept in the permissible range, which in practical terms, means relatively small values that must verify at the same time the compatibility condition $\int_{z_b}^{z_{tr}} \bar{R}es dz = 0$, which appears integrating vertically the momentum equation for \bar{u} . In fact, defining $\bar{I} = \int_{z_b}^{z_{tr}} \bar{u} dz$, the depth-integrated equation for \bar{u} gives:

$$\frac{\partial \bar{I}}{\partial t} + A \bar{I} - \left(\nu_t \frac{\partial \bar{u}}{\partial x} \right) \Big|_{z_b}^{z_{tr}} + \bar{T} h = \int_{z_b}^{z_{tr}} \bar{R}es dz \tag{16}$$

Assuming that $\bar{u}(t = 0) = 0$ and considering $\nu_t \frac{\partial \bar{u}}{\partial x} = \frac{\langle \tau \rangle}{\rho}$ in z_b and z_{tr} , $\forall t$ (2 Neumann-type boundary conditions), it can be seen that a necessary and sufficient condition for $\bar{I} = \bar{0}$ (the integral condition that must satisfy \bar{u} by definition) is $\int_{z_b}^{z_{tr}} \bar{R}es dz = 0$.

3.-Numerical Solution

3.1.- Equations for \bar{u}

The unknowns are \bar{u}, \bar{v} and p_t (equivalently $\langle \eta \rangle$). The available equations are continuity and the x and y momentum equations (vertically integrated and time-averaged). The equations are solved with an explicit finite-differences method based on a MAC-type grid (see figure 3). The solution algorithm uses an upwind and Euler-type discretization (SOLA-type) allowing for variable h and ν_t .

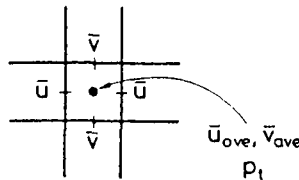


Figure 3.

The \tilde{u}/\tilde{v} interaction effects are considered via \hat{R}_{ij} and $\langle \hat{\tau} \rangle$. Initially, all terms related to \hat{u}/\hat{v} are assumed zero, when solving the \tilde{u} equations. The possible a posteriori correction effects have not been evaluated yet, leaving this as a still open point.

3.2- Equations for \tilde{u}

Using a forward Euler-type discretization for the time-derivative (error $O(\Delta t)$):

$$\frac{\partial u}{\partial t} = \frac{\tilde{u}^{\bar{n}+1} - \tilde{u}^{\bar{n}}}{\Delta t} \quad (17)$$

We obtain an equation for $\tilde{u}^{\bar{n}+1} = \tilde{u}((n+1)\Delta t)$ which turns out to be a set of linear coupled second order ordinary differential equations for \tilde{u}/\tilde{v} .

$$A_t \tilde{u}^{\bar{n}+1} - \frac{\partial}{\partial z} (\Delta t \nu_t \frac{\partial \tilde{u}^{\bar{n}+1}}{\partial z}) = \tilde{R}^n(z) \quad z_b \leq z \leq z_{tr} \quad (18)$$

Where:

$$\begin{aligned} A_t &= I + \Delta t A \\ \tilde{R}^n &= \tilde{u}^{\bar{n}} + \Delta t (-\tilde{T}^n + \tilde{R}es^n) \end{aligned} \quad (19)$$

The solution technique for this set of equations relies on essentially, three ideas:

i) Uncoupling the \tilde{u}/\tilde{v} , equations with an adequate change of variable $w = Vu$, so that:

$$A_t = V \Lambda V^{-1} \quad \text{with} \quad \Lambda = \begin{pmatrix} \lambda_1 & 0 \\ 0 & \lambda_2 \end{pmatrix}; \lambda_1, \lambda_2 \in \mathbb{R}. \quad (20)$$

This change of variables may not always be possible, with cases in which the A_t eigenvalues can be complex or where it cannot be diagonal (in which case it should be replaced by the corresponding Jordan matrix). However, the numerical treatment is essentially identical in all cases, so that without a significant loss of generality, it will be supposed that this kind of situation will never arise in practice. On the other hand if $\frac{\partial \tilde{u}}{\partial y} = 0$ or $\frac{\partial \tilde{v}}{\partial x} = 0$, the equations become automatically uncoupled. The resulting equations can thus be written as:

$$a w_i + \frac{\partial}{\partial z} (K_t(z) \frac{\partial w_i}{\partial z}) = r_i(z) \quad i = 1, 2 \quad (21)$$

ii) The use of a power series decomposition to reproduce the vertical variation of variables such as:

$$u_i(z) = \sum_{j=0}^n a_j z^j \quad (22)$$

$$\nu_t(z) = \sum_{j=0}^p b_j z^j \quad (23)$$

$$\tilde{R}es(x, y, z) = \tilde{R}es(x, y) \left(\frac{z_b + z_{tr}}{2} - z \right) \quad (24)$$

$\bar{Res}(x, y)$ represents the extra degree of freedom inserted to adjust the redundant boundary condition since it is mainly associated to neglected terms. The variation of $\bar{Res}(x, y, z)$ with z has been assumed linear (simplest possible solution satisfying the integral condition).

The power series technique is, among other possible choices, one of the simplest and cheapest, presenting advantages over a finite-differences scheme in z . The reason is that with a power series approach an analytical solution is obtained, whose precision and cost are controlled by the number of terms considered allowing an increase of the vertical resolution where desired in line with the quasi-3D philosophy. An additional advantage is that this approach allows recovering expressions comparable to the polynomial solutions \hat{u}/\hat{v} proposed elsewhere in the literature (see De Vriend and Stive, 1987; Svendsen, '87 '88 '89)

iii) Application of the power series approach to the uncoupled ordinary differential equations associated to the new variables w_i . With this, a recurrent relationship is obtained for the w coefficients:

$$a_{i+2} = f(a_{i+1}, a_i) \quad i = 0, 1, \dots, n - 2 \tag{25}$$

These are $n-1$ equations with $n+1$ unknowns. Additionally there are three extra equations arising from the boundary conditions for $\langle \hat{r}_r \rangle_i, w_i$ and $\langle \hat{r}_b \rangle_i$. The missing unknown, needed to balance the number of equations and unknowns is provided by the degree of freedom associated to $Res_i(x, y)$.

This system of equations is only slightly more expensive than existing 1DV models, since if the equations are adequately ordered, the matrix associated to a_i 's unknowns is approximately lower-triangular.

4.-Closure Submodels

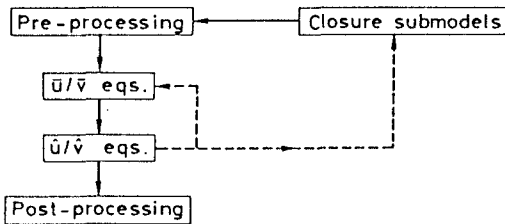


Figure 4.

In this section, some closure submodels will be briefly described, since they are similar to other existing state-of-art models. These submodels, although related, will be separately presented (see figure 4). All closure submodels not mentioned below can be considered identical to those used in De Vriend and Stive (1987).

4.1- Wave Propagation

Wave propagation properties are computed with a pair of equations for the wave number vector \vec{K} , obtained from the Kinematic Conservation Principle, together with a third coupled equation for the amplitude "a", obtained from the energy balance equation (see Yoo, 1986; Yoo and O'Connor, '86a,b). The numerical solution is based on a classical finite differences scheme, with a mesh as schematized in figure 5. This closure submodel reproduces adequately and at reasonable cost wave/current interactions, refraction/diffraction phenomena, and energy dissipation. The current driving terms are considered to be proportional to D (Dingemans et al,1987), which in turn is computed by means of the formula proposed by Battjes and Janssen (1978). The trough level, z_{tr} , is obtained using cnoidal theory.

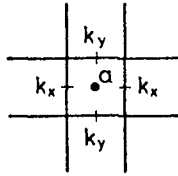


Figure 5.

4.2- Eddy Viscosity

To model $\nu_t(z)$ the simplest possible approach (based on an algebraic model) has been once again selected. This algebraic model (see for a review De Vriend and Kitou, 1990), includes the contributions of breaking waves and currents (influenced by the presence of the waves). The ν_t value satisfies the relation; $\nu_t^2 = \nu_c^2 + \nu_{br}^2$, equivalent to adding the corresponding values of K (turbulent kinetic energy) for waves and currents (Deigaard et al,1986). Following De Vriend and Stive (1987), the vertical profile of $\nu_c(z)$ is assumed constant in the upper half of the middle layer and quadratic in the lower half, although in both cases the profile is modelled as a function of the shear velocity enhanced by wave-effects. The profile of $\nu_{br}(z)$ is assumed constant in the whole middle layer, as a function of $(\frac{D}{\rho})^{\frac{1}{2}}$ (Svendsen,1987).

The evaluation of turbulent stresses remains nevertheless, an open problem that must be solved in a near future, in view of their strong influence on ν_t . The crucial effect of ν_t on the vertical profile of \bar{u} can be easily illustrated by solving the homogeneous equation for w_i , which looks as:

$$\lambda w + \frac{\partial}{\partial z}(K_t(z) \frac{\partial w}{\partial z}) = 0 \tag{26}$$

Table 1 shows a summary of the wide range of possible expressions for $w(z)$.

Tabla 1: Illustration via of homogeneous eq. for w

$K_t(z)$	$\rightarrow \lambda$	$w(z)$
const > 0	> 0	Exponential
const > 0	< 0	Sinusoidal
Linear	=0	logarithmic
quadratic	Varying	Varying (dep. on BC and λ)

It is important to remark that although the order-of-magnitude analysis carried out in

previous sections assumed equal values of the eddy viscosity for the horizontal and vertical directions (see Svendsen, 1988), several authors have proposed different values. As a matter of fact, some references suggest the horizontal ν_{tH} two orders-of-magnitude larger than the vertical ν_{tV} (see De Vriend and Kitou, 1990).

4.3- Boundary conditions

The expression considered for the shear stress $\langle \hat{\tau}_{tr} \rangle$ is very similar to the formulation proposed by De Vriend and Stive (1987).

The shear stress $\langle \hat{\tau}_b \rangle$ is modelled using the formulation of Nishimura (1983), because of its ability to reproduce adequately the directional features of this stress (Yamaguchi, 1988).

To evaluate $\tilde{u}(z_b)$ there are several available options, though none of them appears, at this stage, to be very convincing. Conceptually, it seems that the clearest solution would be to solve the middle and bottom boundary layers in a coupled way, imposing a non-slip condition at the real bottom. This approach, however, as previously indicated presents some additional difficulties. As a starting point, $\tilde{u}(z_b)$ will be derived from the identity $\tilde{u}(z_b) = \bar{u} + \tilde{u}(z_b)$, with \bar{u} obtained from the depth-averaged equations, and $\tilde{u}(z_b)$ given by a wall-law profile:

$$u_i(z) = \frac{u_{*i}}{\kappa} \log\left(\frac{u_{*i} E}{\nu_{mol}} z\right) \quad (27)$$

where:

$$\begin{aligned} u_{*i} &= \left(\frac{\tau_{bi}}{\rho}\right)^{\frac{1}{2}} \\ E &= 9.0 \\ \kappa &= 0.41 \text{ (Von Karman's constant)} \end{aligned} \quad (28)$$

5.-Validation

To begin with, it must be stressed that the calibration/validation processes is far from finished. The present status can be summarized as follows:

- The code for the 1DV model is already developed, but has not been validated yet.
- The two modules (2DH + 1DV) have not been run yet in a coupled way.
- For the time being, results can only be interpreted in a qualitative manner.

In any case, the list of test cases as follows:

2DH CODE (\tilde{u}):

- Normal and oblique incidence on a plane beach (setup, v_i) (Stive and Wind, 1982; De Vriend and Stive, 1987).
- Circulation behind a detached breakwater (Nishimura et al, 1985; Horikawa, 1987).
- Circulation on a variable bottom topography (Noda, 1974; Yamaguchi, 1986).

1DV CODE (\tilde{u}):

- Undertow (Hansen and Svendsen, 1984; Stive and Wind, 1986; Nadaoka, 1986).
- Long-shore Current (Visser, 1984).

The only case here presented is the 2DH nearshore circulation over a symmetric concave topography with normal wave incidence (Noda, 1974; Yamaguchi, 1986). It has been selected because it is a particularly interesting 2DH problem whose bathymetry can be numerically generated. The obtained results (see figure 6 and 7), are qualitatively similar to those reported

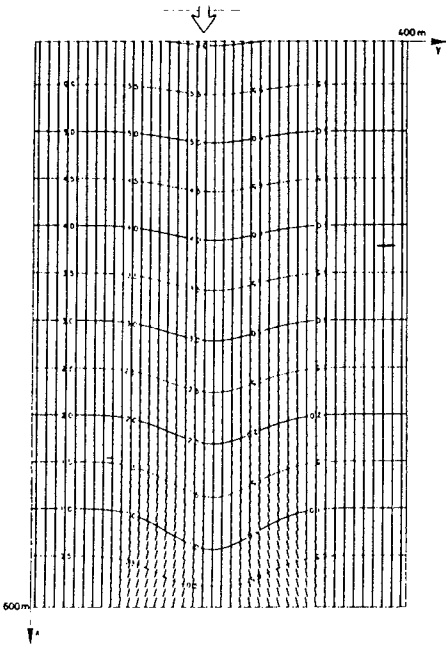
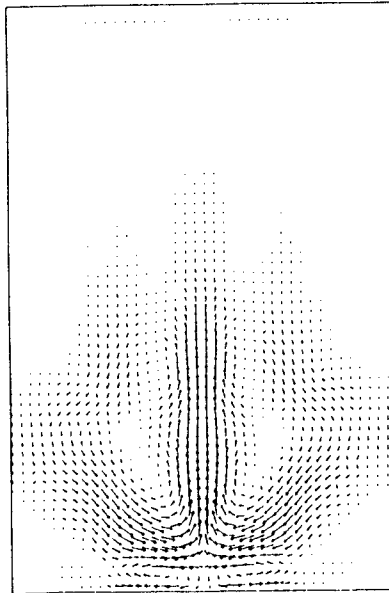


Figure 6
 - Bottom topography and associated wave number vector field for the Noda, 1974 test case.

Figure 7.
 - Current velocities field for the same case of figure 6.



by other authors, showing the presence of two circulation cells near the breaker line, together with another pair of flatter cells near the shoreline.

6.-Conclusions

A newly developed quasi-3D model for nearshore circulation has been presented. The most outstanding features are:

- Same solution domain and boundary conditions for both current-flow components, \vec{u} and \vec{v} (so as to give a consistent physical and mathematical meaning to the algebraic sum of both components).

- Some degree of interaction between \vec{u} and \vec{v} is retained.

- A new treatment for solving the depth-varying component is proposed (allowing local increases in resolution where desired).

- The same grid is used for waves and currents, avoiding thus, spurious effects due to interpolations.

Finally, it's important to point out that a certain number of points remain still open. Among them, the following are worthwhile mentioning:

- **Specific of the model:**

- a) Effects of \vec{u} / \vec{v} interaction.

- b) Effects of G term (Volume flux over z_{tr}).

- c) Effects of introducing the residual \vec{Res} (to accommodate the third boundary condition and other uncertainties).

- d) Effects of \vec{W} evaluated up to z_{tr}

- **General for nearshore circulation code:**

- a) Empirical modelling of wave characteristics inside the surf-zone.

- b) Use and validation of an eddy viscosity model inside the surf-zone.

- c) Effects of solving in a coupled way the middle and bottom boundary layer.

Acknowledgments

The authors wish to express their acknowledgments to the MOPU-PCM for partially supporting this study. They also want to thank CIMNE-UPC for contributing to the financial support of the study.

REFERENCES

- [1] Battjes, J.A. (1974): *Surf similarity*. ICCE, ASCE, pp. 466-480.
- [2] Battjes, J.A. and Janssen, J.P.: (1978) *Energy loss and set-up due to breaking of random waves*. ICCE, ASCE, pp. 569-587.
- [3] Battjes, J.A., Sobey, R.J., Stive, M.J.F. (1988) *Nearshore circulation*, Internal publication, Dep. of Civil Eng., Delft Univ. of Tech.
- [4] De Vriend, H. and Stive, M.J.F. (1987) *Quasi-3D modelling of nearshore currents*. Special issue JONSMOD'86, J. Coastal Eng.
- [5] De Vriend, H.J and Kitou, N. (1990) *Incorporation of wave effects in a 3D current model*. (Submitted to Coastal Eng.).

- [6] Deigaard, R., Fredsoe, J. and Hedegaard, I.B. (1986) *Suspended sediment in the Surf Zone*. J. of Waterway, Port, Coastal and Ocean Engineering, Vol. 112, pp. 115-128.
- [7] Dingemans, M.W., Radder, A.C. and de Vriend, H.J. (1987) *Computation of the driving forces of wave-induced currents*. J. Coastal Eng. JONSMOD'86.
- [8] Hansen, J.B. and Svendsen, I.A. (1984) *A theoretical and experimental study of Undertow*. ICCE, ASCE, pp. 2.246-2.262.
- [9] Horikawa, K. (1987) *Nearshore dynamics and coastal process*. University of Tokio Press.
- [10] Nadaoka, K., Kondoh, T. (1982) *Laboratory measurements of velocity field structure in the Surf Zone by LDV*. Coastal Eng in Jpn, Vol 25, pp. 125-146.
- [11] Nishimura, H. (1982) *Numerical simulation of nearshore circulation*. Coastal Eng. in Jpn, JSCE, pp. 333-337.
- [12] Nishimura, H., Maruyama, K. and Sakurai, T. (1985) *On the numerical computation of nearshore currents*. Coastal Eng. in Jpn, Vol. 28, pp. 137-145.
- [13] Noda, E.K. (1974) *Wave Induced Nearshore Circulation*. Journal of Geoph. Research, vol. 79, number 27.
- [14] Stive, M.J.F. and de Vriend, H. (1987) *Quasi-3D nearshore current modelling: wave induced secondary currents*. Coastal Hydrodynamics, ed. R.A. Dalrymple, ASCE, pp. 356-383.
- [15] Stive, M.J.F. and Wind, H.G. (1982) *A study of radiation stress and setup in the nearshore region*. Coastal Eng., Vol 6, pp. 1-26.
- [16] Stive, M.J.F. and Wind, H.G. (1986) *Cross shore mean flow in the Surf Zone*. J. Coastal Engineering.
- [17] Svendsen, I.A. (1984a) *Wave heights and setup in a Surf-Zone*. Coastal Engineering, Vol 8, pp. 303-329.
- [18] Svendsen, I.A. (1984b) *Mass Flux and Undertow in a Surf-Zone*. Coastal Engineering Vol 8, pp. 347-365.
- [19] Svendsen, I.A. and Hansen, J.B. (1988) *Cross-shore current in Surf-Zone Modelling*. Coastal Eng, Vol 12, pp 23-42.
- [20] Svendsen, I.A., Schaffer, H.A. and Hansen, J.B. (1987) *The interaction between the Undertow and the boundary layer flow on a beach*. Journal Geoph. Res. vol. 92, pp. 11.845-11.856.
- [21] Svendsen, I.A. (1989) *Velocity in combined Undertow and longshore currents*. Coastal Eng, Vol 13, pp. 55-79.
- [22] Visser, P.J. (1984) *Uniform longshore current measurements and calculations*. ICCE, ASCE, pp. 2.192-2.207.
- [23] Wind, H.G. and Vreugdenhil (1986) *Rip current generation near structures*. J. Fluid Mech. 171, pp. 459-476.
- [24] Yamaguchi, M. (1986) *A numerical model of nearshore currents based on a finite amplitude wave theory*. ICCE, ASCE, pp. 849-863.
- [25] Yamaguchi, M. (1988) *A numerical model of nearshore currents due to irregular waves*. ICCE, ASCE, pp. 1.113-1.124.
- [26] Yoo, D. and O'Connor, B.A. (1986a) *Mathematical modelling of wave induced nearshore circulations*. ICCE, ASCE, pp. 1.167-1.681.
- [27] Yoo, D. and O'Connor, B.A. (1986b) *Ray model for caustic gravity waves*. Proceedings 5th. Congress of Asian and Pacific Division, IAHR, Vol. 3, pp. 1-13.

CHAPTER 25

Wave Attenuation on an Offshore Coral Reef

T.A. Hardy¹, I.R. Young², R.C. Nelson², & M.R. Gourlay³

ABSTRACT

The wave climate along the northeastern tropical coastline of Australia is controlled by The Great Barrier Reef (GBR). However, the processes by which the GBR attenuates and transforms waves are little understood. As the first part of an on-going study of the interaction between waves and coral reefs, a field experiment was conducted to study the processes that occur as waves break on an offshore reef and proceed across the reef flat into the lagoon. Eighteen wave, water level, and current measuring instruments were deployed and data for a wide range of tide and wave conditions were collected. Preliminary results for wave attenuation are presented. Results for wave attenuation across the reef show that wave heights on the reef flat and in its lagoon are controlled by the depth of water over the windward reef flat. As the waves travel across the reef flat, the ratio of significant wave height to water depth reduces to a value of 0.40, and the ratio of maximum wave height to water depth reduces to a value of 0.6 to 0.8. In the deeper water in the middle of the reef lagoon both the ratios of significant wave height to the depth over the reef flat and maximum wave height to the depth over the reef flat remain in the above ranges. However, at the mid-lagoon position these results are less general as wave heights inside a lagoon are also dependant on wind speed, direction, and fetch length inside the lagoon.

INTRODUCTION

The Great Barrier Reef (GBR) stretches for approximately 2000 km along the eastern tropical coast of the state of Queensland in northeastern Australia. Much of the GBR is relatively inaccessible as the reefs are usually more than 50 km, and often much farther, offshore. This is particularly the case in the lower two-thirds of GBR which is

1 Lecturer, Department of Civil and Systems Engineering, James Cook University, Townsville, Queensland, Australia

2 Senior Lecturer, Department of Civil and Maritime Engineering, Australian Defence Force Academy, Canberra, ACT, Australia

3 Senior Lecturer, Department of Civil Engineering, University of Queensland, Brisbane, Queensland, Australia

nearer to populated areas. Because of its remoteness and the relatively small population on the tropical coast, visits to the GBR were relatively few until the last few years. However a recent boom in overseas tourists who are eager to enjoy the pleasures of snorkelling and SCUBA diving has initiated improvements in transportation including large wave piercing catamarans that have greatly reduced travel times to the reef.

Even with the fast catamarans, the trip out to the reef can be long (over two hours at some locations) and uncomfortable. Few of the reefs have any land permanently above the water; therefore, tourist operators are eager to provide stable platforms at their reef destinations. Numerous pontoons have been anchored inside the lagoons of individual reefs. Furthermore, a "floating hotel" was located for one year inside the lagoon of one reef. The design and operation of such facilities requires information about waves after they have proceeded from relatively deep water across the reef front and into the reef lagoon. Such information is needed for both normal operational conditions, as well as during tropical cyclones.

Coral reefs have a marked effect on waves as the waves reflect, refract, and break on the almost vertical seaward reef front, and also as the waves travel over the shallow and rough coral surfaces on the shallow reef flats. Despite this obviously important role, very little is known about the physics of wave energy reflection, dissipation, and transmission on coral reefs. There have been few studies in the GBR. A preliminary experiment was conducted by Young (1989) at Yonge Reef, one of the outer barrier ribbon reefs near Lizard Island in the Far Northern Section of the Great Barrier Reef Marine Park. Measurements between the GBR and the mainland coast north of Cairns and outside the GBR near Myrmidon Reef, offshore of Townsville, have been published by Murray and Ford (1983) and Wolanski (1985), respectively. In addition, laboratory experiments by Nelson and Leslighter (1985) have been used as a basis for engineering design. These sources confirm that the GBR is a significant barrier to wave penetration but none of the studies is extensive enough to provide understanding of the processes involved.

Published studies of waves on coral reefs from outside Australia have concentrated on landbacked or fringing coral reefs. Gerritsen (1981) and Lee and Black (1979) report on the wave-induced processes occurring on a fringing reef in Hawaii. However, this work has limited application for the GBR, not only because a fringing reef was studied, but also because the Hawaiian wave climate is dominated by longer period swell unlike the shorter period sea which dominates much of the GBR. Other studies include those by Roberts (1981) in the Caribbean and by Kono and Tsukayama (1980) for Okinawa.

In order to gather data on the interaction of waves and coral reefs, a field study was conducted in 1988 on an offshore coral reef in the Great Barrier Reef region. An extensive set of wave, water level, and current data was collected on the windward edge of the reef. The purpose of this paper is to present preliminary results on wave attenuation from this investigation.

DESCRIPTION OF THE STUDY REEF

John Brewer Reef, located approximately 70 km northeast of Townsville, Queensland in the Central Section of the Great Barrier Reef Marine Park (Figure 1), was selected as the experimental reef primarily because of the logistical support that was available. John Brewer was the site of the floating hotel which was located in the lagoon for just over a year encompassing the duration of the experiment. In addition, there was a daily catamaran service to John Brewer from Townsville. It would have

been difficult if not impossible to conduct the experiment without the availability of transport and a safe and stable haven from rough conditions for both computer equipment and researchers.

The Central Section of the Great Barrier Reef Marine Park is one of the least densely reefed segments of the GBR. John Brewer Reef is on the inner (landward) edge of the reef matrix and is elliptical in shape (6 km by 3 km) (Figure 2), with the major axis approximately normal to the southeast which is the predominate wind direction. The elevation of the seabed surrounding the reef drops rapidly to a depth of approximately 50 m below Lowest Astronomical Tide (LAT). The windward edge of the reef is a continuous reef flat which is 200 to 300 m wide and uniform in elevation at approximately 0.1 m above LAT. This reef flat extends along not only the southeastern edge but wraps around both the southwestern and northeastern ends of the reef extending approximately three-fifths of the perimeter of the reef. The leeward edge of John Brewer is much less continuous, being composed of coral heads or "bommies", which reach just higher than LAT and are separated by sandy patches with depths of 10 to 20 m. Whereas the windward reef edge could be considered to be 100% solid reef, from aerial photographs, the leeward edge is estimated as being approximately 50% solid.

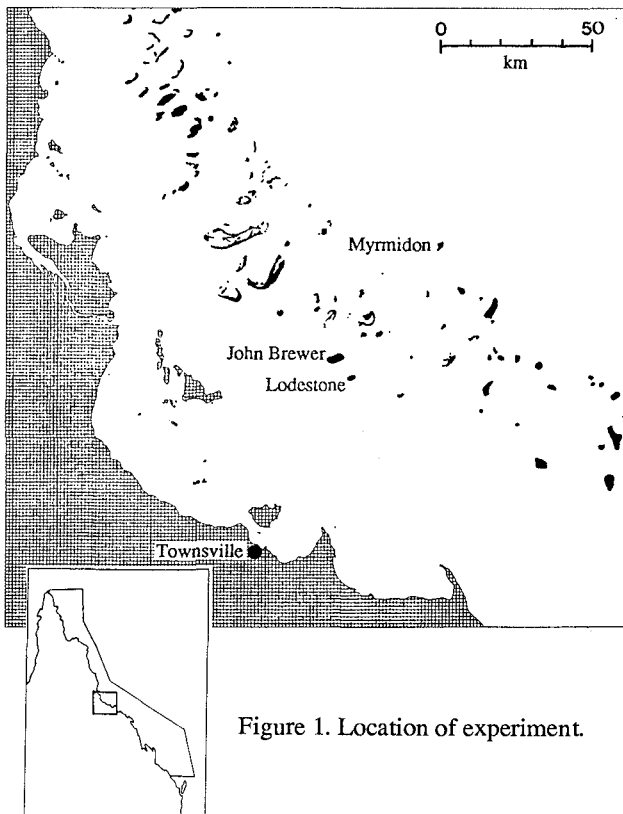


Figure 1. Location of experiment.

The lagoon of John Brewer is mostly sandy bottom and is interspersed with hundreds of medium to large sized bommies most of which remain under water at LAT. The lagoon can be separated into two categories based on depth. The deep lagoon occupies approximately 50% of the area of John Brewer and averages about 10 m in depth. A shallower lagoon provides a transition band of several hundred metres between the windward reef flat and the deep lagoon.

In comparison to reefs in most of the other sections of the GBR, John Brewer is relatively isolated from other reefs. However, being on the inner edge of the reef matrix means that John Brewer seldom receives direct wave energy from seaward of the GBR. The nearest reef in the windward directions (east to southeast) is Lodestone which is approximately 7 km southeast of John Brewer.

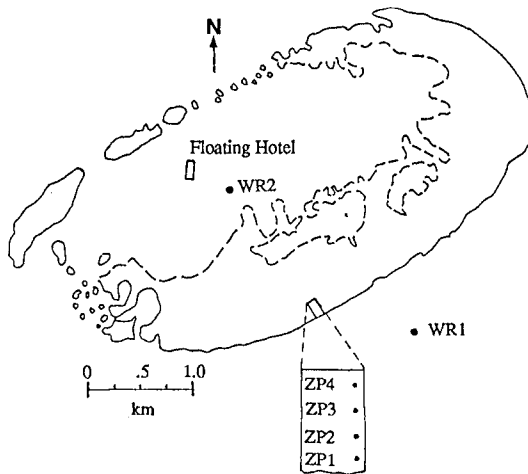


Figure 2. Instrument positions on John Brewer Reef.

A primary criterion in the design of the experiment involved selecting an experimental site that offered a simple geometry so that the physics of the problem could be more easily understood and also so that results from this site could be more easily transferred to other sites. With this in mind, a linear array was envisioned normal to the reef front and parallel to the predominate direction of the wind, which is from the southeasterly direction. It was anticipated that most of the wave attenuation would be caused by wave breaking and bottom friction over the several hundred metres of the relatively shallow reef flat. Therefore, it was decided to concentrate the wave measuring instruments in this zone.

DESCRIPTION OF THE INSTRUMENTS

A combined total of 18 wave, current, tide, and wind measuring instruments were deployed during the experiment. These were made up of two Waverider buoys, four surface piercing wave measuring staffs, six S4 current meters, four tide gauges, one pressure sensing wave gauge, and one anemometer. Since the purpose of this paper is to present wave attenuation data, only the wave measuring instruments will be discussed.

The two Waverider buoys were specially purchased for the experiment. They were imported from Datawell, The Netherlands and were calibrated in Sydney, before being flown to Townsville. Both the buoys were equipped with telemetry and the data signals were captured by a receiver located in the radio room of the Floating Hotel.

The wave measuring staffs used in the field experiment were first proposed by Zwarts (1974). Each staff was six metres long and consisted of two pipes, one inside the other, forming a coaxial cable. Three of the staffs were made of copper pipe, with diameters of 50 mm and 25 mm for the outer and inner pipes, respectively. Slots in the outer pipe allow the movement of water into the space between the outer and inner pipes. The fourth staff was made of aluminium and was of similar design to the copper staffs.

These wave staffs employ a principle commonly used in the telephone industry to detect the location of faults in coaxial cables. The set up of the pipes in a coaxial cable configuration acts as the tuning element of an electronic oscillator. The battery powered electronics located at the head of the pole direct an electromagnetic wave down the pole. This wave reflects off the discontinuity in the dielectric constant at the air-water interface. The length of the unimmersed section of the staff is directly proportional to the period of the oscillation of the electronic signal. The output of the system is a time series of the number of reflections of the electronic signal during a very small time interval.

A battery powered programmable data logger, developed at the Australian Defence Force Academy for the project, controlled the discrete time interval, the length of the time series, and the start of each time series, as well as stored the data. One logger serviced two wave staffs. Approximately 200 time series (100 from each of two staffs) could be stored.

Each of the staffs had to be calibrated so that the counts resulting from the data collection could be translated into water level. Static calibration tests were conducted several times during the design and testing of the loggers in addition to pre- and post-experiment tests. The results were always extraordinarily linear. That is, the recorded points fell on a straight line of water level vs reflection count with a high degree of accuracy. Also, for a given material (i.e. copper or aluminium) the slope of the plotted line was a constant. The slope did not change from one copper staff to another or from one test to another of the same staff. Therefore, the raw counts recorded by the logger could be reduced to water level through a highly accurate linear relationship.

Although the static calibration results are used to convert the instrument counts to water level, it is important to consider the errors that might affect the measurement of the more rapid movement of the water up and down the pole that will occur with waves. At the conclusion of the field work at John Brewer Reef, dynamic tests were conducted on one of the copper staffs. The testing set up was similar to the static tests. The staff was placed in a PVC tube and supported vertically, the tube was half filled with water, and the electronics connected to the logger and computer. But instead of lowering and raising the water level, the staff was moved vertically by the use of a cable and pulley system driven by a variable speed electric motor. An eccentric cam fitted to the flywheel of the motor caused the position of the water surface on the pole to follow a sinusoidal pattern when plotted against time. The response of the system was excellent, the difference between the sinusoidal input signal and the wave staff output was much less than 1%, even with conditions equivalent to wave periods of 1 s and with wave steepnesses near breaking.

Although the primary purpose of the wave staffs was to obtain wave data, tide data is available from the wave records by averaging over a time period much longer than the 3 to 7 seconds of the predominate wave periods. The water level information would give insight into the wave induced water level changes as well as the tide levels at which the wave records were taken.

EXPERIMENTAL SETUP

Figure 2 shows the experimental layout. The primary instruments of the experiment were the two Waverider buoys and the four wave staffs. The "outside" Waverider, WR1, was located approximately 500 m seaward of the reef front in a depth of 50 m. The four wave poles were aligned in a linear array normal to the reef front. The seaward most staff, ZP1, was 27 m from the reef front and staffs ZP2, ZP3, and ZP4 were located at intervals of 42 m, 49 m, and 50 m, respectively. The "inside" Waverider, WR2, was located in the middle of John Brewer lagoon, approximately 1.5 km from the reef edge and in a depth of 12 m.

The deployment of the wave staffs was a formidable task. Not only was the experimental site on the windward edge of the reef, but the site was 70 km from the mainland. Each wave staff was supported by an aluminium tower which was held in place by rope stays attached to metal fence posts that were driven into the reef flat by hand. The towers had to support the wave staffs and logger, but also had to allow access to the top for researcher and portable computer for downloading of data. Each tower was deployed separately during a two day trip. This one-at-a-time deployment allowed for alterations to the design, as the towers were designed especially for the project and the original design was untested. The position of ZP1 was in the breaker zone and this made it difficult to erect the tower, as well as keep it standing. This front tower was toppled during the first strong winds after its initial establishment. However, after re-deployment with extra stays and continual maintenance (the constant pounding of the waves tended to bend the anchor posts) the tower remained functional during the duration of the experiment. All four towers were erected and were well tested in operational conditions several weeks before the deployment of the wave staffs.

The outside Waverider was deployed in early March 1988. The rest of the instruments were deployed during the period of 12-15 August 1988. There were some initial difficulties with the wave poles and it was necessary to reprogramme the loggers and re-deploy the poles during 1-2 September 1988. The wave poles were removed on 15 October 1988. The Waverider buoys were left in position at the end of the main experiment and were removed on 11 July 1989.

DATA ANALYSIS AND RESULTS

A time series containing 2048 samples of water level at a discrete time interval of $\Delta t = 0.3906s$ was collected once an hour from both Waverider buoys. For the wave poles, a time series of water level with 4800 samples or 20 minutes at $\Delta t = 0.25s$ was collected each hour during the first five days of the experiment and every two hours for the rest of the experiment.

The data collection from the six primary instruments was a great success. More than 3000 individual time series were gathered from these main instruments. There were 286 times when all 6 instruments were operating and of these, 254 were when waves were approaching from the East to South directions for which the experiment was designed. Data were collected for a wide range of tide and wind conditions. We believe that this data set is the largest and most comprehensive ever collected in this environment.

Preliminary analysis for wave height attenuation has been completed on the large data set from the six primary wave measuring instruments. A frequency domain analysis was conducted by transforming the time series into frequency space using an FFT. Significant wave height was calculated as $H_{m_0} = 4.0\sqrt{m_0}$, where m_0 is the zeroth moment of the variance spectral density. A time domain analysis has also been conducted using a zero downcrossing technique, and the maximum wave height, H_{max} , was calculated for each wave record. Each of the time series and spectra were plotted. A twenty second time period surrounding the time of the maximum wave in each time series has also been plotted to aid in the discovery of bad data points.

Figures 3-5 contain plots of the time series of wind speed (Myrmidon Reef, see Figure 1), water level, and significant wave height, at three of the wave measuring stations (WR1, ZP4, and WR2) for 5-6 September 1988. During this period wind speed reached 10.8 m/s (21 knots) during a 2 m tidal range. The influence of the tide is apparent in the plots of H_{m_0} , except for the outside Waverider (WR1). At higher water levels, there is a noticeable reduction in H_{m_0} from the outside Waverider, WR1, through the inner most pole, ZP4, and into the inner Waverider, WR2. At lower water levels the reduction is more dramatic. This is certainly the expected result since all the mechanisms that will reduce wave height (reflection, refraction, wave breaking, and bottom friction) have a greater effect at lower water levels.

Figures 6-11 contain the plots of H_{m_0} vs water depth over the reef flat for WR1, ZP1, ZP2, ZP3, ZP4, and WR2, respectively. The plot (Figure 6) for the outside Waverider (WR1) shows no indication of a dependence of wave height on water level. It is not expected that tidal variations in the inter-reefal areas would significantly effect the wave results because these depths average 50 m and the maximum tidal range at John Brewer is less than 4 m. Therefore, any tidal effect on wave height at WR1 would have to result from the effect of other reefs upwind of John Brewer. There would be a lag between tide level and the effect at WR1 caused by the time the wave train took to travel the distance between reefs. However, studying the time series of tide, wind speed and wave height reveals no obvious trends. The lack of stationarity (the wind does not remain constant) complicates a rigorous statistical correlation analysis.

In contrast to Figure 6, Figures 7-11 all show a marked dependence of H_{m_0} on tide level. The envelope is well defined and reasonably linear, especially at lower water levels. Using the relationship, $H_{m_0} = \gamma d$, where d is the water depth over the reef flat and γ is the slope of the upper envelope of the H_{m_0} vs water level relationship, γ reduces from 0.7 at the outermost pole (ZP1) to 0.4 at the innermost pole (ZP4). These results are similar to results from laboratory experiments conducted by Horikawa and Kuo (1967) in which waves broke on the seaward edge of a horizontal shelf fronted by a sloping offshore bottom, a topography similar to that of a coral reef. Values of γ from their experiment decreased from 0.80 at the shelf edge (recall that ZP1 was 27 m in from the reef edge) to 0.35 to 0.40 landward along the shelf.

Figures 7 to 9 for ZP1, ZP2, and ZP3 show, that for water depths greater than 1.5 m, the larger waves do not reach the limiting value corresponding to the envelope determined for water depths less than 1.0 to 1.5 m. However at ZP4 (Figure 10) the larger waves at depths greater than 1.5 m do approach the same limiting envelope as determined for smaller depths. This behaviour suggests that width of the surf zone may be extending past the location of ZP4 during more extreme conditions at higher tide

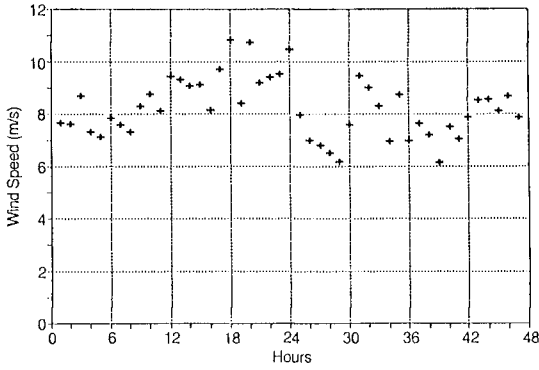


Figure 3. Wind Data, September 5-6 1988.

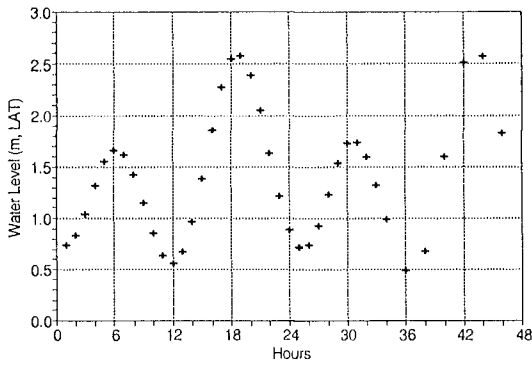


Figure 4. Tide Data, September 5-6 1988.

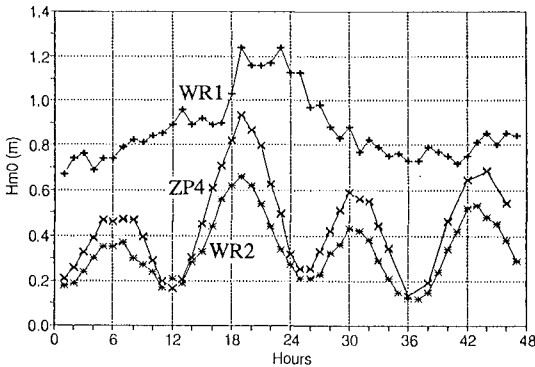


Figure 5. Significant wave heights, September 5-6 1988.

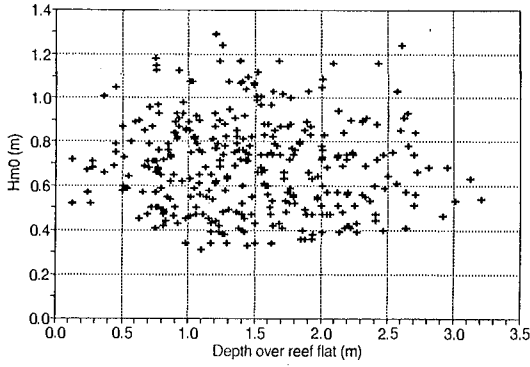


Figure 6. Significant wave height vs water depth over reef, WR1

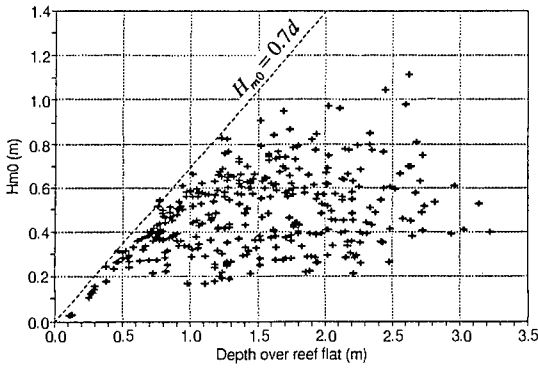


Figure 7. Significant wave height vs water depth over reef, ZP1

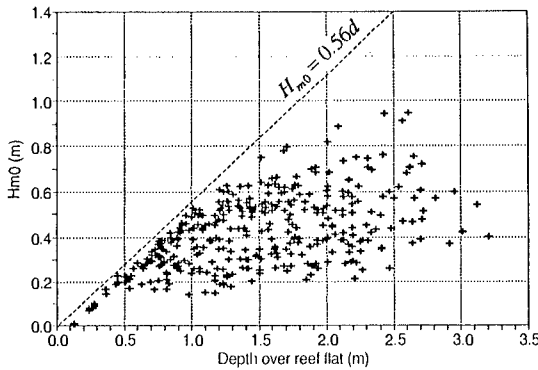


Figure 8. Significant wave height vs water depth over reef, ZP2

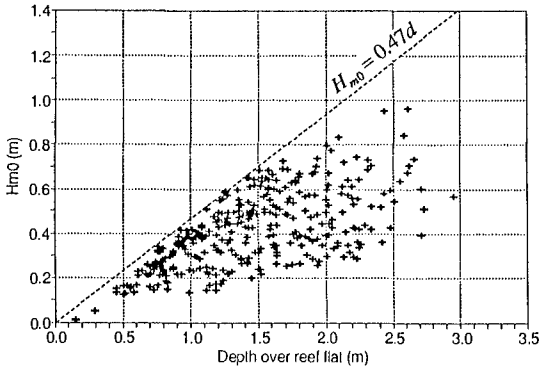


Figure 9. Significant wave height vs water depth over reef, ZP3

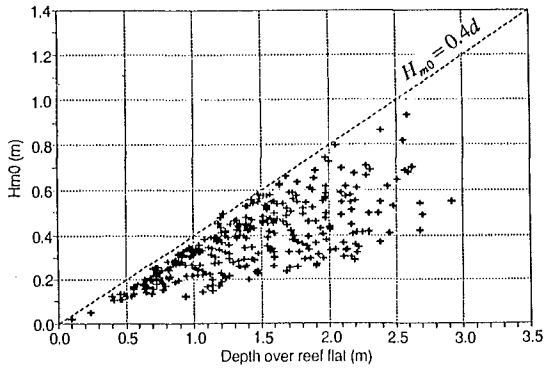


Figure 10. Significant wave height vs water depth over reef, ZP4

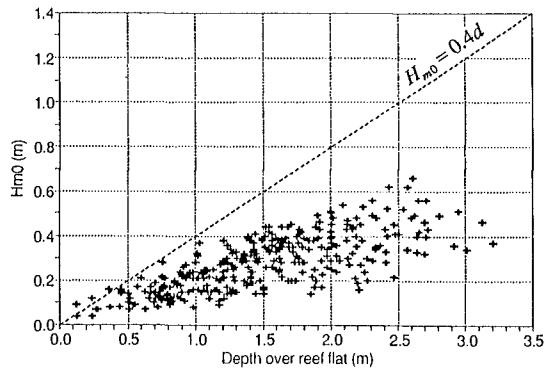


Figure 11. Significant wave height vs water depth over reef, WR2

levels. Visual observations indicated that ZP4 was almost always free of wave breaking activity (especially at lower tide levels), but these observations did not include severe conditions at higher tide levels.

The analysis of the wave height data at WR2 is more complicated than at the wave staffs. Wave heights at WR2 were not limited by the depth at that instrument. Recall that WR2 was located in the middle of the reef lagoon in an average depth of 12 m. Wave heights at WR2 generally are smaller than at ZP4. This may be partially explained by the negative shoaling effect as the waves propagated from the shallow water over the reef flat into the deeper water in the lagoon. Also, although outside energy that reached WR2 was limited by the depth of water over the reef front, this outside energy will not necessarily be that which came past the wave staffs. Furthermore, observations while travelling by boat across the lagoon indicated that there could be significant wave growth during periods of high wind speed. Since the distance that locally generated waves travelled across the lagoon to WR2 varied with wind direction, the results shown in Figure 11 should be a function of local wind speed and direction, as well as water depth over the reef front. Although the upper envelope in Figure 11 is not as well defined as those shown in Figures 7-10, the depth of water over the reef flat is clearly an important control on the amount of wave energy reaching WR2. This conclusion is also strongly suggested in Figure 5, where, as previously mentioned, the wave height and water depth over the reef are strongly correlated.

For higher water levels at WR1, there is a trend for the larger waves to fall short of the linear extension of the envelope defined by the lower water levels. This is similar to the trend noted above for ZP1, ZP2, and ZP3. There is a temptation to suggest that using a linear trend, based on the lower water levels, to predict the larger significant wave heights might result in over-prediction. However, it is expected that the envelope would be more poorly defined at higher water levels, since there are fewer wave heights greater than the depth limiting condition as compared with the lower water levels, and (in the case of WR2) the wind speeds and directions for maximizing the wave height may not have been encountered during the experiment. Fortunately, data were collected outside the main experiment which help define the envelope for WR2 at higher water levels. Cyclone Aivu passed approximately 100 km to the south of John Brewer Reef on the morning of 4 April 1989. At 07:32 the high astronomical tide in Townsville was predicted to be 3.6 m, just 0.1 m short of highest astronomical tide. At 07:00 the largest significant wave heights, $H_{m0} = 2.89\text{m}$ and $H_{m0} = 1.65\text{m}$ were measured at WR1 and WR2, respectively. (The wave staffs were not deployed.) There were no water level measurements at John Brewer Reef, but using an estimate of 4.0 m (adding cyclone induced water levels to the astronomical tide) for the depth of water over the reef front, $\gamma \approx 1.65/4.0 = 0.41$, which agrees well with the estimate of $\gamma = 0.4$ taken from the lower portion of Figure 11.

Plots of H_{\max} vs d for all six wave measuring instruments are shown in Figures 12 to 17. Since the maximum wave height is a single wave as opposed to the significant wave height which characterises the whole of the wave field, the upper envelope of the plots of H_{\max} vs d are not as well defined as those of H_{m0} vs d (all records with values of the ratio of H_{\max} to H_{m0} greater than 2.0 were checked for bad data points). Still, as expected, the dependence on depth is clear for the four wave poles (Figures 13-16) and WR2 (Figure 17). Again there is no apparent dependence of H_{\max} on depth over the reef flat for WR1 (Figure 12).

The ratio of maximum wave height to water depth, (γ_{\max} , reduced from approximately 1.1 at ZP1 to between 0.6 and 0.8 at ZP4. As with significant wave height, the results for WR2 are less linear and not as well defined as for the wave staffs. The maximum wave height recorded at WR2 during cyclone Aivu was $H_{\max} = 2.33$ m at an estimated $d \approx 4.0$ m, which gives $\gamma_{\max} = 0.58$. This indicates that at higher water levels the results for γ_{\max} lie more closely on a linear extension of an estimate of $\gamma_{\max} = 0.6$ taken from the lower portion of Figure 17 than the plotted data would indicate. It should be noted that laboratory data for the maximum height of regular waves on horizontal or very flat bottoms, i.e. conditions similar to reef tops give a maximum value of $\gamma = 0.55$ (Nelson, 1985).

The results from WR2 must be used with caution for application to other locations. Although depth over the windward reef flat is clearly an important and perhaps the most important variable for wave heights inside the lagoon, other site specific variables will also play a role. The width of the reef flat will be important, as will the local wind speed, direction, and the length and depth of the fetch inside the lagoon.

FUTURE WORK

The analysis of the wave data has not been completed. For example, the effect of wave breaking on wave frequency is still to be investigated. As a final product, it is hoped to incorporate knowledge gained on the attenuation and transformation of waves on coral reefs into an improved spectral wave model for both inter- and intra-reefal regions. As the first step in this process the partitioning of the energy losses into the components of refraction, breaking, bottom friction, and reflection will be attempted.

Wave induced water levels and currents are important for both engineering and biological requirements. Observations at John Brewer reef indicate that wave induced currents could significantly affect the circulation in the reef lagoon. The current and water level data have not yet been analysed. However, as part of the overall study of wave and reef interaction, laboratory measurements of wave setup and wave generated currents across an idealised two dimensional reef have been completed and are being prepared for publication.

Another component of the overall research is the study of wave induced processes affecting coral cay formation and stability. The construction of a physical model of a planar coral reef with a cay has been completed in the University of Queensland wave basin. Experiments using this physical model to study the wave-induced water levels and currents on a three dimensional planar reef are on-going.

ACKNOWLEDGEMENTS

This research was sponsored by the Marine Science and Technologies Grant Scheme. The considerable help and support of the Australian Institute of Marine Science is gratefully acknowledged. Many people had a hand in the success of this field experiment. Volunteers at James Cook University, including Ian Dight, Lance Bode, and Lou Mason, have been essential especially in the deployment of the instruments. Two people who must be singled out as providing excellent and essential assistance throughout the experiment are Ray McAllister from the Australian Institute of Marine Science who designed, built, and was foreman for the erection of the towers, and Daryl Winterbottom from the Australian Defence Force Academy who designed and built the data loggers.

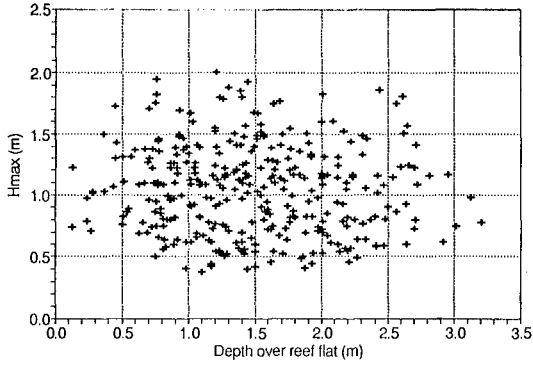


Figure 12 Maximum wave height vs water depth over reef, WR1

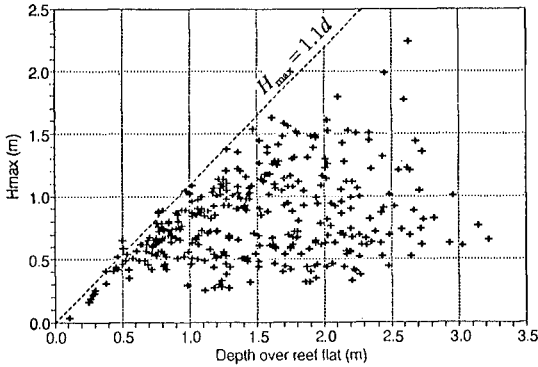


Figure 13. Maximum wave height vs water depth over reef, ZP1

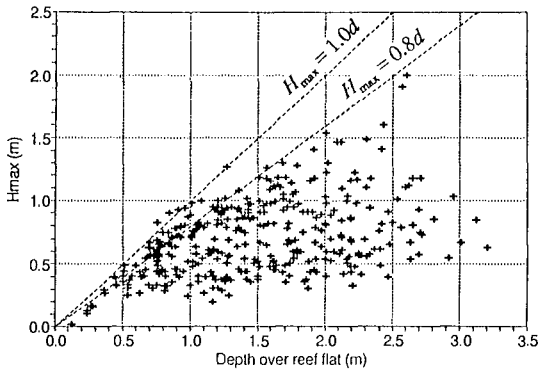


Figure 14. Maximum wave height vs water depth over reef, ZP2

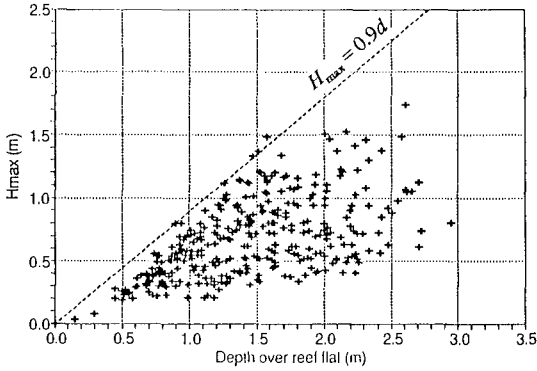


Figure 15. Maximum wave height vs water depth over reef, ZP3

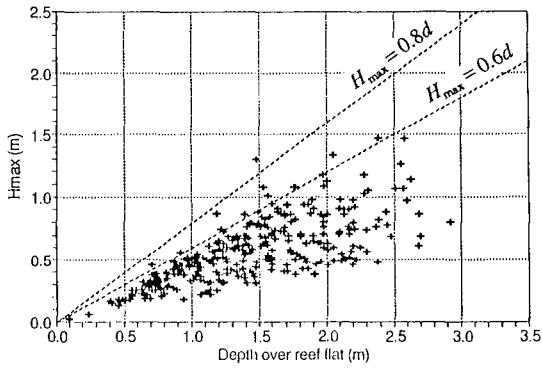


Figure 16. Maximum wave height vs water depth over reef, ZP4

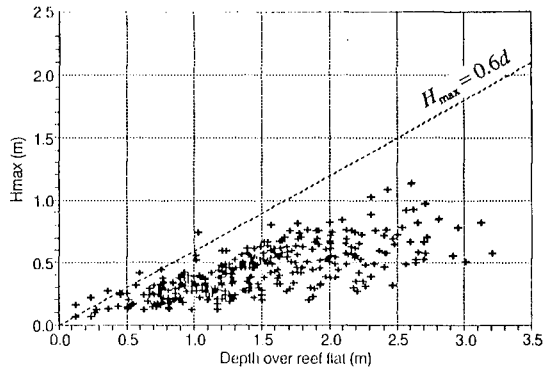


Figure 17. Maximum wave height vs water depth over reef, WR2

REFERENCES

- Gerritsen, F. 1981. "Wave Attenuation and Setup on a Coastal Reef", Look Lab. Tech Report No. 48, Univ. of Hawaii, 416 pp.
- Horikawa, K. and Kuo, C.T. 1967. "A Study of Wave Transformation Inside the Surf Zone", Proc. 10th International Conf. Coastal Eng., ASCE, vol. 1, pp. 217-233.
- Kono, T. and Tsukayama, S. 1980. "Wave Transformation on Reef and Some Consideration on its Application to Field", Coastal Eng. in Japan, vol. 23, pp. 45-57.
- Lee, T.T. and Black, K.P. 1979. "The Energy Spectra of Surf Waves on a Coral Reef", Proc. 16th International Conf. Coastal Eng., ASCE, vol 1, pp. 588-608.
- Murray, R.T. and Ford, L.R. 1983. "Problems in the Analysis of Data for the Assessment of Longshore Sediment Transport: an Example from North Queensland", 6th Aust. Conf. Coastal and Ocean Eng., Inst. Engrs. Aust., pp. 21-26.
- Nelson, R.C. 1985. "Wave Heights in Depth Limited Conditions", Trans. Inst. Engrs. Aust., Civil Eng., vol CE 27, pp 210-215.
- Nelson, R.C. and Lesleighter, E.J. 1985. "Breaker Height Attenuation over Platform Coral Reefs", 7th Aust. Conf. Coastal and Ocean Eng., Inst. Engrs. Aust., vol. 2, pp. 9-16.
- Roberts, H.H. 1981. "Physical Processes and Sediment Flux Through Reef-Lagoon Systems", Proc. 17th International Conf. Coastal Eng., ASCE, vol. 1, pp. 946-962.
- Wolanski, E.J. 1985. "Some Properties of Waves at the Queensland Shelf Break", 7th Aust. Conf. Coastal and Ocean Eng., Inst. Eng. Aust., vol. 2, pp. 61-70.
- Young, I.R. 1989. "Wave Transformation over Coral Reefs", Journal of Geophysical Research, vol. 94, no. c7, pp. 9779-9789.
- Zwarts, C.M.G. 1974. "Transmission Line Wave Height Transducer", Proc. International Symposium on Ocean Wave Measurement and Analysis, New Orleans, ASCE, vol. 1, pp. 605-620.

CHAPTER 26

APPLICATION OF LOGNORMAL TRUNCATED DISTRIBUTION TO PREDICTION OF LONG TERM SEA STATE USING VISUAL WAVE HEIGHT DATA.

Angel González¹ Javier Martínez² Rafael Blázquez³

ABSTRACT

The purpose of this paper is to analyze the behaviour of the lognormal distribution function in wave studies, when visual observations are used to predict the long term wave height distribution.

We are focused our attention on the problem of visual biased samples. For this kind of data the lognormal model does not fit accurately the sample leading to wrong extrapolations.

One possible solution to avoid this problem is to consider the sample as truncated. According to this procedure the distribution function is estimated based only on data higher than the point of truncation.

1.-INTRODUCTION

It is well known that the knowledge of wave parameters, mainly the wave height, is indispensable to carry out projects in maritime engineering, that is the reason why at the present most of the developed countries are trying to improve their measuring networks.

The very best state would be to have a great deal of recorded wave data concerning the area of each particular study, but unfortunately the fact of the matter is that in many cases instrumental data either are not available or do not exist at all, and it is necessary to use other sources of wave data.

-
- 1-CENTRO DE ESTUDIOS DE CARRETERAS, CEDEX, Madrid, Spain.
2-CENTRO DE E. DE PUERTOS Y COSTAS, CEDEX, Madrid, Spain.
3-INSTITUTO EDUARDO TORROJA, CSIC, Madrid, Spain.

Sources of wave data may be considered under the three groups: instrumental, hindcast and visual data.

Instrumental data usually come from wave buoys records and they are preferred because of their reliability and quality, but among their shortcomings are the reduced area of coverage and the limited availability which is often due to commercial restrictions.

The hindcast wave data can be obtained from wind field analysis. Wave heights are estimated from knowledge of the wind speed and fetch, covering large areas. On the other hand hindcasting methods are not very accurate.

The third source is visual data. Visual observations provide additional information about wave parameters, for instance wave direction, and also cover large sea areas. The reliability of visual data has been fully criticized for different reasons. In this paper we are focused our attention on the problem of visual biased samples.

2.-STATEMENT OF PROBLEM

Visual data usually come from ship reports, that is why an important part of them are concentrating on the main shipping routs.

These data bring up some shortcomings due to the observation itself:

- Wave heights reported in adverse climatic conditions tend to be overestimated by the observer (Jardine,1979).

- More ships sail in good weather conditions consequently samples are biased towards lower wave height values.

The result is that these samples lead to wrong extrapolations of the long term wave height distribution when the observations reported as calms are included in the sample.

3.-METHODOLOGY

3.1.-Fundamentals

Since the lognormal distribution function is by

and large considered appropriate for wave studies, Jasper (1956), Darbyshire (1956), Khanna and Andru (1974), the cumulative distribution function (CDF) corresponding to the sample we are dealing with (figure 1) has been plotted in the lognormal probability paper (figure 2).

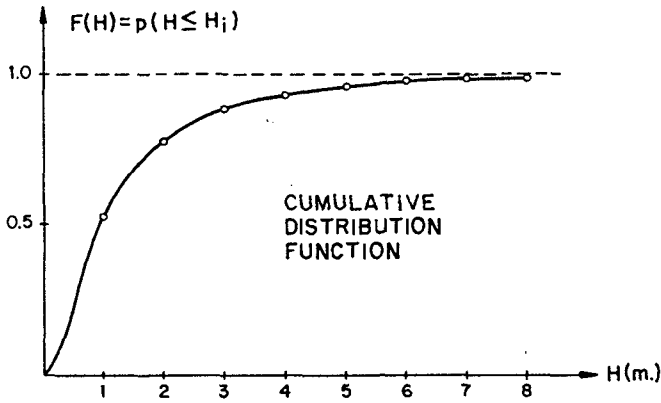


Figure 1

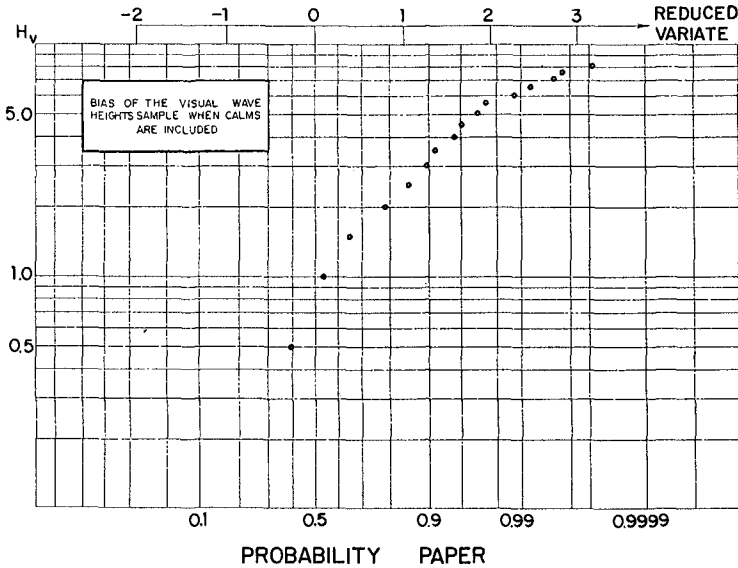


Figure 2

It can be seen that, when the calms are included in the sample, a simple straight line does not fit the points accurately enough.

One possible solution to overcome this problem is to consider the sample as truncated in order to get rid of those data causing a biased sample.

A variable may be such it appears to be lognormal except in that part of the distribution for which the values of the variable either can not occur or are not observed. The distribution of such a variable is said to be incomplete or, more commonly, truncated.

The resulting distribution might then have a shape like figure 3 shows, if the distribution of the original population was lognormal.

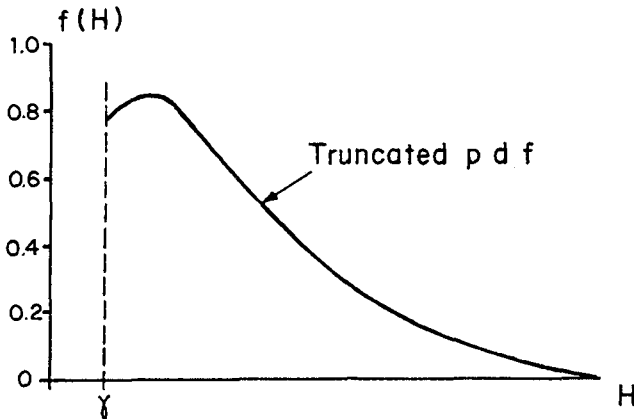


Figure 3

In this case the members of the population below γ have been eliminated. Below γ point there are no values of random variable, and their probabilities are removed.

Censored distributions differ slightly in application in that the total population is present but the exact frequencies are known only up to (or beyond) a certain value.

In these cases the distribution is assumed to

have the probability below (or above) γ lumped at that γ point. (See figure 4).

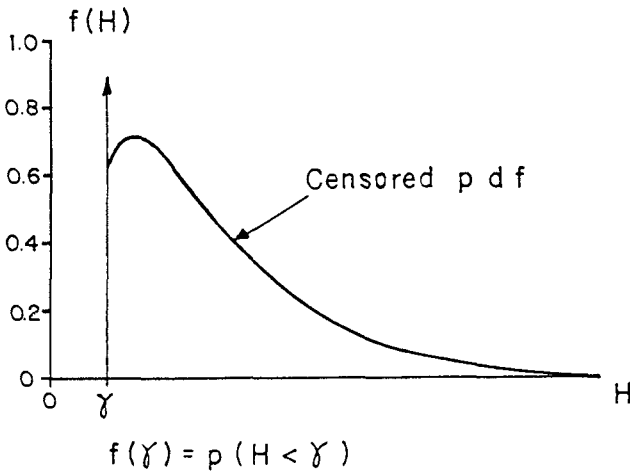


Figure 4

The distribution between truncation and censorship arises from the fact that in the first, the available information is confined to the range (γ, ∞) , whereas in the second a limited knowledge of the variable in the range $(0, \gamma)$ permits consideration of the complete range $(0, \infty)$, (Benjamin, 1981).

In practice truncated samples arise with several types of experimental data in which recorded measurements are available over only a partial range of the variable.

In our case the random variable is the visual wave height and the point of truncation does not physically exist. Obviously there are wave heights below the point of truncation and the low wave heights, even calms, occur in Nature.

Strictly speaking we are dealing with a lower bound censored distribution in which probabilities below a certain value are unreliable. However, if the distribution is considered as truncated and we assume that the point of truncation is known, the problem becomes mathematically tractable.

So, a correct value for the point of truncation has to be chosen and the distribution function will be estimated based only on data higher than the point of truncation.

3.2.-Procedural steps

Figure 5 shows the shape of both untruncated and truncated lognormal density functions.

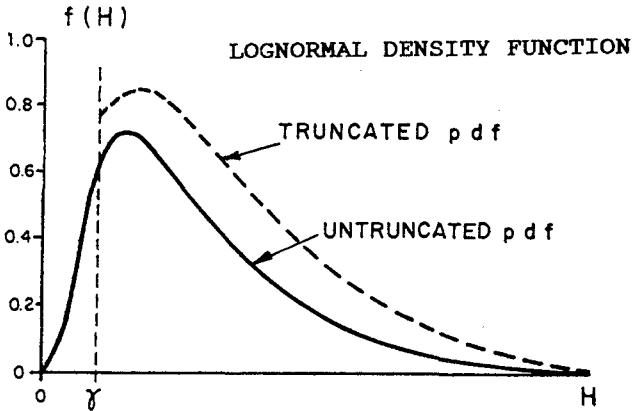


Figure 5

The truncated probability density function only exists above γ point, and obviously its area must equal one, so the PDF is zero up to γ and K times the untruncated probability density function above that point.

Thus, if the original population has a lognormal PDF :

$$f(x) = \frac{1}{x B \sqrt{2\pi}} e^{-1/2 \left(\frac{\ln x - A}{B} \right)^2}$$

then, the truncated PDF may be written as

$$f_t(x) = 0 \quad , \quad x < \gamma$$

$$f_t(x) = K f(x) \quad , \quad x \geq \gamma$$

The probability axiom

$$\int_{\gamma}^{\infty} f(x) dx = 1$$

leads to

$$K = \frac{1}{1 - F(\gamma)}$$

where $F(\gamma)$ is de CDF value at γ point.

Although in principle it would be possible to apply the method of moments to estimate A and B parameters there seems to be no easy way of solving the resulting equations for the first and second sample moments.

Therefore the method of maximun likelihood is a good choice to obtain the estimators of those parameters.

A technique frequently appropriate in maximun likelihood estimation problems is to find the maximun of the loglikelihood function. If the sample is $x_1, x_2, x_3, \dots, x_n$ then the likelihood function of the sample is

$$V = f(x_1) f(x_2) \dots f(x_n) = \prod_{i=1}^n \frac{1}{x_i B \sqrt{2\pi}} e^{-1/2 \left(\frac{\ln x_i - A}{B} \right)^2} \frac{1}{1 - F(\gamma)}$$

and so the loglikelihood function may be written

$$L = \ln V =$$

$$= \sum \ln \left[\frac{1}{x_i B \sqrt{2\pi}} e^{-1/2 \left(\frac{\ln x_i - A}{B} \right)^2} \frac{1}{1 - F(\gamma)} \right]$$

The derivatives with respect to the parameters when set equal to zero, permit to obtain A and B by means of a function which was tabulated by Hald, (Aitchison and Brown, 1957).

4.-APPLICATION OF PROPOSED METHODOLOGY

The application of the truncation method has been carried out using a sample of visual data from the National Climatic Center (Asheville, North Carolina, USA).

The sample concerns the Spanish northern coast, in the Bay of Biscay near Bilbao, exactly from 43.3° to 44.0° North and from 2.5° to 3.5° West.

Figure 6 shows the exact location where the sample was obtained.

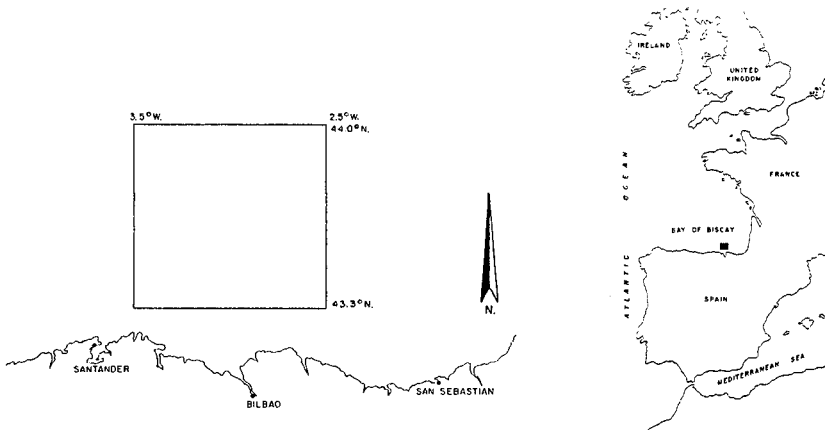
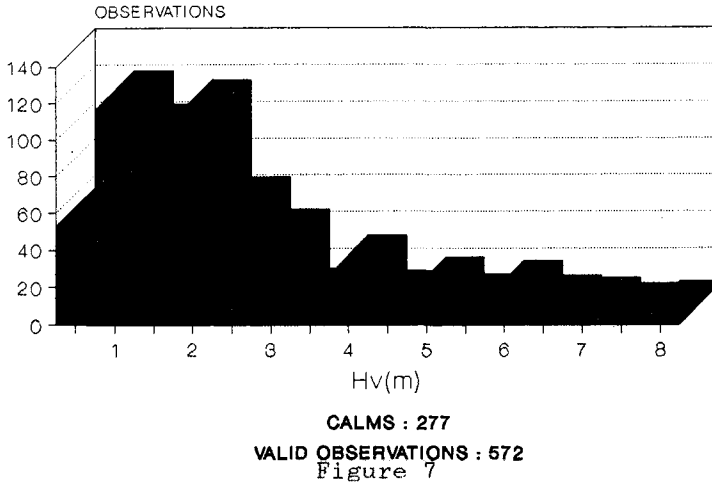


Figure 6

This sample has 572 valid observations and 277 calms. In the histogram (figure 7) the calms are not included and it can be seen how it takes a lognormal distribution shape.



The lowest range of the variable has 53 observations, when the calms are not included, and its probability is almost 0.1, exactly 0.09.

Subsequently the calms have been included in the sample and the cumulative frequencies have been plotted in the lognormal probability paper (Figure 8).

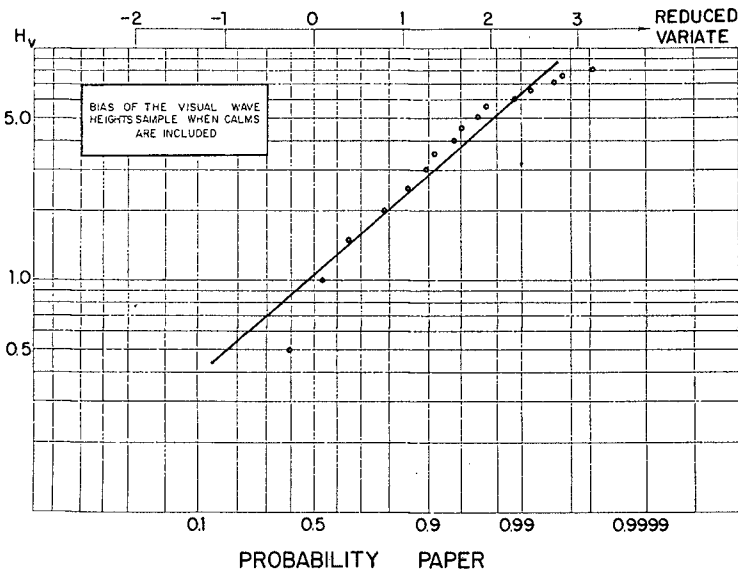


Figure 8

This drawing shows that the probability of the lowest range of the variable is almost 0.4 whereas it hardly was 0.1 when the calms were not included.

At this moment we should consider if the sample is either biased or unbiased. In the second case, there is no problem to include the calms in the lowest range of the variable, but if the sample is biased, as it happens in our present case, a standard fitting of cumulative distribution shows that the straight line does not fit the data points very accurately (see figure 8).

The methodology has been carried out by choosing two different points of truncation, $\gamma = 0.1$ m and $\gamma = 0.5$ m.

In the figure 9 we can see how both truncated distributions are very close whereas the untruncated is quite different.

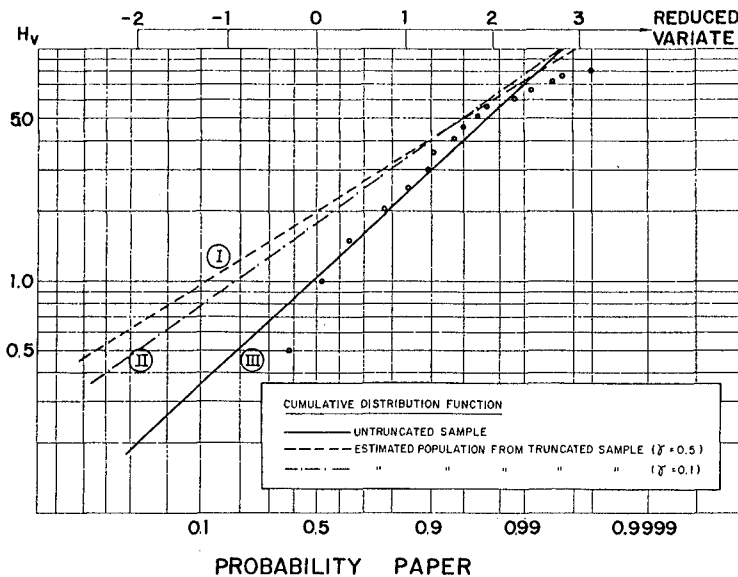


Figure 9

The prediction given by then show how the truncated distributions are in good agreement. Table I represents wave heights versus cumulative probabilities.

TABLE I

Hv(m)	Probability		
	I	II	III
1.5	0.33	0.41	0.67
2.0	0.52	0.59	0.79
2.5	0.67	0.72	0.86
3.0	0.90	0.91	0.92

\ /
good agreement

5. -GOODNESS OF THE METHOD

In spite of the fact that instrumental data are unbiased, a sample collected by a wave buoy has been truncated at the point $\delta = 0.5$ m in order to test the goodness of the truncated distribution.

So, all the data up to 0.5 m have been removed and the truncation method has been applied.

Thus, we have two populations, the original untruncated sample and the truncated sample in which data below 0.5 m have been removed.

The result is that both, truncated and untruncated CDF's are very close. (See figure 10).

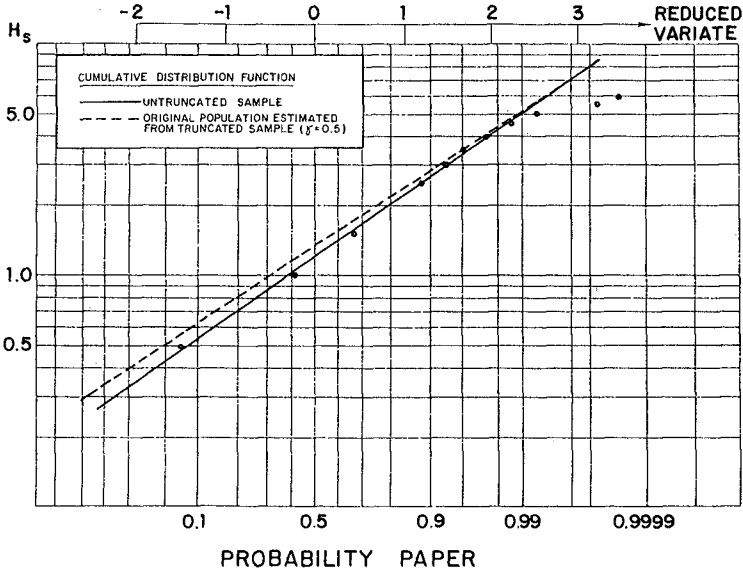


Figure 10

Consequently both of them lead to similar predictions (see Table II).

TABLE II

Hv(m)	Probability	
	Truncated	Untruncated
1.5	0.57	0.64
2.0	0.75	0.80
2.5	0.85	0.88
3.0	0.92	0.93

6.-CONCLUSIONS

1.-In many cases visual wave samples are biased towards lower height values.

2.-The lognormal model, which is usually appropriate for wave studies, does not fit accurately the sample when the calms are included.

3.-For visual wave data the truncation method improves current procedures and avoids wrong extrapolations from observations below the point of truncation.

4.-For instrumental wave data predictions of CDF's of wave heights of both, truncated and untruncated samples, are in good agreement.

5.-The method reported herein is consistent and permits a more effective and accurate use of available visual wave data for coastal and harbour engineering projects.

REFERENCES

AITCHISON, J. and BROWN, J.A.C. (1957), "The lognormal Distribution", Cambridge University Press, London.

BENJAMIN, J.R. and CORNELL, C.A. (1970), "Probability Statistics and Decision for Civil Engineers", Mc Graw-Hill, New York.

DARBYSHIRE, J. (1956), "The Distribution of Wave Heights", Dock and Harbour Authority, May.

JARDINE, T.P. (1979), "The Reliability of Visually Observed Wave Heights", Coastal Engineering, Vol.3, pp. 33-38.

JASPER, N.H. (1956), "Statistical Distribution Patterns of the Ocean Waves and of Wave-Induced Ship Stresses and Motions, with Engineering Applications", Soc. Nav. Archit. Mar. Eng. Trans, 64.

HALD, A. (1949), "Maximun Likelihood Estimation of the Parameters of a Normal Distribution which is Truncated at a Known Point", Skand. Aktnar.Tidskr.32,119.

KHANNA, J. and ANDRU, P. (1974), "Lifetime Wave Height Curve for Saint John Deep, Canada", Proc. Ocean Wave Meas. Anal. 1. pp 301-319.

CHAPTER 27

EXTREME WAVES AND WAVE COUNTS IN A HURRICANE

Rodney J. Sobey¹, Bruce D. Chandler² and Bruce A. Harper³

Abstract

Estimates of wave conditions within a storm event must recognize the variability of wave conditions during the storm and not just the peak conditions. A methodology is presented for the estimation of the probability distribution of the maximum wave in a storm event and the wave count in the same storm event. The predictions are compared with field observations of wave conditions in tropical cyclones from Australia's North West Shelf.

1. INTRODUCTION

The spatial and temporal complexity of wave conditions within a hurricane must be succinctly summarized for the benefit of designers of offshore structures. Conventional limit design is commonly based on a characterization of the wave climate in terms of the maximum wave height and the associated period, whereas fatigue analysis utilizes a wave count distribution.

The classical analysis of wave record statistics involves an explicit assumption that the typical 20 minute wave record is one realization of a stationary stochastic process. Analysis leads to a prediction of the probability density function for the maximum wave in the record, whose mean value is highly sensitive to both the intensity of the sea state and the duration adopted for comparative purposes (e.g. 20 minutes or 3 hours or whatever).

In a storm event however, the sea state is not a stationary stochastic process. Reasonable estimates of maximum wave conditions and wave counts must recognize the slowly-varying evolution of the sea state. Attention must also be given to the restrictions imposed by gravitational instability, especially in

¹Professor of Civil Engineering, University of California, Berkeley, CA 94720, USA

²Riedel & Byrne Consulting Engineers P/L, Mount Lawley, W.A. 6050, Australia

³Senior Ocean Engineer, Woodside Offshore Petroleum P/L, Perth, W.A. 6000, Australia

regard to estimates of maximum wave conditions which likely approach limiting conditions.

A methodology is presented for the estimation of the probability distribution of the maximum wave in a storm event and the wave count in the same storm event. The predictions are compared with field observations of wave conditions in tropical cyclones from Australia's North West Shelf.

2. WAVE OBSERVATIONS DURING TROPICAL CYCLONES

Tropical cyclone (or hurricane or typhoon) conditions are extreme and mercifully infrequent. The intensity is often maintained over a relatively large time and spatial scale and large wave conditions are experienced even at sites relatively distant from the storm track. The available data base of wave observations during hurricane conditions is not extensive. This is a consequence of the rarity of the meteorological event and the erratic nature of storm paths, together with the instrument survival threat posed by such extreme conditions when they do materialize.

In many cases, the measured record includes only a handful of standard 20 minute records during the life of the storm, which generally extends over several days. Where the record is relatively comprehensive, it is often a distant or minor storm. Among the most comprehensive records available are those collected by Woodside Offshore Petroleum on Australia's North West Shelf. The better records are not especially extreme when measured against the brief segment recorded during the infamous Hurricane Camille. They nonetheless loom large in the local wave climate on the North West Shelf and are sufficiently large to characterize expected response patterns.

Wave data from Tropical Cyclone Victor is representative of North West Shelf conditions. TC Victor in early March 1986 reached a minimum central pressure of 930 mb and the storm track was 200 km from the North Rankin data site at closest approach. The standard measuring program of 20-minute records every 6 hours was increased to continuous recording for over two days during the closest approach of the storm. Despite some small data loss, the overall record is comprehensive and provides an excellent illustration of the wave conditions at the North Rankin site during the storm. The water depth at the data site is 125 m, essentially deep water for the measured wave conditions.

The mean rms wave height H_{rms} evolution of the separate 20-minute records is shown in Figure 1. The evolution in the wave height follows the hydrograph pattern of river elevations or flows during flood (i.e. storm) conditions. There is a rapidly rising limb towards a peak, followed by a rather more slowly falling limb to ambient conditions.

There is no such clear trend in the mean zero-up-crossing period τ_z evolution of the separate 20-minute records, which is shown in Figure 2. Also included on Figure 2 are the one standard deviation error bands, which are relatively wide. The change in period during the storm is apparently quite small, which conflicts with the expectation of wind-generated waves in more uniform wind conditions. This somewhat unexpected feature of wave conditions in

hurricanes had previously been noted (Sobey and Young 1986) in the context of peak period. It is also predicted by the Sobey and Young discrete spectral model of wind wave generation in hurricanes.

3. PREDICTIVE CAPABILITY OF RAYLEIGH THEORY FOR STATIONARY RECORDS

Before attempting to accommodate time-varying wave conditions in an analysis of extreme waves and wave counts, it is useful to review the predictive capability of existing approaches to the prediction of extreme waves and wave counts in stationary sea states.

The familiar approach follows Longuet-Higgins (1952) in representing the probability distribution of wave heights within a stationary sea state by the Rayleigh distribution, with probability density function (PDF) and cumulative distribution function (CDF) respectively as

$$\begin{aligned} f(R) &= 2Re^{-R^2} \\ F(R) &= 1 - e^{-R^2} \end{aligned} \quad (3.1)$$

where $R = H/2(2m_0)^{1/2}$ is the normalized wave height. Comparisons of field data provide reasonable visual support for this distribution for near-average wave conditions, with the data being sparse and scattered for the more extreme waves.

The wave count, the number of waves n in a stationary record of N waves whose height equals or exceeds a given height, is related to the exceedence probability as

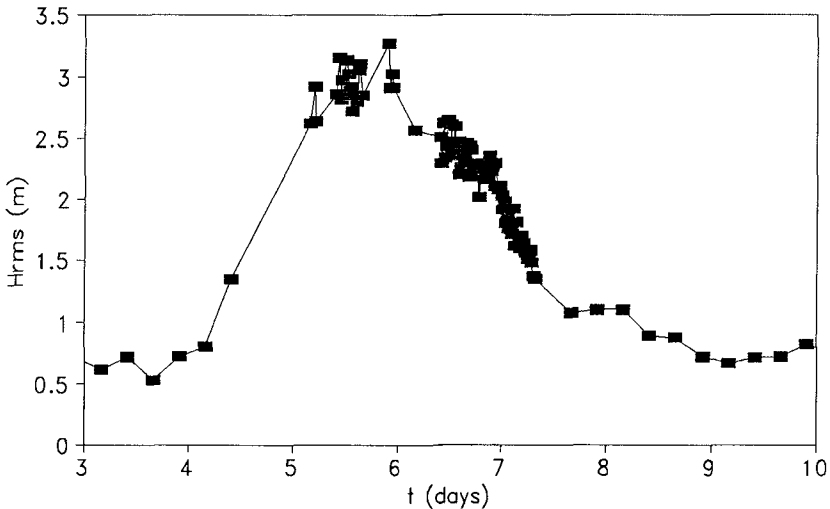


FIGURE 1
Rms wave height evolution in TC Victor during March 1986.

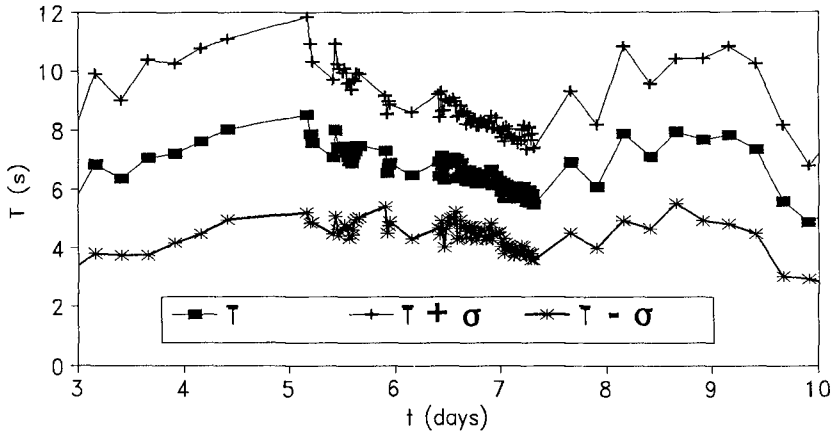


FIGURE 2
Zero-up-crossing period evolution in TC Victor during March 1986.

$$n(R) = N[1 - F(R)] \quad (3.2)$$

The present writers are not aware of any published comparisons of this wave count distribution with field data. Its reliance however on the Rayleigh distribution leads to the expectation that there would be reasonable visual support for near-average waves with a wider scatter for more extreme waves.

Assuming that consecutive waves are independent, the CDF for the maximum wave in a stationary record of N waves is (Longuet-Higgins 1952)

$$F_{\max}(R) = F^N(R) \quad (3.3a)$$

The PDF for the maximum wave in a stationary record of N waves is then

$$f_{\max}(R) = \frac{d}{dR} F_{\max}(R) = Nf(R)F^{N-1}(R) \quad (3.3b)$$

where $f(R)$ and $F(R)$ are the PDF and CDF for individual wave heights in the record. This distribution for the maximum wave in a stationary record of N waves is strongly dependent on N , as shown in Figure 3 for N values from 10 to 1000, a value of 100 being typical of a 20-minute record. The distribution remains relatively wide for all wave counts in the expected range. The Rayleigh distribution has been included in Figure 3 for perspective.

Evaluation of this prediction with field data is complicated by the sparse data set that is available, each 20-minute data set for example yielding only a single observation for wave counts of order 100. Estimates of the distribution are not available and observations of the maximum wave can only be compared with the mean of the distribution, estimated as (Longuet-Higgins 1952)

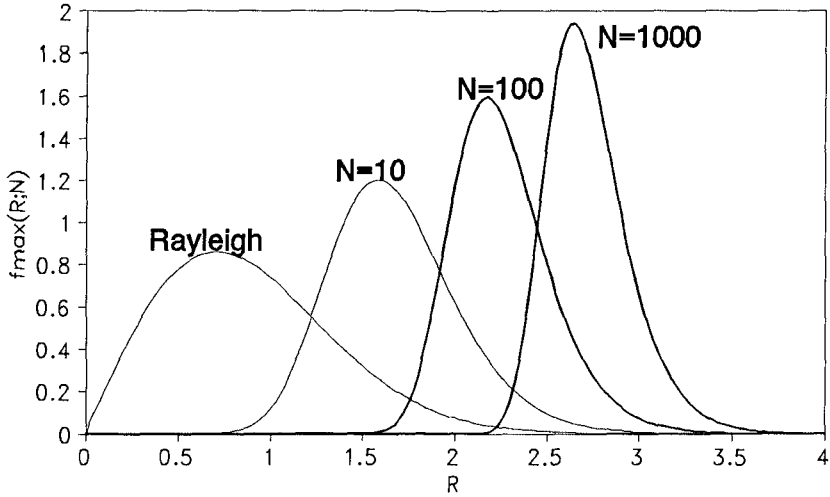


FIGURE 3
Rayleigh-theory predictions of maximum wave in N waves.

$$\bar{R}_{\max} = \int_0^{\infty} r f_{\max}(r) dr \approx \ln^{1/2} N + \frac{\gamma}{2} \ln^{-1/2} N \quad (3.4)$$

where γ is Euler's constant.

The predictive capacity of Equations 3.3 and 3.4 was evaluated from the TC Victor data set introduced as Figures 1 and 2. Each of the separate 20-minute records was considered as representative of a stationary sea state. The theoretical estimate of the expected value of H_{\max} for each segment was computed from Equation 3.4 and the Rayleigh distribution, using the measured H_{rms} and N . This was compared with the measured H_{\max} in Figure 4. Although the distribution of H_{\max} is relatively wide, the TC Victor data base nonetheless identifies a systematic overprediction of order 10% by the "Rayleigh" theory.

As this systematic overprediction would likely feed through to predictions of extreme waves in a complete storm, alternatives to the Rayleigh distribution were reviewed. Field observations of amplitude distributions in intense seas have been represented as the empirical Weibull distribution

$$F(\rho; \alpha, \beta) = 1 - \exp\left(-\frac{8}{\beta} \rho^{\alpha}\right) \quad (3.5)$$

where $\rho = H/H_{\text{rms}}$ and H_{rms} , α and β are the parameters defining the distribution. α and β parameter values of 2 and 8 respectively retrieve the Rayleigh distribution. Forristall (1978) estimates 2.13 and 8.42 from Gulf of Mexico data and Krogstad (1985) typically estimates 2.38 and 12.9 from North

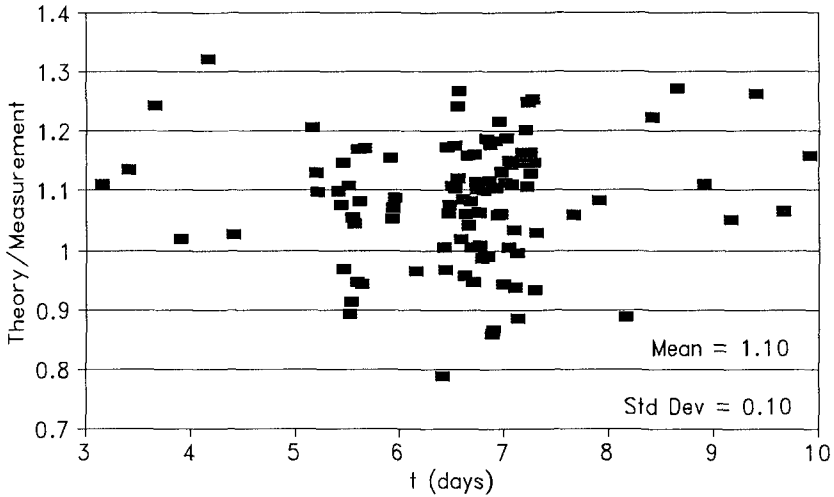


FIGURE 4

Comparison of Rayleigh-theory predictions of maximum wave in N waves and measurements for stationary 20-minute record segments from TC Victor.

Atlantic data. Interestingly, these empirical distributions bracket the Rayleigh distribution in the high amplitude tail, the Forristall distribution predicting a lower probability for the higher waves in the sea state and the Krogstad distribution a higher probability. These distributions are based on theoretical arguments or data that are biased towards average conditions in an albeit intense sea state. Confidence levels in the tail are not especially high, although it is the region of potentially major concern in consideration of maximum wave conditions in a storm. Estimates of the PDF for the maximum wave in N waves follow directly from Equation 3.3b and are compared with the "Rayleigh" estimate in Figure 5. As expected, they bracket the Rayleigh estimate. An estimate based on the Krogstad distribution would increase the overprediction to approximately 20%. An estimate based on the Forristall distribution would marginally decrease the overprediction but not significantly.

Also included on Figure 5 is an estimate based on a tabulated $f(R)$ established by Sobey (1990). This estimate is based on a mean Jonswap spectrum and was established by simulation of one hundred separate realizations of wave sequences, each containing in excess of one thousand waves. This methodology gives reasonable recognition to the more extreme waves in the stationary sea state. The tabulated $f(R)$ used together with Equation 3.3 still appears to predict high, though it does come rather closer to the TC Victor than any of the other predictors.

4. A SLOWLY-VARYING SEA STATE

Wave conditions in a stationary sea state may be characterized by the probability distribution of wave amplitudes, represented by either the probability density function $f(a)$ or the cumulative distribution function $F(a)$, where $a = H/2$ is the wave amplitude and H is the wave height. In a slowly-varying seas state, this distribution can be expected to vary slowly with time, the cumulative distribution function, for example, becoming $F(a;t)$.

Within a short interval of time Δt , the wave count is $\Delta t/\tau_z(t)$ where $\tau_z(t)$ is the mean zero-crossing period in the short interval. Under the assumption (Longuet-Higgins 1952) that consecutive wave in the interval are independent, the cumulative distribution function for the maximum wave amplitude in the interval is

$$F_{\max}(a;t) = [F(a;t)]^{\Delta t/\tau_z(t)} \tag{4.1}$$

A storm event from time A to time B may be characterized as J consecutive intervals of duration Δt_j centered at time t_j such that

$$B - A = \sum_{j=1}^J \Delta t_j = \int_A^B dt \tag{4.2}$$

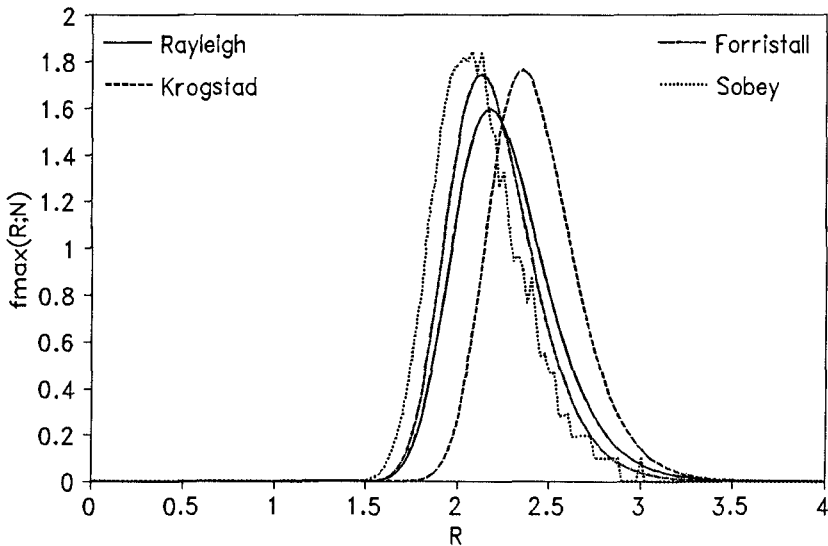


FIGURE 5
Alternative predictions of PDF for maximum wave in 100 waves.

If wave conditions between consecutive intervals remain independent, then the cumulative distribution function for the maximum wave in the storm event is (Borgman 1970)

$$\begin{aligned} F_{\max}(a) &= [F(a; t_1)]^{\Delta t_1/\tau_z(t_1)} [F(a; t_2)]^{\Delta t_2/\tau_z(t_2)} \dots [F(a; t_j)]^{\Delta t_j/\tau_z(t_j)} \\ &= \exp \int_A^B \frac{1}{\tau_z(t)} \ln F(a; t) dt \end{aligned} \quad (4.3)$$

The wave count distribution with amplitude within a storm event will be termed $n(a)$ to distinguish it from the total mean wave count N within the storm event. The number of waves in the short interval Δt that exceed a is

$$\Delta n(a) = [1 - F(a; t)] \frac{\Delta t}{\tau_z(t)} \quad (4.4)$$

For a storm of duration $B - A$, again characterized as J consecutive intervals of duration Δt_j centered at time t_j , the number of waves in the complete storm that exceed a is

$$\begin{aligned} n(a) &= \Delta n_1(a) + \Delta n_2(a) + \dots \Delta n_j(a) \\ &= \int_A^B \frac{1}{\tau_z(t)} [1 - F(a; t)] dt \end{aligned} \quad (4.5)$$

where it has again been assumed that wave conditions between consecutive intervals remain independent.

The time history of the local zero-crossing period and the local cumulative distribution function remains to be specified.

5. PARAMETERIZATION OF SEA STATE IN A STORM EVENT

Statistical summaries (such as significant wave height and zero-crossing period) of measured wave conditions at a fixed site during a storm event typically display the familiar "hydrograph" shape from surface water hydrology. This is especially true of significant wave height and the equivalent rms amplitude. There is a base wave amplitude (analogous to the base flow in surface water hydrology) that is sustained at a reasonably constant level well before and after the storm event. The storm hydrograph itself has the familiar asymmetric rising and falling limbs. In some cases, the time scale of the falling limb is significantly longer than the rising limb but in other cases it is more nearly equal. Storm duration above the base level may range from several hours to several days. The zero-crossing period might be expected to follow a similar trend, although the variation would be much less dramatic. Figures 1 and 2 provide examples of measured hydrographs during TC Victor.

A suitable schematic form for these hydrographs would be

$$q(t) = q_b + \frac{1}{2}(q_p - q_b) \left[1 + \cos\left(2\pi \frac{t - t_p}{4\tau_*}\right) \right] \tag{5.1}$$

where q represent either the local rms wave amplitude $a_{rms}(t)$ or the local zero-crossing period $\tau_z(t)$. The subscripts b and p identify the base and peak hydrograph levels respectively, t_p is the time of the hydrograph peak and τ_* is the half life of the hydrograph, as sketched in Figure 6. Separate half lives of the rising and falling limbs (τ_1 and τ_2) are defined such that the storm event extend from time $t_p - 2\tau_1$ to time $t_p + 2\tau_2$. The finite duration of the storm event is a significant feature in defining the expected maximum wave conditions. A truncated Gaussian form would be equally appropriate.

The adopted form for the local cumulative distribution function has been based on the review of predictive capabilities for extreme waves in stationary conditions, summarized in Figure 4 and 5. It is apparent from these figures that all of the viable alternatives resulted in overprediction of the maximum wave in a typical 20-minute record. The tabulated distribution of Sobey (1990) gave the best agreement with measured data and has been used in the present analysis. It must be anticipated that the overprediction apparent in the stationary sea state analysis will be at least equally apparent in the slowly-varying sea state analysis.

Finally, in recognition of the upper bound imposed by gravitational instability, an empirical modification to the probability distribution was introduced to restrict the maximum wave conditions to the limit wave. The adopted local cumulative distribution function is

$$F(\rho) = \begin{cases} F'(\rho) & \text{for } \rho < \rho_m \\ 1 & \text{for } \rho \geq \rho_m \end{cases} \tag{5.3}$$

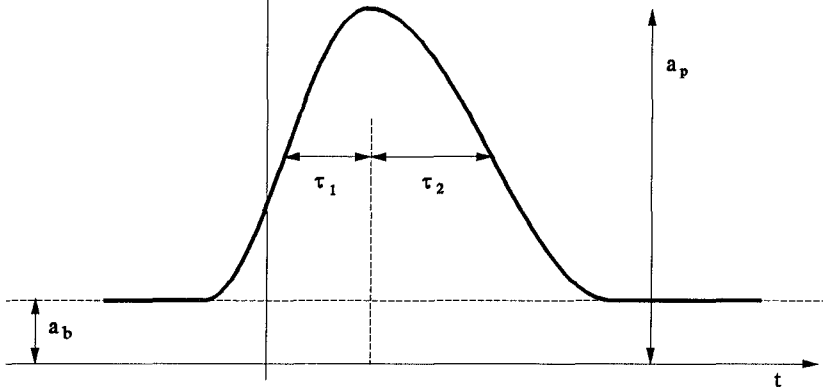


FIGURE 6
Schematic storm hydrograph.

where $F'(\rho)$ is the tabulated CDF for a stationary sea state and $\rho_m = H_m/(2a_{rms})$, H_m being the limit wave height appropriate for the local wave period, water depth and current. This expedient has the additional benefit of limiting the significance of the tail to the local population distribution.

The limit wave height has been defined by interpolation from the Williams (1985) tables. This limit wave cutoff should have only marginal influence on the wave count and will likely influence the maximum wave distribution only near the hydrograph peak of the more intense storms.

6. WAVE CONDITIONS IN A HURRICANE

In application to tropical cyclones or hurricanes on Australia's North West Shelf, it was noted in Figure 2 that measured time histories of zero-crossing periods did not change significantly during the storm. Accordingly, the zero-crossing period was assumed to be constant for the duration of the storm. With the rms wave amplitude following the cosine hydrograph, the standard deviate of the local probability distribution becomes

$$\rho(t) = \frac{A}{B + \frac{1}{2}(1-B)(1 - \cos s)} \quad (6.1)$$

where $A = a/a_p$, $B = a_b/a_p$ and $s = 2\pi(t - t_p)/4\tau_*$.

The cumulative distribution function for the maximum wave in the storm then becomes

$$F_{\max}(A) = \exp\left[\frac{N}{\pi}\Phi(A, B, \alpha, \beta, A_m)\right] \quad (6.2)$$

where N is the mean wave count in the complete storm, $A_m = (H_m/2)/a_p$ and Φ is the dimensionless definite integral

$$\Phi = \int_0^\pi \ln F(s; A, B, \alpha, \beta, A_m) ds \quad (6.3)$$

In like manner, the wave count becomes

$$n(A) = \frac{N}{\pi}\Psi(A, B, \alpha, \beta, A_m) \quad (6.4)$$

where Ψ is the dimensionless definite integral

$$\Psi = \int_0^\pi [1 - F(s; A, B, \alpha, \beta, A_m)] ds \quad (6.5)$$

Both integrals were evaluated numerically.

7. COMPARISONS WITH FIELD DATA

Tropical cyclone Victor in February-March 1986 was a reasonably intense storm, having a minimum central pressure of 930 mb. The peak and base rms wave heights were 3.16 m and 0.70 m respectively and the mean wave count in the hydrograph was 62000. The predicted probability density function for the maximum wave in the storm is shown in Figure 7. The distribution is moderately wide. The maximum wave measured during the storm was 8.04 m, which corresponds to a H_{max}/H_p of 2.53. There is order of magnitude agreement between this prediction and the single measurement during TC Victor. It would appear however that the maximum wave in the storm is over-predicted by the theory, as was anticipated with the adoption of the tabulated CDF. The adoption of the Forristall, Rayleigh and Krogstad distributions for the CDF further widens the gap between theory and measurement. A similar trend resulted from the only other storm in the North Rankin data base (TC Ilona) with near-continuous records during the storm.

Figure 7 compares the measured and predicted wave count distributions. Agreement is good for the more frequent waves of average height but the trend at the more extreme wave heights is again over-predicted by the theory.

8. CONCLUSIONS

A methodology has been established for the prediction of the PDF for the maximum wave in a storm event. The maximum wave in the storm appears to

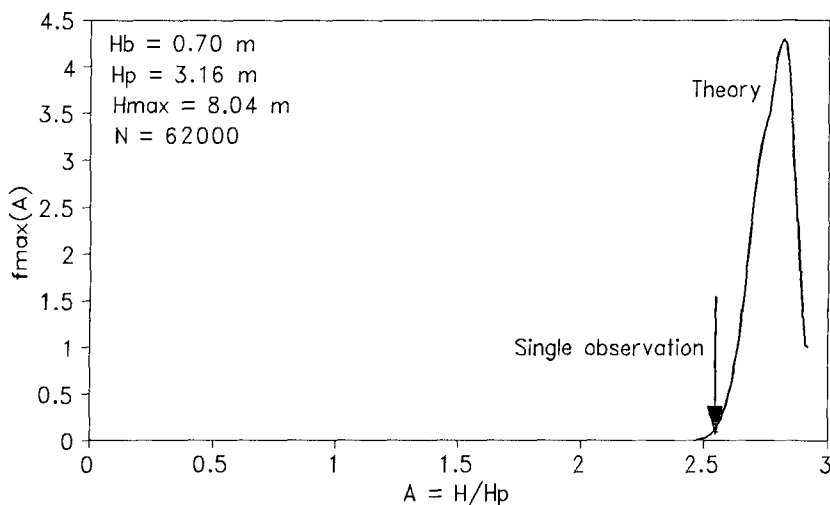


FIGURE 7
Predicted PDF for maximum wave in TC Victor.

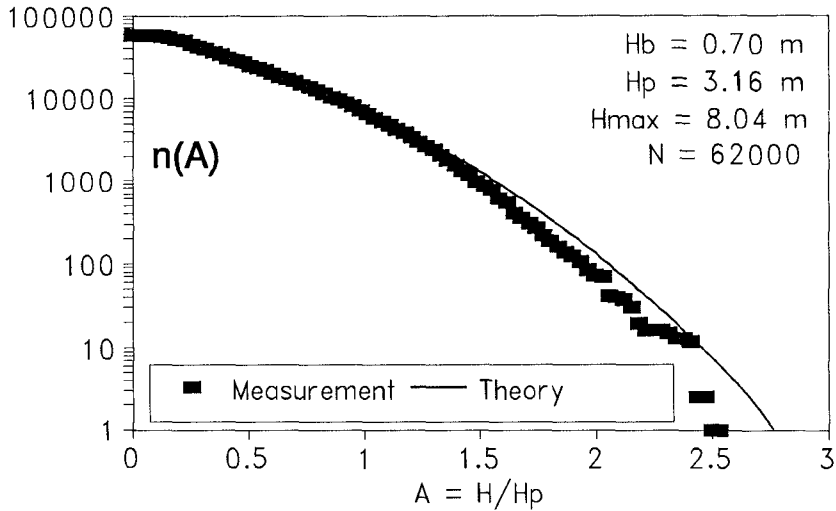


FIGURE 8
Predicted and measured wave count in TC Victor.

be marginally over-predicted for hurricane waves on Australia's North West Shelf. Almost exactly the same systematic trend is identified in the prediction of the maximum wave in the (stationary) 20-minute record segments making up the complete data base.

A parallel methodology for the wave count in the same storm event provided good agreement with field data for average wave heights but again over-predicts at the more extreme waves.

ACKNOWLEDGEMENTS

The authors wish to thank the North West Shelf joint venture participants and the management of Woodside Offshore Petroleum Pty. Ltd. for permission to publish this paper. The participants in the North West Shelf joint venture are Woodside Petroleum Ltd. (through subsidiaries), Shell Development (Australia) Pty. Ltd., BHP Petroleum (North West Shelf) Pty. Ltd., BP Developments Australia Ltd., Chevron Asiatic Ltd. and Japan Australia LNG (MIMI) Pty. Ltd.

REFERENCES

- Borgman, L.E. (1970). Maximum wave height probabilities for a random number of random intensity storms. *Procs., 12th ICCE, Washington, D.C., ASCE*, 1:53-64.
- Forristall, G.Z. (1978). On the distribution of wave heights in a storm. *Journal of Geophysical Research*, 83:2353-2358.

- Krogstad, H.E. (1985). Height and period distributions of extreme waves. *Applied Ocean Research*, 7:158-165.
- Longuet-Higgins, M.S. (1952). On the statistical distribution of the heights of sea waves. *Journal of Marine Research*, 11:245-266.
- Sobey, R.J. (1990). The distribution of wave heights and periods in a stationary record. Manuscript under review.
- Sobey, R.J. and Young, I.R. (1986). Hurricane wind waves - A discrete spectral model. *Journal of Waterway, Port, Coastal and Ocean Engineering*, ASCE, 112:370-389.
- Williams, J.M. (1985). *Tables of Progressive Gravity Waves*. Pitman, Boston.

CHAPTER 28

A PREDICTION MODEL OF IRREGULAR WAVE RUN-UP HEIGHT ON COASTAL STRUCTURES

Cheong-Ro Ryu¹ and Hong-Yoon Kang²

ABSTRACT

The characteristics of irregular wave run-up on coastal structures are discussed related with spectrum shape and grouping parameters of incident waves using the results of 200 cases of hydraulic model experiments. It is clarified that wave run-up is affected by the effects of the irregularity of incident waves and the slope configurations of structures.

A statistical model to estimate the run-up height from the incident wave properties is proposed considering 90 % confidence intervals. Also, the simple probability distribution model of irregular wave run-up height is developed and proved to be useful to the design of coastal structures.

1. INTRODUCTION

Irregular wave run-up is an important factor for the design of coastal structures. However, the published data on the irregular wave run-up are fairly limited and hardly applicable to the design (e.g., Bruun, 1985 ; Ahrens , 1988). It has been emphasized that the characteristics of run-up waves according to the wave grouping or spectrum shapes of the incident waves should be clarified, and there is necessity for developing a prediction model to estimate the irregular wave run-up height (e.g., Kobayashi and Cox, 1990).

In this study, the characteristics of irregular wave run-up on rough permeable coastal structures have been investigated through a series of model experiments to develop a statistical prediction model of irregular wave run-up height on the structures. Among the many governing factors on wave run-up, the effects of the irregularity of incident wave and the slope configurations of structures are studied and discussed in priority in order to improve the predictive capability of the model. To verify the applicability of the model,

¹ Visiting Prof., Dept. of Civil Engineering, University of Delaware, Newark, DE 19716, USA

Professor, Dept. of Ocean Engineering, National Fisheries University of Pusan, Pusan 608-737, KOREA

² Research Associate, Dept. of Ocean Engineering, National Fisheries University of Pusan, Pusan 608-737, KOREA

some comparative discussions are made using some reported experimental data and / or some conventional formulas for run-up height estimation.

MODEL EXPERIMENTS AND DATA ANALYSIS

Important governing parameters on wave run-up related with irregularity of ocean waves can be summarized as follows with conventionally considered parameters in equation(2).

$$\frac{R_{u1/n}}{H_{1/n}} = f \{ \overline{j(\cdot)}, Q_p(\varepsilon), \xi_{1/n}, \dots \} \quad (1)$$

$$\frac{R_u}{H} = f \{ h_c/h_o, h_o/L_o, d/l_a, H/h_o, \theta(\text{slope type}), k, i, \dots \} \quad (2)$$

where, R_u is the run-up height, H the incident wave height, $\overline{j(\cdot)}$ the mean run-length of a wave group, Q_p the spectrum peakedness parameter, ε the spectrum width parameter, ξ the surf similarity parameter, subscript $1/n$ means the $1/n$ significant value, h_c/h_o relative crest height, h_o/L_o relative water depth, d/l_a relative roughness, θ the slope angle, k the permeability, i the sea bottom slope.

Assuming the conditions of permeable deep-water breakwater, infinite crest height, constant roughness, and bottom slope $i = 1/40$, a series of model experiments are carried out to discuss only the effects of eq.(1) and slope type. In the experiments, A 2-dimensional wave flume with 30m length, 0.7m width and 0.95m height is used. A separator in the middle of the wave flume is set up in order to measure both the incident and run-up waves simultaneously as shown in Fig. 1. The incident wave height is measured by a capacitance type wave gauge, and the run-up height is measured by the run-up measuring gauge which is set along the surface of structure slope. Model structures which are made up of core and revetment layer have the uniform slopes of $1/3$, $1/2$, and $1/1.5$ and composite slope. Irregular waves are simulated by the impulse response function method. Using 3 kinds of Pierson-Moskowitz spectrum and 3 kinds of Neuman spectrum with different peak frequencies f_p , 200 cases of experiments with variation of the power level of wave generator are carried out. More details on experimental conditions are described in Ryu and Sawaragi(1986).

The flow for analyzing the statistical characteristics of both incident and run-up waves is shown in Fig.2. Individual incident and run-up waves are defined by zero-upcrossing method. The data of incident waves and run-up waves recorded in an analog data recorder were digitized at 0.05 sec interval for 20 minutes by the A-D transducer and are analyzed by the wave by wave and the spectral analysis method. The real time comparative analysis between the incident and the run-up waves was also applied for the analysis of grouping characteristics of irregular wave run-up.

STATISTICAL CHARACTERISTICS OF THE INCIDENT WAVES

The characteristics of the spectral shape, the statistical wave height/ period distributions and wave grouping properties used

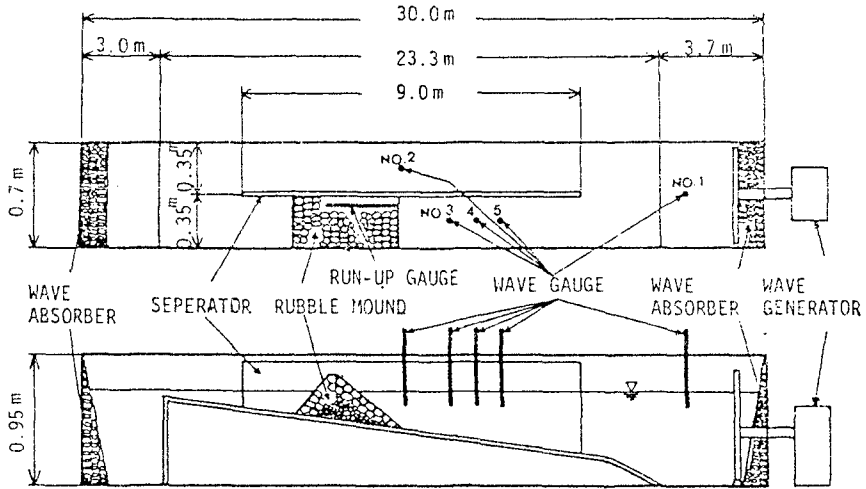


Fig.1. Layout of test flume and model structure.

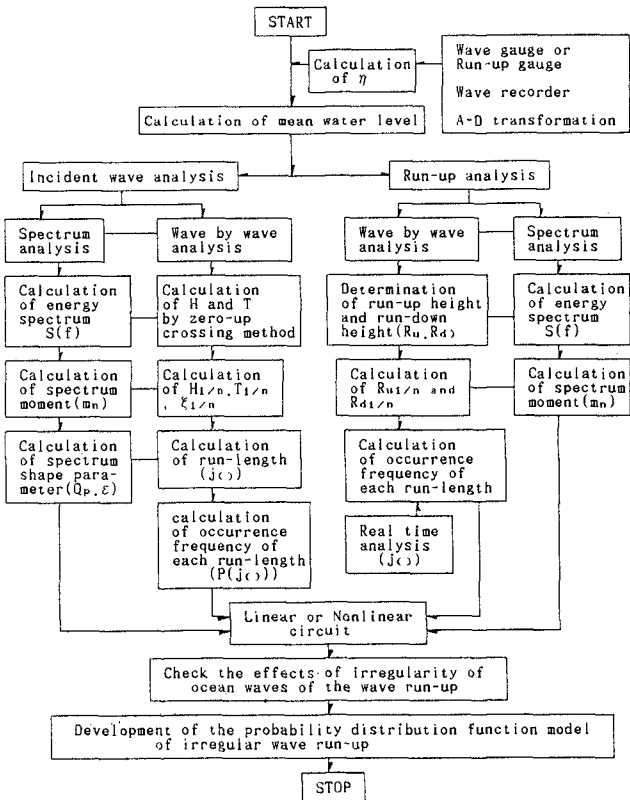


Fig.2. Flow for the analysis of incident and run-up waves.

in the experiments were compared with those of random ocean waves for the reliability of the study.

Wave height and period are very important factors in wave-structure interaction such as wave run-up. An example of the joint distribution of relative wave height (H/\bar{H}) and period (T/\bar{T}) of experimental waves is shown in Fig. 3. In the figure it can be seen that wave period (T/\bar{T}) increases with the increase of wave height in the smaller waves ($H < \bar{H}$), but wave periods are distributed around $T/\bar{T} = 1.1$ in the wave field higher than arbitrary critical value ($H > \bar{H}$). Therefore, the relations among the representative wave periods can be expressed as follows:

$$T_{1/3} \cong T_{1/10} \cong T_{\max}$$

It is identified from the above results that joint distribution of wave height and period has a good agreement with the analyzed results of field data by Goda(1985). In other words, it can be stated that the simulated irregular waves used in model tests represent random ocean waves fairly well.

Fig. 4 shows the distribution of spectral peakedness parameter Q_p by means of the irregular wave data used in model tests compared with field data at Utsira. It can be understood from the figure that most of ocean waves exist mainly in the range of spectral peakedness parameter $1.0 \leq Q_p \leq 3.0$ and that the distribution of Q_p from model tests is also satisfactorily simulated compared with irregular waves in the ocean. Where Q_p have been defined as following equation by Goda (1985).

$$Q_p = \frac{2}{m_0^2} \int_0^{\infty} f S^2(f) df$$

where the spectral moments is

$$m_n = \int_0^{\infty} f^n S(f) df$$

f the frequency, $S(f)$ the energy density of the frequency f .

RUN-UP CHARACTERISTICS OF IRREGULAR WAVES

Grouping Characteristics of Run-up Waves

The grouping characteristics of run-up waves related with the incident wave grouping is important for the stability analysis of rubble mound structures and overtopping control measures on the design of coastal structures (Ryu and Sawaragi, 1986).

One typical example of time histories of incident waves and their corresponding run-up waves is phenomenally shown to examine the cross-correlation in Fig. 5. In the experiment, both incident wave data and run-up wave data are obtained at the same time. In the figure, it can be known that the higher run-up wave groups appear under the the higher incident wave groups attack on steep slopes.

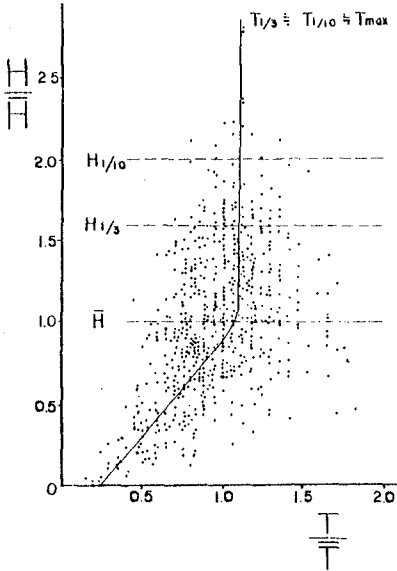


Fig.3. Joint distribution of wave height(H/\bar{H}) and wave period(T/\bar{T}).

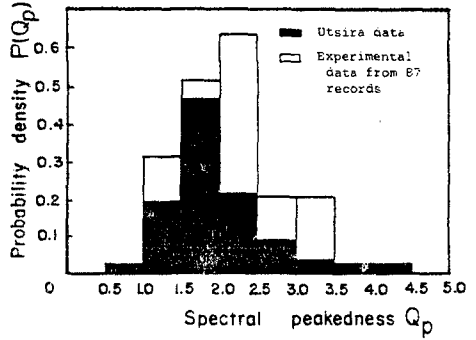


Fig.4. Occurrence probability $P(Q_p)$ of spectral peakedness parameter Q_p .

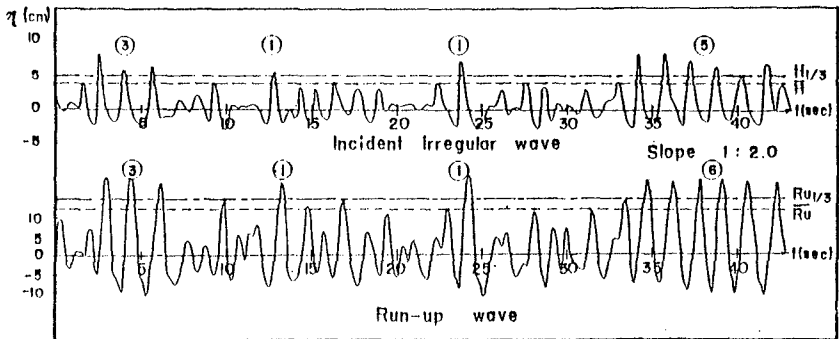


Fig.5. Time histories of incident and run-up waves.

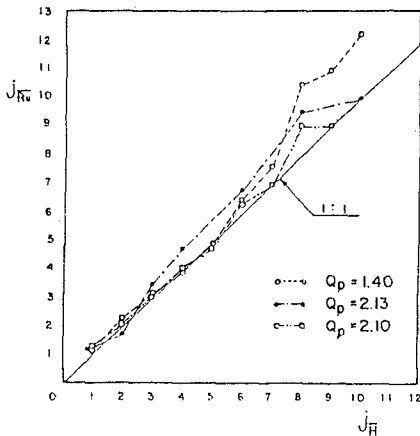


Fig.6. Relations between the run-lengths of higher incident waves ($j_{\bar{H}}$) and those of run-up waves ($j_{\bar{R}u}$).

Where the number inside the circle indicates the run-length.

Fig. 6 shows some examples of the analyzed results for 3 different cases of Q_p by the real time analysis technique. In the figure, it is shown that the run-lengths of run-up waves ($\overline{j_{R_u}}$) exceeding mean run-up height $\overline{R_u}$ are nearly the same or a little larger than those of incident waves ($\overline{j_H}$) exceeding mean wave height \overline{H} . This means that foregoing broken waves or back washes do not affect so much on the motion of following waves on steep, permeable and rough slopes contrary to the results on gentle slopes (Sawaragi and Iwata, 1984).

The Effects of the Irregularity of Ocean Waves on the Wave Run-up

Fig.7 shows the relative run-up heights of irregular waves according to spectrum shape parameters Q_p and ϵ , respectively. It can be understood from the figure that the statistical run-up height becomes larger with the decrease of spectral peakedness parameter Q_p and with the increase of spectral width parameter ϵ as the corresponding tendency with the above illustrated Q_p . This tendency is more remarkable in higher run-up heights ($R_{u1/10} / H_{1/3}$, $R_{u1/3} / H_{1/3}$) than in mean run-up height ($\overline{R_u} / H_{1/3}$).

The results of this study are similar to those of Van Oorschot and D'Angremond(1968) on steep slopes but opposite to those of Mase et al.(1983) on gentle slopes. Therefore, it can be stated that the characteristics of wave run-up heights due to spectrum shapes reverse at the boundary of structure slope 1/4 or 1/5.

In order to analyze the wave grouping effects on the wave run-up, various definitions which can represent the grouping effects are used such as the mean run-length of higher waves ($\overline{j_{H_c}}$), that of ξ^* ($\overline{j_{\xi^*}}$) and that of conditional ξ^* of higher waves ($\overline{j_{(H_c) \xi^*}}$) satisfying the resonance condition on the slope (Ryu and Sawaragi, 1986).

As the same tendency with Fig.7, the extreme run-up heights decrease with increasing the mean run-length of $\overline{j_{H_c}}$, $\overline{j_{\xi^*}}$ and $\overline{j_{(H_c) \xi^*}}$ as shown in Fig.8, Fig.9 and Fig.10. This is remarkably apparent with increasing of slope angle.

A Prediction Model of Irregular Wave Run-Up Heights

Fig. 11 shows the statistical distribution of irregular wave run-up heights on various slopes. In the figure, the distribution of irregular wave run-up heights provides a good approximation to the Rayleigh distribution on the slope steeper than 1 on 2, but it is overestimated in higher run-up on the slope milder than 1 on 3. It seems mainly due to the permeability effects but more detail experiments are required to discuss the above mentioned mechanism.

It is not possible that the irregular wave run-up height can be directly estimated from the incident wave characteristics in the above mentioned distribution. Therefore, it is necessary to derive the relations between surf similarity parameter $\xi_{1/n}$ and normalized irregular wave run-up height $R_{u1/n}/H_{1/n}$.

Non-dimensional run-up heights of irregular waves with respect to surf similarity parameter $\xi_{1/n}$ are shown in Fig. 12. Where solid

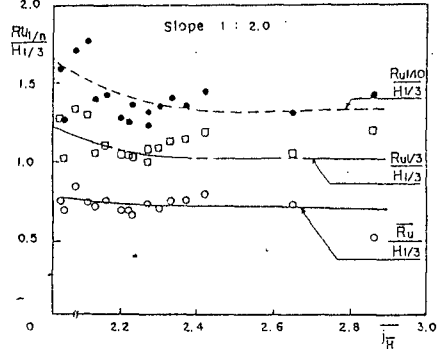
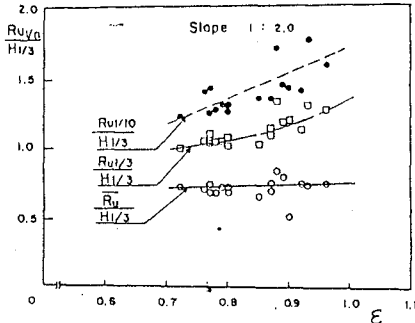
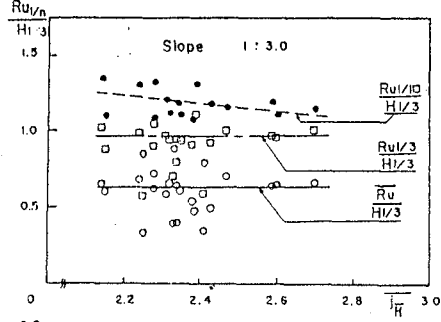
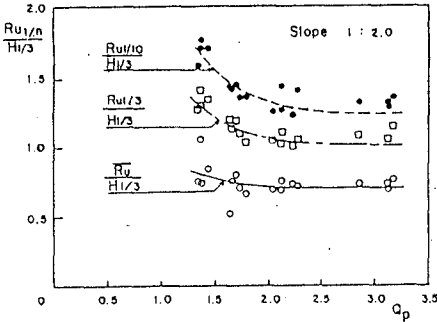


Fig.7. Spectral shape effects on wave run-up heights.

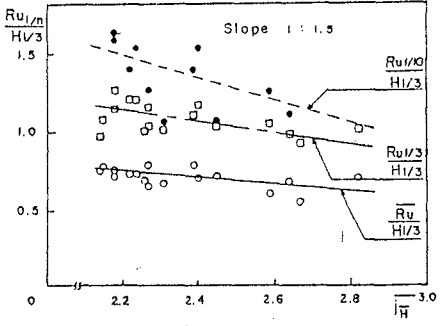
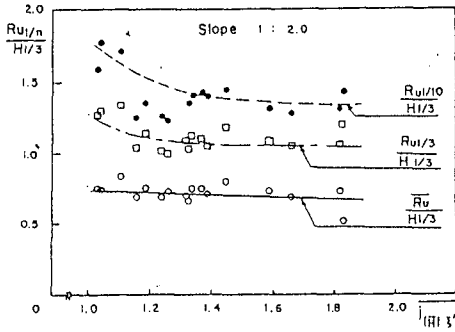


Fig.8. Irregular wave run-up versus jH .

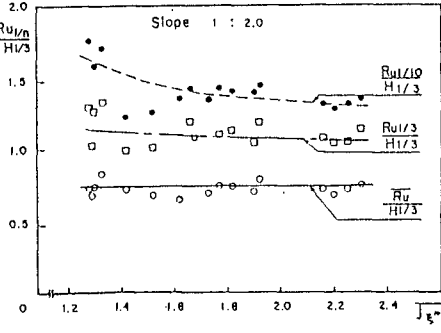
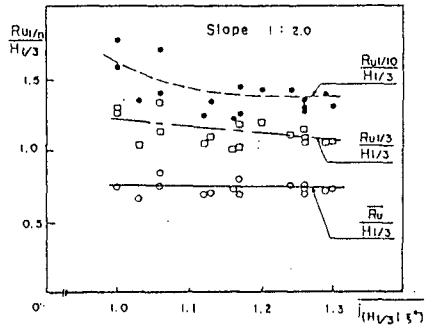


Fig.10. Irregular wave run-up versus $j(H1/3)^2$.

Fig.9. Irregular wave run-up versus jH^* .

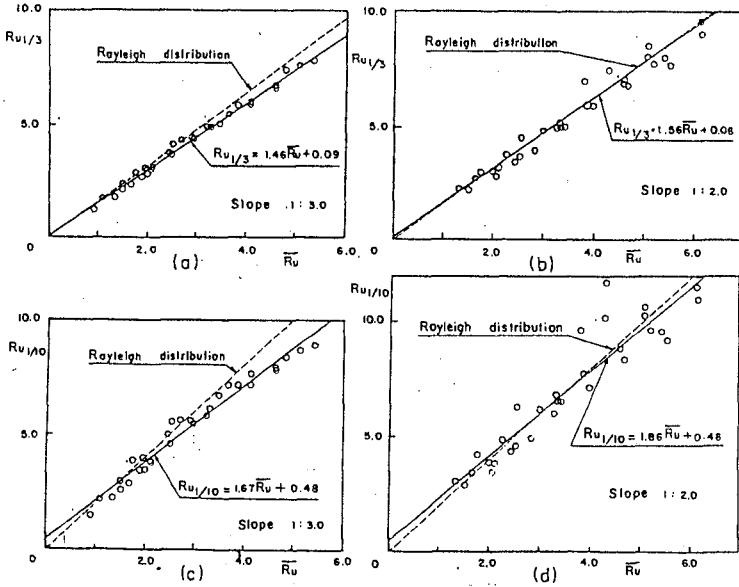


Fig.11. The statistical distribution of irregular wave run-up heights on various slopes.

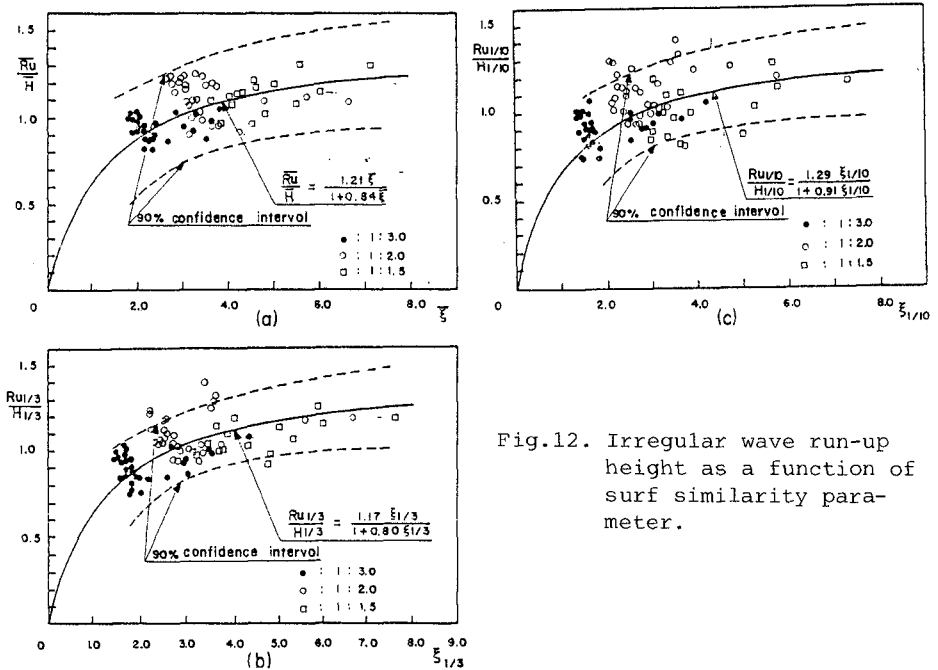


Fig.12. Irregular wave run-up height as a function of surf similarity parameter.

lines denote the regression curves and dashed lines denote 90% confidence interval by eqs. (7), (8) and (9).

The basic formula for estimating the wave run-up height is given as follows

$$R_u = \frac{a \xi}{1 + b \xi} H \tag{3}$$

The regressive curve fitting formulas of the relative run-up heights are as follows

$$\frac{\bar{R}_u}{\bar{H}} = \frac{1.21 \bar{\xi}}{1 + 0.84 \bar{\xi}} \tag{4}$$

$$\frac{R_{u1/3}}{H_{1/3}} = \frac{1.17 \xi_{1/3}}{1 + 0.80 \xi_{1/3}} \tag{5}$$

$$\frac{R_{u1/10}}{H_{1/10}} = \frac{1.29 \xi_{1/10}}{1 + 0.91 \xi_{1/10}} \tag{6}$$

The formulas of 90% confidence interval for regression curves are as follows:

$$\begin{aligned} \frac{\bar{R}_u}{\bar{H}} - (1.66)(0.17) \sqrt{1 + \frac{1}{83} + \frac{(\bar{\xi} - 3.34)^2}{107.90}} < \mu \frac{\bar{R}_u}{\bar{H}} \mid \bar{\xi} \\ < \frac{\bar{R}_u}{\bar{H}} + (1.66)(0.17) \sqrt{1 + \frac{1}{83} + \frac{(\bar{\xi} - 3.34)^2}{107.90}} \end{aligned} \tag{7}$$

$$\begin{aligned} \frac{R_{u1/3}}{H_{1/3}} - (1.66)(0.12) \sqrt{1 + \frac{1}{83} + \frac{(\xi_{1/3} - 3.11)^2}{137.27}} < \mu \frac{R_{u1/3}}{H_{1/3}} \mid \xi_{1/3} \\ < \frac{R_{u1/3}}{H_{1/3}} + (1.66)(0.11) \sqrt{1 + \frac{1}{83} + \frac{(\xi_{1/3} - 3.11)^2}{137.27}} \end{aligned} \tag{8}$$

$$\begin{aligned} \frac{R_{u1/10}}{H_{1/10}} - (1.66)(0.15) \sqrt{1 + \frac{1}{81} + \frac{(\xi_{1/10} - 2.86)^2}{110.77}} < \mu \frac{R_{u1/10}}{H_{1/10}} \mid \xi_{1/10} \\ < \frac{R_{u1/10}}{H_{1/10}} + (1.66)(0.15) \sqrt{1 + \frac{1}{81} + \frac{(\xi_{1/10} - 2.86)^2}{110.77}} \end{aligned} \tag{9}$$

where μ is a function of confidence interval.

The probability distribution function of ξ proposed by Bruun and Günbak(1978) is as follows:

$$P(\xi) = \frac{8 \cdot \xi_d^4}{\xi^5} \exp(-2 \xi_d^4 \cdot \xi^{-4}) \quad (10)$$

$$\text{where } \xi_d = \frac{\tan \theta}{[(2\pi/g)(H_{1/3}/\bar{T}^2)]^{1/2}} \quad (11)$$

where θ is slope angle, $H_{1/3}$ significant wave height and \bar{T} mean wave period.

Using eq.(5) among eq.(4), eq.(5) and eq.(6), one may solve for $\xi_{1/3}$ as follows

$$\xi_{1/3} = \frac{Ru_{1/3} / H_{1/3}}{1.17 - 0.8(Ru_{1/3} / H_{1/3})} \quad (12)$$

Changing random variable from $\xi_{1/3}$ to $Ru_{1/3} / H_{1/3}$ in eq.(12) through Jacobian transformation, the following formulas are obtained:

$$d\xi_{1/3} = \frac{1.17}{[1.17 - 0.80(Ru_{1/3} / H_{1/3})]^2} d \frac{Ru_{1/3}}{H_{1/3}} \quad (13)$$

$$\frac{d\xi_{1/3}}{d \frac{Ru_{1/3}}{H_{1/3}}} = \frac{1.17}{[1.17 - 0.80(Ru_{1/3} / H_{1/3})]^2} \quad (14)$$

combining eq.(10), eq.(11) and eq.(14), eq.(15) is obtained as:

$$p\left(\frac{Ru_{1/3}}{H_{1/3}}\right) = \frac{8 \xi_d^4}{\left[\frac{(Ru_{1/3} / H_{1/3})}{1.17 - 0.80(Ru_{1/3} / H_{1/3})}\right]^5} \cdot \exp[-2\xi_d^4 \left(\frac{Ru_{1/3} / H_{1/3}}{1.17 - 0.80(Ru_{1/3} / H_{1/3})}\right)^{-4}] \frac{d\xi_{1/3}}{d \frac{Ru_{1/3}}{H_{1/3}}} \quad (15)$$

Consequently, substituting eq.(14) into eq.(15), the probability distribution function of irregular wave run-up height can be expressed as eq.(16):

$$p\left(\frac{Ru_{1/3}}{H_{1/3}}\right) = \frac{9.36\xi_d^4(1.17 - 0.80 \frac{Ru_{1/3}}{H_{1/3}})^3}{\left(\frac{Ru_{1/3}}{H_{1/3}}\right)^5} \cdot \frac{\frac{Ru_{1/3}}{H_{1/3}}}{\exp[-2\xi_d^4 \left(\frac{Ru_{1/3}}{H_{1/3}}\right)^{-4}]}{1.17 - 0.80 \frac{Ru_{1/3}}{H_{1/3}}} \quad (16)$$

In order to identify the applicability of the model, the probability distribution of wave run-up height is shown with the experimental data

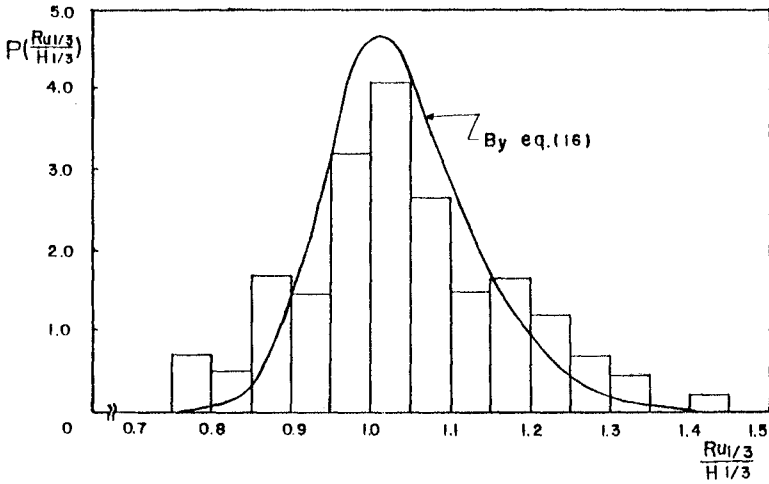


Fig.13. Probability distribution of irregular wave run-up heights on uniform slope.

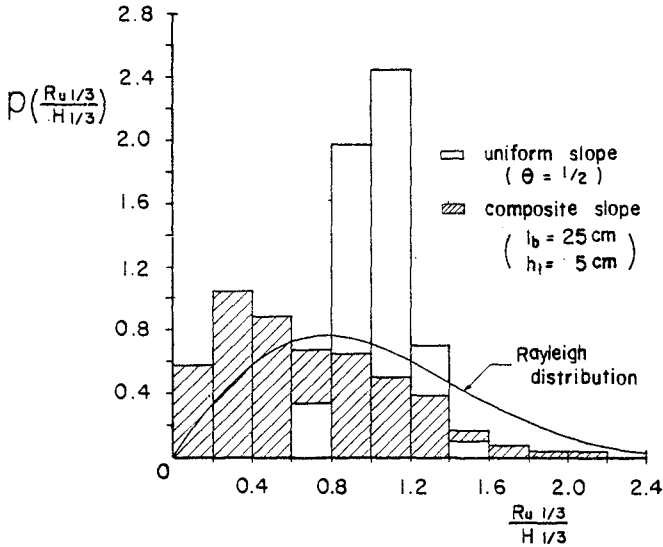


Fig.14. Probability distribution of irregular wave run-up heights on the berm type composite slope.

in Fig. 13. It can be stated from the figure that the proposed model is very useful to predict the run-up height on the permeable rough mound type structures.

In addition, applying the technique used for the uniform slopes, the probability distribution of irregular wave run-up heights on the berm type composite slope is investigated compared with that on the uniform slope and Rayleigh distribution as shown in Fig.14. It is seen that the irregular wave run-up heights are more widely distributed than those on uniform slope and also that the probability density of the run-up height on composite slope is higher in the lower values of $Ru_{1/3} / H_{1/3}$ than that on uniform slope. This means that the attenuation effect of wave run-up height on composite slope is stronger than that on uniform slope due to wave-structure interaction. Furthermore, it can be identified that the distribution of the irregular wave run-up height normalized by wave height has different trend with the Rayleigh distribution.

CONCLUSIONS

Statistical and real time characteristics of irregular wave run-up were studied including the effects of spectral shape and grouping characteristics of incident waves. And the simple probability distribution function of irregular wave run-up heights was developed as a prediction model of the run-up height, and proved to be useful to the deterministic design and applicable to the optimal design concept of coastal structures. However, the experimental conditions could not cover all of the sea state and structural characteristics. Furthermore, the proposed model does not include the effect of grouping of incident waves. These problems will be required to be investigated to develop the more accurately and extensively applicable model.

ACKNOWLEDGEMENTS

The authors would like to thank Dr. Nobuhisa Kobayashi of the University of Delaware and Dr. Hajime Mase of the Kyoto University for their valuable discussions and helpful suggestions at the University of Delaware.

Part of this work was sponsored by the KOSEF (Grant No. 858-1307-001-2). The support is gratefully appreciated.

REFERENCES

Ahrens, J.P. and Heimbaugh, M.S.(1988). Irregular wave run-up on riprap revetments. J. Waterway, Port, Coastal and Ocean Eng., ASCE, 111(4),524-530.

Bruun, P., Ed.(1985) Design and construction of mounds for breakwaters and coastal protection. Elsevier, New York, NY, 938 P.

- Bruun, P. and Günbak, A.R.(1978). Stability of sloping structures on relation to $\xi = \tan\alpha / \sqrt{H/L_0}$. Coastal Engineering, 1(4), 287-322.
- Kobayashi, N. and Cox, D.T.(1990). Permeability effects on irregular wave run-up and reflection. J. Coastal Research(will appear).
- Ryu, C.R. and Sawaragi, T.(1986). Wave control functions and design principles of composite slope rubble mound structures. Coastal Engineering in Japan, 29, JSCE, 227-240.
- Ryu, C.R. and Sawaragi, T.(1986). A new design method of rubble mound structures. Proc. 20th Conf. on Coastal Eng., ASCE, 2188-2202.
- Sawaragi, T. and Iwata, K.(1984). A nonlinear model of irregular wave run-up height and period distribution on gentle slopes. Proc. 19th Conf. on Coastal Eng., ASCE, 415-434.
- Goda, Y.(1985). Random seas and design of maritime structures. University of Tokyo Press, pp.1-323.
- Van Oorschot, J.H. and D'Agremond, K.(1968). The effects of wave energy spectra on wave run-up. Proc. 11th Coastal Eng. Conf., ASCE, 888-900.
- Mase, H. and Iwagaki, Y.(1983). The effects of wave grouping on wave run-up characteristics of irregular waves (in Japanese). Proc.30th Japanese Conf. on Coastal Eng., JSCE, 114-118.

CHAPTER 29

Effects of the Gulf Stream on nearby coastal waves

L.H. Holthuijsen¹ and H.L. Tolman²

Abstract

In the present study a third-generation numerical wave model is used to study effects of a straight Gulf Stream and a Gulf Stream ring, on ocean waves along the coast in swell and storm conditions. The model accounts for all relevant processes of propagation, generation and dissipation of the waves (including current effects) without imposing a priori restraints on the spectral development of the waves. The dominating mechanism affecting the waves appears to be current induced refraction even though the short-crestedness of the incoming waves tends to mask its effects. Depending on wind and wave conditions, refraction may trap locally generated waves in the straight Gulf Stream or it may reflect wave energy back to the open ocean. In the Gulf Stream ring, refraction induces a considerable variation in significant wave height and short-crestedness but it hardly affects the mean wave direction. In storm conditions the processes of generation and dissipation are considerably enhanced in counter-current situations and reduced in following-current situations.

1. Introduction

Observations from ships, aircraft and spacecraft show that ocean waves approaching the east coast of the United States are affected by the presence of the Gulf Stream (e.g. Meadows et al., 1983; McLeish and Ross, 1985; Mapp et al., 1985). The currents tend to create a confused sea state, often with waves that are higher than the incoming waves. In this study a distinction is made between a straight Gulf Stream and a Gulf Stream ring. In the straight Gulf Stream, the wave-current interactions will obviously modify the waves uniformly along the coast whereas down-wave from the ring, the along-shore variations may be appreciable. Several studies have

¹ Delft University of Technology, Department of Civil Engineering, P.O. Box 5048, 2600 GA Delft, the Netherlands

² Delft University of Technology, presently at NASA, Goddard Space Flight Center, Laboratory for Atmospheres, Code 911, Greenbelt, MD 20771, U.S.A.

been carried out to model such modifications of waves across a shear-current or a ring (e.g. Kenyon, 1971; Gutshabash and Lavrenov, 1986; Mathiesen, 1987) but no attempt seems to have been made to include the effects of wind. We therefore use in the present study a numerical wave propagation model extended with source terms representing wave generation and dissipation to propagate waves across a straight Gulf Stream and across a Gulf Stream ring in swell and storm conditions.

2. The wave model

The wave model which we use is a numerical wave prediction model for random, short-crested waves in arbitrary conditions of wind, currents and bathymetry (Tolman, 1989, 1990a, 1990b). It is a discrete spectral wave model accounting for such wave-current interactions as Doppler shifts, radiation stresses and current-induced refraction. It also explicitly models all relevant processes of wave generation by wind and dissipation by white-capping, including an explicit treatment of the nonlinear resonant wave-wave interactions (the WAMDI group, 1988). The model is based on the discrete spectral action balance (e.g. Hasselmann et al., 1973):

$$\frac{\partial N(\omega, \theta)}{\partial t} + \frac{\partial C_x N(\omega, \theta)}{\partial x} + \frac{\partial C_y N(\omega, \theta)}{\partial y} + \frac{\partial C_\omega N(\omega, \theta)}{\partial \omega} + \frac{\partial C_\theta N(\omega, \theta)}{\partial \theta} = \frac{S(\omega, \theta)}{\sigma} \tag{1}$$

where $N(\omega, \theta)$ is the action density of the waves as a function of absolute frequency ω and direction of wave propagation θ (normal to the wave crest) and σ is the relative frequency (as observed in a frame of reference moving with the current).

The left hand side of Eq. 1 represents the local rate of change of the action density (first term), rectilinear propagation in geographic space (second and third term with C_x and C_y), shifting of the absolute frequency due to time variations in depth and currents (fourth term with C_ω) and refraction (fifth term with C_θ). The propagation speeds in geographic space (C_x and C_y) are the group velocity components in x- and y-direction respectively (current speed included). The propagation speeds C_ω and C_θ are given by (Christoffersen, 1982; Mei, 1983):

$$C_\omega = \frac{\partial \sigma}{\partial d} \frac{\partial d}{\partial t} + \mathbf{k} \cdot \frac{\partial \mathbf{U}}{\partial t} \tag{2}$$

$$C_\theta = -\frac{1}{k} \left[\frac{\partial \sigma}{\partial d} \frac{\partial d}{\partial m} + \mathbf{k} \cdot \frac{\partial \mathbf{U}}{\partial m} \right] \tag{3}$$

in which d is depth, \mathbf{k} is the wave number vector, \mathbf{U} is the current velocity vector and m is a coordinate orthogonal to the wave direction. These propagation speeds fully account for the depth and current effects on propagation within the linear theory of slowly-varying surface gravity waves. The depth induced variations of C_x and C_y are normally referred to as "shoaling". To include the current induced variations we use the term "straining" instead. We consider stationary situations in deep water so that all terms involving finite depth and time derivatives of the current are zero (i.e. no shoaling, no depth refraction and no shift of absolute frequencies).

The right hand side of Eq. 1 (the net production of wave action) represents all effects of generation and dissipation of the waves. The processes which are included in the model are:

wave generation by wind (Snyder et al., 1981), nonlinear resonant wave-wave interactions (Hasselmann, 1960; Phillips, 1960), white-capping (Komen et al., 1984) and bottom induced dissipation (Madsen et al., 1988). The actual formulations which are used are those of the WAM model (the WAMDI group, 1988) except for the formulation of the bottom dissipation (but as it has no relevance for the present study, it will be ignored in the following). The model is therefore, like the WAM model, a third-generation wave model in which the wave spectrum develops free of any a priori restraints. All of these processes of generation and dissipation are formulated in a frame of reference moving with the current (implying the use of the relative wind speed). The effects of currents are accounted for by a Jacobian transformation of the computed source term $S(\omega, \theta)/\sigma$ to a stationary reference frame in each time step in the model. The numerical schemes that are used to propagate the waves are predominantly second-order accurate (also refraction). Occasionally the schemes reduce to first-order accuracy when the gradients in the wave field are too sharp. The geographic resolution of the model is $\Delta x = \Delta y = 13.9$ km for the straight Gulf Stream and 15 km for the ring respectively. The spectral resolution is $\Delta f = 0.1f$ in frequency and $\Delta \theta = 15^\circ$ (storm cases) and $\Delta \theta = 7.5^\circ$ (swell cases) in direction. The time step is $\Delta t = 7.5$ min.

3. The Gulf Stream

The current field for this study has been provided by Scott Glenn of Harvard University who used the Harvard Gulf Stream Forecasting Program (Glenn et al., 1987; Robinson et al., 1988) with the Gulf Stream at its climatological location and a warm core ring in a typical location. The currents thus obtained vary sufficiently slowly in time to treat the current field as stationary. For reasons of computational capacity the wave hindcast experiments have been carried out for an infinitely long and straight Gulf Stream and for a ring separately. To obtain the infinitely long, straight Gulf Stream we synthesize a 150 km-wide transverse surface-current profile by averaging the surface-current profile of the forecasted Gulf Stream over a 250 km-long section (Fig. 1). For convenience of discussion, we take the current in this synthesized Gulf Stream to run from south to north (the actual direction is immaterial as only the relative directions of waves and currents are relevant). The surface-current field of the ring (radius to maximum current about 45 km) has been obtained by isolating a 250×250 km² area from the forecasted field (Fig. 2).

4. The waves

We take uniform wave boundary conditions at the open-ocean side of the current fields (some distance up-wave from the current-boundary). The wave condition there are characterized in the storm (wind speed at 10 m elevation $U_{10} = 20$ ms⁻¹) with a two-dimensional JONSWAP spectrum (Hasselmann et al., 1973) of nearly fully developed waves with a $\cos^{2s}((\theta - \theta_0)/2)$ -directional energy distribution. The value of the directional width parameter s is taken from Hasselmann et al. (1980). The swell is characterized with a Gaussian-shaped frequency energy spectrum (standard deviation σ_f) and a $\cos^{20}(\theta - \theta_0)$ -directional energy distribution. Details of the spectral characteristics are given in Table 1. We consider two incoming wave directions relative to the Gulf Stream (swell and storm): 45° from a counter-direction (i.e. waves from north-east) and 45° from a following direction (i.e. waves from south-east). In the case of the

ring the direction of approach is not relevant as the current field is practically rotationally symmetrical. We therefore consider for the ring only one mean wave direction (from east to west for convenience of the discussion).

spectral characteristics		storm	swell
peak frequency	f_{peak}	0.073 Hz	0.071 Hz
peak width	σ_a	0.07	--
	σ_b	0.09	--
	σ_f	--	0.007 Hz
peak enhancement	γ	1.49	--
sign. wave height	H_s	8.10 m	1.99 m
directional width	σ_θ	34.5°	12.4°

Table 1. The spectral characteristics of the wave boundary conditions in the storm and swell cases. For the definition of σ_a , σ_b and γ see Hasselmann et al. (1973).

5. Results for the straight Gulf Stream

5.1 Waves from NE

In the NE swell case the significant wave height shows rather small variations (Fig. 1). An analytical inspection for a monochromatic wave with the same frequency as the peak frequency of the incoming waves shows that this mild variation is mostly due to the opposing effects of refraction on the one hand (which would decrease the significant wave height in the centre of the Gulf Stream) and straining and radiation stresses on the other (which would increase the significant wave height there). The mean wave direction turns only 6° at the centre of the Gulf Stream (more orthogonal to the current) where they are slightly more long-crested than at the open ocean side (quantified with the rms directional width σ_θ of the energy distribution of 12.2° versus 9.5°). The wave field has returned to its undisturbed state after crossing the Gulf Stream.

In the NE storm case the significant wave height increases across the Gulf Stream with an overshoot at the center of the Gulf Stream (Fig. 1) and the relative variations are much larger than in the above swell case. The variations in the other wave parameters such as the mean

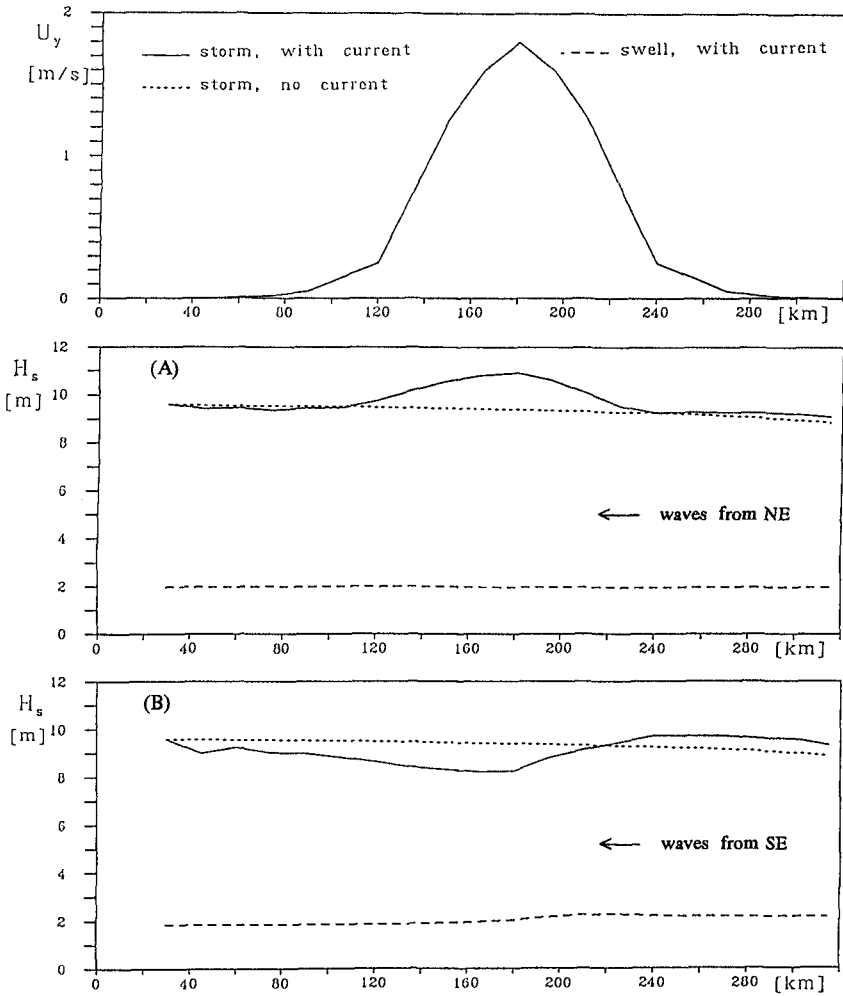


Fig. 1 Profiles in the straight Gulf Stream: current speed (U_y) and significant wave height (H_s). Panel A: waves from counter-current direction (NE). Panel B: waves from following direction (SE).

wave direction are also rather different from those in the swell case. In fact the tendencies are opposite to those in the swell case (e.g. waves turn counter-clockwise towards the centre of the Gulf Stream instead of clock-wise). An inspection of the two-dimensional spectra in this case shows that this is due to wave energy from northerly directions which is added to the incoming spectrum. An analytical inspection shows that this energy propagates along undulating wave rays near the center of the Gulf Stream. It is locally generated by the wind and cannot escape (it is trapped). Our computations therefore confirm the possibility of trapping locally generated waves as suggested earlier by Johnson (1947) and Kenyon (1971). In this storm case the generation and dissipation are much more active in the Gulf Stream than outside the Gulf Stream (in the centre the wind input is enhanced by 48%, dissipation by 80% and nonlinear interactions by 96%, compared with the undisturbed situation). These considerable effects are probably due to a large extent to the trapping of the locally generated waves. They increase the wave steepness, thereby increasing the nonlinear wave-wave interactions and the white-capping. The increase in apparent wind speed (due to the counter-current) may also have some effect.

5.2 Waves from SE

If swell enters the Gulf Stream from the SE direction, the variations in the wave field are somewhat larger than in the NE case (Fig. 1). The behaviour of the significant wave height to increase up-wave from the Gulf Stream and to decrease down-wave from its centre is related to the reflection of some wave energy back to the open ocean. This is clearly visible in the two-dimensional spectra at various locations (not shown here). It is also noticeable in the short-crestedness: the reflected waves travel across the incoming waves at the open ocean side and consequently increase the short-crestedness there (σ_0 increases from the undisturbed value of 12.4° to 24.9°). Beyond the center of the Gulf Stream the absence of the reflected energy turns the mean wave direction slightly counter-clockwise. The spectrum there has a correspondingly narrower directional distribution. Such reflection in a straight (or meandering) shear current is a well-known phenomenon (e.g. Kenyon, 1971; Jonsson and Skovgaard, 1979; Hayes, 1980; Irvine and Tilley, 1988).

In the case of the SE storm, the variations in the wave field are fairly similar to those in the above swell case and reflection is even more important than in the swell case (Fig. 1). This is evident in a sharp decrease of the computed significant wave height near the center of the Gulf Stream and some increase at the up-wave side of the Gulf Stream. However, at some distance beyond the Gulf Stream the wind has generated sufficient wave energy to compensate the reflected energy. In contrast to the NE storm, the intensity of all processes of generation and dissipation are somewhat reduced in the center of the Gulf Stream compared with the undisturbed situation and somewhat enhanced at the boundaries. This is probably due to the current-induced decrease in wave steepness in the following current (lower and longer waves) and a reduction of the apparent wind speed.

The above effects of the Gulf Stream are uniform along the coast so that no variations occur in the wave field along the coast (only across the Gulf Stream). In a more realistic, meandering Gulf Stream, along-shore variations will occur. The wave field in the most extreme meander, a ring, is considered next.

6. Results for the Gulf Stream ring

In the swell case for the ring, the significant wave height increases from 2.0 m up-wave from the ring to 2.7 m just down-wave from the counter-current region and it decreases to 1.4 m just beyond the following-current region (Fig. 2). A ship may therefore encounter nearly a doubling of the significant wave height when travelling from south to north along the lee side of the ring in this situation. In the storm case the pattern of the significant wave height is fairly similar to that in the swell case but with some obvious differences (Fig. 3). The location and extent of the perturbation of the wave field is more confined to the ring and the relative variations are smaller (but still considerable). The variations are largest within the ring (storm case) or just down-wave from the ring (swell case). From there they dampen in the down-wave direction to a situation almost equal to the undisturbed situation (in all respects except that some bimodality in the directional energy distribution is maintained; not shown here). The extent of the disturbance is about one ring diameter in the storm case down-wave from the ring (90 km, affecting coastal waves only if the coast is within this range) whereas in the swell case the effects are still noticeable after two ring diameters (180 km, affecting coastal waves only if the coast is within this range). These wave height variations are well understood from refraction and straining effects. Refraction induces convergence of wave propagation in and beyond the counter-current region and divergence in and beyond the following-current region. Fig. 4 shows the ray pattern for a monochromatic wave with the same frequency as the peak frequency of the swell propagating across the ring. The regions of ray convergence and divergence just beyond the regions of counter-current and following current respectively correspond well with the areas of maximum and minimum significant wave height in the swell case. Such convergence and divergence of wave rays has also been shown by others (e.g. Mathiessen, 1987). The differences in extent and location of the wave field disturbance between the swell case and the storm case seems to be mostly due to the difference in short-crestedness of the incoming waves (see below).

The mean wave direction varies only mildly across the ring (12° maximum in the swell case) and it returns to nearly its undisturbed value at a few diameters distance beyond the ring (swell case) or earlier (storm case). This mild variation of the mean wave direction seems to contrast with the strong refraction effects in the wave ray pattern of Fig. 4. Not only is this variation milder than the variation of individual ray directions, it is also not as lasting as the ray pattern suggests. The reason is that beyond the areas of divergence and convergence, the refracted rays diverge so that the energy represented by these rays decreases and the undisturbed rays dominate. In other words, the divergence of the refracted rays dilutes any effect that they may have on the mean wave direction. In addition, beyond the ring the short-crestedness of the incoming waves mixes disturbed and undisturbed wave components rapidly. It also determines the extent and location of the ring-induced disturbance of the wave field. These effects are stronger in the storm case (with a relatively wide directional energy distribution of the incoming waves, $\sigma_\theta = 34.5^\circ$) than in the swell case (with a relatively narrow directional energy distribution of the incoming waves, $\sigma_\theta = 12.4^\circ$). Across the ring the short-crestedness varies

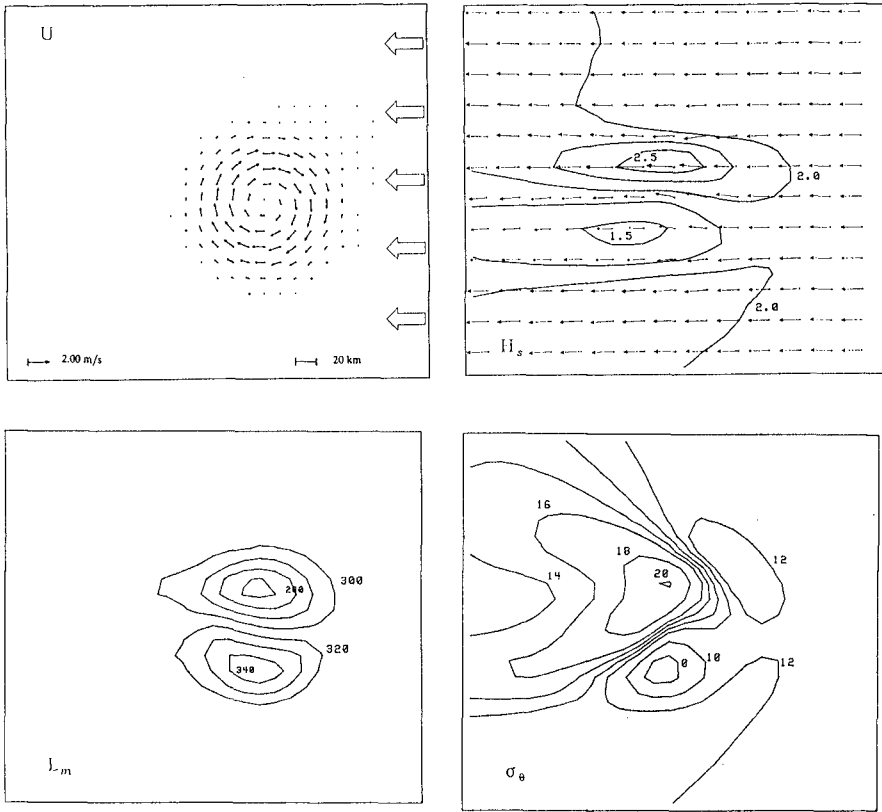


Fig. 2 Contour line plots in the ring area for swell: significant wave height (H_s in m), mean wave length (L_m in m) and directional spread (σ_θ in $^\circ$). Vectors indicate current and mean wave direction.

considerably in the swell case. In the storm case it varies only slightly. Well defined cross-seas (i.e. bimodal spectral directional energy distributions) occur only beyond the counter-current region in the swell case.

Again, as in the Gulf Stream storm cases, the physical processes of wind generation, dissipation and nonlinear wave-wave interactions are considerably affected by the currents. Compared with the undisturbed situation, the wind input is enhanced by 46% (maximum, near the maximum counter-current) and reduced with 26% (minimum, near the maximum following-current). The dissipation is similarly enhanced or reduced with 89% and 46% and the nonlinear wave-wave interactions by 80% and 45% respectively. The computations show that the work done by the radiation stresses when the waves enter the ring is returned when the waves leave the ring.

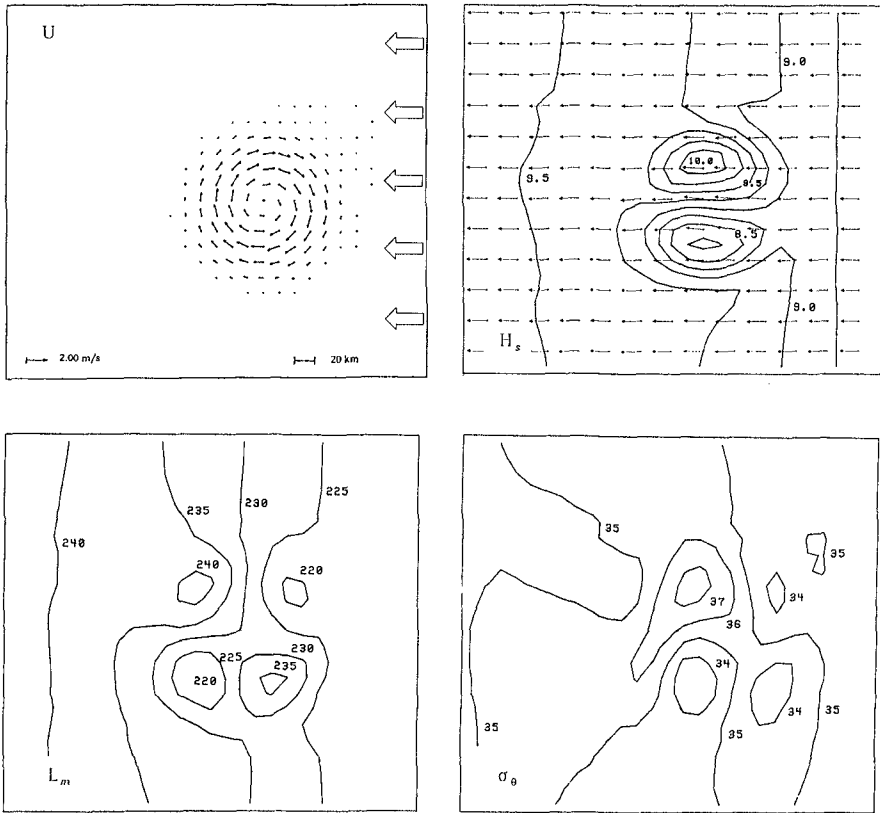


Fig. 3 Contour line plots in the ring area for storm condition: significant wave height (H_s in m), mean wave length (L_m in m) and directional spread (σ_θ in $^\circ$). Vectors indicate current and mean wave direction.

7. Conclusions

If waves from the open ocean travel across the straight Gulf Stream, refraction is the dominating mechanism affecting the waves. Its most notable effect is the trapping of locally generated waves in an adverse-wind situation (wind against the current) and reflection of incoming waves if waves approach from a following direction (waves travelling with the current). In a Gulf Stream ring, refraction affects considerably the significant wave height and the short-crestedness but it affects the mean wave direction only slightly. Well-defined cross-seas occur beyond the ring in swell conditions but not in storm conditions. These effects are not as persistent as refraction computations for monochromatic, unidirectional waves suggest.

In fact, they disappear after a few ring diameters due to the diluting effect of frequency and direction dispersion of the waves. Along the United States east coast the presence of the Gulf Stream will therefore be noticeable in the wave field only from an occasional reduction of incoming swell and from along-shore swell variations at the lee-side of nearby rings (or meanders). In storms practically no effects on the wave field along the coast will be noticeable.

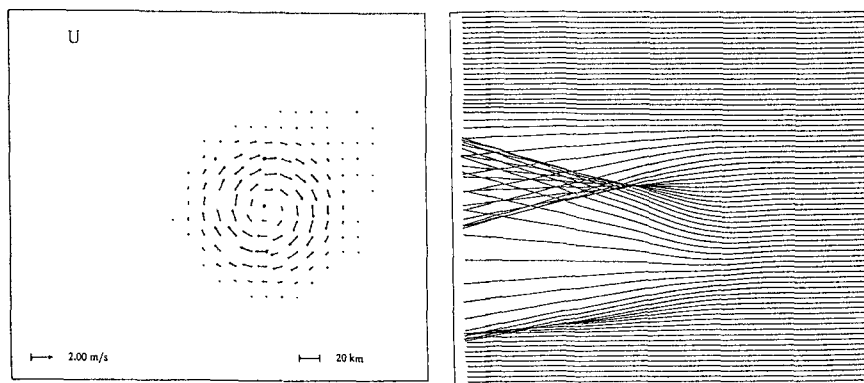


Fig. 4 Wave ray pattern for a 14 s period wave crossing the Gulf Stream ring of this study (courtesy Delft Hydraulics).

Acknowledgements

We sincerely thank Scott Glenn of Harvard University for providing the current fields and Johan Dekker of Delft Hydraulics for providing the wave ray pattern in the ring.

References

- Christoffersen, J.B., 1982, Current depth refraction of dissipative water waves, Institute of Hydrodynamics and Hydraulic Engineering, Techn. Univ. Denmark Series, paper no. 30
- Glenn, S.M., et al., 1987, Recent results of the Harvard Gulf Stream Forecasting Program, *Oceanographic Monthly Summary*, 7, 4, pp. 3 + 12 - 13.
- Gutshabash Ye. Sh. and I.V. Lavrenov, 1986, Swell transformation in the Cape Agulhas Current, *Izvestiya, Atmospheric and Ocean Physics*, Vol. 22, No. 6, pp. 494 - 497
- Hayes, J.G., 1980, Ocean current interaction study, *Journal of Geophysical Research*, Vol. 85, No. 9, pp. 5025 - 5031
- Hasselmann, D.E., M. Dunkel, and J.A. Ewing, 1980, Directional wave spectra observed during JONSWAP 1973, *Journal of Physical Oceanography*, Vol. 10, No. 8, pp. 1264 - 1280
- Hasselmann, K., 1960, Grundgleichungen der Seegangsvoraussage, *Schiffstechnik*, Vol. 7, Heft 39, pp. 191 - 195
- Hasselmann, K., T.P. Barnett, E. Bouws, H. Carlson, D.E. Cartwright, K. Enke, J.A. Ewing, H. Gienapp, D.E. Hasselmann, P. Kruseman, A. Meerburg, P. Muller, D.J. Olbers, K.

- Richter, W. Sell, and H. Walden, 1973, Measurements of wind-wave growth and swell decay during the Joint North Sea Wave Project (JONSWAP), *Deutsches Hydrographisches Zeitschrift*, A8, No. 12, 95 p.
- Irvine, D.E. and D.G. Tilley, 1988, Ocean wave directional spectra and wave-current interaction in the Agulhas from the Shuttle imaging radar-B synthetic aperture radar, *Journal of Geophysical Research*, Vol. 93, No. C12, pp 15389 - 15401
- Jonsson, I.G. and O. Skovgaard, 1979, Wave refraction across a shearing current, *Proc. 16th Coastal Engineering Conference*, 722 - 741, ASCE, New York
- Johnson, J.W., 1947, The refraction of surface waves by currents, *EOS Trans. Am. Geoph. Un.*, 28 (6), pp. 867 - 874
- Kenyon, K.E., 1971, Wave refraction by currents, *Deep Sea Research*, Vol. 18, pp. 1023 - 1034
- Komen, G.J., S. Hasselmann and K. Hasselmann, 1984, On the existence of a fully developed wind-sea spectrum, *Journal of Physical Oceanography*, 14, pp. 1271 - 1285
- Madsen, O.S., Y.-K. Poon and H.C. Graber, 1988, Spectral wave attenuation by bottom friction: theory, *Proc. 21st Intl. Conf. Coastal Eng.*, Malaga, pp. 492 - 504
- Mapp, G.R., C.S. Welch and J.C. Munday, 1985, Wave refraction by warm core rings, *Journal of Geophysical Research*, Vol. 90, No. C4, pp. 7153 - 7162
- Mathiesen, M., 1987, Wave refraction by a current whirl, *Journal of Geophysical Research*, 92, pp. 3905 - 3912
- McLeish, W. and D.B. Ross, 1985, Wave refraction in an ocean front, *Journal of Geophysical Research*, Vol. 90, No. C6, pp. 11929 - 11938
- Meadows, G.A., R.A. Shuchman, Y.C. Tseng and E.S. Kasischke, 1983, SEASAT synthetic aperture radar observations of wave-current and wave-topographic interactions, *J. Geoph. Res.*, 88, C7, pp. 4393 - 4406
- Mei, C.C., 1983, *The applied dynamics of ocean surface waves*, Wiley, New York
- Phillips, O.M., 1960, On the dynamics of unsteady gravity waves of finite amplitude. Part I, *Journal of Fluid Mechanics*, Vol. 9, pp. 193-217
- Robinson, A.R. et al., 1988, Gulf Stream simulation in the dynamics of ring and meander process, *Journal of Physical Oceanography*, 18, 12, pp. 1811 - 1853.
- Snyder, R.L., F.W. Dobson, J.A. Elliott and R.B. Long, 1981, Array measurements of atmospheric pressure fluctuations above surface gravity waves. *Journal of Fluid Mechanics*, 102, pp. 1 - 59
- Tolman, H.L., 1989, The numerical model WAVEWATCH: a third generation model for hindcasting of wind waves on tides in shelf seas. *Communications on Hydraulic and Geotechnical Engineering*, Delft University of Technology, Faculty of Civil Engineering, Rep. No. 89-2, ISSN 0169-6548, 72 p.
- Tolman, H.L., 1990a, Wind wave propagation in tidal seas, doctoral thesis, Delft University of Technology, also *Communications on Hydraulic and Geotechnical Engineering*, Delft University of Technology, ISSN 0169-6548, Rep. No. 90-1, 135 p.
- Tolman, H.L., 1990b, A third generation model for wind waves on slowly varying, unsteady and inhomogeneous depths and currents, accepted for publication in the *Journal of Physical Oceanography*
- WAMDI Group, S. Hasselmann, K. Hasselmann, E. Bauer, P.A.E.M. Janssen, G.J. Komen,

L. Bertotti, P. Lionello, A. Guillaume, V.C. Cardone, J.A. Greenwood, M. Reistad, L. Zambresky, J.A. Ewing, 1988, The WAM model - A third generation ocean wave prediction model, *Journal of Physical Oceanography*, 18, 12, pp. 1775 - 1810.

CHAPTER 30

IMPROVED CALCULATION OF THE SHOALING WAVE FIELD

Masataro Hattori¹ and Tetsuyuki Katsuragawa²

Abstract

Nonlinear wave theories was improved to describe the asymmetry in time histories of the wave elevation and associated particle velocities under relatively steep nonbreaking waves. The improvement was based on the idea that the asymmetry causes both the amplitude changes of the primary and harmonic Fourier components, and the relative phase shifts between the primary and harmonic components.

Relationships between the asymmetry and local wave parameters were prerequisite to the improved calculation, and were derived by using experimental data. The improved calculation proposed was made for a specified local wave condition, without aids of direct numerical simulation techniques. Good agreements of the improved calculation with measurements confirmed applicability of the calculation to the practical use.

1. INTRODUCTION

Coastal engineers have been fully aware of the fact that nonlinearity as well as irregularity in wave motions plays an essential part in various coastal processes, such as the cross-shore sediment transport and the wave-structure interaction. In examining such problems, especially under relatively steep waves, time-dependent characteristics of the kinematic field of wave motions at a certain location are usually predicted from flat bottom solutions of nonlinear theories of permanent waves.

When a surface wave advances over a gently rising slope, it is subjected various nonlinear effects due to convective inertia and bottom friction. The inertia effects bring about asymmetric wave forms both about the horizontal and vertical planes, as shown in Fig. 1. Nonlinear theories of constant wave forms describe reasonably well the vertical asymmetry in wave form about mean water level, but they do not allow the horizontal asymmetry about the wave crest, the front slopes of the waves become steeper than the back slopes. In this sense, no appropriate nonlinear wave theory exists for practical use.

The present paper discusses the asymmetry in shoaling wave profiles, with taking into account the bottom slope effect as well as the incident wave property. Based on wave elevation records, empirical

1. Professor, Department of Civil Engineering, Chuo University, Kasuga 1-13-27, Bunkyo-ku, Tokyo, 112, Japan.

2. Research Engineer, Toyo Construction Co., Ltd., Kanda Nishikicho 3-7-1, Chiyoda-ku, Tokyo, 101, Japan.

equations for the asymmetry in the wave form are derived. Improvement of nonlinear wave theories is made by using the empirical equations. This study is concerned with modified versions of the Stokes 5th order wave theory, ST 5, (Isobe, Nishimura, and Horikawa, 1978; Fenton, 1985) and Dean's 10th order stream function representation of theoretical waves, SFMB 10 (1965), because they are computationally simpler.

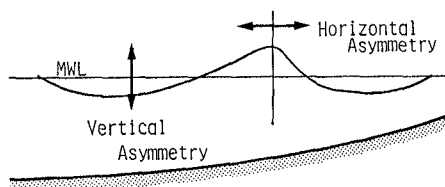


Fig. 1 Asymmetry in the wave profile.

2. OBJECTIVE

Objective of this study is to develop an improved calculation of the wave elevation and particle velocities, with respect to time, under relatively steep nonbreaking waves. From a practical viewpoint, the improved calculation is made for a specified local wave condition: wave height H , wave period T , water depth D , and bottom slope m . In so doing, four sub-objectives are defined: (1) To examine the transformation of shoaling waves by experiments, (2) to obtain empirical relationships of the wave profile asymmetry in terms of the local wave properties and the bottom slope, (3) to modify the theoretical solutions so as to describe the horizontal asymmetry, and (4) to evaluate applicability of the improved calculation by comparisons with measurements.

3. EXPERIMENTAL SETUP AND MEASUREMENTS

Experiments were made in a glass-walled wave flume, 0.30m wide, 0.55m high, and 20m long. Regular waves were generated by a reflection-absorbing type wave maker. Model beaches with slopes of 1:10 and 1:20 were used for all the surface and velocity measurements. The water depth in the flat portion of the flume was between 0.33m and 0.43m.

Simultaneous measurements of the wave elevation and particle velocities were made at various locations over sloping bottom. Wave elevations were measured with a resistance-type wave gage having excellent linearity and high frequency response. Horizontal and vertical particle velocities at the wave measurement section were measured with a two-component LDA velocimeter. These outputs were recorded on a digital recorder with a sampling frequency of 200Hz for extensive processing by computer.

Individual waves in a time series of wave elevation at a certain location were defined by means of the zero-up-crossing method. Based on the individual wave data, the time series of wave elevation and particle velocities were averaged 50 waves with respect to the phase. The harmonic amplitudes were computed from the time series by fast Fourier transform (FFT).

4. EVALUATION OF THE IMPROVED CALCULATION

Applicability of the improved calculation was examined by the overall root-mean-square E of difference between the measurement and calculation of wave elevation and particle velocities for one wave cycle, given by Eq. (1).

$$E = \left(\sum_{i=1}^N (X_i - Y_i)^2 / \sum_{i=1}^N X_i^2 \right)^{1/2} \quad (1)$$

, in which X_i and Y_i are the measured and calculated values at evenly spaced phases ($\Delta\theta = N/T$) for one wave period of the time history, determined by ensemble averaging technique. Taking account of the experimental validity range of water wave theories (Hattori, 1986), the applicability limit of the improved calculation was set as $E < 1.0$.

5 EXPRESSION OF THE SKEWED WAVE FORM

5.1 Brief review of previous studies.

A number of experimental and theoretical studies have been made to examine physical processes in the skewed kinematic field under steep waves propagating on the sloping bottom. However, physical processes of the horizontal asymmetry, wave front faces are steeper than back faces, are still poorly understood.

As to the asymmetric characteristics, Adeyemo (1968 and 70) conducted extensive experiments focused on the asymmetry in wave forms and particle velocity changes with respect to time. He tried to parametrize the asymmetry with respect to various incident wave characteristics. However, he did not succeed to derive any synthetic relationship between the asymmetry and wave parameters.

Hedges and Kirkoz (1981), based on wave elevation data, proposed the transformation zone, which is the region between the point where waves start to lose horizontal symmetry and the breaking point. They found that the rate of horizontal asymmetry transformation increases as the bottom slopes get steeper (Galvin, 1967). In addition, the transformation zone tends to broaden with decreasing in the incident wave steepness.

Flick, Guza, and Inman (1981) presented a very interesting approach for examining the horizontal asymmetry in shoaling wave profiles. Fourier analysis of measured wave elevation records revealed the two following facts, on which the improvement is based:

(1) Harmonic amplitude data provide the principal control over the vertical asymmetry, and are predicted well by the nonlinear theories of permanent waves.

(2) The skewed wave profile causes relative phase shifts ζ_n between the primary and nth harmonic components, given by Eq. (2).

$$\zeta_n = \arctan(S_n/C_n) - n \cdot \arctan(S_1/C_1), \quad (2)$$

where S_n and C_n are the sine and cosine Fourier coefficients. Thus, the measured wave elevation $\eta(t)$ as a function of time can be written as

$$\eta(t) = a_1 \cos \omega t + \sum_{n=2}^M a_n \cos(n \omega t + \zeta_n), \quad (3)$$

in which a_1 and a_n : the amplitudes at primary and nth harmonic frequencies, and ω : the frequency of the primary wave. According to Flick et al. (1981), the harmonic phase shifts ζ_n start to increase from zero as the waves advance over a rising slope, and increase toward the asymptotic values $\zeta_n = (\pi/2)(n-1)$.

5.2 Formulation of the harmonic phase shift ζ_n

The previous studies disclosed the horizontally asymmetric or skewed wave profile is closely related to the local wave parameters and the bottom slope. After careful examination of the experiments by the authors ($m = 1/10$ & $1/20$) and Flick et al. ($m = 1/25$), we found that Goda's nonlinearity parameter Π (1983), given by Eq. (4), is of the most

acceptable, for representing synthetically effects of the incident wave properties on the harmonic phase change inside the transformation zone (Hedges and Kirko³ 1981).

$$\Pi = (H/L) \cot^3 kD, \tag{4}$$

where H is the wave height, L is the wavelength, computed from Airy wave theory, $k(=2\pi/L)$ is the wave number, and D is the water depth. As a consequence, the harmonic phase shifts ζ_n are given by Eq. (5), in terms of the Π parameter and the bottom slope m .

$$\left. \begin{aligned} &\text{For } \Pi < 10^{-2} (B_n/A_n) \\ &\zeta_n / (n-1) = 0, \\ &\text{and for } \Pi > 10^{-2} (B_n/A_n), \\ &\zeta_n / (n-1) = A_n \log \Pi + B_n, \end{aligned} \right\} \tag{5}$$

in which $A_n = (n-1)/30 + 0.60$ and $B_n = 1.33 \cdot m^{1/4}$.

Figures 2 and 3 are comparisons of Eq. (5) with the harmonic phases ζ_n computed from the wave elevation records for the bottom slopes of 1/10, and 1/25. Figure 3 is depicted by utilizing the experimental data of Flick et al. (1981; Fig. 5). The fairly good agreements persuade that the asymmetric wave profile is expressible by substituting Eq. (5) into the analytical solutions of nonlinear wave theories.

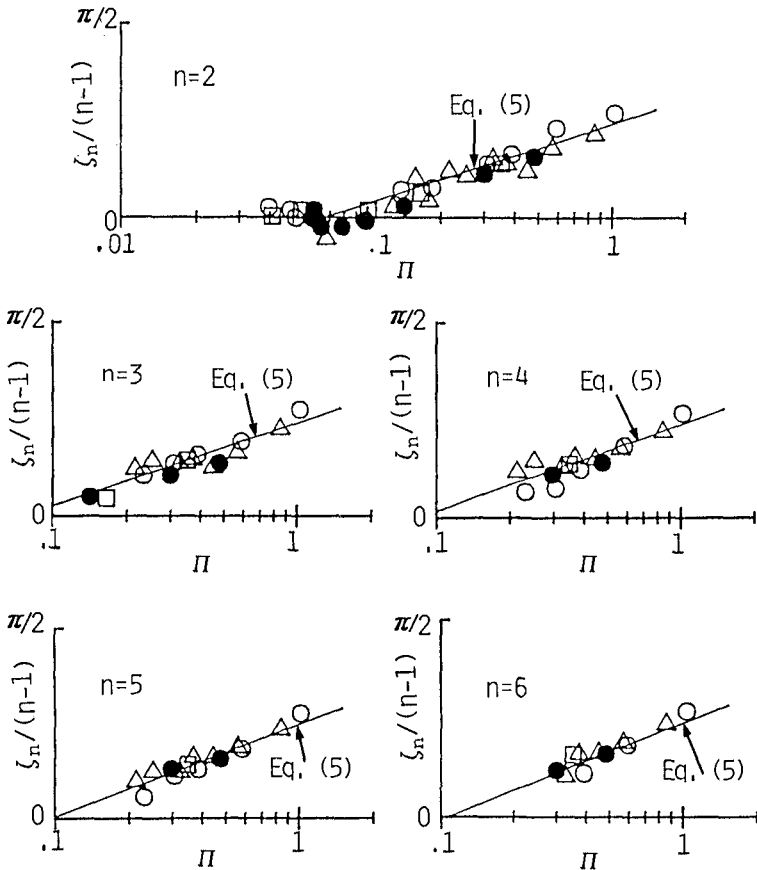


Fig. 2 Relative phase shifts $\zeta_n / (n-1)$ and Goda's Π .
[$n=2-6, m=1/10$]

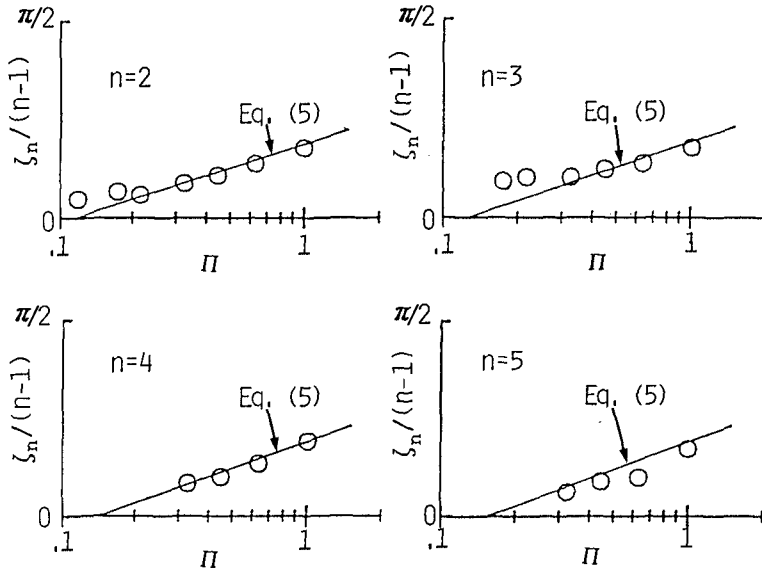


Fig. 3 Relative phase shifts $\zeta_n/(n-1)$ and Goda's Π .
 [$n=2-5$, $m = 1/25$; Flicks et al., 1981]

6. IMPROVED CALCULATIONS

The improved calculation is based on the idea that the horizontal asymmetry in wave elevations and particle velocities, as a function of time, is expressible by the nonlinear wave theory, when the relative harmonic phase shifts are taken into account (Flick et al., 1981). Therefore, this study is concerned with the improvement in the Stokes 5th order wave theory, ST 5, and Dean's 10th order stream function representation of theoretical waves, SFMB 10 (1965). The cnoidal wave theory is excluded from the present study, because the cnoidal solutions are analyzed into the Fourier components in order to generate the horizontal asymmetry by means of the harmonic phase shift. This is very tremendous and barely suitable for practical use.

6.1 Improved Stokes 5th order theory, ST' 5

Figure 4 shows the details of improved calculation of the Stokes 5th order theory. After inputting a specified local wave condition and bottom slope, ST 5 starts to calculate the wave elevation and to determine the primary and harmonic amplitudes. In parallel with this step, the harmonic phase shifts ζ_n are computed from Eq. (5).

Substitution of ζ_n into the phase functions of ST 5 solutions, yields the first approximation of skewed free surface elevation. However, it usually brings about a slight deviation of wave height from the inputted one. Thus, the wave height is iteratively corrected by changing only the primary wave amplitude, because the harmonic amplitudes and their contribution to the wave height deviation are relatively smaller than these of the primary. After determining the skewed wave elevation, the horizontal and vertical velocities are calculated.

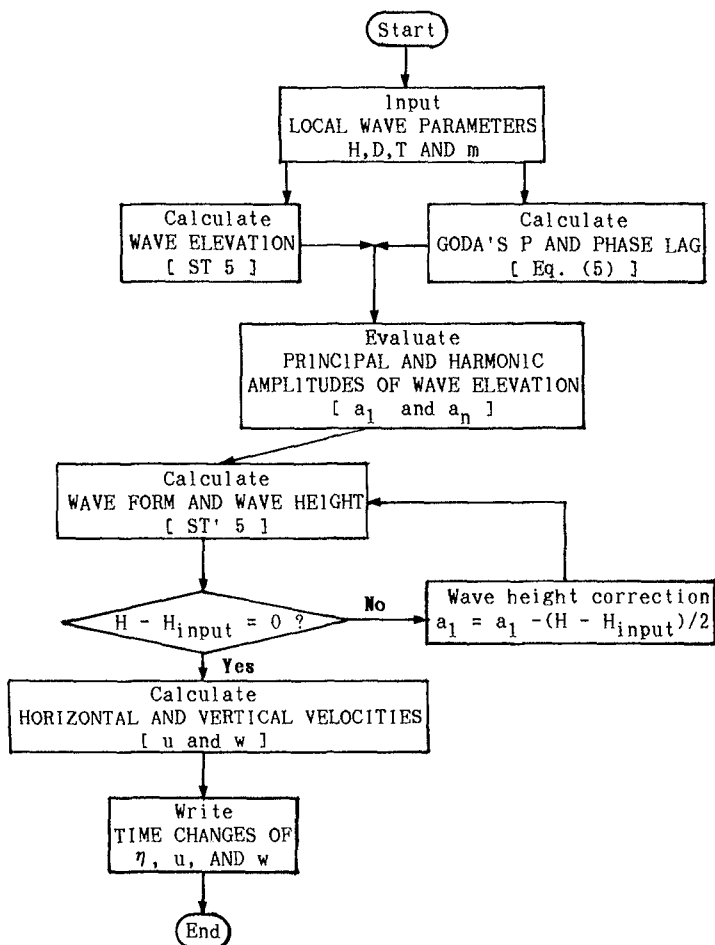


Fig. 4 Flow chart showing the details of ST' 5

Figures 5 and 6 are examples of the comparisons of ST 5 and ST' 5 with measurements of the wave elevation, η , and particle velocities, u and w . The solid and broken lines represent the measured and calculated. Since the local wave conditions are very close to the convergence limit of the Stokes wave theory (Dean and Dalrymple, 1984), instability is clearly observed in the calculated wave elevation after the crest phase. Nevertheless, the ST' 5 yields better agreements with the measurements than the ST 5.

Equation (5) for the harmonic phase shift was derived only from the wave elevation data. It is, therefore, necessary to survey its applicability to the particle velocities. Figure 7 illustrates comparisons between the calculated and measured velocities at the middle and near bottom levels of the water column, for the same case shown in Fig. 6. As in Figs. 6 and 7, ST' 5 predicts fairly well the measured velocity changes in the wave crest, where their profiles are steeper and significantly asymmetric. The agreement, in visual, appears to be reasonably

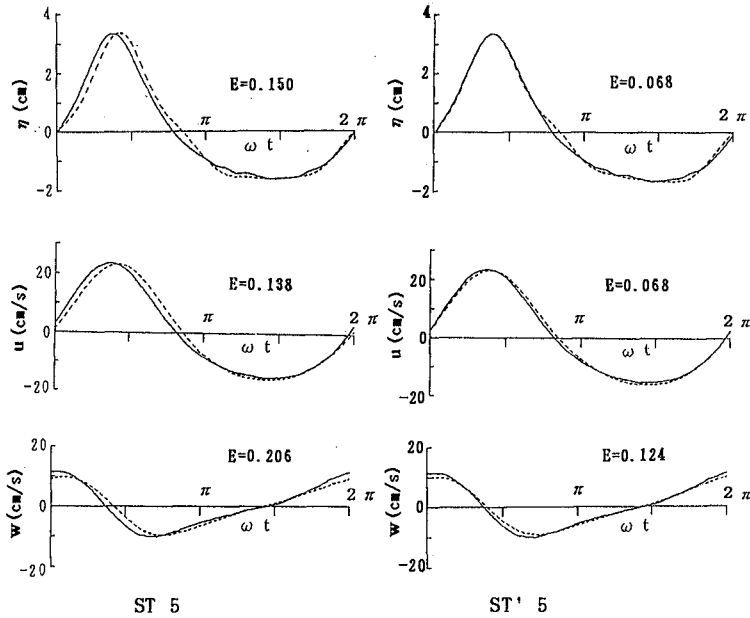


Fig. 5 Comparison of ST 5 and ST' 5 with the measurements.
 (H=5.03 cm, T=0.84 s, D=10.0 cm, z/D=-0.40, Ur=28.4, m=1/20)
 [— : measured, ---- : calculated]

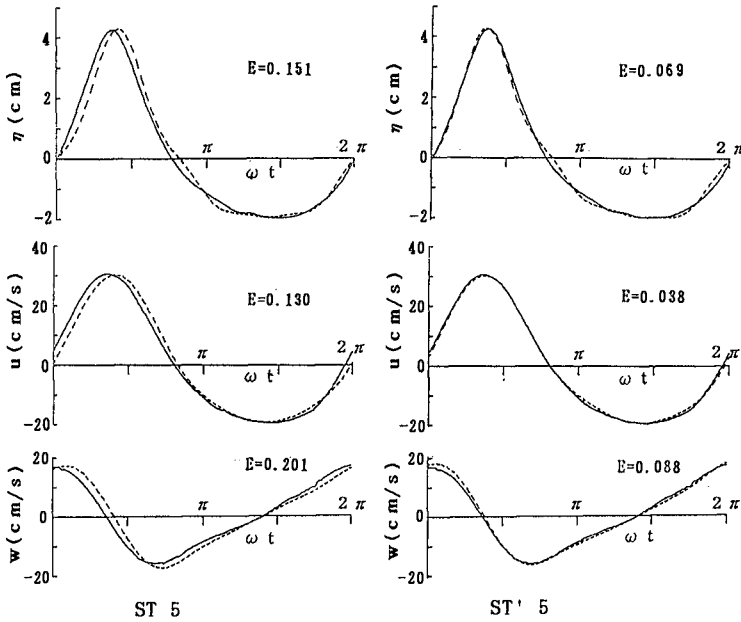
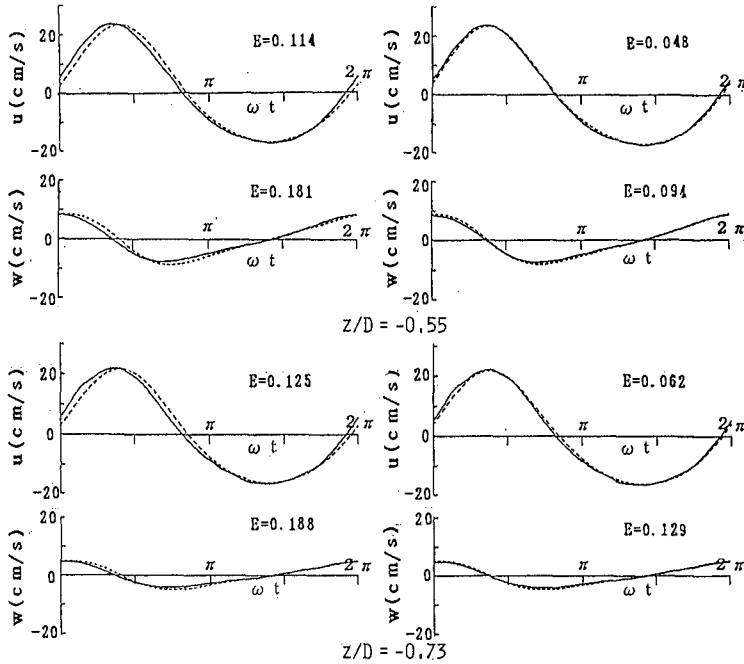


Fig. 6 Comparison of ST 5 and ST' 5 with the measurements.
 (H=6.15 cm, T=0.80 s, D=11.0 cm, z/D=-0.18, Ur=25.1, m=1/20)



ST 5 ST' 5
 Fig. 7 Comparisons between the measured and calculated
 particle velocities by ST 5 and ST' 5.
 (the same case for Fig. 6)

good. However, the overall-rms value E increases gradually toward the bottom. This implies that (1) since the velocity profile get the symmetry with the depth, ζ_n for particle velocities changes at different rates, and (2) decreasing the vertical velocity magnitude toward the bottom gives rise to the increase in E value, even for very small difference between the measured and calculated velocities.

6.2 Improved Stream Function: SFMB' 10 and SFMC' 10

As the wave shoals and wave form becomes more asymmetric, the SFMB tends to overestimate the wave elevation and horizontal particle velocity around wave crest phase (Dean, 1965). To reduce such stream function errors, Saito and Isebe (1987) proposed a modified version of SFMB, using the wave crest height η_c above the mean water level, instead of the wave height (SFMC). Better representation of the wave surface profile is prerequisite to the improvement of the SFMB. Thus, an improved version of SFMC is proposed as an alternative to the SFMB.

In calculations by the SFMC, the wave crest height needs to evaluate from the given wave condition. Steepening of the wave crest as well as skewing the wave form relates both to the wave property and the

bottom slope. Empirical equation for the relative wave crest height, η_c/D , with respect to the relative wave height H/D and the bottom slope m , is determined by using the measuring data of the present authors ($m=1/10$ & $1/20$), Eagleson ($m=1/15$, 1956), Hansen and Svendsen ($m=1/34$, 1979), and Goda ($m=1/100$, 1964).

$$\eta_c/D = m f_1(H/D) \cdot \text{Exp}[f_2(H/D)], \tag{6}$$

in which

$$\left. \begin{aligned} f_1(H/D) &= (H/D) \{2.44(H/D)^2 - 9.24(H/D) + 3.18\} \times 10^{-2}, \\ f_2(H/D) &= (H/D) \{-1.93(H/D)^2 + 1.05(H/D) + 5.58\} \times 10^{-1}. \end{aligned} \right\} \tag{7}$$

Figure 8 is comparisons of Eq. (6) with the measurements for the bottom slopes of $1/20$ and $1/100$, and shows fairly good agreements. The solid lines labeled $\eta_c=H$ and $\eta_c=H/2$ correspond to the solitary and Airy waves.

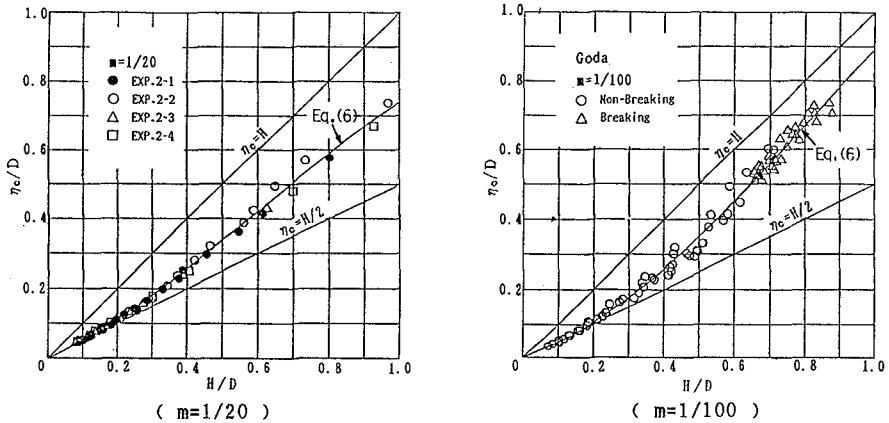


Fig. 8 Relative crest height η_c/D and H/D .

The 10th order stream function method, SFMB 10, can be improved by the almost similar procedure adopted to the ST 5 theory. Figure 9 shows the details of the improved stream function methods, SFMB'10 and SFMC' 10. After determining the asymmetric wave profile with aids of the relative phase shifts ζ_n , the velocities associated are calculated with the aid of SFMA 10 for irregular waves (Dean, 1965).

Comparisons between the measured and calculated wave elevations near wave breaking, as shown in Figs. 10 and 11, indicate superiority of the SFMC' 10 over SFMB' 10. SFMC' 10, and represent reasonably well the asymmetry as well as the maximum elevation of the wave profile in wave crest phase.

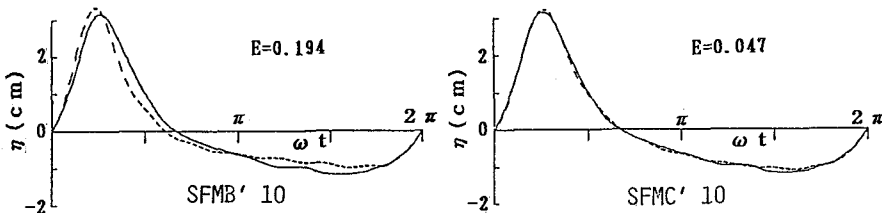


Fig. 10 Comparison of SFMB' 10 and SFMC' 10 with the measured wave elevation. ($H=4.3$ cm, $T=0.99$ s, $D=7.0$ cm, $Ur=84.3$, $m=1/20$)

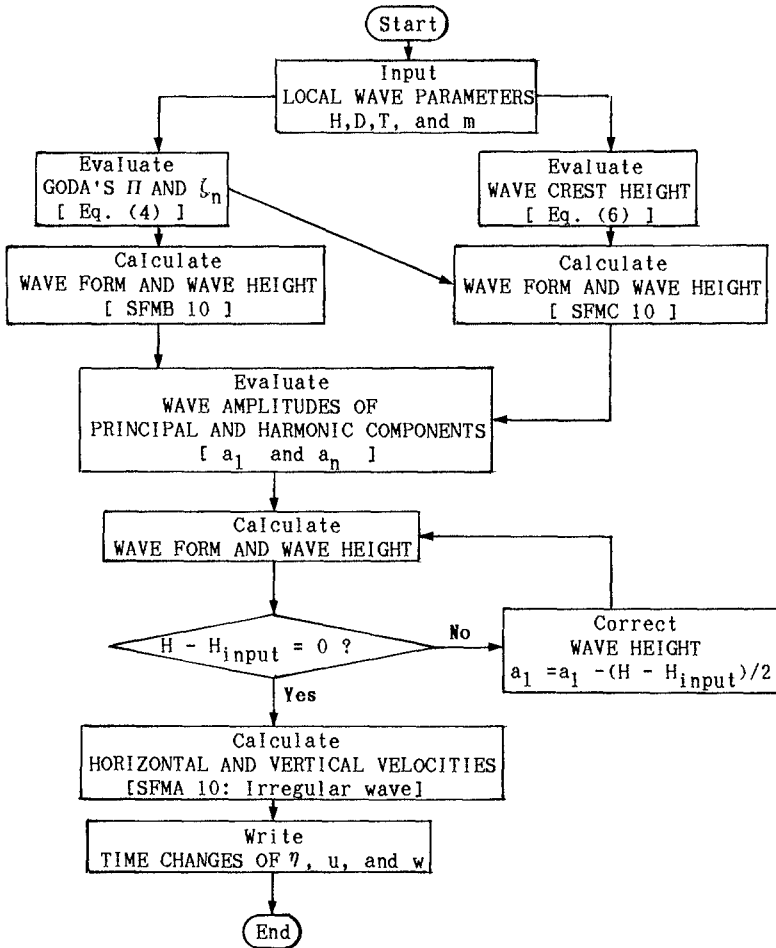


Fig. 9 Flow chart showing the details of SFMB' 10 and SFMC' 10.

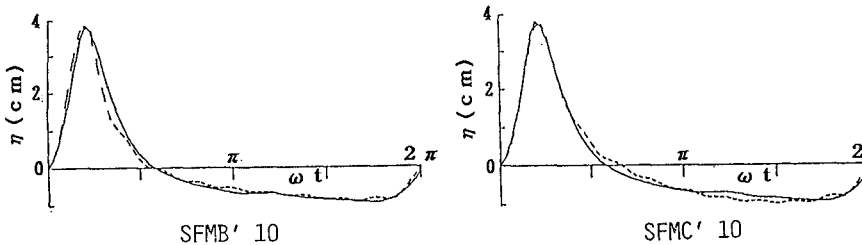


Fig. 11 Comparison of SFMB' 10 and SFMC' 10 with the measured wave form near wave breaking. (Buhr Hansen & Svendsen, 1979) (H=4.7 cm, T=1.0 s, D=6.0 cm, Ur=127.9, m=1/34) [---- : calculated, — : measured]

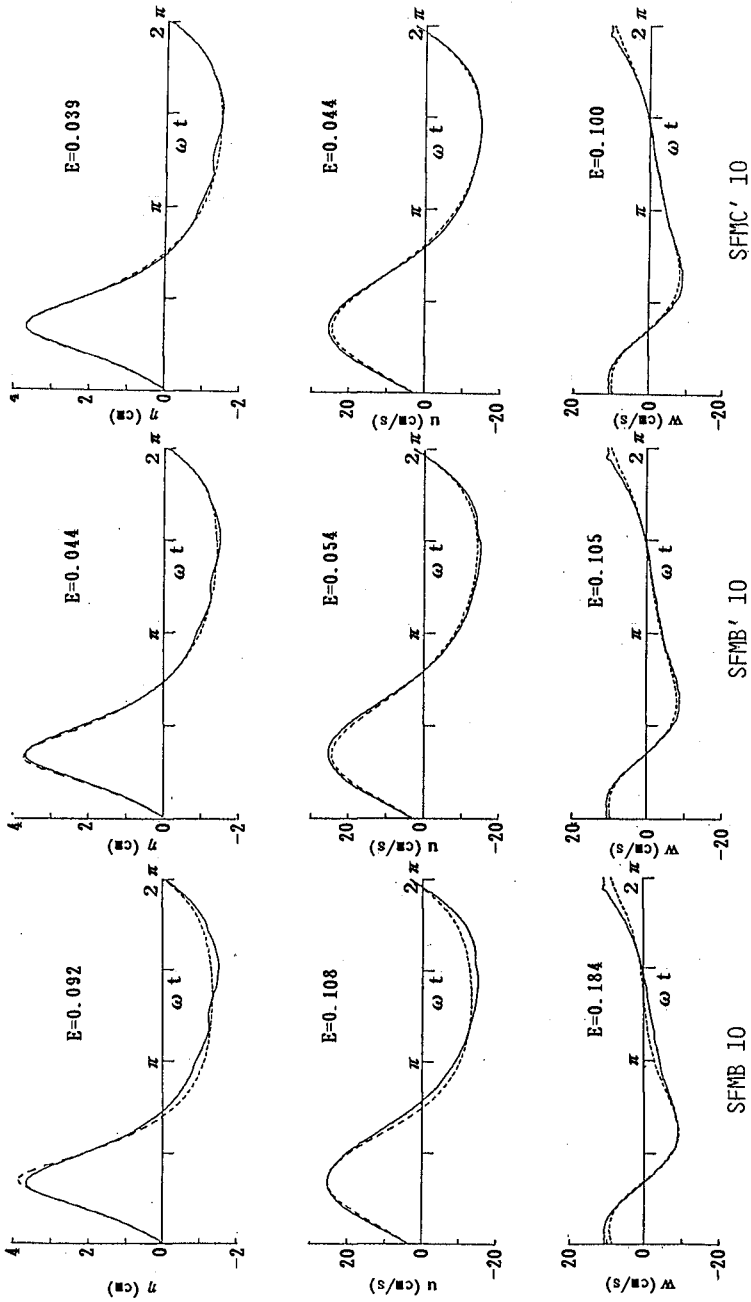


Fig. 12 Comparisons of SFMB 10, SFMB' 10, and SFMC' 10 with the measured wave profile and particle velocities. ($H=5.2$ cm, $T=0.84$ s, $D=9.0$ cm, $z/D=-0.444$, $Ur=44.4$) (—: measured, - - -: calculated)

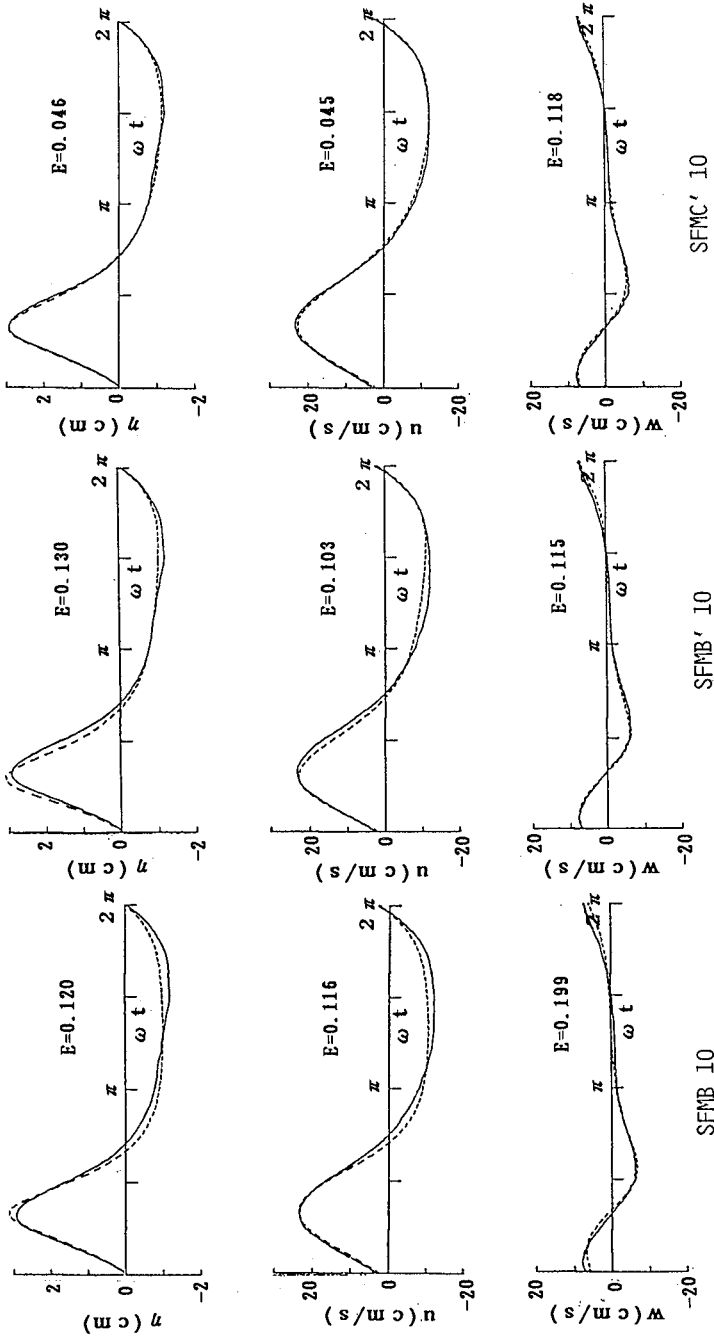


Fig. 13 Comparisons of SFMB 10, SFMB' 10, and SFMC' 10 with the measured wave profile and particle velocities. ($H=4.3$ cm, $T=0.99$ s, $D=7.0$ cm, $z/D=-0.786$, $Ur=84.3$) (—: measured, - - -: calculated)

Figures 12 and 13 illustrate comparisons of the measured wave elevation and particle velocities with the computed ones by SFMB 10, SFMB' 10, and SFMC' 10. Measured velocities under breaking waves tend to lag the surface elevation (Adeyemo, 1972; Flick et al., 1981), while these of the nonbreaking wave occur in phase with the wave profile, as seen in Figs. 11 and 12. This supports that the particle velocities are predicted with aid of the SFMA 10, using the calculated wave elevation. The good agreement of SFMC' 10 with the measurements around the crest phase brings about the better agreement in the trough phase.

It is concluded that the improvement in SFMC' 10 successfully achieves demonstration of the highly asymmetric variation of the wave kinematics even near the wave breaking. Moreover, the improved calculation yields the reasonable prediction both of the magnitude and phase of the peak velocities, which are of fundamental importance to the cross-shore sediment transport.

7. CONCLUSIONS

(1) The improved calculation of the kinematic field under relatively steep and nonbreaking waves was developed to describe asymmetric characteristics of wave kinematics. The improvement is made for the Stokes 5th order theory and Dean's 10th order stream function theory.

(2) The improvement is based on the idea that the vertical asymmetry in the wave elevation can be described by the harmonic amplitude of the nonlinear solution, and the horizontal asymmetry is caused by the relative phase shifts between the primary and harmonic wave component.

(3) Based on the experiments, the harmonic phase shifts are determined as a function of Goda's nonlinearity parameter H and the bottom slope.

(4) Agreements of the calculations with the measured wave elevation and particle velocities confirm that the improved calculations, ST' 5, SFMB' 10, and SFMC' 10, predict reasonably the temporal changes in one wave period.

In concluding, the improved calculation can predict the strongly nonlinear wave field for specified local wave conditions, without aids of direct numerical simulation techniques.

8. REFERENCES

- Adeyemo, M. D. (1968): Effect of beach slope and shoaling on wave asymmetry, Proc. 11th ICCE, pp. 145-172.
- Adeyemo, M. D. (1972): Velocity field in the wave breaker zone, Proc. 13th ICCE, pp. 436-460.
- Buhr Hansen, J. and I.A. Svendsen (1979): Regular waves in shoaling water experimental data, IHHI, Tech. Univ. of Denmark, Series Paper 21.
- Dean, R.G. (1965): Stream function representation of nonlinear ocean waves, Trans. AGU, 70, 18, 4561-4572.
- Dean, R. G. and R. A. Dalrymple (1984): Water Wave Mechanics for Engineers and Scientists, Prentice-Hall, Inc., Chapter 11, pp. 295-325.
- Eagleson, P. S. (1956): Properties of shoaling waves theory and experiment, Trans. AGU, Vol. 37, No. 5, pp. 565-572.
- Fenton, J. D. (1985): A fifth-order Stokes theory for steady waves, Proc. ASCE, Jour. Waterways, Port, Coastal and Ocean Eng., No. 2, pp. 216-234.
- Flick, R.E., R.T. Guza, and D.L. Inman (1981): Elevation and velocity measurements of laboratory shoaling waves, JGR, Vol. 86, 5, 4149-4160.
- Galvin, G. J. (1969): Breaker travel and choice of design wave height, ASCE, Jour. Waterways & Harbor Div., Vol. 95, No. WW2, pp. 175-200.

- Goda, Y. (1964): Wave forces on a vertical circular cylinder: Experiments and a proposed method of wave force computation, Rept. Port and Harbour Tech. Res. Inst., No. 8, 74p.
- Goda, Y. (1983): A unified nonlinearity parameter of water waves, Rept. Port and Harbour Tech. Res. Inst., Vol. 3, 4-30.
- Hattori, M. (1986): Experimental study on the validity range of various wave theories, Proc. 20th ICCE, 232-246.
- Hedges, T. S. and M. S. Kirkoz (1981): An experimental study of the transformation zone of plunging breakers, Coastal Engineering, Vol. 4, pp. 319-333.
- Isobe, M., H. Nishimura, and K. Horikawa (1978): Expressions of perturbation solutions for conservative waves by using wave height, Proc. 33rd Annual Conv. of JSCE, Part 2, pp. 760-761 (in Japanese).
- Saito, E. and M. Isobe (1987): Modified version of the Dean's stream function representation, Abstract of 42nd Annual Conv. of JSCE, II, 484-485. (in Japanese)

CHAPTER 31

A Model for Long Waves at Grazing Angle to a Rubble-Mound Jetty

Eloi Melo *
R.T.Guza †

Abstract

The main features of a model proposed recently by the authors for the propagation of long waves at grazing angle to a rubble-mound jetty are reviewed. Model results for a single jetty and for a jettied channel are shown.

1 Introduction

The behavior of ocean waves normally incident upon a rubble-mound breakwater has received considerable attention. Models describing wave reflection and transmission, the stability of the breakwater, energy dissipation, wave run-up and so on, are available for normal incidence. The case of oblique wave approach is less studied. Recently Melo & Guza (1990 a,b) proposed a linearized model for the propagation of long waves at grazing angle to a rubble-mound jetty. The model combines earlier work on waves normally incident on permeable breakwaters [Sollitt & Cross (1976), Madsen & White (1976)] with the localized dissipation diffraction model of Dalrymple, Kirby & Hwang (1984). Model results for a channel bounded by jetties compared favorably to an extensive data set obtained at the Mission Bay entrance channel in San Diego, California. This paper reviews the main features of the grazing angle model and briefly illustrates its applications.

*Ocean Engineering Graduate Program, COPPE/UFRJ - Federal University of Rio de Janeiro, Caixa Postal 68508, Rio de Janeiro, Brazil. FAX (021) 290-6626

†Center for Coastal Studies, A-009, Scripps Institution of Oceanography, La Jolla, California 92093, USA. FAX (619) 534-0300

2 Model Description

Following the idea of Madsen & White's (1976) model for normally incident waves, the grazing angle model also divides the dissipation of wave energy in the rubble-mound jetty into "external" and "internal" components. The "external" dissipation is associated with fluid motion over the sloped face, and the "internal" dissipation with fluid motion within the pores of the structure. Internal dissipation is modeled with a permeable, surface piercing, homogeneous core of rectangular cross-section. External dissipation caused by run-up over the rough, sloped face is simulated with a surrounding region of comparable *bottom* roughness (Figure 1). The dimensions of the core and external dissipation regions and the representative stone size are estimated from the actual (usually trapezoidal and multi-layered) structure. Incident waves are assumed to be long, linear (nonbreaking), monochromatic and to approach the jetty at grazing angle with respect to the jetty axis (Figure 1).

The key model equation is the Helmholtz equation

$$\nabla^2 \phi + \bar{k}^2 \phi = 0 \quad (1)$$

where ∇ is the horizontal (x, y) gradient, and $\phi(x, y)$ the wave potential, proportional to the free surface displacement. Energy dissipation is accounted for in the model by allowing \bar{k} to be complex.

$$\bar{k} = \sigma(gh)^{-\frac{1}{2}} (1 - if)^{\frac{1}{2}} \quad (2)$$

where σ is the wave frequency, g the acceleration of gravity, h the water depth and f a linearized dissipation coefficient discussed in section 3.

As opposed to the normal incidence situation, the grazing angle case has a wave crest propagating *simultaneously* over three distinct regions: "open" water, the external dissipation region and the permeable core. The portion of the wave within the dissipative zones will be locally damped; gradients in wave height will be generated and a diffraction pattern will appear. Plane wave solutions (with a fixed amplitude and propagation direction) are not possible. Dalrymple, Kirby & Hwang (1984) were the first to study wave diffraction caused by areas of energy dissipation and their solution method is also utilized here (section 4).

3 Linearized Dissipation Coefficients

The linearized dissipation coefficient quantifies the amount of dissipation taking place in each region. In "open" water, dissipation is usually negligible compared to that associated with the jetty, so $f = 0$ away from the jetty.

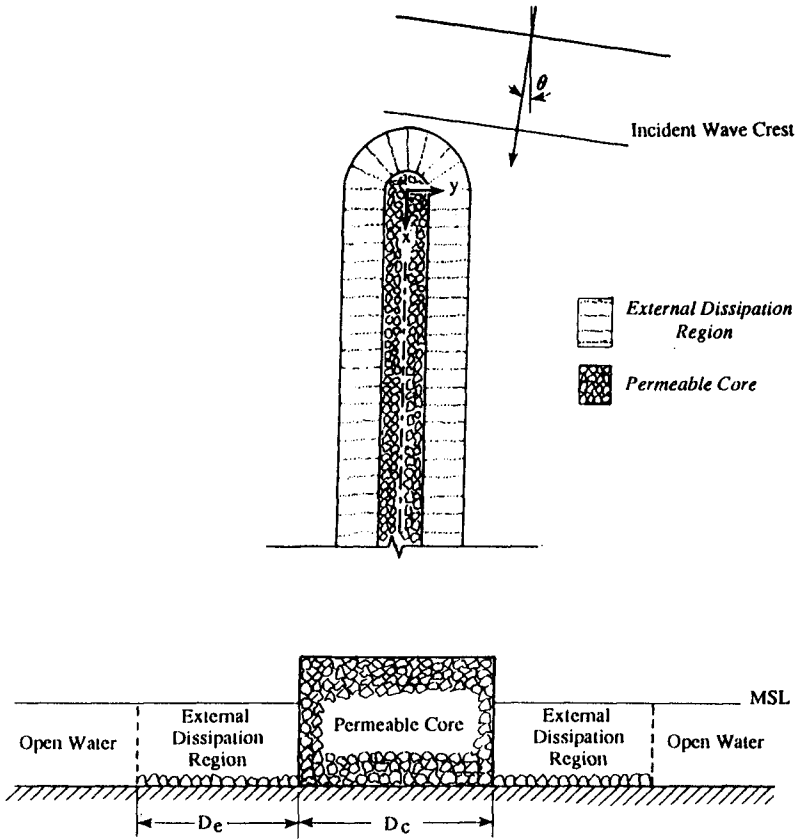


Figure 1: Plan view (upper) and cross-section (lower) of model breakwater.

The evaluation of f in the external region (f_{ext}) requires an estimate of the energy dissipated over a rough, steep slope by a wave at an arbitrary incidence angle. Until more is learned about this very complex problem, a representative value of f_{ext} is obtained from Madsen & White's (1976) reflection measurements of long waves *normally incident* on an impermeable, rough slope

$$f_{ext} \approx \frac{1 - R^2}{kD_e} \quad (3)$$

where R is a reflection coefficient, D_e is the width of the external dissipation region and k is the wavenumber. Madsen & White (1976) found that R was nearly independent of the incident wave height when $kl_s < 2$, where l_s is the length of the sloped face. The above condition is usually satisfied for swell waves in relatively shallow water and steep jetty faces, and makes f_{ext} indeed linear.

Nonlinear turbulent dissipation in the permeable core is included in the linearized model by means of the Lorentz principle of equivalent work [Sollitt & Cross (1976), Madsen & White (1976), Madsen (1983) and others]. In the general case, the internal dissipation coefficient, f_{int} , takes different values at different positions within the core (i.e. $f_{int}(x, y)$). The present model uses the fact that the core width is small compared to the wavelength (for relatively long waves) and assumes f_{int} to be constant in the transverse direction (y -dir). However, (slow) variations in the wave height within the core in the direction of wave propagation (x -dir.) make f_{int} a function of x . The iteration procedure used to calculate f_{int} and the parameterization of the porous medium are exactly the same ones utilized for normally incident waves (see, for example, Madsen (1983)).

4 Solution Method

The solution method suitable here is the parabolic approximation [Radder (1979), Booij (1981), Dalrymple, Kirby & Hwang (1984), Liu, Yoon & Dalrymple (1986), Kirby (1986)]. The governing Helmholtz equation (1) is split into parabolic equations for the transmitted and back-reflected fields. The back-reflected field is neglected and the resulting parabolic equation for the transmitted part is solved numerically. The equation to be solved, if the lower-order parabolic approximation is used, is

$$2i\bar{k} \frac{\partial A}{\partial x} + \left[2\bar{k}(\bar{k} - k) + i \frac{\partial \bar{k}}{\partial x} \right] A + \frac{\partial^2 A}{\partial y^2} = 0 \quad (4)$$

where A is the complex amplitude of the forward scattered wave field (ϕ^+)

$$\phi^+(x, y) = A(x, y) e^{ikx} \quad (5)$$

The applicability of the parabolic method relies on two assumptions:

- (i) That the wave propagates nearly along the axial direction of the jetty.
- (ii) That the back reflected (i.e. in the $-x$ -dir) wave field is negligible.

Assumption (i) is in accordance with the grazing angle requirement. For assumption (ii), the jetty head is the only place capable of producing strong back scattering. Elsewhere, x -variations in the medium of propagation are slow and no significant back reflection should occur. However, the effect of head scattering is expected to be small in the area of interest (i.e. for $x > 0$, Figure 1). Of course, assumption (ii) also implies the existence of a nonreflective boundary at the down-wave side (like a dissipative beach for example).

Numerical solutions are obtained by the Crank-Nicolson finite-difference scheme for a given initial condition. Solutions in the different regions must satisfy continuity of pressure and mass flux at the separating interfaces. This is straight forward at the interface between “open” water and the external dissipation region. However, at the permeable core interface there is a change in the porosity of the medium; a discontinuity in the normal velocity is required to assure mass conservation, and special matching conditions are necessary. Note also that the marching forward nature of the parabolic method is very convenient for the calculation of f_{int} by the Lorentz principle. The correct value of f_{int} is obtained after about 5 iterations.

5 Application Examples

In this section we illustrate the model results with two examples: a single jetty and a jettied channel.

Figure 2 shows the solution for a wave incident at 0° on a crib-style (rectangular cross-section) permeable jetty. In this particular application, all dissipation takes place in the permeable core and there is no external dissipation region. The opposite case of a virtually impermeable, sloped face structure can be treated by considering only external dissipation in the model. It is clear that the presence of the jetty alters significantly the wave field around it, even for a 0° incident wave. Even though the net effect of the jetty is to dissipate wave energy, the diffraction-reflection pattern can result in normalized wave heights greater than 1 (Figure 2). The solution for f_{int} is shown in Figure 3. The current example is for water of constant depth. However, this is *not* a constraint of the model, depth variations of mild slope can also be included. Preliminary tests show satisfactory results for incidence angles as large as 30° . More detailed studies of the single jetty case are under

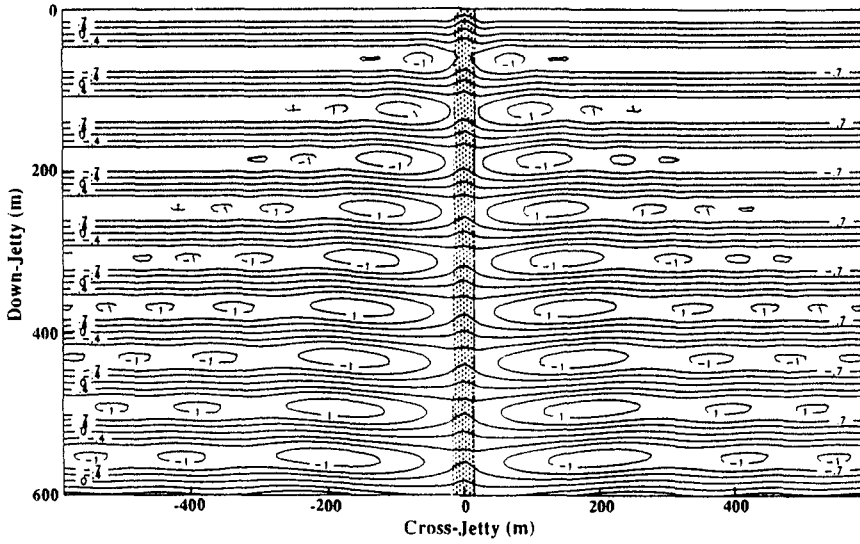


Figure 2: Normalized, instantaneous surface elevation field. Incoming wave: incidence angle = 0° , period = 14 sec, height = 0.8 m, length = 120 m. Model jetty: core width = 32 m, stone diam. = 1.25 m, porosity = 0.45. The origin of the semi-infinite jetty is at (0,0).

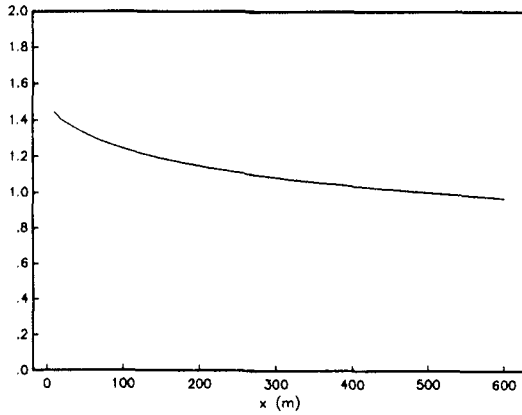


Figure 3: Corresponding f_{int} for Figure 2.

way and will be presented in a forthcoming paper.

Figure 4 shows the solution for a wave propagating in a constant depth channel bounded by nontransmitting (sealed) rubble-mound jetties. The wave is initially at 0° to the channel axis and the model jetties have both external and internal dissipation. As we anticipated, energy dissipation occurring along the jetties generate cross-channel gradients in wave height and the initially plane wave is deformed by diffraction. A damped plane wave is not possible in a wide channel with strong energy dissipation localized at the edges. The solution is a modulated wave with bent crests in spite of the constant water depth. The down-channel variation in f_{int} , shown in Figure 5, corresponds to regions of higher and lower wave heights within the permeable cores.

Model results for a jettied channel compared favorably to an extensive data set obtained at the straight, 1-km long, 250-m wide, 8-m deep Mission Bay entrance channel. The model predicted both the observed rapid wave height decay on the channel centerline and the observed insensitivity of the normalized rate of decay to variations in wave conditions (Figure 6). In the Mission Bay study, the linearized dissipation coefficients were evaluated with the methodology summarized in this paper, *not* by fitting to the data. A complete account of the jettied channel application can be found in Melo & Guza (1990 a,b).

6 Concluding Remarks

The linearized model proposed by Melo & Guza (1990 a,b) for the propagation of long waves at grazing angle to a rubble-mound jetty has been reviewed. Although a crude approximation to the full problem of a directional spectrum of waves propagating about a permeable, multi-layered, sloped structure, we believe it realistically captures the main physical mechanisms of dissipation in the jetty and diffraction in the wave. The model may be a useful engineering tool and, with further refinements, may serve as a basis for dealing with obliquely incident waves on many types of dissipative structures.

Acknowledgements

This work was supported by the Coastal Sciences Branch of the Office of Naval Research, contract N00014-89-J-1055. The California Department of Boating and Waterways (CDBW) supported the Mission Bay data analysis as part of its continuing program of studies to enhance boating safety and access

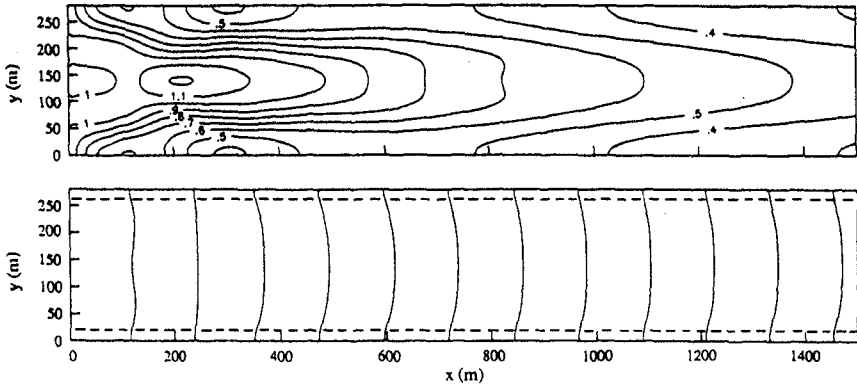


Figure 4: Normalized wave height contour (upper) and wave crests (lower) for a jettied channel. Non-transmitting model jetties are indicated by dashed lines. Incoming wave: same as in Figure 2. Model jetties: permeable core width = 10 m, external diss. width = 10 m, stone diam. = 1.25 m, porosity = 0.45.

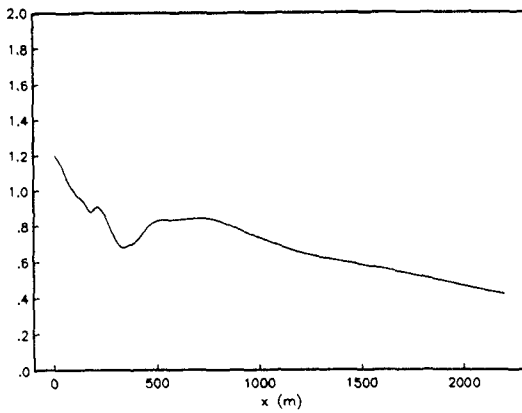


Figure 5: Corresponding f_{int} for Figure 4; $f_{ext} = 0.5$ (constant).

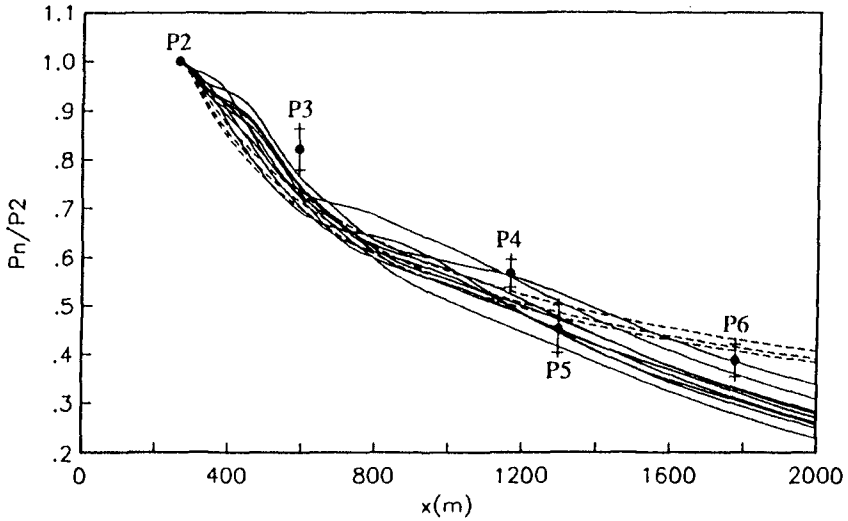


Figure 6: Full lines: model results for the wave height on the channel centerline at location P_n normalized by the height at P2, the sensor located nearest the channel mouth ($x = 0$), for a range of initial conditions including: $0.5 \leq H_o \leq 2.0 m$, $-10^\circ \leq \theta \leq 10^\circ$ and $14 \leq T \leq 20 sec$. Dashed lines: gap diffraction solutions with gap width equal to the waterway width, $-10^\circ \leq \theta \leq 10^\circ$ and $14 \leq T \leq 20 sec$. Also shown are the observed mean (circle) and standard deviation (brackets) of the P_n/P_2 ($n=2,3,4,5,6$) wave height ratio for runs when energy in the period range $13.5 \leq T \leq 23.3 sec$ was at least 70% more than at higher frequencies where the model assumption of long waves is violated.

in California. E.M. received personal support from "Conselho Nacional de Desenvolvimento Científico e Tecnológico" (CNPq, Brazil) and from CDBW.

References

- Booij, N., Gravity waves on water with non-uniform depth and current, Ph.D. dissertation, *Technical University of Delft, the Netherlands*, 130 pp, 1981.
- Dalrymple, R.A., Kirby, J.T. and Hwang, P.A., Wave diffraction due to areas of energy dissipation, *Jour. Waterway, Port, Coastal and Ocean Engineering*, 110(1), pp 67-79, 1984.
- Kirby, J.T., Higher-order approximations in the parabolic equation method for water waves, *Jour. Geophys. Res.*, 91(C1), pp 933-952, 1986.
- Liu, P.L.-F., Yoon, S.B. and Dalrymple, R.A., Wave reflection from energy dissipation region, *Jour. Waterway, Port, Coastal and Ocean Engineering*, 112(6), pp 632-644, 1986.
- Madsen, O.S. and White, S.M., Reflection and transmission characteristics of porous rubble-mound breakwaters, *USACOE, CERC, Misc. Rep. No. 76-5*, 138 pp, 1976.
- Madsen, P.A., Wave reflection from a vertical permeable wave absorber, *Coastal Engineering*, 7, pp 381-396, 1983.
- Melo, E. and Guza, R.T., Wave propagation in a jettied entrance channel, *Scripps Institution of Oceanography, Reference series 90-1*, 82 pp, 1990a.
- Melo, E. and Guza, R.T., Wave propagation in a jettied entrance channel, *Jour. Waterway, Port, Coastal and Ocean Engineering (in review)*, 1990b.
- Radder, A.C., On the parabolic equation method for water-wave propagation, *Jour. Fluid Mech.*, 95, part I, pp 159-176, 1979.
- Sollit, C.K. and Cross III, R.H., Wave reflection and transmission at permeable breakwaters, *CERC, Tech. paper No. 76-8*, 172 pp, 1976.

CHAPTER 32

Movable Bed Friction Factors for Spectral Waves

Ole S. Madsen¹, Paul P. Mathisen², M. Michel Rosengaus³

Abstract

This paper presents a summary of carefully conducted laboratory experiments on the attenuation of simulated spectral waves propagating over an 18-m-long bottom section covered by 10-cm-thick layers of 0.12- and 0.2-mm-diameter uniform quartz sands. The measured attenuation is used in conjunction with the theory for spectral wave attenuation developed by Madsen et al. (1988) to determine values of the movable bed friction factor for spectral waves. When the values of movable bed friction factors, f_{wr} , are plotted against a fluid-sediment interaction parameter, the ratio of skin friction Shields parameter for an equivalent monochromatic wave, ψ_{mr}' , and the critical value of Shields parameter for initiation of sediment motion, ψ_c , a well-defined relationship between f_{wr} and ψ_{mr}'/ψ_c emerges. This relationship is independent of spectral shape (both finite-depth Jonswap and Neumann spectra were simulated) and is the same for the two sediment types tested. Although limited by the range of experimental conditions achieved in the laboratory study the results suggest a simple methodology for the evaluation of spectral wave attenuation from knowledge of sediment and wave characteristics.

¹Professor of Civil Engineering, R. M. Parsons Laboratory, MIT, Cambridge, MA 02139, USA

²Graduate Research Assistant, R. M. Parsons Laboratory, MIT, Cambridge, MA 02139, USA

³Hydraulics Specialist, Instituto Mexicano de Tecnologia del Agua, Jiutepec, Morelos, Mexico

Introduction

In order to predict the attenuation by bottom friction for waves propagating in finite water depth over a movable bottom, it is necessary to estimate the value of the bottom roughness or alternatively the wave friction factor. For wave conditions exceeding the threshold of sediment movement, bottom roughness or wave friction factor is governed by wave-sediment interaction and is related to the characteristics of the wave-generated bedforms. Based on rather limited experimental evidence obtained for wave-sediment interaction, corresponding exclusively to simple periodic waves, predictive relationships for the roughness of movable beds subjected to wave agitation have been proposed, e.g., Grant and Madsen (1982). Neither theoretical nor experimental justification appeared to exist for the transfer of this "knowledge" to the more realistic description of waves in terms of their spectrum until Madsen et al. (1988) presented a theoretical model for the attenuation of spectral waves propagating over a rough bottom, described by its equivalent roughness, k_b . Based on this model Madsen and Rosengaus (1988) developed a methodology for the prediction of spectral wave attenuation by bottom friction. This methodology consisted of:

- 1) representing the spectral wave condition by a representative monochromatic wave having the same root-mean-square near-bottom orbital velocity, u_{br} , and excursion amplitude, A_{br} , as the spectral wave;
- 2) using the representative wave in conjunction with empirical relationships established for monochromatic waves to predict the geometry, relative height, η/A_{br} , and steepness, η/λ , of the wave-generated bottom bedforms;
- 3) obtaining the relative equivalent bottom roughness from an empirical relationship giving k_b/A_{br} as a function of bedform geometry.

The empirical relationships necessary for the implementation of the procedure outlined above were established through extensive and carefully conducted experiments with monochromatic waves (Madsen and Rosengaus, 1988) and the proposed methodology for the prediction of spectral wave attenuation by bottom friction was tested against experimental data. However, the experimental data on which the methodology was based were *limited* by having been obtained for a single sediment, a 0.2-mm quartz sand, and the test of the spectral wave attenuation methodology was *limited* to wave conditions exceeding only slightly the critical condition for initiation of sediment motion. For these reasons Madsen and Rosengaus (1988) emphasized that

their proposed spectral wave attenuation methodology "should be regarded as preliminary until further experiments, covering a wider range of experimental parameters, can support its general validity."

The objective of the present study was to remove the limitations of the previous experimental investigation by: i) performing experiments with a different sediment (a 0.12-mm quartz sand); and ii) extending the range of spectral wave conditions tested to values well above those corresponding to initiation of sediment motion.

The philosophy behind the experimental methodology and procedures used in the present study is unchanged from that of Madsen and Rosengaus (1988). Simply stated, it is to measure the attenuation of water waves (periodic as well as simulated spectral waves) propagating over a long section of movable bed and from the measured attenuation of each incident wave component backfigure the appropriate value of the wave friction factor for each incident wave component using the theoretical model for spectral wave attenuation developed by Madsen et al. (1988). Attempts to relate the experimentally obtained values of friction factors through the corresponding equivalent bottom roughness to geometry of the bottom bedforms, i.e., using the Madsen and Rosengaus (1988) procedure in reverse, were unsuccessful. Therefore, in contrast to Madsen and Rosengaus (1988), the friction factor values obtained here are used directly in an attempt to establish a *friction factor relationship* without the intermediate steps of relating friction factors to equivalent roughness and then relate equivalent roughness to geometry of the wave-generated bottom bedforms.

Methodology and Procedures

The experimental set-up, methodology, and procedures used in this study are identical to those described by Madsen and Rosengaus (1988).

Experimental Set-up. Laboratory experiments were performed in a 0.75-m-wide, 0.90-m-deep, and 30-m-long wave flume in the R. M. Parsons Laboratory. This wave flume is equipped with a programmable piston-type wave maker and has a 1-on-10 sloping absorber beach, which in the present experiments was covered by 7.5-cm-thick horsehair mats to further decrease reflections. At the wavemaker a trapezoidal wooden ramp provided a smooth transition to a level 10 cm above the flume bottom. The region between the ramp--approximately 3 m from the

wavemaker--to the start of the absorber beach--approximately 19 m from the wavemaker--was covered by a 10-cm-thick layer of very uniform 0.12- or 0.2-mm-diameter quartz sand. The water depth above the movable bed test section was 0.6 m for the majority of the experiments with a few experiments conducted at a depth of 0.5 m.

Waves. In order to mobilize the bed material it was necessary to generate waves of large amplitudes and wave length. The standard wave condition of Madsen and Rosengaus (1988) corresponded to a 6-cm-amplitude, 2.65-sec-period wave for which the depth-to-wavelength ratio $h/L = 0.1$ in the 0.6-m-deep section. In the present investigation the wavemaker motion was programmed to simulate the generation of an incident wave spectrum with a peak period corresponding to a depth to peak period wave length ratio of 0.1 in the test section and a root-mean-square wave height ranging from 8.4 cm to 13.4 cm. Both broad-banded Pierson-Neumann spectra and narrow-banded finite-depth Jonswap ($\gamma = 3.3$) spectra were simulated by five frequency components of equal energy.

Measurements. The incident and reflected wave spectra were determined from measurements of surface profiles obtained by two three-gauge arrays located 3 m and 18 m from the wavemaker, respectively. Although not used directly in the analysis of the experimental data obtained in the present study bottom bedform geometry was determined photographically by taking pictures of 1-m sections of the bed profile at four stations along the test section. These pictures, including horizontal and vertical scales, were then projected onto a digitizing tablet and analyzed. Using a vertically mounted laser to trace the bottom profile at different distances from the flume sidewalls it was shown that the trace along the sidewalls accurately represented the bedform geometry.

Procedures. Given the philosophy behind the experiment as outlined in the Introduction the procedure to be followed is quite simple. From the analysis of Madsen et al. (1988) we may write the energy conservation principle for each wave component when only bottom dissipation is considered

$$c_{gn} \rho g a_n \left[\frac{\partial a_n}{\partial x} \right]_{bf} = -E_{d,n} = -\frac{1}{4} \rho f_{wn} u_{br} u_{bn}^2 \quad (1)$$

where ρ is the fluid density, g is gravity, a_n and c_{gn} are the amplitude and group velocity of the wave

component of frequency ω_n , respectively, and for a finite number of wave frequency components

$$u_{br} = \sqrt{\sum_n u_{bn}^2} \quad (2)$$

$$A_{br} = \sqrt{\sum_n (u_{bn}/\omega_n)^2} = u_{br}/\omega_r \quad (3)$$

Thus, for a single wave component--whether it is alone or one of two or more--we have from Eqs. (1) through (3) and linear wave theory

$$\left[\frac{\partial a_n}{\partial x} \right]_{bf} = -f_{wn} \frac{u_{br}}{4gc_{gn}} \left[\frac{\omega_n}{\sinh k_n h} \right]^2 a_n \quad (4)$$

In principle the experimental determination of a_n at two stations, Δx apart, suffices to determine a value of f_{wn} from Eq. (4). In practice, however, life is unfortunately not that simple.

All the experimental determinations of Δa_n involve the "small" difference between two "large" quantities. As an example we may take the standard periodic wave ($a_n = 6$ cm, $T_n = 2\pi/\omega_n = 2.65$ sec, $h = 0.60$ m) and a friction factor of $f_{wn} = 0.2$ to obtain a change in amplitude of $\Delta a_n \approx 7$ mm over the 15-m-long test section. While this value of Δa_n is well above the accuracy with which the individual amplitude is determined experimentally--estimated to be of the order 0.5 mm--it should be recalled that component amplitudes of the order 2 to 3 cm are used in spectral simulations. In fact, the decision to simulate the wave spectra by five frequency components was arrived at precisely from consideration of desired accuracy. Nevertheless, we are in some cases attempting to measure differences of the order a mm or less, i.e., approaching the magnitude of uncertainty of each measurement used to determine the difference. For this reason alone it is essential that the experiments be conducted with great thoroughness and repeated several times in order to minimize the effect of experimental errors. In the present investigation all experimental determinations of wave attenuation for a given wave condition were repeated five to ten times.

As a result of the inherent experimental difficulties associated with an accurate determination of Δa_n the variability in friction factors for the individual frequency components, f_{wn} , obtained from Eq. (4) is quite large. However, the theory developed by Madsen et al. (1988) assumed the friction factors for

the individual frequency components, f_{wn} , to be the same for all frequency components. For these reasons the wave attenuation data were used to obtain values of f_{wn} from Eq. (4) and these values were then used to obtain a single "representative" wave friction factor, f_{wr} , from

$$f_{wr} = \frac{\sum_n f_{wn} u_{bn}^2}{\left[\sum_n u_{bn}^2 \right]} \quad (5)$$

In passing, it should be noted that the representative wave friction factor, defined by Eq. (5), will conserve total spectral dissipation when applied to each individual frequency component.

However, other effects in addition to those directly related to measurement accuracy play a role in these experiments. Owing to the requirement of long waves of substantial amplitude--to set the bottom sediment in motion--it can be expected that nonlinear effects come into play. To illustrate this, assume the change of amplitude, Δa_n , to have been determined experimentally over a distance Δx . Formally, we may then write

$$\frac{\partial a_n}{\partial x} \simeq \frac{\Delta a_n}{\Delta x} = m = m_{nl} + m_{sw} + \left[\frac{\partial a_n}{\partial x} \right]_{bf} \quad (6)$$

in which m_{nl} denotes amplitude changes associated with non-linearity, m_{sw} the changes associated with dissipation along the side walls, and $(\partial a_n / \partial x)_{bf}$ is the quantity expressing the contribution of bottom friction, i.e., the quantity we are looking for. A priori we cannot neglect the unwanted contributions, m_{nl} and m_{sw} , in particular when the overall requirement of accuracy is kept in mind.

To evaluate the magnitude of the terms m_{nl} and m_{sw} in Eq. (6) a series of experiments was first conducted in which the incident wave characteristics at the two measurement stations were determined corresponding to flat-bed conditions, i.e., sufficient time following the start of the wavemaker was allowed for transients to die out and the bed was covered by thin steel plates to prevent bedform development. Experiments of this type were performed 5 to 10 times and the measured amplitude change in these experiments (denoted by subscript p)

$$\left[\frac{\Delta a_n}{\Delta x} \right]_p = m_p \simeq m_{nl} + m_{sw} + m_{fb} \quad (7)$$

was taken to represent nonlinear and sidewall effects also in the movable bed runs. The bottom friction

effect, m_{fb} in Eq. (7), was calculated theoretically--the bottom boundary layer remained laminar for flat bed conditions.

Following the preliminary runs the wave condition was maintained in the flume for sufficiently long time to ensure the bedforms on the bottom to be fully developed (in some cases this took several hours). Several wave measurements were then performed corresponding to fully developed bed conditions with bottom bedform geometry determined between individual wave measurements (to ensure that the bed indeed was fully developed). Combining the preliminary and the fully developed wave measurements produced experimental results for the isolated effect of wave attenuation

$$\left[\frac{\partial a_n}{\partial x} \right]_{bf} \approx \left[\frac{\Delta a_n}{\Delta x} \right]_{bf} = m - m_p + m_{fb} \quad (8)$$

caused by the movable bed, which in turn were used in Eqs. (4) and (5) to obtain friction factors.

Results

The experimental values obtained for the representative spectral wave friction factor, f_{wr} , are presented as full symbols (with one standard deviation error bars indicated) in Figure 1 versus the representative value of a fluid-sediment interaction parameter

$$S_r = \frac{\psi_{mr}'}{\psi_c} \quad (9)$$

in which

$$\psi_{mr}' = \frac{\tau_{bm}'}{(s-1)\rho g d} \quad (10)$$

is the Shields parameter obtained from the maximum bottom shear stress predicted for the representative monochromatic wave defined by Eqs. (2) and (3) based on grain-size bottom roughness, i.e., for $k_b = d$, and ψ_c is the critical shear stress for initiation of sediment movement obtained from Shields criterion (Madsen and Grant, 1976). Thus the parameter S_r represents the extent to which threshold conditions are exceeded. For comparison the wave friction factors obtained from monochromatic wave experiments are included as open symbols in Figure 1.

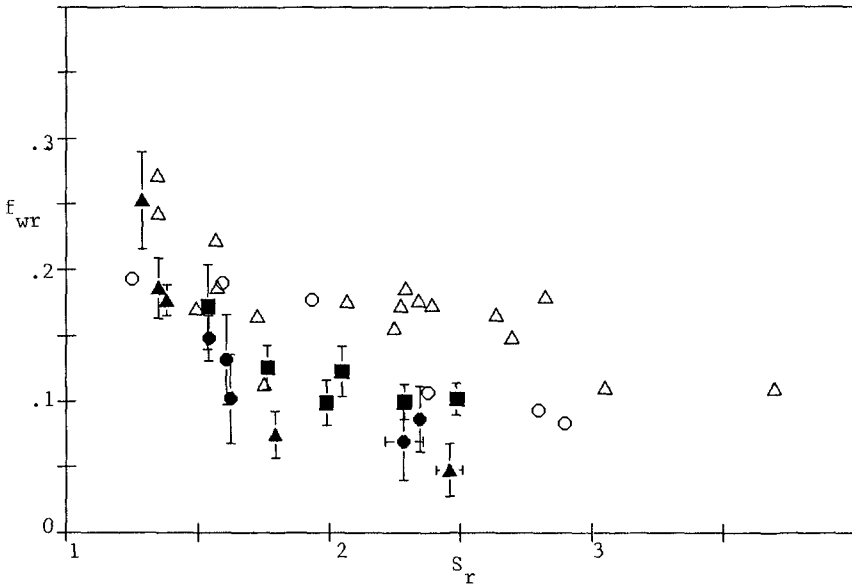


Figure 1. Movable bed friction factors for spectral waves (solid symbols) and periodic waves (open symbols). Triangles: 0.2-mm, Pierson-Neumann spectrum; circles: 0.12-mm, Pierson-Neumann spectrum; squares: 0.12-mm, finite-depth Jonswap spectrum

A striking feature of the spectral wave friction factors presented in Figure 1 is that they appear to form a unique relationship $f_{wr} = f_{wr}(S_r)$, despite the fact that the values were obtained for different sediments (0.2-mm- and 0.12-mm-diameter quartz sands) and for different spectral shapes (broad-banded Pierson-Neumann and narrow-banded finite-depth Jonswap spectra with $\gamma = 3.3$). While this finding is extremely fortunate from the point of view of practical application of the results it is of some concern that the spectral wave friction factors consistently fall considerably below the values of their monochromatic counterparts for $S_r > 1.5$.

The methodology for the determination of spectral wave friction factors proposed by Madsen and Rosengaus (1988) should result in a negligible difference between spectral and monochromatic wave friction factors so long as their associated bottom bedforms are similar. Examination of the height and length of bedforms generated by spectral and monochromatic waves reveals that the spectral bedforms have a slightly smaller

height and a somewhat smaller steepness than their monochromatic counterparts. However, accounting for this difference in bedform geometry would at most account for a 20-percent decrease in the spectral wave friction factors relative to the monochromatic values when the bedform geometry is used in conjunction with the empirical relationship for bottom roughness proposed by Madsen and Rosengaus (1988). Referring to the results presented in Figure 1 it is evident that a larger-than-20-percent reduction of the monochromatic wave friction factors is called for to bring them in line with the spectral results. It is therefore concluded that the methodology for the evaluation of spectral wave friction factors proposed by Madsen and Rosengaus (1988) indeed is limited by the limited range of their experiments. In fact, it worked for them only because their spectral experiments were limited to values of $S_r < 1.5$, i.e., those represented in Figure 1 by the three points with $S_r \approx 1.3$, which just happened to overlap with the monochromatic results.

In an attempt to explain the reduction of spectral wave friction factors the digitized records of the bottom profiles, obtained from photographs of the fluid-sediment interface along the glass side-walls of the flume, were carefully examined with particular emphasis on the characteristics of the ripple crests. In this manner it was found that ripple crests generated by spectral waves were somewhat more rounded than those generated by monochromatic waves. Clearly, the rounding of a sharp ripple crest only reduces the ripple height slightly (as observed) but results in a significant reduction of the strength of flow separation over the crest. It is hypothesized that the larger waves in a spectral simulation shave off the sharp ripple crests thereby causing the observed reduction in dissipation and friction factors for spectral waves. Since maximum near-bottom orbital velocities associated with spectral waves are approximately Rayleigh-distributed regardless of spectral shape, this hypothesis supports our finding that spectral dissipation is independent of spectral shape.

Summary and Conclusions

The spectral wave friction factors obtained from our experiments and presented in Figure 1 may be represented with a 20-percent error by the following movable bed friction factor relationship

$$f_{wr} = 0.29 S_r^{-1.5} \quad \text{for} \quad S_r > 1.2 \quad (11)$$

This expression may in turn be used with the spectral wave boundary layer theory of Madsen et al. (1988) to obtain a relationship, accurate to within 30 percent, for the movable bed roughness associated with spectral waves

$$k_b/A_{br} = 1.5S_r^{-2.5} \quad \text{for} \quad S_r > 1.2 \quad (12)$$

It is tentatively proposed that these relationships are generally valid for cohesionless sediments regardless of spectral shape. Having been burned once, it should be *emphasized* that experimental support of these expressions is limited to values of $S_r < 2.5$. However, some comfort in extrapolating the expressions beyond this limit may be found in the dependency of the relative roughness on S_r to the negative 2.5 power being identical to the S_r -dependency of the bottom bedform roughness of Grant and Madsen (1982) for large values of S_r .

Acknowledgments

The research presented here was funded as project RC-18 by the MIT Sea Grant College Program under federal grant NA86 AA-D-SG089 from the National Sea Grant College Program, National Oceanic and Atmospheric Administration, U.S. Department of Commerce. The assistance of Chris Rehmann, UROP student on the project, is acknowledged as are the expert typing skills of Read Schusky.

References

- Grant, W. D., O. S. Madsen. 1982. Movable bed roughness in oscillatory flow. *J. Geophys. Res.* 87(C1):469-481.
- Madsen, O. S., W. D. Grant. 1976. Quantitative description of sediment transport by waves. Proc. 15th ICCE, ASCE 2:1093-1112.
- Madsen, O. S., M. M. Rosengaus. 1988. Spectral wave attenuation by bottom friction: Experiments. Proc. 21st ICCE, ASCE 1:849-857.
- Madsen, O. S., Y.-K. Poon, H. C. Graber. 1988. Spectral wave attenuation by bottom friction: Theory. Proc. 21st ICCE, ASCE 1:492-504

CHAPTER 33
2ND ORDER WAVE GENERATION
AND APPLICATION TO SHOALING INVESTIGATIONS

by

A. Götschenberg and K.F. Daemrich¹

ABSTRACT

Model tests have been carried out in a wave channel with and without consideration of 2nd order wave components in the control signal for the wave paddle. The wave channel was equipped with a 1:30 sloped bottom starting 57.00 m in front of the paddle. The water depth was 1.00 m during all tests.

The Self-Correcting System was proved to be able to suppress unwanted free higher and lower harmonics during the generation process.

On the slope measured amplitudes of the 2nd order waves were lower than predicted by 2nd order theory. Commonly used wave height parameters are not influenced significantly by the type of control signal.

1. Introduction

A large number of shoaling investigations have been carried out in the last two decades. Starting with pure regular wave investigations, later on tests were performed with irregular seastate and finally with directional spectra in the increasing number of 3D wave basins in the world. On the other hand with the increasing amount of computer hardware power available, software tools were developed to calculate shoaling phenomena in 2D or 3D models. But still there is a lack of information concerning the behaviour of non-linear waves generated in a wave channel either in a horizontal section and especially over a sloping bottom.

This paper deals with the generation of 1st and pertinent 2nd order waves in a wave channel. A technique is presented leading to proper 2nd order wave components without unwanted free waves in the horizontal section of the channel. Measured values of 2nd order wave amplitudes and commonly used wave height parameters are plotted for the shoaling area.

1 Res. Engineers, FRANZIUS-INSTITUT, Univ. of Hannover,
Nienburgerstr. 4, D-3000 Hannover 1, Germany

2. 2nd Order Wave Theory for Wave Groups and Spectra

The theoretical solution of 2nd order wave phenomena is referred to SAND (1982, "Long Wave Problems ...") and SAND/MANSARD (1986, "Reprod. of Higher Harmonics..."). They present transfer function formulas which allow the computation of the amount of 2nd order wave components in irregular wave trains. Fig. 1 shows a time series of a simple wave group, composed of two frequencies f_1 and f_2 . The extension of 1st order theory to 2nd order shows that additional wave components appear at frequencies $f_2 - f_1$ (bounded long wave) and $f_1 + f_2$ (higher harmonic). Furthermore the higher harmonics $f_1 + f_1$ and $f_2 + f_2$, known from the regular wave theory, are 2nd order effects related to each basic frequency component. The superposition of 1st and 2nd order waves shows the typical flatter troughs and sharper crests compared to the linear wave train. Lower and higher harmonics are bound to the group of the basic linear waves, i.e. they do not propagate as linear waves with similar frequencies but with the group velocity.

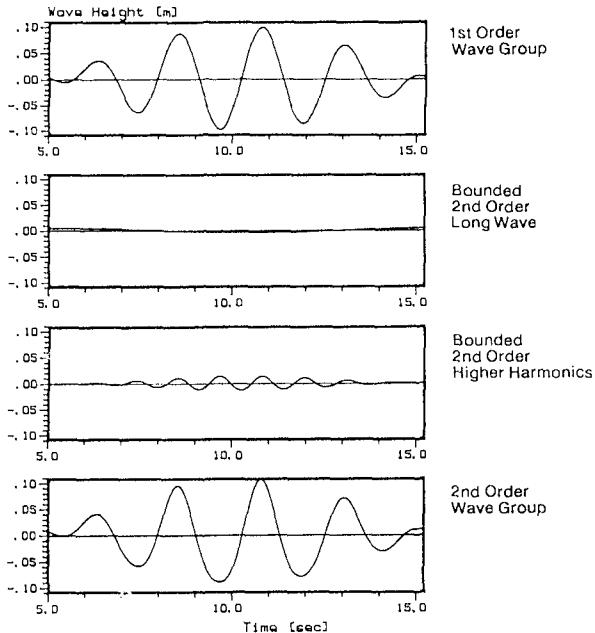
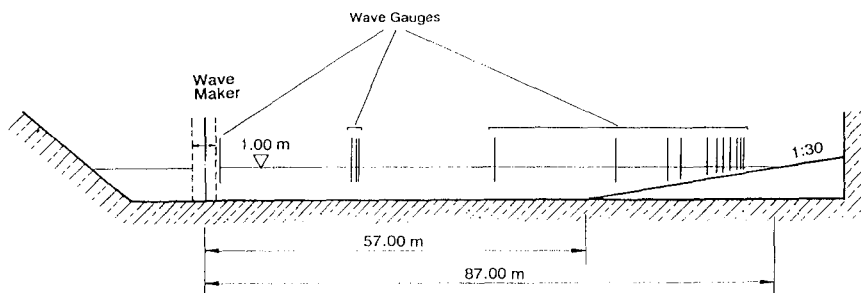


Fig. 1: Example of a Wave Group and Pertinent 2nd Order Components

2nd order waves of an irregular wave train are calculated by superposition of lower and higher harmonics of all possible combinations of frequencies in the 1st order spectrum.

The amplitudes of lower and higher harmonics are calculated from transfer functions given in the above mentioned papers.

When a 1st order wave train is generated in a hydraulic model, a transformation process occurs near the wave paddle generating the group bounded long wave (f_2-f_1) and also the bounded higher harmonics f_1+f_1 , f_1+f_2 , and f_2+f_2 . During this process also free long waves and free higher harmonics are created which are about 180° out of phase at the paddle compared to the bounded wave components and move independent from the basic linear wave combinations. At a certain frequency (i.e. f_2+f_1) two waves are existent in the channel: the bounded one which belongs to the 1st order waves and should not be suppressed and the unwanted free one which should be suppressed because it is only due to the technique of wave generation in the model and may cause problems in model test interpretation.



Gauge No.	Distance to Paddle	Water-depth	Gauge No.	Distance to Paddle	Water-depth
[-]	[m]	[m]	[-]	[m]	[m]
1	1.00	1.000	9	78.20	0.360
2	23.01	1.000	10	79.90	0.205
3	23.41	1.000	11	80.92	0.170
4	23.67	1.000	12	81.88	0.135
5	45.22	1.000	13	82.54	0.115
6	63.62	0.750	14	83.03	0.100
7	71.85	0.478	15	83.63	0.080
8	73.94	0.410			

Fig. 2: Experimental Setup

3. Model Test Layout

Fig. 2 shows the experimental setup during the tests in the wave channel at FRANZIUS-INSTITUT. The channel has a horizontal bottom of 57.00 m length and a 1:30 sloped plywood beach at the end. The width of the channel is 2.20 m and the water depth is 1.00 m. The wave paddle was driven in "pusher mode" during all tests. Some wave gauges are installed in the area with the horizontal bottom. The greater part is concentrated on the slope, mainly in the region with low water depth. Test series contained regular waves, bichromatic waves (groups composed of two frequencies) and spectra with different incident wave steepness and peak enhancement factors.

The sequence length of the wave groups was 20.48 sec and the sequence length of the spectra was 102.4 sec. All signal creation and measurement analysis work was done on a HP1000/A600+ computer equipped with DA/AD converter. The sampling rate of signal input and output was 80 msec in the case of wave groups and 100 msec in the case of spectra. The measurement of the gauge signals starts when the wave paddle starts to move and lasts 4 minutes if wave groups are generated and 6 minutes for wave spectra respectively.

4. Generation of Wave Groups

4.1. Analysis over Test Duration

In order to value the existence of bounded and free waves an FFT-analysis of the measured time series was performed for several time windows. Fig. 3 shows results from tests with 1st order wave generation. The variation of the measured amplitudes of the frequency component f_2-f_1 with increasing test duration is plotted in different water depths ($f_1=0.25$ Hz, $f_2=0.30$ Hz). In comparison the theoretical amplitudes according to the formula of SAND applied to the measured components f_1 and f_2 is shown. The control signal in this test contains no 2nd order amplitude, especially no (f_2-f_1) -component. It clearly can be stated, that the amplitude of this component is different in space and time dimension. The top frame contains the component at gauge 1 (water depth $h=1.00$ m) near the paddle. The amplitude is about 2 mm, increasing to 15 mm after 70 sec test duration due to reflection. At gauge 4 ($h=1.00$ m) the amplitude increases from 4 to 13 mm and at gauge 9 ($h=0.27$ m), where still no breaking occurs, the amplitude reaches 25 mm and decreases to 18 mm after 100 sec. From

the results in the time windows without reflection it can be seen that in the channel a system of two waves, both with the frequency f_2-f_1 , a bounded and a free one, exists. The superposition leads to different resultant amplitudes in space because of different propagation velocities in the channel.

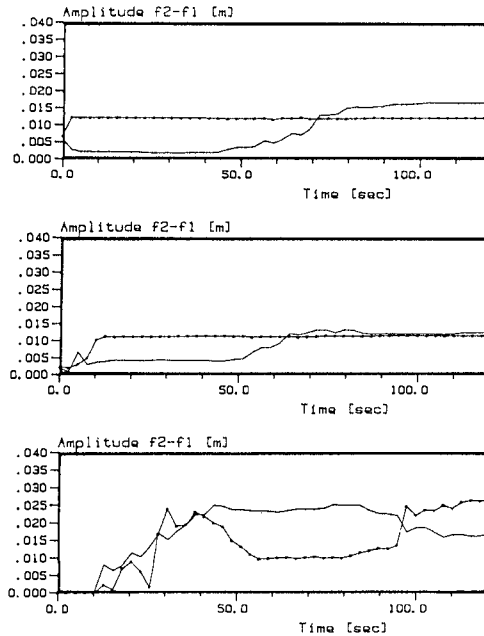


Fig. 3: Amplitude of 2nd Order Frequency Component f_2-f_1 versus Test Duration without Compensation ($f_1 = 0.24$ Hz, $f_2 = 0.29$ Hz, dotted line: Theory)

A proper generation method should create the bounded lower and higher components without parasitic free waves. Measured amplitudes would then be constant in space and, as long as there is no influence from reflection, in time. Ignoring the theoretical solution of 2nd order theory for computation of the control signal we have used the "Self-Correcting System" (DAEMRICH, EGGERT, 1981) for the generation of the control signal with the higher and lower harmonic components.

The target wave train was computed first with lower and higher harmonics according to the theory. Then a control signal for the wave paddle was calculated using linear

hydromechanic transfer functions as a first input. 3 or 4 test runs with the Self-Correcting System were made to find the best fitting of desired and target wave train at the reference gauge. For an easy and definite detection of deviations from the target wave train the reference wave gauge has to be chosen close to the wave paddle. In our test it was chosen to be the gauge 1 m in front of the wavemaker.

Fig. 4 shows the component f2-f1 now with compensation of 2nd order waves in the above mentioned way. Top and middle curve are gauges in the horizontal section of the channel. The third graph is again gauge 9 on the slope. The wave group reaches this point after 30 sec, at that time the amplitude of the component f2-f1 starts to increase.

Amplitudes fit the theoretical values very well in the horizontal section up to the time step 40 sec. The amplitudes of the basic linear components f1 and f2 are stable during the whole test run. The increasing amplitude after 40 sec indicates a reflected wave at the frequency component f2-f1. From our analysis it cannot

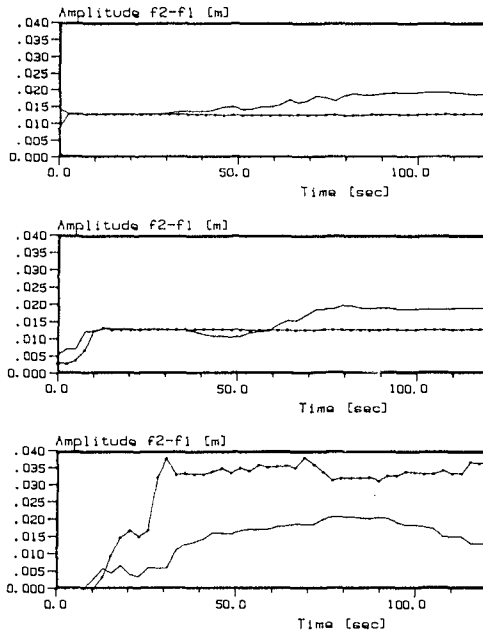


Fig. 4: Amplitude of 2nd Order Frequency Component f2-f1 versus Test Duration with Compensation (f1 = 0.24 Hz, f2 = 0.29 Hz, dotted line: Theory)

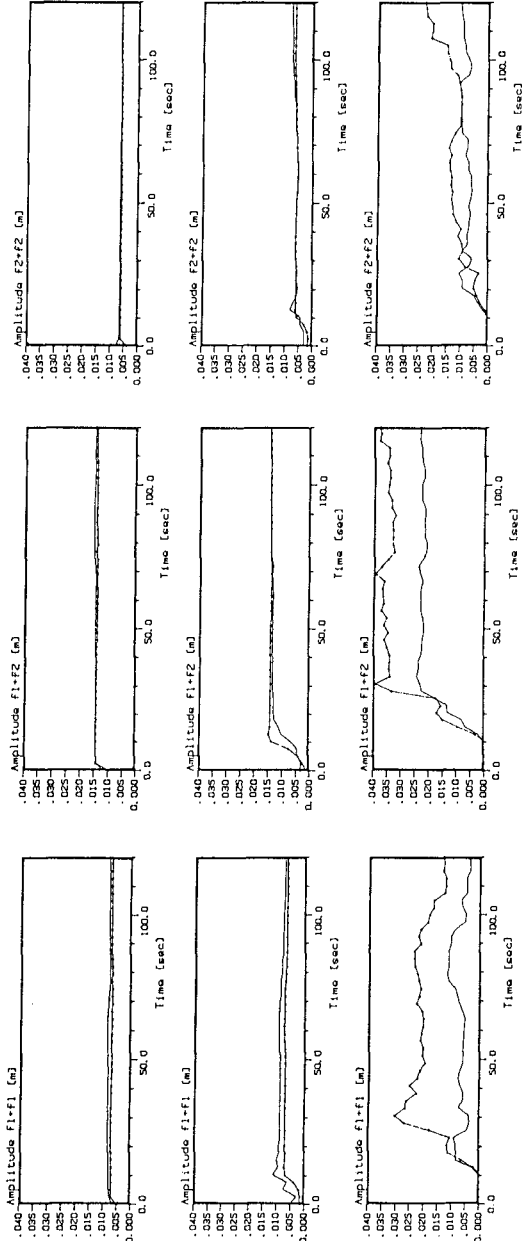


Fig. 5: Amplitude of 2nd Order Frequency Components f_1+f_1 , f_1+f_2 , and f_2+f_2 versus Test Duration with Compensation ($f_1 = 0.24$ Hz, $f_2 = 0.29$ Hz, dotted line: Theory)

be clearly stated whether it is a reflected bounded long wave or a reflected free wave, created during the propagation of the basic linear waves over the sloping bottom at the end of the channel.

At gauge 9 in a water depth of 0.27 m (bottom curve, Fig. 4) the measured amplitude was always lower than the theoretical one, but both curves are nearly stable over time when the group reaches this point.

The time variation of the amplitudes of the higher harmonics are similar to the variation of the lower component in Fig. 4. In Fig. 5 the higher harmonics are plotted over test duration for the case with 2nd order compensation in the control signal. The measurements fit very well with calculations and are stable over time. In the higher harmonic components almost no free parts are detectable. On the slope the measured amplitudes are always lower than predicted by theory.

4.2. Analysis over Channel Length

In Fig. 6 the measured amplitude of the lower harmonic ($f_2 - f_1$) is plotted over the channel length with (Fig. 6, top) and without (Fig. 6, bottom) compensation of 2nd order waves. The FFT-analysis starts 40 sec after start of the wave paddle movement. Test conditions are the same as in the previous plots. If no free wave component exists in the channel, the curves labeled "theory" and "model test" should be parallel to x-axes and have similar course in the horizontal section of the channel. Without compensation of 2nd order waves the amplitudes differ in space, indicating the existence of both bounded and free components. With compensation nearly no free component is detectable.

In Fig. 7 the 2nd order higher harmonic wave amplitudes are plotted from tests with and without compensation. The tendency is the same as for the lower harmonic: Without compensation of 2nd order waves, the amplitude differs over the channel length, a free wave exists. With compensation almost no free wave is detectable in the horizontal section.

Fig 8 and 9 are similar plots like Fig. 6 and 7 but for a shallow water wave group.

The results reported were obtained from tests with groups that only contain two frequencies. The tests with spectra were performed in a similar way with the Self-Correcting System. However, the principle of generating free and bounded harmonics can be studied easier in

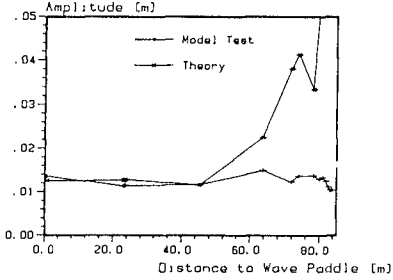
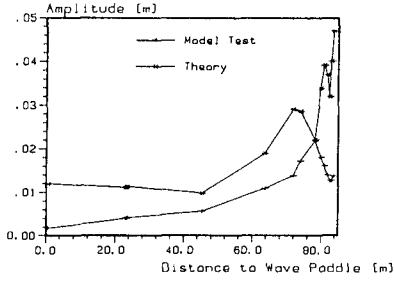


Fig. 6:
Amplitude of 2nd Order
Component $f_2 - f_1$
without (top) and with
(bottom) compensation
($f_1 = 0.24$ Hz, $f_2 = 0.29$ Hz)

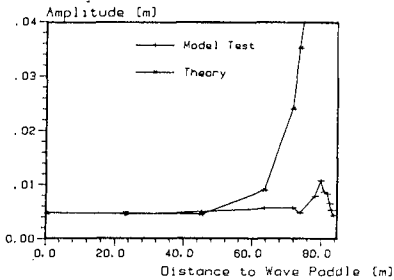
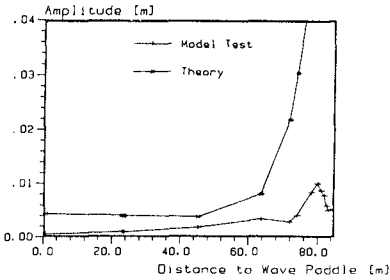


Fig. 8:
Amplitude of 2nd Order
Component $f_2 - f_1$
without (top) and with
(bottom) compensation
($f_1 = 0.20$ Hz, $f_2 = 0.24$ Hz)

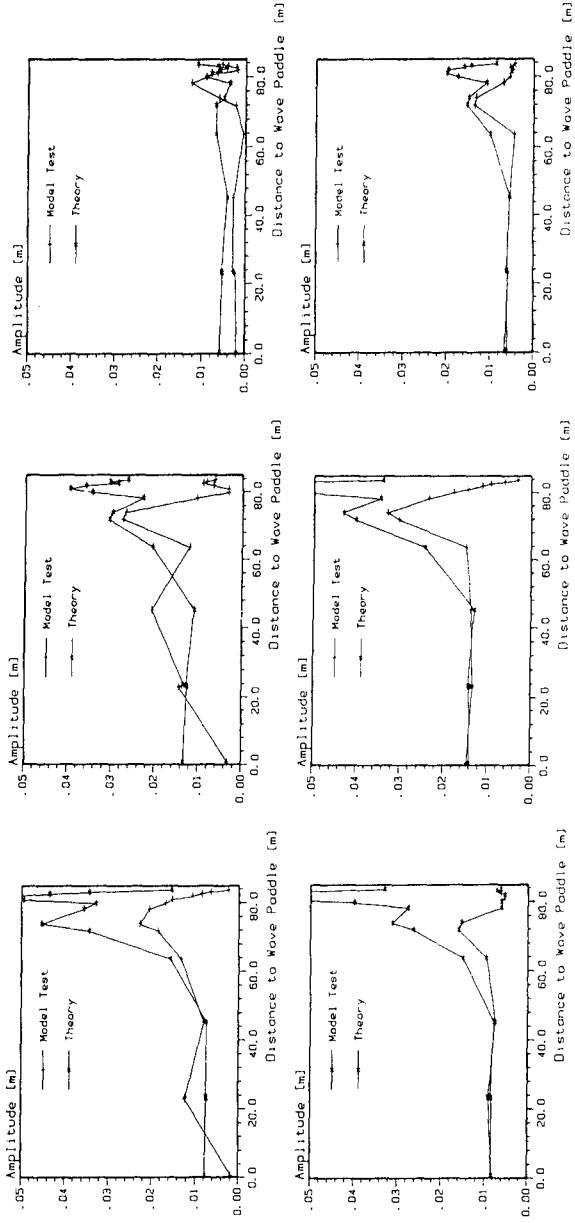


Fig. 7: Amplitude of 2nd Order Component $f_1 + f_1, f_1 + f_2, f_2 + f_2$ without (top row) and with (bottom row) compensation ($f_1 = 0.24$ Hz, $f_2 = 0.29$ Hz)

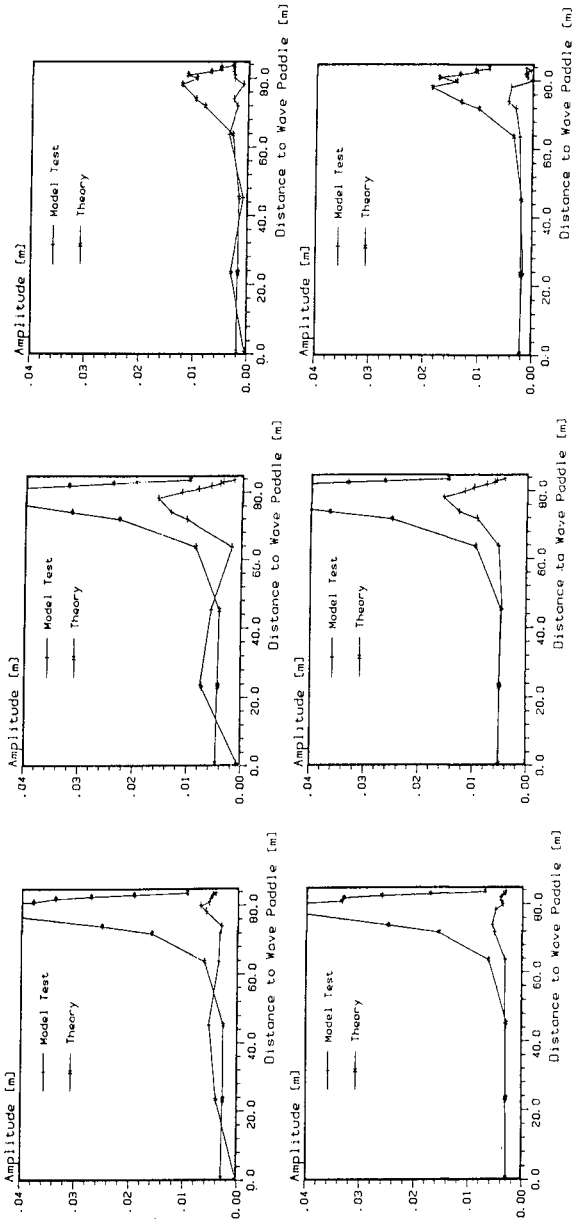


Fig. 9: Amplitude of 2nd Order Component
 $f_1 + f_1$, $f_1 + f_2$, $f_2 + f_2$
without (top row) and with (bottom row)
compensation ($f_1 = 0.20$ Hz, $f_2 = 0.24$ Hz)

simple wave groups because every higher and lower harmonic has only one pair of basic linear waves as source. In a spectrum a lot of combinations of frequency components will contribute to a lower and higher harmonic frequency, each with a bounded and free part. A separation to each source couple f_1 and f_2 and verification and analysis in the hydraulic model seems to be a Sisyphean task.

4.3. Analysis in the Shoaling Area

The difference of 2nd order wave amplitudes between measurement and theory is obvious in the area of the slope and detectable in all cases (Fig. 6 - 9).

In Fig. 8 and 9 the incident linear waves are shallow water waves. There is good agreement in the horizontal bottom section but no agreement of theory and measurement in the area with low water depth. Although the measured amplitudes increase, they never reach the theoretical ones.

The analysis of 2nd order waves on the slope is dominated by the fact that measured amplitudes are lower than the predicted ones. Theoretical values are obtained by using only the two basic linear components as a source, although spectral deformation on the slope occurs (s.Ch. 5). Incorporating the complete spectrum to calculate the higher harmonics on the slope as well as considering wave setup only leads to insignificant reduction of theoretical values.

This leads to the question whether 2nd order waves can be generated stable in time and space dimension for significant lower water depth.

5. Spectral Deformation

It was the aim of the test to prove whether in the shoaling area a difference occurs in measured wave parameters with and without compensation of 2nd order waves in the control signal.

In a first step the ratio of $H_{1/3}$ over H_{m0} is plotted against relative water depth (Fig. 10). The two graphs in one frame are tests without and with compensation. Starting with the common value of 0.95 for deep water the ratio increases up to 1.2 in the first case and 1.10 in the second. A general tendency in the behaviour of 2nd order and 1st order spectra is not detectable.

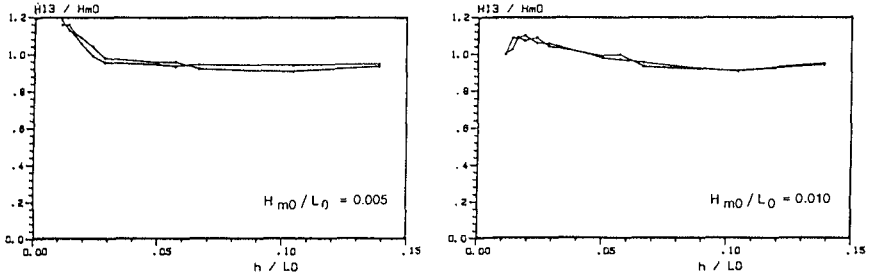


Fig. 10: Ratio of Waveheight Parameters

Fig. 11 shows a plot of H_{13} over H_{130} against the ratio of water depth over incident wave height. Again no difference can be detected whether compensation of 2nd order was used or not. The curve without dots shows the result of GODA's theory for the irregular wave deformation process. Regarding the results of all tests it can be stated that theory and measurements are in good agreement in shallow water but for values of h/H_0 between 1.6 and 4.0 the theory overestimates the measurement.

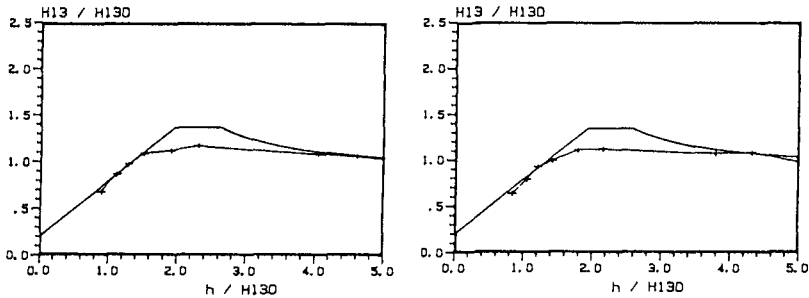


Fig. 11: Variation of Significant Waveheight H_{13}

6. Conclusion

The Self-Correcting System was found to produce irregular waves with strongly reduced unwanted free 2nd order waves when theoretical 2nd order time series served as target wave trains.

It has been shown, that in the case of wave groups the amplitudes of the 2nd order waves in the shoaling area differ dependent on the consideration of 2nd order waves in the control signal. In both cases they are lower than predicted by theory.

In a wave spectrum, wave height parameters seem to be not significantly changed whether a compensation of 2nd order waves was used or not.

7. Acknowledgement

The investigations described in this paper were carried out as part of the research programme of the Sonderforschungsbereich 205 at the FRANZIUS-INSTITUT for Hydraulic Research and Coastal Engineering, University of Hannover. The authors gratefully acknowledge the Deutsche Forschungsgemeinschaft for their financial support throughout the investigations.

8. References

- DAEMRICH, K.-F. and EGGERT, W.-D.: Self-Correcting System for Wave Generation in Hydraulic Models. Proceedings XIX IAHR Congress, New Dehli, 1981.
- SAND, S.E.: Long Wave Problems in Laboratory Models. Journal of the Waterway, Port, Coastal and Ocean Division, ASCE, Vol.108, WW4, 1982.
- SAND, S.E. and MANSARD, E.P.D.: Reproduction of Higher Harmonics in Irregular Waves. Ocean Engineering, Vol.13, No.1, 1983.
- GODA, Y.: Irregular Wave Deformation in the Surf Zone. Coastal Engineering in Japan, Vol. 18, 1975..

CHAPTER 34

COMPUTATION OF 3-D WIND-DRIVEN CURRENTS BY RESPONSE FUNCTION METHOD

Shiao-Kung Liu and Jan J. Leendertse

1. INTRODUCTION

The paper describes the principle and the computational procedure for the calculation of coastal wind-driven circulation by means of the response function technique. Response functions for a specific coastal seas are derived by use of a three-dimensional model of the area. This method computes the dynamic features associated with the coastal circulation via numerical convolution. Consequently, it is several orders of magnitude more efficient than using the direct integration of the three-dimensional coastal model itself.

2. TECHNIQUES USED

For computing coastal wind-driven currents, the traditional, simple fixed drift-ratio method has many difficulties when applied in shallow coastal area with complicated boundaries. Strictly speaking, the fixed ratio method is applicable only for cases of steady wind with constant speed blows over water with infinite depth and with no boundaries. However the concept is rather good and simple. The proposed response function method is the extension of this basic idea except it includes the nonlinear dynamics associated with a specific coastal area.

The RAND Corp. Santa Monica, CA. 90406

When used in conjunction with a verified model, the wind driven currents of different vertical levels can be calculated using numerical convolutional technique. When deriving the response function, local parameters such as the inertial period, tidal regime and tidal dissipation effect associated with the particular coastal area are all included. To generate a complete set of response functions, five computer simulation runs are needed. One computer run is without wind but with tide. The other four computer runs are with tides and with winds from each of four directions. The four response function sets are derived from the difference between them and the one with tide as the only forcing function. The magnitude of tidal currents at different coastal areas produces variable wind responses under the same wind, so the tide has to be included when deriving wind response functions, otherwise they will be overestimated. This is why in a coastal area with strong tidal currents the drift ratio would be lower than in the open ocean because of the quadratic nature of the bottom friction.

Wind driven currents over stratified waters vary with the degree of vertical stability associated with the stratification. Shore effect further complicates the three-dimensionality of the hydrodynamics of the coastal wind driven currents. To illustrate this point we use a simple case where the E-W and N-S components of the response function of water movement at two nearby locations in Norton Sound is plotted (Figs. 1 and 2). These response functions for the easterly wind are derived by applying east wind for a duration of 12 hours (close to the inertial period) over the water. The response of surface water at two nearby locations is not the same to satisfy the continuity principle of water within the bay. Response functions over the water column of the entire modeled area are calculated by the three-dimensional model.

When response functions are saved in discrete time intervals (usually 15 to 30 minutes) the drift velocity under a future wind scenario at a certain time is computed by numerical convolution.

$$U_{ijk}(n\Delta t) = \Delta t \sum_{m=0}^n (W^2) h_{ijk}(n\Delta t - m\Delta t)$$

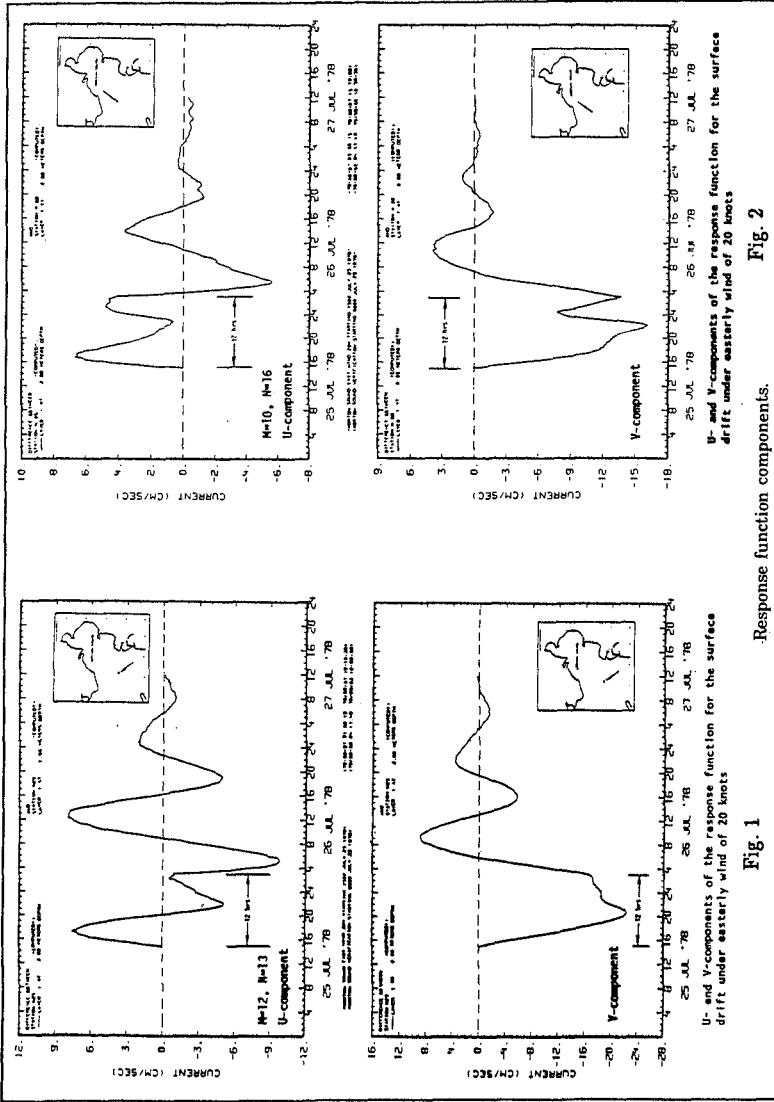


Fig. 1

Response function components.

Fig. 2

U- and V-components of the response function for the surface drift under easterly wind of 20 knots

Two sets of wind response functions for the surface layer of two neighboring coastal locations showing the difference due to the effects of shore distance, depth, bottom friction, and vertical stratification.

where W = wind speed from a certain direction,

U_{ijk} = velocity at a particular point

in space (i,j,k)

h_{ijk} = time domain response function between

squared wind speed and velocity at
point (i,j,k)

With this formula the velocity at point i,j,k can be determined if the wind speed from a specific direction is known, as well as the response function. The same principle applies for complex wind scenarios, then the vectorial decomposition is involved. Similarly, the principle has been extended to simulating movements and dispersion of pollutant, oil movements under ice, multivariant system analysis involving environmental impact due to multiple sources, etc. (Liu and Leendertse, 1987, 1989, 1978). Figure 3 shows a typical results of coastal drift as computed with numerical convolution. Computer time required by this method is approximately two orders of magnitude lower than the direct 3-D simulation method.

3. ACKNOWLEDGEMENTS

The study was supported by the Mineral Management Service, Department of the Interior, through an interagency agreement with the National Oceanic and Admospheric Administration, under which a multiyear program responding to the needs of petroleum development of the Alaskan continental shelf is managed by the Outer Continental Shelf Environmental Assessment Program office.

4. REFERENCES

Liu, S. K., and J. J. Leendertse (1978): Multi-dimensional Numerical

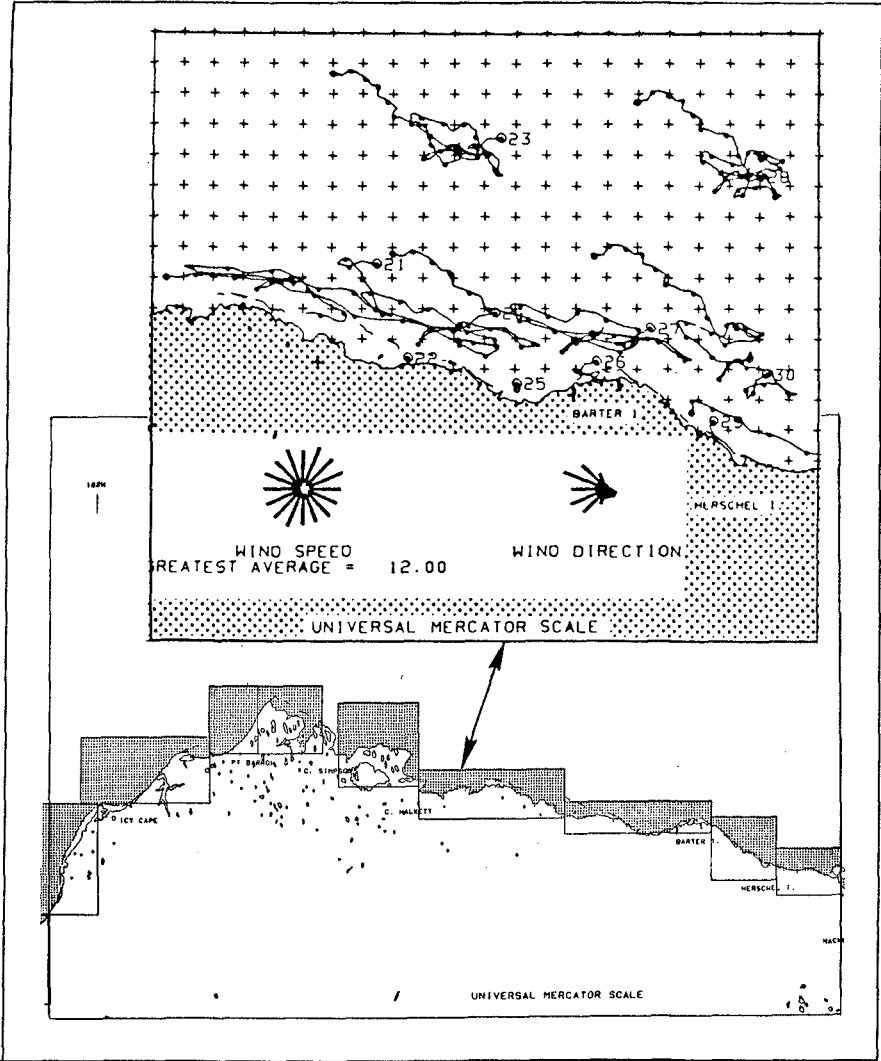


Fig. 3 Daily movements of coastal surface current under identical weather scenario as computed by the convolutional process using 3-D response functions. These trajectories shows the coastal wind drift as a function of shore configuration, , cal depth, vertical stratification, latitude, and the presence of ice.

Modeling of Estuaries and Coastal Seas, in *Advances in Hydro-Sciences*, Vol. 11, 1978, Academic Press, New York.

Liu, S. K., and J. J. Leendertse (1987): *Modeling the Alaskan Continental Shelf Waters*, RAND R-3567-NOAA/RC, 136 pages

Liu, S. K., and J. J. Leendertse (1989): *A Modeling System for Coastal Oil Spill Risk Analysis*, Coastal Engineering XXI, ASCE.

CHAPTER 35

Velocities and Bed Friction in Combined Flows

J.F.A. Sleath*

Abstract

Velocity measurements have been made with a laser doppler anemometer in a steady flow flume with an oscillating bed. The velocity profiles in these tests, for which the oscillation was at right angles to the steady current, were found to be qualitatively similar to those observed in previous measurements with currents collinear with the direction of oscillation. Measured time-mean velocity profiles show moderate agreement with the predictions of the models of Grant & Madsen (1979) and Christoffersen & Jonsson (1985) in the outer layer (the 'current boundary layer') but poor agreement close to the bed (the 'wave boundary layer').

1. Introduction

The problem of wave/current interactions is of importance in many areas of coastal engineering. The present paper is concerned with the velocity profiles, and hence the shear stresses, in the boundary layer near the bed. There have been a great many theoretical studies of this problem (see, for example, Sleath, 1990) and also several experimental studies for current collinear with the wave direction (Kemp & Simons, 1982, 1983, Van Doorn, 1981). But, as far as the writer is aware, there have been no systematic boundary layer measurements for waves at right angles to the current. The aim of the present study was to provide such measurements although, as will be seen from the next Section, the experimental situation investigated was not quite the same as that of waves at right angles to a current.

*Lecturer, Cambridge University Engineering Department,
Trumpington Street, Cambridge CB2 1PZ England.

2. Experimental equipment

One of the reasons for the absence of systematic laboratory measurements of boundary layer profiles for waves at right angles to a current is that a very large apparatus is required. It is difficult to obtain in a wave tank Reynolds numbers high enough to ensure fully-developed turbulence in the wave-induced boundary layers. In order to get round this problem it was decided to replace the wave motion by an oscillatory flow produced by oscillating the bed. It may be shown that, relative to axes fixed in the oscillating bed, the velocity profiles obtained in this way are identical with those which would be obtained in an oscillatory flow water tunnel with a steady current at right angles to the direction of oscillation. In other words, the oscillatory flow is that which would be produced in the vicinity of the bed by waves of infinite length. Second-order effects, such as the wave-induced mass transport current, are not reproduced.

Figure 1 shows a plan view of the experimental apparatus. It consists, essentially, of a steady flow re-circulating flume with a section of bed replaced by an oscillating plate. The direction of oscillation of the plate is at right angles to that of the steady current. Its length is 0.81 m in the direction of the steady flow and it extends across the full width of the flume, through slits in the walls, into outer chambers fitted with compensating cylinders. The oscillation of the plate is produced by a Scotch Yoke mechanism driven by a variable speed motor. The amplitude of oscillation can be varied from 0 to 0.19 m and the period from 0.5 to 6 sec. The steady flow flume is of length 5 m and width 1.2 m. Meshes are fitted at the upstream end to produce a uniform entry flow. In these tests the depth of water was usually held at about 0.26 m. Under these circumstances the pumps can produce mean velocities in the test section of up to 0.2 m/s.

Three different bed roughnesses were investigated: smooth stainless steel plate, sand of median diameter D equal to 1.64 mm, and gravel of median diameter 8.1 mm. The sand and gravel were glued to the oscillating section of bed. A thin layer of contact adhesive, diluted with petrol, was spread uniformly over the bed and then the sediment was sprinkled on top. The same roughness was spread for a distance of 1.7 m upstream of the oscillating section of bed and for a distance of 1.0 m downstream. The Nikuradse roughness length k_s was determined from the steady flow velocity profiles on the assumption that for rough beds the zero intercept of the

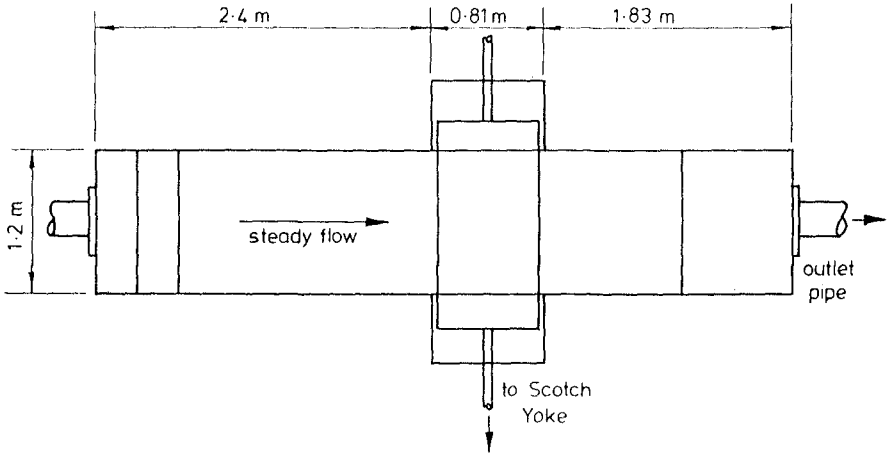


Figure 1. Plan view of the flume

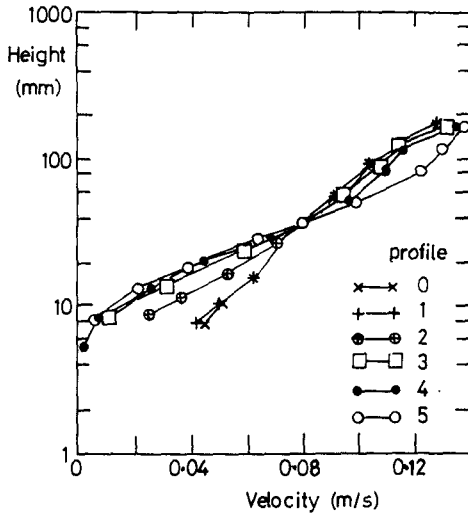


Figure 2. Steady current velocity profiles on the centre line of the flume. Distances downstream of the upstream edge of the oscillating bed are: (0) - 0.05 m, (1) - 0.05 m, (2) 0.09 m, (3) 0.22 m, (4) 0.47 m, (5) 0.72 m. For all profiles except (0) the cross-channel oscillation of the bed was of amplitude ± 0.14 m and period 2.9 sec.

logarithmic velocity profile is equal to $k_s/30.2$. The values of k_s obtained in this way were 20.3 mm for the 8.1 mm^s gravel and 1.49 mm for the 1.64 mm sand. The explanation for the surprisingly low values of k_s for the 1.64 mm sand is probably that the grains were very rounded and that the glue tended to fill the voids between grains.

The velocities were measured with a single component fibre optic laser doppler anemometer manufactured by DANTEC. The probe was operated in back-scatter mode with a 30 mW He-Ne laser. Further details of this instrument and of the flume are given by Lee Young (1989).

3. Boundary layer growth with downstream distance

Most of the velocity profiles in the main test series were measured, on the centre line of the flume, at a distance of 0.65 m from the upstream edge of the oscillating plate. Since a new boundary layer will grow from the edge of the oscillating plate it is reasonable to ask whether this distance is large enough for the velocity profile to have reached an equilibrium value. Figure 2 shows examples of the steady current velocity profiles at various distances from the upstream edge of the oscillating plate. Profile (0) was measured without oscillation of the plate whereas all of the other profiles were measured with a plate oscillation of amplitude 0.14 m and period 2.9 sec. The mean flow rate was the same for all profiles. Profiles (0) and (1) were each measured at a distance of 0.05 m upstream of the oscillating plate. The fact that these two profiles are almost identical suggests that the upstream influence of the plate oscillation is very slight. On the other hand, the effect of plate oscillation on the steady current profiles downstream of the upstream edge is significant. As might be expected, the change in velocity profile with downstream distance is most rapid just downstream of the leading edge of the oscillating plate. At 0.47 m from the upstream edge the velocity profile appears to have reached an equilibrium up to a height of about 40 mm from the bed.

4. Time-mean currents and shear stresses

The time-mean velocities and shear stresses discussed in this Section are in the direction of the mean current. With the present experimental apparatus time-mean quantities perpendicular to this direction are zero.

4.1 Smooth beds

The velocity profiles in Figure 2 were measured with the 8.1 mm gravel. Very similar results are obtained with the 1.64 mm sand but the smooth bed profiles are

different. Figure 3 shows two smooth bed time-mean velocity profiles measured on the centre line of the flume 0.65 m from the leading edge of the oscillating plate. The pump setting was the same for both profiles but in one case there was a plate oscillation of amplitude 0.125 m and period 2.41 sec and in the other there was no oscillation. It is clear that oscillation of the smooth plate has a negligible effect on the time-mean velocity profile. The reason is probably that the oscillatory flow is not at a sufficiently high Reynolds number to generate additional turbulence with this smooth plate. On the other hand, oscillation of the rough beds generates significant additional turbulence and it is this which changes the time-mean velocity profile, as shown in Figure 2.

4.2 Rough beds

One of the aims of the present study was to provide new data with which to test the predictions of theoretical models. Figure 4 shows a typical comparison of two measured time-mean velocity profiles with the curve obtained from the model of Grant & Madsen (1979). We see that there is quite good agreement between the measurements and the predictions of the model in the outer layer (the 'current boundary layer') but that the agreement is much less good close to the bed (the 'wave boundary layer'). Similar discrepancies are found with other models. This suggests that the assumptions of existing models for the wave boundary layer are not adequate.

Figure 5 shows how the measured values of the apparent roughness k_a compare with the values predicted by the models of Grant & Madsen (1979) and Christoffersen & Jonsson (1985). The predicted value has been obtained by assuming that the measured and predicted velocities are the same at a height of 25.4 mm above the bed. This allows k_a and the time-mean shear velocity to be calculated independently.

We see that the theoretical models predict the value of k_a/k_s quite well at low values of this parameter but that the agreement is less good at high values. It should be emphasized, however, that there is considerable uncertainty in the estimation of k_a even when, as in the present case, a least-squares technique is adopted. This is because the velocity profile is only logarithmic over a restricted range of heights so that experimental error in a velocity measurement can cause an appreciable change in the apparent value of k_a .

On the whole, Christoffersen & Jonsson's model appears to give closer agreement with experiment when $n = 2.0$ and $r = 0.925$ than when $n = 0.367$ and $r = 0.450$.

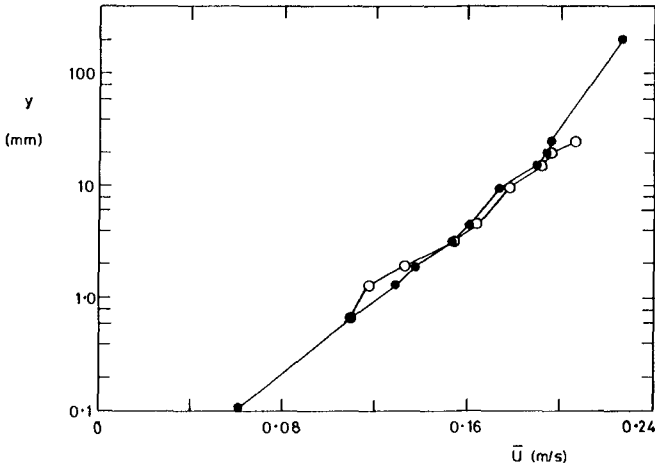


Figure 3. Time-mean velocity profiles over a smooth bed.
 O—O:— oscillation amplitude = + 0.125 m, period = 2.41 sec. ●—●:— no oscillation

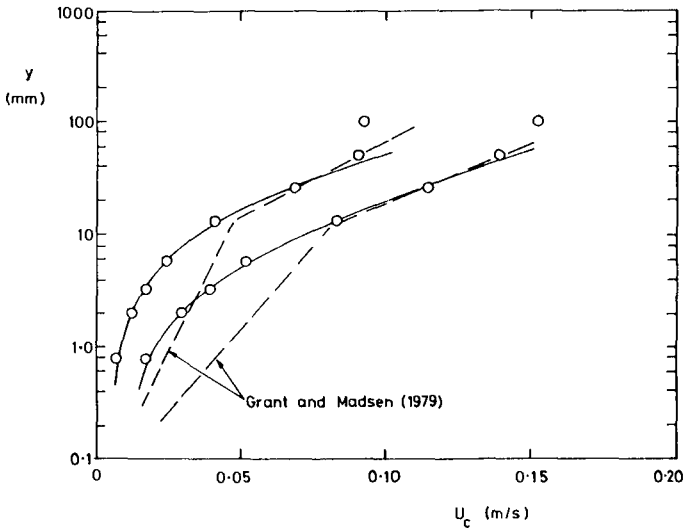


Figure 4. Comparison of two measured time-mean velocity profiles with predictions of the model of Grant & Madsen (1979). Oscillation amplitude = + 0.14 m, period = 1.76 sec. 1.64 mm sand

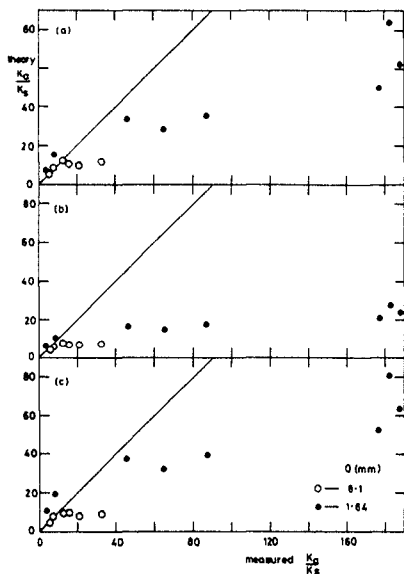


Figure 5. Comparison of predicted and measured values of combined flow roughness k_a divided by steady flow roughness k_s , (a) Grant & Madsen (1979) (b) Christoffersen & Jonsson (1985) with $n = 0.367$, $r = 0.450$ (c) Christoffersen & Jonsson (1985) with $n = 2.0$, $r = 0.925$

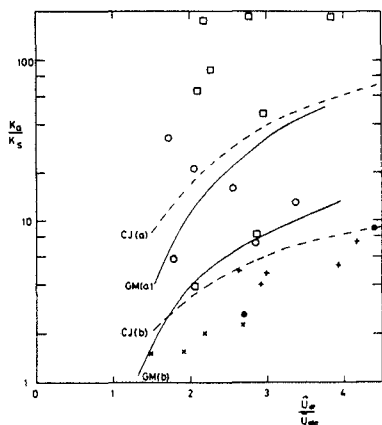


Figure 6. k_a/k_s versus $\hat{u}_{*c} / \bar{u}_{*c}$. GM and CJ represent the predicted curves of Grant & Madsen (1979) and Christoffersen & Jonsson (1985) for (a) $a/k = 94.8$ and (b) $a/k = 6.9$. Symbols are: \square - present tests $D = 1.64$ mm, O - present tests $D = 8.1$ mm, \bullet - Van Doorn (1981), x - Kemp & Simons (1982), $+$ - Kemp & Simons (1983)

A different way of predicting the apparent roughness k_a was suggested by Coffey & Nielsen (1986). They observed that existing laboratory measurements could be represented by a single curve if k_a/k_s was plotted against \hat{u}_*/\bar{u}_{*c} , where \hat{u}_* is the amplitude of the fluctuation in shear velocity at the bed and \bar{u}_{*c} is the time-mean value. Figure 6 suggests that the same curve would not be valid for the present measurements. This may be because the present measurements are for currents at right angles to the oscillation whereas the previous measurements were for currents collinear with the oscillation or it may be that another parameter is important. The models of Grant & Madsen and Christoffersen & Jonsson both suggest that the ratio of orbital amplitude a to Nikuradse roughness k_s is important. Figure 6 shows the curves predicted by these models for the two bed roughnesses. In the present tests $a/k_s = 6.9$ for the 8.1 mm gravel and 94.8 for the 1.64 mm sand. We see that the predicted change in k_a/k_s with a/k_s is quite large.

Another quantity of interest which may be obtained from the slope of the time-mean velocity profiles in the outer region is the time-mean shear velocity \bar{u}_{*c} . This may be used to calculate the time-mean friction coefficient:

$$\bar{f}_c = \frac{2 \bar{u}_{*c}^2}{U_o^2}, \quad (1)$$

where U_o is the amplitude of the velocity of the oscillating plate. Figure 7 shows how the measured values of \bar{f}_c for the present tests compare with the values predicted by the models of Grant & Madsen (1979) and Christoffersen & Jonsson (1985). It is difficult to draw definite conclusions because the experimental scatter is considerable. On the whole, the agreement between theory and experiment is closer than for the apparent roughness k_a . However, there does seem to be a consistent tendency for the theory to underestimate the friction factor at large values of this parameter. In this case the choice of the values of n and r in Christoffersen & Jonsson's model appears to make little difference to the overall comparison.

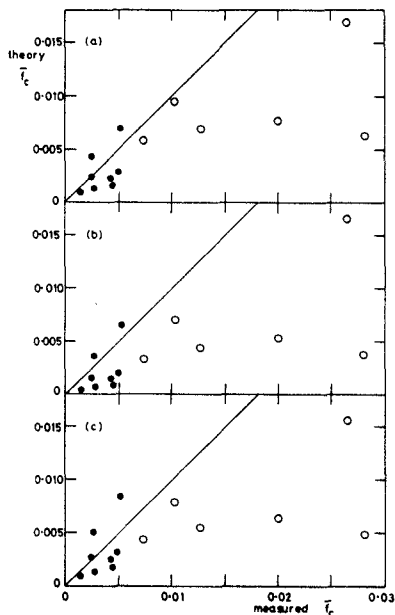


Figure 7. Comparison of predicted and measured values of time-mean friction factor \bar{f}_c . (a) Grant & Madsen (1979) (b) Christoffersen & Jonsson (1985) with $n = 0.367$, $r = 0.450$ (c) Christoffersen & Jonsson (1985) with $n = 2.0$, $r = 0.925$. Symbols as for Figure 5.

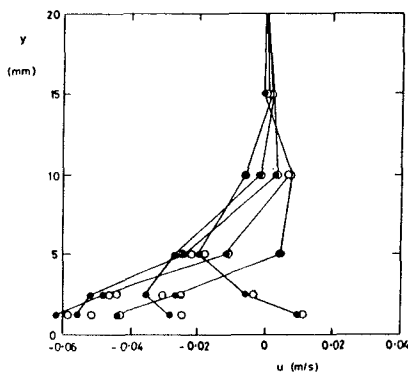


Figure 8. Oscillatory velocity profiles at phase intervals of 45° . Oscillation amplitude = $+ 0.14$ m, period = 2.75 sec in each case. $D = 1.64$ mm. \bullet - no steady current, \circ - steady current with $\bar{u}_{*c} = 0.0094$ m/s.

5. Oscillatory velocities and shear stresses

5.1 Velocities and shear stresses parallel to the direction of oscillation

In the present tests the influence of the steady current on the oscillatory velocity profile was much less marked than the influence of the oscillation on the steady current. This is illustrated in Figure 8 which shows typical velocity profiles at various phases of oscillation with, and without, a steady current.

The same situation is shown in Figure 9 which represents the ratio of the oscillatory friction factors with and without a steady current. In this figure

$$f_w = \frac{\hat{\tau}_{\omega t}}{\frac{1}{2}\rho U_o^2} \quad (2)$$

where $\hat{\tau}_{\omega t}$ is the amplitude of the shear stress at the bed in the absence of a steady current. The definition of f_{wC} is the same except that the shear stress amplitude is that in the presence of a steady current. The values of f_w and f_{wC} used in this Figure are those determined from the experimental measurements, with the aid of the momentum integral. Figure 9 shows that for this range of \bar{u}_{*c}/U_o the experimental results are in good agreement with the predictions of Grant & Madsen and Christoffersen & Jonsson.

5.2 Oscillatory velocities and shear stresses parallel to the mean current

The oscillation of the rough plates also generates an oscillatory velocity, and hence a shear stress, in the direction of the mean current. This is because the additional turbulence generated by the oscillatory flow fluctuates in intensity during the course of the cycle (Sleath, 1987). If the angular frequency of the oscillation is ω the frequency of the fluctuation in turbulence intensity is 2ω . Consequently the fundamental frequency of the oscillatory velocity and shear stress in the direction of the mean current is also 2ω . Interaction between the various oscillatory components also produces higher-order harmonics both parallel and perpendicular to the mean current direction but the magnitude of these harmonics is much less than that of the fundamental components.

The fluctuating component of velocity in the mean current direction is relatively weak but the shear stress it generates at the bed is not negligible, as indicated in Figure 10. We see that the amplitude $\hat{\tau}_{2\omega t}$ of the

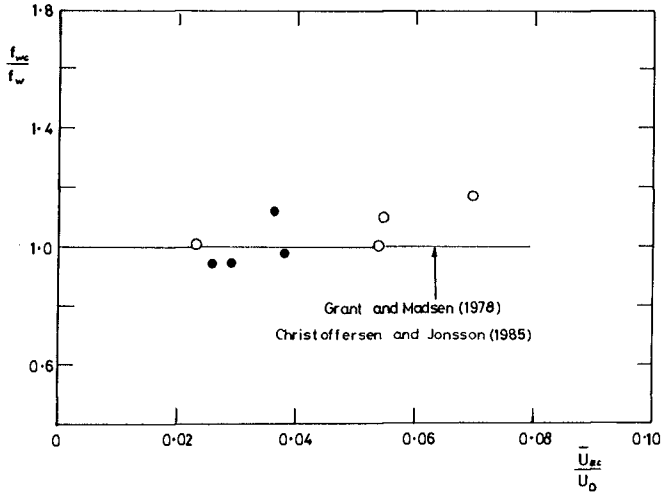


Figure 9. Ratio of oscillatory friction factors measured with and without a superimposed steady current.
 O - 8.1 mm gravel, ● - 1.64 mm sand

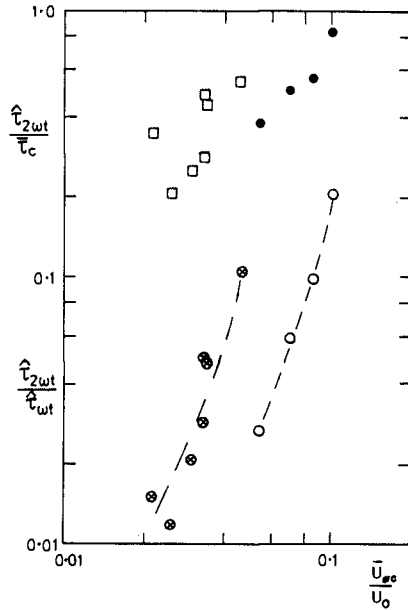


Figure 10. Amplitude of oscillatory shear stress $\hat{\tau}_{2wt}$ in the mean current direction.
 O, ● - 8.1 mm gravel; ⊗, □ - 1.64 mm sand

fluctuating shear stress ranges from about 20 % to 80 % of the time-mean shear stress $\bar{\tau}_c$. However, this fluctuating stress in the mean current direction is still small compared with the amplitude $\hat{\tau}_{\omega t}$ of the fluctuating shear stress in the direction of oscillation. As shown in Figure 10, the ratio of these two shear stresses was usually significantly less than 10 % in these tests.

In Figure 10, the shear stress $\hat{\tau}_{\omega t}$ in the direction of oscillation was calculated from Jonsson's (1963) expression for friction factor whereas the component $\hat{\tau}_{2\omega t}$ in the mean current direction was determined from the momentum integral

$$\tau = \int_0^{\infty} \frac{\partial}{\partial t} (u_{\infty} - u) dy$$

where u is the fluid velocity at height y and u_{∞} is the fluctuating velocity outside the wave boundary layer. In these tests u_{∞} was either zero or very nearly so. It is well known that calculations of shear stress based on the momentum integral tend to be inaccurate and this is particularly true in the present case because the boundary layer for the 2ω component of velocity is very thin. The values of $\hat{\tau}_{2\omega t}$ in Figure 10 should consequently be treated with caution.

6. Conclusions

(1) Velocity measurements show that equilibrium profiles are established relatively quickly above the oscillating section of bed. For example, 0.47 m downstream of the leading edge of the oscillating bed the velocity profile was in equilibrium to a height of about 0.04 m above the bed.

(2) The measurements with smooth beds showed no significant effect of the oscillation on the velocity profile of the steady current. This lack of interaction is probably because the oscillatory Reynolds numbers were not high enough for additional turbulence generation with smooth beds.

(3) In contrast, the measurements with the rough beds showed significant modification of the time-mean velocity profile when an oscillation was superimposed on the flow. The modification was qualitatively similar to that observed, by previous investigators, for steady currents parallel to the direction of oscillation.

(4) The effect of the steady current on the oscillatory flow was small, even for the rough beds, for the present test conditions.

(5) Measured time-mean velocity profiles are in quite

good agreement with the profile predicted by Grant & Madsen's (1979) model in the outer layer (the 'current boundary layer') but in poor agreement close to the bed (the 'wave boundary layer'). Measured outer layer quantities such as apparent roughness and mean shear velocity also show moderate agreement with Grant & Madsen's model and with that of Christoffersen & Jonsson (1985) with $n = 2.0$ and $r = 0.925$.

(6) With the rough beds it was possible to observe a fluctuating shear stress at right angles to the direction of oscillation. The amplitude of this shear stress was small compared with the shear stress in the direction of oscillation but quite significant compared with the time-mean shear stress.

7. Acknowledgements

The author is grateful to the Natural Environment Research Council for a grant towards the cost of equipment.

References

- Christoffersen, J.B & Jonsson, I.G. 1985 Bed friction and dissipation in a combined current and wave motion. *Ocean Engng.*, 12(5), pp 387-423.
- Coffey, F.C. & Nielsen, P. 1986 The influence of waves on current profiles. *Proc. 20th Int. Conf. on Coastal Eng. Taipei*, pp 82-96.
- Grant, W.D. & Madsen, O.S. 1979 Combined wave and current interaction with a rough bottom. *J. Geophys. Res.* 84 (C4), pp 1797-1808.
- Jonsson, I.G. 1963 Measurements in the turbulent wave boundary layer. *Proc. 10th Congr. IAHR London*, pp 85-92.
- Kemp, P.H. & Simons, R.R. 1982 The interaction between waves and a turbulent current. *Waves propagating with the current. J. Fluid Mech.* 116, pp 227-250.
- Kemp, P.H. & Simons, R.R. 1983 The interaction between waves and a turbulent current. *Waves propagating against the current. J. Fluid Mech.* 130, pp 73-89.
- Lee Young, J.S. 1989 Bed mechanics in combined steady and oscillatory flow. Ph.D. thesis, University of Cambridge.

Sleath, J.F.A. 1987 Turbulent oscillatory flow over rough beds. *J. Fluid Mech.* 182, pp 369-409.

Sleath, J.F.A. 1990 Seabed boundary layers. In 'The Sea', Vol. 9 B. Le Mehaute and D. Hanes Eds., Wiley, New York, pp 693-727.

Van Doorn, T. 1981 Experimental investigation of near bottom velocities in water waves with and without a current. Delft Hydraulics Lab. TOW-Report 1423.

amplitude (m)	period (s)	temperature (°C)	\bar{u}_{*c} (m/s)	k_a/k_s	$\frac{\hat{\tau}_{2\omega t}}{\bar{\tau}_c}$	$\frac{U_o}{(\omega v)^{1/2}}$
$D = 1.64 \text{ mm}, k_s = 1.49 \text{ mm}$						
0.141	2.22	18.3	0.019	177	0.22	231
0.141	2.19	21.2	0.020	65	0.45	242
0.141	2.18	21.6	0.011	183	0.35	244
0.141	4.58	19.0	0.007	8.1	-	162
0.141	4.49	21.1	0.010	3.9	0.54	169
0.141	4.44	21.8	0.007	46	0.25	171
0.141	1.76	19.3	0.023	87	0.49	263
0.141	1.75	20.0	0.019	188	0.28	266
$D = 8.1 \text{ mm}, k_s = 20.25 \text{ mm}$						
0.140	2.43	14.2	0.026	7.5	0.50	208
0.140	2.43	14.7	0.022	13	0.38	210
0.140	4.39	17.4	0.023	5.8	0.83	161
0.140	4.39	17.9	0.020	21	0.55	162
0.140	2.92	18.9	0.024	16	-	202
0.140	2.82	19.8	0.037	33	-	208

Table I. Test conditions for the measurements in line with the mean current direction

CHAPTER 36

ON THE FITTING OF JONSWAP SPECTRA TO MEASURED SEA STATES

E.P.D. Mansard¹ and E.R. Funke²

ABSTRACT

A new technique has been described for the optimal fitting of JONSWAP model spectra to measured sea states. This technique, validated by numerical simulations, can provide enhanced estimations of the peak frequency, the peak enhancement factor and the significant wave height of natural seas.

1.0 INTRODUCTION

The variability of spectral estimates resulting from conventional variance spectral density analysis of relatively short wave records, is appreciable. It is, therefore, difficult to obtain from them a reliable appraisal of spectral parameters that reflect the properties of the sea state prevailing over a large area and over a long duration. Furthermore, wave data recorded in nature are frequently corrupted with background noise, such as transmission interference or data loss due to buoy submergence. As a result, the variance spectral densities of such wave data must usually be band-limited at arbitrarily chosen upper and lower cut-off frequencies. This truncation can have a significant effect on the values of estimated wave parameters, particularly those which depend on the calculation of spectral moments.

Various algorithms for the estimation of spectral wave parameters exist. Some of these are published in the IAHR/PIANC List of Sea State Parameters (1986). Other authors have also described methods for the determination of spectral sea state parameters (Houmb and Øyan, 1981). So far these techniques have been evaluated only by application to field recorded wave data, for which the expected values are not known accurately. It was therefore not possible to determine how well these methods succeeded in recovering the underlying process parameters from the analysis of relatively short samples of the sea state.

¹ Senior Research Officer

² Principal Research Officer
Hydraulics Laboratory, National Research Council of Canada
Bldg. M-32, Montreal Road, Ottawa, Ontario K1A 0R6

Mansard and Funke (1988b) investigated a several of the known computational methods for spectral parameter estimation and evaluated their ability to recover the known process parameters by a numerical simulation of waves. This study used 200 numerically simulated wave records, each containing approximately 110 waves. These were derived from JONSWAP spectra with γ -values of 1 and 3.3, using the "random complex spectrum" method (Funke and Mansard, 1987). The JONSWAP parametric spectrum was chosen for this study because it is the most commonly used model, and it covers also the Pierson-Moskowitz as well as the Bretschneider (i.e. the ITTC or ISSC) spectra as special cases.

The "random complex spectrum" method of numerical wave synthesis is based on the Fourier transform, but is akin to a simulation of waves from long term "white noise" and is, therefore, a spectrally non-deterministic method. Miles and Funke (1988) demonstrated that the spectral domain characteristics of wave records produced by this method, mimic the natural variability of stationary, linear stochastic processes. This is to say, that individual realizations of synthesized waves exhibit the same variability of spectral estimates as would be encountered from filtered white noise. Whereas the properties of the underlying generating process are not known for natural sea states, they are known completely for numerically synthesized wave data. A numerical simulation of waves and subsequent spectrum analysis permits, therefore, the evaluation of conventional methods of parameter estimation by comparing the mean, the standard deviation, the maximum and the minimum values of the spectral parameters to the known simulation inputs.

Estimations of some spectral characteristics are linked to a basic assumption of the spectral shape characteristics. For deep water waves, one usually assumes a JONSWAP type of spectrum of which the Pierson-Moskowitz and the Bretschneider are special cases. For these parametric model spectra, one must know three fundamental parameters, i.e. the peak frequency, the significant wave height and a spectral width measure. (The peak width parameters σ_a and σ_b will be assumed in this study to have the same values as those suggested by JONSWAP, i.e. 0.07 and 0.09 respectively).

Various spectral width measures have been proposed, such as the peakedness factor, Q_p , or the spectral width parameters ϵ_2 or ϵ_4 (IAHR/PIANC, 1986). Mansard and Funke (1988a) have shown that the peakedness factor is highly sensitive to the choice of cut-off frequencies. Because the spectral width parameters ϵ_n are derived from higher spectral moments, the same problem applies to these as well (see also Rye, 1977). In any case, for a JONSWAP spectrum, the most suitable spectral width measure would be the peak enhancement factor, γ . Knowledge of this parameter would permit matching of the parametric model spectrum to the measured sea state spectrum. LeBlond (1982) published a technique for this purpose, which will be described below.

The work presented both here and in Mansard and Funke (1988b), was undertaken to enhance computational methods for the discovery of the underlying spectral parameters of a sea state, and to provide the means of assigning confidence limits to such estimates. The authors consider it important that relatively short samples

of ocean waves, taken at a single point in an area of interest, should reveal the generally prevailing sea state over the storm area with as much confidence as possible. This would then allow the use of such wave data for the verification of hindcasting or forecasting techniques. It would also permit a more credible use of this data for design or simulation applications, where wave recording stations had been deployed at some distance from the site of interest.

A particular case in point is the situation which the authors encountered with the Ocean Ranger capsizing investigations during 1982. At the time of the accident, only one wave recording buoy was operational and was located some 37 km from the accident site. However, prior to the accident, 3 buoys were operational, with the second 17 km from the Ocean Ranger and the third quite near the platform. Comparative analysis between the three buoys indicated considerable differences in peak frequency (Mogridge, 1985). A preliminary reanalysis of the data from two of these stations was carried out recently, using the enhanced method of analysis presented here. It was then found, that the differences were relatively small and that data from the two sites could be used interchangeably.

2.0 PRELIMINARY RESEARCH

By applying the technique of numerical wave simulation, Mansard and Funke (1988b) evaluated traditional algorithms for the estimation of three principal spectral parameters, i.e. the peak frequency, the peak enhancement factor and the significant wave height. The investigation was carried out for a range of JONSWAP γ -values varying from $1 \leq \gamma < 12$. From this it became apparent that the results of the analysis are:

- in most cases, highly dependent on the arbitrary higher and lower cut-off frequencies, which are used for the analysis;
- a function of the resolution of the spectral density analysis;
- a function of the γ -value of the JONSWAP spectrum;
- biased due to the skewed profile of wave spectra.

Because it was the ultimate objective of the study to devise a technique of optimally fitting a parametric model spectrum to the simulated sample spectra, and because it was known that any multi-parameter optimal fit relies heavily on the initial guesses of the parameters to be optimized, it was considered essential to improve on existing algorithms for the estimation of the three above mentioned spectral wave parameters before attempting the use of optimization procedures.

2.1 Estimation of the Peak Frequency

2.1.1 Initial guess of the peak frequency

Mansard and Funke (1988b) considered 5 algorithms for the estimation of the peak frequency. The simplest of these is the detection of that frequency that corresponds to the largest value of the sample spectrum, S_{\max} (i.e. $f_p = f(S_{\max})$). Because of the large variability of spectral estimators, this method also leads to a large variability

in the estimation of the peak frequency.

For this reason, some researchers prefer to use the "Delft" method (IAHR/PIANC List of Sea State Parameters, 1986). This is defined as the frequency computed as the centroid of the spectral band between the lower and the upper intercepts of the spectral density and the threshold which is 80% of $S_{\eta}(f_p)$, i.e.

$$f_{pD} = \frac{\int_{f_1}^{f_2} f \cdot S_{\eta}(f) \cdot df}{\int_{f_1}^{f_2} S_{\eta}(f) \cdot df} \quad (1)$$

where f_1 and f_2 are the upper and lower frequencies corresponding to the intercepts. This parameter is also referred to here as f_{pD8} .

A third option is similar to the second, except that the threshold is chosen to be 60% rather than 80% of the spectral peak value. It offers an advantage over the second method by including a larger portion of the spectrum, and thereby reducing variability. To distinguish it from the f_{pD8} parameter, it is referred to here as f_{pD6} .

The fourth and the fifth methods were used by Read (1986). The peak frequency estimator, referred as f_{p5} , is given by:

$$f_{p5} = \frac{\int_0^{f_2} f \cdot S^5(f) \cdot df}{\int_0^{f_2} S^5(f) \cdot df} \quad (2)$$

The fifth method yields f_{p8} , which is similar in definition to f_{p5} , except that the power coefficients are 8 instead of 5.

These five estimators of peak frequency (f_p , f_{pD8} , f_{pD6} , f_{p5} and f_{p8}) were evaluated by Mansard and Funke (1988b) through numerical simulation using a Pierson-Moskowitz model spectrum with a peak frequency of 0.55 Hz as a generating function. Using the random complex spectrum method, 200 wave trains, each 200 seconds long, were synthesized and then subjected to spectral analysis. The various estimates of peak frequency derived from these spectra were then subjected to statistical analysis. In order to evaluate the effect of spectral resolution on these statistics, three different resolutions, corresponding to 10, 20 and 30 degrees of freedom were also used. The main conclusions of this study are given below.

The traditional estimate of peak frequency (i.e. f_p) has by far the largest variability, which improves however, as the degrees of freedom of spectral analysis increase. The mean values of peak frequency from all five methods demonstrate a bias toward higher values. In terms of variability, the f_{p5} algorithm is superior to others and can be computed with relative simplicity, i.e. without bidirectional threshold detection, as required for f_{pDx} calculations. Because of this, f_{p5} was selected as the basis for the development of an enhanced wave parameter estimator, for which it will serve as the "initial guess".

2.1.2 The bias corrected estimate for the peak frequency

The JONSWAP parametric model spectrum is not symmetrical about its peak frequency f_0 . The leading edge of the spectrum is steeper than its trailing edge. As

a result, any peak frequency definition based on centroid calculation is expected to provide a bias in the estimation of peak frequency. However, this bias does not constitute a serious concern since it can be corrected, and furthermore, it becomes insignificant as the peakedness of the spectrum increases.

The bias correction function for f_{p5} as a function of γ can be determined by applying the f_{p5} -calculation to smooth theoretical JONSWAP spectra, for which the peak frequency is predefined and therefore known. Such a calculation is free of variability. This was carried out and the result was subjected to a multivariate regression analysis, which in turn yielded to the following function:

$$C_f = 1.005 + 1 / [50.746 \cdot (\gamma - 0.2397)^2] \quad (3)$$

This function can only be evaluated once the γ -value is known. As this information is available only at a later stage of the analysis, C_f is initially estimated as $C_f \approx 1.02$ for the purpose of computing γ . This bias correction is applied as follows:

$$f'_{p5} = \frac{1}{C_f} \cdot \int_0^{\infty} f \cdot S^5(f) \cdot df \bigg/ \int_0^{\infty} S^5(f) \cdot df \quad (4)$$

As will be described later, this bias corrected estimate will be used as the initial condition in an optimization procedure for the determination of an enhanced peak frequency estimator.

2.2 Estimation of the Peak Enhancement Factor.

2.2.1 The initial guess of the peak enhancement factor

It was shown in Mansard and Funke (1988b), that the peak enhancement factor γ may be estimated through the use of the parameter of a bivariate Rayleigh probability density, κ_f , given by Battjes and van Vledder, (1984). This is approximated by:

$$\kappa_f^2 \hat{m}_0^2 \approx \left[\int_{f_1}^{f_2} S(f) \cdot \cos(2\pi f\tau) \cdot df \right]^2 + \left[\int_{f_1}^{f_2} S(f) \cdot \sin(2\pi f\tau) \cdot df \right]^2 \quad (5)$$

where $S(f)$ is the spectral value, $\tau = \sqrt{\hat{m}_0/\hat{m}_2}$, and \hat{m}_0 and \hat{m}_2 are the estimators of the zeroth and the second spectral moment functions respectively. These were computed over the spectral range from $0.5f_{p5}^l$ to $2.5f_{p5}^l$. In this computation, f_{p5}^l is evaluated using $C_f = 1.02$ in Equation (4).

By applying linear regression analysis to the κ_f -values, as derived from smooth JONSWAP parametric model spectra for various values of γ ranging from 1 to 12, a conversion formula was derived that established the relationship between κ_f and γ . This formula was given in Mansard and Funke (1988b) as:

$$\begin{aligned} \gamma_0 &= 50.69 - 404.97\kappa_f + 1211.2\kappa_f^2 - 1599.6\kappa_f^3 + 817.26\kappa_f^4 \quad \text{for } \kappa_f \geq 0.4 \\ &= 1 \quad \text{for } \kappa_f < 0.4 \end{aligned} \quad (6)$$

The results of applying this formula to simulated wave data were reported in Mansard and Funke (1988b).

2.2.2 Enhanced estimator of the peak enhancement factor

When applying Equation (6) to sample spectra derived from a 10-degrees of freedom spectral density analysis of 200 numerical simulation of wave trains, synthesized from JONSWAP class of spectra and using the "random complex spectrum" method of wave synthesis, it was found that an additional bias of the recovered γ -values for the range of $\gamma < 2.5$ occurred. Whereas the relation in Equation (6) was established from smoothed parametric model spectra, during the application of Equation (6) to numerically synthesized data, estimates of γ with values less than 1 were found to occur. By rounding these values up to 1, the mean value of the γ -estimator tends to be increased slightly. For this reason, an improvement to the relationship between κ_γ and γ was derived here. This new peak enhancement factor is now given by:

$$\begin{aligned} \gamma' &= -0.835 + 1.797\gamma_0 - 0.2011\gamma_0^2 && \text{for } \gamma_0 < 2.5 \\ &= \gamma_0 - 0.10 && \text{for } \gamma_0 \geq 2.5 \end{aligned} \tag{7}$$

Applying this estimation formula to a numerical simulation leads to the statistics given in Table 1

REQUIRED	1.0	3.3	7.0
MEAN	1.13	3.33	7.09
STD. DEV.	0.26	1.06	2.14
MAX.	2.49	8.81	12.00
MIN.	1.00	1.00	1.56

TABLE 1. Variability of Enhanced γ -Values by Equation (7)

2.3 Estimation of the Significant Wave Height

2.3.1 Initial guess of the significant wave height

The significant wave height (H_{m0}) is computed from:

$$H_{m0} = 4\sqrt{m_0} \tag{8}$$

where m_0 is the zeroth moment, i.e. the area under the population variance spectral density function. Because of the presence of both high and low frequency noise, the zeroth moment is traditionally derived by spectral integration between some arbitrarily chosen upper and lower cut-off frequencies. As a result, the total variance is consistently underestimated by an amount corresponding to the spectral areas that have been eliminated by truncation. This energy loss can easily be

recovered as a cut-off frequency dependent bias correction. Because the authors have usually carried out wave data analysis for the band of $0.5f_p \leq f \leq 2.5f_p$, this was adopted for this investigation as well, using f_p^1 for the peak frequency.

2.3.2 Enhanced estimate of the significant wave height

Mansard and Funke (1988b) determined the truncation induced bias by integrating smooth parametric JONSWAP class spectra over the range of $0.5f_p \leq f \leq 2.5f_p$. The resultant values of the zeroth moment were then subjected to regression analysis, which yielded a bias correction function. This was incorporated into an equation for the enhanced estimation of the significant wave height, namely:

$$m'_0 = C_m^2(\gamma) \cdot \int_{f_1}^{f_2} S_\eta(f) \cdot df \quad (9)$$

where:
$$C_m(\gamma) = 1.0015 + \frac{1}{[19.9178(\gamma' + 2.6937)]} \quad (10)$$

The variability of the enhanced estimate of the significant wave height, H_{m0}^1 , obtained by Equations (8) and (9) is given in the following table for the numerical simulations described in Section 2.2.2.

	$\gamma = 1.0$	$\gamma = 3.3$	$\gamma = 7.0$
MEAN	.150	.150	.150
STD. DEV.	.007	.009	.011
MAX.	.167	.183	.193
MIN.	.134	.127	.122

TABLE 2. Variability of Enhanced Estimates of the Significant Wave Height, H_{m0}^1

3.0 FITTING OF PARAMETRIC MODEL SPECTRA

The concept of optimally fitting a parametric model spectrum to spectral density estimates, as derived from the analysis of relatively short samples of a stochastic process, is founded on the hypothesis that knowledge of the spectral profile (i.e. a parametric model spectrum such as the JONSWAP class of spectrum), will improve the recovery of spectral parameters, because all spectral estimates are expected to contribute equally to the recovery process. Spectral fitting could be achieved as a multi-parameter or a single parameter optimization. In the former, several parameters are optimized concurrently, whereas only one is optimized at each pass in the latter case.

Optimization procedures must always start with some initial guess of the unknown parameters. The enhanced estimates of the spectral parameters described above,

such as the peak frequency f_{p5}^I , the peak enhancement factor γ^I and the spectrally derived significant wave height H_{m0}^I , were considered to be the best possible initial guesses for this purpose. (Any spectral fit which uses just these initial guesses will be called as initial guess fit).

Optimization is achieved through the application of a criterion, which is generally computed from some error function between the measured spectral density and the theoretical spectral density evaluated with the optimally fitted parameters. The evaluation of the criterion at the end of the optimization process is also a measure of the goodness of fit obtained through the use of the particular criterion.

For this study, a 3-parameter optimization was attempted first and the fitting method used was the Simplex Algorithm (Caceci and Cacheris, 1984). This method has the advantage of permitting multiple parameter optimization with arbitrary optimization criteria. Four different criteria were investigated for this purpose.

After carrying out extensive experiments, it was found that in most cases, the optimal values achieved through a 3-parameter fit were different from those known to be correct. The only exception to this was the fitting of Pierson-Moskowitz spectra (i.e. for γ values of 1). At this stage of the development, it appears that multi-parameter optimization cannot be used. Since an extensive discussion of the optimizing criteria and the results of the multi-parameter fitting are beyond the scope of this paper, they will be reported separately in Mansard and Funke (1991).

As indicated earlier, optimization can also be employed by fixing one or two of the parameters, and then optimizing the remainder. This approach led to a very satisfactory result in the improvement of the estimation of the peak frequency.

The technique, which is now used, computes the initial guesses for all three spectral wave parameters, as described above. The best guess for H_{m0} and γ is then fixed, (i.e. H_{m0}^I and γ^I) and optimal fitting is applied to find the best peak frequency f_0^I . The optimizing criterion used for this purpose can be defined as follows:

$$\sum_{j=1}^N [(\sqrt{S_m(f_j)} - \sqrt{S_s(f_j)}) \cdot \sqrt{W_j}]^2 \text{ is to be a minimum} \tag{11}$$

where $S_m(f_j)$ is the fitted model spectrum, $S_s(f_j)$ is the sample spectrum and W_j is the weighting function. The weighting function can be defined as follows:

$$W_j = \begin{cases} \frac{S_m(f_0)}{S_m(f_j)} & \text{if } S_m(f_0) < 100 \cdot S_m(f_j) \\ 0 & \text{otherwise} \end{cases} \tag{12}$$

where f_0 is the peak frequency.

A brief discussion of this criterion can be found in Mansard and Funke (1988b).

The results of this one parameter fitting are shown in Figure 1 for γ -values from 1 to 7, together with the results obtained from traditional and bias-corrected estimations. From this it is evident, that the spectral fitting, in combination with a carefully selected criterion function, can significantly enhance the estimation of a process parameter.

Generally, the spectral resolutions used in this fitting procedure correspond to 10 degrees of freedom (DOF). By using a small resolution such as this, a large number of statistically independent spectral estimates are included in the optimization procedure.

Figure 1 shows that for broad spectra (i.e. $\gamma = 1$), the standard deviation of peak frequency obtained by the traditional estimate can be improved by a factor of about 7 through spectral fitting. Preliminary results indicate that, even if a coarser resolution such as DOF = 30 is used in the traditional estimate of f_p , the improvements that can be achieved by the spectral fitting would be in the order of 6. Effects of the resolution will be discussed separately in Mansard and Funke (1991).

Figure 2 illustrates an example of one sample spectrum, derived by synthesis of a random wave train, and subsequently submitted to spectral analysis with 10 degrees of freedom. The figure also shows the population spectral density (JONSWAP with $\gamma = 1$), the "initial guess" spectral fit, and the optimally fitted spectrum using criterion given in Equation (11). This example illustrates the improvements which may be achieved over the more traditional methods of analysis.

4.0 THE LEBLOND METHOD FOR THE ESTIMATION OF THE PEAK ENHANCEMENT FACTOR

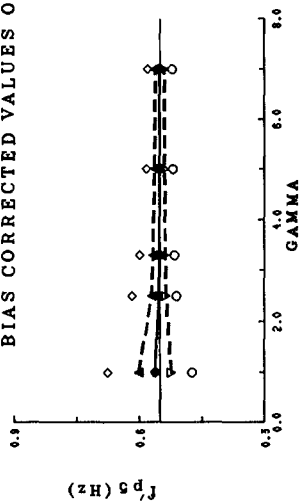
LeBlond (1982) developed and used a technique for the estimation of the JONSWAP peak enhancement factor. This technique is based on an assumption that a certain relationship exists between the spectra's Phillip's constant α and the significant wave height H_{m0} (Mitsuyasu et al, 1980). The method is also limited to γ -values that are less than 4.

LeBlond analyzed his wave data with very low resolution, corresponding to 30 DOF, and determined the spectral peak frequency by the traditional method; that is, by taking the frequency of the largest spectral value. After this, LeBlond integrated the spectrum from 0.05 to 0.5 Hz (full scale units) to get the significant wave height, and used the formula:

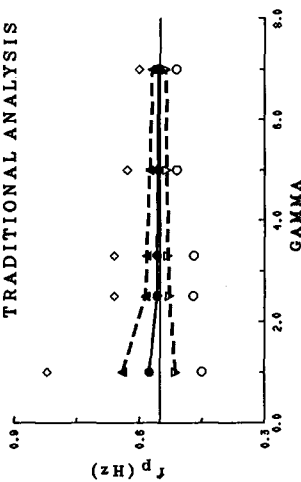
$$\gamma = \left[\frac{S(f_p)}{\frac{5}{16f_p} H_{m0}^2 e^{-5/4}} \right]^{3/2} \quad (13)$$

to compute the JONSWAP peak enhancement factor.

BIAS CORRECTED VALUES OF f_{p5}



TRADITIONAL ANALYSIS



OPTIMALLY FITTED VALUES

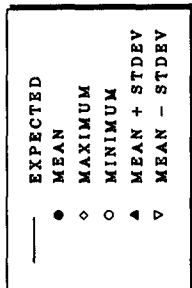
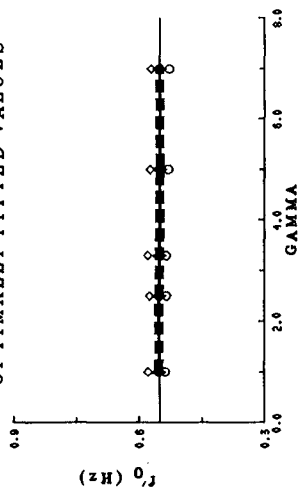


FIGURE 1

RANGE OF ESTIMATES FOR PEAK FREQUENCY UNDER DIFFERENT COMPUTATIONAL METHODS
 (RANDOM COMPLEX SPECTRUM METHOD OF SYNTHESIS)
 ($T_R=200s$ $f_0=0.55$ Hz $H_{m0}=0.15m$ $N_B=200$ $DOF=10$)

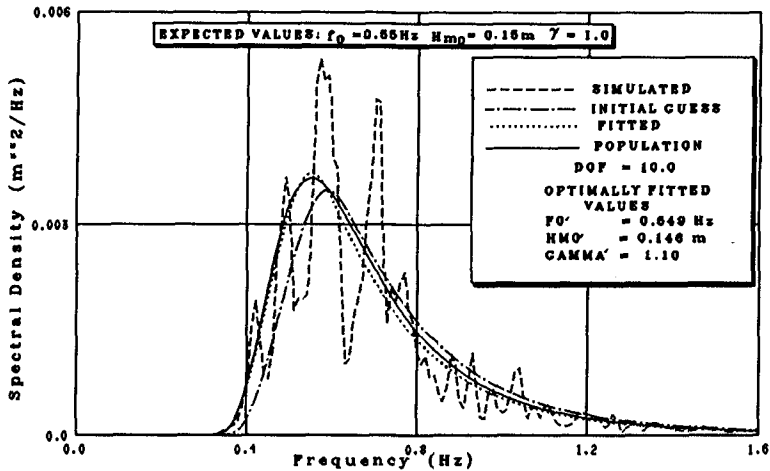


Fig.2 EXAMPLE OF AN OPTIMAL FIT

Table 3 summarizes the result of an analysis carried out by the LeBlond method, using 200 numerically simulated waves with approximately 110 waves derived from a JONSWAP spectrum with a peak enhancement factor $\gamma=3.3$ and a peak period of 0.55 Hz.

	PEAK FREQUENCY f_0^t (HZ)	EST. SIG. WAVE HEIGHT H_{m0}^t (m)	PEAK ENHANCEMENT FACTOR, γ^t
MEAN	.557	.150	2.817
STD. DEV.	.018	.009	0.689
MAX.	.595	.183	4.849
MAX.	.490	.127	1.177

TABLE 3. Results of LeBlond Analysis

The important result from Table 3 is the fact that the standard deviation of the LeBlond estimator for γ -values is only 65% of that obtained with the authors' method. The mean value of γ and peak frequency values are, however, not as satisfactory, and the significant wave height estimators look good only because the numerical simulation used here was free of noise, and the integration limits could be extended from 0 to the Nyquist frequency.

However, the positive result from the LeBlond example suggests that further improvements in the estimation of the peak enhancement factor may be possible.

5.0 EXAMPLE ANALYSIS OF OCEAN WAVE DATA

Figure 3 compares the peak frequency, estimated by the spectral fitting, for two wave recording stations at the Ocean Ranger and the Sedco 706, nearly 17 km apart. Although there were 3 sites near the Ocean Ranger platform, only these two stations were chosen for this preliminary investigation since continuous wave records were available from them. The third station, Zapata Uglund, which was 30 km away from the Ocean Ranger, had records only at 3 hour intervals during that period.

For purpose of comparison, the traditional estimates of peak frequency and the bias-corrected values of f_{p5} are also shown in Figure 3. This figure clearly illustrates the improvements that can be achieved in the interpretation of prototype data through optimal fitting. It can be seen from this figure that, while the traditional and bias-corrected estimates show considerable differences in the peak frequencies at these stations, the optimally fitted values indicate the similarity of the two sites during the time of the storm. For these two stations, the variability of peak frequency between consecutive records of 20 minutes is reduced considerably when spectral fitting is applied.

6.0 CONCLUSIONS

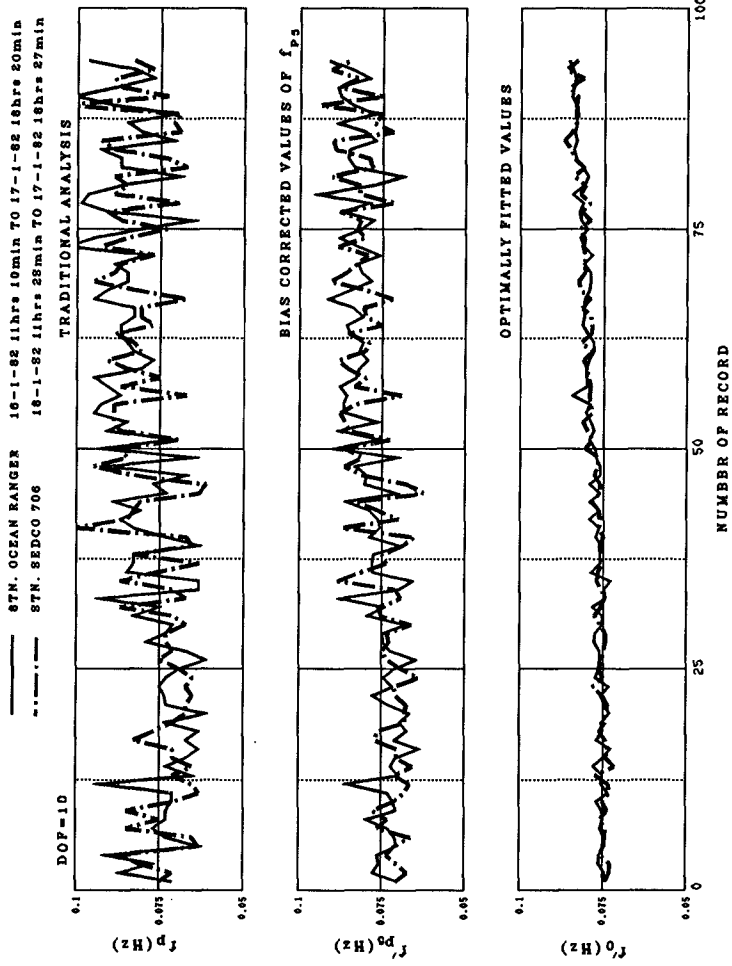
An enhanced method for estimation of the spectral peak frequency for ocean wave data has been presented. The method was tested by numerical simulation of short wave records. For JONSWAP spectra with $\gamma = 1$, the variability of the peak frequency estimate can be improved by a factor of 7. Two methods for the estimation of JONSWAP peak enhancement factors are presented, but neither is considered satisfactory.

Further work will seek improvements in the estimation of the JONSWAP peak enhancement factor, establish suitable bias correction functions for the significant wave height as a function of spectral cut-off frequencies, and establish convenient confidence bands for the estimation of the three principal spectral wave parameters. Improvements in computational efficiency and the effects of spectral resolution will also be investigated.

The new method is believed to improve the validation of hindcasting and forecasting numerical models. At this time, the method applies only to the deep water situation, where spectral estimates of contributing frequencies are statistically independent. Future development may be able to address the intermediate and shallow water depth situation as well, where the spectral estimates are interdependent because of nonlinear interactions.

7.0 REFERENCES

- Battjes, J.A. and van Vledder, G.Ph., "Verification of Kimura's Theory for Wave Group Statistics", Proc. of 19th Int. Conf. on Coastal Engg., Houston, USA. 1984.
- Caceci, M.S. and Cacheris, W.P., "Fitting Curves to Data", BYTE, May 1984.



ESTIMATES OF PEAK FREQUENCY AT STATIONS OCEAN RANGER AND SEDCO
FIGURE 3

Funke, E.R. and Mansard, E.P.D., "A Rationale for the Use of the Deterministic Approach to Laboratory Wave Generation", Proc. of the Seminar on Wave Generation and Analysis in Laboratory Basins, 22nd IAHR Conf., Lausanne, Switzerland, 1987.

IAHR/PIANC, "List of Sea State Parameters", PIANC Supplement to Bulletin No. 52, General Secretariat of PIANC, Résidence Palace, Quartier Jordaens, rue de la Loi, 155, 1040 Brussels, Belgium, 1986.

Houmb, O.G. and Øyan, T., "Fits Between Empirical Spectra and the JONSWAP Model" Report no. 5, Division of Port and Ocean Engineering, The University of Trondheim, Trondheim, Norway, 1981.

LeBlond, P.H., "Wave Spectra in Canadian Waters", Report prepared for the Canadian Marine Environmental Data Service by Seaconsult Marine Research Limited, June 1982.

Mansard, E.P.D. and Funke, E.R., "Physical Experiments in Laboratories: Contrast of Methodologies and Results". Lecture notes for the short course on "Planning and Design of Maritime Structures", 21st Int. Conf. on Coastal Engg., Malaga, Spain, 1988a.

Mansard, E.P.D. and Funke, E.R., "On the Fitting of Parametric Models to Measured Wave Spectra", "Proc. 2nd. Int Symp. on Waves and Coastal Engg, Univ. of Hannover, Hannover, W. Germany, 1988b.

Mansard, E.P.D. and Funke, E.R., "A Discussion on Spectral Fitting of Parametric Models to Measured Sea States", Hydraulics Laboratory Technical Report in progress, National Research Council of Canada, Ottawa, Canada, to be published in 1991.

Miles, M.D. and Funke, E.R., "Numerical Comparison of Wave Synthesis Methods", Proc. 21st Int. Conf. on Coastal Engg. Malaga, Spain, June, 1988.

Mitsuyasu, H., Tasai, F., Suhara, T., Mizuno, S., Ohkusu, M., Honda, T. and Rikiishi, K. "Observations of the Power Spectrum of Ocean Waves using a Cloverleaf Buoy", J. Phys. Oceanogr., 10, 1980.

Mogridge, G.R., "Hydrodynamic Model Tests of the Semi-Submersible Ocean Ranger" Hydraulics Laboratory Technical Report TR-HY-007, National Research Council of Canada, Ottawa, Canada, 1985.

Read W.W., "Time Series Analysis of Wave Records and the Search for Wave Groups", Ph.D. thesis, James Cook University of North Queensland, Australia. 1986.

Rye, H. "The Stability of Some Currently Used Wave Parameters", Coastal Engineering, Vol. 1, No.1, March, 1977.

CHAPTER 37

AN EFFICIENT METHOD FOR THE REPRODUCTION OF NON-LINEAR RANDOM WAVES

Gert Klopman ¹ and Peter Jan Van Leeuwen ²

Abstract

For the laboratory study of many random-wave induced phenomena, wave-board control signals according to linear wave theory are not sufficient: apart from bound sub- and superharmonic waves, spurious free waves are generated. Wave generation according to a higher-order wave theory is necessary in order to suppress these spurious waves. The perturbation method of multiple scales is used to derive formulas for the second-order wave-board control signal, assuming the carrier-wave spectrum is narrow banded. The resulting algorithm is much faster than the one based on the full second-order theory. Furthermore, the applicability of the narrow-band approximation is indicated for carrier-wave spectra frequently used in coastal and ocean engineering.

1 Introduction

For the extrapolation of laboratory data to full scale sea conditions it is essential to have a realistic reproduction of the sea in laboratory experiments. In a natural wave train, with the spectral energy density concentrated around the peak frequency, the non-linearity of the free-surface boundary conditions introduces sub- and superharmonics which are phase locked to the primary wave components. When the system under investigation is perceptible to these sub- and superharmonics, it is important to reproduce them correctly in the laboratory.

The subharmonics (or bound long waves) can generate the forcing for long-period harbour oscillations, slow-drift motions of moored vessels and tension-leg platforms, and offshore sand-bar formation due to sediment transport. The superharmonics introduce sharper-peaked wave crests and flatter troughs, they are important for sediment transport due to wave asymmetry and can be of importance for forces on offshore structures.

¹Delft Hydraulics, P.O. Box 152, 8300 AD Emmeloord, The Netherlands.

²Delft University of Technology, Dept. of Civil Engineering, P.O. Box 5048, 2600 GA Delft, The Netherlands.

An incorrect (linear) reproduction in the laboratory generates free waves at the same frequencies as the bound sub- and superharmonics, but travelling at a different speed. This difference in speed between the free and bound wave components results in spatial variations in the root-mean-square (rms) free-surface fluctuations, for instance obscuring the interpretation of the results from models with a movable bed.

The problem of reproducing the subharmonics correctly up to second order, for long-crested random waves in the laboratory, has been solved for translating wave boards by Sand (1982), and for translating and rotating wave boards by Barthel et al (1983). The reproduction of superharmonics is dealt with by Sand & Mansard (1986), both for translating and rotating wave boards.

Both the sub- and the superharmonic second-order corrections to the wave-board control signal are determined at every frequency by computing an integral over an appropriate frequency range (involving the Fourier transform of the first-order free-surface elevation and a second-order transfer function). The work needed for generating a control signal correct up to second order is thus proportional to the square of the work needed for generating the first-order signal.

Since most engineering applications deal with sea conditions characterized by quite narrow-banded spectra, the perturbation method of multiple scales is an alternative to generate second-order long-crested random waves in the laboratory. All operations to compute the second-order control signal from the first-order free-surface elevation can be performed in the time domain, and involve only a few simple algebraic operations on the first-order free-surface signal. Therefore, the work needed for generating the second-order control signal is proportional to and only slightly more than the work for generating the first-order signal.

The application of the perturbation method of multiple scales for the present random-wave generation problem, is very similar to the use of the same method by Agnon & Mei (1985) and Agnon, Choi & Mei (1988) for determining the slow-drift motion of two-dimensional bodies in beam seas.

In this paper we first consider some aspects of the usefulness of the narrow-band approximation, for coastal and ocean engineering applications. Next, the perturbation method of multiple scales is applied to the present problem of generating second-order wave-board control signals. Here, we only present results for the subharmonic bound-wave corrections, and not for the superharmonics.

2 Applicability of narrow-band approximation

The accuracy of the multiple-scales method increases as the spectral width decreases. The errors, introduced by the use of the narrow-band approximation in the multiple-scales approach, should be small for the wave spectra normally used in coastal and ocean engineering. In order to get some indication of the usefulness of the multiple-scales perturbation-series method, some comparisons

were made between second-order free-surface elevation spectral densities obtained with the multiple-scales perturbation-series method, as described by Mei (1989, Chapter 12), and those obtained by a full second-order theory, as described by Laing (1986). This comparison only gives an indication of the accuracy, since a non-linear random process is not fully characterized by its autospectrum.

Here, we consider gravity waves on the free surface of a fluid domain of initially constant depth h . The fluid is assumed to be homogeneous, inviscid and incompressible, and the flow is assumed to be irrotational. Surface tension effects and effects of the air above the free surface are neglected. The flow can be described by a velocity potential Φ , with the fluid velocity vector equal to the gradient of the velocity potential.

The perturbation method of multiple scales was used to simulate a finite duration realization of the second-order free-surface elevation in the time domain. The free-surface elevation $\zeta(x, t)$ and the velocity potential $\Phi(x, z, t)$ are expanded into perturbation series:

$$\begin{aligned}\zeta &= \sum_{n=1}^{\infty} \varepsilon^n \zeta_n(x, t), \\ \Phi &= \sum_{n=1}^{\infty} \varepsilon^n \phi_n(x, z, t),\end{aligned}\tag{1}$$

with x the horizontal space coordinate, positive in the wave propagation direction, z the vertical space coordinate, with $z > 0$ above the still water elevation. The time coordinate is denoted by t and ε is a small non-linearity parameter proportional to the wave slope.

Because we are considering propagating wave phenomena, the terms from the perturbation series are expanded into harmonic functions. The amplitudes of the harmonic functions are assumed to vary only slowly in space and time, i.e. the carrier waves are assumed to have narrow-banded spectra. This slow modulation is formalized by the introduction of fast coordinates (x_0, t_0) and a cascade of slow coordinates $(x_1, t_1), (x_2, t_2), \dots$ in the horizontal space and the time direction:

$$\begin{aligned}x_0 &= x, & x_1 &= \varepsilon x, & x_2 &= \varepsilon^2 x_2, \dots, \\ t_0 &= t, & t_1 &= \varepsilon t, & t_2 &= \varepsilon^2 t_2, \dots,\end{aligned}\tag{2}$$

where it has been assumed that the modulation effects are of the same order as the non-linearity effects.

The (quadratic) non-linearity of the problem, due to the non-linear free-surface boundary conditions, introduces higher harmonics into the higher-order solutions:

$$\begin{aligned}\zeta &= \sum_{n=1}^{\infty} \varepsilon^n \sum_{m=-n}^{+n} \zeta^{(n,m)} E_0^m, \\ \Phi &= \sum_{n=1}^{\infty} \varepsilon^n \sum_{m=-n}^{+n} \phi^{(n,m)} E_0^m,\end{aligned}\tag{3}$$

with:

$$E_0 = e^{ix_0}, \quad \chi_0 = k_0 x_0 - \omega_0 t_0, \tag{4}$$

and

$$\begin{aligned} \zeta^{(n,m)} &= \zeta^{(n,m)}(x_1, x_2, \dots; t_1, t_2, \dots), \\ \phi^{(n,m)} &= \phi^{(n,m)}(x_1, x_2, \dots; z; t_1, t_2, \dots), \end{aligned} \tag{5}$$

expressing the slow variation of these complex-valued amplitude functions $\zeta^{(n,m)}$ and $\phi^{(n,m)}$. In (4), k_0 is the carrier wave number and ω_0 is the carrier-wave angular frequency. Because ζ and Φ are real-valued functions, $\zeta^{(n,-m)}$ and $\phi^{(n,-m)}$ have to be the complex conjugates of respectively $\zeta^{(n,m)}$ and $\phi^{(n,m)}$.

The solution of both the first-order and the second-order problem can for instance be found in Mei (1989, Chapter 12):

$$\begin{aligned} \zeta_1 &= \frac{1}{2} (Ae^{ix_0} + *), \\ \phi_1 &= \phi^{(1,0)}(x_1, t_1) - \frac{1}{2} \frac{g \operatorname{ch} Q}{\omega_0 \operatorname{ch} q} (iAe^{ix_0} + *), \end{aligned} \tag{6}$$

and

$$\begin{aligned} \zeta_2 &= \left\{ -\frac{1}{g} \frac{\partial \phi^{(1,0)}}{\partial t_1} - \frac{\omega_0^2}{4g \operatorname{sh}^2 q} |A|^2 \right\} + \\ &\quad + \frac{k_0 \operatorname{ch} q}{8 \operatorname{sh}^3 q} (2 \operatorname{ch}^2 q + 1) (A^2 e^{2ix_0} + *), \\ \phi_2 &= \phi^{(2,0)} - \frac{1}{2} \frac{g \operatorname{ch} Q}{\omega_0 \operatorname{ch} q} \left(\frac{1}{\omega_0} + \frac{q \operatorname{th} q - Q \operatorname{th} Q}{k_0 C_g} \right) \left(\frac{\partial A}{\partial t_1} e^{ix_0} + * \right) + \\ &\quad - \frac{3}{16} \frac{\omega_0 \operatorname{ch} 2Q}{\operatorname{sh}^4 q} (C A^2 e^{2ix_0} + *), \end{aligned} \tag{7}$$

with $q = k_0 h$, $Q = k_0(z+h)$, $C_g = d\omega_0/dk_0$ the group velocity, g the gravitational acceleration, $A(x_1, t_1)$ the complex-valued amplitude of the carrier waves and an asterisk (*) denoting the complex conjugate of the preceding term. We have chosen $\zeta^{(2,1)}$ equal to zero, i.e. the first-order solution ζ_1 completely describes the free-surface elevation spectral density near the peak frequency. The wave number k_0 is related to the angular frequency ω_0 by the linear theory dispersion relation:

$$\omega_0^2 = g k_0 \operatorname{th} q, \tag{8}$$

and further use has been made of

$$\frac{\partial A}{\partial t_1} + C_g \frac{\partial A}{\partial x_1} = 0, \tag{9}$$

which is correct up to second order.

The second-order correction (7) to the free surface elevation ζ still contains $\phi^{(1,0)}$. This is determined from the solvability condition for the third-order zeroth-harmonic $(n, m) = (3, 0)$ problem, see e.g. Mei (1989, Chapter 12), and assuming

that the waves propagate according to Stokes's second definition of wave celerity (i.e. the mean mass flux through a vertical plane perpendicular to the wave propagation direction is equal to zero), resulting in $\langle \zeta \rangle = 0$, with $\langle \cdot \rangle$ denoting a time average. The second-order correction ζ_2 becomes:

$$\zeta_2 = \frac{1}{2} \frac{g}{C_g^2 - gh} \left\{ \frac{C_g}{C_0} + \frac{q}{\text{sh } 2q} \right\} (|A|^2 - \langle |A|^2 \rangle) + \frac{k_0 \text{ch } q}{8 \text{sh}^3 q} (2 \text{ch}^2 q + 1) (A^2 e^{2i\chi_0} + *), \quad (10)$$

with $C_0 = \omega_0/k_0$ the phase velocity.

Equations (6) & (10) are used to simulate part of a realization of the second-order random free-surface elevation. The first-order complex-valued random wave signal $A \exp(i\chi_0)$ is generated from a given first-order free-surface elevation spectrum with the random-amplitude/random-phase method (Tucker et al.; 1984).

The second-order free-surface spectrum can be computed without making the narrow-band approximation with the formulations of Laing (1984). The (one-sided) non-linear free-surface elevation spectrum $S_{\zeta\zeta}(\omega)$ is expanded into a perturbation series:

$$S_{\zeta\zeta}(\omega) = \sum_{n=1}^{\infty} \varepsilon^n S_{\zeta\zeta}^{(n)}(\omega), \quad (11)$$

of which we consider only the first two terms. For a given first-order spectrum $S_{\zeta\zeta}^{(1)}(\omega)$, the second-order correction $S_{\zeta\zeta}^{(2)}(\omega)$ becomes:

$$S_{\zeta\zeta}^{(2)}(\omega) = \int_{\frac{1}{2}\omega}^{\infty} D_{20}(\omega, \omega') S_{\zeta\zeta}^{(1)}(\omega') S_{\zeta\zeta}^{(1)}(\omega' - \omega) d\omega', \quad (12)$$

with $D_{20}(\omega, \omega')$ the second-order transfer function, given by:

$$D_{20} = \frac{2 (D_2(\omega, \omega'))^2}{g^2 (1 - \omega^2/g\kappa \text{th } \kappa h)^2}, \quad (13)$$

$$D_2 = \frac{1}{2} \left\{ (\omega')^2 + (\omega - \omega')^2 + \omega'(\omega - \omega') - \omega'(\omega - \omega') \coth k'h \coth(\kappa - k')h + \omega\omega' \coth \kappa h \coth k'h + \omega(\omega - \omega') \coth \kappa h \coth(\kappa - k')h \right\}, \quad (14)$$

with κ the wave number of the bound waves, and:

$$\begin{aligned} (\omega')^2 &= gk' \text{th } k'h, \\ (\omega - \omega')^2 &= g(\kappa - k') \text{th } (\kappa - k')h, \end{aligned} \quad (15)$$

the dispersion relationships for the free waves. Equation (12) shows that an integral over all frequency pairs has to be computed, in order to obtain the second-order spectrum.

Both descriptions of the second-order free surface elevation, i.e. the multiple-scales perturbation method as well as the full second-order theory in the frequency domain, include the subharmonic as well as superharmonic bound waves. Both methods were used to obtain second order spectra, assuming the first-order spectrum to be of JONSWAP shape:

$$S_{\zeta\zeta}^{(1)}(f) = \frac{\beta H_{rms}^2}{f_p} \left(\frac{f}{f_p}\right)^{-5} \exp\left[-\frac{5}{4}\left(\frac{f}{f_p}\right)^{-4}\right] \gamma^{-\frac{1}{2}} \left(\frac{f-f_p}{\sigma f_p}\right)^2, \quad (16)$$

with $f = \omega/(2\pi)$ the frequency, H_{rms} the rms wave height, f_p the spectral peak frequency, γ the peak enhancement factor, σ the peak width parameter and β a form factor chosen in such a way that $H_{rms}^2 = 8 \int_0^\infty S_{\zeta\zeta}^{(1)}(f) df$.

The results of three simulations will be shown, all with a rms wave height $H_{rms} = 0.7062[m]$, a peak frequency $f_p = 0.25[Hz]$, a still water depth $h = 3[m]$, and with the mean JONSWAP values for σ , i.e. $\sigma = 0.07$ for $f < f_p$ and $\sigma = 0.09$ for $f \geq f_p$. The simulation with the multiple-scales perturbation method in the time domain had a duration of 6400[s] and a sample rate of 5.12[Hz]. The following three values for the peak enhancement factor γ were used:

$\gamma = 20$, a very narrow-banded first-order spectrum,

$\gamma = 3.3$, the mean JONSWAP value, and

$\gamma = 1$, the Pierson-Moskowitz spectrum.

Figures 1-3 show a comparison between the autospectra of the free-surface elevation, obtained from the multiple-scales perturbation method and from the full second-order theory. The relative differences between both approaches become larger when the spectral width increases, and are of the order of 10% of the square root of the spectral density (a measure for corresponding wave amplitude) near $f = 0.02[Hz]$, where the subharmonic spectral density is high. It should also be noted that the relative importance of the bound long waves decreases as the spectral width increases. The difference between the spectrum obtained from the multiple-scales perturbation-series simulation and the theoretical first-order spectrum is due to the random-amplitude approach during the generation of the first-order signal and the finite duration of the numerical simulation (therefore also H_{rms} , obtained from finite-duration realizations, is a random variable). Since the mean free-surface elevation is equal to zero, the spectral density falls off near $f = 0[Hz]$ for the spectra obtained from the numerical simulation, but is not exactly equal to zero due to the computational method used for obtaining the spectra (Fast Fourier Transform on half-overlapping segments, with Van Hann data window).

The deviations, due to the narrow-band approximations implied by the use of the multiple-scales perturbation-series method, were considered to be very acceptable for the spectra commonly used in coastal and ocean engineering.

3 Second-order random-wave generation method

The generation of subharmonic waves, both bound and free waves, is described by Agnon & Mei (1985) in their study of the small-amplitude slow-drift motion due to beam seas of a two-dimensional rectangular block, sliding over the sea bed. Agnon, Choi & Mei (1988) extended this analysis to the case of floating two-dimensional cylinders undergoing both small- and large-amplitude slow-drift motions ('large' meaning motions comparable to or even greater than the motions at the carrier-wave frequency). Here, we use the results of Agnon & Mei (1985) for the determination of the low-frequency wave-board control signal, in such a way that only bound long waves are generated, and no spurious free long waves.

The horizontal wave-board position is denoted by $X(t)$, and the still position is at $x = X = 0$. As in (1), the free-surface elevation $\zeta(x, t)$, the velocity potential $\phi(x, z, t)$, and now also the wave-board position $X(t)$ are expanded into perturbation series:

$$\begin{aligned}\zeta &= \sum_{n=1}^{\infty} \varepsilon^n \zeta_n(x, t), \\ \Phi &= \sum_{n=1}^{\infty} \varepsilon^n \phi_n(x, z, t), \\ X &= \sum_{n=1}^{\infty} \varepsilon^n X_n(t).\end{aligned}\tag{17}$$

The terms in the perturbation series are again expanded into harmonic functions, as in (3). We introduce a cascade of slow variables, cfm. (2). However, now the amplitudes of the harmonic functions vary fast in space near the wave board due to the presence of evanescent modes. Therefore, the solution is assumed to be of the following form:

$$\begin{aligned}\zeta &= \sum_{n=1}^{\infty} \varepsilon^n \sum_{m=-n}^{+n} \zeta^{(n,m)} e^{-im\omega_0 t}, \\ \Phi &= \sum_{n=1}^{\infty} \varepsilon^n \sum_{m=-n}^{+n} \phi^{(n,m)} e^{-im\omega_0 t}, \\ X &= \sum_{n=1}^{\infty} \varepsilon^n \sum_{m=-n}^{+n} X^{(n,m)} e^{-im\omega_0 t},\end{aligned}\tag{18}$$

with:

$$\begin{aligned}\zeta^{(n,m)} &= \zeta^{(n,m)}(x_0, x_1, x_2, \dots; t_1, t_2, \dots), \\ \phi^{(n,m)} &= \phi^{(n,m)}(x_0, x_1, x_2, \dots; z; t_1, t_2, \dots), \\ X^{(n,m)} &= X^{(n,m)}(t_1, t_2, \dots),\end{aligned}\tag{19}$$

i.e. the harmonic functions $\zeta^{(n,m)}$ and $\phi^{(n,m)}$ are also functions of x_0 , and it is not assumed that the first-order solution only contains propagating waves $A \exp [i(k_0 x_0 - \omega_0 t_0)]$, but also evanescent modes fixed to the wave board.

The derivation of the first-order solution and the second-order subharmonic solution can be found in Agnon & Mei (1985), including how to remove the evanescent mode contributions from the subharmonic solution. These derivations will not be repeated here, but we only present the results for our problem of second-order wave-board control. The first-order first-harmonic solution is:

$$\begin{aligned}
 \zeta^{(1,1)} &= \frac{1}{2} A(x_1 - C_g t_1) e^{ik_0 x_0} + \\
 &\quad - i \frac{\omega_0 C_g}{C_0} \frac{1}{2} A(-C_g t_1) \sum_{l=1}^{\infty} \frac{1}{k_l} \frac{1}{C_g - \frac{1}{2}(q_0^2 + q_l^2)/(k_D h)} e^{-k_l x_0}, \\
 \phi^{(1,1)} &= -i \frac{g \operatorname{ch} Q_0}{\omega_0 \operatorname{ch} q_0} \frac{1}{2} A(x_1 - C_g t_1) e^{ik_0 x_0} + \\
 &\quad - \frac{g C_g}{C_0} \frac{1}{2} A(-C_g t_1) \sum_{l=1}^{\infty} \frac{1}{k_l} \frac{\cos Q_l}{\cos q_l} \frac{1}{C_g - \frac{1}{2}(q_0^2 + q_l^2)/(k_D h)} e^{-k_l x_0}, \\
 X^{(1,1)} &= i \frac{C_g}{C_0 \operatorname{th} q_0} \frac{1}{2} A(-C_g t_1),
 \end{aligned} \tag{20}$$

with $k_D = \omega_0^2/g$, $q_l = k_l h$, $l = 0, 1, 2, \dots$ and $Q_l = k_l(z + h)$, $l = 0, 1, 2, \dots$. The propagating wave number k_0 and the evanescent-mode wave numbers k_l , for $l = 1, 2, \dots$ satisfy the linear-theory dispersion relationships:

$$\omega_0^2 = \begin{cases} g k_0 \operatorname{th} q_0 & , l = 0, \\ g k_l \tan q_l & , l = 1, 2, \dots \end{cases} \tag{21}$$

The first-order zeroth-harmonic solution is:

$$\begin{aligned}
 \zeta^{(1,0)} &= 0, \\
 \phi^{(1,0)} &= \frac{g^2 [2\omega_0 k_0 + C_g(k_0^2 - k_D^2)]}{4\omega_0^2 (C_g^2 - gh)} \left(\int_{-\infty}^{x_1 - C_g t_1} |A(\psi)|^2 d\psi \right), \\
 X^{(1,0)} &= -\frac{g^2}{4\omega_0^2 C_g} \left(\frac{2\omega_0 k_0 + C_g(k_0^2 - k_D^2)}{C_g^2 - gh} + \frac{2\omega_0 k_0}{gh} \right) \times \\
 &\quad \times \int_{-\infty}^{-C_g t_1} (|A(\psi)|^2 - \langle |A|^2 \rangle) d\psi,
 \end{aligned} \tag{22}$$

where $X^{(1,0)}$ is the desired subharmonic bound-wave contribution to the wave-board control signal X . Note that $\phi^{(1,0)}$ and $X^{(1,0)}$ are proportional to $|A|^2$, and thus in fact higher-order quantities. This is due to the fact that their derivatives $\partial\phi^{(1,0)}/\partial x_1$ and $\partial X^{(1,0)}/\partial t_1$ are the relevant physical quantities which are second-order quantities within the multiple-scales perturbation-series approach.

From the second-order zeroth-harmonic contribution to the solution, only the $\zeta^{(2,0)}$ -term is needed:

$$\zeta^{(2,0)} = -\frac{1}{g} \left\{ \frac{\partial \phi^{(1,0)}}{\partial t_1} + \left[\left| \frac{\partial \phi^{(1,1)}}{\partial x_0} \right|^2 - k_D^2 |\phi^{(1,1)}|^2 \right]_{z=0} \right\}. \quad (23)$$

In summary, $\zeta^{(1,1)}$, $\phi^{(1,1)}$ and $X^{(1,1)}$ in (20) are the terms proportional to the wave amplitude A , and $\zeta^{(2,0)}$, $\phi^{(1,0)}$ and $X^{(1,0)}$ in (22) & (23) are the subharmonic terms proportional to $|A|^2$.

The first-order random free-surface signal $A \exp(-iC_g t_1)$ is generated with the random-amplitude/random-phase method (Tucker et al.; 1984), for a given first-order free-surface elevation spectrum, as in Section 2. Next the wave-board control signal, correct up to second order, is computed. Required time integrations are performed with the modified midpoint rule, and time differentiation with central finite differences, both of second-order accuracy, i.e. $O(\Delta t^2)$. Also deterministic waves, such as monochromatic and bichromatic waves, can be generated correctly up to second order with these equations.

At the moment, flume tests are performed at Delft University of Technology, for the experimental verification of the second-order wave-board control system.

4 Concluding remarks

The perturbation-series method of multiple scales has been used to derive an efficient method for the generation of second-order random waves in wave flumes with a translating wave board. The method is presented in detail for the subharmonic corrections to the wave-board control signal, but can easily be extended to include the superharmonic corrections.

The amount of work to generate the second-order corrections with the proposed method is proportional to the amount of work to generate the first-order signal. In previously used second-order frequency-domain methods, this amount of work was proportional to the square of the effort for generating the first-order signal.

Furthermore, the narrow-band approximation, implied by the use of the multiple-scales perturbation-series approach, seems to be very acceptable for the first-order spectral shapes most frequently used in coastal and ocean engineering problems.

Acknowledgments

This research has been sponsored by the Netherlands Organization for the Advancement of Research (N.W.O.) and Delft Hydraulics's Long-Term Research Theme for Experimentation Techniques.

The authors wish to thank Mr. L. Verhage for performing the computing analysis and coding of the wave-board control software package, and Mr. H.A.H. Petit for checking the formulas.

References

- Agnon, Y. and Mei, C.C. (1985) "Slow-drift motion of a two-dimensional block in beam seas", *J. Fluid Mech.* **151**, pp. 279-294.
- Agnon, Y., Choi, H.S. and Mei, C.C. (1988) "Slow drift of a floating cylinder in narrow-banded beam seas", *J. Fluid Mech.* **190**, pp. 141-163.
- Barthel, V., Mansard, E.P.D., Sand, S.E. and Vis, F.C. (1983) "Group bounded long waves in physical models", *Ocean Engng.* **10**(4), pp. 261-294.
- Laing, A.K. (1986) "Nonlinear properties of random gravity waves in water of finite depth", *J. Phys. Oceanogr.* **16**(12), pp. 2013-2030.
- Mei, C.C. (1989) "*The applied dynamics of ocean surface waves*", World Scientific Publ., Singapore.
- Sand, S.E. (1982) "Long wave problems in laboratory models", *J. Waterway, Port, Coastal, Ocean Engng.* **108**(WW4), pp. 492-503.
- Sand, S.E. and Mansard, E.P.D. (1986) "The reproduction of higher harmonics in irregular waves", *Ocean Engng.* **13**(1), pp. 57-83.
- Tucker, M.J., Challenor, P.G. and Carter, D.J.T. (1984) "Numerical simulation of a random sea: a common error and its effect upon wave group statistics", *Appl. Ocean Res.* **6**(2), pp. 118-122.

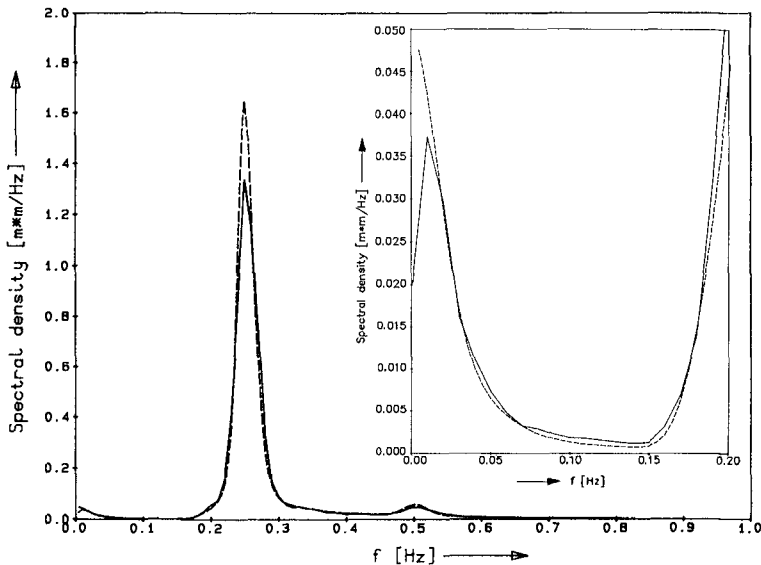


FIGURE 1. Second-order spectral energy density of free-surface elevations ($\gamma = 20$), ——— multiple-scales perturbation-series simulation (Mei; 1989), - - - - full second-order theory (Laing; 1986).

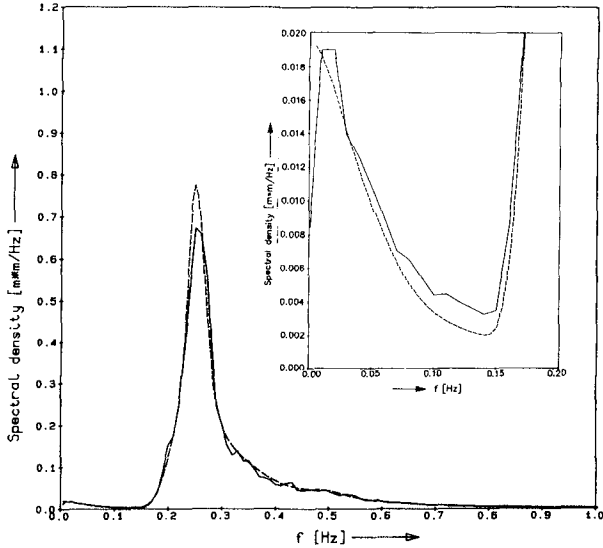


FIGURE 2. Second-order spectral energy density of free-surface elevations ($\gamma = 3.3$; mean JONSWAP spectrum), ——— multiple-scales perturbation-series simulation (Mei; 1989), - - - - full second-order theory (Laing; 1986).

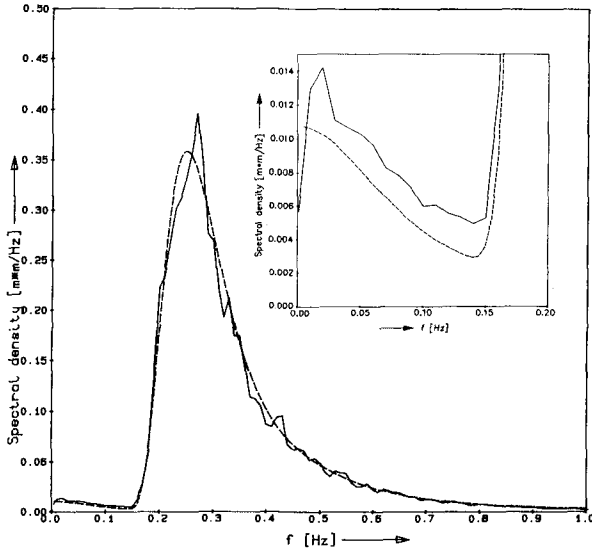


FIGURE 3. Second-order spectral energy density of free-surface elevations ($\gamma = 1$; Pierson-Moskowitz spectrum), ——— multiple-scales perturbation-series simulation (Mei; 1989), - - - - full second-order theory (Laing; 1986).

CHAPTER 38

An Experimental Study of Waves on a Strongly Sheared Current Profile.

Christopher Swan.*

Abstract.

This paper describes a series of observations within a combined wave-current flume. A two dimensional progressive wave train was superimposed upon a co-flowing current profile. The direction of this current was reversible, thereby allowing the formation of both a "favourable" current velocity (one in which the current is in the same direction as the wave celerity), and an "adverse" current velocity. The combined flow field was measured using laser Doppler anemometry. The nature of the current profile was modified so as to allow an investigation of the interaction resulting from both a uniform current and a sheared current profile.

In the case of a uniform current, there was no observable phase change between the surface elevation and the velocity profile. In this respect the present measurements are very different from the observations presented by Brevik (1980a). Indeed, they confirm that a description of the oscillatory motion merely requires the introduction of a Doppler shift as was suggested by Fenton (1985). In the case of a sheared current profile the oscillatory component of the wave motion is found to be strongly dependant upon the vorticity within the current profile. The analytical solution proposed by Kishida and Sobey (1988) appears to underestimate the extent of the interaction, while the numerical solution proposed by Chaplin (1990) provides a better description of the combined flow field. The departure from irrotational theory is significant. In the case of waves superimposed on a strongly sheared "adverse" current the horizontal velocity component may be as much as 80% larger than the predicted irrotational motion.

* Lecturer, Imperial College, Dept. of Civil Engineering, London SW7 2BU. U.K.

1.0 Introduction.

The interactions resulting from the combination of waves and currents has been the subject of numerous publications. Thompson (1949) presented the first solution for waves on a linear shear current (ie. the current varies linearly in the vertical direction, but does not vary in the horizontal direction). Tsao (1959) also considered this problem, and established that the wave motion will remain irrotational provided the vorticity profile is uniform with depth. He conducted a classical Stokes' expansion, and obtained the third order expressions for the surface displacement and the velocity field in conditions of arbitrary depth. Dalrymple (1973) obtained the dispersion equation for finite amplitude waves on a bi-linear current profile. Using a stream function expansion he obtained a higher order numerical solution for waves on a linear, bi-linear, and arbitrary current profile. Further investigations of finite amplitude waves on a sheared current profile are given in Brink-Kjær and Jonsson (1975), Brink-Kjær (1976), Dalrymple (1977), and Kishida and Sobey (1988). These articles, together with the many other aspects of wave-current interaction, have been discussed in a number of review articles, of which Peregrine (1976) and Jonsson (1990) are two very good examples.

Despite the large number of theoretical solutions, the quantity of experimental data is extremely limited, and that which is available has tended to concentrate on the flow features within the near bed region (eg. Van Doorn, 1981). Brevik (1980a) investigated a number of different wave forms on an essentially uniform current profile (some shear did exist within the near bed region). Much of this work was directed towards the determination of the combined wave-current friction factor, and the reduction in wave height along the length of the experimental flume. However, he did take some measurements of the horizontal velocity component using a MIC-PAC micro-propeller. Unfortunately, the velocity measurements are limited to the case of a co-flowing "favourable" current (in the same direction as the wave motion), and because of the measuring system the velocity could only be determined within the lower half of the flow field. Nevertheless, the results are important in that there appeared to be a phase change between the velocity field and the surface profile. In two separate cases the horizontal water particle velocity was observed to lag behind the surface elevation by approximately 30° . The magnitude of this phase change was found to be uniform with depth. In a second series of observations Brevik and Aas (1980b) considered the interaction of waves and currents over a rough bed.

Kemp and Simons (1982 & 1983) provide the only other measurements of wave-current interactions. In the first

paper they considered the case of a "favourable" co-flowing current, and in the second an "adverse" co-flowing current. In both cases the experimental measurements are concentrated within the near bed region, and have been used to determine the variation in the turbulence intensity, the bed stress, and the nature of the bottom boundary layer. A limited number of measurements were taken at greater heights above the bed. However, because the current was introduced through the bed of the wave flume (similar to Brevik, 1980a) the current profile at these positions is essentially uniform with depth.

In many practical cases it may, of course, be assumed that the current velocity is approximately uniform with depth. Examples of this type of behaviour would include the large scale ocean currents, and the majority of tidal flows. However, in many other instances the current velocity will vary significantly with depth leading to the creation of a vorticity profile. Perhaps the most important example of this type of behaviour is the wind driven current where the magnitude of the current velocity varies exponentially with depth, leading to a very strong shearing action within the upper layers of the flow field.

The purpose of the present investigation was to obtain experimental data describing the interaction between waves and currents throughout the depth of the flow field for a number of different current profiles. In particular, to observe the modification of the oscillatory motion in the presence of a strongly sheared current velocity, and to compare this data with the existing theoretical solutions.

2.0 Apparatus.

The experimental observations were made in the Cambridge University Engineering Department's wave flume. This facility is 0.6m wide, 18m long, and allows a maximum water depth of 0.45m. The waves were generated via a hinged paddle, located within a deepened section at one end of the wave flume. The bed conditions were smooth (covered with plate glass), and the beach slope was maintained at 1:20. At this angle the effects of beach reflection were eliminated in all but the very longest waves considered. In these cases, an additional wave absorber was placed approximately half way up the beach slope. With this in place the reflection coefficient was never larger than 2.7%.

The re-circulating current was introduced via two loops of 50mm diameter pipework each connected to a self priming centrifugal pump. The total volume flow could be adjusted up to a maximum of 0.05m³/s. In the first half of the experiment the current was in the same direction as the wave celerity, and therefore constituted a co-flowing

"favourable" current. In the second half, the pipework was reversed, and the case of waves on a co-flowing "adverse" current was considered. In each of these cases the nature of the current profile, $U(z)$, was found to be dependant upon the height of the inlet and outlet pipes above the bed. To reinforce this pattern the outflow pipes, (the high pressure ends), were fitted with an appropriately shaped diffuser; while the inflow pipes (the low pressure ends), were located beneath a horizontal plate to prevent the formation of a vertical vortex and the resulting air entrainment. To further stabilise the flow field a small thickness of honeycomb, or flow straightener, was placed directly in front of both the in-flow and out-flow pipes. Figure 1 indicates the general arrangement of the experimental apparatus. This corresponds to the first case of a co-flowing current.

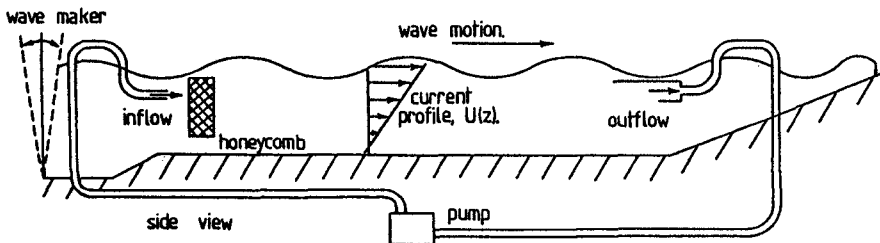


Figure 1. Experimental apparatus.

The velocity field was measured using laser Doppler anemometry. A 15mw. Helium-Neon laser was mounted above the wave flume. This was used to create a two beam system from which the horizontal component of the velocity field could be determined within a measuring volume which was estimated to be approximately 1.0mm^3 . Using this system the velocity could be determined to $\pm 3\%$.

3.0 Measuring technique.

Unfortunately, the introduction of a current within a wave flume is not as straight forward as indicated on figure 1. There are a number of practical problems which limit the superposition of a current profile and a progressive wave train. When the pumps were initially switched on, a long wave was generated leading to a seiching motion within the wave flume. Although the wave absorber reduced the effective life span of this motion, it was still found to take approximately 45 minutes until the variation in the surface elevation could be considered negligible ($< 1\text{mm}$). Furthermore, the action of the current itself leads to the formation of surface ripples. If these features are allowed to develop along the length of the flume, they can reach an appreciable height, often having

an amplitude in excess of 12mm. However, the addition of teepol in approximately 15 ppm. reduces the surface tension and thereby limits the formation of these features. This disturbance was never larger than 1.5mm in amplitude, and was for the most part considerably less.

The generation of a two dimensional current was rather more difficult to achieve. After a large number of experimental tests it was concluded that the honeycomb placed directly in front of the inflow and outflow pipes was critical in the development of an appropriate current profile. If the flow straightener was removed, or was of insufficient thickness, then the flow field would develop a three dimensional component, and in many cases become unstable within the central portion of the wave flume. Figure 2 shows the variation in the current profile across the tank width with the honeycomb in place. Although the magnitude of the current velocity does appear to be slightly larger along the centre line, the general form of the current profile is surprisingly consistent. In figure 3 the time variation in the current profile is shown throughout the duration of a test run. The current profile appears to be relatively unchanged even after a period of 8 hours. These measurements were obtained with a 75mm thickness of honeycomb as indicated on figure 1.

While the addition of honeycomb allows the development of a suitable current profile, its presence within the wave flume produces an important source of wave reflections. A problem which is further complicated by the horizontal plate located above the inflow pipes. As a result of these difficulties it became apparent that the creation of a reasonable current profile, and a continuous progressive wave train was not possible using the present arrangement. However, it was possible to achieve the required current profile and superimpose the effects of 5 or 6 gravity waves before the flow field is disrupted by the presence of the reflected waves. The measuring technique thus developed along the following lines. The required current profile was established within the wave flume. The long wave seiching was allowed to dissipate before the commencement of the experimental run. The wave maker was switched on, but the sampling procedure was delayed until the first two or three waves had passed the measuring section. At this point the wave profile will have achieved a regular form. The combined velocity field is then sampled for the duration of three or four wave cycles, but ceases before the reflected components start to disrupt the established order. The resulting pattern is shown on figure 4.

For this technique to provide information about the vertical variation in the horizontal velocity, it must be repeatedly applied at a number of different locations in the same vertical section. If the resulting data is to be

Figure 2. The variation in the current profile across the width (W) of the wave flume.

- ▲ —▲ —▲ $y=0.25W.$
- —■ —■ $y=0.50W.$
- —● —● $y=0.75W.$

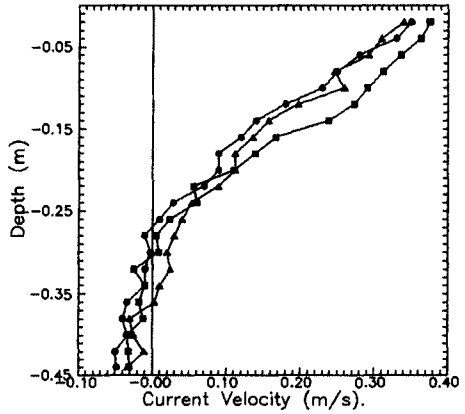


Figure 3. The variation in the current profile with time t.

- ▲ —▲ —▲ $t=1.0hr.$
- —■ —■ $t=4.0hr.$
- —● —● $t=8.0hr.$

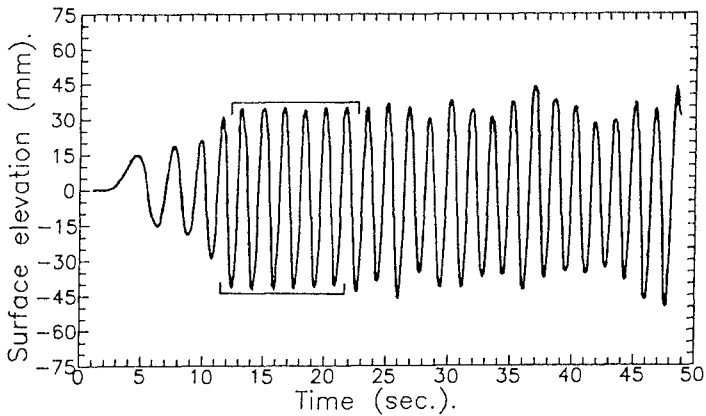
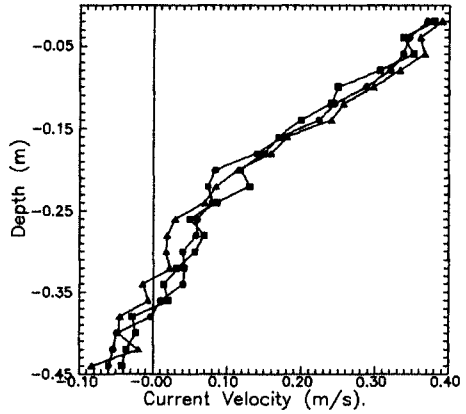


Figure 4. The development of the surface profile.

representative of the combined wave-current motion, then it is essential that the wave maker is capable of generating the same wave form throughout the duration of a test run (approximately 8 hours). To ensure that this requirement did not cause any difficulties, the wave amplitude was continuously monitored. The variation was generally found to be small ($<3\%$). However, this variation did become more significant as the wave length was reduced. In an attempt to average out these fluctuations extreme waves, or those waves in which the surface amplitude differed from the mean value by more than $\pm 5\%$, were neglected. Furthermore, the measured kinematics at any one depth were based on an average of five bursts, each containing three complete wave lengths.

In addition to the repeatability requirement, the wave motion should reduce to the irrotational solution proposed by Stokes (1880) in the absence of a current. Figure 5 shows the variation in the horizontal velocity at a number of different depths for the case $U(z)=0$. Although the current velocity was zero, the experimental arrangement is as indicated on figure 1. Both the flow straightener and the pipework were still located within the wave flume. The agreement with the third order irrotational solution is remarkably good.

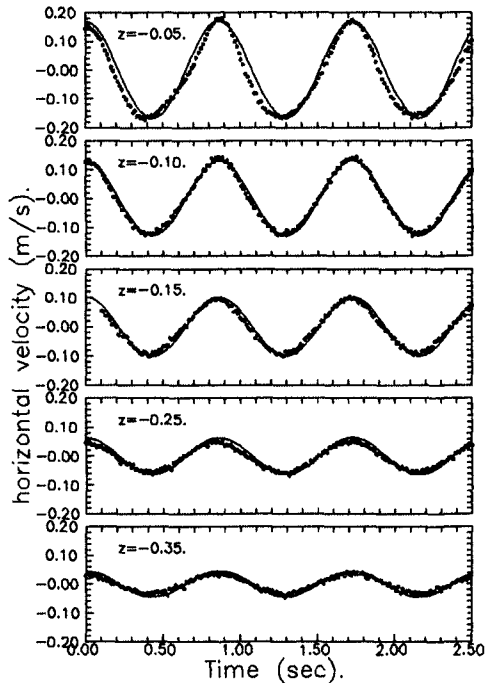


Figure 5. Horizontal velocity component (Waves only).

4.0 Experimental results.

A total of six different types of interaction were considered, the experimental details of which are given in table 1.

Case	Wave form.	Current profile.
(1)	a=35.1mm, h=0.35m, T=1.412s.	Uniform, favourable.
(2)	a=35.7mm, h=0.45m, T=0.877s.	Uniform, adverse.
(3)	a=22.5mm, h=0.45m, T=0.869s.	Linear, favourable.
(4)	a=31.5mm, h=0.35m, T=1.418s.	Linear, favourable.
(5)	a=45.5mm, h=0.45m, T=0.998s.	Linear, adverse.
(6)	a=61.5mm, h=0.35m, T=1.420s.	Linear, adverse.

Table 1. Experimental parameters.

The first two cases correspond to a preliminary set of measurements in which the current profile was essentially uniform with depth. Case (1) considers the effects of a "favourable" current velocity ($U_{mean}=0.108m/s$,

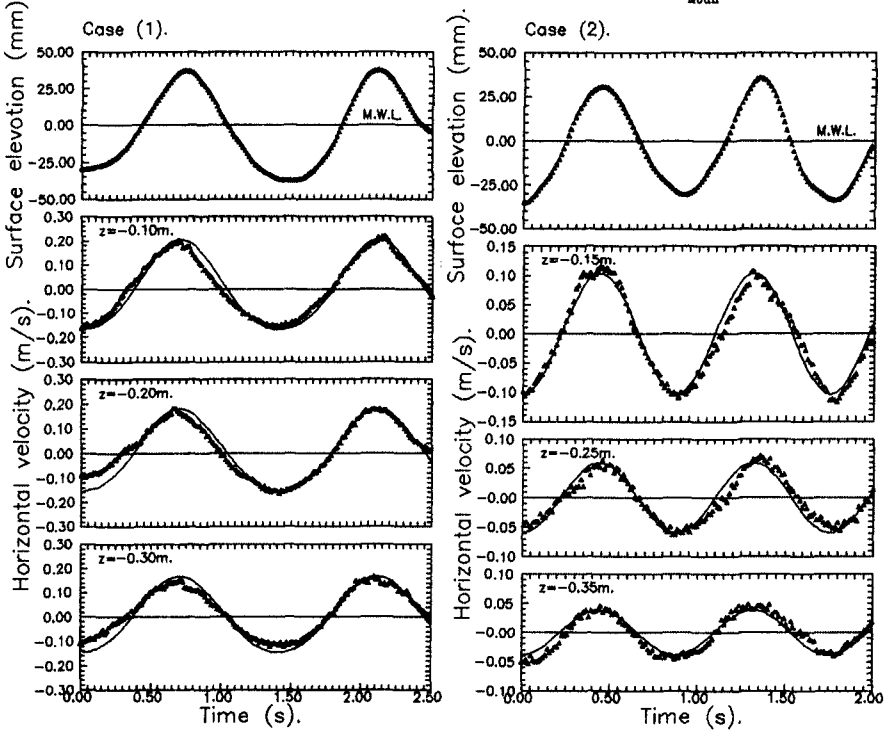


Figure 6. Waves on a uniform current.
 _____ Fenton (1985).

and case (2) the effects of an "adverse" current velocity ($U_{\text{mean}} = -0.120 \text{ m/s}$). In each case the only significant shearing motion occurred within a relatively thin layer directly above the bed. The oscillatory motion resulting from this type of wave-current interaction is shown on figures 6a and 6b respectfully. In both cases, the observed kinematics are shown to be in phase with the surface elevation. Furthermore, the magnitude of the oscillation appears to be in agreement with Fenton's (1985) Doppler shifted solution.

The remaining experimental results all concern the interaction with a sheared current profile. In cases (3) and (4) a "favourable" current profile with positive shear is considered (ie the velocity increases with height above the bed), while in cases (5) and (6) an "adverse" current with negative shear is considered. In each case the variation in the current velocity with depth is approximately linear. The importance of this assumption will be considered in section 5. One interesting feature of each current profile is the reversal in the current

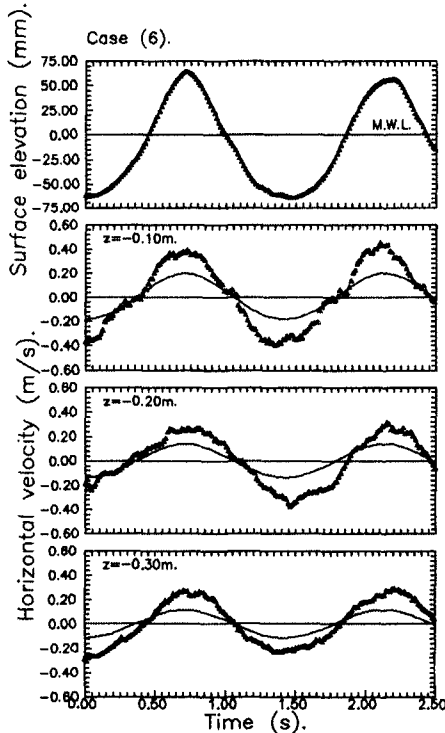


Figure 7. Waves on a linear shear current.
 Fenton (1985).

velocity within the near bed region. This would appear to correspond to a large scale longitudinal circulation along the length of the wave flume. It was consistently observed throughout the working section (figure 2.), and was small in comparison with the magnitude of the surface current ($U_{z=0}$).

In each of the above cases the oscillatory motions were again found to be in phase with the surface elevation. Figure 7 concerns the flow conditions in case (6) and shows the characteristics of the surface elevation together with the time variation in the horizontal velocity at a number of different depths ($z=-0.1m$, $-0.2m$, and $-0.3m$). The amplitude of the oscillatory motion for cases (3)-(6) are shown on figures 8a-8d.

5.0 Comparisons with other work.

The experimental data appertaining to waves on a uniform current (Cases 1 and 2) differs from previous measurements (Brevik, 1980a) in that there is no observable phase change between the velocity profile and the surface elevation. In this respect, the present measurements appear to be in agreement with the existing analytical solutions (Fenton, 1985) and the recent numerical simulations (Chaplin, 1990). The accumulated evidence therefore suggests that the phase change observed by Brevik (1980a) does not represent a true wave-current interaction. A possible explanation of these results may well be found in the nature of the velocity measurements. Indeed, Brevik comments on the suitability of a horizontal micro propeller in the presence of a substantial vertical velocity component, ie. at significant heights above the bed. Wave reflection may also have contributed to the creation of the observed phase change. This latter point is at least partially substantiated by the asymmetrical nature of the measured surface profile.

The amplitude of the oscillatory motion produced by waves on a uniform current (figures 6a and 6b) shows good agreement with the Doppler shifted solution proposed by Fenton (1985). This clearly indicates that provided the magnitude of the surface drift velocity is taken into account within a modified dispersion equation, the measured characteristics of the velocity field for waves on a uniform current may be described on the basis of a modified Stokes' (1880) expansion.

In contrast, the measurements shown in figures 7 and 8 cannot be explained by the introduction of a simple Doppler shift. The shearing motion within the current profile produces an associated vorticity profile which must be taken into account when describing the combined flow field. However, in the case of a linear shear current the vorticity profile is constant with depth.

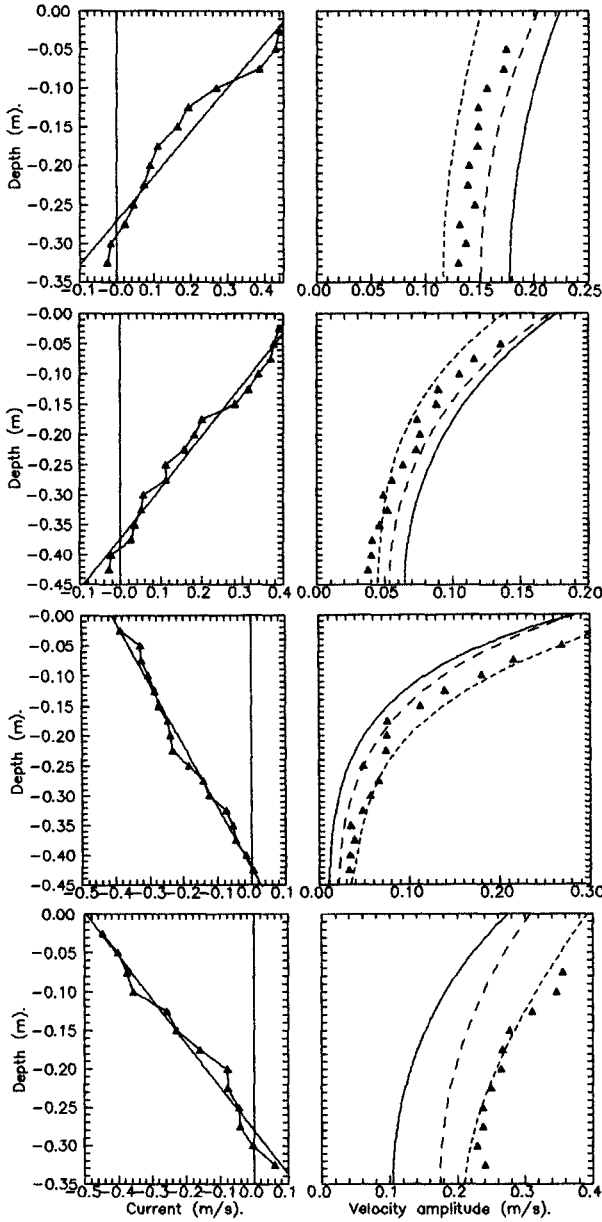


Figure 8a-8d. Waves on a linear shear current.
 — Doppler shifted solution (Fenton, 1985).
 - - - Linear shear solution (Kishida et al,1988).
 - · - · - Numerical solution (Chaplin, 1990).

Tsao (1959) considered this situation and concluded that the waves would remain irrotational, though different from Stokes' (1880) classical expansion. Kishida and Sobey (1988) extended this argument and obtained a 3rd. order solution for waves on a linear shear current. The results of this theory are shown on figures 8a-8d. The numerical solution proposed by Chaplin (1990) is also shown on figures 8a-8d. This solution allows a "best fit" cubic approximation of the current profile to interact with the required wave motion. There are no prior assumptions regarding the nature of the vorticity profile, and convergence is achieved after the summation of a large number of terms within a stream function expansion.

It is clear from figure 8 that the solutions proposed by Kishida and Sobey (1988) and Chaplin (1990) both predict the nature of the observed departure from the Doppler shifted solution (Fenton, 1985). The interaction with a co-flowing "favourable" current having positive shear is shown to produce a reduction in the amplitude of the horizontal velocity component; while the interaction with a co-flowing "adverse" current having negative shear is shown to increase the amplitude of the horizontal velocity component.

The analytical solution proposed by Kishida and Sobey (1988) appears to underestimate the extent of these interactions. This is particularly noticeable in the case of an "adverse" current having negative shear. In case (6) the observed velocity amplitude was as much as 81% larger than the Doppler shifted solution (Fenton, 1985), and 42% larger than the 3rd. order solution for waves on a linear shear current (Kishida and Sobey, 1988). Although this case corresponds to the steepest wave form investigated, it is, according to the classification code proposed by Dean (1970), a third order wave. As a result, the apparent discrepancies between the solution proposed by Kishida and Sobey (1988) and the experimental observations is rather surprising. One possible explanation for this observation is that the wave-current interaction increases the non-linearity of the wave form by enhancing the relative contribution of the higher harmonics. As a result, the wave energy is transferred to the higher harmonics, and consequently the traditional classification codes used for progressive gravity waves may be less appropriate in the presence of a significant wave-current interaction. The numerical solution shown on Figures 8a-8d (Chaplin, 1990) appears to support this view. By incorporating the full effects of the higher harmonics within a stream function expansion it provides a very good description of the experimental data in all cases.

6.0 Concluding remarks.

The present observations have shown the importance of the interaction resulting from a combination of waves and currents. In many practical cases it may, of course, be assumed that the current velocity is approximately uniform with depth. Under these conditions the horizontal velocity component remains in phase with the surface elevation, and the Doppler shifted solution proposed by Fenton (1985) is shown to provide a good description of the velocity field.

In many other instances the current velocity will vary significantly with depth. This leads to the creation of a vorticity distribution which must be taken into account when defining the characteristics of the oscillatory motion. Under these conditions the introduction of a simple Doppler shift within the dispersion equation is no longer sufficient to define the flow field. The third order analytical solution proposed by Kishida and Sobey (1988) is shown to predict the general effects of the vorticity profile. However, in the case of a strongly sheared "adverse" current profile it appears to underestimate the extent of the resulting interaction, thereby hinting at the increasing importance of the higher harmonics. In contrast, the numerical solution proposed by Chaplin (1990) is shown to provide a good description of the flow field in all cases.

The modification of the wave induced flow field in the presence of a strongly sheared "adverse" current profile is of particular importance, and undoubtedly warrants further study. The effect of this type of interaction is to significantly increase the amplitude of the oscillatory motion. Indeed, the effect is so pronounced that an interaction of this type may, under some circumstances, represent a possible "loading criteria" for the design of coastal and near-shore structures.

7.0 Acknowledgements.

The author would like to express his appreciation to Professor J. Chaplin for providing the results of his numerical model.

References.

- BREVIK, I. (1980a) Flume experiment on waves and currents II. Smooth bed. Coastal Eng., 4:89-110.
BREVIK, I. & AAS, B. (1980b) Flume experiment on waves and currents I. Rippled bed. Coastal Eng., 3:149-177.
BRINK-KJÆR, O. (1976) Gravity waves on a current: the influence of vorticity, a sloping bed, and dissipation. Tech. Univ. Denmark, Inst. Hydrodyn. & Hydraul. ser. paper No. 12.

- BRINK-KJÆR, O. & JONSSON, I.G. (1975) Radiation stress and energy flux in water waves on a shear current. Tech. Univ. Denmark, Inst. Hydrodyn. & Hydraul. Prog. Rep. 36:27-32.
- CHAPLIN, J.R. (1990) Computation of steep waves on a current of arbitrary profile. Water wave kinematics, Kluwer Acad. Pub.
- DALRYMPLE, R.A. (1973) Water wave models and wave forces with shear currents. Univ. Florida, Lab. Rep. No. 20.
- DALRYMPLE, R.A. (1977) A numerical model for periodic finite amplitude waves on a rotational fluid. J. Comput. Phys., 24:29-42.
- DEAN, R.G. (1970) Relative validities of water wave theories. J. Waterw. Harbors Coastal Eng., 96:105-119.
- FENTON, J.D. (1985) A fifth order Stokes' theory for steady waves. J. Waterw., Port, Coastal and Ocean Eng. 111:216-234.
- JONSSON, I.G. (1990) Wave-current interactions. The Sea. Vol 9. Ocean Engineering Science. Chapter. 1.1.3.
- KEMP, P.H. & SIMONS, R.R. (1982) The interaction of waves and a turbulent current: waves propagating with the current. J. Fluid Mech. 116:227-250.
- KEMP, P.H. & SIMONS, R.R. (1983) The interaction of waves and a turbulent current: waves propagating against the current. J. Fluid Mech. 130:73-89.
- KISHIDA, N. & SOBEY, R.J. (1988) Stokes' theory for waves on a linear shear current. J. Eng. Mech. 114:1317-1334.
- PEREGRINE, D.H. (1976) The interaction of water waves and currents. Adv. Appl. Mech., 16:9-117.
- STOKES, G.G. (1880). On the theory of oscillatory waves. Math. Phys. Papers. vol 1. Cambridge University Press.
- THOMPSON, P.D. (1949) The propagation of small surface disturbances through rotational flow. Ann. N.Y. Acad. Sci., 51:463-474.
- TSAO, S. (1959) Behaviour of surface waves on a linearly varying flow. Moscow. Fiz. Tech. Inst. Issl. Mekh. Prikl. Mat. 3:66-84.
- VAN DOORN, T. (1981) Experimental investigation of near bottom velocities in water waves without and with a current. Delft Hydraul. Lab. Rep. M1423

CHAPTER 39

WAVE KINEMATICS IN THE SURFACE ZONE

James E. Skjelbreia¹, Member ASCE
Alf Tørum²

Abstract

An extensive series of laboratory experiments have been carried out with regular and irregular waves travelling over a horizontal bottom. Velocity measurements of the flow were obtained at numerous vertical positions with major emphasis given to the surface zone. The flow measurements were made possible by use of a custom designed LDV having the special characteristic of being operative very near the free surface. Presented is an overview of the study and some of its majors results.

1 Introduction

The study of the flow within water waves has a long history, yet, it seems, some of the fundamental aspects of the phenomenon are poorly or not satisfactorily understood. Specifically, how reliable is current knowledge on details of wave surface shape, velocity field, induced current, or effects of ambient current over the spectrum of wave heights, periods, and water depths? Even for regular waves, let alone irregular waves, the answers to this question are far from complete. For more complex situations, say, for instance, three-dimensional ocean waves, the present methods for predicting the flow field are, at best, dubious. Clearly the problem is difficult and is one that deserves continued yet careful study—even at the most fundamental level.

¹ Senior Research Scientist, MARINTEK, Box 4125, 7002 Trondheim, Norway

² Head of Research, SINTEF NHL, 7034 NTH, Norway

Presently, designers for the offshore environment are often faced with the problem of using flow descriptions, and hence loading information, that might be of uncertain reliability. For fixed structures, one can take steps to alleviate the uncertainties by use of a safety factor and/or a wave theory that has proven to be conservative. Although this approach may solve the problem it can add substantially to overall development costs. For structures affected dynamically by waves, the problem is more acute; an overly conservative approach may render a design impractical due to excessive motion, for instance, when, in fact, if more realistic knowledge of the flow were known, the design might be completely acceptable.

The number of studies concerning measurement of wave kinematics is few and their scope often limited. These facts are a reflection of the difficulties, partially described above, that one encounters in such endeavors. Recent reports on field measurements and comparison to theory have been made, e.g., Lambroskos (1981), Forristall (1986), and one on the WADIC experiment presented at this forum. Among others, laboratory measurements of wave kinematics have been reported by Vis (1980), Bosma and Vugts (1981), Anastasiou *et al.* (1982), Bullock and Short (1985), and Gudmestad *et al.* (1988). Though each of these reports contain interesting and useful information, they still lack unification and presentation of sufficient evidence in a way that, say, designers can utilize the information with confidence. This is a problem, and in fact it is quite unlikely that generalized procedures to tackle the wave kinematics issue will be available soon.

The primary intent of this paper is to present examples of and discuss an extensive series of laboratory experiments that have been carried out with regular and irregular waves travelling over a horizontal bottom. Velocity measurements of the flow were obtained at numerous vertical positions with major emphasis given to the surface zone. The flow measurements were made possible by use of a custom designed LDV having the special characteristic of being operative very near the free surface.

2 Theoretical and Experimental Considerations

Linear Random Wave Theory. As a first approach to the problem of irregular waves, one can assume the flow to be composed with the sum of many individual *linear* waves each with its own frequency, direction, phase and celerity as predicted by the linear dispersion relation. This technique is often referred to as *linear random wave theory* (see Forristall, 1981 for a description). Bosma and Vugts (1981) performed experiments using one-dimensional irregular waves and reported on comparisons of velocity measurements obtained by laser Doppler velocimetry to linear random wave theory. They show that the agreement far

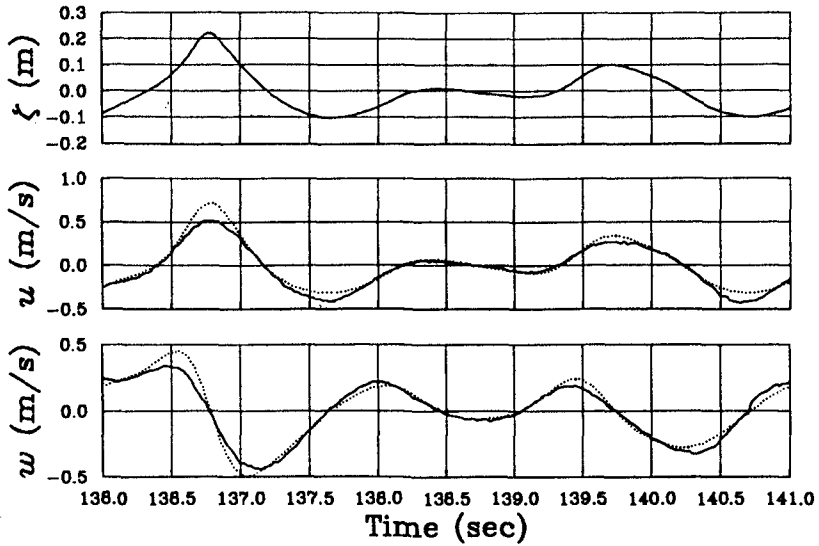


Figure 1 Example of linear random wave theory, — measurement, ··· linear random wave theory (Case 6, $z = -0.10\text{ m}$).

below the mean water level is reasonable, but tends to deviate increasingly with increasing elevation. This tendency of deviation can be explained, at least partially, by the significance of the higher wavenumber components *riding atop* the lower wavenumber components and hence may be displaced many of their own wavelengths from the mean water line. For large wavenumber, k , the amplitude of the velocity contribution is proportional to e^{kz} , where z is the coordinate measured vertically upward from the mean water line. The higher wavenumber contributions can become excessively large when $z > k^{-1}$ and similarly, significantly diminished when $z < -k^{-1}$. The net effect is that contributions from the higher wavenumber components will be over-represented in crests and under-represented in troughs. A good example of this can be seen in Figure 1. Shown are measurements of ζ , u , and w , the surface elevation, and the horizontal and vertical velocities respectively. The dotted line is the velocity obtained using linear random wave theory. The velocity shown in Figure 1 was measured at 0.1 m below the mean water line using the facility described in the next section; the wave conditions correspond to Case 6 of Table 1. We see significant departure of measurement from theory in the crests and troughs, on the other hand when ζ is near zero the comparison is better. This latter feature should be

expected if one believes in the linear superposition of waves since all wave components are, at least momentarily, at the elevation that linear theory presumes they are, namely $z = 0$, the mean water line.

Stretching Approximations. The notion of predicting kinematics beneath irregular waves from a spectral decomposition of the surface elevation, such as that done with linear random wave theory, is very attractive for its simplicity and speed of computation. Suggestions to cope with the problems inherent with linear wave theory have been made by Chakrabarti (1971) and Wheeler (1979), though both approaches fail to satisfy the Laplace equation Forristall (1981) mentions that use of Wheeler's method results in a lower error in the kinematics boundary condition when compared to linear random wave theory. With Wheeler's approach the variable z in the linear solutions for flow velocity is substituted as follows:

$$z \leftarrow \frac{z - \zeta}{1 + \zeta/d} \quad (1)$$

where d is the undisturbed water depth. The new expression for z is never greater than zero and for each wavenumber will effectively *stretch* or *compress* the velocity profile from the mean water line to the instantaneous free surface. For the case of irregular waves the higher wavenumber components, which tend to be of lesser amplitude than the low wavenumber components they ride atop, will be more reasonably represented. Taking the same example as shown in Figure 1 and using Wheeler's approach, we see in Figure 2 that a better

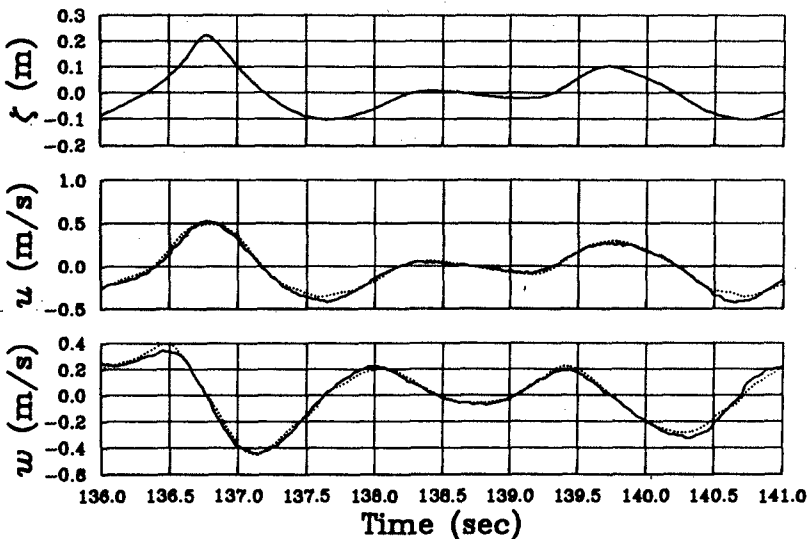


Figure 2 Example of a stretching approximation, — measurement, ... Wheeler's method (Case 6, $z = -0.10$ m).

approximation to the measured velocity over linear random wave theory is obtained. Still there are differences and this is but one comparison. The velocity in this case was computed using similar steps as for linear random wave theory; the procedure is complicated somewhat by the fact that ζ now appears in the equations for flow velocity such that it is not possible to form a simple transfer function relating surface elevation information to the flow velocity beneath.

3 Experimental Equipment and Procedures

The experiments for this investigation were carried out using the wave tank illustrated in Figure 3, which is located at the Norwegian Hydrotechnical Lab-

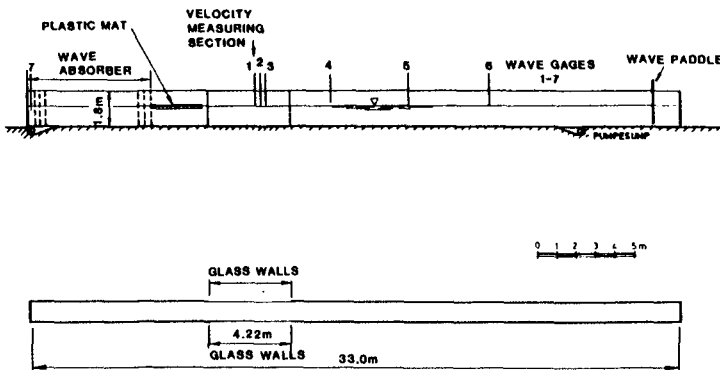


Figure 3 Wave Tank.

oratory in Trondheim. The tank is 33 m long, 1.02 wide and 1.8 m deep. It is constructed of concrete with a glass section 4.22 m wide, located approximately 10 m from the end of the tank, that allows viewing over the full depth. The wave generator is hydraulically driven and can be discretely varied from a pure hinge mode to a pure piston mode. At the end of the tank, opposite the wave generator, is located a passive wave absorber developed by the National Research Council of Canada. This device consists of a series of vertical perforated steel plates and has a reflection coefficient of approximately 5% over a broad frequency range that encompassed the range of frequencies with significant wave energy typical in this study. (For more details on this device see Jamieson and Mansard, 1987). Just ahead of the absorber, in the direction of the wave generator, is a positively buoyant mat 2.5 m in length that floats on the water surface. Usage of the mat significantly reduces high frequency reflections from the absorber and helps to reduce cross waves.

Flow velocity was measured on the centerline at a single longitudinal position along the tank, coinciding with gage 1, but at several different elevations (see next section) by a two-component laser Doppler velocimeter (LDV). The two velocity components measured were in a plane parallel to the side walls of the tank with a measurement volume cross-section of approximately $100\ \mu\text{m}$ in diameter. Frequency shifting was utilized enabling the resolution of directional ambiguities in the flow. The LDV was specifically designed for this study and has the special feature of using only a *single* laser beam in the flow. This feature allows measurements very near arbitrarily oriented surfaces, including the free surface. This device is similar to and based on one described by Skjelbreia (1987).

The surface elevation was measured with standard resistive-type gages having streamlined supports to minimize disturbances. One wave gage was positioned at the LDV station, it was displaced from the wave tank's centerline $0.34\ \text{m}$ to avoid disturbance to the flow in the vicinity of the LDV measurement point. The wave generator control signal was constructed from a JONSWAP target wave spectrum using $\gamma = 3.0$. The spectrum was divided into 1000 frequency components and each component assigned a random phase. Great care was given to maintaining reproducible wave conditions in the tank. This was necessary to construct a *snap-shot* of the flow throughout the depth since the LDV is capable of only a single point measurement. Careful control of the water depth was found to be very important for reproducibility and it was maintained to within $\pm 1\ \text{mm}$ by an overflow connected by tubing to the tank and by having a water inflow of $0.11/\text{min}$ into the tank to offset small leaks in the overall system.

4 Test Program

The complete test program consisted of nine wave conditions, six irregular wave cases, two regular wave cases, and one case that the control signal to the wave generator was constructed from two sinusoids, these are listed in Table 1. In total there were 269 runs recorded.

Listed in Table 1, the peak period, T_p , is the value used to create the control signal for driving the wave generator and the significant wave height, H_s , was determined from the measured energy spectrum at the LDV station. For the two period case, the values for H_s/gT_p^2 and d/gT_p^2 are based on the average of the two periods and for the regular wave cases, T_p and H_s are simply T and H , the period and waveheight.

Velocity measurements of the flow were obtained at as many as fifteen separate elevations for each of the nine cases considered. The majority of the elevations were clustered in the surface zone with a few covering the flow on down to the bottom.

Table 1 Test Program.

Case	Type	T_p (s)	H_s (m)	d (m)	H_s/gT_p^2	d/gT_p^2
1	Irregular	1.2	0.11	1.3	0.0078	0.092
2	Irregular	1.4	0.16	1.3	0.0083	0.068
3	Irregular	1.65	0.17	1.3	0.0064	0.049
4	Irregular	1.65	0.17	0.6	0.0064	0.022
5	Irregular	1.8	0.21	1.3	0.0066	0.041
6	Irregular	2.4	0.25	1.3	0.0044	0.023
7	Two Per.	2.1&2.4	0.18	1.3	0.0036	0.026
8	Regular	1.5	0.26	1.3	0.0118	0.059
9	Regular	1.5	0.23	0.6	0.0104	0.027

5 Presentation and Discussion of Results

The results to be presented have been selected from Case 6 listed in Table 1. There have not been any adjustments to the velocity measurements to account for a current that may be present or to remove the effects of reflected or resonant waves. Instead, all measurements presented are the raw, unfiltered information that was obtained by the wave gages and the LDV. A note on the flow velocity time traces to be presented: measurements near the surface have varying degrees of intermittent behavior depending on what level they were obtained. This occurs when the water surface drops below the probe volume of the LDV and the measurement ceases. Until the water surface moves back up to the level of the LDV the signal holds at the last measured value, these *drop-out* periods will be noted as the flat portions in the time traces. Occasionally when the water surface just crosses the LDV level, a spike in the measurement occurs, these should not be interpreted as valid measurements.

Irregular Waves. We will present a few comparisons to contrast the differences between linear random wave theory and Wheeler's method. In Figure 4 are shown measurements taken from Case 6 of the horizontal velocity at elevations throughout the depth together with predictions using linear random wave theory. The upper measurements illustrate the well know fact of the unsuitability of linear random wave theory in the surface region (the ordinates for $z = 0.20, 0.10,$ and 0.05 m have multiplying factors of $10^{21}, 10^9,$ and 10^3 respectively). Beginning at $z = 0.00$ (mean water level) we note the near 250% over-prediction of velocity beneath the crest located at 136.7 s. The surface is relatively steep about this crest and hence has energy at the higher wavenumbers as compared to other portions of the signal where there is not the same

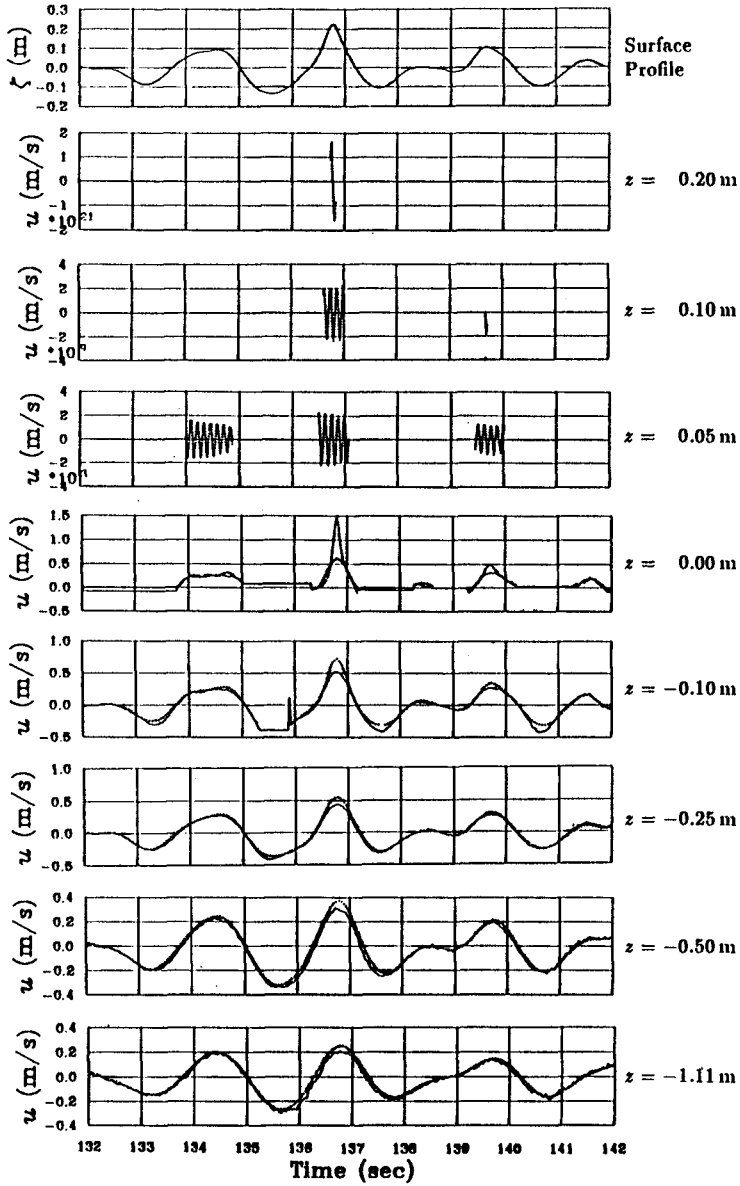


Figure 4 Measurements (—) of surface elevation and horizontal velocity compared with linear random wave theory (···), Case 6.

degree of error. The measurement level at $z = -0.10$ m is beneath nearly all the troughs in this segment, note that the velocity is consistently under-predicted in magnitude. Moving further down the comparison improves, still the velocity at $z = -1.11$ m under the crest at 136.7 s is over-predicted by 25%.

In Figure 5 we move on with the same case and time segment as the previous figure but now the horizontal velocity is compared with Wheeler's method. There is general improvement in the comparison. In the surface region reasonable values are now predicted and the actual measurement have become visible. In particular, the velocity measurements beneath the crest at 136.7 s are all within 8% of the predicted values with the exception of the two measurements nearest the bottom. The trough values at $z = -0.10$ m are under-predicted as was the case with linear random wave theory. There are a number of interesting features we can observe in this figure, for instance note the rapid increase in horizontal velocity as the surface is approached in the crest located at 136.7 s, pointing out the importance of wave steepness and the need for measurements near the surface. A good example of the frequency dependence of the velocity can be seen by comparing the wave with its crest at 134.5 s to the one with its crest 136.7 s. For example the measurement made at $z = 1.11$ m shows the horizontal velocity in each wave to be similar while the surface profile indicates that one wave has nearly twice the waveheight as the other. One can see this type of feature elsewhere in the signal as well.

To complete our comparison, shown in Figure 6 are measurements of vertical velocity and predictions according to Wheeler's method corresponding to the same time segment as in the two previous figures. In general, the comparison is good. The maximum vertical velocity is consistently over-predicted just ahead of the crest at 136.7 s in the surface region, $z = 0.05$ to -0.10 m. At $z = -1.11$ m the magnitude of the flow is low and near the resolving level of the LDV, the jaggedness in the signal is not necessarily turbulence. In contrast to the horizontal velocity, the vertical velocity is better predicted at this level.

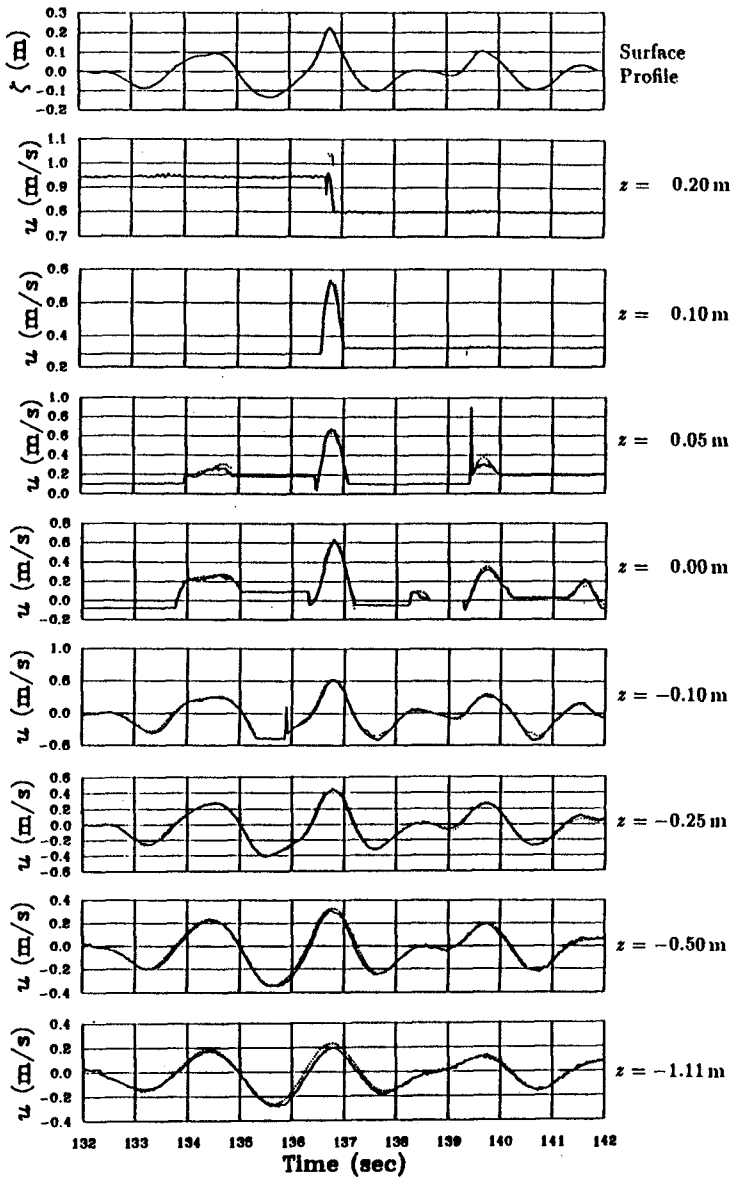


Figure 5 Measurements (—) of surface elevation and horizontal velocity at various levels compared with Wheeler's method (···), Case 6.

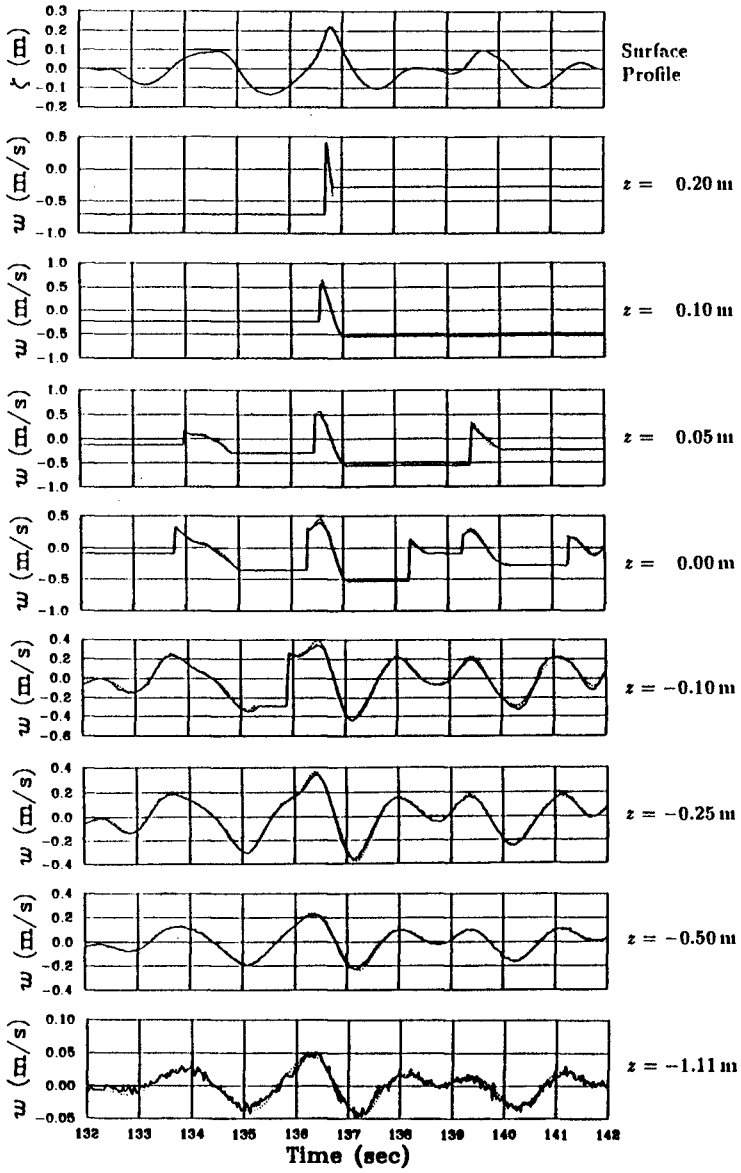


Figure 6 Measurements (—) of surface elevation and vertical velocity at various levels compared with Wheeler's method (···), Case 6.

6 Conclusions

Presented has been an overview of, what we consider, a systematic and well planned series of experiments to investigate the wave kinematics problem. Preliminary analysis has shown Wheeler's method to compare well with the presented measurements, including a regular wave case during the early stages of a run.

7 Acknowledgements

We greatly appreciate the financial support from NTNF, Amoco, Conoc, Exxon, Mobil and Statoil. An additional special thanks to Amoco Norway who provided the funds needed to design and construct the LDV, an essential component in this study.

8 References

- ANASTASIOU, K., TICKELL, R. G., & CHAPLIN, J. R. 1982 Measurement of particle velocities in laboratory-scale random waves. *Coastal Eng.*, **6**, pp. 233–254.
- BOSMA, J. & VUGTS, J. H. 1981 Wave kinematics and fluid loading in irregular waves. *Proc. Int. Symposium on Hydrodynamics in Ocean Eng.*, The Norwegian Institute of Technology, pp. 136–165.
- BULLOCK, G. N. & SHORT, I. 1985 Water particle velocities in regular waves. *J. Waterway, Port, Coastal and Ocean Eng.*, ASCE, Vol. 111, No. 2, pp. 189–200.
- CHAKRABARTI, S. K. 1971 Discussion on 'dynamics of single point mooring in deep water.' *J. Waterways, Harbour and Coastal Eng. Div. ASCE*, Vol. 97, pp. 588–590.
- FORRISTALL, Z. GEORGE 1981 Kinematics of directionally spread waves. *Proc. Conf. on Directional Wave Spectra Applications*, 14–16 Sept., Univ. of Calif., Berkeley. Published by ASCE.
- FORRISTALL, Z. GEORGE 1986 Kinematics in the crests of storm waves. *Proc. 20th Coastal Eng. Conf.*, Taipei, Taiwan pp. 208–222.
- GUDMESTAD, O. T., JOHNSEN, J. M., SKJELBREIA, J., & TØRUM, A. 1988 Regular water wave kinematics. *Proc. Int. Conf. on Behaviour of Offshore Structures, Boss '88*, Trondheim, Norway, June 21–24, pp. 789–803.

- JAMIESON, W. W. & MANSARD, E. P. D. 1987 An efficient upright wave absorber. ASCE Speciality Conference on Coastal Hydrodynamics, Univ. of Delaware, June 29 to July 1.
- LAMBRAKOS, KOSTAS F. 1981 *J. Waterway, Port, Coastal and Ocean Division ASCE*, Vol. 107, WW3, pp. 159–174.
- SKJELBREIA, JAMES ERIC 1987 Observations of breaking waves on sloping bottoms by use of laser doppler velocimetry. Ph.D. thesis, California Institute of Technology, Pasadena, California.
- VIS, F. C. 1980 Orbital velocities in irregular waves. *Proc. 17th Coastal Eng. Conf.*, Sidney, Australia. pp. 173–185.
- WHEELER, J. D. 1970 Method for calculating forces produced by irregular waves. *J. Petroleum Tech.*, March, pp. 119–137.

CHAPTER 40

STOCHASTIC MODELING OF SURFING CLIMATE

William R. Dally¹, M. ASCE

Abstract

A continued increase in the popularity of surfing, coupled with the potential for adverse impacts by coastal construction projects on favored surfbreaks, has recently confronted engineers with the problem of defining and quantifying a 'good' surfbreak. A rudimentary analysis of surfing mechanics demonstrates that conditions can be examined in terms of the joint statistical climate of 1) breaker peel rate, and 2) attainable board speed as characterized by the Irribarren Number. Assuming a planar beach and using linear wave theory, two theoretical models for the joint probability density of peel rate and Irribarren Number can be used to appraise short-term surfing conditions. Results indicate that the short-crested character of real waves plays a primary role in enhancing surfbreak. For practical calculations of long-term surfing climate at specific sites, offshore wave gage data can be transformed across a measured beach profile to predict breaker conditions in the outer surf zone. Application of such a numerical algorithm to the beach at Duck, North Carolina indicates that the waves are suitable for surfing roughly 25% of the time.

Introduction

Often the major impetus for beach nourishment and structural projects is not only erosion control and the protection of upland real estate, but also the preservation of the recreational opportunities afforded by a fronting beach. Surfing is one such activity, and although Morahan

¹ Assistant Professor, Oceanography and Ocean Engineering, Florida Institute of Technology, 150 W. University Boulevard, Melbourne, Florida 32901, U.S.A.

(1971) and others have assigned substantial monetary value to surfing recreation, the economic and cultural benefits of surfing have usually been overlooked during the development of beach projects. Consequently the physical impact of a particular project on the local surfbreak, and the subsequent impact on surfing recreation, have rarely been considered.

In recent years, surfers have begun to increase public awareness as to the importance of preserving good surfbreaks (see Pratte, 1987), and some engineers and planners have begun to at least take surfing into consideration during project design. This immediately gives rise to the problem of how to define and quantify a 'good' surfbreak and the suitability of a particular beach for surfing. Viable engineering models for beach 'surfability' are required in order to prevent negative impacts on surfing, to guide mitigation if such impacts are unavoidable, and to perhaps even enhance the surfbreak at a project site.

Background

Criterion for a Ridable Wave

According to Walker (1974) and Dally (1989), the qualitative definition of 'surfable' is a wave on which a surfer can maintain a mean speed (termed 'board speed') that is as fast or faster than the rate at which the point of incipient breaking translates along the wave crest (termed 'peel rate'). If the breaking segment of the wave overtakes the surfer, the wave 'closes out' and becomes unsurfable. In the most basic sense, it is the joint statistical climate of attainable board speed and peel rate that determine the surfing climate of a particular beach.

Board Speed

To date there appears to have been no comprehensive studies which specifically address the speeds attainable on surfboards. Using aerial photographs, Walker (1974) was able to infer mean board speed from estimates of the peel rate of waves that were surfed, and found maximum speeds on the order of 12 m/s (27 mph). Although direct measurements of board speed have yet to be obtained, parameters currently found in engineering practice can be utilized to provide insight.

Attainable board speed is a function of the size and shape of the face of the breaker, the weight of the surfer, and board characteristics. For a given board shape and surfer weight, the board speed can be inferred by using the

wave height at incipient breaking (H_b) to quantify the size and the Irribarren Number (I) to represent shape of the wave face. Irribarren Number is defined as

$$I_b = m/[H_b/(gT^2/2\pi)]^{1/2} \quad (1)$$

$$I_o = m/[H_o/(gT^2/2\pi)]^{1/2} \quad (2)$$

in which m is bottom slope, T is wave period, g is gravitational acceleration, and the subscripts "b" and "o" denote conditions at incipient breaking and in deep water, respectively. The Irribarren Number has been shown to characterize breaker type (Galvin, 1968 and Battjes, 1974). Spilling breakers are surfable, but not as desirable as plunging breakers. Collapsing breakers are unsurfable and in fact are quite dangerous to surfers. Table 1 presents surf climate classifications in terms of Irribarren Number and breaker type.

TABLE 1 - Surf Climate Classifications

Irribarren Number	Breaker Type	Surfing Terminology
$I_b < 0.4$ $I_o < 0.5$	Spilling	'mushy'
$0.4 < I_b < 2.0$ $0.5 < I_o < 3.3$	Plunging	'tube' or 'hollow'
$2.0 < I_b$ $3.3 < I_o$	Surging or Collapsing	'cruncher'

Peel Rate

The peel rate, V_{bp} , as defined by Walker (1974) is given by

$$V_{bp} = c_b/\sin(\alpha_b) \quad (3)$$

where α_b is (in planform) the angle between the wave crest and the path scribed by the moving break point. This angle is determined by the gradient in wave height along the wave crest, which has contributions from both oblique incidence and longshore variation in wave height. Referring to Figure 1 for definitions, and assuming the bottom contours are locally straight and parallel, α_b is given by

$$\tan \alpha_b = ds/dn = \tan \theta_b + ds_*/dn \quad (4)$$

where ds is the incremental path length scribed by the breakpoint projected in the direction of wave propagation. As mentioned, a portion of this distance, ds_* , is associated with the local longshore gradient in wave height, i.e. the short-crestedness of the breakers. This quantity is given by

$$ds_* = (H_b - H_*) / (dH/ds) \quad (5)$$

where H_* is the height of the wave as it passes the bottom contour. If there is no longshore gradient, the breakpoint simply moves along the bottom contour. Assuming that the ratio of wave height to water depth at incipient breaking (K) is spatially uniform, it can be shown that

$$ds_*/dn = \frac{-(dH/dy)}{[(dH/ds) \cos \theta_b] + (K m \cos^2 \theta_b)} \quad (6)$$

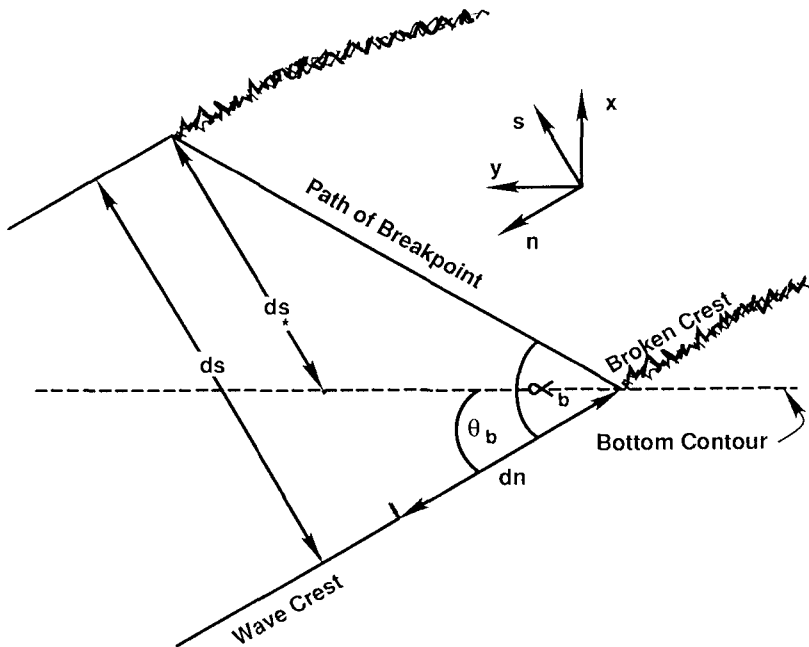


Figure 1 - Schematic diagram of breakpoint mechanics showing movement of breakpoint during an increment of time.

The rate of shoaling, dH/ds , required in Eq.6 can be derived from conservation of energy flux. For a planar beach and adopting shallow water linear wave theory, this is given by

$$dH/ds = (H/4h) m \cos \theta_b + (H/2) \tan \theta_b (d\theta_b/ds) \quad (7)$$

If it is assumed that $d\theta_b/ds$ is small, at the breakpoint Eq.7 becomes

$$dH/ds = (K/4) m \cos \theta_b \quad (8)$$

and Eq.4 becomes

$$\tan \alpha_b = \tan \theta_b + \frac{-(dH/dy)}{(5/4) K m \cos^2 \theta_b} \quad (9)$$

Based on this background, stochastic models for the joint statistical behavior of board speed (Irribarren Number) and peel rate can be developed to assess the surfing climate at a beach. In order to study the relative importance of wave obliqueness versus short-crestedness in determining peel rate and surfing climate, two stochastic models are derived below. The first one neglects short-crestedness whereas the second neglects obliqueness. As will be seen, they are based on the assumption of stationarity in the incident wave climate, and so may be used to assess surfing climate in only a short-term sense.

Stochastic Model for Short-Term Surfing Climate #1

If it is assumed that the bottom contours are straight and parallel and that there is no longshore variation in wave height, $\alpha_b = \theta_b$ (see Eq.9). From Eq.4, Snell's Law then dictates that V_{bp} is predetermined in deep water, i.e.

$$V_{bp} = c_o / \sin(\theta_o) \quad (10)$$

where $c_o = gT/2\pi$. By utilizing Eqs.2 and 10, surfing conditions can be characterized entirely in terms of deepwater conditions. With a given constant bottom slope, a joint probability distribution function (pdf) of the three random variables H_o , T , and θ_o is required. It is further assumed that wave direction is independent of height and period, i.e.

$$\text{pdf}(H_o, T, \theta_o) = \text{pdf}(H_o, T) \cdot \text{pdf}(\theta_o) \quad (11)$$

From Longuet-Higgins (1983), the pdf(H_o, T) is given by

$$\text{pdf}(R_o, \tau) = C_1 (R_o/\tau)^2 \exp\{-R_o^2[1+\epsilon^{-2}(1-\tau^{-1})^2]\} \quad (12a)$$

where

$$R_o = H_o/H_{\text{rmso}} \quad (12b)$$

$$\tau = T/\bar{T} \quad (12c)$$

$$C_1 = [4/(\pi\epsilon)^{1/2}][1+(1+\epsilon^2)^{-1/2}]^{-1} \quad (12d)$$

H_{rmso} is the root mean square wave height in deep water, \bar{T} is the mean period, and ϵ is a band width parameter. Adopting a cosine-squared type distribution for pdf(θ_o), i.e.

$$\text{pdf}(\theta_o) = (2/\pi) \cos^2(\theta_o - \bar{\theta}_o) ; \quad -90^\circ \leq (\theta_o - \bar{\theta}_o) \leq 90^\circ \quad (13)$$

straightforward transformation of random variables leads to

$$\text{pdf}(I_o, \tau) = 2 C_1 \frac{m^6 \tau^4}{I_o^7 \bar{S}_o^3} \exp\{-\frac{m^4 \tau^4}{I_o^4 \bar{S}_o^2} [1+\epsilon^{-2}(1-\tau^{-1})^2]\} \quad (14)$$

$$\text{pdf}(\hat{V}_{\text{bp}}) = (2/\pi) \frac{\tau}{[1-(\tau\hat{V}_{\text{bp}})^2]^{1/2}} \cos^2[\sin^{-1}(\tau\hat{V}_{\text{bp}}) - \bar{\theta}_o] \quad (15)$$

where \hat{V}_{bp} is dimensionless peel rate defined by

$$\hat{V}_{\text{bp}} = (g\bar{T}/2\pi)/V_{\text{bp}} \quad (16)$$

and \bar{S}_o is a deepwater wave steepness defined as

$$\bar{S}_o = H_{\text{rmso}}/(g \bar{T}^2/2\pi) \quad (17)$$

The marginal pdf of I_o and \hat{V}_{bp} is found by integrating numerically with respect to wave period.

Sample results are shown in Figures 2a, b, and c. The lines separating surfable from unsurfable conditions are shown only conceptually, with the exception that the upper limit on Irribarren Number is dictated by the exclusion of collapsing breakers. Integrating the volume of probability density contained in the surfable region

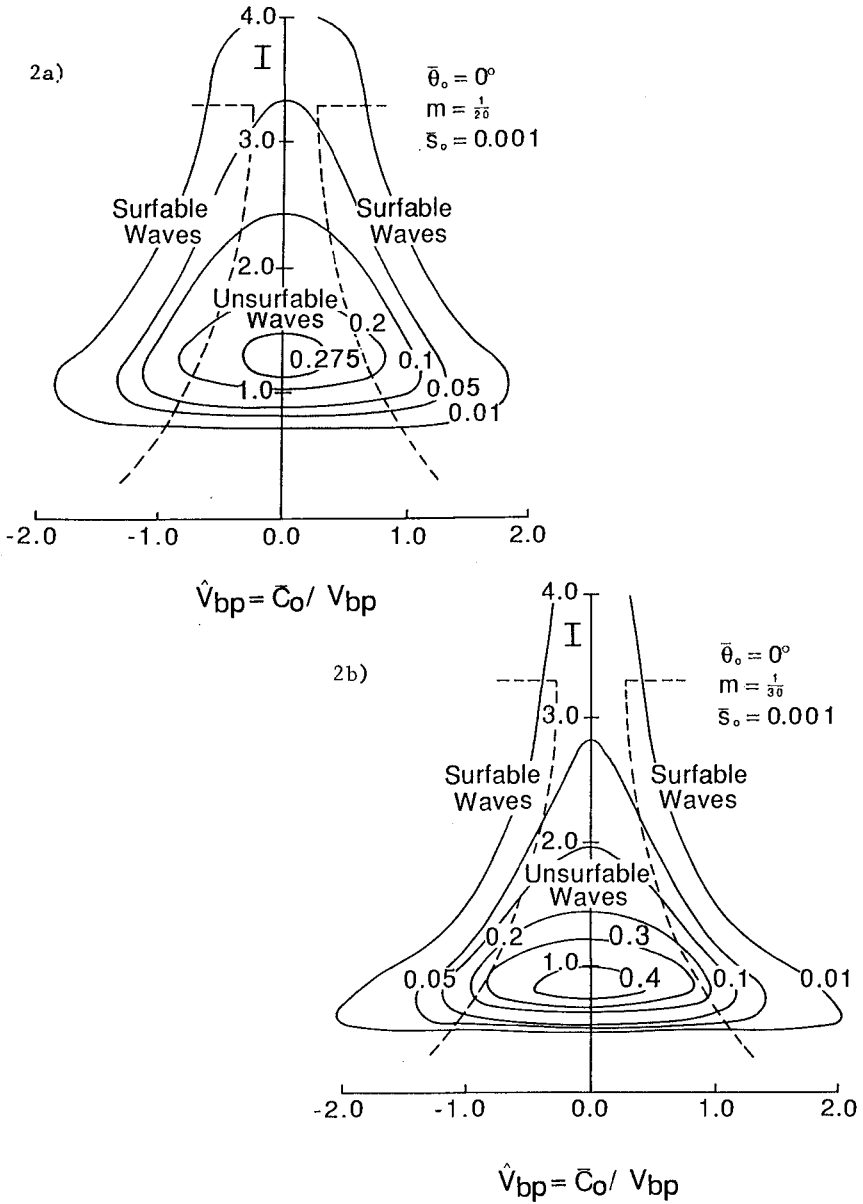


Figure 2 - Sample results of theoretical model for surfing climate given by numerical integration of Eqs.14 and 15. Volume contained in surfable region represents the proportion of incoming waves that are surfable.

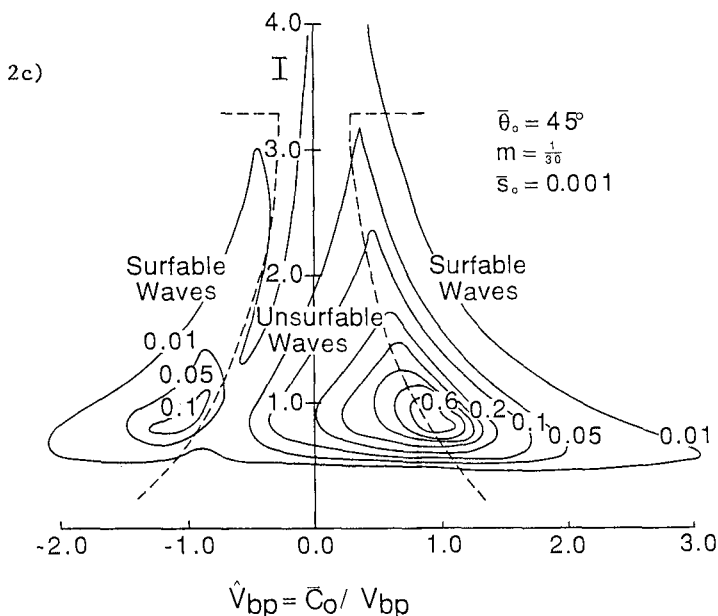


Figure 2 - concluded

yields the proportion of the incoming waves that can be regarded as surfable, and provides a number that can be used to quantify the surfing climate for a particular beach and incident wave conditions.

Figures 2a and b are for a mean angle of incidence of zero, but for different bottom slopes. Note that more probability density is shifted into the unsurfable region if the bottom slope is decreased from 1/20 to 1/30. If the mean angle of incidence is oblique to the shoreline as in Figure 2c, the pdf changes shape significantly and more density falls within the surfable region.

Stochastic Model for Short-Term Surfing Climate #2

In this model it is assumed that all waves break parallel to the bottom contours of a planar beach, and that a single uniform value can be used to represent the longshore gradient in wave height. Starting again from Eq.12, and employing Eq.2 and linear wave theory to shoal waves from deep water to the break point, transformation of random variables leads to

$$\text{pdf}(I_o, \hat{C}_b) = C_1 \frac{m^2 \hat{C}_b^4 K^2}{I_o^3 \bar{S}_o^3 \pi^2} \exp -\left\{ \frac{m^4 \hat{C}_o^4}{I_o^4 \bar{S}_o^2} [1+\epsilon^{-2}(1-\hat{C}_o^{-1})^2] \right\} \quad (18a)$$

in which

$$\hat{C}_o = \hat{C}_b [(K^2/2\pi^2)(I_o/m)^4]^{1/5} \quad (18b)$$

Using Eqs.3 and 9 yields the relation

$$\hat{C}_b = \hat{V}_{bp}^{-1} [\Omega(1+\Omega^2)^{-1/2}] \quad (19a)$$

in which

$$\Omega = [(-dH/dy)/(1.25 K m)] \quad (19b)$$

and a final transformation leads to

$$\text{pdf}(I_o, \hat{V}_{bp}) = C_1 \frac{m^2 K^2}{I_o^3 \bar{S}_o^3 \pi^2} \frac{[\Omega(1+\Omega^2)^{-1/2}]^5}{\hat{V}_{bp}^6} \exp -\left\{ \frac{m^4 \hat{C}_o^4}{I_o^4 \bar{S}_o^2} [1+\epsilon^{-2}(1-\hat{C}_o^{-1})^2] \right\} \quad (20)$$

Sample results for a value of dH/dy of -0.005 are displayed in Figure 3. In comparison to Figures 2b and 2c, it is clear that for the same bottom slope and mean deepwater steepness a much greater proportion of waves fall within the bounds of the surfable region. Although the two models are quite simple and heuristic, these results do indicate that the contribution to the peel rate from the short-crestedness of waves is more important than that from wave obliqueness. Future investigations and modeling of surfing climate should be focused accordingly.

Computational Model for Long-Term Surfing Climate

Because the formulations above inherently assume that the incident waves are a stationary random process, they can only be valid on a time scale on the order of several hours to perhaps several days. To quantify the surfing climate of a site on a seasonal or yearly time scale, a long-term model or methodology is required. In addition, surfers usually line up at the outer edge of the surf zone and choose to ride only the higher waves in the incoming groups. Therefore it appears that a reasonable description of the long-term surfing climate would be the joint distribution of board speed and peel rate associated with

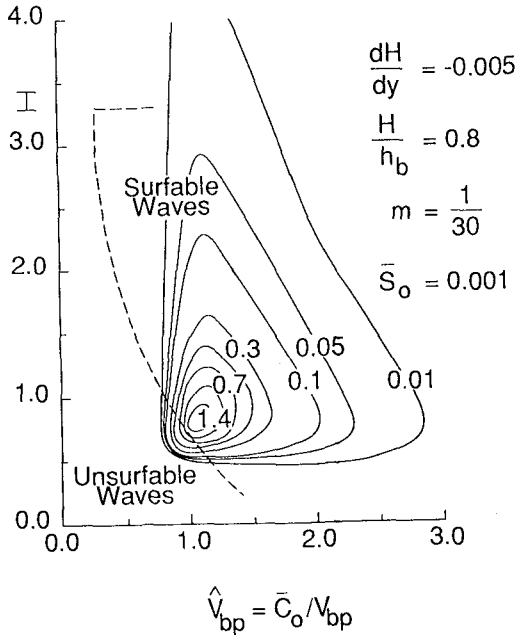


Figure 3 - Sample results of second theoretical model for short-term surfing climate given by Eq.20.

only the larger breaking waves (e.g. $H_{1/10}$), analyzed at intervals of several hours.

Wave height and period provided by long-term wave gage records, hindcast predictions, or even manual observations might be used to calculate Irribarren Numbers. However, wave direction information needed to partially determine peel rate is more difficult to obtain, plus observations of the longshore gradient in breaker height are almost nonexistent. At present, development of usable methodologies to assess long-term surfing climate must therefore be guided by available data.

As an example, detailed, long-term wave information is available in the Monthly Data Summaries published by the Field Research Facility in Duck, North Carolina. The data utilized herein is derived from pressure gage time series collected for 34 min, once every six hours, and is reported in the form of energy based significant wave height, H_{m0} , and associated peak spectral period, T_p . The gage is located at a nominal water depth of 8 m.^p Concurrent tide measurements are also provided, plus high quality nearshore bathymetry is available from CRAB surveys.

Numerical Algorithm

H and T can be used as the input required by the joint probability density function of wave height and period derived by Longuet-Higgins (1983) by assuming that $H_{rms} = H_{po}/\sqrt{2}$ and $\bar{T} = 0.8 T$. With the pdf discretized into a joint histogram, the routine steps landward along a measured beach profile, shoaling each representative wave according to the theory of Shuto (1974):

$$H^2 C_g = \text{const. (linear theory)} \quad \text{for } gHT^2/h^2 < 30 \quad (21a)$$

$$Hh^{2/7} = \text{const.} \quad \text{for } 30 < gHT^2/h^2 < 50 \quad (21b)$$

$$Hh^{5/2} [(gHT^2/h^2)^{1/2} - 2\sqrt{3}] = \text{const. for } 50 < gHT^2/h^2 \quad (21c)$$

where C_g is the group velocity. Each representative wave shoals until the condition for incipient breaking developed by Weggel (1972) is satisfied:

$$(H_b/h) = b(m) - a(m) H_b/gT^2 \quad (22a)$$

where

$$a(m) = 43.8(1.0 - e^{-19m}) \quad (22b)$$

$$b(m) = 1.56/(1.0 + e^{-19.5m}) \quad (22c)$$

Because the bottom profile at the FRF is irregularly shaped and often contains a bar formation, an estimate of the effective bottom slope is needed in Eq.22. This estimate is determined from the section of profile immediately seaward of the point of interest, by averaging the slope over a distance of one wave length. The routine continues to step across the profile until 10% of the waves have broken. At this point the average incipient breaker height and average of the associated Irribarren Numbers at breaking ($H_{b.1}$ and $I_{b.1}$) are calculated for this 10% of the waves that broke first.

Sample results from this algorithm are presented in Figure 4 for the month of January, 1989, and in Figure 5 for the month of July, 1989. It is interesting to note that the predicted Irribarren Numbers fall predominantly in the range of spilling breakers, and that $H_{b.1}$ and $I_{b.1}$ are inversely correlated - unfortunate from the surfer's point of view.

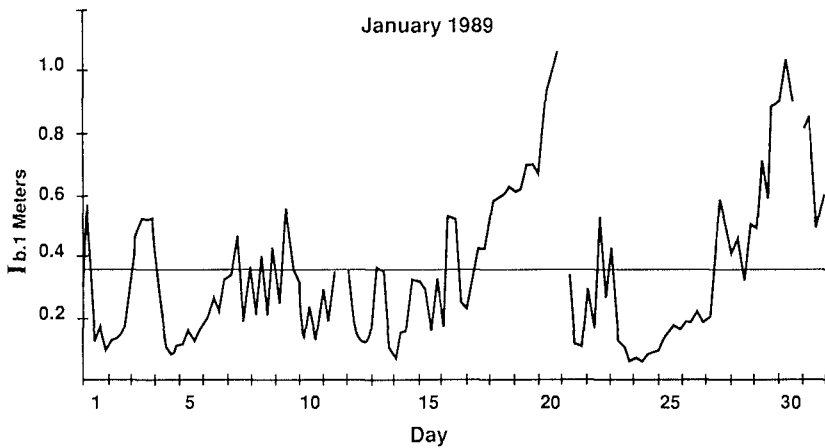
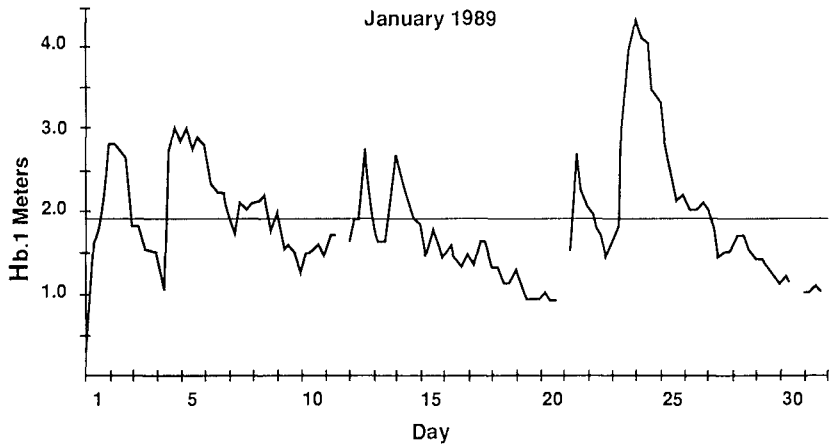


Figure 4 - Results from the numerical algorithm for the long-term surf climate at Duck, North Carolina during the month of January, 1989. The correlation between Hb.1 and Ib.1 is -0.71 .

If a criterion for surfable conditions is imposed such that $Hb.1 > 1.25m$ and $Ib.1 > 0.3$, the waves were surfable roughly 35% of the time in January and 33% of the time in July. Raising the requirement on Hb.1 to 1.5m reduces January to 20% surfable, and July to 15%.

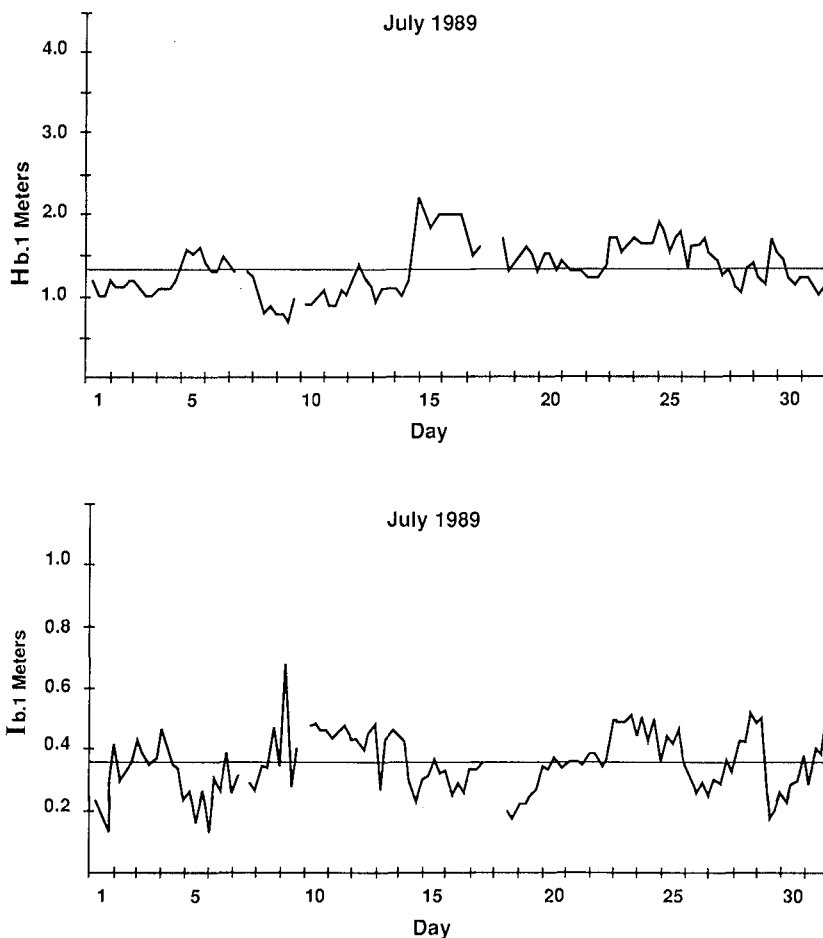


Figure 5 - Results from the numerical algorithm for the long-term surf climate at Duck, North Carolina during the month of July, 1989. The correlation between Hb.1 and Ib.1 is -0.23.

Summary and Conclusions

Viable engineering models and methodologies that can be used to evaluate the surfing climate at a beach are needed to preserve the recreational benefits of the coast. A rudimentary analysis of surfing mechanics demonstrates that the basic parameters in need of study are 1) the peel

rate of a breaking wave, and 2) the attainable board speed. Assuming a planar beach and using linear wave theory, two heuristic models have been presented that can be used to appraise short-term surfing conditions, given beach and incident wave characteristics. Results indicate that it is essential to include the short-crested character of real surf in model formulations. Also presented is a numerical algorithm which utilizes arbitrary beach profiles and measured offshore wave data to evaluate surfing conditions on a seasonal or yearly time scale.

Future investigations of surfing should include a better parameterization of attainable board speed in terms of wave and wind characteristics, with verification to direct measurements. Another important aspect to consider is the paddling effort required in order to catch a wave, i.e. the interplay of the mechanics of catching a wave and the transformation of the individual wave as it approaches breaking. This can play a major role in assessing the surfbreak on a particular day.

References

- Battjes, J.A., 1974, "Surf Similarity," Proc. 14th Conf. Coast. Eng., ASCE, pp.466-480.
- Dally, W.R., 1989, "Quantifying Beach 'Surfability'," Proc. Beach Techno. Conf., Tampa, FL, pp.47-58.
- Galvin, C.J., 1968, "Breaker Type Classification on Three Laboratory Beaches," J. Geophys. Res., Vol.73, No.12, pp.3651-3659.
- Longuet-Higgins, M.S., 1983, "On the Joint Distribution of Wave Periods and Amplitudes in a Random Wave Field," Proc. Royal Soc. London, A389, pp.241-258.
- Morahan, E.T., 1971, "The Economic Value of Surfing Sites on Oahu; A Preliminary Estimate," Dept. Agriculture and Resource Economics, Univ. Hawaii, Honolulu.
- Pratte, T.P., 1987, "Ocean Wave Recreation," Proc. Coastal Zone '87, pp.5386-5398.
- Shuto, N., 1974, "Nonlinear Long Waves in a Channel of Variable Section," Coastal Eng. Japan, JSCE, Vol.17, pp.1-12.
- Walker, J.R., 1974, "Recreational Surf Parameters," U. of Hawaii Look Lab. Rep. No.30, 311 pp.
- Weggel, J.R., 1972, "Maximum Breaker Height," J. Wtrys., Hrbrs., Coast. Eng. Div., ASCE, Vol.98, No.WW4, pp.529-548.

CHAPTER 41

WAVE MODEL APPLICATION IN A WADDEN SEA AREA

J.D. den Adel (1), H.D. Niemeyer (1), A.F. Franken (1),
N. Booij (2), J. Dekker (3), J.A. Vogel (4)

ABSTRACT

A verification study of the numerical 2D wave propagation model HISWA is presented for a complex coastal area. Model predictions are confronted with field measurements. Also the effects of specific model possibilities and limitations are examined. Results have been fair: mean errors in wave height of 12% and in wave period of 4%, at a distance of 4 km from the incoming boundary over which measured wave heights reduced 40% and periods 21%.

1 INTRODUCTION

The aim of using wave propagation models, is to estimate nearshore wave conditions from offshore available wave data, by considering the onshore wave processes. In this paper the performance of the wave propagation model HISWA in a German part of the Frisian Wadden Sea (fig. 1) is discussed. As the study is still continuing, only intermediate results will be presented, unsolved questions might be answered in the near future.

-
- 1 Coastal Research Station/NLWA-Forschungsstelle Küste, Norderney/East Frisia, Federal Republic of Germany
 - 2 Delft University of Technology/TU Delft, Delft, The Netherlands
 - 3 Delft Hydraulics/Waterloopkundig Laboratorium, Emmeloord, The Netherlands
 - 4 Ministry for Public Works/Rijkswaterstaat, The Hague, The Netherlands

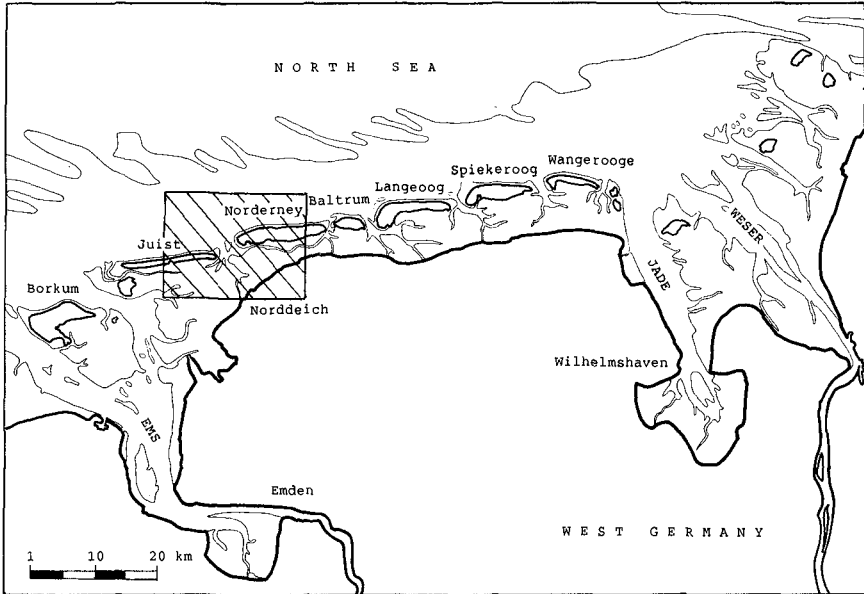


fig. 1 location of the investigation area

2 THE MODEL HISWA

To get an idea of the sort of model, the basic formulation of HISWA and the physical processes involved will be discussed briefly. Detailed information can be found in papers by BOOIJ et al. (1985) and HOLTHUIJSEN et al. (1988).

HISWA is a numerical, 2D wave propagation model, based on the action balance equation for stationary conditions. Action is an energy derived quantity, by dividing energy by the relative frequency. Unlike energy, action is also conserved in the presence of a current. The action balance equation has the following shape:

$$\frac{\partial(c_x A)}{\partial x} + \frac{\partial(c_y A)}{\partial y} + \frac{\partial(c_\theta A)}{\partial \theta} = S \quad (1)$$

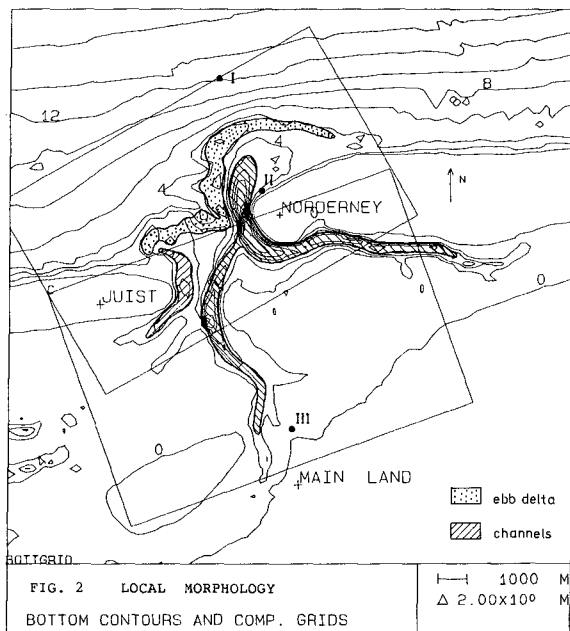
On the left hand side the transport terms (gradients) of the action density integrated over the frequency (A) are written. c_x and c_y denote the translation speeds of A , c_θ the speed with which A changes its direction. The transport terms cause a redistribution of existing energy in

space and over the directions, which implies propagation and shoaling and refraction but not diffraction.

On the right hand side the S , denoting sinks and sources, stands for the sum of all external processes removing wave energy from or introducing wave energy into the system. These are wave breaking, bottom friction, current dissipation and wind growth. They are represented by suitable semi-empirical functions.

The frequency is not constant; there is an equation similar to (1) from which the action averaged frequency can be found. By employing the θ -dimension, the concept of a directional wave spectrum is retained. The action balance is projected on a regular grid (x, y, θ) for numerical operation.

HISWA can produce several types of output, for a number of wave parameters. In this study the wave height and period serve as test parameters. HISWA operates with a significant wave height $H = 4(M_0)^{0.5}$ and a mean period $T = M_{-1}/M_0$ in which M_0 and M_{-1} are the 0th and the -1st frequency moments of the wave spectrum. Anywhere in this paper H and T are those given by the above definitions.



3 MORPHOLOGY

Because of its relevance for wave propagation, a short outline of the local morphology is given (fig. 2). The area of interest lies in the surroundings of the barrier islands Norderney and Juist. North of the islands initially there is a mildly sloping bottom. This smooth topography is interrupted by an ebb delta, lying at a distance of at most 2 km out of the northwest coast of Norderney. It partly shelters the tidal inlet between Norderney and Juist. In the tidal inlet two main channels have formed. The larger eb channel in the east splits up into two tributaries, one bending around the west end of Norderney and another directed to the main land coast in the middle. The flood channel in the west, bends around the eastern shore of Juist.

South of the islands physiographically quite a different situation occurs. Here the area consists of a system of tidal flats and narrow channels, a typical part of the Wadden Sea stretching along the Dutch, German and Danish coasts. But currently the investigations are focussed on the northern part.

Two dominating features with respect to wave propagation are the ebb delta and the tidal channels. The ebb delta causes a lot of wave breaking during storm occasions. The channels are corridors through which wave energy penetrates. Also the course of wave directions along the channels remains rather constant for a wide range of incoming wave directions (NIEMEYER, 1986).

The frames in fig. 2 indicate the computational areas, measuring about 7.5 x 12 km and 9 x 12 km north and south. Points I, II and III are observation points.

4 FREQUENCY SHIFT

HISWA simulates the frequency change associated with each of the dissipative or generative processes. For wave breaking and bottom friction the frequency change can optionally be switched on or off. The change of frequency is based on certain assumptions of the frequency spectrum in relation to energy dissipation. As indicated by DINGEMANS (1987) these assumptions do not fully match physical reality. Compared with a laboratory experiment (DINGEMANS, 1987) the frequency would get too high (or the period too low). A constant frequency on the other hand, is physically also unrealistic in relation to wave breaking and bottom friction.

A change in frequency will affect the processes on both sides of the action balance equation and thus the wave height. Refraction, getting weaker with increasing frequency, has especially much influence on the steep slopes of the main channel along Norderney. So it is of importance to have a good estimation of the frequency. To examine the effect of the frequency change, ratios between the wave height computed at a constant frequency and at a changing frequency were calculated for regularly spaced points over the area. It was found that these ratios lie between 0.60 in the eastern main channel and 1.25 at the western part of the ebb delta. Just as an example fig. 3 shows a block print of such ratios for a part of the area. (A block print is a table of values for a grid of regularly spaced points, like a value map with different x,y-scales).

VOGEL et al. (1988) applied HISWA in a comparable sort of area with the frequency change switched on. Instead of the expected underestimation of the wave period by letting the frequency change, their computations showed a small overestimation of the period of 7% on average.

1.16	1.15	1.13	1.10	1.07	1.05	1.05	1.05	1.05	1.07	1.08
1.17	1.15	1.11	1.07	1.03	1.03	1.04	1.04	1.05	1.06	1.08
1.16	1.13	1.08	1.03	1.01	1.01	1.02	1.03	1.05	1.07	1.08
1.14	1.09	1.04	1.00	0.99	1.00	1.01	1.03	1.05	1.08	1.09
1.11	1.05	1.00	0.97	0.98	0.99	1.01	1.03	1.06	1.08	1.09
1.08	1.01	0.97	0.96	0.96	0.98	1.01	1.05	1.07	1.09	1.10
1.03	0.97	0.94	0.94	0.95	0.98	1.02	1.06	1.09	1.10	1.11
0.98	0.94	0.92	0.92	0.94	0.98	1.04	1.08	1.11	1.12	1.13
0.95	0.91	0.90	0.91	0.94	1.01	1.07	1.11	1.14	1.15	1.16
0.92	0.88	0.87	0.90	0.97	1.07	1.12	1.14	1.15	1.16	1.15
0.89	0.85	0.85	0.90	1.02	1.13	1.25	1.37	1.29	1.32	1.41
0.86	0.81	0.83	0.92	1.08	1.37	1.74	nney	nney	nney	nney
0.83	0.78	0.81	0.92	1.17	1.17	nney	nney	nney	nney	nney
0.79	0.77	0.83	0.95	1.42	1.42	nney	nney	nney	nney	nney
0.76	0.77	0.85	0.95	nney	nney	nney	nney	nney	nney	nney
0.75	0.77	0.84	0.92	nney	nney	nney	nney	nney	nney	nney
0.74	0.76	0.82	0.90	nney	nney	nney	nney	nney	nney	nney
0.74	0.75	0.82	0.91	nney	nney	nney	nney	nney	nney	nney
0.74	0.77	0.85	0.95	nney	nney	nney	nney	nney	nney	nney
0.74	0.78	0.87	1.00	1.14	1.14	nney	nney	nney	nney	nney
0.74	0.79	0.87	0.93	0.92	0.92	nney	nney	nney	nney	nney
0.73	0.77	0.83	0.87	0.87	0.87	nney	nney	nney	nney	nney
0.71	0.73	0.79	0.85	0.86	0.86	nney	nney	nney	nney	nney
0.69	0.70	0.76	0.83	0.85	0.83	0.80	nney	nney	nney	nney
0.68	0.68	0.72	0.78	0.83	0.80	0.79	nney	nney	nney	nney
0.67	0.66	0.69	0.72	0.75	0.73	0.72	0.71	nney	nney	nney
0.66	0.64	0.64	0.67	0.71	0.69	0.67	0.68	0.71	nney	nney
0.65	0.63	0.61	0.62	0.65	0.66	0.63	0.60	0.64	0.94	nney
0.66	0.62	0.60	0.59	0.60	0.61	0.60	0.58	0.54	0.68	1.01

fig. 3 ratios of the wave height obtained with the frequency switches turned off and turned on

In order to decide for this area whether to run HISWA with a changing or a constant frequency, tests were done both with the frequency change switched on and off. For both situations the calculated wave periods and wave heights were compared with field measurements. For the wave period an overall better performance was found by having the frequency change switched on, as can be seen in figure 4 and table 1: a mean percent error $e(T)$ of -4% with the frequency change switched on against 29% with the frequency change switched off. The percent error of the period is defined as $e(T) = 100\% * (T_{his} - T_{obs}) / T_{obs}$, with the subscripts his and obs referring to HISWA and observed values. For the wave height there is hardly any difference between cases with a changing or a constant frequency: mean errors $e(H)$ of 12% for both cases (fig. 5, table 1). This could be due to the position of the observation point (II) in front of the deep channel along Norderney, where the wave height is still relatively unaffected by refraction. The scatter (standard deviation sd) gets a little lower when the frequency change is switched on. On account of the improvement of the wave period, it was decided to run HISWA with the frequency change switched on.

TABLE 1 : FIELD MEASUREMENTS AND HISWA PREDICTIONS

INCIDENT WAVES		INSHORE WAVE HEIGHTS H (m)			INSHORE WAVE PERIODS T(s)		
height H (m)	period T (s)	observed	HISWA freq. switch on	HISWA freq. switch off	observed	HISWA freq. switch on	HISWA freq. switch off
2.69	6.4	1.50	1.53	1.69	6.1	4.6	6.4
2.69	6.4	0.98	1.08	0.97			
2.61	8.1	1.48	1.64	1.59	4.3	5.4	8.1
1.53	5.5	1.13	1.12	1.16	5.2	4.3	5.5
1.70	6.2	1.20	1.34	1.40	4.8	4.8	6.2
1.65	6.2	1.32	1.51	1.52	4.7	5.2	6.2
1.69	5.4	1.14	1.38	1.36	4.6	4.5	5.4
1.77	5.7	0.92	1.07	1.07	4.6	4.1	5.7
1.69	5.7	0.91	1.30	1.34	4.7	4.5	5.7
1.93	6.6	0.98	0.89	0.84	4.7	4.0	6.6

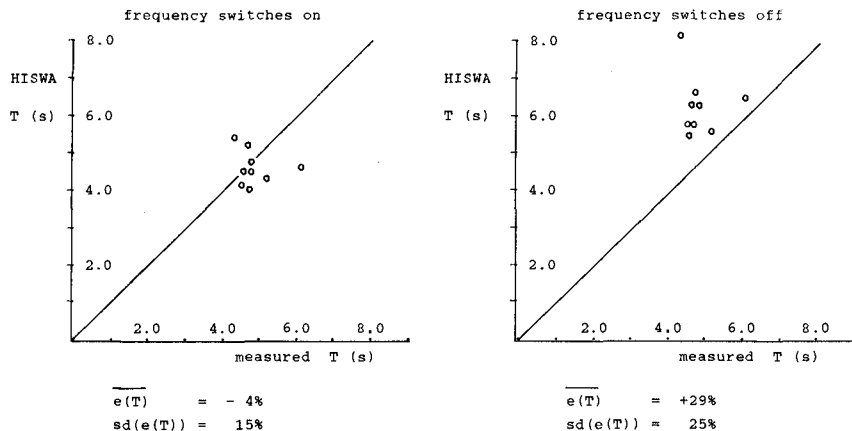


fig. 4 WAVE PERIOD TESTS WITH THE FREQUENCY SWITCHES TURNED ON AND TURNED OFF

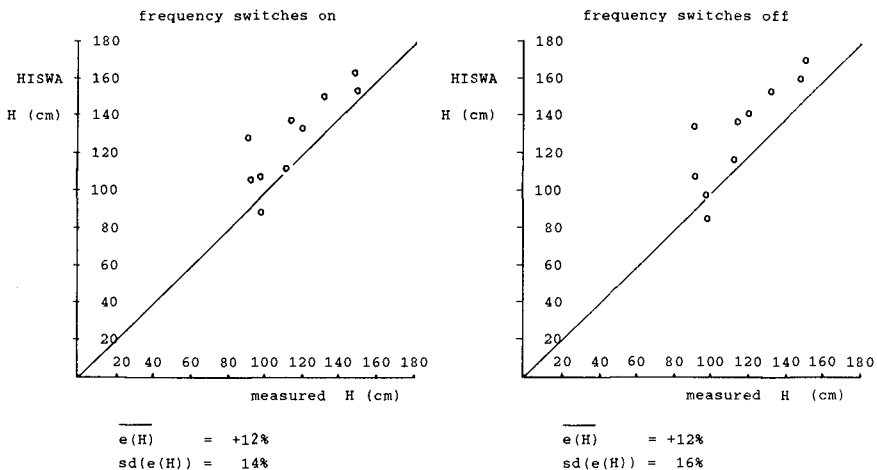
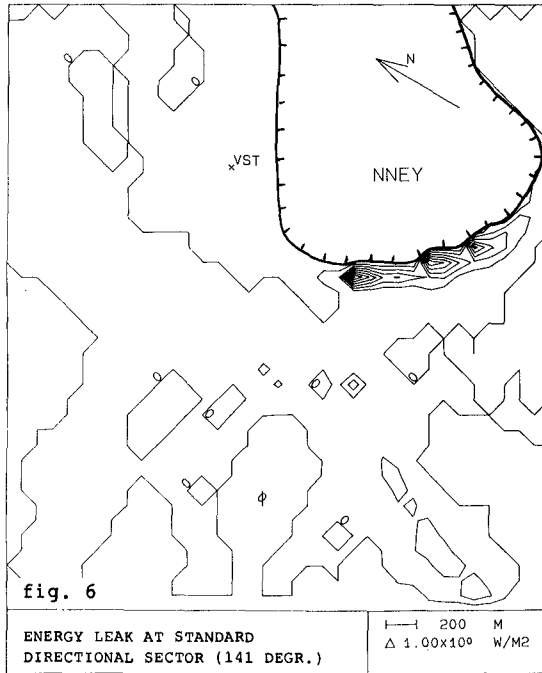


fig. 5 WAVE HEIGHT TESTS WITH THE FREQUENCY SWITCHES TURNED ON AND TURNED OFF

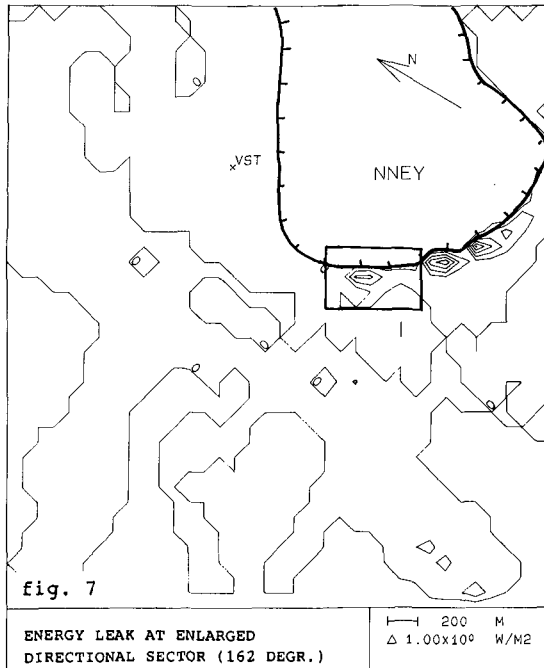
5 ENERGY LEAK

For reasons of numerical stability HISWA can only operate within a directional sector of limited range. The sector width should be predefined and usually is taken near 120 degrees. Energy transported beyond the directional limits



is removed out of the system. This unintended energy loss, called (energy) leak, is thus caused by numerical restrictions and should not physically occur. So leak arises when the wave energy is distributed over a wider directional range than the predefined directional sector.

In the area of investigation leak occurs on the steep slopes of the deep channel along Norderney due to strong refraction (fig. 6). To get an idea of the error in the wave height caused by leak, the directional sector was enlarged to 162 degrees (which is about the maximum attainable and not suited for operational purpose). By this, leak will be reduced and the wave height increased and so a link can be made between leak and wave height. In the region where leak was largest, it was reduced strongest by expanding the directional sector as can be seen in figs. 6 and 7 (within the small rectangle). By means of block prints it was found that leak reduced here about three times whereas the wave height only increased 4%. This is about the largest effect leak can have upon the wave height, because here leak reduces from the highest value to a rather low value. So leak has only little effect upon the wave height.



Besides expanding the directional sector there are some other ways to influence the leak. The computational grid can for instance be rotated in such a way that as much energy as possible falls within the directional limits (fig. 8). In this way an orientation with lowest leak was found, the x-axis directing 150 to 160 degrees clockwise from the north. Because wave directions in the tidal channels are rather consistent, this orientation will be suited for incoming waves of all relevant (on-shore) directions.

Leak will also be influenced by the use of the frequency switches. Switching on the frequency change will reduce refraction because of an onshore frequency increase. Thus the energy will be spread over a smaller directional range and the leak will be reduced. In case of a changing frequency leak is about 3 times less than in case of a constant frequency.

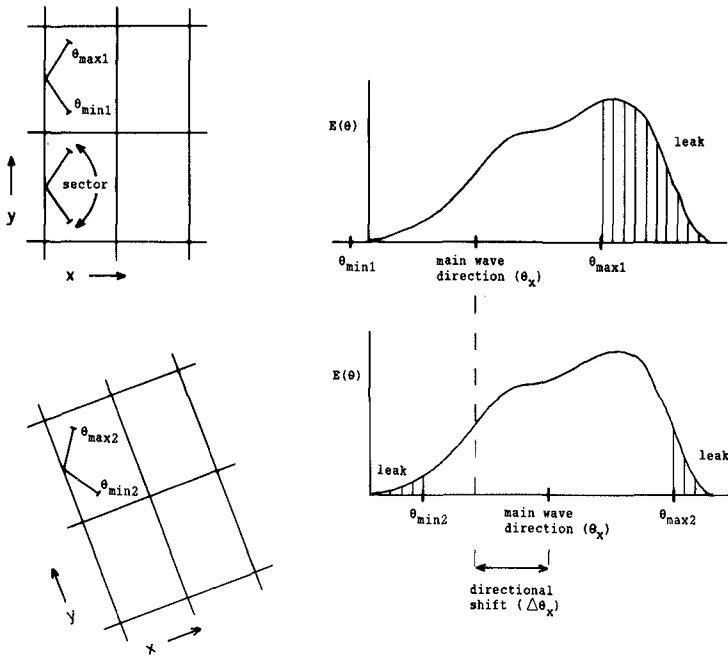


fig. 8 turning the computational grid and energy leak

6 MODEL RESULTS

Before looking at the results it should be noted that the sink and source functions of HISWA contain some empirical coefficients for which default values are assumed, which can however be adjusted. A calibration took place, based on two storm occasions, after which both wave breaking coefficients of Miche were lowered. They were given values of 0.75 and 0.90 for shallow and deep water respectively. Their standard model values were 0.8 and 1.2.

As test conditions, wind speeds ranged from 10.3 to 18.6 m/s at 10 m height, wind directions from 280 to 340 degrees and wave directions from 270 to 320 degrees (going clockwise from the north to the incoming direction). Currents were not included, but computations were generally done at low stream conditions.

Results have already been shown at the tests with the frequency switches (table 1, figs. 4 and 5). It might

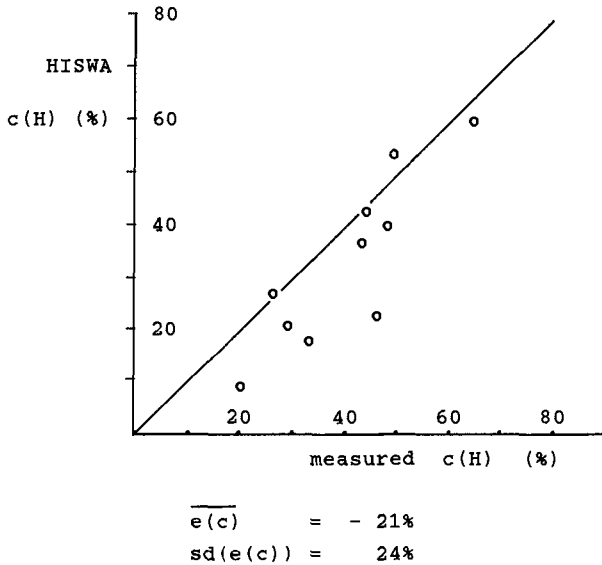
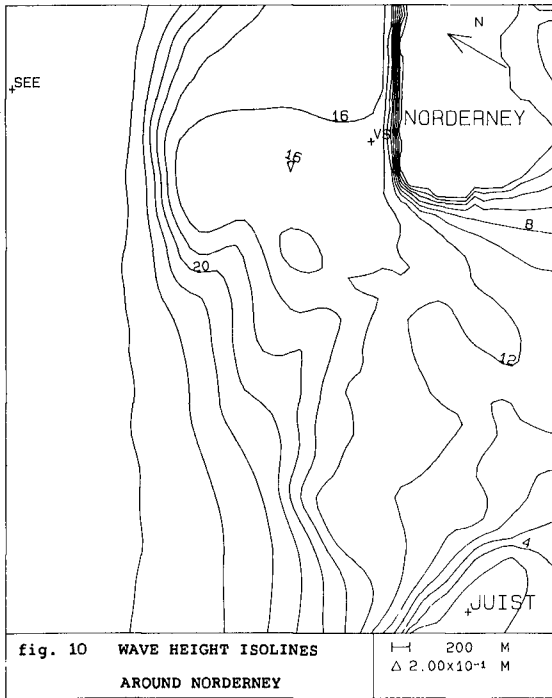


fig. 9 COMPARISON OF PREDICTED AND MEASURED
ONSHORE WAVE HEIGHT CHANGES

however be more convenient to use the change in wave height between offshore boundary and nearshore observation point as test parameter, rather than the wave height. By this it will be more apparent whether the predictions concern situations of substantial onshore change or not, indicating the quality of the tests. In fig. 9 the percent onshore wave height change of the HISWA computations is plotted against the measurements. The percent onshore wave height change is defined as $c(H) = 100\% * (H_{off} - H_{near}) / H_{off}$, with the subscripts off and near referring to offshore and nearshore observation points. As is seen HISWA predicts too small changes which means wave heights are still too high despite the downward adjustment of the wave breaking coefficients. The mean percent error $\overline{e(c)}$ of the percent onshore wave height change is -21% at a standard deviation $sd(e(c))$ of the percent error of 24% .

Fig. 10 shows a typical wave height plot for onshore directed waves. A rapid wave height decrease occurs along the ebb delta. In the inlet channels wave heights are more persistent.



7 SINKS AND SOURCES

The sensitivity of the model to the processes of wave breaking, bottom friction and wind growth was tested by putting alternately one of these processes out of order and comparing the results with the normal case (all processes functioning). In fig. 11 wave height profiles between incoming boundary and observation point show the evolution of the wave height for each case. It is seen that wave breaking is a most dominating process, reducing the wave height up to 45% (beach margins excluded, as waves totally diminish there). The influence of bottom friction and wind growth is much less, at most 4% and 3% respectively. The calculated value comes closest to the measurement when all processes are considered or when the wind growth is not functioning. The wave height reduction between the incoming boundary and the observation point calculated by HISWA is 43%. This lies close to the 42% which NIEMEYER (1987) found as a mean value over a large range of field measurements.

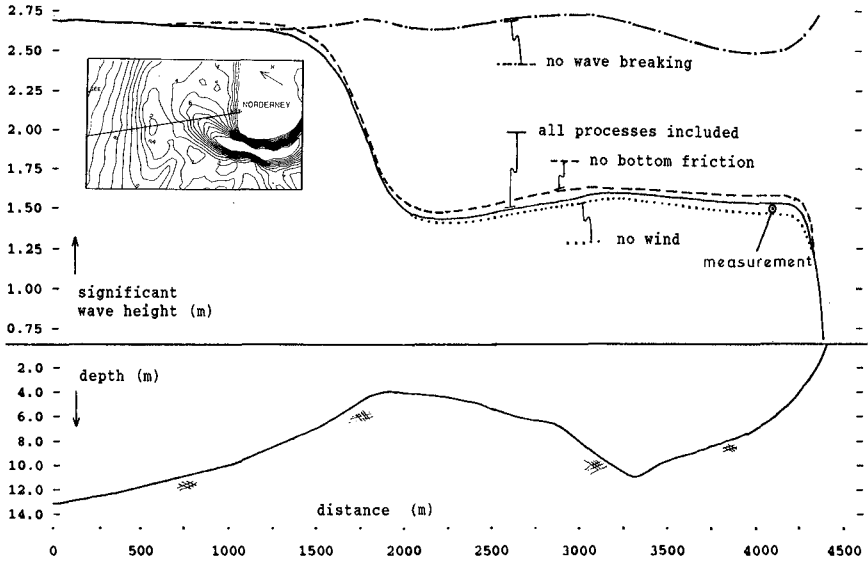


fig. 11 onshore wave height evolution in dependence of energy sinks and sources

The distribution of the percent changes over the total area was examined by means of block prints. Wave breaking can reduce wave heights up to 60% in the centre of the tidal inlet. In the same way the maximum reduction by bottom friction was found to be 7% and the maximum increase by wind growth 9% (at the end of the fetch). Of course these figures depend upon each situation individually and only serve to get an idea of the relative importance of the various sinks and sources in this area. In the study by VOGEL et al. (1988) it was for instance shown that under their conditions, wind growth can be a much more dominating process.

CONCLUSIONS

- Running HISWA with the frequency changes switched on has a positive effect on the wave period and the energy leak. The computed wave height in the observation point hardly improved by use of the frequency switches.
- The presence of leak does not harm the model results significantly.

- Of the various energy sinks and sources, wave breaking has the largest influence upon the wave height.
- HISWA does give fair results in the area of investigation where wave breaking is a dominating process.

ACKNOWLEDGEMENTS

This study is sponsored by the GERMAN FEDERAL MINISTRY FOR SCIENCE AND TECHNOLOGY (BMFT) in the framework of the research programme managed by the GERMAN COMMITTEE FOR COASTAL ENGINEERING RESEARCH (KFKE). The authors also wish to thank all colleagues who gave support to this study, especially those of the section of coastal hydrodynamics of the COASTAL RESEARCH STATION.

REFERENCES

- BOOIJ N., HOLTHUIJSEN L.H. AND HERBERS T.H.C., 1985, The shallow water wave hindcast model HISWA, Part 1: physical and numerical background. Delft University of Technology, Dept. of Civil Engng., Group of Fluid mechanics. Report no. 6-85.
- DINGEMANS M.W., 1987, Verification of numerical wave propagation models with laboratory measurements. Delft Hydraulics Laboratory, Report H-228.
- HOLTHUIJSEN L.H., BOOIJ N. AND HERBERS T.H.C., 1988, A prediction model for stationary, short-crested waves in shallow water with ambient currents. Coastal Engineering, vol. 12, pp. 23 - 54.
- NIEMEYER H.D., 1986, Wave propagation and damping in the offshore and Wadden Sea area near Norderney (in German: Ausbreitung und Dämpfung des Seegangs im See- und Wattengebiet von Norderney). Jahresbericht 1985, Forschungsstelle Küste, Band 37
- NIEMEYER H.D., 1987, Changing of wave climate due to breaking on a tidal inlet bar. Proc. 20th Intern. Conf. Coast. Engng. ASCE, Taipei, vol. 2, pp 1427 - 1443.
- VOGEL J.A., RADDER A.C. AND DE REUS J.H., 1988, Verification of numerical wave propagation models in tidal inlets. Proc. 21st Intern. Conf. Coast. Engng. ASCE, Malaga, vol. 1, pp 433 - 447.

CHAPTER 42

THE MASS TRANSPORT OF WAVES PROPAGATING ON A SLOPING BOTTOM

H.H. Hwung¹ and C. Lin²

ABSTRACT

This paper presents the experimental results on Eulerian mass transport which is induced by waves propagating on a sloping bottom. The measurements are carried out by laser Doppler velocimeter(LDV) in wave flume. A particular installation of measuring system is required to detect the boundary layer flow extremely close to the point of 0.15mm above the sloping bottom. From the experimental results, it is clear to see that the off-shore mass transport takes place inside the region from the proximity of bottom up to wave trough. Around the elevation of wave trough, the mass transport velocity changes its direction to on-shore rapidly, and it reaches the maximum value at still water level, then it decreases to zero at crest. Further, the vertical distribution and similarity profile of Eulerian mass transport inside boundary layer are also obtained and discussed in this paper.

1. INTRODUCTION

Eulerian mass transport of wave shoaling process is a

1. Professor of Hydraulic and Ocean Engineering Department and Director of Tainan Hydraulics Lab. National Cheng Kung University. Tainan, Taiwan, R.O.C.
2. Dr. Engineering, National Cheng Kung University. Tainan, Taiwan, R.O.C.

very important hydrodynamics, which is closely related to the on-shore and off-shore sediment transport, the vertical distribution of suspended materials and the dispersion of pollutants in coastal waters. Within the last decade, Watanabe et al. (1980), Isobe and Horikawa (1981) and Nadaoka et al. (1982) employed hot-film anemometer and LVD (Laser Doppler Velocimeter) to measure the Eulerian mass transport in wave tank, respectively. Moreover, Sleath (1984) detected the mass transport inside boundary layer as wave propagating on a rough bed. Although the previous studies paid more attention on Eulerian mass transport of wave motion, however, the characteristics of mass transport of waves propagating on a sloping bottom has not been fully understood. Accordingly, in this paper the mass transport of wave shoaling from crest through the bottom, including the bottom boundary layer are detected by LDV and the results are discussed.

2. EXPERIMENTS

The experiments were carried out in a $9.5\text{m} \times 0.7\text{m} \times 0.3\text{m}$ wave tank in which the bottom was adjusted on one-fifteenth slope. The testing sections of internal field and boundary layer of waves shoaling on the sloping bottom are sketched in Fig.1. Four kinds of wave steepness were made in wave flume and the experimental conditions are listed in Table 1. In

Table 1. The experimental conditions

case	T (sec)	H (cm)	d_o (cm)	H_o/L_o	Breaker
1	1.41	5.3	33.0	0.0186	plunging
2	1.23	6.6	33.0	0.0313	plunging
3	0.96	5.3	33.0	0.0405	plunging
4	0.96	8.2	33.0	0.0617	spilling

order to understand the distribution of mass transport , it had more fifty points measured by LDV in every testing section. Especially in the boundary layer within about 0.5cm height, it even had twenty-five measuring points detected by LDV in the experiment.

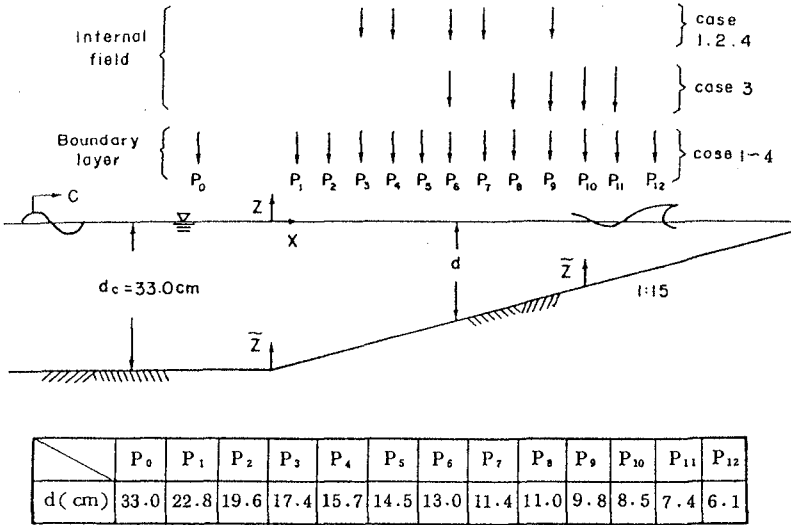


Fig.1 The sketch diagram of testing sections.

Because the light beam of LDV system would be obstructed by the edge of sloping steel plate in the proximity of the bottom, that a particular installation of LDV system was required in order to detect the flow fields extremely close to the point of 0.15mm above the sloping bottom . The sketch diagram of the measuring installation is shown in Fig.2 . According to the experience , water quality control is very important for the fluid dynamic experiments employed by LDV. In this paper two sets of 5 μ m filter screen are used to remove the larger natural particles suspended in water before the fresh water discharges into wave flume. After that , the signals drop-out would be reduced and the experimental quality would keep in good condition.

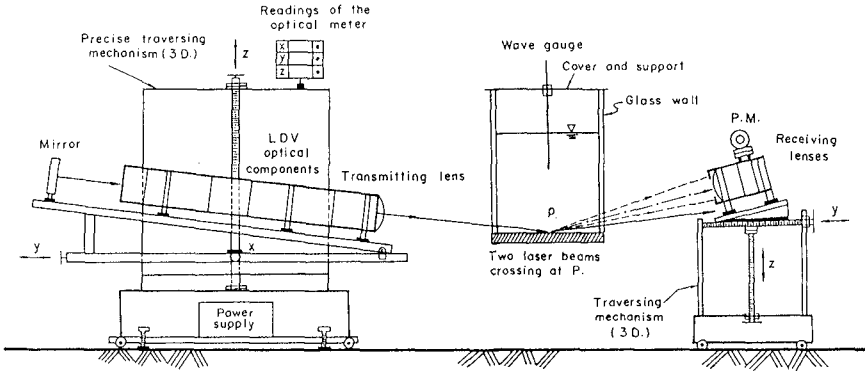


Fig.2 The sketch diagram of measuring installation.

The water surface elevation and the corresponding water particle velocity from crest through bottom were detected by wave gages and LDV simultaneously. All the sampling interval and rate were set with 18~36 seconds and 100Hz respectively . The wave reflection was also examined in this experiments . Since all the reflection coefficient were less than 4.5% , that the effects of reflection was ignored in this paper.

3. RESULTS AND DISCUSSIONS

One case of the experimental results listed in Table 1 are shown on following figures. Fig.3(a) \ (b) are the measuring records of the time series of water surface elevation and horizontal particle velocity on a testing section which the water depth is $d=17.4\text{cm}$, and the measuring point is $\bar{z}=6.8\text{cm}$ above the bottom. Fig.4 (a) \ (b) are the same results at $\bar{z} = 15.7\text{cm}$. It is obviously to see from Fig.4(b) that the part of negative velocity records become straight line . This is because the measuring volume of LDV exposes into air , that the signals drop-out take place as wave trough passing by . In this situation the signals of the above mentioned straight line should be replaced by zero, as we calculate the horizontal velocity and mass transport from LDV measuring records.

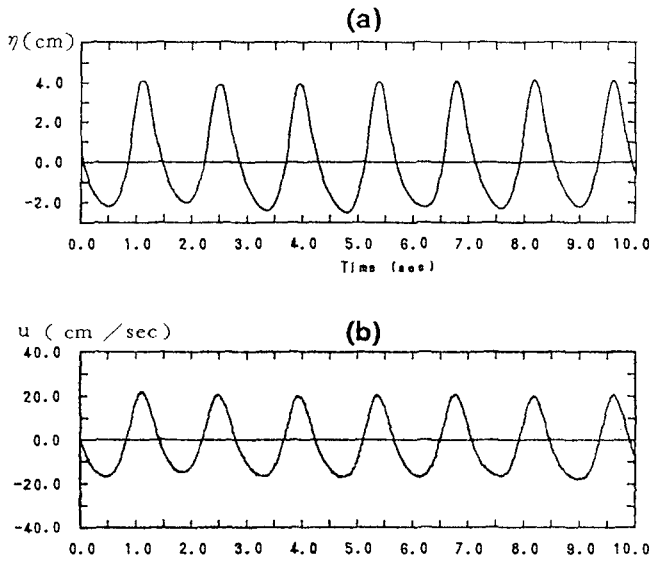


Fig.3 Time series of water surface elevation and horizontal particle velocity at $d=17.4$ cm and $\bar{z}=6.8$ cm for case 1.

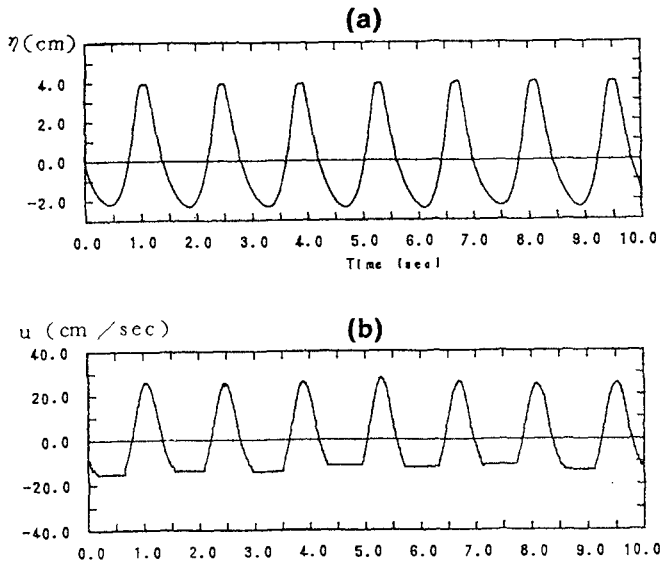


Fig.4 Time series of water surface elevation and horizontal particle velocity at $d=17.4$ cm and $\bar{z}=15.7$ cm for case 1.

After employing the phase average method and then taking average for wave period, the vertical profiles of Eulerian mass transport can be obtained and the results are shown in Fig.5(a) \ (b) \ (c) respectively. Furthermore, the comparison between our experiments and some of the theoretical calculations proposed by Longuet-Higgins(1953), Dalrymple(1976) and Nadaoka et al. (1982) are also made in those figures. From the above results, it is clear to see that the off-shore mass transport takes place inside the region from the proximity of bottom up to wave trough. Around the elevation of wave trough, the mass transport changes its direction to on-shore rapidly, and it reaches the maximum value at still water level, then the mass transport decreases to zero at crest. Further, we can see the magnitudes of on-shore and off-shore mass transport velocity increases in the process of wave shoaling on a sloping bottom. Additionally, it is obvious that the theoretical calculations of mass transport from Longuet-Higgins (1953) have more difference with our experiments. As for the results obtained from stream function by Dalrymple(1976), the calculations are coincident with experiments in the region from wave trough to crest. And the results from Nadaoka et al. (1982) are in agreement with our experiments in deep water, but it has more difference in shallow water area.

Fig.6 and Fig.7 show the experimental results of surface profiles and the corresponding horizontal flow fields inside boundary layer at the testing section of $d=15.7\text{cm}$ and 9.8cm , respectively. In above figures, the parameter δ is defined as $\delta = \sqrt{2\nu/\sigma}$ which is the characteristic length scale of boundary layer, ν is kinematic viscosity and σ is angular frequency of wave. From the experimental results inside boundary layer of waves propagating on a sloping bottom, it shows apparently that the flow fields change its direction periodically as wave passed from crest to trough. The on-shore and off-shore flow patterns become asymmetrical gradually, due to the effects of wave shoaling process, and the magnitudes of horizontal particle velocity increases as water depth decreases. Further, the overshooting induced by wave motion taking place near the bottom is also displayed from our experiments.

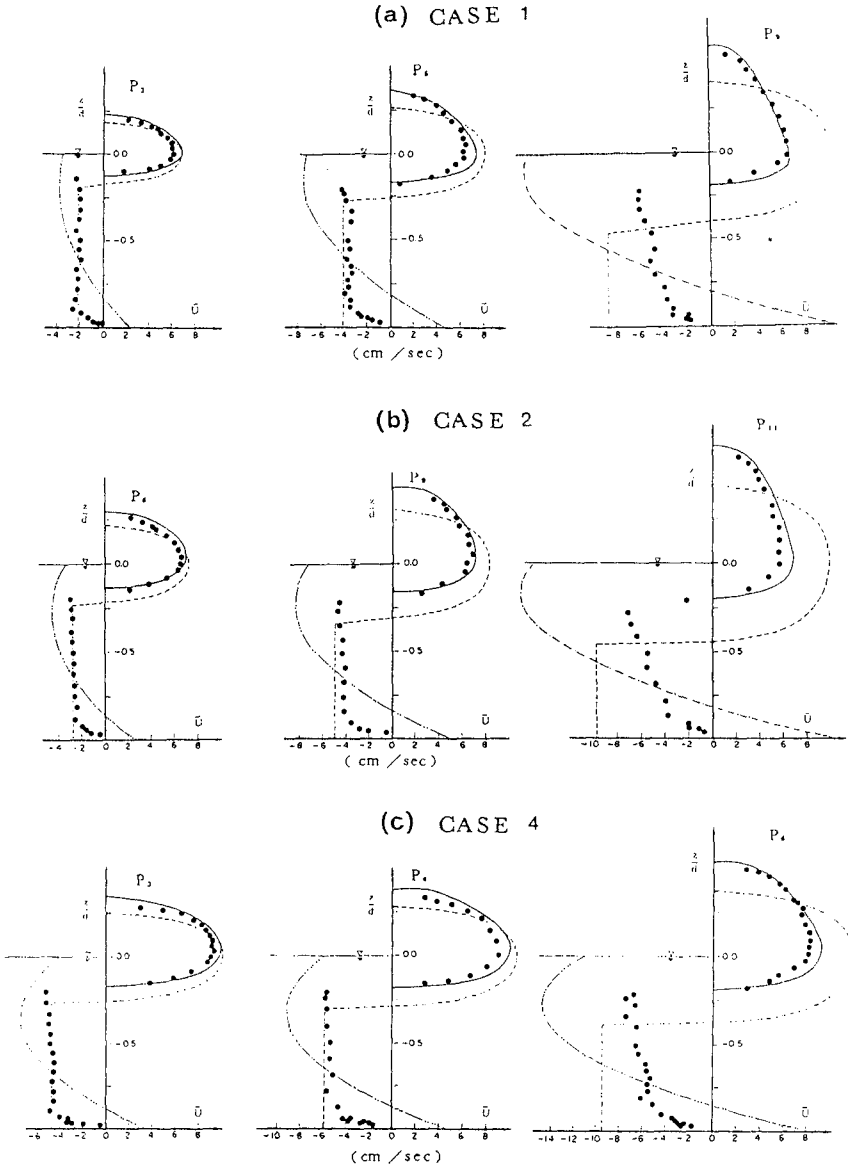


Fig.5 Comparison between experiments and theoretical calculations [● experiments, --- Longuet-Higgins(1953), — Dalrymple(1976), - - - Nadaoka(1982)].

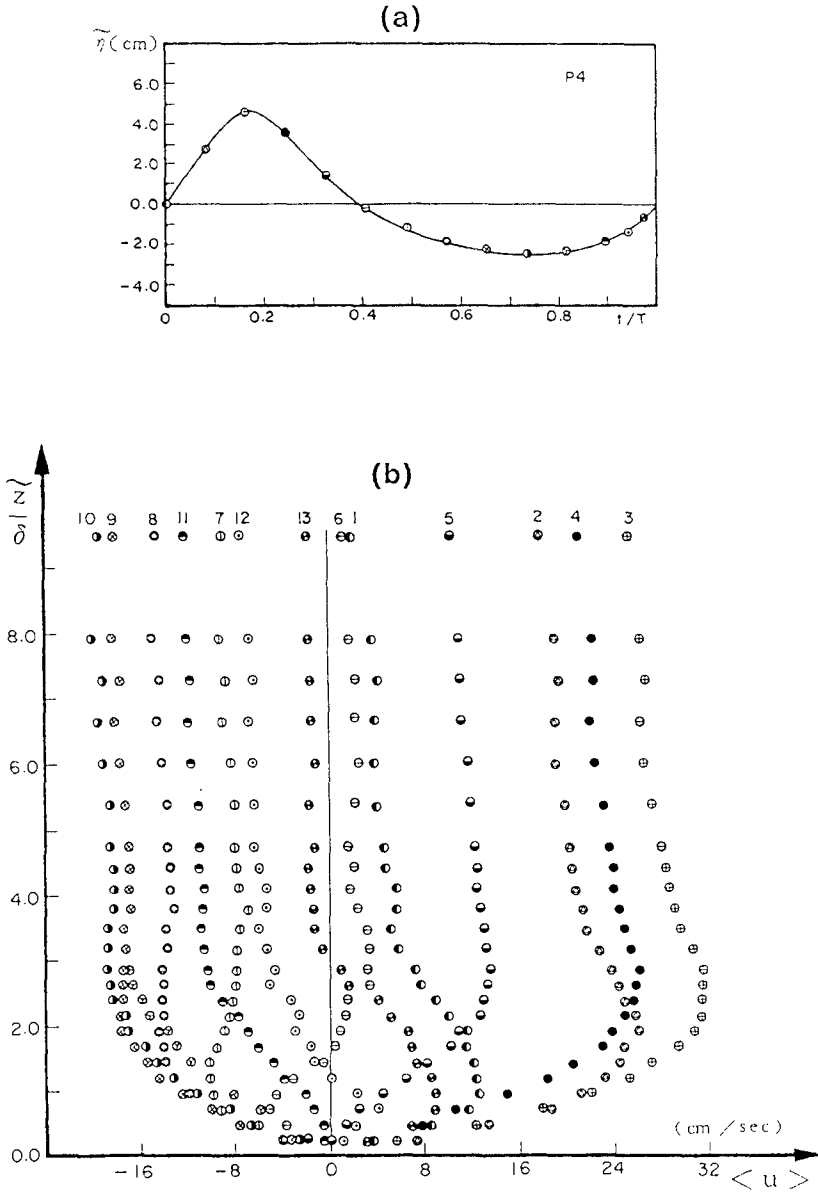


Fig.6 Water surface elevation and horizontal particle velocity inside boundary layer at $d=15.7\text{cm}$ for case 2.

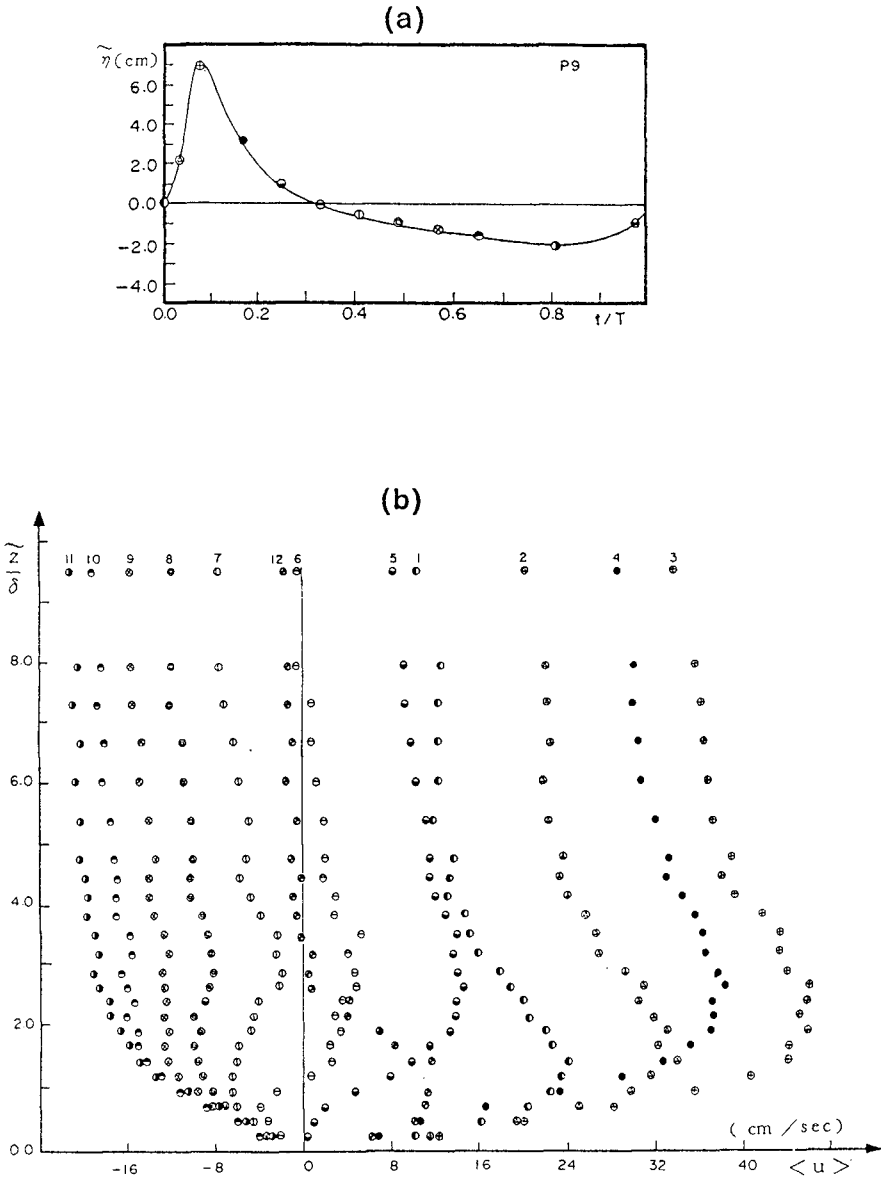


Fig.7 Water surface elevation and horizontal particle velocity inside boundary layer at $d=9.8\text{cm}$ for case 2.

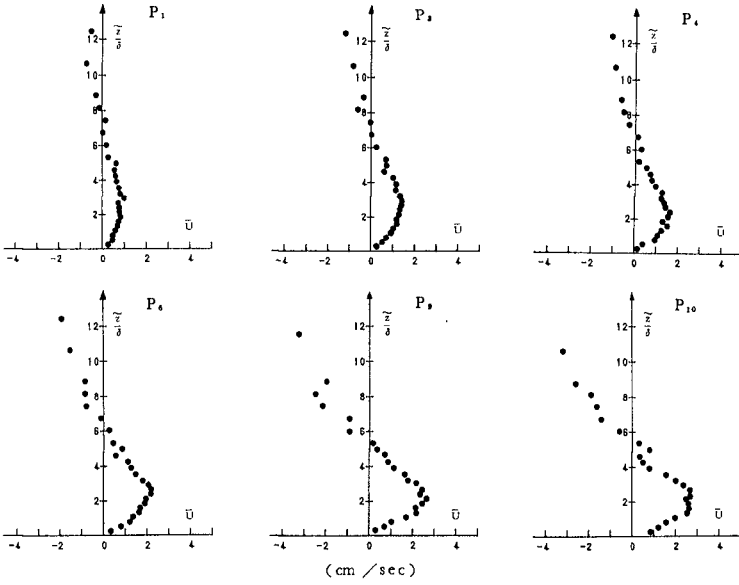


Fig.8 Vertical profiles of Eulerian mass transport inside boundary layer for case 1.

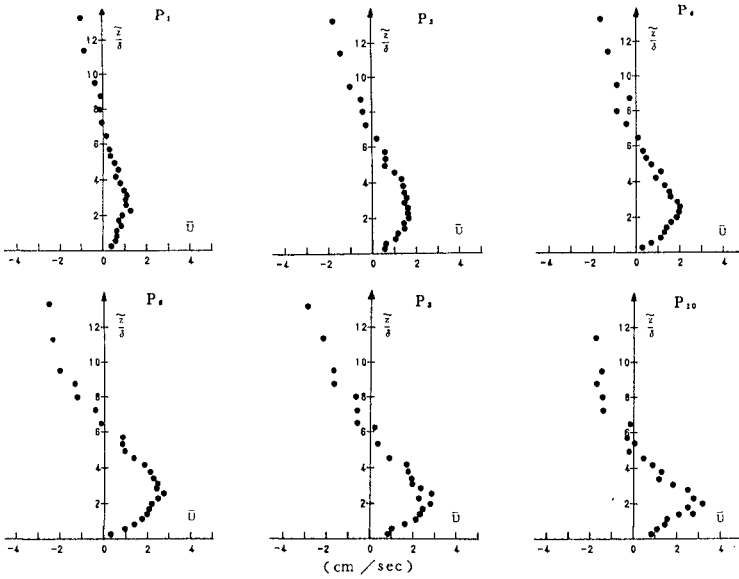


Fig.9 Vertical profiles of Eulerian mass transport inside boundary layer for case 2.

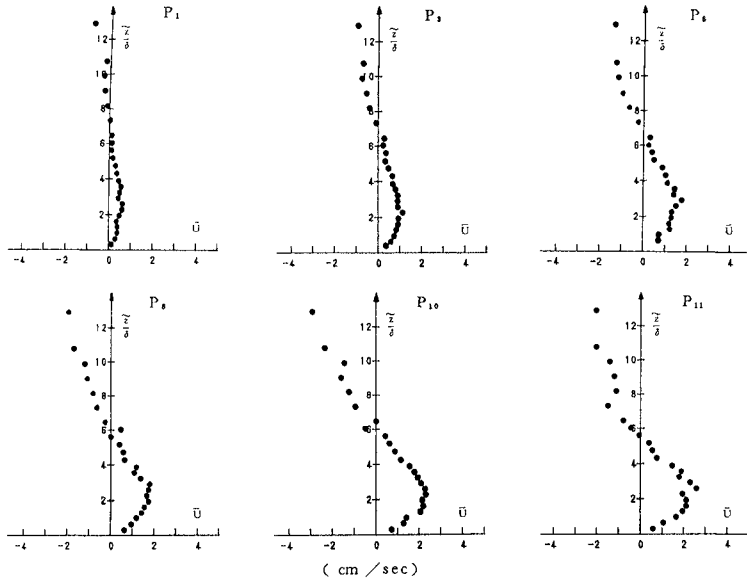


Fig.10 Vertical profiles of Eulerian mass transport inside boundary layer for case 3.

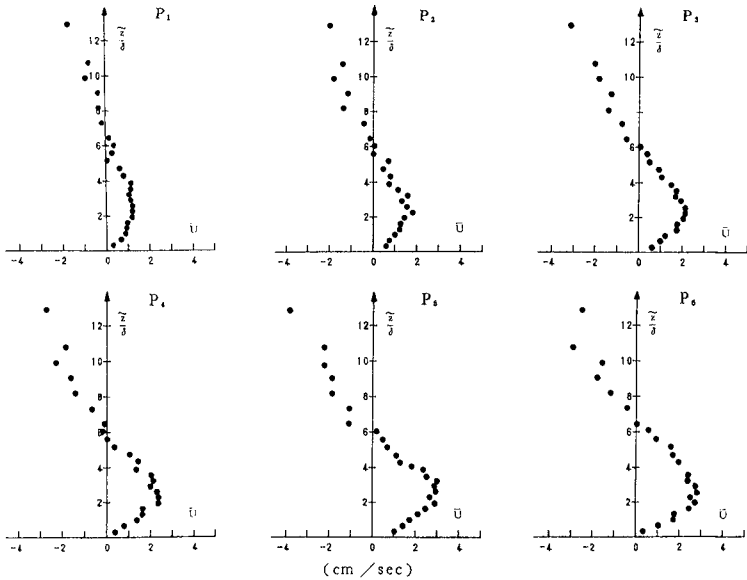
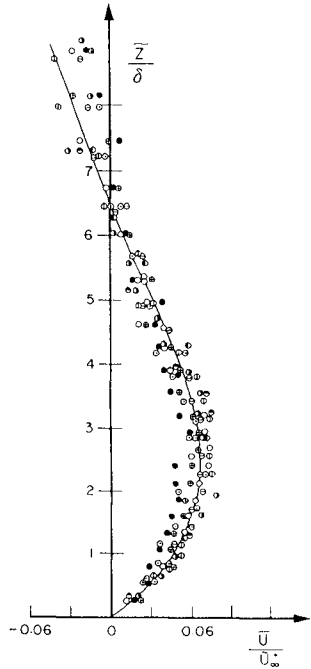


Fig.11 Vertical profiles of Eulerian mass transport inside boundary layer for case 4.

According to all of measuring results , the Eulerian mass transport velocity inside boundary layer are plotted from Fig.8 through Fig.11 , respctively. We can see that the vertical profiles of mass transport increase from bottom and reaches the maximun at the dimensionless distance $\bar{z}/\delta = 2\sim 3$, then decreases gradually to zero at $\bar{z}/\delta = 6.5$. Beyond the above region , Eulerian mass transport becomes negative (off- shore) as the dimensionless distance increasing. Moreover, the similarity profile of Eulerian mass transport velocity inside boundary layer has found from the definition of characteristic velocity proposed by Lin & Hwung(1989),and the result is shown in Fig.12 .Finally, the distribution of the above similarity profile is obtained from regressive analysis and it can be expressed by the combinations of hyperbolic functions as follows:



$$\frac{\bar{u}}{\bar{u}_\infty} = \begin{cases} 0.21 \tanh\left(0.3 \frac{\bar{z}}{\delta}\right) - 0.17 \tanh^2\left(0.3 \frac{\bar{z}}{\delta}\right) & \text{for } 0 \leq \frac{\bar{z}}{\delta} \leq 2.5 \\ -0.087 + 0.39 \operatorname{sech}\left(0.3 \frac{\bar{z}}{\delta}\right) - 0.25 \operatorname{sech}^2\left(0.3 \frac{\bar{z}}{\delta}\right) & \text{for } 2.5 \leq \frac{\bar{z}}{\delta} < 6.5 \end{cases}$$

Fig.12 The similarity profile of Eulerian mass transport inside boundary layer.

4. CONCLUSIONS

The characteristics of Eulerian mass transport of waves propagating on a sloping bottom are described in the paper . From the bottom , the magnitude of on-shore mass transport increases gradually and reaches the maximun at the point of $\bar{z}/\delta = 2\sim 3$, then it decreases to zero at $\bar{z}/\delta = 6.5$.Beyond the

above region, the mass transport becomes off-shore up to the elevation of wave trough, then the mass transport velocity changes its direction to on-shore rapidly, and it reaches the maximum value at still water level. After that the mass transport decreases to zero at crest. From the experiments, the similarity profile of mass transport inside boundary layer is also found in this paper.

5. REFERENCES

1. Dalrymple, R.A. (1976) : Wave-induced mass transport in water waves. *J. of Waterways, Harbors and Coastal Eng. ASCE.* pp.225~264.
2. Hwung, H. H., Lin, C. (1989) : The characteristics of internal flow field and bottom boundary layer of waves propagating on sloping bottom. Dissertation No.16, Tainan Hydraulics Lab. National Cheng Kung University.
3. Isobe, M., Horikawa, K. (1981) : The study on flow field of shoaling waves near surf zone. *Proceeding of 28th Coastal Engineering in Japan.* pp.5~9.(Japanese)
4. Lin, C., Hwung, H. H.(1989) : The experimental study on the boundary layer flow of waves propagating on a sloping bottom. *The Chinese Journal of Mechanics.* Vol.4, No.2, pp. 67~76.(Chinese)
5. Longuet-Higgins, M. S. (1953) : Mass transport in water waves, *Phil, Trans, Royal Society of London, Series A, No.903, Vol.245,* pp.535~581.
6. Nadaoka, K., Kondoh, T. and Tanaka, N (1982): The structure of velocity field within the surf zone revealed by means of laser-Doppler anemometry. *Rept. Port and Harbour Res. Inst. Vol.21,* pp.49~106.
7. Sleath, J. F. A. (1984) : Measurements of mass transport over a rough bed. *Proc. 19th Conf. Coastal Eng.,* pp.1149~1160.
8. Watanabe et al.(1980) : Velocity measurement near breaking point on a sloping bottom. *27th Engineering in Japan.* pp.40~44.(Japanese)

CHAPTER 43

TURBULENCE SCALES IN THE SURF AND SWASH

Reinhard E. Flick

California Department of Boating and Waterways

and

Ronald A. George

Center for Coastal Studies-0209

Scripps Institution of Oceanography

La Jolla, California, USA 92093-0209

Abstract

Ocean surface gravity waves breaking on gently sloping beaches generate substantial turbulent velocity fluctuations, both from overturning at the surface bore and from shear stresses at the bottom. We have used measurements made with laboratory-style hotfilm anemometers in the surf and swash on a *natural beach* to determine the relevant length and velocity scales. Battjes (1975) has pointed out the importance of determining the turbulence scales in the surf zone. Modelers, such as Svendsen and Madsen (1984), for example, rely on length and velocity scale estimates to parameterize and solve the complicated equations that govern surf zone flows. We find that turbulence length scales depend essentially on the bore height, and therefore on the local depth, but may decrease sharply under the bore. We also determine that at least the horizontal velocities approach isotropy at frequencies of 2 to 3 Hz, which turn out to also correspond to length scales on the order of the local depth.

Introduction

The determination of "scales" plays an important role in turbulence research, since turbulent flows must be described by their characteristic times, lengths, velocities, kinetic energies, Reynolds stresses, eddy viscosities and dissipation rates. Much of the theory of turbulence is concerned with establishing connections and relationships between these parameters and much experimental effort has gone into guiding these concerns. The basic reason why this approach is necessary, is that turbulent flows typically contain velocity fluctuations at a broad range of length scales, particularly small ones, so that direct analytical or numerical solution of the governing equations is unmanageable. The parameterizations that arise more or less

naturally from the flow conditions then become the description of that flow. The two key scales are turbulence length and velocity, and we concentrate on characterizing these from measurements.

In a shear flow, any sharp vertical gradients in horizontal velocity, $U(z)$, makes the flow unstable and causes turbulent velocities (u, v, w) to grow in all three directions. The turbulence serves to smooth the mean velocity profile by exchanging momenta, and \overline{uv} , \overline{uw} and \overline{vw} , which are respectively proportional to the Reynolds stresses, τ_{xy} , τ_{xz} and τ_{yz} determine how efficient this is. The Reynolds stresses cannot be calculated in closed form using the original equations of motion (this is the closure problem of turbulence) and they are difficult to measure, even in laboratory flows.

Some of the earliest efforts to understand turbulence were aimed at parameterizing the Reynolds stresses in terms of mean flow quantities (Boussinesq, 1877; Prandtl, 1925; von Karman, 1930), so that:

$$\frac{\tau_{xz}}{\rho} = -\overline{uw} = \nu_t \frac{dU}{dz}, \quad (1)$$

where ν_t represents the turbulent eddy-viscosity, ρ is the fluid density, and dU/dz is the mean shear. This formulation introduced the parameter ν_t which is analogous to the kinematic viscosity and has the dimensions L^2/T , or λq , where λ and $q = \sqrt{k}$ represent respectively turbulence length and velocity scales, and k is the turbulent kinetic energy scale. The turbulent kinetic energy dissipation rate turns out to be $\epsilon = q^3/\lambda$ (Tennekes and Lumley, 1972). Svendsen and Madsen (1984) use (1) and the form $\nu_t = k^2/\epsilon$, as the basis for a model of flow in a surf zone bore.

In considering the role of horizontal turbulent eddies in smoothing the profile of longshore currents in the surf zone, Battjes (1975) arrived at a relationship very similar to (1). He argued that the mean shear (cross-shore gradient in longshore current, in this case) must give rise to anisotropy that is measured by $-\overline{uv}/q^2$ and decays at a rate λ/q , balanced only by the mean shear rate itself, or

$$-\overline{uv} \approx q\lambda \frac{\partial V}{\partial x}. \quad (2)$$

Many different formulations of ν_t are possible, involving different combinations of λ , q , k and ϵ , and each implies a different solution procedure which determines exactly how the closure is made. A spectral method (due to Kolmogorov) can also be used to make estimates of ϵ based on assumptions of local isotropy in an equilibrium range of length scales (see, for example Grant, et al, 1961) but we do not pursue this in the present paper. In principle, such determinations could serve as consistency checks on estimates made in other ways.

We describe our instrumentation and calibration and deployment procedures in the next section. This is followed by a discussion of several experiments we have conducted in the surf zone over the last few years, and the results that are relevant to the determination of turbulence scales.

Instrumentation and Calibration

Experiments have been performed over a number of years at the moderate-energy, gently sloping beach adjacent to Scripps Institution of Oceanography at La Jolla, California. Wave conditions on this beach are highly variable, but we are confined to carrying out measurements when breaking wave heights are under about 2 m. Instruments are generally mounted on pipe supports cantilevered from other pipes which are jettied into the sand and braced to avoid vibration, as illustrated in Figure 1. We deploy instrumentation in the surf zone during times of low tide and then take data when the tide has brought the waves to the sensors. Tide changes of 1 to 2 m are common during spring tide times of the month, particularly in winter and summer, when local tide ranges are highest. This approach also serves to allow measurements at different mean water depths, or relative position in the surf zone, without the need to move the instruments.



Figure 1. Instrument mounting frame hardware showing typical set-up for measurements in the inner surf zone.

We have deployed current meters, pressure sensors, wave staffs, thermistors and two styles of hotfilm sensors. The current meters were standard, 2-axis, spherical, electromagnetic instruments 4 cm in diameter manufactured by Marsh-McBirney, Inc. The calibration of these meters is linear and relatively stable, the only disadvantages being that the frequency response is limited to about 3 Hz, and there is a severe response distortion when the probes are within a few diameters of the free surface (Guza, et al, 1988).

We have made bottom pressure measurements using standard, strain-gauge type sensors with a resolution of several parts per thousand in equivalent water

elevation. The pressure signal is a relatively smooth version of the actual sea surface profile, since the high frequency portions of the velocity potential decay with depth. Pressure signals have been mainly used to have a continuous depth record and a qualitative indication of the wave elevation and phase available for comparison with the higher frequency, turbulence signals. Surface piercing, resistance wire wave staffs have been used extensively in the laboratory, and when carefully prepared and cleaned, can achieve resolutions of better than 1 part per thousand (Flick, et al, 1981). We have found resistance wire wavestaffs to be generally unsatisfactory for routine, unattended data acquisition in the surf zone since debris floating on and in the water, particularly kelp, often stretches or even breaks the wires.

We have used thermistor probes to continuously record water temperature for use in calibrating the hotfilm anemometers. Our probes were "Fastip" model FP-07 microbead thermistors, manufactured by Thermometrics, Inc. The calibrations were done in a water bath and are linear and reproducible to about $\pm 0.1^\circ \text{C}$, absolute. Relative temperature changes are accurate to about $\pm 0.02^\circ \text{C}$, with a half-power frequency response cutoff of about 22 Hz.

Hotfilm Probes

We have successfully adapted laboratory-style hotfilm probes for use in the natural surf zone. We have used Thermo Systems, Inc. (TSI) model 1230-NaCl, quartz-coated platinum, cone shaped sensors, as well as the less rugged model 1210-NaCl cylinder-shaped probes. Despite many difficulties, particularly with breakage and calibration drift reminiscent of the critical and pessimistic review of Frey and McNally (1973), we believe that hotfilm technology is the only one currently capable of providing high-frequency, small scale measurements of velocity fluctuations in the surf. The presence of bubbles and debris in the surf zone greatly inhibits the use of either laser-doppler or acoustic measurement systems, assuming these could be made small enough to avoid serious flow interference, as with fiber optic techniques.

One of the serious drawbacks of single hotfilm sensors is that they do not discriminate direction. In fact, their response is closer to omnidirectional than it is to a much more convenient cosine of the angle of attack. The rectification of the velocity signal is an advantage, however, in one sense, since it selects out the longitudinal component of the turbulence fluctuations u , in the presence of a strong, although oscillating "mean" flow, U . We have had some success in de-rectifying calibrated hotfilm time series in selected instances, by either using current meter records or high shutter-speed video camera images to identify the time of flow reversal. The cone probes were generally deployed pointing offshore, into the oncoming wave flow. The cylinder probes were oriented with their axes aligned in the longshore direction, thus minimizing interference from longshore directed currents.

Hotfilm anemometry rests on the principal that the heat conducted away from the probe by the moving fluid is proportional to some function of the flow speed, S past the probe and the difference in temperature (overheat) of the sensor, T_p and the water, T_w (King, 1914). The sensor is kept at a constant temperature (in our case) by

a bridge feedback circuit (TSI model 1755) that provides an overall frequency response of several hundred Hz. The output (bridge voltage) E is related to the flow speed by King's law

$$E^2 = (A + B S^n) (T_p - T_a), \quad (3)$$

where A , B and n are calibration constants.

Probe calibrations do not stay stable sufficiently long to simply calibrate the sensors in the laboratory and then shift them to the surf. We have consequently constructed a scheme where we calibrate the hotfilm sensors continuously by comparison with a co-located current meter. Results have been very satisfactory for deployment off the end of Scripps Pier, in 5 m water depth well outside the surf zone. With minor adjustments to this method, we have achieved calibration accuracies of about ± 5 cm/sec in peak flows of up to 200 cm/sec, even in the surf zone.

Operating temperatures of the hotfilm probes were generally set to about 25° C above ambient water temperature, which at La Jolla varies from about 14 to 21° C. This resulted in a relatively low overheat ratio of between 5 and 8% to prevent the formation of bubbles on the probes. The equivalent velocity sensitivity, ΔS , of the probes to fluctuations in ambient water temperature can be determined from relation (3) to be

$$\frac{\Delta S}{S} = - \frac{\delta}{\Delta T} \frac{1}{n} \left(1 + \frac{A}{B S^n} \right),$$

where $\delta/\Delta T$ is the fractional change in temperature relative to the overheat, and is assumed small. Assuming E is measured in volts, S in cm/sec and the temperatures are in ° C, typical values for the calibration coefficients are $A = 0.2$, $B = 0.1$ and $n = 0.5$. For an overheat of $\Delta T = 30^\circ$ C and water temperature fluctuations of $\delta = 0.1^\circ$ C, the fractional speed error, $\Delta S/S$ is less than about 2%, so long as flow speeds are larger than about 10 cm/sec.

Surf Zone Turbulence Scales

Figure 2 shows time series data from two hotfilm cone probes and a (rare) wavestaff signal measured in the surf zone at a depth of about 35 cm, with a bore about 25 cm passing the sensors. These data were taken on 21 April 1988, at a sampling rate of 2560 Hz. No current meter data are available, so we were forced to rely on laboratory calibrations of the hotfilm probes, which we believe to be accurate to $\pm 25\%$. The hotfilm data are labelled "upper" and "lower" and represent, respectively, the probe at elevation 38 cm off the bottom and the probe at 20 cm off the bottom. The lower probe was essentially submerged over the entire data run, while the upper probe was out of the water until arrival of the bore at time 12:58:19.

Four seconds of data from this run have been analyzed and Figure 3 shows the autocorrelation functions for the upper and lower probe signals. Note that these functions do not, to first order, depend on the probe calibrations. The temporal lag correlations, $\theta(\tau)$ have been adjusted to equivalent spacial lag correlations, $\theta(r)$, by

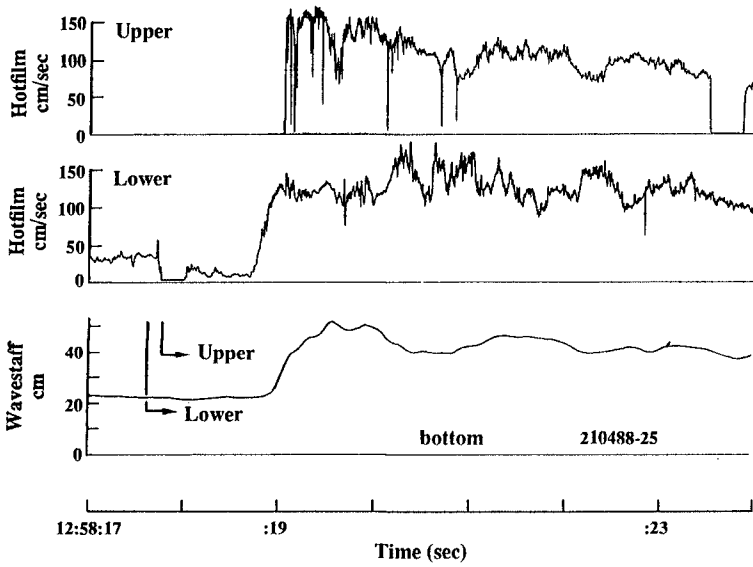


Figure 2. Time series from upper (38 cm) and lower (20 cm) hotfilm probes (upper two traces) and wavestaff signal (lowest trace).

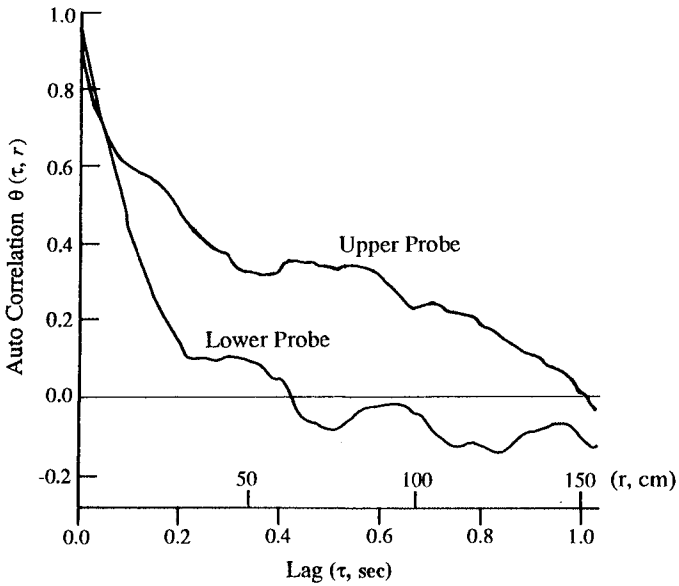


Figure 3. Autocorrelation function from upper and lower hotfilm data (Figure 2) Length scale derived from time scale with $U=150$ cm/sec.

choosing a mean advective speed, $U = 150$ cm/sec and invoking Taylor's hypotheses, $r = U\tau$. The upper and lower rms turbulence levels are about 30 and 20 cm/sec, respectively, so that $q_{rms} \ll U$ is satisfied. We can use the correlation function $\theta(r)$ to estimate the integral scale of the turbulence, defined as

$$\lambda_i = \int_0^{\infty} \theta(r) dr.$$

Results show a decrease in both decorrelation scale and integral scale with depth in the water column. Decorrelation length at the upper probe is on the order of 150 cm, while the integral scale is about 50 cm. The respective lengths at the lower probe turn out to be about 60 and 25 cm, about half the upper values. This supports the intuitive idea that the turbulent eddy length scales are on the order of the bore height in the bore, and that they are therefore of the same order of magnitude as the local depth. It also suggests that length scales and turbulence levels are both smaller below trough level than in the actively overturning bore. With respect to the turbulence intensity, this conclusion is not new or surprising, but there may be some new information in the suggestion that turbulence length scales decrease from the surface downward.

Note that the actual values of these estimates *do* depend on the hotfilm calibrations (through U in Taylor's hypotheses). However, the *relative difference* in length scales would be exaggerated for any plausible calibration corrections, since the mean advective velocity at the upper probe could not be smaller than that at the lower probe. This would *increase* the length scale estimate at the upper level, relative to the lower one. The same argument holds for the turbulent velocity scale.

Corresponding estimates of dissipation rates, $\epsilon = q^3/\lambda$ range from about 100 to 300 cm^2/sec^3 at the lower sensor, and from about 200 to 400 cm^2/sec^3 at the upper sensor, depending on the choice of length scale. It is noteworthy that any of these values far exceed corresponding estimates of dissipation rates in tidal channels, which range from 10^{-3} to 1 cm^2/sec^3 (Grant, et al, 1961). By comparison, it has been estimated that the dissipation rate of oceanic tide motions is on the order of 10^{-5} cm^2/sec^3 (Grant, et al, 1961).

Figure 4 shows the first 32 sec of a 256 sec time series of hotfilm data (dark line) and the cross-shore component of a current meter signal (dashed line). These data were taken on 14 March 1990, at a sampling rate of 4096 Hz. The current meter was mounted 64 cm above the bottom, and total water depth during the data run varied between 75 and 100 cm, with breaking wave heights of about 1.2 m. The current meter record has been offset downward by 20 cm/sec for clarity. The hotfilm measurement has been calibrated and de-rectified using the current meter data as a standard. The agreement is quite good.

Figure 5 shows the ratio of longshore to cross-shore velocity measured by the current meter as a function of frequency. The velocity ratios were calculated from spectral levels of each component. It is clear that V/U increases from values around 0.2 at frequencies corresponding to the incoming wave period of about 10 sec, to

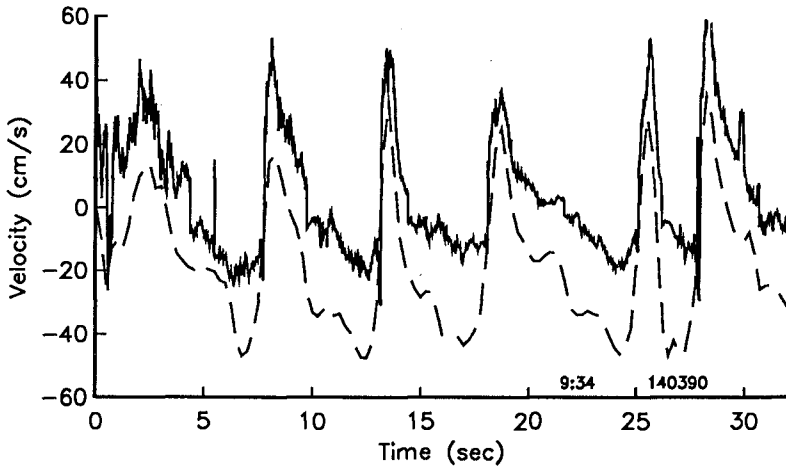


Figure 4. Time series from hotfilm probe (solid trace) and current meter (dashed) in mid surf zone, showing good de-rectification and calibration agreement. Current meter trace is offset -20 cm/sec for clarity.

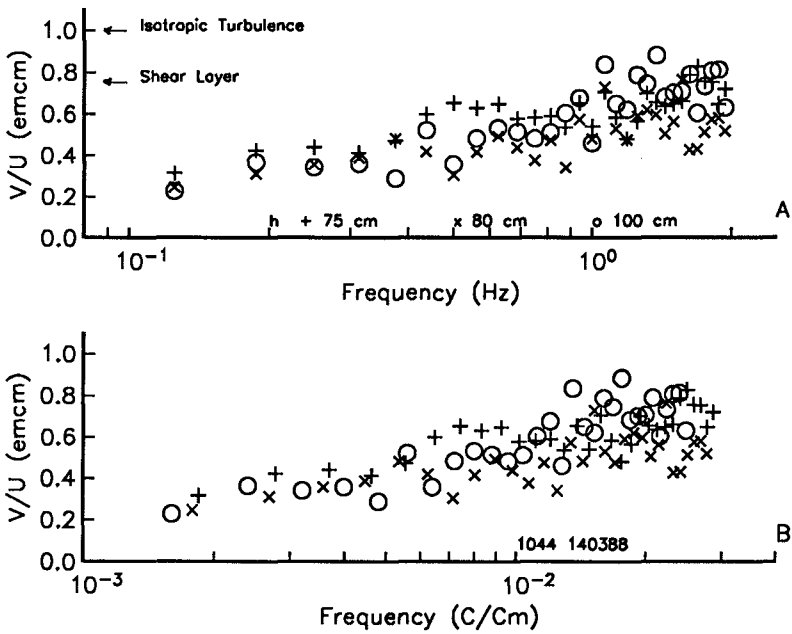


Figure 5. Ratio V/U from current meter data in mid surf zone as a function of frequency and depth, showing approach to isotropy at about 2 or 3 Hz.

values approaching 1 at the current meter cut-off frequency around 2 or 3 Hz. The indicated levels, 0.76, labelled "Shear Layer," and 1.0, labelled "Isotropic Turbulence" correspond to the expected value of V/U for these flows.

Even though fluctuations were only measured in two directions, these data strongly suggest that passing bores generate local turbulent velocities in all three directions. This result should not be surprising, and supports the idea that turbulence under surf zone bores may resemble shear layer turbulence in the transition regime between frequencies associated with wave orbital motions and about 2 or 3 Hz. We would expect the turbulent fluctuations to become increasingly isotropic at higher frequencies, but cannot confirm this with the present measurements. The scatter in the ratio estimates is too large to distinguish a dependence on total depth, which only changes about 20% in the experiment.

Rigorous estimates of the length scales associated with these time scale estimates cannot be made by a straightforward application of Taylor's hypothesis, since the mean flow is unsteady (Figure 4). However, a rough estimate is possible by noting that the peak advective velocities are on the order of $0.25c$, where $c = \sqrt{gh}$ is the shallow water phase velocity, and $g = 980 \text{ cm/sec}^2$, is the acceleration of gravity. Invoking Taylor's hypotheses with $h = 80 \text{ cm}$, results in an upper bound estimate of the length associated with the maximum frequency (2 or 3 Hz) shown in Figure 5, which turns out to be about 35 cm. This reveals that the length scales of the eddies at the lowest frequencies that are "fully" turbulent, here assumed to be those approaching isotropy levels consistent with values expected in a shear layer, are on the order of the waveheight. The wave (or bore) height, H in the surf zone is approximately proportional to the local depth, $H = \gamma h$, where $\gamma \approx 0.7$ is an empirical constant. Therefore, we expect that the turbulent length scale is likewise proportional to the local depth.

Considering all the assumptions, not to mention the limited data, this is remarkably consistent with the above derived result from the auto correlation analysis of the "lower" hotfilm probe. There is again nothing particularly surprising about this, indeed, it would be surprising if it were otherwise. The results are noteworthy, however, since these seem to be the first published field measurements that tend to confirm our intuitive expectations. Furthermore, these suggestions also support the idea stated explicitly by Battjes (1975), that turbulent eddies in the surf zone scale according to the depth, or vertical dimension, and *not* a horizontal dimension, such as distance to the shore, or length between bore crests. The horizontal scales are larger than the depth by a factor on the order of β^{-1} , where β is the beach slope. On a gently sloping shore such as La Jolla, this factor typically ranges from 50 to 100.

It is interesting to consider the expected ratio of longshore to cross-shore orbital velocity in a plane wave that has been subject to refraction into water depths equivalent to those in our experiments. Assuming that Snell's law is valid for waves with period 10 sec, in a water depth of only 1 m, it can be shown that a deep water approach angle of 10° is reduced by linear refraction to a shallow water angle of only 2° . This results in $V/U \approx 0.03$, a ratio much smaller than observed.

Swash Turbulence Scales

Measurements were made in the swash region using a cylinder type hotfilm probe on 8 March 1990. The swash region is defined as that part of the beach which is alternately dry and then covered by water as a result of the wave runup. Due to the prevalence of significant low frequency surf beat, and a mild beach slope of about 1:75, the swash region can be tens of meters wide and each bore may or may not reach the sensor location (Guza and Thornton, 1982; 1985). Equivalently, each individual backwash event may or may not drain the beach at the sensor location. The probe was mounted 1 cm off the bed. Figures 6a and 6b show time series from the hotfilm that have been de-rectified using video tape images. We used the 1/4000 sec shutter speed available on our video camera to ensure clear images at the (fixed) 30 frame/sec sampling rate. We were thus able to resolve the flow reversals to approximately 1/30 sec.

Figure 6a shows 64 sec of data which include 4 prominent up-rush and backwash cycles, but the probe does not get dry until the very last cycle, shortly after $t = 64$ sec. The maximum water depth, h_0 , during each bore was about 30 cm. Unfortunately, we had no direct measure of the depth except what could be estimated from the (oblique) video images. Each swash cycle is characterized by a sharp reversal from offshore (negative) to onshore (positive) flow, followed by a gradual, nearly linear slowing and finally a turning to offshore flow as the wedge of water drains off the beach face. This sequence forms the characteristic sawtooth shape of the velocity time series.

There is turbulent motion with amplitude scales on the order of 5 cm/sec apparent in each of the deceleration phases, but the most prominent occurs starting at about $t = 50$ sec (Figure 6a). Apparently due to the build-up of water on the beach face over a number of preceding uprushes, enough offshore momentum was built up to change the character of this particular backwash. It lasted longer than was typical, and as shown in Figure 6a, reached a larger offshore velocity than normal. Viewing of several hours of video tape shows that this type of event occurs at surf beat intervals, which means in perhaps 5 to 10% of the bores.

This portion of record is plotted in Figure 6b on an expanded scale. Inspection of the video tape corresponding to this time reveals that the strong turbulence was accompanied by a thick cloud of suspended sediment in the layer of water which was approximately 15 cm deep at $t = 50$ sec. The sediment essentially erupted from the bottom at about this time, and remained in suspension at the sensor location until it ran dry. The water surface also noticeably changed character at about $t \approx 52$ sec, from a smooth layer to an extremely rough one. This transition is readily apparent on the video images since reflections of the straight mounting pipes, which are very clear at one instant, suddenly become jagged and then disappear. We interpret this transition in roughness as the surface manifestation of the bottom boundary layer turbulence reaching the water surface.

A low-pass trend shown as a dashed line in Figure 6b was subtracted from the signal to leave an estimate of the turbulence residual. This residual was examined using a scheme that measured the time interval between zero-crossings and averaged

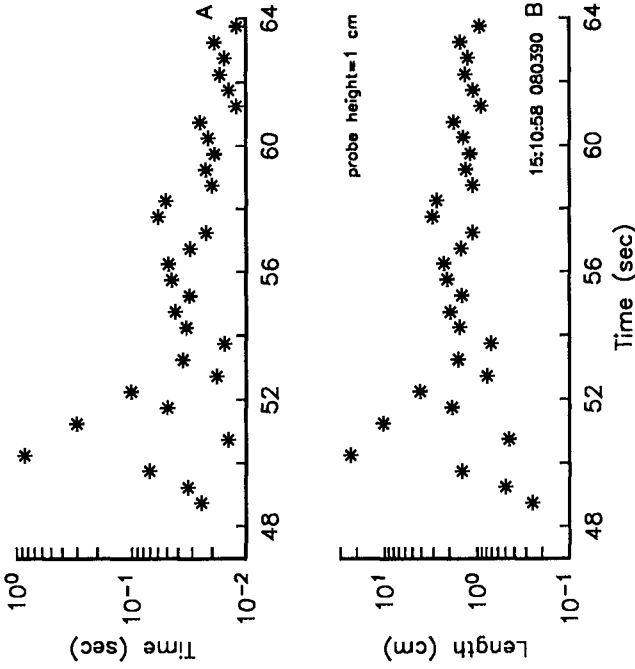


Figure 7. Turbulent time scale (A, upper panel) and length scale (B, lower panel) calculated from zero down-crossings of time series shown in Figure 6b, after removal of low-pass mean. Mean velocity also used to adjust time scale to length scale using Taylor's hypotheses.

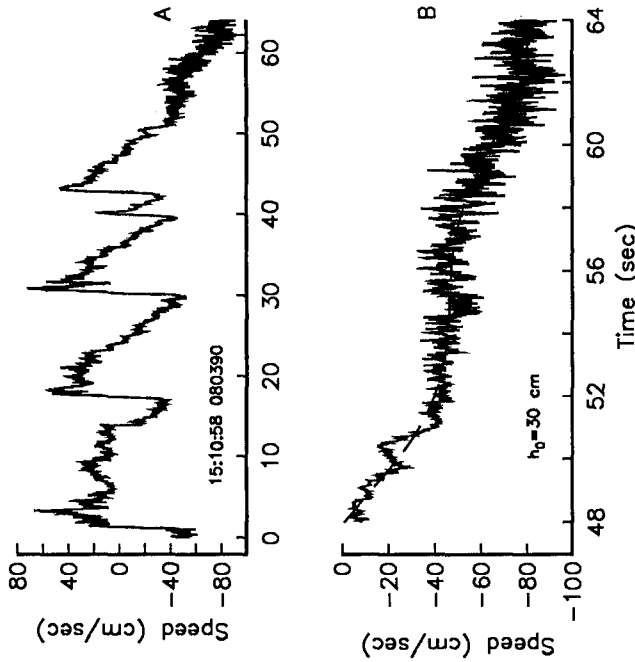


Figure 6. Time series of swash cross-shore velocity measured with hotfilm anemometer. Upper panel (A) shows entire 64 sec record, lower panel (B) shows time 48 to 64 sec. Dashed line is low-passed, mean velocity.

the results over 0.5 sec periods. The method was insensitive to the precise shape chosen for the trend filter. The results are shown in Figure 7a, and suggest that the average zero-crossing time decreases as the flow continues its offshore acceleration.

Application of Taylor's hypothesis to this data, using the low-pass velocity signal mentioned above, yields the results shown in Figure 7b. Here it is revealed that the mean eddy scale is just slightly over 1 cm after $t \approx 52$ sec and remains constant until the end of the record. This result is consistent with the expectation that the eddy scales of flow near a boundary must be on the order of the distance from the boundary. Turbulent eddies cannot transfer momentum in the direction perpendicular to a wall at scales larger than the distance from the wall (Tennekes and Lumley, 1972). This is one characteristic, actually an assumption, that leads to the so-called law-of-the-wall.

Conclusions

Our primary conclusion is that the length scale of turbulence in the surf zone is on the order of the local wave (or bore) height, or equivalently, on the order of the local depth. We also find that turbulent velocity scales are indeed a modest fraction of the local shallow water wave phase speed, $c = \sqrt{gh}$, consistent with laboratory results, but we do not have measurements over a sufficient range of depth to establish the functional dependence, or to quantify the proportionality.

Turbulence length and velocity scales seem to decrease with distance from the surface under a bore. This suggests that the turbulent eddy viscosity, $\nu_t = \lambda q$, and the dissipation rate $\epsilon = q^3/\lambda$, may be strong functions of vertical position in the water column, as well as functions of depth. These findings may have some bearing on detailed models of both longshore currents and undertow (shore normal currents), since the turbulence quantities enter into the current structure through relations like (1) and (2).

At least the horizontal components of velocity in the surf zone approach isotropy at frequencies on the order of 2 or 3 Hz. This is found to be a gross violation of Snell's law, which predicts that ratios of V/U should be only a few percent. This is a clear manifestation of the generation of turbulence by wave breaking in the surf zone.

Limited data in the swash suggest that the length scales in the boundary layer flow near the bottom during backwash events are proportional to the distance from the bottom. Video tape images of swash flow suggest that fully developed backwash events, where the turbulent bottom boundary layer thickness reaches the full flow depth, occur at beat periods and *not* at individual wave periods.

Acknowledgements

The authors gratefully acknowledge the longterm support of the Office of Naval Research (grant N00014-89-J-1095 with the University of California, San Diego, Scripps Institution of Oceanography) and the continued support of the California Department of Boating and Waterways.

References

- Battjes, J.A., 1975, "Modeling of Turbulence in the Surf Zone", *Proc. Symp. Modeling Tech.*, Amer. Soc. Civil Eng., p. 1050-1061.
- Boussinesq, J., 1877, "Theorie de l'ecoulement tourbillant," *Mem. Pre. par. Div. Sav.*, v. 23, Paris.
- Flick, R.E., R.T. Guza and D.L. Inman, 1981, "Elevation and Velocity Measurements in Laboratory Shoaling Waves," *Jour. Geophys. Res.*, v. 86, n. C5, p. 4149-4160.
- Frey, H.R., and G.J. McNally, "Limitations of Conical Hot Platinum Measurements in Laboratory Shoaling Waves," *Jour. Geophys. Res.*, v. 78, n. 9, p. 1449-1461.
- Grant, H.L., R.W. Stewart and A. Moilliet, 1961, "Turbulence spectra from a tidal channel," *Jour. Fluid Mech.*, v. 12, p. 241-268.
- Guza, R.T., M.C. Clifton and F. Rezvani, 1988, "Field Intercomparisons of Electromagnetic Current Meters," *Jour. Geophys. Res.*, v. 93, n. C8, p. 9302-9314.
- Guza, R.T. and E.B. Thornton, 1982, "Swash Oscillations on a Natural Beach," *Jour. Geophys. Res.*, v. 87, n. C1, p. 483-491.
- Guza, R.T. and E.B. Thornton, 1985, "Observations of Surf Beat," *Jour. Geophys. Res.*, v. 90, n. C2, p. 3161-3172.
- King, L.V., 1914, On the Convection of Heat from Small Cylinders in a Stream of Fluid: Determination of the Convection Constants of Small Platinum Wires with Applications to Hot-Wire Anemometry," *Phil. Trans. Roy. Soc. A.*, v. 214, p. 373-433.
- Prandtl, L., 1925, "Bericht ueber Untersuchungen zur ausgebildeten Turbulenz," *ZAMM*, v. 5, p. 136.
- Svendsen, I.A. and P.A. Madsen, 1984, "A turbulent bore on a beach," *fIJour. Fluid Mech.*, v. 148, p. 73-96.
- Tennekes, H. and J.L. Lumley, 1972, *A First Course in Turbulence*, The MIT Press, Cambridge, Mass., 300 pp.
- von Karmann, T.H., 1930, "Mechanische Aehnlichkeit und Turbulenz," *Proc. 3rd Int. Cong. Applied Mech.*, Stockholm, pt. 1, p. 85.

CHAPTER 44

REFLECTION FROM SWASH ZONE ON NATURAL BEACHES

Susumu Kubota¹, Masaru Mizuguchi² and Mitsuo Takezawa³

ABSTRACT

For separating incident and reflected waves, three methods based on linear long-wave theory, small-amplitude wave theory, and quasi-nonlinear long-wave theory were applied to field data recorded on a steeply sloping beach and on a gently sloping beach. The method based on the quasi-nonlinear long-wave theory gave the best results and described well the observed, incident, and reflected wave field.

I INTRODUCTION

The understanding of wave dynamics in the swash zone on natural beaches is important for determining beach erosion, designing coastal structures, and estimating beach deformation after the construction of such structures. However, the properties of the waves are not yet well understood because measurement of waves on natural beaches is difficult to perform. The authors measured the swash oscillation and waves and wave particle velocities in the surf zone by using 16 mm memo-motion cameras, capacitance-type wave gages, and electromagnetic current meters. A part of the results was presented at the 21st Coastal Engineering Conference (Takezawa et al., 1988), where separation of the incident and reflected waves was carried out with good results using the linear long-wave theory. However, application of the linear long-wave theory to field data collected later at a gentle beach gave poor results. Therefore, the small-amplitude wave and the quasi-nonlinear long wave theories were employed for the wave separation. The small-amplitude wave theory

1 Research Associate, Dept. of Civil Eng., College of Science and Technology, Nihon University, Kanda-Surugadai 1-8-14, Chiyoda-ku, Tokyo 101 Japan.

2 Dr. Eng., Professor, Dept. of Eng., Faculty of Science and Technology, Chuo University, Kasuga 1-13-27, Bunkyo-ku, Tokyo 112 Japan

3 Dr. Eng., Professor, Dept. of Civil Eng., College of Science and Technology, Nihon University

did not improve the previously obtained results. However, using the quasi-nonlinear long-wave theory produced better results. The present paper describes the analytical procedures and the results from analysis of the field observations.

11 THEORETICAL BACKGROUND FOR SEPARATING INCIDENT AND REFLECTED WAVES

2.1 Method Based on Linear Long-wave Theory

The separation method which employs linear long-wave theory was given by Guza, Thornton and Holman (1984),

$$\eta_I = \frac{1}{2} \left\{ \eta + \alpha \left[\frac{h}{g} \right]^{1/2} u \right\} \text{----- (1)}$$

$$\eta_R = \frac{1}{2} \left\{ \eta - \alpha \left[\frac{h}{g} \right]^{1/2} u \right\} \text{----- (2)}$$

where η , η_I and η_R are the water surface elevation of the observed, incident and reflected waves, u is the on-offshore component of water particle velocity, g is the acceleration due to gravity, h is the water depth, and α is a constant. The constant α theoretically takes the value of unity.

2.2 Method Based on Small-amplitude Wave Theory

If it is assumed that the observed wave is a result of linear superposition of the incident and reflected waves, then,

$$\eta = \eta_I + \eta_R \text{----- (3)}$$

$$u = u_I - u_R \text{----- (4)}$$

where u_I and u_R are the on-offshore component of water particle velocity of the incident and reflected waves respectively. It is also assumed that the incident wave is a sum of sinusoidal waves with different frequencies. Then, the following expressions are obtained,

$$\eta_I = \sum_{i=1}^{\infty} A_i \cos(\sigma_i t + \epsilon_i) \text{----- (5)}$$

$$\left. \begin{aligned} u_I &= \sum_{i=1}^{\infty} H_i A_i \cos(\sigma_i t + \epsilon_i) \\ H_i &= \frac{\sigma_i \cosh k_i (h+z)}{\sinh k_i h} \\ \sigma_i^2 &= g k_i \tanh k_i h \end{aligned} \right\} \text{----- (6)}$$

where t is the time, z is the vertical distance taking the origin of the coordinate system at the still sea water level, $\sigma_i = 2\pi / T_i$, $k_i = 2\pi / L_i$, and A_i , ε_i , L_i , and T_i are the wave amplitude, the phase difference, wavelength and wave period of an elementary wave. Expression for u_R is similarly,

$$u_R = \sum_{i=1}^{\infty} H_i B_i \cos(\sigma_i t + \varepsilon_i') \text{ ----- (7)}$$

where B_i and ε_i' are the amplitude and the phase difference. A finite Fourier series is used for expressing u as,

$$u = \sum_{i=1}^N (C_i \cos \sigma_i t + D_i \sin \sigma_i t) \text{ ----- (8)}$$

where C_i and D_i are the Fourier coefficients. A sum of independent elementary waves is considered, therefore, or each elementary wave, the following relation can be stated:

$$\begin{aligned} C_i \cos \sigma_i t + D_i \sin \sigma_i t \\ = H_i A_i \cos(\sigma_i t + \varepsilon_i) - H_i B_i \sin(\sigma_i t + \varepsilon_i') \text{ ----- (9)} \end{aligned}$$

Dividing both sides of Eq. 9 by H_i and adding terms i from 1 to N , we have:

$$\begin{aligned} \sum_{i=1}^N \frac{1}{H_i} (C_i \cos \sigma_i t + D_i \sin \sigma_i t) \\ = \sum_{i=1}^N A_i \cos(\sigma_i t + \varepsilon_i) - \sum_{i=1}^N B_i \sin(\sigma_i t + \varepsilon_i') = \eta_I - \eta_R \text{ ----- (10)} \end{aligned}$$

From Eq. (10) and Eq. (3), the final equations for the wave separation is obtained as:

$$\eta_I = \frac{1}{2} \left\{ \eta + \sum_{i=1}^N \frac{1}{H_i} (C_i \cos \sigma_i t + D_i \sin \sigma_i t) \right\} \text{ ----- (11)}$$

$$\eta_R = \frac{1}{2} \left\{ \eta - \sum_{i=1}^N \frac{1}{H_i} (C_i \cos \sigma_i t + D_i \sin \sigma_i t) \right\} \text{ ----- (12)}$$

A problem is the proper choice of N . Measurement noise is usually inherent in the high-frequency region. The power of the noise becomes predominant if a large number is taken on N . Thus, a suitable value on N must be chosen.

2.3 Method Based on Quasi-nonlinear Long-wave Theory

Ignoring any interaction between the incident and reflected wave, it may be assume that Eqs. (3) and (4) are valid. The basic equations in nonlinear long-wave theory of constant depth becomes:

$$\frac{\partial \eta}{\partial t} + \frac{\partial}{\partial x} \{ (h + \eta) u \} = 0 \quad \text{-----} \quad (13)$$

$$\frac{\partial u}{\partial t} + u \frac{\partial u}{\partial x} + g \frac{\partial \eta}{\partial x} = 0 \quad \text{-----} \quad (14)$$

Expanding u in a series and considering up to second order, the following relation between u and η is assumed:

$$u = \left[\frac{g}{h} \right]^{1/2} \eta + \beta \eta^2 \quad \text{-----} \quad (15)$$

Substituting Eq. (15) into the equation of continuity, Eq. (13), β is determined:

$$\beta = -\frac{1}{h} \left[\frac{g}{h} \right]^{1/2} \quad \text{-----} \quad (16)$$

Equation (16) does not satisfy the equation of motion, Eq. (14). In order to satisfy Eq. (14), β should be:

$$\beta = -\frac{1}{2h} \left[\frac{g}{h} \right]^{1/2} \quad \text{-----} \quad (17)$$

Equation (14) itself is originally only approximately correct for the real waves, and the second order terms of Eq. (14) partially vanish. Therefore, it was assumed that Eqs. (13) and (14) would be better satisfied if Eq. (16) was used instead of Eq. (17). Substituting Eq. (16) into Eq. (15):

$$u = \left[\frac{g}{h} \right]^{1/2} \eta \left(1 - \frac{\eta}{h} \right) \quad \text{-----} \quad (18)$$

From Eqs. (3), (4) and (18), Eqs. (19) and (20) result in

$$\eta_I = \frac{1}{2} \left\{ \eta + \alpha u \left[\frac{h}{g} \right]^{1/2} \frac{h}{h - \eta} \right\} \quad \text{-----} \quad (19)$$

$$\eta_R = \frac{1}{2} \left\{ \eta - \alpha u \left[\frac{h}{g} \right]^{1/2} \frac{h}{h - \eta} \right\} \quad \text{-----} \quad (20)$$

III FIELD OBSERVATIONS

3.1 Field Observation Sites

Data analyzed here were measured at Oarai Beach on July 29 (Takezawa et al., 1988) and at Hasaki Beach on July 30, 1987. Oarai Beach is located about 100 km north of Tokyo facing the Pacific Ocean. The Beach is bounded by a commercial harbor at its northern end, and groins were constructed for protecting the harbor against intruding sand from the south. Sand accumulates immediately south of groins and erosion is occurring in an area approximately 2 km south of the largest groin. The observation site was located approximately 1.8 km south of the largest groin. The sand in the swash zone was well sorted with a median diameter of 0.45 mm and a sorting coeffi-

cient, defined as $S=d_{75}/d_{25}$, where d_p is the grain diameter at which p percent of the sand weight is finer, of around 1.25.

Hasaki Beach is located at the southern part of Tokai Coast facing the Pacific Ocean about a distance of 100 km from Tokyo. A research pier belonging to the Hasaki Oceanographical Research Facility, the Port and Harbor Research Institute, Ministry of Transportation, is located here for facilitating field studies in the nearshore zone. The average tidal range at the beach is about 1.2 m and beach slope was considered to be gentle. The beach is composed of sand with a grain size in the range of 0.1 to 0.5 mm. The median grain diameter on the swash zone was around 0.18 mm. Figure 1 shows a location map of the field observation sites.

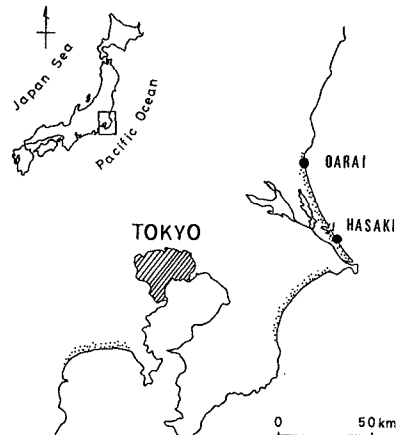


Fig. 1 Location map of field sites.

3.2 Measurement Procedure

Figure 2 shows the beach profile and the arrangement of the instrumentation at both beaches ((a) at Oarai Beach and (b) at Hasaki Beach).

In the swash zone, a target stick array of iron bars painted yellow was installed normal to the shoreline for photographic recording by 16 mm memo-motion cameras. The stick array consisted of 41 bars with an interval of 50 cm covering 20 m of the swash zone at Oarai and of 31 bars with an interval of 1 m covering 30 m of the swash zone at Hasaki. For photographing the waves from the side, a scaffold was elevated at the midpoint of the swash zone approximately 50 m south of the stick array at Oarai. Two sets of cameras recorded the waves from the scaffold. At Hasaki, waves in the swash zone were photographed by two sets of cameras on the pier.

The run-up meter, a capacitance-type wave gage with a modified measuring range, was also stretched parallel to the stick array and 50 cm beside it. The capacitance wire was held at a constant height of 2 cm above the sand surface by supporting rods installed at an interval of 2 m. A plastic scale was pasted to each supporting rods. In order to keep the wire at a constant height, two men were engaged in adjusting the movable supporting device of the wire to follow the sand surface fluctuations.

To record the sea surface variation, target poles for the 16 mm cameras were installed in the sea. A capaci-

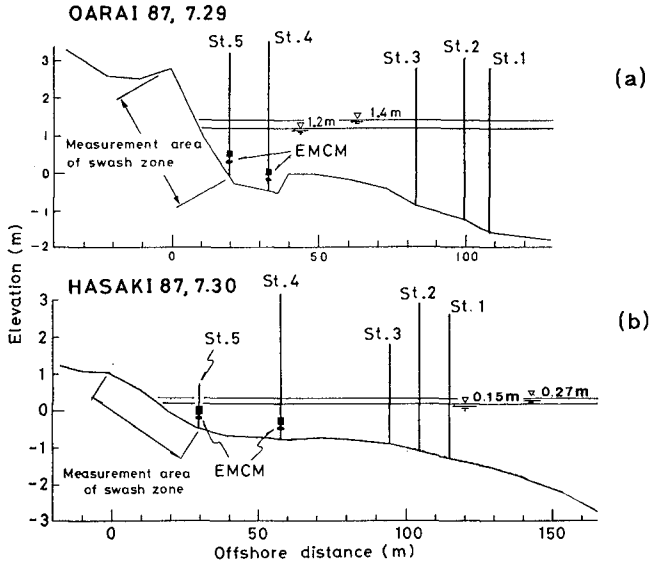


Fig. 2 Beach profiles and arrangement of measuring instruments.

tance-type wave gage and a two-component electromagnetic current meter (EMCM) were attached to the target poles of St. 4 and St. 5 at both beaches. Waves were photographed by two sets of 16 mm cameras on a scaffold elevated at the berm crest at Oarai and on the pier at Hasaki. Figure 3 shows the arrangement of the sticks on the swash slope.

At Oarai, data collection was started on 16:10 and ended 17:50, giving a 100 min experimental duration. During the experiment the tide rose about 20 cm. Average breaking wave height and period estimated by visual observation were about 1m and 12 sec. The average breaker line was located between Sts. 2 and 3. The type of breaker was plunging and the wave direction was almost normal to the shoreline. Additional information may be found in Takezawa et al. (1988). At Hasaki the measurements started on 17:15 and ended on 18:31, with seventy six minutes of data collection. During the measurements the tide rose about 20 cm. The average breaker line was located near St. 2 and an

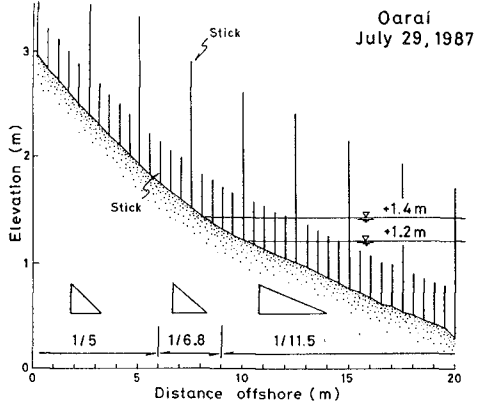


Fig. 3 (a)

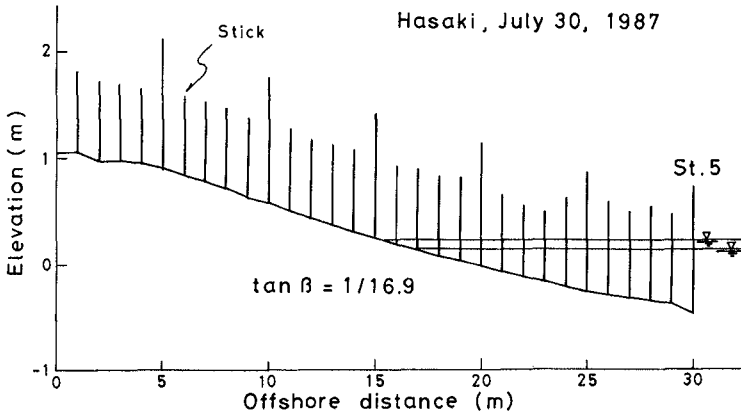


Fig. 3(b) arrangement of the sticks on the swash slope.

average breaking wave height of 0.95 m and a wave period of 12.1 sec were recorded. The waves broke as the plunging type.

Analyzing data obtained by EMCM, no significant power was found in the longshore velocity at both sites except in the very low frequency range.

IV WAVE SEPARATION

In the following, results analyzed at St.4 on Oarai Beach (Hereafter this case will be abbreviated as OA87.St.4) and St.4 on Hasaki Beach (Hereafter abbreviated as HA87.St.4) are described and discussed. Wave data obtained by 16 mm cameras were analyzed in the present study and the wave data obtained with the capacitance-type wave gages were not employed.

Before the results of the analysis are shown, some supplementary information is given. The data collection with the electrical instruments and the photographing with the 16 mm cameras were simultaneously started by hand. No electrical synchronization between the measuring systems were done. The target poles and the electromagnetic current meters were placed close to each other but they were not placed exactly at the same location. It is expected that there was some time lag between the sea surface variation and the water particle velocity. In order to find the time lag, cross-spectral analysis was carried out and the time lag of 0.6 sec (OA87.St.4) and 0.4 sec (HA87.St.4) were obtained between the data records. The time lag was removed in the later analysis.

In the wave separation using Eqs. (11) and (12), a suitable value of N had to be chosen. There are no guide lines for selecting a value of N . Therefore, considering the power spectral functions, three critical frequencies, 0.35 Hz, 0.6 Hz, and 1.0 Hz for OA87.St.4 and 0.4 Hz, 0.9 Hz and 1.2 Hz for HA87.St.4, were evaluated. The three chosen frequencies did not give any noticeable difference

when analyzing the data records. The results obtained for the frequency 1.0 Hz at OA87.St.4 and for 1.2 Hz at HA87.St.4 are discussed later.

In the wave separation using Eqs. (1) and (2) and Eqs. (19) and (20) a value of α has to be determined. The value of α was chosen as the ratio of $(\overline{\eta^2}/\overline{u^2})^{1/2}$ between the observed and the calculated from small-amplitude wave theory, in the primary frequency range of progressive wave domain.

The most suitable value α of was 1.54 for OA87.St.4 and 1.26 for HA87.St.4.

4.1 Wave Separation

Figure 4 shows a portion of the resolved waves by the three methods at OA87.St.4, and Fig. 5 displays results from HA87.St.4. The incident and corresponding reflected waves are easily identified for primary individual

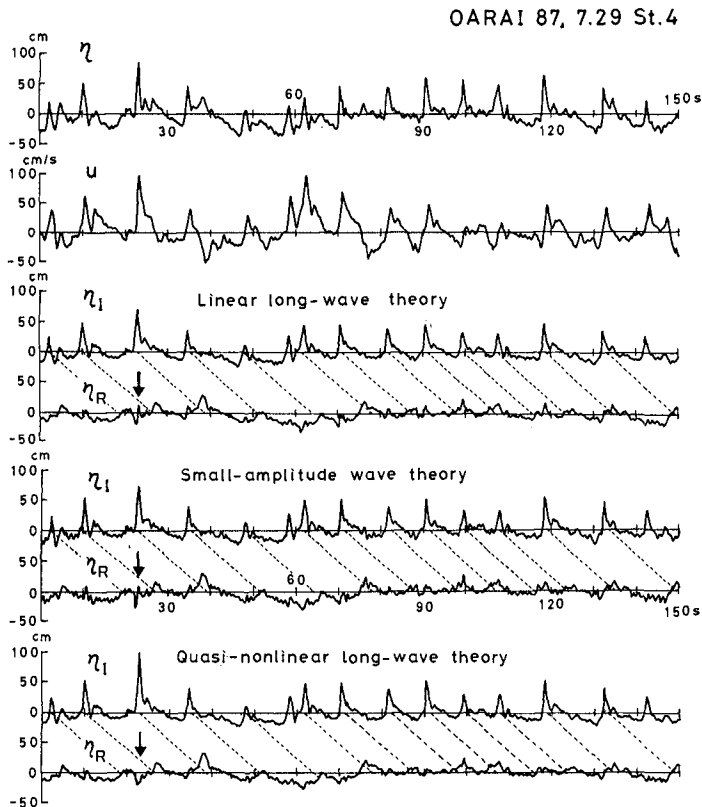


Fig. 4 Observed wave profiles, and separated incident and reflected wave profile by the three methods.

waves (Mizuguchi, 1982) at Oarai Beach, which had a steep swash zone slope. In contrast, reflected waves do not appear at Hasaki Beach, which had a gentle swash zone slope. It is difficult to recognize the correlation between the incident waves and the reflected waves, instead long-period waves appears predominantly in the reflected waves. This implies that primary individual waves ranging from about 5-20 sec in period, having the main power of the incoming waves, lost their energy in the swash zone, resulting in negligible reflection, and only the remaining long-period waves were reflected.

There is no standard method for determining the best separation technique. However, there is a tendency that an excess rise in sea water level appears for a portion of the reflected wave profile separated with linear long-wave theory (Eqs. (1) and (2)), and small-amplitude wave theory (Eqs. (11) and (12)), where this portion corresponds to the crest of the incident wave, when the reflected wave profiles are examined in detail.

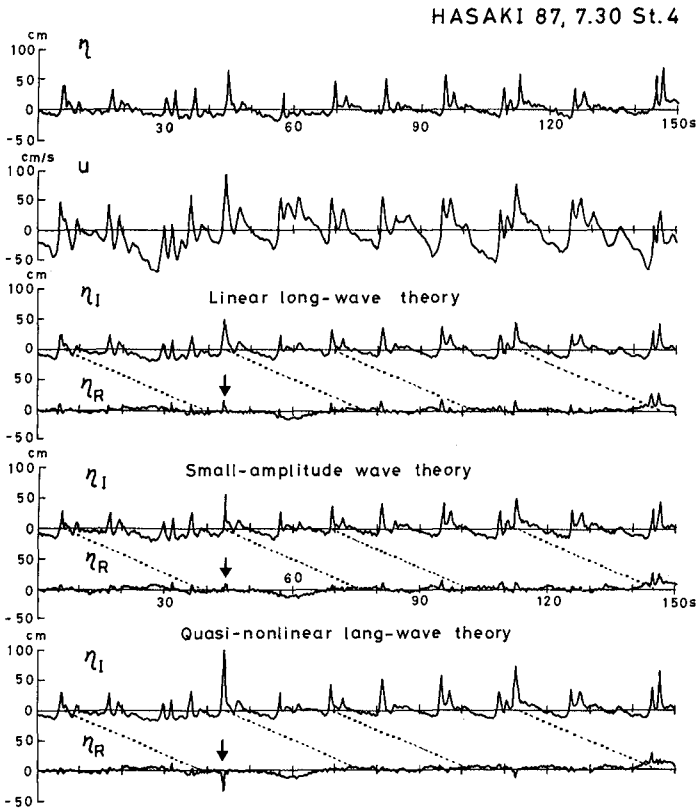


Fig. 5 Observed wave profiles, and separated incident and reflected wave profile by the three methods.

The excess rise does not appear in the reflected wave profile separated with the method based on quasi-nonlinear long-wave theory, (Eqs. (19) and (20)). An example is found at an elapsed time of 23 sec for OA87.St.4, indicated by arrows. This is because the water particle velocity is smaller to apply Eqs. (1) and (2), and Eqs. (11) and (12). However, in the reflected wave profiles separated using Eqs. (19) and (20) for HA87.St.4, an abrupt sharp depression is found at an elapsed time of 45 sec. This was due to an exceptionally large observed water particle velocity, although it is not clear why this occurred.

As a measure to evaluate the different methods, the cross-correlation functions between incident and reflected waves were calculated and are shown in Fig. 6. Close to the time lag zero, the cross-correlation function derived from small-amplitude wave theory and linear long-wave theory fluctuate in comparison with quasi-nonlinear long-wave theory for both OA87.St.4 and HA87.St.4. This means that wave separation using Eqs. (1) and (2) and Eqs. (11) and (12) involves some uncertainty. In addition, the value of the maximum cross-correlation coefficient obtained by the method based on Eqs. (19) and (20) was the highest among the three methods compared at OA87.St.4, where waves were highly reflected because of the steep swash slope. According to the preceding discussion, it is concluded that the separation method based on the quasi-nonlinear long-wave theory is the best among the three investigated methods.

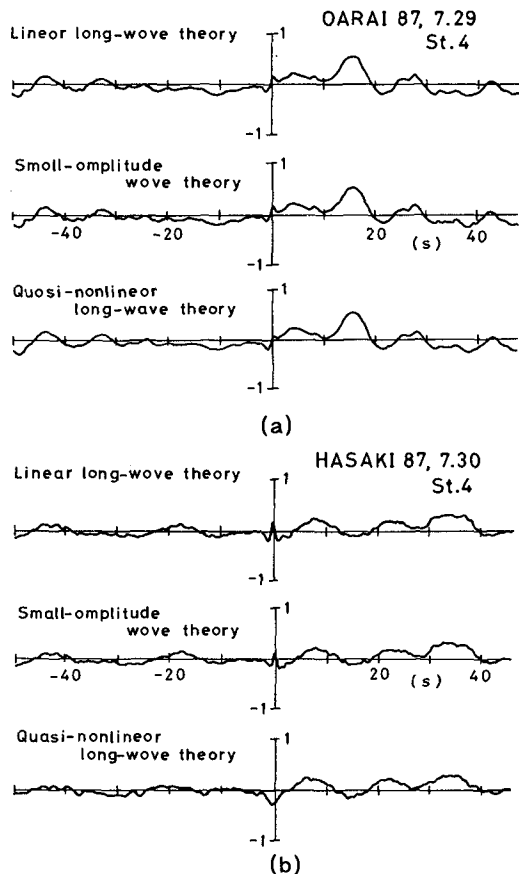


Fig. 6 Cross-correlation function between the incident and the reflected waves.

4.2 Spectral Considerations

Figure 7 shows the power spectral density function for the observed waves, and for incident and reflected waves at OA87. St.4 and HA87. St.4. Figure 8 shows the cross-spectral function between the incident and reflected waves.

At OA87. St.4, in the range below 0.15 Hz, which include the peak frequency, the power spectral shape of the incident and reflected waves are similar and the coherence function is nearly 1.0. This suggests that signifi-

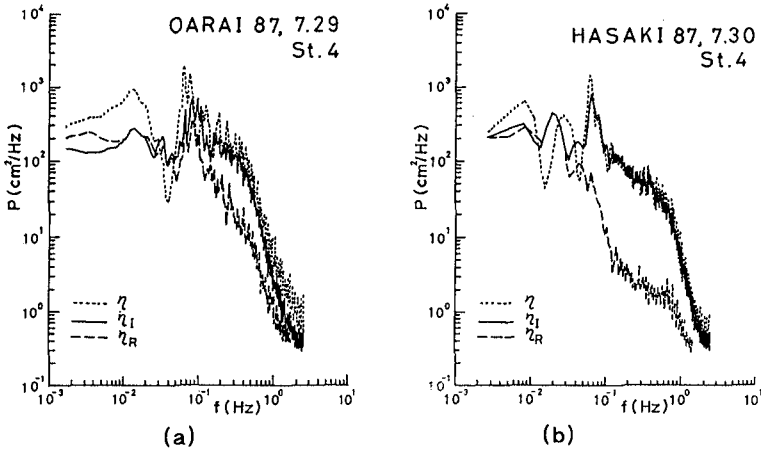


Fig. 7 The power spectral density function of the observed, incident and reflected waves.

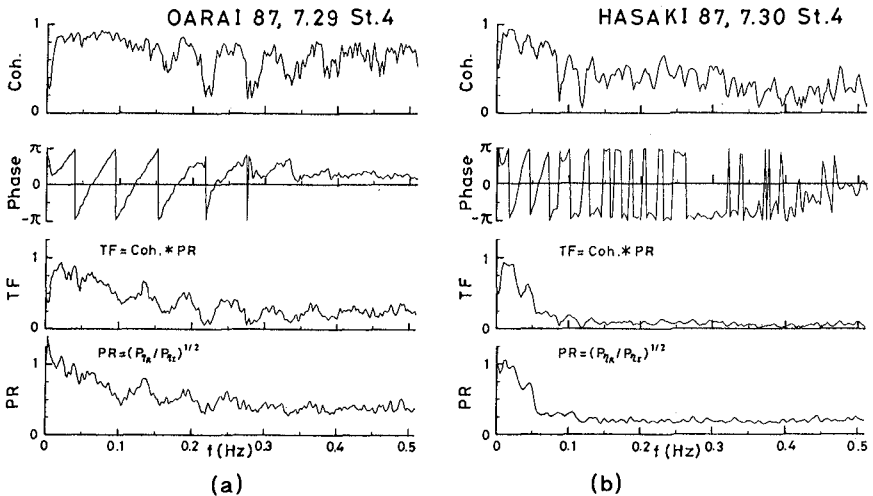


Fig. 8 Cross-spectral function between the incident and reflected waves.

cant wave reflection occurred. In the range higher than 0.15 Hz, the power of the reflected waves is considerably smaller than that of the incident waves. The energy in this range, were lost during the swash process, resulting in a small amount of reflection.

At HA87.St.4, in the range higher than 0.05 Hz, which includes the main power of the incident waves, the power of the reflected waves is very small compared with the power of incident waves, and coherence function is also small. In the range below 0.02 Hz, the power of the incident and reflected waves are of almost the same magnitude and coherence function is almost unity. This indicates that the significant reflection occurred only for long period components.

4.3 Joint Distribution of Wave Height and Period

Figure 9 shows the joint distribution of wave height and period for observed, incident, and reflected waves. The distribution of the observed waves is similar to that of the separated incident waves at both observation sites, OA87.St.4 and HA87.St.4, apart from that the distribution of the incident waves has two maxima. This implies two wave groups, with primary individual waves coming from the off-shore and secondary waves with small heights and periods mainly produced by disturbances in the surf zone. It was noted in the analysis of the

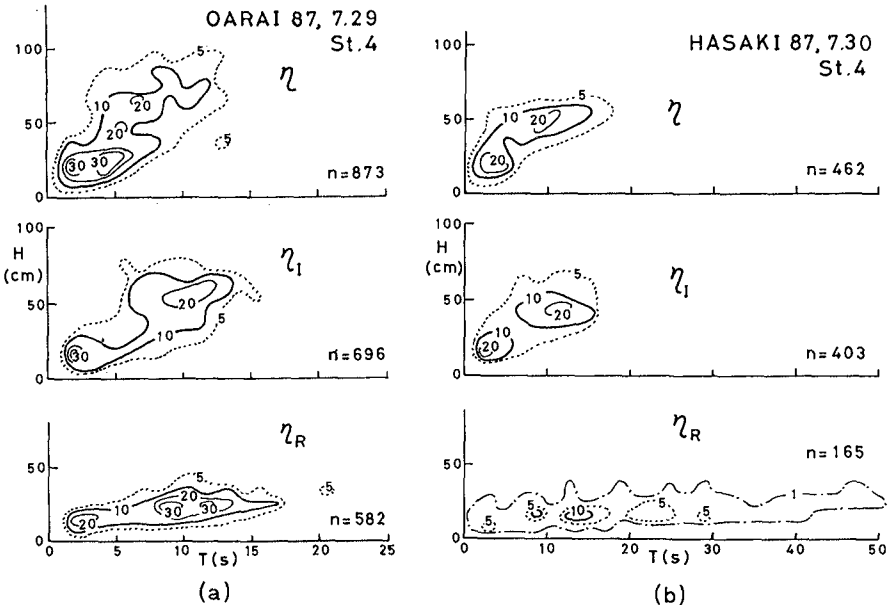


Fig. 9 The joint distribution of wave height and period for the observed, incident and reflected waves.

distributions of incident and reflected waves at OA87.St.4, that the number of defined waves somewhat decreased in the reflected wave field compared to the incident wave field, and the distribution of the reflected waves spread a little towards longer periods. However, the decrease in the number of waves mainly occurred for waves with small height and period, and the decrease did not occur for the primary individual waves ranging from 5 to 20 sec in period although they were reduced in height. This means that primary individual waves in the incident wave field return to the offshore with a decreased height.

The corresponding development does not appear for the waves at HA87.St.4. The number of defined waves considerably decreases and long-period waves not identified in the incident wave field appear in the reflected wave field. These long-period waves are found in the reflected wave profile in Fig. 4(b) and in the range below 0.06 Hz in the power spectral density function shown in Fig. 7(b). Thus, the waves that had the main energy in the period range 8 to 20 sec in the incident wave field lost their energy due to wave breaking on the slope and disappeared in the reflected wave field, implying no reflection. Instead, the long-period waves, which are difficult to distinguish in the incident wave field, are more easily identified in the reflected wave field. Following the above discussion, it is noted that the distribution of the observed waves at OA87.St4 is a result of superimposed incident and reflected waves, which does not show the proper characteristics of an incident wave distribution. The distribution of the observed waves at HA87.St.4 gives almost the same distribution as that of the incident waves. In summary, we need to consider wave reflection when the characteristics of incident waves on steep beaches are estimated.

V CONCLUDING REMARKS

The wave separation method based on quasi-nonlinear long-wave theory gave reasonable results using field data observed at a steeply sloping beach and also from a gently sloping beach. The separated incident and reflected wave field well described the wave characteristics in the surf zone, that is, high frequency waves lost their energy due to breaking and disappeared in the reflected wave field. The waves ranging in period from 5 to 20 sec, which have the main power of the incident waves and are ordinary wind waves, partially lost their energy due to wave breaking and returned to the offshore as reflected waves on the steep foreshore beach. Individual reflected waves were well related to the corresponding incident waves. However, on the gently sloping beach the waves lost their energy on the foreshore slope

and no reflection occurred. Low-frequency waves not easily identified in the incident wave field emerged in the reflected wave field and formed on-offshore standing waves without any breaking on the slope.

The critical frequencies to distinguish between perfect and partial reflection, and partial and no reflection depended on the gradient of the foreshore beach slope. Further field studies at beaches with different slopes should be carried out in order to qualify the wave characteristic in the nearshore zone. Also, further improvement of measurement instruments and development of the theoretical considerations are needed.

ACKNOWLEDGEMENTS

The authors would like to thank the Port and Harbor Research Institute, Ministry of Transportation, for permission to use the observation pier. We also gratefully acknowledge the assistance of Dr. S. Hotta, Professor, Dept. of Civil Eng., College of Science and Technology, Nihon University, during the field observation and in the preparation of this paper. We would also like to express our appreciation to our universities students who provided considerable supports during the field work. Without their help we could not have carried out this field experiment.

A portion of this study was supported by the Research Grant for Assistants and Young Researchers, Nihon University Research Grants for 1989 (Kubota) and Joint Research Grant, College of Science and Technology Research Grants for 1989, Nihon University (Takezawa and Kubota).

REFERENCES

- Guza, R. T., E. B. Thornton and R. A. Holman (1984): Swash on steep and shallow beaches, Proc. 19th Coastal Eng. Conf., ASCE, pp. 708-723.
- Mizuguchi, M. (1982): Individual wave analysis of irregular wave deformation in the nearshore zone, Proc. 18th Coastal Eng. Conf., ASCE, pp. 485-502.
- Takezawa, M., M. Mizuguchi, S. Hotta and S. Kubota (1988): Wave run-up on a natural beach, Proc. 21st Coastal Eng. Conf., ASCE, pp. 151-165.

CHAPTER 45

Instabilities in the Longshore Current

N. Dodd¹, J. Oltman-Shay² and E.B. Thornton³

Abstract

Measurements made during one day of the 1986 SUPERDUCK experiment at Duck, North Carolina are used in order to investigate the model of Bowen & Holman (1989). This model explains low-frequency oscillations in the longshore current, which were observed during that experiment, in terms of a shear instability in that flow. The model is extended to include dissipation (in the form of bottom friction), and it is found that there is good agreement between it and observation.

1. Introduction.

During the 1986 Superduck experiment, at Duck, North Carolina, Oltman-Shay et al. (1989) noticed considerable along-shore progressive wave-like motions. These motions possessed periods of up to the order of 1000 seconds, and can therefore be described as low frequency. However, their associated wavelengths were of the order of 100 metres; this distinguishes them from infragravity waves which possess much longer wavelengths. Furthermore, they were only observed in the presence of a strong longshore current, which was a feature of most days of this experiment: when this current subsided, the oscillations were no longer apparent.

The measurements were made in about 1 to 2 metres of water, in the trough of the offshore bar which developed during the experiment. The incident swell had a period of about 5 seconds and approached the north-south tending beach at large angles. The longshore current was generated when these waves broke on the offshore bar. The waves then reformed and finally broke at the shore. Outside the surf zone, a corresponding long-time modulation of the incoming wave train was not noticed.

¹Adjunct Research Professor, Oceanography Dept., Naval Postgraduate School, Monterey, CA 93943, U.S.A.

²Senior Scientist, Quest Integrated, Applied Physics Division, 21414 68th Avenue South, Kent WA 98032, U.S.A.

³Professor, Oceanography Dept., Naval Postgraduate School, Monterey, CA 93943, U.S.A.

Bowen & Holman (1989) have since presented a model, based on the inviscid, linear 2-dimensional shallow water equations, (under the rigid-lid assumption), to describe these motions. Their hypothesis is that these oscillations are manifestations of a shear instability in the along-shore shear flow (longshore current). This approach is in contrast with those of Symonds et al. (1982), Tang and Dalrymple (1989), and Shemer et al. (1990), all of whom assume low frequency nearshore motions to be forced phenomena.

In the analysis of Bowen & Holman, the mean longshore current is considered time independent and known a priori. The assumption of along-shore (y) uniformity is introduced, which allows the governing equations to be reduced to a single equation, analogous to the Rayleigh stability equation; the difference being due to the dependence of the water depth, h , on the cross-shore coordinate, x . Normal mode analysis then predicts a spectrum of eigenvalues/functions, each of which corresponds to a temporally stable or unstable perturbation, (or mode), of the shear flow. The authors assume the observed perturbations to be the fastest growing unstable modes, for a particular wavelength, λ ; i.e. the unstable modes with the largest growth rates. The spectrum of eigenvalues/functions is defined by the cross-shore depth, ($h(x)$), and longshore current, ($V(x)$), profiles. The situation is depicted in figure 1. They supported their hypothesis by applying this model to a highly simplified set of profiles. Dodd & Thornton (1990) have since shown more rigorously that the model agrees with observation on the non-dispersive nature of the oscillations in frequency-wavenumber (f,k) space.

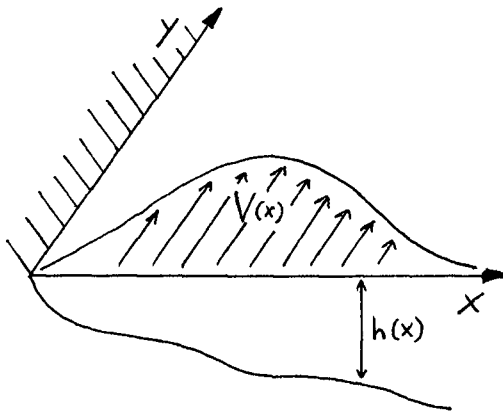


Figure 1. Nearshore bathymetry, $h(x)$, and longshore current, $V(x)$, and their relation to the coordinate system used.

In the following work we examine results from one day of the SUPERDUCK experiment, and we apply the model of Bowen & Holman to the measured V and h profiles for that day. Being a linear analysis, no information concerning the absolute amplitudes of these perturbations can be obtained. Therefore, we concentrate our efforts on comparing observed and predicted (f,k) spectra. In doing this it must be assumed that V and h are dependent only on the cross-shore coordinate, x . Though the bathymetry was mildly three-dimensional, this is a reasonable assumption.

2. Theoretical and Numerical Background.

We consider the domain $0 < x < \infty$, $-\infty < y < \infty$, with the shoreline situated at $x=0$. The total velocity vector, \underline{u}^* , is defined as

$$\underline{u}^* = (u(x,y,t), v(x,y,t) + V(x)). \quad (1)$$

Thus u and v represent the perturbed velocity field and V represents the longshore current. When (1) is introduced into the shallow water equations, which are linearized under the assumption $V_0 \gg u_0$, (where V_0 is a representative amplitude of the longshore current and u_0 is a similar quantity for the perturbed velocity field), we get:

$$\begin{aligned} u_t + Vu_y &= -g\zeta_x \\ v_t + uV_x + Vv_y &= -g\zeta_y \end{aligned} \quad (2)$$

where t is the time coordinate, ζ is the free-surface elevation, and g is the gravitational acceleration constant. Under the rigid-lid assumption, a stream function, $\Psi(x,y,t)$, is introduced into (2), where $u = -\Psi_y/h$ and $v = \Psi_x/h$; this allows the equations (2) to be combined into a single equation. Making the further assumption that the along-shore behavior is simple harmonic, then

$$\Psi(x,y,t) = \Re\{\psi(x)e^{i(ky-\omega t)}\} \quad (3)$$

Thus, the cross-shore structure is described by $\psi(x)$. The resulting linearized equation is

$$(V-c)\{\psi_{xx} - (h_x/h)\psi_x - k^2\psi\} = h(V_x/h)_x\psi. \quad (4)$$

The wavenumber, $k=2\pi/\lambda$, is assumed to be real. The phase velocity, c , (and therefore the frequency, $\omega=c k$), will in general be complex. Thus if c possesses a positive imaginary part, Ψ will be a temporally unstable mode, with wavelength $2\pi/k$, real radian frequency $\Re(\omega)$, and growth rate $\Im(\omega)$. One condition for there to be an instability is that the potential

vorticity associated with the shear flow, V_s/h , should possess a local extremum. This condition is satisfied for all the profiles examined here.

In general, (4) must be solved numerically. Here we use a finite difference solution. In this scheme, (4) is discretized at N nodes on the domain $0 < i\Delta x < (N-1)\Delta x = L$, ($i=1, \dots, N-2$), where Δx is the distance between nodes, and L is some suitably large value. The scheme is accurate to $O(\Delta x^4)$, and the relevant finite-difference approximations for the derivatives in (4) can be found in Collatz (1960). At the boundaries, non-symmetric approximations are derived to the same order of accuracy, although it should be noted that the comparatively large coefficient of the truncation error term, due to the non-symmetric nature of the boundary conditions, degrades accuracy somewhat. The problem may then be posed as a generalized algebraic eigenvalue problem,

$$A\underline{\psi} = cB\underline{\psi}, \quad (5)$$

(where $\underline{\psi} = (\psi_0, \dots, \psi_N)$, and $\psi_i = \psi(i\Delta x)$), and solved subject to the no-normal-flow boundary conditions: $\psi_0 = \psi_N = 0$. In fact, (5) may be solved more rapidly as a classical eigenvalue problem by operating on it with B^{-1} , which is easily calculated since B is well-conditioned. Such a solution yields $N-1$ eigenvalues, c_i , each with an associated eigenfunction, $\underline{\psi}_i$. This method of solution has the disadvantage of being computationally expensive, in both storage and cpu time, and of being generally less accurate than initial-value methods. It is usually used in order to generate initial estimates to eigenvalues, which can then be more accurately estimated using a shooting method. Here this method is used by itself, because the profiles we will be looking at are not smooth, analytic functions, but discrete and numerically generated. This severely restricts the usefulness of shooting methods for this problem. A value of $N = 201$ was the largest that the available storage and cpu time would allow on an IBM 3033. This was adequate for the investigation.

3. Bottom Friction.

The model presented in the preceding section neglects dissipative effects. However, such effects can be important in damping unstable modes. Bowen & Holman included a damping factor, $e^{-\nu t}$, in (3), and estimated that ν would be $O(10^{-2}-10^{-3} \text{ s}^{-1})$, implying that $\Im(\omega)$ must be larger than this for an instability to develop. In fact, dissipative effects can be included in the momentum equations on a rational basis. The equations (2) represent a decoupling of higher order effects, (i.e. perturbations in the longshore current), from the lowest order balance. This balance is between the radiation stress gradients, which are generated by waves breaking at a beach and which lead to the formation of a longshore current, and the bottom friction, and is discussed by Longuet-Higgins (1972). In the higher-order balance wave breaking is absent, and so the most significant dissipative effect is bottom friction. This effect may be included by adding an appropriate term to the momentum equations:

$$\begin{aligned} u_t + V u_y &= -g \zeta_x - \mu u \\ v_t + V v_y + V_x u &= -g \zeta_y - \mu v \end{aligned} \quad (6)$$

Thus the term μ represents the dissipation in the problem. It may be derived on the assumption that the amplitude of the orbital velocity of the incoming gravity wave, U_0 , is much greater than the representative longshore velocity, V_0 ; i.e. $U_0 \gg V_0$. Thus,

$$\mu = \frac{2}{\pi} c_D U_0 \quad (7)$$

where c_D is a dimensionless drag coefficient. (In fact, this assumption is invalid for Duck. However, it is the size of μ which is of importance here and not its form). These equations can then be combined as before to give

$$\left(V - \frac{i\mu}{kh} - c \right) \{ \psi_{xx} - (h_x/h) \psi_x - k^2 \psi \} = h(V_x/h)_x \psi - \frac{i\mu}{kh} (h_x/h) \psi_x \quad (8)$$

It can be seen that μ is always accompanied by i ($= +(-1)^{1/2}$).

The equation (8) can be solved by the method already outlined in the previous section. It is this equation which will be applied to measured V and h profiles from the SUPERDUCK experiment.

4. Observations.

We examine observations from one day of the SUPERDUCK experiment, October 16th, which exhibited the most energetic low frequency motions. For a full description of the field site and the methods of data collection the reader is referred to Oltman-Shay et al. (1989).

Some of the strongest evidence presented by Oltman-Shay et al. for the existence of low frequency perturbations in the longshore current is in the form of iterative maximum likelihood estimated (IMLE) frequency-cyclic wavenumber (f, K) spectra, (where $K = k/2\pi$). Figure 2 shows one such diagram for Oct. 16th, which was constructed from the along-shore component of velocity as measured on that day. Note that the frequency is cut off at 0.05 Hz (20 seconds), thus excluding the incoming swell. The diagram therefore shows only low frequency motions, (compared to the incoming wave train). The figure shows theoretical edge wave dispersion lines for 0 mode and two higher mode edge waves (for a plane beach). Note that frequency bins are now of width about $\Delta f = 0.001$ Hz, and are thus better resolved than the original figures of Oltman-Shay et al.; otherwise, the diagram is similar to those presented, (for other days), by Oltman-Shay et al.

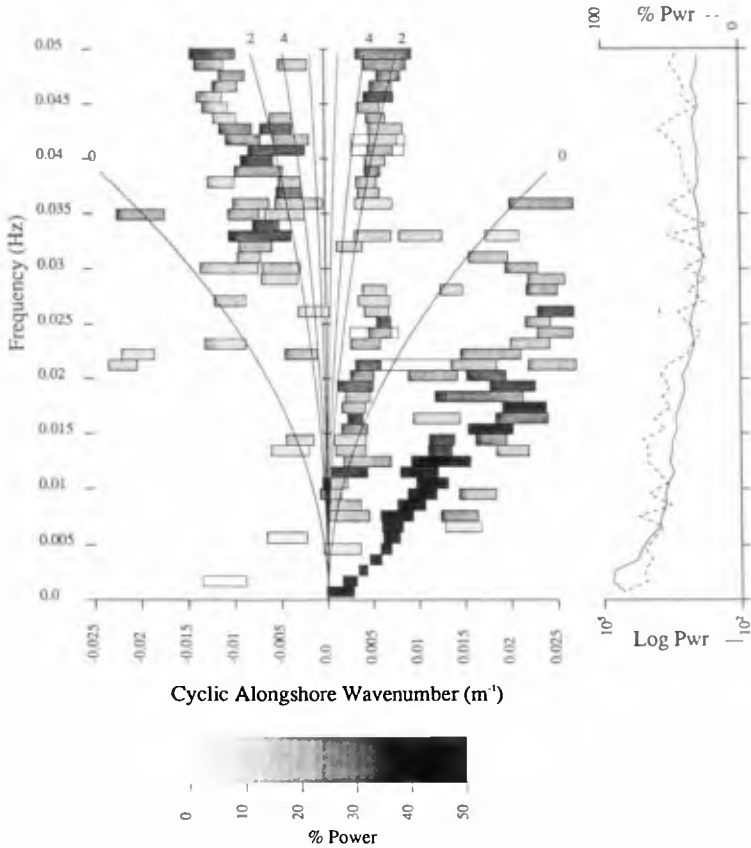


Figure 2. IMLE frequency-cyclic wavenumber spectrum of along-shore velocity on October 16th. Positive wavenumbers indicate southward propagation. Rectangular boxes indicate position of variance peaks defined as those wavenumber maxima having an adjacent valley below their half-power. The wavenumber width of each box is the half-power bandwidth of the peak. Shading density indicates the percent variance in the frequency bin that lies within the half power bandwidth of the peak. Theoretical edge wave dispersion curves (0, 2 and 4), and leaky-trapped boundary are shown. Log power density (cm²/s, solid) and total percent variance displayed in the frequency-wavenumber spectrum (dashed) as a function of the frequency are shown alongside. $\Delta f = 0.00098$ Hz.

There is evidence of edge wave activity in the diagram, which is mostly restricted to frequencies above 0.01 Hz, though it is hard to tell which modes are present. This is partly due the array being too short to successfully resolve them. However, the shorter, low frequency motions do not suffer from this problem; in fact, the most well defined variance

peaks lie well outside the edge wave dispersion curves, and below 0.015 Hz. They appear to describe a roughly linear relation between frequency and wavenumber. As Oltman-Shay et al. noted, these lines are not attributable to advected edge waves, (due to the longshore current), or to deviations of the edge wave dispersion curves from the theoretical form indicated on the figure, (due to deviations of the beach profile from its theoretically plane form). These oscillations can be seen to be progressive, with a phase speed of about 0.9 m/s. They are in the same direction as the longshore current on that day, the maximum value of which was about 1.2 m/s. On this and other days examined, the measured phase speeds were about one half to three quarters the corresponding maximum longshore current value. This is in agreement with theory.

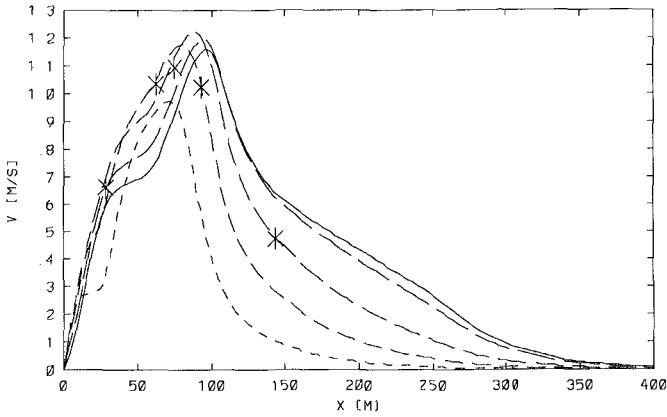
5. Computations.

In order to use the model (8) the cross-shore bathymetry, $h(x)$, and longshore current profile, $V(x)$, must be constructed for October 16th. In the case of h this presents no problems, but for V things are not so simple. This is because there were very few measurements of longshore current made; in fact there are only five such measurements for the 16th. It is therefore difficult to know what the true profile is. However, small differences in this profile can substantially affect the predicted stability characteristics for that day. It is therefore important that we have reasonable confidence in the profile used. Another problem, which is linked to the first, is that the profile was measured sequentially, over a period of about four hours, as a sled was moved in a transect across the foreshore. Although this process was centered about low tide, the depth changed by about 0.2 m during the time the measurements were made. This, combined with other changes which may have occurred in the incoming wave field, may be enough to considerably affect the mean longshore current profile and thus render any profile interpolated from the measured profile dubious at best.

Unfortunately, there is little or no analytical work available for longshore current generation on a barred beach. Therefore, we use the model of Thornton & Whitford (1990) to generate a set of V profiles for the period during which the measurements were taken, to allow for the affects of tidal variations. There are five such profiles in all, (denoted cases A to E), each with an associated depth profile, which covered the tidal range. They are shown in figures 3(a) and 3(b). The actual measured values of V are also shown in figure 3(a). It can be seen that there is a fairly large difference between the first and the last profiles, (A and E), and that the measured values agree closely with profiles C and D. Case E is markedly different from the rest. Moving beach-ward from offshore, each profile is, however, qualitatively similar: there is a maximum in V , followed by a sharp decrease, then a slowing of the decrease, and finally a rapid decay to zero at the shoreline. The large peak in each profile is due to the waves breaking on the bar, and the slowing of the rate of decrease, (which results in a "kink" in the onshore shear), is a result of waves finally breaking at the shore. These features are typical of longshore current profiles on barred beaches. It is easy to see that merely interpolating from the measured values will lead to a qualitatively different profile. There will be no such secondary breaking modeled. The drag coefficient, c_D , was measured at about 0.003, and this value is used throughout the following analysis.

The profiles shown in figures 3(a) and 3(b) are now inserted into (8) and the resulting eigenvalue problem solved. Recall that it is the fastest growing unstable modes which will be of importance; other unstable modes may be present but the modes with the

(a).



(b).

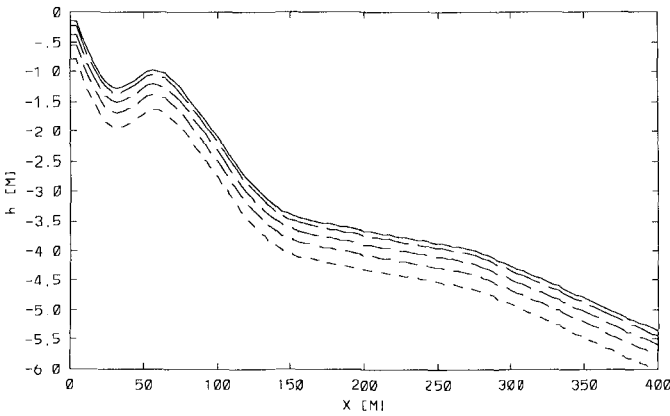


Figure 3. Longshore current (a). and depth (b). profiles used in the stability analysis. Case A is shown by the solid line and cases B to E by dashed lines with progressively shorter dash lengths. Measured longshore current values are indicated in 3(b) by an asterisk.

largest growth rates are expected to be apparent first. We denote the growth rates: $G = \Im(\omega)$. Each of these unstable modes possesses an associated real frequency, $F = \Re(\omega)/2\pi$. In figure 4 we compare the predicted frequencies with the measured frequency-cyclic wavenumber spectra. In this diagram the shading present in figure 2 is omitted so that the

comparison can be seen more clearly.

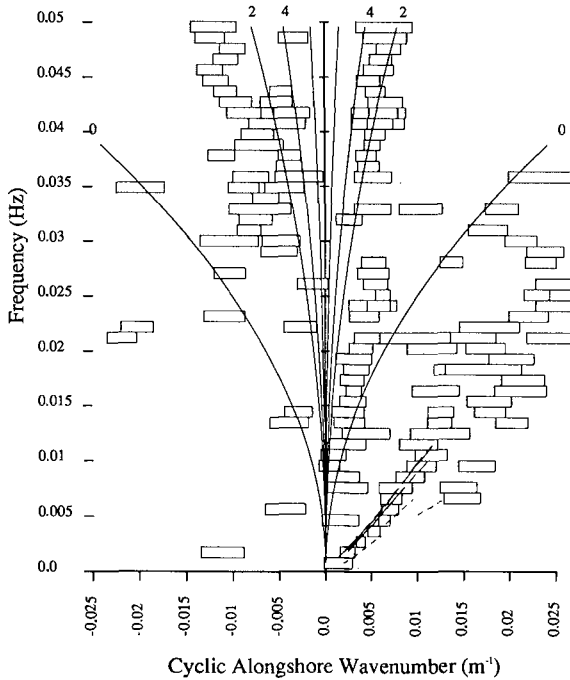


Figure 4. Reproduction of IMLE spectrum shown in figure 2, without shading. Also shown are the predicted dispersion curves, corresponding to the fastest growing unstable modes, for each of the cases A to E. Case A is shown as a solid line, and thereafter cases B to E are shown as dashed lines with progressively shorter dash lengths.

It can be seen that cases A to D give similar dispersion curves. They agree well with measurement. Case E differs substantially from these. Considering the aforementioned difference between this V profile and the rest, this is not surprising. The dispersion curve predicted in this case agrees comparatively poorly with the measured spectra, and for these reasons we now discard case E. Note also that a number of the cases give discontinuous dispersion curves. In these cases, each segment of the curve corresponds to a different unstable mode (eigenvalue) from adjacent segments. They result from G increasing as K increases, for one mode, while for another G decreases. Hence there is a "jump" from one mode to another as the growth rate of the latter exceeds that of the first.

It should be remembered that no information concerning the absolute amplitudes of these oscillations may be obtained from this linear analysis. Thus only relative intensities

can be compared. The model of Bowen & Holman explains perturbations of a shear flow as instabilities in that flow. On this assumption it is natural to extend this interpretation to explain more vigorous perturbations as more unstable modes; i.e. modes with larger growth rates. To make this comparison the IMLE diagram shown in figure 2 is rescaled. In the original figure degrees of shading represent wave energy at a particular wavenumber as a percentage of total energy in that frequency bin. In figure 5, although the original IMLE "boxes" are retained, the shading now represents absolute variance, (or energy), thus allowing comparisons between different frequencies to be made.

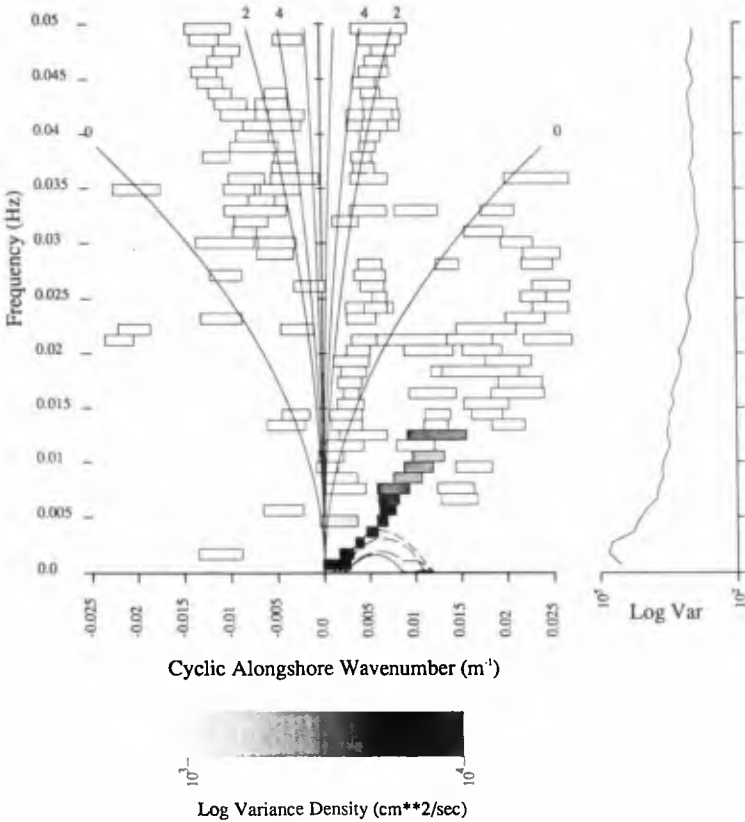


Figure 5. IMLE frequency-cyclic wavenumber spectrum for along-shore velocity, on October 16th. Shading indicates absolute log variance density. Log variance density in the frequency-cyclic wavenumber spectrum as a function of frequency is shown alongside. $\Delta f = 0.00098$ Hz. Also shown are the predicted growth rates, G , (units, rad/s) for the cases A to D. A is shown by the solid line, and B to D by dashed lines with a progressively decreased dash length.

In this figure, measured variance is virtually all concentrated below 0.01 Hz, showing that these motions are far more energetic than any other low frequency motions. In the accompanying log variance plot, the variance can be seen to increase, from very low frequencies, up to a peak in the second frequency bin, (about 0.001 to 0.002 Hz), and decrease thereafter.

The predicted growth rates, G , are shown in the same diagram, (excluding case E). Each of these shows an increase in G , from low wavenumbers, and frequencies, (see the corresponding frequencies in figure 4), to a peak growth rate, and then a decrease as K increases further. This is in rough agreement with the observed spectra. The main area of disagreement is at very small wavenumbers, (very low frequencies), where theory predicts no instability, but quite energetic motions were measured. As we proceed from case A through to case D, the maximum growth rates of the predicted instabilities becomes larger. That this is not solely due to differences in the V profiles can be discovered by re-solving the eigenvalue problem (8) using the longshore current profile for case A and the depth profile for case E. Larger growth rates are found for this case than for case A alone.

6. Discussion and Conclusions.

The further analysis of the observations made on one day of the SUPERDUCK experiment provides some further support for the hypothesis of Bowen & Holman: these motions are manifestations of a shear instability in the longshore shear flow. The improvement in resolution of the IMLE spectrum shown here, ($\Delta f=0.00098$ Hz as opposed to 0.002 Hz), clearly indicates the presence of these motions, lying in a straight line. They also clearly dominate other wave activity. They also reveal the existence of a peak in the energy of these motions, (lying between 0.001 and 0.002 Hz). Theory concurs. The predicted dispersion lines agree well with observation. The results for the 16th are typical for those on other days.

There are some notable discrepancies however. The range of the predicted instability, though in general agreement with measurement, is not the same, and in particular, energetic motions at very low frequencies and wavenumbers are shown by the measurements, and these are not predicted by the theory. These discrepancies may be explained by the fact that there is, in each case, more than one unstable mode. The existence of the motions at larger frequencies may be a result of interactions between such modes. Dodd et al. (1990) have also shown strong evidence of an offset (non-zero intercept) of the linear dispersion lines in IMLE spectra constructed from the cross-shore component of velocity. They thought that this could be caused by the existence of a rip current, and this could explain the existence of intense motions at very low frequencies. Dissipation, as modeled here, appears to be play the important role of damping unstable modes with very small growth rates. This is in agreement with Bowen & Holman.

Finally, we consider the stream function, ψ . For case A, the unstable mode with the maximum growth rate exists at about $K=0.006$ m^{-1} ; see figure 5. At this wavenumber another unstable mode exists. It is not shown in figure 5 because its growth rate, for this value of K , is smaller than that of the first mode by a factor of about 5. The growth rates shown in figure 5 are, of course, the eigenvalues in the problem (8), and with each of these is associated an eigenfunction. We denote these ψ_1 for the fastest growing mode (at $K=0.006$ m^{-1}), and ψ_2 for the second. In figure 6, we show $|\psi_1|^2$ and $|\psi_2|^2$ as functions of x . Also shown in this figure is the cross-shore potential vorticity profile (V_x/h) defined by case A. Note that the peaks in $|\psi_1|^2$ and $|\psi_2|^2$ occur in different places: the first at the local

maximum in V_x/h , and the second at the second local minimum. Looking at figures 3(a) and 3(b), it can be seen that the minimum is associated with the offshore facing shear in V , and that the maximum is associated with the onshore facing shear. Specifically it is due to the "kink" in the V profile due to waves breaking at the shore. If this kink is removed, then the most unstable mode, ψ_1 , disappears, leaving ψ_2 as the most unstable mode. This can be tested by either redefining the V profile between about $x = 40$ m and 100m, or by cubic interpolation between the measured V values shown in figure 3(a). A little further smoothing results in stability; i.e. the problem defined by (4) may be unstable, but the dissipative effects included in (8) damp such instabilities, since the growth rates associated with them are very small. All of this is also true of cases B, C and D. What it seems to indicate is that the instabilities associated with the longshore current profile at a barred beach are due specifically to the form of the onshore shear, and not the offshore (or back) shear, as first suggested by Bowen & Holman (1989).

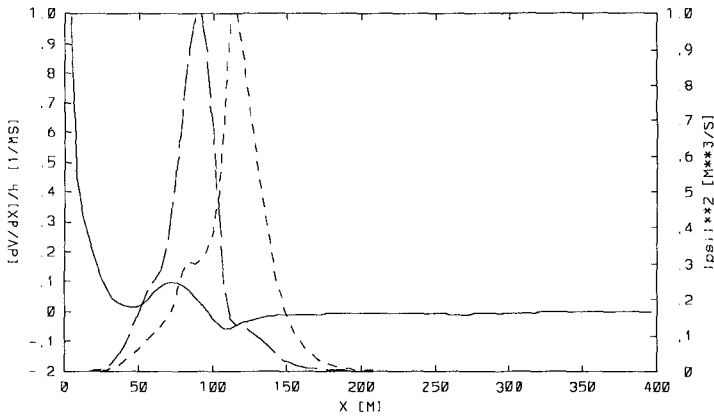


Figure 6. Potential vorticity of shear flow case A (solid line, left scale) and $|\psi_1|^2$ and $|\psi_2|^2$, (moduli squared of the stream functions of the first and second fastest growing modes in case A for $K = 0.006 \text{ m}^{-1}$) (long and short dashed lines respectively, right scale) as functions of x .

7. Acknowledgments.

The work by N. Dodd and E.B. Thornton was direct funded by the Naval Postgraduate School under sponsorship of the Office of Naval Research. J. Oltman-Shay was funded by Office of Naval Research grant N00014-90-J-1118.

References.

- Bowen, A.J. & R.A. Holman. 1989. Shear Instabilities of the Mean Longshore Current: 1. Theory. *J. Geophys. Res.*, 94, 18023-18030.
- Collatz, L. 1960. The Numerical Treatment of Differential Equations. Springer-Verlag. 568p.
- Dodd, N. & E.B. Thornton. 1990. Growth and Energetics of Shear Waves in the Nearshore. *J. Geophys. Res.*, (to appear).
- Dodd, N., J. Oltman-Shay & E.B. Thornton. 1990. Instabilities in the Longshore Current: A Comparison of Theory and Observation. (Submitted to *J. Geophys. Res.*).
- Longuet-Higgins, M.S. 1972. Recent Progress in the Study of Longshore Currents. In *Waves on Beaches and Resulting Sediment Transport*, 203-248. ed. R.E. Meyer. Academic Press.
- Oltman-Shay, Joan, P.A. Howd and W.A. Birkemeier. 1989. Shear Instabilities of the Mean Longshore Current: 2. Field Observations.
- Thornton, E.B. & D.J. Whitford. 1990. Longshore currents over a barred beach, I. Field experiment. (Submitted to *J. Phys. Ocean.*).

CHAPTER 46

A comparison of the performance of three mathematical models of wave disturbance in harbour approaches

Jane V Smallman¹ and Nigel P Tozer²

Abstract

In many design studies for coastal harbours mathematical models are used to define wave conditions in the vicinity of their entrance. There is a wide variety of models available for this purpose, each with their own characteristics. This paper compares the performance of three models which are in use for this type of study. The advantages and drawbacks of each of the models is considered by comparison with results from a physical model of a typical harbour approach bathymetry.

Introduction

Mathematical models of wave disturbance are in frequent use for predicting wave conditions both within and in the approaches to a harbour. Information on wave activity in the approaches to a harbour will be required to make a full assessment of ship manoeuvrability, and the movement of sediments. In the case of a harbour entered by a dredged channel, estimating wave disturbance will often be of importance in studies directed towards optimising channel depth and alignment.

There are presently available a wide variety of models which can be used to estimate wave disturbance. In this work attention is directed towards situations in which wave conditions are to be calculated at many locations, rather than at a few isolated points, in the harbour approaches. The performance of the models within a harbour is not considered here, either because their behaviour in such circumstances has already been examined, or they are unsuited to that type of application.

In developing wave disturbance models comparisons are often made between their results, and those from analytical solutions to

¹ Manager, Ports and Harbours Section, Maritime Engineering Department, Hydraulics Research, Wallingford, Oxon, OX10 8BA, UK
² Scientist, Ports and Harbours Section, Maritime Engineering Department, Hydraulics Research, Wallingford, Oxon, OX10 8BA, UK

idealised problems. In this case the technique which is used is to compare the results from the three mathematical models, with those from a physical model for a typical harbour approach bathymetry. Four sets of results from the physical model were available covering different incident wave conditions. In addition to the accuracy of the representation achieved by the mathematical models, consideration was also given to the speed of the calculation procedure.

The three mathematical models used in the comparison were a wave ray model and two finite difference models. The three models, and the physical assumptions inherent in their mathematical derivation, are described in detail in the following section. In subsequent sections the physical model test case is described and the performance of the models examined. In the final section the overall conclusions resulting from this work are given.

Description of the mathematical models

The three models used in this comparison were PORTRAY (see Smallman, 1987) and two finite difference wave models based on alternative formulations of the mild slope equation. PORTRAY, which is based on a ray tracking technique, was developed at Hydraulics Research, and is in frequent use in site specific studies. Both of the finite difference models were developed at UK Universities and were transferred to Hydraulics Research during 1987. The finite difference models are based on hyperbolic, see Copeland (1985), and parabolic, see Dodd (1988), approximations to the mild slope equation. The mild slope equation is given by

$$\nabla \cdot (c c_g \nabla \phi) + \omega^2 \phi c_g / c = 0 \quad (1)$$

where $\phi(x,y)$ is the velocity potential, c is the phase velocity, c_g the group velocity and ω the radian frequency. The equation, first derived by Berkoff (1972), describes the propagation of periodic, small amplitude surface gravity waves over a seabed of mild slope and will represent the combined effects of refraction, shoaling and diffraction. A more detailed description of each of the models follows.

PORTRAY is based on a ray tracing technique developed from the theory of light. Under the assumptions that the waves are linear, and that a wave in water of local depth, d , will behave similarly to a wave in water of constant depth d , wave refraction and shoaling can be shown to be governed by Snells law. Rays are tracked in the direction of wave propagation, and wave heights are calculated using the principle of conservation of energy between neighbouring rays. This approach has a limitation in that diffraction, ie a lateral transfer of wave energy, which can be caused by rapid gradient changes in the bed, is not included explicitly in the governing assumptions of the model. This can lead to some difficulties in applying the model, particularly in

areas where relatively long period waves are incident along the line of a dredged channel. The model has, however, been extensively validated against physical models and in most situations, particularly in harbour wave disturbance studies, found to provide accurate results, see Smallman (1987).

A set of linear hyperbolic equations to model refraction and diffraction processes in coastal zones was put forward by Ito and Tanimoto (1972) at about the same time as the elliptic mild slope equation was derived. Later Copeland (1985) derived similar equations from the transient form of the mild slope equation. This hyperbolic form can be written as

$$\begin{aligned} \frac{\partial Q}{\partial t} + \frac{c^2}{n} \nabla(n \eta) &= 0 \\ \frac{\partial n}{\partial t} + \nabla \cdot Q &= 0 \end{aligned} \quad (2)$$

Here the water surface elevation η is

$$\eta = A(x,y)e^{-i(\chi - \omega t)}$$

where A is the amplitude of the water surface fluctuation and χ is the phase angle.

Also, $n = \frac{c}{g}$ and Q is a dummy variable representing the flow rate, defined as a vertically integrated function of particle velocity. The equations can represent diffraction, refraction and reflections under the assumptions made in their derivation.

By creating a hyperbolic form from the original equation the mild slope problem has been embedded in a larger space (x,y,t) . This appears to be an unnecessary complication as the time dependence, $e^{-i\omega t}$, is known in advance. Therefore time stepping will produce only a phase change. If it does not then there is a basic inconsistency in the derivation.

This point has been explored by Madsen and Larsen (1987). They make the observation that the time stepping is actually only an iteration towards the steady state, and that only the steady state solution is a solution to the mild slope equation. This accounts in part in the difficulties which are known to occur in getting the hyperbolic form to converge to the steady state. A difficulty which needs to be resolved more satisfactorily before the method can be used reliably in practice.

The time taken to solve the elliptic mild slope equation computationally, and the mathematical uncertainties of the hyperbolic form, means that attention has been given to the parabolic approximation. This will be computationally efficient to solve and mathematically more rigorous in its derivation. However, this is achieved at the expense of accuracy in the representation of physical problems. That is, whilst refraction

and diffraction are represented in the parabolic approximation, reflections are not. A consequence of this is that it is therefore not suitable for representing wave disturbance in harbours where reflected waves will be important.

The first comprehensive account of a parabolic approximation to the mild slope equation was given by Radder (1979). The equation modelled here is based on an improvement to this work given by Booij (1981). The derivation assumes that the reflected wave field is negligibly small so that only forward travelling waves are considered. This leads to the equation

$$\frac{\partial \phi}{\partial x} = \frac{i}{2k} \frac{\partial^2 \phi}{\partial y^2} + \left\{ ik - \frac{1}{2k} \frac{\partial k}{\partial x} \right\} \phi \quad (3)$$

where x is the main direction of wave propagation, y is the transverse direction. Deviations from the x direction are considered in the equation as oblique amplitude modifications. The parabolic approximation will allow refraction, shoaling and seabed diffraction to be modelled. The approximation works best where the important effects occur in the direction of wave propagation, as transverse effects are only included in a weak sense. A detailed account of the deviation of the governing equation for the parabolic model used in this work, and its application to a number of test problems, is given in Dodd (1988).

The equation (3) can be solved numerically using an evolutionary finite difference technique; this type of method only requires storage of one or two adjacent rows of solution points and, as a consequence, is considerably less expensive in terms of cost and storage than the equivalent numerical solution to an elliptic equation. Thus, the main advantage of the parabolic equation is that it permits a more rapid and straightforward method of solution than would be possible for the elliptic equation.

Finally, all three of the models were modified to include the effects of wave breaking. This was done using an empirical formulation put forward by Weggel (1972).

Physical model

The physical model layout is shown in Figure 1. In the tests carried out random waves tests for two spectra from each of two directions were carried out. The characteristics of the incident conditions are given in Table 1.

Test No	Significant wave height H_s (m)	Peak wave period T_p (s)	Direction ($^\circ$)	
1	4.3	8.6	0	Storm
2	1.9	6.0	0	Typical
3	6.0	10.0	25	Storm
4	3.2	7.5	25	Typical

Table 1. Incident wave conditions for physical model tests.

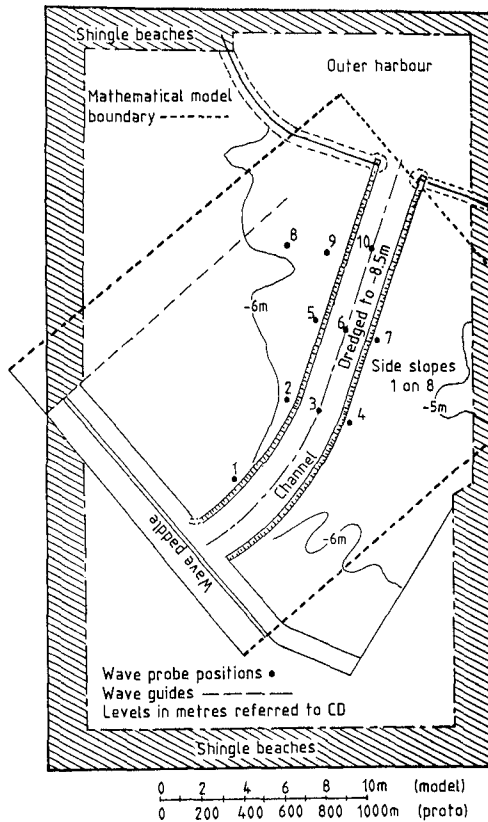


Figure 1 Physical model layout

All of the physical model tests were run at a fixed still water level of +1.9m CD. Measurements of wave height (H_s) were made in the physical model at the ten locations shown on Figure 1. These positions were selected to be representative of conditions within and at the sides of the channel. This particular bathymetry is typical of a dredged harbour approach channel and, as such, will provide a good test of the capabilities of the models for a range of incident wave conditions.

Mathematical model set up

All of the mathematical models require the bathymetry to be described as a set of depth values over a regular grid. Firstly, the bed contours were digitised and then output on a 7m (prototype) mesh. This mesh size gave at least ten points per wave length to the incident wave conditions given in Table 1. This choice of mesh size satisfied the accuracy of representation constraints of the two finite difference models. PORTRAY is not reliant on such grid constraints, so a second set of grid data, each node 35m (prototype) apart, was generated without significant loss of resolution in the description of the bathymetry. PORTRAY was run both for the 35m and 7m mesh layouts.

The mathematical model grid systems were deliberately aligned to one of the wave propagation directions. This was done because, in the derivation of the parabolic model, the coordinates are assumed to be in the main wave propagation direction. It is possible for the model to include wave effects in directions up to 45° different from the main direction, but with its accuracy reducing as the angle increases. This point will need to be borne in mind when considering the parabolic model results for the 25° direction cases.

All of the mathematical models are monofrequency, unidirectional models. It is possible to run each of them repeatedly for different frequency components, and then use linear superposition to achieve a spectral description of wave propagation. This would give a true comparison with results from a random wave physical model. However, for this study monofrequency runs were made using the peak period of the incident wave spectrum to represent the random wave train. This is not ideal, but has been found in many applications to give a reasonable approximation to an incident wave spectrum. It is intended that this research will be extended subsequently to include mathematical models with random wave incident conditions.

For the hyperbolic finite difference model it remained to select a time step. To satisfy the stability criterion of this model, time steps were selected such that 25 elapse in each wave period. To achieve convergence for this model it was typically necessary to run it for 10 wave periods. Neither the parabolic model nor PORTRAY are time dependent models, so no time step was required for either.

Comparison of results

For the purposes of discussion of the results each of the conditions in Table 1 will be referred to as 'typical' or 'storm' waves with an associated direction. For example, the condition storm (25°) will refer to results from test 3.

For each of the four test cases wave height coefficients at analysis points corresponding to the probe positions of the physical model were calculated. These are presented in Tables 2 to 5 for the physical model, each of the mathematical models on the 7m grid and PORTRAY over the 35m grid (referred to as PORTRAY CG). Each of the tabulated values is averaged over nine grid points centred at the analysis point, thus providing values which can be confidently accepted as representative of wave conditions at the given locations.

Discussion of results

Before examining the numerical results in more detail it is worth observing some of the more quantitative aspects of the results which are shown in Figure 2.

Figure 2 represents the calculated significant wave heights for each of the model tests for the storm (0°) condition. Figures 2a and 2b represent the results of PORTRAY for the fine and coarse grid solutions respectively. Figures 2c and 2d represent the calculated wave field for the hyperbolic and parabolic models.

Considering Figures 2a and 2b, it can be seen that PORTRAY models the wave effects on a fine and coarse mesh in a similar manner. The ray approximation means that diffraction by the channel is not represented, and the rays are reflected at the channel sides. This leads to the formation of caustics, and consequently excessively large wave heights at the channel sides. Physically, there will be an area of higher wave activity in this location, but the lack of representation of seabed diffraction in ray models will exaggerate this effect. This behaviour is more clearly seen in the finer grid case, where distinctive regions of large wave heights can be seen. Figure 2b shows how PORTRAY over a coarser grid has led to a more even distribution of the wavefield. This is because the averaging procedure (Southgate, 1984), used to calculate wave heights in the ray models, has effectively introduced a type of numerical diffraction. Also of note are the regions of very low wave heights. Since the PORTRAY model is based on tracing out wave orthogonals there will be some regions where no rays have been able to penetrate. Wave heights in these regions will be physically low, but PORTRAY predicts zero or negligibly small wave heights. It should be observed that, as far as the ray models are concerned, the storm (0°) was the most stringent of the four cases tested. This is because it represents long period waves incident along the line of a dredged channel, ie the case where physical diffraction will be an important mechanism. It will be seen from the numerical results that its performance improves for shorter period waves (typical (0°)), and more markedly for waves from 25° .

Considering the two finite difference models, Figures 2c and 2d, both hyperbolic and the parabolic models produce a similar

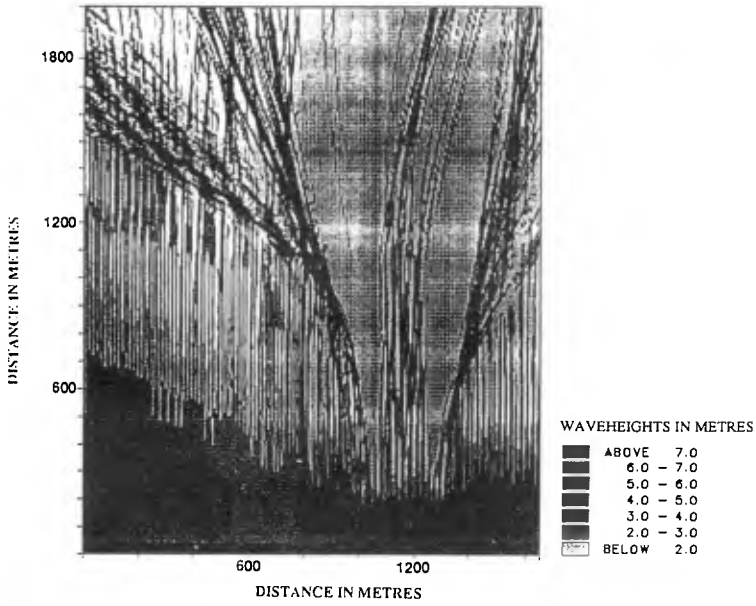


Figure 2a. Waveheight contours. PORTRAY. Storm(0°).

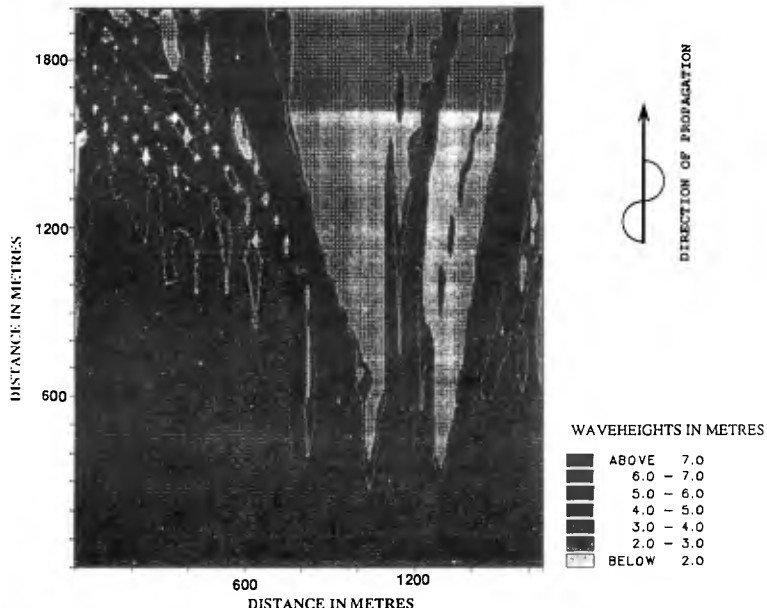
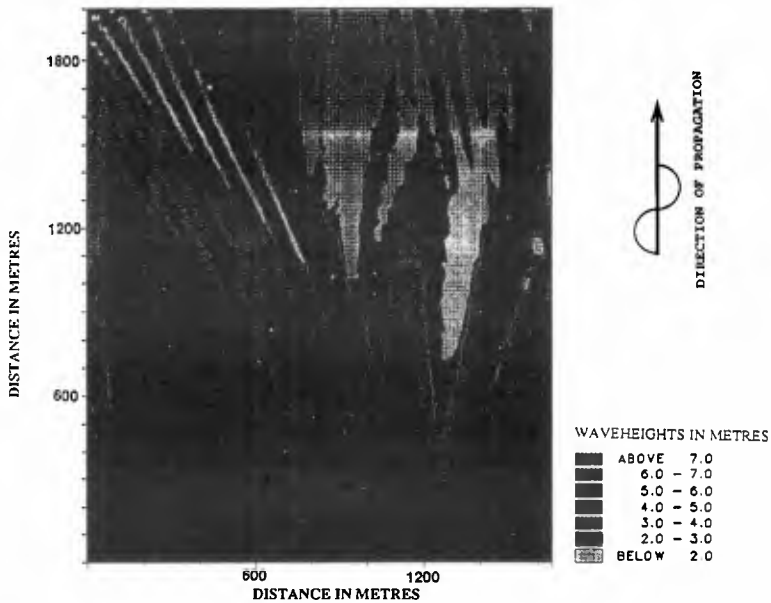
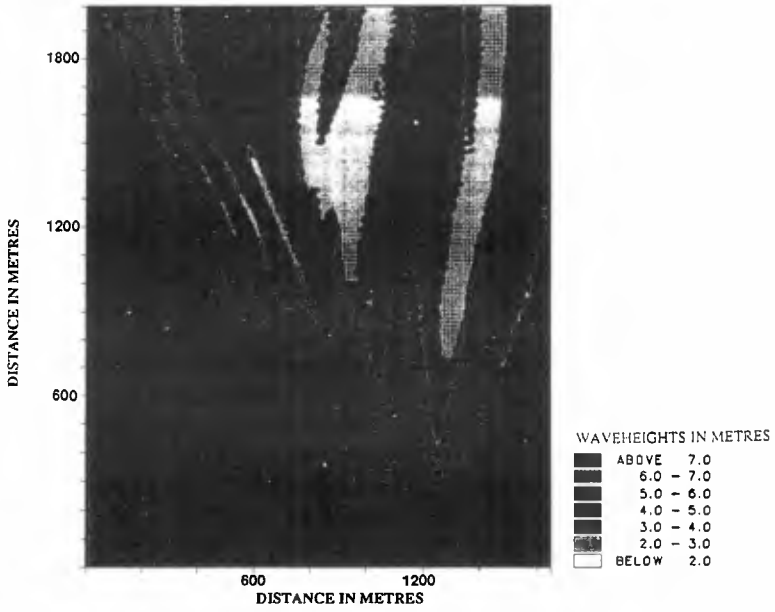


Figure 2b. Waveheight contours. PORTRAY_CG(Coarse Grid),Storm(0°).



wave pattern to that of PORTRAY, and compare more favourably with the coarse grid solution. Diffraction of waves in the vicinity of the channel results in a more even distribution of wave heights. At the channel sides waveheights are generally larger than in the channel region itself. It can be seen that the patterns of wave activity produced by these two models differ away from the channel. The hyperbolic model appears to concentrate energy close to the channel whereas the parabolic model spreads this diffractive energy out more evenly over a larger region.

Examination of the tabulated results allows a quantitative comparison with the measured data. The following discussion will consider positions along the centre, to the left and to the right of the channel, for each test case, in turn. The results shown in Table 2 correspond to measured and predicted waveheight coefficients at the prediction points, see Figure 1, for the illustrated storm (0°) condition, see Figure 2. At positions 3 and 6, along the centre of the channel, all of the models underpredict the waveheights compared with the measured values. The finite difference models are more reliable, within 30% of the measured data, than the PORTRAY solutions. This will be due to an insufficient number of rays penetrating into this region. Further along the channel, shorewards, at position 10, each model predicts significantly higher waveheights than was measured, although the predictions lie within 20% of their combined average. Considering positions to the left of the channel, at points 1, 2, 5, 8 and 9, the finite difference models' results are more consistent with the measured data, notably at position 1 and 5 where the results lie within 10% of the recorded values. Elsewhere, for all the models there are some discrepancies for which there is no apparent trend. To the right of the channel at point 4 each model overpredicts slightly compared with the measured value. However, at position 7 the numerical models underpredict conditions compared with those measured.

The tabulated results in Table 3 corresponding to the typical (0°) condition indicate that each model's performance will change for different incident wave periods. Only some of the trends discussed above are repeated. At position 3 improvement in the predictions is limited to PORTRAY-CG, although the finite difference models' prediction is only slightly worsened. The underprediction shown at position 6 for the storm (0°) condition is reversed for the typical (0°), and at position 10 the finite difference models' prediction is much improved at just over 20% difference. Only at position 1 to the left of the channel do one of the PORTRAY solutions differ from the measured values by more than the finite difference models do. However, the largest variations from the measured value oscillates between the models. The trend for the storm (0°) condition at position 4 and 7 is repeated for the typical (0°); the trends worsened at 4 but improved at 7.

It is clear from Table 3 that the performance of the finite

Analysis point	Physical model	PORTRAY	Parabolic	Hyperbolic	PORTRAY_CG
1	0.9	0.6	1.0	1.0	0.7
2	0.9	1.3	1.2	1.7	1.2
3	0.7	0.1	0.5	0.5	0.0
4	0.6	0.6	0.7	0.7	0.8
5	0.7	0.5	0.7	0.7	1.5
6	0.7	0.3	0.6	0.5	0.5
7	0.6	0.5	0.3	0.2	0.0
8	0.8	0.8	0.9	1.1	0.7
9	0.7	0.6	1.1	1.1	1.1
10	0.6	1.3	1.4	1.5	1.7

Table 2. Waveheight coefficients ,Storm(0°)

Analysis point	Physical model	PORTRAY	Parabolic	Hyperbolic	PORTRAY_CG
1	1.1	0.7	1.0	1.0	0.8
2	1.4	1.4	1.4	1.7	1.5
3	0.3	0.0	0.4	0.4	0.2
4	0.6	0.9	0.9	1.1	0.9
5	1.0	1.0	0.9	1.0	1.2
6	0.8	1.9	1.0	1.3	1.5
7	0.4	0.4	0.4	0.4	0.2
8	0.7	1.1	0.9	1.0	0.9
9	0.9	1.1	1.4	1.2	1.0
10	0.9	1.5	0.7	0.7	2.2

Table 3. Waveheight coefficients ,Typical(0°)

Analysis point	Physical model	PORTRAY	Parabolic	Hyperbolic	PORTRAY_CG
1	0.6	0.6	0.9	1.1	0.8
2	0.5	0.5	0.9	1.1	0.6
3	0.4	0.9	1.2	1.5	0.8
4	0.6	0.2	0.7	0.8	0.4
5	0.6	0.5	0.9	1.0	0.5
6	0.5	0.4	1.0	1.2	0.5
7	0.4	0.2	0.8	0.9	0.4
8	0.6	0.5	0.8	1.0	0.5
9	0.6	0.4	0.9	1.0	0.5
10	0.4	0.9	1.1	1.2	0.6

Table 4. Waveheight coefficients ,Storm(25°)

Analysis point	Physical model	PORTRAY	Parabolic	Hyperbolic	PORTRAY_CG
1	0.9	1.0	1.0	1.0	1.0
2	0.9	0.9	0.9	1.0	0.9
3	1.1	1.5	1.6	1.4	1.0
4	0.9	0.8	0.7	0.9	0.6
5	0.8	0.9	1.1	1.0	0.9
6	0.8	0.8	1.2	1.2	0.9
7	0.8	0.2	0.8	0.7	0.7
8	0.9	0.8	0.9	1.0	0.9
9	0.9	0.8	1.1	1.1	0.8
10	0.6	1.3	1.3	1.2	1.0

Table 5. Waveheight coefficients ,Typical(25°)

difference models for the storm (25°) conditions is considerably worse than that of the PORTRAY solutions with the parabolic model performing slightly better, but results which vary considerably from the measured values are commonplace. The results also indicate that the PORTRAY-CG solution offers the best comparison with the physical model result. Along the centre of the channel the finite difference models show the largest discrepancies with the measured values. To the left of the channel PORTRAY-CG and PORTRAY compare well with the measured data with PORTRAY-CG marginally better at 5, 8 and 9. Predictions by the finite difference models offer slightly better solutions to the left of the channel than along the centre, but still differ markedly from the measured values. Along the positions to the right of the channel, these discrepancies are reduced at position 4, but are again large at 7. Again the performance of PORTRAY-CG is best overall.

The tendency for the finite difference models to overpredict the waveheights for the storm (25°) is not apparent for the typical (25°) condition. Along the centre of the channel the PORTRAY-CG offers the best solution. To the left of the channel all the models perform well with results rarely more than 20% different, and in general closer to 10% different. To the right of the channel at positions 4 and 7 the largest deviation from the measured data are predicted by PORTAY-CG and PORTRAY respectively, with the results within 20% from the measured data at position 4, and 10% at position 7. The results from the finite difference models in this region are in good agreement with the physical model values.

Summary of results

The numerical models in general tend to exaggerate the physical features. In particular they display large spatial variations in wave height, which are not seen in the physical model. However, the mathematical models all give a reasonable representation of the overall physical behaviour.

For waves incident along the line of the channel, the finite difference models perform better in general than PORTRAY, although for incident waves in the off normal direction, notably the storm (25°) condition, the accuracy of the difference models is reduced. This confirms the expectation implied in the assumption made in the derivation of the parabolic approximation, but is less easy to explain in the case of the hyperbolic model.

Running the PORTRAY model over a carefully selected coarser grid has the effect of introducing numerical diffraction into the solution. This leads to a better representation, compared with the physical model, than the fine grid case.

In general the hyperbolic model took considerably longer, of the order of 8 to 10 times, to run than the parabolic and PORTRAY

models. The formulation of the hyperbolic model, which introduces the time variable, also gives rise to difficulties in determining the converged solution. For the test cases described here the parabolic and PORTRAY models took approximately 30 minutes elapsed time on a SUN 3/50 workstation.

Conclusions

All of the mathematical models tested give a reasonable description of the overall physical effects of waves propagating in the vicinity of a dredged channel. This was certainly good enough to justify their use in comparison of harbour approach schemes. Further calibration of the models, against a physical model or site specific measurements, is recommended if they are to be used for calculation of absolute values.

The PORTRAY model performed better for shorter period waves, and incident directions not along the line of the channel: For longer period waves, and where the waves were directly incident along the channel, the parabolic model gave a good representation, but does require that the grid is aligned in the main wave propagation direction. The combination of these two models appears to encompass most of the important physical features. The hyperbolic model did not appear to offer any significant advantages in terms of accuracy over the parabolic model and PORTRAY in these situations, and its run-times were significantly longer.

These conclusions are based on the comparisons made with the physical model tests described here, but are consistent with the anticipated behaviour inherent with the governing assumptions made for each of the mathematical models. Further work is in progress to examine improvements in the mathematical models' performance when random incident conditions are represented.

Acknowledgements

The authors would like to thank staff from Bristol University Mathematics Department and Liverpool University Civil Engineering Department for their advice and assistance with the finite difference models. The work described in this paper was funded as part of Hydraulics Research inhouse research programme.

References

- Berkhoff, J C W (1972). Computations of combined refraction-diffraction. ASCE Proc 13th Conf Coastal Eng, Chapter 24.
- Booij, N (1981). Gravity waves on water with non-uniform depth and current. Report 81-1, Delft University of Technology.
- Copeland, G J M (1985). A practical alternative to the mild slope equation. Coastal Engineering 9, p125-145.

Dodd, N (1988). Parabolic approximations in water wave refraction and diffraction. PhD thesis, Mathematics Department, University of Bristol.

Ito, Y and Tanimoto, K (1972). A method of numerical analysis of wave propagation-application to wave diffraction and refraction. ASCE Proc 13th Conf Coastal Eng, Chapter 26.

Madsen, P A and Larsen, J (1987). An efficient finite difference approach to the mild slope equation. Coastal Engineering II, p329-351.

Radder, A C (1979). On the parabolic equation method for water wave propagation. J Fluid Mech, Vol 95, p159-176.

Smallman, J V (1987). The application of a computational model for the optimisation of harbour layout. Proc 2nd International Conf on Coastal and Port Engineering in Developing Countries (COPEDEC) Beijing, China.

Southgate, H N (1989). Techniques of ray averaging. Int J for Num Meth in Fluids, Vol 4, p725-747.

Weggel, J R (1972). Maximum breaker height. Journal Waterways, Harbour and Coastal Division. ASCE, Vol 98, WW4, p529-548.

CHAPTER 47

OBSERVATIONS OF WIND WAVE NONLINEARITY

T. H. C. Herbers and R. T. Guza

*Center for Coastal Studies, A-009,
Scripps Institution of Oceanography,
La Jolla, California 92093, U.S.A.*

Abstract

Observations of pressure fluctuations at the sea floor in 13 m depth are compared to an existing theory for weakly nonlinear surface gravity waves (Hasselmann, 1962). In this depth, free surface waves (obeying the dispersion relation) at sea and swell frequencies (0.05 - 0.3 Hz) are weakly attenuated, but free waves at frequencies higher than about 0.4 Hz do not reach the sea floor. However, nonlinear interactions between (primary) free waves of about the same frequency, propagating in nearly opposing directions, theoretically excite long wavelength, double frequency (secondary) forced waves that are only weakly attenuated at the sea floor. Bottom pressure spectra observed in 13 m depth show an ($O(10^2)$) increase in high frequency (0.35 - 0.6 Hz) forced wave energy levels in only a few hours after a sudden large veering in wind direction. Estimates of the free wave frequency-directional spectrum show a correspondingly rapid change with unidirectional seas when forced wave energy levels are low before the wind veering, and two nearly directionally opposing seas (0.15-0.3 Hz) when forced wave energy levels are high, consistent with the theoretical generation mechanism. The observed forced wave energy levels are in good agreement with theoretical predictions based on the directional spectrum estimates. Estimates of average wave numbers verify that sea and swell obey the dispersion relation, and show that double sea frequency forced waves have longer wavelengths than the interacting free waves, consistent with theory. Observed third order statistics confirm that the double frequency forced waves are coupled to the directionally opposing seas with a phase relationship predicted by theory.

Introduction

Wind generated surface gravity waves can be represented approximately by a linear superposition of statistically independent wavelets obeying the linearized equations (e.g., Kinsman, 1965). Observations presented here concern some of the weak, but interesting, nonlinear properties of natural wind waves. Theories for weakly nonlinear surface gravity waves, based on a perturbation expansion for small wave steepness, have been developed by various authors (Phillips, 1960; Hasselmann, 1962; and others). The lowest order wave

field is a frequency-directional spectrum $E(f, \theta)$ of free linear waves obeying the dispersion relation

$$f = \frac{1}{2\pi} [g |\mathbf{k}| \tanh(|\mathbf{k}| h)]^{1/2} \quad (1)$$

where \mathbf{k} is the vector wave number, h the water depth and g the acceleration of gravity. At the next order, forced (i.e., not obeying Eq. 1) secondary waves are generated in non-resonant triad interactions with two free wave components. Each pair of primary (free) waves, with frequencies and wave numbers (f_1, \mathbf{k}_1) and (f_2, \mathbf{k}_2) , is accompanied by a pair of secondary waves with the sum and difference frequency and wave number $(f_1 \pm f_2, \mathbf{k}_1 \pm \mathbf{k}_2)$. These lowest order nonlinearities theoretically result in weakly nonGaussian statistics and possibly large deviations from the dispersion relation (e.g., Phillips, 1960; Hasselmann et al., 1963). For example, if $E(f, \theta)$ is narrow and unimodal, then the dominant secondary wave contribution to sea surface elevation is due to the interactions of free wave components with nearly equal frequency ($f_1 \approx f_2$) and wave number ($\mathbf{k}_1 \approx \mathbf{k}_2$). The sum interaction yields the familiar $(2f, 2\mathbf{k})$ Stokes forced wave, in phase with the free wave components, that theoretically distorts the sinusoidal linear wave surface to a profile with sharper crests and flatter troughs. The Stokes correction, which in deep water has double the wavelength of a free wave with the same frequency, contributes a positive skewness to sea surface statistics.

At great depth the theoretically expected local nonlinear effects are markedly different than at the sea surface. Surface gravity waves (both free and forced components) are very strongly attenuated at depths below the sea surface that exceed about half their wavelength. Free waves obeying the dispersion relation (Eq. 1) with typical sea and swell frequencies (0.05-0.3 Hz) are therefore confined to the upper 10-300 m of the ocean, as are the Stokes-type $(2f, 2k)$ secondary waves. Forced waves, however, can have very long wavelengths if $\mathbf{k}_1 \approx \pm \mathbf{k}_2$ and penetrate virtually unattenuated to the ocean floor. A long wavelength, double frequency forced wave $(2f, \mathbf{k} \approx 0)$ can be generated by the sum interaction of two free waves of nearly equal frequency travelling in opposing directions ($f_1 \approx f_2, \mathbf{k}_1 \approx -\mathbf{k}_2$, Miche, 1944). This nonlinear effect is believed to cause high frequency sea floor pressure oscillations and microseisms in the deep ocean (e.g., Longuet-Higgins, 1950).

The present study examines the properties of high frequency secondary forced waves in natural wind waves. Array measurements of wave pressure were collected offshore of Chesapeake Bay in a water depth of 13 m. In this depth locally generated seas (0.15-0.3 Hz) are only weakly attenuated at the sea floor while free waves at double sea frequencies (> 0.35 Hz) are very strongly attenuated, so that relatively weak (at the sea surface) double sea frequency forced waves with longer wavelengths are theoretically dominant at the sea floor. The present observations show, in agreement with theory, that long wavelength high frequency forced waves are generated by the sum interactions of seas travelling in nearly opposing directions. The experiment is described in section 2. In section 3, frequency spectra of pressure on the sea floor are presented that show a rapid increase in forced wave energy levels at double sea frequencies after a large veering in local wind direction, as a result of the nonlinear interactions of nearly directionally opposing seas. The observed energy levels of forced waves are consistent with weakly nonlinear theory. In section 4, deviations from the dispersion relation and nonGaussian statistics associated with weakly nonlinear waves are examined with estimates of average wave numbers and third order

statistics of the bottom pressure field. The results are summarized in section 5. A full account of the observations is given in Herbers and Guza (1990 b, c).

Experiment

Arrays of pressure transducers were deployed at the Chesapeake Light Tower, as part of the SAXON (SAR and X-band Ocean Nonlinearities) experiment. The tower is situated on an exposed shoal approximately 30 km offshore of Cape Henry, Virginia, U.S.A.. The water depth at the tower is 13 m with approximately 0.5 m tidal fluctuations. Two arrays were deployed, each consisting of seven capacitance sensing pressure transducers. One of the arrays (dimensions 20 m x 20 m) was mounted on the tower structure at mid-depth and the other array (dimensions 12 m x 12 m) on the seabed (Fig. 1). The primary purpose of the mid-depth array was to provide estimates of the frequency-directional spectrum $E(f, \theta)$ of (free) sea and swell. The bottom array was deployed to measure the secondary pressure

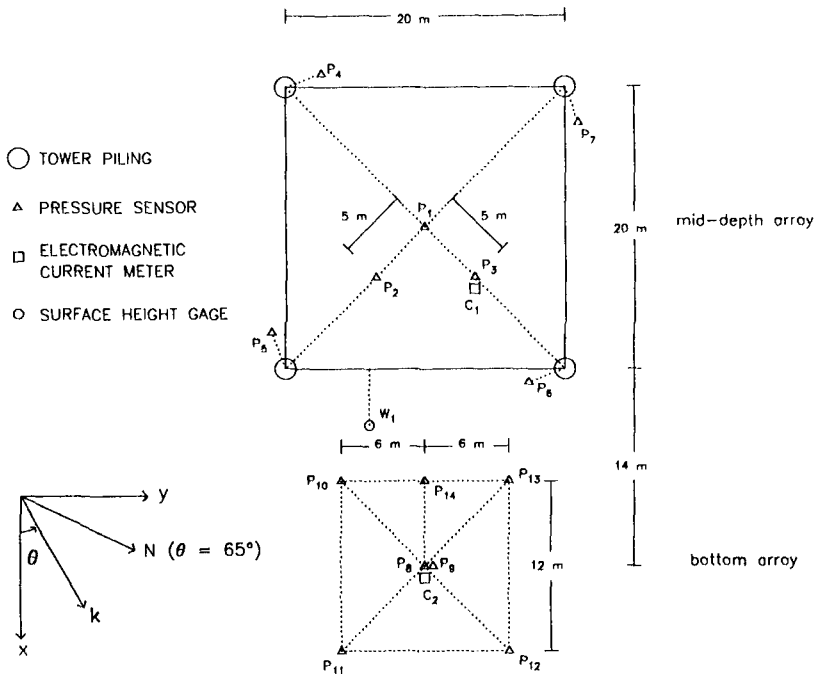


Figure 1. Plan view of mid-depth (6 m below Mean Sea Level) and bottom (13 m below Mean Sea Level) array geometries and analysis coordinate frame. k is the wave number vector and θ is the wave propagation direction. $\theta = 65^\circ$ corresponds to waves arriving from the South.

field. It is better suited for detecting weak high frequency forced waves than the mid-depth array because high frequency free waves are more strongly attenuated at the sea floor than at mid-depth. The bottom array was displaced approximately 24 m East from the center of

the tower (Fig. 1) to reduce tower interference, all bottom sensor locations were accurate to within 5 cm, and the sensors were buried about 10 cm in the sand to reduce flow noise. Data was collected with a 2 Hz sample frequency on a nearly continuous basis from 17 September through 14 October, 1988, spanning a wide range of conditions. Surface elevation data (sampled at 30 Hz) from a surface piercing wire gage, located on the East side of the tower (Fig. 1), was collected intermittently by A. T. Jessup (1989, personal communication). Throughout the experiment the predominantly tidal mean flows, observed at mid-depth and on the bottom, were smaller than about 25 cm/sec and their effect is negligible.

3. Forced Wave Energy and Directionally Opposing Seas

Fig. 2 shows the evolution of the average (over all bottom sensors) bottom pressure frequency spectrum $E_b(f)$ during a 85 hour period, 9 through 13 October 1988. The local wind during this period was highly variable with moderate speeds less than 15 m/sec (Fig.

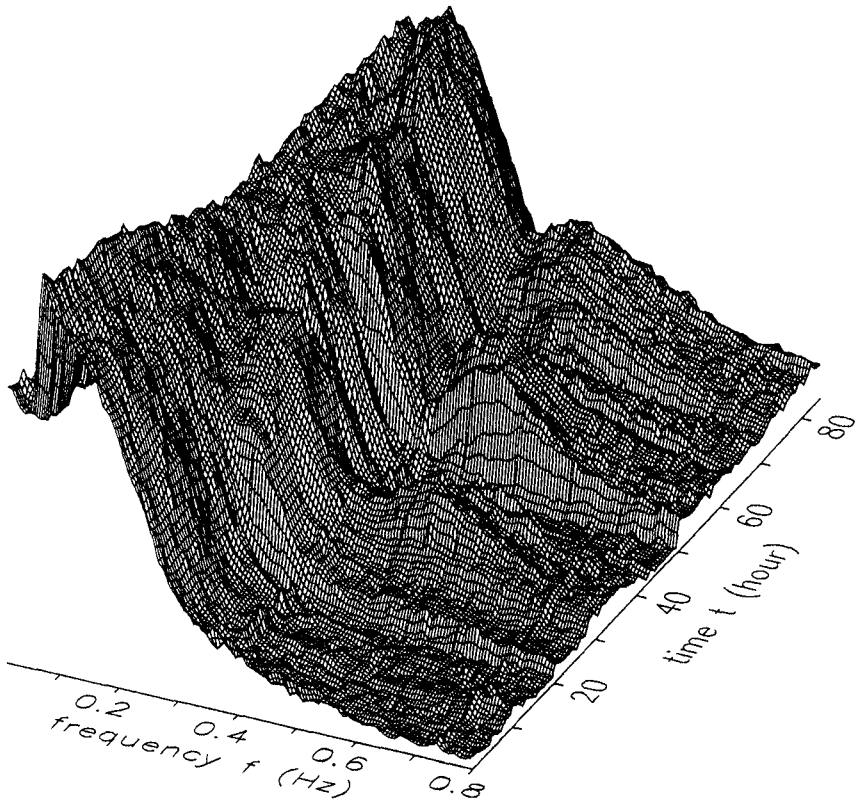


Figure 2. A 3-dimensional surface of $\log E_b(f)$ from 9 October 20:30 h through 13 October 09:30 h, 1988 (local time) at hourly intervals.

3) and significant wave heights ranged from 0.5 to 1.5 m. The high variability in the bottom pressure spectra in the frequency range of 0.35 - 0.7 Hz is striking. In particular, between $t \approx 49$ and 53 h the energy in this range suddenly increases by more than 2 orders of magnitude and a broad feature develops with its peak at approximately 0.47 Hz (Fig. 4). The present study is focused on this event; Herbers and Guza (1990 b, c) discuss the entire period. These high frequency pressure fluctuations cannot be explained with linear wave theory because of the strong attenuation of high frequency free waves. For example, for a surface gravity wave component with frequency $f = 0.5$ Hz, that obeys the linearized equations, the attenuation of pressure at the sea floor relative to the surface is approximately 10^6 . Sea surface excursions of $O(1$ km) would be needed to generate free 0.5 Hz bottom pressure oscillations with $O(1$ mm) amplitude (approximately the root mean square value of the high frequency pressure fluctuations at $t = 53$ h). Wave staff data and visual observations show significantly smaller seas.

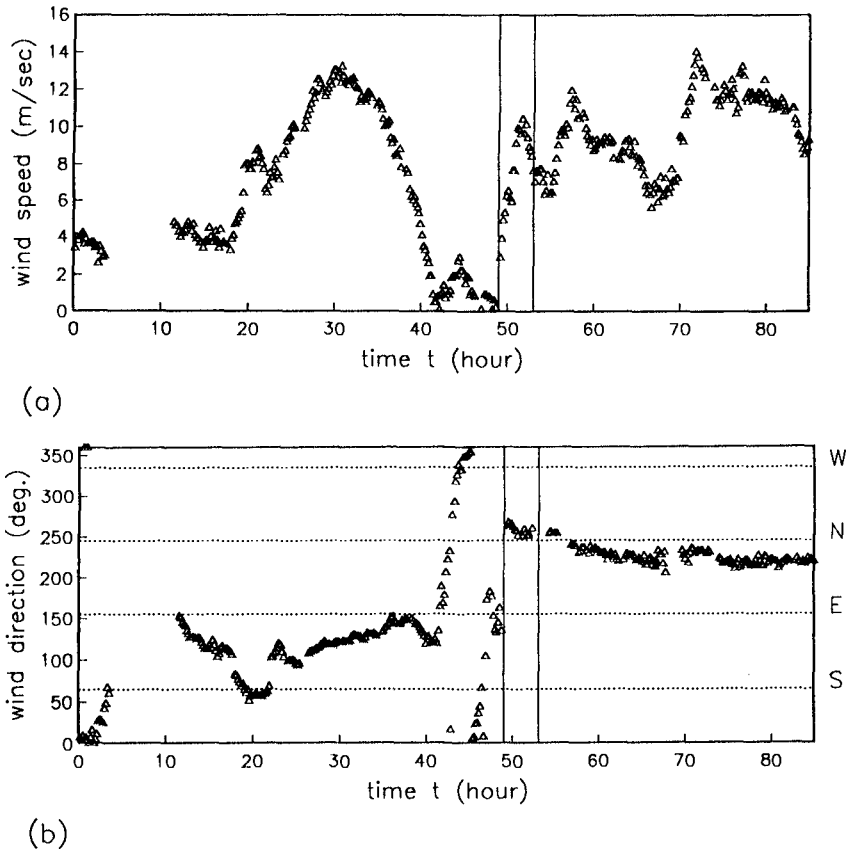


Figure 3. Ten minute averages of wind speed (a) and direction (b) measured 42 m above the sea surface on top of the light tower (edited data provided by A.T. Jessup, personal communication). The vertical lines indicate times selected for detailed analysis.

Between $t = 20$ h and 40 h, the wind was relatively steady in direction from the South-East ($\approx 110^\circ$) with speeds increasing from 4 m/sec to a maximum of 13 m/sec at $t = 30$ h and decreasing to near calm at $t = 40$ h (Fig. 3). During the period $t = 40 - 50$ h, the wind remained calm, followed by a rapid increase to about 10 m/sec at $t = 50$ h, with a direction from the North ($\approx 260^\circ$) nearly opposing the wind direction 20 hours previous (Fig. 3). The dramatic increase in high frequency energy levels between $t = 49$ h and $t = 53$ h (Fig. 4) is related to this change in local winds, but the nonlinear interactions are more complicated than the familiar Stokes second harmonic corrections. In a narrow band surface elevation frequency-directional spectrum $E_s(f, \theta)$ with peak frequency f_p and peak direction θ_p , generation of high frequency secondary waves on the sea surface is dominated by the ("self-self") interactions of energetic components near the spectral peak ($f_1 \approx f_2 \approx f_p$, $\theta_1 \approx \theta_2 \approx \theta_p$). However, these $(2f_p, \theta_p)$ second harmonics have double the wave number k_p of the free wave components and are very strongly attenuated at the sea floor if $k_p h \gg 1$. For the present observations of local seas with periods of 4 to 5 sec in 13 m depth, $k_p h \approx 3$. Stokes self-self interactions in this relatively deep water are both weak at the sea surface (i.e., not amplified by near-resonance) and very strongly attenuated at the sea floor. Longer wavelength forced waves that are generated by the interactions of seas and swell propagating in (nearly) opposing directions are expected to dominate the secondary bottom pressure spectrum.

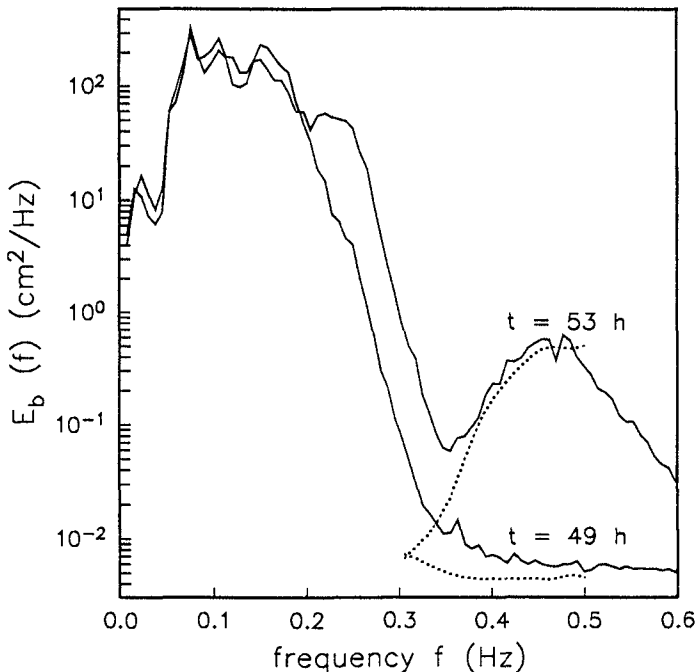


Figure 4. Observed (solid, an average of all bottom sensors) and predicted (dotted, at double sea frequencies 0.3 - 0.5 Hz) bottom pressure frequency spectra, before and after a large increase in forced wave energy levels.

To verify that the observed forced waves are generated by directionally opposing seas, frequency-directional spectra $E_s(f, \theta)$ of free waves (i.e., obeying the dispersion relation, Eq. 1) were estimated from the mid-depth pressure array data. $E_s(f, \theta)$ is expressed as

$$E_s(f, \theta) = E_s(f) S(\theta; f) \tag{2}$$

where $E_s(f)$ is the surface elevation frequency spectrum and $S(\theta; f)$ is the directional distribution at frequency f . On a frequency band by frequency band basis the "smoothest" $S(\theta)$ "consistent" with the array data is obtained by minimizing a roughness measure of the form

$$\int d\theta \left[\frac{d^2 S(\theta)}{d\theta^2} \right]^2$$

subject to the constraint that $S(\theta)$ is a nonnegative function with unit integral that fits the array cross-spectra within a 75 % confidence level (Herbers and Guza, 1990a). Fig. 5 shows estimates of $E_s(f, \theta)$, obtained from the mid-depth array cross-spectra (200 degrees of freedom), at $t = 49$ and 53 h in the frequency range 0.05 - 0.3 Hz, where the energy spectra are energetic and assumed to be dominated by free waves obeying the dispersion relation. This assumption is verified in section 4. At $t = 49$ h, when forced wave energy levels are low, the $E_s(f, \theta)$ estimate shows nearly unidirectional seas from the South with peak frequency 0.18 Hz (Fig. 5a). Four hours later (Fig. 5b), more energetic, slightly higher frequency ($f_p \approx 0.26$ Hz) locally generated seas arriving from the North are also present in a bimodal $E_s(f, \theta)$. The sudden, nearly 180° veering in wind direction from South to North between approximately $t = 40$ h and $t = 50$ h is consistent with the observed change in $E_s(f, \theta)$. Predictions of the forced wave bottom pressure spectrum in the frequency range 0.3 - 0.5 Hz, based on the two $E_s(f, \theta)$ estimates (Fig. 5) and weakly nonlinear theory (Hasselmann, 1962; see Herbers and Guza, 1990b, for the details of the calculations), are compared to the

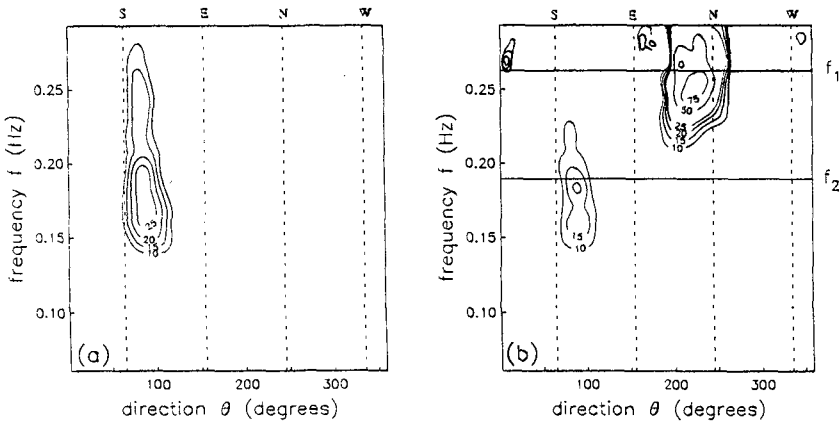


Figure 5. Estimates of the surface elevation frequency-directional spectrum (units $\text{cm}^2/\text{Hz}^\circ$) at $t = 49$ h (a) and 53 h (b). Solid lines (b) indicate bispectral peak frequencies (Fig. 8).

observed bottom pressure spectra (an average of all bottom sensors) in Fig. 4. At frequencies below 0.35 Hz the observed pressure spectrum shows increasingly more power than the forced wave prediction because free waves reach the sea floor. In the frequency range 0.35 - 0.5 Hz, predicted forced wave spectra show the dramatic increase in forced wave energy after the wind veered, due to the interactions of opposing seas, and are in good agreement with the observed forced wave energy levels. However, a change in local wind conditions is not the only mechanism for generation of directionally opposing seas and associated long wavelength forced waves. The double sea frequency forced wave peaks at $t \approx 32$ h and $t \approx 80$ h (Fig. 2) are generated by a similar change in the directional wave spectrum, but the bi-directional seas are the result of the arrival of nonlocally generated wind waves rather than a veering wind (Herbers and Guza, 1990b).

Fig. 6 shows the frequency spectra of all pressure sensors in the mid-depth and bottom array, and a surface elevation spectrum computed from surface piercing wire gage data (provided by A.T. Jessup, personal communication) at $t = 53$ h. The observed vertical decay of sea and swell (0.05 - 0.3 Hz) is consistent with the dispersion relation for free waves (Herbers and Guza, 1990b). The relative decay between mid-depth and bottom pressure at the double sea frequency forced wave peak is not only much weaker than the theoretical value for linear waves but also weaker than the decay of the interacting seas, consistent with the long wavelengths of forced waves generated by opposing seas. As expected from theory, free wind generated waves dominate surface elevation at high frequencies but are very strongly attenuated below about mid-depth (at 0.5 Hz the predicted power decay of free waves at the mid-depth array, relative to the surface, is 10^{-5}). Forced

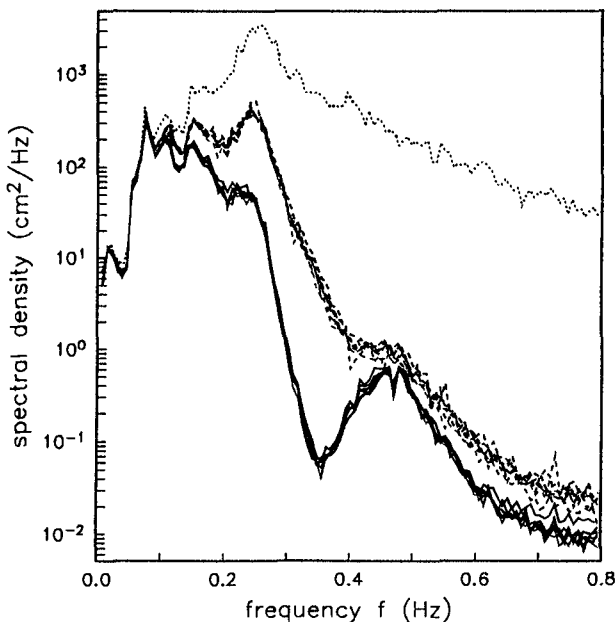


Figure 6. Pressure frequency spectra on the sea floor (solid) and at mid-depth (dashed) at $t = 53$ h. The dotted line is a surface elevation spectrum (data provided by A.T. Jessup, personal communication).

waves smaller in amplitude, but with longer wavelengths, are only weakly attenuated and dominate the high frequency pressure field in the lower part of the water column.

4. Average Wave Numbers and Third Order Statistics

Secondary forced wave components cause nonGaussian statistics and deviations from the dispersion relation. Third order statistics of weakly nonlinear waves are nonzero owing to a statistically consistent phase relationship between free and forced wave components. The resulting nonzero skewness of the bottom orbital velocity field may be important to sediment transport on the shelf. The deviations of forced waves from the dispersion relation can be very large and cause errors in the interpretation of bottom pressure measurements which is often based on the linear dispersion relationship. This is true in particular at frequencies high enough that free waves are strongly attenuated and forced waves contribute significantly to the spectral density. In this section deviations from the dispersion relation and statistical coupling of free and forced waves are examined in the bottom pressure data at $t = 53$ h with high forced wave energy levels (Fig. 4).

A bulk averaged wave number $k_{rms}(f)$ defined as

$$k_{rms}(f)^2 \equiv \int dk |k|^2 E_b(f,k) / \int dk E_b(f,k) \quad (3)$$

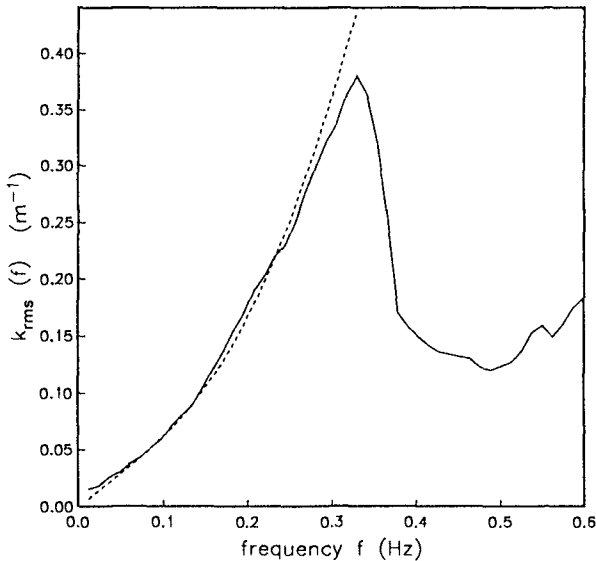


Figure 7. A $k_{rms}(f)$ estimate at $t = 53$ h. The dashed curve is the surface gravity wave dispersion relation.

with $E_b(f, k)$ the bottom pressure wave number-frequency spectrum, can be estimated from a compact array of bottom pressure sensors with spacings L_{ij} small compared to the surface wavelength. The details of the technique, which utilizes a linear combination of the cross-spectral elements, are described in Herbers and Guza (1990c). Fig. 7 shows a $k_{rms}(f)$ estimate at $t = 53$ h. In the frequency range 0.05 - 0.3 Hz, the wave number estimate agrees with the linear dispersion relation within a few percent, consistent with the assumption (used when estimating $E_s(f, \theta)$, Eq. 2) that this part of the spectrum is dominated by free sea and swell. In the spectral valley between the wind wave and double frequency peaks $k_{rms}(f)$ drops sharply and reaches a minimum near the double sea frequency peak ($f \approx 0.5$ Hz). In fact the observed forced waves (that do not obey the dispersion relation) have longer wave lengths than the free waves forcing them, qualitatively consistent with the theory for forced waves excited by the observed directionally opposing seas (Fig. 5).

To examine statistical coupling between the directionally opposing sea peaks and the double frequency forced wave peak, bispectra (Hasselmann et al., 1963; Elgar and Guza, 1985; and others) were computed from the bottom pressure data. Fig. 8 shows an estimate of the normalized bispectrum $b(f_1, f_2)$

$$b(f_1, f_2) \equiv \frac{B(f_1, f_2)}{[E_b(f_1) E_b(f_2) E_b(f_1 + f_2)]^{1/2}} \quad (4)$$

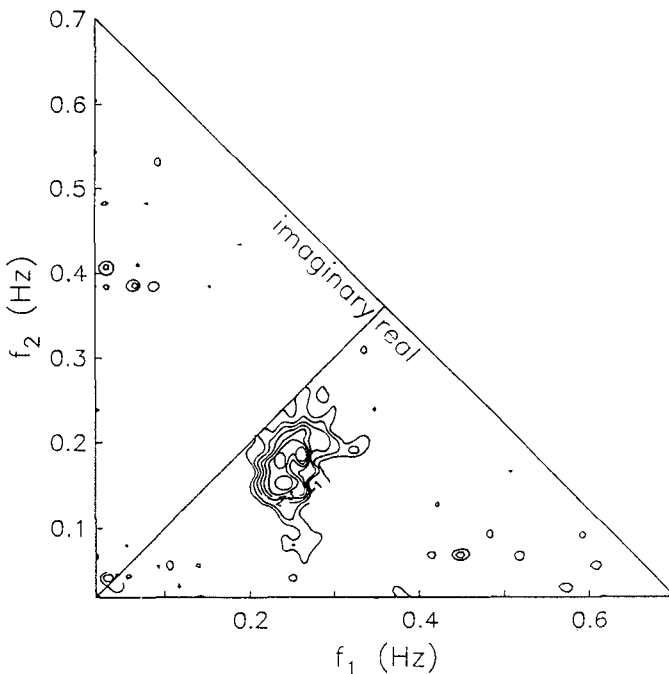


Figure 8. A $b(f_1, f_2)$ estimate (spectra averaged over all bottom sensors) at $t = 53$ h. Contours at levels -6, -5, -4, -3, -2, 2, 3, 4, 5, and 6 $\text{Hz}^{-1/2}$ are shown.

with the bispectrum $B(f_1, f_2)$ defined as the expected value of the third order moment of the bottom pressure Fourier-Stieltjes transform $dZ(f)$:

$$B(f_1, f_2) df_1 df_2 \equiv 2 E\{dZ(f_1) dZ(f_2) dZ(-f_1-f_2)\} \quad (5)$$

The bispectrum vanishes for the wind generated Gaussian free waves and statistically significant deviations of $b(f_1, f_2)$ from zero can be interpreted as nonlinearity of the bottom pressure field associated with the presence of forced waves. Theoretically, the contributions of triad interactions between f_1 (free), f_2 (free) and $f_1 + f_2$ (forced) wave components to $b(f_1, f_2)$ are real (Hasselmann et al., 1963), which means that the bottom pressure field is skewed (i.e., different crest and trough profiles) but statistically symmetric about a vertical plane (i.e., wave crests are not pitched forward or backward). In 13 m depth, the bispectrum at double sea frequencies is theoretically negative and these long forced waves may contribute to a negative skewness of sea floor pressure and orbital velocity fields, rather than the positive skewness of Stokes waves (Herbers and Guza, 1990b). Fig. 8 shows that the observed $b(f_1, f_2)$ is real (deviations of the imaginary part from zero are statistically insignificant), negative, and has a large peak centered at $f_1 \approx 0.26$ Hz, $f_2 \approx 0.18$ Hz. These frequencies are very close to the peak frequencies of the two directionally opposing wind wave systems (Fig. 5b). The observed bispectrum is thus consistent with the theoretical phase relationship between directionally opposing primary waves and secondary long waves (Herbers and Guza, 1990b). Integrals of $B(f_1, f_2)$ along constant sum frequency $f_1 + f_2$ (not shown here, discussed in Herbers and Guza, 1990c) show that nearly all of the wave energy in the range 0.4 - 0.5 Hz is statistically coupled to the two directionally opposing seas. The bispectral estimate thus provides an independent verification of the hypothesis that the observed forced waves are generated by directionally opposing seas.

5. Summary and Conclusions

To examine local nonlinear effects on natural wind generated surface gravity waves, arrays of pressure transducers were deployed at mid-depth and on the sea floor in 13 m deep water, approximately 30 km offshore of Cape Henry, Virginia. Bottom pressure data show enhanced energy at double sea frequencies that appears to be nonlinearly driven by local seas. These nonlinear bottom pressure observations are explained using an existing theory for weakly nonlinear waves (e.g., Hasselmann, 1962). The perturbation solution to second order in wave steepness consists of (primary) free waves obeying the dispersion relation and (secondary) forced waves that do not obey the dispersion relation, generated by interactions between pairs of free waves. Free and forced wave components are both strongly attenuated at depths exceeding about half a wavelength, but forced waves excited by the interactions of directionally opposing free waves of nearly equal frequency have much longer wavelengths than free waves of the same frequency, and thus penetrate to greater depths. In narrow band directional spectra the dominant nonlinear interactions at the sea surface are between waves near the spectral peak having nearly equal frequency and propagation direction. However, in 13 m depth the bottom pressure energy levels of "Stokes harmonics" at double sea frequencies are strongly attenuated, approximately 10^4 - 10^6 weaker than the energy levels of relatively unattenuated forced waves generated by two narrow seas of equal frequency and energy, travelling in nearly opposing directions. Forced wave energy levels on the sea floor in 13 m depth at double sea frequencies are thus theoretically expected to be weak in unidirectional seas and increase dramatically when directionally opposing seas are present.

After the local wind veered, the observed bottom pressure spectra show a large ($O(10^2)$) increase in forced wave energy levels over only a few hours. Estimates of the frequency-directional spectrum of free sea and swell were extracted from the mid-depth array data, before and after this large increase in forced wave energy levels. The estimates show nearly unidirectional free waves when forced wave energy levels were low, and seas travelling in opposing directions when forced wave energy levels were high. Theoretical predictions of forced wave energy spectra, obtained using the estimated free wave directional spectra, confirm that the observed forced waves are generated by the interactions of 0.15 - 0.3 Hz seas travelling in much different directions. The observed large fluctuations in forced wave energy levels are in good agreement with the theoretical predictions. Estimates of average wave numbers confirm that sea and swell obey the dispersion relation and double sea frequency forced waves have longer wavelengths than the interacting seas. Observed third order statistics show nonlinear coupling between directionally opposing seas and forced waves with a phase relationship predicted by theory.

Acknowledgments

This work is a result of research sponsored by the Office of Naval Research, under grants N00014-89-J-3097 and N00014-86-K-0789. The staff of the Center for Coastal Studies (Scripps Institution of Oceanography), led by R. L. Lowe, W. A. Boyd, and M. C. Clifton, installed and maintained the arrays and data acquisition systems. We thank A. T. Jessup for generously providing wind and sea surface elevation data, and S. Elgar for helpful discussions and sharing his bispectra code with us.

References

- Elgar, S. and R. T. Guza, 1985: Observations of bispectra of shoaling surface gravity waves. *J. Fluid Mech.*, 161, 425-448.
- Hasselmann, K., 1962: On the non-linear energy transfer in a gravity-wave spectrum, Part 1. General theory. *J. Fluid Mech.*, 12, 481-500.
- Hasselmann, K., W. Munk and G. MacDonald, 1963: Bispectra of ocean waves, in *Times Series Analysis*, M. Rosenblatt (ed.), John Wiley, New York, 125-139.
- Herbers, T. H. C., and R. T. Guza, 1990a: Estimation of directional wave spectra from multi-component observations. *J. Phys. Oceanogr.*, in press.
- Herbers, T. H. C., and R. T. Guza, 1990b: Wind wave nonlinearity observed at the sea floor. Part I: Forced wave energy. Submitted to *J. Phys. Oceanogr.*
- Herbers, T. H. C., and R. T. Guza, 1990c: Wind wave nonlinearity observed at the sea floor. Part II: Wave numbers and third order statistics (manuscript in preparation).
- Kinsman, B., 1965: *Wind Waves: Their Generation and propagation on the ocean surface*, 676 pp., Prentice-Hall, Englewood Cliffs, N.J.
- Longuet-Higgins, M. S., 1950: A theory of the origin of microseisms. *Philos. Trans. R. Soc. London, A* 243, 1-35.
- Miche, M., 1944: Mouvements ondulatoires de la mer en profondeur constante ou décroissante. *Ann. Ponts Chaussees*, 114, 25-87, 131-164, 270-292, 396-406.
- Phillips, O. M., 1960: On the dynamics of unsteady gravity waves of finite amplitude. Part 1. The elementary interactions. *J. Fluid Mech.*, 9, 193-217.

CHAPTER 48

APPLICABILITY OF A NEW HYBRID PARAMETRIC WAVE PREDICTION MODEL

Yoshio Hatada¹ and Masataka Yamaguchi²

ABSTRACT

DOLPHIN-I is a new hybrid parametric deep water wave prediction model developed by the authors. This paper examines the applicability of DOLPHIN-I, on the basis of the comparison of the computation with the data of significant waves obtained in five sea areas with different horizontal scales around Japan during monsoons and typhoons. In particular, the wave data in Osaka Bay includes frequency and directional spectra. It is verified that the model practicality is excellent, because it reproduces well the wave data observed in any concerned sea area.

1. INTRODUCTION

In the past 10 years, a number of hybrid parametric wave prediction models such as HYP A, TOHOKU, GONO (SWAMP, 1985), HYPAS (Günther et al., 1984) and Graber & Madsen's model (1988) have been proposed. The advantages of these models which imply the effects of wind input, wave-wave interaction and wave breaking in a parametric representation, are the capability to save computer processing time, as compared with the discrete spectral model, and to give reasonable estimation of wave growth under a gradually-varying simple wind field.

However, the degree of freedom in the models is not enough to properly resolve the directional characteristics of a confused wave field in the rapidly-varying wind field of a typhoon and in the sea area enclosed by complicated shorelines, because wave direction is approxi-

1 Research Assistant, Dept. of Ocean Eng., Ehime Univ., Bunkyocho 3, Matsuyama 790, Ehime Pref., Japan

2 Prof., Dept. of Ocean Eng., Ehime Univ., Bunkyocho 3, Matsuyama 790, Ehime Pref., Japan

mated by only one parameter such as a mean wave direction averaged with respect to frequency and direction.

Yamaguchi et al.(1988) developed a new directionally-decoupled hybrid parametric wave prediction model in deep water, hereafter referred to as DOLPHIN-I, in order to improve this situation. DOLPHIN-I assumes that the directional energy of wind-sea defined separately for each direction grows according to a parametric equation derived from an analysis of observed wave growth data under the assumption of ideal generation conditions and that each swell component propagates independently, undergoing energy dissipation. It is formulated so as to make it possible to estimate the time variation of directional spectra at a prescribed location through the computation along the straight wave rays focusing at the location. The computed results for test cases given in SWAMP(1985) showed physically sound behavior in each case (Yamaguchi et al., 1988).

The aim of this paper is to examine the applicability of DOLPHIN-I, based on the comparison between computation and observation. First, a brief explanation of the model is provided from the view points of model formulation and computation method. Wave hindcast is conducted in five sea areas with different horizontal scales during monsoons and typhoons, and wave observation data used in the comparison include not only significant waves but also frequency and directional spectra.

2. OUTLINE OF DOLPHIN-I

(1) Model Formulation

The radiative transfer equation is given as

$$\frac{\partial E(f, \theta)}{\partial t} + C_g(f) \cos \theta \frac{\partial E(f, \theta)}{\partial x} + C_g(f) \sin \theta \frac{\partial E(f, \theta)}{\partial y} = G(f, \theta) \quad (1)$$

where $E(f, \theta)$ is the directional spectrum, f the frequency, θ the direction, $C_g(f) (= g/4\pi f)$ the group velocity of a wave component, g the acceleration of gravity and $G(f, \theta)$ the source function modeling inflow and outflow of wave energy. When a straight propagation path of a wave component is selected such that $dx/ds = \cos \theta$ and $dy/ds = \sin \theta$, Eq.(1) is rewritten as

$$\frac{\partial E(f, \theta)}{\partial t} + \frac{\partial C_g(f) E(f, \theta)}{\partial s} = G(f, \theta) \quad (2)$$

The integration of Eq. (2) over frequency yields the following equation which describes the evolution of directional energy density of wind waves $E(\theta)$

$$\left. \begin{aligned} \frac{\partial E(\theta)}{\partial t} + \frac{\partial \bar{C}_g E(\theta)}{\partial s} &= \int_0^\infty G(f, \theta) df \\ E(\theta) &= \int_0^\infty E(f, \theta) df, \quad \bar{C}_g = \int_0^\infty C_g(f) E(f, \theta) df / E(\theta) \end{aligned} \right\} \quad (3)$$

where \bar{C}_g is the frequency-averaged group velocity.

We assume that wind waves grow under the ideal generation condition, in which case directional spectrum is expressed as a product of the JONSWAP spectrum (Hasselmann et al., 1973) and $\cos^4\theta$ -type angular spreading function and that evolutions of spectral parameters such as saturation range constant α , dimensionless peak frequency ν , and peak enhancement factor γ are governed by the energy-dependent relations which are derived from the empirical expressions of Mitsuyasu et al. (1980). Then, the frequency-averaged group velocity and source function in Eq. (3) can be determined, and evolution of the directional energy of wind-sea $E^*(\theta)$ is described as

$$\left. \begin{aligned} \frac{\partial E^*(\theta)}{\partial t} + \frac{\partial}{\partial s} [C_g(f_m) f(\gamma) E^*(\theta)] &= 2.851 \times 10^{-4} \left\{ \frac{E^*(\theta)}{D^*(\theta)} \right\}^{0.3273} \cdot \exp \left[-0.0875 \right. \\ &\cdot \left. \left\{ \frac{E^*(\theta) |D^*(\theta)|}{1.43 \times 10^3 - E^*(\theta) |D^*(\theta)|} \right\}^{0.8542} \right] \cdot \frac{u_*^3}{g} \cos(\theta - \theta_w) D^*(\theta) \\ D^*(\theta) &= \begin{cases} (8/3 \pi) \cos^4(\theta - \theta_w); & |\theta - \theta_w| < \pi/2 \\ 0 & ; |\theta - \theta_w| \geq \pi/2 \end{cases} \\ f(\gamma) &= 0.8572 \gamma^{0.0426} \end{aligned} \right\} \quad (4)$$

where f_m is the peak frequency, u_* the friction velocity, θ_w the wind direction and $D(\theta)$ the angular spreading function. The asterisk means the ideal generation condition.

Propagation of a swell component is formulated by the above-mentioned one-dimensional radiative transfer equation with an energy dissipation term. It is given as

$$\frac{\partial E_s(f, \theta)}{\partial t} + \frac{\partial C_g(f) E_s(f, \theta)}{\partial s} = \begin{cases} -0.25(u_*|C|)^2 f E_s(f, \theta); & |\theta - \theta_w| < \pi/2 \\ -\beta_M(f, \theta) E_s(f, \theta) & ; |\theta - \theta_w| \geq \pi/2 \end{cases} \quad (5)$$

where $E_s(f, \theta)$ is the directional spectrum of a swell component, $C (=g/2\pi f)$ the wave celerity, and β_M the damping rate due to opposing wind.

In the general sea state, directional spectra of sea waves $E(f, \theta)$ are divided into frequency-integrated directional energy of wind-sea $E_s(\theta)$ and directional spectra of swell components $E_s(f, \theta)$. The directional energy of wind-sea is defined by

$$E_s(\theta) = \int_{\partial f_{m0}}^\infty E(f, \theta) df \quad (6)$$

where $f_{m\theta}$ is the peak frequency of directional spectra for each direction and $\delta(=0.6)$ the correction factor used for the separation of wind-sea and swell. Setting $E_\delta(\theta)$ equal to $E^*(\theta)$ at the growth stage of wind-sea, evolution of wind-sea energy for each direction is computed from Eq. (4) and then total wave energy parameter of wind-sea $\tilde{\epsilon}^*$ is evaluated by $\tilde{\epsilon}^* = E^*(\theta)/D^*(\theta)$. Directional spectra of wind-sea $E_w(f, \theta)$ are established using both the JONSWAP spectrum with the spectral parameters related to dimensionless wave energy and the angular spreading function $D^*(\theta)$. On the other hand, change of directional spectrum for each swell component $E_s(f, \theta)$ is obtained from Eq. (5).

Directional spectrum in general sea state at the same place is evaluated by simply summing up the directional spectral component for the same frequency and direction of both wind sea and swell as

$$E(f, \theta) = E_w(f, \theta) + E_s(f, \theta) \tag{7}$$

The wave statistics are obtained by the numerical integration of directional spectra over wave direction and frequency using the relations such as

$$\left. \begin{aligned} E(f) &= \int_0^\pi E(f, \theta) d\theta, \quad \epsilon = \int_0^\infty E(f) df, \quad H_{1/3} = 4\sqrt{\epsilon} \\ T_{1/3} &= 1.20\sqrt{\epsilon / \int_0^\infty f^2 E(f) df}, \quad \bar{\theta} = \tan^{-1} \left\{ \frac{\int_0^\infty \int_0^\pi E(f, \theta) \sin \theta d\theta df}{\int_0^\infty \int_0^\pi E(f, \theta) \cos \theta d\theta df} \right\} \end{aligned} \right\} \tag{8}$$

where $E(f)$ is the frequency spectrum, ϵ the total wave energy, $H_{1/3}$ the significant wave height, $T_{1/3}$ the significant wave period, and $\bar{\theta}$ the mean wave direction.

(2) Method of Numerical Computation

DOLPHIN-I estimates the time variation of directional spectra of sea waves at a prescribed point by following growth, decay, and propagation of sea waves along a wave ray radiating separately from the point for each direction, as shown in Fig. 1.

The evolution equation of directional energy, Eq. (4) is solved by a finite difference method of the two-step Lax-Wendroff scheme. It is given as

$$\left. \begin{aligned} e_{i+1/2}^{n+1/2} &= \frac{e_i^n + e_{i+1}^n}{2} - \frac{\Delta t}{2 \Delta s} (K_{i+1}^n - K_i^n) + Q_{i+1/2}^n \frac{\Delta t}{2} \\ e_i^{n+1} &= e_i^n - \frac{\Delta t}{\Delta s} (K_{i+1/2}^{n+1/2} - K_{i-1/2}^{n+1/2}) + Q_i^{n+1/2} \Delta t \end{aligned} \right\} \tag{9}$$

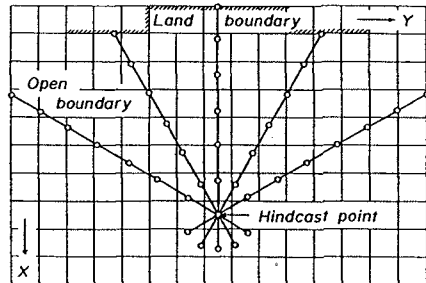


Fig. 1 Wave ray and computation of propagation.

where $e = E^*(\theta)$, $K = \overline{C_g} E^*(\theta)$, Q is the source term in Eq.(4), n the index of the time step, i the grid number on a wave ray, and Δs the grid spacing on a wave ray. The value of e is specified in a parametric manner at the upwave open boundary and it is set at zero in the case of the land boundary. At the downwave boundary, directional energy is freely transmitted, and the upwind difference scheme indicated by

$$e_N^{n+1} = e_N^n - \frac{\Delta t}{\Delta s} (K_N^n - K_{N-1}^n) + Q_N^n \Delta t \tag{10}$$

is used, because Eq. (9) is not applicable, where N is the grid number at the boundary. It should be noted that one grid point is added to the grid system for each direction in order to keep the accuracy of computation at the hindcast point.

The computation of the radiative transfer equation, Eq. (5), makes use of a fractional time step method in which the propagation equation and the forcing equation are solved alternatively. The propagation step uses a piecewise ray method with the Lagrange third order spatial interpolation formula expressed as

$$\left. \begin{aligned} E_s(f, \theta) &= a_1 E_{s_{i-2}}^n(f, \theta) + a_2 E_{s_{i-1}}^n(f, \theta) + a_3 E_{s_i}^n(f, \theta) + a_4 E_{s_{i+1}}^n(f, \theta) \\ a_1 &= -(r-2)(r-1)r/6, \quad a_2 = (r-2)(r-1)(r+1)/2, \\ a_3 &= -(r-2)r(r+1)/2, \quad a_4 = (r-1)r(r+1)/6, \quad r = 1 - C_d(f)\Delta t/\Delta s \end{aligned} \right\} \tag{11}$$

At the grid point next to the upwave boundary and at the downwave boundary, the interpolation formulas with the first and second order accuracy

$$\left. \begin{aligned} E_s(f, \theta) &= (1-r)E_{s_i}^n(f, \theta) + rE_{s_{i+1}}^n(f, \theta) \\ E_s(f, \theta) &= a'_1 E_{s_{i-2}}^n(f, \theta) + a'_2 E_{s_{i-1}}^n(f, \theta) + a'_3 E_{s_i}^n(f, \theta) \\ a'_1 &= (r-1)r/2, \quad a'_2 = (1-r)(1+r), \quad a'_3 = r(r+1)/2 \end{aligned} \right\} \tag{12}$$

are applied respectively as well as in the above-mentioned case. The computation of the forcing step is conducted with the analytical solution given by

$$\left. \begin{aligned} E_s^{n+1}(f, \theta) &= E_s(f, \theta) \exp\{-0.25(u_*^2/C)^2 f \Delta t\} \quad ; \quad |\theta - \theta_w| < \pi/2 \\ E_s^{n+1}(f, \theta) &= E_s(f, \theta) \exp(-\beta_w \Delta t) \quad ; \quad |\theta - \theta_w| \geq \pi/2 \end{aligned} \right\} \tag{13}$$

3. APPLICABILITY OF DOLPHIN-I

(1) Conditions in Wave Hindcast

As shown in Fig. 2, wave hindcast is conducted in the five sea areas with different horizontal scales: Lake Biwa with an extension of 15 to 30 km, Osaka Bay and the Kii Channel with an extension of 30 to 100 km, the western part of the Seto Inland Sea with an extension of 150 km, the Japan Sea with an extension of 800 to 1300 km, and the Northwest Pacific Ocean with an extension of more than 2000 km. In the Pacific Ocean, typhoon-generated waves are hindcast, in which case wind distribution is

estimated by a simple parametric typhoon model. In the other sea areas, waves associated with monsoons are computed, in which case evaluation of wind distribution over the sea is based on a spatial interpolation method of the measured wind data or a weather map analysis.

Table 1 is the computational conditions used in wave hindcast on each sea area. The directional range of -180° to 180° , number of directional data N_θ of 37 and directional increment $\Delta\theta$ of 10° are the same in all cases.

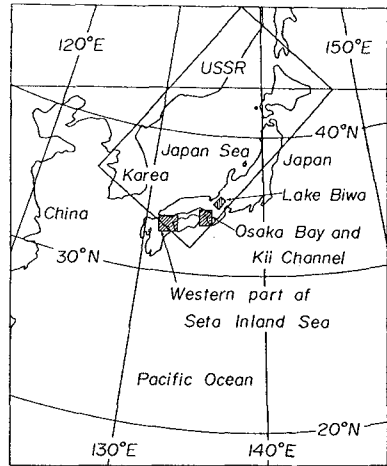


Fig. 2 Five sea areas with different horizontal scales used in wave hindcast.

Wind velocity at the height of 10 m over sea level U_{10} in each sea area is estimated with the method given in Table 1. Friction velocity u_* in DOLPHIN-I is computed from U_{10} by use of a modified form of Mitsuyasus's empirical formula (1984). It is written as

$$C_d = (u_* / U_{10})^2 = \begin{cases} (0.581 + 0.063 U_{10}) \times 10^{-3} & ; U_{10} \geq 10 \text{ m/s} \\ 1.211 \times 10^{-3} & ; U_{10} < 10 \text{ m/s} \end{cases} \quad (14)$$

where C_d is the drag coefficient of the sea surface. Wind characteristics at grid points on each wave ray are evaluated every 30 minutes through linear interpolations with respect to time and space of wind data given every 1 hour at the rectangular grid points.

Table 1 Numerical conditions used in wave hindcast.

	Lake Biwa	Osaka Bay & Kii Chan.	Seto Inland Sea	Japan Sea	Pacific Ocean
MxN	20x15	36x28	30x35	25x44	43x43
$\Delta x = \Delta y$ km	2.5	3	5	40	80
Δs km	2.5	3	5	40	80
Δt min	7.5	6	10	30	60
f_{\min} Hz	0.176	0.1	0.1	0.05	0.04
f_{\max} Hz	2	1.5	1.5	1	1
N_f	22	23	23	24	30
method of wind estimation	interpolation of measured winds	ditto	ditto	weather map analysis	typhoon model

M, N: number of grids in x and y direction, Δx , Δy : grid spacing
 Δs : grid spacing on a ray, Δt : time increment, N_f : number of frequency
 f_{\min} : minimum frequency, f_{\max} : maximum frequency

In the hindcast on the sea areas, except for the Pacific Ocean, land boundary condition in which case the directional spectrum is zero is imposed. On the other hand, directional spectra computed by a product of JON-SWAP-type frequency spectrum referred to as the Ross hurricane model(1976) and $\cos^4\theta$ -type angular spreading function are given at the grid points corresponding to the open boundary of the Pacific Ocean area, in which case input data are local wind characteristics and distance between the concerned grid point and the position of the typhoon center.

In order to initiate DOLPHIN-I, which does not have any term for initial generation of wind waves, directional spectra computed from the before-mentioned model under the conditions of $H_{1/3} = 0.1$ m and $u_* = 0.12$ m/s are provided as an initial condition.

(2) Wave Hindcast in Lake Biwa

Fig. 3 shows the grid system with spacing of 2.5 km placed over Lake Biwa. During winter monsoons, strong winds of more than 10 m/s continue to blow over the lake for two or three days with repetitions of gradual increase and decrease of wind velocity, and the resulting wind fields are quasi-homogeneous and quasi-steady. The wind distribution is obtained by linear interpolation of the wind data measured at three points(B, C and D) with respect to the y direction, in which case uniformity of the wind field in the x direction is assumed.

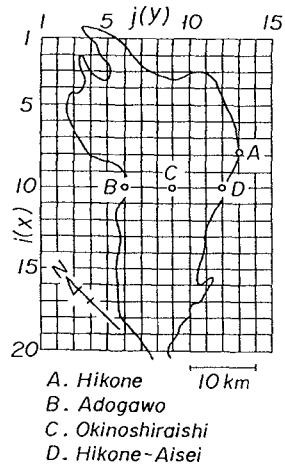


Fig. 3 Grid system used in Lake Biwa.

Fig. 4 indicates the comparison between time variations of significant wave heights and

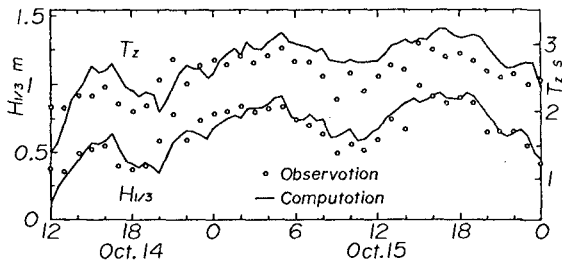


Fig. 4 Comparison between the computed and observed significant waves in Lake Biwa.

mean wave periods observed and hindcast at Hikone-Aisei point, where T_z is the mean period defined by the zero and second moments of frequency spectra, as is indicated in Eq. (10). This is typical of wave variations occurring during seasonal winds in Lake Biwa. The figure shows excellent agreement between the computation and the measurement of significant wave height variation, but hindcast mean periods are slightly greater than the observed results. The reason is that the formulation of DOLPHIN-I is based on Mitsuyasus's empirical relation between spectral parameters and dimensionless fetch, which gives smaller estimation than spectral parameters obtained from the analysis of wave data in Lake Biwa. So, improvement of the model applicability to wave evaluation in Lake Biwa is possible by changing the expressions of spectral parameters.

(3) Wave Hindcast in Osaka Bay and the Kii Channel

Fig. 5 is the grid system with a spacing of 5 km used in wave hindcast, in which small circles are the wind observation stations deployed around the concerned sea area. Wind distribution over the area every 1 hour is estimated from the application of a linear interpolation formula to measured wind data on each of the triangular meshes made by connecting the wind observation stations together (Yamaguchi et al., 1981).

Fig. 6 is the comparison between the computation and the observation for time variation of significant waves at the MT station in Osaka Bay during a strong storm brought about with a typical pressure pattern in the winter of Japan. Wave heights show rapid growth to over 2 m high because of the duration of strong winds of maximum 20 m/s with the direction of SW to W and then they reduce to about 1 m high with a change into moderate winds of 10 m/s or so with the direction of WNW, while wave periods of about 4 s do not vary so much as wave heights. DOLPHIN-I reproduces well the observed time variation of wave heights, but gives a slight overestimation of that

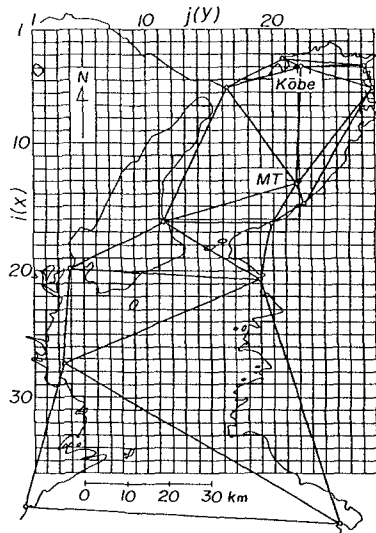


Fig. 5 Grid system used in Osaka Bay and the Kii Channel.

of wave periods.

Another comparison of the time variation of significant waves at the MT station is indicated in Fig. 7. Strong stormy winds during the period of wave hindcast were brought about by a developing low system which proceeded easterly over the Japan Sea. DOLPHIN-I again results in good resolution for the observed time variation of significant waves associated with strong winds whose velocity increases rapidly and then decreases with change of the wind direction from SW to NW. But in detail, DOLPHIN-I tends to give a slight underestimation before the peak period of the storm.

Fig. 8 is the comparison between the computation and the observation for frequency spectra and directional spectra at the MT station. DOLPHIN-I behaves well even for reproduction of the observed wave spectra, but the directional spectra in measurement have a smoother distribution than those in computation, because the directional spectra are evaluated with the Fourier series method of poor directional resolution from current records of the three components. A slight difference in the dominant wave direction in directional spectrum is also found because of possible errors in orientation of the instrument and variability of the measured wind direction.

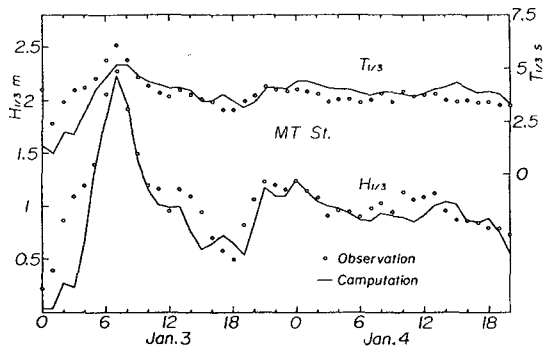


Fig. 6 Comparison between the computed and observed significant waves at the MT station in Osaka Bay (1).

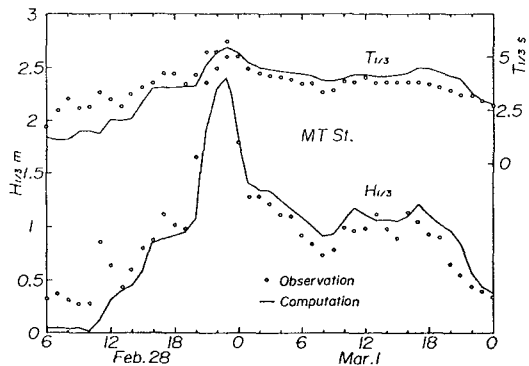


Fig. 7 Comparison between the computed and observed significant waves at the MT station in Osaka Bay (2).

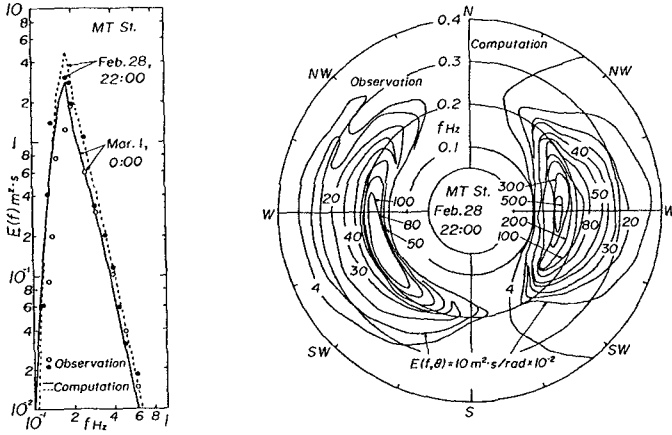


Fig. 8 Comparison of the computed and observed frequency spectra and directional spectra at the MT station in Osaka Bay.

(4) Wave Hindcast in the Western Part of the Seto Inland Sea

Wave hindcast in this sea area is conducted for the period of seasonal winds on the grid system given in Fig. 9, in which case estimation of wind distribution is based on a linear interpolation of measured wind data on triangular elements as well as the case for Osaka Bay. The seasonal winds occurred with the passage of twin low pressure systems over the Japan Sea and the resulting moderately strong winds of over 10 m/s with the direction of WNW to NW continued to blow over the sea area.

Fig. 10 is a simultaneous plot of the time variations of the significant waves at Kanda and Iyo obtained from the computation and the observation. At Kanda with longer fetch for predominant wind direction,

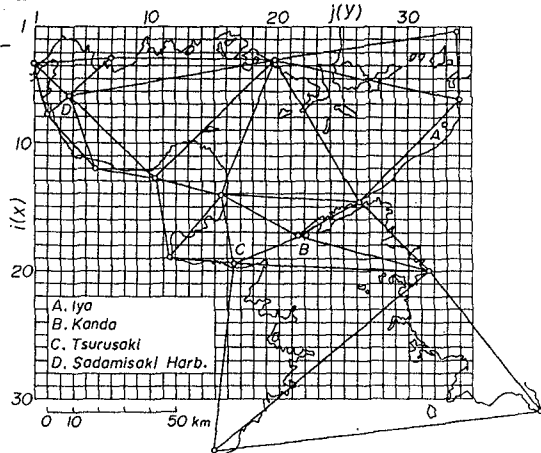


Fig. 9 Grid system used in the western part of the Seto Inland Sea.

correspondence of the computation with the observation is excellent through all periods of the storm, and reasonable agreement between them is also achieved at Iyo with longer fetch, though the observed results are limited in a short period under high wave conditions. The reason why the observed wave periods are slightly greater than the computed ones may be due to the fact that the observation was made with a pressure-type wave gauge.

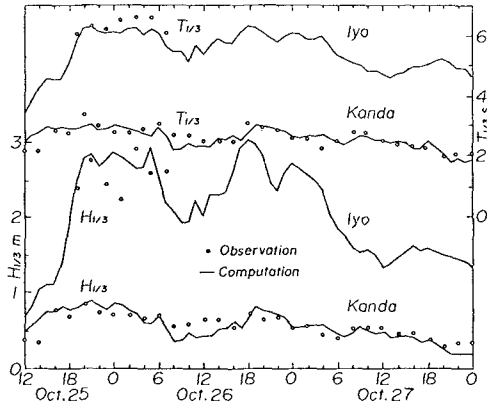


Fig. 10 Comparison between the computed and observed significant waves at Iyo and Kanda.

(5) Wave Hindcast in the Japan Sea

Fig. 10 is the grid system with spacing of 40 km used in wave hindcast on the Japan Sea. The winter storm of interest was generated by a low system whose time history was that two lows, one proceeding northeasterly along the Japan Sea and the other similarly along the Pacific Ocean side of the Japanese coast, came together over the eastern sea area of north Japan and the central pressure lowered to 970 mb at the severest period. Wind distribution over the area is given by the method (Yamaguchi et al., 1984) which estimates gradient winds by approximating curvature of the isobar line and pressure gradient with a spline function and then converts them to winds over the sea, multiplying a constant coefficient (=0.67) by gradient wind velocity and rotating gradient wind direction by 17° counter-clockwise.

The computed and observed time variations of significant waves at

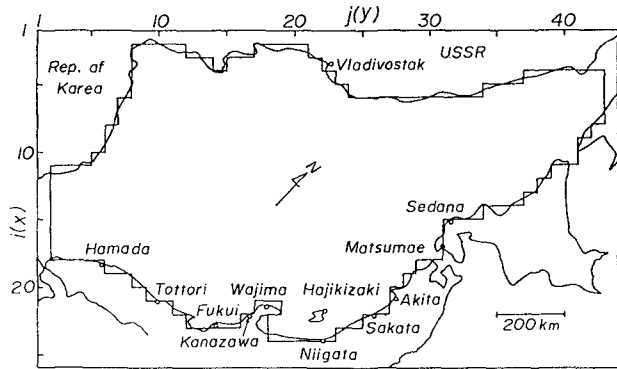


Fig. 11 Grid system used in the Japan Sea.

Wajima with a water depth of 50 m and Tottori with a water depth of 30 m are compared in Fig. 12. The model takes into account the effect of water depth on waves in an expedient way by multiplying the frequency spectrum computed at the hindcast point by a correction factor of $\Phi(kh)=\tanh^2 kh$, where k is the wave number and h the water depth. DOLPHIN-I with a correction for water depth effect predicts the variation of waves with the change of winds in a general sense better than the original DOLPHIN-I, but the degree of agreement between the computation and the observation is not as accurate as in the above-mentioned cases in which wind distribution is estimated with interpolation of measured wind data, because of less accuracy of hindcast winds. In particular, the computed time variation of waves at Wajima is about 4 hours behind the observed one, reflecting the time lag between the computed winds and the measured winds.

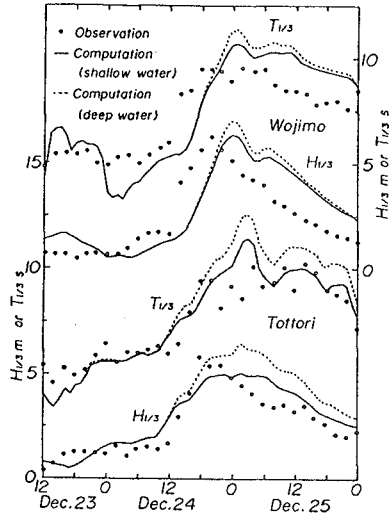


Fig. 12 Comparison between the computed and observed significant waves at Wajima and Tottori.

(6) Wave Hindcast in the Northwest Pacific Ocean

Waves caused by a typhoon with rapidly-varying wind fields is hindcast in the Pacific Ocean. Fig. 13 is the grid system with a spacing of 80 km placed on the Pacific Ocean, in which the tracks of two typhoons to be hindcast for wave conditions - Typhoon 8115 and Typhoon 8210 - are also drawn. The estimation of wind distribution in a typhoon relies on the use of a parametric typhoon model. The model in which the exponential function is assumed for the pressure distribution, computes the wind fields in a typhoon

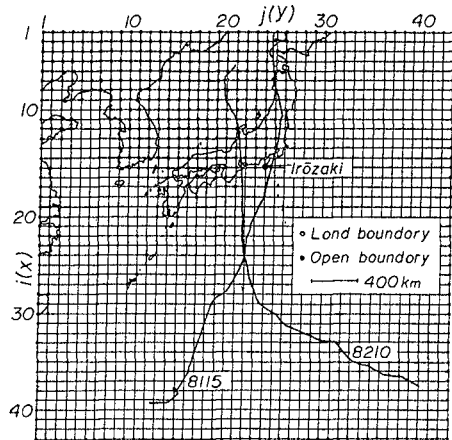


Fig. 13 Grid system used in the Pacific Ocean.

by using parameters such as central pressure, position of the typhoon center, radius to maximum winds and wind inflow angle to the typhoon center. These data are given every 6 hours and through a linear interpolation, wind field is estimated at intervals of 1 hour.

Fig. 14 is the time variation of significant waves at Irouzaki situated on the Pacific Ocean side of the Japanese coast, as is indicated in Fig. 13. The computation is in close agreement with the observation showing propagation of swell with a distant typhoon and rapid growth and decay of wind waves with approach and passage of a typhoon. Accordingly, the model predicts general characteristics of typhoon-generated waves in the northern hemisphere such that waves during Typhoon 8210 when Irouzaki was situated on the right hand side of the typhoon track give more rapid growth and decay associated with approach and passage of a typhoon than those during Typhoon 8115 when Irouzaki was situated on the left hand side of the typhoon track. When the effect of water depth on wave characteristics at Irouzaki where water depth is 50 m deep is introduced in the same way as in the Japan Sea case, the computed results might be slightly smaller than the observed ones.

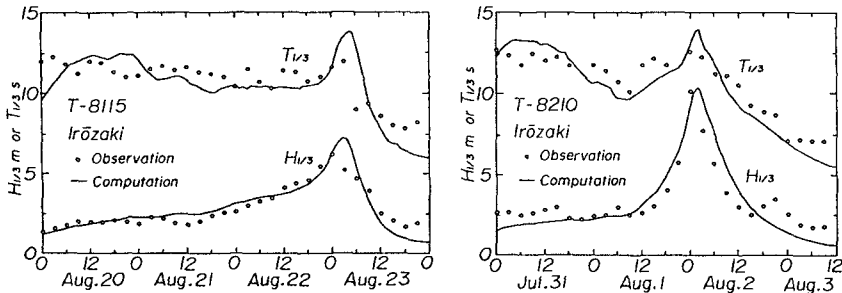


Fig. 14 Comparison between the computed and observed significant waves at Irouzaki.

4. CONCLUSIONS

Practical applicability of the wave prediction model developed by the authors, DOLPHIN-1, was confirmed by reasonable agreement between the hindcast results and the wave data, including directional spectrum, which were acquired in five sea areas with different horizontal scales around Japan.

5. ACKNOWLEDGEMENTS

The authors thank the Bureaus of Harbor Construction, Ministry of Transportation and the Prefectural Offices for kindly offering the valuable wind and wave data.

REFERENCES

- Graber, H.C. and Madsen, O.S. (1988): A finite-depth wind-wave model, Part 1-Model description, *J. Phys. Oceanogr.*, Vol.18, pp. 1465 - 1483.
- Günther, H., Komen, G.J. and Rosenthal, W. (1984): A semi-operational comparison of two parametrical wave prediction models, *Deutsch. Hydrogr. Zeit.*, No. 37, Heft 3, pp. 89-106.
- Hasselmann, K. et al. (1973): Measurements of wind-wave growth and swell decay during the Joint North Sea Wave Project(JONSWAP), *Deutsch. Hydrogr. Zeit.*, A8, Heft 12, pp. 1 - 95.
- Mitsuyasu, H. et al. (1980): Observation of the power spectrum using a cloverleaf buoy, *J. Phys. Oceanogr.*, Vol. 10, pp. 286 - 296.
- Mitsuyasu, H. and Kusaba, T. (1984): Drag coefficient over water surface under the action of strong wind, *J. Natural Disas. Sci.*, Vol. 6, No. 2, pp. 43 - 50.
- Ross, D.B. (1976): A simplified model for forecasting hurricane generated waves (abstract), *Bull. American Meteorol. Soc.*, No. 113.
- SWAMP Group (1985): *Ocean Wave Modeling*, Plenum Press, 256pp.
- Yamaguchi, M. et al. (1981): Spatial distribution of winds over Osaka Bay, *Proc. 28th Conf. on Coastal Eng. in Japan*, pp.168 - 172 (in Japanese).
- Yamaguchi, M. et al. (1984): A method for estimating surface winds from weather map analysis based on spline function approximation, *Proc. 31st Conf. on Coastal Eng. in Japan*, pp. 128 - 132 (in Japanese).
- Yamaguchi, M., Holthuijsen, L.H., Hatada Y. and Hino, M. (1988): A new hybrid parametric wave prediction model taking the wave directionality into account, *Proc. JSCE*, Vol. 399/II-10, pp. 193-202 (in Japanese).

CHAPTER 49

Bottom Shear Stress and Friction Factor Due to the Asymmetric Wave Action

C. T. Kuo ¹

W. J. Chen ²

Abstract

A micro shear gauge was used to measure the bottom shear stress under the shallow water wave on the smooth bed, the data show that bottom shear stress have an asymmetric form similar to the surface water elevation due to the non-linearity of wave. The bottom friction factor under wave crest and wave trough were very different with that defined by Jonsson's and the results were contrary when the bottom particle velocity were defined by linear and non-linear wave theory respectively. Empirical formula were obtained for practical use.

Introduction

Because of the development of economic and increase of population, in recent years, utilization of coastal areas has steadily been increasing for human activities such as transportation and industry. All of the development were taken in the nearshore area and the wave phenomena occurred in this area almost influenced by the bottom shear stress, directly or indirectly.

Therefore wave induced bottom shear stress and friction has an impacted relativity with energy decay, sediment transport rate and wave induced current, etc. About two decades, there were many researchers paid their attention to the bottom boundary layer problems, such as Riedel(1972), Jonsson(1976), Kamphuis(1976)

1 Professor, Graduate school of Hydraulics and Ocean Eng., National Cheng Kung University, Tainan 70101 Taiwan, Republic of China.

2 Lecturer, Dept. of Civil Engineering., National Chiayi Institute of Agriculture, Chiayi 60083 Taiwan, Republic of China.

, Iwagaki (1974), John (1982), Kuo & Chuan (1981) etc. Though they have obtained some basic results, those researchs haven't discussed the variation of bottom shear stress and friction affected with the asymmetry of wave profile in shallow water; therefore, the phenomena described by the above may have an important parameter to determine the sediment moving direction and the on-offshore sediment transport rate.

Sawaragi(1974), Tanaka(1987), Iwagaki(1987), etc. have presented that the non-linear effect of shallow water wave could be made a obviously difference on bottom shear stress and friction factor under the wave crest and wave trough passed respectively. Tanaka (1987) used the stream function theory to calculate the shear stress under non-linear wave and took their results to derive the on-offshore sediment transport rate. In spite of there have a few paper mentioned about the bottom shear stress influenced by the non-linear wave, those research haven't analyzed the shear stress under crest and trough detailly, also they haven't measured the bottom shear stress to verify their results.

In this paper, we use a micro shear gauge to measure the bottom shear stress under shallow water wave acting, the data collected from this experiment were taken to analyze the stress under wave crest and trough respectively, the results were compared with the stress that calculate from linear wave theory. Also we use the non-linear wave theory to calculate the bottom friction factor, and the analyzed results show a visible difference which compared to the results that obtained from linear wave theory by Jonsson etc.

Experimental Facilities and Conditions

The experiment of this paper is taken in a 40 m long, 1.0 m wide, and 1.0 m deep wave flume. The bottom shear stress is measured by a micro shear gauge which was set up in a steely box and installed into the bottom of flume. The sketch of the experimental equipments were show in Fig. 1. The maximum capacity of this shear gauge is 0.2 g and the diameter of the sensible plate is only 1 cm, therefore the sensitive area is too small when compared to the shear plate, so the measured error which occurred at the shear plate; such as sensitive accuracy of the gauge and the

pressure gradient difference at the each side of plate , etc. could be reduce to minimum; therefore the data measured by this micro shear gauge may be more reasonable.

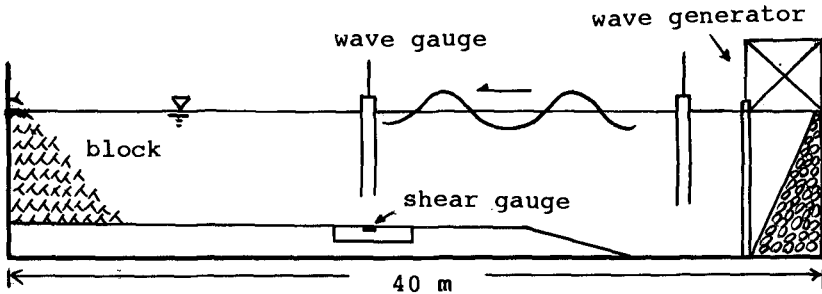


Fig. 1 Sketch of experimental wave flume.

Fig. 2 shows the sketch of the micro shear gauge used by this paper.

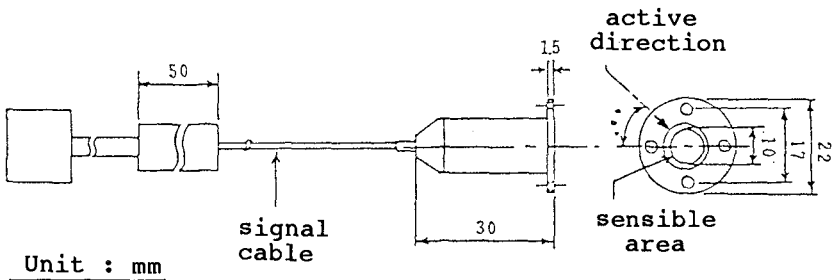


Fig. 2 Sketch of shear gauge.

The test conditions of this experiment are :

- (1) bottom type : smooth bed.
- (2) water depth : 20 cm, 25 cm, 30 cm, 35 cm
- (3) wave period : 1.0, 1.2, 1.4, 1.6, 1.8, 2.0 sec
- (4) wave height : enlarged gradually from 2 cm to before breaking

Fig. 3 shows a example of time series of surface wave height and bottom shear force that just measuring from experiment. In this figure, we could find the asymmetry of bottom shear stress were related to the surface wave profile.

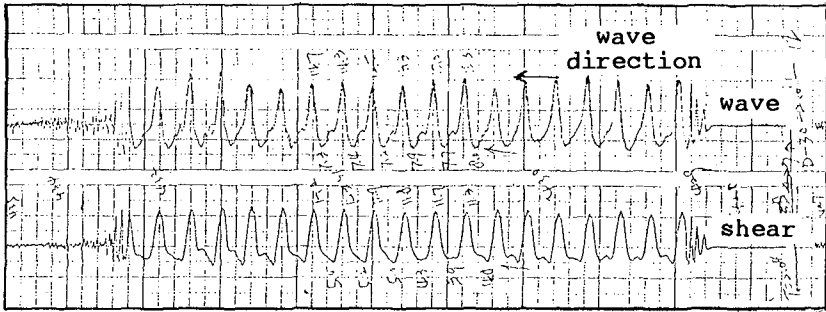


Fig. 3 Time history of measured wave and shear.

Experimental Results and Discussion

(1) Shear stress

In general case, the maximum bottom shear stress τ_{omax} is defined as

$$\tau_{omax} = \mu (\partial u / \partial z)_{z=-h} \dots\dots\dots (1)$$

If the horizontal particle velocity is calculated by linear wave theory and we transformed Eq. 1 to a non-dimensional form, then a dimensionless equation can be represented as Eq. 2

$$\tau_{omax} / \rho g H = \sqrt{2} / [g \sinh(kh)] (\pi / T)^{3/2} \dots\dots\dots (2)$$

where h is water depth, H wave height, k wave number, T wave period, ρ water density, ν is kinematic viscosity and τ_{omax} is the maximum bottom shear stress calculated from Eq. 2.

Fig. 4 represents the non-dimensional measured maximum shear stress under the wave crest (postive direction) and wave trough (negative direction) passed related to the parameter h/L_0 , and the curves on the diagram represent the value that obtained from Eq. 2 which was derived by linear wave theory. From this diagram, we could find that the postive maximum shear stress are large than the negative maximum shear stress obviously, and the measured positive value are large than the value were got from linear wave theory and the measured negative value are small than τ_{omax} , the reason is that in shallow water, wave profile

are no longer be maintained a sine form, it just has a sharp crest and a flat trough, this non-linear effect influence on bottom directly, so the shear stress on bottom also has a profile similar to the surface water elevation. The fluctuation of the measured data were due to the constant value of ν in Eq. 2 and the different bottom friction in each test condition.

The symbol of τ_c , τ_t in the figure represents the measured bottom shear stress under wave crest and wave trough respectively.

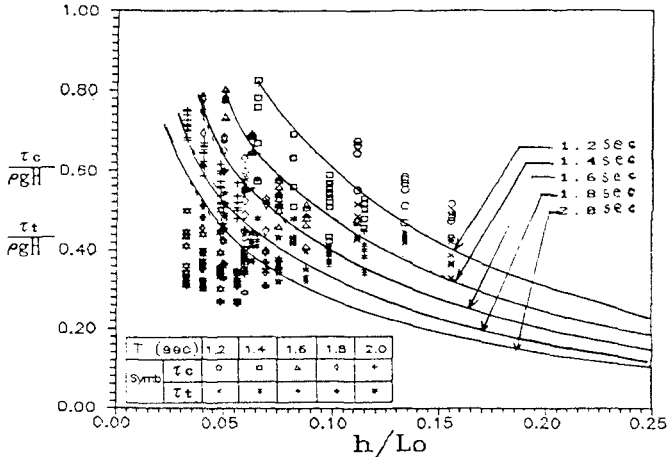


Fig. 4 Relation between $\tau_c / \rho g H$, $\tau_t / \rho g H$ and h / L_o .

Fig. 5 shows the relation between τ_c / τ_a , τ_t / τ_a and Ursell number Ur , the data in the figure indicate that the ratio of τ_c / τ_a are great than 1, τ_t / τ_a are less 1, the reason were due to the asymmetric wave action, that just described above. There also exist a obvious tendency of that τ_c / τ_a , τ_t / τ_a were enlarged and reduced gradually related to the increase of Ur respectively, this phenomenon could emphasized that when wave non-linearity increased, the postive shear stress also increased, but the negative shear stress were decreased. The increment of postive direction are more obvious than negative direction. This may has an important effect on the initial motion of sand and the on-offshore sediment transport rate, so this topic will be studied more detail. The regressive equation from data is expressed as Eq. 3 for practical use.

$$\tau_c/\tau_a = 0.903Ur^{0.081} , \quad \tau_t/\tau_a = 1.211Ur^{-0.149} \quad \dots(3)$$

Here $\tau_a = f_w u_a^2 / 2$ and f_w is the friction factor, u_a the maximum bottom horizontal particle velocity by linear theory. Ursell number Ur was defined as

$$Ur = HL^2/h^3 \quad \dots\dots\dots(4)$$

where L is the wave length at water depth h .

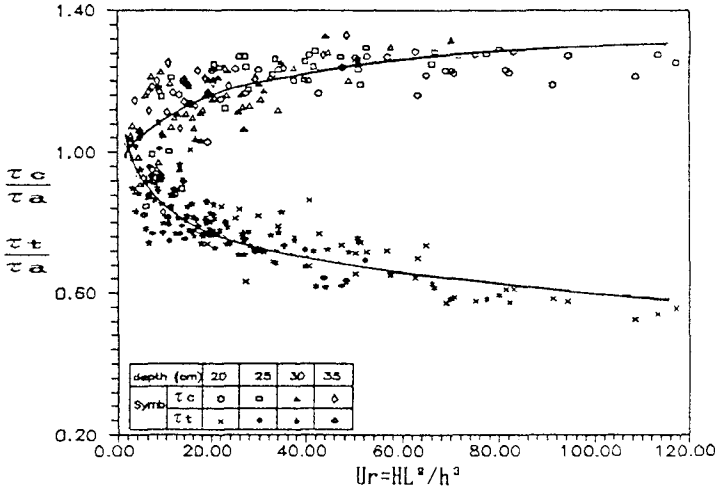


Fig. 5 Relation between τ_c/τ_a , τ_t/τ_a and Ur .

(2) Bottom Friction Factor

Fig. 6 shows the relation between Reynold number (RE) and bottom friction factor f_w , f_{ac} , f_{at} Where f_w is defined by Jonsson etc., f_{ac} \ f_{at} respresent the bottom friction factor under wave crest and wave trough action. Where

$$f_w = 2. / \sqrt{RE} , \quad f_{ac} = 2. \tau_c / \rho u a^2 , \quad f_{at} = 2. \tau_t / \rho u a^2 \quad \dots(5)$$

From this diagram, we can find that when linear wave theory was defined to compute the horizontal bottom velocity, the friction f_{ac} is larger than f_w , and f_{at} is smaller than f_w , furthermore, this tendency is more visible when RE increased. The experimental data can be regressed by two empirical formula like Jonsson's ,

$$f_{ac} = 1.386RE^{-0.448} \quad , \quad f_{at} = 4.093RE^{-0.505} \quad \dots(6)$$

Also, we could express f_{ac} , f_{at} in another form, just like Eq. 7

$$f_{ac} = 0.724f_{\omega}^{0.875} \quad , \quad f_{at} = 1.611f_{\omega}^{1.183} \quad \dots(7)$$

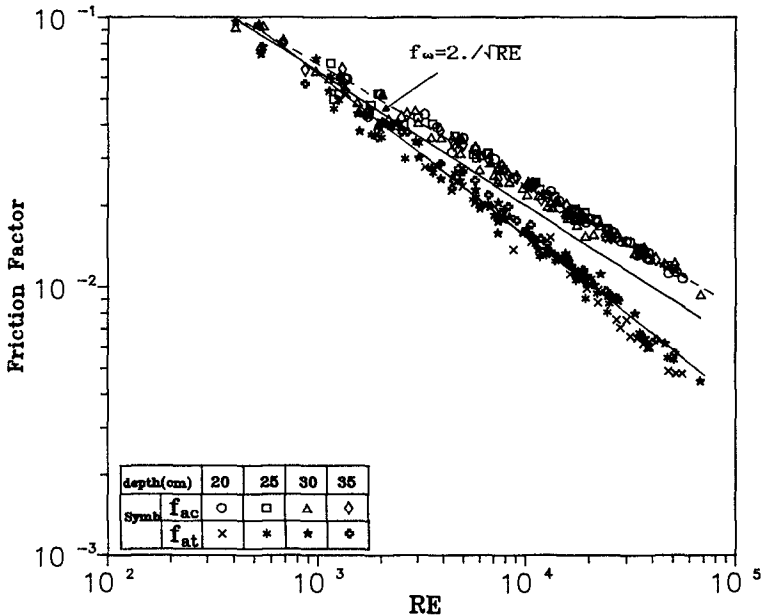


Fig. 6 Relation between friction factor and RE

In nearshore area, linear wave theory is unsuitable to describe the wave phenomena. For more realistic conditions, we use the non-linear wave method to define the bottom particle velocity, and use those to calculate the bottom friction factor under wave crest and trough, which were defined as Eq. 8

$$f_{sc} = 2\tau_c / \rho u_{sc}^2 \quad , \quad f_{st} = 2\tau_t / \rho u_{st}^2 \quad \dots\dots\dots(8)$$

where

$$u_s = c \{ F_1 \cosh[k(h+z) \cos(kx - \sigma t)] + F_2 \cosh[2k(h+z) \cos^2(kx - \sigma t)] + F_3 \cosh[3k(h+z) \cos^3(kx - \sigma t)] \} \quad | \quad z = -h$$

$$F_1 = ak / [\sinh(kh)]$$

$$F_2 = 3a^2 k^2 / [4 \sinh^4(kh)]$$

$$F_3 = 3a^3 k^3 [13 - 4 \cosh^2(kh)] / [64 \sinh^7(kh)]$$

When the friction factor were defined by Eq. 8, the relationship between f_{sc} , f_{st} and RE were show in Fig. 7. It shows that f_{sc} is smaller than f_{st} and f_w , but f_{st} is larger than f_{sc} and f_w . These results are just contrary to those obtained from linear wave theory which were defined in Eq. 5, the reason is that when velocity is calculated by finite amplitude wave theory ,there were a sharply velocity under wave crest and a flatly velocity under wave trough due to the wave non-linearity in shallow water. So how are the real bottom friction factor change with wave condition must be studied detailly. For avoid the complex calculation , the data shows in Fig. 7 can be expressed by a empirical formula as Eq. 9 or Eq. 10

$$f_{sc}=2.596RE^{-0.540} \quad , \quad f_{st}=0.613RE^{-0.341} \quad \dots(9)$$

or

$$f_{sc}=0.724f_w^{0.875} \quad , \quad f_{st}=1.611f_w^{1.183} \quad \dots(10)$$

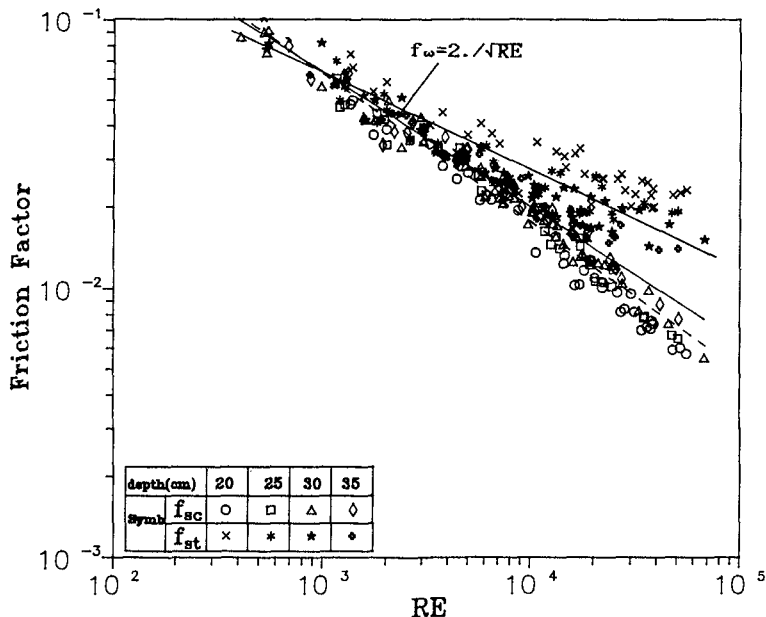


Fig. 7 Relation between friction factor and RE.

Fig. 8 shows the comparisons of f_w , f_{ac} , f_{at} , f_{sc} , f_{st} from this diagram the differences between these factors can be viewed more clearly. When RE

were near transitional flow condition , the data begin scattered away from f_w and f_{st} scattered more obviously, the reason were due to the slowly increased of bottom velocity under wave trough action. There exist a 10% ~ 40% difference between f_{sc} 、 f_{st} and f_w , the variation were depended on the Reynolds number. If we have measured the velocity near bottom simultaneously , then how the friction factor varied may be verified more accurately.

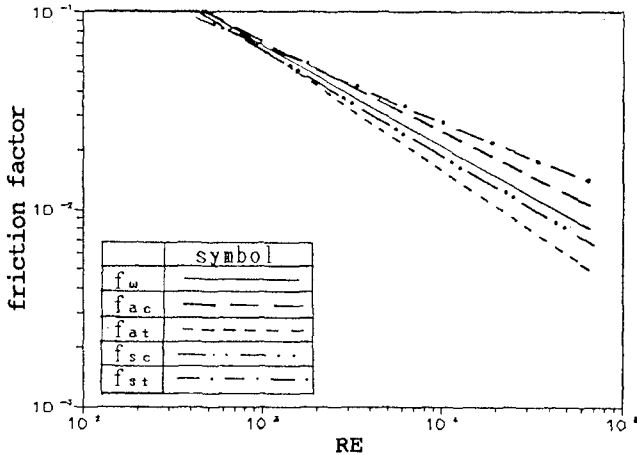


Fig. 8 Comprisions of friction factor and RE.

Conclusion and Suggestion

It shows that the bottom shear stress has a asymmetric form similar to the surface wave profile in shallow water. The positive maximum shear stress (under wave crest) are much larger than the negative maximum shear stress (under wave trough) and those computed from linear wave theory. In addition, the friction factor were varied with what the wave theory was adopted, thers show a constray results when the bottom velocity were defined by the linear and non-linear wave respectively. Phenomena which induced by wave just mentioned above are an important parameter on wave energy decay, nearshore current and may have a determination on the on-offshore sediment transport rate and the particle moving mechanics etc., so how they are changed by the asymmetric wave profile must be study more detailly. If the wave profile, bottom

velocity and shear stress are measured simultaneously, the advanced discussion may get a more reasonable explanation. The next work for us are to improve the experiment and extend to the rough bed condition.

Moreover, we attempt to research a function to express the shear stress and friction factor under a asymmetric wave action and to correlate the results with the on-offshore sediment transport rate.

References

1. Asano, I., Y. Iwagaki, (1986) "Non-Linear Effects on Velocity Fields in Turbulent Wave Boundary Layer", Coastal Engineering in Japan, Vol. 29, pp. 51-63.
2. Horikawa, K. (1978) "Coastal Engineering", University of Tokyo Press.
3. Jonsson, I.G., (1966) "Wave Boundary Layers", Proc. of 10th Coastal Engineering Conference, pp. 127-148.
4. Jonsson, I.G., (1982) "A New Approach to Oscillatory Rough Turbulent Boundary Layers"; Ocean Engng. Vol. 7, pp. 109-152.
5. Kajiwara, K., (1968) "A Model of the Bottom Boundary Layer in Water Waves", Bulletin of the Earthquake Research Institute, Vol. 46, pp. 75-123.
6. Kamphuis, J.W., (1975) "Friction Factor under Oscillatory Waves", Journal of the Waterways Harbors and Coastal Engineering Division, ASCE, Vol. 101, No. WW2, pp. 135-144.
7. Kuo, C.T., K.J. Chung, (1981) "Study on the bottom shear stress on smooth bed due to wave action", Proc of 1st Hydraulic Engineering Conference, pp. 491-510, (Chinese).
8. Masahika, Isobe, (1985) "Calculation and Application of First-Order Cnoidal Wave Theory", Coastal engineering, 9, pp. 309-325.
9. Sleath, J.F.A., (1984) "Sea Bed Mechanics", John Willey & Sons.

CHAPTER 50

Estimation of Directional Spectrum Expressed in Standard Form

Masahiko Isobe ¹

Abstract

A standard directional spectrum is determined by a finite number of parameters included in its mathematical expression. In this paper, a theory is developed to estimate the parameters from a given data set on the basis of the maximum likelihood method. The theory is applied to estimating the parameters in the Mitsuyasu-type standard directional spectrum from data obtained by a three-component array. Main results of analysis of field data are 1) the peak wave direction agrees well with the mean direction defined at each wave frequency, 2) the peakedness parameter can be approximated by that estimated from the long-crestedness parameter at each wave frequency, and 3) the peakedness parameter takes its maximum at the frequency slightly lower than the peak frequency.

1. Introduction

A random sea state is described by a directional spectrum. In recent years, field observations of directional spectra have often been carried out using varieties of measuring instruments developed. At the same time, many theories have been developed for the accurate estimation of directional spectrum (Isobe *et al.*, 1984; Kobune and Hashimoto, 1986; Hashimoto and Kobune, 1988). Cross and power spectra, from which the directional spectrum is estimated, are statistically random quantities. However, the statistical variability is not appropriately taken into account in the theories developed so far.

A standard form of the directional spectrum such as the Mitsuyasu-type directional spectrum is determined by a finite number of parameters. This way of describing directional spectra is convenient for practical uses such as establishing a data base of random sea waves or specifying a design wave condition. Hence, it is necessary to develop a theory to estimate the values of these parameters on a reasonable basis.

¹Associate Professor, Dept. of Civil Eng., Univ. of Tokyo, Bunkyo-ku, Tokyo, 113 Japan

In this paper, a general theory is presented to estimate the parameters included in a standard directional spectrum on the basis of the maximum likelihood method, in which the statistical variability of the Fourier coefficients is taken into consideration. Then, an explicit expression is given for the Mitsuyasu-type directional distribution function. The theory is applied to data obtained from field experiments and the characteristics of directional sea state are discussed.

2. Theory

2.1 Probability density of Fourier coefficients

Suppose M kinds of time series data, $\xi^{(m)}(\mathbf{x}_m, t)$ ($m=1$ to M , \mathbf{x}_m : coordinates at measuring points, t : time), of various wave properties at various points are given. The time series $\xi^{(m)}$ are expanded into Fourier series as

$$\xi^{(m)}(\mathbf{x}_m, t) = \sum_{i=1}^{\infty} (A_{ci}^{(m)} \cos 2\pi f_i t + A_{si}^{(m)} \sin 2\pi f_i t) \quad (1)$$

From the central limit theorem, the coefficients $A_{ci}^{(m)}$ and $A_{si}^{(m)}$ have normal distributions with zero means. Hereinafter we deal only with the i th component, f_i , of the frequency and drop the subscript i . Then the coefficients $A_{ci}^{(m)}$ and $A_{si}^{(m)}$ are expressed in a vector form as

$$\mathbf{A} = \begin{pmatrix} \mathbf{A}_c \\ \mathbf{A}_s \end{pmatrix} \quad (2)$$

and the cross covariance matrix, $\Xi \Delta f$, of \mathbf{A} is expressed in terms of co-spectrum matrix, C , and quadrature-spectrum matrix, Q , as

$$\Xi \Delta f = [\langle \mathbf{A} \mathbf{A}^t \rangle] = \begin{bmatrix} C & Q \\ -Q & C \end{bmatrix} \Delta f \quad (3)$$

Where Δf is the frequency range that the coefficient \mathbf{A} represents and $\langle \rangle$ denotes an expected value. The cross-power spectrum matrix, Φ , are defined as $\Phi_{mn} = C_{mn} - iQ_{mn}$ and related with the directional spectrum, $S(f, \theta)$, as

$$\Phi_{mn}(f) = \int_0^{2\pi} H_m(f, \theta) \bar{H}_n(f, \theta) \exp[-i\mathbf{k}(\mathbf{x}_n - \mathbf{x}_m)] S(f, \theta) d\theta \quad (4)$$

(Isobe *et al.*, 1984). Where f is the frequency, θ the wave direction, \mathbf{k} is the wave number vector, H_m the transfer function from the water surface elevation to the m th measured quantity, and $\bar{}$ denotes the complex conjugate.

From the cross-covariance matrix expressed by Eq. (3), the joint normal distribution, $p(\mathbf{A})$, of the Fourier coefficients \mathbf{A} is given as

$$p(\mathbf{A}) = \frac{1}{(\sqrt{2\pi\Delta f})^{2M} \sqrt{|\Xi|}} \exp\left[-\frac{1}{2\Delta f} \mathbf{A}^t \Xi^{-1} \mathbf{A}\right] \quad (5)$$

(Rice, 1944). Where $|\Xi|$ and Ξ^{-1} are the determinant and inverse matrix of Ξ .

Now a complex variable, ζ , is defined as

$$\zeta = \mathbf{A}_c - i\mathbf{A}, \tag{6}$$

then the right hand side of Eq. (5) is expressed in terms of ζ as

$$p(\mathbf{A}) = \frac{1}{(2\pi\Delta f)^M |\Phi|} \exp\left[-\frac{1}{2\Delta f} \zeta^t \Phi^{-1} \zeta\right] \tag{7}$$

in which the dimension of the matrix reduces to M . In deriving the above equation,

$$\Phi \Delta f = [\langle \bar{\zeta} \zeta^t \rangle / 2] = (C - iQ) \Delta f \tag{8}$$

and the relationship, $|\Xi| = |\Phi|^2$, is used.

2.2 Definition of likelihood function

If the directional spectrum is given, Φ can be calculated by Eq. (4) and the joint distribution function of \mathbf{A} is determined by Eq. (7). Since \mathbf{A} is obtained by the Fourier analysis of given time series data, Eq. (7) gives the probability density with which the given \mathbf{A} occurs.

A set, $\mathbf{A}^{[j]}$ ($j=1$ to J), of the Fourier coefficients \mathbf{A} is obtained by dividing the time series into segments or from a small but finite range of frequency. The joint probability with which the set $\mathbf{A}^{[j]}$ ($j=1$ to J) occurs at the same time is obtained by multiplying each probability density. Its J th root, L , is expressed as

$$\begin{aligned} L(\mathbf{A}^{[j]}; \Phi) &= \{p(\mathbf{A}^{[1]}) \times p(\mathbf{A}^{[2]}) \times \dots \times p(\mathbf{A}^{[J]})\}^{1/J} \\ &= \frac{1}{(2\pi\Delta f)^M |\Phi|} \exp\left[-\sum_{m=1}^M \sum_{n=1}^M \Phi_{mn}^{-1} \hat{\Phi}_{nm}\right] \end{aligned} \tag{9}$$

where

$$\hat{\Phi}_{nm} = \frac{1}{2J\Delta f} \sum_{j=1}^J \hat{\zeta}_n^{(j)} \zeta_m^{(j)} \tag{10}$$

From the above definition, $\hat{\Phi}_{nm}$ is regarded as the quantity which can be obtained by operating a rectangular filter to the periodogram $\hat{\zeta}_n^{(j)} \zeta_m^{(j)} / 2\Delta f$ and this means that $\hat{\Phi}_{nm}$ is the cross or power spectrum obtained by the Fourier analysis.

The quantity L expressed by Eq. (9) means the possibility or likelihood that the set $\mathbf{A}^{[j]}$ occur at the same time and called the likelihood function. From field measurements, $\mathbf{A}^{[j]}$ ($j=1$ to J) is given but Φ is unknown. In the maximum likelihood method, Φ is determined so that the possibility becomes maximum.

As seen from Eq. (4), the cross-power spectrum matrix Φ is a function of the parameters included in the standard directional spectrum. However, we

first assume that every component in the cross-power spectrum matrix changes independently and find the maximum value of the likelihood function in a global sense. To obtain the value of Φ which maximizes L , we take the derivative of Eq. (9) with respect to every component, Φ_{kl} (k and $l=1$ to M), of the matrix Φ and make every derivative vanish.

Let the cofactor of the matrix Φ be denoted by ϕ , the following relationships are obtained from mathematical theorems concerning a matrix.

$$|\Phi| = \sum_{k'=1}^M \phi_{lk'} \Phi_{k'l} \quad (11)$$

$$\Phi_{mn}^{-1} = \frac{\phi_{mn}}{|\Phi|} \quad (12)$$

And hence

$$\frac{\partial |\Phi|}{\partial \Phi_{kl}} = \phi_{lk} = |\Phi| \Phi_{lk}^{-1} \quad (13)$$

$$\frac{\partial \Phi_{mn}^{-1}}{\partial \Phi_{kl}} = -\Phi_{ln}^{-1} \Phi_{km}^{-1} \quad (14)$$

Now the derivative of Eq. (9) is expressed as

$$\frac{\partial L}{\partial \Phi_{kl}} = L \times \left\{ -\Phi_{lk}^{-1} + \sum_{m=1}^M \sum_{n=1}^M \Phi_{ln}^{-1} \hat{\Phi}_{nm} \Phi_{mk}^{-1} \right\} \quad (15)$$

To make the derivative vanish, we obtain

$$\Phi_{nm} = \hat{\Phi}_{nm} \quad (16)$$

and then the maximum value of L is obtained as

$$L_{\max} = \frac{e^{-M}}{(2\pi\Delta f)^M |\Phi|} \quad (17)$$

Equation (16) means that the cross-power spectra Φ_{nm} should agree with the quantity which is obtained by operating a rectangular filter to the periodogram.

2.3 Estimation of parameters in standard directional spectrum

Once we choose a standard directional spectrum, the components of the cross-power spectrum matrix are not independent of each other. The cross-power spectrum matrix, Φ_{nm} , is now a function of the parameters, λ_i ($i=1$ to I), in the standard directional spectrum through Eq. (4) and is written as $\Phi_{nm}(\lambda_i)$. Hence, to determine the value of λ_i by the maximum likelihood method, we take the derivative of Eq. (9) with respect to λ_i ($i=1$ to I) and make every derivative vanish.

The derivative of the likelihood function with respect to λ_i can be obtained by the chain rule as

$$\frac{\partial L}{\partial \lambda_i} = \sum_{k=1}^M \sum_{l=1}^M \frac{\partial L}{\partial \Phi_{kl}} \frac{\partial \Phi_{kl}}{\partial \lambda_i} \tag{18}$$

On substituting Eq. (15) into the above equation and setting the derivative equal to zero, the following equation results:

$$\sum_{k=1}^M \sum_{l=1}^M \{-\Phi_{lk}^{-1} + \sum_{m=1}^M \sum_{n=1}^M \Phi_{ln}^{-1} \hat{\Phi}_{nm} \Phi_{mk}^{-1}\} \frac{\partial \Phi_{kl}}{\partial \lambda_i} = 0 \tag{19}$$

From the above equation with $i=1$ to I , we can determine the values of λ_i ($i=1$ to I) and then the directional spectrum.

Once λ_i are determined, the value, \hat{L}_{max} , of the likelihood function corresponding to λ_i is calculated. Since the global maximum L_{max} is given by Eq. (17), the adaptability of the standard directional spectrum can be defined as \hat{L}_{max}/L_{max} . This is an advantage of the present method.

The concept of the maximum likelihood used in the present study is similar to that used in Hashimoto and Kobune (1988). However, in the present study, the joint normal distribution of the Fourier coefficients is taken into consideration, whereas in Hashimoto and Kobune (1988) the cross-power spectra are assumed to be independent of each other. For example, when two time series data are obtained at very close locations, it is more rational to take into consideration the correlation between the Fourier coefficients as in the present study.

In the numerical calculation of Eq. (19), the Newton-Raphson procedure can be employed. Let the left hand side of Eq. (19) be denoted as

$$f_i(\lambda_{i'}) = \sum_{k=1}^M \sum_{l=1}^M \{-\Phi_{lk}^{-1} + \sum_{m=1}^M \sum_{n=1}^M \Phi_{ln}^{-1} \hat{\Phi}_{nm} \Phi_{mk}^{-1}\} \frac{\partial \Phi_{kl}}{\partial \lambda_i} \tag{20}$$

then the second derivatives are expressed as follows:

$$\begin{aligned} \frac{\partial f_i}{\partial \lambda_{i'}} &= \sum_{k=1}^M \sum_{l=1}^M \{-\Phi_{lk}^{-1} + \sum_{m=1}^M \sum_{n=1}^M \Phi_{ln}^{-1} \hat{\Phi}_{nm} \Phi_{mk}^{-1}\} \frac{\partial^2 \Phi_{kl}}{\partial \lambda_{i'} \partial \lambda_i} \\ &+ \sum_{k'=1}^M \sum_{l'=1}^M \sum_{k=1}^M \sum_{l=1}^M [-\Phi_{l'k}^{-1} \Phi_{lk}^{-1} + \{\Phi_{lk}^{-1} \sum_{m=1}^M \sum_{n=1}^M \Phi_{ln}^{-1} \hat{\Phi}_{nm} \Phi_{mk}^{-1} \\ &+ \Phi_{l'k}^{-1} \sum_{m=1}^M \sum_{n=1}^M \Phi_{ln}^{-1} \hat{\Phi}_{nm} \Phi_{mk'}^{-1}\}] \frac{\partial \Phi_{k'l'}}{\partial \lambda_{i'}} \frac{\partial \Phi_{kl}}{\partial \lambda_i} \end{aligned} \tag{21}$$

By the linear approximation of $f_i(\lambda_{i'})$ the following iteration formula can be obtained:

$$\lambda_i^{(j+1)} = \lambda_i^{(j)} - \sum_{i'=1}^I \left[\frac{\partial f_i}{\partial \lambda_{i'}} \right]^{-1} f_{i'}|_{\lambda_i = \lambda_i^{(j)}} \tag{22}$$

where $\lambda_i^{(i)}$ and $\lambda_i^{(i+1)}$ are the values of λ_i at i th and $(i+1)$ th iteration steps. The above formula is repeatedly used until a converged solution is obtained.

2.4 Expression for Mitsuyasu-type directional spectrum

The Mitsuyasu-type directional distribution function is expressed as

$$S(f, \theta) = P(f) \frac{2^{2s+1} \Gamma^2(s+1)}{\pi \Gamma(2s+1)} \left[\cos \frac{\theta - \theta_o}{2} \right]^{2s} \quad (23)$$

where $P(f)$ is the frequency spectrum, and Γ represents the gamma function. To estimate the directional spectrum for a certain frequency f , the unknown parameters are P , θ_o and s which are denoted by λ_1 , λ_2 and λ_3 , respectively.

In the following, we derive the equations for data obtained by a three-component array in which the water surface elevation, η , and two components, u and v , of the horizontal water particle velocity are measured. By denoting $\xi^{(1)} = \eta$, $\xi^{(2)} = u$ and $\xi^{(3)} = v$, the cross-power spectra for Eq. (23) are

$$\Phi_{11} = P(1 + \epsilon) \quad (24)$$

$$\Phi_{12} = PH_u m_1 \cos \theta_o \quad (25)$$

$$\Phi_{13} = PH_u m_1 \sin \theta_o \quad (26)$$

$$\Phi_{22} = PH_u^2 \left(\frac{1}{2} + m_2 \cos 2\theta_o \right) (1 + \epsilon) \quad (27)$$

$$\Phi_{33} = PH_u^2 \left(\frac{1}{2} - m_2 \cos 2\theta_o \right) (1 + \epsilon) \quad (28)$$

$$\Phi_{23} = PH_u^2 m_2 \sin 2\theta_o \quad (29)$$

where

$$m_1 = \frac{s}{(s+1)} \quad (30)$$

$$m_2 = \frac{s(s-1)}{2(s+1)(s+2)} \quad (31)$$

and H_u is the transfer function from the water surface elevation to the magnitude of the horizontal water particle velocity. Though the quantity H_u can be evaluated by the small amplitude wave theory, the following formula obtained from the relationship among the power spectra is used to eliminate the error included in the data.

$$H_u = \sqrt{\frac{P_u(f) + P_v(f)}{P_\eta(f)}} \quad (32)$$

Equations (24), (27) and (28) are expressions for power spectra and are multiplied by $(1 + \epsilon)$ on assuming that a noise component with a relative power of ϵ is included in the data. Hence, ϵ becomes the fourth unknown parameter, λ_4 , to

be determined by the maximum likelihood method. If another assumption that the noise component is due to a component of the directional spectrum with a uniform directional distribution is adopted, ϵP , $\epsilon PH_u^2/2$ and $\epsilon PH_v^2/2$ should be added to the power spectra Φ_{11} , Φ_{22} and Φ_{33} , respectively. Which assumption should be adopted can be discussed in terms of the adaptability \hat{L}_{\max}/L_{\max} .

It is easy to differentiate Eqs. (24) to (29) with respect to λ_i ($\lambda_1 = P$, $\lambda_2 = \theta_0$, $\lambda_3 = s$, $\lambda_4 = \epsilon$) up to the second order and by substituting the derivatives into Eqs. (20) and (21) the right hand side of Eq. (22) can be determined and then modified values $\lambda_i^{(i+1)}$ are calculated. The initial values of λ_i ($i=1$ to I) are taken to be the power spectrum of η , the mean direction, the value of s obtained from the long-crestedness parameter, and zero, respectively.

Numerical instability sometimes occurred in the algorithm of the original Newton-Raphson method. Hence additional procedures are employed. When modified λ_i gives a smaller value of the likelihood function, the magnitude of the modification by Eq. (22) is made half. When a convergent solution is not obtained within 10 iterations, the procedure is continued by neglecting the second derivatives in Eq. (21). This modification made the numerical calculation convergent for all the cases tried.

3. Application

3.1 Field experiment

The data used in application of the present theory were obtained from three series of field experiments. Sets of an ultra-sonic wave gage and an electromagnetic current meter were installed at the sea bottom. The first and second field experiments were performed from 1 to 2 of October, 1987, and from 29 to 30 of August, 1988, respectively, at Oarai beach, Ibaraki prefecture, Japan, facing the Pacific Ocean. One segment of data record contains 2046 data with the sampling frequency of 0.5s, and 95 and 75 segments were recorded in Oarai 1987 and 1988 experiments, respectively. The bottom topography and the arrangement of the instruments are shown in Fig. 1 for the Oarai 1988 experiment, as an example. The third experiment was performed from 11 to 18 of January, 1989, at Ogata beach, Niigata prefecture, Japan. This experiment was performed as a part of a comprehensive, inter-institutional field experiment, SWAN 89 (Sediment, Wave and Nearshore Circulation Observation, 1989), managed by Professor Tsuchiya, Kyoto University. Data segments with a 17 min. duration were recorded every one hour and total number of segments is 134. The average wave statistics during the observation are shown in Table 1.

3.2 Result of data analysis

Assumptions of noise components are examined first. Figure 2 shows the

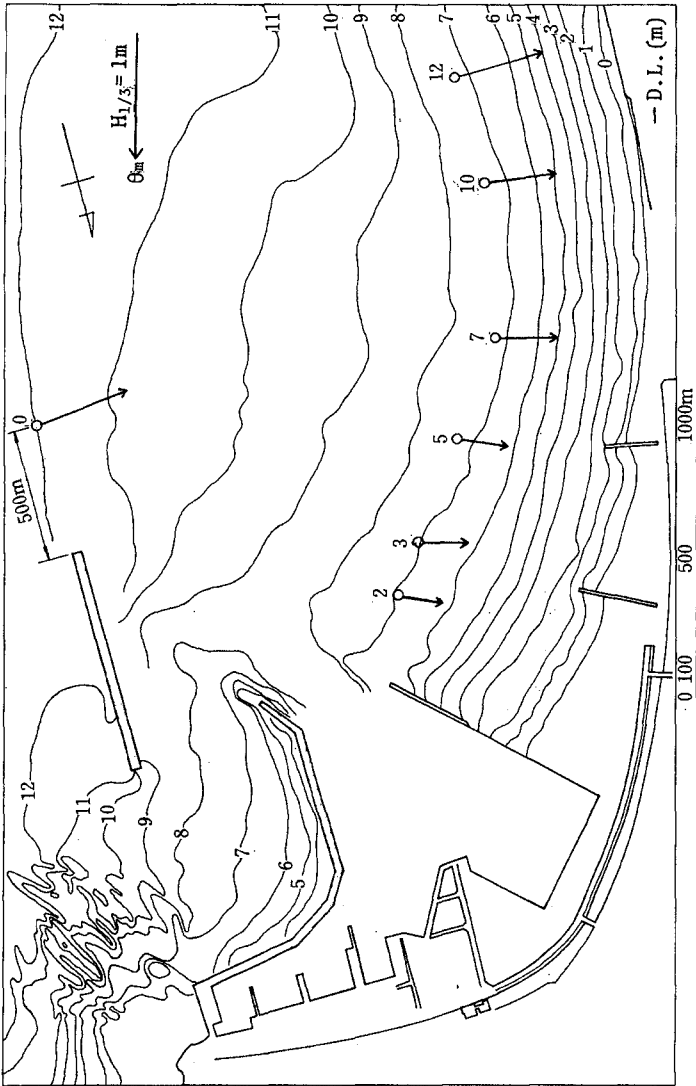


Fig. 1 Arrangement of measuring points (Oarai, 1987.10.01-02).

Table 1: Wave statistics during field experiments.

Observation	Measuring point	h (m)	$H_{1/3}$ (m)	$T_{1/3}$ (s)	θ_m	$\bar{\gamma}$
OA87	0	12.5	0.63	6.3	174	0.61
OA88	1	13.2	1.09	7.4	165	0.43
	2	12.1	-	-	-	-
	3	10.9	1.04	7.5	175	0.40
	4	7.3	1.02	7.6	-179	0.33
OG89	1	25.0	1.67	6.8	-77	0.44
	2	15.3	1.31	6.5	-51	0.42
	3	11.3	1.19	6.2	-50	0.40

OA: Oarai, OG: Ogata, h : water depth,

$H_{1/3}$: significant wave height, $T_{1/3}$: significant wave period,

θ_m : mean direction measured anti-clockwise from east,

$\bar{\gamma}$: long-crestedness parameter.

result of data analysis for three assumptions of noise component. From the top to bottom figures, average values during the observation are shown for the frequency spectrum, $P(f)$, the peak direction, θ_o , the peakedness parameter, s , and the adaptability, \hat{L}_{\max}/L_{\max} , are plotted. In each figure, the solid line corresponds to the assumption of the noise component proportional to the frequency spectrum, and the dotted line to the assumption of the noise component with uniform directional distribution. The broken line represents the result when the noise component is neglected. Without noise component, the adaptability \hat{L}_{\max}/L_{\max} decreases significantly. The adaptabilities are almost the same for the two assumptions of noise component, but the difference of the estimated s between the two assumptions is large. Since the assumption of noise component proportional to the frequency spectrum gives a slightly higher adaptability and gradual increase of s with decreasing water depth, this assumption is adopted in the following analysis.

In the top of each figure through Figs. 3 to 6, P is the frequency spectrum, ϵP the noise component, and P_η the frequency spectrum of the water surface elevation. In the second figure, θ_o denotes the estimated peak direction. The symbols θ_m and θ_p represent the mean and principal directions, respectively, which are calculated from the power and cross spectra (Horikawa, *ed.*, 1985). In the third figure, s is the estimated peakedness parameter, and s_γ represents s

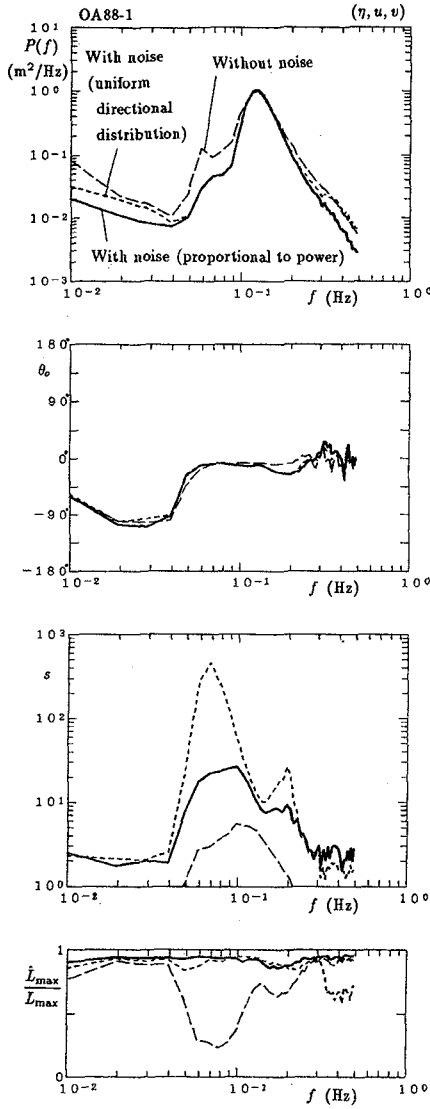


Fig. 2 Effect of formulation of noise component on directional spectrum estimation.

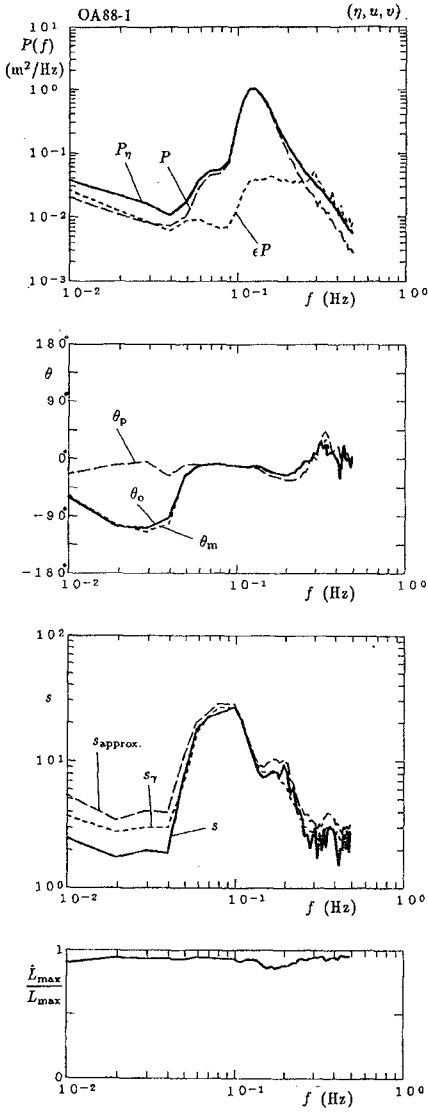


Fig. 3 Result of directional spectrum estimation (1).

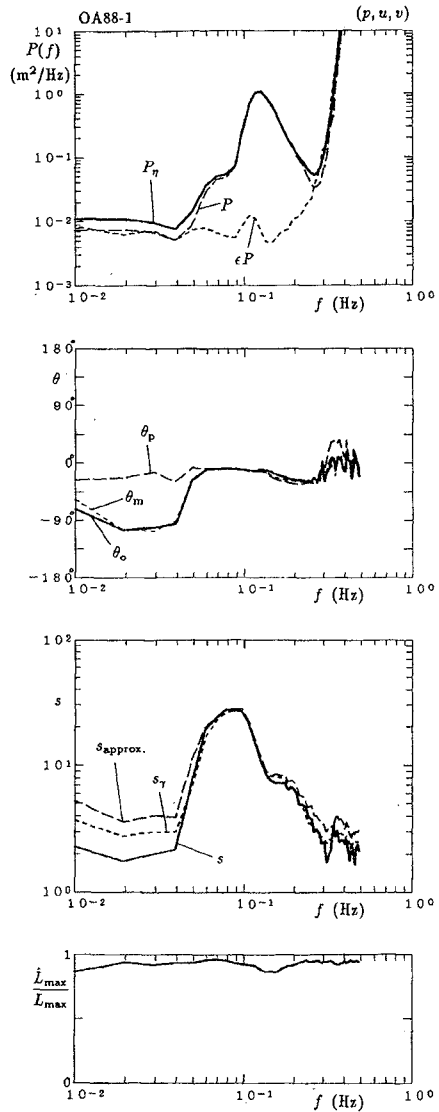


Fig. 4 Result of directional spectrum estimation (2).

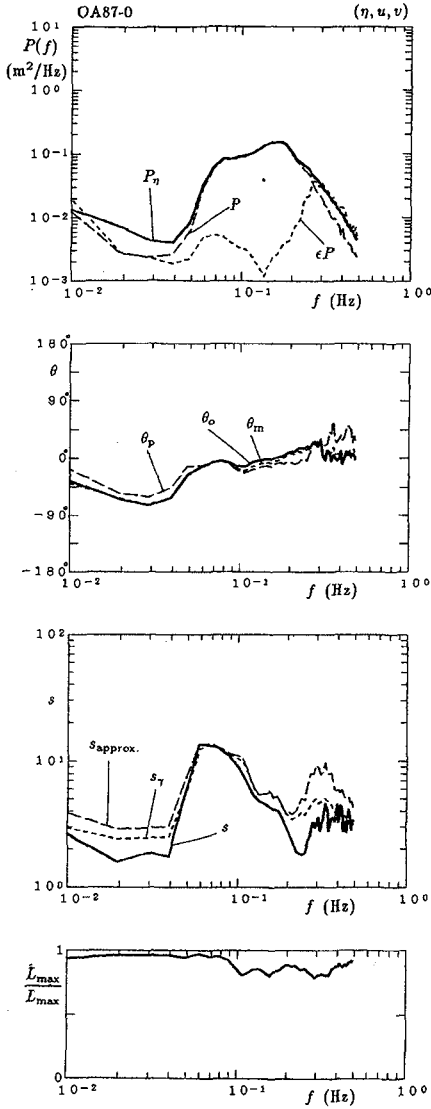


Fig. 5 Result of directional spectrum estimation (1).

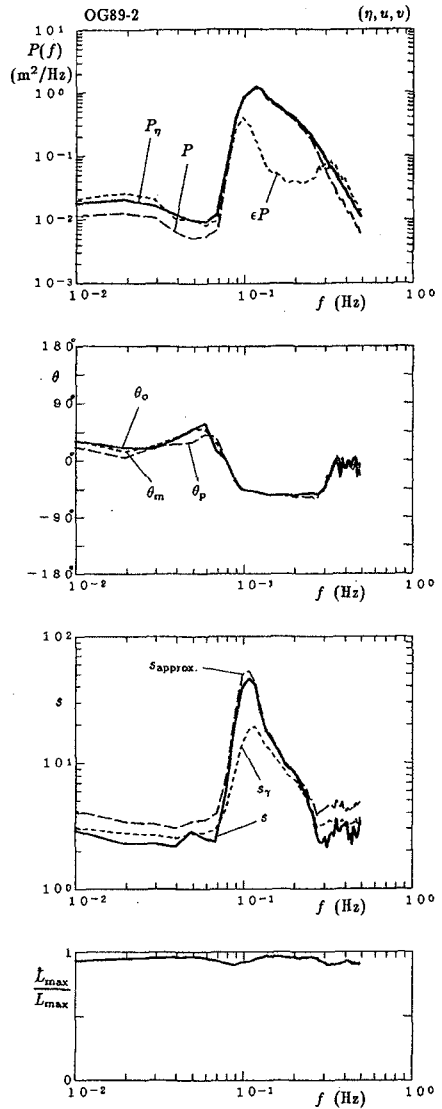


Fig. 6 Result of directional spectrum estimation (2).

calculated by the following equations:

$$\gamma^2 = \frac{\hat{\Phi}_{20} + \hat{\Phi}_{02} - \sqrt{(\hat{\Phi}_{20} - \hat{\Phi}_{02})^2 + 4\hat{\Phi}_{11}^2}}{\hat{\Phi}_{20} + \hat{\Phi}_{02} + \sqrt{(\hat{\Phi}_{20} - \hat{\Phi}_{02})^2 + 4\hat{\Phi}_{11}^2}} \quad (33)$$

$$\gamma^2 = \frac{2s + 1}{s^2 + s + 1} \quad (34)$$

Equation (33) is the definition of the frequency-dependent long-crestedness parameter and Eq. (34) gives the relationship between the long-crestedness parameter and the peakedness parameter. The quantity s_{approx} is an approximation of s which is obtained by substituting γ_α for γ in Eq. (34). The quantity γ_α is calculated by the following equations:

$$\left(1 - \frac{\gamma_\alpha^2}{\gamma^2}\right) = \alpha \frac{\sin^2 2\theta_m}{4 - 2\sin^2 2\theta_m} \left(1 - \frac{\gamma'^2}{\gamma^2}\right) \quad (35)$$

$$\alpha = 0.859 - 0.174\gamma^2 - 0.104\sin^2 2\theta_m \quad (36)$$

where γ is calculated by Eq. (33) and γ' denotes the value of γ which is calculated from Eqs. (34) and (37).

$$\frac{s}{s + 1} = \sqrt{\frac{\hat{\Phi}_{10}^2 + \hat{\Phi}_{01}^2}{\hat{\Phi}_{00}(\hat{\Phi}_{20} + \hat{\Phi}_{02})}} \quad (37)$$

For Fig. 4, the pressure variation is used instead of the water surface elevation. The small amplitude wave theory is used to determine the transfer function from the water surface elevation to the pressure variation. The results are almost the same as those shown in Fig. 3 in which the water surface elevation is used.

Figures 5 and 6 shows the results for Oarai 1987 and Ogata 1989 experiments, respectively. From these figures, it can be concluded that the estimated value P of the frequency spectrum, the peak direction θ_o , and the peakedness parameter s agree well with the power spectrum P_η of the water surface elevation, the mean direction θ_m , and the approximated value s_{approx} , respectively. Since the latter parameters are very easy to calculate, the computational time can greatly be reduced.

In the frequency spectrum, the high frequency range seems to follow the -4 power law. The maximum s occurs at the frequency slightly lower than the peak frequency and the dependence of s on the frequency is different from the formula proposed by Mitsuyasu *et al.* (1975). Accumulation of much more data is necessary for a further and more reliable discussion.

4. Conclusion

A general procedure is given on the basis of the maximum likelihood method for estimating the parameters included in a standard directional spectrum. As

an example, formulas are given for estimating the parameters in the Mitsuyasu-type directional spectrum from the data of the water surface elevation and two components of the horizontal water particle velocity. The present method is applied to the data obtained by three series of field experiments. It is found that the parameters in the Mitsuyasu-type directional spectrum can be approximated by the parameters which can be calculated with much less computational time. Accumulation of much more data is necessary to discuss the characteristics of directional sea states such as the functional dependence of the peakedness parameter s on the frequency. The appropriate assumption on the noise component remains to be studied in the future work.

Acknowledgement

This study is financially supported by the Grant-in-Aid for Scientific Research, Ministry of Education, Science and Culture.

Reference

- Hashimoto, N., and K. Kobune (1988): Estimation of directional spectrum through a Bayesian approach, *Coastal Eng. in Japan*, Vol. 31, pp. 183-198.
- Horikawa K., (*ed.*) (1988): *Nearshore Dynamics and Coastal Processes*, Univ. Tokyo Press, 522p., Part V, Chap. 3, pp.407-422.
- Kobune, K., and N. Hashimoto (1986): Estimation of directional spectra from the Maximum Entropy Principle, *Proc. 5th Int. Offshore Mech. and Arctic Eng. Symp.*, Tokyo, pp. 80-85.
- Isobe, M., K. Kondo, and K. Horikawa (1984): Extension of MLM for estimating directional wave spectrum, *Proc. Symp. on Description and Modelling of Directional Seas*, Copenhagen, pp.A-6-1 - A-6-5.
- Mitsuyasu, H. *et al.* (1975): Observation of the directional spectrum of ocean waves using a cloverleaf buoy, *J. Phys. Oceanogr.*, Vol. 5, pp. 750-760.
- Rice, S. O. (1944): Mathematical analysis of random noise, *Bell Syst. Tech. J.*, Vol. 23, pp. 282-332.

CHAPTER 51

CHARACTERISTICS OF OSCILLATORY FLOW OVER RIPPLE MODELS

Kiyoshi Horikawa¹ F.ASCE
Syunsuke Ikeda² M.ASCE

ABSTRACT

The results of extensive laboratory investigations on the oscillatory flow over ripple models were presented. The ripple models were installed in an oscillatory flow flume. A two-dimensional laser doppler velocimeter was utilized to measure the fine structure of flows in the vicinity of the whole length of a ripple model which was induced by various types of oscillatory flow. The results of measurements were displayed in the form of distributions of mean fluid velocity, stationary velocity, fluid turbulence intensity and Reynolds stress. By using these data the characteristics of oscillatory flow, such as the formation and decay of vortices, the generation of stationary velocity and the variation of kinematic eddy viscosity were discussed.

INTRODUCTION

More than 40 years ago Bagnold (1946) made his laboratory investigations on the oscillatory flow over sand ripples by oscillating the arced bottom harmonically through still water. Since then considerable amount of laboratory investigations have been attempted to clarify the stated phenomena in connection with various subjects, such as the mechanism of ripple formation, the ripple geometry, the sediment transport in the vicinity of sand ripples, and the wave energy dissipation due to the existence of sand ripples.

1. Professor, Department of Foundation Engineering, Saitama University, 255 Shimo-Okubo, Urawa, Saitama 338, Japan. Professor Emeritus, The University of Tokyo.
2. Professor, Department of Civil Engineering, Tokyo Institute of Technology, 2-12-1 O-okayama, Meguro-Ku, Tokyo 152, Japan.

During the last decade the laser doppler velocimeters (LDV) have been adopted together with the data acquisition system to display precisely the fields of mean velocity and turbulence intensity within the domain which was set for the measurement (Du Toit et al., 1980 ; Sawamoto et al., 1981 ; Sato, 1987 ; Sleath, 1987).

Therefor our knowledge on the fine structure of oscillatory boundary layer flow has been deepend during the last decade. The most remarkable phenomenon observed around sand ripples is the generation of vortices separated from a certain location near the ripple crest. It has been realized that the life of vortices from generation to decay is an important element for determining the structure of flow field which has strong influence on the suspension of sediment near the sand ripple and on the decay of wave energy (Ikeda, et al., 1989). In order to clarify more the detailed structures of the oscillatory boundary layer flow, we have continued to carry out a series of laboratory investigations in an oscillatory flume in which sand ripple model was installed. The model of sand ripples has a characterized shape with a sharpened crest as shown in Figure 1. The reason why we adopted such a peculia sharp-crested ripple, which is quite different from the actual sand ripples with a rounded crest, is, for the sake of simplicity, to fix the separation point of flow at a definite point; that is at its crest (Longuet-Higgins, 1981).

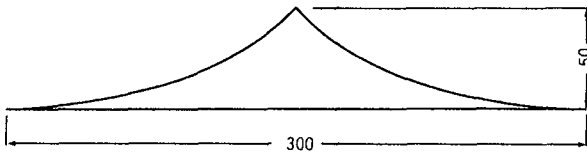


Fig.1 Profile of the ripple model. (unit:mm)

EXPERIMENTAL FACILITIES AND PROCEDURES

An oscillatory flow flume with 13 m in length and 0.3 m x 0.3 m in cross-section was used for the laboratory experiment, the observation section of which was 2 m long and was made of glass except the flume bottom (Figure 2). The oscillatory fluid motion was produced by a piston driven by a DC-motor, and the maximum amplitude of the fluid motion was 70 cm. The period of fluid oscillation was variable between 1 s and 20 s.

The height and length of the ripple model were selected to be 5 cm and 30 cm, respectively (Figure 1).

The surface of the ripple was finished smoothly. Seven of model ripples were placed at the test section, among which the region between the 3rd and the 4th crests was selected for the precise velocity measurement. We took four cases as experimental runs as shown in Table 1. The periods of test runs varied from 3 s to 9 s. The measuring points were decided to be 316 points in total as indicated in Figure 3. That is to say, one wave length of ripple was divided into 12 sections, and the vertical spacing were taken to be 5 mm, 10 mm and 20 mm from the bottom to a certain elevation as shown in Figure 3.

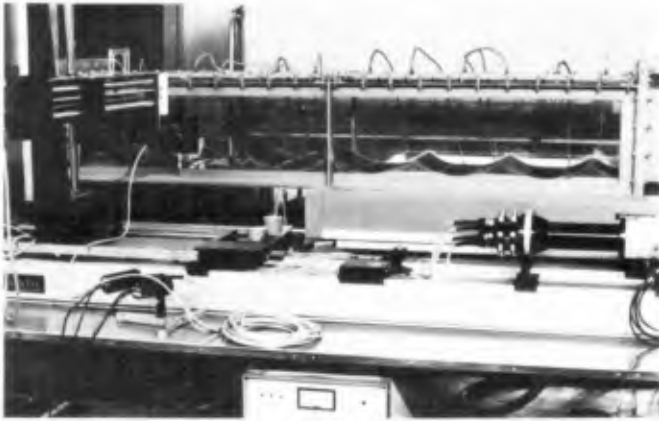


Fig.2 Experimental apparatus.

Table 1 Experimental conditions.

Run	1	2	3	4
T(s)	9.0	6.0	3.0	6.0
\hat{U} (cm/s)	13.9	20.9	20.9	10.5
Re	2.7×10^4	4.2×10^4	2.1×10^4	1.1×10^4

\hat{U} : amplitude of the oscillatory flow velocity

$$Re = \frac{\hat{U}a}{\nu} = \frac{\hat{U}^2 T}{2\pi \nu} \quad : \text{Reynolds number}$$

a : amplitude of the oscillatory flow motion

ν : kinematic viscosity of fluid

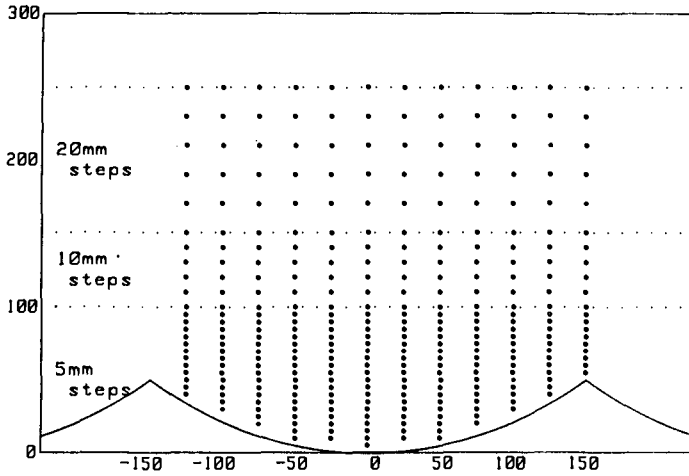


Fig.3 Data sampling points.

At each measuring point the velocity measurement was made for 30 cycles of waves by using a 2-D LDV. The lens of the velocimeter was moved by a 3-D traverse facility controlled by a mini-computer with a minimum displacement of 0.5 mm. Thus horizontal and vertical velocity components were measured. The commencement of data sampling was controlled by an electric signal generated at the piston. The phase 0 was selected at the instant when the movement of the piston became stationary, i.e. the cross-sectionally averaged fluid velocity became zero. The sampling time was selected to be 0.0195 s, during which 5 data were obtained. Therefore, 150 data were acquired for one phase at a measuring point. The interval of the sampling phases was $\pi/8$. The local mean fluid velocity, the intensity of fluid turbulence, the Reynolds stress, the kinematic eddy viscosity and the stationary velocity components were calculated by using 150 data at one phase and at one point and displayed in a graphical form.

RESULTS OF LABORATORY INVESTIGATION AND DISCUSSION

Mean Fluid Velocity

The boundary layer developed along a ripple surface can be divided into two parts. The first one is the inner boundary layer or the Stokes layer existing very close to the bottom boundary, where the fluid flow is strongly controlled by fluid viscosity. The second one is the outer boundary layer where the flow structure is characterized by the behavior of organized vortices

separated from the crest of the ripples. The thickness of the inner boundary layer is very thin with the order of $\sqrt{\nu T}$, where ν is the kinematic viscosity of fluid and T is the oscillation period.

Variation of the mean velocity fields during the phases 0 to $7\pi/8$ for Run 3 was illustrated in Figure 4 with a time interval of $\pi/8$. Through the careful observation of time variation of velocity field illustrated in Figure 4, the behavior of an organized vortex covering its growing and then decaying processes can be realized. This phenomenon is a remarkable feature of the outer boundary layer of the oscillatory flow.

In order to clarify the characteristic behavior of the flow in the inner boundary layer, the velocity distribution at the section just above a ripple crest was measured. The reason is that the thickness of the boundary layer at the crest must be specified in predicting the circulation of the vortices. Based on the result of velocity measurement, the temporal variation of the boundary layer thickness for two selected cases were plotted as shown in Figure 5. It is clearly noticed that the thickness reduces considerably at flow accelerating phases, while the thickness tends to increase at decelerating phases. Even though the boundary layer thickness shows such a temporal variation as stated above, the temporally averaged value of the thickness is reasonably well described by $\sqrt{\nu T}$ as seen in this figure.

It has been predicted theoretically that stationary cells are generated in the outer boundary layer of the oscillatory flows over a wavy boundary. In our study the stationary velocity component was derived by averaging the fluid velocity for one period of oscillatory flow at each measuring point. The result for Runs 2 and 3 were drawn in Figure 6, from which it can be clearly observed that two stationary cells were generated. The maximum steady flow velocity seems to occur near the bottom close to the ripple crests. The ratio of the maximum steady velocity to the velocity amplitude of the undisturbed flow, U , was calculated and shown in Table 2. From this table it is found that the stated ratio was affected by the period of fluid oscillation. For $T = 3$ s, the ratio was about 0.76, while it was about 0.58 for $T = 9$ s. These results indicate that the magnitude of stationary velocity is very large near the bottom. This fact suggests that the stationary cell has an important role in amplifying the height of ripples. It can also be observed that the

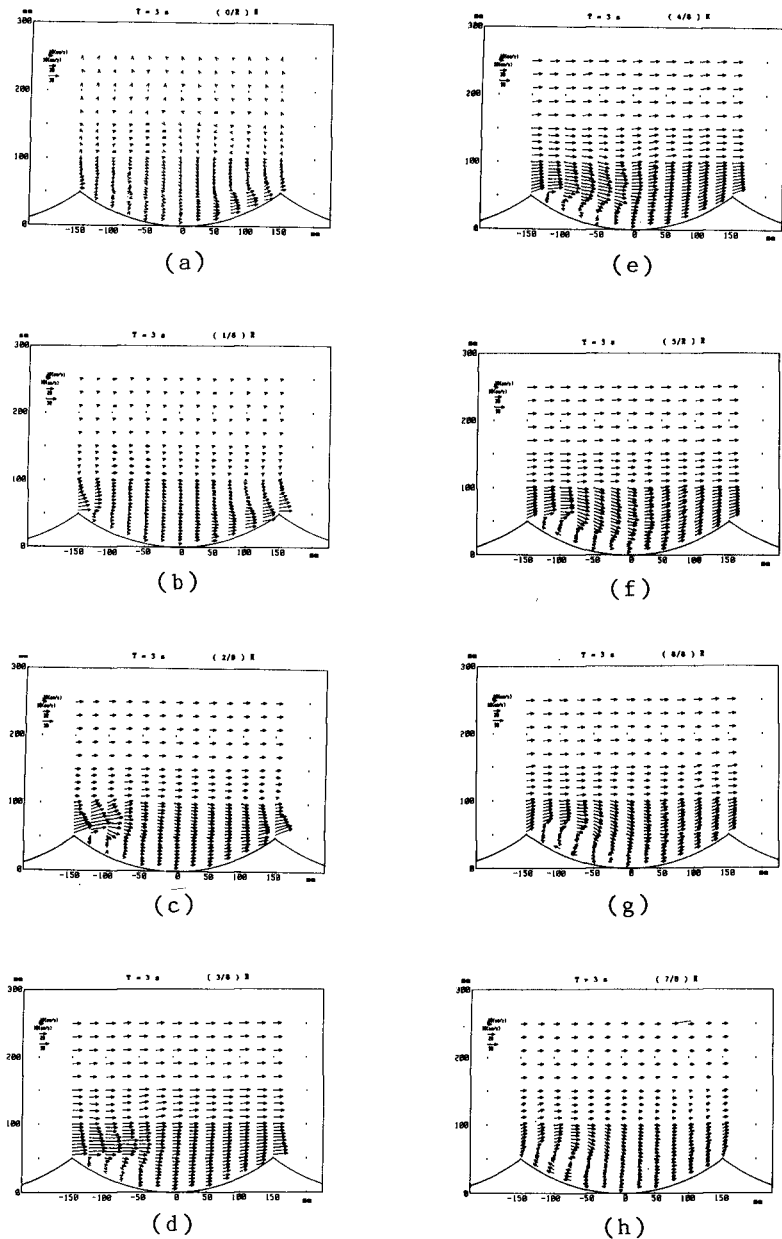


Fig.4 Distributions of temporally averaged fluid velocity for Run 3.

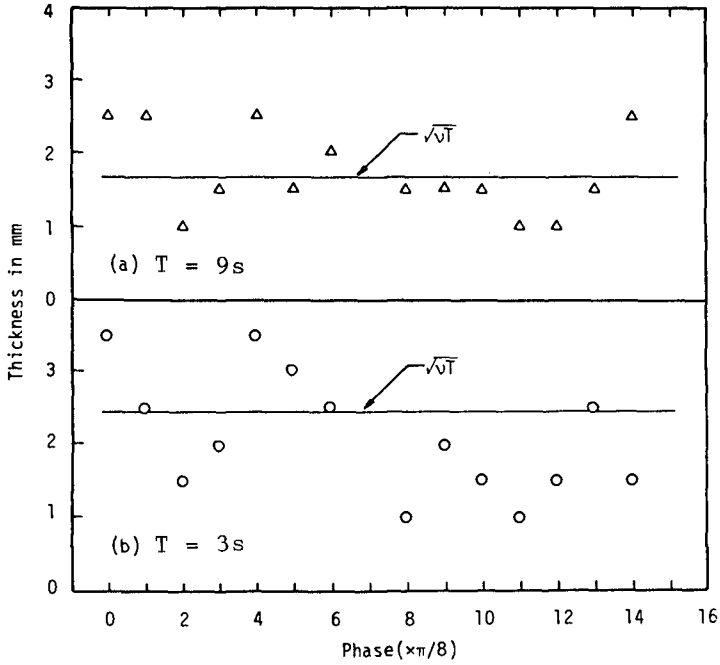


Fig.5 Temporal variation of the inner boundary layer thickness above the ripple crest.

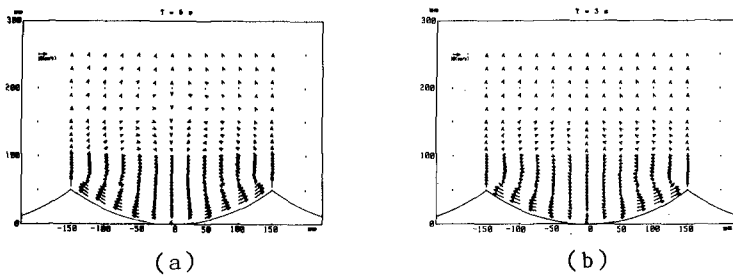


Fig.6 Stationary velocity distributions for (a) Run 2 and (b) Run 3.

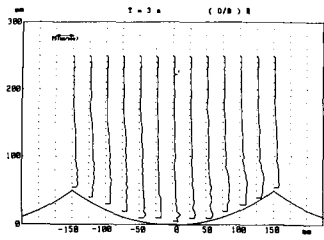
Table 2 Maximum speed of stationary current, V_{\max} .

T (s)	3	6	9
\hat{U} (cm/s)	20.9	20.9	13.9
V_{\max} (cm/s)	15.8	13.3	8.02
$\frac{V_{\max}}{\hat{U}}$	0.76	0.64	0.58

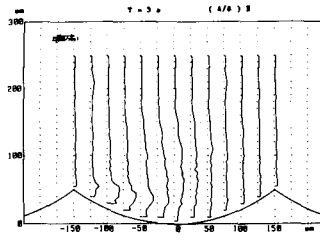
stationary cells are significantly correlated with the vortices which seem to strengthen the stationary velocity component compared with that predicted for rolling grain ripples. The laboratory data at the University of Tokyo (Hamamoto, et al., 1982) obtained by using a sinusoidal shape bottom boundary indicated that the questioned ratio was about 0.3, considerably smaller than the present results. Therefore the circulation of the vortices generated over the round-crested ripples is expected to be smaller than that over sharp-crossed ripples. The second series of our experiment using a round-crested ripple model, which is now going on, is expected to give more definite conclusions on this subject.

Fluid Turbulence Intensity

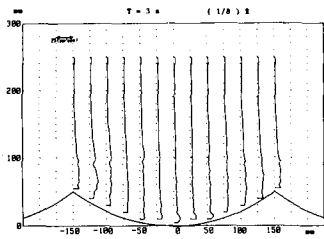
The intensity of fluid turbulence was calculated by using 150 data for each velocity component obtained for each phase at each measuring point. Figure 7 shows the variation of the vertical distribution of turbulence intensity expressed in the form of RMS value during a half-cycle of fluid oscillation. The intensity of fluid turbulence was slightly large in the area where the vortex separated from the right hand side crest in the preceding period was still existing at the phase of $(0/8)\pi$ and gradually attenuated in due course. On the contrary to this, the turbulence intensity in the right hand side area of the left crest increased and the area with large turbulence intensity increased its size. The turbulence intensity reached the maximum at the phase $4\pi/8$ near the center of the vortex, the value of which became as large as 80 % of the velocity amplitude of the undisturbed oscillatory flow, \hat{U} . The fluid turbulence was convectively transported toward the down stream, and prevailed in almost all over the boundary layer between the two neighbouring crests at the phase $6\pi/8$. The turbulence intensity became to decrease its magnitude at



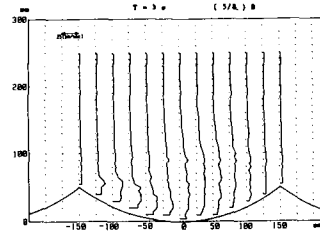
(a)



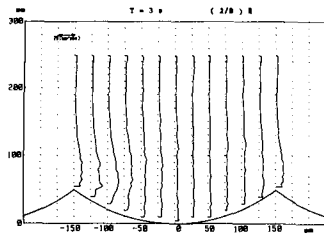
(e)



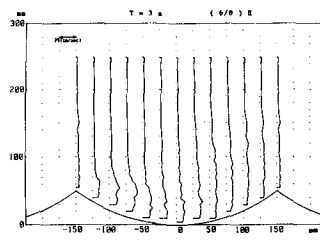
(b)



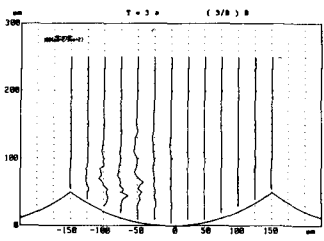
(f)



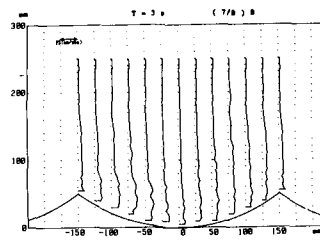
(c)



(g)



(d)



(h)

Fig.7 Distributions of the fluid turbulence intensity for Run 3.

the phase $7\pi/8$, but the intensity still kept the level of 60 % of the velocity amplitude.

The Reynolds Stress

The kinematic Reynolds stress, $-\overline{u'v'}$, was also obtained as depicted in Figure 8. The distributions of the Reynolds stress show more clearly the effect of the vortices on the turbulent fluid. At the phase $(0/8)\pi$, the Reynolds stress was almost zero everywhere except the limited region on the right hand side where a weak negative Reynolds stress was observed corresponding to the vortex shed from the right hand side ripple crest. At the phase $\pi/8$ a weak positive Reynolds stress began to appear in the downstream of the left crest corresponding to the release of vorticity from the crest. The Reynolds stress increased very rapidly at the phase $2\pi/8$, where the value was positive below the prescribed streamline with the maximum fluid velocity and negative above the streamline. The region of large Reynolds stress moved downstream, and the absolute value of the Reynolds stress reduced considerably at the phase $3\pi/8$. This reduction corresponds to the fact that the vertical distribution of mean fluid velocity became more uniform near the crest. The Reynolds stress took positive value almost everywhere, and reached its maximum at the phase $4\pi/8$ in the vortex region.

The Reynolds stress began to appear in the region above the ripple trough, and was probably induced by a large fluid velocity transported convectively from the left hand side ripple crest. The maximum fluid velocity at the trough located at about $y = 70$ mm, below and above which the Reynolds stress was positive and negative respectively. The overall Reynolds stress gradually decreased toward the phase $7\pi/8$.

These observations reveal that the Reynolds stress is significantly correlated with the release of the vorticity from the ripple crest and is essentially zero in the area where the vorticity is not supplied from the ripple crest even if the turbulence intensity has non-zero value there.

Kinematic Eddy Viscosity

The kinematic eddy viscosity, \mathcal{E}_v , was calculated at a few fixed points as well as at the center of the organized vortex. Because the generation of the Reynolds stress is significantly correlated with the vortex formation as revealed previously, the temporal variation of the kinematic eddy viscosity at the vortex

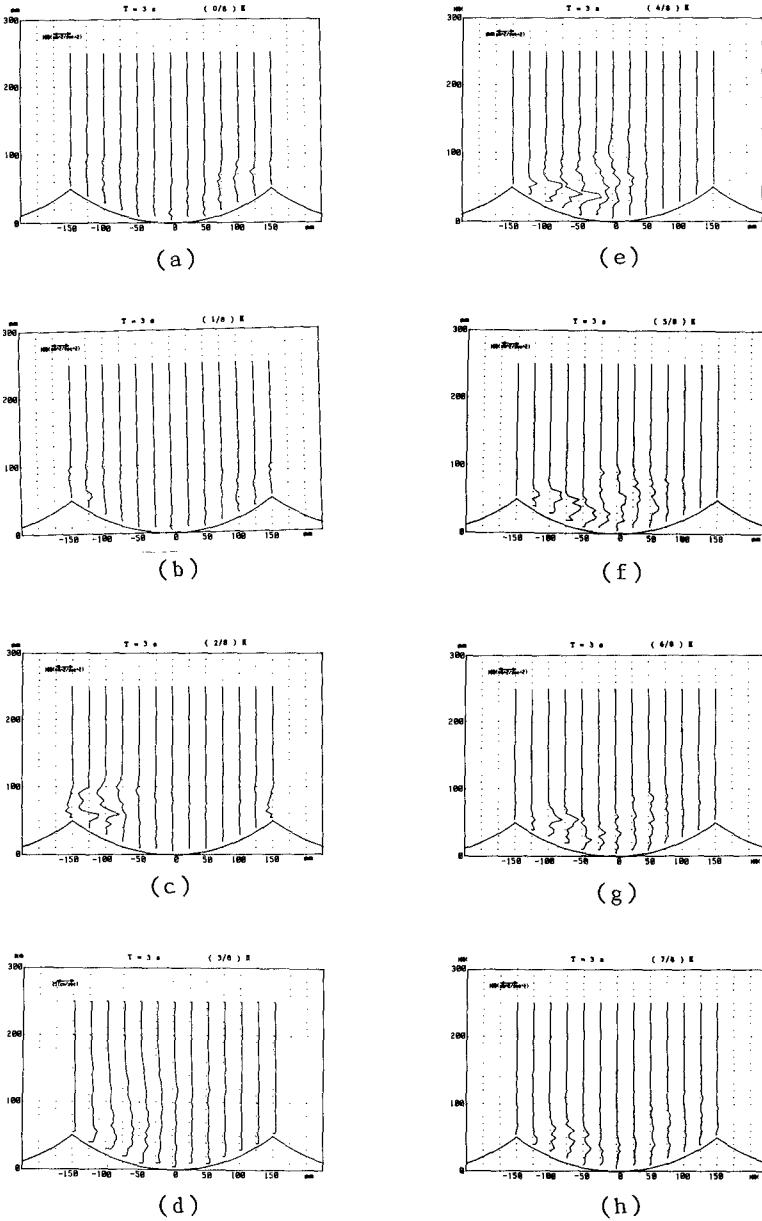


Fig.8 Distribution of kinematic Reynolds stress for Run 3.

center will be described here. The results were given in Figure 9, in which the kinematic eddy viscosity was calculated from the raw data, without smoothing, of the distribution of the fluid velocity and the Reynolds stress. A large variety of the kinematic eddy viscosity with time is almost in accordance with the undisturbed oscillatory flow for each case. It is clearly seen that the kinematic eddy viscosity increased linearly with phase until the phases $4\pi/8$ and $12\pi/8$, at which the fluid velocity reached its maximum. The kinematic eddy viscosity, then, decreased rather gradually, and therefore it indicated a slightly unsymmetrical distribution with respect to the phase. The above feature was common for each run. The distribution of the kinematic eddy viscosity non-dimensionalized by the velocity amplitude of the undisturbed oscillatory flow and the ripple height, becomes nearly identical as shown in Figure 10. The results obtained here suggests that the assumption of constant kinematic eddy viscosity does not hold in the present type of flow, and a turbulent model such as two equation model must be employed to predict the flow field.

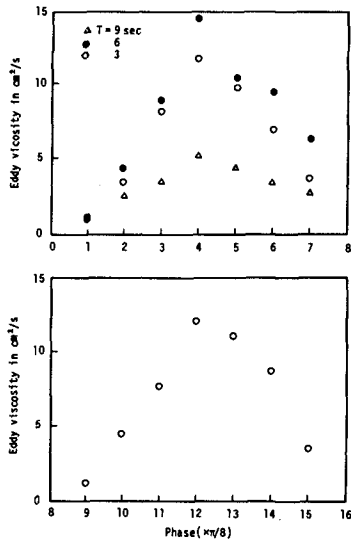


Fig.9 Temporal variations of kinematic eddy viscosity at the vortex center.

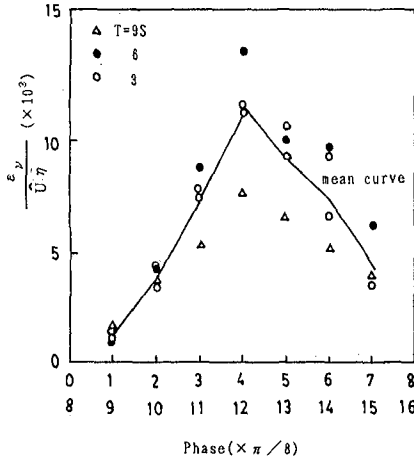


Fig.10 Temporal variation of the non-dimensionalized kinematic eddy viscosity.

CONCLUSIONS

A detailed measurement was performed for the oscillatory boundary layer flow over a sharp-crested ripple model by using a 2-D LDV controlled by a computer. The conclusions are summarized as follows:

- (1) The oscillatory boundary layer over a ripple model is separated into two parts ; the inner and the outer boundary layers. The thickness of the inner boundary layer is well expressed by $\sqrt{\nu T}$. The feature of the outer boundary layer is characterised by the organized vortices, and the growth of the vortices has a phase-lag against the undisturbed main flow.
- (2) The stationary velocity component constitutes two cells between two ripple crests, the distribution of which is similar regardless of the test conditions. The flow is moving toward the crests, and the velocity is very large near the bottom boundary close to the ripple crests.
- (3) The fluid turbulence is found to be closely correlated with the vortices. The generation of the Reynolds stress is limited essentially within the vortex region. Some minor part of the vortices is convectively transported downstream, and yields weak Reynolds stress there.

- (4) The kinematic eddy viscosity obtained at the near-center of the organized vortices reveals that it varies sinusoidally in accordance with the oscillatory flow. The variation of the kinematic eddy viscosity with respect to the phase is similar to the other regardless of the test conditions reported herein.
- (5) The three-dimensional structure of the oscillatory boundary layer is still left as a future subject.

ACKNOWLEDGMENT

This study has been supported by the Grant-in-Aid for Scientific Research from the Ministry of Education and Culture of Japan (Grant No.01460180).

REFERENCES

- Bagnold, R. A. : Motion of waves in shallow water, Interaction between waves and sand bottoms, Proc. Royal Society, London, A187, pp.1-18, 1946.
- Ikeda, S., S. Kizaki, S. Ishii and S. Kuribayashi : Flow near sand ripples and dissipation of wave energy, Coastal Eng. in Japan, Vol.32, No.1, pp.15-36, 1989.
- Du Toit, C. G. and J. F. A. Sleath : Velocity measurements close to rippled beds in oscillatory flow, J. Fluid Mech., Vol.112, pp.71-96, 1981.
- Hamamoto, K., N. Mimura and A. Watanabe : Experimental study on oscillatory boundary layer over sand ripples (2), Proc. 29th Japanese Coastal Eng. Conf., JSCE, pp.254-258, 1982 (in Japanese).
- Longuet-Higgins, M. S. : Oscillating flow over steep sand ripples, J. Fluid Mech., Vol.107, pp.1-35, 1981.
- Sato, S. : A Fundamental Study on Shoaling and Velocity Field Structure of Water Waves in the Nearshore Zone, Dr. Thesis. The University of Tokyo, Feb. 1987.
- Sawamoto, M., T. Yamashita and M. Kitamura : Distributions of turbulent intensity and suspended sediment concentration, Proc. 28th Japanese Coastal Eng. Conf., pp.232-236, 1981 (in Japanese).
- Sleath, J. F. : Turbulent oscillatory flow over rough beds, J. Fluid Mech., Vol.182, pp.369-409, 1987.

CHAPTER 52

SENSITIVITY ANALYSIS FOR MULTI-ELEMENT WAVEMAKERS

Gordon S. Harkins,¹ Robert A. Dalrymple² and Miguel A.
Losada³

1 Abstract

Lateral variations in wave height have been observed in directional wave basins when generating monochromatic plane waves. Two numerical schemes are presented to examine wave height sensitivity to perturbations in stroke length between paddles and gaps between either adjacent paddles or the sidewall of the basin. A non-uniform wavemaker front generates both the desired wave and can generate waves at an angle and at the same frequency as the main wave.

2 Introduction

Simulation of realistic sea states requires the use of directional wave basins which can produce directional spectra. These basins generally consist of numerous wavemakers along one side of the tank and either reflecting or absorbing walls for the other sides. Before realizing the full potential of these tanks one must first understand the production of uniform monochromatic waves by a multi-element wavemaker system and the errors inherent in any possible nonuniform wavemaker front.

A numerical procedure is developed to examine wave height sensitivity to gaps which may exist between paddles and variations in paddle stroke length in a wave basin with reflecting

¹Coastal Engineer, Sea Engineering, Inc., Makai Research Pier, Waimanalo, Hawaii 96795, USA.

²Professor, Center for Applied Coastal Research, Department of Civil Engineering, University of Delaware, 137 DuPont Hall, Newark, Delaware 19716, USA.

³Professor, Departamento de Ciencias y Tecnicas, del Agua y del Medio Ambiente, Universidad de Cantabria, Santander, Spain.

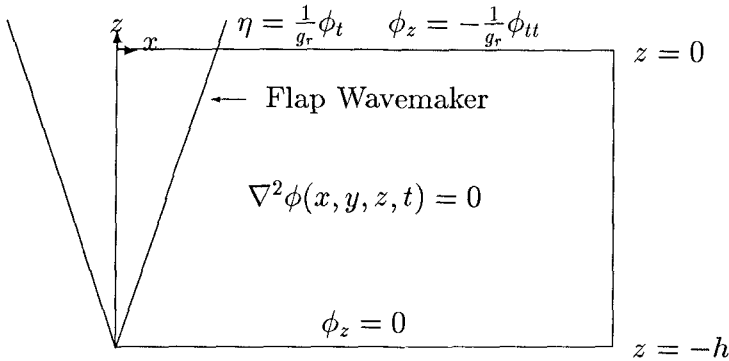


Figure 1: Boundary value problem specifications for both numerical models

sidewalls. To study variations in paddle motion for a multi-element wavemaker system a technique was developed to numerically model individual paddles. A sinusoidally varying “top hat function” consisting of the difference of two Heaviside functions is used to represent the paddle motion. This allows each paddle to have its own stroke length. For small amplitude waves the total wave height at a particular location in the tank can be found from the summation of waves produced by each individual paddle. No-flow gaps between paddles are created by positioning the “top hat functions” a small distance apart.

A second technique was used to specify the flow through gaps for uniform motion of a multi-element wavemaker system. A dual series relation is developed by matching the water particle velocity across the gaps and wavemakers and matching the velocity potential in the gaps. The perturbations in the wave field produced by the gaps is examined for two cases. The first involves an infinitely long tank with infinitely wide wavemakers placed in the middle of the tank. The second cases involves wavemakers placed a finite distance away from a fully reflecting backwall.

3 Formulation of the Boundary Value Problem

For an incompressible fluid with irrotational motion Laplace’s equation

$$\nabla^2\phi(x, y, z, t) = 0$$

holds throughout the domain of the problem. Laplace’s equation is elliptic and can only be solved uniquely if boundary conditions are given around the domain of the problem. For small amplitude waves the boundary conditions can be seen in Figure

1. Along the free surface the dynamic free surface and the combined free surface boundary conditions are applied. A no flow condition is specified for the bottom at $z = -h$. Applying the bottom boundary condition and the linear combined free surface boundary condition the velocity potential can be written as

$$\Phi = \phi(x, y) \cosh k(h + z)e^{-i\sigma t} \quad (1)$$

where a temporally periodic solution has been assumed. The angular frequency is given by the usual dispersion relationship

$$\sigma^2 = g_r k \tanh k(h + z)$$

where g_r is gravity, k is the wave number defined as $\frac{2\pi}{L}$ where L is the wavelength. Since we are interested in the cause of the lateral variation along the whole length of the tank, the vertically evanescent modes have been neglected because of their rapid decay away from the paddles.

We will also specify a no flow condition through the side walls given as

$$\phi_y = 0 \text{ at } y = \pm b$$

Two families of solutions exist that satisfy the side wall condition. The first family of solutions is symmetric about the x -axis and is referred to as the even modes and is given by the y portion of the velocity potential below

$$\phi_e(y) = \cos \lambda_j y$$

where

$$\lambda_j \equiv \frac{j\pi}{b} \text{ for } j = 0, 1, 2, \dots$$

One should note that the usual plane progressive mode is the $j = 0$ mode which has no variation in wave height across the tank. The second family of solutions is anti-symmetric about the x -axis and is referred to as the odd modes and the y component of the velocity potential is

$$\phi_o(y) = \sin \gamma_l y$$

where

$$\gamma_l \equiv \frac{l + \frac{1}{2}\pi}{b} \text{ for } l = 0, 1, 2, \dots$$

In general the y component of the velocity potential is just the sum of the even and odd modes.

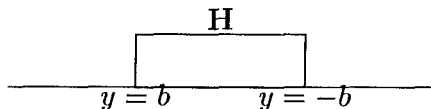


Figure 2: Top hat function generated by the difference of two Heaviside function

The x component of the velocity potential which satisfies Laplace's can be written as

$$\phi(x) = e^{i\sqrt{k^2 - \alpha^2}x}$$

where α represents either the even or odd mode wave number.

The velocity potential can be separated into its even and odd contributions and be written as the sum of

$$\phi_e = \sum_{j=0}^{\infty} A_j e^{i(\sqrt{k^2 - \lambda_j^2}x - \sigma t)} \cosh k(h + z) \cos \lambda_j y$$

$$\phi_o = \sum_{l=0}^{\infty} B_l e^{i(\sqrt{k^2 - \gamma_l^2}x - \sigma t)} \cosh k(h + z) \sin \gamma_l y$$

This is the same solution Dalrymple (1989) found for a constant depth wave basin. To solve for the unknowns A_j and B_l we will use the wavemaker boundary conditions.

3.1 Wavemaker Boundary Conditions for Perturbations in Stroke Length

For a wave tank whose paddle spans the width of the tank the usual linearized kinematic wavemaker boundary condition can be shown to yield

$$u(0, z, t) = -iU_0 e^{-i\sigma t} \text{ for } |y| < b \quad (2)$$

where U_0 is the magnitude of the paddle velocity at $x = 0$ along the z^{th} plane and i is the $\sqrt{-1}$.

A more attractive technique exists for specifying (2) which can be expanded to account for a multi-element wavemaker. We will denote the Heaviside function as H and define $H(y - b)$ as

$$H(y - b) = \begin{cases} 0, & \text{for } y < b \\ 1, & \text{for } y \geq b \end{cases}$$

We can also combine two Heaviside functions to generate a "top hat function". Figure 2 was generated using the difference of two

Heaviside function as given below

$$\mathbf{H} = H(y + b) - H(y - b). \tag{3}$$

Multiplying the “top hat function” by $U_0(z)$ and a complex exponential of time yields the wavemaker boundary condition in terms of Heaviside functions and can be written as

$$u(0, y, z, t) = -iU_0\mathbf{H}e^{-i\sigma t}$$

The “top hat function” approach can be expanded to account for a multi-element wavemaker. The width of the Heaviside functions and placement controls the paddle width and the no flow gap width between paddles. In general the wavemaker boundary condition for the n^{th} paddle can be written as

$$u_n(x = 0, y, z, t) = -iU_{0,n}\mathbf{H}_n\mathbf{e}^{-i\sigma t}$$

and the full wavemaker boundary condition is the sum of the contribution from each wavemaker

$$u(0, y, z, t) = \sum_{n=1}^N u_n \tag{4}$$

where N is the number of wavemakers and the constant $U_{0,n}$ allows for non-uniform paddle motion. For stroke length perturbations $U_{0,1} \neq U_{0,2} \neq \dots U_{0,N}$. This is different from waves that are generated at an angle to the wavemaker in which there is a sinusoidal variation in the phase between paddles but the stroke length for each paddle is the same.

For an N wavemaker system a summation over the N paddles must also be added and the even and odd velocity potentials reduce to

$$\phi_e = \sum_{n=1}^N \sum_{j=0}^{\infty} A_{n,j} e^{i(\sqrt{k^2 - \lambda_j^2}x - \sigma t)} \cosh k(h + z) \cos \lambda_j y \tag{5}$$

and

$$\phi_o = \sum_{n=1}^N \sum_{l=0}^{\infty} B_{n,l} e^{i(\sqrt{k^2 - \gamma_l^2}x - \sigma t)} \cosh k(h + z) \sin \gamma_l y. \tag{6}$$

The constants $A_{n,j}$ and $B_{n,l}$ can be solved uniquely by applying the wavemaker boundary condition given in (4) for the n^{th} paddle and the orthogonal relationship between trigonometric series and the hyperbolic cosine function. For the even coefficients we first multiply by the $\cos \lambda_j y$ term and integrate over the

width of the tank and then multiply by $\cosh k(h+z)$ term and integrate over the depth. Similarly for the odd coefficients except we multiply by the $\sin \gamma_l y$ series instead of the cosine series. The coefficients are given as

$$A_{n,j} = -\frac{\int_{-b}^b U_{0n}(y) \mathbf{H}_n \cos \lambda_j y dy \int_{-h}^0 U(z) \cosh k(h+z) dz}{\sqrt{k^2 - \lambda_j^2} \int_{-b}^b \cos^2 \lambda_j y dy \int_{-h}^0 \cosh^2 k(h+z) dz} \quad (7)$$

$$B_{n,l} = -\frac{\int_{-b}^b U_{0n}(y) \mathbf{H}_n \sin \gamma_l y dy \int_{-h}^0 U(z) \cosh k(h+z) dz}{\sqrt{k^2 - \gamma_l^2} \int_{-b}^b \sin^2 \gamma_l y dy \int_{-h}^0 \cosh^2 k(h+z) dz} \quad (8)$$

The free surface elevation can be found from the linear dynamic free surface boundary condition.

3.2 Wavemaker Boundary Condition for Flow between Paddles

In the previous formulation Heaviside functions were used to model wavemakers where a perturbation between paddle stroke length could be analyzed. In this section a numerical procedure is introduced to study the wave field created by gaps between paddles for uniform paddle motion. These gaps allow flow between the paddles unlike the previous section where no flow gaps were assumed. Since there is a transmission of fluid through the gaps, an eigenfunction expansion method describes the wave field on each side of the wavemakers.

Two cases will be analyzed for the gap problem. The first case involves an infinitely long tank with an infinitely wide wavemaker located in the center of the tank. In the second case, the gap problem is solved in a semi-infinite long tank with infinitely wide wavemakers placed next to a reflecting backwall.

3.2.1 Infinitely Long Tank

The solution technique Dalrymple and Martin (1990) applied to the problem of waves impinging on an infinite row of offshore breakwaters can be applied to the problem of wavemakers with gaps. Following the coordinate convention Dalrymple and Martin introduced, the wavemakers are modelled as infinitely thin barriers, centered at $y = \pm nb$ where $n = 1, 2, 3, \dots, \infty$ and are separated by gaps of width $2g$. The lines $y = \pm nb$ are lines of symmetry assuming the wavemaker motion is uniform. Instead of solving the problem for an infinitely long row of wavemakers an analogous problem in which a sidewall or barrier is placed

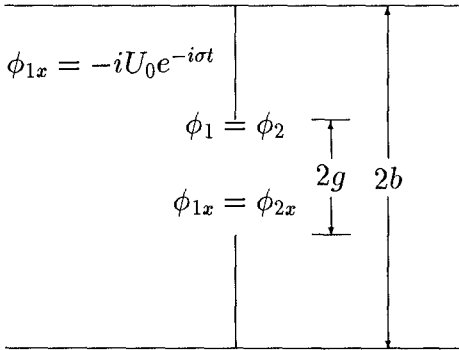


Figure 3: Boundary conditions for an infinitely long tank

along the lines of symmetry will be solved. Waves that initially travelled across these lines are now reflected back and the wave pattern seen is unchanged.

For uniform paddle motion the wave field is symmetric about the center of the wavemakers and thus only the even family of solutions should be retained in the y component of the velocity potential. The velocity potential for $x < 0$ can be written as

$$\phi_1(x, y) = \sum_{j=0}^{\infty} A_j \cos \lambda_j y e^{-i\sqrt{k^2 - \lambda_j^2} x}$$

where the negative complex exponential allows waves traveling to the left and for $x > 0$

$$\phi_2(x, y) = - \sum_{j=0}^{\infty} B_j \cos \lambda_j y e^{i\sqrt{k^2 - \lambda_j^2} x}$$

where the minus sign has been kept for convenience. The full velocity potential can be found using equation (1).

The wavemaker boundary conditions shown in Figure 3 will be used to solve for the constants A_j and B_j . Three conditions are specified. The first is the kinematic wavemaker boundary condition matching the wavemaker velocity with the water velocity. In the gaps we match the velocities and the velocity potentials to ensure a matching of the free surface. Setting the velocities and the velocity potentials in the gaps equal we find that

$$\sum_{j=0}^{\infty} A_j \cos \lambda_j y = 0 \quad \text{for } |y| \leq g \tag{9}$$

Matching the velocity at the wavemaker

$$\sum_{j=0}^{\infty} (A_j \sqrt{k^2 - \lambda_j^2} \cos \lambda_j y - U_0) = 0 \text{ for } g < |y| \leq b \quad (10)$$

Sneddon (1966) termed the two conditions (9) and (10) a dual series relation which can be combined to make one mixed boundary condition given as $G(y) = 0$ where

$$G(y) = \begin{cases} \sum_{j=0}^{\infty} A_j \cos \lambda_j y, & \text{for } |y| \leq g \\ \sum_{j=0}^{\infty} A_j \sqrt{k^2 - \lambda_j^2} \cos \lambda_j y - U_0, & \text{for } g < |y| \leq b \end{cases} \quad (11)$$

The above expression can not be solved analytically and we will resort to using a least squares techniques to solve for the unknown coefficients A_j . This requires that the following equation be a minimum

$$\int_{-b}^b |G(y)|^2 dy. \quad (12)$$

by definition $|G(y)|^2 = GG^*$ where the $*$ denotes the complex conjugate. If we minimize the above integral with respect to A_j we find

$$\frac{\partial}{\partial A_m} \int_b^b |G| dy = 0$$

or

$$\int_b^b G^* \frac{\partial G}{\partial A_m} dy = 0 \text{ for } m = 0, 1, \dots$$

where

$$\frac{\partial G}{\partial A_m} = \begin{cases} \cos \lambda_m y & \text{for } |y| \leq g \\ \sqrt{k^2 - \lambda_m^2} \cos \lambda_m y & \text{for } g < |y| \leq b \end{cases}$$

3.2.2 Semi-Infinite Tank

The above problem of an infinitely long tank only needs to be slightly modified to account for a reflecting backwall located behind the wavemakers. This problem can be seen in Figure 4 where the backwall is located a distance ℓ behind the wavemakers. To account for the backwall an additional term must be added to ϕ_1 and is shown below

$$\phi_1(x, y) = \sum_{j=0}^{\infty} (B_j e^{-i\sqrt{k^2 - \lambda_j^2} x} \cos \lambda_j y + C_j e^{i\sqrt{k^2 - \lambda_j^2} (x + \ell)} \cos \lambda_j y)$$

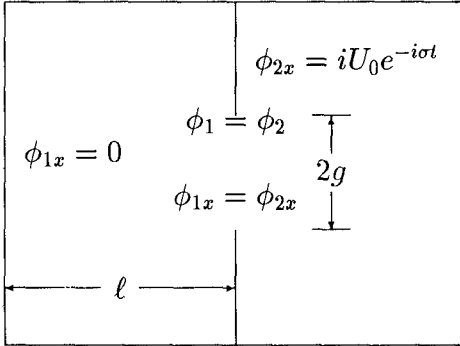


Figure 4: Boundary conditions for a semi-infinite tank

Applying the no-flow condition at $x = -\ell$ we can first find an expression for B_j in terms of C_j and re-write ϕ_1 as

$$\phi_1(x, y) = \sum_{j=0}^{\infty} B_j \cos \lambda_j y [e^{-i\sqrt{k^2 - \lambda_j^2} x} + e^{i\sqrt{k^2 - \lambda_j^2} (x+2l)}].$$

By matching the velocities in the gap we find

$$B_j = -\frac{A_j}{1 - e^{2i\sqrt{k^2 - \lambda_j^2} l}}$$

thus ϕ_1 can be written as

$$\phi_1 = \sum_{j=0}^{\infty} -A_j \frac{\cos \lambda_j y}{1 - e^{2i\sqrt{k^2 - \lambda_j^2} l}} (e^{-i\sqrt{k^2 - \lambda_j^2} x} + e^{i\sqrt{k^2 - \lambda_j^2} (x+2l)})$$

We will use the remaining two boundary conditions to find a new dual series relationship given as

$$G(y) = \begin{cases} \sum_{j=0}^{\infty} A_j \cos \lambda_j y (1 + \beta) = 0, & \text{for } |y| \leq g \\ \sum_{j=0}^{\infty} A_j \sqrt{k^2 - \lambda_j^2} \cos \lambda_j y - U_0, & \text{for } g < |y| \leq b \end{cases}$$

where β is

$$\beta = \frac{1 + e^{2i\sqrt{k^2 - \lambda_j^2} l}}{1 - e^{2i\sqrt{k^2 - \lambda_j^2} l}}$$

4 Numerical Results

4.1 Perturbed Paddle Motion

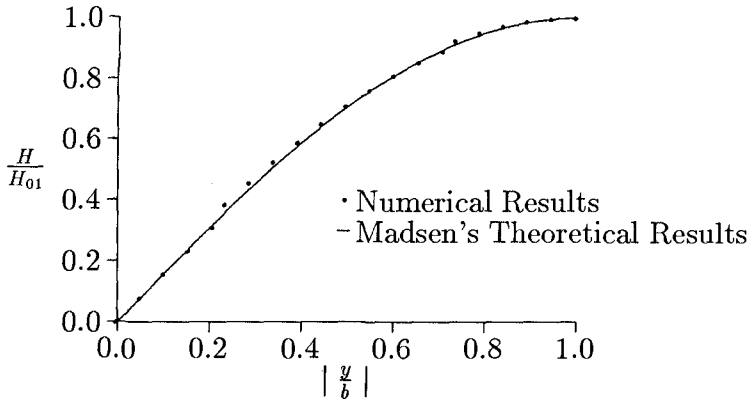


Figure 5: Relative wave height variation where H is the calculated wave height divided by the theoretical wave height H_{01} versus the dimensionless position across the tank $\frac{y}{b}$.

Madsen (1974) analyzed the results of a two wave paddle system in which the paddles were 180° out of phase located between reflecting sidewalls and a flat impermeable bottom. Madsen's numerical results which correspond very closely with his experimental results are plotted versus the authors numerical results in Figure 5. The horizontal axis shows the nondimensional position across the tank, and the vertical axis is the nondimensional wave height given by the calculated wave height H divided by the theoretical wave height along the sidewalls. The figure shows very good agreement between the two models.

We will again use the two wavemaker system utilized by Madsen but instead of 180° phase difference between paddles we allow a 10% variation in the stroke length between paddles. The importance of the lateral variation can be calculated by the ratio of a_{max}/a_0 where a_{max} is the combined amplitude of the non-plane modes and a_0 is the amplitude of the plane progressive mode (the $j = 0$ mode). Figure 6 shows the importance of the non-plane modes for varying kb values. This problem is purely anti-symmetric and cross tank resonance occurs at $kb = \pi/2$ and $3\pi/2$.

The usefulness of the first model is not limited to a two wave-maker system. Figure 7 was produced by a 10 paddle system with a 10% variation in the paddle stroke where the no flow gaps between paddles are 10% of the paddle width and $kb = 5.6$. The figure is a computer generated instantaneous picture of only the perturbed wave field where the wave crests are the darker regions and the wave troughs are the lighter regions. The paddles are located at the bottom of the figure and the reflecting sidewalls are

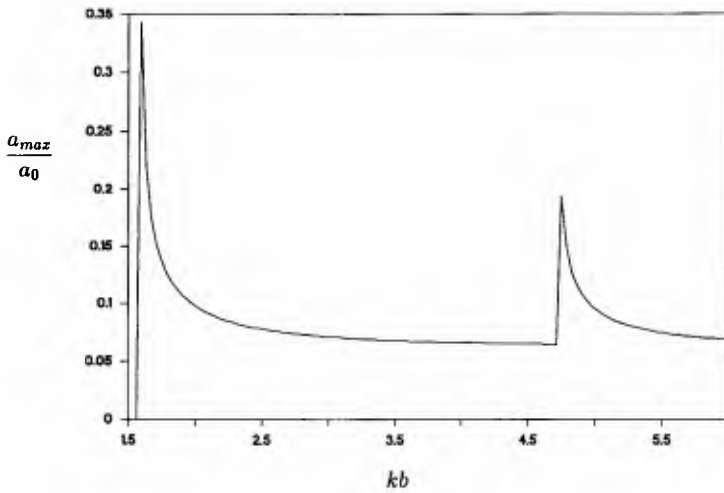


Figure 6: The lateral variation produced by a 10% stroke length difference for a two paddle system.



Figure 7: Instantaneous picture of the perturbed wave field. The paddles are located at the bottom of the figure and the sidewalls are located on the left and right margins.

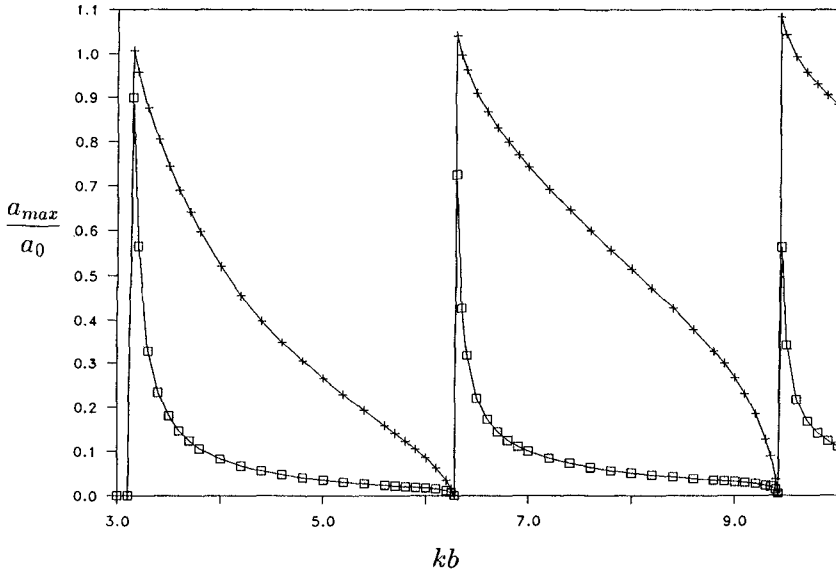


Figure 8: Resonance curves for an infinitely long tank. A gap width of 5% of the paddle width is marked with \square and a 10% gap width is marked with $+$.

located on the left and right margins. A 15% variation in the waveheight was found for this case.

4.2 The Gap Problem

A lateral variation in the wave field can also be produced by flow through the gaps between paddles for an infinitely long tank. For the gap problem we assumed symmetric motion about the center of the tank and resonance should occur at $kb = n\pi$. Graphing kb versus a_{max}/a_0 defined previously, Figure 8 clearly shows the first three resonance peaks. Decreasing the gap width by 5% greatly reduces the lateral variation generated.

The wave field produced by placing a reflecting backwall just over a half wavelength behind the wavemaker can be seen in Figure 9. In this case the location of the backwall is near resonance and with $kb = 3.6$ the tank is near resonance across the tank. Graphs showing lateral variation as a function of kb for different gap sizes and backwall distances can be found in Harkins (1990).



Figure 9: Instantaneous picture of the wave field produced by gaps between paddles. The backwall is located at the bottom of the figure.

5 Conclusions

Both the generated wave length and the basin geometry are important in creating a clean monochromatic plane wave. Even small perturbations in the paddle stroke length as well as flow between paddles can generate large lateral variations in the wave field especially near resonance conditions.

Heaviside functions can accurately represent discrete paddles of a multi-element wavemaker. This technique is useful in analyzing perturbations in the stroke length between paddles since the stroke length of each paddle is easily defined. Lateral variations will be present whenever the tank width is wider than the half wavelength of the generated wave and can be significant when the kb is a multiple of $\frac{\pi}{2}$. For small amplitude waves, the wave field is produced by the contribution of each paddle and thus the complexity of the wave field increase with the number of paddles.

If water is allowed to flow through the gaps between paddles, then an eigenfunction expansion can be used to describe the wave field produced. Since the wavemaker motion was assumed to be uniform, lateral variation will be present when the paddle plus gap width is greater than the wavelength of the generated wave. The lateral variation can be significant when the kb ratio is a multiple of π and when the flow through the gaps is stronger.

References

- Dalrymple, R. A. (1989).
Directional Wavemaker Theory with Sidewall Reflection, J. Hydraulic Research, 27, pp. 23-34.
- Dalrymple, R.A. and P. A. Martin (1990)
Wave Diffraction Through Offshore Breakwaters, J. Waterway, Port, Coastal and Ocean Engineering, 6, 1990.
- Harkins, G. S. (1990) Sensitivity Analysis For Multi-Element Wavemakers, Thesis to be presented to the University of Delaware, Newark, Delaware, in 1990 in partial fulfillment of the requirements of the Degree of Masters of Applied Sciences.
- Madsen, O.S. (1974).
A Three Dimensional Wavemaker; Its Theory and Application, J. Hydraulic Research, 12, pp.205-222.
- Sneddon, I.N. (1966).
Mixed Boundary Value Problems in Potential Theory, Amsterdam:North Holland Publishing Co.,pp. 282.

CHAPTER 53

A MODEL TO PROPAGATE NONLINEAR WATER WAVES

J. M. Chambel Leitão*

J. L. M. Fernandes**

Abstract

The aim of the work presented here is to propagate random waves from deep or intermediate water depth to the nearshore region with a Boundary Integral Equation Method (BIEM) which is able to handle the nonlinear effects that occur in the process. A two-dimensional (x,z) mild nonlinear model to propagate waves over an uneven bottom is presented here. It takes into account 2nd order nonlinear effects of the wave transformation entering into shallow water. If energy dissipation is neglected, the flow field generated by the wave propagation can be described by a velocity potential formulation which is governed by the Laplace's equation in the domain. The results obtained from the model are time-dependent. The model is tested with solitary and irregular waves and compared with analytical and experimental results.

Introduction

The previous work done by the authors, (Fernandes, 1988) and (Leitão and Fernandes, 1989), led to the evidence that the computer CPU time required by a linear BIEM model (which cannot handle nonlinear effects) was relatively small whereas the nonlinear one was prohibitively expensive for real problems. This high cost is primarily due to the moving free surface boundary because the operation count includes forming a new coefficient matrix and solving the system every time step.

* PhD student

** Assistant Professor

Instituto Superior Técnico, Dep. Mechanical Engineering
Av. Rovisco Pais, 1096 LISBOA, PORTUGAL

A mild nonlinear model, was developed to meet the needs of affordable computer time and significant nonlinear effects. A Stokes-like expansion provided second order terms of the kinematic and the dynamic free surface boundary conditions that were introduced into a BIEM model. The important advantage of this is that these free-surface conditions are now applied at the mean water level which precludes moving elements. A constant coefficient matrix is used in this case. The boundary is discretized into linear elements and the time stepping is based on multistep integrators.

Basic Equations

Considering the flow to be irrotational and inviscid and the fluid to be incompressible, the Laplace's equation for the velocity potential (ϕ) is valid.

$$\nabla^2 \phi = 0 \quad (1)$$

This equation is subjected to a number of boundary conditions, namely: a) prescribed velocity (at the bottom or vertical boundaries),

$$\frac{\partial \phi}{\partial n} = \gamma(x, z, t), \quad (2)$$

where n is the unit outward normal; b) radiation (at vertical boundaries),

$$\frac{\partial \phi}{\partial t} + c \frac{\partial \phi}{\partial n} = 0, \quad (3)$$

where c is the outgoing wave celerity; c) two nonlinear conditions (dynamic and kinematic) for the free-surface:

$$\frac{\partial \phi}{\partial t} + \frac{1}{2} |\nabla \phi|^2 + g\eta = 0; \quad z = \eta \quad (4)$$

$$\frac{\partial \eta}{\partial t} + \frac{\partial \phi}{\partial x} \frac{\partial \eta}{\partial x} - \frac{\partial \phi}{\partial z} = 0; \quad z = \eta \quad (5)$$

where η is the surface elevation.

2nd order free surface equations

In order to avoid problems and costs caused by a moving boundary on the numerical model, a Taylor series expansion of both dynamic and kinematic conditions is made about the level $z=0$.

$$\phi(x, \eta, t) = \phi(x, 0, t) + \eta \frac{\partial \phi(x, 0, t)}{\partial z} + \eta^2 \frac{\partial^2 \phi(x, 0, t)}{\partial z^2} + O(\eta^3) \quad (6)$$

The following expressions result for the free-surface conditions, considering only the two first terms of the Taylor series:

$$\frac{\partial \phi}{\partial t} + \eta \frac{\partial^2 \phi}{\partial z \partial t} + g\eta + \frac{1}{2} \left(\frac{\partial \phi}{\partial x} \right)^2 + \eta \frac{\partial \phi}{\partial x} \frac{\partial^2 \phi}{\partial x \partial z} + \frac{1}{2} \left(\frac{\partial \phi}{\partial z} \right)^2 + \eta \frac{\partial \phi}{\partial z} \frac{\partial^2 \phi}{\partial z^2} = 0; \quad z = 0 \quad (7)$$

$$\frac{\partial \eta}{\partial t} + \frac{\partial \phi}{\partial x} \frac{\partial \eta}{\partial x} + \eta \frac{\partial^2 \phi}{\partial x \partial z} \frac{\partial \eta}{\partial x} - \frac{\partial \phi}{\partial z} - \eta \frac{\partial^2 \phi}{\partial z^2} = 0; \quad z = 0 \quad (8)$$

In order to assess the importance of each term, dimensionless variables are introduced as follows:

$$\phi = \frac{AL}{T} \phi'; \quad x = Lx'; \quad z = h z'; \quad t = Tt'; \quad \eta = A\eta'$$

The typical scales used are: A - wave amplitude; L - wave length; T - wave period; h - depth. Using also parameters $\epsilon = A/h$ and $\delta = h/L$ (dropping primes) expressions (7) and (8) result in:

$$\begin{aligned} \frac{\partial \phi}{\partial t} + \epsilon \eta \frac{\partial^2 \phi}{\partial z \partial t} + \frac{T^2}{L} g\eta + \epsilon \delta \frac{1}{2} \left(\frac{\partial \phi}{\partial x} \right)^2 + \epsilon^2 \delta \eta \frac{\partial \phi}{\partial x} \frac{\partial^2 \phi}{\partial x \partial z} + \frac{\epsilon}{\delta} \frac{1}{2} \left(\frac{\partial \phi}{\partial z} \right)^2 + \\ + \frac{\epsilon^2}{\delta} \eta \frac{\partial \phi}{\partial z} \frac{\partial^2 \phi}{\partial z^2} = 0 \end{aligned} \quad (9)$$

$$\frac{\partial \eta}{\partial t} + \epsilon \delta \frac{\partial \phi}{\partial x} \frac{\partial \eta}{\partial x} + \epsilon^2 \delta \eta \frac{\partial^2 \phi}{\partial x \partial z} \frac{\partial \eta}{\partial x} - \frac{1}{\delta} \frac{\partial \phi}{\partial z} - \frac{\epsilon}{\delta} \eta \frac{\partial^2 \phi}{\partial z^2} = 0 \quad (10)$$

Neglecting terms of $O(\epsilon^2)$, $O(\epsilon^2/\delta)$ or larger and getting back to dimensional form, the free-surface conditions read:

$$\text{- Dynamic} \quad \frac{\partial \phi}{\partial t} = -g\eta - \frac{1}{2} |\nabla \phi|^2 - \eta \frac{\partial^2 \phi}{\partial z \partial t} \quad (11)$$

$$\text{- Kinematic} \quad \frac{\partial \eta}{\partial t} = \frac{\partial \phi}{\partial z} - \frac{\partial \phi}{\partial x} \frac{\partial \eta}{\partial x} + \eta \frac{\partial^2 \phi}{\partial z^2} \quad (12)$$

These equations are both valid at level $z = 0$ which allows the upper boundary in the numerical model to be constant in time. The last two terms of (11) and (12) account for the most important nonlinear effects while the others represent the linear ones.

Boundary Integral Element Method

The Laplace's equation with prescribed Dirichlet, Neumann, Robin and mixed boundary conditions is an elliptic problem which can be suitably solved by the BIEM. Our problem for the velocity potential is an hyperbolic one which includes variable time. Thus, we can use that method for the spatial discretization and let the time dependency be handled by a finite difference stepping scheme. A direct boundary element formulation, based upon Green's second identity, relates potential and normal velocity at the boundary. This way, the discretization involves only the boundary. For each element, x , z , ϕ , $\partial\phi/\partial n$ and η are piecewise linearly interpolated using their nodal values. Boundary conditions and unknowns can then be manipulated to form a system of equations. Having done this, one obtains an approximate solution that is equally accurate on both potential and normal velocity. The computation, upon request, of the potential and the velocity vector at interior points is explicit.

Time Marching Procedure

The free-surface equations for the second order model include linear terms, which are integrated by a trapezoidal rule (implicit), plus second order terms for which Adams predictor-corrector formulas are adequate. The blended predictor formulae are as follows:

$$\text{Dynamic} \quad \frac{1}{\Delta t} (\phi^{i+1} - \phi^i) = -\frac{g}{2} (\eta^{i+1} + \eta^i) + D_P^{(i,i-1)} \quad (13)$$

$$\text{Kinematic} \quad \frac{1}{\Delta t} (\eta^{i+1} - \eta^i) = \frac{1}{2} (\phi_z^{i+1} + \phi_z^i) + K_P^{(i,i-1)} \quad (14)$$

Here D_P and K_P represent differences from linear equations and can be predicted as:

$$D_P^{(i,i-1)} = \frac{1}{4} (\phi_x^2 + \phi_z^2)^{i-1} - \frac{3}{4} (\phi_x^2 + \phi_z^2)^i + \frac{1}{2} (\eta^{i-1} \phi_{zt}^{i-1} - 3 \eta^i \phi_{zt}^i)$$

$$K_P^{(i,i-1)} = \frac{1}{2} (-3 \phi_x^i \eta_x^i + \phi_x^{i-1} \eta_x^{i-1} - 3 \phi_{xx}^i \eta^i + \phi_{xx}^{i-1} \eta^{i-1}).$$

The corrector step makes use of the formulas:

$$\text{Dynamic} \quad \frac{1}{\Delta t} (\phi^{i+1} - \phi^i) = -\frac{g}{2} (\eta^{i+1} + \eta^i) + D_C^{(i+1,i)} \quad (15)$$

$$\text{Kinematic} \quad \frac{1}{\Delta t} (\eta^{i+1} - \eta^i) = \frac{1}{2} (\phi_z^{i+1} + \phi_z^i) + K_C^{(i+1,i)} \quad (16)$$

where D_C and K_C are given by:

$$D_C^{(i+1,i)} = -\frac{1}{4} (\phi_x^2 + \phi_z^2)^{i+1} - \frac{1}{4} (\phi_x^2 + \phi_z^2)^i - \frac{1}{2} (\eta^{i+1} \phi_{zt}^{i+1} + \eta^i \phi_{zt}^i)$$

$$K_C^{(i+1,i)} = -\frac{1}{2} (\phi_x^{i+1} \eta_x^{i+1} + \phi_x^i \eta_x^i + \phi_{xx}^{i+1} \eta^{i+1} + \phi_{xx}^i \eta^i).$$

The numerical computation of the derivatives is omitted for brevity, being the vertical acceleration (ϕ_{zt}) the most unstable. A linear relation between ϕ and $\partial\phi/\partial n$ is sought with these formulae and it is accomplished by substitution of η^{i+1} in (13) with the corresponding expression taken from (14). The same is done for the correction procedure. Due to their linearity, other boundary conditions are of straightforward discretization in time.

Test Case 1

This first example aims to test the model with solitary waves propagating over a constant depth channel. Amplitudes were made to vary from 0.1 to 0.4 times the depth. From figure 1 an amplitude decay can be observed near the generation region and becoming less apparent as the wave moves rightwards. For

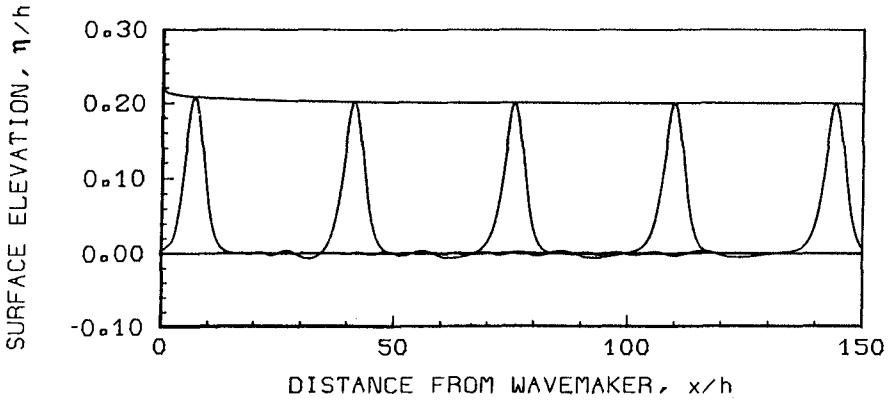


Figure 1. water surface profiles, for several time instants, and maximum amplitude curve along the channel; BIEM numerical results

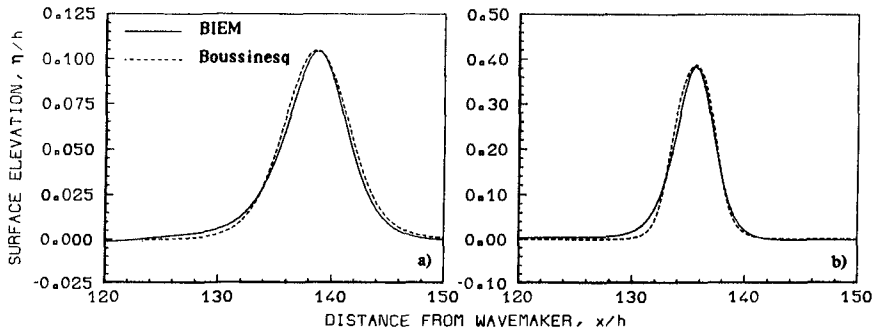


Figure 2. Comparison between numerical and Boussinesq's solitary wave profiles: a) $A/h \approx 0.1$; b) $A/h \approx 0.4$

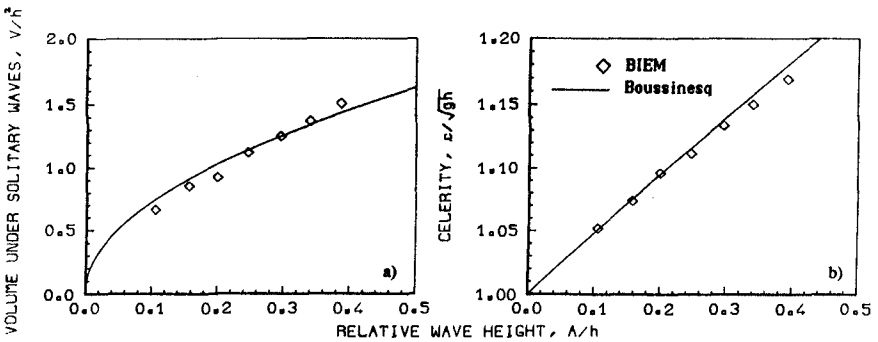


Figure 3. Comparison between numerical and analytical results for: a) volume under solitary waves; b) celerity

higher amplitudes this decay is more pronounced. Also a dispersive tail can be seen as the wave propagates. In figures 2a and 2b comparisons are made between the numerical profiles and the analytical solution of Boussinesq. These numerical profiles were taken when the wave reached the right end of the channel and had already an almost constant amplitude. The agreement seems good. Computations of celerity and of the volume under the solitary waves are also compared with their corresponding analytical values available from Boussinesq's theory (figure 3). Again both numerical and analytical values agree well and even the different trend that can be identified in the numerical results of celerity is also present on some experimental results (Goring, 1978). The CPU time needed for each run (1000 time steps and 620 nodes) was about 6m30s on a CONVEX C220.

Test Case 2

A solitary wave propagating over a step is tested and results are compared with experiments by (Goring, 1978). In figure 4 time series of surface elevation at several points are displayed along with some experimental values. The effects of viscosity and bottom and wall shear, present when a real wave propagates on a channel, tend to decrease the amplitude of the wave. Since those effects are not accounted for on the numerical model, differences found both in amplitude and phase should be expected. The second wave on gauge 1 is the one reflected from the step which, after reflecting again on the generation plate, appears once more on that same gauge. This second reflection on the generator is not present on the experimental results maybe because that wavemaker had a nonreflecting surface. After passing over the step, the solitary wave evolves into three solitary waves. On gauge 5 those three waves, going to and coming from the right wall, can be very distinctly observed. Figure 5 shows the free-surface numerical profile when the first and second waves are almost completely formed. They are compared with two analytical Boussinesq's profiles of equal amplitudes. The CPU time needed for this example (3500 time steps and 683 nodes) was 22 min on a CONVEX C 220.

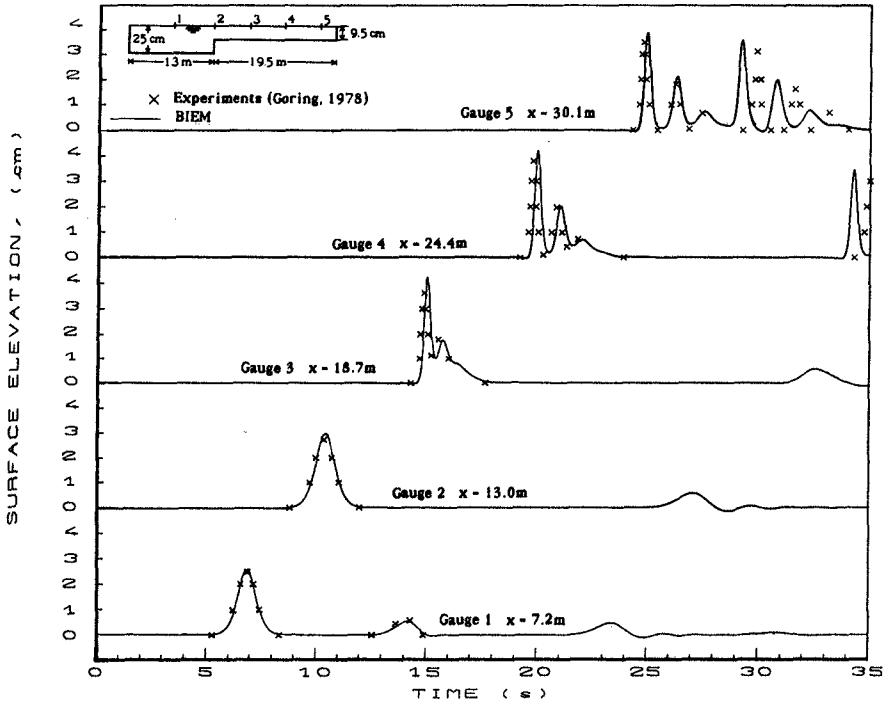


Figure 4. Water surface elevation time histories at five gauges along the channel; comparison between BIEM and experimental results

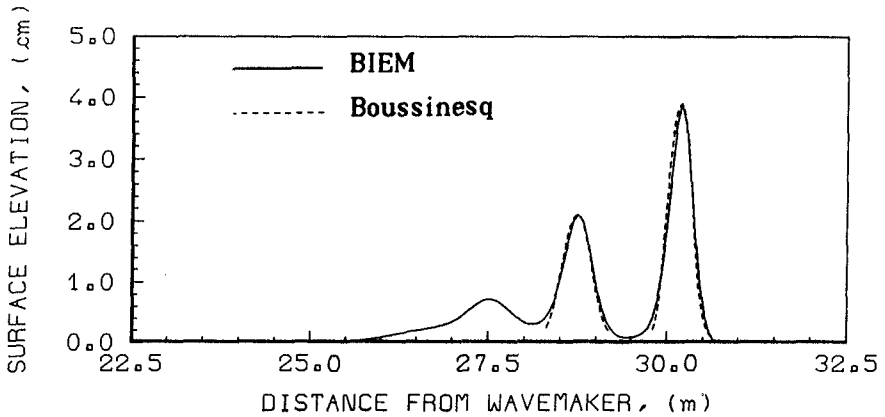


Figure 5. BIEM water surface profile; comparison with Boussinesq's theoretical solitary wave profiles

Test Case 3

The shoaling of random waves is a problem of current interest and it is addressed here in the perspective of comparing experimental and field results with numerical BIEM results. A limitation of this numerical model is that it cannot include breaking effects on shoaling studies. As this is a second order model, propagating waves of two individual frequencies, say f_i and f_j , would produce waves of frequency f_i+f_j and f_i-f_j . For a continuous spectrum, energy is transferred to lower and higher harmonics of the peak frequency; see for example (Mansard et al.,1988).

Three random wave cases were simulated with three different significant wave heights (5.0, 8.0 and 8.5 cm) each corresponding to a Bretschneider spectrum with 0.6 Hz peak frequency. The effects of shoaling, on a 1/20 slope, upon spectral shape, groupiness factor, shape factor of Weibull Distribution and skewness of water surface variation are investigated and compared, when it was possible, with experiments from (Mase, 1989). Although Mase's experiments were made by taking several samples from a spectrum (Pierson-Moskowitz with peak frequency of 0.6 Hz) but with different groupiness factors, the 3 numerically generated samples of random waves used in this study had 3 different spectra for each one and no imposed groupiness factor.

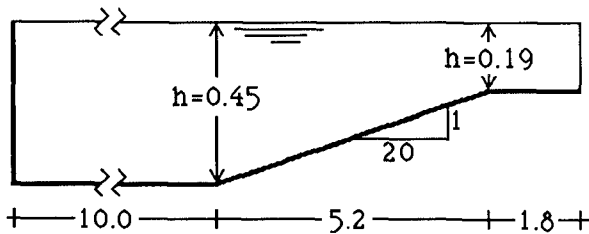


Figure 6. Numerical flume (dimensions in meters)

The "numerical flume" in figure 6, had the generation region at 45cm depth, and a slope of 1/20 until 19 cm depth. At the right end of the channel a radiation boundary is used. The referred experiments of (Mase, 1989) also include the breaking region. Records of surface elevation were stored for 50 nodes of

the free-surface during 250 sec., containing about 170 waves, and for each one a time and frequency analysis was done. The spectra in fig. 7 are: the one imposed, with a significant wave height of 8.5 cm and source of the random wave sample, and the other three result from the frequency analysis at 45cm (toe of the slope), 23.5cm and 19 cm depth. Sub and superharmonics appear very clearly for decreasing depths in fig. 7. This energy transfer inside the spectrum, a nonlinear effect, is present when waves reach shallow water.

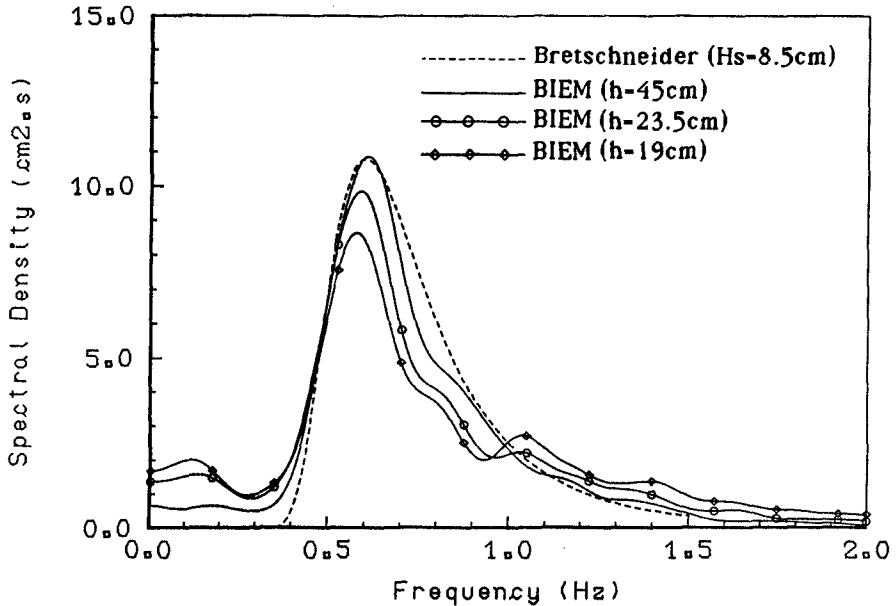


Figure 7. Spectra resulting from numerical BIEM data frequency analysis at several depths and source spectrum of the random waves introduced at the left end of the channel

The most important parameters computed were:

- The groupiness factor (GF) calculated from SIWEH (Funke and Mansard, 1979);
- The shape factor of the one parameter Weibull Distribution (m) (Cohen, 1965);
- The skewness of water surface variation ($\sqrt{\beta_1}$);
- The spectral width parameter Q_p defined by (Goda, 1970).

In fig. 8 the variation of Q_p along the slope can be seen and, though no comparison is made with other results, the trend seems to be correct according to data from (Thompson and Vincent, 1985). In fig. 9 the variation of the groupiness factor and the skewness along the slope is shown. When compared with results from (Mase, 1989) it can be seen that for similar tests similar values and trends are encountered. A correlation between the groupiness factor and the shape factor of Weibull Distribution proposed by (Mase, 1989) is presented in fig. 10 with some of the numerical results. These seem to fit quite well in the 95% confidence interval.

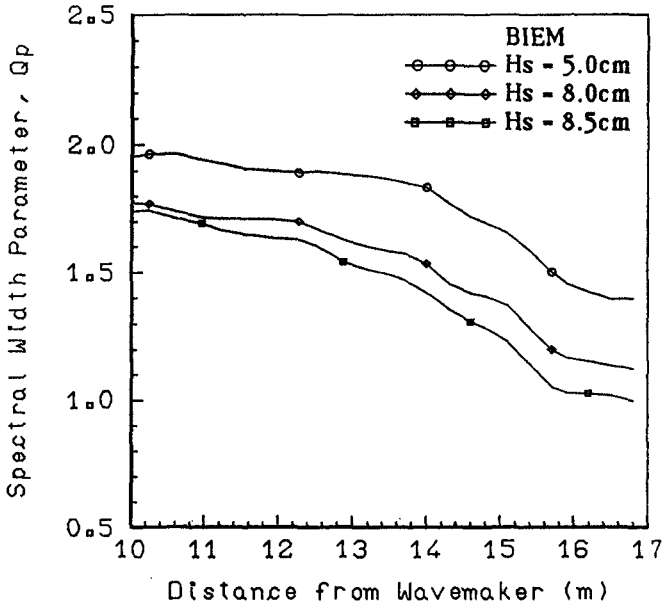


Figure 8. Spectral Width Parameter along the 1/20 slope

Conclusions

A 2nd order BIEM model to propagate waves in intermediate and shallow water was presented. The tests made with solitary and irregular waves showed that it can handle quite well nonlinear waves up to, at least, 0.4 of relative wave height. Although it cannot include breaking effects, studies of irregular wave propagation are possible within a moderate range of relative wave heights (this limit would be about $0.5Hm_0/h$)

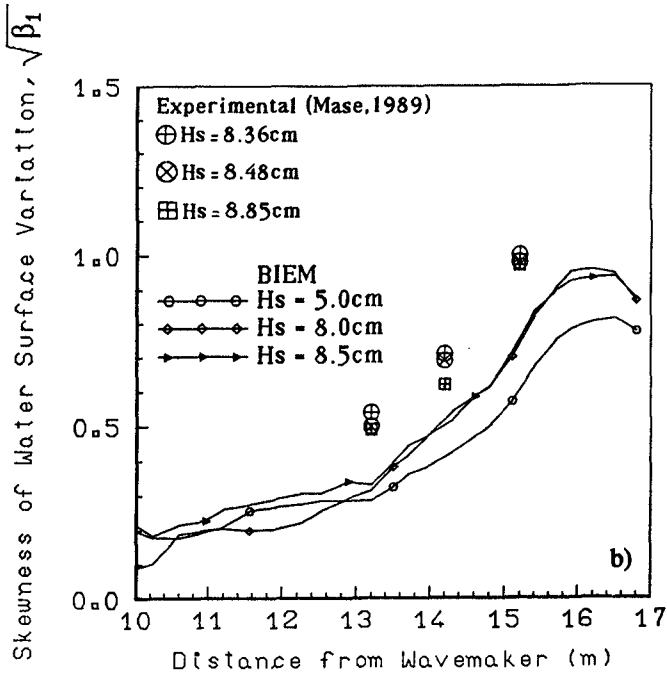
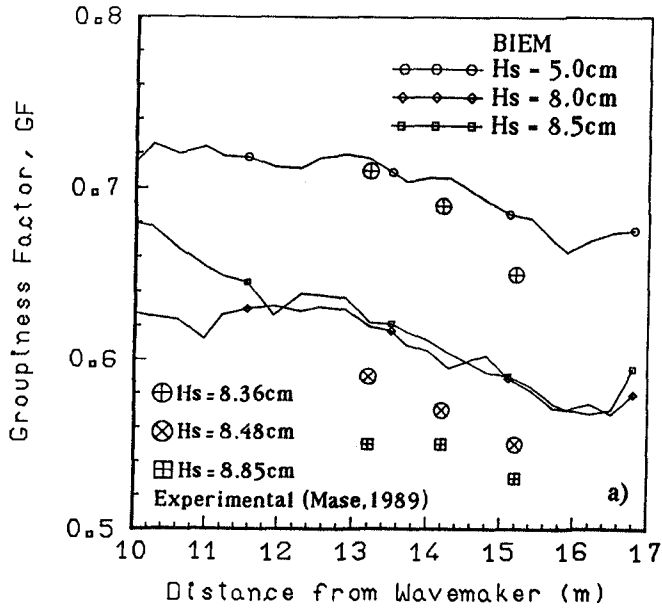


Figure 9. Variation along the 1/20 slope of: a) the Groupiness Factor; b) the Skewness of Water Surface Variation

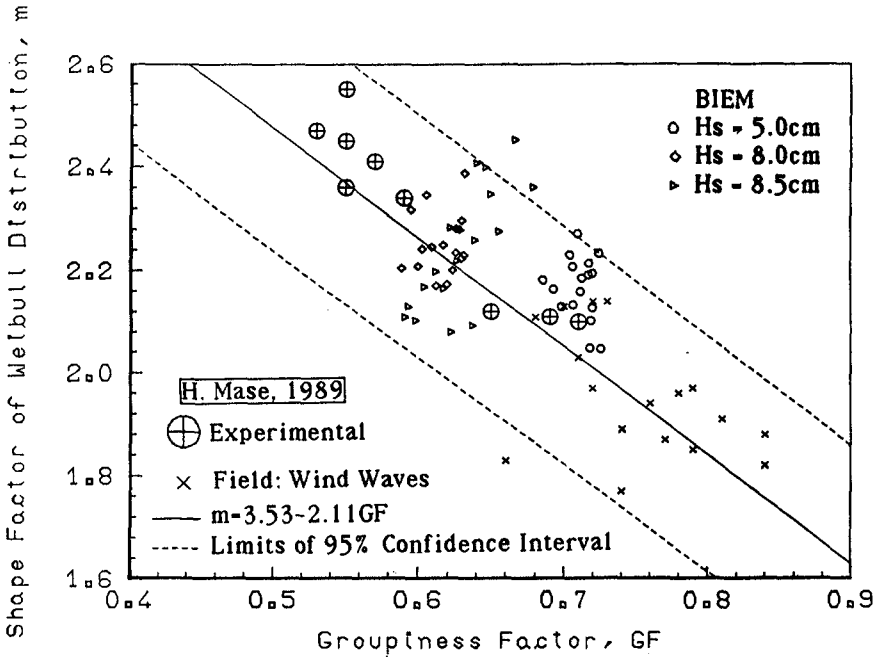


Figure 10. Relationship between Groupiness Factor and Shape Factor of Weibull Distribution

although it was not thoroughly studied). In that range of relative wave heights it is possible to compute pressure inside the 2D domain which allows also to evaluate forces acting on submerged bodies. Depending on the size of the discretization, this model is about 10 times faster than a fully nonlinear BIEM model. The ideas presented here can be extended to three-dimensional problems as more computer power becomes available.

Acknowledgements

This work and the first author are supported by Junta Nacional de Investigação Científica e Tecnológica under contract nº 87472.

References

Cohen, A. C., "Maximum likelihood estimation in the Weibull Distribution based on complete and on censored samples", *Technometrics*, Vol.7, No. 4, November 1965.

Fernandes, J.L.M., "A boundary element method for nonlinear water waves", *Proc. Computer Modelling in Ocean Engng*, Eds B. A. Schrefler & O. C. Zienkiewicz, Balkema, September 1988.

Funke, E.R., Mansard, E.P.D., " On the synthesis of realistic sea states in a laboratory plume", *Hydraulics Laboratory, Report n° LTR-HY-66*, National Research Council of Canada, Ottawa, Canada, August 1979.

Goda, Y., "Numerical experiments on wave statistics with spectral simulation", *Report of the Port and Harbour Research Institute*, 9(3), 1970.

Goring, D.G. "Tsunamis - The propagation of long waves into a shelf", *W.M. Kech Laboratory of Hydraulics and Water Resources, Report n° KH-R-38*, California Institute of Technology, Pasadena, California, November 1978.

Leitão, J.M.C. and Fernandes, J.L.M., "Numerical solution of linear wave propagation problems", *Proc. 4º Simpósio Luso-Brasileiro de Hidráulica e Recursos Hídricos*, Ed. APRH, Lisboa (in Portuguese), June 1989.

Mansard, E. P. D., Sand, S. E., Klinting, P., "Sub and Superharmonics in natural waves", *Journal of Offshore Mechanics and Arctic Engineering*, Vol. 110, August 1988.

Mase, H., "Groupiness factor and wave height distribution", *Journal of Waterway, Port, Coastal and Ocean Engineering*, Vol. 115 n° 1 , January 1989.

Thompson, E.F., Vincent, C.L. "Significant wave height for shallow water design", *Journal of Waterway, Port, Coastal and Ocean Engineering*, Vol. 111, n° 5, September 1985.

CHAPTER 54

WAVE DIRECTION MEASUREMENT USING MARINE X BAND RADAR

Hiromaru Hirakuchi, Masaaki Ikeno

ABSTRACT

Spatial radar signals received by a conventional marine radar are digitized as a 8-bit word by means of an A/D converter. The numerical procedure is discussed to estimate the two-dimensional radar spectrum from a digitized radar image. Directional spectra of sea waves are also observed by a 3-component wave array. A comparison of the mean wave direction and period estimated from the radar spectrum with the results from the array spectrum shows that the developed data acquisition system and numerical procedure represent a reliable and very cost-effective means to observe the properties of sea waves.

1. INTRODUCTION

In addition to wave height and period, wave direction has great influence upon the coastal problems. The measuring techniques for wave direction can be classified into two major groups, the direct measurement method and the remote sensing method. In recent years, considerable interest has been showed in the application of the remote sensing techniques; a synthetic aperture radar (SAR) mounted on a satellite or an airplane, a shore-based high frequency (HF) radar. One of such studies has dealt with the use of a marine X band radar.

Ijima et.al.(1964) and Wright(1965) were the first to report the use of the marine radar for imaging ocean waves. Willis and Beaumont(1971), Evmenov et.al.(1973), and Mattie and Harris(1978) have also presented photographic radar images. In order to estimate the mean wave direction and period, these early researchers visually inspected the radar images as displayed on the plane position indicator (PPI).

Making use of the digitized radar images, Hoogeboom and Rosenthal(1982) and Young et.al.(1985) have calculated the 2- and 3-dimensional spectra of the spatial radar images. It appears that the numerical procedure is very useful to determine the properties of ocean waves. In these studies, however, the radar images displayed on the PPI were once recorded on photographic films, and the

Senior Research Engineer, Central Research Institute of Electric Power Industry, Abiko, Abiko-Shi, Chiba, Japan.

photographic images were digitized by means of an image processor. Therefore, it is difficult to apply a marine radar to routine data collection.

The purpose of this study is to overcome some of the technical difficulties associated with the routine data collection and to verify the numerical procedure employed for analysis of digitized radar images through comparison with the directional wave spectra obtained by the direct measurement method.

2. MARINE RADAR SYSTEM

The marine X band radar used in this study is of the conventional rotating type. Parameters of the radar system are as follows: frequency of 9.4GHz, antenna type of 2.81m slotted wave guide, nominal peak power of 25kW, pulse length of 20ns at 5.6km range, pulse repetition frequency of 2000Hz, antenna rotation speed of 24rpm, HH polarization, and horizontal/vertical beam width of $0.8^{\circ}/25^{\circ}$.

The data acquisition system is shown schematically in Fig.1. The intensity of the reflected signals from nearby sea surface is stronger than that from distant sea surface. In order to extend the measurable range of distance, the received signals were fed into a log-amplifier, and the resultant signals were digitized as a 8-bit word (0-255) by means of an A/D converter controlled by a personal computer. The digitized images were stored on floppy disks.

Two successive radar images, having time delay of the antenna rotation period, can be observed by the system. Each radar image in a quadrant area with the angle of 90° consists of 256 pixels along a radar beam and 512 pixels along an arc. The sampling frequency along a radar beam is 10MHz; the distance resolution and range are 15m and 3.84km, respectively. The azimuthal signals of the rotating antenna are used to collect the proper azimuthal data; The azimuthal resolution is about 0.176° .

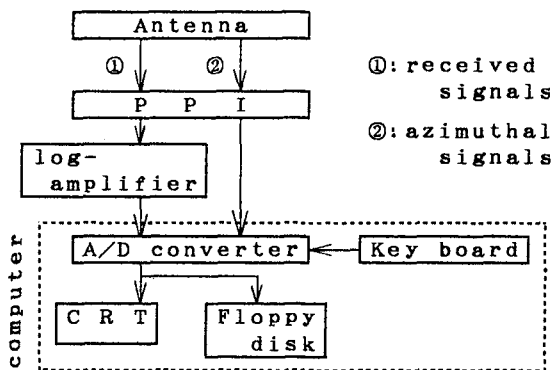


Fig.1 Flow diagram of data acquisition system.

3. FIELD OBSERVATION

A field observation was carried out near the coast of Kashiwazaki, Japan, in Feb., 1988. The marine radar was mounted on a rooftop at the distance of 50m from the shoreline: the height of the antenna is about 20m above the sea level. Fig.2 shows the observation area. Four radar images each with a different direction were observed every 2 hours during two periods; from 18:00 on 15 to 12:00 on 17, and from 16:00 on 27 to 12:00 on 29. As shown in Fig.2, the direction of the first radar image is from 200° to 290°, second 220°-310°, third 245°-335°, and fourth 290°-20°. Where the direction is defined clockwise from the north.

In addition to the radar system, five wave arrays were also deployed to observe the directional spectra of sea waves, as shown in Fig.2, where ST.1-ST.5 represent the wave observation points. ST.1 and ST.4 are 10m deep, ST.3 and ST.5 are 20m deep, and ST.2 is 15m deep. A 3-component wave array was used for the direct wave measurement; a supersonic wave gauge and a two-component electro-magnetic current meter. The wind speed and direction during this observation were measured by Tokyo Electric Power Company at the point A and B in Fig.2. The heights of A and B are 10m and 78m from the ground level, respectively; 20m and 160m from the sea surface, respectively.

An example of the digitized radar images of the 3rd quadrant (245°-335°) are shown in Fig.3(a)-(c), which were observed at 6:00 on Feb. 16 (CASE-1), at 0:00 on Feb. 17 (CASE-2), and at 20:00 on Feb. 27 (CASE-3). Incident wave directions in Fig.3(a) and Fig.3(c) are about 290° and 0°, respectively. The striking feature in Fig.3(b) is the pronounced bi-directional sea state.

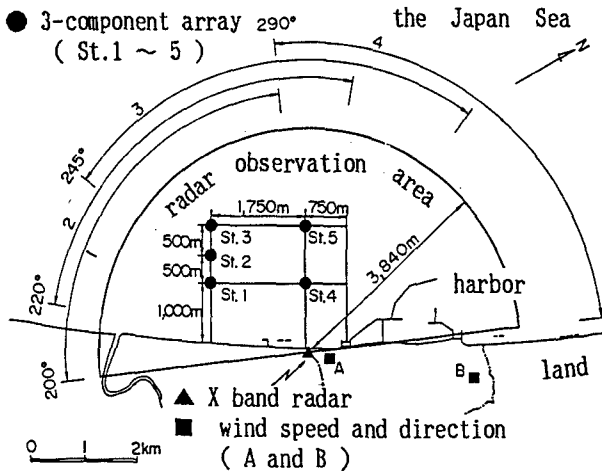
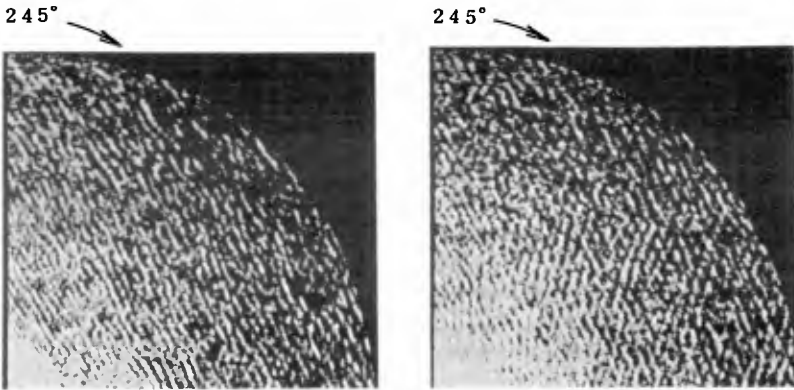


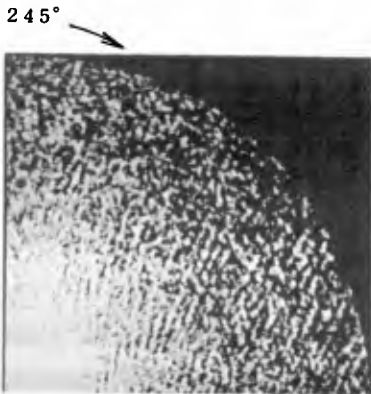
Fig.2 Field observation area.

In this study, radar images for CASE-1, 2 and 3 are examined. Wind data at point A and wave data are shown in Table 1, together with the data observed before and after 2 hours of each radar observation.



(a) CASE-1 (at 6:00 on Feb. 16)

(b) CASE-2 (at 0:00 on Feb. 17)



(c) CASE-3 (at 20:00 on Feb. 27)

Fig.3 Observed radar images.

4. DATA PROCESSING

4.1 DISTANCE CORRECTION

The intensity of the radiated energy decreases with the square of the distance from the antenna, and the intensity of the backscattered energy also decreases with the square of the distance from the target.

Table 1 Wind and wave data summary.

Date & Time 1988 Feb.	Wind Speed & Direction (m/s)	Wave Height (cm)					Wave Period (T _{1/3} (sec) f _p (Hz))					Wave Direction (deg)				
		ST.1	ST.2	ST.3	ST.4	ST.5	ST.1	ST.2	ST.3	ST.4	ST.5	ST.1	ST.2	ST.3	ST.4	ST.5
16, 4:00	15.3 NNW	---	213	253	215	213	---	6.32	6.31	6.33	6.37	---	327	340	322	
16, 6:00	15.7 NNW	268	273	309	276	263	7.34	7.15	7.04	6.82	7.03	322	320	320	323	
16, 8:00	16.8 NNW	280	283	313	279	275	0.125	0.133	0.121	0.111	0.123	320	316	314	312	
17, 00:00	8.4 NNW	279	269	263	254	254	7.36	7.10	6.89	7.15	6.79	318	322	323	325	
17, 2:00	12.6 NNW	190	178	216	184	183	0.119	0.117	0.119	0.145	0.115	318	318	320	316	
17, 00:00	11.9 NNW	205	189	231	199	219	0.119	0.117	0.127	0.182	0.193	324	312	326	318	
17, 2:00	8.4 NNW	180	170	181	183	174	6.73	6.06	6.83	7.11	6.96	322	319	326	324	
17, 4:00	8.4 NNW	189	178	194	193	199	0.109	0.111	0.107	0.107	0.104	328	318	322	320	
17, 6:00	8.4 NNW	161	157	157	153	157	7.33	6.89	6.75	6.71	7.49	321	325	322	322	
17, 8:00	9.2 NW	174	174	168	169	189	0.117	0.109	0.111	0.113	0.109	330	336	322	318	
18, 00:00	9.0 NW	79	90	91	86	91	4.60	5.16	4.69	4.75	4.99	360	350	339	342	
18, 2:00	9.0 NW	90	102	102	96	98	0.260	0.125	0.258	0.133	0.260	330	2	4	348	
18, 4:00	9.0 NW	101	94	112	106	119	4.58	5.01	4.93	4.77	4.85	331	334	330	335	
18, 6:00	12.9 NW	112	103	121	113	124	0.109	0.107	0.223	0.115	0.238	330	4	350	338	
18, 8:00	12.9 NW	130	135	119	129	116	4.79	4.87	4.89	5.01	4.83	322	327	335	326	
18, 10:00	12.9 NW	137	142	128	138	126	0.195	0.201	0.123	0.197	0.203	326	326	352	316	

①

②

③

H_{1/3}, T_{1/3} : significant wave height and period defined by zero-crossing method.
 4√m₀ : representative wave height estimated from 0th moment (m₀) of wave power spectrum.
 f_p : peak frequency of wave power spectrum.
 θ_m : mean wave direction calculated from 1st moment of directional spectrum.
 θ₀ : peak direction of integrated directional spreading function.
 ①, ②, ③ : CASE-1, 2 and 3

However, the clutter cross-section is proportional to the distance from the antenna, because the depression angle of the antenna is very small. Therefore, the intensity of the received signals varies inversely as a cube of the distance, rather than inversely as the fourth power as is the case for point targets. In the radar system, the received signals were fed into a log-amplifier, so that the digitized radar signals are expressed as follows:

$$\zeta = \log C = \log \lambda + \log \sigma_0 - 3 \log R \quad \text{----(1)}$$

where ζ is the signal through the log-amplifier, C is the received signal, σ_0 is the cross section per unit area, R is the distance from the antenna, and λ is defined as

$$\lambda = P_t G A_e \theta_B (c \tau / 2) / (4 \pi)^2 \quad \text{---(2)}$$

Where P_t is the transmitter power, G is the antenna gain, A_e is the antenna effective aperture, θ_B is the azimuthal beam width, c is the velocity of radar propagation, and τ is the radar pulse width.

$\log \lambda$ in Eq.(1) is a constant value, because λ is associated with the only specifications of the radar antenna as shown in Eq.(2). Since the distance range considered in this study is from 1 to 4km offshore, $\log R$ in Eq.(1) is approximated to a linear line over this range. $\log \sigma_0$ in Eq.(1) represents the intensity of sea clutter, so that its spatial variation is very important to estimate the wave direction and period.

If the characteristics of the sea surface are spatially homogeneous, a spatially averaged value of $\log \sigma_0$ is in close proximity to a constant value. On these assumptions, the signals after correcting the distance effect along a radar beam were expressed as follows:

$$\xi = \zeta - \delta(R), \quad \delta(R) = a + b R \quad \text{---(3)}$$

where ξ is the distance corrected signal, $\delta(R)$ is the fitting line, a and b are coefficients of a least square approximation.

Examples of the digitized radar signals along a radar beam are shown in Fig.4. Fig.4(a) represents the typical signals reflected from the wind wave surface. The signals in the range of 1km are saturated owing to the strong echo. However, the signals over that range show the images of the irregular sea waves. The fluctuated curve around 0 level indicates the signals after distance correction which was carried out over the range of 1km. This figure shows the property of the distance correction method described above.

Fig.4(b) represents the signals observed under the snowy weather condition. Characteristics of this case are that intensity level is high, but the fluctuation of the signals is very small. It is difficult to recognize the wave image in Fig.4(b) owing to the radar scattering from snow.

Fig.4(c) was observed under the calm condition. Wind speed was less than 2m/s, and the significant wave height and period were about 1.2m and 8s, respectively. Swell can not be detected outside the breaker zone. This figure indicates that short ripples generated by the wind are essential to the detection of long waves.

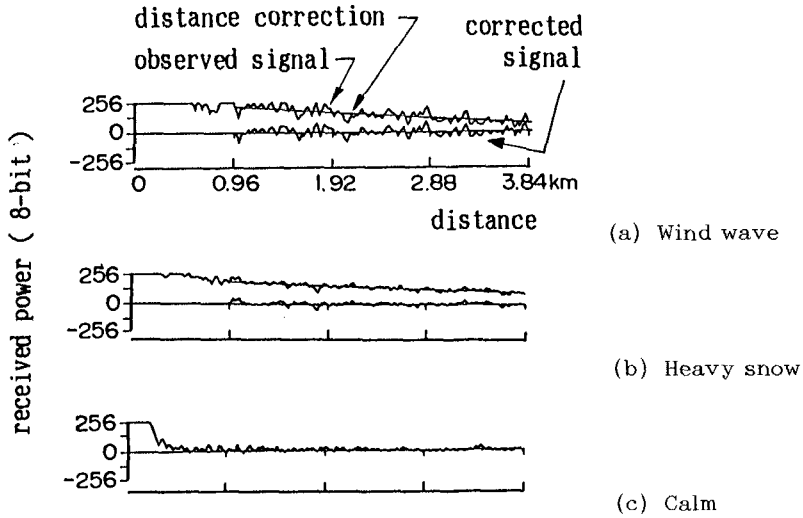


Fig.4 Example of digitized radar signals along a radar beam.

4.2 RADAR SPECTRAL ESTIMATION

The data analysis procedure is shown in Fig.5(a). After correcting the distance effect, the digitized radar image defined in the polar coordinate system is converted to the Cartesian coordinate system. A square region with a length of 960m as shown in Fig.5(b) is extracted from the converted data.

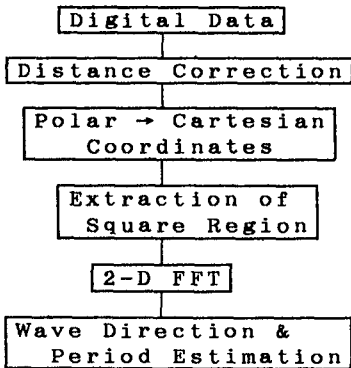


Fig.5(a) Data analysis procedure.

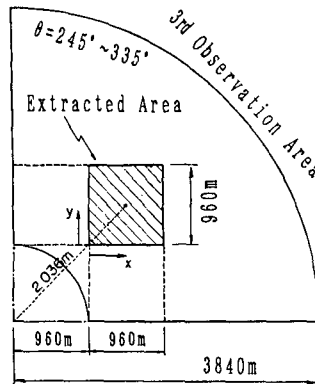
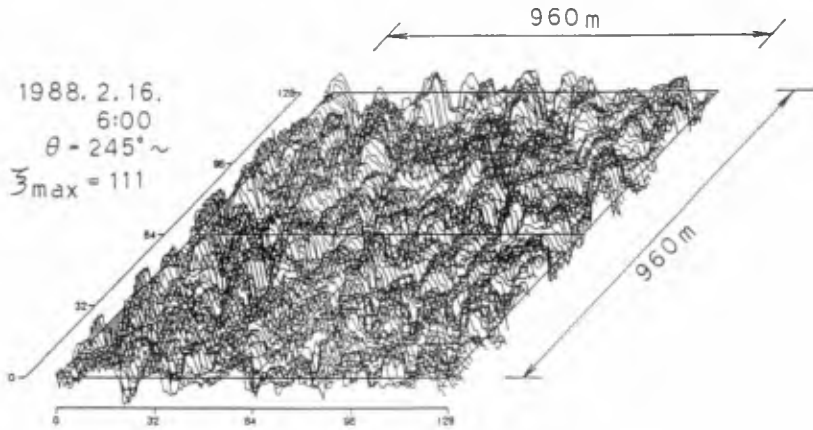
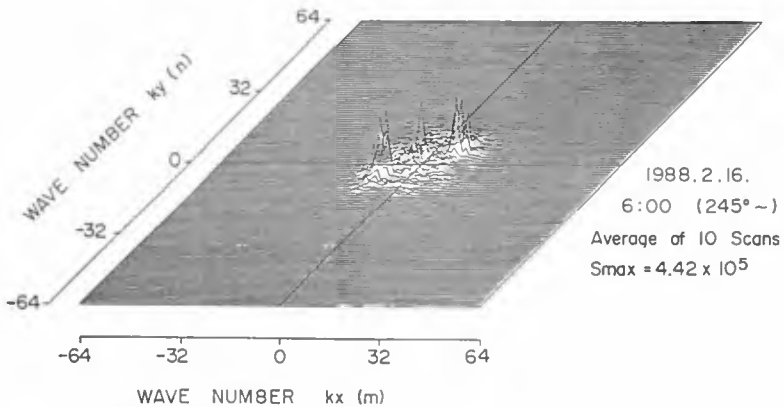


Fig.5(b) Analyzed area.

Fig.6 shows an example of the extracted spatial radar image and the wave number spectrum calculated from the 2D-FFT procedure. It is difficult to estimate the wave direction from Fig.6(b), because a 180° directional ambiguity exists in Fig.6(b) which has point symmetry. It is possible to remove this ambiguity by use of two successive images (Atanassov et.al.(1985)). However, this ambiguity can be removed by assuming that the reflected waves from the beach are very weak and most of the waves are coming from the offshore. Using this assumption, mean wave direction and period can be estimated from the wave number at the radar spectral peak, making use of the dispersion relationship.



(a) Spatial radar image



(b) Wave number spectrum

Fig.6 Example of spatial radar image and wave number spectrum.

5. RESULTS

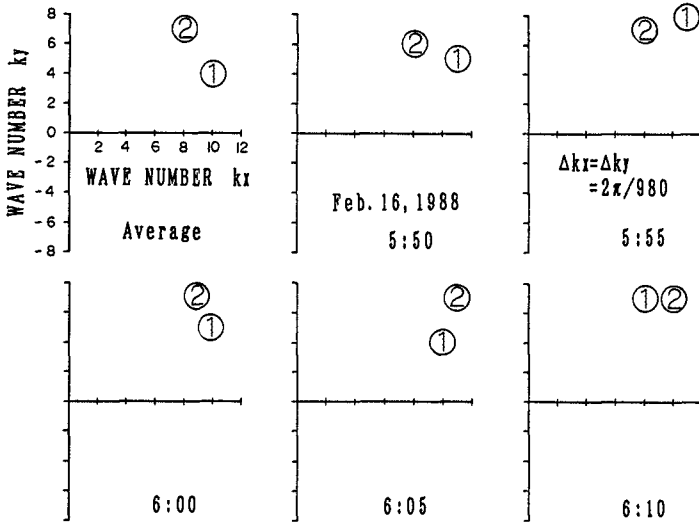
Fig.7(a) for CASE-1 represents the wave numbers at the radar spectral peaks observed every five minutes from 5:50 to 6:10 on 16, together with the results of the averaged radar spectrum. ① and ② denote a first and second spectral peak, respectively. The wave numbers observed every five minutes represent slightly different values owing to the statistical variation of the random sea surface; the directional estimate from a radar image has a statistical error of about 10° . The averaged radar spectrum should be used to estimate the mean wave direction and frequency.

The wave direction and period estimated from the averaged radar spectrum were compared with those observed by the 3-component wave array. The contours in Fig.7(b) represent the directional wave spectrum observed at ST.3, making use of the extended maximum likelihood method (EMLM) proposed by Isobe et.al.(1984). As shown in Fig.7(b), the peak of the directional spectrum and integrated directional function represent the directions of 304° and 314° , respectively. The first peak of the radar spectrum is the direction of 313° , which is in good agreement with the array estimate.

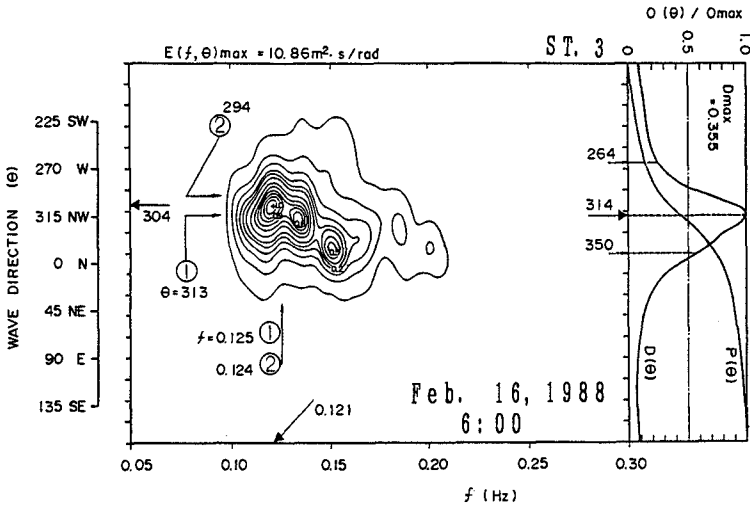
Fig.8(a) for case-2 shows the results observed every five minutes from 23:50 on 16 to 0:10 on 17. Since the wave number ① and ② in Fig.8(a) are rather stable results in five radar spectra, the radar spectrum exhibits a bimodal directional distribution with the major peak at 341° and 313° , the frequency of 0.11Hz and 0.125Hz. However, the direction and period at the radar spectral peaks are much different from the results of the array spectrum, as shown in Fig.8(b).

The array spectrum observed 4 hours later than CASE-2 measurement are shown in Fig.9, together with the results of wave number ① and ② obtained in CASE-2. In Fig.9, the directions of the array spectrum which represents the bimodal structure show good agreement with ① and ②, although the frequencies of the array spectrum are slightly low. Fig.9 shows that the bimodal structure observed by the radar spectrum in Fig.8(b) is probably a true indication of the wave field.

Fig.10 for case-3 represents the results observed at 20:00 on 27. In this case, only one radar image is used for wave number estimation. The array spectrum in Fig.10 observed at ST.3 represents the two distinct spectral peaks; the long and short waves with the frequency of 0.12Hz and 0.22Hz, respectively. The direction of the long waves is about 345° , which is in good agreement with the results of radar spectral peaks (346°). The wave direction of the long waves in CASE-3 is approximately 45° further to the north than that of CASE-1.

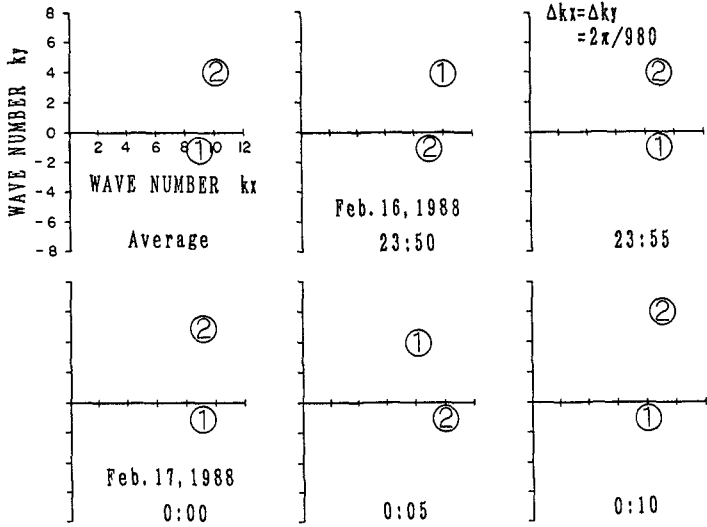


(a) Wave numbers at first and second peak of radar spectrum.

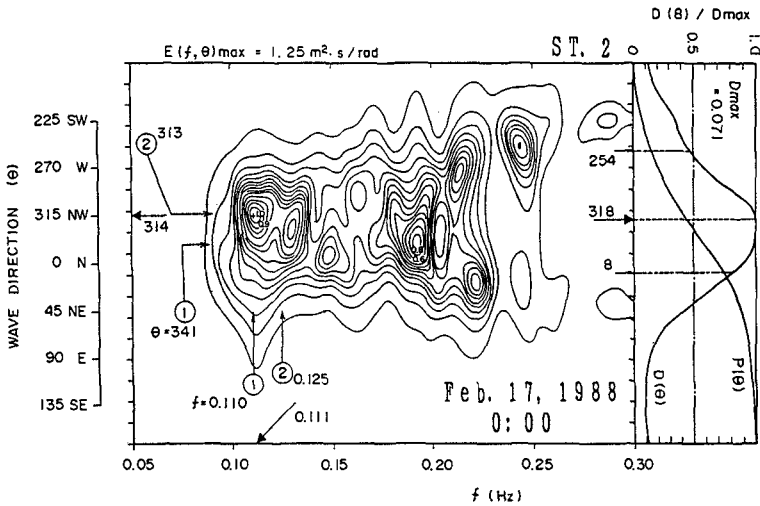


(b) Directional spectrum observed by wave array.

Fig.7 Comparison of wave direction and period for CASE-1.



(a) Wave numbers at first and second peak of radar spectrum.



(b) Directional spectrum observed by wave array.

Fig.8 Comparison of wave direction and period for CASE-2.

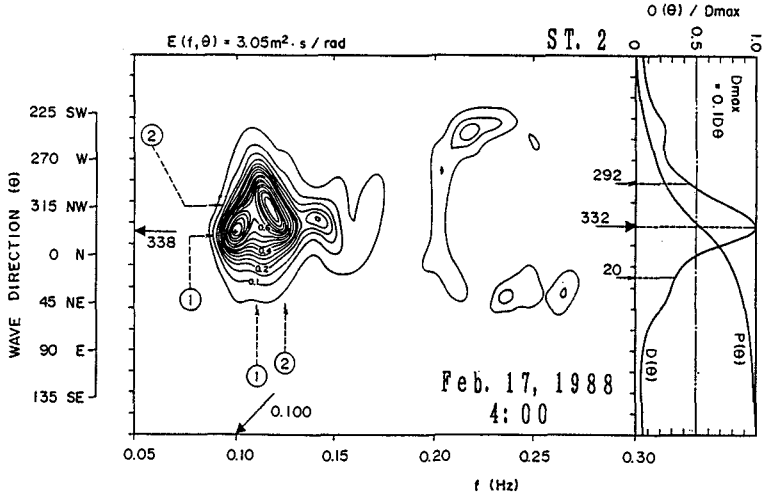


Fig.9 Directional spectrum observed 4 hours later than CASE-2.

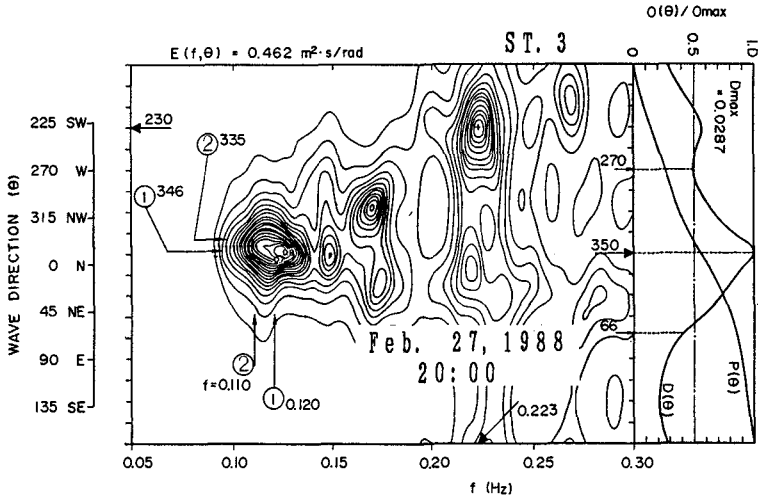


Fig.10 Comparison of wave direction and period for CASE-3.

6. CONCLUSIONS

The data acquisition system has been developed to record the spatial radar signals, and the numerical procedure employed for analysis of the digitized radar images has been proposed. Using this radar system and numerical procedure, the mean wave direction and period in the uni- and bi-modal wave field can be estimated more easily than the conventional method. Moreover, it will be possible to record the consecutive radar images by means of this system and to calculate the three-dimensional radar spectrum.

REFERENCES

- Atanassov, V., W. Rosenthal, and F. Ziemer (1985) : Removal of ambiguity of two-dimensional power spectra obtained by processing ship radar images of ocean waves, *J.G.R.*, Vol.90, No.C1, pp.1061-1067.
- Ijima, T., T. Takahashi, and H. Sasaki (1964) : Application of radars to wave observations, *Prod. of 11th Japanese Conf. of Coastal Eng.*, pp.81-88. (in Japanese)
- Isobe, M., K. Kondo, and K. Horikawa (1984) : Extension of MLM for estimating directional wave spectrum, *Proc. Symp. Description and Modelling of Directional Seas*, Tech. Univ. Denmark, Paper No.A-6, pp.1-15.
- Evmenov, V.F., I.V. Kozhukhov, N.T. Nichiporenko, and G.D. Khulop (1973) : Test of the radar method of defining ocean wave elements, *Fluid Mechanics - Soviet Research*, Vol.2, No.5, pp.141-145.
- Hoogeboom, P., and W. Rosenthal (1982) : Directional wave spectra in radar images, *International Geoscience and Remote Sensing Symposium*, IEEE.
- Mattie, M.G., and D.L. Harris (1978) : The use of imaging radar in studying ocean waves, *Proc. of 16th Conf. on Coastal Eng.*, pp.174-189.
- Willis, T.G. and H. Beaumont (1971) : Wave direction measurement using sea surveillance radars, *Tech. Memo. TR 118*, Royal Aircraft Establishment.
- Wright, F.F. (1965) : Wave observation by shipboard radar, *Ocean Sci. and Ocean Eng.*, Vol.1, pp.506-514.
- Young, I.R., W. Rosenthal, and F. Ziemer (1985) : A three-dimensional analysis of marine radar images for the determination of ocean wave directionality and surface currents, *J.G.R.*, Vol.90, No.C1, pp.1049-1059.

CHAPTER 55

Variation of Surf Zone Turbulence in A Wave Period

Y. Tada¹, T. Sakai², M. ASCE and E. Obana³

Abstract

The phase variation of turbulent intensity in the surf zone during one wave period is discussed. The existing data show a peak near the wave crest phase and a following gentle decrease. The peak delays downwards. The model by Deigaard et al. (1986) which uses the one equation model for the turbulent kinematic energy transportation explains the above mentioned trend roughly. The vertical convection term has no significant effect on the phase variation. The production term given by Deigaard et al. overestimates the energy production at the water surface by wave breaking.

Introduction

It is well known that the turbulence generated by wave breaking is responsible to the suspension of sediment in the surf zone. Also it determines the vertical profile of the undertow. At present, its time average over the wave period is important for practical purpose. To discuss these phenomena more in detail, however, we have to know its phase variation during one wave period.

In this study, the phase variation of the surf zone turbulence is discussed by using existing data. Then, the calculated results by using the existing analytical prediction techniques are compared with the data. Especially the application of the one equation model of

1 Daiichi-Sekkeibu, Doboku-Sekkei-Honbu, Kajima Corporation, Akasaka 6-5-30, Minato-Ku, 107 Tokyo, Japan.

2 Dept. of Civil Eng., Kyoto Univ., Yoshida-Honmachi, Sakyo-Ku, 606 Kyoto, Japan.

3 Osaka Prefectural Government, Tanimachi 2-3-4, Chuoh-Ku, 540 Osaka, Japan.

the turbulent kinematic energy transportation is discussed.

Experimental Data on Phase Variation

Stive(1980) published his data on the turbulent intensity in a surf zone on a uniform slope beach in a wave tank. The experimental conditions are shown in Table 1. The breaking water depth h_b was about 26cm. He presented the results in several figures. Fig.1 is an enlarged copy of one of his figures. The mean water depth d at the measuring point was 18.6cm. The abscissa shows the wave phase. The ordinate shows a non-dimensional height above the mean water level. The curves are the contour lines of turbulent intensity. It is clear that the turbulent intensity is large under the wave crest.

Table 1 : Experimental Conditions

	Stive(1980) test 2	Sakai et al.(1982) case H2
i	1/40	1/28
T(sec)	3.0	1.16
H_o (cm)	14.2	
h_b	26.0	17.7
H_b	22.6	12.8
H_o/L_o	0.010	0.066

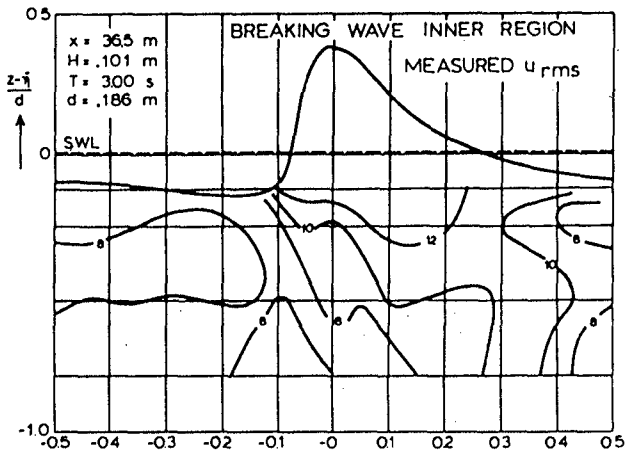


Fig.1 Experimental result by Stive(1980) ($d = 18.6\text{cm}$)

To make clear the phase variation of the turbulent intensity, its values were read from his figure at several levels, and plotted in a usual phase-intensity figure. Fig.2 shows the result at $d = 14.3\text{cm}$. z is a vertical coordinate and positive upwards. The origin is at the still water.

As seen in the curve at $z = -2.4\text{cm}$, the profile of phase variation of turbulent intensity is similar to that of the water level. It has a peak near the wave crest phase. At $z = -4.7\text{cm}$, this trend still exists. At $z = -7.4\text{cm}$, the trend is not so clear. At least at the upper two levels there is a peak and then a gradual decrease follows. One interesting fact is that the phase of the peak delays downwards. In the case of 18.6cm water depth (Fig.1) the same trend is seen. The peak under the

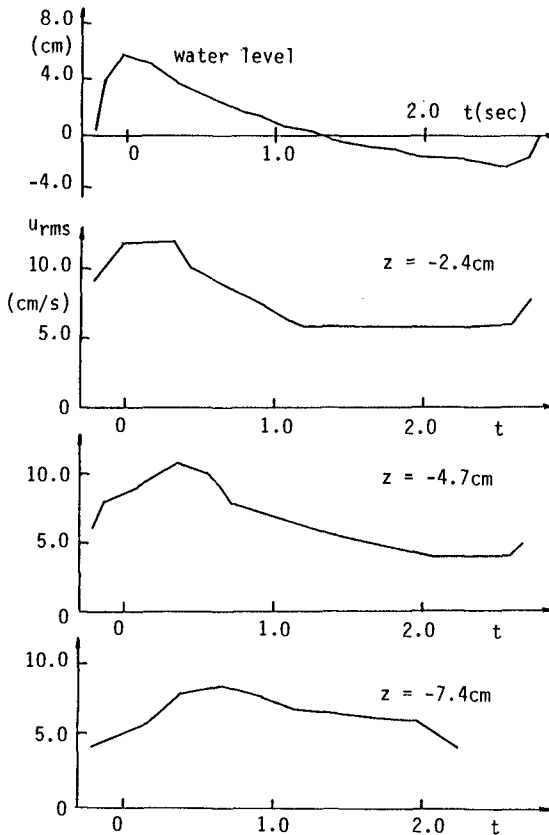


Fig.2 Phase variation of turbulent intensity (Stive, 1980, test 2, $d = 14.3\text{cm}$)

wave crest and the following gradual decrease are seen. The peak phase delays downwards.

To examine whether or not other data show the similar trend, other data are checked. One of the authors measured the turbulent intensity in a surf zone in a wave tank (Sakai, Inada and Sandanbata, 1982). The experimental conditions are shown in Table 1, and compared with Stive's conditions. Fig.3 is one example of the results. The still water depth h was 12.3cm. The similar trend is found. The data of Nadaoka (1986) shows a long tail of the contour lines. This also means the downward delay of the peak phase.

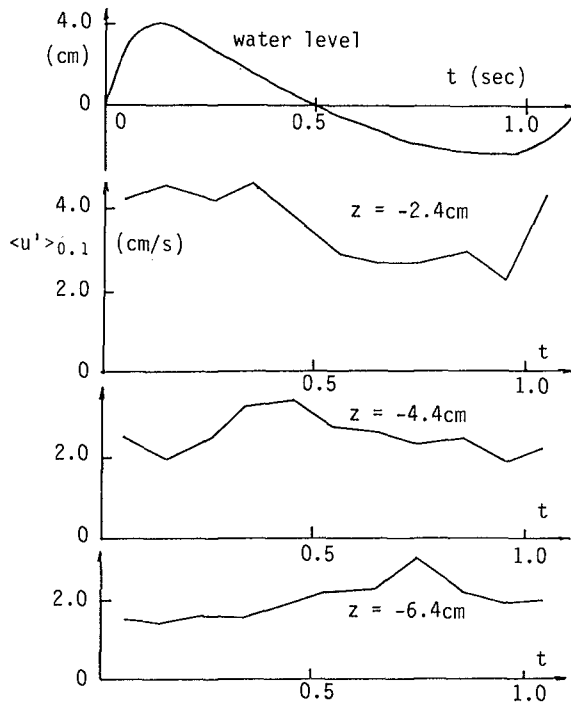


Fig.3 Phase variation of turbulent intensity (Sakai, et al., 1982, case H2, $h = 12.3\text{cm}$)

Models on Phase Variation

Deigaard et al. (1986) applied the one equation model for the turbulent kinematic energy transportation to simulate the phase variation of turbulent intensity during one wave period in a surf zone. The equation which they used is given as follows :

$$\frac{\partial k}{\partial t} = \frac{\partial}{\partial y} \left(\frac{\varepsilon}{\sigma_k} \frac{\partial k}{\partial y} \right) + \frac{\text{PROD}}{\rho} - c_d \frac{k^{3/2}}{l} \quad , \quad (1)$$

where k is the turbulent kinematic energy, y is the vertical coordinate directed upwards from bottom, ε is the turbulent eddy viscosity given by $l\sqrt{k}$, l is the length scale of turbulence, $\sigma_k = 1.0$, ρ is the density of water and $c_d = 0.08$.

Eq.(1) is a simplified equation of one equation model for the turbulent kinematic energy transportation. The three terms in the right hand side represent the diffusion of turbulent kinematic energy by the turbulence itself, the production of it and the dissipation. They thought that the turbulence energy is generated at the water surface, diffused downwards by itself and dissipated.

The production of turbulent energy at the water surface is given by

$$\text{PROD} = E_{loss} \frac{36}{(H\beta T)^2} z \left(1 - \frac{z}{H}\right) t \left(1 - \frac{t}{\beta T}\right) \quad (2)$$

$$: 0 \leq z \leq H, \quad 0 \leq t \leq \beta T$$

$$E_{loss} = \frac{H^3}{(4D^2 - H^2)} \gamma D \quad , \quad \beta = 2 \frac{D + H/2}{L} \quad ,$$

where H is the wave height, D is the mean water depth, γ is the unit weight of water, L is the wave length, T is the wave period and z is the vertical coordinate directed downwards with its origin at the surface. This expression is based on experimental data of a hydraulic jump.

They calculated the phase variation of turbulent intensity for the conditions of the experiment by Stive. They presented the calculated result in the similar manner as Stive did(Fig.1).

The values are read from their figures, and compared with the experimental result by Stive. Fig.4 is the case of 18.6cm water depth. The experimental result is shown with thick full line. The calculated result by Deigaard et al. is shown with chain line. It explains the experimental result roughly.

The dotted line is the calculated result by using a model of one of the authors(Sakai et al., 1982). The broken line is the calculated result by using a model of

Svendsen(1987). The model of Sakai et al. also explains the experimental result roughly. In the model of Svendsen, the production and diffusion terms were neglected. So this model explains only the gradual decrease. Although the model of Sakai et al. explains the experimental result as roughly as the model of Deigaard et al., the model of Deigaard et al. is most suitable physically.

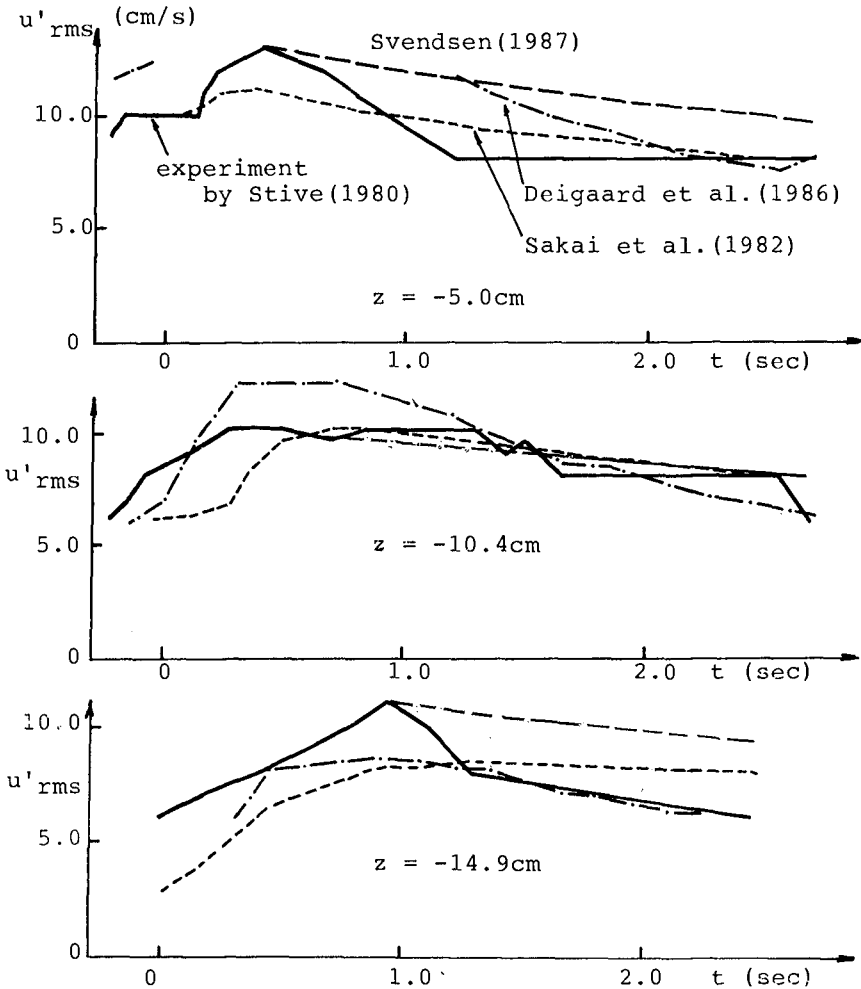


Fig.4 Comparison of predicted results with experimental result(Stive, test 2, $d = 18.6\text{cm}$)

Convection Terms

Svendsen(1987) compared the vertical distribution of mean turbulent intensity of Stive's experiment with that of Deigaard et al.(Fig.5). The calculated vertical distribution by Deigaard et al.is steeper than that of the experimental result by Stive. Svendsen thought that this was due to the neglecton of the convection term in the turbulent kinematic enery transportation equation.

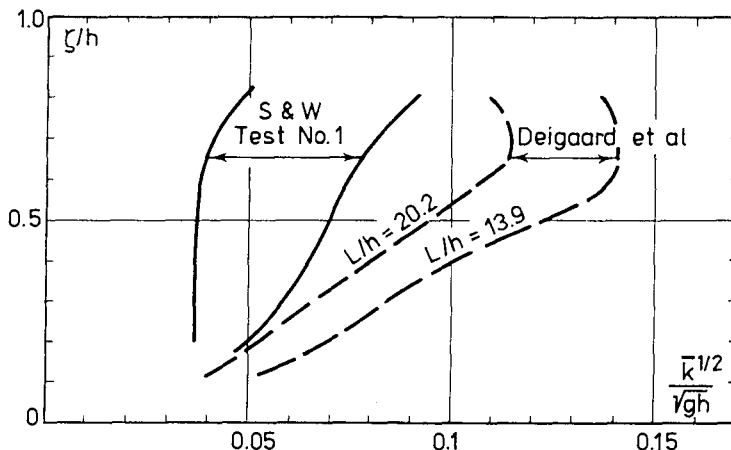


Fig.5 Comparison of predicted mean turbulent intensity (Deigaard et al., 1986) with experimental data (Stive, 1980) (Svendsen, 1987, Fig.9)

$$\frac{\partial k}{\partial t} + u \frac{\partial k}{\partial x} + v \frac{\partial k}{\partial y} = \frac{\partial}{\partial x} \left(\frac{\epsilon}{\sigma_k} \frac{\partial k}{\partial x} \right) + \frac{\partial}{\partial y} \left(\frac{\epsilon}{\sigma_k} \frac{\partial k}{\partial y} \right) + \frac{\text{PROD}}{\rho} - c_d \frac{k^{3/2}}{l} \quad (3)$$

Eq.(3) is the full equation of the one equation model for the turbulent kinematic enery transportation. This equation was originally developed for the two-dimensional boundary layer flow. The second and third terms in the left hand side are the convection terms. The first and second terms in the right hand side are the horizontal and vertical diffusion terms respectively. Deigaard et al. neglected the convection terms and the horizontal diffusion term. From the data by Stive, the magnitude of the vertical diffusion term was estimated. It was found that the magnitude of the vertical convection term might be same order as that of diffusion term.

To check the effect of the convection terms, a similar calculation to that by Deigaard et al. is done. Fig.6 shows the discretization of the wave phase and the height above the bed for the case of $d = 18.6\text{cm}$ of Stive's experiment. The i' and j' values indicate the discretization of the phase and the height above the bed. Only the vertical convection term is included. In Stive's paper, there was no data on the vertical water particle velocity. It was assumed, therefore, that the velocity field is similar in the surf zone. The vertical water particle velocity was calculated from other data (Nadaoka, 1986).

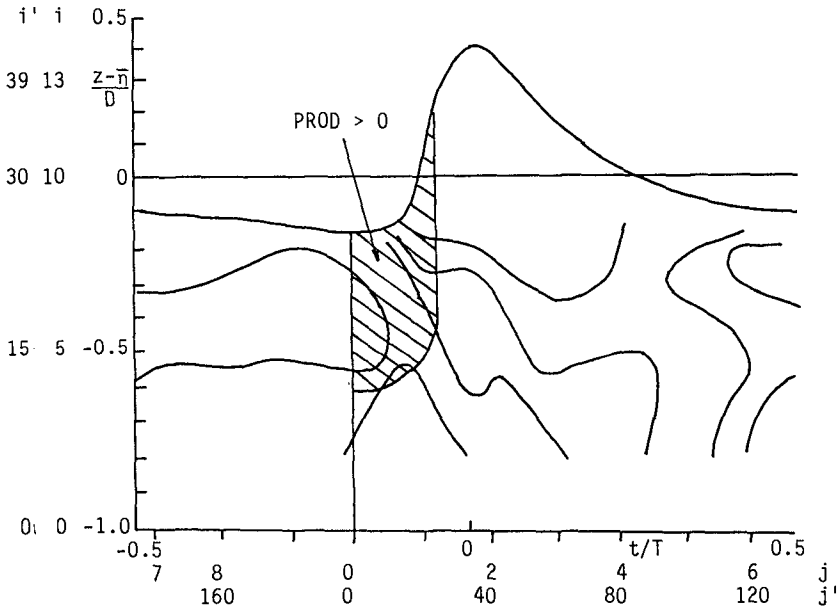


Fig.6 Discretization of wave phase and height above bed for case of $d = 18.6\text{cm}$ of Stive's experiment

The dotted line in Fig.7 is the calculated result in which the vertical convection term is included for the case of $d = 18.6\text{cm}$ of Stive's experiment. The production and dissipation terms are multiplied by 0.3 and 0.5 respectively (explained later). The full line is the calculated result without the convection terms. The cross points are the measured result by Stive. There is no significant improvement on the calculated result.

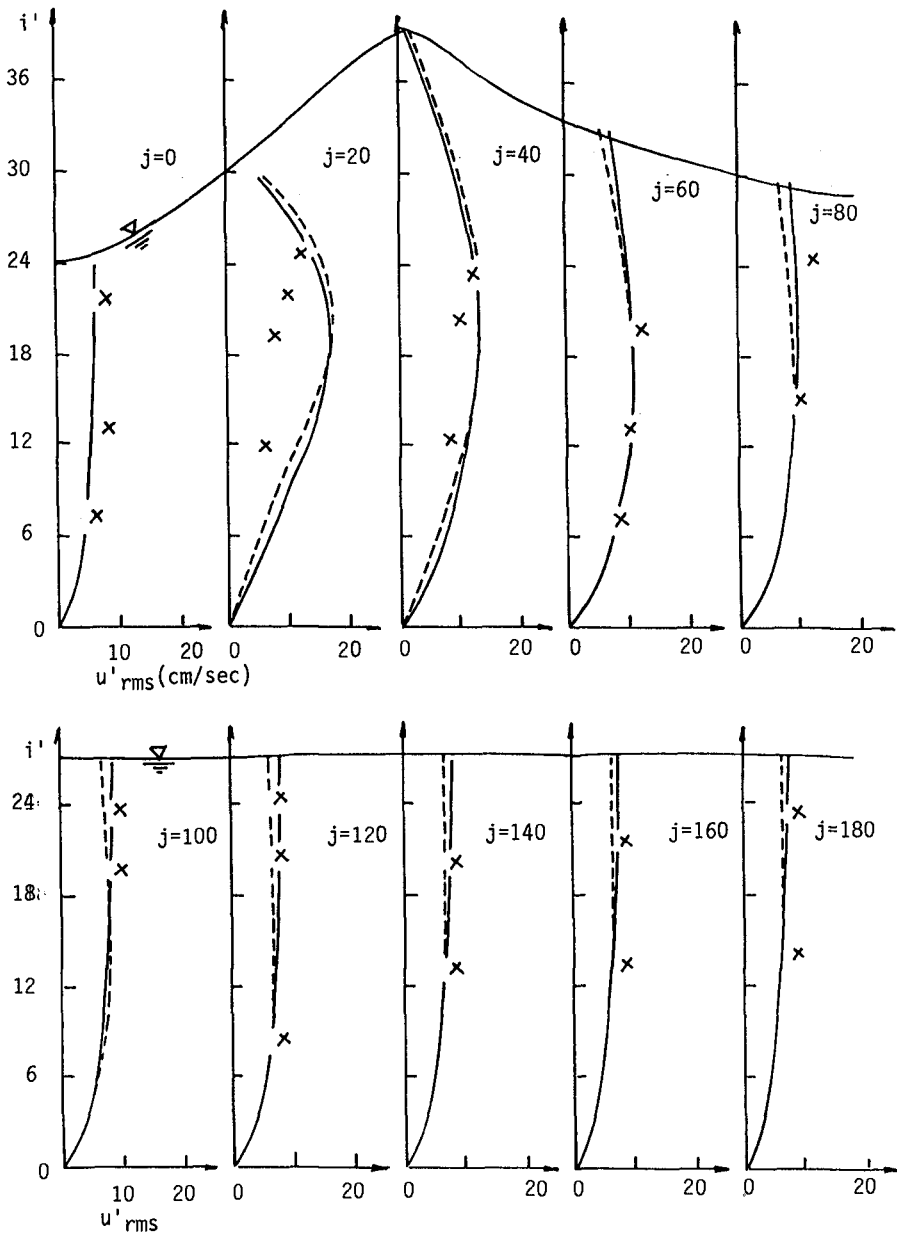


Fig.7 Effect of vertical convection term on phase variation of turbulent intensity

Production Term

Then the production term was also estimated from the data by Stive. It was found that the production term was predominant at least under the wave crest. The production of turbulent energy is expressed by Eq.(4). It is a product of the Reynolds stress and the vorticity.

$$\overline{-u'_\alpha u'_\beta} \left(\frac{\partial U_\alpha}{\partial x_\beta} \right) \approx \overline{-u'v'} \frac{\partial U}{\partial y} \approx \overline{u'v'} \left(\frac{\partial V}{\partial x} - \frac{\partial U}{\partial y} \right) \quad (4)$$

In the 20th Conference on Coastal Engineering, one of the authors presented a numerical simulation of the motion after wave breaking on a beach (Sakai et al., 1986) (Fig.8).

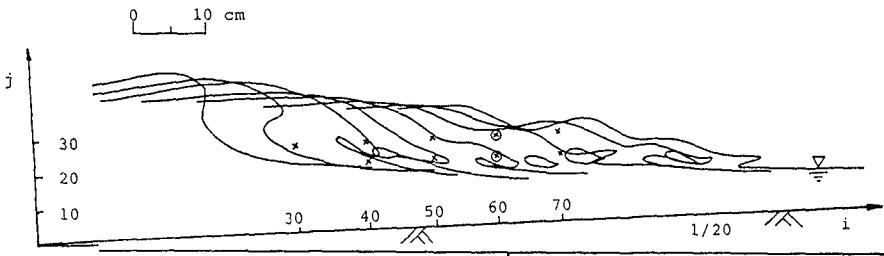


Fig.8 Numerical simulation of motion after wave breaking on beach (Sakai et al., 1986)

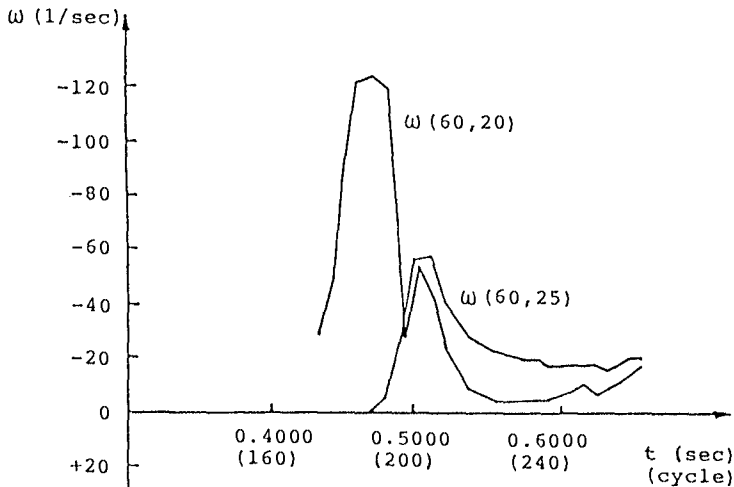


Fig.9 Time variation of vorticity (Sakai et al., 1986)

The vorticity was estimated from the simulation result at two points indicated by the circled cross point. Fig.9 is the time variation of vorticity.

The vorticity increases and decreases very rapidly. The time interval is about 0.1sec. In the model of Deigaard et al., the time interval of the production term is given by δT in Eq.(2). The calculated value of δT for the simulated case is about 0.3sec. The Deigaard et al.s' model may overestimate the time interval of the production term.

To check the effect of the production term, a similar calculation to that by Deigaard et al. is done. In this case, the discretization of the phase and the height above the bed is rather rough as indicated by the i and j values in Fig.6. The full curves in Fig.10 show the result when the Deigaard et al.s' equation is used for the case of $d = 18.6\text{cm}$ of Stive's experiment..

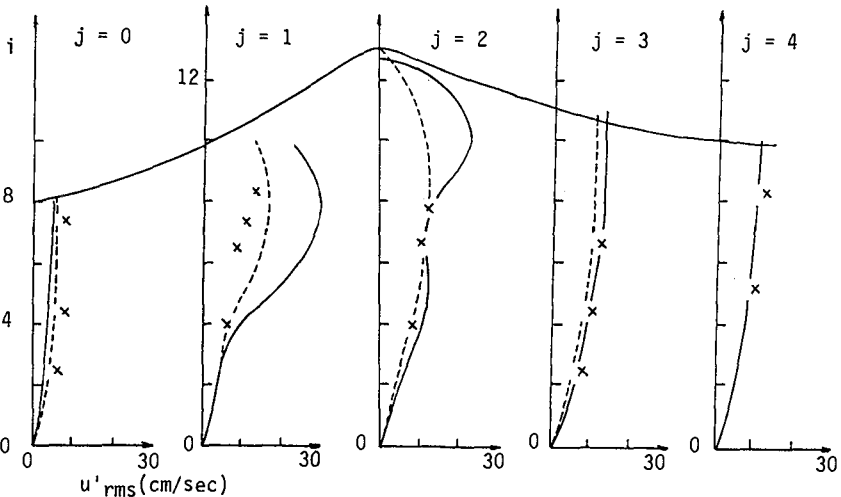


Fig.10 Effect of production term on phase variation of turbulent intensity

The calculated result overestimates the turbulent intensity under the wave crest. Then, the production term was multiplied by 0.3. And the dissipation term was multiplied by 0.5. The calculated value decreases as indicated by the dotted curves. This means that the production given by Deigaard et al. is too large, and its 30% is enough to reproduce the measured result.

In fact, from a personal communication with Deigaard, it was found that he himself did a similar

correction in his calculation. The production term is strongly related to the slope of the vertical distribution of turbulent intensity(Fig.5). The correct estimation of the production is, therefore, necessary to improve the prediction.

The reason for the reduction of the dissipation remains unclear.

Conclusions

(1) The existing data on the phase variation of turbulent intensity in surf zone during one wave period show a peak near the wave crest and a following gentle decrease. The phase of the peak delays downwards.

(2) The model of Deigaard et al.(1986) which utilized the one equation model for the turbulent kinematic energy transportation, explains the experimental results roughly.

(3) The vertical convection term in the turbulent kinematic energy transportation equation has no significant effect on the variation.

(4) The production term of Deigaard et al. gives a longer time interval than the vorticity in a numerical simulation of motion after wave breaking by Sakai et al.(1986).

The production term of Deigaard et al. gives a steeper slope of the vertical mean turbulent intensity distribution than the existing experimental results.

The production multiplied by 0.3 and the dissipation multiplied by 0.5 gives a reasonable result.

It is necessary to refine the production term to predict more accurately the phase variation of turbulent intensity during one wave period in the surf zone.

Acknowledgement

The authors would like to express their appreciation to Emeritus Prof. Y. Iwagaki, Faculty of Eng. and Prof. Y. Tsuchiya, Disaster Prev. Res. Inst., Kyoto Univ. for their helpful discussions. A part of this study is supported by a Grant-in-Aid for Co-operative Research, No.63302048, The Japanese Ministry of Education, Science and Culture.

References

- Deigaard, R., Fredse, J. and Hedegaard, I.B.(1986) : Suspended sediment in the surf zone, Jour. of Waterway, Port, Coastal and Ocean Eng., ASCE, Vol.112, No.1, pp.115-128.
- Nadaoka, K.(1986) : A Fundamental Study on Shoaling and Velocity Field Structure on Water Waves in The Nearshore Zone, Tech. Rep. No.36, Dept. of Civil Eng., Tokyo Inst. of Tech..
- Sakai, T., Inada, Y. and Sandanbata, I.(1982) : Turbulence generated by wave breaking on beach, Proc. of 18th Conf. on Coastal Eng., ASCE, pp.1-21.
- Sakai, T., Mizutani, T., Tanaka, H. and Tada, Y.(1986) : Vortex formation in plunging breaker, Proc. of 20th Conf. on Coastal Eng., ASCE, pp.711-723.
- Stive, M.J.F.(1980) : Velocity and pressure field of spilling breakers, Proc. of 17th Conf. on Coastal Eng., ASCE, pp.547-566.
- Svendsen, I.A.(1987) : Analysis of surf zone turbulence, Jour. of Geophy. Res., Vol.92, No.C5, pp.5115-5124.

CHAPTER 56

WAVE GROUP FORCED NEARSHORE CIRCULATION

Rachel E. Fowler¹ and Robert A. Dalrymple,² F.ASCE

Abstract

Forcing of the nearshore circulation system by incident wave groups is examined. Attention is focused on the generation of migrating rip currents and development of low frequency motion. Analysis of experimental results categorises the migrating rip currents as very low frequency motion in the FIG energy band. It is suggested that migrating rip currents, in addition to shear waves, are a valid generation mechanism for very low frequency motion in the nearshore region.

Introduction

The primary currents in the nearshore area are longshore currents, cross-shore currents (or undertow), and rip currents. Longshore currents, generated by incident waves with an oblique approach to the shoreline, flow parallel to the beach carrying sediments downwave. Cross-shore currents develop to maintain the mass flux balance in the surf zone. They can transport sediments offshore, although they can not carry sediments far beyond the breaker line. Rip currents are more powerful surface currents and are a major mechanism for water exchange across the breaker line. They can transport large amounts of sediment a considerable distance beyond the surf zone. Numerous theories exist for the presence of rip currents as discussed by Dalrymple (1978). All these features of the nearshore circulation system are generally considered stationary processes.

Underlying the nearshore currents is a low frequency motion which is typically unsteady and periodic in nature. This motion includes surf beat, edge waves, and far-infragravity motions. Much attention has been given to the characterization of these wave motions, but as yet, their generation mechanisms are not totally understood.

The fundamental aim of the research work described in this paper was to study the nearshore circulation system and evaluate its response to forcing by offshore wave groups. In particular, we examined the generation of slowly migrating rip currents by the offshore wave groups, and the corresponding development of low frequency motions in the surf zone.

¹Graduate Research Assistant, Center for Applied Coastal Research, University of Delaware, Newark, Delaware 19716 USA

²Professor, Center for Applied Coastal Research, University of Delaware, Newark, Delaware 19716 USA

Wave Groups and Low Frequency Motion in the Nearshore Region

Initial discoveries of low frequency motion (frequencies $<$ incident wave frequency, periods 30–300s) in the nearshore region are attributed to Munk (1949) and Tucker (1950). They observed oscillations in the water surface elevation which had periods of several minutes. Munk named these long, low frequency waves 'surf beat'. Tucker found the best evidence of surf beat during periods of long, regular groups of incident waves, and noted that the long waves were out of phase with the wave groups.

Longuet-Higgins and Stewart (1962, 1964) demonstrated theoretically, using radiation stresses, that a small second-order undulation accompanies a first-order wave group, leading to the development of a set-down wave, a long, forced wave in the nearshore region. It was shown that the forced wave has the same wave length and period as the incident wave group and is 180° out of phase with the group, as observed by Tucker. They suggested that the surf beats seen by Munk and Tucker were seaward propagating free waves formed by the release of the forced, set-down waves as they are reflected near the coastline.

Following these initial surf beat studies, the majority of research on the interaction of wave groups and the nearshore circulation system has focused on edge waves. Gallagher (1971) showed that non-linear interactions between wind waves, leading to an inter-frequency energy transfer, can initiate forced edge waves in the surf zone which can grow resonantly. In a laboratory study, Bowen and Guza (1978) considered both resonant and non-resonant interactions between incoming wave trains and confirmed that, when the frequency and longshore wave number of incident wave groups satisfy the edge wave dispersion relationship, theoretically predicted edge wave motions can be generated and maintained.

Huntley, Guza and Thornton (1981) summarised that there are three different generation mechanisms for nearshore low frequency motion: progressive edge waves, standing edge waves (caused by an obstruction or topographic form), and forced second-order waves under incident wave groups. From their analyses of data from the National Sediment Transport Study field experiment at Torrey Pines Beach, California, they found the most important of these generation mechanisms to be progressive edge waves. They observed long-wave motion in the surf zone with frequencies and wave lengths that corresponded to those predicted by the edge wave dispersion relationship. However, they also found that other generation mechanisms were important, primarily forced motion due to standing edge waves.

Tang and Dalrymple (1989) also worked with the NSTS data set, but concentrated on nearshore motions at much lower frequencies than those in the edge wave band. Figure 1 shows the edge wave energy identified by Huntley, Guza and Thornton, but there is also a significant pocket of energy in the lowest frequency band. Tang and Dalrymple demonstrated, through various statistical analysis methods, that offshore wave groups were significantly correlated with the measured, very low frequency motion ($<$ 0.0015 Hz, periods $>$ 660 sec.). During the field experiment, observations were made of slowly migrating rip current cells in the surf zone which had the same wave length as the very low frequency motion. Tang and Dalrymple hypothesised that the incident wave groups forced a response in the surf zone in the form of migrating rip currents, which, in turn, had a very low frequency motion signature in wave number-frequency space.

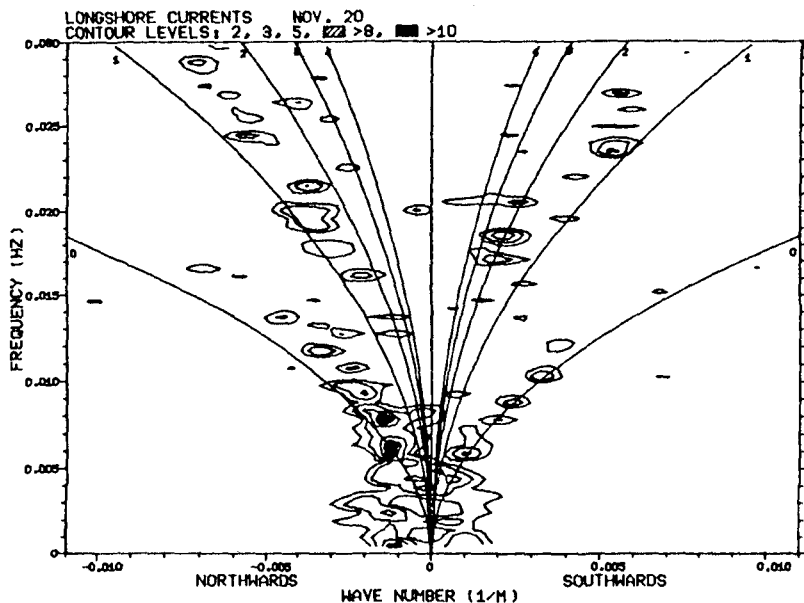


Figure 1: Wave number-frequency spectrum derived from cross-shore current measurements at an offshore location. Torrey Pines Beach, California, USA. (Fig. 10B-5 of Tang and Dalrymple, 1989)

Data from the SUPERDUCK field experiment (see Crowson *et al.* (1988)) conducted at Duck, North Carolina, were analysed by Oltman-Shay, Howd and Birkemeier (1989) and produced solid evidence of high energy motion at very low frequencies. These low frequency oscillations can be clearly seen in the velocity records (fig. 2), particularly in the longshore velocity records. Oltman-Shay *et al.* also analysed their data in wave number-frequency space and clearly demonstrated that the high energy, low frequency motion is distinct from edge wave motion (fig. 3). An approximately linear relationship between wave number and frequency was also revealed, implying that the low frequency motion is non-dispersive. This very low frequency motion was observed only in the presence of a mean longshore current, and changed speed and direction with that mean current. Oltman-Shay *et al.* named this kinematically distinct, low frequency band of energy the 'far infra-gravity (FIG) band' and, in a companion paper by Bowen and Holman (1989), it was suggested that the observed motions were generated by instabilities in the mean longshore current. These instabilities lead to the formation of a longshore-progressive shear wave, which has the restoring force of vorticity rather than gravity.

Theoretical Considerations

Since incident wave groups appear to be important to the dynamics of the nearshore circulation system, we examine their simplest form. Consider the summation of two sinusoidal incident wave trains, as described by linear theory. The

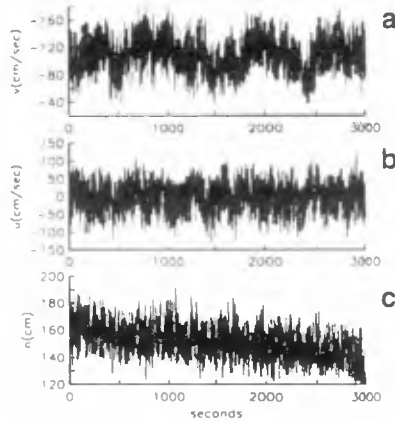


Figure 2: Time series measurements of (a) longshore (v), (b) cross-shore (u) velocity, and (c) surface displacement (η) collocated in the surf zone. Duck, North Carolina, USA. (Fig. 2 of Oltman-Shay *et al.*, 1989)

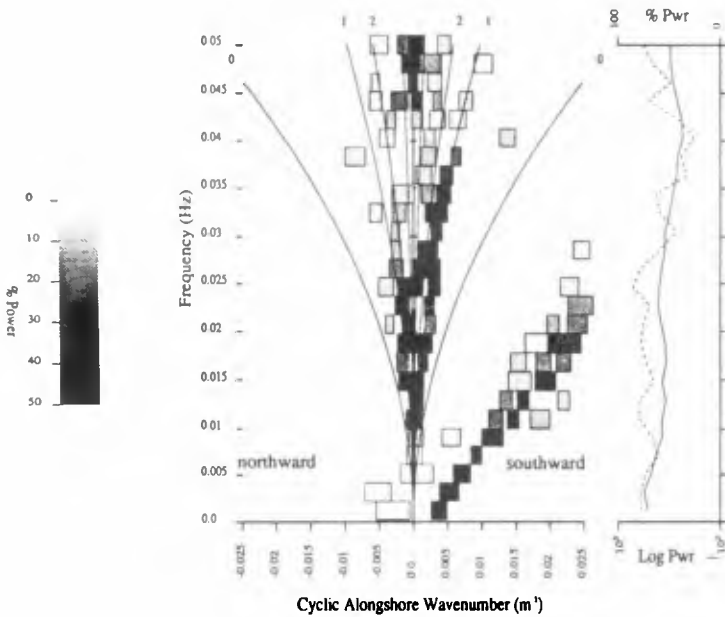


Figure 3: Wave number-frequency spectrum derived from cross-shore velocity measurements in the surf zone. Duck, North Carolina, USA. (Fig. 6b of Oltman-Shay *et al.*, 1989)

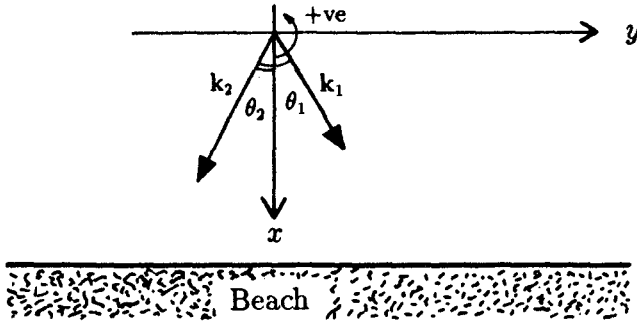


Figure 4: Coordinate system.

velocity potential and water surface elevation are given by:

$$\phi(\mathbf{x}, z, t) = \frac{ga_1 \cosh k_1(h+z)}{\omega_1 \cosh k_1 h} \cos \psi_1 + \frac{ga_2 \cosh k_2(h+z)}{\omega_2 \cosh k_2 h} \cos \psi_2 \quad (1)$$

$$\eta_t(\mathbf{x}, t) = \left. \frac{1}{g} \frac{\partial \phi}{\partial t} \right|_{z=0} = a_1 \sin \psi_1 + a_2 \sin \psi_2 \quad (2)$$

where $\psi_i = (\mathbf{k}_i \cdot \mathbf{x} - \omega_i t)$, phase function of wave train, $i = 1, 2$
 $\mathbf{k}_i = |\mathbf{k}_i| \cos \theta_i = k_i \cos \theta_i$, wave number of wave train, $i = 1, 2$
 $\omega_i =$ frequency of wave train, $i = 1, 2$
 $a_i =$ amplitude of wave train, $i = 1, 2$
 $g =$ acceleration due to gravity
 $h =$ water depth
 $\mathbf{x} = (x, y)$

The wave numbers, \mathbf{k}_i , are related to the angular frequencies of the waves by the linear dispersion relationship. Note from figure 4 that the x axis is positive onshore.

Through the use of various trigonometric identities, the total water surface elevation can be rewritten and expressed as the sum of a modulated sine wave and a plane wave train:

$$\eta_t(\mathbf{x}, t) = 2a_1 \sin \left(\frac{\psi_1 + \psi_2}{2} \right) \cos \left(\frac{\psi_1 - \psi_2}{2} \right) + (a_2 - a_1) \sin \psi_2 \quad (3)$$

By introducing the definitions:

$$\left. \begin{aligned} \omega_1 &= \omega - \frac{\Delta\omega}{2} \\ \omega_2 &= \omega + \frac{\Delta\omega}{2} \end{aligned} \right\} \begin{aligned} \omega &= \frac{\omega_1 + \omega_2}{2} \\ \Delta\omega &= \omega_2 - \omega_1 \end{aligned} \quad \left. \begin{aligned} \mathbf{k}_1 &= \mathbf{k} - \frac{\Delta\mathbf{k}}{2} \\ \mathbf{k}_2 &= \mathbf{k} + \frac{\Delta\mathbf{k}}{2} \end{aligned} \right\} \begin{aligned} \mathbf{k} &= \frac{\mathbf{k}_1 + \mathbf{k}_2}{2} \\ \Delta\mathbf{k} &= \mathbf{k}_2 - \mathbf{k}_1 \end{aligned}$$

we develop η_t in terms of the average frequency, ω , the average wave number

vector, \mathbf{k} , and their difference terms, $\Delta\omega$ and $\Delta\mathbf{k}$:

$$\eta_t(\mathbf{x}, t) = 2a \underbrace{\sin(\mathbf{k} \cdot \mathbf{x} - \omega t)}_{\text{carrier wave}} \underbrace{\cos\left(\frac{1}{2}(\Delta\mathbf{k} \cdot \mathbf{x} - \Delta\omega t)\right)}_{\text{wave envelope}} + (a_2 - a_1) \sin\left(\underbrace{\mathbf{k} \cdot \mathbf{x} - \omega t - \left(\frac{1}{2}(\Delta\mathbf{k} \cdot \mathbf{x} - \Delta\omega t)\right)}_{\psi_2}\right) \quad (4)$$

For $a_1 = a_2$, the second term is eliminated. The total water surface elevation now consists of a carrier wave, propagating in the $(\mathbf{k}_1 + \mathbf{k}_2)/2$ direction, at speed $(\omega_1 + \omega_2)/|\mathbf{k}_1 + \mathbf{k}_2|$, modulated by a wave envelope, which propagates at speed

$$Cg = \frac{\omega_1 - \omega_2}{|\mathbf{k}_1 - \mathbf{k}_2|} \quad (5)$$

in the $\mathbf{k}_1 - \mathbf{k}_2/2$ direction. The longshore component of the speed of propagation of the wave envelope, Cg_y , is easily obtained from equation 5.

From the velocity potential (eq 2), expressions can also be developed for the longshore and cross-shore velocities:

$$u = -\frac{\partial\phi_t}{\partial x} = g\mathbf{k}f(\mathbf{k})(a_1 \cos\theta_1 \sin\psi_1 + a_2 \cos\theta_2 \sin\psi_2) + O(\Delta\mathbf{k}, \Delta\omega) \quad (6)$$

$$v = -\frac{\partial\phi_t}{\partial y} = g\mathbf{k}f(\mathbf{k})(a_1 \sin\theta_1 \sin\psi_1 + a_2 \sin\theta_2 \sin\psi_2) + O(\Delta\mathbf{k}, \Delta\omega) \quad (7)$$

where

$$f(\mathbf{k}) = \frac{\cosh k(h+z)}{\cosh kh}$$

From these expressions it can be noted that the cross-shore velocity and the water surface elevation (eq 2), are in phase at both the incident wave frequency and the group frequency. However, the longshore velocity moves in and out of phase at the incident wave frequency and is 180° out of phase at the wave group frequency. Similar phase differences at the group frequency were observed in the field by Kim and Huntley (1986).

As the incident wave trains propagate towards the shore they alternatively reinforce and cancel each other out, creating periodic, longshore variations in wave height. Lines of cancellation, or nodal lines, can be seen in the wave field. For the special case where the intersecting wave trains are of the same frequency $Cg = 0$, and the wave groups do not propagate. At the intersection of the nodal lines with the beach, rip currents develop, as demonstrated by Dalrymple (1975). The longshore spacing of the nodal lines, and hence the rip currents, can be predicted by:

$$Lg_y = \frac{2\pi}{k_2 \sin\theta_2 - k_1 \sin\theta_1} \quad (8)$$

In general, for two incident wave trains with slightly different frequencies, $\omega_1 \neq$

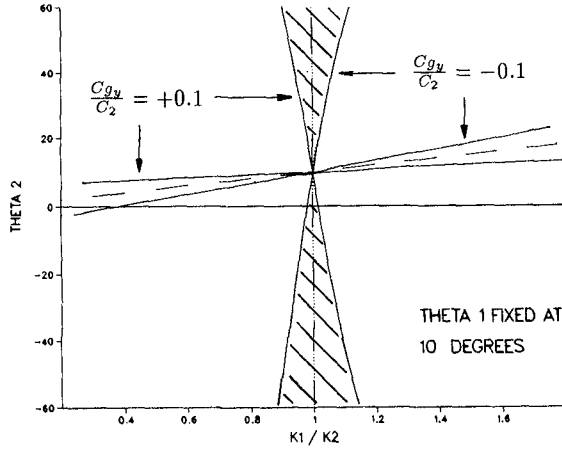


Figure 5: Graphical representation of the incident wave conditions suitable for the development of migrating rip currents.

ω_2 , the speed of propagation of the wave envelope is no longer zero. Therefore, the nodal lines in the wave field are no longer stationary. Since we know that rip currents can develop in the surf zone for $Cg_y = 0$, we now suggest that for $Cg_y \approx 0$ rip currents can be generated and will migrate slowly along the beach with the nodal lines. To facilitate prediction of suitable conditions for migrating rip currents, a dimensionless expression is developed from equation 5:

$$\frac{Cg_y}{C_2} = \frac{(k_r - 1)(k_r \sin \theta_1 - \sin \theta_2)}{k_r^2 + 1 - 2k_r \cos(\theta_1 - \theta_2)} \quad (9)$$

using the shallow water assumption, $\omega_1/\omega_2 = k_1/k_2$, and where $k_r = k_1/k_2$, the ratio of the wave numbers of the two wave trains, and C_2 is the celerity of the second wave train. This expression must be $\ll 1.0$ to enable rip currents to develop. Equation 9 is represented graphically in figure 5 which is for the case where θ_1 is fixed at $+10^\circ$.

The lines represent contours of Cg_y/C_2 . The dashed line represents the conditions for stationary rip currents. The graph shows two families of solutions. The horizontally oriented lines represent conditions when the nodal lines are propagating in the on/offshore direction, at large angles to the beach normal. These conditions do not lead to the development of rip currents on the beach, but instead create a surf beat effect. The vertically oriented family of solutions represent conditions which do lead to the development of rip currents. Values of $Cg_y/C_2 = \pm 0.1$ were arbitrarily selected as limits for the development of migrating rip currents, and several test cases were selected within these limits for the experimental work. Care was taken to avoid incident wave conditions that would initiate edge waves.

Experimental Facilities and Procedures

The migrating rip currents were simulated in the directional wave basin at the University of Delaware. The basin measures 20m x 20m x 1.1m. Along

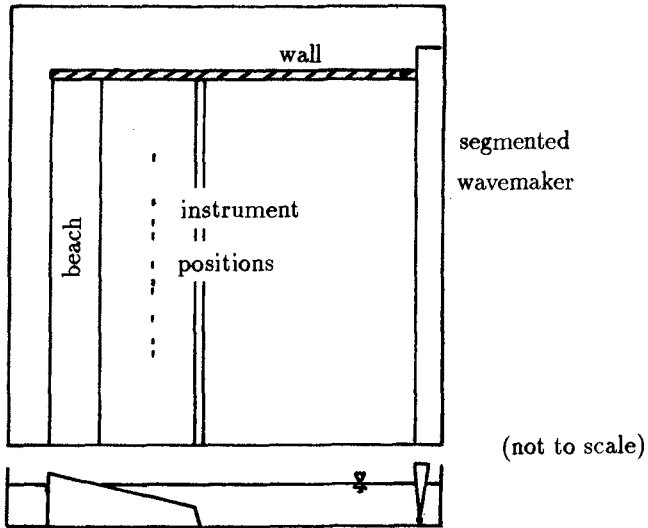


Figure 6: Plan and elevation of the directional wave basin at the University of Delaware, showing the experimental set-up.

one wall there is a segmented wavemaker composed of thirty individually actuated paddles (fig. 6). A wooden beach, 14.65m in length, was installed in the basin providing an idealised, planar slope of 1:10. A closed basin condition was maintained as required for wave generation using the 'designer waves' technique, Dalrymple (1989). The water depth was maintained at 81cm for the duration of the experiments.

Cross-shore and longshore currents were measured at ten locations along the beach using Marsh-McBirney electromagnetic current meters. The instrument locations were in the form of a ten-point, linear array, 1.52m seaward from the still water line, outside the surf zone. The data sampling frequency was set at 10Hz and record lengths containing 4096 data points were obtained.

Four experimental cases were run and are summarised in figure 7. The first two cases, RTEST and PTEST, are identical except for their wave heights. The fourth experimental case, STEST, is of note since the rip currents propagate along the beach in a direction opposite to that of the incident waves. Further details of the laboratory experiments are presented in Fowler (1990).

Results

Cross-shore and longshore velocity records were obtained for each experimental case at all ten locations in the linear array. Typical velocity records from one location are presented in figure 8. The cross-shore record clearly shows the wave groups arriving in the nearshore region. The two records are seen to be out of phase as suggested by the theory, although quantitative evaluation of this has not been performed. The longshore velocities have about half the magnitude of

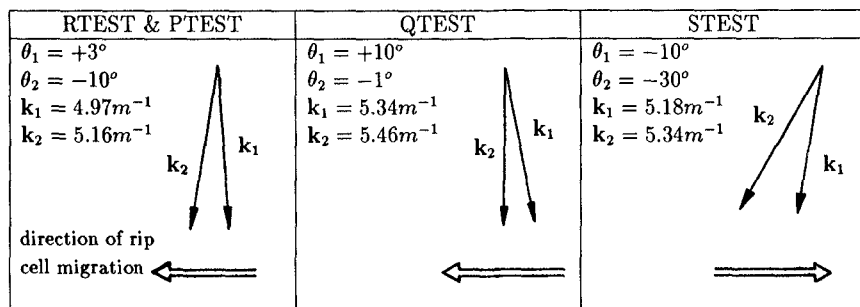


Figure 7: Summary of the four experimental cases.

the cross-shore velocities, but the low frequency modulation is very prominent. This low frequency modulation can be very clearly seen in the frequency spectrum (fig. 9). The incident waves are easily identifiable, but the spectrum is dominated by a low frequency peak due to the rip currents migrating along the beach. This conclusion is confirmed by visual observations of the period of the rip cells in the laboratory.

With the exception of the RTEST data, for each experimental case the cross-shore velocity records from all ten instrument locations were combined and analysed using either a direct Fourier transform method (DFT), or a maximum likelihood method (MLM), to create a wave number-frequency spectrum. Frequency is represented on the vertical axis, and alongshore wave number, here defined as $2\pi/L$, where L = wave length, is along the horizontal axis. Within this framework, contour lines of energy are plotted. The curved lines represent the theoretical edge wave dispersion relationship for modes 0, 1 and 2. For the RTEST experimental case, data from three locations were considered unreliable and discarded. A wave number-frequency spectrum was produced from the remaining seven velocity records.

The low frequency portion of the wave number-frequency spectra for each of the four experimental cases are presented in figures 10 through 13. In each graph the occurrence of low frequency motion is clearly represented and cannot be due to edge wave motion as it is not coincident with any of the edge wave dispersion relationship curves. The frequency of the energy in each case corresponds to visual observations in the laboratory of the period of the migrating rip cells passing a fixed point.

Compared to QTEST and STEST, the PTEST and RTEST experimental cases produced stronger rip currents, which flowed further offshore before dissipating. Consequently, the current meters were further from the head of each passing rip current and the offshore velocities due to the rip were more pronounced. The rip current signature in the cross-shore velocity records is sharper for these cases. When their experimental results were analysed in wave number-frequency space, a second pocket of energy appeared at twice the frequency and half the wave length of the primary feature, a harmonic of the fundamental mo-

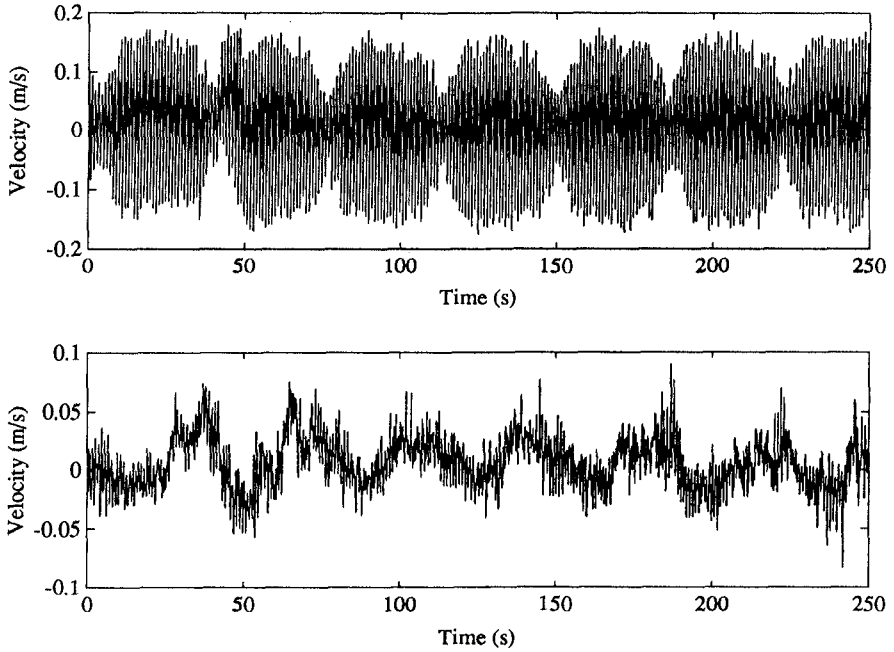


Figure 8: Typical cross-shore (top) and longshore (bottom) velocity records from one location in the instrument array.

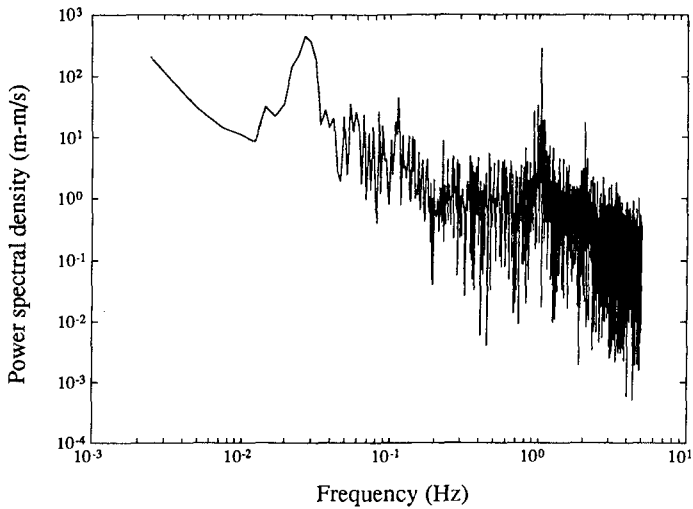


Figure 9: Typical frequency spectrum from one longshore velocity record.

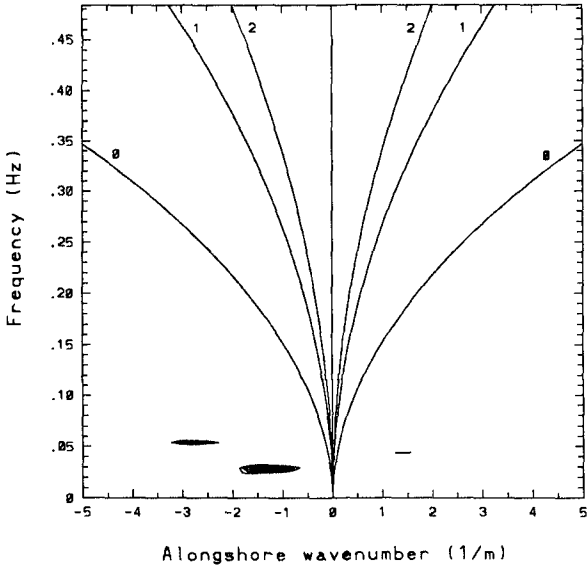


Figure 10: Wave number-frequency spectrum derived from cross-shore velocity records for the RTEST experimental case.

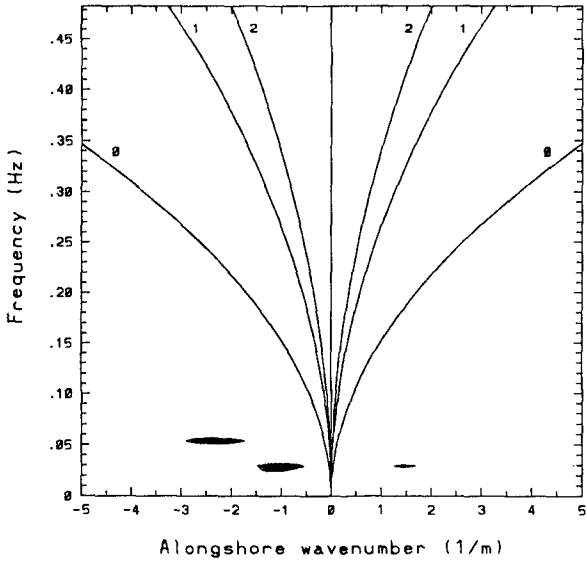


Figure 11: Wave number-frequency spectrum derived from cross-shore velocity records for the PTEST experimental case.

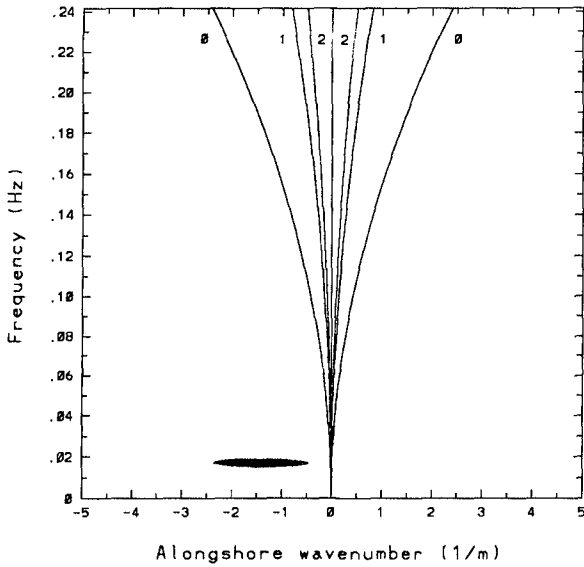


Figure 12: Wave number-frequency spectrum derived from cross-shore velocity records for the QTEST experimental case.

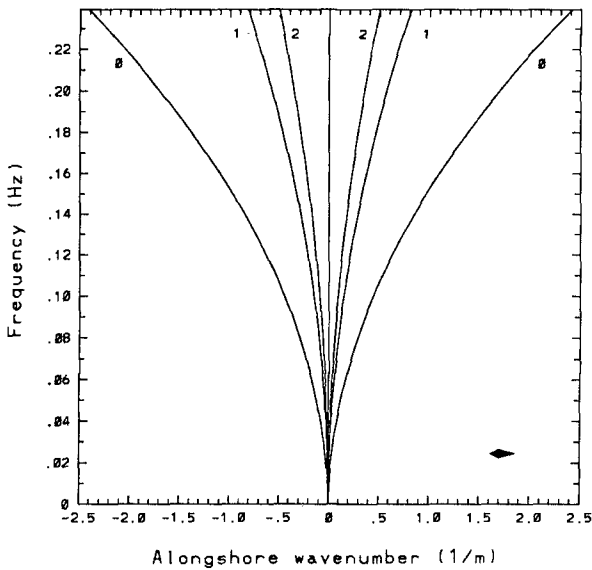


Figure 13: Wave number-frequency spectrum derived from cross-shore velocity records for the STEST experimental case.

tion. This is seen in figures 10 and 11.

The first three experimental cases, RTEST, PTEST, and QTEST, were analysed using the DFT method. Peak splitting due to large directional spread ruled out the use of an MLM for these cases. The DFT method tended to spread the energy over several wave number bins, but the central wave number is still in fairly good agreement with the observed wave lengths. The theoretically calculated wave numbers are over-predicted compared to the wave number-frequency spectra results. However, it must be remembered that equation 8 is based on linear wave theory and includes a shallow water assumption.

MLM analysis was successful on the STEST results producing a better definition of the low frequency motion in the wave number-frequency spectrum. The pocket of low frequency energy is located in the positive wave number region, unlike the previous cases, simply because the rip currents were migrating in the opposite direction.

Conclusions

Incident wave groups have been shown to be important to the dynamics of the nearshore circulation system. Simple linear theory, based on two incident wave trains with $\omega_1 \approx \omega_2$, provided a generation mechanism for slowly migrating rip currents. This suggested mechanism was verified in a laboratory wave basin. Rip currents developed in the surf zone where nodal lines in the offshore wave field intersected the beach. The rip currents propagated along the beach at the same speed as the nodal lines propagated through the wave field.

The longshore spacing of the rip currents can be predicted with some limitations. All the rip spacings were somewhat over predicted and this is thought to be due to the use of linear theory and the shallow water assumption.

The theory predicted the cross-shore and longshore velocities to be out of phase by 180° , a phenomenon previously observed in the field and qualitatively seen in the laboratory results.

Offshore, incident wave groups have been shown to force a response of the nearshore circulation system in the form of migrating rip currents. In turn, these migrating rip currents have a signature in wave number-frequency space that classifies them as very low frequency motion in the nearshore region, in the previously named 'FIG' energy band. It is therefore proposed that migrating rip currents are an alternative to shear waves as a generation mechanism for very low frequency motion in the nearshore region. Future research should include consideration of how to uniquely identify these two mechanisms in the field.

Acknowledgement

Support provided by the National Science Foundation, under grant # MSM 8712203, is hereby gratefully acknowledged.

References

- Bowen, A.J. and Guza, R.T. (1978). "Edge waves and surf beat", *J. Geophys. Research*, 83, C4, 1913-1920.

- Bowen, A.J. and Holman, R.A. (1989). "Shear instabilities of the mean longshore current; 1. Theory", *J. Geophys. Research*, 94, C12, 18023–18030.
- Crowson, R.A., Birkemeier, W.A., Klein, H.M., and Miller, H.C. (1988). "SUPERDUCK nearshore processes experiment: Summary of studies CERC Field Research Facility", *Tech. Rep. CERC-88-12*, Coastal Eng. Res. Cent. Vicksburg, Mississippi.
- Dalrymple, R.A. (1975). "A mechanism for rip current generation on the open coast", *J. Geophys. Research*, 50, 24, 3485–3487
- Dalrymple, R.A. (1978). "Rip currents and their causes", *Proc. 16th Intl. Coastal Engineering Conf.*, ASCE, Hamburg, 2, 1414–1427.
- Dalrymple, R.A. (1989). "Directional wavemaker theory with sidewall reflection", *J. Hydraulic Research*, 27, 1, 23–33.
- Fowler, R.E. (1990). "Wave group forced nearshore circulation: a generation mechanism for migrating rip currents and low frequency motion", Thesis to be presented to the University of Delaware, Newark, Delaware, in 1990, in partial fulfillment of the requirements for the degree of Master of Civil Engineering.
- Gallagher, B. (1971). "Generation of surf beat by nonlinear wave interactions", *J. Fluid Mechanics*, 49, 1–20.
- Huntley, D.A., Guza, R.T., and Thornton, E.B. (1981). "Field observations of surf beats; 1. Progressive edge waves", *J. Geophys. Research*, 86, C7, 6451–6466.
- Kim, C.S., and Huntley, D.A. (1986). "On time delays in the nearshore zone between onshore and longshore currents at incident wave frequencies", *J. Geophys. Research*, 91, C3, 3967–3978.
- Longuet-Higgins, M.S., and Stewart, R.W. (1962). "Radiation stress and mass transport in gravity waves, with application to 'surf beats'", *J. Fluid Mechanics*, 13, 481–504.
- Longuet-Higgins, M.S., and Stewart, R.W. (1964). "Radiation stress in water waves; a physical discussion, with applications", *Deep Sea Res.*, 11, 529–562.
- Munk, W.H. (1949) "Surf beats", *Trans. Am. Geophys. Union*, 30, 849–854.
- Oltman-Shay, J., Howd, P.A., and Birkemeier, W.A. (1989). "Shear instabilities of the mean longshore current; 2. Field observations", *J. Geophys. Research*, 94, C12, 18031–18042.
- Tang, E.C.-S., and Dalrymple, R.A. (1989). "Nearshore circulation: Rip currents and wave groups", in *Nearshore sediment transport*, R.J. Seymour, ed., Plenum Press.
- Tucker, M.J. (1950) "Surf beats: sea waves of 1 to 5 min. period", *Proc. Royal Soc.*, A202, 565–573.

CHAPTER 57

BORE-LIKE SURF BEAT ON REEF COASTS

Eizo NAKAZA,¹⁾ Seiko TSUKAYAMA²⁾ and Mikio HINO³⁾

Abstract

Reef coasts, because the wave height of incoming stormy high waves are extremely dampened by coral reef, have been believed as calm sea areas. However, many coastal structures have actually been damaged by stormy waves dampened by the reef. Surf beat with large wave height was discovered through field observations. The surf beat has been named as "Bore-like Surf Beat". The wave height and the wave velocity of the Bore-like surf beat is larger than that of individual waves. Numerical simulation taking into account of non-linear effect of surf beat phenomenon on the reef shows good agreement with laboratory data.

The main reason of the disasters of coastal structures on the reef coasts is existence of the Bore-like surf beat resonantly excited incoming wave groups.

Introduction

The coasts around the Southwest Islands of Japan are what is called the reef coast, which is surrounded by natural coral reef. On the reef coasts, the sea area is made comparatively calm due to the energy dissipating effect of the reef to the incoming waves, as the natural submerged breakwater. Therefore, it has been believed that the existence of the reef is contributed for the safety of the coastal structures. But actually, disasters caused by Typhoon waves have frequently occurred on reef coasts and is contradictory to the general concept that "the reef coast is a calm sea area".

1) Research Associate, 2) Associate Professor, Dep. of Civil Engineering, Faculty of Engineering, Ryukyu University, Japan.

3) Professor, Dep. of Civil Eng., Faculty of Eng., Dep. of Tokyo Institute Technology.

Since 1973, the waves on reef coasts have been investigated by Kohno and Tsukayama. They mainly clarified the wave deformation on the reef by laboratory experiments and/or field observations. Takayama et al. (1977) experimentally investigated the waves on the reef with irregular waves, and proposed an empirical estimating formula for the wave height and wave set-up on the reef. After Takayama et al., the estimating formula of the wave height on the reef has usually been used in design for coastal structures in reef coasts of the Southwest Islands of Japan. The wave height expected by Takayama's empirical equation gives about 1m for incoming waves with the wave height above 10m. As for the wave set-up, it is about 1.5m. In the traditional design concept, as generally speaking, the reef area is one of the calm sea.

Surf beat phenomena on the reef were discussed by Seelig (1983). He firstly showed that the surf beat contributes the wave run-up. But no characteristic of surf beat is clarified.

Recently, Tsukayama and Nakaza clarified the wave deformation due to the large roughness of the coral reef as well as the wave breaking deformation.

There are many studies on the individual waves in sea areas with the reef, as shown above. But the surf beat on the reef coasts has not been studied enough. In this paper, first of all, the actual condition of wave disasters on the reef coasts is shown, and then it is disclosed that the main reason of the severe coastal disasters is the existence of surf beat with the wave height larger than one of individual waves. Secondly, the surf beat phenomena resonantly excited by incoming wave groups on the reef are shown by field observation data as well as experimental and numerical ones.

2. What happened on reef coasts ?

- (i) A typical topography of the reef coasts in the Okinawa Islands of Japan, and waves on there

Figure-1 shows a topography of typical reef coast of the Okinawa Islands in Japan. It may be the same type as the reef in Australia, which is well known as the Great Barrier Reef. The width of the reef is about 300m to 1000m, and the water depth at high tide is about 2m to 3m. The heel of the beach is called as beach front, and the offshore edge of the reef flat is called as reef front. As shown in Fig.-1, many coral reefs of the Okinawa Islands have a steep slope, which is about 1/10 in front of the reef flat. In some cases, the offshore side of the reef flat edge becomes more sharply sloped.

Photograph-1 shows the wave condition on the reef when the deep water wave height is about 4m. As shown in this photograph, the incoming waves are rapidly dampened. Therefore, the wave height on the reef is extremely small, except near the reef front. For example, as seen in photo.-1(b), near the shore line, a child can play with the waves, for its height is very small.

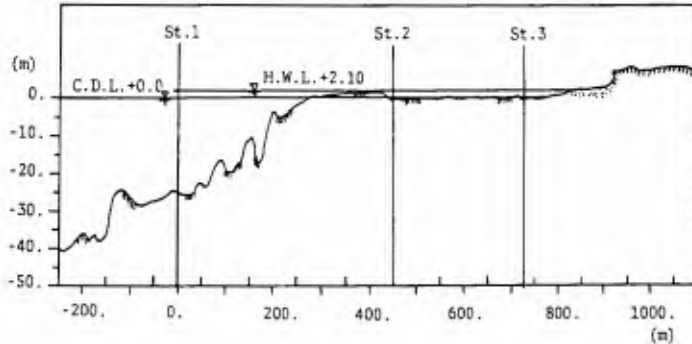


Fig. 1 Cross-sectional topography of a typical reef coast of Okinawa Islands in Japan



(a) Wave braking near the reef front



(b) waves near the shore line

Photo.-1 waves on a reef coast under a Typhoon condition

In Okinawa Islands, the coastal structures have usually been constructed in the reef zone. Existence of a coral reef has been believed that it acts as safety guard for coastal structures against incoming high waves. Because the water depth on the reef is about 2m, and it has a wide breaking zone which perfectly reduces the height of incoming waves.

(ii) Damages of coastal structures by stormy high waves due to Typhoon

The results of recent surveys of coastal disasters on the reef have shown that many coastal structures severely been destroyed. These disasters are due to extremely high storm surges (flood-like waves) which are higher than 5.0m above Datum Level.

Photograph-2 shows a seawall, roads, and houses damaged by a typhoon. The elevation of foundations of the houses and roads is between 5.5m and 7m above the high water level. And the elevation of seawall crown near the shore line is 5.5m above the high water level.

Figure-2 shows a sketch drawn by three civil engineers who happened to have been there during that typhoon disaster. They explained the disaster as follows.



Photo. -2 Destroyed seawall and road due to storm surges (Sosu coast, Typhoon T8613)

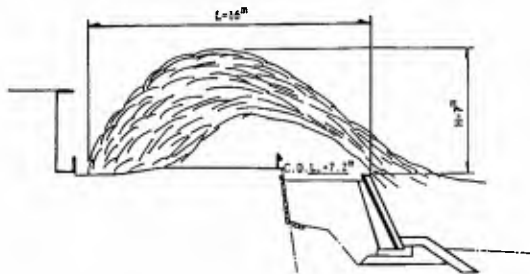


Fig. -2 Sketch of an overtopping wave

The damage was caused by big floods, meaning stormy surges. The big floods surged on the seawall and overtopped it at about 10-minutes intervals (as will be shown, which corresponds to the natural period of the reef coast).

From the traditional estimating method, the wave set-up for a 10m wave in deep water is estimated as about 1.5m. Such a extremely high surge on coral reef zones can not be supposed from the traditional design concept.

(iii) Bore-like surf beat

Photograph-3 shows a reef coast when the tide is high and at a calm sea condition. In this Photograph, The solid line shows the shore line at high water level condition. And the crown level of the coastal cliff is between 6m and 7m above datum level. The pole held by the man is 2m in height.

Photograph-4 was successively taken with time interval of about 15sec. when a typhoon approached the Okinawan main Island on 9:22 at Aug. 29th in 1987. In photo. (a), the waves superimposed on the surge induced by incoming high wave groups can be seen. When this photo. was taken, the significant wave height at the offshore was about 6m. Photograph-(b) was taken after 15sec from the state in Photo. (a). The white line can seen as the breaking wave near the middle of this Photo. is the front of a surge advancing to the shore. And the short period wave, so-called individual waves, can be seen too. After 15sec from that, the surge attacked the near shore cliff. Photograph(c) shows the attack of the surge.



Photo. -3 Shore line under a calm sea condition (high water level)



(a) 9:22:00



(b) 9:22:15



(c) 9:22:30

**Photo. -4 Bore-like surf beat Occurred on Aug. 29, 1987
(Minatogawa coast, T8712)**

As seen in photo.-3, the storm surge or surf beat phenomenon on the reef is one of violent wave phenomena. The surf beat very resembles to the Tsunami, so the authors (1988(a) (c), 1990) named it "Bore-like surf beat" or "Tsunami-like surf beat."

Usually, the surf beat has been believed to be a kind of mild and static wave phenomenon compared to the wave with short period. However, as mentioned before, the surf beat phenomenon in the coral reef zone is a violent wave phenomenon. So, we can conclude that they can cause the severe damage on the coastal structures in the reef coasts, where are usually thought that merely the small individual waves exist. And it is clarified that the above mentioned disaster, explained by three engineers, is due to the Bore-like surf beat. Because the interval of the surge attacking the seawall coincided with the natural period of the reef basin.

3. Theory

For the long period fluctuations of mean sea level, the long wave equations has been normally used. Because the violent surf beat phenomenon on the reef is considered, the nonlinear term in the governing equations can not be ignored. Therefore, the Bore-like surf beat, one of the fluctuations of mean sea level, is governed by the long wave equations,

$$\frac{\partial \eta}{\partial t} + \frac{\partial u(h+\eta)}{\partial x} = 0 \quad (1)$$

$$\frac{\partial u}{\partial t} + u \frac{\partial u}{\partial x} + g \frac{\partial \eta}{\partial x} + \frac{1}{\rho(h+\eta)} \frac{\partial S_{xx}}{\partial x} + \frac{f}{h+\eta} u|u| = 0 \quad (2)$$

where t : time, x : onshore distance from the reef front, η : mean sea-level elevation, u : cross-sectional mean velocity in the vertical section, h : water depth measured from the still water surface, S_{xx} : x -component of radiation stress, ρ : water density, f : bottom friction coefficient, and g : acceleration of gravity. In the momentum equation, a predominant forcing factor of the nonstationary periodic response of water is the term of radiation stress, which is proportional to the square of incident short period wave heights, and varying with time.

The radiation stress at a x from the reef front is given by

$$S_{xx} = \frac{1}{8} \rho H(x, t)^2 \left(\frac{2kh}{\sin h 2kh} + \frac{1}{2} \right) \quad (3)$$

where $H(x, t)$ is the wave height on x at time t . the time variation of the wave height on the reef can be calculated by

$$\frac{H(x, t)}{H_o(t)} = B \exp\{-Ax/L\} + ah/H_o(t) \quad (4)$$

$$H_o(t) = \overline{H_o}(1+0.5 \sin \sigma_o t) \quad (5)$$

where $H_o(t)$: incident wave height at the time t , h : still water depth on the reef, σ_o : angular frequency of incident wave groups. And mean wave set-up on the reef is given by the equation,

$$\overline{\eta} = \overline{H_o} \left[C - \frac{3}{8} \beta \left(\frac{H(x)}{\overline{H_o}} \right)^2 \right]^{1/2} - h \quad (6)$$

The coefficients A , B , C , α and β are proportionality constants to be determined by experiments.

Figure-3 shows the numerical simulation of surf beat taking into account of the non-linear effect of long period fluctuation of mean sea-level, for the wave group period is 27.2sec, and the mean incident wave height $\overline{H_o}=6.5\text{cm}$. On the other hand, fig.-6 shows the result of simulation by Symonds' Method (1982, 1984) which ignored the non-linear effect. As seen in Fig.-5, compare to the result from liner simulation, the surf

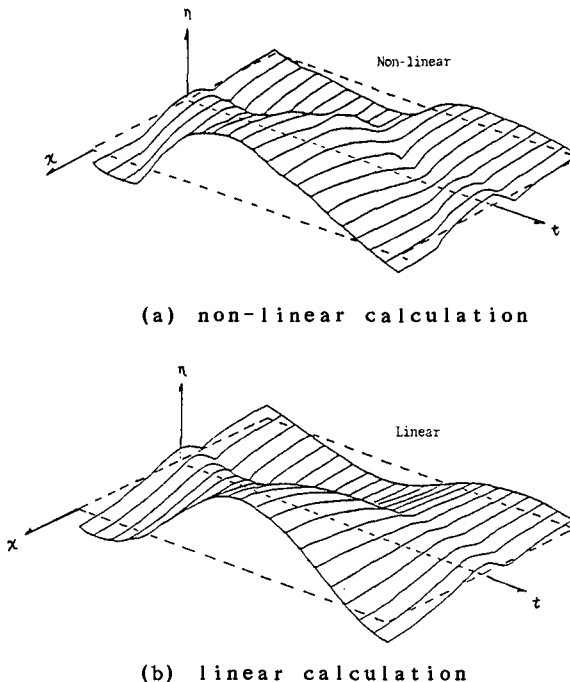


Fig. -3 Numerical simulation of Bore-like surf beat

beat profile at shore line very inclines onward. And it shows one of the future of the Bore-like surf beat.

4. Experiment

4.1 Experimental equipments and method

Two-dimensional experiment has been performed using laboratory equipments in Fig.-4. The wave tank is 27m long, 0.7m wide and 1.0m deep. The prototype of reef coast has the reef flat of 400m in width and the steel water depth of 2m. The experiments were conducted with two types of regular and irregular incident wave groups. In this paper, only the results from the case with regular incident wave groups will be explained.

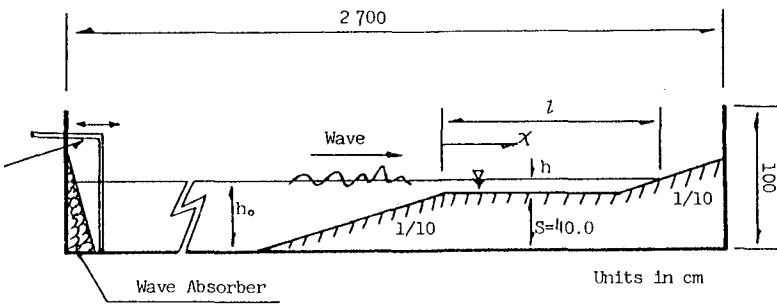


Fig.-4 Experimental equipment

4.2 Results

Figure-5 shows an example of the bore-like surf beat. The upper trace is the profile of deep water waves, and the lower one is the profile of sea surface oscillation on the near shore line. As shown in this figure, the Bore-like surf beat phenomenon is excited by incoming wave groups.

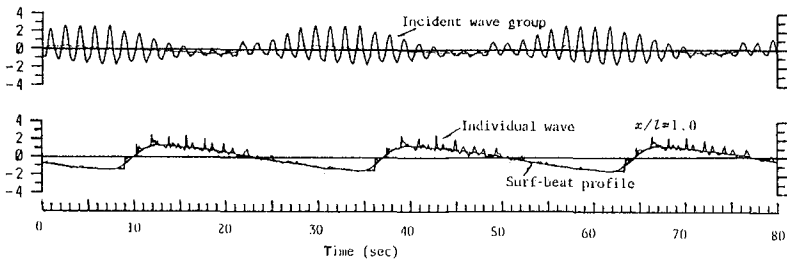


Fig.-5 Example of the experimental waves in deep area and near shore line

Figure-6 shows the comparison of the numerical simulation with the experiments for long period sea oscillation at near shore line. In the figure, circles indicate the experiments, and the solid line represents the results of the numerical simulation. The numerical simulation shows good agreement with the experiments.

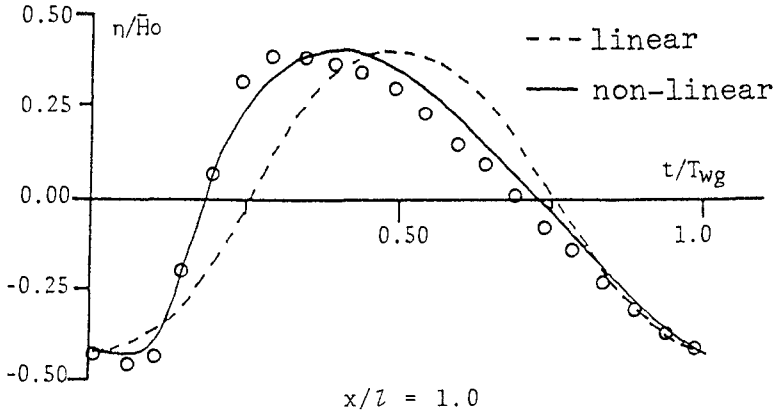


Fig. -6 Comparison of numerical simulation with experiments for long period sea oscillation

Reef coast has the natural period of the seich in a reef basin. Figure-7 shows the oscillation mode of the sea surface in the reef basin. The natural period of the reef coast can be approximately estimated by equation (7).

$$T_0 = \frac{4l}{(2n+1)\sqrt{gh}} \quad (n=0,1,2 \dots) \tag{7}$$

where l : width of the reef flat, and h : still water level.

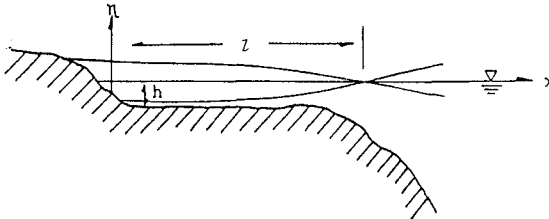


Fig. -7 Long period oscillation mode of sea surface on the reef basin

Figure-8 shows the resonance diagram of sea surface oscillation plotted against the non-dimensional period of wave groupiness. The solid line in the figure corresponds to the numerical solution. As seen in this figure, clear resonant responses are induced when the periods of groupiness of the incoming waves coincide with the natural periods of the reef basin. And the results of numerical solution show good agreement with the experimental results.

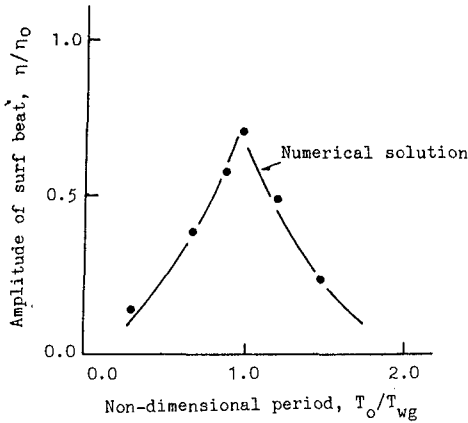


Fig.-8 Resonance diagram
(η_0 , T_{wg} :root mean square amplitude
and period of incident wave groups)

5. Field observation of surf beat on the reef

Figure-9 shows records by pressure-type wave gages simultaneously obtained under the Typhoon at three different locations as shown in Fig.1. The station point 1 is located at 250m offshore from the reef front, the point 2 is located near the reef front and point 3 is located near shore line. As seen in these wave records, wave profile observed at St.1 shows only the feature of wave groupiness, while the other wave profiles observed at St.2 and St.3 show the low frequency oscillation of the mean sea level with period of from 1 to 5 minutes. At St.3 the high mean sea elevations occurred between 10 and 17 minutes corresponding to the clear incoming wave grouping.

Figure-10 shows the power spectrum of the low frequency oscillation of mean sea level at St.3. In this Figure, the arrows n_1 , n_2 , and n_3 indicate the natural frequency of the reef coast for the fundamental mode, second mode, and third mode respectively. The power spectrum has the two peaks corresponding to the natural

frequency of the reef coast. Estimating the power spectrum for the lower frequency than the peak frequency nearly corresponding to the significant wave period of the incident waves, we can obtain the frequency response of mean sea level. But straightly calculating from the sea surface oscillation obtained by wave recorder, the low frequency power spectrum of incident waves can not be obtained. In this study, for the slowly varying wave height time history, the smoothed instantaneous wave energy history proposed by Funke-Mansard(1980) is used.

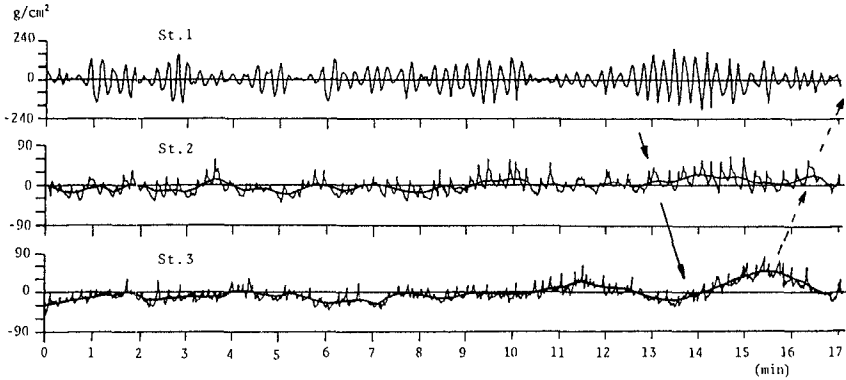


Fig. -9 Wave gage records simultaneously obtained for Typhoon T8520 at three different locations

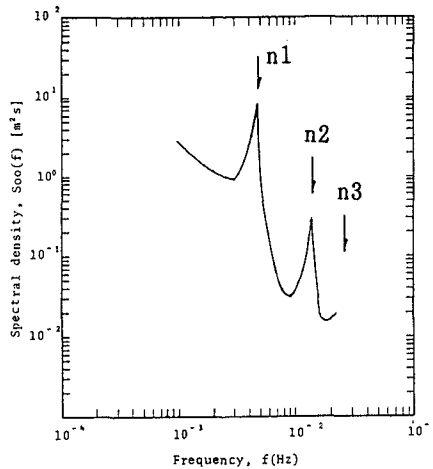


Fig. -10 Power spectrum of the low frequency oscillation of mean sea level at point 3

Figure-11 shows the low frequency power spectrum of incident wave energy. Seeing this figure attentively, it can be noticed that there are two peaks of the low frequency spectrum. The second peak from the lowest frequency is corresponds to the frequency for the repetition length of high waves (Goda's j_2). But what does the first peak mean ?. the period for the first peak is about twice of the second peak. The authors has been thought that the surf beat on the reef coasts has resonantly excited by the wave energy on the second peak, because the period corresponds to the natural period of the reef coasts around the Okinawan Islands.

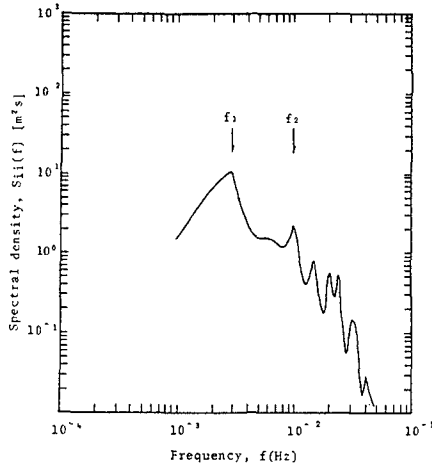


Fig. -11 Low frequency power spectrum of a incident wave groups

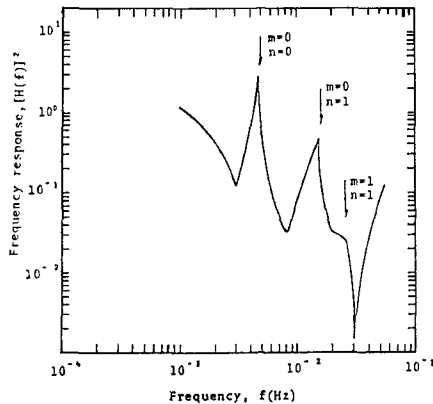


Fig. -12 Frequency response of mean sea level in a reef basin

Considering the linear wave phenomenon, the frequency response of mean sea level with long period is estimated by

$$S_{00}(f) = |H(f)|^2 S_{11}(f)$$

Figure-12 shows the frequency response $|H(f)|$. The frequency response has two clear resonant frequency corresponding to estimated ones by equation (2). As seen in this figure, the surf beat (that is to say, Bore-like surf beat) should be considered that it is resonantly excited by incoming wave groups.

6. conclusion

In a coral reef zone, resonant long period oscillations with the predominant natural frequency have been induced by incoming wave groups. The wave groups may resonantly excite Bore-like surf beat on the reef, and the severe disasters of coastal structures on the reef have always been induced by Bore-like surf beat. The simulation taking into account of the non-linear effect of the surf beat is good agreement with experimental one. A method for estimating the low frequency spectrum of incident waves is proposed. The frequency response of mean sea level with long period can be estimated by the method proposed in this study. And it indicates one of the resonant diagram for the long period fluctuation of mean sea level. The frequency response for a reef coast is identified. The periods for the first and/or second peak of the low frequency spectrum can be used in the estimation of occurrence of resonant response of mean sea-level in bays, harbor, and coasts with clear natural frequency.

References

- Goda, Y.: Random seas and design of maritime structures, University of Tokyo Press, p.323, 1985.
- Hino, M., et al. (1988a): A study on a bore-like surf beat induced by wave groupiness, Proc. 35th Japanese Conf. on Coastal Eng., pp.197-201. (in Japanese)
- Nakaza, E. and Hino, M. (1988b): Coastal disasters due to Bore-like surf beat on reef coasts, Proc. 35th Japanese Conf. on coastal Eng., pp.202-206. (in Japanese)
- Naksza, E., et al. (1988c): Wave force due to Tsunami-like surf beat, Proc. 35th Japanese Conf. on coastal Eng., pp.597-601. (in Japanese)
- Nakaza, E. and Hino, M. (1990): Reef-zone disaster caused by Bore-like surf beat. Coastal Eng. in Japan.
- Seelig, W. (1983): Laboratory study of reef-lagoon system hydraulics, J. waterway, Port, Coastal and Ocean Eng., ASCE, Vol.109, No.4, pp.380-391.
- Symonds, G. and Bowen (1984): Interaction of near shore bars with incoming wave groups, J. Geophysical Research, Vol.89, No.C2, pp.1953-1959.
- Takayama, T., et al.: Wave deformation on the reef coasts, Tech. Rep. of the Port and Harbor Res. Inst., No.278. (in Japanese)
- Tsukayama, et al. (1989): Wave deformation on reef corals, Proc. 36th Japanese conf. on coastal Eng., pp.70-74. (in Japanese)
- Tsukayama, S., et al. (1990): wave transformation due to the big roughness of coral reef on sea bottom, Proc. 45th Annual Conf. of the Japan Society of Civil Eng., 2, pp.756-757. (in Japanese)

CHAPTER 58

BRAGG REFLECTION OF WAVES BY ARTIFICIAL BARS

James T. Kirby¹, Jeffrey P. Anton²

Abstract

We consider the extension of previous theories for Bragg reflection of surface waves by parallel bars to the case of artificial bars placed discretely on the seabed. The case of non-resonant, weak reflection is considered first, followed by a consideration of the application of resonant interaction theory to the dominant Fourier mode of the bar field. Both theories are compared to numerical results, and discrepancies are seen in both cases. Finally, experimental results are compared to theory.

Introduction

The discovery that the Bragg reflection mechanism leads to strong reflection of incident surface waves by periodic bottom undulations has led to speculation that artificial bars could be constructed which would partially shelter shores or localized structures from wave attack. Possible bar configurations of this sort have been discussed previously by Mei et al. (1988) and Naciri and Mei (1988). The paper by Bailard et al. (1990) in this conference describes an effort which was made to install and test an artificial bar field offshore of a natural beach.

The purpose of the present study was to extend the scope of available theory and techniques which were available for predicting wave reflection from bars, in support of the proposed field study. Here, we discuss the application of analytic perturbation methods for both non-resonant and resonant cases. We also discuss numerical results, which point out limitations present in both analytic approaches. Finally, experimental results largely provide a qualitative verification but in turn show some limitation of the small amplitude bar theory.

Theory for Small Amplitude Bars

The theory which provides the framework for analysis here is given by an extended mild-slope equation derived by Kirby (1986).

We treat the water depth $h'(x, y)$ as the superposition of a mildly-sloping bottom $h(x, y)$ and a rapidly-varying but small-amplitude undulation $\delta(x, y)$:

$$h'(x, y) = h(x, y) - \delta(x, y) \quad (1)$$

¹Assoc. Prof., Center for Applied Coastal Research, Dept. of Civil Engrg., Univ. of Delaware, Newark, DE 19716

²Formerly, Grad. Stud., Coastal and Oceanographic Engineering Department, University of Florida, Gainesville, FL 32611

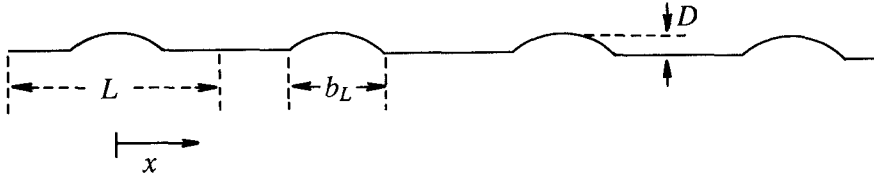


Figure 1: Bar field with four discrete bars.

Using $h(x, y)$ as the reference depth in the mild-slope sense, the model equation

$$\nabla_h \cdot (CC_g \nabla_h \phi) + k^2 CC_g \phi = \frac{g}{\cosh^2 kh} \nabla_h \cdot (\delta \nabla_h \phi) = 0 \tag{2}$$

is obtained, where ϕ is the value of the linear wave potential at the still water surface. The model coefficients are obtained from

$$\omega^2 = gk \tanh kh ; C = \frac{\omega}{k} ; C_g = \frac{\partial \omega}{\partial k} \tag{3}$$

and are determined by the value of $h(x, y)$ in all cases.

The Artificial Bar Field

In the absence of appropriate field data, we have restricted our attention here to the study of periodically spaced bars ($\delta = \delta(x)$) and an otherwise uniform depth $h = \text{constant}$. In principal, δ is arbitrary aside from the small amplitude restriction. In the present study, we have chosen a bottom consisting of rectified sine waves, given by

$$\delta(x) = \begin{cases} D \cos \frac{\pi}{b_L}(x - NL) ; & NL - \frac{b_L}{2} \leq x \leq NL + \frac{b_L}{2} \\ 0 & \text{otherwise} \end{cases} \tag{4}$$

$N = 0, \dots, N_b - 1$

where N_b is the number of bars, L is the periodic bar spacing, b_L is the footprint of the bar on the bottom, and D is the bar height. The rectified cosine form is chosen mainly for its convenience in later analysis. An example bar field is shown in Figure 1. The bar field is periodic over intervals of width L , and can be conveniently represented by the cosine series,

$$\delta(x) = \sum_{n=0}^{\infty} D_n \cos(n\lambda x) ; \lambda = \frac{2\pi}{L} \tag{5}$$

where

$$D_0 = \frac{D}{\pi} ; D_1 = -\frac{D}{2} ; D_n = D \frac{\cos\left(\frac{n\pi}{2}\right)}{\pi(1 - n^2)} (1 + \cos n\pi) \tag{6}$$

Non-resonant Reflection

For the case of h constant, the model equation (2) may be written as

$$\nabla_h^2 \phi + k^2 \phi = \alpha \nabla_h \cdot (\delta \nabla_h \phi) \quad (7)$$

where

$$\alpha = \frac{4k}{2kh + \sinh 2kh} \quad (8)$$

With $\delta(x)$ representing bars varying in the x -direction, we represent oblique waves according to

$$\phi(x, y) = \tilde{\phi}(x) e^{imy}; \quad m = k \sin \theta \quad (9)$$

and obtain

$$\begin{aligned} \tilde{\phi}_{xx} + \ell^2 \tilde{\phi} &= \alpha (\delta \tilde{\phi}_x)_x - m^2 \alpha \delta \tilde{\phi}, \\ \ell^2 &= k^2 - m^2 = k^2 \cos^2 \theta \end{aligned} \quad (10)$$

This equation has been obtained by Miles (1981) who used it to study reflection from a single isolated obstacle.

For $\delta(x)$ confined in a finite region of space, we may write

$$\begin{aligned} \tilde{\phi}(x \rightarrow \infty) &= T e^{i\ell x} \\ \tilde{\phi}(x \rightarrow -\infty) &= e^{i\ell x} + R e^{-i\ell x} \end{aligned} \quad (11)$$

where T and R are complex transmission and reflection coefficients. With δ small, we expand $\tilde{\phi}$, T and R as series in the small parameter $\epsilon = D/h$, and obtain

$$\phi_0 = e^{i\ell x} \quad R_0 = 0 \quad T_0 = 1 \quad (12)$$

at leading order. At second order, the reflection coefficient R_1 for an arbitrary topography $\delta(x)$ is

$$R_1 = -\frac{i\alpha}{2\ell} (\ell^2 - m^2) \int_{-\infty}^{\infty} \delta(x) e^{2i\ell x} dx \quad (13)$$

as found by Miles (1981). Note that R_1 is singular in the limit as $\theta \rightarrow \pi/2$. This effect has not been previously noted and its practical implications are unclear.

For the case of a simple sinusoidal bottom

$$\delta(x) = D \sin(\lambda x); \quad 0 \leq x \leq N_b L \quad (14)$$

we obtain the expression

$$|R| = \begin{cases} \frac{\alpha D}{2} \left(\frac{\ell^2 - m^2}{\ell^2} \right) \frac{2\ell/\lambda}{\frac{2\ell^2}{\lambda} - 1} \left| \sin \left(\frac{2\ell}{\lambda} \pi N_b \right) \right|; & \frac{2\ell}{\lambda} \neq 1 \\ \frac{\alpha D}{2} \left(\frac{\ell^2 - m^2}{\ell^2} \right) \frac{\pi N_b}{2}; & \frac{2\ell}{\lambda} = 1 \end{cases} \quad (15)$$

This result extends the non-resonant theory of Davies and Heathershaw (1984) to include obliquely incident waves.

For the periodic bar field described by (5) and (6), we substitute (5) in (13) and obtain the expression

$$R_1 = \frac{-i\alpha}{2} \left(\frac{\ell^2 - m^2}{\ell} \right) \sum_{n=0}^{\infty} D_n I_n, \quad (16)$$

where the integrals I_n are given by

$$I_n = \int_{-\frac{\ell}{2}}^{(N_b-1)L+\frac{\ell}{2}} \cos(n\lambda x) e^{2itx} dx. \quad (17)$$

As in the case of a single sinusoidal bar, the integral I_n takes on special values when $2\ell/n\lambda = 1$ for the corresponding value of n . We further simplify the notation by setting

$$\gamma = \frac{2\ell}{\lambda} \quad (18)$$

Then, for $\gamma \neq n$, we obtain the expression

$$I_n(\gamma) = \frac{\gamma^2}{\ell(\gamma^2 - n^2)} e^{i\ell N_b L} \sin \ell N_b L; \quad \gamma \neq n \quad (19)$$

For $n = \gamma$, we obtain the expression

$$I_n(\gamma = n) = \frac{N_b L}{2} \quad (20)$$

We thus obtain the general solution for obliquely incident waves

$$R_1 = -\frac{i\alpha}{2} \left(\frac{\ell^2 - m^2}{\ell^2} \right) \left\{ \sum_{n=0, \gamma \neq n}^{\infty} \frac{\gamma^2 D_n}{(\gamma^2 - n^2)} e^{i\ell N_b L} \sin \ell N_b L + D_n \delta(n - \gamma) \frac{\ell N_b L}{2} \right\} \quad (21)$$

where $\delta(n - \gamma)$ is the delta function, and there $n = \gamma$ can only occur for one wavenumber component for a fixed value of ℓ . For the case of normally incident waves (studied further below), we let $\ell \rightarrow k$, $m \rightarrow 0$ and obtain

$$R_1 = -\frac{i\alpha}{2} \left\{ \sum_{n=0}^{\infty} \frac{\gamma^2 D_n}{(\gamma^2 - n^2)} e^{ik N_b L} \sin k N_b L + D_n \delta(n - \gamma) \frac{k N_b L}{2} \right\} \quad (22)$$

From the form of the solution, it is apparent that each harmonic of the bar field contributes to the reflection process, with the dominant contribution of the n^{th} harmonic coming from the neighborhood $\lambda \approx n$. An example plot of reflection coefficient $|R_1|$ is shown in Figure 2 for a case of 4 bars with crest-to-crest spacing equal to the unrectified wavelength ($b_L = L/2$). Waves are normally incident on the bar field. The peak in $|R_1|$ at $2k/\lambda = 1$ corresponds to the usual Bragg interaction between the surface wave and the fundamental harmonic of the bar field, when the surface wave length is twice the bar spacing. A second prominent peak is located at $2k/\lambda = 2$, corresponding to a surface wavelength equal to twice the length of the second harmonic of the bar field (and thus equal in length to the bar spacing). This strong second peak is absent when the bar

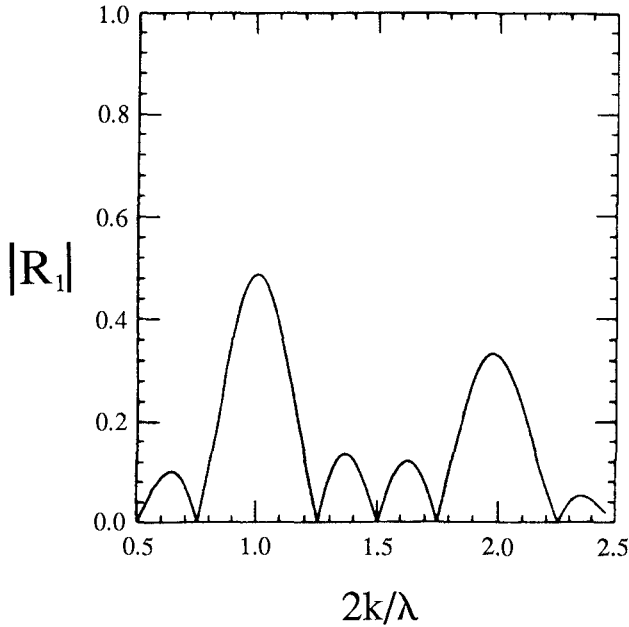


Figure 2: Reflection for four discretely placed bars. Non-resonant theory, equation (22).

field being considered is a simple sinusoid, as in Davies and Heathershaw (1984) and Mei (1985).

In general, the relative amplitude of the peaks in the reflection coefficient may be adjusted by changing the spacing of artificial bars, assuming the cross-section of each bar to stay the same. Pushing bars closer together makes the bar field more sinusoidal and reduces the importance of higher harmonics. Placing the bars further apart makes them into relatively more “solitary” features, and thus emphasizes the relative importance of higher harmonics. Two cases illustrating these extremes were investigated in the experiments described below.

Resonant Reflection

The reflection coefficient described in (21) is defective for the cases $2\ell \approx n\lambda$, where the coefficient can become arbitrarily large as $N_b \rightarrow \infty$. While this limit would never be reached in practice, the result shows that the theory is not strictly valid in the neighborhood of the resonances. The problem lies with assuming that R_1 is $O(1)$ in the perturbation series used above. Mei (1985) has developed a resonance theory which allows for $O(1)$ reflection in the neighborhood of each resonance. Mei et al. (1988) further suggested that, for the case of a bar field with multiple Fourier components, the reflection could be estimated using the resonance theory applied to the Fourier mode corresponding to the bar wavelength. This approach would not account for the occurrence of multiple strong peaks. In the present study, we define a neighborhood of each resonance $2\ell/\lambda = n$ to be the range $n - 1/2 \leq 2\ell/\lambda \leq n + 1/2$. Then, in each range, Mei's theory is used with $2\ell/\lambda^*$ replacing $2\ell/\lambda$, with $\lambda^* = n\lambda$. We refer the reader to Mei (1985) for the expressions defining the reflection coefficients. The only necessary modification to the theory account for oblique incidence and the presence of multiple resonant peaks. The frequency ω_n of the n^{th} resonant peak is given by

$$\omega_n^2 = \frac{gn\lambda}{2 \cos \theta} \tanh \left(\frac{n\lambda h}{2 \cos \theta} \right) \quad (23)$$

The cutoff condition Ω_0 defined by Mei is replaced by

$$\Omega_{0n} = \frac{\ell^2 - m^2}{\ell^2} \frac{\omega_n k D_n}{2 \sinh 2kh} ; \quad k = \frac{\ell}{\cos \theta} \quad (24)$$

where the D_n are the amplitudes of the bar Fourier coefficients, and there Ω_{0n} refers to the n^{th} resonant peak.

An example of the reflection calculated for the case of normal incidence is given in the following section, in comparison with numerical results and results of the non-resonant theory.

Numerical Solutions

In order to study the validity of each of the perturbation solutions, direct numerical solutions of equation (10) were also performed. For a bar field in the region $0 \leq x \leq N_b L$, an incident wave boundary is established at $x = A < 0$, and a downwave, transmitting boundary is established at $x = B > N_b L$. For an incident wave $\tilde{\phi}_I = e^{i\ell x}$, the appropriate boundary conditions are

$$\tilde{\phi}_x = \begin{cases} i\ell(2\tilde{\phi}_I - \tilde{\phi}) ; & x = A \\ i\ell\tilde{\phi} ; & x = B \end{cases} \quad (25)$$

Equations (10) and (25) are finite-differenced using central differences, leading to a tridiagonal system which is solved using the Thomas algorithm.

Figure 3 shows a sample of calculated reflection coefficients obtained with the numerical solution and the two analytic solutions, for the bar field described in Figure 2. As expected, the non-resonant solution over-predicts reflection at $2k/\lambda = 1$, in comparison with the resonant theory of Mei (1985). The discrepancy is relatively minor at the second peak $2k/\lambda = 2$, where the resonance is relatively weaker. In contrast to both analytic theories, the numerical results

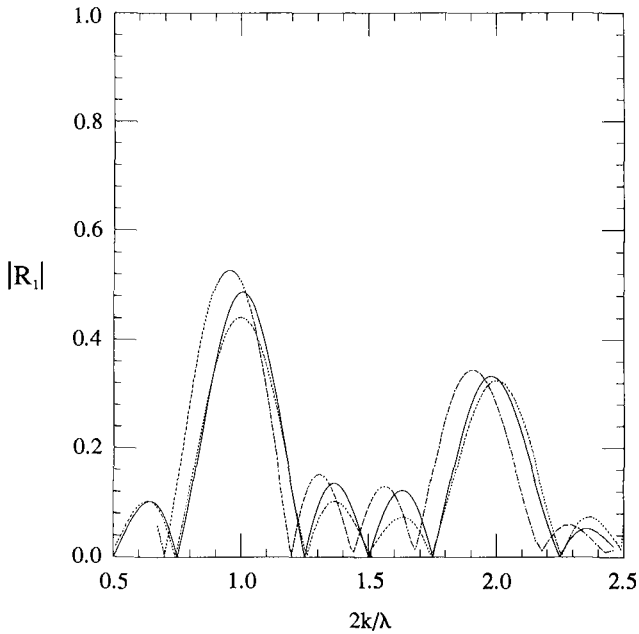


Figure 3: Comparison of non-resonant, resonant and numerical solutions for a bar field with $N_b = 4$. ———, non-resonant theory; - - -, resonant theory; - · -, numerical results.

show a strong downshift of the reflection peaks to lower values of $2k/\lambda$. This downshift is related to the simultaneous interaction between the wave field and several bottom modes; a similar effect occurs for the case of a sinusoidal bar field, but it is much more subtle. The numerical scheme also predicts a higher reflection coefficient at each peak. The large downshifts and higher peaks are largely validated by data described below. These results indicate that either of the two analytic solutions are at best qualitatively accurate when used to describe reflection from the type of bars that could be built in an actual construction project.

Experimental Results

Experiments were conducted in the 60 cm wide wave flume in the Coastal and Oceanographic Engineering Laboratory, University of Florida, in order to verify the basic aspects of the theory for normally incident waves. For the experiments, a water depth $h = 15$ cm was used. Bar height D was 5 cm, giving $D/h = 0.33$, which is relatively large and could contribute to some of the discrepancies between theory and data noted below. The bar footprint $b_L = 50$ cm. Two bar spacings, $L = 80$ cm and 120 cm, were tested, corresponding to cases with bar field higher harmonics of low importance and great importance,

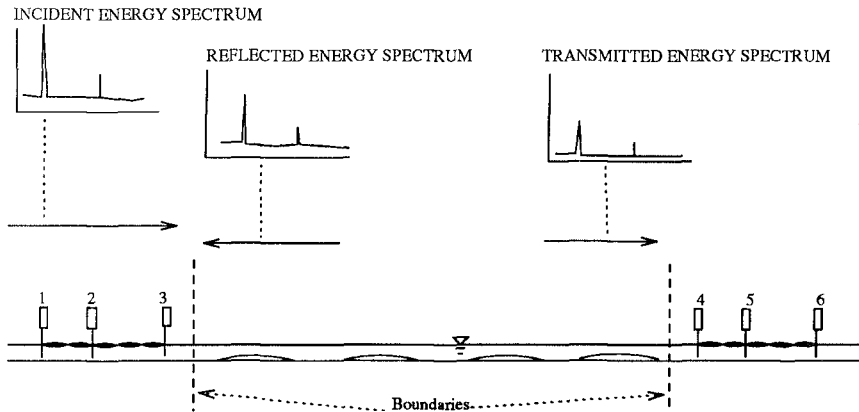


Figure 4: Bar field and wave gage placement

respectively. The bar fields tested contained four discrete bars.

In order to maintain a close correspondence between the assumed linearity of the wave theory and the experiments, incident waves on the order of 1 cm in height were generated. (Actual height varied with wave frequency, as would be expected from wavemaker theory.) Wave heights were measured using capacitance wave gages mounted with 6 cm-long wires, which were calibrated over their full length. Data was sampled using 12-bit digitization, giving a resolution of 0.012 mm/division. The wavefield was sampled at a $10Hz$ frequency, with experimental waves being generated in the range $0.4Hz \leq f \leq 1.6Hz$.

Due to the small wave heights being used, there was an additional source of noise in the data associated with mechanical vibration in the wavemaker and other high-frequency effects. In retrospect, it would be better to use slightly higher waves in future experiments unless great care were taken to isolate mechanical vibration. (For a particularly spectacular example of clean data in a related low-amplitude wave experiment, see Benjamin et al. (1989)).

The three-gage, least squares method developed by Funke and Mansard (1980) was used to separate incident and reflected waves. The gage layout relative to the bar field is shown in Figure 4. The incident-reflected separation was performed both upwave and downwave of the experimental bar field. The downwave separation indicated a reflection from the absorbing beach on the order of 5–6%. This reflected energy was neglected in subsequent processing and the downwave region was assumed to be perfectly transmitting.

Figure 5 shows the measured reflection coefficient for the case of $L = 80cm$, when bar field harmonics are relatively unimportant. Also included in the figure is the prediction of the numerical model described in the previous section. The data largely validates the theory, although there is a great deal of scatter. (It also appears that shifting the data to higher values of $2k/\lambda$ would bring the data into fairly close agreement with theory. No systematic error was ever detected in the experimental procedure which could account for such a shift, unfortunately.)

Figure 6 shows corresponding data for the case of $L = 120cm$, where the

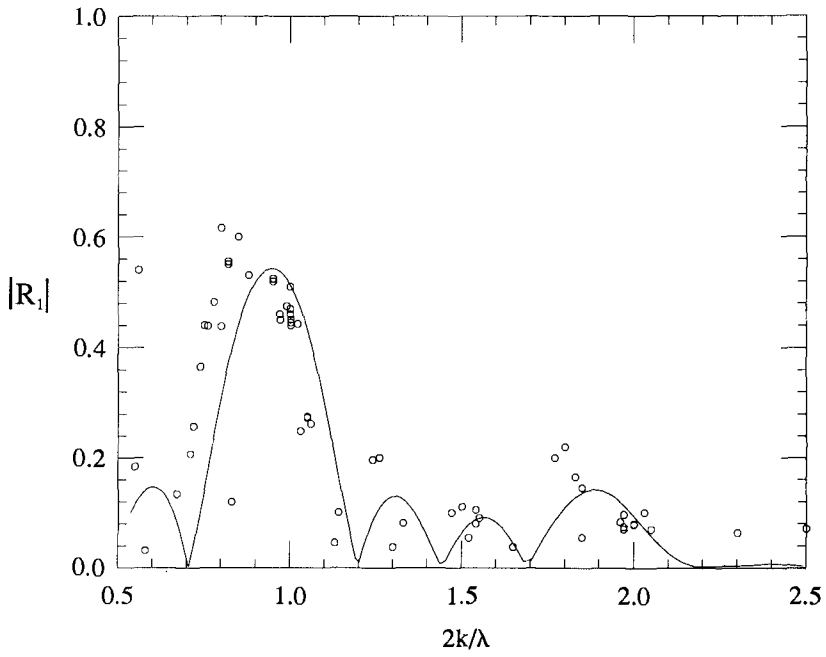


Figure 5: Experimentally measured reflection coefficient, $L = 80\text{cm}$.

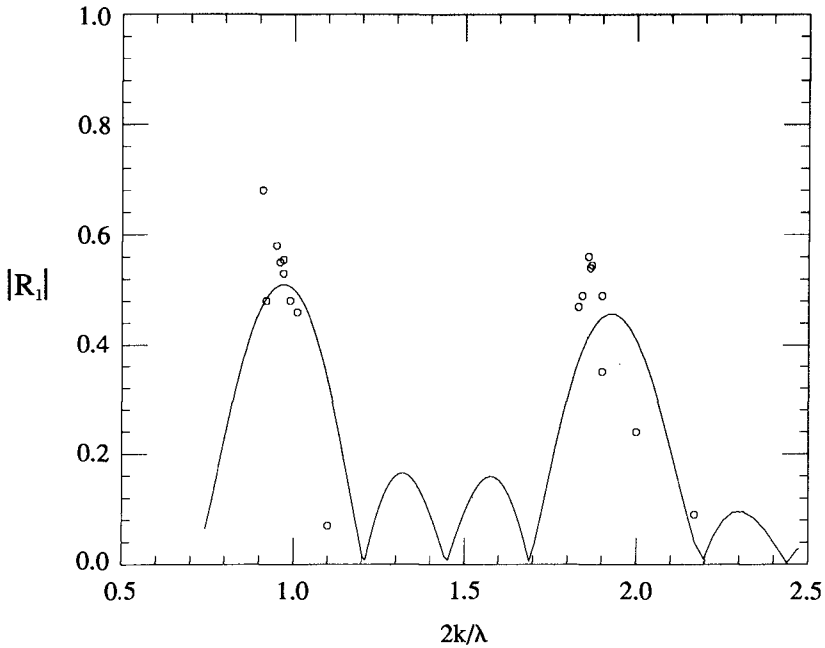


Figure 6: Experimentally measured reflection coefficient, $L = 120\text{cm}$.

second harmonic component of the bar field is comparable in height to the fundamental harmonic. Due to time constraints, the data here is relatively sparse, and tests were grouped in order to show the relative heights of the two reflection peaks. Both the presence and the relative importance of the two numerically-predicted peaks are substantiated by the data.

Response of a Closed-end Channel

One question that arises in response to the realization that bars can reflect significant amounts of incident energy is whether or not a region downwave of a bar field experiences a less severe wave condition than the region on the incident site. The answer to this question can be positive or negative, depending on the geometry of the downwave region and the reflectivity of the end boundary. For cases where reflection from the end wall is nearly complete, waves travelling back towards the bar field are partially re-reflected into the sheltered region. The possibility of resonating the sheltered region exists, as does the possibility of reducing the wave activity, and depends primarily on whether the sheltered region contains an integer multiple of one-half the surface wavelength.

Figure 7 shows the numerically predicted amplitude at a vertical wall situated four barfield wavelengths downwave of a bar field with four bars, as in the previous examples. The incident wave has an amplitude of unity, and so an amplitude of 2 represents simple reflection. The figure shows that the amplitude at the wall can reach as high as 3.6 and as low as 1, representing a range of

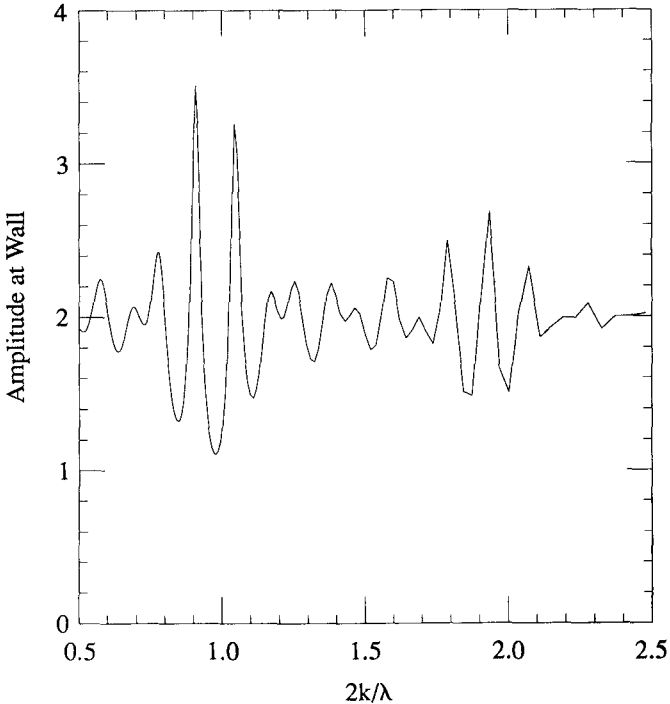


Figure 7: Wave Amplitude at End Wall of a Channel Sheltered by an Artificial Bar Field

resonance and sheltering conditions.

For the case where the channel end is primarily absorbing (due to wave breaking or frictional effects), the possibility of resonating the sheltered region is greatly reduced. This virtually guarantees that a bar field designed to shelter a beach from wind-wave band waves would not resonate the shoreline. However, as the wave frequency becomes low, even a mildly-sloped shoreline can become essentially reflective. It is thus possible that broad, low bars contribute significantly to amplifying long wave energy on the beach face. The long waves that could be amplified or resonated by this mechanism may be locally generated by nonlinear processes in the surfzone, or they may be arriving as part of the forced or free long wave climate incident from offshore. Problems of this sort need further investigation to determine the relative importance of bottom interaction in influencing the nearshore wave climate.

Acknowledgements

The work described in this paper was supported by the Office of Naval Research and the Naval Civil Engineering Laboratory through contracts N00014-86-K-0790 and N00014-89-J-1717. Both authors were affiliated with the Coastal and Oceanographic Engineering Department, University of Florida at the start of this study; use of the facilities there is greatly appreciated. Conversations with Jim Bailard, Bob Guza, and Dan Hanes were instrumental in the early stages of problem formulation.

References

- Baillard, J., DeVries, J., Kirby, J.T. and Guza, R.T., 1990, "Bragg reflection bars: A new shore protection concept?" *Proc. 21st Int'l. Conf. Coastal Engrg.*
- Benjamin, T.B., Boczar-Karakiewicz, B. and Pritchard, W.G., 1987, "Reflection of water waves in a channel with corrugated bed," *Journal of Fluid Mechanics*, 185, 249-274.
- Davies, A.G. and Heathershaw, A.D., 1984, "Surface-wave propagation over sinusoidally varying topography," *Journal of Fluid Mechanics*, 144, 419-433.
- Funke, E.R. and Mansard, E.P.D., 1980, "Measurement of incident and reflected spectra using a least squares approach," *Proc. 17th Int'l. Conf. Coastal Engrg.*, 1, 154-172.
- Kirby, J.T., 1986, "A general wave equation for waves over rippled beds," *Journal of Fluid Mechanics*, 162, 171-186.
- Mei, C.C., 1985, "Resonant reflection of surface water waves by periodic sand-bars," *Journal of Fluid Mechanics*, 152, 315-335.
- Mei, C.C., Hara, T. and Naciri, M., 1988, "Note on Bragg scattering of water waves by parallel bars on the seabed," *Journal of Fluid Mechanics*, 186, 147-162.
- Miles, J.W., 1981, "Oblique surface-wave diffraction by a cylindrical obstacle," *Dynamics of Atmospheres and Oceans*, 6, 121-123.
- Naciri, M. and Mei, C.C., 1988, "Bragg scattering of water waves by a doubly periodic seabed," *Journal of Fluid Mechanics*, 192, 51-74.

CHAPTER 59

GENERATION MECHANISM OF ABNORMAL WAVES ALONG THE JAPAN COAST

by
Tomoaki Komaguchi¹
Yoshito Tsuchiya² M.ASCE.
and
Naofumi Shiraishi³

Abstract

The conditions under which abnormal waves occur in the western part of the Japan Sea and the northwestern part of the Pacific Ocean are examined. A numerical study of the abnormal waves was performed for a selected monsoon condition in winter. The mechanism of abnormal wave development is clarified using a wave spectrum model. It was found from the directional spectra that the effect of wind duration plays a key role in abnormal wave generation. For typhoon conditions, the relation between a standard project typhoon and the abnormal waves induced, is considered and the simulation method of the typhoon model is improved by introducing the typhoon stagnation effect. Finally, it was shown that abnormal waves generated by typhoons are due to long typhoon stagnation.

1. Introduction

Recently, as urbanization develops around the coastal zone, more regard to safety against coastal disaster is required. It is essential to take the enormous disaster potential of the low probability of occurrence of storm surge, high waves, etc. into account when planning and designing coastal structures. Abnormal waves which are the primary cause of coastal disasters

¹ Civil Engineer, Hydraulic Laboratory, Nippon Tetrapod Co., Ltd., 2-7, Higashi-Nakanuki, Tsuchiura, Ibaraki Pref., 300 Japan

² Professor, Disaster Prevention Research Institute, Kyoto University, Goka-sho, Uji, Kyoto 611, Japan

³ Chairman, Nippon Tetrapod Co., Ltd., 2-7-1, Nishishinjuku, shinjuku-ku, Tokyo 163, Japan

along the Japan coast, are generated by monsoons in winter and typhoons in summer. They often cause severe damage to the coast, so prevention of coastal disaster by predicting the possibility of occurrence for waves of long return period, location of appearance, etc. is important. Unfortunately, even in this day and age, the mechanism of abnormal wave development is still not satisfactorily clear.

The major causes of abnormal wave generation are geographical features, such as sea bottom topography, and wind properties, such as wind duration. The effect of wind duration is of particular importance in developing waves. Figure 1 shows the location map of Japan and the representative typhoon courses. The Japan Sea, located between Japan and the Asiatic continent is almost enclosed by Sakhalin, Hokkaido, Korea and Kyushu. During winter, convection currents, the so-called monsoon, occur between the Asiatic continent and the Pacific Ocean and low pressures often take place. If low pressure stagnation occurs on the northern side of

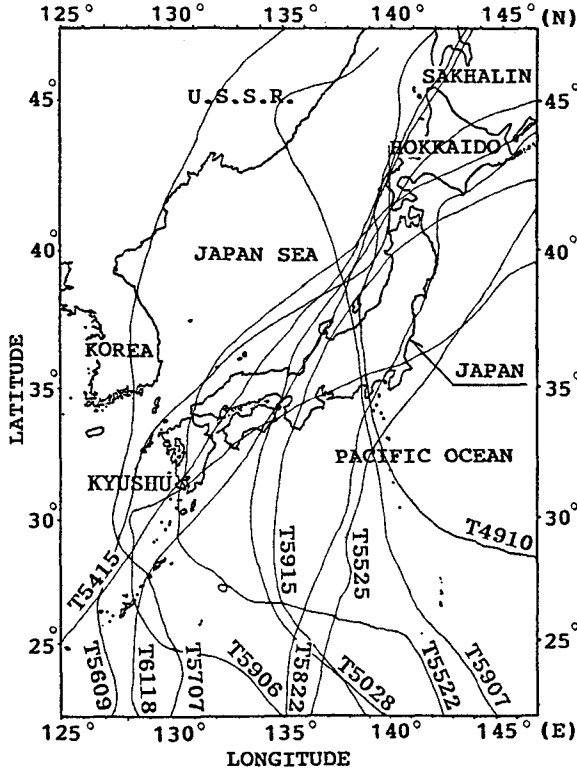


Figure 1. Location map of Japan and representative typhoon courses

Hokkaido, the typical meteorological condition of winter exists and waves develop to a great extent due to duration of the monsoon.

In a typhoon situation, on the other hand, high waves are also generated. These also cause damage. A typhoon is a very large air vortex and wind field, so it is considered that waves induced by typhoons yield duration-limited wave growth curves. In general, a typhoon first moves in low latitude from south to north or northwest, but a change of course to Japan mainland occurs. Stagnation of the typhoon occurs at this turning point. If a typhoon stagnates at low latitude, swell develops rapidly due to the long duration propagating from the wind fields to the coast. This can occur from distances even as great as 2000 km.

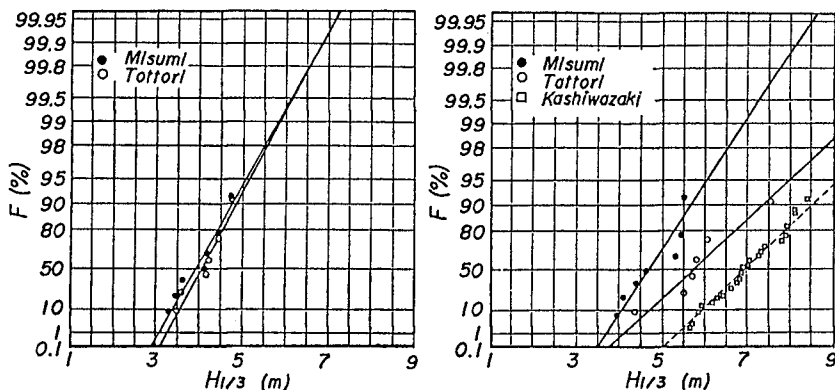
One of the ways to investigate the occurrence and conditions of abnormal waves is statistic approach using observed and hindcasted wave data (Yamaguchi et al., 1978) and wave prediction model studies for the greatest typhoon to date (Yamaguchi et al., 1986). In Japan, the typhoon model simulation is usually employed. This is an effective method for the investigation of abnormal waves induced by a typhoon. Nevertheless, it does not satisfactorily take the effect of typhoon stagnation into account, so the mechanism of abnormal waves of very long return periods is not made clear. As mentioned above, waves can develop great energy due to the long duration and it is considered that the wind field of a typhoon is a duration-limited condition. Therefore, abnormal waves induced by a typhoon can be predicted using an extension of typhoon model by introducing the typhoon stagnation effect.

In this paper, using the wave data observed at harbors on the western Japan Sea coast, extremal wave statistics are examined to consider the actual wave conditions induced by monsoons and typhoons in the Japan Sea. The mechanism of abnormal wave development was then clarified using a wave spectrum model. For typhoon conditions, a method for direct investigation of abnormal waves is considered and the typhoon model was improved by introducing the typhoon stagnation effect. Consequently, the statistic properties of duration of typhoons were examined. Furthermore, using the improved typhoon model, it is shown that if a typhoon stagnated at a low latitude and the duration is extremely long, waves would develop to a remarkable extent along the Japan coast.

2. Methodology

2.1 Wave conditions in the Japan Sea

First, we discuss the actual wave conditions for the occurrence of abnormal waves in the western part of the Japan Sea. Extremal statistics of wave heights observed at Misumi and Tottori harbors on the Japan Sea coast were obtained. These are shown in Figure 2. It is confirmed that the waves induced by monsoons are indeed larger than those from typhoons, at both locations.



(1) Typhoon (induced waves) (2) Monsoon (induced waves)

Figure 2. Applicability of Gumbel distribution to extremal wave statistics. Locations of each harbor are indicated in Figure 3.

As already mentioned, the Japan Sea is almost closed, so that it is considered that waves induced by monsoons follow the fetch-limited wave growth curves. Monsoon wind speeds are generally lower than those of typhoons. Even so, in the winter monsoon condition, the wind direction is nearly constant and the duration is very long, so waves receive great energy from them. If a monsoon wind changes its direction, waves turn into large swell and wind waves rapidly develop in the new direction. These waves interfere with each other. It can be assumed herein that abnormal waves induced by monsoon may be generated as a result of a combination of energy from swell that develop due to long duration and wind waves. Using a wave model, the mechanism of this process is confirmed for a selected monsoon condition.

2.2 Wave model

The model used for the numerical experiments is the wave spectral model proposed by Yamaguchi and Tsuchiya (1979). It is a so-called Second Generation (SWAMP, 1985) spectral wave model based on the two-dimensional properties of ocean waves. The total energy is evaluated by integrating the energy balance equation (Hasselmann, 1968)

$$\frac{\partial E(f, \theta, \mathbf{X}, t)}{\partial t} + \nabla \cdot (E(f, \theta, \mathbf{X}, t) \cdot \mathbf{C}_g) = S(f, \theta, \mathbf{X}, t) \quad (1)$$

where E is the two-dimensional energy density spectrum for frequency f and direction θ at x , y , and t , and \mathbf{C}_g is the group velocity derived from linear theory. The source function S is represented for the three stages of the sea state, i.e. the growing, decaying and opposing wind states.

In the growing stage, the generation term is composed of a linear (Phillips, 1957) and exponential growth (Miles, 1957), such as $A + B \cdot E$. In the model, the term A represents Phillips' external turbulent pressure forcing and the term $B \cdot E$ corresponds to the Miles' linear feedback mechanism. The numerical values of A and B are calculated using two formulae proposed by Inoue (1967). The fully developed JONSWAP spectrum is assumed and the energy-subtracting term is introduced according to the hypothesis that a fully developed sea state exists in equilibrium. Using the modified parameter as written down by Barnett (1968), the resonant nonlinear wave-wave interaction effects are also incorporated. In the second decaying stage, dissipation due to the nonlinear effect is assumed to play a part. For opposing winds conditions, adding the second stage, it is assumed that the winds produce the reverse effect to Miles' exponential growth.

2.3 Hindcast results

Numerical studies on the mechanism of wave development and propagation for a selected monsoon condition experienced in 1989 were conducted. High waves were observed along the Western Japan Sea coast on that occasion. Figure 3 shows the computational domain of the study. The domain covers the total Japan Sea area. Points A, B, C and D indicate the locations of Misumi, Tottori, Kyogamisaki and Kashiwazaki. Estimated significant wave heights and periods are compared with those measured at these points. Figure 4 shows comparisons of measured and estimated values at point C. As shown in this figure, it is concluded that the wave characteristics can be predicted satisfactorily by this wave model.

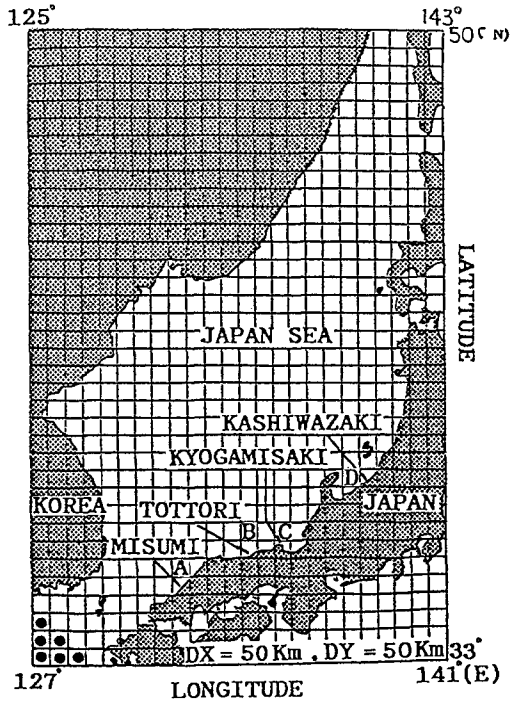


Figure 3. Computational domain for monsoon condition

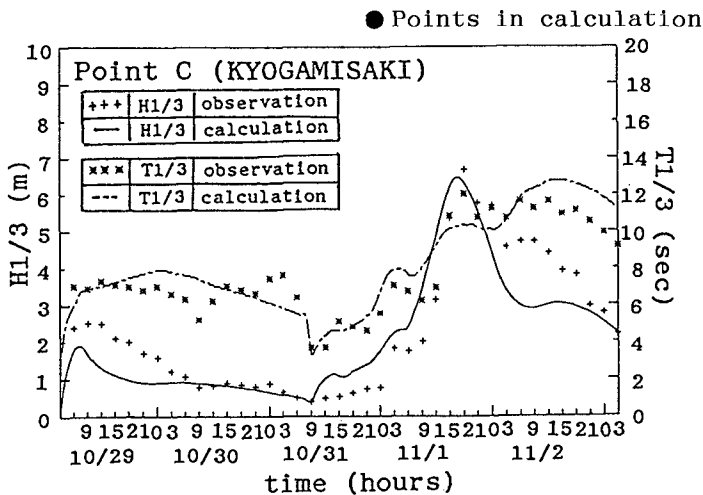


Figure 4. Comparisons between estimated significant wave heights and periods and those measured at point C(KYOGAMISAKI)

The Custer diagrams shown in Figures 5(a) and (b) show wave fields using the calculated wind fields. The unit arrows in each figure indicate the wind direction and mean wave direction. As can be seen in the figures, the wind first blew from SW in the same direction. When the wind field changed its direction from SW to NE because of the low pressure movement, waves develop sufficiently from the NE direction due to the long duration and long fetch. Furthermore, after the low pressure passed through the Japan Sea, it became the typical monsoon condition of winter and the wind blew strongly from the NW or N direction. The influence of this wind caused waves to change into large swell and wind waves developed from the NW direction. The net results of this process is that the waves change their directions from NE to NW and came to the Western Japan Sea coast.

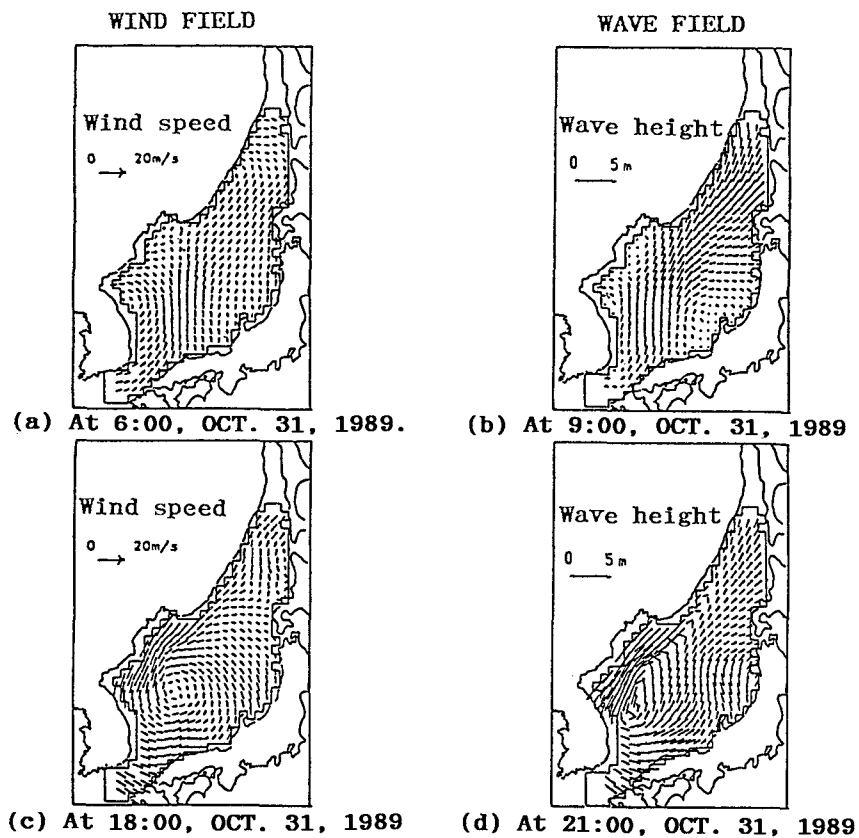


Figure 5(a). Changes in wind and wave field calculated
 (see also Figure 5(b))

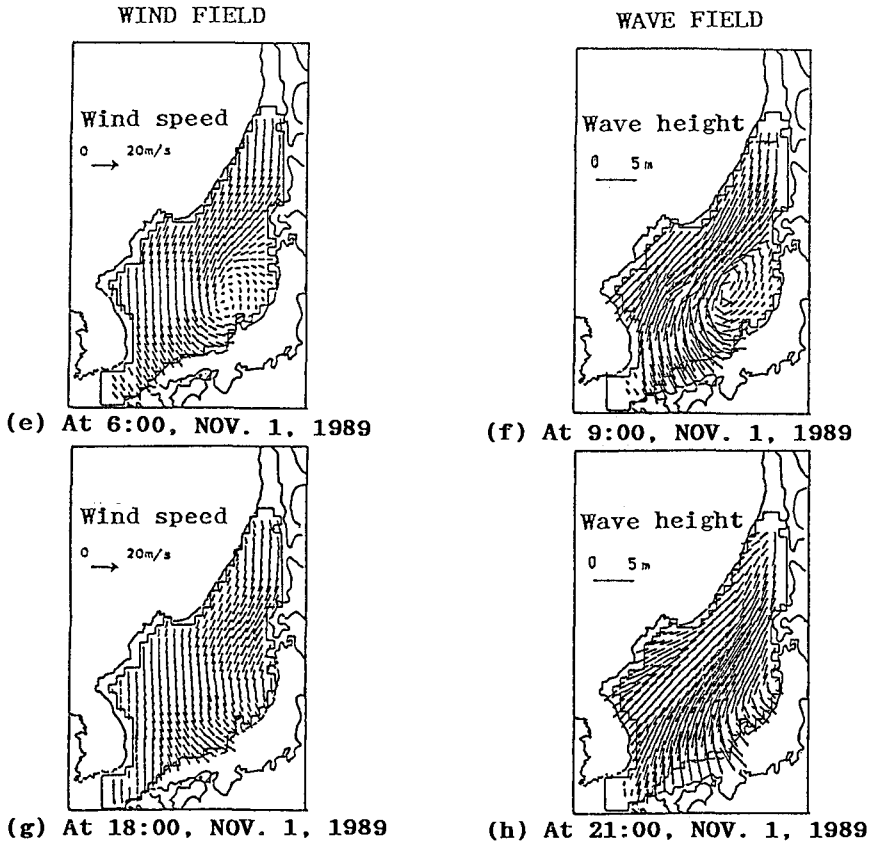
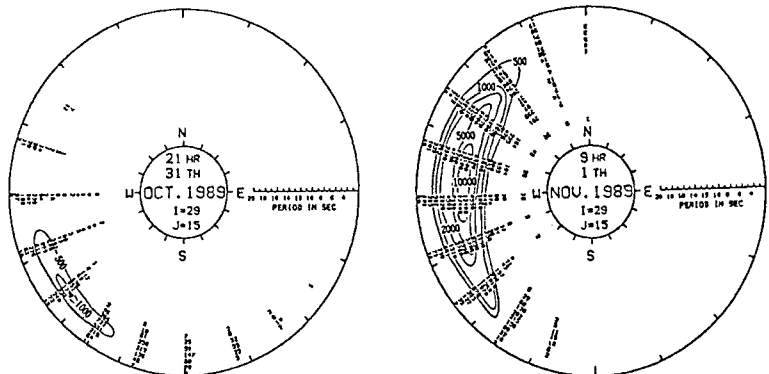


Figure 5(b). Changes in wind and wave fields calculated

2.4 Discussion

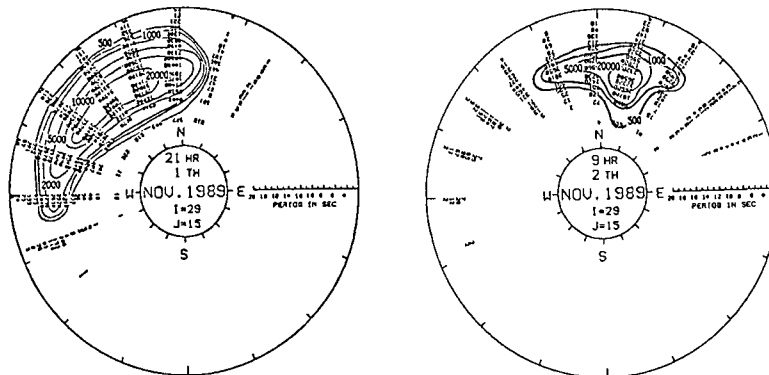
Figure 6 shows the changes of distributions of directional spectra at Point C. The top and bottom of the circle indicate the North and South direction and right and left side correspond to East and West. The energy densities of all wave components are distributed inside the circle. The center area of each circle indicates the components of swell and the area of near circumference also indicates wind waves. As can be seen, at first the energies of wind waves developed from the SW direction, but their energies are of low level. However, after the waves accumulated a lot of energies from the NW direction, swell developed rapidly and their energies increased dramatically due to the monsoon duration. It can be concluded for the Western Japan Sea that abnormal waves are generated as a result

of a combination of energy from swell that develop due to the long duration of monsoons and wind waves. Thus, we emphasize here that wind duration is an important factor in abnormal wave development.



(a) At 21:00, OCT. 31.

(b) At 9:00, NOV. 1.



(c) At 21:00, NOV. 1.

(d) At 9:00, NOV. 2.

Figure 6. Directional spectra calculated by selected monsoon condition.

From the monsoon results, it is clear that wind duration plays a key role in abnormal wave generation, so a method to investigate abnormal waves directly using typhoon model simulation was considered. Usually, as a wind field of a typhoon is quite large, waves induced by typhoons yield the duration-limited wave growth curves. If a typhoon stagnates at low latitude for a very long time and the wind duration increases to an extreme, waves can develop their energies rapidly. Therefore, the generation of abnormal waves from a typhoon can be predicted by a numerical model if the typhoon duration is very long and the intensity and magnitude of the typhoon just before and after landing is taken into consideration.

Figure 7 shows correlation between T_d and P_c , where T_d is the wind duration when the eye of the typhoon passes from $25^\circ N$ to $29^\circ N$ in latitude and P_c is the central atmospheric pressure depth. The figure indicates that T_d and P_c are independent of each other.

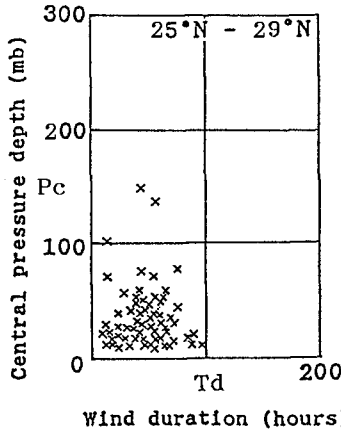


Figure 7. Correlation between central pressure depth P_c and duration of typhoon T_d .

The extremal statistics of annual maximum T_d are shown in Figure 8. The solid line is a regression analysis line obtained from the Gumbel distribution. The correlation coefficient between the solid line and T_d is 0.969, so that applicability of the Gumbel distribution to extremal statistics of annual maximum T_d is very good. It is concluded from these results that we must treat the duration of typhoon as a statistic parameter.

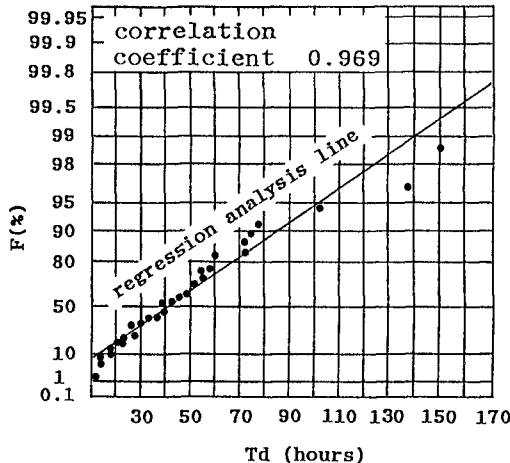


Figure 8. Extremal statistics of annual maximum duration of typhoons.

3. Simulation and Results

3.1 Improved typhoon model

In this paper, it is considered that the way to investigate abnormal waves directly is to use a typhoon which has a low probability of occurrence. As a first step, the relation between a Standard Project Typhoon (Mitsuta, 1965, Fujii and Mitsuta, 1986) and the abnormal waves induced is considered and it is concluded that the abnormal waves induced by the typhoon are predicted by a typhoon model. The statistic properties of duration of typhoon are investigated. From these results, the simulation metho of the typhoon model was improved upon by introducing the typhoon stagnation effect (Tsuchiya and Komaguchi, 1987).

Table 1 shows the return period of typhoon duration in the region of low latitude. According to the table, the extended duration of a 50 year return period is around 120 hours.

Table 1. Return period of typhoon duration in the region of low latitude.

Return period T_m (year)	Extended duration T_d (hours)
10	82.84
20	99.30
30	108.76
50	120.58
100	136.52
150	145.81
200	152.40
300	161.67
500	173.34

As already mentioned, in Japan, wave hindcast model studies are usually conducted for the greatest typhoon, such as in the case of the Isewan typhoon. The duration time of the typhoon is only 15 hours. Using the improved typhoon model, it is shown that the situation for abnormal waves can be predicted under the condition of an extremely long duration.

3.2 Results

The domain of computation for the typhoon model is shown in Figure 9. The duration time of typhoon 8218 is actually 36 hours. The conditions for calculation are $DX = DY = 50$ km and $DT = 30$ minutes. As initial and boundary wave conditions, the parametric model of Ross(1976) is used and the directional spectrum assumed to be a JONSWAP spectrum with a cosine square angular spreading.

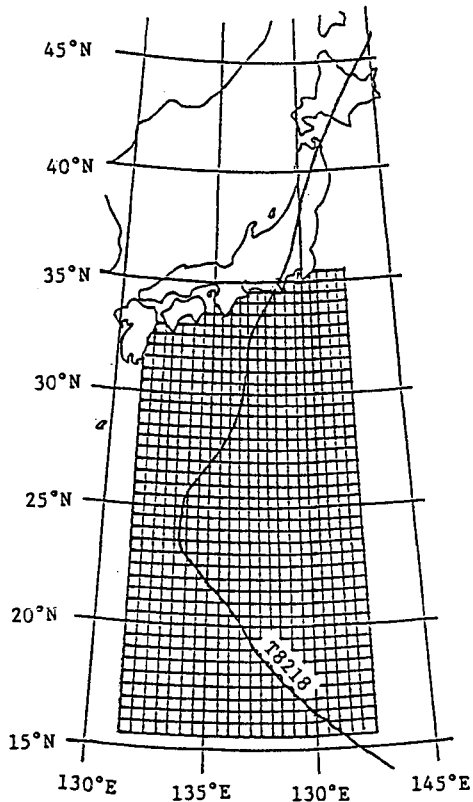
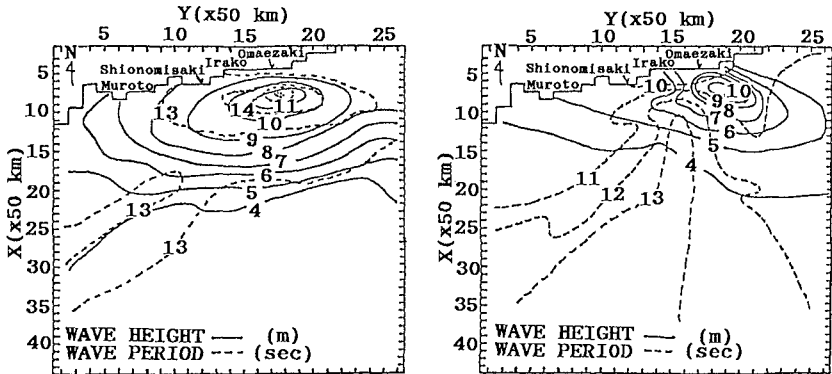


Figure 9. Domain of computation for typhoon model

Figure 10 shows a comparison of the distribution of the wave fields made in a case (a) where an extreme duration of a 500 year return period of T_d was taken and compared with a case (b) where typhoon stagnation was not considered. The figures indicate that when a typhoon stagnates at low latitude and the wind duration is extremely long, waves will develop to a remarkable extent along the Northwestern Pacific Ocean coast.



(a) Typhoon stagnation occurred. (b) Typhoon stagnation did not occur.

Figure 10. Comparison of the distribution of the wave field along the Northwestern Pacific Ocean coast.

4. Conclusions

The major conclusions of the study are as follows:

- (1) It was considered in the Western Japan Sea that waves induced by monsoons have a possibility of obtaining energies larger than those from typhoons. From the directional spectra, it was clarified that abnormal waves are generated as a result of a combination of energy from swell that develop due to the long duration of the monsoon and wind waves.
- (2) By consideration of the relation between the standard project typhoon and abnormal waves induced by the typhoon, the typhoon model was improved by introducing typhoon stagnation.
- (3) The statistic properties of typhoon duration were examined. It was concluded from the results that the duration of a typhoon must be introduced as a statistic parameter.
- (4) The results of numerical simulation using an improved typhoon model showed that if typhoon stagnation occurred and the duration was extremely long, waves would develop to a remarkable extent along the Japan coast.

Acknowledgement

We would like to express our sincere thanks to Professor Yasushi Mitsuta, D.P.R.I., Kyoto University, for his useful comments on typhoon properties.

References

Barnett, T. P. : On the generation, dissipation, and prediction of ocean wind waves., J.Geophys. Res., 73, 513-529, 1968

Fujii, T., and Y. Mitsuta (1986): Synthesis of a stochastic typhoon model and simulation of typhoon winds. *Annals, Disas. Prev. Res. Inst., Kyoto Univ., No.29 B-1*, pp. 229-239. (in Japanese)

Hasselmann, K.: "Weak-interaction theory of ocean waves". *Basic Development in Fluid Dynamics, 2*, 117-182, Academic Press Inc., New York, 1968

Inoue, T. : On the generation of the spectrum of a wind generated sea according to a modified Miles-Phillips mechanism and its application to wave forecasting., *Dept. of Meteorol. and Oceanogr., New York Univ. TR-67-5, 74p.*, 1967

Miles, J. W. : On the generation of surface waves by shear flows. *J. F. M., 3*, 185-204, 1957

Mitsuta, Y.(1965): Standard Project Typhoon (1). *Annals, Disas. Prev. Res. Inst., Kyoto Univ., No. 8*, pp. 605-612. (in Japanese)

Phillips, O. M. : On the generation of waves by turbulent wind. *J. F. M., 2*, 417-445, 1957

Ross, D. B. : A simplified model for forecasting hurricane generated waves (abstract)., Presented at Conference on Atmospheric and Ocean Waves, Seattle, *Bull. American Meteorological Society, 113.*, 1976

The SWAMP Group : The sea wave modeling project, part 1.; Principal results and conclusions., *Proc. Symp. on Wave Dynamics and Radio Probing of Ocean Surface, Miami, 1981*, in *Ocean Wave Modeling*, Plenum Press, 3-153

Tsuchiya, Y., and T. Komaguchi (1987): The huge wave prediction by numerical model of ocean waves. *Annals, Disas. Prev. Res. Inst., Kyoto Univ., No. 30 B-2*, pp. 663-693. (in Japanese)

Yamaguchi, M., Y. Tsuchiya, and T. Shibano (1978): A Consideration of Wave Extreme Statistics. *Proc. 25th Japanese Conf. Coastal Eng., JSCE*, pp. 70-74. (in Japanese)

Yamaguchi, M., Y. Tsuchiya, H. Koyata and T. Watanabe (1979): Numerical Prediction of Wind Waves in Limited Fetch. *Proc. 26th Japanese Conf. Coastal Eng., JSCE.*, pp.99-100. (in Japanese)

Yamaguchi, M., Y. Hatada, K. Kobuchi, and M. Hino (1987): Estimation of alongshore distribution of typhoon-generated maximum wave height around the Japanese coast based on wave hindcasting. *Proc. JSCE., Vol. 381 II-7, JSCE*, pp. 131-140. (in Japanese)

CHAPTER 60

FIELD MEASUREMENTS AND ANALYSIS OF WAVE INDUCED NEARSHORE CURRENTS

H. D. NIEMEYER

Coastal Research Station/NLWA-Forschungsstelle Küste
Norderney/East Frisia, Federal Republic of Germany

ABSTRACT

Two data sets of field measurements of wave-induced nearshore currents are analyzed and discussed with respect to cross-shore transport phenomena and the effectiveness of beach groynes. The results are discussed in order to improve future artificial beach nourishments.

1. BACKGROUND AND SETUP OF INVESTIGATIONS

Subject of this contribution are the results of field measurements carried out on beaches of the East Frisian island of Norderney at the southern North Sea coast (FIG. 1). These investigations are part of a research programme for the optimization of future beach nourishments in the framework of interactions between hydrodynamics and existing solid structures.

In the past the East Frisian barrier islands were enforced to migrate their shape due to migra-

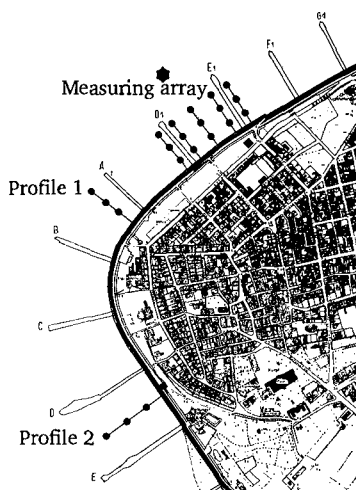
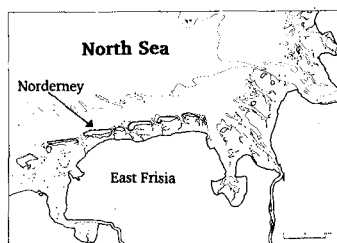


Fig. 1: Island of Norderney in the southern North Sea with measuring array and profiles

tion of tidal inlets creating a new ebb delta geometry with a furthermore updrift overlap of the ebb delta along the downdrift inlet shoreline. The sediment transport due to the eastward directed littoral drift bypasses the inlet in the form of large, migrating swash bars via the ebb delta and leads finally to a welding process of swash bars and island shore. Downdrift of their landfall the beaches suffer therefore from insufficient sediment supply causing erosion. For almost the last two centuries the morphological development of the western part of the island of Norderney was particularly governed by these processes (LUCK 1977). In order to stop further shoreline retreat solid structures have been erected since the middle of the last century. In spite of the construction of groynes, revetments and seawalls the problems remained unsolved till the introduction of repeatedly executed artificial beach nourishments as a successful tool of coastal protection which each remedied the grievance for a certain period of time (KRAMER 1960).

Though artificial beach nourishments have appeared as a rather successful tool to counterbalance the effects of continuous beach erosion, the demand for further improvements has been steadily present and has recently been more and more growing with respect to the effects of an expected acceleration of sea-level rise. Therefore in 1988 an intensive monitoring programme was started including hydrodynamical field measurements, beach and foreshore survey and sediment sampling.

Waves and currents are measured in one array with 16 and in 2 profiles with 3 measuring stations. Each station is equipped with both a pressure gage and an electromagnetic current meter, whose sensor heads are fixed closely to the bottom in order to measure velocities and directions of the currents there. First results gained from data in the measuring array (FIG. 2) are presented here. Special emphasis is laid on cross-shore transport phenomena and effectiveness of groynes. Due to limited space the discussion is focused on two data sets being representative of storm surge conditions and of swell occurring at ordinary tide water levels. In order to get a better in-

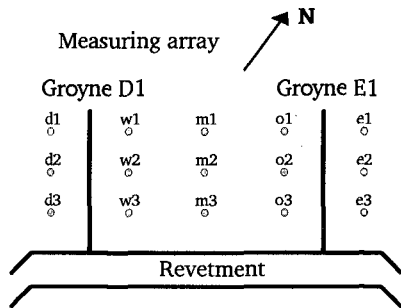
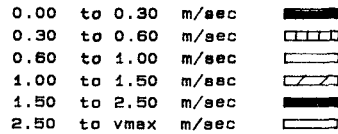


Fig. 2: Marks of measuring points in the measuring array and velocity ranges of the current roses

sight into the complex structure of the near-bottom currents on the beach the following analysis procedures were applied for this study:

- Any with a sampling rate of 11,78 Hz measured vector for a time series of twenty minutes are distinguished for sectors of $22,5^\circ$ and five classes of velocity ranges and plotted as current roses (FIG. 5, 6, 14). Additionally resulting current roses are gained by the addition of any counterdirectional components of the original rose (FIG. 7).
- The total amount of spectral energy is summarized for sectors of 5° and plotted as directional spectra (FIG. 8, 10-12).

2. HYDRODYNAMICAL BOUNDARY CONDITIONS

The mean tidal range in the area of Norderney is about 2.4 m with variations of ± 0.7 m due to spring and neap. The tide is lunar semidiurnal with a mean period of 12 h 25'. Until now the highest measured storm surge set-up was some 3 m above MHWL. The averaged yearly exceedence frequencies of storm surge peaks above MHWL due to German standard classification are 10 for 0,93 m; 0,5 for 1,95 m and 0,05 for 2,86 m (NIEMEYER 1987a). Tidal currents are rather weak on the beaches with mean velocities of about 10 cm/s and a range of maximum velocities of 2,5 to 29,8 cm/s for flood and 5,1 to 39,5 cm/s for ebb tide with respect to 21 continuously measured tides (NIEMEYER 1987b).

High energy wave conditions occur for winds from west to northeast generating landward traveling waves in the southern North Sea. On the island's shoreface on the average the sector of wave directions is reduced from 135° to 85° for mean conditions due to refraction. The predominantly western and northwestern directions of wind and swell create a system of longshore currents with north-eastern direction on the northwestern beach and south-eastward in the vicinity of the main channel of the tidal inlet (NIEMEYER 1986). The ebb delta overlaps in longshore direction the island's shoreface seaward of the beaches which have to be nourished from time to time and are now subject of this investigation. Waves propagating onshore from sea into this area have to pass the ebb delta with its shoals forcing higher waves to break. The energy dissipation due to that process effects not only a reduction of wave heights and a transformation of periods, lengths and steepness but also as well an energy shifting to higher frequencies as a decay of energy concentration leading to multi-peak spectra (NIEMEYER 1987c).

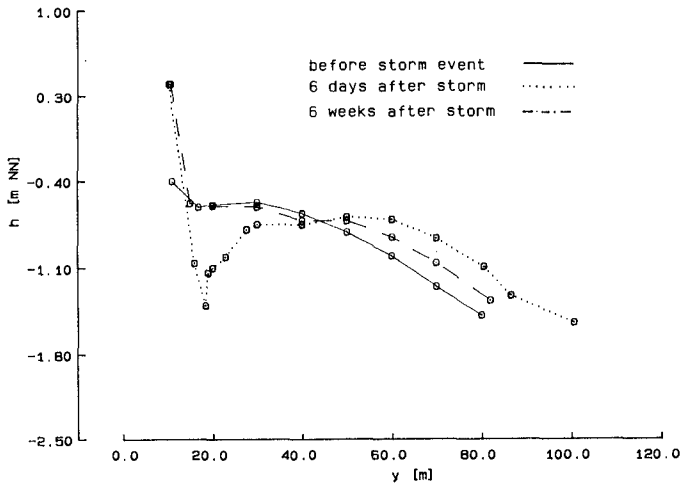


Fig. 3: Beach erosion due to storm surges and aftermath recovery

3. WAVE-INDUCED CURRENTS AND CROSS SHORE TRANSPORT PHENOMENA

3.1 Recovery of erosion profiles

The typical seasonal shift of beach profiles due to changing wave conditions is a well known as the phenonema of summer and winter profiles (BASCOM 1954). After the occurrence of numbers of severe storm surges HOMEIER (1976) investigated the behaviour of beaches on the East Frisian islands including those in the suppletion area of Norderney. The most important result was that even a recovery of those beaches takes place which suffer from continuous erosion. The beach erosion due to storm surges was balanced by an accumulation of material on the shoreface which moves slightly back shoreward within a few weeks. After that period the rate of erosion has decreased to mid-term tendency. A typical example of storm surge erosion and following recovery for a beach profile in the investigation area is shown in FIGURE 3. One major subject of this study is to get to know the governing hydrodynamical processes of this phenonema in order to make eventually use with respect to the design of future beach nourishments.

3.2 Analysis of Storm Surge Current Measurements

Storm surges are usually accompanied by high energy waves. For these conditions there is a broad surf zone on the



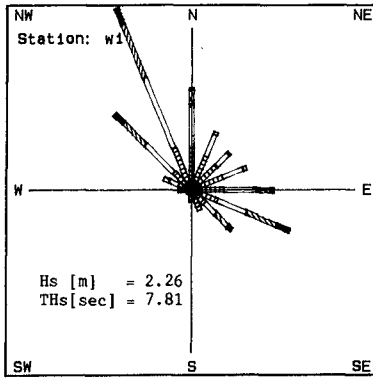
Fig. 4: Broad surf zone with white rollers during a storm surge

beaches of the investigation area characterized by subsequently following white rollers (FIG. 4). The energy dissipation of the waves establishes a complicated secondary system superimposing the incident waves. In this study data of a storm surge at high tide with a set-up of approximately 1,5 m above MHWL are taken. Wind direction was 290° with speeds between 15 and 16 m/s within the last three hours before. Significant wave heights ranged from 1,96 m (station m3; waterdepth $h = 2,6$ m) close to the revetment to 2,21 m (m1; $h = 3,3$ m) in the most seaward row of the measuring array (FIG. 5 + 6).

The current roses for the most seaward (FIG. 5) and for the most shoreward measuring row (FIG. 6) show a shoreward increasing overbalance of seaward directed components. This effect becomes more apparent, if resulting current roses are used. The example of the inner line of the array (FIG. 7) shows evidently that at least there are only resulting components in updrift longshore and especially in offshore direction with a reasonable part of high velocities. The same results are gained if data analysis is carried out with directional spectra (FIG. 8).

This data seem to be a reasonable hydrodynamical explanation for the high erosion rates and especially the shoreward increase of seaward directed currents explains sufficiently the scouring in front of revetments due to storm surges. The deposition of eroded material on the shoreface is possible as the overbalance and intensity of offshore directed currents decreases with distance from the shore.

Date : 24-dec-88
Record : 11:34 - 11:54
100 Promille



Date : 24-dec-88
Record : 11:34 - 11:54
100 Promille

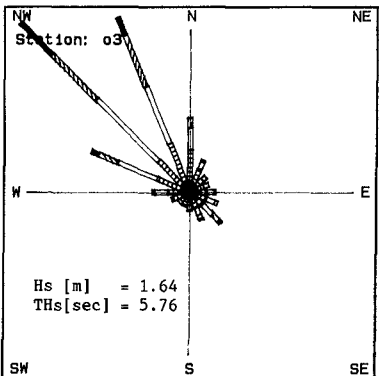
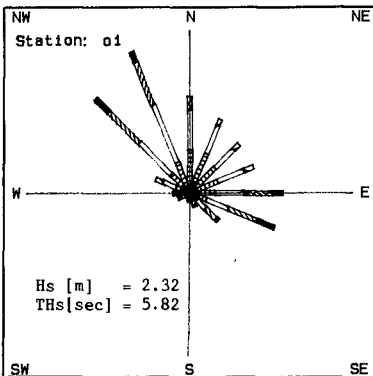
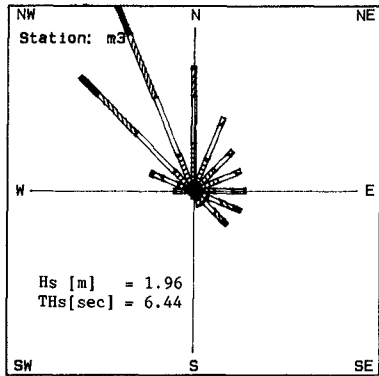
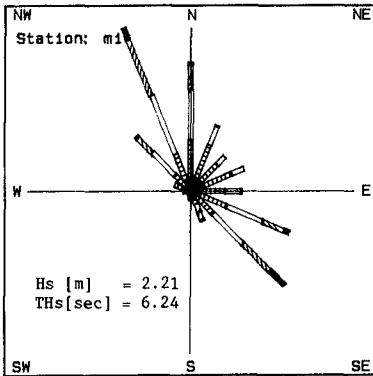
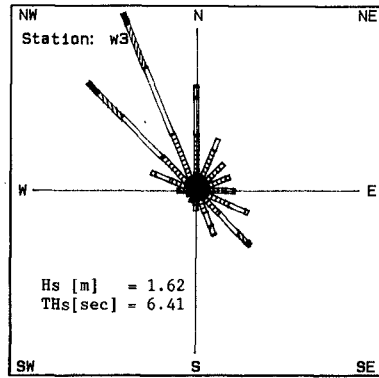


Abb. 5: Current rose of the measuring points w1, m1, o1 (storm surge)

Abb. 6: Current rose of the measuring points w3, m3, o3 (storm surge)

Date : 24-dec-88
 Record : 11:34 - 11:54
 100 Premille

Date : 24-dec-88
 Record : 11:34 - 11:54
 70 m² s⁻²

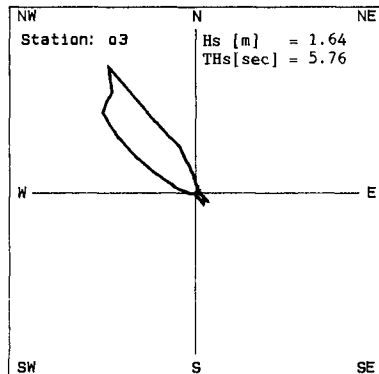
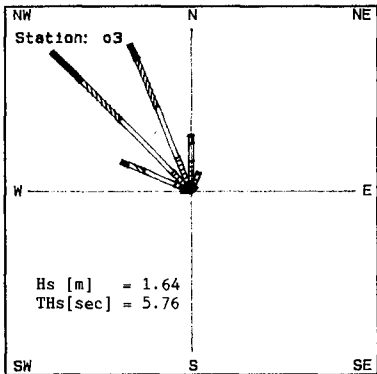
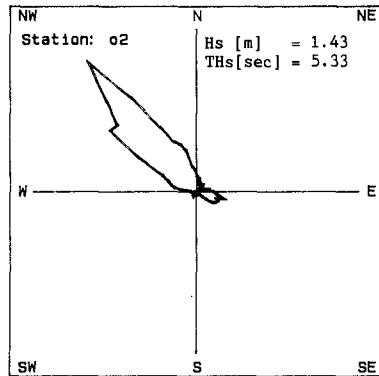
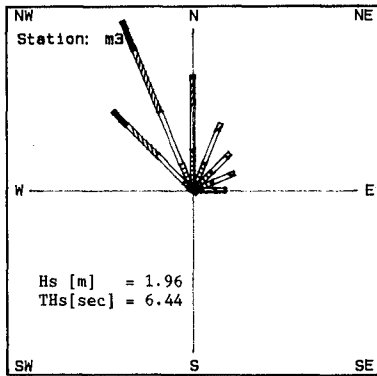
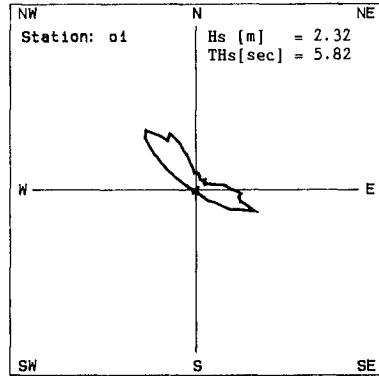
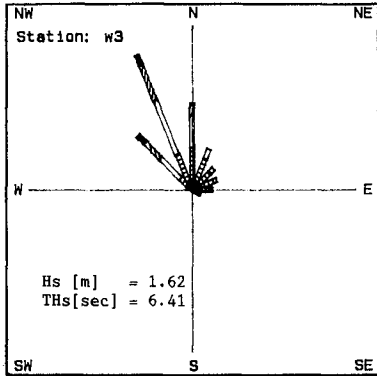


Abb. 7: Resulting current rose of the measuring stations w3, m3, o3 (storm surge)

Abb. 8: Directional current spectra of the measuring stations o1, o2, o3 (storm surge)

The overbalance of seaward directed currents is expected to be an undertow effect (SVENDSEN 1984; STIVE & WIND 1986) due to breaking waves which occur -as explained before- across the whole breadth of the beach as white rollers. Their onshore directed mass flux must be compensated by a "relatively strong seaward flow below trough level" (BATTJES 1988). The high turbulence in the surf zone creates high suspension rates so that the transport capacity of the undertow does not only base on bed load. This might be a further explanation for the short term erosion created by storm surges.

3.3 Wave Induced Currents for Swell Conditions

Contradictory to storm surges with its broad surf zone for usual conditions wave breaking takes place in a narrow area in front of the revetment with a swash zone (FIG. 9). The waves on the shoreface and especially on the beach steepen due to shoaling before they break finally. Here a data set is taken from a normal tide with a peak height of 0,3 m below MHWL. There were offshore directed winds with speeds of about 5 m/s. The significant waves in the center line of the array range from 0,93 m (m_1 ; $h = 1,8$ m) to 0,66 m (m_3 ; $h = 0,6$ m).

The directional current spectra for the data from the array (FIG. 10-12) indicate a well established circulation in the groyne field. The primarily driving force is the overbalance of onshore directed energy along the updrift groyne E1 which is intensified by an also resulting



Abb. 9: Waves on the beach with narrow breaker line and swash zone

Date : 17-feb-89
 Record : 21:18 - 21:38

Date : 17-feb-89
 Record : 21:18 - 21:38

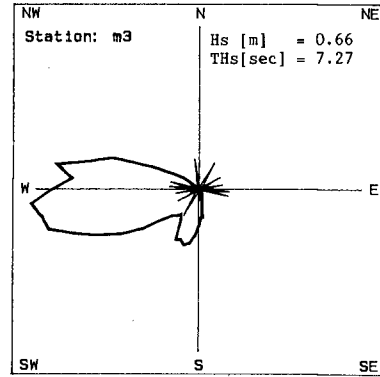
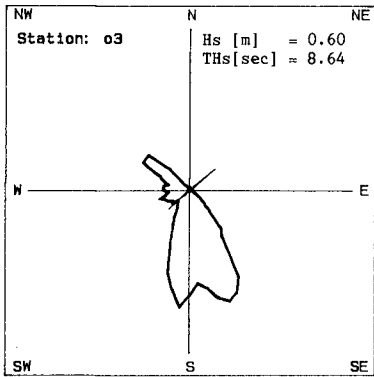
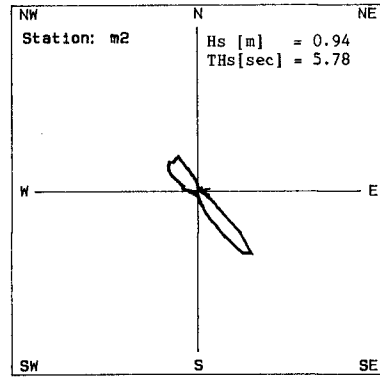
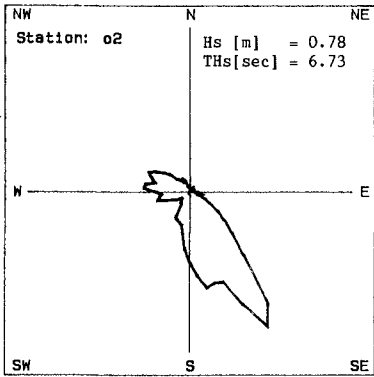
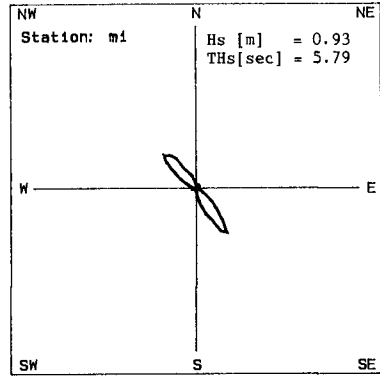
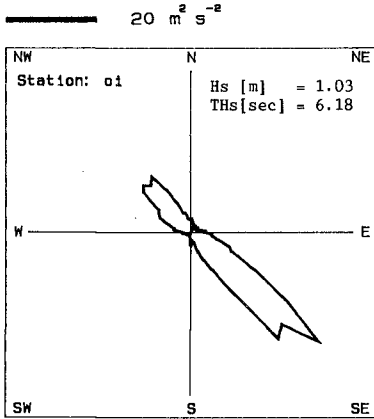


Abb. 10: Directional current spectra of the measuring stations o1, o2, o3 (normal tide)

Abb. 11: Directional current spectra of the measuring stations m1, m2, m3 (normal tide)

shore-ward directed energy in the center point m2 of the array. This onshore drift creates especially close to the revetment a downdrift longshore current and due to the guiding effect of the downdrift groyne D1 concentrated seaward directed currents, which are superimposed by the return flow from the swash zone. This circulation pattern does doubtlessly depend on the geometry of the existing groyne-revetment system, especially if considered that the return flow does not occur in the place of the minimum breaker height. But its driving force must be the measured onshore near bottom drift which might be explained as an effect of very steep nonlinear waves (VAN RHIJN 1990).

As these waves are still non-breaking suspension is much lesser than in the high turbulent surf zone. Sediment transport takes place therefore mainly or even only as bed load. This explains the lower capacity in comparison with the undertow created by storm waves on the beach. If it is expected that onshore drift effects like those observed here cause the recovery of eroded beaches the longer duration of this process compared to the short period necessary for the erosion is reasonable.

In this case fortunately data of a beach profiling are available for the same period (FIG. 13). A comparison of the levelling in the three measuring lines w, m and o is in good agreement with the expected transport processes:

Date : 17-feb-89
Record : 21:18 - 21:38

50 m² s⁻²

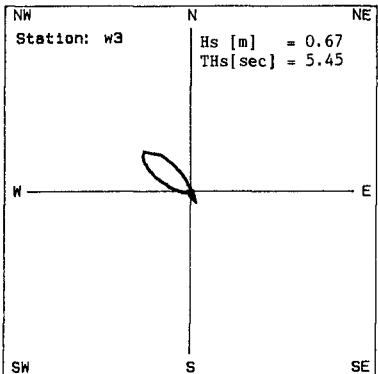
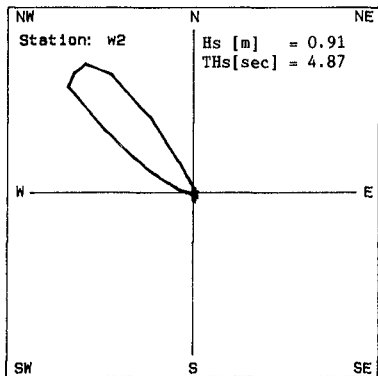
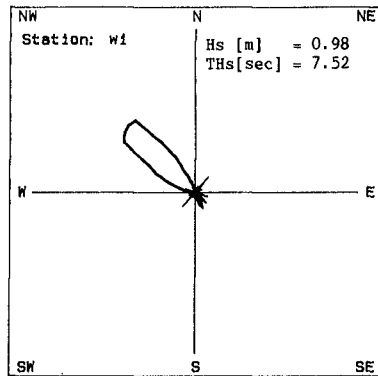


Abb. 12: Directional current spectra of the measuring stations w1, w2, w3 (normal tide)

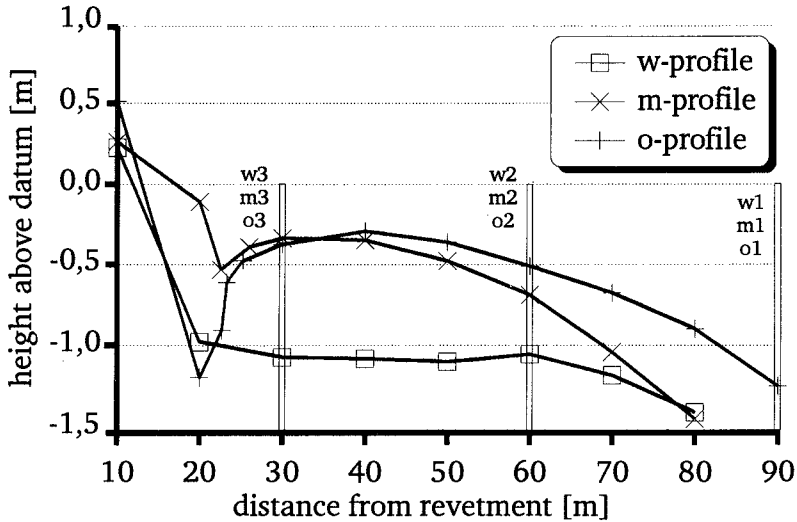


Abb. 13: Beach profiles of the measuring array

the beach is relatively high where onshore directed drift has been measured whereas it is remarkable lower in its other parts.

4. EFFECTIVENESS OF GROYNES

The purpose of beach groynes is to reduce or even to prevent longshore currents and the caused sediment transport. The effectiveness of the groyne system has already been shown by the example of forced circulation. Furthermore the two data sets will be used to get a better insight in the interactions between waves and wave-induced currents with groynes.

Exemplary the effectiveness of the updrift beach groyne E1 is investigated here. The data of the storm surge event show a remarkable longshore current both the points m1 and m3. The longshore components in the position o1 close to the updrift groyne are at least of the same order of magnitude as those measured in m1 which may be explained by the fact that the groyne has no effect on the longshore currents (FIG. 5). In contrast to position o3 the longshore components of the currents are remarkably reduced in comparison with those in m3 (FIG. 6). Obviously the greater height of the groyne in this place causes this effect.

The same effect becomes apparent for the data of the normal tide (FIG. 14) by comparison with the current roses in the measuring points o1, o2 and o3. Whereas the longshore components in the positions o2 and especially o3 are remarkably reduced, in the most seaward situated measuring point the incident waves induce significant up-drift longshore components which are independent of the provoked circulation in the groyne field (FIG. 10-12).

A comparison of the geometrical boundary conditions of both data sets shows that the water depth above the groyne crest at position o3 for the storm surge is greater than in position o1 at the normal tide (FIG. 15). Apparently this parameter is not a reasonable measure for the effectiveness of groynes. Considering additionally the groyne elevation above the beach it is likely that the relative reduction of the total water column above the beach by the groyne is a more reasonable geometrical parameter for the effectiveness of groynes than the water depth above the groyne crest. In order to get a deeper insight in the physical background of the interactions between beach, groynes, waves and wave-induced currents systematical data analysis additionally considering hydrodynamical parameters has to be carried out in the next future.

Date : 17-feb-89
Record : 21:18 - 21:38

100 Promille

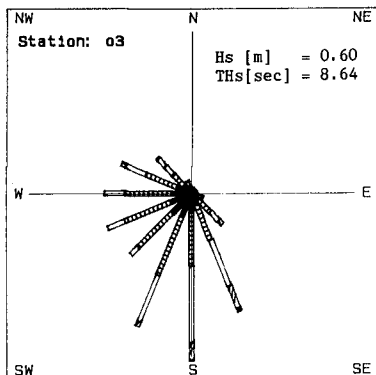
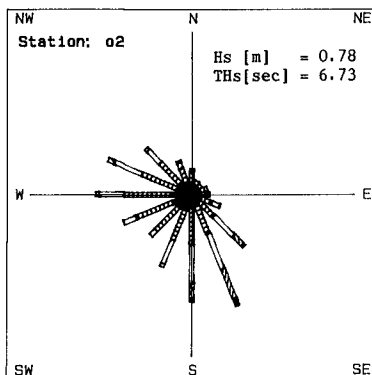
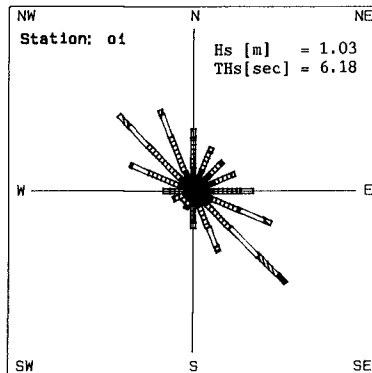
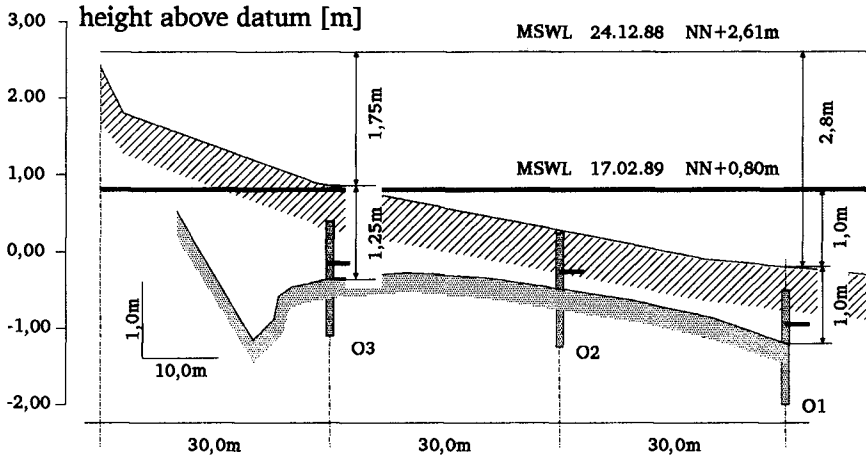


Abb. 14: Current rose of the measuring stations o1, o2, o3 (normal tide)



o-profile 17.02.1989

Abb. 15: Geometrical boundary conditions for groyne effectiveness

5. CONCLUSIONS

The results give a good indication of the driving hydrodynamical forces which govern storm surge erosion and afterward recovery of beaches with revetments and groynes. It is evident that a shoreward increasing tendency of resulting seaward directed currents effects the enormous scour which become especially visible in front of revetments after storm surges. It is also apparent that their seawardly decreasing overbalance allows the sedimentation of the eroded beach material on the shoreface. It seems to be reasonable that the overbalance of seaward directed currents could be explained as undertow effects created by breaking waves. Due to the high turbulence in the surf zone sediment transport does not only occur as bed load but also as suspension which intensifies its efficiency leading to high erosion rates on the beach and correspondently high deposition rates on the shoreface.

The high nonlinearity of steep shoaling but still non-breaking waves creates drift effects which might effect onshore directed bed load transport. But its capacity is much lesser than that of combined suspension and bed load due to undertow currents in the surf zone. This might be a sufficient explanation for the much longer duration of the recovery process compared with the short time event of storm surge erosion.

Furthermore the data discussed here give the impression that the effectiveness of groynes depends primarily on the relative reduction of the total water column due to the groyne elevation above the beach and not on the water depth above the groyne crest.

The application of these results on future beach nourishments implies that the deposition of material on the shoreface is more effective than on the beach itself. A replenishment on the beach reduces the groyne elevation above its bottom and consequently the the relative reduction of the water column. This would again lead to a diminished effectiveness of the groynes with respect to longshore transport which would effect an increase of material losses in the first period after the execution of the nourishment decreasing with the progress of erosion.

Furthermore a nourishment on the shoreface might be better adjusted to natural transport phenonema. The provoked sediment transport due to the disturbance of the existing dynamical equilibrium by artificial deposition of additional material is mainly directed onshore in the first phase after the execution of the nourishment. As this event usually takes places in late spring or early summer, there will be shift of material from the shoreface to the beach which is expected to build up a slowly growing deposit for the erosion due to harvest and winter events with strong sea conditions including storm surges. The main advantage will be that it takes a certain period of time to build up the deposit and within this period the nourished material will be mainly in a position where it is less sensitive to erosion by longshore currents. In contrast to a nourishment on the beach itself will expose the material from the beginning totally to their eroding capacity. Additionally the reduction of water depth would provoke the breaking of even relative small waves and intensify suspension and erosion. Therefore a nourishment on the shoreface might be a successful solution in order to reduce the high losses in the first phase after the execution and to extend the period of effectiveness of nourishments.

6. ACKNOWLEDGEMENT

This study was sponsored by the GERMAN FEDERAL MINISTRY FOR SCIENCE AND TECHNOLOGY (BMFT) in the framework of the GERMAN COMMITTEE FOR COASTAL ENGINEERING RESEARCH (KFKI). The author is grateful for the support he got from his colleagues of the Section of Coastal Hydrodynamics at the COASTAL RESEARCH STATION.

7. LITERATURE

- BASCOM, W. H. (1954):** Characteristics of Natural Beaches. Proc. 4th Conf. o. Coast. Eng., ASCE
- BATTJES, J. (1988):** Surf-Zone Dynamics. Ann. Rev. Fluid Mech. 1988, 20
- DEAN, R. G. (1983):** Principles of Beach Nourishment. in: CRC Handbook of Coastal Processes and Erosion (ed. P. KOMAR); CRC Press, Boca Raton/Fl.
- HOMEIER, H. (1976):** Effects of Severe Storm Surges on East Frisian Island Beaches and Dunes (in German: Die Auswirkungen schwerer Sturmtiden auf die ostfriesischen Inselstrände und Randdünen). Jber. 1975 Forsch.-Stelle f. Insel- u. Küstenschutz, 27
- KRAMER, J. (1960):** Beach Rehabilitation by Use of Beach Fills and Further Plans for the Protection of the Island of Norderney. Proc. 7th Conf. o. Coast. Eng. Richmond, ASCE
- LUCK, G. (1977):** Long-termed Development of Tidal Inlets between Eastfrisian Islands. Proc. 15th Intern. Conf. o. Coast. Eng. Honolulu, ASCE, New York
- NIEMEYER, H. D. (1986):** Wave Propagation and Damping in the Offshore and Wadden Sea area of Norderney (in German: Ausbreitung und Dämpfung des Seegangs im See- und Wattengebiet von Norderney). Jber. 1985 Forsch.-Stelle Küste, 37
- NIEMEYER, H. D. (1987a):** Classification and Frequency of Storm Surges (in German: Zur Klassifikation und Häufigkeit von Sturmtiden) Jber. 1986 Forsch.-Stelle Küste, 38
- NIEMEYER, H. D. (1987b):** Measurements of Tidal Currents in Groyne Fields (in German: Tidestrommessungen in Bühnenfeldern). Jber. 1986 Forsch.-Stelle Küste, 38
- NIEMEYER, H. D. (1987c):** Changing of Wave Climate due to Breaking on a Tidal Inlet Bar. Proc. 20th Intern. Conf. o. Coast. Eng. Taipei, ASCE, New York
- SVENDSEN, I. A. (1984):** Mass Flux and Undertow in a Surf Zone. Coast. Eng., Vol. 8, No. 4
- STIVE, M. J. F. & WIND, H. G. (1986):** Cross-Shore Mean Flow in the Surf Zone. Coast. Eng., Vol. 10, No. 4
- VAN RHIJN, L. (1990):** Sediment Transport by Currents and Waves. Civ. Eng. Europ. Courses Progr. o. Europ. Comm. Cont. Educ., Syllabus Delft Univ. o. Techn. - Int. Civ. Eng.

CHAPTER 61

Directional Random Waves Propagation on Beaches José María GRASSA¹

Abstract

The paper deals with a method for the simulation of irregular, directional waves over large coastal areas using a linear model based on a energetically equalized discretization of wave spectrum and a parabolic approximation to the Berkhoff equation for wave evolution. A sensitivity analysis based on a comparison with physical model tests gives some ideas about the applicability of the method.

Introduction

Waves on the coast often shows little directional spreading due to the effect of refraction and diffraction. However, there is now sufficient evidence about the critical importance that directionality can have in the transformation of wave characteristics from deep to shallow waters, as shown through numerical experiences by Goda (1985) and Isobe (1987) and in physical model tests by Vincent and Briggs (1989).

Evolution models for spectral parameters including wave refraction and diffraction and assuming no wave generation or dissipation can be made applying the linear superposition of component waves transformed according to Berkhoff's (1974) equation if wave non-linearities can be disregarded for the specific problem to be studied or not important due to particular wave characteristics. However, over the very large areas often appearing in coastal studies, even the application to a single component of the mild-slope equation can be a formidable task. A solution for that can be the use of a parabolic approximation to the Berkhoff equation. In fact, parabolic equation method (PEM) extension for use with irregular directional waves has been done by Isobe (1987) applying the Radder's (1979) wave equation in the ray - front coordinates system. Very recently, Panchang et al. (1990) have also presented irregular directional results for the Vincent and Briggs tests (1989) using Radder's equation over an orthogonal grid, with a good agreement between computed and physical model results.

The present paper deals with the application of higher order, large angle PEM (Booij, 1981), (Kirby, 1986a, 1986b) to directional wave propagation on large coastal areas. At first, a brief review of the methodology employed is given. Some basic

¹Director, Centro de Estudios de Puertos y Costas, CEDEX - MOPU. c/ Antonio Lopez, 81, 28026 Madrid, SPAIN

questions arise about the method for wave spectrum discretization and they are studied suing a comparison with physical model tests by Vincent and Briggs(1989). Then, the method is applied to an idealized coastal area showing some of the implications that directionality can have on coastal environments.

Methodology

Under the assumption of validity for linear superposition as a method for the description of irregular waves, simulation of directional waves can be made trough the application to a number of monochromatic waves representing the whole wave spectrum of a wave equation for the evolution of monochromatic waves over an irregular bed.

Given a wave spectrum $S(f, \theta) = S(f) G(f, \theta)$ where $G(f, \theta)$ is a normalized shape function for directional distribution, a representation between given cut-off values, (f_{min}, f_{max}) , $(\theta_{min}, \theta_{max})$ in N_f, N_θ components each of which defined by a corresponding frequency, a direction and a wave amplitude $(f_i, \theta_{ij}, a_{ij}, i = 1, N_f, j = 1, N_\theta)$ can be made by a constant step method:

$$\Delta f = \frac{f_{max} - f_{min}}{N_f} \quad \Delta \theta = \frac{\theta_{max} - \theta_{min}}{N_\theta} \tag{1}$$

$$f_i = f_{min} + (i - 0.5) \Delta f$$

$$\theta_{ij} = \theta_{min} + (j - 0.5) \Delta \theta \tag{2}$$

$$a_{ij} = \sqrt{2S(f_i, \theta_{ij}) \Delta f \Delta \theta}$$

The method employed in the present work for an energetically equalized discretization of the spectrum consists of:

$$f_i \text{ given by: } \int_{f_{min}}^{f_i} S(f) df = \left(\frac{m_0}{N_f} \right) (i - 0.5)$$

$$\theta_{ij} \text{ given by: } \int_{\theta_{min}}^{\theta_{ij}} G(f, \theta) d\theta = \left(\frac{1}{N_\theta} \right) (j - 0.5) \tag{3}$$

$$a_{ij} = \sqrt{\frac{2m_0}{N_f N_\theta}}$$

being m_0 the zero order moment of the frequency spectrum. In the context of wave propagation, a similar approach has been presented by Goda (1985); at least for the frequential part of the spectrum.

Having obtained a representation of the irregular waves as a number of simple monochromatic waves, a PEM is employed for solving the wave potential field over the area of interest. It is possible then to recover some wave characteristics as significant wave height, instantaneous free surface, etc, through linear superposition of results for the components. Given the limitation of PEM that assumes a main wave propagation

direction one alternative is to obtain a specific calculation grid over the area modelled as a function of the direction of the incident wave, thus overcoming this limitation. That approach has been taken by Panchang et al.(1990). However, the use of large angle parabolic models such as (Kirby, 1986b), allows for the use of only one calculation grid in some cases even with some quite broad directional spectrum, avoiding the need for an interpolation of results of components in order to recover the irregular wave characteristics of interest.

For his application on wave propagation studies, equalized discretization shows some basic advantages:

1. Grouping of wave components around the spectrum peak, both in the frequency and direction domains (as seen in fig. 1). This is important in connection with PEM, given its intrinsic angular limitations. This makes easier the design and orientation of a calculation grid for a given area and can avoid the need of an arbitrary truncation of the spectrum.

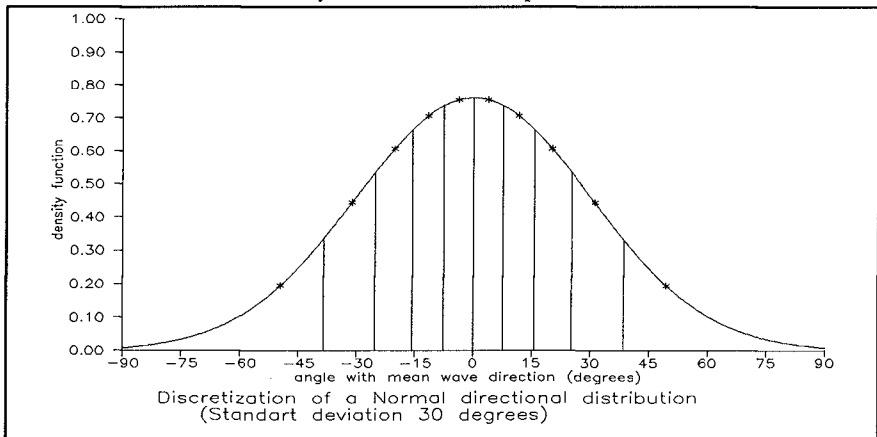


Figure 1.- Equalized discretization for a directional shape.

2. Each one of the equalized components has a same amount of energy and can, in a first approximation, contribute equally to the disturbance in a given point. Then, computational effort is optimized for a given number of wave components.

The main disadvantage is that equalization is more complex and time consuming (when the spectral shape is not directly integrable) than constant step procedures; in the present context, however, equalization is a trivial task in comparison with the effort involved in the propagation of the wave components.

In the present application, solution of equations (3) for the equalized discretization of an arbitrary spectrum shape has been made using standard library routines (Morris, 1987) for evaluation of integrals over finite intervals and equation solving.

From a practical point of view, two main questions should be assessed:

1. Order of magnitude in the number of wave components needed to obtain accurate results, within the intrinsic limitations of the method (linear superposition, approximate PEM).
- 2.- Optimal distribution of the computational effort between the frequency and directional domain.

That points are going to be examined by comparison between the results applying the proposed methodology and some physical model test.

Comparison with Physical Model Tests

A numerical model built within the methodology exposed has been compared with the results of some tests on irregular directional wave propagation performed by Vincent and Briggs (1989) in a wave basin with a directional irregular wave generator. For the irregular waves target spectrum has been a TMA shape (Bouws et al., 1985) in the frequency domain and a wrapped around the circle normal distribution shape for directions. The bathymetry modelled has been a elliptic shoal similar to the one studied by Berkhoff et al. (1982), but over an horizontal bed instead of a sloping one. Figure 2 shows the layout of the model.

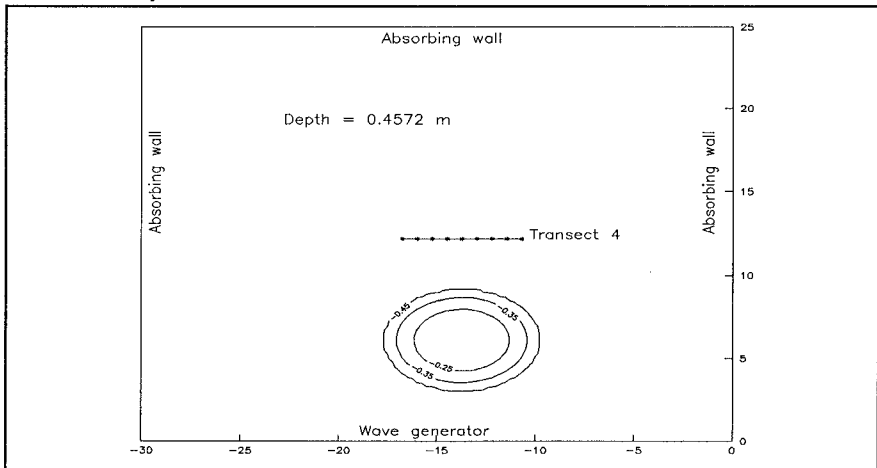


Figure 2.- Layout of the model

Cases selected are shown in table 1, and covers both wide and narrow shapes both in the frequency and direction domains for low steepness waves in intermediate water depth, making at first reasonable the use of linear theory. A monochromatic test and two unidirectional tests have also been computed.

<u>Test Id.</u>	<u>Waves</u>	<u>Peak Factor</u>	<u>Standard Deviation</u>
M2	Regular	-	-
U3	Irregular	2	0
U4	Irregular	20	0
N3	Irregular	2	10
N4	Irregular	20	10
B3	Irregular	2	30
B4	Irregular	20	30

Table 1.- Tests selected for comparison

In the numerical calculation, for the irregular cases the equalized discretization of the spectrum has been made taking only 10 frequency components by 10 directional (when required) components with the same frequency cutoff as in the physical model. Then for the narrow directional spreading tests, initial wave direction over the grid has an obliquity of up to around 16 degrees with the assumed main wave direction, avoiding the need for an arbitrary wrapping of the directional distribution in order to satisfy the PEM assumptions. Otherwise, for tests B3 and B4, maximum initial obliquity is around 49 degrees, and is going to be higher given the expected wave pattern after the shoal, thus some truncation should be applied.

The area modelled has been discretized in a calculation grid of 101 x 121 nodes with node distance of 0.25 ms. Wave propagation for each component over the same grid has been calculated using a Crank - Nicholson finite difference scheme based on higher order, large angle Kirby's minimax parabolic equation (Kirby, 1986b) in a linear version and without friction terms. Initial condition for complex wave amplitude ϕ for each oblique component ij in the first row of the grid are:

$$\phi_{ij} = a_{ij} \exp(i(k_i \sin\theta_{ij} y + (S_0)_{ij})) \quad (4)$$

being k_i the wave number corresponding to wave component i,j , and y the coordinate values corresponding to the grid nodes along the first row (x being the main propagation direction). A pseudo random value S_0 , equally distributed between 0 and 2π is added to the initial phase function for each component in order to obtain realistic instantaneous free surfaces.

Minimax parameters for the computations have been taken for 70 degrees of aperture, and a dissipative filter (Kirby, 1986a) has been applied to the computed results.

Figures 3 - 4 shows results of significant wave height along measurement section 4, with the reference of physical model results. The continuous line presents numerical results and the broken line physical results from the graphs of Vincent and Briggs (1989).

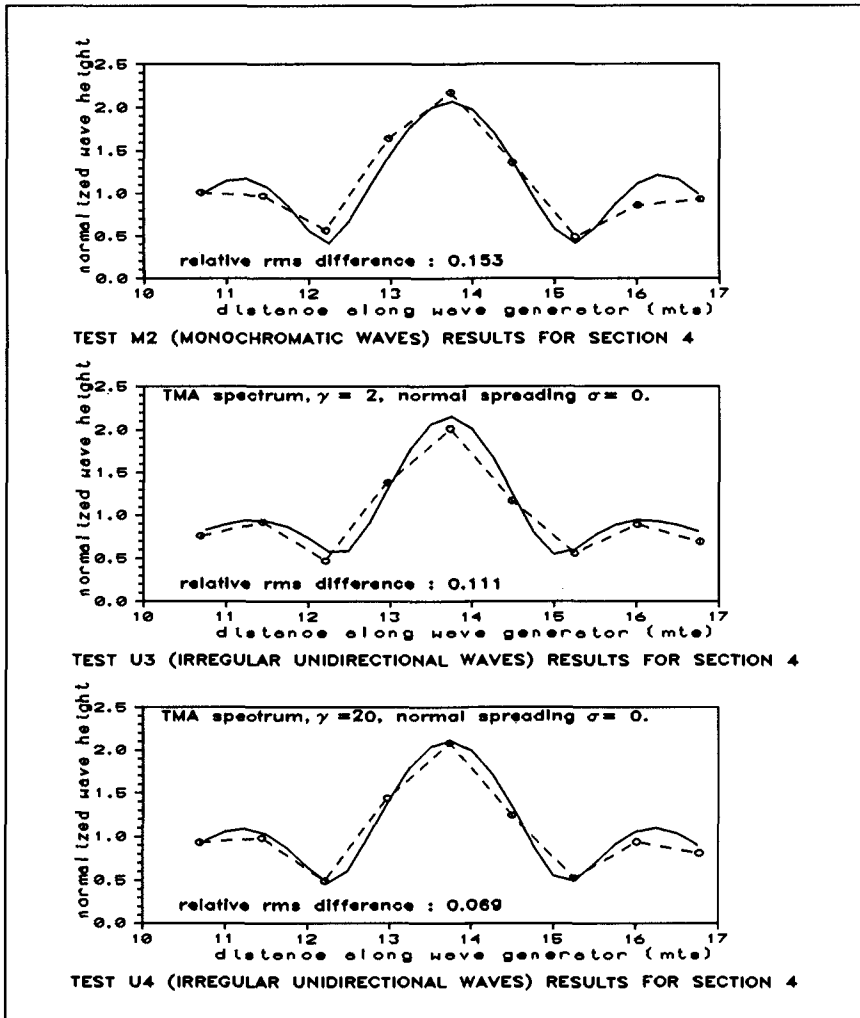


Figure 3.- Results for non directional tests

As signaled by Vincent and Briggs (1989), the non-directional cases show very similar features to the ones in the regular test. However, the qualitative agreement is better in tests U3, U4 than in M2, featuring both numerical and physical results the lateral linear caustics that develops behind the shoal, not present in the physical model results for the monochromatic case.

For the directional tests, the magnitude of the caustic shows an intense decrease, practically disappearing for wide spreading tests. Similarly, numerical and physical results fits well, except in the test B4, with a narrow frequency spectrum and

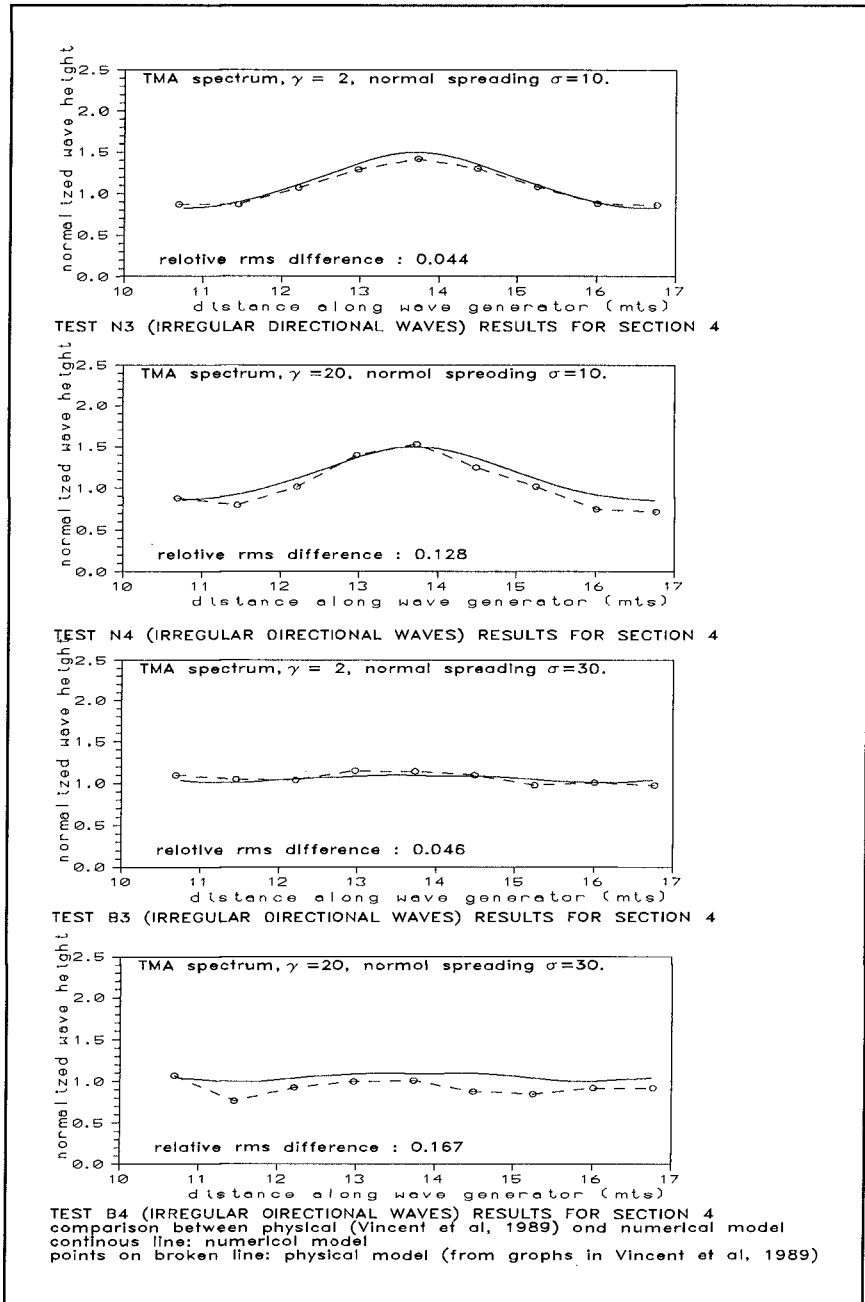


Figure 4.- Test results for directional cases

wide directional spreading, where physical model results shows a systematic trend towards lower values than the numerically computed, perhaps due to some amount of dissipation over the shoal.

A quantitative measure of the quality of results has also been made, using a relative root mean square difference between physical and numerical model for that section:

$$dif_{rms} = \sqrt{\frac{\sum \left(\frac{H_{pm} - H_{nm}}{H_{pm}} \right)^2}{N}} \quad (5)$$

where:

H_{pm} : Wave height in physical model (from graphs in Vincent and Briggs, 1989)

H_{nm} : Wave height in numerical model

N : number of measurement points along section 4

Table 2 summarizes the results.

Test id.	Relative root mean square difference
M2	0.153
U3	0.111
U4	0.069
N3	0.044
N4	0.128
B3	0.046
B4	0.167

Table 2.- Comparison between numerical & physical results

Then it appears that in the cases modelled an irregular linear wave propagation model based on an equalized discretization of the spectrum and the application of a higher order PEM provides a similar quality of results as with PEM applied to monochromatic test.

Sensitivity Analysis

A sensitivity analysis of the results as a function of number of wave components has been made for test case N3, trying to obtain information about which number of wave components is needed for a correct reproduction of irregular propagation in that test and also studying the stability of the numerical model. Results have been evaluated with eq. 5 for an increasing number of discrete components (equal number in frequency and directions) from 4 (2 x 2) to 900 (30 x 30), obtaining the relative difference with physical model tests.

Results are plotted in figure 5 (solid line), together with similar data for results obtained through a constant increment discretization of the spectrum (dashed line).

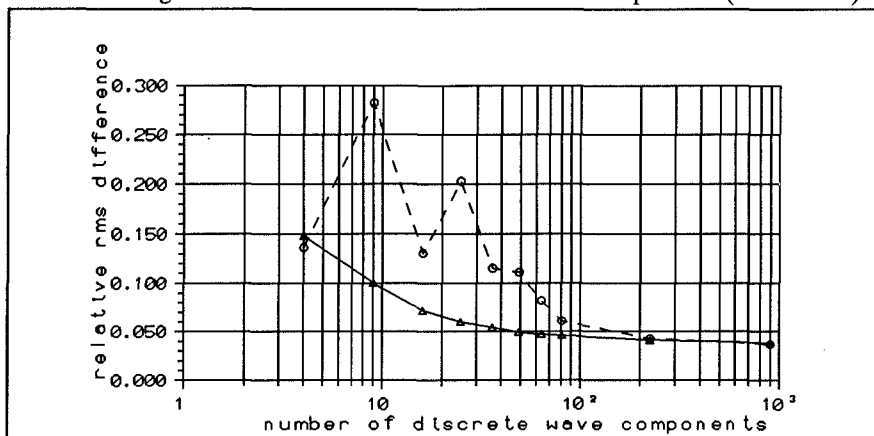


Figure 5.- Sensitivity to number of components (test N3)

As can be seen, results obtained with equalized discrete components converge in a stable way towards the asymptotic solution for the numerical model and a very little improvement is obtained with more than 100 components. Otherwise, results with constant step shows larger errors with a small number of components and an anomalous behavior when the number of intervals in the directional domain is odd, due to the fact that then a component is placed on the spectral peak, with a predominant amount of wave energy which implies results more similar to the monochromatic situation. Of course, with an increasing number of wave components, differences between both approaches vanishes, but it is still noticeable at the number of wave components used in the present work.

Then it can be concluded that equalized discretization gives, from the point of view of wave propagation, a more reliable representation of irregular waves than constant step methods, in particular if the number of wave components used is not high. The need of a low number of components for the obtention of good quality results is a hopefully conclusion, making possible the application of the methodology over large areas with reasonable computing resources, and implies also the possibility of application of more complex models such as the elliptic mild-slope equation using a similar approach.

Another question is the optimum relationship between number of directional and frequency components involved in the computations. That question is to be solved in a case basis, but given the greater importance of directionality over frequency shape at least in cases involving diffraction, it appears likely to use a larger number of directional components. From a computational point of view, it should be noted that the coefficients in the discretized parabolic equation do not have any dependence on the wave direction (except for the independent term that depends also on initial conditions), being a function of wave frequency, wave number and related quantities (phase and group velocity). Then, when a component has been computed for a given

frequency, only a minor modification on the independent term of the parabolic equation system is needed in order to setup the equation for a new wave direction with the same frequency. Figure 6 shows results for test B3 computed using double number of directional components (dashed line) that of frequency ones and an equal number (solid line).

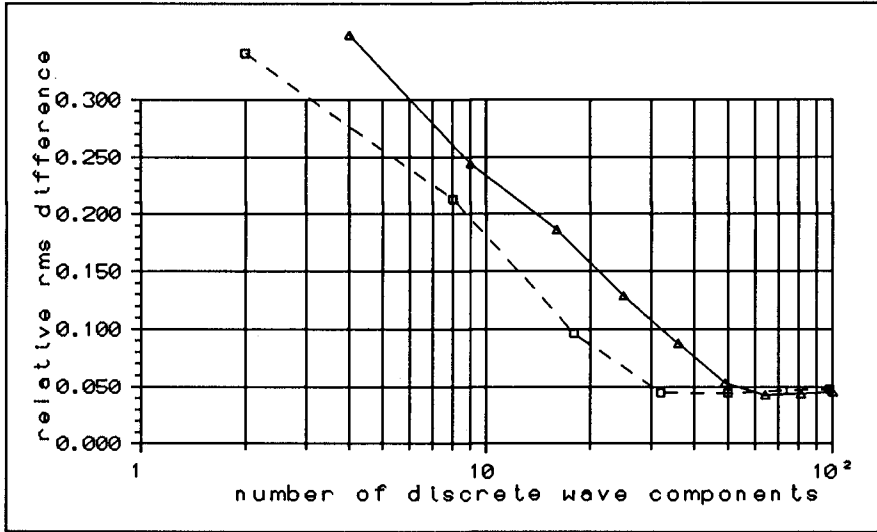


Figure 6.- Comparison of results with $N_0 = 2 N_f$ (Test B3)

A similar quality of results is obtained with $(N_f = 4, N_0 = 8)$ and $(N_f = 7, N_0 = 7)$ with the added advantage of the low computational cost of computing an additional directional component for a given frequency as compared with the cost of the setup of the coefficients of the system of equations that arises from PEM, needed if more frequencies are involved.

Application over an idealized bathymetry

An application has been made over an idealized bathymetry given by:

$$z(x,y) = -10 + 0.001 * x \tag{6}$$

$(0 \leq y \leq 1500.)$
 $(0 \leq x \leq 1000.)$

with x, y and z in meters and representing a plane sloping beach. A shore-parallel breakwater is located at a depth of 7. mt and extends from y = 750 to y = 1500 mt.

Three different wave conditions have been tested:

- a) Monochromatic waves with period 10 sec. and normal incidence.
- b) Swell-like waves, defined by a Jonswap spectrum with $\gamma = 7.$ and directional spread modelled according to the Mitsuyasu - Goda - Suzuki(Goda, 1985) shape

function with $S_{\max} = 100$.

c) Sea-like waves, with $\gamma = 2$, and a broader directional distribution given by $S_{\max} = 25$, at the offshore boundary of the modelled area.

The discretization has been made taking 101×151 equally spaced nodes (distance between nodes 10 mt) and the irregular runs have been made with 5×15 components. Simulation of wave breaking has been artificially introduced in the model in a way similar to Ebersole (1985), trying to obtain qualitative information about breaking along the beach.

Computed results for significant wave height field are given in figures 7 - 9.

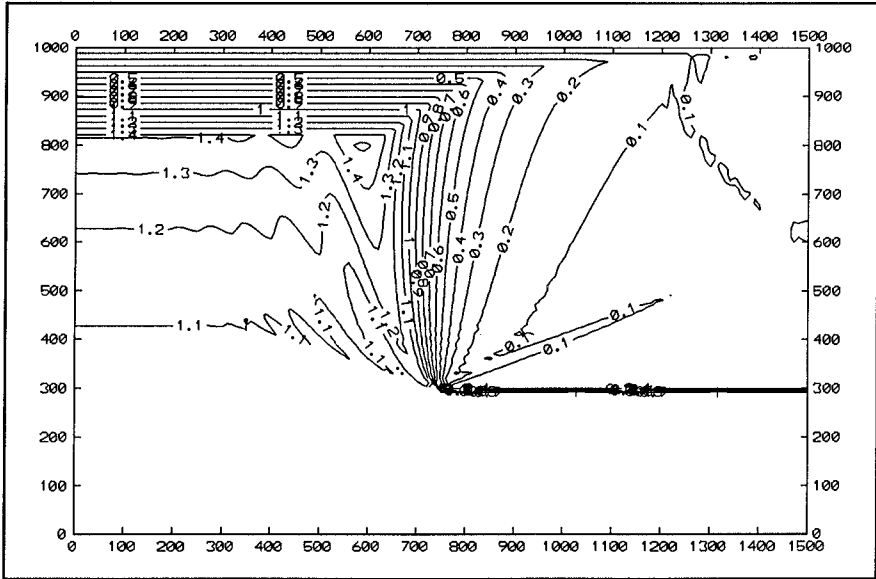


Figure 7.- Wave height field for monochromatic test

As can be seen, there are significant differences between for monochromatic and irregular wave results. At first, wave height field seems to be smoother on the coast in the irregular waves tests (the "wavy" variation in wave height associated to wave diffraction vanishes). It is to be noted that for all the tests, a dissipative interface (Kirby, 1986b) has been applied and is needed due to the numerical noise that arises in higher order parabolic schemes. Also, as signaled by Goda (1985) wave penetration along the line between the toe of the breakwater and the coast is higher for the irregular, broad directional test than for the monochromatic and the swell-like test.

Then, it appears than for narrow-directional distributions, wave irregularity can have a main effect of smoothing some of the special characteristics of monochromatic wave response, having a more fundamental effect for sea wave states.

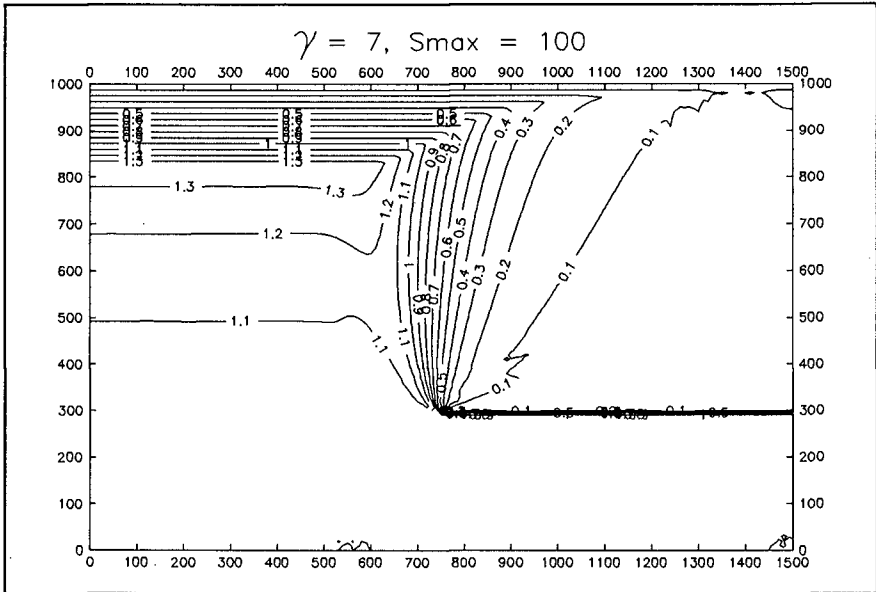


Figure 8.- Wave height field for swell conditions test

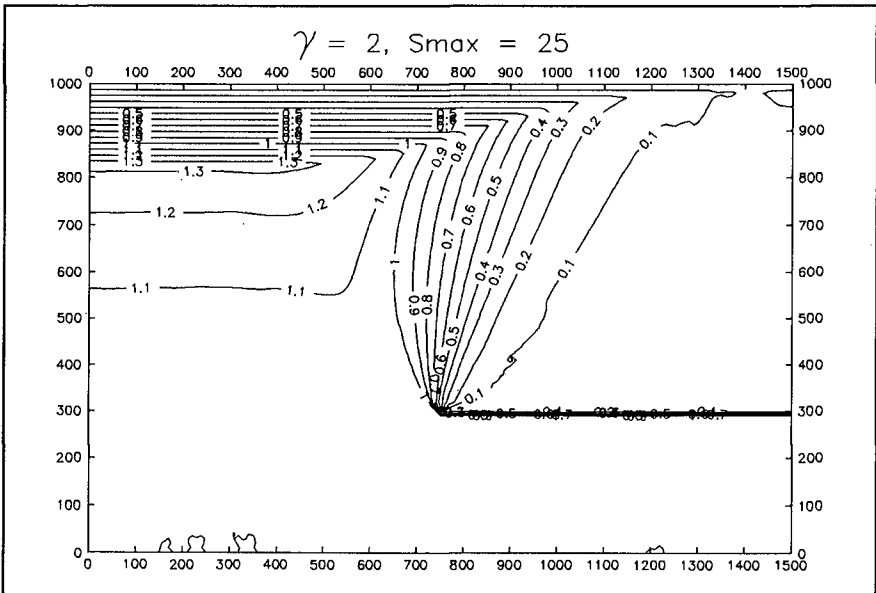


Figure 9.- Wave height field for sea wave conditions

Figure 10 shows breaking wave height along the beach for the three tests, being a main characteristic the more slowly decrease in wave height along the diffraction area for sea waves.

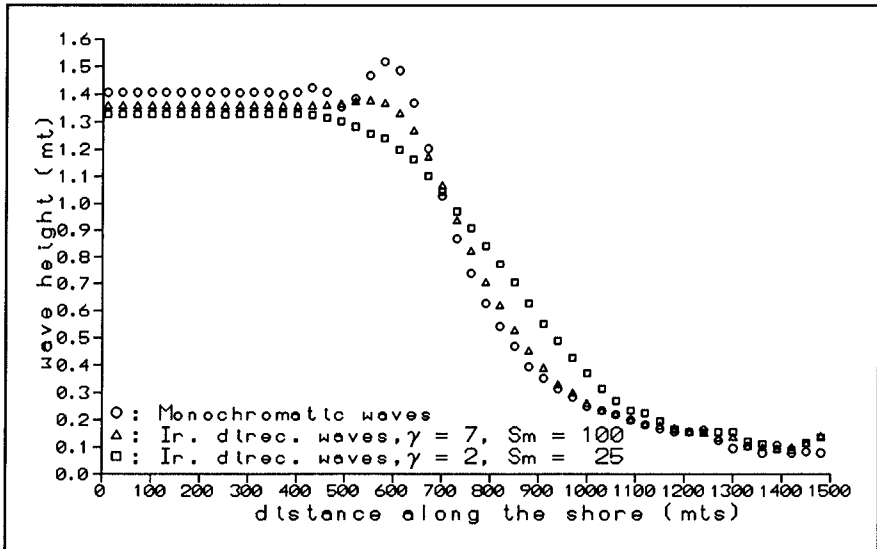


Figure 10.- Breaking wave height along the shore

Conclusions

A methodology for the study of irregular directional waves that can be applied to large areas has been presented, based on linear superposition of energetically equalized components of the target spectrum and the application of higher order parabolic approximations to the Berkhoff equation. Comparison with low steepness physical model tests by Vincent and Briggs (1989) and a sensitivity numerical experiment shows that it is possible to obtain quite accurate results even with a very low number of components, and that it could be more interesting to take a higher number of directional components than frequential ones. That should apply also for models builded from the elliptic mild slope equation.

A more extensive comparison including the high steepness tests of Vincent and Briggs (1989) is to be made for studying the expected degradation of predictive capability of the method for situations in which nonlinearities play an important role. As an alternative, another approach, perhaps based on more general equations for free surface flow simulation should be considered. Unfortunately, however, most of those models cannot be applied over the total range of depths to be considered for wave transformation from deep to shallow waters.

An application for an idealized coastal area shows some interesting features in the wave height field along the shore for the test with sea waves condition, giving

results in qualitative agreement with those obtained by Goda (1985) for directional wave diffraction applying semi-analytical models. Additional work is to be done for incorporating a more realistic description of wave breaking into the model.

One of the actual weaknesses for application of directional wave propagation to studies on coastal areas is the absence of information about directional wave conditions and propagation characteristics on nature. Then an effort should be made in order to obtain field data and validate numerical models against that information.

References

- Berkhoff, 1974: Computation of combined refraction - diffraction. Proc. 13th ICCE, p. 471 - 490, ASCE.
- Radder, A.C., 1979: On the Parabolic Equation Method for Water Wave Propagation. J. Fluid Mech. Vol. 95, part 1, pp. 159, 176.
- Booij, N., 1981: Gravity Waves on water with non-uniform depth and current. Thesis, T.U. Delft.
- Berkhoff, J.C.W., Booij, N., and Radder, A.C., 1982: Verification of numerical wave propagation models for simple harmonic linear water waves. Coastal Eng., 6, 255 - 279.
- Bouws, E., Gunther, H., Rosenthal, W., and Vincent, C., 1985: Similarity of the wind wave spectrum in finite depth water. J. Geophys. Res., 90(C1), 975 - 986.
- Goda, Yoshimi, 1985: Random seas and design of maritime structures. University of Tokio press
- Ebersole, B. A., 1985: Refraction - Diffraction model for linear water waves. J. Waterways, P., C., and Ocean Eng., ASCE, Vol. 111, No. 6, 939-953.
- Kirby, J.T., 1986a: Higher order approximations in the parabolic equation method for water waves. J. Geophys. Res., 91(C1), 933 - 952.
- Kirby, J.T., 1986b: Rational approximations in the Parabolic Equation Method for water waves. Coastal Eng., 10, 355-378.
- Morris, A.H., 1987: NSW library of mathematics subroutines. NSW TR 86-251.
- Isobe, M., 1987: A parabolic equation model for transformation of irregular waves due to refraction, diffraction and breaking. Coastal Eng. in Japan, Vol. 30, No. 1, 33 - 47.
- Vincent, C.L. and Briggs, M.J., 1989: Refraction - diffraction of irregular waves over a mound. J. Waterways, P., C., and Ocean Eng., ASCE, Vol. 115, No. 2, 269-284.
- Panchang, V.G., Wei, G., Pearce, B.R., Briggs, M.J., 1990: Numerical simulation of irregular wave propagation over shoal. J. Waterways, P., C., and Ocean Eng., ASCE, Vol. 116, No. 3, 324 - 340.

CHAPTER 62

Spatial variation of wave group statistics and representative wave-heights of swell

Akiyuki UKAI^{*}, Takashi YASUDA^{**}, Kazunori ITO^{***}

Abstract

This study derives a practical equation that can describe the weakly nonlinear waves having an arbitrary spectral form and propagating unidirectionally from deep to shallow water, and carries out the numerical simulation using the equation. Based on the simulated results, some investigations are made on the characteristics of spatial variation of wave group and representative wave-heights in the propagation process.

1. Introduction

Characteristics of grouped waves propagating from deep to shallow water are clearly important for engineering purpose, but are little made clear because of the difficulty of the observation in field. Regretably, most of usual investigations are concerned with the statistics of wave grouping derived from temporal wave registrations obtained at fixed locations and lack a view point that the statistics may change spatially during the propagation of the grouped waves.

Hence, in order to investigate on the spatial variations of the characteristics during the propagation from deep to shallow water, it is essentially required to develop a tractable equation that can be easily solved for the nonlinear waves having an arbitrary spectral bandwidth and propagating from deep to shallow water and employ a theoretical approach using the equation, instead of the approach based on the field observation.

* Eng., Civil Eng. Dept., Penta-Ocean Construction Co., Ltd., Koraku 2-Chome, Bunkyo-ku, Tokyo 112, JAPAN

** Prof., Dept. of Civil Eng., Gifu Univ., Gifu 501-11, JAPAN

***Graduate student, ditto

In this study, we suggest a single tractable equation of spatial evolution type for describing the unidirectional propagation of swell and carry out numerical simulations using the equation. Further, based on the simulated results, we investigate intensively on the characteristics of spatial variations of wave group statistics and representative wave-heights in the propagation process.

2. A model equation for swell

2.1 Derivation

we derive a tractable equation that can easily describe weakly nonlinear waves having an arbitrary spectrum and propagating unidirectionally from moderately deep to shallow water, by modifying the dispersion term of the following perturbed KdV equation so as to give the correct linear dispersion relation of surface gravity waves.

$$\eta_x + \frac{1}{\sqrt{gh}}\eta_t + \frac{3}{2} \frac{1}{h\sqrt{gh}}\eta\eta_t + \frac{1}{6} \frac{h^2}{(gh)^{3/2}}\eta_{ttt} + \frac{1}{4} \frac{h_x}{h}\eta = 0 \tag{1}$$

where the subscripts x and t denote partial differentiations with regard to them, x the horizontal coordinate, t the time, η the temporal water surface elevation, h the mean water depth in the propagation process and g the acceleration of gravity.

To our best knowledge, there is no equation of spatial evolution type such that can describe actually the propagation process of weakly nonlinear waves having arbitrary spectrum. The necessary conditions for the equation are as follows:

- i) Only if the temporal water surface elevation at any fixed location is given as a boundary condition, the equation can describe its spatial evolution over a sloping bottom from deep to shallow water.
- ii) The equation can be applied to the swell having an arbitrary spectrum.
- iii) The equation should be tractable so as to be for numerical simulation of the long distance propagation.

An equation of wave motion of spatial evolution type can be written for linear waves having correct dispersion relation and propagating on the moving coordinate with the speed of \sqrt{gh} as

$$\partial_x \eta + \int_{-\infty}^{\infty} F(\tau - \sigma) \partial_\sigma \eta d\sigma = 0 \tag{2}$$

where

$$\left. \begin{aligned} F(\tau - \sigma) &= \frac{1}{2\pi} \int_{-\infty}^{\infty} \frac{c(\omega) - \sqrt{gh}}{c(\omega)} e^{-i\omega(\tau - \sigma)} d\omega \\ \tau &= \int dx / \sqrt{gh} - t, \quad \omega = 2\pi f \end{aligned} \right\} \tag{3}$$

and $c(\omega)$ is the wave speed of linear dispersive waves.

Here, assuming its solution as

$$\eta = \sum_{-\infty}^{\infty} A_m(x) \exp(i\omega_m \tau), \quad (4)$$

and treating this equation on the frequency domain, we obtain the following mode rate equation.

$$\frac{dA_m}{dx} + ik(\omega_m)[C(\omega)/\sqrt{gh} - 1]A_m = 0, \quad m: -\infty \sim \infty \quad (5)$$

Further, introducing the nonlinear term $3/2\eta\eta_x$ and the shoaling term $h_x\eta/4$ included in the perturbed KdV equation shown in eq(1), we obtain a single tractable equation of spatial evolution type and call it as a model equation for swell unidirectionally propagating from moderately deep to shallow water.

$$\begin{aligned} d\tilde{A}_m/dx^* + ik_m^*(c^* - h^{*1/2})\tilde{A}_m \\ + \sum_{j=-\infty}^{\infty} i \frac{3}{2} k_m^* h^{*-1/4} \tilde{A}_{m-j} \tilde{A}_j = 0, \end{aligned} \quad (6)$$

$m: -\infty \sim \infty$

$$\left. \begin{aligned} x^* &= x/h_0, \quad k_m^* = k(\omega_m)h_0, \quad h^* = h/h_0, \\ c^* &= c(\omega_m)/\sqrt{gh_0}, \quad A_m/h_0 = \tilde{A}_m h^{*-1/4}, \end{aligned} \right\} \quad (7)$$

This equation has two conserved quantities of 1st and 2nd order are derived from the model equation as

$$\frac{d}{dx} I_1 = -\frac{3}{4} \frac{\eta^2}{\sqrt{gh^3}} \Big|_0^{T_0} - \int_0^{T_0} L[\eta] dt, \quad I_1 = \int_0^{T_0} \eta dt, \quad (8)$$

$$\frac{d}{dx} I_2 = -\frac{\eta^3}{2\sqrt{gh^3}} \Big|_0^{T_0} - \int_0^{T_0} \eta L[\eta] dt, \quad I_2 = \int_0^{T_0} \frac{\eta^2}{2} dt, \quad (9)$$

where

$$L[\eta] = \sum_{m=-\infty}^{\infty} i [\sqrt{(k_m/h)\tanh k_m h} - k_m] A_m e^{i\omega_m t}, \quad (10)$$

Assuming the periodicity of η with an observation period T_0 on time domain, we can put the right hand sides of eqs(8) and (9) zero, because of the relation $A_m = A_{-m}$ and the fact that $\omega(k_m)$ is the odd function of k_m . Thus, we can evaluate the accuracy of the numerical solution by examining the conservativeness of I_1 and I_2 . Here, the equation was solved under the accuracy that the errors for both the conservation laws are kept within 0.1 %.

Furthermore, it should be emphasized that the modulational instability occurs in the wave train governed by the model equation, although the nonlinear term of the equation is identical with that of the KdV

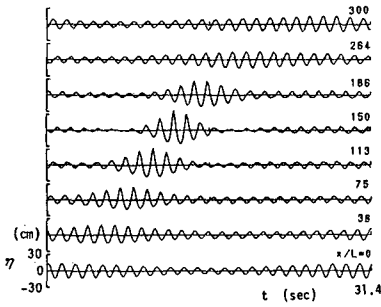


Fig. 1
Wave train of a quasi-monochromatic wave train.

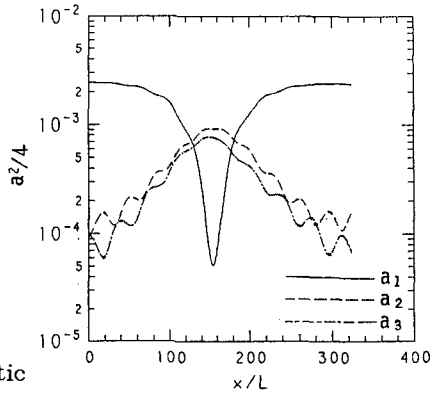


Fig. 2 Modulation of peak and its side band modes.

equation which cannot express the instability. Figure 1 shows the spatial evolution of a quasi-monochromatic wave train governed by the model equation. Figure 2 shows the modulation of the peak mode and its side-band modes and explains clearly that the modulation and demodulation successively occur.

2.2 Accuracy

Since the model equation is not derived consistently from the fundamental equation of hydrodynamics, we are required to examine the applicability before carrying out the numerical simulations of long distance propagation of swell through the model equation.

At first, we examined the accuracy of the model equation by comparing with the exact Stokes waves. Figure 3 [Yasuda et al., 1989] shows the applicable region of the model equation and the KdV equation. The boundaries in this figure indicate the critical values of ka and kh under which the maximum value of the error E_1 , defined by

$$E_1(t) = \int_{-\pi/k}^{\pi/k} [\eta(x, t) - Y(x - ct)]^2 dx \bigg/ \int_{-\pi/k}^{\pi/k} Y^2 dx, \tag{11}$$

is kept within 0.06. Here, η denotes the numerical solution of the model equation, Y the exact Stokes wave solution and c is phase speed. Hence, E_1 can be used as an error criterion indicating the accuracy of the numerical solution to the exact solution of steady wave. It could be said that the model equation is applicable within the boundaries shown in figure 3 and that the model equation is superior to the KdV equation in the range of $kh > 0.8$. However, the model equation does not unexpectedly work so well for the waves in

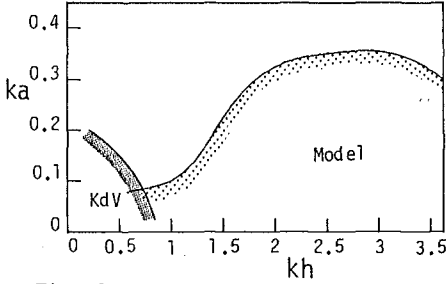


Fig. 3

Applicable region derived from the comparisons with the exact Stokes wave.

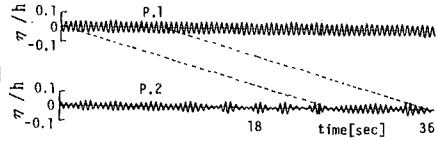


Fig. 4

Temporal water surface elevations measured at P.1, and P.2

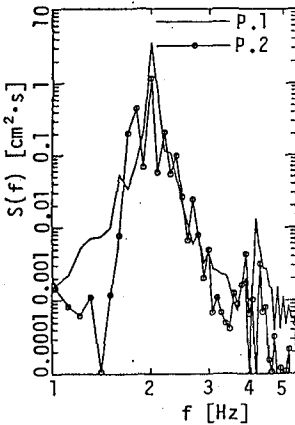


Fig. 5

Power spectra measured at P.1 and P.2

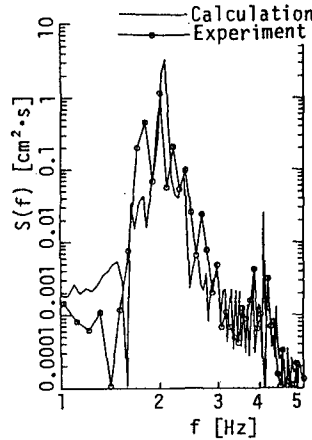


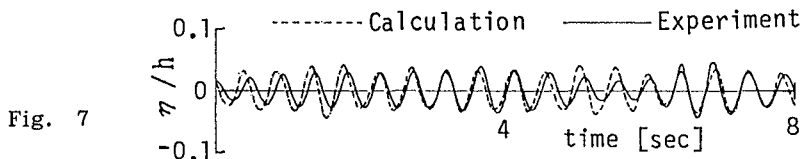
Fig. 6

Comparison of power spectra at P.2 between the experimental result and the calculated one.

deeper water than $kh > 3.3$, because its nonlinear term is valid only for long waves with $kh \ll 1$.

Secondly, we examined experimentally the applicability of the model equation to the quasi-monochromatic waves suffering from the modulational instability. Figure 4 shows the temporal water surface elevations at P.1 and P.2 of a modulational wave train generated in a wave flume [1m x 1m x 54m] having a servo-controlled wave maker. The distance between the measuring location P.1 and P.2 is $kx = 42\pi$ in this case. It is conjectured from Fig. 5 that the modulation observed at P.2 is primarily due to the growth of the side-band modes of the spectral peak.

Figure 6 shows the comparison of power spectra at P.2 between the measured result and the simulated one.



Comparison of water surface profile at P.2 between the experimental result and the simulated one.

Figure 7 indicates the comparison of temporal wave profile at P.2 between both the results. The simulation carried out by making the waves measured at P.1 propagate to P.2 through the model equation. Both the results corresponds to each other in rough trend. However, it should be noticed that the modulation of the simulated waves is considerably weak and the side-band modes of the simulated waves are not so strengthened in comparison with those of the measured waves. Hence, it should be noted that the growth of the modulation is evaluated a little weakly as far as the model equation is used.

Finally, we examined the applicability of the model equation to irregular waves having various spectral bandwidth, by generating the desired waves of which initial spectra are the Wallops type in the aforementioned wave flume and comparing the measured wave profiles at P.2 with the results simulated as well as the case of the quasi-monochromatic waves mentioned above. The error criterion E_2 for evaluating the applicability of the model equation to the irregular waves is defined as

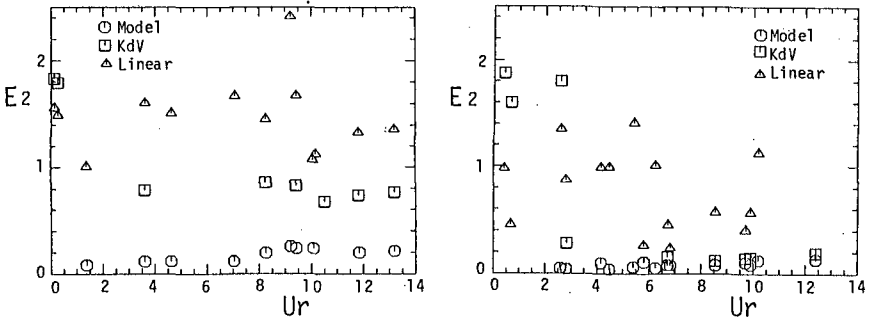
$$E_2(x) = \int_0^{T_0} (\eta_{ob} - \eta_{ca})^2 dt / \int_0^{T_0} \eta_{ob}^2 dt \quad , \quad (12)$$

This denotes the difference with the water surface elevation including the propagation speed between the simulated result η_{ca} and the measured one η_{ob} at P.2. The relation between the error criterion E_2 and the Ursell number(Ur) is shown in Fig. 8. Qp in the figure denotes the spectral peakedness parameter.

Figure 9 shows the comparison of temporal wave profile at P.2 between the measured result and the simulated one in the case that the aforementioned error E_2 is 0.23.

3 Propagation of swell

Numerical simulations using the model equation are made in order to investigate on the characteristics of spatial variations of wave grouping, by giving the following temporal water surface elevation with the desired statistics to the model equation as the



(a) $Q_p \approx 2$ (b) $Q_p \geq 4$
 Fig. 8 The relation between error criterion E_2 and U_r .

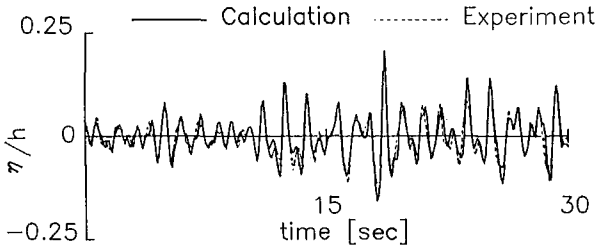


Fig. 9 Comparison with experimental wave profile in the case of the value of $E_2 = 0.23$.

boundary condition at origin.

$$\eta(0, \tau) = \sum_{n=0}^{\infty} 2|A_n| \sin(2\pi f_n \tau + \varepsilon_n) \quad , \quad (13)$$

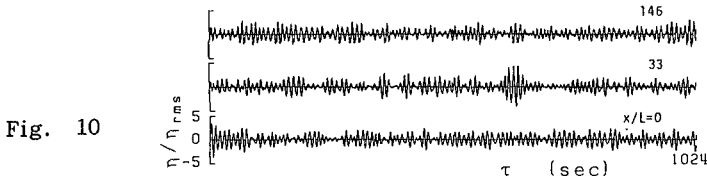
where, ε_n is the random phase angle distributed uniformly between 0 and 2π , M the number of the Fourier modes and 2^{11} in this study, A_n denotes the amplitude of the n th Fourier mode and is related to the spectral density $S(f)$ as

$$A_j = \sqrt{2 \int_0^{\infty} S(f) \delta(f - f_j) df / T_0} \quad , \quad (14)$$

The initial spectrum $S(f)$ is given so as to have the Wallops type and the values of parameters governing the spectral form are determined for the initial waves so as to have the desired statistics with the dispersion parameter kh , the nonlinear parameter ka and the spectral bandwidth parameter m . Here, k is the wave number which is correspondent to the frequency at the spectral peak and is calculated through the

Tablu 1 The relation between m and Q_p .

m	5	15	30	55
Q_p	2.00	4.04	5.90	8.07



Wave profile of numerically simulated waves during the propagation ($kh=2.0$, $ka=0.15$ and $m=15$).

linear dispersion relation, and the amplitude equals to the half of the significant wave-height $H_{1/3}$. The value of m is about 5 in the case of wind waves and is over 15 for swell. Table 1 indicates the present relation between m and Q_p .

Figure 10 shows the temporal water surface elevations at $x/L=0$, 33 and 146 of the waves simulated with using the model equation under the initial statistics of $kh=2.5$, $ka=0.15$ and $m=15$.

4 Spatial variation of wave grouping

Groupiness Factor(GF) defined by Funke and Mansard[1979] is employed here as statistics of describing wave grouping and its spatial variation dependent on the initial values is investigated for the simulated waves. Figure 11 indicates the spectral forms

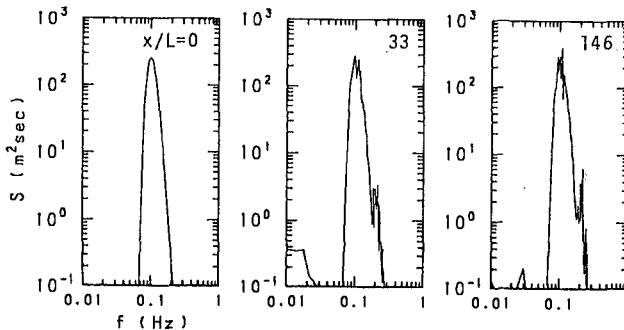


Fig. 11

Variation of the spectral form of the wave shown in Fig.10.

of nonlinear waves shown in Fig. 10. The remarkable growth of the modulation at $x/L=33$ is supposed to be due to the pronounciation of side-band modal components.

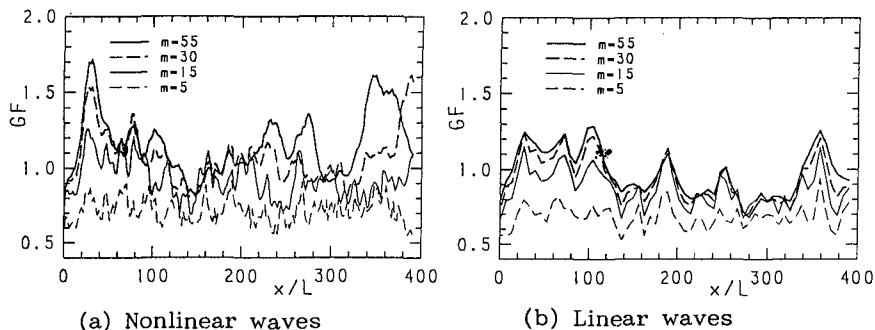
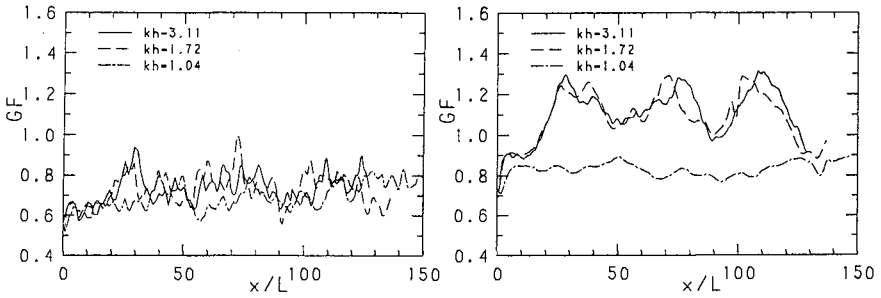


Fig. 12

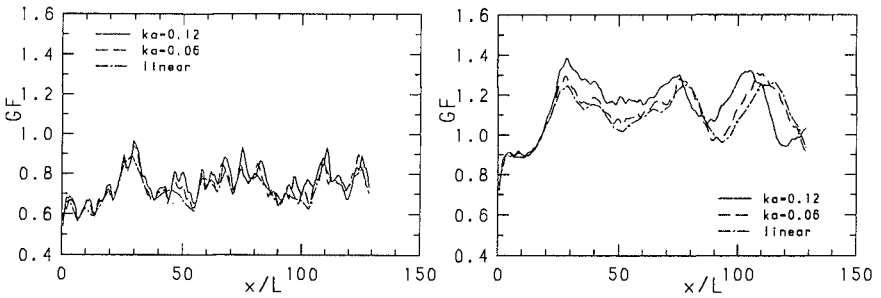
Influences of bandwidth parameter m on the spatial variation of GF of nonlinear and linear waves. ($kh=2.5$, $ka=0.15$)

Figure 12(a) shows the spatial variation of GF of the waves simulated with the model equation under the initial statistics of $kh=2.5$, $ka=0.15$ and some spectral bands of $m=5, 15, 30$ and 55 . The spatial variations of GF of linear waves under the same initial statistics are in Fig. 12(b), in order to show the influence of nonlinearity on wave grouping. It is found from the figures that not only the value of GF of nonlinear waves but also that of linear waves varies spatially during the propagation. The former variation is conjectured to be caused by the modulational instability, while the latter one is clearly due to linear combination of the Fourier modes. However, the former variation gets to exceed greatly the latter one and the influence of the nonlinearity becomes dominant as the value of m increases, that is, the spectral bandwidth becomes narrower.

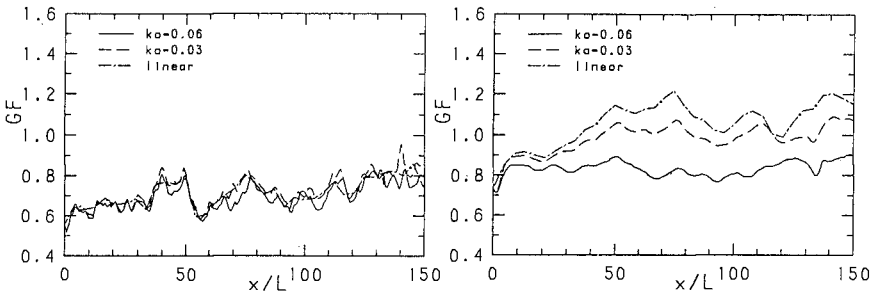
The influence of kh on the spatial variations of GF is examined. Figure 13 shows the influence under the initial statistics of $ka=0.12$, $m=5$ and 30 and $kh=1.04$, 1.72 and 3.11 . In the broad band case of $m=5$, the spatial variation of GF is not so dependent on the value of kh and the influence of kh is not so conspicuous. However, under the narrow band spectrum of $m=30$, the difference between the case of $kh=1.04$ and those of $kh=1.72$ and 3.11 is very large. This remarks that wave grouping catastrophically changes at the vicinity of $kh=1.40$, which is the critical point of the modulational instability in the model equation, under the spectrum of finite bandwidth.



(a) $m=5$ (b) $m=30$
 Fig. 13 Influences of kh on the spatial variation of GF.



(a) $m=5$ (b) $m=30$
 Fig. 14 Influences of ka on GF under $kh=3.11$.



(a) $m=5$ (b) $m=30$
 Fig. 15 Influences of ka on GF under $kh=1.04$.

In order to investigate the nonlinear effect on the variation of GF, we carried out some numerical simulations. Figures 14 and 15 show the influence of the value of ka on the variation of GF. The statistics of initial waves are $kh=3.11$, $ka=0.06$ and 0.12 , $m=5$ and 30 in the Fig. 14. And, those of initial waves in Fig.

15 are $kh=1.04$, $ka=0.03$ and 0.06 , $m=5$ and 30 . In these cases, the growth of wave grouping becomes strengthened as the spectral bandwidth get to be narrower from $m=5$ to $m=30$. These results show that the effect of nonlinearity on the growth of wave grouping could be almost ignored so long as the value of ka is less than 0.12 .

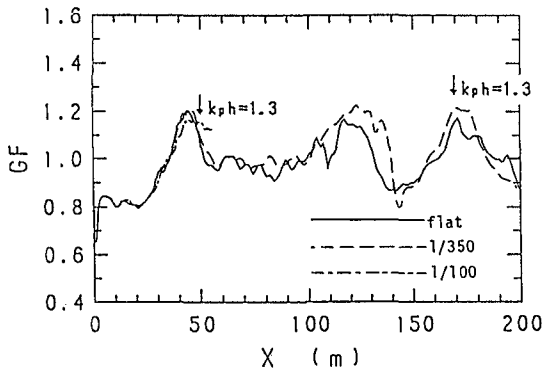


Fig. 16

Influences of bottom slope on the spatial evolution of GF

In order to investigate the effect of bottom slope on the variation of GF, we carried out the numerical simulation for three different values of bottom slope. The statistics of the initial waves are $kh=3.11$, $ka=0.06$ and $m=15$, and the simulation results are shown in Fig.16. It is found that the bottom slope has little influence on the behavior of GF so long as the value of kh is larger than 1.3 . From this result, we can conclude that the spatial variation of wave grouping should be considered as a result of the modulational instability rather than that of shoaling wave.

6. Spatial variations of representative wave-heights

If wave grouping is a consequence of finely tuned focussing of linear wave trains or modulational instability of nonlinear wave trains, it is natural that the influence of wave grouping comes not only to a time sequence of zero-cross waves but also to representative wave-heights. Figure 17 shows spatial variations of representative wave-heights of the swell of which initial statistics are $kh=2.5$, $ka=0.15$, $m=5$ and 30 . Since the swell propagate on a flat bottom, the values of η_{rms} , \bar{H} and $H_{1/3}$ are almost invariant as the matter of course. On the other hand, the value of H_{max} varies greatly in the propagation process and the

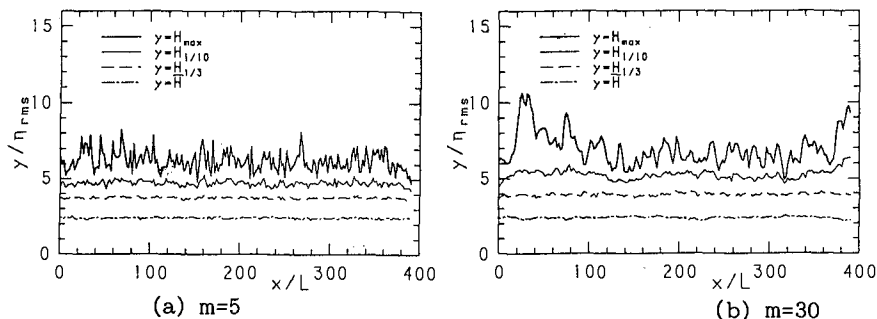


Fig. 17 Spatial evolution of representative wave-heights.

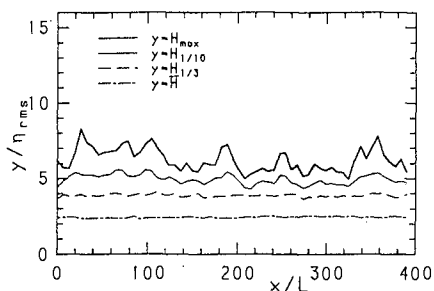


Fig. 18 Spatial evolution of representative wave-heights in linear wave field

ratio of $H_{max}/H_{1/3}$ often exceeds 2.0 that is the value employed in the design of offshore structures. Figure 18 shows spatial variations of representative wave-heights of the linear wave under the initial statistics of $kh=2.5, ka=0.15$ and $m=30$. The value of \bar{H} , $H_{1/3}$ and $H_{1/10}$ are similar to those shown in Fig.17(b). The value of H_{max} varies in the propagation process, but the ratio of $H_{max}/H_{1/3}$ never exceed 2 in this linear calculation. Therefore the appearance of a region with $H_{max}/H_{1/3} > 2$ which was observed in Fig. 18 can be ascribed to the nonlinear interaction. Figure 19 shows the relation between GF and H_{max} under the initial statistics of $kh=2.5, ka=0.15$ and $m=30$. The variation of GF agrees well with that of H_{max} . This indicates that the variation of H_{max} is dependent on GF in the propagation process. Figure 20 shows the relative frequency of the ratio H_{max}/\bar{H} derived from the surface elevation at each location in the propagation process. A solid line denotes the relative frequency of the waves of which zero-cross wave-heights obey the Rayleigh distribution. Although there is no significant

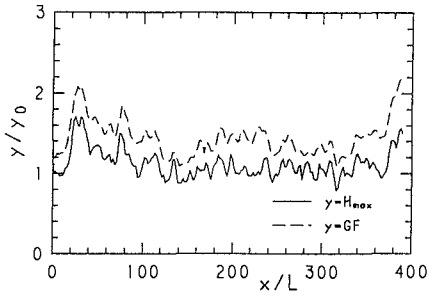


Fig. 19
the present relation between GF and H_{max}

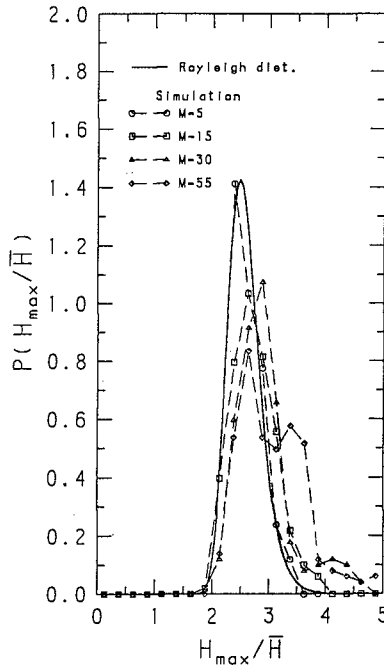


Fig. 20
Relative frequencies of the ratio H_{max}/\bar{H} at each location in the propagation process.

difference in the case of $m=5$ between the result simulated by the model equation and that based on the Rayleighan, the difference between both the results becomes significant in the case of $m=30$. This

demonstrates that the consideration of the influence of wave grouping becomes necessary in the reliable prediction of design waves as the spectral band-width gets to narrower.

7. Conclusions

The accuracy and applicable region of the model equation was made clear with respect to the wave statistics of kh and ka or U , through experimental examinations. Wave groups seen in the swell having $kh \geq 0.14$, $ka \geq 0.12$ and $m \geq 30$ are originated primarily by the modulational instability, although the other wave groups are generally consequences of linear combination of different, independent Fourier modes. Wave packets exhibited generally in the swell varies spatially during the propagation differently from the envelope solitons and should be treated as unsteady phenomena. The characteristics of their spatial variations were made clear through GF and representative wave-heights and were found to be dependent on the statistics of kh , ka and m . The maximum wave-height H_{max} is closely related with the wave grouping and the relative frequency of the ratio H_{max}/\bar{H} considerably deviates from that based on the Rayleigh distribution under the narrow band spectrum of $m \geq 30$.

The authors wish to express their thanks to Dr.M.Tanaka for his valuable advices.

References

- Yasuda,T.,M.Tanaka,A.Ukai and Y.Tsuchiya(1988)
Proc. of Coastal Eng., Vol. 35, JSCE pp.93-97.
Yasuda,T.,M.Tanaka,K.Ito (1989)
Proc. of Coastal Eng., Vol. 36, JSCE pp.104-108.
Funke,E. and E.Mansard(1979)
Hyd. Lab. Rep. LTR-HY-66, NRC Canada, 54p.

CHAPTER 63

SEA-AIR INTERACTIONS IN THE COSTAL CIRCULATION AROUND GRAN CANARIA ISLAND (SPAIN)

Begoña Tejedor¹, Miguel Alejo², Luis Tejedor³

Abstract

This paper presents the results of analyzing six months of simultaneous records of water levels, currents, wind and atmospheric pressure that have been collected outside the surf zone at three locations in the eastern coast of Gran Canaria (Canary Islands, Spain). The results shown in this paper concern mainly one of the coastal stations, placed at the port of Las Palmas city. Although tides and currents use to be astronomically dominated, a non-permanent term appears in certain time intervals, identified as a long wave -rotary type- with a frequency very close to the inertial one. Another interesting result is the appearance of harmonic tidal periodicities in the atmospheric variables, which suggest a higher importance of the meteorological tides or/and a strong interaction sea-air.

Introduction

As it is well known, nearshore currents outside the surf zone use to be mainly dominated by tide and wind. Wind affects the upper layer of water and does not use to produce permanent periodic terms in the currents. But meteorological variations may give rise to important effects in the current patterns, either by enhancing or weakening some existing periodic terms or by generating new ones, that appear in the spectrum as new peaks which can only be explained via sea-air interaction.

¹Assoc. prof.; ²Acting full prof.; ³Senior Full prof.
Univ. of Las Palmas de Gran Canaria. Dept. of Physics.
Faculty of Marine Sciences.
35017 Tafira. Las Palmas de Gran Canaria. SPAIN.

The Canary Islands are a privileged place for observing oceanographic phenomena, as they are oceanic islands that are in the path of a general oceanic circulation and they are wide enough to perturbate it and to super-impose a very interesting local pattern. Moreover, the archipelago is placed between the northern parallels $27^{\circ}30'$ and $29^{\circ}30'$, in the zone where the intense solar radiation and the local earth parameters enhance sea-air interaction and resonance phenomena, and trade winds are dominant.

In the present work, the attention has been focussed in the eastern coast of Gran Canaria Island (fig. 1), where 3 coastal stations were established and at least six months of simultaneous and continuous records of tide, currents and meteorological variables were collected. The results now shown are mainly obtained from the station No. 3 (port of Las Palmas).

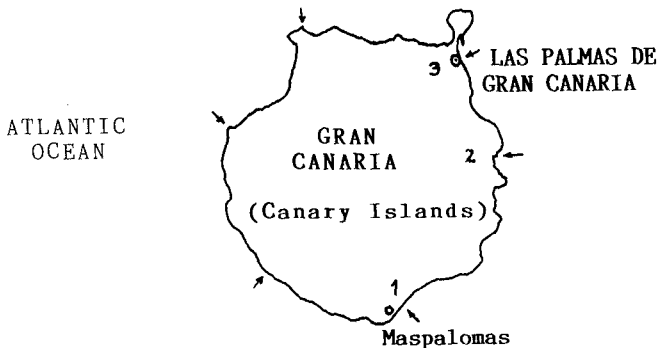


Figure 1.- Location of measurement stations

Data collection and analyzing methods

The measurements of currents are performed by 2 current meters placed at 15 and 30 m depth, in areas of about 45 m total depth. The meteorological data recorded are pressure, temperature and wind velocity at 10 m above the sea surface. The instruments are made by Aanderaa, and the sampling interval is set to 30 minutes.

Current and wind velocities were split into North-South and East-West components, approximately corresponding to longshore and transverse directions. For data from station No. 1, another pair of axes was also considered, resulting from linear regression in the polar diagram.

As only long period constituents were to be studied, a low pass filter was applied to the series, after which a final lag of 1 hour resulted.

The main analyses were achieved by both harmonic and spectral methods. The harmonic analysis uses 69 astronomical constituents, being possible to add 77 more ones for including shallow water terms. The least-square technique is applied with nodal corrections for the longest constituents that can be resolved over the length of the record. If the record length does not allow to determine a certain constituent, an estimate may be obtained by inference.

The term "component" has been used for longshore or transverse series, while the term "constituent" was used for harmonics.

The results are amplitude and Greenwich phase of every constituent, as well as the axis length and orientation of the ellipses with respect to the reference system and the phase angle.

By means of spectral analysis, the same results are obtained, as well as the cross-spectra between pairs of variables and the clockwise and anticlockwise rotary spectra.

The study was performed for months, quarters and half-years, what allows to estimate the stability of the constituents as a function of time.

Constituent	Current Component			
	East - West		North - South	
	Mean	σ	Mean	σ
Shallow Water	11.52 %	4.40	4.12 %	1.94
Long Period	4.11 %	2.28	16.83 %	5.13
Diurnal	20.56 %	6.58	20.05 %	4.11
Semidiurnal	30.20 %	12.51	36.85 %	5.75
Third-diurnal	4.36 %	2.21	2.64 %	2.43
Residual	29.25 %	8.48	19.51 %	2.74

Table 1.- Distribution of variance in the current measurements at the Port of Las Palmas. Depth: 15 m

Results of harmonic analysis

Table 1 shows the spectral distribution of the mean variance of the current -a measure of the energy-, with the standard deviation, obtained from the half-year records of station No. 3, at a depth of 15 m.

The maximum flood (south-going) reaches 40 cm/s, and the maximum ebb (north-going) attains a value of 30 cm/s. The currents flow predominantly along the North-South direction (longshore). The transverse current records exhibit a higher variability and a strong level of noise.

The frequency band with the greatest amount of energy is the semidiurnal one in both components, what means a 30.2% for the longshore one and a 12.5% for the transverse one. The diurnal band amounts to 20.6% and 6.5% respectively for the longshore and transverse components.

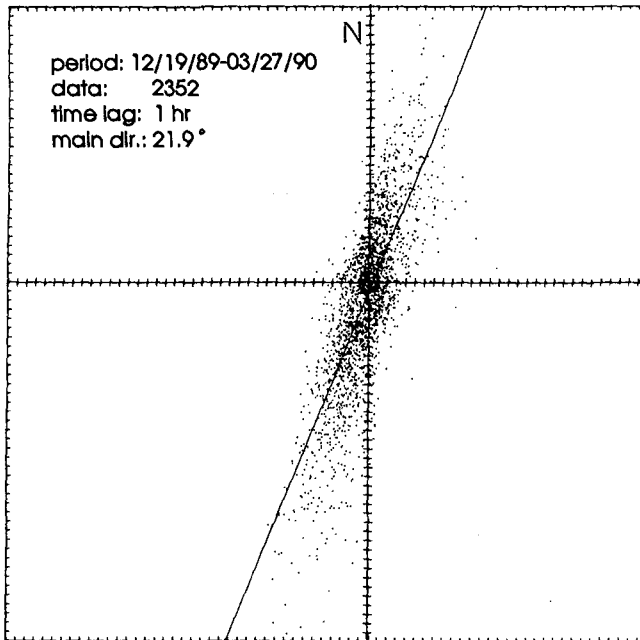


Figure 2.- Polar diagram of currents at the Port of Las Palmas. Depth: 15 m

In the polar representation (fig. 2) it may be seen that the main direction of the current is almost North-South, with a certain asymmetry: data toward the south and with high speed are deflected to the east, probably due to the gradient currents generated after the strong and persistent trade winds blowing to the south and given rise to an over-elevation at the coast.

The amplitudes and phases of the main tidal constituents in the 3 stations are shown in table 2. It can be seen the relative importance of the semidiurnal and diurnal terms. The stability of the tidal constituents was obtained after analyzing monthly records. The greatest deviations correspond to the S_2 constituent, what suggests that this band may be affected by non-tidal phenomena. Some characteristics of the tide at Las Palmas can be deduced from table 3. The ratio $(K_1+O_1)/(M_2+S_2)=0.11$ means a semidiurnal tide.

With respect to the currents, table 4 offers the characteristic parameters of the ellipses of the main constituents (after Godin, 1972): major and minor half-axis, angle with respect to the East-West axis and rotation sense. The axes of the main constituents are orientated parallelly to the coast.

	Station 1		Station 2		Station 3	
	H(cm)	G(°)	H(cm)	G(°)	H(cm)	G(°)
MSF	0.87	254.8	1.25	251.2	1.64	61.5
$2Q_2$	0.78	317.4	0.73	158.1	0.15	297.6
O_1	4.91	81.0	4.62	268.8	4.95	278.4
NO_1	0.31	194.5	0.68	320.7	0.47	246.1
K_1	6.70	204.0	5.90	7.6	6.05	40.9
N_2	16.72	329.6	14.76	323.5	13.23	348.6
M_2	61.28	343.6	71.01	338.4	73.45	0.4
S_2	29.66	16.8	22.02	7.3	31.07	35.8
MO_3	0.05	295.2	0.09	76.2	0.10	173.6
M_3	0.43	236.1	0.55	67.3	0.49	114.8
M_4	0.66	353.5	0.64	21.0	0.75	47.8

*Table 2.- Tidal constituents at the various stations
(H: amplitude; G: phase Greenwich)*

	M_2/S_2		K_1/O_1		$\frac{K_1+O_1}{M_2+S_2}$		K_1/NO_1	
Analyses Six Months	2.67		1.31		0.11		21.77	
Analyses Monthly	Mean	σ	Mean	σ	Mean	σ	Mean	σ
	2.69	0.24	1.31	0.08	0.11	0.01	35.42	26.63

Table 3.- Characteristics of tide at the Port of Las Palmas

	Station 1				Station 2				Station 3			
	M	m	θ	*	M	m	θ	*	M	m	θ	*
MSF	1.59	0.01	137.7	A	0.69	0.16	23.0	C	1.77	0.12	76.8	A
2Q ₁	0.60	0.02	139.9	C	0.35	0.13	47.3	A	0.12	0.02	79.8	C
O ₁	1.44	0.06	137.2	A	0.16	0.01	94.7	C	0.36	0.08	63.6	C
NO ₁	0.81	0.02	131.6	C	0.41	0.16	179.4	A	2.26	0.48	76.8	C
K ₁	3.07	0.05	137.1	C	0.29	0.08	15.3	A	2.44	0.30	75.3	C
N ₂	0.89	0.04	134.7	C	0.48	0.08	28.7	C	0.63	0.07	86.0	C
M ₂	2.78	0.04	139.8	A	1.96	0.03	26.6	A	5.7	0.24	75.7	C
S ₂	1.23	0.11	144.8	A	0.72	0.22	19.9	A	2.60	0.08	74.2	C
MO ₃	0.05	0.01	110.4	C	0.21	0.03	36.2	C	0.30	0.03	85.3	C
M ₃	0.04	0.01	115.5	C	0.29	0.07	34.2	A	0.24	0.18	112.9	C
M ₄	0.15	0.01	118.8	A	0.88	0.01	35.3	A	0.62	0.03	82.3	C

Table 4.- Ellipses of the current constituents at the various stations.
Depth 15 m.

M: major half-axis; *m*: minor half-axis; θ : inclination
*: sense of rotation (C: clockw.; A: anticlockw.)

The stability of the characteristic parameters is shown in table 5, where their amplitudes and phases can be seen. As usual, the stability of the surface displacements is higher than the stability of the currents. Nevertheless, S₂ makes an exception.

The ratio between tidal amplitudes and current amplitudes for the diurnal and semidiurnal bands is not a constant. It gives a significantly higher value for the constituents NO₁ and 2Q₁ (more important for the first one),

		A (cm)				G (°)			
		Mean	σ	Max	Min	Mean	σ	Max	Min
MSF	u	0.26	0.24	0.67	0.07	227.1	85.3	301.2	183.8
	v	1.20	0.89	2.36	0.14	244.3	91.6	331.4	158.2
2Q ₁	u	0.28	0.20	0.59	0.09	184.5	60.2	220.7	140.6
	v	0.95	0.49	1.56	0.21	148.1	50.2	170.8	110.1
O ₁	u	0.43	0.16	0.53	0.15	172.1	30.0	190.3	155.3
	v	1.31	0.51	1.91	0.50	142.7	20.6	158.3	138.5
NO ₁	u	1.18	0.38	1.66	0.67	136.1	40.7	150.8	100.1
	v	3.23	1.15	4.13	1.50	90.7	30.8	110.7	58.4
K ₁	u	0.52	0.24	0.90	0.30	38.9	18.1	49.3	22.1
	v	2.33	1.18	3.69	0.62	12.3	11.1	22.4	1.9
N ₂	u	0.46	0.14	0.66	0.30	359.6	25.7	358.9	330.4
	v	1.75	0.68	2.79	0.88	302.1	18.8	309.4	298.4
M ₂	u	2.10	1.20	4.02	0.98	288.1	27.1	290.6	254.3
	v	6.77	1.46	8.32	4.37	278.0	15.6	283.4	268.1
S ₂	u	0.67	0.24	0.94	0.37	12.5	10.5	17.2	4.5
	v	2.45	1.12	3.73	0.87	6.0	10.1	9.1	0.3
MO ₃	u	0.23	0.08	0.31	0.10	297.7	30.3	320.0	253.2
	v	0.46	0.08	0.53	0.33	245.9	22.3	250.6	222.8
M ₃	u	0.37	0.28	0.84	0.08	243.7	25.7	259.7	220.4
	v	0.82	0.83	2.26	0.25	143.4	18.9	155.2	130.6
M ₄	u	0.44	0.52	1.33	0.06	79.5	30.2	100.8	50.1
	v	1.08	0.82	2.50	0.45	60.1	15.2	71.8	46.2

Table 5.-Stability of current constituents at the Port of Las Palmas from monthly analyses. Depth 15 m

	M ₂ /S ₂		K ₁ /O ₁		$\frac{K_1+O_1}{M_2+S_2}$		K ₁ /NO ₁	
Analyses Six Months	2.72 (2.83)		1.78 (1.84)		0.39 (0.34)		0.72 (0.64)	
Analyses Monthly	Mean	σ	Mean	σ	Mean	σ	Mean	σ
	3.3 (3.1)	2.1 (1.6)	3.2 (3.2)	2.4 (2.4)	0.39 (0.34)	0.04 (0.03)	0.83 (0.93)	0.4 (0.5)

Table 6.-Characteristics of currents at the Port of Las Palmas. N-S component at 15 m. Major half-axis of the ellipse: ()

what is coherent with the presence of non-tidal terms. Some characteristics of the currents can be appreciated in table 6. Although the ratio $(K_1+O_1)/(M_2+S_2) = 0.39$ suggests a mixed tidal current with semidiurnal predominance, the high value of the NO_1 constituent or other waves with close frequencies causes a certain modulation with diurnal effect, which in certain occasions results in more energy in the diurnal band than in the semidiurnal one.

Results of spectral analysis

The spectral analysis of the records confirms the information given by the harmonic analysis. Figure 3 shows a typical spectrum of the longshore component of the current, at 15 m depth and corresponding to station No. 3 (Port of Las Palmas). Maxima corresponding to diurnal, semidiurnal, third-diurnal, quarter-diurnal periods, etc. can be observed, as well as low frequency maxima for 38 hrs., 50 hrs. and 4.7 days. Analogous results are obtained for depth 30 m.

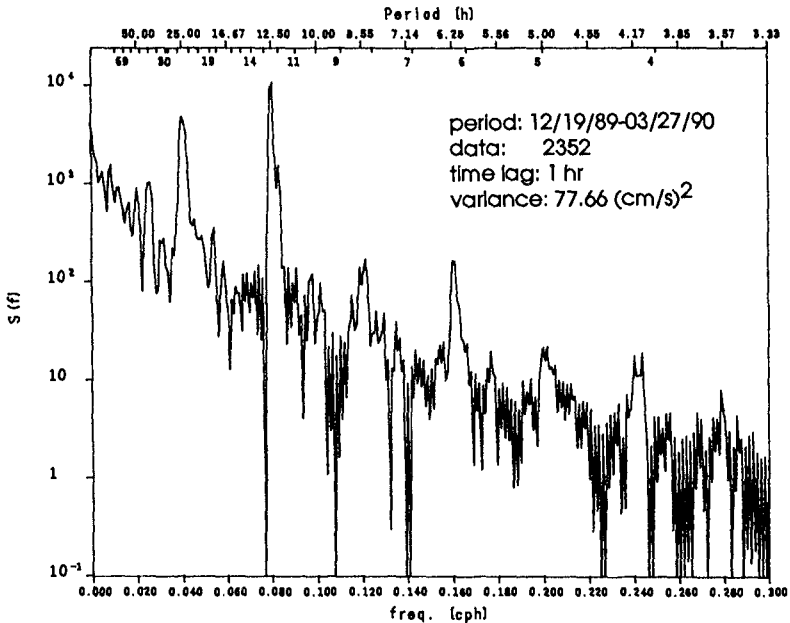


Figure 3.-Power spectrum of the longshore component (N-S) of the current at the Port of Las Palmas. Depth 15 m

In the transverse components of the current (fig. 4) there is less energy and the ratio signal/noise is lower, for what only for the diurnal, semidiurnal, third-diurnal and quarter-diurnal bands maxima are well defined:

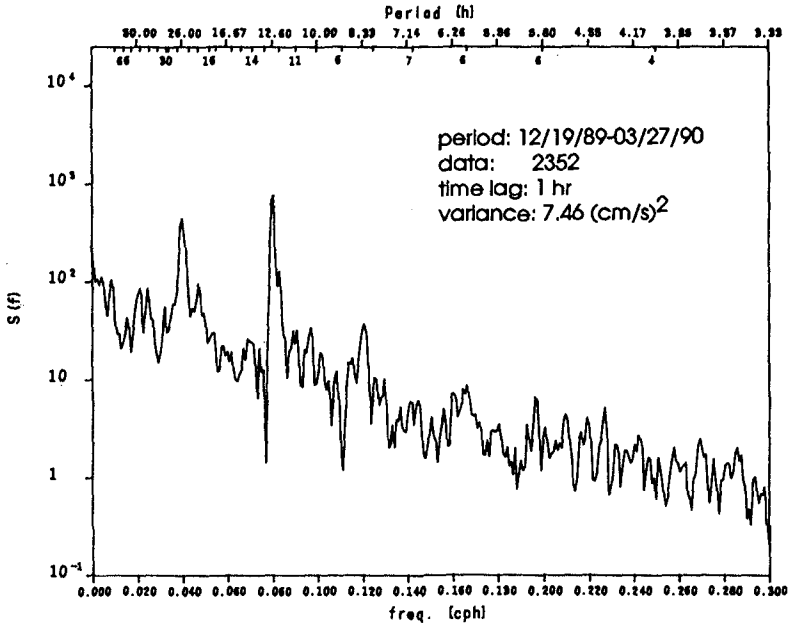


Figure 4.-Power spectrum of the transverse component (E-W) of the current at the Port of Las Palmas. Depth 15 m

Cross-spectra between the series at 15 m and at 30 m below the surface allow to deduce a high coherence (fig. 5), and the phase shift is negligible in the most significant frequencies. Rotary spectra for both depths confirm the clockwise rotation in the astronomical frequencies. So a barotropic movement may be inferred.

In order to correlate the meteorological variables with the currents, the power spectra of the atmospheric pressure and temperature were computed. Figure 6 shows the power spectrum of the pressure. Perhaps surprisingly, the similitude in the energetic distribution is quite high, and what is more, there are maxima at the diurnal, semidiurnal, third diurnal, quarter-diurnal bands, etc. This is not common at all, and a similar trend may be observed in the temperature.

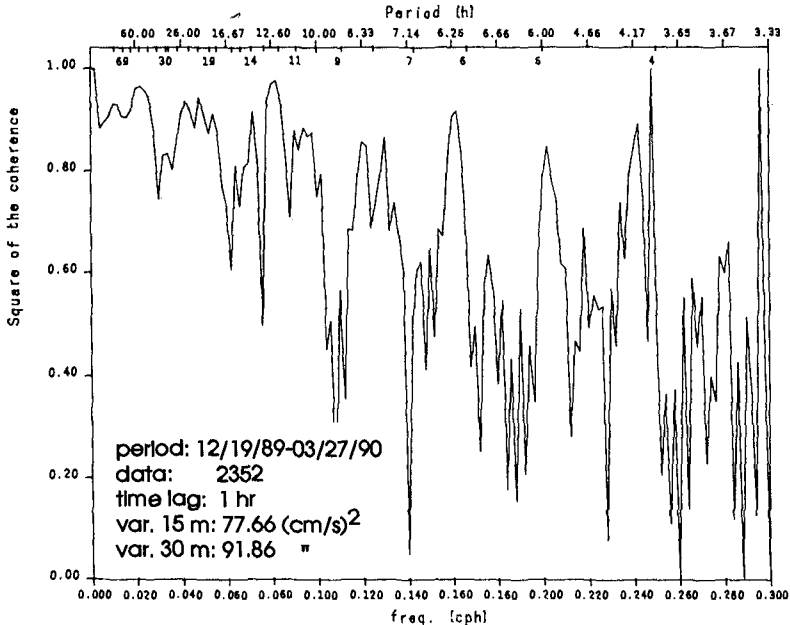


Figure 5.-Cross spectrum of the longshore components (N-S) of the current at the Port of Las Palmas at 15 and 30 m. Square of the coherence function.

Nevertheless, wind analysis does not provide significant results with respect to this phenomenon, but it may be explained taking into account the strong energy and persistence of the trade winds, which mask weaker terms such as breeze.

Other results

When comparing monthly analyses with the analysis of the whole record, two other significant results appear:

- The constituents with frequencies close to 0.0263 cph use to appear in all records.
- While in the complete half-year record of currents the semidiurnal band has more energy (almost 40% of the total energy) than the diurnal one (25%), in some monthly analyses both bands seem to have similar amounts of energy and, in some cases, the diurnal band even overtake the semidiurnal one. The only logical ex-

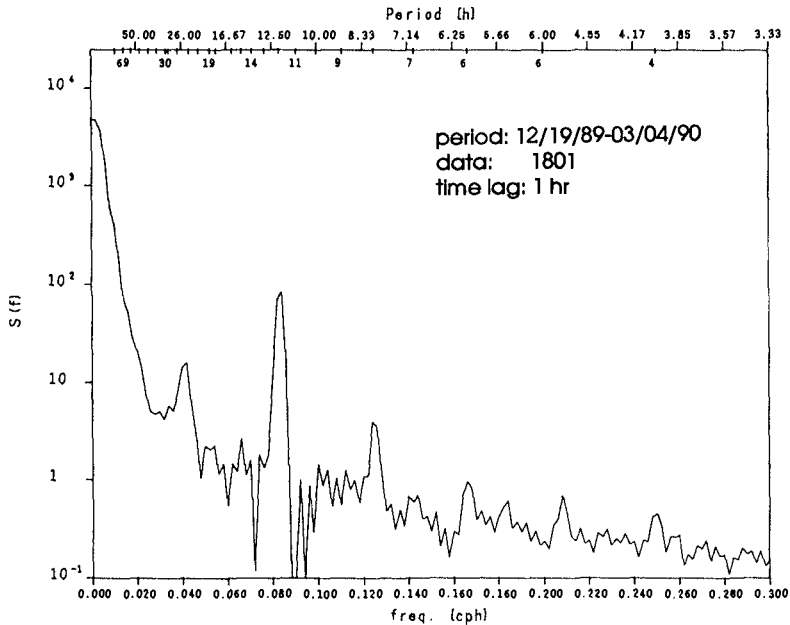


Figure 6.—Power spectrum of the atmospheric pressure at the Port of Las Palmas

planation for this phenomenon is the presence of non-tidal terms in the diurnal band, what is not strange as the inertial frequency is here 0.0391 cph.

In order to catch this wave, analyses were focussed on sections of the records that fulfil the conditions of having more energy in the diurnal band than in the semi-diurnal one and corresponding to neap tide, with the aim of getting the highest signal/noise ratio.

An example of this occurred between the 15th of February and the 4th of March of 1990 (fig. 7). The energy in the diurnal band is 36.9% and in the diurnal one is only 26.3%. Tides were in the neap cycle. In this period, harmonic and spectral analysis provide different importance for the astronomical constituents. The term NO_1 is the paramount one by spectral analysis, but it is of second order by harmonic analysis. So, one may deduce that a wave with frequency close to that of the NO_1 term is present. Its former energy need not be strong, as non-linear interaction and resonance with the astronomical term may give rise to the significant peak reached in the spectrum.

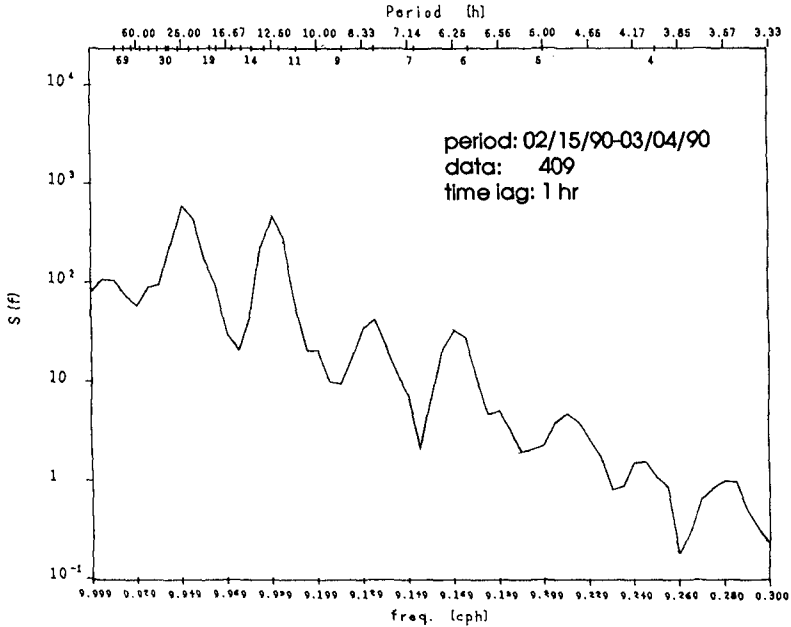


Figure 7.-Power spectrum of the longshore component (N-S) of the current at the Port of Las Palmas. Depth 15 m

An iterative approach was used in order to define the parameters of this wave. A scanning of the frequencies between the O_1 and the K_1 on the residual series resulting after subtracting the predicted series due to astronomical terms only from the recorded series (Pugh and Vassie, 1976), and fitting by least squares, gives an amplitude of 2.16 cm/s (for the major half-axis) and a frequency of 0.0398 cph, very close to the inertial frequency 0.0391 cph. The generation and propagation of this wave are presently being studied, but a rotary, Kelvin wave is assumed, as water over-elevations are negligible. After subtracting this term to the observed series, the results of the spectral analysis are normal and they are coherent with those obtained by harmonic analysis.

Finally, it is interesting to compare the power spectra of currents and meteorological variables (fig. 8).

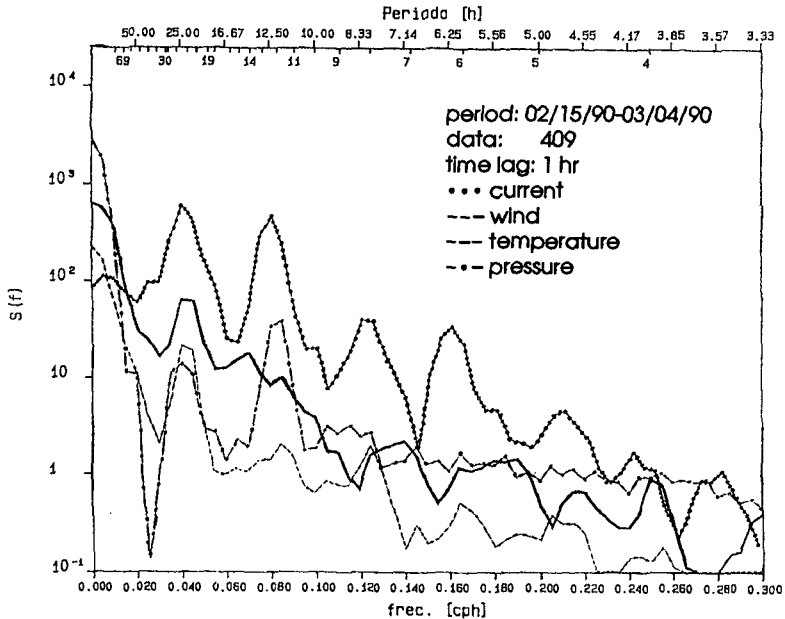


Figure 8.-Power spectra of the longshore components (N-S) of the current at 15 m and the wind, the atmospheric temperature and the atmospheric pressure at the Port of Las Palmas

Conclusions

As main conclusions of this work, we can underline:

- The characteristics of the tides and currents use to be astronomically dominated, with a clear influence of the wind in the layer close to the surface.
- A non-permanent term appears in certain intervals of the current records. This term is identified as a long wave with a frequency very close to the inertial one. As there is small correspondence with the elevation of the surface, a rotary wave is assumed.
- Rather surprisingly, the periodicities involved in the meteorological variables go beyond the traditionally assumed ones, showing a pattern very similar to that of the oceanic tide and currents. This important observation agrees with other recent observations (Cartwright *et al.*, 1985), and suggests a higher importance of the meteorological tides or/and a strong interaction sea-air.

References

CARTWRIGHT, D.E., SPENCER, R. AND VASSIE, J.M., 1985. *Some minor but interesting properties of the Atlantic Ocean Tides*. 10th Internatl. Symp. on Earth Tides. Madrid.

GODIN, G., 1972. *The Analysis of Tides*. Univ. of Toronto Press.

PUGH. D.T., and Vassie, J.M., 1976. *Tide and Surge Propagation Off-shore in the Downing Region of the North Sea*. Deut. Hydrogr. Zait. 29, p. 163-213.

CHAPTER 64

A NUMERICAL METHOD OF SOLITARY WAVE FORCES ACTING ON A LARGE VERTICAL CYLINDER

Takumi Ohyama ¹

ABSTRACT

Solitary wave forces acting on a large vertical cylinder are calculated using a time-stepping method which improves upon the conventional boundary element approaches. The effect of this improvement on the numerical solution is a more realistic solitary wave profile. Nonlinear effects on the solitary wave forces are investigated by comparing the numerical results with the first approximations given by Isaacson. The first approximation for overturning moment is underestimated remarkably when the incident wave height is relatively high.

1. INTRODUCTION

In order to design coastal or offshore structures, accurate prediction of wave forces is necessary. In general, the incoming wave height considered during design is substantial, so that the nonlinear wave effects cannot be ignored and the linear potential theory may not predict realistic values of wave forces. Among various numerical studies applied to this problem, the methods of approach may be classified into two groups. One approach is based on a perturbation method. Using Stokes' wave theory, second approximations for wave forces acting on a large vertical cylinder have been recently introduced by many researchers. For example, Hunt and Buddour (1981) gave the solution for deep water, and Eatock Taylor and Hung (1987) attempted to derive the definite solution for arbitrary water depth. However, this type of approach cannot be directly extended to higher-order expansions because of difficulties in the treatment of the free surface condition and the nonlinear radiation condition.

¹Institute of Technology, SHIMIZU CORPORATION, Etchujima 3-4-17, Koto-ku, Tokyo 135, JAPAN

The other approach is a time-stepping method in which the boundary integral equations based on Green's theorem are solved at successive time steps. In this approach, the complete boundary value problem of velocity potential is considered without using the assumption of weak nonlinearity. For example, Isaacson (1982) applied this boundary integral equation method to the problem of nonlinear wave scattering around three-dimensional bodies. A similar method was proposed by Nakayama and Washizu (1981) for two-dimensional sloshing problems. However, the potential values on free surfaces were not estimated accurately in the time-stepping procedure of these conventional methods.

This paper studies interactions between a solitary wave and a large vertical cylinder using a newly developed numerical method. The proposed technique treats the interaction as a three-dimensional transient problem, and it improves the time-stepping procedure of the conventional boundary element methods. The effect of the improvement on the numerical solution is investigated by fundamental examinations. Nonlinear effects on wave forces exerted by a solitary wave on a circular cylinder are discussed by comparing the numerical results with first approximations given by Isaacson (1983). The results obtained from this study may be applicable to the design of coastal structures in shallow water.

2. THEORETICAL FORMULATION

2.1 Boundary Integral Equations

Consider a three-dimensional fluid region Ω as shown in Fig. 1. The region is enclosed by the free surface S_F , the body wetted surface S_V , the wave generating boundary S_C , the wall boundaries S_{W1} , S_{W2} , S_{W3} , and the seabed S_B . The boundaries, S_C , S_{W1} , S_{W2} , and S_{W3} , are located sufficiently far from the body so that the diffracted waves will not reach these boundaries during the duration of computation. The fluid is assumed to be incompressible, inviscid and irrotational, so that the fluid motion can be described by a velocity potential ϕ . The velocity potential can be given as the solution satisfying the following governing equation and the associated boundary conditions:

$$\nabla^2 \phi = 0 \quad (\text{in } \Omega), \quad (1)$$

$$\partial \phi / \partial n = 0 \quad (\text{on } S_B, S_{W1}, S_{W2}, S_{W3}), \quad (2)$$

$$\partial \phi / \partial n = 0 \quad (\text{on } S_V), \quad (3)$$

$$\partial \phi / \partial n = -\partial \phi / \partial x = -U(z, t) \quad (\text{on } S_C), \quad (4)$$

$$\partial \phi / \partial n = n_z (\partial \eta / \partial t) \quad (\text{on } S_F), \quad (5)$$

$$\partial \phi / \partial t + (1/2)(\nabla \phi)^2 + g\eta = 0 \quad (\text{on } S_F), \quad (6)$$

in which n and n_z are the direction and the z -component of outward unit normal vector n defined on the boundary surfaces, respectively, and η is the free surface elevation above the still water level. U in Eq. (4) denotes the water particle velocity in the x -direction of the solitary wave given by the analytical solutions. Equation (1) corresponds to the continuity equation of the fluid motion. Equations (2) and (3) relate to the impermeable conditions on the seabed and the walls and the body surface, respectively. In generating waves, the still-water condition is applied as an initial condition, and the kinematic condition as indicated in Eq. (4) is imposed on S_C . Equations (5) and (6) represent the kinematic and the dynamic conditions on S_F , which are considered to be nonlinear.

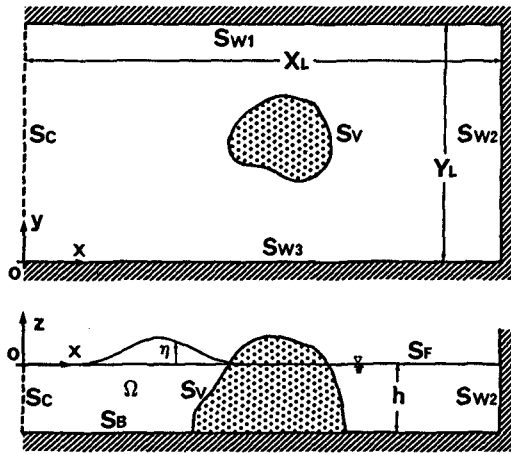


Fig. 1 Coordinate system.

Applying the second form of Green's theorem over the closed surface S containing the fluid region Ω , a boundary integral equation is introduced in which the boundary values of the potential ϕ are related to those of the normal derivative $\partial\phi/\partial n$. The potential $\phi(P)$ at the point $P(x_P, y_P, z_P)$ which lies on S is expressed as

$$\phi(P) = -\frac{1}{\alpha(P)} \int_S \left\{ \phi(Q) \frac{\partial G}{\partial n}(P, Q) - \frac{\partial \phi}{\partial n}(Q) G(P, Q) \right\} ds, \tag{7}$$

where $Q(x_Q, y_Q, z_Q)$ is a point lying on S where the integration is performed and G represents a Green function. $\alpha(P)$ denotes a coefficient calculated by

$$\alpha(P) = - \int_{S_F \cup S_C \cup S_{W3} \cup S_V} \frac{\partial G}{\partial n} ds. \tag{8}$$

The Green function involved in Eq. (7) is chosen to account for the symmetry about the boundaries, S_B, S_{W1} , and S_{W2} , such that

$$G(P, Q) = \frac{1}{r_0} + \sum_{n=1}^7 \frac{1}{r_n}, \tag{9}$$

$$\left. \begin{aligned}
 r_0 &= \sqrt{(C_x)^2 + (C_y)^2 + (C_z)^2}, & r_1 &= \sqrt{(C_x)^2 + (C_y)^2 + (D_z)^2}, \\
 r_2 &= \sqrt{(C_x)^2 + (D_y)^2 + (C_z)^2}, & r_3 &= \sqrt{(C_x)^2 + (D_y)^2 + (D_z)^2}, \\
 r_4 &= \sqrt{(D_x)^2 + (C_y)^2 + (C_z)^2}, & r_5 &= \sqrt{(D_x)^2 + (C_y)^2 + (D_z)^2}, \\
 r_6 &= \sqrt{(D_x)^2 + (D_y)^2 + (C_z)^2}, & r_7 &= \sqrt{(D_x)^2 + (D_y)^2 + (D_z)^2}, \\
 C_x &= x_P - x_Q, & D_x &= x_P + x_Q - 2X_L, \\
 C_y &= y_P - y_Q, & D_y &= y_P + y_Q - 2Y_L, \\
 C_z &= z_P - z_Q, & D_z &= z_P + z_Q + 2h,
 \end{aligned} \right\} \quad (10)$$

in which X_L and Y_L are the length and the width of the fluid region, respectively, as shown in Fig. 1. This Green function satisfies $\partial G/\partial n = 0$ on S_{W1} , S_{W2} and S_B , so that the integrals over these boundaries can be excluded from Eq. (7). Substituting Eqs. (2), (3), (4) and (5) into Eq. (7), the following integral equation is introduced:

$$\phi(P) = -\frac{1}{\alpha(P)} \left\{ \int_{S_F \cup S_C \cup S_{W3} \cup S_V} \phi \frac{\partial G}{\partial n} ds - \int_{S_F} G n_z \frac{\partial \eta}{\partial t} ds + \int_{S_C} G U ds \right\}, \quad (11)$$

The dynamic condition on S_F can be transformed into another integral equation by applying the method of weighted residuals. Substituting Eq. (5) into Eq. (6) and integrating it over S_F after multiplying both sides by a weighting function ω , the following integral equation can be obtained:

$$\int_{S_F} \omega \left[\frac{\partial \phi}{\partial t} + \frac{1}{2} \left\{ n_z^2 \left(\frac{\partial \eta}{\partial t} \right)^2 + \left(\frac{\partial \phi}{\partial X} \right)^2 + \left(\frac{\partial \phi}{\partial Y} \right)^2 \right\} + g \eta \right] ds = 0, \quad (12)$$

where (X, Y) is a local coordinate system on the surface plain normal to the vector n as shown in Fig. 2.

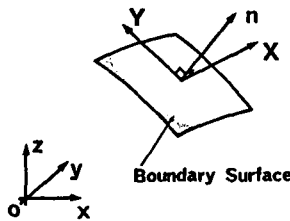


Fig. 2 Local coordinates on the free surface.

2.2 Spatial Discretization of Integral Equations

The boundary surfaces, S_F , S_C , S_{W3} , and S_V , are discretized into finite numbers of triangle elements. The local coordinate system (X, Y) is defined as indicated in Fig.3 over each element. In this figure, $j1, j2, j3$ are nodal point numbers comprising the J -th element, and R denotes a point on the element. Representing the variables of ϕ, η, U and ω as Γ , the values of Γ and $\partial\Gamma/\partial t$ on R can be written as

$$\Gamma = N_J^T \Gamma_J, \quad \Gamma_J^T = \{\Gamma_{j1}, \Gamma_{j2}, \Gamma_{j3}\}, \quad (13)$$

$$\frac{\partial \Gamma}{\partial t} = N_J^T (\Gamma_t)_J, \quad (\Gamma_t)_J^T = \left\{ \left(\frac{\partial \Gamma}{\partial t} \right)_{j1}, \left(\frac{\partial \Gamma}{\partial t} \right)_{j2}, \left(\frac{\partial \Gamma}{\partial t} \right)_{j3} \right\}, \quad (14)$$

in which N_J represents interpolation function vector. If linear distributions of Γ and $\partial \Gamma / \partial t$ over the element are assumed, N_J can be expressed as

$$N_J^T = (1/S_J) \{ S_{j1}, S_{j2}, S_{j3} \}, \quad (15)$$

where S_{j1} , S_{j2} and S_{j3} are defined in Fig. 3 and S_J is the area of the J -th element ($= S_{j1} + S_{j2} + S_{j3}$).

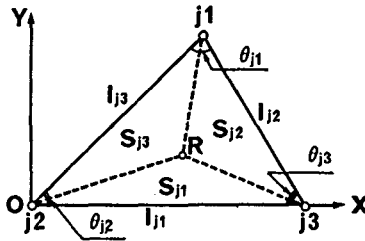


Fig. 3 Definition sketch in the J -th element.

Using the expressions of Eqs. (13) and (14), the integral equation (11) is transformed into

$$\alpha_i \phi_i + \sum_{J=1}^M A_{iJ}^T \phi_J - \sum_{J=1}^{M_F} (n_z)_J B_{iJ}^T (\eta_t)_J + \sum_{J=M_F+1}^{M_F+M_C} B_{iJ}^T U_J = 0 \quad (i = 1, 2, \dots, N), \quad (16)$$

$$A_{iJ} = \int_{S_J} N_J \frac{\partial G}{\partial n} ds, \quad B_{iJ} = \int_{S_J} N_J G ds, \quad (17)$$

in which M and N are the total numbers of triangle elements and the nodal points, respectively. M is made up of M_F elements over S_F , M_C elements over S_C , M_V elements over S_V , and M_W elements over S_{W3} . The surfaces are treated in order S_F , S_C , S_V and S_{W3} as J increases from 1 to M . The vectors, A_{iJ} and B_{iJ} can be calculated numerically, even when i coincides with $j1$ or $j2$ or $j3$. Numerical integrals over all the elements, however, may require time-consuming computational efforts. Therefore, the calculations of A_{iJ} and B_{iJ} are simplified by assuming those values to be constant over the J -th element, when $i \neq j1$ nor $j2$ nor $j3$. Thus

$$A_{iJ} \simeq \frac{S_J}{3} \left(\frac{\partial G}{\partial n} \right)_{iJ} \mathbf{E}, \quad B_{iJ} \simeq \frac{S_J}{3} G_{iJ} \mathbf{E} \quad (i \neq j1, j2, j3), \quad (18)$$

$$\mathbf{E}^T = (1, 1, 1), \quad (19)$$

where $(\partial G/\partial n)_{iJ}$ and G_{iJ} are the corresponding values at the center of gravity in the J -th element.

Substituting Eqs. (13) and (14) into Eq. (12), we obtain

$$\sum_{J=1}^{M_F} \left[\int_{S_J} N_J N_J^T ds (\phi_t)_{iJ} + \frac{(n_z)_J^2}{2} \int_{S_J} N_J N_J^T (\eta_t)_{iJ} N_J^T ds (\eta_t)_{iJ} + \frac{1}{2} \{ (\phi_X)^2 + (\phi_Y)^2 \}_{iJ} \int_{S_J} N_J ds + g \int_{S_J} N_J N_J^T ds \eta_{iJ} \right] = 0. \quad (20)$$

The velocity squared on the surface plain, $\{(\phi_X)^2 + (\phi_Y)^2\}_{iJ}$, is assumed to be constant over the J -th element. That is,

$$\begin{aligned} \{(\phi_X)^2 + (\phi_Y)^2\}_{iJ} &= \frac{1}{4S_J^2} \{ (l_{j1}\phi_{j1})^2 + (l_{j2}\phi_{j2})^2 + (l_{j3}\phi_{j3})^2 \} \\ &\quad - \frac{1}{S_J} \left\{ \frac{\phi_{j1}\phi_{j2}}{\tan \theta_{j3}} + \frac{\phi_{j2}\phi_{j3}}{\tan \theta_{j1}} + \frac{\phi_{j3}\phi_{j1}}{\tan \theta_{j2}} \right\}. \end{aligned} \quad (21)$$

The integrals involved in Eq. (20) can be calculated analytically and may be transformed into the form

$$\sum_{j=1}^{N_F} \gamma_j \omega_j = 0, \quad (22)$$

where N_F is the number of the nodal points on the free surface. γ_j involves ϕ_j , $(\partial\phi/\partial t)_j$, η_j , $(\partial\eta/\partial t)_j$ ($j = 1, 2, \dots, N_F$) as unknown variables (see Ohyama, 1989 b). The arbitrariness of the weighting function ω leads to the equation

$$\gamma_j = 0 \quad (j = 1, 2, \dots, N_F). \quad (23)$$

2.3 Time-Stepping Procedure

The discretized equations (16) and (23) are solved simultaneously for successive time steps to estimate the wave motion transition. The surface elevation and the velocity potential at the n -th time step, $\eta^{(n)}$ and $\phi^{(n)}$, are given as

$$\eta^{(n)} = \eta^{(n-1)} + \Delta\eta^{(n)}, \quad \phi^{(n)} = \phi^{(n-1)} + \Delta\phi^{(n)}, \quad (24)$$

in which $\Delta\eta^{(n)}$ and $\Delta\phi^{(n)}$ represent the increments of η and ϕ during the time increment Δt , respectively. Using Taylor expansions around the corresponding values at the $(n-1)$ -th time step and neglecting the higher order terms with respect to Δt , $(\partial\eta/\partial t)^{(n)}$ and $(\partial\phi/\partial t)^{(n)}$ can be expressed as

$$\left(\frac{\partial\eta}{\partial t}\right)^{(n)} = \frac{2\Delta\eta^{(n)}}{\Delta t} - \left(\frac{\partial\eta}{\partial t}\right)^{(n-1)}, \quad (25)$$

$$\begin{aligned} \left(\frac{\partial\phi}{\partial t}\right)^{(n)} &= \frac{2\Delta\phi^{(n)}}{\Delta t} - \left(\frac{\partial\phi}{\partial t}\right)^{(n-1)} - \frac{2\Delta\eta^{(n)}}{\Delta t} \left(\frac{\partial\phi}{\partial z}\right)^{(n-1)} \\ &\quad - \Delta t \left(\frac{\partial\eta}{\partial t}\right)^{(n-1)} \left(\frac{\partial^2\phi}{\partial z\partial t}\right)^{(n-1)} + \left(\frac{\partial\eta}{\partial t}\right)^{(n-1)} \left(\frac{\partial^2\phi}{\partial z^2}\right)^{(n-1)} \quad (\text{on } S_F). \end{aligned} \quad (26)$$

It should be noted that Taylor expansions, with respect not only to time but also to spatial displacement, must be applied to the estimation of the potential values on S_F . The last three nonlinear terms on the right-hand side of Eq. (26) correspond to the change in location of the nodal point on S_F . In the method proposed by Nakayama and Washizu (1981) for two-dimensional sloshing problems, only the expansions with respect to time were considered, so that these nonlinear terms were entirely neglected. Isaacson (1982) also omitted the effect of spatial displacement from the time-stepping procedure. However, the partial effects were taken into account in a recent paper (Isaacson and Zuo, 1989).

Substituting Eqs. (24), (25) and (26) into Eqs. (16) and (23), the linear algebraic equations for $\Delta\phi_j^{(n)}$ ($j = 1, 2, \dots, N$) and $\Delta\eta_j^{(n)}$ ($j = 1, 2, \dots, N_F$) can be obtained. The quantities associated with the boundary surface profile, S_J , $(n_x)_J$, A_{iJ} , B_{iJ} , and so on, are unknown when solving the equations at each time step, since $\Delta\eta_j^{(n)}$ are involved in the equations as unknown variables. Thus, in order to obtain the successful solutions associated with the corresponding free surface profile, the iteration procedure is applied using the surface profile at the previous time step as the initial profile (see Ohyama, 1985). It usually takes two or three iterations to obtain the convergence.

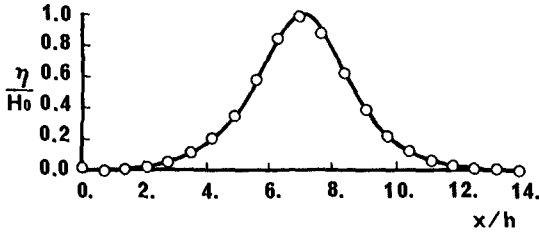
3. ACCURACY AND FUNDAMENTAL EXAMINATIONS

Fundamental examinations were carried out to confirm the validity of the proposed method. Solitary waves with various wave heights, H_0 , were generated numerically in a three-dimensional wave channel with a constant depth h and a constant width Y_L . In the computations, the still water condition ($\phi = \eta = 0$) inside the region was considered as an initial condition, and the third approximation given by Fenton (1972) was applied to the velocity U imposed on S_C . The numerical results were compared with the third approximation in terms of the generated wave profile and the hydrodynamic pressure. Once the velocity potential ϕ is given at successive time steps, the pressure p can be obtained from the Bernoulli equation

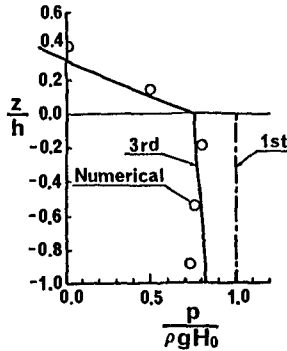
$$p = -\rho \left\{ (\partial\phi/\partial t) + (1/2)(\nabla\phi)^2 + gz \right\}, \quad (27)$$

where ρ is the fluid density. The results for the case of $H_0/h = 0.4$ are shown in Figs. 4 (a) and 4 (b) together with the corresponding approximations. In this calculation, X_L/h and Y_L/h were fixed at 14.0 and 2.1, respectively. According to the results of the previous study for a two-dimensional numerical model (Ohyama, 1989 a), the maximum horizontal distance between the neighboring nodal points on S_F , Δl , and the time increment Δt were varied with H_0/h . In the case of $H_0/h = 0.4$, $\Delta l/h$ and $\Delta t\sqrt{g/h}$ were set at 0.7 and 0.4, respectively. As shown in Figs. 4 (a) and 4 (b), the agreements between the numerical result and the third approximation

are fairly good, whereas the first approximation predicts a remarkably larger value for hydrodynamic pressure under the still water level. It may indicate that the proposed method can well predict the wave motion and the induced force even in the case of a relatively high wave height.



(a) Generated solitary wave profile ($y/h = 0$)



(b) Distribution of hydrodynamic pressure under the wave crest

Fig. 4 Comparisons with the corresponding approximation for $H_0/h = 0.4$;
 ○, numerical result; —, third approximation; ---, first approximation.

Additional examinations were performed to ascertain the effect on the numerical solutions of taking into account the nonlinear terms in Eq. (26). Figure 5 shows the numerical result of the generated wave profile with $H_0/h = 0.4$, together with the third approximation. The results calculated by the proposed method and those by the conventional method, in which the nonlinear terms in Eq. (26) are neglected, are denoted by circles and triangles, respectively. It should be noted that the proposed method can eliminate the numerical error accumulation which occurs in the conventional analysis.

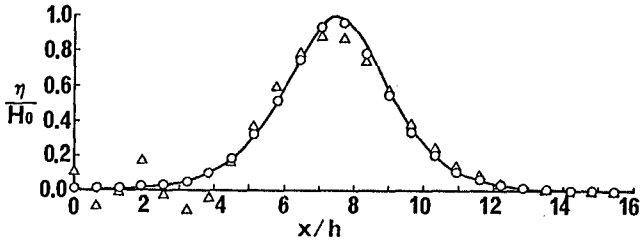


Fig. 5 Generated solitary wave profile with $H_0/h = 0.4$;
 ○, numerical result taking into account the nonlinear terms in Eq. (26);
 △, numerical result neglecting the nonlinear terms in Eq. (26);
 —, third approximation given by Fenton, 1972.

4. NONLINEAR EFFECTS ON SOLITARY WAVE FORCES

First approximation for the solitary wave diffraction around a circular cylinder was already given in closed form by Isaacson (1982). According to this approximation, a maximum force coefficient, C_F , and a maximum overturning moment coefficient, C_M , are conveniently described by the single number $(a/h)\sqrt{H_0/h}$, in which C_F and C_M are defined as

$$C_F \equiv \frac{F_{max}}{\rho g H_0 a h}, \quad C_M \equiv \frac{M_{max}}{\rho g H_0 a h^2}, \quad (28)$$

where F_{max} and M_{max} denote the maximum horizontal force and the maximum overturning moment, respectively, and a is the cylinder radius. However, the first approximations were introduced on the assumption of a small wave height. Thus, nonlinear effects on solitary wave forces acting on the cylinder may be discussed by comparing the numerical result with the first approximation.

Figure 6 shows the free surface elevation computed by the proposed method in the case of $(a/h)\sqrt{H_0/h} = 2.0$ and $H_0/h = 0.4$, when the horizontal force acting on the cylinder is at the maximum. Only the half side of the fluid region was considered in the calculation because of the symmetry of the circular cylinder. In the case indicated in Fig. 6, the surfaces S_F , S_C , S_V and S_{W3} were discretized into 846, 120, 112, and 176 elements, respectively, and the total number of the nodal points was 680.

The corresponding numerical results of the temporal variations of the horizontal force F_x and the overturning moment M_y are indicated in Figs. 7 (a) and 7 (b), together with the first approximation. The abscissa in these figures represents nondimensional time, where t' denotes time measured from the instant when the crest of the incident wave passes the center of the cylinder. The calculation was carried out for H_0/h being 0.1 and 0.4. In the case of $H_0/h = 0.1$, the agreements between the numerical result and the first approximation are fairly good for both the horizon-

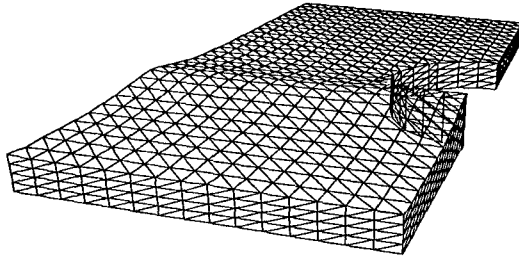
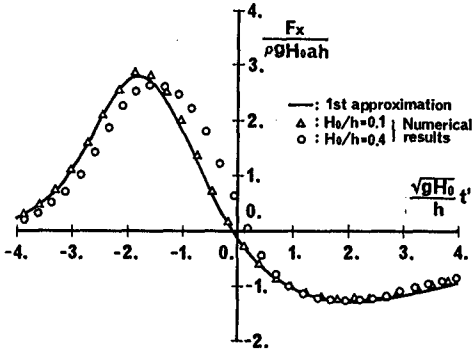


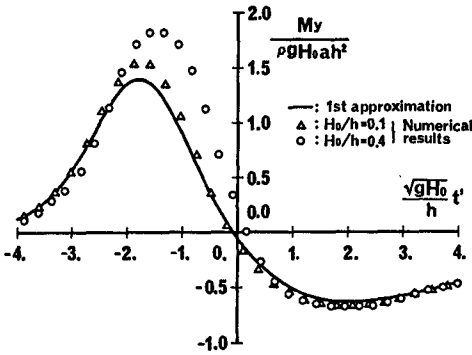
Fig. 6 Free surface elevation with $(a/h)\sqrt{H_0/h} = 2.0$ and $H_0/h = 0.4$.

tal force and the overturning moment. For $H_0/h = 0.4$, however, the prediction of the maximum overturning moment is remarkably larger than the first approximation, whereas the difference in the maximum horizontal force may not be notable. The reason why the prediction of the overturning moment for $H_0/h = 0.4$ is larger than the first approximation may be explained by the following facts. First, **Figure 8** shows the distribution of hydrodynamic pressure in a horizontal cross section when the horizontal force is at the maximum. For $H_0/h = 0.4$, the pressure over the cylinder surface is found to be smaller than the value predicted by the approximation. This characteristic is the same as the progressive solitary wave, as indicated in **Fig. 4 (b)**. Second, the proposed method takes into account the pressure distribution above the still water level, whereas it is neglected in the first approximation. These two facts have contrary effects on the prediction of the horizontal force, so that the numerical results of the horizontal force may differ slightly from the approximation, even for the case of $H_0/h = 0.4$. Furthermore, the second fact explains that the point of the resultant force shifts upward as the incident wave height increases. Thus, compared to the approximation, the proposed method predicts a larger value for the overturning moment.

Figures 9 (a) and **9 (b)** show the variations of C_F and C_M with $(a/h)\sqrt{H_0/h}$, respectively. When the value of $(a/h)\sqrt{H_0/h}$ is small, the differences between the numerical result and the first approximation are not significant, even for the overturning moment. As this parameter $(a/h)\sqrt{H_0/h}$ becomes larger, however, the approximation predicts a much smaller magnitude of overturning moment. The prediction obtained from the numerical calculation shows a 40% larger value than the approximation for $(a/h)\sqrt{H_0/h} = 3.0$ and $H_0/h = 0.4$.



(a) horizontal force



(b) overturning moment

Fig. 7 Temporal variations of horizontal force and overturning moment for $(a/h)\sqrt{H_0/h} = 2.0$.

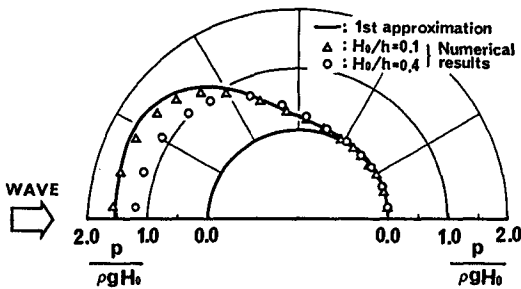
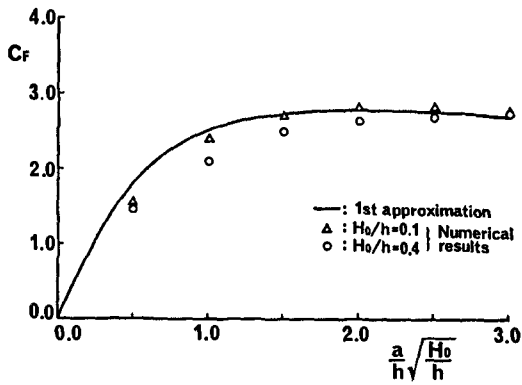
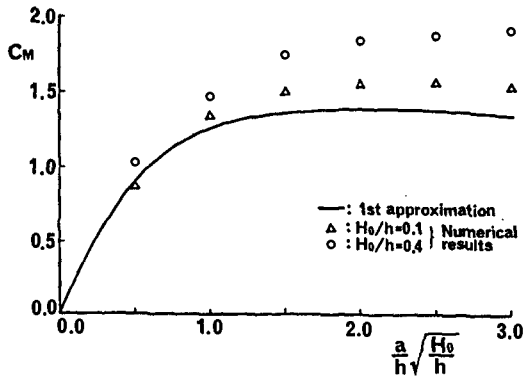


Fig. 8 Distribution of hydrodynamic pressure at $z/h = -0.1$ when F_x is at the maximum with $(a/h)\sqrt{H_0/h} = 2.0$.



(a) C_F



(b) C_M

Fig. 9 Variations of C_F and C_M with $(a/h)\sqrt{H_0/h}$.

5. CONCLUSION

A numerical method has been developed for simulating solitary wave diffraction around large structures. The proposed method is based on the nonlinear potential theory, and it improves the time-stepping procedure of the conventional boundary element methods to provide greater accuracy. The effect of the improvement on the numerical solution has been shown by the simulation of a more realistic solitary wave profile.

Comparisons have been carried out with the first approximation for the horizontal

force and the overturning moment, acting on a circular cylinder. The first approximation gives reasonable results when H_0/h is about 0.1. When $H_0/h = 0.4$, however, the same approximation remarkably underestimates the overturning moment.

REFERENCES

- Eatock Taylor, R., and Hung, S. M., 1987: Second order diffraction forces on a vertical cylinder in regular waves, *Appl. Ocean Res.*, **9** (1), 19-30.
- Fenton, J.D., 1972: A ninth-order solution for the solitary wave, *J. Fluid Mech.*, **53**, 257-271.
- Hunt, J. N., and Baddour, R. E., 1981: The diffraction of nonlinear progressive waves by a vertical cylinder, *J. Mech. Appl. Math.*, **34**, 69-87.
- Isaacson, M de St Q., 1982: Nonlinear-wave effects on fixed and floating bodies, *J. Fluid Mech.*, **120**, 267-281.
- Isaacson, M de St Q., 1983: Solitary wave diffraction around large cylinder, *J. Waterway, Port, Coastal and Ocean Eng.*, ASCE, **109**, 121-127.
- Isaacson, M de St Q., and Zuo, Q.-H., 1989: Nonlinear wave forces on a circular cylinder, *Can. J. Civ. Eng.*, **16**, 182-187.
- Nakayama, T., and Washizu, K., 1981: Boundary element method applied to analysis of two-dimensional nonlinear sloshing problems, *Int. J. Numer. Methods Eng.*, **17**, 1631-1646.
- Ohyama, T., 1985: Boundary element analysis for solitary wave reflection and induced forces, *Proc. 32nd Japanese Conf. Coastal Eng.*, 555-559 (in Japanese).
- Ohyama, T., 1989 a: Boundary element analysis for run-up of nonlinear water wave, *Tech. Papers ISCFD-NAGOYA*, 377-382.
- Ohyama, T., 1989 b: A boundary element analysis for nonlinear wave diffraction around large structure, *Proc. JSCE*, **411**, 197-206 (in Japanese).

CHAPTER 65

A NUMERICAL MODEL OF THE ROUGH TURBULENT BOUNDARY LAYER IN COMBINED WAVE AND CURRENT INTERACTION

HUYNH-THANH Son and TEMPERVILLE André
Institut de Mécanique de Grenoble
B.P. 53X, 38041 Grenoble Cedex, France

ABSTRACT

The turbulent boundary-layer flow over flat rough beds due to a wave or a combined wave-current interaction is studied by using a simplified numerical second-order turbulence model. The model results are compared with many sets of experimental data. Excellent predictions for ensemble-averaged velocities and favourable predictions for turbulence quantities are obtained. Variations of kinematic and dynamic characteristics of boundary-layer flow with wave, current and bed roughness parameters are determined. The model is also modified to simulate the oscillatory turbulent flow over rippled beds. The mean velocity field and the distribution of time-averaged turbulence quantities are calculated. The validity of the model is verified through comparison with experimental results. The performance and the limitation of the model are discussed.

I. INTRODUCTION

A knowledge of the boundary layer flow in the vicinity of the sea bed is important for problems of coastal engineering, in particular for investigations of coastal erosion, sediment transport and the transport of pollutants.

Bodies of water that are subjected to currents and waves, according to their characteristics, produce a flat, generally rough bed, or a rippled bed. In order to quantify sediment transport, the amplitude and direction of the velocities and shear stresses in the boundary layer close to these different shapes of bed must be known.

Enquiries into the turbulent boundary layer generated by a sinusoidal wave are not recent. The experiments of Jonsson (1963), Horikawa and Watanabe (1968), Kamphuis (1975), Jonsson and Carlsen (1976) are noteworthy. Recently, experiments have been performed using laser velocimetry, e.g. the experiments of

Sumer et al. (1986), Sleath (1987) and Jensen et al. (1989). Theoretically, numerous investigations exist : from the analytical models of Kajiura (1968), Brevik (1981), Myrhaug (1982), Trowbridge and Madsen (1984) to the numerical models of Bakker (1974), Johns (1975), Sheng (1984), Fredsoe (1984), Asano and Iwagaki (1986), Blondeaux (1986), Justesen (1988), Sheng and Villaret (1989). Also to be mentioned is the semi-empirical model of Jonsson (1980), which proposed a universal distribution law for the velocity in the boundary layer.

As far as the boundary layer due to the interaction between a current and a wave is concerned, few experiments are available, among which only those of Van Doorn (1979), Simon et al. (1988) pertain to the turbulent and hydraulically rough case that is of interest to us. After the analytical model of mixing length due to Bijker (1967), other analytical models are based on the time-invariant turbulent viscosity, as in the case of a wave : Lundgren (1973), Smith (1977), Grant and Madsen (1979), Tanaka and Shuto (1984), Myrhaug (1984), Asano and Iwagaki (1984). For numerical models, that of the mixing length due to Bakker and Van Doorn (1978), Van Kerstern and Bakker (1984) as well as that of Fredsoe (1984), which assumes a logarithmic velocity distribution. Models with more or less complicated turbulent closure are also applied to this problem : Sheng (1984), and Davies et al. (1988).

To investigate the effect of wave and current on the boundary layer, we have selected the second order turbulence model that was originally suggested by Lewellen (1977) and simplified by Sheng (1984), Sheng and Villaret (1989) for the one dimensional flows. A simplified three dimensional version of the model is actually developed for the case of a wave without and with current. The numerical results are compared with experimental results in order to verify the validity of the model. In the last section, the model is written in orthogonal curvilinear coordinates in order to investigate oscillatory turbulent flow over a rippled bed. The results obtained are also compared with the experimental results for the case of symmetric and asymmetric ripples.

II. BOUNDARY LAYER ABOVE A FLAT BED

II-1. Equations of the model

The problem is treated in cartesian coordinates (x,y,z) with the z axis directed upwards (Fig. 1). The flat horizontal bottom is fixed at $z = z_0 = k_N/30$, where k_N represents the equivalent Nikuradse roughness.

The system of equations is established with the following assumptions: (a) the thickness of the boundary layer is much smaller than the wavelength of the wave; (b) the amplitude of the wave velocity \hat{U}_h is much smaller than the wave celerity C .

In these conditions, the momentum equations for the two horizontal components of velocity (u,v) along x and y can be written:

$$(1) \quad \frac{\partial u}{\partial t} = -\frac{1}{\rho} \frac{\partial P}{\partial x} + \frac{\partial}{\partial z} (-\overline{u'w'}) ; \quad (2) \quad \frac{\partial v}{\partial t} = -\frac{1}{\rho} \frac{\partial P}{\partial y} + \frac{\partial}{\partial z} (-\overline{v'w'})$$

where the Reynolds stresses $-\overline{u'w'}$ and $-\overline{v'w'}$ can be modelled in the form :

$$(3) \quad -\overline{u'w'} = \nu_t \frac{\partial u}{\partial z}, \quad -\overline{v'w'} = \nu_t \frac{\partial v}{\partial z}$$

where ν_t represents the turbulent viscosity.

The pressure gradients are expressed as follows :

$$(4) \quad -\frac{1}{\rho} \frac{\partial P}{\partial x} = \frac{\partial U_{hx}}{\partial t} - \frac{1}{\rho} \frac{\partial P_c}{\partial x}, \quad -\frac{1}{\rho} \frac{\partial P}{\partial y} = \frac{\partial U_{hy}}{\partial t} - \frac{1}{\rho} \frac{\partial P_c}{\partial y}$$

where (U_{hx}, U_{hy}) are the two horizontal components of the wave velocity and P_c represents the pressure due to the current.

Turbulent closure is performed by means of two equations for the turbulent kinetic energy K and for the length scale L of the turbulence (Lewellen, 1977) :

$$(5) \quad \frac{\partial K}{\partial t} = \nu_t \left[\left(\frac{\partial u}{\partial z} \right)^2 + \left(\frac{\partial v}{\partial z} \right)^2 \right] - \frac{\nu_t}{L^2} K + 1.2 \frac{\partial}{\partial z} \left(\nu_t \frac{\partial K}{\partial z} \right)$$

$$(6) \quad \frac{\partial L}{\partial t} = 0.175 \frac{\nu_t}{K} \left[\left(\frac{\partial u}{\partial z} \right)^2 + \left(\frac{\partial v}{\partial z} \right)^2 \right] L + 0.075 \sqrt{2} K + 1.2 \frac{\partial}{\partial z} \left(\nu_t \frac{\partial L}{\partial z} \right) - \frac{0.375 \sqrt{2}}{\sqrt{K}} \left[\frac{\partial (\sqrt{K} L)}{\partial z} \right]^2$$

The assumption of local equilibrium of the turbulence made by Sheng (1984) allows ν_t to be put in the form :

$$(7) \quad \nu_t = \sqrt{2} \frac{\sqrt{K} L}{4}$$

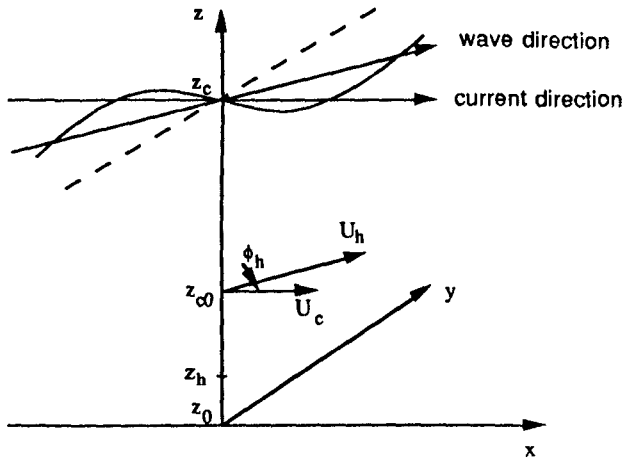


Fig. 1 Outline of physical system and reference system of axes (flat bed)

At the bottom ($z = z_0$) the boundary conditions in all cases are the following :

$$(8) \quad u = v = 0 \quad ; \quad \partial K / \partial z = 0 \quad ; \quad L = \alpha z_0 \quad \text{with } \alpha = 0.67,$$

where the von Karman constant is taken as $k = 0.4$.

The conditions at the upper limit of the boundary layer depend on the particular case studied, and will be described later.

The set of equations (1) to (8) is discretised using the implicit finite control volume method (Patankar, 1980) on a grid whose step size increases exponentially from bottom to top, thus giving good resolution near the bed where gradients are important. The time step is constant over the whole period of the wave. Each discretised equation corresponds to a tridiagonal matrix which can be solved by means of Thomas's algorithm (Roache, 1976).

II-2. Case of the wave

In the case of a unidirectional wave, the above set of equations is solved by taking $v = 0$. The pressure gradient is given by :

$$(9) \quad -\frac{1}{\rho} \frac{\partial P}{\partial x} = \frac{\partial U_h}{\partial t}$$

where $U_h = \hat{U}_h \sin \omega t$ is the wave velocity at the upper limit of the boundary layer defined by $z_h = \delta_K$, δ_K corresponds to the thickness beyond which K is zero. The following approximation was obtained :

$$(10) \quad \frac{\delta_K}{k_N} = 0.246 \left[\frac{\hat{a}_h}{k_N} \right]^{0.81} \quad \text{with } \hat{a}_h = \frac{\hat{U}_h}{\omega}$$

For $z = z_h$ the boundary conditions are :

$$(11) \quad K = L = 0 \quad \text{and} \quad U = U_h$$

* *Comparison with experimental results* : The model results were compared with the experiment of Sumer et al. (1986). The lower boundary is at $z_0 = k_N/30 = 0.0133$ cm, and the upper boundary is taken to be at $z_h = 20$ cm. The magnitude of the wave velocity is $\hat{U}_h = 210$ cm/s and the period $T = 2\pi/\omega = 8.1$ s. Good agreement can be seen in Figure 2 for the velocities, except at $z = 0.1$ cm. The values of the friction velocity $u_* = \text{sign}(-\overline{u'w'}) \sqrt{|\overline{u'w'}|}$ are slightly lower than found experimentally (Fig. 3). In Figure 4 the profiles of the fluctuating velocities $\sqrt{u'^2}$ and $\sqrt{w'^2}$ are compared. It can be seen that there is agreement for $\sqrt{u'^2}$ for phases between 30° and 120° , and for $\sqrt{w'^2}$ for the other phases.

* *Wave friction coefficient* : In investigations of the wave boundary layer, the friction coefficient f_h introduced by Jonsson (1963) is often used : $\hat{\tau} = \frac{1}{2} f_h \hat{U}_h^2$ where $\hat{\tau}$ is the amplitude of the shear stress at the bed. The formula for f_h that arises

from the present model as follows :

$$(12) \quad f_h = 0.00278 \exp \left[4.65 \left(\frac{\hat{a}_h}{k_N} \right)^{-0.22} \right]$$

For comparison, Figure 5 shows the curves obtained from the formulae of Kajiura (1968), Kamphuis (1975), Jonsson and Carsen (1976). The curve given by (12) is close to the results of Kamphuis.

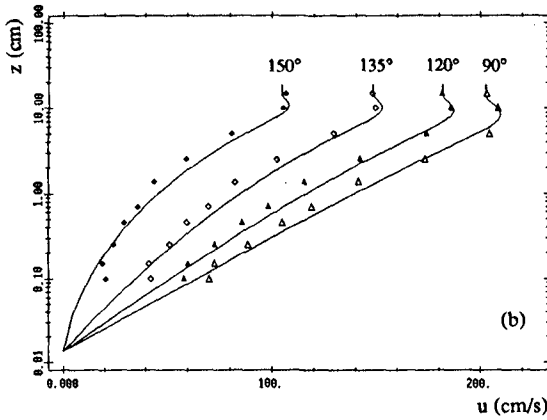


Fig. 2 Comparison between the calculated velocity profiles (—) and those measured by Sumer et al (1986) (symbols) for the different phases.

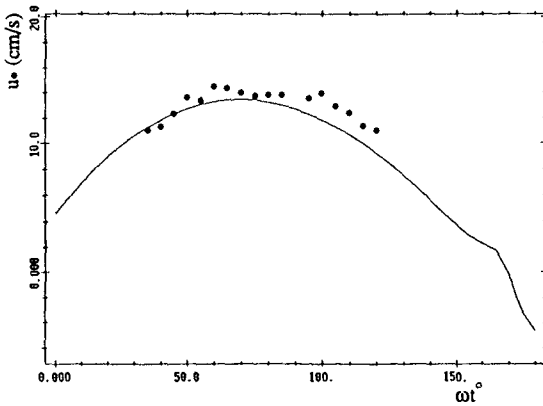


Fig. 3 Comparison between the shear velocity calculated by the present model (—) and that obtained experimentally by Sumer et al (1986) (●)

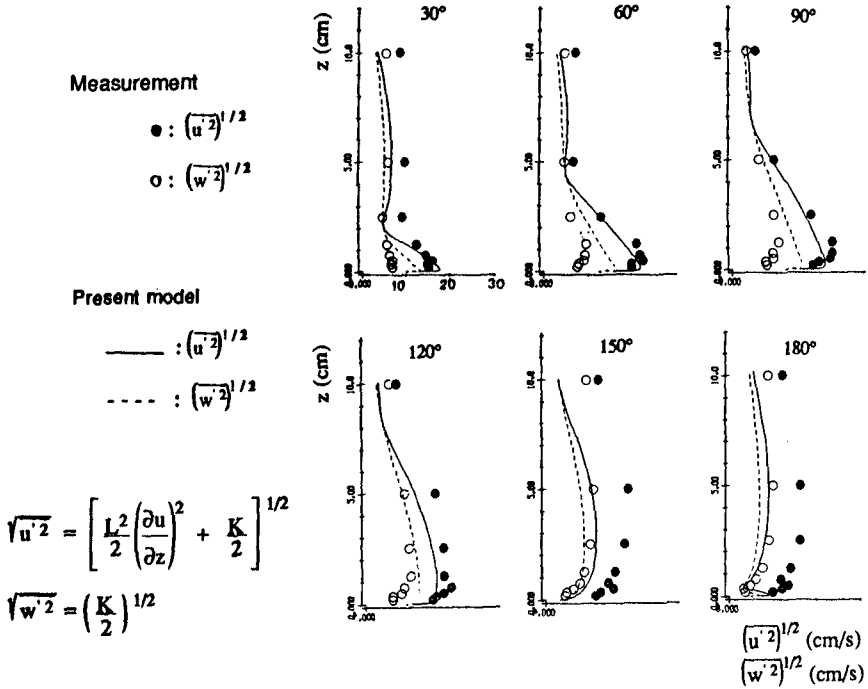


Fig. 4 Comparison between the fluctuating velocity profiles calculated by the present model and those obtained experimentally by Sumer et al. (1986) for the different phases.

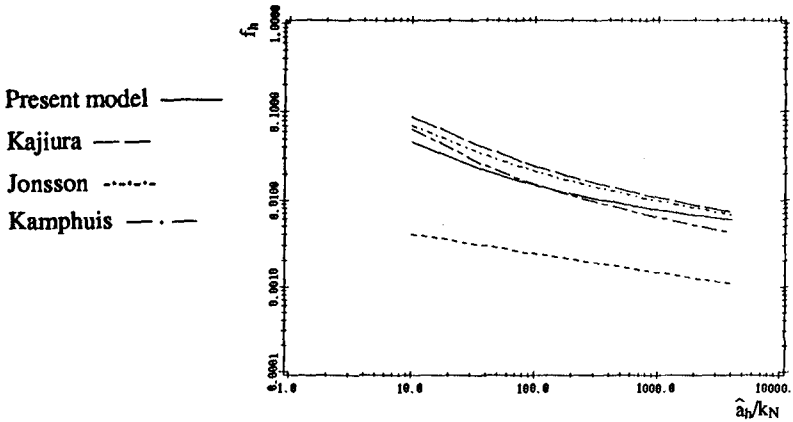


Fig. 5 Variation of the friction coefficient f_h as a function of \hat{a}_h/k_N

II-3. Case of wave and current interaction

The investigation of the wave-current interaction is performed using equations (1)+(8). The wave propagates in a direction at an angle ϕ_h to the current, which is parallel to the direction x (Fig. 1). The upper boundary conditions apply at $z = z_{c0}$ located in the inertial layer of the current and which is taken to be at $(0.10+0.15) z_c$, where z_c is the total height. The two components of the velocity at z_{c0} are assumed to be known :

$$(13) \quad U = U_c + U_{hx} = U_c + U_h \cos \phi_h \quad ; \quad V = U_{hy} = U_h \sin \phi_h$$

where U_c is the current velocity.

In addition, the following boundary conditions are applied:

$$(14) \quad u = U ; v = V ; \partial K / \partial z = 0 ; L = \alpha z ; \partial P_c / \partial x = \partial P_c / \partial y = 0$$

* *Comparison with experimental results* : The results of the model are compared with the experiments of Van Doorn (1981) for the case of colinear wave-current interaction ($\phi_h = 0^\circ$). We selected the test V20RA, for which the upper limit z_{c0} is equal to 4.5 cm. In Figure 6 is shown the mean velocity profile. Good agreement is found with the experiment. The upper limit can be also treated at the surface libre $z_c = 30$ cm (Huynh Thanh and Temperville, 1989).

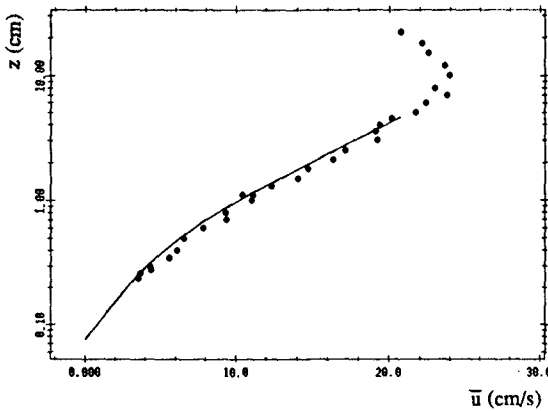


Fig. 6 Comparison between the mean velocity profiles calculated with the present model (—) and those measured by Van Doorn (1981). Test V20RA.

* *Friction coefficients* : The friction coefficients f_{ch} and f_c are defined as follows :

$$(15) \quad \frac{\hat{\tau}_{ch}}{\rho} = \frac{1}{2} f_{ch} \hat{U}_h^2 \quad ; \quad \frac{\bar{\tau}_c}{\rho} = \frac{1}{2} f_c \hat{U}_h^2$$

where $\hat{\tau}_{ch}/\rho$ and $\bar{\tau}_c/\rho$ are the maximum and mean shear stresses respectively.

Figures 7 and 8 show the variation of f_{ch} and f_c as a function of \hat{a}_h/k_N for different values of z_{c0}/k_N , U_0/\hat{U}_h , and ϕ_h . From these curves, it can be noted that for fixed z_{c0}/k_N and ϕ_h , f_{ch} and f_c increase for increasing U_0/\hat{U}_h . The change in f_c with ϕ_h is substantial only for $U_0/\hat{U}_h < 1$. When the current is stronger than the wave ($U_0/\hat{U}_h \geq 1.5+2$), the influence of ϕ_h on f_c is not marked, which means that in this case the mean characteristics of the current practically do not change under the action of the wave.

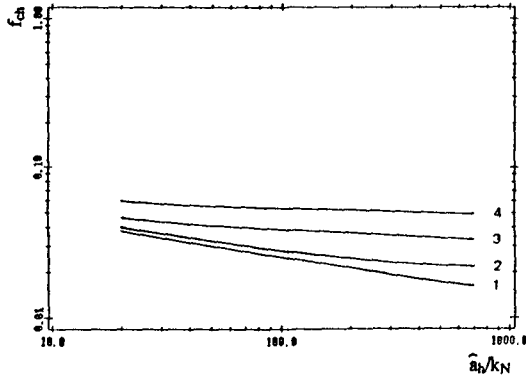


Fig. 7. Variation of the friction coefficient f_{ch} as a function of \hat{a}_h/k_N , z_{c0}/k_N , U_0/\hat{U}_h and ϕ_h . $z_{c0}/k_N = 100$ $\phi_h = 0^\circ$

- (1) $U_0/\hat{U}_h = 0.5$ (2) $U_0/\hat{U}_h = 1$ (3) $U_0/\hat{U}_h = 1.5$ (4) $U_0/\hat{U}_h = 2$

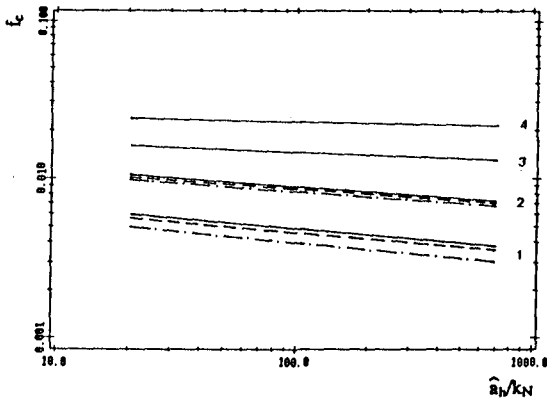


Fig. 8 Variation of the friction coefficient f_c as a function of \hat{a}_h/k_N , z_{c0}/k_N , U_0/\hat{U}_h and ϕ_h . Parameters and notations as in Fig. 7.

- $\phi_h = 0^\circ$; - - - $\phi_h = 45^\circ$; - . - . $\phi_h = 90^\circ$

III. BOUNDARY LAYER ON A RIPPLED BED

III-1. Formulation of the model

The physical problem is outlined in Figure 9 : under the action of a wave of wavelength L_h , maximum velocity \hat{U}_h and period T, two-dimensional vortex ripples are assumed to be present on the bed. Laboratory and *in situ* measurements have shown that $L_h \gg L_r$. This allows us to restrict the zone of the calculation : rather than investigating the problem over the whole of the wavelength L_h , we shall only consider the wavelength L_r as shown in Figure 9. Moreover, to simplify the description of the boundary conditions at the surface of the ripple and also to eliminate the unknown pressure gradient due to the bed form, it is convenient in this case to transform the cartesian coordinates (x,z) into orthogonal curvilinear coordinates (X,Z) , and to use the variables ψ (stream function) and ξ (vorticity) instead of the velocities u and w .

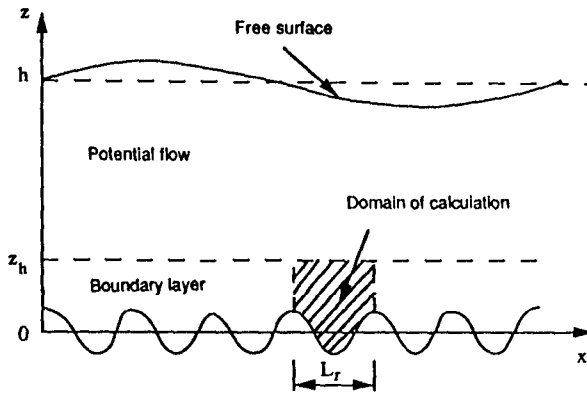


Fig. 9 Scheme of the physical system (rippled bed).

In general, the coordinate transformation is given by :

$$(16) \quad \begin{aligned} X &= x + \sum_{n=1}^N a_n \cdot \exp(-n k_r Z) \cdot \sin(n k_r X - \theta_n) \\ Z &= z - \sum_{n=1}^N a_n \cdot \exp(-n k_r Z) \cdot \cos(n k_r X - \theta_n) \end{aligned}$$

where a_n and θ_n are the amplitude and phase difference of the n th harmonic describing the ripple, and $k_r = 2\pi/L_r$ is the wave number associated with L_r .

The stream function ψ and the vorticity ξ are defined by :

$$(17) \quad u = \frac{\partial \psi}{\partial z} \quad ; \quad w = -\frac{\partial \psi}{\partial x} \quad ; \quad \xi = \frac{\partial u}{\partial z} - \frac{\partial w}{\partial x}$$

In coordinates (X,Z) , the set of equations to be solved is :

$$(18) \quad J \nabla^2 \psi = \xi$$

$$(19) \quad \frac{1}{J} \frac{\partial \xi}{\partial t} - \frac{\partial (\psi, \xi)}{\partial (X, Z)} = \nabla^2 (v_t \xi) - J \zeta$$

$$(20) \quad \frac{1}{J} \frac{\partial K}{\partial t} - \frac{\partial (\psi, K)}{\partial (X, Z)} = 1,2 \frac{\partial}{\partial X} \left(v_t \frac{\partial K}{\partial X} \right) + 1,2 \frac{\partial}{\partial Z} \left(v_t \frac{\partial K}{\partial Z} \right) \\ + v_t J \left[\left(\frac{\partial^2 \psi}{\partial X^2} \right)^2 + \left(\frac{\partial^2 \psi}{\partial Z^2} \right)^2 \right] - \frac{1}{J} \cdot v_t K - \frac{1}{J} \frac{v_t}{L^2} K$$

The length scale L is assumed to vary as follows :

$$(21) \quad L = \alpha Z \sqrt{1 - \frac{Z}{Z_h}}$$

and the turbulent viscosity v_t is determined by (7).

In the previous set of equations, ζ and K are terms pertaining to the partial derivatives of ψ and v_t ; J is the jacobian of the coordinate transformation ; ∇^2 is the laplacian operator. The following boundary conditions are applied :

- At the lower limit of the boundary layer ($Z = Z_0 = k_N/30$)

$$(22) \quad \frac{\partial \psi}{\partial Z} = \frac{\partial \psi}{\partial X} = \psi = \frac{\partial K}{\partial Z} = 0 \quad ; \quad \xi_0 = \frac{2 J \psi_1}{(Z_1 - Z_0)^2}$$

where ψ_1 is the stream function at height Z_1 on the second node of the grid (Roache, 1976).

- At the upper limit of the boundary layer ($Z = Z_h$)

$$(23) \quad \psi = Z_h U_h(t) \quad ; \quad K = \xi = 0$$

- At the lateral boundaries ($X = 0$ and $X = L_r$), we assume spatially periodic conditions for ψ , ξ and K .

The above set of equations is discretized using implicit finite difference schemes (centred in space and forward in time). The alternating direction implicit (A. D. I.) method is used to solve the equations for ξ and K . The Poisson equation for ψ is solved by the bloc-cyclic reduction method (Roache, 1976) which allows a huge saving in calculation time compared with the Gauss-Seidel iteration method. The spatial grid contains $M \times N$ nodes with step $\Delta X = \text{const}$, and ΔZ varying exponentially from the bottom upwards. The time step is $\Delta t = T/360$ s. In all the test cases, convergence is obtained after 20 calculation periods.

III-2. Comparison with the experimental results of Du Toit and Sleath (1981)

The dimensional parameters in the test for comparison are the following :

- Symmetric ripple with $L_r = 17.2$ cm, $h_r = 2.9$ cm, $d = 0.04$ cm

- Cosinusoidal wave : $U_h = \hat{U}_h \cos \omega t$, where $\hat{U}_h = 14.3$ cm/s, $T = 2\pi/\omega = 5.37$ s

For the numerical calculation, a 17x25 node grid was chosen with $\Delta X = 1.0625$ cm and ΔZ varying from 0.056 cm to 0.5 cm. The equivalent Nikuradse roughness is $k_N = 2.5 d = 0.1$ cm. The upper limit is chosen to be equal to $Z_h = 5$ cm.

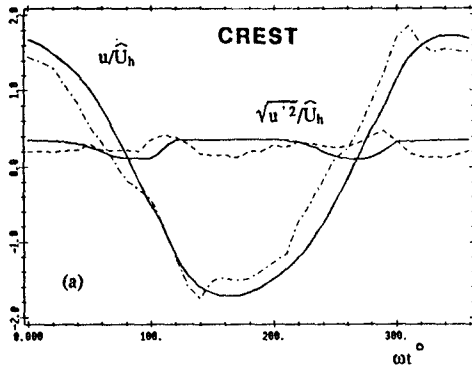


Fig. 10 Comparison between the results of present model (—) and those of the measurements of Du Toit and Sleath (1981) for the time variation of the horizontal velocity u and of the horizontal fluctuating velocity $\sqrt{u'^2}$. Measurements at height $z = 1.65$ cm above the crest

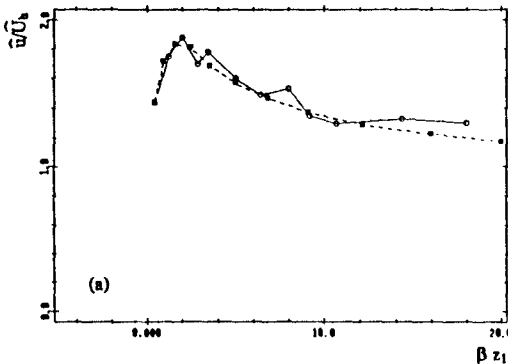


Fig. 11 Vertical variation of the amplitude of the velocity u calculated (+ -) and measured (o -) by Du Toit and Sleath (1981) above the crest.

At height $z = 1.65$ cm above the crest (Fig. 10), good agreement can be seen between the amplitude of the calculated and measured horizontal velocities u , as well as for the fluctuating horizontal velocity $\sqrt{u'^2}$. There is, however, a discrepancy of 25° between the measured local peak ($\omega t = 140^\circ$) and that calculated ($\omega t = 165^\circ$).

The vertical variation of the amplitude of the velocity u , designated by \hat{u} , obtained from the model coincides with that measured above the crest (Fig. 11). Note that the z axis is normalized by the parameter $\beta = \sqrt{\omega/2\nu} = 7.2 \text{ cm}^{-1}$ and z_1 is measured from the ripple crest.

III-3. Comparison with the experimental results of Sato et al. (1987)

The test parameters are the following:

- The ripple is asymmetric with $L_r = 12 \text{ cm}$, $h_r = 2 \text{ cm}$, $d = 0.02 \text{ cm}$.

- The potential flow is a third-order Stokes wave ($T = 2\pi/\omega = 4 \text{ s}$):

$$U_h = -29,5 (\cos \omega t + 0,258 \cos 2\omega t + 0,048 \cos 3\omega t) \text{ (cm/s)}$$

For the modelling, after determining the amplitudes a_n and the phase shifts θ_n of the simulated ripple, we choosed a grid of 13×25 nodes with $\Delta X = 1 \text{ cm}$, and ΔZ varying from 0.06 cm to 0.6 cm . The time step is $\Delta t = 0.011 \text{ s}$. The upper limit is choosen at $Z_h = 6.5 \text{ cm}$.

Figure 12 shows the comparison between the results of the model and those of the measurement for the velocity field and the turbulent kinetic energy K for phase $\omega t = 54^\circ$. It can be seen that the vortex obtained with the model on the right hand leeside of the ripple is weaker than that measured, and the calculated intensity K is smaller in the model than found experimentally.

IV. DISCUSSION AND CONCLUSION

We have examined the problem of the oscillatory turbulent boundary layer on a rough sea bed using different versions of a turbulent closure model with two equations, one for the turbulent kinetic energy K and the other for the length scale L .

* *Performance of the model* : For a flat bed, a simplified three dimensional model was used to investigate the hydrodynamic characteristics of the flow in the boundary layer as a function of the different wave, current, angle of interaction and bed parameters. For the oblique wave-current interaction, the model requires further experimental verifications.

For a rippled bed, we have used a two-dimensional model that can reproduce the velocity and the vorticity fields as well as other turbulent quantities. Comparison with the experimental results shows that this model is able to predict quite well the complex flow properties over a rippled bed. Before applying the model to general cases, it would be necessary to confirm the numerical results by conducting further tests, particularly for the Reynolds stresses and the turbulent quantities.

* *Limitation of the model* : As for all models of turbulent closure (Rodi, 1980), the present model was originally designed for permanent flows in the fully developed turbulent regime at high Reynolds numbers. When the flow is oscillatory, the condition of local equilibrium of the turbulence, which is valid for a permanent flow,

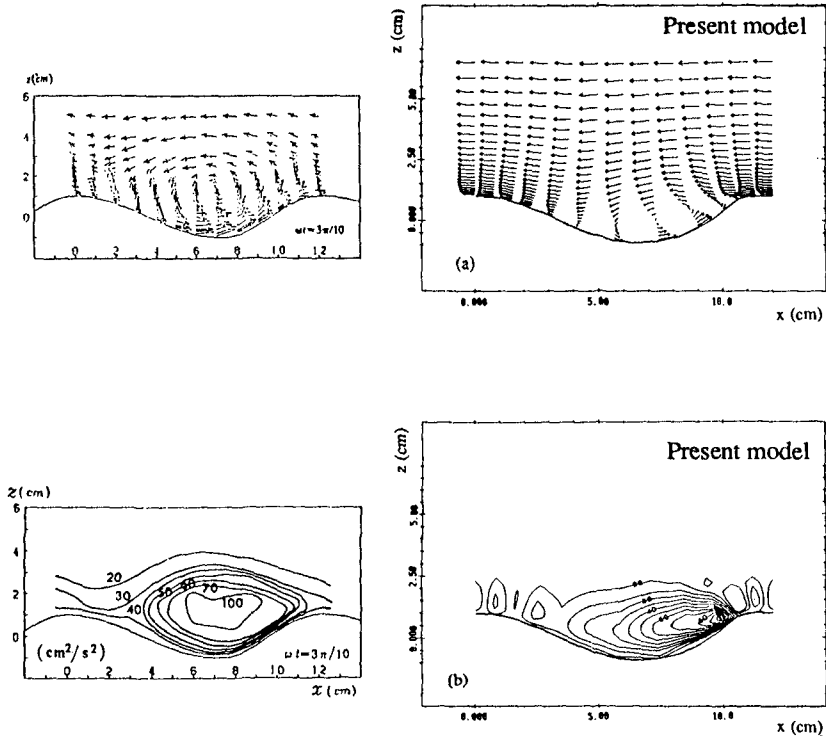


Fig. 12 Comparison between the results of the present model and the measurements of Sato et al. (1987) at phase $\omega t = 54^\circ$.

(a) velocity field; (b) turbulent kinetic energy field

is no longer completely satisfied, particularly at the times when the velocity of the potential flow is small. Consequently there is a time variation of the friction in the oscillatory boundary layer, which induces the change of flow regime in the course of a period. No such change was included in the model. Thus, to obtain more precise results, it is necessary to improve the model not only for high Reynolds numbers but also for moderate Reynolds numbers.

In parallel with investigations into improvements, we shall apply the model to the prediction of certain important parameters of the natural boundary layer, together with analysis of sea measurements in the framework of the GDR Manche project.

REFERENCES

- ASANO T. and IWAGAKI Y. (1984). *Proc. 16th Conf. Coastal Eng.*, pp. 2397 - 2413.
- BAKKER W. T. (1974). *Proc. 14th Conf. Coastal Eng.*, pp. 1129 - 1148.
- BAKKER W. T. and VAN DOORN Th. (1978). *Proc. 16th Conf. Coastal Eng.*, pp. 1394-1413.
- BIJKER E. W. (1967). *Delft Hydraul. Lab. Rep.* 50.
- BLONDEAUX P. (1987). *J. Hydraul. Res.*, 25 (4), pp. 447 - 463.
- BREVIK I. (1981). *J. Waterway Port Coastal Ocean Div.*, 107 (WW 3), pp. 175 - 188.
- DAVIES A. G., SOULSBY R. L. and KING H. L. (1988). *J. Geophys. Res.*, 93 (C1), pp. 491-508.
- DU TOIT C. G. and SLEATH J. F. A. (1981). *J. Fluid Mech.*, 112, pp. 71 - 96.
- FREDSOE J. (1984). *Inst. Hydrodyn. Hydraul. Eng. Tech. Univ. Denmark. Series paper 35.*
- GRANT W. D. and MADSEN O. S. (1979). *J. Geophys. Res.*, 84 (C4), pp. 1797 - 1808.
- HORIKAWA K. and WATANABE A. (1968). *Coastal Eng. Jpn.*, 11, pp. 13 - 28.
- HUYNH THANH S. and TEMPERVILLE A. (1989). *Proc. 23th Cong. IAHR*, pp. A247-A254.
- JENSEN B. L., SUMER B. M. and FREDSOE J. (1989). *J. Fluid Mech.*, 206, pp. 265 - 297.
- JONSSON I. G. (1963). *Proc. 10th Congr. IAHR*, pp. 85 - 92.
- JONSSON I. G. and CARLSEN N. A. (1976). *J. Hydraul. Res.*, 14 (1), pp. 45 - 60.
- JONSSON I. G. (1980). *Ocean Eng.*, 7, pp. 109 - 152.
- JUSTESEN P. (1988). *Coastal Eng.*, 12, pp. 257-284.
- KAJIURA K. (1968). *Bull. Earthquake Res. Inst.*, 46, pp. 75 - 123.
- KAMPHUIS J. W. (1975). *J. Waterw., Harbors Coastal Eng. Div.*, 101 (WW 2), pp. 135 - 144.
- LEWELLEN W. S. (1977). In Handbook of turbulence, Plenum Publishing Corp., Vol. 1, pp. 237-280.
- MYRHAUG D. (1982). *Ocean Eng.*, 9, pp. 547 - 565.
- PATANKAR S. (1980). Numerical heat transfer and fluid flows. McGraw Hill Book Co..
- ROACHE P. J. (1976). Computational fluid dynamics. Eds. Hermosa Publishers.
- RODI W. (1980). Turbulence models and their applications in hydraulics. Monograph, IAHR, Delft, The Netherlands.
- SATO S., SHIMOSAKO K. and WATANABE A. (1987). *Coastal Eng. Jpn.*, 30, pp. 89 - 98.
- SHENG Y. P. (1984). *Proc. 19th Conf. Coastal Eng.*, pp. 2380 - 2396.
- SHENG Y. P. and VILLARET C. (1989). *J. Geophys. Res.*, 94 (C10), pp. 14,429 - 14,444.
- SIMON R. R., KYRIACOU A., SOULSBY R. L. and DAVIES A. G. (1988). *IAHR Symposium on Mathematic Modeling of Sediment Transport in the Coastal Zone*, pp. 33 - 47.
- SLEATH J. F. A. (1987). *J. Fluid Mech.*, 182, pp. 369 - 409.
- SMITH J. D. (1977). In The Sea, vol. 6, Eds. Wiley-Interscience, New York, pp. 539 - 578.
- SUMER B. M., JENSEN B. L. and FREDSOE J. (1986). In Advances in Turbulences, pp. 556-567.
- TANAKA H. and SHUTO N. (1984). *J. Hydraul. Res.*, 22 (4), pp. 245 - 261.
- VAN DOORN Th. (1981). *Delft Hydraul. Lab. Rep.* M1423. Part 1.

CHAPTER 66

RUNUP, SETUP AND THE COASTAL WATERTABLE

Peter Nielsen *

Abstract

The three related phenomena of wave runup, wave setup and the dynamics of the coastal watertable are considered and their inter-relations are investigated via a comprehensive field study. The measured runup distributions confirm the expectation that the Rayleigh distribution is a reasonable model and that the vertical scale of the distributions is proportional to $\sqrt{(H_{orms} L_o)}$ as in Hunt's (1959) formula but that the proportionality to the beach slope, also prescribed by this formula, only applies for fairly steep beaches. The measured setup profiles are quite different from the ones predicted on the basis of $H=\gamma h$ and linear wave theory in the surf zone. The measured profiles are flatter in the outer surf zone and steeper close to the beach. The shoreline setup is generally about $0.4 H_{orms}$, which is somewhat higher than the previously suggested values. This is because the previous values of the shoreline setup were rarely measured but generally extrapolated with insufficient recognition of the steepening of the profile near the shoreline. The watertable data show that the inclined beach face acts as a strongly non-linear filter which makes the watertable variation at a point inside the beach far from sinusoidal (when the tide is approximately sinusoidal) and elevates the average position of the watertable considerably compared to the mean sea level.

1. Introduction

The concepts of wave runup, setup and the coastal watertable have been described previously in the literature but articles dealing with the three together are virtually absent. One notable exception to this rule is Longuet-Higgins (1983).

Articles about wave setup tend to be "geographically" restricted to the area seaward of the swash zone, i.e. where the sand surface is always under water, while papers about the watertable have been restricted to the area landward of the runup limit. Thus the setup profiles and the watertables of the literature rarely meet, see Figure 1. Consequently, since the runup literature, which rules the swash zone, has

Supervising Engineer, Coast and Rivers Branch, Public Works Department, 1 Chifley Square, Sydney 2000, AUSTRALIA.

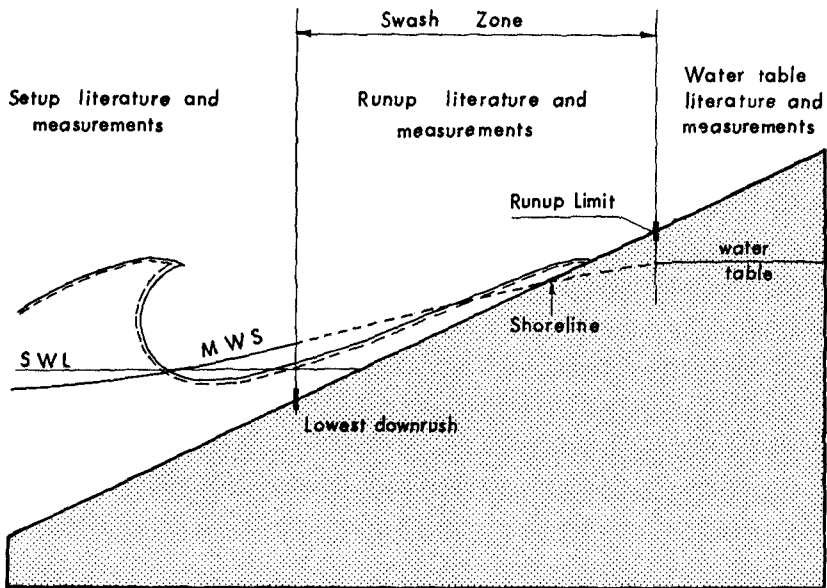


Figure 1: The literature on setup, runup and the coastal watertable is geographically separated into three non-overlapping areas: the setup literature considers the surf zone seaward of the point of lowest downrush, the runup literature considers the swash zone and the watertable literature considers only the area landward of the runup limit.

has been generally uninterested in the MWS, the latter can only be drawn as a broken line through the swash zone. This is particularly unfortunate because a most important part of the MWS namely the shoreline always falls within the swash zone where the MWS is but vaguely described.

The present study presents an attempt to give an integrated description of the three phenomena with the aid of new field data sets which include runup-, setup- and watertable measurements taken simultaneously.

2. Field equipment

The system of manometer tubes which was applied to get the setup measurements has been described and discussed in detail by Nielsen (1988) and Nielsen et al (1988), it consists of hard though flexible nylon tubes extending up to 500 metres into the surf zone and a separate line has been laid out through the Brunswick River entrance extending from well upstream of the point where the waves normally die out to about 150 metres outside the entrance breakwaters. Additional mean water levels in the inner surf zone and the swash zone and

watertable heights inside the beach were taken with simple stilling wells.

Quantitative information about the runup distributions were obtained simply by counting the number n_i of waves which went past each of the stilling wells or other fixed points on the beach face with known elevation z_i .

3. Wave runup

The following includes quantitative data on runup distributions measured on a wide variety of beaches in New South Wales, Australia.

The runup distributions were, in the present study, measured in terms of the number of waves transgressing certain points on the beach face. It was found (in agreement with Battjes 1971) that the Rayleigh distribution is a good model i e

$$P\{z_{wm} > z\} = \exp[-(\frac{z-z_{100}}{L_R})^2] \quad \text{for } z > z_{100} \quad (1)$$

where z_{wm} is the maximum level reached by a given wave, z_{100} is the highest level which was transgressed by all the waves and L_R is the vertical scale of the runup distribution.

Based on the classical work by Hunt (1959) on the runup of regular waves and the subsequent work by Saville (1961) and Battjes (1971) for irregular waves, it seemed reasonable to expect the vertical scale L_R to be close to the offshore rms-wave-height times the surf similarity parameter i e

$$L_R \approx (H_{orms} L_o)^{0.5} \tan\beta \quad (2)$$

However, the fact that most beach profiles are curved means that the definition of "the beach slope" $\tan\beta$ for use in this formula is not trivial, see Figure 2.

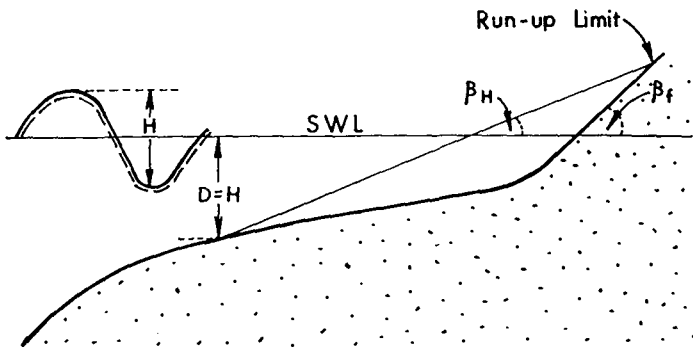


Figure 2: "The beach slope", applicable to the whole surf zone, is not well defined for most beaches, but the beach face slope, $\tan\beta_F$ generally is.

Because of this lack of a good definition, it was decided to leave out the slope in the initial analysis. That is, in order to analyse the measured runup distributions, we plotted the transgression probability in the form $\sqrt{(-\ln n_i/N)}$, where N is the total number of waves, against $(z_i - SWL)/\sqrt{(H_{orms} L_o)}$ and performed linear regression analysis in accordance with

$$\sqrt{(-\ln n_i/N)} = \frac{z_i - SWL}{C_1 \sqrt{(H_{orms} L_o)}} - C_2 \tag{3}$$

where the constant C_1 then has taken the place of "the beach slope" in Equation (2) and the second constant C_2 [= $(z_{100} - SWL)/L_R$] is the dimensionless elevation of z_{100} above the still water level, see Figure 3. A summary of the runup distributions collected so far is presented in Table 1. For a detailed description of the field sites see Nielsen & Hanslow (1991).

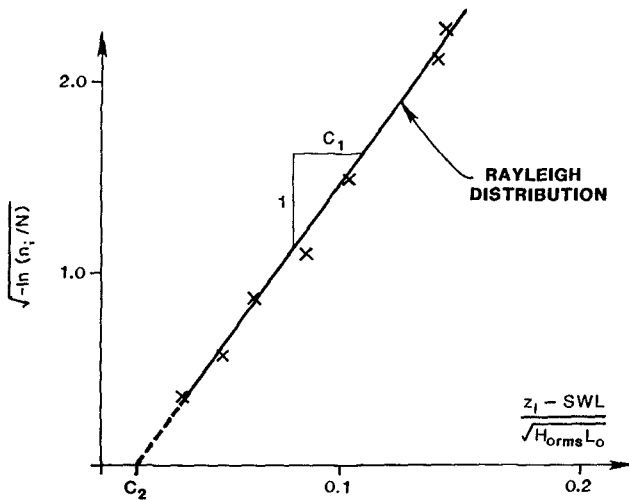


Figure 3: Runup data from Palm Beach north of Sydney, 3/8-1990, 13:40-13:55. The Rayleigh distribution is seen to provide a reasonable model.

The Rayleigh distribution (1) combined with Hunt's formula in the form (2) provides a good model for runup by irregular waves onto steep structures, but for the wide range of beach topographies covered in the present study that is not the case. For very flat beaches, the dependence upon the "beach slope" disappears and a relation of the form

$$L_R = 0.05 \sqrt{(H_{orms} L_o)} \quad \text{for } \tan \beta_F \leq 0.10 \tag{4}$$

where $\tan\beta_F$ is the slope of the beach face, seems to hold. See Figure 4.

For the steeper beaches the vertical scale is roughly proportional the slope of the beach face, but because $\tan\beta_F$ is generally larger than "the beach slope" which is probably more like the average slope β_H between the point where $h=H_{orms}$, see Figure 2, a factor of roughly 0.6 applies:

$$L_R \approx 0.6 \tan\beta_F \sqrt{(H_{orms} L_o)} \quad \text{for } \tan\beta_F \geq 0.10 \quad (5)$$

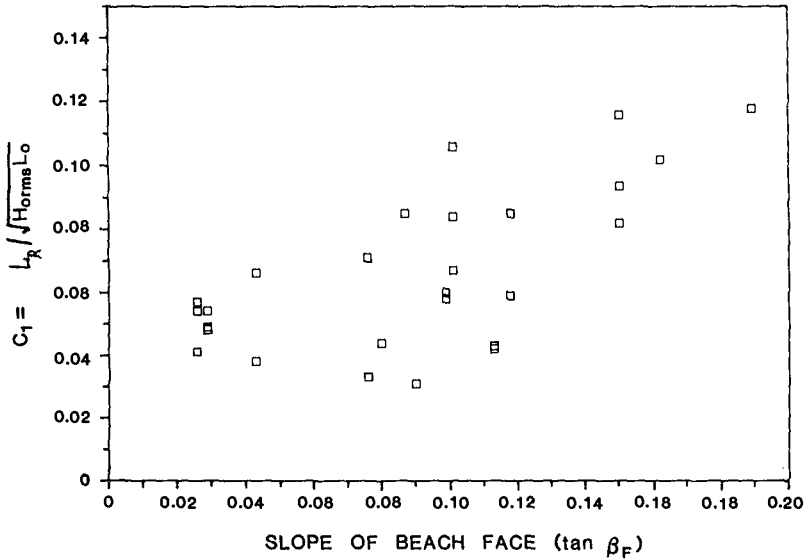


Figure 4: For very flat beaches the vertical scale of the runup distribution is independant of the slope of the beach face.

The second parameter in the Rayleigh distribution (1), namely the highest level z_{100} transgressed by all waves is plotted against the beach face slope in Figure 5. From this figure it can be seen that for very flat beaches ($\tan\beta_F \leq 0.08$), z_{100} is significantly below the still water level, while it is uniformly scattered around the SWL for the steeper beaches. The fact that z_{100} moves seaward of the still water line on very flat beaches is mainly due to the fact that strong surf beats are common on such beaches and; when the surf beat is down, most waves are transformed into bores seaward of the still water line and several pairs of bores will coalesce by overtaking through the surf zone. This deminishes the number of waves which are counted at the still water line.

Table 1. Summary of runup data

Location	Date	Time (EST)	H_{orms} [m]	T_s [s]	$\tan\beta_F$	C_1	r	$P(z_g)$	$C_1/\tan\beta_F$	C_2
Brunswick	1/12-88	1040	0.53	7.0	0.043	0.038	0.999	0.33	0.88	-0.45
	22/12-88	1622	1.13	8.1	0.029	0.049	0.990	0.06	1.69	-0.53
	22/12-88	1702	1.13	8.3	0.029	0.054	0.988	0.19	1.86	-0.59
	22/12-88	1808	1.07	8.4	0.029	0.048	0.966	0.27	1.66	-0.67
	21/3-89	1635	1.20	11.5	0.090	0.031	0.987	0.38	0.34	0.29
	31/3-89	1515	1.91	8.0	0.080	0.044	0.993	0.37	0.55	-0.34
	22/8-89	1345	1.30	10.5	0.043	0.066	0.995	0.27	1.53	-0.58
	22/8-89	1515	1.25	10.2	0.043	0.038	1.000	0.04	0.88	-0.12
Dee Why	13/7-89	1010	2.92	11.3	0.113	0.042	0.999		0.37	0.24
	13/7-89	1050	2.95	11.4	0.113	0.043	0.996		0.38	0.23
	26/7-89	1045	2.58	8.5	0.118	0.059	0.984	0.37	0.50	-0.27
	26/7-89	1145	2.17	7.6	0.118	0.085	0.993	0.43	0.72	-0.39
Ocean Beach *	24/7-89	1218	0.78	7.1	0.076	0.071	0.998		0.93	-0.37
	24/7-89	1442	0.74	7.8	0.076	0.033	0.995		0.43	0.15
Palm Beach	18/4-89	1612	0.62	8.3	0.189	0.118	0.992	0.78	0.62	0.00
	19/4-89	743	0.98	7.9	0.162	0.102	0.999	0.91	0.63	0.03
	6/6-90	1415	0.96	6.8	0.101	0.067	0.988	0.24	0.67	-0.28
	6/6-90	1445	0.96	6.8	0.101	0.084	0.997	0.30	0.84	-0.43
	6/6-90	1515	0.96	6.4	0.101	0.106	0.967	0.40	1.05	-0.45
	2/8-90	1445	0.95	9.7	0.087	0.085	0.995	0.51	0.98	0.26
	3/8-90	1348	2.90	9.6	0.099	0.058	0.997	0.32	0.58	0.28
	3/8-90	1445	2.55	9.7	0.099	0.060	0.991	0.46		0.32
Pearl Beach *	30/6-89	1615	1.55	8.8	0.150	0.094	0.991	0.60	0.63	-0.13
	30/6-89	1650	1.58	8.7	0.150	0.116	0.980	0.50	0.77	-0.14
	30/6-89	1713	1.58	8.8	0.150	0.082	0.997	0.51	0.55	0.26
Seven Mile Beach	21/8-90	1645	1.07	7.5	0.026	0.057	0.979	0.07	1.69	-0.84
	22/8-90	1015	1.16	7.0	0.026	0.054	0.979	0.10	2.07	-0.81
	22/8-90	1245	1.10	7.4	0.026	0.041	0.971	0.01	1.57	-1.10

*): Data from Turner (1989).

4. Wave setup on beaches.

While the wave setup data of the present study are geographically restricted to a few beaches on the coast of New South Wales they do form the most comprehensive set of field data available to day.

The first major conclusion to be drawn from the data is that the measured setup profiles are quite different from the ones that result from assuming periodic waves, constant height to depth ration [$H=\gamma(D+B)$] in the surf zone, and radiation stress given by linear wave theory. These are the simplifying assumptions suggested by Bowen et al (1968).

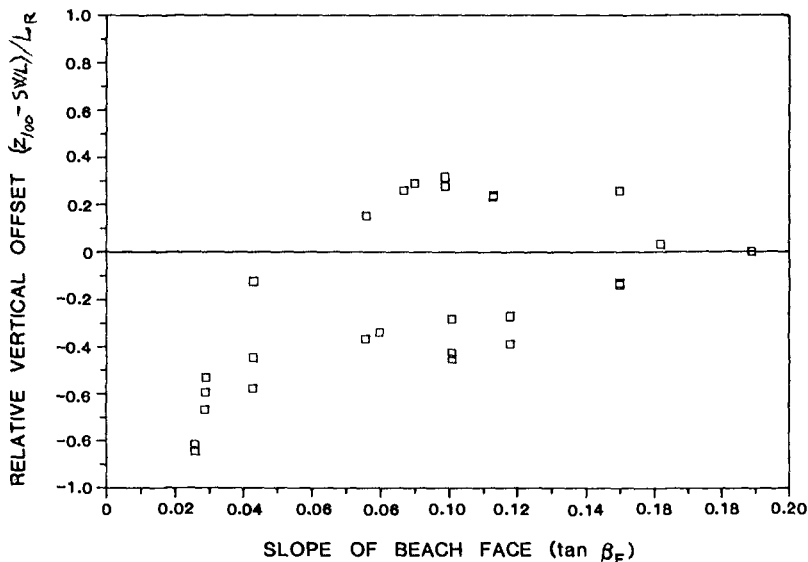


Figure 5: For very flat beaches z_{100} is significantly below the still water level, but for the steeper beaches the deviation is insignificant.

The difference emerges most clearly when the setup B is plotted against total depth, h as in Figures 6. In such a diagram the setup profile according to the above assumptions is a straight line with slope $S = 3\gamma^2/8$ while the typical field data set shows a very different trend. A contributing factor to the difference of shape is wave irregularity as discussed by Battjes and Janssen (1978) and by Nielsen et al (1988). However, wave height variability can only explain the upward concavity of the profile, not the higher values of the shoreline setup, B_s . The measured values of the B_s ($= z_s - SWL$) are generally about $0.4 H_{orms}$ which is significantly above the Bowen-et-al-model's prediction of $\frac{3}{8} \gamma H_b$ with reasonable values of γ and H_b/H_o .

The difference between observed and expected setup profiles must result from a combination of the following effects:

1. Real waves near breaking carry much less momentum flux than sine waves of the same height (Nielsen et al 1988 and Dean 1974).
2. The momentum flux does not decay as rapidly as H^2 in the outer surf zone (Svendsen 1984).
3. The bores in the swash zone carry considerably more momentum flux than sine waves of the same height.

A theoretical description of the setup profile which accounts for the observed features is not yet available so the best design guidance is probably gained from the data.

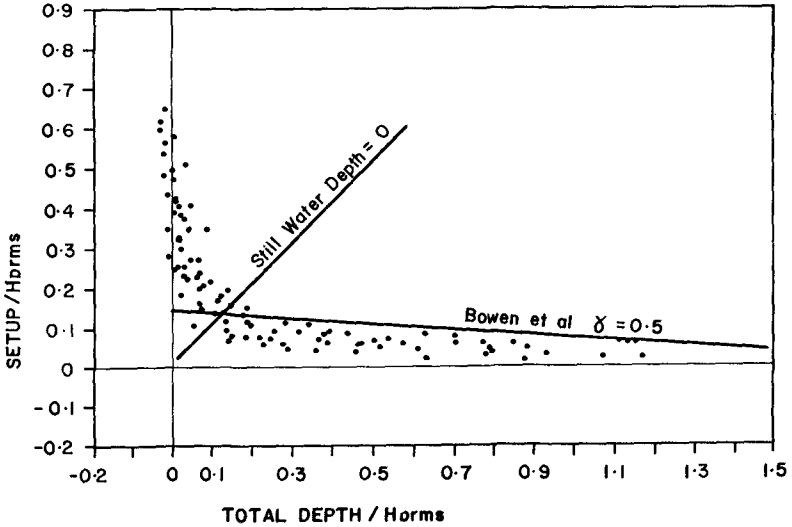


Figure 6: Wave setup at Dee Why Beach, Sydney on August 4 1987, $(H_{orms}, T_p) = (1.6m, 8.2s)$.

A close-up look at the setup profile near the shoreline is provided by Figure 7 for a range of beach shapes and wave heights. This plot differs from Figure 6 in

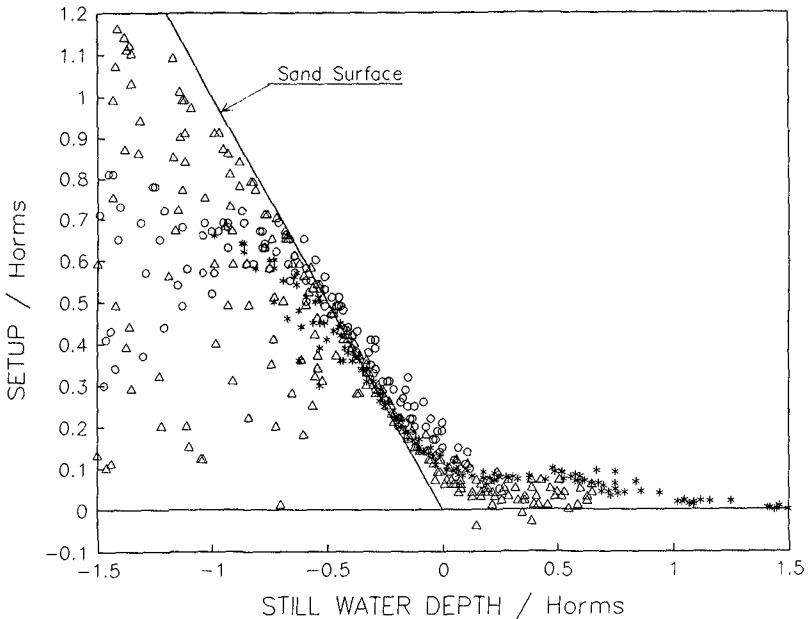


Figure 7: Relative Setup from the swash zones at Brunswick Heads 22/6-89 (*), Palm Beach 6/6-90 (o), and Seven Mile Beach 21/8-90 (Δ). Data details in Table I.

that the abscissa is the dimensionless still water depth rather than the total depth.

One step towards achieving an integrated picture of wave setup, wave runup and coastal watertable dynamics is to determine the position of the shoreline in the runup distribution i.e. what fraction of the waves are expected to transgress the shoreline on a given beach. One example involving a steep beach of coarse sand (Palm Beach) is shown in Figure 8. Such beaches drain rather efficiently and hence the Mean Water Surface will establish itself at a fairly low position relative to the runup/infiltration distribution, with most of the waves transgressing the shoreline. For the shown example, the shoreline was transgressed by about 78 percent of the waves, i.e. $P\{z_g\} = 0.78$.

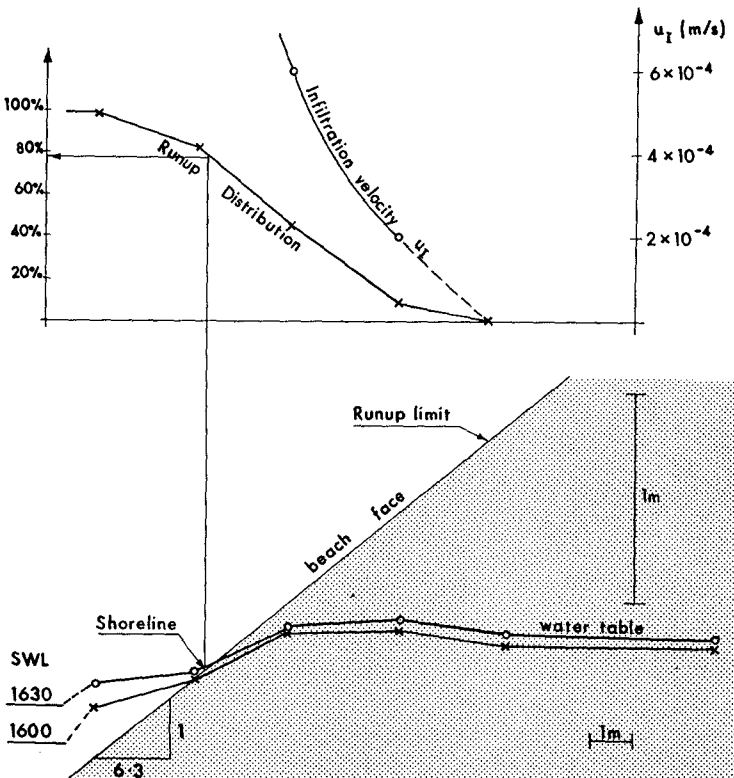


Figure 8: The relation between wave transgression statistics and the position of the shoreline at the Northern end of Palm Beach. The preceding low tide was at 13:51, the following high at 20:08 with a range of 1.0m. The offshore wave data were $(H_{orms}, T_p) = (0.62m, 8.3s)$.

The position of the shoreline and hence $P\{z_s\}$ is a function of the relative tidal range $A_{\text{tide}}/H_{\text{rms}}$ and the tidal phase as well as of the beach slope and permeability. Still, the data in Table 1, which correspond to mixed tidal phases show a clear relationship between the relative shoreline elevation and the beach slope, see Figure 9.

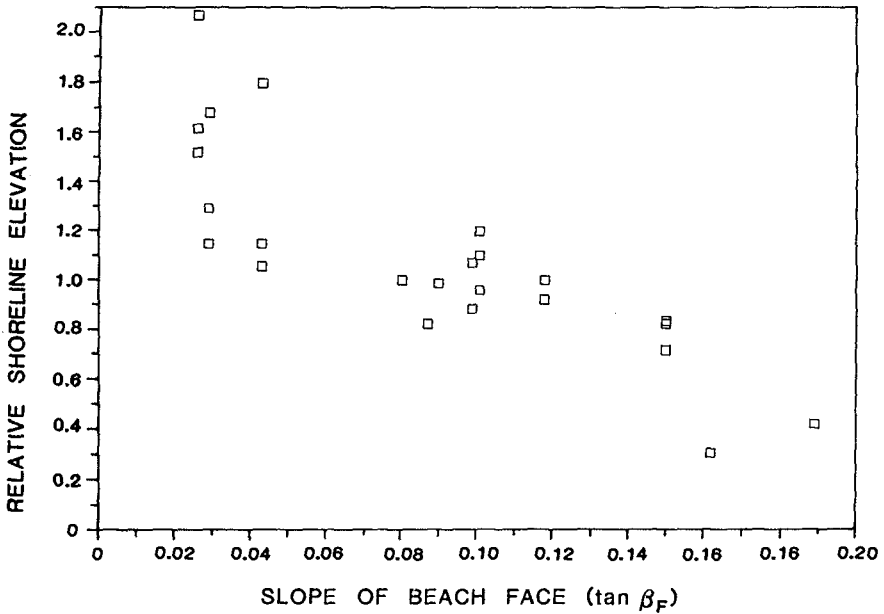


Figure 9: The relative shoreline elevation $(z_s - \text{SWL})/L_R$ is a decreasing function of the beach face slope because steeper beaches generally drain more efficiently than flat beaches.

Although the combination of Figures 4 and 9 points towards a predictive formula of the form

$$B_s = F[\sqrt{(H_{\text{orms}} L_o)}, \tan \beta_F] \tag{6}$$

the data can also give a rough indication of B_s as function of the offshore wave height irrespective of beach morphology, namely

$$B_s = 0.4 H_{\text{orms}} \tag{7}$$

see Figure 10

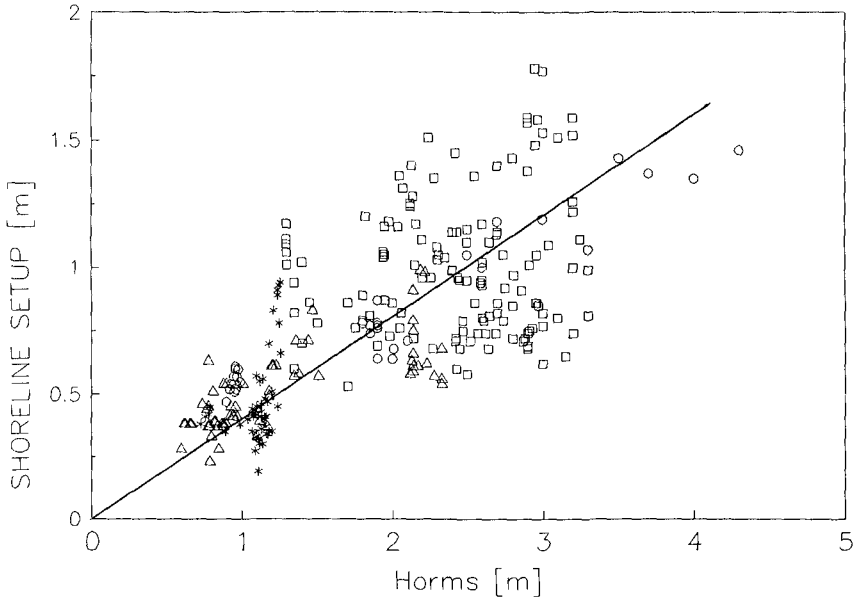


Figure 10: Shoreline setup, B_s , as function of offshore wave height. The straight line is given by Equation (7). Legend: * Seven Mile Beach, o Palm Beach, [] Brunswick Heads, Δ Dee Why Beach.

5. Watertable data

Two methods were applied for collecting watertable data. For short records (25 hours or less) an array of simple stilling wells were used. These were monitored with a dip-meter which is a measuring tape with a conductivity sensor on the end. For long term records a self recording pressure sensor in a single well was used.

Figure 11 shows a series of MWS/watertable measurements from Dee Why Beach on the rising tide (high tide at 20:00). Estimated shoreline elevations based on (7) are given on the right. Note that the watertable continues to rise landward of the shoreline due to the infiltration from runup.

One long term record is shown in Figure 12 together with the corresponding wave-, tide- and rainfall data. Rainfall had little impact because the well was located on the narrow sand barrier in front of Dee Why Lagoon but the influence

from waves and tides is very clear. We see that the watertable was at all times more than one metre above MSL, and the tidal variation is highly asymmetrical. That is, the watertable rises very sharply and falls of very slowly in response to an essentially sinusoidal tide. A considerable fraction of the overheight as well as the skewness is due to asymmetry in the boundary condition at the beach face. In qualitative terms we may say that the infiltration at high tide is much more efficient than the draining at low tide.

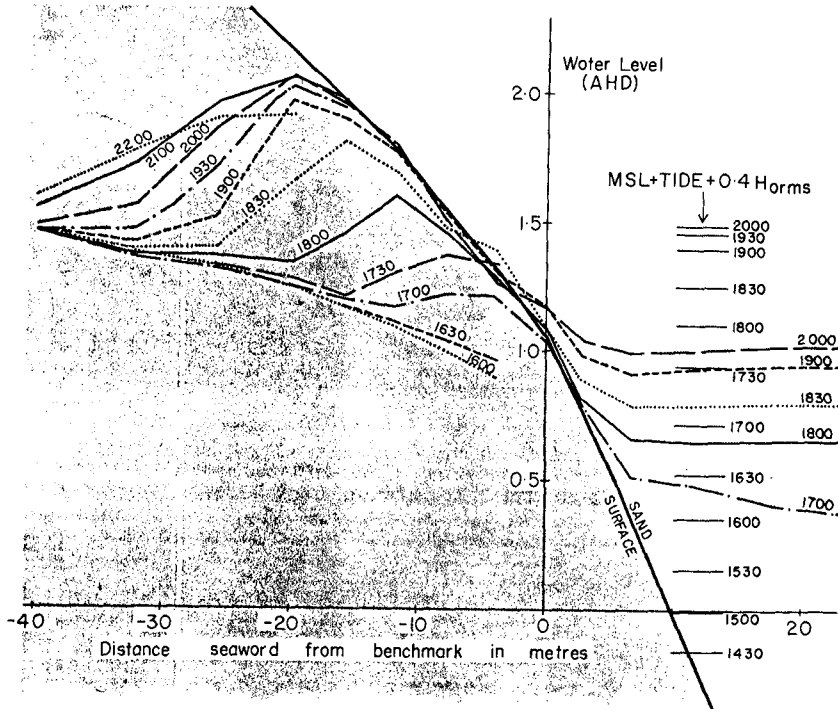


Figure 11: Successive watertable measurements taken at Dee Why Beach 7/9-87, ($H_{orms}, T_g \approx (1.1m, 8s)$)

6. Watertable modelling

The dynamics of the watertable as forced by waves and tides has been modelled using the following theoretical framework. The flow inside the sand is governed by Darcy's law and the conservation of volume which leads to

$$\frac{\partial \eta}{\partial t} = -\frac{KD_a}{n} \frac{\partial^2 \eta}{\partial x^2} + u_I \tag{8}$$

where K is the permeability, D_a is the depth of the sand body below the average watertable, n is the relative pore volume and u_I is the infiltration velocity due to wave runup.

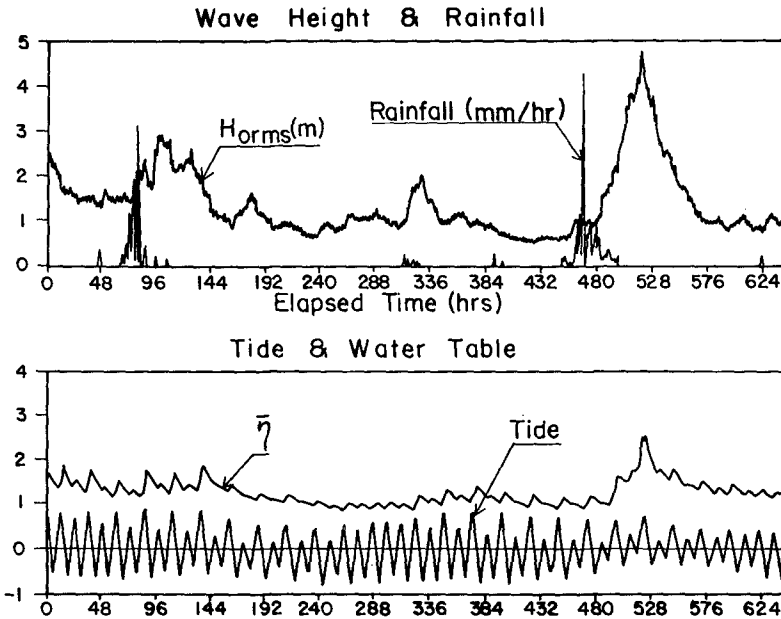


Figure 12: Watertable record from Dee Why Beach. The measurements were taken in a well situated about 30 metres from the average shoreline position where the sand level was approximately 2.6m AHD.

Analytical solutions to (8) can be found for the two special cases of pure wave forcing and pure tidal forcing, under the additional assumption that the shoreline position can be prescribed, see Nielsen et al (1988). For the pure wave case it can then be shown that the asymptotic inland watertable height above the shoreline is proportional to the horizontal length scale of the runup distribution squared divided by the aquifer depth i e

$$\bar{\eta}(\infty) - \text{SWL} = \text{const } H_{\text{orms}} L_o / D_a \quad (9)$$

It is independent of the beach permeability because greater permeability equally enhances infiltration and drainage.

For pure tidal forcing a perturbation solution has been used to describe the average overheight above MSL as well as the skewness shown by the data in Figure 12. It turns out that the magnitude of the overheight is $0.5kA^2 \cot \beta$ where k is the wavenumber of the tidal watertable wave and A is the tidal amplitude. With typical k -values of 0.08m^{-1} this tidal overheight ranges typically from 0.2 to 0.5 metres on the coast of New South Wales.

7 References

- Battjes, J.A., and J.P.E.M. Janssen, Energy loss and setup due to random breaking waves, paper presented at Proc 14th Int Conf Coastal Engineering, Am. Soc. Civ. Eng., Hamburg, 1978.
- Battjes, J.A., Runup distributions of waves breaking on slopes, *J. Waterways, Harbours and Coastal Engineering Division, A.S.C.E.*, vol. 97, WW1, pp 91-114, 1971.
- Bowen, A.J., D.L. Inman, and V.P. Simmons, Wave setdown and setup, *J. Geophys. Res.*, 73(8), 2569-2577, 1968.
- Dean, R.G., Evaluation and development of water wave theories for engineering application, Spec. Rep. 1, CERC, Washington, D.C., 1974.
- Guza, R.T., and E.B. Thornton, Wave setup on a natural beach, *J. Geophys. Res.*, 86 (C5), 4133-4137, 1981.
- Holman, R.A., Extreme value statistics for wave runup on a natural beach, *Coast. Eng.*, 9, 527-544, 1986.
- Holman, R.A., and A.H. Sallenger, Setup and swash on a natural beach, *J. Geophys. Res.*, 90 (C1), 945-953, 1985.
- Hunt, I.A., Design of seawalls and breakwaters, *Proc. Am. Soc. Civ. Eng.*, 85 (WW3), 123-152, 1959.
- Longuet-Higgins, M S, Wave Setup, Percolation and Undertow in the surf zone, *Proc Roy Soc Lond Ser A* 390, pp 283-291, 1983.
- Nielsen, P., Wave Setup: A Field Study, *J. Geophysical Res.*, Vol. 93, (C12), pp 15643-15651, 1988.
- Nielsen, P & D Hanslow (1991): Runup distributions on natural beaches, *J Coastal Res.*
- Nielsen, P., G.A. Davis, J. Winterbourne, and G. Elias, Wave setup and the water table in sandy beaches, Tech. Rep. 88/1, Coast and Rivers Branch, Public works Dep., Sydney, New South Wales, Australia, 1988.
- Svendsen, I.A., Wave heights and setup in a surf zone, *Coast. Eng.*, 8 (3), 303-329, 1984.
- Turner, I LL (1989): The total water content of sandy beaches, B Sc Hons Thesis, Dept of Geography, University of Sydney.

CHAPTER 67

Application of The Second-order Mode Coupling Equation to Coastal Engineering Problems

Mitsuhiro Tanaka†

Abstract

The Second-order Mode Coupling Equation (SMCE) is applied to the 3-dimensional evolution of a solitary wave the crest-line of which is not straight but bent initially. It is found that the bent solitary wave recovers a straight crest-line spontaneously by producing a nonuniform distribution of waveheight and hence that of propagation speed along the crest-line.

1. The Second-Order Mode Coupling Equation

1.1 The Mode Coupling Equation

As pointed out by Zakharov(1968), the motion of water waves can be expressed as a Hamiltonian system by using the total energy as the Hamiltonian and the complex amplitude spectrum $b(\vec{k}, t)$ defined by

$$b(\vec{k}, t) = \sqrt{g/2\omega(k)} \bar{\eta}(\vec{k}, t) + i\sqrt{\omega(k)/2g} \tilde{\phi}^s(\vec{k}, t) \quad (1)$$

as the canonical variable. Here $\bar{\eta}(\vec{k}, t)$ and $\tilde{\phi}^s(\vec{k}, t)$ are the Fourier transform of the free surface displacement $\eta(\vec{x}, t)$ and the velocity potential $\phi(\vec{x}, z, t)$ evaluated at the free surface respectively, and $\omega(k) = \sqrt{gk \tanh kh}$, with $k = |\vec{k}|$.

† Assistant, Department of Applied Mathematics, Faculty of Engineering, Gifu University 1-1 Yanagido, Gifu 501-11 JAPAN

When the Hamiltonian is approximated by a power series of $b(\vec{k}, t)$ truncated at the $(n+1)$ th-order, the resulting Hamilton's equation which governs the evolution of $b(\vec{k}, t)$ contains n -th power of $b(\vec{k}, t)$ and is called here the n -th-order mode coupling equation.

In the derivation of the mode coupling equation, it is usually assumed that the nonlinearity of the underlying wave field is small (i.e., $ak \ll 1$) and that the bottom is flat (i.e., $h = \text{const.}$) and impermeable. With regard to the value of kh , however, no assumption is made and the equation can be applied to waves of any wavelength so long as the above-mentioned assumptions hold.

The third-order mode coupling equation reduces to the well-known Zakharov's equation if only the near resonant interactions are taken into account among all the possible four-wave interactions. Zakharov's equation is further simplified to give the nonlinear Schrödinger equation when the assumption of narrow-bandedness of the wave field is added.

Here in this work, we focus our attention to the Second-order Mode Coupling Equation which we'll call the SMCE for short. Following the notation of Stiassnie and Shemer(1984), the SMCE can be expressed as follows,

$$\begin{aligned} \frac{db(\vec{k})}{dt} + i\omega(k)b(\vec{k}) \\ + i \iint V^{(1)}b(\vec{k}_1)b(\vec{k}_2)\delta(\vec{k} - \vec{k}_1 - \vec{k}_2)d\vec{k}_1d\vec{k}_2 \\ + i \iint V^{(2)}b^*(\vec{k}_1)b(\vec{k}_2)\delta(\vec{k} + \vec{k}_1 - \vec{k}_2)d\vec{k}_1d\vec{k}_2 \\ + i \iint V^{(3)}b^*(\vec{k}_1)b^*(\vec{k}_2)\delta(\vec{k} + \vec{k}_1 + \vec{k}_2)d\vec{k}_1d\vec{k}_2 = 0. \quad (2) \end{aligned}$$

This equation reduces to the well-known K-dV equation under the assumptions that the water is shallow (i.e., $kh \ll 1$) and all the wave components propagate only in the positive x -direction.

There are two major reasons why we choose the SMCE here and discard all the higher order nonlinear interaction terms. The

first reason is; It can be shown that the magnitude of the third-order terms of the mode coupling equation relative to the second-order ones is given by the wave steepness ak of the underlying wave. This implies that the third-order terms as well as all the higher order terms would give only negligibly small contributions to the motion of a solitary wave which we focus our attention to in this work, because it is generally true for a long wave like a solitary wave that a/h may be $O(1)$ while kh is very small, resulting in a very small value of ak .

The second reason to choose SMCE is much more pragmatic. The n -th order mode-coupling equation generally contains n -tuple convolution sums, and the number of operations required per each time step would increase as N^n with N being the number of Fourier modes involved in the calculation. However, the operation count necessary for the evaluation of the second-order convolution terms increase only as $N \ln N$ instead of N^2 . This is because these terms can be rewritten to a form to which the pseudospectral method is applicable and so can be evaluated fast by a series of FFT's and inverse FFT's. This reduction of the number of numerical operations becomes crucial when one is to pursue a 3-dimensional problem like the one shown in Sec. 2 of this work, because for such a 3-D problem the number of Fourier modes required for a reasonably accurate expression of the wave field inevitably becomes large. For such a problem with large number of Fourier modes, the higher order mode coupling equations like Zakharov's equation, however valuable they may be from the theoretical point of view, would require unrealistically vast amount of CPU time on the computing facilities now available and would have only a very limited practical value.

1.2 Accuracy of The SMCE

Before proceeding to an application of the SMCE to a practically interesting problem, it may be sensible to know how better the SMCE approximates the behaviour of long waves than the K-dV equation which is one of the most standard equations for long wave problems.

What we've done is to input the steady periodic solution of

fully nonlinear water wave equations to the SMCE and the K-dV as the initial condition and observe how strongly this steady profile is deformed at later times. In the calculation shown below, we tentatively fix the water depth so that $kh = 0.5$. For this value of kh , the linear dispersion relation of the K-dV equation $\omega(k) = \sqrt{gh}k \{1 - (kh)^2/6\}$ is a very good approximation of the exact one $\omega(k) = \sqrt{gk} \tanh kh$ with the error being only less than 0.3%. In this sense the water is sufficiently shallow and we expect that the K-dV equation approximates the steady translation very well.

The deformation of the wave form is measured by a quantity $D(t)$ defined by

$$D(t) = \int_0^L \{\eta(x, t) - H(x - ct)\}^2 dx / \int_0^L H^2 dx, \quad (3)$$

where H is the profile of the steady periodic wave solution employed as the initial condition and c its propagation speed. As the initial condition is an exact steady solution of the fully nonlinear problem, the deformation $D(t)$ should remain zero if the approximation is 'ideal'. Therefore, we can discuss the accuracy of various different approximations by comparing the magnitude of $D(t)$ given by those approximations.

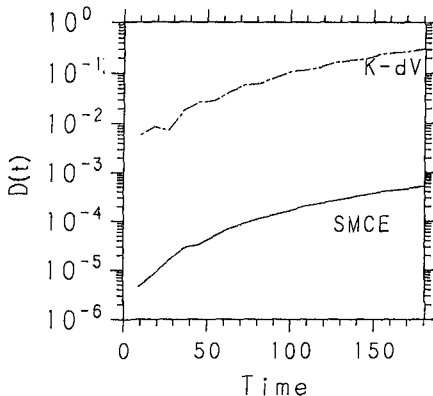


Fig. 1 Growth of Deformation $D(t)$ for a steady periodic solution with $ak = 0.1$ and $kh = 0.5$

Figure 1 shows the growth of $D(t)$ for the steady wave with $ak = 0.1$. It can be seen that $D(t)$ given by the SMCE remains about 500 times smaller than that of the K-dV equation during the period of time considered, implying that the SMCE gives 500 times more accurate result than the K-dV equation does, at least for the steady translation of the particular wave considered here. It may be noted that the length of time shown in Fig.1 is fairly long for the particular steady wave, and during which the wave has propagated more than 250 times the water depth.

If the nonlinear terms of both the SMCE and the K-dV are calculated by the pseudospectral method, and the time-stepping of both equations are carried out by Runge-Kutta-Gill method, the SMCE requires about three times longer CPU time than the K-dV equation does.

2. Three-Dimensional Evolution of A Bent Solitary Wave

2.1 Initial Condition

As an application of the SMCE to a 3-dimensional problem, we investigate the time evolution of a wave which is basically a Boussinesq solitary wave propagating in the positive x -direction but the crest-line of which is slightly bent initially. More specifically, we've prescribed the initial condition as follows:

$$\eta(x, y, 0) = a_0 \operatorname{sech}^2 \{(x - x_c(y))/D\} \quad (4a)$$

$$\phi^s(x, y, 0) = \sqrt{4a_0/3} \tanh \{(x - x_c(y))/D\} \quad (4b)$$

where D is the width of the solitary wave which is related to the waveheight a_0 by $D = \sqrt{4(1 + a_0)/3a_0}$. In the calculation reported here, the initial shape of the crest-line $x_c(y)$ is chosen tentatively as $x_c(y) = x_0 - \epsilon \cos(2\pi y/L_y)$ with x_0 being some appropriate constant. The parameter ϵ determines the magnitude of the y -variation of the crest position, while L_y determines its length-scale. For the sake of numerical computation, the wave field is assumed to be periodic both in the x - and y -direction with the period L_x and L_y , respectively. The period in the x -direction L_x is taken sufficiently long so that the existence of the

periodic boundary would not affect the evolution of the wave field seriously. The water depth is normalized as 1.

Figure 2 shows the bird's-eye view of the wave form at $t = 0$ (Fig. 2a) and $t = 30$ (Fig. 2b) when the crest is not bent initially. The values of parameters chosen for this calculation are $a_0 = 0.2$, $L_x = 61.3$, $L_y = 5$, $N_x = 128$, $N_y = 12$ and $\Delta t = 0.5$. Here N_x and N_y are the number of mesh points in the x - and y -direction, respectively, and Δt is the step-size of the time-integration which is carried out by Runge-Kutta-Gill scheme. The total CPU time is about 57 sec. on FACOM M780 of the Computation Center of Nagoya University. Although the initial condition is not a steady solution of the SMCE but of the Boussinesq equation, the solitary wave seems to be propagating almost steadily on the SMCE as well. This is quite reasonable because the Boussinesq soliton should be a good approximation of the steady solution of the SMCE when the waveheight is not large as in the present case where $a_0 = 0.2$.

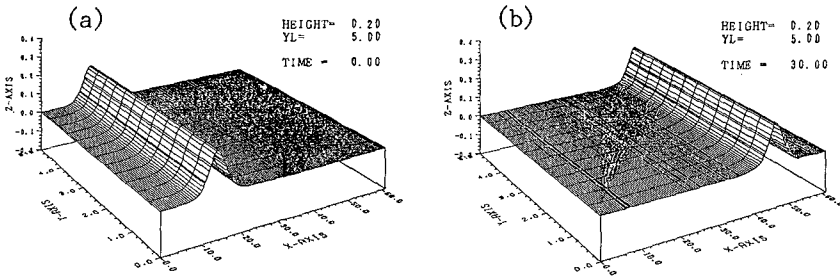


Fig. 2 Wave-form when the solitary wave is not bent initially.
(a) $t = 0$, (b) $t = 30$.

2.2 Scenario of 3-D Evolution

An example of the evolution of a bent solitary wave is shown in Fig. 3. All the parameters are the same as the previous case, the only difference being that the amplitude of the initial bend ϵ is set equal to 1 instead of 0. Figure 3a shows the bird's-eye view of the initial wave form, and the time evolution that follows is shown in Figs. 3b–3f. The scenario of the evolution may be summarized as follows:

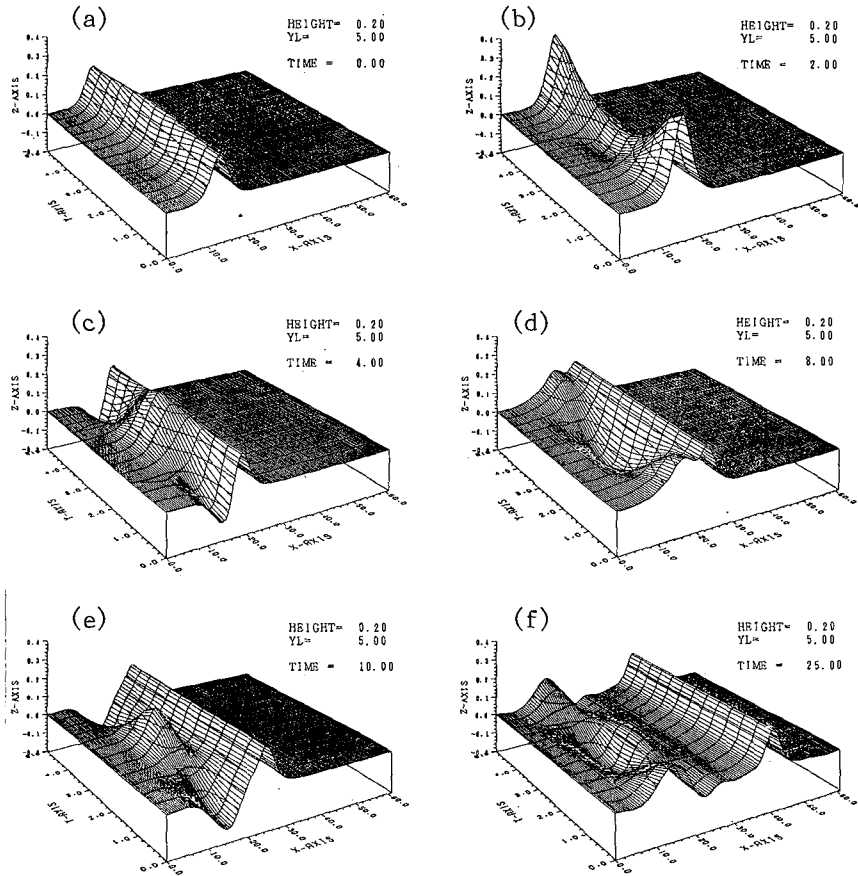


Fig. 3 3-D evolution of a bent solitary wave. $a_0 = 0.2$, $L_y = 5$ and $\epsilon = 1$.

(1) The waveheight spontaneously starts to increase around $y = 0$ and $y = L_y$ where the wave crest is made behind initially, while it starts to decrease around $y = L_y/2$ where the crest is put forward. As it is generally true for long waves that the higher waves propagate faster than the lower, this unevenness of the waveheight brings out such a distribution of propagation speed along the crest-line that would help the bent crest-line go back to a straight line. (Fig.3b)

(2) Around $y = 0$ and $y = L_y$ where the crest is now propagating faster because of the increased waveheight, the water just behind the crest appears not to be able to keep up with the crest, and as a result of that, a depression of water surface appears. On the other hand, around $y = L_y/2$, the water just behind the crest seems to be overtaking the crest which is now propagating by a reduced speed, and a swell up of water surface is observed behind the crest. (Fig.3c)

(3) The lateral distribution of the free surface displacement behind the crest-line that has appeared in (2) evolves into a standing wave-like oscillation. The period of oscillation coincides approximately with that of a linear long wave with wavenumber $k = 2\pi/L_y$. By this time, the recovery of a straight crest-line has been accomplished, and a 2-dimensional solitary wave with a straight crest-line is emerging out of the transient wave motion. (Figs.3d and 3e)

(4) The initial condition finally splits into two parts. One is a 2-D solitary wave with a straight crest-line which propagates steadily with a speed given approximately by $1 + a/2$, and the other is a standing wave-like oscillation which appears to stay around the position for all the time, the position where the wave was given initially. This difference between the propagation speed of these two parts brings out the appearance of a region with a calm free surface between them. This calm region grows wider as time goes on and the solitary wave propagates further from the initial position. (Fig.3f)

Figure 4a shows the top-view of the crest-line at various time-steps in which it can be seen clearly how the crest-line approaches a straight line. In order to see this phenomenon more quantitatively, we show in Fig.4b the evolution of a quantity X_{dev} defined by

$$X_{\text{dev}}(t) = \int_0^{L_y} \{x_c(y) - \bar{x}_c\}^2 dy, \quad (5)$$

where $x_c(y)$ is the x -coordinate of the crest-line in terms of y and \bar{x}_c is the average of $x_c(y)$. By its definition, X_{dev} vanishes when the crest-line is straight.

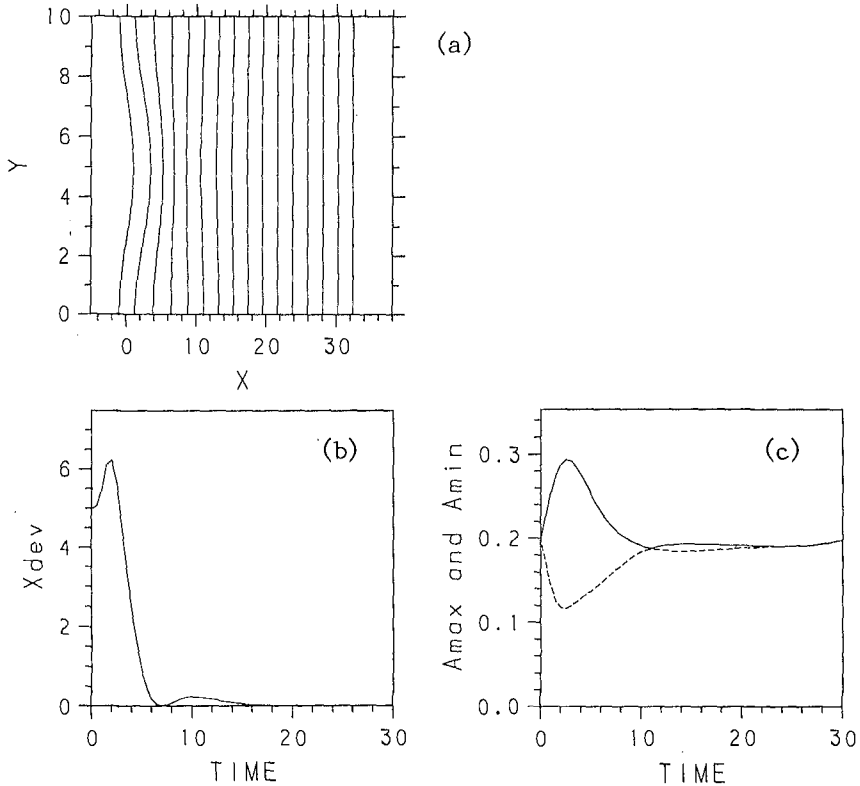


Fig. 4 (a) The top-view of the crest-line for $0 \leq t \leq 30$. (b) X_{dev} , i.e., the deviation of the crest-line from a straight line. (c) The evolution of the maximum and the minimum waveheight along the crest-line ($a_0 = 0.2$, $L_y = 10$ and $\epsilon = 1$)

Figure 4c shows the evolution of the maximum and the minimum waveheight along the crest-line. This figure shows clearly the spontaneous appearance of a nonuniformity of the waveheight right after the initial time, as well as its gradual relaxation and the return to a state of uniform waveheight.

2.3 L_y – Dependence

We've shown above that a solitary wave seems to have an ability to make its crest-line straight when it's bent initially by producing a nonuniform distribution of the waveheight along the crest.

There are two important quantities that characterize this phenomenon. One is the characteristic time-scale of the phenomenon and the other is the size of the highest wave that appears during the transient motion. Figure 5a shows the L_y -dependence of the characteristic time-scale which is defined as the time when $X_{\text{dev}}(t)$ of eq.(5) attains its first local minimum. In the same figure is also shown by a dashed line the period of oscillation of a linear long wave with wavelength L_y . The result shows that the longer the length-scale of the initial bend, the longer it takes to return to a straight crest-line.

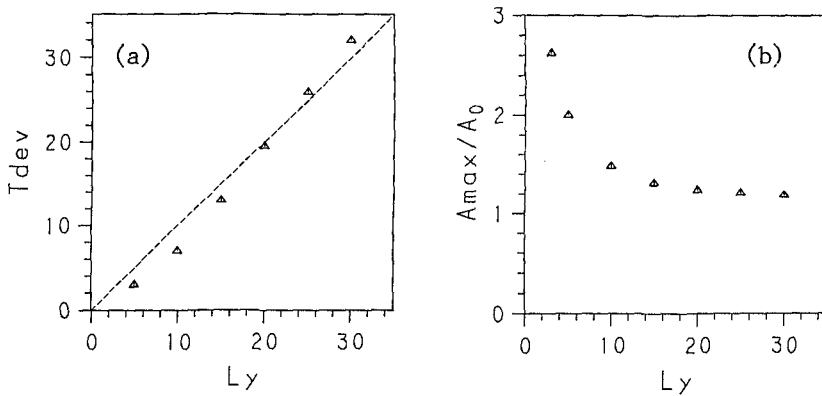


Fig. 5 (a) L_y -dependence of the characteristic time-scale (b) L_y -dependence of the maximum waveheight that appears during the transient motion

The maximum waveheight that appears during the transition divided by the initial height is shown in Fig.5b as a function of L_y . This figure shows that the higher wave appears as the length-scale of the initial bend is shortened or as the curvature of the initial crest-line is increased. For the type of initial condition we are now using, we can get a wave which is 2.6 times as high as the initial wave by bending its crest-line such that $L_y=3$ and $\epsilon = 1$. This result strongly suggests that it might be possible to make a solitary wave break without decreasing the water depth but by just bending its crest-line somehow. We've also investigated the dependence of the phenomenon on the initial waveheight a_0

by changing a_0 from 0.1 to 0.5, but no appreciable change in the characteristic time-scale or the maximum waveheight was observed.

The crest-line of solitary waves that are observed on the beach are usually very long and nearly straight in spite of the uneven bottom topography over which they may have propagated. This might be related to the ability of a solitary wave as that shown above to keep its crest-line straight by adjusting the waveheight distribution along the crest when it is deformed by some external cause.

3. A Simple Model

In this section, we try to reproduce the phenomenon shown in the previous section by a simple model in order to understand intuitively the principle that underlies the phenomenon. The model the detail of which is explained below is derived by an analogy with the motion of an axisymmetric (or cylindrical) solitary wave.

The waveheight of a diverging axisymmetric wave which can be produced quite easily by throwing a stone into a pond is observed to decrease as the wave propagates outward and the crest-line of the wave is stretched. On the other hand, the waveheight of a converging axisymmetric wave which occurs when one hits a circular basin filled with water increases as the wave propagates inward and the crest-line is shortened. It is quite obvious that these changes of waveheight are the result of conservation laws.

3.1 Assumptions of the Model

Bearing this in mind, we now propose a very crude model to understand intuitively the 3-D evolution of a bent solitary wave. The followings are the assumptions on which the model is constructed;

- (1) Each point that constitutes the crest-line moves in the direction normal to the crest-line at that point with velocity v given by $v = (1 + a/2)$, where a is the local waveheight of the crest.
- (2) The waveheight a changes in such a way that *mass* or *energy* is conserved. (see Assumption (3) below.)

(3) The shape of normal cross-section at any point of the crest-line is similar to that of the K-dV soliton, and its horizontal length-scale is proportional to $1/\sqrt{a}$ when the local waveheight is a .

3.2 Evolution Equations

The shape of the crest-line and the distribution of the waveheight along it at time t is assumed to be described as $x = x(\sigma)$, $y = y(\sigma)$ and $a = a(\sigma)$, where σ is a parameter which plays a role of the *Lagrangian* coordinate. With this parametric representation of the crest-line, the Assumption (1) can be expressed as

$$\left. \frac{\partial \vec{x}}{\partial t} \right|_{\sigma} = \vec{v} = \{1 + a(\sigma)/2\} \vec{n}, \quad (6)$$

with

$$\vec{n} = (y_{\sigma} \vec{i} - x_{\sigma} \vec{j}) / \sqrt{x_{\sigma}^2 + y_{\sigma}^2}.$$

This is the evolution equation for the shape of the crest-line. On the other hand, the evolution of $a(\sigma)$ is governed by the Assumptions (2) and (3) which require the following relations to hold. When *mass* conservation is assumed,

$$a(x_{\sigma}^2 + y_{\sigma}^2) = \text{const.} \quad (7)$$

along a ray (i.e., $\sigma = \text{const.}$), while

$$a^3(x_{\sigma}^2 + y_{\sigma}^2) = \text{const.} \quad (8)$$

if *energy* conservation is assumed instead.

3.3 Result

Figures 6.a and 6.b show the top-view of the crest-line at various times and the evolution of X_{dev} defined by eq.(5), respectively, that are obtained by the model with *energy* conservation. Although the model is quite a crude one and there would be a lot of possibilities to elaborate on it, it nevertheless expresses, at least qualitatively, the approach of a bent crest-line to a straight line as shown by these figures.

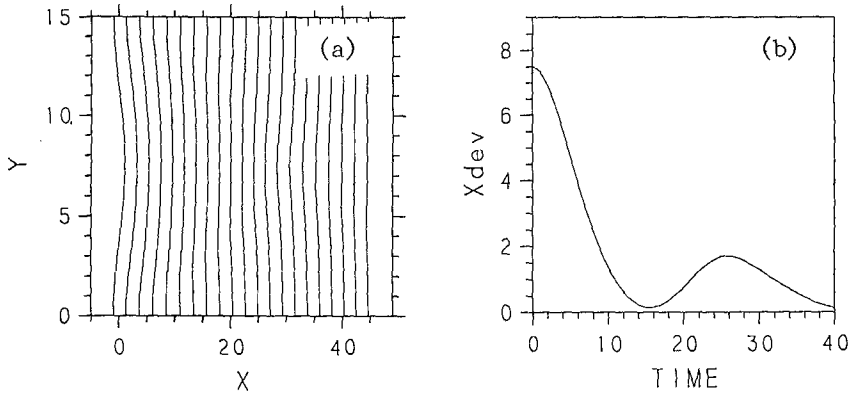


Fig. 6 (a) The top-view of the crest-line for $0 \leq t \leq 40$. (b) X_{dev} , i.e., the deviation of the crest-line from a straight line. ($a_0 = 0.2$, $L_y = 15$, $\epsilon = 1$ and the energy conservation eq.(8) is assumed.)

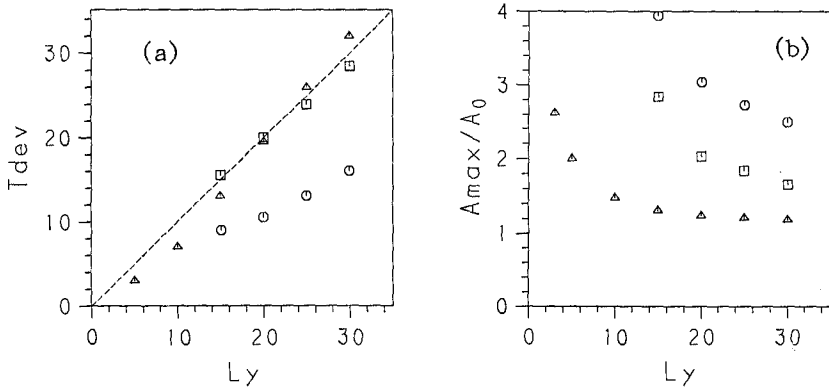


Fig. 7 (a) L_y -dependence of the characteristic time-scale (b) L_y -dependence of the maximum waveheight that appears during the transient motion. \odot : model with mass conservation, \square : model with energy conservation, \triangle : SMCE.

The L_y -dependence of the characteristic time-scale and the maximum waveheight obtained by the present model are shown in Figs. 7a and 7b respectively. In these figures, the open squares show the result of the model with energy conservation, while the open circles show that of the model with mass conservation. The

result of the SMCE is also shown in the same figures by open triangles for the sake of comparison.

It can be seen from these figures that the model with *energy* conservation generally gives much better results than the model with *mass* conservation. Especially, the characteristic time-scale predicted by the model with *energy* conservation almost coincides with that predicted by the SMCE as shown in Fig. 7a. This reminds us of the well-known fact in the perturbation theory of the K-dV equation that the amplitude modulation of one-soliton induced by a small perturbation can be calculated correctly by using any of the infinite number of conservation laws except the first one which corresponds to the mass conservation. This somewhat peculiar fact can be explained in terms of the non-secular condition of the perturbation analysis. (see for example Tanaka (1980))

References

- STIASSNIE, M. AND SHEMER, L. (1984)
On modification of the Zakharov equation for surface gravity waves.
J. Fluid Mech. 143, 47–67.
- TANAKA, M. (1980)
Perturbations on the K-dV solitons
– An approach based on the multiple time scale expansion –
J. Phys. Soc. Jpn. 49, 807–812.
- ZAKHAROV, V.E. (1968)
Stability of periodic waves of finite amplitude on the surface of a deep fluid.
J. Appl. Mech. Phys. 2, 190–194.

CHAPTER 68

FULL-SCALE MEASUREMENTS OF WAVE RUN-UP AT SEA DYKES

Uwe Sparboom 1)
Joachim Grüne 2)
Sven Grosche 3)
Mark Haidekker 3)

ABSTRACT

Wave run-up phenomena due to breaking waves acting on sea dykes are focussed in this paper. Field measurements at two locations of the North Sea Coast are reviewed and compared with full-scale investigations in the Large Wave Channel, Hannover. Commonly used design approaches on wave run-up at sea dykes are discussed. For some naturally shaped shallow wave spectra (Pierson-Moskowitz type) estimations are proposed for wave run-up, run-down and water front velocity in relation to the wave height and to the breaker number.

1. INTRODUCTION

Wave run-up and overtopping phenomena are mostly responsible for dyke failures during storm surge tides at the German North Sea Coast. Recently, this again was demonstrated at dyke profiles near Dagebüll harbor, Northfrisian Coast. Looking towards the discussed possible sea level rise in the near future, reliable wave run-up design criteria for sea dykes are very important.

-
- 1) Dr.-Ing., Senior Research Engineer
 - 2) Dipl.-Ing., Senior Research Engineer
 - 3) cand.-ing., Senior Students of Electrical Eng.

Large Wave Channel-Joint Institution of the University of Hannover and the Technical University of Braunschweig,

Hannover University, Merkurstrasse 11, 3000 Hannover 21, Germany

Wave run-up field measurements at Eastfrisian sea dykes were reported by Erchinger (1974). An estimation of the maximum wave run-up - based on levelling the marker-line of flotsam after storm tides - was proposed by Niemeyer (1976). Results on wave run-up field measurements at the North Sea Coast, also correlated to synchronously measured wave spectra, were published by Coldewey (1982) and Grüne (1982).

In this paper, field measurements (Grüne, 1982) and full-scale measurements in the Large Wave Channel (Führböter, Sparboom and Witte, 1989) were compared with calculated wave run-ups using the empirical approaches derived by Wassing (1957) and by Hunt (1959). Extensions of the Hunt-approach which were published by van Oorschot and d'Angremond (1968) and by Battjes (1971) were also taken into account for comparison.

2. FIELD MEASUREMENTS

In order to verify empirically developed formulae field measurements on wave run-ups and wave spectra were carried out previously (Grüne, 1982). A special run-up probe was used at two different locations of the North Sea Coast (WANGEROOGE and EIDERDAMM). The investigated dyke profiles with 1:4 and 1:6 slopes were constructed by a sand core which was covered by an impermeable layer made from asphalt concrete (Fig. 1). The data of the storm surge measurements were analyzed in the time domain.

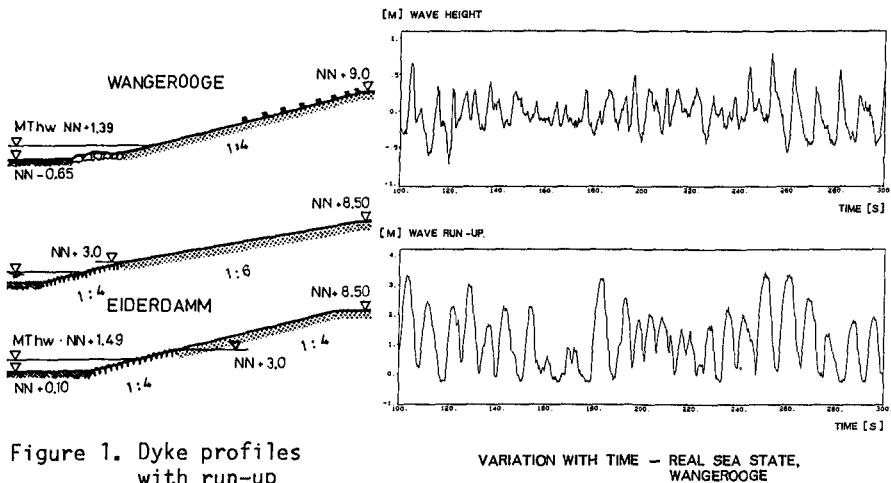


Figure 1. Dyke profiles with run-up gauges (Grüne, 1982)

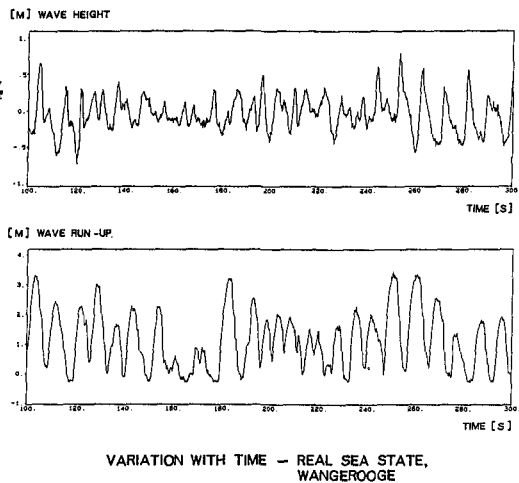


Figure 2. Synchronous records of waves and wave run-ups

An example for synchronously measured records of the wave height and the wave run-up is given in Fig. 2 for a short time slice. Corresponding log-normal distributions of a nearly 15 minutes time interval are plotted in Fig. 3.

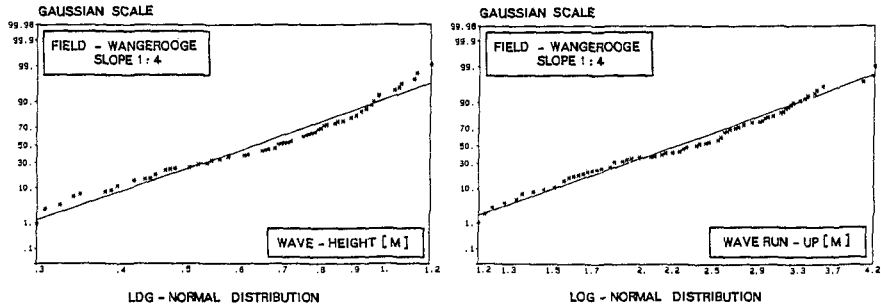


Figure 3. Log-normal distributions of 15 minutes records

Comparing measured and calculated run-ups it was found that the measured run-ups were considerably higher than the predicted run-ups. Two design formulae were used for the run-up with 2 % exceedance:

a) Wassing, 1957 $R_{98} = K \cdot H_{1/3} \cdot \frac{1}{N}$

with the empirical factor $K = 8$,
the significant wave height $H_{1/3}$
and the slope angle N .

b) Hunt, 1959 $R_{98} = C' \cdot \bar{T} \cdot \sqrt{G \cdot H_{1/3}} \cdot \frac{1}{N}$

with the empirical factor $C' = 0.5$,
the mean period \bar{T} ,
the acceleration due to gravity G ,
the significant wave height $H_{1/3}$
and the slope angle N .

Remark:

The original Hunt-formula (e.g. Techn. Advis. Comm., 1974) yields the run-up $R=0.4 \cdot \bar{T} \cdot \sqrt{gH} \cdot 1/N$ and is derived from experimental laboratory tests on smooth and uniform slopes. Applying this formula to field conditions the wave parameters usually are used as statistic values (\bar{T} and $H_{1/3}$). After Führböter (1976) the run-up estimation by Hunt should be increased by a factor 1.25 which goes back to a proposal presented by Vinjé during a meeting of the so-called North Sea Coastal Engineering Group in the year 1972. The empirical factor C' therefore becomes $C' = 1.25 \cdot 0.4 = 0.5$.

Results of the comparison were plotted in Fig. 4 for the WANGEROOGE location. For the 1:4 slope the mean K-factor (Wassing) increased up to 11.32 and the mean C' - factor (Hunt) increased up to 0.71. Results of the EIDERDAMM location were given in Fig. 5 for both slopes 1 : 4 and 1 : 6. Comparing the results for the 1:4 slope with those of the WANGEROOGE location a larger increase of the empirical factors is shown.

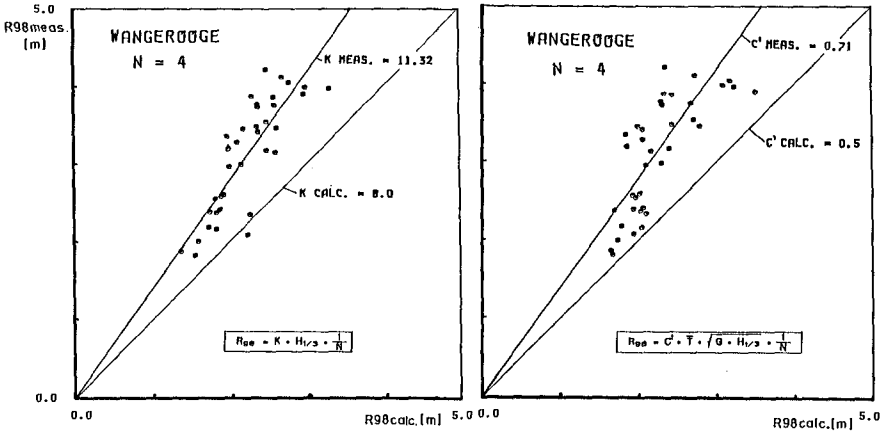


Figure 4. Comparison of measured and calculated wave run-up (after Grüne, 1982)

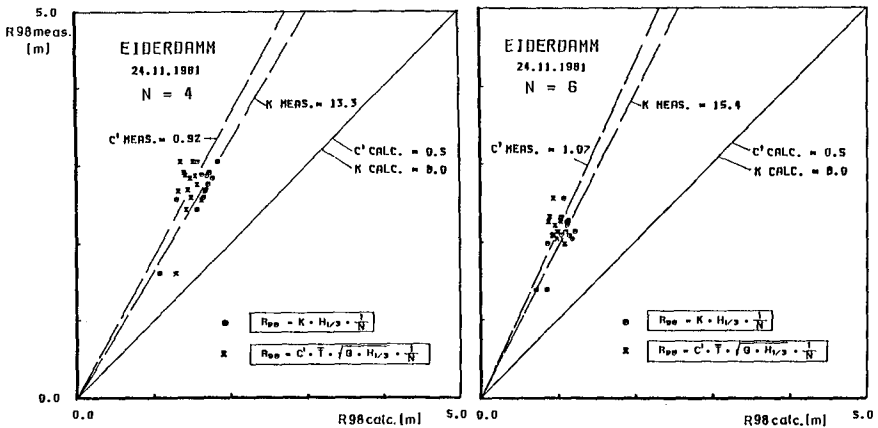


Figure 5. Comparison of measured and calculated wave run-up (after Grüne, 1982)

In order to compare the field measurements with the extended Hunt-approach established by van Oorschot and d'Angremond (1968), some field records of the WANGE-ROOGE location were additionally analyzed in the frequency domain in the same manner as the new data from full-scale laboratory investigations. The results will be discussed in chapter 4.2.

3. LARGE WAVE CHANNEL MEASUREMENTS

3.1 Test set-up

The Large Wave Channel (LWC) in Hannover allows to investigate wave attack phenomena in full-scale. The main dimensions of the channel are: depth 7.0 m; width 5.0 m and length 324 m. Regular and random waves can be generated up to wave heights of 2.5 m with a waterdepth of 5.0m. Details on the Large Wave Channel were published by Grüne and Führböter (1975). Design criteria and technical works were reported by Grüne and Sparboom (1982).

A cross-section of the prototype dyke slope which was investigated in the Large Wave Channel shows Fig. 6. The dyke core was constructed by sand. The compact cover layer was made by asphalt concrete with a smooth surface. Wave run-ups were measured by a special step gauge (Grüne, 1982). The waves were measured near the toe of the dyke slope by a wire gauge. The tests were carried out with a waterdepth of 4.8 m (SWL).

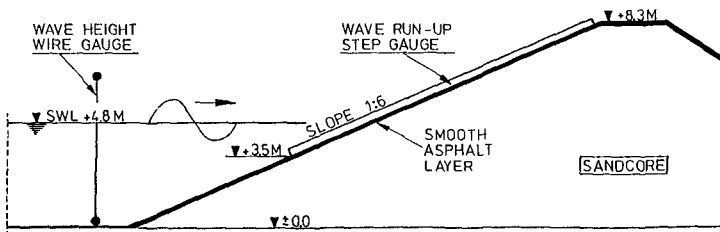


Figure 6. Test slope 1:6 in the Large Wave Channel (LWC)

3.2 Wave conditions

With reference to natural wave conditions at sea dykes two main test series were run (Führböter et al., 1989):

- a) regularly generated waves with wave heights up to 2.3 m and wave periods up to 15 s;
test duration: 110 waves

- b) irregularly generated waves; P-M-type spectra with significant wave heights up to 1.2 m and peak periods up to 11 s ;
test duration: nearly 25 minutes

For all generated waves an integrated absorption control system was applied to minimize wave reflexions at the wave generator. The wave parameters for all tests including the corresponding breaker numbers ξ (Iribarren number) are plotted in Fig. 7.

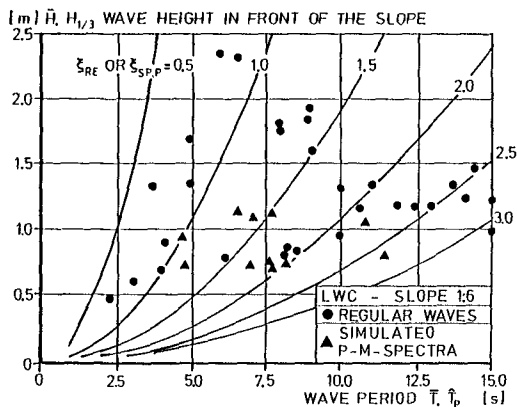


Figure 7. Wave test parameters for 1:6 dyke slope

3.3 Data evaluations

The measured data were analyzed in the time domain as well as in the frequency domain using the computer equipment (HP 1000/A 900) at the Large Wave Channel (Sparboom and Grosche, 1986/1987; Sparboom and Haidekker, 1987).

The test data for regular waves (Fig. 8) were characterized by mean parameters (\bar{H} , \bar{R} , \bar{T}). Because each regularly generated wave produced a run-up, the mean period had the same value for both signals.

The test data for irregular waves (Fig. 9) were characterized by mean parameters (\bar{H} , \bar{T}) and by extreme statistics (R_{98} , $H_{1/3}$). The waves were evaluated by the zero-down crossing method and the run-ups were found by crest values above SWL. An example of the calculated log-normal distributions of the synchronously recorded waves and run-ups is given in Fig. 10. Frequency characteristics (e.g. peak period T_p) were calculated using the frequency analysis (Fast Fourier Transformation method). One window had 8192 data points. The Nyquist frequency was 20 Hz and the number of degrees of freedom was 54 with respect to combined averaging.

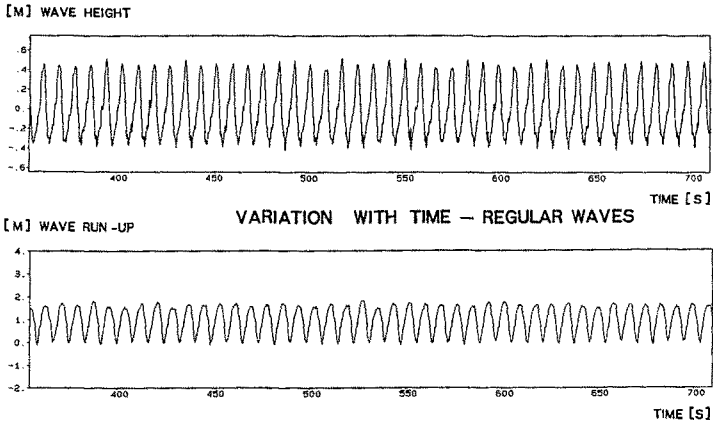


Figure 8. Synchronous records of waves and run-ups

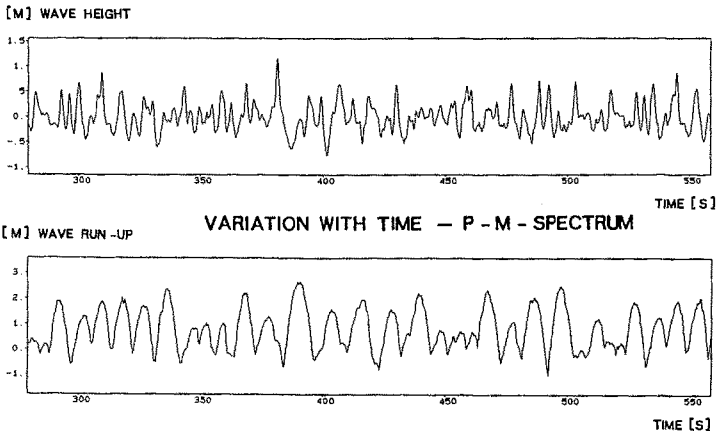


Figure 9. Synchronous records of waves and run-ups

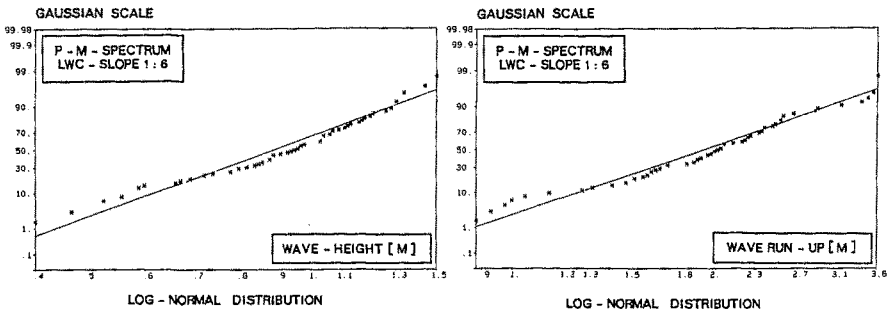


Figure 10. Log-normal distributions of 25 minutes records

4. COMPARISON OF CALCULATED AND MEASURED WAVE RUN-UP

4.1 Regular waves

The so-called Delft-formula was derived by Wassing (1957). Regular waves with steepnesses of 5 and 7 percent were investigated in a small-scale model (Tab. 1). Another formula was published by Hunt (1959). After this formula the run-up depends linearly on the breaker number which contains the influence of the wave height, the wave length or wave period and the slope angle (Tab. 1).

In Fig. 11 the measured run-ups were compared with calculated ones using these two formulae. For plunging breakers the Hunt-approach underpredicts run-up about 20 percent and the Wassing-approach overpredicts run-up about 35 percent. As shown later, run-up phenomena under sea state conditions cannot be described sufficiently basing only on laboratory tests with regularly generated waves. The dynamic response due to a random process differs significantly from a response due to a regular process.

Table 1.

WAVE RUN-UP DUE TO REGULAR WAVES
BREAKING ON SMOOTH DYKE SLOPES

WASSING, 1957

$$R = 7.5 \cdot H \cdot \frac{1}{N} ; \frac{H}{L} = 0.05$$

$$R = 7.0 \cdot H \cdot \frac{1}{N} ; \frac{H}{L} = 0.07$$

HUNT, 1959

$$R = 0.4 \cdot T \cdot \sqrt{G \cdot H} \cdot \frac{1}{N} \quad \text{OR}$$

$$R = H \cdot \xi ; \xi = \frac{T}{N} \cdot \sqrt{\frac{g}{2\pi \cdot H}}$$

ξ = BREAKER NUMBER

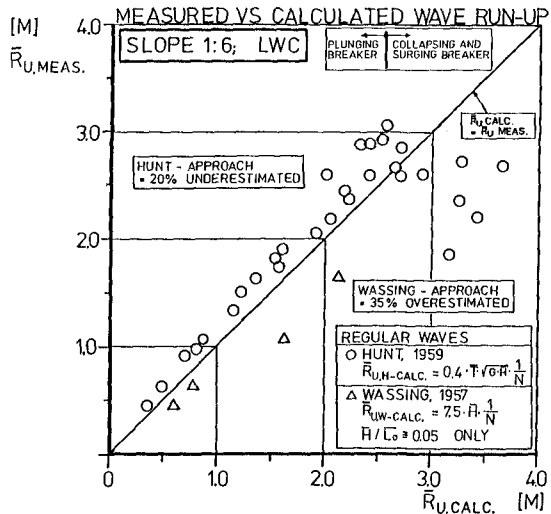


Figure 11. Comparison of measured and calculated wave run-up

4.2 Irregular waves

The formulae derived by Wassing and Hunt were extended to sea state conditions. From a practical point of view the extreme wave run-up mostly is defined by R 98 which means that the highest two percent of the wave run-ups are acceptable for overtopping. Van Oorschot and d'An-

gremond (1968) published results derived from spectral wave simulations in a small-scale model. They found that the run-up values vary with the spectral width parameter (formula see Tab. 2). According to the Rayleigh-distribution of waves and run-ups Battjes (1971) proposed coefficients for narrow and wide band wave spectra (Tab. 2).

In Fig. 12 some results of run-up values $R_{u,98}$ from field measurements by Grüne (1982) (WANGEROOGE location) and the results from full-scale measurements in the Large Wave Channel are compared with theoretical ones. The approach by Wassing -neglecting the wave period- is far from being reliable; the theoretical values are 60 percent underestimated. The Hunt/Battjes-formula -in the case of wide wave spectra- underestimates the run-up nearly 20 percent and the Hunt/v.Oorschot,d'Angremond-formula overestimates the run-up nearly 20 percent. The differences of the data seem to be caused by using different wave periods. Therefore in the opinion of the authors, for using the formulae the choice of the periods should be paid more attention. From various spectra in Fig. 13 it can be seen that the peak periods of both the waves and the run-ups seem to tend into the same range. A strongly smoothing procedure of the energy shape is exemplarily shown in Fig. 14 for one field and one LWC-test. The changes of the spectral density shapes are indicated by the transfer function with integrator characteristic. Higher frequencies of the

Table 2.

WAVE RUN - UP DUE TO IRREGULAR WAVES (SPECTRA) BREAKING ON SMOOTH DYKE SLOPES

WASSING, 1957

$$R_{98} = 8 \cdot H_{1/3} \cdot \frac{1}{N}$$

HUNT, 1959
VAN OORSCHOT / D'ANGREMOND, 1968

$$R_{98} = C_{98}(\hat{\tau}) \cdot \hat{\tau}_P \cdot \sqrt{G \cdot H_{1/3}} \cdot \frac{1}{N}$$

$\hat{\tau}_P$ = PEAK PERIOD OF WAVE SPECTRUM
 $\hat{\tau}$ = SPECTRAL WIDTH PARAMETER
 (NARROW) 0.22 < $\hat{\tau}$ < 0.59 (WIDE)
 0.55 < $C_{98}(\hat{\tau})$ < 0.74

HUNT, 1969
BATTJES, 1971

$$R_{98} = 0.60 \cdot \bar{T} \cdot \sqrt{G \cdot H_{1/3}} \cdot \frac{1}{N}$$

CASE OF NARROW WAVE SPECTRA

$$R_{98} = 0.75 \cdot \bar{T} \cdot \sqrt{G \cdot H_{1/3}} \cdot \frac{1}{N}$$

CASE OF WIDE WAVE SPECTRA

\bar{T} = MEAN WAVE PERIOD

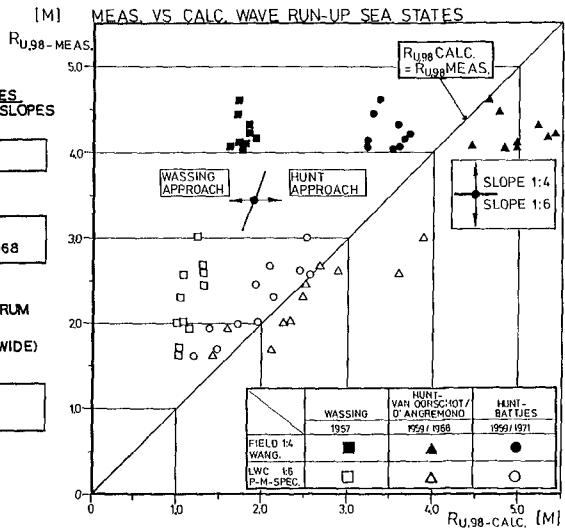


Figure 12. Comparison of measured and calculated wave run-up

wave process are lost in the run-up response process. Lower frequencies are found for the run-up process which are not present in the incident wave process (see also Mase, 1988). In the range of the peak frequency a quasi linear relation between both processes seems to exist. Further detailed research work on this topic is recommended.

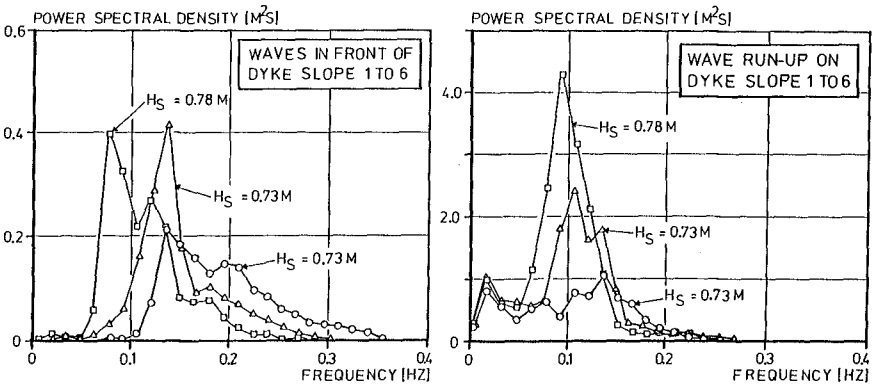


Figure 13. Corresponding wave and run-up spectra of LWC-tests

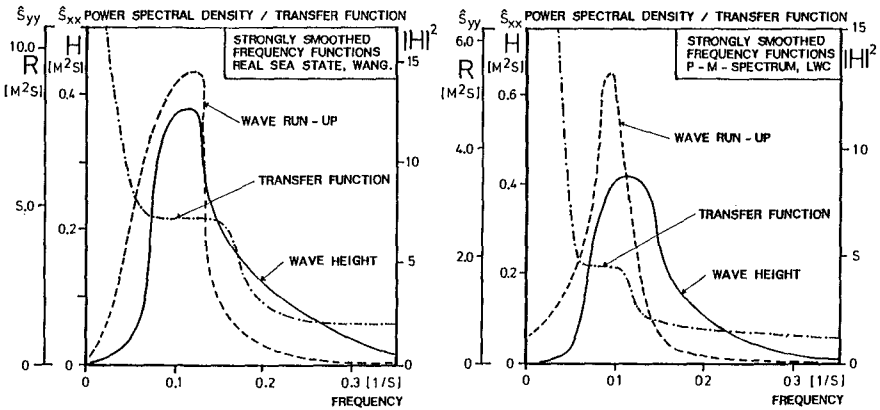


Figure 14. Spectral functions of waves and run-ups

5. WAVE RUN-UP, RUN-DOWN AND WATER FRONT VELOCITY AS A FUNCTION OF THE BREAKER NUMBER

In this chapter the results from the full-scale measurements with regular waves and with wave spectra at the prototype 1:6 dyke slope (Large Wave Channel) are referred to the well-known breaker number ξ as mentioned by Bruun and Günbak (1977). Wave run-up (Fig. 15) and run-down (Fig. 16) were calculated as relative values with reference to the wave height. The water front velocities (Fig. 17) were referred to $\sqrt{g \cdot H}$ (Roos and Battjes, 1976).

In the range of plunging breakers the data for regular waves as well as for irregular waves (Fig. 15) do not fit the relation $R_u = H \cdot \xi$ derived by Hunt (1959). If the wave spectra are described by $H^{1/3}$ (or $H^{1/2}$) and T_p , for the investigated wide banded Pierson-Moskowitz spectra which have a similar energy density shape as shallow water spectra (e.g. WANGEROOGE location) a rough run-up estimation is proposed for plunging breakers $0.5 < \xi < 2.5$:

$$\frac{R_{u,gs}}{H^{1/3}} = 1 + \xi \quad \text{with } \xi = \frac{T_p}{N} \cdot \sqrt{\frac{G}{2\pi \cdot H^{1/3}}}$$

$$\text{or } \frac{R_{u,gs}}{H} = 1.5 \cdot (1 + \xi) \quad \text{with } \xi = \frac{T_p}{N} \cdot \sqrt{\frac{G}{2\pi \cdot H}}$$

with N = front slope ($1/N = \tan \alpha$)
and G = acceleration due to gravity.

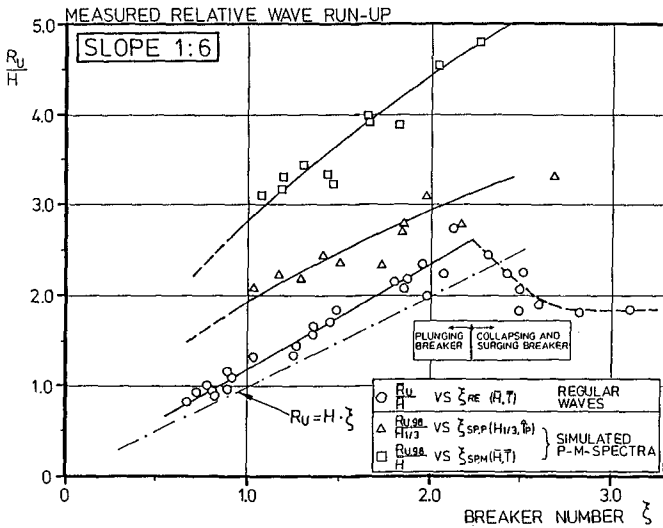


Figure 15. Relative wave run-up of Large Wave Channel tests

The relative run-down is shown in Fig. 16. The run-down of regular waves remains above SWL up to $\xi \approx 2.0$ whereas in the case of irregular waves the run-down always remains under SWL. For the investigated P-M-type spectra the wave run-down can roughly be described for plunging breakers $0.5 < \xi < 2.5$:

$$\frac{RD_{.98}}{H_{1/3}} = -0.23 \cdot \xi \text{ with } \xi = \frac{\Delta T_P}{N} \cdot \sqrt{\frac{G}{2\pi \cdot H_{1/3}}} .$$

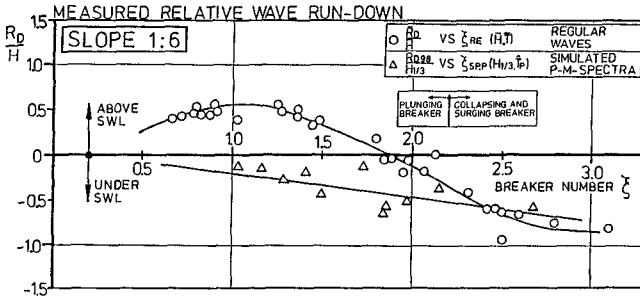


Figure 16. Relative wave run-down of Large Wave Channel tests

The water front velocities (Fig. 17) were evaluated from the time records of the wave run-up signals (Fig. 8 and 9). The mean velocities were calculated with the time in which the run-up or the run-down reached the maximum or the minimum. The maximum velocities were found by the first derivative of the run-up/run-down signal. High velocity values were found -as expected- in the lowest range of run-down; they were acting roughly near SWL. Mean and maximum velocities due to regularly generated waves confirm earlier small-scale measurements by Roos and Battjes (1976) up to $\xi \approx 2.0$. It should be noted that relative velocities due to irregular waves are definitely larger than those found for regular waves. For the investigated spectra a rough estimation of the local maximum water front velocities (up and down the slope) may be given for plunging breakers $0.5 < \xi < 2.5$:

$$\frac{MAX V_{98}}{\sqrt{G \cdot H_{1/3}}} = 1.5 + 0.25 \cdot \xi \text{ with } \xi = \frac{\Delta T_P}{N} \cdot \sqrt{\frac{G}{2\pi \cdot H_{1/3}}}$$

with $max V_{98}$ = statistical value with two percent exceedance .

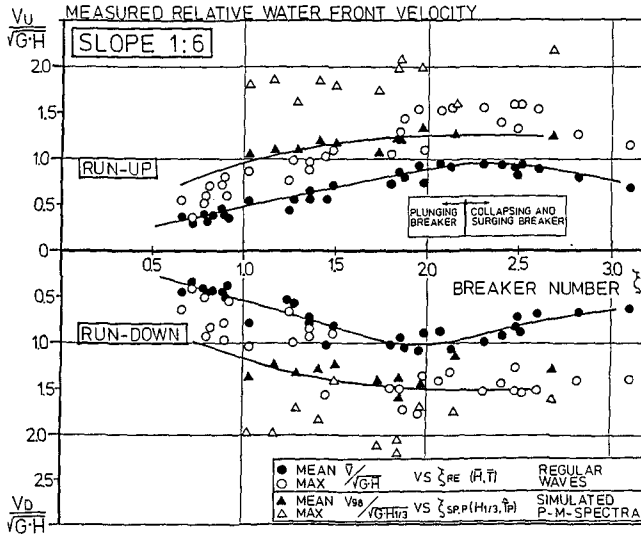


Figure 17. Relative water front velocities of Large Wave Channel tests

6. CONCLUDING REMARKS

The approach by Wassing (1957) disregarding the wave period cannot be used for real sea state conditions.

The approach by Hunt (1959) can be verified for full-scale and real sea state conditions. Nevertheless, the selection of the wave spectra parameter for the wave period and the wave height has to be investigated in more detail with different sea state conditions to enable a standardization for general application.

Results from measurements with regular waves even in full-scale do not describe the wave run-up process under sea state conditions sufficiently and should therefore not be used for practical engineering purposes.

7. ACKNOWLEDGEMENT

The authors would like to acknowledge very gratefully the German Research Foundation (DEUTSCHE FORSCHUNGSGEMEINSCHAFT) sponsoring the research program on safety and reliability of dykes and revetments for coastal protection (SFB 205 / A1). The project is running under supervision of Prof. Dr.-Ing. A. Führböter.

8. REFERENCES

- Battjes, J.A.: Run-up distributions of waves breaking on slopes. Journal of the Waterways, Harbors and Coastal Engineering Division, ASCE, Vol.97, No WW1, 1971
- Bruun, P., Günbak, A.R.: Stability of sloping structures in relation to $\xi = \tan \alpha / H / L_0$ risk criteria in design. Coastal Engineering, Elsevier Science Publishers B.V., Amsterdam, Vol. 1, 1977
- Coldewey, H.-G.: Naturmessungen zur Erfassung des Watt-seegangs und des Wellenaufbaus auf Seedeiche. Berichtswerk Intermaritec '82, Hamburg, 1982 (in German)
- Erchinger, H.F.: Wellenaufbau an Seedeichen-Naturmessungen an der ostfriesischen Küste. Mitteilungen Leichtweiß-Institut der Technischen Universität Braunschweig, Heft 41, 1974, (in German)
- Führböter, A.: Äußere Belastung der Seedeiche. In "Seedeichbau-Theorie und Praxis", Vereinigung der Naßbaggerunternehmen e.V., Hamburg, 1976 (in German)
- Führböter, A., Sparboom, U., Witte, H.-H.: Großer Wellenkanal Hannover: Versuchsergebnisse über den Wellenaufbau auf glatten und rauhen Deichböschungen mit der Neigung 1 : 6. Die Küste, Westholsteinische Verlagsanstalt Boyens & Co, Heide, Heft 50, 1989 (in German)
- Grüne, J.: Wave run-up caused by natural storm surge waves. Proc. of the 18th Int. Conf. on Coastal Eng., Cape Town, ASCE, 1982
- Grüne, J., Führböter, A.: Large Wave Channel for full-scale modelling of wave dynamics in surf zones. Proc. Symp. on Modelling Techniques, San Francisco, ASCE, 1975
- Grüne, J., Sparboom, U.: Großer Wellenkanal-Problemstellung und Lösung aus versuchstechnischer und konstruktiver Sicht. Technischer Bericht, SFB 79, Universität Hannover, 1982 (in German)
- Hunt, I.A.jr: Design of seawalls and breakwaters. Journal of the Waterways and Harbors Division, ASCE, Vol. 85, No WW 3, 1959
- Niemeyer, H.D.: Zur Abschätzung des maximalen Wellenaufbaus an Seedeichen aus der Einmessung von Teekgrenzen. Die Küste, Westholsteinische Verlagsanstalt Boyens & Co, Heide, Heft 29, 1976 (in German)
- Mase, H.: Spectral characteristics of random wave run-up. Coastal Engineering, Elsevier Science Publishers B.V., Amsterdam, Vol. 12, 1988
- Oorschot van, J.H., d'Angremond, K.: The effect of wave energy spectra on wave run-up. Proc. of the 11th Int. Conf. on Coastal Eng., London, ASCE, 1968
- Roos, A., Battjes, J.A.: Characteristics of flow in run-up of periodic waves. Proc. of the 15th Int. Conf. on Coastal Eng., Honolulu, ASCE, 1976
- Sparboom, U., Grosche, S.: Meßergebnisse des Wellenaufbaupiegels am 1 : 6 geneigten Asphaltdeich im Großen Wellenkanal. Technischer Bericht, SFB 205, Universität Hannover, 1986/1987 (in German)
- Sparboom, U., Haidekker, M.: Rechnerorientierte Signalanalyse im Frequenzbereich. Technischer Bericht, SFB 205, Universität Hannover, 1987 (in German)
- Technical Advisory Committee on Protection Against Inundation: Wave run-up and overtopping. Government Publishing Office, The Hague, 1974
- Wassing, F.: Model investigation on wave run-up carried out in the Netherlands during the past twenty years. Proc. of the 6th Int. Conf. on Coastal Eng., Gainesville, ASCE, 1957

CHAPTER 69

STATISTICAL CHARACTERISTICS OF OFFSHORE CURRENTS

Michel K. Ochi*

ABSTRACT

This paper presents the analytical derivation of probability density functions applicable for tidal (high frequency components), residual (low frequency components), and total (the vector sum of tidal and residual) current velocities. The theoretical probability density functions are compared with histograms constructed from measured data. A method to estimate the extreme current velocities in a specified time period is presented by applying extreme value statistics.

INTRODUCTION

The magnitude of current velocity measured in offshore areas fluctuates randomly with frequencies covering a wide range from 0.0008 to 0.08 cycles per hour (period range from 1200 to 12 hours). Measured current data may be decomposed into high and low-frequency components. Here, high-frequency components are considered to be currents associated with tides, while low-frequency components (called residual currents) are those attributed to wind and all other environmental conditions.

It may be of considerable interest to obtain the statistical distributions applicable for the tidal (high frequency components), residual (low-frequency components), and total (the vector sum of tidal and residual) current velocities, and therefrom to estimate the extreme velocities expected to occur in a specified time period.

This paper presents the analytical derivation of probability density functions applicable for the tidal and residual as well as total current velocities. The theoretical probability density functions are compared with histograms constructed from measured data. Based on these probability density functions, extreme current velocities are estimated from knowledge of variances of high and low-frequency components in two rectangular directions.

* Professor, Coastal & Oceanographic Engineering Department
University of Florida, Gainesville, Florida, 32611, U.S.A.

High Frequency (Tidal) and Low Frequency (Residual) Currents

Offshore current velocity records, in general, represent the average velocities consisting of various frequencies measured during a certain time period. For example, Figure 1 taken from Reference 1 shows a portion of measured current velocities recorded at a 26 meter depth off Newfoundland, Canada. The data represent the hourly mean current velocities measured at 10 minute intervals in a dominant hourly current direction. Figure 2 shows a polar diagram indicating the magnitude and direction of the measured current velocities. Unfortunately, statistical information on high frequency (tidal) and low frequency (residual) current velocities cannot be obtained from Figure 2. Nor is it possible to obtain this information by simply separating the time history shown in Figure 1 into high and low frequency components, since the components thusly obtained merely represent the high and low frequency current velocities in the dominant hourly current direction. The tidal and residual currents flow independently in constantly changing direction.

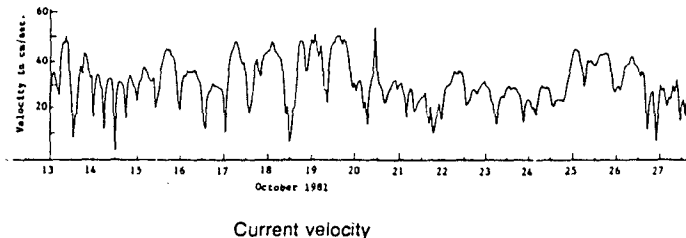


Figure 1 Time history of current velocity

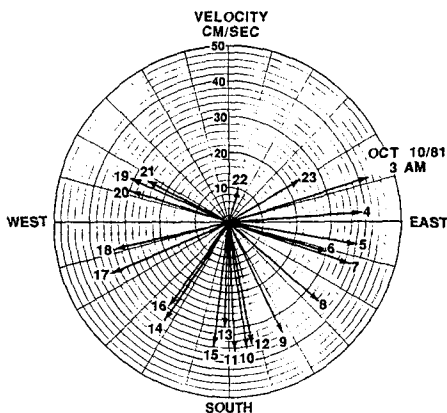


Figure 2 Polar diagram indicating the magnitude and direction of current velocity as a function of time

In order to obtain the statistical properties of tidal components and residual components of current velocity, it is first necessary to decompose the measured current velocity into two rectangular components as shown in Figure 3. Here, for convenience, we consider the East-West and North-South directions. Each of these two velocity components, denoted by U and V respectively, is then further decomposed into a high frequency (tidal) velocity component and a low frequency (residual) velocity component. In the present study, a cutoff frequency of 0.035 cycles/hour (28.5 hour period) is used to separate the two components [1]. This is because the results of spectral analysis of the records indicate that a small amount of energy exists beyond the 24.0 hour period (0.042 cycles/hour). Thus, the time history of current velocity constructed from measurements at one hour intervals is decomposed into the following four components:

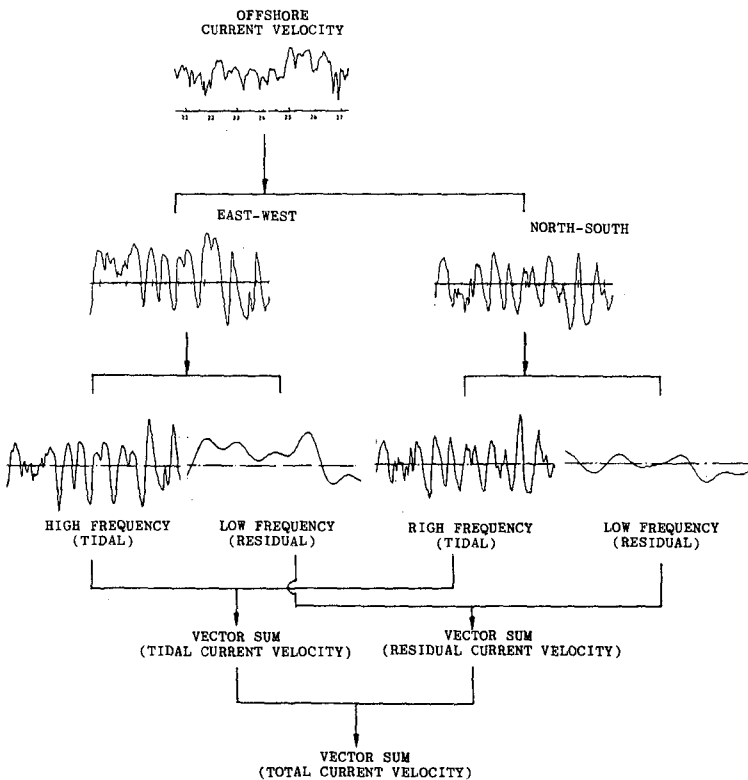


Figure 3 Diagram illustrating analysis of offshore current velocity data

In the East-West direction

- High frequency (tidal) component, H_u
- Low frequency (residual) component, L_u

In the North-South direction

- High frequency (tidal) component, H_v
- Low frequency (residual) component, L_v

From these four time histories, the magnitude of high frequency (tidal) velocity can be obtained by combining H_u and H_v in vector form, while that for the low frequency (residual) velocity is obtained by combining L_u and L_v . The current velocities thusly combined at one hour intervals, denoted by H and L, respectively, have individual directions and provide information on tidal and residual current velocities. The high and low frequency currents are hereafter referred to as tidal and residual currents, respectively.

Figures 4 and 5 show examples of polar diagrams indicating the magnitude and direction of the tidal and residual current velocities, respectively, as a function of time. As can be seen in Figure 4, the tidal current velocities show approximately the same pattern of rotation as the measured current velocities shown in Figure 2. However, the residual velocity rotates very slowly clockwise through 180 degrees in approximately 20 hours in this example, and then rotates counter-clockwise through 90 degrees in approximately 12 hours. The residual current velocity does not have a consistently rotating directionality in contrast to the tidal velocity.

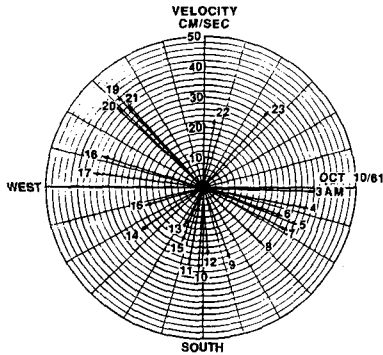


Figure 4 Polar diagram indicating the magnitude and direction of tidal (high frequency) current velocity as a function of time

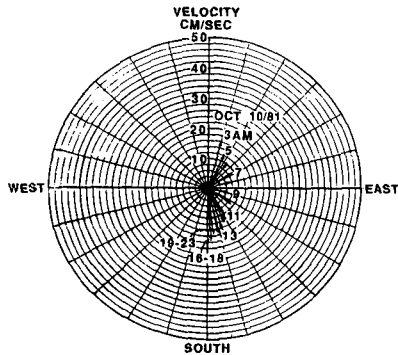


Figure 5 Polar diagram indicating the magnitude and direction of residual (low frequency) current velocity as a function of time

It is noted that the tidal current and the residual current are statistically uncorrelated. The correlation coefficient between them is extremely small, on the order of 0.05. Hence, the possibility of simultaneous occurrence of large tidal current and large residual current is almost nil.

PROBABILITY DISTRIBUTIONS OF TIDAL AND RESIDUAL CURRENT VELOCITIES

The probability density function applicable for the tidal current velocity can be derived as follows: It is found from statistical analysis of measured data that both the East-West and North-South components of high frequency current velocities approximately follow the Gaussian probability distribution with zero mean and variance which is equal to the area under the spectral density function obtained for each direction [1]. It is also found that the East-West and North-South components, H_u and H_v , are statistically independent. Let us write the variance of H_u and H_v as σ_{HU}^2 and σ_{HV}^2 , respectively. Since the two random variables, H_u and H_v are statistically independent, the joint probability density function can be written as

$$f(H_u, H_v) = \frac{1}{2\pi\sigma_{HU}\sigma_{HV}} \exp \left\{ -\frac{1}{2} \left(\frac{H_u^2}{\sigma_{HU}^2} + \frac{H_v^2}{\sigma_{HV}^2} \right) \right\}, \quad (1)$$

$$0 \leq H_u < \infty, \quad 0 \leq H_v < \infty.$$

Let H be the vector sum of the two components. Then, H_u and H_v can be written as

$$H_u = H \sin\theta \quad H_v = H \cos\theta, \quad (2)$$

where θ = directional angle of H measured from North.

By applying the technique of changing random variables, the joint probability density function of H and θ can be obtained as

$$f(H, \theta) = \frac{H}{2\pi\sigma_{HU}\sigma_{HV}} \exp \left\{ -\frac{H^2}{2} \left[\frac{1}{\sigma_{HU}^2} + \left(\frac{1}{\sigma_{HV}^2} - \frac{1}{\sigma_{HU}^2} \right) \cos^2\theta \right] \right\}, \quad (3)$$

$$0 \leq H < \infty, \quad 0 \leq \theta \leq 2\pi.$$

The probability density function of the vector sum can then be obtained as the marginal probability density function of Eq.(3). That is,

$$f(H) = \frac{H}{2\pi\sigma_{HU}\sigma_{HV}} e^{-\frac{H^2}{2\sigma_{HU}^2}} \int_0^{2\pi} \exp\left\{-\frac{H^2}{2}\left(\frac{1}{\sigma_{HV}^2} - \frac{1}{\sigma_{HU}^2}\right)\cos^2\theta\right\} d\theta. \quad (4)$$

By expanding the exponential function and by integrating with respect to θ , we have

$$\begin{aligned} f(H) &= \frac{H}{\sigma_{HU}\sigma_{HV}} e^{-\frac{H^2}{2\sigma_{HU}^2}} \left[1 - \frac{H^2}{4}\left(\frac{1}{\sigma_{HV}^2} - \frac{1}{\sigma_{HU}^2}\right) + \frac{H^4}{64}\left(\frac{1}{\sigma_{HV}^2} - \frac{1}{\sigma_{HU}^2}\right)^2 + \dots \right] \\ &\sim \frac{H}{\sigma_{HU}\sigma_{HV}} e^{-\frac{H^2}{2\sigma_{HU}^2}} \cdot e^{-\frac{H^2}{4}\left(\frac{1}{\sigma_{HV}^2} - \frac{1}{\sigma_{HU}^2}\right)} \\ &= A \frac{H}{\sigma_{HU}\sigma_{HV}} \exp\left\{-\frac{H^2}{4}\left(\frac{1}{\sigma_{HU}^2} + \frac{1}{\sigma_{HV}^2}\right)\right\}, \end{aligned} \quad (5)$$

where A is a normalization factor to be determined such that the area under the probability density function becomes unity. It can be obtained as

$$A = 2\sigma_{HU}\sigma_{HV} \left(\frac{1}{\sigma_{HU}^2} + \frac{1}{\sigma_{HV}^2}\right). \quad (6)$$

Hence, the probability density function of tidal current velocity becomes

$$f(H) = \frac{H}{2} \left(\frac{1}{\sigma_{HU}^2} + \frac{1}{\sigma_{HV}^2}\right) \exp\left\{-\frac{H^2}{4}\left(\frac{1}{\sigma_{HU}^2} + \frac{1}{\sigma_{HV}^2}\right)\right\}. \quad (7)$$

This is the Rayleigh probability density function whose parameter is given as a function of the variances of the East-West and North-South components. Figure 6 shows a comparison of the probability density function given in Eq.(7) and the histogram of tidal current velocity constructed from measured data. Good agreement between them can be seen.

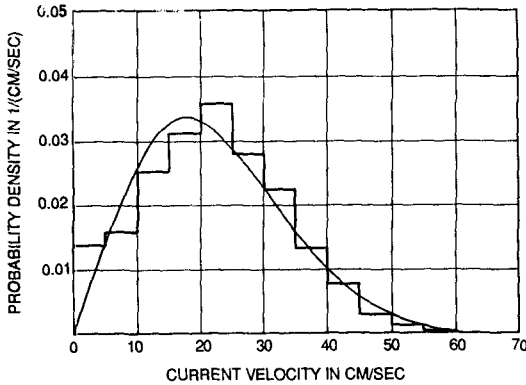


Figure 6 Comparison between histogram and probability density function of tidal (high frequency) current velocity

The probability density function of the residual current velocity can be derived through the same procedure as that used for the tidal current velocity. That is, by writing the variances of the East-West and North-South components of residual currents as σ_{LU}^2 and σ_{LV}^2 , respectively, the probability density function of the residual current velocity, L, can be given by

$$f(L) = \frac{L}{2} \left(\frac{1}{\sigma_{LU}^2} + \frac{1}{\sigma_{LV}^2} \right) \exp \left\{ -\frac{L^2}{4} \left(\frac{1}{\sigma_{LU}^2} + \frac{1}{\sigma_{LV}^2} \right) \right\} \quad (8)$$

A comparison between the probability density function and the histogram constructed from measured data is shown in Figure 7.

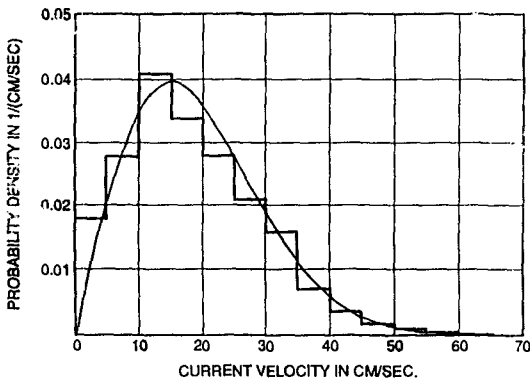


Figure 7 Comparison between histogram and probability density function of residual (low frequency) current velocity

PROBABILITY DISTRIBUTION OF TOTAL CURRENT VELOCITY

In this section, the probability density function of the vector sum of tidal and residual current velocities, hereafter called the total current velocity, will be derived. Here, the total current velocity is equal to the measured current velocity illustrated in Figure 1.

The magnitude of the total current velocity, denoted by C , can be written by the following vector sum of tidal and residual velocities:

$$C = \{ H^2 + L^2 + 2HL \cos(\theta_H - \theta_L) \}^{1/2}, \quad (9)$$

where H = magnitude of tidal current velocity, L = magnitude of residual current velocity, θ_H = directional angle of tidal current velocity, θ_L = directional angle of residual current velocity.

It was obtained in the previous section that the random variables H and L both follow the Rayleigh probability law. Hence, the probability distribution of the sum of the first two terms of Eq. (9), $(H^2 + L^2)$, can be obtained as follows:

It can easily be derived that the square of the Rayleigh probability distribution becomes the exponential probability distribution. That is, by writing H^2 and L^2 as H_* and L_* , respectively, we can derive the following probability density functions of H_* and L_* .

$$f(H_*) = \frac{1}{R_H} \exp\{-H_*/R_H\}, \quad f(L_*) = \frac{1}{R_L} \exp\{-L_*/R_L\}, \quad (10)$$

where

$$R_H = 4 / \left(\frac{1}{\sigma_{HU}^2} + \frac{1}{\sigma_{HV}^2} \right) \quad \text{and} \quad R_L = 4 / \left(\frac{1}{\sigma_{LU}^2} + \frac{1}{\sigma_{LV}^2} \right). \quad (11)$$

Since the random variables H and L are statistically independent [1], the probability density function of the sum of the random variables H_* and L_* , denoted by X , can be obtained as

$$\begin{aligned} f(x) &= \int_0^x \frac{1}{R_H} \exp\{-H_*/R_H\} \cdot \frac{1}{R_L} \exp\{-(x-H_*)/R_L\} dH_* \\ &= \frac{1}{R_H - R_L} \left(e^{-\frac{x}{R_H}} - e^{-\frac{x}{R_L}} \right), \quad 0 \leq x < \infty. \end{aligned} \quad (12)$$

Next, let us derive the probability density function of the third term of Eq.(9). For this, first the probability density function of $L \cos(\theta_H - \theta_L)$ is considered. Results of analysis show that the difference of the two angles $\theta_H - \theta_L$ scatters in random fashion over the range from $-\pi$ to $+\pi$; therefore, we may assume that $\cos(\theta_H - \theta_L)$ is a random variable and it has a uniform distribution over the range -1 to $+1$ with a density of $1/2$. It can also be assumed that the random variables L and $\cos(\theta_H - \theta_L)$ are statistically independent. Then the probability distribution of the product of $L \cos(\theta_H - \theta_L)$, denoted by Y , can be written as

$$f(y) = \begin{cases} \int_y^\infty \frac{1}{2} \frac{1}{L} f(L) dL & \text{for } y > 0 \\ \int_{-|y|}^\infty \frac{1}{2} \frac{1}{L} f(L) dL & \text{for } y < 0, \end{cases} \quad (13)$$

where $1/L$ is the Jacobian associated with the change of random variables, and $f(H)$ is given in Eq.(8). The probability density function $f(L)$ is symmetric with respect to $y=0$. Hence, we may write the function as

$$f(y) = \frac{1}{R_L} \int_{|y|}^\infty \exp \left\{ -L^2/R_L \right\} dL = \sqrt{\pi/R_L} \Phi \left(-\sqrt{2/R_L} |y| \right), \quad (14)$$

where $Y = L \cos(\theta_H - \theta_L)$ and R_L is given in Eq.(11).

The probability density function of $HL \cos(\theta_H - \theta_L)$ can be derived as the density function of the produce of two random variables H and $Y = L \cos(\theta_H - \theta_L)$ which are statistically independent. However, the derivation is extremely complicated in practice because of the density function $f(y)$. Hence, the probability density function $f(y)$ is approximated by the following normal probability density function:

$$f(y) = \sqrt{2/\pi R_L} \exp \left\{ -2|y|^2/R_L \right\}. \quad (15)$$

A comparison of Eq.(14) with its approximation given by Eq.(15) is shown in Figure 8 in which the random variable Y is non-dimensionalized by letting $Y = \sqrt{R_L}/2 X$.

By applying this approximation, the probability density function of $HL \cos(\theta_H - \theta_L)$, denoted by Z , can be derived from Eqs.(7) and (15). That is,

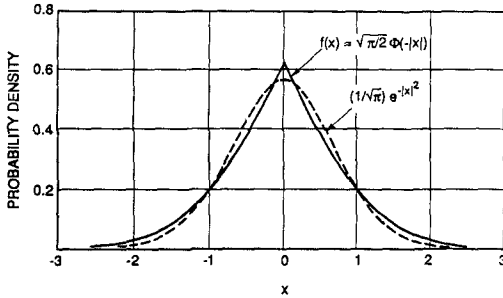


Figure 8 Comparison between $f(x)$ and its approximation by $(1/\sqrt{\pi})\exp\{-|x|^2\}$, where $y = \sqrt{R_1/2} x$ in Eq.(15)

$$f(z) = \int_0^u \frac{2}{R_H} \sqrt{\frac{2}{\pi R_L}} \exp\left\{-\frac{H^2}{R_H}\right\} \exp\left\{-\frac{2}{R_L}\left(\frac{z}{H}\right)^2\right\} dH$$

$$= \sqrt{\frac{2}{R_H R_L}} e^{-2\sqrt{\frac{2}{R_H R_L}} |z|}, \quad -\infty < z < \infty . \tag{16}$$

From the above equation, the probability density function of $2Z = 2HL \cos(\theta_H - \theta_L)$ which is the third term of Eq.(9) can be obtained. That is, by writing $2Z = W$, we have

$$f(w) = \frac{1}{\sqrt{2R_H R_L}} e^{-\frac{2|w|}{\sqrt{2R_H R_L}}}, \quad -\infty < w < \infty . \tag{17}$$

The probability density function of C^2 can now be evaluated as the density function of the sum of the two random variables X and W which are considered to be statistically independent and whose probability density functions are given in Eqs.(12) and (17), respectively. Since the random variable C^2 is positive only, we consider the following two cases for both of which the sum of X and W is positive.

(i) For $X > 0$ and $W > 0$.

By writing the random variable $C^2 = U = X + W$, we can derive the probability density function $f(u)$ from Eqs.(12) and (17) as

$$f(u) = \int_u^\infty \frac{1}{R_H - R_L} \left(e^{-\frac{x}{R_H}} - e^{-\frac{x}{R_L}} \right) \frac{1}{\sqrt{2R_H R_L}} e^{-\frac{2(u-x)}{\sqrt{2R_H R_L}}} dx$$

$$\begin{aligned}
 &= \frac{1}{\sqrt{2}} \left[\frac{1}{(\sqrt{2R_H} - \sqrt{R_L})(\sqrt{2R_L} - \sqrt{R_H})} e^{-\sqrt{\frac{2}{R_H R_L}} u} \right. \\
 &\quad \left. + \frac{\sqrt{R_H}}{(R_H - R_L)(\sqrt{2R_H} - \sqrt{R_L})} e^{-\frac{u}{R_H}} - \frac{\sqrt{R_L}}{(R_H - R_L)(\sqrt{2R_L} - \sqrt{R_H})} e^{-\frac{u}{R_L}} \right] \tag{18}
 \end{aligned}$$

(ii) For $x > 0$ and $W < 0$ but $U = X + W > 0$.

By writing $|W| = X - U$ in Eq.(17), we have

$$\begin{aligned}
 f(u) &= \int_u^\infty \frac{1}{R_H - R_L} \left(e^{\frac{x}{R_H}} - e^{\frac{x}{R_L}} \right) \frac{1}{\sqrt{2R_H R_L}} e^{-\frac{2(u-x)}{\sqrt{2R_H R_L}}} dx \\
 &= \frac{1}{\sqrt{2}} \frac{1}{R_H - R_L} \left[\frac{\sqrt{R_H}}{\sqrt{2R_H} + \sqrt{R_L}} e^{-\frac{u}{R_H}} - \frac{\sqrt{R_L}}{\sqrt{2R_L} + \sqrt{R_H}} e^{-\frac{u}{R_L}} \right] \tag{19}
 \end{aligned}$$

The sum of Eqs.(18) and (19) yields the probability density function of U . However, we consider only positive U in the above and discard the sum of the two random variables X and W for which U becomes negative. Hence, it is necessary to normalize the resultant probability density function so that the area under the density function is unity. By taking normalization into consideration, we have

$$\begin{aligned}
 f(u) &= L \left[\frac{1}{\sqrt{2}} \frac{1}{(\sqrt{2R_H} - \sqrt{R_L})(\sqrt{2R_L} - \sqrt{R_H})} e^{-\sqrt{\frac{2}{R_H R_L}} u} \right. \\
 &\quad \left. + \frac{2}{R_H - R_L} \left(\frac{R_H}{2R_H - R_L} e^{-\frac{u}{R_H}} - \frac{R_L}{2R_L - R_H} e^{-\frac{u}{R_L}} \right) \right], \quad 0 \leq u < \infty \tag{20}
 \end{aligned}$$

where

$$L^{-1} = \frac{1}{2} \frac{\sqrt{R_H R_L}}{(\sqrt{2R_H} - \sqrt{R_L})(\sqrt{2R_L} - \sqrt{R_H})} - \frac{2(R_H^2 - R_H R_L + R_L^2)}{(2R_H - R_L)(2R_L - R_H)} \tag{21}$$

Finally, by changing the random variable U to C where C is the square-root of U, we can derive the probability density function applicable for the total current velocity given in Eq.(9) as follows:

$$f(C) = L \left[\frac{\sqrt{2} C}{(\sqrt{2R_H} - \sqrt{R_L})(\sqrt{2R_L} - \sqrt{R_H})} e^{-\sqrt{\frac{2}{R_H R_L}} C^2} + \frac{4 C}{R_H - R_L} \left(\frac{R_H}{2R_H - R_L} e^{-\frac{C^2}{R_H}} - \frac{R_L}{2R_L - R_H} e^{-\frac{C^2}{R_L}} \right) \right], \quad 0 \leq C < \infty. \quad (22)$$

A comparison between the theoretical probability density function derived in Eq.(22) and the histogram of the total current velocity constructed from measured data is shown in Figure 9. Good agreement can be seen in the figure. The values of R_H and R_L of Eq.(22) are computed by Eq.(11) in which variances are evaluated through spectral analysis [1]. These are

$$\sigma_{HU}^2 = 334.3 \text{ (cm/sec)}^2, \quad \sigma_{HV}^2 = 293.7 \text{ (cm/sec)}^2, \\ \sigma_{LU}^2 = 248.7 \text{ (cm/sec)}^2, \quad \text{and} \quad \sigma_{LV}^2 = 214.2 \text{ (cm/sec)}^2.$$

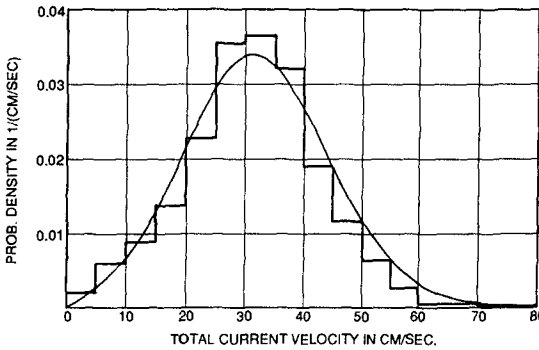


Figure 9 Comparison between histogram and probability density function of total current velocity

Next, let us evaluate the magnitude of extreme current velocity expected to occur in 20 and 50 years. For this, the cumulative distribution function of the total current velocity is obtained by integrating Eq.(22) as follows:

$$\begin{aligned}
 F(C) &= \int_0^C f(C) dC \\
 &= L \left[\frac{\sqrt{R_H R_L}}{2(\sqrt{2R_H} - \sqrt{R_L})(\sqrt{2R_L} - \sqrt{R_H})} \left(1 - \exp \left\{ -\sqrt{\frac{2}{R_H R_L}} C^2 \right\} \right) \right. \\
 &\quad + \frac{2R_H^2}{(R_H - R_L)(2R_H - R_L)} \left(1 - \exp \left\{ -\frac{C^2}{R_H} \right\} \right) \\
 &\quad \left. - \frac{2R_L^2}{(R_H - R_L)(2R_L - R_H)} \left(1 - \exp \left\{ -\frac{C^2}{R_L} \right\} \right) \right] \tag{23}
 \end{aligned}$$

Then, by applying extreme value statistics, the probable extreme value most likely to occur in n-observations can be evaluated as a solution of the following equation:

$$\frac{1}{1 - F(C)} = n \tag{24}$$

Here, n is the number of samples in a specified time period. Since n = 1911 in 4 months for this example, the extreme values in 4 months, 20 years and 50 years are estimated as shown in Figure 10. For convenience, the logarithm of Eq.(24) is shown in the figure. The estimated extreme current velocity in 4 months is 76 cm/sec as compared with 74 cm/sec observed in the data. The extreme values expected in 20 and 50 years are 92.0 cm/sec and 94.5 cm/sec, respectively, as indicated in the figure.

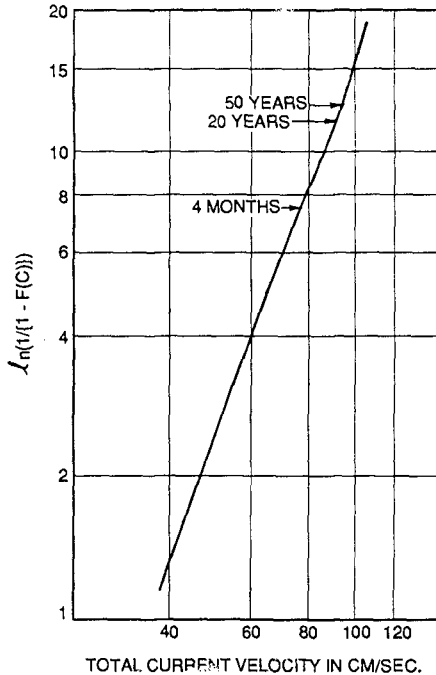


Figure 10 Estimation of extreme current velocity in 4 months, 20 and 50 years

CONCLUSIONS

This paper presents the results of a study on stochastic analysis of offshore currents. The objective of the study is to estimate the extreme magnitude of offshore current velocities based on the probability density functions applicable for tidal (high frequency components), residual (low frequency components), and total (the vector sum of tidal and residual) current velocities. From the results of the analysis, the following conclusions are derived:

(1) It is found theoretically that the tidal (high frequency components) current velocity follows the Rayleigh probability law. The probability density function is given in Eq.(7). The parameter of the probability density function is given as a function of variances of high frequency components in two rectangular directions.

(2) Similarly, the magnitude of residual (low frequency components) current velocity follows the Rayleigh probability law and its density function is given in Eq.(8).

(3) The probability density function of the total current velocity (the vector sum of tidal and residual current velocities) is analytically derived as given in Eq.(22).

(4) The theoretical probability density functions are compared with histograms constructed from measured data and good agreement between them is obtained.

(5) A method for estimating the extreme value of the total current velocity expected in a specified time period is developed from knowledge of the variances of high and low frequency components in two rectangular directions.

ACKNOWLEDGEMENTS

This research was sponsored by the Office of Naval Research, Ocean Technology Program, through contracts N00014-88-K-0537 to the University of Florida. The author would like to express his appreciation to Drs. E.A. Silva and S.E. Ramberg for their valuable technical discussions received during the course of this project. The author is grateful to Dr. Max Sheppard for his kind help in obtaining the current data used in this study. The author also wishes to express his appreciation to Ms. Laura Dickinson for typing the manuscript.

REFERENCES

1. Ochi, M.K. and McMillen, R.I., "Stochastic Analysis of Offshore Currents", Proc. 21st Int. Conf. on Coastal Eng., Vol.3, 1988, pp.2536-2546.

CHAPTER 70

BREAKING AND REFLECTION OF A STEEP SOLITARY WAVE CAUSED BY A SUBMERGED OBSTACLE

Takashi Yasuda, Masanori Hara

ABSTRACT

A fully nonlinear potential flow theory is solved numerically but almost exactly for a solitary wave passing over a submerged obstacle by using BIM. Based on the numerical solutions, the reflection characteristics and the breaker type and criterion are made clear for a solitary wave up to breaking caused by a step.

1. INTRODUCTION

A sound knowledge on the transformation including the breaking of steep coastal waves over a submerged obstacle is important for planning and designing submerged coastal structures. However, few knowledge is obtained on the breaking caused by a submerged obstacle including a discontinuity in depth.

It has often been remarked that waves on beaches resemble solitary waves. In fact, steep coastal waves are demonstrated to be representable as a random train of solitons (Tsuchiya & Yasuda, 1986). Hence, it may be better to consider each wave crest as a solitary wave and investigate its transformation, rather than to examine directly that of steep coastal waves.

A computational model to be used here is based on BIM and has already developed by authors (1989). It can describe almost exactly the transformation up to overturning of the solitary wave propagating over a bed

* Prof., Dept. of Civil Eng., Gifu Univ., Gifu 501-11, JAPAN

** Eng., Civil Eng. Dept., Idemitsu Engineering Co., Ltd., 37-24 Shinden cho, Chiba 260, JAPAN

containing a submerged obstacle.

This study aims to make clear the breaker criterion and reflection characteristics of steep solitary waves passing over a step by using the computational model (Yasuda et al., 1989) which can describe almost exactly the transformation up to overturning of the solitary wave.

2. COMPUTATIONAL MODEL

In this study, the solitary wave given by the exact steady solution of fully nonlinear potential-flow theory is supposed over the planar of left side from the obstacle, and the still water is supposed over the obstacle and its right side planar in a two-dimensional domain. Further, the Cauchy integral theorem is introduced to solve Laplace's equation under the condition on the rigid boundary. The updating of the free surface profile and the velocity potential is based on the second-order Taylor expansion in a mixed Eulerian-Lagrangian formulation as well as Dold & Peregrine (1986).

3. VALIDITY OF THE MODEL

The first check of the time stepping accuracy is provided by examining the growth of the error energy defined by

$$E(t) = \frac{1}{2} \int_{-\infty}^{\infty} [\eta(x, t) - Y(x - ct)]^2 dx, \quad (1)$$

where Y is the surface displacement of the steady solitary wave mentioned above, c its propagation speed and η the water surface profile given by the present numerical solution. A test is made on the solitary wave in still water up to the dimensionless time $t\sqrt{g/h}=12$. Here, h is the undisturbed water depth and g the acceleration of gravity. While the wave has propagated on the distance of $15h$, $E(t)$ remains less than 3×10^{-5} in value. (Note, for comparison, that for the wave under consideration $(1/2) \int Y^2 dx = 0.42$.)

The second check is provided by examining the validity of the model against carefully controlled experiments in a wave tank (1m×1m×54m). The desired steep solitary wave is generated by using a servo-controlled, hydraulically activated wave maker. The

free surface displacement is measured with the capacitance-type wave gauges installed at three locations, P.1, P.2 and P.3 which are placed at the front of the obstacle, just behind of it and at the breaking point of the transmitted solitary wave, respectively. The breaking point is defined as the onset of the formation of a jet or bubble plume. The location of P.3(breaking point) is decided for each incident solitary wave by using a high speed video camera and observing the presence of the jet or bubble plume.

Figure 1 shows an example of the computed shape of the free surface at some evolution times. The initial wave-height H/h of the incident solitary wave is 0.4, and the relative height R/h and length B/h of the submerged breakwater model are $4/7$ and $24/7$, respectively. It is found that while the transmitted

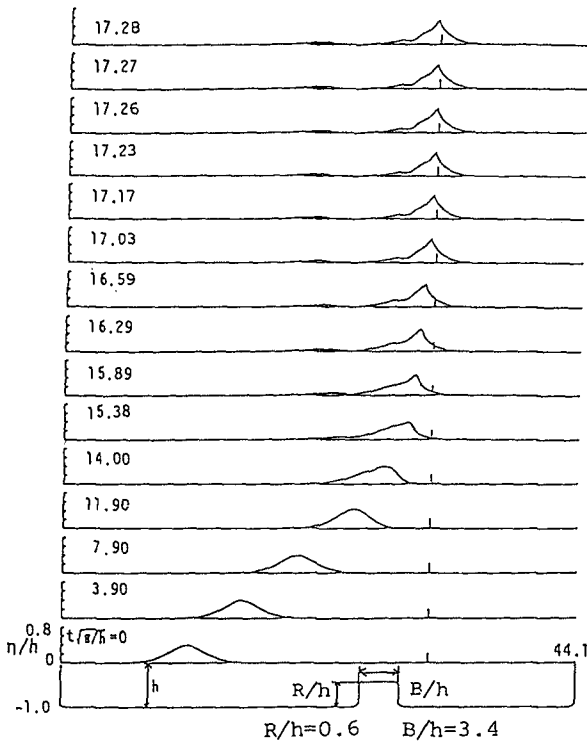


Fig.1 Transformation of a solitary wave passing over a submerged break-water

solitary wave makes its front face overturn at the location of P.3, the reflected wave propagates backward as a small but noticeable solitary wave.

Figure 2 describes the temporal changes of the crest-height η_c/h and the horizontal water particle velocity U_c/\sqrt{gh} and the gradient angle of the front face θ at the top of the solitary wave shown in Fig.1. It is found that the gradient angle θ reaches -90 degrees and the front face becomes vertical at the onset when the top of the wave passes through the location of P.3 where the formation of a jet was observed in the experiment. Hence, the onset of overturning can be defined as the breaking point in the computational model.

Figure 3 shows the comparisons of the temporal surface elevation of the solitary wave shown in Fig.1 between the results computed by the model and the experimental results measured with the wave gauges installed at P.1, P.2 and P.3. The computed and measured profiles can not be quite distinguished up to the overturning location(P.3), nevertheless the formation of vortex was observed behind the end of submerged breakwater. This remarks that the numerical

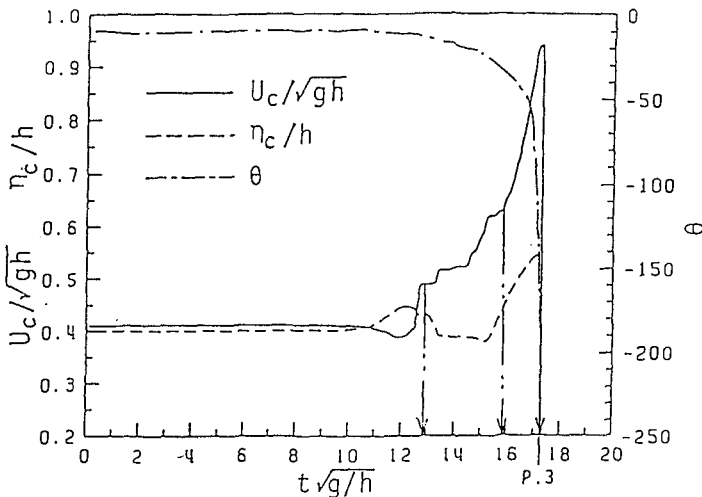


Fig.2 Temporal changes of the quantities η_c/h , U_c/\sqrt{gh} and θ .

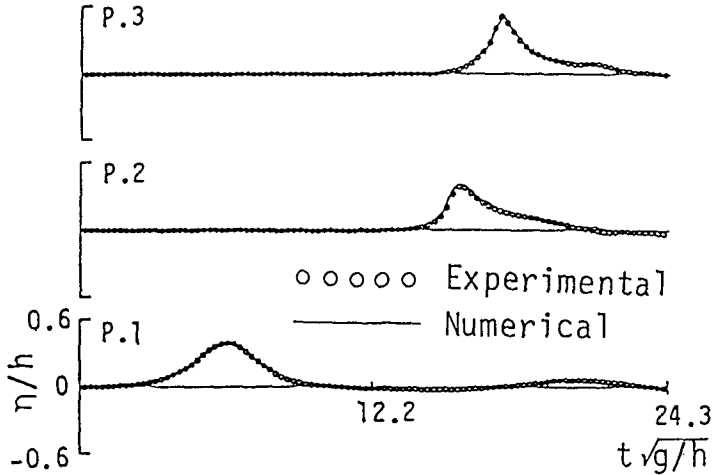


Fig.3 Comparisons with temporal water surface elevation between numerical and experimental results

results for the transformation of steep solitary waves over submerged obstacles are in excellent agreement with tank measurements up to overturning and the present model makes it possible not only to describe the transformation including overturning but also to predict the breaking point.

Further, in order to demonstrate the accuracy of the numerical solution obtained by using the present scheme, we carried out some numerical simulations of solitary waves propagating over a gently sloping bottom under the same initial wave-height H/h and bottom slope $\tan \theta$ with Papanicolaou and Richlen's experiment (1988). The breaker wave-height H_b/h was compared between the numerical results, where the breaker point is defined as the onset of overturning and experimental results by Papanicolaou and Richlen (for brevity P-R). Table 1 shows the results of the comparisons. It can be easily recognized from this table that the breaker wave-heights computed with the present model agree with those obtained by P-R within the error degree of 1%. This remarks that the breaking criteria could be established for the solitary waves without carrying out experimental works in a wave tank.

Table 1 Comparison with the breaker wave-height between the present numerical results and experimental ones by P-R

H / h	tan θ	H _b /h	
		Experi. (P-R)	Numeri.
0.2	0.0141	1.222	1.218
0.3	0.0126	1.086	1.077
0.4	0.0126	1.071	1.080

4. DEFORMATION UP TO BREAKING AND REFLECTION

Figure 4 shows the propagation processes of solitary waves up to breaking points. While the wave profile at the breaker point shown in Fig.4(a) seems to be a spilling breaker, the wave profile shown in Fig.4(b) could be regarded clearly as a plunging breaker. From these results, we can be convinced that both breaker types of spilling and plunging occur even in the case except for sloping bottoms and depend on a parameter ξ_s defined by authors (Yasuda, Hara & Sakakibara 1990) as

$$\xi_s^* = (R/h)/(H/h)^{2/5}, \quad (2)$$

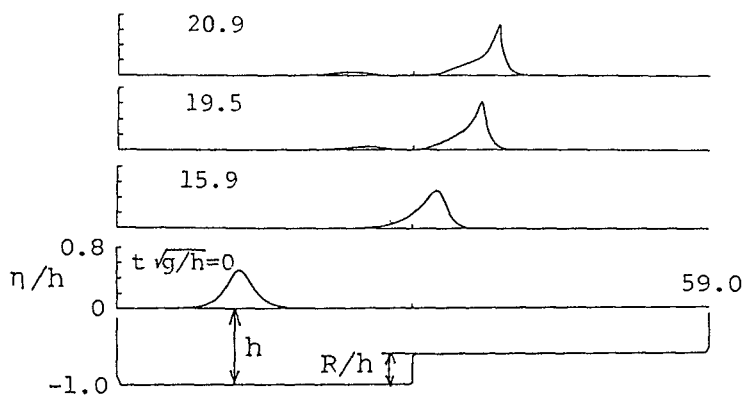
where H denotes the initial wave-height of an incident solitary wave, h the still water depth in front of the rectangular step and R its height.

Further, we define a horizontally asymmetric parameter β_4

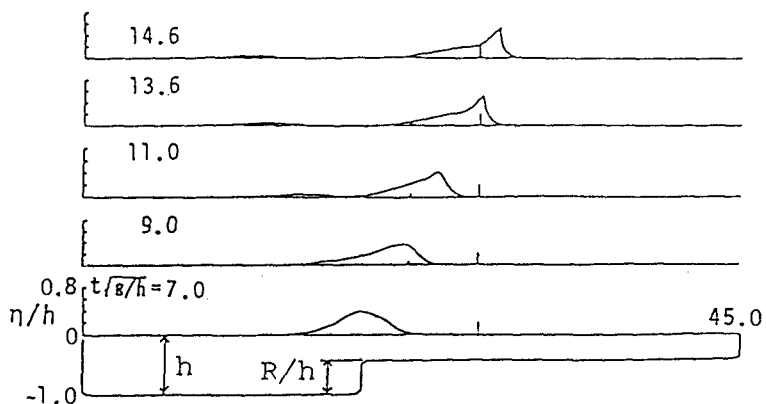
$$\beta_4 = \frac{-1}{2B} \int_{-B}^B \eta_x dx, \quad (3)$$

as the breaker type index, since the breaker type could be supposed to correspond directly to horizontal asymmetry. Here, the integral region B in the equation is indicated in Fig.5 Figure 6 shows the relation between the values of the parameter ξ_s of incident solitary waves and the parameter β_4 calculated from their wave profiles at breaker points.

Figure 7 indicates the backward propagation process of a reflected wave from a rectangular step. The reflected wave also seems to propagate as a steady solitary wave. Hence, we can easily define the reflection coefficient Kr of a solitary wave as a ratio



(a) Spilling breaker
 ($H/h=0.50$, $R/h=0.4$, $\xi_s = 0.032$)



(b) Plunging breaker
 ($H/h=0.36$, $R/h=0.6$, $\xi_s = 0.100$)

Fig.4 Temporal changes of wave profile of a solitary wave passing over a step

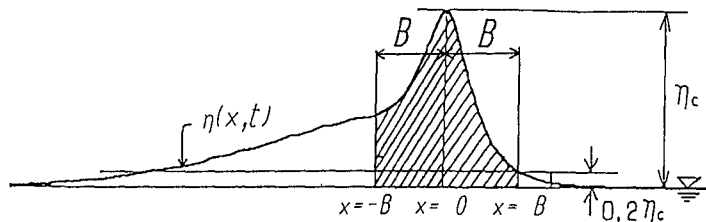


Fig.5 Region of integration for a horizontally asymmetric parameter β_4

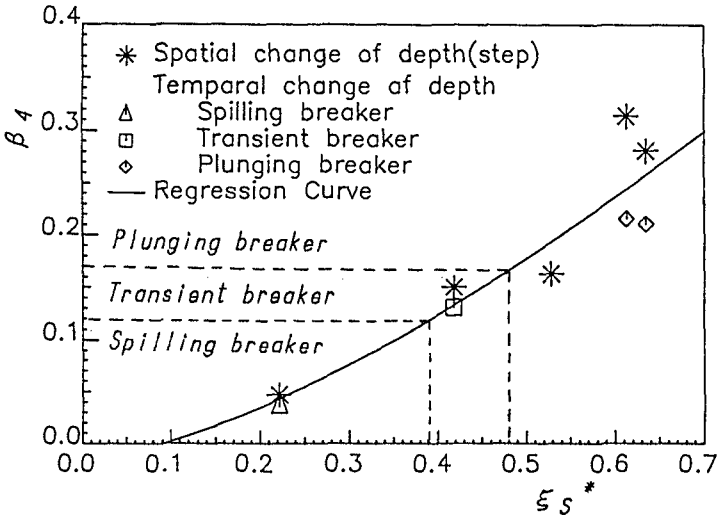


Fig.6 Relation with the breaking of a solitary wave caused by a step between ξ_s^* and β_4

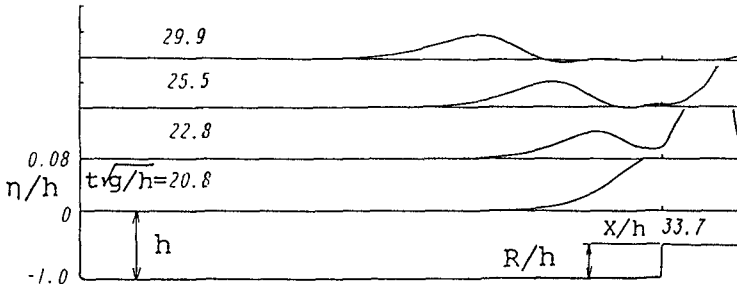


Fig.7 Backward propagation of a reflected wave from a step

of an incident wave-height H to a wave-height of the reflected solitary wave. Figure 8 shows the comparison of the relation of the reflection coefficient K_r to the relative step-height R/h between the computed results by the present model and the experimental ones by Seabra-Santos et al(1987). In the figure, a solid line indicates the result calculated by Lamb's formula

$$K_r = \frac{1 - \sqrt{1/(1 - R/h)}}{1 + \sqrt{1/(1 - R/h)}} \quad , \quad (4)$$

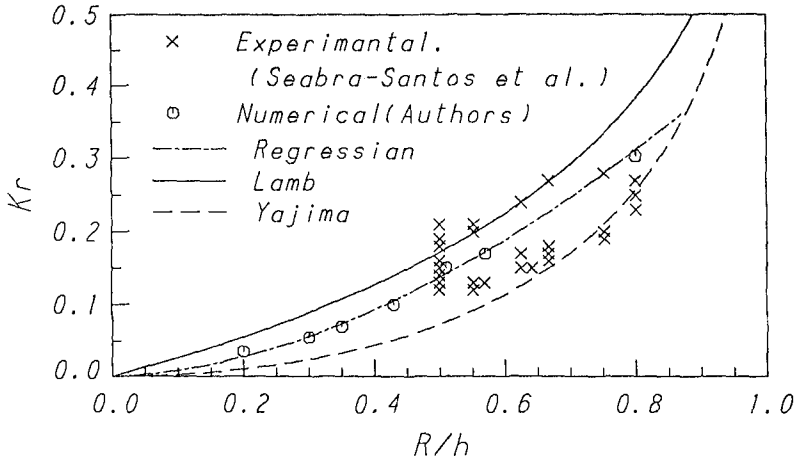


Fig.8 Relation of the reflection coefficient K_r from a step to its relative step height R/h

and a broken line denotes the theoretical result suggested by Yajima(1984) who solved the reflection problem of the KdV soliton using the inverse scattering method.

$$K_r = \frac{1}{4} \left\{ \sqrt{1 + 8 \frac{\sqrt{1/(1-R/h)} - 1}{\sqrt{1/(1-R/h)} + 1}} - 1 \right\}^2 \quad (5)$$

The regression curve is drawn with the following equation

$$K_r = 0.460(R/h)^{1.745} \quad (6)$$

It is made clear that the reflection coefficients obtained by the present model are independent of the amplitudes of incident waves as well as both the results of Lamb and Yajima, although they reveal the intermediate characteristics between eq.(4) and eq.(5). This remarks that the reflection coefficient of steady waves from a step is almost independent of the order of their nonlinearity but mainly depends on the relative step-height R/h alone.

5. BREAKING CRITERIA

Figure 9 shows the relation between the wave-height H/h of incident solitary wave of which front face

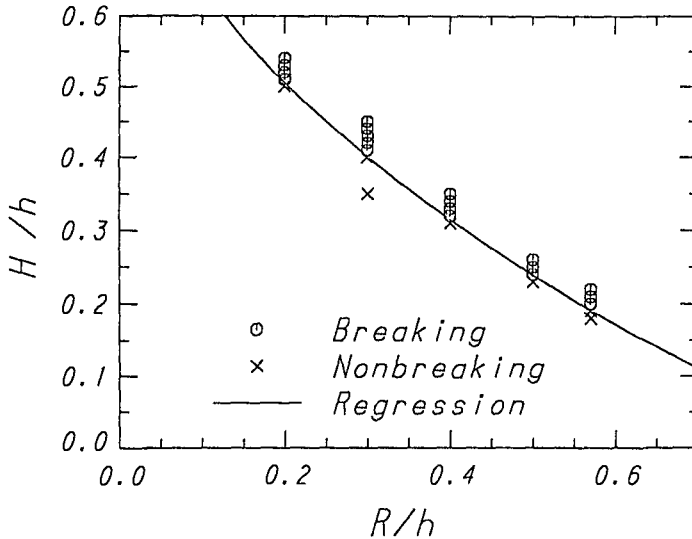


Fig.9 Relation of the presence of breaking caused by a step to the initial wave-height of incident solitary wave H/h and relative step-height R/h

overtURNS or not on a step and the relative step-height R/h . The solid line indicates the limiting wave-height H_c/h of the solitary wave which can be transmitted without breaking. The limiting wave-height is almost inversely proportional to the step-height. From the relation between H/h and R/h , the value of the critical step-height comes to light against each incident solitary wave which propagates over the step without breaking.

Figure 10 shows the breaking criteria of a solitary wave over a step, that is, the relation of the crest-height at the onset of breaking η_b/d and the limiting wave-height H_c/d to the relative step-height R/h . Here, d is the water depth on the step and is equal to $h-R$. It should be noted that the value of η_b/d is almost constant and is nearly 0.9, independently of the step-height. This remarks that the solitary wave having the crest-height under about 0.9 does not break on the step, even if the crest-height exceeds 0.78 which is the maximum crest-height of the steady solitary wave on a flat bottom. The solitary wave having the crest-height between 0.78 and 0.9 suffers fission on the

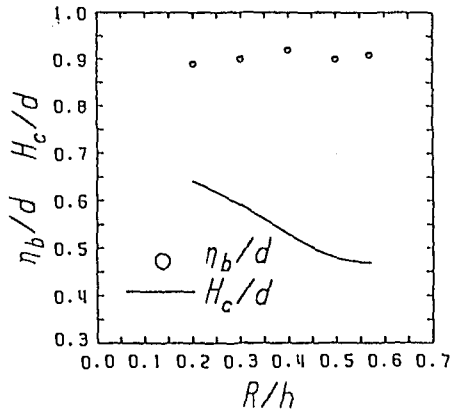


Fig.10 Breaking criterion of a solitary wave over a step

step, instead of breaking.

6. CONCLUDING REMARKS

It is verified through carefully controlled experiments that the present model enables us to compute very accurately the transformation of a steep solitary wave leading to breaking. Many numerical simulations using the model yield the breaker criterion and reflection coefficients of steep solitary waves over a step and further make clear the characteristics of reflected waves consisting of the positive solitary wave from the submerged breakwater.

7. ACKNOWLEDGEMENT

The authors wish to express their thanks to Dr. M. Tanaka of Gifu Univ. for his valuable advice.

REFERENCES

- DOLD, J.W. and D.H. PEREGRINE(1984).
Proc. 19ICCE, 955-967.
- Papanicolaou, P. and Reichlen, F. (1988).
Sea Surface Sound (Ed. B. Kerman, Kluwer
Academic Pub.), 97-109.
- Seabra-Santos, F. J., Renouard, D. P. and Temperville, A. M.
J. Fluid Mech., Vol. 176, 117-134, (1987)

- TSUCHIYA, Y. and T. YASUDA(1984).
Proc. 19ICCE, 435-451.
- YAJIMA, N.(1984).
Bull. RIAM, Kyushu Univ., No.60, 277-291.
- YASUDA,T., M.HARA and M.TANAKA(1989).
Proc. 3ISCFD, 1049-1054.
- YASUDA,T.,M.HARA and Y.SAKAKIBARA(1990).
Proc. of Coastal Eng.,Vol.37,JSCE,61-65.

CHAPTER 71

REPORT FROM THE NATO ARW ON WATER WAVE KINEMATICS, MAY 1989

by
Alf Tørum¹ and Ove T. Gudmestad²

ABSTRACT

A report is given on the NATO Advanced Research Workshop on "Water Wave Kinematics" held in Molde, Norway, 22 - 25 May 1989. The reports from the five working groups set up during the workshop are included in full.

1. INTRODUCTION

Water wave kinematics is a central field of study in ocean and coastal engineering. The wave forces on structures as well as sand erosion on coastlines and in the ocean are to a large extent governed by the local distribution of velocities and accelerations of the water particles.

Our knowledge of waves has generally been derived from measurements of the water surface elevations. The reason for this is that the surface elevations have been of primary interest and fairly cheap and reliable instruments have been developed for such measurements. The water wave kinematics has been derived from the surface elevation information by various theories. However, the different theories for the calculation of water particle velocities and acceleration have turned out to give significant differences in the calculated responses of structures. In recent years new measurement techniques have made it possible to make accurate velocity measurements. Hence, the writers deemed it to be useful to bring together a group of experts working actively as

¹ Head of Research/Professor. Norwegian Hydrotechnical Laboratory/Norwegian Institute of Technology, 7034 Trondheim, Norway.

² Dr. Scient/Dicipline Leader, Statoil, P.O. Box 300, 4001 Stavanger, Norway.

researchers in the field of water wave kinematics. These experts included theoreticians as well as experimentalists on wave kinematics. It was also deemed useful to include experts on the response of structures to have their views on what information is needed on water wave kinematics.

The objectives of the workshop were:

- to summarize research related to wave kinematics (state-of-the-art)
- to define approaches for design of safe and cost efficient offshore and coastal structures
- to exchange ideas and methodologies and to serve as a forum for idea generation
- to define further research needs and the most efficient methods to solve those needs.

A grant from NATO International Scientific Exchange Programme made it possible to hold a NATO Advanced Research Workshop in Molde, Norway, 22 - 25 May 1989. Additional funding was obtained from Statoil, Norway, the Royal Norwegian Council for Scientific and Industrial Research, Norway (NTNF) and from the Foundation for Scientific and Industrial Research at the Norwegian Institute of Technology, (SINTEF), Norway.

The workshop was organized as a series of lectures, including invited lectures, with discussions. Five working groups were also set up on five different subjects: Deep water waves, shallow water waves, breaking and freak waves, measurements and forces. The discussions and conclusions of the working groups were summarized in reports.

The scientific committee for the workshop had the following members:

Professor A. Tørum
Norwegian Hydrotechnical Laboratory/
Norwegian Institute of Technology, Norway.
Director of the Workshop.

Dr. Scient. O.T. Gudmestad
Statoil, Norway
Director of the Workshop

Professor R.G. Dean
University of Florida, USA

Professor D.H. Peregrine
University of Bristol, United Kingdom

Dr. S. Sand
Danish Maritime Institute, Denmark

60 persons from 13 different countries attended the workshop.

The proceedings from the workshop have been published by Kluwer Academic Publishers, The Netherlands. The title of the proceeding is "Water Wave Kinematics" with A. Tørum and O.T. Gudmestad as editors. 35 papers and 13 written short contributions are included in the proceedings. The proceedings also contain the reports of the working groups.

It is not possible within the framework of the paper to ICCE'90 to give proper justification to all the papers and discussions. However, it is felt that the summary reports from the working groups give state-of-the-art reports as well as recommendations for further research. They are therefore included in this paper.

2. REPORT FROM THE WORKING GROUP ON DEEP WATER WAVE KINEMATICS

2.1. INTRODUCTION AND SUMMARY

There are presently many wave kinematics procedures that are used by the offshore engineer to calculate design kinematics. These procedures include the highly nonlinear, two-dimensional breaking wave methods, the linear, random three-dimensional methods and others. In many cases the application determines the procedure to be used, e.g. for steel piled jacket (SPJ) static design the Stokes type procedures have traditionally been used. In other instances, the choice of the procedure depends on regulatory agency requirements, familiarity, available experimental verification, and also simplicity. The argument can be made that all these procedures have served the offshore industry well since there have been no major offshore platform failures that are directly attributed to wave kinematics inaccuracies. This success, however, may be due to general conservative approaches used in platform design, and to compensating factors. All procedures represent approximations to the real offshore kinematics problem, and as design procedures become more sophisticated, aiming to improve safety while reducing platform costs, there is a two-fold need (1) for additional verification and improvement of the various available procedures and (2) for development of procedures that solve satisfactorily the general problem of three-dimensional irregular waves with currents. The additional verification and establishment of ranges of applicability of present pro-

cedures is of utmost importance since some of the procedures, e.g. stretching methods for irregular waves, give significantly different kinematics in the wave crest region.

2.1.1. Statement of the problem

The general problem of wave kinematics and currents in deep water is quite complex, and needless to say it has not been solved. The physical model assumed for this discussion is deterministic (stochastic aspects of wave kinematics are not considered) and includes:

- regular or irregular finite height, non breaking waves
- wave conditions with or without energy spreading
- wave conditions with or without current.

In the case of waves only or waves with uniform current, the fluid is assumed irrotational and incompressible. For the case of nonuniform current with waves, the appropriate vorticity is assumed to be included. It is believed that any accurate solution to the analytical relationships describing this stated problem will give sufficiently accurate kinematics. Of course this will need to be substantiated with data.

2.1.2. Status

A satisfactory method for calculating kinematics in the general irregular wave with energy spreading cases that satisfies to high degree of accuracy Laplace's equation and boundary conditions is not presently available. For practical application, however, there are many analytical and empirical procedures that can be used depending on application. These procedures are backed up by varying degrees of experimental and/or analytical verification.

The extension of the two-dimensional wave procedures to three-dimensional waves is not straightforward neither from the analytical or technical nor from the wave input description side. Available solutions (empirical or low order analytical) are approximate, and, no extensive comparisons with data have been carried out.

The presence of storm tide or other non-uniform currents adds to the difficulty of the general wave only problem. Analytical solutions for regular waves (Stokes) with arbitrary current profiles are available. Also, empirical solutions are available for the general case, but those solutions can benefit from additional data.

2.1.3. Recommendations

Further measurements in the laboratory followed by carefully defined field tests are required. Test programs should be based on the need of the offshore industry. The industry should define the acceptable levels of accuracy in the kinematics, which would normally depend on application.

It is also required to develop analytical or numerical methods which solve the more general problem of kinematics for currents plus irregular, three-dimensional waves. In order to achieve this goal there is need for international cooperation and data sharing. Definition of standard bench-mark wave and current cases would also expedite verification of the procedures.

2.2. KINEMATICS MODELS

There are four major classes of wave kinematics problems that are discussed below which represent different levels of difficulty in the search for solutions. These are: two dimensional waves with and without current, three-dimensional waves with and without current.

2.2.1. Two dimensional waves

There is no kinematics procedure or theory presently available for the general case which satisfies the governing equations and the boundary conditions. The relatively new boundary integral methods hold promise but at present have computational and free boundary limitations.

Simple procedures (e.g. Wheeler stretching, delta stretching, Gudmestad method etc) which represent extrapolations of linear theory to finite height irregular waves have been successfully compared to available data according to published results. Since these procedures are basically empirical, their use far outside the range of wave parameters for which they have been verified should be done with caution. Additional kinematics data (laboratory and field) are needed in the wave crest to further verify and define the range of applicability of these methods. Theoretical efforts to assess the methods are also worthwhile.

There exist analytically robust procedures (Stokes methods, boundary integral methods, etc) to treat regular or or limited groups of waves with high accuracy although further testing against available data is necessary for these procedures, also. Verified methods

for using these procedures with irregular waves are yet to be established.

Numerical procedures (e.g. stream function, EXVP method, etc) that treat irregular single or multiple waves can also be used. These procedures fit with high accuracy one or both boundary conditions. The applicability of these procedures is limited by the assumptions they are based on (rigid shape or changing shape waves) and the required length of the wave trace that can be treated.

Linear theory could be used for low wave steepness or for elevations beyond one wave height below the deepest wave trough. Higher order theories (2nd order) are available and are applicable for low steepness. These theories, however, require additional comparisons with data, also.

2.2.2. Three dimensional waves

There is no general theory presently available apart from general linear wave theory and there is no procedure under development which is computationally efficient for the nonlinear case. Some of the available two-dimensional empirical procedures (stretching methods) may in principle be extended to the three-dimensional wave case. Test data will be needed to verify the accuracy of such extensions.

The linear wave theory could be used for the low wave steepnesses. Higher order numerical procedures (e.g. Forristalls KBCF-method) could be used if made computer efficient. Here also there is a need for data verification.

2.2.3. Current with waves

There is no analytical procedure available for the general case. There are, however, empirical procedures which are used by the offshore industry; these procedures have not been validated with data. For two-dimensional, steady regular waves and collinear current of arbitrary profile new theories exist and insight can be gained with these theories as to how waves interact with currents. Measurements are needed in the wave zone in particular to test the goodness of these various procedures.

2.3. RECOMMENDATIONS

The recommendations below address both short term and long term needs. The wave kinematics problem remains

still a challenging problem for the theorists and experimentalist, and will require good imagination to bring about new and improved solutions that can be put to use in offshore design.

2.3.1. Data

It is recommended that the industry clearly define the required accuracy of new data needed for the different applications. Laboratory measurements on kinematics for the following wave cases are needed:

- 2D regular waves and groups of waves for a larger range of parameters to verify analytical and numerical procedures;
- 2D irregular waves to verify and extend the test data base;
- 2D current with regular and irregular waves;
- 3D irregular waves in order to extend methods and procedures presently used for 2D waves;
- 3D irregular waves with current.

The laboratory tests should also aim towards definition of field tests which subsequently should be carried out.

2.3.2. Analysis methods

Research should concentrate on the following main tasks:

- Develop fully consistent 2D theory for irregular waves;
- Develop empirical procedures for current with waves;
- Develop fully consistent 2D theory for current with regular and with irregular waves;
- Extend empirical procedures from 2D to 3D,
- Develop higher order analytical and numerical procedures for 3D irregular waves with and without current;
- Clarify further the mean flow in the kinematics in waves.

2.4. COOPERATION

In order to successfully develop the analytical tools needed and to fully benefit from future testing in the laboratory and in the field, international cooperation is required. It is recommended that standard test cases be defined through the cooperation of the offshore industry and research institutions in order to verify procedures. For advancing the kinematics procedures, it

is essential that there be data sharing. Also, the offshore industry must continue to provide data for long term research projects at the institutions and the research institutions must continue to carry out basic research to solve engineering needs.

3. REPORT FROM THE WORKING GROUP ON SHALLOW WATER WAVE KINEMATICS

INTRODUCTION

The Working Group on Shallow Water Wave Kinematics (WGSWK) defined "shallow water" as extending from the conventional deepwater limit, $h/L_0 = 0.5$, to the shoreline. A decision was made to focus on the needs for the next two or so decades with criteria of methodology and data required by the designer and a generally improved understanding of the phenomena related to shallow water wave kinematics. Although of importance, wave hindcasting was not considered as within the Group's scope. Finally, in order to provide focus to our recommendations, only six problem areas have been selected for emphasis.

STATUS

The shallow water region is characterized as one of substantial nonlinearity, and directionality with the possibility of strong currents and large tidal fluctuations. At present, substantial variability in methodology ranging from ad hoc to sophistication is employed in the prediction of shallow water wave kinematics. The range of methodology encompasses regular vs irregular waves, deterministic vs stochastic representation and various methods of combining waves and currents. Although each of them can play useful roles, a better understanding is needed of the strength and relatively applicability and differences to be expected. Regulatory agencies prefer straight forward procedures suitable for codification. A need exists to develop and introduce procedures that have greater realism and physics and can be readily applied by industry.

The workshop addressed a number of problems relative to shallow water kinematics. It was concluded that for the case of regular waves without currents, existing wave theories are adequate. However, more emphasis needs to be directed to the problems of regular waves with a current which varies over depth. Of particular concern is the appropriateness of methods for predicting near surface kinematics. Due, in part, to the high nonlinearity of the surf zone and the significance of sediment transport in this area, more effort here is needed.

Other areas of research need are described in the following sections of this Working Group Report.

LONG-TERM CLIMATE DESCRIPTION

A Long-term climate description of a region is an important engineering activity which requires research in order to improve its reliability. In the absence of long-term widespread measurements, emphasis is thrown onto the use of recently developed shallow water codes such as -3 GWAM. The hindcasting is performed for adjacent deep water and wave energy is then radiated in towards the shallow water region. Inherent difficulties with this systematic approach centre around the influence of current-interaction, shoaling, and large variations of still water level with time. Areas of immediate research concern include the following:

- Algorithms to optimize long-term information whilst reducing the bulk of wind and pressure fields processed. (Such as sequential bootstrapping techniques and other sub-sampling procedures).
- Improving storage techniques for time-step and spatial interpolation.
- Statistical methods for addressing questions of simultaneity of water depth, current wave fields.

B. Although many platforms are equipped to record sea-state data, this is still done on a systematically intermittent basis (e.g. 20 minutes for each 3 hours). This appears to be satisfactory for most spectral and statistical requirements, but cannot be expected to record the more extreme events which may occur whilst the instruments are on stand-by. Without resorting to continuous recording, and hence involving storage and servicing problems, it would be highly desirable to develop methods of recording the extreme events in as much detail as possible.

WAVE TRANSFORMATION & DETERMINISTIC MODELS

A In the analysis of nearshore wave phenomena, the starting point will most often be information (e.g., the directional wave spectrum) of the wave field in deep water. Therefore, one needs wave transformation models that can transfer this information into the shallow water area of interest and to provide input for surf zone models.

The different model employed are chosen according to the scale and distance from the shore of the area under consideration:

- Outer area:
Depth-Current refraction models (linear)
Ray theory, finite difference
Mesh size 100 m - 1 km
Size of area modelled 25 km² - 1000 km²
- Intermediate area:
Models based on mild slope equation (linear, extended to include dissipation and boundary absorption) the parabolic approximation (linear or weakly nonlinear and dissipative).
Mesh size: 5 m - 20 m.
Size of area modelled: 1 km² - 25 km².
- Harbour areas:
Models based on "Boussinesq equation". (Weakly nonlinear).
Helmholz equation or 30 linear potential solutions
Mesh size: 5 m - 20 m.
Size of area modelled: < 5 km².

Research needs:

- Spectral model including refraction, diffraction, frequency shifts due to wave breaking.
- Generation of long waves by short waves, and their transformation.

B As the water depth becomes small and/or the waves become high, the analytical wave models cease to be valid: The prediction of maximum waves of constant form (with or without current) require the use of stream-function-like theories. In some cases these data can also be fitted to extreme wave data to account for the asymmetry found in nature. Asymmetry statistics or realistic methods of generalizing wave asymmetry should be developed. The wave models for prediction of kinematics under waves should be evaluation with high quality data.

2D models based on potential flow can now solve fully nonlinear problems from deep to shallow water. Up to now they are however limited:

- to the first breaking wave
- lack of a radiation boundary for arbitrary waves
- cannot model friction and flow separation

Research should be directed toward:

- introducing variety
- investigating post-breaking extensions of such models
- developing a free boundary (i.e. weakly reflective boundary conditions)
- 3D potential flow models

WAVE-CURRENT INTERACTION

Waves interact with current in a number of important, and often nonlinear ways within the upper frictionless part of the water column and through their combined friction at the bed. These strongly influence the wave propagation characteristics, the current distribution, the resulting sediment transport, and forces on structures. The State of the Art and the Research Needs on various modes of interaction are as follows:

A Refraction

At the moment, refraction of linear waves by horizontally sheared, vertical uniform currents can be calculated. It is however, necessary to extend these methods to nonlinear waves.

B Kinematics

Methods for the computation of regular nonlinear waves on codirectional vertically sheared currents have recently appeared. They should be extended to non-codirectional cases, and to random waves. Also, they should be combined with above mentioned item to predict refraction and kinematics due to horizontally and vertically sheared currents.

C Mass transport

Theories exist to calculate the mass transport of water near the bed for a laminar wave boundary layer in the absence of currents. These should be extended, first to the turbulent wave boundary layer, then to the case where an external (e.g. tidal) current is imposed.

D Bottom friction

Several theories exist to calculate mean and peak bed shear stresses due to sinusoidal waves superimposed on a current. These prediction methods need to be simplified (without offering much of their accuracy) to be applicable in wave phase averaged numerical wave and current models. Also, extensions should be made toward

irregular (frequency and direction) waves, breaking waves and to distinguish the wave propagation direction.

All the above topics require advances through theoretical and numerical methods, and laboratory and field measurements.

The topics require to be combined together to provide fully interactive 2D numerical models of wave and current fields, leading possibly (on the long term) to 3D models.

NONLINEAR DIRECTIONAL WAVE THEORY

A constant reoccurring problem in ocean engineering consists of finding the best choice for a given application between random, linear, directional wave theory and nonlinear unidirectional deterministic wave theory. Each approach seems to be optimal for some class of problems, but there are other types of problems for which neither is quite right. A nonlinear, directional, wave theory is sorely needed to bridge between the two extremes. In recent years, several new approaches to the problem have emerged. This, coupled with the increasing power of available computers, makes now an appropriate item to undertake the solution of this reoccurrent problem, both for deep and shallow water.

One potential direction of attack is to combine waves from several directions while forcing satisfaction of the wave equation and free surface conditions. A second direction consists of an iterative procedure which starts with a linear, directional sea surface and, in a stepwise fashion, proceeds to modify the surface toward a better satisfaction of free surface conditions while maintaining the proper directional spectrum and any conditioning constraints.

There probably are other alternatives also available. The development of such a general random directional wave theory would be of great value in future ocean engineering investigations.

SPLASH ZONE KINEMATICS

The wave kinematics at or near the free water surface are very critical in determining overturning moment and other load parameters in an offshore structure. It is difficult to make field measurements of wave kinematics in this zone since the measuring devices are alternately submerged and in the air. The abrupt shock to the instrument at the moment of passing through the air-water interface typically induces transients in the

measurements which are difficult to interpret. Measurements of forces in the splash zone experience similar shock problems. Non intrusive measurement scheme for both kinematics and forces need to be developed and studied.

From an analytical perspective relative to random, linear directional wave theory, the prediction of kinematics and forces for locations above mean water level are perplexing and create paradoxes within linear wave theory. Linear theory assumes infinitesimal amplitudes and so kinematics above mean water level are contradictory. If the theory is used without modification above mean water level, the velocities are overestimated in a part of the force regime critical to most structural computations. Various "stretching" schemes have been proposed and used, but these are quite "ad hoc" in nature and theoretically unsatisfactory. It would be much more desirable to have some scheme which closely satisfies the free surface boundary conditions.

Some experiments have been carried out to investigate splash zone kinematics and forces under laboratory conditions. Use of these results demands a knowledge of scale effects which for these processes are poorly understood. In field conditions also there is likely to be a thin wind-induced surface current which may locally enhance particle velocities and forces.

In summary there is a research need for (a) improved instrumentation for measuring forces and kinematics in the wave splash zone, and (b) more theoretically sound ways to modify random linear directional wave theory for loading points in the splash loading zone. (c) improved understanding of scale effects and (d) of the importance of wind-induced surface currents.

SURF ZONE HYDRODYNAMICS SEDIMENT TRANSPORT

To further our understanding of the processes that shape our coastline, it is essential that we understand the hydrodynamics of the surf zone. Of particular interest are the distribution over depth of wave induced longshore and onshore-offshore currents and the momentum fluxes which drive them. Advances in this area will enable more refined studies of sediment transport modes and rates.

As has been stressed by Dr. N. Barltrop during this workshop it is important to determine the appropriate wave theory to use for a particular study. Waves in the surf zone are non-linear. The hydrodynamics of the surf zone is further complicated by the geometry of the

bottom. Therefore it is suggested that shallow water wave theories (for constant and variable depth) be evaluated for applicability over various geometries (starting with planar and simple curved geometries and eventually extending to geometries which include bars). In parallel with the theoretical studies numerical approaches (such as the Stream Function Wave Theory or the Numerical Wave Tank) should be considered. Infragravity waves can also cause substantial velocity fluctuations and water surface displacements in the surf zone.

The turbulence associated with wave breaking causes the wave height to decay which is directly related to the momentum fluxes. Thus studies to determine the variation of eddy viscosity over depth and across the surf zone are essential. Another process to be further studied is the reforming of waves as they propagate over the troughs between bars.

Further research is also required in including the effects of the bottom boundary layer on the wave induced currents. In the area of sediment transport studies are required to model sediment transport across the surf zone and over depth. Shallow water symmetrical and asymmetrical waves and their interactions with currents should be considered as driving mechanisms.

Sediment transport driven by random waves is also an area requiring research efforts.

Better models to quantify longshore and crossshore sediment transport rates for suspended and bedload load transport are required. The threshold of motion and sediment pick-up rates are topics still requiring better understanding. One area of particular interest is the determination of the extent over depth of the breaking induced mixing and its effects on sediment transport. In this respect breaker types should be considered in analysis. Equilibrium beach profiles also need further research. To obtain a broader understanding of the mechanisms shaping coastal regions the sediment transport outside the surf zone requires attention. The study of the transport in this zone including tidal and storm surge currents is of importance. Surf zone and non-surf zone models of transport need to be connected in attempts to obtain a global model.

The verification of the results of the investigations suggested through laboratory and especially field testing is of utmost importance.

4. REPORT FROM THE WORKING GROUP ON BREAKING AND FREAK WAVES

DEEP-WATER BREAKING

Presentations at the workshop have included discussion of waves breaking in deep-water but details are only given in the context of wave tank simulations. Conventional measurements at sea do not distinguish broken from unbroken waves.

We wish to emphasize that the physics of breaking waves can differ between wave tanks and waves at sea. In particular, the most frequent and important occurrences of deep-water breaking are in wind-driven waves. The character of wind-driven waves varies with their age, but at any time breaking is intermittent and short-crested. This makes it difficult to quantify and measure breaking events.

Statistics of breaking would be invaluable. Some statistics of white caps have been collected and are clearly related to breaking events. Efforts to quantify the relation would be welcome and should be contrasted with statistics of breaking based on spectral distributions which only present the exceeding of a mathematical criteria. Such criteria need to be established from the physics of wind-wave interaction. An initial approach based on measurements following the mariner's type of observation is recommended, e.g. the percentage of braking waves as a function of wind speed, the size and duration of white caps, depth of air entrainment etc. We consider relations between sea state and Beaufort number could be confirmed and compared with modern wind casting methods.

Short-crestedness implies a need to account for three-dimensional breaking in multi-directional seas, but first the behaviour of ideal regular waves needs clarification both experimentally and theoretically.

The important effects of wind, with its pressure distribution driving the waves and the vorticity that wind drift induces in the surface layer have yet to be quantified, although, their qualitative importance has been demonstrated. This research is urgently needed since wave breaking is intimately linked with wave generation, and this linkage produces the most severe states that ships and offshore structures encounter.

We propose that measurements of breaking wind-waves be first conducted in wind-wave flumes, where it should be possible to measure all significant parameters,

though some development of instrumentation may be needed, especially to recognise wave breaking. In particular local properties worth measuring include elevation, velocity, vorticity, turbulent intensity, in both air and water as well as air or water entrainment. General properties to be examined include the type of breaking, three-dimensional structure and the role of breaking in frequency downshifting.

Theoretical studies need to be encouraged into quantifying the effects of surface drift and of three-dimensionality. Current numerical models can describe two-dimensional irrotational waves as they break. Addition of a layer of vorticity at the surface is feasible. Three-dimensional irrotational programs are likely to be developed but combination with vorticity seems unlikely in that case.

SHALLOW-WATER BREAKING

Breaking induced by bottom topography is a well-studied area because of its importance in all aspects of coastal engineering. For the purposes of this working group we ignore its implications for and interactions with surf-zone processes, other than the basic hydrodynamics. The presentations in the workshop reflect current research frontiers. That is investigation of the complex but deterministic flow field that occurs after breaking is represented by Tallent's detailed description of the eddies and splashes for a wave on a beach, the numerical modelling of wave behaviour before any splash occurs is described by Grilli and by Peregrine. These are all two-dimensional studies. For shallow-water breaking this limitation is not serious since such breaking is usually longcrested.

A number of substantial field experiments in the last decade are giving a good appreciation of surf-zone kinematics. However, for many practical purposes results from regular wave trains are used, often with extremely simplified models of the surf zone.

At the research level, many detailed aspects need study as mentioned below but the only major gaps in our knowledge concern the flow once breaking starts, until, on gentle slopes, the wave has become a turbulent bore; and the flow when breaking stops as when a broken wave enters deeper water. Further study is required because of the importance of the breaking phase in processes such as sediment transport, the generation of nearshore circulation which influences dispersion of pollution etc, the determination of set-up and run-up with relevance to flooding, and the severe conditions that break-

ing provides for structures such as breakwaters and sea walls.

Research is needed in the experimental area to clarify the strong effects of wind which at the present time are mainly recorded in books on surfing. Onshore winds lead to a dominance of spilling breakers, whereas offshore winds encourage plunging breakers. Several aspects of breaking need to be quantified, although we can recognise spilling and plunging breakers, intermediate cases are not readily described. That is, we still lack good definition for the relative size and strength of breakers.

The present initial studies on breaker structure need to be developed and extended since for many applications this is the most significant phase of wave development. There are still distinct experimental difficulties, and instruments or measuring techniques need to be developed, e.g. to measure air-water ratios.

Experiments and characterization of irregular waves as they break are required, especially on steeper slopes where backwash has a significant influence on breaker character.

Field observations have provided substantial data banks which can be usefully studied with further analysis and interpretation. We note however that conventional measurements can be of much greater value if simultaneous film or video records are made since it is not always easy to recognise wave breaking from other records.

Theoretical study is hampered by the difficulties of describing the breaking process, though there is a good chance of progress if the simple turbulence modelling of Svendsen and Madsen (1984) is developed. Verification of the potential flow models up to breaking by comparison with a wider range of experiments is desirable, and these models can be improved in a number of ways, e.g. inclusion of vorticity layers may mimic wind drift, or a sheared backwash flow.

Mathematical models of a simpler kind, such as those using the finite-amplitude shallow-water equations could provide insight into the interaction between the dominant waves and longer period waves (infra-gravity waves) whose origin may be in the surf-zone region and which have a dominant influence on run-up on gentle beaches.

FREAK WAVES

The workshop presentations of Kjeldsen and Sand give a good indication of the "state of the art" in this area. The following definition of freak waves has been proposed by Kjeldsen

$$H_{max}/H_s > 2.0$$

since this will in most cases (number of waves $n = 1000-2000$) represent a clear exceedance of the most probable maximum wave according to the Rayleigh distribution (c.f. Sand et al.). On the basis of observations in the Gulf of Mexico, the North Sea, the Irish Sea, off the coast of Norway, etc. it is believed that the phenomenon appears in both deep and shallow water, and is dependent on locality.

It is proposed that the following causes be further investigated:

Wave phenomenon causing freak waves:

- wave focusing
- waves arising from different directions
- super-position of waves of different scales

Amongst the physical causes are:

- topographical refraction, diffraction and reflection on different scales
- wave-current refraction
- colliding low pressure systems (e.g. collisions between polar lows and ordinary low pressures)
- combination of swell and wind seas
- response of the wave field to a turning wind field such as a hurricane

In many cases freak waves appear as a result of combinations of the phenomena mentioned above (see Kjeldsen).

Recommendations for future research are listed under the following headings:

- Full scale freak wave measurement program (selection of instrumentation, site platforms, etc)
- Extended analysis of existing data.
- Correlation of meteorological information and freak wave occurrence.
- Further description of freak wave categories as non-breaking, spilling or plunging breakers.

- Kinematic theory of 3-D freak waves (especially above MWL).
- Ultimate and accidental limit state design guidelines and possible forecasting for ships and the oil industry.

(See also recommendations given by ISSC on ship subject in August, 1988).

5. REPORT FROM THE WORKING GROUP ON MEASUREMENT OF WAVE KINEMATICS

5.1. INTRODUCTION

It was the position of this group that the other working groups in this workshop would provide the needs and justification for additional wave kinematics measurements. Consequently, our recommendations will focus more on the means of implementing measurements and making suggestions for improving the state-of-the-art. Given the very different natures of field and laboratory measurements requirements, this group felt it best to consider the requirements independently. It is important to note that our recommendation philosophy will not be limited to currently available methods and techniques but to also include technology and techniques that show promise for future wave kinematic measurements.

5.2. STATUS

5.2.1. Field

The quantity of field measurements available is inadequate and the quality, with respect to wave kinematics, is, in general, low. Furthermore, available measurements are often severely limited in usefulness due to the measurement locations, structural influence and lack of one or more velocity components. Instrument reliability is very uncertain as instruments are often improperly calibrated and maintenance and recalibration are infrequent or non-existing. Not infrequently, valuable information in severe storms is lost due to equipment failure.

5.2.2. Laboratory

In contrast to field measurements, the quantity and variety of laboratory measurements available is significant, but are still lacking in the important near-surface and bottom zones. The possibility of excellent quality in measurements is high given: the opportunity for assured reliable instrument operation through frequent testing and calibration; the disturbance to the flow, by

the measuring instrument or its support structure, can be made negligible or completely eliminated altogether; and that three-component measurements are attainable. Despite this, laboratory measurements must be viewed cautiously due to the possibility of improper modelling and uncontrollable tank effects.

5.3. USE OF MEASUREMENTS

5.3.1. Field

In general measurements are made for a specific purpose. Field measurements are though focusing on topics not covering the wave kinematics. Instead oceanographic knowledge is sought in order to define statistical parameters, for example:

- wave height
- tidal and ocean currents
- wind speed

However, time series of more severe events are in general available.

5.3.2. Laboratory

Laboratory experiments are, in general, conducted to verify the validity of theories and extensions to theories. Therefore laboratory measurements are, for the present, limited to unidirectional problems and most often to shallow or very shallow water cases since theoretical efforts are extensive here.

Laboratory measurements, therefore, do not cover the complex situation as found in nature that we attempt to learn more about.

5.4. MEASURING TECHNIQUES

5.4.1. Field

The most frequently used velocimeters are of the electromagnetic flow meter type. A few acoustic meters are also now available, their applicability to wave kinematics is uncertain. For current measurements, mechanical propeller meters are commonly applied for short term measuring programs. They are all kept at fixed positions by mounting directly to fixed structures or suspended from buoyant bodies. In general, none of the above mentioned meter types are suitable for measurements in the splash zone.

5.4.2. Laboratory

Commonly used types of velocimeters are electromagnetic, acoustic, and micropropeller meters. Optical techniques such as Laser Doppler Velocimetry have become increasingly used providing measurements without disturbing the flow.

5.5. RECOMMENDATIONS

5.5.1. Field

- a. Equipment operation should be kept at a level securing high fidelity, i.e. sufficient calibration and verification are needed.
- b. Equipment should be made durable.
- c. Measurements are to be taken at sufficient distance from structural influence. All three velocity components are needed.
- d. Equipment for near surface measurements needs development.
- e. Three-component LDV should be developed.

5.5.2. Laboratory

Techniques in general should be improved to allow for a more free choice in setting up an experiment. Whole-field measurements may prove excellent for verification after improvement of the recording and processing techniques. Maintenance and reliability should be given the utmost attention.

6. REPORT FROM THE WORKING GROUP ON FORCES

The discussions of this working group were an example of the dialogue and international co-operation that is personally rewarding for all participants and leads to valuable consolidation of the state-of-the-art and also points to future research needs.

This has been a workshop on water wave kinematics. Forcing on ocean and coastal structures is fundamentally related to kinematics - the two subjects should not be considered independently. However, the discussions of this working group were focussed on the issue of how knowledge of kinematics can lead to predictions of forcing. The discussions began with consideration of Morison's equation, and expanded to include other topics such as freak waves, laboratory standards, and the need

for an accessible complete information data base of field and laboratory data.

We have seen that the determination of force coefficients for an irregular wave case cannot be expected to follow from any regular flow situation. The case of coexisting waves and current should also be considered separately. It has been suggested that the use of random process theory to determine the variance and statistics of extreme Morison equation forcing in irregular waves leads to very encouraging results.

It is generally recognized that kinematics in the near field are more significant than those in the far field. Further study of wave effects on force coefficients is recommended.

More data is needed on force coefficients in situations typical of the real ocean environment. Continued research into force coefficients appropriate for: multi-directional seas, coexisting waves and currents, clusters of cylinders, and relative velocity situations, is recommended. The emphasis of this research should remain on understanding the physics of the forcing process, particularly the importance of kinematics in the near field.

Having called for more research and more data, the working group considers it important to recommend that the data be available to researchers around the world, and that it be reported in a sufficiently complete manner so that results from various sources may be compared. Probabilistic format and methods should be more systematically used in the processing and presentation of experimental results in order to:

- a) make them objectively comparable, and
- b) provide the information needed for reliability design methods.

A common data base for force coefficient values, together with the ability to inter-compare the results from various sources, would encourage more rigorous application of the Morison equation.

The accident at the Ekofisk field in 1984 in which a control room wall was damaged by a wave crest at least 22 m above mean water level has been mentioned by both Kjeldsen and Sand et al. This event provides graphic evidence that "freak" waves are a definite hazard to ocean structures. There is a need to learn more about the processes through which these waves are formed, their kinematics, and their probability of occurrence.

Efforts to understand the influence of crossing seas, topography, and co-existing current, on the frequency and formation of these extreme waves should continue. More good field data is needed to extend our understanding of "freak" waves. It has been suggested that the wave rider buoy is not capable of making these measurements.

A related topic is the forcing caused by breaking waves which may not necessarily be "freaks". Breaking and very steep asymmetric waves can exert significantly larger forces on ocean structures than steady symmetric waves of similar height and period. Such unsteady waves exist in real seas, and they should be considered by the designers of ocean structures. It is recommended that research into the probability of occurrence of wave breaking in a variety of realistic multidirectional seas should continue. It is also recommended that study of the forcing due to unsteady and breaking waves should continue.

A gap still exists between regulations - and therefore, engineering practice - and state-of-the-art research. There is a need for continual upgrading of design specifications to reflect advances made by the research community.

There was some discussion of the need for quality assessment of wave basin tests. Information of reflection characteristics, wave generator capabilities, and the vertical distribution of kinematics measured in the basin at various distances from the wave generator, should be documented and made available by basin operators.

More research on long waves and their influence on the slow drift motions of floating structures is recommended.

In summary, we would like to encourage the participants of the other working groups to continue to advance on many of the kinematics-related issues discussed at this workshop. This will help those of us in the forcing working group to solve some of our own problems. Expressed in a different way, learning more about hydrodynamic forcing on coastal and ocean structures is intimately linked to greater understanding of wave kinematics.

7. ACKNOWLEDGEMENT

The reports from the working groups presented in this paper has been reprinted from the proceedings of the NATO ARW (ref. 1). We acknowledge the permission of Kluwer Academic Publishers to reprint them.

REFERENCES

1. TØRUM, A. and GUDMESTAD, O.T.(editors): Water Wave Kinematics. Proceedings of the NATO Advanced Research Workshop on Water Wave Kinematics, Molde, Norway, 22-25 May 1989. Kluwer Academic Publishers, The Netherlands, 1990. 771 pages. Published in cooperation with NATO Scientific Affairs Division.

CHAPTER 72

Prediction of the dimensions of a rip current system on a coast with bars

Julio Zyserman¹, Jørgen Fredsøe², Rolf Deigaard²

Abstract

A method to determine the dimensions of rip current systems (distance between rip currents, and width and depth of the rip channels) is presented for the case of a coast with longshore bars. The method is based on an overall sediment balance in the nearshore region. The balance is determined by application of a model for the wave-induced flow combined with a sediment transport model. The influence of the wave height, the wave period, and the direction of wave propagation, as well as of the sediment size is analyzed.

1. Introduction

Rip currents are strong narrow currents flowing seaward across the breaker zone, which return the water transported landward by the breaking waves. These currents influence the characteristics of the wave-induced flow and the associated sediment transport, and thereby the nearshore morphology. While a diversity of analytical and numerical models has been developed to determine the features of rip-current systems on plane beaches, the references regarding rip currents on coasts with longshore bars are rather scarce.

The main purpose of the present paper is to develop a method which can describe the characteristics of a rip-current system on a coast with bars taking an overall balance of the sediment transported in the nearshore region into account.

¹ Laboratorio de Hidráulica Aplicada, INCYTH, Casilla de Correo 21, 1802, Aeropuerto de Ezeiza, Ezeiza, ARGENTINA.

² Institute of Hydrodynamics and Hydraulic Engineering, Building 115, Technical University of Denmark, DK-2800 Lyngby, DENMARK.

2. The model for the wave-induced flow

Hydrodynamics in the uniform condition

Consider the situation shown in Fig. 1. A train of waves propagates obliquely towards a coast with a longshore bar. The bottom contours are straight, and parallel to the shoreline. The adopted system of reference is also shown in the figure. The x-axis is coincident with the still-water shoreline, and the y-axis has its origin at the coast and extends offshore. As the waves approach the coast, the effect of refraction makes the wave fronts turn, and the combined effects of shoaling and refraction do that the waves become steeper, until they break on the bar. The subscript "br" is used to indicate characteristics of a given variable at the line of breaking. The broken waves pass over the crest of the bar to the deeper water of the trough where the process of wave breaking is reduced or completely stopped. As the waves further propagate towards the beach, they are shoaled and refracted until they eventually break on the inner beach.

Under these conditions, a longshore current is generated by the breaking waves. The driving force for the

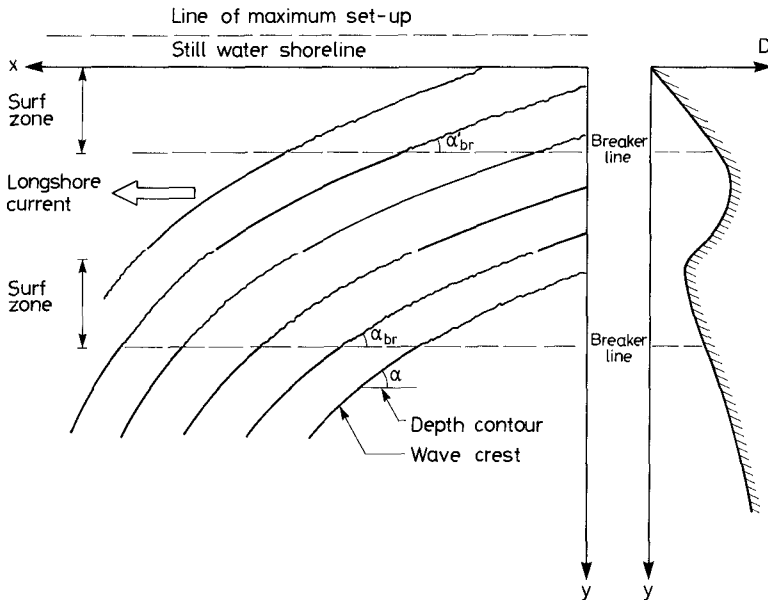


Figure 1. Definition sketch for uniform case.

current is provided by the cross-shore gradient of the shear component of the radiation stress tensor S_{xy} . Since the value of $\partial S_{xy} / \partial y$ is directly proportional to the rate of dissipation of wave energy (Longuet-Higgins, 1972), the forcing term and therefore the induced current will be greater where the dissipation of wave energy is more intense, i.e. in the vicinity of the lines of breaking.

The waves also cause a deviation of the mean water surface from the still water level. Seaward of the breaker line a depression of the mean water level or "set-down" exists, whereas a raise of the water surface with respect to the still water level or "set-up" appears in the surf zone.

As an example the velocity profile of the depth-integrated longshore current calculated over a bar-trough profile is shown in Fig. 2.

The calculation have been made for irregular waves, and the wave conditions have been determined by the model of Battjes and Janssen (1978) for the transformation of Rayleigh distributed waves, with the breaker index given by Battjes and Stive (1985).

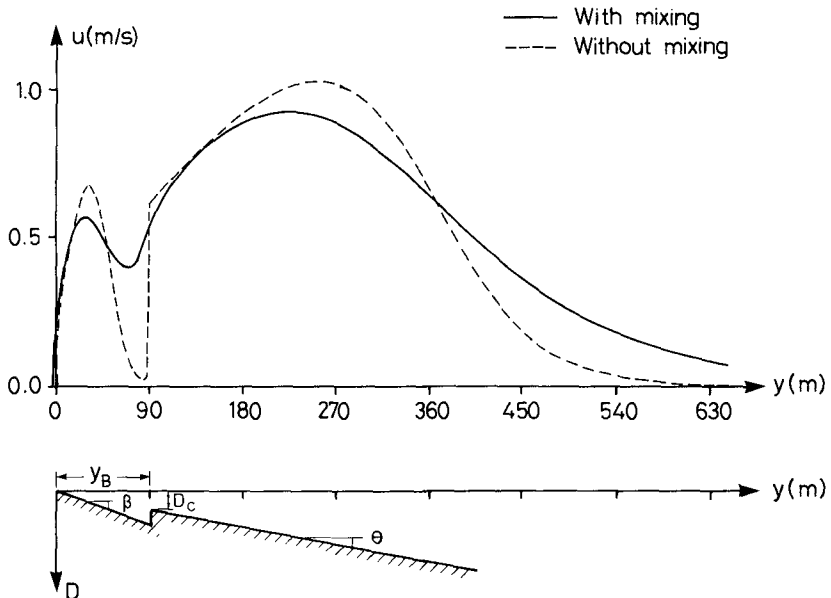


Figure 2. Calculated profiles of longshore current, and the bar-trough profile.

Refraction was determined by application of Snell's law using the peak period of the irregular waves, and disregarding the influence of the currents on wave refraction. Bottom friction was modelled according to Fredsøe (1984), and the turbulent stresses were represented by the usual gradient diffusion of momentum, with the coefficient for lateral exchange of momentum given by Battjes (1983). More details about the representation of the forcing terms can be found in Zyserman (1989).

The variables were chosen as: deep water wave height $H_{rms,0} = 1.2$ m, peak wave period $T_p = 7.5$ s, mean direction of wave propagation in deep waters $\alpha_0 = 45^\circ$, distance from still water shoreline to the crest of the bar $y_B = 90$ m, still water depth over the bar $D_c = 1$ m, slope of the inner beach $\tan(\beta) = 0.02$, slope of the seaward face of the bar $\tan(\theta) = 0.01$, and mean diameter of the bed material $d = 0.20$ mm. The profile labeled as "without lateral mixing" in Fig. 2 was determined disregarding the cross-shore exchange of momentum.

Hydrodynamics in the non-uniform condition

Figure 3 shows the non-uniform coastal geometry. The cross section through the bar is similar to the uniform profile considered above, but the bar is interrupted by rip channels of width W_H and depth D_H , so that the length of the bar between adjacent holes is L_B . The rip channels are taken to have a rectangular section, where they cross the bar.

The waves still break on the bar, but the water depth in the channels is so large that the wave breaking here is much less intense than on the bar, if the waves break at all. The tendency to build up the wave set-up is therefore much stronger over the bars than in the channels.

This means that the mean water level is higher behind the bar than at the holes, and that a pressure gradient directed towards the rip channels exists. This pressure gradient will accelerate the mass of water at the trough in the longshore direction, until it turns seaward and flows through the holes in the form of a rip current. The amount of water discharged by the rips is compensated by the water flowing over of the bar into the trough.

The wave-induced currents can be described by means of depth-integrated equations for conservation of x-momentum and of y-momentum and the continuity equation. In the general form these equations read:

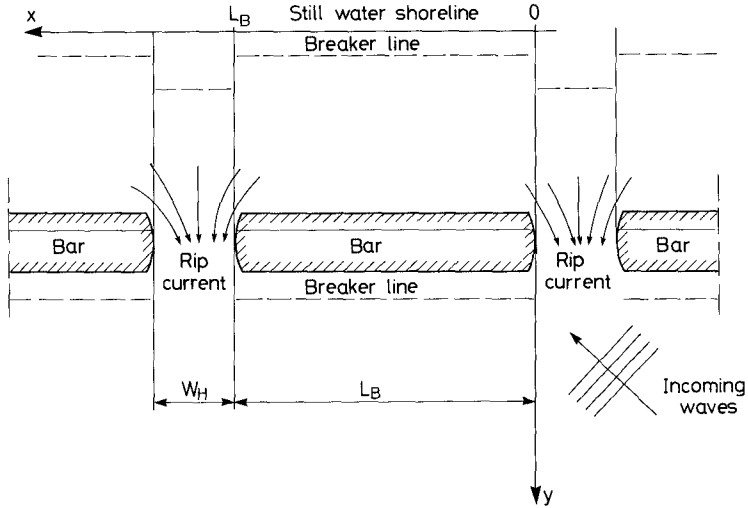


Figure 3. Definition sketch for the non-uniform case.

$$\rho h \left(\frac{\partial U}{\partial t} + U \frac{\partial U}{\partial x} + V \frac{\partial U}{\partial y} + g \frac{\partial \bar{\eta}}{\partial x} \right) + \frac{\partial S_{xx}}{\partial x} + \frac{\partial S_{xy}}{\partial y} - \frac{\partial T_{xx}}{\partial x} - \frac{\partial T_{xy}}{\partial y} + \bar{\tau}_{bx} = 0 \tag{1}$$

$$\rho h \left(\frac{\partial V}{\partial t} + U \frac{\partial V}{\partial x} + V \frac{\partial V}{\partial y} + g \frac{\partial \bar{\eta}}{\partial y} \right) + \frac{\partial S_{xy}}{\partial x} + \frac{\partial S_{yy}}{\partial y} - \frac{\partial T_{xy}}{\partial x} - \frac{\partial T_{yy}}{\partial y} + \bar{\tau}_{by} = 0 \tag{2}$$

$$\frac{\partial \bar{\eta}}{\partial t} + \frac{\partial (hU)}{\partial x} + \frac{\partial (hV)}{\partial y} = 0 \tag{3}$$

where U and V are the time-mean and depth-averaged components of the flow, t is time, h is the total depth $h = D + \bar{\eta}$, D is the local depth measured from the still water level and $\bar{\eta}$ is the water surface elevation, g is the acceleration of the gravity, S_{xx} , S_{xy} , and S_{yy} are the longshore, shear, and cross-shore components of the radiation stress tensor respectively, T_{xx} , T_{xy} , and T_{yy} are the analogous values of the Reynolds stresses produced by the turbulence, and $\bar{\tau}_{bx}$ and $\bar{\tau}_{by}$ are the components of the resulting bed shear stress over a wave period.

Solution of equations (1), (2), and (3) gives the three variables U, V , and $\bar{\eta}$ in the domain of interest.

A numerical solution of equations (1) to (3) requires large and laborious calculations, and considerable amounts of computing time. It has therefore been preferred to adopt some physically well based simplifying assumptions, in order to reduce the computations involved in the solution. This has been done because a large number of study cases involving different wave characteristics and shore configurations was to be analyzed.

The assumptions adopted are listed below. A detailed discussion of the procedure is given by Zyserman (1989).

- A steady state is considered.
- The diffusion of momentum due to turbulent fluctuations of the velocity is not taken into account.
- It is assumed that the wave characteristics are uniform alongshore between two holes.
- The cross shore discharge of water per unit length over the crest of the bar produced by the breaking waves q_w is given by

$$q_w = h_c V = h_c \sqrt{2g(\bar{\eta}_0 - \bar{\eta})} \quad (4)$$

according to Deigaard (1986). $\bar{\eta}_0$ is the value of the set-up for the uniform situation, $\bar{\eta}$ is the real value of the set-up, and h_c is the mean-water depth over the crest of the bar.

- It is assumed that the cross-shore component of the current V varies linearly behind the bar, and that cross shore discharge is constant offshore the bar:

$$V = V_{\max} y / y_B \quad \text{for } 0 < y < y_B \quad (5)$$

$$hV = \text{constant} \quad \text{for } y > y_B \quad (6)$$

V_{\max} being the maximum value of V in the through just behind the bar crest.

- The contribution of the wave set-up $\bar{\eta}$ to the total depth h is disregarded, so now $h = D$.
- The mean water surface behind the bar is horizontal.

With these simplifications, the set of three equations can be reduced to the following two partial differential equations:

$$\rho D \left(U \frac{\partial U}{\partial x} + V \frac{\partial U}{\partial y} + g \frac{\partial \bar{\eta}}{\partial x} \right) + \frac{\partial S_{xy}}{\partial y} + \bar{\tau}_{bx} = 0 \quad (7)$$

$$\frac{\partial(DU)}{\partial x} + \frac{\partial(DV)}{\partial y} = 0 \quad (8)$$

which can be solved by an iterative procedure.

The numerical solution is performed using a finite difference formulation of Eqs. (7) and (8). The unknowns are determined in a domain having the length of the bar L_B in the x-direction, and being bounded by the still-water shoreline and an offshore limit y_L , which is taken as the position where the value of $\partial S_{xy}/\partial y$ becomes smaller than a chosen limiting value.

The boundary conditions for the variables are:

$$U = 0 \quad \text{for } y = 0 \quad \text{and} \quad 0 < x < L_B \quad (9)$$

$$U = 0 \quad \text{for } y = y_L \quad \text{and} \quad 0 < x < L_B \quad (10)$$

$$V = 0 \quad \text{for } y = 0 \quad (11)$$

$$DV = \text{constant} \quad \text{for } Y_B < y < y_L \quad (12)$$

The boundary condition for $\bar{\eta}$ is determined from the expansion-loss of the rip current flowing through the rip channels:

$$\bar{\eta}_H = \frac{|\bar{v}_{rip}|^2}{2g} \quad (13)$$

The subscript "H" indicates a value of the variable determined at the hole, \bar{v}_{rip} is the velocity in the rip channel.

Figure 4 shows the longshore current velocity profiles obtained for $H_{rms,0} = 1.2$ m, $T_p = 7.5$ s, $\alpha_0 = 45^\circ$, $\tan(\beta) = 0.02$, $\tan(\theta) = 0.01$, $D_c = 1$ m, $L_B = 180$ m, $Y_B = 90$ m, $W_H = 22.5$ m, $D_H = 3$ m, and $d = 0.2$ mm. The velocity in the rip channel equals 1.22 m/s in this situation.

The results obtained can be compared with the velocity profile without lateral mixing of Fig. 2. The same data were used in the two examples, so the observed differences are due to the presence of the rip currents.

A striking difference is the smoothness of the velocity profiles in the case of non-uniform flow conditions, even when the effect of turbulent momentum transfer is disregarded. This is due to the cross shore flow which effectively transfers longshore momentum in the

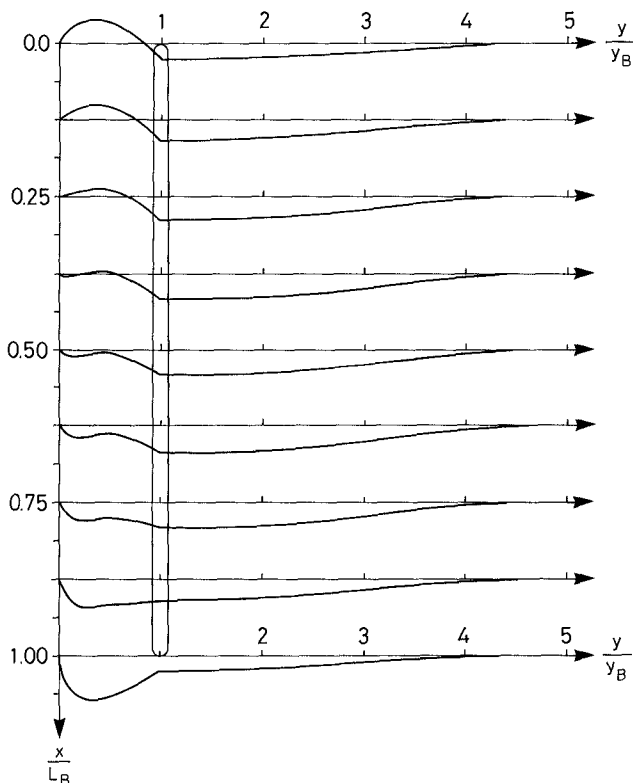


Figure 4. Calculated longshore current flow in presence of rip currents.

cross shore direction. The shore parallel velocities on the bar are reduced because water from offshore continuously is moving into the field of driving forces from the wave breaking. Similarly the longshore momentum is convected into the trough, giving a continuous velocity profile.

The flow model which gives the flow field and the wave conditions in the near-shore area is used as basis for the sediment transport calculations.

3. The sediment transport model

The model used to calculate sediment transport has been described in detail in a series of papers by Fredsøe, Andersen, and Silberg (1985), and Deigaard, Fredsøe, and Hedegaard (1986a, 1986b), so only the main features of the model are presented here.

The total load transport of sediment per unit width q_t is determined as the sum of two contributions: the bed load transport q_b and the suspended load transport q_s .

The instantaneous bed load transport is related to the instantaneous dimensionless bed shear stress or Shield's parameter θ according to the findings of Engelund and Fredsøe (1976). θ is determined at each instant from the model developed by Fredsøe (1984) for the boundary layer in combined wave-current situations. The mean value of the bed transport during a wave period is then found by integration of the instantaneous values.

The concentration profile of suspended sediment is determined at every instant by solving the diffusion equation for the sediment. The turbulent exchange factor for the suspended sediment is taken equal to the eddy viscosity of the flow. The turbulent eddy viscosity is determined as the combination of contributions from the current boundary layer, the wave boundary layer and from the wave breaking.

The mean value of the suspended transport in the direction of the mean current over a wave period is determined by time-averaging the product between the concentration of suspended sediment and the total (current + wave) horizontal velocity in the direction of the current. This product is integrated between the bed level and the water surface to give the transport rate.

4. The prediction of the dimensions of the rip-current system

Based on the sediment transport calculations the dimensions of the bar-rip channel system is determined. The dimensions considered are: the bar length L_B , the width of the rip channel W_H and the depth D_H of the rip channel. The geometry of the system is then determined for a given bar profile, sediment characteristics and incoming wave conditions. Equilibrium conditions are assumed and no erosion or deposition must occur. The basis for the analysis are the sediment budgets for two cells, Fig. 5.

The sediment transported in the trough by the longshore currents flowing toward the rip must equal the amount of sediment flushed through the hole by the rip. This condition can be written as:

$$Q_{S,rip} = Q_{S,end} \quad (14)$$

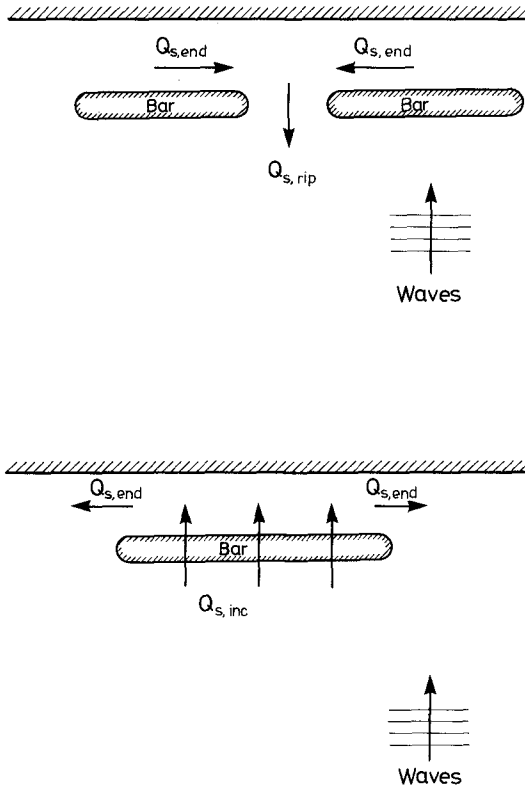


Figure 5. Sediment balances.

The total amount of sediment transported over the bar must be equal to the amount of sediment transported toward the rip, giving:

$$Q_{S,inc} = Q_{S,end} \quad (15)$$

where the the sediment transport per unit width q_t has been integrated along the bar, and across the rip channel and the trough, in order to determine $Q_{S,inc}$, $Q_{S,rip}$, and $Q_{S,end}$, respectively.

These two conditions make it possible to determine the bar length L_B and rip depth D_H for a given value of the rip width W_H . The solution is made by iteration, calculation the ratio between the in- and outgoing sediment of each cell. An example of the calculations is shown in Fig. 6 with the following input data: $H_{rms,0} = 1.2$ m, $T_p = 7.5$ s, $\alpha_0 = 0^\circ$, $\tan(\beta) = 0.02$, $\tan(\theta) = 0.01$, $D_c = 1$ m, $L_B = \text{variable}$, $Y_B = 90$ m, $W_H = 22.5$ m, $D_H = \text{variable}$, and

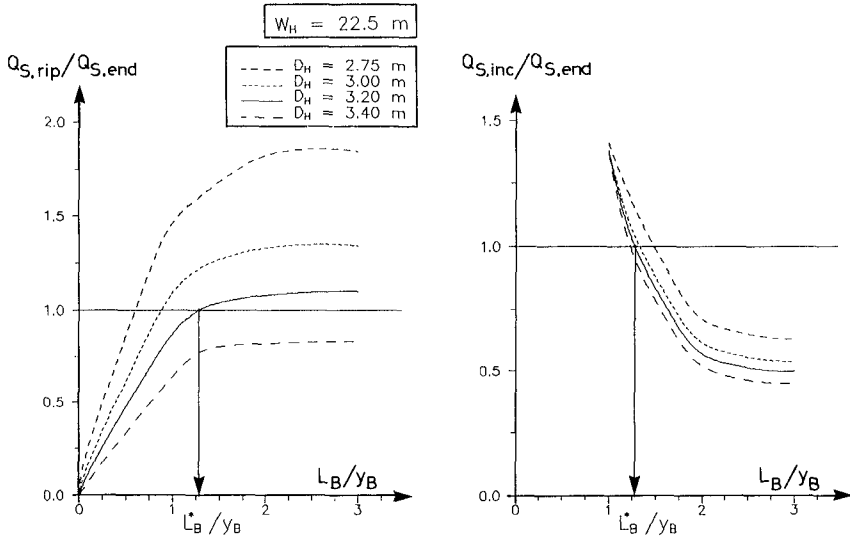


Figure 6. The determination of the length of the bar.

$d = 0.2$ mm. The solution in this case is found for $D_H = 3.2$ m and $L_B = 1.3 y_B = 120$ m.

When this method is applied for different widths of the hole W_H , it is possible to obtain a set of curves representing the equilibrium length of the bar L_B , the depth of the hole D_H , and the total sediment transport of the rip $Q_{S,rip}$ as functions of the width of the hole W_H , for a given wave situation, bar-trough profile, and bed material. Fig. 7 shows the equilibrium value of $Q_{S,rip}$ and D_H as function of and the width of the hole. The data are similar to Fig. 6, except for the wave approach angle which is now $\alpha_0 = 45^\circ$. The equilibrium bar length is very insensitive to changes in W_H being constant about $L_B = 1.37 y_B = 123$ m.

$Q_{S,rip}$ is a measure of the flushing capacity of rip channel, and the situation with maximum $Q_{S,rip}$ can therefore be taken as the optimal configuration where the rip current has the highest capacity to flush sediment in the seaward direction. This criterion gives a rip channel width of $W_H = 25$ m and a depth of $D_H = 2.8$ m.

A sensitivity analysis has been made to illustrate the influence that the wave height, the wave period, and the diameter of the bed material have on the solution. The situation illustrated in Fig. 7 with $\bar{\alpha}_0 =$

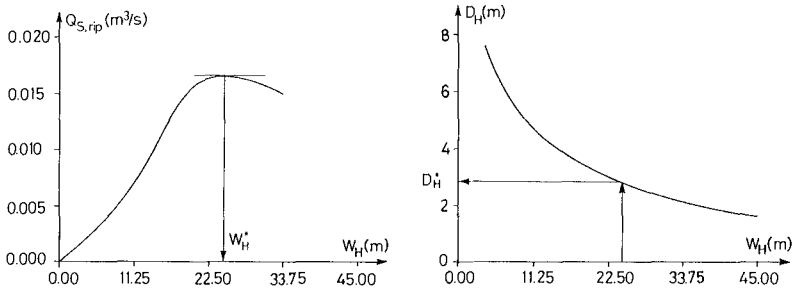


Figure 7. The determination of the dimensions of the rip channels based on $(Q_{S,rip})_{max}$.

45° is taken as Case I, and used as a basis for the comparison. All the other cases are obtained by changing the value of one of the independent variables with respect to its value in this case. Case II is the situation already considered in which the angle of wave incidence was changed to $\alpha_0 = 0^\circ$. In Case III the wave height is taken as $H_{rms,0} = 2$ m. In Case IV the wave period is taken as $T_p = 10$ s, and in Case V the grain size is taken as $d = 0.4$ mm, giving $w = 0.05$ m/s. The results are presented in Table 1.

An alternative criterion for determining the rip channel width has been proposed by Skou and Fredsøe (1990). The idea is that nature should select the

Case	$H_{rms,0}$ (m)	T_p (s)	$\bar{\alpha}_0$ (°)	d (mm)	L_B (m)	W_H (m)	D_H (m)
I	1.2	7.5	45	0.20	123	25	2.80
II	1.2	7.5	0	0.20	120	25	3.00
III	2.0	7.5	45	0.20	146	11	5.25
IV	1.2	10.0	45	0.20	126	23	3.15
V	1.2	7.5	45	0.20	123	43	1.65

$$D_C = 1 \text{ m} \quad Y_B = 90 \text{ m} \quad \tan(\beta) = 0.02 \quad \tan(\theta) = 0.01$$

Table 1. The equilibrium dimensions as function of the input parameters.

condition giving the maximum slope of the $Q_{S,rip} - W_H$ curve, as this represents the maximum strength of the response of the system to a perturbation imposed on it. If for instance the width of the channel is reduced by a random infill of sediment, then the increase of $Q_{S,rip}$ due to the decrease in W_H is a measure of how fast the rip channel will erode to reestablish the equilibrium. Fig. 8 illustrates the application of this criterion to Case III, giving $W_H = 17.6$ m and $D_H = 3.6$ m.

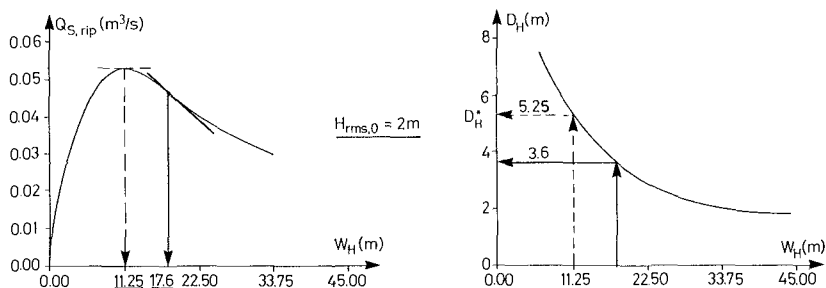


Figure 8. Determination of the dimensions of the rip channels based on $(dQ_{S,rip}/dW_H)_{max}$.

5. Conclusions

A method for determining the features of a stable shore when a rip-current system exists on a bar-trough shore profile has been developed. The calculated characteristics of the coast comprise the length of the bar or spacing between rip currents L_B , and the dimensions of the rip channel: width W_H and depth D_H .

The method reproduces some characteristics of the rip-current systems that can be observed in nature fairly well, such as the larger distance between rip channels and the deeper holes associated with heavy breakers, see Case III of Table 1.

No perceptible influence of the grain diameter on the length of the bar was found, but coarser grains led to wider and shallower holes. It was also determined that waves of normal incidence produce slightly shorter bars and deeper holes than waves of oblique incidence.

6. References

- Battjes, J.A. and Janssen, J.P.F.M. (1978): Energy loss and set-up due to breaking of random waves. *Procs. 16th. Int. Conf. on Coast. Eng., Hamburg, Vol. 1*, pp. 569-587.
- Battjes, J.A. and Stive, M.J.F. (1985): Calibration and verification of a dissipation model for random breaking waves. *Jour. of Geophys. Res., Vol. 90, No. C5*, pp. 9159-9167.
- Battjes, J.A. (1983): Surf zone turbulence. *Procs. of Seminar on Hydrodynamics of Waves in Coastal areas. I.A.H.R., Moscow, U.S.S.R.*, pp. 137-140.
- Deigaard, R. (1986): Longshore current behind bars. *Prog. Rep. 64, ISVA, Techn. Univ. of Denmark*, pp. 25-29.
- Deigaard, R., Fredsøe, J. and Hedegaard, I.B. (1986a): Suspended sediment in the surf zone. *Jour. of Waterway, Port, Coast. and Ocean Eng., ASCE, Vol. 112, No. 1*, pp. 115-128.
- Deigaard, R., Fredsøe, J. and Hedegaard, I.B. (1986b): Mathematical model for littoral drift. *Jour. of Waterway, Port, Coast. and Ocean Eng., ASCE, Vol. 112, No. 3*, pp. 351-369.
- Engelund, F. and Fredsøe, J. (1976): A sediment transport model for straight alluvial channels. *Nordic Hydrology, Vol. 7*, pp. 293-306.
- Fredsøe, J. (1984): Turbulent boundary layer in wave-current motion. *Jour. of Hydr. Eng., ASCE, Vol. 110*, pp. 1103-1120.
- Fredsøe, J., Andersen, O.H., and Silberg, S. (1985): Distribution of suspended sediment in large waves. *Jour. of Waterway, Port, Coast. and Ocean Eng., ASCE, Vol. 111, No. 6*, pp. 1041-1059.
- Longuet-Higgins, M.S. (1972): Recent progress in the study of longshore currents. In: *Waves and Beaches and Resulting Sediment Transport*. Edited by R.E. Meyer. Academic Press, pp. 203-248.
- Skou, A. and Fredsøe, J. (1990): Application of the Escoffier curve to determine cross section areas of tidal inlets. *Prog. Rep. 71, ISVA, Techn. Univ. of Denmark*, pp. 51-60.
- Zyserman, J.A. (1989): Characteristics of stable rip current systems on a coast with a longshore bar. *Series Paper 46, ISVA, Techn. Univ. of Denmark*, 178 pp.
- Zyserman, J.A., and Fredsøe, J. (1988). The influence of rip currents on the longshore sediment transport. *Procs. of the 2nd Int. Symposium on Wave Res. and Coastal Eng. Published by the Special Research Group 205 of the University of Hannover*, pp. 125-138.

CHAPTER 73

SCALE EFFECTS IN BREAKING WAVES

Toumazis¹, A.D. and Anastasiou², K.

Abstract

A breaking wave model, which is partly physical and partly analytical, is proposed. This model is based on observations that up to a certain moment the wave presents a long, smooth, horizontal, cylindrical edge, which then segments due to surface tension effects. A disturbance on a cylindrical surface, withdrawn from the influence of gravity, becomes unstable when its wavelength exceeds the circumference of the cylinder. The rate of growth of the instability, is a function of the radius of the cylinder and the wavelength of the disturbance. Using the theory describing the evolution of the assumed hyperbolic shape of the tip of a breaking wave, the radius of the cylindrical edge is approximated to the radius of curvature of the hyperbola. The model describes the three-dimensional evolution of the curling wave crest. Scale effects are then derived which show good agreement with experimental results.

Introduction

During the overturning process of a breaking wave, the plunging jet is in a state of free fall. Assuming that the wave is two-dimensional, with no transverse inertial forces, and air friction is negligible, surface tension is the predominant force acting on the fluid particles.

Under similar ambient conditions, the behaviour of the overturning face of the breaking wave is the same to that of a liquid cylinder. If a liquid cylinder is constructed and liquid is drawn out gradually, the diameter of the cylinder decreases until the length of the cylinder becomes just about three times as great as its diameter. Soon afterwards instability begins, and the cylinder alters its form; it narrows at the waist, so passing into an unduloid and the deformation progresses quickly until the cylinder breaks in two, and its halves become portions of spheres. This behaviour is due to surface tension effects. Plateau (1863) established experimentally that the distance between the spheres is proportional to the diameter of the cylinder. In the case of a very long cylinder, when many spheres are formed, the parts between consecutive

¹ Engineer, Noble Denton Consultancy Services, 131 Aldergate Street, London EC1A 4EB, U.K.

² Lecturer, Civil Engineering Department, Imperial College of Science, Technology and Medicine, London SW7 2BU, U.K.

dilations or constrictions undergo identically and simultaneously the same modifications as described above (fig. 1).

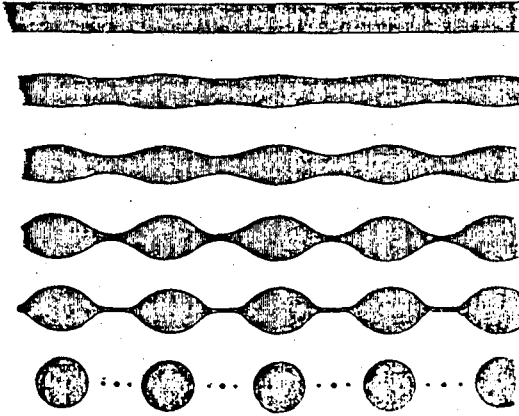


Fig. 1 Stages of the segmentation of a liquid cylinder

Plateau (1863) also noted that the phenomenon of the formation of lines and their resolution into spherules is not confined to the case of the rupture of the equilibrium of liquid cylinders; it is always manifested when one of the liquid masses, whatever may be its figure, is divided into partial masses. The phenomenon is also produced when liquids are submitted to the free action of gravity.

Worthington (1908) discussed the effect of surface tension on breaking waves. He observed that a wave that has just impetus enough to curl over and break, up to a certain moment it presents a long, smooth, horizontal, cylindrical edge, from which, at a given instant, are shot out a large array of little jets which speedily break into foam, and at the same moment the back of the wave, hitherto smooth, is seen to be furrowed and combed (fig. 2). He proposed that these jets are due to the segmentation of the cylindrical rim according to Plateau's law, and the ridges between the furrows mark the lines of easier flow determined by the jets. Further observations of this phenomenon were made by Toumazis (1989) from video and photographic records.



Fig. 2 Diagrams of a breaking wave (Worthington 1908)

Regarding scale effects in breaking waves, Fuhrboter (1986) studied impact loading by breaking waves on slopes and found that scale effects do exist.

Skladnev and Popov (1969) measured impact pressures induced by waves breaking on a slope in a more systematic way. Waves of the same steepness but of wave height ranging between 3 and 120 cm were tested. Prototype conditions were considered the ones with the 120 cm wave height. The results were presented in graphical form (fig. 3). The abscissa is the ratio of the model to the prototype (120cm) wave heights and the ordinate is the ratio of the model to the prototype impact pressure factor K_p , defined as the ratio of the measured pressure to the static pressure ρgh , where h is the wave height. From these results it is evident that, it is not permissible to use Froude criteria to scale up experimental results on breaking waves with model breaker height less than about 0.5m.

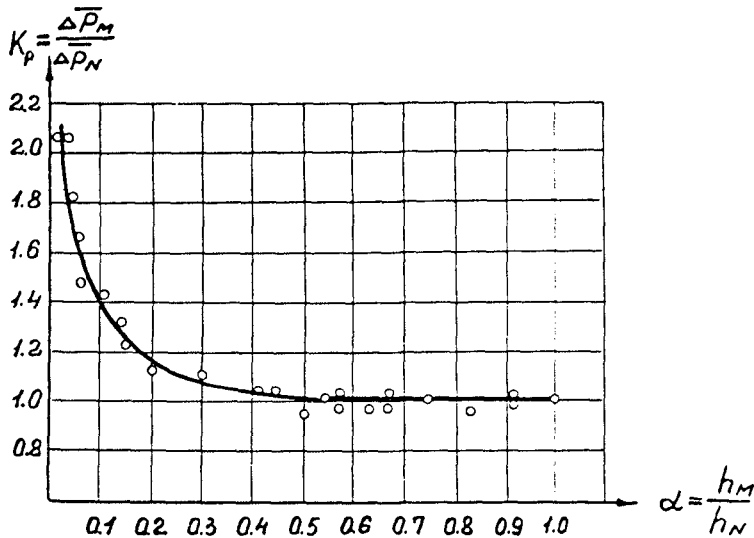


Fig. 3 Effects of wave height on the relative wave pressure value in the wave impact zone. (Skladnev and Popov, 1969)

Stive (1984) reached the same conclusion, stating that in order to avoid disturbing influence of the surface tension on the amount of air absorption in the broken wave, the incident wave height in the model must exceed approximately 0.5m.

The primary objective of this work is to formulate a model for the effects of surface tension on breaking waves and to establish a quantitative threshold beyond which scale effects are negligible. It will be shown that this threshold agrees well with available experimentally derived indicators.

Surface Tension Effects on Free Falling Liquid Cylinders

Any small disturbance on a liquid cylinder may be considered, according to Fourier's theorem, as the summation of a series of sinusoidal wave disturbances. The surface area of the cylinder will change whereas the volume of the liquid

remains the same. As surface tension results in contracting the volume to the minimum possible surface area, an increase of the surface area due to the disturbance will be opposed by surface tension, whereas a contraction of the surface will be enhanced. The criterion for stability is therefore the change of surface area for a given volume after the appearance of a small disturbance. In the following derivations the effects of only one sinusoidal disturbance will be considered, bearing in mind that the principle of linear superposition must be applied when a full range of Fourier components must be taken into account.

If a cylinder with radius r is slightly deformed so that

$$y = r + a \cos \frac{2\pi}{L} x \quad (1)$$

where x is measured parallel to the axis, y is the distance normal to the axis, a is the amplitude of the deformation, and L is the wavelength of the deformation. Plateau (1863) showed that the cylinder is stable if

$$L < 2 \pi r \quad (2)$$

The theory is hereby extended to consider a sector of a liquid cylinder with a slight sinusoidal deformation

$$y = r + a \cos(kx) \quad , \quad \text{where } k=2\pi/L \quad (3)$$

The mean surface area between two consecutive crests, σ , is then

$$\sigma = r \theta + \frac{1}{2} r \theta a^2 k^2 \quad (4)$$

where θ is the angle between the radii of the sector. Assuming the volume of water in the cylindrical sector remains the same, the mean volume S is

$$S = \frac{1}{2} \theta r^2 + \frac{1}{4} \theta a^2 \quad (5)$$

Combining the two expressions for σ and S ,

$$\sigma = \sqrt{2 \theta S} + \frac{\theta}{4} \frac{a^2}{r} (k^2 r^2 - 1) \quad (6)$$

The surface area of the undisturbed liquid ($a=0$) is,

$$\sigma_0 = \sqrt{2 \theta S} \quad (7)$$

Therefore, the change in the surface area is,

$$\sigma - \sigma_0 = \frac{\theta}{4} \frac{a^2}{r} (k^2 r^2 - 1) \quad (8)$$

If $k.r > 1$ the surface area increases and hence the liquid is stable, while if $k.r < 1$ the surface area decreases and instability results.

The obtained result is independent of the angle θ . The cylinder is a special case of the considered case, with $\theta=2\pi$. Plateau (1864) and Rayleigh (1878) reached the same result by considering the cylindrical shape as the initial condition.

The mode of falling away from unstable equilibrium necessarily depends on the small deformations to which the system is subjected. In an ideal situation of no deformations, even if $L>2\pi r$ the cylinder would still be in equilibrium. In practice however, some kinds of disturbances are always present. Although all disturbances corresponding to $L>2\pi r$ are unstable, the rate of change of the shape due to each wavelength, L is different.

Assuming that the amplitude of the disturbance, a , once unstable, grows exponentially with time, that is

$$a = a_0 e^{qt} \quad (9)$$

where a_0 is the initial amplitude, Lord Rayleigh (1878) showed that for a cylindrical surface,

$$q^2 \approx \frac{T}{\rho r^3} \left[x^2 - \frac{9}{8} x^4 + \frac{7}{24.3} x^6 - \frac{25}{210} x^8 + \frac{91}{211.3.5} x^{10} \right] \quad (10)$$

where $x=kr=2\pi r/L$. For given r , all disturbances with wavelength, L , less than $2\pi r$ ($2\pi r/L>1$) are stable. For L greater than $2\pi r$ the disturbances grow with time, the fastest growing one having $L\approx 9r$.

Gravity and Inertial Effects

The mathematical description of the free surface area of a two-dimensional overturning wave, as governed by inertial and gravitational forces, was presented by Longuet-Higgins (1980). A frame of reference was used in which the x -axis is longitudinal horizontal, in the same direction as the propagation of the wave, the y -axis is transverse horizontal and the z -axis is vertical. The saddle-point, the point where the pressure gradient vanishes, follows a free fall trajectory. Its motion therefore satisfies

$$x = x_1 + U (t-t_1) \quad (11)$$

$$\text{and} \quad z = z_1 - 1/2 g (t-t_1)^2 \quad (12)$$

where x_1 , z_1 , t_1 and U define the initial coordinates, time and horizontal velocity respectively. The tip of the wave is approximated by the hyperbola

$$\frac{x^2}{\alpha^2} - \frac{z^2}{\beta^2} = 1 \quad (13)$$

Taking γ to represent the angle between the asymptotes, δ the angle of rotation of the principal axes, and r the radius of curvature at the tip of the breaker (fig. 4),

$$\tan \frac{\gamma}{2} = \frac{\beta}{\alpha} \quad (14)$$

$$r = \left| \frac{\beta^2}{\alpha} \right| \quad (15)$$

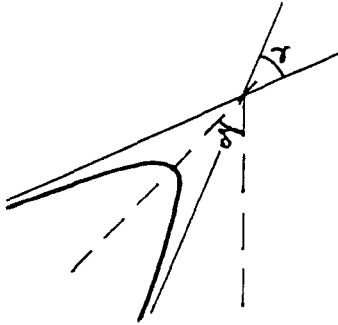


Fig. 4 Hyperbola approximating the tip of the wave.

Given the initial conditions, the two-dimensional evolution of the crest of the wave as depicted in Fig. 5 may be completely described, as shown by Longuet-Higgins (1980). It should be noted that in this reference there is a misprint in equation 5.8; the term f^2 should be included in the numerator of the right hand side.

The Proposed Model for the Breaker

Worthington's proposition (1908) is adopted as the fundamental assumption on which the presented model is based. That is, the crest of the overturning wave presents a long, smooth, horizontal, cylindrical edge.

The horizontal cylindrical edge, in the state of free fall, is modified in a manner governed by surface tension principles. The radius of the cylindrical edge is assumed to be independent of surface tension effects and only governed by inertial and gravitational forces. The formulations derived by Longuet-Higgins (1980) are therefore applicable to this problem. The radius of the cylindrical edge (Worthington, 1908) is equated to the radius of curvature of the hyperbolic edge of the wave (Longuet-Higgins, 1980). The proposed model is therefore a combination of two distinct analytical descriptions. The problem is studied by considering the evolution of monochromatic sinusoidal disturbances on the tip of an overturning wave.

Consider a small sinusoidal disturbance of amplitude a_0 , and wavelength L , on a liquid cylindrical edge. Surface tension considerations suggest that the amplitude of the disturbance will start growing when the wavelength, L , exceeds $2\pi r$, with an exponential rate of growth, $a_t = a_0 \exp(qt)$ (equation 9). The value of q is obtained from equation 10. For a cylindrical edge with a continuously varying radius, r , it is more appropriate to rearrange equation 9 so that,

$$a_{t+\delta t} = a_t \exp(q \delta t) \quad (16)$$

Given the initial conditions of the overturning wave, that is the conditions at breaking point, the evolution of the breaker shape is computed. For any time t , the values of the variables δ and γ as defined by Longuet-Higgins (1980) are thus obtained. These values together with the coordinates of the point of intersection of the axes of the hyperbola, which are determined from equations 11 and 12 describe completely the evolution of the tip of the breaker in the two-dimensional plane of the wave. The radius of curvature of the tip of the breaker is equal to

$$r = \left| -\frac{\beta^2}{\alpha} \right| = r_0 \tan^{3/2}(\gamma/2) \quad (17)$$

Assuming that the rate of increase of the amplitude of a disturbance on the tip of the breaker is the same as that for a cylinder, as derived by Rayleigh (1878), the amplitude of a disturbance of wavelength L is then obtained using equations 16 and 10.

Figure 5 shows the time dependent characteristics of six distinct sinusoids with the same initial amplitude. It is clear that, as the radius of curvature of the curling wave crest decreases with time, the long disturbances start growing first. The rate of growth of the amplitude decreases with increasing wavelength of the disturbance (eqn. 10). A long wavelength starts growing early and slowly, whereas a short wavelength starts growing late and rapidly. There is consequently a particular wavelength which attains the maximum amplitude at the instant of hitting the water surface. This predominant wavelength is therefore a function of the type and size of the breaker (initial radius of curvature, breaker height and horizontal velocity) and the form of the initial disturbance.

Short wavelengths are in general associated with small breaker heights and small radii of curvature at the tip of the breaker. The duration of overturning is short. Sinusoidal disturbances of long wavelengths although unstable, grow very slowly and the short duration of overturning does not allow them to become dominant. The smaller the breaker, the shorter the predominant wavelength.

On the other hand, big breakers have large radii of curvature even at plunging point. Disturbances of short wavelengths do not become unstable. As a result, the bigger the breaker, the longer the predominant disturbance.

Derivation of Scale Effects from the Proposed Model

As it has already been noted, in breaking waves apart from the gravitational and inertial effects, surface tension also plays a significant role. In scaling surface tension effects the ratio of the inertial to the surface tension forces must be the same. The Weber number

$$W_e = u \sqrt{(l\rho/T)} \quad (18)$$

must be the same in both prototype and model conditions, where ρ and T are the density and surface tension of the fluid, u and l are velocity and length scales respectively.

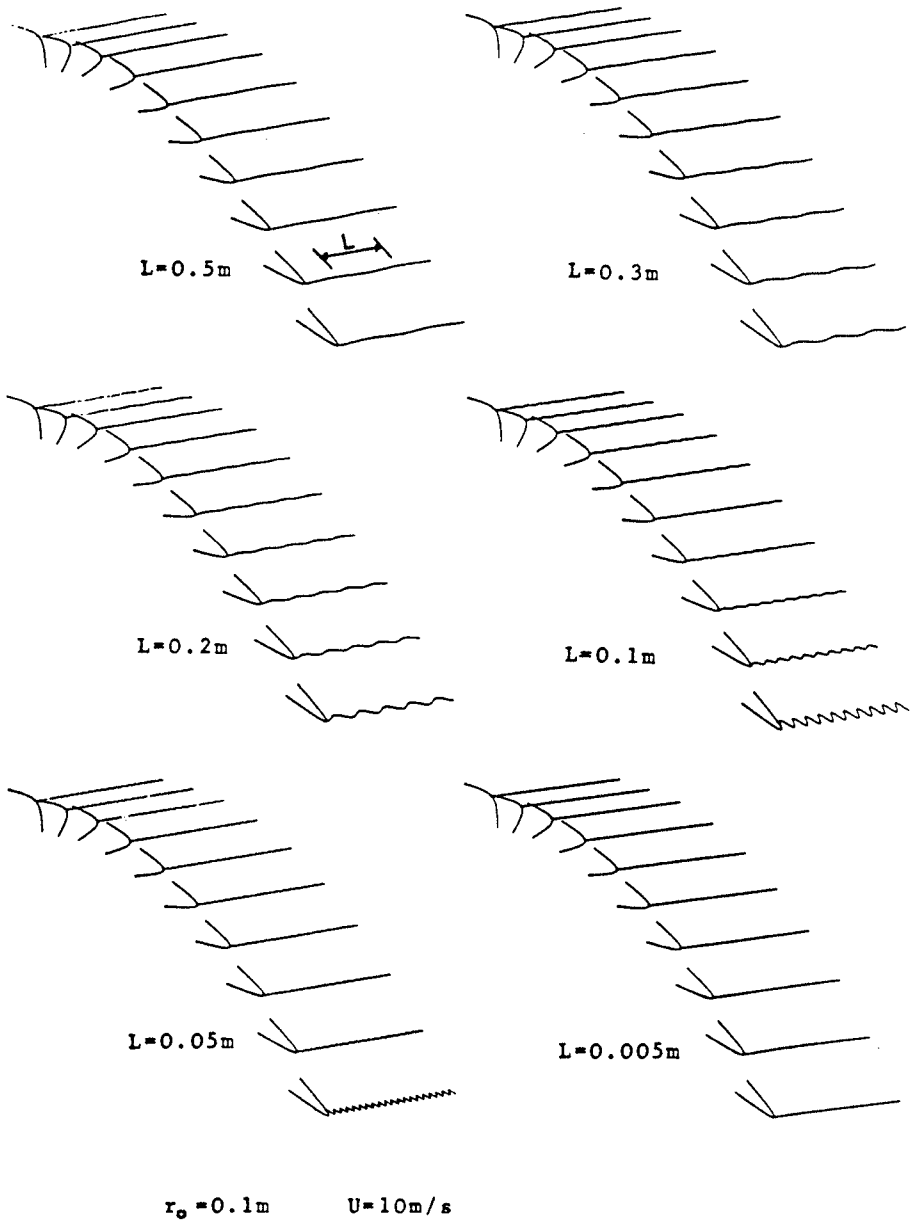


Fig. 5 Evolution of six sinusoids, of different wavelength, on the tip of an overturning wave.

It is evident that the Froude and Weber criteria cannot be satisfied simultaneously. In model tests involving breaking waves, Froude scaling is usually the adopted criterion, as it models satisfactorily the overall conditions, although the details of the breaking process are not fully modelled. It is of vital importance, in the interpretation of the model test results, to know how the non-scaling of surface tension effects affects the prototype conditions.

The developed physical/computational model, which takes into consideration both gravitational and surface tension effects, is now used to quantify scale effects in breaking waves. Consider a wave breaking in shallow water (fig. 6), which has the following characteristics

$$\begin{aligned} L_b &\sim T \sqrt{gh} & (19) \\ \text{and } H_b &\sim h & (20) \end{aligned}$$

where \sim means order of, L_b is the wavelength of the breaking wave, T is the wave period, h is the water depth at breaking point, and H_b is the breaker height.

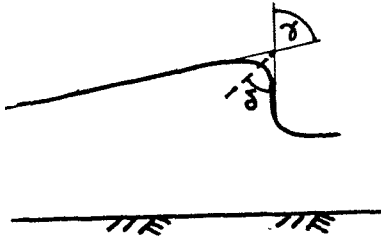


Fig. 6 Breaking wave in shallow water depth.

In order to determine the angle γ when the forward face of the wave becomes vertical, the assumption is made that the backward face of the wave is straight such that,

$$\tan \gamma \sim \frac{L_b}{H_b} = \frac{T\sqrt{gH_b}}{H_b} = T \sqrt{\frac{g}{H_b}} \quad (21)$$

The initial conditions are therefore

$$\gamma_0 \sim \tan^{-1} \left(T \sqrt{g/H_b} \right) \quad (22)$$

$$\delta_0 \sim 1/2 \gamma_0 \quad (23)$$

$$r_0 \sim 1.4 H_b \quad (24)$$

The duration of overturning is equal to the time required for a free fall from height H_b

$$t_b \sim \sqrt{2H_b/g} \quad (25)$$

For a given breaking wave height, H_b , and wave period, T , the evolution of a transverse sinusoidal disturbance on the wave crest, with wavelength L , and amplitude a_0 , is traced up to plunging point. The ratio of the amplitude of the disturbance at plunging point, a_p , to the initial amplitude, a_0 , i.e. a_p/a_0 , is a measure of the surface tension effect on the wave breaking process for the assumed wavelength of initial disturbance.

When the above procedure is followed for a range of wavelengths of disturbance, the maximum value of a_p/a_0 , corresponding to the predominant wavelength of disturbance, is deduced. Any given breaker is therefore associated with a predominant wavelength of disturbance, whose amplitude at plunging point is amplified by the factor a_p/a_0 .

Figure 7 presents the computed values of the ratio a_p/a_0 for a wide range of wave conditions. The variation of this ratio reflects the effects of scaling. A constant value for a_p/a_0 implies that the shape of the breaker does not change between large and small waves.

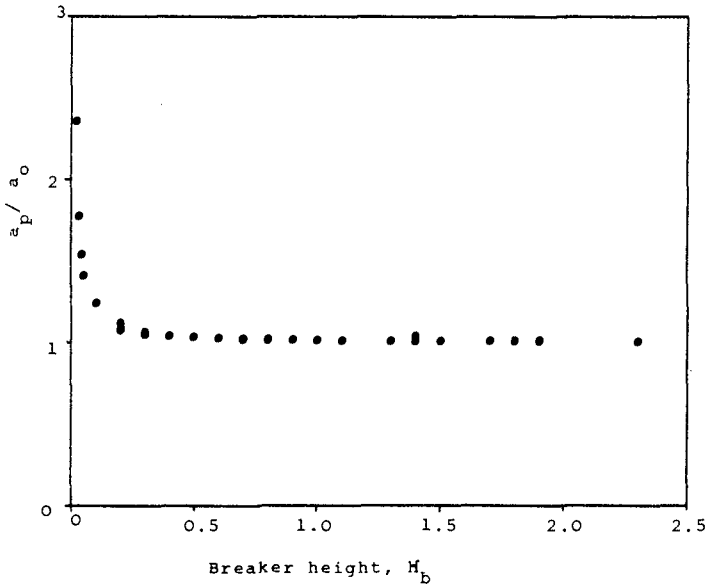


Fig. 7 Model results showing the relative growth of predominant disturbance as a function of breaker height.

It is evident from this plot that, surface tension effects are the same for breaking waves bigger than about 0.5m in height, whilst they become increasingly important for smaller waves. This observation suggests that, assuming the curling face of the wave retains a hyperbolic shape, big waves, which have small curvatures, do not feel the surface tension forces. This is in agreement with the broad characteristics of surface tension; surface tension is a molecular effect which becomes important for high curvatures.

The presented model is in agreement with the experimental results of Skladnev and Popov (1969) and Stive (1984), who both found that scale effects do exist for breaking waves smaller than 0.5m high. The results from the present model and the available experimental observations, however, appear to disagree with regard to the following point. The present model predicts no segmentation of the tip of the wave for big waves, whilst the experimental results suggest that big waves are highly aerated and spayed, whilst in small waves aeration is negligible or does not occur at all (Skladnev and Popov,

1969). This apparent contradiction may be justified by considering the 0.5m cut-off point as the point at which the physical process of wave overturning changes. For breaker heights up to 0.5m, the global surface tension effects are more significant than the microscopic ones. For bigger waves, as the results from the proposed model suggest, the global surface tension effects are negligible.

The radius of curvature of an assumed irregularity on the tip of the wave is very small compared to that of the tip of the breaker. When unstable, the short wavelength disturbances grow much faster than the longer ones. These properties imply that, the short sinusoidal transverse disturbances, which are stable from the macroscopic point of view, are now unstable and fast growing. They thus prevail on the tip of the wave. The described process is illustrated in figure 8. The evolution of the same monochromatic disturbance is presented, as predicted from the numerical model, for four different radii of curvature. The fast growth of the disturbance associated with the small radii of curvature is evident. Irregularities on the tip of the breaker, therefore tend to produce closely spaced jets. These jets are easily observed on the curling crest of two-dimensional overturning waves, breaking in both deep and shallow water conditions.

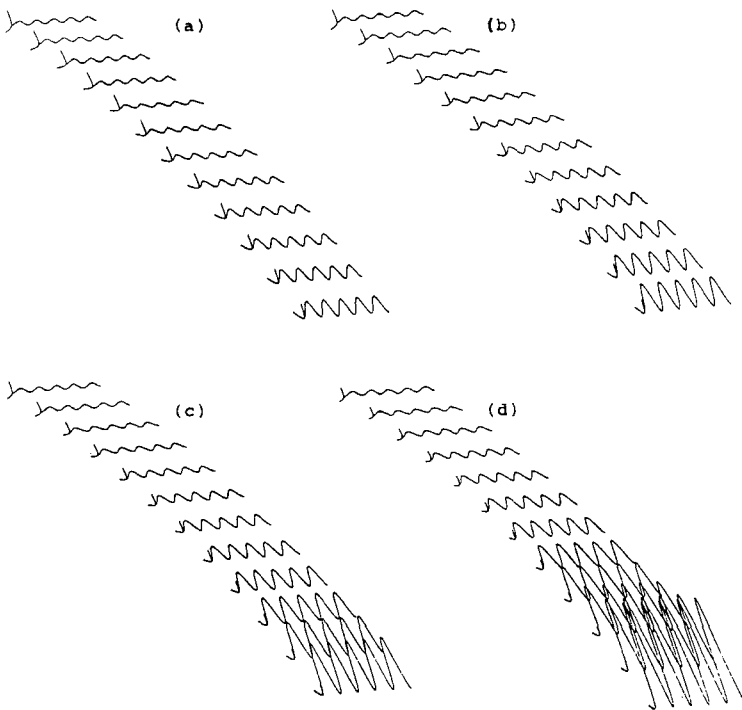


Fig. 8 Evolution of a transverse disturbance ($L=40\text{mm}$), on 4 waves of different curvatures: $r_0 =$ a) 14mm, b) 12mm, c) 10mm, d) 8mm. Time interval = 0.02 seconds.

Critical Assessment of the Proposed Model

The accuracy of any model depends on the validity of the assumptions inherent in the modelling. In the proposed model two distinct theories are used, the first one dealing with the segmentation due to surface tension effects, and the second with the stretching of the tip of the plunging jet, due to gravity and inertia effects.

The formulations on surface tension used in the proposed model are based on linear theory. Non-linear solutions have been developed since the original formulations by Plateau and Rayleigh. Bogy (1979) presented a literature review on the problem of the segmentation of liquid jets. Recent theories take into account finite amplitude disturbances, non-linear interactions, viscosity and air friction. The approximations inherent in the proposed model are such that the use of linear theory in describing surface tension effects is quite reasonable.

Regarding the formulations derived by Longuet-Higgins (1980) on the change of form of the tip of the curling wave, no experimental work has been done to test the theory. The reason for the absence of such a work becomes apparent when one looks at photographs showing the overturning process. The curling face loses its continuity, as it spreads into jets and the free surface boundary is no longer two-dimensional, making the description of the cross sectional profile a most difficult task. The theory and assumptions however, on which the derivations are based are reasonable and, overall, the results are broadly in agreement with observations.

The assumptions inherent in the proposed model introduce their own limitations. Firstly, it is assumed that the tip of the overturning wave behaves like a horizontal liquid cylinder. The surface tension formulations for liquid cylinders are based on the assumption that there is no flow across the surface of the cylinder, a condition which is not necessarily valid in a breaking wave. The effect of this assumption is that the model is strictly applicable to the very tip of the wave crest.

The ridges formed at the back of the wave are not treated by the proposed model. Their formation may be explained by the physics on which the model is built. The back of the wave has its own radius of curvature and any transverse disturbance on its surface will grow or diminish according to surface tension principles. The segmentation of the tip of the wave spreads in the vicinity of the crest. The long wavelengths of the enhanced transverse disturbances are further amplified, as the radius of curvature at the back of the wave is longer than at the tip. These disturbances appear as ridges, or channels of easier flow according to Worthington's (1908) terminology, spaced at wider intervals as their distance from the tip of the breaker becomes greater.

A further assumption built in the model is that the two theories used, namely surface tension and gravity, do not affect each other. That is, the radius of the cylinder is not modified by the growth of the disturbance. This assumption affects mostly the short disturbances which rapidly form thin jets, in which case the horizontal cylinder loses its physical meaning.

Conclusions

Surface tension has been shown to play an important role in the overturning stage of a breaking wave. During this stage, any unstable disturbances on the tip of the breaker will grow as the curling face follows a free fall trajectory. The effects of the two main forces, namely gravity and surface tension have been combined together to produce an analytical/numerical model that describes the evolution of the overturning face of a breaking wave.

The initial conditions of the overturning face were related to the breaker height and period, after making certain approximations. The most important result derived from the model is that breaking characteristics are independent of surface tension effects, for breakers larger than 0.5m high, a result which is in agreement with earlier experimental results.

References

- Bogy, D.B. (1979), 'Drop formation in a circular liquid jet', *Ann. Rev. Fluid Mech.*, vol. 11, pp. 207-228
- Fuhrboter, A. (1986), 'Model and prototype tests for wave impact and run-up on a uniform 1:4 slope', *Coastal Eng.*, vol. 10, pp. 49-84.
- Longuet-Higgins, M.S. (1980), 'On the formation of sharp corners at a free surface', *Proc. of the Royal Soc. of London, Series A*, vol. 371, pp. 453-478.
- Plateau, J. (1863), 'Experimental and theoretical researches on the figures of equilibrium of a liquid mass withdrawn from the action of gravity', *Annual Report of the board of the Smithsonian Inst.*, pp. 207-285.
- Plateau, J. (1864), 'Experimental and theoretical researches on the figures of equilibrium of a liquid mass withdrawn from the action of gravity', *Annual Report of the board of the Smithsonian Inst.*, pp. 285-369.
- Rayleigh, Lord (1878), 'On the instability of jets', *Proc. London Math. Soc.*, pp. 4-13.
- Skladnev, M.F. and Popov, I.Y. (1969), 'Studies of wave loads on concrete slope protections of earth dams', *Symp. on Wave Action, Delft*, paper no. 7.
- Stive, M.J.F. (1984), 'Energy dissipation in waves breaking on gentle slopes', *Proc. 19th Int. Conf. on Coastal Eng.*, pp. 99-127.
- Toumazis, A.D. (1989), 'An investigation of the physics of breaking/broken waves', Ph.D thesis, University of London.
- Worthington, M.A. (1908), 'A study of splashes', Longmans, Green and Co., London.

ACKNOWLEDGEMENTS

The authors would like to thank SERC and MTD Ltd for funding the project entitled 'The Kinematics of Breaking/Broken Water Waves', which the presented work is part of.

CHAPTER 74

Comparison of Wave Hindcast Methods for Lower Gulf of Thailand

Sutat Weesakul¹
Supot Charulakana²

Abstract

The practical wave hindcast methods namely, SMB (Sverndrup-Munk-Bretchneider), PM (Pierson-Moskowitz) and SPM 1984 (Shore Protection Manual) were evaluated and accessed for their accuracy using the one year recorded of the available oceanographic data at the lower gulf of Thailand in 1987. It was found that all models show the comparable accuracies of significant wave height (H_s) and significant wave period (T_s) but SPM (1984) rather gave the lowest root mean square error when H_s exceeds 1 m. The empirical formulae of land-wind velocity relationship was simply established in a exponential form. The value of constants in the expression between the 5 meteorological stations on land in the southern part of Thailand and the offshore platform were obtained as well. Using the land-wind velocity empirical formulae and a selected wave hindcast method to predict H_s and T_s , the better result was obtained by the low RMSE value.

Introduction

In developing countries, long term wave record is always lacked due to the high cost of instrument used. This make the unreliable of wave forecasting from the limited number of data for planning and design of coastal projects. A wave hindcast model utilizing local wind velocity will provide more quantitative data of wave climate. The design parameters of two large ports in Thailand is also obtained from the result of wave hindcast models. The selection of appropriate models is quite important and it will govern the project cost. In this study, the result of practical wave hindcast models were compared with the real field measurement to access their accuracy. The empirical relationships of land-wind velocity were established in order to improve the wave hindcast

¹D.Eng, Dept. of Civil Eng, Faculty of Engineering, Chulalongkorn University, Bangkok 10330, Thailand

²Graduate Student, ditto

procedure at specific sites. The better result was obtained and shown with the lower root mean square error for both wave height and period.

Procedure

A comparison of three wave hindcast models was carried out using the oceanographic information recorded at the offshore platform at the lower gulf of Thailand during a period of one year in 1987. The available data were significant wave height, period, wind velocities and their direction respectively. Fig.1 shows the location of offshore platform. The conventional Sverdrup-Munk-Bretschneider (SMB) model was compared with the Pierson-Moskowitz (PM) model and with the relatively new model from shore protection Manual (SPM, 1984).

The SMB wave hindcast model was used as the standard method for wave prediction and its procedure was published and referred to SPM (1977). The PM wave hindcast model was an accepted method and Silvester (1977) and Muangman (1973) described the detail for hindcast deep water wave height and period including the energy transfer concept from the previous wind velocity. Recently, the standard method for wind wave prediction in Shore Protection Manual (1984) was changed. The simplifying equation was based on the parametric approach of Hasselmann et al (1976). This method will refer to as SPM (1984) and it will be tested for its accuracy as well.

The significant data for wave hindcast method was wind direction and velocity overwater or oversea. The problem in wave hindcast method in practical is that how to transform the available recorded overland wind velocity to the overwater wind.

In this study, land-wind velocity relationship was empirically formulated using the Meteorological information observed at the 5 stations at the southern part of Thailand and the offshore wind velocity data. Since the altitude of the meteorological station was not much higher than the sea level, the data between overwater and overland wind velocity was related instead of using pressure gradient. Lag time of wind data was also taken into considered and computed by measuring the distance between the platform and each land station in different wind direction and divided by average velocity. The lag time was used to select the over land data which corresponded to over water wind.

Results

The significant finding from the study will be highlighted associated with the example results herein.

Comparisons of Wave Hindcast Models

The results of all three wave hindcast models were shown by

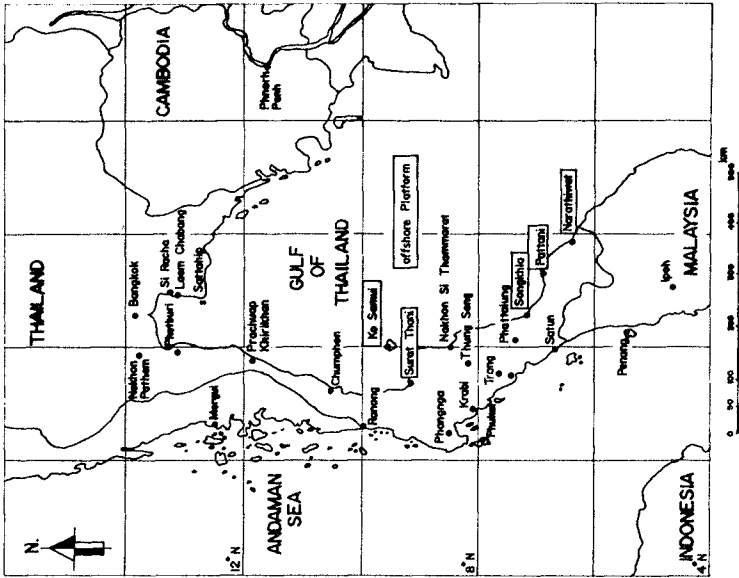


Fig. 1 Location of the Study Area

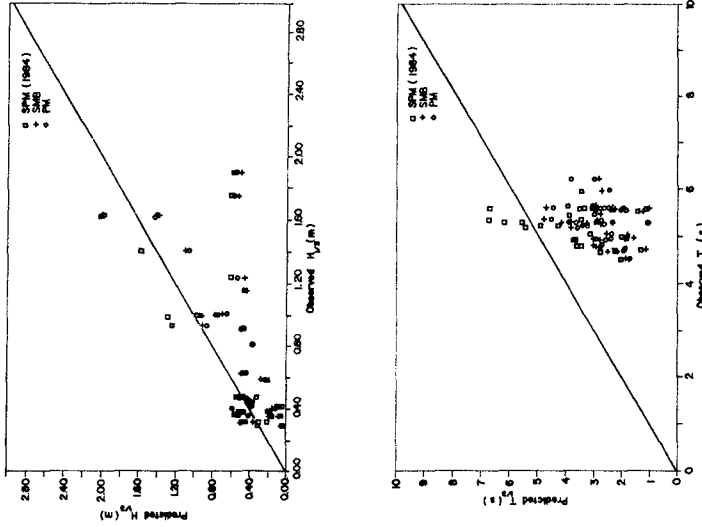


Fig. 2 Comparison of Predicted and Observed $H_{1/3}$ and $T_{1/3}$ in March 1987

comparing predicted and observed values of significant wave height and period. In Thailand, there are 3 seasonal classified by wind direction. The wind from North East Monsoon always blow from period of December to March. The South West Monsoon start from June to September. Finally the transition period is from April to May and October to November. Examples taken from March, July and December 1987 were depicted in Figs.2 to 4. The predicted values from SPM (1984) were rather overestimated when wave height exceeds approximately 1 m. while the rest is underestimated. The wave period showed the same trend while that from SMB and PM were underestimate. The accuracy of each models were accessed using the root mean square error (RMSE). Figure 5 showed RMSE of wave height and period. SPM (1984) has the less RMSE of wave height compared with the rest when its value exceeds 1 m. while the wave period show scatter RMSE for and model. However, the accuracies in predicting wave height and wave period were comparable for all models. In addition, It was found that most of the time wave condition was duration limited case independent of method used.

Land-Wind Velocity Relationship

Relation of over water wind velocity, i.e at the offshore platform, and that of over land, i.e at the nearby 5 meteorological station on land, were simply established and expressed as

$$R_L = a+b.exp(c.U_L) \quad (1)$$

Knowing over land wind velocity (U_L), the over water wind velocity (U_W) can be computed using the ratio $R_L (=U_W/U_L)$ in the above equation. Fig.6 shows land-wind velocity relationship. Table 1 summarizes the constants, a, b and c, of each stations. It was found that the ratio R_L increased as the station more away from shoreland.

A better result of wave hindcasting, using the over land wind data and the above equation, are depicted in Fig.7. The RMSE reduced from 0.595 m. to 0.383 m. and 6.676s to 5.025s for both significant wave height and period. The improved accuracy are 55% and 33% respectively.

Conclusions

Wave climate at a specific site in the study area can be predicted using the empirical formulae of land-wind velocity relationship and a selected wave hindcast model. Any models give the comparable accuracies of the wave hight prediction but SPM (1984) rather give the high value when wave height exceeds 1 m. with the less RMSE compared with the rest and most of the time the wave period is somewhat lower than the measured one. The procedure described above is useful and practical for engineering application in developing countries which deal with coastal problems since local wave climate is necessarily and basically needed when few field date is available.

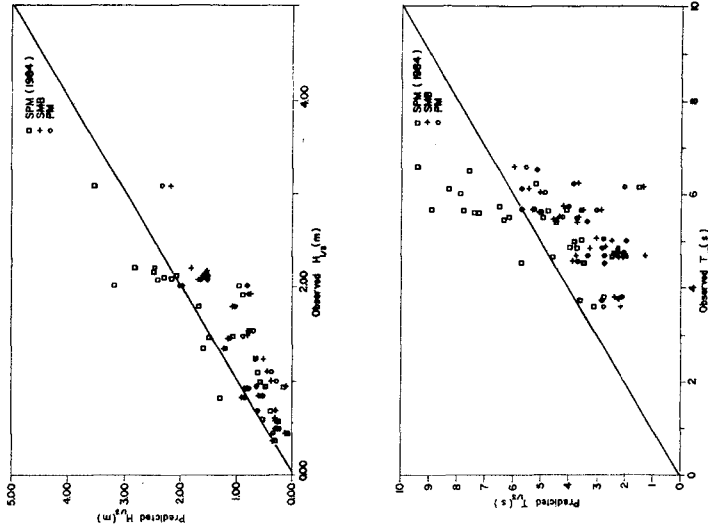


Fig. 4 Comparison of Predicted and Observed $H_{1/2}$ and $T_{1/3}$ in December 1987

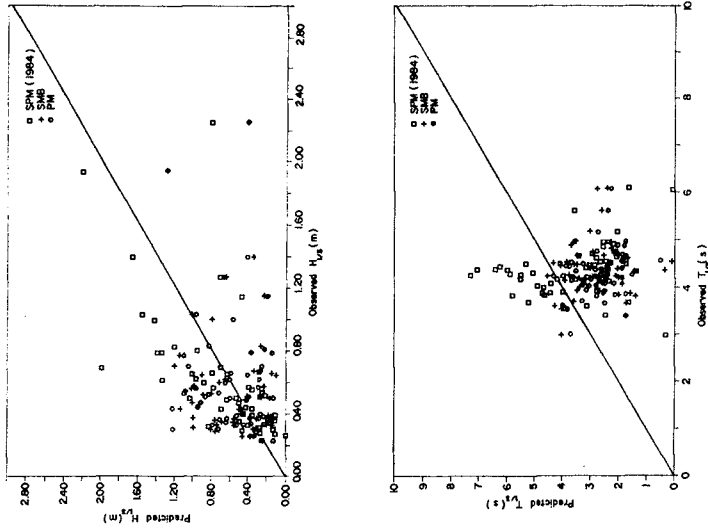


Fig. 3 Comparison of Predicted and Observed $H_{1/2}$ and $T_{1/3}$ in July 1987

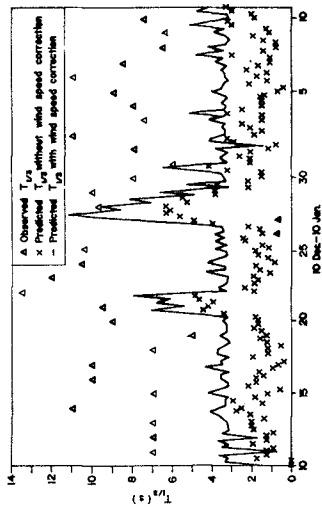
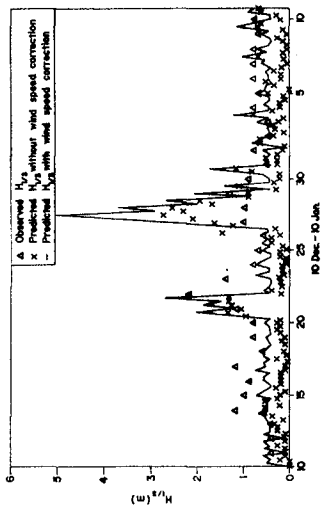


Fig. 7 Comparison of Predicted and Observed $H_{1/3}$ and $T_{1/3}$ at Narathiwat

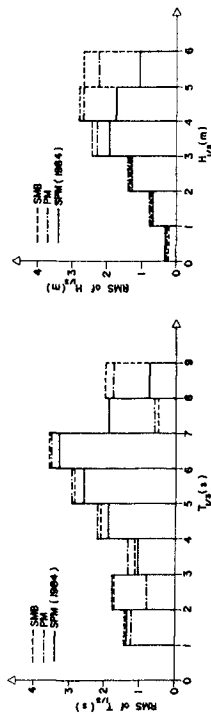


Fig. 5 Root Mean Square Error of $H_{1/3}$ and $T_{1/3}$

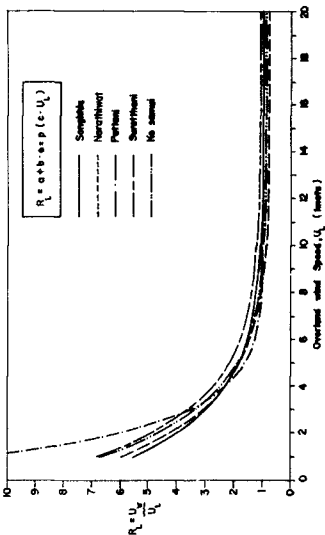


Fig. 6 Relationship of $H_{1/3}^2/U_{1/3}^2$ and $U_{1/3}$

References

1. Muangman (1973), "Wave Climate Forecasting in Gulf of Thailand", Master Thesis no. 569, Asian Institute of Technology, Bangkok, Thailand.
2. SILVESTER, R (1979) "Coastal Engineering" Vol I Elsevier 457 p.
3. US ARMY CORPS OF ENGINEERS, CERC, (1977) "Shore Protection Manual" 3rd ed. 3 Vol.
4. US ARMY CORPS OF ENGINEERS, CERC, (1984) "Shore Protection Manual" 4th ed. 2 Vol.

Table 1 Constants of Over land and Over water wind velocity Relationship

Station	Distance from shoreline (m)	a	b	c
Ko samui	300	0.819	9.196	-0.436
Songkhla	900	0.935	6.921	-0.411
Narathiwat	1,800	0.762	7.985	-0.418
Suratthani	6,100	1.062	8.818	-0.421
Pattani	8,300	0.969	20.189	-0.696

CHAPTER 75

Developing Wave-Current Boundary Layers

Richard R.Simons¹
Andreas G.Kyriacou²

Abstract

When applied to real engineering problems, mathematical models of combined wave-current flows usually assume that both wave and current properties remain in a quasi-steady state. Shear stresses and other flow parameters are calculated for instantaneous values of wave height and current strength, regardless of the changes being induced by tides, winds, or wave grouping.

This paper describes tests carried out in a wave flume to investigate velocity profiles, bottom shear stresses and water surface characteristics under gradually developing flow conditions, such as those created when a group of waves is superimposed onto a pre-existing current or when a steady current is added to a train of regular waves. Results indicate that, at laboratory scale, the water surface characteristics adapt within a few wave periods to changes in superimposed waves or current, but that mean velocity profiles and shear stresses may take considerably longer to respond to the new flow conditions.

Introduction

In the assessment of sediment transport at the seabed or in the design of structures to stand in coastal waters, a large number of mathematical models

¹Lecturer, Civil Engineering Dept, University College London.

²Project Manager, Santa Fe Laboratory, UCL, London WC1E 6BT
ENGLAND

are now available to describe the local wave and current processes. Approximately thirty of these models include the effects of wave-current interactions, and their calibration has generally been based on the assumption of a quasi-steady relationship between the wave properties and the current strength [Simons et al. (1988)]. In practice, with coastal hydrodynamics dominated by cyclic tidal currents and storm-generated currents and waves, this is not the case, although it remains to be shown whether the quasi-steady approach gives an adequate prediction. Some models [Christoffersen and Jonsson (1985); Davies, Soulsby and King (1988)] have included the effects of unsteady currents, but these are the exceptions. The DSK (1988) model predicts a rapid change in boundary layer characteristics if the net flow rate, rather than the driving pressure gradient, is maintained after the addition of the waves. However, if instead, the pressure gradient is held constant, then the change to stable wave-current conditions is far less rapid.

The present paper describes a laboratory study aimed at measuring the characteristics of developing flows, in particular looking at the rate at which bottom shear stresses and water surface properties in wave-current flows adapt to varied currents and isolated wave groups.

Wave-Current Interaction

Before going on to consider cases where current strengths are being varied or where short groups of waves are being superimposed on a current, it is worth noting the results from previous studies carried out under "steady" combined wave-current conditions, when regular waves of constant height propagate onto a steady unidirectional current.

Results from earlier experiments in flumes and in the field indicate that the properties of both waves and currents are changed from their separate values. These observations have been used to calibrate and to confirm the physical assumptions necessary in the derivation of wave-current mathematical models. For instance, the addition of wave-induced oscillatory motion has been shown to be capable of inducing orders-of-magnitude increases in the apparent bed roughness and the bottom shear stress felt by the mean current, although the mean

velocity profile retains a logarithmic region [Bakker & Doorn (1978); Brevik & Aas (1980); Kemp & Simons (1982), (1983); Tanaka, Chian & Shuto (1983)]. Turbulence intensities determined from the fluctuations about the ensemble averaged velocities are increased within the oscillatory boundary layer; Simons et al. (1988) found that the increase in u' is of the same order as the increase in u_* defined from the mean velocity profiles.

As a result of the extra frictional resistance at the bed, it has been demonstrated in flume tests that the mean water level slope increases if a constant volume flow rate is to be maintained. Also, rates of wave energy dissipation change in the presence of co-existing currents. Simons, Grass & Kyriacou (1988) showed that attenuation rates decrease if waves propagate over a following current, but that they can increase if the current flows against the direction of wave propagation. It was suggested that this phenomenon could be explained in terms of a wave friction factor, using the definition proposed by Jonsson (1966).

Experiments

The present test programme was performed in a recirculating laboratory flume 610 mm wide and 30 m long, with a still water depth of 300 mm and a horizontal bed roughened with 10 mm limestone chippings. A two channel laser Doppler anemometer was used to determine instantaneous Reynolds stresses and simultaneous horizontal and vertical velocities. The experimental set-up was similar to that described by Simons et al. (1988).

During the test programme, 10 different developing flow cases were investigated, where waves were gradually superimposed onto an existing steady current or vice versa. Seven tests involved running a steady current for one minute, adding waves for 6 minutes, then returning to the current-only state for a further minute. In the other three tests, waves were first propagated through still water for a minute, a current introduced gradually over an 80 second period and run for a further 5 minutes, then the waves turned off and a steady current left to flow for another minute. The experimental conditions are set out in **Table 1**.

Each test was repeated 10 times, with the 2-channel

Run	Initial State:			Superimposed flow:			Final state:		
	u	T	H	u	T	H	u	T	H
	mm/s	s	mm	mm/s	s	mm	mm/s	s	mm
WK4.D	75	-	-	75	0.7	22.6	75	-	-
M4.D	190	-	-	190	0.7	18.2	190	-	-
ST4.D	250	-	-	250	0.7	16.2	250	-	-
ST4.I	250	-	-	250	1	36.9	250	-	-
ST3.I	250	-	-	250	1	27.7	250	-	-
M4.I	190	-	-	190	1	40.7	190	-	-
WK4.I	75	-	-	75	1	50.5	75	-	-
US4.I	-	1	50.7	250	1	27.7	250	-	-
UM4.I	-	1	50.7	190	1	40.7	190	-	-
UW4.I	-	1	50.7	75	1	50.5	75	-	-

Table 1. Parameters for the developing flow tests.

laser anemometer set at different heights above the bed. Water surface (wave height and MWL) was also recorded simultaneously at 10 points along the flume in 3 groups such as to make it possible to identify and compensate for reflected waves moving back up the flume from the beach. Water surface data were recorded on computer disc every 140ms through a high speed analogue to digital converter, while velocities were stored on magnetic tape for subsequent processing.

In order to analyse the results from these varied flow tests, it was necessary to develop a series of computer programmes capable of synchronizing a large number of independent data files. Each of these files contained a time series of velocities or Reynolds stresses at the chosen measuring positions through the boundary layer, from which full depth profiles of mean velocity, turbulence and Reynolds stress could be generated at different stages through the tests (using appropriate short-term averaging). Simple ensemble-averaging was not possible because of the imposed variation in the "mean" velocities. Time series of MWL and wave height at 3 widely spaced locations along the flume were also required, from which it was possible to derive information on wave attenuation and mean water

surface slope. This process was complicated by having only 10 simultaneous sets of water surface data, closely spaced in three groups (5m, 15m, and 25m from the wave paddle) from which to interpret the significance of reflected waves in the flume.

Two wave periods [0.7s, 1.0s.] and two wave heights [25mm, 40mm.] were considered in combination with three co-directional currents [75mm/s, 190mm/s, 250mm/s].

Results

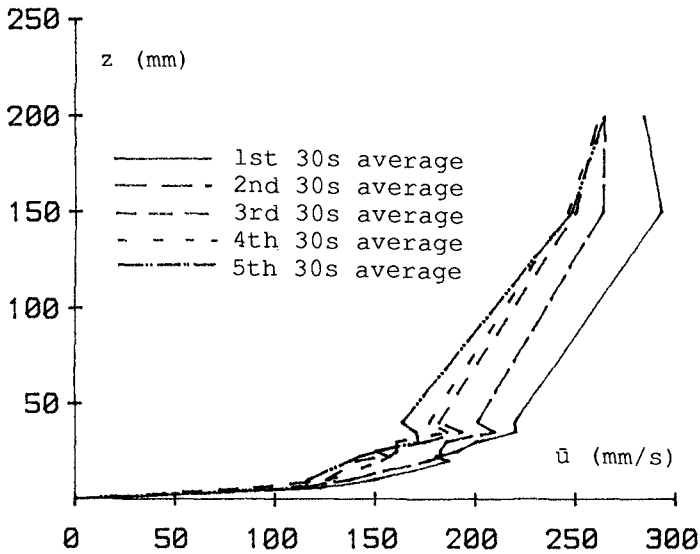


Fig.1 Boundary layer profiles of horizontal velocity at 30s intervals after the superposition of waves [T=1s;].

In the tests where waves were superimposed onto a pre-existing steady current, it was found that the mean velocity profile took approximately 200 wave periods to stabilize under the new combined flow conditions. The increase in shear stress at the boundaries slowed the mean current, causing a redistribution of flow across the channel. Fig.1 shows mean velocity profiles at 30 second intervals after generation of the first wave at the paddle 15 m upstream. Despite the scatter caused by

such a short averaging period, the mean velocities can be seen to be more or less established in a stable profile after 150s; over the next 50s, velocities increase towards their initial current-only values near mid-depth, but with slower flow maintained near the bed and at the surface. It should be remembered here that the mean velocities reflect not just the superimposed current flow but also wave-induced mass transport.

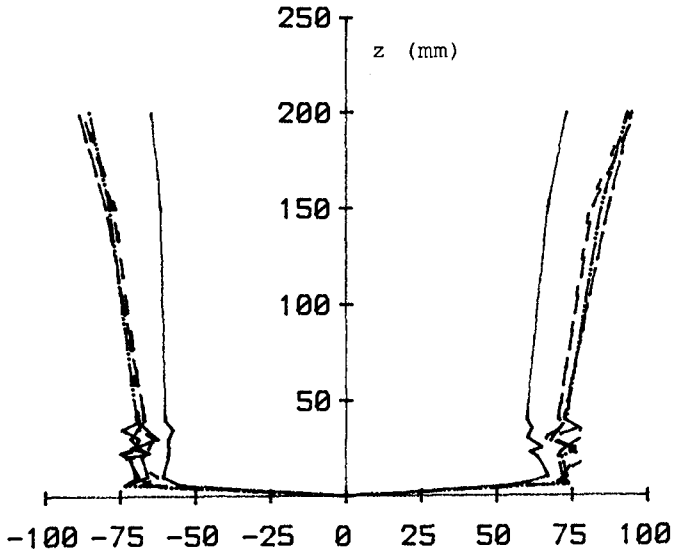


Fig.2 Development of Horizontal Oscillatory Velocities at 30s intervals after the start of wave generation.

In order to determine orbital velocity amplitudes and turbulence intensities during the transitional period after the addition of the waves, a second order curve fit was applied to the unprocessed velocity data to establish the oscillatory component. The short term mean velocity and the reconstituted 2nd order orbital velocity were then subtracted from the raw data, leaving the turbulent velocity fluctuations. The root-mean-square of these short samples (5 s; 30 s) were then used to quantify the instantaneous turbulence intensities.

The same procedure was applied to horizontal and vertical velocity components and to Reynolds stresses. Fig.2 shows the variation in horizontal orbital amplitude through the depth at time intervals corresponding to those in fig.1; the wave motion was found to be stable after the generation of 20 or so waves.

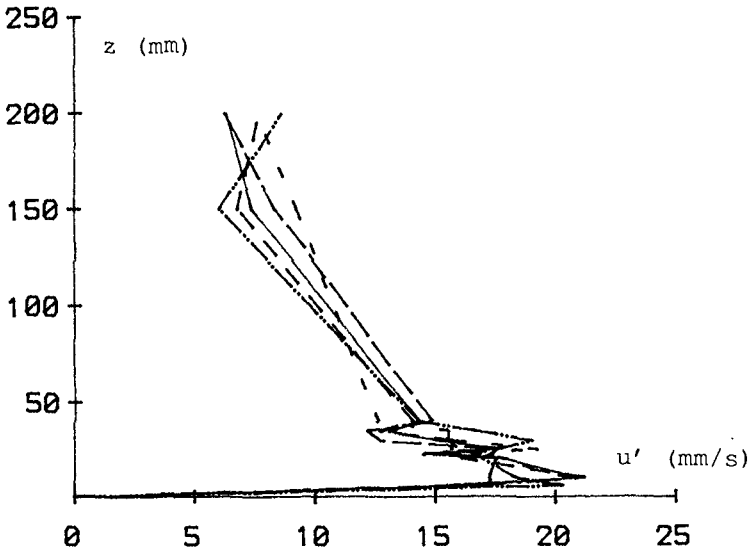


Fig.3 Development of Horizontal Turbulence Intensities at 30s intervals after waves are superimposed.

Profiles of turbulence intensity through depth showed considerable scatter, as the 30s averages plotted in fig.3 demonstrate. The profile containing the highest values near the bed relates to data sampled early in the test, and is probably attributable more to the change in mean velocity during the initial 30s sample rather than to real turbulence. Careful study of the profiles of u' and v' could justify a conclusion that stable wave-current conditions have been established after 30 or so wave periods, but such a view must be taken as tentative.

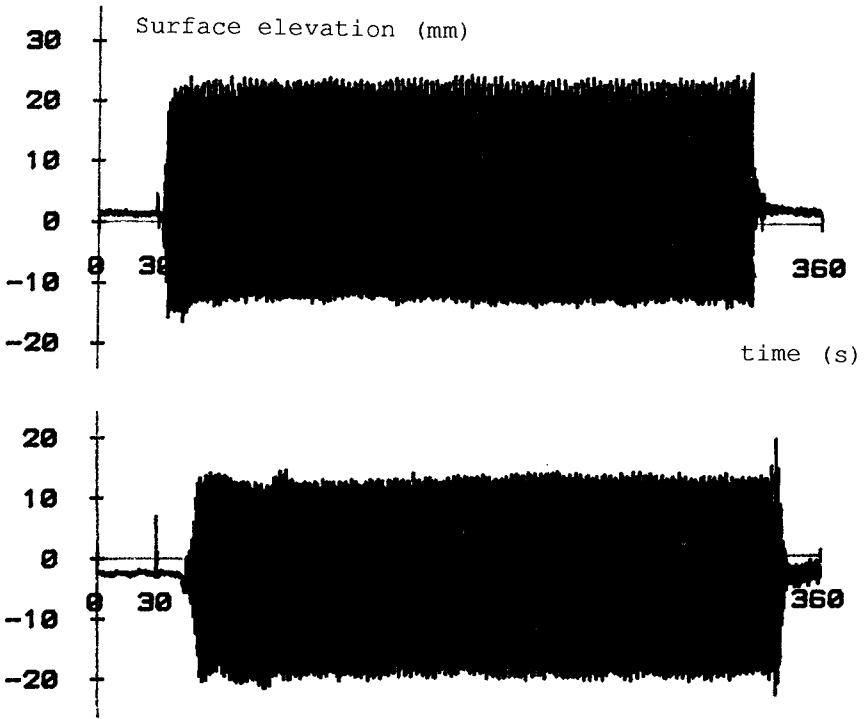


Fig.4 Variation in water surface elevation when waves are added to a steady current: a) 5m from the wave paddle; b) 25m from the wave paddle.

Turning now to the behaviour of the water surface, fig.4 records the water surface movement at the measuring station closest to the wave paddle (top) and near the beach, 20m. downstream (bottom). Using the second order curve-fitting routine, it was possible to analyse these data further to yield time series of wave heights (fig.5) and "mean" water levels (fig.6) for the corresponding tests. These results confirm earlier observations that the mean water level slope is increased by the addition of waves. Figs.4 and 6 both show the water level rising at the paddle end of the flume by between one and two millimetres, with a corresponding fall at the beach end. This change takes approximately 30s. to stabilize, whereas wave heights build up to a constant value within three or four seconds of the arrival of the first wave. The regular oscillation apparent in the MWL traces is due to the use

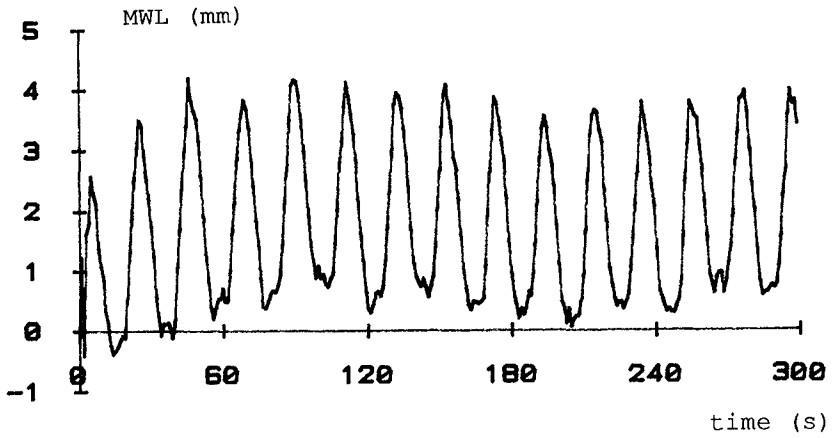


Fig.6 Time series of mean water level 5m from the paddle when waves are added to a steady current.

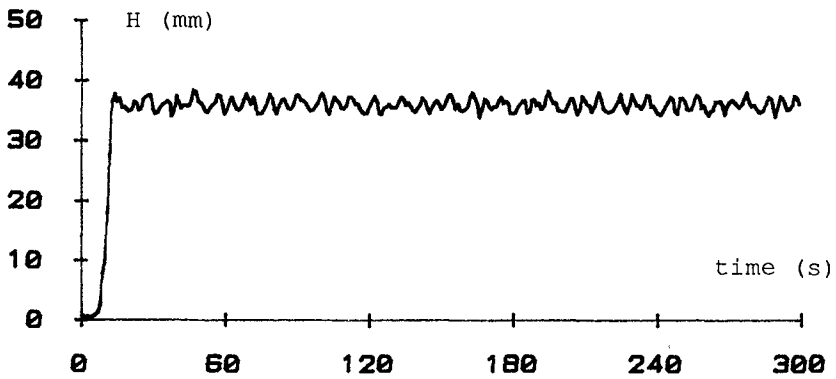


Fig.5 Time series of wave heights 5m from the paddle when waves are added to a steady current.

of a digitizing interval which does not exactly repeat at the same phase each wave cycle.

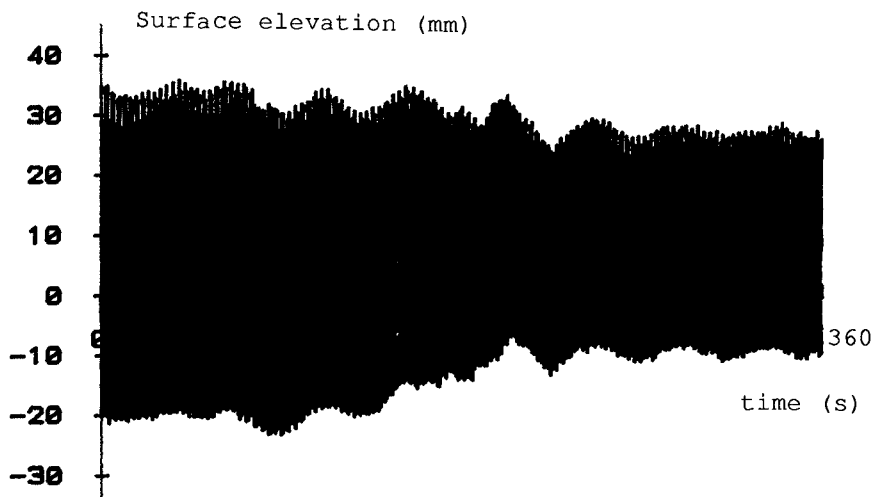


Fig.7 Time series of wave heights 5m from the paddle when waves are added to a steady current.

All the results described above relate to the first series of tests where waves are added to a pre-existing current. Analysis is still to be completed for the tests where a current was gradually imposed onto regular waves. However, fig.7 shows the water surface movement at the 5m position along the flume during one of these runs. Despite the great care exercised in opening the current control-valve, a seiche wave has clearly been set up in the flume. This emphasizes the difficulty in carrying out and analysing data from these unsteady tests.

Conclusions

From the profiles of mean velocity and turbulence characteristics, it has been shown that stable wave-current conditions may not be established until nearly

200 waves have passed the LDA measuring position. However, a far more rapid time-scale (say 15 wave periods) was evident in the changes in hydraulic gradient along the flume induced by the addition of waves to a current.

These results suggest that care needs to be taken when using wave-current models in coastal engineering for the prediction of mean velocities and consequential sediment transport rates if wave conditions are changing rapidly. However, a quasi-steady approach appears appropriate where changes in wave characteristics and mean water levels are the only consideration.

Acknowledgements

The authors are grateful to Hydraulics Research, Wallingford, for the use of their experimental facilities, and to the Science and Engineering Research Council for their support during the work described in this paper.

References

- Bakker W.T. and van Doorn T. 1978 Near-bottom Velocities in Waves with a Current. Proc. 16th Int.Conf. on Coastal Engng, Hamburg, pp.1394-1413.
- Brevik I. and Aas B. 1980 Flume experiments on waves and currents: rippled beds. Coastal Engineering, 3, pp149-177.
- Christoffersen J.B. and Jonsson I.G. 1985 Bed friction and dissipation in a combined current and wave motion. Ocean Engng. Vol.12, No.5, pp.387-423
- Davies A.G., Soulsby R.L. and King H.L. 1988 A numerical model of the combined wave and current bottom boundary layer. J. Geophysical Research.
- Jonsson I.G. 1966 The friction factor for a current with superimposed waves. Prog.Rep. 11, Coastal Engng. Lab., Tech. Univ. Denmark
- Kemp P.H. and Simons R.R. 1982 The interaction between waves and a turbulent current: waves propagating with the current. J.Fluid Mech., 116, pp.227-250

Kemp P.H. and Simons R.R. 1983 The interaction between waves and a turbulent current: waves propagating against the current. J.Fluid Mech., 130, pp.73-89

Simons R.R., Kyriacou A., Soulsby R.L. and Davies A.G. 1988 "Predicting the Nearbed Turbulent Flow in Waves and Currents". Proc. IAHR Symp. on Math.Modelling of Sediment Transport in the Coastal Zone, Copenhagen, Denmark, 1988, pp.33-47.

Simons R.R., Grass A.J. and Kyriacou A. 1988 "The Influence of Currents on Wave Attenuation". Proc. ASCE 21st Coastal Engng. Conf, Malaga, Spain, June 1988, Chapter 25, pp.363-376.

Tanaka H., Chian C.S. and Shuto N. 1983 Experiments on an oscillatory flow accompanied with unidirectional motion. Coastal Engng. in Japan, Vol.26, pp.19-37

CHAPTER 76

INCORPORATION OF WAVE EFFECTS IN A 3D HYDROSTATIC MEAN CURRENT MODEL

H.J. de Vriend¹⁾ and N. Kitou²⁾

Abstract

The consistency of the mathematical formulation of a 3D hydrostatic current model for coastal areas is discussed. At various points, widely accepted concepts and formulations are shown to lead to inconsistencies, and more consistent alternatives are proposed. Besides, some essential lacunae in our physical knowledge of 3D wave-driven currents are indicated.

Introduction

Nearshore currents have a three-dimensional structure, which plays an important part in coastal dynamics. Mathematical models in this field ought to take this into account. Especially if the wave-induced "cross-shore" sediment transport is concerned, descriptions of the near-bed current velocity based on a 2D depth-integrated current model will fail (cf. De Vriend, 1986). Also 2D-vertical models will fail in many practical cases, by lack of longshore uniformity. Quasi-3D models, coupling a 1D-vertical and a 2D depth-integrated model to describe a 3D current field, may bring relief here. This type of models, however, needs further substantiation before being ready to describe nearshore currents (Arcilla et al., 1990; Svendsen and Putrevu, 1990). Fully 3D current models, therefore, have their part to play here, if it were only as a reference for simpler models (e.g. Q3D).

The present paper describes the incorporation of wave-effects into a 3D-hydrostatic mean current model. It concerns the form and the consistency of the basic mathematical formulation, rather than the actual numerical implementation.

Model concept

We will start from a 3D hydrostatic current model, with the vertical plane mapped onto a rectangle via the so-called sigma-trans-

-
- 1) DELFT HYDRAULICS, P.O.B. 152, 8300 AD Emmeloord, The Netherlands
 - 2) Demokritos Univ. of Xanthi, Dept. of Civil Engrg., 67100 Xanthi, Greece

formation. It is essential for the concept presented herein, that the vertical is discretized into a fixed number of steps (layers), the uppermost of which covers at least the full height of the sea waves (Fig. 1).

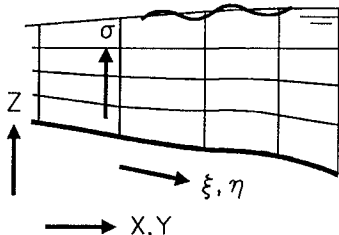


Fig. 1 Discretization of the vertical plane

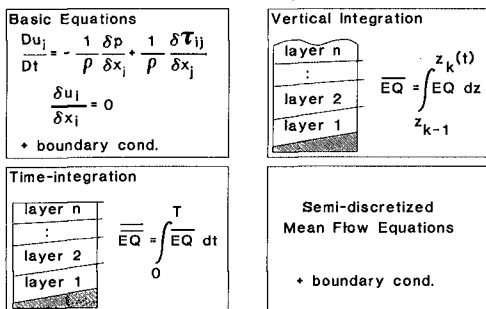


Fig. 2 Derivation of semi-discretized wave-averaged equations

The net wave effects are included in the constituting equations for the mean current by formal integration of the Reynolds equations over the vertical elements of the computational grid and over the time scale of the waves (Fig. 2).

The resulting semi-discretized equations contain a number of wave residual terms, viz.

- mass flux terms in the equation of continuity,
- mass flux terms in the momentum equations, and
- wave-induced effective stresses in the momentum equations.

Besides, the waves influence the turbulent exchange of momentum and the effective bottom shear stress.

In the next sections, we will discuss these effects one by one, supposing the wave parameters to be given, i.e. we will not go into the matter of fully interactive wave-current systems.

Wave-induced mass flux

In the case of periodic waves, the wave-averaged equation of continuity contains no net wave-effects in layers entirely below the wave trough level, i.e. in all layers but the one adjacent to the water surface.

The wave-averaged equation for this top layer reads

$$\frac{\partial \Delta_k}{\partial t} + \frac{\partial}{\partial X_i} \left(U_{i,k} \Delta_k + \frac{M_i}{\rho} \right) + T.T. = 0 \tag{1}$$

in which:

- t = time,
- X_i = horizontal co-ordinates (i=1,2),
- Δ_k = thickness of the k-th layer,

- $U_{i,k}$ = horizontal mean velocity components, averaged over the k-th layer,
- M_i = wave-induced mass flux components,
- ρ_i = mass density of the fluid,
- T.T. = terms related to the sigma-transformation.

The wave-induced mass flux components in this equation are defined by

$$M_i = \frac{1}{T} \int_t^{t+T} dt \int_{z_{n-1}}^{z_n} \rho \tilde{u}_{i,n} dz \tag{2}$$

in which T denotes a significant time scale of the wave motion, long enough to yield a meaningful average, $\tilde{u}_{i,n}$ is the wave orbital velocity in the top layer, and n is the index of this layer.

On the basis of a wave theory, Eq. (2) can be elaborated in terms of wave field parameters (height, direction, etcetera). We will discuss this in a later section.

At the physical level, Eq. (2) means an extension with respect to 2D-vertical and 2D-horizontal situations: the mass flux can give rise to 3D circulations, as is illustrated in Fig. 3.

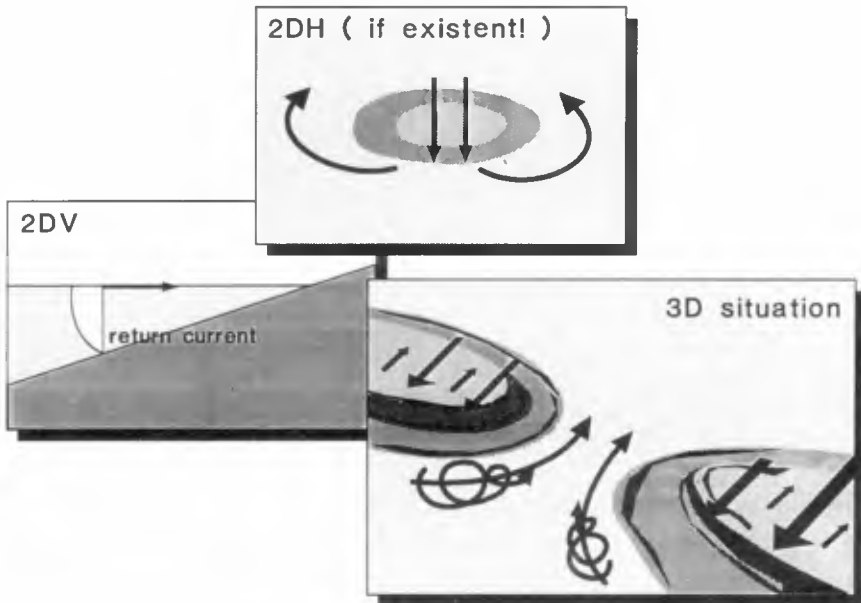


Figure 3 3D effect of wave-induced mass flux

Wave-induced momentum flux

The procedure outlined in Figure 2, when applied to the momentum equations, yields residual wave-effects through the non-linear advection terms. Using

$$\frac{1}{T} \int_t^{t+T} dt \int_{z_{k-1}}^{z_k} u_{i,k} u_{j,k} dz = U_i U_j \Delta_k + U_i \frac{M_i}{\rho} + U_j \frac{M_j}{\rho} + \frac{1}{T} \int_t^{t+T} dt \int_{z_{k-1}}^{z_k} \tilde{u}_{i,k} \tilde{u}_{j,k} dz \quad (3)$$

we can split the residuals of the horizontal advection terms into a mean-flow part, a mass-flux related part (two terms), and a part that contributes to the radiation stress.

The vertical advection term also yields a wave-residue, which should not be disregarded a priori (also see Svendsen and Lorenz, 1989, and Deigaard and Fredsøe, 1989).

The resulting semi-discretized equation for the k-th layer reads

$$\begin{aligned} \frac{D}{Dt} \left(U_{i,k} \Delta_k + \frac{M_i}{\rho} \right) + (U_i W)_{z_{k-1}}^{z_k} = \\ - g \Delta_k \frac{\partial z_s}{\partial X_i} + \frac{1}{\rho} \frac{\partial}{\partial X_j} (\Delta_k \bar{\tau}_{ij,k}) + \frac{\bar{\tau}_{i,z}}{\rho} \Big|_{z_{k-1}}^{z_k} + \\ + \frac{1}{\rho} \frac{\partial}{\partial X_j} (\Delta_k \bar{\sigma}_{ij,k}) - \langle \tilde{u}_i \tilde{w} \rangle \Big|_{z_{k-1}}^{z_k} + T.T. \end{aligned} \quad (4)$$

in which:

W = mean vertical velocity component,

g = acceleration due to gravity,

z_s = water surface level,

$\bar{\tau}_{ij}$ = Reynolds stress components in vertical planes,

$\bar{\tau}_{i,z}$ = Reynolds stress components in horizontal planes,

$\bar{\sigma}_{ij}$ = wave-induced effective stress,

\tilde{u}_i, \tilde{w} = wave-orbital velocity components,

T.T. = terms due to the co-ordinate transformation.

The mass flux component, non-zero in the top layer only, is defined by (2). The definition of the wave-induced effective stress reads

$$\bar{\sigma}_{ij,k} = \frac{1}{T} \int_t^{t+T} \frac{dt}{\Delta_k} \int_{z_{k-1}}^{z_k} \rho \tilde{u}_{i,k} \tilde{u}_{j,k} dz + \frac{\delta_{ij}}{T} \int_t^{t+T} \frac{dt}{\Delta_k} \int_{z_{k-1}}^{z_k} (\bar{p} - \rho \langle \tilde{w}^2 \rangle) dz \quad (5)$$

in which \bar{p} denotes the instantaneous hydrostatic part of the pressure and δ_{ij} is the Kronecker delta.

In general, the wave-induced mass flux will be small as compared with the mass flux related to the mean flow. If not, the mean flow velocity will be so small, that the advection terms are negligible, anyway. We will therefore disregard the mass-flux related residual advection terms.

The remaining residue of wave-induced horizontal advection basically acts as an effective stress, comparable to the Reynolds stress. In depth-integrated models, it adds up to the radiation stress (Longuet-Higgins and Stewart, 1964); in the present 3D model, this stress is distributed over the vertical. Consequently, the wave-induced current forcing, composed of the divergence of the effective stress and the vertical advection residue, also has a vertical distribution.

In addition to the wave-induced terms in (4), which vanish in the absence of waves, there are also wave-influenced terms, which are just modified by wave effects. The shear stress terms are of this type, and so are the near-bed boundary conditions.

In the next sections, we will discuss how the mass flux, the effective stress and the wave-induced current forcing can be elaborated in terms of global wave field properties, such as energy density, energy dissipation rate, etcetera. The other wave-influenced terms will receive further attention in a later section.

Evaluation for harmonic waves

Wave-induced mass flux

Using linear wave theory, Eq. (2) for the wave-induced mass flux can easily be elaborated to

$$M_i = \frac{E}{c} e_i^w \quad (6)$$

in which E is the energy density of the wave field, c is the wave celerity, and e_i^w denotes the components of the unit vector in the direction of wave propagation.

Wave-induced forcing ("classical" approach)

In depth-integrated models, it is customary to evaluate the radiation stresses on the basis of linear wave theory for a quasi-uniform domain (mild-slope approximation).

When applied to the present vertically resolved model, this theory yields for the effective stresses

$$\begin{aligned} \bar{\sigma}_{ij,k} &= \left(N - \frac{1}{2}\right) E f_{ij}(z_k) + \frac{1}{2} \delta_{kn} E \\ \langle \tilde{u}_{i,k} \tilde{w} \rangle &= 0 \end{aligned} \quad (7)$$

in which N is the ratio of group and phase celerity, and f_{ij} is a function of z only. Note that the last term of the expression for $\bar{\sigma}$ exists only in the top layer.

The corresponding wave-induced driving force per unit area (henceforth called "force", as the term "stress" has already been used for the effective stress tensor) can be elaborated to

$$F_{i,k} = \frac{D}{c} e_i^w f_D(z_k) - \frac{1}{2} \frac{\partial E}{\partial X_i} f_E(z_k) + \dots \tag{8}$$

in which D denotes the dissipation rate of the wave field, and f_D and f_E are functions of z only.

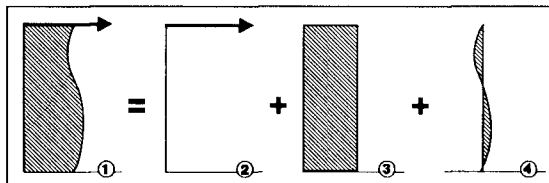


Figure 4 Decomposition of wave-induced force ("classical" theory)

The wave-induced force according to (8) can be split into three parts, viz. (also see Fig. 4)

- a surface part: $F_{s_i} = - \frac{1}{2} \frac{\partial E}{\partial X_i}$ (9)

- a depth-invariant part: $\bar{F}_i = h \frac{\partial}{\partial X_i} \left\{ \frac{(n-\frac{1}{2})E}{h} \right\} + \frac{1}{2} \frac{\partial E}{\partial X_i}$ (10)

- a depth-varying part: $F_{z_i} = \frac{E}{h} f_1(z) + \frac{1}{2} \frac{\partial E}{\partial X_i} f_2(z) + \frac{D}{c} f_3(z)$ (11)

The depth-invariant part of the force is fundamentally unable to drive a circulation current and is therefore disregarded here. The depth-varying part is basically able to drive a circulation, but it is usually assumed weak enough to be disregarded. This leaves the surface part, which acts at the mean water surface like a wind stress. It corresponds with the force at the wave trough level in various undertow models (Svendsen, 1984; Stive and Wind, 1986).

According to Eq. (9), the force will be non-zero in non-breaking (e.g. shoaling) wave fields. This is a major inconsistency of the model. If there is no ambient current and no wave breaking, all of the above results stem from a description of an ideal fluid in irrotational motion. The surface force resulting from this theory, however, will give rise to an infinite vorticity when applied to an ideal fluid body.

Wave-induced forcing (revised theory)

In a genuinely uniform situation, there will be no gradients in global parameters, such as E, and hence there will be no surface force and no inconsistency. From a practical point of view, however, a model should cover more than this trivial case.

Any deviation from uniformity in the "classical" model gives rise to the aforementioned inconsistency. Upon closer investigation, this is basically due to the assumption of quasi-uniformity of the domain and the global wave field parameters, which underlies the description of the vertical structure of the wave motion in the "mild-slope" approximation (Berkhoff, 1976):

$$\begin{Bmatrix} \tilde{\eta} \\ \tilde{u} \\ \tilde{p} \end{Bmatrix} = \begin{Bmatrix} \hat{\eta} \\ \hat{u}(z) \\ \hat{p}(z) \end{Bmatrix} \cos\chi \quad \text{with: } \chi = \omega t - kX \quad (12)$$

$$\tilde{w} = \hat{w}(z) \sin\chi$$

In this approximation, each of the amplitude functions \hat{u} , \hat{p} and \hat{w} is strictly similar in every vertical of the domain. Spatial non-uniformities only affect their scaling.

In order to achieve consistency of the model, we shall relax the mild-slope approximation. Going back to irrotational motion in a domain with a mildly sloping bottom and weakly non-uniform global wave parameters, we can take the classical solution as a basis and perturb this for small non-uniformities. In a horizontally 1D case, oriented along the X-axis, this yields in a first-order approximation (see De Vriend and Kitov, 1990, for further details)

$$\tilde{\eta} = \hat{\eta} \cos\chi \quad (13)$$

$$\tilde{u} = \hat{u}(z) \cos\chi + f_u \left(\frac{\partial z_b}{\partial X}, \frac{\partial z_s}{\partial X}, \frac{\partial k}{\partial X}, \frac{\partial \hat{\eta}}{\partial X}; z \right) \sin\chi \quad (14)$$

$$\tilde{w} = \hat{w}(z) \sin\chi + f_w \left(\frac{\partial z_b}{\partial X}, \frac{\partial z_s}{\partial X}, \frac{\partial k}{\partial X}, \frac{\partial \hat{\eta}}{\partial X}; z \right) \sin\chi \quad (15)$$

in which the functions f_u and f_w depend linearly on the gradients of the global parameters z_b , z_s , k and $\hat{\eta}$.

Substituting this result into the expressions for the effective stresses yields

$$\bar{\sigma}_{ij,k} = (N - \frac{1}{2}) E f_{ij}(z_k) + \frac{1}{2} \delta_{kn} E \quad (16)$$

$$\langle \tilde{u}_{i,k}, \tilde{w} \rangle = (N - \frac{1}{2}) E f_E \left(\frac{\partial z_b}{\partial X}, \frac{\partial z_s}{\partial X}, \frac{\partial k}{\partial X}; z \right) + f_E(z) \frac{\partial E}{\partial X} \quad (17)$$

in which f_{ij} and f_E are functions of z only, and f_E depends linearly on the gradients of z_b , z_s and k . Note that, unlike Eqs. (14) and (15), the effects of the amplitude variation are separated and yield the energy-gradient term of (17).

Also note that (16) is identical to (7), i.e. in a first-order approximation the residue of the horizontal momentum flux is not affected by the global non-uniformities.

In contrast with the classical theory, however, the vertical momentum flux is deviating from zero now!

Although we have only derived the revised theory for a 1-D case, it seems reasonable to assume, that similar results will be found when applying the same idea to horizontally 2-D situations.

Let us therefore assume, without formal proof, that in such a situation the vertical momentum flux contribution (17) can simply be rotated into the direction of wave propagation.

In that case, elaboration of the wave-induced driving forces yields

$$F_{i,k} = \frac{D}{c} e_i^w f_D(z_k) + \text{irrot. terms} \quad (18)$$

The irrotationality of the last terms in this equation refers primarily to the horizontal plane, but, upon closer inspection, these terms are also irrotational (uniformly distributed) in the vertical. Hence this part of the force is basically unable to drive a circulation current and can be disregarded here. The remaining part is proportional to the energy dissipation rate of the wave field (cf. Longuet-Higgins, 1970; Battjes, 1988), and it turns out to be concentrated in the top layer, where the $\langle \tilde{u}\tilde{w} \rangle$ -term reaches its highest value and where the dissipation actually takes place (Fig. 5).

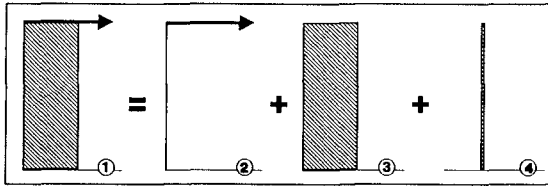


Figure 5 Decomposition of wave-induced force (revised theory)

The inconsistency of the classical model has now been removed: if the flow is inviscid, there is neither dissipation, nor wave-induced current forcing. Apparently, the vertical momentum flux term, which is the only part of the forcing influenced by the present extension of the wave model, plays a key role in achieving consistency (cf. Svendsen and Lorenz, 1989, for waves on a sloping bottom, and Deigaard and Fredsøe, 1989, for breaking waves). This may seem to be in contrast with Stive and Wind's (1986) observation, that the $\langle \tilde{u}\tilde{w} \rangle$ -term, when evaluated on the basis of measured data, is relatively small. We would like to point out, however, that the principal effect of this term is concentrated in the top layer of the fluid, between the troughs and the crests of the waves. Stive and Wind's data set does not extend to this area.

Role of bottom friction and wind-input

Although the formal derivation of (18) is based on the inviscid flow assumption, the wave boundary layer can easily be included. There, again, the $\langle \tilde{u}\tilde{w} \rangle$ -term plays a prominent part (Longuet-Higgins, 1953; also see Craik, 1982): it yields the driving force of the boundary layer streaming.

In general, the forcing will be located where the dissipation of organized motion actually takes place (cf. Nairn et al., 1990). As illustrated by Fig. 6, this will be in the surface layer for wave-breaking and wind-input (negative dissipation!), in the bottom boundary layer for bottom friction, and probably throughout the water column for wave-turbulence interaction in an ambient turbulent flow.

It may be clear, that in a depth-integrated current model outside the surf zone the contributions of the various types of wave energy dissipation ought to be weighted according to their location in the vertical. They cannot simply be piled up in a current-driving body force, which is implicitly assumed (via the assumptions under-

lying the depth-averaging) to be uniformly distributed over the vertical. This would imply too much emphasis on the forcing associated with bottom friction, and too little on the wind-induced forcing. Unfortunately, this is exactly what is done when putting the results of a wave model, including effects of wind-input and bottom friction, into a classical radiation stress and wave-induced force computation, and driving a depth-averaged current model with the resulting forces. Models of this type covering large areas with mainly non-breaking waves should therefore be considered with caution.

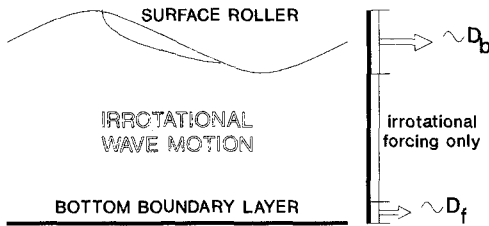


Figure 6

Location of wave-induced current forcing

Evaluation for broken waves

Roller concept

According to a concept introduced by Svendsen (1984), a broken wave of the spilling type can be considered as a harmonic carrier wave with a surface roller at its front face. This roller introduces an additional complication for the surf zone.

Since the roller moves with the wave celerity c , its contributions to the wave-averaged fluxes of mass, momentum and energy are given by (also see Deigaard and Fredsoe, 1989)

$$\text{mass flux: } \rho \frac{Ac}{\lambda} \tag{19}$$

$$\text{momentum flux: } \rho \frac{Ac^2}{\lambda} \tag{20}$$

$$\text{energy flux: } \rho \frac{Ac^3}{\lambda} \tag{21}$$

where λ denotes the wave length and A the cross-sectional area of the roller. According to Svendsen (1984), the latter quantity can be estimated at $0.9 H_{cw}^2$, if H_{cw} is the height of the carrier wave.

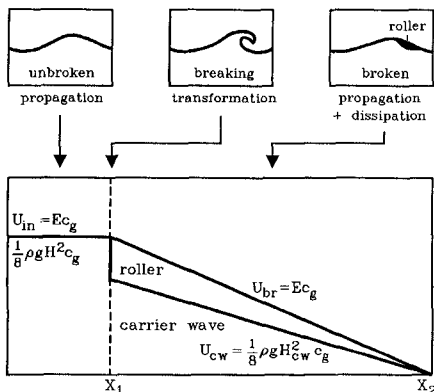
The total mean energy flux due to a broken wave follows from

$$E_{br}c_g = \frac{1}{8} \rho g H_{cw}^2 c_g + \rho \frac{Ac^3}{\lambda} \tag{22}$$

in which c_g is the group celerity of the waves. With the above approximation of A and the shallow water approximation of the phase and group celerities, this leads to (cf. De Vriend and Stive, 1987)

$$E_{br} = E_{cw} \left(1 + 7 \frac{h}{\lambda} \right) \tag{23}$$

Both (22) and (23) express, that there is a difference between the energy contents of the carrier wave and the broken wave as a whole, due to the contribution of the roller (Fig. 7).



Hence it makes a difference, whether we describe the waves by their bulk energy density, e.g. by solving an energy balance equation including a dissipation term, or by the height of the carrier wave, e.g. via a breaker height criterion. In the former case, the roller effect is already included in the computed energy density, E_{br} , whereas in the latter case the roller contribution has to be accounted for explicitly.

Figure 7 Energy flux due to broken waves

Wave-induced mass flux

The wave-induced mass flux, found by adding the contributions of the carrier wave and the roller, reads

$$M_{br} = \frac{E}{c} + \rho \frac{Ac}{\lambda} \tag{24}$$

or, making use of Eq. (23) and the underlying assumptions,

$$M_{br} = \frac{E_{br}}{c} \tag{25}$$

Apparently, the mass flux, at least in this approximation, can be expressed in terms of the bulk energy density of the broken waves, without any additional term to account for the roller contribution.

Note, however, that this is only valid as long as the shallow water approximation applies to c and c_g .

Wave-induced forcing

Eq. (18) gives the wave-induced forces in terms of the energy dissipation rate, including the effect of breaking. Hence, it is the most convenient to derive these forces from a wave model that describes the decay of the bulk energy density by solving an energy balance equation including dissipation. In that case, the roller contribution in D needs not be calculated explicitly.

If the wave model describes the height of the carrier wave, e.g. via the breaker height criterion $H_{br} = yh$, the dissipation rate has to be calculated from

$$D = - \frac{\partial}{\partial X} \left[\frac{1}{8} \rho g H_{cw}^2 c_g + \rho \frac{Ac^3}{\lambda} \right] \tag{26}$$

Here the roller contribution has to be taken explicitly into account.

Wave influence on turbulence effects

Waves also exert their influence on the mean current through turbulence and boundary shear stress. Non-breaking waves affect the

near-bed water motion and the bed shear stress (for instance, see Van Kesteren and Bakker, 1984, or Davies et al., 1988), and they are also suspected to interact with the turbulence higher up in the water column.

Broken waves introduce an additional turbulence production mechanism, which can be of significant influence in a large part of the vertical (Justesen et al., 1986), and possibly also in the horizontal (Wind and Vreugdenhil, 1986).

In the transition zone, where waves start breaking, there is a transformation of organized wave motion, through overtopping and roller formation, into turbulence. Nairn et al. (1990) show, that this transition process should be taken into account when modelling the currents in this zone.

Starting from the Boussinesq hypothesis, so from a scalar eddy viscosity, there is a range of turbulence models and bed stress models at our disposal. Very few of these models, however, include wave effects in a well-validated manner.

Without going into details, we will consider three types of models, indicate how wave effects can be included and assess the state of the art.

Partial-slip model

Leendertse (1987), in his 3D-hydrostatic current model, uses a combination of a constant eddy viscosity and a partial-slip condition at the bottom

$$\nu_t \left. \frac{\partial U}{\partial z} \right|_{z_b} = A |U_1| U_1 \quad (27)$$

in which the factor A is the key element of the model. It has to be derived from known shear stress descriptions, such as Chezy's or Manning's model.

This technique, sometimes referred to as Bazin's method, has proved rather successful in plane or slightly disturbed steady shear flow (e.g. in rivers and well-mixed estuaries; Engelund, 1974). As far as we know, it has never been shown to work equally well for strongly distorted oscillatory shear flow.

When attempting to apply this concept to the coastal situation, with its strongly distorted 3D flow and its complex shear stress relationships, the determination of A becomes rather laborious, if possible, at all. In view of the rather weak physical basis, the effort to further work out this concept seems not justified.

Algebraic eddy viscosity model

Algebraic eddy viscosity models are widely used in engineering applications. Very often, this is combined with a similarity assumption, which, for a simple pressure-driven shear current, boils down to

$$\nu_t = \bar{\nu}_t f_v(z) \quad (28)$$

A parabolic shape function f_v , combined with appropriate boundary conditions, leads to the well-known logarithmic velocity profile. The depth-invariant scaling factor, $\bar{\nu}_t$, reflects the turbulence production mechanism. In plane shear flow, for instance, $\bar{\nu}_t$ is proportional to the bottom shear velocity.

A way of including wave effects into this type of model is to adjust \bar{v}_t for wave-induced turbulence generation. In principle, this can concern only turbulence generated at the bottom, since other production mechanisms are likely to correspond with other vertical shape functions. This means, that breaker-generated turbulence is not included, nor the interaction of waves and turbulence throughout the water column.

It may be possible to model the various wave-effects on turbulence separately and to superimpose the results. The eddy viscosity is a non-physical artefact, which is unsuited for superposition, but superimposing turbulence kinetic energy contributions seems a defensible case (Deigaard et al., 1986).

At the eddy viscosity level, this would mean a quadratic composition

$$v_t = \left[\left\{ \bar{v}_t f_v(z) \right\}_{\text{bottom}}^2 + \left\{ \bar{v}_t f_v(z) \right\}_{\text{breaking}}^2 + \dots \right]^{\frac{1}{2}} \quad (29)$$

shear

In practical model applications, a vertical resolution which is sufficient to describe the details of boundary layers is seldomly feasible. In those models, the boundary layer is described with a separate, semi-analytical boundary layer model, which is matched with the numerical solution, e.g.

$$U = \frac{U_*}{\kappa} \ln \frac{z}{z_0} \quad (30)$$

in which U_* denotes the wall shear velocity and z_0 is the point of zero intersection of the velocity profile. In general, z_0 is given in terms of roughness parameters, and the matching with the numerical model goes via U_* .

Waves are known to influence both quantities: they tend to enhance the effective wall shear stress, and they shift the point of zero intersection of the mean velocity further away from the wall (see, for instance, Van Kesteren and Bakker, 1984).

Higher-order turbulence closure

A more sophisticated way of describing turbulence is the so-called higher-order closure, based on one or more coupled transport equations for turbulence properties, such as the kinetic energy. Typical examples are the k-model (e.g. Deigaard et al., 1986) and the k- ϵ model (e.g. Wind and Vreugdenhil, 1986).

Higher-order turbulence models have proven their value for intra-wave current modelling (e.g. Davies et al., 1988). At the level of wave-averaged current modelling, however, their present applicability is limited by a lack of basic knowledge. Possibly important turbulence production mechanisms (wave-turbulence interaction) are still poorly known, and the knowledge of the intra-wave processes has hardly been parameterized in terms of mean-current and global wave properties.

On the other hand, depth-averaged models including wave breaking as a source of turbulence production (Battjes, 1983; Wind and Vreugdenhil, 1986) seem to work well. It has to be pointed out, however, that these models have only been tested critically for the inner surf zone, where this type of production is predominant.

For other areas, wave-averaged higher order turbulence models have not yet been substantiated.

Conclusions

The principal conclusions from the work presented herein can be summarized as follows.

- The wave-induced mass flux has to be included in the equation of continuity for the top layer. It will not always be compensated by a return current in the same water column, but can give rise to 3D circulations.
- The $\langle \bar{u}\bar{w} \rangle$ -term in the wave-averaged momentum equation plays an essential part in the consistency of the model in spatially non-uniform situations.
- The classical mild-slope approximation leads to inconsistency of the model, because it yields inappropriate estimates of the $\langle \bar{u}\bar{w} \rangle$ -term. An extended linear wave model for mildly non-uniform situations leads to consistent results.
- Wave-induced current forcing is located there, where the wave energy dissipation actually takes place. This means, that the forcing due to spilling breakers takes place near the water surface, and that forcing associated with bottom dissipation takes place near the bottom.
- The necessity to include a roller contribution when modelling wave-driven currents depends on whether the bulk energy density of the breaking waves is described, or the carrier wave height. Only in the latter case, a roller contribution has to be taken explicitly into account.
- So far, the application of higher-order turbulence models in wave-averaged current models is not supported by sufficient physical knowledge, except maybe for very specific situations.

Acknowledgement

The major part of the work presented herein was carried out during the second author's stay at DELFT HYDRAULICS, in 1988, which was co-financed by the University of Xanthi, Greece. The results will be implemented and utilized by both authors in Project 0035-C, "G6 Coastal Morphodynamics" of the Marine Science and Technology (MAST) Programme of the Commission of the European Communities.

References

- Arcilla, A.S., Collado, F.R., Lemos C.M. and Rivero, F., 1990. Another quasi-3D model for surfzone flows. Proc. 22nd ICCE, Delft (in press).
- Battjes, J.A., 1983. Surf zone turbulence. Proc. XXth IAHR-Congr., Moscow. Sem. "Hydrodynamics of waves in coastal areas".
- Battjes, J.A., 1988. Surf zone dynamics. Ann. Rev. Fluid Mech., 20, p. 257-293.
- Berkhoff, J.C.W., 1976. Mathematical models for simple harmonic linear water waves; wave diffraction and refraction. Doct. thesis, Delft Univ. of Techn., 103 pp.
- Craik, A.D.D., 1982. The drift velocity of water waves. J. Fluid Mech., 116, p. 187-205.

- Davies, A.G., Soulsby, R.L. and King, H.L., 1988. A numerical model of the combined wave and current bottom boundary layer. *J. Geoph. Res.*, 93,C1, p. 491-508.
- Deigaard, R., Fredsøe, J. and Hedegaard, I.B., 1986. Suspended sediment in the surf zone. *J. Waterway, Port, Coastal, Ocean Engrg.*, 112,1, p. 115-128.
- Deigaard, R. and Fredsoe, J., 1989. Shear stress distribution in dissipative water waves. *Coastal Engrg.*, 13, p. 357-378.
- De Vriend, H.J., 1986. 2DH computation of transient sea bed evolutions. Proc. 20th ICCE, Taipei, Taiwan, p. 1689-1712.
- De Vriend, H.J. and Kitou, N., 1990. Incorporation of wave effects in a 3D hydrostatic current model. Delft Hydraulics, Rept. H 1295 (in preparation).
- De Vriend, H.J. and Stive, M.J.F., 1987. Quasi-3D modelling of near-shore currents. *Coastal Engineering*, 11,5&6, p.565-601.
- Engelund, F., 1974. Flow and bed topography in channel bends. Proc. ASCE, Jnl. Hydr. Div., 100,HY11, p. 1631.
- Justesen, P., Fredsoe, J. and Deigaard, R., 1986. The bottle-neck problem for turbulence in relation to suspended sediment transport in the surf zone. Proc. 20th ICCE, Taipei, p. 1225-1239.
- Leendertse, J.J., 1987. A three-dimensional alternating direction implicit model with fourth order dissipative non-linear advection terms. Rijkswaterstaat, Rept. WD-3333-NETH.
- Longuet-Higgins, M.S., 1953. Mass transport in water waves. *Phil. Trans. Royal Soc.*, A254, p. 535-581.
- Longuet-Higgins, M.S., 1970. Longshore currents generated by obliquely incident waves. *J. Geoph. Res.*, 75, p. 6778-6801.
- Longuet-Higgins, M.S. and Stewart, R.W., 1964. Radiation stresses in water waves; a physical discussion with applications. *Deep Sea Res.*, 11, p. 529-562.
- Nairn, R.B., Roelvink, J.A. and Southgate, H.N., 1990. Transition zone width and implications for modelling surfzone hydrodynamics. Proc. 22nd ICCE, Delft, (in press).
- Stive, M.J.F. and Wind, H.G., 1986. Cross-shore mean flow in the surf zone. *Coastal Engineering*, 10, p. 325-340.
- Svendsen, I.A., 1984. Mass flux and undertow in the surf zone. *Coastal Engineering*, 8, p. 303-329.
- Svendsen, I.A. and Lorenz, R.S., 1989. Velocities in combined undertow and longshore currents. *Coastal Engrg.*, 13, p. 55-79.
- Svendsen, I.A. and Putrevu, U., 1990. Nearshore circulation with 3-D current profiles. Proc. 22nd ICCE, Delft, (in press).
- Van Kesteren, W.G.M. and Bakker, W.T., 1984. Near bottom velocities in waves with a current; analytical and numerical computations. Proc. 19th ICCE, Houston, p. 1161-1177.
- Wind, H.G. and Vreugdenhil, C.B., 1986. Rip-current generation near structures. *J. Fluid Mech.*, 171, p. 459-476.

CHAPTER 77

Nonsteady computations of undular and breaking bores

A.F.Teles da Silva ¹ and D.H.Peregrine ²

1. Introduction

A bore occurs when water with local depth h_1 , say, moves over shallower water with depth h_2 , necessarily moving at a lower speed, in a scale in which horizontal distances are a few times bigger than either h_1 or h_2 . The bore is the region of transition between the two uniform depths and speeds. If the slopes are initially gentle, the bore gets gradually steeper and develops into one of three types depending on the ratio $\Delta = \frac{h_1-h_2}{h_2}$. For small enough values of Δ , $\Delta < \simeq 0.3$, the bore front develops into a smooth succession of long waves. The difference between the upstream and downstream levels is fitted with undulations which are long at the front and short at the back. These are called undular bores. For big enough values of Δ , $\Delta > \simeq 0.7$, bore fronts break and the whole bore takes the aspect of a turbulent breaking zone extending over some depths and advancing at a constant speed (over a flat bed); outside this turbulent zone the water is flat. For intermediate values of Δ breaking and turbulence at the front precede a train of smooth undulations. Here the difference in level between upstream and downstream is fitted partially with breaking and turbulence in the front and partially with undulations. these bores are called undular breaking bores.

The classical bore theory, Lamb (1932) article 187, supposes a well developed bore advancing at constant speed and calculates the fluxes of mass, momentum and energy across the bore in a frame of reference moving with the bore speed. It is shown that if mass and momentum are preserved, energy must be necessarily lost. Benjamin and Lighthill (1954), applied this approach, within the approximation of Kortweg & De Vries' equation, to the first

¹ Instituto de Matemática, Univ. Fed. do Rio de Janeiro & Lab. Mec. Fluidos, Prog. Eng. Mec., COPPE, CP68503, CEP21910, Rio de Janeiro - RJ, Brazil

² School of Maths, Univ. of Bristol, Bristol BS8 1TW, England

undulation of an undular bore; they show that, if mass momentum and energy are preserved, the wave is necessarily a solitary wave, if energy is lost the wave is a cnoidal wave. A limitation to the applicability of the classical approach to the whole of an undular bore is that, at any time, the flow at its back is unsteady; because new undulations are continually forming and growing, turning the bore into an intrinsically unsteady phenomenon even if waves in the front assume a nearly steady aspect. Hence, in order to understand the bore as a whole, with its upstream and downstream regions, the evolution must be followed from an initial state. The simplest unsteady model is provided by shallow water equations; although, these are unable to predict undulations because vertical components of velocity are neglected. A higher order unsteady modelling is obtained by either Boussinesq's or Kortweg & De Vries' equations. Peregrine (1966), using a smooth transition as initial state, integrates Boussinesq's equations, numerically, in order to follow the evolution of gentle undular bores. The characteristic formation of smooth undulations is compared with the continuous steepening predicted by shallow water theory. Using K. & De V.'s equation, Gurevich & Pitaevskii (1973), calculate analytically, an asymptotic solution valid for large values of time, the evolution of a step like initial condition. It is found that the separation between successive crests increases logarithmically and the height of the solitons at the head of the bore is 2Δ for an initial step of magnitude Δ .

In the present work we model the unsteady evolution of an initially gentle transition using a completely nonlinear mathematical formulation. The only approximations are the ones inherent to perfect fluid modelling. The flow is described by a potential of velocities ϕ which at any time obeys to:

$$\nabla^2 \phi = 0 \quad (1)$$

$$\phi_t + \frac{1}{2} \nabla \phi^2 + gY = 0 \quad \frac{D\mathbf{R}}{Dt} = \nabla \phi \quad (2)$$

$$\phi_y = 0 \quad (3)$$

$$\lim_{x \rightarrow -\infty} Y = h_1 - h_2 \quad \lim_{x \rightarrow \infty} Y = 0$$

$$\lim_{x \rightarrow -\infty} \nabla \phi = (U_1, 0) \quad \lim_{x \rightarrow \infty} \nabla \phi = (U_2, 0) \quad (4)$$

(1) is to be valid inside the fluid region; equations (2) are to be satisfied on the free surface which is described parametrically by $\mathbf{R} = (X, Y)$ to allow for overturning, g is the acceleration of gravity; equation (3) is valid on the flat bed placed at $y = -h_2$; the four

equations (4) are valid on the extremities, $x = \pm\infty$ and h_1, h_2, U_1 and U_2 are given constants. Moreover we re scale distances by the downstream depth h_2 and accelerations by the acceleration of gravity g . The evolution of the free surface is calculated by a numerical method which is a modification of Dold & Peregrine's (1986) boundary integral scheme from the initial free surface profile

$$Y = \frac{\Delta}{2}[1 - \tanh(\alpha X)] \quad (5)$$

For most of the computations the value of α has been set to $\alpha = 0.25$.

2. Numerical Results

Figure 1a shows the evolution of a strong bore, for $\Delta = 0.8$, for times 0, 2, 4, 6, 8, 10, 12 and 14, (from top to bottom in that order). Figure 1b shows the bore overturning at time 14.95. Figure 2a shows the evolution of an undular breaking bore, for $\Delta = 0.35$, for times 0, 10, 20, 30, 40, 60 and 70, with a vertical magnification of 10. This bore breaks at time 71.9; the breaking crest is shown in Figure 2b.

In order to assess the influence of Δ on the bore evolution we follow the growth of the first wave. Figure 3 shows graphs of height of the first crest, (x axis), against time, (y axis), for several values of Δ : 0.1, 0.2, 0.25, 0.28, 0.3, 0.3125, 0.325, 0.35, 0.4, 0.5, 0.6, 0.7, 0.8, 0.9, 1.0, 1.2 and 1.5 (from bottom to top). Waves have been followed until time 140, for cases in which breaking did not occur, and until the moment when a slope of 90° first appear. Waves can, approximately, be grouped into three types:

- i*) the crest grows towards an asymptotic value;
- ii*) the crest first behaves as if in *i*) and then steepens and rapidly breaks;
- iii*) the crest grows at an accelerated rate until breaking.

These types correspond to the three bore types: undular, breaking and undular breaking. More details of the computations are given in Table 1. Table 1, below, gives the nondimensional time of breaking, t_b , which is the time when a slope of 90° first appear, in $\sqrt{\frac{h_2}{g}}$ units; the height of breaking y_b ; the horizontal distance travelled before breaking, x_b , in h_2 units. The front of the stronger bores break at a height that is slightly bigger than the original ($= \Delta$); also shown in Table 1 are H_1 and H_2 which are the distances from the first and second crests to the bed, respectively, divided by $1 + \Delta$, (upstream level); for Δ greater than 0.7, H_2 is nearly 1. meaning that secondary undulations almost cease to exist. As Δ grows beyond 1.5,

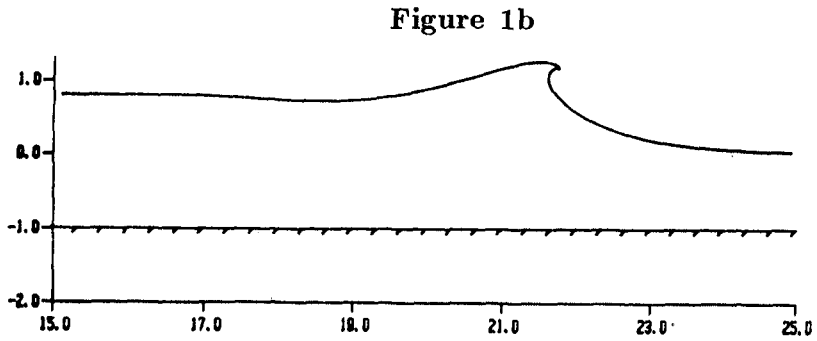
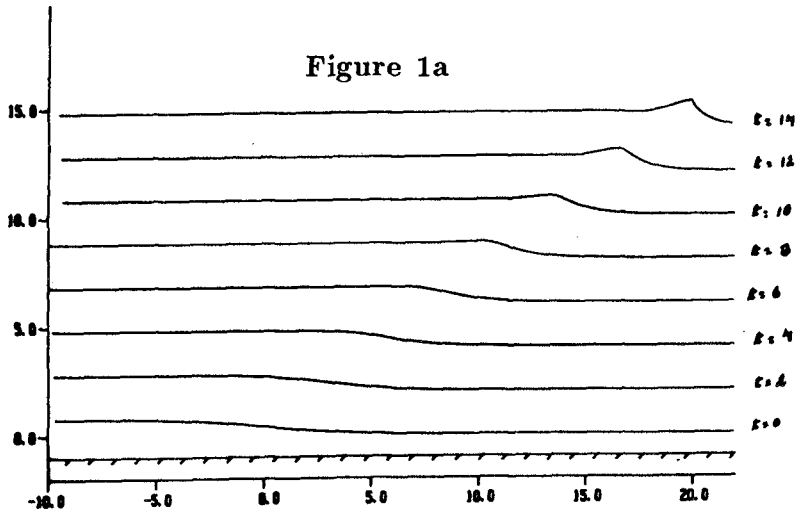


Figure 2a

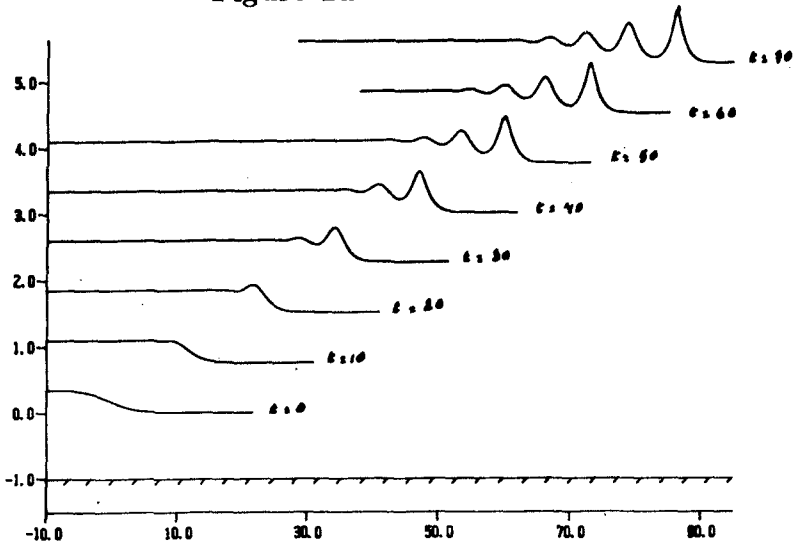


Figure 2b

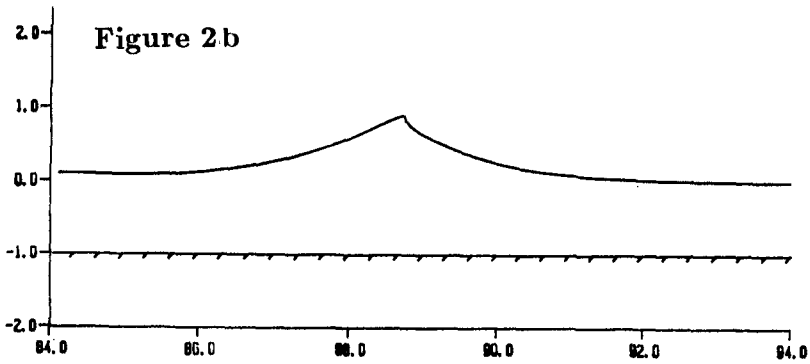


Figure 3

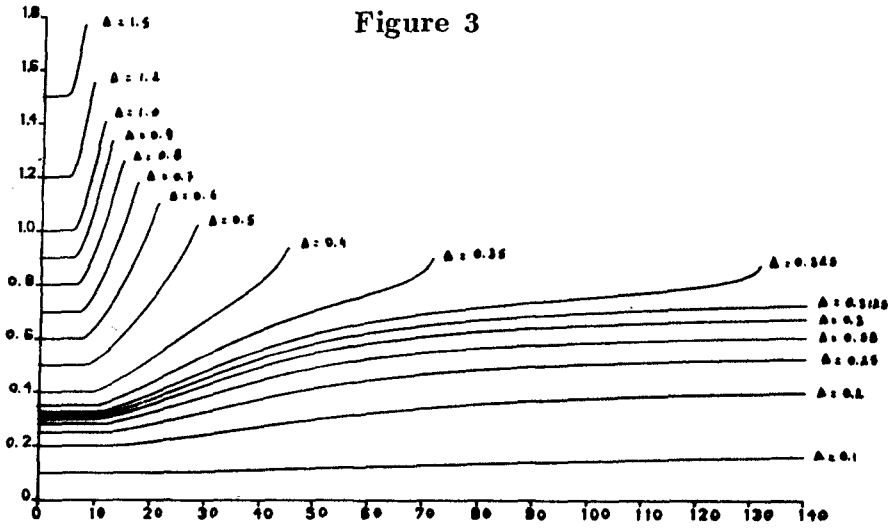
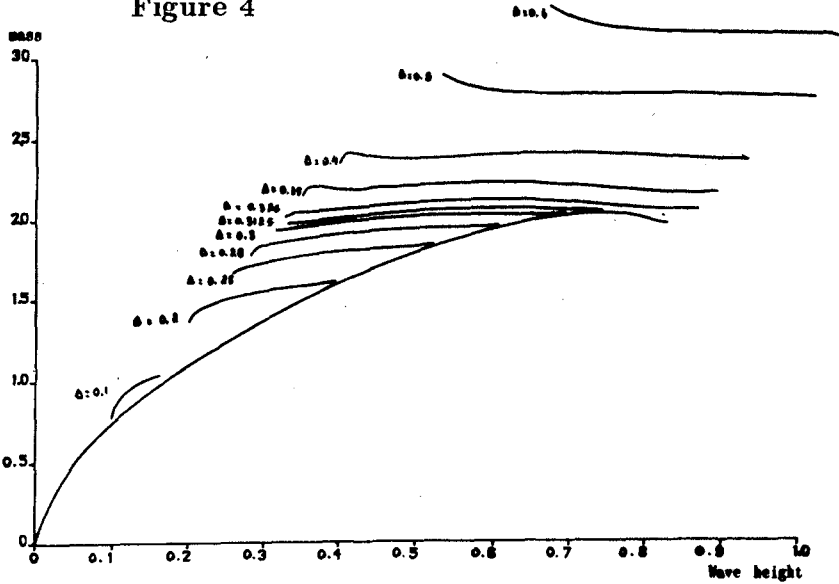


Figure 4



H_1 approaches 1.0; for higher values of Δ the bore breaks before a single wave forms; these facts also appear in the values of $\theta_1, \theta_2, \theta_3$ and θ_4 which are respectively the maximum slopes, in degrees, of the front and back faces of the first and second waves. Note that after breaking the values of H_1 will be reduced.

Δ	t_b	x_b	y_b	H_1	H_2	θ_1	θ_2	θ_3	θ_4
0.325	131.7	164.4	0.87	1.42	1.28	81.5°	26.4°	11.9°	11.1°
0.35	71.9	88.7	0.89	1.40	1.19	88.5°	25.3°	4.3°	3.0°
0.4	45.3	56.2	0.93	1.40	1.12	84.9°	23.0°	1.2°	0.5°
0.5	28.3	36.3	1.02	1.35	1.05	83.5°	21.9°	0.0°	0.0°
0.6	21.1	28.0	1.10	1.31	1.03	85.7°	20.2°	0.0°	0.0°
0.7	17.1	23.5	1.18	1.28	1.00	84.8°	18.6°	0.0°	0.0°
0.8	14.4	20.5	1.26	1.25	1.00	86.2°	17.0°	0.0°	0.0°
1.0	11.1	17.0	1.41	1.20	1.00	84.2°	14.1°	0.0°	0.0°
1.2	9.2	15.0	1.55	1.16	1.00	89.5°	11.5°	0.0°	0.0°
1.5	7.4	13.1	1.77	1.11	1.00	85.5°	7.6°	0.0°	0.0°
2.0	-.	-.	-.	1.05	1.00	87.2°	3.3°	0.0°	0.0°
3.0	-.	-.	-.	1.03	1.00	91.8°	-.°	0.0°	0.0°

Table 1

According to Benjamin and Lighthill (1954) the first wave of a well developed bore is a solitary wave. We expect the computed bores either to break or to develop into solitary waves. For this reason we compare properties of first waves in the bore with properties of solitary waves. Figure 4 shows graphs of mass of the first wave against wave-height for values of Δ equal to 0.1, 0.2, 0.25, 0.28, 0.3, 0.3125, 0.325, 0.35, 0.4, 0.5 and 0.6 (from bottom to top); also shown is the same relationship for the same range of solitary waves for comparison (the longer curve starting at the origin). Some remarkable facts can be observed: waves which are not going to break tend to assume the mass of a solitary wave even if wave-lengths at this stage, $t \leq 140.$, are all less than 4.5 depths; this fact have equally been observed for phase speed and maximum slope; waves which break have more mass than the maximum possible for solitary waves. Nonbreaking waves in Figure 4 tend to approach the solitary wave curve in a way that enables a rough estimate of asymptotic heights of undulations of nonbreaking bores. On this basis we conjecture that $\Delta \simeq 0.3$ is the highest limit for undular bores.

Another result about the evolution of bores is shown in Figure 5 where curves of wave-length of the first undulation is plotted against

Figure 5

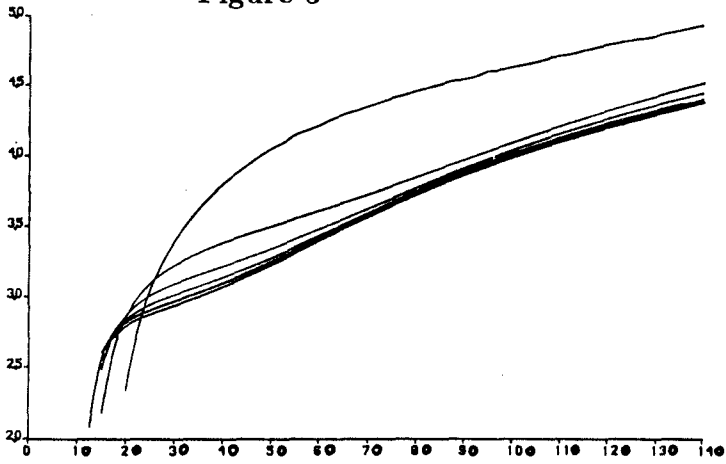
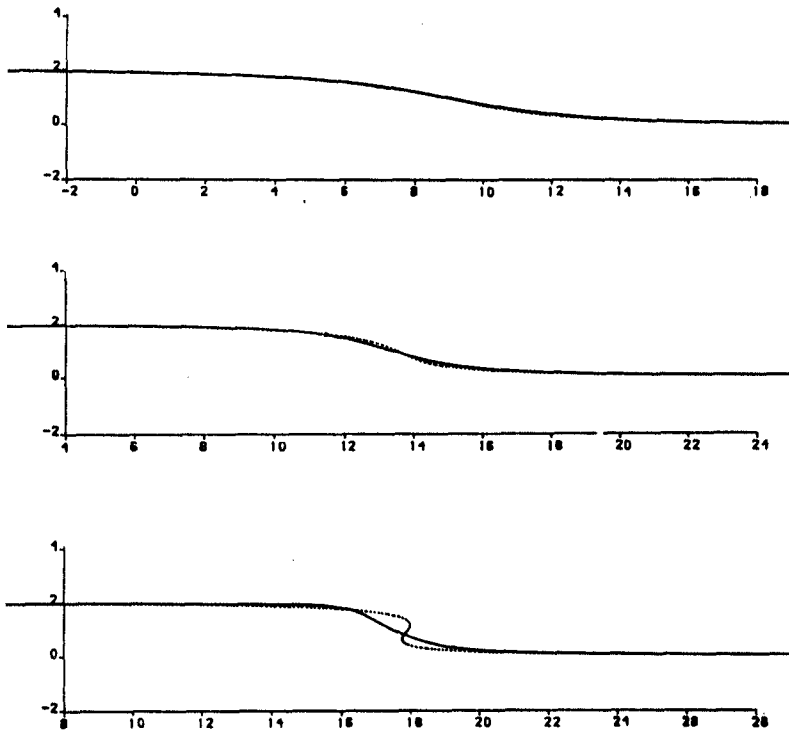


Figure 6



time; the wave-length of the first wave has been calculated as twice the horizontal distance from the crest to the trough just behind. A feature of Figure 5 that is important in the comparison with experiments is that bores undulations stretch faster for the gentler bores.

4. Comparison with weakly nonlinear results

In order to assess ranges of effectiveness of weakly nonlinear modelling we calculate the evolution of the initial free surface condition (5) using both shallow water and Boussinesq's equations and compare the results with the ones obtained by means of fully nonlinear calculations. Shallow water equations provide a good approximation for the initial stages of steepening of initially gentle bore fronts; for large values of Δ , where secondary undulations are not present, shallow water equations remain accurate for slopes up to $\simeq 20^\circ$. Boussinesq's equations are more suitable to model the initial stages of evolution of very small undulating bores. Figure 6 shows the comparison with shallow water equations for the initial condition (5) with $\alpha = 0.125$ and $\Delta = 2.0$; times shown are 4.0, 6.0, and 8.0 (from top to bottom).

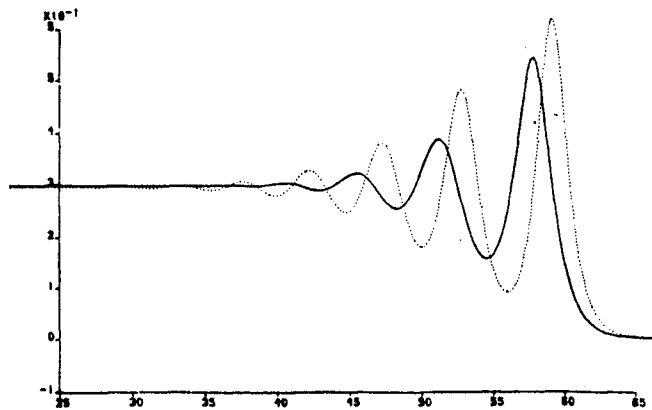
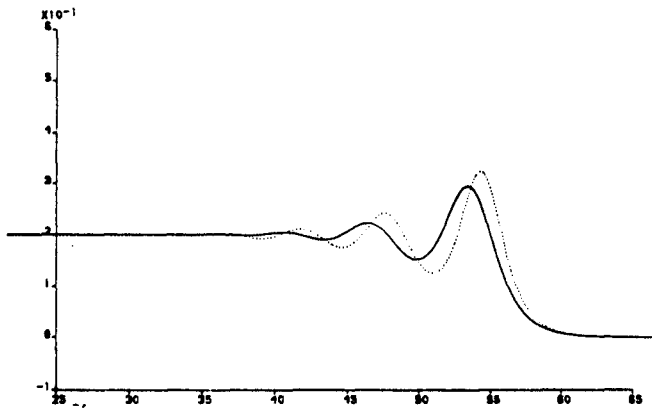
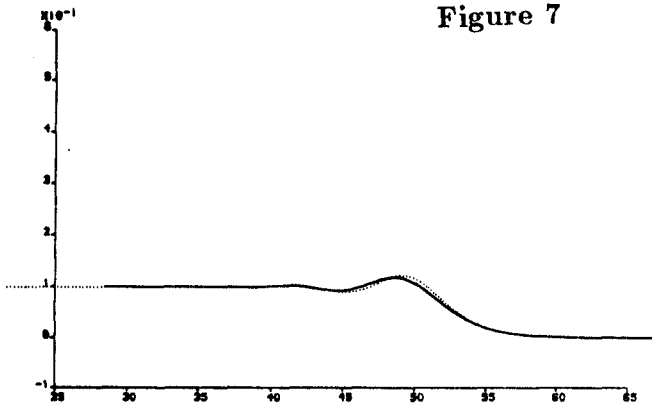
There is a good agreement until time 6.0 when slopes are $\simeq 20^\circ$; after this point shallow water equations predict a too quick steepening and breaking.

Figure 7 shows a comparison between results from Boussinesq's equations (dashed lines) and full nonlinear computations (full lines) for $\alpha = 0.25$, time = 50 and $\Delta = 0.1, 0.2$ and 0.3 (from top to bottom). Boussinesq's equations overpredict undulation growth, bore speed and number of undulations in a way that errors increase with Δ and time for a fixed value of α .

5. Comparison with experiments

Favre (1935) conducts experiments in a canal 75.58m long and 0.41m wide; from Favre's experiments we are specially interested in his first and third sets in which depth of water is $\simeq 0.2050m$ and $\simeq 0.1075m$, respectively. Results for 0.2050m of depth compares well with our computational experiments. In this set Δ varies from 0.062 to 0.278 depths. It is found that, at the end of the tank, after travelling for about 300 depths, the first waves acquire a nearly steady aspect; final wave-lengths range from $\lambda = 10.8$ depths to $\lambda = 8.6$ depths. Of special interest for comparisons are the bores with $\Delta = 0.202$ and $\Delta = 0.278$ depths which produce waves that at the end of the canal are respectively 0.395 and 0.570 depths of height. According to results in Figure 3 we can expect our calculated bores with $\Delta = 0.2$ and $\Delta = 0.28$ depths to produce solitary waves which are $\simeq 0.41$ and $\simeq 0.62$ depths high respectively. These figures

Figure 7



are respectively 3.8% and 8.8% higher than Favre's; the small differences can still be accounted for viscous dissipation of long waves travelling over long distances.

For depth 0.1075*m*, Favre's third set, viscous effects are more conspicuous and results do not match as well with our calculations. In this set Δ ranges from 0.080 to 0.500 depths. One mismatch appears in the measured wave-lengths. In the previous set, undulations at the bore front for $\Delta = 0.238$ have a wave-length of 9.024 after travelling for about 300 depths; in depth 0.1075*m*, with a bore with $\Delta = 0.230$, a wave-length of 8.47 depths is found at the end of the canal which is about 600 depths long. In a completely inviscid situation we should expect this later bore to attain greater wave-lengths for two reasons: gentler bores should stretch faster and bores continually stretch as they travel further; (see Figure 5). The results of Figure 5 are confirmed by Favre's experiments of the same set. Another important difference between our inviscid results and Favre's third set is the breaking, spilling, of the bore front for $\Delta = 0.281$, at a distance of about 350 depths from the start of the canal; in his first set the bore with $\Delta = 0.278$ produces waves which are 0.570 depths high; one could expect smaller waves for $\Delta = 0.281$ because of a stronger viscous dissipation in shallower waters; this wave must break at a height smaller than 0.6 depths which is too small when compared with results for y_b in Table 1.

6. Bores on water of constant vorticity

Favre's results for depth 0.1075*m* are certainly more affected by viscosity than these for depth 0.2050*m*. One of the effects of viscosity is dissipation of energy; but the sole dissipation of energy cannot be accounted for differences found in the comparison between inviscid results and Favre's experiments. Another important manifestation of viscosity, for long waves, is the shedding of vorticity generated at the boundary layer on the bed. Negative vorticity produced at the bed is difused into the fluid and its distribution varies with time and location which makes mathematical modelling a difficult task. For mathematical convenience we adopt a simple model in which vorticity is a constant. A perturbation in a 2D flow with constant vorticity can be represented by a potential flow. Hence, in order to introduce constant vorticity into the flow, we modify the boundary value problem for the potential ϕ given in equations (1) to (4) adding to the first and second equations (2), the terms:

$$-\omega(Y\phi_x - \psi)$$

to the left hand side of the first of equations (2), where ω is the value for the constant vorticity and ψ is a complex conjugate of ϕ

and

$$-\omega Y_i$$

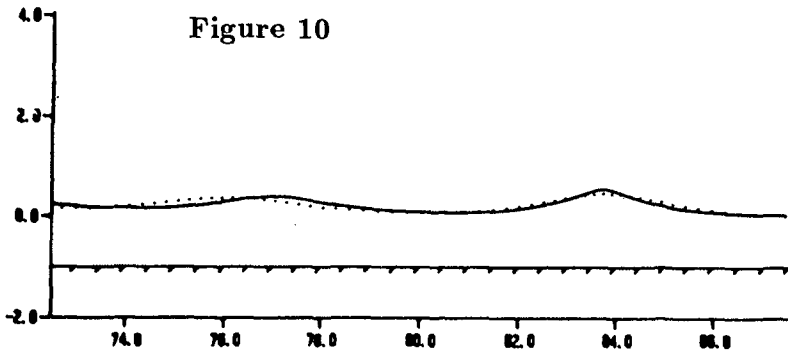
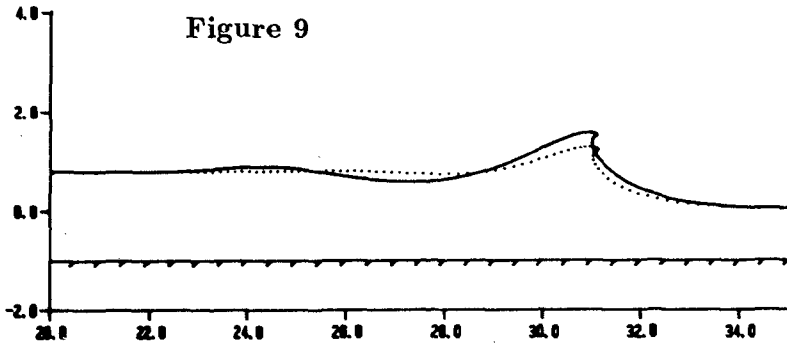
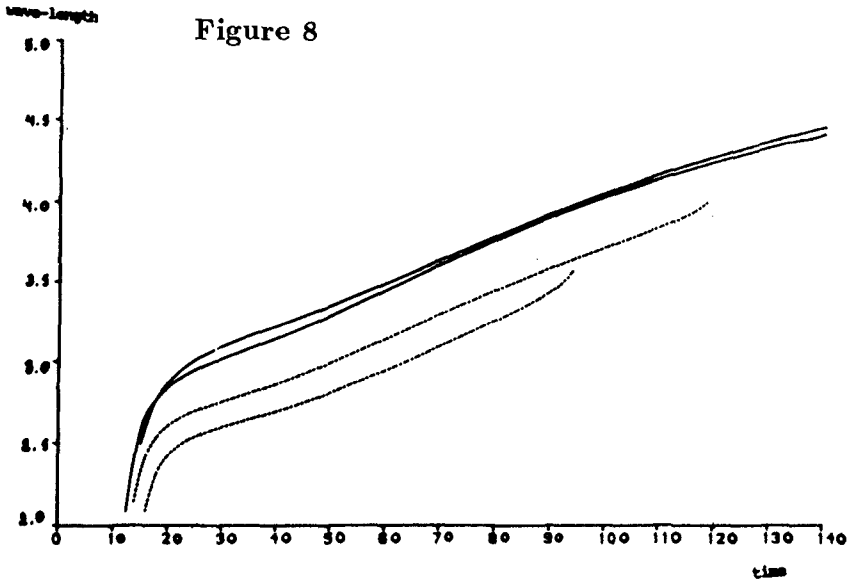
to the right hand side of the second of equations (2).

Despite the simplicity of constant vorticity modelling, features of the third set of, depth = 0.1075m, of Favre's experiments are present in our computations. Figure 8 shows the evolution of wave-length with time for irrotational and rotational bores: the full line curves are irrotational bores for $\Delta = 0.25$, upper curve, and $\Delta = 0.28$, lower curve; the dashed lines are rotational bores: for $\Delta = 0.28$ and $\omega = -0.125$, upper curve, and for $\Delta = 0.25$ and $\omega = -0.25$, lower curve. The two irrotational bores show the usual pattern in which the lower one is longer at any given time. Negative vorticity affects wave-lengths: the rotational bores are shorter than the corresponding irrotational ones, moreover the lower rotational bore, $\Delta = 0.25$ is made shorter by the use of stronger negative vorticity, $\omega = -0.25$ compared with $\omega = -0.125$. Another feature reproduced by constant negative vorticity modelling is breaking at smaller wave-heights; Figure 9 shows breaking of two bores with $\Delta = 0.8$, the dashed line bore is irrotational and the full line one moves in water of vorticity $\omega = -0.25$; the legend to the graph belongs to the rotational bore and the profile shown is for time 12. Results in Table 1 show that the corresponding irrotational bore breaks (with an angle of 90°) at time 14.4 and its crest is, at the moment of breaking, at $x = 20.5$, hence negative vorticity causes premature breaking. About the profile of the bore $\Delta = 0.281$, Favre comments that it has the shape of a cycloid; such a comment cannot apply to irrotational waves. Figure 10 compares the profiles of the first two undulations of two bores, both with $\Delta = 0.25$; the one in dotted lines is an irrotational bore and the one in full lines represents the profile of a bore with vorticity $\omega = -0.25$. We notice that not only wave-lengths are shorter but crests are more peaked and troughs are flatter.

Positive vorticity has an opposite effect: Undulations tend to get longer, acquire a round sinusoidal shape and break at bigger heights when compared with irrotational ones. Bores which move up estuaries, probably, travel on water in which vorticity is mainly positive, generated by the boundary layer of the downstream river current. These bores should look rounder and move faster than bores running over still water.

7. Conclusions

Comparisons between Favre's first and third sets of experiments show that depth of water and width of the channel play an important role on results. Sandover and Zienckiewicz (1957), conducted experiments on bores for channel depths of 2", 3", 4" and 6". They present



results for nondimensional discharge of water against wave-height at the end of the canal. These results show that for the same discharge wave-heights consistently increase with channel depth. They also show results for a channel in which the bed is rough and crests at the end of the canal are consistently lower when compared with results for the same discharge and depth on smooth beds.

Favre's and Sandover and Zienkiewicz's results show that interaction with the boundary layer at the bed may be important in the analysis of results of experiments with bores. The presence of a boundary layer has two important effects: dissipation of energy and generation of vorticity. Dissipation of energy contributes to lower wave heights and the presence of vorticity will have an effect on breaking, on wave-lengths, on wave shape and on the limit on maximum Δ for undular bores.

Results in Figure 4 and Table 1 lead to the conclusion that maximum height of bores divided by upstream depth, H_1 , grows with Δ for $\Delta < \simeq 0.3$ and then decay for breaking bores, ($\Delta > \simeq 0.3$). The limiting figures 0.3 and 0.7 have been found through an irrotational modelling; how this figures will change in real situations may depend on average values of vorticity. In situations in which vorticity is negative, as it happens in bores running over still water, the only vorticity is produced at the bed by the undulations, these figures will be smaller. In situations in which the bore moves upstream a current, the average vorticity can be positive and the limiting waves higher.

8. References

- Benjamin, T. B. & Lighthill, M. J. (1954)
On cnoidal waves and bores. *Proc. Roy. Soc. A*, 224, 448-460.
- Dold, J. W. & Peregrine, D. H. (1986)
An efficient boundary int. meth. for steep unsteady waves.
Numerical methods for fluid dynamics II, eds: K. W. Morton
& M. J. Baines, pp 671-679. Clarendon Press, Oxford.
- Favre, H. (1935)
Etude théor. et expérimental des ondes de translation.
Dunod, Paris.
- Gurevich, A. V. & Pitaevskiï, L. P. (1973)
Nonstationary structure of a collisionless shock wave.
Zh. Eksp. Theor. Fiz. 65, 590-604
- Lamb, H. (1932)
Hydrodynamics. Dover, New York.

CHAPTER 78

Experimental and Numerical Study on Solitary Wave Breaking

Hitoshi Nishimura¹ and Satoshi Takewaka²

Abstract

Interior flow fields under drastically transforming solitary waves were visualized and recorded using a high-speed video system. Flow velocities were estimated by tracing fluid particles through spatial correlation analysis of video images. A Lagrangian equation system was successfully employed to numerically simulate two-dimensional wave transformations in a vertical plane.

Introduction

In these years, remarkable progresses have been achieved in techniques for analyzing nearshore wave transformation. However, our knowledge on the fundamental mechanism of wave breaking is rather limited as well as on after-breaking wave transformation. Existing breaking indices are by no means enough for application to a complicated field of composite and/or irregular waves. For future study of this problem, introduction of new methods is of particular importance in both experimental and theoretical approaches.

Since wave transformation such as breaking is quite unstable, exactly the same phenomenon cannot be reproduced even in a well-designed wave flume. It is therefore difficult to obtain an entire picture of interior fluid motion by repeating velocimeter measurements. At least, the accuracy of thus obtained velocity distribution cannot be sufficient for succeeding estimation of pressure, vorticity, and so forth. In this

¹ Professor, Inst. of Eng. Mechanics, Univ. of Tsukuba, Tsukuba, Ibaraki, 305, Japan.

² Research Associate, Dept. of Civil Eng., Tokyo Inst. of Tech., O-okayama, Meguro, Tokyo, 152, Japan.

context, observation and measurement with visual devices are much more promising.

On the other hand, a Eulerian equation system is normally employed in computational approach to two-dimensional fluid motions. Numerical schemes in the Eulerian framework, however, have a weakness in handling moving boundaries. Note that the fluid motion under a wave is essentially prescribed by surface conditions and that the surface profile rapidly deforms under a breaking condition. Although the Lagrangian equations have some disadvantages in particular in their numerical integration process, they may provide a useful means for wave transformation analysis, allowing much more rigorous treatment of surface boundaries.

Methods of Picture Analysis

Techniques of flow visualization and video image analysis are employed here to investigate the hydraulic mechanisms of solitary wave runup on a vertical wall and its breaking on a uniform slope. Once if a precise velocity field in a wave is obtained, then corresponding distributions of pressure, vorticity, etc., will be easily deduced.

A conventional method of neutral buoyancy float tracing is not quite appropriate for such a purpose. It is not easy to keep the floats with finite sizes in suspension and they may not move in the same manner as water particles. The number of floats is limited for computerized tracing and, furthermore, their location cannot be well controlled. A flow field is more conveniently visualized by densely scattering small solid particles in the fluid. In this case, flow velocity at an arbitrary position is estimated from the variation of a local brightness pattern through either temporal or spatial correlation analysis.

Figure 1 describes the principle of temporal correlation analysis (for example, Miike et al., 1986), in which time-series data of brightness variations at adjacent two points are compared. Time-lag between the variations is considered to be the traveling time of a water particle for the distance between these two points. The flow direction can also be detected since the correlation will be highest between two points along a local path-line. This method is suitable to real time measurement of flow velocity at a fixed point, but is not applicable to strongly unsteady flows, requiring steady shift of brightness variation for a finite time interval.

The spatial correlation analysis (for example, Kimura and Takamori, 1986), in principle, is more similar to the normal float tracing. A recorded image of visualized fluid at each time is converted into a matrix of digital brightness gradation data at all the pixels. A small square body of fluid is specified by a reference frame fixed in a matrix, whereas a test frame with the same size is moved in another matrix for an adjacent time as shown in Figure 2. The spatial correlation between brightness patterns in these two frames is evaluated in terms of the correlation coefficient R defined by

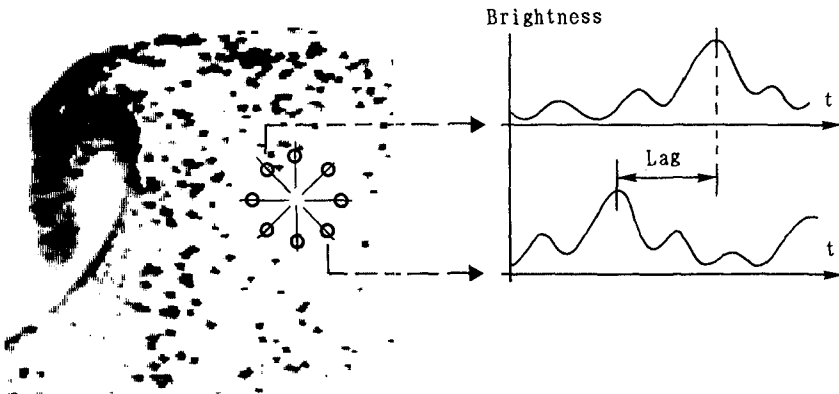


Figure 1. Temporal Correlation Analysis

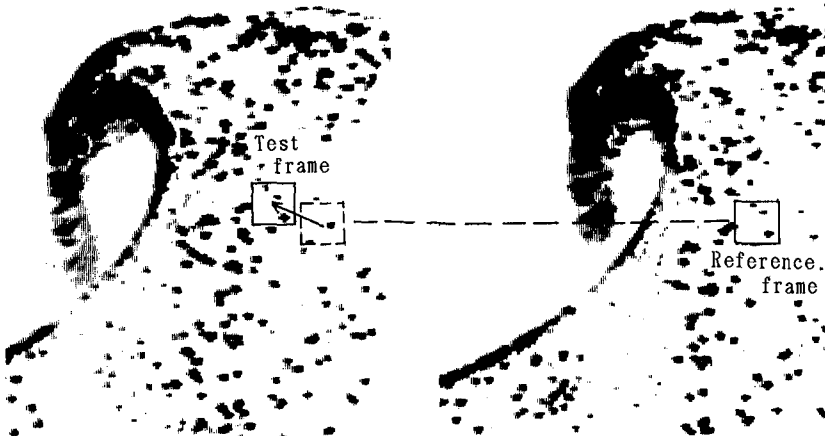


Figure 2. Spatial Correlation Analysis

$$R = \frac{\sum (m_i - \bar{m})(n_i - \bar{n})}{\sqrt{\sum (m_i - \bar{m})^2 \sum (n_i - \bar{n})^2}} \quad (1)$$

where m_i and n_i represent the brightness gradations at the i -th pixels in the reference and test frames, and \sum and $\bar{\quad}$ respectively denote summation and average over the frames. Higher correlation will be obtained as the test frame gets closer to the new location of the fluid body in question. Spatial displacement of the fluid body during a prescribed time interval is thus estimated. This method is adopted in the following, since it is obviously applicable even to unsteady flows.

When brightness variation is smooth both in time and in space, introduction of gradient method is recommended to notably reduce the computational load for the above-explained fitting test. Provided that the apparent brightness of a water particle is kept unchanged as it moves, the total derivative of the brightness B should vanish: that is,

$$dB/dt = B_t + UB_x + VB_y \quad (2)$$

where t is the time, x and y are the horizontal and vertical coordinates, U and V are the velocity components in the x - and y -directions, and suffices denotes partial derivatives. The above relationship gives the flow direction from temporal and spatial gradients of brightness.

It should be also noted that the angle of fluid particle rotation can be directly detected by rotating the test frame and seeking for better fit, where the brightness values have to be interpolated for the pixels in the rotated frame. The local vorticity can be thus estimated possibly more accurately than from velocity gradients. Pre-processing of image data using filters may be helpful in these advanced analyses (Huang, 1981).

Experimental Setup and Data Processing

For each case of experiment, either a vertical wall or a uniform slope were installed in a wave flume 17m long, 40cm wide and 60cm deep. A solitary wave was generated by a single forward motion of a piston-type wave board driven by compressed air. In order to lessen the effect of parallax in video recording, the flume width was reduced to 10cm by a partition wall with a gradual contraction in front of the wave generator.

The time-scale of the present experiments required the use of high-speed monochromatic video system, by which 1000 scenes can be recorded per second. A scene was resolved into 256x256 pixels when converted to a

matrix of digital brightness gradations. Flow was visualized by scattering yellow polyethylene beads with diameter of roughly 0.5mm in the water. The beads are originally heavier than water, but their specific gravity is adjustable by heating because of gas containment. The density of bead distribution was determined on trial and error basis so as to produce the best video images. The material of background wall and the directions of lighting had also to be carefully decided. Reflected lights from water surface and basin walls badly disgrace the reliability of image data.

Figure 3 shows the outline of data acquisition and processing system, where the arrows indicate the flow of data. A set of digitized image data is enormous in its volume, while a high-speed video tape can be rewound only several times. Obtained analogue data, therefore, were first copied on a normal tape, and only necessary parts of the data for each analysis were stored on a hard disk after A-D conversion. For efficient processing of data by a micro-computer, it is desirable to write programs in a machine language.

Results of Experiments

Photo 1 shows video images describing runup and return flow motions of a solitary wave on the vertical wall. This can also be regarded as the formation process of a standing wave. It was observed that the lower layer water starts to fall slightly before the maximum runup height is reached. A very slender runup profile is thus formed. After that, the crest water gets into nearly

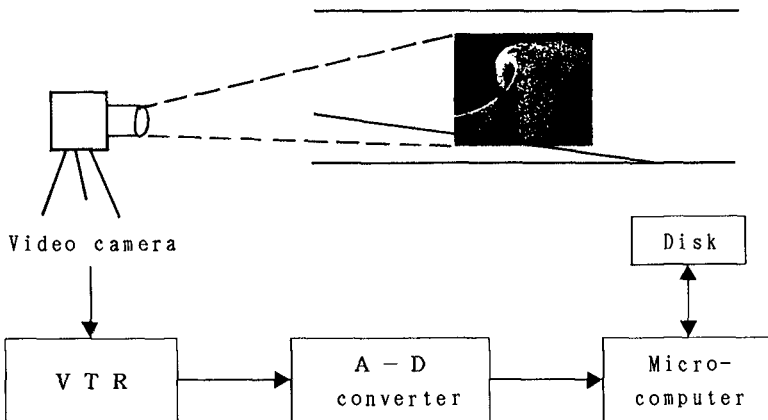


Figure 3. Data Acquisition and Processing System

free fall motion and plunges into lower water layer, yielding a vortex motion at the foot of the wall. Slow replay of video record in fact well exhibit such details of rapid wave deformation. A result of image analysis is given in Figure 4, which shows an instantaneous flow field in the rising stage. Obvious misevaluations of velocity appear at several points in the figure. In the fitting tests, the frame size of 9×9 pixels were adopted, and displacements of water particles were evaluated in pixel unit. More precise velocities will be obtained by estimating sub-pixel fractions of displacements through two-dimensional interpolation.

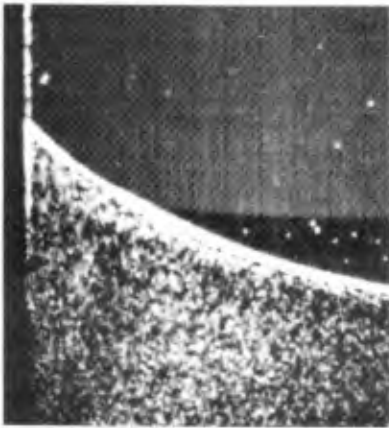
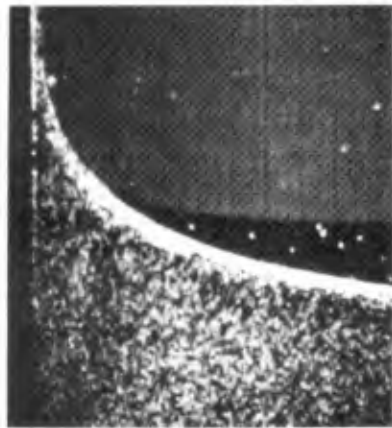
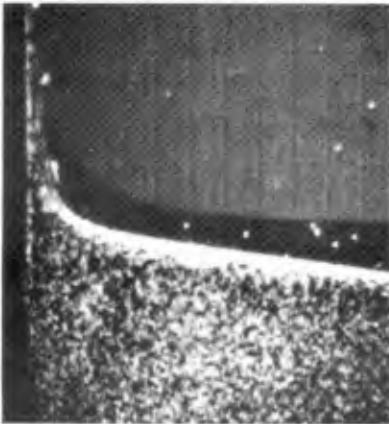
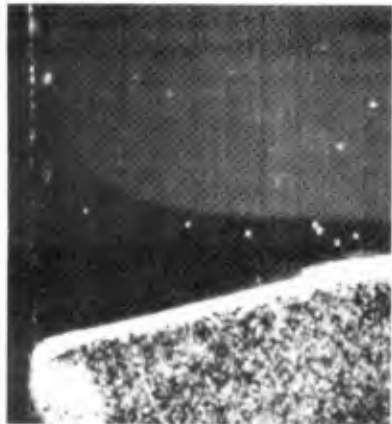
(a) $t = 6.46s$ (b) $t = 6.56s$ (c) $t = 6.64s$ (d) $t = 6.84s$

Photo 1. Solitary Wave Runup on a Vertical Wall

Photo 2 shows a visualized breaking motion of a solitary wave on the 1/20 slope. A shadow region appears under the overturning wave crest, since light source was located on the upper flange of wave flume. Figure 5 is an example of obtained velocity field. The velocity vectors were plotted only for the points where larger correlation coefficients than 0.7 was obtained in the fitting tests. This criterion of minimum reliability could not be attained for the shadow region, indicating the fatal importance of lighting technique for thorough estimation of velocities over the whole region.

Lagrangian Equation System

For theoretical treatment of fluid motion in a vertical plane, it is here assumed that the fluid is inviscid and incompressible. A further assumption is that only the gravity is exerted as an external force.

The continuity equation in the Lagrangian framework is given as

$$X_a Y_b - X_b Y_a = J \quad (3)$$

where a and b are the Lagrangian parameters to identify a water particle, X and Y are the horizontal and vertically upward coordinates to indicate the location of the water particle at an arbitrary time, J is at most a function of a and b , and suffices again denotes partial derivatives. The above equation is differentiated with

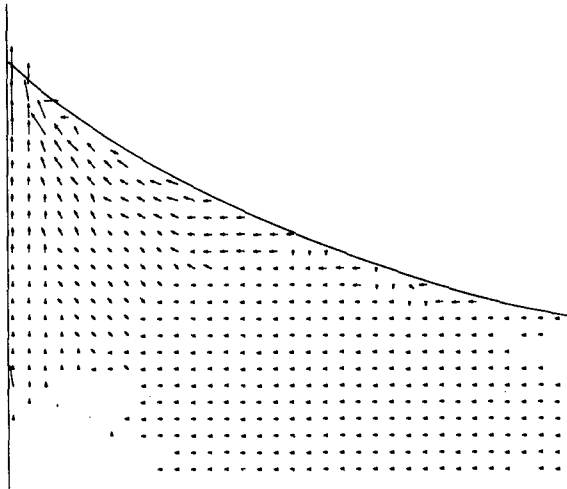


Figure 4. Observed Flow Velocities in a Solitary Wave Running Up on a Vertical Wall



(a) $t = 5.140s$



(b) $t = 5.165s$



Photo 2. Solitary Wave Breaking on a Uniform Slope

respect to time t to yield

$$U_a Y_b - U_b Y_a - V_a X_b + V_b X_a = 0 \tag{4}$$

in which the velocity components U and V are simply related to X and Y as

$$U = X_t, \quad V = Y_t \tag{5}$$

On the other hand, the momentum equations are written as

$$X_{tt} X_a + (Y_{tt} + g) Y_a = -P_a / \rho \tag{6}$$

$$X_{tt} X_b + (Y_{tt} + g) Y_b = -P_b / \rho \tag{7}$$

where P is the pressure, g is the gravitational acceleration, and ρ is the fluid density. Elimination of force terms in the above equations through cross-differentiation and single integration of the obtained equation with respect to time lead to the following law of vorticity conservation.

$$U_a X_b - U_b X_a + V_a Y_b - V_b Y_a = C \tag{8}$$

where C is an arbitrary function of a and b .

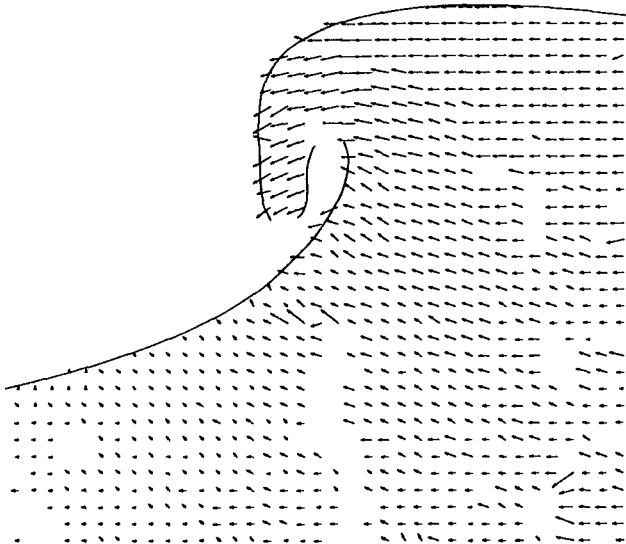


Figure 5. Observed Flow Velocities in a Breaking Solitary Wave

For simplicity, a and b are defined as the positional coordinates of a fluid particle at a reference time $t=0$ when the fluid is at rest. It is most convenient to define the coordinate system in such a way that either a or b takes a constant value along every boundary. For a solid boundary, the expression of boundary configuration in terms of X and Y by itself gives a kinematic condition. Along a free surface, $P=0$ is imposed as a dynamic condition, which can be easily rewritten in terms of the other unknown variables with reference to the momentum equations (6) and (7).

Numerical Simulation Using Lagrangian Equations

Numerical analysis with experimental verification is a useful means for investigating the detailed dynamics of wave transformation. Behavior of surface waves is essentially governed by the boundary conditions at the free surface. Although the Lagrangian coordinate system is possessed of a definite advantage in describing a moving boundary (Chan, 1975), it has been rarely employed in wave computations, perhaps because of 1) second order derivatives with respect to time involved in the equations of motion, 2) nonlinearity of both the equations of motion and continuity, and 3) weakness against large deformation of computational grids. These difficulties, however, became less significant nowadays as computational technology rapidly progressed. For this sort of simulation, two alternative formulations are available.

One is a velocity solution method, where the continuity equation (4) and the irrotationality constraint (8) are discretized and solved simultaneously with given boundary conditions for velocity components at all the grid points. The computation proceeds to the next time step through integration of Eq. (5). It is obvious that this method is applicable only to irrotational fluid motion.

The other is a pressure solution method, in which the original set of equations is directly treated, that is, discretized pressures in the momentum equations (6) and (7) are determined so that the resultant deformation of every fluid particle satisfies the continuity equation (3). This formulation for the pressure yields in principle a Poisson-type equation, which is numerically solved through easier operation of matrices with a smaller dimension. Furthermore, the pressure formulation is more flexible in taking into account secondary factors such as fluid viscosity and surface tension. A shortcoming of this formulation lies in weaker constraint against the generation of non-physical vorticity,

which often results in computational instability of checkerboard-split type.

It proved from trial computations of the solitary wave transformations that two methods mentioned above yield no significant difference in their results. Computed distributions of velocity and pressure for the case of solitary wave runup are shown in Figure 6, where both the coordinates and pressure are nondimensionalized with the still water depth as length-scale. Water particles are either at rest or slowly falling except near the wave crest as observed in the corresponding experiment. Extremely mild pressure gradient in the upper layer gives a theoretical background to the observed free-fall motion of crest water. The computation fails immediately after this as fatal distortion of computational grids emerges in the crest region.

Computed velocity and pressure in the breaking wave are shown in Figure 7. Mild pressure gradient in the crest region implies less dynamical interaction between water particles. Further decrease in the local pressure will lead to a free motion of the crest water and possibly to air entrainment. On the contrary, verti-

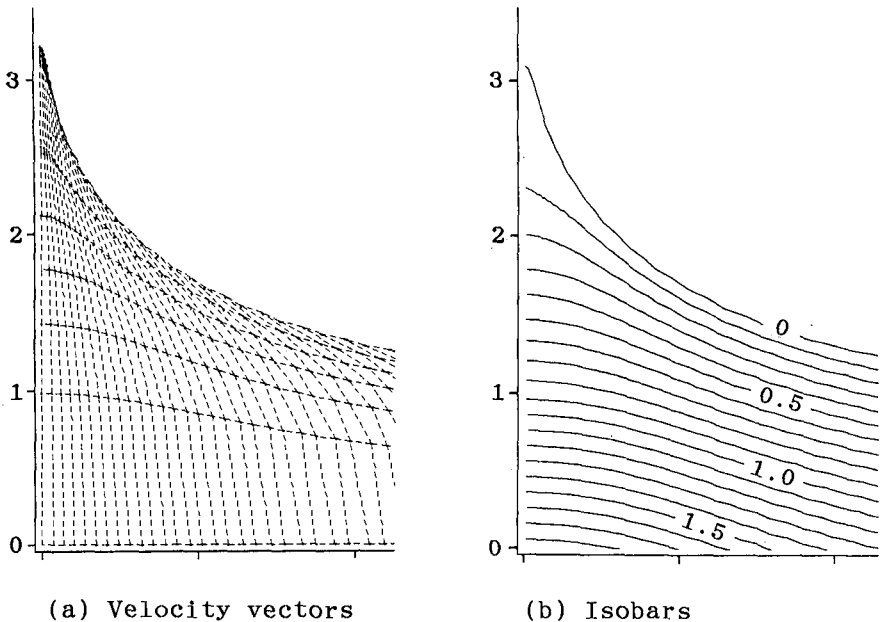
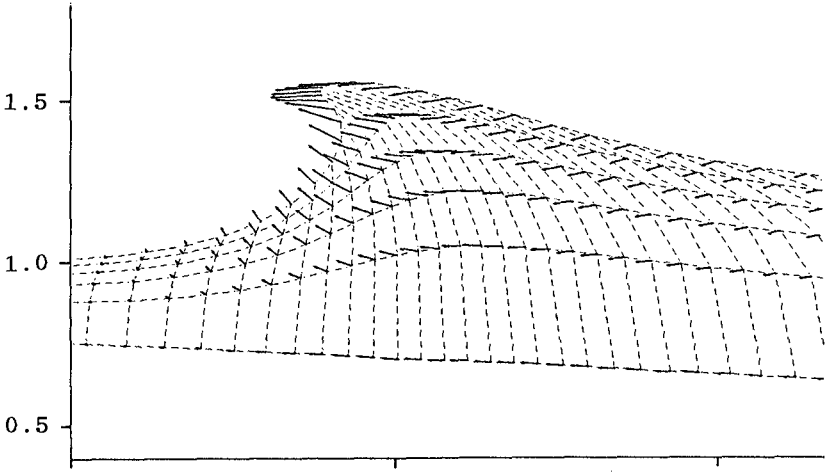
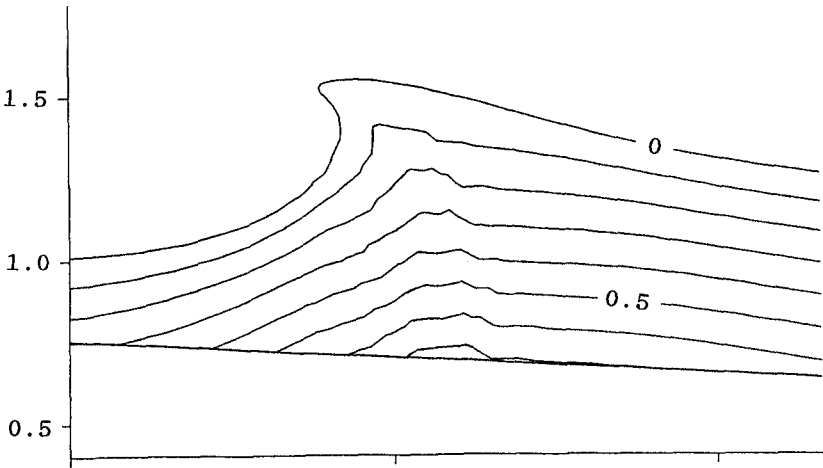


Figure 6. Computed Distributions of Velocity and Pressure in a Solitary Wave Running Up on a Vertical Wall

and possibly to air entrainment. On the contrary, vertical pressure gradient at the foot of the breaker front is rather steep, providing a good circumstance for sediment suspension. In general, numerical simulation excluding the effect of surface tension allows unrealistic formation of a sharp plunging nose.



(a) Velocity vectors



(b) Isobars

Figure 7. Computed Distributions of Velocity and Pressure in a Breaking Solitary Wave

Concluding Remarks

For better understanding of wave breaking phenomena, combined experimental and theoretical investigations are required particularly on their dynamical aspects with more attention to the process of local pressure reduction. The spatial correlation analysis of video images provides a useful means in such studies as well as the numerical analysis in the Lagrangian framework. The accuracy of velocity estimation by means of image analysis is expected to largely improve in the near future as video systems with higher resolution become available.

References

- Chan, R.K.C. (1975): A generalized arbitrary Lagrangian-Eulerian method for incompressible flows with sharp interfaces, Jour. Comp. Phys., Vol. 17, pp. 311-331.
- Huang, T. S. (1981): Image Sequence Analysis, Springer Verlag, 437 p.
- Kimura, I. and T. Takamori (1986): Image processing of flow around a circular cylinder by using correlation technique, Proc. 4th Int. Symp. Flow Visualization, pp. 221-226.
- Miike, H., Y. Kurihara, H. Hashimoto and K. Koga (1986): Velocity field measurement by pixel-based temporal mutual-correlation analysis of dynamic image, Trans. IECE Japan, Vol. E69, No. 8, pp. 877-882.

CHAPTER 79

WAVE REFLECTION BY A NUMBER OF THIN POROUS PLATES FIXED IN A SEMI-INFINITELY LONG FLUME

S. W. TWU¹ and D. T. LIN²

ABSTRACT

The reflection of small-amplitude surface waves by a number of vertical porous plates is investigated. The plates are fixed in a semi-infinitely long channel of constant depth. Analytic solutions in dimensionless closed form are presented for the surface wave profiles in the several regions separated by these plates. And from them the reflection coefficient is obtained. Three cases, one to three porous plates, are evaluated. The results show that for incident waves in the range of $1/20 < \text{water depth/wave length} < 1/2$, it is appropriate to maintain the spacing between every two adjoining plates, and between the end wall and its nearest plate at a value of 0.88 times the water depth. As two or three porous plates are used for damping wave, an arrangement would be more effective if the front porous plate has a larger porosity and the back one has a smaller porosity. Several experimental tests for these porous-plate wave absorbers are conducted and the reflection coefficients are measured by using Goda's method. It is found that the theoretical solutions agree fairly well with the experimental results.

I. INTRODUCTION

The reflection and transmission of small-amplitude surface waves by a thin vertical barrier were first studied by Dean (1945). In Dean's analysis, the vertical barrier was submerged in water with its top edge at a distance below the free surface. Since then, several similar problems have been analyzed by authors, such as Wiegel (1960), Newman (1965), Mei (1969), Macaskill (1979), etc. In most of their analysis, the obstacles are assumed to be placed in a spacious water area without any boundary effect. It is known that if there is any other structure existing around the barriers, such as a back wall, the estimating results will be different. Chwang (1984) analyzed the reflection of small-amplitude surface wave by a thin porous plate fixed near the end of a semi-infinitely long channel of constant depth. Chwang found that as the distance

-
1. Professor, Hydraulics & Ocean Eng'ng Dept.; Researcher, Tainan Hydraulic Laboratory, Cheng-Kung Univ., Tainan (70101), Taiwan, R.O.C.
 2. Engineer, Taiwan Fishery Technical Consultants. 6F, 14 Wen-Chow Street, Da-An District (10616). Taipei, Taiwan, R.O.C.

between the porous plate and the channel end wall (l) is equal to a quarter wave length plus a multiple of half-wave length of the incident wave, then the reflected wave amplitude is reduced to a minimum. In water areas where the waves have a variety of wave length, it is unlikely to keep a constant value for l/λ (λ the wave length). Then in this situation, The problems of how the spacing between the porous plate and the end wall may affect the reflection coefficient if a single plate is used, and what might be the appropriate spacing among these plates if a number of porous plates are adopted are investigated in this paper.

II .THEORETICAL CONSIDERATION

Three thin porous plates are assumed to be located in a semi-infinitely long channel of constant depth shown in Figure 1. The first plate is located at $x=0$, the second at $x=-l_1$, the third at $x=-(l_1+l_2)$, and the end wall at $x=-(l_1+l_2+l_3)$. An incident wave propagating in the negative x direction toward the porous plates is represented by

$$\eta_i = a \sin (\omega t + K_0 x) \dots \dots \dots (1)$$

where η_i is measured from the undisturbed mean free surface at $y=h$, K_0 is the wave number, ω is the circular wave frequency and a is the incident wave amplitude which is assumed to be very small in comparison with the water depth(h).

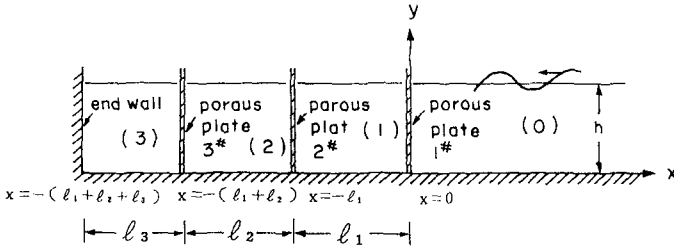


Fig.1. Sketch of three porous plates in a semi-infinitely long flume.

The fluid in the channel is assumed to be inviscid and incompressible, and its motion irrotational. Therefore, the velocity potentials $\Phi_j(x,y,t)$ exist in all regions and the velocity of the fluid can be expressed as

$$\vec{V}_j = \nabla \Phi_j \quad (j=0,1,2,3) \dots \dots \dots (2)$$

where the subscript j refers to the j th fluid region. Region (0) represents the region $x>0$, region (1) represents $-l_1 < x < 0$, region (2) represents $-(l_1+l_2) < x < -l_1$, and region (3) represents $-(l_1+l_2+l_3) < x < -(l_1+l_2)$. The velocity potentials satisfy the two-dimensional Laplace equation

$$\nabla^2 \Phi_j = 0 \quad (j=0,1,2,3) \dots \dots \dots (3)$$

The linearized free-surface kinematic and dynamic condition are, respectively

$$\frac{\partial \Phi_j}{\partial y} = \frac{\partial \eta_j}{\partial t} \quad \text{at } y=h \quad (j=0,1,2,3) \dots \dots \dots (4)$$

$$\frac{\partial \Phi_j}{\partial t} + g \eta_j = 0 \quad \text{at } y=h \quad (j=0,1,2,3) \dots \dots \dots (5)$$

Where g is the gravitational constant . From equation (4) and (5) we obtain the linearized free-surface condition for the velocity potentials Φ_j

$$\frac{\partial^2 \Phi_j}{\partial t^2} + g \frac{\partial \Phi_j}{\partial y} = 0 \quad \text{at } y=h \quad (j=0,1,2,3) \dots \dots \dots (6)$$

The normal velocity of the fluid must vanish at the bottom of the channel. Hence

$$\frac{\partial \Phi_j}{\partial y} = 0 \quad \text{at } y=0 \quad (j=0,1,2,3) \dots \dots \dots (7)$$

Let the normal velocity of the fluid passing through the porous plate from region 0 to region 1 be $W_1(y,t)$, that from region 1 to region 2 be $W_2(y,t)$ and that from region 2 to region 3 be $W_3(y,t)$. Then, the boundary conditions on both sides of each thin porous plate are

$$\frac{\partial \Phi_j}{\partial x} = -W_1 \quad \text{at } x=0 \quad (j=0,1) \dots \dots \dots (8)$$

$$\frac{\partial \Phi_j}{\partial x} = -W_2 \quad \text{at } x=-l_1 \quad (j=1,2) \dots \dots \dots (9)$$

$$\frac{\partial \Phi_j}{\partial x} = -W_3 \quad \text{at } x=-(l_1+l_2) \quad (j=2,3) \dots \dots \dots (10)$$

The end wall is assumed to be solid and vertical, and the normal velocity vanishes at the wall. Therefore

$$\frac{\partial \Phi_3}{\partial x} = 0 \quad \text{at } x=-(l_1+l_2+l_3) \dots \dots \dots (11)$$

It is assumed that the flow inside the porous plate obeys the Darcy's law. Hence the flow velocity inside the porous plate W is

linearly proportional to the pressure difference between the two sides of each porous plate.

$$W_1(y,t) = \frac{b_1}{\mu} (P_0 - P_1) \quad \text{at } x=0 \dots\dots\dots(12)$$

$$W_2(y,t) = \frac{b_2}{\mu} (P_1 - P_2) \quad \text{at } x=-\ell_1 \dots\dots\dots(13)$$

$$W_3(y,t) = \frac{b_3}{\mu} (P_2 - P_3) \quad \text{at } x=-(\ell_1 + \ell_2) \dots\dots\dots(14)$$

where μ is the dynamic viscosity and b_1, b_2, b_3 are material constant, having the dimension of length. The hydrodynamic pressures $P_j(x, y, t) (j=0, 1, 2, 3)$ are related to the velocity potentials through the linearized Bernoulli equation

$$P_j = -\rho \frac{\partial \Phi_j}{\partial t} \quad (j=0, 1, 2, 3) \dots\dots\dots(15)$$

where ρ is the density of the fluid. Since the incident wave is a periodic wave, the velocity potentials, porous flow velocities and the hydrodynamic pressures are assumed to have a time factor $\exp(i\omega t)$.

$$\Phi_j = \phi_j(x, y) \exp(i\omega t) \quad (j=0, 1, 2, 3) \dots\dots\dots(16)$$

$$\bar{w}_j = w_j(y) \exp(i\omega t) \quad (j=0, 1, 2, 3) \dots\dots\dots(17)$$

$$P_j = p_j(x, y) \exp(i\omega t) \quad (j=0, 1, 2, 3) \dots\dots\dots(18)$$

Here, a complex expression is used and only the real parts should be taken to represent physical quantities.

The solutions of equation (3), satisfying boundary conditions (6), (7), (11) for each region are, respectively,

$$\begin{aligned} \phi_0 = & A_0 \cosh K_0 y \exp(ik_0 x) + A_0^* \cosh K_0 y \exp(-ik_0 x) \\ & + \sum_{m=1}^{\infty} A_{0m}^* \cos K_m y \exp(-K_m x) \dots\dots\dots(19) \end{aligned}$$

$$\begin{aligned} \phi_1 = & B_0 \cosh K_0 y \exp(ik_0 x) + \sum_{m=1}^{\infty} B_{0m} \cos K_m y \exp(K_m x) \\ & + B_0^* \cosh K_0 y \exp(-ik_0 x) + \sum_{m=1}^{\infty} B_{0m}^* \cos K_m y \exp(-K_m x) \\ & \dots\dots\dots(20) \end{aligned}$$

$$\begin{aligned} \phi_2 = & C_0 \cosh K_0 y \exp(ik_0x) + \sum_{m=1}^{\infty} C_{0m} \cos K_m y \exp(K_m X) \\ & + C_0^* \cosh K_0 y \exp(-ik_0x) + \sum_{m=1}^{\infty} C_{0m}^* \cos K_m y \exp(-K_m X) \end{aligned} \dots\dots\dots(21)$$

$$\begin{aligned} \phi_3 = & D_0 \cosh K_0 y \cos K_0(x + \varrho_1 + \varrho_2 + \varrho_3) \\ & + \sum_{m=1}^{\infty} D_{0m} \cos K_m y \cosh K_m(x + \varrho_1 + \varrho_2 + \varrho_3) \dots\dots\dots(22) \end{aligned}$$

where the first term on the right hand side of equation (19) corresponds to the incident wave. A_0 is the incident wave constant and is related to the incident wave amplitude, a , by

$$A_0 = \frac{ag}{\omega \cosh k_0 h} \dots\dots\dots(23)$$

k_0, k_m ($m=1, 2, 3, \dots\dots\dots$) satisfy the dispersion relation

$$\omega^2 = gK_0 \tanh K_0 h = -g K_m \tan K_m h \dots\dots\dots(24)$$

Noting that $\cosh k_0 y$ and $\cos K_m y$ ($m=1, 2, 3, \dots$) form a complete set of orthogonal functions over the range from $y=0$ to $y=h$, substituting equations (19)~(22) into equations (8) ~ (11) by using equations (12)~(18), then equating the coefficients of terms with the same function, we obtain

$$A_{0m}^* = B_{0m} = B_{0m}^* = C_{0m} = C_{0m}^* = D_{0m} = 0 \dots\dots\dots(25)$$

($m=1, 2, 3, \dots$)

$$\left. \begin{aligned} \frac{A_0^*}{A_0} &= F_1^* + i F_2^* \quad , \quad \frac{B_0}{A_0} = F_3^* + i F_4^* \\ \frac{B_0^*}{A_0} &= F_5^* + i F_6^* \quad , \quad \frac{C_0}{A_0} = F_7^* + i F_8^* \\ \frac{C_0^*}{A_0} &= F_9^* + i F_{10}^* \quad , \quad \frac{D_0}{A_0} = F_{11}^* + i F_{12}^* \end{aligned} \right\} (26)$$

in which

$$F_1^* = \frac{F_9 F_{11} + F_{10} F_{12}}{F_{11}^2 + F_{12}^2} \quad , \quad F_2^* = \frac{F_{10} F_{11} - F_9 F_{12}}{F_{11}^2 + F_{12}^2}$$

$$\begin{aligned}
 F_3^* &= \frac{-2G_1 (F_7 F_{11} + F_8 F_{12})}{F_{11}^2 + F_{12}^2} , & F_4^* &= \frac{-2G_1 (F_8 F_{11} - F_7 F_{12})}{F_{11}^2 + F_{12}^2} \\
 F_5^* &= \frac{-2G_1 (F_5 F_{11} + F_6 F_{12})}{F_{11}^2 + F_{12}^2} , & F_6^* &= \frac{-2G_1 (F_6 F_{11} - F_5 F_{12})}{F_{11}^2 + F_{12}^2} \\
 F_7^* &= \frac{-4G_1 G_2 (F_3 F_{11} + F_4 F_{12})}{F_{11}^2 + F_{12}^2} , & F_8^* &= \frac{-4G_1 G_2 (F_4 F_{11} - F_3 F_{12})}{F_{11}^2 + F_{12}^2} \\
 F_9^* &= \frac{-4G_1 G_2 (F_1 F_{11} + F_2 F_{12})}{F_{11}^2 + F_{12}^2} , & F_{10}^* &= \frac{-4G_1 G_2 (F_2 F_{11} - F_1 F_{12})}{F_{11}^2 + F_{12}^2} \\
 F_{11}^* &= \frac{-8G_1 G_2 G_3 F_{12}}{F_{11}^2 + F_{12}^2} , & F_{12}^* &= \frac{-8G_1 G_2 G_3 F_{11}}{F_{11}^2 + F_{12}^2}
 \end{aligned}$$

in which

$$G_1 = \frac{\rho \omega b_1}{\mu k_0} , \quad G_2 = \frac{\rho \omega b_2}{\mu k_0} , \quad G_3 = \frac{\rho \omega b_3}{\mu k_0} \dots\dots(27)$$

G_1, G_2 and G_3 are known as porous-effect parameter(Chwang 1984) for the three porous plates, respectively,

$$\begin{aligned}
 F_1 &= (G_3 - 1) T_3^* (T_1 T_2 - T_1^* T_2^*) + G_3 T_3 (T_1^* T_2 + T_1 T_2^*) \\
 F_2 &= G_3 T_3 (T_1 T_2 - T_1^* T_2^*) - (G_3 - 1) T_3^* (T_1^* T_2 + T_1 T_2^*) \\
 F_3 &= (G_3 + 1) T_3^* (T_1^* T_2^* - T_1 T_2) - G_3 T_3 (T_1^* T_2 + T_1 T_2^*) \\
 F_4 &= G_3 T_3 (T_1 T_2 - T_1^* T_2^*) - (G_3 + 1) T_3^* (T_1^* T_2 + T_1 T_2^*) \\
 F_5 &= (2G_2 - 1) F_1 + (T_1^2 - T_1^{*2}) F_3 + 2T_1 T_1^* F_4 \\
 F_6 &= (2G_2 - 1) F_2 - 2T_1 T_1^* F_3 + (T_1^2 - T_1^{*2}) F_4 \\
 F_7 &= (T_1^{*2} - T_1^2) F_1 + 2T_1 T_1^* F_2 + (2G_2 + 1) F_3 \\
 F_8 &= -2T_1 T_1^* F_1 + (T_1^{*2} - T_1^2) F_2 + (2G_2 + 1) F_4 \\
 F_9 &= -(2G_1 - 1) F_5 - F_7 , & F_{10} &= -(2G_1 - 1) F_6 - F_8 \\
 F_{11} &= F_5 - (2G_1 + 1) F_7 , & F_{12} &= F_6 - (2G_1 + 1) F_8
 \end{aligned}$$

$$\begin{aligned}
 T_1 &= \cos k_0 \varrho_1 , & T_2 &= \cos k_0 \varrho_2 , & T_3 &= \cos k_0 \varrho_3 \\
 T_1^* &= \sin k_0 \varrho_1 , & T_2^* &= \sin k_0 \varrho_2 , & T_3^* &= \sin k_0 \varrho_3
 \end{aligned}$$

(j) From equation (5), we have the free-surface equation for region

$$\eta_j = - \frac{1}{g} \frac{\partial \Phi_j}{\partial t} \quad (y=h) \quad j=0,1,2,3 \dots\dots\dots(28)$$

Substituting equation (16) into (28) , by using equation (19), (25) and (26), then taking the real part, we obtain the free-surface elevation, ζ_0 , for region(o)

$$\zeta_0 = R_e (\eta_0) = a [\sin(\omega t + k_0 x) + F_1 \sin(\omega t - k_0 x) + F_2 \cos(\omega t - k_0 x)] \dots\dots\dots(29)$$

in which

$$a = \frac{\omega A_0 \cosh k_0 h}{g}$$

The first term on the right hand side of equation(29) represent the incident wave , and the second and third term represent the reflected wave with a wave amplitude a_r as

$$a_r = (F_1^2 + F_2^2)^{1/2} a \dots\dots\dots(30)$$

If we define the reflection coefficient as ratio of wave amplitude of the reflected to incident wave , then we have the reflection coefficient C_r as

$$C_r = (F_1^2 + F_2^2)^{1/2} \dots\dots\dots(31)$$

The free-surface elevation for regions (1) , (2) and (3) could also be obtain in the same way. They are respectively

$$\zeta_1 = a [F_3 \sin (\omega t + k_0 x) + F_4 \cos (\omega t + k_0 x) + F_5 \sin (\omega t - k_0 x) + F_6 \cos (\omega t - k_0 x)] \dots\dots\dots(32)$$

$$\zeta_2 = a [F_7 \sin (\omega t + k_0 x) + F_8 \cos (\omega t + k_0 x) + F_9 \sin (\omega t - k_0 x) + F_{10} \cos (\omega t - k_0 x)] \dots\dots\dots(33)$$

$$\zeta_3 = a \{ F_{11} \sin \omega t \cos [k_0(x + \varrho_1 + \varrho_2 + \varrho_3)] + F_{12} \cos \omega t \cos [k_0(x + \varrho_1 + \varrho_2 + \varrho_3)] \} \dots\dots\dots(34)$$

The first and second term in equation (32) , (33) represent waves progressing from right to left, with amplitude $(F_3^2 + F_4^2)^{1/2} \cdot a$ and $(F_7^2 + F_8^2)^{1/2} a$ for regions (1) and (2), respectively. The third and fourth term are waves from left to right with amplitude $(F_5^2 + F_6^2)^{1/2} a$ and $(F_9^2 + F_{10}^2)^{1/2} a$, respectively. In region (3) , the wave is in a situation of fully standing wave , with the same wave amplitude in both directions.

III .THEORETICAL RESULTS

Based on equation (31), the theoretical reflection coefficient is computed. Letting $\varrho_2 = \varrho_3 = 0$ we obtain the theoretical reflection coefficient for a single porous plate , showing the same result as Chwang's (1984). The porous plate produces the smallest reflection coefficient if the single porous plate is located at a distance of $m/4$ times the wave length ($m=1,3,5, \dots$) in front of the end wall. Letting $\varrho_3 = 0$ we obtain a case for two porous plates. For a constant value of $\varrho_2/\lambda = 0.25$, the relationship between C_r and ϱ_1/λ is calculated and shown in Figure 2 . With four G values presented

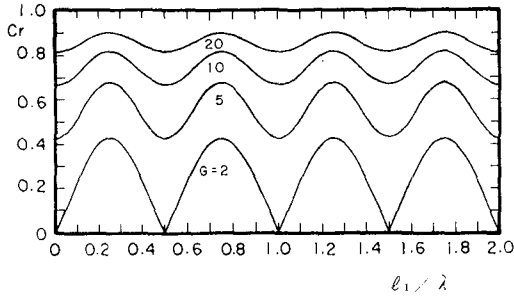


Fig.2. Reflection coefficient versus l_1/λ for two porous plates with $l_2/\lambda=0.25$.

, it shows that the two porous plates produce the smallest reflection coefficient if the distance between the two porous plates is maintained at a distance of a multiple of half wave length. For $G=2$ a zero reflection coefficient can be reached. In the case of three porous plates, letting $l_3/\lambda=0.25$ and $l_2/\lambda=0.5$ the relationship between C_r and l_1/λ is presented in Figure 3. Again, it is found that as long as the distance between the first and second plate is maintained at a multiple of half wave length, the best wave absorption can be observed. For $G=3$, a zero reflection coefficient can be obtained. From the above-mentioned cases, it is concluded that the best wave absorption could be achieved by locating every porous plate at a position where a clapotis node may occur. Both porous plates in Figure 2, or three porous plates in Figure 3, have a uniform G value for each solution curve. Now,

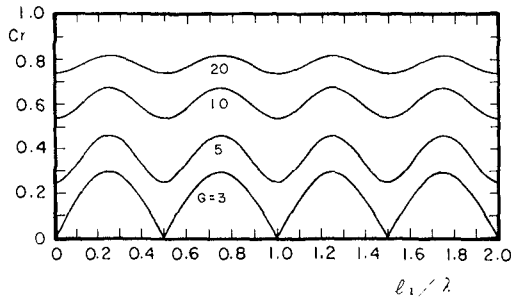


Fig.3. Reflection coefficient versus l_1/λ for three porous plates with $l_2/\lambda=0.5$, $l_3/\lambda=0.25$.

we shall see what would happen if we use different G values for the two or three porous plates. Firstly, each plate of the two-porous-plate wave absorber is placed at where a clapotis node may occur. And two cases are calculated. One of them is that the first plate has a G value twice as large as that of the second plate. The other case has a reverse arrangement. Their results are shown in Figure 4 by the curve indicating C_r versus G. It is easily seen that for two porous plates with different G values, whether the first or the second plate has a larger porous-effect parameter does not have any effect on the reflection coefficient, if each

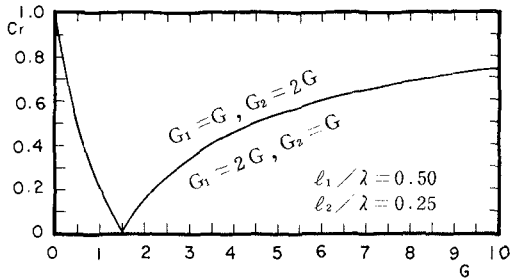


Fig.4. Comparison of reflection coefficient between two arrangements of two porous plates.

plate is located at a position where a clapotis node may occur. However, if one of the plates is not located at such a position, a different phenomenon happens. This can be seen in Figure 5, in which the first porous plate is not located at such a position. It is indicated that the two-porous-plate wave absorber with a larger G value for the first porous plate than for the second porous plate always give a lower reflection coefficient than the one with reverse G values. The same phenomenon also happens in the three-porous-plate wave absorber. Figure 6 shows the case of three porous plates having each plate located at a position where a clapotis node would occur. And it is observed that whether the porous plates have an increasing order or decreasing order of G values from the front to the back of the wave absorber does not have any effect on the reflection coefficient. But in Figure 7, in which only one

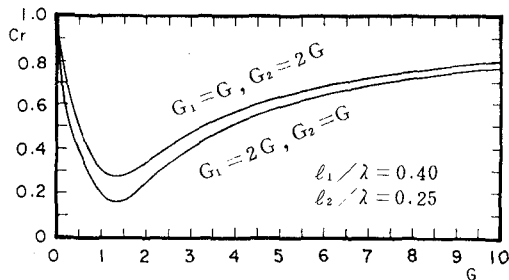


Fig.5. Comparison of reflection coefficient between two arrangements of two porous plates.

of the three porous plates is located at the particular position mentioned above, the reflection coefficient is quite different. The wave absorber with decreasing order of G values for those plates along the incident wave direction tends to give a lower reflection coefficient in comparison with the increasing order case. According to the previous statement, we know that it is the most efficient way to locate each porous plate at a position where a clapotis node may occur, if a number of porous plates are adopted. However, in actual situation it is impractical to maintain a porous plate at such a position because of the variable incident wave length. The nondimensional parameter Q_s/λ is evidently a variable rather than

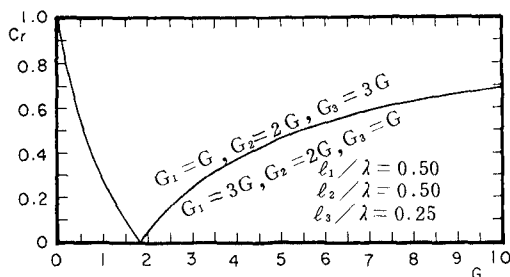


Fig.6. Comparison of reflection coefficient between two arrangements of three porous plates.

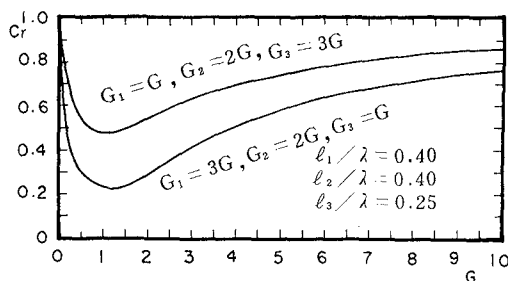


Fig.7. Comparison of reflection coefficient between two arrangements of three porous plates.

a constant. Therefore, a value of another dimensionless parameter Q_s/h is more suitable to be sought in an attempt to find a proper spacing among those plates. For incident waves corresponding to the range $0.095 < \omega^2 h/g < 3.13$, the reflection coefficient of the wave absorber has been calculated for various values of Q_s/h from 0.05 to 1.0. And it is found that whether it contains one, two or three porous plate(s), the wave absorber gives a more homogenous lower reflection coefficient as $Q_s/h=0.88$. The reflection coefficient of these cases at this particular value of Q_s/h will be shown later in section (IV) and compared with the experimental results.

IV. EXPERIMENTAL TESTS

Three kinds of porous plates with different G values have been used for the model tests. They are (i) Plate No.1 : a stainless steel screen with 7 strings per cm, (ii) Plate No.2 : four layers of plate No.1 attached together, (iii) Plate No.3 : a layer of sponge of one cm in thickness and a plate No.1 attached together. To determine the material constant b of the porous plates, a water tank with a water head of 3 cm is used. The porous plate is placed at the outlet of the water tank, and the flow velocity passing through the porous outlet is measured. From equation (12) or (13), (14), we have.

$$\frac{W}{\gamma} = \frac{b}{\mu} \left(\frac{\Delta p}{\gamma} \right) \dots\dots\dots(35)$$

in which $\frac{\Delta p}{\gamma}$ represents the water head in tank . Based on equation (35) , with μ , γ , $\frac{\Delta p}{\gamma}$ and W being known, the material constant can be calculated. The material constant thus obtained for the porous plates is as follows:(i)porous plate No.1: $b=1.49 \times 10^{-6}m$, (ii) porous plate No.2: $b=1.01 \times 10^{-6}m$, (iii) porous plate No.3: $b=3.25 \times 10^{-7}m$. Substituting the material constant for these porous plates into equation (27), the porous-effect parameter is obtained. And based on this , the theoretical reflection coefficient is computed. Finally , several comparisons between the theoretical solution and the experimental result are made.

Experiments for the wave reflection by the wave absorber are conducted in a 75 m long wave flume with a cross section of $1.2m \times 1.0m$. Two wave gauges are located in front of the wave absorber at proper positions suggested by Goda . Then the experimental reflection coefficients are calculated by Goda's method for separation of the incident and reflected waves. The advantage of Goda's method is that there is no need to adjust the positions of the two wave gauges whenever the wave period changes . Let $\Delta \ell$ be the distance between the two wave gauges and X_1 the distance between the first porous plate and its nearest wave gauge . Goda suggests

$$X_1 \geq 0.1 \lambda_{max}$$

$$0.05 \lambda_{max} < \Delta \ell < 0.45 \lambda_{min}$$

In the experimental test a water depth of 50 cm is adopted. Wave period varies from 0.85 to 3 secs and the wave length varies from 112.0 to 639.6 cm. Hence, $X_1=120cm$ and $\Delta \ell=40cm$ used here are both within the Goda's suggested range . In measuring the reflection coefficient two different ways have been conducted. One of them is fixing the wave period at a constant , 2 secs, and then varying the distance between the porous plate and the end wall. This is conducted for a case of single porous plate . The ℓ/λ value has been changed from 0.5 to 1.5 with an interval of 0.05 and its result is shown in Fig 8 . Whereas the other is fixing ℓ/h at a

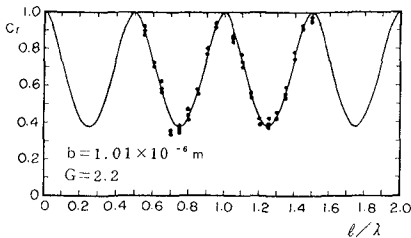


Fig.8. Reflection coefficient versus ℓ/λ for single porous plate with wave period=2.5.

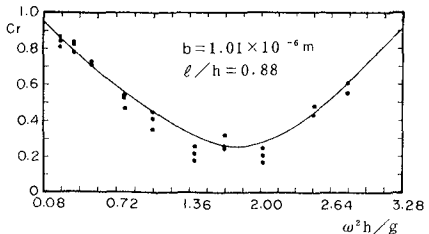


Fig.9. Reflection coefficient versus $\omega^2 h/g$ for single porous plate.

constant and then changing the wave period during the experiment and its results are shown in Figure 9 to 13. In all these figures the theoretical value is presented by curve and the experimental result by dot. Figure 8 shows the reflection coefficient in terms of Q/λ for a single porous plate with material constant $b = 1.01 \times 10^{-6} \text{m}$. It is found that the experimental data agree very well with the theoretical solution. The wave absorber gives the lowest reflection coefficient if the porous plate is located at where the clapotis node may take place, i.e. $Q/\lambda = 1/4, 3/4, 5/4, 7/4, \dots$. Figure 9 to 13 show the reflection coefficient in terms of $\omega^2 h/g$ with $Q_s/h = 0.88$, which is the proper spacing found after series of calculation. Figure 9, 10, 11 are the results for single porous plate, two porous plates and three porous plates, respectively, with the same material constant, $b = 1.01 \times 10^{-6} \text{m}$, for all these porous plates. Good agreement is found between the theoretical solution and the experimental result. It is observed that a three-porous-plate wave absorber is more effective in damping wave than a two-porous-plate one, and the two-porous-plate wave absorber is also more effective than the single-porous-plate one. Figure 12 shows the reflection coefficient for a two-porous-plate wave absorber with different material constants for the plates, one with $b = 1.01 \times 10^{-6} \text{m}$, the other with $b = 3.25 \times 10^{-7} \text{m}$. Two arrangements have been performed, one with the larger b value for the front porous plate and the smaller b value for the back one, the other with the reverse order. Results of this two arrangements have been presented in this figure. It is shown, both theoretically and experimentally, that an arrangement with a larger b value for the front porous plate and a smaller b value for the back plate tends to give a lower reflection coefficient than the arrangement with a reverse order does. For a three-porous-plate wave absorber, a similar phenomenon can be found by referring to Figure 13. Their material constants are $1.49 \times 10^{-6} \text{m}$, $1.01 \times 10^{-6} \text{m}$, $3.25 \times 10^{-7} \text{m}$, respectively. It is also found that the case that has a decreasing order of material constant for the porous plates gives a lower reflection coefficient, thus works better in wave absorption, than the other case does. In general speaking, theoretical curves in Figure 12 and 13 agree well with the experimental results. But the agreement is not as good as that in previous figures. This is because the present wave absorbers contain a porous plate No.3 each, with material

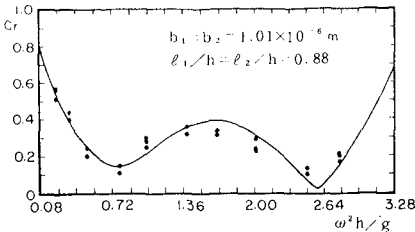


Fig.10. Comparison between the theoretical solution and the experimental result for two porous plates.

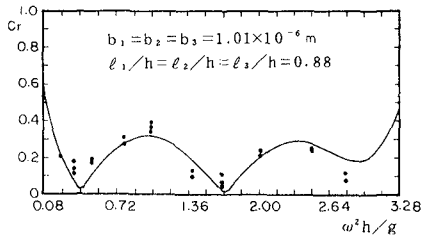


Fig.11. Comparison between the theoretical solution and the experimental result for three porous plates.

constant $b = 3.25 \times 10^{-7} \text{ m}$, which is a sponge attached together with a steel screen. This porous plate bends as the waves pass through. And this bending motion causes a discrepancy from the theoretical assumption that these porous plates are fixed in place, thus leading to a little worse agreement between the experimental data and the theoretical value.

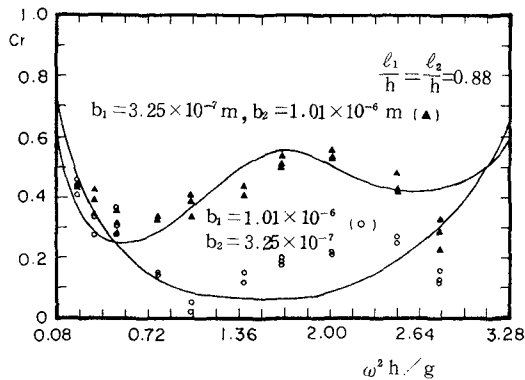


Fig.12. Comparison between the theoretical solution and the experimental result for two arrangements of two porous plates.

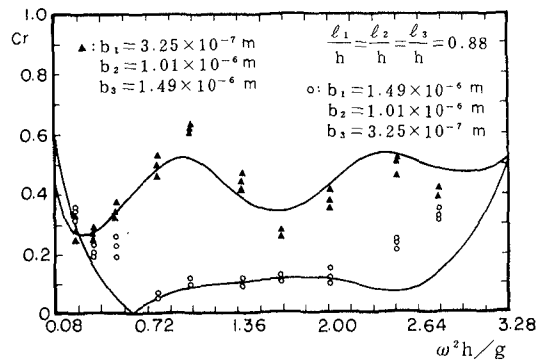


Fig.13. Comparison between the theoretical solution and the experimental result for two arrangements of three porous plates.

V. CONCLUSIONS

To damp wave by porous plate structure, the locations and the number of porous plates and the arrangement of material constant all play an important role in estimating the reflected waves from the structure. According to theoretical analysis, the best location for a porous plate is a position where a clapotis node may take

place . This measure could be applied to a wave absorber containing more than one porous plate . But in practical consideration ,it is much unlikely to choose a clapotis-node location for a porous plate because of the variable wave length.In this situation it is preferable to take a distance of 0.88 times the water depth for the space between any two adjoining porous plates, and between the end wall and its nearest one . In water areas with waves of varied wave periods, more than one porous plate would be more effective in wave damping than a single porous plate as long as the locations of the plates are properly selected . Likewise , a wave absorber containing more than two porous plates would be more effective than that containing only two porous plates . Furthermore, if more than two porous plates are adopted and an arrangement is used such that the material constants for these porous plates are in a decreasing order from the front to the back of the wave absorber, it would give a very low reflection coefficient.

REFERENCES

- Chwang, A. T. and Dong, Z. 1984 , Wave-trapping due to a porous plate. Proc. 15th ONR Symposium on Naval Hydrodynamics. pp.407-417.
- Dean, W. R. 1945, On the reflexion of surface waves by a submerged plane barrier. Proc. Phil. Soc., Vol.41, pp.231~238.
- Goda, Y. and Suzuki, Y. 1976, Estimation of incident and reflected waves in random waves experiments. Proc. 15th Coastal Eng. Conf., pp.628-650.
- Macaskill, C. 1979, Reflexion of water waves by a permeable barrier. J. Fluid Mech., Vol.95, pp.141-157.
- Mei, C. C. and Black, J. L. 1969, Scattering of surface waves by rectangular obstacles in waters of finite depth. J. Fluid Mech., Vol.38, pp.499-511.
- Newman, J. N. 1965, Propagation of water waves past long two-dimensional obstacles . J. Fluid Mech., Vol.23, pp.23-29.
- Wiegel, R. L. 1960, Transmission of waves past a rigid vertical thin barrier. J. Waterways and Harbours Division. March, pp.2413-1-12.

CHAPTER 80

MODELING OF WAVE TRANSFORMATION ON SUBMERGED BREAKWATER

Somchai Rojanakamthorn¹, Masahiko Isobe², and Akira Watanabe³

ABSTRACT

A mathematical model of wave transformation over a submerged permeable breakwater is developed on the basis of the equations for waves on a porous layer which are newly derived under the mild-slope assumption. The model equation is given as a two-dimensional elliptic equation analogous to the mild-slope equation on an impermeable bed. The model of wave breaking on a submerged permeable breakwater is proposed on the basis of the modified mild-slope equation. The validity of the model is confirmed through comparison with the experiments for a trapezoidal breakwater and with strict solution for a rectangular breakwater.

I. INTRODUCTION

A submerged breakwater has been shown as an effective wave control structure with less environmental impacts. Prediction of the wave transformation over a submerged permeable breakwater and the resultant effects on wave action is important in planning and designing structures for the coastal protection. So far, investigations have mostly been carried out on the basis of laboratory and field experiments such as Dattari *et al.* (1978). Though some theoretical studies were made by Liu (1973) and others, a simple and general predictive model has not been established yet.

In this study, a model equation is derived based on the mild slope assumption to analyze the transformation of waves over a submerged permeable breakwater. The resultant equation is given as a two-dimensional elliptic equation and is analogous to the standard mild-slope equation for an impermeable bed. A mathematical model based on the present mild-slope equation is used to compute the wave transformation for a general bottom configuration. The applicability of the model is demonstrated through comparison with laboratory data obtained from model experiments in a wave flume. The validity of the model is also examined by comparing with the strict solution for a rectangular submerged breakwater.

¹M. Eng., Dept. of Civil Eng., Univ. of Tokyo, 7-3-1 Hongo, Bunkyo-ku, Tokyo, 113 Japan.

²D. Eng., Associate Professor, ditto.

³D. Eng., Professor, ditto.

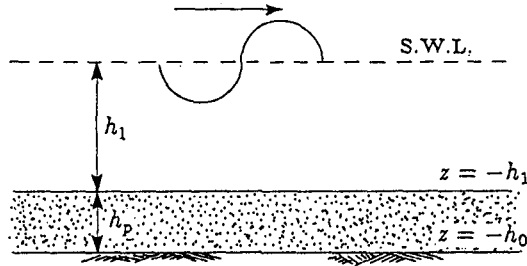


Fig.1 Definition sketch; waves propagating over a horizontal porous layer.

II. MODELING OF WAVE TRANSFORMATION

The mathematical derivation of the basic equation for the transformation of non-breaking waves over an inclined porous layer is given in Rojanakamthorn *et al.* (1989). In the following, the derivation is briefly reviewed and the model of breaking wave transformation is formulated.

2.1 Wave Transformation over an Inclined Porous Layer

The analytical approach starts with the formulation of the wave transformation over a horizontal porous layer. A definition sketch is shown in Fig.1 in which the depth of water, h_1 , and the thickness of the porous layer, $h_p = h_0 - h_1$, are constant. The governing equations describing the motion of an incompressible fluid inside the porous medium under the assumption of irrotational flow can be shown by Eqs.(1) and (2) in terms of the seepage velocity potential ϕ_s and pressure p_s .

$$\nabla^2 \phi_s = 0 \tag{1}$$

$$C_r \frac{\partial \phi_s}{\partial t} + \frac{1}{\rho}(p_s + \gamma z) + f_p \sigma \phi_s = 0 \tag{2}$$

where C_r is the inertia coefficient, ρ the mass density of water, γ the unit weight of water, f_p the linearized friction factor, σ the angular frequency of the periodic wave motion, $\nabla = (\partial/\partial x, \partial/\partial y, \partial/\partial z)$ the gradient operator, and $\partial/\partial t$ the partial differential operator with respect to time. The friction factor f_p is evaluated from the Lorentz' condition of equivalent work. The relationship can be expressed as

$$f_p = \frac{\int_V \int_0^T \left(\frac{\epsilon^2 \nu}{K_p} |\vec{u}_s|^2 + \frac{\epsilon^3 C_t}{\sqrt{K_p}} |\vec{u}_s|^3 \right) dt dV}{\sigma \int_V \int_0^T \epsilon |\vec{u}_s|^2 dt dV} \tag{3}$$

in which \vec{u}_s is the seepage velocity vector, ϵ the porosity of the medium, ν the kinematic viscosity, K_p the permeability, C_t the turbulent friction coefficient, V the volume under consideration, and T the wave period.

Equations (1) and (2) represent the Laplace equation and the unsteady Bernoulli equation for a seepage flow, respectively. The equations for the flow outside the porous medium can be obtained by substituting the coefficient C_r by unity and the friction

factor f_p by zero. The governing equations yield a potential flow problem. An analytical solution is derived for a monochromatic progressive wave train. The solutions for the velocity potentials were obtained as follows.

$$\phi = \frac{ig\eta}{\sigma} \frac{\epsilon \sinh(kh_p) \exp\{k(z+h_1)\} - \delta \cosh\{k(z+h_1)\}}{\epsilon \sinh(kh_p) \exp(kh_1) - \delta \cosh(kh_1)} \tag{4}$$

$$\phi_s = \frac{ig\eta}{\sigma} \frac{\cosh\{k(z+h_0)\}}{\epsilon \sinh(kh_p) \exp(kh_1) - \delta \cosh(kh_1)} \tag{5}$$

where

$$\eta = a \cdot \exp\{i(\sigma t - kx)\} \tag{6}$$

$$\delta = \epsilon \sinh(kh_p) - (C_r - if_p) \cosh(kh_p) \tag{7}$$

in which a is the amplitude of the incident wave prescribed at $x = 0$, g the gravitational acceleration, and $k = k_r - ik_i$ the complex wave number which is determined from the following relationship.

$$\sigma^2 = gk \frac{\epsilon \exp(kh_1) \sinh(kh_p) - \delta \sinh(kh_1)}{\epsilon \exp(kh_1) \sinh(kh_p) - \delta \cosh(kh_1)} \tag{8}$$

It is noted that without a porous layer the above results reduce to the following linear wave solution (9) and the dispersion relation (10).

$$\phi = \frac{ig\eta}{\sigma} \frac{\cosh\{k(z+h_0)\}}{\cosh(kh_0)} \tag{9}$$

$$\sigma^2 = gk \tanh(kh_0) \tag{10}$$

A mild-slope equation is then derived for an inclined porous layer in a general bottom configuration. Referring to Fig.2 in which waves propagate over a submerged permeable breakwater, the governing equations derived from the equations of an incompressible fluid are expressed in terms of the amplitudes of velocity potentials as

$$\nabla_h^2 \Phi + \frac{\partial^2 \Phi}{\partial z^2} = 0 \quad , \quad \nabla_h^2 \Phi_s + \frac{\partial^2 \Phi_s}{\partial z^2} = 0 \tag{11}, (12)$$

where $\nabla_h = (\partial/\partial x, \partial/\partial y)$ is the horizontal gradient operator, and

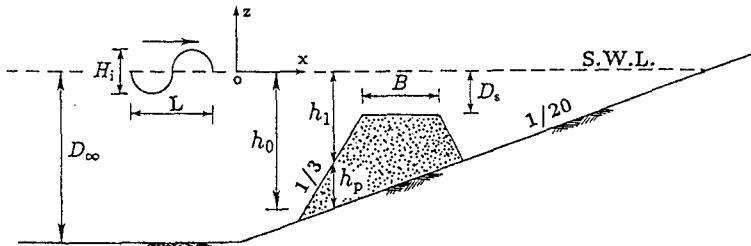


Fig.2 Definition sketch; waves propagating over a submerged permeable breakwater.

$$\Phi = (ig\hat{\eta}/\sigma)G(z) \quad , \quad \Phi_s = (ig\hat{\eta}/\sigma)H(z) \tag{13},(14)$$

in which $\hat{\eta}$ is the complex amplitude of the water surface displacement, and

$$G(z) = \frac{\epsilon \sinh(kh_p) \exp\{k(z + h_1)\} - \delta \cosh\{k(z + h_1)\}}{\epsilon \sinh(kh_p) \exp(kh_1) - \delta \cosh(kh_1)} \tag{15}$$

$$H(z) = \frac{\cosh\{k(z + h_0)\}}{\epsilon \sinh(kh_p) \exp(kh_1) - \delta \cosh(kh_1)} \tag{16}$$

Equations (13) to (16) are assumed to be applicable to the slowly varying depth condition by using the local values of k , h_0 , h_1 and h_p . The mild-slope equation is derived by the vertical integration of Eqs.(11) and (12) after multiplying by appropriate functions.

$$\int_{-h_1}^0 \left[G \left(\nabla_h^2 \Phi + \frac{\partial^2 \Phi}{\partial z^2} \right) \right] dz + \int_{-h_0}^{-h_1} \left[\epsilon(C_r - if_p)H \left(\nabla_h^2 \Phi_s + \frac{\partial^2 \Phi_s}{\partial z^2} \right) \right] dz = 0 \tag{17}$$

By utilizing the relevant boundary conditions and the solutions of Φ and Φ_s with the form of Eqs.(13) to (16) are invoked and the variations of depth are taken into consideration, Eq.(17) is thus expressed as

$$\begin{aligned} & \nabla_h \int_{-h_1}^0 G^2 \nabla_h \hat{\eta} dz + \int_{-h_1}^0 k^2 G^2 \hat{\eta} dz \\ & + \epsilon(C_r - if_p) \left[\nabla_h \int_{-h_0}^{-h_1} H^2 \nabla_h \hat{\eta} dz + \int_{-h_0}^{-h_1} k^2 H^2 \hat{\eta} dz \right] \\ = & - \left[\int_{-h_1}^0 G \nabla^2 G \hat{\eta} dz + G \nabla_h G \cdot \nabla_h h_1 \hat{\eta} \right]_{-h_1} \\ & + \epsilon(C_r - if_p) \left\{ \int_{-h_0}^{-h_1} H \nabla_h^2 H \hat{\eta} dz + H \nabla_h H \cdot \nabla_h h_1 \hat{\eta} \right\}_{-h_1} \\ & + H \nabla_h H \cdot \nabla_h h_0 \hat{\eta} \Big|_{-h_0} \Big\} \end{aligned} \tag{18}$$

The assumption of slowly varying depth, *i.e.*, the mild slope assumption is imposed. The contributions of the terms on the right-hand side of Eq.(18) which are the second order of the bottom slope are considered negligible. The following elliptic equation is finally obtained.

$$\nabla_h(\alpha \nabla_h \hat{\eta}) + k^2 \alpha \hat{\eta} = 0 \tag{19}$$

where

$$\alpha = \alpha_1 + \epsilon(C_r - if_p)\alpha_2 \tag{20}$$

$$\alpha_1 = \beta_1^2 h_1 [(\beta_2^2/2kh_1)\{1 - \exp(-2kh_1)\} - (\beta_3^2/2kh_1)\{1 - \exp(2kh_1)\} - 2\beta_2\beta_3] \tag{21}$$

$$\alpha_2 = \frac{1}{2}\beta_1^2 h_p \left\{ 1 + \frac{\sinh(2kh_p)}{2kh_p} \right\} \tag{22}$$

$$\beta_1 = [\epsilon \exp(kh_1) \sinh(kh_p) - \delta \cosh(kh_1)]^{-1} \tag{23}$$

$$\beta_2 = \epsilon \exp(kh_1) \sinh(kh_p) - (1/2)\delta \exp(kh_1) \quad (24)$$

$$\beta_3 = (1/2)\delta \exp(-kh_1) \quad (25)$$

Equation (19) is the mild-slope equation describing wave transformation on a mildly sloping porous layer and is an extension of the standard mild-slope equation derived by Berkhoff (1972) for an impermeable bed.

2.2 Breaking Wave Transformation on a Submerged Breakwater

(1) Modified mild-slope equation on porous layer

A submerged breakwater usually has a principal function of premature breaking of high waves to diminish the heights of waves transmitted to the shore. To develop a general predictive model for the breaking wave transformation, Eq.(19) is modified by incorporating an energy dissipation term as

$$\nabla_h(\alpha \nabla_h \hat{\eta}) + (k^2 \alpha - i\sigma \alpha f_D) \hat{\eta} = 0 \quad (26)$$

where f_D is an energy dissipation function. The energy dissipation function f_D due to wave breaking will be derived on the basis of energy equation.

(2) Energy dissipation function of breaking wave

For a uniform porous layer and water depth condition, the value of α is constant and independent of horizontal coordinates. Equation (26) then reduces to

$$\nabla_h^2 \hat{\eta} + (k^2 - i\sigma f_D) \hat{\eta} = 0 \quad (27)$$

The complex amplitude of the water surface displacement is now defined in terms of wave amplitude a as

$$\hat{\eta} = a \cdot \exp(-i\chi) \quad (28)$$

where χ is the phase angle.

Substituting Eq.(28) into (27) and grouping the real and imaginary terms, we obtain

$$\nabla_h \chi \cdot \nabla_h \chi = k_r^2 \{1 - (k_i/k_r)^2\} + (1/a) \nabla_h^2 a \quad (29)$$

$$\nabla_h (a^2 \nabla_h \chi) = -(2k_i k_r + \sigma f_D) a^2 \quad (30)$$

The contribution from the last term in Eq.(29) may be considered negligible and the ratio k_i/k_r may be small, and hence Eq.(29) is approximated as

$$\nabla_h \chi = (k_r \cos \varphi, k_r \sin \varphi) \quad (31)$$

where φ is the wave angle. If a unidirectional wave is considered, Eq.(30) reduces to

$$\frac{\partial}{\partial n} (a^2) = -(2k_i + \frac{\sigma f_D}{k_r}) a^2 \quad (32)$$

where n represents the coordinate in the direction of wave propagation.

Equation (32) is an energy equation of waves propagating over a horizontal porous layer in which the wave energy is dissipated due to porosity and wave breaking. The

standard mild-slope equation describing the transformation of breaking waves on an impermeable bed is shown by Eq.(33).

$$\nabla_h(cc_g \nabla_h \hat{\eta}) + (k^2 cc_g - i\sigma f'_D) \hat{\eta} = 0 \tag{33}$$

where f'_D is the energy dissipation function, c the wave celerity, and c_g the group velocity. The energy dissipation function f'_D due to wave breaking was proposed by taking into account the processes of wave decay and recovery (Watanabe and Dibajnia, 1988).

$$f'_D = \alpha_D \tan \zeta' \sqrt{\frac{g}{h}} \sqrt{\frac{\vartheta' - \vartheta'_r}{\vartheta'_s - \vartheta'_r}} \tag{34}$$

where

$$\vartheta' = (|\hat{\eta}|/h), \quad \vartheta'_s = 0.4(0.57 + 5.3 \tan \zeta'), \quad \vartheta'_r = 0.4(|\hat{\eta}|/h)_b \tag{35}, (36), (37)$$

in the above equations α_D equals 2.5, $\tan \zeta'$ the bottom slope at the breaking point, and the subscript b denotes the value at the breaking point. The parameters ϑ'_s and ϑ'_r are expressed according to the results of experiment.

Under the same condition of uniform water depth, an energy equation of breaking wave transformation is derived in a similar fashion. The equation is expressed as

$$\frac{\partial}{\partial n}(a^2) = -\frac{f'_D}{c_g} a^2 \tag{38}$$

Supposing that the mechanism of energy loss due to wave breaking on a submerged permeable breakwater is similar to those on an impermeable bed, we obtain the following expression through comparison of Eqs.(32) and (38).

$$f_D = (k_r/\sigma c_g) f'_D \tag{39}$$

Equation (39) gives an energy dissipation function due to wave breaking on an inclined porous layer. Here, an effective depth is introduced to take into account the porosity of the structure.

$$h'_1 = h_1 + \epsilon h_p \tag{40}$$

The energy dissipation function due to wave breaking on a submerged permeable breakwater is finally expressed as

$$f_D = \frac{k_r}{\sigma c_g} \cdot \alpha_D \tan \zeta \sqrt{\frac{g}{h'_1}} \sqrt{\frac{\vartheta - \vartheta_r}{\vartheta_s - \vartheta_r}} \tag{41}$$

where $\tan \zeta$ is the equivalent bottom slope at the breaking point which is defined as a mean slope in the distance $5(h'_1)_b$ offshoreward from the breaking point, and

$$\vartheta = (|\hat{\eta}|/h'_1), \quad \vartheta_s = 0.4(0.57 + 5.3 \tan \zeta), \quad \vartheta_r = 0.4(|\hat{\eta}|/h'_1)_b \tag{42}, (43), (44)$$

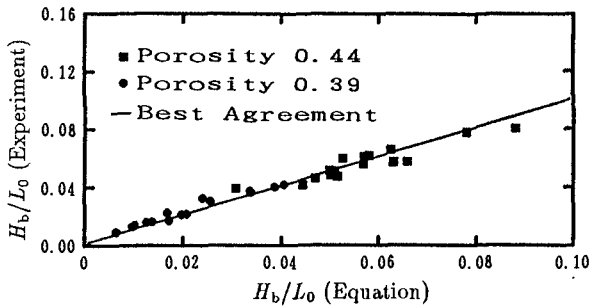


Fig.3 Breaking wave condition on submerged permeable breakwater.

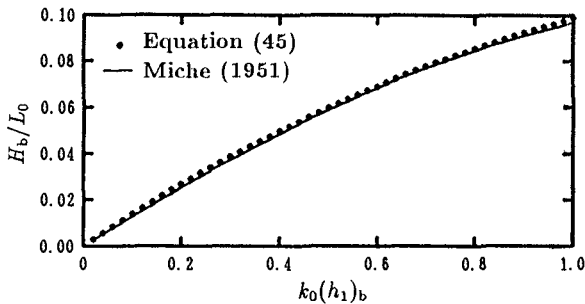


Fig.4 Comparison of breaking wave condition.

(3) Breaking criterion

Wave breaking is usually detected from the condition which is determined by breaking indices. The information of wave breaking on a submerged permeable breakwater is scarce. Therefore, the wave breaking phenomena were preliminary investigated through a series of laboratory experiments.

The model experiments of submerged permeable breakwater were conducted with two sizes of gravel on a uniformly sloping bed and a horizontal bottom. The porosity of gravel were 0.39 and 0.44, respectively. On the basis of the experimental results, an empirical formula for the condition of wave breaking on a submerged permeable breakwater is proposed.

$$H_b/L_0 = 0.127 \tanh\{k_0(h_1)_b\} \tag{45}$$

where H_b is the wave height at the breaking point, L_0 the deep water wavelength, $k_0 = 2\pi/L_0$ the deep water wave number, and $(h_1)_b$ the depth of breakwater surface at the breaking point. The agreement of Eq.(45) with the experimental results is shown in Fig.3. The breaking wave condition in Eq.(45) has a similar form as that presented by Miche (1951).

$$H_b/L_b = 0.142 \tanh\{k_b(h_1)_b\} \tag{46}$$

in which L_b is the wavelength at the breaking point, and $k_b = 2\pi/L_b$ the breaking wave number. Equation (45) is plotted in comparison with Eq.(46) in Fig.4. It is shown that both equations give almost the same results for breaking wave height. However, the definition of the breaking wavelength and wave number for a submerged permeable breakwater is implicit. For the sake of the present application, Eq.(45) will be adopted as an index to detect the wave breaking.

2.3 Numerical Computation

A method of numerical computation is utilized for the computation of wave transformation in general breakwater configurations. A detailed description is also given in Rojanakamthorn *et al.* (1989). The governing equation is discretized by using a finite difference scheme. In this paper, a two-dimensional problem as in the wave-flume experiments is analyzed to examine the validity of the present model. Then, Eq.(26) reduces to

$$\frac{d}{dx} \left(\alpha \frac{d\hat{\eta}}{dx} \right) + (k^2 \alpha - i\sigma \alpha f_D) \hat{\eta} = 0 \quad (47)$$

The study area is divided into grids in the x-direction and a finite difference form of Eq.(47) is formulated. The computation is performed with the following boundary conditions. At the offshore boundary, an open boundary condition is imposed in which the water surface displacement is composed of incident and reflected wave components. Under the assumption of linear superposition, the complex amplitude of the water surface displacement is expressed as

$$\hat{\eta} = a_i \exp(-ik_0 x) + a_r \exp(ik_0 x) \quad (48)$$

where a_i and a_r represent the amplitudes of incident and reflected waves, respectively, and k_0 the complex wave number at the offshore boundary.

At the shoreline boundary, a non-reflective condition is imposed by considering that the wave energy is dissipated due to breaking on the shore. Therefore, the water surface displacement is the resultant of the transmitted waves.

$$\hat{\eta} = a_t \exp(-ik_{sh} x) \quad (49)$$

where a_t is the amplitude of transmitted waves, and k_{sh} the wave number in the shoreline region.

The solutions are obtained through an iteration. An initial value of the friction factor f_p is first assumed with zero energy dissipation due to wave breaking, $f_D = 0$. With a given incident wave condition, the complex wave number k at every grid is calculated from Eq.(8) via an iteration technique. The coefficient α is next evaluated from Eqs.(20) to (25) and then coefficients of the amplitudes $\hat{\eta}$ at every grid are determined. This results in a set of linear equations which can be solved by using the method of Gauss elimination. Wave breaking on the breakwater is then examined by Eq.(45) and the energy dissipation due to wave breaking is included from Eqs.(41) to (44). The calculation is iterated until the convergent results are obtained. The friction factor f_p is next evaluated from Eq.(3). The computed value of f_p is compared with the assumed one and the computation is iterated when required.

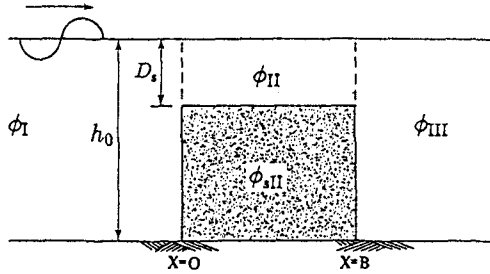


Fig.5 Definition sketch; waves propagating over a rectangular submerged breakwater.

For irregular waves, a technique of individual wave analysis is utilized. The advantage of this technique has been clarified in the analysis of wave breaking. In the computation, individual waves are defined from an irregular wave train through zero-downcrossing method and the transformation of each wave component is calculated.

2.4 Rectangular Submerged Breakwater

The validity of the mild-slope equation is examined by comparing with an analytical solution for a rectangular submerged permeable breakwater. A breakwater of finite width B is considered as shown in Fig.5. A monochromatic incident wave encounters the breakwater face at $x = 0$. Then, some part of the wave energy is reflected while the other part is transmitted through the breakwater. The flow field is separated into three regions. The solution in each region is shown in terms of unknown amplitudes as follows.

Region I ($x < 0$)

$$\begin{aligned} \phi_I = & \{a_i \exp(-ikx) + a_r \exp(ikx)\} \frac{\cosh\{k(z+h_0)\}}{\cosh(kh_0)} \exp(i\sigma t) \\ & + \sum_{m=1}^{\infty} a_{rm} \exp(k_m x) \frac{\cos\{k_m(z+h_0)\}}{\cos(k_m h_0)} \exp(i\sigma t) \end{aligned} \quad (50)$$

Region II ($0 < x < B$)

$$\phi_{II} = \sum_{n=0}^{\infty} [a_{1n} \exp(-ik_n x) + a_{2n} \exp\{ik_n(x-B)\}] G_n(z) \exp(i\sigma t) \quad (-h_1 < z < 0) \quad (51)$$

$$\phi_{sII} = \sum_{n=0}^{\infty} [a_{1n} \exp(-ik_n x) + a_{2n} \exp\{ik_n(x-B)\}] H_n(z) \exp(i\sigma t) \quad (-h_0 < z < -h_1) \quad (52)$$

Region III ($x > B$)

$$\begin{aligned} \phi_{III} = & a_t \exp\{-ik(x-B)\} \frac{\cosh\{k(z+h_0)\}}{\cosh(kh_0)} \exp(i\sigma t) \\ & + \sum_{m=1}^{\infty} a_{tm} \exp\{-k_m(x-B)\} \frac{\cos\{k_m(z+h_0)\}}{\cos(k_m h_0)} \exp(i\sigma t) \end{aligned} \quad (53)$$

In the above equations, a_{rm} and a_{tm} represent the amplitudes of evanescent modes of reflected and transmitted waves, a_{1n} and a_{2n} the amplitudes of progressive and evanescent modes of the transmitted waves through the front face and reflected waves from the rear face of the breakwater, and

$$G_n(z) = \frac{\epsilon \sinh(k_n h_p) \exp\{k_n(z + h_1)\} - \delta_n \cosh\{k_n(z + h_1)\}}{\epsilon \sinh(k_n h_p) \exp(k_n h_1) - \delta_n \cosh(k_n h_1)} \tag{54}$$

$$H_n(z) = \frac{\cosh\{k_n(z + h_0)\}}{\epsilon \sinh(k_n h_p) \exp(k_n h_1) - \delta_n \cosh(k_n h_1)} \tag{55}$$

in which

$$\delta_n = \epsilon \sinh(k_n h_p) - (C_r - i f_p) \cosh(k_n h_p) \tag{56}$$

The wave number k is determined from Eq.(10) while k_m and k_n can be determined from Eqs.(57) and (58).

$$\sigma^2 = -g k_m \tan(k_m h_0) \tag{57}$$

$$\sigma^2 = g k_n \frac{\epsilon \exp(k_n h_1) \sinh(k_n h_p) - \delta_n \sinh(k_n h_1)}{\epsilon \exp(k_n h_1) \sinh(k_n h_p) - \delta_n \cosh(k_n h_1)} \tag{58}$$

In Eqs.(50) to (53), unknown parameters are a_r , a_{rm} , a_t , a_{tm} , a_{1n} and a_{2n} . These unknowns are solved with the boundary conditions, namely the continuity of pressure and mass flux at the interfaces. The orthogonality of the eigenfunctions is utilized. After mathematical manipulations, the amplitudes a_{1n} and a_{2n} can be solved from the following equations.

$$\begin{aligned} & \sum_{n=0}^{\infty} \left[a_{1n} \left\{ \left(1 + \frac{k_n}{k} \right) \lambda_{10n} + \left(C_r - i f_p + \epsilon \frac{k_n}{k} \right) \lambda_{20n} \right\} \right. \\ & \left. + a_{2n} \exp(-i k_n B) \left\{ \left(1 - \frac{k_n}{k} \right) \lambda_{10n} + \left(C_r - i f_p - \epsilon \frac{k_n}{k} \right) \lambda_{20n} \right\} \right] \\ = & \frac{2a_i}{\cosh(k h_0)} \left\{ \frac{h_0}{2} + \frac{\sinh(2k h_0)}{4k} \right\} \tag{59} \end{aligned}$$

$$\begin{aligned} & \sum_{n=0}^{\infty} \left[a_{1n} \left\{ \left(1 + \frac{i k_n}{k_m} \right) \lambda_{3mn} + \left(C_r - i f_p + \epsilon \frac{i k_n}{k_m} \right) \lambda_{4mn} \right\} \right. \\ & + a_{2n} \exp(-i k_n B) \left\{ \left(1 - \frac{i k_n}{k_m} \right) \lambda_{3mn} \right. \\ & \left. \left. + \left(C_r - i f_p - \epsilon \frac{i k_n}{k_m} \right) \lambda_{4mn} \right\} \right] = 0 \quad (m = 1, 2, 3 \dots) \tag{60} \end{aligned}$$

$$\begin{aligned} & \sum_{n=0}^{\infty} \left[a_{1n} \exp(-i k_n B) \left\{ \left(1 - \frac{k_n}{k} \right) \lambda_{10n} + \left(C_r - i f_p - \epsilon \frac{k_n}{k} \right) \lambda_{20n} \right\} \right. \\ & \left. + a_{2n} \left\{ \left(1 + \frac{k_n}{k} \right) \lambda_{10n} + \left(C_r - i f_p + \epsilon \frac{k_n}{k} \right) \lambda_{20n} \right\} \right] = 0 \tag{61} \end{aligned}$$

$$\sum_{n=0}^{\infty} \left[a_{1n} \exp(-ik_n B) \left\{ \left(1 - \frac{ik_n}{k_m} \right) \lambda_{3mn} + \left(C_r - if_p - \epsilon \frac{ik_n}{k_m} \right) \lambda_{4mn} \right\} + a_{2n} \left\{ \left(1 + \frac{ik_n}{k_m} \right) \lambda_{3mn} + \left(C_r - if_p + \epsilon \frac{ik_n}{k_m} \right) \lambda_{4mn} \right\} \right] = 0 \quad (m = 1, 2, 3 \dots) \tag{62}$$

where

$$\lambda_{10n} = \int_{-h_1}^0 G_n(z) \cosh\{k(z+h_0)\} dz, \quad \lambda_{20n} = \int_{-h_0}^{-h_1} H_n(z) \cosh\{k(z+h_0)\} dz \tag{63}$$

$$\lambda_{3mn} = \int_{-h_1}^0 G_n(z) \cos\{k_m(z+h_0)\} dz, \quad \lambda_{4mn} = \int_{-h_0}^{-h_1} H_n(z) \cos\{k_m(z+h_0)\} dz \tag{64}$$

The amplitudes of reflected and transmitted waves a_r and a_t are then calculated from Eqs.(65) and (66).

$$a_r = \frac{1}{\frac{2}{\cosh(kh_0)} \left\{ \frac{h_0}{2} + \frac{\sinh(2kh_0)}{4k} \right\}} \sum_{n=0}^{\infty} \left[a_{1n} \left\{ \left(1 - \frac{ik_n}{k} \right) \lambda_{10n} + \left(C_r - if_p - \epsilon \frac{k_n}{k} \right) \lambda_{20n} \right\} + a_{2n} \exp(-ik_n B) \left\{ \left(1 + \frac{k_n}{k} \right) \lambda_{10n} + \left(C_r - if_p + \epsilon \frac{k_n}{k} \right) \lambda_{20n} \right\} \right] \tag{65}$$

$$a_t = \frac{1}{\frac{1}{\cosh(kh_0)} \left\{ \frac{h_0}{2} + \frac{\sinh(2kh_0)}{4k} \right\}} \sum_{n=0}^{\infty} \{ a_{1n} \exp(-ik_n B) + a_{2n} \} \{ \lambda_{10n} + (C_r - if_p) \lambda_{20n} \} \tag{66}$$

The reflection and transmission coefficients, K_r and K_t , are by definition equal to the absolute value of ratio of the complex wave amplitudes.

$$K_r = |a_r/a_i|, \quad K_t = |a_t/a_i| \tag{67}$$

Equations (59) to (67) are the strict analytical solution for a simple rectangular submerged permeable breakwater.

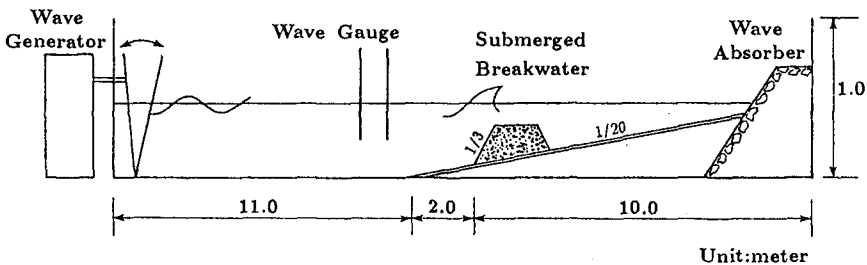


Fig.6 Model experiment of submerged breakwater.

III. VERIFICATION OF THE WAVE MODEL

The validity of the present model is examined by comparing the results from the numerical computation with experimental data obtained in a laboratory experiment and a strict solution for a rectangular submerged breakwater.

The experiments on the wave transformation over a submerged permeable breakwater were carried out in a laboratory wave flume as shown in Fig.6. The model breakwater composed of gravel with average diameter of 2.5 cm was placed on a 1/20 uniformly sloping bed. The offshore slope of the breakwater was 1/3. Tests were conducted for various wave conditions of regular and irregular waves with different values of the breakwater crown width. The water surface displacement was measured along the center line of the test section from offshore to onshore region. Sample of the experimental data for the distributions of root mean square value of water surface fluctuation are presented in Fig.7. In the figures, H_i and T represent the incident wave height and period for regular waves while $H_{1/3}$ and $T_{1/3}$ represent the significant wave height and period for irregular waves. The symbols X_t and X_c indicate the locations of the toe and crown of the breakwater, and X_{sh} the location of the shoreline. It is found that the wave amplitude considerably decreases over the breakwater which indicates a significant loss of the wave energy.

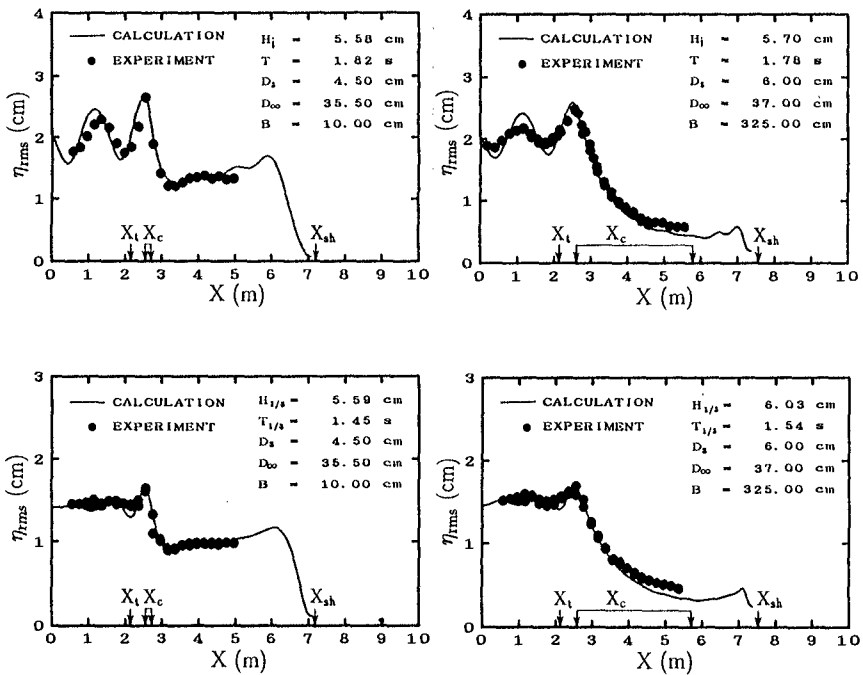


Fig.7 Distribution of root mean square value of water surface fluctuation.

The mathematical model based on the present mild-slope equation is applied to the computation of wave transformation over a submerged breakwater. Some important parameters are evaluated from given properties of the model breakwater; the porosity is 0.39. Values of the permeability K_p and turbulent friction coefficient C_f are interpolated from the results of laboratory tests under steady flow conditions which were presented by Sollitt and Cross (1972). In the present computation, the values of $K_p = 3.77 \cdot 10^{-7} \text{ m}^2$ and $C_f = 0.332$ are adopted. The inertia coefficient C_r is approximately regarded as unity after Sollitt and Cross (1972). The computation is performed by the iteration procedure. Results of the numerical computation are also shown in Fig.7 in comparison with the experimental data. The agreement between the model computation and experiment is generally good although the computation gives a transmitted wave component slightly smaller than the measured one. The computation also shows a slight overestimation of reflected wave due to the energy dissipation.

The present model is applied to a rectangular submerged breakwater and the reflection and transmission coefficients are compared with the strict solutions. A breakwater of width $B = 3 \text{ m}$ with the same physical properties as mentioned is considered. The amplitudes of reflected and transmitted waves are obtained from the potential in the offshore and onshore region of the breakwater. Then, the reflection and transmission coefficients are calculated. The computation was performed for various conditions. Sample results of the comparison are shown in Fig.8 as a function of relative water depth, h_0/L_0 . The agreement is fairly good in spite of the assumption of mild slope used in the derivation.

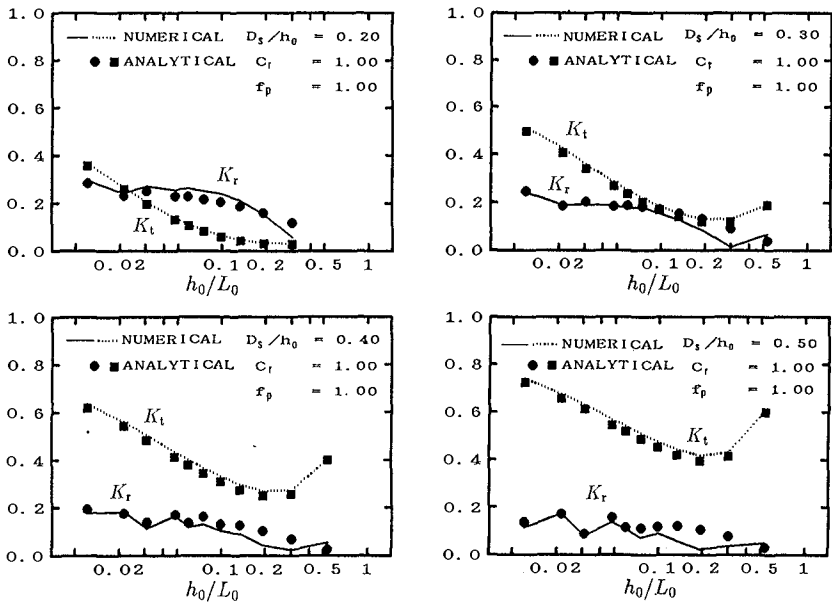


Fig.8 Reflection and transmission coefficients of rectangular submerged breakwater.

IV. CONCLUDING REMARKS

A mathematical model for the computation of wave transformation over a submerged permeable breakwater has been proposed on the basis of newly-derived mild-slope equation. The model equation is simple and helpful in understanding the physical behavior of the phenomenon. Its application was described by means of a numerical computation and the validity of the model was confirmed through comparisons with the experimental data and with a strict solution for a rectangular submerged breakwater. The present model is applicable for a wide range of breakwater configurations. However, the extension of the present model for a three-dimensional problem is essential to make the model more practical and useful for the prediction of wave field around the submerged breakwater.

REFERENCES

- [1] Berkhoff, J.C.W. (1972): Computation of combined refraction-diffraction, Proc. 13th Coastal Eng. Conf., ASCE, pp.471-490.
- [2] Dattari, J., H. Raman, and N.J. Shankar (1978): Performance characteristics of submerged breakwater, Proc. 16th Coastal Eng. Conf., ASCE, pp.2153-3171.
- [3] Liu, P.L.F. (1973): Damping of water waves over porous bed, J. Hydraulics Division, ASCE, Vol. 99, pp.2263-2271.
- [4] Miche, R. (1951): Le pouvoir réfléchissant des ouvrages maritime exposés à l'action de la houle, Annales Ponts et Chaussées, 121^e Année, pp.285-319.
- [5] Rojanakamthorn, S., M. Isobe, and A. Watanabe (1989): A mathematical model of wave transformation over a submerged breakwater, Coastal Eng. in Japan, Vol.32, No.2, pp.209-234.
- [6] Sollit, C.K. and R.H. Cross (1972): Wave transmission through permeable breakwaters, Proc. 13th Coastal Eng. Conf., ASCE, pp.1827-1846.
- [7] Ward, J. C. (1964): Turbulent flow in porous media, J. Hydraulic Div., ASCE, Vol. 90, No. HY5, pp.1-12.
- [8] Watanabe, A., and M. Dibajnia (1988): A numerical model of wave deformation in surf zone, Proc. 21st Coastal Eng. Conf., ASCE, pp.578-587.

CHAPTER 81

Wind-induced Cross-shore Water Flows

J B Crowley* and D H Swart**

1. Abstract

To cater for the effect of wind-driven nearshore processes on the prediction of nearshore onshore/offshore sediment transport a series of field experiments were carried out to establish a reference framework to be used as basis for the modelling of wind-driven cross-shore currents. The results indicate a clear relationship between bottom return current, wind speed and the water depth. This implies that a mathematical framework can be established using the conservation of mass and momentum and the similarity criterion.

2. Background

Nearshore sediment transport takes place as the combined action of wind, waves and tides. The processes are characterised by extreme turbulence under the action of breaking or near-breaking waves. Predictive techniques for the magnitude of the resulting nearshore transport rate, whether it be in the alongshore or the cross-shore direction, proliferate but they have all got but one commonality - the extreme simplifications and assumptions that have to be made. Typically what is done is that both wind and tide effects are neglected and only wave effects are considered. If we concentrate on cross-shore sediment transport, the best and/or most-used techniques today are those of Baillard (1981), Nairn (1988), Larson (1989), Stive (1987) and Swart (1974, 1986). Apart from the last technique, which has a broad theoretical basis with empirical coefficients which has proved extremely robust and accurate over a

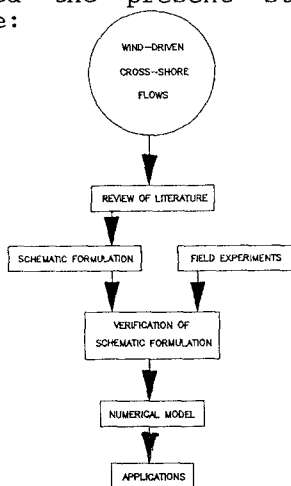
* CSIR, P O Box 320, Stellenbosch, 7600, South Africa.

** CSIR, P O Box 395, Pretoria, 0001, South Africa.

wide range of conditions, the other methods all utilise a momentum approach and are more theoretical of nature.

Experience has shown that these techniques are reasonably reliable (Seymour *et al.*, 1988, Möller *et al.*, 1988) but that specifically wind effects can totally upset the predicted results. Swart (1987) showed, e.g. that whereas all known predictors of the direction of cross-shore wave-driven transport would indicate offshore-directed sediment movement (beach erosion), the beach in the centre of a large bay of the south coast of South Africa accreted heavily whilst being attacked by normally-incident storm waves with a significant incident height of about 7 m and a deep-water steepness of 0,05. At the time a 20 m/s offshore wind was blowing, with presumably onshore return flow at the bed to compensate for water blown seawards.

This inspired the present study, which has the following outline:



The present paper concentrates on the field work and covers all aspects but the last two, namely, the numerical model and potential applications.

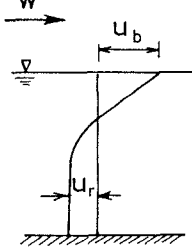
2. Review of Literature

A scan of the literature reveals a wide selection of papers dealing with the prediction of wind-driven water flow, e.g. Kranenburg (1987), Hubertz (1987), Kullenberg (1976), Winant (1980), Komen and Riepma (1981), Thomas (1975), Eidnes (1986), Bennett (1974, 1979), Birchfield (1972), Grant (1979), Madsen (1976), Kuzmic (1989) and Van Dorn (1953). However, although these papers contain valuable insights into the theoretical treatment of

wind-driven flows in general, they contain virtually nothing on cross-shore flows.

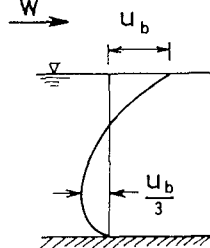
The only two papers with an applicable treatment of cross-shore flows are those by Kranenburg (1987) and Van Dorn (1953). In these two cases the following representation of the vertical flow profile was postulated on the basis of data:

a. Kranenburg (1987)



- Laboratory data
- Theoretical framework sketchy

b. Van Dorn (1953)



- Theoretical framework
- Sketchy data in pond

Figure 1. Postulated Wind-driven Flow Profile

Theoretical treatment. If one considers the various theoretical treatments in the whole body of the literature referred to above, it can be concluded that these are both numerous and varied. A short summary is included below.

The **basic equations** typically are

- the conservation of mass; and
- the equations of motion.

The **boundary conditions** used to solve these are then:

- the mean vertical surface flow is equal to zero; and/or
- the bottom shear stress is specified; and/or
- the surface shear stress is specified; and/or
- the surface drift velocity is related to the wind speed at some elevation above the water surface.

If one looks at the assumptions made by the various investigators, one sees the following spread:

- Direction of wind
 - on/offshore
 - longshore

- Water surface slope - horizontal
- sloping
- Homogeneous wind stress - all
- Coastal alignment - straight
- curved
- arbitrary
- Wave effects - included
- excluded
- Temporal variability - yes
- no
- Vertical averaging - yes
- no
- Hydrostatic pressure - yes
- no
- Dynamic pressure terms - included
- excluded
- Return flow - yes
- no
- Bed friction - neglected
- linear
- quadratic
- Geometry of water body - arbitrary
- rectangular
- two-dimensional

3. Schematic Formulation

On the basis of an analysis of the literature, the following first approximate approach is formulated.

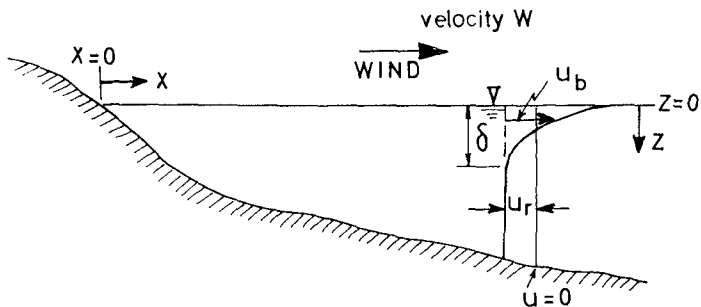


Figure 2. Definition Sketch

The following assumptions are made:

- ♦ the rigid-lid approximation is used;

- ♦ wave effects are neglected;
- ♦ the water surface slope is horizontal;
- ♦ the pressure distribution is hydrostatic;
- ♦ turbulent pressures are neglected;
- ♦ shear stresses in the return flow area are disregarded;
- ♦ the velocity profiles in the boundary layer agree to similarity, that is, the surface drift is proportional to the shear velocity U_* .

With these assumptions as basis, the following formulation is found:

Equation of motion

$$U_r \frac{dU_r}{dx} + \frac{1}{\rho} \frac{\partial \bar{p}}{\partial x} = 0 \quad \dots (1)$$

Conservation of mass

$$- U_r d + \int_0^{\delta} U_b(x, z) dz = 0 \quad \dots (2)$$

Integral conservation of momentum

$$d \frac{\partial \bar{p}}{\partial x} + \frac{d}{dx} \left[\rho \int_0^{\delta} \left\{ -U_r + U_b(x, z) \right\}^2 dz \right] = \rho U_*^2 \quad \dots (3)$$

Similarity criterion

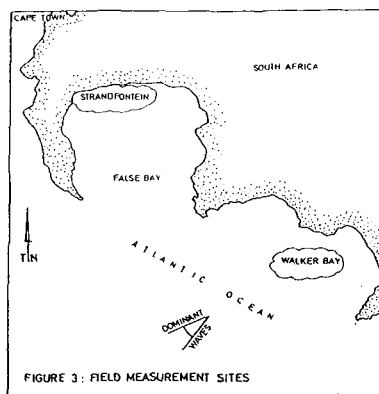
$$u_b(x, z) = U_* f(\zeta) \quad \text{where } \zeta = z/\delta \quad \dots (4)$$

The function $f(\zeta)$ determines the shape of the velocity profile inside the boundary layer. Kranenburg (1987) manipulated his data into a form where an expression could be found for $f(\zeta)$.

For the case where the bed slope is constant and with the surface shear velocity u_* proportional to the wind velocity W , it can be show that

$$\frac{U_r}{W} \propto d^{-1} \quad \dots (5)$$

This relationship will be used later as framework to plot the field data.



4. Field Experiments

The field measurements to quantify bottom return current as a result of a cross-shore wind were done at two sites on the south-western coast of South Africa. As can be seen on Figure 3, both of these bays face the predominant south-westerly swells although False Bay due to its dimensions is more protected than Walker Bay. Storm waves arrive at the latter nearly unabated.

In all three experiments were done, namely, in September 1986 and February 1990 in Walker Bay and in March 1990 in False Bay. The Walker Bay exercises were part of much bigger field measurement campaigns into nearshore coastal processes but the False Bay exercise was done solely for the purpose of determining wind-driven currents.

At Walker Bay the strongest wind events are from the north-west (May to August) and from the south-east during the rest of the year. Cross-shore wind events are therefore less prevalent. Nevertheless, a few useful blows in roughly the cross-shore direction did occur during the two exercises. The strongest wind events at False Bay occur from the same directions but due to the orientation of the bay and more specifically the prominent mountain ranges around it, the strong winds are nearly always roughly aligned in the cross-shore direction.

In doing the experiments during the three field programmes it was generally strived to deploy the equipment in the bottom 20 % of the water column and seaward of the dominant breaker line. Deployment water depth varied from 4 m to 20 m and in some of the shallower cases the current meters were at times inside the surf zone or very close to it, thus measuring wave-driven currents. It is easily visible on the plots of current velocity when this occurred.

As a result of the manner of deployment (location, depth, etc.) the results represent a breadth of varying influences, e.g. in incident waves (surface roughness), wave effects (rip currents, orbital velocity) and the bottom roughness (False Bay generally has a smoother bottom than Walker Bay).

Walker Bay : September 1986 Figure 4 gives an overview of the type of data gathered during this exercise. Figure 4c summarises all the available data points obtained with a vector-averaging current meter in 20 m water depth every 15 min. between 21 and 26 September 1986.

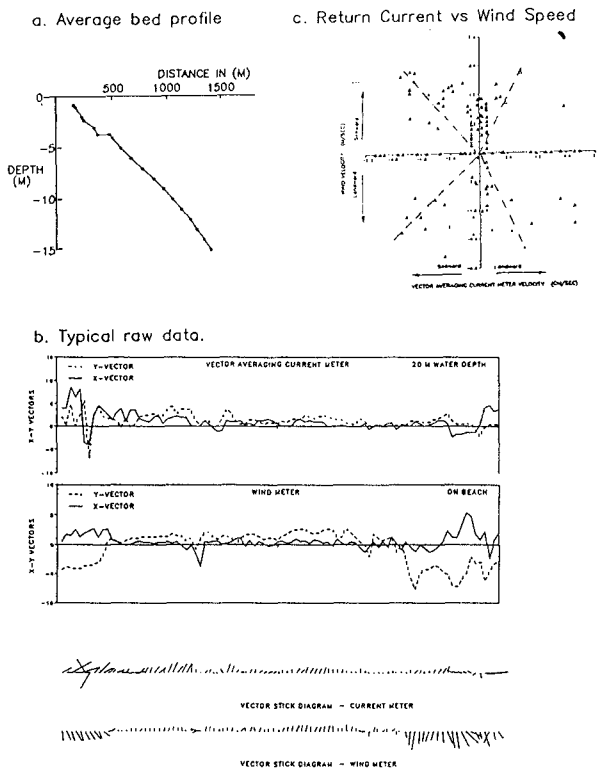
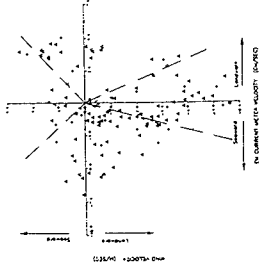
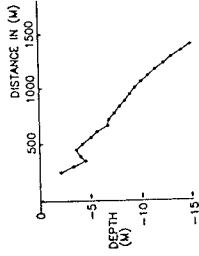


FIGURE 4: WALKER BAY DATA : September 1986

c. Return Current vs Wind Speed



a. Average bed profile



b. Typical raw data.

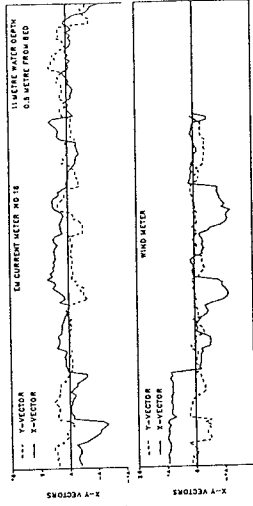
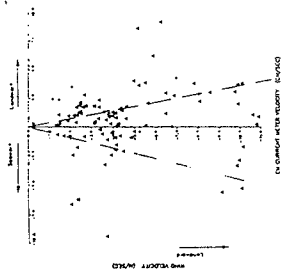
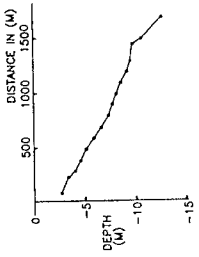


FIGURE 5 : WALKER BAY : February 1990

c. Return Current vs Wind Speed



a. Average bed profile



b. Typical raw data.

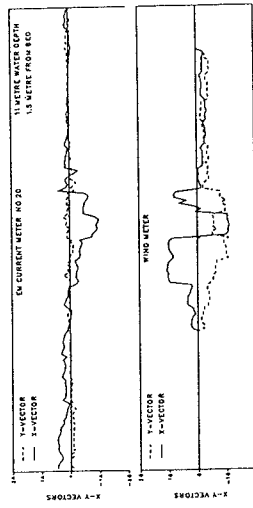


FIGURE 6 : STRANDFONTEIN : March 1990

During this period the incident, offshore wave climate varied as follows:

	Maximum	Mean	Minimum
* Significant height (m)	4,1	2,9	2,1
* Peak period (s)	15,5	12,3	7,5

The beachline was characterised by prominent cusps at 300 m centres, but the nearshore contours were nearly straight. As a result of the cusped shoreline rip currents occurred along the beach at 300 m intervals leading to breaches in the main breaker bar at 5 m water depth, also at 300 m centres. At the position of the meter, well outside the breaker line, the contours were nearly parallel.

Walker Bay : February 1990. During this exercise 'bottom' current meters were deployed in 4 m and 11 m water depth, in each case at 0,5 m and 1,5 m above the bed. Figure 5 gives an overview of the data for the 11 m depth, 1,5 m above the bed case. The duration of the measurement campaign was from 9 to 22 February 1990, for a period of 2 hours around each day time high and low tide. Electromagnetic current meters were used for all four deployments.

During this period the incident, offshore wave climate varied as follows:

	Maximum	Mean	Minimum
* Significant height (m)	3,8	2,1	1,2
* Peak period (s)	13,5	10,3	6,6

The nearshore topography was fairly complex with no clear, well-developed breaker bar. Thus the contours were also complex, characterised by rapidly changing bars, troughs and gullies in 4 m depth but with a reasonably stable, straight set of contours in 11 m depth. The location of the breaker bar in Figure 5a in relation to the measuring stand also shows the potential for variability.

False Bay : March 1990. During this exercise the configuration of the February 1990 Walker Bay experiment was repeated, except that the deeper stand now had current meters at 0,5 m, 1,5 m and 2,5 m above the bed. Unfortunately, the meter closest to the bed at this deep stand malfunctioned and no data was obtained for that elevation above the bed.

Measurements were obtained for 2 hours around each day time high and low tide for the period 11 March to

21 March 1990. During this period the incident wave climate varied as follows:

	Maximum	Mean	Minimum
* Significant height (m)	3,0	1,8	1,0
* Peak period (s)	13,5	10,3	5,5

Figure 6 shows an overview of the data for the meter at 2,5 m above the bed in 11 m water depth. Figure 6c clearly shows some predominant wave effects, associated with a macro-rip current occurrence in the area.

This site is characterised by a very much flatter bottom profile than at Walker Bay, a very straight beach with fine sand, a smooth calcareous surface offshore and nearly straight contours at both deployment stands.

5. Verification of Schematic Representation

It was shown earlier that for a constant bed slope, which is a realistic assumption for all cases as can be seen, in Figures 4 to 6, the ratio U_r/W is proportional to the inverse of the water depth. To test this hypothesis the data in figures like Figures 4 to 6, but for all instruments, were fitted with a best-fit straight line through the origin. It is important to note that the wind condition varied between onshore and offshore, thus giving two possible data points per graph. The data, given in Figure 7a, show clearly that the correct tendency is prevalent in the plot. The scatter is to be expected, since the experiments were done under very different wave conditions and with varying seabed configurations. It is interesting that ratios between approximately 0,01 and 0,02 are found for the return current, whereas earlier studies have shown that the surface drift velocity varies between 3 % and 7 % of the wind speed (Kullenberg, 1976).

What is interesting, however, is that not only do those cases conform where the bottom current is a return current when compared to the wind direction, but this is also the case for those situations when the bottom current is in the same direction as the wind direction (Figure 7b). Presumably this represents cases where the whole water column is moved by wind action and continuity is achieved through horizontal water circulation.

The problem with field observations of wind-induced drift, or for that matter with laboratory observations, is that the drift takes place in a part of the nearshore area characterised by fairly vigorous currents, to

mention but nearshore circulation with frequently stormy rip currents, orbital velocities and mass transport. All but the last are up to an order of magnitude higher than the wind-induced drift. Separation of the wind drift from the complex composite of currents in the nearshore area is at best a guesstimate. However, the analysis done herein is not intending to provide absolute values for the drift, but rather to indicate qualitative final estimates of what appears to be the wind drift. As was shown, some clear guidelines emerged, obviously keeping the above comments in mind.

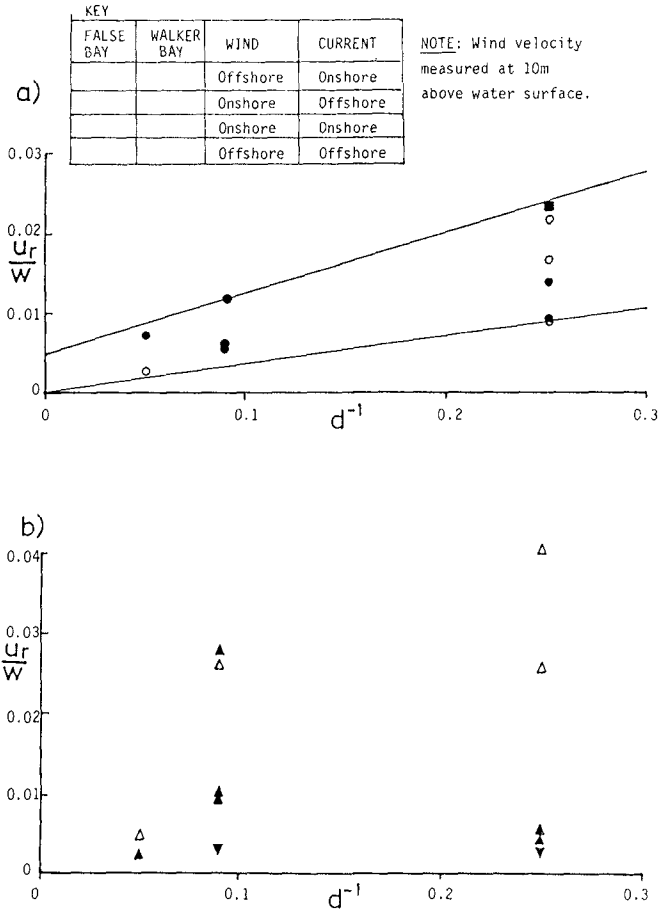


Figure 7. Schematic Framework for Prediction of Return Velocity U_r as a Function of Wind Velocity W and Water Depth d .

6. Conclusions and Recommendations

The main conclusions reached to date in this study on wind-induced cross-shore water flows are the following:

(1) The theoretical framework represented by Equations (1) to (4) is promising.

(2) The bottom 'return' layer concept seems reasonable, although the field data show that there are also cases where the return flow does not take place in the same cross-section. Presumably this latter case is strongly related to irregularities in the sea bottom and the obliqueness of the incident waves.

(3) The effect of bed slope on the results in Figure 7a and 7b appears to be fairly minimal.

(4) At present it is not sure to what extent waves will influence the results.

Therefore, with this as basis, we are taking the following approach:

♦ We are developing a numerical model for an arbitrary bottom profile; and

♦ We are further investigating the effect of varying surface roughness caused by variations in wave height.

Having made these advances, we hope to in time be in a position to predict the wind-driven cross-shore flows in a situation such as depicted below.

References

Bailard, J A (1981). An energetics bedload model for a plane sloping beach: local transport. *Journal of Geophysical Research*. Vol. 86, No. C3.

Bennett, J R (1974). On the dynamics of wind-driven lake currents. *Journal of Physical Oceanography*, Vol. 4, pp 400-414.

Bennett, J R and Magnell, B A (1979). A dynamical analysis of currents near the New Jersey Coast. *Journal of Geophysical Research*, Vol. 84, pp 1165-1175.

- Nirchfield, G E (1972). Theoretical aspects of wind-driven currents in a sea or lake of variable depth with no horizontal mixing. *Journal of Physical Oceanography*, Vol. 2, pp 355-362.
- Eidnes, G, Utnes, T and McClimans, T A (1986). Wind mixing a stratified shear flow. *Continental Shelf Research*, Vol. 6, pp 597-613.
- Hubertz, J M (1987). A wind- and wave-driven nearshore current model. Department of the Army, US Army Corps of Engineers, Washington. *Final Report February 1987*.
- Komen, G J and Riepma, H W (1981). The generation of residual vorticity by wind and bottom topography in a shallow sea. *Oceanological Acta*, Vol. 4, pp 267-277.
- Kranenburg, C (1987). Turbulent surface boundary-layer induced by an offshore wind. *Journal of Hydraulic Research*, Vol. 25, pp 53-65.
- Kullenberg, G E B (1976). On vertical mixing and the energy transfer from the wind to the water. *Tellus XXVIII*, Vol. 2, pp 159-165.
- Kuzmic, M (1989). A numerical study of wind-induced motions in shallow coastal seas: model and basic experiment. *Appl. Math. Modelling*, Vol. 13, pp 178-191.
- Larsen, M (1989). S beach: numerical model for simulating storm-induced beach change. Department of the Army, US Army Corps of Engineers, Washington. *Report 1*.
- Madsen, O S (1976). A realistic model of the wind-induced Ekman boundary layer. *Journal of Physical Oceanography*, Vol. 7, pp 248-255.
- Möller, J P and Swart, D H (1988). Extreme erosion event on an artificially nourished beach. *Proc. 21th International Conference on Coastal Engineering*. Malaga, Spain.
- Nairn, R B (1988). Prediction of wave height and mean return flow in cross-shore sediment transport modelling. *IAHR Symposium in Mathematical Modelling of Sediment Transport in the Coastal Zone*. Copenhagen.

- Seymour, R J, Castel, D (1988). Validation of cross-shore transport formulations. *21st International Conference on coastal Engineering*. Malaga.
- Stive, M J F (1987). A model for cross-shore sediment transport. *Proc. 20th International Conference on Coastal Engineering*. Taipei.
- Swart, D H (1974a). Offshore sediment transport and equilibrium beach profiles. Doctoral thesis, Technische Hogeschool. Delft.
- Swart, D H (1974b). A schematisation of on/offshore transport. *Proc. 14th International Conference on Coastal Engineering*.
- Swart, D H (1976). Predictive equations regarding coastal transports. *Proc. 15th International Conference on Coastal Engineering*. Honolulu, Hawaii.
- Swart, D H (1986). Prediction of beach changes and equilibrium beach profiles. Lecture notes for short course on: *Dynamics of sand beaches*. Taipei, Taiwan.
- Thomas, J H (1975). A theory of steady wind-driven currents in shallow water with variable eddy viscosity. *Journal of Physical Oceanography*, Vol. 5, pp 136-142.
- Winant, C D (1980). Coastal circulation and wind-induced currents. *Ann. Rev. Fluid Mech.*, Vol. 12, pp 271-301.

CHAPTER 82

Irregular Waves on a Current

H.-H. Prüser and W. Zielke ¹

1 Introduction

In coastal areas interacting currents and waves are quite frequent. The currents are generated by the tides or the discharge of a river; the waves are irregular short crested, generated by the wind. A suitable numerical wave model for this situation is presented in this paper. It is based on the Boussinesq-Wave-Equations (BWE) which were extended to simulate the influence of a current on a wave as well as the effects of nonlinear wave-wave interaction in a propagating wave spectrum.

An analytical approach to describe wave-current interaction was given by Longuet-Higgins/Steward (1960) [3]. They investigated linear small amplitude waves in a moving medium and introduced the concept of radiation stress to determine the change of wavelength and wave amplitude as a function of the current and the direction of wave propagation. Their fundamental work was the basis for the development of various numerical models, which were reviewed recently by Jonsson (1989) [2]. Most of these models are restricted to linear (small amplitude) wave theory.

The wave climate in shallow water is generated by the influence of bottom topography as well as by nonlinear wave-wave interaction in a propagating wave spectrum, which cannot be described by linear wave theory. Instead, such weakly nonlinear waves are frequently modeled using the BWE. The development of models based on these equations first began in the late 70's. Since then, a number of studies have been carried out to verify their capabilities. It has been shown that they are able to simulate accurately combined refraction, diffraction, reflection and shoaling (see for example Madsen/Warren (1984)[4] as well as the nonlinear wave-wave interaction in a wave spectrum propagating over an uneven bed (see for example Prüser/Schaper/Zielke (1986)[7]). Boussinesq wave models have now become a practical tool for engineering applications.

In this paper, a numerical model based on an extended form of the BWE which takes into account the influence of an ambient current on waves is used to investigate irregular waves propagating and refracting on an ambient current. After presenting the equations, a comparison based upon linear (small amplitude) wave theory is conducted to illustrate the range of application. The numerical model was used to simulate irregular waves with a current in a flume and in a basin. The results were in good agreement with the solution of Longuet-Higgins/Steward.

¹Institute of Fluid Mechanics, University of Hannover, Appelstr. 9A, 3000 Hannover, F.R.G.

2 The mathematical model

2.1 The Extended Boussinesq-Wave-Equations

Nonlinear wave behaviour in shallow water and in intermediate depth can be simulated using the BWE. These equations have been extended in order to include the effect of wave-current interaction, which is often necessary in coastal areas. *Mathematically, the general case of waves propagating through a current field over an arbitrary bottom topography is a complex initial boundary value problem. However, since the length and time scales of the wave motion are usually much smaller than those of the current, it is possible to solve the current field and the wave field in two separate steps*². Consequently, for the derivation of the extended BWE, it is assumed that the current field is known from numerical simulations or measurements. A step by step description is given by Prüser (1991)[6]. The extended BWE used in this paper and the equation of continuity are as follows (the index '0' refers to the ambient current and '*' to the combined flow of waves and currents. Variables without indices refer to waves only) :

$$\begin{aligned}
 u_{,t} + u^*u_{,x} + v^*u_{,y} + g\zeta_{,x} &= -\frac{D^2}{6}(u_{,xxt} + v_{,xyt}) + \frac{D}{2}((u_{,t}D)_{,xx} + (v_{,t}D)_{,xy}) \\
 &\quad + u_0\frac{D^2}{3}(u_{,xxx} + v_{,xxy}) + v_0\frac{D^2}{3}(u_{,xxy} + v_{,xyy}) \quad (1)
 \end{aligned}$$

$$\begin{aligned}
 v_{,t} + u^*v_{,x} + v^*v_{,y} + g\zeta_{,y} &= -\frac{D^2}{6}(u_{,xyt} + v_{,yyt}) + \frac{D}{2}((u_{,t}D)_{,xy} + (v_{,t}D)_{,yy}) \\
 &\quad + u_0\frac{D^2}{3}(u_{,xxy} + v_{,xyy}) + v_0\frac{D^2}{3}(u_{,xyy} + v_{,yyy}) \quad (2)
 \end{aligned}$$

$$(D + \eta)_{,t} + (u^*(D + \eta))_{,x} + (v^*(D + \eta))_{,y} = 0 \quad (3)$$

with: $u^* = u + u_0 \quad v^* = v + v_0$

The fluid velocities u^* , v^* are comprised of the ambient current field u_0 , v_0 and the wave flow field u , v . The current appears in the convective terms of the left hand side of the equations and also produces additional third order terms. The numerical BOUSSINESQ-WAVE-MODEL (BOWAM) which was available for the solution employs a formulation involving fluxes and surface elevations [8] [9]. Therefore, it was necessary to transform the equations by substituting $h = D + \zeta$, $p = uh$ and $q = vh$. The equations were solved by an implicit third order corrected finite difference method using two time levels and central differences.

2.2 Range of application, harmonic waves

The range of application depends on the wavelength to water depth ratio L/D . Shallow water is defined if the wavelength is larger than 20 times the water depth whilst deep water is defined if the wavelength is smaller than twice the

²cited from Jonsson[2]

wavelength; the region between these limits is referred to as intermediate depth. The BWE are limited to shallow water with an extension to include intermediate depth. In a nonlinear study with periodic waves, McCowan (1987)[5] has shown that the equations are valid provided the wavelength is at least 6 times the water depth. In this paper, the range of application for the extended BWE will be checked by a comparison with linear (small amplitude) wave theory. In a first step, the dispersion relations will be investigated. These results are necessary to subsequently verify the extended BWE using analytical solutions of wave-current interactions.

The wave profile is given by a harmonic function with amplitude a , wave number $k = 2\pi/L$ and frequency $\omega = 2\pi/T$.

$$\eta(x, t) = a \sin(\omega t - kx) \tag{4}$$

For simplicity, the investigation is limited to the one-dimensional case with constant water depth. The BWE and the equation of continuity reduce to:

$$u_{,t} + (u_0 + u)u_{,x} + g\eta_{,x} - \frac{1}{3}D^2u_{,xxt} - \frac{1}{3}D^2u_0u_{,xxx} = 0 \tag{5}$$

$$\eta_{,t} + u_0\eta_{,x} + Du_{,x} = 0 \tag{6}$$

The velocity u can be eliminated by differentiating (5) with respect to x and substituting (6) in (5). Finally, nonlinear terms of order $O(a^2)$ are neglected.

$$-\eta_{,tt} + (gD - u_0^2)\eta_{,xx} - 2u_0\eta_{,xt} + \frac{D^2}{3}(\eta_{,xxtt} + 2u_0\eta_{,xxxxt} + u_0^2\eta_{,xxxxx}) = 0$$

Inserting the wave profile (4) into the above equation gives Equ. (7). Nontrivial solutions for the frequency ω (8) are obtained if the first parenthesis is set to zero.

$$\left(\omega^2 - 2ku_0\omega + k^2u_0^2 - \frac{k^2gD}{1 + \frac{1}{3}D^2k^2}\right) a \sin(\omega t - kx) = 0 \tag{7}$$

$$\omega_{1,2} = ku_0 \pm \sqrt{\frac{k^2gD}{1 + \frac{1}{3}k^2D^2}} \tag{8}$$

The sign in front of the square root is chosen according to whether the wave is propagating in the direction of the current u_0 or in the opposite direction. The differentiation of ω with respect to the wave number k gives the group velocity:

$$c_g = \frac{\partial\omega}{\partial k} = \frac{1}{2}c^B(1 + G^B) + u_0$$

$$\text{mit: } G^B = \frac{1 - \frac{1}{3}k^2D^2}{1 + \frac{1}{3}k^2D^2} \tag{9}$$

Table 1 summarizes the analytical formulae for the dispersion relation of the linear theory and of the Boussinesq theory in the case of small amplitude waves.

and Steward. The wavelength in the presence of a current is given by an implicit function of the corresponding wave in still water (frequency ω ; phase velocity c) and the current u_0 :

$$L^c = 2\pi k^c \quad \text{with} \quad (\omega - k^c u_0)^2 = k^c \omega c \quad (10)$$

The change of wave amplitudes depends on the manner in which the ambient current is generated. Longuet-Higgins/Steward investigated two different situations, which were defined as *upwelling from below* and *inflow from the sides*. These definitions will be explained in the Chap. 3.1. In the case of *upwelling from below*, an adequate formula describing the situation with a current (a^c, L^c, G^c) and the situation in still water (a, L, G) is given by Brevik/Aas (1980)[1]. The change of amplitudes tends towards infinity as the Froude number tends towards $Fr \rightarrow -0.5$:

$$\frac{a^c}{a} = \sqrt{\frac{1 + G}{\left(\frac{L^c}{L} - \frac{u_0}{c}\right)(1 + G^c) + \frac{2u_0}{c}\left(1 - \frac{L}{L^c} \frac{u_0}{c}\right)}} \quad (11)$$

The parameters G, G^c, L^c and c can be substituted by the dispersion relations summarized in Table 1. Fig. 2 shows the change of wavelength L^c/L and Fig. 3 shows the change of wave amplitude a^c/a as a function of the Froude number $Fr = u_0/\sqrt{gD}$ for three different wavelengths ($L/D = 20, 10, 6$). The solid lines indicate the results obtained from the formulae (10) and (11) using linear theory whilst the dashed line indicate the results from Boussinesq theory. A negative Froude number indicates that the current and waves are propagating in opposite directions. The formulae are evaluated for Froude numbers $-0.3 < Fr < 0.5$. For most coastal engineering purposes, however, Froude numbers lie in the range of $-0.2 < Fr < 0.2$. With regard to the change of wavelength L^c/L , the following can be stated:

- The wavelength increases if the direction of wave propagation is the same as that of the current ($Fr > 0$) and decreases in the case of opposite directions. This effect is more pronounced in deeper water.
- The Boussinesq approximation is very good for the complete range of Froude numbers in Fig. (2) provided the wavelength is larger than 10 times the water depth.

With regard to the change of wave amplitude a^c/a , the following can be stated:

- The wave amplitude increases if the direction of wave propagation and that of the current are different ($Fr < 0$) and decreases when the directions are the same.
- The influence of the relative wavelength L/D on the change of amplitudes is very slight for Froude numbers greater than zero, but significant for Froude numbers less than zero.

	linear theory	Boussinesq theory
phase velocity $c^c = u_0 + c$	$c^L = \sqrt{gD} \sqrt{\frac{1}{kD} \tanh kD}$	$c^B = \sqrt{gD} \sqrt{\frac{1}{1 + \frac{1}{3} k^2 D^2}}$
group velocity $c_g^c = u_0 + \frac{1}{2} c(1 + G)$	$G^L = \frac{2kD}{\sinh 2kD}$	$G^B = \frac{1 - \frac{1}{3} k^2 D^2}{1 + \frac{1}{3} k^2 D^2}$

Table 1: Dispersion relation in linear and Boussinesq theory

The superscript *c* indicates currents, *L* indicates Linear theory, and *B* indicates Boussinesq theory. The comparison indicates a high degree of similarity between linear and Boussinesq theory. If an ambient current is present, then the phase velocity *c^c* and the group velocity *c_g^c* are superposed on the current *u₀* and the corresponding velocity in still water. For shallow water conditions (*kD* → 0), linear and Boussinesq theory are identical. In deeper water however, the solution obtained by Boussinesq theory is an approximation to linear theory.

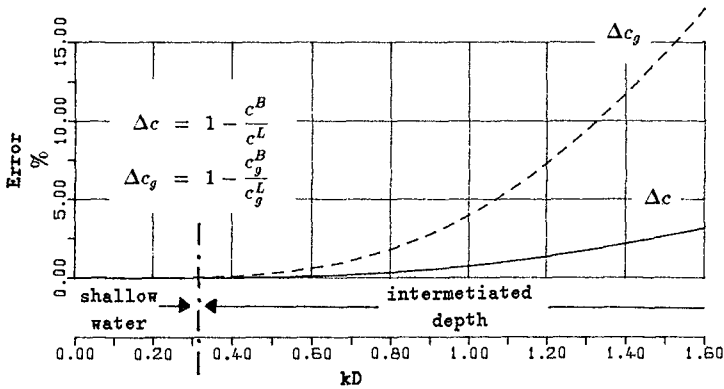


Figure 1: Dispersion relation in linear and Boussinesq theory as a function of the parameter *kD*

Fig. 1 displays the relative errors of the phase velocity Δc (solid line) and the group velocity Δc_g (dashed line) as a function of the parameter *kD*. As expected, an excellent agreement is found between linear and Boussinesq theory for shallow water conditions ($L/D > 20, kD < 0.3$). Moving into deeper water ($kD > 0.3$), Boussinesq approximation for the phase velocity is much better than for the group velocity. A priori we will allow errors in phase and group velocity less than 5%, which gives a limit for the range of application of $kD < 1.0$ (see Fig. 1). This is in agreement with McCowan who indicated that the wavelength should be larger than 6 times the water depth.

The change of wavelength and wave amplitude due to the ambient current can be determined by analytical solutions based on the work of Longuet-Higgins

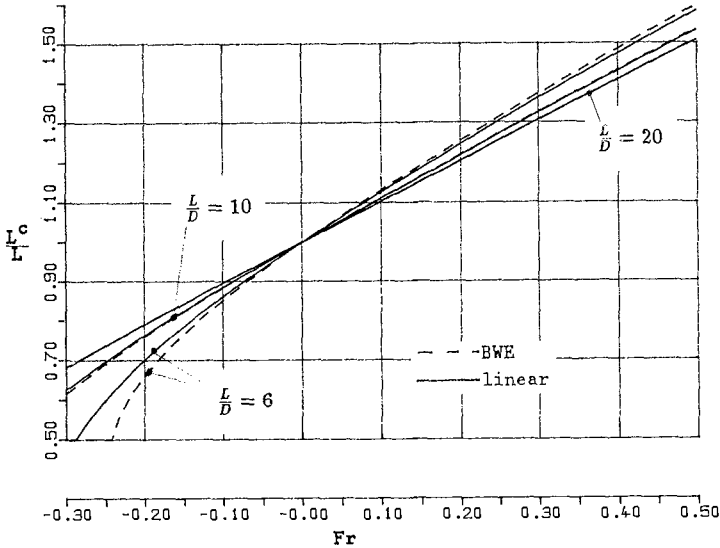


Figure 2: Change of wavelength due to an ambient current. Comparison with the corresponding wavelength in still water.

- For negative Froude numbers, the wavelength must be larger than 10 times the water depth.

In conclusion: Within limits of linear wave theory, extended BWE are valid for simulating the interaction of an ambient current on waves if the corresponding wavelength in still water is larger than 10 times the water depth and the Froude number is in the range of $-0.2 < Fr < 0.2$. If the corresponding wavelength in still water is smaller than 10 times the water depth and larger than 6 times the water depth, the extended BWE are applicable only if wave and current are in the same direction. If the waves are even shorter than 6 times the water depth, they are outside the range of Boussinesq theory, independent upon the current direction.

2.3 Range of application, irregular waves

The investigation on the basis of the dispersion relation, as presented in Chap. 2.2, is necessarily limited to harmonic waves with particular frequencies and wavelengths. The natural sea state, however, contains various interacting wave components. There is a need to define, which type of spectra and which frequency range can be modeled properly with BWE. Due to the nonlinear character of the waves there is no analytical theory available to define the range of validity. On the basis of experience, which has been obtained in a quite number of BOWAM-Simulations the following statements can nevertheless be made:

In irregular wave trains short waves are often related to longer waves. One ex-

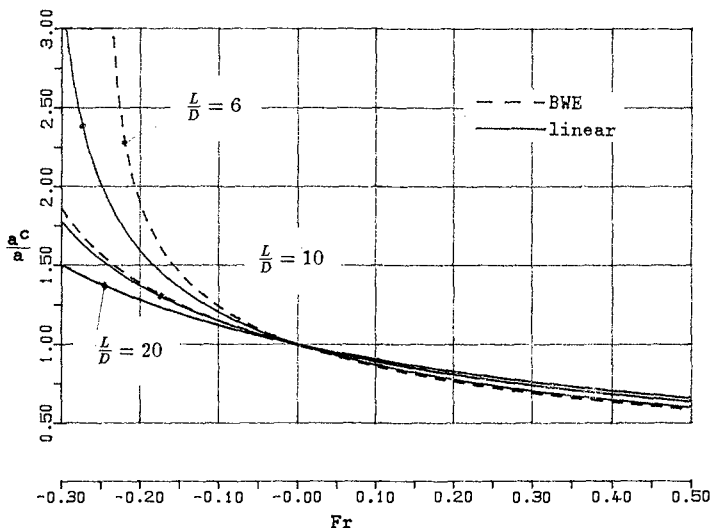


Figure 3: Change of wave amplitude due to an ambient current. Comparison with the corresponding wave amplitude in still water.

ample is the behaviour of wave groups. Hydraulic measurements and the theory of biharmonic waves have shown, that bounded-long waves as well as bounded-short waves are generated. Another example is the propagation of a wave spectrum from deeper to shallower water. A transformation of energy towards higher harmonics can be observed. The centre-row of Fig. 6 demonstrates this quite clearly. In both cases, the high frequency components (short waves) which are created in the transformation may be outside of the range of validity of BWE as defined in Chap. 2.2. However, they can be properly modeled with BWE as long as the corresponding long waves are in the range of validity.

3 Waves on a current in a flume

3.1 Generation of the current

The current can be generated by pumping water into the flume through an inlet (or outlet) located at the bottom or in the walls. In the following it will be assumed that this volume flux is constant in time. The current velocity u_0 can be changed, however, by increasing or decreasing the cross-section of the flume. The change of wave amplitudes caused by the ambient current depends on *how* the current is generated. In the case of an upwelling of water from below (inlet at the bottom, varying water depth), it is larger than in case of inflow from the sides (inlet in the wall, narrowing of the width of the flume). Both cases will be investigated numerically. In Fig. 4, the corresponding analytical solutions for shallow water conditions and constant water depth are shown. A negative current with a Froude number of $Fr = -0.2$ shows an increase of the amplitudes of about

10% for the case of *inflow from the sides* and of about 25% for the case of *upwelling from below*. The change of wavelength is the same in both cases.

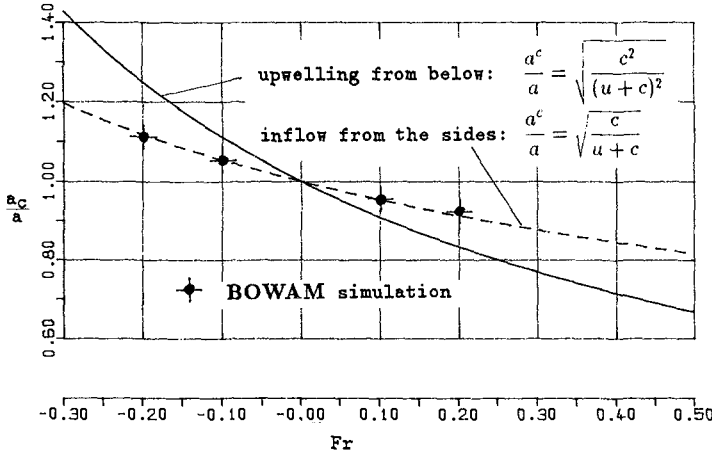


Figure 4: Change of amplitudes in shallow water. Comparison of the situations *upwelling from below*, *inflow from the sides* and BOWAM-Simulation.

3.2 Inflow from the sides

The behaviour of a wave spectrum propagating in a wave flume with constant water depth was investigated using the BWE. The upper part of Fig. 5 displays the experimental set-up: A numerical wave flume with a wave maker on the left hand side and three velocity/water elevation gauges A, B, C is shown. The water depth ($D = 0.5m$) as well as the width of the flume are constant. A number of inlets in the walls enable an ambient current to be generated between the gauges A and B by an *inflow from the sides*. The current u_0 is assumed to be zero at gauge A, increasing linearly to gauge B and remaining constant between gauges B, C.

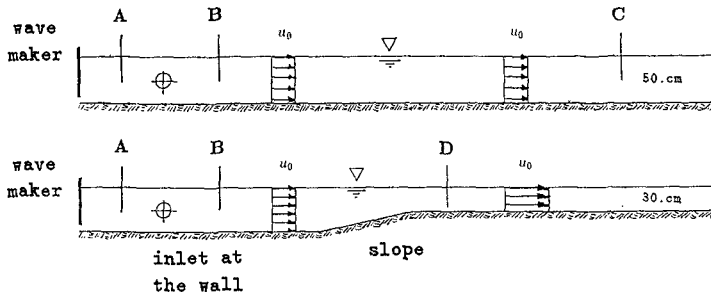


Figure 5: Experimental set-up: Waves with an ambient current in a wave flume

Pierson–Moskowitz spectra are introduced into the flume by the wave maker. The simulated time series of the surface elevation η are recorded at the gauges. These were transformed by FFT into the frequency domain to investigate the change of the spectral shape along the flume. Fig. 6 displays the calculated wave spectra at the gauges A, B, C for different ambient currents. The total amount of energy is given by the spectral moment of zero order m_0 . Assuming a *Rayleigh* distribution, the significant wave height can be calculated from:

$$H_s = H_{m0} = 4\sqrt{m_0} \quad (12)$$

The spectra along the centre-row of Fig. 6 are the results of a simulation in still water ($Fr = 0.$). The significant wave height m_0 is the same for all gauges. For deep water conditions the incoming Pierson–Moskowitz spectrum is stable. In Fig. 6 the wavelength corresponding to the peak period of the spectrum ($T_p = 4.5s$) is about 20 times the water depth, which indicates shallow water conditions. Therefore, due to nonlinear wave–wave interaction in shallow water, the spectral shape changes considerably. Higher harmonics and low frequency components bounded to wave groups have been generated. This is visible in the spectral shape. A double peaked spectrum and lower frequency components not included in the input spectrum appear at gauge C. The numerical simulation without a current has been verified very successfully by hydraulic measurements for a number of different wave spectra (Prüser/Schaper/Zielke [7]). It can be used to estimate and compare the influence of the ambient current.

The first and third row of Fig. 6 display the influence of wave–current interactions. The Froude number of the ambient current was $Fr \pm 0.1$, i.e. the investigation deals with waves propagating in the direction of the current as well as in the opposite direction. The recorded time series at gauge A is equal in both cases because the current is zero at this location. The wave spectrum at gauge A is given in the centre-row. The influence of the ambient current on the wave spectrum can be separated into two phenomena:

The first one concerns the change of significant wave heights H_s between gauges A and B. If waves and currents are propagating in the same direction, the amplitudes i.e. the energy corresponding to the individual frequency components have decreased. The spectral moment of first order changes from $m_0 = 8.6 \cdot 10^{-5}$ to $7.8 \cdot 10^{-5}$ (the reverse effect occurs if waves and current are propagating in opposite directions $m_0 = 8.6 \cdot 10^{-5}$ to $9.6 \cdot 10^{-5}$). This gives significant wave height ratios of $H_s^c/H_s = 0.95$ and $H_s^c/H_s = 1.06$, respectively). Further investigations show, that these ratios are nearly independent upon the incoming wave height H_s , but they do depend on the peak–period of the spectrum. This is in agreement with Fig. 11. For shallow water conditions and a current, generated by an *inflow from the sides*, the results of BOWAM are very close to the analytical solution, as shown in in Fig. 4. The second phenomenon concerns nonlinear wave–wave and wave–current interactions. These can be obtained by comparing the wave spectra at the gauges B and C for the three test conditions displayed in Fig. 6. Double peaked spectra are generated and the total amount of energy

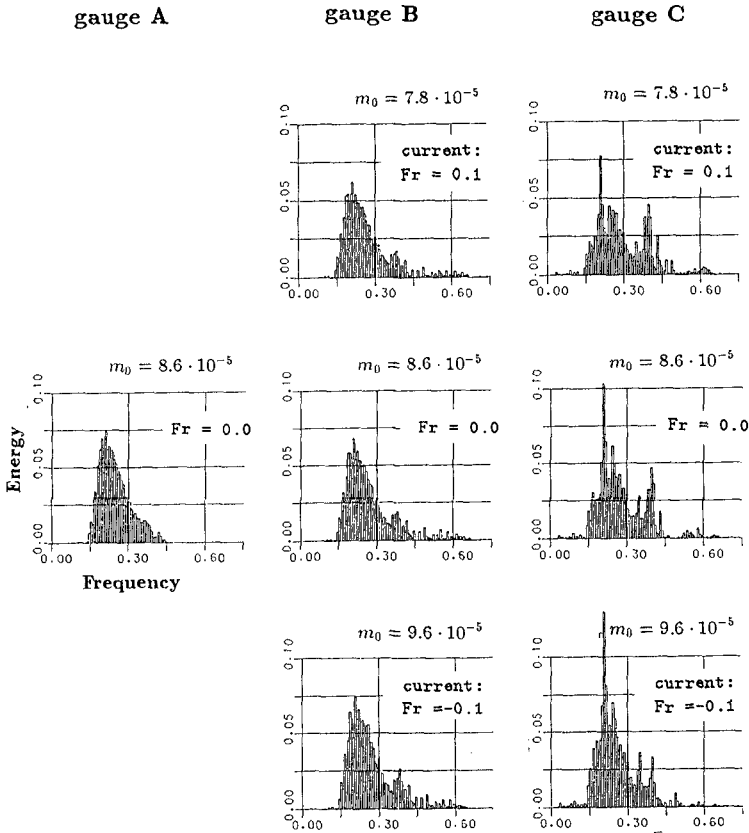


Figure 6: Wave-current interaction in the frequency domain

is constant for each test. However, the behaviour of the peaks at a frequency of $\approx 0.2Hz$ and $\approx 0.4Hz$ is different. The first peak decreases if waves and current are propagating in the same direction and increases otherwise. This is again in agreement with Fig. 4. The behaviour of the second peak is almost the reverse of the latter. It remains constant or increases if waves and current are in the same direction and decreases otherwise. This cannot be explained by the theory of Longuet-Higgins/Steward. Although the significant wave height of the spectrum is relatively small compared to the water depth ($H_s \approx 4.cm$ $D = 50.cm$), the nonlinear wave-wave interaction between the individual frequency components dominates the influence of wave-current interaction. Contrary to the first phenomenon there is a significant dependency on the incoming wave height, indicating the necessity of nonlinear numerical simulations.

3.2 Upwelling from below

The bottom picture of Fig. 5 displays the experimental set-up. This is almost the top picture, except that a slope is present between gauges **B** and **D** and the water depth reduces from 50.cm to 30.cm. Consequently, the wave transformation is even more complicated. Due to the different cross-sections, the ambient current is larger at gauge **D** than at gauge **A**. The change of the current takes place above the slope by an upwelling of water from below. In addition to this, the propagating wave spectrum shoals over the slope.

Assuming a linear, monochromatic wave, the change of its amplitude between gauges **B** and **D** can be calculated using the formula³

$$\frac{a^D}{a^B} = \sqrt{\frac{(u_{0,B} + \frac{1}{2}c_B(1 + G_B)L_B)c_D}{(u_{0,D} + \frac{1}{2}c_D(1 + G_D)L_D)c_B}} \quad (13)$$

If the ambient current is zero at both gauges ($u_{0,B} = u_{0,D} = 0$), then (13) gives the shoaling coefficient. If $u_{0,B} = 0$ and the water depths are equal at both gauges, then (13) is identical to Equ. (11). It is important to notice that the change of amplitudes results from a combination of wave-current interaction and shoaling.

As indicated in Chap. 3.2, the significant wave height of the spectrum H_s is affected by an ambient current as predicted by the analytical solution of Longuet-Higgins/Steward. This chapter is to investigate further changes in a combined current-shoaling situation. A suitable numerical model has to take into account that waves are transformed by an upwelling of water from below. In other words, it has to take into account a vertical component of the fluid velocity above the slope. Although the variables of the extended BWE are the depth-averaged horizontal velocities u, v , a vertical velocity w varying linearly from the bottom to the surface is assumed during the derivation. This enables the equations to simulate the wave behaviour above the slope which is influenced by water *upwelling from below*.

Several numerical simulations have been carried out using a Pierson-Moskowitz spectrum with different peak periods T_p and different significant wave heights H_s . Also, a comparison is made using Equ. (13), involving a monochromatic wave with a period equal to the peak period of the spectrum. Table 2 summarizes the results for a spectrum with $T_p = 4.5s$ and different current conditions: Column *BOWAM* displays the results of the numerical model whereas column *combined* shows the results of the analytical solution (13). It is common practice in simple linear wave modelling to approximate combined effects as a superposition of individual effects. For comparison, column k_s and column k_u are the results of separate shoaling and separate wave-current interaction, respectively. Column $k_{s,u} = k_s k_u$ displays the results of the linear superposition.

It can be stated that the results of BOWAM are in very good agreement with the analytical solution. The linear superposition of separate shoaling and

³This formula has been developed based on the concept of the *conservation of wave action*. For details, see Jonsson [2] and Prüser[6].

gauge B		gauge D		$H_{s,D}/H_{s,B}$				
u_0	Depth	u_0	Depth	BOWAM	combined	k_s	k_u	$k_{s,u}$
0.100	0.50	0.167	0.30	1.068	1.070	1.125	0.970	1.091
-.100	0.50	-.167	0.30	1.200	1.192	1.125	1.036	1.166
0.150	0.50	0.250	0.30	1.039	1.048	1.125	0.957	1.077
-.150	0.50	-.250	0.30	1.241	1.232	1.125	1.057	1.189

Table 2: Combined modelling of waves on a current and shoaling

separate wave current interaction is a relatively good approximation regarding wave heights. It should not be used, however, if one is interested in locating a breaker zone, which depends on the ratio of wave height to water depth; irregular wave trains will produce a time-varying breaker zone. This has to be simulated in nonlinear wave models.

4 Waves on a current in a basin

The corresponding two-dimensional extension of the test described in Chap. 3.2 will be investigated here. In a wave basin of constant water depth ($D = 50\text{cm}$), a Pierson-Moskowitz spectrum ($T_p = 4.5s$, $H_s \approx 4\text{cm}$) is generated by the wave maker and propagates from left to right. An ambient current with a Froude number of $Fr = \pm 0.1$ is assumed in a part of the computational domain.

The situations: a) waves and current propagating in the same direction; b) no current; c) waves and current propagating in opposite directions are displayed from top to bottom in Fig. 7.

The wave crests at a specific time step are given on the left hand side. The darker the wave crests, the higher is the surface elevation. A numerical, directional wave gauge is placed in the basin to obtain the spectral shape of the spectrum and the distribution of the mean direction as a function of the frequency. In the case of still water, the transformation is the same as displayed along the centre-row of Fig. 6. The mean direction is constant at $\Theta = 90^\circ$ and the spectral moment $m_0 = 8.6 \cdot 10^{-5}$.

In the presence of a current, the wave fronts change their direction. In the case of waves and current in the same direction, the waves are refracted with an average angle of $\Delta\Theta = 10^\circ$ at the gauge (For waves and current in opposite directions the angle of refraction is $\Delta\Theta = 12^\circ$). The quantity $\Delta\Theta$ depends on current and frequency. High components are refracted more than low components.

At the transition between still water and current, the crests are drawn apart. This produces a two-dimensional effect in which wave energy propagates along the crests. A decrease or increase of the spectral moment m_0 was recorded. This depends on the current condition and on the position in the computational domain. The change can be very much higher than predicted in the one-dimensional test (Chap. 3.2). Fig. 7 shows that in the case of waves and current in the same direction, the spectrum remains single-peaked ($m_0 = 5.1 \cdot 10^{-5}$) at the chosen

gauge. A double-peaked spectrum ($m_0 = 11.5 \cdot 10^{-5}$) is generated if waves and current are in opposite directions.

The numerical model was also used to simulate arbitrary angles between the current and the wave direction. Although, the results were very promising, they are not presented here because corresponding hydraulic measurements were not available for verification purposes.

5 Conclusions

A numerical model based on the extended Boussinesq-Wave-Equations (BWE) was applied to simulate irregular waves with an ambient current. The current alters wave height, wavelength and the direction of wave propagation. The equations may be used to simulate the generation or the change of a current by an *inflow from the sides* as well as by an *upwelling from below*.

The range of validity has been checked, comparing Boussinesq theory with linear wave theory. Regarding harmonic waves, the BWE are valid provided the wave length is at least 10 times the water depth and the Froude number of the current is smaller than ± 0.2 . Regarding irregular waves, even shorter waves of a spectrum can be simulated as long as they are related to long waves (bounded-short waves, the generation of higher harmonics).

The change of the significant wave height of a Pierson-Moskowitz spectrum can be predicted by the theory of Longuet-Higgins/Stewart using a monochromatic wave with the peak period of the spectrum. The change depends on the period of the wave, the strength of the current and the water depth. The wave amplitude itself has a minor effect. The results of the numerical model are in very good agreement with the theory. The numerical model also simulates the development of the spectral shape.

References

- [1] I. Brevik and B. Aas. Flume experiments on waves and currents. *Coastal engineering*, 3, 1980.
- [2] I.G. Jonsson. Wave-current interactions. *Report No. S 49*, 1989. The Danish Center for Applied Mathematics and Mechanics. Institute of Hydrodynamics and Hydraulic Engineering.
- [3] M.S. Longuet-Higgins and R.W. Stewart. The changes in amplitude of short gravity waves on steady non-uniform currents. *Journal of fluid mechanics*, 10, 1961.
- [4] P.A. Madsen and I.R. Warren. Performance of a numerical short-wave model. *Coastal Engineering*, 8, 1990.
- [5] A.D. McCowan. The range of application of Boussinesq type numerical short wave models. In *IAHR-Congress*, 1987. Lausanne.

- [6] H.-H. Prüser. Zur Interaktion von Wellen und Strömung im flachen Wasser. *Report No. 30*, Institut für Strömungsmechanik und elektronisches Rechnen im Bauwesen, Universität Hannover, 1991.
- [7] H.-H. Prüser, H. Schaper, and W. Zielke. Irregular wave transformation in a Boussinesq wave model. In *20nd International Conference on Coastal Engineering*, 1986. Taipei.
- [8] H. Schaper. Ein Beitrag zur numerischen Berechnung von nichtlinearen kurzen Flachwasserwellen mit verbesserten Differenzenverfahren. *Report No. 21*, Institut für Strömungsmechanik und elektronisches Rechnen im Bauwesen, Universität Hannover, 1985.
- [9] H. Schaper and W. Zielke. A numerical solution of the Boussinesq type wave equations. In *19nd International Conference on Coastal Engineering*, 1984. Houston.

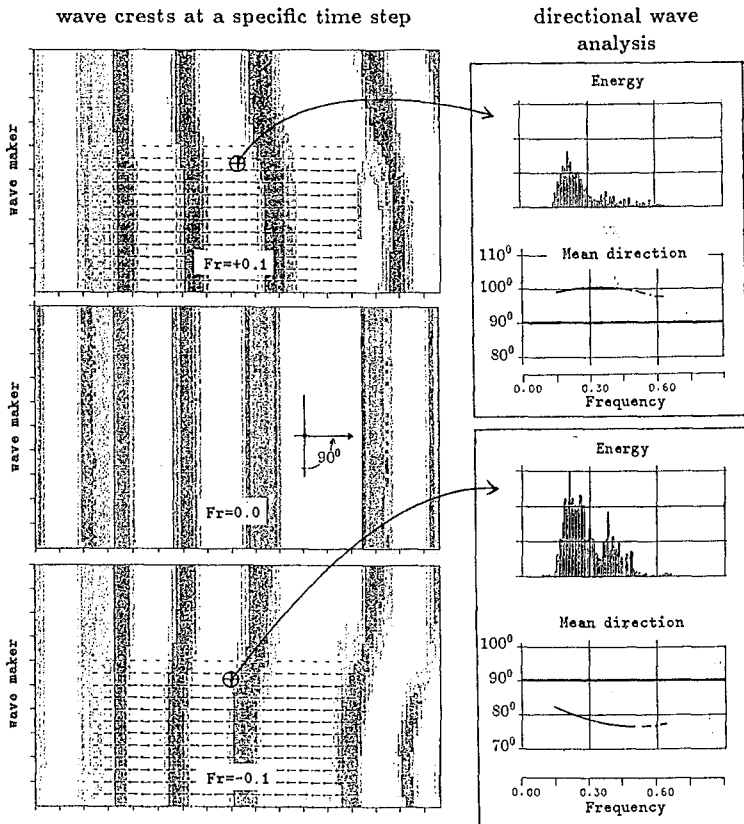


Figure 7: Waves with a current in a basin

CHAPTER 83

WAVE SPECTRA TRANSFORMATIONS

Giancarlo Chiaia, Leonardo Damiani, Antonio Petrillo *

Abstract

In this paper the transformations of sea waves, reproduced by a JONSWAP spectrum in a laboratory channel, have been studied both in frequency and time domain. In frequency domain the occurrence of non-linearities producing energy transfers to high and low frequencies was studied. The reported experimental results enabled us to compare the two approaches and to define the limits within which they give the same results.

INTRODUCTION

The transformations of a sea state when moving from deep to shallow waters can be studied by analyzing how the values of its characteristic quantities vary in the time as well as in the frequency domain.

Although describing the same physical phenomenon, these two approaches are not always equivalent and often give quite different results, especially when great transformations have already occurred.

The study of the correlation between the results of the two methods is particularly important both for setting up and applying mathematical models to foresee the pattern of spectral shapes, as well as for application purposes, such as the estimate of the significant wave height for the design of sea works. Moreover, the knowledge of local sea states is indispensable for the study of solid transportation.

In this work the two types of analyses were made, referring to one-dimensional JONSWAP spectra generated in a wave channel with a sand bar-shaped bed, in order to define their applicability limits. We analyzed the occurrence of non-linearities by introducing first Ursell number and then a

*Hydraulics and Hydraulic Constructions Institute
Bari University - Via ReDavid, 200 - BARI (ITALY)

dimensionless depth and by establishing the limits of linear propagation (Thompson and Vincent, 1985).

Some singularities observed in the pattern of parameters calculated in the frequency domain led us to study the energy components at low frequencies, especially near the shore. These were studied according to the theory of reflection of small amplitude waves, which, despite the approximation due to the non-linearity of the problem, enabled us to identify the presence of an almost standing component (surf-beat) with remarkable energy quantities in the surf-zone.

Finally, the analysis in the time domain enabled us to establish the limits within which the knowledge of the energy spectrum can be applied to estimate the quantities of interest to engineers.

DESCRIPTION OF EXPERIMENTAL SET-UP AND FACILITIES

Experiments were carried out in the wave channel at the laboratory of the Hydraulics and Hydraulic Constructions Institute of Bari University.

The channel is about 45 m long and 1 m wide; its walls consist of 1.2 m high crystal glass sheets supported by iron frames with a center to center distance of about 0.44 m, resulting in 100 gauging cross-sections along the whole length of the channel (the 100th cross-section coincides with the wave generator paddle location). The channel bottom is covered with a sand layer of a pretty uniform size $d_{50}=0.15$ mm and with a corresponding fall velocity $\omega = 0.018$ m/s. Experiments are also being carried out to assess the performance of some submerged breakwaters (Lamberti et al., 1985); therefore, at a distance of 4.5m from the wave generator, the channel has been longitudinally subdivided into two parts in order to simulate the evolution of an unprotected beach, in one part, and the evolution of a protected beach under the same wave attack in the other. The experimental measurements reported in this paper were all made in the former. Two bars, whose crests were approximately located at cross-sections 60 and 30, were observed in the channel during the tests.

The wave generation system consists of a flat paddle which receives a rotatory-translational motion: the kinematic mechanism which drives the paddle is designed for the axis of rotation to be lower than the channel bottom, this being a better condition to generate waves at shallow depths. The paddle is set in motion by an oleo-dynamic system driven by an electrical valve which, through an electrical signal, sends pressurized oil to the two ends of the cylinder in which the piston moves. The piston displacements, measured by a transducer, control the system in a closed chain circuit and give it a good stability in the applied field of frequencies. The whole system is controlled by a processing computer.

The small water losses occurring in the channel, especially between the paddle and the channel walls, are compensated by an automatic supply system driven by an electrical water gauge equipped with a band-pass filter which eliminates wave-generated surface oscillations. During the tests, the water depth near the paddle was 0.8 m with level fluctuations of about 0.1 mm.

In Froude undistorted similarity with 1:10 length scale, the tests reproduce some meteomarine conditions of mid-Adriatic sea (Italy).

The sea states in the channel were represented by energy density JONSWAP spectra with amplification parameter $\gamma=3.3$ and shape factor $\omega=0.07$ for $f < f_p$ and $\omega=0.09$ for $f > f_p$. The wave attacks tested in the channel have off-shore significant heights (H_s) ranging from 8.34 to 24.17 cm and significant period (T_s) ranging from 1.49 to 2.13 s, corresponding to JONSWAP spectra with peak frequencies in the range $(0.44-0.63 s^{-1})$ and zero-th order moments m_0 of the spectra varying from 5 to 42 cm^2 .

In this study we analyzed the results referring to five wave attacks of the same peak frequency $(0.507 s^{-1})$ and m_0 (evaluated at the first monitoring cross-section) ranging between 5.20 and 36 cm^2 . For these attacks measurements are available at all the gauge stations of the channel, this being indispensable to describe a complete wave pattern.

The measurements in the channel were made through capacitive probes, calibrated before each experiment and connected to a processing computer through an analogue-digital converter. For each measurement the data acquisition was made simultaneously with three probes, for a time of 102,4 s and a sampling interval of 0.1 s. The three probes were also used to assess the incident and reflected spectra (Lamberti et al., 1986).

The probes could measure the wave state up to cross-section 8, since the low water depth near the shoreline makes the measurements poorly reliable because of the presence of air mixed with water.

Telecamera shots were used to measure the wave flow also in the area between cross-sections 8 and 5, where the swash-zone starts (Damiani and Ranieri, 1989), and to check the data obtained from the probes between cross-sections 13 and 8 where the presence of air bubbles can invalidate the probe measurements. The frame by frame shot enabled to have the time pattern of the free water level fluctuations.

The data taken by the probes or the telecamera were processed both in the time (up-zero-crossing method) and the frequency domain.

In the latter case, the n-th order spectral density moments were calculated through numerical integration; hence the average spectral periods ($T_{01} = m_0/m_1$ and $T_{02} = \sqrt{(m_0/m_2)}$) as well as the parameters of spectral width ($\epsilon_2 = (m_0 m_2/m_1^2 - 1)^{0.5}$ and $\epsilon_4 = (1 - m_2^2/(m_0 m_4))^{0.5}$) were obtained.

Through partial integration of the spectrum the energy content in the neighbourhood of the peak frequency and its two first harmonics (E_1, E_2, E_3) were calculated assuming, in agreement with other authors (Guza and Thornton, 1980), $0.9nf_p$ and $1.1nf_p$ with $n=1, 2, 3$ as integration limits.

The equivalent and significant wave heights $H_{rms} = \sqrt{8m_0}$ and $H_s = 4\sqrt{m_0}$ were calculated for an infinitely narrow spectrum.

For the study of low frequency waves (among which the surf-beat) the energy and the height H_{rms} of the examined frequencies were also calculated by integrating the spectrum on a $3\delta f$ large band, centered on the concerned frequency, with δf being the resolution frequency of the spectrum.

By applying the up-zero-crossing method for each cross-section all the statistical characteristics of the wave state were calculated. The water level rise distribution was also analyzed with respect of Gauss distribution by applying χ^2 test and calculating the skewness and the the kurtosis ($\beta_1, \sqrt{\beta_2}$).

The definitions and symbols of quantities were taken from the "List of Sea State Parameters" (I.A.H.R., 1987).

ANALYSIS OF EXPERIMENTAL RESULTS

Linear Propagation Field

In figure 1 the configuration of the sand bed of the channel with the two previously mentioned bars is illustrated. It also shows the energy spectra measured at some representative cross-sections and referred to a wave attack of a peak frequency equal to 0.507 s^{-1} and a zero-th order moment of the spectrum equal to

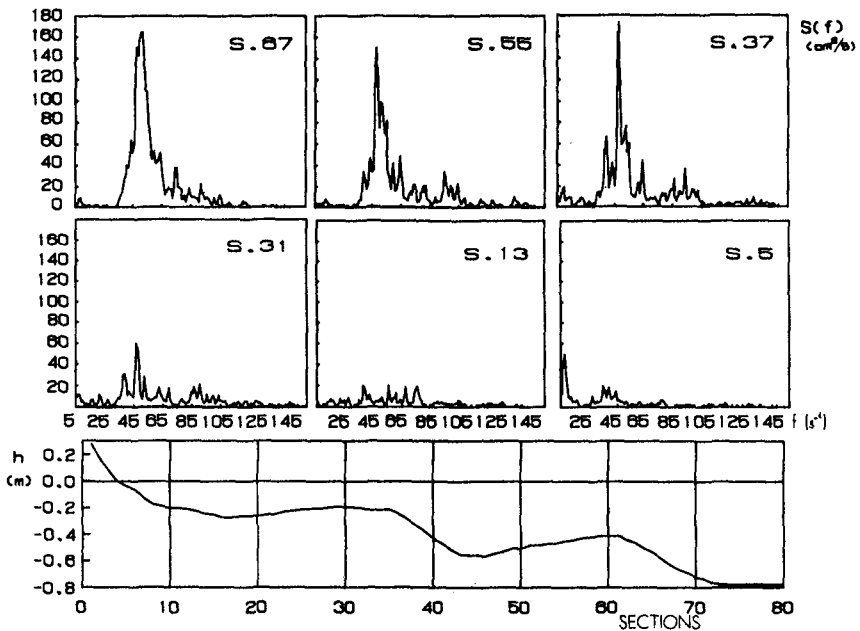


Figure 1. Beach profile and sample of spectra assessed in different cross-sections.

28 cm^2 at the first gauging cross-section.

This figure emphasizes the transformations of the spectrum in its propagation up to the shoreline. Already in the zone off-shore the first bar, where only shoaling is present (cross-section 67), the spectrum transformations result in an energy transfer to high frequencies; afterwards, flowing over the off-shore bar,

it is noticed a first wave breaking, which produces a decline of the energy content at the peak frequency and an increase of the above said transfers. It then follows a recombination phase in which the energy content at peak frequency grows up and energy quantities at low frequencies start being remarkable. The high energy dissipations, due to the wave breaking on the on-shore bar, cause a remarkable flattening of the spectrum at cross-section 31. The spectrum completely changes its initial shape at cross-section 13, so that it is no longer possible to detect any energy content at the peak frequency. Near the shoreline (cross-section 5) the only significant energy content is the one at low frequency (surf-beat): this points out that very slow oscillations of the mean sea level occur in this area.

Definitely, moving from off-shore to the shoreline, waves basically undergo three kinds of transformations: energy transfers towards high frequencies, breaking dissipations and energy transfers towards low frequencies. The energy transfer towards high frequencies shows that non-linearities occur in the propagation of spectra.

The non-linearities were studied by analyzing the ratios of the energy quantities around the first and the second harmonic to the peak frequency energy (Guza and Thornton, 1980; Petrillo, 1988). These ratios were taken as a function of Ursell number calculated through $Ur = H_{rms} L_p^2 / h^3$, where h is the local depth and L_p is the local wave length at the peak frequency (Figure 2).

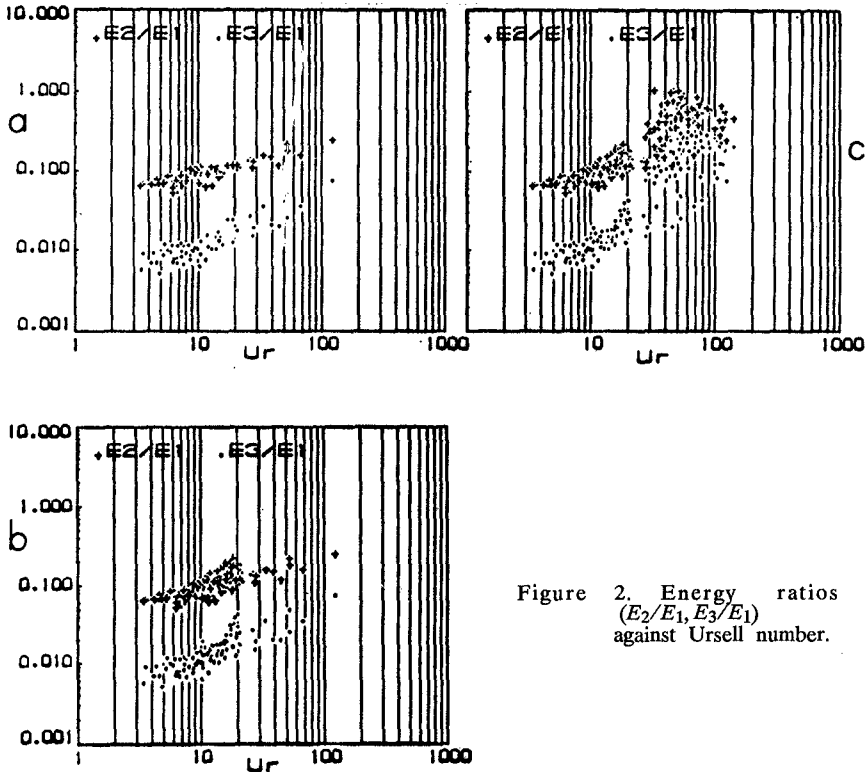


Figure 2. Energy ratios ($E_2/E_1, E_3/E_1$) against Ursell number.

In order to emphasize the shoaling, the breaking and the bar-effects, the pattern of these ratios was studied by plotting first the data off-shore the first bar (i.e. before breaking) (figure 2.a), then those before the on-shore bar (including the previous ones, but always excluding data of cross-sections where waves break) (figure 2.b) and, at last, the values of the ratios for all the cross-sections, including those of breaking (figure 2.c).

By comparing figures 2.a and 2.b it is noticed that the presence of bars locally creates some non-linearities. When flowing over the on-shore bar, wave breaking occurs and non linearities increase as shown in the figure 2.c.

From the analysis of the enclosed and examined diagrammes, considering that for a theoretical JONSWAP spectrum with $\gamma=3.3$ the E_2/E_1 and E_3/E_1 ratios are respectively equal to 0.083 and 0.008, it can be stated that the non-linearities on the first harmonic appear when Ursell number values are higher than 6, whereas the non-linearities on the second harmonic appear at higher Ur values (about $Ur > 10$). These results are in agreement with those found by Guza and Thornton (1980) and other authors.

Instead of Ursell number, the dimensionless depth $K_{p0}h$ (where $K_{p0}=2\pi/L_0$ is the wave number, calculated by referring to the peak frequency), which is easier to determine, can be applied to study the occurrence of non linearities at high frequencies.

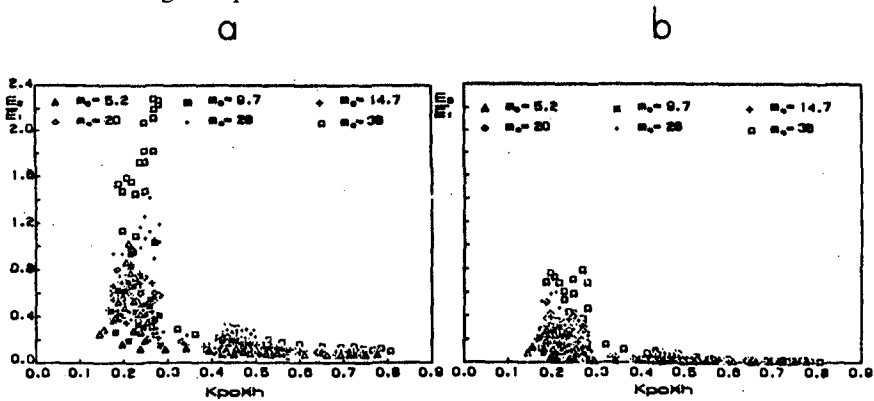


Figure 3. Energy ratios ($E_2/E_1, E_3/E_1$) versus $K_{p0}h$.

From the analysis of figure 3, reporting the data for all the gauging cross-sections and all the wave attacks, it is shown that non-linearities occur both on the first and the second harmonic when $K_{p0}h$ is greater than 0.8.

It has to be observed that, since the examined attacks have all the same peak frequency, and so the same L_p , and since the non-linearity depends on the H/h and h/L_p ratios (Petrillo, 1988), h being equal, non-linearities increase with the increase in energy of the wave attack.

The pattern of ϵ_2 , and ϵ_4 as a function of Ursell number is reported in figure 4; for values of $Ur < 6$, the two parameters have values quite close to those

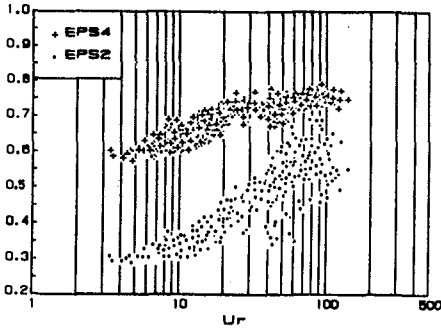


Figure 4. Spectral width parameter (narrowness parameter and broadness factor) against Ursell number.

of the undistorted JONSWAP spectrum ($\epsilon_2=0.329$ and $\epsilon_4=0.658$); they increase with the increase of Ursell number in a way qualitatively similar to that of the E_2/E_1 and E_3/E_1 ratios; the same behaviour is observed for ϵ_2 and ϵ_4 as a function of $K_p h$.

Figure 4 also shows that ϵ_2 , which has higher relative variations, is more significant than ϵ_4 in representing the phenomenon; this is in agreement with Thornton and Guza (1983).

Analysis in the Frequency Domain

Referring to the wave attack with $m_o=36 \text{ cm}^2$, figure 5 illustrates the pattern of H_{rms} calculated on the basis of the energy content of the whole spectrum and then of the spectrum around the surf-beat frequency (0.0781 s^{-1}); the figure also reports the pattern of the $T_{0.2}/T_p$ and $T_{0.1}/T_p$ ratios and the beach profile.

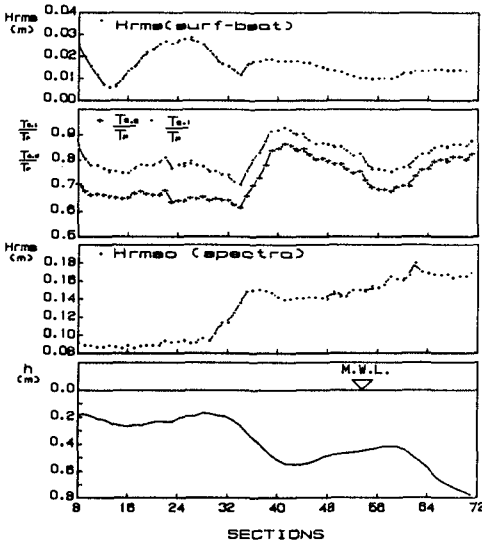


Figure 5. Beach profile; H_{rms} , $T_{0.2}/T_p$, $T_{0.1}/T_p$ values, assessed across the shore.

The pattern of H_{rms} of the whole spectrum is indicative of the kind of transformations which spectrum undergoes when approaching the shoreline: shoaling until reaching the off-shore bar; small wave breaking on the bar; then recomposition; shoaling again up to the on-shore bar; large wave breaking on it and, at last, spectrum reaches the shoreline with a saturated energy content in the wind-wave band.

The mean spectral periods decrease in the shoaling area and on the bar because of the energy contents increase on the second and the third harmonic; during recomposition, periods increase, go back to normal values, then they decrease again because of shoaling on the

on-shore bar and, at last, they become minimum in the area of highest wave breaking. Downstream of the on-shore bar (see figure 1), the spectrum is flat and so the values of average periods remain basically constant. Nevertheless the

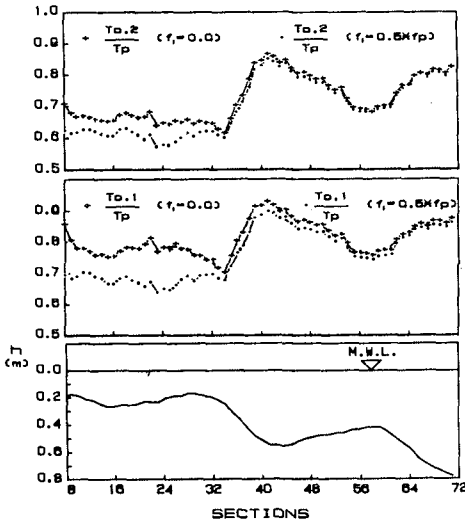


Figure 6. Dimensionless mean spectral periods H_{rms} , $T_{0.2}/T_p$, $T_{0.1}/T_p$ across the shore, evaluated with different integral limits in n-th order moments calculation.

pattern of mean periods in this area shows an increase in the proximity of cross-sections 22 and 8 where the surf-beat energy values are maximum.

The influence of surf-beat at the cross-sections downstream of the on-shore bar on the the first and second order moments, and then on the mean spectral periods, can be observed in figure 6 which also illustrates the pattern of the mean spectral periods, calculated by integrating the spectrum starting from the frequencies $f_1=0$ and $f_1=0.5f_p$. It is noticed that the two quantities are the same up to the cross-section of maximum wave breaking (cross-section 34), whereas they greatly differ downstream the on-shore bar, where the surf-beat energy is greater. In this area the value of the $T_{0.2}/T_p$ ratio fluctuates, for the considered wave attack, in the range 0.62–0.67, and it decreases (about 10%) if the contribution due to low frequencies is omitted. Near

the shoreline, where the surf-beat reaches its absolute maximum value, such a ratio becomes equal to 0.72 and it reduces (15%) if the surf-beat contribution is omitted. The same pattern is observed for the parameter $T_{0.1}/T_p$.

The mean spectral periods, for all the examined wave attacks, are plotted in figures 7a and 7b, as a function of $k_p h$. It is noticed that for $k_p h > 0.6$, independently of the energy of attacks, the dimensionless periods remain rather constant ($T_{0.1}/T_p = 0.87$ and $T_{0.2}/T_p = 0.846$). These values are slightly different

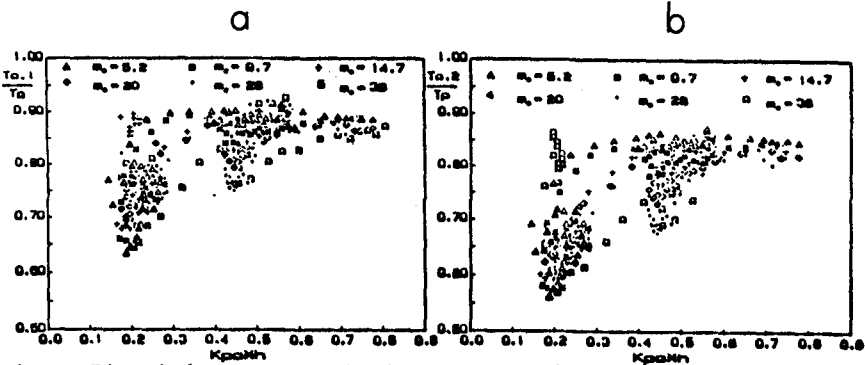


Figure 7. Dimensionless mean spectral periods versus $K_p h$ for all the wave attacks.

from the theoretical ones of JONSWAP spectrum with $\gamma=3.3$, respectively equal to 0.844 and 0.801. These deviations, (3% for $T_{0.1}/T_p$ and 6% for $T_{0.2}/T_p$) are to be attributed to the inevitable errors produced in spectrum generation and survey. Nevertheless, the previous figures show the same trend found by other authors (Bendykowska, 1986; Liberatore and Petii, 1988).

For $K_{po}h > 0.6$, on the average, $T_{0.2}/T_p$ and $T_{0.1}/T_p$ tend to decrease with $k_{po}h$, but, differently from the results by other authors (Bendykowska, 1986), who found a monotone and always decreasing pattern, in the present experiments a high variability was observed as a function of the wave energy.

This behaviour is clearly linked to the non-linearities which occur during propagation (shoaling, bars, wave breaking) and to low frequency standing waves, both related to the wave energy and to the shape of the beach profile.

In order to show that surf-beat is really a standing wave produced by reflection from the beach, the small amplitude wave theory was applied (in spite of the approximations due to the non-linearity of the phenomenon). According this theory the resulting wave amplitude should be enveloped by the curves representing respectively the sum and the difference between the incoming and reflected waves. Figure 8 illustrates, for some frequencies, the heights of the resulting monochromatic waves, the sum of the incoming and reflected waves heights and their difference, along the channel. The above mentioned heights have been calculated by integrating around the considered frequency, respectively the spectrum surveied in the cross sections and the incoming and reflected spectra, assessed through the three probe method.

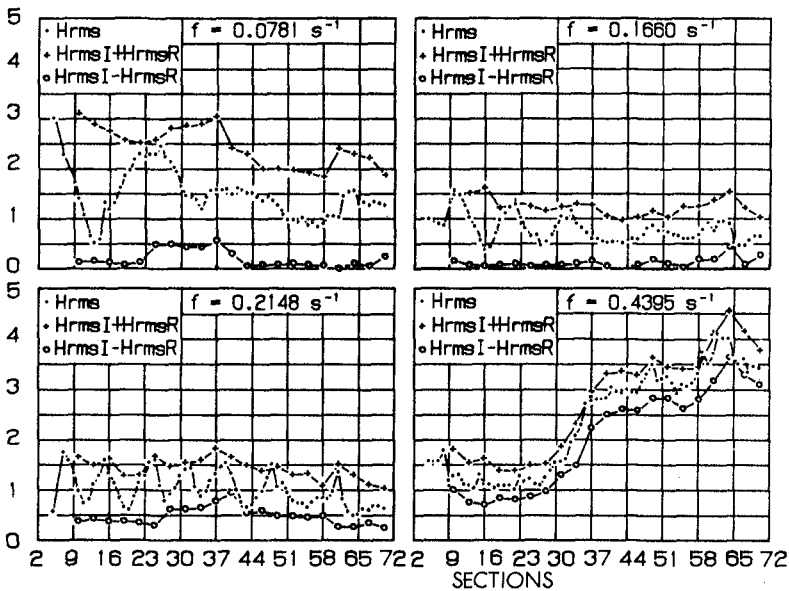


Figure 8. Envelope of monochromatic components according to small amplitude wave theory.

It can be observed that surf-beat component (at the frequency $0.0781s^{-1}$ in model scale) is a quasi pure standing wave because the progressive component (represented by the difference between the incoming and reflected waves) is very little if compared with the standing one (difference between the two lines representing the sum of the incoming and reflected wave heights and their difference): that means an almost complete reflection from the beach at the surf-beat frequency.

For the monochromatic components with frequencies higher than the surf-beat one, the progressive component is larger, but a standing component is still present: that means a partial reflection; the reflection lessens with frequency increasing and it becomes negligible near the peak frequency where monochromatic components can be represented by pure progressive waves.

Analysis in the Time Domain

The patterns of T_s/T_p and T_z/T_p (with T_s and T_z , respectively significant and average periods, both assessed in the time domain) for the attack with $m_o=36 cm^2$ and $f_p=0.507 s^{-1}$, as well as the beach profile are illustrated in figure 9.

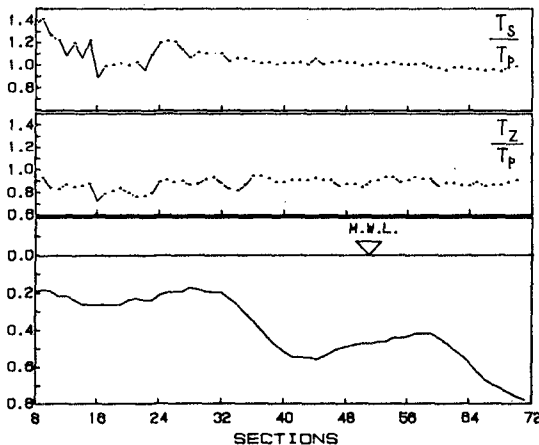


Figure 9. Dimensionless wave periods (T_s/T_p and T_z/T_p), evaluated in time domain, across the shore.

In agreement with the results by other authors (Liberatore and Petti, 1988) T_z/T_p is not so much affected, at least up to the on-shore bar, by the transformations of the spectrum when passing from higher to lower depths. This ratio ranges around 0.9, higher than the theoretical value referred to JONSWAP spectrum with $\gamma=3.3$; such a difference is similar to the one observed in the analysis of the mean periods in frequency domain. The T_s/T_p ratio is, on the average, equal to 1.00 up to the on-shore bar, with a slightly decreasing trend. This enables to refer to the peak frequency of the

spectrum, rather than to the significant one, when using the models for studying the wave transformations. This is always true far from breaking; after breaking the T_s/T_p ratio is sensitive to the distortions of the spectrum, especially near the shoreline, where it is also affected by low frequency standing waves and the dimensionless significant period reaches the value 1.40.

Figures 10.a and 10.b report dimensionless wave periods, for all the examined wave attacks, as a function of $K_p h$. The two figures show quite the same behaviour.

For $K_p h > 0.6$, T_s/T_p is almost constant, with an average value equal to 0.975, whereas for $0.3 < K_p h < 0.6$, a dispersion of experimental data is observed with a slightly decreasing pattern. For values of $K_p h < 0.3$, the behaviour of different wave attacks greatly differs: the significant period increases with the increase of the attack energy and, hence, of the surf-beat it produces. In this area the data referring to the attacks with $m_o = 5; 10; 15 \text{ cm}^2$ fall below the straight line representative of the mean value off-shore, whereas, for higher energy, they fall above. These results are in agreement with those reported in figure 3. The same conclusions may be drawn from the analysis of the behaviour of T_s/T_p as a function of Ursell number: it is constant for $Ur < 10$; for $10 < Ur < 30$ the data are scattered around the mean value despite the presence of a band of variability; whereas for $Ur > 30$ the points form a cloud with increasing T_s/T_p values for the wave attacks of higher energy.

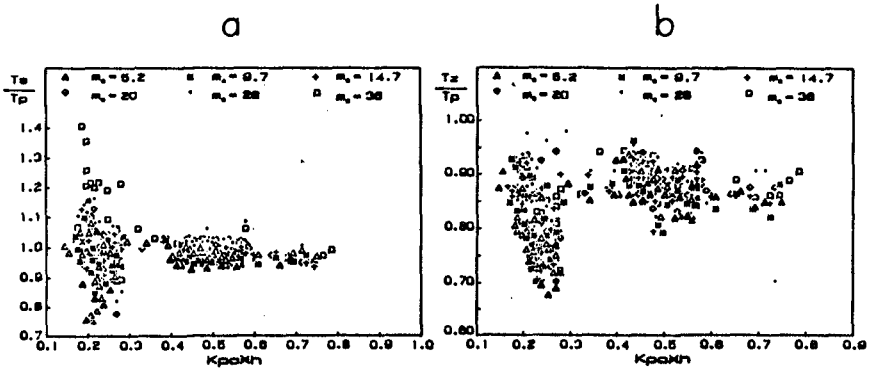


Figure 10. Dimensionless periods, evaluated in time domain, versus $K_p h$ for all waves attacks.

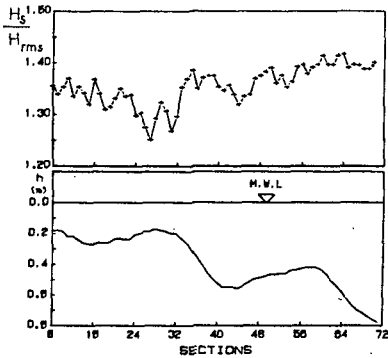


Figure 11. Beach profile and H_s/H_{rms} across the shore.

For the previously examined attack, figure 11 reports the pattern of H_s/H_{rms} ratio, calculated in the time domain. It is noticed that, except at some cross-sections, H_s/H_{rms} is not greatly influenced by the wave transformations: it decreases from 1.40 to 1.34 from off-shore to the shoreline, with lower values between cross-sections 24 and 32, where it reaches the minimum value 1.25. These results are partly in agreement with those found by Thornton and Guza (1983). In their experiments on gentle slope beaches, they found that the ratio H_s/H_{rms} is constant and equal to 1.42 for a sea state following wave heights Rayleigh distribution.

Figure 12 reports the ratio between the wave energy calculated in the time domain ($E_{td} = 1/8 \rho g H_{rms}^2$) and the energy assessed by integration of the spectrum (given by $E_{fd} = \rho g m_o$) and the skewness and kurtosis of elevations along the shore.

The figure shows that at the cross-sections off-shore the first bar, where the spectrum is not markedly affected by non-linearities, both the skewness and the kurtosis have values close to those of Gauss distribution and E_{td}/E_{fd} approaches to 1, that is the time and frequency domain analyses give the same results.

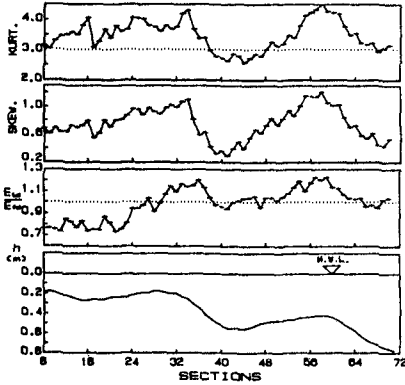


Figure 12. Beach profile, time domain energy rated to frequency domain energy, Skewness, and Kurtosis of surface elevations.

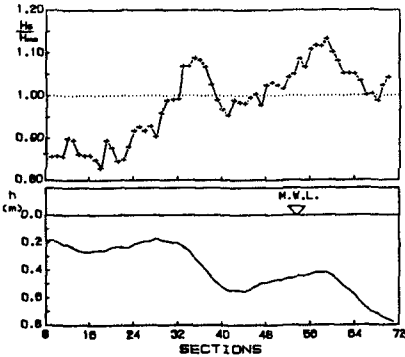


Figure 13. Comparison between significant wave height values calculated in the time domain and through the zero-th order moment of the spectrum.

When the spectrum is affected by non-linearities (produced by shoaling, bar-effect and breaking), both the kurtosis and the skewness increase: the former because of decreasing of maximum wave heights and hence of a greater probability around the average value, the latter because of energy transfers at high frequencies which makes the waves similar to cnoidal waves. In this case E_{td}/E_{fd} increases and reaches the maximum value of about 1.2.

In the inner surf-zone, the strong dissipations due to wave breaking produce a notable flattening of the spectrum, thus, as it is reported by other authors (Dally and Dean, 1988), the H_{rms} height, calculated in the time domain, declines and the E_{td}/E_{fd} ratio becomes lower than 1. Finally, from the figure it can be stated that the assumption $H_{rms} = \sqrt{8}m_o$, which links a quantity calculated in the time domain to a quantity obtained in the frequency domain, can be applied only when the non-linearities are far away. This is partly in disagreement with the results by other authors (Thornton and Guza, 1983), who noticed that the above said relationship can be applied also in the case of breaking waves.

Figure 13 illustrates the ratio between the significant height, H_s , calculated by the up-zero-crossing method and the significant height, H_{smo} , obtained from the spectrum which, in the case of JONSWAP spectrum with $\gamma=3.3$, is related to the zero-th order moment through the relationship $H_{smo} = 3.866\sqrt{m_o}$.

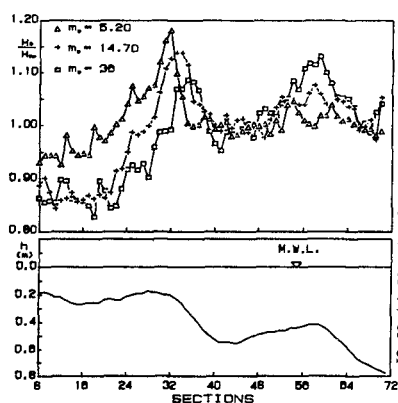


Figure 14. Behaviour of (H_s/H_{smo}) ratio for different wave attacks.

This ratio has a pattern qualitatively similar to that of E_{id}/E_{fd} illustrated in figure 12.

The pattern of H_s/H_{smo} , for three wave attacks of different energy (figure 14), shows that the deviations of the ratio from 1 depend on the attack energy. This is in agreement with the results found by Thompson and Vincent (1985) who relate the deviations of H_s/H_{smo} to the local steepness, which is a strictly increasing function of the energy for each cross section, since all the described wave attacks have the same peak frequency.

CONCLUSIONS

The analysis of the experimental results, confirms how difficult it is to establish a direct correlation between the characteristic quantities of a wave state in the frequency and in the time domain.

In fact, the results from the two types of analysis are well correlated only in a limited field of linear propagation with values of the parameter $k_p h > 0.6$, or $Ur < 10$.

Out of this field, the evaluation of the characteristic quantities in the time domain based on the knowledge of those in the frequency domain, entails big errors in that the spectrum, because of the great non-linearities occurring during propagation, can no longer represent the physical phenomenon correctly; in these zones it is better to refer to the time domain.

It was shown that, for values of $k_p h < 0.3$, a decreasing trend of the mean spectral periods $T_{0.1}$ and $T_{0.2}$ was observed, due to the presence in this zone of low frequency standing waves which greatly affect them, whereas the characteristic periods in time domain (T_s and T_c) are less affected by non-linearities.

Following on the lack of direct correlation of the results from the two methods, it is difficult to evaluate the significant wave height (needed to design sea structures) based on the knowledge of the spectrum.

The analysis in frequency domain pointed out some monochromatic components at low frequencies and, among them, the surf-beat ($f = 0.0781s^{-1}$ in model scale) with a great energy content in the surf-zone and a maximum value near the coast. Some authors (Bredshaw, 1980) assumed that the genesis of the phenomenon is related to the fact that, after breaking, the wave recomposes and generates new bigger waves which capture and incorporate smaller ones. This mechanism should produce a gradual change in the spectrum, passing from the

breaking point to the shoreline, in that going towards shallow waters a gradual absorption of smaller waves is supposed to occur. The present experiments, although not showing such a gradual absorption, showed, in the surf-zone, the presence of energy quantities at frequencies between the surf-beat and the peak one. It is thought, however, that although the above-said mechanism may contribute to the energy transfer to low frequencies, the presence of surf-beat is essentially due to the reflection of the beach (Guza and Thornton, 1985) which generates a standing wave at low frequency.

References

- Bendykowska, G., Spectral characteristics of irregular waves over sloping bottom, Atti del XX Convegno di Idraulica e Costruzioni Idrauliche, Padova, 1986.
- Bredshaw, M.P., Topographic control of run-up variability, Proc. 17th Intern. Coast. Eng. Conf., 1980.
- Dally, R.W., G.R. Dean, Closed-form solutions for the probability density of wave height in the surf-zone, Proc. 21th Intern. Coast. Eng. Conf., 1988.
- Damiani, L., M. Ranieri, Oscillazioni sottocosta prodotte da onde random, Atti del II Congresso A.I.O.M., Napoli, 1989.
- Goda, Y., Statistical variability of sea parameters as a function of wave spectrum, XXII Conf. I.A.H.R., Seminar Maritime Hydraulics section, 1987.
- Guza, R.T., E.B. Thornton, Local and shoaled comparisons of sea surface elevations, pressures and velocities, J. of Geophys. Res., Vol. 85, 1980.
- Guza, R.T., E.B. Thornton, Observations of surf beat, J. of Geophys. Res., Vol. 90, 1985.
- International Association for Hydraulics Research List of Sea State Parameters, XXII Conf. I.A.H.R., Lausanne, 1987.
- Lamberti, A., A. Petrillo, M. Ranieri, A comparative analysis of some types of submerged barriers as beach defense structure, XXI Conf. I.A.H.R., 1985.
- Lamberti, A., A. Petrillo, M. Ranieri, Generation of irregular waves in an experimental channel, V Conf. Asian and Pacific Reg. Div. I.A.H.R., 1986.
- Liberatore, G., M. Petti, Modification of random waves characteristics in shoaling waters, Excerpta, Vol. 3, 1988.
- Petrillo, A., Evoluzione delle onde di mare su bassi fondali sabbiosi con pendenza variabile, IX Congr. A.I.M.E.T.A., Bari, 1988.
- Thompson, E.F., C.L. Vincent, Significant wave height for shallow water design, J. of Waterway, Port, Coastal and Ocean Eng., Vol.3, 1985.
- Thornton, E.B., R.T. Guza, Transformation of wave height distribution, J. of Geophys. Res., Vol. 88, 1983.

SUBJECT INDEX

Page number refers to first page of paper.

- Accretion, 1975, 2580
Advection, 1186
Alaska, 1687
Algorithms, 136, 255, 478, 516
Analytical techniques, 2682
Anemometers, 450, 489, 557
Arctic regions, 1687
Armor units, 1270, 1306, 1334, 1375,
1403, 1417, 1446, 1460, 1538, 1552,
1578, 1620, 1634, 1716, 1730, 1755,
1805, 1819, 2768, 2782, 2796, 3194
Artificial islands, 2768
Assessments, 41
Asymmetry, 396, 637
Atmospheric pressure, 95, 826
Australia, 2241, 2265
- Backwashing, 2360
Bank erosion, 2385
Barges, 1648
Barrier design, 2950
Barrier islands, 783, 3254
Barriers, 1564
Bars, 959, 2101, 2145, 2265
Bars, riverine, 757, 2964
Bathymetry, 597, 1292, 2279, 2416,
2782
Bays, 2047
Beach cusps, 2101
Beach erosion, 95, 570, 1862, 1975,
2010, 2020, 2073, 2173, 2241, 2304,
2360, 2385, 2457, 2471, 2580, 2644,
2710, 2726, 2740, 2782, 2796, 2810,
3063, 3254
Beach nourishment, 783, 1984, 1998,
2020, 2241, 2304, 2394, 2542, 2796,
3183, 3227, 3254
Beaches, 109, 227, 281, 516, 557, 570,
798, 867, 1292, 1702, 2061, 2117,
2159, 2265, 2291, 2443, 2481, 2552,
2566, 2682
Bed load movement, 2332, 2536,
3037
Bed ripples, 661, 2186, 2200
Bed roughness, 450
Bedforms, 2318
Berms, 1730, 2073, 2101, 2304, 3194,
3207, 3222
Blocks, 1606
Boring, 1019
- Boundaries, 2227
Boundary conditions, 1292, 1948
Boundary element method, 840,
1270, 1389, 3140
Boundary layer, 281, 2360
Boundary layer flow, 450, 544, 661,
853, 993
Boundary shear, 2536
Brazil, 3207
Breaking waves, 32, 68, 123, 136, 150,
164, 218, 306, 330, 516, 716, 895,
923, 973, 1019, 1033, 1060, 1362,
1473, 1827, 2145, 2159, 2173
Breakwaters, 136, 164, 306, 1060,
1200, 1270, 1320, 1348, 1362, 1375,
1403, 1473, 1538, 1592, 1620, 1634,
1675, 1702, 1716, 1730, 1755, 1781,
1805, 1827, 1837, 1851, 2020, 2034,
2416, 2603, 2616, 2740, 3194, 3207,
3222, 3239
Bridge foundations, 3268
Bridges, 3268
Building design, 2908
Bulkheads, 1837
Buried pipes, 2508
- Caissons, 1403, 1675, 1827
Channel stabilization, 2922, 2975
Channels, waterways, 2430, 2936,
2975, 3024, 3088, 3126
Characteristics, 82
China, People's Republic of, 82, 2047
Cnoidal waves, 109, 1144
Coastal engineering, 1, 7, 516, 769,
881, 935, 1005, 1513, 1862, 1984,
1998, 2010, 2975, 3112, 3281
Coastal environment, 177, 867, 959,
1088, 1144, 1172, 2047, 2768, 2894,
2908
Coastal management, 7, 41, 1895,
1909, 2589, 2824
Coastal morphology, 1876, 1888,
1948, 1962, 1975, 2589, 2682, 2922,
2950, 2964, 3050, 3171
Coastal processes, 444, 557, 743,
1074, 1876, 1895, 1909, 1935, 1962,
1975, 2061, 2087, 2101, 2117, 2227,
2265, 2332, 2346, 2402, 2443, 2457,
2481, 2522, 2552, 2566, 2589, 2682,
2710, 2810, 3037, 3154

Volume 1, 1-1116 Volume 2, 1117-2172 Volume 3, 2173-3308

- Coastal structures, 371, 743, 757, 923, 1200, 1306, 1375, 1431, 1446, 1460, 1487, 1499, 1524, 1552, 1578, 1592, 1687, 1795, 2457, 2726
- Cohesive sediment, 2984, 3012, 3037
- Computation, 164, 191, 444, 1019, 1060, 1513, 1909, 2255
- Computerized simulation, 1172
- Concrete, 1687, 2768
- Concrete blocks, 1431
- Concrete construction, 1578, 1634, 1755, 1819
- Conferences, 1, 7
- Construction, 1280, 2020, 2950, 3239
- Construction materials, 1648, 3222
- Construction methods, 1648, 1675, 3207
- Contamination, 2894, 3194, 3222
- Control structures, 1060
- Coral reefs, 330
- Coriolis effect, 95
- Critical load, 2671
- Currents, 95, 205, 241, 316, 384, 444, 450, 489, 853, 993, 1074, 1088, 1186, 2131, 2227, 2443, 2495, 2866, 3171
- Cyclones, 358, 2852
- Cylinders, 973, 1280, 1389, 1795
- Cylindrical shells, 1675
- Dam construction, 3050
- Damage, 743, 1446, 1552, 1851, 2416, 2908, 3074
- Damage estimation, 2796
- Damping, 1592
- Data analysis, 345
- Decision making, 1
- Deep water, 623, 1827
- Deltas, 2984
- Design, 136, 597, 923, 1160, 1254, 1320, 1362, 1403, 1417, 1431, 1487, 1524, 1552, 1819, 1827, 1837, 2020, 3102, 3194, 3207, 3239, 3268
- Design criteria, 1634, 3024, 3074
- Design storms, 2304
- Design waves, 18, 647, 1306
- Diffusion, 1186
- Diffusion coefficient, 2998
- Dikes, 895, 1254, 1431, 1487, 1662, 2010, 2087, 2671, 2880, 2998, 3171, 3183
- Dimensions, 959
- Disposal, 2430
- Distribution functions, 18, 345
- Disturbances, 597
- Dolos, 1417, 1805, 1819
- Drag coefficient, 1716, 1769
- Dredge spoil, 1362, 2430, 2824
- Dredging, 2964, 3024, 3088, 3126
- Drift, 3140
- Dunes, 1922, 1984, 2304, 2471
- Dynamic characteristics, 1837
- Dynamic loads, 1755
- Dynamic models, 2265
- Dynamic stability, 1270, 1730
- Dynamic tests, 1755
- Dynamics, 2227, 2346
- Ecology, 2984
- Economics, 2796
- Embankments, 1662, 2754
- Energy dissipation, 123, 1334, 1499, 1620, 2522
- Energy transfer, 123
- Entrainment, 2200
- Environmental effects, 3171
- Environmental impacts, 3024
- Equations of motion, 881, 1513, 3112
- Equilibrium, 2291, 3050, 3063
- Erosion, 935, 1922, 2087, 2998, 3012
- Erosion control, 1662, 2740
- Estimates, 464
- Estuaries, 1962, 2047, 2542, 2866, 2922, 2936, 2950, 2964, 2984, 2998, 3012, 3050, 3154
- Evolution, development, 1876, 1962
- Experimental data, 1242
- Experimentation, 584, 1592
- Extraction procedures, 1998
- Failures, 1755, 2087, 2671
- Failures, investigations, 3222
- Feasibility studies, 1702
- Fences, 2754
- Field investigations, 82, 867, 2047, 2710
- Field tests, 330, 703, 1074, 1702, 2087, 2471, 2644
- Filters, 1524
- Floating bodies, 3140
- Floating structures, 1320, 2740, 2852
- Flood control, 1254, 1862, 1895
- Flood plain insurance, 41
- Flood plain regulation, 2908
- Flooding, 218
- Flow characteristics, 316
- Flow measurement, 489, 503
- Flow profiles, 1922
- Flow visualization, 1033, 2186
- Fluid-structure interaction, 1564
- Flumes, 255, 489, 544, 661, 993, 1046, 1538, 1730, 2536, 2552, 2630

- Forecasting, 986
Foundation construction, 1648
France, 2936, 3088
Frequency analysis, 293, 1102
Friction factor, 420, 637
- Geography, 2589
Geomorphology, 2984
Geotextiles, 1524, 1687
Granular materials, 1524, 2616
Grasses, 1662
Gravity waves, 55, 557, 611
Great Lakes, 2291
Grid systems, 2255
Groins, structures, 783, 2173, 3227, 3254
Groundwater flow, 2644
Gulfs, 986
- Harbors, 597, 1935, 2481, 2894, 3074, 3102, 3154, 3183, 3239
Histograms, 909
History, 1876
Hurricanes, 358
Hydraulic design, 3102
Hydraulic jump, 2880
Hydraulic loading, 1564
Hydraulic models, 267, 371, 1446, 1460, 1538, 2402, 2950, 3207
Hydraulic performance, 1578
Hydraulics, 1033, 1186, 1228, 2880
Hydrodynamics, 68, 123, 241, 1186, 1769, 2213, 2824, 3154
Hydrographic surveys, 3024
Hydrostatics, 1005
- Ice forces, 2768
Image analysis, 1033
Impact, 1473
Implementation, 2241
In situ tests, 2671
Indonesia, 2385
Inertia, 1716, 1769
Information systems, 2589
Inlets, waterways, 2522
Installation, 2852
Instrumentation, 1634
Interactions, 450, 489, 826, 853, 1088, 1200, 1389, 2443, 2696, 3112, 3140
International treaties, 935
Islands, 826, 2010
Italy, 218
- Japan, 18, 623, 769, 1280, 2726, 2754
Jetties, 410
- Kalman filter, 1769
Kinematics, 503, 935, 1513
- Laboratory tests, 255, 420, 503, 661, 1131, 1662, 2471, 2495, 2552, 2668, 2740, 2975
Lagoons, 330, 2880
Land reclamation, 2964
Landfills, 3227
Lasers, 544
Least squares method, 464
Limit design, 358
Littoral currents, 68, 281, 584, 729, 783, 826, 1005, 1118, 1242, 2061, 2173, 2402, 2603
Littoral drift, 783, 2542, 2710, 2880, 3183
Loads, 1606, 1742, 1769
Long waves, 410, 570, 1131, 1144, 1200, 1228, 1270, 1781, 2073
- Maintenance costs, 2010
Mapping, 2279
Marinas, 3239
Marine terminals, 3074, 3207
Mass transport, 544, 2998
Mat foundations, 1687, 2768
Mathematical models, 218, 597, 1060, 1473, 2131, 3126, 3281
Measurement, 584, 909, 1118, 2332, 2668
Methodology, 1592, 2894
Microcomputers, 2159
Mixing, 2346
Mixtures, 2696
Model studies, 2964, 3194
Model tests, 430, 1348, 1606, 1805, 1837, 2782
Model verification, 109, 191, 530, 1564
Modeling, 109, 123, 973, 1131, 1487, 1975, 2213, 2346, 2443, 2566, 2984, 2998
Models, 55, 150, 241, 316, 410, 584, 716, 769, 923, 959, 986, 1922, 1935, 2061, 2087, 2471, 2603
Monitoring, 1564, 3227
Monsoons, 623, 769
Mooring, 3074
Moorings, 1320
Movable bed models, 420, 2372, 2457, 2536, 2566
Mud, 2936, 2975, 2998, 3037
- National Flood Insurance Program, 2908

- Navigation, 2430, 2936, 2975, 3088, 3126
- Nearshore circulation, 150, 241, 267, 316, 444, 729, 783, 826, 1074, 2061, 2241
- Netherlands, 1, 1160, 1254, 1862, 1876, 1888, 1895, 1909, 1935, 1948, 1962, 1984, 1998, 2010, 2984
- New Jersey, 2020
- Nonlinear analysis, 55
- Nonlinear systems, 396
- Nonuniform flow, 281
- North Sea, 1214, 1888, 1948, 2589, 2824, 2838, 3254
- Numerical calculations, 150, 306
- Numerical models, 68, 136, 191, 205, 384, 623, 853, 1088, 1186, 1306, 1320, 1389, 1742, 1795, 2034, 2173, 2186, 2304, 2372, 2430, 2508, 2668, 2824, 2866, 3012, 3024, 3037, 3112, 3140
- Ocean disposal, 2824
- Ocean engineering, 935
- Ocean waves, 82, 384, 410, 503, 557, 623, 703
- Oceanographic surveys, 986
- Offshore structures, 1280
- Oil pipelines, 3171
- Oscillations, 584
- Oscillatory flow, 661, 2186, 2346, 2372, 2495, 2616
- Overtopping, 177, 1348, 1375, 1487
- Overturning tests, 840
- Paddles, 675
- Parameters, 2922
- Peak values, 647
- Performance, 2020, 2768
- Permeability, 1060, 1499, 2616
- Perturbation theory, 478
- Pipelines, 2508
- Planning, 3102
- Plates, 1046, 1228
- Plunging flow, 895, 973
- Policies, 1862
- Pontoons, 2852
- Pore pressure, 1334, 1499
- Porosity, 2616, 2754
- Porous media, 2616
- Porous media flow, 1046
- Ports, 82, 1675, 2975, 2998
- Potential flow, 923
- Predictions, 55, 241, 345, 358, 371, 530, 623, 853, 959, 1446, 1795, 1922, 1935, 1975, 2034, 2145, 2265, 2508, 2603, 3063, 3281
- Pressure distribution, 1606
- Pressure measurement, 1144
- Pressures, 164, 191, 611
- Probabilistic models, 1160
- Probability density functions, 909
- Probability distribution, 371
- Probes, instruments, 2936
- Profile measurement, 2682, 2710
- Profiles, 2566
- Projects, 1984
- Protective structures, 1160, 2810, 3254, 3268
- Prototype tests, 2630
- Prototypes, 2671
- Public opinion, 2394
- Radar, 703, 2279
- Radioactive tracers, 2710
- Random waves, 41, 68, 255, 478, 647, 689, 798, 1102, 1460, 2117
- Reefs, 743, 1375, 1781, 2852
- Reliability analysis, 1403
- Remote sensing, 703
- Repairing, 2416
- Reports, 935
- Research, 729, 935, 1538, 1975, 2471
- Revetments, 1306, 1431, 1524, 1606, 1662, 1837, 2810
- Rheological properties, 2936, 2975
- Rip currents, 729, 959
- Riprap, 2810
- Rock structures, 1306, 1446, 1460
- Roughness, 41
- Rubble-mound breakwaters, 177, 410, 1334, 1417, 1499, 1552, 1578, 1620, 1648, 1805, 1819
- Safety programs, 1254
- Salinity, 2866
- Salt water intrusion, 2866
- Salt water-freshwater interfaces, 2866
- Sand, 1362, 1998, 2087, 2291, 2416
- Sand transport, 1895, 1909, 1948, 1962, 2173, 2213, 2318, 2360, 2495, 2508, 2580, 2668, 2696, 2754, 3154, 3183, 3227
- Sand waves, 2508, 2668
- Scale effect, 973, 1716
- Scale models, 2394, 2457, 3088
- Scour, 2457, 2782, 2950, 3227, 3268
- Scouring, 1795
- Sea floor, 757, 853, 2279, 2508, 2668
- Sea level, 95, 867, 1160, 1862, 1876, 1948, 1962, 2644, 2838, 3063
- Sea state, 345, 358, 464, 478, 647, 675,

- 895, 1851
 Sea walls, 1292, 1742, 2241, 2782, 2810
 Sediment, 2894
 Sediment concentration, 716, 1922, 2047, 2318, 2360, 2630
 Sediment control, 2603
 Sediment transport, 68, 123, 281, 293, 420, 637, 783, 959, 1074, 1795, 1922, 1935, 2087, 2101, 2131, 2145, 2159, 2186, 2200, 2227, 2255, 2291, 2318, 2332, 2346, 2372, 2402, 2430, 2443, 2481, 2495, 2508, 2522, 2536, 2552, 2603, 2630, 2668, 2682, 2710, 2726, 2824, 2880, 3012, 3037, 3102, 3171
 Sedimentation, 2047, 3239
 Sedimentology, 2394
 Sensitivity analysis, 675, 798
 Sensors, 2227, 2279
 Shallow water, 267, 293, 637, 812, 895, 1019, 1088, 1200, 2213, 3126
 Shear flow, 584, 2696
 Shear stress, 637, 993, 2145, 2536
 Shear tests, 2696
 Shear waves, 729, 1242
 Ship motion, 3074, 3088, 3112, 3126
 Shoaling, 55, 109, 267, 396, 430, 530, 1102, 2481
 Shore protection, 1160, 1431, 1592, 1687, 1702, 1837, 1862, 1895, 1935, 1984, 1998, 2010, 2265, 2385, 2542, 2589, 2603, 2796, 2810, 3254
 Shoreline changes, 1292, 1998, 2020, 2034, 2101, 2522, 2566, 2726, 2740, 3281
 Silts, 3088
 Simulation, 255, 267, 420, 464, 675, 798, 812, 1033, 1270, 1606, 2318, 2443, 2726, 3102
 Slope stabilization, 1687, 2768
 Slopes, 293, 306, 371, 544, 570, 1060
 Social aspects, 7
 Solitary wave, 689, 840, 881, 923, 1019, 1033, 1144, 1200, 1270, 1487
 Spain, 826, 3154, 3183
 Spatial data, 812
 Spectral analysis, 32, 703
 Speeches, 1
 Stability, 1306, 1362, 1375, 1403, 1446, 1552, 1716, 1805, 2922
 Standing waves, 1033, 1742
 Static tests, 1755
 Statistical analysis, 516, 909, 2838
 Statistical models, 371, 1851
 Statistics, 18, 358, 812
 Steady flow, 2495
 Steel construction, 2852
 Stochastic models, 516
 Stochastic processes, 255
 Stones, 1837
 Storm surges, 1214, 1564, 1895, 1922, 2304, 2950
 Storms, 18, 218, 227, 358, 743, 1118, 1702, 1851, 2073, 2332, 2372, 2457, 2580, 2671, 2908, 3222
 Stratification, 1186, 2047
 Stratified flow, 3024
 Strength, 2671
 Stress, 1417, 1578, 1819
 Structural design, 1634, 1819
 Structural response, 1634
 Structural stability, 1578, 1578
 Structural strength, 1417
 Surf beat, 32, 743, 1102, 1131, 1781
 Surf zone, 32, 68, 95, 123, 150, 177, 227, 241, 316, 330, 516, 557, 716, 867, 1118, 1348, 2073, 2145, 2402
 Surface waves, 55, 293, 396, 503, 611, 757, 840, 1046, 1228, 3012
 Surfing, 516
 Suspended sediments, 716, 2117, 2131, 2159, 2200, 2227, 2824
 Taiwan, 1675
 Testing, 1592
 Thailand, 986
 Theories, 647, 757
 Thermal stresses, 1755
 Thickness, 1805
 Three-dimensional flow, 2255
 Three-dimensional models, 267, 444, 1005, 1186, 2131, 2159, 2255, 2402, 2481, 2782
 Tidal currents, 909, 1214, 2430, 2964
 Tidal power plants, 3050
 Tidal waters, 1948, 2522, 2838, 2922, 3063
 Tides, 2644, 3050, 3171
 Time dependence, 205, 293
 Time series analysis, 2838
 Time studies, 1102
 Topography, 2101, 2117, 2173, 2213, 2279, 2332, 2481
 Transducers, 1280
 Transformations, 1102
 Transport phenomena, 2998
 Tsunamis, 1172
 Turbulence, 150, 557, 661, 716, 1019
 Turbulent boundary layers, 853
 Two phase flow, 2346, 2372
 Two-dimensional models, 689

- Typhoons, 623, 769
- Undertow, 123, 150, 227, 783, 2061
- Unsteady flow, 993, 2880
- Urban areas, 2394
- Velocity, 191, 227, 503, 557, 909
- Velocity distribution, 661, 2866
- Velocity profile, 281, 450, 993, 2372
- Vertical cylinders, 840, 1769
- Visual perception, 345
- Vortex shedding, 3171
- Vortices, 661, 1019, 1242, 2186, 2200
- Walls, 164
- Waste site cleanup, 2894
- Water depth, 205, 3268
- Water flow, 3063
- Water level fluctuations, 2291, 2838
- Water levels, 826, 1909
- Water quality, 2394
- Water surface, 227, 993, 1144, 1172, 1742
- Water table, 867, 2644
- Water tunnels, 2318
- Water waves, 164, 503, 689, 881, 935, 1389, 1769, 2213, 3140
- Wave action, 41, 191, 205, 895, 1131, 1306, 1730, 1795, 1805, 1819, 1935, 2061, 2073, 2117, 2385, 2542, 2552, 2580, 2630, 2644, 2768, 2908, 3037, 3112, 3194
- Wave attenuation, 330, 420, 1228
- Wave climatology, 986, 1088, 1292, 1888, 2159, 2416, 2542
- Wave crest, 396, 973
- Wave damping, 743, 1046, 1334
- Wave diffraction, 840
- Wave energy, 267, 530, 611, 1118, 1131, 1228, 1242, 1292, 1334, 1375, 1499, 1620, 2522
- Wave equations, 306
- Wave forces, 95, 164, 241, 840, 935, 1005, 1280, 1320, 1334, 1348, 1362, 1389, 1403, 1446, 1473, 1513, 1538, 1606, 1716, 1742, 1781, 1827, 2131, 3126, 3140
- Wave generation, 384, 430, 478, 675, 689, 769, 1172, 1214
- Wave groups, 32, 82, 177, 371, 729, 743, 812, 1131, 1552, 2117
- Wave height, 18, 177, 205, 293, 330, 345, 358, 464, 530, 675, 812, 881, 986, 993, 1102, 1742, 1851, 1888, 2034, 2117, 2145, 2402, 2630
- Wave measurement, 330, 430, 703, 895
- Wave pressure, 1473, 1564, 1620, 1781
- Wave propagation, 32, 306, 316, 384, 410, 420, 530, 544, 611, 689, 703, 798, 812, 881, 1088, 1172, 1214, 1228, 2186, 2213, 3112
- Wave reflection, 109, 136, 306, 570, 757, 923, 1046, 1172, 1460, 1702
- Wave refraction, 109, 205, 384, 530, 1088
- Wave runup, 41, 68, 191, 371, 557, 570, 867, 895, 1200, 1242, 1270, 1662, 2360, 2471
- Wave spectra, 32, 109, 177, 205, 267, 430, 464, 478, 623, 647, 703, 769, 798, 1102, 1320
- Wave velocity, 396, 853, 2200
- Wavelength, 2034
- Waves, 55, 450, 489, 597, 637, 993, 2318, 2332, 2443, 2495
- Weirs, 1487
- Wetlands, 2542
- Wind direction, 1888
- Wind forces, 95, 218, 444, 1074, 1118, 1888, 2385, 2754
- Wind pressure, 826
- Wind tunnel test, 2754
- Wind velocity, 986
- Wind waves, 32, 218, 611, 1214

AUTHOR INDEX

Page number refers to first page of paper.

- Ahrens, John P., 1837
 Alejo, Miguel, 826
 Allsop, N. W. H., 1446, 1460
 Alonso, Ignacio, 2580
 Al-Salem, Abdullah, 2318
 Alvarez, Ricardo, 2580
 Anastasiou, K., 973
 Andrassy, Christopher J., 41
 Anglin, C. D., 1634
 Anton, Jeffrey P., 757
 Araújo, Luiz C., 3171
 Asano, Toshiyuki, 2372
- Bailard, James A., 1702
 Bakker, K. J., 1524
 Bakker, W. T., 1935, 2360
 Bakker, Willem T., 2696
 Bandeira, Jefferson V., 3171
 Basco, David R., 1292
 Battjes, J. A., 32, 1975
 Bellessort, Bernard, 2394
 Bertotti, L., 218
 Bezuijen, A., 1431, 1606
 Bijker, Romke, 2508
 Bjordal, S., 3074
 Blázquez, Rafael, 345
 Blondeaux, Paolo, 2186
 Boczar-Karakiewicz, B., 2213, 2265
 Bodge, Kevin R., 2796
 Booij, N., 530
 Borgman, Leon E., 255
 Bosman, D. E., 3239
 Bowen, Anthony J., 2061, 2227
 Bowers, E. C., 3126
 Bradbury, A. P., 1446
 Breteler, M. Klein, 1431, 1524
 Breteler, Mark Klein, 191
 Briand, Marie-Hélène G., 2159
 Briggs, Michael J., 267
 Brosen, Michael, 3140
 Brossard, C., 3088
 Bundgaard, Henrik I., 3140
 Burcharth, H. F., 1417
 Burcharth, Hans F., 1819
 Burger, A. M., 1431
 Bürger, W. W., 1578
- Caldas, Felipe, 3194
 Canestrelli, P., 218
 Cavaleri, L., 218
 Chandler, Bruce D., 358
 Chang, J. J., 1172
 Chapalain, G., 2213
- Charulakana, Supot, 986
 Chen, W. J., 637
 Chiaia, Giancarlo, 1102
 Chian, Chimin, 1270
 Collado, F., 316
 Cooker, M. J., 164, 1473
 Costa, Rui G., 2047
 Cox, Daniel T., 1306
 Craeymeersch, Johan A., 2984
 Crapps, David K., 3268
 Crowley, J. B., 293, 1074
- Daemrich, K. F., 430
 Dally, William R., 516
 Dalrymple, Robert A., 675, 729
 Damiani, Leonardo, 1102
 Davis, A. B., 3227
 de Jong, H., 2922
 de Kok, J. M., 2824
 De Rouck, J., 1755
 de Vriend, H. J., 1005
 de Vriend, Huib J., 1962
 de Vroeg, J. H., 1935
 Dean, Robert G., 2145, 2522
 Dean, William L., 3268
 Dedeysne, R., 1755
 Degrieck, J., 1755
 Deguchi, Ichiro, 2603
 Deigaard, Rolf, 959
 Dekker, J., 530
 Delouis, A., 3088
 den Adel, H., 1524, 1606
 den Adel, J. D., 530
 Dette, Hans H., 2566
 DeVries, Jack, 1702
 Diez, J. J., 3154
 Dijkman, M. J., 1935
 Dijkzeul, Johan C. M., 2255
 do Valle, Antonio B., 3171
 Dodd, N., 584
 Drapeau, G., 2710
- Edge, B. L., 3268
 Ekebjærg, Lars C., 1186
 Elgar, Steve, 55
 Endo, Taiji, 1403
 Escobar, V. A., 3154
 Eysink, W. D., 1948
- Farrell, Stewart C., 2020
 Fassardi, Claudio, 1552
 Feral, Alain, 2936
 Fernandes, J. L. M., 689

- Fernández, José, 3183
 Fisher, J. S., 2471
 Fleming, C. A., 2589
 Flick, Reinhard E., 557
 Fournier, Charles P., 3194
 Fowler, Jimmy E., 2457
 Fowler, Rachel E., 729
 Franken, A. F., 530
 Fredsøe, Jørgen, 959
 Freilich, M. H., 55
 Funke, E. R., 464
- Gadd, P. E., 2768
 Gadd, Peter E., 1687
 Galichon, P., 3088
 Galichon, Pascal, 2936
 George, Ronald A., 557
 Gerritsen, F., 2922
 Gerritsen, Franciscus, 1270
 Giménez, Marcos H., 255
 Goda, Yoshimi, 18
 Gómez Pina, Gregorio, 1592, 3183
 González, Angel, 345
 González Madrigal, B., 1348
 Gordon, A. D., 2880
 Götschenberg, A., 430
 Gourlay, M. R., 330
 Granboulan, J., 3088
 Granboulan, Jérôme, 2936
 Grassa, José María, 798
 Green, Malcolm O., 2200
 Greenwood, Brian, 227, 2061, 2227
 Griggs, Gary B., 2810
 Grilli, Stéphan T., 1200
 Grosche, Sven, 895
 Grummitt, Alan Albert Campbell, 2852
 Grüne, Joachim, 895
 Gudmestad, Ove T., 935
 Guifen, Wang, 2430
 Guza, R. T., 55, 410, 611
 Guza, Robert T., 1702
- Haidekker, Mark, 895
 Hall, Kevin R., 1620, 1730, 2616
 Hallermeier, Robert J., 41
 Hallie, Frank P., 1998, 2984
 Hamerlynck, Olivier, 2984
 Hamm, Luc, 2975
 Hansen, Niels-Erik Ottesen, 3024
 Hanson, Hans, 2034, 2173
 Hara, Masanori, 923
 Hardy, T. A., 330
 Harkins, Gordon S., 675
 Harper, Bruce A., 358
 Hatada, Yoshio, 205, 623
- Hattori, Masataro, 396
 Hay, Alex E., 2227
 Hayashi, Katsuyuki, 177
 Hazen, David G., 2061, 2227
 Headland, John R., 1320
 Herbers, T. H. C., 611
 Herbich, John B., 2894
 Hino, Mikio, 743, 1781
 Hirakuchi, Hiromaru, 703
 Hirasawa, Mitsunari, 1280
 Holman, Rob, 1118, 1242
 Holthuisen, L. H., 384
 Holtzhausen, A. H., 1805
 Hoozemans, Frank M. J., 1888
 Horikawa, Kiyoshi, 661, 2754
 Hotta, Shintaro, 2754
 Hou, Ho-Shong, 1827
 Houston, Samuel H., 2145
 Howd, Peter, 1242
 Howd, Peter A., 1118
 Howell, Gary L., 1417, 1819
 Hudspeth, R. T., 1513
 Hudspeth, Robert T., 255, 1552
 Hughes, Steven A., 2457
 Hunter-Blair, A., 2589
 Hwung, H. H., 544
- Ijima, Takeshi, 1228
 Ikeda, Syunsuke, 661
 Ikeno, Masaaki, 703
 Irie, Isao, 2998
 Isobe, Masahiko, 123, 136, 647, 1060, 2495
 Ito, Kazunori, 812
 Iwata, Koichiro, 2740
 Izumiya, Takashi, 306
- Jackson, L. A., 2241, 2265
 Jasińska, Ewa, 2866
 Jeng, Dong-Sheng, 1742
 Jensen, John, 2671
 Jensen, Jürgen, 2838
 Jensen, Ole Juul, 1538, 3074, 3102, 3222
 Jones, J. Sterling, 3268
 Jongeling, Tom, 1564
 Jonsson, Ivar G., 1131, 1389
 Juhl, Jørgen, 1538
- Kadono, Takashi, 1280
 Kai, Yen, 2964
 Kajima, Ryoichi, 1716
 Kamphuis, J. W., 2710
 Kamphuis, J. William, 2159, 2402
 Kang, Hong-Yoon, 371
 Kao, Joseph S., 1730

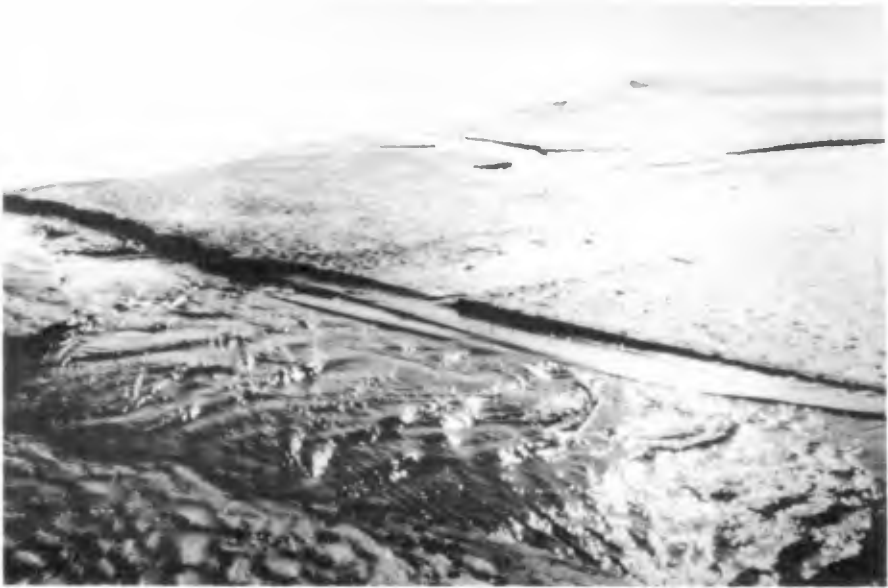
- Kapp, J. F., 3239
 Kardana, 2385
 Katoh, Kazumasa, 95, 2073
 Katopodi, Irene, 2131
 Katsuragawa, Tetsuyuki, 396
 Kawata, Yoshiaki, 281, 2332
 Kim, Ga-Ya, 2603
 Kirby, James T., 109, 757, 1702
 Kitou, N., 1005
 Klatter, Leo, 1564, 2950
 Klomp, Wim H. G., 2696
 Kloos, M., 3239
 Klopman, Gert, 478
 Kluger, J. W. J., 2416
 Kobayashi, Nobuhisa, 1306
 Kobune, Koji, 18
 Kojima, Haruyuki, 1228
 Komaguchi, Tomoaki, 769
 Komar, Paul, 1242
 Komar, Paul D., 1118
 Kondo, Hideo, 3063
 Kondo, Kosuke, 2481
 Konter, Jan, 1564, 2950
 Kraus, Nicholas C., 2034, 2173
 Kriebel, David L., 2304
 Kubota, Susumu, 570
 Kuik, Ton (A) J., 1862
 Kunz, H., 3254
 Kuo, C. T., 637
 Kuo, Shih-Duenn, 1675
 Kyriacou, Andreas G., 993
- Langerak, A., 2922
 Larson, Magnus, 2173
 Latham, J. -P., 1446
 Laubscher, W. I., 3227
 Laustrup, Chr., 2671
 Lean, G. H., 3126
 Lee, J. J., 1172
 Leendertse, Jan J., 444, 2255
 Leidersdorf, C. B., 2768
 Leidersdorf, Craig B., 1687
 Leitão, J. M., 689
 Lemos, M., 316
 Lin, C., 544
 Lin, D. T., 1046
 Lionello, P., 218
 Liu, Shiao-Kung, 444
 Liu, Shu-xue, 82
 Long, B., 2710
 Losada, Miguel A., 675
 Louisse, Cees (C) J., 1862
 Louisse, Cees J., 1998
 Louters, Teunis, 2984
 Lundgren, J., 3074
- McDougal, W. G., 1417
 McDougal, William G., 1687
 McLaren, P., 2589
 Madsen, H. Toxvig, 2671
 Madsen, Ole S., 420
 Madsen, Per A., 3112
 Manoha, Bruno, 2542
 Mansard, E. P. D., 464
 Martinez, Javier, 345
 Martínez, Jesús, 2580
 Mase, Hajime, 177
 Mathisen, Paul P., 420
 Matsumi, Yoshiharu, 1648
 Medina, Josep R., 255, 1552
 Mehta, Ashish J., 2047
 Melo, Eloi, 410
 Migniot, Claude, 2975
 Mitsunobu, Norihiko, 2668
 Mizuguchi, Masaru, 570
 Mizumura, Kazumasa, 1403
 Mizuno, Yuzo, 1280, 1362
 Møller, Jacob Steen, 3024
 Monadier, P., 3088
 Moutzouris, C. I., 2552
 Mügge, Hans-Eckart, 2838
 Mulder, Herman P. J., 3012
 Mulder, Jan P. M., 2984
 Muñoz, Angel, 3183
 Murakami, Kazuo, 2998
 Murakami, Noritaka, 2740
 Murray, Malcolm, 3207
- Nadaoka, Kazuo, 2346
 Nagai, Yutaka, 1280
 Nairn, Robert B., 68
 Nakamura, Kazuo, 2117
 Nakaza, Eizo, 743, 1781
 Nelson, R. C., 330
 Nicholson, John, 3050
 Nielsen, Peter, 867
 Niemeyer, H. D., 530, 783, 2360
 Nishi, Ryuichiro, 2117
 Nishimura, Hitoshi, 1033
 Nnadi, Fidelia N., 2536
 Nodani, Hitoshi, 2481
 Nosek, Kevin B., 41
- Obana, E., 716
 Ochi, Michel K., 909
 O'Connor, Brian, 3050
 Ohnaka, Susumu, 2443
 Ohyama, Takumi, 840
 Okayasu, Akio, 123
 Okuno, Masakazu, 3037
 Olivares Prud'Homme, J., 1348
 Oltman-Shay, J., 584
 Oltman-Shay, Joan, 1118, 1242

- Osborne, Philip D., 227, 2227
 Ostrowski, R., 2101
 Oumeraci, H., 1334, 1578
 Overton, M. F., 2471
 Özhan, Erdal, 1487
- Partensky, H. W., 1334, 1578
 Peregrine, D. H., 164, 1019, 1473
 Petrillo, Antonio, 1102
 Pfaff, W. M., 3227
 Philipse, Leo, 1662
 Pilarczyk, K. W., 1431
 Pilarczyk, Krystian W., 1375
 Pluijm, Marco, 2010
 Postma, Renske, 2984
 Poulsen, L., 2671
 Prins, J. E., 7
 Prtšer, H. -H., 1088
 Pruszek, Z., 2101
 Putrevu, Uday, 241
- Raichlen, Fredric, 1144
 Ramsden, Jerald D., 1144
 Rasmussen, Erland B., 1186
 Rayner, Ralph, 3050
 Refaat, Hossam El-din A. A., 281
 Retief, G. de F., 3239
 Rhee, Joon P., 1819
 Ribberink, Jan S., 1998, 2131, 2318
 Ridge, A. B., 3239
 Rivero, F., 316
 Roelse, Piet, 1984
 Roelvink, Dano (J) A., 1962
 Roelvink, J. A., 1909, 1998
 Roelvink, J. A. (Dano), 68
 Rogers, Spencer M., Jr., 2908
 Rojanakamthorn, Somchai, 1060
 Romafczyk, W., 1769
 Rosengaus, M. Michel, 420
 Rouch, Franck, 2394
 Ryu, Cheong-Ro, 371
- Saito, Eiichi, 1795
 Sakai, T., 716
 Sakakiyama, Tsutomu, 1716
 Sánchez-Arcilla, A., 316
 Sánchez-Carratalá, Carlos R., 255
 Sand, Stig E., 3102
 Sato, Michio, 2117, 2644
 Sato, Shinji, 1795, 2668, 3037
 Sawaragi, Toru, 2603
 Sayao, Otavio J., 3194, 3207
 Schäffer, Hemming A., 1131
 Schönfeld, Wolfgang, 2838
 Schoonees, J. S., 2416, 3227
 Scott, Katherine, 2810
- Scott, R. D., 1634
 Seiffert, Jan Willem, 1662
 Shibayama, Tomoya, 1795, 3037
 Shih, Robert W. K., 1499
 Shimizu, Takuzo, 2481
 Shimoda, Naokatsu, 2740
 Shiraiishi, Naofumi, 769, 1403
 Silvester, Richard, 2726
 Simons, Richard R., 993
 Skjelbreia, James E., 503
 Skourup, Jesper, 1389
 Sleath, J. F. A., 450
 Smallman, Jane V., 597
 Smith, Gregory M., 2616
 Smith, Jane M., 267
 Sobey, Rodney J., 358
 Sobierajski, E., 1769
 Son, Huynh-Thanh, 853
 Sørensen, Ole R., 3112
 Sørensen, Torben, 3222
 Southgate, Howard N., 68
 Spanhoff, R., 2824
 Sparboom, Uwe, 895
 Spencer, J. M. A., 3126
 Staub, Carsten, 2508
 Steetzel, Henk J., 1922
 Stive, M. J. F., 1909
 Stive, Marcel J. F., 1876, 1962
 Stockberger, M. Todd, 2291
 Stolk, A., 1895
 Stone, A. L., 2471
 Struik, P., 1254
 Suriamihardja, Dadang Ahmad, 150
 Svendsen, Ib A., 241, 1200
 Swan, Christopher, 489
 Swart, D. H., 293, 1074, 3227
 Syamsudin, 2385
- Tada, Y., 716
 Taerwe, L., 1755
 Tait, James F., 2810
 Takewaka, Satoshi, 1033
 Takezawa, Mitsuo, 570
 Tanaka, Mitsuhiro, 881
 Teisson, Charles, 1851, 2542
 Tejedor, Begoña, 826
 Tejedor, Luis, 826
 Teles da Silva, A. F., 1019
 Temperville, André, 853
 Terwindt, J. H. J., 1975
 Thomsen, J., 3074
 Thornton, E. B., 584
 Tokikawa, Kazuo, 1280
 Tolman, H. L., 384
 Tolman, Hendrik L., 1214
 Tomlinson, R. B., 2241

- Torum, Alf, 503, 935
 Toue, Takao, 2566, 2782
 Toumazis, A. D., 973
 Townend, I. H., 2589
 Tozer, Nigel P., 597
 Tsai, Ching-Piao, 1742
 Tsuchiya, Yoshito, 150, 281, 769,
 2332, 2726
 Tsukayama, S., 743, 1781
 Tsuruya, Hiroichi, 2998
 Tuah, Hang, 255
 Turcke, D. J., 1634
 Twu, S. W., 1046
- Udink, Connie, 3012
 Ukai, Akiyuki, 812
 Uliczka, Klemens, 2630
 Umezawa, Nobutoshi, 1362
- Valdés Fernández de Alarcón, J. M.,
 1592
 Vallianos, Limberios, 1320
 van Alphen, Jos S. L. J., 1998
 Van Beurden, I. J. C. A., 1160
 Van Damme, L., 1755
 van de Graaff, Jan, 2682
 van der Burg, G., 2279
 van der Meer, Jentsje W., 191, 1375
 van Halsema, D., 2279
 van Heuvel, Tj., 2824
 van Kesteren, Walther G. M., 2696
 van Leeuwen, P. J., 32
 Van Leeuwen, Peter Jan, 478
 van Vessem, P., 1895
 Verhagen, H. J., 2087
 Vested, Hans Jacob, 1186
 Viggosson, G., 3074
 Viguier, Jacques, 2936
 Vincent, Christopher E., 2200
 Visser, P. J., 2087
 Vittori, Giovanna, 2186
 Vogel, J. A., 530
 Vogelzang, J., 2279
- von Amsberg, Claus, 1
 Vrijling, J. K., 1160, 2087
 Vrouwenvelder, A. W. C. M., 1254
- Walker, James R., 1144
 Wang, Hsiang, 2566, 2782
 Watanabe, Akira, 123, 136, 1060,
 2443, 2495
 Weesakul, Sutat, 986
 Weggel, J. Richard, 2020
 Wensink, G. J., 2279
 Wiersma, Hans (J.), 1876
 Wilde, P., 1769
 Wilson, Kenneth C., 2536
 Wind, H. G., 3281
 Work, Paul A., 2522
 Wouters, J., 1606
 Wurjanto, Andojo, 1306
- Yagi, Hiroshi, 2346
 Yalçmer, Ahmet Cevdet, 1487
 Yamaguchi, Masataka, 205, 623
 Yamamoto, Masato, 1403
 Yamashita, Takao, 150, 177, 2726
 Yanagishima, Shin-ichi, 95, 2073
 Yanase, Tomoyuki, 1362
 Yano, Kenji, 1362
 Yasuda, Takashi, 812, 923
 Yixin, Yan, 2964
 Yoshida, Akinori, 1228
 Yoshioka, Hiroshi, 2332
 Young, I. R., 330
 Yu, Xiping, 136
 Yu, Yu-xiu, 82
 Yu, Z., 2360
- Zeidler, R. B., 2101
 Zhou, Liu, 1417
 Zielke, W., 1088
 Zitman, Tjerk J., 1876
 Zude, Cao, 2430
 Zwamborn, J. A., 1805, 2416
 Zyserman, Julio, 959

PART II

Long Waves and Storm Surges



CHAPTER 84

EVOLUTION OF INFRAGRAVITY VARIANCE DURING A STORM

Peter A. Howd¹, Joan Oltman-Shay^{1,2}, Rob Holman¹, and Paul D. Komar¹

Abstract

Data from an alongshore array of bidirectional current meters located in the surf zone were analyzed to provide estimates of the behavior of three bands of wave energy during the passage of a moderate storm. The variance in the incident wave band is found to be saturated, as is expected of depth-limited waves. The infragravity band variance is found to depend most strongly on the offshore wave height. Shear wave variance is found to be correlated with the magnitude of the measured longshore current. During a period of nearly constant high waves, the composition of the low frequency band motions ($f < 0.05$ Hz) changed dramatically. This change is thought to be related to the directional characteristics of the incident band wind waves.

Introduction

A primary interest in the study of nearshore processes has been the characterization of two frequency bands of surface gravity waves, incident wind waves ($0.05 < f < 0.33$ Hz) and infragravity waves ($f < 0.05$ Hz). The recent discovery of shear waves (Oltman-Shay, et al., 1989a; Bowen and Holman, 1989) has added additional complexity to the problem of quantifying coherent sources of energy in the nearshore.

The objective of this paper is to present data documenting the evolution of the low frequency waves during the passage of a moderate storm. The instruments used for this study were located in the trough of a nearshore bar system in approximately 1.5 m of water. In the next section we will briefly review previous work on

1. College of Oceanography, Oregon State University, OC Admin. Bldg. #104, Corvallis, Oregon, U.S.A. 97331-5503

2. Now at: Quest Integrated, 21414 68th Ave. So., Kent, Washington, U.S.A. 98032

these low frequency waves, then move on to the data collection and analysis techniques used in this study. We then present our findings and some preliminary conclusions.

Background

Infragravity waves are traditionally considered to be the surface gravity waves which result from the second order interaction of incident wind waves. The free infragravity waves can be broken into two distinct groups, a set of discrete edge wave modes which are trapped to the shoreline, and a continuum of leaky waves which reflect from the shoreline and radiate energy back out of the nearshore zone. Bounded waves, the forced displacement of the free water surface by the structure of wave groups also contribute to infragravity wave energy. Edge waves on a plane sloping beach must have alongshore wavenumbers, k , in the range $\sigma^2/g \leq |k| \leq \sigma^2/g\beta$ (where $\sigma = 2\pi f$ and $k = 2\pi/L$) satisfying the relationship $\sigma^2 = g|k| (2n+1)\beta$ (Eckart, 1951), while for leaky waves there is a continuum of alongshore wavenumbers $|k| < \sigma^2/g$ (Suhayda, 1974; Guza and Bowen, 1976).

It is important to note that measurements of infragravity waves obtained in the surf zone underestimate the maximum variance of the infragravity band for two reasons. First, while incident waves decrease in height from breaking to the shore-

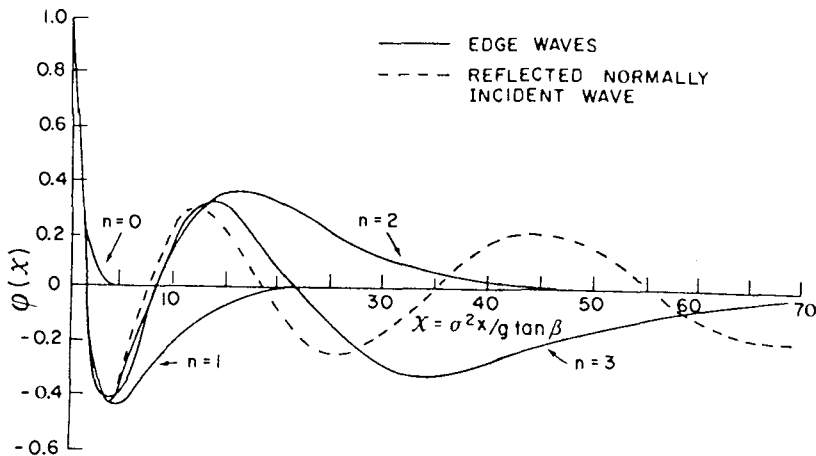


Figure 1. Cross-shore shape of the first three edge wave modes and the normally reflected leaky wave plotted versus dimensionless cross-shore distance.

line, infragravity waves have their maximum height at the shoreline and decay offshore (Figure 1). Secondly, infragravity waves have complicated cross-shore structures which contain zero crossings. Thus at any position seaward of the shore-

line, measurements are influenced not only by the offshore decay of the wave amplitudes, but by the nodal structure.

Shear waves, a new class of nearshore wave, are distinguished by large alongshore wavenumbers, well outside the range of surface gravity waves, $|k_{sw}| > \sigma^2/g\beta$ (Oltman-Shay, et al., 1989a). On the one beach studied to date, a typical energetic period is 200 s with an alongshore wavelength of 200 m. This distinctive signature permits their contribution to total current variance to be separated in alongshore wavenumber-frequency space. Bowen and Holman (1989) present a theoretical derivation of these waves as an instability of the mean longshore current which depends on the conservation of potential vorticity. The cross-shore shear of the mean longshore current provides background vorticity. Using a simple model they show there is a frequency range where a perturbation to the mean current (the shear wave) will grow exponentially at a rate which depends on the magnitude of the shear on the seaward face of the current.

Field Site and Methods

The data used for this study were collected as part of the SUPERDUCK experiment (Crowson, et al., 1988). This was a large multi-agency experiment hosted by the Coastal Engineering Research Center's Field Research Facility (FRF) in Duck, North Carolina during October, 1986. This beach is located on the mid-Atlantic coast of the United States in the center of a 100-km long barrier spit (Figure 2). The mean foreshore slope is approximately 1:10 and decreases offshore to 1:100.

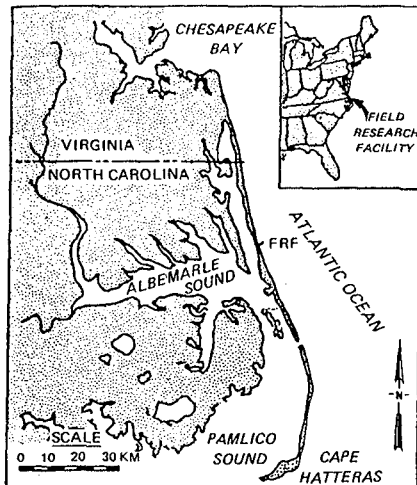


Figure 2. Location of the Coastal Engineering Research Center's Field Research Facility.

Sand bars are common, are usually three-dimensional, but become linear during

storms (Lippmann and Holman, 1990). The extreme tide range during the experiment was 137 cm.

The primary source of data for this work was an array of bidirectional electromagnetic current meters deployed approximately 55 m seaward of the mean shoreline position (Figure 3). The sampled array length was 290 m, sufficient to resolve typical wavelengths at this site. Sensors were oriented such that +V currents (alongshore) flow 'north' parallel to the beach and +U (cross-shore) currents flow offshore. All gages remained submerged at low tide. The gages were hard wired to the computer and collected at 2 Hz for four hour periods surrounding high and low water. The incident wind wave climate was sampled in 8 m depth using a 255 m long array of 9 bottom mounted pressure sensors.

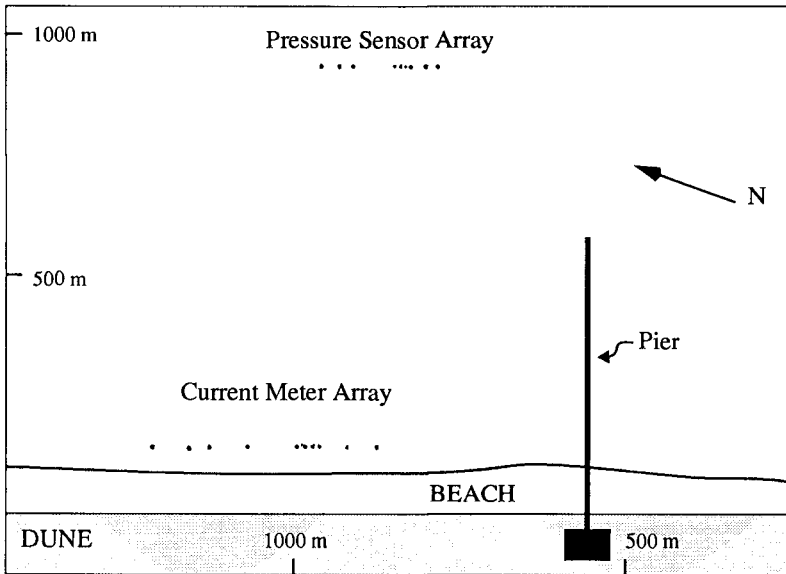


Figure 3. Plan view of the SUPERDUCK field site at CERC'S Field Research Facility in Duck, NC. Shown are the nearshore current meter array and the offshore wind wave directional array relative to the location of the pier.

A total of 37 4-hour data runs were recorded over the course of the experiment. From those, 21 were selected for further analysis on the basis of spatial homogeneity over the length of the arrays and stationarity over the 4 hour run duration. The current meter data were used to calculate the alongshore wavenumber-frequency spectra for both the cross-shore and alongshore components of flow. First each 4-hour time series was divided into 13 ensembles with 50% overlap, each 2048 s in length. The ensembles were demeaned and quadratically detrended and tapered with a Kaiser-Bessel data window. After application of an FFT, the cross-spectral constituents were calculated between all sensor pairs. Finally, alongshore wave-

number-frequency spectra were estimated using the Iterative Maximum Likelihood Estimator (IMLE) developed by Pawka (1983) and previously applied to surf zone data by Oltman-Shay and Guza (1987). The pressure sensor array in 8 m depth allowed similar alongshore wavenumber-frequency analysis.

Variance was then partitioned between the three bands in alongshore wavenumber-frequency space as shown in Figure 4. Integrated variances for each band were calculated using

$$s_{INC}^2 = \int_{0.05-k_{NY}}^{0.33 k_{NY}} \int (S(k, f)) dkdf$$

$$s_{IG}^2 = \int_0^{0.05 k_0} \int_{-k_0} (S(k, f)) dkdf$$

$$s_{SW}^2 = \int_0^{0.05 k_{NY}} \int_{-k_{NY}} (S(k, f)) dkdf - s_{IG}^2$$

where s^2 is the integrated variance for each of the bands, k_{NY} is the Nyquist alongshore wavenumber of the array, k_0 is the estimated mode zero wavenumber and $S(k, f)$ is the spectral density. The subscripts refer to **INC**ident, **Infra**Gravity, and **Shear** Waves, respectively.

Results

During the 14-day period of the experiment, the root mean square (rms) wave height $(8s^2)^{1/2}$ in 8 m water depth ranged from 50 cm to over 200 cm. During the peak of the storm the wave height remained very near 200 cm for a total of 18 hours. In the surf zone, the cross-shore component of the infragravity band reached a maximum rms value of 63 cm/s and averaged 32 cm/s for the 21 4-hour runs. The alongshore component of the infragravity band had a maximum rms flow of 33 cm/s and a mean of 20 cm/s. The shear wave band had maximum rms values of 41 and 35 cm/s with means of 25 and 20 cm/s for the cross-shore and alongshore components, respectively, for the 21 runs. First we will examine the general behavior of each of the wave bands (after Howd, et al., 1991), followed by a more careful examination of two data runs from the period of high waves.

Given the position of the current meter array in the inner surf-zone shoreward of the sand bar crest, we expect to observe that the incident band was limited

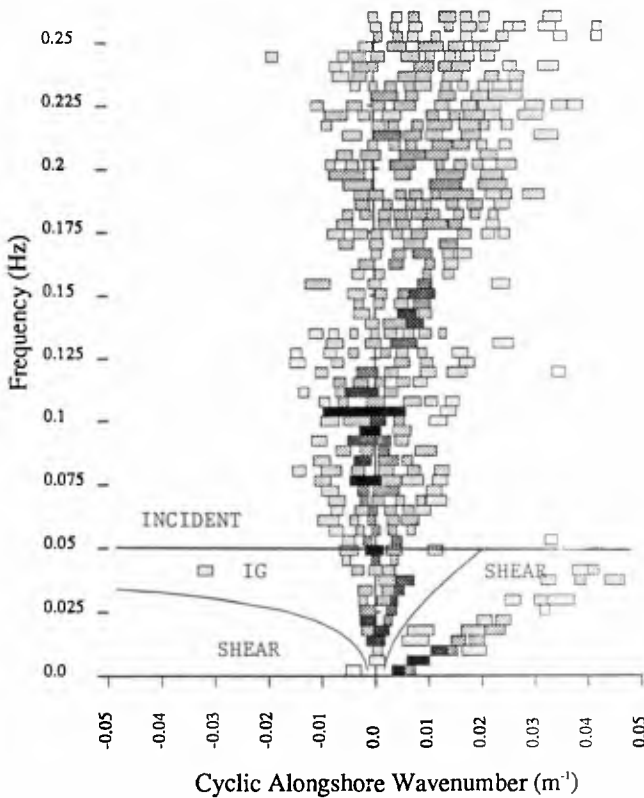


Figure 4. Cyclic alongshore wavenumber ($1/L$) vs. frequency spectrum with lines showing the bounds of each of the three wave types. The shaded boxes indicate peaks in $S(k,f)$ with the darkness indicating the higher variance. The width of the box indicates the half-power wavenumber bandwidth.

by the water depth, either at the array or further seaward at the bar crest. The strongest evidence for saturation of the incident band was the lack of statistically significant correlation (at the 95% level) between the incident wave heights at the array (calculated using linear theory) and the offshore wave height ($r^2 = 0.16$). There was however a significant correlation between the tide and the incident band wave height at the array ($r^2 = 0.80$) indicating the measurements were, as expected, a function of the water depth.

The infragravity wave motions were found to be significantly correlated with the offshore wave height ($r^2 = 0.73$ and 0.75 for the cross-shore and alongshore components, respectively). This finding is in agreement with current meter data from similar water depths on three other beaches (Holman, 1981; Guza and Thornton, 1985; Howd, et al., 1991).

Shear waves are expected to scale with the shear on the seaward face of the longshore current (Bowen and Holman, 1989), but because of the array design, no measurements of longshore current shear were available. Thus we have tested the absolute value of the mean longshore current $|\langle V \rangle|$, as a proxy for the shear. As expected from the preliminary observations of Oltman-Shay, et al. (1989a), significant correlations (95% level) were found ($r^2 = 0.25$ and 0.42 for the cross-shore and alongshore components respectively), but, as the low values suggest, considerable scatter exists in the data.

We will now compare two data runs taken during the storm. The first, taken just as the storm was reaching its peak, began at 1030 EST on October 10, 1986, and was characterized by an offshore rms wave height of 185 cm, peak period of 7.3 s and a 24.3 degree angle of incidence. The mean longshore current at the surf zone array was 160 cm/s to the south. The second run we will present was collected toward the end of the storm event and began at 1820 EST on October 11, 1986. The offshore wave height was 190 cm, the peak period was 10 s and the waves were near normally incident. The mean longshore current at the surf-zone array was 13 cm/s to the south.

Figure 5 shows the alongshore wavenumber-frequency spectra from the 8 m pressure sensor array for the two runs. To the right of each f - k spectrum is the more typical frequency spectrum (solid line). The different characteristics of the incident band are readily visible. The oblique approach of the wind waves on the 10th ($f \sim 0.125$ Hz) is clearly contrasted with the more shore-normal (at the variance peak, $f \sim 0.08$ Hz) approach on the 11th. Notice how the incident waves are clearly bounded by the line marking the relation $\sigma^2/g = k$, which is the cutoff for waves not trapped in the nearshore (i.e., they are either of deep water origin or are leaky waves reflected from the shoreline).

The infragravity band also shows surprising structure, despite the location of the sensors in 8 m of water nearly 1 km offshore. The distinctive linear trend of variance peaks from $f \sim 0.0$ to 0.10 Hz and k from 0. to 0.006 m^{-1} seen on the 10th has been shown to be the result of high mode edge waves, progressing in a southern direction (Elgar, et al., 1989; Oltman-Shay, et al., 1989b). While the high mode edge wave signature is still present on the 11th, the lowest frequencies ($f < 0.025$ Hz) appear to be more leaky in nature. There is a distinct lack of a shear wave signal at alongshore wavenumbers greater than the mode 0 dispersion curves as expected for pressure signals this far offshore (Bowen and Holman, 1989).

Figure 6 presents the alongshore wavenumber-frequency spectra computed from the alongshore component of flow in the surf-zone. As expected, the incident peaks are not visible. Most striking are the differences in the low frequency portion of the f - k spectra. On the 10th, the infragravity field was dominated by southward progressing edge waves and shear waves. The unique linear trend of the edge wave field which extends well into the incident band is unexplained, but was observed on

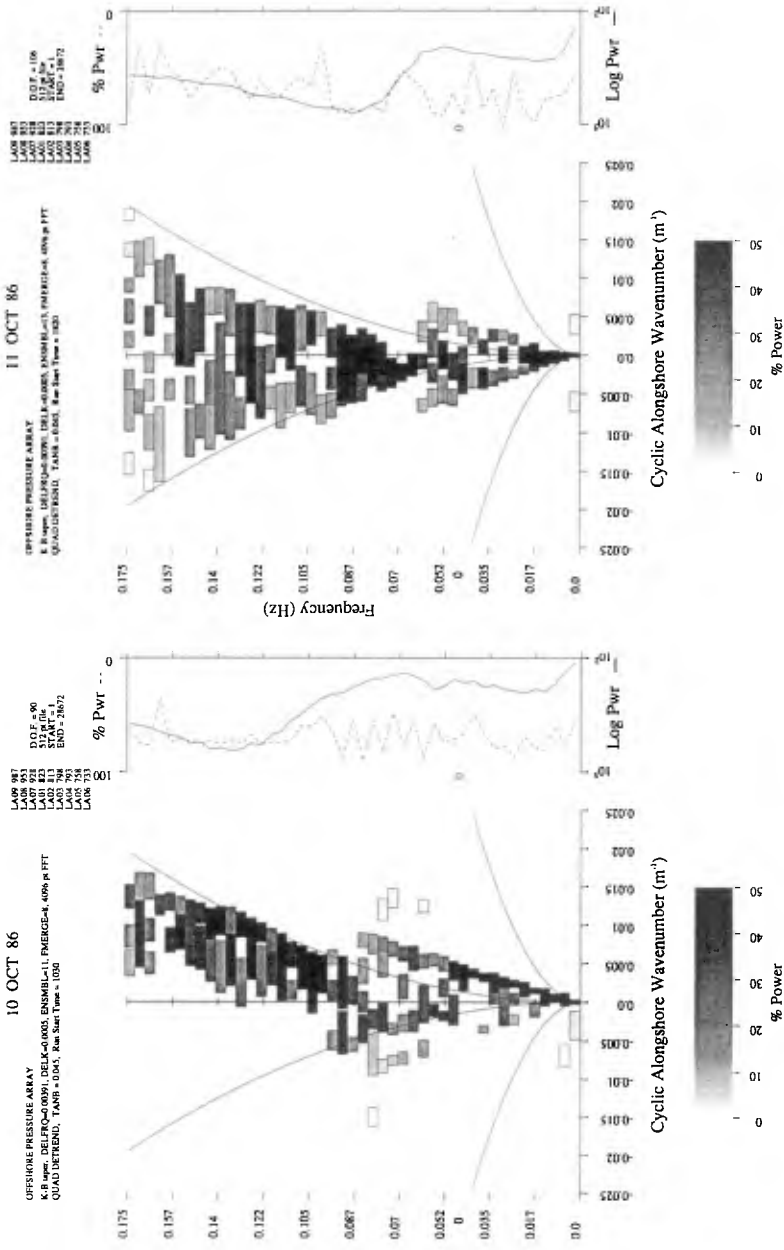


Figure 5. Frequency-alongshore wavenumber spectra from the pressure sensor array in 8 m depth. Positive wavenumbers indicate southward progressive waves. The height of the boxes indicates the frequency bandwidth, the width of the boxes indicates the half-power wavenumber bandwidth. The shading of the boxes indicates the percentage of that frequency band's variance contained in that peak. To the right of each $f-k$ spectrum is the frequency spectrum (solid line) and a representation of the percent of that frequency's variance contained in the identified peaks (dashed line). See text for interpretation of the data.

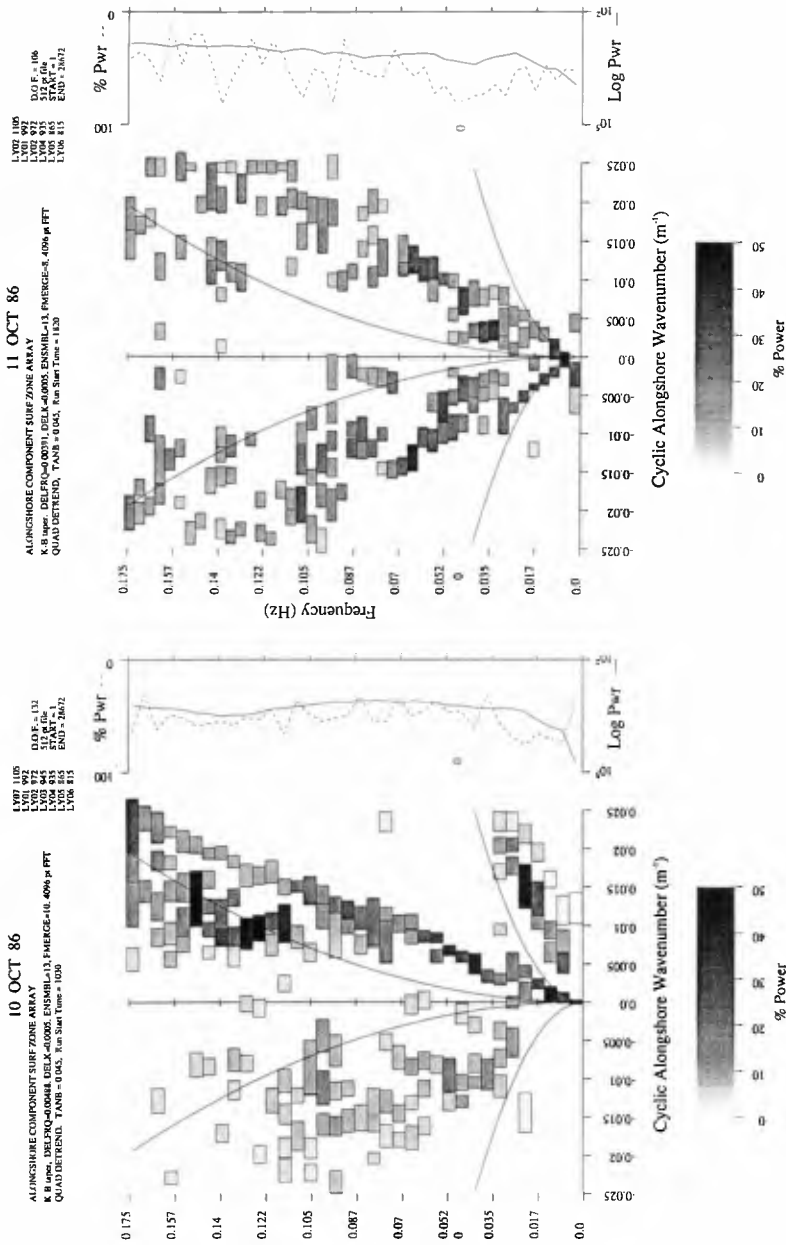


Figure 6. Frequency-wavenumber spectra calculated from the alongshore component of flow measured by the array of current meters in 1.5 m depth.

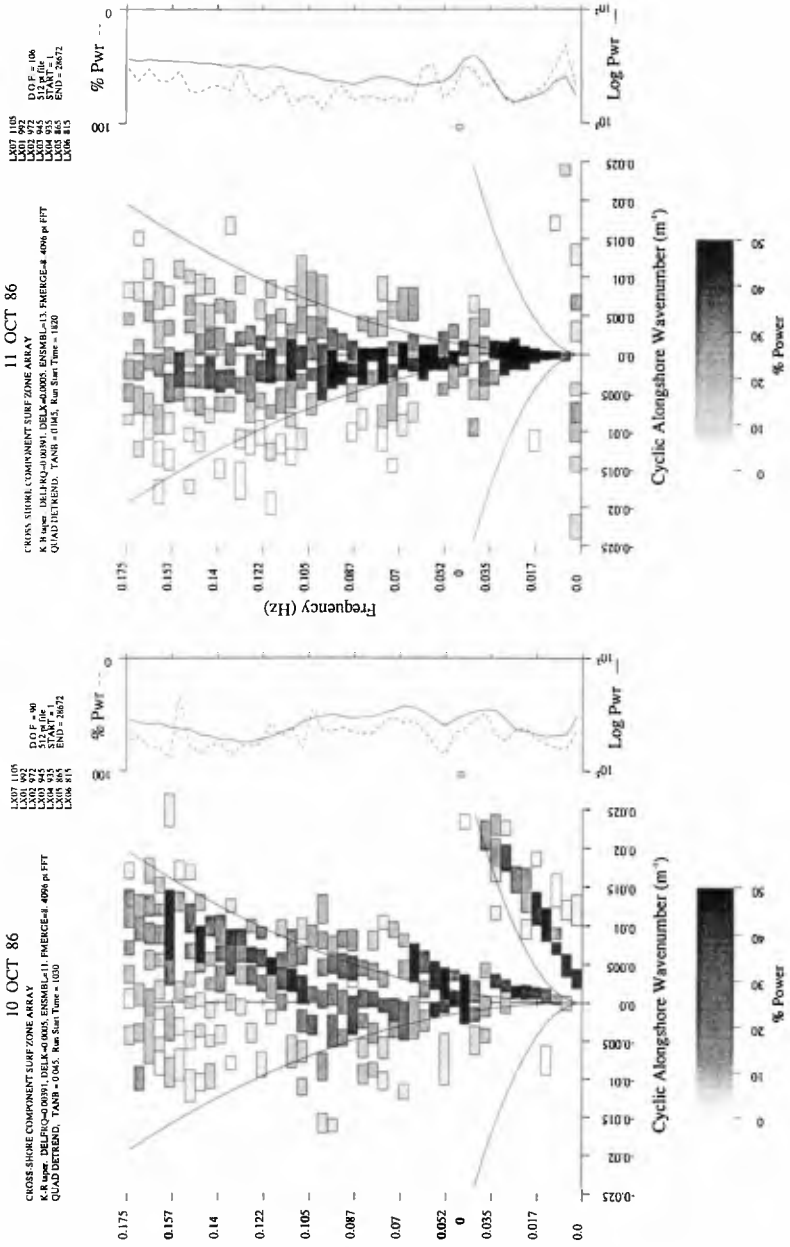


Figure 7. Frequency-wavenumber spectra calculated from the cross-shore component of flow measured by the array of current meters in 1.5 m depth.

other days with similar conditions. The rms infragravity oscillations measured 27 cm/s. The shear wave field was strong (rms oscillation of 28 cm/s) as would be expected in the presence of 160 cm/s mean currents. On the 11th, the infragravity wave field is again dominated by edge waves, but now with nearly equal contributions from the northward and southward progressive modes. The coherent structure of the shear wave band has vanished. The infragravity wave rms alongshore oscillation has remained steady at 29 cm/s while the shear wave rms value has dropped to 21 cm/s.

Figure 7 shows the equivalent spectra calculated using the cross-shore component of flow from the surf-zone sensors. The incident peaks are visible in the frequency spectra, but much less dominant than at the 8 m array (Figure 5). The differences between the low frequency motions on the two days are clear. On the 10th, not only is there a strong shear wave signal (rms oscillation of 38 cm/s), but the infragravity waves are dominated by low mode edge waves with an rms oscillation (as a band) of 36 cm/s. In contrast, on the 11th, the infragravity band is dominated by what appear to be either leaky waves or high mode edge waves. The rms oscillation of the infragravity band has nearly doubled from the 10th to 63 cm/s. As was also the case for the alongshore component of flow, the coherent structure has disappeared from the shear wave band.

While interpretation of the marked increase in the magnitude of cross-shore infragravity oscillations remains preliminary, it is safe to say that it is not due to an increase in the broad band forcing of low mode edge waves on the 11th. Oltman-Shay and Guza (1987) have shown that this should result in a simultaneous increase in the alongshore component of flow. Remembering that the alongshore rms oscillations for the two days were essentially unchanged, the increase in cross-shore oscillations is suspected to be due to an increase in the forcing of leaky waves or high mode edge waves, neither of which contribute greatly to alongshore velocity variance. A detailed study of the modal amplitudes of infragravity waves during this period is forthcoming.

Conclusions

We have used 21 4-hour data runs collected over a wide range of incident wave conditions to quantify the behavior of the alongshore and cross-shore components of wave motion for three different wave types. The incident band oscillations in the surf-zone were not significantly correlated with the offshore wave height, but were strongly correlated with the tide elevation indicating saturation due to depth limited breaking. The infragravity wave rms velocities were significantly correlated with the offshore wave height but the composition of the band appears to depend on the directional nature of the incident wind wave field. Shear waves were observed during times of strong longshore currents, but the magnitude of the current at the surf-zone array of instruments was found to be only a marginal predictor of the rms oscillations of the shear waves.

In addition there is significant evidence that the composition of the low frequency gravity wave field (edge, leaky and bound) changed considerably during the course of the storm. At the beginning of the storm when the incident waves approached the beach obliquely, the rms velocities of both components of flow in the infragravity band were nearly equal. As the angle of wave approach became nearly normal, the rms cross-shore velocity of the infragravity band grew, becoming a factor of two greater than the alongshore velocity.

Acknowledgements

We would like to thank the staff of CERC's Field Research Facility once again for the fine support they provided during the SUPERDUCK experiment. CERC also funded the deployment of the gages and the distribution of the data. The funding for the analysis of the data has been provided from grants to Oregon State University from the National Science Foundation (OCE87-11121) and the Office of Naval Research, Coastal Sciences Program (N00014-87-K0009).

References

- Crowson, R., W. Birkemeier, H. Klein, and H. Miller, 1988, SUPERDUCK near-shore processes experiment: Summary of studies CERC Field Research Facility, *U.S. Army Tech. Report CERC-88-12*.
- Bowen, A.J. and R.A. Holman, 1989, Shear instabilities of the mean longshore current; I. Theory, *J. Geophys. Res.* 94: 18032-18041
- Elgar, S., J. Oltman-Shay, and P. Howd, 1989, Observations of infragravity frequency long waves; I. Coupling to wind waves, *EOS, Trans. Am. Geophys. Union*, 70:1133.
- Guza, R. and E. Thornton, 1985, Observations of surf beat, *J. Geophys. Res.*, 90:3161-3172.
- Guza, R. and A.J. Bowen, 1976, Resonant interactions for waves breaking on a beach, *Proc., 15th ICCE* 560-579.
- Holman, R.A., 1981, Infragravity energy in the surf zone, *J. Geophys. Res.*, 86:6442-6450.
- Howd, P.A., J. Oltman-Shay, and R.A. Holman, accepted, Wave Variance Partitioning in the Trough of a Barred Beach, *J. Geophys. Res.*
- Lippmann, T.C. and R.A. Holman, 1990, The spatial and temporal variability of sand bar morphology, *J. Geophys. Res.*, 95:11575-11590.

- Oltman-Shay, J. and R.T. Guza, 1987, Infragravity wave observations on two California beaches, *J. Physical Oc.*, 17: 644-663.
- Oltman-Shay, J., P.A. Howd, and W.A. Birkemeier, 1989a, Shear instabilities of the mean longshore current; II. Field observations, *J. Geophys. Res.* 94: 18031-18042.
- Oltman-Shay, J., S. Elgar, and P. Howd, 1989b, Observations of infragravity frequency long waves; II. Comparison with a 2-D wave group generation model, *EOS, Trans. Am. Geophys. Union*, 70:1133.
- Pawka, S., 1983, Island shadows in wave directional spectra, *J. Geophys. Res.*, 86:2579-2591.
- Suhayda, J., 1974, Standing waves on beaches, *J. Geophys. Res.* 72: 3065-3071.

CHAPTER 85

THEORY VERSUS EXPERIMENTS IN TWO-DIMENSIONAL SURF BEATS

Hemming A. Schäffer† and Ivar G. Jonsson‡

Abstract

Comparison is made between a deterministic infragravity-wave model and existing laboratory experiments. The theoretical model considers incident bichromatic waves including the effects of the accompanying incident long, bound wave, an oscillating position of the break point, and the intrusion of short-wave grouping into the surf zone, whereas frictional effects are neglected. A measure of the infragravity wave activity is the amplitude of a seaward progressing free, long wave. For this amplitude the qualitative agreement between theoretical results and experiments is excellent. Quantitatively the theory overestimates the infragravity waves by typically 50–100%. This may in part be attributed to the neglect of frictional effects.

1 Introduction

Numerous field experiments have shown that low frequency oscillations (periods of the order of several minutes) can account for a substantial part of the energy in a surf zone. The closer to the coastline, the more this feature is pronounced. These low frequency motions, which have been termed surf beats or infragravity waves have even been reported to exceed the magnitude of the breaking wind waves. It is widely recognized that surf beats are of major importance for the development of longshore bars in the two-dimensional case. Three-dimensional waves at infragravity frequencies account for more complicated ways of sediment transport and changes in coastal morphology.

Usually one distinguishes between the “trapped” and the “leaky” modes, where the trapped modes as opposed to the leaky ones are trapped to the coastline by refraction. In the present paper we confine ourselves to two dimensions so that only the leaky modes are considered. Three-dimensional results will be published elsewhere.

It is well known that groups of short waves induce long (low frequency) bound waves which are phase-locked to the short-wave envelope and travel with the group velocity. These bound waves are known to be a possible source of surf beats. Another effect of the modulation in the short waves is the resulting oscillations of the break point position. This further induces a time-varying

† Danish Hydraulic Institute, Agern Allé 5, DK-2970 Hørsholm, Denmark. The present work was conducted while H. A. Schäffer was a PhD-student at ISVA.

‡ Institute of Hydrodynamics and Hydraulic Engineering (ISVA), Technical University of Denmark, DK-2800 Lyngby, Denmark

set-up which also contributes to the low frequency motion.

A theoretical model which takes both of these effects into account has been developed. In this paper we concentrate on the comparison of the model results with laboratory measurements by Kostense (1984), and the underlying theory is only briefly discussed. A short theoretical description is given in Schäffer et al. (1990), and for a full report on the theory we refer to Schäffer (1990).

2 Mathematical model

The phenomenon of infragravity waves forced by short waves involves two scales in time as well as in space. Typically the timescale of the short waves is $O(10s)$ and of the infragravity waves $O(100s)$. One way to treat this problem is to separate the two scales explicitly as in a WKB-expansion. Here we have used another approach, which is perhaps less stringent, but probably more transparent, physically as well as mathematically. Regardless of the approach the same equations evolve.

From the “narrow-minded” short-wave point of view the infragravity motion is merely a slowly varying current. In comparison with the large length scale of the infragravity wave, the water will be shallow and accordingly the current will be uniform over depth (we neglect bottom friction). Thus we can use the depth-integrated and time-averaged conservation equations of mass and momentum for waves on a slowly varying uniform current, where the time averaging is taken over one short wave period. Upon linearizing these equations, the current can be eliminated to get the equation governing the elevation of the mean water surface $\bar{\zeta}$

$$\frac{\partial}{\partial x} \left(gh \frac{\partial \bar{\zeta}}{\partial x} \right) - \frac{\partial^2 \bar{\zeta}}{\partial t^2} = -\frac{1}{\rho} \frac{\partial^2 S_{xx}}{\partial x^2} \quad (1)$$

(cf. Symonds et al., 1982, Mei and Benmoussa, 1984, and others). Here S_{xx} is the radiation stress associated with the incident short waves

$$\frac{1}{\rho g} S_{xx} = \frac{1}{2} |A|^2 \left\{ \frac{2c_g}{c} - \frac{1}{2} \right\} \quad (2)$$

where A is a complex amplitude allowed to have a slow variation in time as well as in space, c and c_g are phase and group velocities, respectively, h is depth, x is cross-shore coordinate, ρ is density and g is acceleration of gravity. The right hand side of (1) is responsible for the forcing of infragravity waves, and it is important how it is modelled. Thus a description of the radiation stress or essentially of the variation of A is needed. Given conservative circumstances of no dissipation, the forcing outside the surf zone follows from conservation of energy. After breaking sets in, assumptions concerning the variation of the break point position and the decay of the short waves are required.

2.1 The breaking of incident waves

The model used for the breaking and shoreward decay of modulated incident waves is a combination of two simple, but basically different models.

The first one is obtained by assuming that the short-wave modulation is totally destroyed by the breaking, so that the wave height in the surf zone is solely dependent on the local water depth. This implies an oscillation of the break point position which is essentially harmonic in time. This model was used

by Symonds et al. (1982) to study the effect of a time-varying position of the break point, neglecting the incident bound wave.

The second model postulates a fixed initial break point position letting the short-wave modulation be fully transmitted into the surf zone. This model was used by Schäffer and Svendsen (1988) when studying the nearshore behaviour of an incident long bound wave.

A hybrid model is now obtained by combining these two. After some manipulations the new model can be shown to correspond to a time-varying breaker depth given by

$$h_b(t) = \frac{\bar{a}_b}{\gamma_0} (1 + \kappa \mu \delta \cos \omega t + O(\delta^2)) \quad (3)$$

where $\delta = a^{(2)}/a^{(1)}$ is a small modulation parameter ($a^{(1)}$ and $a^{(2)}$ are the amplitudes of the two waves constituting the wave groups), \bar{a}_b is the mean amplitude at the mean break point, γ_0 is the amplitude to depth ratio for vanishing short-wave modulation ($\delta = 0$) and κ is a parameter at our disposal. Furthermore, μ is a factor which accounts for the short-wave shoaling within the region where the initial breaking takes place. This shoaling effect was disregarded by Symonds et al. (1982), Schäffer and Svendsen (1988), and Schäffer et al. (1990) corresponding to the assumption of $\mu \equiv 1$. However, we may as well include it, and after some manipulations we obtain

$$\mu \equiv \frac{1}{1 + \nu} \quad (4)$$

where

$$\begin{aligned} \nu &= - \left[h \sqrt{c_g} \frac{d}{dh} \frac{1}{\sqrt{c_g}} \right]_{h=\bar{h}_b} \\ &= \left[\frac{1}{2} \frac{h}{c_g} \frac{dc_g}{dh} \right]_{h=\bar{h}_b} \end{aligned} \quad (5)$$

so that $0 \lesssim \nu \leq \frac{1}{4}$ and thus $\frac{4}{5} \lesssim \mu \leq 1$. According to (5) ν can in principle be negative, but since this corresponds to breaking at intermediate water depth it will not happen in practice. The above two models appear for $\kappa = 1$ (short-wave modulation destroyed) and $\kappa = 0$ (fixed initial break point), respectively. The value of κ reflects the extent to which the modulation of the incident waves is "used" to produce an oscillating break point position and consequently the "amount" of grouping which is transmitted into the surf zone. On the basis on experimental results for monochromatic waves collected by Goda (1970), we have estimated κ to be in the range $1 < \kappa < 1.2$. From the empirical relations given by Hansen (1990), κ appears as a universal constant (i.e. independent of the steepness of the incident short waves) and we get $\kappa \equiv 1.09$, see Schäffer (1990). Results for γ_0 versus the deep water short-wave steepness $\hat{a}_\infty \equiv a_\infty k_\infty$ are adapted from Goda (1970) and Hansen (1990), and they are depicted in Fig. 1 for various beach slopes h_x . An estimate of the deviation from unity of the parameter κ can be shown to equal minus the slope of these curves in the double logarithmic plot, i.e. $\kappa = 1 - d(\log \gamma_0)/d(\log \hat{a}_\infty)$.

That $\kappa > 1$ actually means that the higher waves break so early that they end up being the lower ones inside the surf zone.

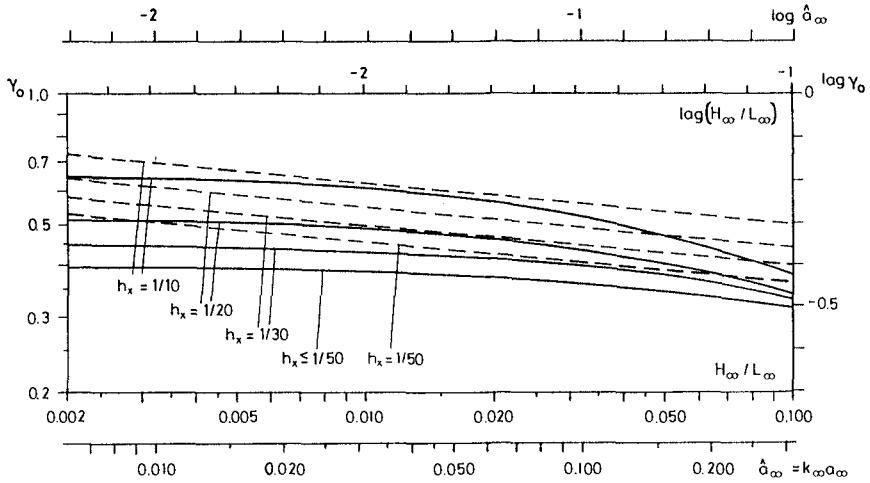


Figure 1 Index $\gamma_0 \equiv a_b/h_b$ versus deep water steepness \hat{a}_∞ for different bottom slopes $h_x = \tan \beta$. Results for monochromatic waves adapted from Goda (1970) (—) and from Hansen (1990) (---).

3 Method of solution

We restrict ourselves to a plane sloping beach $h = h_x x$ connected with an offshore shelf, and consider only periodic solutions. Fourier expansions of S_{xx} and ζ turn (1) into ordinary differential equations for the different regions, which are solved by the method of variation of parameters. Solutions of different regions are matched using standard conservation considerations with regard to mass, momentum, and energy. The boundary conditions are those of finite shoreline amplitudes and absence of incident free long waves — not to be confused with the incident bound long wave which is an important part of the solution.

Special action is taken in the region of initial breaking i.e. within the inner and outer limits of the initial break point. In this region substantial forcing of infragravity wave motion takes place as first shown by Symonds et al. (1982). The solution is developed to the leading order in the short-wave modulation parameter δ . To this order it can be shown that infragravity waves are only forced at the fundamental group frequency so that no higher harmonics appear. Furthermore, a large gradient of the infragravity wave surface elevation over the region of initial breaking is for convenience concentrated in a discontinuity at the mean break point depth \bar{h}_b as can be seen in the example shown in Fig. 2.

For a detailed description of the mathematical development we refer to Schäffer (1990).

4 Results and comparison with experiments

A sample of the model results is shown in Fig. 2. The figure shows the envelope of the infragravity wave (not to be confused with the envelope of the incident

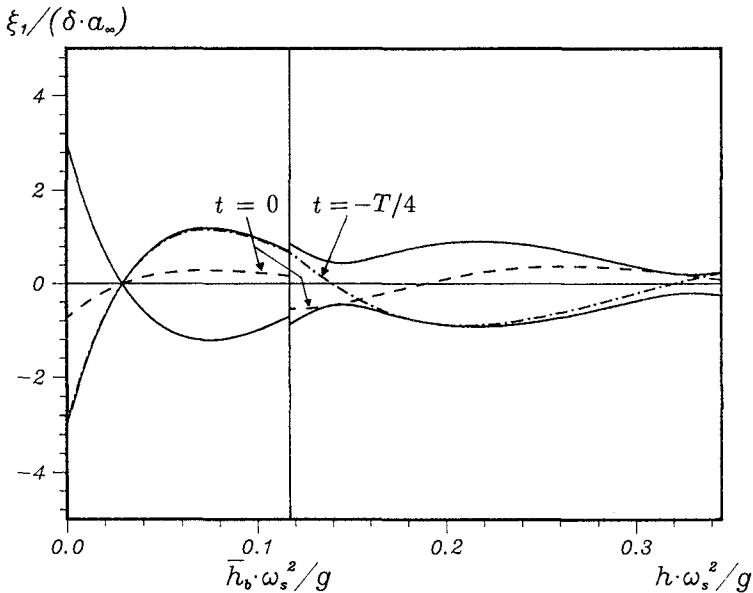


Figure 2 Sample result for $\kappa = 1.1$ of the spatial variation of the infra-gravity wave elevation (normalized by the modulation of the short wave amplitude in deep water) versus depth (normalized by the (inverse value of the) deep water short-wave number ω_s^2/g). T is the group period, and the mean depth at the break point is \bar{h}_b . The abscissa is limited by the depth of the offshore shelf. The figure corresponds to the “•” at $\chi = 5.8$ in Fig. 6a.

short waves) and the elevation at $t = 0, -T/4$ where T is the group period. The discontinuity at the mean break point position at $t = 0$ is a consequence of the substantial forcing around the mean break point position mentioned above, together with a consistent development of the solution to the leading order in the short-wave modulation parameter. The latter can be shown to be consistent with letting the spatial extent of the region of initial breaking tend toward zero leaving a discontinuity behind.

The solution shows a gradual change from an almost standing wave in the vicinity of the shoreline to an almost purely seaward progressive wave some distance offshore.

A series of high quality laboratory experiments on long waves forced by short-wave groups, conducted at the Delft Hydraulics Laboratory, were reported by Kostense in 1984. Fortunately his experimental setup exactly meets the assumptions behind the present theoretical model. This applies to the bathymetry as well as the incident short-wave groups, and his measurements include the respective amplitudes of the incident, bound, long wave and the seaward progressive, free, long wave. The movement of the wave-maker paddle included second-order generation as well as active absorption of free, long waves returning to the wave maker. Consequently free, long, standing waves arising from the

Series	$a_o^{(1)}$	$a_o^{(2)}$	$\omega^{(1)}$	$\omega^{(2)}$	ω	χ
	(cm)	(cm)	(rad/s)	(rad/s)	(rad/s)	
A-1	5.5	1.1	3.062	2.145	0.917	5.81
A-2	5.5	1.1	3.062	2.296	0.766	4.05
A-3	5.5	1.1	3.065	2.456	0.609	2.55
A-4	5.5	1.1	3.077	2.618	0.459	1.44
A-5	5.5	1.1	3.063	2.755	0.308	0.65
B-1	5.5	1.1	4.295	3.372	0.923	5.57
B-2	5.5	1.1	4.065	3.293	0.772	3.93
B-3	5.5	1.1	4.070	3.455	0.615	2.48
B-4	5.5	1.1	4.071	3.609	0.462	1.39
B-5	5.5	1.1	4.070	3.762	0.308	0.62
C-1	8.0	1.6	4.294	3.522	0.772	5.33
C-2	5.5	1.1	4.065	3.293	0.772	3.93
C-3	3.5	0.7	4.295	3.523	0.772	2.65
D-1	5.5	1.1	3.065	2.456	0.609	2.55
D-2	3.5	0.7	3.065	2.456	0.609	1.76
D-3	3.0	0.6	3.065	2.456	0.609	1.55

Table 1 Short-wave characteristics for the experiments by Kostense (1984). The listed χ -values (based on $\gamma_o = 0.4$) differ a little from the ones used by Kostense, due to his neglect of short-wave shoaling.

reflection of free, long waves at the paddle were avoided, and the measurements provide an excellent test of the present theory.

Five series of experiments are reported, and the first four of these correspond to a short-wave modulation parameter of $\delta = 0.2$. This meets our assumptions of $\delta \ll 1$, considering the limited accuracy expected from the theoretical model due to the complicated physical mechanisms in question. The characteristics of the incident short waves for these four series (A–D) is given in Table 1. Here ($a_o^{(1)}, a_o^{(2)}$) and ($\omega^{(1)}, \omega^{(2)}$) are the amplitudes (over the shelf) and angular frequencies of the two wave trains, ω is the difference frequency (group frequency), and χ is a parameter defined by $\chi \equiv \omega^2 \bar{x}_b / (g h_x)$, \bar{x}_b being the position of the mean break point ($x = 0$ at the shoreline). In the fifth experimental run δ equals 0.8, and no comparison is made.

The relevant parameters describing the geometry of the experimental facility are the depth $h_o = 0.5m$ on the shelf and the beach slope $\bar{h}_x = 0.05$.

In series A and B the short-wave amplitudes are kept constant while the difference frequency ω is changed. The resulting amplitude of the incident, bound, long wave $|\xi_b|$ is compared with the theoretical values in Fig. 3a. The excellent agreement is indeed a manifestation of the thoroughness of the experiments. The theory of the bound, long wave is due to Longuet-Higgins and Stewart (1962, 1964). Kostense presents a comparison similar to that of Fig. 3 based on an equivalent formulation given by Ottesen Hansen (1978). Fig. 3b shows $|\xi_b|$ for series C and D for which the respective difference frequencies are

kept constant, while the amplitudes of the short-wave components are changed. Again the theory and the measurements compare very well.

We now turn to the results for the amplitude of the outgoing, free, long wave $|\xi_f|$, the generation of which is far more complex. The physical mechanisms of generation involve complicated surf zone dynamics, and thus the results of the mathematical model can hardly be expected to match the measurements as closely as the results for the incident bound, long wave. One aspect of the model can be expected to give a one-sided error, and that is the neglect of frictional effects. Thus, everything else being equal we can expect the model to overestimate the long-wave activity.

Fig. 4 compares $|\xi_f|$ (at the shelf) from the theory and measurements, and the qualitative agreement is seen to be excellent. Furthermore, we recognize the expected overestimation, which for most runs is approximately 50–100%. At least part of this mismatch may be attributed to the neglect of friction.

The results for $|\xi_f|$ are repeated in Fig. 5 with $\chi \equiv \omega^2 \bar{x}_b / (gh_x)$ as the abscissa. Note that the extraordinary trend of a straight line for the measurements of series D is reproduced by the theory. The measurements of series A, B, and C all show a convex trend as also given by the theoretical results.

In order to compare with the theory of Symonds et al. (1982) we have used Green's law to assign the computed as well as the measured values of $|\xi_f|$ to their values $|\xi_f(\bar{x}_b)|$ at the break point. Furthermore, $|\xi_f(\bar{x}_b)|$ was normalized by the variation about the mean of the stationary shoreline set-up for infinitely long groups, denoted $\Delta\zeta$. The results are shown in Fig. 6a together with the theoretical curve of Symonds et al., which is seen to be inadequate. Here $(\gamma_o, \kappa) = (0.4, 1.0)$ was used. Fig. 6b is equivalent to Fig. 6a, only the results are based on the dashed curve for $h_x = 1/20$ in Fig. 1, which gives γ_o -values ranging from 0.47 to 0.53 and $\kappa = 1.09$. The general picture is seen to be the same. (Note that the compression of the abscissa χ in Fig. 6b as compared with Fig. 6a (which is due to the larger γ_o -values used) affects the measured and computed results equally much, and it has nothing to do with how well they compare).

Fig. 7a is adapted from Kostense, and it shows $|\xi_f|$ versus $|\xi_b|$. As noted by Kostense, the correlation is very poor (as could be expected). This also applies to our theoretical results as shown in Fig. 7b.

The theoretical $|\xi_f|$ -values of this section were calculated with the assumptions of full long-wave reflection from the coastline. Corrections for partial reflection can be introduced by requiring the maximum shoreline amplitude of the elevation of the standing infragravity wave to be $|\xi_1(0)|_{max} = gh_x^2 / \omega^2$. This limit is valid for a free standing long wave on a plane sloping beach as indicated by the solution of the nonlinear shallow water equations by Carrier and Greenspan (1958) (see Meyer and Taylor, 1972). However, when these modifications are incorporated, the only correction is a 10% reduction of theoretical $|\xi_f|$ -value in the first run of series A, the rest of the runs being unchanged. Thus no conclusions are changed.

Kostense mentions three possible reasons for the limited validity of the theory by Symonds et al. These are the neglect of the incident, long, bound wave, the preclusion of short-wave grouping inside the surf zone, and the assumption of full long-wave reflection at the shoreline. The present model accounts for all these effects, and particularly inclusion of the incident, long, bound wave is of great importance. The next step towards a correct mathematical model should be the inclusion of frictional effects such as turbulence in the surf zone and bottom friction.

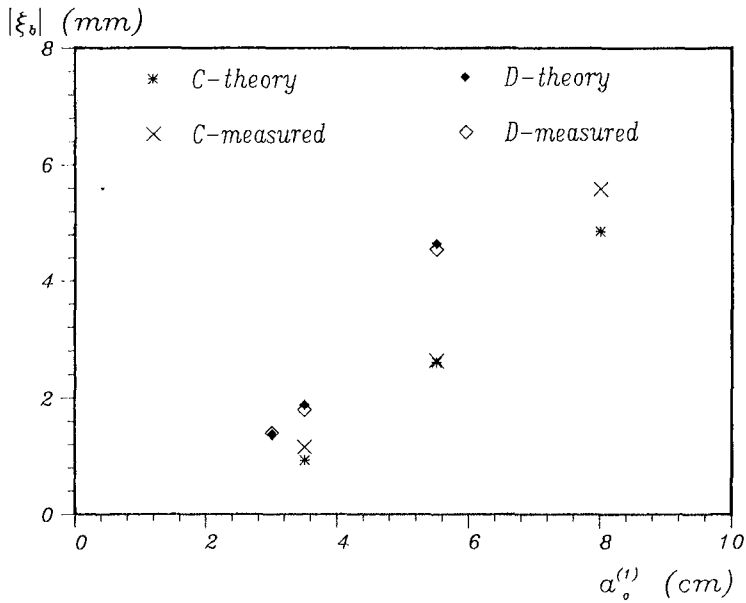
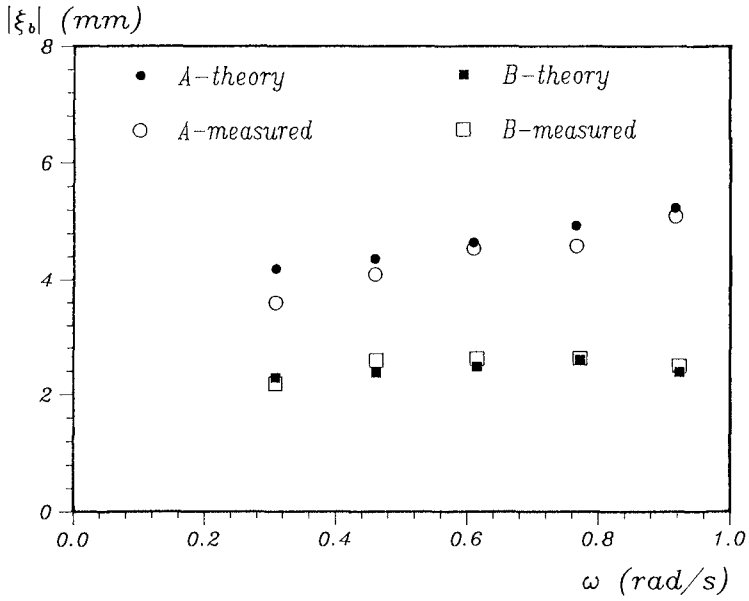


Figure 3 Amplitude of incident bound, long wave $|\xi_b|$ versus (a) the difference frequency ω (series A and B), and (b) the amplitude of the largest short-wave component $\alpha_o^{(1)}$ (series C and D).

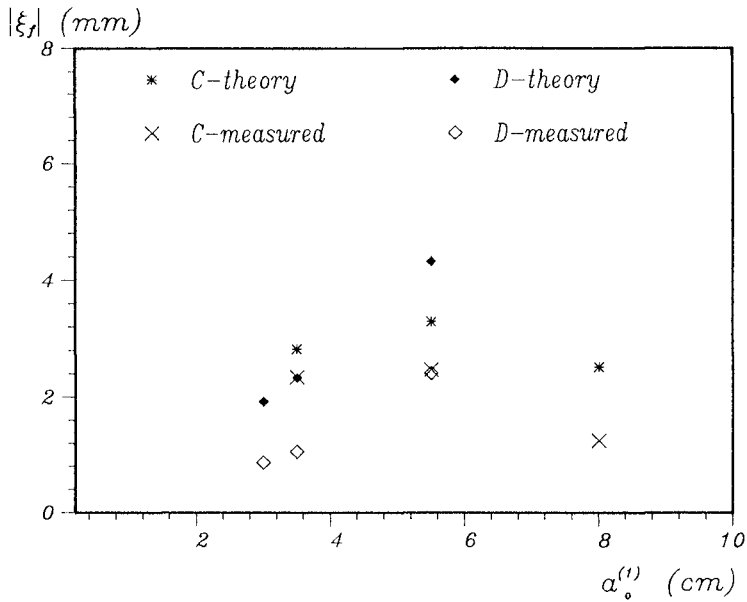
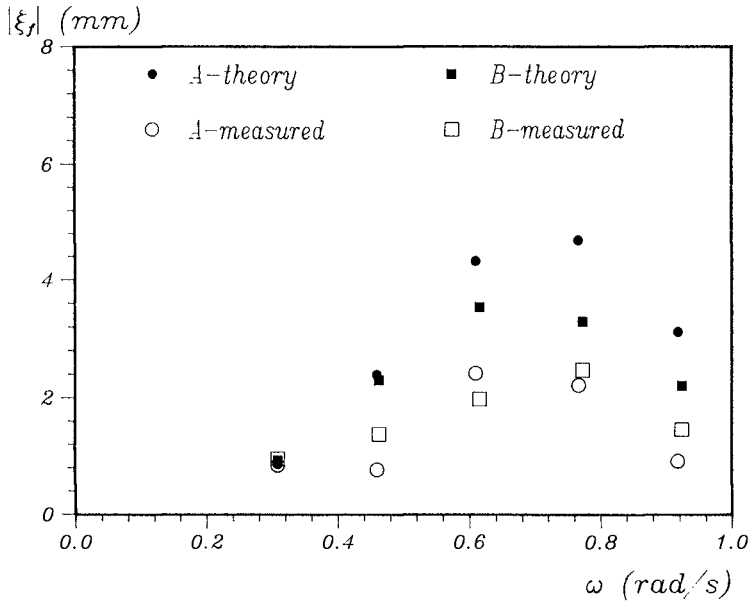


Figure 4 Amplitude of outgoing free, long wave $|\xi_f|$ versus (a) the difference frequency ω (series A and B), and (b) the amplitude of the largest short-wave component $\alpha_o^{(1)}$ (series C and D). $(\gamma_o, \kappa) = (0.4, 1.0)$.

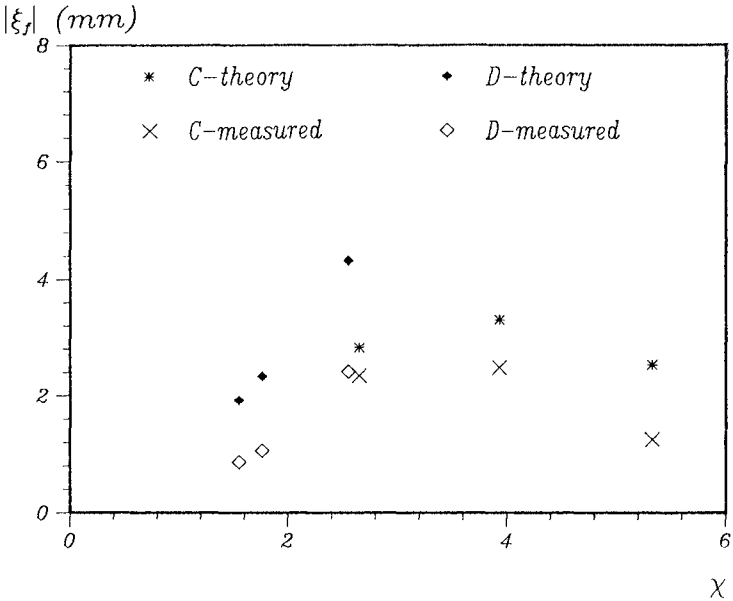
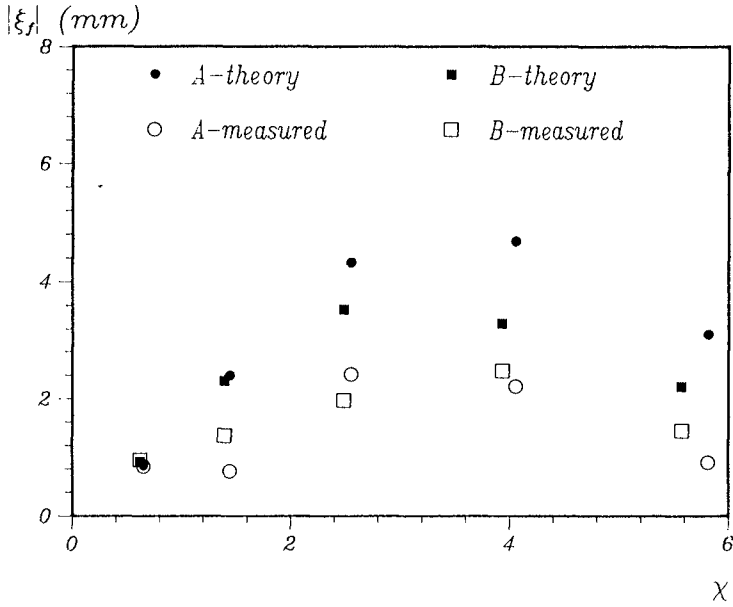


Figure 5 Amplitude of outgoing free, long wave $|\xi_f|$ versus χ for (a) series A and B, and (b) series C and D. $(\gamma_o, \kappa) = (0.4, 1.0)$.

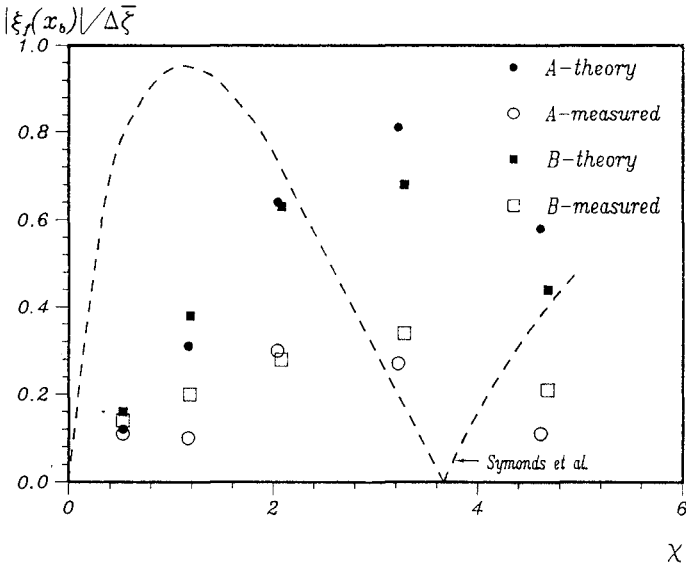
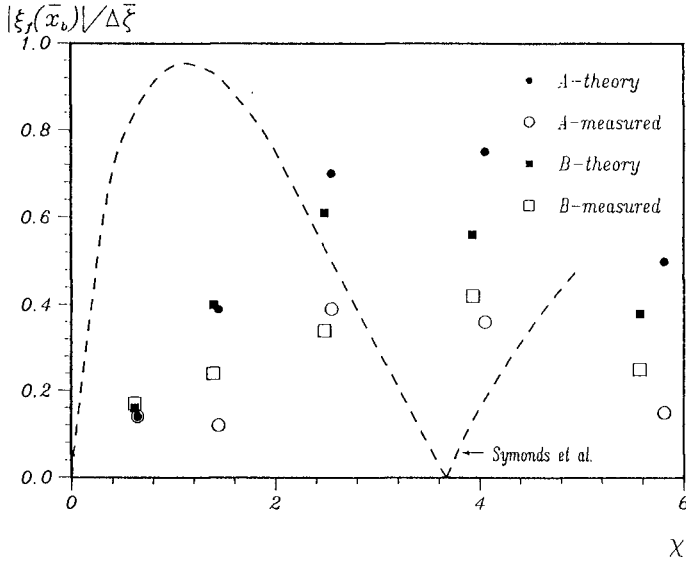


Figure 6 Normalized amplitude of outgoing free, long wave $|\xi_f(\bar{x}_b)|/\Delta\bar{\xi}$ at the mean initial break point position versus χ for series A, B, C, and D. Comparison with the theory of Symonds et al. (1982) (---). (a) $(\gamma_o, \kappa) = (0.4, 1.0)$ and (b) $(\gamma_o, \kappa) = (0.47-0.53, 1.09)$ as given by the dashed curve for $h_x = 1/20$ in Fig. 1.

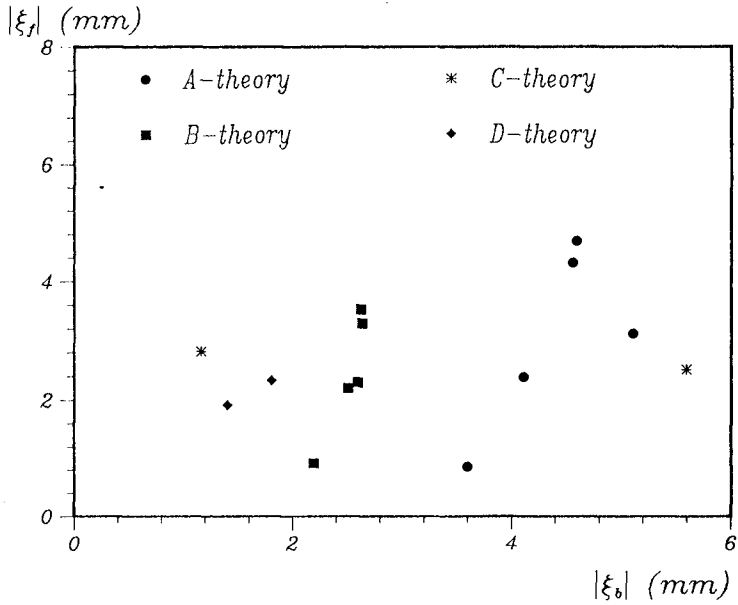
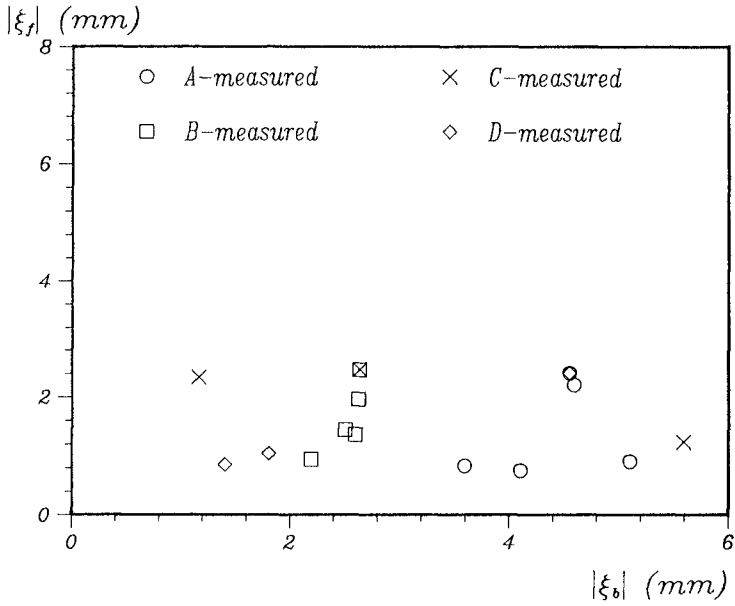


Figure 7 Amplitude of outgoing free, long wave $|\xi_f|$ versus amplitude of incident, bound, long wave $|\xi_b|$ for series A, B, C, and D. (a) measurements, and (b) theory for $(\gamma_o, \kappa) = (0.4, 1.0)$.

REFERENCES

- Carrier, C. F. and H. P. Greenspan (1958). Water waves of finite amplitude on a sloping beach. *J. Fluid Mech.*, **4**, 97-109.
- Goda, Y. (1970). A synthesis on breaker indices. *Trans. Jap. Soc. Civ. Engrs.*, **2**, Part 2, 227-230.
- Hansen, J. Buhr (1990). Periodic waves in the surf zone: Analysis of experimental data. *Coastal Eng.*, **14**, 19-41.
- Kostense, J. K. (1984). Measurements of surf beat and set-down beneath wave groups. *Proc. 19th Int. Conf. Coastal Eng.*, Houston, Texas, 1984, ASCE, New York, 1985, **1**, 724-40.
- Longuet-Higgins, M. S. and R. W. Stewart (1962). Radiation stress and mass transport in gravity waves with application to 'surf beats'. *J. Fluid Mech.*, **13**, 481-504.
- Longuet-Higgins, M. S. and R. W. Stewart (1964). Radiation stresses in water waves: A physical discussion with applications. *Deep Sea Research*, **11**, 529-562.
- Mei, C. C. and C. Benmoussa (1984). Long waves induced by short-wave groups over an uneven bottom. *J. Fluid Mech.*, **139**, 219-35.
- Meyer, R. E. and A. D. Taylor (1972). Run-up on beaches. In *Waves on Beaches*, R. E. Meyer (ed.), Academic Press, New York, 357-412.
- Ottesen Hansen, N.-E. (1978). Long period waves in natural wave trains. *Prog. Rep.* **46**, Inst. Hydrodyn. Hydr. Eng. (ISVA), Tech. Univ. Denmark, 13-24.
- Schäffer, H. A. and I. A. Svendsen (1988). Surf beat generation on a mild slope beach. *Proc. 21st Int. Conf. Coastal Eng.*, Malaga, Spain, 1988, ASCE, New York, 1989, **2**, 1058-1072.
- Schäffer, H. A. (1990). Infragravity water waves induced by short-wave groups. Series paper **50**, Inst. Hydrodyn. Hydr. Eng. (ISVA), Tech. Univ. Denmark, 168 pp.
- Schäffer, H. A., I. G. Jonsson, and I. A. Svendsen (1990). Free and forced cross-shore long waves. In *Water Wave Kinematics*, A. Tørum and O. T. Gudmestad (eds.), Kluwer Academic Publishers, Dordrecht, 367-385.
- Symonds, G., G. A. Huntley and A. J. Bowen (1982). Two dimensional surf beat: Long wave generation by a time-varying break point. *J. Geophys. Res.*, **87**, C1, 492-498.

CHAPTER 86

BOTTOM PRESSURES DUE TO LONG WAVES: LABORATORY AND FIELD MEASUREMENTS

Fredric Raichlen¹, Jerald D. Ramsden², and James R. Walker³

1. INTRODUCTION

A convenient and attractive way of determining the nearshore wave environment is through the use of bottom (or near bottom) pressure measurements. However, it has been realized for some time that care must be taken in interpreting such pressure measurements and relating them to the local waves amplitudes in the region where the waves become highly nonlinear and shoal near the shore, e.g., see Grace (1978), Guza and Thornton (1980), Bishop and Donelan (1987), Lee and Wang (1984), Bodge and Dean (1984), and Nielsen (1989) among others. This study is directed to questions raised in connection with the interpretation of the water surface time-history from bottom pressure measurements for highly nonlinear long waves. In particular the waves which were primarily of interest were large solitary and cnoidal waves, i.e., non-periodic and periodic long waves.

The motivation for this work was the requirement to document the water surface-time histories of near breaking waves, nearly solitary in shape, with heights up to 2 m in a large fresh water wave basin. Wave staffs, either capacitance or resistance types, were not readily available for these measurements. In place of this technique, video recordings were made of the water surface at the location of surveyor's staff gages, but data reduction of these video recordings, except for a few cases, was estimated to be excessively time consuming. Hence, pressure transducers mounted near the bottom were installed at the wave staff locations to obtain simultaneous measurements which could be related to the variation of the water surface elevation with time.

To assist in defining the corrections to be used to convert the pressure measurements obtained in the large wave basin to wave heights, an experimental study in the laboratory and an analytical study were undertaken using solitary and cnoidal waves. For solitary waves pressure correction factors based on linear wave theory were not adequate to determine the wave amplitudes from the pressure measurements. Therefore, the correction factors were obtained first from theories

¹ Prof. of Civil Engr., W.M.Keck Laboratory of Hydraulics and Water Resources, California Institute of Technology, Pasadena, CA 91125, USA

² Graduate Student, W.M.Keck Laboratory of Hydraulics and Water Resources, California Institute of Technology, Pasadena, CA 91125, USA

³ Vice President, Moffatt & Nichol, Engineers, P.O.Box 7707, Long Beach, CA 90807, USA

accurate to the second and third approximations as presented by Grimshaw (1971) and given in slightly different form by Fenton (1972). The pressure correction factors for nonlinear periodic long waves were obtained using stream function theory as presented by Dean (1965,1974), and higher order cnoidal wave theories presented by Isobe, Nishimura, and Horikawa (1978) and summarized by Horikawa (1988). The approach of Dean(1974) also was extended for use with solitary waves. This paper will compare the nonlinear theories mentioned for solitary and cnoidal waves to the results of laboratory experiments in addition to the limited field experiments conducted in a large fresh-water wave facility. Some discussion will be given herein regarding the use of pressure transducers for dynamic pressure measurements; this will be presented in Section 3.

As a convenience to the reader, expressions for the solitary wave from Fenton (1972) which are accurate through the third order are presented in this section; these will be compared with experimental results. The wave train is stationary in the x,y plane with the origin of the coordinates at a point on the bottom; x is measured in the direction of wave propagation. The amplitude of the solitary wave can be expressed as:

$$\eta = 1 + \epsilon s^2 - \frac{3}{4} \epsilon^2 s^2 t^2 + \epsilon^3 \left(\frac{5}{8} s^2 t^2 - \frac{101}{80} s^4 t^2 \right) + 0(\epsilon^4) \quad (1)$$

where η is the wave amplitude normalized with the depth, h , ϵ is the ratio of wave height to depth, H/h , $s = \text{sech } \alpha x$, $t = \tanh \alpha x$, and:

$$\alpha = \left(\frac{3}{4} \epsilon \right)^{1/2} \left(1 - \frac{5}{8} \epsilon + \frac{71}{128} \epsilon^2 \right) + 0(\epsilon^{7/2}) \quad (2)$$

The pressure measured on the bottom can be written as:

$$\frac{p}{\gamma h} = 1 + \epsilon s^2 + \epsilon^2 \left(\frac{3}{4} s^2 - \frac{3}{2} s^4 \right) + \epsilon^3 \left(-\frac{1}{2} s^2 - \frac{19}{20} s^4 + \frac{11}{5} s^6 \right) + 0(\epsilon^4) \quad (3)$$

where p is the total bottom pressure and γ is the specific weight of the fluid. The ratio of the wave height to the dynamic pressure head under the wave, accurate to second order, can be obtained from Eq 3 as:

$$\frac{H}{p_d / \gamma} = \frac{1}{1 - \frac{3}{4} \epsilon} \quad (4)$$

and to third order also from Eq 3 as:

$$\frac{H}{p_d / \gamma} = \frac{1}{1 - \frac{3}{4} \epsilon + \frac{3}{4} \epsilon^2} \quad (5)$$

For convenience, in the following, the subscript used in the dynamic pressure, p_d , will be dropped and the dynamic pressure will be denoted simply as: p . Experimental data obtained in a wave tank will be compared to Eqs. 4 and 5.

For the long periodic waves, cnoidal wave theory and stream function theory were used to describe the water surface-time history and the variation with time of the dynamic pressure. Due to the complexity of the resulting expressions, they will not be presented here. In lieu of that, the interested reader is referred to Horikawa (1988) and Dean (1974) for a presentation of the cnoidal wave theory and the stream function theory, respectively.

2. EXPERIMENTAL EQUIPMENT AND PROCEDURES

The laboratory experiments were conducted in a wave tank which is 15.24 m long, 0.38 m wide, and 0.61 m deep, with glass walls throughout and a programmable bulkhead wave generator located at one end. The trajectory of the wave generator was determined from the method described by Goring and Raichlen (1980). In this approach, used for long waves, the position of the vertical bulkhead with time is based on the condition that the velocity of the plate must be equal to the depthwise average of the water particle velocity under the wave at that instant. Thus, the plate trajectory includes nonlinear aspects of wave generation. Voltage-time histories were constructed with this approach and used in the electro-hydraulic servo system of the wave generator for both solitary and cnoidal waves. Resistance wave gages were used to determine the water surface-time history of the wave.

Pressures were measured in the laboratory using a variable reluctance pressure transducer (Pace Model P7D) with a pressure sensing diaphragm which was 0.0267 cm thick and 2.54 cm in diameter. The transducer pressure port was connected directly to the bottom of the wave tank by a 5.28 cm long and 0.46 cm inside diameter brass tube. In unsteady pressure measurements care must be taken to obtain as high a natural frequency of the instrument as is possible relative to the frequency content of the pressure signal while still maintaining adequate sensitivity to insure accuracy. Since air entrainment in a water filled pressure transducer can significantly lower its natural frequency, the pressure gage was filled carefully with water by flushing it for a substantial period of time. An analysis presented by Ippen and Raichlen (1957) showed that the internal dimensions of the tube which connected the transducer to the pressure source could have an important effect on the natural frequency of the gage. By careful attention to this feature of the gage-wave tank connection and to air entrainment, a measured natural frequency of the transducer of about 70 hz was attained.

As implied above, it is not the natural frequency of the gage alone which is important, but the magnitude of the natural frequency of the gage **relative** to the maximum frequency of the important portion of the pressure signal, (or the incident wave). It can be shown that the amplitude spectrum of a solitary wave when analyzed as a linear signal is:

$$\frac{S(\omega)}{S(0)} = \frac{\xi\omega}{\sinh \xi\omega} \quad (6)$$

where:

$$\xi = \frac{\pi}{\sqrt{3}} \sqrt{\frac{h}{g}} \frac{1}{\sqrt{\frac{H}{h} \left(1 + \frac{H}{h}\right)}}$$

and $S(\omega)$ is the amplitude of the frequency component ω , H is the wave height, and h is the water depth, see, e.g., Synolakis (1986). For the wave heights and water depths used in the laboratory experiments, the frequency at which $S(\omega)$ has decreased to about 1% of its value at zero frequency, i.e., $S(\omega)/S(0) = 0.01$, is about 4 hz. Thus, the natural frequency of the gage was significantly greater than the important frequencies in the wave. This resulted in relatively undistorted measurements.

Measurements of water waves were to be made in the field in a large fresh

water wave basin which consists of a wave channel 130 feet wide and 180 feet long with depths varying from 8 feet to approximately 5 feet, opening into a larger basin where the depth decreased uniformly to zero. The latter has a width of about 500 feet and a length in the direction of wave propagation of about 250 feet. The depth variations in the wave channel were as follows: a constant 8 ft depth extending 15 ft from the wave generator, followed by a 40 ft section with a 4.3% slope where the depth decreases from 8 ft to 6.28 ft, followed by 72 ft of constant depth, with the remaining 53 ft of the wave channel having a bottom slope of 2.2% reaching a final depth of 5.11 ft. Waves are generated at one end of the 130 foot wide channel by releasing a fixed volume of water into the channel during a short time interval.

Wave measurements were conducted at three locations in the wave channel; the location which is of interest in this study is in the constant depth region, 6.28 ft deep, about 90 ft from the wave generator. Thus, the position for which the wave measurements will be discussed here was about 35 ft, i.e., nearly six depths, from the beginning of the constant depth section. A pressure transducer was attached to the tripod at a distance from the bottom equal to 0.317 times the depth ($y/h = 0.317$). The pressure gage (Senso-Metric semiconductor pressure transducer Model SP91) had a natural frequency in air of approximately 30 KHz. For a near-breaking solitary wave in this region of the wave channel, 99% of the energy would be at frequencies less than approximately 2 Hz. Although the natural frequency of the transducer in water would be less than in air, little dynamic distortion would be expected using this gage. Simultaneous with the pressure measurements, video recordings were made of the wave as it passed the wave staff. In addition, visual observations were taken of the height of the first major wave as it propagated past the wave staff. In Section 3 theoretical results will be compared to the pressure measurements using the visual observations of the height of the first wave as it propagated past the pressure transducer.

3. RESULTS AND DISCUSSION OF RESULTS

Several theories for long waves will be compared to experimental results obtained in the laboratory and in the field. The variation of both the pressures and the amplitude-time histories of these waves will be presented.

It is useful, first, to look in a general way at the influence of non-linearities and vertical accelerations, i.e., frequency dispersion, on the pressures under solitary waves. (It should be remembered that if linear wave theory were applied to long waves such as solitary waves, the pressures under the waves would be distributed hydrostatically.) Evidence of these effects is shown in a qualitative fashion in Fig. 1. This three-dimensional plot was obtained from Eq. 3 and shows the variation of the wave amplitude normalized by the dynamic pressure head on the bottom, as a function of relative wave height and of relative distance measured from the crest for a solitary wave. The abscissal range of relative wave height is: $0 < H/h < 0.65$. In the ordinate, for convenience, only the value: $\eta/(p/\gamma) = 1$ is indicated. This corresponds to hydrostatic pressure conditions and it is seen to apply only for small relative wave heights independent of location, x/h . However, as the relative wave height increases, the effects of nonlinearities and vertical accelerations become apparent, and linear theory, i.e., a hydrostatic pressure distribution under the wave, is not applicable. For example, at $H/h = 0.65$, under the crest, the dynamic pressure head is less than the wave amplitude. Conversely, at $x/h \approx 2$, the dynamic pressure head is greater than the amplitude. If care were not taken in interpreting the pressure measurements properly for such large waves, the wave height would be significantly under-

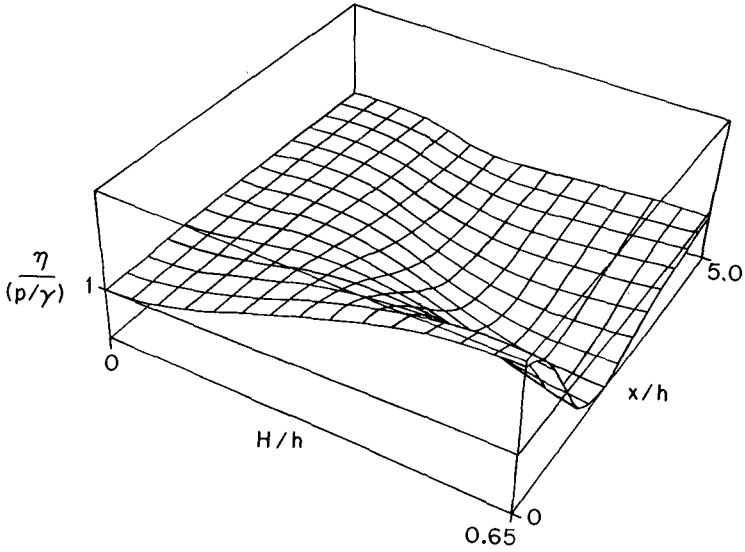


Fig. 1 The Variation of Wave Amplitude Normalized by Dynamic Bottom Pressure with Relative Wave Height and Distance for a Solitary Wave

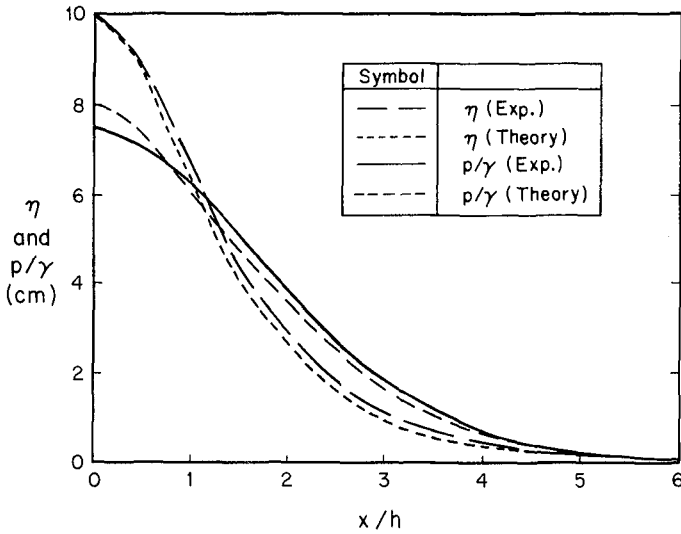


Fig. 2 Variation of Amplitude and Dynamic Bottom Pressure With Relative Distance for a Solitary Wave: $H/h = 0.54$

estimated and the wave shape distorted.

This variation is more clearly shown in Fig. 2 where the results of experiments conducted in the laboratory are presented. The ordinate corresponds to both the wave amplitude and the dynamic pressure head, each expressed in centimeters, and the abscissa is the distance from the crest normalized with respect to the depth. The depth for these experiments was 18.6 cm and the relative wave height was: $H/h = 0.538$. Theoretical pressures and amplitudes as obtained from Fenton (1972), Eqs. 1 and 3, are shown along with the experiments. It is seen that the dynamic pressure under the crest is approximately 75% of the amplitude. Therefore, if simple linear theory were used the wave height obtained from pressure measurements would be underestimated by approximately 25%. As distance from the crest increases, the correction factor becomes equal to unity at approximately $x/h = 1.5$, where the dynamic pressure is equal to the amplitude. For $x/h > 1.5$, because of the vertical water particle accelerations, the dynamic pressure becomes larger than hydrostatic.

The variation of the ratio of the wave height to the dynamic pressure head on the bottom with relative wave height for a solitary wave is shown in Fig. 3. Data are presented from two separate experiments. In Experiment A the pressure transducer used was as obtained from the manufacturer, and in Experiment C the internal pressure ports in the gage were enlarged as much as possible, limited only by the gage dimensions. It appears that the internal gage modifications did not affect the pressure measurements; thus, any change of the frequency response of the gage accomplished by the internal modifications were not important for these waves. No doubt one important reason for this is that for these solitary waves, as mentioned earlier, 99% of the energy was at frequencies less than approximately 4 hz whereas the natural frequency of the gage was about 70 hz.

Three analytical curves are shown in Fig. 3, corresponding to second and third order solitary wave theories and to the stream function theory. The analytical curves obtained from Eqs. 4 and 5 are shown as dotted and dashed, respectively. The solid curve which is labeled stream function theory was obtained from a numerical algorithm based on the development by Dean (1965) and from computations at higher orders than the results presented by Dean (1974). To use this method for solitary waves, first the variation of the ratio of wave height to dynamic pressure head with depth-to-wave length, h/L , was defined for long periodic waves. The curves corresponding to constant H/h so obtained were extrapolated to $h/L = 0$ to define a stream function result which might be applicable to solitary waves. (This will be discussed later in detail.) It is seen in Fig. 3 that the stream function theory agrees well with the experimental results for the full range of relative wave heights which were investigated.

These data have been replotted in Fig. 4 as the ratio of the dynamic pressure head on the bottom to the depth as a function of relative wave height. Experimental data shown in Fig. 4 compare well with the stream function theory and poorly with the linear theory except for $H/h < 0.1$. In essence Fig. 4 emphasizes problems which can occur when interpreting pressure gage measurements under long waves. For example, consider the case of a relatively large wave where the pressure has been measured and the wave height is to be determined. Fig. 4 shows that for solitary waves with $H/h > 0.7$ the dynamic pressure is essentially constant. This means that although the wave height is increasing, the vertical accelerations also change in such a way that the pressure remains relatively unchanged. Thus, for this range of relative wave heights it is difficult, if not impossible, to actually define the solitary wave

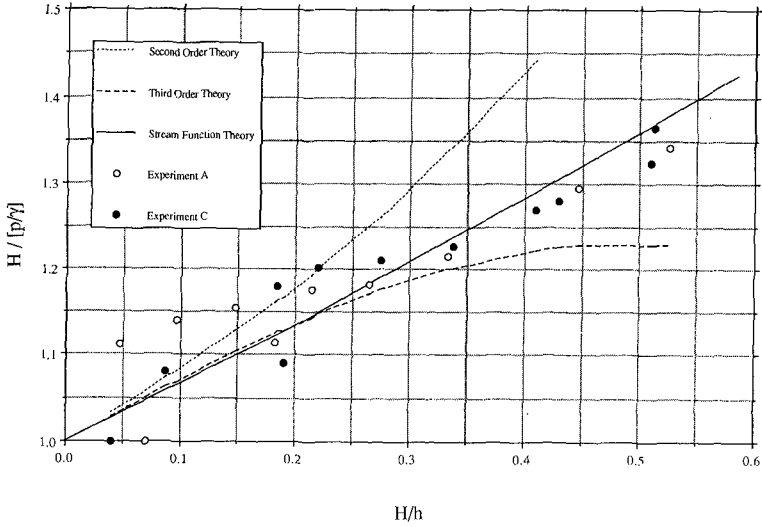


Fig. 3 Comparison of Theories to Experiments for Dynamic Bottom Pressures Under the Crest of a Solitary Wave: $H/(p/\gamma)$ vs. H/h

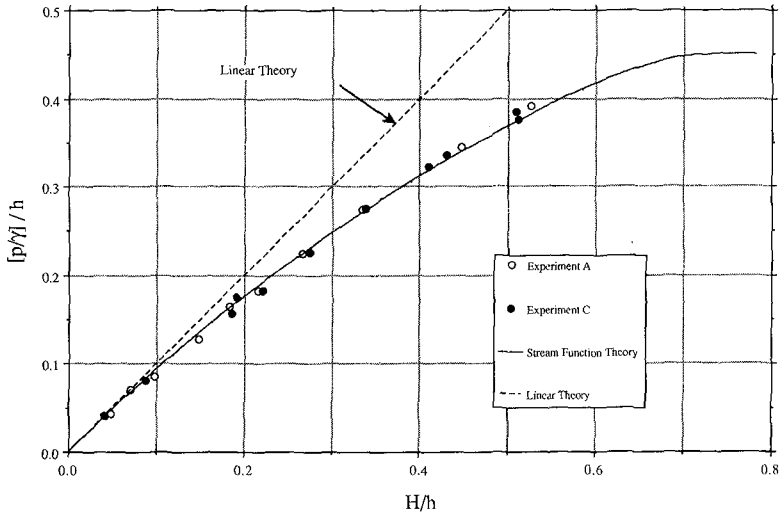


Fig. 4 Comparison of Theories to Experiments for Dynamic Bottom Pressures Under the Crest of a Solitary Wave: $(p/\gamma)/h$ vs. H/h

height from bottom pressure measurements. Unfortunately, at times, it is for just these large waves that one would like to obtain a good estimate of wave height. Thus, for such large long waves, bottom or near bottom pressure measurements may be inappropriate for accurate water surface time histories.

The pressures under large periodic long waves were also investigated in the laboratory and certain of these results are presented in Figs. 5a and 5b. The ordinate in Fig. 5a is the ratio of the wave amplitude to the depth. In Fig. 5b the ordinate is the dynamic pressure measured on the bottom normalized with respect to depth. For both Figs. 5a and 5b the abscissa is the relative distance in the direction of wave propagation. The depth for these experiments was 20.01 cm, the wave period was 1.98 seconds, $H/h = 0.565$, and the non-dimensional period parameter was: $gHT^2/h^2 = 108.6$. The cnoidal wave theory presented in Figs. 5a and 5b is a third-order long wave solution from Horikawa (1988). Included also is the result from the stream function theory carried out to the 21st order. It is seen that the two theories for the wave shape agree reasonably well with the experiments with some divergence in the trough region. The pressures measured are generally less than those predicted by the two theories although the stream function theory agrees better with the experiments near the crest than does the higher order cnoidal wave theory. This result is similar to that observed in the solitary wave phase of the study.

The theoretical and experimental variation of the wave height divided by the total dynamic pressure for periodic waves is shown in Fig. 6 as a function of depth to wave length for constant values of wave height-to-depth. The total pressure is defined in the ordinate as the difference between the pressure measured under the crest and that measured under the trough. The theoretical curves are determined from stream function theory computed to a high enough order so there is little variation in the ordinate value when the order of the computations is increased. For these computations the maximum order was 51 for the longer waves. (It is these curves, for given relative wave heights, which were extrapolated to $h/L = 0$ to define the stream function relationship for solitary waves presented in Fig. 3; the extrapolated curves are shown dashed.) The results from the linear theory, also presented in Fig. 6, appear to converge with the stream function theory for smaller wave height-to-depth ratios only as the depth-to-wave length becomes large. Included in Fig. 6 are the results of four experiments conducted with long cnoidal waves with the relative wave height for each experiment presented in brackets next to the data point. It is seen that the theory agrees reasonably with the experimental data.

The amplitude at the crest and the amplitude at the trough divided by the corresponding pressure head are plotted in Figs. 7 and 8, respectively, as a function of depth-to-wave length and relative wave height. The agreement of the theory with the experimental data appear to be reasonable with respect to the crest amplitude shown in Fig. 7, but appears to be less so for the trough measurements in Fig. 8. The primary reason for the latter is probably experimental error due to the relatively small pressures in the trough region. In both Figs. 7 and 8, the linear theory is shown for comparison, and it is seen, as expected, that for long waves the divergence from the linear theory increases significantly as the relative wave height increases. For example, for $h/L = 0.05$, the so-called limit of shallow water waves, the amplitude at the crest relative to the dynamic pressure head on the bottom for a wave with a relative wave height of: $H/h = 0.6$ predicted by the stream function theory is approximately 1.6 compared to a value of about unity for linear theory. This means that the pressure head under the crest is only about 60% of the amplitude. In Fig. 8 similar data are shown for the trough region where it is seen that, as the relative wave height increases for a given depth to wave length, the wave becomes

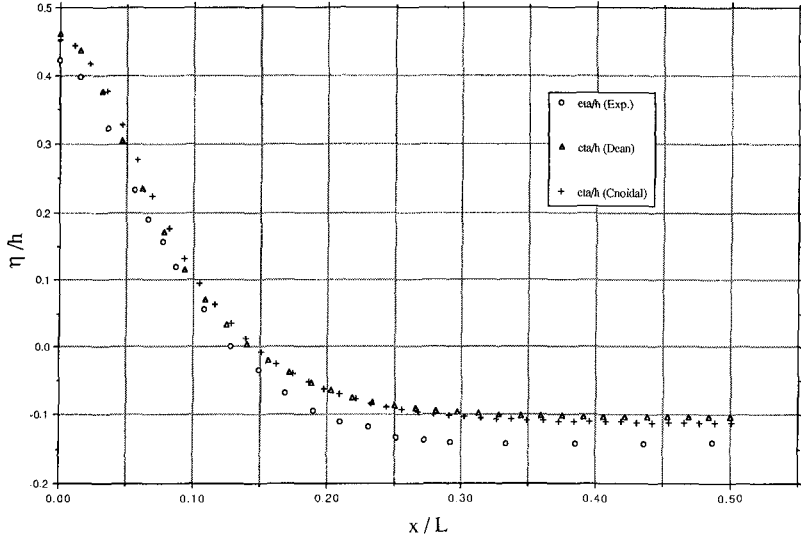


Fig. 5a Comparison of Theories to Experiments for Relative Amplitude of a Cnoidal Wave: $H/h = 0.57$, $gHT^2/h^2 = 108.6$

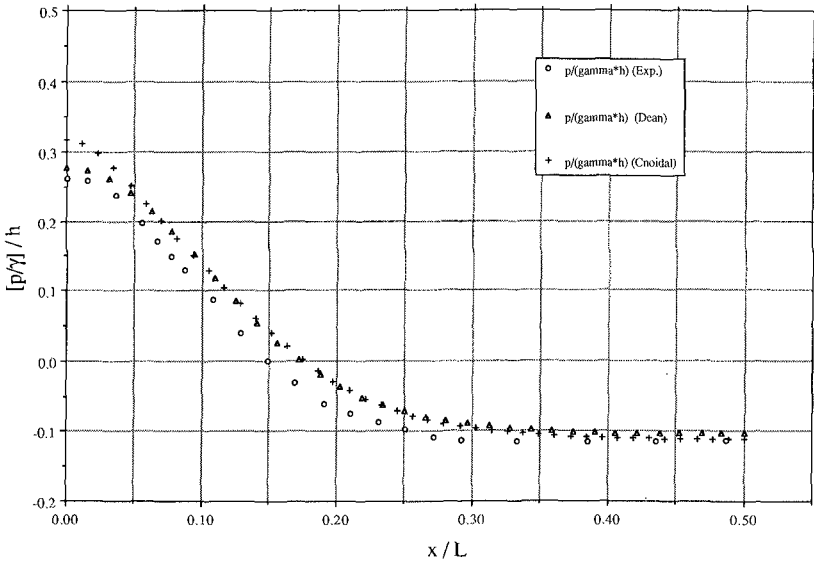


Fig. 5b Comparison of Theories to Experiments for Dynamic Bottom Pressures Under a Cnoidal Wave: $H/h = 0.57$, $gHT^2/h^2 = 108.6$

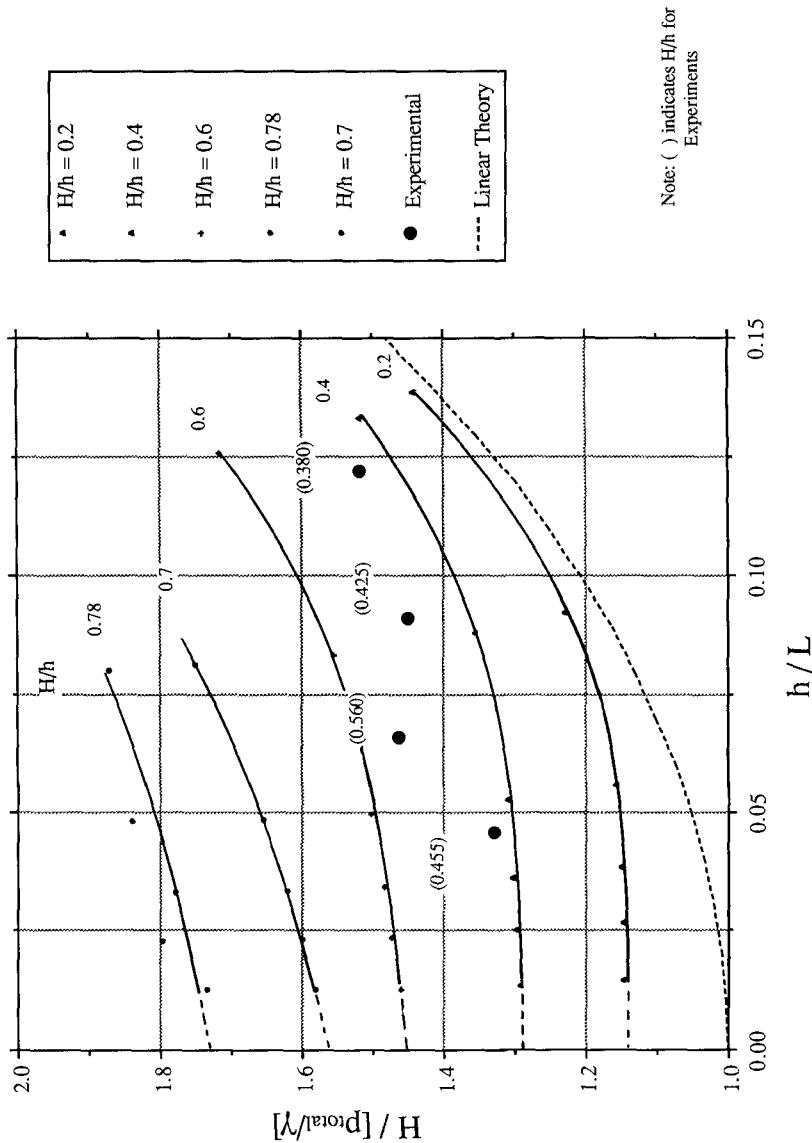


Fig. 6 The Ratio of Wave Height to Dynamic Bottom Pressure as a Function of Relative Depth and Height from Stream Function Theory

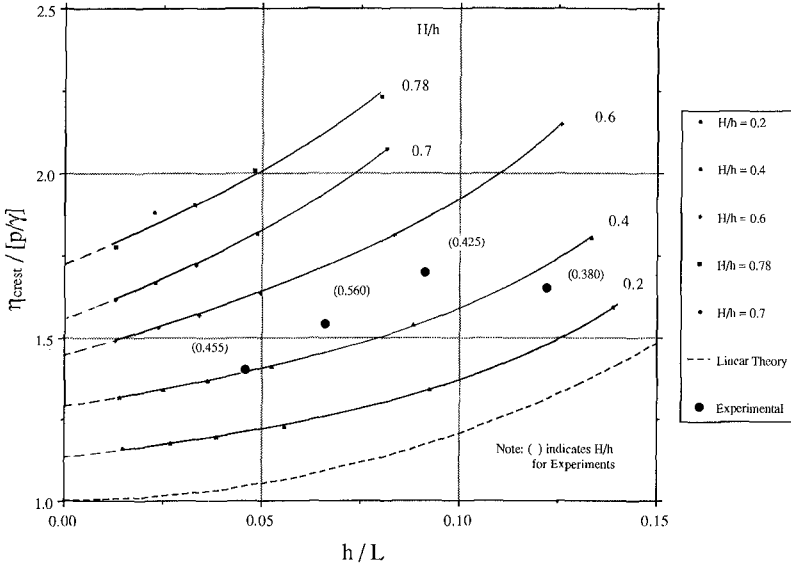


Fig. 7 The Ratio of Crest Amplitude to Dynamic Bottom Pressure as a Function of Relative Depth and Height from Stream Function Theory

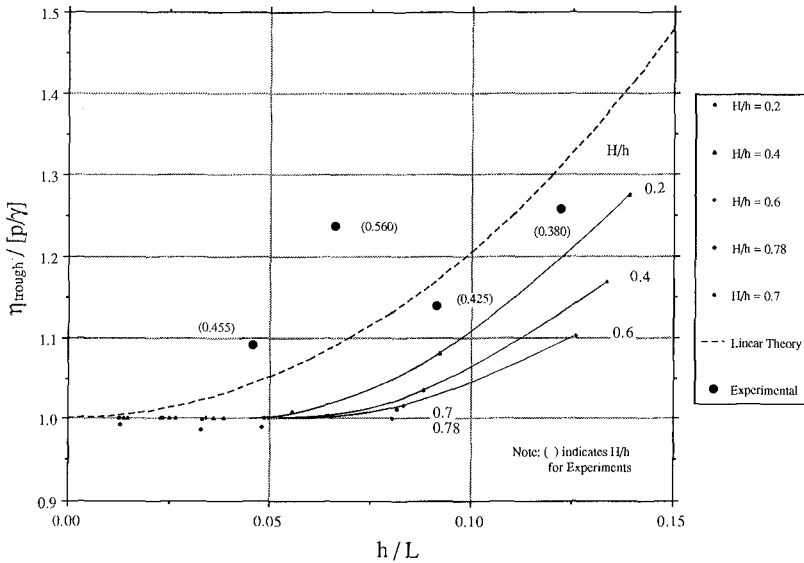


Fig. 8 The Ratio of Trough Amplitude to Dynamic Bottom Pressure as a Function of Relative Depth and Height from Stream Function Theory

more solitary-like so that in the trough region the influence of vertical accelerations becomes less. Thus, contrary to the crest region, the correction factor for a large long wave is nearly unity in the trough region whereas linear theory indicates much larger factors due to the sinusoidal shape of the latter.

To some extent, these data can be summarized as shown in Fig. 9 where the ordinate is the dynamic pressure on the bottom normalized by depth and the abscissa is the wave height-to-depth. Theoretical results are shown for the solitary wave and for two long periodic waves with a relative depth to wave length of: $h/L = 0.05$ and 0.1 . Included also are curves labeled: "Linear (Solitary Wave)" and "Linear ($h/L = 0.1$)". These curves correspond to linear wave theory applied to a solitary wave and to a periodic wave ($h/L = 0.1$). The divergence of the nonlinear theories and the linear theories begins at about $H/h \approx 0.1$ for both the solitary and the periodic waves and increases thereafter. This indicates that care must be taken in applying linear theory to determine the wave height from pressure measurements for long periodic and non-periodic waves. As before, for large waves, the pressure becomes relatively insensitive to increasing wave heights. This again suggests the problem discussed earlier with regard to interpreting wave heights from pressure measurements for H/h greater than 0.6 to 0.7. It is interesting to note the similarity between the results for periodic waves with $h/L < 0.1$ and solitary waves.

Pressure measurements were made in the field in the large fresh water wave facility described in Section 2 at a distance from the bottom of $y/h = 0.317$. An example of pressure measurements for six different tests with an observed relative wave height of: $H/h = 0.79$ are shown in Fig. 10. The ordinate is the dynamic pressure in feet and the abscissa is the number of data points obtained when sampling at a rate of 16 samples per second. The reasonable agreement among the six runs demonstrates good wave generation reproducibility considering the scale of the waves being generated and the type of wave generator used. It should be recalled from Section 2 that these waves have propagated up a slope of about 4.3% before reaching the horizontal section where the pressure measurements were made. A distinctive solitary wave-like shape of the leading part of this wave is apparent as well as the shelf-like trailing part of the first wave. The latter has been found by others for solitary waves propagating up a slope in the laboratory, e.g., Skjelbreia (1987).

In Fig. 11 data are presented from field experiments conducted in the large wave channel on two different days. The ordinate is the wave height normalized by the dynamic pressure head and the abscissa is the relative wave height. (As mentioned earlier, the wave height which is used corresponds to the height which was observed on the wave staff as the wave propagated past the location of the pressure gage.) Included in this figure is a theoretical curve obtained from stream function theory for $y/h = 0.317$ and $h/L = 0$. Considering the shape of the waves as described by the pressure-time histories presented in Fig. 10, the agreement of the theory and the data are surprisingly good. Relative wave heights corresponding to $H/h > 0.8$ are realized due to the 4.3% slope which precedes the horizontal section where the measurements are made and the short distance from the beginning of that section to the location of the pressure transducer. Thus, to some extent, it appears that the leading portion of the wave can be described by a solitary wave reasonably well.

When the dynamic pressure head normalized by the depth is plotted as a function of relative wave height, as shown in Fig. 12, the variation is similar to that seen in Fig. 4. The field data for large relative wave heights appear to reach an asymptotic value of normalized pressure between 0.45 and 0.5. These data show, as

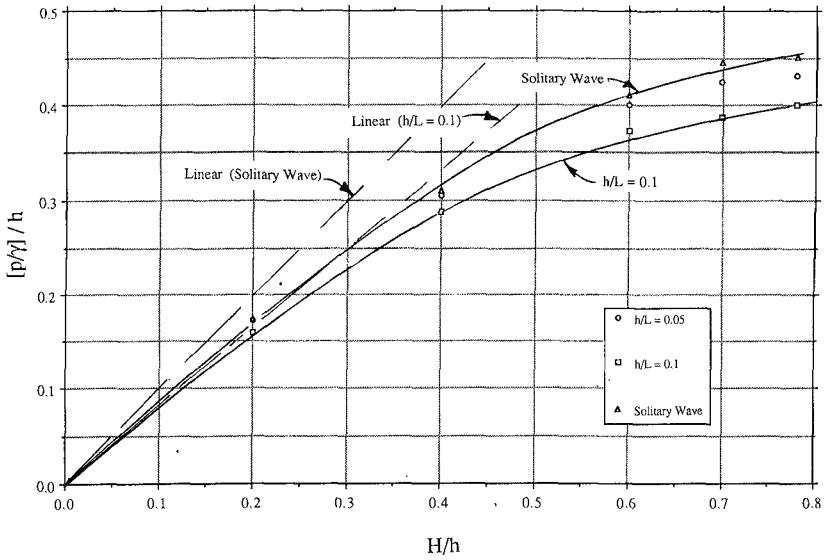


Fig. 9 Variation of Normalized Dynamic Bottom Pressure Under the Crest with Relative Wave Height: Stream Function and Linear Theories

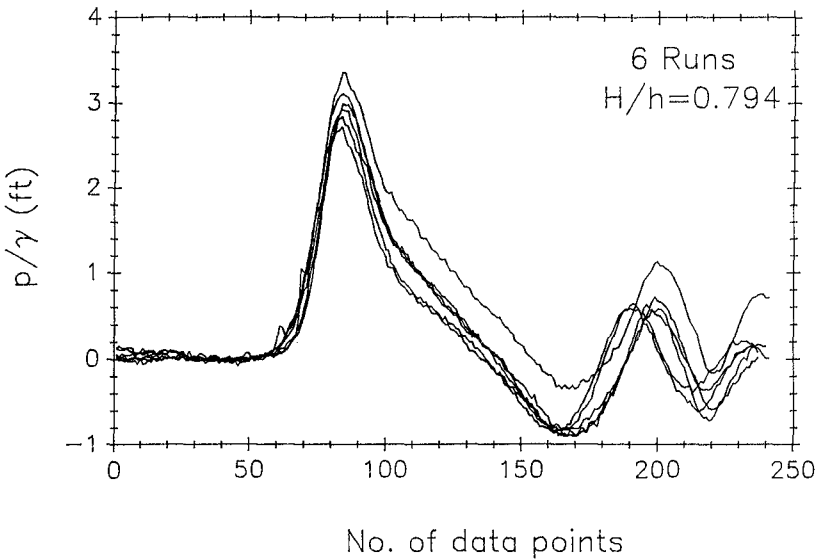


Fig. 10 Field Measurements of Dynamic Bottom Pressure with Time (Data Rate = 16 Samples per sec)

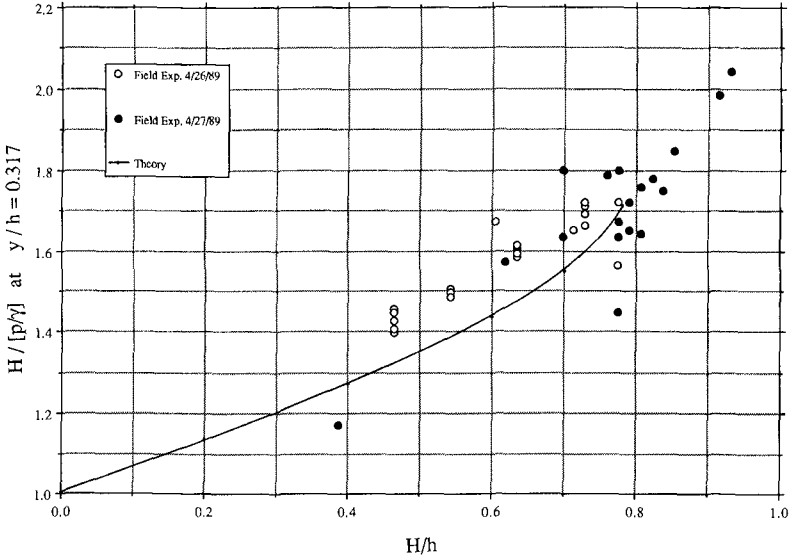


Fig. 11 Comparison of Stream Function Theory as Extrapolated for Solitary Waves to Field Experiments: $H/(p/\gamma)$ vs H/h at $y/h = 0.317$

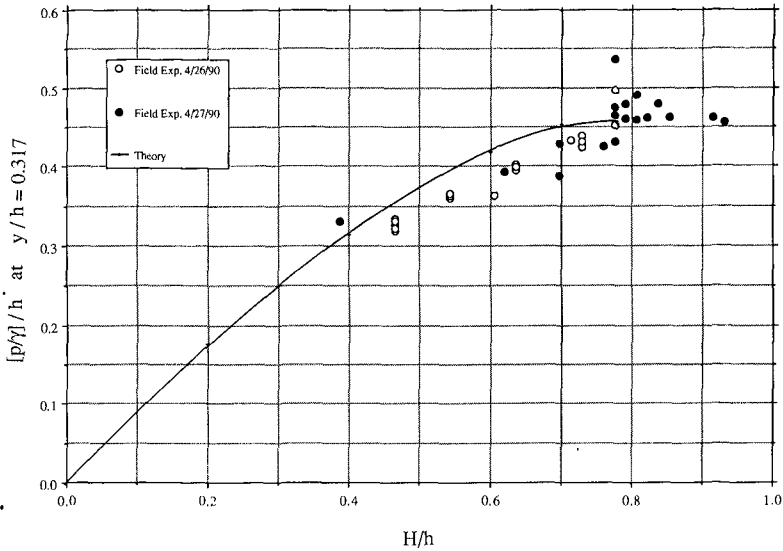


Fig. 12 Comparison of Stream Function Theory as Extrapolated for Solitary Waves to Field Experiments: $(p/\gamma)/h$ vs H/h at $y/h = 0.317$

before for the laboratory results, that for large, long, nonperiodic waves it is inaccurate to define the wave height from the pressure measurements alone.

4. CONCLUSIONS

The following major conclusions can be drawn from this study:

1. For solitary and cnoidal waves, nonlinear effects and vertical accelerations (frequency dispersion) are important in defining the pressures under the waves.
2. For $H/h > 0.1$ linear theory should not be used to evaluate the wave height from pressure measurements for long waves.
3. The extrapolated stream function theory appears to agree best with the experimental data for solitary waves. Solitary wave theories corresponding to the second and third orders in the parameter H/h agree reasonably well with the data only for small relative wave heights. For such non-periodic waves it is inaccurate to define the wave height from pressure measurements alone.
4. For relatively large solitary waves and cnoidal waves the ratio of the dynamic pressure under the wave crest, on or near the bottom, to the depth appears to approach a constant value of 0.45, or somewhat less.

5. REFERENCES

- Bishop, C.T. and Donelan, M.A., "Measuring Waves with Pressure Transducers", Coastal Engr., Vol 11, 1987.
- Bodge, K.R. and Dean, R.G., "Wave Measurement with Differential Pressure gages", Proc. 19th Coastal Engr. Conf., 1984, pp 755-769
- Dean, R.G., "Stream Function Representation of Nonlinear Ocean Waves", Journ. Geoph. Res., vol 70, No 18, pp 4561-4572, Sept. 1965
- Dean, R.G., "Evaluation and Development of Water Wave Theories for Engineering Application", Spec. Report No. 1, USACE, CERC, Nov. 1974
- Fenton, J., "A Ninth Order Solution for the Solitary Wave", Jour. Fluid Mech., Vol. 53, 1972
- Goring, D.G. and Raichlen, F., "The Generation of Long Waves in the Laboratory", Proc. 17th Coastal Engr. Conf., 1980
- Grace, R.A., "Surface Wave Heights from Pressure Records", Coastal Engr., Vol. 2, 1978, pp 55-67
- Grimshaw, R., "The Solitary Wave in Water of Variable Depth", Journ. Fluid Mech., Vol. 46, Part 2, 1971
- Guza, R.T. and Thornton, E.B., "Local and Shoaled Comparisons of Sea Surface Elevations, Pressures, and Velocities", Journ. Geoph. Res., vol 85, C3, March 20, 1980, pp 1524-1530
- Horikawa, K., "Nearshore Dynamics and Coastal Processes", Univ. of Tokyo Press, 1988
- Ippen, A.T. and Raichlen, F., "Turbulence in Civil Engineering: Measurements in Free Surface Streams", Jour. of Hyd. Div., ASCE, Vol. 83, No. HY 5, Oct. 1957

- Isobe, M., Nishimura, H., and Horikawa, K., "Expressions of Perturbation Solutions for Conservative Waves by Using Wave Height", Proc. 33rd Annl. Conf. of JSCE, II, pp 39-43 (in Japanese), 1978
- Lee, D.-H. and Wang, H., "Measurement of Surface Waves from Subsurface gage", Proc. 19th Coastal Engr. Conf., 1984
- Nielsen, P., "Analysis of Natural Waves by Local Approximations", Journ. of Waterways, Port, Coastal, and Ocean Engineering, ASCE, Vol. 115, No. 3 May 1989
- Skjelbreia, J.E., "Observations of Breaking Waves on Sloping Bottoms by Use of Laser Doppler Velocimetry", W.M.Keck Lab. Report KH-R-48, Calif. Inst. of Tech., Pasadena, CA, 1987
- Synolakis, C., "The Run-up of Long Waves", PhD Thesis, Calif. Instit. of Tech., Pasadena, CA, USA, 1986

CHAPTER 87

SEALEVEL RISE : A PROBABILISTIC DESIGN PROBLEM

prof. ir. drs. J.K. Vrijling ¹⁾
ir. I.J.C.A. Van Beurden

Abstract

An economic model is developed to calculate the optimal height of sea defences in case of sealevel rise. The optimal amount and the optimal period of heightening are found, for the single period as well as for the multi-period case. Finally the optimal strategy of heightening of sea defences in case of an uncertain sealevel rise is formulated.

1.0 Introduction

The relative sealevel rise is a well-known fact. In the period from 1682 to 1930, a rise has been measured at the official benchmarks in Amsterdam. The velocity of the rise however appeared to be a function of time. Initially the velocity was 0.04 m per century but after 1850, the sealevel rise increased up to 0.17 m per century. The Delta Committee therefore chose a value of 0.20 m per century for this phenomenon. During the last 20 years, measurements have confirmed this estimate.

However recently experts have come to doubt this figure. In studies several causes are mentioned that may increase the velocity of the sealevel rise :

- melting of the polar ice pack.
- thermal expansion of the oceans.
- tectonic movement of the crust of the earth.
- settlement of alluvial soils due to dewatering.

Estimates of the future sealevel rise based on these ranging from 0.20 to 1.20 m per century are mentioned.

1) Professor hydraulic engineering,
T.U Delft, Stevinweg 1, 2628 CN, Delft

facts differ considerably. For the year 2050 values However these extreme values have not yet been confirmed by observations.

If the sealevel starts to rise, it will pose a significant threat to the low lying countries. The question is when and to what extent should these countries strengthen their sea defences, considering the uncertainty in the relative sealevel rise.

2.0 An economic model

Although the question of the strengthening of sea defences allowing for sealevel rise is multi-faceted, it is readily schematised to an economic decision problem. Solutions for planning period and height are found by minimising the total costs TC consisting of the investment in heightening of the sea defences I and the present value of the expected loss in case of inundation R :

$$TC = I + R \quad (1)$$

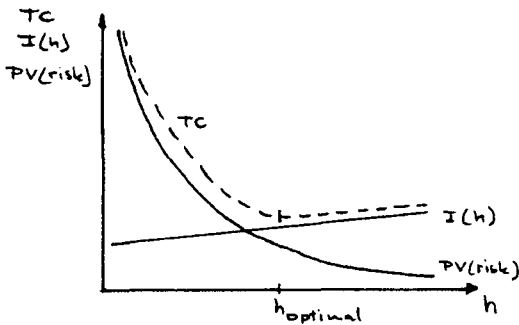


figure 1
Optimisation of the
height of a sea
defence.

In this paper the problem as stated by Van Dantzig[1960] is used as a starting point for the analysis.

2.1 Base case

To allow for sealevel rise, it will be necessary to heighten the sea defence after a certain period. If only one planning period is considered the investment I is schematised by :

$$I = I_0 + I_1(H - H_0) \quad (2)$$

where I_0 = initial cost of heightening [DF1]

I_1 = cost per meter heightening [DF1]

H = height after heightening [m]

H_0 = initial height [m]

The present value of the expected loss in case of inundation R is given by :

$$R = \int_0^{T_p} W P_f(H) e^{-rT} dt = \frac{W P_f(H)}{\gamma} (1 - e^{-\gamma T_p}) \quad (3)$$

where W = damage by inundation [DF1]

T_p = planning period [year]

$P_f(H)$ = probability of failure, schematised by :

$$P_f(H) = e^{-\frac{H - \eta t - A}{B}} \quad (4)$$

η = sealevel rise [m/year]

A, B = parameters of the distribution [m]

γ = $r - \eta/B$

r = real rate of interest [/year]

It is assumed that the parameters A en B of the probability of failure, are not affected by the sealevel rise.

The optimal probability of failure can be found by solving :

$$\frac{\partial TC(H, T_p)}{\partial H} = 0 \quad (5)$$

which yields :

$$P_{f_{opt}}(T_p) = e^{-\frac{H_{opt} - A}{B}} = \frac{I_1 B}{W} \frac{\gamma}{1 - e^{-\gamma T_p}} \quad (6)$$

In the following calculations values for the various parameters according to Van Dantzig have been used :

$I_0 = 40 \cdot 10^6$ [DF1]	$I_1 = 1 \cdot 10^6$ [DF1]
$H_0 = 3.00$ [m]	$W = 24 \cdot 10^9$ [DF1]
$A = 1.96$ [m]	$B = 0.33$ [m]
$r = 0.015$ [/year]	

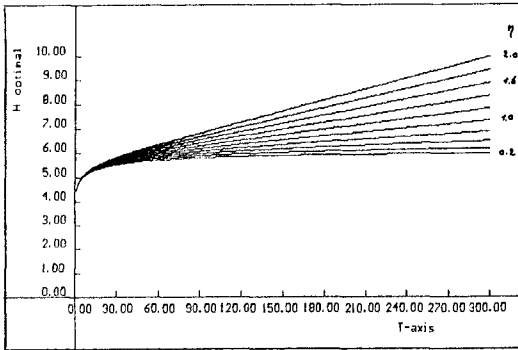


figure 2
Optimal height of
for single period.

In figure 2 the optimal height derived from $P_{f,opt}(T)$ is shown.

The additional heightening ($H - H_{(n=0)}$) of the sea defence to allow for sealevel rise can also be expressed as a fraction of the occurring rise during the planning period ($\cdot T_p$). This is shown in figure 3. From this figure it can be seen that to allow for sealevel rise not the total occurring rise during the planning period has to be added to the height of the sea defence as should be expected, but only a part of it.

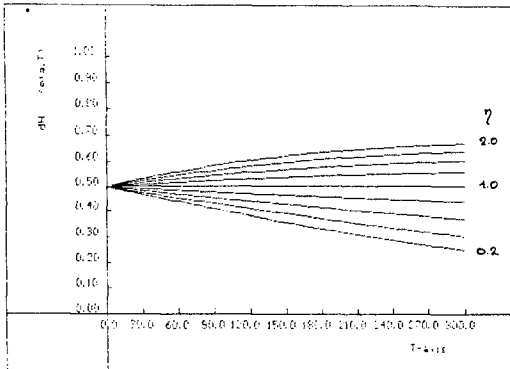


figure 3
Additional heightening
to allow for sealevel
rise as fraction of
occurring sealevel
rise

Additionally the condition for an economical solution is $TC_0 \geq TC$:

$$P_f(H_0) \geq \frac{\gamma}{W} \frac{(I_0 + I_1(H - H_0))}{1 - e^{-\gamma T_p}} + P_f(H) \tag{7}$$

Substitution of the optimal value of the height given by equation (6) yields :

$$P_f(H_0) \geq \frac{I_0 + I_1(H - H_0 + B)}{1 - e^{-\gamma T_p}} \frac{\gamma}{W} \quad (8)$$

2.2 Regular heightening

For a consistent solution of the optimal strategy however, not only the first heightening of the sea defence has to be taken into account, but also the subsequent future adaptations. In this case terms have to be added to I and R for future investments and risks. If all following planning periods are considered, this yields :

$$I = I_0 + I_1(H - H_0) + (I_0 + I_1\eta T_p) \frac{1}{e^{rT_p} - 1} \quad (9)$$

$$R = \frac{W}{\gamma} P_f(H) \frac{1 - e^{-\gamma T_p}}{1 - e^{-rT_p}} \quad (10)$$

The condition for an economical solution can be found by substitution of $T_p = \infty$ in equation (8) :

$$P_f(H_0) \geq (I_0 + I_1(H - H_0 + B)) \frac{\gamma}{W} \quad (11)$$

Optimum height

By solving equation (5), the optimal value for the probability of failure as a function of the planning period is found :

$$P_{f_{opt}} = \gamma \frac{BI_1}{W} \frac{1 - e^{-rT_p}}{1 - e^{-\gamma T_p}} \quad (12)$$

In figure 4 the optimal height computed from $P_{f_{opt}}$ and the optimal minimum height given by $H_{min} = H_{opt} - \eta T$ are shown for several values of η . From this figure it can be seen that for higher sealevel rises and longer planning periods, the optimal height increases and the optimal minimum height decreases. In figure 5 the relative extra-heightening to allow for sealevel rise is shown. The allowance factor is in the order of 0.5. Only for extreme values of the sealevel rise and long planning periods this factor is significantly exceeded.

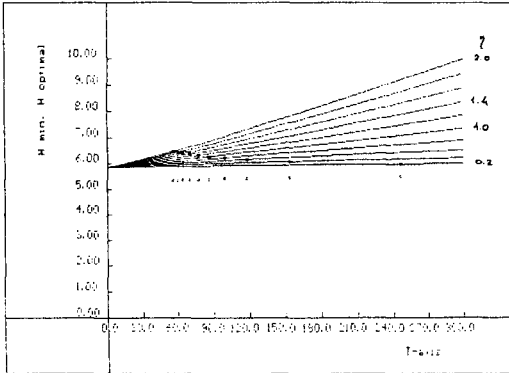


figure 4
Optimal height and
optimal H_{\min}

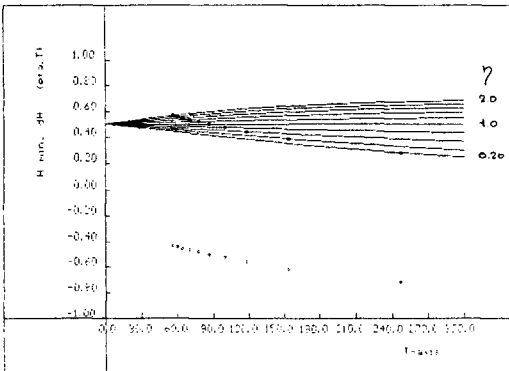


figure 5
Additional heightening
as fraction of occur-
ring sealevel rise
(regular heightening)

Optimum planning period

Additionally total cost can be optimized by differentiating TC with respect to the planning period. Algebraically a solution cannot be found, however for the examples above, values for the optimal planning period $T_{p,opt}$ have been found numerically as shown by dots in figure 4 and figure 5.

In figure 6 total cost TC is shown as a function of the planning period. Early non-optimal adaptations appear to be more expensive than later non-optimal adaptations, especially for less severe sealevel rises.

As a result of the optimal height and the optimal planning period, the crest of the sea defence should be kept in a band between the optimal design level and a certain minimum. In figure 7 is shown an optimal scenario.

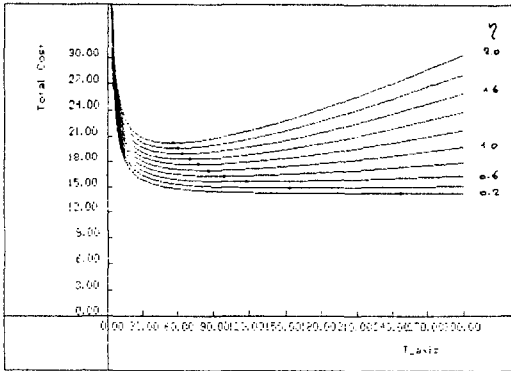


figure 6
Total cost as
function of the
planning period.

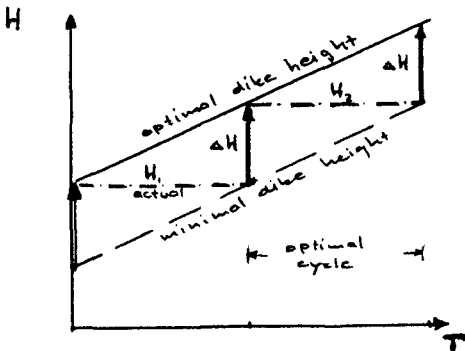


figure 7
Optimal scenario for
heightening.

2.3 Optimum waiting period

If the sea defence already has an non-optimal height or if some of the parameters change, the question arises, when and to what extent the sea defences should be heightened. To solve this problem, equations (9) and (10) have to be changed into:

$$I = [I_0 + I_1(H + \eta T_w - H_0) + (I_0 + I_1 \eta T_{opt}) \frac{1}{e^{rT_{opt}} - 1}] e^{-rT_w} \tag{13}$$

$$R = \frac{W}{Y} P_f(H_0) (1 - e^{-rT_w}) + \frac{W}{Y} P_f(H) \tag{14}$$

where T_w = waiting period

Again the optimal height can be solved by differentiating TC with respect to H. This leads to the same result as given before.

The optimal waiting period has not been solved

algebraically, but numerical solutions give the impression that a simple solution of the following form exists :

$$T_w = T_{p,opt} - \frac{H_{opt} - H_0}{\eta} \quad (15)$$

Optimal scenarios based on this equation are shown in figure 8. As for severe sealevel rises, optimal heights are higher and minimal heights are lower, in case of sudden increase of the sealevel rise immediate action will not be necessary. Only when the lower bound of the new regime is reached the sea defence should be heightened.

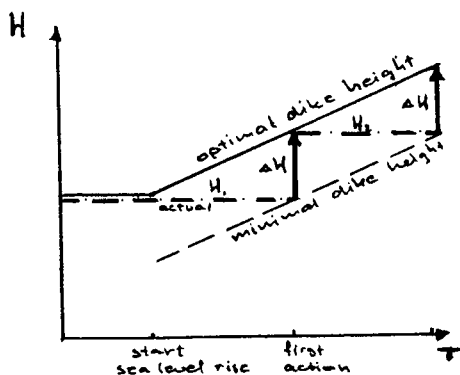


figure 8
Optimal action

2.4 Optimal design sealevel rise

So far the optimal scenario has been calculated for a certain known value of the sealevel rise. However as mentioned above, this value is uncertain. The occurring sealevel rise may vary from 0.20 to 1.20 meter per century according to various estimates. It will be clear that this will affect the total cost of the regular heightening.

In the following calculations the actual value of the occurring sealevel rise is supposed to be known at the moment the sea defences need to be heightened due to this sealevel rise.

Total cost in the case of a different assumed sealevel rise and occurring sealevel rise is given by :

$$TC(\eta_a, \eta_o) = I(\eta_a, \eta_o) + R(\eta_a, \eta_o) \quad (16)$$

where :

$$I(\eta_a, \eta_o) = I_0 + I_1(H_{opt\eta_a} - H_0) + (I_0 + I_1\eta_o T_{opt\eta_o}) \frac{1}{1 - e^{-rT_{opt\eta_o}}} e^{-rT_w} \quad (17)$$

$$R(\eta_a, \eta_o) = \frac{W}{\gamma} (P_f(H_{opt\eta_a}) (1 - e^{-\gamma T_w}) + P_f(H_{opt\eta_o}) \frac{1 - e^{-\gamma T_{opt\eta_o}}}{1 - e^{-rT_{opt\eta_o}}} e^{-rT_w}) \quad (18)$$

T_w is can be calculated using equation (15) :

$$T_w = T_{opt\eta_o} - \frac{H_{opt\eta_o} - H_{opt\eta_a}}{\eta_o} \quad (19)$$

In figure 9 the extra total cost due to different values for the design and occurring sealevel rise is shown for a design sealevel rise of 20 cm per century. As can be expected, the extra cost is higher for lower occurring sealevel rises.

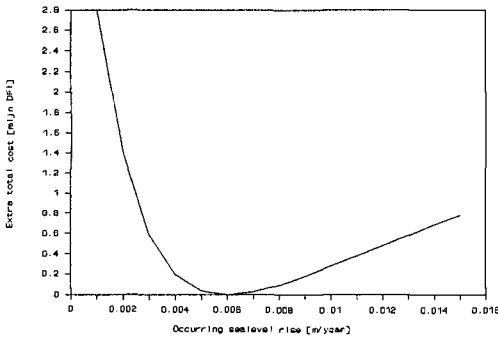


figure 9
Extra total cost for
 $\eta_d = 0.006$ m/year

Assuming a certain probability density function for the occurring sealevel rise $f(\eta_o)$ the expected total cost for an assumed value of the sealevel rise can be calculated :

$$TC_{unc}(\eta_a) = \int_0^{\infty} TC(\eta_a, \eta) f(\eta) d\eta \quad (20)$$

In case of a discrete probability density function this equation can be written as:

$$TC_{unc}(\eta_a) = \sum_{i=1}^N TC(\eta_a, \eta_i) P(\eta_i) \quad (21)$$

The optimal design sealevel rise η_d can be found by minimising $TC_{unc}(\eta_d)$. Calculations have been made for three probability density functions (figure 10) :

- 1) : Uniform distribution
- 2) : Normal distribution :
- 3) : Gumbel distribution :

All distributions having $\mu = 0.006$ and $\sigma = 0.002$ m/year.

The value of the expected total cost as a function of the sealevel rises is shown in figure 11.

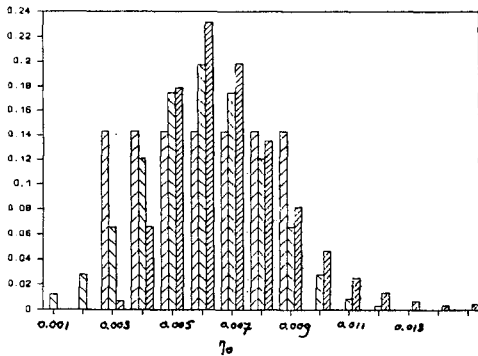


figure 10
The probability density functions of sealevel rise

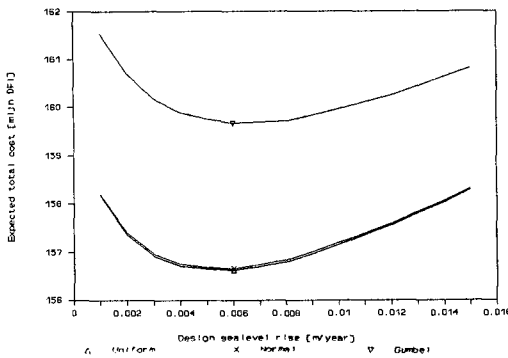


figure 11
Expected value of the total cost.

The minimal value of the expected cost is approximately found at the average value of the sealevel rise. Further it is observed that the cost is less sensitive for an over-estimate of the occurring sealevel rise than for an under-estimate. It seems therefore advisable to choose a safe value for the design sealevel rise, if the sea defences have to be heightened.

3.0 Conclusions

The question when and to what extent the sea defences of low-lying countries should be strengthened in case of an increasing sealevel rise can be answered by an economic probabilistic model.

To allow for sealevel rise not the occurring sealevel rise has to be added to the height of the sea defence but only a part of it. This part is depending on the several parameters in the order of 0.5. Only in case of very high values of the sealevel rise this factor is significantly exceeded and approaches 0.7.

If the sea defences are well maintained, immediate action is not advised in case of an increase of sealevel rise. Action should be taken when the lower bound of the new regime as defined in this paper is reached.

In case of action under uncertainty of the future occurring sealevel rise, do not under-estimate this value, as the total cost of a sea defence that is constructed to low, exceeds the cost of a sea defence constructed sufficiently high.

Appendix 1 : Reference

Van Dantzig (1960) The economic decision problem concerning the security of the Netherlands against storm surges.

Appendix 2 : Mathematical tools

The following formulas have been used in this paper :

Present value of a future amount A_T

$$PV(A_T) = A_T e^{-rT} \quad (22)$$

Present value of a flow F

$$PV(F) = \int_0^T F e^{-rt} dt = \frac{F}{r} (1 - e^{-rT}) \quad (23)$$

Present value of a future flow F_f

$$PV(F_T) = \int_T^{T+\Delta T} F_T e^{-rt} dt = \frac{F_T}{r} e^{-rT} (1 - e^{-r\Delta T}) \quad (24)$$

Present value of a returning future cost

$$PV(A, T) = \sum_{n=0}^{\infty} A e^{-rnT} = A \frac{1}{1 - e^{-rT}} \quad (25)$$

CHAPTER 88

NEARFIELD TSUNAMIS GENERATED BY THREE DIMENSIONAL BED MOTIONS

J.J. Lee* & J.J. Chang**

ABSTRACT

A theoretical and computer simulation has been conducted on near field tsunamis generated by three dimensional bed motion. Linear dispersive wave theory has been used. Nonlinear effect has been found to be negligible for nearfield tsunami generation problem, as nonlinear effect is significant primarily for propagation over long distances. The specified bed deformation takes into account many possible dipole dislocation patterns with different aspect ratio. Three dimensional pictures of the water surface elevation were constructed from the array of computer data.

For the nearfield tsunamis problem, the distance between the generation area and the shoreline is relatively short, thus the main generated wave quickly interact with the reflected leading wave from the coastal boundary to create an even more complicated wave profile. The coastal boundary can either focus or diffuse these waves, resulting in large variations in wave amplitude in the coastal region.

(I) PROBLEM FORMULATION

Let (x, y, z) constitute a Cartesian coordinate system with $z = 0$ as the undisturbed water surface as shown in Fig. 1. Initially, the fluid is at rest with the free surface and solid boundary defined by $z = 0$ and $z = h$ respectively, where h is a constant. For $t > 0$, the solid boundary is moved as prescribed by $\xi(x, y; t)$. The resulting deformation of the free surface is to be determined as $z = \eta(x, y; t)$. Assuming irrotational flow and an inviscid

* Jiin-Jen Lee, Professor of Civil Engineering, Department of Civil Engineering, University of Southern California, Los Angeles, CA 90089-2531

** John J. Chang, President of John Chang & Associates, 1116 Loganrita Ave., Arcadia, CA 91006 (Formerly, Research Engineer in Civil Engineering, University of Southern California, Los Angeles, CA 90089-2531).

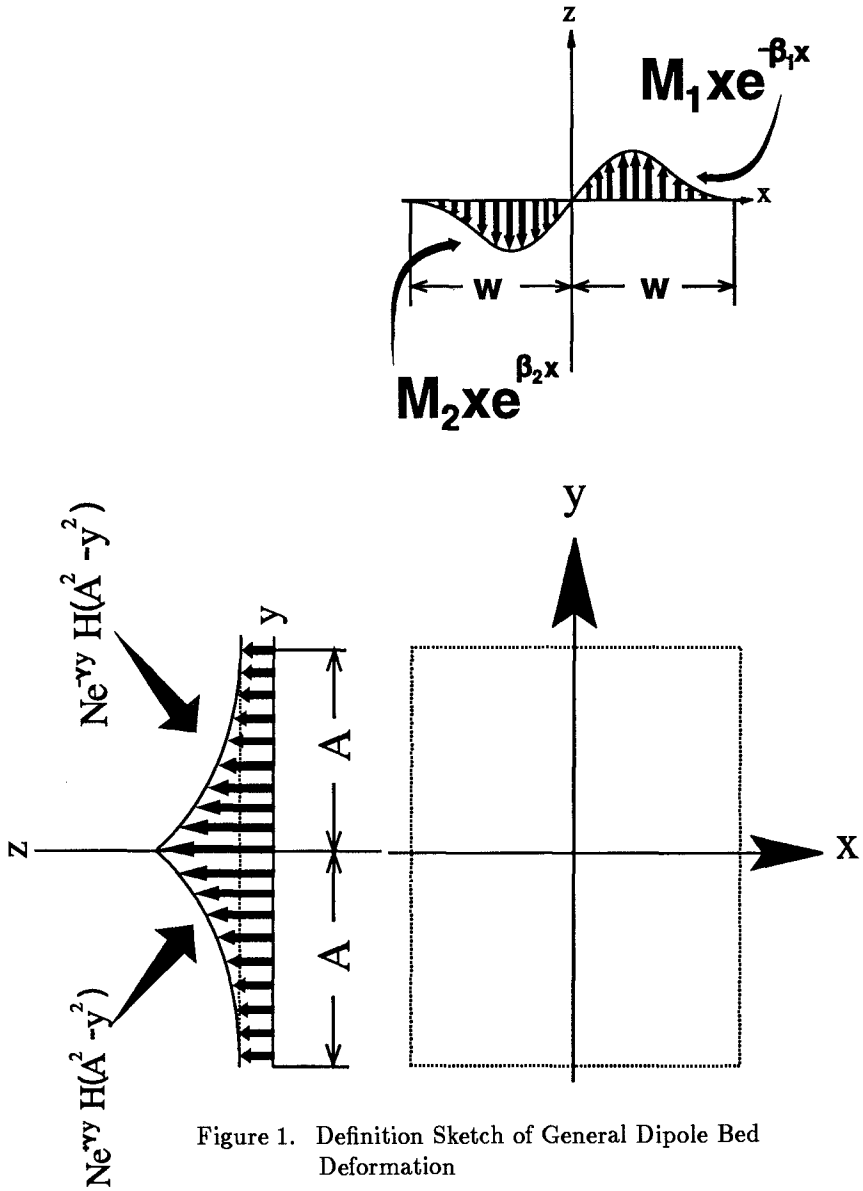


Figure 1. Definition Sketch of General Dipole Bed Deformation

fluid, the fluid kinematics can be expressed in terms of a velocity potential $\varphi(x, y, z; t)$. The differential equation and the linearized boundary conditions that φ must satisfy can be listed as follows:

$$\Delta^2 \varphi = 0 \quad 0 < t < \infty, -\infty < x, y < \infty, -h < z < 0 \quad (1)$$

$$\varphi_{tt} + g\varphi_z = 0 \quad z = 0 \quad (2)$$

$$\varphi_z = \xi(x, y; t) \quad z = -h \quad (3)$$

In these equations, the subscripts denote partial derivatives and g denotes the gravitational acceleration.

The linearized relation between the water surface displacement, η , and the velocity potential, φ , is

$$\eta(x, y; t) = -\frac{1}{g}\varphi_t(x, y, 0; t) \quad (4)$$

The solution for φ (and hence, η) is obtained by using the Fourier transform for the spatial variables x, y and the Laplace transform for the time variable t defined by:

$$\hat{f}(K_1, K_2, s) = \int_0^\infty e^{-st} \int_{-\infty}^\infty e^{iK_2 y} \int_{-\infty}^\infty e^{iK_1 x} f(x, y; t) dx dy dt \quad (5)$$

By applying the transformation of equation (5) to the governing equation and boundary conditions with the subsequent inversion, one obtains the water surface elevation as:

$$\eta(x, y; t) = \frac{1}{(2\pi)^2} \int_{-\infty}^\infty \int_{-\infty}^\infty \left[\frac{1}{2\pi i} \int_{B_\gamma} \frac{s^2 e^{-iK_1 x} e^{-iK_2 y} e^{st} \hat{\xi}(K_1, K_2, s)}{(s^2 + \omega^2) \cosh \sqrt{K_1^2 + K_2^2} h} ds \right] dK_1 dK_2 \quad (6)$$

where $\omega^2 = g\sqrt{K_1^2 + K_2^2} \tanh \sqrt{K_1^2 + K_2^2} h$ and $\int_{B_\gamma} \equiv \lim_{\Gamma \rightarrow \infty} \int_{\mu - i\Gamma}^{\mu + i\Gamma}$ is the Bromwich constant, μ is a positive constant and Γ is a real number.

In order to obtain the specific wave profile as defined in equation (6), one must specify the bed deformation history $\xi(x, y; t)$. The bed deformation is assumed to be a rectangular block with a dipole type of deformation in x axis, and exponential variation in time:

$$\xi(x, y; t) = T(t)X(x)Y(y) \quad (7)$$

where

$$\begin{aligned}
 T(t) &= \xi_0(1 - e^{-\alpha t}) \quad t \geq 0 \\
 X(x) &= \begin{cases} M_1 x e^{-\beta_1 x} & x \geq 0 \\ M_2 x e^{\beta_2 x} & x < 0 \end{cases} \\
 Y(y) &= N e^{-\gamma|y|} H(A^2 - y^2)
 \end{aligned}$$

ξ_0 is the maximum amplitude of the vertical displacement, α is the time constant defined as $1.11/t_c$, and t_c is the characteristic time defined by $\xi/\xi_0 = 2/3$ at $t = t_c$. M_1 , M_2 , β_1 and β_2 , are real and positive constant, A is a half length of the rectangular block. The heavy side step function is defined as:

$$H(A^2 - y^2) = \begin{cases} 1, & A^2 - y^2 > 0 \\ 0, & A^2 - y^2 < 0. \end{cases}$$

The transformation of equation (7) yields:

$$\begin{aligned}
 \hat{\xi}(K_1, K_2; s) &= \left\{ M_1 \left[\frac{\beta_1^2 - K_1^2 + 2i\beta_1 K_1}{(\beta_1^2 + K_1^2)^2} \right] \right. \\
 &\quad \left. - M_2 \left[\frac{\beta_2^2 - K_1^2 + 2i\beta_2 K_2}{(\beta_2^2 + K_1^2)^2} \right] \right\} 2Ni. \tag{8} \\
 &\quad \left\{ \frac{e^{-\gamma A}}{\gamma^2 + K_2^2} [-\gamma \cos K_2 A + K_2 \sin K_2 A] + \frac{\gamma}{\gamma^2 + K_2^2} \right\} \cdot \\
 &\quad \xi_0 \left[\frac{\alpha}{s(s + \alpha)} \right]
 \end{aligned}$$

Substituting equation (8) into equation (6) and solving for the surface elevation one obtains:

$$\begin{aligned}
 \eta(x, y; t) &= \frac{-2\xi_0 Ni}{(2\pi)^2} \int_{-\infty}^{\infty} \int_{-\infty}^{\infty} \left\{ M_1 \left[\frac{\beta_1^2 - K_1^2 + 2i\beta_1 K_1}{(\beta_1^2 + K_1^2)^2} \right] \right. \\
 &\quad \left. - M_2 \left[\frac{\beta_2^2 - K_2^2 + 2i\beta_2 K_1}{(\beta_2^2 + K_1^2)^2} \right] \right\} \cdot \\
 &\quad e^{-iK_1 x} \cdot \left\{ \frac{e^{-\gamma A}}{\gamma^2 + K_2^2} [-\gamma \cos K_2 A + K_2 \sin K_2 A] + \frac{\gamma}{\gamma^2 + K_2^2} \right\} \cdot e^{-iK_2 y} \cdot \\
 &\quad \frac{1}{\cosh \sqrt{K_1^2 + K_2^2} h} \cdot \left[\frac{\alpha^2}{\alpha^2 + \omega^2} (e^{-\alpha t} - \cos \omega t - \frac{\omega}{\alpha} \sin \omega t) \right] dK_1 dK_2
 \end{aligned}$$

where

$$\omega^2 = g \sqrt{K_1^2 + K_2^2} \tanh \sqrt{K_1^2 + K_2^2} h \tag{9}$$

To obtain a simplified solution from equation (9) the bed deformation is assumed to be axially symmetrical. A sketch of such specific fluid domain is

set in Fig. 1 for the case of $M_1 = M_2 = M$, $\beta_1 = \beta_2 = \beta$, $\gamma = 0$ and $N = 1$. Thus, equation (9) becomes:

$$\eta(x, y; t) = \frac{2\xi_0\beta M}{\pi^2} \int_{-\infty}^{\infty} \int_{-\infty}^{\infty} \frac{\sin K_2 A}{K_2} \frac{K_1}{(\beta^2 + K_1^2)^2} \cdot e^{-iK_1 x} \cdot e^{-iK_2 y} \cdot \frac{1}{\cosh \sqrt{K_1^2 + K_2^2} h} \left[\frac{\alpha^2}{\alpha^2 + \omega^2} (e^{-\alpha t} - \cos \omega t - \frac{\omega}{\alpha} \sin \omega t) \right] dK_1 dK_2$$

where

$$\omega^2 = g\sqrt{K_1^2 + K_2^2} \tanh \sqrt{K_1^2 + K_2^2} h \quad (10)$$

Equation (10) contains poles at $K_2 = 0$. This singularity can be treated easily by L' Hospital's rule.

Introducing $K_1 = -2\pi k_1$ and $K_2 = -2\pi k_2$, equation (10) can be rewritten as:

$$\eta(x, y; t) = 8\beta M \xi_0 \int_{-\infty}^{\infty} \int_{-\infty}^{\infty} e^{i2\pi k_1 x} e^{i2\pi k_2 y} f(k_1, k_2) dk_1 dk_2 \quad (11)$$

where

$$f(k_1, k_2) = \frac{-2\pi k_1}{[\beta^2 + (2\pi k_1)^2]^2} \cdot \frac{\sin 2\pi k_2 A}{2\pi k_2} \cdot \frac{1}{\cosh \sqrt{(2\pi k_1)^2 + (2\pi k_2)^2} h} \left[\frac{\alpha^2}{\alpha^2 + \omega^2} (e^{-\alpha t} - \cos \omega t - \frac{\omega}{\alpha} \sin \omega t) \right]$$

and

$$\omega^2 = g\sqrt{(2\pi k_1)^2 + (2\pi k_2)^2} \tanh \sqrt{(2\pi k_1)^2 + (2\pi k_2)^2} h$$

It should be recognized that equation (11) is a two dimensional Fourier transform of $f(k_1, k_2)$, and can be computed by using the fast Fourier transform (FFT).

(II) NUMERICAL IMPLEMENTATION

Suppose that $f(k_1, k_2)$ is defined in the interval of $-T/2 < k_1, k_2, \frac{T}{2}$ and is zero for $|k_1|, |k_2| > T/2$, equation (11) can then be written as:

$$\eta(x, y; t) = 8\beta M \xi_0 \int_{-\frac{T}{2}}^{\frac{T}{2}} \int_{-\frac{T}{2}}^{\frac{T}{2}} e^{i2\pi k_1 x} e^{i2\pi k_2 y} f(k_1, k_2) dk_1 dk_2 \quad (12)$$

It should be noted that the advantageous procedure of computing $\eta(x, y; t)$ in equation (12) is to fix a time $t = t_i$ and evaluate all possible x and y by recognizing equation (12) as a double Fourier transform of $f(k_1, k_2; t)$.

The integral in equation (12) can be approximated by Reimann sum. Thus, equation (12) became as two-dimensional discrete Fourier Transform form:

$$\eta(k_1, k_2; t) = 8\beta M \xi_0 \Delta k_1 \Delta k_2 \sum_{n_1 = -\frac{N_1}{2} + 1}^{N_1/2} \sum_{n_2 = -\frac{N_2}{2} + 1}^{N_2/2} f(n_1, n_2) \omega_1^{k_1 n_1} \omega_2^{k_2 n_2}$$

$$\text{for } \frac{-N_1}{2} + 1 \leq k_1 \leq \frac{N_1}{2}, \quad \frac{-N_2}{2} + 1 \leq k_2 \leq \frac{N_2}{2} \quad (13)$$

where

$$f(n_1, n_2) = \frac{-2\pi n_1 \Delta k_1}{[\beta^2 + (2\pi n_1 \Delta k_1)^2]^2} \cdot \frac{\sin 2\pi n_2 \Delta k_2 A}{2\pi n_2 \Delta k_2} \cdot \frac{1}{\cosh \sqrt{(2\pi n_1 \Delta k_1)^2 + (2\pi n_2 \Delta k_2)^2} h} \cdot \left[\frac{\alpha^2}{\alpha^2 + \omega^2} (e^{-\alpha t} - \cos \omega t - \frac{\omega}{\alpha} \sin \omega t) \right],$$

and

$$\omega^2 = g \sqrt{(2\pi n_1 \Delta k_1)^2 + (2\pi n_2 \Delta k_2)^2}$$

$$\tanh \sqrt{(2\pi n_1 \Delta k_1)^2 + (2\pi n_2 \Delta k_2)^2} h$$

N_1 and N_2 are the number of discrete points which correspond to the x and y axis, respectively; $n_i = -\frac{N_i}{2} + 1, -\frac{N_i}{2} + 2, \dots, \frac{N_i}{2}$ for $i = 1, 2$. The constant length, $\Delta k_i = 2T/N_i$ for $i = 1, 2$. This definition of Δk_i , implies that $\Delta x = \Delta y = \frac{1}{2T}$, and $x = k_1 \cdot \Delta x, y = k_2 \cdot \Delta y$.

It should be noted that $\omega_1 = e^{2\pi i/N_1}$ and $\omega_2 = e^{2\pi i/N_2}$ introduced in equation (13) are $N_1 - th$ and $N_2 - th$ roots of unity in the complex number field, respectively.

An array of 256×256 points was used to compute equation (13), i.e. $N_1 = N_2 = 256$ and $m = 8$. To avoid the spurious short-period oscillations, Δk should be kept small. However, a small Δk implies that the region of computation is also correspondingly limited. All numerical results presented in this study are obtained for $\Delta k = 0.03$. This value was arrived at through a series of numerical experiments.

In order to obtain the wave profile as defined in equation (13), one must specify the parameters M and β , for the comparison study, the results

obtained for the water wave generated by equation (13) will be compared with the previously published half-sine type dipole dislocation results (Chang (1981)). It should be noted that the bed deformation of half-sine type dipole dislocation is also assumed to be rectangular block with a dipole type of deformation in x -axis and exponential variation in time. This is specified as follows:

$$\xi(x, y; t) = \xi_0(1 - e^{-\alpha t})\left(\sin \frac{\pi x}{2B}\right)[H(B^2 - x^2)H(A^2 - y^2)]. \quad (14)$$

In order to set the resulting bed deformation specified by equation (7) and (14) to have the the same deformation energy as well as the same displacement volume the parameter M is equal to 5.8 and β is equal to 2.134.

(III) RESULTS AND DISCUSSION

Numerical results obtained from equation (13) for a general case dipole dislocation of a rectangular block have been obtained. A series of three-dimensional pictures of the wave surface elevation are presented in figure 2 for different dimensionless time parameters, $t\sqrt{g/h}$. The dimensionless parameters for this case are: $t_c\sqrt{g/h}/B = 0.069$, $B/h = 12.2$ (B is the effective half width of a rectangular block, let $B = \frac{1}{2}W = 2.0$ as shown in Fig. 1), $\xi_0/h = 0.2$. The time history of bed motion is an exponential form as seen in Equation (7) with a characteristic time parameter, $\alpha = 18.46$. These three-dimensional pictures were constructed from 256×256 pixel using image processing technique, and represent the overall pictorial view of the wave profile at $t\sqrt{g/h} = 4.20, 12.61, 21.02$ and 29.43 . The vertical viewing angle for these pictures is 60° and the horizontal angle is 60° . The wave amplitude, η , has been normalized by the total bed displacement, ξ_0 . By inspecting these three-dimensional pictures the wave along the x -axis are transformed from the original exponential form into waves of two opposite directions outward from the generation region. The waves along the y -axis disperse from the original wave form as time increase. Due to radiation of wave in every direction, the extent of the generated regions are presented as approximately elliptic region. The complex nature of generated wave patterns due to three-dimensional bottom dislocation is shown in these pictures.

In order to demonstrate the transformation of wave profile as a function of time, the water surface profile along any arbitrarily chosen coordinates by a generalized digital mathematical phantom is also obtained. Figure 3 show the water surface profile along x axis ($y = 0$ for $x > 0$). For convenient comparison of the results for the two different bed motion.

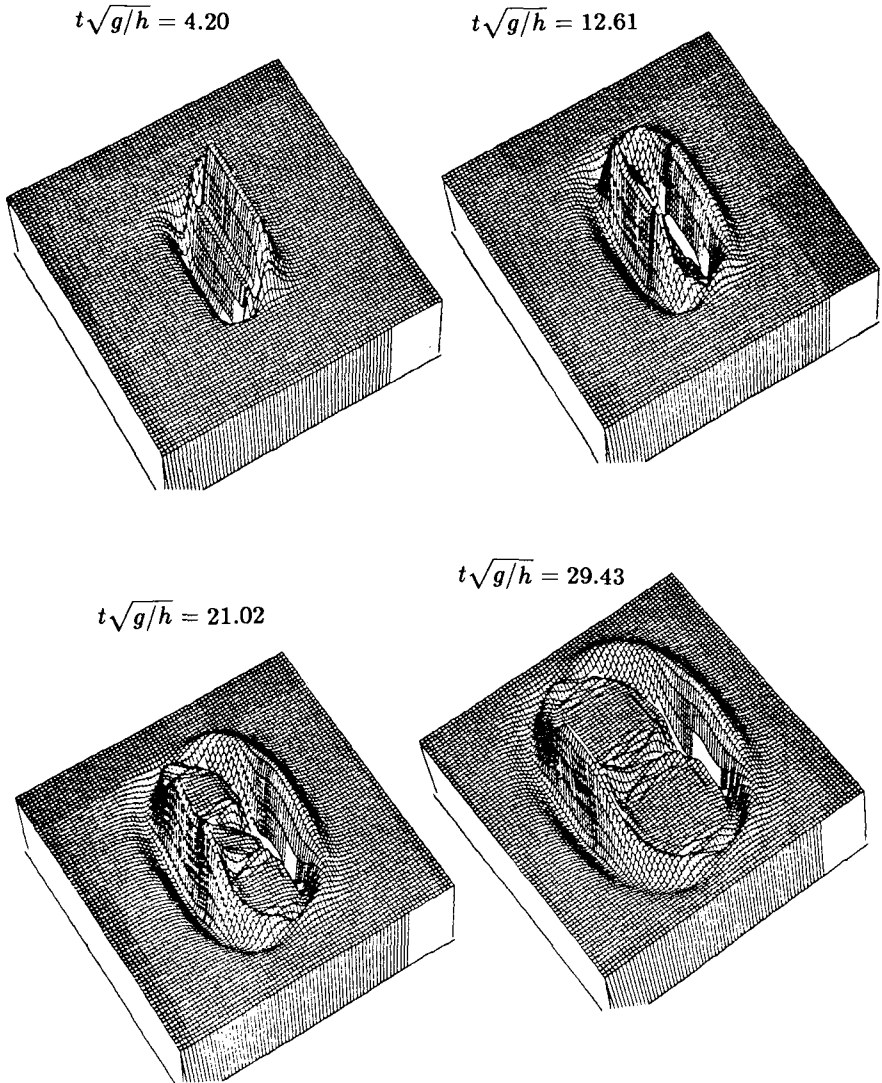


Figure 2. Three Dimensional Pictures Due to General Case Dipole Dislocation Bed Motion Showing the Wave Pattern Near the Generation Region for Specified Time Parameters (Viewing Angle: $\theta_h = 60^\circ$, $\theta_v = 60^\circ$)

The water profiles for a half-sine type dipole dislocation are also superimposed in Figures 3. These profiles are obtained by cutting the three-dimensional pictures such that shown in Figure 2. This series of water surface profiles shows how detailed waves are propagated from the origin of disturbance towards the surrounding region. By studying these wave profiles at different time parameters for both types of bed motion as shown in Figures 3, a number of observations can be made:

- (a) The limit of undisturbed water surface is consistent for all time parameters, even when the bottom disturbances differ.
- (b) The water surface profiles for both dipole bed motions obtained, show an asymmetric behavior due to the asymmetric bottom deformation. The wave amplitude along the y -axis is also zero at all the time. It should be noted that the present theoretical analysis does not treat the nonlinear effect, although the dispersive effect is allowed. Using these wave profiles, the propagation speed is also computed as 2.2 ft/sec, this is very close to the longwave celerity $c = \sqrt{gh} = 2.3$ ft/sec.
- (c) At a small time parameter, $t\sqrt{g/h} = 8.41$, the wave profiles due to general case dipole dislocation differ from the wave patterns due to the half-sine type dipole dislocation. This has provided an aspect showing the end effect of the generation region arriving at the x -axis. The generated wave profiles are dependent upon the shape of bed motion.
- (d) For the general type dipole dislocation, the wave amplitude decay rapidly in arbitrary direction (see Figures 3) the rate of decay is faster than the case of half-sine dipole dislocation the wave profiles exhibited larger negative wave trailing the positive leading wave.

The water surface profiles for two different bed deformations as a function of time at three locations away from the generated region are shown in Figure 4. The three locations are chosen along the minor axis ($y = 0$) at $x = 1.5B$, $2.0B$ and $2.5B$. It is seen that the wave profiles in these three locations shows the same time of arrival for different bed motion. The negative leading wave trailing the positive wave propagates away from the generation region, and oscillates in a manner which appears to be approaching the still water surface level as time increase. For the case of general dipole dislocation the negative leading wave trailing the positive wave occurs at a smaller value of $t\sqrt{g/h}$, than that for the case of half-sine bed motion.

To demonstrate the effect of coastal boundary on the nearfield tsunamis generated by the current bed motion models eight computer graphics are presented in Figure 5. These computer graphics show wave patterns for various time after the start of the bed motion as they approach the coastal boundary. The orientation of the coastal boundary is inserted in Figure 5. The computer graphics are generated by different viewing angles providing the

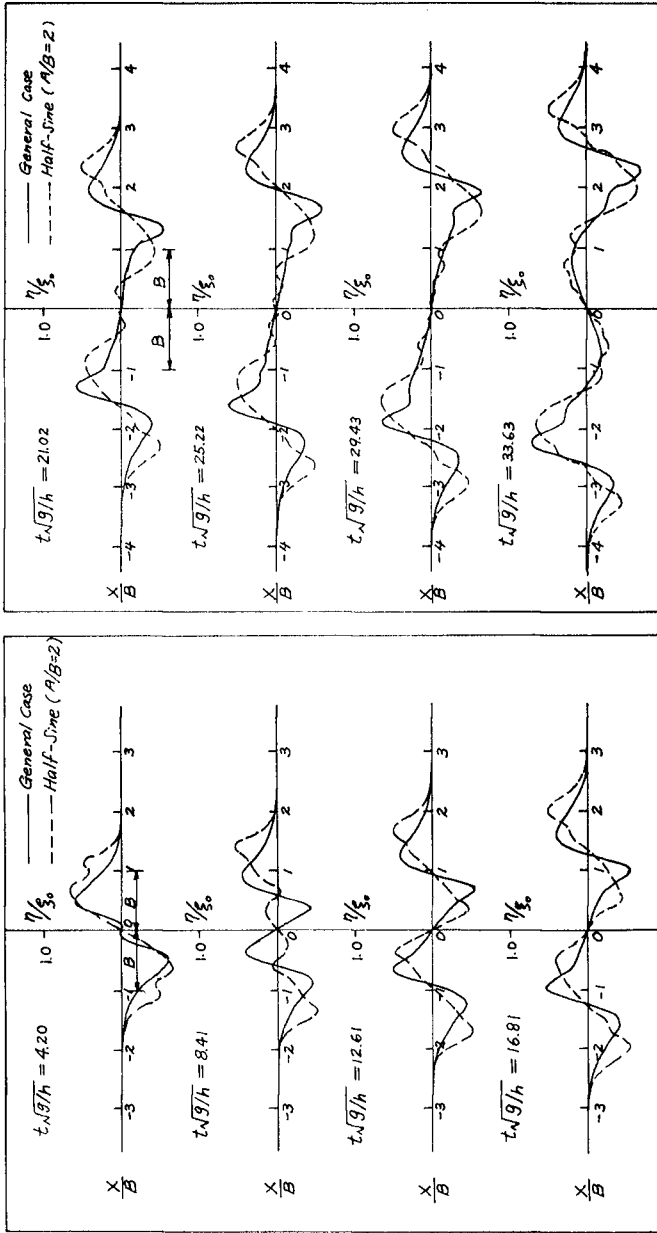


Figure 3. Water Surface Profile Along the x -Axis for Two Different Bed Deformation Models

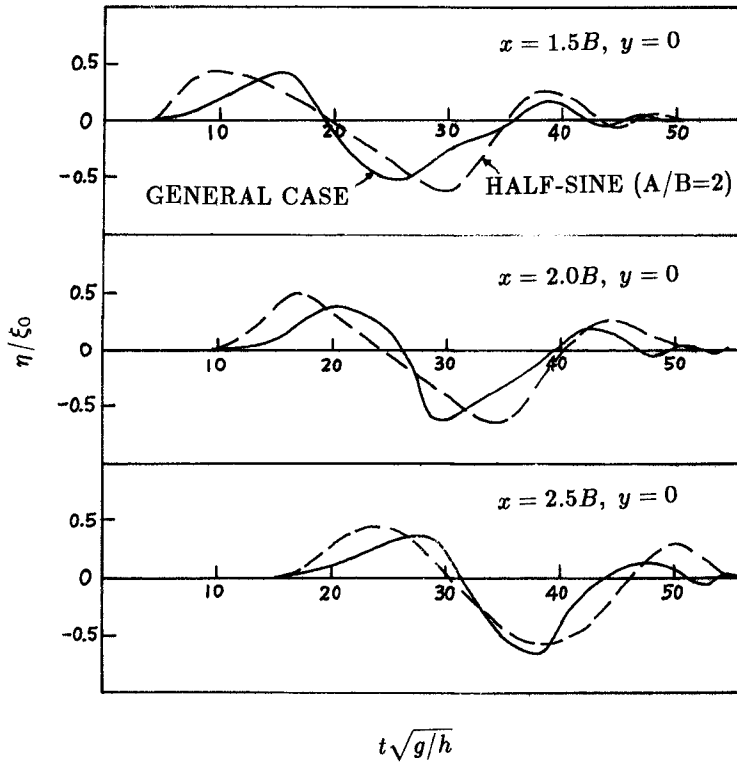


Figure 4. Water Surface Profiles for Two Different Bed Deformation Models at $x = 1.5B, 2.0B$, and $2.5B; y = 0$

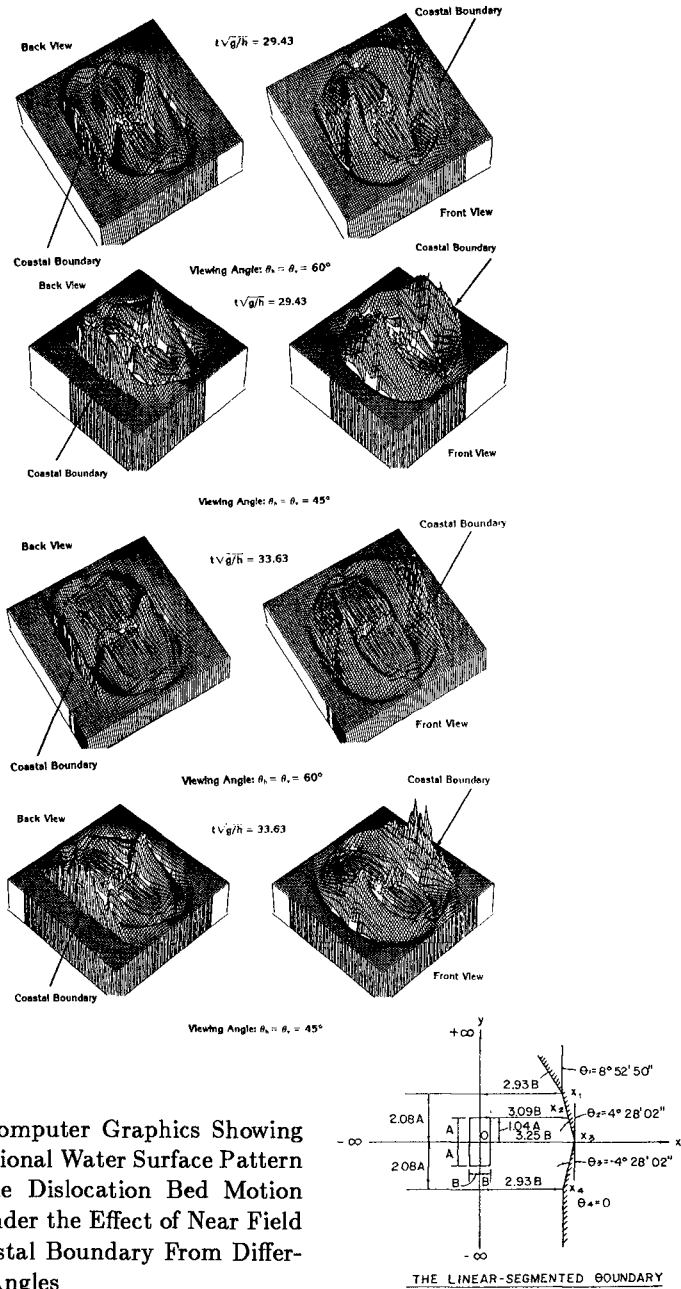


Figure 5. Computer Graphics Showing Three Dimensional Water Surface Pattern Due to Dipole Dislocation Bed Motion ($A/B = 2$) Under the Effect of Near Field Irregular Coastal Boundary From Different Viewing Angles

wave pattern from different perspective. From these, one can readily see the effect of the reflecting boundary and realize the variation of the transient wave amplitudes along the coastal boundary associated with nearfield tsunamis. This feature confirms the field experience which showed a great variation in wave amplitudes at nearby locations along the coastline. It should be noted that the water depth throughout the computational domain has been assumed constant. The resulting water surface profile for variable depth medium would even be more complicated than those shown.

REFERENCES

1. Andrews, H.C., *Computer Techniques in Image Processing*, Academic Press, New York, 1970.
2. Brigham, E.O., *The Fast Fourier Transform*, Prentice-hall, Inc., Englewood Cliffs, New Jersey, 1974.
3. Chang, J.J., "Water Wave Generated by Three-Dimensional Bed Motion," *Ph.D. Dissertation*, University of Southern California, Dec., 1981.
4. Driessche, P.V.D., and Braddock, R.D., "On the Elliptic Generating Region of a Tsunami," *Journal of Marine Research*, Australia, 1972, pp. 217-226.
5. Hammach, J.L., "A Note on Tsunamis: Their Generation and Propagation in an Ocean of Uniform Depth," *Journal of Fluid Mechanics*, Vol. 60, Part IV, 1973, pp. 769-799. (For more details, see Report No. KH-R-28, W.M. Keck Laboratory of Hydraulics and Water Resource, California Institute of Technology, Pasadena, CA, 1972.)
6. Kajiura, K., "Tsunami Source, Energy and the Directivity of Wave Radiation," *Bulletin of the Earthquake Research Institute*, Tokyo University, Vol. 48, 1970, pp. 835-869.
7. Lee, J.J., and Chang, J.J., "Wave Generated by an Impulsive Bed Motion of Finite Size," *Proceeding of the Second Congress of the Asian and Pacific Regional of IAHR*, International Conference on Water Resources Development, Taipei, Taiwan, 12-14 May 1980, pp. 759-768.
8. Lee, J.J., and Chang, J.J., "Water Waves Generated by an Impulsive Bed Upthrust of a Rectangular Block," *Applied Ocean Research*, Vol. 2, NO. 4, 1980, pp. 165-170.
9. Oppenheim, A.V., and Schafer, R.W., *Digital Singal Processing*, Prentice-Hall, Inc., Englewood Cliffs, NJ, 1975.

10. Reed, I.S., Glenn, W.V. Jr., Truong, T.K., Kwoh, Y.S., and Chang, C.M., "X-Ray Reconstruction of the Spinal Cord, Using Bone Suppression, Appendix I and III," *IEEE Transactions on Bio-medical Engineering*, Vol. BME-27, No. 6, 1980, pp. 293-298.
11. Sabatier, Pierre C., "Formation of Wave by Ground Motion" Chapter 17 of *Encyclopedia of Fluid Mechanics*, Gulf Publishing Company, 1986, pp. 723-759.
12. Van Dorn, W.G., "Tsunamis," *Advances in Hydroscience*, Vol. 2, 1965, pp. 1-48.

CHAPTER 89

NUMERICAL 3-D CURRENT MODELLING OF STRATIFIED SEAS

Erland B. Rasmussen¹, Hans Jacob Vested¹
and Lars C. Ekebjærg¹

Abstract

A detailed knowledge of the velocity field is often needed, e.g. for environmental impact assessment and the presence of a continuously stratification often necessitate the use of three-dimensional models. The present paper describes such a three-dimensional numerical model. Its ability to model situations involving stratification is illustrated through two classical hydraulic problems and a practical application. The problems of boundary data in the three dimensions are discussed and a possible way of overcoming these problems is devised.

1. INTRODUCTION

The coastal sea will in many cases be stratified due to variations in temperature or salinity, and even very small differences in density may have a decisive influence upon the properties of the flow considered. During the last decade two dimensional layered models integrated over the layers have been developed to simulate stratified flow. These models typically describe two layers, and have been successfully applied in situations where a pronounced stratification exists. However, in practice the density varies often continuously and the mixing of the water can only be adequately described from a knowledge about the three-dimensional flow field. This has led to the development of three-dimensional numerical current

¹M.Sc. in Civil Engineering, Danish Society of Civil Engineers, Computational Hydraulics Centre, Danish Hydraulic Institute, Agern Allé 5, DK-2970 Hoersholm, Denmark

models capable of calculating the three-dimensional velocity field and density differences in a continuously stratified sea.

In the present paper a three-dimensional numerical hydrodynamic and advection-diffusion flow model is described. The model takes into account density variations, bathymetry and external forcing from, for example, wind and hydrographic boundary conditions. The model is suitable for applications where a detailed description of the flow is necessary, such as water exchange in estuaries, and for environmental impact assessment.

An important aspect of three-dimensional modeling is the need for accurate boundary data that must be known a priori to the simulations. Often these are, however, not known or can only be poorly estimated in practice. Inconsistent boundary data will inherently lead to numerical instability in the model and this problem is more evident in the presence of density variations. A possible solution to this problem has been devised in the present paper.

2. DESCRIPTION OF A THREE-DIMENSIONAL MODEL

The mathematical model is based upon the equations for conservation of mass and momentum (the Reynolds-averaged Navier-Stokes equations) in three dimensions together with an advection-diffusion equation for the scalar quantities salt and temperature,

$$\frac{D\vec{u}}{Dt} + 2 \Omega \times \vec{u} = - \frac{1}{\rho} \nabla P - \vec{g} + \nabla \cdot \{\nu_e \nabla \vec{u}\} + \vec{F}_{\text{ext}} \quad (1)$$

$$\frac{D\rho}{Dt} + \rho \nabla \vec{u} = \nabla \cdot \{D_m \nabla \rho\} \quad (2)$$

$$\frac{D}{Dt} \{\rho S\} = \nabla \cdot \{D_s \nabla S\} \quad (3)$$

$$\frac{D}{Dt} \{\rho T\} = \nabla \cdot \{D_T \nabla T\} \quad (4)$$

where

\vec{u}	is the velocity vector,
P	is the fluid pressure,
ρ	is the density,
ν_e	is the effective viscosity,
\vec{F}_{ext}	is an external forcing such as wind shear,
D_m	is the dispersion coefficient due to fluctuations in density,
Ω	is the Coriolis tensor,
\vec{g}	is the gravitational vector,
S	is the salinity,
T	is the temperature,
D_s and D_T	are dispersion coefficients for salt and temperature, respectively, and
t	is time.

The conservation equations for mass and momentum are discretized with a second order accuracy into a finite difference formulation imposed on a space-staggered rectangular grid. The weak coupling between the fluid pressure and the three velocity components is solved by the artificial compressibility method which first was proposed by Chorin (1967).

The fractional step technique and a special handling of the convective terms allow for a non-iterative ADI (Alternating Directions Implicit) method to be applied for advancing the solution in time.

Simultaneously, the advection-diffusion equation is solved by an explicit quadratic upwind method, the so-called QUICKEST scheme proposed by Leonard (1979) and extended to two and three dimensions by Justesen et al. (1989).

3. MODELLING OF CLASSICAL HYDRAULIC PROBLEMS

Stratified seas are often characterized by migrating fronts of water with different density. The classical example of such flow is often referred to as the lock-exchange flow, as it is observed when a sluice gate separating saline and fresh water is opened. A numerical simulation of this test accentuates the properties of the model with respect to maintaining the density difference at the fronts and thereby the properties to simulate the flow correctly.

Consider a 4 km, 20 m deep channel. Initially the water is at rest, with the less dense water to the

left (salinity 20 ppt.) and the more dense to the right (salinity 32 ppt.), separated by a vertical wall. When the wall is suddenly removed, the two water bodies will start to move. A gridsize of $\Delta x = 100$ m and $\Delta z = 1$ m has been chosen. The time step is set equal to 2.5 sec. There is no wall friction applied and a constant eddy viscosity equal to 0.001 m/s² is used.

Fig. 3.1 shows the development in time of the flow. The very unsteady and complicated flow field at the two density fronts are clearly revealed. Due to the free surface, the flow is not symmetric.

Assuming a balance between the potential and kinetic energy the propagation speed, U_0 , of the density front can be expressed as

$$U_0 = 0.5 \sqrt{\Delta g H_0} \quad (5)$$

where H_0 is the water depth and $\Delta = \Delta \rho / \rho$.

The factor 0.5 in Eq. (5) refers to symmetrical flow and to non-viscid flow. In the presence of a free surface, laboratory experiments yield a deviation of the factor 0.5 in Eq. (5). According to Simpson (1987) the factor becomes 0.465 and 0.59 for the underflow and overflow, respectively.

A comparison between the model estimates and the empirical estimates has been listed in Table 1.

	Emp. Expression	Num. Model
Underflow	0.62	0.62
Overflow	0.66	0.78

TABLE 1 Propagation Speed (m/s) of Density Fronts Based on an Empirical Expression and the Present Model.

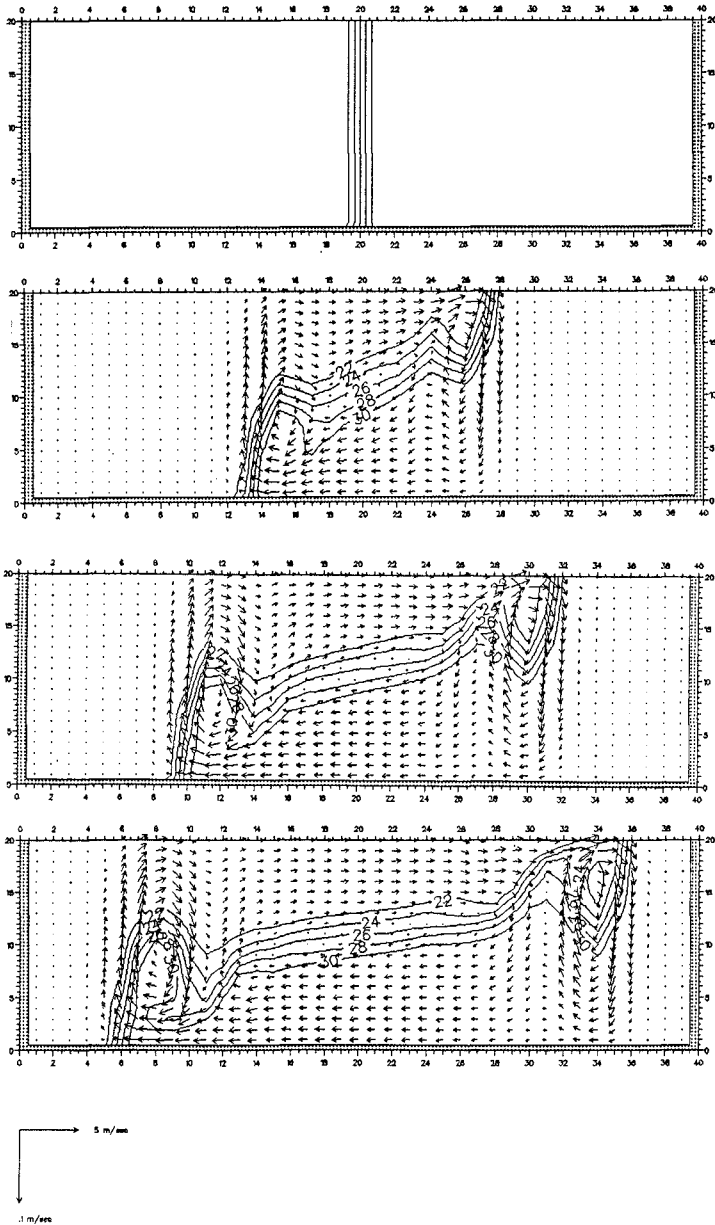


Fig. 3.1 Development of lock-exchange flow. Notice the characteristic head of the fronts which is also seen in laboratory experiments (cf. Simpson (1987)).

As seen from Table 1 there is an excellent agreement regarding the underflow whereas the model tends to overestimate the overflow compared to the empirical expression.

Another classical hydraulic problem in stratified seas is the wind-driven circulation and tilting of the interface. Consider again the 4 km and 20 m deep open channel; but with a stable, horizontal stratification at 10 m depth. The external force is a wind shear stress τ_w equal to 0.58 Pa. The wind causes a set-up in the wind direction and a set-down in the opposite. This tilting of the surface induces additional water movements, resulting in a reversed tilting of the interface, and a wind induced, clockwise rotating current in the upper layer. In the lower

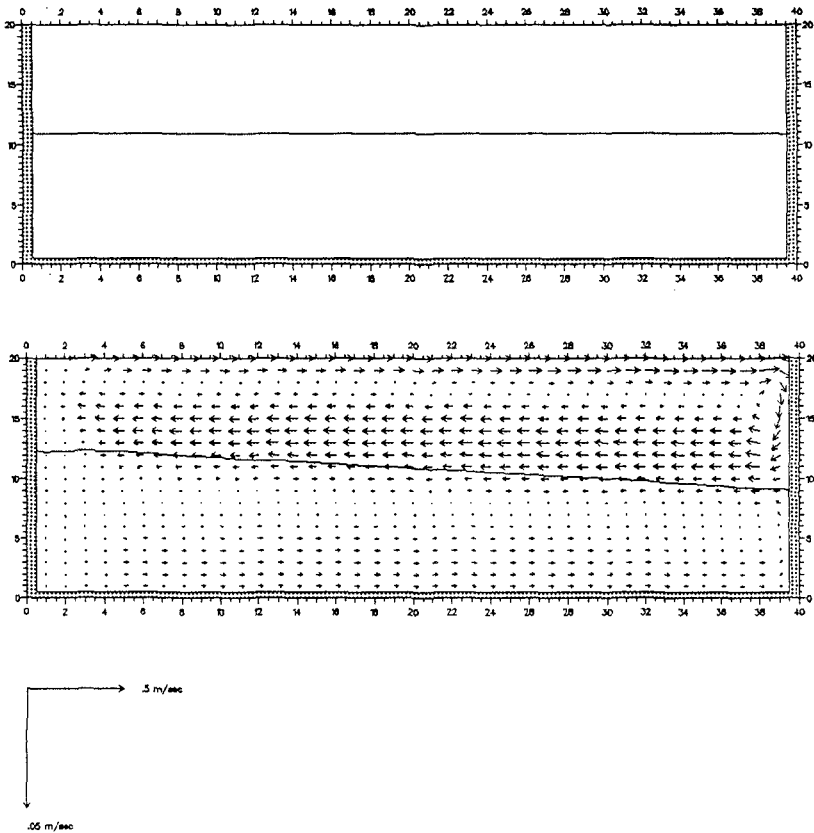


Fig. 3.2 Wind driven circulation. Initial and steady state conditions.

layer a weaker, counter clockwise rotating current is generated. The steady state situation has along with the initial conditions been shown in Fig. 3.2. Assuming a static equilibrium between the wind set-up and the wind shear stress, the set-up can be determined from

$$\Delta\eta = \frac{\tau_{\omega} L}{\rho gh} \quad (6)$$

where L is the length of the channel and h the mean depth of the upper layer. The reversed tilting of the interface $\Delta\eta_i$ can be determined from

$$\Delta\eta_i = - \Delta\eta / \Delta \quad (7)$$

assuming the lower layer is at rest. Inserting the actual values gives $\Delta\eta = 30$ cm and $\Delta\eta_i = 3.18$ m. These values are to be compared with the model results $\Delta\eta = 2,6$ cm and $\Delta\eta_i = 2,76$ m. With the given approximation this is a reasonable agreement.

4. APPLICATION IN THE GREAT BELT AREA

The three-dimensional model briefly described in Section 2 has been set up for the Great Belt which connects the Baltic Sea with the Kattegat (see Fig. 4.1).

The flow in the Great Belt may be very unsteady due to the meteorological changes and the water masses are often stratified with less dense water from the Baltic Sea above the more dense water from the North Sea. In connection with the building of a link across the Great Belt between Funen and Zealand a large field measurement programme has been carried out, providing an excellent basis for comparing model results with field data.

On basis of the available field data a five days period in November 1987 has been selected for simulation. The three-dimensional model has been set up with a horizontal grid spacing of 500 m and with 4 m in the vertical. The time step has been set to 10 min. The relatively high velocities that are observed and the length scales present in the Great Belt imply a significant influence of the Coriolis force. Thus, the effect of Coriolis has been included in the model, also. For simplicity, a bed friction based on a

quadratic law with a constant bed friction coefficient has been applied.

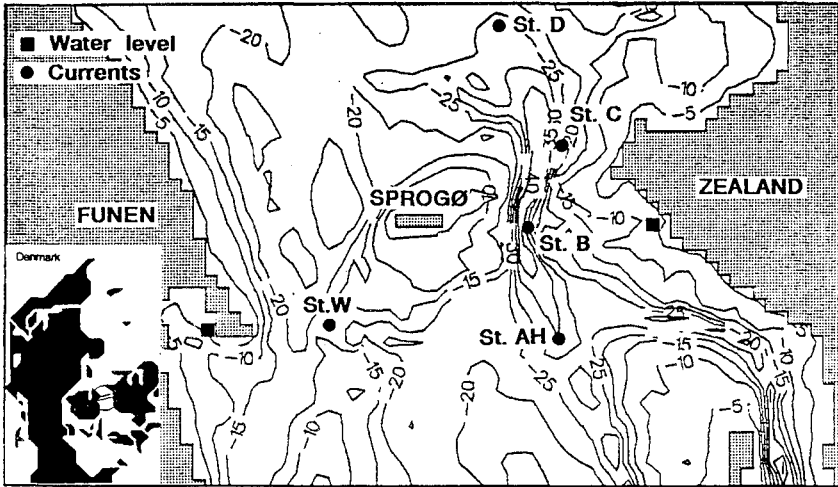


Fig. 4.1 Bathymetry of the Great Belt area with the locations of the measuring stations. Horizontal grid spacing is 500 m.

To describe the turbulence a Smagorinsky formulation of the eddy viscosity (see e.g. Smagorinsky (1963); Aupoix et al. (1982)) has been used. A simple damping function dependent on the gradient Richardson number has been introduced to account for the reduction of the shear stress across a density interface,

$$\nu_e = \frac{\nu_e}{1 + \psi Ri} \quad , \quad Ri = - \frac{g \frac{\partial \rho}{\partial z}}{\rho \left(\frac{\partial \vec{u}}{\partial z} \right)^2} \quad (8)$$

where Ri is the gradient Richardson number and ψ is a calibration factor.

The boundary conditions for the three-dimensional model have in the present study been extracted from a two-layered model assuming hydrostatic pressure and uniform velocity and density profiles for each layer

at the boundaries. Although this approximation is relatively rude, the model will within few grid points from the boundaries adjust itself to a non-uniform velocity distribution. This technique is known to be reliable and will prevent any inaccuracy and contradiction in the prescription of the boundary data.

A total of five stations with between two and four current devices on each string have been deployed during the simulation period. Also, two water level stations near Funen and Zealand, respectively, have been available. The approximate locations of these stations have been shown in Fig. 4.1.

The simulation period begins at 00:00 November 1, and ends at 12:00 November 5, 1987 of which the first 12 hours are a spin-up period. Initially, the density interface is positioned horizontally at 16 m depth.

In Fig. 4.2 a time series of the measured and calculated water levels at the two water level stations have been shown. It is seen that the water level is dominated by the semi-diurnal tide and that the Coriolis effect causes a difference of approximately 10 cm across the Belt under conditions with southward flow. A persisting southerly wind direction throughout the simulation period prevents a northward flow in the upper water masses and hence, neutralizes the Coriolis effect under ebb-tide conditions. Due to the limited model area the water level is strongly influenced by the boundary data and evidently - as seen in Fig. 4.2 - there must be a good agreement between the measured and calculated water levels.

In Fig. 4.3 an example of the horizontal velocities at the surface, at 16 m depth and 24 m depth, have been shown. At this particular time a strong southward flow is present in the upper water masses yielding at a Coriolis tilting at the surface (cf. Fig. 4.2). The reversed tilting of the density interface approximately positioned at -16 m causes a westward flow of dense water through a narrow trench south of the small island Sprogø in the middle of the Great Belt. This feature is also observed in many of the measurements, taken from a research vessel, carried out in parallel to the fixed stations measuring programme.

Typical examples of time series of measured and calculated current speeds have been given in Fig. 4.4.

The discrepancies between the measured and calculated speeds are more pronounced compared with the water levels. Naturally this is to be expected, due to the complexity of the physical (and numerical) velocity fields.

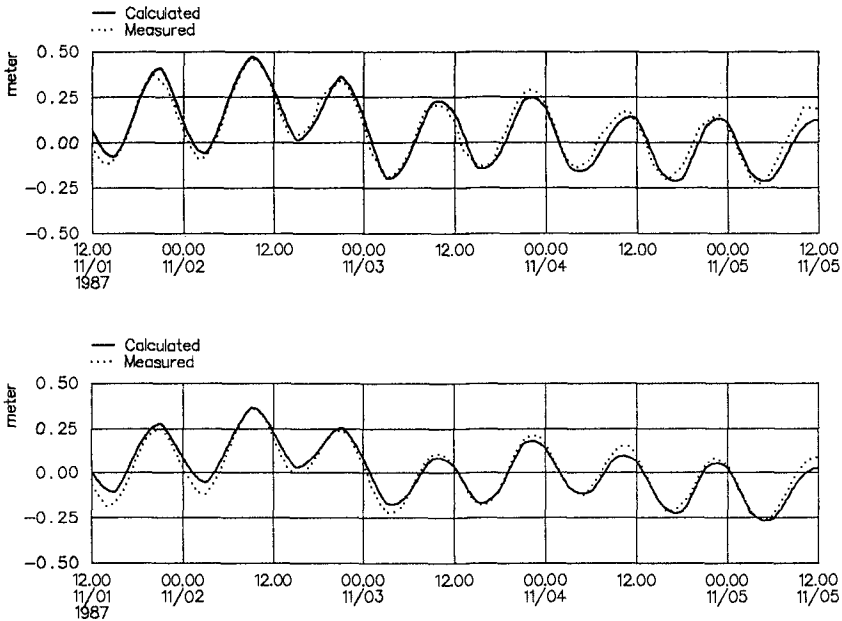
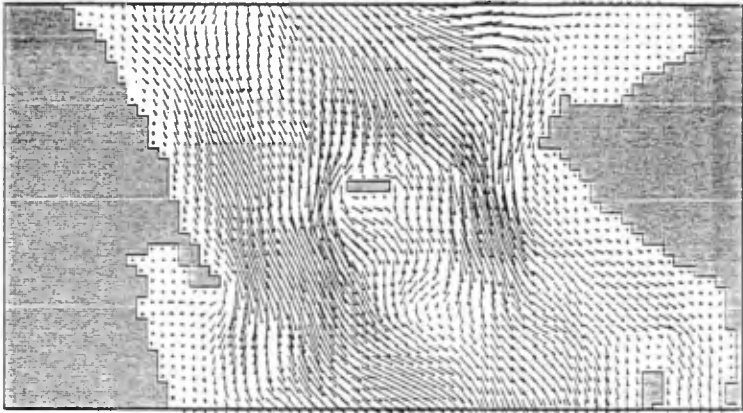


Fig. 4.2 Time series of measured and calculated water levels in Slipshavn (upper) and Korsør (lower)

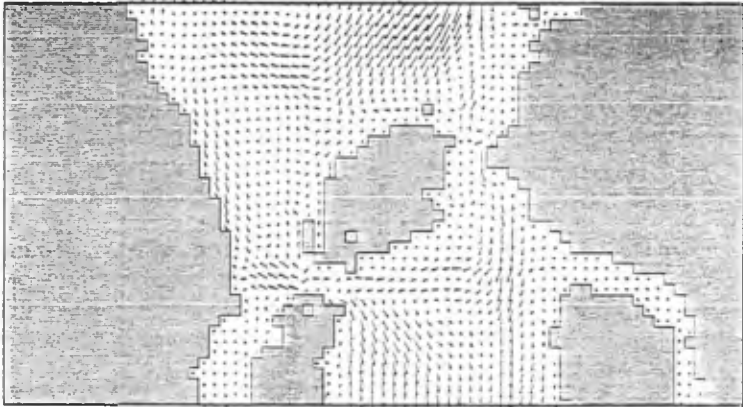
As a qualitative assessment of the model performance the 12 hourly peak values of the current speeds have been extracted from the time series of each current meter along with the corresponding model data. In Fig. 4.5 the calculated vs measured peak values have been shown for all stations and all levels.

Station AH, B and C are deployed on the hillside of a deep, narrow trench (see Fig. 4.1) and thus, provide difficulties in the calibration due to an often inadequate spatial resolution. Comparing these three stations it is seen that there is a reasonable

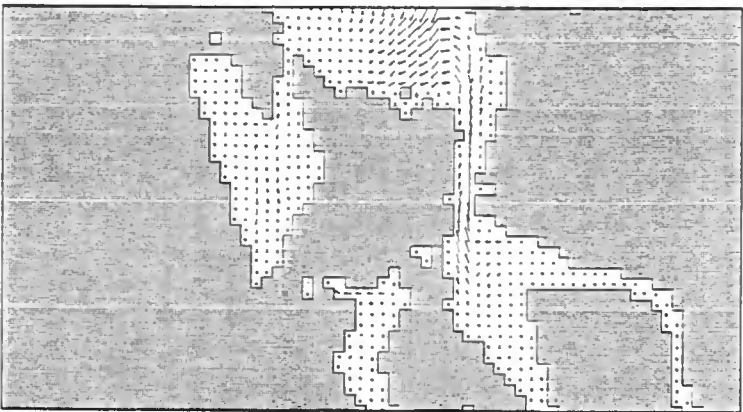
A.



B.



C.



— 0.25 m/s

Fig. 4.3 Calculated horizontal velocities at the surface (A), -16 m (B) and -24 m (C) on November 4, 1987 at 12:00.

agreement for the upper levels except for station AH which seems to overpredict the current speed generally. At station B the model tends to underpredict the peak values at the lower levels which probably is due to a discrepancy in the actual and modelled density interface and the associated damping of the shear stress.

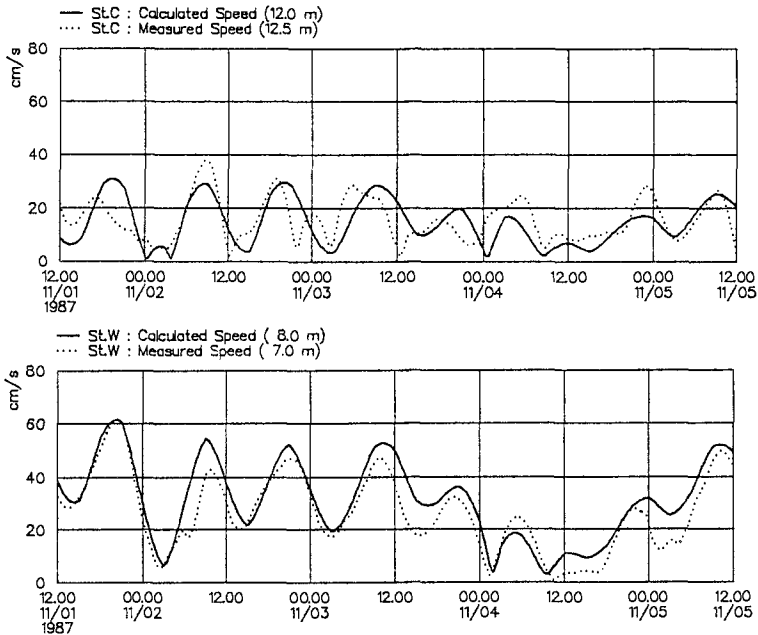


Fig. 4.4 Time series of measured and calculated current speed at Station C (upper) and Station W (lower)

The lower levels at station D show a fairly good agreement whereas the upper levels tend to overpredict. As station D is positioned close to the boundary the prescribed uniform velocity profile is a likely explanation for this behaviour. In nature the highest velocities are observed at the surface and decreasing downwards under the present meteorological and hydrographical conditions. At station W a good agreement is found at the upper level whereas the model overpredicts the peak values at the lower level. Similar to station B the likely explanation for this behaviour is the density interface.

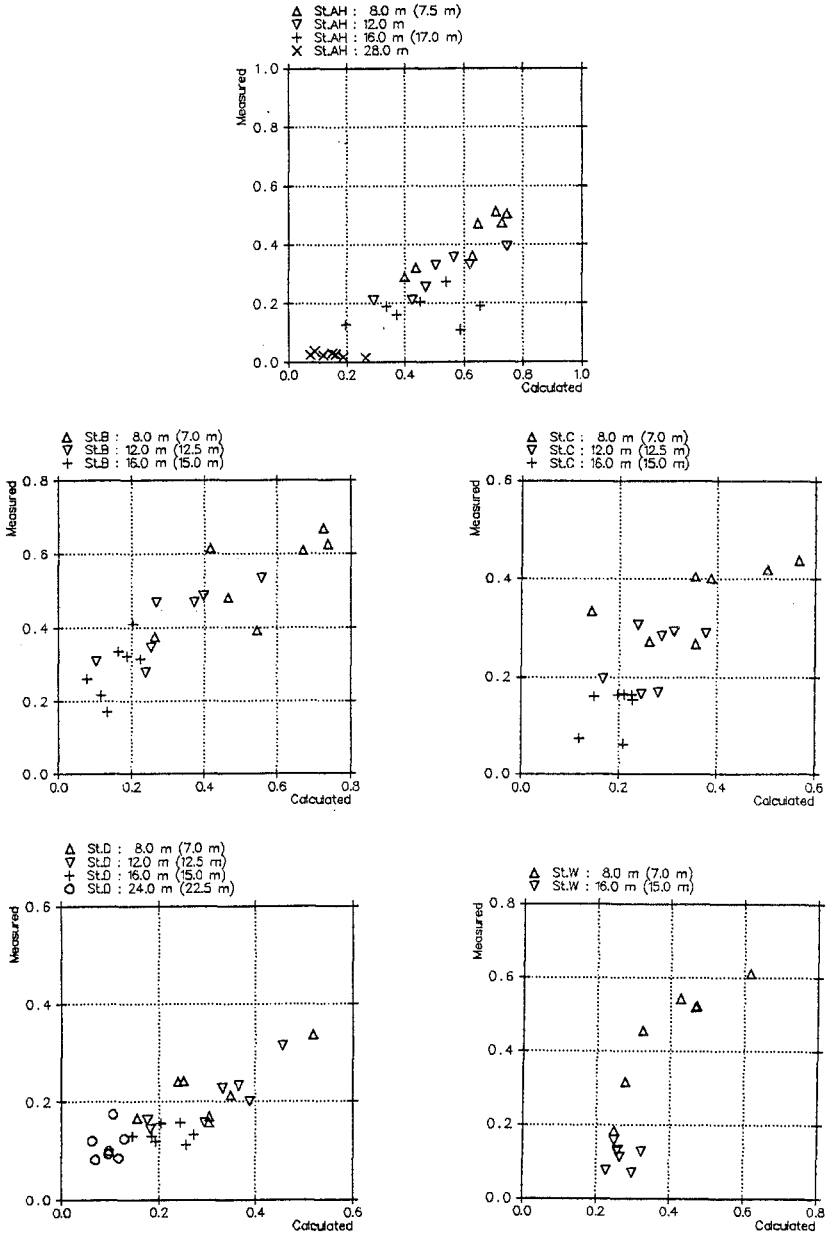


Fig. 4.5 Calculated vs measured 12 hourly peak values of current speeds (m/s) for all stations and all levels

The overall assessment of the model performance with respect to current modelling in stratified seas illustrates the importance of consistent boundary data and the ability of accurate modelling of stratification.

Although the present technique for establishing the boundary data for the three-dimensional model is not generally applicable and, furthermore, is time-consuming, it is a possible way out of the boundary data dilemma. On the other hand, this technique of utilizing results from layered models implies that only the area of interest needs to be modelled in detail and hence, often implies reduced computational costs. Alternatively, the three-dimensional model can be set up for so large an area that the open boundaries are better prescribed, e.g. so far away from the area of interest that the water masses can be regarded as homogeneous.

The problems associated with the boundaries may limit the practical applications of three-dimensional models seriously. Thus, further attention to these problems and especially those regarding the stratification is considered essential.

REFERENCES

- Aupoix, B. and Cousteix, J. (1982): "Subgrid Scale Model for Isotropic Turbulence", Proc. of Symposium on Refined Modelling of Flows, Paris.
- Justestén, P., Olesen, K.W. and Vested, H.J. (1989): "High Accuracy Modelling of Advection in Two and Three Dimensions", XXIII Congress IAHR, Ottawa.
- Leonard, B.P. (1979): "A Stable and Accurate Convective Modelling Procedure Based on Quadratic Upstream Interpolation", Computer Methods in Applied Mechanics and Engineering, 19, 59-98.
- Simpson, J.E. (1987): "Gravity Currents: In the Environment and in the Laboratory", Ellis Horwood Ltd., Chichester.
- Smagorinsky, J. (1963): "General Circulation Experiments with the Primitive Equations, 1. The Basic Experiment", Monthly Weather Review, 91, 99-164.

Long Wave Interaction with Steeply Sloping Structures

Stéphan T. Grilli ¹ and Ib A. Svendsen ², M. ASCE

Abstract : A fully nonlinear model for free surface potential flows is used to analyze the transformation of solitary waves above a mild slope, from intermediate to shallow water (shoaling, overturning), and to study the interaction of these waves with coastal structures located in the shallow area. Computations include wave runup, overturning and reflection from steep slopes or vertical wall, and from a combination of a slope and a submerged breakwater. Results are compared with other numerical, analytical and experimental results. Effects of the submerged breakwater, of making horizontal velocities more uniform over depth and of reducing wave runup on the slope, are further detailed.

Introduction

In this paper, the Boundary Element Model (BEM) for fully nonlinear waves developed by Grilli, *et al.* 1989, is used to analyze the runup and reflection of solitary waves from steep plane slopes and their transformation over a combination of a mild slope and coastal structures (submerged breakwater in front of a steep slope). The model solves two-dimensional free surface flows, in cases where potential flow is a good approximation. Under such conditions, Green's identity makes it possible to transform Laplace's equation into a Boundary Integral Equation (BIE). Instantaneous solution to this equation is then updated in time using the fully nonlinear kinematic and dynamic boundary conditions at the free surface. Along solid boundaries, no-flow conditions or conditions for generating or radiating waves can be imposed as well.

This approach to nonlinear wave flows has been very successful over the last decade. Particularly noteworthy for important steps in its development are contributions by Longuet-Higgins & Cokelet 1976, Vinje & Brevig 1981 and Dold & Peregrine 1986. Most of the applications so far, however, solved the problem in a transformed space or used complex variable formulations, and introduced the assumption that waves are periodic in space.

¹Visiting Research Faculty, *Center for Applied Coastal Research*, Department of Civil Engineering, University of Delaware, Newark-DE 19716, USA, Ph.Nb.: 302-4516383

²Professor and Chairman (same address)

In our model, the equations are solved directly in the physical space (i.e., without any mapping). This yields a method which is capable of directly adapting to almost any geometry of the boundaries and to periodic as well as non-periodic wave conditions. The BIE is solved using a higher-order Boundary Element Method (first introduced by Brebbia 1978), and the time integration is explicit and of second-order accuracy in time, based on the method of Dold & Peregrine 1986. In the model, wave generation can be done by a wavemaker, by internal sources, or by imposing the potential on the free surface (see Grilli & Svendsen 1989b, 1990). In the present paper, only the numerical wavemaker is presented and used to generate solitary waves.

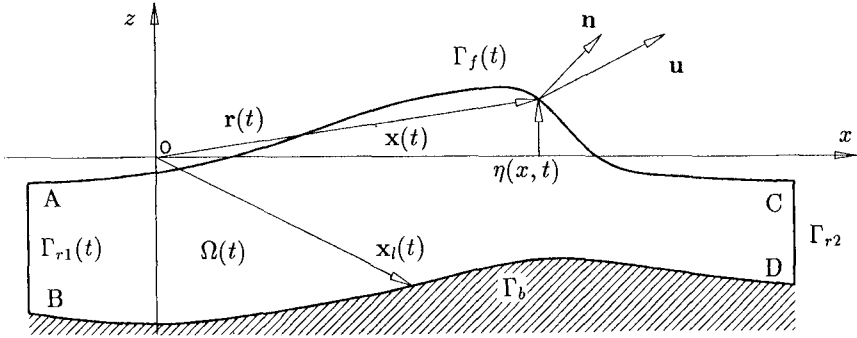


Figure 1: Sketch of the region used in the numerical computations. Definition of geometrical parameters.

Mathematical formulation

Governing equations.— We consider an inviscid irrotational 2-D flow described by a velocity potential $\phi(\mathbf{x}, t)$, and the velocity field is given by $\mathbf{u} = \nabla\phi = (u, w)$. Thus, the continuity equation in the fluid domain $\Omega(t)$ with the boundary $\Gamma(t)$ becomes a Laplace equation for ϕ (Figure 1),

$$\nabla^2\phi = 0 \quad \text{in } \Omega(t) \tag{1}$$

Using the free space Green’s function $G(\mathbf{x}, \mathbf{x}_l) = -\frac{1}{2\pi} \log |\mathbf{x} - \mathbf{x}_l|$, (1) becomes the Boundary Integral Equation (BIE),

$$\alpha(\mathbf{x}_l)\phi(\mathbf{x}_l) = \int_{\Gamma(\mathbf{x})} \left[\frac{\partial\phi}{\partial n}(\mathbf{x})G(\mathbf{x}, \mathbf{x}_l) - \phi(\mathbf{x})\frac{\partial G(\mathbf{x}, \mathbf{x}_l)}{\partial n} \right] d\Gamma(\mathbf{x}) \tag{2}$$

where $\mathbf{x} = (x, z)$ and $\mathbf{x}_l = (x_l, z_l)$ are position vectors for points on the boundary, \mathbf{n} is the unit outward normal vector. and $\alpha(\mathbf{x}_l)$ is a geometric coefficient.

On the free surface $\Gamma_f(t)$, ϕ satisfies the kinematic and dynamic boundary conditions,

$$\frac{D\mathbf{r}}{Dt} = \left(\frac{\partial}{\partial t} + \mathbf{u} \cdot \nabla \right) \mathbf{r} = \mathbf{u} = \nabla\phi \quad \text{on } \Gamma_f(t) \tag{3}$$

$$\frac{D\phi}{Dt} = -gz + \frac{1}{2} |\nabla\phi|^2 - \frac{p_a - p_o}{\rho} \quad \text{on } \Gamma_f(t) \quad (4)$$

with \mathbf{r} , the position vector of a free surface fluid particle, g the acceleration due to gravity, z the vertical coordinate (positive upwards and $z = 0$ at the undisturbed free surface), p_a the pressure at the surface, p_o a reference pressure (e.g. at infinity) and ρ the fluid density.

General boundary conditions.— In the present applications waves are generated by simulating a plane wavemaker motion on the boundary $\Gamma_{r1}(t)$. In this case, the motion and normal velocity are specified over the paddle by,

$$\nabla\phi \cdot \mathbf{n} \equiv \overline{\frac{\partial\phi}{\partial n}} = \mathbf{u}_p(\mathbf{x}_p(t), t) \cdot \mathbf{n} \quad \text{on } \Gamma_{r1}(t) \quad (5)$$

where the overline denotes a specified value, and $(\mathbf{x}_p, \mathbf{u}_p)$ are prescribed wavemaker motion and velocity respectively. Along the stationary bottom Γ_b and the tank extremity Γ_{r2} representing a fixed structure (not necessarily vertical as in Figure 1), we have,

$$\nabla\phi \cdot \mathbf{n} \equiv \overline{\frac{\partial\phi}{\partial n}} = 0 \quad \text{on } \Gamma_b \text{ and } \Gamma_{r2} \quad (6)$$

Time stepping method.— The time stepping, described in detail in Grilli, *et al.* 1989, follows the Eulerian-Lagrangian approach used by Dold & Peregrine 1986. It consists of integrating the two nonlinear free surface conditions (3) and (4) at time t , to establish both the new position of the free surface $\Gamma_f(t)$ and the relevant boundary conditions of Laplace's problems at the next time step $t + \Delta t$. It uses Taylor expansions in terms of the Lagrangian time derivative (as defined in (3)) and the small time increment Δt , for both the position $\mathbf{r}(t)$ and the potential $\phi(t)$ on the free surface, which corresponds to following in time the pathline of a fluid particle, identical to a node of the discretization used for solving the BIE (2). We have so far limited the series to second order in Δt , which requires solving two Laplace problems at each time step (for ϕ and $\frac{\partial\phi}{\partial t}$), to get the coefficients in the series.

After solving a first Laplace problem for $(\phi, \frac{\partial\phi}{\partial n})$ at time t , boundary conditions of a second problem for $(\frac{\partial\phi}{\partial t}, \frac{\partial^2\phi}{\partial t\partial n})$ are determined. Along the free surface, Bernoulli's equation yields,

$$\overline{\frac{\partial\phi}{\partial t}} = -gz - \frac{1}{2} |\nabla\phi|^2 - \frac{p_a - p_o}{\rho} \quad \text{on } \Gamma_f(t) \quad (7)$$

and along the fixed boundaries, we get,

$$\overline{\frac{\partial^2\phi}{\partial t\partial n}} = 0 \quad \text{on } \Gamma_b \text{ and } \Gamma_{r2} \quad (8)$$

For a plane wavemaker, we have,

$$\overline{\frac{\partial^2 \phi}{\partial t \partial n}} = \left[\frac{d(\mathbf{u}_p \cdot \mathbf{n})}{dt} - \mathbf{u}_p \cdot \nabla(\mathbf{u}_p \cdot \mathbf{n}) \right] \quad \text{on } \Gamma_{r1}(t) \quad (9)$$

Boundary conditions for a plane wavemaker.— Development of (9) for a rigid body motion, with translation α and rotation θ yields (Cointe 1989),

$$\overline{\frac{\partial^2 \phi}{\partial t \partial n}} = (\ddot{\alpha} \cdot \mathbf{n}) + \dot{\theta}[(\dot{\alpha} \cdot \mathbf{s}) - \frac{\partial \phi}{\partial s}] - \frac{\partial^2 \phi}{\partial n \partial s}(\dot{\alpha} \cdot \mathbf{s}) + \frac{\partial^2 \phi}{\partial s^2}(\dot{\alpha} \cdot \mathbf{n}) \quad (10)$$

where the dots denote time derivatives ($\frac{d}{dt}$) following the body motion.

A *piston wavemaker* represents a flat vertical plate moving with horizontal displacement $x_p(t)$ and velocity $u_p(x_p(t), t) = \dot{x}_p(t)$. Hence from (5),(10), the boundary conditions read after some calculations,

$$\overline{\frac{\partial \phi}{\partial n}} = -u_p, \quad \overline{\frac{\partial^2 \phi}{\partial t \partial n}} = -\dot{u}_p - u_p \frac{\partial^2 \phi}{\partial s^2} \quad \text{on } \Gamma_{r1}(t) \quad (11)$$

A *Flap wavemaker* corresponds to a flat plate, hinged at the bottom at $\mathbf{x}_g = (0, -d)$ and rotating an angle $\theta(t) \in [\frac{\pi}{2}, 0]$ (negative clockwise). We define $x_p(t)$ and $u_p(x_p(t), t) = \dot{x}_p(t)$, the flap horizontal displacement and velocity respectively at the undisturbed free surface $z = 0$. Hence, from (5),(10), the boundary conditions read after some calculations,

$$\overline{\frac{\partial \phi}{\partial n}} = r_g \dot{\theta}, \quad \overline{\frac{\partial^2 \phi}{\partial t \partial n}} = r_g \ddot{\theta} + \dot{\theta} \left(r_g \frac{\partial^2 \phi}{\partial s^2} - \frac{\partial \phi}{\partial s} \right) \quad \text{on } \Gamma_{r1}(t)$$

$$\dot{\theta} = -R u_p, \quad \ddot{\theta} = -R \left[\dot{u}_p - 2u_p \frac{x_p}{d} \right], \quad r_g = R \sqrt{d^2 + x_p^2} \left[\alpha \frac{x_p}{d} + \beta + d \right] \quad (12)$$

where $R = d/(d^2 + x_p^2)$, and (α, β) represent points along the flap.

Numerical implementation

The BIE (2), equivalent to the Laplace's problems (1) for ϕ and the equivalent BIE problem for $\frac{\partial \phi}{\partial t}$, is solved by a Boundary Element Method (BEM, Brebbia 1978) using a set of collocation nodes on the boundary and higher-order elements to interpolate between the collocation nodes. Quasi-spline elements (Longuet-Higgins & Cokelet 1976) are used on the free surface, and isoparametric elements elsewhere (linear to quartic).

Each integral in (2) is transformed into a sum of integrals over each boundary element. Non-singular integrals are calculated by standard Gauss quadrature rules. A kernel transformation is applied to the weakly singular integrals, which are then integrated by a numerical quadrature exact for the logarithmic singularity. An adaptive numerical integration is used for improving the accuracy of the regular integrations near corners (A-D, Fig. 1) and other places, like the overturning jet in breakers (as, e.g., in Fig. 8c,d), where elements on different parts of the boundary get close to each other.

Details of the numerical implementation can be found in Grilli, *et al.* 1989, 1989b, 1990, along with a discussion of problems associated with surface piercing bodies, such as wavemakers.

Generation of a solitary wave

By a piston wavemaker.—In the following, primes denote dimensionless variables: lengths are non-dimensionalized by d , times by $\sqrt{\frac{d}{g}}$, velocities by \sqrt{gd} and accelerations by g .

For a wave of permanent form, Goring 1978 determined to the first-order, the motion required by a piston wavemaker to generate a specified water surface elevation η immediately in front of the wavemaker (see Grilli & Svendsen 1989a, for detail) as,

$$x_p(t) = \int_0^t \frac{c\eta(x, \tau)}{d + \eta(x, \tau)} d\tau \quad (13)$$

A *first-order* solitary wave profile of amplitude H' in water of constant depth $d' = 1$ is given by,

$$\eta'(x', t') = H' \operatorname{sech}^2[\kappa(x' - c't')] \quad (14)$$

where $\kappa = \frac{\sqrt{3H'}}{2}$ and the celerity $c' = \sqrt{1 + H'}$. Substituting (14) into (13) with $x' = x'_p(\tau')$ required throughout the integration gives the piston motion. The profile (14), however, is truncated at a distance $x' = \lambda'$ from the origin, before it is used in the computations. Setting $x' = x'_p + \lambda'$ in (14) and integrating (13) we get $x'_p(t')$ and, by derivation, $u'_p(t')$ and $\dot{u}'_p(t')$ (see Grilli & Svendsen 1990, for the complete expressions), which, introduced into (11), define the boundary conditions at the wavemaker.

Solitary waves of small amplitude ($H' < 0.2$) are well generated by this method. For such waves, the *first-order* profile (14) is indeed quite close to the exact solution. For steep waves ($H' \geq 0.2$), however, due to nonlinear effects, solitary waves generated by the piston adjust their shape as they propagate, and shed a tail of oscillation behind them (Grilli & Svendsen 1989a). In fact, this was already observed by Goring 1978, in his experiments.

Numerically exact solitary waves.—Solitary waves which are as close to being exact as the discretization allows—"numerically exact waves"—are also used in the computations. They are computed using the method developed by Tanaka 1986, and established as initial condition in the constant depth part of the computational domain.

Reflection from a vertical wall

Reflection of solitary waves from a vertical wall has been used to validate the numerical model, and to compare results with other numerical, analytical or experimental results. In this application, numerically exact solitary waves have also

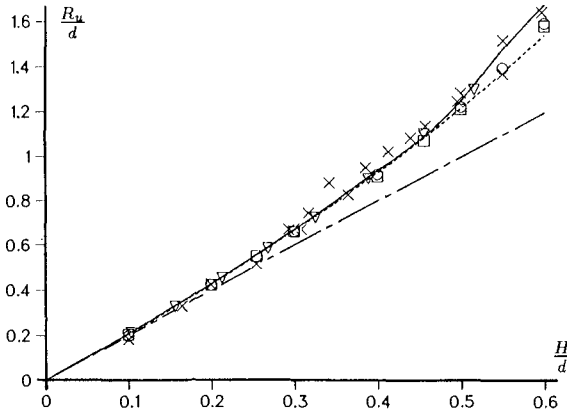


Figure 2: Maximum runup $\frac{R_u}{d}$ for reflection from a vertical wall of solitary waves of height $\frac{H}{d}$. Results of : (—) spline fitting to BEM for the *exact* waves, (\square) BEM for the *first-order* waves, (\circ) Chan & Street 1970 Euler eq., (∇) Fenton & Rienecker 1982 Fourier Method, (\times) Camfield & Street 1969 exper., (- - -) Su & Mirie (1980) 3rd-order analytical solution and (— — —) linear solution.

been used along with the approximate waves generated by the piston wavemaker.

Runup.—In Figure 2, maximum runup values $\frac{R_u}{d}$ obtained with the BEM model for the exact and the approximate (1st-order) waves, are compared with a finite difference solution of Euler equations by Chan & Street 1970 (CH&S), a higher-order Fourier solution by Fenton & Rienecker 1982 (F&R), experimental results by Camfield & Street 1969 (CA&S), and a 3rd-order analytical solution by Su & Mirie 1980 (S&M). One sees that, up till about $\frac{H}{d}=0.45$, all theoretical methods predict similar runups. Above that value, the 3rd-order theory predicts smaller runups, implying that contributions of order higher than third are becoming important. For high waves, F&R's solution coincides closely with our results for the exact waves, and CH&S's solution agrees well with those of our 1st-order waves. This is likely due to the approximate way CH&S generated their initial waves, which makes them qualitatively closer to waves generated by a wavemaker. Finally, CA&S's experiments agree well with the higher-order results.

Pressure force.—Once the BEM solution for the wave motion has been computed, essentially all details of the flow pattern are known, including pressures. We can therefore also calculate the forces and moments exerted on the structure. We found that maximum forces and moments predicted by the BEM closely correspond to F&R and S&M results, up till $\frac{H}{d}=0.5$. For higher waves, a somewhat surprising result of the BEM is a double maximum found in the time variation of the force and moment (Figure 3).

Reflected wave.—A detailed analysis of the reflected waves shows that an os-

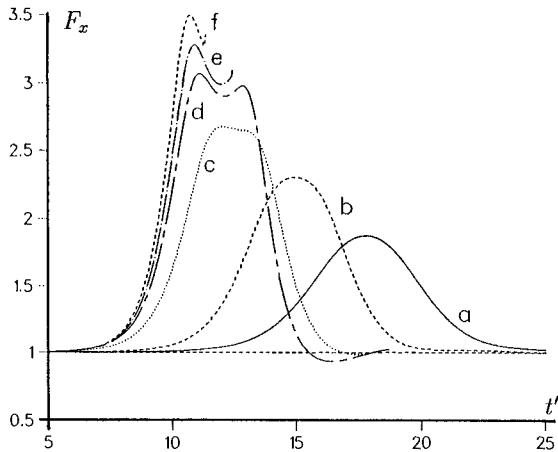


Figure 3: Development in time of total dimensionless pressure force F_x on a vertical wall during reflection of an *exact* solitary wave. $\frac{H}{d}$: (a) 0.2, (b) 0.3, (c) 0.4, (d) 0.5, (e) 0.55, (f) 0.6.

cillatory tail is created by the reflection process, along with negative rundown values on the wall (of about 10% $\frac{H}{d}$ for $\frac{H}{d}=0.5$). Energy is transmitted from the main leading wave to the tail, which results in a slight decrease in wave amplitude after reflection (of about 10% $\frac{H}{d}$ for $\frac{H}{d}=0.5$). These observations tie well in with the 5th-order analytical results by Byatt-Smith 1988. Right after reflection, the reflected wave is also found slightly faster than the incident wave, even though it is smaller (by about 0.5% for $\frac{H}{d}=0.5$). This is due to highly transient changes in shape, energy partition and celerity of the wave, which take place over large propagation distances.

Reflection from a steep slope

Reflection from steep slopes (45° and 70°) has been examined for solitary waves generated by a piston wavemaker, the same way as in the laboratory experiments by Losada, *et al.* 1986 (LVN). Comparison with the measurements shows that phenomena such as generation, propagation and runup on a steep slope of large amplitude waves can be accurately predicted by our model. Even small scale oscillations in the experiments (like the oscillatory tail after reflection) are reproduced quite accurately. An example is given below.

Runup and rundown.—Reflection is computed on both the 45° and 70° slopes for waves of $\frac{H}{d} \approx 0.26, 0.45$. Results show maximum runup values $\frac{R_u}{d}$ are in good agreement with LVN's experiments (within 2.5% for $\theta = 45^\circ$ and 2.0% for $\theta = 70^\circ$). The agreement for the rundown figures $\frac{R_d}{d}$ is somewhat less good but it should be noted that LVN found this quantity quite difficult to measure. Details

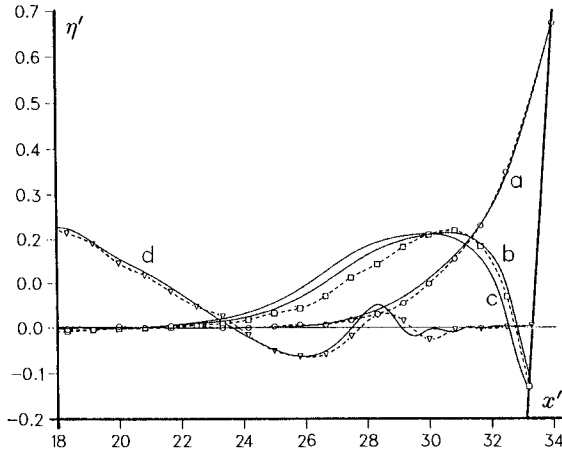


Figure 4: Comparison between computations (—) and measurements (- - -) by Losada, *et al.* 1986 for reflection from a 45° slope of a solitary wave of $\frac{H}{d}=0.269$. The symbols mark data points and the dotted curve is a spline fit to these points. (a) Instant of maximum runup. (b) 0.44 time unit before rundown. (c) Instant of lowest position of water surface. (d) Back of the reflected wave.

can be found in Grilli & Svendsen 1989a.

Free surface elevation.—Figure 4 shows results for the reflection of a wave of $\frac{H}{d}=0.269$ from a 45° slope. The computations are compared with the surface profiles measured by LVN at three different times, of which the first available is the instant of maximum runup (curves a) used for synchronization. In general, the agreement is considered good. Results, however, do not quite coincide at the time of rundown (curve c). The agreement is somewhat better with a profile computed at a time slightly before the instant of rundown (curve b). This shows that, as pointed out by LVN, both rundown and instant of rundown are quite difficult to measure since the surface motion along the slope is important over a very short time (the whole rundown process only lasts a small fraction of a second in the experiments).

Internal velocities.—Motivated by the accuracy of the computations the method has also been used to analyze flow properties such as velocity and pressure fields that have not been measured during the experiments. Water particle velocities have been computed above 30° and 45° slopes, during runup-rundown of a wave of $\frac{H}{d}=0.46$. Figure 5 shows quite complex flows above a 30° slope, with jet-like details (Fig. 5a,b) and a stagnation point (Fig. 5b) climbing up the slope during runup. It is found, the flow is never completely at rest at any moment of the wave reflection (even at the instant of runup in Fig. 5c). Finally, Figure 5d shows the initiation of breaking during the rundown process (backwash), at the rearside of

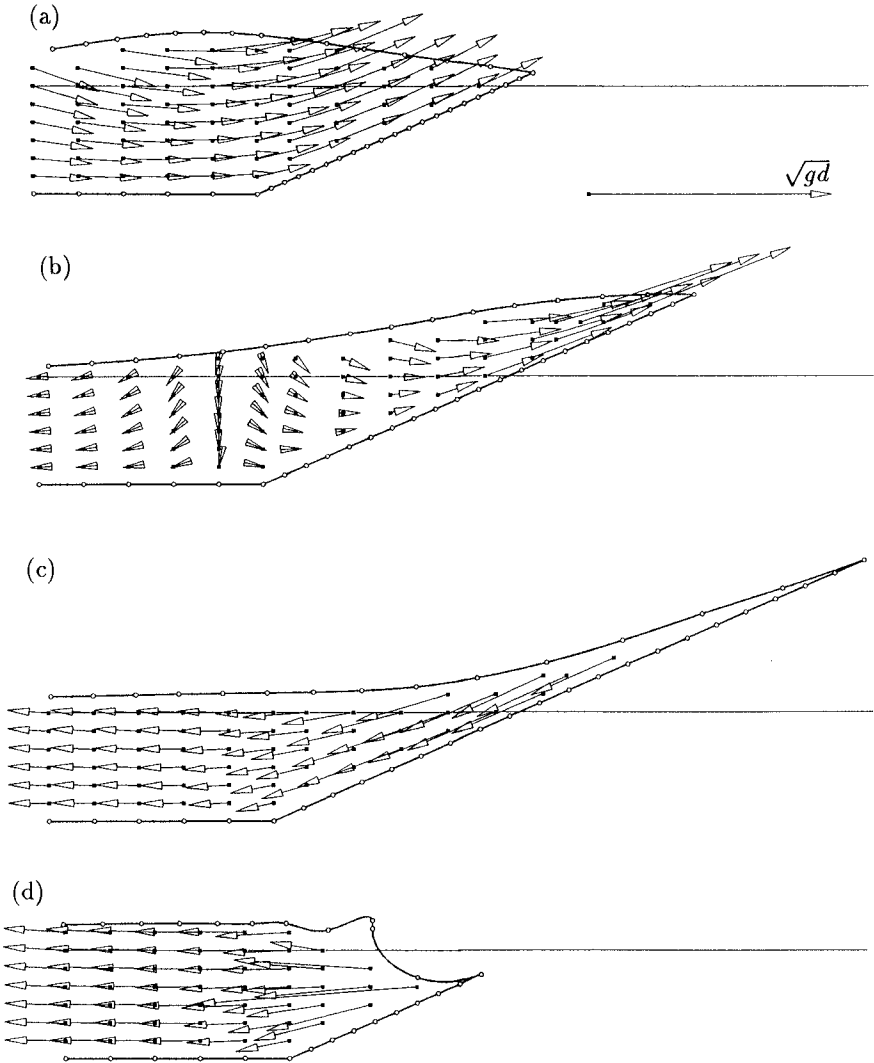


Figure 5: The internal velocity field during runup of a first-order solitary wave with $\frac{H}{d} = 0.46$ on a 30° slope, at time $t' - t'_a =$ (a) : 0, (b) : 0.40, (c) : 0.95 (maximum runup), (d) : 1.90.

and in the direction opposite to the propagation of the reflected wave.

Detailed analysis of the results (Svendsen & Grilli 1990) shows that, for both slopes, horizontal velocities are significantly non-uniform over the depth (with variations of 25-35%) and that, accordingly, important non-hydrostatic pressures are generated (up to 80% on a 45° slope and 180 % on a 30° slope). This invalidates the assumptions underlying the Nonlinear Shallow Water equations and makes their use questionable in these situations. The maximum runup, however, is found to compare reasonably well with the analytical results obtained by, e.g., Synolakis (1987) using those approximate equations.

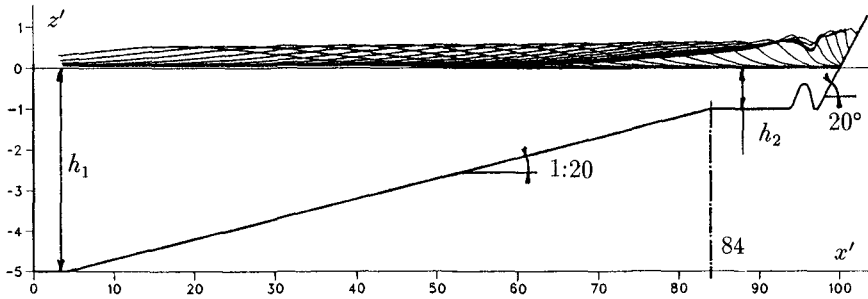


Figure 6: Sketch of composite domain : The shoaling zone is defined for $x' \leq 84$, and the shallow zone for $x' > 84$. Solitary waves are generated by a piston wavemaker at the leftward boundary.

Shoaling and reflection over a complex geometry

Solitary waves are propagated from deep to shallow water, in a domain with the bottom configuration of Figure 6. Waves of $\frac{H_1}{h_1} = 0.05$ to 0.2 are generated by a piston wavemaker, at the left hand boundary, in water of depth $h_1 = 5$, and are propagated over a mild 1:20 slope towards a region of depth $h_2 = 1$. At the extremity of this region, there is a combination of a submerged breakwater and a 20° slope. The length of the domain is $100h_2$, and the regions with $x' = \frac{x}{h_2} < 84$ (the end of the mild slope), or > 84 are named the shoaling and the shallow zones, respectively.

Shoaling zone.—Shoaling of waves of $\frac{H_1}{h_1} = 0.05, 0.10, 0.15$ and 0.2 has been computed. In a logarithmic scale, results in Figure 7 show that, for $-\log\left(\frac{h}{h_1}\right) \leq 0.45$ (i.e., $x' \simeq 60$), the rate of shoaling is close to, but not quite, the one predicted by Green's law. The average slope of the 4 curves in Figure 7 actually is closer to 1:5 in this region. During shoaling, incident waves reflect on the 1:20 slope. Due to the finite length of the computational domain, however, reflected waves propagating backward in the domain also reflect on the wavemaker. This leads to a slight increase in water level in the shoaling zone. Since smaller solitary waves are longer, the relative increase in level is somewhat more pronounced for

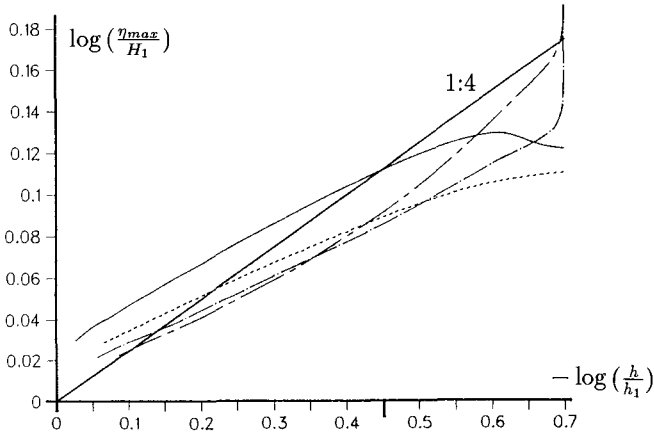


Figure 7: Maximum wave amplitude $\frac{\eta_{max}}{H_1}$ in shoaling zone, as a function of relative depth $\frac{h}{h_1}$ for $\frac{H_1}{h_1}$: (—) 0.05, (- - -) 0.10, (- · -) 0.15, (— —) 0.20. The straight line represents theoretical Green's law: $\frac{\eta_{max}}{H_1} \propto \left(\frac{h}{h_1}\right)^{-\frac{1}{4}}$

the smallest waves. This is illustrated by the vertical shifts between the curves in Figure 7.

Further up the slope, for $-\log\left(\frac{h}{h_1}\right) > 0.45$ (i.e., $x > 60$), the rate of shoaling of the two smallest waves reduces, whereas the two largest waves shoal up even more and at an increasing rate. This is likely because the smallest waves, being longer, start earlier feeling the influence of the shallow water zone ($h = h_2$).

Shallow zone.—Figure 8c and d show that the largest waves of initial height $\frac{H_1}{h_1} = 0.15$ and 0.20 continue shoaling in the shallow zone, even though it is of constant depth. Their profile becomes more and more asymmetric, and their amplitude peaks up to $\frac{\eta_{max}}{h_2} \simeq 1.4$ and 1.6. They eventually become plunging breakers, somewhat before reaching the submerged breakwater. Hence, this shows, highly transient waves can reach breaking heights of more than twice the classical 0.78 times the local depth.

The two smallest waves of $\frac{H_1}{h_1} = 0.05$ and 0.1 (Figure 8a and b) shoal up to $\frac{\eta_{max}}{h_2} \simeq 0.55$ and 0.80 (at $x' \simeq 95$), respectively, propagate over the submerged breakwater and run on the slope up to heights of $\frac{R_w}{h_2} \simeq 0.90$ and 1.5 respectively. Even higher relative heights of $\frac{\eta_{max}}{h} = 1.26$ and 1.66 respectively, are locally reached above the submerged breakwater.

Figure 8b also shows the wave of $\frac{H_1}{h_1} = 0.1$, eventually, is similar to a collapsing breaker. Computations of internal velocities above the slope, for a time slightly before the collapsing, show that velocities are close to being uniform over the depth. This is unlike the results obtained (e.g., in Fig. 5) for wave runup on steep slopes without a submerged breakwater at their toe, where the non-uniformity of the horizontal velocity was as high as 35%. Computations

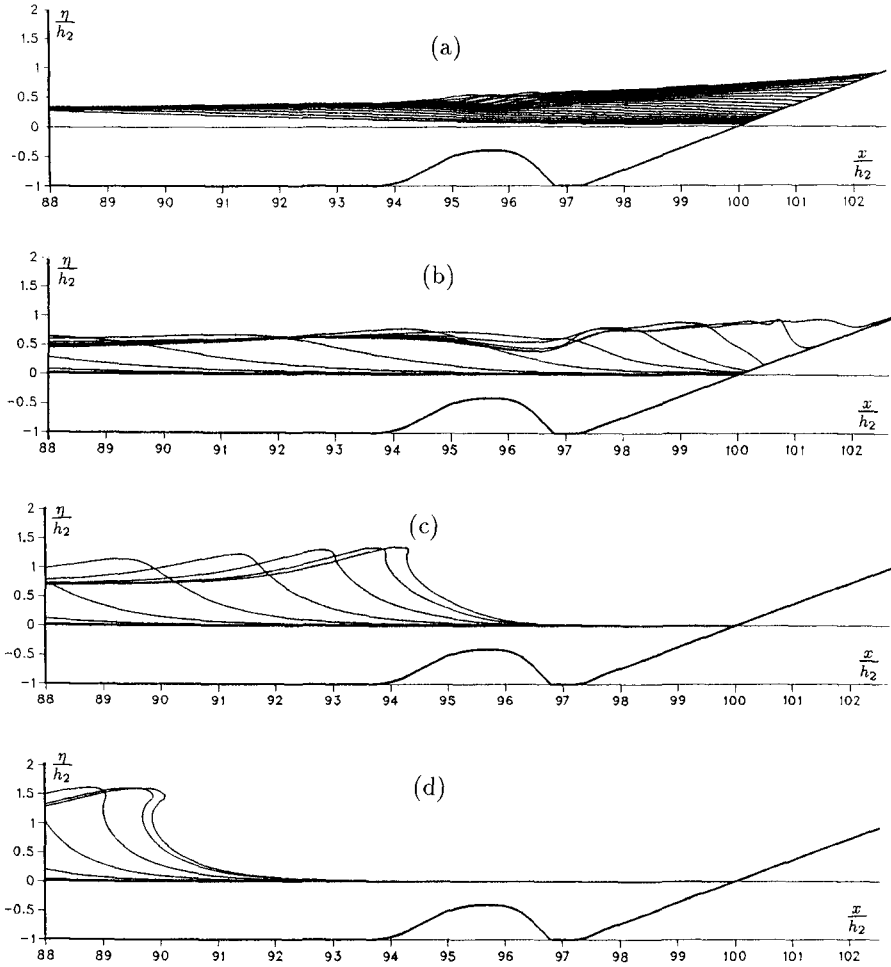


Figure 8: Free surface elevation $\frac{\eta(x)}{h_2}$ in the shallow zone for $\frac{H_1}{h_1}$: (a) 0.05, (b) 0.10, (c) 0.15, (d) 0.20. Profiles are plotted each 10 (varying) time steps.

made in the same domain, for the same wave as in Figure 8b, but without the submerged breakwater, give a maximum runup of more than twice the previous result ($\frac{R_u}{h_2} = 3.16$). This shows, the submerged breakwater has the effect, not only of making velocities more uniform (i.e., decreasing the maximum velocity), but also of reducing wave runup. Both these effects mean reduction of wave action on the steep slope.

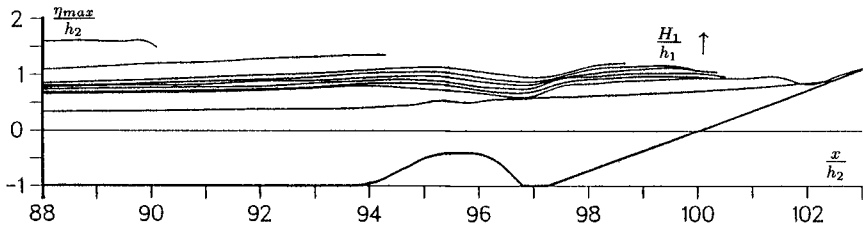


Figure 9: Envelope of maximum surface elevation $\frac{\eta_{max}}{h_2}$ in the shallow zone : curves represent, from down to up, $\frac{H_1}{h_1}$: 0.05, 0.10, 0.105, 0.110, 0.115, 0.120, 0.125, 0.15, 0.20.

In order further to analyze the transition between situation (b) and (c) in Figure 8, computations have also been made for intermediate wave heights of $\frac{H_1}{h_1} = 0.105, 0.110, 0.115, 0.120$ and 0.125 . Figure 9 shows envelopes of the water elevations $\frac{\eta_{max}}{h_2}$ obtained for these waves, as well as for the waves used in Figure 8. When wave height is slightly increased above $\frac{H_1}{h_1} = 0.1$, results show, the breaking type changes from collapsing to surging and plunging. At the same time, the breaking point (i.e., the abscissa of the maximum amplitude of the last computed profile) moves slightly backward on the slope and the breaking height becomes slightly larger. For all waves, there is a trough in the envelope, slightly downstream of the submerged breakwater, corresponding to where velocities are becoming more uniform. Further downstream, about at the toe of the slope, wave height is building up again. This process corresponds to the transformation of kinetic energy into potential energy and seems to occur, here, at a faster rate than in the situation without the submerged breakwater. Hence, wave height builds up more and over a larger area above the slope, and runup values are reduced.

References

- Brebbia, C.A. (1978) *The Boundary Element Method for Engineers*. John Wiley & Sons, U.K..
- Camfield, F.E. & Street, R.L. (1969) "Shoaling of Solitary Waves on Small Slopes." *ASCE, WW95*, 1-22.
- Chan, R.K. & Street, R.L. (1970) "A Computer Study of Finite-amplitude Water Waves." *J. Comp. Phys.* **6** 68-94.
- Coite, R. (1989) "Quelques aspects de la simulation numérique d'un canal à houle." *Thèse de Docteur de l'Ecole Nationale des Ponts et Chaussées*, 284 pps.

- Dold, J.W. & Peregrine, D.H. (1986) "An Efficient Boundary Integral Method for Steep Unsteady water Waves." *Numerical methods for Fluid Dynamics II* (ed. K.W. Morton & M.J. Baines), pp. 671-679. Clarendon Press, Oxford.
- Fenton J.D. & Rienecker, M.M. (1982) "A Fourier Method for Solving Nonlinear Water-Wave Problems : Application to Solitary-Wave Interactions." *J. Fluid Mech.* **118**, 411-443.
- Goring D.G. (1978) "Tsunamis - The Propagation of Long Waves onto a Shelf." *W.M. Keck Laboratory of Hydraulics and Water Resources, California Institute of Technology, Report No. KH-R-38.*
- Grilli, S., Skourup, J. & Svendsen, I.A. (1989) "An Efficient Boundary Element Method for Nonlinear Water Waves." *Engineering Analysis with Boundary Elements*, **6** (2), 97-107.
- Grilli, S. & Svendsen, I.A. (1989a) "Computation of Nonlinear Wave Kinematics during Propagation and Runup on a Slope." In *Water Wave Kinematics* (Proc. NATO ARW, Molde, Norway, May 89) (ed. A. Torum & O.T. Gudmestad), NATO ASI Series E: Applied Sciences Vol. **178**, 387-412. Kluwer Academic Publishers.
- Grilli, S. & Svendsen, I.A. (1989b) "The Modelling of Highly Nonlinear Waves : Some Improvements to the Numerical Wave Tank." In *Advances in Boundary Elements (Proc. 11th Intl. Conf. on Boundary Elements, Cambridge-Massachusetts, USA, August 89)*, Vol. 2 (ed. C.A. Brebbia & J.J. Connor), pp. 269-281. Computational Mechanics Publication. Springer-Verlag, Berlin.
- Grilli, S. & Svendsen, I.A. (1990) "Corner Problems and Global Accuracy in the Boundary Element Solution of Nonlinear Wave Flows." *Engineering Analysis with Boundary Elements* **7** (4) (in press).
- Longuet-Higgins, M.S. & Cokelet, E.D. (1976) "The Deformation of Steep Surface Waves on Water - I. A Numerical Method of Computation." *Proc. R. Soc. Lond.* **A350**, 1-26.
- Losada, M.A., Vidal, C. & Nunez, J. (1986) "Sobre El Comportamiento de Ondas Propagándose por Perfiles de Playa en Barra y Diques Sumergidos." *Dirección General de Puertos y Costas Programa de Clima Marítimo. Universidad de Cantabria. Publicación No. 16.*
- Su, C.H. & Mirie, R.M. (1980) "On Head-on Collisions between two Solitary Waves." *J. Fluid Mech.* **98** 509-525.
- Svendsen, I.A. & Grilli, S. (1990) "Nonlinear Waves on Steep Slopes." *J. Coastal Research* **SI 7**, 185-202.
- Synolakis, C.E. (1987) "The Runup of Solitary Waves." *J. Fluid Mech.* **185**, 523-545.
- Tanaka, M. (1986) "The Stability of Solitary Waves." *Phys. Fluids* **29** (3), 650-655.
- Vinje, T. & Brevig, P. (1981) "Numerical Simulation of Breaking Waves." *Adv. Water Resources* **4**, 77-82.

CHAPTER 91

NORTH SEA WIND WAVES ON TIDES AND STORM SURGES

Hendrik L. Tolman *

ABSTRACT

The influence of tide- and surge-induced currents and surface level variations on wind wave generation and propagation in the North Sea is investigated. The main interest is focussed on the shift of the absolute frequency due to time varying currents. For several North Sea storms calculations have been performed with a third-generation wave model, which includes all relevant effects of wave-current interactions and wave generation. Results of several hindcasts have been compared with data. The study shows that tides and surges result in relatively small but distinct modulations of mean wave parameters (5 - 10%), and large variations of spectral energy densities (50%). The tide-induced modulations of in particular wave periods are strongly influenced by the unsteadiness of depth and current. Observed modulations of mean wave parameters with periods comparable to that of the tide appear to be wind-induced for a significant part.

1 Introduction

In the present study effects of tides and storm surges on North Sea wind waves are assessed. Such effects have been recognized by people living of the sea for centuries; charts of shelf seas like the North Sea indicate that tidal races (e.g. severe current induced breaking) occur near many headlands and offshore shoals. Theoretically the interactions between (wind) waves and currents have also been recognized. The subject is treated in many textbooks and review papers (e.g., Whitham 1974; Peregrine 1976; Phillips 1977; Mei 1983; Peregrine and Jonsson 1983; Jonsson 1990).

The separate modeling of waves (and currents) is well developed; all relevant kinematic and dynamic aspects of waves (including sources and sinks of wave energy) can be accounted for explicitly (e.g. WAMDI group 1988). In models for waves on currents, however, only a limited part of this knowledge is used. Source terms for input and

* Department of Civil Engineering, Delft University of Technology. Presently: Code 911, NASA / Goddard Space Flight Center Greenbelt, MD 20771, USA

dissipation are usually not considered at all (e.g., Dobson and Irvine 1983; Gutshabash et al. 1986; Liu et al. 1989), or highly parameterized (e.g., Holthuijsen et al. 1989). Furthermore all these models assume quasi-stationary current fields.

In the present study two aspects are added to the scope of previous studies on wave-current interactions. First, the present study deals with unsteady currents, accounting for the corresponding shift of absolute frequency. As is indicated in previous papers (Tolman 1988, 1990b), this effect of unsteadiness should not be neglected if waves on tides are considered. Secondly both wave-current interactions *and* wave growth and decay are fully accounted for. For the scale of shelf seas such an approach seems necessary, since scales of wave-current interactions and of growth and dissipation of wave energy are approximately equal (i.e. of the order of 1000 km and 1 day). To obtain both qualitative and quantitative results, the present study deals with some practical storm cases in the (southern) North Sea.

This paper presents a selection of the results of the authors PhD study (1990a). Formulations and models are described briefly. For an extensive review of the governing equations, numerical models and results, reference is made to Tolman (1989, 1990a).

2 Wave-current interactions

Wind waves are usually described with a variance (or energy) density spectrum F as a function of wave phase parameters such as the wavenumber k , the intrinsic or relative frequency σ (as observed in a frame or reference moving with the mean current \mathbf{U}), the absolute frequency ω (as observed in a fixed frame) and the direction θ (normal to the wave crest of the component). In the linear theory for (quasi-) uniform surface gravity waves on slowly varying depths and currents (e.g., LeBlond and Mysak 1978; Phillips 1977; Whitham 1974), the wavenumber k is related to the frequencies σ and ω in the dispersion relation (surface tension neglected, d is the water depth averaged over the wave field):

$$\sigma = \sqrt{gk \tanh kd} = \omega - \mathbf{k} \cdot \mathbf{U} \quad (1)$$

Wind wave propagation in an unsteady and inhomogeneous medium is (within the linear wave theory) most conveniently described with the spectral action balance equation (e.g., Whitham 1965; Bretherton and Garrett 1968; Hasselmann et al. 1973; Willebrand 1975). In the present study, the following version of the action balance equation is used:

$$\frac{\partial N}{\partial t} + \nabla_x \cdot [(\mathbf{c}_g + \mathbf{U})N] + \frac{\partial}{\partial \omega} [c_\omega N] + \frac{\partial}{\partial \theta} [c_\theta N] = \frac{S}{\sigma} \quad (2)$$

$$N = \frac{F(\omega, \theta, \mathbf{x}, t)}{\sigma}$$

$$c_g = \frac{\sigma}{k} \left[\frac{1}{2} + \frac{kd}{\sinh 2kd} \right] \quad (3)$$

$$c_\omega = \frac{\partial \sigma}{\partial d} \frac{\partial d}{\partial t} + \mathbf{k} \cdot \frac{\partial \mathbf{U}}{\partial t} \quad (4)$$

$$c_\theta = -\frac{1}{k} \left[\frac{\partial \sigma}{\partial d} \frac{\partial d}{\partial m} + \mathbf{k} \cdot \frac{\partial \mathbf{U}}{\partial m} \right] \quad (5)$$

where N is the action density spectrum, the quantities c represent propagation velocities in several spaces (see below) and S represents the net source term for wave variance. The energy propagation velocity c_g has the direction θ and m is a coordinate perpendicular to θ .

The left hand side of (2) represents conservative action propagation. The first term of Eq. (2) is the local rate of change of the action density. The second term of Eq. (2) represents convection in the physical space due to the wave energy propagation velocity c_g and the mean current velocity U . This term includes straining of the wave field due to spatial variation of $c_g + U$ (which is usually called shoaling if depth variations are considered). The third term of Eq. (2) represents the change of absolute frequency due to the unsteadiness of depth and current (e.g., Barber 1948; Mei 1983 page 96). The fourth term of Eq. (2) represents refraction.

The right hand side of Eq. (2) describes non-conservative processes. A distinction is made here between four separate source terms: (i) wind input; (ii) nonlinear resonant wave-wave interactions; (iii) dissipation due to deep-water wave breaking (whitecapping) and (iv) dissipation due to bottom friction. Formulations for the first three terms are taken directly from the WAM model (WAMDI group 1988). The formulation for the fourth term is taken from Madsen et al. (1988). For slowly varying currents, these formulations are valid in a frame of reference moving with the mean current velocity. Expressions for a fixed frame of reference are obtained using a straightforward Jacobian transformation and some minor adaptations to the original expressions (see Tolman 1990a).

3 Method of investigation

Wind wave hindcasts for this study have been performed with the third-generation wave model WAVEWATCH (Tolman 1989, 1990a), which has been developed specially for this study. The model includes all relevant wave-current interactions and explicit formulations for all source terms for wave growth and dissipation as described in the previous section. The model utilizes second order accurate propagation schemes in all discrete spaces (x, ω, θ). The numerical treatment of source terms is taken from the WAM model (WAMDI group 1988). In the hindcasts the spectrum is described with 24 discrete directions ($\Delta\theta = 15^\circ$) and with 26 frequencies (0.041 Hz - 0.453 Hz, $f_{i+1}/f_i = 1.1, f = \omega/2\pi$). The spatial resolution $\Delta x = 24$ km and the time step $\Delta t = 15$ min. The bathymetry of the North Sea is shown in figure 1.

Wind fields for the hindcasts consist of UK6 wind fields of the British Meteorological Office (BMO). Input current and water level fields for WAVEWATCH have been calculated with the model DUCHESS (e.g. Wang 1989), which solves the depth integrated shallow water equations on a fixed grid. The current fields have been calculated using both tidal constituents and wind forcing, so that the current and water level fields consist of both tides and surges. Wave boundary conditions at the open northern model boundary have been calculated with the deep-water no-current ocean wave model DOLPHIN (Holthuijsen and De Boer 1988).

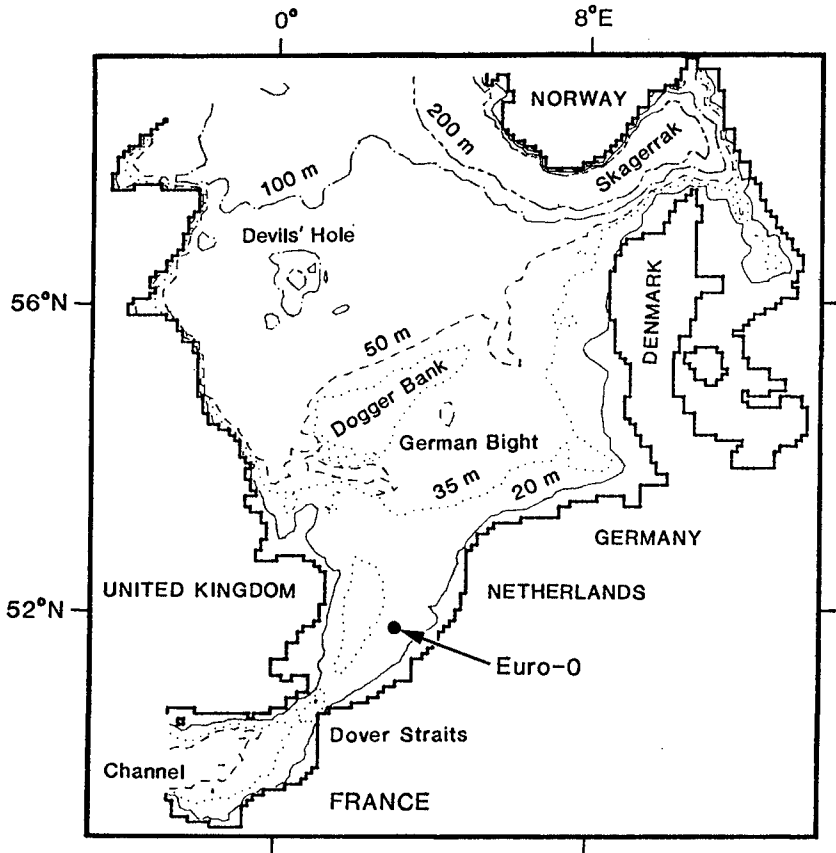


Fig. 1: The North Sea bathymetry.

Three storm cases on the North Sea are considered. Cases I (Jan. 1-4 1988) and II (Sept. 26-28 1987) consist of tide-dominated conditions with moderate SW and NW winds, respectively. For these cases wave observations were available. Case III consists of a surge-dominated case (Feb. 28-29 1988), for which no sufficient observations were available. The effects of the surge in this case are illustrated in Fig. 2 with water levels and the northerly current component U_N at location Euro-0 (see Fig. 1).

The tide- and surge-dominated cases are discussed separately below. In the discussion of the results for the tide-dominated cases the attention will be focussed on tide induced modulations of mean wave parameters and of parts of the spectrum, the specific effects of the unsteadiness of the tidal currents, the spatial distribution of tide-induced modulations of mean wave parameters and on a comparison of observed modulations of mean wave parameters with data. The results for the surge-dominated case will be

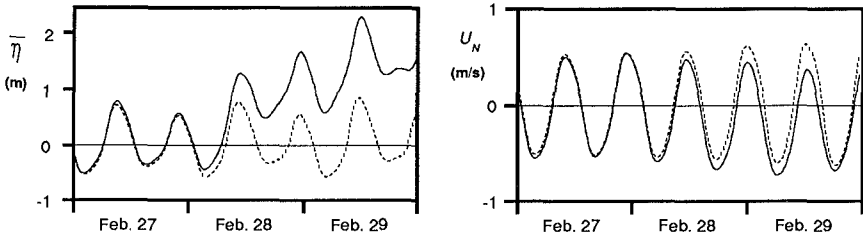


Fig. 2: Water levels $\bar{\eta}$ and northerly current components U_N for case III at location Euro-0. — : with wind forcing; ···· : without wind forcing.

discussed only for as far as they differ from the results of the tide-dominated cases. The mean wave parameters assessed here are the significant wave height H_s , the absolute period T_a and the mean wave direction $\bar{\theta}$:

$$H_s = 4\sqrt{\overline{\int \int F(\omega, \theta) d\omega d\theta}} \quad (6)$$

$$T_a = \overline{2\pi/\omega} \quad (7)$$

$$\bar{\theta} = \arctan \frac{b}{a} \quad (8)$$

The overbar notation at the right hand side of these equations denotes a straightforward average over the spectrum $F(\omega, \theta)$; a and b are the first two Fourier coefficients of the directional distribution (e.g., Kuik et al., 1988).

4 Results for tide-dominated cases

In the tide-dominated cases I and II, mean wave parameters show a small but distinct tide-induced modulation, as is illustrated in Fig. 3 with the significant wave height and the mean absolute period at Euro-0 for case I. In this figure, tide-induced modulations are observed as the difference between results of calculations in which tides are accounted for (solid lines) and where tides are neglected (dotted lines). As expected, the tide-induced modulations reflect the tidal period. The mean wave direction $\bar{\theta}$ is not presented in the figure, since it did not show significant tidal influences (tide-induced modulations less than 2°). The negligible tide-induced modulation of the mean wave direction suggest that current refraction has negligible influences on mean wave parameters. This is confirmed by practically identical results of repeated calculations, in which refraction is neglected altogether. Note that depth refraction is not relevant here, since waves are relative short (due to the moderate wind speeds) and are therefore not influenced by the bathymetry (e.g., deep water waves).

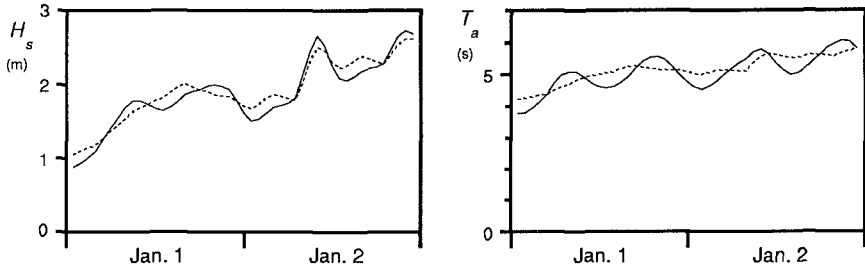


Fig. 3: Mean wave parameters at Euro-0 in case I (1988). — : with tides and surges; ···· : without tides and surges.

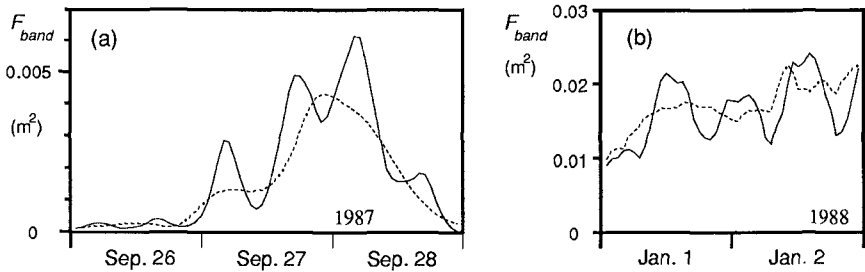


Fig. 4: Energy in fixed spectral bands (F_{band}) at Euro-0. (a) Case II, 0.1 - 0.2 Hz (b); case I, 0.3 - 0.5 Hz. — : with tides and surges; ···· : without tides and surges.

Modulations within the spectrum can be much larger than modulations of mean wave parameters, as is illustrated in Fig. 4 with the total energy in selected frequency bands at location Euro-0. Modulations of the order of 50% have been found in all frequency bands in the cases considered here. Since such large modulations have not been found in the significant wave height, modulations of different parts of the spectrum obviously have opposite signs and therefore largely cancel out in spectral averages.

The unsteadiness of tidal currents mainly manifests in modulations of the absolute period, since the unsteadiness explicitly causes a modulation of the absolute frequency (Eqs. (2) and (4), see also Tolman 1988, 1990b). The tide-dominated cases indeed show a significant modulation of the absolute period, as is illustrated in Fig. 3. The unsteadiness proved to have only a mild effect on the wave height modulation, as follows from results of repeated calculations in which the effects of unsteadiness are neglected (figures not presented here). The effects of unsteadiness are furthermore illustrated in Fig. 5 with the tide-induced modulations of the absolute period (ΔT_a , the difference between results of calculations with an without tides) for Euro-0 in case II, plotted as a function of the current velocity in the mean propagation direction of the waves, U_p (θ_U is the current direction).

$$U_p = |U| \cos(\theta_U - \bar{\theta}). \quad (9)$$

Plotted are both the results as obtained with a fully unsteady approach (solid line) and results as obtained with a quasi-stationary approach (dashed line) where $c_\omega \equiv 0$. In this case, the modulation of the absolute period completely disappears if depth and current unsteadiness are neglected. Apparently the entire modulation of the absolute period in this case is caused by the unsteadiness of depth and current. Figure 5 furthermore indicates, that the modulations of the wave parameters do not have a one-on-one relation with the local current velocity. Since the relation between modulations of wave parameters and the local current was found to vary with location and storm case, effects of wave-current interactions cannot be estimated from local parameters of tides only. This contrasts with the results of a analysis of effects of quasi-stationary currents, where many interaction effects can be estimated directly from the local current velocity.

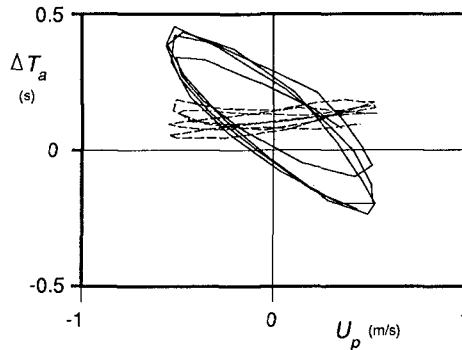


Fig. 5: Modulations of the absolute period ΔT_a as a function of the current velocity in the propagation direction of the waves U_p at Euro-0 for case II.

— : unsteady [c_ω given by (4)] ; --- quasi-stationary ($c_\omega \equiv 0$).

The spatial distribution of effects of tides (and surges) on wind waves is assessed by considering the normalized rms modulation of wave parameters (i.e., the coefficient of variation CV). For example, the coefficient of variation of the wave height $CV(H_s)$ is defined as:

$$CV(H_s) = \frac{\sqrt{T^{-1} \int \Delta H_s^2 dt}}{T^{-1} \int H_s dt} \quad (10)$$

where T is the duration of the averaging period (typically several tidal periods). The largest effects of the tides occur in the southern North Sea, as was expected, since the largest current velocities also occur in this region. In fact, the spatial distribution of the coefficients of variation of the wave heights, periods and lengths is similar to that of the

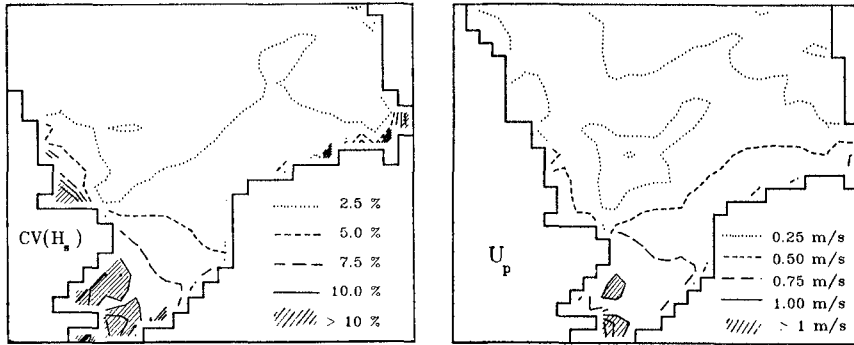


Fig. 6: Spatial distribution of the coefficient of variation of the significant wave height ($CV(H_s)$, total effect of wave-current interactions) and the distribution of the maximum current velocities in the mean wave direction (U_p) for case I (Jan. 1-2 1988).

maximum current velocities in the mean wave direction U_p , as is illustrated in Fig. 6. This figure shows values of $CV(H_s)$ of up to 15 % in the southernmost North Sea. The absolute period, relative period and the wave length show coefficients of variation of up to 10 %, 5% and 10% respectively. In case II coefficients of variation and current velocities U_p are somewhat smaller, with maxima concentrated near the British coast (figures not shown here).

Observed data were available for both tide-dominated cases. To compare the relatively small observed modulations as found in the calculations with observations, the modulations have been isolated. In the calculations modulations are the difference between results of repeated calculations in which tides and surges are either incorporated or ignored; the modulations in the observations have been defined as modulations with periods between approximately 9 h and 15 h (obtained by filtering the observed data). Calculated tide-induced modulations of the significant wave height (ΔH_s) and of the mean absolute period (ΔT_a) show some agreement with observed modulations, but also significant differences. This is illustrated in Fig. 7 with observed and calculated modulations for Euro-0 in case I. However, the residual modulations of the significant wave height and the mean absolute period, defined as the difference between observed and calculated modulations, proved to be highly correlated with observed wind speed variations with periods between approximately 9 h and 15 h. This is illustrated in Fig. 8. The high correlation suggests that the differences between observed and calculated modulations of wave parameters in Fig. 7 are caused by wind speed variations, and are not due to model errors.

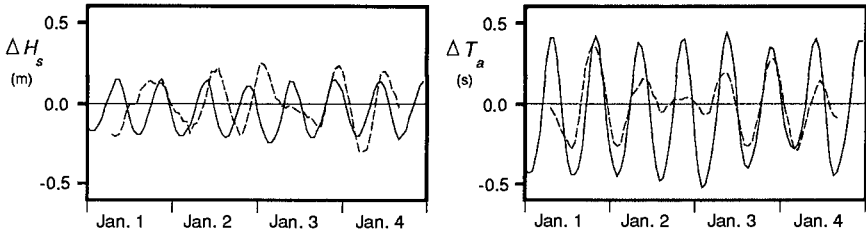


Fig. 7: Observed and calculated modulations (dashed and solid lines respectively) of the significant wave height and the mean absolute period at Euro-0 in case I (1988).

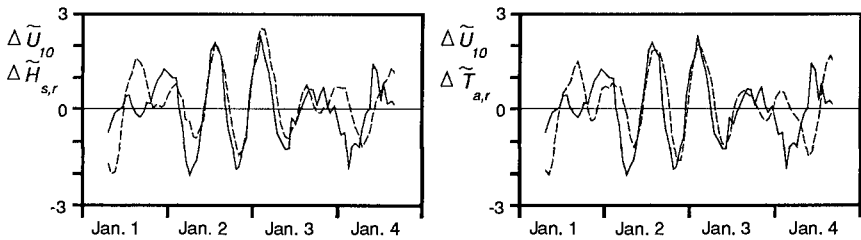


Fig. 8: Residual modulations of the significant wave height and the mean absolute period ($\Delta H_{s,r}$, dashed line and $\Delta T_{a,r}$, dotted line, respectively) and observed wind speed modulations (solid line) at Euro-0 in case I (1988).

5 Results for surge-dominated case

Results for the surge-dominated case III are presented, for as far as the results differ systematically from those of the tide-dominated cases (as mentioned above).

In the surge-dominated case, waves are essentially in shallow water, so that interactions can be caused by both surface level variations and currents. The numerical calculations indeed show effects of surface level variations and of currents on mean wave parameters; results of calculations with and without tides and surges, with surface level variations only and with currents only all show significant differences. This is illustrated in Fig. 9 with the corresponding wave heights at Euro-0. Since the time scale of computed interactions as presented in Fig. 9 is clearly larger than that of the tide, the interactions appear to be surge-dominated. For the effects of surface level variations this was expected, since surface level variation are surge dominated (see Fig. 2). For the effects of the currents this is somewhat surprising, since local currents are still tide dominated (see Fig. 2). It seems that the systematic nature of small wind driven currents results in more lasting (i.e. accumulated) effects than the larger, but oscillating tidal currents.

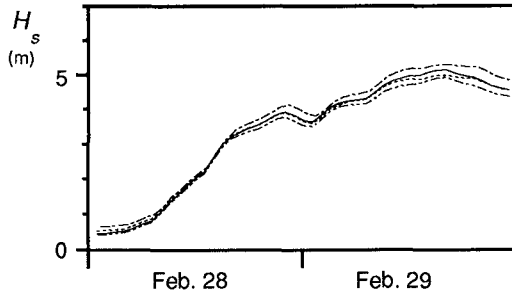


Fig. 9: Significant wave heights at Euro-0 in case III. — : with tides and surges; ···· : without tides and surges; - · - · : surface level variations only; - · - · - : currents only

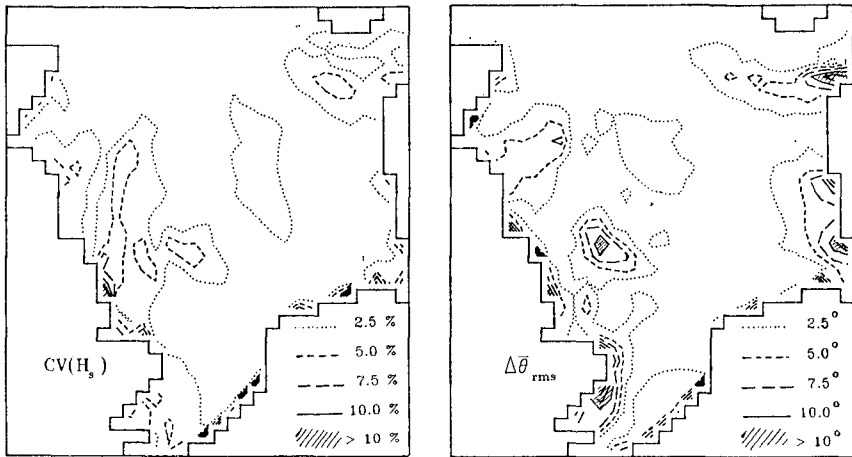


Fig. 10: Spatial distribution of the coefficient of variation of the significant wave height and rms differences of the mean wave direction due to refraction (case III, Feb. 28-29 1988).

The higher surface level and corresponding larger depth due to the surge result in higher waves (dash-dot lines versus dotted lines in Fig. 9), probably due to a reduced bottom-induced energy dissipation due to the increased water depths. On the other hand currents reduce wave heights and periods (dash-dot-dot lines versus dotted lines in Fig. 9). This might be explained from the wind-induced currents, which in the southern North sea are systematically in the propagation direction of the waves, reducing the effective

fetch and wind speed. The separate contributions of surface level variations and currents to the interactions are opposite and largely cancel out, resulting in a practically negligible total effect of all interactions.

Furthermore the surge-dominated case differs from the tide-dominated cases since depth refraction plays a distinct role in case III. This is illustrated in Fig. 10 with coefficients of variation for the significant wave height and rms differences of mean wave directions, obtained by comparing model results in which refraction was either incorporated or ignored. Effects of refraction are observed in areas with large gradients in the bottom level (compare Fig. 1), but do not spread over larger areas.

6 Discussion

The results of the North Sea hindcasts presented here show that the unsteadiness of tidal currents has a significant influence on wave-tide interactions. The relative importance of unsteadiness and inhomogeneity varies in space and time, so that effects of wave-tide interactions cannot be estimated from local depth and current parameters only, nor with a quasi-stationary or quasi-homogeneous approximation. Nevertheless effects of tides and surges seem to be restricted to areas with significant tide- and surge-induced currents and surface level variations.

The tidal currents result in modulations of mean wave parameters with an oscillating character (see e.g. Fig. 3), whereas currents and surface level variations of surges result in more monotonic variations (see e.g. Fig. 9). Wave-tide interactions seem to accumulate much less than wave-surge interactions, since case III shows that current-induced interactions appear to be surge dominated, although the local currents are clearly tide-dominated (as discussed in section 5). In the storm surge case considered here, effects of currents and surface level variations largely cancel out and resulting relative modulations of mean wave parameters are much smaller than in the moderate cases. It might therefore be concluded that the relative importance of wave-tide and wave-surge interactions decreases with increasing storm severity. However, the cancelling out of effects of currents and surface level variations cannot be expected to occur in any complex storm case. The potential magnitude of wave-surge interactions therefore is given by the potential magnitudes of effects of water level variations and currents separately, which are roughly of the same order of magnitude as the effects of tides in the tide-dominated conditions considered here. Consequently, it can not be concluded from the present results that the relative importance of interactions decreases with increasing storm severity.

This paper focuses on modulations of mean wave parameters. However, modulations of spectral densities or of energy in fixed frequency bands in general are much more pronounced than those of the mean wave parameters (modulations of 50% or more in all parts of the spectrum, e.g., Fig. 4). In particular the effects of the tides and surges on the low frequency variance (or energy) is striking, since wave-current interactions for monochromatic waves suggest a decreasing effect of currents with decreasing frequency due to decreasing Doppler shifts kU_p and relative current velocities U/c_g . This large impact is explained from the steep gradients in the low frequency flank of frequency spectra, where small shifts of the spectral peak frequency (or mean frequency) can cause large modulations of the total variance in fixed frequency bands. Like the

frequency shifts, these modulations of spectral densities are strongly influenced by the unsteadiness of depth and current and cannot be estimated from local depth and current parameters only, or with conventional quasi-stationary approaches (as discussed above). Considering the relatively small magnitude of effects of wave-tide and wave-surge interactions on the significant wave heights H_s and the mean wave period T_a (typically 5 to 10%), the implications for North Sea wave forecasting seem to be small. Such a conclusion is supported by the fact that observed modulations appear to be mainly wind-induced. However, the calculated modulations might be significant when assessing design wave heights for e.g. offshore platforms. Furthermore the large modulations of spectral densities due to tides has implications for e.g. the dynamic analysis of structures, as is illustrated by a study of the wave-induced movements and accelerations of the Euro-0 platform (tide-induced modulations of the order of 50%, Peters and Boonstra 1988).

7 Conclusions

This study on effects of tides and storm surges on wind waves in the North Sea has given rise to the following conclusions. Tides and storm surges in the North Sea should be treated as an unsteady medium for wind wave propagation. Both the unsteadiness and the inhomogeneity of depth and current play a significant role in the interactions so that neither a quasi-stationary nor a quasi-homogeneous approximation to wave-current interactions can be used. In moderate wind and wave conditions interactions are predominantly caused by (tidal) currents, whereas in severe conditions both currents and (mean) surface level variations contribute to the interactions. Due to accumulation of effects, relatively small currents of surges might have larger impacts on mean wave parameters than larger (but oscillating) tidal currents. Tide- and surge-induced modulations of mean wave parameters such as the significant wave height and the mean wave periods are relatively small (typically 5 to 10%). Tide-induced variations of spectral densities can be of the same order of magnitude as the average spectral density over a tidal period. Observed modulations of mean wave parameters (in particular the wave height) appear to be wind-dominated rather than tide-dominated.

Acknowledgements. The author acknowledges with pleasure that the Dutch Ministry of Public Works and Transportation (Rijkswaterstaat) has supplied the bottom schematization of the North Sea, the tidal boundary conditions and observed wind and wave data. The the Royal Netherlands Meteorological Institute (KNMI) has supplied the wind fields for this study. In this, the help of in particular J. de Ronde, R. van Dijk, A.J. van der Kerk, H. Ligtoet (Rijkswaterstaat), H.W. Riepma and E. Bouws (KNMI) was greatly appreciated. Permission to use the numerical wave model DOLPHIN of Digital Hydraulics Holland B.V. is highly valued. Furthermore, the support, suggestions and comments of colleagues at the Delft University of Technology, KNMI, Delft Hydraulics and Rijkswaterstaat, and of members of the WAM group, in particular L.H. Holthuisen, J.A. Battjes and N. Booij was of great help. This study has been performed

while the author was working at the Delft University of Technology. This paper has been written while the author held a National Research Council - NASA Research Associateship.

REFERENCES

- Barber, N.F., 1949: Behaviour of waves on tidal streams. *Proc. Roy. Soc. London, A* **198**, 81-93.
- Bretherthon, F.P., and C.J.R. Garrett, 1968: Wave trains in inhomogeneous moving media. *Proc. Roy. Soc. London, A* **302**, 529-554.
- Dobson, E.B., and D.E. Irvine, 1983: Investigation of Gulf Stream ring detection with spaceborne altimeter using mean sea height, wave height and radar cross section. The Johns Hopkins University, Applied Physics Laboratory, Space Department, Rep. JHU/APL S1R3U-005, 51 pp.
- Gutshabash Ye. Sh., and I.V. Lavrenov, 1986: Swell transformation in the Cape Agulhas Current. *Izvestiya, Atmospheric and Ocean Physics*, **22** No. 6, 494-497.
- Hasselmann, K., T.P. Barnett, E. Bouws, H. Carlson, D.E. Cartwright K. Enke, J.A. Ewing, H. Gienapp, D.E. Hasselmann, P. Kruseman, A. Meerburg, P. Müller, D.J. Olbers, K. Richter, W. Sell and H. Walden, 1973: Measurements of wind-wave growth and swell decay during the Joint North Sea Wave Project (JONSWAP). *Ergänzungsheft zur Deutschen Hydrographischen Zeitschrift, Reihe A (8°) Nr. 12*, 95 pp.
- Holthuijsen, L.H., and S. de Boer, 1988: Wave forecasting for moving and stationary targets. In: *Computer modelling in ocean engineering*, Eds. B.Y. Schrefler and O.C. Zienkiewicz, Balkema, Rotterdam, 231-234.
- Holthuijsen, L.H., N. Booij and T.H.C Herbers, 1989: A prediction model for stationary, short crested waves in shallow water with ambient currents. *Coastal Engineering*, **13**, 23-54.
- Jonsson, I.G., 1990: Wave-current interactions. In: *The Sea volume 9: Ocean engineering science*. Le Mehaute Ed., Wiley, 65-120
- Kuik, A.J., G.Ph. van Vledder and L.H. Holthuijsen, 1988: A method for the routine analysis of pitch-and-roll buoy wave data. *J. Phys. Oceanogr.*, **18**, 1020-1034.
- LeBlond, P.H. and L.A. Mysak, 1978: *Waves in the Ocean*. Elsevier, Amsterdam, 602 pp.
- Liu, A.K., F.C. Jackson, E.J. Walsh and C.Y. Peng, 1989: A case study of wave-current interaction near an oceanic front. *J. Geophys. Res.*, **94**(C11), 16189-16200.
- Madsen, O.S., Y.-K. Poon and H.C. Graber, 1988: Spectral wave attenuation by bottom friction: theory. *Proc. 21st Int. Conf. Coastal Eng.*, Malaga, 492-504.
- Mei, C.C., 1983: *The applied dynamics of ocean surface waves*. Wiley, New York, 740 pp.
- Peregrine, D.H., 1976: Interaction of water waves and currents. *Adv. Appl. Mech.*, **16**, 9-117.
- Peregrine, D.H., and I.G. Jonsson, 1983: Interaction of waves and currents. Miscellaneous Report No. 83-6, CERC, U.S. Army Corps of Engineers.
- Peters, H.C. and H. Boonstra, 1988: Fatigue loading on a single pile platform due to combined action of waves and currents. *Proc. 5th Int. Conf. on the Behaviour of Offshore Structures*, 1015-1034.
- Phillips, O.M., 1977: *The dynamics of the upper ocean*. 2nd edition. Cambridge University Press, 336 pp.

- Tolman, H.L., 1988: Propagation of wind waves on tides. *Proc. 21st Int. Conf. Coastal Eng.*, Malaga, 512-523.
- Tolman, H.L., 1989: The numerical model WAVEWATCH: a third generation model for the hindcasting of wind waves on tides in shelf seas. *Communications on Hydraulic and Geotechnical Engineering*, Delft Univ. of Techn., ISSN 0169-6548, Rep. No. 89-2, 72 pp.
- Tolman, H.L., 1990a: Wind wave propagation in tidal seas. Doctoral thesis Delft Univ. of Techn., also *Communications on Hydraulic and Geotechnical Engineering*, Delft Univ. of Techn., ISSN 0169-6548, Rep. no. 90-1, 135 pp.
- Tolman, H.L., 1990b: The influence of unsteady depths and currents of tides on wind wave propagation in shelf seas. *J. Phys. Oceanogr.*, **20**, 1166-1174.
- Wang, Z.B., 1989: Mathematical modelling of morphological processes in estuaries. Doctoral thesis Delft Univ. of Techn., also *Communications on Hydraulic and Geotechnical Engineering*, Delft Univ. of Techn., ISSN 0169-6548, Rep. no. 89-1.
- WAMDI group, 1988: The WAM model - a third generation ocean wave prediction model. *J. Phys. Oceanogr.*, **18**, 1775-1810.
- Whitham, G.B., 1965: A general approach to linear and non-linear dispersive waves using a Lagrangian. *J. Fluid Mech.*, **22**, 273-283.
- Whitham, G.B., 1974: *Linear and nonlinear waves*, Wiley, New York, 636 pp.
- Willebrand, J., 1975: Energy transport in a nonlinear and inhomogeneous random gravity wave field. *J. Fluid Mech.*, **70**, 113-126.

CHAPTER 92

DECOMPOSITION AND INTERCEPTION OF LONG WAVES BY A SUBMERGED HORIZONTAL PLATE

Haruyuki Kojima¹, Takeshi Ijima² and Akinori Yoshida³

Abstract

The results of two-dimensional hydraulic experiments are presented on the decomposition of regular and irregular surface waves by a fixed, submerged horizontal plate with a finite length. Nonlinear interactions, containing the near-resonant interaction as well as the self- and mutual-interactions, among the waves affected by the submerged plate are found to induce the generation of higher harmonic components which propagate independently in the lee side, and to result in appreciable disintegration of wave form. This wave decomposition may produce considerable modification of the spectrum of a transmitted-wave train through the nonlinear transfer of energy from primary wave components to higher frequency components and consequently reduce its significant wave period. With the above mechanism, thus, the submerged horizontal plate may serve as an effective interception device against waves, especially of long wave length.

1 Introduction

There are three conceivable mechanisms by which a submerged horizontal plate intercepts incoming waves: (1) linear interaction between surface waves passing over the plate and an oscillatory fluid motion beneath the plate, resulted from the phase differences between them; (2) wave breaking on it and turbulence around it which result in decreasing transmitted-wave height through energy loss; (3) wave decomposition due to nonlinear effects taking place in the shallow water region over the plate, which would cause the frequency band of transmitted waves to be diversified, thereby reducing the impact of individual waves. The first two mechanisms and their wave attenuation effects, which numerous researchers have studied theoretically and experimentally (for example, Ijima et al, 1970; Siew & Hurley, 1977; Patarapanich, 1984 and Tabuchi et al, 1987), are well known. Although the observation of wave disintegration by a submerged object like a submerged breakwater has been reported (Horikawa, 1960; Jolas, 1960), little attention has been placed on the third mechanism in the light of wave interception effects, nor extensive study has been performed to understand its phenomenon.

The purpose of this study is to examine the phenomenon of wave decomposition accompanied with the generation of higher harmonics by a submerged horizontal plate

¹Research Associate, Dept. of Civil Eng. Hydraulics, Kyushu Univ., Higashi-ku, Fukuoka, Japan

²Professor Emeritus, Faculty of Engineering, Kyushu University

³Associate Professor, Dept. of Civil Engineering Hydraulics, Kyushu Univ.

and their propagation in the water region over the plate and in the transmitted-wave side in order to discover the conditions under which a significant energy transfer and shortening of wave length can take place. We also evaluate the effects of decomposing a wave into higher harmonic components on its statistical properties and attenuation.

2 Experimental Procedure and Analysis

A wave tank used is 29m long, 0.3m wide and 0.5m deep with the piston-type wave generator, which can generate both regular and irregular waves and absorb more than 90% of reflected waves. The tank ends in a very efficient wave absorber, the reflection coefficient of which is less than 10%. The water depth h is maintained constant at 0.38m. A horizontal plate was fixed at a certain depth h_s from the water surface. The length of the horizontal plate B was varied, and for a comparative purpose one plate was extended to the end of the tank, which plate was regarded to be infinitely long (hereafter referred to as the infinite plate).

The laboratory experiment has three phases:

- (1) The first phase involves regular wave tests where a monochromatic sinusoidal wave and a composite wave of two primary frequency components are used. To investigate the mechanism of wave decomposition by a submerged horizontal plate, we observed wave profile transformation in the regions over and past the plate of various lengths. Measurement of the wave profile was made with four capacitance wave gages at a number of stations along the tank, successive stations being 20cm apart. At each station the passage of the first 20 to 30 wave data was recorded, which were then converted at the sampling rate of 0.05sec. to digital data. The Fourier analysis was applied to the profile data to obtain the spatial distribution of harmonic component amplitudes.
- (2) The second phase is irregular wave tests where forced disintegration of random incident waves associated with real ocean waves is examined. The random waves generated in the experiments are based on the Bretschneider-Mitsuyasu spectrum. The range of significant wave periods $T_{1/3}$ used in the tests was 0.8 to 2.42 sec. ($h/L_{1/3} = 0.387$ to 0.085; $L_{1/3}$: the incident wave length associated with the significant wave period) and a significant wave height was 4.5cm ($H_{1/3}/h = 0.118$). Spectral densities for incident, transmitted and reflected waves were estimated from smoothing estimated periodgrams by the resolution technique (Goda and Suzuki, 1976). We also obtained statistical properties of the transmitted waves which may be modified by the nonlinear interactions.
- (3) The third phase deals with evaluation of the effects of wave disintegration on wave interception. The case where a vertically-slitted wall was placed behind a submerged horizontal plate was experimented and possible changes in wave transmission-reflection coefficients and wave force exerted on the permeable wall due to disintegration of incoming waves were studied.

3 Test Results and Discussions

3.1 Evolution of Wave Profiles

Figure 1 shows the evolution of wave profiles when a monochromatic wave of an infinitesimal amplitude ($H_I/L = 0.0066$) enters and travels over the infinite plate (Figure

1-(a)) and the finite plate of $B/h = 5.25$ (Figure 1-(b)). The wave profiles for two wave periods (T) are depicted from the data of every other station and each of the highest wave crest is aligned at zero on the abscissa for a comparative purpose. It is seen that waves propagating over the infinite plate will break down into multiple secondary peaks in their profiles, as observed by Multer and Galvin(1967) and Boczar-Karakiewicz(1972) in a wave tank of constant depth. Since the higher crest propagates faster than the smaller ones, the primary crest approaches the preceding secondary crest from behind. When the two crests encounter and interact each other, the large crest decreases in height while the smaller one increases, and the wave form is nearly identical with the initial wave form. Then they exchange roles in both amplitude and speed and start to separate each other. This event is repeated at a certain distance called the recurrence distance. The event clearly indicates that the well-known soliton effects occur in the shallow water region over the infinite plate.

Markedly different evolution of wave profiles is observed once waves passed over the finite plate and entered the original water depth(see Figure 1-(b)). One of the obvious features is that the wave profiles appear somewhat irregular so that it is difficult to follow a particular wave crest. Another is that as the wave train of a primary wave and secondary waves travels down the tank, some of the secondary waves grow as nearly great as the primary wave. A consequence of increase in the height of secondary waves would be apparent reduction in period of the wave train.

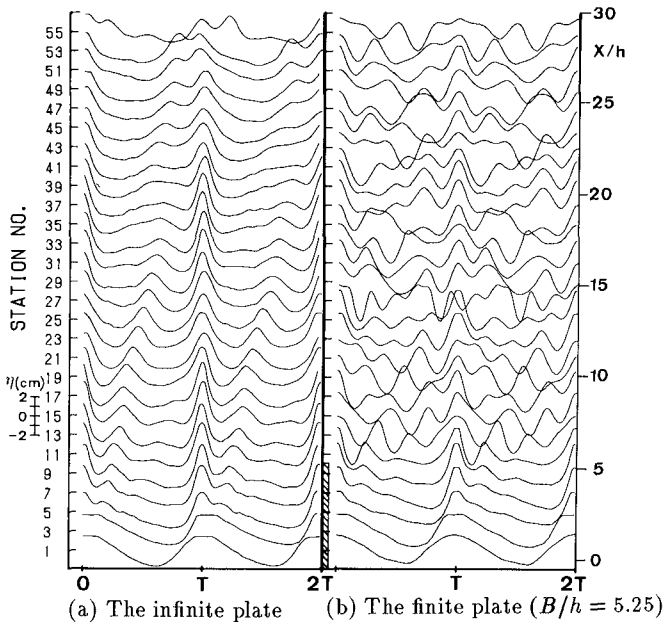


Figure 1 Wave profile transformation along the wave tank ($h/L = 0.100, H_I/L = 0.0066$).

3.2 Fourier Analysis

We study quantitatively wave profile data based on Fourier analysis. Applying this analysis to wave profile data yields the amplitude of any Fourier component, A_i ($i = 1, 2, 3, \dots$) associated with corresponding angular frequency σ_i at each measuring station. Figures 2 and 3 depict the spatial distribution of the amplitudes of the 1st, 2nd and 3rd harmonic components (A_1, A_2, A_3), normalized by the incident wave amplitude a_0 , for the case of the infinite and the finite plates, respectively. The heights of the two largest waves (primary and the largest secondary), Hm and Hs , normalized by the incident-wave height are also plotted versus distance from $x = 0$, the front end of the plate. The prominent difference between the results of the infinite and the finite plates lies in the variation of harmonic amplitudes in the region beyond the extent of the finite plate; the amplitude variation in the transmitted-wave side becomes nearly constant, independent of space, although small disturbances (or undulations) of spatial periodic manner is seen, while variation of the wave heights (Hm, Hs) is still spatially periodic. This implies that each of the harmonic component waves generated over the plate by nonlinear interactions should propagate independently and without mutual interactions in the water of the original depth with the phase speed corresponding to its own frequency. Thus the height of the primary wave would rise to the maximum when other harmonics are in phase with it; the height would decrease as phase is shifted.

Of interest here is the magnitude of harmonic component amplitudes in the lee side of the finite plate, because the increase in their amplitudes, comparable to the first harmonic one, indicates considerable transformation of surface wave form, which may consequently reduce an apparent wave period. As seen from the figures, the harmonic amplitudes are equivalent to those at the end of the plate, their magnitudes being related to the length of a submerged horizontal plate. It is then obvious that if the plate length is half of the recurrence distance, the amplitude of the first and third harmonics is minimum, while that of the second harmonic maximum. Similar results are discussed by Mei(1988) through the theory of nonlinear resonant interactions in water of constant depth.

3.3 Generation and Growth of Higher Harmonics

We examine factors affecting on the generation and growth of higher harmonics, which include fluid motion under the plate and water depth above the plate. In doing so, we introduce a parameter indicating the magnitude of the higher harmonics, namely, the square root of the ratio of the energy flux of harmonic components to the incident wave energy flux T_{p_i} ($i = 1$ through 3), referred to as the energy flux ratio. When $i = 1$, T_{p_1} is equivalent to a transmission coefficient of the first harmonic component.

The energy flux ratios versus relative water depth for the submerged horizontal plate and impermeable rectangular body are shown in Figure 4-(a) and Figure 4-(b), respectively. The solid line in the figure indicates the transmission coefficient obtained from the linearized computation of the boundary element method proposed by Ijima, Chou and Yoshida(1976). A distinct difference between the horizontal plate and rectangular body lies in the energy flux ratio of the first harmonic component, i.e., the transmission coefficient. The results of the horizontal plate show a strong tendency of selectively intercepting wave of a certain wave length, the measured value of T_{p_1} being

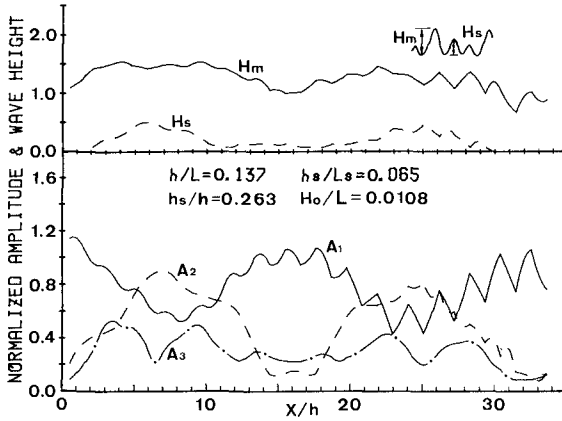


Figure 2 Spatial distribution of the amplitude of harmonic components for the infinite plate ($h/L = 0.100$).

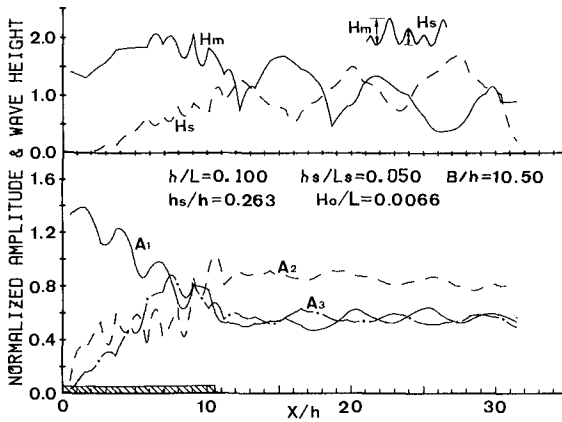


Figure 3 Spatial distribution of the amplitude of harmonic components for the finite plate ($B/L = 10.50$, $h/L = 0.100$).

less than 0.4 at $h/L = 0.15$. In contrast, the rectangular body has no such tendencies and the measured value of T_{p1} appears to be around 0.75 in the entire range of h/L . The energy flux ratio of higher harmonics for the both cases has similar trends showing the maximum values of about 0.5 at around $h/L = 0.225$ for T_{p2} , except in the lower range of relative water depth where the energy of the higher harmonics generated by the rectangular body is relatively greater. Since the amplitude of the first harmonic component in that range is quite small for the horizontal plate, however, the relative magnitude of the second harmonic amplitude to the first is much larger in the case of the horizontal plate than the impermeable rectangular body. These results lead to

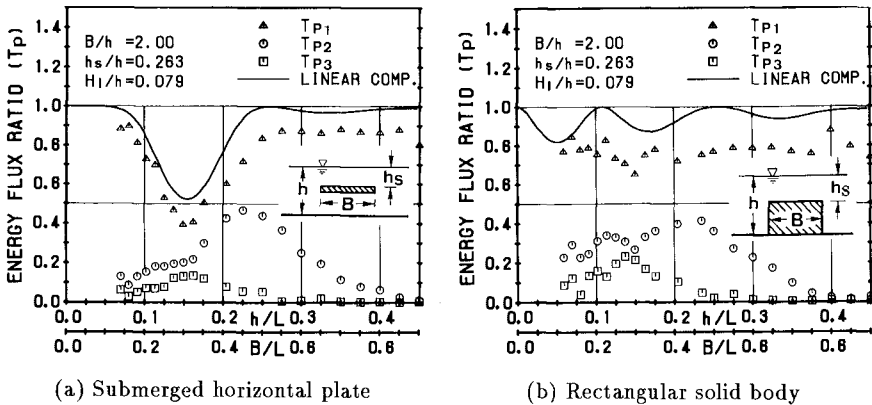


Figure 4 The magnitude of harmonic components in the transmitted waves.

conclusions that the fluid motion beneath the plate has little effect on the generation of higher harmonics and a submerged horizontal plate is more effective in reduction of wave period than a impermeable rectangular body.

The effects of a plate length B and water depth over the plate h_s on the generation and growth of higher harmonics are also studied. A brief summary is discussed here; detailed results can be seen elsewhere (Kojima and Ijima, 1989). Increase in the plate length results in heightening the maximum values of T_{p2} and T_{p3} as well as shifting these values to lower relative water depth. A horizontal plate of longer length will thus more effectively generate higher harmonics against waves of longer wave length. Decrease in the plate depth h_s results in augmenting the values of T_{p2} in the larger relative water depth and the maximum value of T_{p3} as well.

3.4 Decomposition of Two Primary Waves

Figure 5 shows an example of the normalized amplitude spectra of the incident waves of two primary frequencies $f_1 = 0.500_{Hz}$ and $f_2 = 0.667_{Hz}$ (upper) and those of the transmitted waves (lower). The amplitude spectra of the incident waves are measured at constant water depth without existence of a submerged plate and those of the transmitted waves are obtained from the data measured at the point $4.75h$ away from the rear end of the plate. It is obviously seen that many modes of harmonics are present in the transmitted waves, where the sum interaction components and the difference interaction components are generated other than the self-interaction modes, i.e., $2f_1, 2f_2, 3f_1$ and $3f_2$, the sum interactions being dominated. Secondary waves ($f_1 + f_2, f_2 - f_1$), the products of binary interactions between primary components, are evident together with tertiary waves ($2f_1 + f_2, f_1 + 2f_2$), the components arising from the interactions between primary and secondary wave; the sum interactions of these are appreciably larger than any of the components resulting from the self-interaction effects.

It has been shown in the theory of nonlinear resonant interactions by Phillips (1960)

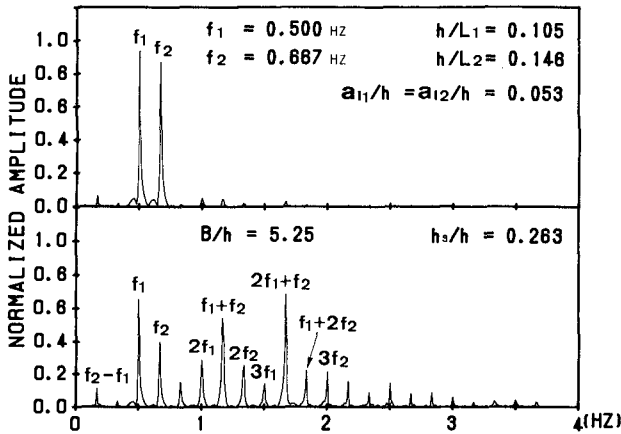


Figure 5 Amplitude of spectra of the incident wave of two primary components(upper) and the transmitted wave (lower).

and Longuet-Higgins(1962) that in the case of deep water the secondary interactions will not occur since the phase velocity of the secondary components is always different from the phase velocity of a free infinitesimal wave of the same wave number, whereas the tertiary interaction will occur. In the case of waves transmitting over the submerged plate where the ratio of water depth to wave length becomes considerably small, however, the near-resonant interaction(Bryant, 1973) would give rise to secondary waves due to the fact that the wave dispersion relation approaches asymptotically a straight line as non-dimensional wave number kh becomes small. The harmonic modes present in the transmitted waves may thus be generated by the nonlinear interactions comprised of the near-resonant interaction as well as the self- and mutual-interactions among the waves affected by the submerged plate.

The amplitude of the harmonic components together with the amplitude of the two primary components is plotted versus distance from $x = 0$ in Figure 6. As the waves travel over the plate, the amplitudes of secondary and tertiary waves increase with decrease in the amplitudes of the two primary components. Once the waves passed the plate and entered the water of the original depth, however, amplitude variations appear to be independent of space, similar to the results of a monochromatic incident wave. Thus, disintegrated waves of all the harmonics in the transmitted-wave side are most likely to propagate at phase speeds corresponding to their own frequencies.

In order to examine changes in the magnitude of secondary and tertiary amplitudes generated by nonlinear interactions with varying the frequency ratio of two primary waves f_2/f_1 , the energy flux ratio of each harmonic component of the transmitted waves to the incident wave is obtained and depicted in Figure 7. One of the two fundamental frequencies f_1 is kept constant at $f_1 = 0.400$ Hz ($h/L_1 = 0.082$) for the upper figure and $f_1 = 0.667$ Hz ($h/L_1 = 0.148$) for the lower figure, while the other frequency f_2 is varied. Comparison of the two figures reveals an interesting result that when the frequency of one of the two primary waves is low, the frequency range of the other wave

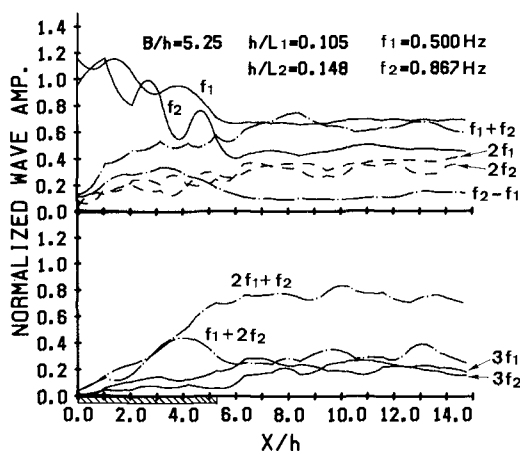


Figure 6 Spatial distribution of harmonic component amplitudes, measured along the tank, for two primary waves.

that induces nonlinear interactions tends to become wider and the frequency range appears to be shifted to the higher range. Another noticeable point is that although a monochromatic wave of high frequency, say $f = 1.314_{Hz}$ ($h/L = 0.425$), striking the submerged plate alone produces hardly any harmonics (see Figure 4), coexistence of a low frequency wave with it could give rise to secondary and tertiary components (see in Figure 7 the energy flux ratio at $f_2/f_1 = 3.285$ for $f_1 = 0.40_{Hz}$ and at $f_2/f_1 = 1.970$ for $f_1 = 0.667_{Hz}$). These results can be taken as evidence that the decomposition of an incident wave by the submerged horizontal plate through the mechanism of nonlinear interactions is much more excited when multiple wave components exist in the incident wave field rather than a single component. It is concluded therefore that a submerged horizontal plate can be considered as a device that effectively transfers the energy of incident waves to higher components of transmitted waves, thereby reducing the impact of primary wave components.

3.5 Decomposition of Random Waves

3.5.1 Transformation of frequency spectrum

Forced wave disintegration by a submerged horizontal plate is examined for irregular incident waves associated with real ocean waves with a sharp spectral peak around a significant wave period. Figure 8 shows the transformation of frequency spectral shape, along the tank, for the random incident wave train with a significant wave frequency $f_{1/3} = 0.625_{Hz}$ ($h/L_{1/3} = 0.105$) and wave height $H_{1/3}/h = 0.118$. It is evident that the spectral shape differs from station to station over the plate. At the front end of the plate ($x = 0.1B$) the spectral shape is similar to that of the incident-wave train, and as the waves propagate further down the tank over the plate, its shape is modified in such manner that some part of the wave energy around the significant wave frequency is transferred to the higher frequency components, thereby flattening the spectral shape. However, little variation of spectral shape is observed when the waves propagate the

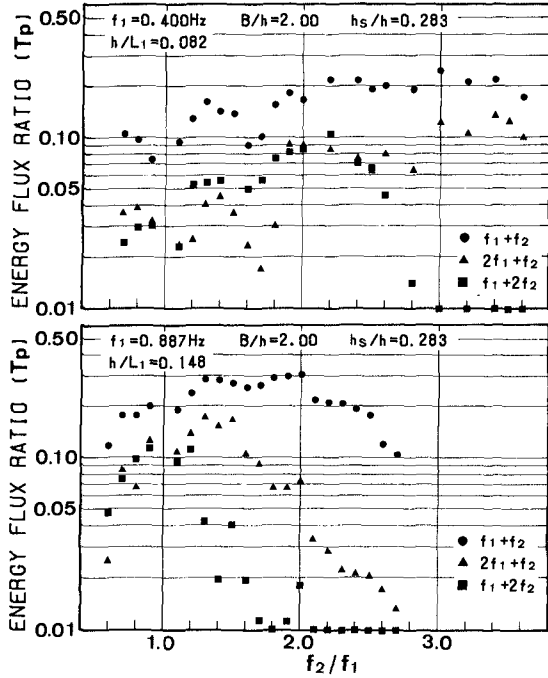


Figure 7 The magnitude of secondary and tertiary components for two primary waves.

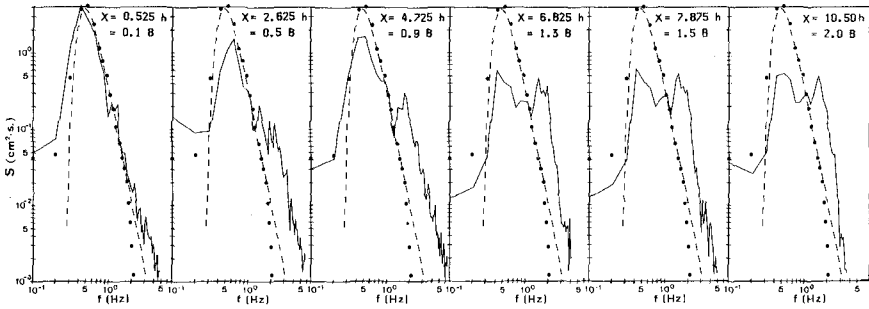


Figure 8 Transformation of the spectral shape of random waves measured along the tank ($h/L_{1/3} = 0.105, H_{1/3}/h = 0.118$); --- target spectrum, ●●●● incident wave, ——— transmitted wave.

water of the original depth after passing the plate ($x > 1.0B$), the spectral shape of which holds the presence of large energy in the high frequency range. This significant energy transfer reflects the effects of the nonlinear interactions taking place over the plate, as discussed in Section 3.4.

3.5.2 Statistical properties of decomposed transmitted waves

We investigate statistical properties of a transmitted-wave train. Wave profile data taken from four wave probes situated 20 to 40cm apart are used. To define individual waves, we utilize the zero-upcrossing method. The number of individual waves sampled is between 400 and 600. All of the statistical values obtained from four probes are averaged to determine one representative value.

One of the main aims for the present research is to confirm the evidence of reduction in wave period of an incoming wave train by a submerged horizontal plate. The significant wave period of a transmitted-wave train $T_{T_{1/3}}$ is compared with that of an incident-wave train $T_{I_{1/3}}$ and their ratios for the cases of $B/h = 2.00, 3.00$ and 5.25 are plotted, in Figure 9, versus relative water depth $h/L_{I_{1/3}}$. Considerable reduction in wave period is seen; the lowest value of $T_{T_{1/3}}/T_{I_{1/3}}$ is about 60% for $B/h = 2.00$ and 45% for $B/h = 3.00$ within the range of relative water depth examined. The lowest value of the wave period ratio tends to be shifted toward the smaller value of relative water depth with increase in the plate length and the ratio comes close to one at the large value of relative water depth (say $h/L_{I_{1/3}} = 0.387$), where the amplitude of higher harmonics may be so small that the form of transmitted-wave profiles would barely alter. Of interest is that when considerable reduction in wave period occurs, the wave height distribution somewhat deviates from the Rayleigh distribution, similar to the wave height distribution for the case of wave transmission over a protruding vertical breakwater, which waves also have shorter periods than those of incident waves, as discussed by Goda and Suzuki(1976).

Figure 10 shows the relationship between the spectrum and the characteristic wave height of a transmitted-wave train and parameters indicating nonlinearity of waves, in which plotted versus relative water depth are the ratio of significant wave height to the square root of the total wave energy (equivalent to the root-mean-square value of the surface elevation) $H_{T_{1/3}}/\sqrt{m_0}$, the skewness $\sqrt{\beta_1}$, and the kurtosis β_2 . The skewness and kurtosis, indicating the extent of the distortion of the statistical distribution of the instantaneous surface elevation from the normal, are expressed as

$$\sqrt{\beta_1} = \frac{1}{\eta_{rms}^3} \frac{1}{N} \sum_{i=1}^N (\eta_i - \bar{\eta})^3, \quad \beta_2 = \frac{1}{\eta_{rms}^4} \frac{1}{N} \sum_{i=1}^N (\eta_i - \bar{\eta})^4 \quad (1)$$

where η_{rms} and $\bar{\eta}$ are the root-mean-square value and the mean value of the surface elevation, respectively.

The theoretical value based on the normal distribution is $\sqrt{\beta_1} = 0$ and $\beta_2 = 3.0$, the latter value of which is drawn with the chain line in the figure. The proportionality constant between $H_{T_{1/3}}$ and $\sqrt{m_0}$ is also plotted at 3.8, with the broken line, the value of which is determined from many wave observation data throughout the world(Goda, 1985). Two distinct trends are obvious: the proportionality constant tends to decrease to a value less than 3.5 in the range of relative water depth between 0.085 and 0.160,

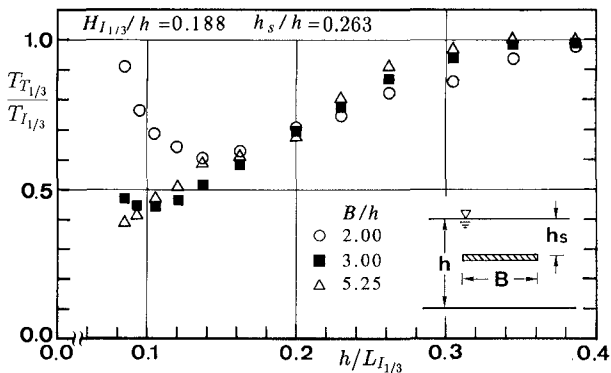


Figure 9 Change in period of transmitted waves for different lengths of the submerged horizontal plate.

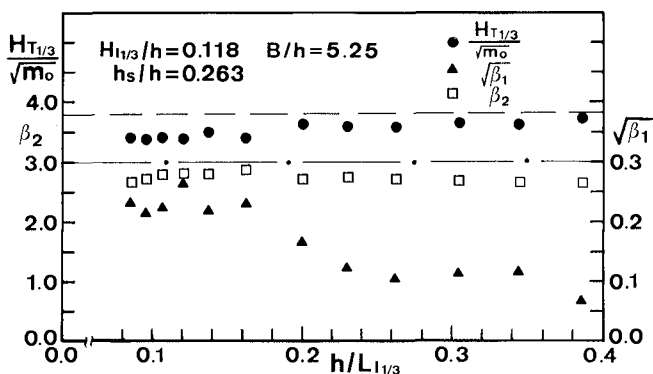


Figure 10 Relationship between the spectrum and the significant wave height and nonlinearity parameters for transmitted-wave trains.

where appreciable reduction in period of the transmitted-wave train occurs, as shown in Figure 9; in the same range the skewness value tends to become a larger value, being more than 0.2. With increase in relative water depth, both the values tend to approach the expected value of 3.8 for $H_{T_{1/3}} / \sqrt{m_0}$ and zero for $\sqrt{\beta_1}$. The value of the kurtosis β_2 has no clear tendencies with respect to relative water depth, but the value stays less than the theoretical value of 3.0 over the entire relative water depth examined, indicating the distribution shows lower peak than the corresponding normal distribution and long tails on both sides.

4 Wave Interception Effects

The disintegration of incoming waves by a submerged plate likely results in shortening of wave length in its shoreward side. We might thus anticipate that any structures located in the lee side of it would be exposed to less wave force and furthermore permeable structures which have a definite drawback in wave dissipation effectiveness against waves of long length would effectively intercept them once their lengths became shorter prior to striking the permeable structures. A schematical description of an experimental setup is shown in Figure 11, where a vertically-slitted wall with porosity $\varepsilon = 0.2$ and thickness $W/h = 0.171$ is placed in the lee side of the submerged horizontal plate. Figure 12 shows one of example of variation of transmission-reflection coefficients and non-dimensional wave force, F/F_s (F_s : standing wave force), acting on the permeable wall with the distance x_w between the plate center and the wall front along the wave channel. With the distance ratio x_w/h the values of a transmission coefficient K_T and wave force vary in a similar manner, while reflection coefficient values K_R vary in an opposite fashion, two peak locations of K_T and F/F_s being at about $x_w/L = 0.3$ and 0.85 where K_R indicates a minimum value.

Taking an average value of these fluctuations over the distance ratio and plotting the average value together with a vertical line indicating the maximum and minimum values of the fluctuations for K_T and F/F_s , with its top and bottom ends respectively, we have a representative value for wave transmission and force versus relative water depth in Figures 13 and 14. In these figures, the results for the case without a horizontal plate (Kojima, et al, 1988) are also plotted with a triangle mark for the measured and a solid line for the computed. It can be easily observed that the existence of the submerged horizontal plate considerably reduces both the wave transmission and force over the entire relative water depth tested. The experimental results for the case of the permeable wall plus the horizontal plate follow the same trend as the wave period changes shown in Figure 9; K_T and F/F_s tend to decrease with the relative water depth to a minimum value at about $h/L = 0.15$ and then increase. This trend can be taken as the evidence of the effects of wave disintegration on wave interception.

5 Conclusions

The major conclusions obtained are as follows:

- (1) Wave decomposition accompanied with the generation of higher harmonics by a submerged horizontal plate can be considered as a phenomenon that is induced by nonlinear interactions including the near-resonant interactions as well as the self- and mutual-interactions, which are much more excited when multiple wave components exist in the incident wave field. The non-spatial variation of harmonic component amplitudes in the lee side of the plate, different from the spatial variation above the plate, suggests that each component wave should propagate independently in that water region at its own phase speed without the self- and mutual-interactions.
- (2) By comparing the harmonic generation by the horizontal plate with that by the submerged rectangular body, the fluid motion beneath the plate was determined to have little effects on the wave decomposition.
- (3) A submerged horizontal plate induces a considerable modification in the ocean

wave spectrum, in such manner that the energy around significant wave frequency is transferred to higher frequency components due to the nonlinear interactions. This modification results in reducing significant wave period of the transmitted wave train by about 50%.

(4) When the significant wave period of a transmitted-wave train is reduced considerably compared with that of an incident wave train, interesting statistical properties of the transmitted-wave train are observed; namely, the wave height distribution somewhat deviates from the Rayleigh distribution, the ratio of the significant wave height to the root-mean-square value of surface elevation becomes about 3.3, and the skewness appears to be over 0.2.

(5) A submerged horizontal plate can serve as one of the effective wave interception devices against waves of long wave length, due to the fact that the energy of the long incident waves is disintegrated or dispersed into that of higher harmonic components

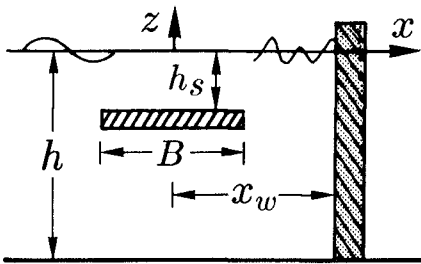


Figure 11 Schematic description of a submerged horizontal plate and vertical permeable wall.

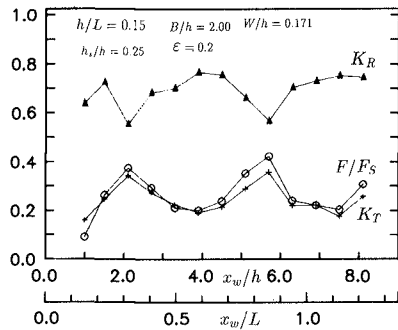


Figure 12 Variation of transmission-reflection coefficients and wave force with the distance ratio x_w/h .

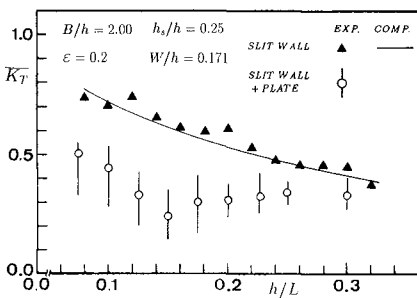


Figure 13 The average, maximum and minimum wave transmission coefficient versus relative water depth.

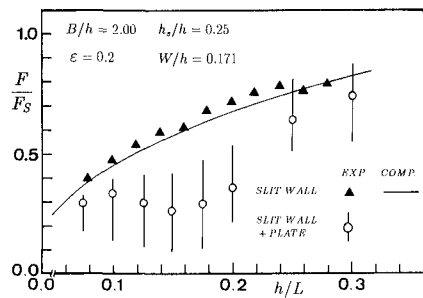


Figure 14 The average, maximum and minimum wave force versus relative water depth.

in the transmitted waves, thereby reducing the impact of the primary waves.

The authors wish to express heartfelt thanks to Mr. A. Nagano (a graduate student, Kyushu University) and Mr. H. Takao (a former student, Kyushu University) for valuable cooperation in the experimental work. Partial support of the Grant-in-Aid for Scientific Research from the Ministry of Education, Science and Culture is acknowledged.

References

- Boczar-Karakiewicz, B., 1972, "Transformation of wave profile in shallow water," *Arch. Hydrotech*, 19, pp. 197-210.
- Bryant, P. J., 1973, "Periodic waves in shallow water," *J. Fluid Mech.*, 59, part 4, pp. 625-644.
- Goda, Y. and Suzuki, Y., 1976, "Estimation of incident and reflected waves in random waves," *Proc. 15th Int'l. Conf. on Coastal Eng., ASCE*, pp. 828-845.
- Goda, Y., 1985, *Random Seas and Design of Maritime Structures*, Univ. of Tokyo.
- Horikawa, K., 1960, "Secondary wave crest formation," *Trans. of Japan Soc. Civil Eng.*, No. 66, pp. 50-58.
- Ijima, T. et al, 1970, "Analytical study of breakwater and quay with horizontal plate," *Proc. of the 17th Japanese Conf. on Coastal Eng.*, pp. 97-106 (in Japanese).
- Ijima, T., Chou, C. R. and Yoshida, A., 1976, "Method of analysis of two dimensional water wave problems," *Proc. 15th Int'l. Conf. of Coastal Eng., ASCE*, pp. 2717-2736.
- Kojima, H., Ijima, T. and Yoshida, A., 1988, "A numerical method for hydraulic properties of a vertical slit-type breakwater against regular and irregular Waves," 6th Cong. A.P.R.D., I.A.H.R., pp. 201-208,
- Kojima, H. and Ijima, T., 1989, "An experimental study on wave decomposition by a submerged horizontal plate," *Memoirs of faculty of Engineering, Kyushu Univ.*, Vol. 49, No. 4, pp. 195-212.
- Jolas, P., 1960, "Passage de la houle sur seuil," *Houille Blanche* 15, pp. 148-152.
- Mei, C. C., 1988, *The Applied Dynamics of Ocean Surface Waves*, pp. 1-740.
- Multer, R. H., and Galvin, C. J., 1967, "Secondary waves: periodic waves of non-permanent form," *Trans. Am. Geophys. Union*, 48, pp. 139.
- Longuet-Higgins, M. S., 1962, "Resonant interactions between two trains of gravity waves," *J. Fluid Mech.*, 12, pp. 321-332.
- Phillips, O. M., 1960, "On the dynamics of unsteady gravity waves of finite amplitude. part 1. the elementary interactions," *J. Fluid Mech.*, 9, pp. 193-217.
- Siew, P. J. and Hurley, D. G., 1977, "Long surface waves incident on a submerged horizontal plate," *J. Fluid Mech.*, Vol.83, Part 1, pp. 141-151.
- Tabuchi, M. et al, 1987, "Study of hydraulic properties of a horizontal plate type breakwater," *Proc. of the 34th Japanese Conf. of Coastal Engineering*, pp. 482-486 (in Japanese).

CHAPTER 93

Observations of the Swash Expression of Far Infragravity Wave Motions

Rob Holman¹, Peter Howd¹, Joan Oltman-Shay², and Paul Komar¹

Abstract

One of the important results from the recent SUPERDUCK experiment was the discovery of very low frequency motions (10^2 - 10^3 second periods) with anomalously short longshore wavelengths (10^2 meters). Subsequent analysis showed the motions to be shear waves, unstable perturbations of the mean longshore current that act to conserve potential vorticity. A specific prediction of the model is that these waves have negligible elevation signal (they are non-divergent), in contrast to gravity waves. Examination of simultaneous run-up data confirms the non-divergent nature of the solutions. While edge wave modes were detected, no significant swash energy was seen in the low frequency, high wavenumber region where shear wave energy was found in the current meter data. This apparently negative result adds support to the interpretation of these motions as shear waves.

Introduction

In September and October, 1986, a large field experiment called SUPERDUCK was held at the U.S. Army Corps of Engineers Field Research Facility (FRF) at Duck, North Carolina, USA. The site features a pronounced and frequently active nearshore sand bar system, and a primary objective of the October phase of the experiment was to study possible mechanisms of sand bar generation. Of particular interest to some participants was validation of models that depend on the presence of edge waves to account for dominant longshore lengthscales.

Detection of edge waves was accomplished using a longshore array of bi-directional electromagnetic current meters placed 50 m offshore, in the expected location of the trough, landward of the bar. Seven instruments were placed with lag spacings of 110, 20, 30, 10, 70, and 50 m, an optimal design for the subsequent maximum likelihood spectral analysis. Four hour time series were collected, and frequency-wave-number (f-k) spectra computed.

1. College of Oceanography, Ocean Admin Bldg 104, Oregon State University, Corvallis, OR, USA 97331-5503

2. Quest Integrated, 21414 68th Ave. So., Kent WA, USA 98032

While edge wave modes were observed in the infragravity band, the highest energy densities occurred at lower frequencies with periods typically on the order of $10^2 - 10^3$ seconds (Oltman-Shay *et al*, 1989). To distinguish this frequency band, the name Far InfraGravity (or FIG) band was adopted, in analogy to the relationship of infrared and far infrared light in the optical spectrum. Most surprising, the wavenumbers of the FIG energy were substantially higher than $\sigma^2/g\beta$, the wavenumber of a mode 0 edge wave, the largest value allowable for gravity waves (σ is radial frequency, g the acceleration of gravity, and β the beach slope). Moreover, the observed motions were very coherent and were always progressive in the direction of the mean longshore current.

A theoretical explanation of these motions was provided by Bowen and Holman (1989). They showed that under some circumstances a strong mean longshore current is unstable to perturbations, such that the perturbation will grow and progress with the current. These motions are called shear waves since their existence depends on the cross-shore shear structure of the current. Using a simple example geometry, Bowen and Holman showed that typical time and length scales of shear waves would be in the FIG band, and at high wavenumber, as was observed in the data.

The underlying dynamics of shear waves depend on the conservation of the total potential vorticity. Thus, a perturbation of the vorticity (shear) of the mean longshore current will be compensated for by the relative vorticity, resulting in a meandering flow pattern. However, an explicit assumption of the theory is that the motions are non-divergent (the rigid lid assumption) so that the rate of change of sea surface elevation is negligible. Thus, the theory specifically predicts that, despite the large energies seen in the velocity data, the sea surface elevation signal of shear waves should be negligible.

Synchronous with the velocity data, run-up measurements were also collected during SUPERDUCK. These data represent sea surface elevation signals at a specific location (the shoreline), so they can be used to test the non-divergent assumption and hence whether the observed motions are, in fact, shear waves. Thus the objective of this paper is to examine swash data to determine the presence or absence of energy at the low frequencies and high wavenumbers seen by the current meter data. A negative result adds support to the interpretation of these waves as non-divergent shear waves.

Field Experiment

Run-up data were collected during SUPERDUCK using videotapes of near-shore wave motion (note that the terms run-up and swash are used interchangeably in this paper to indicate the time series of sea surface elevation at the shoreline). Three cameras were mounted on the top of a high tower on the crest of the sand dune, 43.2 m above mean sea level. Records were 1 hour 55 minutes long and, when possible, were timed to correspond to current meter runs.

Digitization of the swash time series was carried out with an Imaging Technology Series 150 image processing package using the following set of steps. As a

preliminary step, the geometry of the camera view was solved for by digitizing a representative frame and then locating the image coordinates of a set of known ground control points that fall in the field of view. The problem is generally over-determined (more known points than unknown parameters) so that the geometry variables can be solved for in a least squares sense. Then, for each sampling time, the video frame is digitized and the beach profile transects of interest placed on the image, based on the now-known geometry. Figure 1 shows an example frame. A total of 39 transects have been placed on the image at a longshore spacing of 10 m (for a total longshore beach length of 380 m being analyzed). For each transect, the intensities of image pixels are read into the host Sun 4/110 computer and a search algorithm implemented to find the water's edge (the selected run-up location is marked on the screen and in figure 1 with a small vertical tick). This selected horizontal location is then translated into a vertical elevation swash signal based on the measured beach profile, and the resulting value written into the computer file. This search is performed for each of the 39 transects before a new frame is digitized. The whole process is repeated every second for the length of the run. An operator monitors the performance of the system by observing the marked computer "picks" and can tune algorithm parameters for each individual transect during digitization.

Resolution of the technique depends on range from the camera and focal length of the individual lens. Typical horizontal resolutions range from 20 cm (swash elevation of 2.0 cm) for close ranges to 0.73 m (swash elevation of 7.3 cm) for the most distant cases. Worst case resolutions for each of the analyzed runs are listed in Table I.

Four data runs were selected for analysis. The first two were at times when no significant shear wave energy was observed in the current meter records and the second two when shear wave energy was obvious. Times of the runs and associated environmental conditions are listed in Table I.

Table I
Statistics for Selected Data Runs

Name	time (EST)	date	T^1 (sec)	α^2 (°)	H_s^3 (m)	R_s^4 (m)	R_s/H_s	δx^5 (m)
GD097	1135	10/12/86	11.4	+14	2.18	2.47±.47	1.13	0.68
GD105	0745	10/13/86	10.7	+22	1.52	1.78±0.22	1.17	0.73
GM133	1025	10/15/86	6.2	-28	1.34	1.35±0.14	1.01	0.37
GM143	1020	10/16/86	5.0	-50	1.27	1.18±0.14	0.93	0.37

1. peak period from 8 m depth pressure sensor
2. peak direction from 8 m depth linear pressure sensor array. Positive angles from south
3. significant wave height from 8 m depth pressure sensor, (periods from 3 - 20 sec)
4. significant swash height, averaged over entire longshore run-up array
5. horizontal resolution of swash data at farthest transect (worst case)



Figure 1. Example video frame showing waves in the nearshore and run-up. Lines across the beach represent surveyed beach profiles. For automatic digitization, the computer searches out along each line (starting with the left hand tick) until it finds the run-up (marked by the right-hand tick). 39 transects are shown.

General Swash Results

Figure 2 shows an example section of swash time series for 32 of the 39 transects, a total beach length of 310 m. The longshore structure of individual swashes is apparent to the eye; there is little discernible phase lag through the array, implying that the waves were approaching the shoreline at near normal incidence (nearby transects actually appear to lead distant ones slightly, implying a northward propagation, consistent with the observed angle of incidence). The visible coherence with longshore distance lends confidence to the digitization process; longshore variability appears to be a function of the observed wave field, not random noise in the sampling algorithm.

A further check on the believability of the results comes from plotting the longshore variability of the basic time series statistics. Figure 3 shows the significant swash height (calculated as $4 \times$ standard deviation) for each of the four runs. Longshore-averaged values are listed in Table I as dimensional values as well as normalized by the significant wave height measured by offshore pressure sensors. In general, the longshore variability shown in figure 3 is quite small, implying a stability in the digitization process. Most variability that does exist occurs on a number of transects, as would be expected for a natural phenomenon (as opposed to random scatter of the digitizing process). It should be noted that in none of these runs was the beach completely two dimensional. In each case, there was natural longshore variability in the bathymetry that undoubtedly contributed to the variability in the observed swash statistics.

SUPERDUCK Run-up

GD097, 01/12/86, 1135 EST
 (32 of 39 lines, 10 m spacing)

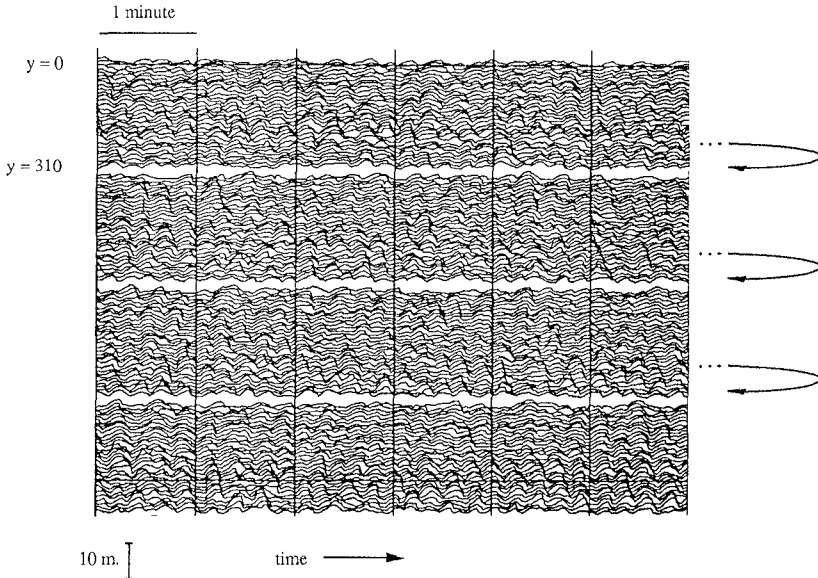


Figure 2. Example swash time series from one data run. Four non-contiguous segments are shown, each of six minute duration. For each segment, 32 adjacent transects are plotted. The longshore coherence and phase of incident wave motions is apparent. 10 m vertical swash scale is shown at bottom.

Spectra were calculated for all transects. Representative examples are shown in figure 4. In each case the peak period observed in 8 m depth is listed above the spectrum, and indicated by an arrow on the plot. For runs GD097 and GD105, there was significant energy at the incident peak. By contrast, for runs GM133 and GM143 (both near low tide) the high frequency incident waves are dissipated over the sand bar so that the spectral peak occurs at a period of about 15 seconds with some lower frequency energy present. GD097 and GD105 also show interesting (and statistically significant) peaks at lower frequency, with a representative period being 35-40 seconds. Intriguingly, this is roughly the period appropriate to an infragravity wave

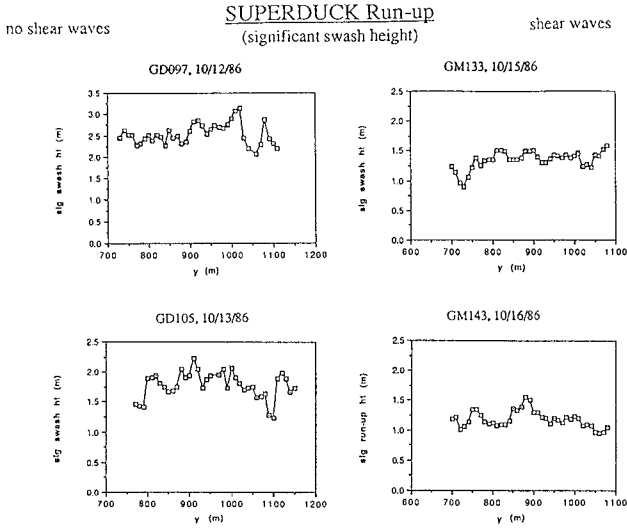


Figure 3. Longshore variability of significant swash height for each of the four selected data runs.

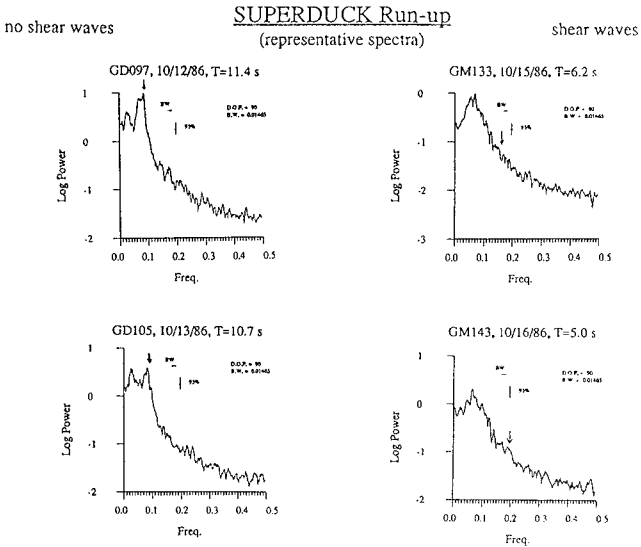


Figure 4. Spectra of swash for selected longshore transects, one for each of the four data runs. Peak periods from offshore pressure gauges are listed above each spectrum and are indicated by arrows on the plots. 90 degrees of freedom.

with a first node at the location of the observed sand bar. Examination of spectra over the length of the “array” shows a smooth variability in the lower frequency peak, suggesting some longshore standingness to this energy. This will be the subject of further work. In no case was the significant energy concentration in the very lowest frequencies associated with the FIG band.

Frequency-wavenumber results

In calculating f-k spectra from current meter measurements, a limited number of instruments (7) were deployed in a configuration optimized to the IMLE spectral analysis technique. In our case, adding “instruments” to the dataset simply involves specifying additional longshore transects to be digitized, and we have arbitrarily specified an array of 39 equally-spaced locations. However, due to technical aspect of the stability of the IMLE analysis, results are best if a subset of 7 transects are chosen, using the same lag spacing as was used for the current meter array. Of course, with so many transects, there are a number of potential choices. Figure 5 illustrates the

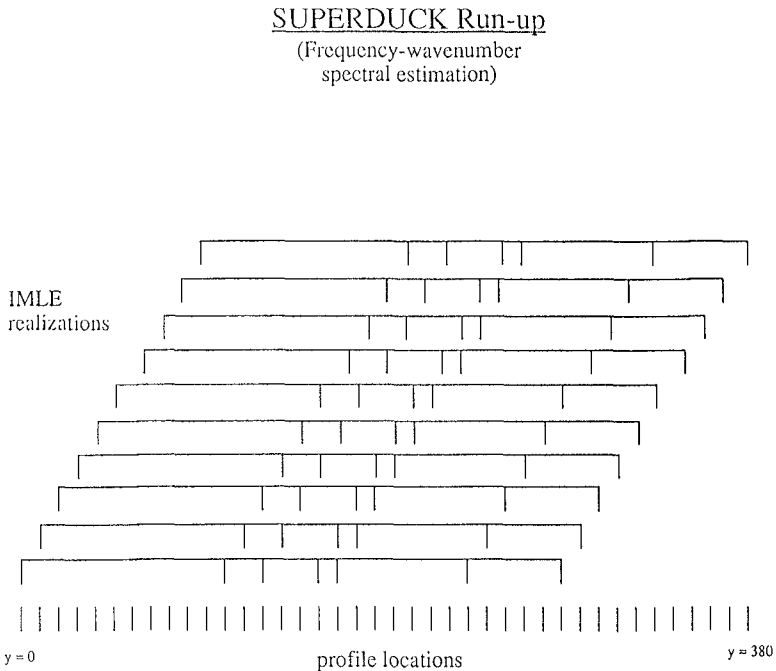


Figure 5. Schematic of “longshore array realizations” used in the analysis. The 39 available transects are shown equally-spaced at the bottom of the figure. Lines above indicate selected arrays for IMLE spectral analysis. Results from the 10 realizations are averaged to yield the final f-k spectra.

options, with the 7 sensor configuration shifted progressively in the longshore. When f-k spectra were calculated for each of these realizations, the basic structure of the spectra were similar, but there was also a great deal of noise that confused the interpretation. To combine the realizations and reduce the noise, the raw f-k spectral data were averaged for the 10 realizations shown in figure 5, yielding a much better result. (We note that many other array designs are also possible and could also be averaged into the result. The simplest of these would just be a reversal of the array. The independence of more and more permutations must gradually decrease, although, at this point, we have not pursued a rigorous quantification of the amount of averaging that is useful. Nor is it clear that averaging the wavenumber spectral results is preferred since IMLE calculations are nonlinear. Averaging of the cross-spectral matrix would be preferred and will be pursued in the future).

Figure 6b shows the resulting averaged f-k spectrum for run GM133, judged the highest quality of our data runs and also one for which shear waves were very clearly observed in the current meter records (figure 6a). Only the sub-incident frequencies are shown. The dispersion lines for modes 0, 1, 2 and cutoff mode edge waves, calculated to account for the true bathymetry as well as the presence of a mean longshore current, are shown to guide the eye.

Several features are seen. In general, there is a significant amount of energy at low wavenumbers, consistent with results from cross-shore velocity data shown in figure 6a. However, there are also clear suggestions of mode 0 edge wave energy propagating in both the southward (positive wavenumber) and northward (negative wavenumber) directions. Interestingly, the modes are asymmetric with respect to the zero wavenumber axis. This result is both predicted by the theoretical dispersion lines, and observed in the data. Identification of possible higher mode edge waves from this diagram is possible, but requires an active imagination.

Figure 7 is an alternate presentation of the same run-up spectrum. However, instead of relying on an algorithm to pick significant peaks in the spectrum, all data are shown with a shading linearly proportional to their energy density (note that each frequency band is still normalized to unit energy so that the shading density indicates relative concentration of energy within the frequency band). When viewed at a distance and with a partial squint, the concentrations of energy along curved dispersion lines are more apparent, with the two modes noted previously being relatively obvious and higher modes being somewhat distinguishable. The asymmetry due to the longshore current is quite obvious.

Figure 6a also clearly shows the region of shear wave energy from the cross-shore velocity data, as the linear feature on the positive wavenumber side of the spectrum. The concentration of energy in the shear waves is evident, particularly at the lower frequencies associated with the FIG band ($<10^{-2}$ Hz). By contrast, the same region, outlined in the run-up spectrum of figure 6b, shows no concentration of energy lying along this ridge. Some energy is observed in the lower frequency, higher wavenumber region (beyond mode 0 edge waves), but there is no correspondence between the f-k location of that energy and the location of the obvious shear waves in the current

SUPERDUCK Spectra 10/15/86

cross-shore velocity

MODELLED DISPERSION
15 OCT 86
LUN BATHYDID, Bath Start Time = 0012
LUN BATHYDID, ENHIB = 15, PNEIGCS = 4, 400, P = FFT
LUN V = 3.14
LUN S = 9.11
LUN Q = 9.11
LUN P = 9.11
LUN V = 3.14

run-up

average of 10 10 11 13 14 17 24 291
LUN BATHYDID, ENHIB = 15, PNEIGCS = 4, 400, P = FFT
LUN BATHYDID, Bath Start Time = 0012
LUN V = 3.14
LUN S = 9.11
LUN Q = 9.11
LUN P = 9.11
LUN V = 3.14

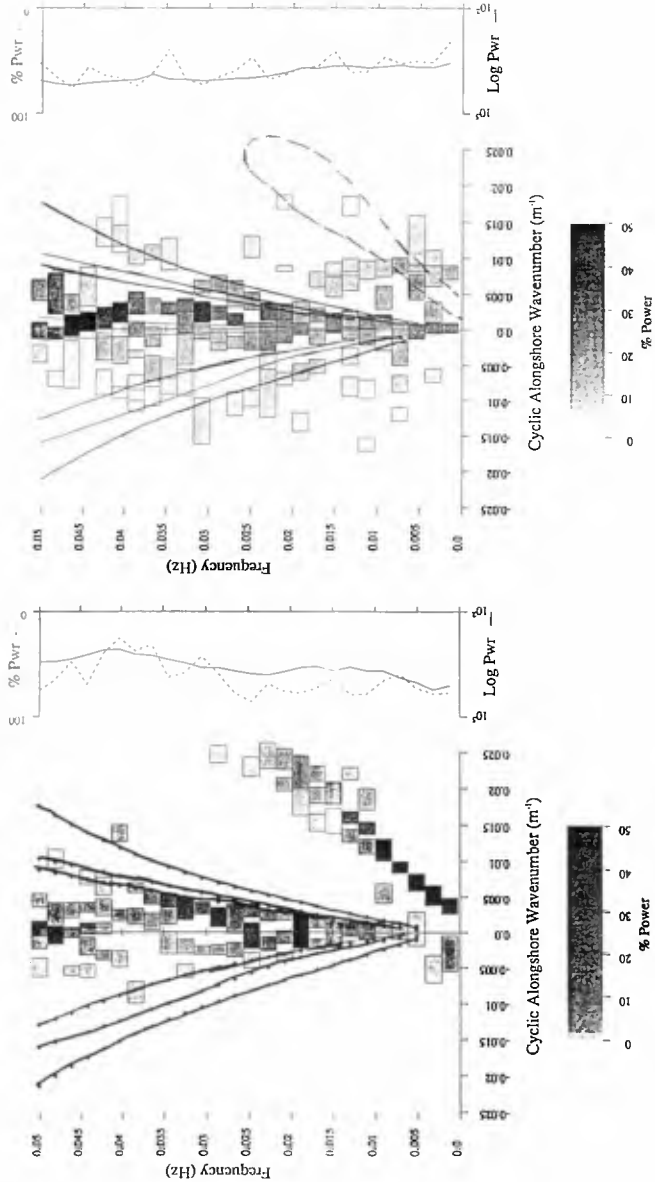


Figure 6. Frequency-wavenumber spectra for a) cross-shore velocity, and b) run-up for 10/15/86. Edge wave mode lines are for modes 0, 1, and 2 and include effects of true bathymetry and mean longshore current. Shear waves are clear in the velocity data, but are absent in run-up.

SUPERDUCK, 10/15/86
 frequency-wavenumber spectrum
 Run-up

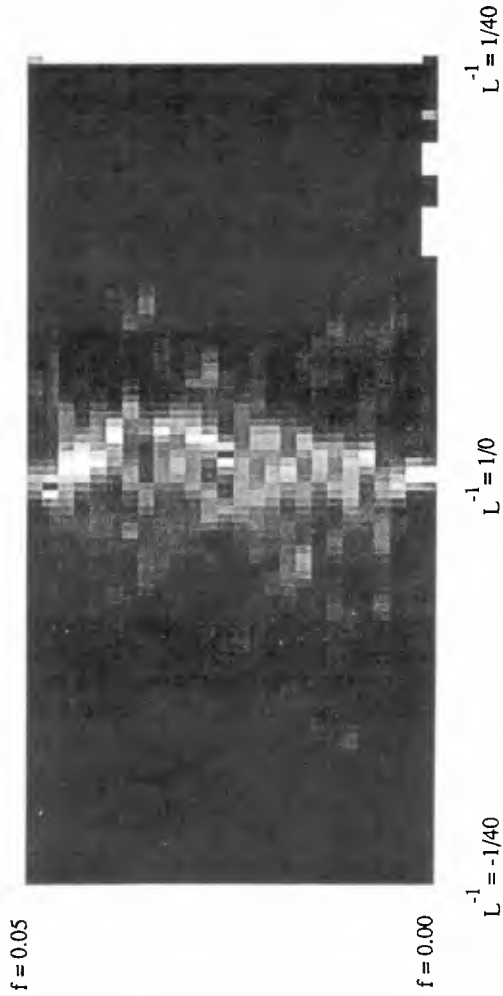


Figure 7. Frequency-wavenumber spectrum for 10/15/86. These are the same data as figure 6b) but the spectral estimates have been shaded for all f-k bins and energy concentrations are indicated by whiteness. Low mode edge waves are shown by the light color ridges curving up into plus and minus wavenumber space.

SUPERDUCK Spectra
10/12/86

cross-shore velocity

run-up

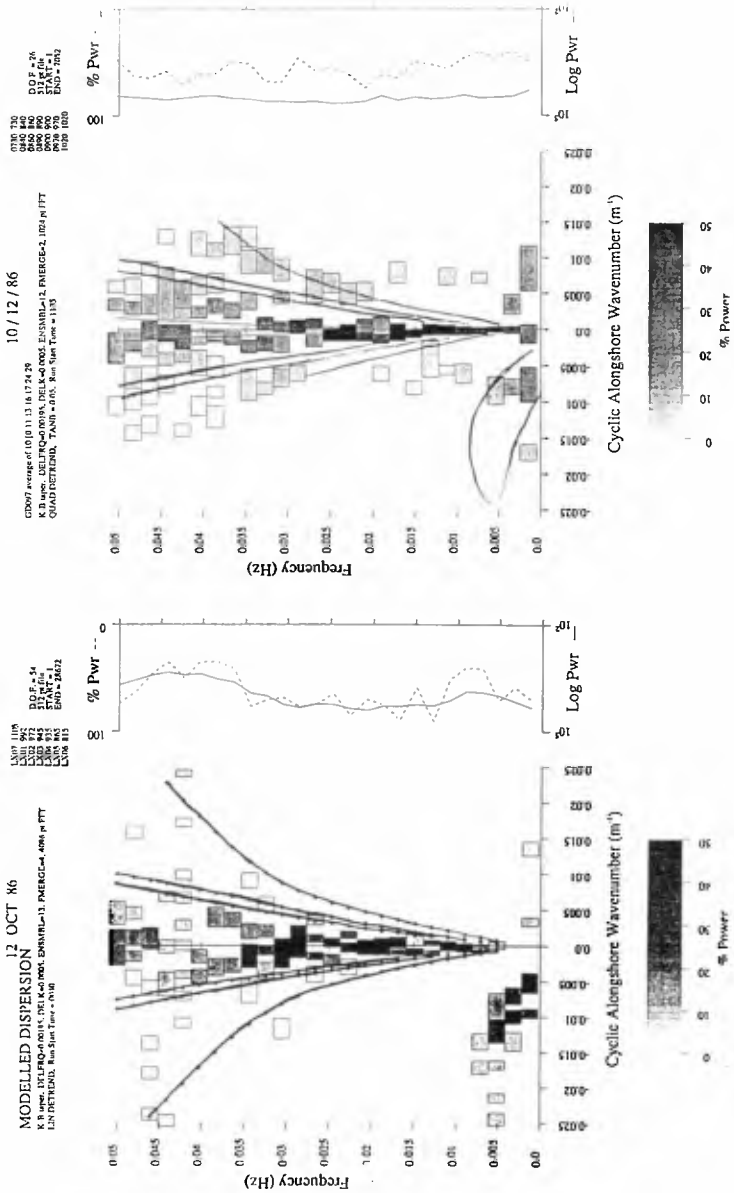


Figure 8. Frequency-wavenumber spectra for a) cross-shore velocity, and b) run-up for 10/12/86, a day for which little shear wave energy was observed in the velocity data. Edge wave mode lines are for modes 0, 1, and 2 and include effects of true bathymetry and mean longshore current. Run-up data clearly shows low mode edge wave energy, but little in the shear wave region.

meter data. At present, we do not know what the observed region of energy represents.

Figure 8 shows f - k spectra for October 12 (run GD097) for the cross-shore velocity data (figure 8a) and for run-up (figure 8b). Again, low mode edge waves are visible in the run-up data, even more than in the cross-shore velocity spectrum. While this run was specifically chosen as one for which shear wave energy was a minimum, we still see a slight concentration in the velocity data at very low frequencies and large negative wavenumber. Again, the same region, marked on the run-up spectrum, shows no particular concentration of energy.

The absence of low-frequency, high-wavenumber energy in the run-up data supports our hypothesis that shear waves are, in fact, just that; shear waves. These motions appear to obey the rigid lid assumption, showing no significant sea surface elevation signal despite large concentrations of energy in velocity time series.

Conclusions

Examination of the sea surface elevation signal (represented by swash time series) at sub-incident band frequencies has shown the presence of a variety of expected gravity wave motions including leaky modes (low wavenumber energy) and low mode edge waves. However, even under conditions when shear wave energy was extremely pronounced in velocity data taken 50 m offshore, there is no indication of such signals in the swash data. This supports the rigid lid assumption made in the theory; these low-frequency high-wavenumber motions appear to be vorticity signals with no significant sea surface elevation signal.

Acknowledgments

We would like to thank Paul O'Neill for the enormous amount of work he put into developing the image processing hardware and software, and in digitizing the data runs. Once again, we would like to acknowledge the excellent work of the Army Corps FRF staff during the SUPERDUCK experiment, and the efforts of Col. Grum in obtaining funding for the tower at Duck. Much of the theoretical and conceptual understanding of this problem has resulted from discussions with Tony Bowen. Funding for this work was from the Office of Naval Research, Coastal Sciences program under contract N00014-90-J-1118.

References

- Bowen, A.J. and R.A. Holman, 1989: Shear instabilities of the mean longshore current, 1. Theory. *J. Geophys. Res.*, **94**, (C12), 18023-18030.
- Oltman-Shay, J.M, Howd, P.A. and W.A. Birkemeier, 1989: Shear instabilities of the mean longshore current, 2. Field observations. *J. Geophys. Res.*, **94**, (C12), 18031-18042.

CHAPTER 94

Safety philosophy for dike design in The Netherlands

A.W.C.M. Vrouwenvelder¹, P. Struik²

Abstract

This paper describes the history and present state of the art with respect to safety philosophy for flood defence systems in the Netherlands. It is explained that present day philosophy is based on a so called dike-ring approach and on a probabilistic treatment of all load and strength parameters. Both target safety levels as well as verification procedures are discussed. Simplification rules for application in every day practice are given.

1. Introduction

In the past decades, the design of dikes and flood-defences has developed from a traditional craft to a scientific approach. Traditionally the crest of the dike was built 1 m above the highest water level known so far. In the late 1930's it was recognized that water levels are statistical quantities and that dike design should be based upon water level exceedence frequencies. The first step from a deterministic to a probabilistic design approach was taken. The next step is to extend this idea to other load and strength parameters, the so called full probabilistic design. This paper describes the main developments in this field and the present state of the art.

¹ Professor of Mechanics, Delft University of Technology, Department of Civil Engineering and Head of the Department of Structural Dynamics, TNO, P.O. Box 49, 2600 AA Delft, The Netherlands

² Coordinating Engineer for the Technical Advisory Committee for Water Defences (TAW), Ministry of Transport and Public Works, Rijkswaterstaat, Hydraulics Section of the Road and Hydraulic Engineering Divison, P.O. Box 5044, 2600 GA Delft, The Netherlands.

2. Floods and flood defence strategies, a historical overview

In 1916 a storm surge flooded the land around the former Zuiderzee (see Figure 1). This inundation led to the decision to close the Zuiderzee, by means of a dam, the Afsluitdijk, and thus creating the IJssel-meer. The Afsluitdijk was completed in 1932. For the design only historical data were taken into account. The dike height was based on the rule that it should be able to withstand the highest known storm level in history.

For the next 20 years, Holland seemed to be safe. Then, on the first of February 1953, a severe storm surge struck the south western coast and drove the water into the delta of the Rhine, Schelde and Meuse, up to an unprecedented level. A great number of dikes collapsed, large parts of land were flooded and over 1800 people drowned.

After this disaster the so called Delta-committee was formed to prevent such a tragedy to ever happen again. The Delta-plan was developed and executed. This meant a 700 km shortening of the coastline, by the closure of all major estuaries, and strengthening of the dikes.

In the preceding decades it was discovered that the observed storm levels plotted on probability paper against their probability of exceedence formed nearly a straight line. Now it was possible to extrapolate this line and base the dike design on a storm level with a chosen probability of exceedence.

The acceptable return-period for the waterlevel that the dikes should still withstand was set by the Delta-committee on 10,000 years for central-Holland and 4,000 years for the other parts of Holland, with less inhabitants and less investments. Also a economical study was carried out, trying to balance the investments in flood defences against the probability of failure and the consequential damage. That study pointed in the same direction for the choice of the return period.

The Delta-plan was still under construction when the next event happened. In 1960 an inland polder dike failed and the polder Tuindorp-Oostzaan, an urban area near Amsterdam, was flooded. After the investigation of the cause of this event it was concluded that it would be better not to wait for the next disaster and then form an other committee of investigation, but to have a permanent committee to safeguard the safety against inundation.

This led to the formation of the Technical Advisory Committee on Water Defences (TAW) by the Minister of Transport and Public Works. The first task of this committee is to advise the minister on all technical-

scientific aspects of water defences and of the protected areas. To do so this committee coordinates research and publishes guides for the design and maintenance of water defence works.

In the early seventies the acceptable return period for river dikes became a matter of discussion. In this case the figures given by the Delta Committee seemed to be too strict. In 1975 the Becht Committee advised a return period of 1250 years for the design water level of the river dikes.

This recommendation was based on the following distinction between river and sea hazards:

- inundation by fresh water causes less damage than inundation by salt water;
- high water level on rivers can be predicted earlier and appropriate measures can be taken;
- the areas threatened by rivers are above mean water level, which means that after the flooding the water disappears and gaps can easily be closed.

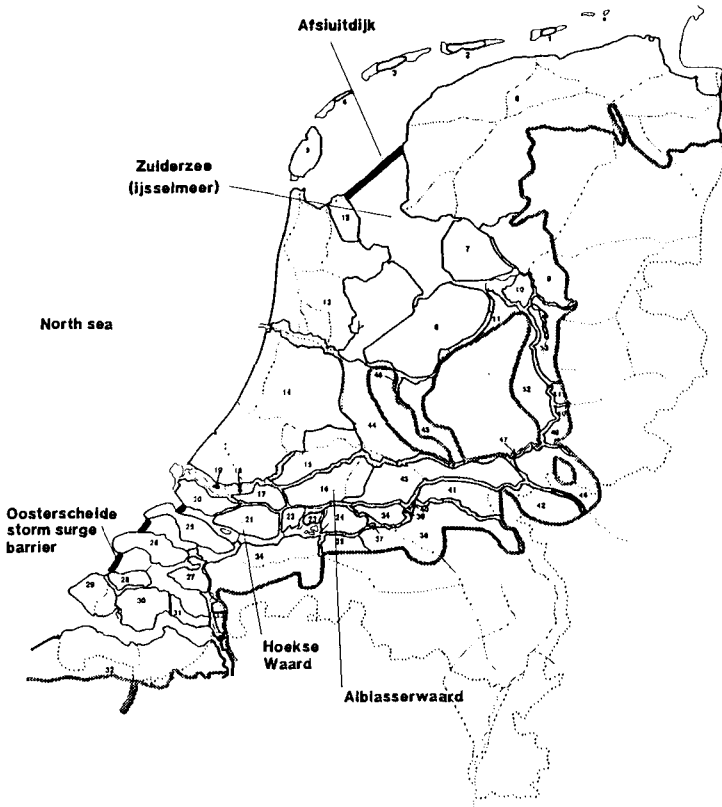


Figure 1: Map of the Netherlands

As a part of the Delta Plan the Eastern Schelde Storm Surge Barrier was build in the period 1980-1988 (see Figure 1). During design it was recognised that probabilistic treatment of the water level should be extended to other load parameters (wind, waves), but also to resistance parameters (soil) and operational factors (electric power, human factors). After this rather succesful introduction of probabilistic methods into practice, other applications followed.

Recently, in 1989, the TAW published the Guide for the Design of River Dikes, especially dealing with tidal-river dikes. This design guide is based on probabilistic starting points and the dike-ring concept (see section 3). It is however stressed that this does not imply that it is possible to actually calculate the probability of inundation.

In 1991 a new Law in Flood Protection is expected to pass the Dutch Houses of Parliament. Target of the new law is to maintain the safety that has been obtained by years of construction, consuming large sums of money. To do so a five-yearly check of the primary waterdefences has to be carried out and a report on the provided safety should be given. The TAW is now working on a guidance document how to carry out this safety-check.

3. Basic concepts of Probabilistic Design

In the Netherlands a polder is often bordered by water on many sides. Therefore the expression "dike-ring" is introduced for referring to the protecting ring of water retaining structures bordering the area (see Figure 2). An important point is that this protecting ring should be considered as a coherent system and not as an arbitrary set of individual elements. If for the time being equal consequences for the failure of all parts of the ring are assumed, the basic safety requirement for the dike-ring can be formulated as:

$$P\{F\} < P\{\text{target}\} \quad (1)$$

In here $P\{F\}$ is the failure probability or probability of inundation for the dike ring (per year) and $P\{\text{target}\}$ is the accepted value. The design problem now can be subdivided into two distinguished parts:

- (1) to determine the target failure probability;
- (2) to judge wether a given dike system (existing or designed) fulfils the basic requirement.

Item (1) is partly a technical matter and partly a matter of political decision. The technical part is related to questions as: what will be the consequences of a dike failure in terms of inundation, loss of property and loss

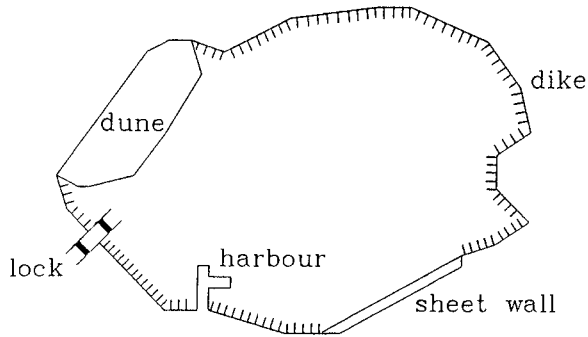


Figure 2: A dike-ring is an area surrounded by a system of water retaining elements as dunes, sheet walls, locks and so on.

of life. Politicians should answer questions as to what losses can be accepted.

Item (2) is a typical technical problem. It is effective to distinguish two different lines of approach. The first line of approach is bottom up: based on physical models for all failure mechanisms and based on statistical models for all random variables, one may calculate the failure probability for the complete system. The second line is top down: starting from a given target probability for the system, one derives targets for individual mechanisms and elements; from there on one derives requirements for the design variables.

As long as all mechanisms are known and full information on all statistical properties exists, both approaches are entirely equivalent. However, as this is not the case, the first approach is deemed to fail at present: the system failure probability for a complete dike-ring simply cannot be calculated. Taking the second approach however, it is possible to deal at least with a substantial part of the design problem, even if not all mechanisms can be treated. As research goes on, the part that can be dealt with using these techniques, will increase.

4. Target reliability

In Figure 3 the flow chart for a target reliability estimation has been indicated. Based on the hydraulic conditions at the river, sea or lake on one side and the gap growth characteristics for the failing dike element on the other, the discharge through the breach can be calculated. Given the resulting inundation pattern, the material losses and the losses of human lives must be estimated. An example is shown in Figure 4.

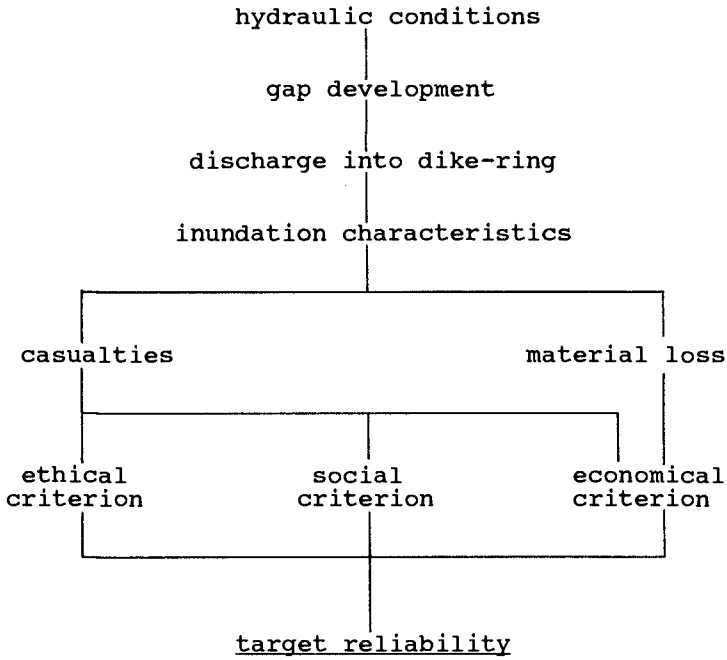


Figure 3: Determination of target reliability

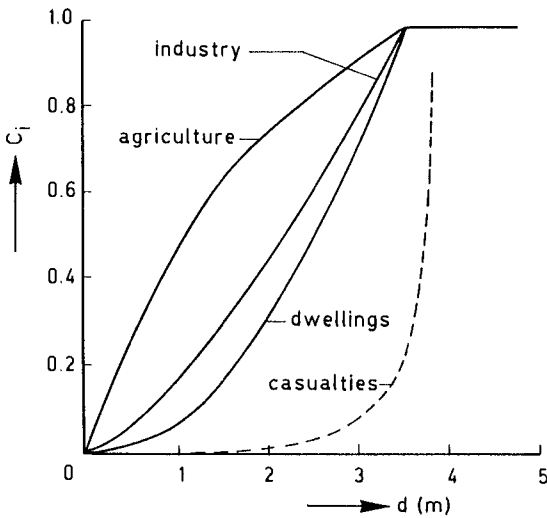


Figure 4: Material loss and number of casualties as a function of the inundation depth (examples)

These losses should give indications for target reliabilities. In the Netherlands a three criterion system is under development:

1. An ethical or personal risk criterion. According to this criterion it is not allowed to let an arbitrary person run a risk for drowning which is substantially higher than the risk for an accident in normal life;
2. A socially accepted risk, which is concerned with the aversion a society has against large accidents including many casualties;
3. An economic criterion: the cost of improving a dike system should (at least) be balanced by the save of losses.

For further information the reader is referred to [TAW]. An interesting application, involving also time dependency and maintenance aspects is presented in [Vrijling]. If the three criteria give different answers, as they usually do, a possible strategy is to maintain the most severe requirement as the governing one. However, as said before, in matters of this kind the last word is to politicians.

Alblasserwaard case

In order to check the usefulness of the criteria mentioned and the adequacy of the calculation tools, one of the dike rings in the lower Rhine area has been analysed [Vrouwenvelder, Wubs]. The dike ring chosen was the Alblasserwaard which stretches from a river dominated regime at the east to a mixed sea river regime at the west side, see Figure 1. A more detailed map is presented in Figure 5. Figure 6 presents a schematic cross section.

For breaches on various locations along the dikes, the resulting water levels within the dike ring have been calculated (Figure 7). These water levels depend highly on the location of the breach: the most severe inundation occurs when the dike fails at Gorinchem. In that case the water level equals 3.70 m above average sea level, which means inundation depths varying from 1.70 m to 5.20 m. A breach at Alblasserdam, located at the most western point of the dike ring, leads to an inundation depth of no more than 1.5 m; parts of the dike ring even will remain dry.

These results show that it may be necessary to have a safety differentiation within one dike ring. At present this is not common practice. Following this line of thought, safety targets were derived for every location based on inundation depth versus loss diagrams (Figure 4) and the criteria presented before.

For Alblasserdam a target value for the inundation return period of 3,500 years resulted, which almost equals the present value. For Gorinchem this value varied from 8,000

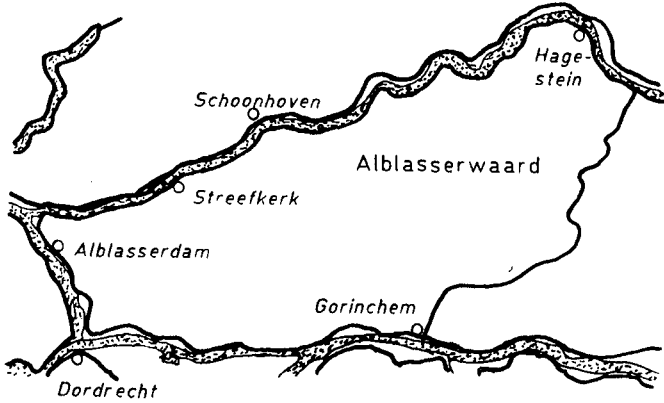


Figure 5: Dike ring Alblasserwaard

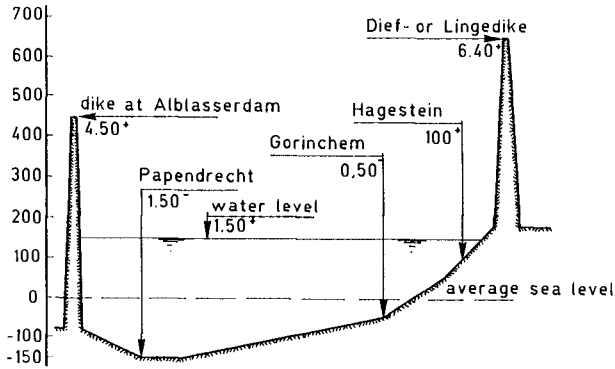


Figure 6: Schematic cross section of Alblasserwaard

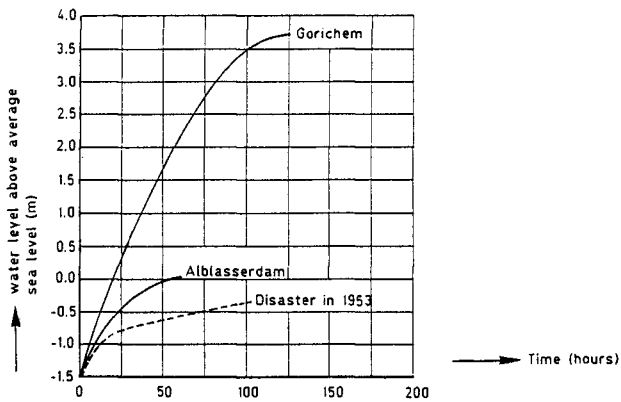


Figure 7: Inundation depth versus time curves for breaches on various locations

to 600,000 years, depending on the casualty-inundation depth relationship. It should be stressed that this relationship is highly uncertain. On the other hand, it is only necessary to oversize the dikes at Gorinchem slightly compared to other ones to reach a very high local safety level.

5. Assessment of a given dike-ring

As mentioned in section 3, a useful strategy is to start from the accepted general failure probability and break it down into acceptable failure probabilities for the various mechanisms and elements (top-down-approach). A demonstration of such a break down is presented in Figure 8. This failure tree shows the dominant failure modes and (by way of example) corresponding individual failure probabilities per mode. All modes have been assumed to be stochastically independent, which is conservative.

Within one mode one might continue the break down and split up the total failure probability for the mode under consideration between all elements of the dike-ring. As an alternative it is sometimes possible to use for one mechanism a bottom up procedure, and calculate the failure probability of the system. This depends on the characteristics of the failure mode, the elements involved and the system properties (serial system, parallel system or mixed). Both procedures will be discussed later on.

Special attention in the analysis of a dike-ring has to be given to structural components as locks and storm surge barriers. In the first place, these structures may give rise to additional mechanisms, resulting from discontinuities in the water retaining system. A second point is that these structures may contain moving parts, which may fail because of jamming, faults in electrical and hydraulic systems, human errors, and so on. The basic philosophy and assessment tools for these types of events can, however, be the same as for natural failure modes.

- Top Down procedures

For discrete elements forming a purely serial system, the break down within one mode can be performed in the same manner as for the break down between the modes; if necessary again independency between the elements or modes can be assumed. So in the case of N elements one has to fulfill:

$$\sum P(F_i) = P(F_1 \text{ or } F_2 \dots \text{ or } F_N) \geq P(F_{\text{system}}) \quad (2)$$

where $P\{F_i\}$ = Failure probability of element i for the failure mode under consideration (e.g. overtopping or sliding) and $P\{F_{\text{system}}\}$ = Target system failure probability for the mode under consideration.

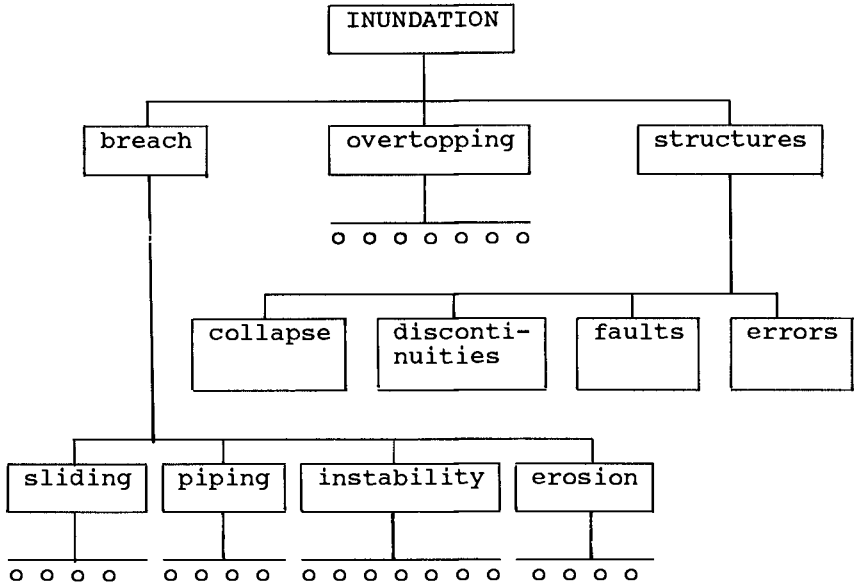


Figure 8: Failure Tree for a Dike-ring

Most straightforward of course is to take equal failure probabilities for all members. However, from the economical point of view some other distribution may be preferred. If there is correlation between the members, one might use some equivalent number of members (see [Vrouwenvelder]).

In the case of continuous elements the concept of the equivalent independent dike section can often be used. As an example consider the mechanism of slope instability. It can be proven [Calle] that the dike may be conceived as a system of independent sections, each section having a length of 30 - 100 m. This length coincides almost with the length of a sliding surface. The probability of failure for a single sliding surface can be found from a standard FORM analysis [TAW]. In the same way the mechanism of piping can be analysed [Calle].

- Bottom Up Procedures

It is sometimes possible to calculate the failure probability of the complete system for the specific mode. Three methods can be distinguished: (1) Monte Carlo, (2) Numerical Integration and (3) First Order Methods.

Monte Carlo may be considered as an appropriate for relatively simple systems. The point is that the number of simulations should be large in order to get a reliable result. However, there are promising developments going on into new techniques as for instance importance sampling and directional sampling [Bjerager].

Numerical integration is feasible as long as the number of random variables is small (say less than 5), or when some special structure of the mathematical problem makes it possible to break the multiple integral into a number of smaller integrals. The model defining the failure domain should not be too complicated.

An example where the technique of numerical integration has been applied with great success is the mechanism of wave overtopping: for all elements of a dike ring this mechanism may depend on the same sea water level, river discharge, wind velocity and wind direction. This enables the evaluation for the dike-ring failure probability by means of a multi dimensional integral. Based on this principle the computer program DIJKRING has been developed [Niemeijer, Volker, Vrouwenvelder]. Consider as an example the dike ring Hoekse Waard (Figure 9), which can be subdivided into 18 dike segments. DIJKRING needs a specification of the orientation, location and geometry for all dike segments. Next, for every combination of the four random variables DIJKRING checks all dike segments for overtopping failure. The resulting failure probability was calculated as once per 600 year. After the construction of a storm surge barrier near Rotterdam this number will be improved.

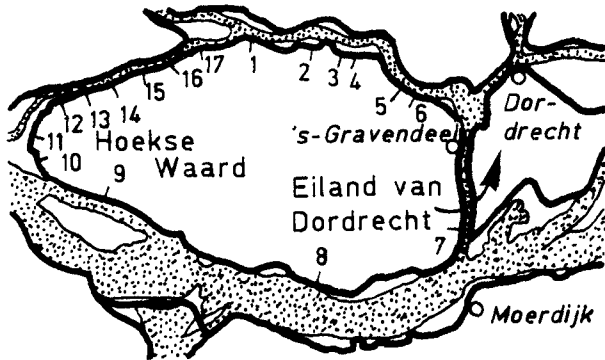


Figure 9: Dike ring Hoekse Waard, subdivision into 18 elements

Especially in structural engineering the method of First Order Methods is very popular. As a first step the individual failure modes are analysed using the FORM or level II procedures [TAW]. Next the combination of failure modes of failure sequences are evaluated using the first order approximation according to [Hohenbichler/Rackwitz], [Ditlevsen] or [Stevenson/Moses]. For this method the number of modes and the correlation between the failure modes should not be too large.

6. Every day practice/code development

Although the basic philosophy for the safety assessment should "always" be a probabilistic one, it is not desirable to perform detailed probabilistic analyses for all mechanisms and all dike-rings. There is a need for simple design methods for the every day practice. Standard procedures to derive simple rules from probabilistic considerations have been developed in the past decades and can be found in the international literature.

The basic idea is that one uses "design values" for the random variables. A design value X_d is the value that one uses in the safety check formulas, and corresponds to a probability of being lower (for strenght parameters) or higher (for load parameters) of:

$$P [X < X_d] = \Phi(-\alpha\beta) \quad (\text{for resistance}) \quad (3)$$

$$P [X > X_d] = \Phi(+\alpha\beta) \quad (\text{for load}) \quad (4)$$

Here β is the so called reliability index (corresponding roughly to $-\log P(\text{target})$) and the coefficient α ($0 < \alpha < 1$) indicates the relative importance of the variable and can be found from a FORM (First Order Reliability Method) or level II analysis. In many codes these α -values have been standardized in the following way:

- leading resistance parameter: $\alpha = 0.80$
- leading load parameter : $\alpha = 0.70$
- other resistance parameters : $\alpha = 0.32$
- other load parameters : $\alpha = 0.28$

In practice, design values are often calculated as the product of characteristic values and partial safety factors. Assuming the characteristic values to equal the mean value and a normal distribution, the partial safety factor is given by:

$$\gamma = 1 + \alpha \beta V \quad (5)$$

V is the coefficient of variation for the variable under consideration. For other distributions similar expressions are available. The concept of "design values", characteristic values and partial safety factors have also found its way into the TAW guides for river dike design and dune reliability assessment.

7. Conclusion

Based on the probabilistic principles and methods outlined in this paper, it is possible to judge in a rational manner the safety of a complete dike system. Consistent assessment on various levels of sophistication is possible. In practice the degree of refinement will depend on the state of the knowledge about the mechanisms under consideration and/or on the economic consequences of nonoptimal solutions.

In the present situation already many basic ideas of the probabilistic design philosophy have found their way into practice, either by design guides, or in the design of specific structures. There is a tendency towards more applications in specific projects. This has to do with the fact that the most difficult parts of the River dike construction works still have to be carried out. Especially the cases with conflicting interests have been postponed until the last stage. These are for instance dikes in cities or through valuable landscapes.

Problems of that type demand extra skills and ingenuity, to take all aspects in account and to find the best possible design. In these cases an integrated approach and an open discussion is necessary to achieve an optimal and generally accepted solution. For large projects, such as the Storm Surge Barrier in the Eastern Schelde, this is already good practice, but smaller projects may also demand the same approach. It may be necessary to change the historically approved opinion that only a water defence system consisting of sand and clay is a good one. Probabilistic methods will help to prove that other solutions can be considered as equivalent reliable alternatives.

References

- Calle, E.O.F., "Probabilistic Analysis of stability of Earth Slopes", ICSMFE-XI, San Francisco, 1985.
- Calle, E.O.F., "Serial system Effects for the Piping Mechanism (in Dutch), CO-294460/21, Grondmechanica Delft, Februari 1989.
- Ditlevsen, O. and Bjerager, P., "Methodes of Structural System Reliability", Structural Safety, 3, 195-230, 1986.
- Ditlevsen, O. and Bjerager, P., "Plastic Reliability Analysis by Directional Simulation", DCAMM Report No. 353, Technical University of Denmark, June 1987.
- Hohenbichler, M. and Rackwitz, R., "First Order Concepts in System Reliability", Structural Safety, Vol. 1, No. 3, April 1983.

Stevenson, J. and Moses, F., "Reliability Analysis of Frame Structures", Journal of the Structural Division, ASCE, Vol. 96, ST11, Nov. 1970, pp. 2409-2427.

TAW, "Probabilistic design of flood defences", CUR-Report 141, Gouda, June 1990

Vrouwenvelder, A., "Partial Safety Factors for the Nieuwe Waterweg Storm Surge Barrier", Short Course on Reliability, Imperial College of Science, Technology and Medicine, September 1990.

Vrouwenvelder A., Niemeyer J., and Volker W., "Overtopping Probability for a Dike-ring", Short Course on Reliability, Imperial College of Science, Technology and Medicine, September 1990.

Vrijling J., van Beurden I. "Sea level rise, a probabilistic design problem", Coastal Engineering, 1990.

PART III

Coastal Structures



CHAPTER 95

DYNAMIC STABILITY OF ARMOR UNITS - A BEM APPROACH

Chimin Chian(1) and Franciscus Gerritsen(2)

ABSTRACT

A method is presented for predicting primary stability of armor units on a breakwater exposed to solitary waves. A 2-D flow model is developed based on a boundary element method for simulating run-up of a nonbreaking solitary wave on an impermeable, smooth slope. Since Laplace equation subject to exact boundary conditions is solved by the model, the 'mild slope' restriction in using a 1-D long wave model is eliminated. Schemes including inductive wave generation, Lagrangian shoreline motion and free surface regridding are proposed. The run-up flow model is then coupled with an armor stability model to predict a stability number for armor units as function of time and location on the slope. Aspects such as applicability of Morison-type approach and selection of lift coefficient are examined. Results of computed wave run-up and armor stability are compared with experimental data.

1. INTRODUCTION

A solitary wave, described as a disturbance of water surface that travels at a supercritical phase speed with a permanent and symmetrical form completely above the still water line, propagates from offshore region shoreward towards a coastal structure which has a sloping seaward face. After the leading tip of the wave reaches the slope, the wave deforms, runs up to a maximum height, and then runs down before propagating seaward. In its passage, the wave generates an unsteady flow field which exerts hydrodynamic forces on the exposed part of the structure. The subject of this study is the primary stability of the protective layer of rocks, or armor units, on the sea-facing slope of the structure under such flow conditions.

Kobayashi et al. (1986, 1987) studied the problem for oscillatory waves with a flow model based on a finite-difference method. A stability model was developed for armor units which predicted a stability number as a function of time and location on the slope

1) Graduate Student University of Hawaii, presently M.I.T., R.M. Parsons Laboratory, Cambridge, MA 02139.

2) Professor of Ocean Engineering, University of Hawaii, Honolulu, Hawaii.

Since a one-dimensional long wave equation was used, their model is applicable only to mild slopes. When the slope is relatively steep, a two-dimensional model is desirable for adequate description of the flow condition along the sloping bed. For this purpose, an approach based on the boundary element method is deemed appropriate if we may assume the slope is, to a good approximation, smooth.

Run-up of solitary waves on a smooth slope has been studied, among a few others by Kim et al. (1983) using a boundary element method. To broaden the range of problems being treated and to reflect the development in our study of nonlinear wave simulation, we present in this paper a model based on the potential theory and a boundary element method (BEM) for evaluating the stability of armor units exposed to solitary waves on relatively steep, impermeable, smooth slopes.

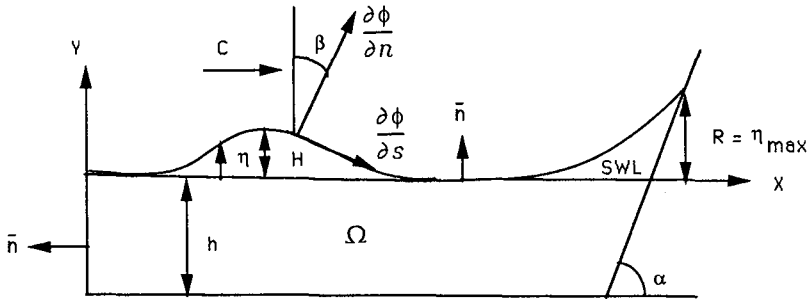


Fig.1 Definition sketch.

2.PROCEDURE

For a problem defined in Fig.1 where potential theory is assumed valid, the appropriate governing equation and boundary conditions are

$$\nabla^2 \phi = 0 \quad \text{in } \Omega, \tag{1}$$

$$\frac{\partial \phi}{\partial n} = 0 \quad \text{on solid bed}, \tag{2}$$

$$\frac{\partial \eta}{\partial t} + \frac{\partial \phi}{\partial x} \frac{\partial \eta}{\partial x} = \frac{\partial \phi}{\partial y} \quad \text{on } y = \eta, \tag{3}$$

$$\frac{\partial \phi}{\partial t} + \frac{1}{2} \left\{ \left(\frac{\partial \phi}{\partial x} \right)^2 + \left(\frac{\partial \phi}{\partial y} \right)^2 \right\} + g \eta = 0 \quad \text{on } y = \eta. \tag{4}$$

Nondimensionalizing variables such that

$$(x^*, y^*, \eta^*) = \frac{(x, y, \eta)}{h}, \quad t^* = t \sqrt{\frac{g}{h}}, \quad \phi^* = \frac{\phi}{\sqrt{gh^3}}, \quad (u^*, v^*) = \frac{(u, v)}{\sqrt{gh}}$$

dropping the stars, and expressing the free surface boundary conditions in surface-fitting coordinates (Liu, 1978), we have

$$\nabla^2 \phi = 0 \quad \text{in } \Omega, \quad (5)$$

$$\frac{\partial \phi}{\partial n} = 0 \quad \text{on solid bed}, \quad (6)$$

$$\frac{\partial \eta}{\partial t} = \frac{1}{\cos \beta} \frac{\partial \phi}{\partial n} \quad \text{on } y = \eta, \quad (7)$$

$$\frac{\partial \phi}{\partial t} + \frac{1}{2} \left\{ \left(\frac{\partial \phi}{\partial n} \right)^2 + \left(\frac{\partial \phi}{\partial s} \right)^2 \right\} + \eta = 0 \quad \text{on } y = \eta. \quad (8)$$

To specify the condition at the offshore (left) boundary, we differentiate between wave generation and run-up simulation. In wave generation, an inductive method is used (Chian, 1989) in which the wave field is generated by gradually introducing a known-a-priori wave form into the computational domain with other variables being solved stepwise in the process until the entire wave (cut at 0.1%H) is in the domain. For this procedure, the condition at the offshore boundary is

$$\frac{\partial \phi}{\partial n} = -u, \quad (9)$$

where u is the horizontal fluid particle velocity. In the ensuing run-up simulation, the generated wave field is taken as the initial condition and the offshore boundary is set open by using an Orlanski condition given by

$$\frac{\partial \bar{\phi}}{\partial t} + c \frac{\partial \bar{\phi}}{\partial n} = 0, \quad (10)$$

where c is the wave phase speed and overbars denote depth-averaged values, all being evaluated at each time step. The assumption underlying eq.(10) is that the shape of the outgoing wave keeps approximately unchanged.

At the shoreline, we write the dynamic free-surface boundary condition (8) as

$$\frac{d\phi}{dt} = \frac{1}{2} \left[\left(\frac{\partial \phi}{\partial n} \right)^2 + \left(\frac{\partial \phi}{\partial s} \right)^2 \right] - \eta \quad \text{on } y = \eta. \quad (11)$$

Assuming that the fluid element at the shoreline consists of the same fluid particles at all times, eq.(11) further reads

$$\frac{d\phi}{dt} = \frac{1}{2} u_s^2 - \eta \quad \text{on } y = \eta, \quad (12)$$

with u_s , the velocity of the fluid element at the shoreline, being evaluated using the boundary solutions of velocity potential along the slope. To match this scheme, Lagrangian nodes are used on the slope to follow fluid motion.

Applying Green's second identity to the boundary value problem governed by the Laplace equation, it may be shown that

$$\epsilon(\zeta)\phi(\zeta, t) = \int_{\Gamma} \left\{ G(\zeta, \omega, t) \frac{\partial \phi}{\partial n}(\omega, t) - \phi(\omega, t) \frac{\partial G}{\partial n}(\zeta, t) \right\} d\Gamma, \tag{13}$$

Where ζ, ω are field and source points, Γ is the boundary enclosing Ω , ϵ is the interior angle of the boundary at ζ , and G is a fundamental solution of the form

$$G(\zeta, \omega, z) = -1/r(z), \text{ with } r \text{ being the distance between } \zeta \text{ and } \omega.$$

Discretizing eq.(13) by dividing Γ into N linear elements, and differencing eqs. (7), (8), (10), (12) in time by a Crank-Nicholson implicit scheme, a set of simultaneous equations subject to boundary conditions may be obtained (Kim et al., 1983; Chian, 1989) and solved in time domain for ϕ and $\partial\phi/\partial n$ around Γ . Differentiating solutions of ϕ along the slope then yields a history of fluid particle velocities at various locations on the slope, which are used as input for the armor stability model as will be discussed later.

In implementing run-up simulation, a regridding scheme is used on the free surface at each time step, with which the size of projections on x of all elements are kept equal so as to avoid excessive elongation or shortening of certain elements and improve the accuracy of numerical differentiation along the free surface in evaluating $\frac{\partial\phi}{\partial s}$ and β . The scheme is given by

$$\begin{aligned} \left(\phi, \frac{\partial\phi}{\partial n}, \frac{\partial\phi}{\partial s} \right)_{i'} &= \xi_1^+ \left(\phi, \frac{\partial\phi}{\partial n}, \frac{\partial\phi}{\partial s} \right)_i + \xi_2^+ \left(\phi, \frac{\partial\phi}{\partial n}, \frac{\partial\phi}{\partial s} \right)_{i+1} && \text{(advancing wave)} \\ \left(\phi, \frac{\partial\phi}{\partial n}, \frac{\partial\phi}{\partial s} \right)_{i'} &= \xi_1^- \left(\phi, \frac{\partial\phi}{\partial n}, \frac{\partial\phi}{\partial s} \right)_i + \xi_2^- \left(\phi, \frac{\partial\phi}{\partial n}, \frac{\partial\phi}{\partial s} \right)_{i+1} && \text{(receding wave)} \end{aligned}$$

where

$$\begin{aligned} \xi_1^+ &= \frac{1}{2} \left(1 - \frac{dS - S_i/2}{S_i/2} \right), & \xi_2^+ &= \frac{1}{2} \left(1 + \frac{dS - S_i/2}{S_i/2} \right), \\ \xi_1^- &= \frac{1}{2} \left(1 - \frac{dS - S_{i-1}/2}{S_{i-1}/2} \right), & \xi_2^- &= \frac{1}{2} \left(1 + \frac{dS - S_{i-1}/2}{S_{i-1}/2} \right). \end{aligned}$$

In the above, S_i and S_{i-1} are the lengths of the i th and the $(i-1)$ th elements. dS is the difference in element length between two time steps. Primes for the subscripts denote the interpolated nodal points. Linear interpolation is chosen in this scheme for consistency with the linear elements used in this study.

To relate wave field with armor stability, Kobayashi et al. (1986) showed, based on analysis of forces acting on armor stones, that the commonly used stability number

could be dynamically represented by the one calculated from the threshold condition against sliding/rolling. Modified in this study, using the scaling relationships given previously, this number is given by

$$N_s = A \frac{H}{u_b^2} \left[\tan \phi \cos \alpha - \frac{u_b}{|u_b|} \left(B \frac{du_b}{dt} - \sin \alpha \right) \right], \quad (14)$$

$$A = \frac{2C_3^{2/3}}{C_2(C_D + C_L \tan \phi)}, \quad B = \frac{C_M}{s-1}, \quad s = \frac{\gamma_s}{\gamma_w},$$

in which u_b is the fluid velocity tangential to the slope, C_D, C_M, C_L are the drag, inertia and lift coefficients, respectively, and C_2, C_3 , , , are, respectively, area and volume coefficients of the stone, frictional angle of the stone, specific gravity of the stone and that of the water.

In this study, the same values for various coefficients in eq.(14) are adopted as in Kobayashi et al. (1986, 1987) except for C_L which is chosen to be 0.18. The value of 0.4 as used for some cases by Kobayashi et al. (1986, 1987) is close to the solution of Milne-Thomson (1960) for low Keulegan-Carpenter number flow and minor effect of wall proximity. These premises are apparently at odds with the present problem.

In coupling the BEM flow model with the stability model, special considerations are given to the fact that the Morison-type approach, on which eq.(14) is based, may be considered valid only when the depth of the flow is sufficiently large compared with the sizes of the stones. Since it is observed that a thin-water sheet trailing the down-running wave usually develops within a section near the shoreline, most obviously when the initial wave is relatively large, eq.(14) does not, and in fact should not be expected to, provide reasonable prediction of N_s . This difficulty is circumvented in this study by starting computing N_s from the location where the difference between the bed slope and the free surface slope becomes larger than 0.2, assuming this difference in slope increases monotonically within a certain distance from the shoreline at all times. This procedure, however, is found not necessary for waves of heights smaller than about 0.2 where no pronounced thin water sheet is observed.

3.RESULTS

Numerical experiments are run for solitary waves due to Boussinesq and Laitone on slopes steeper than 15° . The profile due to Boussinesq (1872) is given by

$$\eta = H \operatorname{sech}^2 \left\{ \left(\frac{3H}{4} \right)^{\frac{1}{2}} (x - ct) \right\}, \quad (15)$$

where

$$c = \sqrt{1 + H},$$

and the one due to Laitone (1960) is given by

$$\eta = H \operatorname{sech}^2[\sigma(x-ct)] \left\{ 1 - \frac{3}{4}H[1 - \operatorname{sech}^2\sigma(x-ct)] \right\} \tag{16}$$

where

$$c = 1 + \frac{1}{2}H - \frac{3}{20}H^2 + O(H^3),$$

$$\sigma = \sqrt{\frac{3}{4}H} \left(1 - \frac{5}{8}H \right) + O(H^{5/2}).$$

For eq.(14), we use $s = 2.71, C_2 = 0.9, C_3 = 0.66, C_D = 0.5, C_M = 1.5,$ and $C_L = 0.18.$

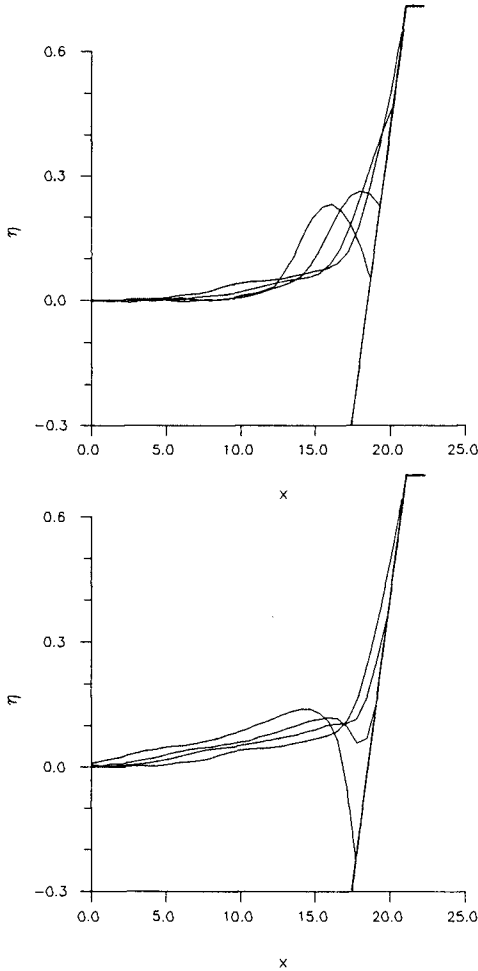


Fig.2 Sequences of free surface evolution during run-up (upper) and run-down (lower); $H=0.2, =15\%.$

Fig.2 shows typical sequences of the evolving free surface profiles during run-up and run-down of a wave of $H=0.2$ on a 15° slope. The deflected shape of the down-running wave with a thin tail near the shoreline when it approaches the still water line is clearly observed, which actually becomes more pronounced for higher waves.

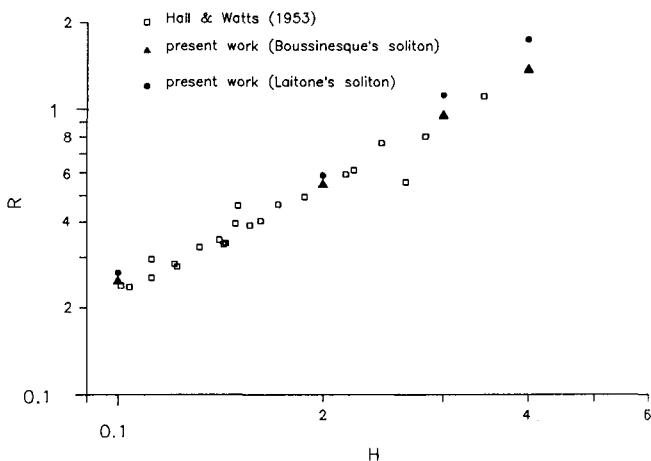


Fig.3 Maximum run-up of two different solitary waves on a 25° slope compared with experimental data by Hall and Watts (1953).

Fig.3 presents the predicted maximum run-up on a 25° slope as compared with experimental data by Hall and Watts (1953). Fairly favorable agreement is achieved for both types of waves. The reflected wave formed after run-down is found to be around $3/4$ of the initial wave height. This reflected wave is observed to pass through the offshore open boundary with less than 3% increase in height and a phase speed agreeing well with the analytical value corresponding to its height. For waves higher than 0.38, backwash breaking is found to occur near the end of run-down, when fatal numerical instability occurs.

Computed stability numbers are compared with the experimental results by Ahrens (1975) where oscillatory waves are used. The reason for using this work for comparison is that no experimental work for the solitary wave has ever been done in this subject area. To seek a common reference parameter for comparison, we use an equivalent Iribarren number given by

$$\xi = \frac{\tan \alpha}{\left(\frac{H}{L_e}\right)^{\frac{1}{2}}}, \quad (17)$$

where L_e is the equivalent wave length defined by the length of the wave truncated at $\eta = 0.1\% H$ on both ends. Figs.4 and 5 present computed N_s as a function of ξ on 1:2.5 and 1:3.5 slopes, respectively. The trends of stability variation over the concerned

range of surf conditions are predicted satisfactorily with locations of minimum stability found at $2.0 < \xi < 3.0$ for cases tested. The value of minimum N_s , however, is somewhat underestimated in the case of 1:2.5 slope, which seems to be related to uncertainties in identifying regimes of applicability for a Morison-type approach in the present problem as mentioned earlier. For a particular wave, the minimum stability is always found to occur in the vicinity of the still water shoreline position during backwash.

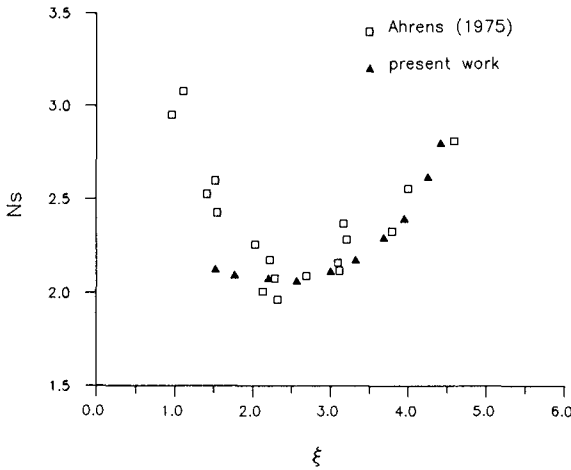


Fig.4 Comparison of computed stability number with experimental data by Ahrens (1975) on a 1:2.5 slope.

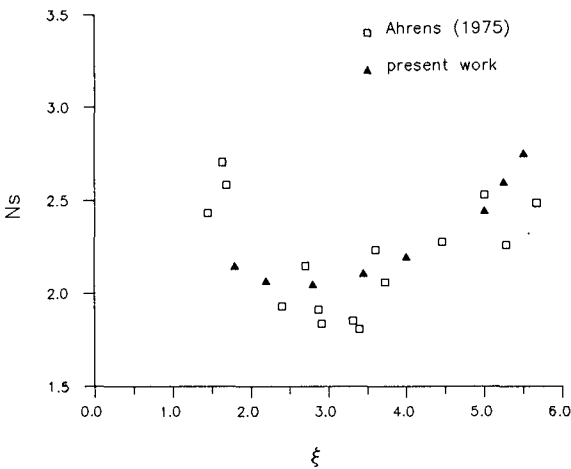


Fig.5 Comparison of computed stability number with experimental data by Ahrens (1975) on a 1:3.5 slope.

4. CONCLUSIONS

The stability of armor units on a breakwater slope exposed to solitary waves can be favorably modelled using the wave field predicted by the procedure of boundary element method as presented in this study. No 'mild slope' assumption is needed.

The proposed schemes including inductive wave generation, Lagrangian shoreline condition and free surface regriding combined yield satisfactory results in run-up simulation. The Orlanski-type radiation condition also exhibits fair performance.

The formulation of stability number based on the Morison equation does not yield realistic results unless the local water depth is sufficiently larger than the characteristic stone size. The simple empirical criterion used in this study to exclude the region where the Morison-type approach does not apply yields reasonable results. Further study is needed to better determine regimes of applicability of the Morison-type approach in the present problem.

A reasonable range of lift coefficients of the armor stones should be close to the lower limit of the range used by Kobayashi et al. (1987), i.e. around 0.18.

5. ACKNOWLEDGEMENTS

Thanks are extended to Professors R.C. Ertekin, H. G. Loomis and J.A. Williams for helpful discussions. Financial support by the Hawaiian Natural Energy Institute, the Pacific Center for High Technology Research, and the National Science Foundation under Grant No. BCS-8958346 is also thankfully acknowledged.

REFERENCES

Ahrens, J.P., (1975). Large wave tank test of riprap stability. Tech. Mem., 51, U.S. Army Corps of Engineers.

Boussinesq, J., (1872). Theorie des ondes et des remous qui se propagent le long d'un canal rectangulaire horizontal, en communiquant au liquide contenu dans ce canal de vitesses sensiblement paralleles de la surface au fond. Journal de Mathematiques Pures et Appliquees, 2nd Serie, Vol. 17, pp. 55-108.

Chian, C. (1989). Simulation of solitary wave run-up and computation of armor-unit stability on a coastal structure by a boundary element method. Thesis, University of Hawaii at Monoa. Hall, J.V. and Watts, G.M., (1953). Laboratory investigation of the vertical rise of solitary waves on impermeable slopes. U.S. Army, Corps of Engineers, Beach Erosion Board, Technical Memorandum No.33.

Kim, S.K., Liu, P. L-F. and Liggett, J.A., (1983). Boundary integral equation solutions for solitary wave generation, propagation and run-up.

Coastal Engineering, v.7: pp. 299-317.

Kobayashi, N., Roy, I. and Otta, A.K., (1986). Numerical simulation of wave runup and armor stability. OTC paper 5088, 18th Offshore Technology Conference, Houston, Texas, pp. 51-56.

Kobayashi, N., and Otta, A.K., (1987). Hydraulic stability analysis of armor units. Journal of Waterway, Port, Coastal, and Ocean Engrg., Vol.113, No.2, pp.171-186.

Laitone, E. V., (1960). The second approximation to cnoidal and solitary waves. J. Fluid Mech., v.9, pp. 430-444.

Milne-Thomson, L. M. (1960). **Theoretical Hydrodynamics.** 4th Edition, The MacMillan Company, New York.

CHAPTER 96

Wave forces on cylindrical members at offshore structure

Yuzo Mizuno¹, Kazuo Tokikawa², Mitsunari Hirasawa¹
Yutaka Nagai³ and Takashi Kadono⁴

1. Preface

Until now, offshore areas have rarely been utilized because of restrictions caused by waves. To utilize offshore areas more fully, it is necessary to develop technology for construction of offshore structures able to withstand large waves. To achieve this, C.E.R.I. of Hokkaido Development Bureau has carried out in situ offshore experiments to investigate structures in an area with large waves as part of studies funded by Funds for Science and Engineering Development: research on utilization of maritime zones by constructing offshore structures. This project has analysed data of wave forces against circular cylindrical members of offshore structures in a large wave area. This type of data has rarely been reported in the past.

2. Experimental structure and observation

The offshore experimental structure is 10mX5m and 18m high, and was constructed in 7.0m deep water off the Ohgon Cape at Rumoi in Hokkaido on the Japan Sea coast in 1984¹⁾.

Phot.1 shows the offshore experimental structure in winter, and Fig.1 shows the location of the omnidirectional wave force transducer, the ultrasonic wave gauge, the current meter, and the strain gauge.

The wave force transducer is shown in Phot.2, it was developed especially for this project and can measure the magnitude and direction of forces on cylindrical members (0.508m in diameter)²⁾. Fig.2 shows a sectional view of the wave force transducer.

1. Civil Engineering Research Institute of Hokkaido Development Bureau, 1-3 Hiragish, Toyohiraku, Sapporo, 062 Japan

2. Hokkaido Development Bureau, Nouth 8-West 2, Kitaku, Sapporo, 060 Japan

3. Tomakomai Port, Hokkaido Development Bureau, Japan

4. Ministry of Transport, Japan



Phot.1 Offshore experimental structure

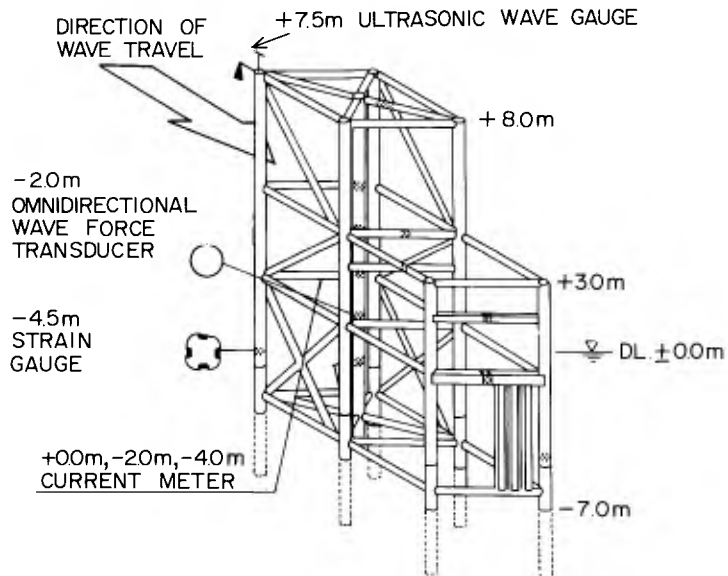
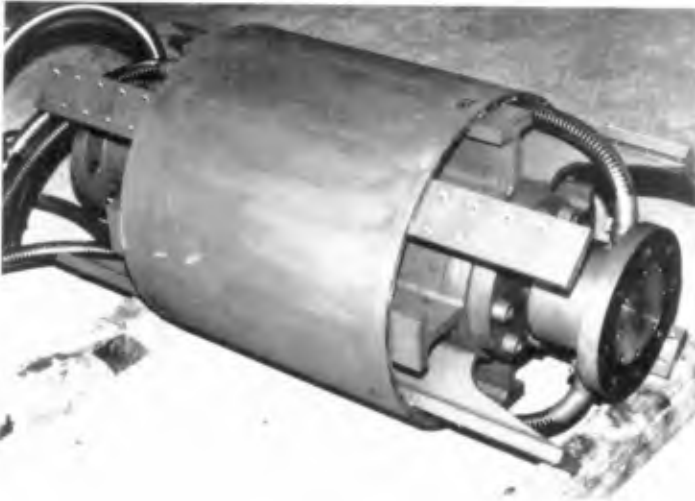


Fig.1 Sensor location



Phot.2 Omnidirectional wave force transducer

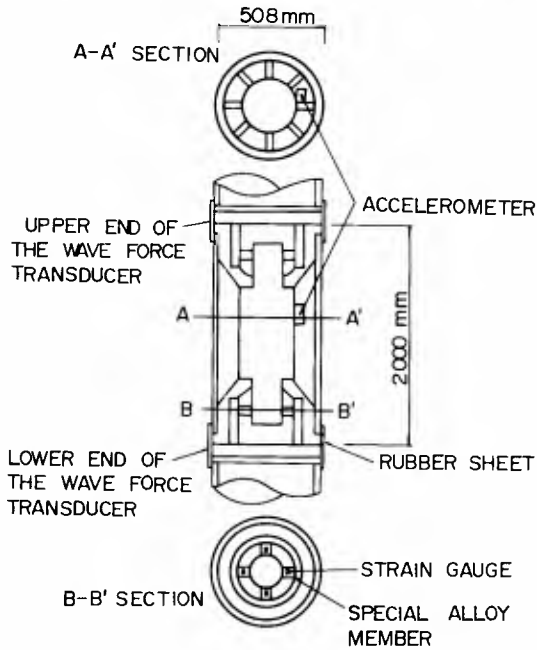


Fig.2 Sectional view of wave force transducer

Wave induced forces were determined from the difference between the highest and the lowest shear forces obtained by measuring the strain along the axes of special alloy members at both the upper and lower ends of the wave force transducer.

Fig.3 shows the distribution of heights and periods of significant waves by the zero-down-cross method using data gathered in 1984-86. It shows some waves higher than 4 meters, and so the data can be used for wave force characteristics in the high Reynolds number range. The subject of the analyses are the largest 14 data sets (2,487 waves) of 48 sets from the winter of 1986: the waves are 2.47m - 4.52m and the periods 6.49sec - 9.64sec. Both total and local wave forces acting on the members were examined. Total wave forces were measured by the strain gauge set at the foot of the experimental structure in Fig.1. Local wave forces were measured by an omnidirectional wave force transducer set on a vertical circular cylindrical member at the center of the structure between 1.0m to 3.0m below the water.

Current velocities were measured by the current meter 2.0m under the water surface 2m from the wave force transducer perpendicular to the wave direction.

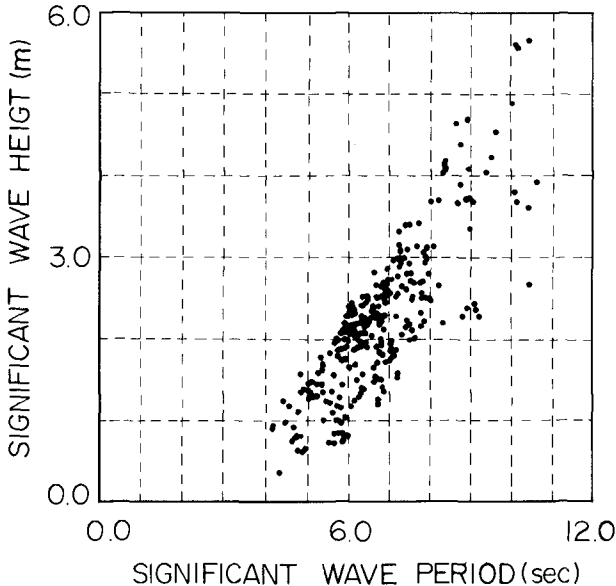


Fig.3 Distribution of heights and periods of significant waves by the zero-down-cross method

3. Drag coefficient and inertial force coefficient of vertical circular cylindrical members.

In general, wave forces acting on submerged cylindrical members can be calculated with Morrison's equation³⁾.

$$\frac{dF}{dz} = C_d \frac{\omega_o}{2g} Du|u| + C_m \frac{\omega_o \pi D^2}{4g} \frac{\partial u}{\partial t} \dots\dots\dots (1)$$

where, dF is the normal force action upon a length dz along the axis of member (tf); u is the water particle velocity acting normal to the member axis (m/s); Cd is the drag coefficient; Cm is the inertial force coefficient; D is the diameter of the member (m); ω_o is the weight of a unit volume of sea water (tf/m³); and g is the acceleration of gravity (m/s²)

The first term on the right side of Eq.(1) represents the drag force and the second the inertial force. The drag and inertial force coefficients are believed to be influenced by Reynolds number(uD/v), KC number(uT/D), and others. Widely deviating experimental data of these wave force coefficients have been reported, and data using Reynolds numbers in the range to 10⁶ are not adequate. There is also no standardized system for measuring wave force coefficients. This paper follows the procedure:

- ① Define each wave with the zero-up-cross time of the water surface-wave profile
- ② The direction of the resultant maximum wave force computed by combining the horizontal wave force components is to be considered the direction of each wave
- ③ The direction component of water particle velocity and its acceleration are derived for each wave
- ④ The Cd and Cm of each wave are derived by the least squares method
- ⑤ The Cd and Cm are corrected to restore peak values

When the residual sum of squares of measured and calculated wave forces is minimized in step ④, wave force coefficients can be given as:

$$C_d = \frac{2g}{\omega_o D} \frac{S_3 S_4 - S_5 S_2}{S_1 S_3 - S_2^2} \dots\dots\dots (2)$$

$$C_m = \frac{\omega_o \pi D^2}{4g} \frac{S_1 S_3 - S_2^2}{S_5 S_1 - S_2 S_4} \dots\dots\dots (3)$$

$$S_1 = \sum u_i^4, \quad S_2 = \sum (\partial u / \partial t)_i u_i |u_i|, \quad S_3 = \sum (\partial u / \partial t)_i^2 \dots\dots\dots$$

$$S_4 = \sum f_i u_i |u_i|, \quad S_5 = \sum f_i (\partial u / \partial t)_i \dots\dots\dots (4)$$

where, f_i and u_i shows the measured wave forces and water particle velocities at time i , and Σ means the sum total of the data of a wave at a particular time.

Fig.4 shows a time-series profile of representative wave forces calculated from measured wave forces and water particle velocities, and water particle accelerations and wave force coefficients calculated by the above equations. Despite its quasi-empirical nature Morrison's equation reproduces the wave force profile fairly accurately. However, since the above method is designed to compute wave force coefficients that on average agree to measured values, there is a danger that the peak values of wave forces - the most important in actual designs - will not always correctly correspond to the measured wave forces.

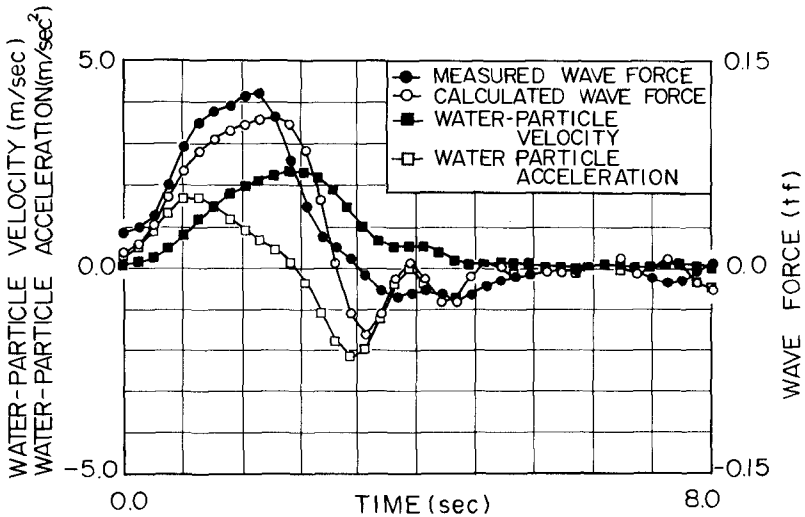


Fig.4 Time-series profile of measured and calculated wave forces

To observe this, a comparison of measured peak wave forces and computed peak wave forces of all analyzed data is made in Fig.5 where the relation between these two values is given by the least squares method. The results show that the calculated values tend to be only 87% of the measured values, and in the following, wave force coefficients are corrected by this factor (1/0.87).

Using the previous procedure, Figs.6 and 7 indicate the relation between the drag coefficient/inertia force coefficient of wave forces obtained by the omnidirectional wave force transducer, (effective measurement range above 0.07tf

(0.686kN)) and Reynolds number, using parameters derived from the KC numbers. The Reynolds and KC numbers are computed with the maximum water particle velocity of each wave.

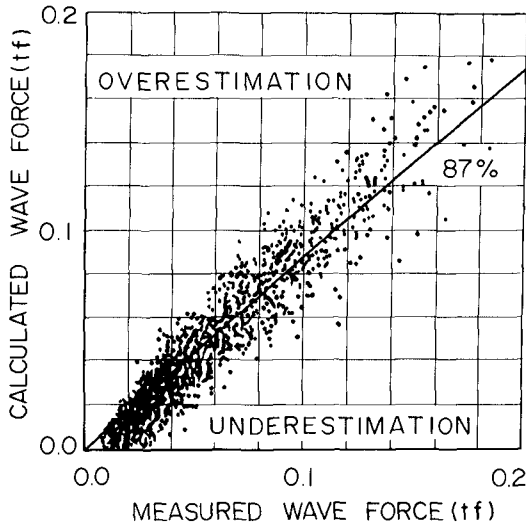


Fig.5 Relation between peak values of measured and calculated wave forces

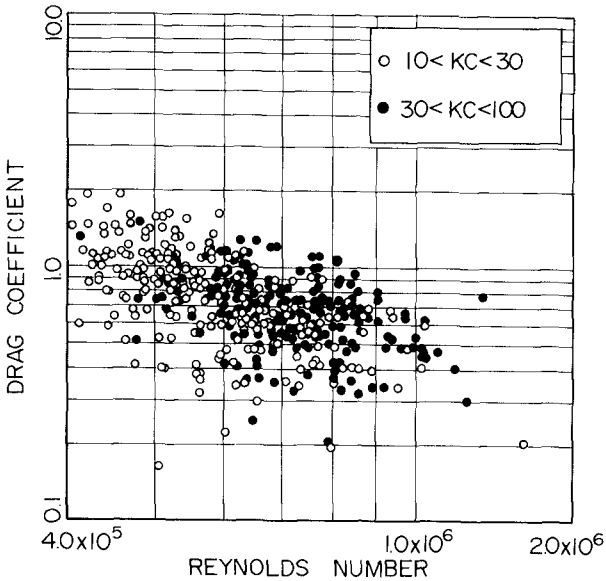


Fig.6 Relation between drag coefficient and Reynolds number

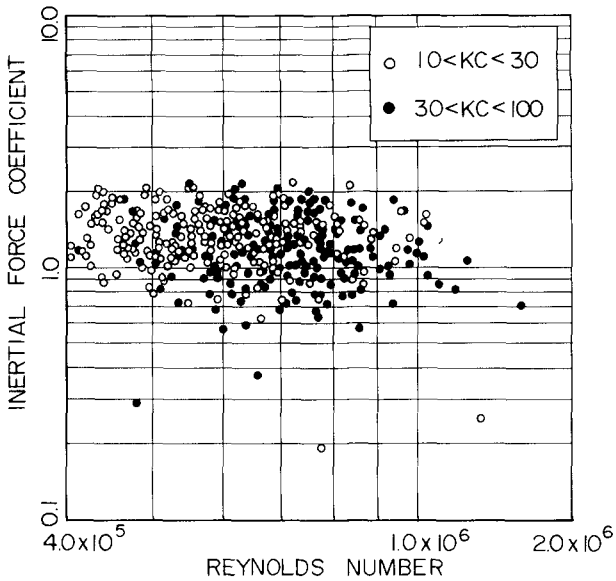


Fig.7 Relation between inertial force coefficient and Reynolds number

The omnidirectional wave force transducer in this experiment was painted to eliminate the growth of organisms, and none were found on the structure prior to the beginning of the measurements. Therefore, the data may be considered applicable for smooth circular cylindrical members.

As seen in Fig.7, there are correlations between wave height and period, and the Reynolds and KC numbers are related, which makes it difficult to determine the exact relation between wave force coefficients and the numbers. However it may be concluded that the drag coefficient will likely decrease with increases in Reynolds number, while the inertial force coefficient remains unaffected by Reynolds number. The dependence of the two wave force coefficients on the KC number is not shown explicitly. The drag coefficient becomes almost independent of Reynolds numbers above 7.0×10^5 . The average values of wave force coefficients of data in this range are $C_d = 0.60 \pm 0.17$ and $C_m = 1.23 \pm 0.34$ considerably less than the $C_d = 1.0$ and $C_m = 2.0$ commonly used.

Reported wave force coefficient measurements are given in Table 1^{4) 5) 6) 7)}. The results cannot simply be compared to these values because of the different Reynolds numbers involved, and the values in this study scatters less than other results. The data are relatively close to the results of Kim et al., but extend to higher Reynolds numbers.

Another point is that the drag coefficient in Kim et al. becomes constant at $Re > 2.0 \times 10^5$ ⁴⁾.

Table 1 Reported wave force coefficient measurements

Researcher	Re	KC	Cd	Cm
Kim	$1.5 \times 10^5 \sim 7.5 \times 10^5$	15 ~ 30	0.61 ± 0.15	1.20 ± 0.26
Bishop	$1.0 \times 10^5 \sim$		0.73	1.24
Yoshida	$2.5 \times 10^5 \sim 7.0 \times 10^5$	3 ~ 28	0.6 ± 1.8	1.7
Dean	$1.0 \times 10^4 \sim 1.0 \times 10^7$	10 ~ 50	0.5 ~ 1.2	1.33
Evan	$1.0 \times 10^5 \sim 5.0 \times 10^6$	10 ~ 80	0.58 ± 0.33	1.76 ± 1.06
Reid	$1.0 \times 10^5 \sim 2.0 \times 10^5$	10 ~ 20	0.53 ± 0.20	1.47 ± 0.36

4. Results of analyses of total wave force data

The values of the total wave force data measured by the strain gauges set at the foot of the experimental structure were compared with values computed by a three-dimensional static structural analysis program, and features of the wave induced forces were examined.

The experimental structure was analyzed by a structural analysis program for complex structures: ISAP-II of TOSBAC 600. Wave forces were calculated by Morrison's equation - wave direction designated by an arrow in Fig.1 - and water particle acceleration was determined by the small amplitude wave theory. Phase differences were not considered when computing wave forces because the structure is small compared with the wave length. Buoyancy acting against the members of the structure above the hydrostatic surface was also considered, buoyancy was applied to the entire cross section of the members on the assumption that the water level in the members was little affected by the waves. The range of wave forces and buoyancy was obtained from calculations of maximum wave heights ⁶⁾.

Fig.8 shows the relation between the measured axial forces and wave heights in six samples (1043 data) where the wave directions were relatively close to the calculations; the axial forces are the peak axial forces of each wave defined from the zero-up-cross time. The solid line (Fig.8) indicates axial force values computed by the typically used wave force coefficients - $C_d=1.0$ and $C_m=2.0$ - and the broken line presents values computed using the coefficients $C_d=0.6$ and $C_m=1.2$ obtained in the preceding section. In both cases, the wave period was assumed to be 10 seconds.

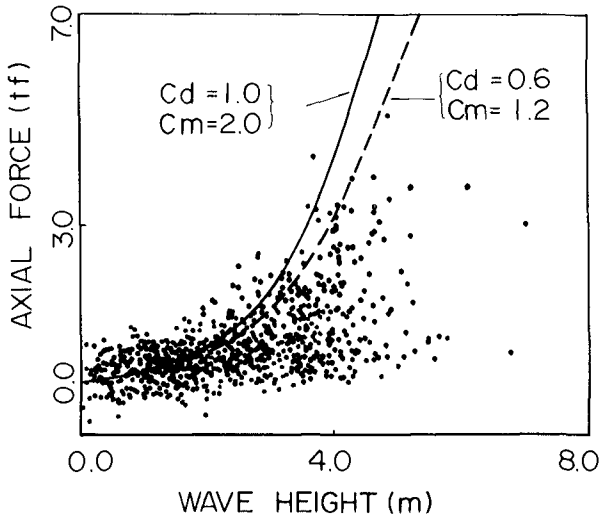


Fig.8 Relation between measured axial forces and wave height

The experimental structure has numerous horizontal members in addition to the vertical ones, and the calculated wave forces increase discontinuously with increases in wave height; however, the lines in Fig.8 are continuous because specific wave heights were chosen for the computation and the results were smoothed to a continuous curved line. This curve is approximately in proportion to the cube of the wave height.

Although the measured values are relatively dispersed as indicated in Fig.8, they tend to correspond well to the calculated values of the three-dimensional static structural analysis. However, even the values calculated with the coefficients $C_d=0.6$ and $C_m=1.2$ are greater than the measured values, especially at large wave heights. According to this figure, the present standard coefficient values ($C_d=1.0$ and $C_m=2.0$) are clearly in a safe range.

Furthermore, it was observed that the shock wave forces on structural members in this experiment were far larger than Morrison's wave forces above the hydrostatic plane⁹; however, no effect of these shock wave forces were found in the total wave force values.

Apparently, this resulted from the shock waves being so localized that there were phase differences among the members, and also because the duration of shock waves is so short that the structure as a whole, was unable to respond.

In the present project the experimental offshore structure was set in shallower water than actual offshore structures. However more members need not be considered when examining the overall stability of an actual offshore structure, except in particular cases.

5. Summary

This report examines features of wave induced forces on circular cylindrical structural members with data from an offshore experimental structure. The main results of the project are as follows:

① Data of wave induced forces on circular cylindrical members in an offshore area were obtained: some of the waves were large and in the high Reynolds number range. Wave induced forces on the members were examined for both total and local wave forces. Local wave forces were measured by an omnidirectional wave force transducer developed for this project.

② On the basis of wave forces (local wave forces) induced on the circular cylindrical members and the simultaneously measured water particle velocity data, the drag coefficient and inertial force coefficient were computed as $C_d=0.6\pm 0.17$ and $C_m=1.23\pm 0.34$, in the Reynolds numbers range above 7.0×10^5 . The drag coefficient decreases with increases in the Reynolds number, whereas the inertial force coefficient is unaffected by fluctuations in Reynolds number.

③ Measured values of total wave forces tended to agree with the three-dimensional static structural analysis calculations. However, the calculated values, even with wave force coefficients of $C_d=0.6$ and $C_m=1.2$, became larger than the measured values. There was no effect of shock wave forces in the measured values

6. Acknowledgments

We wish to thank the committee for offshore structure research and experiments in offshore areas for its cooperation in the preparations for the present project - Director: Akira Ozaki; and Hideo Kondo; Takeo Hori; Shinichi Ishii; Yoshimi Goda; Takafumi Takaishi; Keizo Kuwahara; Tadaaki Itakura.

7. Bibliography

- 1) Nagai Yutaka; Yazu Hideaki; Kadono Takashi: "Offshore structure Experiments in a Real Sea Area," Second report, 28th conference of Industrial Technology Development, Hokkaido Development Bureau, pp,1514-1522,1985. (In Japanese)
- 2) Kadono Takashi; Momose Osamu; Nagai Yutaka: "Development of the Omnidirectional Wave Force Transducer." Monthly report of the civil Engineering Research Institute of

- Hokkaido Development Bureau, No. 391, pp.1-17,1985. (In Japanese)
- 3) Civil Engineering Society: Hydraulics Formulae, 1985 Version, pp.625, 1985.(In Japanese)
 - 4) Kim, Y.Y. and Hibbard, H.C.: "Analysis of Simultaneous Wave Force and Water Particle Velocity Measurements," Proc. OTC, vol. 1. No. 2192, pp. 461 - 469, 1975.
 - 5) Bishop, J.R.: "RMS Force Coefficients Derived from Christchurch Bay, Mechanics of Wave Induced Forces on Cylinders," Pirman Publishing Ltd., pp. 334 - 345, 1979.
 - 6) Yoshida Tsunematsu; Ito Soichi; Tsutsumi Saburo: "A Study of Wave Force Coefficients and Wave Force by an Offshore Experiment on a Jacket Type Structure," 27th Japanese Conferene on Coastal Eng., pp.368-372, 1980.
 - 7) Hogben; N. et al.: "Estimation of Fluid Loading on Offshore Structures," Proc. the Institution of Civil Engineering, 1977.
 - 8) Goda Yoshimi: "Wave Forces on a Vertical Circular Cylinder, Experiments and a Proposed Method of Wave Force Computation," Rept, PHRI, No. 8, 1964.
 - 9) Nagai Yutaka; Kadono Takashi; Yatsu Hideaki: "Field Experiment of a Jacket-type Structure in a Surf Zone," 5th OMAE, 1986.

CHAPTER 97

The Effect of Seawalls on Long-Term Shoreline Change Rates for the Southern Virginia Ocean Coastline

David R. Basco¹

Abstract

This paper examines the relationship between the off shore bathymetry, resulting wave climate, shore boundary conditions (i.e., seawalled versus dune/beach sections) and the shoreline response as represented by long-term shoreline change rates over 120 years for the southern Virginia ocean coastline in the United States. Along the tourist area of the City of Virginia Beach, the data supports the conclusion that a seawall's presence for over 50 years has produced no significant increase in the recession rate. The highest recession rate (3m/yr) occurs at the Sandbridge sector further south. Some now claim that the beach width is narrowing at Sandbridge as a result of recent seawall construction. This allegation completely ignores the root cause of the problem which is shown in this paper to be the steep offshore bathymetry and high wave energy in this region. If we neglect the offshore boundary conditions when making field studies of "hardfacing" versus dune/beach sections, we can reach completely erroneous results.

1.0 Introduction

Coastlines are either stable, accreting or receding when viewed on a long term basis relative to some *fixed* reference. For example, the City of Virginia Beach along the southern Virginia ocean coastline (Fig. 1) exhibits all three shoreline trends as described in detail below. There are numerous reasons for coastline recession, both natural and human-induced. Some form of shore protection

¹Professor of Civil Engineering and Director of the Coastal Engineering Institute, Old Dominion University, Norfolk, VA 23529.

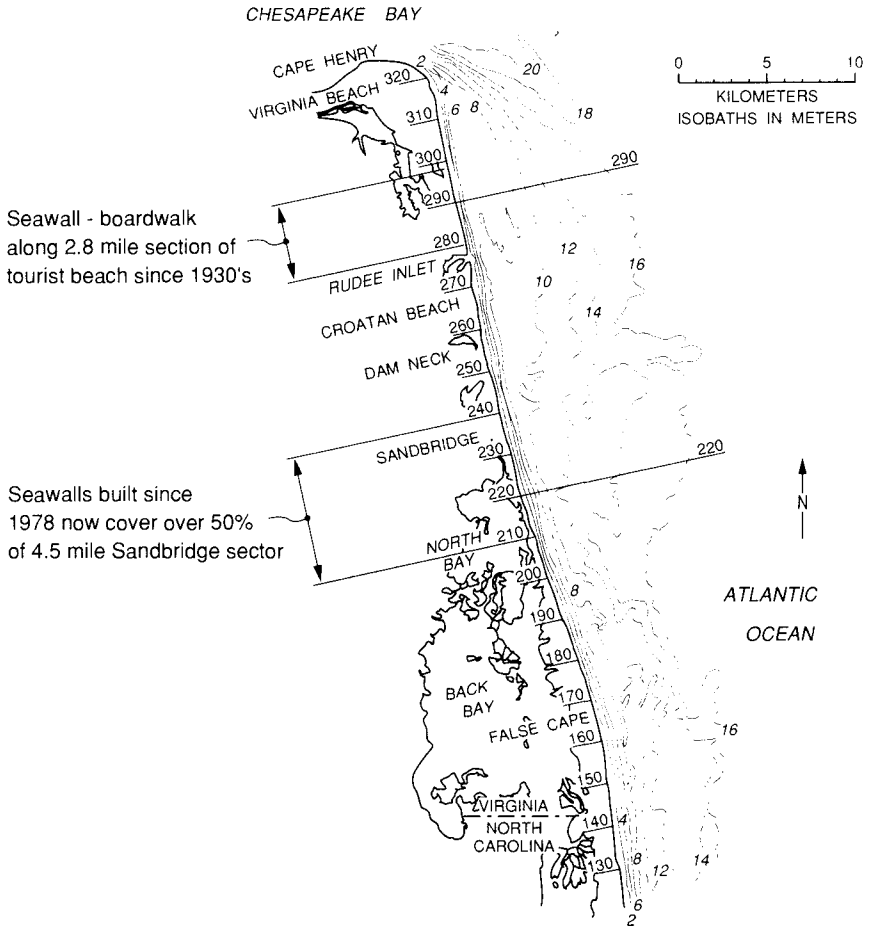


Fig. 1 Coastal Area and Bathymetry of the Study Region.
 (adapted from Wright et al., 1987)

measure is often undertaken when the shoreline recession threatens permanent resources (roads, bridges, buildings, etc.) and if the benefits exceed the costs over the design life of the project.

Three engineering options exist for shore protection: (1) natural defenses including strengthening dunes and beach nourishment; (2) sand trapping systems to widen beaches; and (3) coastal armoring; combinations are also possible. Coastal armoring includes seawalls, bulkheads and revetments, but all such coastal armoring structures will be referred to as "seawalls". Seawalls are usually constructed along developed shorelines experiencing a recessional trend and subject to storm-induced water level rise with accompanying wave energy. In many cases, recreational beaches are also present.

The degree to which a seawall affects the adjacent beach is the focus of much recent attention (e.g., Kraus and Pilkey, 1989, editors). Various allegations on the adverse effects of seawalls on beaches have been made and claimed as common knowledge (without reference). Statements such as "...the seawalls destroyed the beach"; "...bulkheads stir up wave action and increase erosion"; "...costly seawalls and jetties actually increase erosion"; "...bulkheading (does) more damage than it prevents"; "...bulkheads hasten the erosion of surrounding beaches"; etc. have been attributed to "coastal scientists". The most sweeping allegation of all is the claim that "...seawalls actually increase erosion and destroy the beach" (Pilkey and Wright, 1988). These allegations stem from an over emphasis on the land boundary conditions (i.e., "hardfacing" -vs- dune/beach "soft" boundaries) and consequently the almost total neglect of the offshore boundary conditions when discussing shoreline change. These allegations also stem from the "migration barrier beach paradigm" as discussed below.

In this paper, we examine the relationship between the offshore bathymetry, nearshore wave climate, type of landward boundary, and shoreline response as represented by long-term shoreline change rates based on over 127 years of survey records for the southern Virginia ocean coastline. Shoreline change rate data both before and after seawall construction are examined to determine if there is a discernable increase in long-term erosion rate in front of the seawalls. Shorter term variability and changes measured immediately after storms are also of concern but are not considered in this paper.

2.0 Boundary Conditions At Virginia Beach, Virginia

2.1 Offshore Boundary Conditions

The southern Virginia ocean coastline (Fig. 1) is all within the political jurisdiction of the City of Virginia Beach. It extends over 26 miles from Cape Henry at the north on the lower edge of the entrance to the Chesapeake Bay to the border of Virginia and North Carolina (latitude $36^{\circ} 33'$).

2.11 Bathymetry. A three-dimensional, perspective plot of the nearshore bathymetry for over 6000m seaward to depths beyond -15m (MSL) is presented as Fig. 2. The offshore bathymetry is irregular. A relatively broad, flat region is found adjacent to the tourist part of the City (labeled Virginia Beach) resulting in the -9m contour almost 4000m seaward. This -9m depth contour gradually moves closer to shore as the beach profile steepens further south. At the section labeled Sandbridge (a subdivision of the City) the profile is the steepest with -9m being found only about 1200m offshore. Continuing further south, the profile again flattens and a large, permanent offshore bar feature is found at False Cape. Putting sections A & B together reveals the continued variability in nearshore bathymetry along the study region.

The -9m depth is approximately the "closure depth" for the existing wave climate and sand gain size in this area. Beach profiles in the northern end (e.g. Section 290) are flatter and those at Sandbridge (e.g. Section 220) are steeper than the equilibrium shape for the representative sand grain size. Tidal currents through the entrance to Chesapeake Bay are an important factor in shaping local bathymetry as is the existing wave climate and its interaction with the tidal currents.

2.12 Wave Height Variation. The figures above are adapted from a recent report by the Virginia Institute of Marine Science (Wright et al., 1987) in which a computer model was used to transform ocean waves moving toward the shoreline from the northeast, east and southeasterly directions. The RCPWAVE code (Ebersole et al., 1986) was modified to include bottom friction, if desired. Fig. 3 is one example (Wright et al., 1987, p.61) for a deep water wave height of 2.1m and 8 sec period from the northeast and shows the three-dimensional perspective plot of wave height variation everywhere in the computational domain (60 x 160 grid with $\Delta x=100m$ offshore and $\Delta y=250m$ alongshore). The trends along the beach for

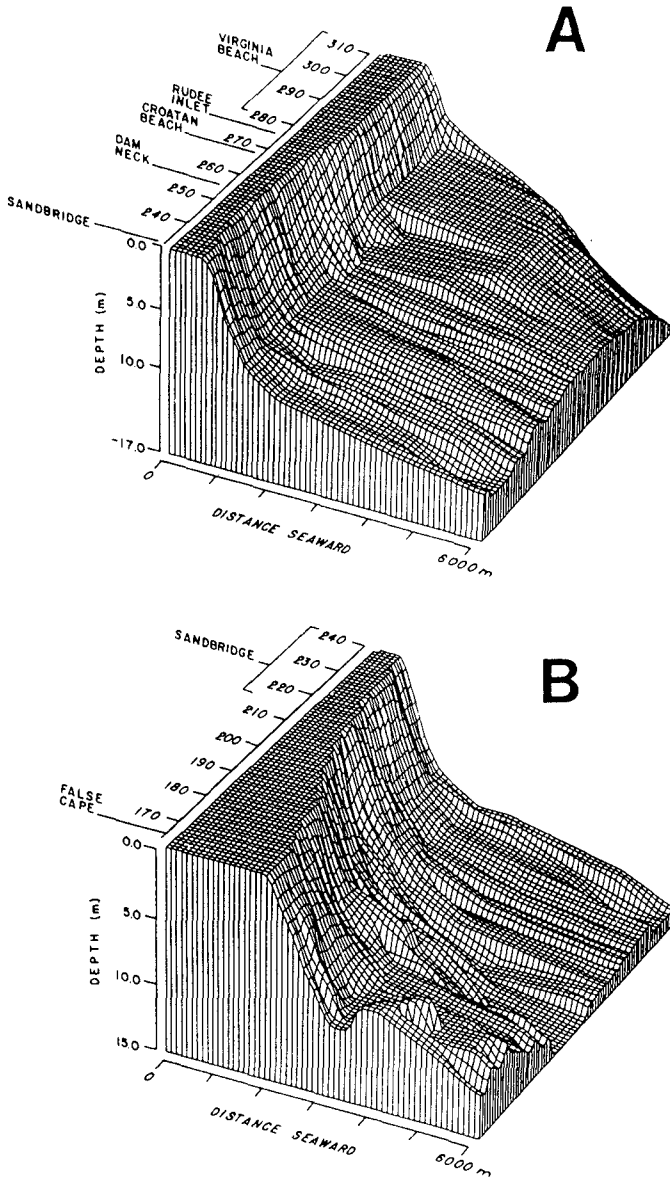


Fig. 2 The Study Region Bathymetry in 3-D Perspective and Split into a Northern (A) and Southern (B) Sector (adapted from Wright et al., 1987).

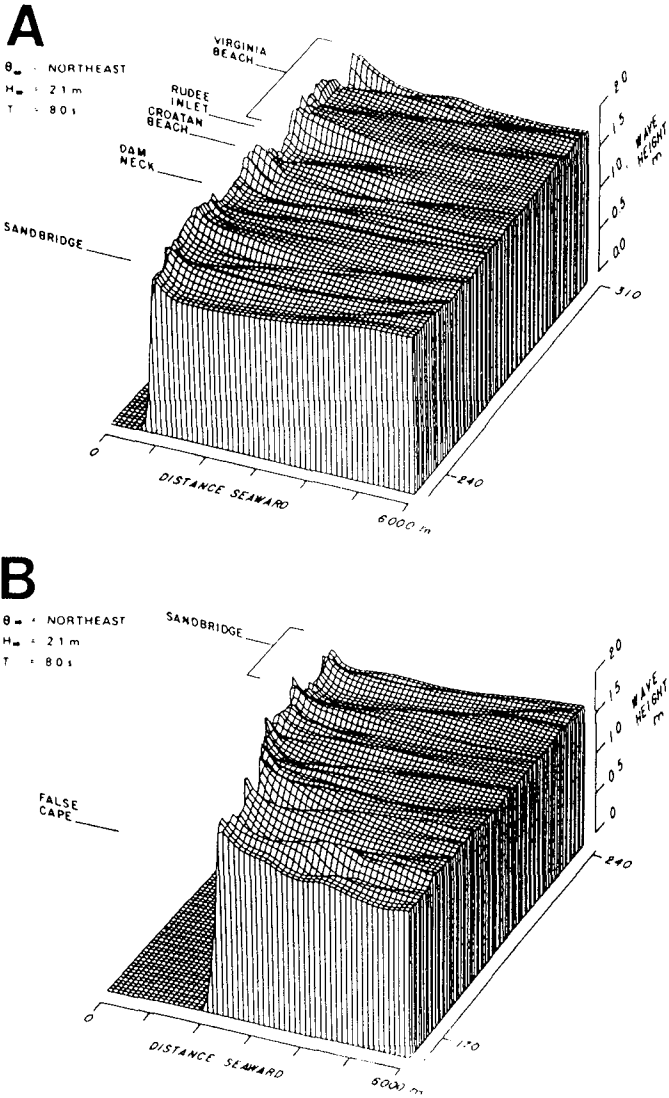


Fig. 3 Spatial Wave Height Variations for the Study Region As Predicted by the RCPWAVE Computer Code With No Bottom Friction. The Wave Conditions Are for a Typical Northeaster (adapted from Wright et al., 1987).

breaking wave height vary considerably but generally show H_b increasing along the Sandbridge sector relative to the northern and southern sectors. These results are with no bottom friction in the model.

Wright et al. (1987) considered the possibility for 55 different wave climate combinations (deepwater height, period, dominant direction) as measured in 1982 at the Corps of Engineers, Field Research Facility pier some 65 miles south of Virginia Beach. The computer model was run for these 55 cases, breaking wave height variations calculated along the coastline and then averaged together. The overall average breaking wave height calculated for the entire study region was 0.58m in 1982. The relative variation of breaking wave height along the shoreline from north(top) to south(bottom) when compared with the overall average is plotted in Fig. 4(rightside). These trends in breaker wave height are consistent with the variation in bathymetry. Higher wave energy at Sandbridge is expected because the deeper, offshore contours are closer to shore at Sandbridge.

2.2 Landward Boundary Conditions

The landward side of the shoreline consists of a sandy beach with natural and artificially created dunes, a small, stabilized tidal inlet and seawalls (with boardwalk) along some regions.

2.21 Seawalled Sections. Seawalls are found in two areas of Virginia Beach as shown in Fig. 1. Along the northern, tourist/resort beach, a seawall/boardwalk structure exists as illustrated in the Corps, Shore Protection Manual (1984), Vol II, p6-7) between Rudee Inlet and 49th Street. Private property seawalls further north extend the length of seawalled beach to about 2.8 miles. Some type of "hardfacing" structure with boardwalk has existed in this location since the 1930's*. Over 3 million people use this beach area during the three primary summer months of the tourist season.

Further south at Sandbridge, seawall construction began in 1978 to protect private property of individual lot owners as year-around residents or renters. Construction

*An 1887 photograph of the Princess Anne Hotel at the tourist beach location showed an extensive length of vertical pile seawall about 5-6ft in elevation above the beach face.

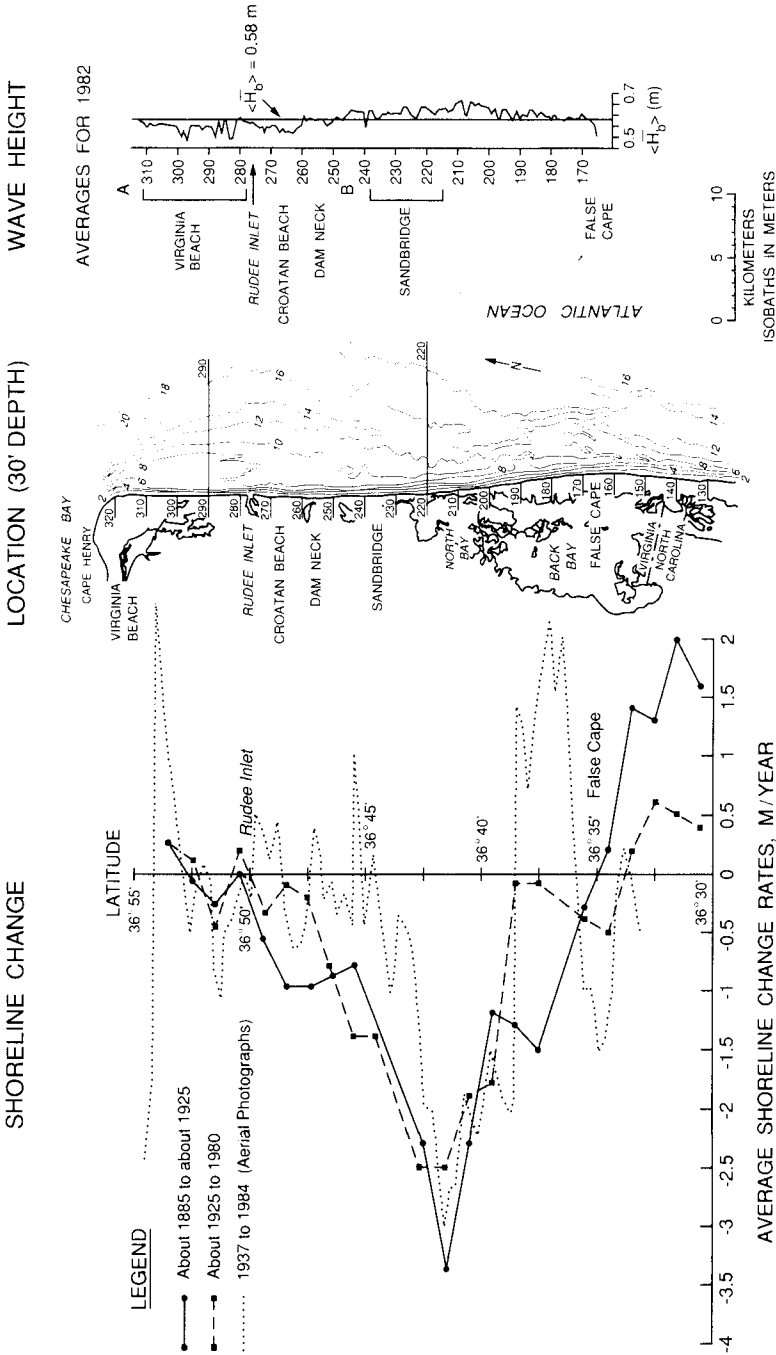


Fig. 4 Composite of Shoreline Change Rates(left), Bathymetry(center) and Breaking Wave Heights(right) and Their Variation Along the 25-mile Atlantic Ocean Coastline of the City of Virginia Beach, Virginia

has accelerated in recent years so that presently, over 50% of the 4.5 mile stretch has vertical, sheet-pile (steel, timber, concrete) bulkhead protection.

2.22 Rudee Inlet. An extremely small water body (Lakes' Rudee and Wesley) is open to the Atlantic Ocean through Rudee Inlet which was fixed in position by two, very short, rock jetties in 1953. Inlet bypassing from south to north and channel maintenance by fixed and floating dredging plant (hydraulic cutterhead and jet-pump systems) occurs each year averaging about 100,000cy per year. The short length of the jetties permits natural inlet bypassing in both directions and results in an accretional beach for less than 500 ft on both sides of the inlet. Consequently, these natural and artificial sand transport systems and the small scale of the tidal flows and jetties produce only local, minor changes along the landward boundary at this location.

2.23 Beach Renourishment. Since 1951, over 10.6 million cy of sandy material (including Rudee Inlet bypassing) has been deposited on the resort strip between Rudee Inlet and about 45th street. The average amount per year (0.27 M cy) is about 5 percent of the total active sand volume (envelope between erosional and accretioned profiles out to the closure depth) in this region. Net sediment transport to the north has changed the shoreline position in this region over the last 40 years as discussed below. Most references consider Sandbridge a nodal point for net sediment transport direction.

3.0 Shoreline Movements

3.1 Long-Term Average Shoreline Change Rates

3.11 Cartographic Information. Federal government surveys and resulting cartographic information has been used by Everts et al., (1983) to calculate the long-term average shoreline change rates in m/yr for 122 years of data as shown in Fig. 4 (far left side). The vertical scale (latitude) coincides with the shoreline location with Cape Henry at the top and the Virginia/NC border at the bottom. Accretion is to the right of zero and recession rates are shown to the left of zero (stable shoreline position) on the horizontal axis.

For a 67 year period between 1858-1925, the solid line reveals some accretion in the far north, a slightly receding shoreline along the tourist beach to Rudee Inlet, considerably recession exceeding 3 m/yr at Sandbridge and then the reverse trends with considerable

accretion (2m/yr) further south at False Cape and beyond the border.

For the next 55 year averaging period (1925-1980) as shown by the dashed line, the trends are very similar or less extreme in all locations. Further refinement by Everts et al., (1983) for the north end above Rudee Inlet using 10-15 years averaging intervals between 1925-1980 reveals increasing accretional rates with time and reflects the last 40 years of beach renourishment with net northerly drift.

3.12 Aerial Photographs. Dolan(1985) used historical aerial photographs between 1937 and 1984 (47 years) to determine long-term average change rates along this same coastline. These results are shown as the fine dotted line in Fig. 4 (far left side). The overall patterns are generally similar. Additional accretional reaches below Rudee Inlet and above Sandbridge may be due to some southerly movement of renourishment materials since 1952. The location and magnitude of the highest recessional rates at Sandbridge are confirmed by these results. The greatest differences in change rates between the mapped and photographically deduced data are found in the False Cape region. No explanation is offered for these discrepancies.

3.2 Short Term and Storm Effects

The results above are for average shoreline movement over very long time intervals. Shorter term "average" variability, seasonal changes and those occurring immediately after storms are also of concern. A study has recently begun at Sandbridge with the goal to investigate shorter term and storm term related effects of seawalls and beaches (Basco, 1990a).

4.0 Boundary Conditions and Shoreline Response

4.1 Virginia Beach, Virginia

Fig. 4 compares the (i)variability of offshore bathymetry and seawall locations (center)(ii)the variability in breaking wave height (far right) and the (iii)variability of long-term shoreline change rates (far left) on the same vertical scale. We must consider both the offshore and the landward boundary conditions when discussing shoreline change. For Virginia Beach, Virginia there exists a strong cause-effect relationship between offshore bathymetry (i.e., profile steepness), breaking wave height variation, and long-term shoreline response.

For the tourist section above Rudee Inlet, a comparison of pre-seawall recession rates (67 years, 1858-1925) and post-seawall recession rates (55 yrs, 1925-1980) allows us the opportunity to tentatively conclude that a seawall/boardwalk for over 50 years has produced no significant change in long term shoreline trends. This conclusion admits some shorter term variability in the data, accuracy of rate estimates and beach renourishment.

At Sandbridge, seawalls have only existed for a relatively short time period. About 90% of the total coverage (2.3 miles) had been constructed since 1986. One thing is clear, however. Seawalls are not responsible for over 130 years of steady shoreline recession of about 3m/yr. To argue now that the beach width is narrowing at Sandbridge as a result of the recent acceleration of seawall construction is to completely ignore the root cause of the problem.

4.2 General

Attempts to develop generalized boundary conditions landward, seaward and along the bottom that influence shoreline position and adjacent subaerial beach response are underway. Weggel has suggested a classification system (Weggel, 1988, p.36) involving six seawall "types" which depend on the location of the seawall with respect to the shoreline. During storm surge events on some coasts, all six "types" or locations could be realized when variable water levels are experienced.

The subsurface boundary is only of recent interest. Drain pipes to artificially lower the water table have produced stable or accretional shorelines in some locations that were previously recessional. More study is needed of the local water table effects on shoreline change rates.

5.0 Barrier Beaches and Adjacent Back Bay Systems

5.1 Barrier Beach Migration Paradigm

Barrier beaches are nature's mechanism for protecting the bays, lagoons, and estuaries that lie behind them. The reduced wave energy environment permits the retention of cohesive sediments and grasses to survive in the tidal marsh areas. Since the 1950's, coastal geologists have done a outstanding job of explaining the migrating nature of barrier beach systems. These educational efforts have influenced public policy regarding development on migrating barrier islands. In short, the beach migration paradigm says:

'Let the barriers migrate landward. All efforts to stabilize migration are "economically unsound" in the long run when *only* the value of property built on the barrier is considered. The government should not subsidize an "economically unsound" policy'.

The first road built on a migrating barrier island becomes a fixed reference line to measure shoreline movements. Barriers migrating landward (transgression) create recessional shoreline movements. Simply put, the distance from the shoreline to the reference line (e.g. road centerline) decreases each year. Efforts to maintain the road at its fixed position result in shrinking beach widths when the road gets close enough to the shoreline. Is the road "... increasing erosion and destroying the beach"?

The presence of the road permits easy access by car, development for commercial, residential and recreational use and when economical, seawall construction to protect upland resources including public facilities. The distance from the shoreline to the seawall (new reference line) continues to decrease each year. Is the "... seawall increasing erosion and destroying the beach"?

As shown in this paper, some coastlines are receding at some locations due to offshore boundary conditions causing wave energy focusing and excess erosional stress. Not all coastlines are protected by barrier islands. And, as conclude by Leatherman, 1988 (p.63):

" Overwash is *not* the dominant process by which *most* barriers move landward since the amount of sediment transported by this means is too small. Inlet formation, when tidal currents cut a channel below sea level, moves far greater quantities of sediment into a lagoon over the long term and is the major process for barrier migration" (p.63).

It is thus clear to the writer that much blame placed on seawalls for shrinking beach widths and disappearing beaches is ill-founded.

5.2 Loss of Tidal Marshes in Back Bay Systems

We need to consider the barrier island *and* the estuarine-bay-lagoon-system behind the migrating island as an

integrated whole. Since the 1950's a wetlands value paradigm for public policy has evolved that says in short:

'America's wetlands are diminishing. Alterations must be monitored and any losses mitigated to conserve existing wetlands. The government is opposed to all destruction of coastal marshes.'

Basco (1990b) discusses the conflict produced by migrating barrier islands that shrink wetlands and calls for an expanded, elevated and shifted new paradigm for public policy decisions that includes the total value of what's behind and on the moving barrier islands in the coastal zone.

6.0 Conclusions

No discernable increase in long-term average shoreline change rate has occurred over a 2.8 mile stretch of Virginia Beach when considering data prior to seawall construction (1858-1925) and in subsequent years (1925-1980) when seawalls have existed. The long-term average change rate in this tourist/resort strip area of the city is about 0.4m/yr recession.

At Sandbridge, fourteen miles south, the 127 year data average (all sources) is about 3m/yr recession. This is attributed to offshore boundary conditions producing an excess erosional stress and a nodal point for sediment transport at this location. Recent seawall construction at Sandbridge (since 1978) provides a new reference line to measure shrinking distances from the shoreline to the seawall. The presence of the seawall is not responsible for a long-term average shoreline change rate of -3m/yr. Only long-term data at this location will provide the necessary evidence to determine if the walls create a recession rate exceeding -3m/yr. Little is known about the proper averaging time necessary to remove short-term variability from the long-term trend.

If we neglect the offshore boundary conditions when making field studies of "hardfacing" sections of coastlines versus "soft" sections and erosion rates, we can reach completely misleading results. As a positive first step toward understanding how seawalls and beaches interact, the science and coastal engineering community must insist upon more complete documentation of field studies when reported in the literature and at conference proceedings.

References

- Basco, D.R. (1990a) "The Interactions of Seawalls and Beaches at Sandbridge Beach, Virginia", Research Proposal for USAE, WES, CERC, Vicksburg, MS.
- Basco, D.R. (1990b) "On the Loss of Estuarine Bay Areas Due to Barrier Island Migration", Proceedings, The Coastal Society, Oct. (in press).
- Dolan, R.H. (1985) *Sandbridge Beach and Back Bay Virginia*, Tech Report, Coastal Research Assoc., Inc., Charlottesville, VA, 120p.
- Ebersole B.A., et al. (1983) *Regional Coastal Processes Numerical Modeling System, Rept. 1, RCPWAVE*, Tech Rept. CERC-86-4, WES, Vicksburg, MS March, 150p.
- Everts, Craig H., et al. (1983) *Shoreline Movements: Cape Henry, Virginia to Cape Hatteras, North Carolina, 1849-1980*, Rept. No.1, Tech. Rept, CERC-83-1, WES, Vicksburg, MS, July, 123p.
- Kraus, N.C. and O.H. Pilkey (editors), (1988) "The Effects of Seawalls on the Beach", *Journal of Coastal Research*, Spec.Iss., No.4, Autumn.
- Leatherman, S.P. (1988) *Barrier Island Handbook*, Laboratory, for Coastal Research, U. of Maryland, College Park, MD, Third Edit, 92p.
- Pilkey, O.H. and Wright, H.L.,III; (1988) "Seawalls Versus Beaches", *Journal of Coastal Research*, Spec. Iss. No.4, pp.41-66.
- Shore Protection Manual (1984), USAE, Vol.II, US Govt. Printing Office, Washington, DC.
- Weggel, J.R. (1988) "Seawalls: The Need for Research, Dimensional Considerations and a Suggested Classification", *Journal of Coastal Research*, Spec. Iss. No.4, pp.29-39
- Wright, L.D., et al. (1987) *Shoreline and Beach Dynamics of the Coastal Region from Cape Henry to False Cape, Virginia*, Virginia Institute of Marine Science, Tech. Rept., September., 105p.

CHAPTER 98

ROCK SLOPES UNDER IRREGULAR WAVE ATTACK

Nobuhisa Kobayashi¹, Andojo Wurjanto², and Daniel T. Cox³

ABSTRACT

The numerical model that was shown to be in fair agreement with six test runs of available data on the stability of rock units under irregular wave attack is used to examine the critical incident wave profile associated with the minimum rock stability for each run. The minimum rock stability computed for the runs with dominant plunging waves on gentler slopes is caused by the large wave with the maximum crest elevation during its uprush on the slope. The minimum rock stability computed for the runs with dominant surging waves on steeper slopes is caused by the downrushing water with high velocities resulted from a large zero-upcrossing wave with a high crest followed by a deep trough. In addition, a simplified model is proposed to predict the eroded area due to the movement and dislodgement of rock units using the probability of armor movement computed by the numerical model. This model is shown to be in qualitative agreement with the empirical formula of Van der Meer (1988).

INTRODUCTION

Kobayashi and Wurjanto (1989a) synthesized their numerical models and presented a computer program called IBREAK, which may be used for the design of rough or smooth impermeable coastal structures of arbitrary geometry against normally incident waves. Kobayashi and Wurjanto (1989c) showed that IBREAK could be calibrated and applied to predict the hydrodynamic forces and sliding motion of dolos units at the Crescent City breakwater. Kobayashi, Cox and Wurjanto (1990) conducted irregular wave tests and showed that IBREAK could be extended to predict irregular wave reflection and runup on a 1:3 rough impermeable slope. On the other hand, Kobayashi and Wurjanto (1989b, 1990) extended IBREAK to predict the flow and armor response on a rough permeable slope as well as the flow in a thin permeable underlayer. Kobayashi, Wurjanto and Cox (1990) applied the extended numerical model and showed that the computed critical stability number for initiation of rock movement under the computed irregular wave motion was in good agreement with the stability number corresponding to the start of damage measured by Van der Meer (1988).

¹Assoc. Prof., Center for Applied Coastal Research, Dept. of Civil Engrg., Univ. of Delaware, Newark, DE 19716

²Graduate Student, Dept. of Civil Engrg., Univ. of Delaware, Newark, DE 19716

³Graduate Student, Dept. of Civil Engrg., Kyoto Univ., Kyoto 606, Japan

In this paper, the temporal and spatial variations of the stability of rock units computed by Kobayashi, Wurjanto and Cox (1990) are analyzed in detail to examine what wave conditions may cause the minimum stability of rock units. Gunbak and Bruun (1979) described the various sequences of waves which may cause severe conditions on a breakwater. Their descriptions were qualitative since it is very difficult to measure the flow and armor response simultaneously.

COMPARISON BETWEEN MEASURED AND COMPUTED STABILITY NUMBERS

In the following, the comparison made by Kobayashi, Wurjanto and Cox (1990) is summarized. They expressed the hydraulic stability condition against sliding or rolling of an armor unit on a rough permeable slope in the form

$$N_s = H'(s - 1)^{-1}(\rho s/W')^{1/3} \leq N_R(t, x) \quad (1)$$

where N_s = stability number; H' = incident wave height used for the normalization of dimensional variables indicated by the prime; s = specific density of the armor unit; ρ = fluid density; W' = median mass of the armor units; and N_R = armor stability function. The dimensionless function N_R varies with the normalized time, $t = t'/T'$, and the normalized horizontal distance from the toe of the slope, $x = x'/[T'(gH')^{1/2}]$, where T' = incident wave period used for the normalization; and g = gravitational acceleration. The expression of N_R as a function of the normalized fluid velocity and acceleration was given in the paper of Kobayashi and Wurjanto (1990) where the input parameters for the computation of the armor stability were specified.

Computation was made for six test runs selected from the test results with the dimensionless damage level, $S=2$, and the number of incident waves, $N = 1000$, listed in Appendix II of the thesis of Van der Meer (1988). These runs corresponded to the start of damage. The incident irregular waves for the six runs were generated using the Pierson-Moskowitz spectrum. The significant wave height, H'_s , and the average period of the zero upcrossings, T'_m , of the incident wave train were used by Van der Meer to characterize the incident irregular waves. As a result, use was made of $H' = H'_s$ and $T' = T'_m$ for the normalization of the dimensional variables. The normalized incident wave train, $\eta_i(t) = \eta'_i/H'$, at the toe of the $1 : \cot \theta'$ slope required as input to the numerical model was generated numerically for the specified spectral density with assumed random phases. Since different sets of the random phases yield different temporal variations of $\eta_i(t)$, the incident irregular wave train specified for each run was not the same as that generated in a wave flume by Van der Meer (1988). In order to reduce the computation time, the duration of the computation was limited to $0 \leq t \leq 256$, corresponding to $N = 256$ instead of $N = 1000$.

Table 1 lists the values of $\cot \theta'$, $H' = H'_s$, $T' = T'_m$, $\xi = T' \tan \theta' / (2\pi H' / g)^{1/2}$ and N_s for each of the six test runs, where ξ = surf similarity parameter based on H'_s and T'_m . The six runs with $\xi = 1.72 - 6.88$ were selected to represent dominant breaker types of plunging, collapsing and surging waves on uniform slopes. Runs R2a and R2b corresponded to run R2 and were based on the same spectral density with given values of H'_s and T'_m . The time series $\eta_i(t)$ for runs R2a and R2b were generated numerically using different sets of the random phases.

Table 1 also lists the computed value of the critical stability number N_{sc} for each run. The value of N_{sc} for each run was taken as the minimum value

Table 1: Six Test Runs Compared with Numerical Model

Run No.	$\cot \theta'$	H' (cm)	T' (sec)	ξ	Measured N_s	Computed N_{sc}
R1	6	10.09	2.63	1.72	1.72	1.56
R2a	6	7.75	3.15	2.36	1.32	1.75
R2b	6	7.75	3.15	2.36	1.32	1.63
R3	4	8.16	3.22	3.52	1.39	1.15
R4	3	8.92	3.13	4.37	1.52	1.36
R5	2	7.98	2.69	5.95	1.36	1.01
R6	2	7.98	3.11	6.88	1.36	1.47

of $N_R(t, x)$ for the ranges of $x \geq 0$ and $8 \leq t \leq 256$ where the normalized horizontal coordinate x was taken to be positive landward with $x = 0$ at the toe of the slope and the duration $0 \leq t < 8$ was excluded to account for the initial transient waves in the computation starting from the initial conditions of no wave action in the region $x \geq 0$ at $t = 0$. The computed critical stability number N_{sc} and the measured stability number N_s are in fair agreement as shown in Table 1 where the values of N_{sc}/N_s are in the range 0.74-1.33. The small difference between the computed values of N_{sc} for runs R2a and R2b indicates the variability caused by the random phases, although a much larger number of simulated runs are required to perform a statistical analysis of the variability. The comparison between N_s and N_{sc} shown in Table 1 is not really rigorous because of the inherent differences between these stability numbers as discussed by Kobayashi, Wurjanto and Cox (1990).

WAVE CONDITIONS FOR CRITICAL ARMOR STABILITY

The wave conditions corresponding to the computed minimum stability of rock units for each run are examined in this paper to identify the wave conditions which are critical to the stability of rock units. In the following, runs R1 and R4 may be regarded as representative runs for dominant plunging and surging waves, respectively, whereas run R3 happens to include an exceptionally large wave.

The free surface displacement above the still water level (SWL) and the depth-averaged horizontal fluid velocity are normalized as $\eta = \eta'/H'$ and $u = u'/(gH')^{1/2}$, respectively, where u is taken to be positive landward. Fig. 1 shows the computed variations of η , u and N_R with respect to x at the time, $t = t_{sc}$, when the minimum value of N_R in the range $x \geq 0$ corresponds to the critical stability number N_{sc} . The values of t_{sc} for runs R1, R3 and R4 are 164.75, 156.38 and 161.55, respectively. The shaded area shown in the figure for η corresponds to the permeable underlayer for each test where the numerical model is presently limited to the case of a thin permeable underlayer (Kobayashi and Wurjanto, 1990). Fig. 1 also shows the computed variation of the local stability number N_{sx} with respect to x where N_{sx} was defined as the minimum value of $N_R(t, x)$ at the specified location during $8 \leq t \leq 256$. The minimum value of N_{sx} with respect to x equals the critical stability number N_{sc} .

The critical stability number for run R1 with $\xi = 1.72$ occurs slightly behind the steep front of the uprushing water with large upslope velocities and accel-

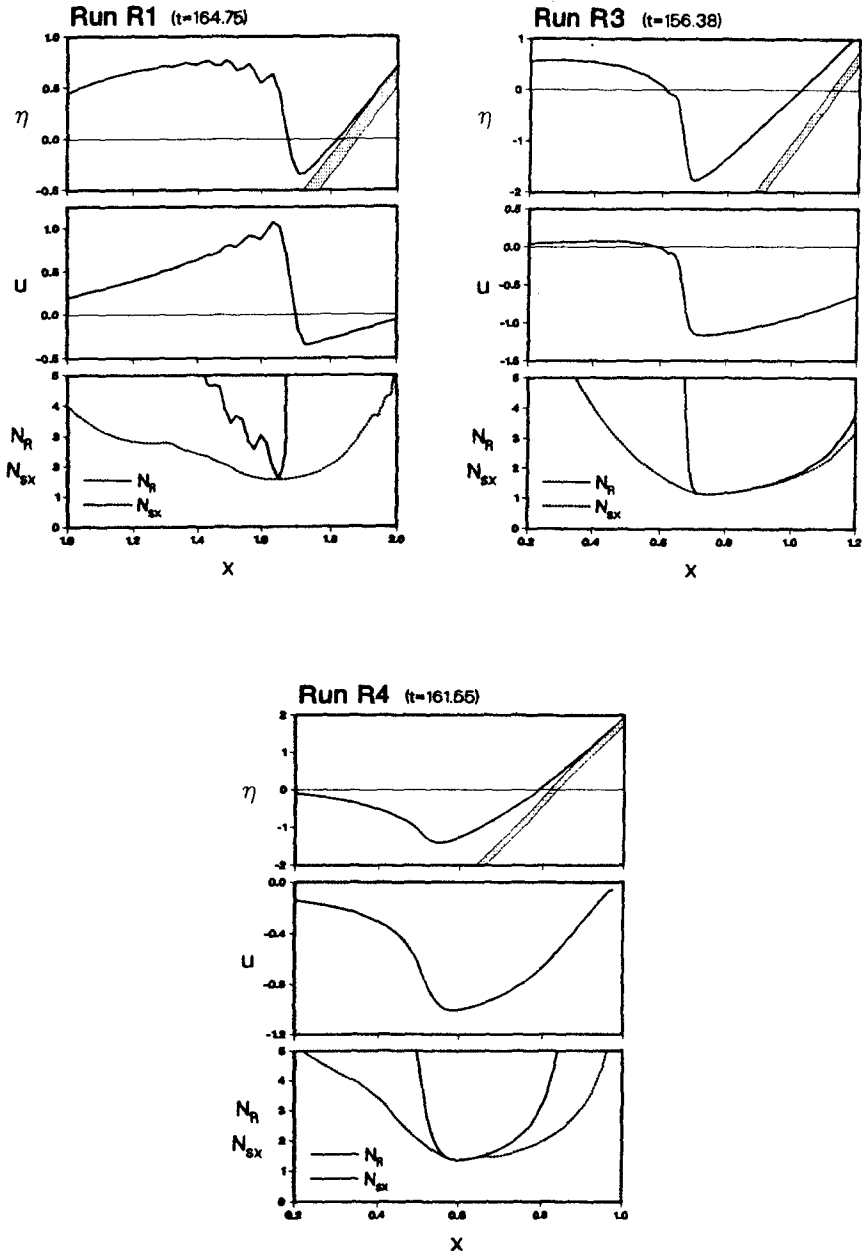


Figure 1: Variations of η , u and N_R with Respect to x at Time of Minimum Stability for Runs 1, 3 and 4

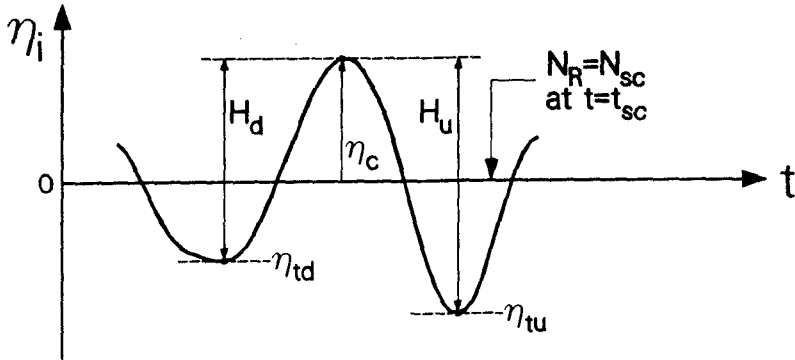


Figure 2: Definition Sketch for Critical Incident Wave Profile

erations. The local stability number in the range $1.5 \leq x \leq 1.9$ is computed to occur when this steep front moves upslope. On the other hand, the critical stability number for run R4 with $\xi = 4.37$ is caused by the downrushing water with large downslope velocities. For the exceptional case of run R3, the downrushing water flows extremely deep below SWL and encounters the uprushing water. The corresponding incident wave profile for run R3 will be shown to exhibit a very high crest followed by a very deep trough. This is one of the dangerous wave conditions identified by Gunbak and Bruun (1979).

The incident wave profile associated with the critical stability number N_{sc} for each run is examined to identify the incident wave profiles which may cause the critical uprushing or downrushing flow on uniform slopes. Fig. 2 shows the incident wave profile $\eta_i(t)$ at the toe of the slope normalized by the zero-upcrossing significant wave height H'_s slightly before the time $t = t_{sc}$ when $N_R(t, x) = N_{sc}$ at the certain location on the slope. The crest elevation η_c above SWL associated with the critical incident wave profile is obtained. The trough elevations η_{td} and η_{tu} adjacent to the crest elevation η_c are then found using the zero-downcrossing and zero-upcrossing methods, respectively. The corresponding wave heights H_d and H_u are given by $H_d = (\eta_c - \eta_{td})$ and $H_u = (\eta_c - \eta_{tu})$.

The values of η_c , η_{td} and η_{tu} for each run are listed in Table 2. These values are compared with the maximum crest elevation η_{cm} and the minimum trough elevation η_{tm} for $\eta_i(t)$ during $0 \leq t \leq 256$. Table 2 shows that $\eta_c = \eta_{cm}$ for runs R1, R2a, R2b and R3 while $\eta_{tu} = \eta_{tm}$ for runs R3 and R4. For runs R5 and R6, η_c is somewhat smaller than η_{cm} and η_{tu} is somewhat larger than η_{tm} .

Table 3 lists the values of H_d , T_d , H_u and T_u for each run where T_d and T_u are the zero-downcrossing and zero-upcrossing periods, respectively, of the individual wave whose crest elevation is η_c . The wave periods are normalized by the average zero-upcrossing period T'_m . Table 3 also lists the ranks of H_d and H_u among the 256 zero-downcrossing and zero-upcrossing individual wave heights, respectively, which are ranked in the descending order. Table 3 suggests that the critical incident wave profile is more related to the zero-upcrossing wave than the zero-downcrossing wave for runs R4, R5 and R6. The zero-upcrossing wave with $\eta_c = 1.052$, $\eta_{tu} = -1.126$ and $H_u = 2.178$ for run R3 appears to be exceptional, although the computed critical stability number N_{sc} for run R3 listed in Table 1 is not exceptionally small.

Table 2: Crest and Trough Elevations of Critical Wave Profile

Run	Crest		Trough		
No.	η_c	η_{cm}	η_{td}	η_{tu}	η_{tm}
R1	0.905	0.905	-0.527	-0.669	-0.934
R2a	0.822	0.822	-0.602	-0.459	-0.833
R2b	0.969	0.969	-0.877	-0.648	-0.933
R3	1.052	1.052	-0.673	-1.126	-1.126
R4	0.605	0.873	-0.034	-0.783	-0.783
R5	0.720	0.787	-0.550	-0.686	-0.793
R6	0.772	0.940	-0.447	-0.712	-0.974

Table 3: Wave Heights and Periods of Critical Wave Profile

Run No.	Zero-Downcrossing			Zero-Upcrossing		
	H_d	Rank	T_d	H_u	Rank	T_u
R1	1.433	4	1.263	1.575	1	1.256
R2a	1.424	3	1.195	1.280	7	1.518
R2b	1.846	1	1.189	1.617	3	1.116
R3	1.726	2	1.134	2.178	1	1.014
R4	0.639	118	0.649	1.388	5	1.213
R5	1.270	5	0.951	1.407	2	0.904
R6	1.219	17	1.066	1.484	4	1.235

Figs. 3-5 show the temporal variations of $\eta_i(t)$ and $Z_r(t)$ in the vicinity of $t = t_{sc}$ for runs R1, R3 and R4, respectively, where $Z_r = Z'_r/H'$ is the normalized waterline elevation on the slope above SWL corresponding to the instantaneous water depth $\delta'_r = 1$ cm (Kobayashi et al. 1990). Figs. 3-5 also show the zero-upcrossing and zero-downcrossing wave height distributions of the specified incident wave train $\eta_i(t)$ for each run as compared with the Rayleigh distribution given by $P = \exp[-2(H_p/H_s)^2]$ where P is the exceedance probability associated with the normalized wave height H_p and H_s is the normalized significant wave height.

The value of P for give H_p is estimated by $P = n/(N_o + 1)$ where $n =$ rank of H_p and $N_o =$ number of individual waves, which is 256 for these runs. Since the zero-upcrossing significant wave height H'_s is used for the normalization, $H_s = 1$ for the zero-upcrossing wave height distribution. The values of H_s for the zero-downcrossing wave height distribution are found to be essentially unity for all runs. Figs. 3-5 also point out the exceedance probability P for H_u and H_d for each of the three runs to indicate the values of H_u and H_d as compared with the rest of the individual wave heights.

Figs. 3-5 together with Figs. 1-2 and Tables 1-3 elucidate the critical wave conditions corresponding to the minimum stability of rock units for each run. For run R1 with $\cot \theta' = 6$ and $\xi = 1.72$, the critical stability number occurs at the time t_{sc} when the large wave with the maximum crest elevation $\eta_c = \eta_{cm}$ uprushes on the slope and encounters the trough of the waterline oscillation on the slope as shown in Fig. 3. The computed results for runs R2a and R2b with

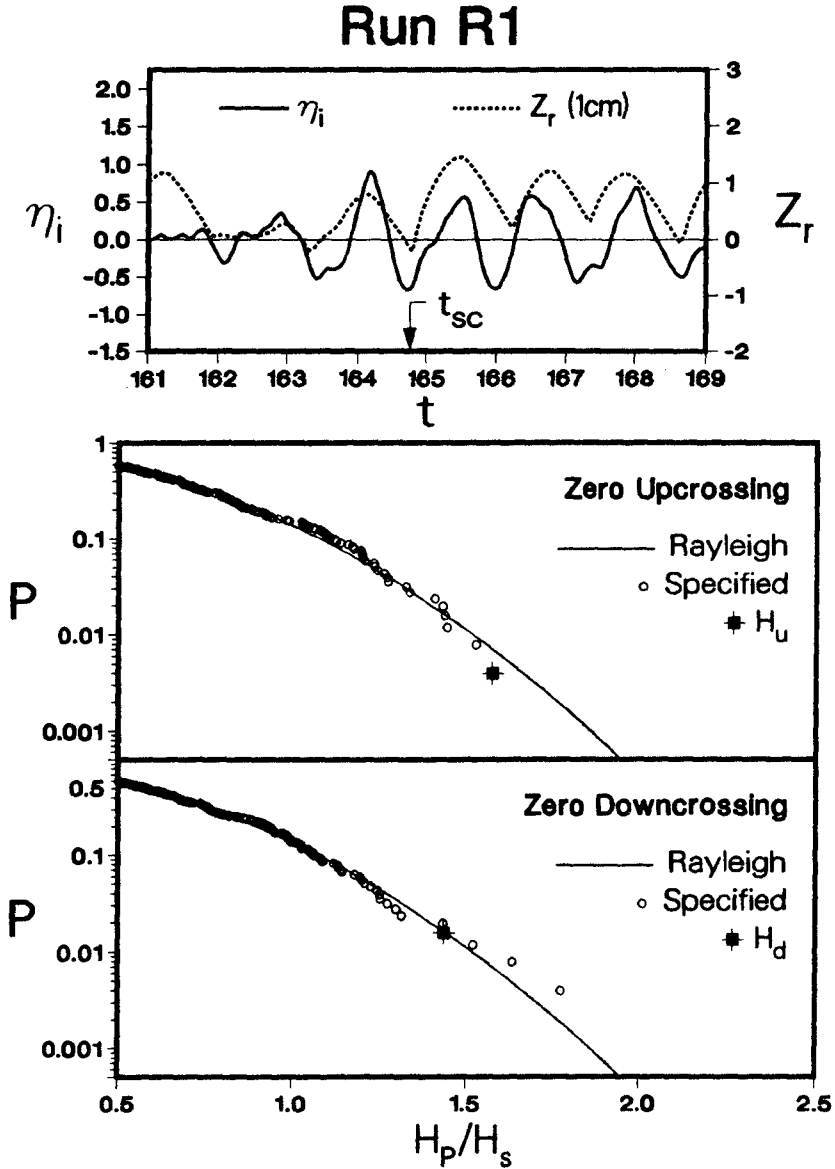


Figure 3: Analysis of Critical Wave Profile for Run R1

Run R3

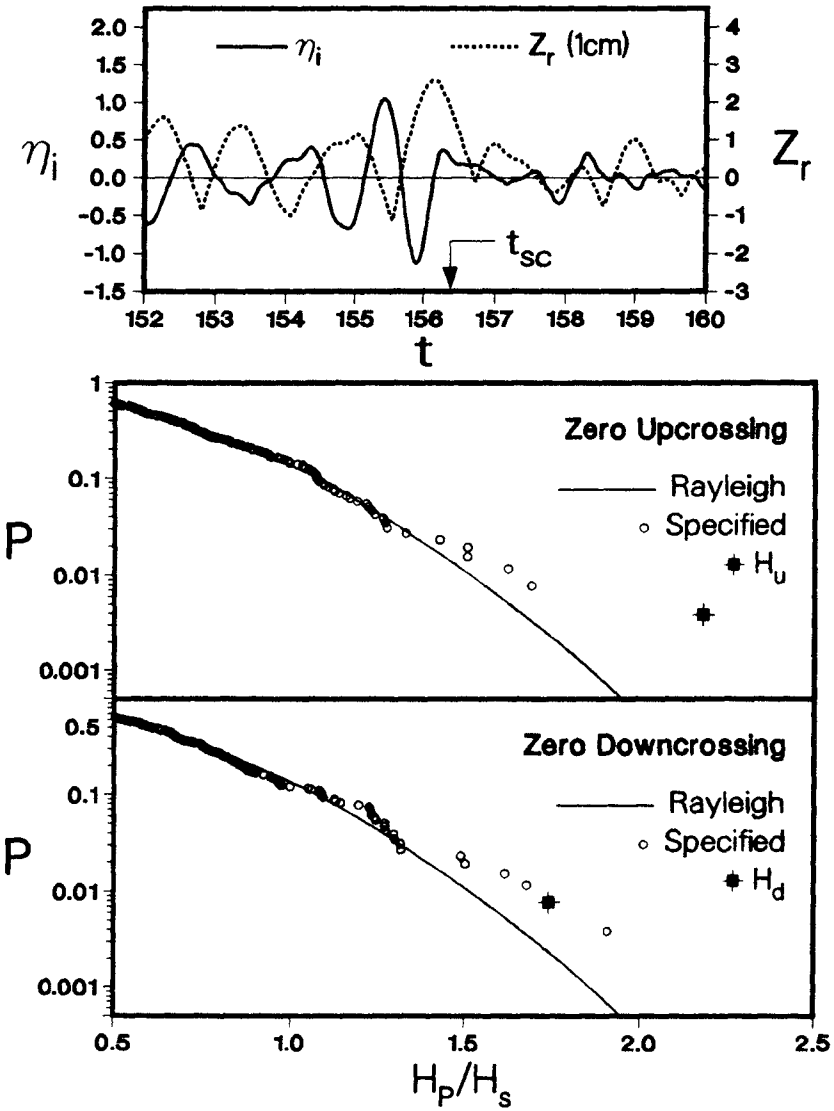


Figure 4: Analysis of Critical Wave Profile for Run R3

Run R4

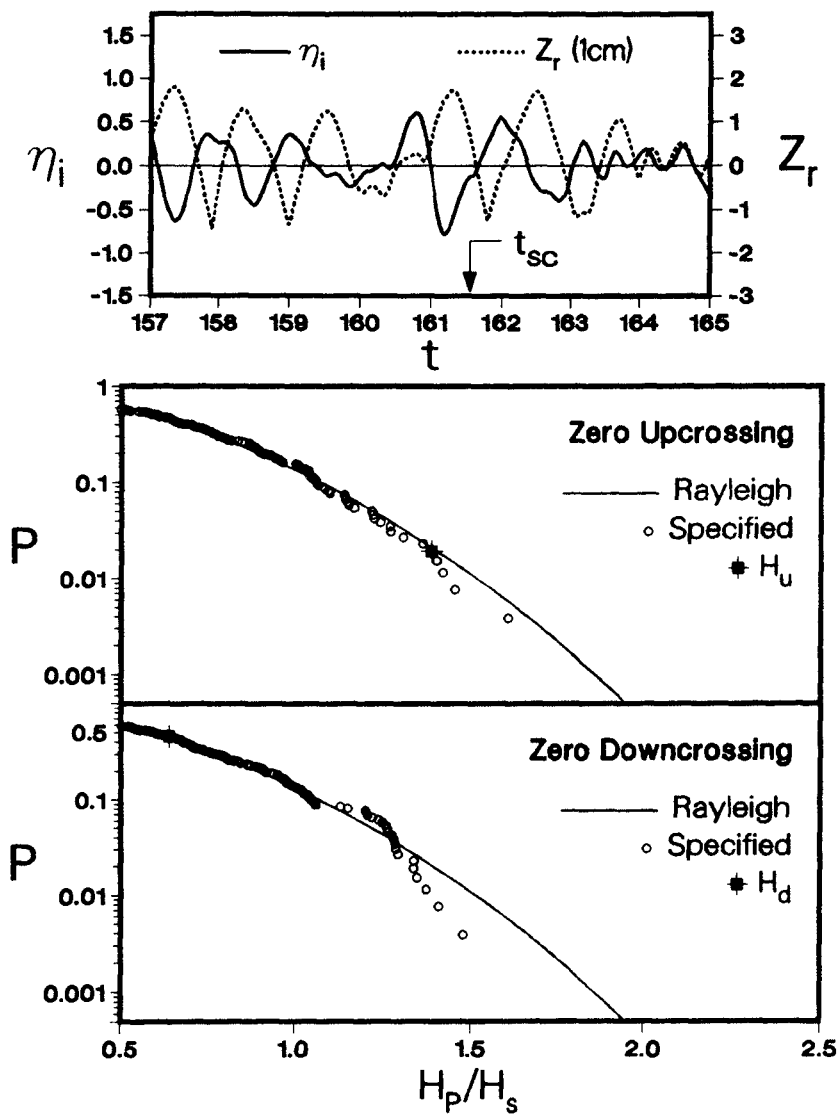


Figure 5: Analysis of Critical Wave Profile for Run R4

$\cot \theta' = 6$ and $\xi = 2.36$ are very similar to those for run R1. Additional runs are required to determine whether these critical wave conditions are limited to relatively gentle slopes such as $\cot \theta' = 6$ or can occur for steeper slopes as long as the surf similarity parameter is roughly two. For run R3 with $\cot \theta' = 4$ and $\xi = 3.52$, the critical stability number occurs at the time t_{sc} when the extremely large wave with the maximum crest elevation $\eta_c = \eta_{cm}$ and the minimum trough elevation $\eta_{tu} = \eta_{tm}$ causes the downrushing water with large velocities following large runup as shown in Fig. 4. For run R4 with $\cot \theta' = 3$ and $\xi = 4.37$, the critical stability number occurs at the time t_{sc} when the relatively large zero-upcrossing wave with the high crest followed by the deep trough causes the downrushing water with large velocities with the waterline on the slope being near SWL as shown in Fig. 5. The computed results for run R5 with $\cot \theta' = 2$ and $\xi = 5.95$ and run R6 with $\cot \theta' = 2$ and $\xi = 6.88$ are similar to those for run R4.

PROBABILITY OF ARMOR MOVEMENT AND DAMAGE LEVEL

The critical incident wave profile and resulting critical stability number N_{sc} is useful for the design of armor units in which $N_s < N_{sc}$ so that armor units will not move under the action of design waves. If the mass of armor units is reduced such that $N_s > N_{sc}$, the degree of armor movement and resulting profile change will need to be predicted.

The computed armor stability function $N_R(t, x)$ depends on the normalized incident wave train $\eta_i(t)$ and the slope and armor characteristics specified as input to the numerical model. In the numerical model, the constant friction factor f' is used to account for the roughness effects of the primary cover layer on the flow over the rough permeable slope, while the effects of the permeable underlayer are taken into account by the volume and momentum fluxes into or out of the permeable underlayer. Since the computed flow field is not very sensitive to the assumed value of f' , the computed temporal and spatial variations of $N_R(t, x)$ for each run in Table 1 may be assumed to remain essentially the same even if the stability number N_s defined in Eq. 1 is increased somewhat by decreasing only the median mass W' of the armor units.

In the following, the probability of armor movement based on the movement duration, P_t , and the probability of armor movement per unit normalized time, P_m , are predicted as a function of the stability number $N_s > N_{sc}$ and the location x of the armor unit along the uniform slope. For given N_s and x , armor movement will occur during the time when $N_s > N_R$. The duration of each event of armor movement is denoted by t_j with $j = 1, 2, \dots, J$ where $J =$ number of armor movement events during the specified duration $t_{min} \leq t \leq t_{max}$. In this paper $t_{min} = 8$ and $t_{max} = 256$. From the computed armor movement statistics, the probabilities P_t and P_m may be defined as

$$P_t = (t_{max} - t_{min})^{-1} \sum_{j=1}^J t_j ; P_m = \frac{J}{(t_{max} - t_{min})} \tag{2}$$

For example, Fig. 6 shows the computed probabilities P_t and P_m for $N_s/N_{sc} = 1.1, 1.3$ and 1.5 for run R1 where the normalized elevation, $z = z'/H'$, of the armor unit on the slope relative to SWL located at $z = 0$ is used instead of x . The computed probabilities of the armor movement occurring mostly below SWL increase with the increase of N_s . For run R1, the computed value of N_{sc} is 1.56 and the measured value of N_s corresponding to the start of the damage was 1.72 as listed in Table 1. This implies that the numerical model predicts the

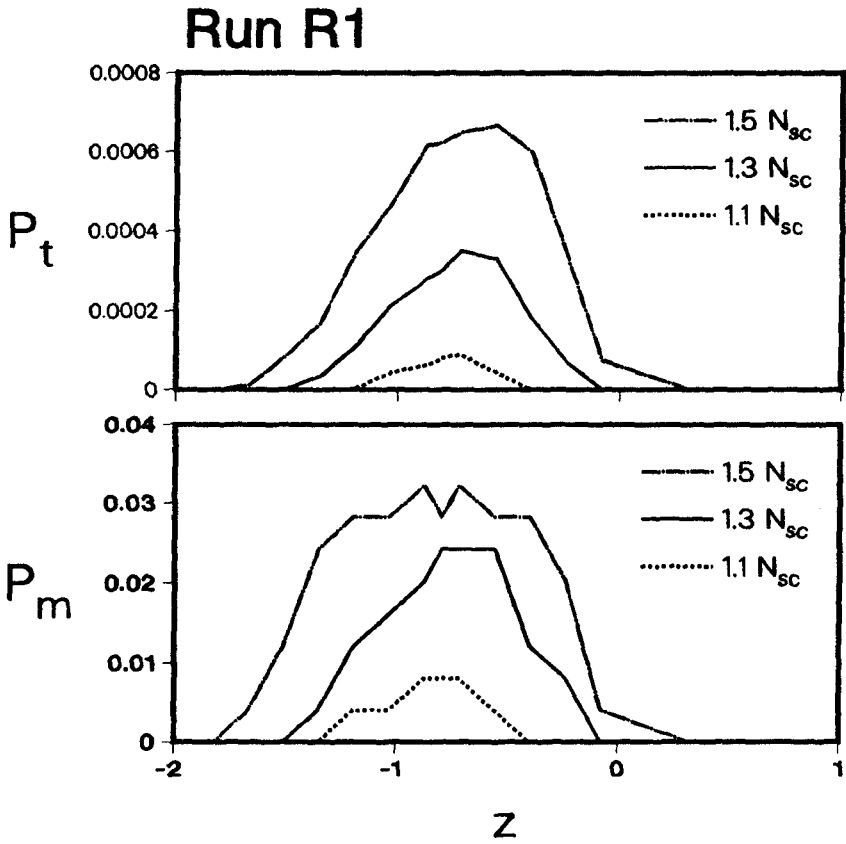


Figure 6: Computed Probabilities for Given N_s of Rock Movement for Run R1

movement of the armor units with $N_s = 1.72$, that is, $N_s/N_{sc} = 1.10$. However, the predicted probabilities for $N_s/N_{sc} = 1.1$ are very small as shown in Fig. 6.

The probability of armor dislodgement per unit normalized time, P_d , is expected to be less than P_m . As a first attempt, it is simply assumed that $P_d = C_d P_m$ where $C_d =$ empirical parameter. The rate of vertical erosion of the primary cover layer may be given by

$$\frac{\partial \eta'_e}{\partial t'} = \frac{C_3(d')^3}{1 - n_a} \frac{1 - n_a}{C_2(d')^2} \frac{P_d}{T'} = \frac{C_3 d' P_d}{C_2 T'} \tag{3}$$

where $\eta'_e =$ vertical erosion depth of the primary cover layer taken positive downward; $t' =$ time associated with the profile change; $d' =$ characteristic length of the armor unit; $C_3 =$ armor volume coefficient; $C_2 =$ armor area coefficient; $n_a =$ porosity of the primary cover layer; and $(P_d/T') =$ probability of dislodgement of a single unit per unit time. In Eq. 3, $C_3(d')^3/(1 - n_a)$ is the volume occupied by a single unit, while $(1 - n_a)/C_2(d')^2$ is the number of armor units per unit area along the slope. Eq. 3 predicts the erosion only since the dislodged armor units are assumed to be deposited in the region where P_d is essentially zero.

In the following, the profile change is assumed to be so small that P_d may be assumed to be independent of t' . Then, Eq. 3 yields $\eta'_e = (C_3 d' P_d t)/C_2$ where $\eta'_e = 0$ at $t' = 0$ and $t = t'/T'$ is the normalized time which is equal to the number of individual waves. Integration of η'_e along the slope in the region $\eta'_e > 0$ yields the eroded area A'_e . Van der Meer (1988) defined the damage level S by $S = A'_e/(W'/\rho_s)^{2/3}$. The present analysis can be shown to yield

$$S = \frac{C_d C_3^{2/3} (s - 1) N_s t}{C_2 \sin \theta'} \int P_m dz \tag{4}$$

where the stability number N_s is defined in Eq. 1 and the integration of P_m with respect to z can be performed for given $N_s > N_{sc}$ using the computed variation of P_m such as those shown in Fig. 6. For the runs listed in Table 1, use was made of $C_3 = 0.66$, $C_2 = 0.90$ and $s = 2.63$ by Kobayashi and Wurjanto (1990). In the following computation, the number of individual waves is taken to be $t = 1000$ and the value of N_s is varied such that $N_s/N_{sc} = 1.1, 1.2, \dots, 2.0$.

Fig. 7 shows the computed damage level S as a function of N_s for runs R1, R3 and R4. The empirical parameter C_d is taken as $C_d = 0.005, 0.01$ and 0.02 so that the computed values of S are of the order of the values of S based on the empirical formula of Van der Meer (1988) which is also plotted for each run in Fig. 7. The computed variations of S with respect to N_s for the other runs are also in qualitative agreement with the empirical formula. Eq. 4 will overestimate the value of S if S becomes so large that the profile change will result in the decrease in P_m and P_d . The major difference between Eq. 4 and the empirical formula is that the probability of armor movement P_m in Eq. 4 is computed for the specified incident wave train $\eta_i(t)$ for each run. It is hence possible to examine the sensitivity of P_m to various incident wave trains.

CONCLUSIONS

The computed results presented herein is not extensive and need to be verified. The numerical model is used to examine the detailed armor response to the specified incident wave trains since the detailed quantitative understanding

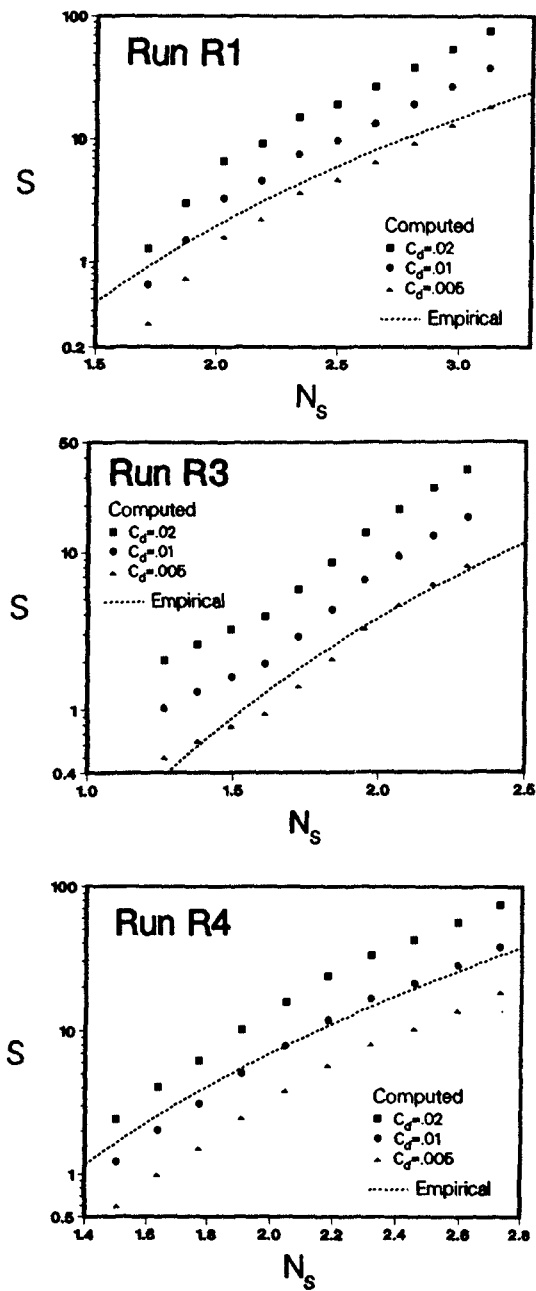


Figure 7: Computed Damage Level S as a Function of N_s for Runs R1, R3 and R4

is essential for improving the design of rock slopes for specified design waves as well as determining the design wave conditions more specifically than those based on the representative wave height and period. Generally, the scatter of data points about an empirical curve used for the design of a coastal structure against irregular waves is fairly large. Some of the scatter appears to be caused by the use of the representative wave height and period.

ACKNOWLEDGEMENT

This work is a result of research sponsored by Coastal Engineering Research Center, U.S. Army Engineer Waterways Experiment Station, under Contract No. DACW39-90-K-0006-P001 and the National Science Foundation, under grant CTS-8900640.

REFERENCES

- Gunbak, A. R. and Bruun, P. M. (1979), "Wave mechanics principles on the design of rubble-mound breakwaters." *Proc. P.O.A.C.*, Norwegian Inst. of Tech., Trondheim, Norway, 1301-1318.
- Kobayashi, N. and Wurjanto, A. (1989a), "Numerical model for design of impermeable coastal structures." *Res. Rept. No. CE-89-75*, Department of Civil Engineering, University of Delaware, Newark, DE 19716.
- Kobayashi, N. and Wurjanto, A. (1989b), "Armor stability on rough permeable slopes of marine structures." *Proc. 23rd I.A.H.R. Congress*, Ottawa, Canada, C, 407-414.
- Kobayashi, N. and Wurjanto, A. (1989c), "Numerical prediction of hydrodynamic forces and sliding motion of dolos units." *Proc. Stresses in Concrete Armor Units*, ASCE, 355-378.
- Kobayashi, N. and Wurjanto, A. (1990), "Numerical model for waves on rough permeable slopes." *J. Coast. Res.*, Special Issue No. 7 on Rational Design of Mound Structures, 149-166.
- Kobayashi, N., Wurjanto, A. and Cox, D.T. (1990), "Irregular waves on rough permeable slopes." *J. Coast. Res.*, Special Issue No. 7 on Rational Design of Mound Structures, 167-184.
- Kobayashi, N., Cox, D.T. and Wurjanto, A. (1990), "Irregular wave reflection and runup on rough impermeable slopes." *J. Wtrway. Port Coast. and Oc. Engrg.*, ASCE, 116(6) (in press).
- Van der Meer, J. W. (1988), "Rock slopes and gravel beaches under wave attack," Delft Univ. of Tech., Delft, The Netherlands, Doctoral Thesis.

CHAPTER 99

DYNAMIC ANALYSIS OF FLOATING BREAKWATER MOORING SYSTEMS

John R. Headland¹ and Limberios Vallianos²

Abstract

This paper presents a numerical model for computation of floating breakwater mooring forces. The model is based on time domain mooring analysis techniques which permit simulation of: (1) nonlinear mooring line load characteristics and (2) mooring line loads associated with second order wave drift forces. Numerical model results are compared to physical model tests (Torum, 1989) and prototype measurements (Nelson and Broderick, 1986). These comparisons demonstrate that the numerical model provides good estimates of floating breakwater mooring line forces. Accordingly, it is concluded that the numerical model serves as a useful engineering tool for analysis and design of floating breakwater mooring systems.

Introduction

Floating breakwaters have been the subject of research for many years. Much of this research, however, has focused on breakwater wave transmission characteristics. Although wave transmission is an important functional design consideration, floating breakwaters and their moorings must also withstand survival environmental loadings. This paper presents a systematic and practical procedure for analysis of floating breakwater mooring systems.

¹ A.M. ASCE, Consultant, Harbor & Coastal Engineering, Naval Facilities Engineering Command 200 Stovall St. Alexandria, VA USA

² M. ASCE, Principle Coastal Engineer, U.S. Army Corps of Engineers, Institute for Water Resources, Fort Belvoir, VA, USA

Previous Investigations

Floating breakwater performance can be evaluated using numerical and physical models. Physical models provide the most reliable estimates of floating breakwater performance, but are generally expensive. Numerical models provide a relatively inexpensive means of assessing floating breakwater performance and are particularly useful in feasibility level analyses which can be used to refine designs prior to physical model testing. Numerical modeling of moored floating breakwaters has most often been performed using frequency domain techniques. Examples of frequency domain numerical models may be found in Adee et al (1976) and Tekmarine Inc. (1986) which can be used to estimate floating breakwater wave transmission characteristics and mooring line forces. Georgiadis and Hartz (1982) developed a numerical model to evaluate the internal loads of a floating breakwater module using both frequency and time domain techniques.

Laboratory and field studies of various floating breakwater installations (Adee et al, 1976) have shown that frequency domain analysis provides a good engineering estimate of floating breakwater wave transmission characteristics. However, as will be discussed below, frequency domain analyses often do not adequately predict breakwater motions and attendant mooring line forces.

Miller et al (1984) found that the frequency domain approach adequately predicted floating breakwater motions in heave and roll, but could not predict the low frequency sway motions which generally dominated mooring forces. Similarly, Adee et al (1976) concluded that mooring forces developed from frequency domain analysis must be increased substantially in order to provide an estimate of actual mooring forces. Figure 1 presents an example force time history reported by Adee et al (1976) for floating breakwater installation at Tenakee, Alaska. Incident waves had periods ranging from 1 to 2 seconds, however, mooring line forces were dominated by long period oscillations with periods of approximately 55-60 seconds. A review of the dynamic characteristics of the floating breakwater mooring system indicated that the recorded sway motion of the floating breakwater was very close to the sway natural period. Similar prototype measurements were reported by the Japanese Ministry of Transport at site near Kumamoto, Japan (see Tekmarine (1986)). Clearly, any numerical analysis of floating breakwater mooring line forces must account for both high and low frequency motions.

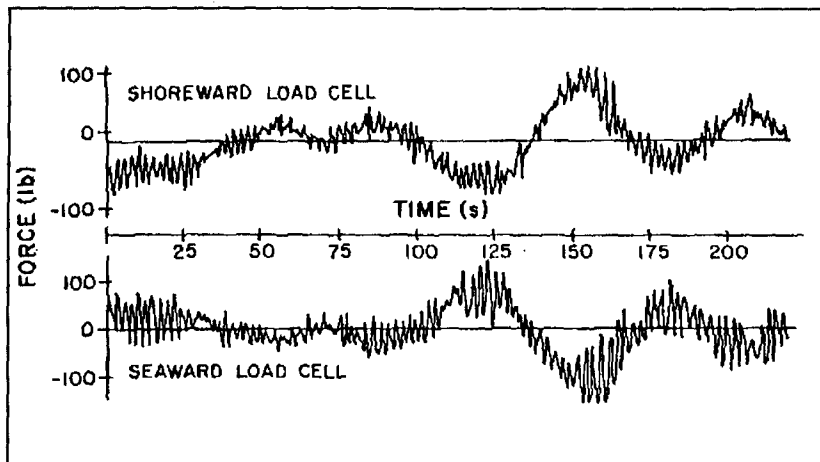


Figure 1. Typical Mooring Force Time History

Low frequency motions of moored structures result from second order wave drift forces (Pinkster, 1980). Such forces are neglected in a first order frequency domain analysis such as that reported in Adey et al (1976) and Tekmarine Inc. (1986) which assume applied hydrodynamic loading and attendant breakwater response are sinusoidal at a frequency equal to the incident wave frequency. As a result, such frequency domain analyses do not account for the "second order" wave drift forces which can dominate mooring line forces. The following paragraphs outline a time domain numerical model capable of estimating first and second order floating breakwater motions and mooring line forces.

Numerical Model Theory

Equations of Motion. Research on the behavior of moored vessels has shown that mooring systems are best modeled in the time domain using the impulse-response method (Van Oortmerssen, 1976). The time domain approach can be used to simulate nonlinear mooring line behavior as well as arbitrary applied loadings. Because an arbitrary applied loading can be specified, the time domain approach can be used to assess first and second order wave forces. The governing equations of motion, which account for time domain motion in six degrees of freedom, are as follows:

$$\sum_{j=1}^6 [(M_{kj}+m_{kj})\ddot{x}_j + \int_{-\infty}^t K_{kj}(t-\tau)\dot{x}_j(\tau) d\tau + C_{kj}x_j] = F_k(t) \tag{1}$$

$$k = 1, 2, \dots, 6$$

Where:

- x_j = motion in the j-th mode
- M_{kj} = inertia matrix
- C_{kj} = hydrostatic restoring force matrix
- K_{kj} = impulse response function matrix
- m_{kj} = constant added mass matrix
- $F_k(t)$ = arbitrary external force in k-th mode due to waves, mooring line reactions, viscous damping, winds, currents, etc.
- k = denotes mode of motion, (i.e. 1 (surge), 2 (sway), 3 (heave), 4 (roll), 5 (pitch), 6 (yaw))

The left hand side of equation (1) contains linear hydrodynamic reaction forces while the right hand side represents an arbitrary forcing function which may include linear terms (e.g. first order wave forces) and nonlinear terms (e.g. second order wave drift forces, mooring line forces, viscous damping, etc.). The primary advantage of the impulse-response function approach is that arbitrary motion over a range of motion frequencies can be simulated correctly. Other time domain methods, such as that used by Georgiadis and Hartz (1982), assume constant values of added mass and damping at a single frequency even though breakwater motion may occur over a range of frequencies.

Hydrodynamic Coefficients. The inertia matrix, M_{kj} , and hydrostatic restoring force matrix, C_{kj} , are computed using standard methods of naval architecture. The impulse-response function matrix, K_{kj} , and the constant added mass coefficient, m_{kj} , are computed as follows (Van Oortmerssen, 1962):

$$K_{kj} = \frac{2}{\pi} \int_0^{\infty} b_{kj}(\omega) \cos \omega t d\omega \tag{2}$$

$$m_{kj} = a_{kj}(\omega^*) + \frac{1}{\omega^*} \int_0^{\infty} K_{kj}(t) \sin \omega^* \tau d\tau \quad (3)$$

Where:

- a_{kj} = frequency-dependent added mass
 b_{kj} = frequency-dependent damping coefficient

The above frequency dependent added mass and damping coefficients may be computed using either strip-theory or diffraction theory hydrodynamic analysis. The Frank Close-Fit strip theory approach, as documented by Kaplan (1989), was used in the present analysis.

Wave Forces. The applied force resulting from waves, $F_{kw}(t)$, can be written as:

$$F_{kw}(t) = \sum_0^n f_k^{(1)}(\omega_n) a_n \cos(\omega_n t + \epsilon_n + \epsilon_k) \quad (4)$$

$$+ \sum_0^n \sum_0^m f_k^{(2)}(\omega_n) a_n a_m \cos((\omega_n t + \epsilon_n) - (\omega_m t + \epsilon_m))$$

Where:

- $f_k^{(1)}(\omega_n)$ = first order wave transfer function in k-th mode for n-th wave component
 $f_k^{(2)}(\omega_n)$ = second order wave transfer function in k-th mode for n-th wave component
 ϵ_k = phase of first order wave transfer function in k-th mode for n-th wave component
 a_n = wave amplitude of n-th wave component
 ϵ_n = phase of n-th wave component
 ω_n = frequency of n-th wave component

The above formula is used to simulate first and second order wave force time-histories resulting from an incident wave spectrum composed of n-waves. The incident wave spectrum is represented in the above formulation by

the wave amplitudes and phases (i.e. a_n and ϵ_n) which correspond to wave frequencies, ω_n . Wave amplitudes and frequencies are determined from an incident wave spectrum using the "equal area" method described by Borgman (1969).

It should be noted that the wave force formulation presented in equation (4) is only valid for long-crested, uni-directional wave conditions. The present version of the model cannot be used to assess mooring loads from directional spectra. Fortunately, the results of Torum et al (1989) indicate that directional spreading has little influence on mooring line forces.

The first order wave transfer functions were also computed using the Frank-Close Fit method documented by Kaplan (1989). The second order wave transfer functions were computed from the first order wave analysis using methods based on the work of Gerritsma and Beukelman (1972) and Newman (1967). As will be discussed later, mooring simulations using these computed drift forces over estimated the sway motions and attendant mooring line forces of scale model and prototype floating breakwaters. This overprediction was believed to be due to the fact that both the physical model and prototype breakwaters were heavily overtopped by waves. In an effort to account for overtopping, wave drift forces were computed using the following expression derived by Longuet-Higgins (1977):

$$f_2^{(2)} = \frac{1}{4} \rho g (a^2 + a_R^2 - a_T^2) \left(1 + \frac{2kh}{\sinh(2kh)} \right) \quad (5)$$

Where:

- a = incident wave amplitude
- a_R = reflected wave amplitude
- a_T = transmitted wave amplitude
- k = wave number
- h = water depth

The reflected wave amplitude can be estimated from the incident and transmitted wave amplitudes as follows:

$$a^2 \sim a_R^2 + a_T^2 \quad (6)$$

Given measured values of the incident, reflected and transmitted wave amplitudes, equation (5) can be used to estimate second wave drift forces. Wave overtopping conditions are taken into account implicitly through the measured incident, reflected and transmitted wave amplitudes.

Viscous Damping Coefficients. Numerous studies (e.g. Wichers, 1988) have shown that potential theory damping terms for surge, sway and yaw motions of moored structures are negligible in comparison to viscous damping terms at low frequency. Accordingly, an additional term is added to the time-varying applied force, $F_k(t)$, to account for viscous damping effects. Both nonlinear and linear viscous sway damping formulations were investigated. In accordance with the findings of Wichers (1988), initial efforts were directed towards evaluation of a quadratic damping term formulated as follows:

$$F_{2D}(t) = -\frac{1}{2} \rho C_{2D} |\dot{x}_2| \dot{x}_2 A_2 \quad (7)$$

Where:

- $F_{2D}(t)$ = nonlinear damping force in sway
- ρ = water density
- A_2 = lateral wetted area of breakwater
- C_{2D} = viscous drag coefficient in sway

After considerable analyses, it was concluded that the above nonlinear damping formulation provided very little damping for typical floating breakwater sway motion velocities and was abandoned in favor of a linear damping formulation as follows:

$$F_{2D}(t) = -B_{2D} \dot{x}_2 \quad (8)$$

Where:

- B_{2D} = linear viscous damping coefficient

A similar formulation has been shown to successfully predict surge damping characteristics of vessels secured to single point moorings in still water (Wichers, 1988). Using the results of a prototype extinction tests, Seelig (1990) demonstrated that the above linear formulation could be used to estimate the sway motions of a spread-moored vessel in still water. Seelig's prototype measurements were used to estimate linear damping coefficient, B_{2D} .

Mooring Forces. Mooring line restoring forces in the numerical model are computed using static catenary theory. Mooring line loads are determined from the instantaneous position of mooring attachment point on the breakwater and from static load deflection curves for each line. The total mooring restoring forces and moments acting on the center of gravity of the breakwater in each mode of motion are computed by summing the force (and moment) contributions from each mooring line. These forces are then added to the $F_k(t)$ term on the right hand side of equation (1). Although Torum et al (1989) suggest that such effects may be important at high frequency, no attempt has been made to incorporate dynamic oscillations of the mooring lines in the numerical model.

MODEL APPLICATION

The U.S. Army Corps of Engineers initiated the Floating Breakwater Prototype Test Program in 1981. A concrete box or caisson-type floating breakwater was constructed, installed and monitored an exposed site in the Puget Sound as part of this program. Results of this study are presented in Nelson and Broderick (1986). The general arrangement of the floating breakwater installation is shown in Figure 2. The particulars of the floating breakwater unit are summarized in Table 1.

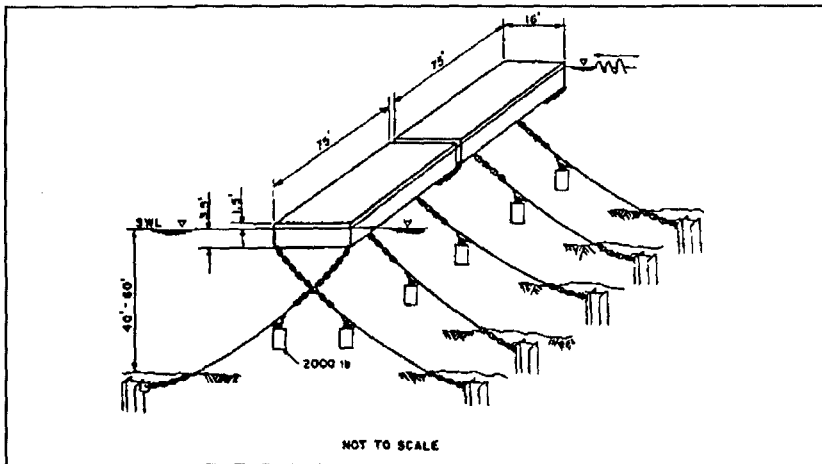


Figure 2. Layout of Puget Sound Floating Breakwater

Table 1
 Characteristics of Puget Sound Floating Breakwater

Length=150 ft (46m)	Natural Period-Sway = 20 sec
Beam =16 ft (4.9m)	Natural Period-Heave = 3.2 sec
Draft=3.5 ft (1.1m)	Natural Period-Roll = 2.4 sec
Mass=16,696 slugs (244,022 kg)	Natural Period-Pitch = 3.4 sec
C.G = 1 ft (.31m)	Natural Period-Yaw = 14 sec
GM = 5.35 ft (1.6m)	

Table 1 also summarizes the natural period for each mode of motion of the breakwater. The natural periods were determined by performing extinction tests with the numerical model for mid-tide conditions. As can be seen in Table 1, the natural periods of motion in sway and yaw are much longer than: (1) heave, roll and pitch natural periods and (2) typical floating breakwater design waves periods.

The U.S. Army Corps of Engineers, Waterways Experiment Station, Coastal Engineering Research Center recently sponsored a series of 1:10 scale physical model tests to evaluate the performance of the prototype structure. The tests are given in Torum et al (1989).

In order to validate the numerical model presented in this paper, the predictions of the numerical model were compared to measurements obtained in the prototype experiment and physical model tests. Results of this comparison are described below.

Physical Model Tests. Torum et al (1989) present physical model test results for both a continuous breakwater structure (i.e. "stiff" model) and a discontinuous series of breakwater pontoons separated by fenders (i.e. "fendered") model. Only the "stiff" model results were used in the evaluation of the time domain numerical model. The linear hydrodynamic coefficients and wave transfer functions for the caisson-type floating breakwater were computed in the frequency domain and converted to time domain functions using the techniques described above. It would be highly desirable to measure these parameters directly with the results of physical model tests. Unfortunately, given the nature of physical modeling program described by Torum et al (1989), there is no way to validate these quantities directly. A systematic series of physical model tests would be

required to evaluate the added mass, damping and wave transfer functions separately. At this juncture, one can only compare the final output of the physical model (i.e. breakwater motions and mooring line forces) to that simulated by the numerical model.

Mooring analyses were prepared for a variety of the wave conditions tested in the physical model. As previously mentioned, second order wave transfer functions were initially computed without accounting for wave overtopping. The resulting mooring dynamic simulations significantly overpredicted breakwater motions and attendant mooring line forces. A systematic variation of the second order wave transfer functions and viscous damping coefficients demonstrated that the floating breakwater response was relatively sensitive to the second order wave transfer functions and less sensitive to the viscous damping coefficient as long as the linear damping formulation was used. Hence, the original method for computing the second order drift forces was abandoned in favor of the method of Longuet-Higgins (1977) presented in Equation (5). In order to apply equation (5) it was necessary to know the incident, reflected and transmitted wave amplitudes for each wave frequency. Fortunately, breakwater transmission characteristics were presented in Torum et al (1989). Hence, the second order wave transfer functions could be estimated directly from equations (5) and (6). Mooring line load deflection curves were estimated from plots presented in Torum et al (1989).

Example numerical model results are presented in Figure 3 which presents time histories of water surface elevation, sway, heave, and roll motions and mooring line forces for beam-on waves with a significant wave height of 1.43 meters and a peak spectral wave period of 4.3 seconds. Figure 3 is actually a portion of the predicted time history as the numerical model was run for a total time of 960 seconds. With the exception of roll, the numerical model provided a good prediction of the breakwater motions. Specifically, the peak values of sway, heave, and roll measured in the physical model were 3.029 meters, .7022 meters, and 10.04 degrees, respectively, while the peak values of sway, heave, and roll predicted by the numerical model were 2.8 meters, 0.65 meters, and 25 degrees, respectively. The maximum mooring line load predicted by the numerical model (31.8 kilonewtons) was comparable to that measured in the physical model tests (32.97 kilonewtons). Figure 3 indicates several facets of the breakwater response, namely: (1) heave and roll response are at the incident wave frequency, (2) sway response and mooring line forces

are dominated by low frequency motion near the natural period of sway motion, and (3) roll motion is overpredicted by the numerical model. Similar results were obtained for other comparisons of the numerical model results with that measured in the physical model.

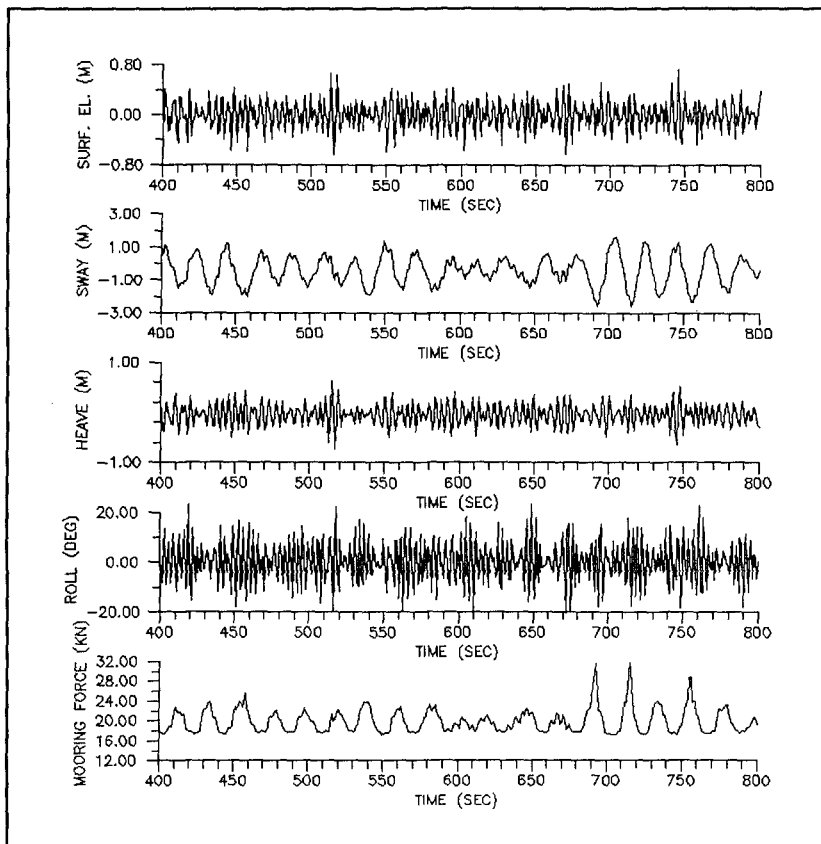


Figure 3. Example Numerical Model Results.

The numerical model results described above are generally consistent with the conclusions presented by Torum et al (1989) who concluded that: (1) floating breakwater sway response was dominated by low frequency motions and (2) mooring line forces were governed by low frequency sway motion and wave frequency roll and heave motions. However, spectral plots of mooring line forces presented in Torum et al (1989) indicate peak spectral energy at or near the wave frequency with a secondary

peak at low frequency. This led Stansberg et al (1990), in a summary of the Torum et al (1989) report, to conclude that mooring line forces were on the average governed by heave and roll motions with extreme events strongly influenced by low frequency sway peaks. The numerical model presented in this paper indicates that mooring line loads are dominated by horizontal sway motions. Additional analyses will be required to evaluate the apparent discrepancies between the sway motion and mooring line force spectra presented in Torum et al (1989).

Prototype Measurements. The numerical model was used to estimate the mooring line loads recorded during the Floating Breakwater Prototype Test Program. Hydrodynamic coefficients and wave transfer functions were computed in the same manner as described above for the physical model. Wave transmission coefficients measured in the physical model tests of Torum et al (1989) were used to estimate the second order wave transfer functions for the prototype structure. Mooring line load-deflection characteristics were estimated on the basis of the field pull tests described in Nelson and Broderick (1986).

Example numerical model results are presented in Figure 4 for an incident significant wave height of 1.29 feet and a peak spectral period of 2.75 seconds. Numerical computations were performed for a total simulation time of 540 seconds to correspond with the results presented in Nelson and Broderick (1986). The results presented in Figure 4 for the prototype breakwater are similar to those presented in Figure 3 for the scale model breakwater. Specifically, breakwater sway response and attendant mooring line force is primarily at low frequency near the natural period of sway motion while the breakwater response in heave and roll is at a frequency corresponding to the incident wave. The maximum mooring line load measured for these wave conditions was 6,346 pounds (28.3 kilonewtons) while the numerical model prediction was 6070 pounds (27.0 kilonewtons). Similar results were found for other numerical model-prototype measurement comparisons.

CONCLUSIONS

A numerical model for dynamic analysis of floating breakwater mooring systems has been presented. Comparisons of numerical model results with physical model and prototype measurements indicate that the numerical model provides reasonable estimates of floating

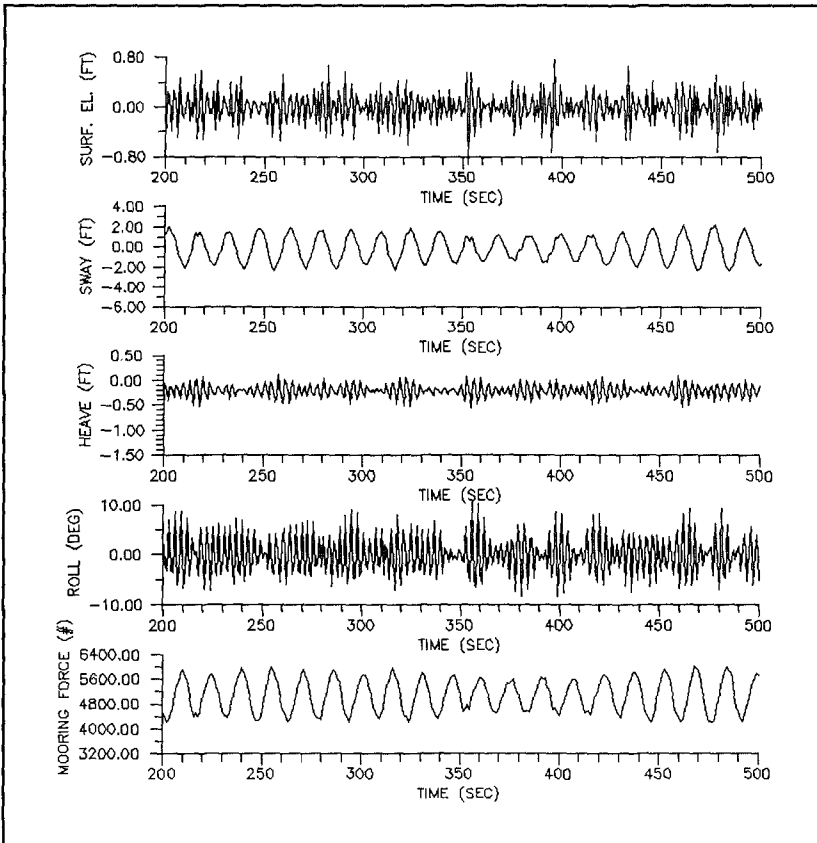


Figure 4. Example Numerical Model Results

breakwater mooring line forces for planning and design use. Moreover, the numerical model can be used as a planning tool prior to physical model studies of final floating breakwater mooring configurations. Additional studies, involving systematic physical model tests, will be necessary to reduce uncertainties associated with: (1) computation of the hydrodynamic coefficients, wave transfer functions, and applied wave force time histories, and (2) importance of roll and heave motions on mooring line loads.

REFERENCES

Adee, B.H., Richey, E.P. and Christensen, D.R., "Floating Breakwater Field Assessment Program, Friday Harbor,

- Washington," Coastal Engineering Research Center, Technical Paper No. 76-17, October, 1976.
- Borgman, L.E.**, "Ocean Wave Simulation for Engineering Design," ASCE WWH, November, 1969.
- Georgiadis, C. and Hartz, B.J.**, "A Computer Program for the Dynamic Analysis of Continuous Floating Structures in Short Crested Waves," Harris Hydraulic Laboratory, Technical Report No. 4, University of Washington, April 1982.
- Gerritsma, J. and Beukelman, E.**, "Analysis of the Resistance Increase in Waves of a Fast Cargo Ship," International Ship Building Progress, Vol. 19, No. 219, September, 1972.
- Kaplan, P.**, "Technical Manual for SCORES II Program-NCEL Finite Depth Version," Report No. 89-77A, January, 1989.
- Longuet-Higgins, M.S.**, "The Mean Forces Exerted by Waves on Floating or Submerged Bodies with Applications to Sand Bars and Wave Power Machines," Proc. R. Soc. Lond. A. 352, 463-480, 1977.
- Miller, R.W., Christensen, D.R., Nece, R.E., and Hartz, B.J.**, "Rigid Body Motion of a Floating Breakwater: Seakeeping Predictions and Field Measurements," Water Resources Series, Tech. Rept. No. 84, U. of Washington, Department of Civil Engineering, February, 1984.
- Nelson, E.E. and Broderick, L.L.**, "Floating Breakwater Prototype Test Program: Seattle, Washington," MP CERC-86-3, Coastal Engineering Research Center, U.S. Army Waterways Experiment Station, March, 1986.
- Newman, J.N.**, "The Drift Force and Moment on Ships in Waves," J. of Ship Research, March, 1967.
- Pinkster, J.A.**, "Low Frequency Second Order Wave Exciting Forces on Floating Structures," Publication No. 650, NSMB, Wageningen, Netherlands, 1980.
- Van Oortmerssen, G.**, "The Motions of a Moored Ship in Waves," NSMB, Wageningen, Netherlands, 1976.
- Wichers, J.E.W.**, "A Simulation Model for a Single Point Moored Tanker," Publication No. 797, MARIN, Wageningen, The Netherlands, 1988.
- Seelig, W.N.**, personal communication, July, 1990.
- Stansberg, C.T., Torum, A., and Naess, S.**, "On a Model Study of a Box Type Floating Breakwater," PIANC, Osaka, Japan, May, 1990.
- Tekmarine, Inc.**, "Development and Verification of Numerical Models for Floating Breakwaters," Coastal Engineering Research Center, U.S. Army Waterways Experiment Station, December, 1986.
- Torum, A., Stansberg, C.T., Ottera, G.O., and Slattelid, O.H.**, "Model Tests on the CERC Full Scale Test Floating Breakwater," Final Report, Norwegian Marine Technology Research Institute, MT51 89-0153, June, 1989.

CHAPTER 100

WAVE-INDUCED PORE PRESSURE IN RUBBLE MOUND BREAKWATERS

Oumeraci, H.; Partenscky, H.W.¹

Abstract

Experimental results from large scale tests are presented for the distribution of wave-induced pore pressure within rubble mound breakwaters, for the reflection coefficients and the damping of wave motion through the armour and under-layer. The results are then discussed with respect to application and further research.

1. Introduction

Previously, the effects of the internal flow field on the armour and geotechnical stability of rubble mound breakwaters were largely ignored. A brief literature review /3/ as well as recent hydraulic and numerical model investigations /14; 7; 1/ highlighted the importance of the motion of pore water for a better understanding of the geotechnical behaviour and of the external flow on and in the armour layer.

At present, numerical modelling efforts appear to be directed towards the elaboration of an integrated code which should describe wave action on and within the breakwater as well as its effect on armour stability.

Considering the present knowledge of scale effects /8; 13; 4/ and owing to the fact that the loading parameters are not controllable under prototype conditions, measurements from large scale model tests at present represent the most suitable data for calibration and verification. Thus, it is one of the main objectives of this paper to provide the necessary information for this purpose.

¹Franzius-Institute, University of Hannover, Germany

2. Oscillatory Flow in Porous Media-Theory

When a wave approaches a non-overtopped rubble mound breakwater, part of the incident energy E_i is dissipated on and within the structure (E_d), part is reflected (E_r) and the rest is transmitted (E_t) through the breakwater:

$$E_i = E_d + E_r + E_t, \quad (1)$$

The dissipated energy (E_d) can in turn be divided in three distinct parts: the energy dissipated on and in the armour layer (E_{da}), the energy dissipated in the under layer filter (E_{df}) and the energy dissipated within the core (E_{dc}):

$$E_d = E_{da} + E_{df} + E_{dc} \quad (2)$$

Most of the studies available on waves in rubble mound breakwaters are directed more toward the determination of averaged transmission and reflection coefficients than toward the understanding of the internal wave motion; i.e. the porous structure is often considered as a kind of a black box system.

Theoretical work which actually deals with the internal oscillatory flow induced by waves was mostly related to the study of permeable wave absorbers and wave filters /2; 9; 11/. In this respect, BIESEL /2/ was the first to identify the form of the spatial and temporal relationships which describe a linearly damped, oscillatory flow. LE MEHAUTE /10/ continued BIESEL's work and applied it to rubble mound breakwaters.

The investigations of BIESEL /2/ and LE MEHAUTE /10/ are considered here because a) they constitute the first attempts to describe wave motion in porous media and b) almost no significant advances on their fundamental approach have been made since then.

A general linearized BERNOULLI equation for an oscillatory flow in a wave filter based on the NAVIER-STOKES equation has been derived by BIESEL /2/.

A parameter $k_v = D/n$ was introduced in this equation by LE MEHAUTE /10/ to account for the porosity n and inertia effects (D) of the porous material:

$$\frac{p}{\rho} + k_v \frac{\partial \phi}{\partial t} + g y + c_f \phi = \text{const.} \quad (3)$$

The time derivative of equ. (3), together with $\frac{\partial y}{\partial t} = \frac{1}{n} \frac{\partial \phi}{\partial y}$ and $p = \text{const.}$ at the free surface $y = f(x,t)$ yields:

$$k_v \frac{\partial^2 \phi}{\partial t^2} + \frac{g}{n} \frac{\partial \phi}{\partial y} + c_f \frac{\partial \phi}{\partial t} = 0 \quad (4)$$

where:

- g = acceleration of gravity
 p = pore pressure
 ρ = water density
 c_f = linearized friction coefficient
 ϕ = potential function of a 2D-wave travelling through a porous medium with a porosity n and subject to a friction force $\vec{F}_R = -c_f \cdot g \vec{\text{grad}} \phi$
 t = time
 x, y = coordinates (Ox-axis is at SWL and Oy-axis is positive upward)

Considering the continuity equation $\Delta \phi = 0$ and the boundary condition at the depth $y = -h$, the following particular solution of equ. (4) is obtained.

$$\phi = \frac{H_w}{2} e^{-\beta k x} \frac{\omega}{k \sinh k h} \left| \cos \beta k (h+y) \cosh k (h+y) \sin (kx - \omega t) + \sin \beta k (h+y) \sinh k (h+y) \cos (kx - \omega t) \right| \quad (5)$$

where:

- H_w = incident wave height at the outer boundary of the porous medium ($x = 0$)
 h = water depth
 k = $2\pi/L'$: wave number
 L' = wave length within the breakwater
 ω = $2\pi/T$: angular wave frequency
 T = wave period
 β = damping coefficient

The wave length L' within the rubble mound breakwater is related to the length L of the incident wave as follows /10/:

$$L' = L/\sqrt{D} \text{ for } h/L < 0,5 \quad (6)$$

where:

$$L = \frac{gT^2}{2\pi} \tanh \frac{2\pi h}{L} \quad (7)$$

- D : Coefficient characterising the relative increase of the seepage length as a result of the deviation of the flow path caused by the presence of the grains. An empirical value $D \approx 1.4$ was given by LE MEHAUTE /10/, whereas a value $D = 1.5$ was determined theoretically by MICHE /12/.

It follows from equ. (5) and (6) that the height of the pressure oscillation $p(x)$ of a wave travelling through a rubble mound breakwater in the x -direction will decrease exponentially according to the following expression:

$$p(x) = p_0 \cdot e^{-\beta \frac{2\pi}{L'} x} \quad (8)$$

where p_0 = pore pressure at $x = 0$

3. Experimental Set-up and Test Procedure

3.1 Description of the breakwater model

The rubble mound breakwater model tested and the experimental set-up have already been described in a previous paper /3/. The cross-section of the large scale model with the position of the pressure cells and the run-up gauges is shown in Fig. 1.

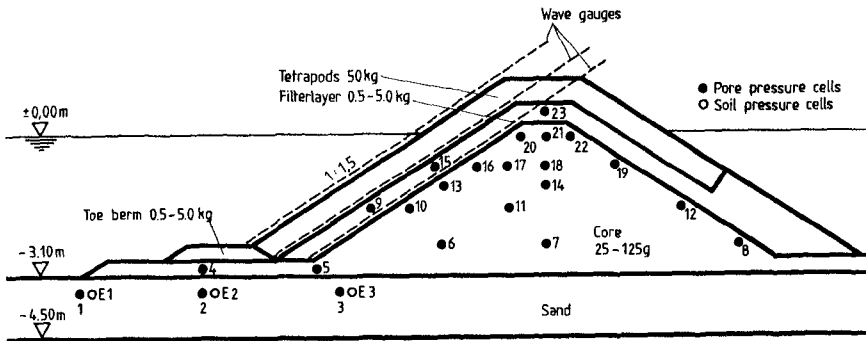


Figure 1. Large scale model of the investigated breakwater

The grain size distribution of the core material used in the model is given in /3/.

The mean diameter is $d_{50} \approx 4$ cm and the uniformity coefficient $U = \frac{d_{60}}{d_{10}} \approx 2.2$. For the wave heights tested the REYNOLDS number related to the grain size is in the range $Re = 5 \cdot 10^4$ to 10^5 ; i.e. scale effects due to viscous flow within the core material can be neglected /13/.

3.2 Test programme and procedure

For each test series the wave period was kept constant, whereas the wave height was increased after each test.

Monochromatic waves with heights up to 2.0 m and periods $T = 3 - 8$ s, as well as irregular waves with significant heights up to 1.0 m and peak periods $T_p = 3 - 8$ s have been used. In addition, 4 test series with the most critical peak period ($T_p = 4.5$ s) were carried out for groupiness factors $GF = 0.6, 0.7, 0.8$ and 0.9 in order to investigate the effect of wave grouping on wave run-up, internal pressure build-up and armour stability.

During the tests, attention has been placed on observations of armour stability as well as on simultaneous measurements of incident waves, pore pressure distribution and wave run-up on the slope of the armour, filter layer and core material.

4. Experimental Results

4.1 Wave reflection

The incident and reflected waves have been determined by means of the commonly used 3-wave gauge procedure. For the range of wave conditions tested, the reflection coefficient K_R is given in Fig. 2 as a function of the surf similarity parameter ξ .

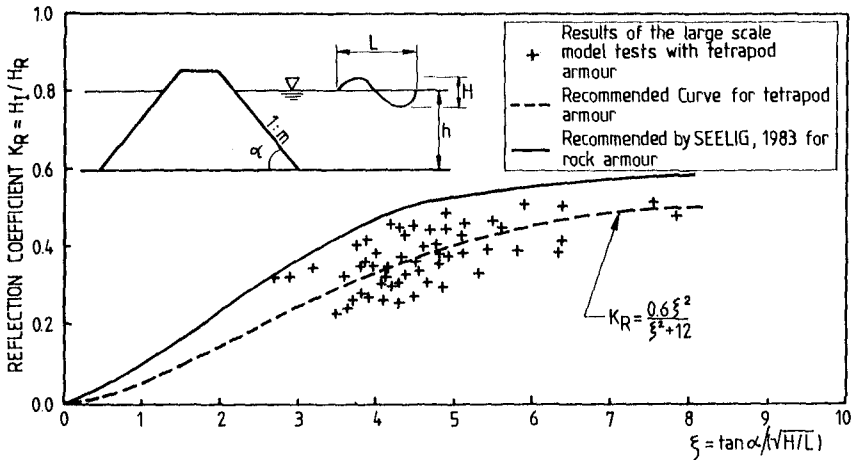


Figure 2. Reflection coefficient K_R vs. surf similarity parameter ξ

The reflection coefficients obtained ($K_R = 0.20 - 0.45$) correspond to the values given by SOFREMÉR and SOGREAH for tetrapods, but are comparatively lower than those given by the empirical relationship derived by CERC /14/ for natural stone armours. The latter appears to rather describe the envelope of the maximum values for the tetrapod armour (Fig. 2).

4.2 Wave damping by the armour and under-layer

The incident waves penetrating into the armour and under-layer as well as into the core are followed by means of 3 wave run-up gauges. They have been specially developed for this purpose and were installed along the slope of the tetrapod armour, of the under-layer and of the core material, respectively ((Fig. 1).

The analysis of the results shows that a considerable part of the incident wave energy is dissipated not only by the armour but also by the under-layer. The degree of dissipation is strongly dependent on the magnitude of the similarity parameter ξ . The smaller this parameter, the more pronounced is the energy dissipation. For instance, the drop of the relative wave height when the wave passes through the armour layer varies from about 30 % to 60 % for surf similarity parameters $\xi = 5$ and $\xi = 2$, respectively. Considering the total attenuation of wave motion taking place within both the armour and the under-layer, the corresponding values become 60 % to 90 %, respectively (Fig. 3).

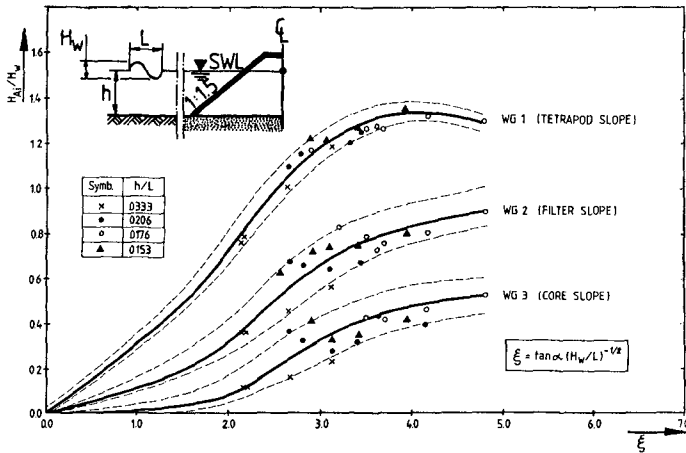


Figure 3. Wave damping by the armour and under-layer vs. surf similarity parameter ξ

The dependence of the energy dissipation on the surf similarity parameter ξ results from the shape of breakers on the outer slope; i.e. spilling and plunging breakers ($\xi \leq 2$) which are associated with a high degree of air entrainment and high impact velocities give the largest damping values, whereas collapsing and surging breakers ($\xi > 2$) yield the lowest ones.

A further result emerging from Fig. 3 is the much lower value of the run-up and run-down heights on the core slope compared to that at the outer slope. This is of importance for the design of the crest level of the core material. However, a set-up of the mean water level inside the breakwater, which may range from 10 to 20 % of the incident local wave height, should be additionally considered.

5. Wave-Induced Pore Pressure

For the measurement of the pore pressure inside the rubble mound breakwater model twenty piezoresistive pressure gauges (Type PDCR NATEC SCHULTHEISS) were installed at different locations (Fig. 1). These locations were selected in such a way that the pore pressure distribution and the boundary values required for the implementation and calibration of numerical models can be gained with sufficient accuracy.

The designation "pore pressure" used in the following is related to the excess pore water pressure which is solely induced by wave action; i.e. all the twenty pressure gauges record zero pressure at still water level (no wave action). Thus, the corresponding hydrostatic pressure head should be added to the recorded pressure values to obtain the total pore water pressure. The terms "pore pressure height" and "pore pressure amplitude" are used on the analogy with waves to designate the height and the amplitude of the pressure fluctuations, respectively.

5.1 Influence of incident wave parameters on pore pressure

5.1.1 Effect of wave height

The effect of the incident wave height on the magnitude of the pore pressure is illustrated for one location in Fig. 4.

Given a wave period and with increasing wave heights the pore pressures first increase rapidly, then at a lower rate, due to higher friction losses associated with larger hydraulic gradients. The pore pressure - wave height curves appear to have a similar shape for the locations and wave periods investigated.

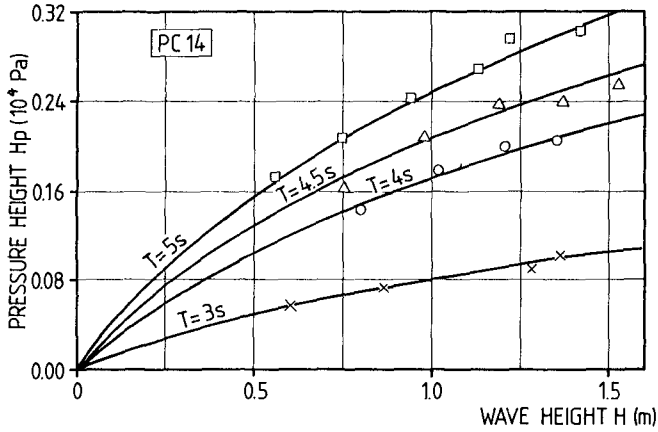


Figure 4. Effect of wave height on pore pressure

5.1.2 Effect of wave period

The effect of the incident wave period on the magnitude of the pore pressure is shown in Fig. 5.

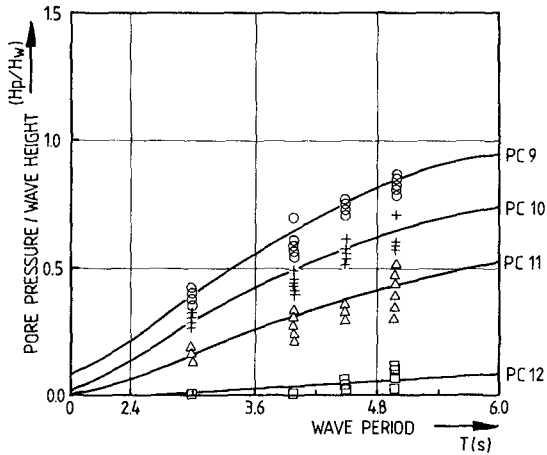


Figure 5. Effect of wave period on pore pressure

Given a wave height and with increasing wave period the pore pressure first increases very slightly, then rapidly and finally at a lower rate.

Similar shapes of pore pressure - wave period curves have been obtained for further locations and various wave heights.

5.2 Spatial distribution of pore pressure

In the following, only the spatial distribution of time averaged values of pore pressure heights is considered. In this respect and for simplification, the horizontal and the vertical distributions are treated separately.

5.2.1 Horizontal pore pressure distribution

In order to verify whether the waves are damped within the breakwater according to the theory outlined in chapter 2, the horizontal plane containing the pressure cells PC 15 to PC 19 is considered (Fig. 1). For this purpose, the ratio between pore pressure $p(x')$ at a distance x' from the origin located at PC 15 ($x' = 0$) and pore pressure p_0 measured at $x' = 0$ is plotted against the relative distance x'/L' .

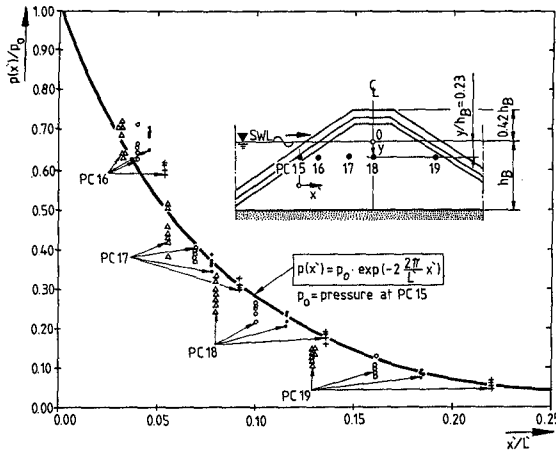


Figure 6. Pore pressure dissipation within the breakwater

For the elevation of the horizontal plane considered, the pore pressure decreases exponentially in the direction of wave propagation according to the following relationship:

$$p(x') = p_0 \cdot e^{-2 \cdot \frac{2\pi}{L'} x'} \tag{9}$$

However, the magnitude of the damping factor β in equ. (8) depends on the elevation of the horizontal plane considered with respect to the still water level (SWL). Further results which will be published in the near future suggest that the lower the location under SWL, the smaller the damping factor β becomes. This can be explained by the friction losses which become smaller as the degree of turbulence decreases, i.e. as the distance from SWL increases.

5.2.2 Vertical pore pressure distribution

The pore pressure does not vary hydrostatically with depth, even in the centre of the breakwater. This may be explained by the dynamic effects which are more pronounced near the front face and just under SWL. In order to identify the relevant parameters which influence the degree of attenuation with depth, the relative pore pressure height $p(y)/H_w$ is plotted against the relative elevation (y/L) under SWL in Fig. 7 for different relative water

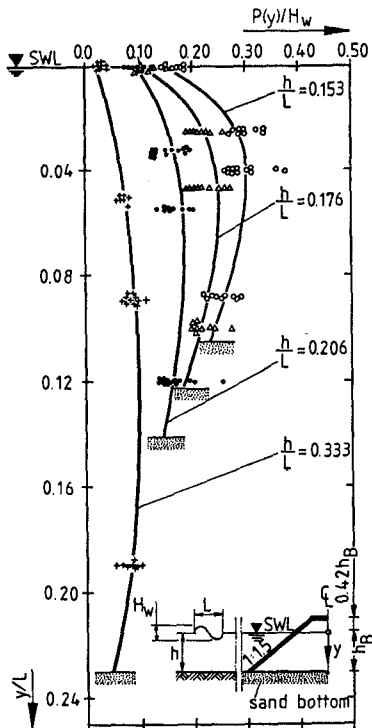


Figure 7. Pore pressure attenuation with depth

depths (h/L). Departing from SWL the pore pressure first increases up to a maximum value with increasing depth, then slightly decreases. The smaller the relative water depth (h/L), i.e. the longer the waves, the higher is the induced pore pressure and the less pronounced is the pressure attenuation.

6. Discussion and Application of the Results

6.1 Reflection coefficient

An accurate evaluation of the reflection coefficient $K_R = \sqrt{E_r/E_i}$ is important, since it is the remaining energy $E_{dt} = E_d - E_t$ (see equ. (1)) which represents the input for the study of energy dissipation on and in the breakwater. Thus rewriting equ. (1) as:

$$E_{dt} = E_d + E_t = (1 - K_R^2)E_i, \quad (10)$$

it follows from the relationship obtained in Fig. 2 that E_{dt} may amount to 80 - 96 %, depending on the surf similarity parameter ξ . For the range of common ξ -values this relationship can be used for tetrapod armours. It is suggested, however, that future work should focus upon the development of more suitable measuring techniques and methods for the determination of reflection coefficients, since the 3 wave gauge procedure commonly used is still not satisfactory.

6.2 Energy dissipation through armour and under-layer

The results shown in Fig. 3 represent the first attempts to follow the wave motion from the sea-structure interface to the core. For this kind of investigation, small-scale model tests are not suitable because of the dissimilarity of air entrainment resulting from breaking waves and flow separation. For the importance of air content for energy dissipation on and in the breakwater see chapt. 6.4. A reliable evaluation of the rate of energy dissipation through the first layers does not only provide the necessary boundary conditions for resolving the equations of motion in numerical codes, but also helps in assessing the forces on armour units.

Together with the relationship given in Fig. 2, the results presented in Fig. 3 allows the evaluation of the different energy components involved in equ. (1) and (2). For instance, given a surf similarity parameter $\xi = 4$, the reflected energy is $E_r = 12$ %, the energy dissipated on and in the armour layer $E_{da} = 54$ %, the part dissipated in the under-layer $E_{df} = 23$ % and the remaining part which

is finally transmitted into the breakwater core is only 11 % of the total incident wave energy.

These results implicitly highlight the importance of the armour and the under-layer for energy dissipation and the question which may arise if a single armour layer is used or an under-layer is omitted.

6.3 Attenuation of pore pressure within the breakwater

The experimental results presented here generally give much higher pressure values when compared to the results from available numerical codes /1; 5; 6/. This is mainly due to the fact that the dynamic component of the pore pressure has not been well accounted for. The latter, however, represents an important part of the total wave-induced pore pressure, particularly in the region under SWL and near the front face where it is more dominant.

6.4 Some remarks on scale effects

The limitations of common small scale model tests when investigating wave energy dissipation on and within rubble mound breakwaters are due to the impossibility of simultaneously fulfilling the similitude criteria of FROUDE, WEBER and REYNOLDS.

a) Scale effects due to the dissimilarity of WEBER's number

The rate of air entrainment into the armour and under-layer resulting essentially from wave breaking, and to a lesser extent from flow separation, is generally higher in prototype; i.e. the rate of wave energy dissipation through the armour and under-layer is lower in the model. The relationship between air entrainment and energy dissipation in breaking waves has already been treated by FÜHRBÖTER /4/. In addition, it has been observed (video records) that a large amount of air bubbles are often driven into the core by breaking waves. The effect of air content α in the two-phase internal flow, however, is known to cause a reduction of the effective hydraulic conductivity of the porous medium /6; 5/:

$$K_{aw} = K_w (1 - \alpha)^3 \quad (11)$$

where K_{aw} , K_w : two-phase and single-phase hydraulic conductivity, respectively.

This means that an air fraction α of only 10 % may cause a reduction of more than 25 % in the hydraulic conductivity. This in turn will considerably reduce the rate of pore pressure attenuation.

- b) Scale effects due to the dissimilarity of REYNOLDS' number

The use of small-scale models generally results in a lower permeability of the core material. This effect is additionally reinforced by the afore mentioned dissimilarity in air entrainment, thus leading to too high viscous forces in the model and affecting the flow regime within the breakwater. A lower rate of energy dissipation will result. This subject has been treated by OUMERACI /13/ and JENSEN et al. /8/.

7. Concluding Remarks and Perspectives

The present results may be used to estimate reflection, run-up and run-down heights as well as the rate of attenuation of a wave as it propagates into a tetrapod armoured breakwater. However, it should be kept in mind that these results present only a small part of a considerable set of data obtained from systematic tests in large and small-scale models which are now being analysed.

Evaluating in a more systematic and fundamental manner the different energy components in equ. (1) and (2) in order to better understand the complex processes of wave energy dissipation on and in rubble mound breakwaters will be the topic of a forthcoming paper. In addition, an attempt will be made to improve the theory presented in chapter 2. However, in view of the variety and complexity of the interrelated processes involved, like wave breaking and air entrainment, virtual mass effects, non-linearity and unsteadiness of the flow together with the uncertainties in the hydraulic properties of the different breakwater layers, it seems obvious that reliable analytical solutions cannot be developed in a straightforward manner. Therefore, the research strategy adopted at the University of Hannover consists in the development of a reliable integrated numerical code which will be calibrated by the data from the large-scale tests and then used as a research tool, the ultimate objective being the development of analytical solutions.

8. Acknowledgements

This investigation is part of an extensive basic research programme in coastal engineering (SONDERFORSCHUNGSBEREICH 205) which is supported by the German Research Council (DFG).

8. References

1. BARENDS, F.B.T.: "Geotechnical aspects of rubble mound breakwaters". - ICE, Proc. Conf. Breakwater '85, London 1986.
2. BIESEL, F.: "Equations de l'écoulement non lent en milieu perméable". - La Houille Blanche No 2, 1950.
3. BÜRGER, W.; OUMERACI, H.; PARTENSKY, H.W.: "Geo-hydraulic investigations on rubble mound breakwaters". ASCE, 21st ICCE, Torremolinos/Spain.
4. FÜHRBÖTER, A.: "Über die Bedeutung des Luftschlages für die Energieumwandlung in Brandungszonen". - Mitteilungen d. Franzius-Instituts, Univ. Hannover, H.36, 1971.
5. HALL, K.R.: "A study of the stability of rubble mound breakwaters". - Ph.D. Thesis, Univ. New South Wales/Australia, 1987.
6. HANNOURA, A.A.: "Numerical and experimental modelling of unsteady flow in rockfill embankments". - Ph.D. Thesis, Univ. Windsor, Ontario/Canada, 1978.
7. HÖLSHER, P.; DE GROT, M.B.; VAN DE MEER, J.W.: "Simulation of internal water movement in breakwaters". - IAHR, SOWAS-Symposium, Delft 1988.
8. JENSEN, O.J.; KLINTING, P.: "Evaluation of scale effects in hydraulic models by analysis of laminar and turbulent flow". - Coastal Eng. Elsevier, Vol. 7, 1983.
9. LEAN, G.H.: "A simplified theory of permeable wave absorbers". - IAHR, J. Hydr. Res., 5 (1967) No 1.
10. LE MEHAUTE, B.: "Perméabilité des digues en enrochements aux ondes de gravité periodiques". - La Houille Blanche No 6, 1957 & No 2, 3, 1958.
11. LE MEHAUTE, B.: "Progressive wave absorber". - IAHR, J. Hydr. Res. 10 (1972) No 2.
12. MICHE, R.: "Recherches théoriques sur les écoulements de filtration non permanents". - 5^e Journées de l'Hydraulique, 1960.
13. OUMERACI, H.: "Scale effects in coastal hydraulic models". - IAHR Symp. on scale effects in modelling hydr. structures, Esslingen, 1984.
14. SEELIG, W.N.: "Wave reflection from coastal structures". ASCE, Proc. Conf. Coastal Structures, 1983.
15. SIMM, J.D.; HEDGES, T.S.: "Pore pressure response and stability of rubble mound breakwaters". - ICE, Breakwater '88, London 1988.

CHAPTER 101

REDUCTION OF WAVE FORCES AND OVERTOPPING BY SUBMERGED STRUCTURES IN FRONT OF A VERTICAL BREAKWATER.

B. González Madrigal (1)
J. Olivares Prud'Homme (2)

1.- ABSTRACT:

This paper describes some of the results obtained from a series of model tests to measure wave forces and overtopping in a vertical breakwater located in a surf zone. The aim of the tests was to better design conditions using submerged structures. With the sections proposed in this study, it is possible to achieve a considerable reduction in wave forces and overtopping on vertical breakwaters.

2.- INTRODUCTION

Most vertical breakwaters in Spain have been constructed at depths where breaking does not occur. It is a well known fact that the wave pressure to which a vertical breakwater is subject in breaking conditions, is much greater than when such conditions are absent, so the design conditions vary considerably. As a result of this, some solutions, including vertical breakwaters with block mounds, have been developed with a view to dissipating energy. Nevertheless, these solutions have not taken into account their possible use for recreational purposes, such as Marinas; in these cases, the question of aesthetics is fundamental as regards the impact that they might have on the coastal environment.

Recently, the C.E.P.Y.C. has carried out tests on a series of sections subject to irregular waves, with a view to improving design conditions for a vertical breakwater situated in a surf zone. The various options studied, are

(1) Head of Maritime Structures Division, Centro de Estudios de Puertos y Costas, (CEPYC-CEDEX), Antonio Lopez 81, Madrid 28026, Spain.

(2) Research Engineer, Centro de Estudios de Puertos y Costas, (CEPYC-CEDEX), Antonio Lopez 81, Madrid 28026, Spain.

based on the geometrical variation that crowns the caisson and on the inclusion of submerged elements in front of the vertical face breakwater, which modify the conditions of the incident wave. These elements consist of a submerged breakwater and rubble toe protection with a small rubble fill between them.

These tests were made for the Marina breakwater at the Olympic Village in Barcelona, whose technical engineers proposed different test solutions. In addition to this work, a series of complementary tests were carried out in order to obtain further information concerning the overtopping rate.

3.- TEST CONDITIONS

The tests took place in a tank with an overall length of 45 m, 6.5 m wide and 0.80 m deep, at the C.E.P.Y.C. laboratories in Madrid.

A channel 1.3 m wide was placed inside the tank, into which the test section was located, facing the normal direction of the wave propagation generated by the paddle.

The depth of the water at the foot of the paddle was 0.70 m, so as to guarantee wave generation in acceptable conditions, and the depth at the foot of the test section was 0.225 m, with a 1:30 gradient at the bottom. A 1:40 scale was used in the tests.

A dynamometer was used for measuring the wave forces, whose ranges of measurement were:

F_x and F_y : 40 Kp (Model units)
 M : 600 Kp.cm (Model units)

As regards the measurement of the overtopping, which included: the amount of these expressed in terms of the number of waves contained in the wave recording, the height reached by the "sheet" of water above the crown and the volume of water that overtopped, we would say that, the recordings of the first two cases were carried out using a device designed in the C.E.P.Y.C., consisting of a transducer made up of a fibreglass plate on which a printed circuit was attached, this being connected to a series of electrodes 1 cm apart. As the water flowed over them, the circuit closed and thus provided the overtopping height (in centimetres) as a sum of the wet electrodes, the abovementioned overtopping also being counted in the overall calculation. The measurement of the volume of water which overtopped was achieved, by a tray attached to the

rear part of the section. The results of this volume are given per linear metre of section of breakwater and per second ($m^3/m/s$).

The output of the analogical signals from the dynamometer and the overtopping gauge are conditioned afterwards, by means of an A/D convertor and digitalized so that they can be read by a computer. A description of of this process is shown in Figure 1.

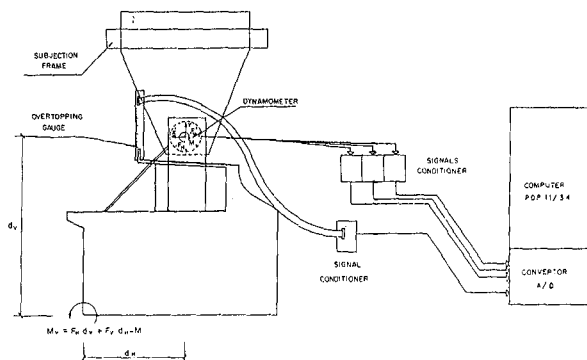


Figure 1. Measures diagram

The tests were carried out in three types of storm conditions, adjusted to a theoretical spectrum of the J.O.N.S.W.A.P. kind, whose characteristics are similar to those that occur in the Spanish Mediterranean; the wave conditions of these storms, are shown in table 1.

Where:

Gamma is the peak enhancement factor of the Jonswap spectrum, T_p is the peak period of the wave spectrum in seconds and H_s is the significant wave height in metres. The calibrated test waves correspond to records of 300 to 325 waves.

STORM	T_p (s)	H_s (m)	GAMMA
I	10	6, 7.5	3.3
II	12	6, 7.5	3.3
III	14	6, 7.5	3.3

Table 1.

On considering the depth of the toe of the structure $d = 10.20$ m, the bed slope $m = 0.033$ and the three peak periods of the storms, it could be concluded that the structure under the different wave calculations, would be subjected to unbroken waves, broken waves and breaking waves, critical conditions being given for waves that break or which are at breaking point over the vertical facing.

4.- PROCEDURE

The sequence of tests was developed in four distinct stages, each one constituting an approximation to the optimization of the section for the design wave conditions

The First Stage, consisted of testing three vertical breakwaters with the same crown height $h_c = 8.4$ m (which did not vary during the different test stages), but having different crown shapes, these included solutions 1,2,3. Figure 2.

The storms that these structures were subjected to were storms I and III, shown in Table 1.

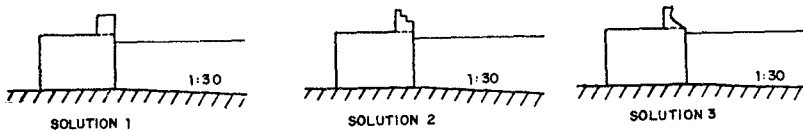


Figure 2. First stage solutions

The second stage consisted of placing a submerged breakwater that would serve as a filter to the incident wave, causing it to break, so that the wave forces and overtopping at the vertical breakwater would be reduced, Figure 3. Initially, the solutions tested were 4, 5 and 6, that vary as regards the distance between the transversal axis of the submerged breakwater and the wall of the vertical breakwater (L) and the crown height of the submerged breakwater (C_c). After this, and with a view to observing the degree of operativity of the combination vertical breakwater - submerged breakwater, complementary overtopping measurements were carried out with the solutions 4a, 4b, 4c, 5a and 6a, whose characteristics can be seen in Table 2.

The wave conditions tested, corresponded to storms II and III in Table 1, with steps for significant waves of 4, 5, 6 and 7.5 metres.

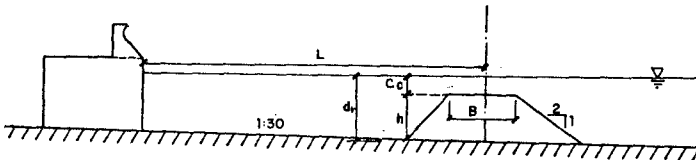


Figure 3. Second stage solutions

SOLUTION	B(m)	Cc(m)	L(m)	dr(m)	ct	tp	Fill
1	-	-	-	-10.2	1	-	-
2	-	-	-	-10.2	2	-	-
3	-	-	-	-10.2	3	-	-
4	18	-3.5	60	-10.2	3	-	-
4A	18	-2.5	60	-10.2	3	-	-
4B	12	-3.5	60	-10.2	3	-	-
4C	12	-2.5	60	-10.2	3	-	-
5	18	-3.5	85	-10.2	3	-	-
5A	12	-3.5	85	-10.2	3	-	-
6	18	-2.5	85	-10.2	3	-	-
6A	12	-2.5	85	-10.2	3	-	-
7	18	-2.5	60	-10.2	3	Y	-
8	18	-2.5	60	- 6.0	3	Y	Y
9	18	-2.5	60	- 4.0	3	Y	Y
10	18	-1.5	60	- 4.0	3	Y	Y
11	18	-1.5	60	- 6.0	3	Y	Y
12	30	-2.5	66	- 6.0	3	Y	Y
13	30	-1.5	66	- 6.0	3	Y	Y
14	30	-1.5	66	- 4.0	3	Y	Y
15	30	-2.5	66	- 4.0	3	Y	Y
16	18	-2.5	60	- 6.0	2	-	Y
17	30	-2.5	66	- 6.0	2	-	Y

TABLE 2.

The Third stage was made up by solutions 7 to 15, and consisted of placing rubble toe protection at the base of the vertical breakwater. As regards the submerged breakwater, the geometrical parameters were varied: Cc, L and B, as well as considering rubble of 8 Tons and different parallelepiped concrete block weights on the crown. Fillings of different depths (dr) were tested between the submerged breakwater and the attached rubble, Figure 4 and Table 2.

The test storms were those referred to as II and III in Table 1.

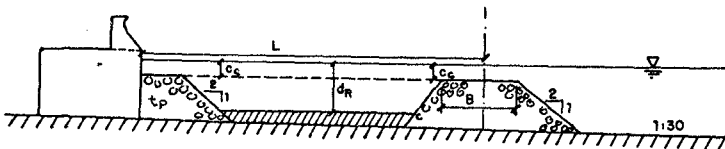


Figure 4. Third stage solutions

The Fourth Stage, comprised solutions 16 and 17. It consisted of testing a tiered superstructure of the type used in solution 2, but occupying the whole width of the caisson. Likewise, the protective rubble attached to the vertical breakwater was removed, one sole thickness of

filling being considered, the variation between the two solutions referred to being determined by the crown width of the submerged breakwater, B, Figure 6 and Table 2.

The test waves at this stage, were storms II and III from Table 1 with step heights for significant waves of 4, 5, 6 and 7.5 metres.

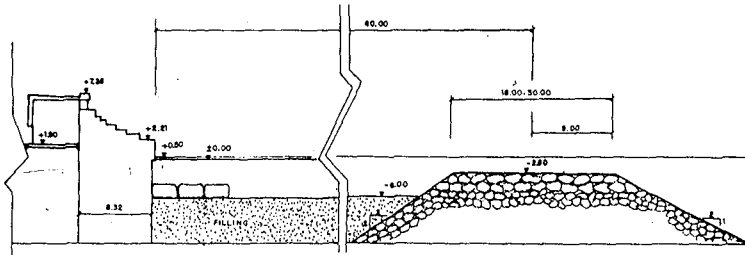


Figure 5. Fourth stage solutions

5.- WAVE FORCE ANALYSIS

The analysis of the results as far as the wave forces is concerned, will only be carried out for the maximum horizontal force recorded by the dynamometer throughout the length of each one of the tests, these being characterized by significant wave height and a specific peak period.

The analysis will be made for the solutions included in each one of the stages outlined in section 4. and, finally all the solutions will be compared as a whole.

The maximum horizontal forces of the first group of tests, corresponding to the first three solutions, can be seen in Figure 6.

The results clearly show, a reduction in the resulting force, undergone in solutions 2 and 3, that at the height +2 present a sloping and tiered surface at the crown of the section, by contrast to solution 1, which has a totally vertical surface. At the same time, the influence of the peak period in the value of the wave force, is clearly shown.

The reduction referred to, as is known, is a result of the lag that exists between the wave action on the two surfaces of the structure; i.e.: that of the caisson, totally vertical, and the tiered sloping surface of the crown. Likewise, the discontinuity that is implied in the sloping plane, also prevents high pressures, known as impulsive breaking wave pressures, from being brought to bear, because they occur slightly above the still water level (S.W.L.); however, this kind of pressure does feature in solution 1, as all the necessary conditions are present.

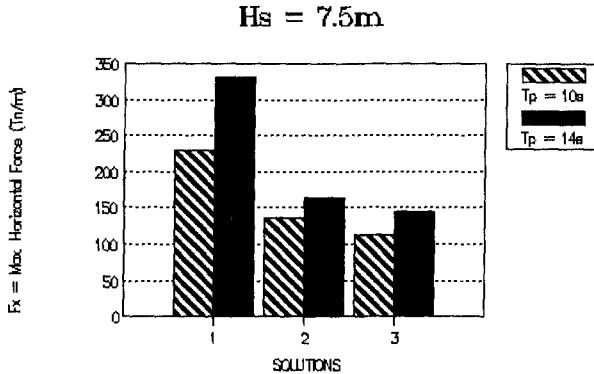


Figure 6. Results from first stage.

Mitsuyatsu (2) demonstrated, on the basis of a series of systematic experiments that, where there is no rubble mound breakwater foundation and as long as the breaking of the wave occurs in front of a vertical wall, impulsive breaking wave pressure could be brought to bear if the sea bed were equal to or greater than 3% and the wave incidence angle were below 20° , as is the case in solution 1.

Nevertheless, in spite of the considerable reduction in the wave force in solutions 2 and 3, as compared to solution 1, neither of the two can be considered acceptable from the viewpoint of values of the safety factors required for the sliding and overturning of a particular caisson, this having been previously designed. So various options were designed in front of the breakwater and this gave rise to the subsequent stages that were commented upon in section 4.

Solutions 4, 5 and 6 made up the second stage of the present work. The results, as far as the maximum horizontal force is concerned, are shown in Figure 7.

The differences that exist between the results, are determined by the variation in depth of the crown of the submerged breakwater (C_c) and by the length (L) between the vertical face of the caisson and the axis of the submerged breakwater.

It can be observed from the comparison of results, how length (L) is the most influential of the abovementioned parameters, while C_c , at least as regards the experimented values (a difference of 1 m), hardly undergoes any variation, if the respective values of solutions 5 and 6 are observed.

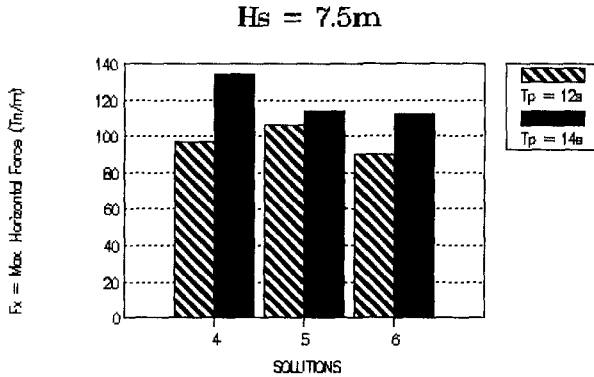


Figure 7. Results from second stage

The reduction in the maximum horizontal force, as a result of the submerged breakwater, in the three solutions, with respect to solution three in the first stage, this serving as a reference, is 8.3 %, solution 4, 18 %, solution 5 and solution 6, 22.75 %. In spite of the reduction in two of the cases being significant when compared to solution 3, it still does not meet the safety factor values that are required for the specific caisson.

The analysis of the next group of tests, belongs to the third stage, and the different solutions are characterized, as was mentioned in section 4, by the variation in some of the geometrical parameters of the submerged breakwater, as a result of a rubble toe protection at the vertical breakwater and by a filling between both breakwaters: vertical and submerged.

The results of this stage can be seen in Figure 8. It can be said that the filling at height -6 m , barely influenced the dissipation of the incident wave energy, once this passed over the submerged breakwater, which can be seen from the values of the figures that correspond to solutions 7 and 8; nevertheless, the same filling, increasing the crown height by 2 m to -4 m , brought about a reduction that lies in a range that goes from 8.5 % to 14 % (compare with solutions 8-9, 13-14 and 12-15).

Solutions 10, 11, 13 and 14 were tested by placing one single layer of parallelepiped elements of concrete blocks of different weights on the crown of the submerged breakwater; as regards this, it could be said that solutions 10 and 11, with respective weights of 20 Tn and 25 Tn , gave worse results than those others where 8 Tn quarry stone units were used on the crown, through the absence of interlocking between the concrete units and, as a result, there was an increase in damage once the first.

test waves attacked: this caused a reduction in the crown height.

45 Tn elements were placed for solutions 13 and 14. Such a great weight difference gave rise to a decrease in the damage and caused an improvement in behaviour, as far as the recording of maximum horizontal force was concerned, and when compared to solutions 10 and 11, although the crown height width went up from $B = 18$ m to $B = 30$ m.

The influence of parameter B in the stretches being tested, can also be seen when comparing the results of solution 8 and solution 12, the latter undergoing a reduction in wave force of 16.6 %.

$H_s = 7.5$ m

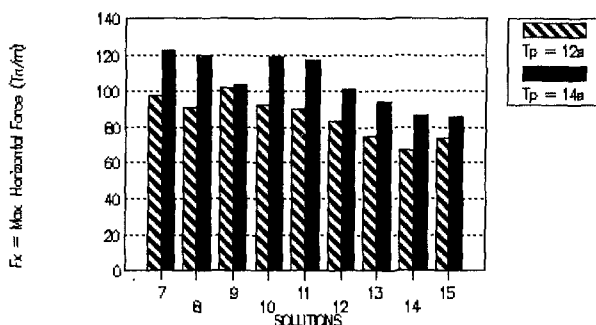


Figure 8. Results from third stage

In the last solutions to be tested, 16 and 17, the configuration of the caisson superstructure was changed, its profile being completely tiered, as can be seen in Figure 5. In addition to this, the rubble attached to the caisson toe was removed, the filling being retained.

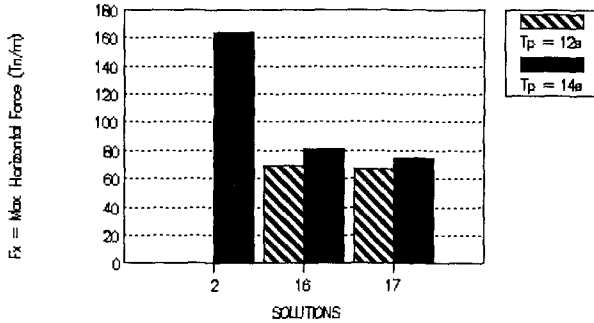
The results of these solutions can be seen in Figure 9. The result of solution 2, that corresponds only to the caisson with tiered superstructure, is also shown. The reduction of the maximum horizontal force exceeds that of solution 2 in both, and by more than 50 %. The different crown widths of the submerged breakwater, $B = 18$ m and $B = 30$ m that were tested, determine the variation in the results of solutions 16 and 17.

In the light of these results, solution 16 was chosen as the definitive one, that on the basis of the maximum simultaneous wave forces recorded on the dynamometer, complied with the advisable and authorised safety factors in the practice, in accordance with the caisson width that had been previously adopted.

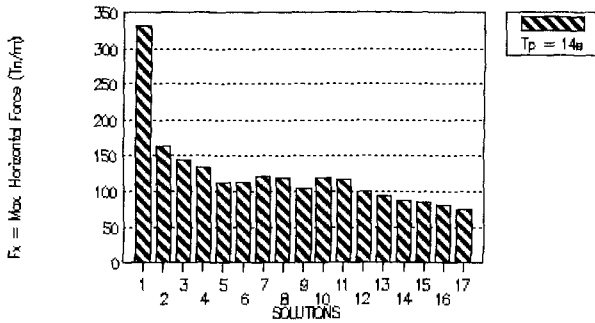
Finally, Figure 10 shows all the results of each one of the solutions tested, corresponding to the maximum horizontal force reached in every one of them.

By mere observation, the reduction that occurs when comparing solution 1 with solution 16, can be considered spectacular, to say the least.

$H_s = 7.5m$



$H_s = 7.5m$



Figures 9 and 10

6.- WAVE OVERTOPPING ANALYSIS

The measures that were taken as regards wave overtopping were; firstly the number of waves that overtopped the breakwater (N), with respect to the total number of waves in the recording (Overtopping %). Secondly, the height of the sheet of water that overtopped the crown of the breakwater, to which, if we add the distance from the water level of the design to the crown height, can be called "overflow wave run-up", from whose values the parameters $R1/3$, R and R_{max} are obtained, through the statistical analysis of the recordings. Finally, the total volume of overtopping during the test storm, expressed in terms of

one m³/s per running metre of vertical breakwater, (average overtopping rate (Q)).

The most important factor for the design engineer concerns the value of Q, because this parameter is the one that determines the flood level behind the breakwater, the capacity that the structure's drainage system requires or the degree of operativity during the storms, of the installations, behind the breakwater.

Making an overall analysis of the overtopping rate obtained for the different solutions tested, we could say that the inclusion, in front of the breakwater, of the different submerged elements, with their respective test sizes, has proved to be effective, as regards the reduction of the overtopping rate; this can be observed in Figure 11, which refers to the most unfavourable wave conditions.

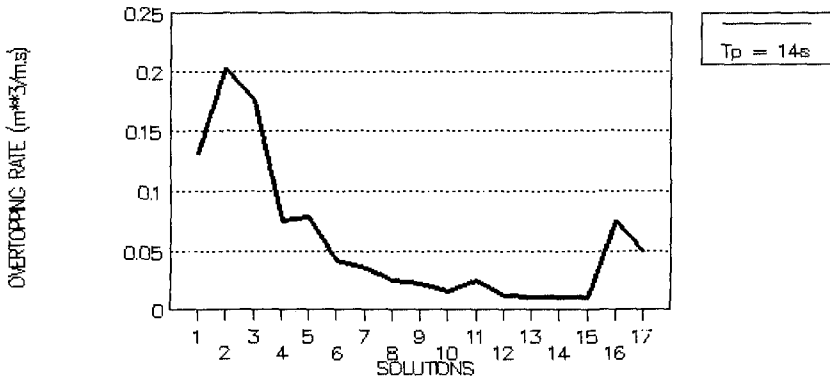


Figure 11. Overtopping comparative graphic, Hs=7.5m

It is not possible to give design recommendations in this work, because in order to do this, it would be necessary to take the geometrical variables of the different element into account, together with a greater number of tests, but, on making an analysis by stages, it is possible to talk of the different effects that could be observed under test conditions.

The first stage of the tests had as main aim to observe the effects, in the wave run-up and overtopping, of the three shapes of crown that were chosen. In figure 12, it can be seen that the least favourable crown was the one used in solution 2. As regards the wave run-up, it can be clearly stated that there are no great differences between the solutions, it turning out to be a very uniform phenomenon for the two test storms (Tp = 10s and Tp = 14s), nevertheless, the final difference in the results is marked by the overtopping percentage that is found in line with the overtopping rate.

Of the different solutions tested at the second stage complementary tests, i.e. solutions 4, 4a, 4b, 4c, 5, 5a, 6 and 6a, see Table 2, firstly it can be said that, compared to the previous stage, reductions have been obtained in the wave run-up and overtopping through the use of the submerged breakwater, Figure 11, and secondly, that for the two phenomena, the least favourable storms were those characterized as $T_p = 14s$, Figures 13 and 14.

$H_s = 7.5m$

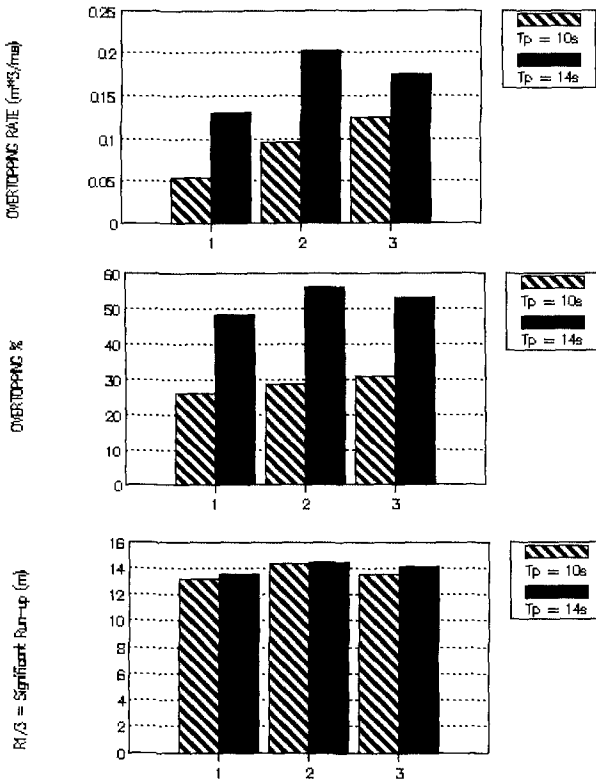


Figure 12. Results from solutions 1,2,3 with $H_s=7.5m$

Thirdly, that, within the magnitude of the values tested in variables L , C_c and B , the run-up phenomenon still shows very uniform behaviour, the best results being observed at this stage for $L = 60 m$ and $B = 12 m$. However, in the case of the overtopping rate, it can be seen that parameters C_c and L do not influence very much, and that it is parameter B , for the solutions that have a greater value ($B = 18 m$), which gives the best results both for $T_p = 12s$ and $T_p = 14s$. Figures 13 and 14.

At the third stage, owing to the fact that the run-up phenomenon is still fairly uniform and unhelpful in the evaluation of the various solutions, it will not be taken into account in this analysis.

On studying the results of the different solutions at this stage (7 to 15) with respect to the overtopping rate, we can say that, simply by including the protection at the toe of the vertical breakwater acting together with the submerged breakwater, solution 7, Figure 15, reductions are obtained in the overtopping with respect to the two previous stages, and then, on reducing the existing depth in the space formed between the two breakwaters using a rubble filling, we continue to obtain improvements the lesser the depth ($dR = -10.2, -6, -4$). Nevertheless, the most influential variable is still the width of the berm (B) of the submerged breakwater, a considerable improvement being observed when it is increased to 30 m.

Finally, of the solutions taken at the 4th stage, it can be seen from Figure 11, how the omitting of the wall protection influences the results, and, also the influence of the width of the berm (B) between 18 m and 30 m.

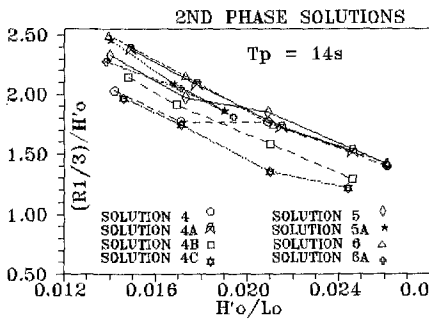


Figure 13. Wave Run-up

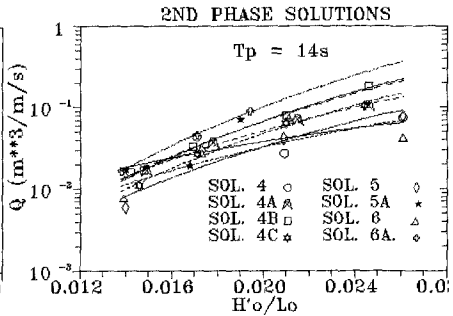


Figure 14. Overtopping

$H_s = 7.5m$

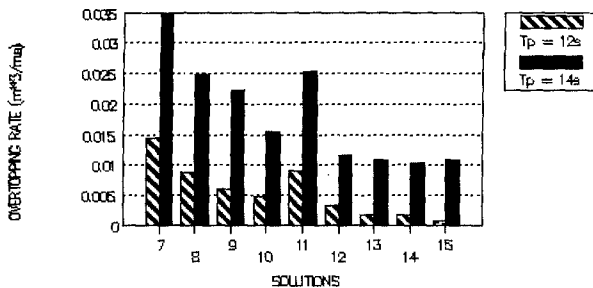


Figure 15. Results from third stage solutions

7.-CONCLUSIONS

The different activity, carried out in front of the vertical designed breakwater, have been shown, at the Marina of the Olympic Village for Barcelona-92, they were designed to optimize the abovementioned breakwater from the point of view of its stability and functionality.

In the light of the tests performed, it is not possible to establish any design criteria to determine the optimum geometrical characteristics of the submerged breakwater situated in front of the vertical one; it would only be possible by the realizing of a larger number of more systematic tests carried out in order to detect the sensitivity of each of the parameters involved in the wave attack (C_c , B , L and dr).

Nevertheless, it can be said that, within the range of values experimented for the above-cited parameters, the crown width of the submerged breakwater, B , turned out to be the most sensitive to both the wave force and the overtopping.

As far as the "overtopping/run-up" is concerned, it can be said that the statistical parameter $R_{1/3}$, used in its analysis, hardly showed significant variations for the different situations tested.

8.-ACKNOWLEDGEMENTS

The authors would like to acknowledge the help given by the persons in charge of the Olympic Village, who provided us with the slides showing the situation of the Marina at the time. These slides made the presentation at the I.C.C.E.'90 easier.

9.- REFERENCES

- 1.- Ahrens, John P. (1987)
Characteristics of Reef Breakwaters.
Coastal Engineering Research Center.
Technical Report CERC-87-17.
- 2.- Mitsuyatsu, H. (1962)
Experimental Study on Wave Force against a Wall.
Rept. Transportation Tech. Res. Inst. Min. of
Transport, Japan, N° 47.
- 3.- Goda, Y. (1985)
Random Seas and Design of Maritime Structures
UNIVERSITY OF TOKYO PRESS.

CHAPTER 102

STABILITY OF BREAKWATERS CONSTRUCTED ON DREDGED SAND MOUND

Kenji Yano, Yuzo Mizuno, Nobutoshi Umezawa and
Tomoyuki Yanase¹

ABSTRACT

The possibility for the construction of "sand mound breakwater", which is a caisson type breakwater on a artificial sand mound, has been studied. First the wave force characteristics acting on the composite sand mound breakwater model are described, to identify the conditions where impulsive breaking wave pressures are generated. Second, the scouring of the toes of rubble mounds is discussed. Finally there is an outline of field experiments, scouring of sand mounds, and the status of the deposits. The results of experiments provide useful information for the design of breakwater constructed on the artificial sand mound or on a similar double-sectioned sea bottom.

1. INTRODUCTION

The construction of composite breakwaters in relatively deep sea areas requires a large rubble mound foundation that takes up a considerable proportion of the total construction cost. This is due to limitations imposed on the capacity of the caisson plant, which force an increase in the height of the rubble mound. In harbors where dredging of waterways and anchorages yields large quantities of good sand, the construction costs of breakwaters and the cost incurred in disposing the dredged sand may be reduced if the sand is used in the breakwater mound.

¹ Port and Harbor Section, Civil Engineering Research Institute, Hokkaido Development Bureau, 1-3 Hiragishi, Toyohira-ku, Sapporo, 062, Japan.

The construction of "Sand Mound Composite Breakwaters" requires a solution to the technical problems with wave force characteristics, scouring, bearing capacity, liquefaction characteristics, all of which are important in breakwaters on the artificial sand mound. Since 1986, the Hokkaido Development Bureau has been conducting experiments with hydraulic models and field demonstration tests at Tomakomai East Port to help solve these problems.

This report presents an evaluation of tests with the hydraulic model, with partial results of the field tests. First the wave force characteristics acting on the composite sand mound breakwater model are described, to identify the conditions where impulsive breaking wave pressures are generated. A number of studies on impulsive breaking pressures (e.g. Tanimoto, 1976) acting on normal composite breakwaters have been carried out, but studies relative to the breakwater on a double-sectioned sea bottom are virtually non-existent.

Second, the scouring of the toes of rubble mounds is discussed. Much effort has been made to avoid the scouring of toes of rubble mound, however, no generally applicable countermeasures have been established to meet particular local requirements. This presents a design method for effective countermeasure work based on tests with hydraulic models: (i) determining the scouring positions of breakwaters by structural types, and (ii) determining the length of effective counter-scouring work.

Finally there is an outline of field experiments, scouring of sand mounds, and the status of the deposits.

2. WAVE FORCE CHARACTERISTICS ACTING ON BREAKWATER

2-1 Testing Equipment and Method

The tests were conducted in a two-dimensional wave tank equipped with an irregular wave generator (24m long, 80cm wide, 1m high). Dimensions were 1/75, with the channel bed slope 1/100. The wave spectrum employed was the modified Bretschneider-Mitsuyasu frequency spectrum. The measurement time was set at the significant wave period $\times 200$ sec., to ensure measurements of more than 200 waves. The data was transformed to digital at the sampling frequency of 100Hz. Figure 1 shows a typical section of the test model.

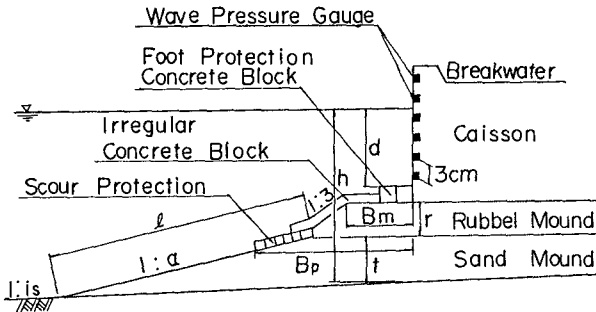


Fig. 1 Typical section of test model

The wave pressures were defined as the maximum average pressures of individual waves, and the representative wave pressures were defined with a same way for the wave heights such as the maximum wave pressure, the 1/10 maximum one-tenth wave pressure, and the maximum one-third wave pressure or significant wave pressure, expressed as p_{max} , $p_{1/10}$, and $p_{1/3}$ respectively.

There are two major types of tests. Test 1 on a fixed bed with the sand mound slope, and thickness and the depth varied. The rubble mound had a standard width of front berm F_m of a minimum 14cm (in-situ size 10.5m) assuming the foot protection concrete block and the armor concrete block as paired. For reasons of economy the thickness was kept as low as possible, 4cm (3m in-situ) including the thickness of the armor concrete block. The breakwaters were then evaluated with significant waves of 6 wave heights \times 3 periods.

Test 2 was performed on a movable bed and the variation in wave pressures after scouring was investigated. A movable bed was prepared in the same section as the fixed bed by replacing the sand mound and seabed with fine sand (median particle size $d_{50}=0.16\text{mm}$). Considering characteristics of littoral drift, this was equivalent to a median particle size of $d_{50}=1\text{mm}$ in-situ. The slope of the sand mound and the width of the counter-scouring works were varied. After measuring the sand surface after scouring by the precision bottom gauge with wave motion for 4 hours, the wave pressures were measured at similar conditions as in Test 1.

2-2 Results and Discussion

(a) The Effect of Slope of Sand Mound

Figure 2 shows variations in the coefficient of wave pressure intensity with the slope of the sand mound

at 1/15, 1/30, and 1/50 and with $t=6\text{cm}$, and $h=24\text{cm}$. The figure indicates that the coefficients often become large when the steepest slope is $a=1/15$, and it also indicates that there are cases where coefficients become greater with the longer periods and flatter slopes. This shows that impulsive breaking wave pressures are possibly generated more commonly with flat sloped sand mounds of moderate slope length.

(b) Shock Wave Pressure Generation

The above confirmed that very strong shockwave pressures could act on the sand mound composite breakwater under various conditions. Figure 3 graphically shows the possibility of shock pressures leading to breaking waves. It uses two sets of nondimensional quantities, and the ratio of significant wave height ($H_{1/3}$) to own depth of mound (d) on the ordinate and mound slope length (l) to wavelength (L) on the abscissa and the coefficients of the maximum cotidal average intensity of wave pressure ($\bar{P}_{\text{max}}/w_0H_{\text{max}}$). The broken and chained lines indicate boundaries where the coefficients exceed 1.5 and 2.0 suggesting the possibility of shock pressure from breaking waves to be significant above these boundaries.

The design of conventional composite breakwaters for sea areas with bedrock and cross sections similar to sand mounds, require special attention to the possibility of producing similar wave pressure characteristics.

(c) The Effect of Scouring of Sand Mound

The wave pressure tests above were all on fixed beds, and relate to the problems of the effect of various conditions of wave on the stabilization of the breakwaters immediately after completion. Another important problem in the stability of sand mound breakwaters is scouring and the possible effects of wave pressures when the shape of the sand mound changes due to scouring in front of breakwaters.

Figure 4 shows results with $h=24\text{cm}$ and $t=6\text{cm}$ as in Table 2, when $H_{1/3}=8.5\text{cm}$, and $T_{1/3}=1.3\text{s}$ was active for 4 hours. The scouring is greater with $a=1/15$ than with 1/50. It is evident that the face of the narrower anti-scouring installations suffers more from scouring. This indicates problems with actual breakwaters as the maximum scouring depth with the model can be assumed to be 1 to 1.5m.

In $\bar{P}_{1/3}$ there are no appreciable changes among the values before and after scouring for different wave pressure intensities. For \bar{P}_{max} , the intensities before

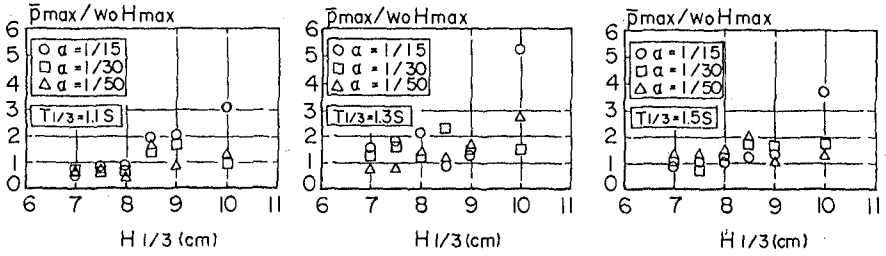


Fig. 2 Differences of wave pressures by sand mound slopes

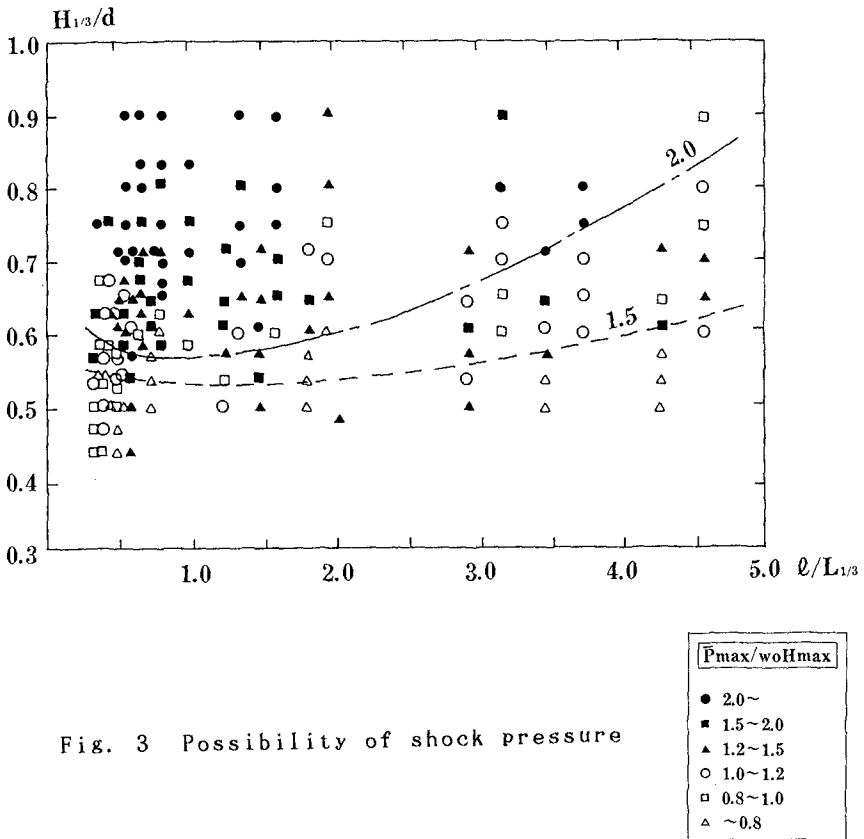


Fig. 3 Possibility of shock pressure

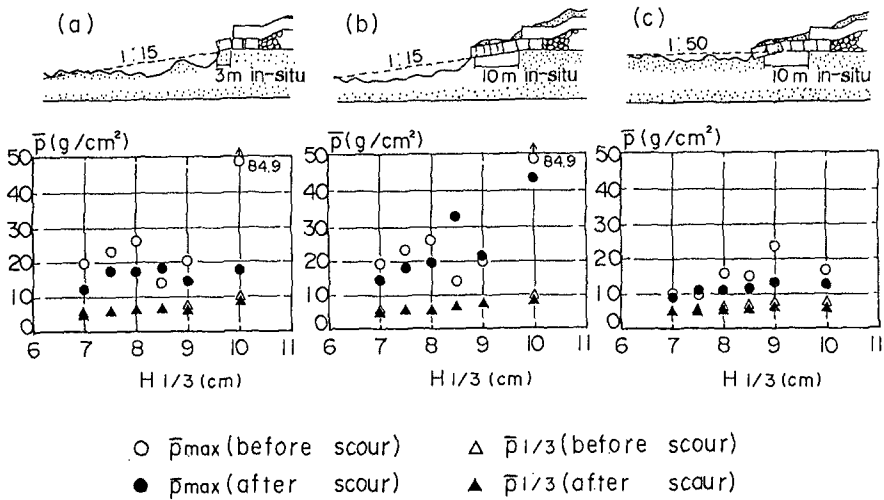


Fig. 4 Differences of wave pressures due to before and after scours

scouring was greater. Other periods show similar results, and it is assumed that there are no significant differences in the characteristics of wave pressures with different scouring configurations.

3. SCOURING IN FRONT OF BREAKWATERS AND ITS PREVENTION

3-1 Test Method

The tests were carried out in the two-dimensional wave tank used for the wave pressure tests. The scale, except for the bottom materials, were based on the Froude Model Law of 1/40 without distortion. The bottom materials were the same as used in the previous wave pressure tests. The particle size of the sand equal a $d_{50}=0.5\text{mm}$ size of bottom materials. The rubble-filled wire cross baskets for the scour prevention were 1/40 of the regular baskets (2.0m x 3.0m x 1.0m) with the weight adjusted to equal 10 tons in-situ. With regular waves as test waves scouring was studied on 3 kinds of wave periods $T=7, 10, \text{ and } 13$ sec.

3-2 Test Results and Discussion

(a) Structural Type of Breakwater and Place of Scouring

Irie (1984) pointed out that because of standing

waves bottom is scoured at nodes and accumulated at loops in front of the actual breakwaters. A remarkable damage of rubble mound would take place when the first node of standing waves $L/4$ comes near the toe of rubble mound where L is the length of a progressing wave.

Introducing this into a design poses problems: (i) establishing a basis for depth determination when calculating L of a composite breakwater, and (ii) determination of the location of the reflection face (the origin for $L/4$) for breakwater armored with wave dissipating blocks or slit caisson breakwater. To evaluate (i) and (ii), these 3 types of breakwater were examined. Figure 5 shows the models of wave dissipating type breakwater. The height of the crown was set so the breakwater would be non-overtopping.

Figure 6 shows an example of the scouring location where: $h=37.5\text{cm}$ (15m in-situ), and $T=2.06\text{sec}$ (13 sec). The \circ mark in the figure indicates the use of (h) as the depth when determining the wave length and Δ indicates when (d) was used. K_r is the reflection coefficient. The locations of $L/4$, $L/2$, and $3L/4$ are shown on the structures. Hence, black indicates the scouring locations and white the deposition. Based on this, the conversion into $L/4$ shows only differences of a few meters with long $T=13$ sec periods, which indicates that it is relevant to the pickup (h) as the depth to determine the wavelength.

Figure 7 shows the scouring locations of the wave dissipating armor block structure and the 2-stage slit breakwater. The \circ and \square in the figure show the locations of $L/4$, $L/2$, and $3L/4$ seen from structures using (h) to calculate the wavelength as with the composite breakwater. The \circ mark indicates upright wall reflection of the wave dissipating armor block structure and the \square mark indicates the intersection between the slope face of the wave dissipating blocks and the still water level.

For the slit caisson breakwater, \circ indicates the offshore side slit wall face and \square indicates the rear upright wall. In wave dissipating armor block breakwaters, visual inspection was considered necessary to establish the upright wall face as a reflector, based on the reflected waves around the structure and the scouring location shown in the figure.

With the slit caisson breakwater, the reflecting face was set on the offshore side of the upright face up to $T=10\text{sec}$. However, for periods of $T=13\text{sec}$, the reflection face of the scouring location is thought to be located somewhere between the offshore side slit wall face and the rear upright wall. In practice it is

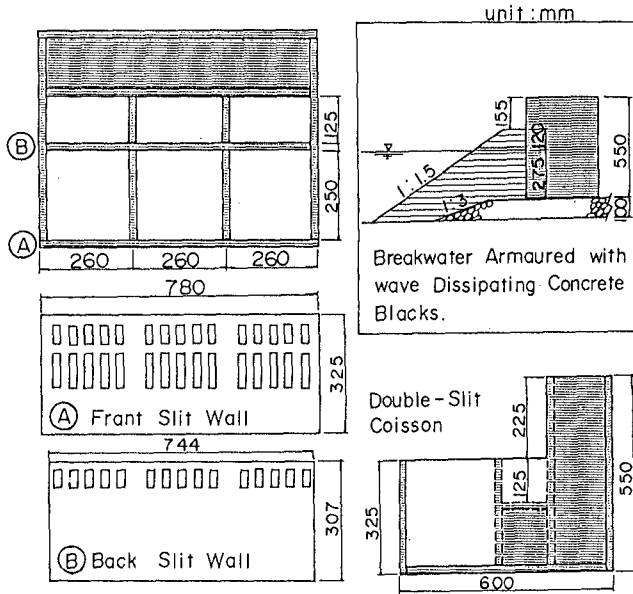


Fig. 5 Models of wave dissipating type breakwater

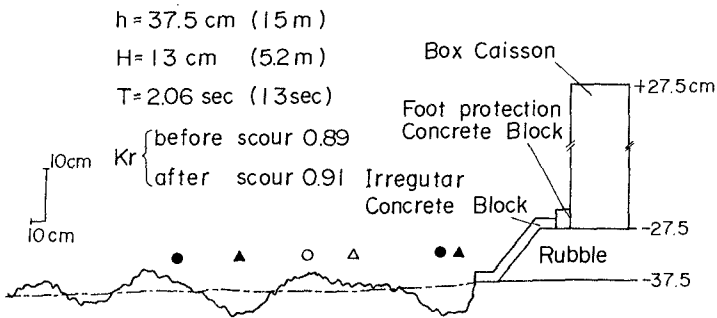


Fig. 6 Scouring location in front of composite breakwater

strongly recommended to set all on the offshore side of the slit wall face.

Comparing the scouring of common composite breakwaters with low-reflection type breakwaters shows that the absolute quantities of scouring and deposition are smaller with the low-reflection type, suggesting that the reduction in reflected waves is more effective to control the scouring.

(b) Length of Scour Prevention Works

The experiments with the composite breakwater used the wavelength as the parameter to attempt to determine the length of rubble-filled wire cross baskets for the scour prevention. Wavelength L was determined with the installation depth, and the scouring conditions were compared by successively increasing the length of the wire crosses from the offshore side (i) $L/4$ ($3L/12$), (ii) $L/3$ ($4L/12$), and (iii) $5L/12$, with the upright wall face as the origin (face of reflection). Two sea bottom slopes were studied $1/100$ and $1/15$.

Figure 8 shows one set of results. The bottom slope did not affect moving the wire crosses nor cause scouring when the basket length was $5L/12$, and these dimensions was considered effective for scour control. Scour control with $L/3$ were also generally effective although there was a slight dipping of one basket at the end. With $L/4$ baskets, the movement of baskets in the front row was significant, and particularly with steep bottom slopes, and the scour quantity at the toe of the slope was the largest. These results showed that using only the wave length parameter L in designs was adequate for scour prevention. There were good results with $L/3$ from the upright wall of the structure as the effective length of scour prevention works.

4. FIELD TESTING

4-1 Construction of Sand Mound

The tests were conducted in a 16m deep sea area at Tomakomai East Port on the Pacific coast by Tomakomai Port and Harbor Construction Office. Figure 9 shows schematic diagram of sand mound breakwater at Tomakomai Port. Figure 10 shows a model of the breakwater with two 12.5m (L) x 20m (W) x 12m (H) caissons installed on the sand and rubble mound. The construction started in November 1986 and was complete in October of the following year.

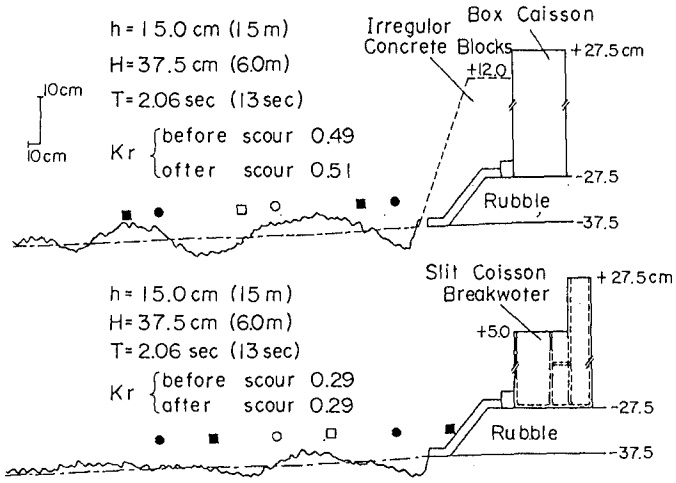


Fig. 7 Scouring location in front of wave-dissipating type breakwater
 (Top) Breakwater armoured with wave dissipating concrete blocks
 (Bottom) Slit caisson breakwater

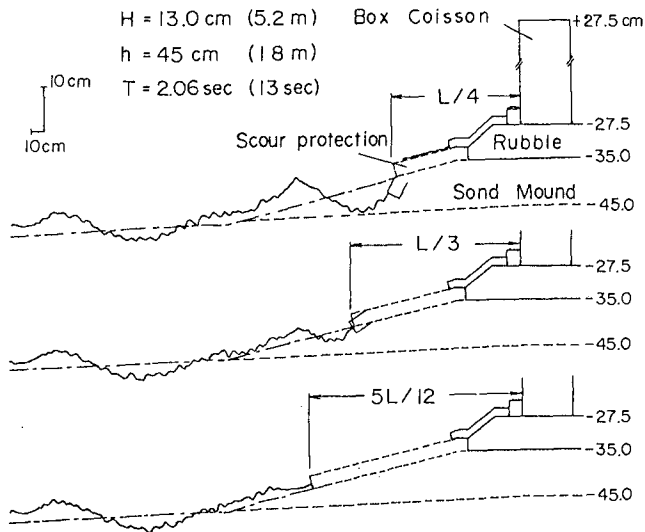


Fig. 8 Scouring shapes in front of breakwater under various length of scour protections.

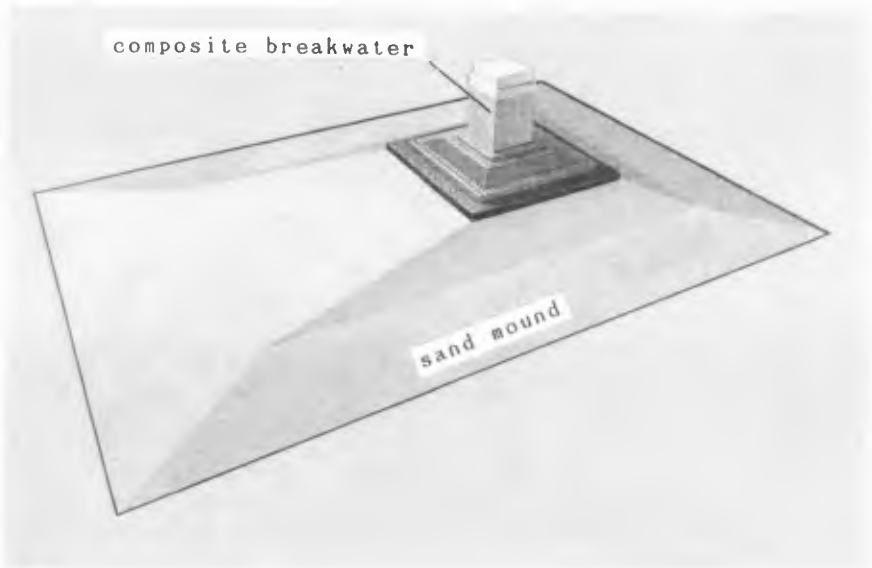


Fig. 9 Schematic diagram of sand mound breakwater for field test at Tomakomai Port



Fig. 10 Test breakwater at Tomakomai Port

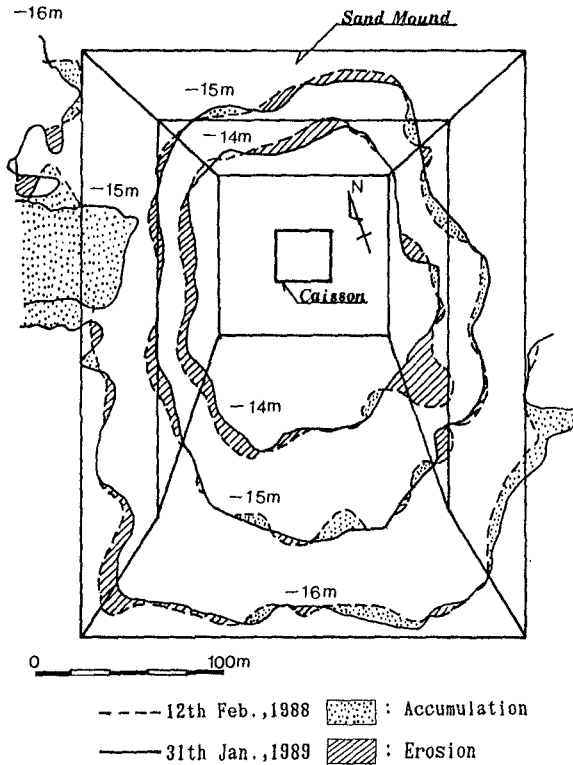


Fig. 11 Comparison of contours

The sand mound used dredged sediment from waterways (the median particle size $d_{50}=0.8\text{mm}$) and other fill material (the median particle size $d_{50}=1.7\text{mm}$, pump dredged and pile-stored on land for several years during which the fine particles were washed out leaving stones as main component). The materials for the sand mound were transported by bottom door hopper barges installed canvas curtain for dispersion prevention, and approximately 1,000,000 cubic meters were dumped for a maximum mound thickness of 3m.

4-2 Stability Against Scouring

Figure 11 shows sounding surveys conducted between the caissons half a year after the initial installation (February, 1988) together with sounding survey of January 1989. The largest significant waves observed during this time was 4.0m, and the variation in the subbase heights lower than 0.5m, indicating that the sand mound remained stable.

5. SUMMARY

The results obtained from the study may be summarized as follows:

(1) The relation between the slope of the sand mound and the generation of shock pressure breaking waves is affected by the angle of the slope, and also particular slopes of sand mounds and lengths of slope are susceptible to the wave conditions generating shock pressure breaking waves.

(2) The nondimensional ratios: significant wave height ($H1/3$) to crown depth of rubble mound (d), and slope length of sand mound (l) to wave length related to the significant wave period in Figure 3, and indicates the possibility of shock pressure breaking wave generation.

(3) There were no significant differences in the intensities of wave pressure before and after scouring.

(4) Comparing the scouring of common composite breakwaters with low-reflection type breakwaters shows that the absolute quantities of scouring and deposition are smaller with the low-reflection type, suggesting that the reduction in reflected waves is more effective to control the scouring.

(5) It is recommended that the effective length of scour prevention work is $L/3$ from the upright wall of the structure.

REFERENCES

- IRIE, I. and K. Nadaoka (1984): Laboratory reproduction of seabed scour in front of breakwaters, Proc. 19th Int. Conf. Coastal Eng., Houston, pp. 1715-1731.
- TANIMOTO, K., S. Takahashi and T. Kitaya (1981): Generation of Breaking Wave-led Shock Pressure by the Mound Configurations of Composite Breakwater and its Countermeasures, Port Research Report, vol. 20, 2nd edition, pp. 3-39 (in Japanese).

CHAPTER 103

STABILITY OF LOW-CRESTED AND REEF BREAKWATERS

Jentsje W. van der Meer¹⁾ and Krystian W. Pilarczyk²⁾

Abstract

Low-crested structures are designed for some or even severe overtopping. The stability of these structures is sometimes higher than the non-overtopped structures, due to the fact that wave energy can pass over the crest, giving lower wave forces on the armour layer of the seaward slope.

Low-crested structures can be classified into three categories: dynamically stable reef breakwaters, statically stable low-crested structures with the crest above swl and statically stable submerged structures. Well described investigations at various institutes (in total about 275 tests) were re-analysed and this has led to practical design formulas and graphs for each of the three classes mentioned above.

Introduction

As long as structures are high enough to prevent overtopping, the armour on the crest and rear can be (much) smaller than on the front face. The dimensions of the rock in that case will be determined by practical matters as available rock, etc.

Most structures, however, are designed to have some or even severe overtopping under design conditions. Other structures are so low that also under daily conditions the structure is overtopped. Structures with the crest level around swl and sometimes far below swl will always have overtopping and transmission.

It is obvious that when the crest level of a structure is low, wave energy can pass over it. This has two effects. First the armour on the front side can be smaller than on a non-overtopped structure, due to the fact that energy is lost on the front side.

The second effect is that the crest and rear should be armoured with rock which can withstand the attack by overtopping waves. For rock structures the same armour on front face, crest and rear is

1) Delft Hydraulics, PO Box 152, 8300 AD Emmeloord, The Netherlands
2) Rijkswaterstaat, PO box 5044, 2600 GA Delft, The Netherlands

often applied. The methods to establish the armour size for these structures will be given here. They may not yield for structures with an armour layer of concrete units. For those structures physical model investigations may give an acceptable solution.

Classification of low-crested structures

Low-crested rock structures can be divided into three categories, see also Figs. 1-3.

Dynamically stable reef breakwaters

A reef breakwater is a low-crested homogeneous pile of stones without a filter layer or core and is allowed to be reshaped by wave attack (Fig. 1). The equilibrium crest height, with corresponding transmission, are the main design parameters. The transmission will not be treated in this paper (one is referred to Van der Meer (1990b)).

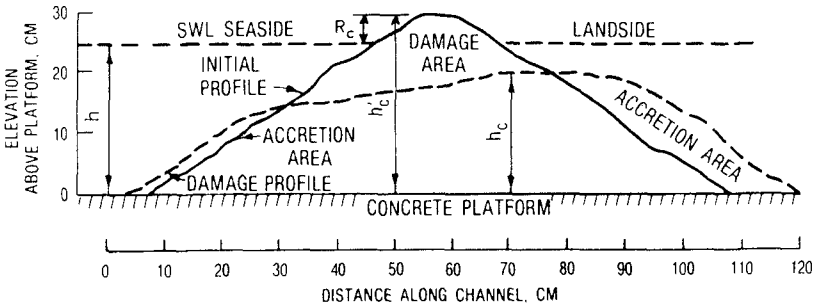


Figure 1 Example of reef type breakwater (Ahrens (1987))

Statically stable low-crested breakwaters ($R_c > 0$)

These structures are close to non-overtopped structures, but are more stable due to the fact that a (large) part of the wave energy can pass over the breakwater (Fig. 2).

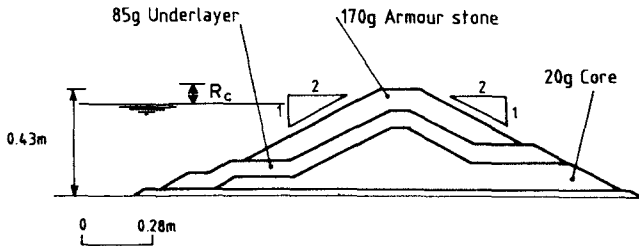


Figure 2 Example of low-crested breakwater (Powell and Allsop (1985))

Statically stable submerged breakwaters ($R_c < 0$)

All waves overtop these structures and the stability increases remarkably if the crest height decreases (Fig. 3).

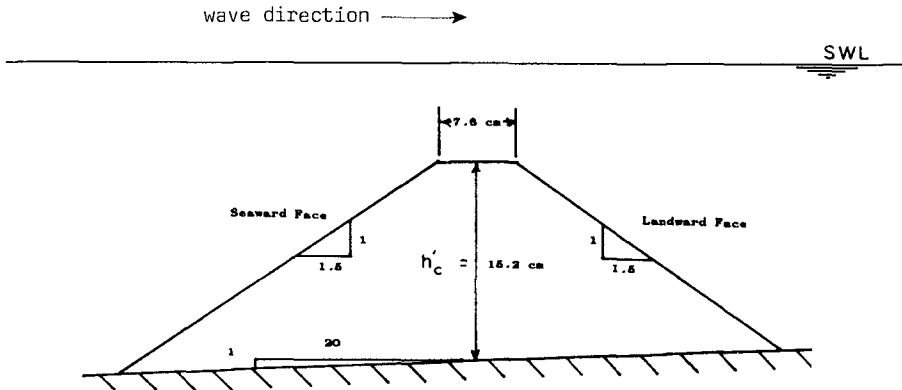


Figure 3 Example of submerged breakwater Givler and Sørensen (1986))

Description of data sets

Ahrens (1987) described the stability of reef type breakwaters. This type of breakwater is little more than a homogeneous pile of stones with individual stone weights similar to those ordinarily used in the armour and first underlayer of conventional breakwaters. The initial crest height is just above the water level. Under severe wave conditions it is allowed that the crest height decreases to a certain equilibrium crest height. Ahrens performed about 15 tests on stability of these structures and gave a formula for the equilibrium crest height.

Allsop (1983) and Powell and Allsop (1985) described about 45 tests on the stability of breakwaters with the crest above swl and which were conventional breakwaters. Only small damage (displacement of stones) was allowed during design conditions.

Givler and Sørensen (1986) described about 45 tests on the stability of submerged breakwaters. The tests were performed with regular waves and included a large range of wave heights, but also wave periods. The damage at the crest was measured and the design criteria are similar to the conventional breakwaters (no or only small damage allowed).

Finally Van der Meer (1988) performed about 45 tests during his very extensive model investigation (in total about 500 tests) on structures with a low crest. These tests cover all three structure types described above (reef type, low-crested above swl and submerged) and were used as a connection between the various structures and data sets.

A more extensive description of the above described data sets together with the complete re-analysis of the data can be found in Van der Meer (1990a).

Reef breakwaters

The analyses of stability by Ahrens (1987, 1989) and Van der Meer (1990a) was concentrated on the change in crest height due to wave attack, see Fig. 1. Ahrens defined a number of dimensionless parameters which described the behaviour of the structure. The main one is the relative crest height reduction factor h_c/h_c' . The crest height reduction factor h_c/h_c' is the ratio of the crest height at the completion of a test, h_c , to the height at the beginning of the test, h_c' . The natural limiting values of h_c/h_c' are 1.0 and 0.0 respectively.

The wave height can be characterised by $H_s/\Delta D_{n50}$ (Van der Meer (1988)) or N_s (stability number: Ahrens (1987, 1989)).

$$H_s/\Delta D_{n50} = N_s \quad (1)$$

where:

H_s = significant wave height, H_s or H_{m0} (H_{m0} was used in this study)

Δ = relative mass density; $\Delta = \rho_a/\rho_w - 1$

ρ_a = mass density of armour rock

ρ_w = mass density of water

D_{n50} = nominal diameter of rock; $D_{n50} = (M_{50}/\rho_a)^{1/3}$

M_{50} = average mass (50% value on mass distribution curve)

Ahrens found for the reef breakwater that a longer wave period gave more displacement of material than a shorter period. Therefore he introduced the spectral (or modified) stability number, N_s^* , defined by:

$$N_s^* = H_s^{2/3} L_p^{1/3} / \Delta D_{n50} \quad (2)$$

where: L_p = the Airy wave length calculated using T_p and the water depth at the toe of the structure h . In fact a local wave steepness is introduced in Eq. 2 and the relationship between the stability number N_s and the spectral stability number N_s^* can simply be given by:

$$N_s^* = N_s \times s_p^{-1/3} = H_s/\Delta D_{n50} \times s_p^{-1/3} \quad (3)$$

where: s_p = the local wave steepness; $s_p = H_s/L_p$

That a longer wave period gives more damage than a shorter period is not always true. Ahrens concluded that it was true for reef breakwaters where the crest height lowered substantially. It is however not true for non-overtopped breakwaters (Van der Meer (1987 or 1988)). The influence of the wave period in that case is much more complex than suggested by Eq. 3.

The crest height (reduction) of a reef type breakwater can be described by:

$$h_c = \sqrt{A_t / \exp(aN_s^*)} \tag{4}$$

where "a" = a coefficient and A_t = area of structure cross-section. Ahrens gave various equations for the coefficient a. The most recent and refined one is given by Ahrens (1989):

$$"a" = 0.046(h_c' - h_c) / h + 0.2083(h_c / h)^{1.5} - 0.144(h_c / h)^2 + 0.4317 / \sqrt{B_n} \tag{5}$$

where:

h = water depth at structure toe and
 $B_n = A_t / D_n^2$ (bulk number)

The structures of Van der Meer (1988) had other crest heights, water depths, bulk numbers and slope angles than Ahrens' structures. A first fit of Eqs. 4 and 5 with these data is shown in Fig. 4. The breakwater response slope is shown on the vertical axis and is defined by:

$$C = A_t / h_c^2 \tag{6}$$

The graph shows the data sets with different bulk numbers B_n and response slopes C . Where Ahrens' data were nicely located around the curve (Eqs. 4 and 5), the data of Van der Meer did not. It is clear from Fig. 4 that the average slope "as built", C' , has also influence on the crest height, besides the parameters h_c' / h and B_n .

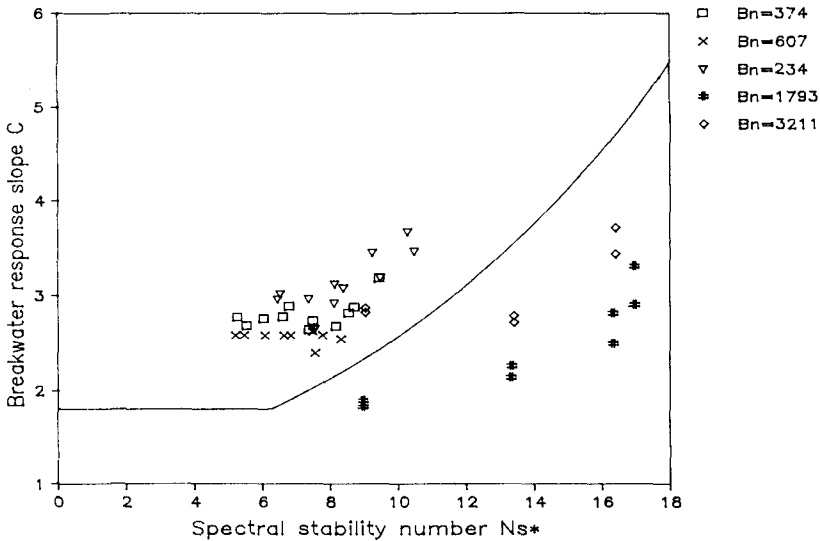


Figure 4 Data of Van der Meer (1988) with Eqs. 4 and 5

Therefore all the data of Ahrens (1987) were re-analysed together with the data of Van der Meer (1988). The complete analysis is given by Van der Meer (1990a), the basis of this paper. It will not be given here.

The final equation that was derived from the analysis is given by:

$$h_c = \sqrt{A_c / \exp(aN_s^*)} \quad (4)$$

$$\text{with "a"} = -0.028 + 0.045C' + 0.034h'_c/h - 6.10^{-9} B_n^2 \quad (7)$$

and $h_c = h'_c$ if h_c in Eq. 4 $>$ h'_c .

The same data as shown in Fig. 4 are given in Fig. 5, but now with the new equations 4 and 7, and with on the vertical axis the relative crest height h'_c/h in stead of the response slope C. The agreement is good. Eq. 7 gives almost the same results for Ahrens' test range as Eq. 5. Eq. 7 is, therefore, valid for a wider range of conditions.

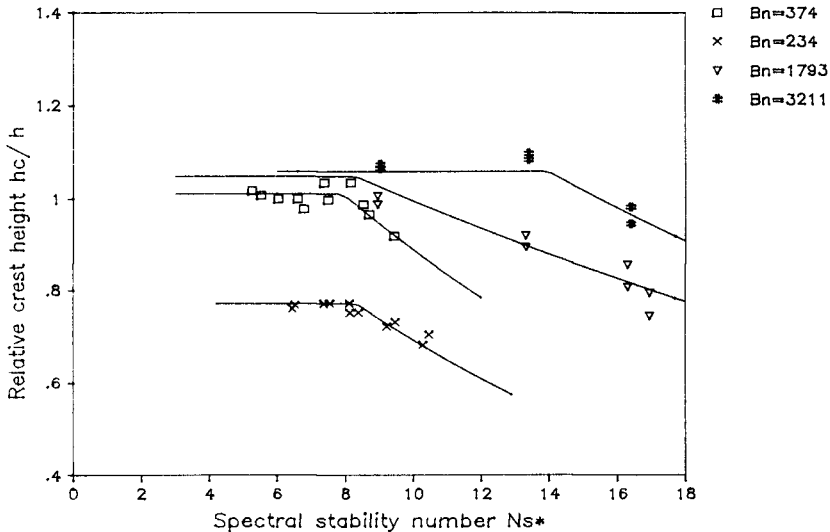


Figure 5 Data of Van der Meer (1988) with Eqs. 4 and 7

The lowering of the crest height of reef type structures as shown in Fig. 1, can be calculated with Eqs. 4 and 7. It is possible to draw design curves from these equations which give the crest height as a function of N_s^* or even H_s . An example of h_c versus H_s (produced by Delft Hydraulic's program BREAKWAT) is shown in Fig. 6. The reliability of Eq. 4 can be described by giving 90% confidence bands. The 90% confidence bands are given by $h_c \pm 10\%$.

Statically stable low-crested breakwaters above swl

The stability of a low-crested conventional breakwater can be related to the stability of a non-overtopped structure. Stability formulas as the Hudson formula or more advanced formulas (Van der Meer (1987, 1988)) can be used for example. The required stone diameter for an overtopped breakwater can then be determined by a reduction factor for the mass of the armour, compared to the mass for a non-overtopped structure.

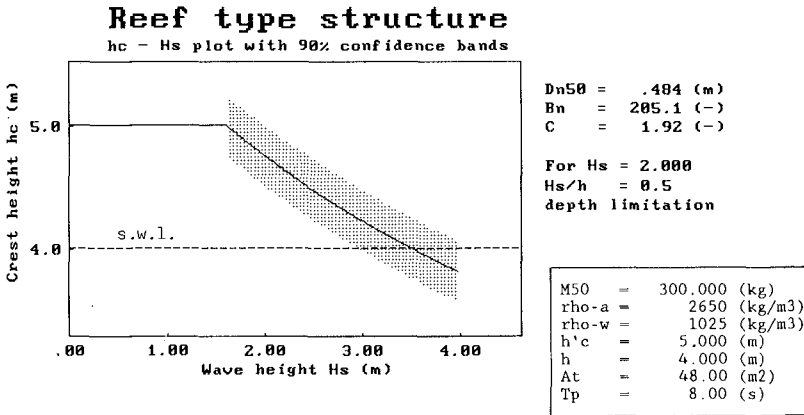


Figure 6 Design graph of reef type breakwater

Data sets that could be used for analysis were a part of Ahrens data (with small damage to the crest), Powell and Allsop (1985) and Van der Meer (1988). Fig. 7 gives the damage curves of a part of Van der Meer's tests with four crest heights, R_c , and for a constant wave period of 1.7 s. From this figure it is obvious that a decrease in structure crest height results in an increase in stability.

Furthermore, from the tests it could be concluded that a longer period of 2.2 s gave an increase in stability for $R_c/H_c \leq 1.3$ and the shorter period of 1.7 s for a lower value of $R_c/H_c \leq 0.8$. This can also be explained in a physical way. A long period gives higher run-up on a slope than a short period. Therefore more energy is lost by overtopping for a long period at the same crest level as for a short period.

The transition height where the increase in stability starts (given as a R_c/H_c value) should in fact be a function of the wave period (or wave steepness) too. From the mentioned data sets the following transition heights R_c/H_c were derived and the corresponding (average) wave steepness $S_{op} = 2\pi H_s/gT_p^2$ was taken from the original data.

Author	transition	
	R_c/H_s	s_{op}
Van der Meer ($T_p = 2.0$ s)	0.8	0.025
Van der Meer ($T_p^D = 2.6$ s)	1.3	0.015
Ahrens	1.3	0.010
Allsop (long wave)	2.0	0.006
Allsop (short wave)	0.7	0.027

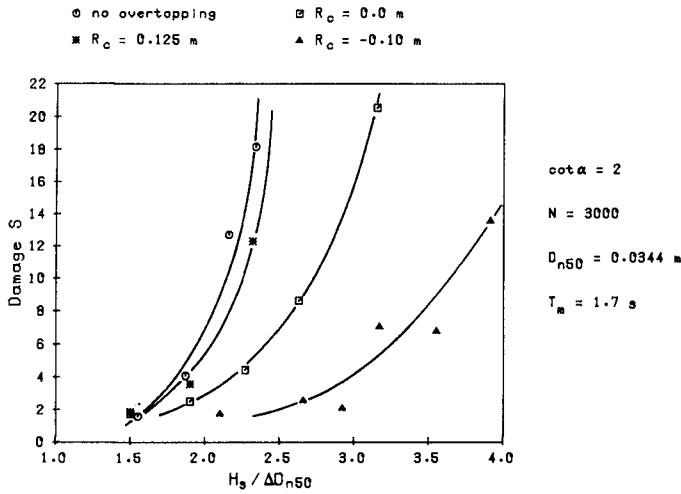


Figure 7 Influence of crest height on damage curves (from Van der Meer (1988))

These data points are shown in Figure 8. Although the points are only a rough estimate, they show a consistent trend: a decreasing transition crest height with increasing wave steepness. The possible maximum steepness in nature will be in the order of $s_{op} = 0.04 - 0.045$, which in fact was not tested by one of the authors. Although not the best fit, the following equation (also shown in Figure 8) gives a good fit with the data:

$$\text{transition crest height: } R_c/H_s = 0.13 s_{op}^{-0.5} \tag{8}$$

In Powell and Allsop (1985) a dimensionless crest height R_p^* was introduced which was used to describe overtopping and which included the wave steepness. The definition is given by:

$$R_p^* = R_c/H_s \sqrt{s_{op}/2\pi} \tag{9}$$

Comparison and rewriting of Eqs. 8 and 9 shows that the transition crest height can simply be described by:

$$R_p^* = 0.052 \tag{10}$$

The average increase in stability ($H_s/\Delta D_{n50}$ or N_s^*) for a structure with the crest at the water level, in comparison with a non-overtopped structure, is in the order of 20-30%. If the increase in stability is set at 25%, independent of wave steepness, and if a linear increase in stability is assumed between $R_p^* = 0.052$ and $R_p^* = 0$, the increase in stability can be described as a function of R_p^* only. Furthermore, if not the increase in stability is taken as a measure, but the reduction in required nominal diameter D_{n50} , the final equation becomes:

$$\text{Reduction factor for } D_{n50} = 1/(1.25 - 4.8 R_p^*) \tag{11}$$

for $0 < R_p^* < 0.052$

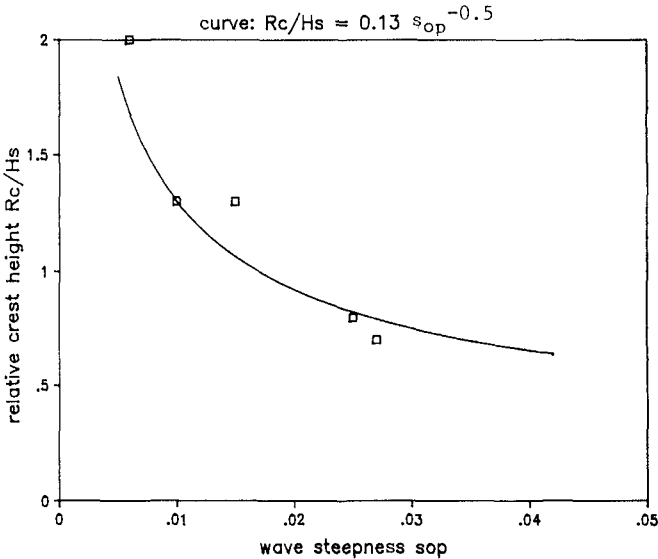


Figure 8 Transition crest height where the influence of a low crest starts, as a function of wave steepness

This final equation 11 describes the stability of a statically stable low-crested breakwater with the crest above swl in comparison with a non-overtopped structure. Eq. 11 is shown in Fig. 9, for various wave steepnesses, and can be used as a design graph. The reduction factor for the required nominal diameter can be read from this graph (or calculated by Eq. 11) in comparison with a non-overtopped structure.

An average reduction of 0.8 in diameter is obtained for a structure with the crest height at the water level. The required mass in

that case is a factor $(1/1.25)^3 = 0.51$ of that required for a non-overtopped structure.

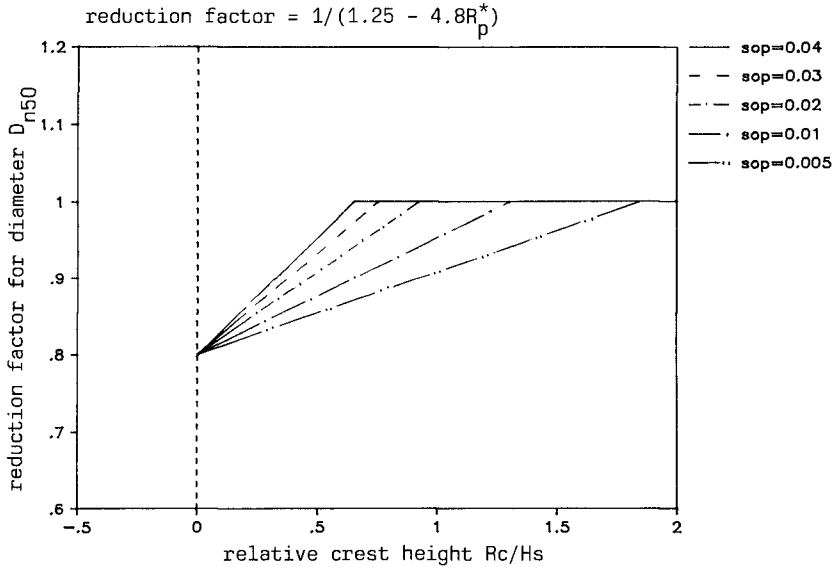


Figure 9 Design graph with the reduction factor for the stone diameter of a low-crested structure ($R_c < 0$) as a function of relative crest height and wave steepness

Submerged breakwaters

The tests of Ahrens (1987, 1989) and Allsop (1983) and Powell and Allsop (1985) had always an initial crest level at or above the water level. Only Van der Meer (1988) and Givler and Sørensen (1986) had initial crest heights below the water level. The total amount of data is limited, however. Van der Meer (1988) tested only a slope angle of 1:2 and Givler and Sørensen (1986) tested only a slope of 1:1.5. The seaward slope angle might have some influence on the stability of the submerged structure. Therefore the analysis of submerged structures here will be only valid for rather steep slopes, say about 1:1.5 to 1:2.5.

The slope angle has large influence on non-overtopped structures. In the case of submerged structures the wave attack is concentrated on the crest and less on the seaward slope. Therefore it might be allowed to exclude the slope angle of submerged structures as being a governing parameter for stability.

The relationship between relative crest height h'/h and spectral or modified stability number N_s^* (Eq. 2) for a fixed damage level of $S = 5$, where S is defined by Van der Meer (1988), is shown in Fig. 10. It is noted again that the tests of Givler and Sørensen were

performed with monochromatic waves and that therefore, differences in results between Van der Meer's tests and Givler and Sørensen's tests might be due to this effect.

The N_s^* values of Givler and Sørensen for $h'_c/h = 0$ are a little smaller than those of Van der Meer. This might be caused by the above described difference in wave testing, but also by a less accurate measuring technique for the damage.

The N_s^* values for $h'_c/h = 0.75$, however, are lower in Van der Meer's tests, see Figure 10. The data points of Van der Meer for this crest height are very close which means that for statically stable submerged structures stability might better be described by N_s^* instead of $H/\Delta D_{n50}$. That this is not the case for low-crested structures with the crest above swl, can also be concluded from Figure 10, where for $h'_c/h > 0$ substantial difference is found for the two wave periods tested by Van der Meer.

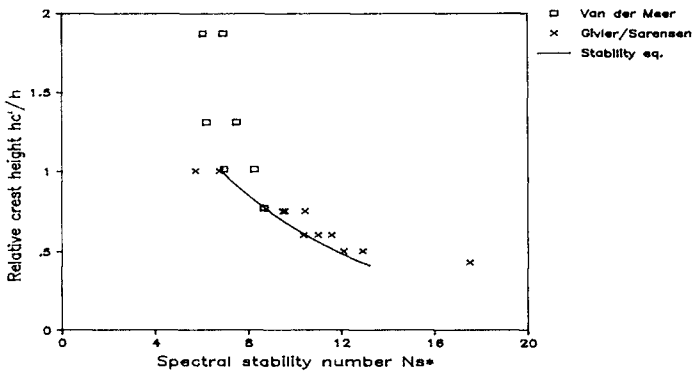


Figure 10 Spectral stability number as a function of relative crest height for submerged structures and for a fixed damage level of $S = 5$

For structures with the crest above swl it was concluded that a reduction of 0.8 in nominal diameter (or an increase of 25% in N_s^*) value can be expected for breakwaters with the crest at the water level, in comparison with non-overtopped structures. This factor is also present in Figure 10. For submerged structures, however, the increase in stability is much larger. The difference in N_s^* between $h'_c/h = 1.0$ and 0.5 is about a factor 2.

Moreover, if $h'_c/h < 0.45$ a remarkable increase in stability is present (the right points in Figure 10). This might be due to a change in phenomenon considered. If the structure becomes too low (and too small) the wave does not "feel" the structure anymore.

Figure 10 can be used to develop a design formula for submerged structures. As the difference between testing with monochromatic or random waves is not known for this type of structure, a design curve

should be at the safe side of the data of Givler and Sørensen. According to the description of the crest height for a reef breakwater (see Eq. 4) the following equation can be fitted to the data:

$$h'_c/h = a \exp(bN_s^*) \quad (12)$$

where "a" and "b" are coefficients. The coefficient "b" was found to be the same for all three damage levels of $S = 2, 5,$ and 12 which were considered, and amounted to $b = -0.14$. The coefficients "a" were respectively 2.33, 2.68 and 3.11 for $S = 2, 5$ and 12 . A linear relationship between "a" and S gives the following equation:

$$a = 2.1 + 0.1 S \quad (13)$$

Eqs. 12 and 13 together give the final stability formula:

$$h'_c/h = (2.1 + 0.1 S) \exp(-0.14 N_s^*) \quad (14)$$

The stability of submerged breakwaters is only a function of the relative crest height, the damage level and the spectral stability number. Eq. 14 is shown in Figure 10 and gives good agreement with the test results.

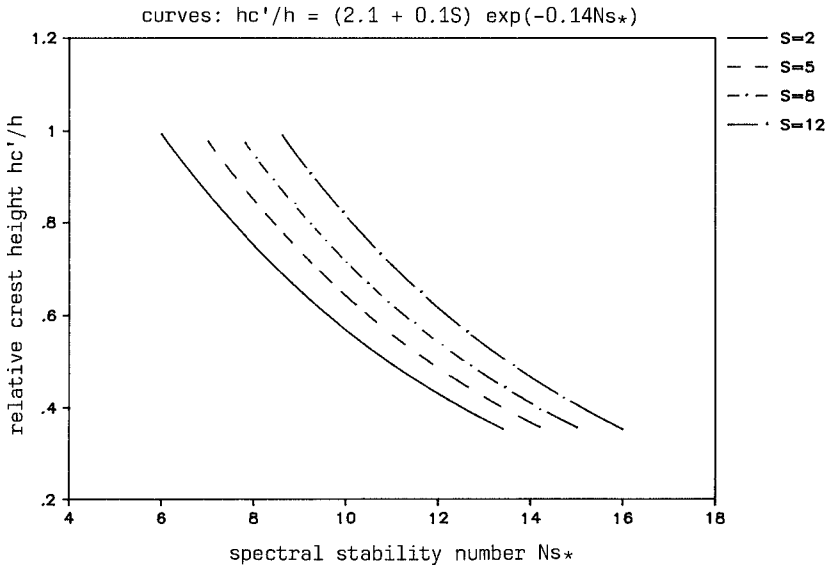


Figure 11 Design curves for a submerged structure

For fixed crest height, water level, damage level, and wave height and period, the required ΔD_{n50} can be calculated, giving finally the required stone weight. Also wave height versus damage curves can be derived from Eq. 14.

Eq. 14 is shown as a design graph in Fig. 11 for four damage levels. Here $S = 2$ is start of damage, $S = 5-8$ is moderate damage and $S = 12$ severe damage (more than one layer removed from the crest).

Conclusions

Low-crested rubble mound structures can be divided into three categories: dynamically stable reef breakwaters; statically stable low-crested breakwaters ($R_c/H_c > 0$) and statically stable submerged breakwaters. All waves overtop these structures and the stability increases remarkably if the crest height decreases.

The stability of reef breakwaters is described by Eqs. 4 and 7. Design curves can be drawn with the aid of these equations and an example is given in Fig. 6.

The stability of a low-crested breakwater with the crest above swl is first established as being a non-overtopped structure. Stability formulas derived by Van der Meer (1987, 1988) can be used. The required stone diameter for an overtopped breakwater can then be determined by multiplying the derived stone diameter for a non-overtopped structure with a reduction factor, given by Eq. 11. Design curves are shown in Fig. 9.

The stability of submerged breakwaters depends on the relative crest height, the damage level and the spectral stability number. The stability is described by Eq. 14 and a design graph is given in Fig. 11.

References

- Ahrens, J.P., 1987.
Characteristics of reef breakwaters.
CERC, Vicksburg, Technical Report CERC-87-17.
- Ahrens, J.P., 1989.
Stability of reef breakwaters.
ASCE, Journal of WPC and OE, Vol. 115, No. 2.
- Allsop, N.W.H., 1983.
Low-crest breakwaters, studies in random waves.
Proc. of Coastal Structures '83, Arlington.
- Givler, L.D. and Sørensen, R.M., 1986.
An investigation of the stability of submerged homogeneous rubble-mound structures under wave attack.
Lehigh University, H.R. IMBT Hydraulics, Report #IHL-110-86.
- Powell, K.A. and Allsop, N.W.H., 1985.
Low-crest breakwaters, hydraulic performance and stability. Hydraulics Research, Wallingford. Report SR 57.
- Van der Meer, J.W., 1987.
Stability of breakwater armour layers - Design formulae.
Coastal Eng., 11, p 219 - 239.

Van der Meer, J.W., 1988.

Rock slopes and gravel beaches under wave attack.

Doctoral thesis, Delft University of Technology. Also: Delft Hydraulics Communication No. 396

Van der Meer, J.W., 1990a.

Low-crested and reef breakwaters.

Delft Hydraulics Report H 986.

Van der Meer, J.W., 1990b.

Data on wave transmission due to overtopping.

Delft Hydraulics Report H 986.

CHAPTER 104

FORCES ON AND PARTICLE MOTIONS AROUND SUBMERGED STRUCTURES IN STEEP WAVES

JESPER SKOURUP ¹ and IVAR G. JONSSON ²

Abstract

A boundary integral equation method combined with a non-linear time stepping procedure for the free water surface is developed for simulations of the interaction between highly non-linear water waves and fixed submerged horizontal cylinders.

The wave forces on the cylinders are computed and a good correspondence is found with other computed results for low Keulegan-Carpenter numbers.

A new method for tracing the orbits of water particles in the fluid domain is developed, and the influence from submerged structures on the orbits is visualized through some computational examples.

Introduction

The numerical modelling of the interaction between highly non-linear water waves and large structures has been a field of growing interest during the last decade. These studies are motivated by the desire to obtain a numerical model in which simulations of wave/structure interactions can be performed, and hence establish an alternative to physical model tests. Among the numerical models based on a potential theory formulation the Boundary Integral Equation Method (BIEM) turns out to be one of the most efficient ones.

The first contribution where the BIEM was used for the modelling of steep and overturning waves was given by Longuet-Higgins & Cokelet (1976). They used a formulation based on Green's 2nd identity, but in a conformably map-

-
- 1) Danish Hydraulic Institute, DK-2970 Hørsholm, Denmark.
 - 2) Institute of Hydrodynamics and Hydraulic Engineering (ISVA), Technical University of Denmark, DK-2800 Lyngby. DENMARK

ped space, and the computations were thus restricted to two spatial dimensions (2-D).

Use of a BIEM based on the Cauchy integral theorem was made by Brevig et al. (1981), and they computed the wave forces on a submerged horizontal circular cylinder (pipeline) caused by breaking waves.

Stansby and Slaouti (1984) also used a formulation based on the Cauchy integral theorem in their computations of wave forces on a horizontal circular cylinder, and they obtained results which were in good agreement with the analytic results of Ogilvie (1963).

An efficient method for the temporal updating of the free water surface was developed by Dold & Peregrine (1984). In this method the influence of the higher order derivatives along the free water surface was taken into account, and this permitted the use of large time-steps with a good accuracy, and the method became very efficient for the modelling of e.g. overturning waves. In their model a conformably mapped space and Cauchy's integral theorem were used, and hence their computations (as in the previous models) were restricted to 2-D problems.

In the present paper a 2-D physical-space, non-linear BIEM is used for the modelling of steep water waves and for wave-structure interactions, and contrary to the 2-D models described above, there are in principle no restrictions for this model to be extended to 3-D.

A simple method (based on the BIEM) for a time-stepping of water particles within the fluid domain is developed and used for tracing particle orbits in time. Fixed structures are incorporated into the model, and the flow field around them are evaluated by use of the time-stepping of interior points.

Furthermore the wave forces on the structures are computed, and the "shielding" and "blockage" effects are shown for the case of two parallel cylinders.

Mathematical Formulation

The irrotational flow of an incompressible fluid with a free surface is considered. Within the frame of potential theory the flow can be described by a velocity potential $\phi(x,t)$, and the fluid velocity is then given by $u = (u,w) = (\phi_x, \phi_z) = \nabla\phi$ where $x = (x,z)$ is a position vector of an "observation point" and t is the time. By use of the mass conservation equation in the fluid domain $\Omega(t)$ (depicted in Fig. 1) we find that ϕ satisfies the Laplace equation throughout the fluid domain, i.e.

$$\nabla^2\phi = 0. \quad (1)$$

The boundary conditions for ϕ on the free surface $\Gamma_f(t)$ are the kinematic condition

$$\frac{D\vec{r}}{Dt} = \left(\frac{\partial}{\partial t} + \vec{u} \cdot \nabla\right)\vec{r} = \vec{u} = \nabla\phi, \quad z = \eta \tag{2}$$

where \vec{r} is a position vector of a water particle at the free surface, and the dynamic condition (Bernoulli's equation)

$$\frac{D\phi}{Dt} = -gz + \frac{1}{2} |\nabla\phi|^2 - \frac{p_a}{\rho}, \quad z = \eta \tag{3}$$

($D\phi/Dt = \phi_t + |\nabla\phi|^2$ is a particle following (Lagrangian) operator, and ϕ_t is an abbreviation of $\partial\phi/\partial t$). In (3), g is the acceleration due to gravity, p_a is the atmospheric pressure, and ρ is the density of water (here taken as 10^3 kg/m^3).

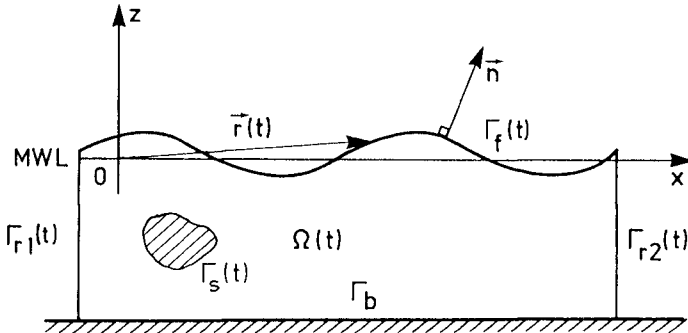


Fig. 1 Calculation domain and definition of boundaries. The x-axis is at the mean water level (MWL).

On the stationary bottom Γ_b (which is horizontal and impermeable) the boundary condition is

$$\phi_n = 0, \quad z = -h \tag{4}$$

where n is the coordinate along the unit normal vector \vec{n} pointing outwards from the fluid domain (and ϕ_n is an abbreviation of $\partial\phi/\partial n$).

When a structure is situated in the computational domain, the boundary condition on its surface $\Gamma_s(t)$ is

$$\phi_n = \nabla\phi \cdot \vec{n} = V_s \tag{5}$$

where V_s is a function describing the velocity of the body surface in the direction of the unit normal vector n . In the case of a fixed structure $V_s = 0$.

Boundary conditions at the lateral boundaries $\Gamma_{r1}(t)$ and $\Gamma_{r2}(t)$ are needed for a closure of the boundary value problem for ϕ . By assuming space periodicity (but not necessarily time periodicity) and no net current

below wave trough level, periodicity conditions can be imposed on the vertical boundaries $\Gamma_{r1}(t)$ and $\Gamma_{r2}(t)$

$$\phi_n[\Gamma_{r1}(t)] = -\phi_n[\Gamma_{r2}(t)], \quad \phi[\Gamma_{r2}(t)] = \phi[\Gamma_{r1}(t)] \quad (6)$$

for the same z-values at the two boundaries. The horizontal distance between $\Gamma_{r1}(t)$ and $\Gamma_{r2}(t)$ has to be an integer number of wave lengths. Periodicity conditions at the lateral boundaries were also used by Brevig et al. (1981) and by Stansby and Slaouti (1984) in their studies of wave/structure interaction by use of the BIEM.

In order to solve the Laplace problem (1) with the fully non-linear boundary conditions we use an integral equation method based on Green's 2nd identity

$$\alpha(\vec{x})\phi(\vec{x}, t) = \int_{\Gamma(t)} \phi(\vec{\xi}, t)G_n(\vec{x}, \vec{\xi}) - G(\vec{x}, \vec{\xi})\phi_n(\vec{\xi}, t) d\Gamma \quad (7)$$

where $\vec{\xi}$ is the position vector of an "integration point" situated at the boundary $\Gamma(t)$.

The kernel function $G(\vec{x}, \vec{\xi})$ is the free space Green's function which in two dimensions is:

$$G(\vec{x}, \vec{\xi}) = \ln|\vec{\xi} - \vec{x}| \quad (8)$$

The factor $\alpha(\vec{x})$ depends on the boundary geometry ($\alpha(\vec{x}) = \pi$ for \vec{x} at a smooth part of the boundary, and $\alpha(\vec{x}) = 2\pi$ for \vec{x} inside $\Omega(t)$).

The derivative of G in the direction of the outwards unit normal vector \vec{n} is

$$G_n(\vec{x}, \vec{\xi}) = \frac{(\vec{\xi} - \vec{x}) \cdot \vec{n}}{|\vec{\xi} - \vec{x}|^2} \quad (9)$$

Following the solution of the Laplace problem for ϕ an updating in time of the computational domain and related boundary conditions to a subsequent time level must be performed. Using the Lagrangian approach developed by Dold & Peregrine (1984), truncated Taylor series in time for the position vector \vec{r} of a free surface particle and for the velocity potential ϕ provide

$$\vec{r}(t+\Delta t) = \vec{r}(t) + \sum_{k=1}^n \frac{(\Delta t)^k}{k!} \frac{D^k \vec{r}(t)}{Dt^k} + O[(\Delta t)^{n+1}] \quad (10)$$

$$\begin{aligned} \phi(\vec{r}(t+\Delta t), t+\Delta t) &= \phi(\vec{r}(t), t) \\ &+ \sum_{k=1}^n \frac{(\Delta t)^k}{k!} \frac{D^k \phi(\vec{r}(t), t)}{Dt^k} + O[(\Delta t)^{n+1}] \end{aligned} \quad (11)$$

where Δt is the time increment, and the Lagrangian (particle following) operator D/Dt is defined in (2).

The expansion coefficients in (10) and (11) are obtained by successive solutions of the Laplace equation for the velocity potential ϕ and its time derivatives, where the solution of one Laplace problem provides the non-linear boundary conditions for the next.

The solution of the Laplace problem for ϕ by use of Green's 2nd identity (7) gives as result ϕ and ϕ_n at the whole boundary of the computational domain. Hence the gradient of the velocity potential can be evaluated, and thereby the first order expansion coefficients in (10) and (11) by use of the free surface boundary conditions (2) and (3).

The boundary condition at the free surface for the Laplace problem involving the first order time derivative is obtained from the Eulerian form of the dynamic condition at the free surface (cf. (3)).

$$\phi_t = -gz - \frac{1}{2}|\nabla\phi|^2 - \frac{p_a}{\rho}, \quad z = \eta \quad (12)$$

The conditions at the remaining part of the boundary are obtained by differentiating (4), (5), and (6) with respect to t .

Just as the governing differential equation (1) and the integral equation (7) are valid for ϕ , these may also be written for time derivatives of any order of ϕ . Hence we have a mathematical problem formulated in the same geometry as before, but now with ϕ_t and ϕ_{tn} as solution at the boundary of the computational domain. The numerical solution of the second (and of subsequent) Laplace problems is computationally very fast compared to the solution of the first Laplace problem since the kernel functions (G, G_n) of the governing integral equation only are functions of the boundary geometry which is unchanged, since all derivatives are computed at the same time level. In the present work the series (10) and (11) are truncated after $n=2$, but it is mentioned that the expansion coefficients are obtained from the fully non-linear boundary conditions at the free surface.

The lateral boundaries of the computational domain are updated by following the horizontal motion of the intersections with the free surface.

After the solutions of the Laplace problems for ϕ and ϕ_t have been found by use of the BIEM, all variables of interest at the boundary of the computational domain are determined. By use of (7) it is thus possible to determine the values of the velocity potential ϕ and its time derivative ϕ_t at any point inside the computational domain $\Omega(t)$. Furthermore, analytical differentiations of (7) provide integral equations to determine the values of $\phi_x, \phi_z, \phi_{xt}, \phi_{zt}, \phi_{xx}$ and ϕ_{xz} at the observation point x .

These functions only appear as unknowns outside the relevant integrals (since G and its derivatives are functions of the geometry, which is known), and the numerical evaluation of them is therefore very fast. From the results we may deduce the particle velocity components u and w , the acceleration components a_x and a_z , and the dynamic pressure p^+ ($= p + \rho gz$) at the interior point given by the position vector \vec{x} as:

$$u(\vec{x}) = \phi_x(\vec{x}) \quad (13)$$

$$w(\vec{x}) = \phi_z(\vec{x}) \quad (14)$$

$$a_x(\vec{x}) = \phi_{xt}(\vec{x}) + \phi_{xx}(\vec{x})\phi_x(\vec{x}) + \phi_{xz}(\vec{x})\phi_z(\vec{x}) \quad (15)$$

$$a_z(\vec{x}) = \phi_{zt}(\vec{x}) + \phi_{xz}(\vec{x})\phi_x(\vec{x}) - \phi_{xx}(\vec{x})\phi_z(\vec{x}) \quad (16)$$

$$p^+(\vec{x}) = -\rho \left[\phi_t(\vec{x}) + \frac{1}{2} \{ (\phi_x(\vec{x}))^2 + (\phi_z(\vec{x}))^2 \} \right] \quad (17)$$

where in (16) $\phi_{zz}(\vec{x})$ has been replaced by $-\phi_{xx}(\vec{x})$.

A time-stepping method for water particles in the fluid domain $\Omega(t)$ similar to the one for updating of particles at the free water surface (i.e. based on truncated Taylor series) may then be written as:

$$x_i(t+\Delta t) = x_i(t) + u(\vec{x})\Delta t + a_x(\vec{x}) \frac{(\Delta t)^2}{2} + O[(\Delta t)^3] \quad (18)$$

$$z_i(t+\Delta t) = z_i(t) + w(\vec{x})\Delta t + a_z(\vec{x}) \frac{(\Delta t)^2}{2} + O[(\Delta t)^3] \quad (19)$$

where the position vector of the water particle is $\vec{x} = (x_i, z_i)$. Hence we have established a visualization technique that enables us to follow the traces of water particles in the fluid domain in time.

Numerical Solution Method

The boundary of the computational domain is subdivided into a finite number of small segments, each segment connecting two adjacent discretization points situated at the boundary curve. By representing the geometry as well as the boundary functions ϕ and ϕ_n at each segment by a prescribed variation, the governing integral equation can be formulated in terms of the values of the variables ϕ and ϕ_n (or ϕ_t and ϕ_{tn}) in the discretization points. Hence we may form a linear algebraic system of equations, in which each element only is a function of the geometry of the boundary and of the interpolation functions used.

In order to model the variation of boundary functions between the discretization points, we use a Hermite

cubic spline representation along each boundary element at the free surface (i.e. between two adjacent discretization points) and a linear variation elsewhere. By this method a continuity up to and including 2nd order derivatives of the free surface representation is kept, and all boundary nodes there are treated equally in the numerical solution of the governing integral equation.

The numerical integration over each regular boundary element (i.e. an element where the integration point does not coincide with the observation point) is performed by use of a standard Gauss-Legendre quadrature. At the singular boundary elements special methods must be used (see Skourup (1989) for details).

Results

During recent years, particular attention has been paid to numerical simulations of the interaction between waves and submerged floating structures with large dimensions. Especially a new concept for crossing of deep fjords and straits with submerged tunnels (which e.g. has been proposed for a strait crossing at Høgsfjord, Norway) has inspired to the work presented in this paper.

In all the following computations the Keulegan-Carpenter number K is smaller than 2 and the predominant contribution to the force on the structure is thus inertial and can be computed by the BIEM.

The total wave force vector \vec{F} on the structure, which is cylindrical, is obtained by integrating the excess pressure p^+ (due to the waves) over the whole surface of the structure.

$$\vec{F} = - \int_{\Gamma_s} p^+ \vec{n} d\Gamma \quad (20)$$

where \vec{n} is the outward normal unit vector from the surface of the cylinder. The excess pressure p^+ is determined from the Bernoulli equation as

$$p^+ = - \rho \left[\phi_t + \frac{1}{2} (\phi_s^2 + \phi_n^2) \right] \quad (21)$$

where ϕ_n vanishes at the surface of the cylinder (since it is fixed and impermeable). The term ϕ_s is found from the spatial derivatives of ϕ at Γ_s .

One Circular Cylinder

The special reference case with computation of the interaction between waves and a submerged horizontal circular cylinder with its axis parallel to the wave crests has been treated widely in the literature, beginning with Dean (1948), who showed that linear deep water waves un-

dergo a phase shift as they pass over a cylinder, and further that there is no reflection from the cylinder. Ursell (1950) used a multipole method, and derived expressions for the first-order forces on the cylinder. Ogilvie (1963) extended Ursell's method and provided expressions for the mean second order ("drift") force at the cylinder. Chaplin (1984a,b) performed experiments to determine the non-linear forces and mass transport around a horizontal submerged cylinder, and experimentally verified that there is a mass-transport around the cylinder, as it could be predicted by use of Milne-Thomson's (1968) circle theorem.

A fluid domain with a horizontal dimension of one wave length L is considered. In this domain we situate a fixed horizontal circular cylinder with diameter $D = 2a$ (a being the radius of the cylinder) and a submergence d of its centre axis as depicted in Fig. 2.

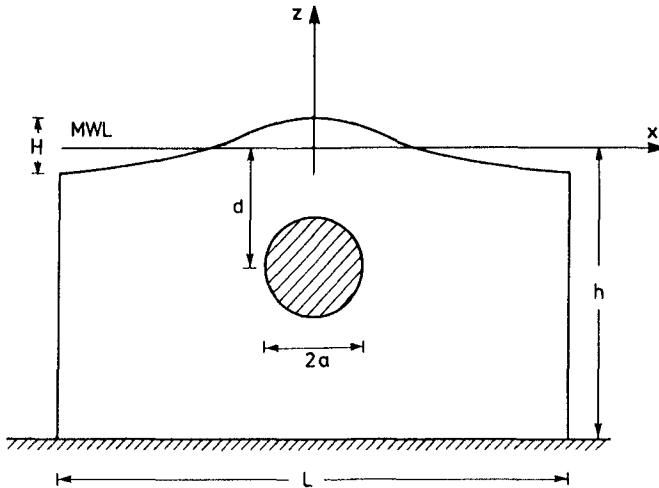


Fig. 2 Definition sketch of submergence d and radius a of horizontal circular cylinder.

The diameter of the cylinder is $D = 10.0$ m and the submergence is $d = 20.0$ m. The wave data are: $H = 10.0$ m, $T = 8.78$ s, at a depth $h = 100$ m and an initial profile given by the stream function wave theory by Rienecker & Fenton (1981). This gives a wave length $L = 128$ m and hence a steepness of the wave of 7.8%, and the Keulegan-Carpenter number $K = 1.2$. Computations are carried out covering 6 wave periods with time steps of $T/100$, and the resulting wave force variation in time on the cylinder is depicted in Fig. 3. The total force on the cylinder is computed as the modulus of the two force components F_x and F_z .

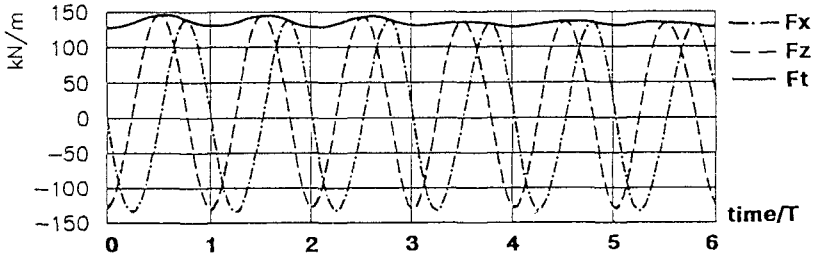


Fig. 3 Wave force on a horizontal cylinder during 6 wave periods. Domain length is L .

By regarding Fig. 3 it is readily seen that the oscillations of the total force tend to decrease as the computations proceed in time. In order to investigate if this is an effect arising from using the periodicity conditions at the lateral boundaries with a distance of just one wave length, the same computation is carried out with identical wave and structure data, but now with the horizontal dimension of the computational domain of either three or five wave lengths (i.e. the spacing of the cylinders is either $3L$ or $5L$).

In Fig. 4 the total force on the cylinder is compared for the horizontal dimension of the computational domain being either one or three wave lengths.

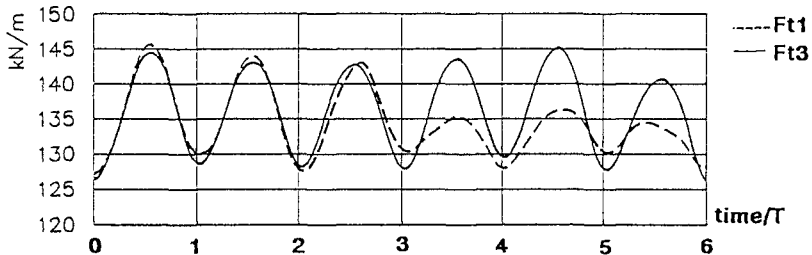


Fig. 4 Total wave forces on a cylinder during 6 wave periods. Domain length is either L or $3L$.

During the first three wave periods the difference between the two results is less than 1.5% of the mean total force on the cylinder. The larger deviation hereafter is probably an effect of the proximity of other cylinders. Extending the horizontal dimension of the computational domain further to five wave lengths provides almost identical results as obtained from the domain, which was three wave lengths long, when the first three wave periods are considered.

From these computational results we conclude that a horizontal dimension of one wave length is sufficient

for computations covering a time span less than three wave periods. It is mentioned that the computational time is proportional to N^3 for large values of N (where N is the number of computational nodes at the boundary), and the desired accuracy of the results therefore must be assessed against the computational time necessary to provide the results.

Numerical results for the interaction between non-linear waves and a submerged horizontal, circular cylinder at low Keulegan-Carpenter numbers, are found in Stansby & Slaouti (1984), in Vada (1987), and in Isaacson & Cheung (1990), and in all cases the inertia coefficients are in the same range as the present results.

Experimental results are also available, and for deeply submerged cylinders Cheong et al. (1989) found the inertia coefficients to be in the vicinity of 2 for low Keulegan-Carpenter numbers. For a cylinder close to the free surface, Chaplin (1984b) and Miyata & Lee (1990) found the inertia coefficients to be much smaller than 2 in their experiments with Keulegan-Carpenter numbers in the range 1-3. Chaplin (1984b) explained this decrease as associated with the circulation generated by steady streaming in the oscillatory boundary layer on the cylinder. It has not been possible in the present work to reproduce these low inertia coefficients. This indicates that the large reduction of the inertia coefficients is an effect due to viscosity, which is omitted in the present work. Miyata & Lee (1990) obtained this large decrease of the inertia coefficient in their computations where they solved the Navier-Stokes equations in a finite difference formulation for Reynolds numbers $1.69 \cdot 10^4$ and $3.87 \cdot 10^4$.

Tracing of the orbits of water particles in the vicinity of the cylinder is performed by use of the time stepping method for particles in the fluid domain (i.e. eqs. (18) and (19)).

In Fig. 5 the particle motion during one (Eulerian) wave period is followed. It is seen that the water particles tend to follow the cylinder contour and that they have all moved to new positions in the clockwise direction around the cylinder after one wave period. This circulation of water particles around a horizontal cylinder is also showed analytically by e.g. Ogilvie (1963), and verified experimentally by Chaplin (1984a). The amplitudes (both in the horizontal and the vertical directions) are by linear wave theory found to be 2.77 m for a water particle at $z = -12.0$ m, and this corresponds quite well with the orbits shown in Fig. 5.

Particle orbits in the vicinity of the cylinder are also computed using the circle theorem (cf. Milne-Thomson, 1968) combined with a time-stepping procedure (as (18) and (19)) for water particles and good agreement was found with orbits computed by the BIEM.

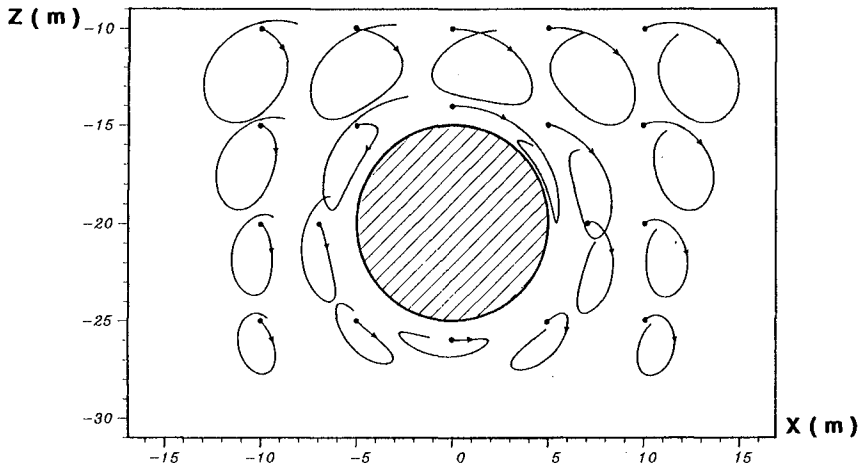


Fig. 5 Traces of the particle motions during one period in the vicinity of a submerged, circular cylinder with diameter $D = 10.0$ m. Wave data: $T = 8.78$ s, $H = 10.0$ m, $L = 128$ m at $h = 100$ m. ●: initial position, ▶: orbital direction. Domain length L .

Two Circular Cylinders

Computations with more than one cylinder in the fluid domain are also performed.

Two parallel horizontal circular cylinders are considered, and the dimensions of the cylinders are kept the same as in the previous case, i.e. with a diameter $D=10.0$ m, and a submergence of their centre lines at $d=20.0$ m. The wave data are also the same as before. The length of the computational domain equals L . In order to investigate the shielding and blockage effects between the two cylinders, computations with different distances between the centre lines have been carried out covering three wave periods. The distances have been chosen as $1.5D$, $2D$ and $3D$ and the main results are given in Table I. Here also the reference-numbers corresponding to an "infinite" distance between the cylinders are given. These reference numbers are computed during the second and third wave period for the case with one cylinder in a domain with length $5L$.

From Table I two different effects from the interaction between the two cylinders appear. Regarding the horizontal force F_x on each of the two cylinders it is seen that the amplitudes are decreasing as the cylinders are approached to each other, and that the force amplitude is larger on the upstream cylinder than on the downstream cylinder. This is due to a shielding effect between the two cylinders.

Cylinder	Centre	$F_{x,max}$	$F_{x,min}$	$F_{z,max}$	$F_{z,min}$	$F_{t,max}$	$F_{t,min}$
	axis dist.						
1 (upstream)	1.5D	138.1	-123.2	160.3	-142.9	162.0	116.4
	2D	139.9	-129.5	151.6	-134.1	154.5	122.3
	3D	142.4	-134.0	145.4	-128.4	149.1	122.8
2 (downstream)	1.5D	126.1	-122.7	155.0	-146.4	155.6	116.9
	2D	131.7	-125.6	145.0	-137.5	146.5	119.9
	3D	134.4	-130.4	138.7	-132.8	141.3	121.7
	"∞"	137.6	-134.2	142.9	-128.4	143.0	128.1

Table I Extreme wave force amplitudes (in kN/m) at two parallel cylinders as function of centre axes distance. The computations cover 3 wave periods.

Regarding the vertical force F_z on each of the two cylinders it is seen that the amplitudes are increasing as they are approached to each other. This result shows that there is a blockage effect between the two cylinders. The maximum force amplitude is slightly larger on the upstream cylinder than on the downstream cylinder.

The sum of the shielding and the blockage effects between the two cylinders appear in the total force variation at the two cylinders, and it is seen that the effect from blockage influences the total force, since the maximum values of the total force on each of the two cylinders increase as the they are approached to each other.

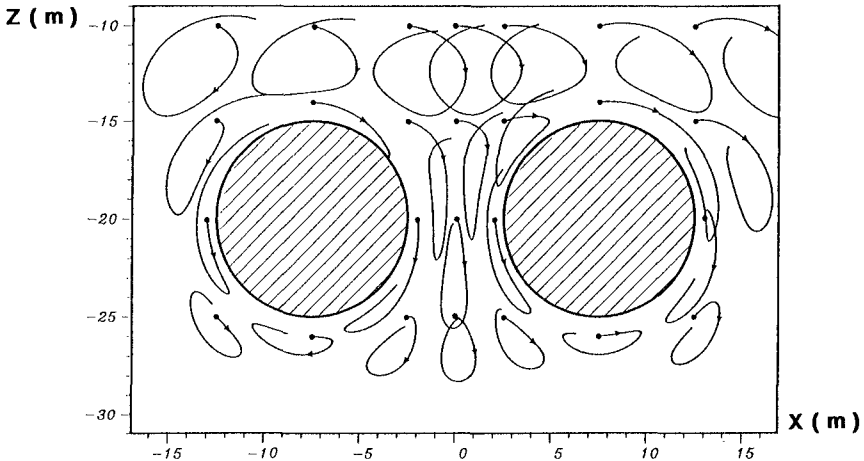


Fig. 6 Particle orbits in the vicinity of two parallel horizontal circular cylinders with centre axis distance 1.5D. Other data as in Fig. 5.

The shielding effect between the two cylinders is seen only to have a small influence on the maximum value of the total force on the two cylinders.

Particle orbits in the vicinity of the cylinders are shown in Fig. 6 for a centre axis distance 1.5D.

Conclusion

It has been demonstrated that a fully non-linear boundary element model with periodicity conditions at the lateral boundaries of the computational domain provides good results for wave forces on and particle orbits around submerged horizontal cylindrical structures (2-D) for small Keulegan-Carpenter numbers. The effects from shielding and blockage between two cylinders are shown by computational examples, and the cylinder distances are found to have some effect on the forces.

There are, in principle, no restrictions in the mathematical formulation that prevent the present model from being extended to 3-D. However, appropriate conditions at the lateral boundaries of the computational domain must be developed in order to be able to perform computations with 3-D waves of not permanent form. Furthermore, faster and more efficient computers than those of today must be developed before an accurate non-linear 3-D model can be developed and used for application as a "numerical wave tank".

A more detailed account of the present study will be published subsequently (Skourup & Jonsson, 1990).

Acknowledgement

Most of the work presented in this paper was done as part of the first author's Ph.D. studies at ISVA at the Technical University of Denmark under the supervision of Assoc. Professor Ib A. Svendsen and later under the supervision of Assoc. Professor Ivar G. Jonsson. Jesper Larsen, Ph.D., acted as co-supervisor.

A large part of the work was performed at the University of Delaware, U.S.A., in close collaboration with Stephan T. Grilli, Ph.D., and Professor Ib. A. Svendsen.

The Danish Technical Research Council (STVF) has financed the present study (J. No. 5.17.3.6.03). This support is gratefully acknowledged.

References

- Brevig, P., Greenhow, M. and Vinje, T. (1981). Extreme wave forces on submerged cylinders. 2nd Int. Symp. on Wave and Tidal Energy. Cambridge, England, Paper E2, 143-166.
- Chaplin, J.R. (1984a). Mass transport around a horizontal cylinder beneath waves. J. Fluid Mech. 140, 175-187.

- Chaplin, J.R. (1984b). Non-linear forces on a horizontal cylinder beneath waves. *J. Fluid Mech.* 147, 449-464.
- Cheong, H.-F., Jothi Shankar, N. and Subbiah, K. (1989). Inertia dominated forces on submarine pipelines near seabed. *J. of Hyd. Res.* 27(1), 5-22.
- Dean, W.R. (1948). On the reflection of surface waves by a submerged cylinder. *Proc. Camb. Phil. Soc.*, 44, 483-491.
- Dold, J.W. and Peregrine, D.H. (1984). Steep unsteady water waves. An efficient computational scheme. *Proc. 19th ICCE, Houston, Texas*, 1, 955-967. ASCE, New York, 1985.
- Grilli, S.T., Skourup, J. and Svendsen, I.A. (1989). An efficient boundary element method for non-linear water waves. *Engineering Analysis with Boundary Elements*. 6(2), 97-107.
- Isaacson, M. and Cheong, K.-F. (1990). Time-domain solution for second-order wave diffraction. *J. of Waterway, Port, Coastal and Ocean Engineering*, 116 (2), 191-210.
- Longuet-Higgins, M.S. and Cokelet, E.D. (1976). The deformation of steep surface waves on water. I. A numerical method of computation. *Proc. Roy. Soc. London, A* 350, 1-26.
- Milne-Thomson, L.M. (1968). *Theoretical Hydrodynamics*. 4th ed. MacMillan, London.
- Miyata, H. and Lee, Y.-G. (1990) Vortex motions about a horizontal cylinder in waves. *Ocean Engineering*, 17 (3), 279-305.
- Ogilvie, T.F. (1963). First and second order forces on a cylinder submerged under a free surface. *J. Fluid Mech.*, 16, 451-472.
- Rienecker, M.M. and Fenton, J.D. (1981). A Fourier approximation method for steady water waves. *J. Fluid Mech.*, 104, 119-137.
- Skourup, J. (1989). A boundary integral equation model for the development of non-linear water waves and their interaction with structures. Ph.D. dissertation. Series Paper No. 47. xvi + 158 pp. Institute of Hydrodynamics and Hydraulic Engineering (ISVA). Technical University of Denmark.
- Skourup, J. and Jonsson, I.G. (1990). Computations of forces and particle orbits around horizontal cylinders under steep waves. Submitted for publication.
- Stansby, P.K. and Slaouti, A. (1984). On non-linear wave interaction with cylindrical bodies: A vortex sheet approach. *Appl. Ocean Res.*, 6(2), 108-115.
- Ursell, F. (1950). Surface waves in the presence of a submerged circular cylinder. *Proc. Camb. Phil. Soc.*, 46, 141-158.
- Vada, T. (1987). A numerical solution for the second-order wave diffraction problem for a submerged cylinder of arbitrary shape. *J. Fluid Mech.*, 174, 23-37.

CHAPTER 105

Reliability Analysis of Composite Breakwaters Protected with Armor Blocks

Masato Yamamoto*
Kazumasa Mizumura**
Taiji Endo***
and
Naofumi Shiraishi****

Abstract

The subject of this present research is to study probabilistic design of caissons of composite breakwaters, rubble-mounds and foundations protected with armor blocks. Concerning caissons, sliding, rocking and overturning motions are considered to be the failure modes. Wave forces acting on a caisson can be calculated using Goda's formulas(1974). The stability of the rubble-mound is estimated by means of Bishop's method while geotechnical problems employ a simplified equation as a reliability function in accordance with the Japanese Standards for Coastal Structures.

Since distribution for occurrence for each failure mode is unknown, Monte Carlo simulation was applied to calculate the risk of each failure. The probability of geotechnical failure was greatest among the failure modes but the rubble-mound was not in danger of collapse.

Introduction

In Japan, breakwaters of the type shown in Fig.1 are the most commonly designed and constructed. They consist of caisson, concrete cap, rubble-mound and armor blocks. Such a breakwater is referred to as "a composite breakwater protected with armor blocks". It has several advan-

*Senior Research Engineer,Hydraulic Laboratory,Nippon Tetrapod Co.,Ltd.,2-7,Higashi-Nakanuki,Tsuchiura,Ibaraki Pref.,300,Japan

**Prof. of Civil Eng.,Dept.,Kanazawa Inst. of Tech.,7-1,Ogigaoka,Nonoichimachi,Ishikawa Pref.,921,Japan

***Director,Overseas Division,Nippon Tetrapod Co.,Ltd.,2-7-1,Nishi-Shinjuku,Shinjuku-Ku,Tokyo,163,Japan

****Chairman, Nippon Tetrapod Co.,Ltd.,ditto

tages, i.e.

- (1)The construction period is short.
- (2)A large sea area within the breakwater is conserved.
- (3)The crest elevation is low.
- (4)Ships are easily moored inside the upright section.
- (5)etc.

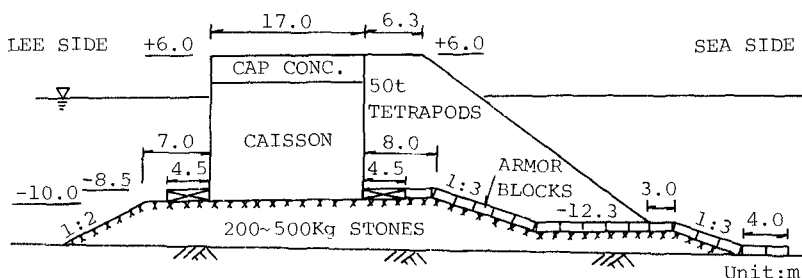


Fig.1 Typical Composite Breakwater Protected with Armor Blocks

In recent years, breakwaters have been constructed in deeper and deeper areas so the armor blocks and upright sections receive large wave forces. As a result, blocks receive damage and caissons slide or overturn. In addition, foundations receive such high pressure from caissons that they collapse.

Engineers in Japan design composite breakwaters protected with armor blocks using a deterministic method introducing a safety factor. The method is based on experiences from construction of breakwaters over many years. However if a new type structure is designed or constructed or conventional breakwaters are placed in a deep sea area where no structure has existed before, the deterministic or safety factor approach is not easily applicable.

Recently, new methodology based on probabilistic and statistical theory has been the subject of study for application to coastal structures e.g. Burcharth(1985), Van der Meer et al(1987), Mizumura et al(1988) and PIANC(1990). In this new design method, ranks of safety between breakwaters can be balanced and structures designed taking into account economical conditions (Yamamoto et al(1988)).

In this paper, the authors applied the probabilistic method to a composite breakwater protected with armor blocks taking wave breaking and retaining wave after breaking into account.

Reliability Analysis

If the external force is represented by S and the resistant force by R in a certain failure mode, the reliability function Z is given by eq.(1).

$$Z = R - S \tag{1}$$

In this case, as Z is greater than 0, failure does not occur. However, if Z is less than 0, failure does occur. In eq.(1) the variables R and S are generally uncertain or probabilistic ones therefore Z is also a probabilistic variable. So if the probabilistic density function of Z is known, the probability where the failure occurs can be calculated as follows;

$$P = \int_{-\infty}^0 f(Z) dZ \tag{2}$$

in which f(Z) is the probabilistic function of probabilistic variable Z.

If m failure modes exist for a breakwater, the total failure probability for the breakwater is obtained as eq.(3).

$$P_f = \text{Prob} \{ (Z_1 < 0) \cup (Z_2 < 0) \cup \dots \cup (Z_m < 0) \} \tag{3}$$

Assuming all m failure modes are independent of each other, the probability for the risk is simply rewritten by eq.(4).

$$P_f = 1 - \prod_{i=1}^m \{ (1 - P_{fi}) \} \tag{4}$$

Concerning the failure modes for the composite breakwater protected with armor blocks as shown in Fig.1, the main modes are (1) movement of armor blocks, (2) slide of the upright section, (3) overturning of the upright section, (4) slide of the rubble-mound and (5) collapse of the foundation that is geotechnical instability shown in Fig.2.

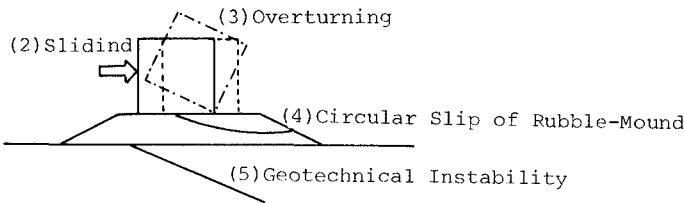


Fig.2 Failure Mode for Composite Breakwater protected with Armor Blocks

The block movement for these failure modes was already discussed by Mizumura et al(1988) and Yamamoto et al (1988) in a previous ICCE in Spain. Therefore in this paper the authors dealt with (2)-(5) as the failure modes of the composite breakwater. The failure modes above were selected as representative, however because the proba-

bility density functions of the failure occurrence, $f(Z)$ was not unknown, Monte Carlo simulation was conducted to calculate the functions.

Wave Forces Acting on Caisson Wall

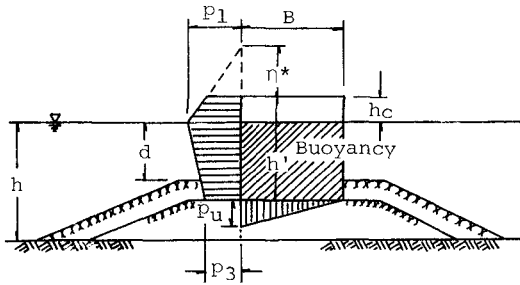


Fig.3 Distribution of Wave Pressure

Fig.3 shows a sketch of a wave pressure distribution along the upright section. Wave pressures acting on the upright section are expressed as below (Tanimoto et al(1976));

$$p_1 = \lambda \alpha_1 w_0 H \tag{5}$$

$$p_3 = p_u = \lambda \alpha_1 \alpha_3 w_0 H \tag{6}$$

$$\eta^* = 1.5 \lambda H \tag{7}$$

where λ is the wave pressure reducing ratio due to the armor block protection, and

$$\alpha_1 = 0.6 + \frac{1}{2} \left[\frac{4\pi h/L}{\sinh(4\pi h/L)} \right]^2 \tag{8}$$

$$\alpha_3 = 1 - \frac{h'}{h} \left[1 - \frac{1}{\cosh(2\pi h/L)} \right]$$

λ refers to the ratio of the wave force in the case of protection as opposed to that without protection. When λ equals to 1, no protection exists in front of the caisson. In the case where λ is less than 1, that indicates that there is the armor block protection. The value of λ is taken to be 0.8 in the case of the composite breakwater protected with armor units according to the Japanese Standards of design of breakwaters based on hydraulic model tests. The total horizontal wave force acting on the vertical wall, up-lift force and moment around the heel

Goda(1974) proposed formulas representing wave forces acting on an upright section of a composite breakwater without armor protection. Tanimoto et al(1976) modified Goda's formulas to apply a composite breakwater protected with armor blocks introducing a wave pressure reducing ratio due to armor blocks.

of the caisson are obtained by eq.(9)-(12).

The horizontal wave force;

$$F = \frac{1}{2} (p_1 + p_3)h' + \frac{1}{2} (p_1 + p_4)h_c^* \quad (9)$$

The moment around the corner of the base due to the horizontal wave force;

$$M_p = \frac{1}{2} (2p_1 + p_3)h'^2 + \frac{1}{2} (p_1 + p_4)h'h_c^{*2} \\ + \frac{1}{6}(p_1 + 2p_4)h_c^{*2} \quad (10)$$

in which

$$p_4 = \begin{cases} p_1 (1 - h_c/\eta^*) & : \eta \geq h_c \\ 0 & : \eta^* < h_c \end{cases}$$

$$h_c^* = \min (\eta, h_c)$$

$\min(a,b)$: smaller of a and b.

The total up-lift force:

$$U = \frac{1}{2} p_u B \quad (11)$$

The moment around the hcel due to the up-lift force:

$$M_u = \frac{2}{3} UB \quad (12)$$

Reliability Functions for Each Failure Mode

When the wave forces F and U operate on the caisson, the resistant force against slide is due to friction represented by eq.(13) and the resistant moment is given by eq.(14).

$$F_r = \mu (W - U) \quad (13)$$

$$M_r = Wt \quad (14)$$

in which W is the weight of the upright section in water, μ indicates a frictional coefficient between the caisson base and the surface of the rubble-mound and t refers to the distance between the caisson heel and the centroid of

the upright section.
So the reliability functions for slide and overturning of the upright section are expressed by

$$Z_S = \mu (W - U) F \tag{15}$$

and

$$Z_O = Wt - M_u - M_p \tag{16}$$

respectively.

Concerning the collapse of rubble-mound slope, the mound slope is assumed to be destroyed by a circular arc of which the center is located at point O as shown in Fig.4.

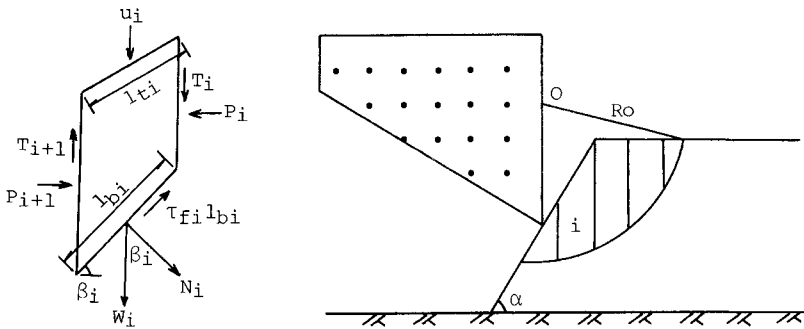


Fig.4 Selection of Center of Circular Arc

The computational method is as proposed by Bishop. The forces exerted on the *i*-th soil element are described in Fig.4. Assuming that $T_i = T_{i+1}$ and $P_i = P_{i+1}$, the sliding and resistant moment with respect to point O are written as;

$$M_S = \sum_{i=1}^n (W_i + u_i) R_o \sin \beta_i \tag{17}$$

$$M_b = \sum_{i=1}^n \tau_{fi} l_{bi} R_o \tag{18}$$

in which W_i is the weight of the *i*-th soil element, β_i is an angle of the sliding arc of the *i*-th soil element to the horizontal, R_o refers to the radius of the circular arc, τ_{fi} indicates the shear stress exerted on the circular arc of the *i*-th soil element, l_{bi} is the length of the circular arc and u_i is the vertical force due to wave action. If the normal force exerted on the circular arc is given by N_i , the shear stress becomes

$$\tau_{fi} = \frac{N_i}{l_{bi}} \tan \phi \tag{19}$$

where ϕ is the friction angle. The balance of the verti-

cal forces exerted on the i -th element gives the normal force as eq.(20).

$$N_i = \frac{W_i + u_i}{\cos\beta_i + \tan\phi \sin\beta_i / F_s} \quad (20)$$

F_s is obtained as follows.

$$F_s = \frac{1}{\sum_{i=1}^n (W_i + u_i) \sin\beta_i} \sum_{i=1}^n \frac{(W_i + u_i) \tan\phi}{\cos\beta_i + \tan\phi \sin\beta_i / F_s} \quad (21)$$

Therefore the reliability function is given by

$$Z_b = M_b - M_s \quad (22)$$

This equation is tantamount to F_s . If $Z_b < 0$ or $F_s < 1$, the rubble-mound slope collapses. F_s should be obtained by iteration in eq.(21).

Concerning the geotechnical instability, the bearing capacity of the foundation engineering for eccentric inclined load. However in this study a simplified technique was employed in order to examine the magnitude of the heel pressure. According to Goda(1985), the largest bearing pressure at the heel P_e is obtained as below;

$$P_e = \begin{cases} \frac{2W_e}{3t_e} & : t_e \leq \frac{1}{3} \\ \frac{2W_e}{B} \left(2 - 3 \frac{t_e}{B} \right) & : t_e > \frac{1}{3} \end{cases} \quad (23)$$

in which $t_e = M_e / W_e$, $M_e = Wt - M_u - M_p$ and $W_e = W - U$. If the allowance for heel pressure is τ , the reliability function for the geotechnical stability is represented by the following equation.

$$Z_g = \tau - P_e \quad (24)$$

The value of τ is usually taken to be 40ton/m²-50ton/m².

Wave Transformation from Offshore to Breakwater Site

The wave force acting on the upright section can be obtained from eqs.(5)-(12) if the wave height at the breakwater is given. The distribution of the wave height in deep water can be regarded as Rayleigh distribution. However, that at the breakwater in shallow water or the surf zone is generally not known. Goda(1975) proposed the numerical method to calculate the wave height of random waves in the surf zone. In this study, the method was

applied to obtain the wave height distribution at the breakwater site. This method is as follows;
 A random wave train of which the height distribution is given in deep water is separated into individual waves defined by the zero-up crossing and deformation of each individual wave due to shoaling or breaking is estimated applying monochromatic wave theory including non-linearity. Goda obtained the wave height distribution in the surf zone taking retaining waves after breaking and surf beat into consideration.

Risk Analysis and Illustrative Examples

In this study, failure probability for the composite breakwater protected with armor blocks was calculated on the basis of the following assumptions.

(1) Uncertain variables are wave heights in deep water, wave periods, frictional coefficients (μ) and wave force reducing ratio (λ). Other variables are deterministic ones.

(2) The distribution of wave heights follows the Rayleigh distribution in deep water. The distribution of wave period of the 2nd power is also Rayleigh distribution.

(3) A frictional coefficient between the caisson base and rubble-mound is distributed in accordance with the normal distribution of which the mean value is 0.57 and the standard deviation is 0.05. This is decided under a condition where 10cm sliding distance of the upright section is allowed (Toyama(1985)).

(4) The wave force reducing ratio is uniformly distributed from 0.4 to 1.0 with reference to the results of hydraulic model tests conducted by Tanimoto et al(1976).

The procedure for risk analysis was as follows;

The distribution of wave height at the site of the breakwater was calculated employing the numerical method described previously. Next, we sampled a wave height coupled with a wave period from their distribution at the breakwater site. In this sampling, the distribution of the wave periods was assumed not to change at the site of the breakwater. The wave force and moment acting on the upright section could be calculated substituting the sampled wave height and period into eq.(5)-(12). We judged whether the failure for each mode occurred or not utilizing the reliability function. This procedure was repeated 5000 times (Monte Carlo simulation). Eventually, the failure probability for each failure mode could be estimated. Total risk of the breakwater is obtained by eq.(25).

$$\begin{aligned}
 P &= P_s + P_o + P_b + P_g \\
 &- P_s P_o - P_o P_b - P_b P_g - P_g P_s \\
 &+ P_s P_o P_b + P_o P_b P_g + P_b P_g P_s + P_g P_s P_o
 \end{aligned}$$

- PsPoPbPg

(25)

in which P:the total failure probability, Ps:the failure probability of slide, Po:the failure probability of over- turn, Pb:the failure probability of mound slip and Pg:the failure probability of geotechnical instability. In the computation, the value 45 ton/m² was taken as the limitation of the heel pressure. Fig.5 shows the model of the breakwater used in this analysis.

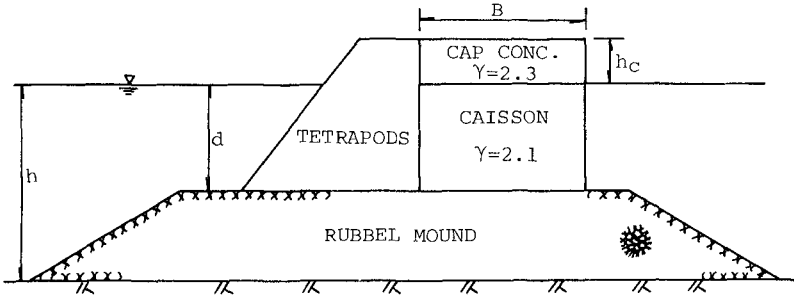


Fig.5 Model of Breakwater

Fig.6 shows variations of the total and each failure probability versus the equivalent deep water wave heights when the wave period(T) is 8.0sec, the water depth(h) is 6.0m, the caisson width(B) is 4.0m, the clearance(a distance between the still water and the top elevation of the upright section hc) is 2.0m and the water depth on the mound(d)is 4.0m.

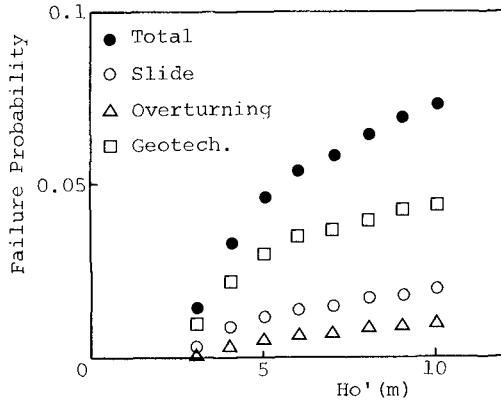


Fig.6 Effect of Wave Height on Failure Probability

The value of the individual and total failure probabilities increases the wave height becomes larger. The risk to the rubble-mound slope is not seen in the figure because that the probability was zero through all computation cases in our simulation. In other words, the rubble-mound is strongest against wave force. In the range where the wave height is smaller than 5m, the geotechnical and total

failure probabilities increase significantly. However when the wave height exceeds 5m, the increment of this risk decreases. This is one reason why the number of the incident wave breaking between the offshore and the site of the breakwater increases when H_o' becomes larger than 5m. Among the failure modes, geotechnical risk is the greatest problem followed by slide of the upright section. Therefore if an incident wave height became large, the foundation would collapse before the upright section slide or overturned.

Change in the failure probability versus the wave period is shown in Fig.7 in the case where the equivalent deep water wave height(H_o') is fixed at 6.0m, $h=6.0m$, $B=4.0m$, $h_c=2.0m$ and $d=4.0m$.

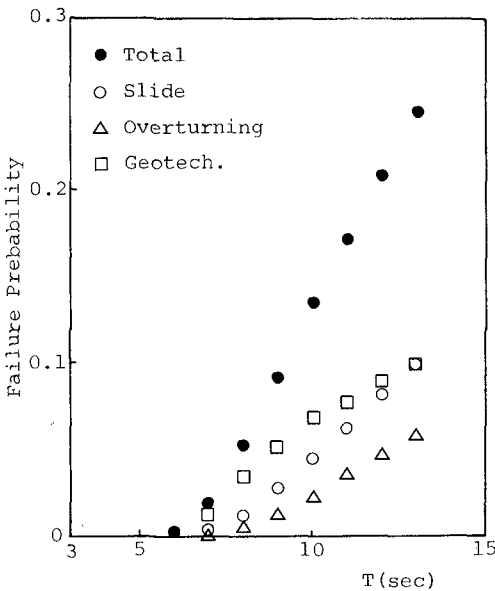


Fig.7 Effect of Wave Period on Failure Probability

The failure probability linearly increases as the wave period becomes long. In this case, the risk for geotechnical instability is greatest, but that for slide of the upright section becomes the same as the risk for geotechnical when the wave period increases. As the wave length becomes large, α_1 and α_3 in eq.(8) increase, therefore the wave force also become large. In addition, when h/L_o (L_o : a wave length in deep water) is small, waves tend not to break. So the wave force becomes large and the failure probability increases as the wave period is large.

Fig.8 indicates the influences of the water depth on a breakwater when $H_o'=6.0m$, $T=8.0sec$, $B=4.0m$, $h_c=2.0m$ and $d=4.0m$.

As the water depth increases, each as well as the total failure probability increases. When the water depth is large, wave heights hitting the breakwater becomes large and their wave lengths also increase. The wave forces acting on the breakwater therefore increase because the number of breaking waves decreases and because of the effects of wave length from the formulae for wave forces. In this case also, in the range where the water depth is greater than 8m, the difference between the risk for foundation collapse and caisson slide is close.

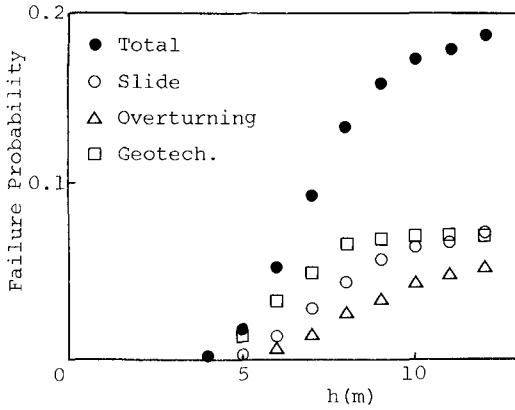


Fig. 8 Effect of Water Depth on Failure Probability

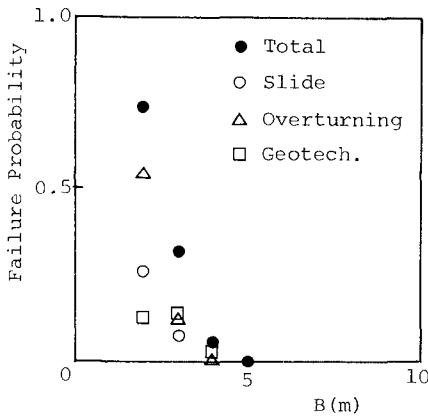


Fig. 9 Effect of Upright Section Width on Failure Probability

The relationship between the width of the upright section and failure probability is shown in Fig. 9 in the case of $H_o' = 6.0m$, $T = 8.0sec$, $h = 6.0m$, $h_c = 2.0m$ and $d = 4.0m$. When the caisson width is narrow, the risk of overturn is greatest. From this figure, it can be seen that in order to reduce risk increase of the upright section is the best way. In particular, the wide caisson effect to decrease the risk of overturning.

Fig. 10 shows the variation of the failure probability as the gradient of the sea bottom slope is changed from 0.01 (1/100) to 0.1 (1/10). The failure probability increases as the sea bottom becomes steeper. The breaking wave height becomes large if the wave period and water depth are fixed. As a result, the incident wave height becomes is so large that the great wave force can lead the breakwater to collapse. Failure probabilities of slide and overturn increase with the steepness of the sea bottom.

Geotechnical risk increases until the gradient of the sea bottom slope is 0.08. This is the plateau and is less than the probability for the slide and overturn when the gradient is greater than 0.08.

From Fig. 6 - Fig. 10, the wave period and gradient of the sea bottom affect the failure probability more significantly than the wave height. The longer the wave period and the steeper the sea bottom, the greater the failure probability for the composite breakwater protected with armor blocks is. In most cases, the probability of geotechnical instability is larger than the slide and over-

turn of the upright section of the composite breakwater protected with armor blocks.

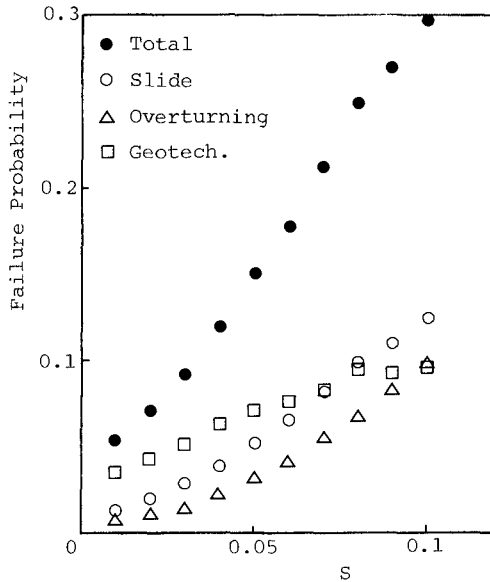


Fig.10 Effect of Gradient of Sea Bottom Slope on Failure Probability

Comparison with Risk for Armor Protection

Mizumura et al(1988) calculated the failure probability for displacement of armor blocks whose weights were obtained using the Hudson formula under the conditions where $H_o'=4.0m$ with all other previous conditions remaining the same.

Fig.11 is a comparison of the failure probability of an upright section with that of motion from armor blocks as obtained by Mizumura et al(1988) versus the wave height and period respectively.

In the figure, the solid lines show the failure probability of the composite breakwater protected with armor blocks designed with a safety factor of one unit concerning slide of the upright section.

The failure probability of the armor units is greater than that of the composite breakwater in the total range of wave height. When the wave period is less than approximately 15sec, the risk to the armor blocks is also greater than that of the composite breakwater protected with armor blocks. This implies that when high waves attack a composite breakwater protected with armor blocks, armor

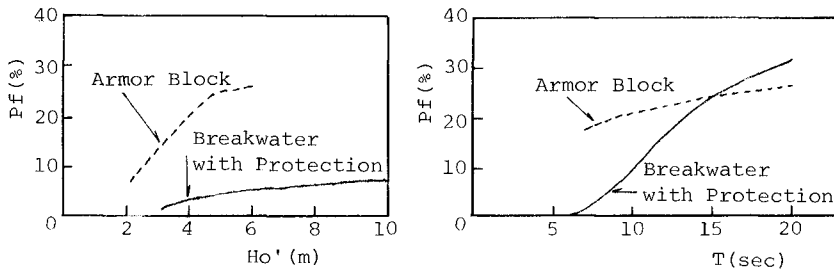


Fig.11 Comparison of Failure Probability of Protection with Upright Section

units collapse sooner than the upright section. However if armor blocks move sooner than the composite breakwater with protection, the width of the protection decreases, the wave force acting on the upright section through the protection increases (Hattori et al). Therefore the risk for motion of the upright section or geotechnical instability of the composite breakwater would become larger. It is therefore necessary to take into account the correlation between the armor blocks and upright section of the breakwater protected with armor blocks.

Conclusions

The following conclusions have been derived from this study.

1. Wave transformation, i.e. wave shoaling, breaking and retaining wave energy after breaking are acceptable for inclusion in simulations from offshore to the site of a breakwater.
2. Wave height is not as significant as wave period, water depth, caisson width and gradient of the sea bottom slope in failure probability of a composite breakwater protected with armor blocks. In particular, it can be seen that wave period is most significant.
3. In order to decrease risk to a breakwater, increases of caisson width proved effective because failure probability is reduced remarkably as the caisson width increases.
4. Geotechnical failure is potentially more dangerous than other failure modes.
5. Comparing the failure probability of armor unit displacement with that of the composite breakwater protected with armor blocks, the former is greater than the latter even when the wave height is increased. The risk of the former is less than that of the latter in the case of

short period waves, while when the wave period becomes longer, the former is greater than the latter. However correlation between collapse of the upright section and blocks should be taken into consideration in the case of a composite breakwater protected with armor blocks.

References

Burcharth, F.H. (1985): "On the reliability of rubble mound breakwater design parameters", *Hydraulics & Coastal Eng. Lab., Dept. of Civil Eng., Univ. of Aalborg, Denmark*, 24p.

Goda, Y. (1974): "A new method of wave pressure calculation for the design of composite breakwater", *Proc., 14th Int. Conf. Coastal Eng., Copenhagen*, pp.1702-1720.

Goda, Y. (1975): "Deformation of irregular waves due to depth controlled wave breaking", *Rept. Port and Harbor Res. Inst., Vol. 14, No. 3*, pp.59-106 (in Japanese).

Goda, Y. (1985): "Random seas and design of maritime structures", *Univ. of Tokyo Press*, p.323.

Hattori, M., K. Inagaki, Y. Noguchi, and T. Endo (1988): "Wave force on breakwaters with concrete block mound", *Proc. 21st Int. Conf. Coastal Eng., Malaga, Vol. 3*, pp. 2144-2158

Mizumura, K., M. Yamamoto, T. Endo and N. Shiraishi (1988): "Reliability analysis of rubble-mound breakwater", *Proc. 21st Int. Conf. Coastal Eng., Malaga, Vol. 3*, pp. 2053-2062.

PIANC (1990): "Introduction of a partial coefficient system for the design of rubble mound breakwaters", *Draft report, Subgroup F, Working Group 12*, 39p.

Tanimoto, K., K. Moto, S. Ishizuka and Y. Goda (1976): "An investigation on design wave force formulae of composite-type breakwaters", *Proc. 23rd Japanese Conf. Coastal Eng.*, pp. 11-16 (in Japanese).

Toyama, S. (1985): "The application of the reliability theory to the breakwater", *Tech. Note of Port and Harbor Res. Inst.*, No. 540, 49p (in Japanese).

Van der Meer, J.W. and K.W. Pilarczyk (1987): "Stability of breakwater armour layers deterministic and probabilistic design", *Delft Hydraulic Communication*, No. 378, 34p.

Yamamoto, Y., K. Mizumura, T. Endo and N. Shiraishi (1988): "Reliability based design of rubble-mound breakwater", *Proc., 21st Int. Conf. Coastal Eng., Malaga, Vol. 3*, pp. 2063-2074.

CHAPTER 106

Stresses in Dolosse

H.F. Burcharth¹ Liu Zhou² Gary L. Howell³ W.G. McDougal⁴

Abstract

Failures of rubble mound breakwaters armoured with complex types of unreinforced concrete armour units are often due to breakage. This happens when the stresses exceed the material strength. Sufficient parametric studies of the stresses are not yet available to produce design diagrams for structural integrity.

The paper presents the results and the analyses of model tests with 200 kg and 200 g load-cell instrumented Dolosse. Static stresses and wave generated stresses were studied as well as model and scale effects. A preliminary design diagram for Dolosse is presented as well.

Introduction

Many of the recent dramatic failures of a number of large rubble mound breakwaters armoured with Dolosse and Tetrapods were caused by breakage of the concrete armour units. Breakage took place before the hydraulic stability of intact units in the armour layers expired. Thus there was an imbalance between the strength (structural integrity) of the units and the hydraulic stability (resistance to displacements) of the armour layer.

While the hydraulic stability can be roughly estimated by formulae and further evaluated in conventional hydraulic model tests, it is much more complicated to assess the structural integrity of the armour units. The increased research activity in this field has not yet resulted in generally applicable design diagrams or formulae by which the armour units can be designed as is the case for other civil engineering structural members.

For dealing with the problem the different types of loads on armour units and their origins might be listed as shown in Fig. 1.

¹Prof. of Marine Civil Engineering, Aalborg University, Denmark.

²Ph.D., visiting researcher, Aalborg University, Denmark.

³Senior Research Engineer, Coastal Engineering Research Center, Waterways Experiment Station, U.S. Army Corps of Engineers, Vicksburg, Ms. USA.

⁴Ass. prof., Oregon State University, Corvallis, Oregon. Visiting prof. University of Aalborg, Denmark, 1987.

TYPES OF LOADS		ORIGIN OF LOADS	
STATIC		Weight of units	
		Prestressing due to: Settlement of underlayers Wedge effect and arching due to movements under dynamic loads	
DYNAMIC	Impact	Rocking/rolling of units Missiles of broken units Placing during construction	} impacting solid bodies
	Pulsating	Gradually varying wave force including slamming Earthquake	
ABRASION		} Suspended material	
THERMAL		} Stresses due to temperature differences during hardening processes Freeze — thaw	
CHEMICAL		} Corrosion of reinforcement Sulfate reactions etc.	

Fig. 1. Types and origin of loads on armour units (from Burcharth, 1981).

It is characteristic for both static and dynamic load conditions that a deterministic calculation of the stresses in the units is practically impossible, mainly because of the stochastic nature of the wave loads, the complex shape of armour units and their random placements.

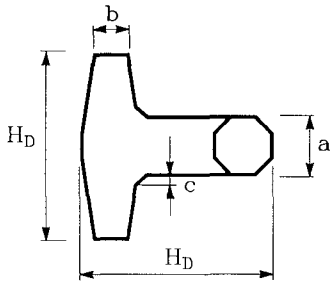
It is also characteristic of these stresses that they do not scale in the same way. Generally speaking the stresses due to non-impact loads increase linearly with the characteristic length of armour units, while impact-induced stress increases with the square root of the characteristic length. The relative importance of these stresses depends on the size and geometry of the units, their position on the slope and so on.

In this paper only static and pulsating stresses are considered.

Dolos static stress experiments in the dry (ramp tests)

Description of the experiment

With the purpose of studying the characteristics of static stresses in Dolosse and the related model and scale effects, a large field experiment programme was started in 1986 in Aalborg Hydraulic Laboratory (AHL) at Aalborg University. It includes comparative compaction experiments with 200 kg and 200 g Dolosse placed on ramps with various slope angles. The geometries of the Dolosse are given in Fig. 2.



		app. 200 kg	app. 200 g
Height H_D	(cm)	80	8
Waist width a	(cm)	26	2.6
Head width b	(cm)	16	1.6
Height of fillet c	(cm)	4.0	0.46
Waist ratio		0.325	0.325

Fig. 2. Geometry of Dolosse.

200 kg strain-gauged Dolosse

Based on the structural consideration and practical experience, it is now generally accepted that Dolos fractures tend to occur in or near the shank-fluke interfaces. Consequently, two shank and two leg cross sections near the shank-fluke interfaces of 200 kg Dolosse were chosen as strain-gauged sections. Because the signals from the surface mounted strain gauges turned out to be too weak a load-cell solution was adopted. Four strain-gauge rosettes were mounted on the surfaces of steel tubes inserted as load cells in each of the chosen sections, cf. Fig. 3.

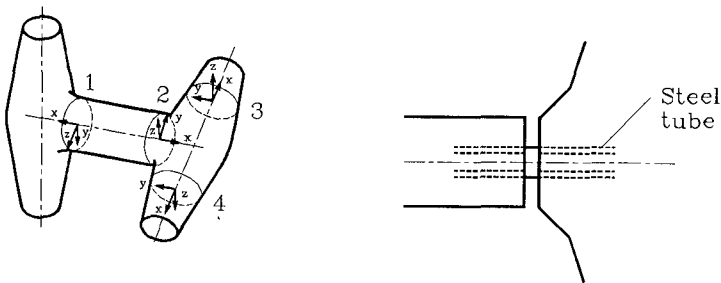


Fig. 3. Instrumented sections. 200 kg concrete Dolosse, Aalborg Hydraulic Laboratory (AHL).

The load cells allowed the following component forces/moments to be recorded, cf. Fig. 4, where the octahedral cross section is the correct one, and the circular cross section is an approximation (Burcharth et al., 1988).

The instrumentation made it possible to verify the relative importance of shear and axial forces.

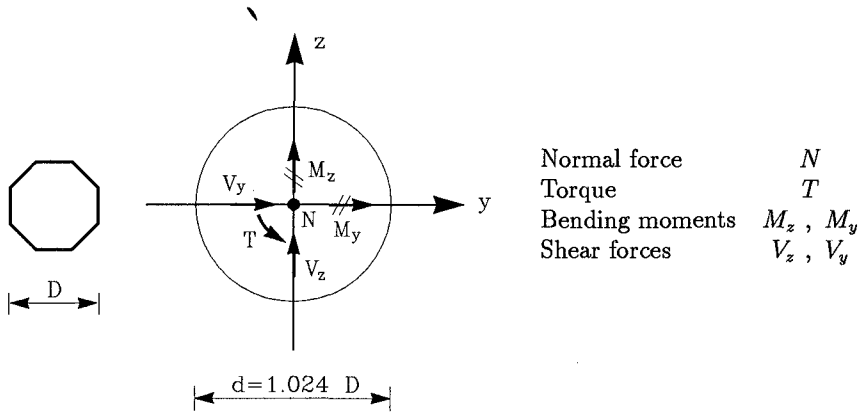


Fig. 4. Component forces/moments recorded in the instrumented sections.

200 g strain-gauged Dolosse

The applied units were developed by CERC and lent to the University of Aalborg (Markle, 1990). One shank cross section in the shank-fluke corner was strain-gauged to obtain two orthogonal bending moments and the torque. The stress contributions from axial and shear forces, which were believed to be of minor importance, were neglected.

The applied signal analysis, i.e. the transformation of the recorded load cell strains to armour unit stresses, is described in Burcharth et al., 1988. The first step in the signal analysis is to calculate the component forces/moments in the steel tube sections according to the recordings of strains. The next step is to transform these component forces into the stresses in the corresponding Dolos sections, and finally to calculate the maximum principal tensile stress, which is chosen as the critical parameter for the structural integrity of the armour units.

A large ramp (5 x 4 m) and a small ramp (0.5 x 0.4 m) with changeable slope angles were built. 72 Dolosse (200 kg or 200 g), including the instrumented ones, were randomly placed in two layers on the ramp. Every experiment involved the following 4 steps and corresponding recordings.

- (i) Zeroing of strain gauges while the two instrumented Dolosse were in a specified position resting unloaded on ground.
- (ii) Placement of the Dolosse on the ramp.
- (iii) Vibration of the ramp.
- (iv) Removal of Dolosse from the ramp and placement of the two instrumented Dolosse in the position described under (i).

Three pre-determined slopes were used: 1 : 0.9, 1 : 1.38 and 1 : 2. The instrumented Dolosse were 'randomly' placed at positions 1 and 2 in the bottom layer, as shown in Fig. 5.

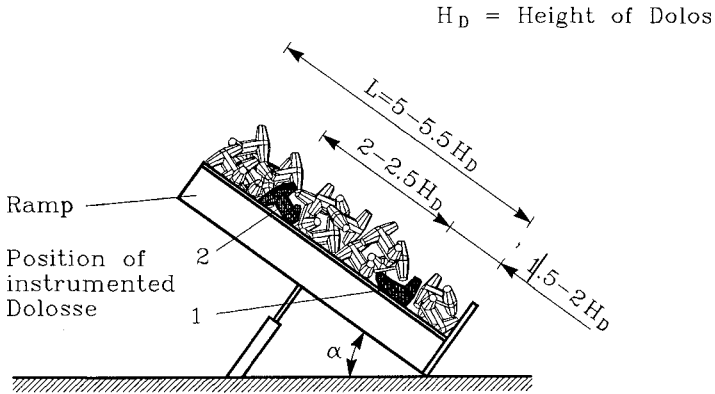


Fig. 5. Dolos compaction experiment set-up, Aalborg Hydraulic Laboratory (AHL).

Results from the static stress experiments (ramp tests)

Comparison of stresses in the shank and fluke cross sections

Because the small scale units cannot for practical reasons be instrumented in the fluke sections it is important to investigate if this implies a model error of any significance. From the tests with the 200 kg Dolosse it is clearly demonstrated in Table 1 that the max principal tensile stresses in the shank cross sections generally are bigger than those in the fluke cross sections.

Table 1. 200 kg Dolos compaction experiment results.

Group	1	2	3	4
Slope	1 : 0.9	1 : 1.38	1 : 1.38	1 : 2
Instrumented Dolos position	1	1	2	1
Average of σ_T in shank (MPa)	0.336	0.167	0.151	0.166
Average of σ_T in fluke (MPa)	0.181	0.157	0.088	0.12
No. of tests	28	40	36	20

σ_T denotes the max principal tensile stress in strain-gauged sections.

It is also seen that when dealing with results based on stresses only measured in the shank section it is necessary to compensate for the influence of fluke failures.

If it is assumed that the only relevant failure modes are fracture in the type of sections shown in Fig. 3, i.e. 2 shank sections and 4 fluke sections, then it is possible to calculate the probability of failure for the Dolos, P_{Dolos} , from the probability of failure in the fluke section, P_{fluke} , and the probability of failure in the shank section, P_{shank} if the correlations between the various failure modes are known. If the Dolos is modelled as a series system, consisting of n elements $i = 1, 2, \dots, n$, i.e. the failure of the Dolos takes place when any one of the element fails, then the probability of failure for the Dolos can be estimated as

$$P_{Dolos}(\sigma_T) \simeq 1 - \Phi_n(\bar{\beta}; \bar{\rho})$$

where $\bar{\beta} = (\beta_1, \dots, \beta_n)$ and $\beta_i(\sigma_T) = -\Phi^{-1}(P_i(\sigma_T))$ is the generalized reliability index corresponding to failure mode i . Each failure mode is approximated by a linear failure function in independent standard normal variables.

$\bar{\rho} = [\rho_{ij}]$ is the correlation matrix for the linear failure functions.

$\Phi_n = n$ -dimensional standardized normal distribution.

Generally calculation of $\Phi_n(\bar{\beta}; \bar{\rho})$ for $n \geq 3$ cannot be performed exactly but the Hohenbichler approximation can be used (Thoft-Christensen et al. 1986). $n = 6$ in the proposed model for a Dolos. Alternatively reliability bounds can be calculated. A simple lower bound is the maximum probability of failure of any element, in this case corresponding to P_{shank} . This lower bound corresponds to full correlation between all elements, i.e. $\rho_{ij} = 1$ for all i and j . A simple upper bound can be found by assuming non-correlated elements in which case we get

$$P_{Dolos}(\sigma_T) = 1 - (1 - P_{shank}(\sigma_T))^2 (1 - P_{fluke}(\sigma_T))^4$$

The assumption of non-correlated elements gives the highest possible probability of failure. More narrow bounds can be found if the correlations are known. The simple lower and upper bounds are shown in Fig. 6 together with an estimate of the real failure probability based on a Hohenbichler approximation. The high stress levels shown in the Figure are due to the inclusion of test results from the very steep 1 : 0.9 slope.

Influence of Dolos position and slope angle

The results in Table 1 show as expected that the dolosse situated in lower positions of the bottom layer have greater stresses than those situated in the higher positions, and the dolos stress increases with steeper slopes, other conditions being equal.

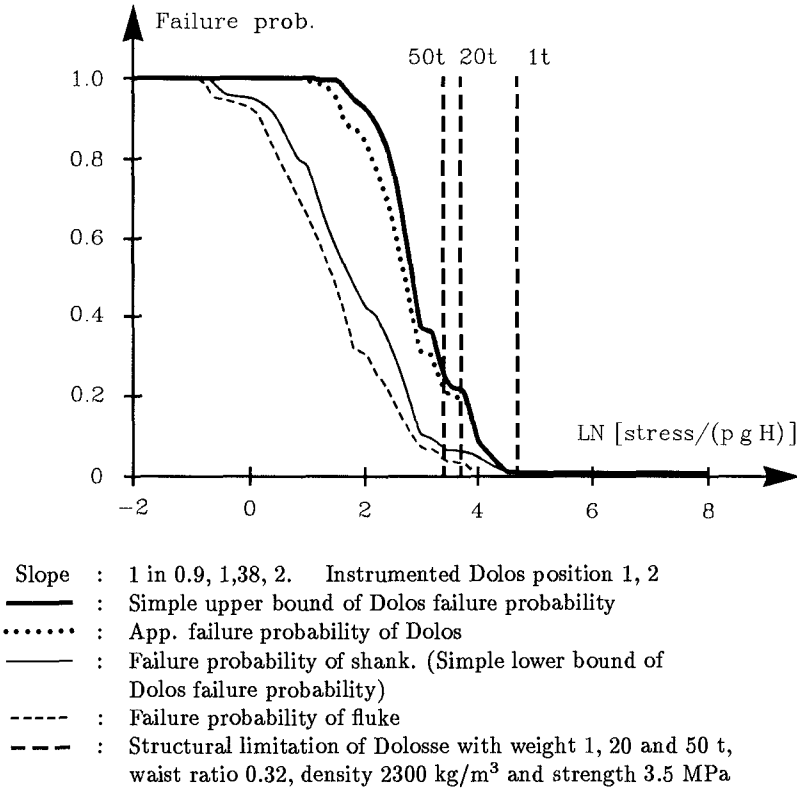


Fig. 6. Failure probability of Dolosse based on recorded static stresses in ramp tests in the dry, AHL experiments.

The stress distribution

The measured maximum principal tensile stresses σ_T followed the log-normal distribution both in the shank and the fluke cross sections. The density function is given by

$$f(\ln \sigma_T) = \frac{1}{\sigma\sqrt{2\pi}} e^{-\frac{1}{2}\left(\frac{\ln \sigma_T - \mu}{\sigma}\right)^2}$$

$$\mu = \frac{1}{N} \sum_{i=1}^N \ln(\sigma_T)_i \quad \sigma^2 = \frac{1}{N-1} \sum_{i=1}^N (\ln(\sigma_T)_i - \mu)^2$$

where μ and σ are average and standard deviation respectively.

The conclusion on stress distribution is consistent with results from small scale tests conducted by D. Turke, Canada (private communication), see also Anglin et al., 1990.

Stress contribution from shear and axial forces

In small scale tests it is difficult or even impossible to mount a sufficient number of strain gauges inside small Dolosse to determine all component forces/moments in a cross section. Generally the stress contributions from axial and shear forces are regarded of minor importance. To check this hypothesis the distribution of $(\sigma_T - \sigma'_T/\sigma_T)$, where σ'_T represents the corresponding maximum principal tensile stress without axial and shear forces, is plotted in Fig. 7. The results are from the fully instrumented 200 kg Dolosse and represent only the conditions in the instrumented shank sections. From this Figure the following can be concluded:

- (i) the bigger σ_T , the smaller $(\sigma_T - \sigma'_T/\sigma_T)$, i.e. reduced influence from axial and shear forces.
- (ii) The negligence of axial and shear forces most likely results in overestimation of the max principal tensile stress. In other words, it is on the safe side.

Slope : 1 in 0.9, 1.38, 2. Instrumented Dolos position 1, 2
 - - - : Fracture limitation of concrete Dolosse
 (density 2300 kg/m³, tensile strength 3.5 MPa)
 - . - : Exceedence probability

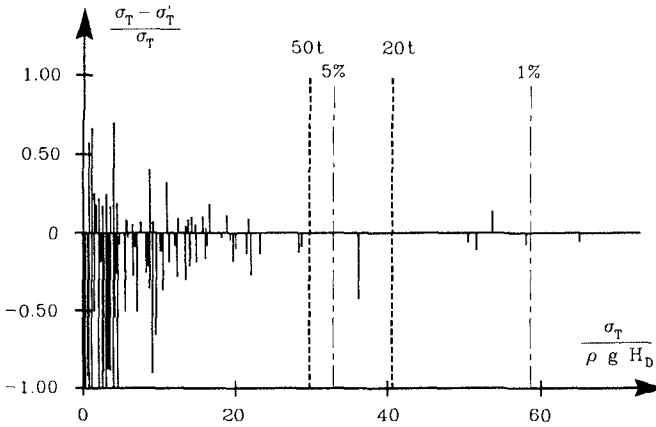


Figure 7. Example of stress contribution from axial and shear forces. Tests with 200 kg Dolosse, Aalborg Hydraulic Laboratory (AHL) experiments.

Comparison of static stress distributions in large and small scale experiments including verification of the scaling law

Fig. 8 shows the exceedence probability of the dimensionless maximum principal tensile stress in 200 kg and 200 g concrete Dolosse in the compaction experiment.

It is consistent (especially for high stress levels), with the theoretical scaling law $\lambda_\sigma = \lambda_\rho \lambda_L$, where λ_σ , λ_L and λ_ρ are scaling factors for stress, length and density, respectively.

- Slope : 1 in 0.9, 1.38, 2. Instrumented Dolos position: 1 and 2.
 - - - : Fracture limitation of concrete Dolosse (density 2300 kg/m³, tensile strength 3.5 MPa)
 — : 200 g concrete Dolos (without shear and axial forces)
 — : 200 kg concrete Dolos (without shear and axial forces)

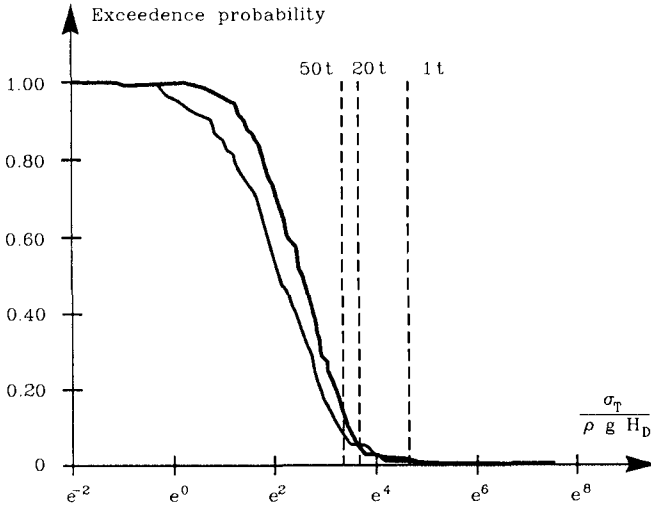


Figure 8. Comparison of stress distributions in shank cross sections of 200 kg and 200 g concrete Dolosse. Influence from shear and axial forces are neglected. AHL experiments.

Influence of compaction and surface roughness

Comparative tests with smooth (polyester) and rough (concrete) Dolosse revealed that the amount of compaction (settlement) and the surface roughness influenced the stresses significantly. The effects should be considered in the model test analysis.

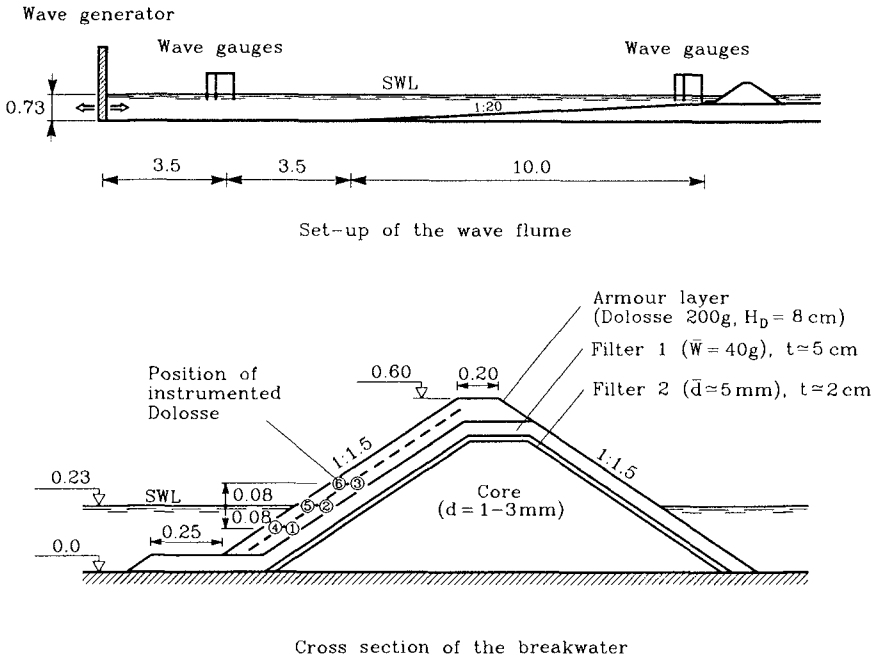
Hydraulic flume tests

The object of the flume tests at AHL is to study the armour unit stresses as functions of the structural and the sea state parameters.

Although a comprehensive parametric study has not yet been completed, enough tests have been made to present some conclusions related to a range of problems. The set-up and procedure for the tests are coordinated with tests at CERC, Vicksburg, in order to establish a more complete parametric study.

Model test set-up and description of the experiments

All tests were conducted in a 1.2 m wide and 1.5 m deep flume with the model situated app. 17 m from the wave paddle, Fig. 9. The flume was divided into two parts with width of 0.75 m and 0.45 m, respectively. The breakwater model was placed in the 0.75 m wide part of the flume at the top end of a 1 : 20 foreshore slope. The water depth at the toe of the breakwater was 23 cm. The 0.45 m wide part of the flume was fitted with an effective non-reflecting array of perforated metal sheets. Fig. 9 also shows the cross section of the breakwater.



Measures and levels in meter

Fig. 9. Set-up of the wave flume and the cross section of the breakwater. Aalborg Hydraulic Laboratory (AHL) experiments.

To compensate for reflected waves two arrays of three wave gauges were installed. The incident wave spectrum was calculated by the least square method presented by Mansard et al., 1980.

The irregular waves were generated by a piston type paddle according to the five parameter JONSWAP spectrum with the peak enhancement coefficient being 4.

Table 2 lists the characteristics of the applied waves propagating towards the breakwater at the paddle and at the toe of the breakwater. L_p is wave length

corresponding to the spectral peak period and $\zeta = T_p \left(\frac{2\pi}{gH_{m0}} \right)^{0.5} \tan\alpha$.

Table 2. H_{m0} and T_p at the wave paddle and at the toe of the structure.

H_{m0}^p	at the paddle (cm)	5	10	15
T_p	at the paddle (sec)	1.5	2	2
H_{m0}^p/L_p	at the paddle	0.016	0.022	0.032
H_{m0}^t	at the toe (cm)	5.7	11.8	17.9
T_p	at the toe (sec)	1.5	2	2
ζ	with H_{m0}^p and $\tan\alpha = \frac{1}{20}$	0.27	0.25	0.21
ζ	with H_{m0}^t and $\tan\alpha = \frac{1}{1.5}$	3.3	3.1	2.5

Definition of peaks of static plus pulsating stresses

In the statistical analyses of the stress peaks presented in the paper a definition of the peaks by zero down crossing identification has been adopted, Fig. 10. This definition is applied due to the fact that static and pulsating stresses scale the same way.

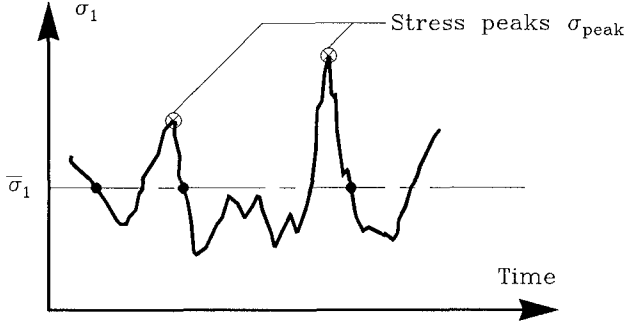


Figure 10. Definition of peaks of stress in time series.

Results from the flume tests

Distribution of static stresses

The distribution of the static stresses which are defined as the average of the Dolos stresses before and after wave attacks is shown in Fig. 11. As is seen the distribution closely follows the log-normal distribution as also found from the ramp tests.

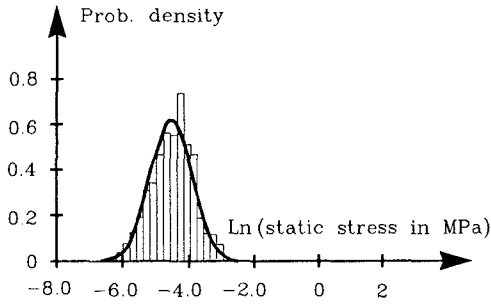


Figure 11. Distribution of static stresses in flume tests with 200 g Dolosse as recorded in one shank cross section.

Distribution of stress peaks for static plus pulsating loads

Fig. 12 shows for three different sea states the stress distributions obtained from the flume tests with 200 g Dolosse only instrumented in one shank cross section. Results are for 6 positions of Dolosse within the area between levels SWL \pm app. 1.5 times the Dolos height.

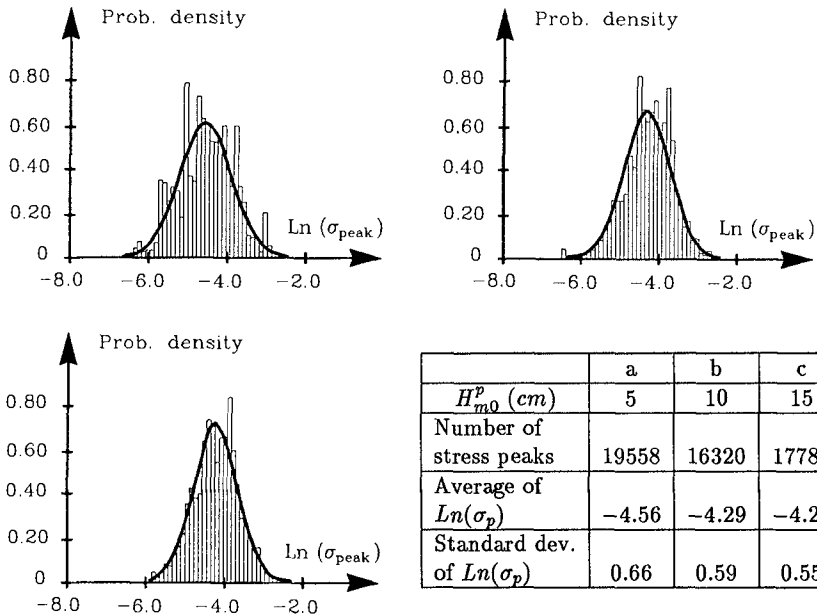


Figure 12. Distribution of peaks of static and pulsating stresses (in MPa).

It is seen that the mean values (mean of \ln) increase with the wave height, but at the same time the standard deviation decreases. Consequently, the stress corresponding to higher exceedence probability levels are found to be almost invariant to the wave height for waves higher than a certain level, cf. also Fig. 12. This tendency can also be seen in model test results with Tetrapods, Bürger et al., 1990.

Preliminary design chart

Fig. 13 is an example of a preliminary design chart. Note that the static stresses (corresponding to zero wave height) are large compared with the total stresses under wave action.

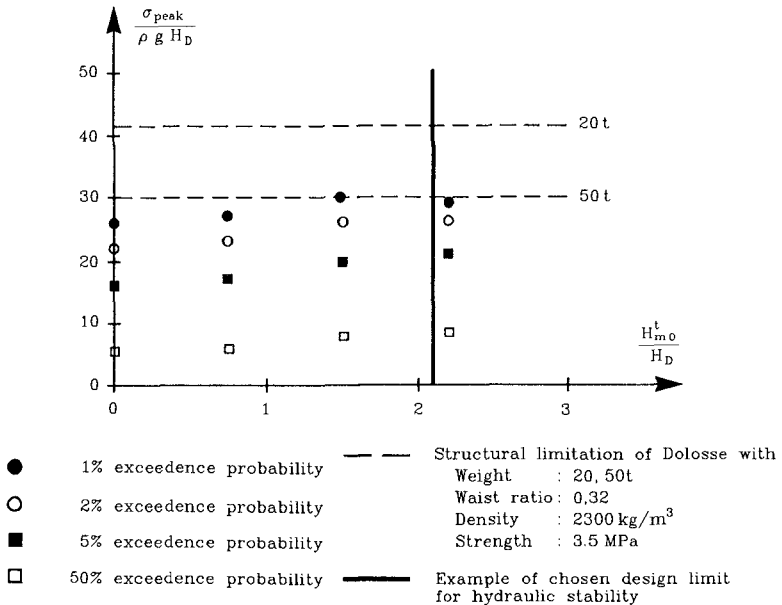


Figure 13. Preliminary design chart for Dolos with waist ratio 0.32. The design chart covers the area between levels SWL \pm app. 1.5 times the Dolos height. The exceedence probabilities are obtained from the fitted log-normal distribution of peaks of static and pulsating stresses. Impact stress, fatigue, failure contribution from flukes and surface roughness correction are not included.

Within the tested range it was found that the wave generated pulsating stresses, in terms of the average of the significant stress wave height, increase almost linearly with the significant wave height.

Acknowledgement

The valuable assistance of Dr. L. Pilegaard-Hansen, Institute of Building Technology, University of Aalborg, in the early phase of the ramp tests is very much appreciated. The work reported here was part of a cooperative effort between the Crescent City Prototype Dolosse Study of the Coastal Engineering Research Center and the University of Aalborg. Permission to publish this paper has been granted by the US Army Corps of Engineers, Office, Chief of Engineers.

References

- Anglin, C.D., R.D. Scott, D.I. Turcke, M.A. Turcke (1990): *The development of structural design criteria for breakwater armour units*. Proc. Seminar Stresses in Concrete Armor Units, ASCE, Vicksburg, U.S.A., 1990.
- Burcharth, H.F. (1981) : *Full-scale dynamic testing of dolosse to destruction*. Coastal Engineering, Vol.4, 1981.
- Burcharth, H.F. and Gary Howell (1988): *On methods of establishing design diagrams for structural integrity of slender complex types of breakwater armour units*. Seminaire International Entretien des Infrastructures Maritimes. Casablanca, Morocco, 1988.
- Burcharth, H.F. and Liu Zhou (1990): *A general discussion of problems related to the determination of concrete armour unit stresses including specific results related to static and dynamic stresses in Dolosse*. Proc. Seminar Stresses in Concrete Armor Units, ASCE, Vicksburg, U.S.A., 1990.
- Bürger, H. Oumeraci, H.W. Partenscky (1990): *Impact Strain Investigations on Tetrapods: Results of Dry and Hydraulic Tests*. Proc. Seminar Stresses in Concrete Armor Units, ASCE, Vicksburg, U.S.A., 1990.
- Mansard, E.P.D., E.R. Funke (1980): *The measurements of incident and reflected spectra using a Least Squares Method*. Proceeding of the 17th International Conference on Coastal Engineering, Sydney, Australia, March 1980.
- Markle, D.G. (1990): *Crescent City Instrumented Model Dolos Study*. Proc. Seminar Stresses in Concrete Armor Units, ASCE, Vicksburg, U.S.A., 1990

CHAPTER 107

VERIFICATION AND PRACTICAL USE OF
METHOD

BLOCK REVETMENT DESIGN

A.M.Burger*, A.Bezuijen**, K.W.Pilarczyk*** and M.Klein Breteler****

ABSTRACT

The research into the physical processes in concrete block revetments under wave attack resulted in three separate design methods. A resume is given of the numerical, analytical and black-box methods and their respective fields of application have been indicated. Special attention is given to the verification of the analytical model with large scale model tests.

INTRODUCTION

Since 1980 Delft Hydraulics and Delft Geotechnics have been involved in a research project for the Dutch Rijkswaterstaat (Ministry of Transport and Public Works). The aim of this research project was to develop a sophisticated design method for placed concrete block revetments under wave attack. This type of block revetments is used throughout the Netherlands for the slope protection of water retaining structures. Separate parts of the design method have been published by Den Boer et al (1983, 1984), Bezuijen et al (1987, 1988), Klein Breteler et al (1987, 1988), Pilarczyk (1990) and Burger et al (1983, 1988, 1990). The present paper gives a resume of the results and a comparison of the results of computations with the results of large scale verification tests. The development of the design method has presently been finished and the ongoing research on block revetments is aimed at developing the probabilistic concept of safety and the residual strength of block revetments after initial failure.

A summary of the results of the entire research project has recently been published by Bezuijen et al (1990-1). The design method covers the schematization and calculation of the external and the internal wave induced loads, on the various structure elements and enables the design of a stable top layer and stable filter and base layers, including stable interfaces between successive layers. The design of the sublayers will not be dealt with in this paper, but has been covered by Bakker et al (1990) and earlier by Van der Knaap et al (1986) and Bezuijen et al (1987).

- * Association of the Netherlands Cement Industry, P.O.Box 3011, 5203 DA 's-Hertogenbosch, the Netherlands
- ** Delft Geotechnics, P.O.Box 69, 2600 AB Delft, the Netherlands
- *** Road and Hydraulic Engineering Division, P.O.Box 5044, 2600 GA Delft, the Netherlands
- **** Delft Hydraulics, P.O.Box 152, 8300 AD Emmeloord, the Netherlands

RESUME OF DESIGN METHOD

The design method has been developed for revetments that are founded on a granular filter layer. A typical cross section is given in fig.1.

The principle of the design is based on a specific perception of the course of events that endanger the structure's stability: Wind waves running on a slope induce time dependent pressures on the top layer of a revetment; these pressures are transmitted through the top layer to the filter layer and influence the ground water flow in the filter layer, causing time and place dependent pressure differences across the top layer, that tend to lift individual blocks from the revetment.

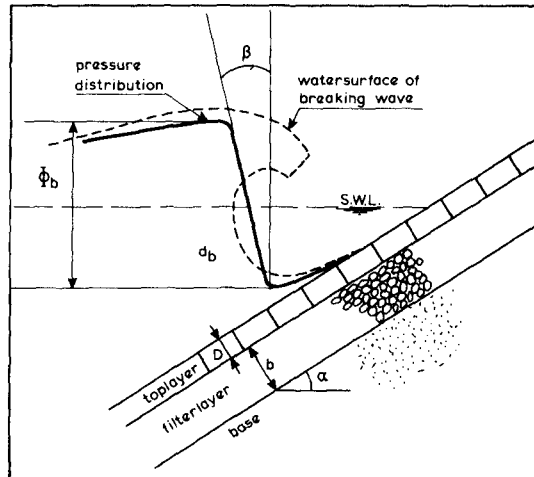


Figure 1 Definition sketch

From the results of large scale model investigations (Burger 1983, 1984) it has been concluded that this failure mechanism can only occur when the relative percentage of openings in or between the blocks is smaller than approximately 10% of the top surface of the blocks.

This covers most of the concrete block revetments in the Netherlands, but excludes all kind of block mats, with mostly perforated blocks or large interspaces between the blocks. Also the stability (or failure) of placed block revetments on a more or less impermeable core is not covered by the perception of the failure mechanism on which the calculation method of the physical processes has been based. For those situations empirical results from mostly large scale model investigations and field experience have been used to develop an empirical extension of the design method.

The design method, based on a mathematical description of the physical hydraulic processes, has been divided into two main parts: the computation of the loads on the various parts of the structure and the computation of the strength of these parts.

For the determination of the hydraulic loads the following steps have been distinguished:

- Transformation of the wave conditions in front of the revetment to the external hydraulic loads on the structure's surface. For this transformation a data base of systematic pressure recordings from model tests has been established to be used in conjunction with numerical models to calculate the time dependent internal pressures and the structure's response (Bezuijen et al 1987, 1988). An empirical simplified description for the wave induced pressures has been developed to be used in an analytical model (Burger et al, 1990).
- Transformation of the external hydraulic loads on the structure's surface to the hydraulic loads in the sublayers of the structure. For the computation of the pore pressures, the hydraulic gradients and the internal water flow in the granular sublayers, a detailed numerical and a schematised analytical method have been developed.

For the computation of the internal hydraulic loads the permeabilities of the different layers of the revetment proved to be essential. For the permeability of granular layers use can be made of existing relations, but for the determination of the permeability of the concrete block top layer an analytical method has been developed and verified. This method has been described by Klein Breteler et al (1998) and enables the calculation of the permeability of a new top layer. It fails, however, for the calculation of the time dependent changes in permeability due to siltation, vegetation and such that have turned out to be decisive for the top layer stability in practical situations.

For the determination of the strength of the relevant parts of the revetment structure the following separation can be made:

- The strength of the placed blocks top layer, that is composed of the weight of the block and the different interaction forces between adjacent blocks. For the latter strength factors a conservative 'common sense' approach has been developed, that accounts for the fact that through friction and clamping forces a top layer of individual blocks may act as an interlocked system. It should be emphasized, however, that this additional strength is mobilized only after that the internal pressures, acting from the filter on the block, tend to lift the block.
- The strength of the granular sublayers of the revetment, which is the resistance to hydraulic loads. For the evaluation of this filter strength a new set of filter rules has been developed and verified by means of model testing. In this way the internal stability of a filter and the stability of granular interfaces can be determined. The development of this method and the final results have been presented by Bezuijen et al (1987) and Bakker et al (1990).

The combination of the methods mentioned above for the determination of loading and strength of different parts of a revetment enables the design of a safe stable structure.

LARGE SCALE VERIFICATION

During the development of the predictive models for loading and strength of the various structure elements each model has been verified by means of schematized, mostly full scale model investigations. Small scale models have been used only for the predictive models for hydraulic external wave induced loads, as it appeared that conflicting scale rules for wave action and ground-water flow (in the sublayers) prohibit the application of small scale models for stability investigations.

Finally, the model as a whole has been thoroughly checked and verified in a full scale model investigation in the large wave flume of Delft Hydraulics. In this model investigation 12 different placed concrete block revetments were exposed to varying wave conditions. The slope angle was kept constant at, $\cotg \alpha = 3$. The core of the structure consisted of well compacted, fine sand. Table 1 indicates the characteristics of the 12 different slope revetment structures.

Identification	TOP LAYER						SUBLAYERS			
	Block size (cm)			Holes (round)		Width of Inter-spaces (mm)	Geotextile		Granular filter	
	L	B	D	number of holes	hole size (mm)		1)	2)	layer thic kn. (cm)	grain-size D ₁₅ (mm)
Slope I, west	30	25	15	0	-	1.5	-	-	25	3.6
Slope I, east	30	25	15	0	-	1.5	-	-	50	3.6
Slope II, west	30	25	15	0	-	2.0	+	-	50	9.2
Slope II, east	50	50	15	0	-	4.0	+	-	50	3.6
Slope III, west	50	50	15	6	51	4.0	+	+	50	8.5
Slope III, east	50	50	15	1	125	4.0	+	+	50	8.5
Slope IV, west	50	50	15	6	70	4.0	+	+	50	8.5
Slope IV, east	50	50	15	1	170	4.0	+	+	50	8.5
Slope V, west	50	50	15	6	91	4.0	+	+	50	8.5
Slope V, east	50	50	15	1	225	4.0	+	+	50	8.5
Slope VI, west	50	50	30 ³⁾	0	-	3.8	-	+	35	17.3
Slope VI, east	30.5	30.5	11.5 ⁴⁾	0	-	2.7	+	+	53.5	8.5

1) Geotextile between top layer and granular filter

2) Geotextile between granular filter and base

3) With run-up reducing surface

4) Interlocking blocks

Table 1 Slope revetments for large scale verification tests

Figure 2 shows a typical model structure, covering the eastern half of the 5 m wide wave flume. The model was equipped with instruments to measure the external wave loads (pressures and water velocities) and the wave induced internal water pressures in the sublayers and acting on the underside of the toplayer. In a special measuring frame the upward motion of a selected block was measured. In this way the loads and the response of the revetment were measured simultaneously. On the interface of base and granular filter layer the hydraulic gradients have been measured to verify the filter rules (Bakker et al, 1990).

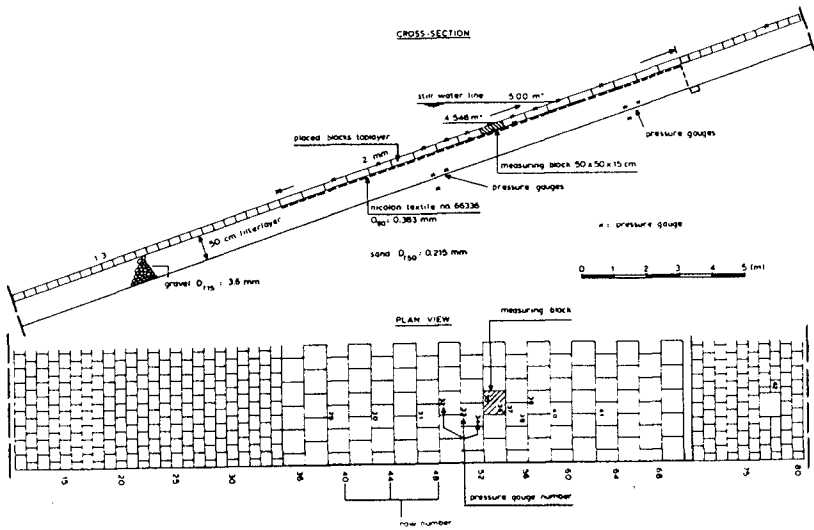


Figure 2 Cross section and plan-view of slope II, east

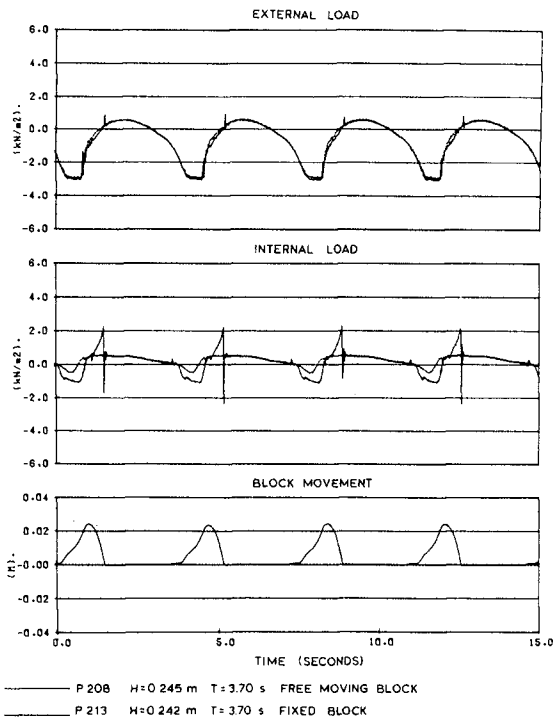


Figure 3 shows an example of the output of the physical model tests. The figure shows the recording of the pressures on top and underneath a free moving block together with the recorded block motion for two almost identical tests. The only difference between the tests was that in one test (P208) the block was free to move (the recording shows a periodic lift of some 2.5 cm) and in the other test (P213) the block was fixed. The influence of block motion on the pressures is clear.

Figure 3 Influence of block movement on internal load

The top part of the figure shows the exact reproduction of the external wave pressures for the two tests; the lower part shows the successive block jumps with a duration of some 1.5 seconds. The central part of figure 3 shows the load reduction during upward block motion, and the pressure increase during downward motion. This confirms qualitatively the phenomenon that the upward motion of a free block reduces the pressures underneath that block. When the resultant upward load on the block exceeds the critical value of potential instability the block starts moving upwards, inducing water flow in the filter towards the space created by the upward motion. Consequently, the pressure difference across the top layer is reduced. This potentially important load reduction can be quantified with the numerical and analytical design methods that have been developed. Bezuijen et al (1990-2) deals with the verification of the numerical model.

The remarkable negative pressure peaks in figure 3 are due to water hammer just after the moment that the block falls back in its initial position. This dynamical phenomenon is neither dealt with in the analytical nor in the numerical model as inertia effects of the revetment are assumed to minimize the effect of impacts. In this specific situation it is considered to be a model effect related to the situation that the block can move up and down almost frictionless; a situation that will never occur in practical situations.

Figure 4 shows the result of a quantitative comparison between the physical model results and the analytical design method presented by Burger et al (1990).

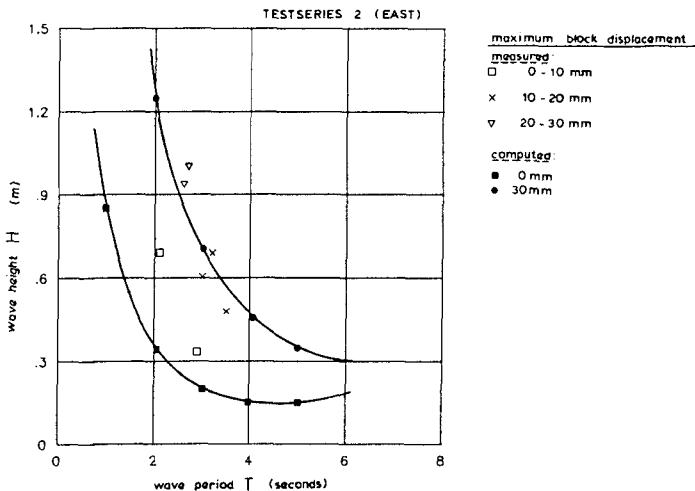


Figure 4 Comparison of analytical model with large scale model results

The figure shows an H-T diagram for one of the tested slopes in which each symbol represents a test. The type of symbol indicates the recorded maximum block displacement (\square = 0-10 mm; \times = 10-20 mm; ∇ = 20-30 mm). The connected solid symbols are the result of calculations with the analytical method for different acceptable block movements (\blacksquare = 0 mm; \bullet = 30 mm).

The general agreement is good and indicates that the analytical design method yields somewhat conservative (= safe) results. Given the fairly rough schematisations of the physical processes involved this result is considered to be quite satisfactory.

PRACTICAL APPLICATION OF THE METHODS

In fact the design method as a whole consists of a number of separate methods to design a block revetment from the first stage of the feasibility study to the stage of detailed engineering. In the following the practical application of those methods will be outlined. The following models will be dealt with:

- analytical model;
- numerical model;
- black box model;
- initial design model.

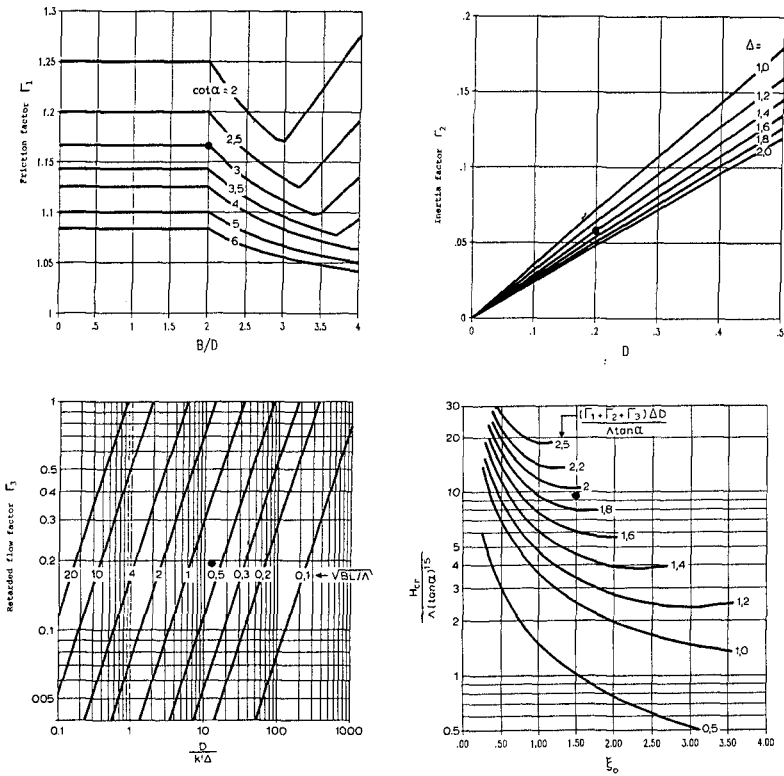
Next, some attention will be given to the general tendencies of the consequences of adaptations to the structure's design.

Analytical model

The analytical model consists of a set of large formulae that discourage their use in stages of preliminary design (see Burger et al, 1990). Those formulae, however, are the results of only a simplified description of only the most relevant physical phenomena of a block revetment under wave attack. To encourage the use of the method the formulae have been presented in figure 5 in the form of a set of graphs.

In the following some remarks to the figure will be made:

- the graphs do not yield a design, but only determine the limit state wave conditions for a given design;
- the input consists of the block dimensions (B,L,D, Δ), the slope steepness (α), the wave steepness (H/Lo) and the permeabilities of top layer and filter, which are incorporated in the leakage factor (λ);
- the upper left figure accounts for the friction between individual blocks, the upper right figure accounts for the inertia of a moving block, the lower left figure accounts for the pressure fall underneath a moving block and the lower right figure integrates those three correction factors and leads to the critical wave height (H_{cr}) for the structure;
- this critical wave height should be larger than the design wave height for the structure.



Example (•): $B = L = 0.4 \text{ m}$ $D = 0.2 \text{ m}$ $\Rightarrow \begin{cases} \Gamma_1 = 1.17 \\ \Gamma_2 = 0.06 \\ \Gamma_3 = 0.19 \end{cases}$ with block motion: $H_{cr} = 1.1 \text{ m}$
 $\cot \alpha = 3$ $\Delta = 1.4 \text{ m}$
 $\Lambda = 0.6 \text{ m}$ $k' = 0.01 \text{ m/s}$ (without block motion:
 $\xi_0 = 1.5$ choose $\Gamma_2 = \Gamma_3 = 0 \Rightarrow H_{cr} = 0.65 \text{ m}$)

Figure 5 Design graphs for analytical model

This analytical model is also very suitable for transformation into a PC-model as has been done for one of the manufacturers of block-mat systems (see figure 6).

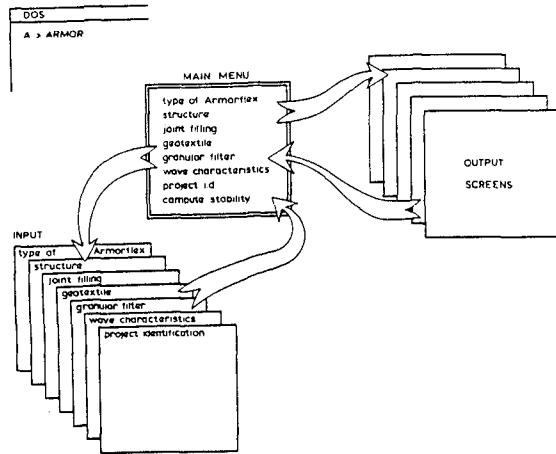
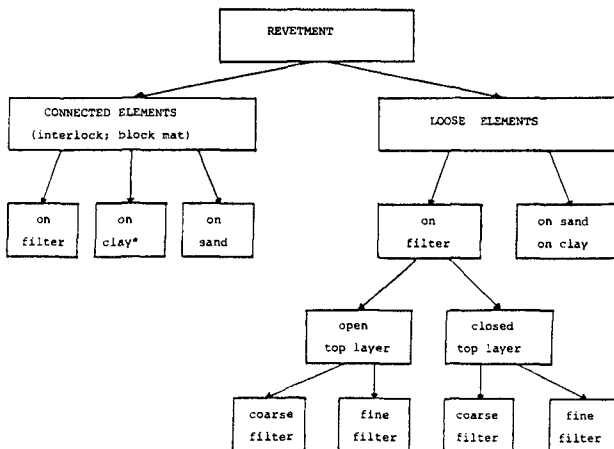


Figure 6 Set-up of Amorflex model

Numerical model

The numerical model can be considered as a specialist's tool. It will be used during the stage of detailed engineering of a revetment structure. It gives the time dependent loads and the structure's response. The average designer will need specialist's assistance to make an optimum use of this sophisticated design aid (see Bezuijen et al 1987, 1988, 1990-2).

Black-box model



* no model data available

Figure 7: Flow diagram for block-box model

This model consists of a system of purely empirical model test results of block revetment failure. In fact the box is not completely black but it is rather a grey-box. The acquired knowledge of the decisive parameters for block revetment stability have led to a division in eight combinations of top layer and sublayer (figure 7). The black-box model is very valuable for situations where the schematisations of the numerical and analytical models are not acceptable; for example for impermeable filter layers.

Initial design model

Finally an attempt has been made to combine all information from analytical, numerical and black-box models with field experience. This attempt has led to a consistent set of graphs to get a first impression of the critical wave height for a given structure.

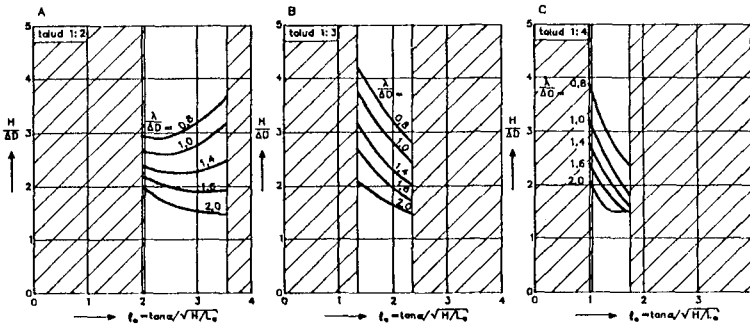


Figure 8 Simple design graph for top layer thickness

Even when using those methods the designer must still be aware of the consequences of his design freedom, also beyond the design of a stable top layer. Adaptation of one structural element may have strong effects on other parts of the structure as will be illustrated by a description of the possible consequences of steepening of an initially flat slope:

The aim of the designer will be to reduce the costs of the revetment by a reduction of the slope length. However, the wave run-up on a steep slope will increase and consequently the length of the revetment or even the volume of the dike will increase. The wave run-down will also increase, due to the higher value of the breaker parameter ξ . This generally will necessitate thicker blocks. Steepening the slope will also reduce the effective block weight but will on the other hand increase the friction between the blocks. For a steeper slope the soil mechanical stability will be more critical and the design of the granular filter and the interfaces between successive layers should be adapted and may even necessitate the application of a geotextile. Steepening the slope may also necessitate a stronger toe structure to support the revetment, and an extension of the toe structure to compensate for additional toe scour. Finally it is expected that an initial small damage will grow faster on a steep slope than on a gentle slope.

Some of the consequences mentioned are covered by the design methods that have been presented, but others are not. The designer himself is finally responsible for the quality of his design.

SAFETY CONSIDERATIONS

Correct application of the design methods lead to a 'safe' concrete block revetment. However, in the following some ideas about safety will be presented, showing the designer that safety is not an absolute and strict design consideration. The functional requirements of the revetment, the statistics of the boundary conditions, the residual strength of the structure and the acceptability of occasional (or even intensive) maintenance influence the selection of the hydraulic design conditions and the structural design itself.

In a very general way a safety consideration for a designer is: a reference for dealing with the possibility of a failing structure. It is the awareness of the designer that the same block revetment can be applied as a channel bank protection and as a protection of a dike surrounding a low lying polder area. The consequences of failure can be completely different and vary from the necessity of some repair measures to the loss of many lives, as will be illustrated in the following:

A revetment along an inland waterway will regularly meet its design conditions, maybe even daily, consisting of the waves induced by a ship sailing at maximum speed. From a maintenance point of view this means that no damage under design conditions is acceptable. Consequently, all attention from the designer is focussed on the initial strength of the structure; the residual strength does not play a role.

But a revetment on a dike enclosing a low laying polder will only at very rare occasions meet its design conditions. In the Netherlands such structures are designed for average storm recurrence frequencies of 1/4,000 or 1/10,000 times per year, because of the enormous potential losses resulting from a dike break-through.

Under such very rare conditions some damage to the top layer might be acceptable when the residual strength of the revetment is sufficient to guarantee the safety of the protected land. Consequently, the designer will explicitly incorporate the residual strength in his design.

A safety consideration is also: dealing with uncertainties. Uncertainties in material performance, construction methods and maintenance discipline.

For given boundary conditions and estimated uncertainties in the design parameters a revetment has been designed and the chance of failure has been calculated, using the three different design procedures: black-box model, analytical model and numerical model. The results of these probabilistic calculations (see table 2) confirm that more advanced design models requiring more detailed input, lead to a more reliable structure.

However, because of the many uncertainties in even the estimates of the parameter uncertainties, the calculated chance of failure will have little or no relation with the frequency of damage to the structure. But, for the comparison of different structures a probabilistic safety analysis may be very valuable.

Applied model	Chance of failure per 100 yr
Black-box	0.16
Analytical model	0.04
Numerical model	0.01

Table 2 Chances of failure for a specific structure

It will be clear that with the present state of the art a safety consideration for a revetment must be much more than the application of a probabilistic design method. The following example, however, will demonstrate that the use of a probabilistic calculation may contribute to the knowledge of the sensitivity of a structure design and is therefore a valuable tool.

Example: the resultant load on the top layer of a revetment is governed by the value of the leakage factor λ that can be calculated from the permeabilities and thicknesses of top layer and filter layer and the slope angle. In a deterministic approach a reduction of the leakage factor yields an increased top layer stability. In a probabilistic approach, however, not only the median leakage factor is taken into account, but also the statistical deviation of this value, based on the statistical deviation of the forementioned constituents. In the case of a reduction of the leakage factor it appears that for a smaller leakage factor the sensitivity of top layer stability for variations in the leakage factor is much greater than for larger values of the leakage factor. For a given acceptable chance of failure for the top layer much of the profit obtained by reducing the leakage factor is lost due to the increased sensibility of the stability for variations in the leakage factor!

This example reveals the validity of the concept of probabilistic design for placed block revetments.

Summarising it can be stated that at present, and probably also during the next decade, the role of probabilistic design for placed block revetments is essential for the analysis of the weaknesses of a design, but is of very limited value for a prediction of the chance of failure.

For the time being those elements of a structure that contribute for a large part to the total uncertainty of its performance should be avoided as much as possible.

The present research on safety aspects of block revetments is therefore focussed at:

- better estimates for the partial safety coefficients for the various parameters of the design models
- and at
- determination of the residual strength of the block revetment after an initial failure.

CONCLUSIONS

The research on placed block revetments has resulted in three design procedures: a black-box model, an analytical model and a numerical model. The models have been verified thoroughly and have been integrated in a set of simple graphs for initial design purposes. A start has been made to include probabilistic concepts in a safety consideration for block revetments. The following conclusions can be drawn from the research so far:

- The presented methods provide a powerful design tool for placed block revetments, based on thorough understanding of the physical processes in the revetment.
- Stochastic phenomena have proved to dominate the actual behaviour of a realised structure. Current research is therefore focussed on gaining knowledge of the statistical distribution of the structure's parameters.
- The effect of time dependent changes in structure parameters is still ignored in the design model. The gradual decrease of the permeabilities of top layer and filter layer in combination with a gradual increase of the friction between individual blocks may lead to a completely different behaviour of the structure than perceived in the design.
- For an optimum design the separate parts of the revetment should be treated completely integrated.
- For the time being the most profitable way to design a good revetment is to reduce the statistical dispersion of the input parameters for the design model.

ACKNOWLEDGEMENT

The development of this design model has been performed by order of the Technical Advisory Committee on Water Retaining Structures of the Dutch Ministry of Transport and Public Works. Their co-operation and permission to publish these results is gratefully acknowledged.

REFERENCES

- BAKKER, K.J., KLEIN BRETELER, M. and ADEL, H. DEN (1990), New criteria for granular filters under revetments. ICCE Delft, the Netherlands.
- BEZUIJEN, A., KLEIN BRETELER, M. and BAKKER, K.J. (1987), Design criteria for placed block revetments and granular filters. Copedec, Beijing.
- BEZUIJEN, A., WOUTERS, J. and LAUSTRUP, C. (1988), Block revetment design with physical and numerical models. ICCE Malaga, Spain.

- BEZUIJEN, A., BURGER, A.M. and KLEIN BRETELER, M. (1990), Placed block revetments. Compilation of research results 1980-1988. ISBN 90-9003232-0 (in Dutch).
- BEZUIJEN, A., WOUTERS, J. and ADEL, H. DEN (1990), Numerical simulation of the motion of a loose revetment block. ICCE Delft, the Netherlands.
- BOER, K. DEN, KENTER, C.J. and PILARCZYK, K.W. (1983), Large scale model tests on placed blocks revetment. Coastal structures 1983.
- BOER, K. DEN and BEZUIJEN, A. (1984), Compilation of slope revetment research between 1980 and 1984. Delft Hydraulics and Delft Geotechnics, M1881, Part XV (in Dutch).
- BURGER, A.M. (1983), Large scale guidance studies for top layer stability. Delft Hydraulics and Delft Geotechnics, M1795, Part IX (in Dutch).
- BURGER, A.M. (1984), Evaluation hydraulic aspects of the Oesterdam large scale model investigations. Delft Hydraulics and Delft Geotechnics, M1795, Part VIII (in Dutch).
- BURGER, A.M., KLEIN BRETELER, M., BANACH, L. and BEZUIJEN, A. (1988) Analytical design method for block revetments. ICCE Malaga, Spain (not published in the proceedings).
- BURGER, A.M., KLEIN BRETELER, M., BANACH, L. and BEZUIJEN, A. (1990) Analytical design method for block revetments. ASCE Journal of Waterway, Port, Coastal and Ocean Engineering, No 5, September 1990.
- KNAAP, F.C.M. VAN DER, KLEIN BRETELER, M. and MEULEN, T. VAN DER (1986), Design criteria for geotextiles beyond the sand tightness requirement. 3rd International Conference on Geotextiles, Vienna, Austria.
- KLEIN BRETELER, M. (1987), Stability of a top layer consisting of loose blocks, Delft Hydraulics, H195.04 (in Dutch).
- KLEIN BRETELER, M. and BEZUIJEN, A. (1988), The permeability of closely placed blocks on gravel, Proceedings SOWAS, Delft.
- PILARCZYK, K.W. (editor) (1990), Coastal protection, Proc. Short Course Delft University of Technology, June/July 1990, ISBN 90 6191 1273

NOTATION

b	= thickness of filter	(m)
B	= width of block	(m)
d_b	= position of minimal external pressure	(m)
D	= thickness of block	(m)
D_f	= characteristic grainsize filter	(m)
g	= acceleration of gravity	(m/s ²)
H, H_{cr}	= wave height, critical	(m)
k	= permeability of filter	(m/s)
k'	= permeability of top layer	(m/s)
L	= block length	(m)
L_o	= deep water wave length $g/2\pi.T^2$	(m)
O	= opening size of geotextile	(m)
T	= wave period	(s)
α	= slope angle	(°)
β	= steepness of pressure distribution	(°)

Γ	= strength increase factor	(-)
Δ	= specific mass of block = $(\rho_a - \rho) / \rho$	(-)
ϕ_b	= maximum external potential	(m)
λ	= leakage factor = $\sin \alpha \cdot \sqrt{k \cdot b \cdot D / k'}$	(m)
Λ	= $\lambda / \sin \alpha$	(m)
ξ_0	= breaker parameter = $\tan \alpha / \sqrt{H / L_0}$	(-)
ρ_a	= specific density of block	(kg/m ³)
ρ	= specific density of water	(kg/m ³)

CHAPTER 108

Rock Armour Stability Formulae-Influence of Stone Shape and Layer Thickness

Bradbury AP¹, Latham J-P² & Allsop NWH³

Abstract

A series of hydraulic model tests of armour rock stability have been carried out on a 1:2 slope armoured with rock of each of 5 different shape types. Results of these tests have been compared with damage predicted by van der Meer's stability formulae. Coefficients are suggested to describe the influence of armour shape and layer thickness in revised stability formulae.

1. Introduction

Coastal structures may be protected from the effects of wave action using rock armour with a variety of rock types, each of different grades and shape properties. The shape characteristics of quarried rock are governed largely by natural jointing and fracturing, and by production techniques. Many quarries can only produce flat slabby armourstone due to the limitations of the bedding. Under circumstances where the bedding and joint characteristics of the source permit, and where special production techniques are used, near equant blocks of armour can be produced.

During service, rock armour may suffer changes to both its shape and size. Previous research by Queen Mary College, and Hydraulics Research (Refs 1,2,3) has demonstrated the importance of rock quality and shown that degradation of armour in service constitutes a major problem for many coastal structures worldwide. Degradation of the armour may occur by fracturing, spalling or abrasion. These may be particularly important in severe wave climates, where there are abrasive sediments, or where the rock is of low grade, or where the rock is too small for the incident wave

¹Coast Protection Group, New Forest District Council, Lymington, SO41 9ZG, UK

²Coastal Engineering Research Group, Queen Mary and Westfield College, Mile End Road, London E1 4NS, UK

³Coastal Structures Section, Hydraulics Research, Wallingford, OX10 8BA, UK

conditions. Recently some structures have been designed for dynamic stability. In such cases the armour will also be more susceptible to degradation due to its movement under wave action.

2. Previous Work

Recent work in the UK and the Netherlands has highlighted the shortcomings of the Hudson formula (Ref 4), traditionally used for the design of rock armour for static stability. The omission of several fundamental hydraulic parameters in the Hudson formula has been addressed by van der Meer (Refs 5,6). These studies included the data from Thompson & Shuttler's work on rip-rap stability (Ref 7), in addition to the results from many other irregular wave tests. The new design formulae are based upon a more comprehensive empirical framework, and allow the designer to explore the influence of mound permeability, storm duration and acceptable damage levels. These formulae do not give quantitative advice on the effects of armour shape stability. Neither do they allow for variations in construction which may result in loose interlock, or armour layers of variable thickness.

The influence of armour shape and placement on stability has been discussed by a number of researchers. The Shore Protection Manual (Ref 4) suggests different stability coefficients for smooth and angular rock. Jensen (Ref 8) and Bergh (Ref 9) have tested rock armour of various shapes, and identified significant influence of armour shape on stability.

Van der Meer did not consider gross shape and roundness as variables in his static stability programme. However, a number of interesting observations arose during his tests which may be related to armour shape. Rounding of material during the extensive testing programme seems to give a likely explanation of some anomalous results. Two repeat tests at the beginning and end of the test programme resulted in 2.5 times more damage in the second test. Tests to investigate the effects of relative mass density identified a systematic effect, apparently uncorrelated to rock density. These differences may have arisen from variations in roundness and surface texture.

These suggest that gross shape and roundness, together with placement technique, have an important effect on stability, but no clear guidance is given to the designer on these effects. This study sought therefore to identify the influence of rock shape on armour stability, for inclusion in empirical design methods.

3. Test Programme

The framework of this study was based on the parameters defined in van der Meer's design formulae. A systematic series of random wave stability tests were carried out on each armour shape, including the effects of wave period, significant wave height and mean wave steepness, for a range of surging and plunging wave

conditions. A number of variables were kept constant throughout these tests:

Median armour weight $W_{50} = 323\text{g} \pm 2\%$
 Relative mass density of rock = 1.73
 Armour slope $\cot \alpha = 2$
 Armour grading (D_{85}/D_{15}) = 1.25
 Spectral shape = JONSWAP
 Approach beach slope = 1:52
 Filter size $D_{50} = 11\text{mm}$
 Construction method, crest level, wave angle
 Water depth at the toe of the structure, $h_s = 0.5\text{m}$

Measurements were made of the armour slope profiles, using a computer driven bed profiler, sampling at intervals of approximately $0.5 D_{n50}$ along each of 10 profiles across the test section. Damage to the test sections was expressed by the dimensionless damage parameter, S , defined:

$$S = A_e / D_{n50}^2 \quad (1)$$

An important variation between this study and previous work was the method of construction of the armour layers. Studies by both van der Meer and Thompson & Shuttler used armour layers constructed to a thickness of $2 - 2.4 D_{n50}$, with bulk placement of rock. Whilst bulk placement is common for rip-rap with a wide armour grading, this study used armour with a narrow grading ratio of $D_{85}/D_{15} = 1.25$. This study therefore used individual placement of the armour blocks to give two layers. The effect of this placement method was that the measured armour layer thickness was about $1.5 - 1.7 D_{n50}$.

Five contrasting shapes of rock were selected to represent the full range of armour shapes. Categories of rock defined in this study are: fresh, equant, tabular, semi-round, and very round. Fresh, crushed rock is used in many model tests and is generally typical of much quarried rock. This shape was initially selected as a base condition for comparison with van der Meer's work. Flat or slabby rock was excluded from this category. Equant or nearly cubic rock was selected as the second armour shape. Flat, slabby or tabular rock, with maximum to minimum lengths in excess of 2, was selected as a third shape, typical of much quarried limestone presently excluded from many design specifications. The effects of changing shape whilst in service were also examined by testing two grades of rounded rock, prepared by tumbling in a concrete mixer. Rounding to a weight loss of 5-10% and 20-25% represented materials subject to varying degrees of abrasion.

4. Shape Analysis

A study has been carried out at Queen Mary College to develop methods for the description of particle shape (Ref 3, 11), and

this has allowed a number of shape parameters to be examined. The median value of the X/Z ratio (maximum and minimum dimensions of the enclosing cuboid) has been used in the past to give a basis for comparing the gross shape of the samples. Recently Latham et al (Ref 11) have developed shape descriptors based on Fourier and/or Fractal analysis of particle outlines and armour slope profiles. These include the Fourier shape factor, P_C , which describes gross shape, and the Fourier asperity roughness, P_R , which is sensitive to roughness, but is also influenced by gross shape. The most useful of these shape descriptors was the Fourier asperity roughness factor, P_R . Blocks that have not undergone rounding but are tabular and elongate will give higher values of P_R than ones that are equant.

5. Test Results

For each test, values of the damage parameter were calculated from the profile data. In the preliminary analysis, damage was compared directly with that predicted by Van der Meer's formulae with a permeability coefficient of $P = 0.1$. For the purposes of further analysis, van der Meer's formulae were re-arranged, replacing the fixed coefficients in the original formulae by variables. The plunging wave formula was rewritten:

$$S^* = H^* / C_{p1} \quad (2)$$

where

$$S^* = (S/\sqrt{N})^{0.2} \quad \text{and} \quad H^* = H_s/\Delta D_{n50} \sqrt{\xi_m} P^{-0.13}$$

where C_{p1} replaces 6.2 in the original.

The surging wave formula was rewritten :

$$S^* = H^{**} / C_{su} \quad (3)$$

where

$$H^{**} = H_s/\Delta D_{n50} \sqrt{\tan \alpha} P^{0.13} \xi_m^{-P}$$

where C_{su} replaces 1.0 in the original equation.

Curve fitting regression coefficients for C_{p1} and C_{su} were calculated, for a permeability of $P = 0.1$ and are given in Table 1. Results from this study for plunging waves are compared with predicted damage from van der Meer's equation in Figure 1. Comparisons with van der Meer's equations indicated that very round rock performed worse than predicted, as did the partially rounded rock. However, equant and fresh rock also performed somewhat worse than predicted. Tabular rock surprisingly performed better than any other shape. Throughout the test programme, the threshold of damage for virtually all conditions was lower than that predicted by van der Meer's formulae. There

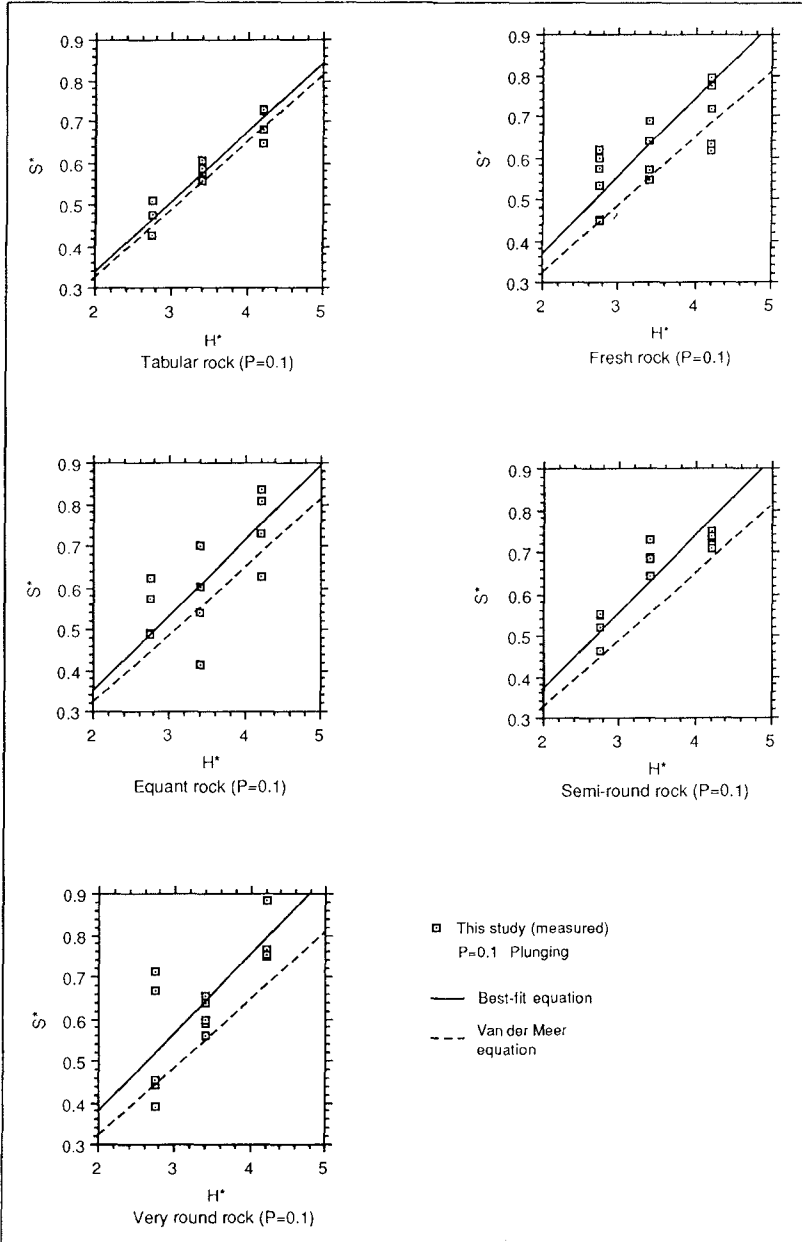


Figure 1 Van der Meer's predictions for plunging waves and curve fitting regression results for C_{p1}

was also noticeable scatter outside of Van der Meers 90% confidence bands, mostly at higher damage levels.

Table 1 Curve fitting regression results for C_{pl} and C_{su} in eqs. (2) and (3) for $P = 0.1$

Shape classes	Plunging C_{pl}	Surging C_{su}
Tabular	5.93	0.999
Fresh	5.63	0.711
Equant	5.61	0.894
Semi-round	5.39	0.830
Very round	5.35	0.713
Van der Meer	6.20	1.000

Initially it was felt that the consistently higher damage observed in this study could have resulted from the lower layer thickness, perhaps giving a lower value of P than the 0.1 limit given by Van der Meer. Subsequent analysis of this variable in the equations given by van der Meer indicated that substitution of a lower value of P cannot give satisfactory results for both surging and plunging formulae. A more reasonable explanation of this anomaly was derived after more detailed analysis and comparison of the results of this study with previous work. Samples of material from the previous studies were analysed using Latham's shape descriptor techniques.

This showed that the bulk of van der Meer's tests were performed with material similar in roughness and degree of rounding to the semi-round rock of this study, but with more equant gross shape. The material used by Thompson & Shuttler had characteristics similar to the equant rock of this study. It was concluded therefore that van der Meer's equations represent the stability of equant and semi-round rock.

6. Effects of Layer Thickness and Particle Shape

For armour with a narrow grading, the procedure most often adopted is to build a two layer system with random block orientation and individual placement of armour. A layer thickness of less than $2D_{n50}$ may therefore be common. Differences in the layer thickness achieved in this study and those in van der Meer's study represent a 30% reduction in layer thickness. It was suspected that this comparative reduction in layer thickness alone gave the increase in damage from that predicted by van der Meer for equant and semi-round materials.

This increase can be explained by replacing some coefficients in the van der Meer equations by variables. Analysis of the results by least squares non-linear regression gave acceptable explanations for the influence of both shape and layer thickness. The shape effects were best described by using the coefficients

C_{pl} and C_{su} . To fix these values at 6.2 and 1.0 for equant and semi-round materials required either that:

- (i) the power coefficients of P, 0.18 and 0.13 must be adjusted to be functions of layer thickness; or
- (ii) the power coefficient of S/\sqrt{N} , must be adjusted.

Both (i) and (ii) were tested, but the most satisfactory results were achieved by adjustment of the power coefficients of S/\sqrt{N} . Conveniently a single adjustment of this coefficient can account for both surging and plunging results as shown in Table 2.

These revised equations may be given:

$$\text{Plunging waves: } S^{*'} = H^*/C_{pl}' \quad (4)$$

$$\text{Surging waves: } S^{*'} = H^{**}/C_{su}' \quad (5)$$

$$S^{*'} = (S/\sqrt{N})^{x(1)} \quad \text{for plunging} \quad (4a)$$

$$S^{*'} = (S/\sqrt{N})^{x(2)} \quad \text{for surging} \quad (5a)$$

Table 2. Derivation of curve fitting power coefficients for S/\sqrt{N} by least squares non linear regression

	Plunging	Surging
	$C_{pl}' = 6.2$	$C_{su}' = 1.0$
Equant	$x(1)=0.236$	$x(2)=0.249$
Round	$x(1)=0.269$	$x(2)=0.260$
Equant & semi-round	$x(1)=0.252$	$x(2)=0.254$

The coefficients $x(i)$ and $x(ii)$ may therefore be reasonably assigned the same value of 0.25. The only difference in the formulae needed to describe the effects of layer thickness on damage for equant and semi-round rock was therefore a change in the power coefficient from 0.2 to 0.25. Thus S in eqn.(4a) and eqn.(5a) can be replaced by:

$$S^{*'} = (S/\sqrt{N})^{0.25} \quad (6)$$

Further curve fitting to establish best fit values of C_{pl}' and C_{su}' in equations (4) and (5), assuming equation (6), was then carried out to quantify the effects of armour shape on stability. The regression results for C_{pl}' and C_{su}' for each armour shape are presented in Figures 2 and 3, and Table 3.

It is important to emphasise that this analysis is only valid for the range of conditions used in this study [i.e 1:2 slope, impermeable core, layer thickness $t_a = 1.5-1.7 D_{n50}$].

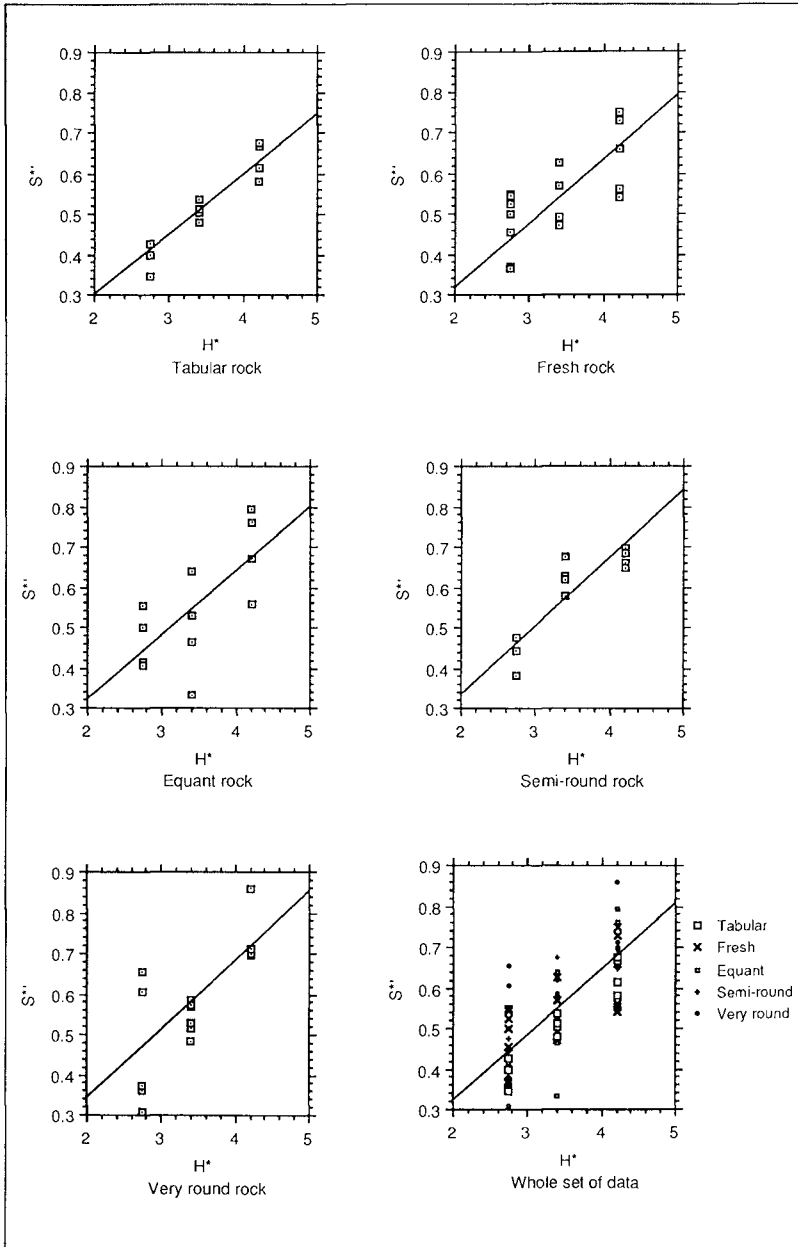


Figure 2 Curve fitting regression results for C_{pl} , plunging wave formula

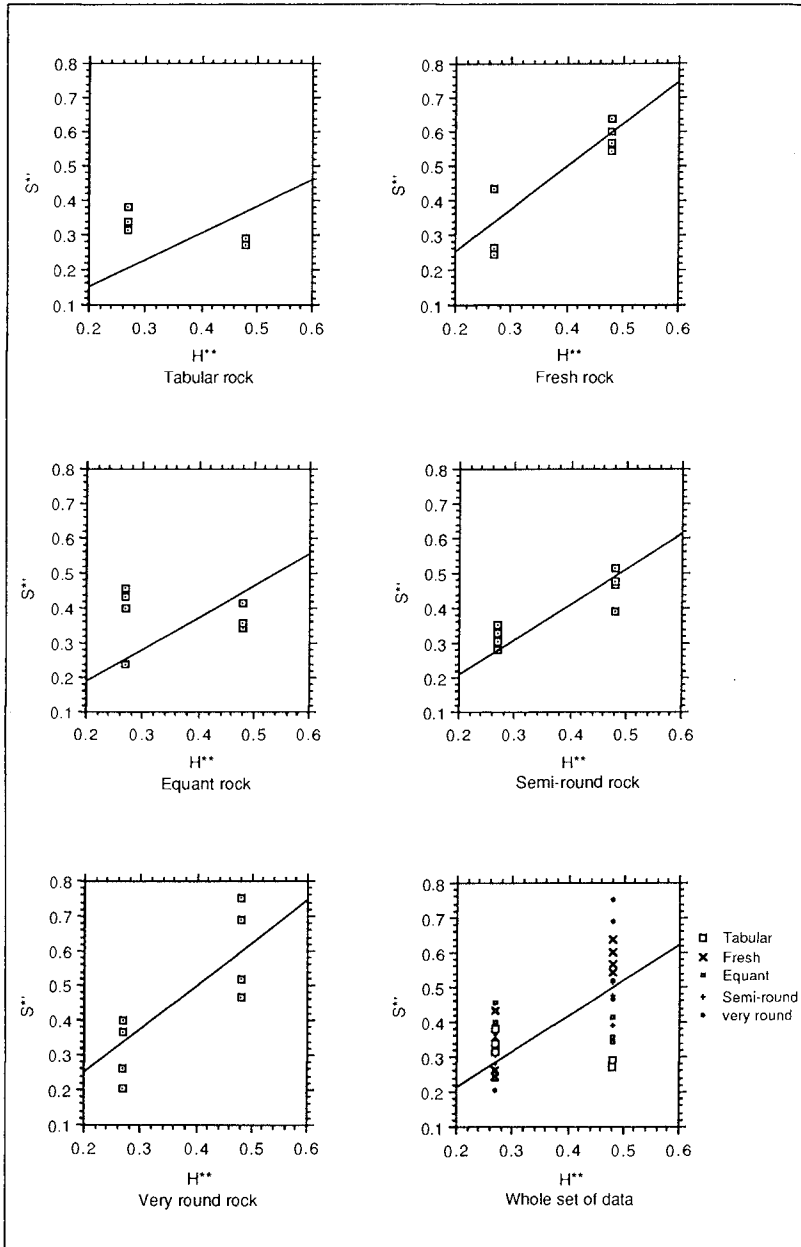


Figure 3 Curve fitting regression results for C_{su}^1 , surging wave formula

Table 3 Curve fitting regression results for C'_{pl} and C'_{su} in eqs. (9) and (10)

Shape classes	Plunging	Surging
	C'_{pl}	C'_{su}
Tabular	6.72	1.301
Fresh	6.32	0.811
Equant	6.24	1.087
Semi-round	5.96	0.989
Very round	5.88	0.810

The results of shape analysis of the armour determined during the test programme can be compared with the stability coefficients C'_{pl} and C'_{su} . From a simple regression of C'_{pl} and C'_{su} on P_R , the following summary equations were derived:

$$C'_{pl} = 5.4 + 70.0 P_R \quad (7)$$

$$C'_{su} = 0.6 + 40.0 P_R \quad (8)$$

Figures 4 and 5 show the results of this analysis including data derived from the original tests carried out by van der Meer, for which values of 6.2 and 1.0 can be assumed for C'_{pl} and C'_{su} .

Van der Meer's equations can now be modified to account for different shaped armour and layer thicknesses. Substituting the new coefficients for 2 layers of armour on an impermeable core at a slope of 1:2, the proposed modifications to van der Meer's equations are given by:

$$H_s/\Delta D_{n50} \sqrt{\xi'_m} = C'_{pl} P^{0.18} (S/\sqrt{N})^{0.25} \quad (9)$$

$$H_s/\Delta D_{n50} = C'_{su} P^{-0.13} (S/\sqrt{N})^{0.25} \sqrt{\cot \alpha} \xi'_m P \quad (10)$$

where C'_{pl} and C'_{su} are shape coefficients given in equations (7) and (8) by the Fourier asperity roughness parameter P_R .

C'_{pl} and C'_{su} have been set to be coincident with C_{pl} and C_{su} respectively for flume tests results from all studies using Equant and Semi-round type test material. However C_{pl} and C_{su} in the general equations (2) and (3) may not have the same influence on stability as eqns. (7) and (8) since, for example permeability in the core may greatly influence the effect of shape on damage.

The implications of these equations are now summarized. The change in damage S as a result of using tabular or very round rock by comparison with equant rock has the following influence.

Damage, S Plunging : Tabular = 0.81 Equant
Very round=1.40 Equant

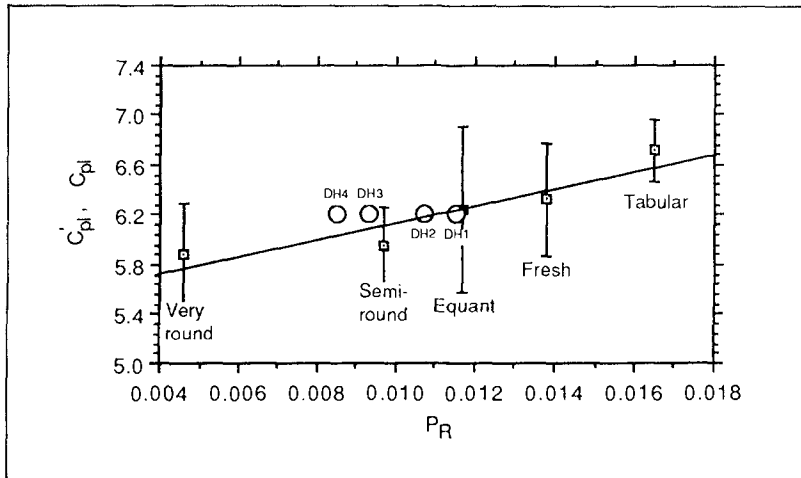


Figure 4 Best fit for shape coefficient C'_{pl} in Equation (7) versus block shape parameter P_R

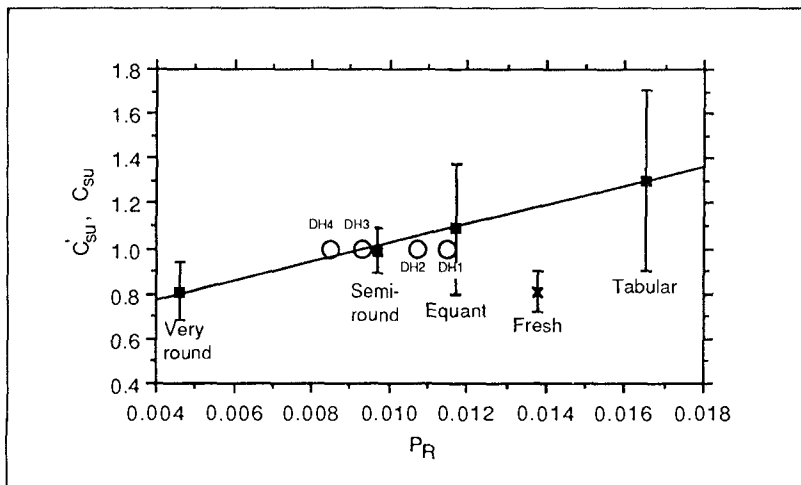


Figure 5 Best fit for shape effect coefficient C'_{su} in Equation (8) versus block shape parameter P_R

Surging : Tabular =0.52 Equant
 Very round=3.44 Equant

This simple summary of the shape effects given by equations (7) and (8) may be an over-simplification of the complexity of shape effects but indicates the potential dangers of underdesign if the effects of shape are ignored.

The surging wave data gave more scatter than the plunging data and gave large standard errors for the curve fitting, whilst the fresh rock results did not conform to summary trends at all, casting some doubts on this simple interpretation of the surging waves results.

10. Conclusions

The results of the study gave consistently higher damage levels than predicted by van der Meers equations for shape classes of material of similar shape characteristics to those from which the formulae were derived.

These differences have been attributed to the lower layer thickness achieved by placing armour in a two layer thickness resulting in a total layer thickness, of $t_a \approx 1.6 D_{n50}$. Such increased damage for thinner armour layers can be predicted by assuming that the power 0.2 for (S/\sqrt{N}) in both surging and plunging equations is replaced by 0.25.

For different armour shapes and conditions represented in the model test series van der Meer's equations can be simply modified, assuming the 0.25 power correction for double armour layers with the introduction of two shape coefficients.

$$C'_{pl} = 5.4 + 70.0 P_R$$

$$C'_{su} = 0.6 + 40.0 P_R$$

into the equations:

$$H_s/\Delta D_{n50} \sqrt{\xi_m} = C'_{pl} P^{0.18} (S/\sqrt{N})^{0.25}$$

$$H_s/\Delta D_{n50} = C'_{su} P^{-0.13} (S/\sqrt{N})^{0.25} \sqrt{\cot \alpha} \xi_m^P$$

11. Acknowledgements

This paper describes the results of model tests funded by the Department of the Environment, the Ministry of Agriculture Fisheries and Food, and the Science and Engineering Research Council. Additional work has been supported by Queen Mary and Westfield College, Hydraulics Research, and New Forest District Council.

The authors are grateful for helpful advice from Dr van der Meer of Delft Hydraulics during the model studies, and for the assistance of Mr H Wang at Queen Mary and Westfield College in the further analysis.

12. References

1. Allsop NWH, Bradbury AP, Poole AB, Dibb TE, & Hughes DW "Rock Durability in the marine environment" Report SR11, Hydraulics Research, Wallingford, March 1985.
2. Bradbury AP & Allsop NWH "Durability of rock on coastal structures" Proc 20th Coastal Eng Conf, Taipei, November 1986.
3. Latham J-P, Mannion MB, Poole AB, Bradbury AP & Allsop NWH. "The influence of armourstone shape and rounding on the stability of breakwater armour layers". Queen Mary College, September 1988.
4. Coastal Engineering Research Centre "Shore Protection Manual" Vols I-II, US Government Printing Office, Washington, 4th Edition, 1984.
5. Van der Meer JW "Rock slope and gravel beaches under wave attack" PhD thesis Delft University of Technology, April 1988, also as Delft Communications No 396.
6. Van der Meer JW & Pilarczyk KW "Stability of breakwater armour layers: deterministic and probabilistic design" Delft Hydraulics Communication No 378, Delft, The Netherlands, February 1987.
7. Thompson DM & Shuttler RM. "Design of riprap slope protection against wind waves", Report 61, CIRIA, London 1976.
8. Jensen OJ "A monograph on rubble mound breakwaters." Danish Hydraulics Institute, Horsholm, November 1984.
9. Bergh H "Riprap protection of a road embankment exposed to waves." Bulletin No TRITA-VB1-123, Royal Institute of Technology, Stockholm, Sweden, 1984.
10. Bradbury AP, Allsop NWH, Latham J-P, Mannion M & Poole AB. "Rock armour for rubble mound breakwaters, sea walls and revetments: recent progress". Hydraulics Research, Report SR150, March 1988.
11. Latham J-P, & Poole AB "The application of shape descriptor analysis to the study of aggregate wear" QJEG, Vol 20, pp297 - 310, 1987.

Summary of notation

ξ_m	Iribarren or surf similarity number
P	Notional Permeability factor
S	Dimensionless damage to a mean profile
N	Number of waves in a storm or test
H_s	Significant wave height
Δ	Relative density
D_n	Nominal particle diameter
C_{su}	Surging wave shape coefficient, defined in equation (2)
C_{pl}	Plunging wave shape coefficient, defined in equation (3)
C'_{su}	Surging wave shape coefficient defined in equation (4)
C'_{pl}	Plunging wave shape coefficient defined in equation (5)
A_e	Cross section area eroded

CHAPTER 109

Reflection Performance of Rock Armoured Slopes in Random Waves

N W H Allsop¹

Abstract

Waves reflected from breakwaters and sea walls may cause navigation or mooring problems in or near harbours, and may increase beach erosion or local scour.

This paper gives results of hydraulic model tests on the reflection characteristics of idealised rock armoured slopes. Examples of the performance of a number of practical structures are also discussed.

1. Wave Reflections

The importance of wave reflections from coastal and harbour structures has historically been given relatively little weight in the design process. Recently it has been appreciated that local problems may often arise due to cumulative increases in wave energy, particularly within harbours. Typically, increased wave reflections may lead to:

- (a) Danger to vessels, often close to the harbour entrance.
- (b) Disruption to handling operations in the harbour due to excessive vessel motions.
- (c) Damage to vessel or mooring systems.
- (d) Local bed scour.
- (e) General increases in erosion at adjoining sites.

Recent studies at Hydraulics Research on wave reflections were prompted by problems experienced in harbours in the Caribbean. Changing wave patterns within these harbours arose from increased reflections from new structures, and from the refraction effects of dredging, (Refs 1, 2). A detailed review of the data available on the wave reflection performance of coastal structures was conducted (Ref 3), and was summarised at the 1988 ICCE (Ref 4). The review noted that data on the reflection performance of rock armoured slopes was sparse, and was restricted

¹Manager, Coastal Structures Section, Hydraulics Research, Wallingford, OX10 8BA, UK)

to regular waves only. It was therefore agreed that a short series of random wave flume tests would be conducted to provide data of general application, and to be used in the numerical modelling of the harbours of interests. This paper presents results from those tests on simple and bermed rock armoured slopes (Ref 5). The paper also presents results from tests on some practical example structures.

2. Measurements and Definitions

In each of the tests considered in this paper, reflections have been measured in a random wave flume. Three wave probes were placed in a constant water depth in front of the test section. Incident and reflected spectra were calculated from the wave probe output by a program developed by Gilbert & Thompson (Ref 6), based on the method of Kajima (Ref 7). This method calculates the reflection coefficient function $C_r(f)$ over the frequency range $0.5f_p < f < 2.0f_p$, where f_p is the frequency at peak energy density for the generated wave spectrum. The reflection coefficient function gives information on the reflection performance with frequency, and is often used in cases where it may be assumed that reflection is a linear process.

At coastal structures wave breaking will have a significant influence on the reflection performance. For this work a total energy approach has therefore been adopted. The reflection coefficient, C_r , is defined in terms of the total reflected and incident energies, E_r and E_i respectively, each parameter measured over the same frequency range:

$$C_r = (E_r / E_i)^{1/2} \quad (1)$$

3. Reflections from Simple and Bermed Slopes

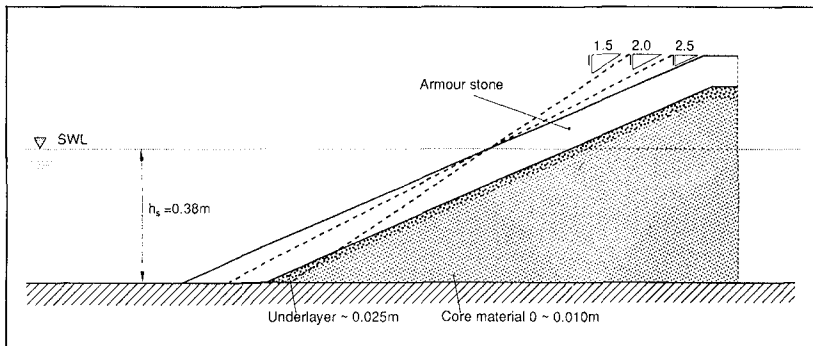


Figure 1 Simple slopes tested

A total of 19 cross-sections were used in these tests to explore the effects of:

- (a) front face slope angle, α ;
- (b) smooth or armoured facing;
- (c) armour layer thickness, t_a ;
- (d) armour unit size, M_{50} , D_{n50} ;
- (e) berm length, B .

For the simple slopes, 3 slope angles were used, $\cot \alpha = 1.5$, 2.0 and 2.5. Smooth and armoured slopes were tested at each angle, Figure 1. A further series of tests explored the influence of 3 berm widths, Figure 2. Armoured slopes were tested with single or double layer armour placement.

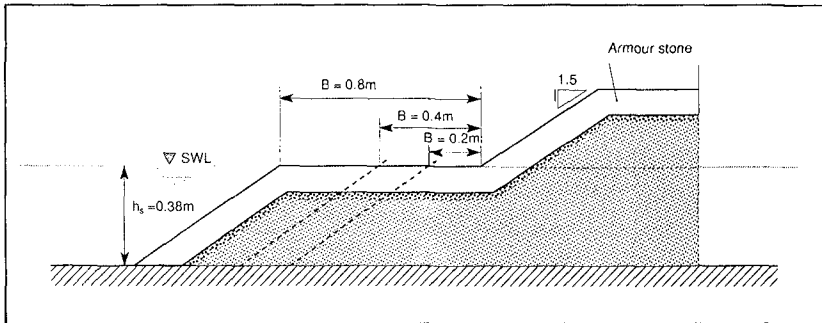


Figure 2 Bermed slopes tested

A set of 9 sea states were used with mean sea steepness, $s_m = H_s/L_m$, from 0.0043 to 0.52. Relative mean local wave lengths, L_{ms}/h_s , varied from 6.2 to 14.8. Values of the Iribarren number for the simple slopes, $I_{r_m} = \tan \alpha / s_m^{1/2}$, varied between 1.7 and 10.2.

4. Test Results

Simple slopes

The results of the tests were presented as graphs of C_r against I_r for the simple slopes. To these results have been fitted simple empirical equations of the form used by Seelig (Ref 8):

$$C_r = \frac{a I_{r_m}^2}{b + I_{r_m}^2} \quad (2)$$

This equation was preferred as it is well-known and simple to use, and has been found to give a good description of the reflection coefficient over most of the range of practical interest, see Reference 4. Values of the empirical coefficient a and b were derived for each of the simple slopes tested, both smooth and armoured.

In the preliminary analysis it was noted that the curves calculated by simple regression did not give a good fit over the full range of values tested, and tended to under-estimate C_r at higher values of I_{rm} for the rock armoured slopes. A revised analysis was therefore attempted in which a weighting was applied at the larger values of I_{rm} . This is not a fully satisfactory approach, it did however give consistently better descriptions of much of the data for smooth and armoured slopes. Examples of the test results are shown in Figures 3 to 6 and values of the empirical coefficients are summarised below:

Test section	a	b
Smooth	0.96	4.80
Rock armour, 2 layer	0.64	8.85
Rock armour, 1 layer	0.64	7.22
Large rock, 2 layer	0.64	9.64
Large rock, 1 layer	0.67	7.87

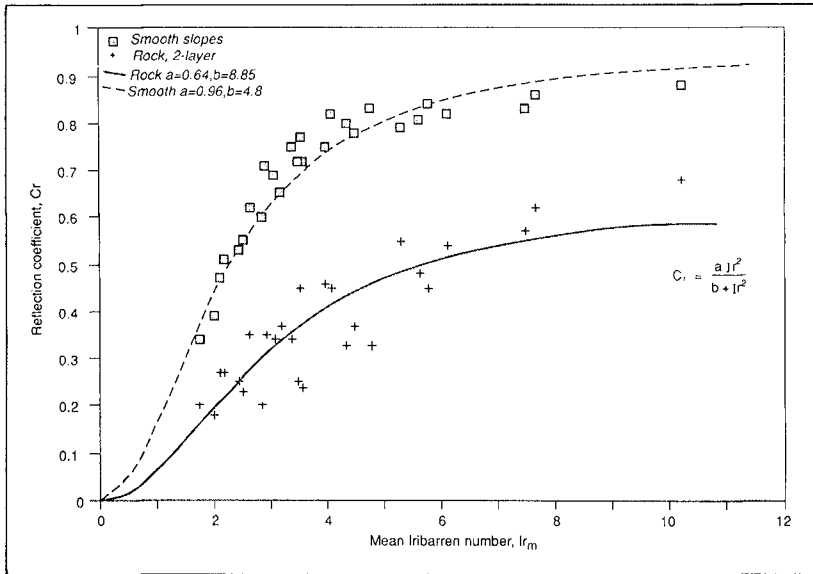


Figure 3 Reflections, smooth and armoured slopes

The results in Figures 3-5 are presented as values of C_r against I_{rm} , where the calculation of I_{rm} is based upon the deep water wave length of the mean wave period, T_m :

$$L_m = g T_m^2 / 2\pi$$

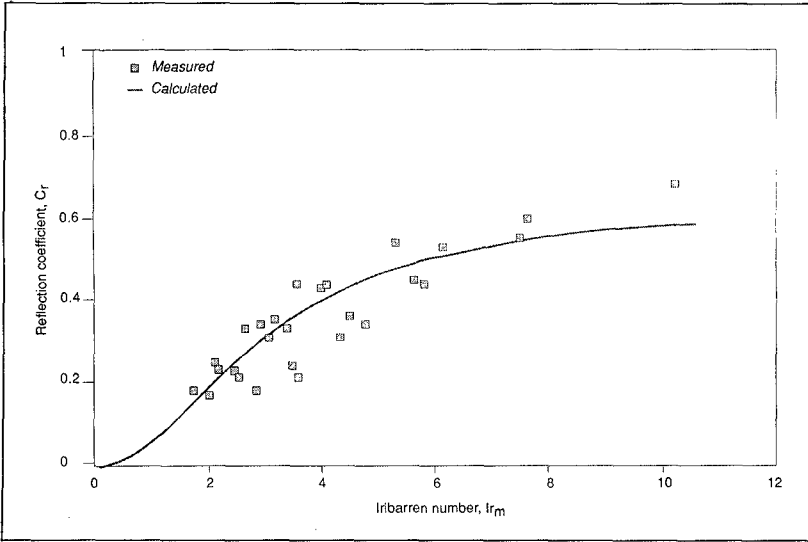


Figure 4 Reflections, large rock, 2 layer

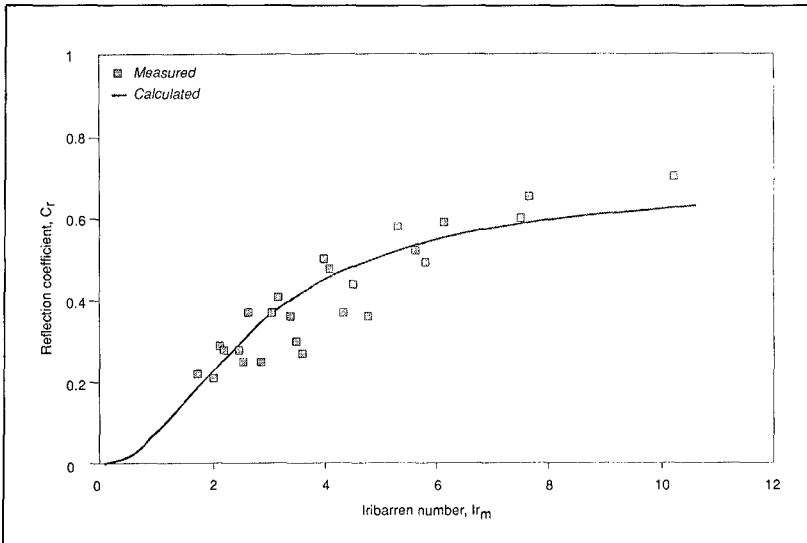


Figure 5 Reflections, large rock, 1 layer

The use of L_m in the calculation of I_r intended to represent the local wave breaking may seem somewhat obstruse. It might be the water depth local to the structure, L_{ms} , would give a more reliable description. The results shown in Figure 3 were therefore re-plotted as C_r against $I_{r_{ms}}$, where $I_{r_{ms}}$ was calculated using the wavelength of the mean period in the water depth at the test section, L_{ms} . These results are shown in Figure 6. Surprisingly there appears to be no improvement through the use of L_{ms} which, being less easy to calculate, complicates the use of any prediction formula based upon it.

This conclusion is similar to one drawn by Yoo (cited by Southgate, Ref 11), who noted the paradox of using an offshore wave parameter to described an inshore process, but found that the use of L_{m0} gave a clearer classification of wave breaking.

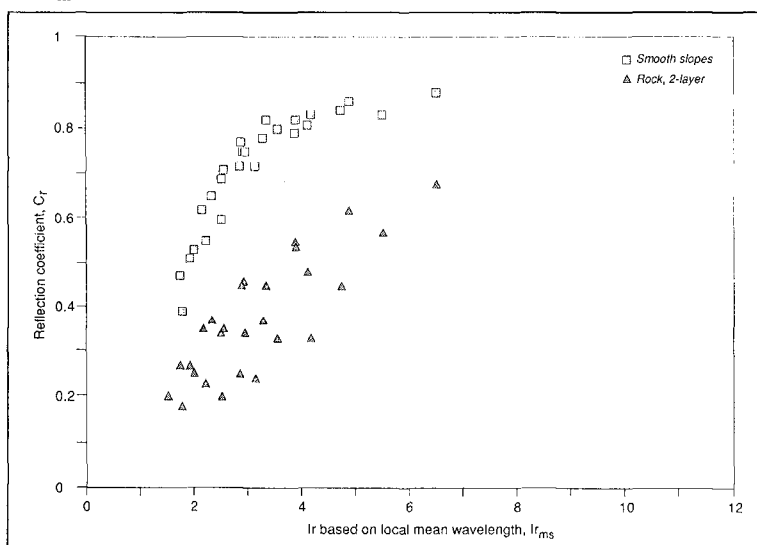


Figure 6 Simple slopes, effect of $I_{r_{ms}}$

Bermed slopes

It is difficult to justify the use of the Iribarren number in analysing the performance of bermed slopes. The dimensionless parameter that has been found most useful for such structures is the ratio of berm length to wave length, B/L . The use of this parameter is however complicated by the choice of which wavelength best represents random wave conditions. In this study the wavelength was calculated for the mean wave period both in deep water and in the test water depth, giving L_{m0} and L_{ms} respectively. No clear difference in the fit of the data emerged, and L_{m0} is used in the results shown in Figure 7.

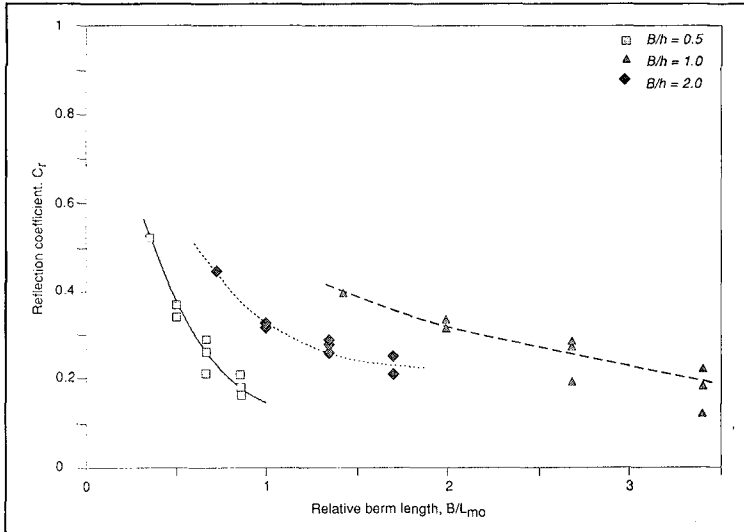


Figure 7 Effect of berm width

Careful consideration of the results shown in Figure 7 suggests that the effect of increasing B on the reflection performance is negligible over the berm widths tested. The separation of the curves for different berm lengths is due primarily to the effect of B in the parameter B/L_{ms} . The data does however suggest that for values of $B/L > 0.05$, the reflections will be reduced to about 50-65% of those from the equivalent simple slope.

5. Comparisons with Other Data

Practical examples of coastal or harbour structures often differ from those for which the test data is used to derive empirical design methods. It is instructive therefore to compare the results of the simple prediction methods available with those measured for realistic structures. Three such examples will be considered here.

Seawall at Blue Anchor Bay

Vertical or slightly battered walls are known to reflect at around 90-100%. These reflections frequently increase local scour, often undermining the wall. Increasingly refurbishment of such seawalls has involved the construction of a rock armoured slope against the wall, reducing wave impacts on the wall, and reducing the level of reflections. Such protection may also improve the wave overtopping performance of the seawall, although some configurations may make matters worse!

In an example described previously (Ref 4), the engineer considered two rock armoured slopes as alternatives to an asphalt grouted toe. The site is subject to a large tidal range, and the wall only experiences significant wave action above about neap high water level, Figure 8.

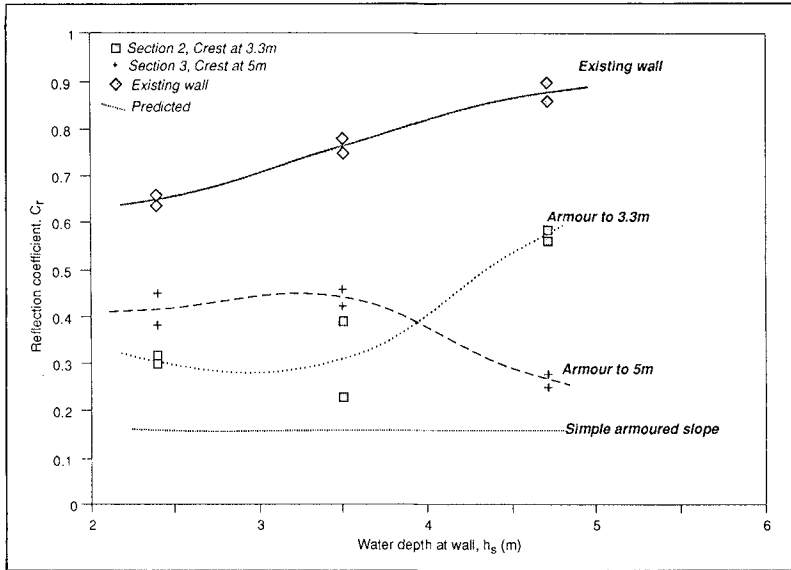


Figure 8 Blue Anchor Bay, sea wall reflections

For the existing structure, C_r reduced from around 0.85 at $h_s = 4.7\text{m}$, to about 0.65 at $h_s = 2.4\text{m}$, principally due to the increasing influence of the (relatively) smooth asphalt slope. Even at the lower test level the rear wall greatly influenced the reflections. A continuous smooth slope at the 1:2.86 angle of the asphalt would reflect at $C_r = 0.30$ using the data in Section 4.1 above. Two protection schemes were considered, each using rock placed at 1:2.5, to crest levels at 3.3m or 5.0m above the toe. Both schemes reduced the reflections significantly, and in the prototype considerable beach material has built up against the rock. Of interest here however is the comparison of the reflections measured, and those predicted for a continuous armoured slope. For the wave conditions tested, the idealised slope would give $C_r = 0.16$, but those measured generally exceeded 0.3.

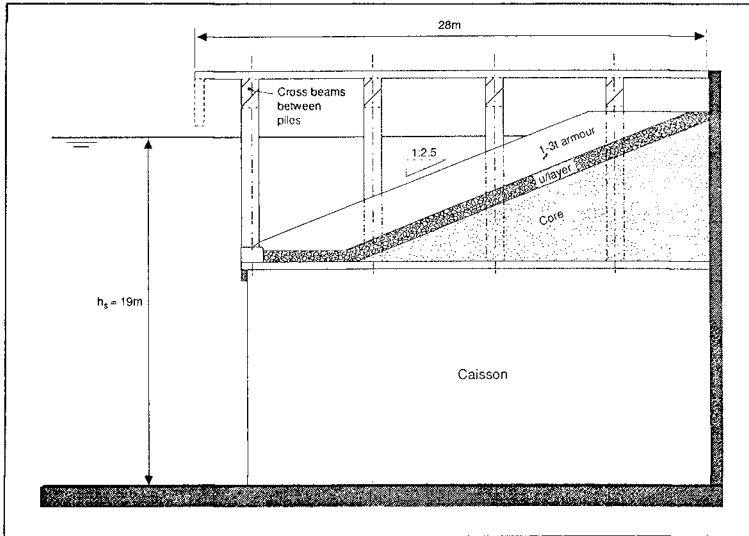


Figure 9 Coal berth quay, option A1/A2

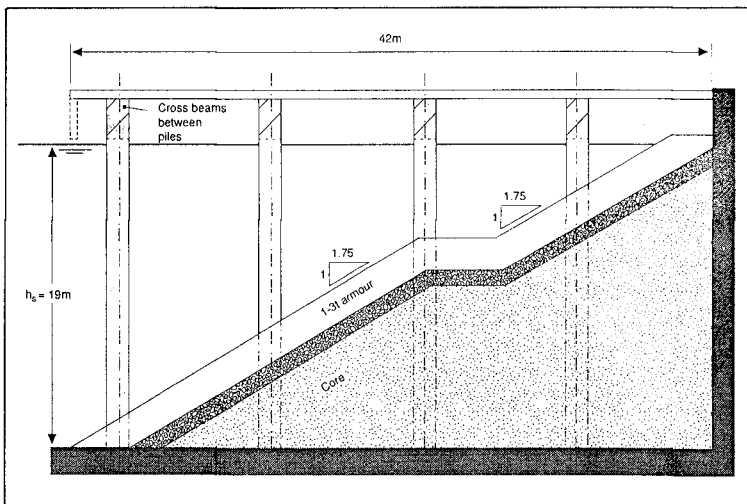


Figure 10 Coal berth quay, option B

Coal berth armoured slopes

Reflections from two alternative harbour structures were compared in a recent study. Both structures were formed by an armoured slope beneath a piled deck. In the first instance, models A1-A3, the rock armoured slope at 1:2.5 was to be constructed on a part-depth caisson, see Figure 9. Models A1 and A2 were very similar, differing only in fine details of the underlayer construction. In both sections waves were able to ride over the crest of the armour. The seaward edge of the armoured slope was about 7m from the impermeable rear wall. Section A3 differed in the crest detail only. For this section the void behind the 4th row of piles was filled, in prototype by a service duct laid on fine fill and concrete footing.

The alternative structure, model B, used a full depth slope at 1:1.75 with a small berm at half water depth, Figure 10. The crest of the armour was very close to the water surface, as was the impermeable rear wall.

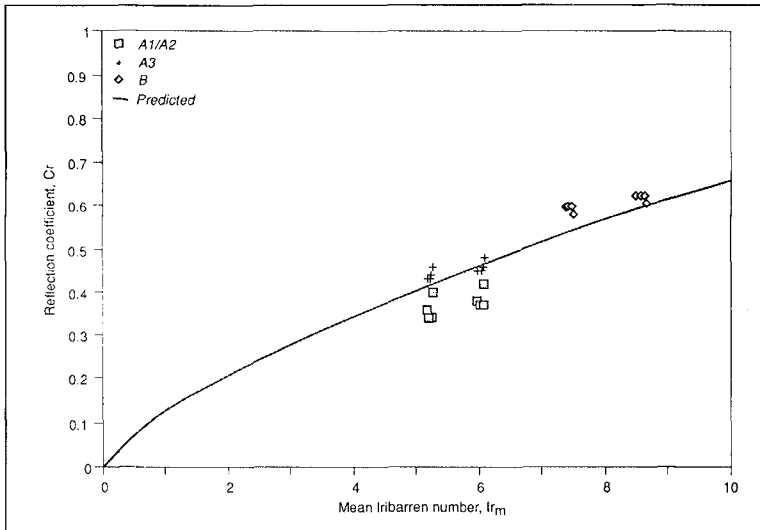


Figure 11 Coal berth quay, reflection performance

The results of the tests may be compared with values of C_r predicted by Seelig's equation with $a = 0.64$ and $b = 8.85$. The results are shown in Figure 11. Somewhat to the designer's surprise, model A reflected least, with values below the prediction. The reflections from model A3 were more severe, due to the proximity of the rear wall. The reflections from model B were significantly greater than for A, but when plotted against Ir_m again lie only slightly above the prediction line.

Analysis of other data by Postma

Reflection data measured by van der Meer (Ref 10) on simple armoured slopes have been analysed by Postma (Ref 9), using the surf similarity parameter, or Iribarren number, defined using the steepness of peak period in deep water, $s_{op} = 2\pi H_s/g T_p^2$. For all of van der Meer's data, Postma derived a simple prediction equation:

$$C_r = 0.14 Ir_p^{0.73} \quad \text{where} \quad Ir_p = \tan \alpha / s_{op}^{1/2} \quad (3)$$

Postma also fitted an equation of the form of (3) to the data in Reference 5:

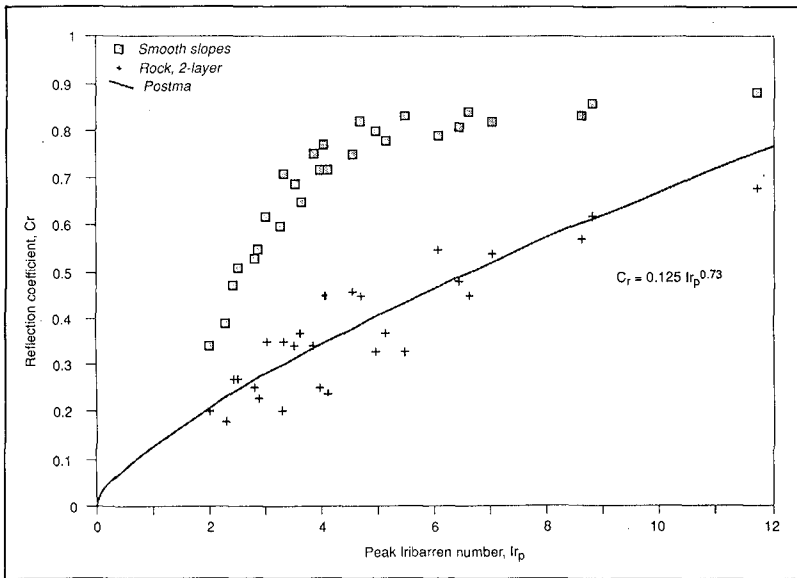


Figure 12 Simple slopes, comparison with Equation 4

$$C_r = 0.125 Ir_p^{0.73} \quad (4)$$

Equation 4 is compared with the smooth and armoured slope results in Figure 12. Postma's simple curve gives a good fit to the data for simple rock armoured slopes over the range $2 < Ir_p < 9$.

6. Conclusions and Recommendations

Tests with random waves on idealised simple slopes have given new values for the empirical prediction equation for C_r derived by Seelig. Comparisons of the performance of practical examples have shown that their reflection performance may be strongly influenced by small geometric variations around the water line. Where the structural geometry departs from the idealised structures tested, particularly close to the water level, hydraulic model tests will be required to quantify the reflections.

7. Acknowledgements

The work covered in References 1-3 was conducted by Hydraulics Research for the British Overseas Development Administration. The preparation of this paper was supported by Hydraulics Research.

8. References

1. Jones D V & Smallman J V. "Wave reflections in Caribbean harbours: studies for Port Castries, St Lucia", Report OD 94, Hydraulics Research, Wallingford, March 1988.
2. Smallman J V & Green A P E. "Wave reflections in Caribbean harbours: studies for St George's harbour, Grenada, and St John's harbour, Antigua", Report OD 109, Hydraulics Research, Wallingford, March 1988.
3. Allsop N W H & Hettiarachchi S S L. "Wave reflections in harbours: the design construction, and performance of wave absorbing structures". Report OD 89, Hydraulics Research, Wallingford, March 1989.
4. Allsop N W H & Hettiarachchi S S L. "Reflections from coastal structures", Proc 21st ICCE, Malaga, June 1988. (Available as HR conference paper No 17).
5. Allsop N W H & Channell A R. "Wave reflections in harbours: reflection performance of rock armoured slopes in random waves". Report OD 102, Hydraulic Research, Wallingford, March 1989.
6. Gilbert G & Thompson D M. "Reflections in random waves, the frequency response function method". HR Report IT 173, Hydraulics Research, March 1978.
7. Kajima R. "Estimation of an incident wave spectrum under the influence of reflection". Coastal Eng. in Japan, Vol 12, 1969.
8. Seelig N W. "Wave reflection from coastal structure". Proc. Conf. Coastal structures 1983, ASCE, Arlington, 1983.

9. Postma G M. Wave reflection from rock slopes under random wave attack. MSc thesis, Delft University of Technology, in preparation. (Cited by van der Meer J W & Allsop N W H. "Physical processes and design tools," 5.1 in Manual on the use of rock shoreline and coastal engineering, CUR C67/CIRIA RP 402, draft January 1990).
10. Van der Meer J W, 1988-1. "Rock slopes and gravel beaches under wave attack" Doctoral thesis, Delft University of Technology, (available as Delft Hydraulics Communication No 396).
11. Southgate H N. "Wave breaking: a review of techniques for calculating energy losses in breaking waves". Report SR 168, Hydraulics Research, Wallingford, March 1988.

CHAPTER 110

A Model for Breaking Wave Impact Pressures

M.J. Cooker* and D.H. Peregrine[†]

Abstract

This paper discusses a mathematical model of the large, short-lived pressures brought about by waves breaking against coastal structures. The idea of pressure impulse, P (the integral of pressure with respect to time from the start to the finish of the impact) is used to simplify the equations of ideal incompressible fluid motion. P satisfies Laplace's equation in a domain which is the mean position of the wave during the very short time of impact. We solve analytically a two-dimensional boundary-value problem, which models an idealized wave striking a vertical wall. Expressions are derived for the impulse on the wall, the peak pressure distribution, and the change in fluid velocity due to impact. The results are insensitive to the shape of the wave far from the wall. The results agree with some experimental measurements, from the literature.

Introduction

This paper is concerned with the very large and sudden pressures exerted by a breaking wave when it slams into a solid surface.

Winter storms in February 1990 caused great damage to sea walls on the UK coast, and there is a long-standing need to understand how breaking waves are able to exert loads on vertical walls, and other structures. Many field measurements and experimental studies since Bagnold (1939) have shown the existence of peak pressures exceeding 10 times the hydrostatic head and which last for periods between 0.1 and 10 milli-seconds (depending on the size of the wave). Figure 1 shows a typical pressure-time curve, for a point on a vertical wall. Blackmore and Hewson (1984) measured impact pressures in the field and high, short-lived loadings have been recorded on sloping beaches (Richert, 1968; Grüne, 1988).

*Research Assistant. †Professor.
School of Mathematics, University of Bristol, University Walk,
Bristol, BS8 1TW, England.

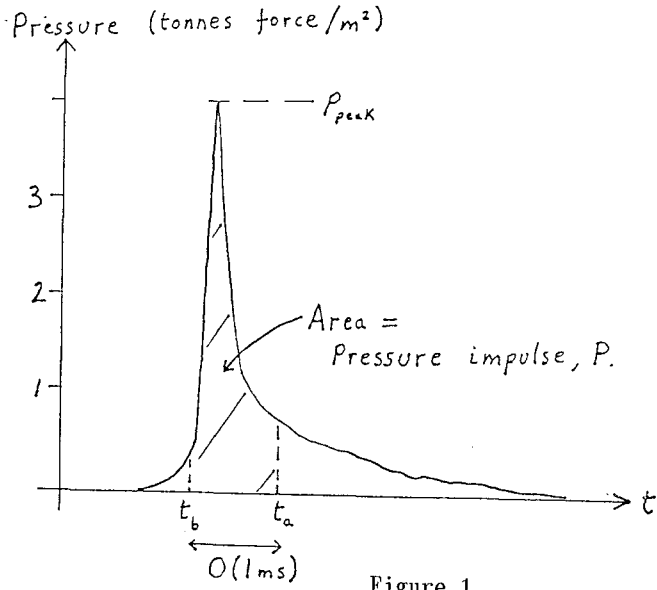


Figure 1.

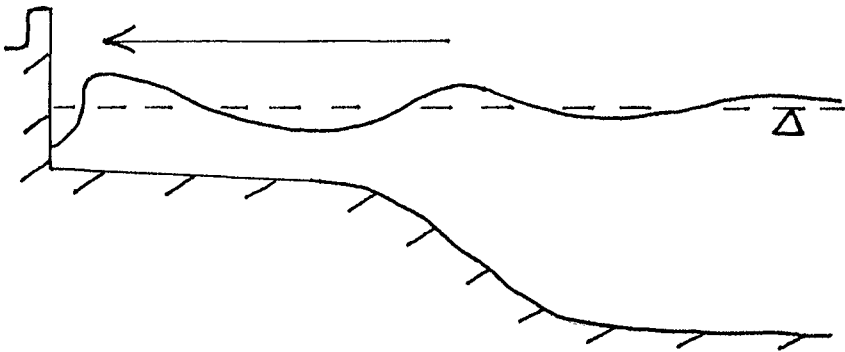


Figure 2. Sketch of wave steepening in shoaling water. A vertical face at the moment of impact, gives the highest peak impact pressures.

A full review of the literature is given by Cooker (1990, chap.6), and here we highlight the laboratory studies of Bagnold (1939), Nagai (1960) and Weggel and Maxwell (1970), all concerned with vertical walls. Current empirical engineering rules for peak pressure distribution p_{PK} at a vertical wall are summarized by Partensky (1988). All these studies suggest that p_{PK} varies up and down the wall with a clear maximum near the water-line and a decrease toward the bed. Computations by Cooker and Peregrine (1990) reproduce these pressure distributions.

This paper puts these empirical rules on a rational basis by using the theory of pressure impulse, (Lagrange 1783),

$$P(x,y) = \int_{t_b}^{t_a} p(x,y,t)dt \quad (1)$$

where t_b and t_a are the start and finish times of the impact. See figure 1.

Many experimenters have noted that under fixed wave conditions there is wide scatter in peak pressure. Bagnold (1939) pointed out that, despite the variations in p_{PK} (and in the impact time, $\Delta t \simeq$ twice pressure rise time), the product $p_{PK} \Delta t$ remains roughly constant;

$$P = p_{PK} \frac{\Delta t}{2} \quad (2)$$

is an approximation to the definition of P in equation (1). Given the unavoidable difficulty of predicting p_{PK} , in this paper we suggest that pressure impulse is a more convenient concept, especially from a mathematical viewpoint. Below we show that $P(x,y)$ satisfies Laplace's equation within a fluid domain which is the mean position of the fluid during the short time of impact. Armed with an analytic expression for P , and an estimate of the impact time Δt , we can use (2) to arrive at reasonable predictions for peak pressure distribution.

An advantage of this approach is that it allows us to model impact pressures due to even turbulent waves and, so far as P is concerned, the fluid can even be slightly aerated. The method can also be applied to more complex and three-dimensional wave impacts such as waves hitting a vertical cylinder. This is the subject of further work in progress.

Mathematical Model

We consider a wave in shoaling water approaching the shore from deeper water, and we expect typically the wave to steepen and break with a height possibly greater than the local still water depth, and with a speed greater than the maximum local wave speed

(gh)^{1/2}. Experiments show that the highest impact pressures occur when the wave face is vertical at the instant it strikes the wall. See figure 2.

We return to this specific problem below, but first consider a body of water striking a rigid surface. Let the impact speed be typically U_0 , and the length-scale of the body of water be L_0 . Let Δt be the impact time. Let $U_0, L_0, \Delta t, p_0$ be independent velocity, length, time and pressure scales for the variables in Euler's equations, for two dimensional inviscid, incompressible flow. After some manipulation we arrive at an equation in dimensionless variables $\underline{U}, t, p, x, y$

$$\frac{\partial \underline{U}}{\partial t} + \frac{\Delta t U_0}{L_0} (\underline{U} \cdot \nabla) \underline{U} = \frac{-\Delta t p_0}{\rho U_0 L_0} \nabla p \quad (3)$$

where $\nabla = (\partial/\partial x, \partial/\partial y)$.

Typically $\Delta t U_0/L_0$ is very small (~ 0.03 in the computations of Cooker and Peregrine, 1990). The smallness of this dimensionless group enables us to discriminate between events which are "impact" and those which are not. If $\Delta t p_0/\rho U_0 L$ is $O(1)$ then we have a balance between the first and last terms in equation (3), and the nonlinear 2nd term can be neglected.

We now integrate (3) with respect to time from $t = t_b$ to $t = t_a$, the duration of the impact. Returning to dimensional variables in (3) this gives us

$$\int_{t_b}^{t_a} \frac{\partial U}{\partial t} dt = \frac{-1}{\rho} \nabla \left\{ \int_{t_b}^{t_a} p dt \right\}.$$

From (1) this reduces to

$$\underline{U}_a - \underline{U}_b = \frac{-1}{\rho} \nabla P \quad (4)$$

where \underline{U}_b and \underline{U}_a are the fluid velocities at times immediately before and after the impact, respectively.

We will also assume that the flow is incompressible so that both $\nabla \cdot \underline{U}_b$ and $\nabla \cdot \underline{U}_a$ vanish. Taking the divergence of (4) we arrive at Laplace's equation in the pressure impulse P

$$\nabla^2 P(x, y) = 0. \quad (5)$$

Note that (5) does not involve time so we must solve boundary-value problems in a fixed domain which is a mean position for the fluid during impact. Finally note this theory admits arbitrary

vorticity and can be extended to 3 dimensions.

Boundary-Value Problem.

Let us turn to the 2 dimensional problem in figure 3 for water wave impact on a vertical wall. Given U_b we want to know $P(x,y)$ by solving (5) with appropriate boundary conditions, and then use (2) to find the peak pressure distribution. Also equation (4) gives us U_a , the flow immediately after impact; once we know P .

The boundary condition at the free surface is $P = 0$ because the pressure is a constant (zero) there. At the bed the vertical component of velocity $V = 0$ throughout the impact, so $V_a = V_b = 0$, hence from the vertical component of (4) we have $\partial P / \partial y = 0$. At the wall, we have chosen an upper region occupying a fraction of the wetted length, called the impact zone. Here the horizontal component of fluid velocity U changes from $U = U_b = -U_o$ before impact, to $U = 0$ after impact. From (4) this gives the boundary condition $\partial P / \partial x = -\rho U_o$ where $U_o > 0$ is a constant. Also $\partial P / \partial x = 0$ on the rest of the wall. Towards infinity $P \rightarrow 0$. Figure 3 summarises the boundary value problem, and we can solve using Fourier analysis. A solution which satisfies the bed, free-surface and infinity boundary conditions is

$$P = \sum_{n=0}^{\infty} a_n \sin(\lambda_n y) e^{-\lambda_n x} \tag{6}$$

where $\lambda_n = (n + \frac{1}{2}) \pi / H$.

The constants a_n are determined by the known values of $\partial P / \partial x$ at $x = 0$, the wall

$$\left. \frac{\partial P}{\partial x} \right|_{x=0} = \sum_{n=0}^{\infty} -a_n \lambda_n \sin \lambda_n y$$

$$\left(\begin{array}{ll} = -\rho U_o & y: -\mu H \leq y \leq 0 \\ = 0 & y: -H \leq y \leq \mu H \end{array} \right)$$

which give
$$a_n = \frac{-2\rho U_o}{H} \frac{(1 - \cos \mu \lambda_n)}{\lambda_n^2} \tag{7}$$

and
$$P(x,y) = \frac{-2\rho U_o}{H} \sum_{n=0}^{\infty} \frac{(1 - \cos \mu \lambda_n)}{\lambda_n^2} \sin(\lambda_n y) e^{-\lambda_n x}. \tag{8}$$

Note that for points $x > 0$ (away from the wall) the series in (8) is rapidly convergent because of the exponential terms. At the wall ($x = 0$) the distribution of pressure impulse is as shown in figure 4, for several values of μ .

Now from (2) we have

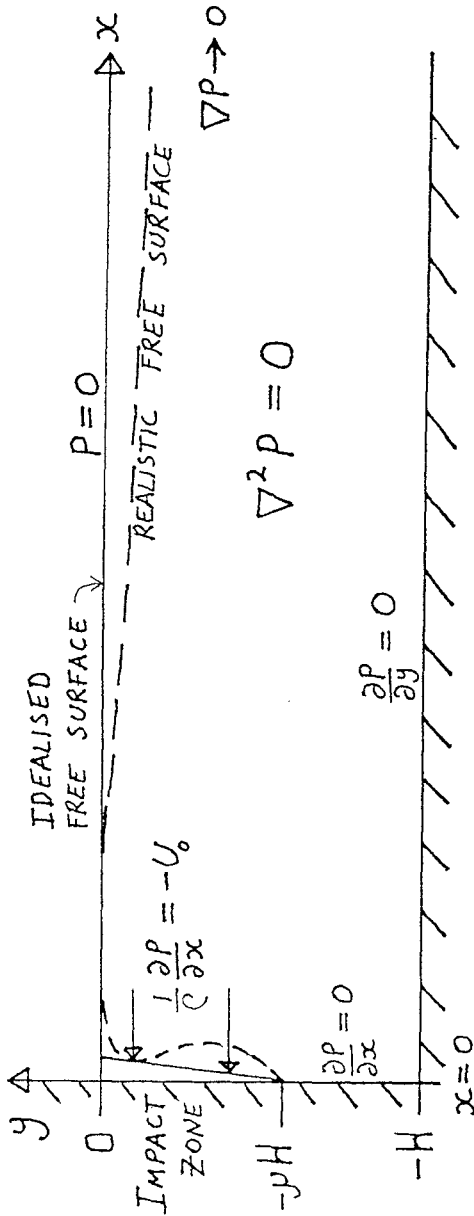


Figure 3. Semi-infinite rectangle geometry. Boundary-value

problem for pressure impulse $P = \int_{t_b}^{t_a} p(x,y,t)dt$.

Note the impact zone occupying the fraction μ of the wall.

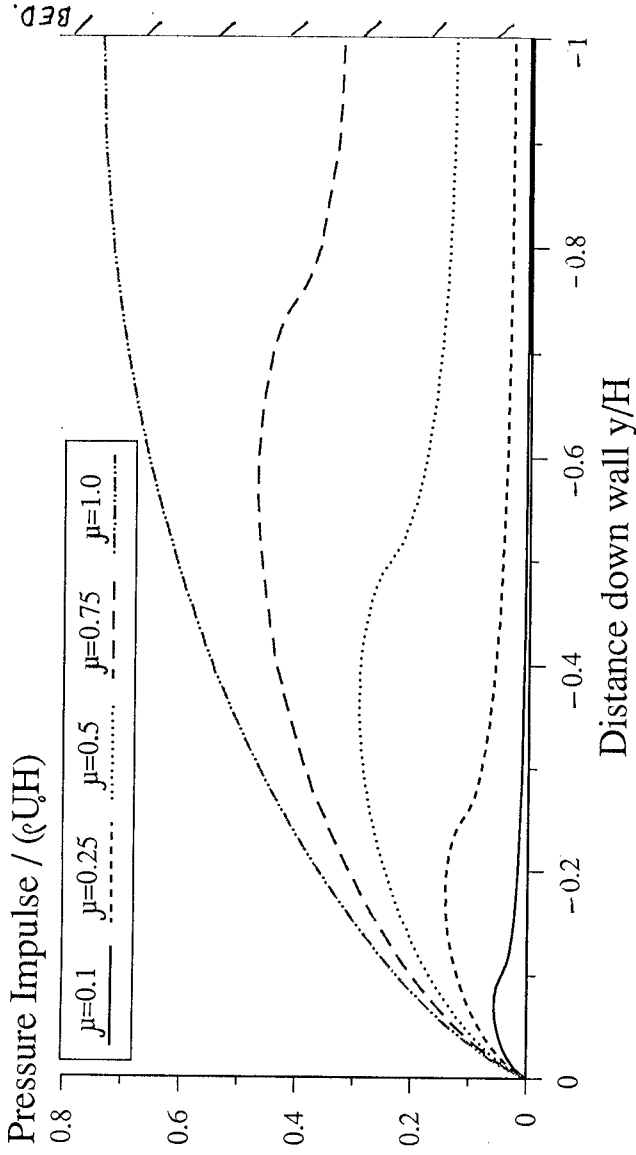


Figure 4. Pressure impulse P from equation (3) at the wall ($x = 0$) for several values of μ . Note that P is directly proportional to the peak pressure.

$$p_{PK} = 2P/\Delta t .$$

The impact time, Δt , is difficult to model because it depends critically on the exact type of breaking at the wall, the air content of the fluid, and the inherent random qualities of impact under "fixed" wave conditions. Following experience from computations in Cooker and Peregrine 1990 it seems reasonable to take $\Delta t \propto \mu H$ e.g. $2\mu H/C_a$ where C_a is the sound speed in aerated water. The authors wish to make it clear that the above theory does not depend on any particular model or choice of Δt (so long as Δt is small, in the sense $\Delta t U_o/L_o \ll 1$). A designer may wish to use values of Δt gleaned from experience or which are related to the resonant frequency of the structure under wave attack.

The peak pressure distribution corresponding to a simple model: $\Delta t = \frac{1}{2}\mu H/U_o$ is shown in figure 5. Small values of μ are of particular interest, and the curves bear a striking resemblance to the empirical diagrams reported in Partensky (1988). Note that the pressure does not decay to zero at the bed and that for $\mu = 1$ the maximum peak pressure lies at the bed.

The impulse on the whole wall, I_w , is the integral of (8) with respect to y , at $x = 0$, over the wall.

$$I_w = \frac{2\rho U_o}{H} \sum_{n=0}^{\infty} \frac{(1 - \cos \mu \lambda_n)}{\lambda_n^3} . \quad (9)$$

See figure 6. In addition the impulse due to a finite triangular wave is shown. This result can also be found analytically. This comparison shows that the impulse is mainly due to the loss of momentum from fluid near the wall. We calculate the significant thickness of fluid L_m (momentum length) for the semi-infinite wave by equating I_w with the momentum of a rectangle of fluid of height μH , speed U_o , density ρ and length L_m . Then

$$L_m = \frac{2}{\mu H^2} \sum_{n=0}^{\infty} \frac{(1 - \cos \mu \lambda_n)}{\lambda_n^3} . \quad (10)$$

Surprisingly L_m is at most $0.543H$ (when $\mu = 1$). This explains why the triangle and the infinite rectangle in figure 6 give impulses which are the same order of magnitude.

Last in this section of theoretical results we can use eqⁿ (4) to predict the fluid velocity after impact, U_a . This is most interesting to evaluate at the free surface. Suppose $V_b = 0$ (i.e. the top of the wave is in horizontal translation before impact) then taking the vertical component of (4) we have

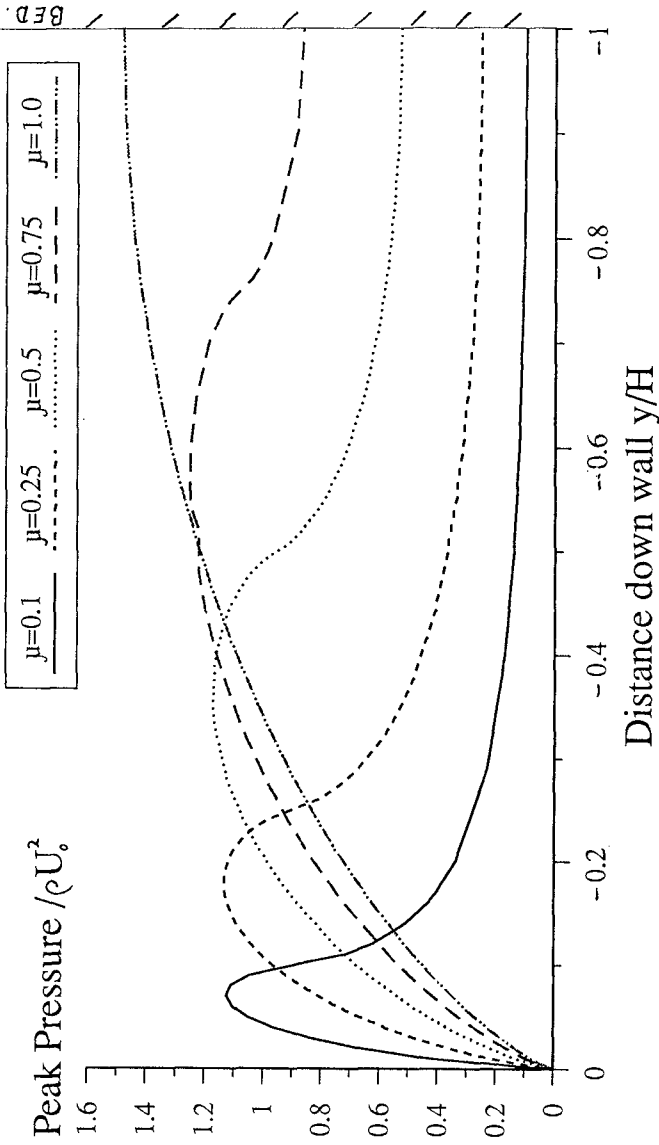


Figure 5. Peak pressure p_{PK} at the wall $p_{PK} = 2P/\Delta t$. Here Δt is modelled by $\frac{1}{2}\mu H/U_0$. Note the non-zero values of p_{PK} at the bed ($y/H = -1$).

Force impulse $\rho U_0 H^3$.

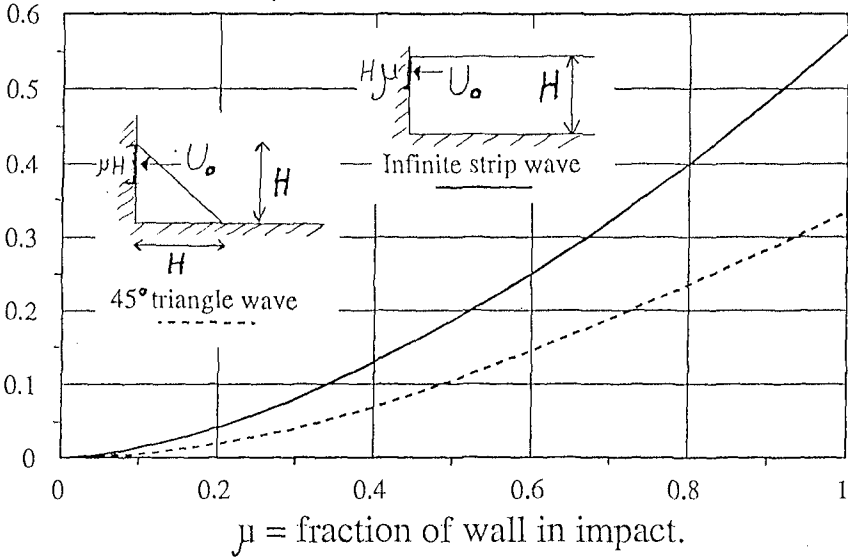


Figure 6. The impulse, I_w , on the wall from equation (9). The impulse due to a triangular wave (see sketch) is also plotted for comparison. The two waves are very different in shape but exert the same order of magnitude of impulse on the wall.

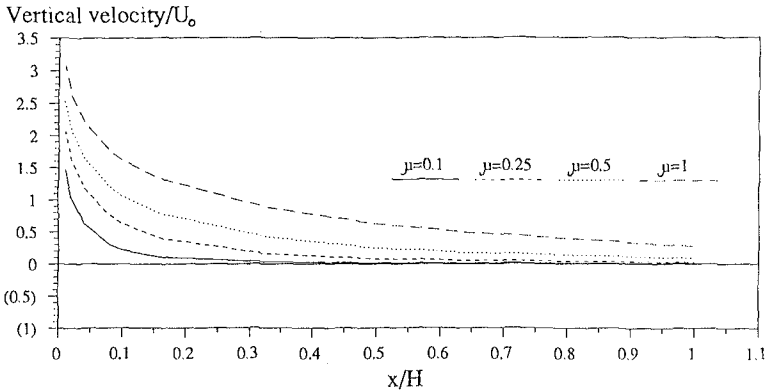


Figure 7. The vertical velocity at the free surface immediately after impact, V_a (with $V_b = 0$) from equation (11) Note these curves are proportional to surface elevation a small time after impact. The velocity near $x = 0$ resembles $\frac{-2U_0}{\pi} \ln(x)$.

$$V_a \Big|_{y=0} = \frac{-1}{\rho} \frac{\partial P}{\partial y} \Big|_{y=0} = \frac{2U_o}{\Pi} \sum_{n=0}^{\infty} \frac{(1 - \cos \mu \lambda_n)}{\lambda_n} e^{-\lambda_n x} \quad (11)$$

$$= \frac{2U_o}{\pi} \ell n \left| \frac{\operatorname{cosech} \pi z / 2 + \operatorname{coth} \pi z / 2}{\operatorname{cosech} \pi x / 2 + \operatorname{coth} \pi x / 2} \right|$$

where $z = x + i\mu$.

At $x = 0$, V_a is infinite, but the vertical flux of fluid between $x = 0$ and any station $x = X$ is finite. V_a is plotted for several values of μ in figure 7. Note that the surface elevation, η , some small time T after impact is given by $\eta(x) = V_a(x) \cdot T$, so that the curves in figure 7 show possible *shapes* of the free surface after impact when the incident wave has a flat top, as in figure 2.

Comparison with Experiment

Figure 8 shows a comparison between the current theory and the peak pressure distributions for two small wave impacts, measured by Weggel and Maxwell (1970). Note that the pressure axis is dimensionless and that we are here comparing shapes of distribution of peak pressure. Our choice of μ accords with that chosen by the experimenters in their own mathematical model.

Figure 9 compares theory with large-scale experiments (Partenscky and Tounsi, (1989): peak values from figure 5). Here we have chosen $\mu = 0.24$, in agreement with the experimenters' choice for their comparison with theory. $\Pi = 2.45\text{m}$, breaker height = 1.5m , so $U_o \approx 3.8 \text{ m/s}$. $\Delta t = 0.015$ (measured) which if $\Delta t = 2\mu\Pi/C_a$ implies $C_a = 230 \text{ m/s}$, (this corresponds to an air volume content of only 0.2%.

These comparisons encourage belief that pressure impulse theory captures the essential fluid mechanics of wave impact.

Conclusions

The theory of fluid pressure impulse has been used to model wave impact on a vertical wall. The results give spatial distributions of peak pressure which agree well with measurements. The theory predicts that the impulse on the wall is similar for two widely differing geometries (semi-infinite rectangle and 45° triangle). This is because the momentum lost from a wave of any shape comes from a narrow zone close to the wall (whose width is the momentum length). An important advantage of this theory is that it can be applied to waves with arbitrary vorticity. Further work is in progress to calculate pressure impulses due to three-dimensional waves.

References

Bagnold, R.A. (1939) Interim Report on Wave-Pressure Research. J.Inst. of Civil Engineers (1938-39), 12, p201-226.

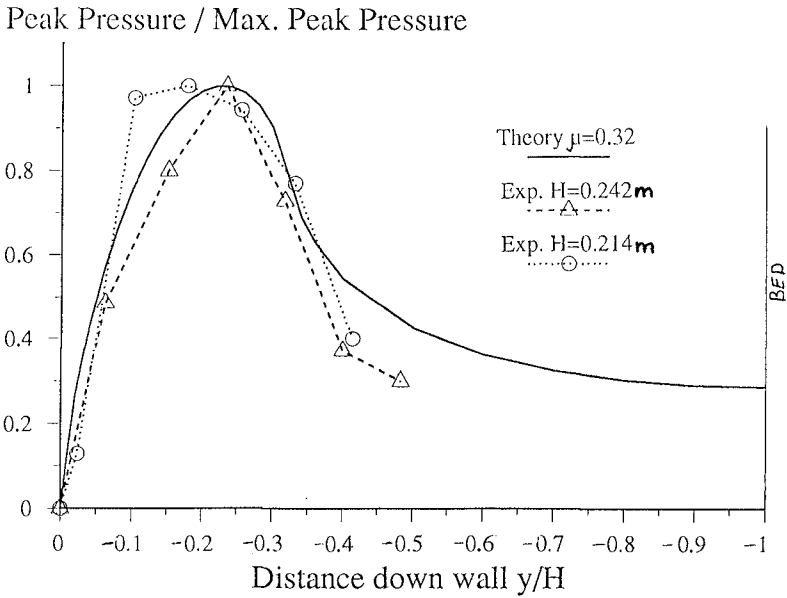


Figure 8. Comparison with experimental measurements of Weggel and Maxwell (1970), for two waves $H = 0.242\text{m}$ and $H = 0.214\text{m}$. Note that the vertical scale is dimensionless and we have chosen $\mu = 0.32$ in agreement with the experimenters' own numerical model.

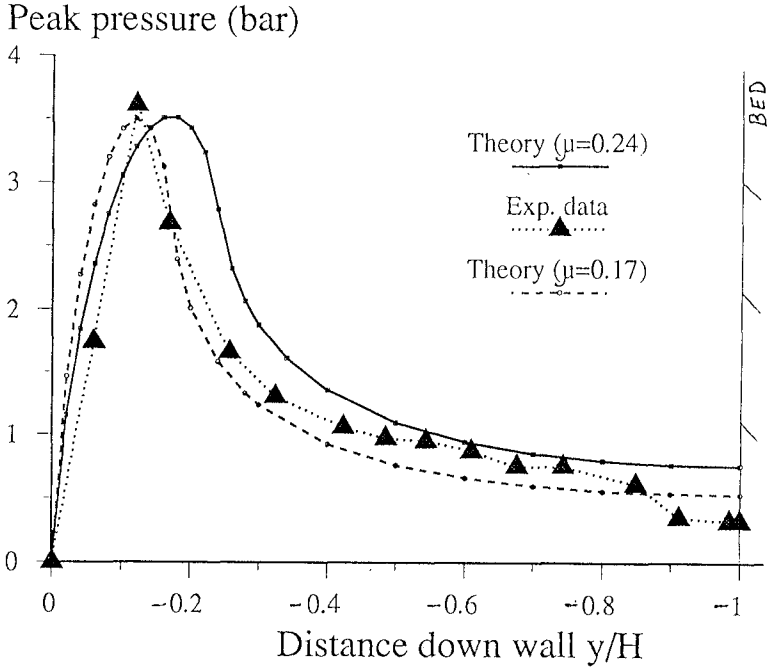


Figure 9. Comparison with experimental measurements of Partenscky and Tounsi (1989) (figure 5). $H = 2.45\text{m}$, $U = \sqrt{gH} = 4.9\text{m/s}$ and $\Delta t = 0.005\text{s}$. (The experimental data is the peak response at each recorder in the impact period). The theory with $\mu = 0.32$ is shown ($\mu = 0.32$ accords with the choice made by those authors for their numerical model). The present theory with $\mu = 0.17$ is also shown.

Blackmore, P.A. and Hewson, P.J. (1984) Experiments on full-scale wave impact pressures. *Coastal Engineering (the journal)*, **8**, pp 331-346.

Cooker, M.J. (1990) The interaction between steep water waves and coastal structures. Ph.D. thesis, Univ. of Bristol, Apr. 1990.

Cooker, M.J. and Peregrine, D.H. (1990) Computations of violent motion due to waves breaking against a wall. 22nd Intl. Conf. on Coastal Engineering, Netherlands 1990, ASCE.

Grüne, J. (1988) Wave-induced shock pressures under real sea state conditions. 21st Coastal Eng. Conf., **3**, p2340-2354.

Lagrange, J.L. (1783) Memoire sur la théorie du mouvement des fluides, *Nouv. Mem. de l'Acad. de Sci. de Berlin*, **12**, p151-188.

Nagai, S. (1960) Shock pressures exerted by breaking waves on breakwaters. *J. Waterways and Harbours Div. Proc.*, ASCE WW2, **86**, [S0-WW] pp1-38.

Partenscky, H.W. (1988) Dynamic forces due to breaking waves at vertical coastal structures. *Proc. 21st Coastal Eng. Conf.* June 1988, pp2504-2518.

Partenscky H.W. and Tounsi, K. (1989) Theoretical analysis of shock pressures caused by waves breaking at vertical structures. Intl. Assoc. for Hydraulic Research XXIII Congress, Ottawa, August 1989, 6 pages.

Richert, G. (1968) Experimental investigation of shock pressures against breakwaters. *Proc. 11th Conf. Coastal Eng. ASCE*, **1**, pp 954-973.

Weggel, J.R. and Maxwell, W.H.C. (1970) Numerical model for wave pressure distributions. *J.W.H.O.E. Div. ASCE* **96**, Aug. 1970, pp 623-642).

CHAPTER 111

Overtopping of Solitary Waves at Model Sea Dikes

Erdal Özhan ¹ and Ahmet Cevdet Yalçmer ²

Abstract

This paper discusses an analytical model for solitary wave overtopping at sea dikes. The model is based on the "weir flow analogy" of Kikkawa et al.(1968). Results of laboratory test on smooth and impermeable model dikes with angles of 45°, 60° and 90° are utilized in constructing the model. Results for solitary waves are compared with those for regular oscillatory waves for the case of vertical dike.

Introduction

Coastal structures are being constructed often low-crested due to economical and/or aesthetic considerations. An important design criterion for such structures is the allowable discharge of wave overtopping. The problem of wave overtopping by oscillatory waves has been studied by various researchers since 1960's. The initial investigations were basically based on laboratory experiments. An analytical model was developed by Kikkawa et al(1968), by following an analogy with the flow over sharp crested weirs. In recent years, following advances on mathematical treatment on wave propagation on steep slopes, some researchers concentrated on numerical modelling of wave deformation on the dike slope and the subsequent overtopping (i.e. Kobayashi and Wurjanto,1989).

¹Prof. Dr. Middle East Technical University, Coastal and Harbor Engg. Res. Cent. 06531 Ankara, Turkey

²Assist. Prof. Dr. Middle East Technical University, Coastal and Harbor Engg. Res. Cent. 06531 Ankara, Turkey

To the knowledge of authors, the problem of solitary wave overtopping at coastal structures has not been studied before. Investigation of this problem is useful for at least two reasons. Firstly findings may contribute to the understanding of the basic mechanism of wave overtopping. Secondly, the results obtained may be used for practical purposes in situations where solitary-like waves interfere with coastal structures.

In this paper, the analogy proposed by Kikkawa et al(1968) is extended and applied to solitary wave overtopping to derive a closed form analytical model. Laboratory experiments are carried out to provide the empirical information required by the model. Solitary overtopping rates at vertical dikes are compared with those of regular oscillatory waves.

Theory

By considering analogy with steady flow over a sharp crested weir, wave overtopping rate at a sea dike may be equated to :

$$q(t) = \frac{2}{3} m (2g)^{\frac{1}{2}} \{z(t) - z_0\}^{\frac{3}{2}} \quad (1)$$

where $q(t)$ = unsteady overtopping rate per unit dike width; $z(t)$ = changing water level elevation measured from still water level; z_0 = crown elevation of the dike; g = gravitational acceleration; m = the weir coefficient which is equal to 0.611 in steady flow. The change of water level elevation during overtopping is written as:

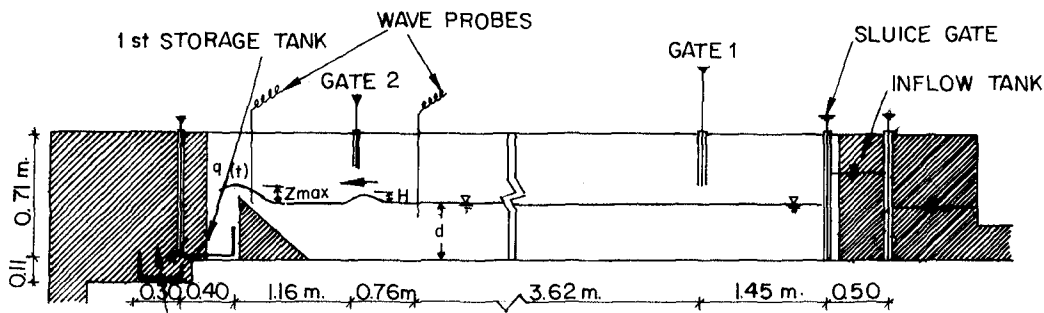
$$z(t) = z_{max} F(t) \quad (2)$$

where z_{max} = maximum rise of the water level; and $F(t)$ = a function having the range of 0 and 1. It is assumed that the maximum water level rise is related to the incident solitary wave height (Fig. 1) as:

$$z_{max} = K H \quad (3)$$

where the maximum rise coefficient K may be a function of wave height-to-water depth ratio ($\frac{H}{d}$), dike angle (α), and wave height-to-crown elevation ratio ($\frac{H}{z_0}$). The water level elevation prior to overtopping is assumed to change in the same way as a deformed solitary wave profile (symmetrical) and the function $F(t)$ is taken as:

$$F(t) = \text{sech}^2(\epsilon \lambda C t) \quad (4)$$



2 nd STORAGE TANK Figure 1: Experimental set-up and parameters

where; $\lambda = (\frac{3H}{4d^3})^{\frac{1}{2}}$, pulse width (phase) parameter; $C = (gd)^{\frac{1}{2}}(1 + \frac{H}{2d})$, celerity of the incident solitary wave; ϵ = an empirical coefficient (called the profile coefficient) which may account for deformation of the wave profile prior to overtopping and nonlinearity in the superposition of incident and reflected waves.

Substitution of Eqns. (2), (3) and (4) into (1) leads to:

$$q(t) = \frac{2}{3}m(2g)^{\frac{1}{2}}K^{\frac{2}{3}}H^{\frac{2}{3}}[Sech^2(\epsilon\lambda Ct) - (\frac{z_0}{KH})^{\frac{2}{3}}] \quad \text{for } |t| \leq \frac{1}{\epsilon\lambda C}Sech^{-1}(\frac{z_0}{KH})^{\frac{1}{2}}$$

$$q(t) = 0 \quad \text{otherwise} \quad (5)$$

Integration of Eq.(5) with respect to time gives the overtopping volume of a solitary wave as:

$$Q = \frac{4}{3}m(2g)^{\frac{1}{2}}K^{\frac{2}{3}}H^{\frac{2}{3}}\frac{I}{\epsilon\lambda C} \quad (6)$$

where Q = overtopping volume of a solitary wave per unit dike width;

$$I = \int_0^{\tau^*} (Sech^2\tau - \frac{z_0}{KH})^{\frac{2}{3}}d\tau$$

and $\tau^* = Sech^{-1}(\frac{z_0}{KH})^{\frac{1}{2}}$. It has been shown that the integral I is approximately equal to (Özhan, 1975):

$$I = \frac{1}{2}sech^{-1}(\frac{z_0}{KH})^{\frac{1}{2}}(1 - \frac{z_0}{KH})^{\frac{2}{3}} \quad (7)$$

Then, the final result giving the overtopping volume of a solitary wave per unit dike width is obtained from (6) and (7) as:

$$\frac{Q(1 + \frac{H}{2d})}{Hd} = \frac{0.6652}{\epsilon}(K)^{\frac{2}{3}}(1 - \frac{z_0}{KH})^{\frac{2}{3}}sech^{-1}(\frac{z_0}{KH})^{\frac{1}{2}} \quad (8)$$

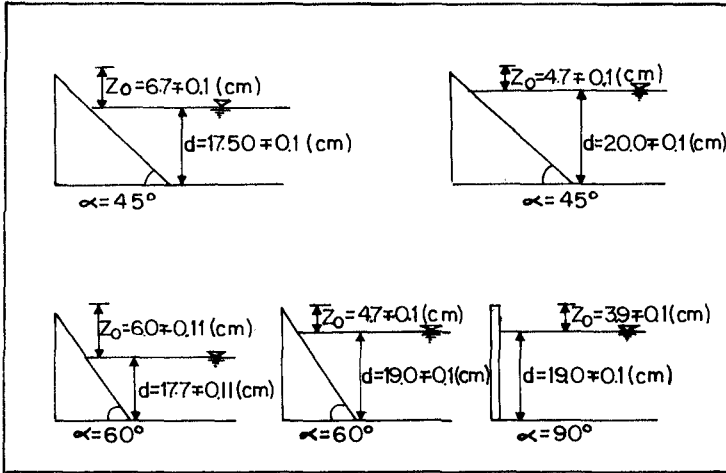


Figure 2: The geometries of model dikes and the water depths used in each experimental group

where $m = 0.611$ is used. This equation includes two empirical coefficients ϵ and K . Laboratory experiments were designed to investigate the values of these coefficients together with their dependence on various parameters.

Laboratory Experiments

The experimental set up is shown in Fig.(1). The solitary waves were generated by a sluice gate operation through introducing suddenly a volume of water into the wave flume. As this deformation evolved into a solitary wave, the trailing disturbances were cut off by closing the vertical gate 1, right after the passage of the solitary wave. The solitary wave moved over a constant water depth up to the dike. Incident solitary wave profiles and water level changes near the dike crown (3 cm in front) just prior to overtopping were measured. The overtopped volume of water was collected successively by two storage tanks. In order to eliminate the possibility of overtopping for a second time by the reflected wave, the gate 2 was closed after the reflected wave moved away from the dike.

The geometries of model dikes and the water depths used in each experimental group are shown in Fig. (2).

Results

In the evaluation of the experimental results, the first consideration was given to the incident solitary wave profile. The measured wave profile was compared with the theoretical Boussinesq profile. The runs which did not show close agreement were disregarded. The experimental data were first used to derive the values of two empirical coefficients, ϵ and K , which appeared in the theoretical model developed in section 2, and then to check the validity of the theoretical model to predict the overtopped wave volume. Finally, the solitary wave overtopping rates were compared with the data available for regular oscillatory waves.

The shape coefficient, ϵ

The shape coefficient, can be written as:

$$\epsilon = \frac{\text{Sech}^{-1}\left(\frac{z(t)}{z_{\max}}\right)^{\frac{1}{2}}}{\left(\frac{3H}{4d^3}\right)^{\frac{1}{2}} Ct}$$

The measured values of $z(t)$ at the location 3 cm in front of the dike crown were used to determine the value of the shape coefficient which provides the best fit to the measured profile. For this purpose, only the water level elevations in excess of the crown elevation (i.e. $z(t) > z_0$) were utilized. The procedure followed minimized the square error in the value of $\text{sech}^{-1}\left(\frac{z(t)}{z_{\max}}\right)^{\frac{1}{2}}$.

The values of ϵ for all three dike slopes are plotted in Fig. (3) against $\frac{H}{z_0}$ ratio. Also shown are the least square lines for each slope. The values of profile coefficient is seen to decrease with increasing $\frac{H}{z_0}$ value for all dike slopes. The least square lines for 60° and 90° dike angles are comparable. However, the slope for the dike with the angle of 45° is somewhat steeper.

The correlation coefficients between ϵ and $\frac{H}{z_0}$ ratio are computed as -0.84, -0.49 and -0.54 respectively for the dike angles of 45°, 60° and 90°. These rather low correlation coefficients indicate the importance of other parameters as well (such as $\frac{H}{d}$ ratio). In the present study however, the least square relationships shown in Fig.(3) were used for the computation of volume of overtopping as it will be discussed later. The intercept and slope (a_1 and b_1) of the linear relationship $\epsilon = a_1 + b_1\left(\frac{H}{z_0}\right)$ for three dike slopes tested are given in Table 1.

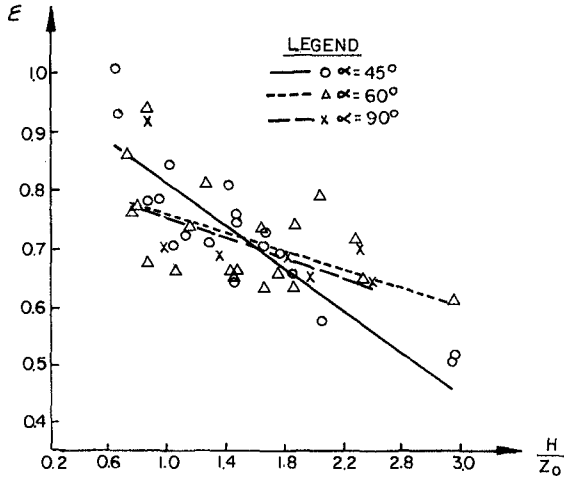


Figure 3: The values of shape coefficient for all three dike slopes

Table 1. The intercept and slope of the linear relationship between ϵ and $\frac{H}{z_0}$

Dike Angle	Intercept, a_1	Slope, b_1
45°	.994	-0.179
60°	.834	-0.076
90°	.839	-0.080

The maximum rise coefficient, K

The maximum rise coefficient defined in Eq.(3) was determined for each experimental run from the water level elevation measured near the dike crown. However, due to the horizontal distance of 3 cm. between the probe location and the dike crown, this value K_m obtained from the maximum recorded water level would be somewhat lower than the actual value corresponding to the maximum level to be reached at the dike crown. Alternatively, the actual value of K could be determined from Eq.8 by using the measured values of overtopped volume and the respective ϵ

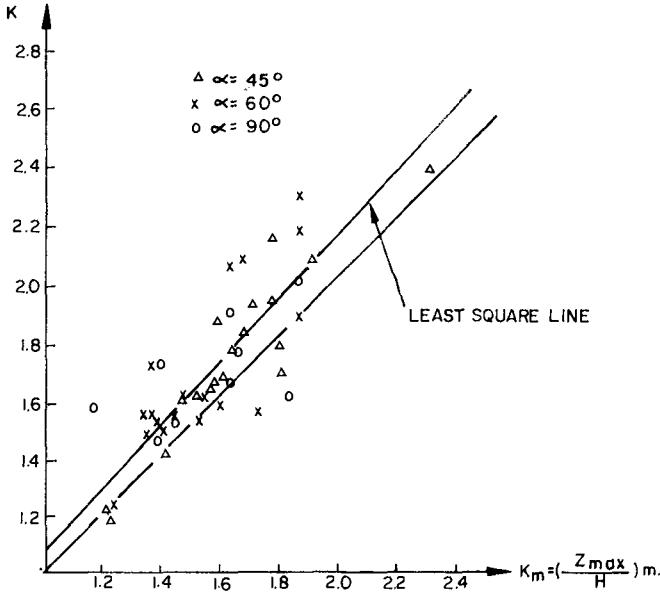


Figure 4: Comparison of theoretical (K) and measured (K_m) values of maximum rise coefficient

value corresponding to the $\frac{H}{z_0}$ ratio of the test. The implicit equation in terms of K which forms after substitution of Q and ϵ for a test, was solved numerically. The maximum rise coefficient, thus obtained are compared with the respective K_m values corresponding to the maximum recorded level in Fig. (4). It is observed that two values are correlated reasonably well. In line with expectations, the maximum rise coefficients computed from the theoretical model by using the measured overtopped volume are larger by 9 % on the average than the respective K_m values. As it was mentioned earlier, this is due to 3 cm. distance between the measurement location and the dike crown.

The maximum rise coefficient K correlates better with $\frac{H}{z_0}$ ratio than the shape coefficient ϵ (Fig. 5). The correlation coefficients were found as (-0.79) to (0.85) for three dike angles tested. For use in conjunction with the theoretical model of overtopping, the least square linear relationships between K and $\frac{H}{z_0}$ ratio were found. These are also shown in Fig. 5. The intercepts and slopes of these equations for 3 dike slopes are given in Table 2.

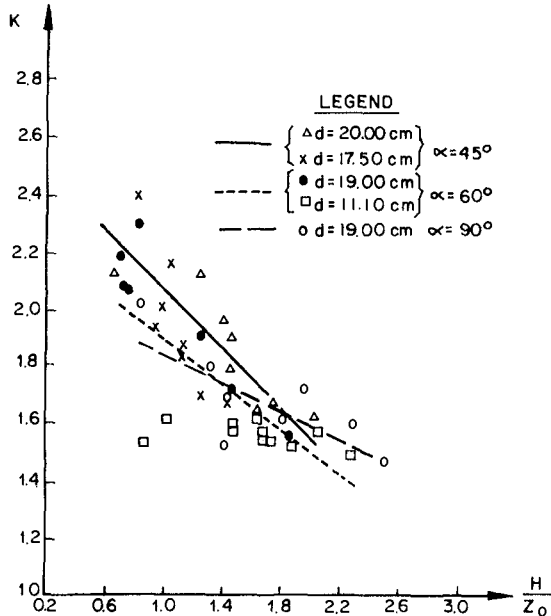


Figure 5: The values of maximum rise coefficient (K) for all three dike slopes

Table 2. The intercept and slope of the linear relationship between K and $(\frac{H}{Z_0})$

Dike Angle	Intercept, a_2	Slope, b_2
45°	2.63	-0.534
60°	2.27	-0.383
90°	2.07	-0.243

The values of maximum rise coefficient K should approach the respective run up coefficients for small values of $\frac{H}{Z_0}$.

Volume of Overtopping

The least square lines for ϵ and K were used in the analytical expression (Eq. 8.) to compute the dimensionless volume of overtopping as a function of $\frac{H}{Z_0}$ ratio. The resulting curves for three dike slopes tested are compared with the experimental data in Fig.(6)- (8). The theoretical model developed together with the empirical

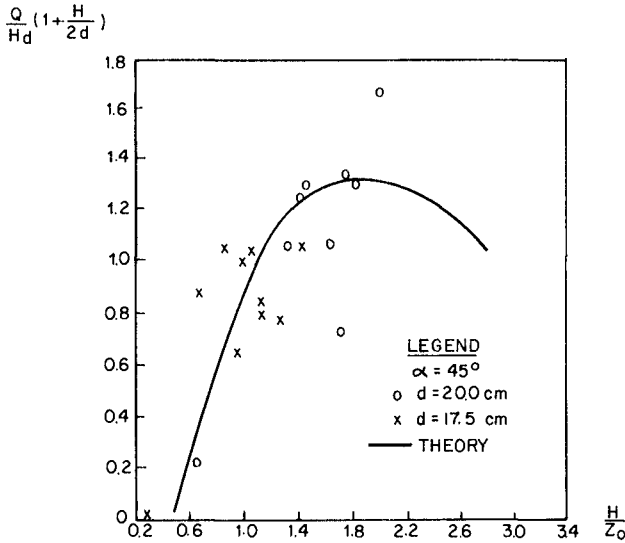


Figure 6: Comparison of measured and calculated overtopping volume $\alpha = 45^\circ$

relationships for ϵ and K are observed to provide reasonable agreement with experimental data for all three dike slopes. For the dikes with 45° and 60° slope angles, the dimensionless overtopping volume is seen to decrease with increasing $\frac{H}{z_0}$ ratio after a critical value of $\frac{H}{z_0}$ 2.0 to 2.1 is exceeded. Within the experimental range covered ($\frac{H}{z_0}$ ratio less than 2.5), such a change of trend is not observed for the vertical dike.

Comparison of the predictions of the presented theoretical model for different dike slopes reveals that the overtopping volume is greater for $\alpha = 45^\circ$ than the other two slopes for $\frac{H}{z_0} \leq 1.9$. The results for 60° and 90° dikes are very similar up to $\frac{H}{z_0} \leq 1.4$. For larger values, the overtopping volume for the vertical dike becomes greater than the respective value for the 60° dike.

Comparison with regular wave overtopping

For comparison of solitary wave overtopping with that of regular waves, it is necessary to define a practical wave period for the solitary wave. This may be done as the time length over which a certain percentage of solitary wave volume passes a fixed point. The resulting expression reads as:

$$T_p = \frac{\sqrt{\frac{g}{d}} \tanh^{-1}(\rho)}{\frac{\sqrt{3}}{4} (\frac{H}{d})^{\frac{1}{2}} (1 + \frac{H}{2d})} \tag{9}$$

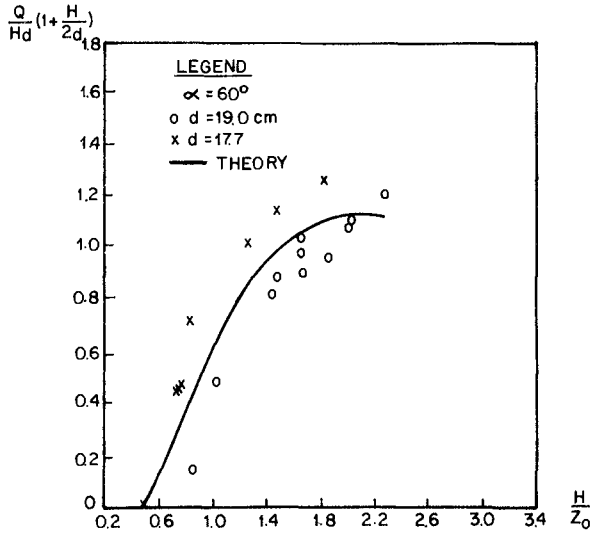


Figure 7: Comparison of measured and calculated overtopping volume $\alpha = 60^\circ$

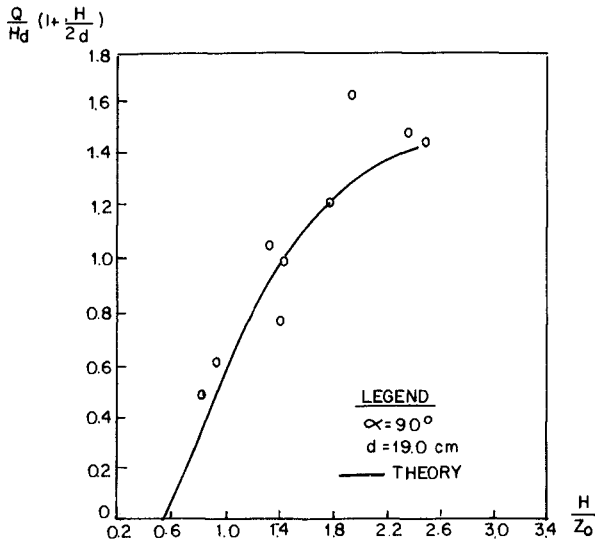


Figure 8: Comparison of measured and calculated overtopping volume $\alpha = 90^\circ$

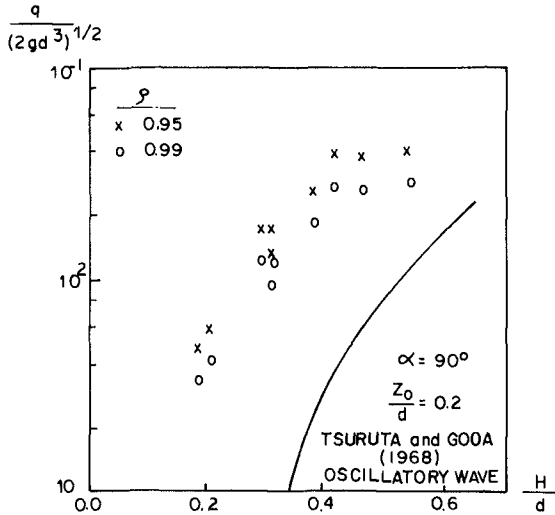


Figure 9: Comparison of solitary and oscillatory wave overtopping rates for a vertical dike

where T_p = the practical wave period; g = gravitational acceleration; and ρ = the percentage of wave volume. Furthermore, the series of solitary waves were treated as a cnoidal wave terrain, and the water depth of the experimental runs was increased by adding the trough amplitude of the respective cnoidal wave. The reanalyzed experimental data in this manner for the vertical dike is compared in Fig.(9) with the curve for regular oscillatory waves given by Tsuruta and Goda (1968). In this comparison, q is the average overtopping discharge over a wave period. The experimental data for solitary waves are plotted twice by using practical wave periods determined from two volume percentages, namely 95 % and 99 %. The presentation in Fig.(9) reveals that the solitary wave overtopping rates are significantly in excess of the respective oscillatory wave discharges.

Conclusions

The results of the present paper can be summarized as follows

1. An analytical expression is derived for the solitary wave overtopping, based on the analogy with sharp-crested weir flow.
2. Empirical data obtained from model dikes with $\alpha = 45^\circ, 60^\circ, 90^\circ$ slope angles is fed into the derived expression.

3. The analogy is shown to be successful for steep dike slopes ($\alpha \geq 45^\circ$).
4. Solitary wave overtopping rates are significantly greater than those for oscillatory waves.

References

- Kikkawa, H., Shi-igai, H. and Kono, T., 1968. Fundamental study of wave overtopping on levees. Coastal Eng. in Japan, 11,107-115.
- Kobayashi, N and Wurjanto, A., 1989. Wave Overtopping on Coastal Structures. ASCE, Journal of Waterways Port Coastal and Ocean Engineering, Vol. 115, No. 2, pp 235-251
- Özhan, E., 1975. Overtopping of solitary waves at vertical sea dikes. T.B.T.A.K. Proc. V. Science Congress, Istanbul. pp 735-747. (In Turkish)
- Tsuruta, S. and Goda, Y., 1968. Expected discharge of irregular wave overtopping. Proc. 11th Conf. Coastal Eng., ASCE, 2, 833-852.
- Yalçiner, A. C. 1981. Overtopping of solitary waves at model sea dikes M.S. Thesis in Civil Engg. Dept., Middle East Tech. Univ., Ankara.

CHAPTER 112

Permeability characteristics of rubble material - New formulae

Robert W K Shih¹

1 Introduction

Rubble mound structures have been used extensively to protect coastal areas of human interest. These include breakwaters, seawalls and related structures. To be successful, a rubble mound structure should absorb most of the energy from the incident waves and be able to withstand the pore pressures generated during the process. These are determined by the geometry of the structure and the hydraulic properties of rubble.

Advances in computer resources enable the interaction between waves and rubble structures to be simulated numerically (Ref 1, 2 and 7). The general approach is to describe the porous medium as a continuum, having properties of dimension, porosity and permeability. The flow of water into and through such a porous continuum may then be described, depending upon the velocities and pore pressures induced. In physical hydraulic modelling of coastal structures various researchers (Ref 5) have considered the importance of permeability characteristics on the scaling of porous rubble core material. Similitude is usually achieved by selecting a model material, of prototype porosity, which yields a comparable hydraulic gradient to the prototype when subjected to an equivalent Froude scaled flow velocity. Both the numerical and physical methods of modelling, however, require a good description of the energy dissipation process which is related to the permeability of the structure. At present, most modellers use formulae which were originally developed for flows in sand. That proposed by Engelund (Ref 4) has been most widely used.

Engelund's formula is expressed in the Forchheimer form which describes the hydraulic gradient (i) in laminar, transitional and turbulent conditions by: $i = au + bu^2$ (Eqn 1) where u is the superficial velocity. The dimensional coefficients a and b are generally referred as the laminar and turbulent coefficients respectively, and are given in terms of particle diameter (D) and

¹Engineer, Coastal Structures Section, Hydraulics Research, Wallingford, Oxfordshire, OX10 8BA, UK

sample porosity (n):

$$a = \alpha_o (1-n)^3 \frac{v}{gn^2D^2}, \quad b = \beta_o \frac{(1-n)}{gn^3D} \quad (\text{Eqn } 2)$$

with appropriate coefficient values:

- (i) uniform spherical particles $\alpha_o = 780$, $\beta_o = 1.8$;
- (ii) uniform rounded sand grains $\alpha_o = 1000$, $\beta_o = 2.8$;
- (iii) irregular angular grains α_o up to 1500 or more, β_o up to 3.6 or more

It should be noted values have been derived for α_o and β_o for materials with diameters much less than 10mm. Large uncertainties are involved when applying these values to rubble materials which have diameters up to or greater than 1m.

The research work presented in this paper is part of a comprehensive study on the hydrogeotechnical performance of rubble mound breakwater. It aims at providing a better insight into the permeability properties of porous media, particularly as they influence the wave/structure interactions. Extensive literature review on previous experimental works and methods of analysis and implementation has been carried out and presented in Ref 8. Based on the review, a new permeameter has been designed, and used to test samples with wide ranges of size and grading under a wide range of flow conditions. Analysis on the results have indicated the inadequacy of the existing formulae and new formulae are proposed in this paper. Results from this study will be implemented in the numerical models which are being developed in parallel.

2 Permeameter design

During the design of the permeameter which was constructed especially for the present study, the following points were considered:

- (i) The main body should be sufficiently large to test material of characteristic diameters up to 50mm. It has been suggested that the permeameter diameter should be at least ten times the diameter of the largest material to be tested (Ref 3).
- (ii) The design should minimise the potential of air entrainment in the material sample.
- (iii) The water supply should be capable of generating a flow velocity through the sample of at least 0.1 m/s.
- (iv) The measured pressure head loss should be representative of the complete sample cross-section.
- (v) The sample should be constrained to retain constant porosity throughout a test without significant dilation or loss of fines.
- (vi) The inflow velocity should be measured precisely.
- (vii) The system should be capable of reproducing and measuring hydraulic gradients in the range 0.01 to 5.

It was decided that a bottom water entry would be most appropriate. This would allow the majority of air entrained in voids between particles to be eliminated by running water through the system for a few minutes before commencement of the test.

The final design solution is presented in Figure 1. The permeameter is cylindrical in shape with overall height and internal diameter equal to 1.45m and 0.6m respectively. Flexible PVC tubes 9mm in diameter were used to allow measurement of a representative pressure head loss at a separation of 0.5m across the entire sample cross-section. Rigid perforated steel plates were incorporated to contain the sample at top and bottom. Water was pumped through the permeameter, initially through a 0.3 metre baffled inlet section, and allowed to flow freely over the upper rim. The system was operated up to a flow velocity of approximately 0.1 m/s. The pumped water was flow gauged using an orifice plate meter in the supply pipe. The discharge water from the permeameter was allowed to drain back freely into the reservoir, within which the pump intake was located, thus providing continuous water cycling.

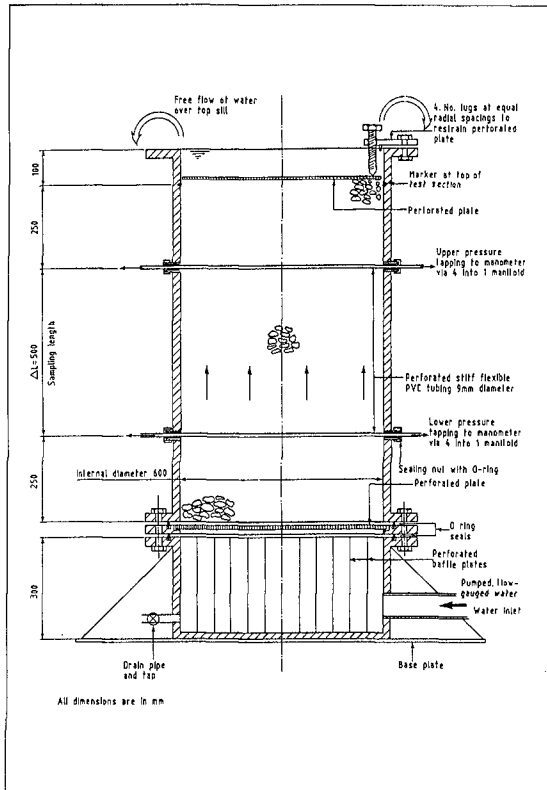


Fig.1 Schematic sectional plan of the present permeameter

3 Testing procedure

The testing procedure is represented by a flow chart in Figure 2. Details of each process are given below.

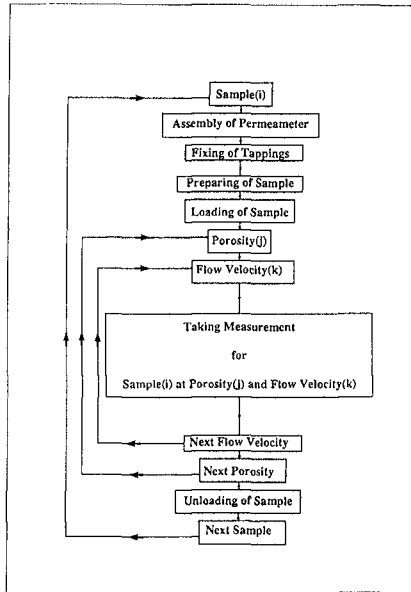


Fig.2 Flow chart for the test procedures

Assembly of the permeameter

Before the permeameter was assembled, it was necessary to ensure that areas such as the flanges, gaskets and bolt holes at the interfaces among the chamber, the perforated base plate, and the base stand, were free from particles.

The perforated base plate was first connected to the chamber hoisted by a gantry. This was done with four 15mm diameter bolts passing from the bottom flange of the chamber into threaded holes in the base plate. This partly assembled permeameter was then hoisted over the top of the base stand. It was lowered down such that the four prefabricated holes on the flange of the chamber, the base plate, and the base stand all lined up with one another. Four 15mm diameters bolts were used to pass through these holes and tighten the three different parts together. The permeameter was then filled with water to check for leakage.

Fixing the tappings

Pressures were measured at two levels, 0.5m apart, inside the permeameter. At each level, the measurement arrangement consisted of a pair of tapping tubes running perpendicularly across the inside diameters of the permeameter. These tubes were made of flexible PVC tubes 9mm in diameter, with perforations at 40mm

intervals. The open ends of these two tapping tubes were connected outside the permeameter via a looped PVC tube. The single outlet from this looped tube was connected to a manometer to provide a representative measurement of pressure at that particular level.

Preparing of samples

The main samples used in the tests were generally limestone with density equal to 2.76 gm/cm^3 . Before use each samples was sieved to produce the required size bands. They were then washed to eliminate fine material which might be washed away during the test, and hence affect the porosity.

Loading of samples

Samples, in small quantities, were carefully loaded into the permeameter. The weight of each sack was recorded so that the total quantity in the permeameter could be determined.

Porosity of the test specimen

Before starting a new series of tests, water was pumped through the sample for 10 minutes at the highest discharge to allow natural settlement to take place. The porosity obtained at the end of this period was defined as the highest porosity that the sample could achieve.

Lower porosities were obtained by compacting the sample with a vibrating poker. This was done by following the procedure below.

- (i) The permeameter was filled with water up to the top surface of the sample.
- (ii) A fixed amount of material was added onto the surface and smoothed by hand.
- (iii) The vibrating poker was used until the water surface just covered the samples.

In cases of high porosities, the poker was only required to be inserted to a depth of about 150mm at two locations. As the samples became more compact, the poker had to be inserted to a greater depth and at more locations. In general, six to eight different porosities were achieved in a series of tests.

Porosity measurements

Porosity was calculated from the weight of the samples loaded, the gross volume of the samples when stabilised, and the specific gravity of the samples.

Flow conditions

For each porosity, up to nine different flow rates were used, increasing regularly from approximately 0.01 m/s to 0.10 m/s .

4 Test conducted

The test samples were produced as a range of single size classes and mixtures derived from them. Each single size class was initially referred to by its nominal upper sieve size, generally significantly greater than either D_{15} or D_{50} which are the diameters of the sample that 15% and 50% of the sample exceed (see Table 1).

Nominal Size (mm)	D_{15} (mm)	D_{50} (mm)	D_{85} (mm)
4	1.49	2.13	2.76
6	4.94	5.42	6.26
10	7.22	8.65	9.74
14	9.35	10.87	12.40
20	12.72	14.65	17.39
28	19.28	21.77	24.58
40	27.61	33.23	37.77
61	54.50	63.00	73.80

Table 1 Single size samples

As quarried rock is more likely to exhibit a "gradual" size grading curve. This is illustrated by Kobayashi et al based on available field data (Ref 6) who describe prototype gradings falling in:

$$1.24 < (D_{50}/D_{15}) < 2.0$$

$$1.24 < (D_{85}/D_{50}) < 1.8$$

$$1.54 < (D_{85}/D_{15}) < 3.6$$

To study the effect due to both the 'size' and 'distribution' of samples within the mixture, a series of tests were carried out on graded samples (see Table 2).

Mixtures (Nominal dia. in mm)	D_{15} (mm)	D_{50} (mm)	D_{85} (mm)	D_{50}/D_{15}	D_{85}/D_{50}	D_{85}/D_{15}
6,10,14	4.09	8.20	11.77	2.00	1.44	2.88
6,10,14,20	4.43	9.77	16.70	2.21	1.71	3.77
6,10,14,20,28	4.76	11.59	22.50	2.43	1.94	4.73
6,10,14,20,28,40	5.70	14.02	29.24	2.46	2.09	5.13
10,14,20	8.04	11.59	17.60	1.44	1.52	2.19
10,14,20,28	8.50	14.02	23.62	1.65	1.68	2.78
10,14,20,28,40	8.97	17.29	30.17	1.93	1.75	3.36
14,20,28	10.66	17.29	24.75	1.62	1.43	2.32
14,20,28,40	11.51	20.59	31.10	1.79	1.51	2.70
20,28,40	16.99	24.38	32.10	1.43	1.32	1.89

Table 2 Wide graded samples

The gradings of the graded sample were chosen based on the following criteria.

- (i) Each mixture should contain at least three different sizes of materials.
- (ii) Sizes of materials should be increased gradually.
- (iii) Ratios of (D_{50}/D_{15}) , (D_{85}/D_{50}) and (D_{85}/D_{15}) should cover the ranges observed in the field data.

5 Analysis of test results

5.1 Single size samples

In considering the large amounts of data produced, it proved to be convenient to describe the flow/resistance relationship for each test in terms of the Forchheimer equation (Eqn 1) with coefficients a and b initially represented by the expressions proposed by Engelund (Eqn 2). A simple assessment of the dependence of coefficients α_0 and β_0 on the particle sizes was carried out. Regression analysis was performed depending on the particle sizes (Eqn 3).

$$\frac{i}{u} \frac{gD_{15}}{u} \frac{n^2}{(1-n)^3} = \alpha_0 + \beta_0 \frac{1}{n(1-n)^2} \left(\frac{uD_{15}}{u} \right) \quad (\text{Eqn 3})$$

Good linear relation was observed (see Figs 3a to 3g).

The laminar constant (α_0) was found to increase in proportion to D_{15} . Its lower limit coincided with the upper limit suggested by Engelund (see Fig 4a). The turbulent constant (β_0) was found to decrease exponentially with D_{15} (see Fig 4b). These results suggest that Engelund's expressions for a and b will need to be modified to represent flow in material larger than 10mm. At its simplest this may be given for formulae for α_0 and β_0 .

The permeability relationship for single size materials is therefore given by $i = au + bu^2$, where i = hydraulic gradient, u = superficial velocity and

$$\begin{aligned} a &= \left[\alpha_1 + \alpha_2 \left(\frac{g}{u^2} \right)^{2/3} D_{15}^2 \right] \frac{(1-n)^2}{n^2} \frac{u}{g} \frac{1}{D_{15}^2} \\ b &= \left\{ \beta_1 + \beta_2 \exp \left[\beta_3 \left(\frac{g}{u^2} \right)^{1/3} D_{15} \right] \right\} \frac{(1-n)}{n^3} \frac{1}{gD_{15}} \end{aligned}$$

where

n = porosity

$\alpha_1 = 1683.71$, $\alpha_2 = 3.12 \times 10^{-3}$

$\beta_1 = 1.72$, $\beta_2 = 1.57$, $\beta_3 = -5.10 \times 10^{-3}$

u = kinematic viscosity of water = $1.14 \times 10^{-6} \text{ m}^2/\text{s}$

g = gravitational acceleration = 9.81 m/s^2

(Eqn 4)

Good agreement was obtained between observed and predicted hydraulic gradients, Fig 5.

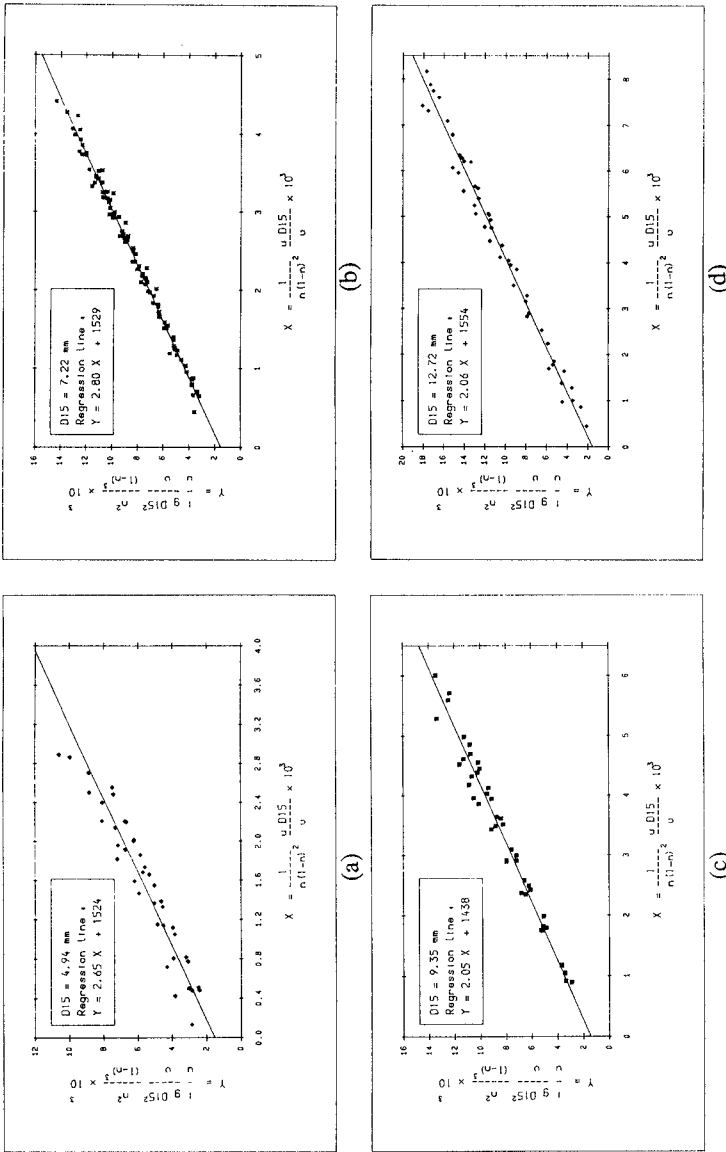
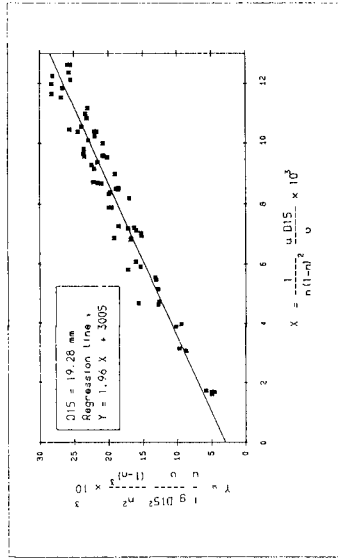
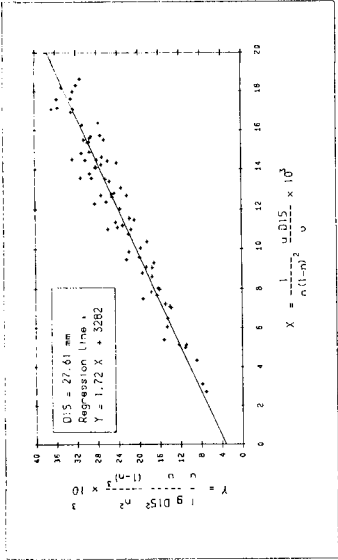


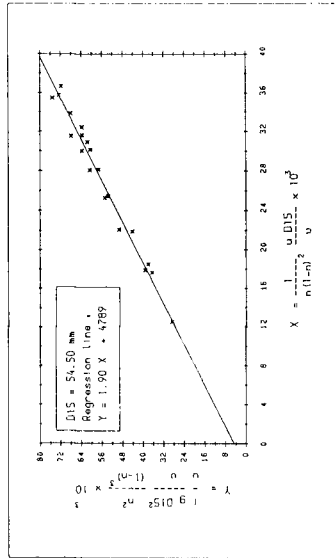
Fig.3 Regression analysis on results of single size materials



(e)



(f)



(g)

Fig.3 cont.

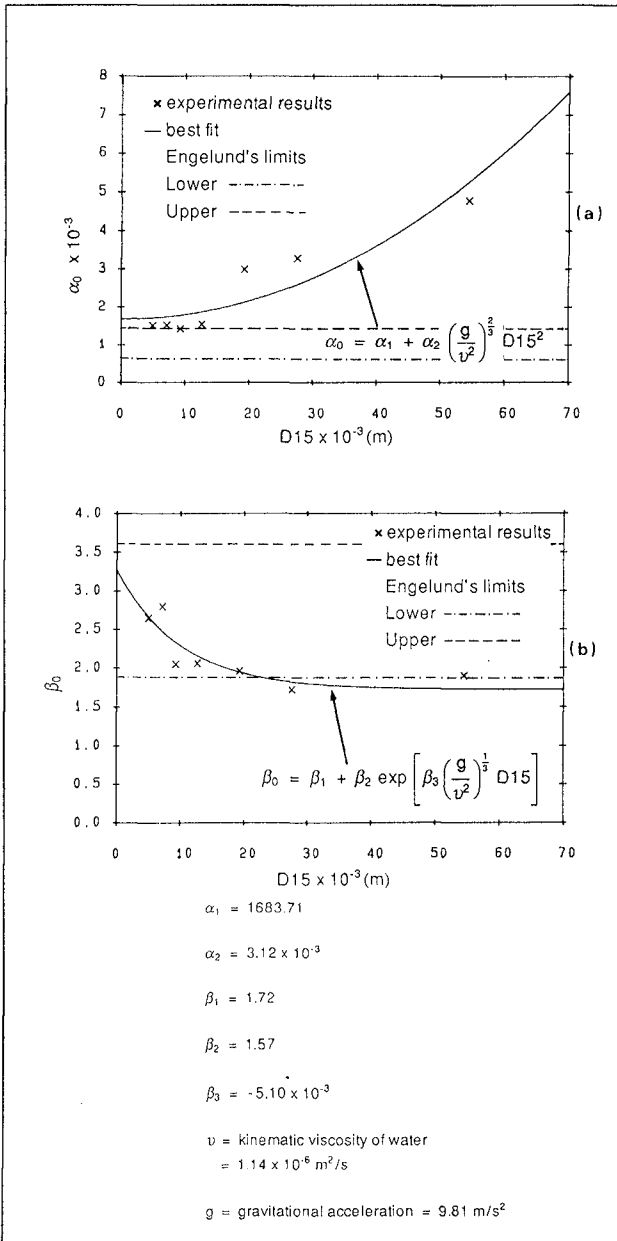


Fig.4 Dependence of α_0 and β_0 on particle diameter D_{15} for single size materials

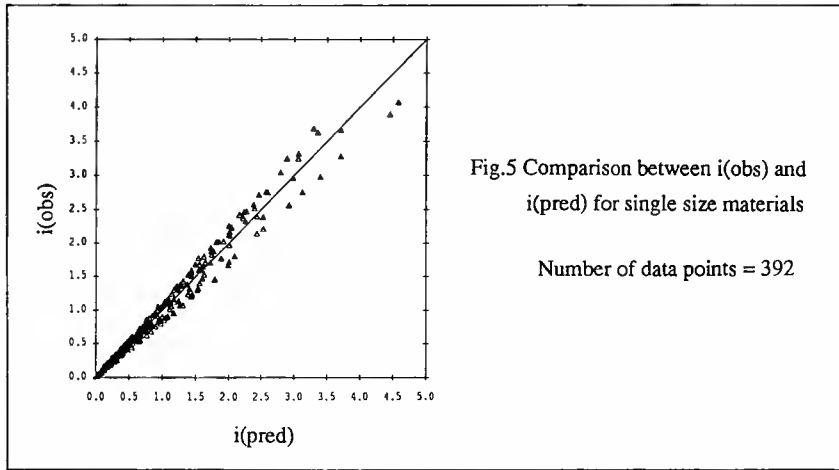


Fig.5 Comparison between $i(\text{obs})$ and $i(\text{pred})$ for single size materials

Number of data points = 392

5.2 Wide graded samples

For wide graded samples, same permeability relationship for single size samples was adopted with D_{15} replaced by D_* where

$$D_* = D_{15} \left(\frac{D_{15}}{D_{50}} \right)^{c1} \left(\frac{D_{50}}{D_{85}} \right)^{c2} \quad (\text{Eqn 5})$$

so as to include the effect due to the grading of the material. Coefficients $c1$ and $c2$ were determined such that the total square errors in hydraulic gradient, $(i_{\text{predicted}} - i_{\text{observed}})^2$, was minimum. This gave $c1 = -1.11$ and $c2 = 0.52$ (see Fig 6).

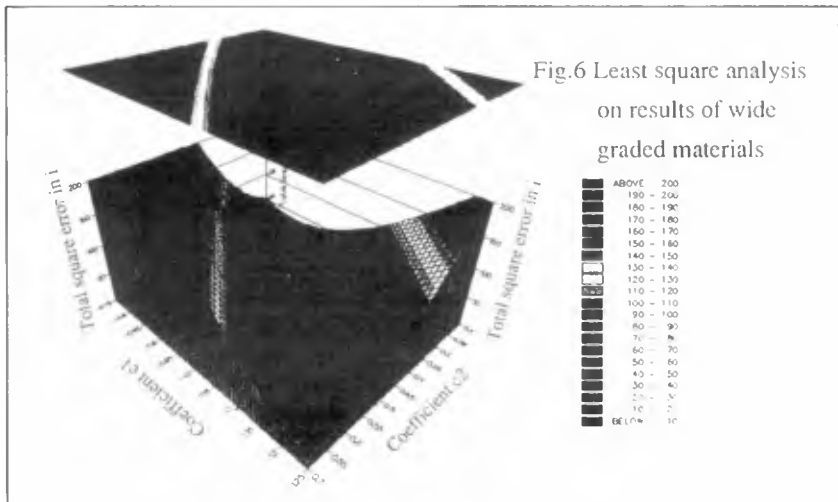


Fig.6 Least square analysis on results of wide graded materials

The permeability relationship for wide graded materials is therefore given by:

$$i = au + bu^2$$

where

i = hydraulic gradient, u = superficial velocity

and

$$a = \left[\alpha_1 + \alpha_2 \left(\frac{g}{U^2} \right)^{2.73} D_*^2 \right] \frac{(1-n^3)}{n^2} \frac{u}{g} \frac{1}{D_*^2}$$

$$b = \left\{ \beta_1 + \beta_2 \exp \left[\beta_3 \left(\frac{g}{U^2} \right)^{1.73} D_* \right] \right\} \frac{(1-n)}{n^3} \frac{1}{gD_*}$$

$$D_* = D_{15} \left(\frac{D_{15}}{D_{50}} \right)^{-1.11} \left(\frac{D_{50}}{D_{85}} \right)^{0.52}$$
(Eqn 6)

where

n = porosity

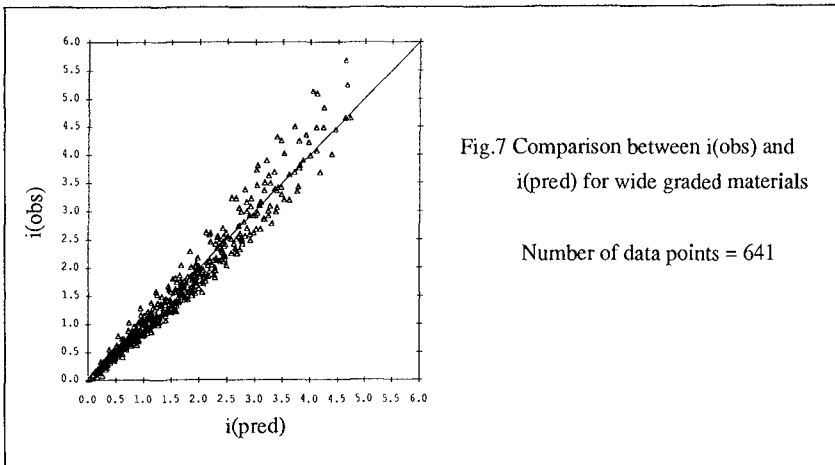
$\alpha_1 = 1683.71, \alpha_2 = 3.12 \times 10^{-3}$

$\beta_1 = 1.72, \beta_2 = 1.57, \beta_3 = -5.10 \times 10^{-3}$

u = kinematic viscosity of water = $1.14 \times 10^{-6} \text{ m}^2/\text{s}$

g = gravitational acceleration = 9.81 m/s^2

Good agreement was obtained between observed and predicted hydraulic gradients Figure 7.



6 Conclusions and recommendations for future work

6.1 Conclusions

A permeameter (Fig 8) with diameter equal to 0.6m was used in the present study. Materials with size varying from 2 mm to 61 mm were tested as single size and wide graded samples. Hydraulic gradients varying from 0.1 to 5.0 were used. New formulae (Eqn 4) and (Eqn 6) for the permeability of rubble materials were proposed to update the existing formulae proposed by Englelund which were originally derived for sand. It should be noted that the newly proposed formulae were based on experimental results carried out in steady state.

6.2 Recommendations for future work

It is recommended that future work should cover the following areas:

- (i) Unsteady/cyclic flows
 - Influence on inertia forces
- (ii) Air entrainment effects
 - External and internal waves breaking
- (iii) Interface loss between different rubble layers
 - Real breakwater composition

7 Acknowledgements

The work on which this paper is based has been funded by the Department of the Environment.

The permeability tests were designed primarily by R V Stephens and conducted by A R Channel. The work was carried out in the Coastal Structures Section managed by N W H Allsop, in the Maritime Engineering Department of Hydraulics Research Limited, Wallingford.



Fig.8 Permeameter in operation

8 References

1. Allsop N W H and Shih R W K. "Permeability of rubble mound coastal structures to wave action: Laboratory and numerical modelling." Proc. of Wave Research and Coastal Engineering, Hannover, 1988.
2. Barends F B J and Holscher P. "Modelling interior processes in a breakwater." Proc. Conf. Breakwaters 88, ICE, Eastbourne, May 1988.
3. Dudgeon C R. "Wall effects in permeameters." Proc. ASCE Journal Hyd. Div, HY5 : 137-148. Paper No 5433, Sept 1967.
4. Engelund F. "On the laminar and turbulent flows of ground water through homogeneous sand." Trans. Danish Academy of Technical Sciences, Volume 3, No 4, 1953.
5. Jensen O J and Klinting P. "Evaluation of scale effects in hydraulic models of laminar and turbulent flows." Coastal Eng 7, 1983, pp 319-329.
6. Kobayashi M, Terashi M and Takahashi K. "Bearing capacity of a rubble mound supporting a gravity structure." Report of the Port and Harbour Research Institute, Vol 26, No 5, pp 215-252. 1987.
7. Madsen O S and White S M. "Reflection and transmission characteristics of porous rubble mound breakwaters." Technical Report No 207, RA M Parsons Laboratory, Dept Civil Eng, MIT, 1975.
8. Stephens R V, Shih R W K and Allsop N W H. "Permeability characteristics of rock fill materials in rubble mound coastal structures." Report IT 340, Hydraulics Research, Wallingford.

CHAPTER 113

MORISON EQUATION COEFFICIENTS AND DATA CONDITION

R.T. Hudspeth¹
Member, ASCE

Abstract

Identification of the Morison equation force coefficients C_m & C_d depends on the condition of the wave force/kinematic data. For simple harmonic kinematics, the data are equally conditioned for identifying C_m & C_d at the critical value of the period parameter ($K = U_m T/D$) defined by Keulegan and Carpenter (1958). Critical values for K are = 11.4 from geometric interpretations and = 13.16 from numerical interpretations. Stable transverse lift forces may also be shown to correlate with the critical values of K from the physical interpretation of the period parameter given by Keulegan and Carpenter (1958). Data from three different types of physical experiments are used to demonstrate the importance of the condition of the data.

Introduction

The Reynolds parameter ($R = U_m D/\nu$) and the Keulegan-Carpenter parameter ($K = U_m T/D$) are the two parameters that are most often used to parameterize the two empirical force coefficients C_m and C_d used in the Morison equation (Dean and Dalrymple, 1981 & 1984). Dean (1976) recognized the importance of the condition of the data when identifying these two empirical force coefficients from wave force data; but he did not correlate the condition of the data with these two parameters. The Dean error ellipse demonstrates geometrically the condition of data for identifying C_m and C_d by the alignment of the axes of the error ellipse as illustrated in Fig. 1.

¹Professor, Ocean Engineering Program, Oregon State University, Corvallis, OR USA 97331

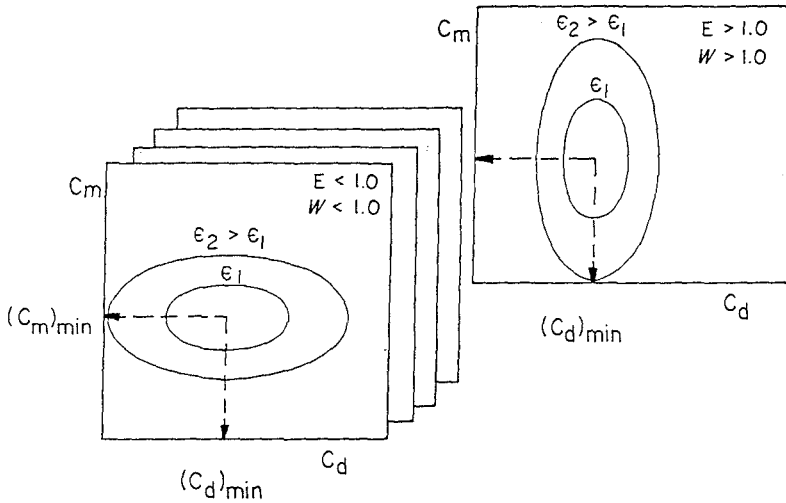


Fig. 1 Dependency of Dean Error Ellipses on $W = |f_d|/|f_m|$

The data are relatively better-conditioned for identifying the empirical force coefficient C_m or C_d on the axis that is parallel to the semi-minor axis of the error ellipse. Dean (1976) correlated the alignment of the axes of these error ellipses with the dimensionless O'Brien force ratio (1952) $W = |f_d|/|f_m|$; but not with either the Reynolds or Keulegan-Carpenter parameters. Hudspeth and Nath (1990) demonstrated that the Dean eccentricity parameter E is proportional to the Keulegan-Carpenter parameter K for kinematic data that are simple harmonic. Consequently, the Dean eccentricity parameter E connects the alignment of the semi-minor axis of the error ellipse to the parametric dependency of C_m and C_d on K . When $E = 1.0$, then $K = 11.40$ and the error ellipse is a circle with zero eccentricity.

The Dean error ellipse (1976) may be extended to include errors in the amplitudes/phases of the kinematics. This extension to include errors in amplitudes/phases demonstrates geometrically the parametric dependency of C_m and C_d on the parameter K (or E) by the magnitude of the slope of the contours of the dimensionless O'Brien force ratio

$W = |f_d|/|f_m|$ passing through the origin for zero error in phase. The advantage of the amplitude/phase error method is that the separate plots required by the Dean error ellipse method for each constant value of $W = |f_d|/|f_m|$ shown in Fig. 1 may be replaced by a single graph with contours of constant values of W . Comparisons of the amplitude/phase analysis with synthetically phase-shifted laboratory data for $E < 1.0$ or $K < 11.40$ and for $E > 1.0$ or $K > 11.40$ are excellent for phase shifts in the range of $|\omega\tau| < \pi/8$.

Data condition is defined as the ability of a least-squares algorithm to locate a global minimum on an error surface for given wave kinematic/force data (cf. Marquardt, 1963). This geometric definition is related to the numerical matrix condition number (cf. Atkinson, 1989). The matrix condition number is computed by four standard measures for the Morison equation. The matrix condition number is identically equal to unity when $K = 13.16$ and $E = 1.15$.

Geometric Interpretations

1) Dean error ellipses: The mean squared error ϵ^2 between the "true" force per unit length (denoted by upper case unprimed letters) $F(\theta)$ and the "computed" force per unit length (denoted by lower case primed letters) $f'(\theta)$ may be estimated from

$$\epsilon^2 = \langle [F(\theta) - f'(\theta)]^2 \rangle \quad (1)$$

where $\theta = 2\pi t/T$; T = wave period; and the temporal averaging operator $\langle (\cdot) \rangle$ is

$$\langle (\cdot) \rangle = \frac{1}{2\pi} \int_0^{2\pi} (\cdot) d\theta$$

If the "computed" force per unit length is given by the Morison equation

$$\begin{aligned} f'(\theta) &= f'_m(\theta) + f'_d(\theta) \\ &= k'_m \dot{u}(\theta) + k'_d u(\theta) |u(\theta)| \quad (2a) \end{aligned}$$

then the "computed" inertia and drag constants are, respectively

$$k'_m = C'_m [\rho \pi D^2 / 4] ; \quad k'_d = C'_d [\rho D / 2] \quad (2b)$$

When simple harmonic kinematics are used in Eq.(2a), Eq.(1) becomes a conic section equation for an ellipse whose origin has been translated and axes rotated (Hudspeth and Nath, 1990; and Thomas, 1965)

$$(\alpha X)^2 + 2HXY + (\beta Y)^2 + 2GX + 2JY + C = 0 \quad (3)$$

where $X = C'_d$ and $Y = C'_m$.

Equation (3) may be written in a form that is more familiar for an ellipse according to (Dean and Dalrymple, 1984)

$$\frac{(X - X_o)^2}{(R/\alpha)^2} + \frac{(Y - Y_o)^2}{(R/\beta)^2} = 1 \quad (4)$$

The eccentricity of the error ellipse may be expressed in terms of the Dean eccentricity parameter E or the Keulegan-Carpenter parameter K or the O'Brien force ratio W by (Hudspeth and Nath, 1990)

$$E = \frac{\alpha}{\beta} = \frac{\sqrt{3}}{2\pi^2} K = \frac{C_m \sqrt{3}}{C_d} W \quad (5)$$

When $K = 2\pi^2/\sqrt{3} \approx 11.40$ then $E = 1.0$ and the error ellipse is a circle and the data are equally conditioned for identifying both C_m & C_d . The eccentricity e^2 of the error ellipse determines geometrically the condition of the data for identifying C_m & C_d . The eccentricity e^2 may be expressed by

$$e^2 = 1.0 - E^{(\pm)^2} \quad (6a, b)$$

where +2 is to be used when $E < 1.0$ and -2 is to be used when $E > 1.0$. Equations (6) imply that a separate error ellipse plot will be required for each constant value of the O'Brien force ratio W (vide Fig. 1 and Dean, 1976).

Specifically, when $E < 1.0$, then $K < 11.40$ and the semi-minor axis of the error ellipse is parallel to the C_m axis. Conversely, when $E > 1.0$, then $K > 11.40$ and the semi-minor axis is parallel to the C_d axis. Note that a value of $K \approx 11.40$ is approximately the value of K at which the peak in C_d and the trough in C_m occur in the replotted Keulegan-Carpenter data shown in Fig. 2 (cf. Sarpkaya and Isaacson, 1981 and Chakrabarti, 1987).

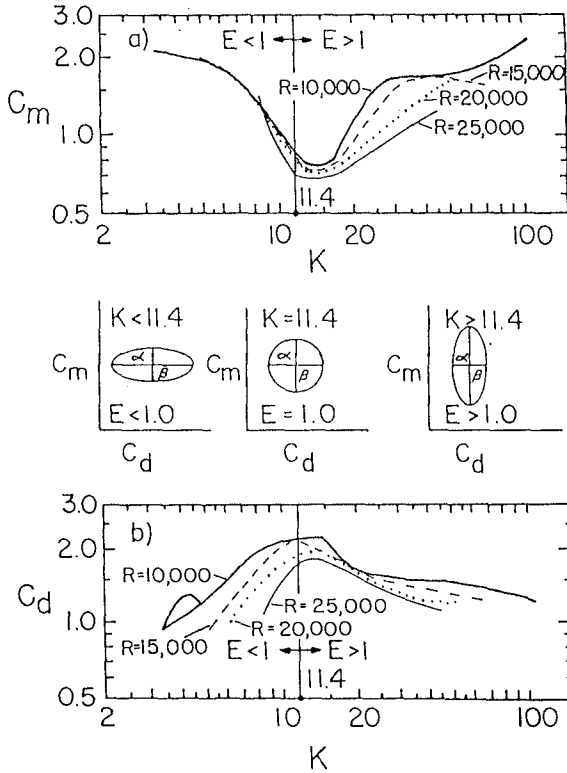


Fig. 2 Correlation of Replotted Keulegan-Carpenter Data with Dean Error Ellipses

2) Amplitude/phase analysis: Hudspeth, et.al. (1988) extended the Dean error ellipse method to include the effects of errors in amplitudes and phases of the wave force/kinematic data. This extension eliminated the need for separate error ellipses for each constant value of the O'Brien force ratio W .

Minimizing Eq.(1) with respect to the computed coefficients C_m and C_d yields 2 equations which may be rearranged to give the following dimensionless inertia coefficient ϵ_m and drag coefficient ϵ_d ratios for small values of the phase shifts $|\omega\tau| \approx 0$:

$$\epsilon_m \approx V[1 - (8W/3\pi)\omega\tau] \tag{7a}$$

$$\epsilon_d \approx V^2[1 + (32/9\pi)(\omega\tau/W)] \tag{7b}$$

with slopes near the origin given by (approximately)

$$S_m = \frac{\partial \epsilon_m}{\partial (\omega\tau)} \approx -\left(\frac{8WV}{3\pi}\right) \tag{8a}$$

$$S_d = \frac{\partial \epsilon_d}{\partial (\omega\tau)} \approx \left(\frac{32}{9\pi}\right)\left(\frac{V^2}{W}\right) \tag{8b}$$

where V = dimensionless velocity amplitude ratio. Note that it is not necessary to construct a separate error ellipse for each constant value of the O'Brien force ratio W .

Figure 3 compares Eqs. (7&8) with synthetically phase-shifted experimental data for $W = 0.49$ (or $E < 1.0$) and for $W = 2.32$ (or $E > 1.0$).

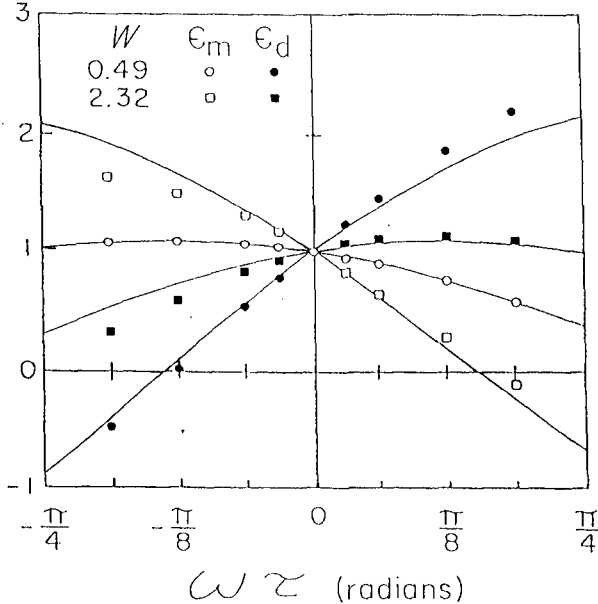


Fig. 3 Comparisons of ϵ_m & ϵ_d with Synthetically Phase-Shifted Laboratory Data (Hudspeth and Nath, 1990)

Numerical Interpretations

Scaling the variables in Eq. (1) by the following:

$$F = \frac{F}{\rho D a^2} \quad u = \frac{u}{a} \quad \dot{u} = \frac{\dot{u}}{a \omega}$$

where a = amplitude of the "computed" velocity; $\omega = 2\pi/T$; and minimizing Eq. (1) with respect to C'_m and C'_d gives the following scaled (or nondimensional) matrix equation :

$$AX = B \tag{9}$$

where the scaled matrices are

$$A = \begin{bmatrix} \frac{4\pi^2}{3K} & 0 \\ 0 & 1 \end{bmatrix} = \begin{bmatrix} \frac{2}{E\sqrt{3}} & 0 \\ 0 & 1 \end{bmatrix}$$

$$X = \begin{bmatrix} C'_m \\ C'_d \end{bmatrix} \quad B = \frac{16}{3} \begin{bmatrix} \langle F\dot{u} \rangle \\ \langle Fu|u| \rangle \end{bmatrix}$$

Matrix A is Hermitian and unitary. It becomes a unit matrix with matrix condition numbers identically equal to unity when $K = 4\pi^2/3 \approx 13.16$ and $E = 2/\sqrt{3} \approx 1.15$.

Table 1. Summary of Matrix Condition Numbers.

Matrix Condition Number (1)	$K < 13.16$ $E < 1.15$ (2)	$K = 13.16$ $E = 1.15$ (3)	$K > 13.16$ $E > 1.15$ (4)	$K = 11.40$ $E = 1.0$ (5)
Cond(A) ₁		1.0		
Cond(A) _∞	$\frac{4\pi^2}{3K} = \frac{2}{E\sqrt{3}}$		$\frac{3K}{4\pi^2} = \frac{E\sqrt{3}}{2}$	1.15
Cond(A) ₂				
Cond(A) _*				

The four standard matrix condition numbers listed in column 1 of Table 1 are defined as follows (Atkinson, 1989):

$$\text{Cond}(A)_1 = \text{Cond}(A)_\infty = \|A\| \cdot \|A^{-1}\|$$

$$\text{Cond}(A)_2 = \left[\frac{\text{Max}|\lambda|}{\text{Min}|\lambda|} \right]^{1/2} ; \quad \text{Cond}(A)_F = \left[\frac{\lambda \in \sigma[A]}{\lambda \in \sigma[A^*A]} \right]$$

where $\|\cdot\|$ = a matrix norm; A^{-1} = matrix inverse; λ = eigenvalue of the matrix A ; $\sigma[\cdot]$ = spectral radius of the matrix $[\cdot]$; and A^* = complex conjugate transpose.

Stable Transverse Lift Forces

Keulegan and Carpenter (p. 439, 1958) gave a physical interpretation of their period parameter in terms of the distance traveled in one direction by a fluid particle in the absence of the cylinder. Accordingly, this definition lead to the ratio between the wave period T and the eddy shedding period T_s being equal to the product between the Strouhal parameter S and the Keulegan-Carpenter parameter K ; or

$$\frac{T}{T_s} = S \cdot K \quad (10)$$

When this ratio is exactly equal to two, then exactly two vortices will be shed during one wave period and the transverse lift force will be stable (Keulegan and Carpenter, 1958). For normal wave conditions, $0.18 < S < 0.20$ and $K \approx 11$ when the ratio $T/T_s \approx 2$.

Data are available that correlate with the critical values of the Keulegan-Carpenter parameter K computed from both the geometric and the numerical interpretations. The only stable transverse lift force seen in the Hayashi and Takenouchi data (1979) shown in Fig. 4 occurs when $K = 11.8$ which is approximately the critical value of K determined from geometric considerations.

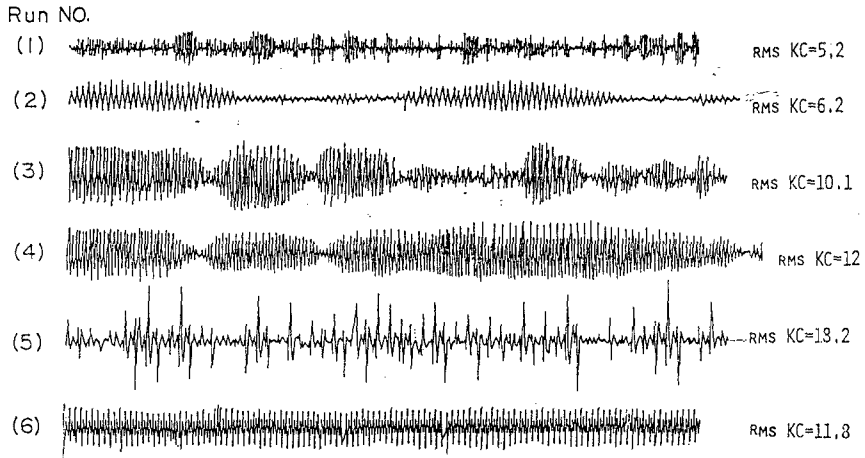


Fig. 4 Transverse Lift Forces on Vertical Circular Cylinders (Hayashi and Takenouchi, 1979)

The only stable transverse lift force seen in the Maull and Milliner data (1979) shown in Fig. 5 occurs in Run 145 when $K = 13.02$ which is approximately the critical value of K determined from numerical considerations.

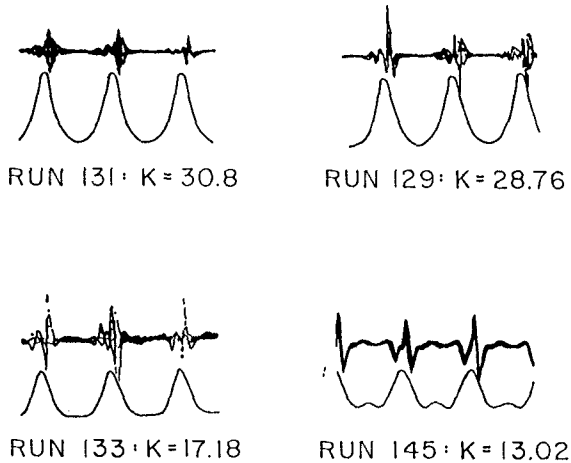


Fig. 5 Forced In-Line Motions and Transverse Lift Forces on a Vertical Circular Cylinder Oscillated in Still Water (Maull and Milliner, 1979)

Conclusions

The critical values of the period parameter $K = U_m T/D$ identified by Keulegan-Carpenter (1958) are shown to correlate with: 1) wave force/kinematic data that are equally conditioned for identifying C_m & C_d ; and 2) stable transverse lift forces. The effects of the condition of the data on the inertia and drag coefficients C_m & C_d are evaluated from two geometric and one numerical interpretations. The two geometric interpretations of the condition of the data proposed by Dean demonstrate that when the Dean eccentricity parameter E equals unity, the data are equally conditioned for determining C_m & C_d . For simple harmonic data, the Dean eccentricity parameter may be shown to be proportional to the Keulegan-Carpenter parameter; i.e., $E = \sqrt{3}K/2\pi^2$. When $E = 1.0$, then $K = 11.40$ and the Dean error ellipse is a circle with zero eccentricity. The numerical interpretation of the condition of the data demonstrates that when the matrix condition number of the 2×2 matrix used to compute C_m & C_d in a best least-squares sense becomes identically equal to unity then $K \approx 13.16$ and $E \approx 1.15$. Stable transverse lift forces occur when the ratio of the wave period T to the period of eddy shedding T_s is exactly equal to two. For a Strouhal parameter $0.18 < S < 0.20$ and $T/T_s = 2$, $K \approx 11$. Three sets of experimental data are compared with the two geometric and one numerical analyses and with the stable transverse force hypothesis. These experimental data represent three very different physical conditions; viz., 1) a horizontal circular cylinder located at the node of standing surface gravity waves, 2) a vertical circular cylinder in propagating surface gravity waves, and 3) a vertical circular cylinder forced to oscillate in otherwise still water.

Acknowledgements

Funding was provided to Oregon State University by the Office of Naval Research under the University Research Initiative (ONR-URI) Contract No. N00014-86-K-0687 .

References

- Atkinson, K.E. (1989). An Introduction to Numerical Analysis, 2nd Ed., John Wiley & Sons, New York, NY, pp. 529-540.
- Chakrabarti, S.K. (1987). Hydrodynamics of Offshore Structures, Springer-Verlag, New York, NY, pp. 168-231.

Dean, R.G. (1976). "Methodology for Evaluating Suitability of Wave and Wave Force Data for Determining Drag and Inertia Coefficients," Proceedings, BOSS '76, pp. 40-64.

Dean, R.G. and Dalrymple, R.A., (1981). "Force Coefficients from Wave Project I and II Data Including Free Surface Effects", Society Petroleum Engineering Journal, AIME, Vol 197, pp. 779-786.

Dean, R.G. and Dalrymple, R.A. (1984). Water Wave Mechanics for Engineers and Scientists, Prentice Hall, pp. 223-227.

Hayashi, K. and T. Takenouchi (1979). "The Fundamental Study of Flow Field Around a Vertical Cylindrical Pile Subjected to Waves," Proceedings, 26th Japanese Conference on Coastal Engineering, Japan Society of Civil Engineers, pp. 406-410

Hudspeth, R.T., J.H. Nath, and P.K. Khare (1988). "Wave Phase/Amplitude Effects on Force Coefficients," Journal of Waterway, Port, Coastal and Ocean Engineering, ASCE, Vol. 114, No. 1, pp. 34-49.

Hudspeth, R.T. and J.H. Nath (1990). "The Dean Eccentricity Parameter and Data Condition," ASME, Journal of Offshore Mechanics and Arctic Engineering (OMAE), Vol. 112, pp. 1-7.

Keulegan, G.H. and Carpenter, L.H. (1958). "Forces on Cylinders and Plates in an Oscillating Fluid," Journal of Research, National Bureau of Standards, Vol. 60, No. 5, Research Paper No. 2857, pp. 423-440.

Marquardt, D.W. (1963). "An Algorithm for Least-Squares Estimation of Nonlinear Parameters," J. Soc. Indust. Appl. Math., Vol. 11, No. 2, pp. 431-441.

Maufl, D.J. and M.G. Milliner (1979). "The Forces on a Circular Cylinder Having Complex Periodic Motion," in Mechanics of Wave-Induced Forces on Cylinders, (ed. T.L. Shaw), Pitman, London, pp. 490-502.

O'Brien, M.P. and Morison, J.R. (1952). "The Forces Exerted by Waves on Objects," Transactions, Amer. Geophysical Union, Vol. 33, No. 1, pp. 32-38.

Sarpkaya, T. and M. Isaacson (1981). Mechanics of Wave Forces on Offshore Structures, Van Nostrand Reinhold Co.

Thomas, G.B. Jr. (1965). Calculus and Analytic Geometry, Addison-Wesley, pp. 473-482; 490-500.

CHAPTER 114

NEW CRITERIA FOR GRANULAR FILTERS AND GEOTEXTILE FILTERS UNDER REVETMENTS

K.J. Bakker¹, M. Klein Breteler²
and Dr. H. den Adel³

Abstract

New criteria for the design of filters under revetments are introduced and verification tests are described. These criteria are based on a hydrodynamic limit instead of the usual geometric limit, assuming a similarity between the flow in open channels and flow in the pores at an interface between filter and base. First a theory was developed for a granular filter only, and later this theory was extended to include the influence of a geotextile. The verification experiments are outlined, and the applicability of the derived formulae is discussed.

Introduction

For the design of coastal structures, such as dike revetments or a breakwater, several aspects have to be considered. Not only the stability of the cover layer is important, but also the stability of the foundation layers, i.e. the filter layers has to be assured. In this paper we restrict ourselves to the filter layers. Until recently the design of these filter layers was based on strict rules demanding geometrically tight filters: the pores in the filter material have to be smaller than the particles of the subsoil to be protected.

The geography of the Netherlands with vast area's of its surface beneath sea level urge a major infrastructure in order to protect its population against flooding hazards. Many dike revetments are necessary, so it is of

-
- 1 Public Works Department, Po Box 20000,
3502 LA Utrecht, The Netherlands
 - 2 Delft Hydraulics Po Box 152,
8300 AD Emmeloord, The Netherlands
 - 3 Delft Geotechnics, Po Box 69,
2600 AB Delft, The Netherlands

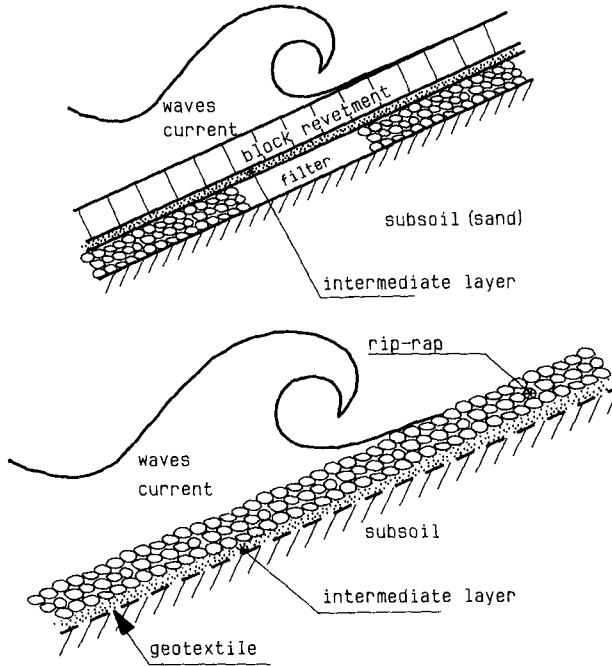


Fig 1. Wave attack on revetments

vital interest to be able to dimension these structures both as safe and as economic as possible. Mainly they can be outlined as in Fig. 1.

For the case we are concerned with, e.g. filter layers between cover layer and base, under a revetment, damage to the filter layer leads to inadmissible settlements of blocks in the cover layer. As a result of research concerning revetments, it was found that the hydraulic gradients in this type of construction are related to the slope gradient. These gradients are relatively small except within the direct vicinity of the surface of the structure.

For transport of grains, forces to activate particle movement have to be present, such as water flowing through the soil skeleton. When hydraulic gradients are small, the "no transport" demand can thus be achieved as well by controlling the pore water velocity; i.e. limiting the permeability of the filter material. In the Netherlands much effort has been put in research to derive new filter rules, based on a combination of geometric and hydrodynamic effects. This has led to filter criteria which might be a factor four less

stringent concerning the ratio of filter to base grain size. After verification of these filter criteria for granular material, the theory was extended to incorporate the influence of a geotextile, at the interface between filter and base material. Assuming that the geotextile has a damping effect on the hydraulic load on the base material, an extended design formula was derived and calibrated with experimental research.

Theory for granular filter interface

Traditionally filter criteria are based on geometric considerations which yield criteria which are based on limiting the diameter of the pore-channels connecting the pore holes in the soil skeleton. These constrictions in the filter must be that small, that the characteristic grain size of the base material is larger, so that base particles cannot pass these constrictions.

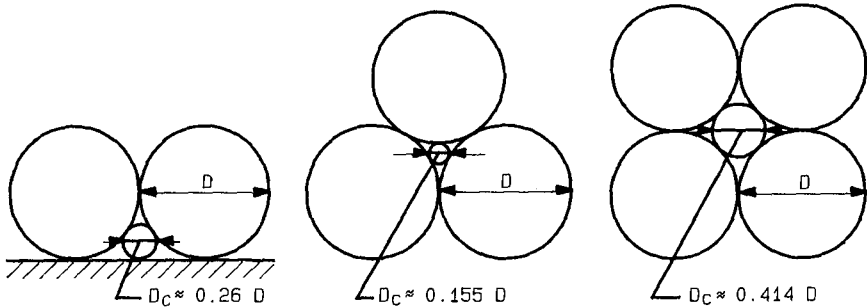


Figure 2 The characteristic constriction size is a function of grain size, and packing of the soil skeleton

In this paper we will distinguish between filter and base material by using D for the diameter of the filter material and d for that of the base material.

According to Kenney (1985), the characteristic constriction in the filter material is

$$D_c^* \leq 0.2 D_{15} \quad (1)$$

and the characteristic grain size of the base material is d_{85} . This leads to a design rule which was conducted first by Terzaghi which says that the ratio D_{15}/d_{85} must be smaller than 4 or 5.

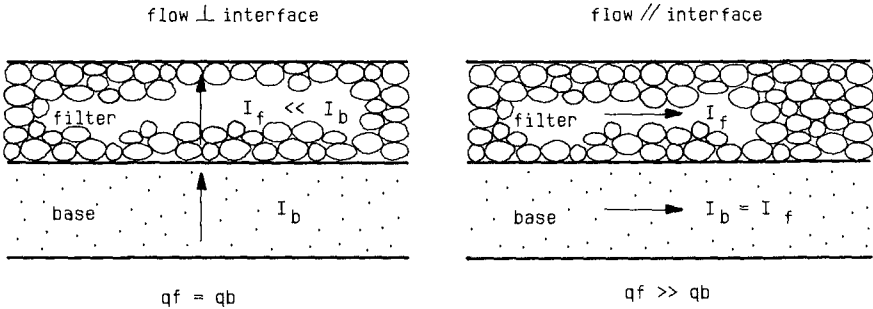


Figure 3 Hydraulic gradients

Yielding;
$$\frac{D_{15}}{d_{85}} < 5 \tag{2}$$

Though later researchers like Thanikachalam (1974) and others have conducted criteria including effects of the grain size distribution, geometric filter criteria are generally tight.

In order to introduce hydraulic criteria we have to classify the loading conditions, see Fig. 3. Traditionally filter experiments to verify for geometric penetration where performed applying flow perpendicular to the filter interface. However, in practical circumstances, the hydraulic loading is often dominated by the hydraulic gradient parallel to the filter interface. As the pore water velocity is determined by the higher permeability in the coarser filter, the hydraulic gradient parallel will lead to higher velocities in the filter than in the base material. On the contrary with perpendicular loading the velocities are approximately the same since continuity must hold.

If the diameter of the pore holes in the filter is large with respect to the grain size of the base-material, the hydraulic loading on the base material can be related to the loading of a sand bottom in an open channel. It is assumed that, given a granular filter with pores much wider than the grains in the base layer, the critical shear over the sand interface is equal to the critical shear in a channel with the same bed material.

Shields related the critical shear stress to the diameter of the base material. As the critical shear stress is related to the water velocity, a relation between the filter velocity and the diameter of base material can be derived, adding corrections for hydraulic conditions in a filter. The threshold of sediment motion

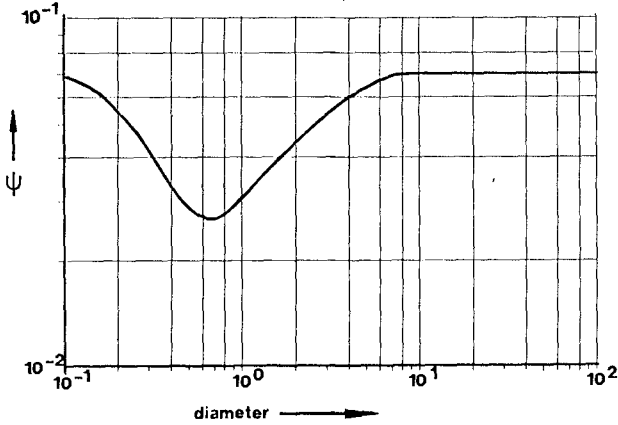


Figure 4 Shields parameter.

in open channels according to Shields is;

$$\tau_{cr} = \psi_s \Delta g D_{50} \rho \tag{3}$$

Where;

τ_{cr} = critical shear stress

ψ_s = Shields parameter

Δ = relative density of sand grains ($\frac{\rho_s - \rho}{\rho}$)

g = acceleration of gravity

D_{50} = grain size corresponding to 50% by weight of finer particles

ρ = mass density of water

ρ_s = mass density of sand

By introduction of the shear velocity $V_* = \sqrt{\tau/\rho}$, equation (1) can be rearranged to yield;

$$V_{*cr} = \sqrt{\psi_s \Delta g D_{b50}} \tag{4}$$

Where V_{*cr} = the critical shear velocity.

Formula (4) was extended in order to calculate the water velocity at threshold of sediment transport for steady flow parallel to a horizontal interface between a filter layer and a base layer, assuming a ratio between the shear velocity and the pore water velocity;

$$q_{cr} = n V_{pcr} = \frac{n}{\kappa} \sqrt{\psi_s \Delta g d_{50}} \tag{5}$$

Where κ is the ratio V_*/V_p between shear velocity, and pore water velocity, and q is the filter velocity. The magnitude of coefficient κ was determined experimentally; κ will be discussed in the next section.

For as far as the inclination concerns, assuming that at threshold of particle motion, there is an

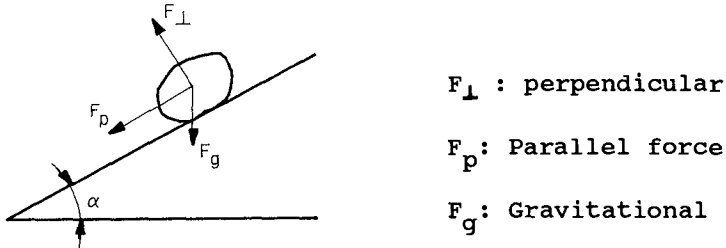


Figure 5 Equilibrium of forces

equilibrium of three forces, see Fig. 5, this leads to:

$$F_p + F_g \sin \alpha = \tan \phi \left\{ F_g \cos \alpha - F_{\perp} \right\} \quad (6)$$

With ϕ : natural angle of repose of single grains of the base material
 α : slope angle

Furthermore the gravitational force, F_g is virtually neutralized when fluidisation occurs:

$$i_f = \Delta(1 - n_b) \quad (7)$$

Where n_b is the porosity of the base material.

Since the shear forces are proportional to v^2 , the critical filter velocity q_{cr} can be written as:

$$q_{cr} = \frac{n}{\kappa} \sqrt{s \Delta g d_{50} \left(\frac{\sin(\phi - \alpha)}{\sin \phi} \right) - \frac{i_{\perp}}{\Delta(1 - n_b)}} \quad (8)$$

where one can identify a part that is related with the hydraulic conditions, a part that accounts for the slope angle, and a part which accounts for the perpendicular hydraulic gradient. A more detailed derivation is given in Bezuijen, Klein Breteler and Bakker (1987)

Finally a permeability relation is needed to relate the filter velocity to the grain size of the filter material. As this filter material is relatively coarse,

we do have to account for the turbulence intensity. Therefore we suggest a non linear permeability relation such as proposed by Forchheimer:

$$i = a q + b q^2 = a q \left(1 + \frac{b}{a} q \right) \tag{9}$$

with;

$$a = 160 \frac{\nu}{g} \frac{(1-n)^2}{n^3 D_{15}^2}$$

$$b = \frac{2.2}{g n^2 D_{15}}$$

where;

$$\nu = \text{kin. visc. of water: } 1.2 \cdot 10^{-6} [\text{m}^2/\text{s}] \quad (13^\circ)$$

This relation which is a quadratic equation in the filter velocity, can be solved directly, and this gives a secant linear expansion in the permeability

$$k^s = \frac{-a + \sqrt{a^2 + 4bi}}{2bi} = \frac{a}{2bi} \left\{ \sqrt{\left(1 + \frac{4bi}{a^2} \right)} - 1 \right\} \tag{10}$$

if $4bi/a^2 \ll 1$ than $\sqrt{1 + 4bi/a^2}$ can be approximated by $1 + 1/2 (4bi/a^2)$; the secant permeability becomes than $1/a$; The Darcy result.

If $4bi/a^2 \gg 1$, than $\left\{ \sqrt{1 + 4bi/a^2} - 1 \right\} \approx (2/a) \sqrt{bi}$

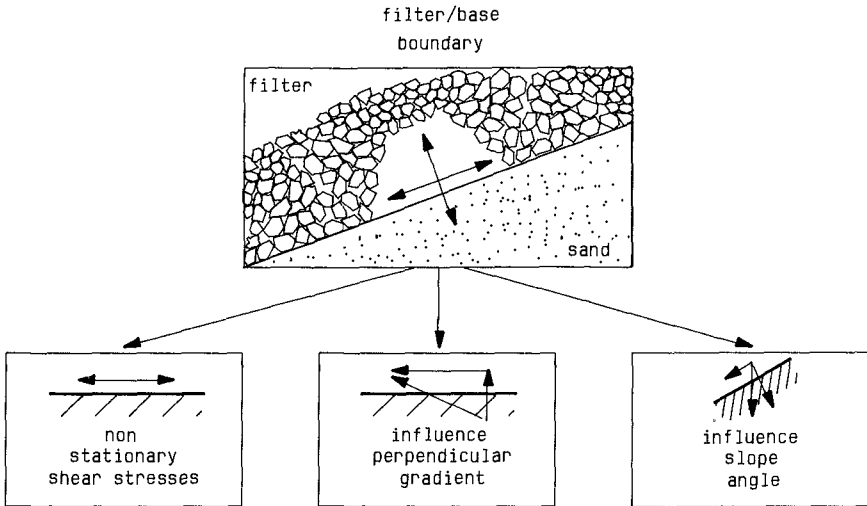


Figure 6 Loading conditions

So than $K^S = 1/\sqrt{bi}$, the result for turbulent flow.

Also experimentally, by measurement it is relatively simple to identify a laminar part, and a turbulent part. Dividing the filter velocity by the hydraulic gradient, one gets;

$$i/q = a + b q \tag{11}$$

By measuring the hydraulic gradient for two values of the hydraulic discharge, a and b can be derived relatively simple.

Verification by model tests for granular filters

The formulae (5) and (8) have been verified by means of laboratory experiments, using non cohesive base materials with steep sieve curves.

In order to verify formula (8), it was tested for the different load components. First stationary flow was verified, both on a horizontal bed, and on sloping beds. Then test were carried out with a perpendicular gradient added to the horizontal flow, and finally the effect of cyclic flow was tested.

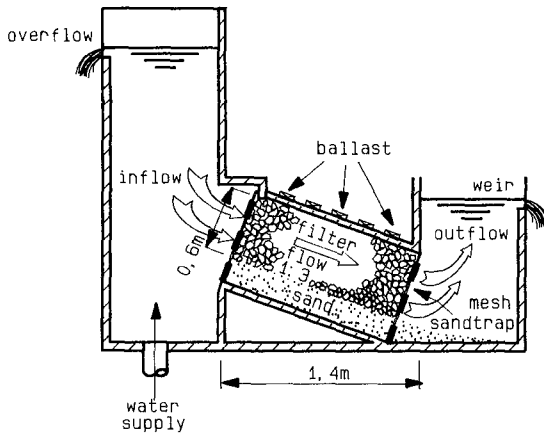


Figure 7 Delft Hydraulics Filter-box, with inclined interface

All these tests were performed in facilities where the sand transport could be measured and where the stability of the interface could be observed visually, except the tests with cyclic flow (visual observation only). The hydraulic loading was increased until there was particle transport. For the stationary flow, both on a horizontal bed, as well as for the inclined beds, the

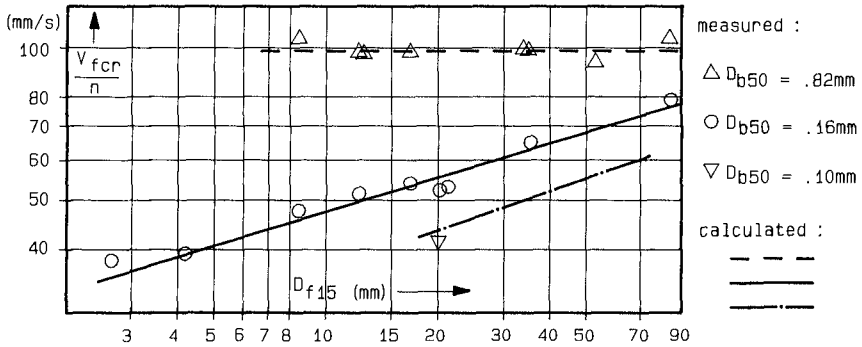


Figure 8 Filter-box test results for stationary flow parallel to a horizontal interface

filter box of Delft Hydraulics was used. see Fig 7. Tests were performed using different base materials with diameters ranging from 0.10 mm up to 0.82 mm and different ratio's D/d . The hydraulic gradient was increased step by step until considerable erosion took place. Sand transport of 0.2 gr/s/m² of dry sand was considered to be critical.

In Fig. 8 some results of the experiments in the filter box are given. The values for the coefficient κ where determined from this figure. As κ becomes constant for larger diameters of the base material the critical filter velocity becomes constant. For the finer base material the critical filter velocity is still a function of the filter material, as this material determines the turbulency conditions. This yielded the following relations for κ ;

$$\kappa = \frac{v^*}{v_p} = 0.8 Re_{cr}^{-0.2} \quad \text{for } 0.1 < d_{50} < 0.3 \text{ mm}$$

$$\kappa = 0.20 \quad \text{for } 0.5 < d_{50} < 1.0 \text{ mm}$$

$$\kappa = 0.35 \quad \text{for } d_{50} > 2 \text{ mm}$$

For $0.1 < d_{50} < 0.3 \text{ mm}$ in formula (8) q_{cr} is a function of Re_{cr} . and therefore a function of q_{cr} , so formula (8) is an implicit relation, however by rearranging q_{cr} , an explicit relation can easily be found.

From tests where a perpendicular gradient was added it was concluded, that though there is a lot of scatter in the results, the proposed formula gives a safe estimate of the critical horizontal filter velocity.

Under practical circumstances the stationary perpendicular gradient is often small, and can than be neglected. For the non stationary component, especially for smaller particles, the stability is enhanced. Since if a particle would move perpendicular to the interface, the removal of the particle from the bed would create an under pressure between particle and subsoil, reducing the gradient, thus giving a greater stability than suggested by the fluidisation gradient.

In order to investigate the influence of a cyclic component in the water velocity, tests were performed in the pulsating water tunnel of Delft Hydraulics. Tests were performed with a wave period of 2 s. which is relatively small compared to wave periods experienced on dikes and bank protection. The experimental results indicated, that for a wave period of at least 2 s. the critical velocity does not differ significantly from the stationary result. The experimental results where discussed in more detail by Bezuijen, Klein Breteler and Bakker (1987)

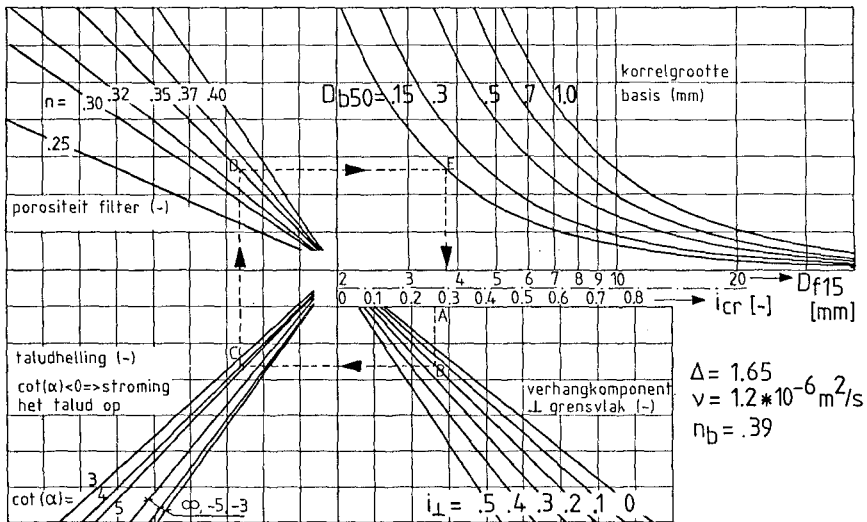


Figure 9 Design diagram for granular filter interface

Finally wave loading tests on a revetment in the Scheldt flume of Delft Hydraulics was performed. In these tests the combination of all loading aspects were present, and the filter was build based on the afore mentioned filter criteria for a critical design. The tests were used to derive wave loading characteristics

too. The verification was both visually, and by measurements of particle transport. No transport of base material was noticed.

Based on the derived theory a design diagram was made. Assuming that hydraulic conditions are known, one can use this, either to find the admissible hydraulic conditions for a given base material, and ratio between filter and base material, as is indicated in Fig. 9, or one can use it the other way round, and derive the filter ratio, when hydraulic conditions are given.

Extension of theory to geotextile interfaces

Once thus far the question arose whether the theory could be extended to include the influence of a geotextile. In comparison to an interface without one, the geotextile reduces the hydraulic loading because the boundary layer of the water flow cannot reach the grains of the base material, so a damping effect will exist. Apart from that, the geotextile, even when it is not geometrically tight, will provide an obstacle for transporting particles.

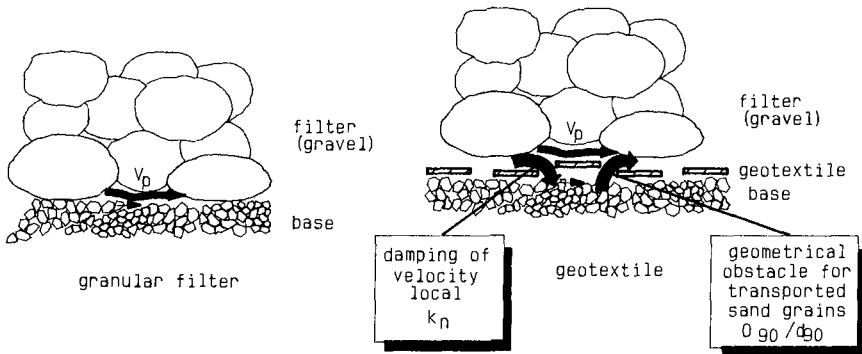


Figure 10 Principle of erosion at interface

Relevant parameters for the stability of particles underneath a geotextile might be;

- the characteristic opening size 0_{90} of the geotextile.
- the permeability k_g of the geotextile, as this

determines whether turbulences in the pore holes in the filter can penetrate to the base material surface, and

- the thickness T_g of the geotextile, which is related to this damping and has a geometric effect too.

The water partly flows just along the geotextile, and gives less shear on the underlying particles. As we assume that the pore water velocity gives the driving force for particle transport, the presence of a geotextile will reduce this pore water velocity. This reduction is a function of the opening size distribution, the permeability, and the thickness of the geotextile, see Fig. 10.

In order to derive a unified theory, the earlier proposed formula for a horizontal bed (without the effect of perpendicular flow) was extended using dimension analysis. An extended formula was derived, see Klein Breteler (1990), where three dimensionless coefficients were introduced in order to quantify these results;

$$q_{cr} = \left(c_1 \left(\frac{T_g}{d_{90}} \right) c_2 \left(\frac{d_{90}}{O_{90}} \right) c_3 \left(\frac{w}{k_g} \right) c_4^{1/m} + \frac{n}{\kappa} \right) \sqrt{\psi_s \Delta g d_{50}} \quad (12)$$

Where c_i are positive coefficients

The geotextile/soil geometry is characterized by the dimensionless thickness of the geotextile, T_g/d_{90} . The critical filter velocity q_{cr} increases with decreasing O_{90}/d_{90} ratio, or with increasing T_g/d_{90} , leading to T_g/d_{90} as a parameter. The geometric effect is characterized by the ratio d_{90}/O_{90} . The ratio w/k_g , where w is the fall velocity of a base particle, is characteristic for flow damping at the threshold of sand motion.

The formula was arranged in such a way, that all parameters will be zero, if no geotextile is present. The formula reduces than to that for granular material (5).

Geotextile interface experiments

Formula (12) was calibrated with experimental testing, quantifying the coefficients c_i . Tests were performed with mesh netting, tape fabric geotextile, and the thicker mat alike geotextile. In these tests base materials ranging from 100 μm up to 200 μm were used under the condition of horizontal flow through a rock layer on a horizontal geotextile.

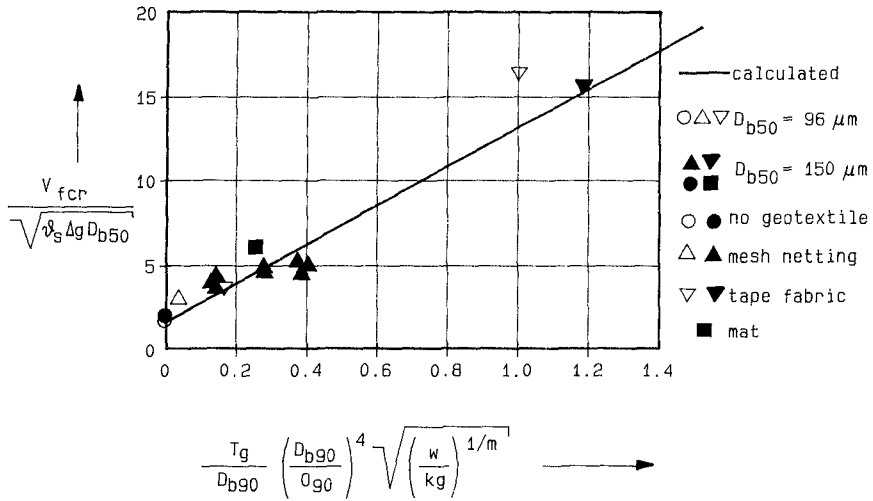


Figure 11 Test results and empirical formula

Since the number of tests performed is relatively small, it is not possible to determine more definite values for the coefficients C_i . Using trial and error methods, acceptable values for C_i were established; $C_1 = 12$, $C_2 = 1$, $C_3 = 4$ and $C_4 = 1/2$, with the test results. This yielded the following formula;

$$q_{cr} = \left(12 \left(\frac{T_g}{d_{90}} \right) \left(\frac{d_{90}}{O_{90}} \right)^4 \left(\frac{w}{kg} \right)^{1/2m} + \frac{n}{\kappa} \right) \sqrt{\psi_s \Delta g d_{50}} \quad (13)$$

In Fig. 11 the test results are gathered in such a way that one can judge the overall behavior of the derived formula. The experiments were described in more detail by Klein Breteler (1990).

Concluding Remarks

The derived formulae give a large extension to the range of applicability for filter materials, because the ratio of filter material and base material can be extended considerably.

The extension of the derived formulae to include the presence and influence of a geotextile filter makes them

more generally applicable. The extended formula can, for example be applied to the design of bottom protections. As the feasible extension to include the influence of the inclination, such as included in the formula for granular filters only, has not been been verified yet.

For other types of structures such as breakwaters, with large elements at the surface structure the use of the criteria should be restricted to that part of the structure for which the interface is not in the direct vicinity of the surface of the structure. Since in the large "pores" between these elements, the dynamic effects of the water flow are not negligible.

A limiting factor to the applicability is that hydraulic loading conditions have to be known, or need to be established, thus for the further introduction of the derived filter criteria a parallel development of design tools to predict the hydraulic loading, in various constructions, is needed.

References

- Bezuijen, A., Klein Breteler M., Bakker, K.J.
Design criteria for placed block revetments and granular filter.
Proc. II Int. Conf. on Coast. & Port Eng. In Dev. Countries, Beijing 1987
- Kenney, T.C. et al,
Controlling constriction sizes of granular filters
Can. Geotech. Journal, 22, 32-43 (1985)
- Thanikachalam, V., Sakthivadivel, R.
Rational design criteria for protective filters, Can. Geotech. Journal 11(1974)309
- Thanikachalam, V., Sakthivadivel, R.
Grainsize criteria for protective filters - an inquiry.
Soil and Foundations, V14 no 4. dec. 1974
Jap. Soc. of Soil Mechanics and Foundation Eng.
- Knaap, F.C.M. van der, Klein Breteler, M., and Meulen, T. van der
Design criteria for geotextiles beyond the sand tightness requirement Proc. 3rd International Conference on Geotextiles, Vienna 1986, Austria.
- Klein Breteler, M., and Verhey, H.J.
Erosion control by hydrodynamic sand tight geotextiles in: Geotextiles, Geomembranes and Related Products, Den Hoedt (ed) Balkema Rotterdam 1990

CHAPTER 115

WAVE FORCES ON BREAKWATER ARMOUR UNITS

Jørgen Juhl¹ and Ole Juul Jensen²

Abstract

The authors have carried out a research project for investigation of the wave forces acting on breakwater armour units. The project included a literature study, hydraulic model testing and analysis of the test results. The hydraulic model testing was made in a wave flume on a 2-dimensional idealised breakwater structure with an armour layer consisting of two rows of horizontal pipes.

Introduction

Many researchers have for many years looked into the question of wave forces on breakwater armour units. Most of the research has concentrated on studying the stability of breakwater slopes armoured with various types of armour units.

Only a few researchers have directly studied the wave forces on armour units by making measurements on idealised armour units in a hydraulic model. Sigurdsson (1962) and Sandström (1974) have made measurements on idealised breakwaters consisting of spherical balls exposed to regular waves.

The present work is of the same nature, but is a pure 2-dimensional case and included testing with irregular waves.

The maximum measured forces on an armour unit, both during run-up and run-down, has been studied as function of wave height, wave period, and position of the unit on the breakwater slope.

¹Senior Hydraulic Engineer, Danish Hydraulic Institute

²Head, Ports and Marine Structures Division, Danish Hydraulic Institute, Agern Allé 5, DK-2970 Hørsholm, Denmark.

In order to make a simplified representation of the acting forces, stability calculations including both measured force components have been carried out.

During run-up large forces in the direction into the breakwater have been measured. These slamming forces were measured both for regular and irregular waves, but are generally more pronounced for irregular waves. The slamming forces are characterised by a rapid growth and a short duration, and occur when the water hits onto the units. This type of forces is not considered to be dangerous for the stability of armour units, but may be dangerous for breakage of slender and fragile concrete armour units.

Results of the study have been published by the authors in Refs. /1/ and /2/.

The Model

The model tests were conducted in a 23 m long and 0.6 m wide wave flume. The flume set-up is shown in Fig. 1.

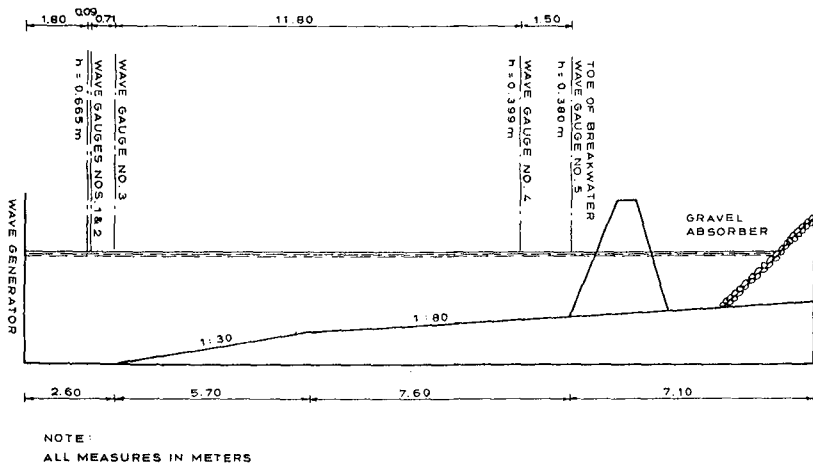


Fig. 1 Set-up of wave flume.

The model tests were conducted on a 2-D breakwater model with a slope of 1:2 of the armour layer. The crest height was chosen not to allow for wave overtopping. The armour layer consisted of two layers of horizontal steel pipes with diameter 50 mm to form an idealised and purely 2-dimensional representation of a breakwater armour layer. The porosity of the armour layer was selected to $p = 0.40$. Details of the model are shown in Fig. 2.

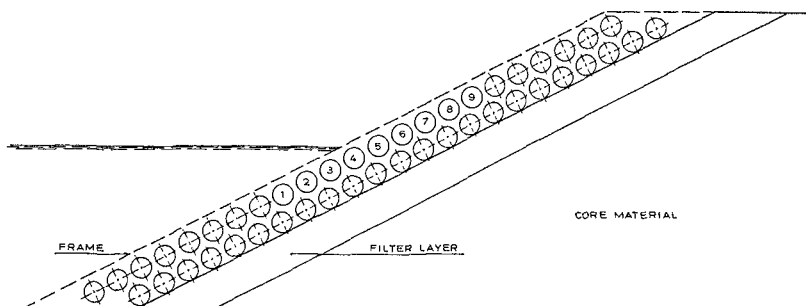


Fig. 2 Details of test set-up.

The wave forces on three of the pipes in the upper layer were measured simultaneously by use of strain gauge transducers giving two force components, i.e. vertically and horizontally. Nine of the pipes in the upper layer were prepared for force measurements. The forces were measured on the 0.2 m wide middle section of the horizontal pipes.

Waves

Regular and irregular waves were used for model testing. The wave combinations covered both non-breaking and breaking waves.

The tests with irregular waves covered a range of wave combinations: Peak periods, T_p , from approximately 1.0 to 3.0 s and significant wave heights, H_s , from approximately 0.05 m to 0.20 m.

The wave heights for the irregular waves were determined as $H_s = 4 \times h_{rms}$, where h_{rms} is calculated as

$$h_{rms} = \sqrt{\frac{1}{m} \sum_{i=1}^m h_i^2}$$

m being the total number of samples and h_i being the surface elevation.

Wave Measurements

The waves in the flume were measured in 5 points by resistance type wave gauges as shown in Fig. 1.

The coefficient of reflection, R , has been determined for each test by a standard three gauge method, wave gauges Nos. 1, 2, and 3.

The measured wave heights have been corrected by a factor of $\sqrt{1+R^2}$ to take into account waves reflected from the breakwater.

The wave height measured 1.5 m in front of the breakwater (wave gauge No. 4) has been used as reference wave height for all test runs.

Measurements of the run-up/run-down was carried out with a wave gauge placed parallel to the breakwater slope and in a distance of 50 mm (one pipe diameter) to ensure no effect from the steel pipes.

Force Measurements

Strain gauge transducers were used for measurements of two force components, i.e. vertically and horizontally.

The natural periods for the 0.2 m test section of the pipes fixed to the strain gauge transducers have been determined:

(a) In air	100 Hz
(b) In water	55 Hz
(c) In half air/half water (pipe No. 5)	60 Hz

It should be noted that the transducers were calibrated to zero-force for still water level. This means that the buoyancy acting vertically upwards has been subtracted for pipes Nos. 1-5 being either totally or partly submerged.

The buoyancy for a totally submerged pipe was 19.30 N/m and for the partly submerged pipe No. 5 the buoyancy was 9.65 N/m. This fact is important in the interpretation and comparison of the test results for the different pipes.

Test Conditions

All tests were carried out with fixed wave conditions, i.e. stationary wave height (H , H_s) and wave period (T , T_s). The water level was identical during all test runs, i.e. a water level of 0.38 m at the toe of the breakwater.

The test runs with regular waves had a duration of 300 s, while the test runs with irregular waves had a duration corresponding to approximately 500 zero-crossing waves.

The signals from the wave gauges and the strain gauge transducers were recorded (with a logging frequency of 40 Hz) and stored by a micro computer.

Wave Forces on a Two-Dimensional Breakwater

The determination of forces acting on the idealised armour units can be compared with forces acting on a pipeline located on or close to the seabed. The following points indicate the complexity for the present model set-up.

- (a) The flow pattern around the pipes is very complex, each individual pipe is influenced by the presence of neighbouring pipes.
- (b) Air entrainment occurs which makes the velocity field uncertain and decreases the density of the fluid.
- (c) The buoyancy varies with time as a result of run-up/run-down. This means that it is impossible to separate the hydrostatic force and hydrodynamic forces.
- (d) Wave breaking results in wave slamming forces.

The positive orientation of the measured forces is shown in Fig. 3.

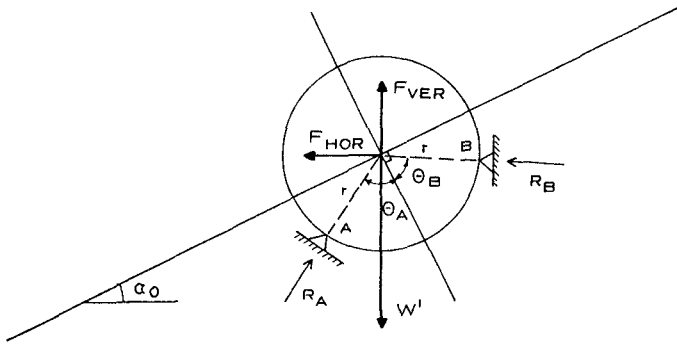


Fig. 3 Definition sketch of the used coordinate system, and simplified stability calculations.

Velocity and Acceleration in Run-up/Run-down

The wave gauge for measuring run-up/run-down was installed 0.05 m above the slope and calibrated so that the run-up/run-down was measured vertically in agreement with the standard procedure for reporting of run-up heights.

The velocity and acceleration of the water in the run-up/run-down front has been calculated by a filter technique as described by Hamming (1977). The filters represented single and double differentiation of the measured time series of run-up/run-down.

It should be noted that the calculated velocity and acceleration refers to the run-up/run-down and not to the flow conditions around the individual pipes.

Stability Calculations

Stability calculations including both force components have been carried out with the aim of making a simplified representation of the acting forces. It is assumed that the armour unit is supported in two contact points as shown in Fig. 3. Only symmetric contact points have been used for the calculations, i.e. $\theta = \theta_A = \theta_B$.

An example of the measured run-up/run-down and measured horizontal and vertical forces is shown in Fig. 4 together with the calculated required weight for no movements. The required effective weight to withstand roll-down, W'_d , is positive whereas the required effective weight to withstand roll-up, W'_u , is plotted as negative values. The required weights presented throughout the paper have been calculated for $\theta = 60$ deg.

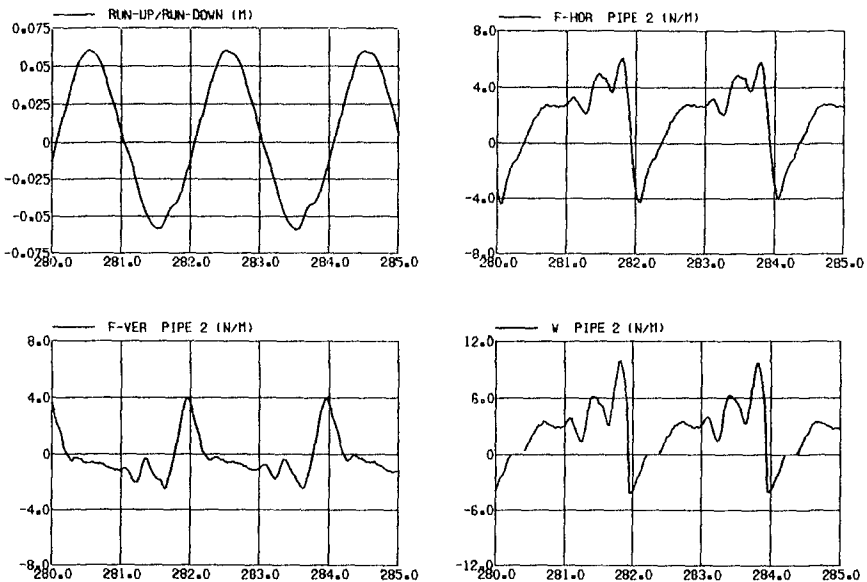


Fig. 4 Recorded and calculated time series for a regular wave with $H = 0.07$ m and $T = 2.0$ s.

Test results for Regular Waves

The following paragraphs include results from testing with regular waves.

Required Weights in Relation to Pipe Position

For regular waves with a wave period of 2.0 s, a series of tests has been carried out for studying the effect of pipe position.

Fig. 5 shows the calculated required weights to withstand roll-up and roll-down, respectively. W'_u and W'_d are presented for the nine pipes on which wave forces have been measured.

The calculated required weights to withstand roll-down shows that a maximum of W'_d is reached at pipes Nos. 1, 2, or 3 depending on the wave height. Also for roll-up, a maximum in required weight is found at pipe No. 1, 2 or 3 and further, a local maximum is found at pipe No. 5. The test results show that the required calculated weights to withstand roll-up are generally less than the required weights to withstand roll-down. This is in good agreement with the experience from physical model tests of rubble mound breakwaters, i.e. the major part of damage occurs during run-down for a slope of 1:2.0.

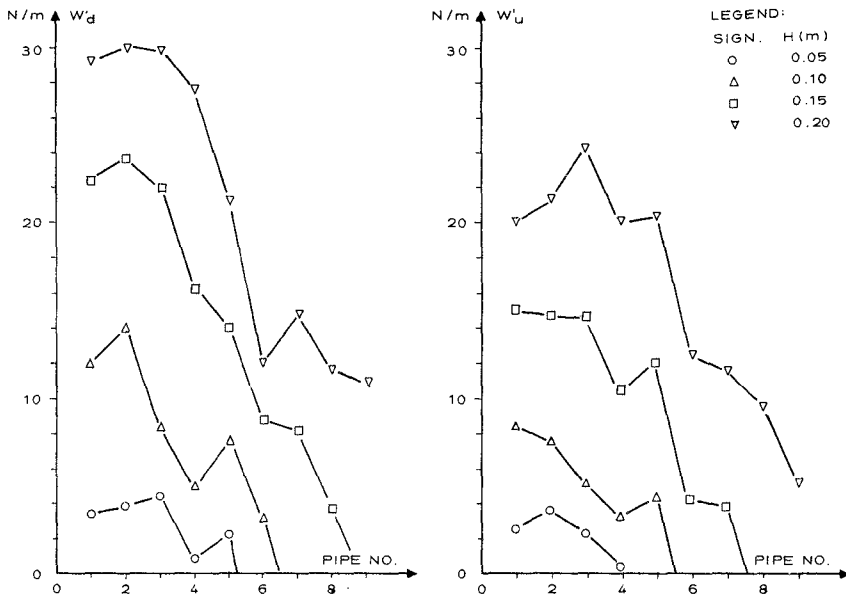


Fig. 5 Required weights to withstand roll-up/roll-down for the nine pipes. Wave period $T = 2.0$ s.

Influence of Wave Period

The calculated required weights to withstand roll-down, W'_d , for pipes Nos. 2 and 5 are shown in Fig. 6 as function of the wave period. The results show that for pipe No. 2, the largest required weight occurs for $T = 1.5$ s, whereas a minimum is found for $T = 2.5$ s. For pipe No. 5, the required weight only varies slightly with the wave period, whereas for pipe No. 8, an increase with the wave period is found, which is due to increasing wave run-up for increasing wave periods. Similar dependencies of the wave period are found for the required weights to withstand roll-up.

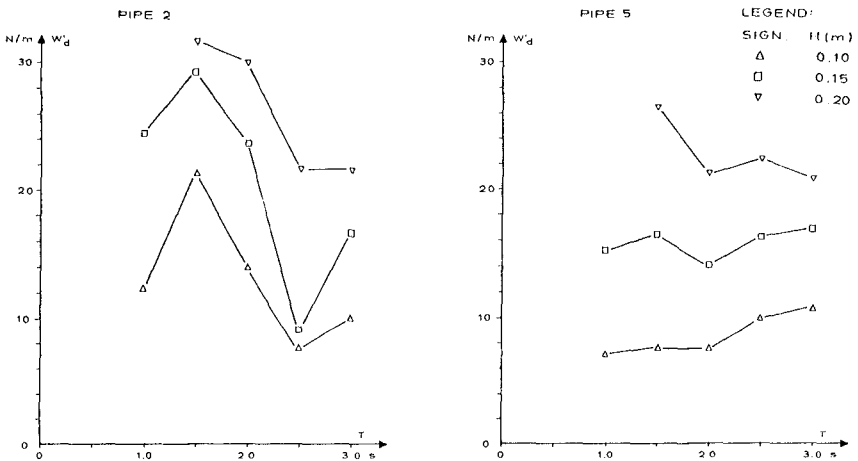


Fig. 6 Required weights as function of the wave period. Regular waves.

The measurements show that it is a rough simplification to aim for one stability formula for description of the stability of the entire seaward armour layer of a rubble mound breakwater.

Influence of Surf Similarity Parameter, $\xi = \tan \alpha_0 \sqrt{H/L_0}$

The influence of the surf similarity parameter on stability has been studied. For fixed values of the required weights to withstand roll-up and roll-down, the corresponding wave heights have been found and the results are for pipe No. 2 presented in Fig. 7. It was found that a minimum in stability occurs for a surf similarity parameter in the order of 2 to 4, which corresponds to peak wave periods in the order of 1.5 s to 2.0 s. It is very important to notice that this range of the ξ -factor corresponds approximately to the transition between plunging and surging wave breaking.

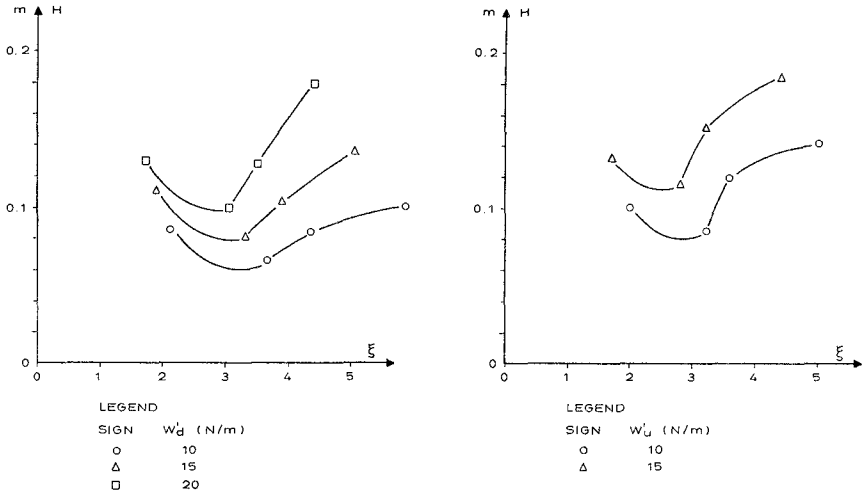


Fig. 7 Relationship between wave height and surf similarity parameter, ξ , for fixed required weights to withstand roll-up and roll-down. Pipe No. 2.

Test Results for Irregular Waves

All results presented in this section are based on model tests with irregular waves generated on basis of a JONSWAP spectrum. The forces were during all tests measured on pipes Nos. 2, 3, and 5.

Analysis of Results

The measured forces and calculated required weights have been analysed statistically by plotting the results on semi-logarithmic paper as shown in Fig. 8. From these plots, the most probable forces and required weights have been found and used for further analyses.

Influence of Wave Height

The calculated required weights to withstand roll-up and roll-down have been plotted for each wave period as function of the wave height. It was found that the relationship between the required weights and the wave height to a high degree depends on the peak wave period and location on the slope.

Influence of Wave Period

The test results for irregular waves show the same tendency, but less pronounced as for regular waves, i.e. a maximum in required weight for $T_p = 1.5$ s for pipe No. 2,

whereas the required weight for pipe No. 5 is almost independent of the wave period.

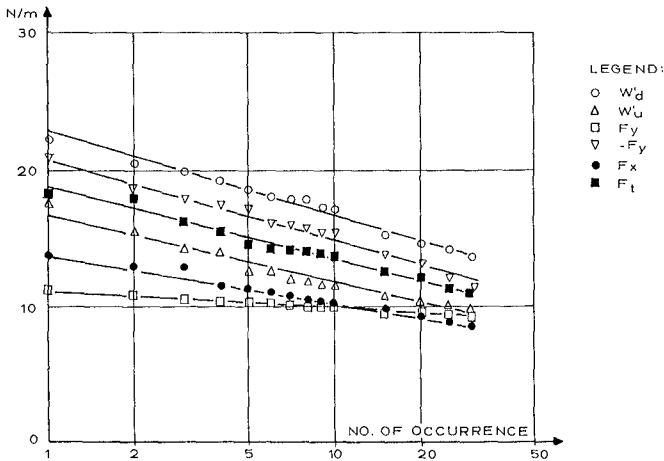


Fig. 8 Distribution of maximum forces and required weights on pipe No. 3. $H_s = 0.13$ m, $T_p = 2.0$ s.

Influence of Surf Similarity Parameter, $\xi = \tan \alpha_o \sqrt{H_s} / L_{op}$

In Fig. 9, the influence of the surf similarity parameter on the stability is shown for pipe No. 2. For fixed values of the required weights to withstand roll-up and roll-down, the corresponding wave heights have been found.

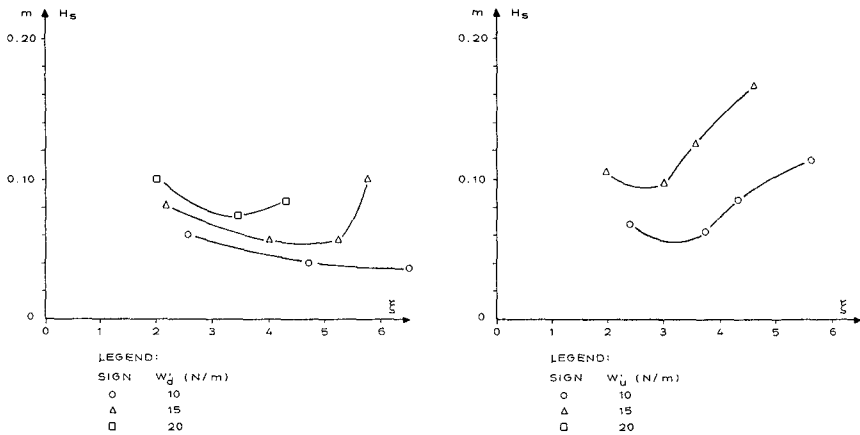


Fig. 9 Relationship between significant wave height and surf similarity parameter, ξ , for fixed required weights to withstand roll-up and roll-down. Pipe No. 2.

For roll-up, a minimum in stability is found for a surf similarity parameter in the order of 2 to 4.

For roll-down, the minimum in stability is not so pronounced as for roll-up or as was the case for regular waves. A minimum in stability was found for a surf similarity parameter of 3-5.

Wave Slamming Forces

The wave slamming forces on the pipes have been analysed by studying the horizontal forces acting into the breakwater, i.e. when $F_{hor} < 0$. The advantage of this method is elimination of the varying buoyancy. It can, however, not be excluded that small buoyancy effects occur due to asymmetrical buoyancy and air entrainment. The duration of the measured slamming forces was approximately 0.1 s with a rising time of approximately half, i.e. 0.05 s. This is significantly longer than slamming forces on a vertical wall, most probably due to the circular shape of the pipe.

Maximum Horizontal Force in Relation to Pipe Position

For regular waves with a period of 2.0 s, a series of tests has been carried out for studying the relationship between the maximum inwards acting horizontal force ($-F_{hor}$) and the pipe position. Fig. 10 shows the results for the nine pipes on which wave forces have been measured.

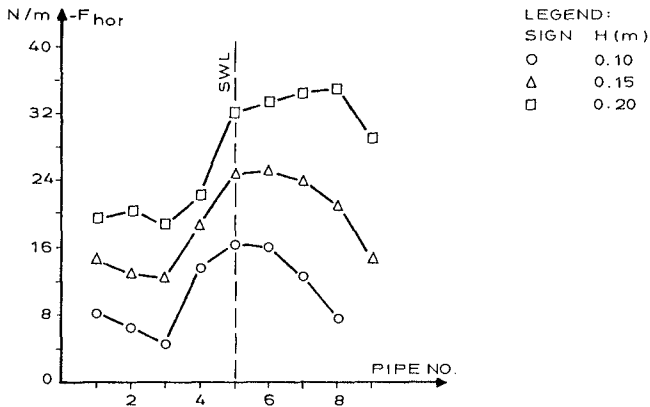


Fig. 10 Maximum inwards acting horizontal forces in relation to pipe position. $T = 2.0$ s. Regular waves.

The results show that for $H = 0.10$ m the largest force is acting on pipe No. 5. When the wave height is

increasing, the wave run-up is increasing and thus the largest force is acting on a pipe further up the slope. For $H = 0.20$ m, the largest force is found to act on pipe No. 8, but this force is only slightly larger than the largest forces acting on pipes Nos. 5, 6, and 7.

For all three wave heights, it was found that the maximum forces acting on pipes Nos. 1, 2, and 3 are approximately half the largest maximum force.

Slamming Forces as Function of Run-Up Velocity

In order to analyse if the run-up velocity is the dominant factor for the horizontal wave impact on the pipes, the maximum measured horizontal force during each run-up period has been determined.

A scatter diagram of the correlation between run-up velocity and maximum inwards acting horizontal force, $-F_{hor}$, on pipe No. 5 is shown in Fig. 11.

The results show that the maximum horizontal force increases almost linearly with the run-up velocity. This result is very surprising as $-F_{hor}$ is expected to be proportional to U^2 .

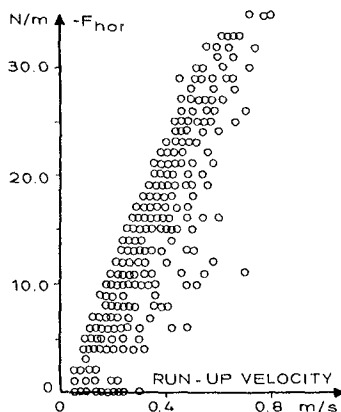


Fig. 11 Scatter diagram of run-up velocity and maximum inwards acting horizontal force on pipe No. 5. $H_s = 0.18$ m, $T_p = 2.0$ m. JONSWAP spectrum.

Summary and Conclusion

Calculations of the required weights to withstand roll-up and roll-down showed that the maximum required weights occur for pipes Nos. 1, 2 or 3 (below SWL), depending on the wave height.

For roll-down, a maximum in required weight for pipe No. 2 is found for a wave period of 1.5 s, whereas the required weight for pipe No. 5 is almost independent of the wave period.

For roll-up, a minimum in stability was found for a surf similarity parameter, ξ , of 2 to 4 for both regular and irregular waves. For roll-down, a minimum in stability was found for a ξ of 2 to 4 for regular waves, whereas the minimum is less pronounced for irregular waves and occurs for a ξ of 3 to 5.

The results show that the slamming forces acting on the pipes vary to a high degree with the wave period resulting in different types of wave breaking and on the position of the pipe relative to SWL.

The largest horizontal slamming forces were measured at the pipes from still water and upwards on the slope. There was a tendency that waves with a period of 1.5 s to 2.0 s caused the largest forces which corresponds to a surf similarity parameter in the order of 2 to 4. This range of the ξ -factor corresponds approximately to the transition between plunging and surging wave breaking.

Analyses have shown that the measured horizontal slamming forces are increasing almost linearly with the run-up velocity.

Acknowledgement

The research study of wave forces on idealised breakwater armour units was partly financed by the Danish Technical Research Council. The support is graciously acknowledged.

Appendix 1 - Reference

- Hamming, R.W. (1977). Digital filters. Prentice-Hall.
- Jensen, O.J. and Juhl, J. (1988). Results of model tests on 2-D breakwater structure. Breakwater '88, Eastbourne, pp. 13-25.
- Juhl, J. and Jensen, O.J. (1989). Wave slamming forces on armour units. Presented at the "Seminar on Stresses in concrete Armour Units" in Vicksburg, U.S.A.
- Sandström, Åke (1974). Vågkrafter på block i vågbrytarslänter (Wave forces on blocks of rubble mound breakwaters), in Swedish with summary in English. Hydraulic Laboratory, Royal Institute of Technology, Stockholm, Bulletin No. 83.

Sigurdsson, Gunnar (1962). Wave forces on breakwater capstones. Journal of the Waterways and Harbors Division, Proceedings of the American Society of Civil Engineers.

Appendix 2 - Notation

The following symbols are used in this paper:

g	=	acceleration due to gravity
F_{hor}	=	horizontal force component (outwards from the breakwater)
$-F_{hor}$	=	horizontal force component (inwards the breakwater)
F_{ver}	=	vertical force component (upwards)
$-F_{ver}$	=	vertical force component (downwards)
F_t	=	total force. Negative when acting into the breakwater
H	=	wave height at wave gauge No. 4
H_s	=	significant wave height at wave gauge No. 4
h^s	=	water depth
h_i	=	surface elevation
h_i^{rms}	=	rms-value of the water surface elevation
L_o	=	deep water wave length, $L_o = g/2\pi \cdot T^2$
L_{op}	=	deep water wave length, $L_{op} = g/2\pi \cdot T_p^2$
m^{op}	=	number of samples
p	=	porosity of armour layer
R	=	reflection coefficient
T	=	wave period
T_p	=	spectral peak wave period
W^p_d	=	required weight to withstand roll-down
W^u_d	=	required weight to withstand roll-up
α	=	slope of breakwater, $\tan \alpha_o = \frac{1}{2}$
θ	=	angle for contact points
ξ	=	surf similarity parameter

CHAPTER 116

EFFECTS OF WAVE GROUPS ON THE STABILITY OF RUBBLE MOUND BREAKWATERS

by

Josep R. Medina¹, Claudio Fassardi²,
and Robert T. Hudspeth³

ABSTRACT

The stability of the armor layer of rubble mound breakwaters has been shown to be highly influenced by some wave grouping characteristics. The measured damage functions are dependent on the Envelope Exceedance Coefficient, α , and also on the Groupiness Factor defined as: $GF = \sigma[H^2(t)]/8m_0$.

INTRODUCTION

Wave groups have been identified as playing an important role in a variety of coastal problems. Medina and Hudspeth (1990) reviewed most of the parameters and methodologies commonly used, as well as the engineering problems associated with wave groupiness. Although the effects of wave groups on the stability of the armor layer of mound breakwaters have been considered by many, a rational method for incorporating wave groups into the design of mound breakwaters has yet to be developed.

Current design methods for armor layers follow the design methodology proposed by the Shore Protection Manual (SPM, 1984) which relates the design of the armor layer to a single representative wave height, H_{10} , which corresponds to a design sea state. The SPM methodology does not incorporate the effects of

¹Prof. Titular, Dep. of Transportation, Univ. Polit cnica de Valencia, Camino de Vera s/n, Valencia 46071, SPAIN.

²Ass. Res., Dep. of Civil Engineering, Oregon State University, Corvallis, OR. 97331, U.S.A.

³Professor, Dep. of Civil Engineering, Oregon State University, Corvallis, OR. 97331, U.S.A.

storm duration, wave period or wave groupiness from the design sea state.

Bruun (1985) reviewed the design of mound breakwaters and emphasized that the stability of these structures is sensitive to wave groups; and, therefore, wave grouping characteristics should be incorporated into their design. On the contrary, Van der Meer (1988) proposed new formulae which considered the influence of duration and wave periods; however, he concluded that wave grouping characteristics and spectral shape have only a minor influence on the stability. Recently, Medina and McDougal (1990) reanalyzed the experimental data from Van der Meer and Pilarczyk (1988); and found that rubble mound breakwaters were more stable against sea states with long wave groups, which appears to be contrary to intuition.

As noted above, there is an apparent contradiction regarding the effects of wave grouping on the stability of rubble mound breakwaters. In order to evaluate the influence of wave grouping on the stability of rubble mound breakwaters and revetments, a series of large scale experiments were conducted at the O.H. Hindsdale Wave Research Facility (OHH-WRF) at Oregon State University. The main goal of these experiments was to resolve the controversy regarding the dependence of damage on the spectral shape and/or the characteristics of wave groups.

ENVELOPE AND WAVE HEIGHT FUNCTIONS

Rye (1982) reviewed the methods for analyzing wave groups and concluded that wave groups measured from field data compared quite well with those obtained from numerical simulations using linear algorithms. The validity of the linear hypothesis was also obtained by Goda (1983) and by Battjes and Vledder (1984) for wave groups in non-shallow waters.

In his classic treatise on random noise, Rice (1954) developed an extensive theory that may also be applied to linear surface gravity waves where the envelope theory appears to be appropriate for analyzing wave groups. Medina and Hudspeth (1987) and Hudspeth and Medina (1988) used the envelope theory of Rice and focused their attention on only some of the more important aspects for analyzing wave groups. The envelope theory, originally applied to 1-D wave analyses, may also be extended rather easily to 2-D and 3-D waves and to wave groups.

Assuming that the sea surface elevation at a point is an ergodic Gaussian stochastic process having a variance spectrum $S_{\eta}(f)$, a realization may be approximated by

$$\eta(t) = \sum_{m=1}^M R_m \cos(2\pi f_m t + \theta_m) \quad (1)$$

where M = the total number of wave components in the realization; R_m , f_m , and

θ_m = the amplitude, the frequency, and a random phase angle, respectively, of the m^{th} wave component. The random phase angle is uniformly distributed in the interval $U[0, 2\pi]$. The Hilbert transform, $\hat{\eta}(t)$, of $\eta(t)$ is given by

$$\hat{\eta}(t) = \sum_{m=1}^M R_m \sin(2\pi f_m t + \theta_m) \quad (2)$$

and the analytical function, $AF(t)$, by

$$AF(t) = \eta(t) + j\hat{\eta}(t) = A(t)\exp(j[\theta(t) + \phi]) \quad (3)$$

where $j = \sqrt{-1}$; $A(t)$ = the envelope function; and $[\theta(t) + \phi]$ = the instantaneous phase angle defined by

$$A(t) = \sqrt{\eta^2(t) + \hat{\eta}^2(t)} \quad (4)$$

$$\theta(t) + \phi = \text{ARCTAN} \left[\frac{\hat{\eta}(t)}{\eta(t)} \right] \quad (5)$$

In the complex plane, Hudspeth and Medina (1988) identified $AF(t)$ as an orbital movement consisting of a vertical displacement of a point floating in the sea surface $\eta(t)$ and a horizontal displacement $\hat{\eta}(t)$. An instantaneous wave height, $H(t) = 2A(t)$, and a local radian frequency, $\Omega(t) = d\theta(t)/dt$, were defined. The statistical properties of these two functions were evaluated and related to the characteristics of wave groups.

The envelope theory may be extended to 2-D experiments in wave flumes using space (x) and time (t) as the independent variables. The water surface elevation in a wave flume may be expressed as

$$\eta(x, t) = \sum_{m=1}^M R_m \cos[2\pi(\lambda_m x - f_m t) + \phi_m] \quad (6)$$

where ϕ_m is a random phase uniformly distributed in the interval $U[0, 2\pi]$; and λ_m is the inverse of the m^{th} wave length computed from by

$$f_m^2 = \left(\frac{g}{2\pi}\right) \lambda_m \tanh(2\pi \lambda_m h) \quad (7)$$

where h is the water depth, and g is the acceleration due to gravity. The Hilbert transform of $\eta(x, t)$ in the space and time domains may be defined as

$$\hat{\eta}(x, t) = \sum_{m=1}^M R_m \sin[2\pi(\lambda_m x - f_m t) + \phi_m] \quad (8)$$

where x and t are considered to be space and time parameters for time and space domain calculations, respectively. The envelope and wave height functions in the wave flume are given by

$$H(x,t) = 2 A(x,t) = 2 \sqrt{\eta^2(x,t) + \hat{\eta}^2(x,t)} \quad (9)$$

The variance spectrum in the space domain, $S_\eta(\lambda)$, may be related to the variance spectrum in the time domain, $S_\eta(f)$, according to the linear dispersion relationship and

$$S_\eta(f) df = S_\eta(\lambda) d\lambda \quad (10)$$

The properties of waves and envelopes in the time domain may be projected to the space domain to obtain

$$4 S_A(\lambda) = S_H(\lambda) \sim (8-2\pi)m_0\Gamma_\eta(\lambda) \quad (11a)$$

$$S_{H^2}(\lambda) \sim 64m_0^2\Gamma_\eta(\lambda) \quad (11b)$$

$$\Gamma_\eta(\lambda) = \frac{2}{m_0^2} \int_0^\infty S_\eta(x+\lambda) S_\eta(x) dx \quad (12)$$

where $S_{H^2}(\lambda)$ and $S_H(\lambda)$ are the variance spectra of $H^2(x,t)$ and $H(x,t)$ in the space domain (t fixed); and $\Gamma_\eta(\lambda)$ is the corresponding spectral density function (unit variance). The envelope spectral density functions in space and time are not related by the linear dispersion relationship.

The spectral density functions for waves and envelopes in space and time may be used to estimate the mean wave velocity and mean group celerity for irregular waves. The flux of energy in a wave flume is approximately proportional to $C_g H^2(x,t)$, where C_g is the mean group celerity. Therefore, it is reasonable to test if $H^2(t)$ at the toe of a rubble mound breakwater affects stability.

Realizations of different discrete waves with the same flux of energy and local wave height and period characteristics may be expressed by

$$\eta_\psi(x,t) = \sum_{m=1}^M R_m \cos[2\pi(\lambda_m x - f_m t) + (\phi_m - \psi)]; 0 \leq \psi \leq 2\pi \quad (13)$$

where ψ is a constant phase shift given to each component. Digital-to-analog simulations make it possible to simulate a desired wave train at the toe of the structure.

DESCRIPTION OF EXPERIMENTS

The effects of wave groupiness on the stability of the armor layer of rubble mound breakwaters do not appear to have been treated in a consistent manner in previous studies. The published results of these experiments do not always give a

precise indication of the wave grouping characteristic that significantly affected the stability. Johnson et al.(1978) indicated that wave trains with long wave runs and high GF are more damaging. However, Burchart (1979) suggested that sea states with short wave runs are the most damaging. Finally, Van der Meer(1988) could not identify any significant differences between wave trains with high GF, long wave runs and narrow spectra and wave trains with low GF, short wave runs and broad spectra.

The apparent contradiction from these published experimental results may possibly be resolved by the wave grouping characterization model proposed by Mase and Iwagaki (1986). They considered two independent characteristics: a) a wave groupiness factor and b) a run length. Our experiments exploit the model of Mase and Iwagaki (1986) using linear wave theory. Our final results will demonstrate those wave grouping characteristics that significantly influence the stability of the armor layer of rubble mound breakwaters.

In order to analyze the influence of wave groups on the stability of the armor layer, two different design methodologies were considered as being representative of the state-of-the-art methods for design: 1) the S.P.M. method (1984); and 2) the highly elaborated Van der Meer method (1988). In both of these two methods, the stability of the armor layer is controlled mainly by

$$N_s = \left[\frac{\rho_r H_s^3}{W \left(\frac{\rho_r}{\rho_w} - 1 \right)^3} \right]^{\frac{1}{3}} \quad (14)$$

where N_s is a stability number; H_s is the significant wave height; W is the median value of the mass distribution of rocks in the armor; and ρ_r and ρ_w are the mass densities of the rocks and water, respectively.

The following secondary factors also affect the stability (or damage function): slope, thickness of armor layer, permeability of the structure, number of waves in a run, surf similarity parameter or mean period, roughness and placement of the armor rocks, and wave groupiness. In our experiments, most of these secondary factors were held constant in order to compare the stability number and the wave grouping characteristics of wave runs with damage (or erosion of the armor layer). The 3.7 m. wide wave channel was divided into two equal halves in order to test simultaneously the same rubble mound breakwater profile but with two different armor layer rock sizes (viz., $W_L=13$ kg. and $W_S=10$ kg.). Consequently, each run provided two different surf similarity parameters in order to evaluate the influence of wave period on stability.

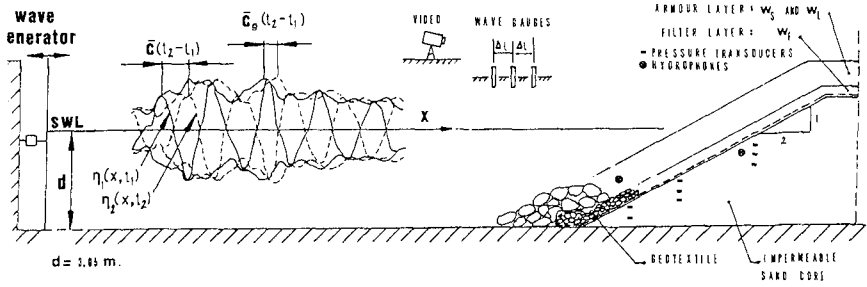


Fig. 1. Schematic of Wave Channel Used for Experiments.

Profiles of the armor layer were recorded after each run in order to measure damage (erosion). A surveying rod with an articulated foot (1 ft. diameter) was used to measure the armor layer profile at every foot. Two hydrophones and nine pressure transducers were placed inside the structure in order to detect rock movement and to measure pressures in the secondary layer.

Two fundamental wave grouping characteristics were considered: 1) the spectral shape related to the mean run length and 2) the energy flux exceedance pattern related to the groupiness factor. The spectral shape and mean run lengths were evaluated using random waves simulated from a Goda-JONSWAP spectra having the same H_s and T_{01} parameters but different peak enhancement factors; viz., $\gamma=1$ and $\gamma=10$. Because breakwaters are subject to damage only from wave heights above a certain threshold level, our experiments were designed to attack the breakwater structure with energy levels above a specified threshold level. Irregular wave trains with envelopes having different energy flux exceedance parameters (related to the groupiness factor) were selected from Monte Carlo realizations of random waves.

Two different realizations of $H^2(x,t)$ were selected for each spectral shape (viz., $\gamma=1$ & $\gamma=10$). These two realizations had relatively high and low envelope exceedance coefficients, α , computed from

$$\alpha = \frac{\alpha'}{E[\alpha']} ; \alpha' = \frac{1}{N} \sum_{n=1}^N \left[\frac{H(n\Delta t) - H_{10}}{H_{10}} \right]^2 \delta(n) \tag{15}$$

where $\delta(n)=1$, if $H(n\Delta t) > H_{10}$ and $\delta(n)=0$, if $H(n\Delta t) < H_{10}$; N is the number of data points in the time series; Δt is the discretization time interval; $H(t)$ is the wave height function measured at the toe of the structure; and $H_{10}=1.27 H_{m0}$. The low and high values for α were selected from one-hundred DSA random wave realizations simulated from two Goda-JONSWAP spectra ($\gamma=1$ & $\gamma=10$), with $T_{01}=3.0$ sec., $f_{min}=0.7 f_p$, and $f_{max}=2.5 f_p$. Four simulations with the maximum and minimum values of α for each spectral shape were selected for the experiment. Initially, a threshold level of H_{10} was used in Eq. 15; however, changing H_{10} to H_s did not change the statistics of α significantly.

For each of the four envelopes, the constant phase shift used in Eq. 13 was $\psi=0, 2\pi/3, 4\pi/3,$ and 2π . Because wave trains having $\psi=0$ & $=2\pi$ are identical, the differences in the measured damage for $\psi=2\pi/3$ & for $\psi=4\pi/3$ means that only the wave height and wave period functions are controlling the stability. Therefore, sixteen wave trains (unit variance) of 650 waves were simulated corresponding to: 1) two spectral shapes ($\gamma=1$ & $=10$); 2) two envelope exceedance coefficients (high and low α); and 3) four phase shifts (viz., $\psi=0, 2\pi/3, 4\pi/3,$ and 2π). The levels of energy in the physical simulations were increased in discrete increments in order to make the stability numbers for the small and large rocks equal in consecutive runs. Seven runs of sixteen wave trains were simulated with significant wave heights determined from

$$H_s(k) = 0.43 \left(\frac{W_L}{W_S} \right)^{\frac{k-1}{3}} ; k=1,2,\dots,7 \quad (16)$$

where $H_s(k)$ is the significant wave height in meters corresponding to the k^{th} run.

Three ultrasonic wave gauges were placed 10 m. from the toe of the structure in order to obtain two records of the incident and reflected wave trains (vide Fig. 1). The wave board did not have direct-digital-control in order to cancel the waves reflected from the structure. Consequently, the measured incident wave trains contained some multi-reflected waves. The method used to separate the incident and reflected wave trains is a modification of the method proposed by Goda and Suzuki (1976).

EXPERIMENTAL OBSERVATIONS

Rock profiles, wave records, video records of run-up, and visual observations of rock movements were recorded during the experiments. The rock profiles were used to calculate the damage defined as the normalized erosion of the armor. The wave records obtained from the three ultrasonic wave gauges located 10 m. in front of the structure were used to measure the waves incident on the structure.

The armor damage was calculated from the eroded area of the mean measured profiles corrected for small errors in measurements and for settlement. Distances along the profiles were normalized by the equivalent cube size (Iribarren) or nominal diameter (Van der Meer), $D_n = (W/\rho_r)^{1/3}$. The Eroded Volume Function (EVF) is defined as the corrected cumulative sum of the differences between the eroded profiles and the original profile. The damage is defined as the maximum value of the EVF.

Two spectral shapes ($\gamma=1$ & $=10$); two envelope exceedance coefficients (high & low α); four phase shifts ($\psi=0, 2\pi/3, 4\pi/3,$ & 2π); two rock sizes ($W_L=13$ kg. and $W_S=10$ kg.); and seven wave runs of increasing energy (Eq. 16)

gave a total number of 512 rock profiles and 224 values of damage. Damage observations from runs $\psi=0$ & $=2\pi$ were used as replicates in order to estimate the statistical variability of the experiments. A comparison between the results obtained from $\psi=2\pi/3$ & $=4\pi/3$ demonstrated that no significant difference was observed by changing the phase shift, ψ . Therefore, the experiments contain four replicates for each of the seven runs with the values of the parameters γ , α , & W held constant.

Measurements of damage at different levels of wave energy were recorded. In order to compare with the definition of damage in the S.P.M. (1984), the breakwater crest elevation was assumed to be equal to the design wave height. The active zone of damage for the experiment ($K_D=4$, $\cot \beta=2$, and $\rho_r/\rho_w=2.74$) was about $31D_n^2$. The data for damage given in the S.P.M. (1984) may then be reasonably approximated by

$$\frac{H_s}{\left[\frac{\rho_r}{\rho_w} - 1 \right] D_n} = N_s = 1.15 [\cot \beta]^{\frac{1}{3}} \sqrt{D} \quad (17)$$

where D is the damage or normalized eroded armor; β is the slope; N_s is the stability number; and $D_n=(W/\rho_r)^{1/3}$ is the nominal diameter. We note that Van der Meer and Pilarczyk (1987) have proposed a different equation.

It would be possible to compare the damage function proposed by Van der Meer (1988) using values for $P=0.2$ (low permeability), $\xi_z=2.2$, and $M=1100$ waves with the damage function estimated from Eq. 17. However, the Van der Meer formulae (1988) were not used for comparisons because they depend critically on the value of the permeability parameter which is too difficult to estimate for design. Van der Meer and Pilarczyk (1987) suggest typical values for P for typical cross sections. However, the two cross sections used in our experiments have values for $0.1 < P < 0.4$. Consequently, estimates of damage may vary by as much as 50% about the average value of $P=0.2$. Because the selection of the parameter P is too subjective to use for design, we have not included the Van der Meer formulae in our comparisons.

Both Eq. 17 and the Van der Meer formulae (1988) suggest a fifth power relationship between damage and the significant wave height. Figure 2 compares the following experimental data for the small size rock: a) envelopes E1 ($\gamma=10$, $\alpha=1.8$) and E3 ($\gamma=10$, $\alpha=0.5$); b) envelopes E2 ($\gamma=1$, $\alpha=1.6$) and E4 ($\gamma=1$, $\alpha=0.5$); c) envelopes E1 and E2; and d) envelopes E3 and E4. The damage function estimated by Eq. 17 and 95% confidence intervals for the experimental data are also included in Fig. 2. Comparisons for the large size rock were similar.

Figure 2 demonstrates that damage produced by envelopes E1 and E2 were similar and clearly higher than damages produced by envelopes E3 and E4. This implies that the mean run length and spectral shape are not relevant for estimating armor stability. On the contrary, the envelope exceedance pattern significantly affects the stability. In addition, the surf similarity parameter significantly affected the stability because all of the damage functions for small size rocks gave systematically higher values than those for large size rocks (with a ξ_z 4.5% lower).

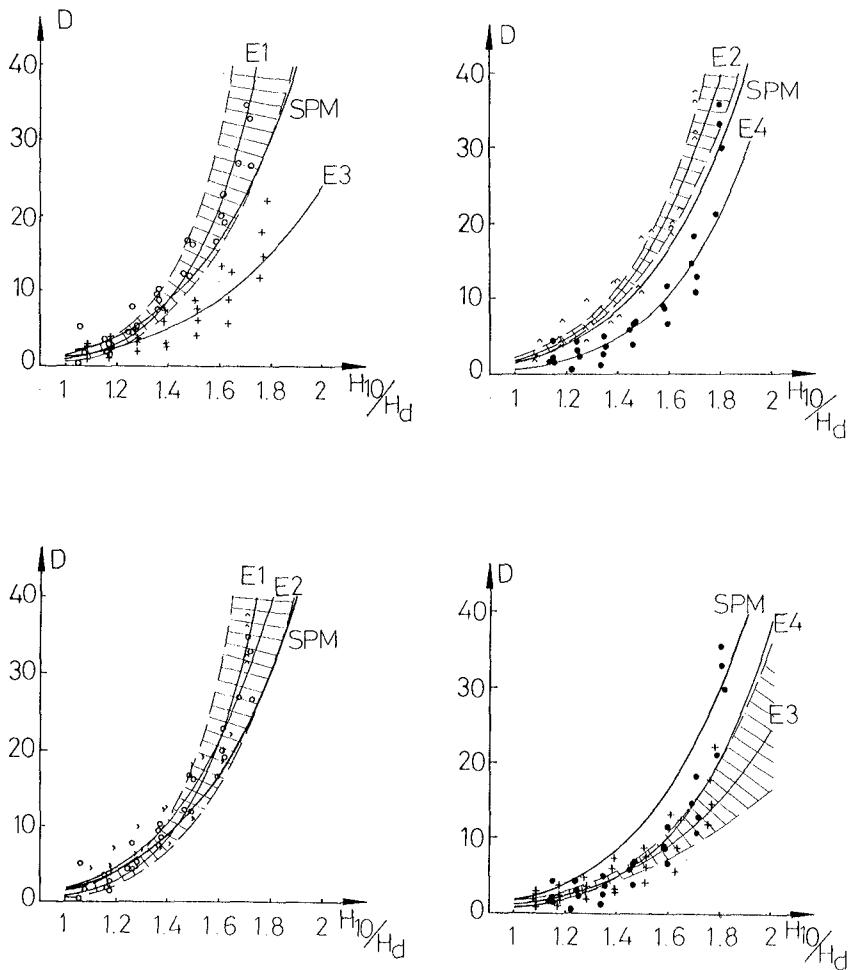


Fig. 2. Comparison of Damage to Small Rocks: a) Narrow & b) Broad Spectra; c) High & d) Low α .

In the past, characteristics of wave groups have only been correlated with spectral peakedness, with mean run lengths, or with other related groupiness parameters. These groupiness parameters have not proven to be completely satisfactory for determining the stability of the armor layers. However, our experimental data demonstrate that wave envelopes may be correlated with stability. Two wave trains incident at the toe of a structure, having exactly the same spectral shape and Rice groupiness parameter, may have significantly different wave envelope functions. By analyzing the wave envelope function as a measure of wave groupiness, it is possible to determine the one that will cause the more damage.

The envelope exceedance coefficient, α , may be related to a groupiness factor, not as defined by Rice, but by $GF = \sigma[H^2(t)]/8m_0$. This definition may not be calculated by the SIWEH as proposed by Funke and Mansard (1979). If the GF were calculated by the SIWEH, it would be biased and would depend on the spectral shape in a way similar to the Rice definition. Our definition for a GF was found to be highly correlated with the envelope exceedance coefficient α computed from analyses of 1000 DSA random simulations for the two spectral shapes used in the experiments (viz., $\gamma=1$ & $=10$). For both of these values of γ , a linear relationship given by $GF=(9+\alpha)/10$ was found to correlate with the simulated data at the 90% confidence level. The mean value of α is $E[\alpha]=1$ by definition and the standard deviation depends on the spectral shape; e.g., $\sigma[\alpha] \approx 0.45$ if $\gamma=10$ & $\sigma[\alpha] \approx 0.30$ if $\gamma=1$.

CONCLUSIONS

The envelope exceedance coefficient, α , defined by Eq. 15 and correlated with the groupiness factor, $GF = \sigma[H^2(t)]$, is a groupiness parameter which controls the stability. Random wave trains in wave flumes may have exactly the same spectral shape, but cause different levels of damage to the armor. The groupiness parameters α or GF may be able to resolve as much as 50% of the variability of the mean damage for a given design sea state and storm duration.

The spectral shape and the number of waves alone are not sufficient to describe the characteristics of wave groups and amount of armor erosion. Wave groups are more appropriately described by the parameters given for the envelope exceedance coefficient, α , or for the groupiness factor defined by $GF = \sigma[H^2(t)]/8m_0$. The spectral peakedness parameter and the mean run lengths are incomplete parameters for analyzing armor stability.

The influence of wave groupiness on armor stability may be of the same order of magnitude as the storm duration. The statistical variability of the observations, and the limited number of cases analyzed in these experiments do not permit a more precise description of the effects of wave groups on the stability of rubble mound breakwaters. However, for a preliminary design, it appears to be

reasonable to modify existing formulae for damage functions by a factor of $(\alpha)^{1/2}$. The envelope exceedance coefficient, α , in random seas demonstrated a log-normal distribution having $E[\alpha]=1$ and $\sigma[\alpha]$ ranging from $[0.30 < \alpha < 0.45]$ depending on the spectral shape.

ACKNOWLEDGEMENTS

We gratefully acknowledge the financial support provided by the following agencies: The Dirección General de Investigación Científica y Técnica, under Grant PB88-0353; The Office of Naval Research under the University Research Initiative (ONR-URI) Contract No. N00014-86-K-0687; and The Oregon Sea Grant and the National Oceanic and Atmospheric Administration, Office of Sea Grant, Dept. of Commerce, under grant no. NA85AA-D-SG095 (project no. R/CE-21) and from appropriations made by the Oregon State Legislature.

REFERENCES

- Battjes, J.A., and Vledder, V. (1984): "Verification of Kimura's Theory for Wave Group Statistics," *Proceedings*, 19th ICCE, 1984, Houston, TX, 642-648
- Bruun, P. (ed.), (1985): *Design and Construction of Mounds for Breakwaters and Coastal Protection*, Elsevier Science Publ., Amsterdam, The Netherlands.
- Burchart, H.F. (1979): "The Effect of Wave Grouping on On-Shore Structures," *Coastal Engineering*, No. 2, 189-199.
- Funke, E.R. and Mansard, E.P.D. (1979): "On the Synthesis of Realistic Sea States in a Laboratory Flume," *HLR Report LTR-HY 66*, National Research Council of Canada, Ottawa.
- Goda, Y. (1983): "Analysis of Wave Grouping and Spectra of Long-Traveled Swell," *Report of the Port and Harbour Research Institute*, Vol. 22, No. 1, 1983.
- Goda, Y., and Suzuki, y. (1976): "Estimation of Incident and Reflected Waves in Random Wave Experiments," *Proceedings*, 15th ICCE, 1976, Honolulu, Hawaii, 828-845.
- Hudspeth, R.T., and Medina, J.R. (1988): "Wave Groups Analyses by the Hilbert Transform," *Proceedings*, 21st ICCE, 1988, Torremolinos, Spain, 884-898.
- Johnson, R.R., Mansard, E.P.D., and Ploeg, J. (1978): "Effects of Wave Grouping on Breakwater Stability," *Proceedings*, 16th ICCE, 1978, Hamburg, Germany, 2228-2243.

Mase, M., and Iwagaki, Y. (1986): "Wave Group Analysis from Statistical Viewpoint," *Proceedings*, Ocean Structural Dynamics Symposium '86, Corvallis, OR, 145-157.

Medina, J.R. and Hudspeth, R.T. (1987): "Sea States Defined by Wave Height and Period Functions," *Proceedings*, IAHR Seminar on Wave Analysis and Generation in Laboratory Basins, 22nd IAHR Congress, Lausanne, Switzerland, 249-259.

Medina, J.R. and Hudspeth, R.T. (1990): "A Review of the Analyses of Wave Groups," Coastal Engineering, (in press).

Medina, J.R., and McDougal, W.G. (1990): "Deterministic and Probabilistic Design of Breakwater Armor Layers" (Discussion), Journal of Waterway, Port, Coastal and Ocean Engineering, 116(4), 508-510.

Rice, S.O. (1954): "Mathematical Analysis of Random Noise," *Bell System Technical Journal*, Vol. 23, 1944, and Vol. 24, 1945. (Reprinted in *Selected Papers on Noise and Stochastic Processes*, N. Wax, Ed., Dover Publications, Inc., New York, NY, 1954, 123-244.)

Rye, H. (1982): *Ocean Wave Groups*, Dept. Marine Technology, Norwegian Institute of Technology, Report UR-82-18.

Shore Protection Manual (1984). Coastal Engineering Research Center, Department of the Army, Waterways Experiment Station, Vicksburg, Miss.

Van der Meer, J.W. (1988): "Deterministic and Probabilistic Design of Breakwater Armor Layer," Journal of Waterway, Port, Coastal and Ocean Engineering, 114(1), 66-80.

Van der Meer, J.W., and Pilarczyk, K.W. (1988): "Stability of Breakwater Armor Layers. Deterministic and Probabilistic Design," Delft Hydraulics Communication No. 378, 12, 18, and 19.

CHAPTER 117

Monitoring hydraulic loads on the Eastern Scheldt Storm Surge Barrier

Leo Klatter¹, Jan Konter² and Tom Jongeling³

1. Abstract

The paper describes the monitoring program that has been set up for the hydraulic loads on the Eastern Scheldt Barrier. The strategy for the measurements will be discussed in detail. The results of the measurements, that have been performed yet, will be presented. These results are discussed only briefly, because the evaluation of the results has not been completed yet.

2. Introduction

The Eastern Scheldt Barrier is located in the mouth of the Eastern Scheldt and is built across the three main channels; Hammen and Schaar both one kilometer wide and Roompot two kilometers wide (See figure 1). The barrier consists of 62 basic sections. Such a basic section is 45 m wide and is built up as following (See figure 2):

The sandbed is covered by a filtermat. On these mat concrete piers are placed. The final flow opening is framed by a concrete sill beam and an concrete upper beam. A steel gate driven by hydraulic cylinders can close the flow opening. On top of the piers a motorway bridge is located. The piers and sill beams are packed in by a rubble sill structure.

All structural elements were prefabricated at a remote construction site, and have been placed by heavy floating equipment.

^{1,2} Rijkswaterstaat, Construction, Hydraulic Department
P.O.box 20.000, 3502 LA Utrecht, The Netherlands

³ Delft Hydraulics, P.O.box 152, 8300 AD Emmeloord, The Netherlands



Figure 1: Location of the Eastern Scheldt Barrier

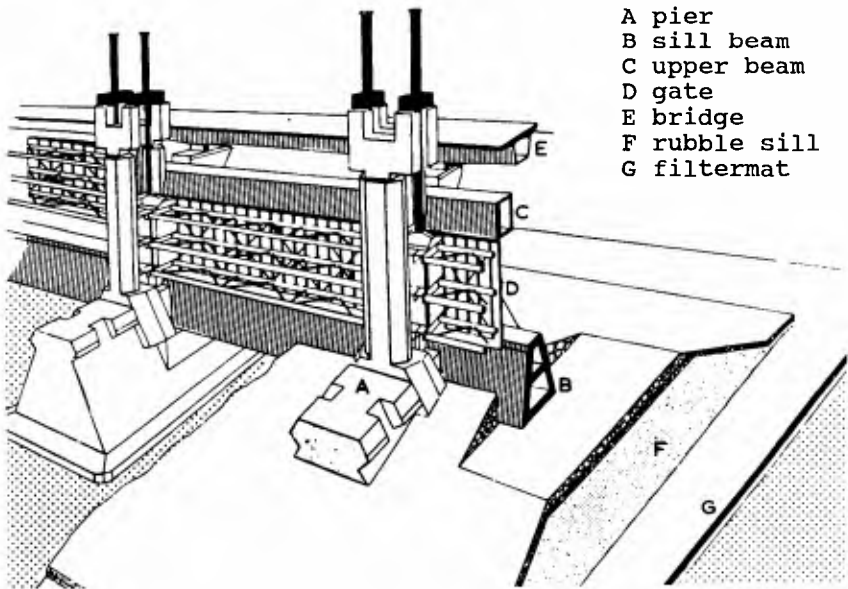


Figure 2: Elements in the Eastern Scheldt Barrier

3. The monitoring system

In an early stage of the design of the barrier it was decided to set up a monitoring program for the entire barrier project (See van Westen, 1990 for the effects of the barrier on environmental aspects).

This paper describes the monitoring system for the hydraulic loads on the barrier itself.

The need for this monitoring system is dictated by the following reasons:

- The innovative design concept called for extrapolation of existing techniques and development of new techniques.
- The probabilistic design coupled the design loads and the rules for operating the barrier. Incertainties in the design are "balanced" against each other.
- The design concept with large prefabricated elements placed on a sand bed foundation made construction tolerances and later deformations critical items.
- The design lifetime of the barrier of 200 years made evaluation of subjects as fatigue of the steel gates and life time expection of geotextiles necessary.

A monitoring system has been designed by the Dutch Rijkswaterstaat and its contractors, in close cooperation with Delft Hydraulics and Delft Geotechnics.

The following items are monitored:

- The hydraulic boundary conditions; waves, waterlevels and currents.
- The loads on the structural elements with special attention for:
 - steel gates; effect of wave impacts, stress variations and response of the gates.
 - upper beam; wave impacts and the response of the beam.
- Foundation aspects (van Heteren et al, 1988). The measurement system is set up to enable a trace back of the forces (by waves and waterlevel difference) through the structure and the response of the foundation; pore pressures and deformations of the subsoil.
- Concrete technological items.
- The behaviour of the rubble sill, bedprotection and scour holes.

It is obvious that it is impossible to measure every item at every pier location. The following strategy has been chosen: extensive measurements are performed at selected locations. In the Schaar-channel at gate S13 and pier S9, in the Roompot-channel around pier R22, gate R21 and upper beam R20 (See figure 3).

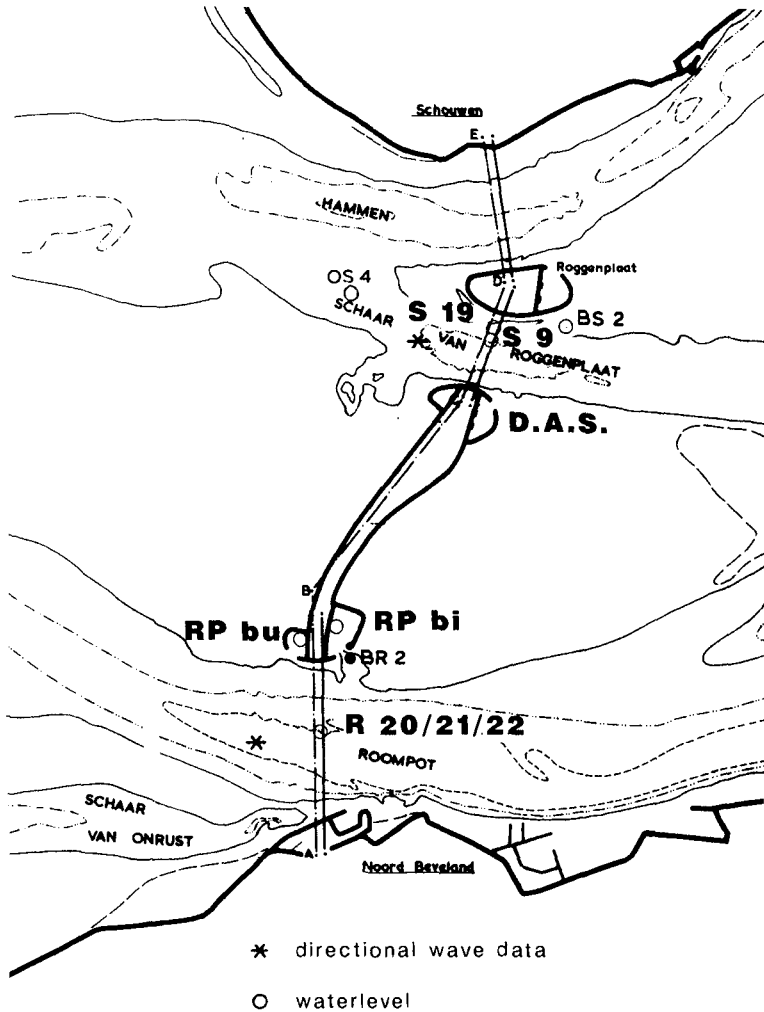


Figure 3: Measurement locations

At all pier locations the overall displacements are measured once a year. Most of the measurements are concentrated during storm closures the of the barrier, with additional campaigns for example to determine natural frequencies of the gates.

All measured data are gathered by a data acquisition system (DAS). The large number of sensors, over 250, with frequencies ranging from 10 - 1000 Hz made a powerful computer system necessary. The DAS is located in the operating post (figure 3).

Before results of the measurements will be presented, attention will be paid to the difference between field measurements and model tests:

- In model tests the boundary conditions that are applied, are mostly even more extreme than the design conditions. Field measurements however are likely to take place under rather moderate conditions.
- Model tests are these days performed in conditioned, sheltered areas while field conditions are relatively rough.
- This is important for the selection of the instruments.
- Model tests are planned operations. Field measurements are occasional operations and the conditions for the measurements are more or less a surprise.
- Model tests are relatively cheap compared to field measurements.
- Model tests can be repeated. In field measurements, of say once a 10 years conditions, failure, one has to wait for another 10 years (statistically) before these measurements can be repeated.

Because of the items mentioned above, translation problems will occur when interpreting field measurements: To evaluate the design, the level of the field measurements has to be translated to the design level, with the complication that the design level of the structure, as built, may differ from the theoretical design level.

The results of the measurements are valid at the measuring locations only. So the results have to be translated to other locations or well, for a complete evaluation of the design of the barrier.

When one compares the results of the field measurements with those from model tests, again a translation to another level and/or other location has to be performed. The translation problems, related to the evaluation of the design with results of field measurements have to be considered thoroughly for the design of a monitoring system.

4. Measurements performed

Since the barrier has been completed in 1986, it still took some time to overcome problems encountered, mainly with the data acquisition system. By the end of 1988 the system became operational.

In december 1988 the first real measurements were performed. These were measuring campaigns were the single gates, R21 and S13 were closed to measure wave impacts and the response of the gates.

In February 1989 the first storm closure of the barrier was performed, and a complete measurement campaign has been performed then (see figure 4).

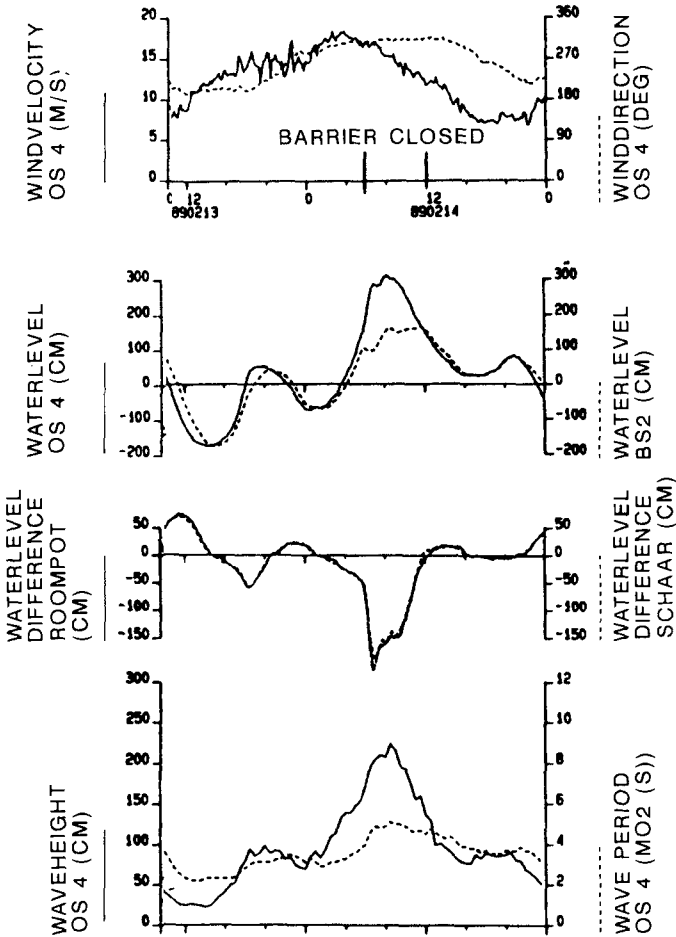


Figure 4: Storm report 13th - 14th February 1989

Westerly winds, with windspeeds between 15 and 20 m/s, caused a maximum waterlevel of 3.08 m above mean sea

level. The maximum waterlevel difference, with the barrier closed was 2 m, with wave heights of over 2 m (significant wave height).

In Oktober 1989 a special measuring campaign was performed to measure the natural frequencies of the gate S13. These are important for the interpretation of the dynamic response of the gates.

February 1990 a heavy storm occurred. This most recent storm was a succesfull one from monitoring point of view; westerly winds, with wind speeds over 20 m/s lasted for more than two days (see figure 5).

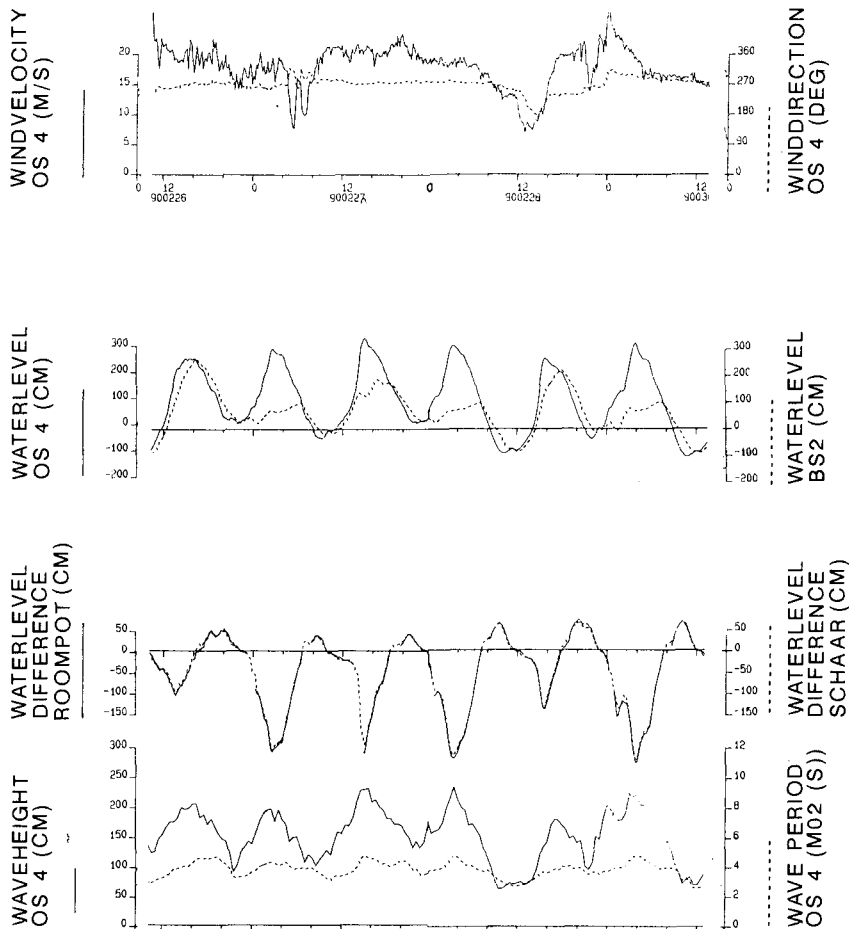


Figure 5: Storm report 26th February - 1st March 1990

The barrier has been closed four times. A maximum water level of 3.61 above MSL was reached. The maximum waterlevel difference was approx 2.4 m with the barrier closed. The significant waveheight reached almost 2.5 m.

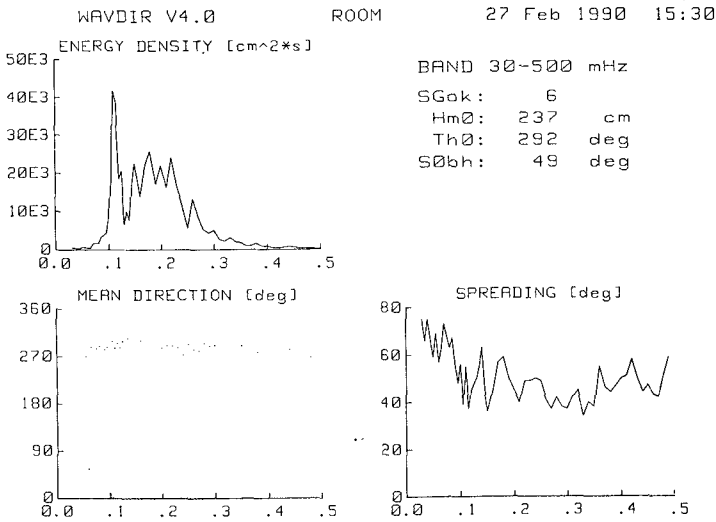


Figure 6: Registration WAVEC buoy

Figure 6 gives the spectral registration of the directional WAVEC buoy. The wave frequencies are in the range of 10 to 3 seconds. The average wave period is 5 seconds.

Rather rough conditions with caused a lot of damage to the Dutch coast. However compared with the design conditions the storm conditions were rather moderate; see table below:

design values	February 1990
waterlevel 5.4 , above MSL	3.6 m
waterlevel difference 5 - 6 m (*)	2.4 m
wave height 5 - 6 m (*)	2.5 m

(*) Due to the probabilistic design an exact design level cannot be given

Until now most of the 1989 data have been processed. The 1990 data are still being processed. Interpretation is planned together for all data.

5. Results

The following paragraph gives an overview of the results of the measurements that were analysed until now. Most of the results are based on the 1989 data.

5.1 Wave impacts on upper beam

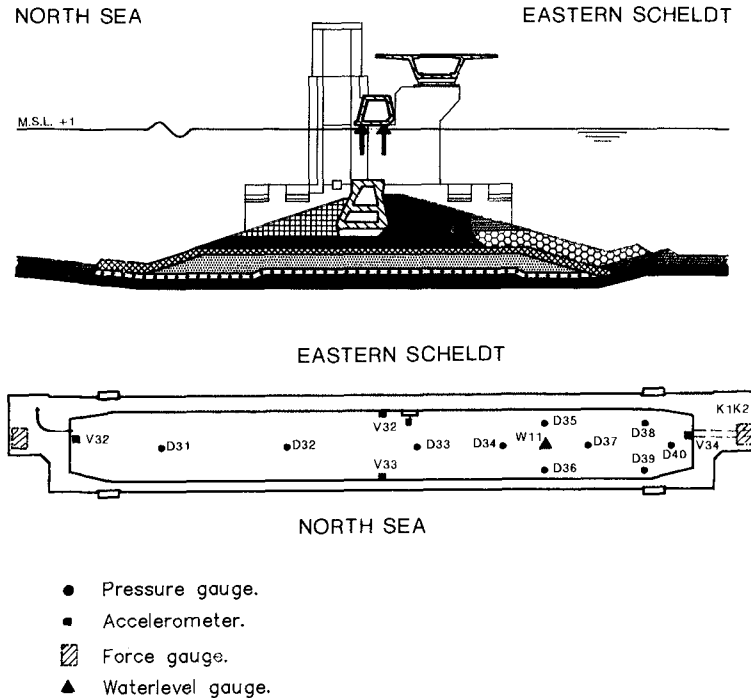


Figure 7: Instrumentation upper beam

When the gate is open, wave impacts against the bottom of the beam can be expected when the water level is in the vicinity of the bottom of the beam, which is at 1 m above MSL. The prestressed concrete beam is relatively light and is sensitive to these loads.

The upper beam is instrumented with pressure gauges, accelerometers, a force gauge in one of the supports and a waterlevel gauge (See figure 7).

As an example of the results, the registration of four pressure gauges are presented in figure 8.

The maximum pressure in this registrations is approx. 30 kN/m^2 with 1 m significant wave height.

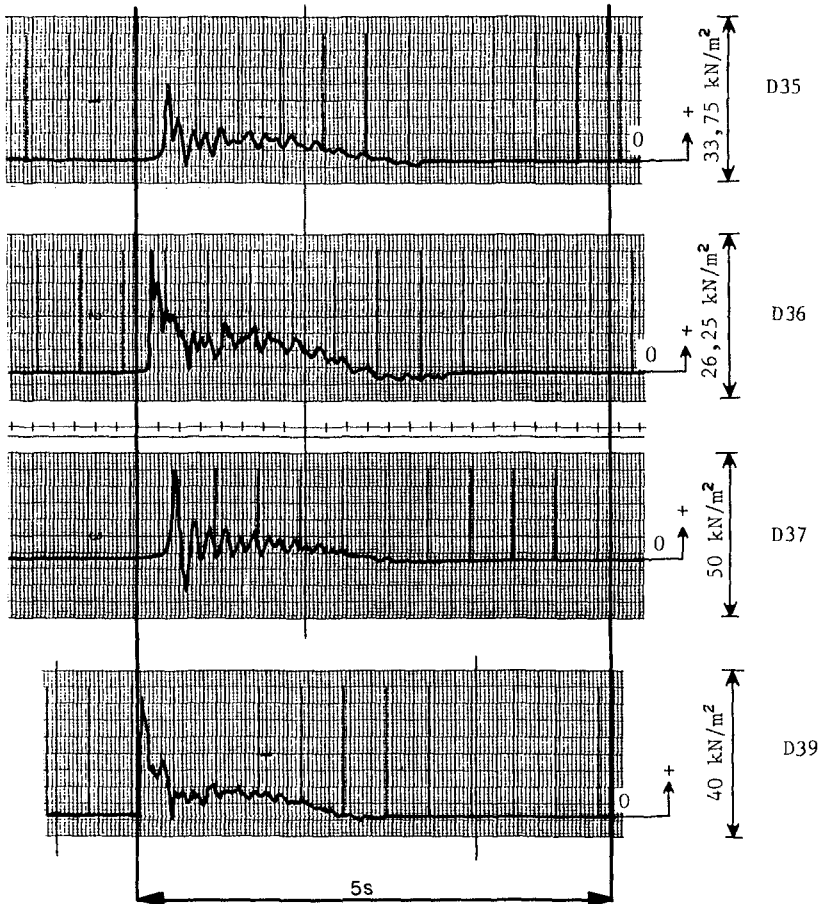


Figure 8: Registrations pressure gauges upper beam.

Figure 9 shows the registration the accelerometers in the middle of the beam and at the support, the registration of the force gauge in the support of the beam and the registration of the waterlevel under the beam. The interpretation and the evaluation of the design still have to be completed. Especially the area opposed to an impact is of importance here.

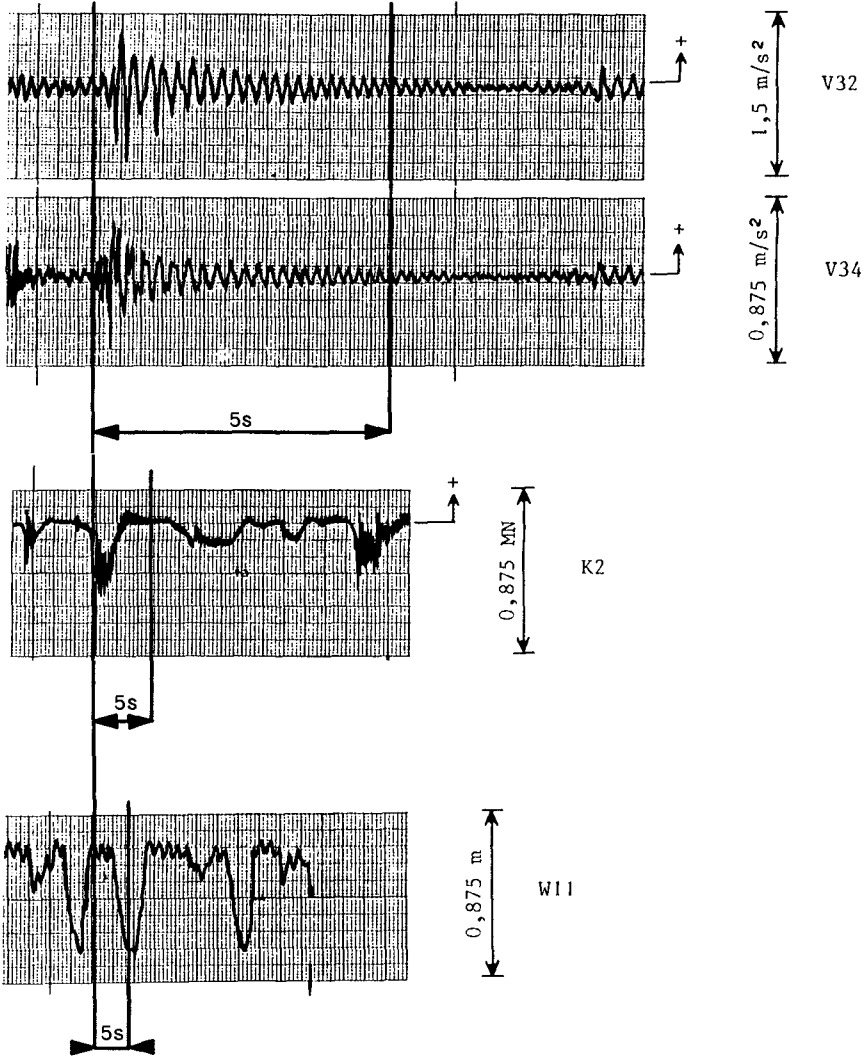


Figure 9: Registrations accelerometers, force gauge and water level gauge upper beam.

5.2 Wave forces on steel gates

The forces in the girder system of the gate are measured by strain gauges attached to the tubes of the girder system.

In this way the force distribution in a single node is measured by instrumenting all five connecting tubes. The horizontal and vertical lateral forces on the gate are measured indirectly by instrumenting six thross girders close to the supports of the gate.

Figure 10 gives an example of one of stress signals related to the lateral force in the gate. The figure gives the stress signal and the exceeding percentage of the stress amplitude.

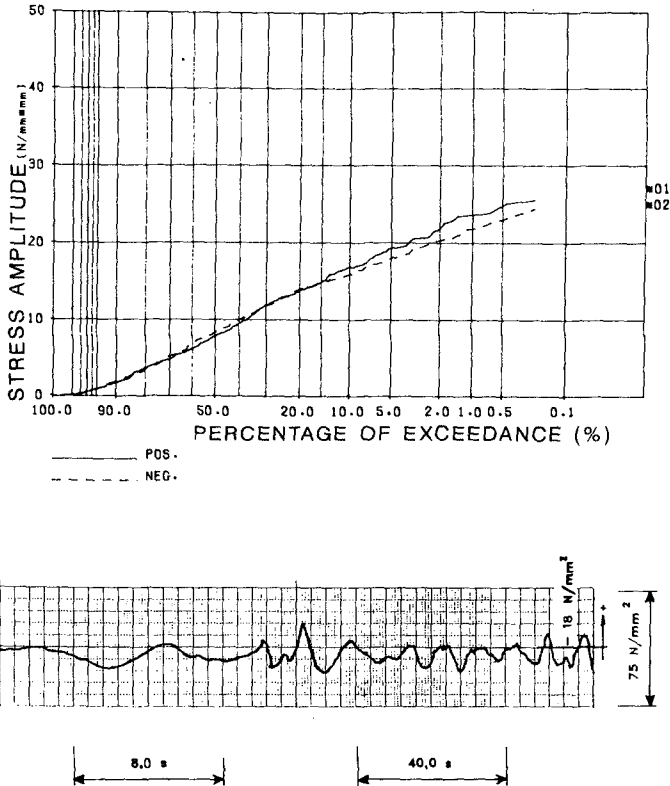


Figure 10: Registration stress signal (below) and exceeding percentage stress amplitude (top) of "lateral force gauge", gate S13.

Evaluation of these results is important, because the gates are constructed of a high strength type of steel that must be inspected on fatigue cracks. The results will be used to evaluate the inspection strategy of the gates.

Wave impacts on the girder system of the gates occur when the girders cross the waterlevel. Impacts have been recorded during the 1990 storms and are under evaluation.

5.3 Boundary conditions

The evaluation of the boundary conditions has been concentrated on waterlevels en flow parameters, and the validation of the flow models that were used for the design (Klatter et al, 1989).

Further the discharge coefficients of the barrier were determined.

Still under evaluation are the result of wave models for reflection coefficient and effects of crest length of the waves.

5.4 Foundation aspects

To evaluate the geotechnical aspects, measurements were performed of pore pressure generation and dynamic deformation of the subsoil. To evaluate these aspects much more measuring data will be needed. The relatively low level of the loads, compared to the design conditions makes an evaluation of the results, especially of the accelerometer data very difficult.

5.5 Bed protection

The bed protection has been monitored by acoustic and visual inspections. These inspections were mainly used to trace damages in the bed protection due to the construction activities of the barrier. Additional field measurements were performed to determine the design load of the critical part of the bed protection close to the barrier. Herefore pilot locations were fitted up with relatively light stones. These locations were carefully monitored and in this way the critical waterlevel difference for initial damage to the bed protection could be determined effectively.

6. Conclusions

The items that have been evaluated so far showed that a monitoring program is highly valuable for:

- optimization of the rules for the barrier operations, the closure and opening strategies of the gates.
- optimization of the inspection program.
- evaluation of the design tools, for example the flow models that were used for the design of the barrier.

Setting up a monitoring system requires much more than just rebuilding a scale model instrumentation at full scale.

- Certain phenomena can better be determined in model tests than in field measurements (eg. stability of rubble stone, liquefaction of the subsoil).
- A selection of a limited number of signals that are representative for the design problems is of vital importance.
- The measuring system should be redundant, critical sensors should be installed double.
- The translation of the measured signals to design conditions must be possible. One has to account for the relatively moderate conditions that can be expected in field measurements.
- The system must be an operational system. The latest high-tech, state of the art systems are likely to fail.
- Optimization is necessary, because the costs of a field monitoring system are extremely high. Not only the construction costs should be considered but also the maintenance costs and operational costs.

The experience is, that it is much easier to record a few giga-bytes of data than to retrieve, analyse and interpret these data.

References

- Heteren, J.v., Lindenberg, J. and Nelissen, H.A.M. (1988).
Verification of Geotechnical Design Criteria for the Eastern Scheldt Storm Surge Barrier.
Proc. IAHR symposium on Modelling Soil-Water-Structure Interactions, Delft, August 1988.
- Klatter, H.E., Dijkzeul, J.C.M., Hartsuiker, G. and Thabet, R.A.H. (1989).
Storm-Surge-Barrier Eastern Scheldt, Evaluation of the Water Movement Studies for the Design and Construction of the Barrier.
Report, Delft Hydraulics, code Z88, 1989
- Westen, C.J. van, Pieters, T. (1990).
The Eastern Scheldt: Monitoring and Evaluation.
Proc. 22nd ICCE, Delft, july 1990.

CHAPTER 118

Stresses in Tetrapods: Results of Large Scale Model Tests

Bürger, W.W.^{*)}; Oumeraci, H.^{**)}; Partenscky, H.W.^{***)}

Abstract

This paper intends to review the experimental research work performed at the University of Hannover on the structural stability of tetrapods. It presents particularly the first results from the hydraulic and pendulum tests which suggest that:

- the most critical location of the armour units with respect to structural stability has been found at and slightly above still water level;
- for regular waves a well defined relationship can be found between incident wave parameters and the induced dynamic and quasi-static stresses. In the case of irregular waves, however a clear relationship appears to exist only for quasi-static loads;
- the critical IRIBAREN-Parameter with respect to structural stability is in the same range as the one found for hydraulic stability;
- a linear relationship has been found between impact bending stress and impact velocity for the tested tetrapods 50 kg - 1.8 t.

1. Introduction

It is now widely accepted that not only the hydraulic stability but also the structural integrity of concrete armour units should be considered in the design of rubble mound breakwaters. Due to a number of diffi-

^{*)} Dipl.-Ing., Research Engineer

^{**)} Dr.-Ing., Senior Research Engineer

^{***)} Prof. Dr.-Ing. Dr.phys.

all University of Hannover, SFB 205, Franzius-Institut,
Nienburger Str. 4, 3000 Hannover 1, FRGermany

culties, no generally applicable criteria and procedures accounting for the breakage of the units and its effect on the whole armour stability are yet available. One of the difficulties is the determination of the actual load history for armour units in a breakwater environment.

The main objective of this paper is to contribute to a better understanding of the actual single impact loads and the subsequent impact stresses.

2. Description of the Research Program

The investigations on the structural behaviour of concrete armour units constitutes a part of an extensive basic research program on rubble mound breakwaters conducted at the University of Hannover and supported by the German Research Council (DFG) within the scope of the "Sonderforschungsbereich 205" (SFB 205). Aside from the research program on structural behaviour of concrete armour units, a number of aspects like hydraulic stability, internal and external flow field as well as geotechnical stability are also being investigated (BÜRGER et al., 1988). The different tests which has been performed on structural stability of the units are given in Fig. 1.

The main purpose of the hydraulic tests with respect to structural stability of the units was to determine the actual response of the units in a breakwater environment as a function of the incident waves and of the location of the units on the slope.

The static tests were primarily destined to calibration as well as to verification purposes related to the sensitivity of the measuring techniques used.

The pendulum tests have been performed, aside from other objectives (BÜRGER et al., 1989), in order to:

- a) compare the impact strain history of tetrapods with full cross section and of the same tetrapods with a reduced cross section,
- b) develop a correlation between the recorded response of the units in the hydraulic model and that in the pendulum tests,
- c) determine impact strain-time functions for instrumented model and prototype tetrapods.

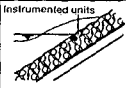

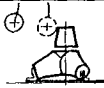

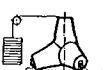
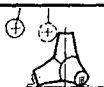

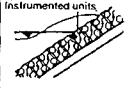
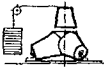
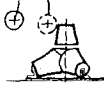

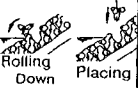

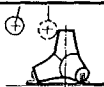


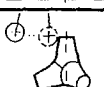


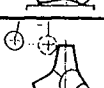

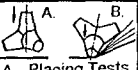
Units	Hydraulic Tests	Static Tests	Pendulum Tests	Drop Tests	Additional Tests
Tetrapods 1 kg (reduced cross section)					
Tetrapods 1 kg (full cross section)					
Tetrapods 50 kg (reduced cross section)					
Tetrapods 50 kg (full cross section)					
Tetrapods 250 kg (full cross section)					
Tetrapods 1.8 t (full cross section)					

Fig. 1 Review of performed tests on structural stability at the University of Hannover

The results of the aforementioned experimental investigations, together with available results from basic research on impact and cyclic loading of concrete are intended to be used for the development of design criteria for the structural stability of the units.

Although a reliable design of concrete armour units with respect to their mechanical strength requires the consideration of all loads and environmental impacts (BÜRGER et al., 1989), the most relevant loads, however, are induced by the combined action of waves and the weight of the units.

3. Large Scale Hydraulic Model Tests

3.1 Description of the Breakwater Model and the Instrumented Units

Fig. 2 shows the cross section of the model in the Large Wave Channel, Hannover.

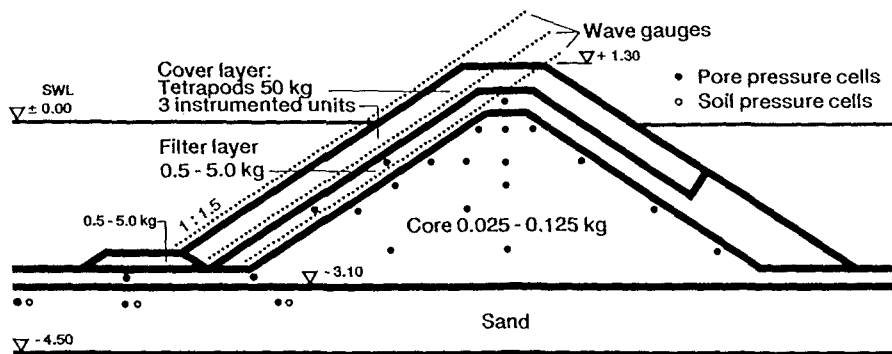


Fig. 2 Cross section in the Large Wave Channel (GWK)

The instrumented tetrapods used in the hydraulic tests had a reduced cross-section in order to measure the wave-induced static loads, quasi-static loads and to a certain extent also dynamic loads (Fig. 3).

Each of the oppositely applied strain gauges on the square steel bar was assigned to one recorder channel. Two signals are thus obtained on channels 1 and 2, respectively, when the tetrapod leg is subjected to load.

3.2 Calibration of the Instrumented 50 kg-Tetrapods

The sensitivity of the measuring instruments and the necessary amplification factor for the tests can be determined by calibration.

By increasing the load, the linearity of the measured values can be checked and both hysteresis and creep effects may be detected.

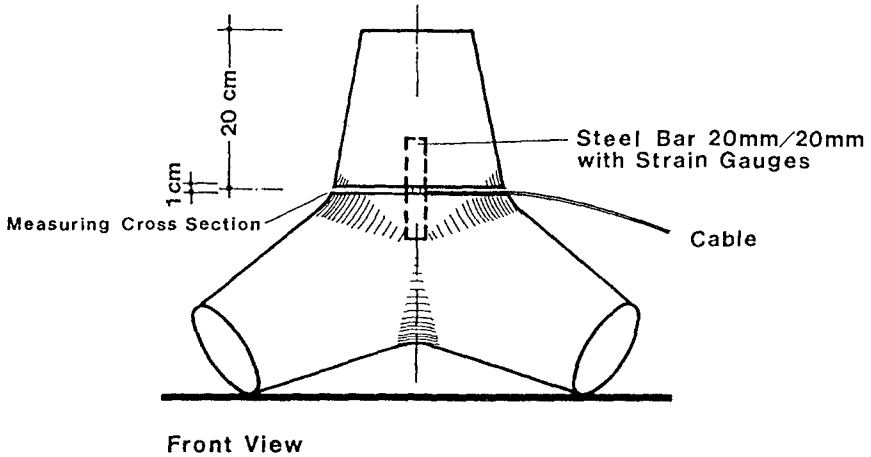


Fig. 3 50 kg-tetrapod with reduced cross section

On the test rig (Fig. 4) the tetrapod is centrally fixed and the load is transferred horizontally to the upwards directed leg by hanging on calibrated weights up to 100 kg in increments of 10 kg.

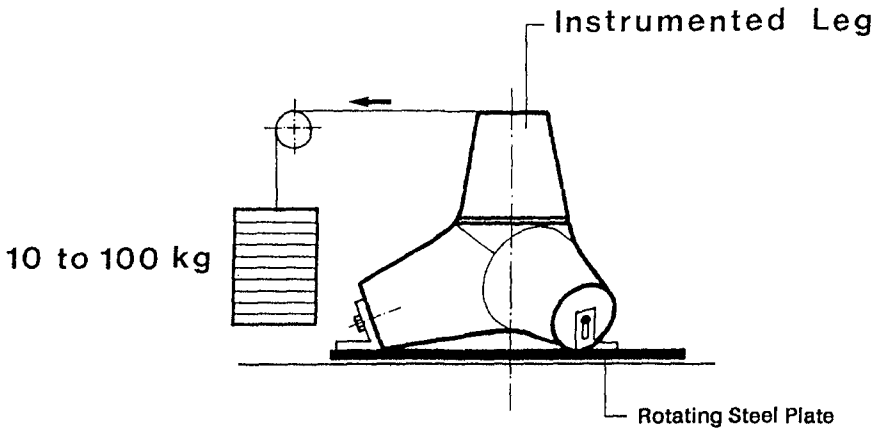


Fig. 4 Set-up for static tests

Strain and bending moments for both axes were recorded at each stage of loading. Thereafter, the leg was unloaded, the steel plate was rotated and the instrumented leg loaded once again.

To check the long-term behaviour of the strain gauge applications and also to determine whether a single calibration value was valid for all tests, a calibration was performed after each series of the hydraulic tests.

3.3 Testing and Recording Procedures for the Hydraulic Tests

3.3.1 Testing Procedure

Since the forces acting on a unit will show a large variability based on the units location and the wave climate, the tests covered up all critical locations on the breakwater (Fig. 5) and were performed with both regular and irregular waves, started with low wave conditions and increased in steps of 10 - 20 cm until a significant unit movement was observed.

After every test series, the cover layer was completely removed and reconstructed by the same persons, to ensure as far as possible similar positions of all tetrapods and similar porosity in all tests.

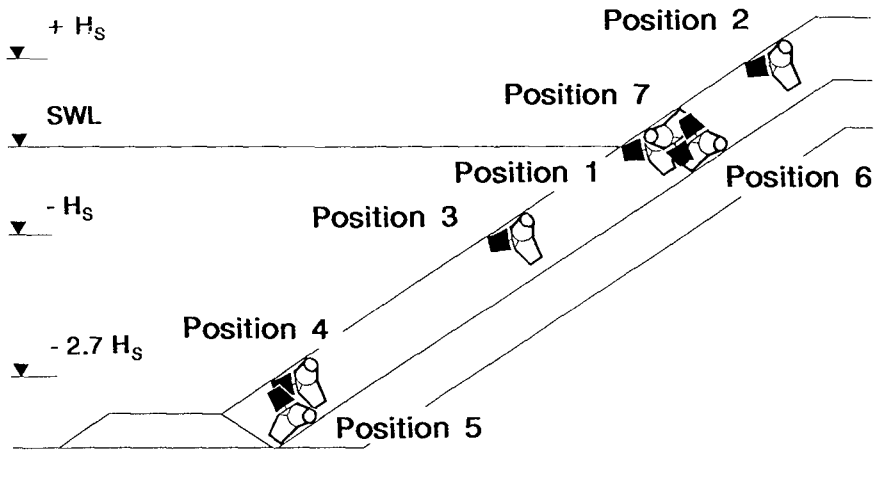


Fig. 5 Positions of the instrumented tetrapods

3.3.2 Data Collection and Recording Procedure

The measured data were recorded at a sampling frequency of 400 Hz. At the same time, the measured values were also registered at a sampling frequency of 11000 Hz by a Video Pulse Code Modulator (Video PCM).

All tests were recorded using two video cameras, one recording the whole armour layer, and the other one the instrumented units. So the movements, rocking or displacement, can be compared with the measured strain data.

Before and after every test, photographs were taken in order to determine the changes which occur in the whole armour layer and the instrumented units.

3.4 Data Reduction

Among the more recent results of hydraulic model tests using instrumented armour units only those of ANGLIN et. al. (1988) are related to the analysis of quasi-static load data. High frequency signals related to impact loading are not measured or are filtered out. However, only regular waves are used for the tests. Therefore, only an averaging procedure for the analysis of the results is adopted; i.e. the average load is determined for each test and then correlated to the wave parameters tested.

In contrast to this approach the tests performed in the Large Wave Channel at the University of Hannover are based on regular and irregular waves and consider all types of loads: static, pulsating and impact loads as well as slamming.

For the irregular wave tests, however, it is necessary to analyse the correlation between the single wave and the induced load. For the tests with more than one thousand waves the interaction between wave parameters and resulting load has to be described individually; i.e. separately for each wave.

The results of the static and dynamic calibration are two calibration factors, one for the static load, pulsating load and slamming (all together called quasi-static load), and the other for the dynamic load. Since the quasi-static and the dynamic load could not be measured separately, the recorded load signal should be splitted into a quasi-static and a dynamic part by a

computer program developed for this purpose. This computer program provides a table containing the wave parameters and the resulting quasi-static and dynamic load for both channels of each tetrapod.

The steps of the program may be described as follows:

1. Identification of the wave occurrence and calculation of the wave duration by analysing the time series of the run-up gauge placed along the slope;
2. Determination of the wave height by analysing the time series of the wave gauge installed in front of the breakwater;
3. Step by step analysis of the measured strain-history for each instrumented tetrapod and both channels;
 - a) Adjustment to zero separately for every time window;
 - b) Calculation of the quasi-static strain by filtering the high-frequency signals;
 - c) Determination of the resulting maximum quasi-static strain according to the following formula:

$$\epsilon_{qs} = \sqrt{\epsilon_{qs1}^2 + \epsilon_{qs2}^2} \quad (1)$$

- d) Evaluation of the dynamic strain by determining the difference between the zero-adjusted raw data and the quasi-static strain;
- e) Determination of the maximum impact strain according to the following formula:

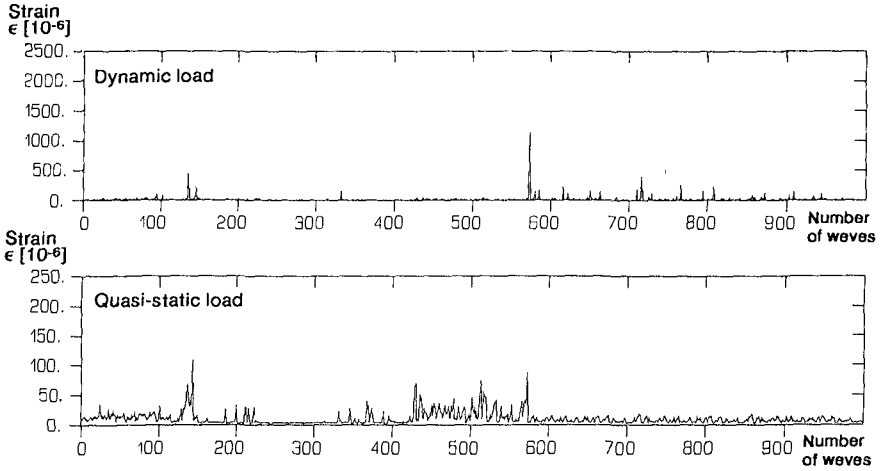
$$\epsilon_d = \sqrt{\epsilon_{d1}^2 + \epsilon_{d2}^2} \quad (2)$$

- f) Print out of the values in a table for each test.

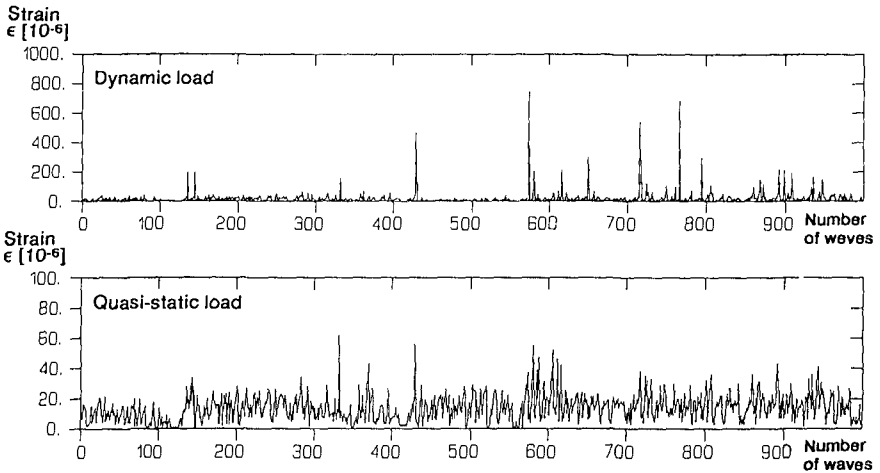
Fig. 6 a) and b) show the separated signals in the same test for both dynamic and quasi-static load and for two different positions of the instrumented tetrapods.

3.5 First Results

The position of each individual tetrapod is of a stochastic nature. When installing the instrumented tetrapods, it is not possible to position the instrumented legs in such a way that the pre-loading



a) Tetrapod D Position 1



b) Tetrapod F Position 7

Fig. 6 Strain records (Wave conditions: JONSWAP-Spectrum, $H_g = 0.90$ m, $T_p = 4.5$ s)

(static loading) is the same from one test series to the next. This also means that the point of contact between an instrumented tetrapod and its neighbouring one is not reproducible. Each reinstallation therefore represents a new loading variant.

Although the tetrapods occupy the same positions shown in Fig. 5 for various periods in the test series, the points of contact, and thus the strain or bending moments, are not directly comparable. As a rule, each test with new wave parameters and settlement during the running tests implies new bearing conditions.

Therefore, a first attempt to determine a relationship between strain and corresponding incident wave parameters resulted in a large scatter of the data, particularly for large wave heights (BÜRGER et al., 1989). Linear regression analysis led to correlation coefficients in the same range as found by ANGLIN et.al. (1988). However, a better correlation could be obtained by considering only the maximum strain-values (BÜRGER et al., 1989).

From the analysis of the data related to the location of the instrumented tetrapods, the highest wave-induced stresses within the tetrapods generally occur at and slightly above the still water level.

Some results from the tests with irregular waves are shown below.

Selected are the locations 1 and 7. The results of one tetrapod with position 1 and those of one tetrapod with position 7 are presented.

Fig. 7 a) & 7 b) show the wave induced strain vs. the IRIBARREN-Parameter for position 1 and for quasi-static and dynamic load, respectively. The same relationship is shown in Fig. 7 c) & 7 d) for position 7. It appears that the maximum dynamic strain is an order of magnitude higher than the quasi-static one. However, both occur at the same IRIBARREN-parameter ($I = 3.0$).

4. First Results of Pendulum Tests

As shown in Fig. 1, pendulum tests have been performed on 1 kg- and 50 kg-Tetrapods with a reduced and a full cross-section, as well as on 250 kg - and 1.8 t - tetrapods with full cross-section.

A detailed description of the tests and some results have already been published (BÜRGER et al., 1989).

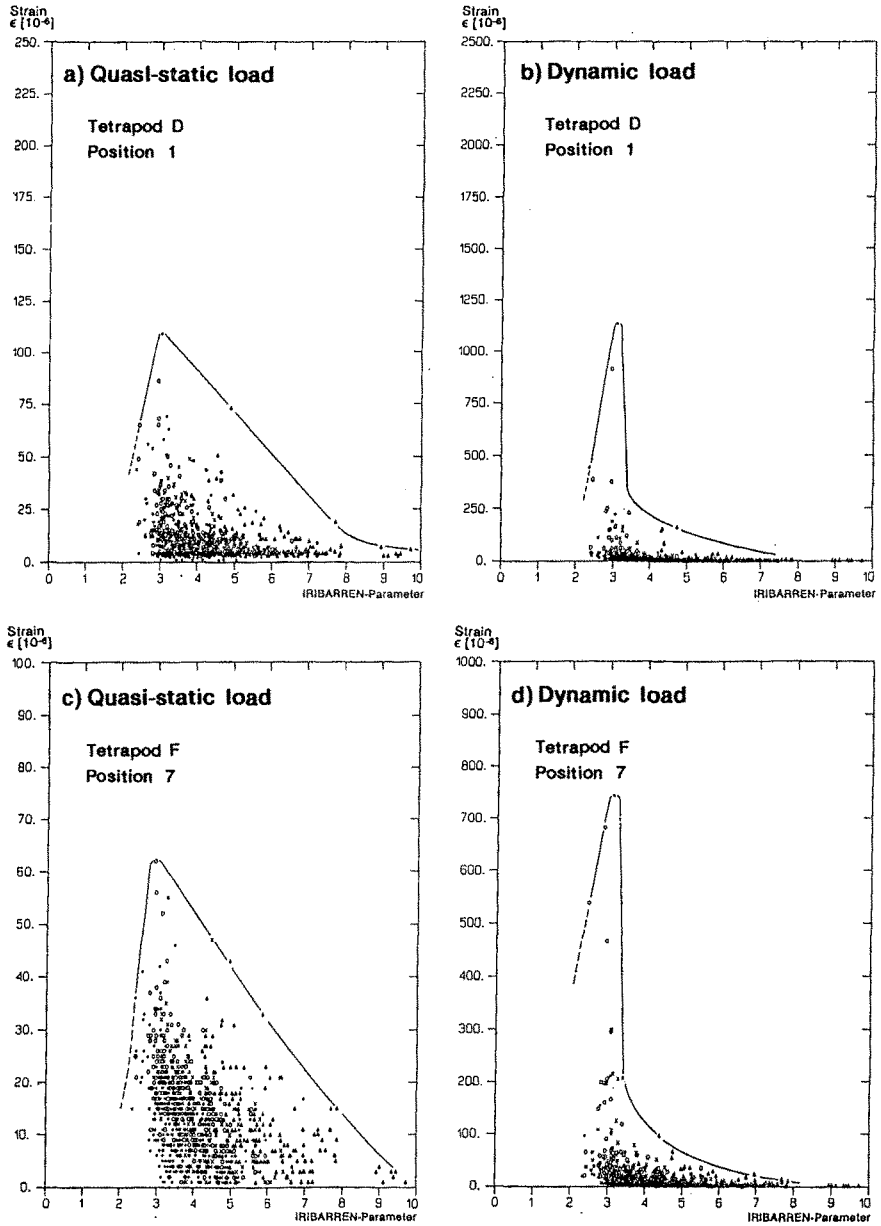


Fig. 7 Quasi-static and dynamic strain vs. IRIBARREN - Parameter (JONSWAP-Spectrum, $H_S = 0.90$ m, $T_p = 4.5$ s)

Considering the range of accuracy of the measurements and the range of the strain rate investigated ($\dot{\epsilon} = 0.061$ to 1.0 s^{-1}) Fig. 8 suggests that a linear relationship between dynamic bending stress σ and impact velocity v appears to exist for the tested tetrapods (50 kg to 1.8 t); i.e. the following relationship holds:

$$\frac{\sigma_{T1.8}}{v_{T1.8}} = \frac{\sigma_{T250}}{v_{T250}} = \frac{\sigma_{T50}}{v_{T50}} \quad (3)$$

where the indices T1.8, T250 and T50 refer to the 1.8 t, 250 kg- and 50 kg-tetrapods, respectively.

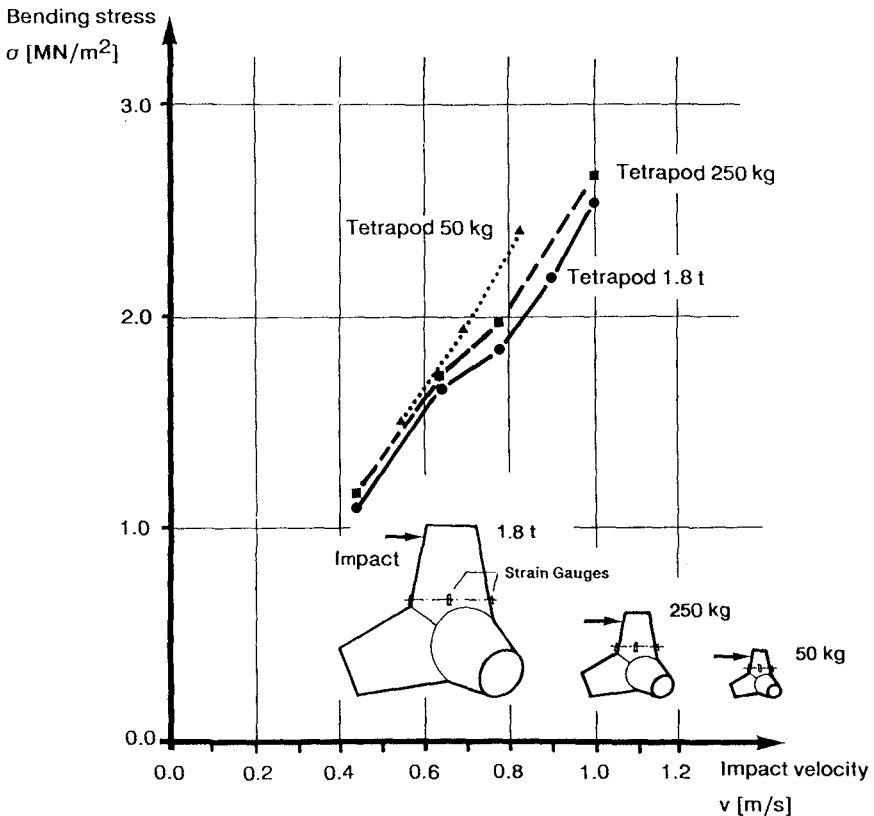


Fig. 8 Bending stress vs. impact velocity for the tested tetrapods

This supports the similitude criterium derived by NISHIGORI, et al. (1985) which suggests that the impact stress in the model (σ_m) is related to that in the prototype (σ_p) by:

$$\frac{\sigma_m}{\sigma_p} = \sqrt{\lambda} \quad (4)$$

where λ is the linear scale factor.

5. Perspectives

Within the scope of the ongoing analysis of the data it is planned to:

- . clarify the similitude problems related to the transfer of the measured impact strains to prototype conditions;
- . include the data related to static loading of the tetrapods in the analysis, so that the total loading can be assessed;
- . elaborate a design procedure with respect to the structural stability of tetrapods based on the experimental results and on an extensive literature study.

6. References

- | | |
|-----------------|--|
| ANGLIN, C.D.: | Wave-Induced Forces in Concrete Armour Units. |
| SCOTT, R.D. | |
| TURCKE, D.J. | IAHR, 23rd Congress, Ottawa, Canada, 1989 |
| BÜRGER, W.W.: | Geohydraulic Investigations of Rubble Mound Breakwaters. |
| OUMERACI, H. | |
| PARTENSKY, H.W. | ASCE, Proc. 21st ICCE, Torremolinos, Spain, 1988 |

- BÜRGER, W.W. : Impact Strain Investigations on
OUMERACI, H. Tetrapods: Results of Dry and
PARTENSKY, H.W. Hydraulic Tests.
Seminar on "Stresses in Concrete
Armor Units", Vicksburg,
Mississippi, U.S.A., 1989
- NISHIGORI, W. : Experiment to measure stress in
KATO, M. tetrapods under wave action
SHIMADA, A. US. Army Corps of Engineers
ENDO, T. CERC, Proc. Workshop on
MATSUMOTO, A. Measurement and Analysis of
Structural Response in Concrete
Armor Units, Vicksburg,
Mississippi, U.S.A., 1985

CHAPTER 119

EXPERIMENTS ON COASTAL PROTECTION SUBMERGED BREAKWATERS: A WAY TO LOOK AT THE RESULTS

Gregorio Gómez Pina¹
J.M. Valdés Fernández de Alarcón²

1. ABSTRACT

In this paper, various damping action on submerged breakwater test results will be analyzed, in order to improve the methodology for future analysis. Experimental data from the authors and other researchers will be analyzed.

2. INTRODUCTION

The use of submerged detached breakwaters has become very attractive in beach restoration projects. The knowledge of how these breakwaters can affect coastal dynamics is necessary for almost any study.

Even though two-dimensional experiments on wave transmission on submerged breakwaters have been carried out by several authors, the application of the results to particular coastal protection projects is difficult and inapplicable in many cases.

Very often, relatively highly sophisticated wave propagation or coastal evolution models consider the influence of the submerged breakwater in a rather simplistic way: by a particular value of the transmission coefficient (K_t).

Furthermore, the application of the coefficient might not respond to realistic situations, depending on model test conditions, data analysis, wave evolution characteristics in the area between the submerged breakwater and the beach, etc.

¹ Coastal Project Manager, MOPU, Dirección General de Puertos y Costas, Paseo de la Castellana 67, Madrid 28046 SPAIN.

² Civil Engineer, Centro de Estudios de Puertos y Costas, (CEPYC-CEDEX), Antonio López 81, Madrid 28026, SPAIN.

3. OBJECTIVE OF THIS STUDY

The purpose of this study is to analyze various damping action on submerged breakwater test results, in order to improve the methodology for future analysis. Due to the breadth of this topic as well as the space limitation, the two following aspects are emphasized in this paper: A) Why it is too simplistic to model all processes by the parameter K_t (normally measured in one position behind the breakwater). B) The potential for mis-interpreting data when analyzing K_t .

4. ANALYSIS OF PHENOMENA INDUCED BY A SUBMERGED BREAKWATER

4.1. Characteristic zones of study

For analyzing hydrodynamic phenomena induced by a submerged breakwater or barrier, five characteristic zones are considered by the authors. This zones are schematized in Fig. 1.

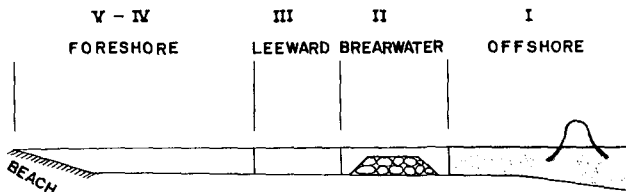


Fig. 1.- Scheme of Characteristic Zones of Study.

Fig. 2 tries to emphasize the two following concepts (which are sometimes ignored or not considered relevant):

- A) Most of experimental data are measured in zone III (near the breakwater) while practical application is needed in zone IV-V (near the beach).

- B) Some hydrodynamic phenomena induced in zones IV-V (difficult to be separated for practical applications) can affect data acquisition in zone III (i.e. wave reflection at the beach).

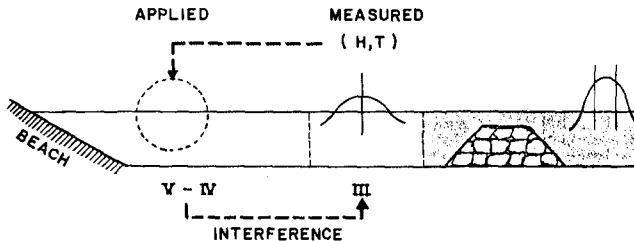


Fig.2.- Interrelation between Characteristic Zones.

4.2. Summary of Hydrodynamic Phenomena

In the authors' opinion, an attempt to show the complexity of the hydrodynamic phenomena induced by a submerged breakwater would help in understanding the existing shortcomings in data acquisition and application. Some of this hydrodynamic phenomena found in the area between the breakwater and the beach were corroborated from some of the experimental results carried out at CEPYC (CEDEX) by the authors (Ref.6, 7, 8 and 15). This will be shown in a very simple, schematic and "descriptive" way (including a few "liberties" with the drawings).

ZONE I

Phenomena: shoaling; wave reflection; breaking (or not) in front of breakwater.

Dimensionless Parameters

$$K_r = H_r / H_i$$

$$I_r = \tan \alpha / \sqrt{H_i / L_i}$$

$$X_B / L_i$$

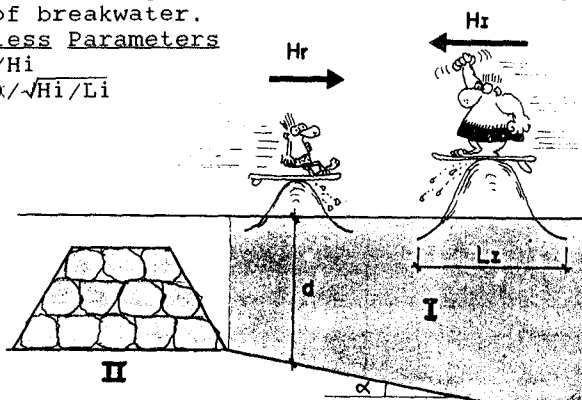


Fig. 3.- Zone I

ZONE II

Phenomena: wave breaking (possible); wave energy losses; long wave pulsative amplification; on/off-shore flow.

Dimensionless Parameters

$$C_L \text{ (breaking, friction, turbulence, percolation)}$$

$$B / L_i \text{ (or } B / gT^2, B / H_i, B / d)$$

$$F / L_i \text{ (or } F / gT^2, F / H_i, F / d)$$

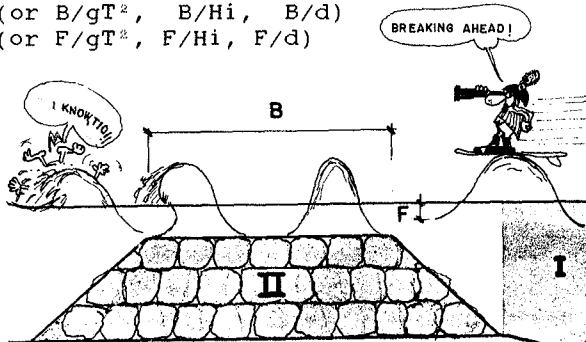


Fig. 4.- Zone II

ZONE III

Phenomena: wave transmission and damping; shifting of transmitted wave periods; wave set-up; periodic on/off-shore flow; possible standing wave patterns; possible longwave oscillations.

Dimensionless Parameters

$K_t = H_t/H_i$
 T_t/T_i
 ξ/H_i

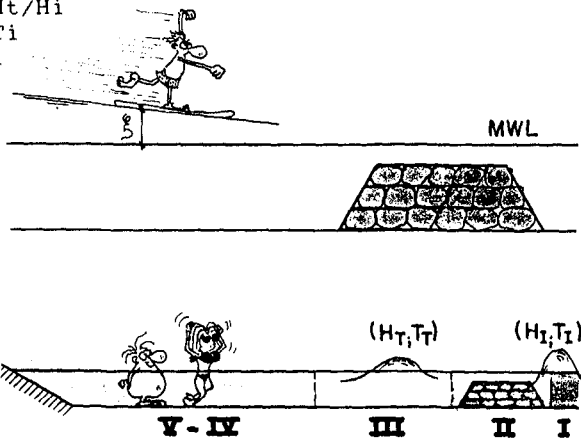


Fig. 5.- Zone III

ZONE IV-V

Phenomena: wave height and period evolution; wave reshaping and possible wave breaking, interference with waves reflected from the beach.

Dimensionless Parameters

Evolution of K_t , T_t/T_i , ξ/H_i
 Influence of (K_r) beach.

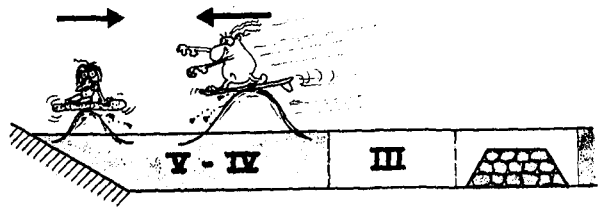


Fig. 6.- Zone IV-V

5. LOOKING AT THE RESULTS IN CHARACTERISTIC ZONES

The two aforementioned concepts (A and B) derived from Fig. 2, should be kept in mind by Coastal Engineers when analyzing experimental data on wave damping action on submerged breakwaters as well as for future model tests. Model tests carried out at CEPYC (CEDEX) (Ref.6, 7 and 8) have shown that in certain

cases, it is not so simple to draw conclusions on wave damping by only analyzing K_t (generally in zone III). In other words: submerged breakwaters could (under certain conditions) be not as "efficient" as one might think, when the evolution of the transmitted wave parameters are compared in the characteristic zones (especially in zone IV-V).

Fig. 7 schematizes the CEPYC model set-up and parameters of study. Notice that waves were measured in 13 points past the breakwater. Also, breaking wave conditions (induced or not by the submerged breakwater) were investigated.

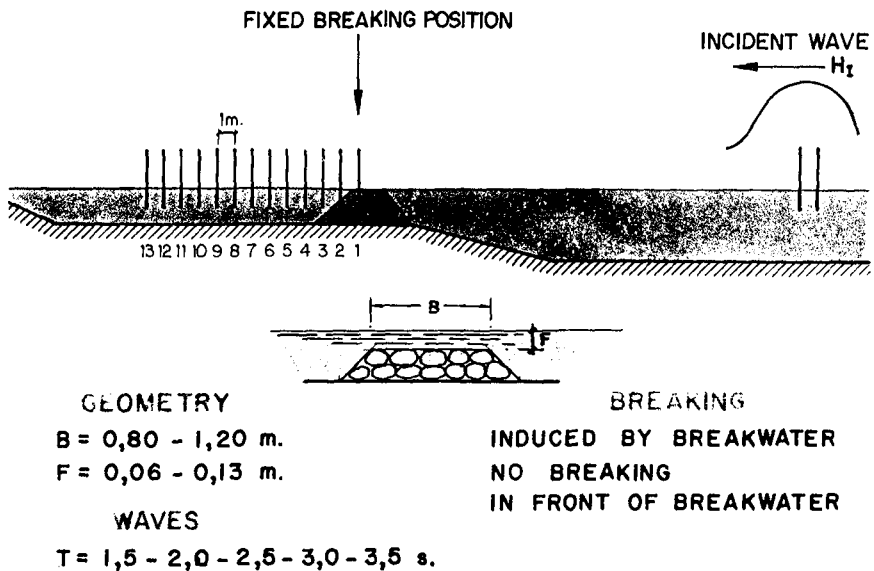


Fig. 7.- Scheme of Transmitted Wave Evolution Model Set-Up.

The two following figures, from the above mentioned model tests, have been chosen as a "reflexion" on the importance of measuring wave characteristics (H , T , ξ) in more than one or two points behind the breakwater.

The first figure is an example of the "relative efficiency" in crest width increment: in zone III (where most of measurements were taken) the increment seems to be very favorable in decreasing transmitted wave height (H_t) while the efficiency is not as clear for zone IV-V (close to the beach).

The second figure remarks the importance of wave reshaping and possible new breaking once the submerged breakwater has induced waves breaking on the breakwater (notice also the set-down points outlined on this figure).

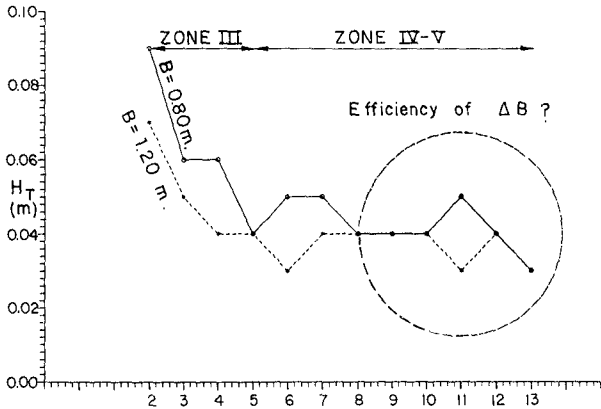


Fig.8.- Example of Wave Transmitted Height (Ht) Evolution

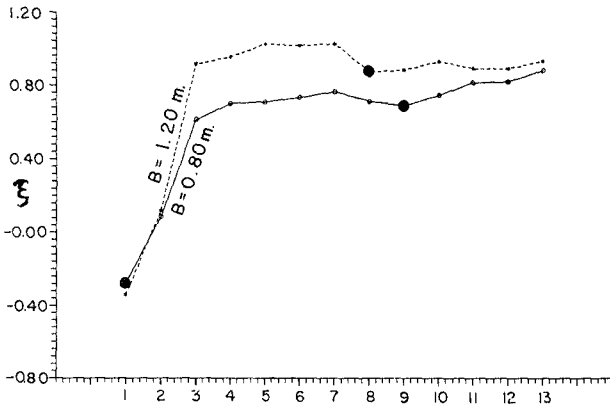


Fig.9.- Example of Wave Set-Up (ξ) Evolution

For a thorough understanding of the main hydrodynamic phenomena induced after wave breaking, including undertow, the authors would like to point out the elegant work carried out by Prof. Svendsen (i.e. Refer.14). New studies trying to "link" the main submerged breakwater parameters and wave evolution in characteristic zones would be very beneficial for coastal engineering applications.

6. LOOKING AT THE RESULTS OF K_t IN ZONE III

The potential for mis-interpreting data, even in the simplest cases of analyzing K_t in zone III will be discussed.

6.1. Transmission Coefficient (K_t) versus relative crest width (B/L)

For coastal engineering applications it is important to know which is the optimum breakwater crest width (B) which gives the minimum transmission coefficient (K_t). From dimensional analysis, the following expression can be derived as one possibility:

$$K_t = f(B/L, H_i/d) \quad (1)$$

To accurately plot the results it is important to note the fact that a change of crest width will also alter the reflection coefficient (K_r) and thus the incident wave height (H_i), according, for instance, to the method of Goda and Suzuki (Ref.5). Therefore, it is not so easy to get the exact values of the term H_i/d unless a large number of model tests are performed. In other words: the plot of K_t versus B/L (Eq. 1) should include the mean value and also the standard deviation of the relative incident wave height term (H_i/d), due to the difficulties in obtaining "exact values" of (H_i/d). This fact, in the authors' opinion, has not been considered in the existing literature.

Even though different authors (Ref.3, 4, 10 and 13) have shown the existence of distinctive maximum and minimum values of K_t in Eq. 1, it has not been remarked whether these curves respond to the spreading characteristics of the results themselves or to the real hydrodynamic problem, according to the equations involved in that modelling.

This fact is important when analyzing experimental results, since one could think (at first) that the obtained results, for instance, might not be valuable due to the large data spread, even when this spread is inherent to the mathematics involved in modelling (i.e. matching conditions).

6.2. Poble Nou Wave Transmission Study

This study, carried out at the CEPYC (Ref.6 and 7), was part of a large project to greatly improve the sea front in Poble Nou, in Barcelona (Spain), for the '92 Olympic Games. Basically, the aim of the model tests was to investigate the efficiency of increasing crest

width on wave damping action.

For that, three crest widths ($B = 34.50$ m. and $\pm 15\%$ on this value), and three wave periods ($T=7, 9$ and 11 secs) were tested, for a crest freeboard $F=0.00$ m. Also a mean water elevation of 0.50 m., associated to the largest wave period was considered.

There were 108 model tests (a relatively large number, in our opinion), in order to get well defined maximum and minimum values in the curves K_t versus B/L , as explained in 6.1. Fig 10 is a typical example of a curve representing Eq. (1):

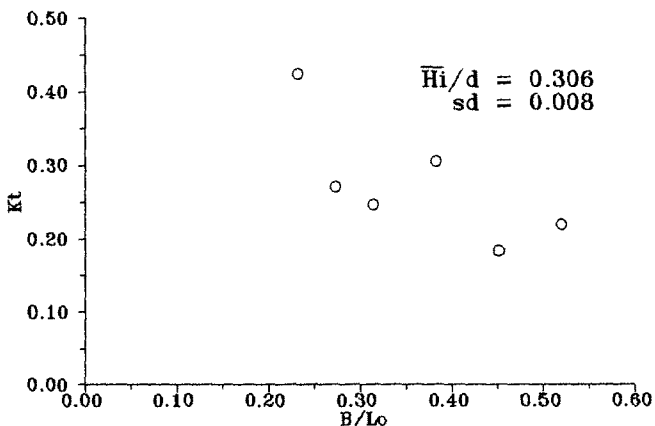


Fig. 10.- A Typical Example of K_t versus B/L_o , for $\bar{H}_i/d=0.306$ (Crest Freeboard $F=0.00$ m.).

From Fig. 10 one could ask the following reasonable questions:

A) Are the results valuable due to the apparently large data spreading shown in Fig. 10 ?

B) Should a fitting curve be used ?

C) Could a figure obtained by connecting all points, and showing distinctive maximum and minimum points, be a real response of the wave transmission phenomenon ?

D) Supposing the above mentioned questions were known, which should be the design value for the relative crest width B/L ?

And, before giving any answer to all these questions, one could also make the following logical reasoning: Which is really the most simple mathematical

answer to these questions?

In Fig. 11, the geometric parameters and also the reflected (R and D) and transmitted (C and T) waves are shown for the three regions in an impervious submerged obstacle. The four variables R, C, D and T are calculated using the four known matching conditions related to velocities and pressure.

A graphic solution is shown in Fig. 12, using the most simple case of short waves, linear theory and no dissipation. Also a crest freeboard of 0.50 m. is adopted, to greatly simplify the problem.

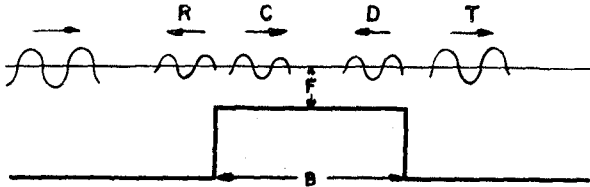


Fig. 11.- Geometric and Wave Parameters for a Submerged Obstacle.

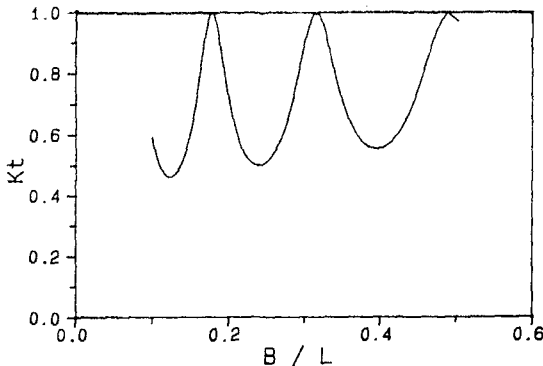


Fig. 12.- A Typical Solution of K_t versus B/L_0 for an Impervious Submerged Obstacle ($F=0.50$ m) Using Linear Theory and Short Waves.

In Fig. 12 it can be seen that in the analysis for the most simple case of short waves, linear theory, and no wave dissipation, the solution for K_t (and also for K_r) shows distinctive maximum and minimum values, as found in other works on submerged obstacles.

However, the theoretical transmission coefficient of linear waves propagating over a submerged porous step decays monotonously with the relative crest width (B/L), but reflection coefficient does oscillate (Losada, personal communication, 1990). This distinct

behaviour is worthy of further research.

Fig. 13 summarizes the results obtained in Ref.6, related to wave transmission (K_t) versus relative crest width (B/L_0) for different relative incident wave height (H_i/d) and zero freeboard ($F=0$) values.

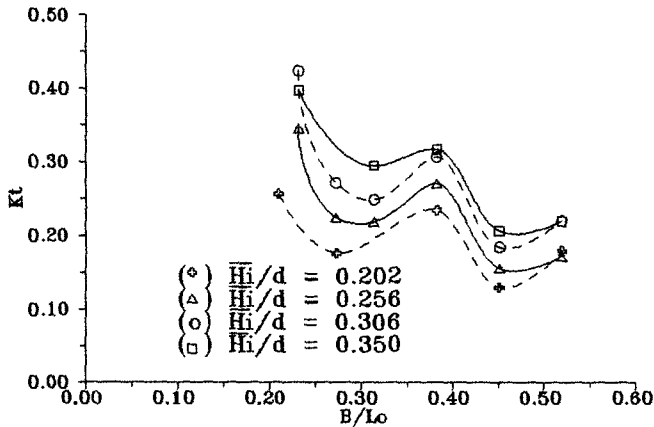


Fig. 13.- K_t versus B/L_0 for Different (H_i/d) and Zero Freeboard ($F=0$).

The following conclusions could be drawn from Fig.13:

- The wave transmission coefficient shows a decreasing oscillatory trend when plotted against the relative crest width (B/L_0) with distinctive maximum and minimum values.

- The relative incident wave height (H_i/d) seems to have influence only on the amplitude of K_t , but not in the values of (B/L_0) corresponding to the maximum and minimum values of K_t .

- Small variations of B/L_0 , corresponding to the minimum values of K_t , gives rise to relatively high values of K_t . Thus, design criteria based on minimum K_t values might be too risky due to the joint appearance of all the complex hydrodynamic phenomena involved and model scale effects in two-dimensional tests.

Unfortunately, the relative small number of model tests considering a freeboard $F=0.50$ m. make the authors unable to compare the results with those obtained applying the most simple theoretical cases of impervious and porous submerged steps, as obtained in Losada's work (Ref.11).

6.3. Influence of Breaking Conditions

The influence of taking into account different breaking conditions (i.e. breaking in front of the breakwater, breaking induced by the breakwater or not breaking) on wave transmission is investigated.

6.3.1. Plotting of Results

The plotting of different dimensionless coefficients versus a new parameter $Ir*(B/F)$, provided a reasonably good fitting in general, as well as a good physical understanding of the results, including the influence of breaking (Ir = the known Iribarren's parameter = $\text{tg}\alpha/\sqrt{H/gT^2}$; $\text{tg}\alpha$ = bottom slope in front of the breakwater; B = crest width; F = crest freeboard).

Space limitations have prevented the authors from presenting some of the results obtained in References 1, 2, 9, 13 and 15, using the above mentioned parameter. However, figure below is the result of analyzing some specific data from Dattatri et al (Ref.3) using the condition of breaking over the breakwater, presented in Nakamura et al (Ref.12).

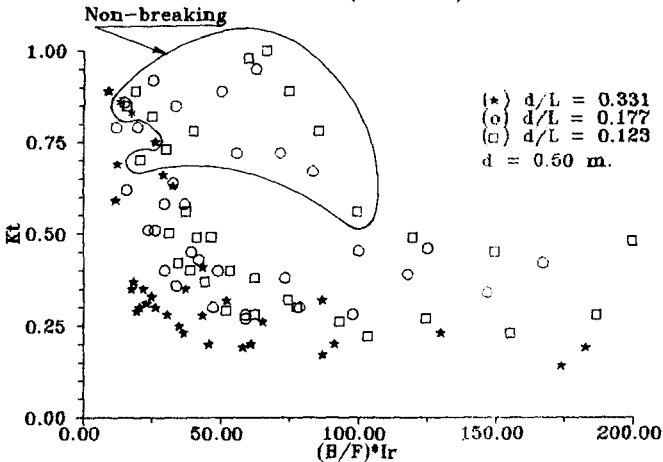


Fig. 14.- Influence of Breaking Conditions on Kt

The following conclusions could be drawn from Fig.14:

- Large data spreading occurs if breaking conditions are not separated adequately.

- The fitting of Kt versus the parameter $Ir*(B/F)$, both for breaking and non-breaking conditions (using Nakamura's criteria), seems to be quite

reasonable: the fitting for breaking condition should show a quasi-asymptotic decreasing curve as expected ($K_t \rightarrow 1$ for relatively small values of B/F and $K_t \rightarrow 0$ for large values of B/F). On the other hand, the pattern for non-breaking condition shows a definitely different shape. This could be also expected since values of $K_t > 1$ are reported for non-breaking conditions (i.e. Ref.12 and 15).

7.-CONCLUSIONS

1) Most of the practical data obtained by different authors is measured in zone III. Thus, one should be aware of this when they are used in zone IV-V for beach application.

2) Since various transmitted wave parameters evolve in different zones as wave propagates landwards, more detailed information should be provided in model tests. In particular, several wave gauges, appropriately separated, should be used for measurements of wave transmitted parameters. Also, reflective beach characteristics and distance from the beach to the breakwater should be reproduced as reliably as possible.

3) When analyzing data in one particular zone, the different processes affecting that zone should, if possible, be separated, for a proper interpretation and application of this data. In particular, breaking conditions (such as breaking induced by the breakwater, breaking in front of the breakwater, or not breaking at all) should be adequately distinguished. This observation should be kept in mind when simple formulae for combined wave transmission data are tried for general design purposes.

4) The use of the parameter $(B/F) \cdot I_r$ versus the other dimensionless parameters (transmission, reflection and losses coefficients, ratio between transmitted and incident wave period and relative wave set-up) seems to improve the fitting of results, especially if the above-mentioned breaking conditions are separated.

5) Experimental studies on wave transmission on submerged breakwaters and zero crest freeboard, as the one explained about Poble Nou, have shown that curves representing transmission coefficients (K_t) versus relative crest width (B/L), for various relative incident wave heights (H_i/d) show, in general, distinctive maximum and minimum values.

Since theoretical studies, with negative crest freeboard, also show in general oscillatory patterns, experimental data should not at first be treated as though they were presenting a large spreading (as is sometimes reported).

6) Even though the above mentioned experimental curves show in general, distinctive maximum and minimum values, the joint appearance of all the complex hydrodynamic phenomena, explained at the beginning of this paper, together with possible model scale effects, make design criteria based on minimum K_t values too risky.

8.-ACKNOWLEDGEMENTS

We would like to thank the Director of CEPYC (CEDEX) for giving permission to publish this paper which has mainly been based on the experimental results carried out by the authors there.

This piece of work could not have been written without the help of most of the people working at the Experimental Division of CEPYC. Space limitation prevents us from writing their names individually. Also the draftsman Mr. Carlos Redondo helped us make the presentation at the ICCE'90 quite enjoyable.

Finally, we would like to thank Professor Miguel Losada and Dr. Raúl Medina, from the University of Santander, for the many helpful discussions we have had with them while writing this paper.

9.-REFERENCES

- 1.- Ahrens, J.P., and Cox, J., 1990. "Design and Performance of Reef Breakwaters". Personal Communication, prepared for the Journal of Coastal Research.
- 2.- Allsop, N.W.H., 1983. "Low-Crested Breakwaters, Studies in Random Waves". Proceedings of Coastal Structures'83, Arlington, pp.
- 3.- Dattatri, J.H., H. Raman and Vothi Sankar, 1978. "Performance Characteristics of Submerged Breakwaters". Proceedings, Coastal Engineering Conference.
- 4.- Dick, T.M. and A. Brebner, 1968. "Solid and Permeable Submerged Breakwaters". Proceedings, Coastal Engineering Conference, Vol. 1.

- 5.- Goda, Y. and Suzuki, Y. 1976. "Estimation of Incident and Reflected Waves in Random Wave Experiments". Proceedings, Coastal Engineering Conference.
- 6.- Gómez Pina, G. 1987. "Ensayos en Modelo del Espigón de Defensa de la Playa de Poble Nou (Barcelona)". Centro de Estudios de Puertos Y Costas (CEDEX). (Unpublished).
- 7.- Gómez Pina, G. and Baonza, A. 1988. "Estudios sobre la Transmisión del Oleaje del Espigón de Defensa de la Playa de Poble Nou (Barcelona)". Revista de Ingeniería Civil N^o 66/1988 (CEDEX).
- 8.- Gómez Pina, G. 1987. "Diseño de un Nuevo Tipo de Barrera Semisumergida Modular para Defensa de Costas". Centro de Estudios de Puertos y Costas (CEPYC), CEDEX. (Unpublished).
- 9.- Hydraulic Research, 1985. "Seaford Frontage-Model Tests of Low Crested Breakwaters, Performance and Stability". HR Report EX 1346.
- 10.- Johnson, J.W., R.A. Fuchs, and J.B. Morison, 1951. "The Damping Action of Submerged Breakwaters". Trans. AGU. 32.
- 11.- Losada, M. 1990. Personal Communication.
- 12.- Nakamura, M., Shiraisi, H., Sasaki, Y., 1984. "Wave Damping Effect of Submerged Dike". Proceedings, Coastal Engineering Conference.
- 13.- Seelig, W.N., 1980. "Two-Dimensional Tests of Wave Transmission and Reflection Characteristics of Laboratory Breakwaters". T.R. No. 80-1, CERC.
- 14.- Svendsen, I.A., 1984. "Waves Heights and Set-Up in a Surf Zone". Coastal Engineering, 8.
- 15.- Valdés, J.M., 1988. "Estudio Experimental sobre Diques de Escollera Sumergidos". Centro de Estudios de Puertos y Costas (CEDEX). (Unpublished).

CHAPTER 120

NUMERICAL SIMULATION OF THE MOTION OF A LOOSE REVETMENT BLOCK

A. Bezuijen¹
J. Wouters ²
H. den Adel³

Abstract

The movement of a block lying loose in a placed block revetment under wave loading was simulated numerically. The results have been compared with the results of large scale model tests in which the motion of a block and the pressure distribution in the filter layer underneath was measured. It appeared that the mechanism concerning the pore pressure distribution and the block movement are described well in the numerical program. The block movement as calculated in the program is higher than measured. The reason for this is described in this paper.

Introduction

A research programme on placed block revetments has led to design rules for the cover layer and filter layer of this type of revetment (Bezuijen et al, 1987, Burger et al, 1990a, Bezuijen et al, 1988). Large scale model test have been performed to verify the design rules. The research programme was commissioned by the Public Works Department of the Ministry of Transport and Public Works in the Netherlands (Rijkswaterstaat) and performed by Delft Hydraulics and Delft Geotechnics.

In this paper the experimental verification of the computer program STEENZET/1+ will be treated. This program is used to calculate the stability of the blocks in a placed block revetment. The program calculates the pore pressures in the filter layer as a function of the geometry, the permeability of both cover layer and filter layer and the wave pressures. For fixed blocks it was shown before that the calculated pore pressures correspond with the measured pore pressures in large scale model tests (Bezuijen et al, 1987). However the displacement of a block will influence the

¹ Research engineer, Delft Geotechnics, P.O. Box 69, 2600 AB Delft, the Netherlands

² Research engineer, Delft Hydraulics, P.O. Box 152, 8300 AD Emmeloord, the Netherlands

³ Research engineer, Delft Geotechnics

pressure distribution below that block, leading to smaller pore pressures underneath the blocks (Burger et al, 1990a). In the model tests described in this paper block motion as well as the pressure underneath a moving block were measured and therefore it is possible to compare measured (and calculated) pore pressures underneath a moving block and its motion.

Model tests

The model tests have been performed in the 230 m long, 7 m deep and 5 m wide wave flume of DELFT HYDRAULICS. All tests were carried out on a slope 1 : 3 and with a water depth of approximately 5 m. Two revetments were tested simultaneously. Hereto the 5 m wide slope at the end of the flume was divided into two sections each 2.5 m wide; these two sections were called East and West, respectively. In total 2 * 6 types of revetments were tested. For the present paper the following 3 revetments are of importance:

	D	B	L	s	b	D _{f15}	n
	[m]	[m]	[m]	[mm]	[m]	[mm]	[%]
I West	.15	.25	.30	1.5	0.25	3.6	38
II West	.15	.25	.30	1.5	0.50	9.2	34
VI West	.30	.50	.50	3.8	0.35	17.3	38

in which: D is the thickness of the blocks, B is the width of the blocks, L is the length of the blocks, s is the width of the joints between the blocks, b is the thickness of the filter layer, D_{f15} is the grain size of the filter material material that is exceeded by 85% of the mass of the grains and n is the porosity of the filter.

An example of two revetments in the Delta flume is shown in photograph 1, a cross-section in figure 1.

With revetment I West as a starting-point the following parameters have been varied: the thickness of the filter layer, the size of the blocks, the grain size of the filter material, and the thickness of the blocks.

In each section there is one block that is completely loose from the adjacent blocks. By means of a displacement gauge the movement of the loose block was measured, see Photograph 2. The wave pressure distribution on top of the revetment as well as the pressure distribution underneath the blocks are of primary importance for the stability of the block revetment and resulting block motion. In order to measure these pressure distributions 19 pressure gauges were placed on top of the revetment and 24 pressure gauges underneath the blocks, viz. 12 on the East and 12 on the West side. The loose blocks and two adjacent blocks, one higher and one lower were provided with both a pressure gauge on top of the block and a pressure gauge under the block. In this way the resulting uplift pressure over these blocks could be measured during the tests.

Three H-T combinations at a constant ξ were tested: a combination for which no block motion was expected, one for the start of block motion and one for a large block motion. H is the wave height, T is the wave period, ξ is the breaker parameter: $\xi = \tan(\alpha)\sqrt{H/L}$, α is the slope angle and L is the wave length.

The following ξ values were used for the tests: $\xi = 1.0, 1.5, 2.0, 3.0$ and 4.0 . The tests used in the simulations were run with regular waves.

Before the actual test, the water level in the flume was adjusted to the level, where the loose block is maximally loaded, providing a maximum block displacement in the actual test.

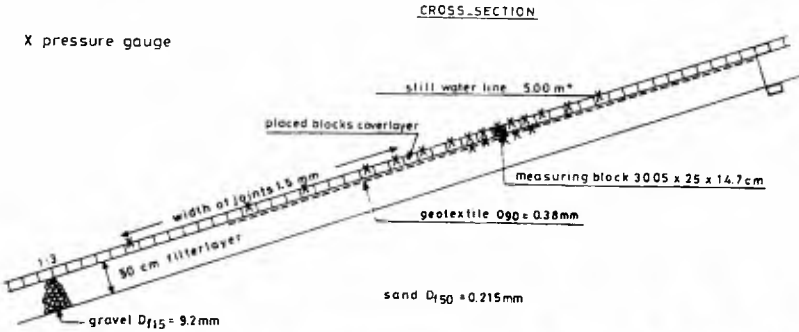


Figure 1. Cross section of revetment II West



Photograph 1. Example of two revetment sections

STEENZET/1+

The basic assumptions of STEENZET/1+ are the same as described for STEENZET/1 (Bezuijen et al, 1988). Both models calculate the pore pressures in a granular filter layer below a cover layer of placed blocks.

The permeability of the subsoil is assumed to be much lower than the permeability of the filter layer and therefore the flow in the subsoil has no significant influence on the flow in the filter

layer. The permeability of the cover layer is also lower than the permeability of the filter layer, resulting in a flow parallel to the slope in the filter layer and perpendicular to the slope in the cover layer.



Photograph 2. Displacement gauges in instrumented blocks next to the moving block

Without any block movement the flow can be described with a finite difference scheme that is shown in figure 2, allowing for flow parallel to the slope in the filter layer and perpendicular to the slope in the joints.

Darcy's equation combined with conservation of mass leads to a description for the potential in each node.

$$\phi_i = \frac{1}{1 + 2 \frac{kbD}{k'L^2}} \left\{ \frac{kbD}{k'L^2} (\phi_{i-1} + \phi_{i+1}) + \phi_{t,i} \right\} \quad [1]$$

where: ϕ_i = piezometric head in the filter layer near joint i (m)

$\phi_{t,i}$ = piezometric head on the revetment near joint i (m)

b = the thickness of the filter layer (m)

D = the thickness of the blocks (m)

k = the permeability of the filter layer (m)

k' = the permeability of the cover layer (m).

At the phreatic surface the piezometric head in the filter layer is equal to the position of the phreatic surface. At the lower end of the revetment the condition $\phi_{i+1} = \phi_{i-1}$ is assumed. If there is no phreatic surface then $\phi_{i-1} = \phi_{i+1}$ for the highest position in the revetment. The potential distribution in the filter layer can be solved if the potential ($\phi_{t,i}$) on the revetment is known. The solution obeys equation [1] for all joints.

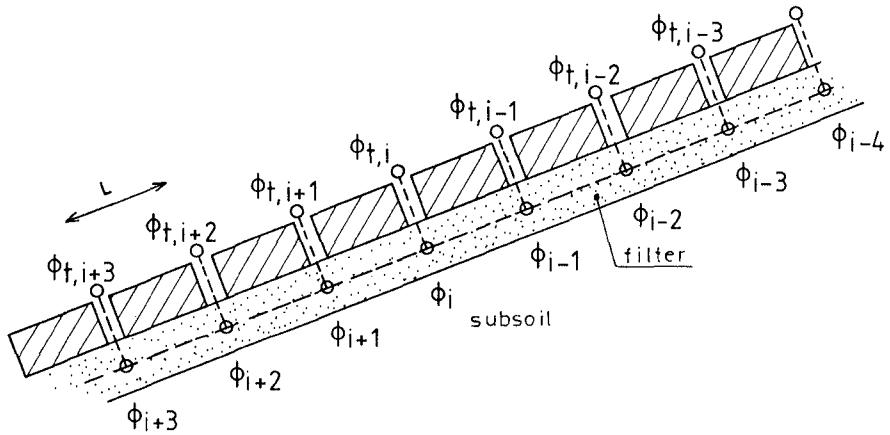


Figure 2. Finite difference scheme of STEENZET/1+

Until now the situation without block movement is described. With block movement the equations change.

In the calculations it is assumed that there is only one loose block. The revetment in the experiments is constructed similarly. This seems to be in contradiction with reality where all blocks might move. However pull-out tests have shown that in a block revetment there are only a few really loose blocks, since clamping forces are high between most blocks.

When a block starts to move, water will flow towards the block from the filter layer underneath the moving block. The water will flow from all sides underneath the block. Far away from the moving block nothing will change and the solution as described by equation [1] can be used. This solution can be used to find the solution with block movement.

The finite difference scheme of figure 3 is applied. This scheme allows for horizontal flow along the slope as well. The solution of equation [1] is used as the solution for the side rows. The row in the middle of the filter layer represents the potential distribution underneath a moving block.

The distance between the side rows and the middle row can be determined from an analytical calculation. It was determined (Bezuijen, 1986) that the right distance equals the leakage factor:

$$\Lambda = \sqrt{\{(k/k')bd\}} \quad [2]$$

This value was used for the horizontal distance in figure 3.

The finite difference scheme of figure 3 allows the flow from 8 directions to the point $\phi_{b,i}$, see figure 4. This flow is assumed to be symmetrical around the moving block which means that only 5 different terms remain. The contributions 3 and 5 are added to the finite difference scheme to describe the more or less radial flow to the moving block. However these terms depend the other

terms and so a correction term on the flow direction 3, 4 and 5 in figure 4 is necessary. By performing a calculation with sheer horizontal flow it was found that this term has to be:

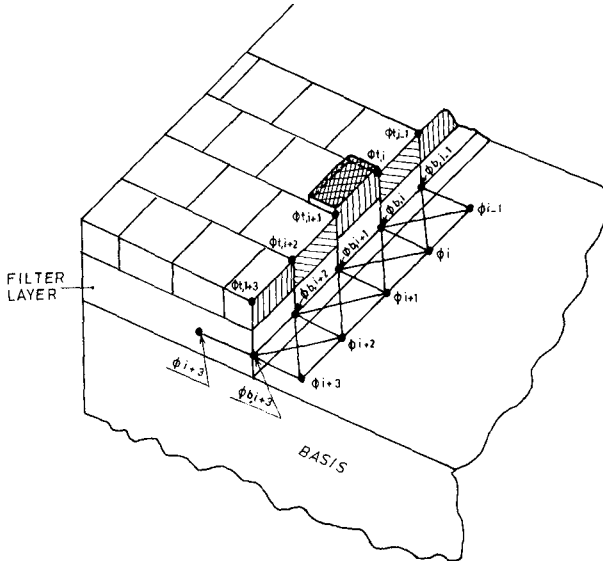


Figure 3. Finite difference scheme of STEENZET/1+

$$c = \left[\frac{2\Delta}{\sqrt{(L^2 + \Delta^2)} + 1} \right]^{-1} \quad [3]$$

The discharge for each contribution in figure 4 can again be determined from Darcy's law. Continuity demands that the sum of all discharges is zero, leading to the set of equations:

$$\begin{aligned}
 kb \frac{\phi_{b,i-1} - \phi_{b,i}}{L} - kb \frac{\phi_{b,i} - \phi_{b,i+1}}{L} + 2kbc \frac{\phi_{i-1} - \phi_{b,i}}{\Delta s [1 - \frac{1}{2} \frac{\Delta L}{\Delta}]} \\
 + 2kbc \frac{\phi_{i-1} - \phi_{b,i}}{\Delta - \frac{1}{2}l} + 2kbc \frac{\phi_{b,i} - \phi_{i+1}}{\Delta s [1 - \frac{1}{2} \frac{l}{\Delta}]} + qb = k' \Delta x \frac{\phi_{b,i} - \phi_d}{\phi} \quad [4]
 \end{aligned}$$

where: $\phi_{b,i}$ = the piezometric head in the column of blocks with the moving block

$s = \sqrt{(\Delta^2 + L^2)}$, the diagonal distance (m) between two different points

$l = L$ for the points of the moving block (otherwise $l = 0$)

This incorporates the fact that underneath the moving block the potential gradient is zero.

Below the non moving blocks $qb = 0$ and the equation (4) can be used to solve $\phi_{b,i}$ for all finite difference points.

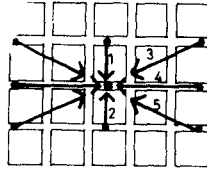


Figure 4. Flow direction towards moving block as schemed in STEENZET/1+

Only directly underneath the moving block the situation is different; the amount of pore water may vary due to the block movement. The piezometric head is not the result of a groundwater flow calculation. Neglecting inertia forces, the piezometric head is determined by the piezometric head on the block, the weight of the block and the friction force:

$$\phi_i = \phi_{t,i} + \Delta D (1 \pm f_c \sin \alpha) \quad [5]$$

where:

$$\Delta = (\rho_c - \rho_w) / \rho_w \text{ the relative density} \quad (-)$$

$$\rho_w = \text{the density of water} \quad (\text{kg/m}^3)$$

$$\rho_c = \text{the density of concrete} \quad (\text{kg/m}^3)$$

$$f_c = \text{the friction coefficient} \quad (-)$$

$$\alpha = \text{the slope angle} \quad (^\circ)$$

\pm means + if the block moves up

means - if the block moves down.

In STEENZET/1+ also the effect of inertia is included, but this is omitted here because the influence of inertia is usually small and including inertia leads to more complex formulae. Substitution of equation [5] in equation [4] for the points underneath the moving block leads to a value for q which determines the block movement for one time step. The remaining difficulty is the term $\pm f_c \sin \alpha$ in equation [4]. It is not known in advance in which direction the block will move. In the STEENZET/1+ program this problem is solved by trial and error. One direction of movement is assumed and equation [4] is solved. If the discharge does not fit with that direction, the other one is tried. It is possible that both do not fit; in that case the piezometric head in the filter layer is too small to push a block further-out of the revetment, but too high to let the block move downwards; this means that the block does not move at all. After some displacement it stops temporarily due to the friction with adjacent blocks and although it is not in contact with the filter layer the solution for non moving blocks equation [1] can be used.

The block starts to move as soon as the difference in piezometric head is larger than the difference that corresponds with the weight of the block, or more mathematically if $\phi_{t,i}$

underneath the possible moving block, calculated with equation [1] is larger than calculated with equation [4]. The block movement is calculated by accumulation of the block displacements during each time step. The calculation of block movement stops if the accumulated displacements lead to a negative block movement, which means inwards the filter layer.

Simulation of tests

The results of the experiments were simulated with STEENZET/1+. In the first simulation test SZ 208 was used. This test was run on revetment II-West, a revetment with a long leakage factor, loaded with a wave with a low steepness. Block movement was measured over 1.5 s in this test. Figure 5 shows the measured pressures in this test together with the pressures measured in test SZ 213. This was exactly the same test, only in test SZ 213 the block was fixed.

Figure 5 shows that when a block starts to move, the pore pressure is reduced as long as the block moves out of the revetment. When the block is pushed backwards to its original position, the pore pressure below the block is higher than for the fixed block. The reason for this is that during the outward directed movement of the block, there is a waterflow towards this block. The water partly flows through the joints around the block and partly pushes the block upwards. When the block drops back to

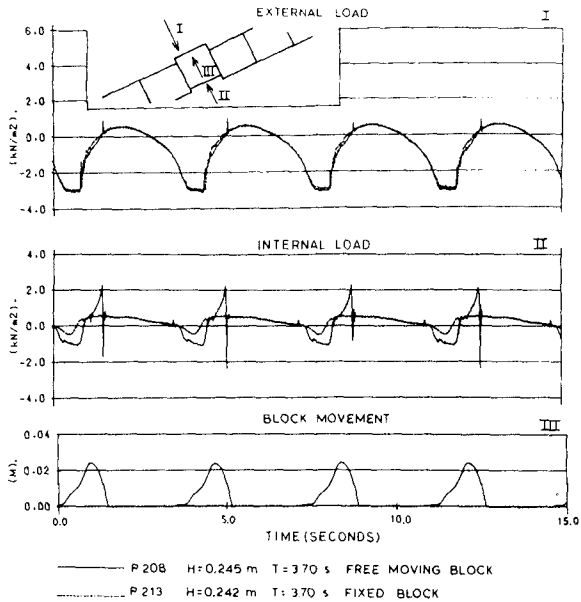


Figure 5. Example of measured pressures and block motion. Pressures with respect to still water. Arrows indicate positive pressure and motion

its original position, the water below the block is 'pushed' into the filter layer, leading to higher pore pressures than in case of no block movement.

Test SZ 208 was used to calibrate the numerical program. It appeared that the friction coefficient between the blocks (see equation [5]) has to be kept zero. This result can be obtained from the test directly by comparing the uplift pressure at which a block starts to move with the pressure corresponding to the weight of the block. The leakage factor see equation [2] of this revetment was also calibrated by means of this test. First the leakage factor was calculated using the results of Den Adel (1987) for the filter layer and of Klein Breteler and Bezuijen (1988) for the cover layer. Thereafter the leakage factor was determined by fitting the results of the calculations with the results of the measurements for test SZ 208. The calculated and 'fitted' leakage factors are shown in table 1.

Test section	Calculated leakage factor (Λ) from literature (m)	by STEENZET/1+ (m)
I	0.67	0.57
II	1.22	1.30
VI	1.13	1.56

Table 1. Leakage factor for the simulated sections, calculated from literature and "fitted" with STEENZET/1+

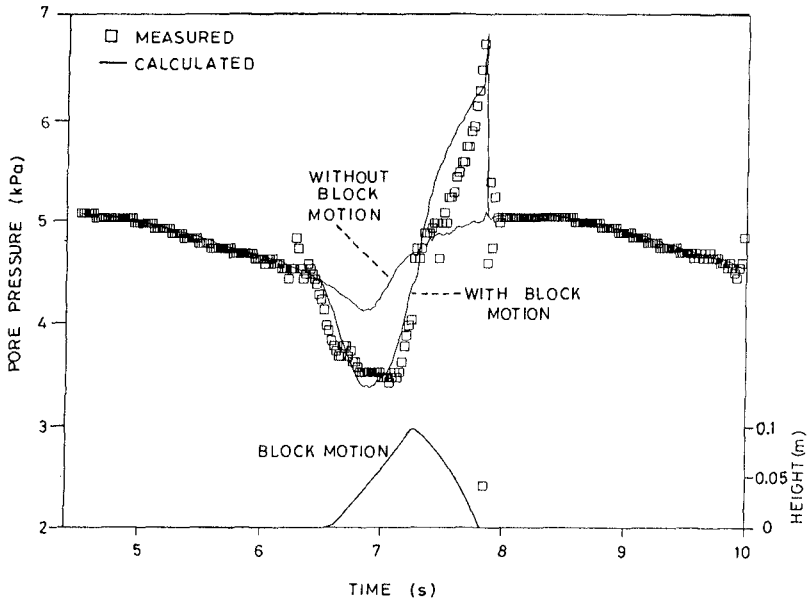


Figure 6. Test SZ 208, measured and calculated pore pressures below the moving revetment block due to wave attack and resulting block motion ($H = 0.25$ m, $T = 3.7$ s, $\xi = 3.11$)

The results of the simulation show good agreement between the measured and calculated pore pressures, see figure 6.

However the simulated block movement is higher than measured (25 mm measured, 120 mm calculated), due to simplifications that have been used to describe the flow directly underneath a moving block. In the simulations it is assumed that the filter layer below the moving block has a very high permeability (due to fluidisation of that part of the filter layer). In the tests fluidisation was prevented by a geotextile that was placed between the blocks and the filter layer.

With the same values of the input parameters (the leakage factor and friction) test SZ210 on the same revetment was simulated. The result is shown in figure 7.

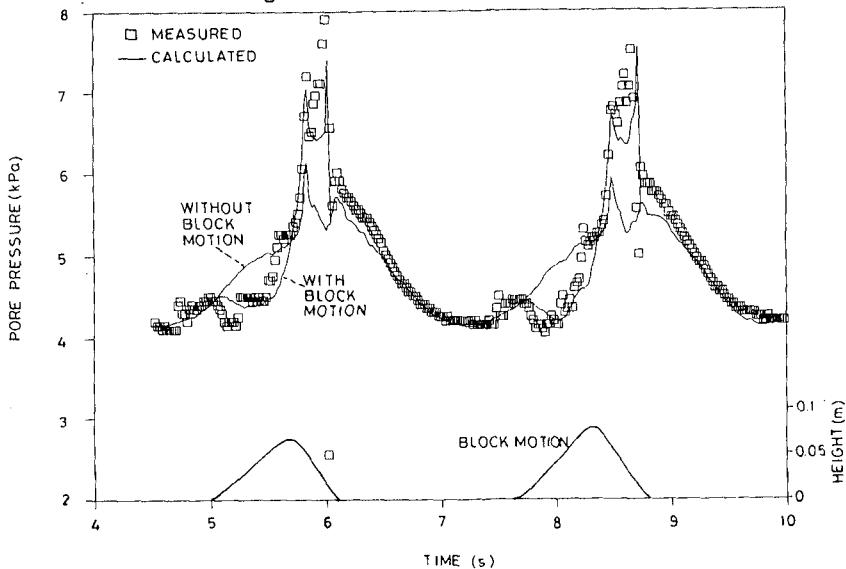


Figure 7. Test SZ 210, measured and calculated pore pressures below the moving revetment block due to wave attack and resulting block motion ($H = 0.49$ m, $T = 2.7$ s, $\xi = 1.6$)

Again the pore pressures agree quite well, but the calculated block movement is too high (15 mm measured, 75 mm calculated).

Figure 8 shows the measured and calculated pore pressures for test SZ152. This test was run on the revetment I-West with a much shorter leakage factor. Again the results of the simulation are the same: good agreement for the pore pressures, but a calculated block movement that is too high (2 mm measured, 10 mm calculated). The results of the measurements as well as the simulations for this revetment can be compared with the results obtained for the revetment II-West with the longer leakage factor.

This shows that in a revetment with a shorter leakage factor the duration of the block movement is much shorter. For the two tests on revetment II-West it was more than a second. For the test on revetment I it was less than 0.5 s.

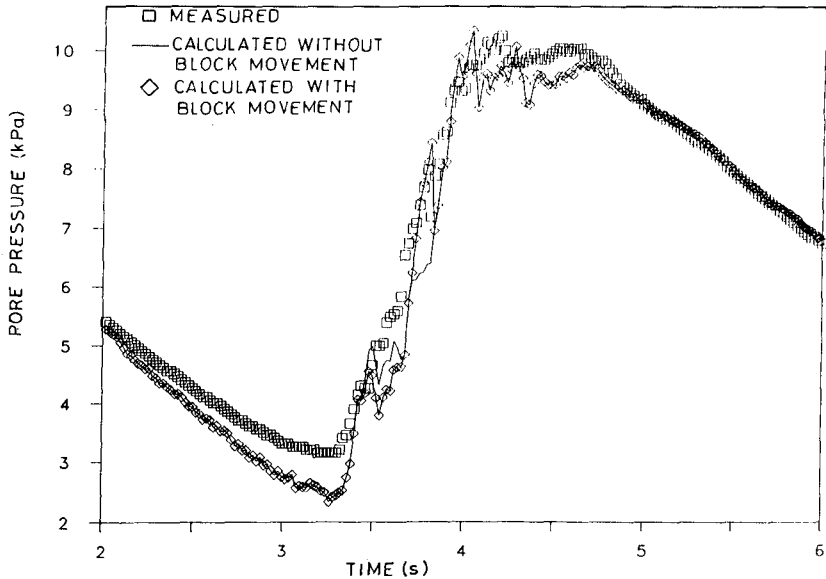


Figure 8. Test SZ 152, measured and calculated pore pressures below the moving revetment block due to wave attack ($H = 1.19$ m, $T = 5.15$, $\xi = 1.94$)

Furthermore the moment of maximum uplift pressure appears to be different. In the test on revetment II-West the maximum uplift pressure was found at the time the wave pressure on the block is at minimum. In the test on revetment I-West it was found that the maximum uplift pressure occurs during the pressure rise of the new incoming wave.

A remarkable result was found when analysing experiment SZ617 on revetment VI-West. The measured and calculated pore pressure are in good agreement as long as the block does not move. However when the block starts to move, a discrepancy was found between measured and calculated pore pressures, see figure 9. The reason for this discrepancy was found by re-analysing the measured pressures. It appeared that the block starts to move before the uplift pressure is larger than corresponding to the weight of the block, see figure 10 where the uplift pressure as measured is plotted together with the block movement. The revetment VI-West consists of relatively large blocks of $0.5 * 0.5 * 0.3$ m, with respect to the wave height. Measuring the uplift pressure over these large blocks on only one position leads to an under-estimation of the pressure. The STEENZET/1+ program uses a linear interpolation over one block. In this case this also leads to a slight under-estimation of the uplift pressure and is probably the reason for the discrepancy between calculated and fitted leakage factor (see table 1).

Influence of cover layer permeability

Since good agreement is found between simulations using

STEENZET/1+ and the tests, we are confident that the program can be used to calculate the effect of changes in parameters on the pressure distribution in the filter layer and the block movement.

As an example the influence of the cover layer permeability was calculated. This example is not purely theoretical but has practical implications. When a block revetment is newly constructed the joints between the block will be clean, leading to a relatively large cover layer permeability. However after some time the wave action will transport sand, silt and shells to the revetment and into the joints causing a decrease in the cover layer permeability.

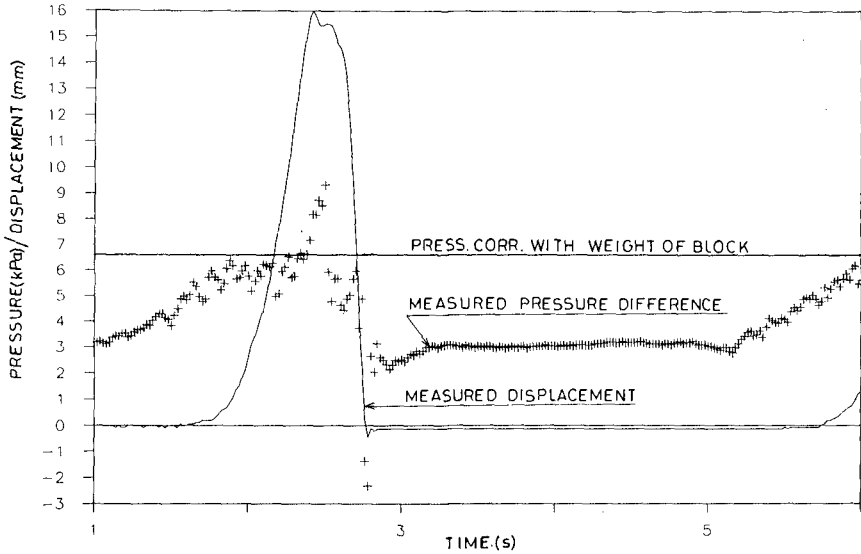


Figure 9. Test SZ 617, measured and calculated pore pressures below the moving revetment block due to wave attack ($H = 0.64$ m, $T = 4.1$ s, $\xi = 2.14$)

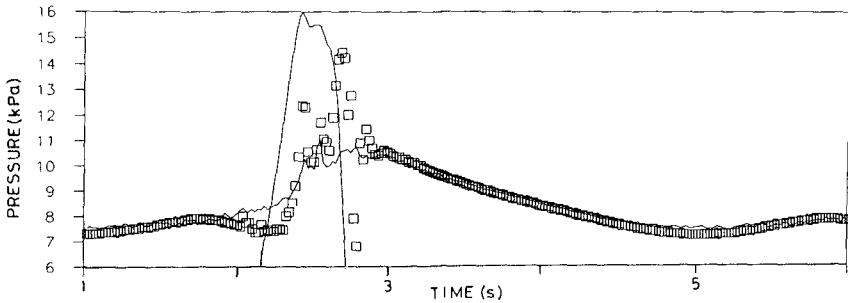


Figure 10. Measured uplift pressure compared with block movement

Recent measurements on a 28 years old revetment have shown a decrease in the cover layer permeability from 10^{-3} m/s to 10^{-6} m/s. It was known from earlier calculations (Bezuijen et al, 1987) that a low cover layer permeability leads to high uplift pressures over the revetment, which can possibly damage the revetment. With the model described in this paper it is possible to investigate what will be the influence of a low cover layer permeability on the block movement. Calculations were performed using the wave loading that was measured by wave SZ208. All calculations were carried out with the same revetment geometry, only the permeability of the cover layer was changed.

The results are presented in figure 11. A very permeable coverlayer results in small uplift pressures, too small to cause any block motion. Decreasing the cover layer permeability leads to higher uplift pressures and in an increase of the block motion, but this block motion has a maximum. For very low values of the cover layer permeability the block motion again decreases. This is caused by the fact that the flow in the filter layer towards the moving block is restricted by these very low values of the cover layer permeability. The calculations also show that the permeabilities that are reached right after construction (between 10^{-3} and 10^{-2} m/s) are most dangerous for the stability of the revetment (the block displacement is then at maximum).

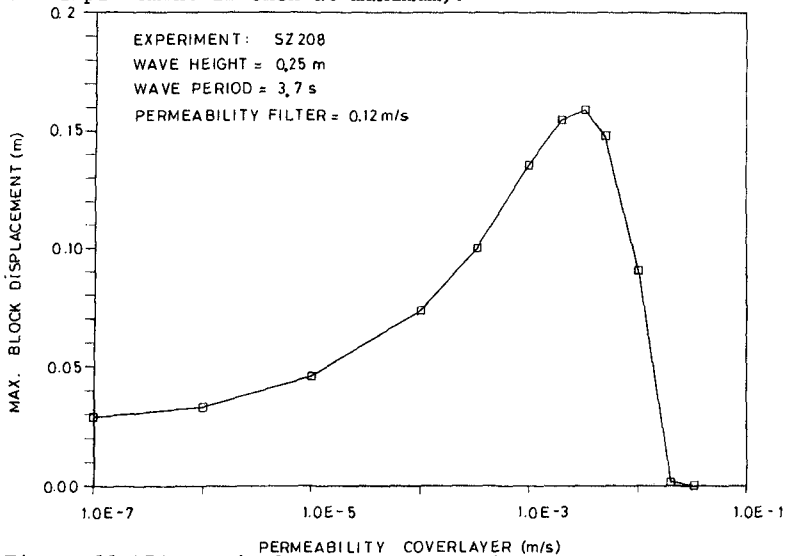


Figure 11. Block displacement as function of the cover layer permeability

Conclusions

The numerical simulations of the large scale model tests lead to the following conclusions:

- It is possible to simulate the motion of a loose revetment block under wave attack with STEENZET/1+. The calculated pore pressures

agree well with the measurements. The calculated block movement is somewhat higher for the structures simulated. This can partly be explained by the presence of a geotextile which prevented fluidisation of the filter layer between the blocks and the filter layer in the model tests and partly by some simplifications in the computer program.

- The influence of friction as well as inertia forces on the results of the calculations is negligible.
- The moment of maximum loading depends on the leakage factor. For a revetment with a long leakage factor (much longer than the wave height) the loading is maximum when the wave pressure on the loaded block is minimum. In case the leakage factor is shorter than the wave height, the maximum uplift pressure is present during the increase in the wave pressure caused by the new incoming wave.
- Measuring the pressure at one location on the block can be insufficient when experiments are performed with block dimensions that are of the same order of the wave height, for example test SZ 617 (wave height 0.64 m and block length = 0.5 m). In this test the inaccuracy in the determined uplift pressure became clear since the block started to move before the uplift pressure was larger than the pressure corresponding with the weight of the loose block.
- Simulation of the block movement for a revetment with different values for the cover layer permeability showed that the block displacement as function of the cover layer permeability has a maximum. Although a revetment with a very low cover layer permeability will be loaded with large uplift pressures, the block movement remains limited because the amount of water that can flow underneath the moving block is restricted by the low cover layer permeability.

References

- ADEL DEN H., Analysing permeability measurements with the Forchheimer relation (in Dutch), Delft Geotechnics, report CO-272550/56, November.
- BEZUIJEN A., WOUTERS J., and LAUSTRUP C. (1980)
Block revetment design with physical and numerical models
Proc. 21st. Conf. on Coastal engineering, Malaga 1988.
- BEZUIJEN A., KLEIN BRETELER M., BAKKER K.J.
Design Criteria for placed block revetments and granular filters.
Proc. 2nd Int. COPEDEC, Beijing, 1987.
- BURGER A.M., KLEIN BRETELER M., BANACH L., BEZUIJEN A. PILARCZYK K.W. (1990a)
Analytical design method for relatively closed block revetments
ASCE, Journ. of Waterway Port Coastal and Ocean Engineering,
Sept./Oct. (pp. 525 - 545).
- BURGER A.M., BEZUIJEN A., PILARCZYK K.W., KLEIN BRETELER M. (1990b)
Verification and practical use of concrete block revetment design method.
To be published Proc. 22nd Int. Conf. Coastal Engineering, Delft
- KLEIN BRETELER M., BEZUIJEN A. (1988)
The permeability of closely placed blocks on gravel
Proc. SOWAS-Symposium, Delft.

CHAPTER 121

WAVE PRESSURE ATTENUATION IN BREAKWATER ARMOUR LAYERS

Kevin R. Hall¹

Abstract

An experimental investigation was conducted to examine the change in fluid pressure through a breakwater armour layer as a function of the incident wave characteristics, breakwater geometry, armour unit type, number of layers of armour and core permeability. Values of internal pressure were found to decrease with the number of layers of armour. The largest percentage decrease occurred within the first few layers; although this trend was somewhat influenced by armour type.

Introduction

A set of experimental studies were undertaken primarily to investigate the mechanism of wave energy dissipation that occurs throughout the various zones (core, filter and armour) of a rubblemound breakwater subjected to monochromatic wave attack. In addition, information regarding the phreatic surface motion within the various zones of the structure was collected. The influence of the armour unit type, relative geometry of the armour layer, breakwater slope and the material used to construct the various layers of the structure on wave energy dissipation, wave runup and rundown on the outer surface of the structure and the internal flow generated within the structure was assessed.

These studies were undertaken in a two dimensional wave flume in which a rubblemound breakwater, instrumented with pressure transducers and capacitance gauges, was subjected to monochromatic wave attack. The rubblemound structure consisted of a core (constructed using either 3.5 mm angular, 16 mm angular or 14 mm rounded stone), a filter layer (constructed using either 16 mm angular or 14 mm rounded stone), and an armour layer (consisting of 1 to 5 layers of either 50 mm stone, 50 mm steel spheres or 60 mm cubes).

Preliminary work was required to determine the flow resistance characteristics of the porous media used in the study. This work was undertaken in a steady flow parameter.

Dept. of Civil Engineering, Queen's Univ., Kingston,
Ontario CANADA K7L 3N6

Test Conditions

The basic geometry of the test section is shown in Figure 1. The outer slope of the breakwater was tested at 1:3, 1:2, and 1:1.5. The slopes of the core and filter layers were made the same as the outer slope. The structure was instrumented with 10 pressure transducers, five on the outer slope of the structure at elevations of -20, -10, two at 0 and +10 cm (all elevations referenced to the still water level) and five on the outer slope of the core at elevations of -20, -10, -5, 0 and +10 cm placed along the centreline of the breakwater. Miniature stainless steel diaphragm pressure transducers (Data Instruments AB-15psig) capable of measuring gauge pressures ranging from 0 - 100 kPa were used. Five capacitance gauges for measuring the internal water surface movement were located along the centreline of the structure.

All tests were undertaken with the still water level located 30 cm above the flume bottom. Eighteen combinations of wave height and wave period were used for each test structure and are summarized in Table 1.

The wave height, H , is the wave height measured at the location of the rubblemound structure in the flume with no structure present. The surf similarity parameter, ξ , uses the breakwater slope, θ , the wave height at the structure, H , and the deep water wave length, L_0 .

Model Materials

(i) Core and Filter Materials

Three types of core material were used during the experimental studies; 3.5 mm river gravel, 14 mm river gravel and 16mm crushed river gravel. Table 2 lists the characteristic geometric properties and the relative density of each material. A filter layer was used in conjunction with the 3.5 mm core material and consisted of the 16 mm crushed river gravel described in Table 2.

(ii) Armour Units

Three types of armour units were utilized during the course of the experimental studies. These are summarized in Table 3.

(iii) Permeability

The flow characteristics of the core and filter materials were tested in a down-flow permeameter connected to a constant head tank. The results are given in Table 3 which lists the porosity and the Forchheimer constants, a and b , for each material.

During each test, the pressures and internal phreatic surface conditions were

ET - EXTERNAL PRESSURE TRANSDUCER
 IT - INTERNAL PRESSURE TRANSDUCER
 SG - PHREATIC SURFACE MONITORING GAUGE

ZONE I ARMOUR LAYER (1 to 5 UNITS THICK)
 ZONE II FILTER LAYER (50 mm THICK)
 ZONE III CORE

ELEVATIONS IN CENTIMETRES

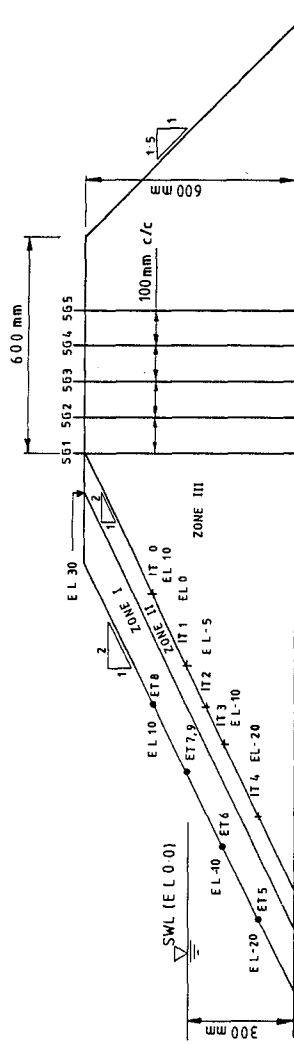


FIGURE 1 CROSS SECTION AND INSTRUMENT LAYOUT FOR BREAKWATER SLOPE 1:2

Table 1
Incident wave conditions for testing

Segment	T	H	$\xi = \tan \theta / [(H/L_o)^{1/2}]$			H/L _o
			Slope			
			1:1.5	1:2	1:3	
1	0.8	30	3.85	2.88	1.92	0.030
2	0.8	60	2.72	2.04	1.36	0.060
3	0.8	90	2.22	1.67	1.11	0.090
4	1.0	30	4.81	3.61	2.40	0.019
5	1.0	60	3.40	2.55	1.70	0.038
6	1.0	90	2.78	2.08	1.39	0.058
7	1.0	120	2.40	1.80	1.20	0.077
8	1.5	30	7.21	5.41	3.61	0.009
9	1.5	60	5.10	3.82	2.55	0.017
10	1.5	90	4.16	3.12	2.08	0.026
11	1.5	120	3.61	2.70	1.80	0.034
12	2.0	30	9.61	7.21	4.81	0.005
13	2.0	60	6.80	5.10	3.40	0.010
14	2.0	90	5.55	4.16	2.78	0.014
15	2.0	120	4.81	3.61	2.40	0.019
16	1.0	180	1.96	1.47	0.90	0.115
17	1.5	200	2.79	2.09	1.40	0.057
18	2.0	200	3.72	2.79	1.86	0.032

Table 2
Characteristic Properties of Core and Filter Materials

Sample	D_{\min} (mm)	D_{50} (mm)	D_{\max} (mm)	Relative Density	Porosity (as tested) percent	$a(\frac{\text{sec}}{\text{cm}})$	$b(\frac{\text{cm}^2}{\text{sec}^2})$
A	1	3.5	8	2.62	35	0.144	0.182
B	2	16	20	2.65	36.5	0.049	0.0109
C	3	14	20	2.65	33.7	0.0951	0.0355

Table 3
Summary of Armour Units

Armour Type	Mass (grams)	Relative Density	Nominal Size (mm)
Stone	$M_{50} = 121$	2.65	$D_{50} = 50$
	$M_{\min} = 80$		
	$M_{\max} = 180$		
Steel spheres	$M = 557$	8.0	50
Cubes	$M = 330$	2.0	60

monitored until steady state conditions were obtained. Time series records of pressure fluctuation at each gauge location were recorded. Post processing was incorporated to decrease the requirement for data storage.

The pressure was measured at a sampling rate of 50 Hz for a total recording length of ten wave periods. Earlier trials in which pressure was sampled at rates of 20 to 50,000 Hz provided sufficient evidence that a sampling rate of 50 Hz would enable determination of peak pressure. The data were subsequently phase-averaged so that each test segment (wave height-wave period combination) was characterized by a time series having a record length equal to the wave period. For the purpose of further analysis, each phase-averaged time series was characterized by a maximum differential pressure head, ΔP , which describes the maximum variation in recorded pressure over the period of the wave divided by ρg , where ρ is the fluid density and g is gravitational acceleration. Therefore, all pressure measurements were reported in terms of the equivalent head of water. The ratio of maximum differential pressure head, ΔP , to wave height, H , was used to provide a non-dimensional expression.

Results

In order to compare the attenuation of pressure between the various layers as a function of the test variables, the percent attenuation of pressure relative to one layer of armour, $\% \Delta P_1$, was calculated where

$$\% \Delta P_1 = \frac{\left(\frac{\Delta P}{H} \right)_n}{\left(\frac{\Delta P}{H} \right)_1} = \frac{\frac{\Delta P}{H} \text{ for } n \text{ layers}}{\frac{\Delta P}{H} \text{ for } 1 \text{ layer}}$$

Values of $\% \Delta P_1$ were calculated for each wave height-period combination. Table 4 shows values of the average and standard deviation of $\% \Delta P_1$ as a function of the number of layers of armour and elevation of the pressure recording.

In order to reduce the number of variables, the data was refined one step further. For each test series, the differential pressure head for a specified number of layers is presented as a percentage of differential pressure head for one layers, that is

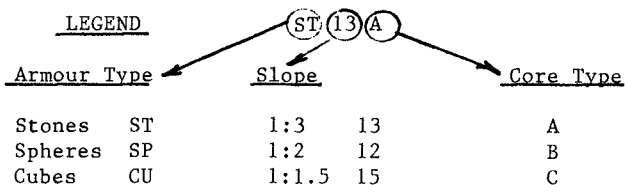
$$\overline{\Delta P / \Delta P_1} = \sum_{i=1}^J \left(\frac{\Delta P_{nj}}{\Delta P_{1j}} \right) / J$$

TABLE 4

Summary of ΔP_1 versus Number of Layers of Armour

Series	EL = 0		EL = -5		EL = -10		EL = -20	
	Avg	(Std)	Avg	(Std)	Avg	(Std)	Avg	(Std)
*								
ST13A	2-1	1.0 (.0)	.58 (.15)	.73 (.09)	.91 (.12)			
	3-1	1.0 (.0)	.57 (.25)	.64 (.15)	.83 (.20)			
	4-1	1.0 (.0)	.44 (.27)	.53 (.12)	.78 (.24)			
SP13A	2-1	1.17 (.3)	.93 (.36)	.97 (.11)	.97 (.27)			
	3-1	.98 (.45)	.65 (.35)	.76 (.15)	.87 (.34)			
	4-1	.94 (.53)	.54 (.36)	.59 (.19)	.78 (.30)			
CU13A	2-1	1.51 (.33)	.68 (.39)	.77 (.64)	.94 (.39)			
	3-1	1.46 (.34)	.76 (.42)	.52 (.28)	.84 (.25)			
	4-1	1.03 (.23)	.62 (.35)	.42 (.23)	.65 (.23)			
	5-1	.96 (.31)	.55 (.38)	.35 (.20)	.40 (.20)			
ST12A	2-1	.88 (.14)	.85 (.59)	.86 (.06)	.96 (.15)			
	3-1	.68 (.14)	.69 (.43)	.75 (.08)	.87 (.26)			
	4-1	.60 (.15)	.56 (.35)	.61 (.07)	.81 (.27)			
	5-1	.50 (.16)	.47 (.34)	.51 (.09)	.76 (.25)			
ST12B	2-1	.38 (.18)	.66 (.13)	.71 (.08)	.85 (.17)			
	3-1	.31 (.10)	.59 (.13)	.60 (.08)	.76 (.18)			
	4-1	.23 (.05)	.48 (.08)	.48 (.08)	.69 (.17)			
	5-1	.27 (.08)	.41 (.14)	.39 (.08)	.58 (.17)			
ST12C	2-1	.77 (.11)	.73 (.11)	.80 (.09)	.98 (.18)			
	3-1	.71 (.15)	.37 (.10)	.58 (.07)	.83 (.22)			
	4-1	.58 (.13)	.28 (.09)	.46 (.08)	.78 (.23)			
	5-1	.53 (.15)	.21 (.06)	.36 (.08)	.65 (.21)			
SP12A	2-1	.82 (.13)	.93 (.08)	.87 (.07)	.95 (.17)			
	3-1	.66 (.16)	.75 (.11)	.76 (.07)	.83 (.26)			
	4-1	.59 (.14)	.64 (.12)	.67 (.09)	.79 (.29)			
CU12A	2-1	.72 (.17)	.74 (.10)	.76 (.10)	.89 (.22)			
	3-1	.49 (.08)	.53 (.14)	.67 (.13)	.92 (.37)			
	4-1	.37 (.11)	.37 (.10)	.44 (.12)	.64 (.21)			
	5-1	.33 (.09)	.29 (.08)	.32 (.11)	.49 (.19)			
ST15A	2-1	.56 (.16)	.84 (.22)	.79 (.21)	.86 (.24)			
	3-1	.47 (.09)	.80 (.09)	.76 (.10)	.89 (.18)			
	4-1	.35 (.05)	.70 (.08)	.64 (.09)	.90 (.19)			
	5-1	.26 (.10)	.58 (.10)	.49 (.12)	.76 (.23)			
SP15A	2-1	.85 (.07)	.83 (.07)	.83 (.08)	.95 (.15)			
	3-1	.71 (.11)	.72 (.11)	.73 (.10)	.93 (.23)			
CU15A	2-1	.74 (.10)	.83 (.11)	.79 (.13)	.91 (.20)			
	3-1	.53 (.12)	.48 (.09)	.51 (.12)	.78 (.21)			
	4-1	.43 (.07)	.34 (.08)	.37 (.10)	.61 (.17)			

* the y-l column represents the difference between tests with y layers and l layer.



where $\Delta P/\Delta P_1$	=	average value of ratio of differential pressure head for n layers to differential pressure head for one layer.
ΔP_{ij}	=	differential pressure head for one layer
ΔP_{nj}	=	differential pressure head for n layers
n	=	number of layers
j	=	test segment number
J	=	total number of test segments

Thus plots of $\overline{\Delta P/\Delta P_1}$ provide a graphical representation of the data in Table 4.

Influence of Elevation

The largest reduction in internal pressure as the number of layers was increased occurred at the still water level, whereas the pressure measured at an elevation of -20 cm showed the smallest reduction as the number of layers of armour was increased. This is illustrated in Figure 2.

Influence of Core Type

The influence of the type of core material on the internal differential pressure head was assessed only for a structure with 50 mm stones in the armour layer and a front slope of 1:2.

Figure 3 provides an example of the variation of $\overline{\Delta P/\Delta P_1}$ with the number of layers of armour as a function of core type. At all elevations, the internal pressure measured in core type A ($D_{50} = 3.5$ mm) were the highest. At all elevations, the internal pressures measured in core type B were approximately 15-20 percent lower than those measured in core type A. The internal pressures measured in core type C varied from being equal to those measured in core type A at elevations of the still water level and -20 cm to a 30 percent reduction at elevation -5 cm and a 15 percent reduction at elevation -10 cm. The reason for this variation with elevation is not quite clear, although it may be a consequence of non-homogeneity in core type C. It was suspected that core material C was non-homogeneous because two separate loads of material were used and these may have had slightly differing characteristics.

The influence of core type was found to be relatively linear with the number of layers of armour.

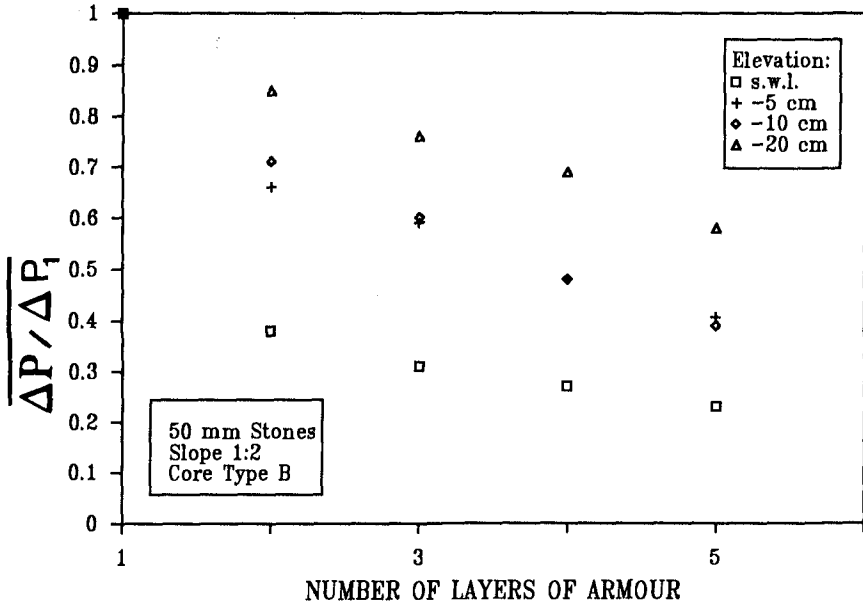


FIGURE 2 INFLUENCE OF ELEVATION ON % ΔP_1

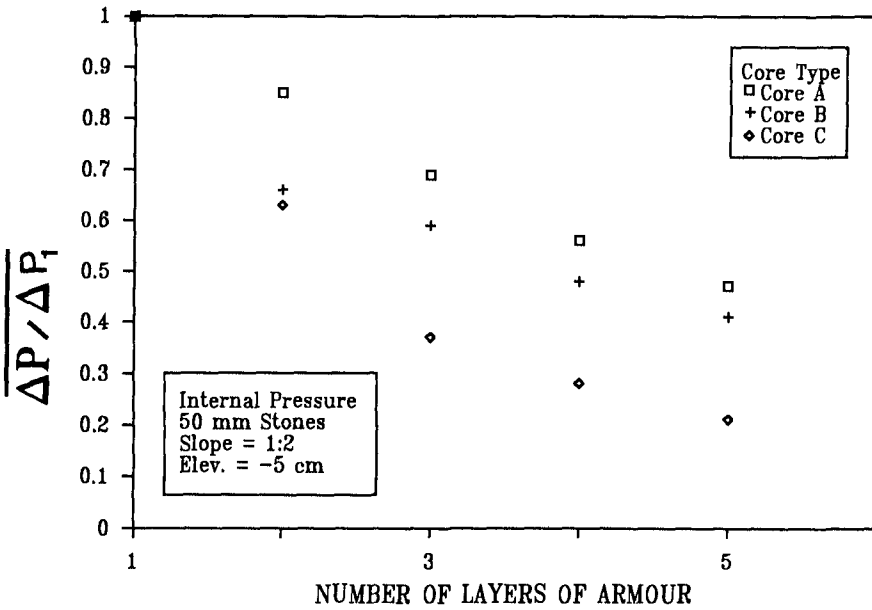


FIGURE 3 INFLUENCE OF CORE TYPE ON % ΔP_1

Influence of Armour Type

The influence of the type of armour unit used in the armour layer on the internal pressure field at the four internal gauge locations is shown in Figure 4 which shows the variation of $\overline{\Delta P / \Delta P_1}$ with the number of layers for a given breakwater slope and pressure gauge elevation.

In general it appears that randomly placed cubes provided the greatest reduction in internal pressures at all elevations on all slopes (with the exception of a few instances). The internal pressures measured for armour layers consisting of stones and spheres exhibited fairly similar trends. Typically cubes provided an additional 10-30 percent reduction in internal pressure, although this usually occurred across the second layer. The rate of change of $\overline{\Delta P / \Delta P_1}$ with the number of layers of armour was similar for all three unit types.

For a breakwater slope of 1:1.5, armour stones exhibited the greatest ability to dissipate internal pressure at the still water level. Cubes exhibited the same trend at all other gauge locations (-20, -10 and -5 cm), with a typical average internal pressure reduction 25-50 percent greater than that of stones, depending upon the number of layers of armour.

For a breakwater slope of 1:2 the greatest internal pressure reduction at all elevations was achieved by using cubes in the armour layer.

As the slope became flatter (1:3), stones and cubes exhibited similar capabilities in providing a reduction in internal pressure, particularly with decreasing gauge elevation.

Influence of Breakwater Slope

Examples of the influence of breakwater slope on the variation of $\overline{\Delta P / \Delta P_1}$ with the number of layers of armour is shown in Figures 5 to 7. One graph is presented for each type of armour unit. An elevation of -10 cm was chosen as representative.

The variation in $\overline{\Delta P / \Delta P_1}$ as a result of slope change was not significant in tests undertaken with armour layers comprised of stones, except at the still water level. A slope of 1:3 consistently provided the greatest internal pressure reduction, although this was only of the order of 5-10 percent greater than that for the other slopes.

This was also true for tests in which the armour layer was constructed of spheres.

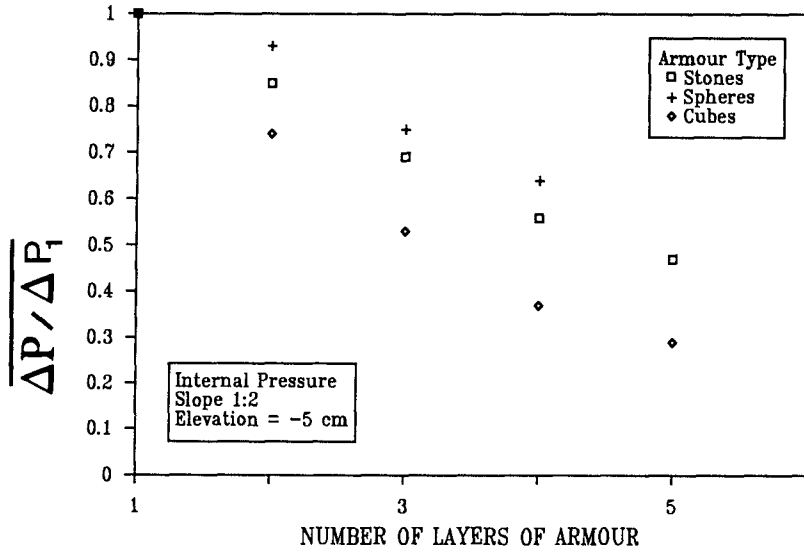


FIGURE 4 INFLUENCE OF ARMOUR TYPE ON $\frac{\Delta P}{\Delta P_1}$

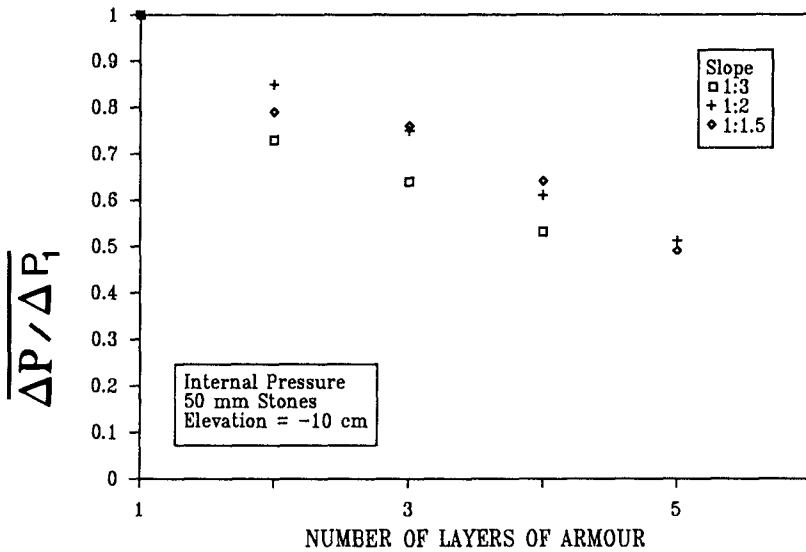


FIGURE 5 INFLUENCE OF SLOPE ON $\frac{\Delta P}{\Delta P_1}$ (Stones)

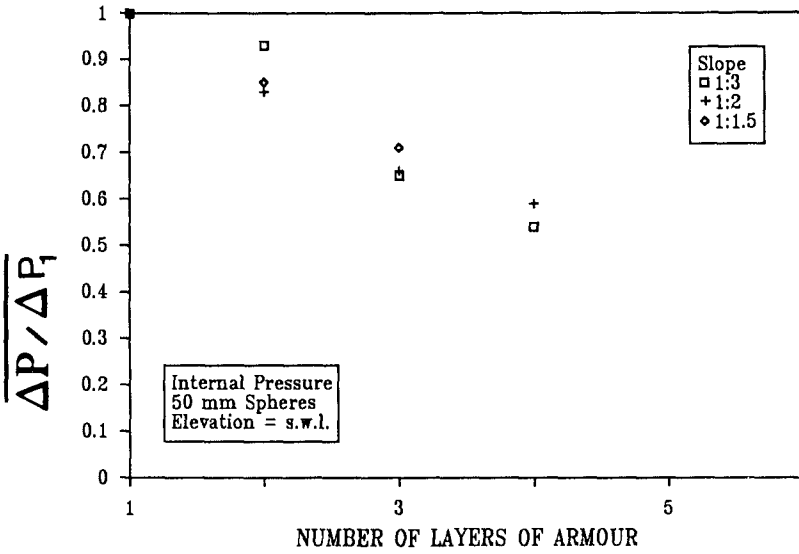


FIGURE 6 INFLUENCE OF SLOPE ON $\overline{\Delta P}_1$ (Spheres)

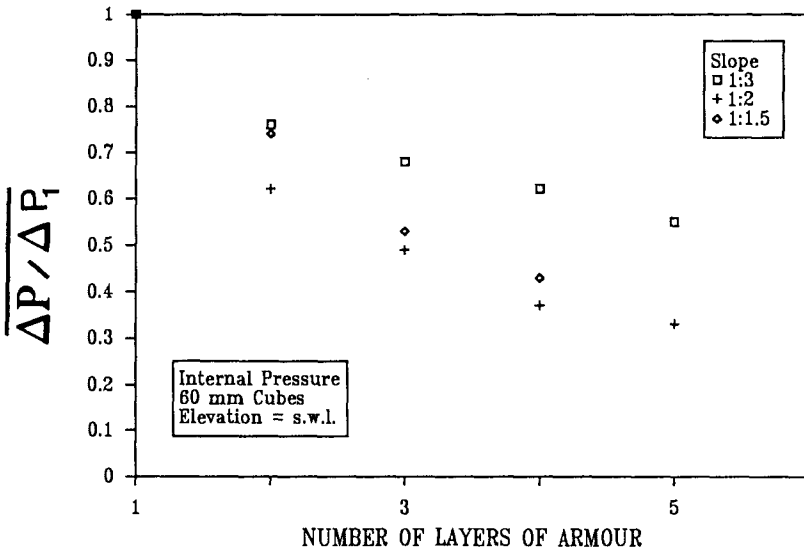


FIGURE 7 INFLUENCE OF SLOPE ON $\overline{\Delta P}_1$ (Cubes)

For these tests, the variation of $\overline{\Delta P/\Delta P_1}$ with slope was not significant at any gauge location. This trend was also observed in tests in which the armour layer was constructed with cubes, except at the still water level.

There were two cases in which the trend described above did not occur. These cases were for measurements made at the still water level. Since the internal pressure at this elevation will be influenced by local variations in the phreatic surface, this may provide an explanation for this effect. The phreatic surface elevation for given test conditions was typically much higher for spheres than for stones or cubes. In tests undertaken with spheres, minor fluctuations in the phreatic surface creates a dynamic pressure component which makes up only a small percentage of the total internal pressure at the still water level. The hydrostatic component was far more significant since the phreatic surface elevation was consistently well above the still water level. However, for tests undertaken with stones and cubes, the local variations in phreatic surface often had a magnitude equal to the average set-up of the phreatic surface. Thus the local variations in phreatic surface elevation became quite significant. These variations were a function of breakwater slope and may indicate why a large variation in

$\overline{\Delta P/\Delta P_1}$ with slope occurred at the still water level in tests undertaken using stones and cubes.

Summary of Findings

- the external pressure response curves were characterized by sharp peaks and rapid rise times whereas internal pressure response was somewhat smooth and gradual as a result of damping within the armour.
- the elevation at which the maximum $\Delta P/H$ on the external slope of the breakwater occurred was found to vary with wave period
- the rate of change of pressure during wave uprush was found to increase with increasing wave height at all gauge elevations
- the core material type had no significant influence on the external pressures but had a marked influence on the internal pressure field. As the number of layers of armour was increased, the magnitude of the peak pressure decreased while the rise time between trough and peak pressures increased
- the number of layers of armour had no influence on the external pressures but had a marked influence on the internal pressure field. As the number of layers of armour was increased, the magnitude of the peak pressure decreased while the rise time between trough and peak pressures increased.

- the type of armour unit used in the armour layer was found to have a small influence on the external pressure field. Using cubes produced the highest value of $\Delta P/H$.
- the maximum $\Delta P/H$ was found to increase with decreasing wave steepness.
- values of internal maximum $\Delta P/H$ were found to decrease with increasing armour layer thickness. The largest percentage decrease was found within the first few layers of armour. This trend was more evident with tests undertaken with stones and cubes in the armour layer. (this is primarily a permeability effect)
- a net downward propagation of wave energy and pressure was found by analyzing phase and elevation relationships between gauge locations
- internal pressures were found to be the highest for tests undertaken using spheres and lowest for tests undertaken using cubes.

CHAPTER 122

CONCRETE ARMOR UNIT STRUCTURAL DESIGN CRITERIA

C.D. Anglin, AM and R.D. Scott, AM ASCE¹
D.J. Turcke²

ABSTRACT

A comprehensive examination of the structural response of breakwater armor units to static and wave-induced loads has been completed using a dolos armor unit load cell in a physical breakwater model. Three extensive test series were completed to assess the influence of a wide range of breakwater and sea state parameters, and data reduction and analyses techniques were developed to estimate the structural response as a function of the critical independent parameters.

Using these data, improved design criteria, which consider both the hydraulic and structural aspects of breakwater design, have been developed for the dolos unit. Perhaps even more significant is the fact that the basic instrumentation scheme, model testing program, and data reduction and analysis procedures could be utilized to develop improved design procedures for other armor units, or to assist in the development of a new armor unit.

INTRODUCTION

Concrete armor units are used to protect rubblemound breakwaters when quarried stone of sufficient size to resist the incident wave climate is not available. The design of these breakwaters considers the hydraulic stability of the armor layer, but does not generally consider the structural integrity of the armor units themselves. The resultant limitations in these design approaches were clearly demonstrated by a number of damages and failures of rubblemound breakwaters in the late 1970's and early 1980's.

A co-operative effort between W.F. Baird and Associates, the Department of Civil Engineering at Queen's University, and the Hydraulics Laboratory of the National Research Council of Canada was initiated in 1980 to investigate the nature and magnitude of the forces acting on breakwater armor units. This effort led to the development of an armor unit "load cell" (Scott, 1986) which could accurately measure static and wave-induced (quasi-static) loads in a hydraulic breakwater model. This instrumentation was used in several extensive test

¹ Project Engineers, W.F. Baird & Associates Coastal Engineers Ltd.
150-38 Antares Drive, Ottawa, Canada, K2E 7V2

² Professor of Civil Engineering, Ellis Hall, Queen's University, Kingston,
Canada, K7L 3N6

series to provide the structural response data required to develop structural design criteria for the dolos armor unit, as discussed in this paper.

INSTRUMENTATION - THE DOLOS LOAD CELL

In this study, the structural response of the dolos armor unit to static and wave-induced (quasi-static) loads was measured in a breakwater model using the armor unit load cell developed by Scott (1986). The load cell utilizes the concept of geometric distortion, and consists of a thin-walled aluminum tube instrumented with strain gauges and inserted into the shank of a hollowed out dolos unit, as shown in Figure 1. Three full strain gauge bridges measure two orthogonal bending moments and the torque at the mid-shank section; instrumentation to measure other load components, such as axial and shear forces, was not provided, as a review of prototype damages and previous analyses for the dolos unit indicated that bending and torsional stresses were dominant. The accuracy and sensitivity of the load cell instrumentation were investigated during calibration by comparing the measured moments and torques to theoretical values.

The original load cell design utilized in the first parametric study (wave-induced loads) was instrumented at the mid-shank section. For the subsequent investigations of static forces and the combined effects of static and wave-induced forces, four improved load cells were constructed, two instrumented at the mid-shank (MS) section and two at the fluke-shank (FS) section. These improvements are discussed in detail in W.F. Baird and Associates (1989b). Details of the two designs were identical except for the location of the split in the dolos shank. In general, all of the load cells utilized in the various testing programs performed well in the harsh environment of a hydraulic breakwater model.

TESTING PROGRAMS

Approximately 2000 tests were undertaken in three separate test series using the dolos load cell in a physical breakwater model in order to measure static and wave-induced (quasi-static) forces in the armor units, and to provide structural response data from which preliminary design criteria could be developed. All tests were undertaken using a "conventional" breakwater cross-section, with a primary armor layer of dolos units (mass of 482 g and density of 2500 kg/m³) placed over a filter layer of crushed stone (mass of 30 to 100 g), as shown in Figure 2. The dolos units had a waist ratio (shank width/overall length) of 0.32 and were randomly placed in two layers with a packing density, ϕ (as defined by Zwamborn, 1978), of 0.8 to 0.9.

The first parametric study of quasi-static (wave-induced) loads was completed using a two-dimensional wave flume at the Hydraulics Laboratory of the National Research Council of Canada (Baird and Associates, 1989a). Over 1000 tests were run with regular waves and approximately 140 tests with irregular waves to assess the effects of breakwater slope, armor unit location, wave period and wave height on armor unit structural response.

After placing two load cells (mid-shank units only) at selected locations in the armor layer, the breakwater was subjected to a short of waves, and the wave gauge and amplified load cell responses (M_1 , M_2 , T) were sampled at 500 Hz for 30 s (regular waves) or 60 seconds (irregular waves). This sample length covered from 10 to 34 wave periods depending on the incident wave period.



Figure 1. The Dolos Armor Unit Load Cell

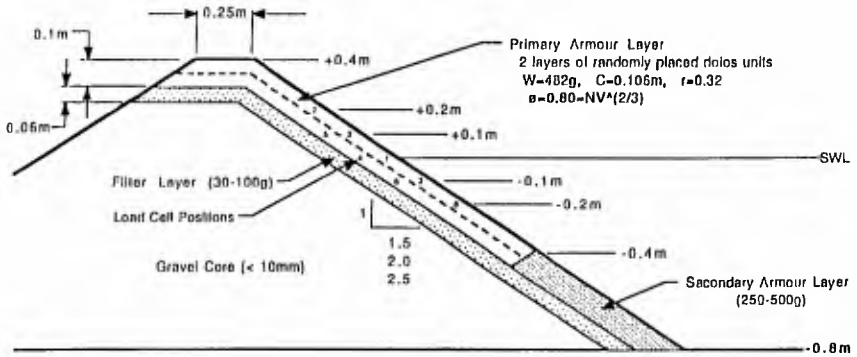


Figure 2. Model Breakwater Cross-Section

The next set of tests, a parametric study of static loads, was completed in a dry environment, with the armor and filter layers constructed on a 0.7 m wide by 1.3 m long plywood ramp. Over 400 tests were run to assess the effects of breakwater slope, load cell location (relative to the "crest" of the breakwater), vibration, and the location of the force measurements (mid-shank section or fluke-shank section).

An additional series of flume tests was then undertaken, using the improved mid-shank and fluke-shank armor unit load cells, in order to measure the combined effects of both static and quasi-static (wave-induced) forces. The primary objective of this test series was to obtain data to allow an assessment of the interaction of the two force components (static and quasi-static). Consequently, a procedure could be developed to combine the results of the two independent parametric studies of these force components to estimate the overall response of the dolos unit to the combined loading conditions. The breakwater cross-section was the same as that used in the earlier flume study (see Figure 2), but the range of parameters tested was reduced as there was no need to repeat all the previous tests to assess the interaction of these forces.

DATA REDUCTION

An initial review of the structural response of the armor unit load cell to wave-induced forces was undertaken using the time series and spectral density plots. An example of these presentations for a selected regular wave test are shown in Figures 3 and 4. The time series plot (Figure 3) shows the repeatability of the response with the wave period, but shows considerable variation between the magnitude and shape of the "response profile" for the three measured load components (M_1 , M_2 and T). The spectral density plot (Figure 4), which shows the energy in the signal as a function of frequency, reveals the presence of an energy peak in the response at the incident wave frequency (f), and also at second and higher harmonic frequencies (i.e. nf , where $n = 1, 2, 3 \dots$). The largest peak in the response was normally located at the incident wave frequency or at the second harmonic frequency. The presence of second and higher harmonics in the response indicates a non-linear interaction between the response and the incident waves. Harmonic peaks in the response signals were observed to occur under the full range of wave conditions and load cell locations tested, although not in every test.

Similar observations were made in reviewing the response of the dolos load cell to irregular waves. The time series plots demonstrated the grouping effect of the incident wave train, with groups of large waves generating a large response in the armor units. The spectral density plots showed that the armor unit response typically had a peak frequency equal to that of the incident wave train (f_p); however, as with the regular wave tests, higher order harmonic peaks were observed in many of the tests.

In order to undertake the various analyses on the load cell response data necessary to develop design criteria, it was desirable to combine the effects of the three measured load components into a single quantity that could be related to a relevant failure criterion for concrete armor units. For unreinforced concrete structures, the exceedance of the tensile cracking strength at any point in the structure is a well accepted failure criterion. Consequently, the measured moment and torque time series (or simply values for the static tests) were used to calculate the time series (or value) of the maximum principal stress (σ) at the measurement location (mid-shank or fluke-shank). This calculation was undertaken using standard structural engineering equations, as summarized below:

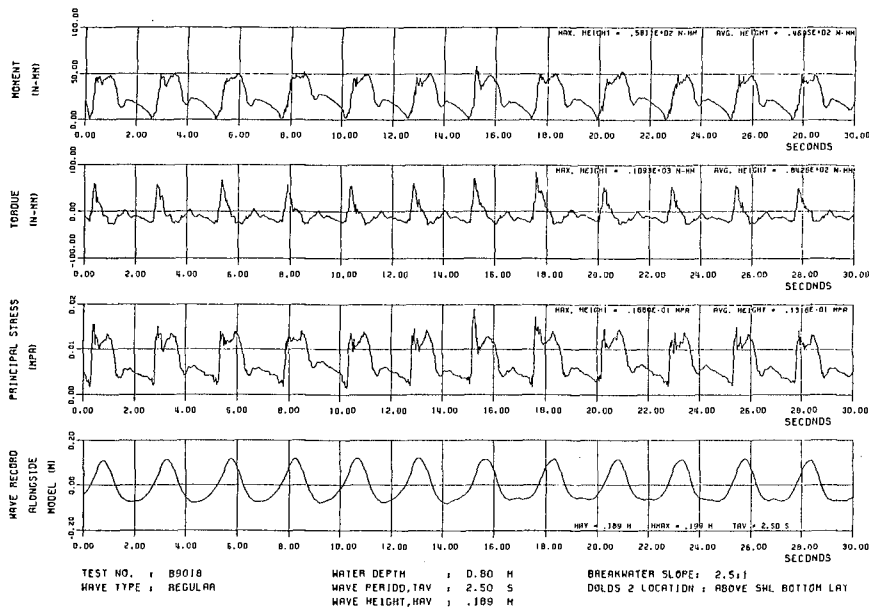


Figure 3. Load Cell Response Time Series

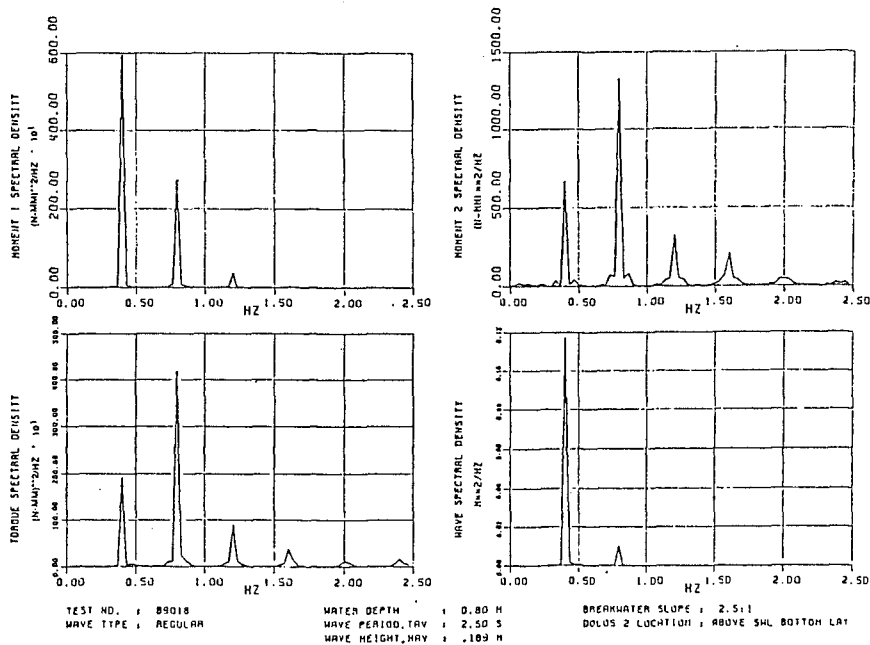


Figure 4. Energy Spectra for Load Cell Response

$$\sigma = 0.5(\sigma_x) + \sqrt{(0.5\sigma_x)^2 + \tau^2} \quad (1)$$

where $\sigma_x = Mc/I$ (longitudinal stress due to resultant bending moment, M) (2)

$\tau = Tc/J$ (shear stress due to torque, T) (3)

with $M = \sqrt{M_1^2 + M_2^2}$ (resultant bending moment calculated from measured moments M_1 and M_2) (4)

T = measured torque

c = distance from neutral axis to surface of dolos shank

I = moment of inertia of dolos shank section

J = polar moment of inertia of dolos shank section

For the static tests, the calculated maximum principal stress value, after scaling to prototype, could simply be compared to the tensile strength of the concrete (ft) to assess the structural integrity of the unit under specified conditions. However, in the case of the quasi-static tests, where the wave-induced principal stress consists of a 30 or 60 s time series rather than a single value, it was desirable to derive a characteristic value of the principal stress time series. Preliminary data analyses were undertaken using the "average stress height" ($\sigma_{avg ht}$) for regular waves and the "one third stress height" ($\sigma_{1/3 ht}$) for irregular waves.

For the development of design criteria, it seemed more appropriate to select an extreme value from the time series with a specific probability of exceedance. Statistical analyses of the regular wave results were undertaken which showed that the distribution of the response peaks within any given sample could be described by a normal distribution. Thus, by calculating the mean (\bar{x}) and standard deviation (s) of the principal stress peaks within a particular sample, a characteristic large value with a specified probability of exceedance could be calculated.

DATA ANALYSES

Initial parametric analyses of the static and quasi-static test data were completed by producing a series of scatter plots for the dependent variable (a characteristic value of the principal stress response) plotted as a function of selected independent variables. The effects of other independent variables was shown by sorting the data into specific ranges for a selected variable and calculating regression lines for the various data subsets.

For example, the principal stress measured in the static armor layer tests was plotted as a function of the vertical distance below the breakwater crest for sixteen data subsets, defined by mid-shank (MS) or fluke-shank (FS) instrumentation, top or bottom layer, before or after vibration, and 1:1.5 or 1:2.5 slope. Figure 5 shows a plot of the full data set for a 1:1.5 slope. In general, the measured stresses tended to be higher on the steeper slope, at locations further down the slope, and in the bottom layer. However, no consistent trend was observed in the results for MS or FS instrumentation location or vibration.

For the quasi-static (wave-induced) test results, the average stress height (for regular waves) or one-third stress height (for irregular waves) was plotted as a function of wave height (H), wave steepness (H/L) and surf similarity parameter ($\xi = \tan \alpha / \sqrt{H/L}$). These plots were produced for selected armor unit locations and periods, as well as for all the data sorted by these parameters, for each breakwater slope tested. A typical plot is shown in Figure 6, which shows $\sigma_{avg ht}$ vs H for all test locations plotted with the different wave periods identified.

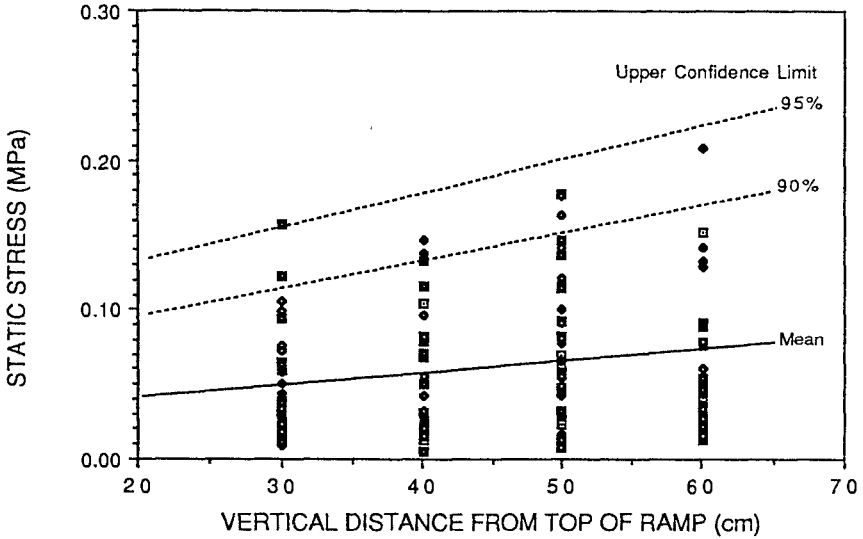


Figure 5. Static Stress as a Function of Vertical Distance (1:1.5 slope, bottom layer)

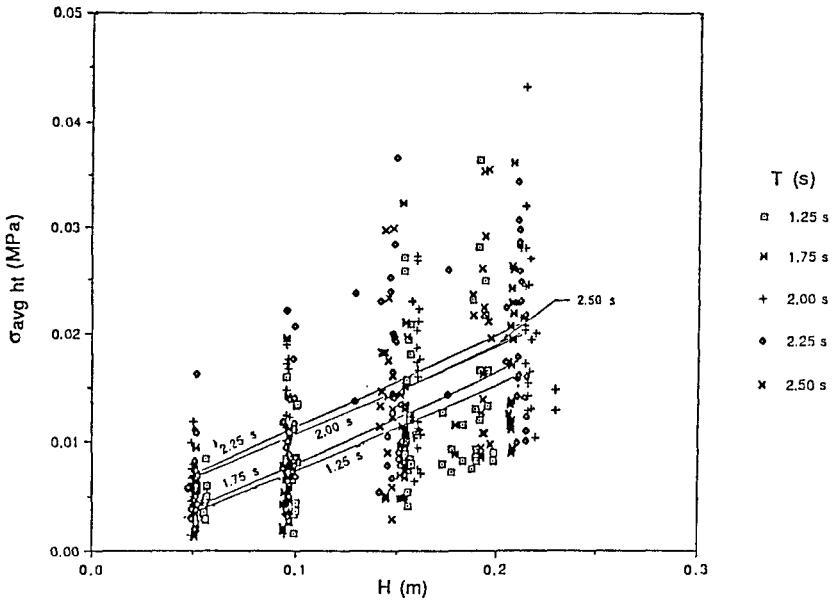


Figure 6. Average Stress vs Wave Height (1:1.5 slope)

In general, wave-induced stresses for both regular and irregular waves were observed to increase with wave height, wave period and wave steepness, while the effects of breakwater slope, armor unit location [top or bottom layer, and position relative to the still water level (swl)] were not as consistent. Wave-induced stresses under regular waves tended to be greatest on a slope of 1:2.0 and lowest on a slope of 1:2.5, with 1:1.5 falling in between; the effect of slope was not investigated in the irregular wave tests. Plots of the average stress height versus the surf similarity parameter (Figure 7) showed that the maximum stresses tend to occur for ξ between approximately 2 and 3.5, which is consistent with earlier literature concerning armor unit stability [for example, Van der Meer and Pilarczyk (1987)].

Multiple regression analyses were undertaken independently on the test results from the static and quasi-static (wave-induced) parametric studies in order to systematically assess the influence of the various independent parameters and to develop a mathematical expression defining the structural response (principal stress) of the dolos unit as a function of the critical parameters. A multiple regression analysis serves to identify three factors: a regression equation; standard error of estimate (s) and coefficient of multiple determination (R^2).

Linear combinations of the independent parameters were tested as an initial model for both the static and quasi-static test results. For the quasi-static test results, the regular and irregular tests were treated separately. In all three cases, it was found necessary to transform the dependent variable (principal stress) by taking its logarithm in order to satisfy the assumption of constant variance in the regression model. This transformation is consistent with the exponential relationship observed between the average stress height and the wave height in the regular wave tests, as mentioned earlier. The resulting regression equations for the three data bases, and their associated standard errors and coefficients of multiple determination, are summarized below:

Static Tests:

$$\log(\sigma_s)_{est} = -2.28 + 0.91(m) + 0.30(D_v - 0.45) + 0.34(layer) \quad (5)$$

$$s = 0.31, R^2 = 0.31$$

Note: the effects of instrumentation location (MS or FS) and vibration (before or after) were found to be insignificant.

Quasi-Static Regular Wave Tests:

$$\log(\sigma_{avg} h)_{est} = -2.70 + 0.18(m) + 0.31(D_{swl}) + 0.13(T) + 2.70(H) \quad (6)$$

$$s = 0.20, R^2 = 0.48$$

Note: the effect of layer (top or bottom) was found to be insignificant.

Quasi-Static Irregular Wave Tests:

$$\log(\sigma_{1/3} h)_{est} = -2.33 - 0.20(D_{swl}) + 0.07(T_p) + 1.91(H_s) \quad (7)$$

$$s = 0.20, R^2 = 0.48$$

Note: the effect of layer (top or bottom) was found to be insignificant.

The parameters in these equations are defined below:

$(\sigma_s)_{est}$	= estimated principal stress from static tests (MPa)
$(\sigma_{avg ht})_{est}$	= estimated average principal stress height, regular wave tests (MPa)
$(\sigma_{1/3 ht})_{est}$	= estimated one-third principal stress height, irregular wave tests (MPa)
m	= tangent of breakwater slope angle (for a 1:2.0 slope, m = 0.5)
D_v	= vertical distance of load cell test location below breakwater crest (m)
D_{swl}	= vertical distance of load cell location from still water level (m) (positive is above the swl)
layer	= categorical variable for layer, top = 0, bottom = 1
T	= average wave period for regular wave tests (s)
H	= average wave height for regular wave tests (m)
T_p	= peak wave period for irregular wave tests (s)
H_s	= significant wave height for irregular wave tests (m)

The standard error of the estimate, which provides a measure of the scatter of the data, can be used to define confidence or exceedance limits for the data if one knows the distribution of the data. Preliminary statistical analyses of the regular wave test results demonstrated that the distribution of the $\log(\sigma_{avg ht})$ values about the regression hyperplane could be described by a normal distribution. Thus, an exceedance limit for the average stress height can be established at any specified probability level using the results of the multiple regression analysis, as shown below:

$$\log(\sigma_{avg ht})_{\alpha} = \log(\sigma_{avg ht})_{est} + \Phi^{-1}(\alpha)s \quad (8)$$

where $(\sigma_{avg ht})_{\alpha}$	= average stress height with a probability of exceedance of α
$(\sigma_{avg ht})_{est}$	= average stress height estimated by the regression equation
$\Phi^{-1}(\alpha)$	= standard normal variate evaluated at probability level α
s	= standard error of the regression equation estimate

This probabilistic approach was incorporated in the development of structural design criteria for the dolos armor unit, as described later in this paper. However, the design criterion for wave-induced loads was developed using a peak stress value with a specified probability of exceedance from each test time series, rather than the average stress height from the time series.

The coefficients of multiple determination were 0.3 for the static tests and approximately 0.5 for the quasi-static tests. This implies that the respective regression models account for only 30 and 50% of the observed variation in the logarithm of the stress value. Some of this variation may be attributed to experimental error; however, a significant portion of this scatter may be explained by the effects of random orientation and boundary conditions of the armor units in the complex armor layer. Quantification of these variables was not attempted in this study. More complex regression models incorporating non-linear terms of the independent variables were investigated, but did not provide any significant improvements over the log-linear models discussed above.

DEVELOPMENT OF DESIGN CRITERIA

Introduction

Design stress level relationships have been derived from the results of the extensive testing programs described earlier for the following loading conditions:

- Static Loads - stresses induced by armor unit self-weight and inter-unit contact
- Quasi-Static Loads - fluctuating stresses induced by wave action
- Total Loads - the total stress due to the combined effects of static and quasi-static (wave-induced) loading

These relationships were derived on a statistical basis such that the designer can select the exceedance probability for the design stress level estimated for a particular set of design conditions. The development of these structural design criteria is presented in detail in Baird and Associates (1989b). Due to space limitations, the following section of this paper summarizes the results for only the total load condition.

Design Equation for Total Loads

A design equation was developed for the total stress occurring in a dolos armor unit due to the combined effects of static and quasi-static loads. The design equation for the combined loading condition is based on a statistical combination of predictive equations for estimating the static and quasi-static stresses. The predictive equations for the static and quasi-static stresses were derived from detailed parametric model studies of the two independent loading conditions using multiple regression analyses, while the statistical combination of these two equations was based on a third model study which investigated the combined effects of the two loading conditions. The resulting design equation for the combined loading condition is presented below.

From a design perspective, we require that:

$$n(\sigma_{tsp})_{\alpha} \leq f_t \quad \text{or} \quad \frac{n(\sigma_{tsp})_{\alpha}}{f_t} \leq 1 \tag{9}$$

where:

- $(\sigma_{tsp})_{\alpha}$ = design total stress level in model armor unit (MPa) with a probability of exceedance of α
- n = model scale factor
- f_t = prototype tensile strength of concrete (MPa)

The design total stress level in the model (MPa) is given by:

$$(\sigma_{tsp})_{\alpha} = (\sigma_{tsp})_{est} + [\Phi^{-1}(\alpha)]s \tag{10}$$

where:

$$(\sigma_{tsp})_{est} = 0.905(\sigma_s)_{est} + 0.639(\sigma_{qsp})_{est} \tag{11}$$

$$(\sigma_s)_{est} = 10^{**}[-2.28 + 0.91(m) + 0.30(D_v/n - 0.45) + 0.34(\text{layer})] \tag{12}$$

$$(\sigma_{qsp})_{est} = 10^{**}[-2.36 + 0.15(m) + 0.10(T/\sqrt{n}) + 0.29(D_{swl}/n) + 2.20(H/n)] \tag{13}$$

s = 0.001 (standard error of the estimate)

$(\sigma_{tsp})_{est}$ is the estimated peak value (5% exceedance) of the principal stress time series for the total loading condition, while $(\sigma_s)_{est}$ is the multiple regression equation estimate of the principal stress due to static loads and $(\sigma_{qsp})_{est}$ is the estimate of the peak value (5% exceedance) of the principal stress time series due to wave-induced loads.

The breakwater geometry parameters in equation 11 have been defined earlier. The representative model scale factor, n , is calculated using the following expression:

$$n = 9.43 \sqrt[3]{\frac{W}{.1549 w_r}} \quad (14)$$

where: W = armor unit mass (tonnes)
 w_r = unit mass of concrete (tonnes/m³)

The design equation presented above can be used to determine the maximum dolos size that is structurally sound, given various breakwater and sea state parameters. For example, given a particular armor unit size (mass) in a specific location, the unit mass of concrete, the breakwater slope, the tensile strength of concrete and the wave height and period, the structural capacity of the unit may be directly computed for different levels of exceedance probability.

For example, Figure 8 presents the maximum permissible dolos mass as given by both the structural capacity criterion (described above) and the hydraulic stability criterion (Hudson's formula) for specified conditions. The design equation for structural capacity was solved for the location within the breakwater producing the highest total stress (i.e.: bottom layer, $D_v/n = 0.6$, $D_{swl}/n = 0.1$).

In a typical breakwater design, the dolos units may be sized initially by means of a hydraulic model study or through use of a stability formula such as Hudson's formula. The structural performance of the armor unit may then be checked by means of the structural design equation for the specified breakwater geometry and sea-state conditions. An appropriate minimum concrete strength may then be selected that ensures the structural integrity of the individual armor units. In addition, the capacity of the dolos unit could be increased by increasing the waist ratio, or by specifying reinforcement as necessary to resist the applied loads. It should be noted that although the design equation is based on dolos load cell data for a waist ratio of 0.32, it is expected that small changes in this variable would not significantly affect the loads acting on the units, but could significantly reduce the stresses in the units due to the increased capacity of the section.

Limitations in the Design Equation

It is important to recognize that in developing this design equation, there are, as in any design equation, a general set of limitations. The general limitations in the application of these results to the structural design of armor units include the following:

- All tests were undertaken in a two-dimensional wave flume; therefore, the results can not be used to assess the influence of three-dimensional effects such as oblique wave action and breakwater layout features (such as heads, corners and transitions).

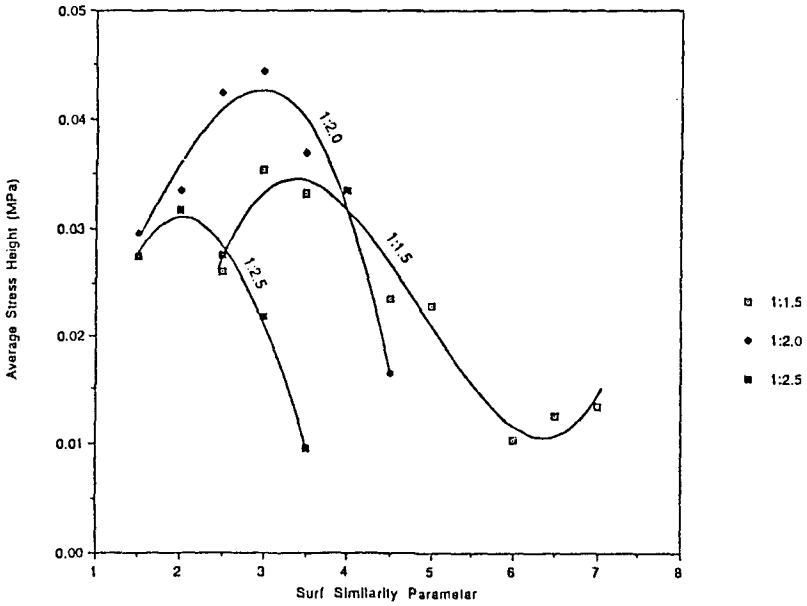


Figure 7. 5% Exceedance Average Stress Envelopes vs Surf Similarity Parameter

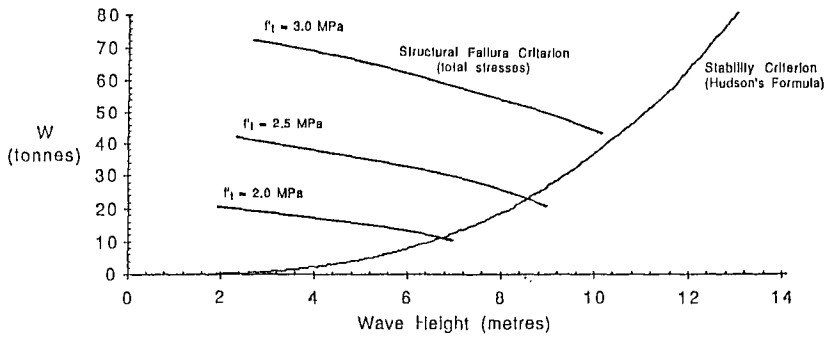


Figure 8. Dolos Hydraulic/Structural Failure Criteria
 ($w_r = 2.4 \text{ t/m}^3$, $K_D = 16$, 1:1.5 slope, $T = 12 \text{ s}$, 5% exceedance limit)

- All tests were completed using non-breaking waves ($H/d < 0.35$); therefore, shallow water effects, most importantly wave breaking, have not been considered.
- The design equation is based on regular waves tests; a limited test series was completed using irregular waves, but was insufficient to develop detailed design criteria. A detailed comparison between the response to regular and irregular waves should be undertaken and incorporated into the design equation.
- The tests were completed using a "no-overtopping" breakwater cross-section. Consequently, the effect of wave overtopping on the structural response of the armor units cannot be assessed.
- The tests were conducted at a single scale; thus, no quantitative assessment of scale effects can be obtained from the test results.
- Stresses derived from the model results are located at the surface of the mid-shank section of the dolos; the stress distribution throughout the dolos unit, in particular stress concentrations at the fluke-shank interface, have not been considered.
- Fatigue effects have not been considered.

Specific limitations on use of the design equations, based on the range of parameters tested, are summarized below:

Location	-with respect to the still water level:	$-0.1 \text{ m} < D_{sw}/n < +0.1 \text{ m}$
	-with respect to the breakwater crest:	$0.3 \text{ m} < D_v/n < 0.6 \text{ m}$
Wave Height:		$0.05 \text{ m} < H/n < 0.25 \text{ m}$
Wave Period:		$1.25 \text{ s} < T/\sqrt{n} < 2.50 \text{ s}$
Breakwater Slope:		$0.4 < m < 0.67$

If any of these quantities are outside these limits, the standard error of the predicted stress will increase, thus decreasing the reliability of the prediction.

So long as one is aware of these limitations, the design equation presented above can be used to provide an initial assessment of the structural integrity of the dolos unit under specified design conditions. However, these limitations must be addressed in future research work, which clearly represents a significant level of effort requiring global co-operation.

Application of the Design Procedure for Other Types of Armor Units

The load cell technology and analyses procedures developed in this study may be readily applied to other types of armor units, particularly those of a slender shape such as the tetrapod, quadripod, etc. As was described in this paper, general design equations may be developed, or it may be desirable to simply verify a preliminary design which has been based on hydraulic stability criteria.

The use of the load cell concept in a physical modelling environment also provides a tool for the development of new types of armor units. This procedure allows one to readily investigate the effects of changes to armor unit shape on both hydraulic stability and structural capacity.

CONCLUSIONS

A comprehensive examination of the structural response of armor units to static and quasi-static (wave-induced) loads has been completed using a dolos armor unit load cell in a physical breakwater model. Predictive equations have been derived which define the stress as a function of the critical breakwater geometry and sea state parameters, and a preliminary structural failure criterion for dolos

armor units has been developed for the first time. In addition, a design chart incorporating both the structural integrity and the hydraulic stability of the dolos unit has been presented. Limitations in the application of these results to the design of armor units have been extensively discussed to ensure that the results are not misused, and to provide guidance for future research. Finally, the procedures and methodologies developed in this study, including the instrumentation, model testing program, and data reduction and analyses techniques, can be readily applied to develop improved design procedures for other armor units, or to assist in the development of new armor units.

ACKNOWLEDGEMENTS

The financial support of the Marine Research and Development Branch of the Canadian Coast Guard, the Natural Sciences and Engineering Research Council of Canada, and W.F. Baird and Associates Ltd. is gratefully acknowledged.

The time and facilities support provided by the Department of Civil Engineering at Queen's University and the Hydraulics Laboratory of the National Research Council of Canada were critical to the successful completion of this work. In particular, Dr. E. Mansard of NRC must be thanked for his contribution to this work. The assistance of Dr. T. Smith of the Queen's STATLAB in overseeing the statistical analyses of the data was an essential element of this study.

REFERENCES

- Anglin, C.D. (1990), "The Structural Response of Breakwater Armor Units to Wave-Induced Forces", M.Sc. Thesis, Department of Civil Engineering, Queen's University, Kingston, Canada, February.
- Baird, W.F. and Associates (1989a), "The Development of a Rational Design Procedure for Concrete Armor Units for Breakwaters - Phase I Report - A Parametric Study of Breakwater Design Variables", report prepared for Marine Research and Development, Canadian Coast Guard, January.
- Baird, W.F. and Associates (1989b), "The Development of a Rational Design Procedure for Concrete Armor Units for Breakwaters - Phase II Report - The Development of Design Guidelines for the Dolos Armor Unit", report prepared for Marine Research and Development, Canadian Coast Guard, May.
- Scott, R.D. (1986), "The Analysis of Concrete Armor Units in a Breakwater", Ph.D. Thesis, Department of Civil Engineering, Queen's University, Kingston, Canada, December.
- Van der Meer, J.W. and Pilarczyk, K.W. (1987), "Stability of Breakwater Armor Layers - Deterministic and Probabilistic Design", Delft Hydraulics Communication No. 378, February.
- Zwamborn, J.A. (1978), "Dolos Packing Density and Effect of Relative Block Density", Proceedings of the 16th International Conference on Coastal Engineering, ASCE, p. 2285-2304, Hamburg, Germany, August-September.

CHAPTER 123

A Fundamental Study on Construction Scheme for Rubble Foundation of Deep Water Breakwater from Hopper Barges

Yoshiharu Matsumi*

ABSTRACT

This study aims to establish the effective construction scheme of the rubble mounds which are constructed by discharging a large amount of rubble from hopper barges. The numerical simulation technique is developed to estimate the spatial geometry of individual rubble mound discharged from a hopper barge. The effective distance between the discharge sites of the barge which makes the uneven property of the mound surface a minimum is discussed in connection with the change in the spatial geometry of the discharged rubble, the water depth and the direction of barge allocation.

1. INTRODUCTION

In general, deep water breakwaters are caisson type structures. The caissons are placed on a rubble foundation which is constructed by discharging a large amount of rubble from a hopper barge. An advantage of this construction method exists in its rapid "executability", since a volume of rubble at one discharge time is extremely large. However, since the rubble landing on the sea floor widely distributes from the discharge point of the barge, the rubble mounds by individual discharges usually form uneven surface foundations. Fig. 1 shows the illustration of the uneven surface of the rubble foundation, the elliptical lines show the plane profile of the individual rubble mound discharged from a hopper barge. When the distance between the discharge sites of the barge becomes larger, the size of the gap between mounds by individual discharges becomes larger. These are the drawbacks of this method of construction.

* Associate Prof. Dept. of Social Systems Engg. Faculty of Engineering, Tottori University, Tottori, Japan.

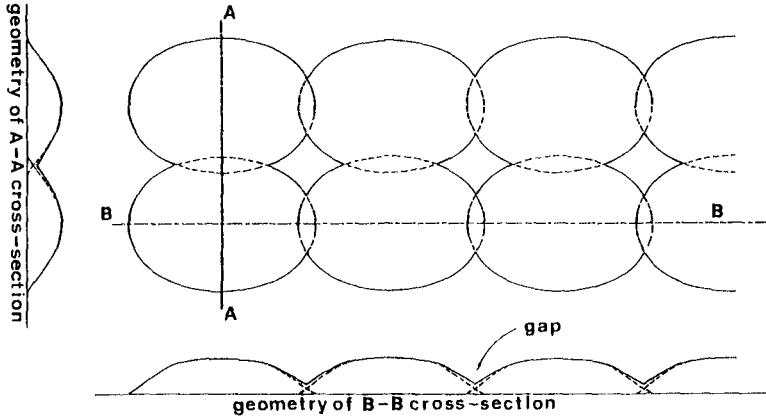


Fig. 1 Illustration of the uneven surface of the rubble foundation.

Recently, the design water depth of breakwaters is becoming deeper and the size of the rubble mound is greater. The portion of the rubble foundation work to the total process of breakwater construction is increasing. Therefore, the technique to construct a mound for breakwaters effectively and economically has become very important. To establish effective construction schemes of the rubble mounds which are constructed by the mentioned techniques, this study investigates the fundamental properties of the rubbles discharged from the barge with numerical techniques. The aim of this study is to make clear the optimal distance between the discharge sites of the barge which makes the uneven property of the rubble mound a minimum.

2. NUMERICAL SIMULATION TECHNIQUE

The spatial geometry of individual rubble mound discharged from a hopper barge can be evaluated by combining the volume of rubble at one discharge with a probability distribution of the plane scatter for the landing rubble on the sea floor. This probability distribution is obtained by analyzing numerically the stochastic differential equations of three dimensional motions for the settling rubble.

2-1 THE EQUATIONS OF MOTION FOR THE SETTLING RUBBLE

The equations of three dimensional motion for one piece of settling rubble are given as

$$M \frac{du}{dt} = -\frac{\rho}{2} C_D A u^2 - C_{Am} \frac{du}{dt} + F_x(t) \quad (1)$$

$$M \frac{dv}{dt} = -\frac{\rho}{2} C_D A v^2 - C_{Am} \frac{dv}{dt} + F_y(t) \quad (2)$$

$$M \frac{dw}{dt} = -\frac{\rho}{2} C_D A w^2 - C_{Am} \frac{dw}{dt} + (M-m)g + F_z(t) \quad (3)$$

where u , v and w are the x , y and z components of the velocity of one piece of settling rubble, A is the projected area of the rubble, M and m are the mass of the rubble and the liquid displaced by the rubble, C_D is the drag coefficient, C_M is the added-mass coefficient, ρ is the fluid density, g is the gravity acceleration. In these equations, the first and second terms on the right-hand side are the drag force and the inertia force exerted on the settling rubble, respectively. The last terms, $F_x(t)$, $F_y(t)$ and $F_z(t)$ indicate the x , y and z components of the drift force exerted on the settling rubble. These drift forces are random external forces. This study focus on the scatter range of the landing rubble on the sea floor. Therefore, in this simulation technique, the z component of the drift force exerted on the settling rubble is neglected.

$$\frac{du}{dt} = -\alpha u^2 + \beta F_x(t) \quad (4)$$

$$\frac{dv}{dt} = -\alpha v^2 + \beta F_y(t) \quad (5)$$

where

$$\alpha = \rho C_D A / \{2(M+C_{Am})\} \quad , \quad \beta = 1/(M+C_{Am}).$$

Eqs. (4) and (5) are non-linear stochastic differential equations (i.e. Langevin equation type). Therefore, in this study, these equations are linearized by using the following equations

$$u^2 = Uu \quad (6)$$

$$v^2 = Vv \quad (7)$$

where U and V are assumed to be of constant value in every time step of the numerical calculation. In this simulation technique, the random drifts, $F_x(t)$ and $F_y(t)$, are expressed by Gaussian random forces with zero mean.

Therefore, the variances (σ_x^2 , σ_y^2) for the x and y components of the landing position on the sea bottom can be obtained as the solution of the linearized stochastic differential equations.

$$\sigma_x^2 = \frac{\gamma\beta^2}{(\alpha U)^3} \left\{ \alpha U t - \frac{3}{2} + 2 \exp(-\alpha U t) - \frac{1}{2} \exp(-2\alpha U t) \right\} \quad (8)$$

$$\sigma_y^2 = \frac{\gamma\beta^2}{(\alpha V)^3} \left\{ \alpha V t - \frac{3}{2} + 2 \exp(-\alpha V t) - \frac{1}{2} \exp(-2\alpha V t) \right\} \quad (9)$$

where γ is the intensity of the white noise which directly influences the scatter range of the settling rubble. The probability distributions of plane scatter for the landing rubble on the sea bottom are given as follows lastly

$$p(x) = \frac{1}{\sqrt{2\pi\sigma_x^2}} \exp\left(-\frac{x^2}{2\sigma_x^2}\right) \quad (10)$$

$$p(y) = \frac{1}{\sqrt{2\pi\sigma_y^2}} \exp\left(-\frac{y^2}{2\sigma_y^2}\right) \quad (11)$$

in which $p(x)$ and $p(y)$ are the x and y components of the probability for one piece of settling rubble.

2-2 SPEED OF THE SETTLING RUBBLE (U,V)

In Eqs. (8) and (9), U and V must be given in consideration of the random drift force acting on the settling rubble. In this study, therefore, U and V are evaluated as the standard deviations (σ_u , σ_v) for the speed of settling rubble at any position. Eqs. (4) and (5) are rearranged in term of x and y, respectively, as

$$u \frac{du}{dx} + \alpha u^2 = \beta f_u(x) \quad (12)$$

$$v \frac{dv}{dy} + \alpha v^2 = \beta f_v(y) \quad (13)$$

where $f_u(x)$ and $f_v(y)$ are assumed to be expressed in the Gaussian random force with zero mean and the intensity of the white noise (γ'). The variances (σ_u^2 , σ_v^2) for the x and y components of the speed of the settling rubble at any position become from Eqs. (12) and (13) as

$$\sigma_u^2 = \beta \left(\frac{\gamma'}{\alpha} \right)^{1/2} \{ 1 - \exp(-4\alpha x) \}^{1/2} \quad (14)$$

$$\sigma_v^2 = \beta \left(\frac{\gamma'}{\alpha} \right)^{1/2} \{ 1 - \exp(-4\alpha y) \}^{1/2} \quad (15)$$

On the other hand, the intensities of the white noise, γ and γ' are included as unknown variables in Eqs. (8), (9), (14) and (15). Basing on the Langevin equation (Hori, 1977), the γ and γ' are related to the mean square of the drift force as following equations

$$2\gamma = \langle F(t)^2 \rangle dt \quad (16)$$

$$2\gamma' = \langle f(\ell)^2 \rangle d\ell \quad (17)$$

where $\langle \rangle$ indicates the expected value, ℓ is the moving distance of the settling rubble. Since $f_u(x)$ and $f_v(y)$ in Eqs. (12) and (13) are assumed to be equivalent to $F_x(t)$ and $F_y(t)$ respectively, γ' becomes from Eqs. (16) and (17) as

$$\gamma' = U\gamma \quad (18)$$

$$\gamma' = V\gamma \quad (19)$$

Therefore, U and V are given as follows lastly

$$U_i = \left[\beta \left(\frac{\gamma U_{i-1}}{\alpha} \right)^{1/2} \{ 1 - \exp(-4\alpha x) \}^{1/2} \right]^{1/2} \quad (20)$$

$$V_i = \left[\beta \left(\frac{\gamma V_{i-1}}{\alpha} \right)^{1/2} \{ 1 - \exp(-4\alpha y) \}^{1/2} \right]^{1/2} \quad (21)$$

in which U_i and V_i are the x and y components of the speed of the settling rubble in the i-th step of the numerical calculation.

2-3 SPATIAL GEOMETRY OF RUBBLE MOUND DISCHARGED FROM HOPPER BARGE

The probability distribution of plane scatter for the landing position of rubbles discharged from a hopper barge can be evaluated as

$$P(j) = \left\{ \sum_{i=1}^N p_i(j) \right\} / N \quad (22)$$

in which $p_i(j)$ is a probability that the rubble which is fallen from the i-th discrete portion in the hopper mouth lands to the j-th discrete portion on the sea floor as shown in Fig. 2. The probability, $p_i(j)$, can be calculated from the probability distribution functions, $p(x)$ and $p(y)$ in Eqs. (10) and (11). Therefore, the spatial geometry of rubble mound discharged from a hopper barge can be simulated by combining this probability with the volume of rubble at one discharge.

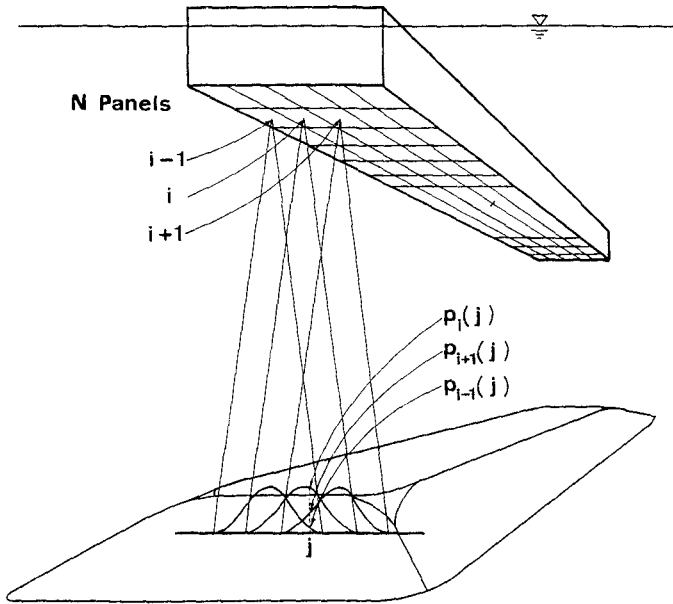


Fig. 2 Mathematical model of hopper barge.

3. OPTIMUM VALUE OF THE INTENSITY OF THE WHITE NOISE

The choice of the value for the intensity of the white noise used in this simulation technique is a problem, because the intensity of the white noise directly influences the scatter range of the settling rubble. In this study, the optimum value of the intensity of the white noise was investigated by comparing the calculated results with the experiments for the probability distribution of the plane scatter of the landing rubble on the sea bottom.

Fig. 3 shows examples of the experimental and calculated probability distribution of the plane scatter for the landing position of rubbles, in which every piece is dropped from the same position. In these cases, the representative size of rubble $d=2.64\text{cm}$ is applied. The upper figures are experiments for three kinds of water depth (i.e. $h=75\text{cm}$, $h=1\text{m}$ and $h=1.5\text{m}$). These experiments were carried out by Okude et al.(1982). P of the ordinate is the amount of the landing rubbles on unit area divided by the total amount of fallen rubbles. In the calculations, figures (A), (B) and (C) are the case for $\gamma=100000$, $\gamma=250000$ and $\gamma=400000$, respectively. All other parameter but γ are the same in these figures. In the

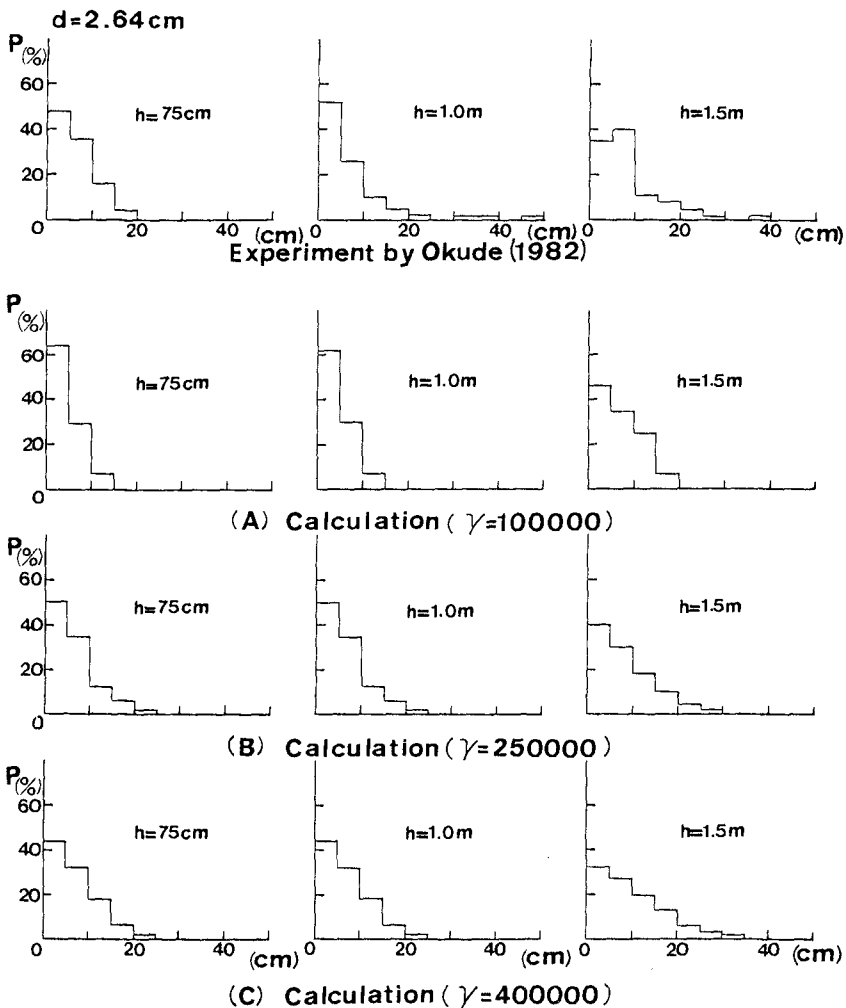


Fig. 3 Experimental and calculated probability distribution of the plane scatter for the landing position of rubbles ($d=2.64\text{cm}$).

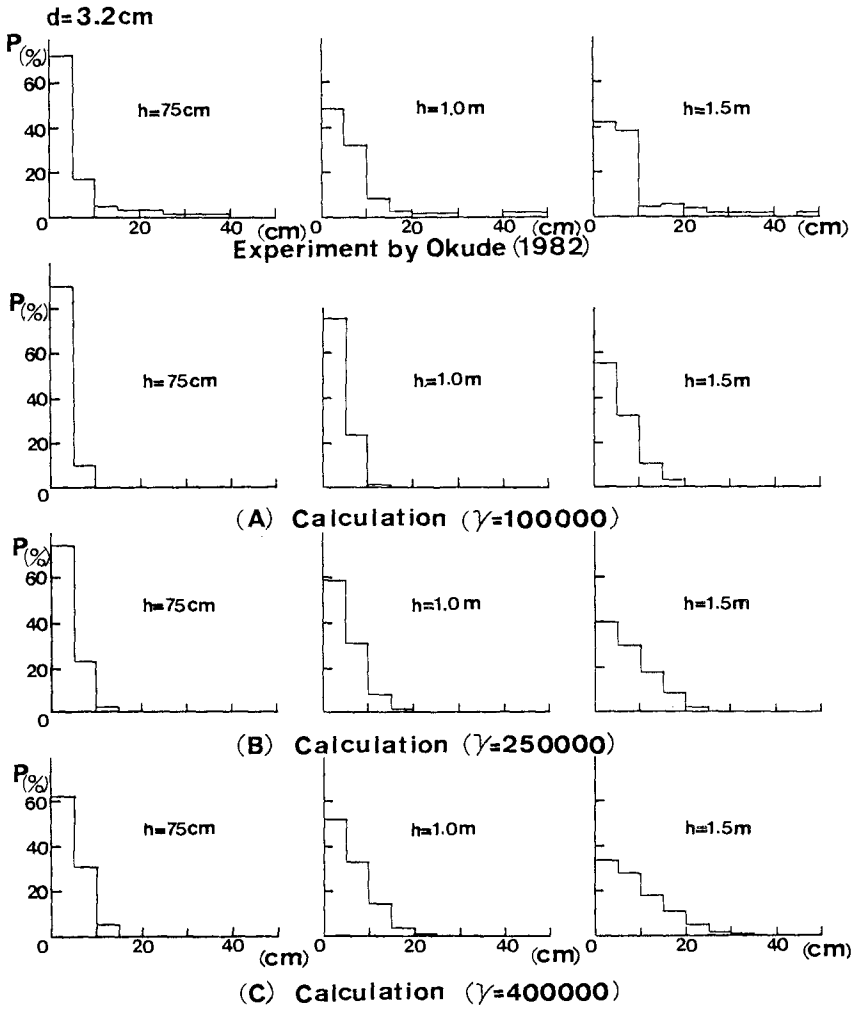


Fig. 4 Experimental and calculated probability distribution of the plane scatter for the landing position of rubbles (d=3.2cm).

calculations, when the value of γ becomes greater, the scatter range for the landing position becomes wider. Comparing these calculated results and the experimental results, it can be found that the calculations of the case for $\gamma=250000$ (Fig. 3 (B)) agree well with the experiments.

Furthermore, Fig. 4 shows the experimental and calculated probability distribution of the plane scatter for the landing position of rubbles in the case of $d=3.2\text{cm}$. The calculations for $\gamma=250000$ (Fig. 4 (B)) agree well with the experiments again. Therefore, from these investigations, it can be concluded that $\gamma=250000$ is the optimum value for the intensity of the white noise in the case of these rubble size. The scale effect of γ is not made clear yet in this study.

4. APPLICATION OF THE NUMERICAL SIMULATION TECHNIQUE

The application of the present simulation technique for the spatial geometry of the rubble mound discharged from a hopper barge was investigated by comparing the calculated results and the experimented results which were carried out by Okude et al.. In their experiment, a 1/20 scale model hopper barge with 100m^3 hopper volume was employed as shown in Fig. 5. The length of the hopper L is 77.3cm , the width W is 24.4cm . In the numerical calculations, the hopper mouth is divided into small panels as shown in Fig. 2. Size of the panel is d times d , d is the representative size of rubble.

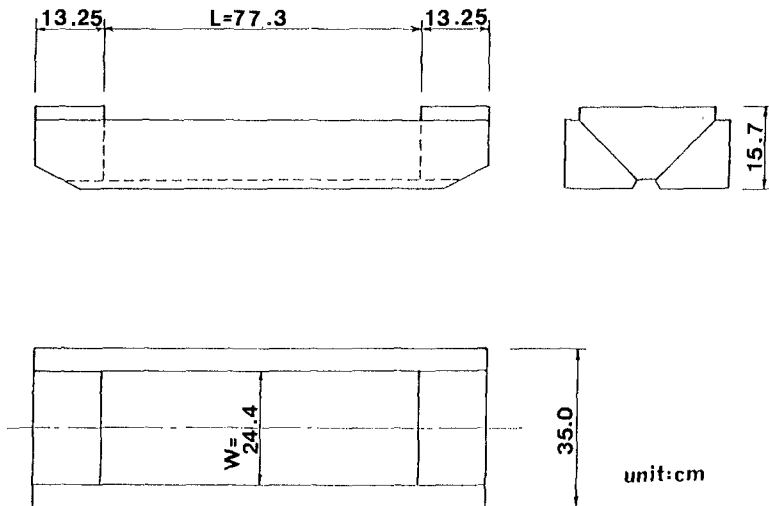


Fig. 5 Definition sketch for the model barge.

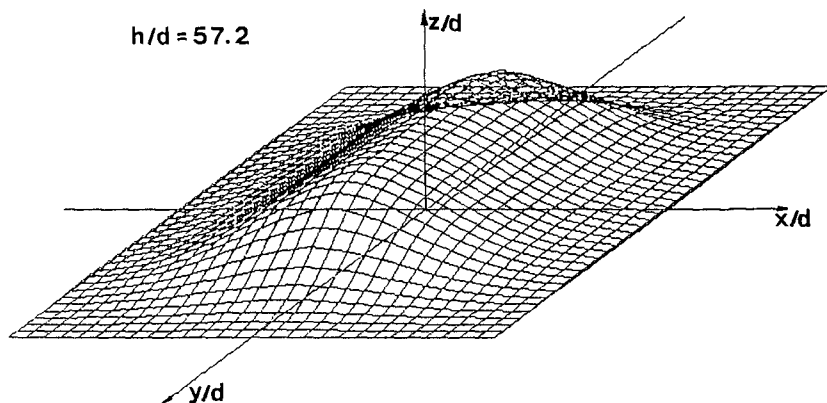


Fig. 6 Calculated spatial geometry of the discharged rubble mound, ($h/d=57.2$)

Fig. 6 shows an example of the calculated spatial geometry of the discharged rubble mound, in which the x and y are taken to be the direction of width and length of the hopper barge, respectively. This calculation is the case for the relative water depth h/d of 57.2. Next, the application of this simulation technique for the spatial geometry of rubble mound was investigated by comparing these calculations with the experimented results by Okude et al..

Fig. 7 shows a comparison between the shape of the calculated cross sections of rubble mound and those obtained in the experiments, figures (A) and (B) are the cases for $h/d=27.2$ and $h/d=57.2$, respectively. The left side from the ordinate in figures shows $x-x$ cross section of the rubble mound (key sketch : top right) and right side shows corresponding $y-y$ cross section. When h/d is 27.2 (Fig. 7 (A)), the simulated results overestimate the experimental results. This simulation technique cannot simulate the rubble sliding down the slope of the mound, which is recognized in the experiments. This overestimate may hence come from this reason. On the other hand, when the water depth becomes deeper, the slope of the mound becomes more mild, therefore the rubble sliding down the slope may hardly occur. In the case of $h/d=57.2$ (Fig. 7 (B)), the calculated and the experimented results agree reasonably well. From these investigations, it can be concluded that the present technique simulates the spatial geometry of the discharged rubble mound for the deeper water depth with sufficient accuracy. However, the applicable limitation of this simulation technique for the shallow water is not made clear in this study.

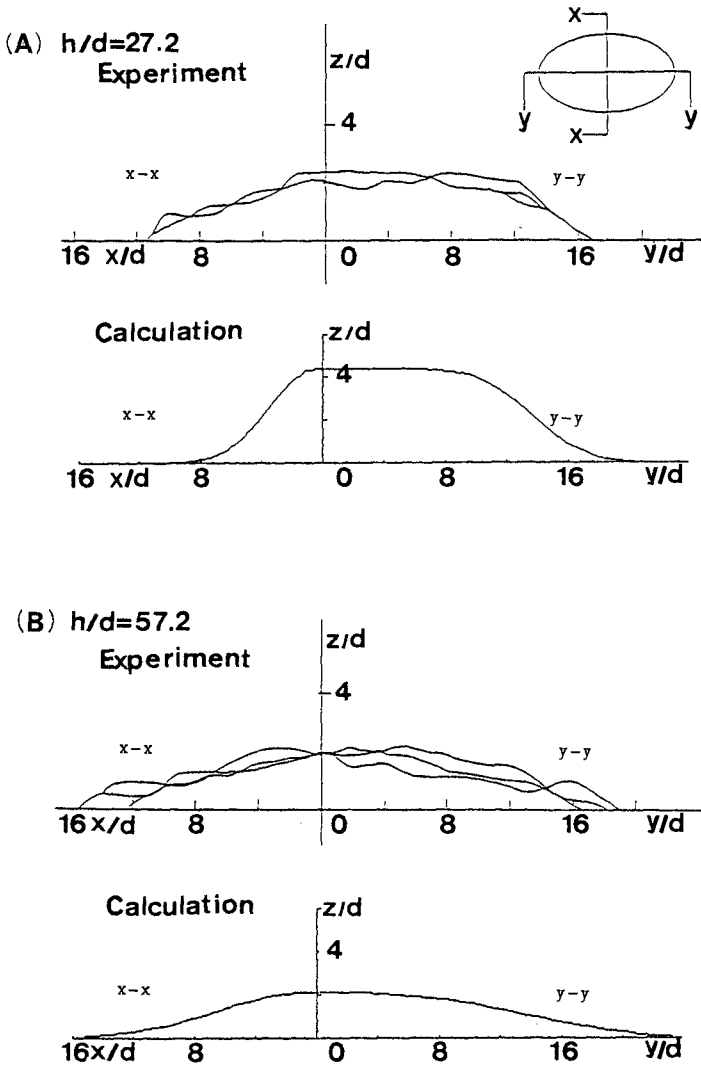


Fig. 7 Comparison between the shape of calculated rubble and experiments.

5. OPTIMAL DISTANCE BETWEEN THE DISCHARGE SITES OF THE BARGE

Fig. 8 shows the change of the calculated spatial geometry of the discharged rubble mound by two barges with respect to the water depth, a is the distance between the discharge sites of the barge. Figure (A) is the case of which the distance a is two times as long as the rubble size d , figure (B) is the case for $a/d=12$. When the distance between two barges is small (Fig. 8 (A)), the mounds by individual discharges form relatively even surfaces in shallow water. On the other hand, when the distance is larger (Fig. 8 (B)), the mounds form remarkably uneven surfaces in deep water. Therefore, it may be concluded that when deciding the distance between the discharge sites of the barge, the design water depth of breakwater becomes an important parameter.

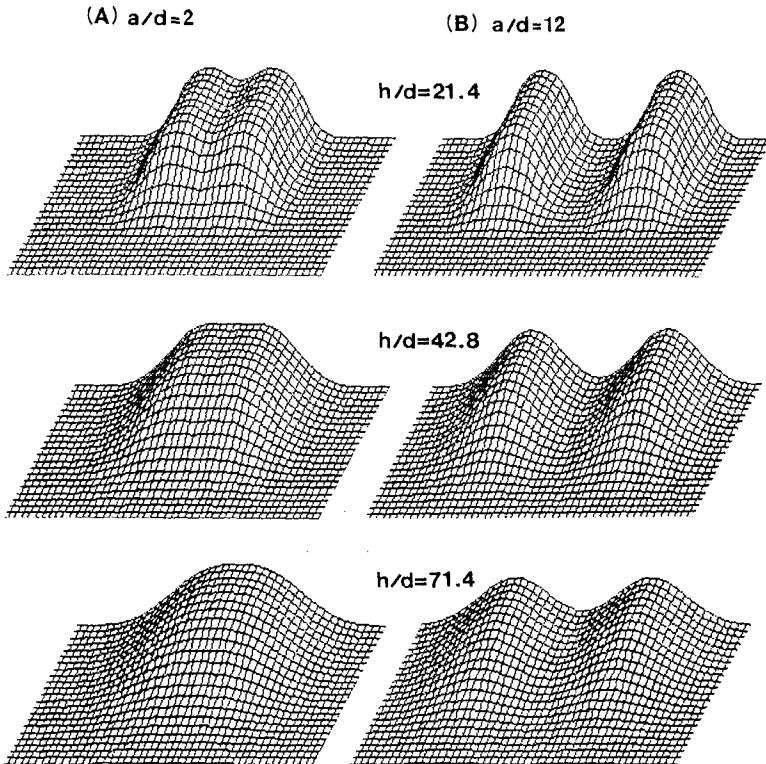


Fig. 8 Change of the discharged rubble mound by two barges with changing water depth.

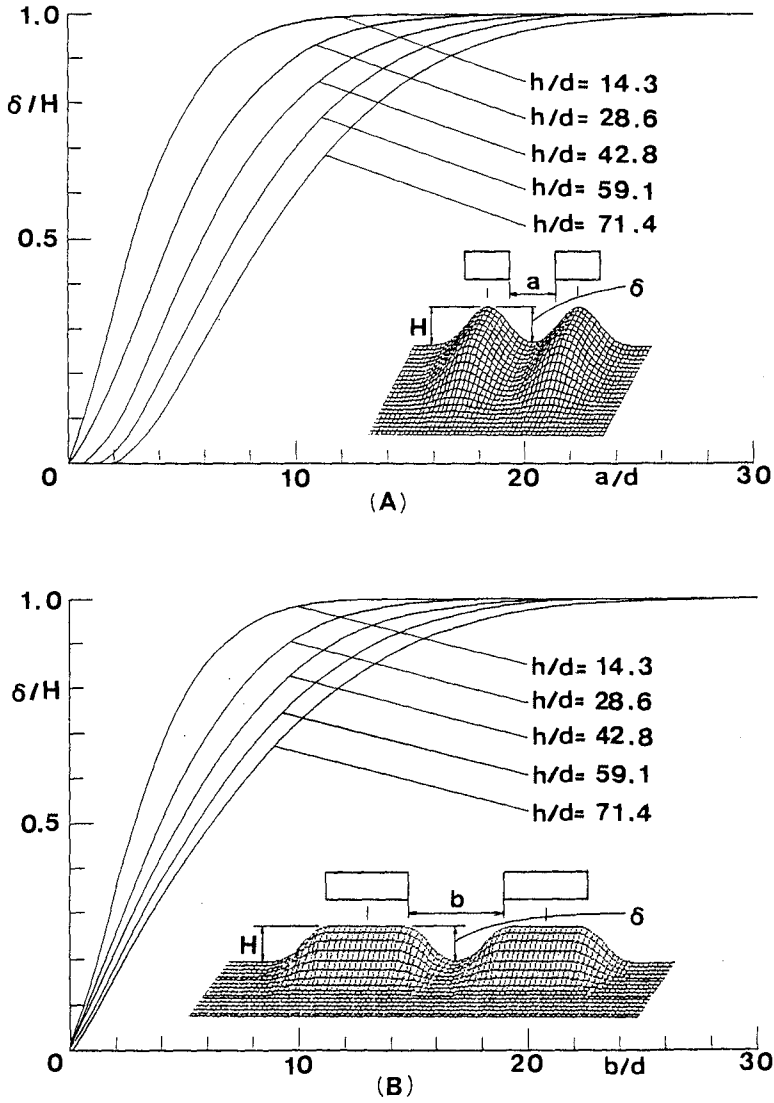


Fig. 9 Change in the size of the gap between the mounds with respect to the distance between the discharge sites of the barge.

Fig. 9 shows the change in the size of the gap between the mounds with respect to the relative distance between the discharge sites of the barge, in which δ is the gap size between individual mounds, H is the representative height of the mound. Figure (A) is the case of which two barges are allocated in the barge width direction, figure (B) is the case for the barge length direction. By using these figures, the effective distance between the discharge sites of the barge which makes the uneven property of the mound surface a minimum can be determined. Comparing the value of δ/H in figure (A) with that in the figure (B), in the region of small distance between the discharge sites of the barge, it is found that a change in the direction of barge allocation gives difference in both values of δ/H , (e.g. focusing the line of $h/d=71.4$, δ/H is equal to about 0.1 at $a/d=4$ in figure (A), on the other hand, at $b/d=4$ in figure (B), δ/H is equal to about 0.3). These extreme difference are caused by the direction of barge allocation. Therefore, it can be concluded that when deciding the distance between the discharge sites of the barge, the direction of barge allocation becomes an important parameter also.

6. CONCLUSION

Concluding remarks are as follows:

- (1) The present technique can successfully simulate the spatial geometry of the discharged rubble mound from the hopper barge in the deep water with sufficient accuracy.
- (2) The effective distance between the discharge sites of the barge which makes the uneven property of the mound surface a minimum is made clear in connection with the change in the spatial geometry of the discharged rubble, the water depth and the direction of barge allocation.
- (3) Applying this simulation technique for the case of the shallow water, the problem of how to deal with the rubbles sliding down the slope of the mound still remains.

REFERENCES

- Hori J.(1977): Equation of Langevin, Iwanami, pp.9-15.
(in Japanese)
- Okude T., et al.(1982):Experimental Study on Construction of Rubble Mound by Split Hopper Barge, Report of the Port and Harbour Research Institute, Vol.21, No.4, pp.132-171. (in Japanese)

CHAPTER 124

RESISTANCE OF GRASSMAT TO WAVE ATTACK

Jan Willem Seijffert¹ and Leo Philipse²

1. SUMMARY

The Dutch dikes along the North Sea and the tidal inlets need protection against erosion by wave attack. In 1983 two tests on full scale were carried out, concerning the resistance of large grass sods taken from Dutch sea-dikes, against wave attack.

For both tests in two different ways grass sods of 7500 to 9000 kg were dug from se-dike slopes, transported and placed in test facilities. In Test 1. the hydraulic load was performed by irregular waves up to $H_s = 1.85$ m, in Test 2. the hydraulic load was a simulated regular wave run-up with velocities until 4 m/s. Test 1. affirmed the possibility of a grassmat to withstand a design storm surge on a dike slope of 1:8 without severe damage. Test 2. showed the limits of erosion resistance and affirmed that the erosion resistance of a grassmat on sandy clay is concentrated in the upper layer of soil and roots.

2. TEST 1.

2.1 The motive of Test 1.

As a part of the realization of the so called Deltaworks in the Netherlands a section of 12 kilometers of the Frisian sea-dike in the northern part of the country should be enlarged (fig. 1).

The dike is situated on the south eastern side of the Waddenzee, a tidal flat of at medium 0.5 to 1 m below Ordnance Datum (O.D.) and a semi-diurnal tidal rise of about 2 m. The foreshore of the dike is a marsh situated about 1.5 m above O.D., that is some decimeters above

¹ J.W. Seijffert, Road and Hydraulic Engineering Division of the Rijkswaterstaat, P.O. Box 5044, 2600 GA Delft;

² L.A. Philipse, Waterschap Fryslân, P.O.Box 147, 8860 AC Harlingen; The Netherlands.

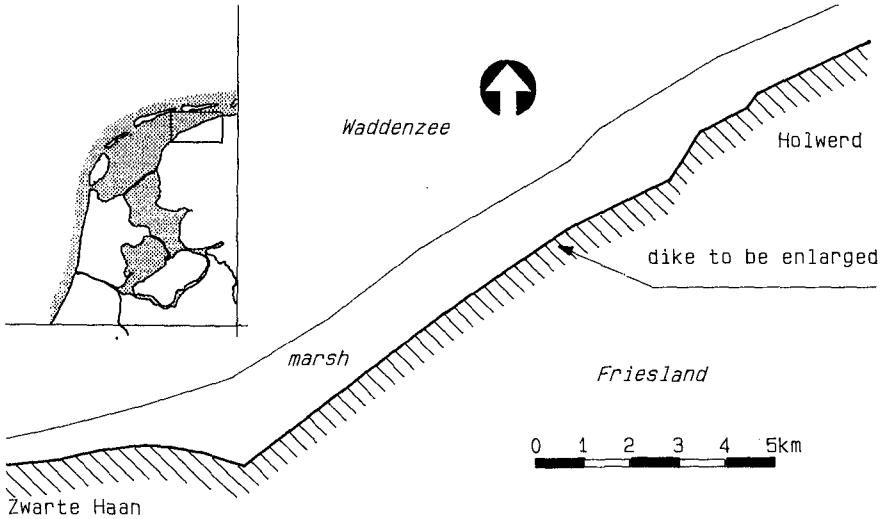


Figure 1. Plan of the Frisian sea-dike to be enlarged

the normal spring tide. Therefore only at storm surge tide a hydraulic load attacks the dike. The design water level is O.D. + 5.50 m, 1.80 m higher than the highest level that appeared in the past, with according wind waves of height $H_s = 1.85$ m, much higher than experienced in situ. The enlarged dike was designed with a relative flat outer slope from 1 : 12 up to 1 : 8 at design water level. Such a wide and rather voluminous cross section was possible because of the local available amount of clay as building material (fig. 2). This raised the question whether or not a non-reinforced grass revetment could be sufficient for the future. Under design conditions the erosive effect of breaking wind waves will be the representative event. In the large wave flume of Delft Hydraulics it is possible to generate

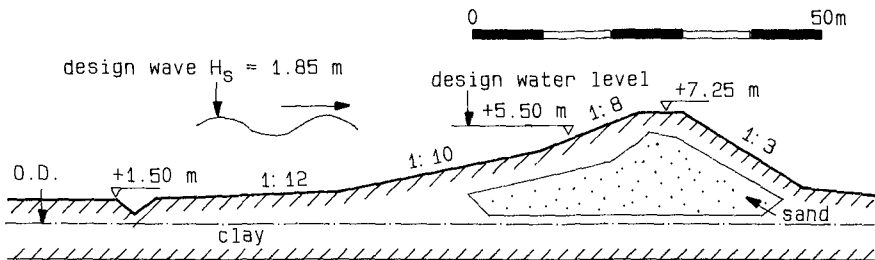


Figure 2. Cross section of enlarged dike

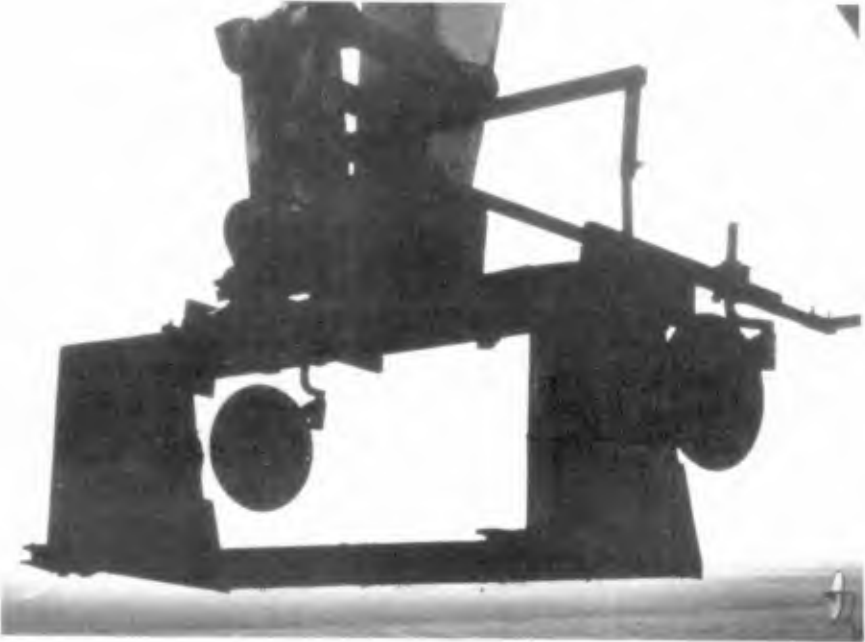


Figure 3. The sod cutting machine



Figure 4. A grass sod being transported

fully realistic the representative hydraulic load, related to water-level and irregular wind waves. The remaining question was the possibility of building a representative and full scale cross section of the outer slope and grass revetment.

2.2 Experimental set-up

As a representative grass revetment the grass of an outer slope angle from 1:5 to 1:6 of about ten years old at a comparable sea-dike was available in the vicinity. To utilize this opportunity a sod cutting machine was designed, and sods of $2.25 \times 5 \times 0.45 \text{ m}^3$ were dug out, transported and placed in the large wave flume.

The cutting machine consisted of a horizontal knife, 2.25 m wide, being pulled underneath the grass at a depth of 0.45 m, followed by a steel plate of 5 m length. Simultaneously two circular steel knives cut the vertical sides of the sods (fig. 3). The steel plate bearded the sod while raising it and during the transport by truck to the large wave flume (fig. 4). For reducing the tractive forces on the horizontal knife and steel plate (and so minimizing the distortion of the grass sod) it was necessary to use some water.

The grass sods were placed in a wave flume of 200 m length, 5 m wide and 7 m depth, under a fixed slope angle of 1:8. The slope reached from the bottom of the flume (Ordnance Datum (O.D.) + 0.5 m) along 55 m up to

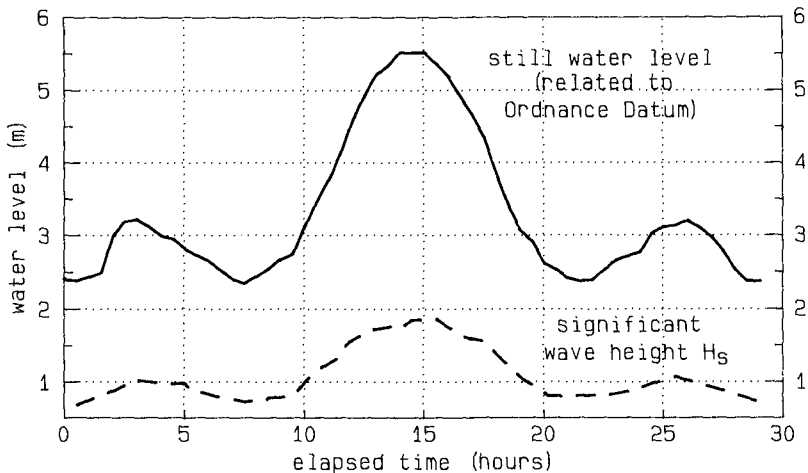


Figure 5. Realized loading conditions (water level and significant wave height) in course of time

O.D. + 7.3 m = crestheight. The grass sods were placed on a clay layer of 1 m thick, with underneath sand with $D_{50} = 225 \mu\text{m}$.

The hydraulic loading was realized by generating irregular waves with a Pierson-Moskowitz spectrum, with varying water level and wave height (fig. 5), with a peak wave period between 5.2 and 5.6 s. This stands for a plunging breaker type, falling on water cushion. The variation of the water level reproduced a storm surge superimposed on a tidal cycle, during 29 hours, reaching a maximum level of O.D.+ 5.50 m and a maximum significant wave height $H_s = 1.85 \text{ m}$. In total the experiment lasted 48 hours, because of two stops between times for lowering the water-level, visual inspection and measuring the erosion level.

The test was executed with fresh water, while in nature the heaviest loading appears with seawater. The clay minerals in the Netherlands are mostly of the illite type (and therefore not very sensitive for dispersion). From experiences in the past with storm surges in the cold season no special effects in respect to dispersion can be derived. Therefore it is assumed that the tests with fresh water are sufficiently reliable.

The water velocities, measured at 0.05 m above the surface, were at maximum 2.2 m/s, at 4% of the waves a speed of 2.00 m/s was exceeded and the mean of the peak velocities was $\pm 1.00 \text{ m/s}$, upward as well as downward, appearing at $H_s = 1.85 \text{ m}$. Run-up and overtopping were measured and were in good accordance with the design values.

Special care has been taken for avoiding erosion due to rim-effects on the grass sods along the walls of the test flume.

Table 1. Vegetational species (percentage)

	Test 1	Test 2	
		sample 1	sample 2
Poa Pratensis (%) (Smooth-Stalked Meadow- or Kentucky Blue Grass)	65	2	2
Festuca Rubra (%) (Red Fescue)	12	20	64
Lolium Perenne (%) (Perennial Ryegrass)	6	76	29
other grasses (%)	7	0	1
other herbs(not grass), (%) among which Trifolium (Clover)	10	2	4
Total	100	100	100

2.3 Description of the grassmat

The grass was in good condition, due to 10 years of treatment, mostly by grazing sheep. The vegetation afforded initially a coverage of the soil of 50 to 80 %, which decreased to 40 to 50 % in the weeks just before the execution of the test. This was due to a lack of direct sunlight by the coverage of the roof on top of the construction hall of the wave flume, in combination with outdoor temperatures up to 25°C. Nevertheless it is not very likely that the root system has weakened significantly in this period. One week before the execution of the test the grass was cut to a length of 0.05 m. A determination of the vegetational species is presented in table 1. Some soil parameters are given in table 2.

Table 2. Soil characteristics

	Test 1	Test 2
Grass turf:		
parts < 0.002 mm (%)	18	20
parts > 0.060 mm (%)	49	46
organic material (%)	< 3	3
Supporting clay layer:		
parts < 0.002 mm (%)	35	-
parts > 0.060 mm (%)	22	-
Plastic Limit (%)	22	24
Liquid Limit (%)	36	42
Specific Weight (dried) (kN/m ³)	14.8	13.9
Sand underneath:		
D ₅₀ (μm)	225	-

2.4 Results

Besides the still water level and wave characteristics being measured during the experiment, the amount of surface erosion was measured during breaks of the execution, by sounding the surface of the turf with a vertical rod in a fixed pattern. Because of the standard deviation of 0.005 m in measuring a single point, the results are presented as a difference between before and after wave loading, of the mean of 30 points in an area of 5 x 5 m (fig. 6). In this way the largest erosion, of about 0.005 to 0.010 m, was measured at levels of about O.D. + 2.45 m and O.D. + 4.25 m as well. In the first mentioned area a wave height of $H_s = 0.85$ m (as a mean) has worked out during 18 hours approx. (fig. 5) and in the second one $H_s = 1.65$ m (as a mean) lasted during 6 hours. Although most of the grass leaves had vanished, the turf was in exceptional good condition without any

visual holes or cracks, caused by erosion. In general it was found that the erosion resistance originated from the upper layer of soil and roots, much more than from the grass leaves. The erosion of the clay surface occurred in a rather even way, without forming obvious cracks or holes. While eroding, a fine root structure of the grass remained on top of the clay. This root structure reduced further erosion rather effectively.

It was remarkable that at the horizontal seams between the successive sods no extra damage occurred, in spite of the presence of little differences in surface height, up to a few centimeters.

Because of the minute erosion after the storm surge simulation during 29 hours, it was decided to restart the experiment after cutting 4 holes in the grass surface. The dimensions of the holes were 0.50 m (width) x 0.20 m (length) x 0.07 m (depth). The wave height was established at $H_s = 1.57$ m and the water level at O.D. + 5.00 m. In the vicinity of the breaker impact the holes eroded progressively, by scouring the soil underneath the upper layer of the turf. The first visible erosion appeared after 5½ hours of loading. After 7 hours two holes were scoured out to the depth of the underlaying, very resistive, clay layer. Conclusive can be stated that the soil material of the grass sods itself was not very resistive to erosion, in contrast to the top layer with roots (of 0.03 m to, at maximum, 0.10 m) which appeared very resistive to erosion under the given loading.

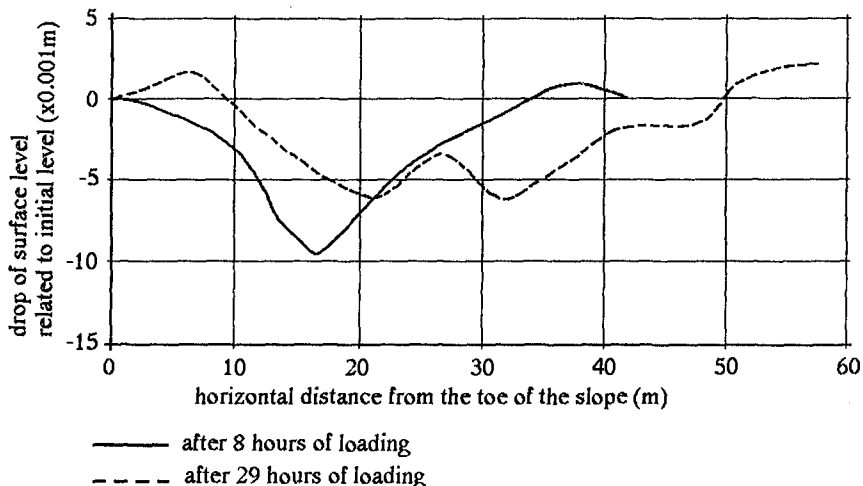


Figure 6. Averaged drop of surface, due to erosion

3. TEST 2.

3.1 The motive of Test 2.

The main objective of test 2. was the development of a quantitative and reproducible full scale test of erosion of vegetation on clayey soil under realistic hydraulic load by run-up, caused by breaking wind waves. This situation is very common on Dutch sea-dikes with a vegetational revetment on top of an armored revetment until the storm surge design water level. In that case the waves brake on the rigid revetment while the grass is only loaded by run-up and run-down.

Therefore 4 problems had to be solved:

1. Cutting and transporting large scale grass sods to a testing location.
2. Generating realistic and reproducible hydraulic loads.
3. To control rim effects and other shortcomings that distorted former experiments in laboratory conditions.
4. Defining a measurable erosion rate parameter.

Only if the conditions mentioned could be satisfied, it would be meaningful to establish an erosion/loading rate on a given grass/soil sample of a well defined condition. Two samples have been taken and tested, under the same conditions, to determine the reproducibility of the test. The two samples originated from the same sea-dike slope in the north of the Netherlands.



Figure 7. Two grass sods for Test 2. being dug out

3.2 Experimental set-up

In Test 2, a grass sod of 0.5 m thick, 1 m wide and 10 m length was dug out as a whole from a sea-dike as follows. An I-girder of 10 m long and 1 m high with one flange cut off was placed with its web horizontally, in a groove, dug out next to the sod to be taken out. The sharp edge of the web was pressed horizontally by hydraulic pistons at 0.5 m below the grass surface underneath the sod. Then the other side of the 1 m wide sod was dug free and the I-girder functioned as a bearer during the take up, the transport as well as during the whole test (fig. 7).

After transport it was put in a test flume with slope angle 1:4. Before starting the experiment, the flange first taken off, and elongating steel plates forming the sides of the flume, were welded on the I-girder. So the test was carried out on an almost undisturbed sample within the steel flume of 1 m wide.

Special care was given to the filling of the slot between the soil and the vertical wall of the steel flume. It was filled by a clay-bentonite mixture and covered by coarse stone-chipping and a strip of Enkamat, a non woven fabric of course filaments. This fabric protects the underlying vulnerable rim, with a roughness according to that of grass, without introducing renewed rim-effects on the transition to the plain grass.

The steel flume described before was placed in a larger (2 m wide) concrete flume next to a weir in the river Meuse. Over this weir a falling water head of about 5 m was available for generating the demanded hydraulic loading. Wave run-up and run-down were generated by simulating a breaking wave. Wave breaking was simulated

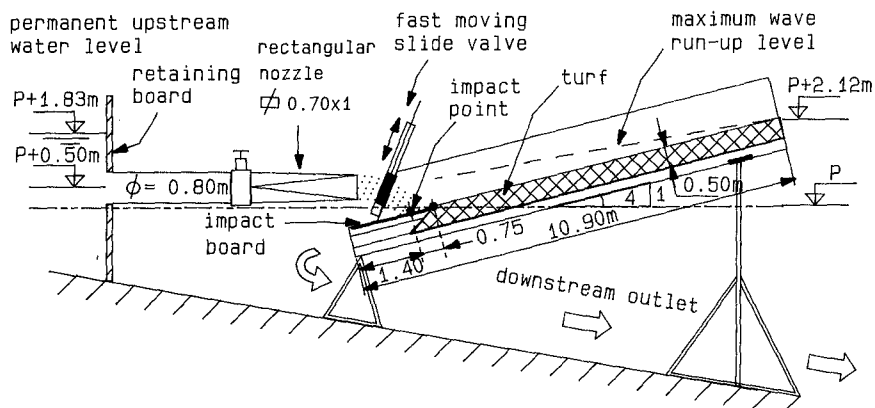


Figure 8. Experimental set-up of TEST 2 with simulation of wave run-up

by periodically (once in 7 seconds) intermitting a water jet of $2.2 \text{ m}^3/\text{s}$, streaming out of a rectangular nozzle (0.7 m high, 1 m wide) at the end of a horizontal pipe (fig. 8).

Designing the set-up for the hydraulic loading, a small scale model was built for testing the lay-out. After building in full scale and placing the grass sod in situ the hydraulic loading was calibrated on a temporary (for some hours only) wooden board, placed 0.10 m above the grass to be tested. For simulating the roughness of grass the board was roughened by placing (and glueing) small wooden cubes of $0.03 \times 0.03 \times 0.03 \text{ m}^3$ in a diamond-shaped pattern with edges of 0.9 m. In this way 3 usable hydraulic conditions were tuned in, each of heavier hydraulic load.

Starting the experiment with sample 1, at first the two lightest conditions were used, each during one hour. After coming out that only the heaviest possible loading should give a significant erosion within reasonable time, only the latter was used.

Free falling (3 s approx.) the water plunged on a roughened wooden board, 0.75 m before the downward rim of the turf, so creating an upward streaming parallel to the grass surface. Before starting the next "wave" the time remaining was enough for all the water running down. The maximum up and down velocities parallel to the grass surface came to 4.0 m/s, and the maximum thickness of the water layer was at maximum 0.70 m at the downward rim of the turf, decreasing uniformly along the grass surface up to the point of maximum run-up, 8 m upward along the slope. This equals, according to the theory of Battjes and Roos (1975), a wave with height $H = 3.6 \text{ m}$ and period $T = 6.8 \text{ s}$.

3.3 Description of the grassmat

The grass was in good shape before starting the tests. The soil coverage by the vegetation was 70-85 % for sample 1 and 70-95% for sample 2. A determination of the vegetational species is presented in table 1.

In the winter before the test the root content as a function of depth was determined at the dike location the grass was taken from. Two samples were taken. The total weight of roots over 0.50 m depth was $29 \text{ g}/\text{dm}^2$ (sample 1) and $35 \text{ g}/\text{dm}^2$ (sample 2), of which 10 and $18 \text{ g}/\text{dm}^2$ (35 and 51 %) in the upper 0.05 m, and 94 and 95 % in the upper 0.40 m.

The most significant difference between the two large sods was the somewhat better condition of the second one at starting the test, and some difference in the dominating grass species in the turf (see table 1).

Some soil parameters of the turf are given in table 2. It

is noticeable that the soil of the samples was not homogeneous, but there were several patches of sand present.

3.4 Results

The amount of erosion was gauged by vertical rods touching the surface in a fixed pattern, during breaks of the simulated wave loading. The erosion at the point of maximum damage at the end of the test of each sample is given in fig. 9. During the first 3 hours of loading hardly any erosion was visible. In the next period from 3 to 10 hours, in the lower 5 m along the slope the grass leaves eroded away. In general it was established that the upper 0.03 m of the turf eroded in a rather even way, without obvious cracks or holes. Thereafter, (between 10 to 15 hours with sample 1, 15 to 25 hours with sample 2) cracks developed.

In sample 1 after 16 hours the rate of erosion increased. After 18 hours, when at 0.6 m from the lower rim the erosion is 0.08 m deep and 0.60 m long, lumps of soil started breaking away and after 22 hours the bottom of the turf was reached.

In sample 2 the increase of the erosion rate appeared after 25 hours at 2.5 m from the lower rim of the turf. After 40 hours the hole was 0.20 m deep and 0.40 m long and the bottom was reached after 41 hours.

As said sample 2 hold out longer than sample 1. Partly this may have been caused by a somewhat better condition of the grassmat as a whole, but it is important to

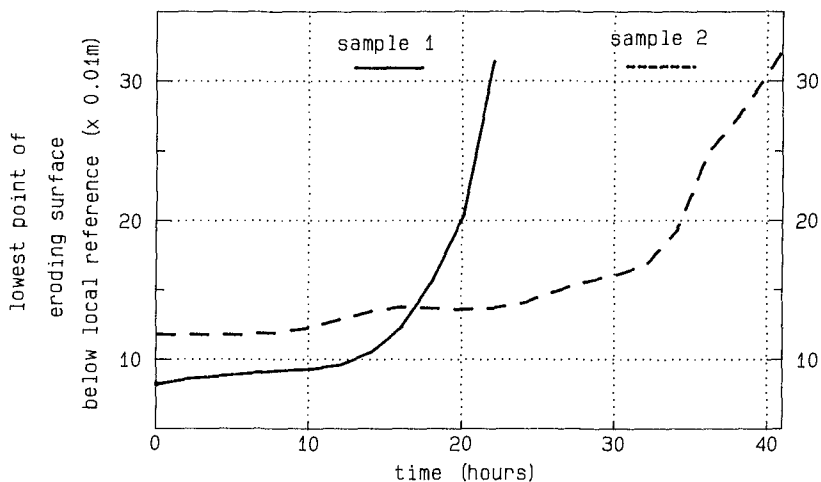


Figure 9. Maximum erosion depth in course of time

mention that sample 1 had a bold patch in the heaviest loaded zone, caused by lack of sunlight during the two months before test by a wall sustaining wooden lath at 0.20 m above the grass. Although 20 hours for sample 1 is significantly shorter than the 40 hours lifetime of sample 2, the top layer caused mainly the total resistivity, even at the bold patch. This confirms the lesser importance of the grass leaves, and shows that the resistivity of the upper root layer can sustain a period of weak growth of the grass, which is likely to be important for the condition of the sea-dike grass in the winter and early spring.

During the process of erosion it was clear that small unevenness of the soil nor small holes such as wormhole were harmful at all. The thick tap-roots such as from the *Taraxacum Officinale* (Dandelion) caused some extra erosion, but not in such a way that the damage that occurred was influenced significantly.

Beyond the detrition of the grass leaves, in general two types of erosion could be distinguished:

1. Areas where the clay remained rather bare behind (up to an erosion of 2 to 3 cm) and
2. Areas where a fine network of roots stayed behind after the soil washed out. This network retards further erosion.

In the first mentioned areas the *Lolium Perenne* (Perennial Ryegrass) dominated, while in the second case *Festuca Rubra* (Red Fescue) dominated. From botanical descriptions it is well known that the *Festuca Rubra* has a wider and finer root system than the *Lolium Perenne*.

From the areas where the grass top layer was eroded 1 to 3 cm, without final distortion, it was hardly possible to grow up the grass in the laboratory from the remaining roots. This means that the grass, after withstanding such a heavy attack, will need one or more growing-seasons for recovery.

Parallel to the full scale test described, laboratory tests were carried out on small cores ($\phi = 66$ mm) taken from the dike location in the winter, from the upper 0.05 m as well as from a depth of about 0.40 m. These erosion test by a rotational water apparatus confirmed qualitatively the large difference between the erosive resistance of the turf at the two depths.

4. CONCLUSIONS

- 4.1 In two different ways the digging out of grass sods of about 0.50 m thick and an area of 10 to 12 m², transporting and placing them as a whole was possible.

- 4.2 Successful simulation was possible of wave attack by direct impact of breaking irregular waves up to $H_s = 1.85$ m and by wave run-up and run-down equivalent to regular waves of about $H = 3.6$ m.
- 4.3 The measures to overcome the influences of rim-effects along the grass sods on the test results were successful.
- 4.4 A general insight and a quantitative description were obtained of the erosion process of the tested grass from real sea-dikes under rather realistic boundary conditions.
- 4.5 It was affirmed that a proper quality grass on sea-dikes can have a high resistance against erosion by storm surges. Thus was decided to enlarge the sea-dike described in paragraph 2.1 as designed, without reinforcement of the grass revetment.
- 4.6 In the two cases with soil of rather sandy clay, the resistance was concentrated in the top layer of 0.03 up to (at maximum) 0.10 m, composed of soil and roots.
- 4.7 The type of erosion depends on the type of grass, particularly the root structure. A wide and fine root-structure (such as *Festuca Rubra*) leaves a fine root-structure behind while eroding, which retards further erosion. Other grasses, such as *Lolium Perenne*, omit this property, which causes a lower erosion resistance.
- 4.8 In two specific cases a quantitative erosion resistance is determined.

REFERENCES

Battjes, J.A. and Roos, A. (1975). "Characteristics of flow in run-up of periodic waves." *Communications on Hydraulics, Report no. 75-3*, Department of Civil Engineering, Delft University of Technology, The Netherlands.

CHAPTER 125

Practical Study on Larger-Scale Cylindrical Caisson Breakwater in Port of Kaohsiung

Kuo, Shih-Duenn

ABSTRACT:

Using cylindrical caisson for a large-scale breakwater is not popular so far in the world. Never-the-less with the completion of Port of Kaohsiung's 2nd Harbor Entrance Project, the engineers in Taiwan has encouraged by the successful experience in this field due to its simple construction method and low cost consideration.

1. INTRODUCTION

Taiwan is an island, most of the economic activities with foreign countries rely on seaport's operation. Therefore, at least 4 international seaports were built successively in last 3 decades. Among them, Port of Kaohsiung is the most important one in terms of cargo handling and foreign trade as a result of the construction of 2nd harbor entrance as shown in Fig. 1.

Although there are many types of breakwaters can be selected for harbor entrance construction project, rectangular caisson breakwater is one of the most popular types in Taiwan, R.O.C. For Kaohsiung 2nd harbor entrance project due to tight schedule, limitative budget and shortage of material, the Harbor Bureau bravely and cautiously used cylindrical caissons as main structure of breakwater to replace the traditional rectangular shape to meet the development of heavy industrial zone surrounding the harbor area. This not only encouraged the engineers in Taiwan, but also set a record in R.O.C.'s harbor engineering.

Perhaps, cylindrical caisson used for breakwater in Kaohsiung was not the first one, but, I think it would be the largest one in the world so far. Kaohsiung's 2nd harbor entrance, navigable by ships up to 125,000 D.W.T. is protected by 2189-meter southern breakwater and 1322-meter northern breakwater, to keep the main channel to a min. depth of 16 meters as shown in Fig. 2. This project, took 8 years to complete from 1967-1975, totally used 136 units of cylindrical caissons including 37 units of $\phi 17^m$ and 99 units of $\phi 24^m$ at a cost of about US\$35 millions at that time.

Kuo, Shih-Duenn, Senior Engineer, Kaohsiung Harbor Bureau
62, Lin-Hai 2nd Road, Kaohsiung, Taiwan

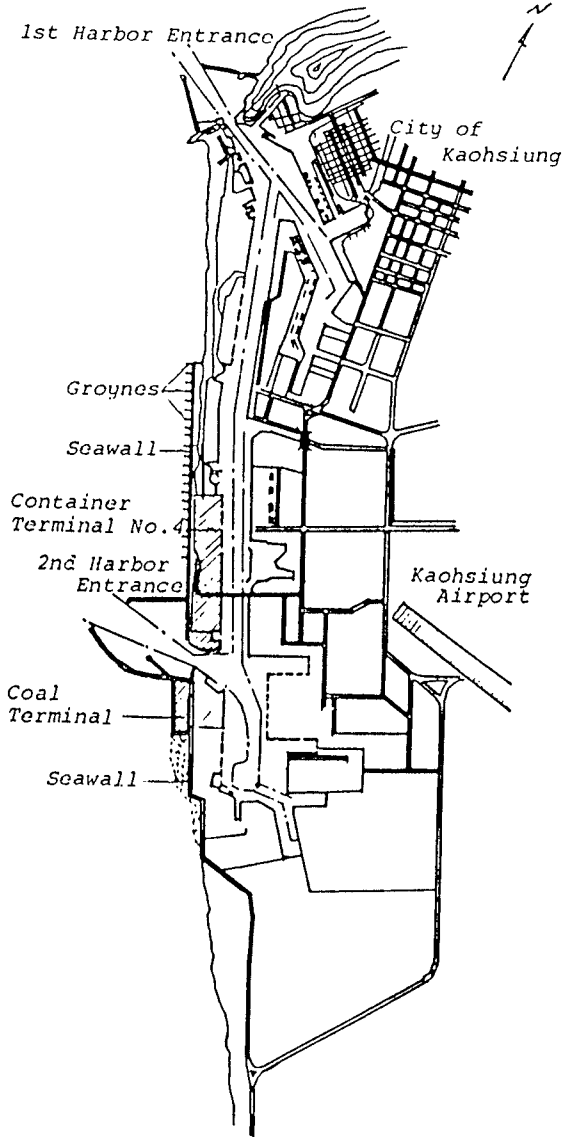


Fig. 1 Port of Kaohsiung

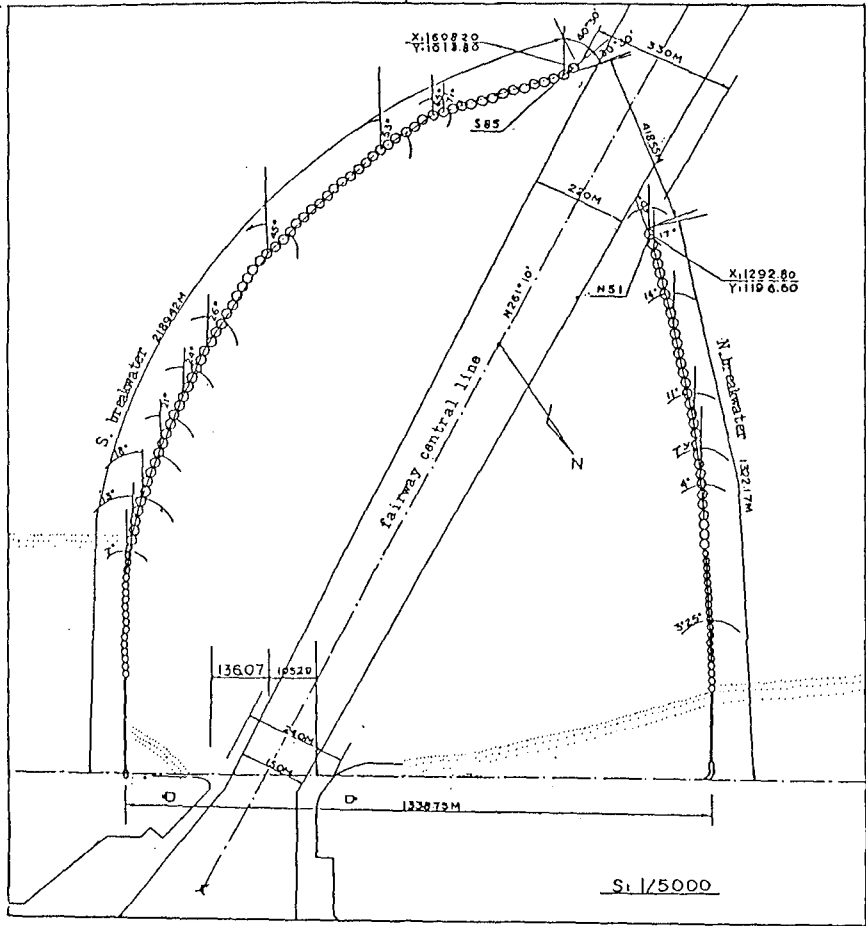


Fig.2. Layout of Kaohsiung 2nd Harbor Entrance
Breakwater (by using cylindrical caisson)

2. PRACTICAL EVALUATION

In view of practical evaluation of cylindrical caisson breakwater, it will be compared its project cost, construction period, construction method, technical problem, damage rehabilitation during construction and maintenance after operation etc. with those of the rectangular type in Taiwan's conditions.

2.1. Initial cost

As conservative evaluation, the construction cost of the cylindrical caisson breakwater could save about 15-20% than that of the rectangular one due to simple construction method and short construction period etc.,

For diver demand, from beginning to the end, divers needed for placing cylindrical caissons in Port of Kaohsiung were only 2-3 teams in comparison with about 50 teams which needed for rectangular types of the same size in doing foundation works and so on in Taiwan's experience. This implied that the cost could reduce in a large amount for cylindrical caisson breakwater.

For rock requirement, due to foundation free, the volumes of rock need for cylindrical caisson breakwater was only half as much as rectangular type. This meant it could save much more money and time in comparing cylindrical caisson breakwater with rectangular one.

For others, it could save about 20% of the budget for equipments and other kinds of material in cylindrical caisson breakwater.

2.2. Construction period:

Using very simple and mass-produced methods for fabricating cylindrical caissons and for the sake of no necessity placing rock base, foundation screed and other sophisticated under-water-works for caissons etc., the construction progress of cylindrical caisson breakwater was much faster than that of the rectangular type. Normally, under the same manpower to complete a same size breakwater, the construction period taken by cylindrical caissons was only half as long as the rectangular one. Taking Port of Kaohsiung's 2nd harbor entrance breakwater into account, placing about 24 units of cylindrical caissons a year were a very high through-put regardless of bad weather in the region lasting for more than 5 months annually.

2.3. Construction method:

Taking average, 2-dozen of cylindrical caissons were needed per year in Port of Kaohsiung's 2nd harbor entrance breakwater construction project. Hence, many possible approaches were used in fabricating works simultaneously to meet the annual demand. At the same time, some other construction methods were also simplified to cope with the actual requirements which were quite different from the rectangular type.

For fabricating works, cylindrical caissons were built either on shore bank, quay side or inside the dock simultaneously to catch the schedule.

2.3.1 Fabricated on shore bank:

Some caissons of 17-meter in diameter were built to complete on the shore bank. After completion, they were launched and floated by cutter dredger, and then, grounded before towing & sinking to prevent them from hitting each other in typhoon season as shown in Fig. 3. Some 20 units of $\phi 24^m$ cylindrical caissons were done in the same way before fabricating dock was available. Simplification and low cost were the advantages, but they needed a lot of land areas and coastal fronts for using.



Fig. 3. Cylindrical Caissons fabricated on shore area.

2.3.2 Fabricated inside the dock:

A total of 81 units of $\phi 24^m$ cylindrical caissons were fabricated inside the dock to the height of 4-meter (draught 3.7^m , freeboard 0.3^m) as shown in Fig. 4, and then, built continuously outside the dock, also in water, till completion and grounded for temporarily setting. This case cost more and took a long time to complete with no other better solution.



Fig. 4. Cylindrical caisson fabricated inside the dock.

2.3.3 Fabricated on quay side:

Some caissons of 17-meter in diameter were constructed to the height of 1.57 meters (draught 0.86^m, free board 0.71^m) on the apron of quay side, and then, hoisted by 200-ton capacity floating crane down to the water to continue the rest part as shown in Fig.5. Being completed, they were grounded temporarily as well. Quay was the requisition for this case.



Fig. 5. Cylindrical caisson fabricated on quay apron.

For foundation built-up, due to caissons being put directly on sea bed of slope ranging from 1:100-1:50 or so, natural sea bed was just the foundation of cylindrical caissons to make the cutting wall to cut through it. Placing rocks or armour units for this kind breakwater aimed at giving appropriate protection to the toes of cylindrical caissons rather than to the foundation, as shown in Fig. 6.

As to the towing & sinking of cylindrical caissons, It's a key point for breakwater construction. The temporarily grounded caissons were refloated before towing. Towing & sinking was done in a continuous process to put the caisson in the right position. Then, the following works, such as sandfill, rock-placing and capping etc. followed up till the caisson come to the absolutely stable condition.

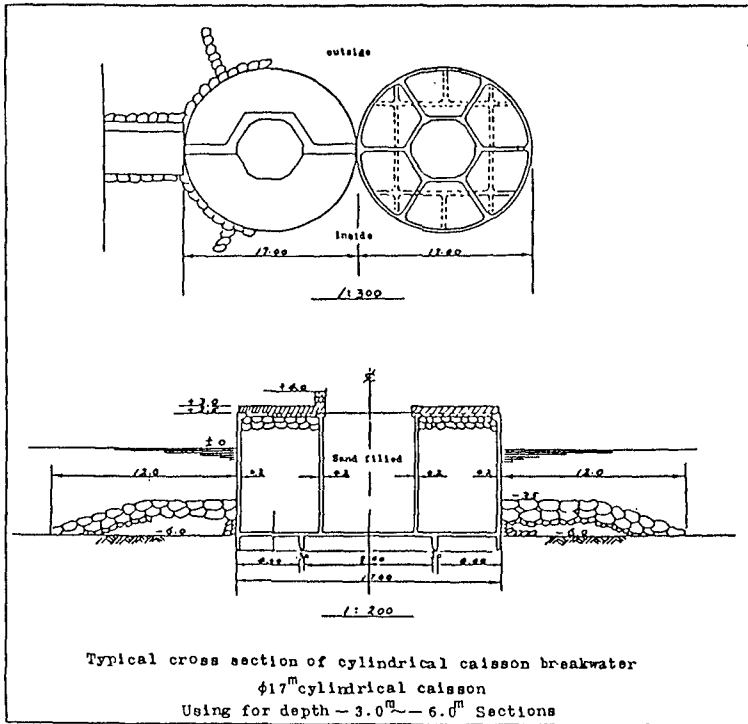
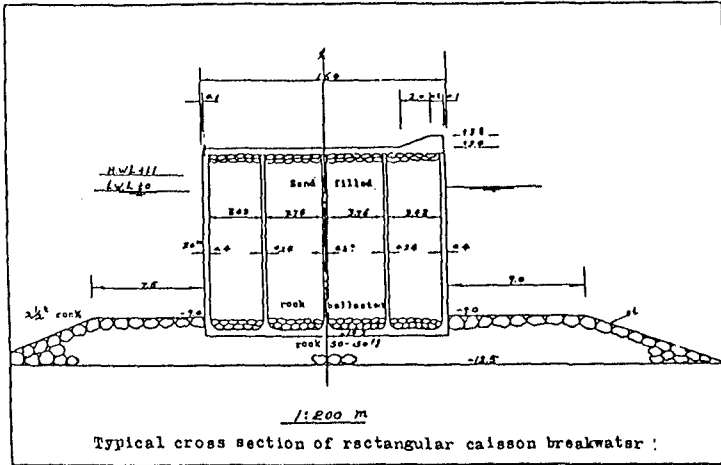


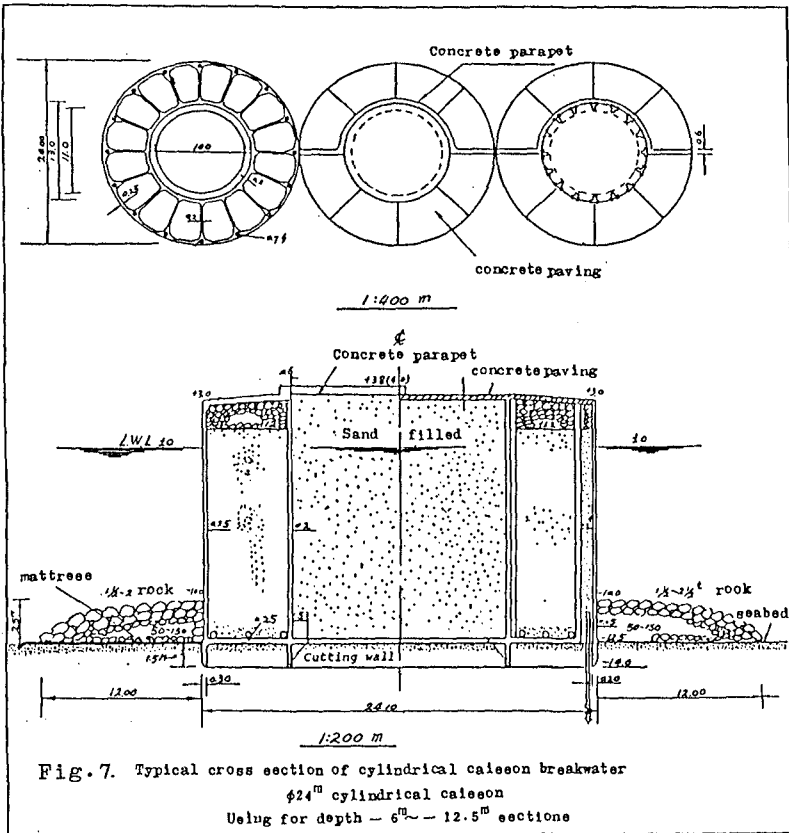
Fig. 6. Different Foundation Methods between cylindrical caisson and rectangular shape breakwaters

2.4. Technical problem:

Some technical problems which play a very important role referring to the cylindrical caisson breakwater were cutting wall installation, gap control, design criteria and so on.

2.4.1 Cutting wall installation:

Cutting wall's design was a very important breakthrough to the cylindrical caisson breakwater. It's installed along the bottom wall with a height of 1.25-1.50 meters as shown in Fig. 7. When cylindrical caissons placed directly on the sea bed, it cut into the sand layer by its self-weight and weight of sand-fill etc. to increase the horizontal resistance forces against sliding. At the same time, it could protect the sand under the caisson from scouring during constructing in monsoon season (wave height under 2 meters). The later was more important than the former due to caisson being placed in monsoon season rather than in typhoon season.



2.4.2 Gap control:

Gaps between each two caissons should be controlled in a proper limit, designed for 40cm in Kaohsiung's case, to avoid wave transmission packing sand from outside the breakwater to silt the channel. Furthermore, the unsuitable arrangement of the gaps could induce wave momentum to wash away the rock or armour units placed in between the gaps. In Kaohsiung's case, we should do routine maintenance by placing about US\$300,000 equivalent armour units (Used 15-20 ton modified tetrapods) annually due to bad control of gaps.

2.4.3 Design criteria

Besides the sand-fill and the weight of caisson itself, the stability design of cylindrical caisson for bearing, sliding and overturning was also controlled by constructing caisson as a hollow type with 1.25-1.5m cutting wall to cut through the sand layer. For the 6 meters designed wave height, the factor of safety of $\phi 24^m$ cylindrical caisson were:

$$F_b = 2.25$$

$$F_s = 1.84$$

$$F_o = 5.40$$

Which were all larger than the standard value 1.2 set for the design criteria.

2.5. Damage rehabilitation during construction

During construction, already placed cylindrical caissons would be declined to about 9 degree or sunk down to the sand bed some 1.5 meters deep, but wouldn't be moved out of the position as hit by big wave forces in case that protection works had not yet completed. If so, the repair and rehabilitation works could be done by mounting precast concrete frame on the top of caisson to the design elevation. This procedure was quite different to the rectangular type which would be damaged in a different way-slide away from its position as shown in Fig. 8. Other damages, such as wall fracture, also could be repaired in a easy way.

2.6. Maintenance after operation:

Although there were many advantages using cylindrical caisson for breakwater, maintenance was the big problem to be solved in comparison with the rectangular one.

For regular maintenance, placing 7.5-20 ton of armour units should be made annually to protect the toes of cylindrical caissons from scouring before typhoon season.

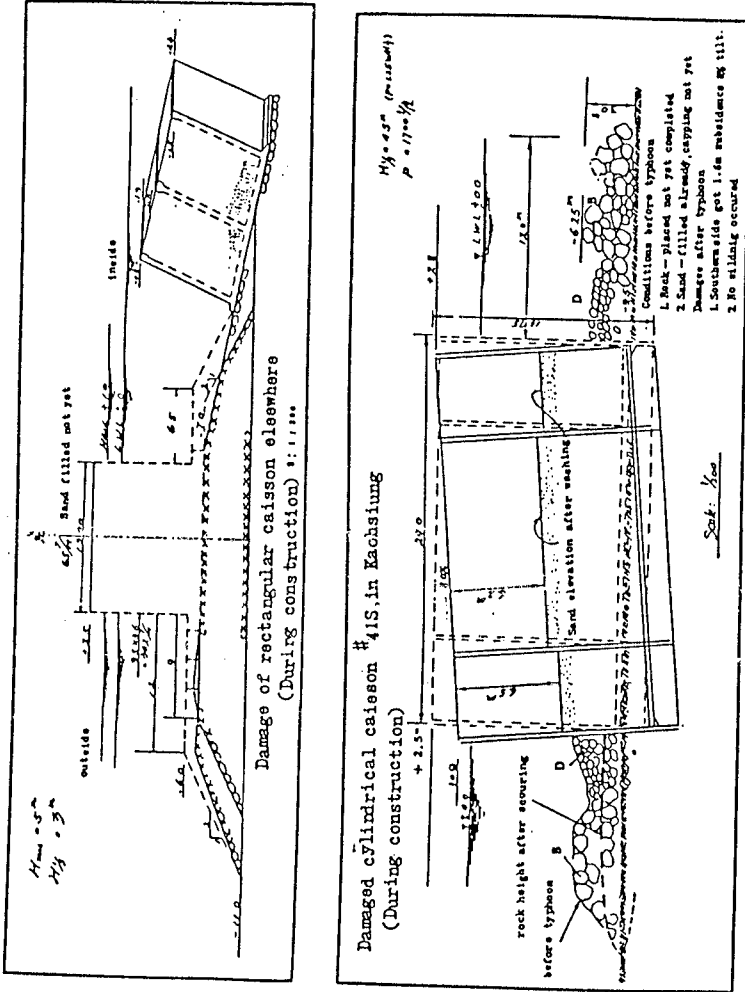


Fig. 8. Different damages for cylindrical and rectangular caissons during construction.

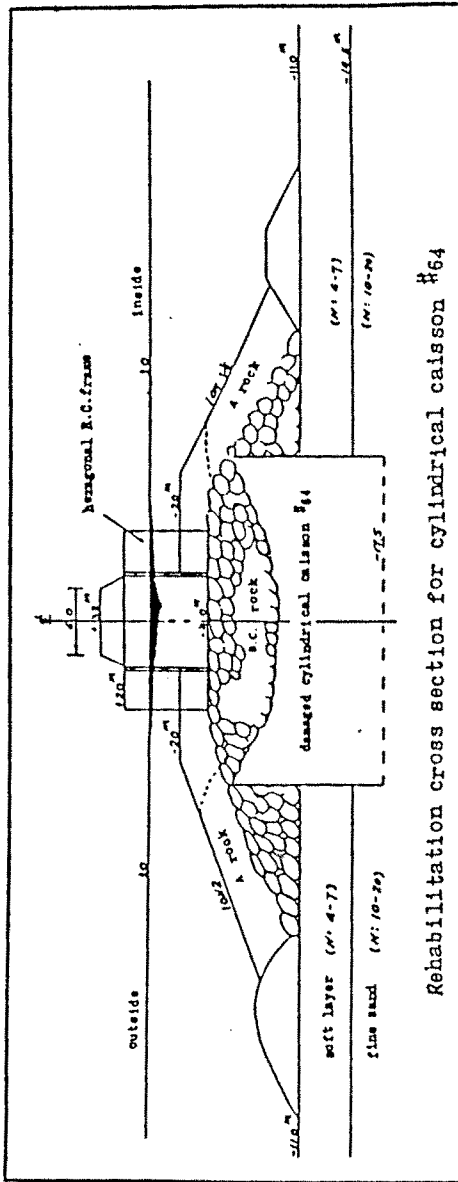


Fig. 9. Repair method... for serious damaged cylindrical caisson breakwater

For emergent disposal, repair works should be carried out as soon as typhoon passed in case of serious damages occurred as shown in Fig. 9.

3. CONCLUSIONS:

(1) Using cylindrical caisson for a large-scale breakwater is encouraged as Port of Kaohsiung's 2nd harbor entrance breakwater has successfully experienced in many typhoon attack (the peak wind speed reached 63 m/sec or 227 km/hour) since it was completed in 1975.

(2) Cutting wall was a key point in cylindrical caisson breakwater design, from which a very good horizontal resistance force against sliding could be given to reduce the damage to the least during/after construction.

(3) Gap design of cylindrical caisson breakwater gave a very close relation with maintenance, Therefore, laboratory model test and mathematics model analysis should be done to find the suitable armor units for long-term stability consideration.

(4) No matter what disadvantages during/after construction are, using cylindrical caisson for the large-scale breakwater project is worthwhile to recommend as it could shorten construction period, simplify construction method and reduce construction cost under the consideration of security and safety. Especially, it will provide a valuable experience for developing countries which run short of funds and need seaport urgently.

4. REFERENCES:

(1) Gong, C.I. et al (1976). Report on improvement study of Kaohsiung 1st Harbor Entrance.

(2) Report on study of construction plan of Kaohsiung 2nd Harbor Entrance (1968)Kaohsiung 2nd Harbor Entrance Construction Department, Kaohsiung Harbor Bureau.

(3) Report on Kaohsiung 2nd Harbour Entrance Construction Project (1976).

CHAPTER 126

ARCTIC SLOPE PROTECTION METHODS

Craig B. Leidersdorf, M. ASCE¹

Peter E. Gadd, M. ASCE¹

William G. McDougal, M. ASCE²

ABSTRACT

This paper reviews knowledge acquired in the Alaskan Beaufort Sea pertaining to three methods of Arctic slope protection: (1) sacrificial beaches, (2) "soft" (geotextile based) armor, and (3) linked concrete mats. Design considerations and performance evaluations are presented for each method, along with recommendations for future use. It is concluded that the existing technology is capable of providing reliable protection for structures located in coastal and nearshore areas, and that more durable systems will be required to withstand the extreme wave and ice loads which can occur at exposed sites in deeper waters.

INTRODUCTION

Since 1976, more than twenty man-made islands, causeways, and coastal pads have been constructed in the Alaskan Beaufort Sea in response to the needs of the petroleum industry. The initial facilities were sited along the coast or at nearshore locations where wave heights and ice forces were limited by the water depth. By the mid-1980's, however, slope protection methods and construction techniques had advanced to the point where islands were installed in exposed locations with water depths to 15 m. Although the rate of new construction decreased in the 1980's with the decline in oil prices,

¹ Principal, Coastal Frontiers Corporation, 9424 Eton Ave., Suite H, Chatsworth, CA 91311, U.S.A.

² Professor, Department of Civil Engineering, Oregon State University, Corvallis, OR 97331, U.S.A.

performance monitoring of many of the facilities has continued through the present date.

The objective of this paper is to review the knowledge of Arctic slope protection which has been acquired from the past fifteen years' experience in the Alaskan Beaufort Sea. Emphasis will be placed upon the three methods which have been most widely employed: (1) sacrificial beaches, (2) "soft" (geotextile-based) armor, and (3) linked concrete mats.

SITE CONDITIONS

The most distinguishing feature of the Arctic offshore environment is the presence of sea ice. First-year ice typically attains a thickness approaching 2 m during the long winter season. When the ice is deformed by pressure, its thickness can increase to 30 m or more, and the resulting pressure ridge can often survive one or more summer melt seasons. Such multi-year floes pose a particular threat to offshore structures, not only because of their great mass, but also because of the drift velocities they can attain during the period of open-water.

Design ice loads generally are based on the crushing strength of the ice (American Petroleum Institute, 1988). Global loads in shallow water are of order 700 to 1000 kPA, while those in deeper water (to 15 m) are of order 1400 to 1700 kPA. Local loads, as might occur on piles or protruding armor units, can exceed the corresponding global load for the entire structure by a factor of three. Damage can also result from the shear forces exerted when ice moves up or along the structure slope, and from ice abrasion.

Hydraulic loads are moderate in the Beaufort Sea due to the limited fetch which results from the proximity of the polar ice pack. At an exposed, deep-water site, representative wave conditions for the 10-year return period storm might consist of a maximum significant wave height of 4-5 m and a peak period of 8-10 sec. Storm surges can significantly increase the water depths and the resulting depth-limited wave heights in nearshore areas.

Experience to date suggests that the most severe damage to slope protection systems often results from a combination of ice and wave loads. Drift ice impacts can damage and displace armor units below the waterline, for example, after which the slope is predisposed to rapid degradation under even moderate wave loads.

Conversely, deformations in the slope profile caused by wave impacts can create local protrusions which serve as focal points for ice forces.

In addition to ice and wave loads, the following factors must be considered in designing slope protection systems for Arctic service: (1) low temperatures (-50°C), (2) a brief open-water season during which construction can be performed (typically 60 to 90 days), (3) a lack of native construction materials (including quarystone and cement in the Alaskan Beaufort Sea), (4) a paucity of environmental data from which to predict extreme events, (5) a lack of specialized construction equipment, and (6) the high cost of importing equipment and non-native construction materials. As a result of these limitations, the slope protection methods which have evolved in the Alaskan Arctic have tended to emphasize simple construction techniques, maximum use of locally available materials, and non-catastrophic modes of failure (in the event that the design conditions have been underestimated).

SACRIFICIAL BEACHES

Sacrificial beach slope protection consists of providing a buffer zone of expendable beach material around the area to be protected (Plate 1). The width of the buffer zone should be sufficient to accommodate the



Plate 1. Sacrificial Beach on Niakuk 4 Island

erosion anticipated from both daily conditions and design storm events. The obvious advantages of such an approach include a low capital cost, ease of construction, and low susceptibility to ice damage. The primary disadvantages are the need for frequent maintenance, and the fact that the degree of protection provided by the system depends not only upon the incident wave heights, but also upon storm duration. Because erosion rates tend to become unacceptably high in exposed locations, sacrificial beaches are most appropriate for coastal or nearshore sites in which the wave heights are depth-limited.

Design Considerations

Of particular benefit in the design of sacrificial beach protection has been the availability of gravel and coarse sand in relict river deposits along the Alaskan coast. To date, all of the sacrificial beaches in the Alaskan Arctic have been constructed from this material rather than from the fine sands and silts found on the sea bottom. The median grain size (D_{50}) has typically ranged from 4 to 8 mm, with a maximum cobble size of 80 mm and a fines content ($D_{50} < 0.075$ mm) of less than 10%. As discussed below, the coarse nature of the sediment has resulted in lower longshore transport rates, and consequently more stable beaches, than those associated with the sand-sized material.

Both cross-shore and longshore transport must be taken into account in determining the required width of the sacrificial buffer zone. To obtain a first approximation of the former, successive profiles were obtained on the slopes of Niakuk 4, a man-made island located in a water depth of 1.4 m, during the three-year period between 1985 and 1988. The change in the configuration of the island which occurred during the monitoring period is illustrated in Fig. 1; representative profile data from the exposed northeast side are presented in Fig. 2.

The data suggest that the gravel tends to assume an equilibrium profile analogous to that reported for sand beaches by a number of investigators (for example, Bruun, 1954; Dean, 1977). The characteristic concave-upward shape of the below-water portion of the profile can be described by the relationship:

$$h = ax^m \quad (1)$$

where h is the depth (m), x is the distance offshore (m), and a and m are empirical constants which provide a best fit to the data with values of 0.39 and $2/3$, respectively.

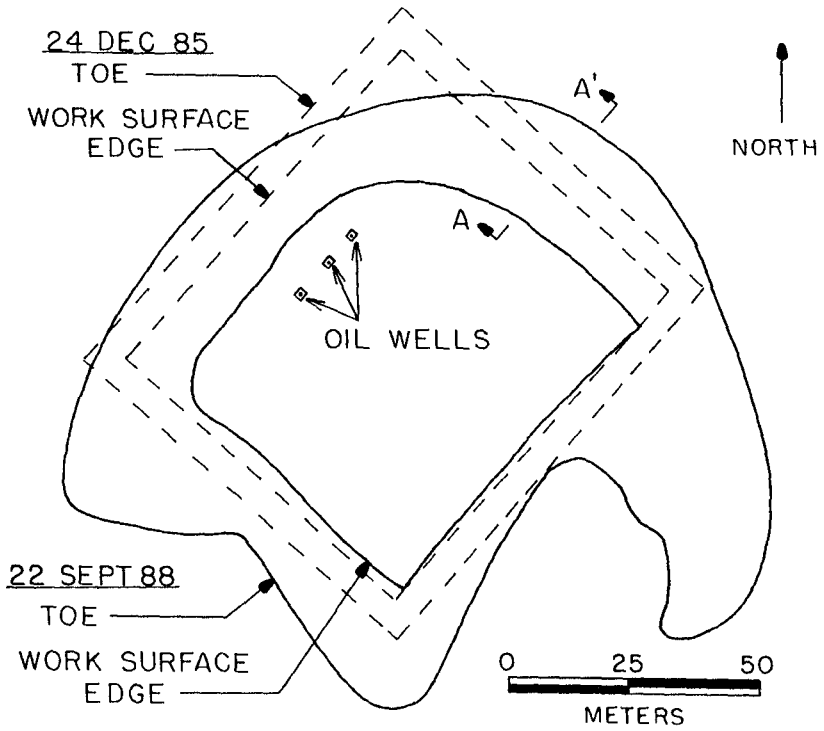


Figure 1. Evolution of Niakuk 4 Island, 1985-88

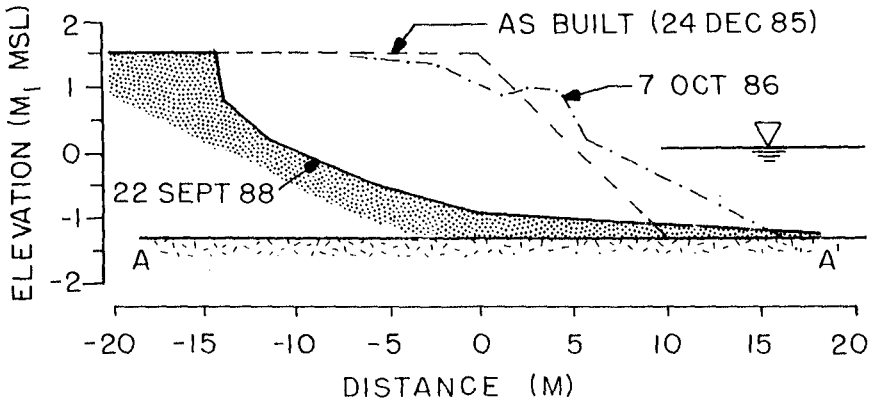


Figure 2. Beach Profiles on Niakuk 4 Island, 1985-88

As reported by Komar (1988), data regarding longshore transport rates for gravel-sized material are extremely sparse. To develop a first order predictive capability for the sacrificial beach material available in the Alaskan Arctic, the average annual net transport rates for the exposed northeast and northwest sides of Niakuk 4 Island (Fig. 1) were calculated from the survey data for the 1985-88 monitoring period. These results were combined with the wave measurements available from a single open-water season prior to the monitoring period (1982) to determine the transport coefficient K in the relationship proposed by Komar and Inman (1970):

$$I_s = KP_1 \quad (2)$$

where I_s is the immersed-weight transport rate and P_1 is the longshore component of wave power based upon the root-mean-square wave height. Values of 0.08 and 0.12 were obtained for the transport coefficient on the northeast and northwest sides, respectively. In view of the limitations of the data set, this range is not surprising. The mean value of 0.10 was therefore adopted as a first approximation of the transport coefficient.

It is noteworthy that the foregoing result, obtained for material with a D_{50} of 4 mm, is substantially lower than the transport coefficient of 0.77 reported for sand (CERC, 1984; note that the value of $K = 0.39$ presented by CERC has been modified to 0.77 to reflect the use of the root-mean-square wave height rather than the significant wave height in calculating P_1 in Eq. 2.) It therefore appears that the use of coarse sediment can significantly improve the performance of sacrificial beaches by reducing the rate of longshore transport.

Performance Evaluation

Four man-made islands and two shore-connected causeways using sacrificial beach slope protection have been constructed in the Alaskan Beaufort Sea to date. Water depths have ranged from 0 to 3 m. The most extensive application has been on the Endicott Oil Production Facility (Munday and Bricker, 1988), where 8 km of causeway in water depths to 2 m are protected by gravel beaches placed at an initial slope of 7H:1V. Fill losses and scarp formation have been modest, and no replenishment has been required since the facility was completed in 1986.

The most thorough documentation of beach performance has been obtained for Niakuk 4 Island (Plate 1; Fig. 1). Constructed in 1984 in 1.4 m of water as a 122 x

107 m rectangle, the island experienced moderate erosion during the 1985 open-water season. It was re-graded to its original configuration during the fall of 1985, at which time the monitoring program referred to previously was undertaken.

During the ensuing three open-water seasons (1986-88), the gravel losses from the exposed northeast and northwest sides of the island averaged only 2,200 m³/yr. More than 75% of this material accumulated in spits which formed at the east and west corners (Fig. 1). During the 1989 open-water season, the spit material was excavated and used to restore the width of the buffer zone on the northeast and northwest beaches. Initial concerns that the gravel would remain frozen during the summer months proved to be unfounded, allowing the backpasing operation to proceed at a rate of 2,900 m³/day.

In contrast to the relative stability evidenced by sacrificial beaches in water depths of 2 m or less, substantial erosion rates have been observed on beaches in deeper water. Such observations encompass islands from which the original armor has been removed (Anderson and Leidersdorf, 1988), as well as purpose-built beaches. Based upon both the rates of erosion and the cost of transporting gravel offshore for beach replenishment, it appears that the 2-m isobath represents a practical limit for the application of sacrificial beach slope protection methods in the Alaskan Arctic.

SOFT ARMOR

"Soft armor" refers the use of geotextile containers filled with sediment as a means of providing slope protection. Although the concept embodies a wide range of devices, the Alaskan experience has indicated that massive units such as tubes and mats are susceptible to rapid deflation when punctured by ice (Leidersdorf, et al., 1981). Large gravel-filled bags (Plate 2) have proven to be best-suited for Arctic service, and are therefore the focus of the discussion which follows.

The advantages of gravel bag slope protection include a moderate capital cost, the ease of performing repairs, and the relative simplicity of the installation procedure. The primary disadvantages are a susceptibility to ice damage, resulting in the need for maintenance, and the environmental nuisance which is created when damaged bags drift away from the slope.



Plate 2. Gravel Bag Armor on Resolution Island

Design Considerations

The central issues to be addressed in the design of gravel bag slope protection are the characteristics of the bags themselves, the placement configuration, and the characteristics of the underlying filter fabric. In the case of the bag characteristics, two sizes, representing capacities of 1.5 and 3.0 m³, have been adopted for most Arctic applications to date. The 3.0 m³ size, with a weight of approximately 5.5 tonnes, has proven to be the largest unit which can be easily handled by conventional construction equipment. It is typically used in exposed locations with relatively energetic wave regimes, while the 1.5 m³ size is applied in cases of more limited wave exposure.

Based on the performance of prototype test sections (Leidersdorf, et al., 1981), bags constructed of a single layer of high-strength fabric are more durable than those comprised of multiple layers of lower-strength material. Woven polypropylene with a grab tensile strength of 700 N/cm has been used to construct the majority of the bags in Arctic service; specifications for this material are provided by Gadd (1988).

Representative placement configurations for gravel bag armor are illustrated in Fig. 3. An inclination of 3H:1V has proven to be the steepest grade at which the

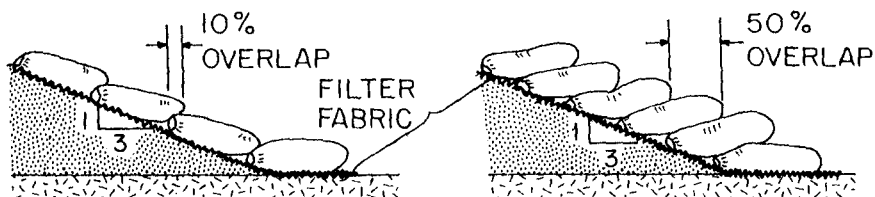


Figure 3. Gravel Bag Placement Configurations

bags are not prone to sliding failure, and has therefore been adopted for most gravel bag installations in Alaska. Maximum stability is achieved by orienting the longitudinal axis of each bag in the on-offshore direction, and by providing a measure of overlap between the bags. A minimum overlap of 10% of the bag length is recommended to insure that the closure end of the bag is protected from direct wave impact by the next bag upslope. Increasing the overlap to 50% requires additional bags, but offers the advantages of greater stability, redundant coverage in the event that bags are damaged, and reduced wave runup elevations.

Based on the results of large-scale model testing, the hydraulic stability of gravel bags in the 50% overlap configuration can be estimated using Hudson's Equation (CERC, 1984) with a stability coefficient K_D of 3.0 (Gadd, 1988). Fig. 4 displays the computed threshold wave heights for bag instability as a function of the cotangent of the slope angle. For the 3H:1V slopes in common use, instability is predicted to occur at a wave height of 1.9 m for 1.5 m³ bags, and 2.4 m for 3.0 m³ bags.

A permeable filter fabric must underlie the gravel bag armor layer to retain the slope fill material (Fig. 3). The experience to date indicates that if the slope is composed of coarse sand and gravel with a low fines content, non-woven material with a grab tensile strength of 525 N/cm provides acceptable performance.

Performance Evaluation

Gravel bags have been used as the primary means of slope protection on nine man-made islands and two coastal pads in the Alaskan Beaufort Sea. Four of the islands were constructed in exposed locations with water depths of 12 to 15 m; the remainder were located in partially sheltered sites with depths to 7 m.

Resolution and Mukluk Islands illustrate the range of performance which has been observed for gravel bag armor systems. Resolution, located in a partially

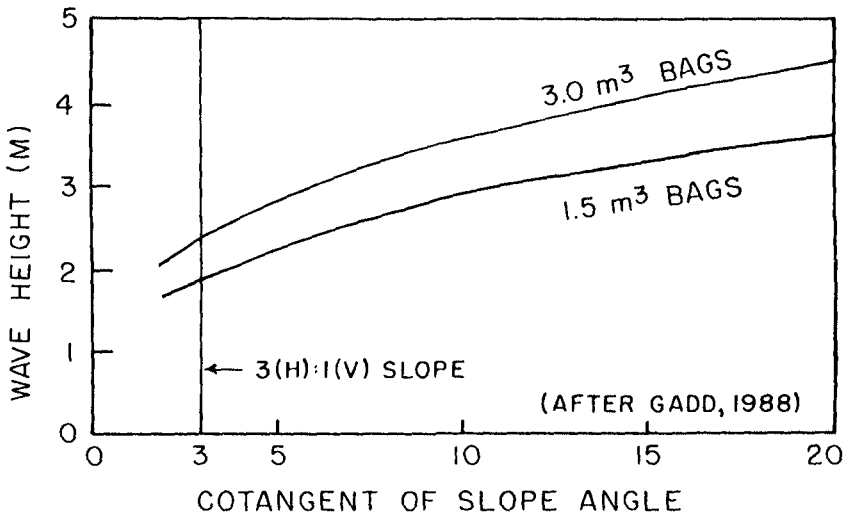


Figure 4. Threshold Wave Heights for Gravel Bag Instability

sheltered location with a water depth of 2.3 m, has sustained damage to its 3,140 1.5 m³ gravel bags at an average rate of about 5% per year since it was constructed in 1980. The primary causes of the damage have been the impacts of drift ice during the summer months, and movements of the ice sheet during the winter months. Repairs have been performed on two occasions to restore the integrity of the armor.

Mukluk Island was constructed in 1983 at an exposed location in 14.6 m of water. During the following two open-water seasons, drift ice impacts ruptured a majority of the 3.0 m³ bags from the waterline to a depth of 8 m. Because the island was no longer needed for oil exploration, the damage was not repaired, leading to an extensive failure of the armor and loss of island fill material in response to two severe storms in 1986 (Anderson and Leidersdorf, 1988).

The foregoing observations, as well as those from other facilities, suggest that gravel bag armor is best suited for applications in shallow and intermediate water depths where wave heights seldom exceed 3 m, and where frequent impacts from large, drifting ice floes are not anticipated. Because ice damage can predispose the armor to failure under wave conditions which are well below the threshold level for hydraulic instability, periodic inspections and repairs are essential to maintaining its functional effectiveness.

LINKED CONCRETE MATS

Linked concrete mat armor consists of concrete blocks which are joined by flexible linkages to form a continuous, articulated cover on the slope to be protected (Plate 3). Rather than depending upon mass alone, the mat derives a significant portion of its stability from the connections between adjacent blocks.



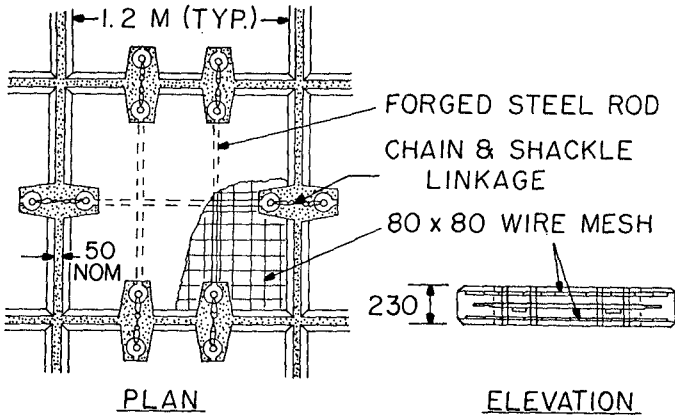
Plate 3. Concrete Mat Armor on the Endicott Project

The primary advantages of the mat concept are a reduced susceptibility to ice damage, a suitability for modular installation, and the ability to accommodate changes in the subgrade without permitting catastrophic fill losses. Disadvantages include a relatively high capital cost, and the difficulty in effecting repairs if significant damage is sustained.

Design Considerations

In recognition of the need to withstand both severe ice loads and the cyclic impact loads resulting from wave-induced uplift, relatively large, reinforced blocks with chain-and-shackle linkages have been selected for most Arctic offshore applications. A representative example of the block design, in which the blocks are 1.2 m square and 230 mm thick, is provided in Figure 5.

A filtration medium is required under the blocks to retain the slope fill material. Permeable geotextiles



(AFTER HAYLEY ET AL., 1987)

Figure 5. Representative Concrete Block Design

have been used for the Arctic projects to date, but graded stone or manufactured concrete rubble may be warranted for projects with a long design life or at exposed locations where the fabric might be damaged by uplift-related abrasion.

Although a semi-analytical model has recently been developed for evaluating the hydraulic stability of unlinked mat systems (Burger, et al., 1990), a comparable design tool for linked mats does not presently exist. Hydraulic model testing is therefore recommended as the most reliable means of refining and confirming the design of linked mat systems for major projects.

The relatively smooth surface of concrete mat armor, although advantageous from the standpoint of reducing ice forces, is ineffective in deterring wave runup. As illustrated in Plate 3, this potential problem can be addressed by restricting the use of the mat to the zone of severe ice and wave impacts, and placing overlapped gravel bags on the upper portion of the slope.

Performance Evaluation

Linked concrete mat armor was tested on a limited scale on two nearshore islands in the early 1980's. Based on the successful performance of these prototype test sections, it has been selected for use in a coastal revetment, and as the primary means of protection for three islands: Northstar, constructed in 1985 in a water depth of 13.7 m (Hayley, et al., 1987), and the two

islands of the Endicott Project, constructed in 1985-6 in depths of 1.8 to 3.6 m (Munday and Bricker, 1987).

At the Endicott site, where the wave and ice conditions are moderated by the water depth, the mat has sustained no significant damage and required no maintenance since it was installed. It is noteworthy that this performance has been achieved despite the occurrence of wave and ice events with sufficient energies to displace 4 m^3 gravel bags on the upper slopes.

Wave and ice conditions have been more extreme at the Northstar Island site, and have included storm waves with heights of 3 to 4 m, and numerous impacts from large multi-year ice floes. Although the mat performed significantly better than the gravel bag armor systems on nearby islands, it nevertheless sustained appreciable damage. As discussed by Gadd and Leidersdorf (1990), wave-induced uplift was of a sufficient magnitude to cause deformation of the subgrade, abrasion of the filter fabric, and localized fill losses. These irregularities in the slope served to intensify the loads imparted by ice impacts, resulting in the breakage of both concrete blocks and steel linkages, and the displacement of groups of blocks in the vicinity of the waterline.

The foregoing observations suggest that the mat systems currently in use are capable of withstanding the wave and ice forces in partially sheltered environments with little or no damage. They are particularly appropriate for projects in such locations with extended service lives, in that their relatively high capital cost will be offset by low maintenance costs. In exposed locations, the existing mat technology is susceptible to damage from the wave and ice forces associated with extreme events. Possible alternatives for improving the armor performance in this regard include increasing the thickness of the blocks and the strength of the linkage system in the vicinity of the waterline, and providing a near-horizontal bench in the slope just below the waterline to dissipate the energy of arriving waves and ice floes (Leidersdorf, et al., 1994).

SUMMARY AND CONCLUSIONS

The experience of the past 15 years indicates that the existing slope protection methods are capable of resisting the hydraulic and ice forces encountered in the coastal and nearshore waters of the Alaskan Arctic. The most cost-effective method of protection for a particular project depends upon the water depth, the degree of exposure to wave and ice impacts, and the project

design life. Sacrificial beaches are well-suited for applications in depths of 2 m or less. Gravel bag armor can withstand more severe wave conditions, but is susceptible to ice damage and requires regular maintenance. Linked concrete mat armor is capable of resisting both the ice and wave impacts commonly encountered in nearshore areas, and is therefore recommended for projects requiring secure protection over an extended period.

Gravel bags and linked concrete mats have also demonstrated the ability to protect facilities at exposed sites in deeper water, but have sustained damage from extreme wave and ice events. Frequent inspection and repair activities are necessary at such locations to prevent catastrophic slope failures.

In order to develop more durable slope protection systems suitable for long-term service at exposed sites, it will be necessary to provide an improved resistance to the impacts of large ice floes, and to the combined effects of wave and ice loads. At the present time, the most promising approach appears to be through modifications to the existing mat technology.

REFERENCES

- American Petroleum Institute, 1988, Recommended Practice for Planning, Designing, and Constructing Fixed Offshore Structures in Ice Environments, API RP2N, Washington, D.C.
- Anderson, L.M. and C.B. Leidersdorf, 1988, "Arctic Island Abandonment: Planning and Implementation for Mukluk Island", Proc. 20th Annual Offshore Tech. Conf., Houston, TX, p. 49-60.
- Bruun, P., 1954, "Coast Erosion and the Development of Beach Profiles", U.S. Army Corps of Engineers, Beach Erosion Board, Tech. Memo 44, Washington, D.C., 79 pp.
- Burger, A.M., M. Klein Breteler, L. Banach, A. Bezuijen, and K.W. Pilarczyk, 1990, Jour. Waterway, Port, Coastal & Ocean Engr., v. 106, n. 5, ASCE, p. 525-543.
- CERC, 1984, Shore Protection Manual, 2 vols., Department of the Army, Coastal Engineering Research Center, U.S. Government Printing Office, Washington, D.C.
- Dean, R.G., 1977, "Equilibrium Beach Profiles: U.S. Atlantic and Gulf Coasts", Dept. of Civil Engr., Ocean Engr. Report No. 12, Univ. of Delaware, Newark, DE.

- Gadd, P.E., 1988, "Sand Bag Slope Protection: Design, Construction, and Performance", in Chen, A.C.T., and C.B. Leidersdorf, eds., Arctic Coastal Processes and Slope Protection Design, ASCE, New York, NY, p. 145-165.
- Gadd, P.E. and C.B. Leidersdorf, "Recent Performance of Linked Concrete Mat Armor under Wave and Ice Impact", Proc. 22nd Coastal Engr. Conf., ASCE, New York, NY.
- Hayley, D.W., P.E. Gadd, and D.A. Horn, 1987, "Advances in Design and Construction of Slope Protection for Gravel Islands, Beaufort Sea, Alaska", Proc. 9th Int. Conf. on Port and Ocean Engr. under Arctic Conditions (POAC'87), Fairbanks, AK.
- Komar, P., 1988, "Environmental Controls on Littoral Sand Transport", Proc. 21st Coastal Engr. Conf., ASCE, New York, NY, v. 2, p. 1238-1252.
- Komar, P.D. and D.L. Inman, 1970, "Longshore Sand Transport on Beaches", Jour. Geophys. Res., v. 75, no. 30, p. 5914-5927.
- Leidersdorf, C.B., 1988, "Articulated Mat Slope Protection for Arctic Applications", in Chen, A.C.T., and C.B. Leidersdorf, eds., Arctic Coastal Processes and Slope Protection Design, ASCE, New York, NY, p. 166-189.
- Leidersdorf, C.B., P.E. Gadd, and W.G. McDougal, 1988, "Articulated Concrete Mat Slope Protection", Proc. 21st Coastal Engr. Conf., ASCE, New York, NY, v. 3, p. 2400-2415.
- Leidersdorf, C.B., R.E. Potter, and R.D. Goff, 1981, "Slope Protection for Artificial Islands off Prudhoe Bay", Proc. 13th Annual Offshore Tech. Conf., Houston, TX, p. 437-447.
- Leidersdorf, C.B., R.E. Potter, and C.J. Sonu, 1984, "Study of Slope Protection Works for the Arctic Ocean", Proc. 31st Annual Coastal Engr. Conf., Japan Society of Civil Engineers, p. 552-556.
- Munday, J.P., and W.F. Bricker, 1988, "Endicott Slope Protection Design and Construction", Proc. 6th Int. Conf. on Offshore Mechanics and Arctic Engr., Houston, TX, p. 47-54.

CHAPTER 127

Bragg Reflection Breakwater: A New Shore Protection Method?

James A. Bailard¹, Jack DeVries², James T. Kirby³
and Robert T. Guza⁴

ABSTRACT

The feasibility of a new type of breakwater is explored through a combined program of theoretical analysis, laboratory experiments and a prototype field test. The breakwater consists of a series of low height, shore-parallel bars which are placed just outside the surf-zone. The incident wave field is strongly reflected when the incident wave length is equal to twice the distance between adjacent bars. The breakwater acts to shelter the beach against storm wave attack and to build a tombolo sand deposit behind the breakwater. Theoretical and laboratory studies indicated that the Bragg reflection breakwater concept may have considerable merit, however, a small scale field test served to demonstrate the many practical difficulties in implementing the concept.

INTRODUCTION

The Naval Civil Engineering Laboratory (NCEL) has been involved in a multi-institutional program to explore low cost, rapidly deployable techniques for reducing beach erosion during storms. One concept under consideration is the Bragg reflection breakwater. Theoretical and

¹ Principal, Bailard Jenkins Technologies, Carpinteria, CA

² Engineer, Naval Civil Engineering Lab, Port Hueneme, CA

³ Professor, University of Delaware, Newark, DE

⁴ Professor, Scripps Institution of Oceanography, La Jolla, CA

laboratory studies have shown that a series of periodically spaced, low height bars, oriented parallel to the beach, can produce a strong reflection of the incident wave field. A resonant condition (termed Bragg reflection) occurs when the incident wave length is equal to twice the separation distance between bars.

The Bragg reflection breakwater concept involves placing a series of artificial bars just outside the surfzone. Referring to Figure 1, the effect of the bar field is two-fold: to shelter the beach from storm wave attack; and, to create a large sand volume behind the breakwater by way of the induced nearshore circulation. Both effects serve to protect the beach against storm wave attack: the first by reducing the rate of offshore sand transport, the second by increasing the erodable sand volume.

The objective of the research program was to explore the feasibility of the Bragg reflection breakwater concept through a combined program of numerical and laboratory modeling and a prototype field test. The present paper presents an overview of the program with an emphasis on the planning and results of a small scale field experiment.

BACKGROUND

Theoretical and Experimental Basis

Davies and Heathershaw (1984), Mei (1985) and others have shown that a series of low amplitude sinusoidal undulations on the seabed can be an effective reflector of surface gravity waves. The reflected wave energy varies as a function of the ratio of the incident wave length to the spacing between bottom undulations. A resonant condition, termed Bragg reflection, occurs when the incident wave length is equal to twice the distance between undulations. When resonance occurs, a small number of bars can reflect a substantial portion of the incident wave energy.

Technical Issues

At the onset of the research program, there were a number of unresolved technical issues relating to the feasibility of the Bragg reflection breakwater concept. These included: the response characteristics of non-sinusoidal bars on a sloping beach; the effects of finite bar length and the resulting wave-induced circulation; the morphological response of the beach in the presence

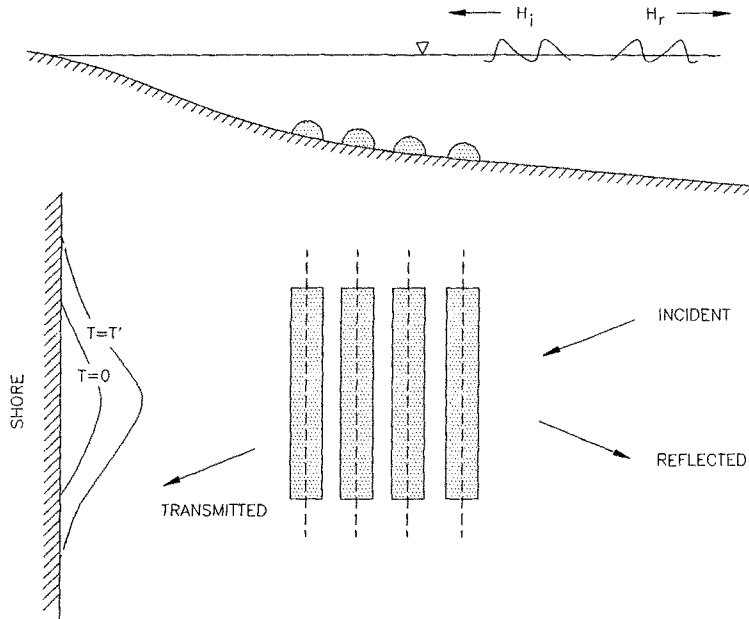


Figure 1. Schematic drawing of Bragg reflection breakwater concept.

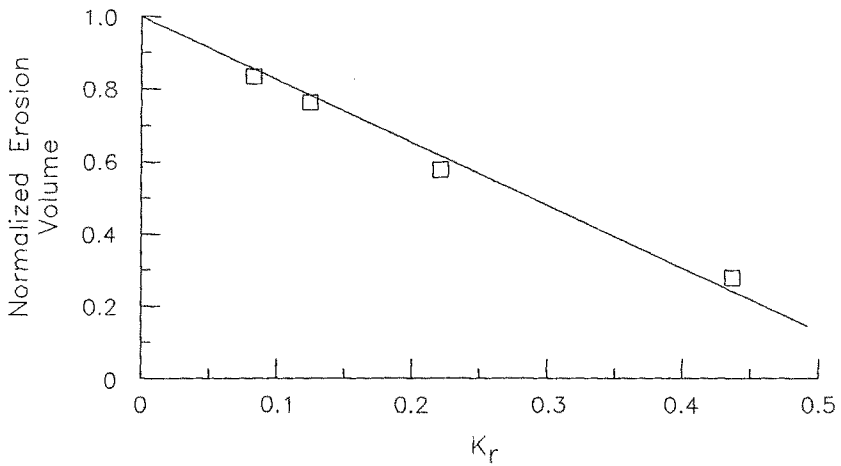


Figure 2. Beach profile response model results.

of the breakwater; the practical design, installation and recovery of a breakwater; and, the effects of waves on bar stability and scour. An additional issue was how to measure spectral wave reflection in the field.

PRELIMINARY ASSESSMENT

As a means of exploring the feasibility of the Bragg reflection breakwater concept, a series of preliminary studies were conducted. These studies were to culminate in a small scale field test of the concept. The results of the preliminary studies can be summarized as follows.

Wave and Current Modeling

Numerical and laboratory modeling studies were conducted at the University of Florida to examine the effects of bar shape, bar placement, beach slope and bar length on the reflection characteristics of a Bragg reflection breakwater. Details of these studies may be found in Anton et al. (1990). Specific results included:

- o The primary effect of beach slope is to require an adjustment in the spacing between each bars to accommodate the change in incident wave length.
- o The reflection from a non-sinusoidal bar field can be calculated by expanding the bottom shape function as a fourier series and linearly summing the response characteristics for each component of the series.
- o Finite bar length causes a longshore variation in the wave-induced setup leading to the formation of a rip current flowing outward over the bar field. The rip current acts to broaden the resonant peak.

These studies indicated that a Bragg reflection breakwater, constructed from a small number of practical-shaped (i.e. non-sinusoidal) bars, could be expected to generate a reflection coefficient in the range of 0.2 to 0.4.

Beach Response Modeling

A Bragg reflection breakwater protects a beach from storm wave attack by reducing the rate of offshore sand transport via decreased wave height and increasing the erodable sand volume via creation of a tombolo behind the breakwater. The former is a two-dimensional effect which is independent of breakwater length. The latter is a three-dimensional effect which results from the formation of a nearshore circulation cell with a rip current flowing outward over the top of the breakwater.

NCEL conducted a numerical model study to determine the impact of a Bragg reflection breakwater on the two-dimensional response of a beach profile during a simulated storm. The model study utilized an energetics-based beach profile response model developed by DeVries and Bailard (1988). The model was run for a simulated 5 day storm assuming varying wave reflection coefficients. The effectiveness of the breakwater was expressed in terms of the normalized erosion volume. This was defined as the ratio of the eroded sand volume in the presence of the breakwater divided by the eroded sand volume without the breakwater.

Model inputs were as follows:

- o Initial equilibrium beach slope = 0.03
- o Grain size = 0.4 mm
- o Storm duration = 72 hr
- o Peak wave height = 2 m
- o Peak wave period = 9 sec

Without the breakwater, the beach eroded approximately 205 cubic meters per meter of beach. Referring to Figure 2, the breakwater reduced the storm erosion volume by an amount which was inversely proportional to the wave reflection coefficient, K_r . The degree of reduction is quite significant, amounting to 35% for a reflection coefficient of 0.2.

A movable bed physical model study was conducted at the University of Florida to qualitatively examine the three-dimensional beach changes induced by a Bragg reflection breakwater. The model confirmed the presence of a nearshore circulation cell with a rip current flowing outward over the bar field. The circulation cell caused a tombolo to form behind the breakwater, with the outer edge of the tombolo perched on the shoreward-most bar.

Bar Module Tests

It was anticipated that developing a practical breakwater would be a significant design challenge. Our limited budget necessitated coming up with a breakwater which could be rapidly assembled, installed and recovered using a minimum of people and equipment. In order to explore various design and installation concepts, NCEL conducted field tests of two bar designs at a Port Hueneme beach. Both designs featured modular constructions consisting of skid-mounted bar modules which could be assembled on the beach and dragged offshore.

Referring to Figure 3, the first design consisted of a geotextile bag attached to a skid-mounted steel frame. The concept was to drag the modules into place with the bags empty, and then fill the bags with sand using a small dredge pump. When the breakwater was no longer needed, the bags could be slit, allowing the sand to disperse and the bars dragged back ashore. The advantage of this design was that the bar modules would be light and easy to move when empty, but heavy and difficult to move when full.

An attempted field test of the geotextile bar design ended in failure. Although assembling and positioning the bar module proved simple, filling the geotextile bag with a small dredge pump proved difficult. The pump was mounted on an amphibious LARC vehicle, parked in the surfzone. The principal difficulties were maintaining an adequate supply of sand to the pump and handling the intake and discharge hoses. When, after a few hours of filling, little sand had been pumped into the bag, the test was abandoned. In retrospect, the test might have been more successful had a larger, perhaps land-based dredge pump had been used. Nevertheless, the installation procedure was judged to be too cumbersome for the planned field experiment.

Referring to Figure 4, the second bar module design consisted of a corrugated steel arch attached to a skid-mounted steel frame. The concept was to assemble the modules on the beach and drag then into position. When the breakwater was no longer needed, the modules would be dragged back onto the beach and removed. The advantage of this design was that the modules were ready to go once they were moved into position. The main drawback was that the modules were relatively light weight and could be moved about by large waves. Although pinning the modules with uplift resisting anchors was considered, it was judged unnecessary for the anticipated wave climate.

The field test demonstrated that the arch module design could be rapidly assembled and installed. Provided wave heights were less than 1 m (rms), the module tended to remain in place. The primary problem was a scouring of the seabed underneath the bar module. This was caused by wave-induced flow passing through the narrow gap between the leading and trailing edges of the bar and the sand bottom. The scour depression acted to further enhance the venting flow, reducing the reflectivity of the bar module.

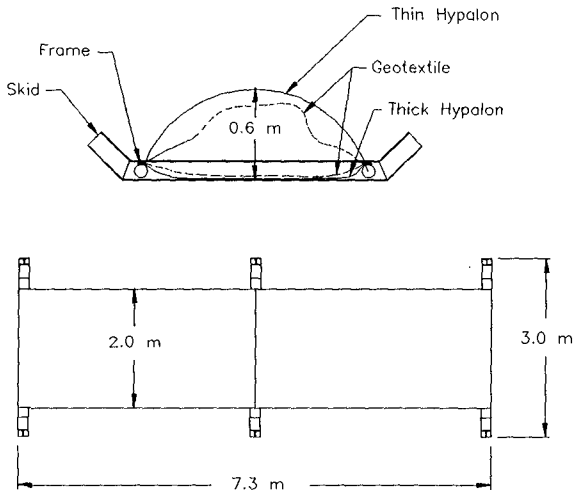


Figure 3. Geotextile bar module design.

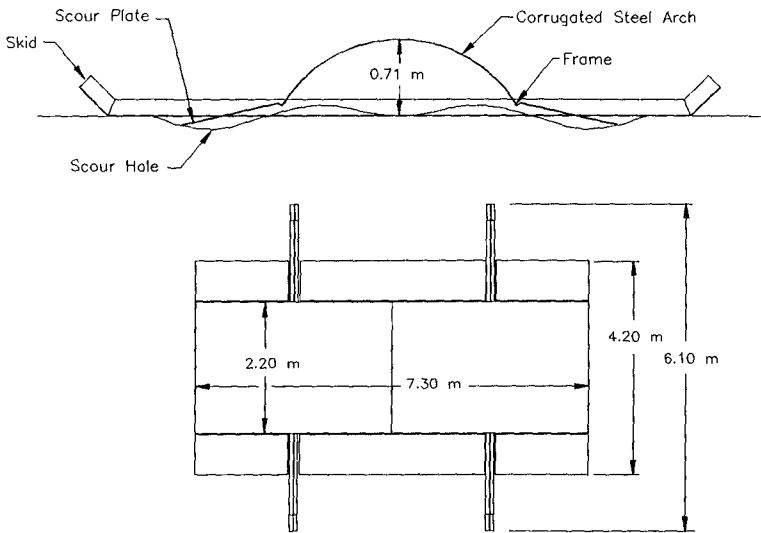


Figure 4. Steel arch bar module design used in the field test.

The venting/scour problem was solved by adding steel plates to the leading and trailing edges of the bar. The plates were attached to the bar by hinges, effectively sealing off the gap underneath the bar. Although some scour continued to occur around the bar module, the plates continued to function by dropping down into the scour depressions. After a period of two days, the scour depressions appeared to stabilize at a depth of about 0.3 m. A few days later, a significant storm passed through the area destroying the bar modules. However, the successful performance of the module prior to the storm convinced us to that the steel arch design would be suitable for the planned field test.

Detection Method

An inverse method was developed to estimate the directional spectrum of the reflected wave field (see Herbers and Guza, 1990). The method requires simultaneous measurement of the incident wave field at a point offshore and the reflected wave field at a point immediately in front of the Bragg reflection breakwater. The procedure is as follows:

- o The incident wave field is estimated using the offshore wave measurements.
- o The incident wave field is transformed to shallow water using linear refraction.
- o The reflected wave field is estimated using the inshore wave measurements and subject to maximum compatibility with the refracted incident wave field.

PROTOTYPE FIELD TEST

Site Selection

In order to maximize the detectable reflected wave energy, we wanted to construct a breakwater that was significantly longer than the incident wave length and which produced a reflection coefficient of about 0.4. To minimize the size of the breakwater and therefore its cost, we decided to carry out our experiment in "super laboratory" conditions. These can be defined as significant wave heights less than 0.25 m, a wave period of about 5 seconds and an installation depth of about 1.5 meters.

A number of sites were considered for the field experiment. The desired site required small amplitude, short period waves, a long planar beach, limited public access

and good logistical support. Based on these criteria, Cape Canaveral Beach, Florida, was selected as the preferred site for the field experiment. The site was located within the confines of Cape Canaveral Air Force Base, limiting public access and providing the necessary logistical support. Two years of wave data from the site indicated that during the month of July, we could expect significant wave heights of about 0.2 m with a 5 second period.

Breakwater Design

Referring to Figure 5, the prototype Bragg reflection breakwater was composed of three bars, 90 meters long. The offshore and middle bars were 0.7 meters high and 2.2 meters wide. The inner bar was 0.6 meters high and 2.4 meters wide. The spacing between the outer and middle bar was 9 meters versus 8 meters between the middle and inner bars. The breakwater was designed to be installed in a water depth of about 0.76 meters MLW.

Referring to Figure 5, each bar module was 7.3 meters long. The modules were fabricated from a pair of corrugated steel arches attached to a steel skid-mounted frame. The frame was composed of a pair of steel angle members attached to two steel skid beams. The angle members served as attachment points for the edges of the corrugated steel arches and the a series of steel scour plates hinged to the front and rear edges of the bar. The bar modules were designed to be assembled by a small crew using a crane and hand tools. Assembly was facilitated by prefabricating the components off-site and using nuts and bolts for fasteners.

The total weight of the bar modules was approximately 3300 lb. An stability analysis indicated that the modules would remain in place without anchoring if rms wave heights were less than 1 m (assuming a wave period of 5 to 6 sec).

Anticipated Performance

Figure 6 shows a plot of the estimated reflection characteristics for the prototype breakwater. These characteristics were estimated using a computer program developed by Kirby (1987). The response function shows a broad peak centered at about 6 seconds with a reflection coefficient value of 0.4. The adjacent narrower peak is the first harmonic resulting from the non-sinusoidal shape of the bar field (i.e. discrete bars resting on a planar bottom).

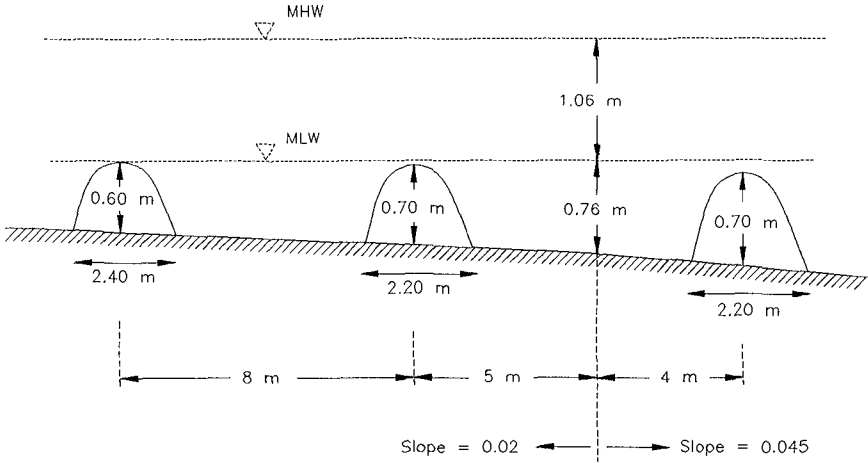


Figure 5. Bragg reflection breakwater design used in the field test.

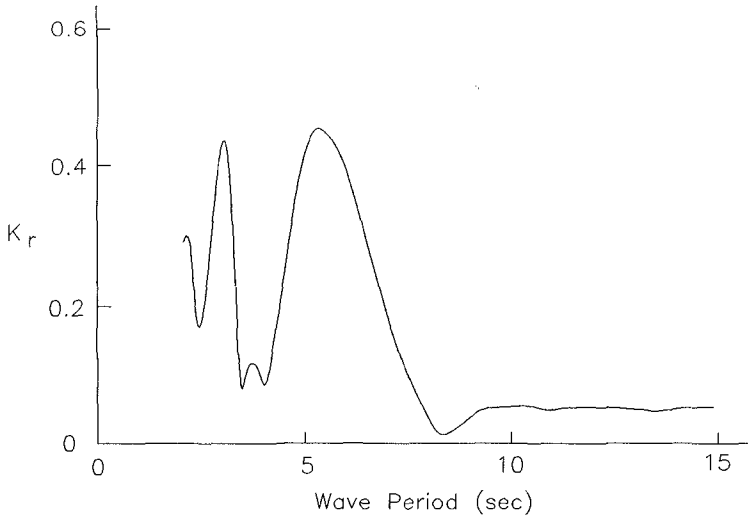


Figure 6. Estimated reflection characteristics for the field tested breakwater.

Installation and Recovery

The bar modules were assembled in a staging area located about 200 meters from the beach. After assembly, the modules were carried to the beach with a large front-end loader. The loader placed the modules on the upper beach face in groups of three, with their skids oriented perpendicular to the shore. Scour plates were attached to each module and tied up out of the way to facilitate module dragging.

Referring to Figure 7, the original installation plan called for dragging the modules into position in groups of three using a shore-based winch and a movable sheave and anchor assembly. In practice, we found that the waves at the site were too large to allow this method of installation. In particular, the LARC vehicle found it difficult to negotiate the surfzone while pulling a heavy anchor and cable. As a result, only one group of modules was installed using this technique. The rest of the modules were installed individually at extreme low tide using the front-end loader. Although rapid (all of the modules were installed in a single low tide), this alternative technique required placing the breakwater approximately 15 meters closer to shore. As a result, the breakwater was situated inside the surfzone for a substantial portion of the tidal cycle.

Monitoring Plan

A survey grid was established in the area of the breakwater and in an adjacent control area. Daily wading profiles were to be conducted in the test and control areas. These were to be supplemented by combined wading and fathometer surveys at the start and end of the experiment.

The incident directional wave spectrum was measured at a depth of 6 meters using a linear array of pressure sensors. A second array of pressure sensors and current meters was to measure the reflected wave field and the induced nearshore circulation field around the breakwater. The offshore array was constructed prior to the installation of the breakwater. The inshore array was to be constructed once the breakwater was in place. Unfortunately, this never occurred due to problems described below.

RESULTS

The Bragg reflection breakwater was deployed on 11 July 1988. During the week prior to installation, the significant wave height at the site averaged about 0.4 m.

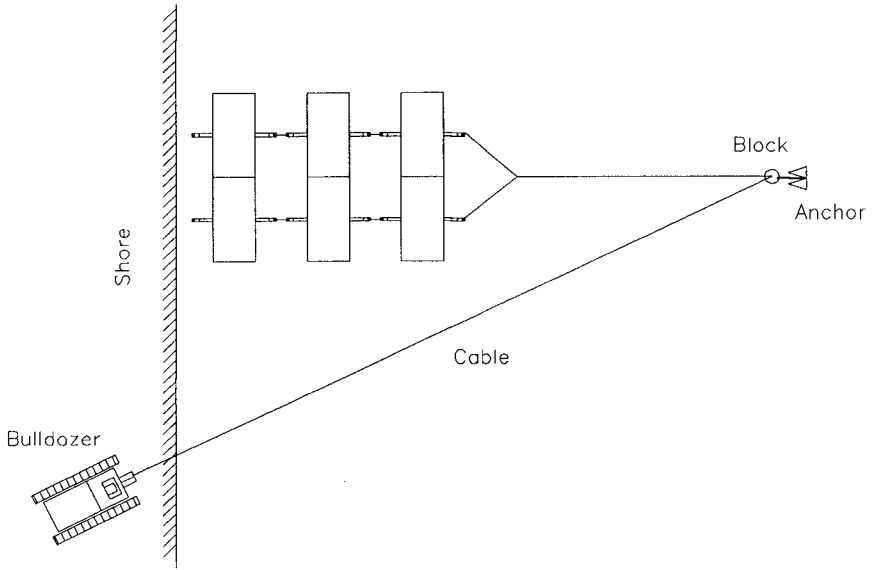


Figure 7. Planned installation method.

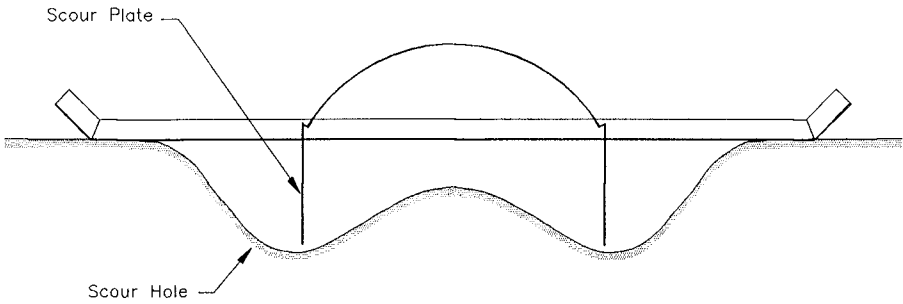


Figure 8. Observed scour pattern in field test.

This was approximately twice the anticipated wave height based on two years of measured wave data and essentially equal to the maximum design wave height for bar stability.

Immediately following breakwater installation, the significant wave height increased to about 0.6 m and remained at this level for the next 36 hours. These waves were significantly greater than the maximum design wave, causing the bar modules to slowly shift their positions. The modules rotated towards the direction of wave attack and moved shoreward about 1 to 2 m. The movement began with the outer-most bar and progressed inward through the middle and inner bars.

Another problem which developed almost immediately after installation of the breakwater was an intense scouring around the bar modules. As the tide rose, the bars were observed to be generating a significant degree of turbidity. On the following day we discovered large scour holes had formed in front of and behind the bars (see Figure 8). The scour holes slowly grew, becoming deeper and wider. Eventually they reached more than 2 meters deep, threatening the stability of the bar modules.

The observed scour was approximately an order of magnitude greater than the scour observed in the Port Hueneme tests. Since wave conditions were similar, we believe that the increased scour was attributable to the different properties of the two beach sands. At Port Hueneme, the sand was well sorted, having a median diameter of 0.25 mm and quartz and feldspar composition. At Cape Canaveral, the sand was poorly sorted, having a medium diameter of 0.14 mm and calcium carbonate composition. Apparently the lighter specific gravity of the Cape Canaveral sand, coupled with its smaller size and higher percentage of fines, resulted in increased sand suspension and enhanced scour.

After two days, the bar modules had become badly scattered. Some of the modules had shifted into their scour holes and begun to become buried. With bar burial becoming a growing problem, the decision was made to terminate the experiment and recover the bar modules while it was still possible. A bulldozer was used to pull the individual modules out of the surfzone and back up the beach face. From there, a front-end loader transported the modules back to the staging area where they were disassembled.

Because of the short duration of the breakwater deployment, the nearshore sensor array was never installed. As a result, no quantitative measurements were obtained.

Visual observations during the first few hours of deployment indicated that some wave reflection was occurring as evidenced by a standing wave pattern in front of the breakwater.

CONCLUSIONS

Theoretical and laboratory studies have indicated that the Bragg reflection breakwater concept may have merit as an expedient shore protection method. The wave sheltering produced by a small number of bars was found to significantly reduce the estimated erosion volume due to a model storm. The small scale field test, however, served to demonstrate many of the difficulties that will need to be overcome before the Bragg reflection breakwater concept becomes practical. Bar stability and sea bed scour appear to be the most troubling problems. Further tests are needed to determine the overall merit of the concept.

REFERENCES

- Anton, J.P., Kaihatu, J.M., Kirby, J.T. and McSherry, T.R. (1990). "Bragg reflection from isolated and finite-length bars," Proc. 22nd International Conference on Coastal Engineering, The Hague, NL.
- Davies, A.G. and Heathershaw, A.D. (1984). "Surface-wave propagation over sinusoidally varying topography," Journal of Fluid Mechanics, Vol. 144, pp 419-443.
- DeVries, J. and Bailard, J.A. (1988). "A simple beach profile response model," Proc. IAHR Symposium on Math Modeling of Sediment Transport in the Coastal Zone, Copenhagen, DK.
- Herbers, T.C. and Guza, R. T. (1990). "Estimation of directional wave spectra from multi-component observations," Journal of Physical Oceanography, in review.
- Kirby, J.T. (1987). "A program for calculating the reflectivity of beach profiles," Univ. of Florida Report No. UFL/COEL-87/004, 43 pp.
- Mei, C.C. (1985). "Resonant reflection of surface water waves by periodic sand bars," Journal of Fluid Mechanics, Vol. 152, pp 315-335.

ACKNOWLEDGEMENTS

This research was funded by the Office of Naval Research

CHAPTER 128

Scale Effect of Wave Force on Armor Units

Tsutomu Sakakiyama¹ and Ryoichi Kajima²

ABSTRACT

This paper describes the scale effect in experiments on the stability of armor units from the point of view of the wave forces. The relationship between the drag coefficient C_D and the stability coefficient K_D of Hudson formula is theoretically derived to be that $K_D \propto C_D^{-3}$ on the condition that the inertia force is negligible. Three kinds experiments were performed by using various sizes of Tetrapods ranging from 16 g to 6800 g according to the Froude law for scaling, 1) to measure wave force on an armor unit placed in an armor layer of a breakwater, 2) to determine the drag and inertia coefficients in wave fields, and 3) to determine the drag coefficient in a steady flow. It is found that the wave force in the small-scale experiments is relatively larger than that in the large-scale experiments. As the wave height increases, the drag force becomes predominant in comparison with the inertia force. It is concluded that the scale effect of the wave force on armor units is mainly due to the change of the relative drag force number as a function of Reynolds number.

1. INTRODUCTION

The weight of armor units in breakwaters and sea walls are usually determined by laboratory experiments or stability formulae. Hudson formula (1959) is prevalently used as a stability formula for its simplicity. In order to apply the experimental results to prototype designs, the scale effect of the experiments on armor units should be taken into account. Thomsen et al.

1 Senior Research Engineer, Central Research Institute of Electric Power Industry, 1646 Abiko, Abiko-city, Chiba, 270-11, Japan.

2 Senior Research Fellow, ditto.

(1972) and Shimada et al. (1986) investigated the scale effect of the stability of armor units by using the large-scale models. Both researches showed that small-scale models were less stable than large-scale models.

In other words, the experimental coefficient in Hudson formula, K_D , at a certain constant damage rate depends on a model scale. As a result, small-scale experiments give conservative stability criteria. The weights of armor units are overestimated when the results are directly applied to prototype designs by the Froude law for scaling. On the other hand, van der Meer (1988) showed that the stability of an armor layer of rock was not influenced by Reynolds number ranging from 4×10^4 up to 7×10^5 .

It was reported that the transmission and reflection coefficients in small-scale tests become smaller than those in large-scale tests (Johnson et al., 1966; Shuto and Hashimoto, 1970; Delmonte, 1972; Wilson and Cross, 1972; Shimada et al., 1986). It means that the energy dissipation in small-scale tests is relatively larger than that in large-scale tests. It also implies that the drag force in small tests is relatively larger than that in large-scale tests. As long as tests are performed by using the Froude law the similarity of the viscosity is neglected.

Although the experimental results of the scale effects were presented in the previous papers and the quantitative evaluation was described, the mechanism of the scale effects has not adequately explained so far.

For the purpose, we focus our attention on the wave forces acting on a single armor unit. This paper firstly aims to theoretically interpret the scale effects of the stability of armor units. Secondly, three kinds of experiments were performed to show that relative wave force depends on the model scales and to approve the theoretically presented relationship between the parameters relevant to the scale effect.

2. THEORETICAL CONSIDERATION

Hudson formula (1959) was derived from the balance between the wave force and the resisting force. The process of the derivation of Hudson formula was reviewed here from the point of view of the scale effect of the wave force. Fig. 1 shows the definition sketch. A wave force is given by Morison equation as shown by eq.(1).

$$F = \frac{1}{2} \rho C_D A u |u| + \rho C_M V \dot{u} \quad (1)$$

where ρ is the fluid density, C_D , C_M the drag and inertia coefficients, A and V the projected area and volume of an armor unit and u , \dot{u} the velocity and acceleration of water particle.

The resisting force is expressed by eq.(2).

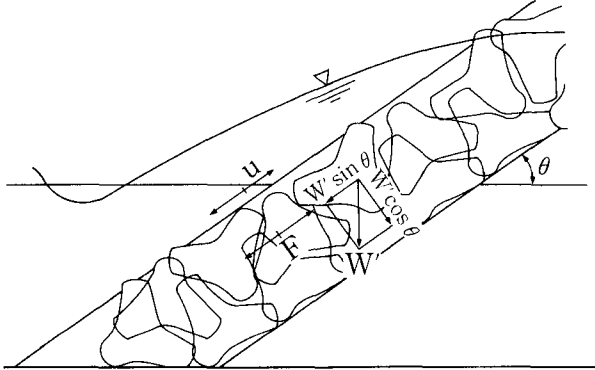


Fig. 1 Definition sketch

$$F_r = \pm fW' \cos \theta - W' \sin \theta \quad (2)$$

where f is the friction coefficient, W' the buoyant weight of the armor unit and θ the angle of the breakwater slope. The signs of "+" and "-" are applied for wave run-down and wave run-up, respectively. For incipient instability of armor units, the wave force is equal to the resisting force. After letting $F=F_r$, the following equation was obtained to describe the relationship between the weight of an armor unit, W , and other parameters.

$$W = \frac{k_a^3 \gamma_r C_D^3 (u | u |)^3}{8 k_v^2 ((\pm f \cos \theta - \sin \theta) (S_r - 1) g - C_M \dot{u})^3} \quad (3)$$

where k_a , k_v are the shape coefficients defined as $A=k_a q^2$, $V=k_v q^3$ and $q=(W/\gamma_r k_v)^{1/3}$ as defined in Hudson (1959).

Hudson formula was derived on some assumptions as follows.

- 1) The inertia force is neglected.
- 2) The velocity u is substituted by that of the linear long wave theory, $u=\alpha \sqrt{gh}$, where α is a proportional coefficient.
- 3) Wave height is assumed as $H=\gamma h$, where γ is a function of the wave steepness. Together with assumption 2), the velocity is given by $u=\alpha \sqrt{gH/\gamma}$.

These assumptions are also introduced into eq.(1). Eq.(1) becomes eq.(2) as follows.

$$W = \frac{k_a^3 \alpha^6 \gamma_r C_D^3 H^3}{8 k_v^2 \gamma^3 ((\pm f \cos \theta - \sin \theta) (S_r - 1) g)^3} \quad (4)$$

In order to investigate the mechanism of the scale effect, the parameters which are functions of Reynolds number should be kept in the formula.

On the other hand, Hudson formula is expressed by eq.(5).

$$W = \frac{\gamma_r H^3}{K_D \cot \theta (S_r - 1)^3} \quad (5)$$

where K_D is the experimentally determined coefficient which is a function of various parameters as mentioned in Hudson (1959).

Hudson (1959) assumed that the resisting force was equal to the buoyant weight of the armor units because an armor unit is isolated for incipient instability. The difference of the term of θ is $\cot \theta$ instead of $\pm f \cos \theta - \sin \theta$ which is equivalent to the term in Iribarren's formula. Hudson introduced the slope of the breakwater θ by the stability number $N_s = (K_D \cot \theta)^{1/3}$.

The rest of the differences are the coefficients which are not related to the scale effects. Comparison between eq.(4) and eq.(5) gives the following relationship between K_D and C_D .

$$K_D \propto C_D^{-3} \quad (6)$$

So far, for the design a value of K_D of a specific kind of armor unit has been considered as a constant at a fixed damage rate. Eq.(6), however, implies that K_D depends on the model scale because the drag coefficient C_D is a function of Reynolds number. It is necessary to ascertain experimentally the relationship between K_D and C_D given by eq.(6). It is also important to check the assumptions which were introduced to the derivation of eq.(4) and Hudson formula. From among them, assumption 1) which is related to the scale effect will be investigated in section 3.2.

3. EXPERIMENTS AND RESULTS

In previous researches the experiments of the stability of armor units were done in the ways of counting the numbers of armor units which rolled down an armor layer of the breakwater and measuring the damaged area due to wave attack. The experimental results might be subjected to the handling of the armor units in the individual experiments. However, it is more accurate to measure wave forces directly than to investigate the damage rate.

3.1 Wave Force on Armor Unit

The first series of experiments was performed in order to measure wave forces acting on an armor unit in an armor layer. Wave force were obtained by using load-cell type wave force gages for various sizes of Tetrapods. Fig. 2

shows the experimental setup which was constructed in a wave flume 51 m long, 0.9 m wide and 1.2 m deep. Wave forces were measured by using the strain gages transducers which transform displacement of armor unit to wave force. The armor unit installed to the wave force gage was protected not to have contact with armor units surrounding it. By the present measuring system, wave force acting on a cylinder which connected the armor unit and the force gage was also included in the data. In order to reduce the wave force acting on the cylinder, as shown by Picture 1 in section 3.2, a pair of wave force gages were used. One force gage was used for the armor unit and the cylinder and the other for the cylinder. Table 1 shows the experimental conditions. According to the Froude law for scaling, the geometric parameters of breakwater model and water depth etc. were determined. Wave heights were chosen by the capacity of the wave generator.

Table 1 Experimental conditions (wave force)

CASE	Tetrapod		breakwater depth h(cm)	period T (s)	wave height H (cm)
	weight W (g)	height b (cm)			
F4	2200	15.0	68.2	2.32	16.9~33.3
F3	570	9.6	43.6	1.85	11.6~27.7
F2	120	5.8	26.4	1.44	6.9~17.6
F1	60	4.6	20.9	1.27	5.7~14.3

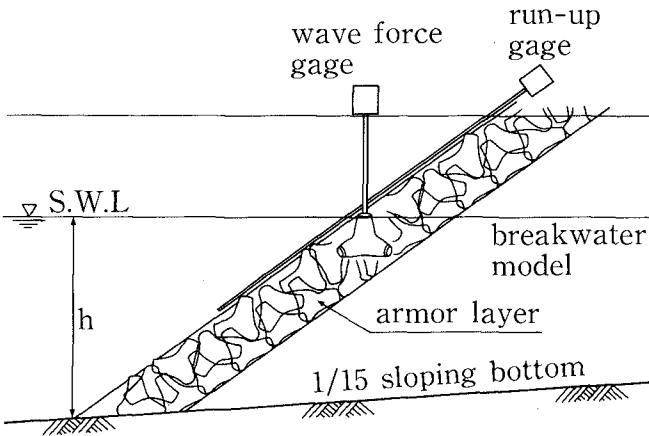


Fig. 2 Experimental setup to measure wave force acting on armor unit in breakwater

Fig. 3 shows an example of time histories of wave run-up, ξ , the wave force F_b in the direction along the breakwater slope and the uplift force F_u . It is observed that the uplift is negative at the moment when a wave hits the

armor unit. It means that wave force works in the direction into the break-water body.

Fig. 4 shows the relationship between the relative wave force F_b/W' and the deep-water wave steepness H_o/L_o for four different sizes of model scales. As this figure shows, the relative wave force increases as model scale becomes small. It means that an armor unit in small-scale experiments becomes unstable under relatively smaller wave action than large-scale experiments.

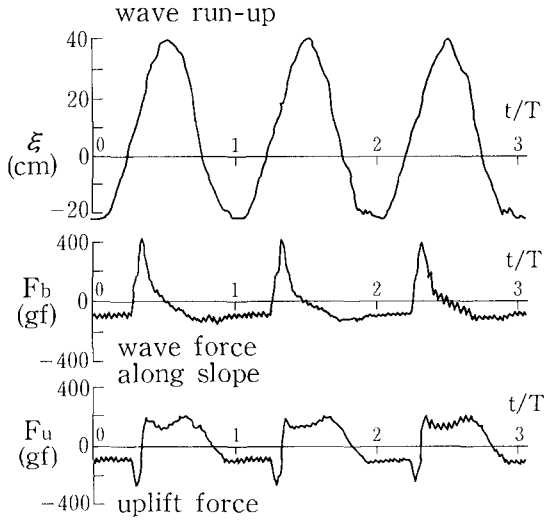


Fig. 3 Time histories of wave forces and wave run-up

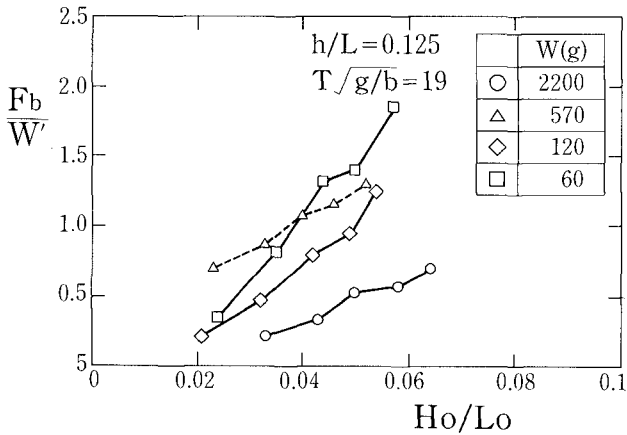


Fig. 4. Relative wave force depending on model scale

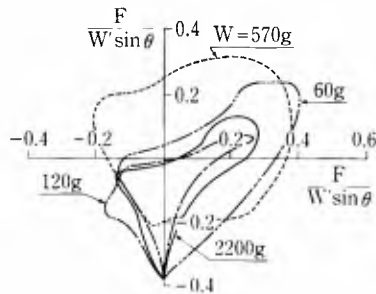


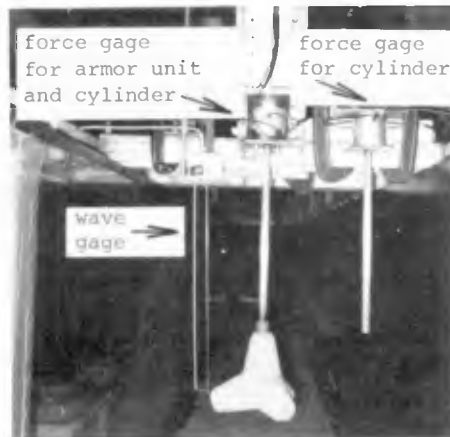
Fig. 5 Hodograph of wave forces

The result of $W=570$ g shows a different tendency. The armor unit of $W=570$ g was set at a different level from the others. Fig.5 shows the hodograph of the wave force. The pattern of $W=570$ g shows acutely different change from the others. When a wave runs down, the wave force is equal to the weight of a part of the armor unit which is under the still water level. The values for $W=60, 120, 2200$ g were about -0.4 but -0.2 for $W=570$ g.

From the above investigation, it is confirmed that the wave force in smallscale experiments is relatively large compared to that in large-scale experiments.

3.2 Drag and Inertia Forces

The second series of experiments was performed in order to check assumption 1), that is, to measure the magnitude of the drag and inertia forces



Picture 1 Experimental setup to determine drag and inertia coefficients

by using five different sizes of Tetrapods. Picture 1 shows the experimental setup. Surface displacement was also measured by using a capacitance-type wave gage. The drag and inertia coefficients were determined by Fourier analysis of the measured wave forces, the estimated wave velocities and accelerations based on Morison equation (Sarpkaya, 1976). Wave velocities and accelerations at the position of Tetrapod were estimated by the fifth order solution of Stokes wave theory (Isobe et al., 1978). The projected area of the armor unit in Picture 1 is $0.59 \times b^2$. Table 2 shows the experimental conditions. The scale of armor units and wave period were determined by the Froude law.

Table 2 Experimental conditions
(drag and inertia coefficients)

CASE	Tetrapod		uniform depth h(cm)	period T (s)	wave height H (cm)
	weight W (g)	height b (cm)			
C5	6800	22.0	92.5	2.87	6.2 ~ 31.8
C4	2200	15.0	90.8	2.36	7.0 ~ 34.3
C3	570	9.6	89.9	1.87	7.3 ~ 35.9
C2	120	5.8	57.3	1.45	4.2 ~ 21.4
C1	60	4.6	49.7	1.28	4.4 ~ 20.9

Fig. 6 shows the comparison between the measured and calculated results of the surface displacement and of the wave forces. At top, the measured surface displacements were in good agreement with the calculated ones. The measured wave force is also in good agreement with the calculated total wave force which consists of the drag and inertia forces as shown by Morison equation.

Fig. 7 shows the ratio of the drag force F_D to the inertia force F_I . Reynolds number Re is defined as $Re = u_c b / \nu$, where u_c is the velocity under the wave crest. As Reynolds number increases, the ratio F_D / F_I increases for each scale model. Since a wave height is large at the incipient instability of armor units, the drag force becomes predominant compared to the inertia force.

Fig. 8 shows the inertia and drag coefficients as functions of Reynolds number and KC number where KC is defined as $KC = u_c T / b$. Since KC number is a ratio of the drag force to the inertia force, as shown in Fig. 7(a), as KC decreases, C_M increases. As Re increases, C_M increases at a certain KC number; on the other hand, C_D decreases. At a constant KC number, Froude number is also constant. It is necessary to concentrate on the changes of C_M and C_D at a constant KC in order to investigate the scale effect of wave force. C_M and C_D are non-dimensional inertia and drag forces, respectively. At a certain constant Froude number, C_M and C_D change depending on Reynolds number.

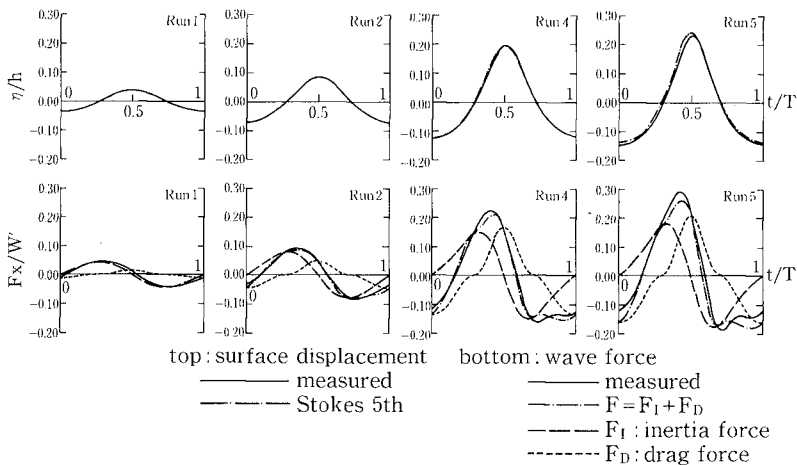


Fig. 6 Surface displacement and wave forces

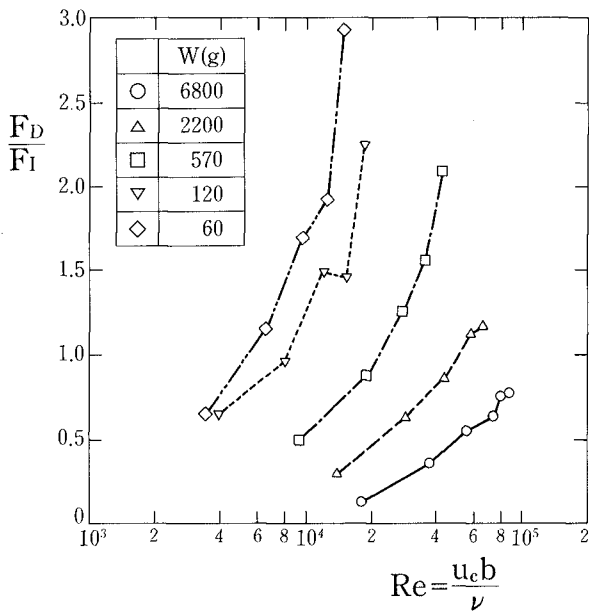
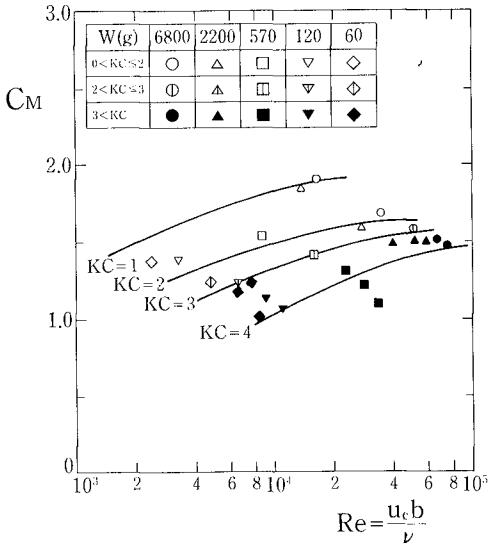
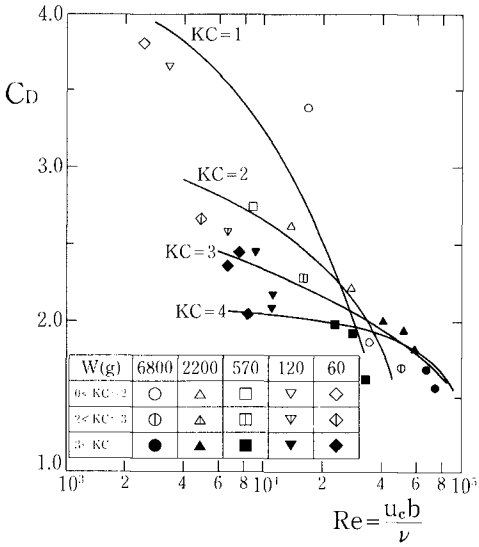


Fig. 7 Ratio of drag force to inertia force



(a) Inertia coefficient C_M



(b) Drag coefficient C_D

Fig. 8 Inertia and drag coefficients depending on model scale

The ratio of the gravity to the inertia force is constant but that of the inertia force to the viscous force changes. The similarity of the dynamics is not kept constant. The inertia force is proportional to wave acceleration and the drag force proportional to the velocity squared. As a result, as wave height increases, the drag force becomes predominant to the inertia force as shown in Fig. 7.

3.3 Scale Effects of Drag Force and Stability

The drag coefficients of various sizes of Tetrapods in a steady flow were obtained by measuring the fall velocities in still water. The weight of Tetrapod ranged from 16 g to 6800 g. A 4-m deep and 2-m by 2-m section water tank as shown in Fig. 9 and a set of video recording system were used to measure fall velocities. Fall velocities were obtained by measuring the falling time for the distance of 1.0 m at three levels ($z = -2.5, -3.0, -3.5$ m). Measurements were repeated from five to ten times for each size of Tetrapod.

By this series of experiments, the determined drag coefficients were obtained on the condition that no inertia force worked and the relative drag force was a constant. It means that the drag force is equal to the buoyant force ($F_D/W'=1.0$) for each size of Tetrapod. If the drag coefficient, which is the relative drag force, is constant, there will be no scale effect due to the viscosity.

Fig. 10 shows vertical changes of the fall velocities of Tetrapods. It was observed that there was no significant change vertically. It is confirmed that the fall velocities were obtained on the condition that no inertia force worked. Maximum fall velocity is up to about 2 m/s at $W=6800$ g on the ex-

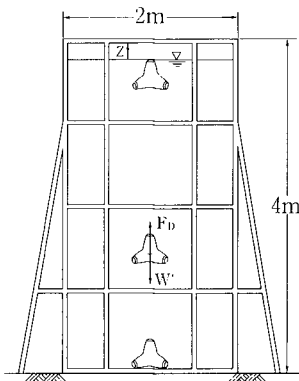


Fig. 9 Water tank to measure drag coefficient in steady flow

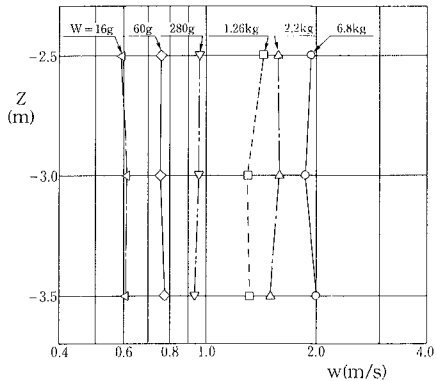


Fig. 10 Fall velocity of Tetrapod

perimental conditions. Vertically averaged values of the fall velocities in Fig. 10 were used in the following analysis. The drag coefficient C_D was calculated with the formula $C_D = 2(S_r - 1)gV/(w^2 A)$, where w is the fall velocity and the projected area $A = 0.65 \times b^2$ was chosen as an averaged value.

Fig. 11(a) shows the normalized drag coefficient C_{Dm}/C_{Dp} depending on Reynolds number, R_b , where C_{Dp} is the prototype drag coefficient and is assumed as 0.6 which is the value of the drag coefficient at $R_b = 10^8$. Reynolds number R_b is defined as $R_b = wb/\nu$. As Reynolds number decreases, C_{Dm}/C_{Dp} increases. It means the relative drag force increases, as a model scale decreases.

The drag coefficient is dependent on conditions of the environment of the armor units. When armor units in an armor layer are attacked by waves, an upper half side of the armor units is exposed to waves. It seems that an armor unit is isolated for incipient instability. It is possible to substitute the drag coefficient of a single armor unit for that in an armor layer in order to discuss the scale effect of the wave force.

Fig. 11(b) shows the scale effect of the stability of armor units (Shimada et al., 1986). This result agrees with that by Thomsen et al. (1972). Although definitions of Reynolds number for R_b and R_N are not exactly same, values of R_b and R_N for a same size of Tetrapod is almost equal. As Reynolds numbers increase from 10^4 to 10^8 , both C_{Dm}/C_{Dp} in Fig. 11(a) and $(K_{Dp}/K_{Dm})^{1/3}$ in Fig. 11(b) reduce roughly to a half. As presented in section 3.2, at large wave height, the drag force becomes predominant compared to the inertia force. However, the inertia force works under wave action. The slight difference between Fig. 11(a) and Fig. 11(B) may be due to the inertia force.

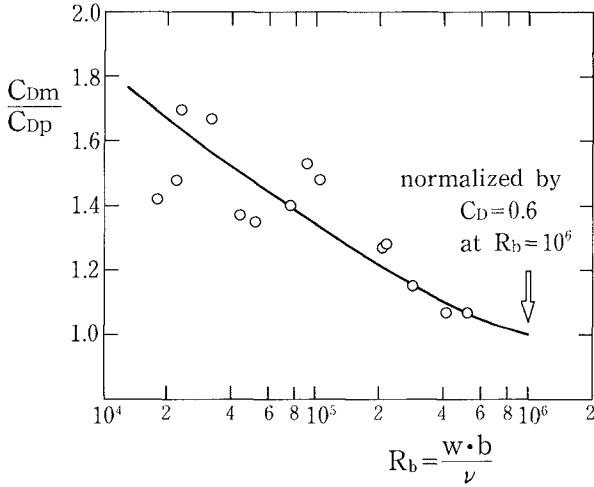
Although the resisting force was not measured in the present study, the result of the scale effect of the stability on the armor units in Fig. 11(b) include both the wave force and the resisting force. The resisting force may be not significantly contribute to the scale effect because an armor unit is isolated when it is unstable.

From the comparison of Fig. 11(a) and (b), eq.(6) which presents that K_D is inversely proportional to C_D cubed, is approved by the experiments.

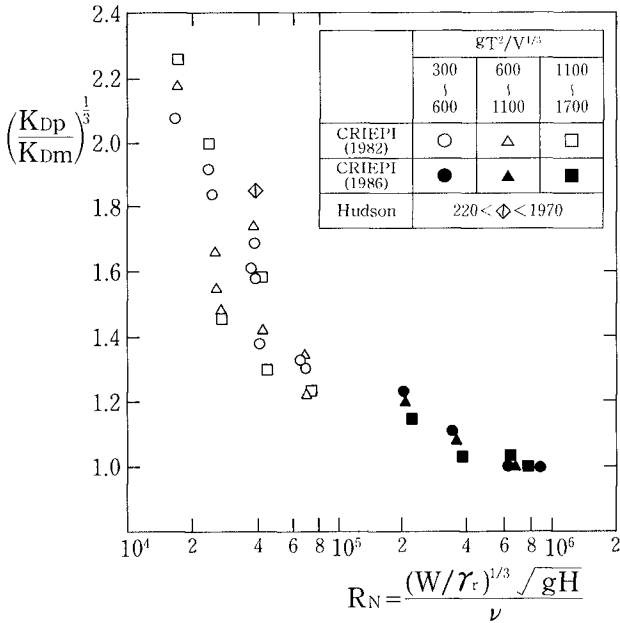
4. CONCLUSION

This paper presented the interpretation of the scale effect of the stability of armor units from the point of view of the wave forces. It is concluded from the results of the theoretical consideration and of the experiments that:

- 1) The relationship between the drag coefficient and the stability coefficient K_D of Hudson formula is theoretically derived to be that K_D is inversely proportional to the drag coefficient cubed on the condition that the inertia force is negligible. That relationship was approved by the experiments.
- 2) Wave force acting on an armor unit in small-scale model tests is relatively large compared with that in the large-scale model tests.



(a) Scale effect of drag force of armor unit



(b) Scale effect of stability of armor units

Fig. 11 Scale effect in experiments on armor units

- 3) For incipient instability of armor units, the drag force is predominant to the inertia force.
- 4) The scale effects of the wave force and of the stability of armor units can be interpreted as the scale-dependent change of the relative drag force because of the neglect of the similarity of the viscosity.

REFERENCES

- Delmonte, R.C. (1972), "Scale effects for wave transmission through permeable structure", Proc. 13th Int. Conf. Coastal Eng., ASCE, Vol. 3, pp. 1867-1872.
- Hudson, R.Y. (1959). "Laboratory investigation of rubble mound breakwaters", Proc. of ASCE Vol. 85, No.WW3.
- Isobe, M., H. Nishimura, and K. Horikawa (1978). "Expressions of perturbation solutions for conservative waves by using wave height", Proc. 33rd Annu. Conf. of JSCE, II, pp. 760-761 (in Japanese).
- Johnson, J.W., H. Kondo, and R. Wallihan (1966). "Scale effect in wave action through porous structure", Proc. 10th Conf. Int. Conf. Coastal Eng., ASCE, Vol. 2, pp. 1022-1024.
- Sarpkaya, T. (1976). "In-line and transverse force on cylinders in oscillatory flow at high Reynolds number", Proc. of the Offshore Technology Conference, Vol. II, pp.95-108.
- Shimada, A., T. Fujimoto, S. Saito, T. Sakakiyama, and H. Hirakuchi (1986). "Scale effects on stability and wave reflection regarding armor units, Proc. 20th Int. Conf. Coastal Eng., ASCE, pp. 2238-2252.
- Shuto, N. and H. Hashimoto (1970). "Hydraulic resistance of artificial concrete blocks", Coastal Eng. in Japan, JSCE, Vol. 13, pp. 43 ~ 54.
- Thomsen, A.L., P.E. Wohlt, and A.S. Harrison (1972). "Rip-rap stability on earth embankment tested in large- and small-scale wave tanks", CERC Technical Memorandum No. 37.
- Van der Meer, J.W. (1988). "Rock slopes and gravel beaches under wave attack", Doctoral thesis, Delft University of Technology, The Netherlands.
- Wilson, K.W. and H.R. Cross. (1972). "Scale effects in rubble-mound breakwaters", Proc. 13th Int. Conf. Coastal Eng., ASCE. Vol. 2, pp. 1873-1884.

CHAPTER 129

Trends in Stability of Dynamically Stable Breakwaters by Joseph S. Kao¹ and Kevin R. Hall²

Abstract

The reshaping of dynamically stable breakwaters was studied subject to variations in armour stone, (gradation and shape), wave characteristics and duration of wave attack from head on waves in a two dimensional wave flume. Tests were undertaken at the Coastal Engineering Research Laboratory of Queen's University, Kingston, Canada using irregular waves. Profiles of the structure during the various stages of reshaping were measured using a semi-automatic profiler developed for this study.

The volume of stones and the initial berm width required for development of a stable profile along with the extent to which the toe of the structure progressed seaward were chosen as the characteristic parameters of the reshaped breakwater. The results indicated that the toe width formed as a result of reshaping and the area of stones required for reshaping were dependent on the wave height, gradation of the armour stone and duration of the storm. The initial berm width required for reshaping was also found to be dependent on the wave height, armour stone gradation, percentage of rounded stones in the armour and the duration of the storm.

Introduction

Dynamically stable breakwaters are formed as a result of reshaping by wave action. Priest et al. (1964), Moutzouris (1978), Kogami (1978), Naheer and Buslov (1983), Hall et al. (1983) and Bruun (1985) reported the formation of S-shaped profiles to be superior in performance to statically stable breakwaters. Van der

¹ Grad. Student, Depart. of Civil Engineering Queen's University, Kingston, Ontario, Canada K7L 3N6

² Assist. Professor, Depart. of Civil Engineering, Queen's University, Kingston, Ontario, Canada K7L 3N6

Meer and Pilarczyk (1987) provided design formulae for rock slopes and gravel beaches and extended them to apply to dynamically stable breakwaters. Breakwaters studied and reported here cover a range of instability number, $H_s/((S_r-1)D_{50})$, from 2 to 5, and utilize the total yield from quarries.

Present Tests

The studies were undertaken in a 1.4 m wide channel located within a 2 m wide wave flume, further details are provided in Hall and Kao (1990).

The rubble mound structure consisted of a core having a D_{50} of 1.2 cm and an armour layer having a D_{50} of 1.9 cm, where D_{50} is the diameter exceeded by 50% of the gradation. Four different gradations of the armour stones were used with D_{85}/D_{15} ratios ranging from 1.35 to 5.4 where D_{85} is the diameter of stone, that is larger by weight, than 85% of the sample and D_{15} is the diameter of stone, that is larger by weight, than 15% of the sample. In particular, gradation 2 has characteristics of quarries used for many previous breakwater projects (Hall et al. (1983), Baird and Hall (1984a, 1984b) and Hall (1987)).

Two other gradations of armour stones having a D_{50} of 1.9 cm and D_{85}/D_{15} ratio of 1.9 that were similar to gradation 2 but with differing percentages of rounded stones were also used in the tests, so that the percentage of rounded stones was varied from 0% to 30%. The characteristics of the armour stones used in the study are summarized in Table 1.

Tests were undertaken on a dynamically stable breakwater whose initial configuration is shown in figure 1. The basic geometry of the test structure was selected based on previous experience and taking into consideration practical aspects which make construction simpler.

Parameters Studied

Three parameters describing various aspects of the profile reshaping were chosen as dependent parameters. The three parameters, illustrated in figure 2, are the volume per unit length of armour stone required on the front slope, (A), the width of berm eroded, (B), and the distance from the control point to the outer extent of the toe following reshaping, (L), formed after the attack of 3000 waves. These parameters were made into

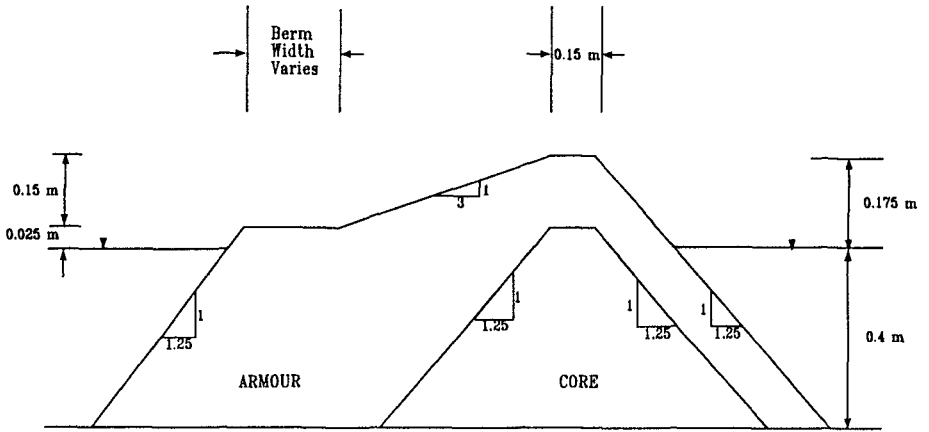


Figure 1 Layout of test breakwater

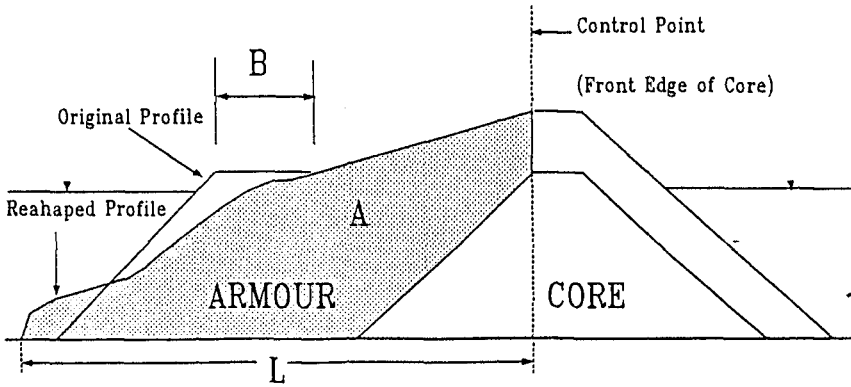


Figure 2 Definition of parameters

dimensionless quantities, A/D_{50}^2 , L/D_{50} and B/D_{50} .

Test Results

Effect of uniformity of stones

Figure 3 shows the relationship between L/D_{50} and the instability number, $H_s / ((S_r - 1)D_{50})$, (where H_s is the significant wave height and S_r is the specific density of armour stone) for the four gradation of stones having a D_{50} of 1.9 cm, and all containing 30% rounded stones. It is seen that gradation 1 is least susceptible to movement offshore indicating that the presence of substantial voids in the armour layer contributes to an efficient wave energy dissipation system. As the relative width of the gradation is increased, there are effectively less voids in the armour stone matrix. Figure 3 shows that the toe width developed increases for gradations 2 and 3. This trend, however, reverses for gradation 4. It appears that as the width of the gradation and thus the maximum stone size increases, the large quantity of stones exceeding a certain upper threshold size has a more dominant effect on stability than does the presence of voids. In gradation 4, a sizeable proportion (20%) of the armour stones exceed 100 gm in weight. The presence of these large stones no doubt had a considerable influence over the stability of the armour layer. Similar trends are observed parameters A/D_{50}^2 and B/D_{50} .

Effect of rounded stones in the gradation

No significant difference was observed regarding the influence of the percentage of rounded stones in the armour layer on L/D_{50} and A/D_{50}^2 following reshaping. Burcharth and Thompson (1983) indicated that in oscillatory flow, there was no appreciable difference in hydraulic stability between rock armour units and dolosse, that is for submerged units, the shape does not significantly influence stability. In the present case, although the berm width, B , of the structure was reduced as a result of wave action, the parameters A and L which are dominated by the underwater profile did not vary with shape. Such behaviour seems to confirm the results of Burcharth and Thompson that when the armour units are completely submerged the shape of the armour unit does not significantly affect the hydraulic stability. However, B/D_{50} was found to depend on the percentages of rounded stones in the armour. Gradation 2A (0% rounded) was found to be more resistant to erosion than gradation 2B (30% rounded), and gradation 2B more resistant to erosion than gradation 2 indicating that the proportion

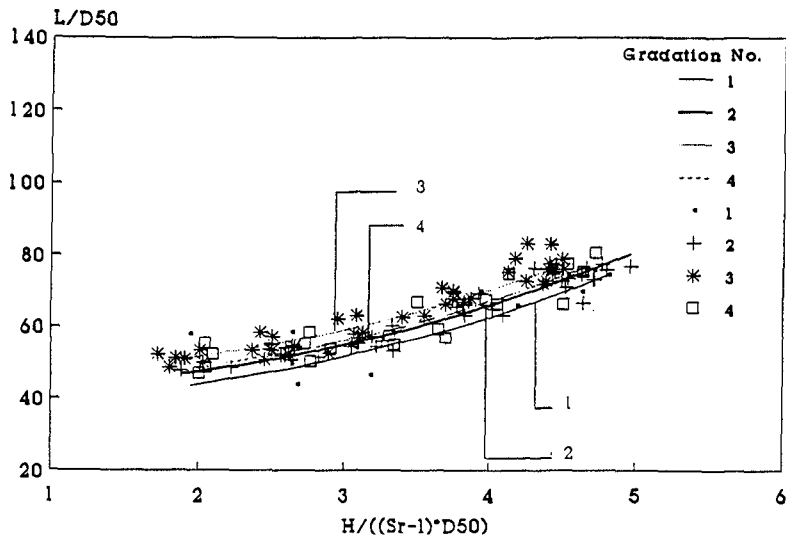


Figure 3 Dimensionless toe width versus instability number, with fitted curves, gradations 1, 2, 3 and 4

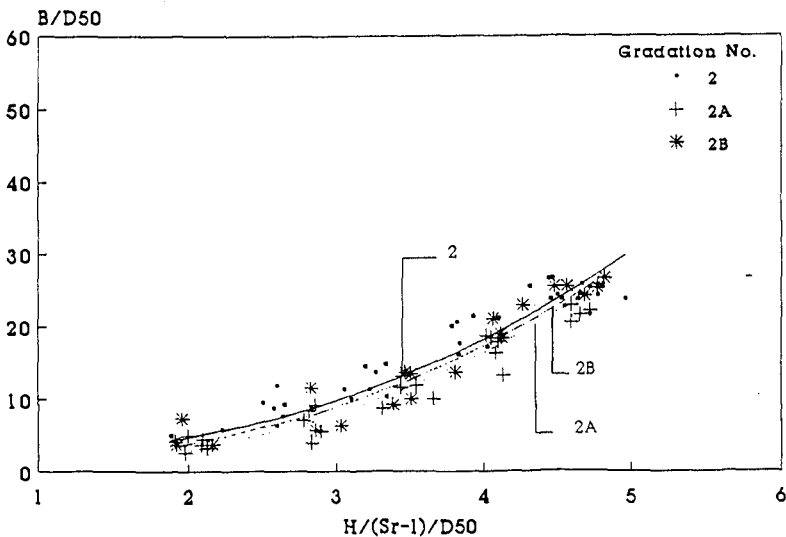


Figure 4 Dimensionless width of berm eroded versus instability number, with fitted curves, gradations 2, 2A and 2B

of rounded stones in the gradation affects initial movement, (stability decreases with increasing "rounding" of stones). Figure 4 shows the influence of the percentage of rounded stones on B/D_{50} .

Effect of duration of storm

Several sets of data were collected for storm durations ranging from 500 to 3600 waves. Such results would be important if there was uncertainty over the expected duration of the design storm. In analyzing these data, the respective areas, A , toe width, L , and width of berm eroded, B ; at any number of waves were divided by the corresponding values formed after the attack of 3000 waves and were called relative area, A_R , relative toe width, L_R , and relative width of berm eroded, B_R , respectively. The number of waves was also divided by 3000 to give the relative number of waves, N_r , (number of waves / 3000). Since relative values are involved, they are independent of wave height, wave period, wave groupiness, gradation and shape.

The relative toe width, $(L/D_{50})_R$, is plotted against the relative number of waves, N_r , in figure 5. The first 500 waves caused most of the reshaping (about 90 % of that of 3000 waves). After 3000 waves, the process of reshaping was found to slow down considerably, but actually never stopped. After the attack of 36000 waves, additional reshaping of about 10 % more than the total toe width formed after 3000 waves attack was observed.

The same trends were observed for A/D_{50}^2 and B/D_{50} .

Effect of other parameters

Wave period and groupiness factor were found to have no significant influence on the three dependent parameters under study. A typical diagram showing the relationship between L/D_{50} and peak spectral wave period T_p is shown in Figure 6. The relationship between L/D_{50} and groupiness factor $g.F.$ is shown in Figure 7.

Derived Relationships for A , B and L .

A multiregression analysis was undertaken using minimization techniques in order to determine the relationship between the three parameters of the reshaped profiles and characteristics of the stone gradations including D_{85}/D_{15} and the percentage of rounded stones (P_R), instability number and number of relative waves, N_R .

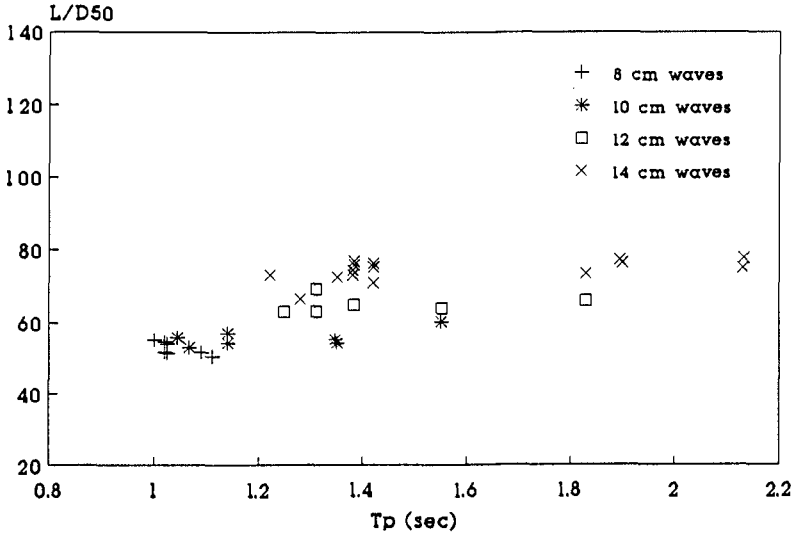


Figure 6 Dimensionless toe width versus spectral peak period, gradation 2

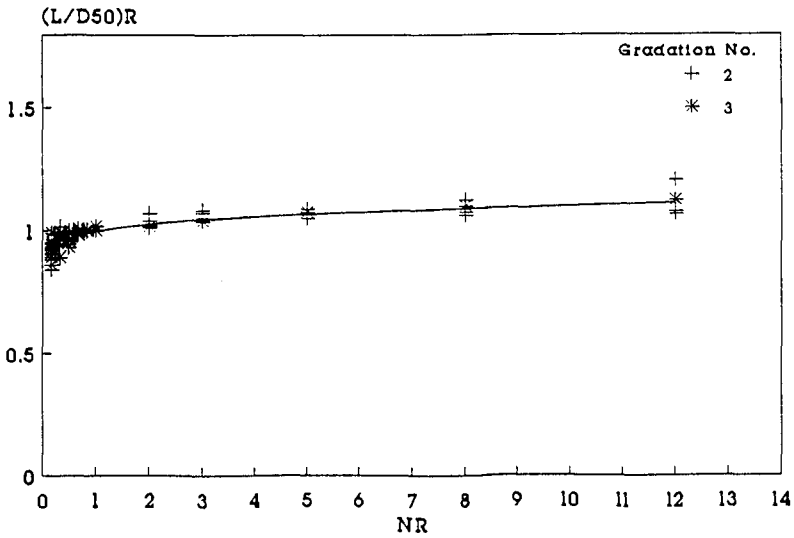


Figure 5 Relative toe width versus relative number of waves, with fitted curves, gradations 2 and 3, all waves

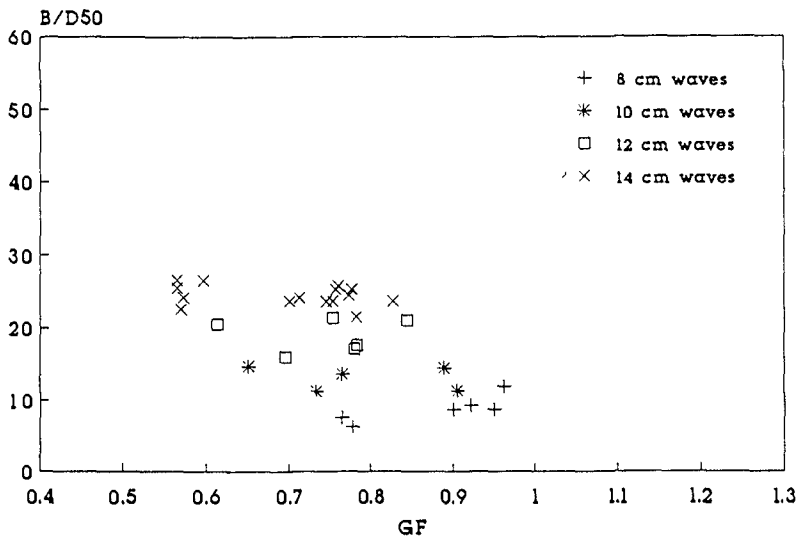


Figure 7 Dimensionless width of berm eroded versus groupiness factor, gradation 2

The relationship between $(L/D_{50})_N$, $(A/D_{50}^2)_N$ and $(B/D_{50})_N$ and N_R are given by

$$\left(\frac{L}{D_{50}}\right)_N = \left[26 + 1.15\left(\frac{H_s}{(S_r-1)D_{50}}\right)^{2.2} + 11\frac{D_{85}}{D_{15}} - 1.5\left(\frac{D_{85}}{D_{15}}\right)^2\right] N_R^{0.042}$$

$$\left(\frac{A}{D_{50}^2}\right)_N = \left[148 + 30\left(\frac{H}{(S_r-1)D_{50}}\right)^{1.9} + 194\frac{D_{85}}{D_{15}} - 27\left(\frac{D_{85}}{D_{15}}\right)^2\right] N_R^{0.043}$$

$$\left(\frac{B}{D_{50}}\right)_N = \left[-10 + 0.51\left(\frac{H}{(S_r-1)D_{50}}\right)^{2.5} + 7.5\frac{D_{85}}{D_{15}} - 1.1\left(\frac{D_{85}}{D_{15}}\right)^2 + 6.1P_R\right] [1 + \ln N_R^{0.11}]$$

where,

- $(A/D_{50}^2)_N$ = dimensionless reshaping area of breakwater after N waves attack
- $(B/D_{50})_N$ = dimensionless width of berm eroded after N waves attack
- $(L/D_{50})_N$ = dimensionless toe width after N waves attack

Conclusions

The present series of tests indicate that for armour stones having the same D_{50} values, the wave height is the single most important factor affecting the reshaping process. Both the porosity of the armour and the fraction of heavy stones in a gradation influence the reshaping of dynamically stable breakwaters. It appeared when the gradation of stones is not very wide ($D_{85}/D_{15} < 3$) narrowly graded armour stones are less prone to reshaping; however, when the gradation of the armour stones is sufficiently wide, the effect of the very large stones start to dominate the effect of the voids inside the armour stone layer. The percentage of rounded stones was found to have an influence only on the width of berm eroded. The other dependent parameters, A and L , are dominated by the submerged section of the structure, where it appears stone mass not shape is more significant. Wave period and wave groupiness were found to have no significant effect on either A , B , or L .

Acknowledgements

The authors would like to express their appreciation to Small Craft Harbours Branch, Department of Fisheries and Oceans, Canada for financial support of the study. The assistance of Mr. M. Mulcahy, Small Craft Harbours is gratefully acknowledged.

List of Symbols

A	volume per unit length of armour stones on the front slope following reshaping.
A/D_{50}^2	dimensionless reshaping volume per unit length of stones after 3000 waves attack
$(A/D_{50}^2)_N$	dimensionless reshaping area of breakwater after N waves attack
B	width of berm eroded
B/D_{50}	dimensionless width of berm eroded after 3000 waves attack
$(B/D_{50})_N$	dimensionless width of berm eroded after N waves attack
D_{15}	diameter of stone, that is larger by weight, than 15% of the sample
D_{50}	diameter of stone, that is larger by weight, than 50% of the sample
D_{85}	diameter of stone, that is larger by weight, than 85% of the sample
D_{90}	diameter of stone, that is larger by weight, than 90% of the sample
H_s	significant wave height
$H_s / ((S_r - 1) D_{50})$	instability number
L	width of the toe
(L/D_{50})	dimensionless toe width after 3000 waves attack
$(L/D_{50})_N$	dimensionless toe width after N waves attack

P_R	percentage of rounded stones in the armour
S_r	ratio of unit weight of armour unit to the unit weight of water

References

Baird, W.F. and Hall, K. R., (1984a): "The Design of Armour Systems for the Protection of Rubble Mound Breakwaters", Canadian Journal of Civil Engineering, Volume 11, pp 164-176.

Baird, W.F. and Hall, K. R., (1984b): "The Design of Breakwaters Using Quarried Stones", Proceedings 19th International Coastal Engineering Conference, Houston, Texas, United States, pp 1024-1031.

Brebner, A, (1978): "Performance of Dolos Blocks in an Open Channel Situation", Proceedings 16th International Conference on Coastal Engineering, Hamburg, West Germany, pp 2305-2307.

Bruun, P., (1985): "Discussion of "Rubble Mound Breakwaters of Composite Slopes", by E. Naheer and V. Buslov", Journal of Coastal Engineering, Volume 9, Elsevier Science Publishers B.V., Amsterdam, The Netherlands, pp 189-191.

Burcharth, H. F., and Thompson, A.C., (1983): "Stability of Armour Units in Oscillatory Flow", Proceedings of a Specialty Conference on the Design, Construction, Maintenance and Performance of Port and Coastal Structures, Arlington, Virginia, United States, pp 71-82.

Hall, K. R., (1987): "Experimental and Historical Verification of the Performance of Naturally Armouring Breakwaters", Proceedings of Workshop on Unconventional Rubble-mound Breakwaters, Ottawa, pp 104-137.

Hall, K.R., Rauw, C.I. and Baird, W.F. (1983): "Development of a Wave Protection Scheme for a Proposed Offshore Runway Extension Unalaska, Alaska", Proceedings of a Specialty Conference on the Design, Construction, Maintenance and Performance of Port and Coastal Structures, Arlington, Virginia, United States, pp 157-170.

Kogami, Y., (1978): "Researches on Stability of Rubble Mound Breakwaters", Coastal Engineering in Japan,

Volume 21, pp 75-93.

Moutzouris, C., (1978): "A Profile of a Sloping Breakwater Based on Recent Results Concerning Wave Propagation and Breaking", Proceedings 7th International Harbour Congress, Antwerp, pp 2.04/1-2.04/7.

Naheer, E., and Buslov, V., (1983): "On Rubble-Mound Breakwaters of Composite Slope", Journal of Coastal Engineering, Elsevier, Amsterdam, The Netherlands, Volume 7, pp 253-270.

Priest, M.S., Pugh, J.W., and Singh, R., (1964): "Seaward Profile for Rubble Mound Breakwaters", Proceedings 9th International Conference on Coastal Engineering, Lisbon, Portugal, pp 553-559.

Van der Meer, J.W., and Pilarczyk, K.W., (1984): "Stability of Rubble Mound Slopes under Random Wave Attack", Publication No. 332, Delft Hydraulics Laboratory, The Netherlands.

Van der Meer, J.W., and Pilarczyk, K.W., (1987): "Dynamic Stability of Rock Slopes and Gravel Beaches", Delft Hydraulics Communication No. 379, Delft Hydraulics Laboratory, The Netherlands.

CHAPTER 130

FORCES ON VERTICAL WALLS DUE TO OBLIQUELY-INCIDENT WAVES

Ching-Piao Tsai * and Dong-Sheng Jeng **

Abstract

The force exerted on a vertical wall due to obliquely-incident waves has been analyzed in this paper from the calculation of short-crested waves system by a numerical scheme. The numerical model preserves the wave elevation in an implicit function form for the dynamic and kinematic boundary equations on water surface, the accuracy is then improved. It is found that the maximum loading in onshore direction may be caused by obliquely-incident waves as the water is greater than intermediate depth. However, the onshore loading does not necessarily be the greatest force for such instance. The greatest force could be produced by the offshore loading under steeper normal standing waves. While the wall is in the shallow water region, the greatest force is occurred in onshore loading at crest by normal standing waves. This research also shows good comparisons from some experimental results.

1. Introduction

Wave forces exerted on vertical walls play a very important role in coastal engineering. The forces produced by standing waves, whose crest parallel to the wall, are usually considered as the maximum loads. However, some evidences have shown that the forces due to obliquely-incident waves, called short-crested waves, could exceed those from waves normal approach to the wall (Silvester 1974, Fenton 1985). The surface of short-crested wave is defined as having a doubly-periodic diamond-shaped crest pattern. Two dimensional progressive and standing waves are physically two limiting cases of short-crested waves as the incident waves are traveling parallel and normal to the wall respectively.

Short-crested waves have been investigated theoretically since Fuchs (1952). The systematic analysis by a third-order approximation in a non-dimensional form was proposed by Hsu et al (1979). While the detailed analysis for the force on vertical walls due to such wave system was first studied by Fenton (1985), with a third-order expansion in wave height. Fenton's solutions showed a number of unusual features which can further be found in this study. Nevertheless, it is found that the third-order

* Associate Professor, Department of Civil Engineering, National Chung-Hsing University, Taiwan 40227, Republic of China

** Master of Engineering, Department of Civil Engineering, National Chung-Hsing University, Taiwan 40227, Republic of China

approximation could produce moderately residual pressures on free surface, which has an influence on the distribution of wave pressures, as the wave is in shallow water, or steeper in intermediate depth in which coastal structures are always located.

To improve the accuracy, the force exerted on a vertical wall is obtained in the study from calculation short-crested waves by a numerical scheme. The numerical model using Fourier series approximation was proposed to calculate the highest periodic short-crested waves on deep water by Tsai et al (1990). Unlike Roberts and Schwartz (1983), the present numerical model preserves the wave elevation function in an implicit form, in analogy to the exact nonlinear nature for the dynamic and kinematic boundary conditions on water surface. Basic formulations are outlined in section 2, and the main procedures for numerical calculations given in section 3. Section 4 demonstrates the results of the force exerted on the wall. The experimental data of standing waves (Goda 1967), one of limiting cases of short-crested waves, are also quoted to compare with the calculation results.

2. Formulations

A sketch diagram of the short-crested wave motion produced by full oblique reflection from a vertical wall is shown in Fig. 1. Assume the fluid to be inviscid, incompressible and of uniform finite depth. The velocity potential ϕ for irrotational motion gives rise to the Eulerian water particle velocity components as

$$u=\phi_x, v=\phi_y, w=\phi_z \tag{1}$$

where the velocity potential $\phi(x,y,z,t)$ satisfies Laplace equation

$$\nabla^2\phi = \phi_{xx} + \phi_{yy} + \phi_{zz} = 0 \tag{2}$$

The dynamic boundary condition at the free surface (DFSBC) is

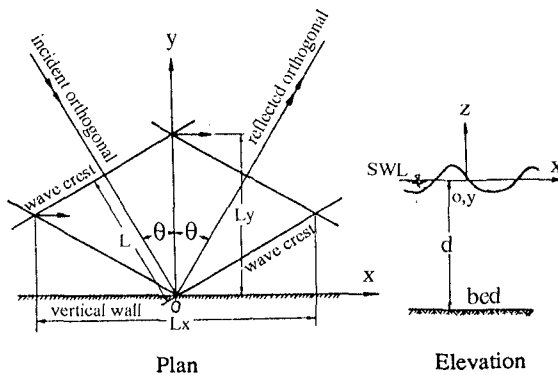


Fig. 1 Sketch diagram of short-crested waves

$$\phi_t + g\eta + \frac{1}{2}(\phi_x^2 + \phi_y^2 + \phi_z^2) = C, \quad \text{at } z = \eta \quad (3)$$

and the kinematic boundary condition at the free surface (KFSBC) is

$$\eta_t - \phi_z + \phi_x \eta_x + \phi_y \eta_y = 0, \quad \text{at } z = \eta \quad (4)$$

while the bottom and wall boundary conditions are

$$\phi_z = 0 \quad \text{at } z = -d; \quad \phi_y = 0 \quad \text{at } y = 0 \quad (5)$$

in which $\eta = \eta(x, y, t)$ is the water surface elevation, g is the acceleration due to gravity, and the subscripts (x, y, z, t) designate differentiation with respect to the Cartesian co-ordinates (see Fig.1) and the time, and C is an arbitrary constant.

Taking the material derivative, D/Dt , of (3) and subtracting g times (4) gives

$$\begin{aligned} \phi_{tt} + g\phi_z + 2(\phi_x\phi_{xt} + \phi_y\phi_{yt} + \phi_z\phi_{zt}) + 2(\phi_x\phi_y\phi_{xy} + \phi_x\phi_z\phi_{xz} + \phi_y\phi_z\phi_{yz}) \\ + (\phi_{xx}\phi_x^2 + \phi_{yy}\phi_y^2 + \phi_{zz}\phi_z^2) = 0 \quad \text{at } z = \eta \end{aligned} \quad (6)$$

The unknown time derivative of η_t in (4) can thus be eliminated, in which η is a priori unknown itself yet to be determined.

As shown in Fig. 1, let L be the wavelength of the incident and reflected waves and L_x and L_y the distances between crests in the x and y directions respectively. The corresponding components of the wavenumber k in these two directions may be defined as

$$k_x = 2\pi / L_x = k \sin\theta = pk, \quad k_y = 2\pi / L_y = k \cos\theta = qk \quad (7)$$

in which $k = 2\pi / L$. By using a reference length $1/k$ and reference time $1/\sqrt{gk}$, the following set of non-dimensional parameters may be introduced,

$$\begin{aligned} \hat{x} = pkx - \sigma t, \quad \hat{y} = qky, \quad \hat{z} = kz \\ \hat{\phi} = \frac{k^2}{\sqrt{gk}}\phi, \quad \hat{\eta} = k\eta, \quad \omega = \frac{\sigma}{\sqrt{gk}} \end{aligned} \quad (8)$$

in which σ is the angular frequency of the incident and reflected wave (i.e. $\sigma = 2\pi / T$ where T is the wave period in seconds).

The carets denoting dimensionless quantities will now be omitted for the sake simplicity, unless otherwise specified. The governing equations may now be transformed in terms of these dimensionless quantities.

$$p^2\phi_{xx} + q^2\phi_{yy} + \phi_{zz} = 0 \quad (9)$$

$$-\omega\phi_x + \eta + \frac{1}{2}(p^2\phi_x^2 + q^2\phi_y^2 + \phi_z^2) = Q, \quad \text{at } z = \eta \tag{10}$$

$$\begin{aligned} &\omega^2\phi_{xx} + \phi_z - 2\omega(p^2\phi_x\phi_{xx} + q^2\phi_y\phi_{xy} + \phi_z\phi_{xz}) \\ &+ 2(p^2q^2\phi_x\phi_y\phi_{xy} + p^2\phi_x\phi_z\phi_{xz} + q^2\phi_y\phi_z\phi_{yz}) \\ &+ (p^4\phi_{xx}\phi_x^2 + q^4\phi_{yy}\phi_y^2 + \phi_{zz}\phi_z^2) = 0, \quad \text{at } z = \eta \end{aligned} \tag{11}$$

$$\phi_z = 0 \quad \text{at } z = -d \tag{12}$$

$$\phi_y = 0 \quad \text{at } y = 0 \tag{13}$$

in which Q is a dimensionless constant.

3. Numerical procedures

A truncated double Fourier series which satisfies both Laplace equation (9) and the bottom and wall boundary conditions (12) and (13) can be given by

$$\phi = \sum_{m=1}^{M-1} \sum_{n=0}^{2N} B_{mn} \frac{\cosh \alpha_{mn} (z + d)}{\cosh \alpha_{mn} d} \sin mx \cos ny \tag{14}$$

in which $\alpha_{mn}^2 = p^2m^2 + q^2n^2$. As (m+n) is odd, then B_{mn} is equal to zero for satisfying the symmetry condition required for the wave motion. The equation (14) yields the appropriate two-dimensional limiting cases of a progressive wave as $p=1$ and $q=0$, and a normal standing wave when $p=0$ and $q=1$. Substituting (14) into DFSBC (10) and KFSBC (11), yields

$$-\omega u + \eta + \frac{1}{2}(p^2u^2 + q^2v^2 + w^2) = Q \tag{15}$$

and

$$\begin{aligned} &\omega^2u_x + w - 2\omega(p^2u_xu + q^2u_yv + u_zw) + 2(p^2uu_zw + p^2q^2uu_yv + q^2vv_zw) \\ &+ (p^4u_xu + q^4v_yv^2 + w_zw^2) = 0 \end{aligned} \tag{16}$$

where

$$\begin{aligned} u &= \sum_{m=1}^{M-1} \sum_{n=0}^{2N} mB_{mn}F_{mn}(\eta) \cos mx \cos ny, & v &= \sum_{m=1}^{M-1} \sum_{n=0}^{2N} -nB_{mn}F_{mn}(\eta) \sin mx \sin ny \\ w &= \sum_{m=1}^{M-1} \sum_{n=0}^{2N} \alpha_{mn}B_{mn}G_{mn}(\eta) \sin mx \cos ny, & u_x &= \sum_{m=1}^{M-1} \sum_{n=0}^{2N} -m^2B_{mn}F_{mn}(\eta) \sin mx \cos ny \end{aligned}$$

$$\begin{aligned}
 u_y &= \sum_{m=1}^{M-1} \sum_{n=0}^{2N} -mnB_{mn}F_{mn}(\eta) \cos mx \sin ny & , & & u_z &= \sum_{m=1}^{M-1} \sum_{n=0}^{2N} m\alpha_{mn}B_{mn}G_{mn}(\eta) \cos mx \cos ny \\
 v_y &= \sum_{m=1}^{M-1} \sum_{n=0}^{2N} -n^2B_{mn}F_{mn}(\eta) \sin mx \cos ny & , & & v_z &= \sum_{m=1}^{M-1} \sum_{n=0}^{2N} -n\alpha_{mn}B_{mn}G_{mn}(\eta) \sin mx \sin ny \\
 w_z &= \sum_{m=1}^{M-1} \sum_{n=0}^{2N} \alpha_{mn}^2 B_{mn} F_{mn}(\eta) \sin mx \cos ny & , & & & \\
 F_{mn}(\eta) &= \frac{\cosh \alpha_{mn}(\eta+d)}{\cosh \alpha_{mnd}} & , & & G_{mn}(\eta) &= \frac{\sinh \alpha_{mn}(\eta+d)}{\cosh \alpha_{mnd}} \tag{17}
 \end{aligned}$$

It is noted that the water surface elevation $\eta(x,y)$ is preserved in an implicit form, instead of a straight double Fourier series by Roberts and Schwartz (1983). This approach is similar to that of Rienecker and Fenton (1981) in solving the problem of two-dimensional progressive waves.

For the purpose of numerical computations, the discretized mesh points (x_i,y_j) are chosen by even symmetric properties given by

$$\begin{aligned}
 x_i &= i \pi / M , & \text{for } i &= 0,1,2,\dots,M \\
 y_j &= j \pi / 2N , & \text{for } j &= 0,1,2,\dots,N
 \end{aligned} \tag{18}$$

For all the mesh points required in (18), the DFSBC of (15) provides $(M+1)(N+1)$ algebraic equations. While (16) is automatically satisfied at points $(x_{M/2},y_N)$, (x_0,y_j) , and (x_M,y_j) for all j , and the value of (16) at points (x_{M-i},y_N) are equal to that of (x_i,y_N) (for $i=1,2,\dots,M/2-1$) from trigonometric symmetry. Then satisfied (16) at remaining points lead to $(M-1)N+M/2-1$ equations. Furthermore, there are two additional equations should be specified, firstly, a wave height relationship ensures that,

$$\eta_{00} - \eta_{M0} - H = 0 \tag{19}$$

where η_{ij} represents $\eta(x_i,y_j)$, H is the waveheight of the short-crested wave. Secondly, the mean water level can be chosen at the coordinate origin, using the simple trapezoidal rule then

$$\frac{\pi^2}{8MN} \sum_{i=0}^{M-1} \sum_{j=0}^{N-1} (\eta_{ij} + \eta_{i+1,j} + \eta_{i,j+1} + \eta_{i+1,j+1}) = 0 \tag{20}$$

Consequently, there are $2MN+3M/2+2$ nonlinear algebraic equations for the same number of unknowns $B_{mn}, \eta_{ij}, \omega, Q$. The system equations can be solved by Newton's iteration scheme. It is noted that M should be taken to be an even integer.

4. Numerical results

Through the numerical scheme stated above, the velocity potential ϕ and wave elevation η of short-crested waves can be calculated completely as both the waveheight and water depth are given. The force exerted on the wall by short-crested waves, produced by obliquely-incident waves reflection from a vertical wall, then may be estimated by integrating the pressure over depth per unit of the wall. The pressure in the wave motion is given by Bernoulli's theorem in terms of dimensionless quantities as

$$\hat{P} = -z - \omega\phi_x - \frac{1}{2}(p^2\phi_x^2 + q^2\phi_y^2 + \phi_z^2) + Q \quad (21)$$

where $\hat{P} = (k/\rho g)P$ is the departure of the wave pressure from that of the atmosphere, ρ being the water density. The force on the wall per unit length due to the wave then performed by

$$F = \int_{-d}^{\eta} P(x, 0, z, t) dz \quad (22)$$

Considering the hydrostatic contribution of the undisturbed water back of the wall, the net force on the wall per unit length then given by

$$[F] = \int_{-d}^{\eta} P(x, 0, z, t) dz - \frac{1}{2} \rho g d^2 \quad (23)$$

In the following results, the term $M=2N=8$ is taken to calculate. Since the wave elevation is preserved in an implicit form in the numerical model, the accuracy can be improved. The accuracy could be measured from the order of residual pressures (the non-zero value of pressures) on the water surface. Although the solution by traditional perturbation method was also obtained from satisfying the conditions of zero-pressure and continuity at the water surface, the pressure computed with the final solution does not necessarily become null at the surface due to the influence of higher order terms neglected in the calculation (Goda 1967). The error is especially occurred in the case of steeper wave in shallow water. In the numerical calculation of present model, however, the error less than 10^{-12} can be under control. Fig. 2 and Fig. 3 show that comparisons of the residual surface pressure / waveheight, in dimensionless \hat{P}_r / \hat{H} , of the steeper wave in the shallow water depth.

The variation of forces in each phase with different angle of incidence are shown in Fig. 4 and Fig. 5, the double peaks appear in small incident angle, such as 0° , 5° . But the phenomenon can not be found in the cases of shallow water and the small steepness in intermediate water depth, which are shown in Fig. 6 and Fig. 7 respectively. From the results, the maximum onshore force does not at the crest but at the intermediate maximum as the wave is small angles of incidence in deep water or larger steepness in intermediate water.

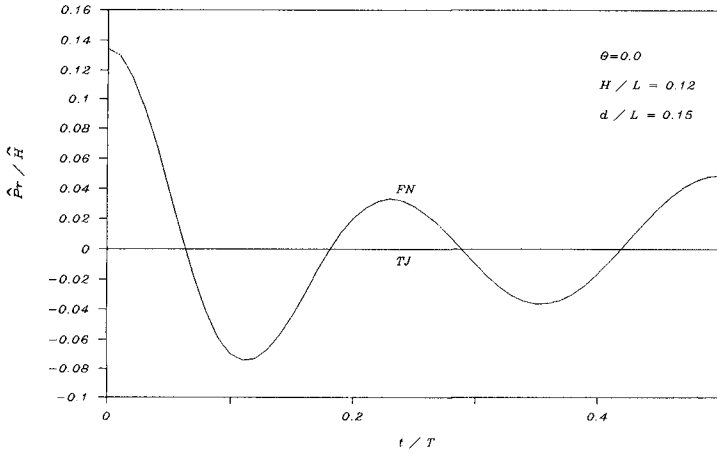


Fig.2 Variations of residual surface pressures with phase of time
 TJ= Tsai & Jeng (present) FN= Fenton (1985)

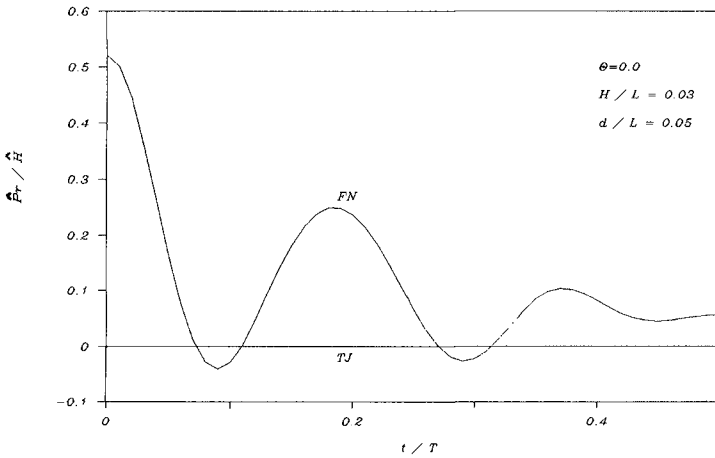


Fig.3 Variations of residual surface pressures with phase of time

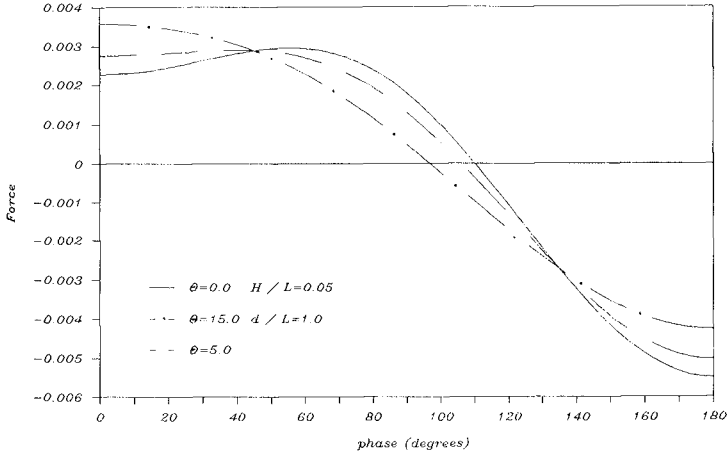


Fig.4 Variation of forces in each phase, Force=[F] / ρgd²

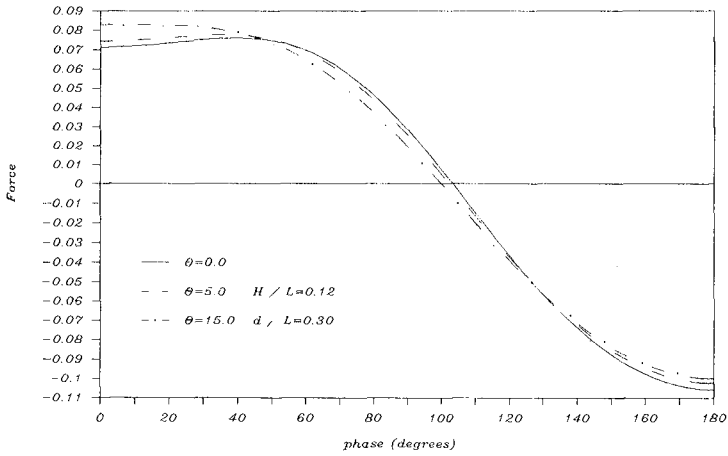


Fig.5 Variation of forces in each phase, Force=[F] / ρgd²

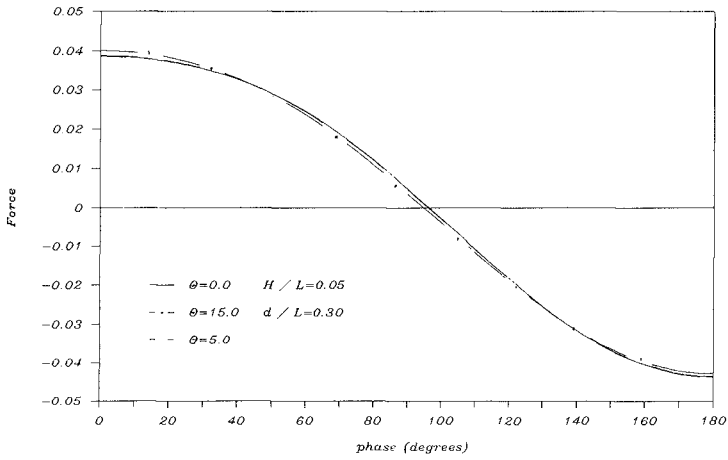


Fig.6 Variation of forces in each phase, Force= $[F] / \rho g d^2$

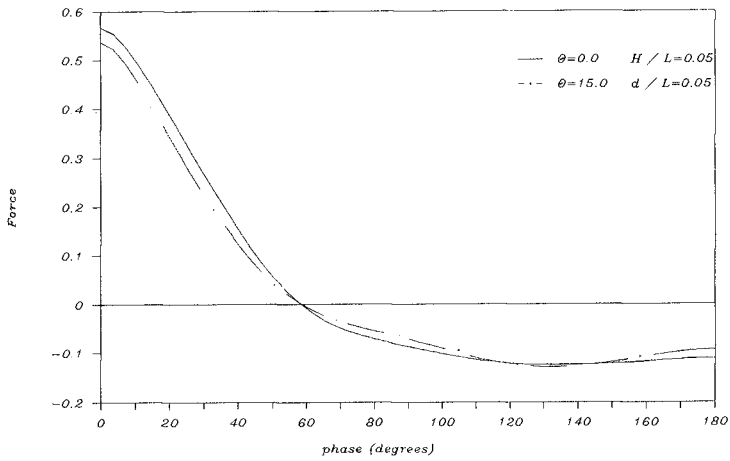


Fig.7 Variation of forces in each phase, Force= $[F] / \rho g d^2$

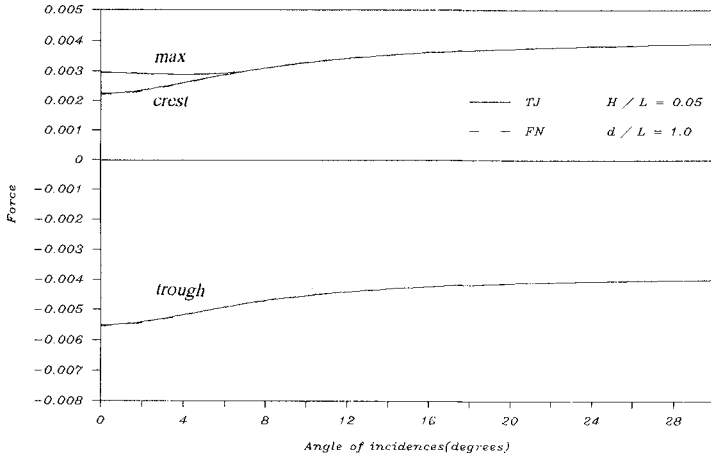


Fig.8 Variation of forces with angle of incidence, Force= $[F] / \rho g d^2$

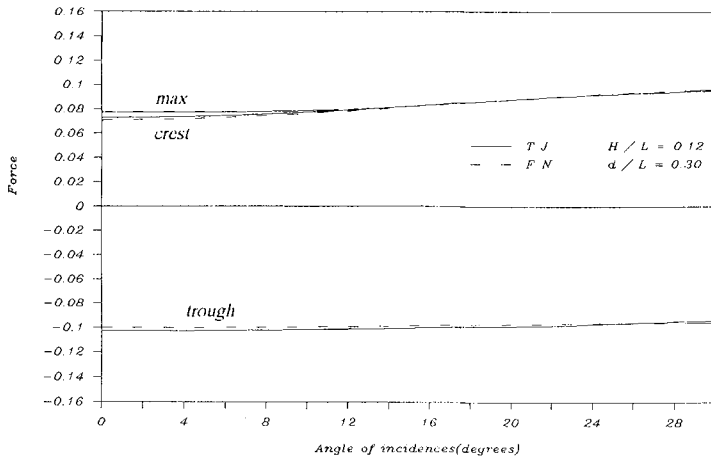


Fig.9 Variation of forces with angle of incidence, Force= $[F] / \rho g d^2$

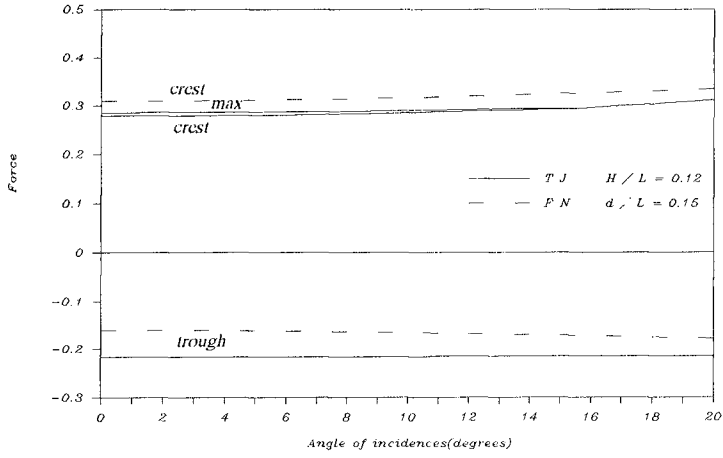


Fig.10 Variation of forces with angle of incidence, Force= $[F] / \rho g d^2$

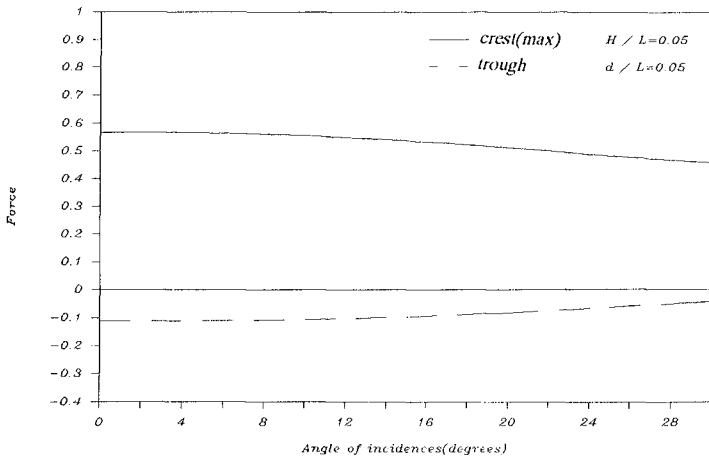


Fig.11 Variation of forces with angle of incidence, Force= $[F] / \rho g d^2$

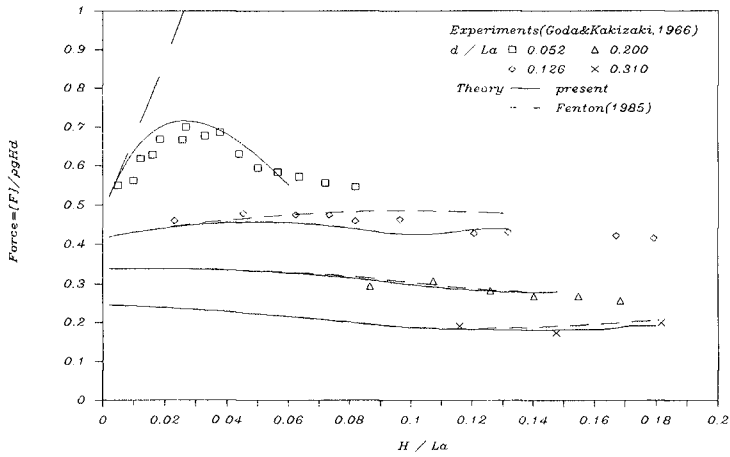


Fig.12 Comparison of maximum onshore wave force, Force= $[F] / \rho g d H$
 (L_a : wavelength of linear approximation)

Fig. 8 to Fig. 11 show the variation of forces per unit length with angle of incidence for each of the wave crest, the trough and the intermediate maximum. Analogous to Fenton (1985), the maximum force for onshore loading may be caused by obliquely-incident waves rather than standing waves. But this behavior is only found to be in water greater than intermediate depth, and opposite in shallow water. These figures also show the greatest net force exerted on vertical walls is occurred in offshore direction under the wave trough, as the water depth is greater than intermediate. And the maximum offshore loading is always produced by normal standing waves. Fig. 12 is the comparison from experimental data of the maximum onshore wave force of standing waves obtained by Goda (1967). The present research shows good agreement with experimental results even though the case of shallow water.

5. Conclusions

Through the calculation of short-crested waves by a numerical model, the force exerted on a vertical wall due to obliquely-incident waves has been obtained. Analogous to Fenton (1985), a number of unfeatures are also found in this paper. Because the wave elevation is preserved in an implicit function form for the dynamic and kinematic boundary equations on water surface, the results in this research show better agreement with some experimental data. Some conclusions can be drawn as the following. As the wave is in the water greater than intermediate depth, the double peaks appear on the time histories of forces in the cases of small incident angle. It is shown that the maximum loading in onshore direction does not be at the crest. From the analysis, it is also investigated that the maximum onshore loading may be caused by obliquely-incident waves rather than those of normal standing waves. Nevertheless, the maximum onshore loading does not necessarily be the greatest force for such instance. The greatest force is always produced by the offshore loading under the wave trough for normal standing waves as waves are steeper. While for shallow water waves, the greatest force is found in onshore loading at crest for normal standing waves.

Acknowledgement

Part of this study is supported by the National Science Council, Republic of China, under Grant No. NSC 77-0209-M005-01 is gratefully acknowledged.

References

- Fenton, J.D. (1985) Wave forces on vertical walls. *J. Waterway, Port, Coastal and Ocean Engr.*, ASCE, 111(4), 693-719.
- Fuchs, R.A. (1952) On the theory of short-crested oscillatory. *Gravity Waves*, U.S. Nat. Bur. Stand. circular 521, 187-200.
- Goda, Y. (1967) The fourth order approximation to the pressure of standing waves. *Coastal Engineering in Japan*, 10, 1-11.
- Hsu, J.R.C., Tsuchiya, Y. and Silvester, R. (1979) Third-order approximation to short-crested waves. *J. Fluid Mech.*, 90, 179-196.
- Rienecker, M.M. and Fenton, J.D. (1981) A Fourier approximation of Stokes expansion of gravity waves. *J. Fluid Mech.* 104, 119-137.
- Roberts, A.J. and Schwartz, L.W. (1983) The calculation of nonlinear short-crested gravity waves. *Phy. Fluid*, 26(9), 2388-2392.
- Silvester, R. (1974) *Coastal Engineering*, Vol. I, Elsevier, Amsterdam, Netherlands.
- Tsai, C.P., Jeng, D.S. and Hsu, J.R.C. (1990) Numerical calculation of the highest periodic short-crested waves on deep water. (to be published)

CHAPTER 131

STATIC AND DYNAMIC LOADING TESTS ON THE HARO ARMOUR UNIT

L. Van Damme¹

J. De Rouck²

L. Taerwe³

R. Dedeyne⁴

J. Degrieck⁵

1. ABSTRACT

During the harbour extension works at Zeebrugge a new armour unit has been developed : the HARO. Tests in wave flume and wave tank showed a very good hydraulic stability, comparable to that of the dolos. Static and dynamic loading tests in the laboratory and pendulum tests on site confirm the HARO's excellent structural performance, comparable to that of the cube. Based on the results of exhaustive investigations one can state that the HARO is a safe and economical solution for the protection of maritime structures.

2. INTRODUCTION

The HARO is a plain concrete block for the protection of maritime structures (breakwaters, sea walls, groynes ...) against wave attack. It found an extensive application in the harbour extension works at Zeebrugge. It is also currently being used for the Gwadar Port in Pakistan. The name HARO is registered by HAECON N.V.

The HARO is a compact concrete block with a large central opening (fig. 1). Both short sides are made wider at the base. The corners are asymmetrically tapered in plan. Thanks to the large central opening, the protuberances at the short sides and

¹Ministry of Public Works, Coastal Department, Ostend, Belgium

²HAECON N.V. and Ghent State University, Ghent, Belgium

³Magnel Laboratory for Reinforced Concrete, Ghent State University, Ghent, Belgium

⁴Bureau SECO, Brussels, Belgium

⁵Department for Mechanics of Materials and Structures, Ghent State University, Ghent, Belgium.

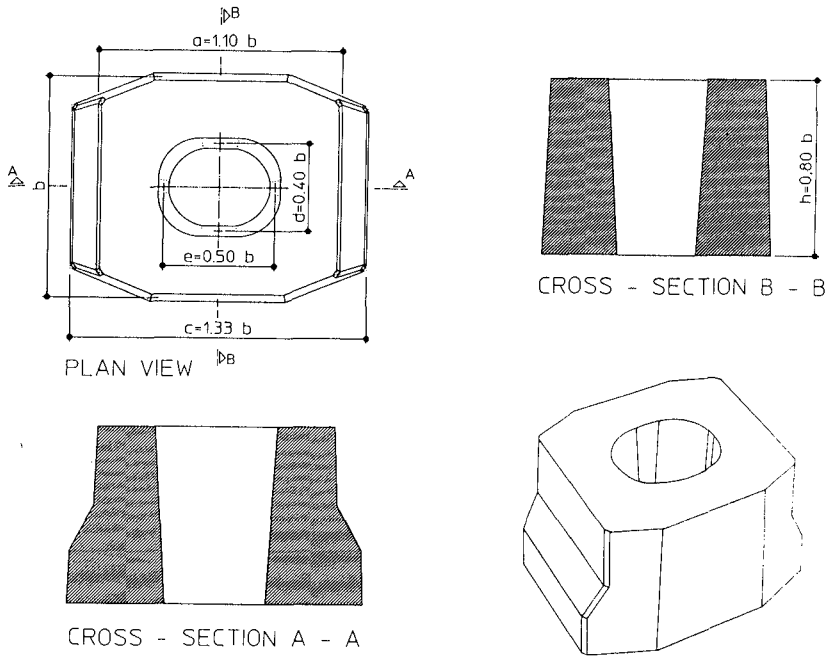


Figure 1. Geometry of the HARO armour unit

conform an appropriate placement pattern, a porosity as high as 51-53 % can be achieved.

An exhaustive laboratory investigation conducted at the Hydraulic Research Laboratory in Borgerhout (Antwerp) showed a very good hydraulic stability which is comparable to that of the dolos (De Rouck et al., 1987; Wens et al., 1990). However, the reliability of the armour layer and thus the whole rubble mound breakwater, not only depends on the hydraulic stability of the armour units but also to a large extent on their structural strength. Unfortunately, failures in the late seventies and in the early eighties showed this point all too clearly. In order to verify the structural strength of the HARO, static and dynamic loading tests were carried out in the Magnel Laboratory of Ghent State University and on the site.

3. STATIC LOADING TEST

The test set-up for the static loading test on a 150 kN HARO is shown in fig. 2. The block was turned on its side and placed on two supporting concrete beams with variable depth. On the upper surface, a circular steel disc (300 mm \varnothing), on which the load P was applied, was placed. This load application point is located on the axis passing through the centroid of cross-section BB (fig. 1). During the test, the total load P was

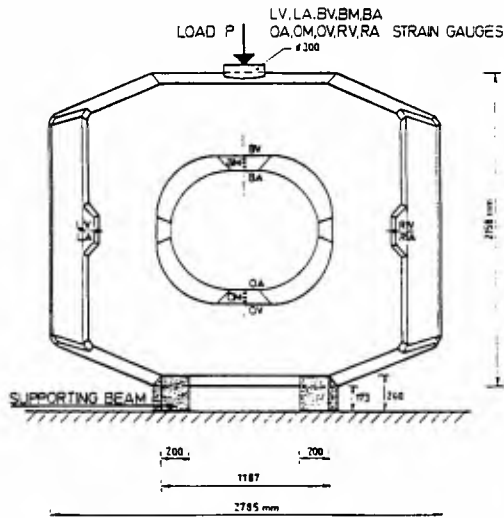


Figure 2. Test set-up for the static loading test

increased by increments of 200 kN. At each load level the deformation of the concrete surface was measured at 10 different points by means of strain gauges with a gauge length of 60 mm. The strain gauges were positioned parallel to the original upper and lower faces of the block. The shortening of the minor axis of the central hole was measured along three verticals.

Rupture of the block occurred at a load level of 2400 kN which corresponds to 16 times the weight of the block itself. Fig. 3 shows the HARO after failure.



Figure 3. Block after the static loading test

The shortening of the short central axis BM-OM in relation to the applied load P is shown in fig. 4. From this figure it appears that the elastic state extends to about 1600 kN. Beyond this value the shortening of the axis BM-OM increases at a higher rate. This non-linear behaviour is confirmed by the strain gauge readings. Measured strains and strains found in a supporting 3-dimensional linear elastic finite element analysis correspond reasonably well for loads up to $P = 1600$ kN, as is shown in fig. 5 for strain gauge LA. From this load level on, the course of the measured strain signals varies rather widely depending on the location of the strain gauges. This is due to the fact that during the loading process the internal stress distribution gradually changes and that only local strains are measured. The maximum measured (tensile) strain equals $190 \cdot 10^{-6}$ (strain gauge BV).

As the static loading test concerns, the total input energy is obtained as the surface under the load-displacement curve. Associating the decrease Δd of the axis BM-OM with the displacement at the point load, one can obtain from fig. 4 the energy values mentioned in table 1.

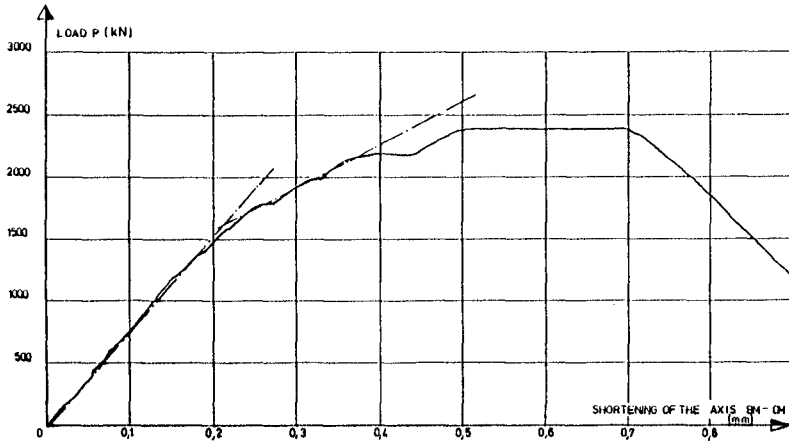


Figure 4. Shortening of the axis BM-OM as function of the load P

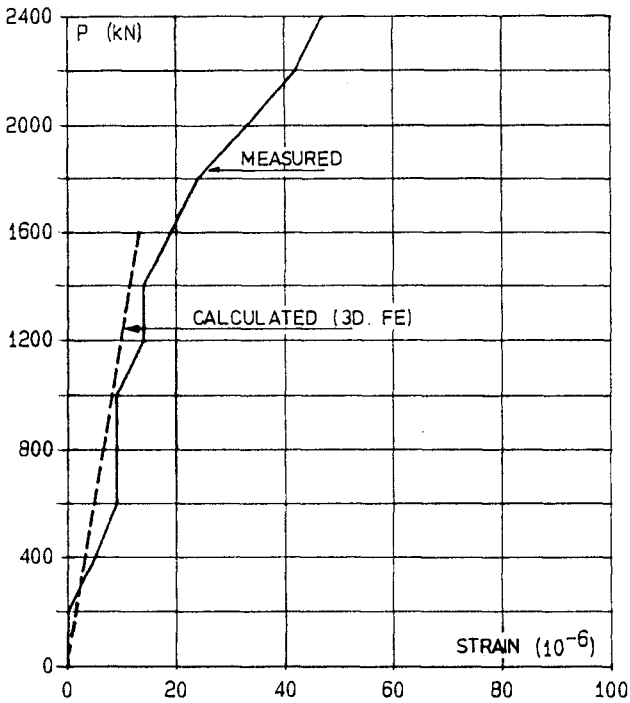


Figure 5. Comparison of measured and calculated strain at LA

TABLE 1 - Static loading test

P (kN)	Δd (mm)	E_i (kJ)
1600	0.21	0.252
2400	0.5	0.800
2400	0.7	1.280

After the test, cores were drilled at the upper and lower face of the block. On the cores (113 mm in diameter and 100 mm in height) compression and splitting tests were performed. Compressive strengths equal to 43.4 MPa and 48.7 MPa were found respectively for the upper and lower surface. Values of 3.08 MPa (upper surface) and 3.67 MPa (lower surface) were obtained for the splitting tensile strength. Each value represents the mean of three test results.

4. DYNAMIC LOADING TEST IN THE LABORATORY

The test set-up for the dynamic loading test is essentially the same as for the static one. The impact is performed by means of a falling steel block, having a mass of 516 kg. The vertical movement of the block is guided by two steel laths which fit, with some margin, in vertical notches at two opposite side faces of the steel block. The lifting hook is designed in such a way that delocking takes place almost instantaneously.

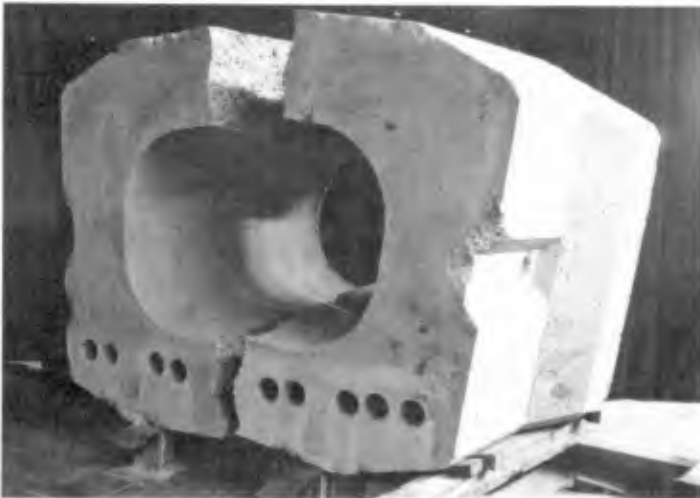


Figure 6. Block after the dynamic loading test

The height of fall, being equal to 50 mm the first time, was successively increased by 50 mm increments until complete failure of the HARO took place. The following cracking sequence could be observed by the naked eye :

- drop height of 650 mm : vertical crack at the upper inner face, extending to the front and back face.
- drop height of 700 mm : vertical crack at the lower inner face.
- drop height of 750 mm : horizontal crack at the left inner face.
- drop height of 800 mm : extension of the vertical cracks and rupture of the block into two parts (fig. 6).

In fig. 7, the maximum tensile strain, recorded during the impact at the locations RA, BM, LA and OM is plotted. It follows that after the impact from 550 mm height, cracking already occurred at the lower inner face (OM). The maximum strain at the upper inner face appears to remain almost constant at a value of 180 microstrain from the impact from 250 mm height on. Noteworthy is that the maximum concrete strain, again corresponds to the usual range i.e. 150-200 10^{-6} , as encountered in the static loading test.

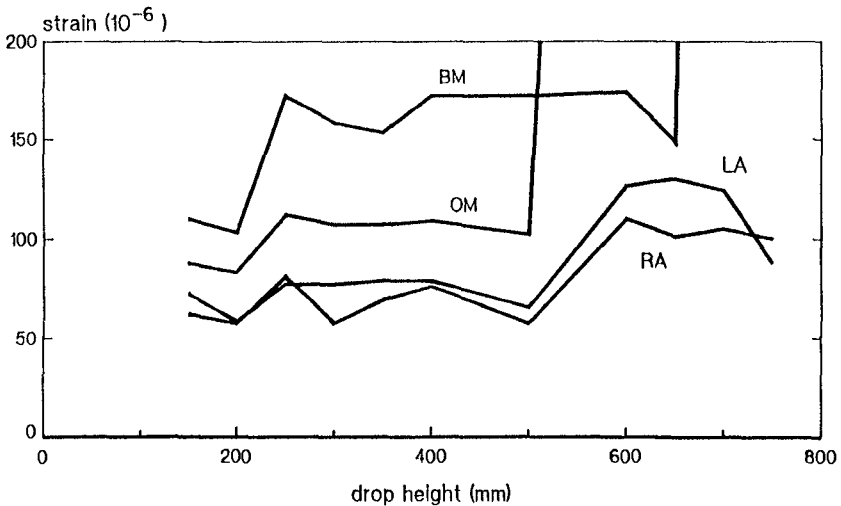


Figure 7. Measured peak strains during impact

The energy input corresponding to the potential energy of the impactor is obtained from

$$E_i = m_i g \Delta h \tag{1}$$

where m_i : mass of the impactor (516 kg)
 g : gravitational acceleration
 Δh : drop height.

For Δh equal to 550 mm (onset of damage) and 800 mm (complete rupture) the values E_i , mentioned in table 2, are obtained. As it was observed that rebound of the impactor

TABLE 2 - Dynamic test in the laboratory

Δh	E_i (kJ)
550 mm	2.784
800 mm	4.050

remained very limited, these values can reasonably be considered as the energy absorbed by the HARO block. The values mentioned in table 1 are considerably smaller than those given in table 2.

From the dynamic measurements, the impact time was calculated as 0.7 ms.

5. PENDULUM TESTS ON THE SITE

5.1. General description

Armour units should be able to withstand impacts from adjacent units. These impacts can occur while placing the units on the slope or under wave attack. In order to simulate these impacts, pendulum tests were carried out on site.

A 150 kN HARO suspended by a cable at the top of a crane jib was first given a horizontal deviation d from its equilibrium position and then swung against other blocks at rest on a rock bed (fig. 8). Two different impact situations were envisaged (fig. 8). In the first test, the impact block hits two blocks of an adjacent row. In the second test, an edge of the impact block hits another block on its weakest side. The first situation results from the design placement pattern (a block of an upper row rests against two blocks of the lower row). The second is deemed to correspond to an exceptional event.

5.2. First test series

The first series of tests is performed according to the first impact situation. The horizontal deviation d before release was progressively increased by 0.50 m. The final deviation amounted to 7.00 m. No further increment was possible due to technical limitations imposed by the crane. None of the blocks was broken. Only the three directly involved blocks were locally damaged at the protuberances.

In table 3, values of the maximum accelerations measured at different locations on the back side of the impact block are mentioned. No reliable strain measurements were obtained during the test series.

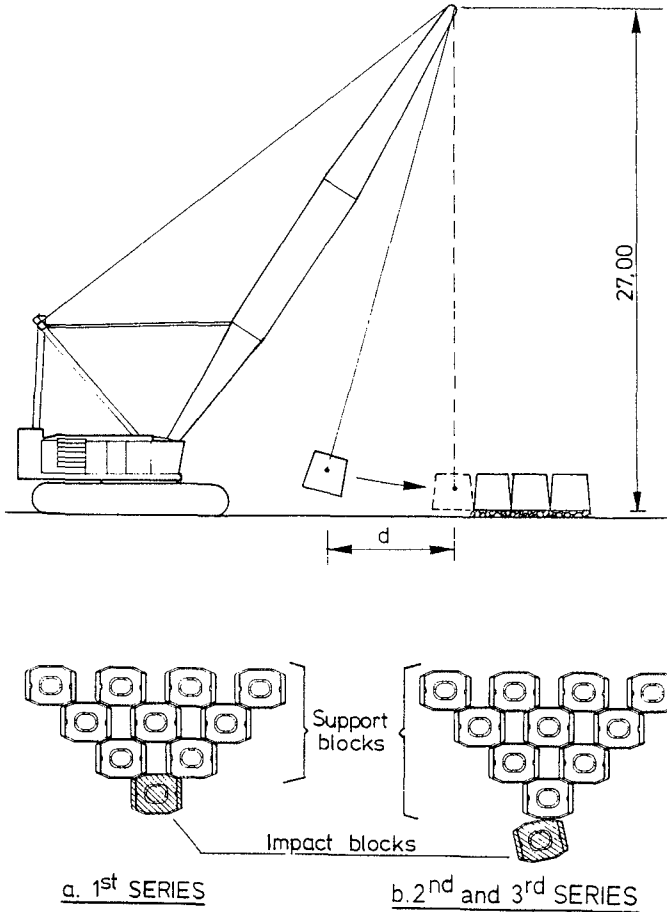


Figure 8. Test set-up for pendulum test on site

The input energy E_i corresponding to the potential energy of the impact block, calculated by (1) is also indicated in table 3. Also indicated is the value $0.5 E_i$, which will be useful for the evaluation of the second and third test series (see sections 5.3 and 5.4). The energy values mentioned in table 3 are considerably larger than those mentioned in tables 1 and 2. However, the impact phenomenon is quite different and obviously the bending stresses are much lower for this first site configuration.

5.3. Second test series

The second series of tests was performed according to the second impact situation envisaged in 5.1. This situation is rather similar to the dynamic loading test performed in the Laboratory (section 4).

TABLE 3 - First test series : accelerations and potential energies E_i

Horizontal deviation d (m)	Δh (m)	Accelerations (m/s^2)				E_i (kJ)	$0.5 E_i$ (kJ)
		A1	A2	A3	Mean		
3.0	0.174	510	220	180	300	25.6	12.8
4.0	0.310	530	340	400	400	45.6	22.8
4.5	0.392	110	30	20	50	57.7	28.8
5.0	0.485	620	270	360	420	71.4	35.7
5.5	0.588	420	370	300	360	86.5	43.3
6.0	0.702	280	200	310	260	103.2	51.6
6.5	0.826	830	1010	750	860	121.5	60.8
7.0	0.960	1000	1020	780	930	141.2	70.6

The deviation was progressively increased by steps of 1 m. The target block showed severe transverse cracks after the impact out from the 4 m deviation. In table 4, peak values of accelerations and strains are mentioned. The locations of the accelerometers A and the strain gauges R are as follows :

- A1 and A2 : back side of target block (opposite to the impact face)
- A3 : front side of impact block (opposite to the impact face)
- R1 : inner back face of target block
- R2 : inner side face of target block
- R3 : inner front face of target block
- R5 : inner back face of impact block
- R6 : inner side face of impact block.

TABLE 4 - Second test series

Deviation d (m)	Peak accelerations (m/s^2)			Peak strains (10^{-6}) (↗ indicates strain gauge failure)				
	A1	A2	A3	R1	R2	R3	R5	R6
1	200	190	210	9	2	3	-	-
2	360	220	140	140	6	14	50	-
3	450	880	330	160	10	25	12	2
4	730	1590	850	↗	41	↗	8	16

The maximum peak strain, before rupture of strain gauge R1, is equal to $160 \cdot 10^{-6}$ which indicates that for the three tests considered so far, the maximum concrete strain could be considered as a useful failure criterion. In fig. 9, the recorded strain signal from strain gauge R3 is shown for the impact from $d = 3$ m. It follows that the impact time is about 12 ms. Fig. 10 shows the acceleration signal A3 for the same impact situation. The second impact at about 295 msec is caused by the rotation of the impact block after the first contact at one of the edges. It has to be noted that the time scales of figs. 9 and 10 are different.

Only in a very limited zone of the front face of the target block, local crushing of the concrete occurred during the first few impacts. This indicates that the energy release in the contact zone remained small. This locally damaged zone had a diameter of about 0.25 m and was located at a height of about 0.50 m.

5.4. Third test series

The third test series was also performed according to the second impact situation. The target block was replaced by a new one but the impact block was the same as in the second test series. Only deviations equal to 1 and 4 m were realized. At the latter impact, severe transverse cracks occurred this time in the impact block. Measured peak accelerations of the impact block are given in table 5.

TABLE 5 - Third test series : accelerations (m/s²)

Deviation d (m)	A1	A2	A3
1	90	20	60
4	720	1350	410

5.5. General remarks

- The results of the tests according to the first impact situation, which could occur during regular placing of the blocks, indicate that under these circumstances no rupture of the blocks seems possible in practice.
- The second, accidental impact situation, appears to be more critical. Comparison of the second and third test series indicates that the stress fields generated both in the impact and the target block, cause damage of comparable magnitude. Hence the mention of $0.5 E_j$ in table 3.
- The input energy at $\Delta h = 800$ mm in the laboratory test equals 4.05 kJ whereas at $d = 4$ m, a value of 22.8 kJ is obtained for the pendulum test. A comparison only based on energy values, appears not to be appropriate.
- Interpretation of the dynamic behaviour on the basis of the acceleration measurements

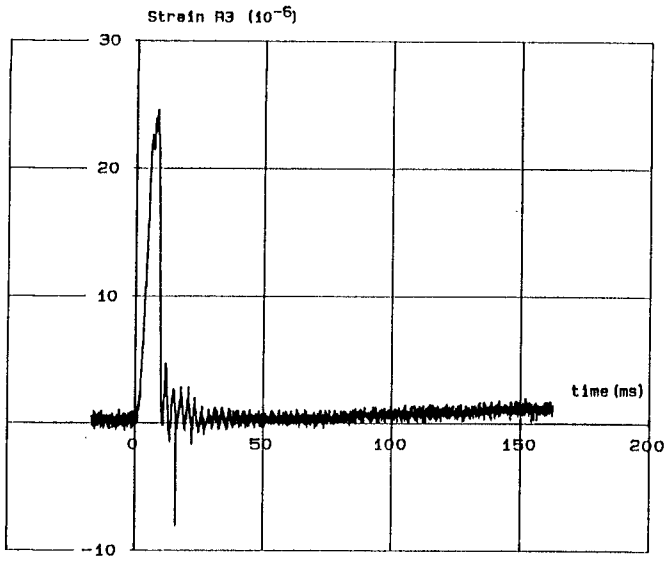


Figure 9. Strain signal R3 during impact from $d = 3$ m (second test series)

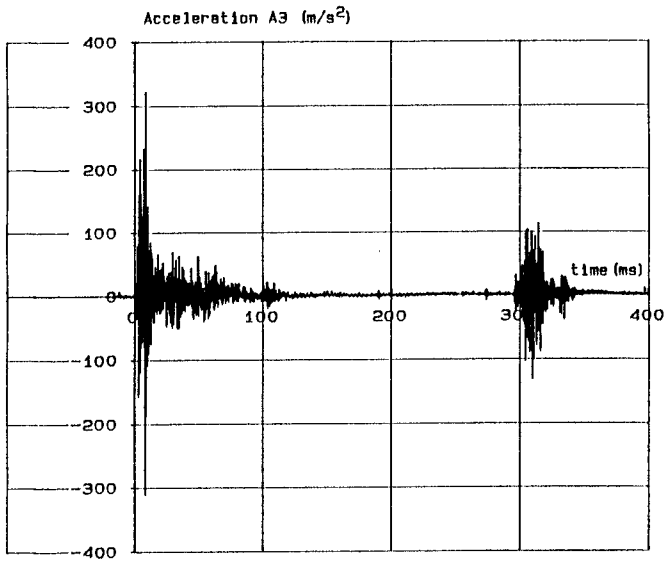


Figure 10. Acceleration signal A3 during impact from $d = 3$ m (second test series)

is not straightforward. Regarding the first impact situation, contact with the two adjacent blocks at rest never occurs simultaneously and hence the energy distribution between the different blocks turns out to be quite complex. In the second impact situation considered, the impact block starts to rotate during the edge contact. This results in a contribution of rotations to the measured total acceleration signal which cannot be separated from the acceleration due to the main pendulum movement.

6. FURTHER CONSIDERATIONS WITH REGARD TO STRENGTH

For plain concrete armour units, structural integrity depends to a large extent on the absence of significant cracks, and thus on the concrete tensile strength. A major problem in this respect is cracking due to thermal stresses caused by the hydration process. Temperature measurements in both grooved cubes and HAROs were carried out during the first days after casting (Van Damme et al., 1988). Due to the central opening in the HARO the temperature increase remained small and resulted in a considerable reduction of the thermal stresses at early age. No thermal cracks are observed in the approximately 11000 HARO units manufactured in Zeebrugge.

7. CONCLUSIONS

- During a static loading test in the laboratory, the HARO block failed at a load of 2400 kN, which represents 16 times its own weight.
- During a dynamic loading test in the laboratory, rupture of a block took place after the impact of a steel block with a mass of 516 kg from a drop height of 800 mm.
- Pendulum tests on the site were performed according to two different configurations (lower part of figure 8). When the impact block was swung in between two other blocks, up from a horizontal deviation of 7 m, only local damage of the blocks occurred. When the impact block hit an adjacent block at its weakest side, failure of the blocks occurred for a horizontal deviation of 4 m.
- Although the general structural shape of the HARO is less robust than a massive cube, the results of static and dynamic loading tests on a 150 kN block confirm the adequate structural performance. Indeed, the tests prove that during regular placing of the individual armour elements no rupture of the blocks seems possible in practice. Even in case of an accident, e.g. dropping of a block during placement, the chance for damage of the blocks remains negligible.
- From a structural point of view the maximum concrete strain can be considered as a useful failure criterion both in static and dynamic loading conditions. Further research on concrete to concrete impact with large-scale tests would provide a better understanding of the failure mechanism.
- It can be stated that all investigations (hydraulic stability, run up, structural strength, durability), the experience on site (fabrication and placement on the slope) and the favourable cost price show that the HARO perfectly fulfils all performance criteria required for armour units.

8. ACKNOWLEDGMENT

The authors gratefully acknowledge the assistance of J. Vyncke (formerly with the Magnel Laboratory, now with the Scientific and Technical Centre for the Building Industry at Brussels) during the dynamic test in the laboratory.

9. REFERENCES

1. De Rouck J., Wens F., Van Damme L., Lemmers J. : Investigations into the merits of the HARO-breakwater armour unit,
Proc. 2nd COPEDEC, Beijing 1987, Vol. II. pp. 1054-1068.
2. Van Damme L., Taerwe L., Dedeyne R., De Rouck J. : Quality and durability of concrete armour units,
Proc. XXIst I.C.C.E., Torremolinos - Malaga, Spain 1988.
Vol. 3. Ch. 156, p. 2102-2115.
3. Wens F., De Rouck J., Van Damme L. : Comparative laboratory investigations on HARO, grooved cubes, dolos and tetrapods,
(to be published in "Coastal Engineering", Delft).

DETERMINATION OF COEFFICIENTS IN MORISON FORMULA BY A KALMAN FILTER

P. Wilde* E. Sobierajski[†]

W. Romańczyk[‡]

Institute of Hydroengineering, Polish Academy of Sciences,
Kościerska 7 Str., 80-953 Gdańsk, Poland

1 INTRODUCTION

In engineering practice semi-empirical formulae are used for the determination of hydrodynamical loads on vertical cylinders due to water waves. The most popular is the Morison formula

$$\frac{dP}{dz} = C_M \rho \frac{\pi d^2}{4} \frac{\partial u}{\partial t} + C_D \frac{\rho d}{2} u |u| \quad (1)$$

where dP is the resultant horizontal force, ρ – the density of the fluid, d – diameter of the cylinder, u – the horizontal component of the orbital velocity in wave motion calculated at the axis of the cylinder. The drag coefficient C_D and inertia coefficient C_M for uniform oscillating flow were determined experimentally by Sarpkaya (1975). The value of these coefficients depend upon the Reynolds and Keulegan – Carpenter numbers. The experiments for the determination of the hydrodynamical forces due to water waves were performed by Chakrabarti (1983), Cotter (1984), Bearman (1985), Sparboom (1987). There are not many data available for this case of loading. A few procedures are established for the determination of the drag and inertia coefficients from the measurements. Some authors claim that the coefficients should be variable in the period of the wave to obtain a good approximation of the real behavior.

*Professor of Civil Engineering

[†]Dr. Eng.

[‡]Research assistant

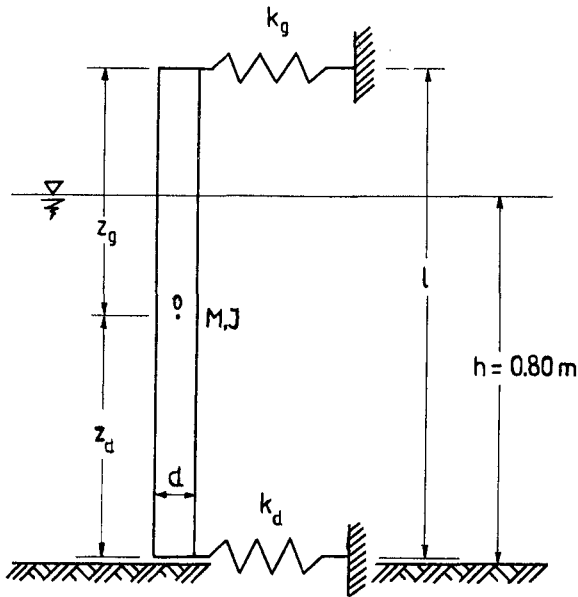


Figure 1: Scheme of dynamical system in one plane.

In the wave flume of the Institute of Hydroengineering in Gdańsk experiments were performed with a vertical rigid cylinder of diameters $d = 76.6 \text{ [mm]}$ and $d = 46.7 \text{ [mm]}$ supported by elastic springs at the bottom and top in the inline and transverse directions (four degrees of freedom). The investigated dynamical system is shown in Figure 1. The water depth was 0.80 [m] , and the wave heights $H = 12, 20, 25 \text{ [cm]}$ were investigated. The displacements at the positions of the springs were measured. Details are given by Wilde and Sobierajski (in print).

A Kalman filter of the type as presented by Wilde and Kozakiewicz (1984) and by Wilde and Romańczyk (1989) were used to decompose the measurements in components with frequencies equal to the multiple of the wave dominant frequency.

2 THE OUTLINE OF THE PROCEDURE

Let us point to some details of the proposed methods of estimation of the C_M and C_D coefficients in the Morison formula. It is necessary to construct a mathematical model for the decomposition of the elevation of the free surface. Let us define two independent stationary random functions $A_1(t)$, $D_1(t)$ defined by the following ITO

stochastic differential equation

$$d \begin{bmatrix} A_0(t) \\ A_1(t) \end{bmatrix} + \eta \begin{bmatrix} 1 & 0 \\ -1 & 1 \end{bmatrix} \begin{bmatrix} A_0(t) \\ A_1(t) \end{bmatrix} = 2\sqrt{\eta P} \begin{bmatrix} 1 \\ 0 \end{bmatrix} dB(u) \tag{2}$$

where η is a parameter with dimension $[s^{-1}]$, P is the asymptotic value of the variance and $dB(u)$ is a Brownian motion process with the variance equal to one. Two random functions $X(t), Y(t)$ are defined by the matrix equation

$$\begin{bmatrix} X(t) \\ Y(t) \end{bmatrix} = \begin{bmatrix} \cos \omega t & \sin \omega t \\ -\sin \omega t & \cos \omega t \end{bmatrix} \begin{bmatrix} A_1(t) \\ D_1(t) \end{bmatrix} \tag{3}$$

where ω is the dominant angular frequency. The mean values of the processes $X(t)$ and $Y(t)$ is equal to zero and the covariance functions are for the stationary case are

$$c_{xx}(\tau) = c_{yy}(\tau) = Pe^{-\eta\tau} [1 + \eta\tau] \cos \omega\tau \tag{4}$$

where $\tau = |t_2 - t_1|$.

Let us define a complex signal

$$Z(t) = X(t) + iY(t) = W(t)e^{-i[\omega t - \psi(t)]} \tag{5}$$

where

$$W(t) = \sqrt{X^2(t) + Y^2(t)} = \sqrt{A_1^2(t) + D_1^2(t)} \tag{6}$$

is the random amplitude and $\psi(t)$ is the random phase shift. Let us assume that the process $X(t)$ has a narrow - band spectral density, such that the amplitude $W(t)$ and phase shift change very little in the wave period.

Two finite sequences of stochastic processes $X_n(t), Y_n(t)$ for $n = 1, 2, \dots$ are defined by the formula

$$X_n(t) + iY_n(t) = Z^n(t) = W^n(t)e^{in[\omega t - \psi(t)]} \tag{7}$$

which have dominant frequencies equal to $n\omega$. It follows from equations (6) and (7) that the function $W^n(t)$ are envelopes for both functions $X^n(t)$ and $Y^n(t)$. If the expression in the square brackets is equal to $r\pi$, where r is an integer then $Y_n(t)$ and $X_n(t)$ touches the envelope for all n . If in the mathematical model (2) the parameter η is equal to zero then the solutions correspond to constant in time functions and the amplitudes and phase shifts are random variables and the real parts correspond to cos and imaginary parts to sin functions. In the stochastic case when η is not equal to zero but is small compared to ω there is a similar behaviour for the sample functions.

From equations (5) and (7) it follows that $X_n(t)$ is the real and $Y_n(t)$ the imaginary part of $Z(t)$ to the power n and thus it is possible to express them as polynomials in $X(t)$ and $Y(t)$ of order n . For example

$$\begin{aligned} X_2(t) &= X^2(t) - Y^2(t) \\ Y_2(t) &= 2X(t)Y(t). \end{aligned}$$

The inverse problem is to express $X^r(t)$ and $Y^r(t)$ as a series in terms of $X_p(t)$ and $Y_s(t)$ where p and s are smaller or equal to r . It may be easily seen that such a

representation is possible with coefficients which depend upon $W^q(t)$ where $q + p = r$ and $q + s = r$. For example

$$\begin{aligned} X^2(t) &= 0.5W^2(t) + 0.5X_2(t) \\ X^4(t) &= 0.375W^4(t) + 0.5W^2(t)X_2(t) + 0.125X_4(t). \end{aligned}$$

In general any polynomial function in $X_r(t)Y_q(t)$ may be expressed as a linear combination of terms of the type $X_p(t)$ and $Y_s(t)$ with coefficients which depend upon $W(t)$.

The surface elevation for the second order Stokes' wave $\zeta(t)$ is described by the formula

$$\zeta(t) = \frac{H}{2} \{ \cos(kx - \omega t) + \frac{2\gamma}{h} \cos[2(kx - \omega t)] \} \quad (8)$$

where

$$\gamma = \frac{kh}{2} \coth(kh) \left[1 + \frac{3}{2\sinh^2(kh)} \right],$$

H is the wave height, h the water depth, ω the angular frequency and k is the wave number. When the wave height and phase shift change very little in the wave period for a fixed position in space $x = 0$, the relation (8) may be generalized for random waves by assuming

$$\zeta = X(t) + \frac{\gamma}{h} X_2(t) \quad (9)$$

where the wave number k is assumed constant and calculated from the dispersion relation for the peak frequency. When the process has very narrow-band spectral density the relations for the regular waves may be used as a first approximation to find the horizontal components $u(t)$ of the velocity vectors and the accelerations. For example the accelerations are

$$\frac{\partial u}{\partial t} = \omega^2 \frac{\cosh[k(h+z)]}{\sinh(kh)} Y(t) + \frac{3}{2} \omega^2 k \frac{\cosh[2k(h+z)]}{\sinh^4(kh)} Y_2(t) \quad (10)$$

where z is the vertical coordinate measured from the still water level.

According to the Morison formula it is necessary to calculate the values of the function $|u|$. It is desirable to express this random function as a sum of random functions with dominant frequencies equal to $n\omega$ and coefficients which are varying slowly in time. Thus we want to approximate a random function $g(X, Y)$ by the following series

$$g(X, Y) = a_0(W) + \sum_{p=1}^n a_p(W) X_p + \sum_{r=1}^n b_r(W) Y_r \quad (11)$$

in the sense that the squared difference J between the left and right side in (11) is minimum. From (7) it follows

$$\begin{aligned} X_p(t) &= W^p(t) \cos[p(\omega t + \psi)] \\ Y_p(t) &= W^p(t) \sin[p(\omega t + \psi)]. \end{aligned} \quad (12)$$

When these functions are substituted it follows that the function J is a function of the random amplitude $W(t)$ and random phase shift $\psi(t)$, and for a fixed time t is a random variable. It is easy to see that when $A_1(t)$ and $D_1(t)$ are independent random variables with Gaussian distributions then $W(t)$ has a Rayleigh distribution

and $\psi(t)$ has a uniform distribution in any interval of length 2π and that they are statistically independent. We may substitute

$$U(t) = -\omega t + \psi(t) \tag{13}$$

and for a fixed t the random variable U has a uniform distribution in the interval $-\pi, \pi$. Thus as a criterion of approximation for a fixed t , in the random formulation we may take that the expected value with respect to the phase

$$I = \int_{-\pi}^{\pi} J(W, u) \frac{1}{2\pi} du \tag{14}$$

is minimized, where the integral is a Riemann integral and $W(t)$ is a fixed value and u is dummy variable.

Similar as in the case of Fourier series, when the necessary condition and the orthogonality properties of the trigonometric functions are used the following expressions for the coefficients are obtained

$$\begin{aligned} a_0(W) &= \frac{1}{2\pi} \int_{-\pi}^{\pi} g(W, u) du \\ a_s(W) &= \frac{1}{2\pi} \int_{-\pi}^{\pi} g(W, u) \cos(su) du \\ b_s(W) &= \frac{1}{2\pi} \int_{-\pi}^{\pi} g(W, u) \sin(su) du. \end{aligned} \tag{15}$$

When these formulas are used for the polynomial functions the same expressions result as before by a direct calculation. For the case $|X|X$ it follows

$$|X|X \simeq \frac{8}{3\pi}WX + \frac{8}{15\pi}W^{-1}X_3 - \frac{8}{105\pi}W^{-3}X_5 + \dots + \tag{16}$$

In Figure 2 a realization of a random function $|X|X$ calculated by a computer is shown and an approximation by two terms. It may be seen that the difference are very small.

With the same approximations as in the expression for the acceleration (10), the horizontal components of the orbital velocities are given by the formula

$$u = \omega \frac{\cosh[k(h+z)]}{\sinh(kh)} X(t) + \frac{3}{4}\omega k \frac{\cosh[2k(h+z)]}{\sinh^4(kh)} X_2(t). \tag{17}$$

Thus the function $|u|u$ depends upon the values of $X(t)$ and $X_2(t)$ and when the integrals according to the expressions (16) are calculated the interval of integration has to be split into parts (absolute value) which depend upon the values of W and the values of z , where the velocity is determined. The coefficients may be determined by numerical methods and the final result is that the expansion in terms is useful and only a few terms are sufficient to obtain a good approximation.

To obtain the resultant force and moment the loads given by the Morison formula (1) have to be integrated along the pile from the bottom to the free surface which changes in time. This is an approximate procedure because the real velocity field in the neighbourhood of the free surface is not very well described by the Stokes' second order approximation. It should be however mentioned that such a procedure is used in an engineering approach and the differences in resultant forces and moments are not great. Due to the integration to the time-dependent free-surface, terms with the double frequency are generated even when the second term

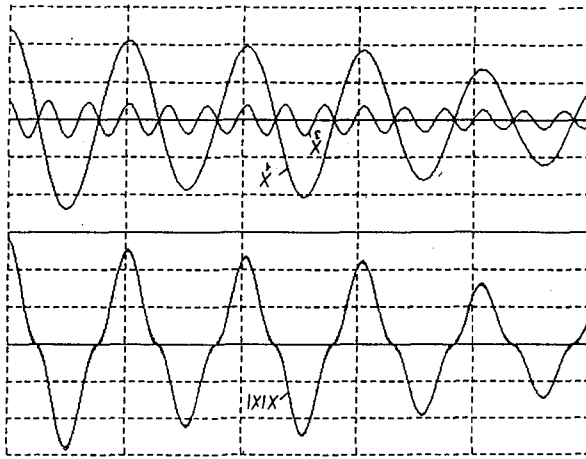


Figure 2: Example of $|X|X$ process and its decomposition

in the Stokes' approximation is very small and the position of the free surface is well described by linear theory of waves.

To avoid complicated algebraic formulae the integrals corresponding to the resultant forces and moments were not expanded in series with the help of the relations (16) but a numerical procedure was applied. From the measured surface elevations by a Kalman filter the functions $X(t)$ and $Y(t)$ with the dominant frequency equal to the peak frequency of the wave were determined. By the relations (10) and (17) the accelerations and velocities as function of z for the times of measurement were calculated and then according to the Morison formula separately for the inertia forces and drag forces. These functions of z were integrated from the bottom of the pile to the free surface to obtain the following relations

$$\begin{bmatrix} R(k) \\ M(k) \end{bmatrix} = \begin{bmatrix} R^M(k) & R^D(k) \\ M^M(k) & M^D(k) \end{bmatrix} \begin{bmatrix} C_M \\ C_D \end{bmatrix} \tag{18}$$

where $R^M(k)$ is the resultant force due to the term with $C_M = 1$, and $R^D(k)$ due to the drag term with $C_D = 1$, $M^M(k)$, $M^D(k)$ denotes moments due to the inertia and drag terms with $C_M = 1$, $C_D = 1$ and k denotes the time step t_k .

When the resultant forces and moments are known the displacements as functions of time may be calculated. In the plane of propagation of water waves the dynamical system has two degrees of freedom. The position of the rigid cylinder is determined by the measured horizontal displacements $x_g(t)$ and $x_d(t)$ at the levels of upper and lower spring respectively. The damping is very small and the natural frequencies are high compared to the peak wave frequency. In the determination of displacements

it is possible to assume the equation for undamped vibrations

$$\begin{bmatrix} M & 0 \\ 0 & J \end{bmatrix} \begin{bmatrix} \ddot{x}(t) \\ \ddot{\varphi}(t) \end{bmatrix} + \begin{bmatrix} k_g + k_d & k_g z_g - k_d z_d \\ k_g z_g - k_g z_d & k_g z_g^2 + k_d z_d^2 \end{bmatrix} = \begin{bmatrix} R(t) \\ M(t) \end{bmatrix} \quad (19)$$

where $x(t)$ is the horizontal displacements of the center of mass, $\varphi(t)$ is the angle of rotation around the center of mass, k_g, k_d are the spring constants of the upper and lower springs, z_g, z_d are the distances from the center of mass to the upper and lower springs, $R(t), M(t)$ are the resultant force and moment of the hydrodynamic forces with respect to the center of mass. The position of center of mass and the mass matrix were calculated with added mass of water and the spring constants were obtained from static loads. The dynamic equation was verified by measuring free vibrations in still water.

The measured displacements $x_g(t), x_d(t)$ are related to the displacements $x(t), \varphi(t)$ by the equation

$$\begin{bmatrix} x_g(t) \\ x_d(t) \end{bmatrix} = \begin{bmatrix} 1 & z_g \\ 1 & -z_d \end{bmatrix} \begin{bmatrix} x(t) \\ \varphi(t) \end{bmatrix}. \quad (20)$$

When the equation of undamped vibrations (19) is used the measured vibrations can not be determined by the solution of this equation because the initial conditions will never be forgotten. The steady - state solution for harmonic vibrations will be used. The hydrodynamic loads (18) are decomposed into components with dominant frequencies corresponding to the multiples of the wave peak frequency and for each component the steady - state harmonic response is calculated. Thus, after simple manipulations the observations model for the time t_k assume the following form

$$\begin{bmatrix} x_g(k) \\ x_d(k) \end{bmatrix} = \begin{bmatrix} H_g^M(k) & H_g^D(k) \\ H_d^M(k) & H_d^D(k) \end{bmatrix} \begin{bmatrix} C_M \\ C_D \end{bmatrix} + \sigma_0 \begin{bmatrix} v_g(k) \\ v_d(k) \end{bmatrix} \quad (21)$$

where $H_g^M(k)$ and $H_d^M(k)$ are the calculated displacements due to the inertia term in the Morison formula for $C_M = 1$, and $H_g^D(k), H_d^D(k)$ due to the drag term for $C_D = 1$, $v_g(k), v_d(k)$ are independent sequences of gaussian white noise with distribution $N(0, 1)$ and σ_0 is the standard deviation of the observation noise.

In the mathematical models for the coefficients C_M and C_D it is assumed that they are statistically independent have constant mean values and fluctuations which are described by the $IT\hat{O}$ stochastic differential equation (2).

The standard Kalman filter procedure is used to estimate the values $C_M(k), C_D(k)$ on the basis of the measured values $x_g(k), x_d(k)$. The procedure was written in the form of an IBM PC computer program.

3 THE EXPERIMENTAL RESULTS

The water depth was 0.80 [m]. Different waves were considered. In Figure 3 the the results for a wave with a small wave height are shown. In this case the wave period was $T = 1.4$ [s] the amplitude of the wave was $\frac{H}{2} = 0.0596$ [m], the horizontal component of the velocity at the still water level calculated on basis of Stockes' theory was $u_{max} = 0.2915$ [$m \cdot s^{-1}$], the corresponding KC number 5.327 and the Reynolds number 1.96×10^4 . According to the data shown in Figure 3 the second term in the Stockes' approximation is negligible. The measured displacements are

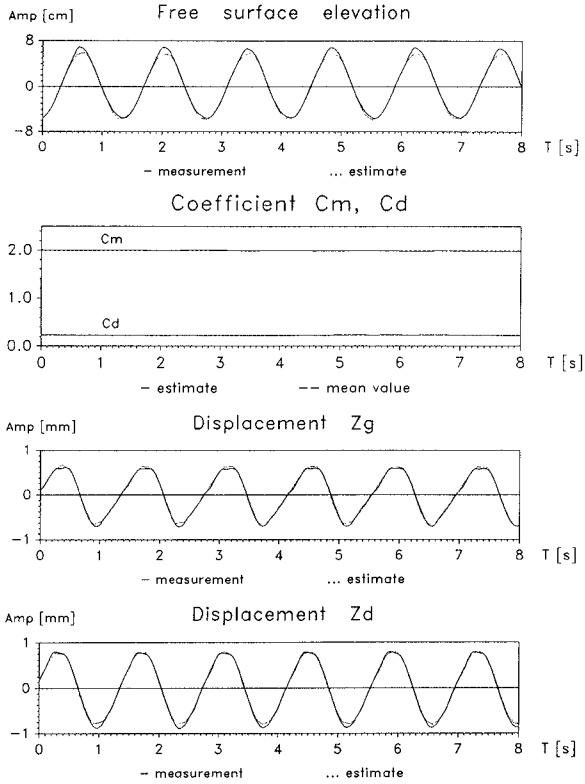


Figure 3: The measured and estimated wave and displacements and the estimated C_M and C_D coefficients for test db1.dat.

very close to trigonometric functions. The estimated coefficients C_M , C_D are very close to constant functions. The average values are $C_M = 1.99$ $C_D = 0.23$. It may be seen that the fluctuations are very small and not regular. Thus the assumption of constant values for the coefficients is justified.

In Figure 4 the data for a steeper wave are shown. In this case the wave period was $T = 1.9$ [s], the amplitude $\frac{H}{2} = 0.113$ [m], the horizontal velocity $u_{max} = 0.527$ [ms⁻¹], the KC number 13.08 the Reynolds number 3.54×10^4 . The wave is a second order Stokes' wave. The measured displacements are not symmetric and the influence of the double frequency of the peak wave is large. It may be seen that also in this case the estimated coefficients C_M , C_D are very close to constant functions. The average values are $C_M = 1.60$, $C_D = 0.70$. It should be stressed however that in this case there are differences between the measured values and the values calculated on the basis of the estimated coefficients. It may be seen from the graph that there are higher harmonics which are neglected in the analysis. The Morison formula introduces approximations, the determination of the velocity and acceleration fields from the Stokes' second order approximation does not correspond exactly to the real behaviour. The description of the dynamical system is simplified because damping is neglected and steady - state harmonic solutions are assumed. It is surprising that with such rude approximation the constant coefficients C_M , C_D may be so adjusted that the calculated solution gives the the basic features of the real behaviour.

The results of all experiments are presented in Figure 5. It should be mentioned that in all experiments the Reynolds numbers are in the range of 10^4 and thus only the relationship with respect of the Keulegan - Carpenter number KC may be shown. If one compares the results with previous investigations they are within the range of the published values. It should be noted that the coefficients C_D are smaller than the values usually used for $Re < 10^5$. As a crude recommendation the results show that for $KC \leq 5$ $C_M = 2$ and it drops to $C_M = 1.5$ for $KC \sim 20$, the values for C_D are $C_D = 0.25$ for $KC = 5$ and they grow up to $C_D = 0.8$ for $KC = 15$ (there are points $C_D = 1.0$). One can not expect to obtain exact values for the considered dynamical system because measurements have a small range in Reynolds numbers.

4 CONCLUSIONS

1. The investigations shown that the Kalman filter procedure is a suitable tool for the analysis of the problem.
2. In the mathematical models it is enough to assume once differentiable random functions described by the $IT\hat{O}$ stochastic differential equation (2).
3. The nonlinear term due to the drag force in Morison formula may be included in the observation model which becomes nonstationary.
4. The simplifying assumptions introduced in the analysis of the dynamical system are justified for practical applications.
5. The results of experiments shown that constant values for the C_M and C_D coefficients may be taken.
6. The procedure may be refined by considering the influence of damping but it looks like it is not possible to expect much better results and the scattering of results must be considerable in view of the complicated physics of the problem.

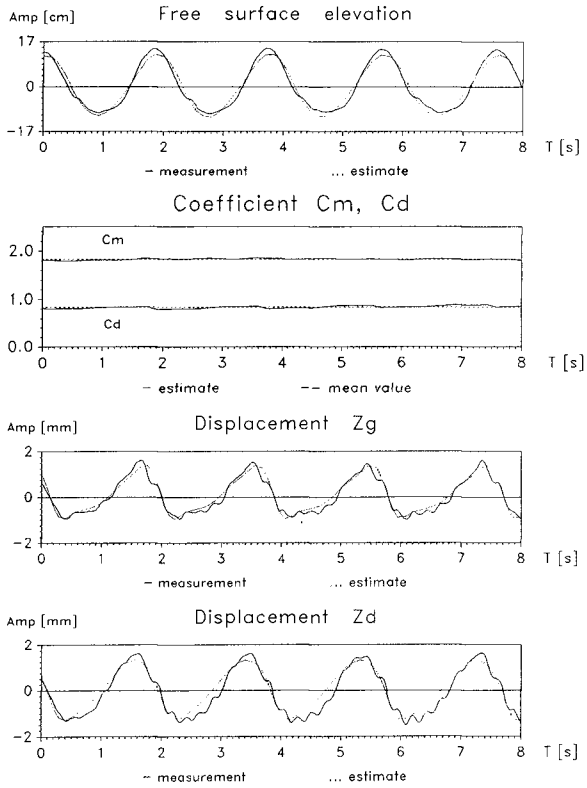


Figure 4: The measured and estimated wave and displacements and the estimated C_M and C_D coefficients for test db5.dat.

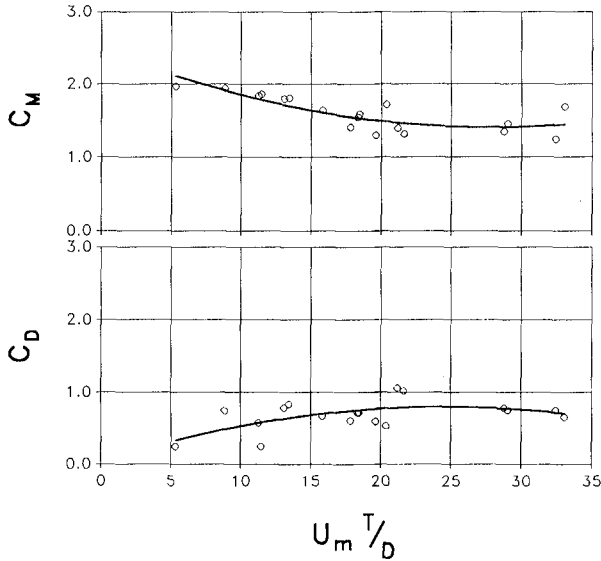


Figure 5: The estimations of the C_M and C_D coefficients

REFERENCE

BEARMAN P. W., CHAPLIN J. R., GREHAM J. M. R., KONSTANCE . K., HALL P. F., KLOPMAN G. (1985)

The loading on a cylinder in post - critical flow beneath periodic and random waves. Proc. Behaviour of Offshore Structures, pp. 213-225.

CHAKRABARTI S. K., COTTER D. C., LIBBY A. R. (1983)

Hydrodynamic coefficients of a harmonically oscillated tower. Appl. Ocean Res., No. 5, pp. 226-233.

COTTER D. C., CHARABARTI S. K. (1984)

Wave force tests on vertical and inclined cylinders. J. Waterways Port and Coastal Eng., No. 110, pp. 1-14.

SARPKAYA, T. (1975).

Forces on cylinder and spheres in a sinusoidal oscillating fluid. Journ. Appl. Mech., Trans. ASME.

SPARBOOM U. (1987)

Über die Seegangsbelastung lotrechter zylindrischer Pfähle im Flachwasserbereich. Diss. Univ. Braunschweig.

WILDE, P., KOZAKIEWICZ, A. (1984).

Application of Kalman filter to the analysis of structure due to waves.

Mitteilungen des Franzius – Instituts, the University of Hanover, Heft 59.

WILDE, P., ROMAŃCZYK, W. (1989).

The mathematical model for the analysis of Stokes' type waves.

Archiwum Hydrotechniki, Gdańsk.

WILDE, P., SOBIERAJSKI, E. (in print).

The added mass of vibrating cylinders in a layer of water with regular waves.

Mitteilungen des Franzius – Instituts, the University of Hanover.

CHAPTER 133

Wave forces on vertical breakwater on Reef Coasts

Eizo Nakaza¹⁾, Seikoh Tsukayama²⁾ and Mikio Hino³⁾

Abstract

The characteristics of the "Bore-like surf beat", one of long wave phenomena occurred on the reef coasts, are clarified by the field observations and experiments. And also, wave forces on breakwaters in the reef coasts are verified through the experiments.

A new pressure formula, taking into account of the wave force due to "Bore-like (Tsunami-like) surf beat", is suggested, and it is shown that the calculations by the formula show good agreement with results of experiments.

1. Introduction

There are a number of wave pressure formula on vertical breakwaters. But, they are derived for the cases of usual breakwaters constructed in sea area having monotonously sloping sea bed, and the accuracy has not been verified when they are applied to the case of breakwater in coasts with reef or multiple topography. As for the waves on the reefs, it is discovered by the authors (1988 (a), (b), (c)), after field observation and experiment, that the "Tsunami-like surf beats" occur when the period of incoming wave groups close to the period corresponding to the resonant frequency of water oscillation in the coastal zone. And this phenomenon may influence to the wave forces.

In this study, first of all, the discussion is made on the main reason of the disaster of coastal structures on the reef coasts due to Typhoon, and the relation between surf beat and fluid forces acting on the vertical breakwater in the reef coasts is clarified. Finally, a new pressure formula taking into account of the wave force due to the surf beat is proposed.

1) Research Associate, 2) Associate Professor, Dep. of Civil Engineering, Faculty of Eng., Ryukyuu University.
3) Professor, Dep. of Civil Eng., Faculty of Eng., Tokyo Institute of Technology. TOKYO, JAPAN

2. Damages of Coastal Structures and Feature of Tsunami-like Surf beat

In this section, some examples of damaged breakwaters are shown firstly, and then the Tsunami-like surf beat just attacking a sea coast is introduced by photographs.

Photograph 1 shows a damaged breakwater by waves due to Typhoon. The caisson of the breakwater was dragged and declined, and armor blocks of tetrapods about 2 tons of weight on harbor side of the breakwater were drawn by fluid forces and dragged about 100 meter from its ordinal position. Photograph 2 shows a destroyed mound breakwaters due to Typhoon. As shown in the photograph, two tons weighted tetrapods were scattered by fluid forces accompanied by the Typhoon. As for the waves conditions on occasion at these site, the wave heights on the places where these breakwater were constructed could not exceed 1.0 meter, because the water depths at the sites are about 2 meters. And significant wave height in offshore at the time, when these disaster were happened, was about 9 meters. Therefore it cannot be supposed that such waves having almost 1.0 meter of height could cause the disasters shown in these photographs.

What was happened on there ?. The answer to this question was discovered by Nakaza. He disclosed that main reason of these damage of break-water is strong flood like currents accompanied by a surf beat, such as Tsunami waves. Nakaza and Hino named this phenomenon as "bore-like surf beat" or "Tsunami-like surf beat", for analogous of its phenomenon to one of Tsunami.

Photograph 3 shows the such " bore-like surf beat" just coming to reef coast, on a occasion of the Typhoon on 6th Oct. 1988. Photograph (a) shows the state when the Bore-like surf beat was outgoing to offshore, and photograph (b) shows coming bore-like surf beat to the shore line, and photograph (c) shows the surf beat just attacking the coastal cliff, after 12 seconds from the time of photograph (b) was taken.

For the existence of such violent phenomenon of bore-like surf beat, wave forces acting on the breakwater or seawall may be different from ones on the same coastal structures built in the usual sea coast having monotonous slope of sea bed. So, ordinal wave pressure formula could not be applied to estimate the wave force in reef zone.

This study devote to clarify the characteristics of wave forces acting on the breakwater on the reef coast under existence of bore-like surf beat by experiments, and suggest a new wave pressure formula taking into account of the wave forces due to the surf beat.

Harbor side

Sea side



Photo. 1 Damaged breakwater due to Typhoon high waves



(a) perspective scene of damaged breakwater



(b) scattering of mound blocks (2t tetrapods)

Photo. 2 Damaged breakwater due to Typhoon high waves



(a) 16:00:00



(b) 16:53:13



(c) 16:53:24

Photo. 3 Bore-like surf beat occurred on Oct. 6, 1988

3. Experiment

Two series of experiments were conducted. The first series of the experiments was carried out to grasp the characteristics of hydraulic phenomena when the bore-like surf beat is attacking the breakwater. The second series of the experiments was conducted for the purpose of characterizing quantitatively the wave forces acting on the breakwaters in relation with the width of the reef flat, and consequently to suggest a new formula for wave pressure under the circumstances above mentioned.

3.1) Experimental equipments and method

Figure 1 shows the arrangement of experimental equipments used in the first series of the experiment. The wave channel shown in the figure, is 22m long, 0.8m wide and 1.0m deep. At the one end of the channel, a flap-type wave generator is installed, which can make regular waves.

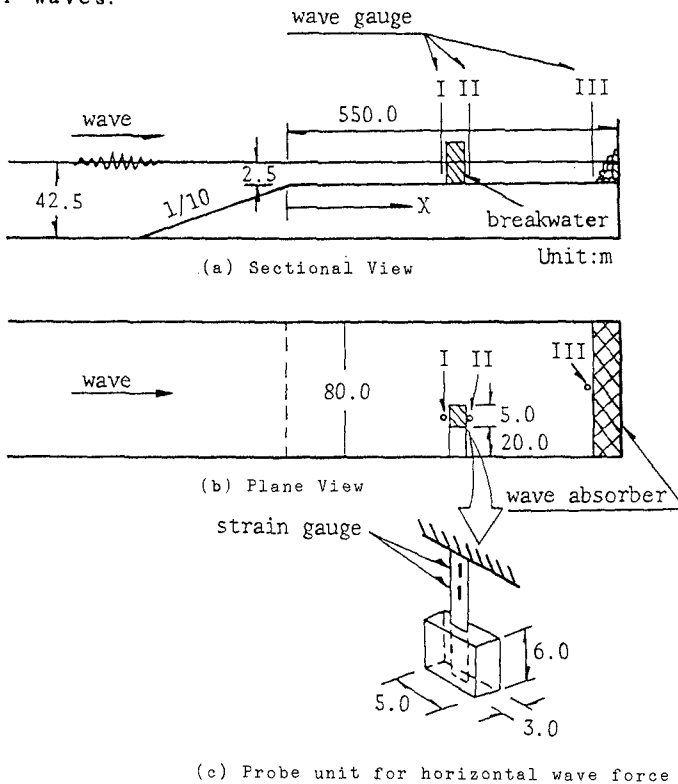


Fig. 1 Experimental equipments (quasi-three dimensional)

The experiments were carried out with two-type of incident waves, one was a continually incoming regular wave groups with constant interval, and the other one was monochromatic wave. The regular wave groups can cause the bore-like surf beat on the model reef as mentioned above, whereas the monochromatic waves cannot excite the surf beat on the reef model.

The method of experiment is as follows; after setting the model, wave generator was started. The wave profiles were recorded by wave gauges, as shown in the Fig. 1, at the suitable points on the reef model. And simultaneously, the wave force acting on the model breakwater was recorded.

Second series of the experiments were conducted utilizing random waves. Figure 2 shows the apparatus used in the experiment. Wave generator for irregular waves are mounted on the wave channel in the figure.

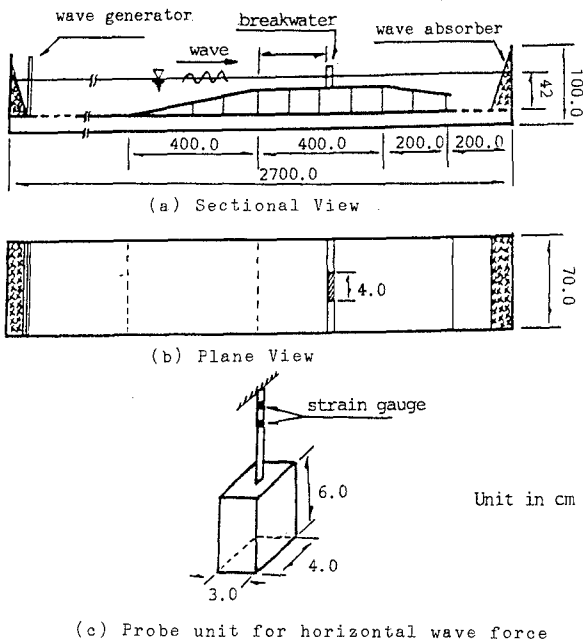


Fig. 2 Experimental equipments (two dimensional)

The experiment was carried out with the method as follows. After setting the model breakwater in the channel, the wave generator was started and the wave profiles and wave forces acting on the breakwater was observed. In the experiment, irregular waves with the spectrum of Bretschneider-Mitsuyasu type was used as

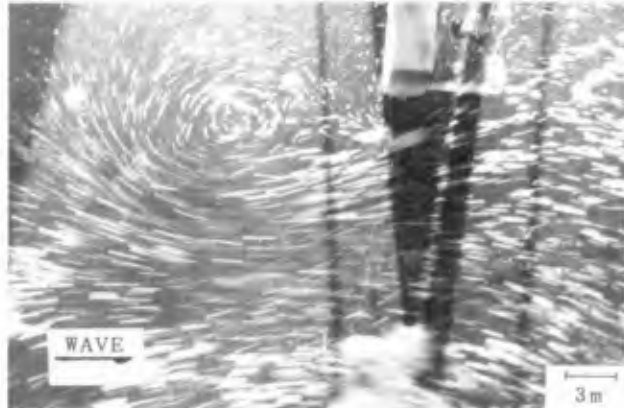
the incident wave. And the distance from the reef front to the breakwater was changed from 0m to 400m .

3.2) Results of first series of the experiments

Photograph 4 shows the vortex shedding from the end of the breakwater. Comparing to dimension of the breakwater, the diameter of the vortex is estimated as more than 30m in prototype scale. Therefore, we cannot ignore the influence of the vortex to the characteristics of the waves transmitted to the sea side of the breakwater, and so as to the wave forces.



(a) in flood stage of the surf beat
(at the time indicated by the arrow A in Fig. 3)



(b) in ebb stage of surf beat
(at the time indicated by the arrow B in Fig. 3)

Photo. 4 Vortex shedding from the edge of a vertical breakwater

Figure 3 shows the profiles of water surfaces and wave forces recorded in the experiment. Figures (a) and (b) show the water surfaces traced by the wave meters, and figure (c) corresponds to the record of wave forces acting on the breakwater. It can be seen, in the figure, the bore-like surf beat results impulsive forces on the breakwater when its incident and reflected wave front struck on the breakwater. The profile of wave force is analogous to one of the water surface in front of the breakwater.

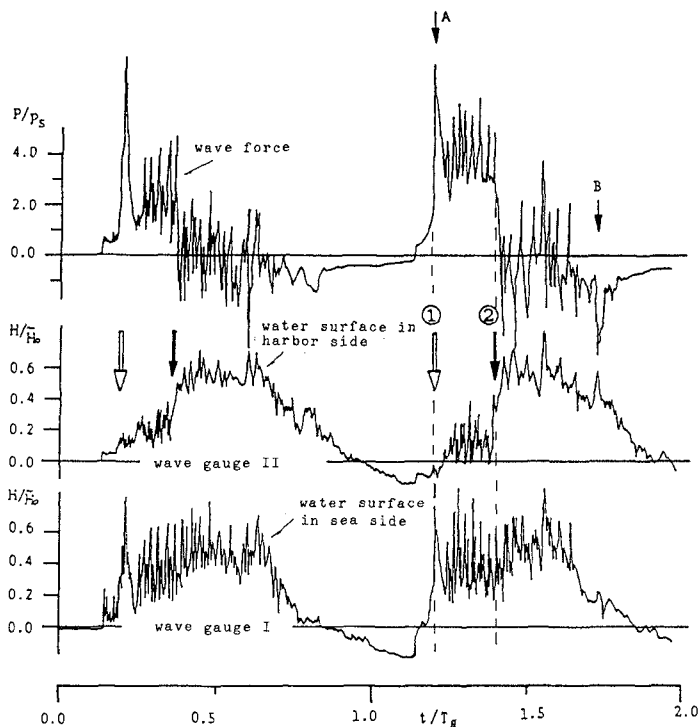


Fig. 3 Profiles of water surface and wave force (in case with surf beat; T_{wg} is the period of incident wave groups)

Figure 4 is similar one to the Figure 2, obtained in the case of experiment with monochromatic incident waves. So there are no occurrence of surf beat such as in the case of upper mentioned. From comparison of figure 2 and figure 3, the difference between these two cases is evident. We can not see in the Fig. 3 the impulsive forces such as seen in the Fig. 2, as though the incident wave heights are equal in both cases.

In estimation of wave forces acting on the breakwaters in the reef areas, therefore, we should take into account such phenomenon mentioned above.

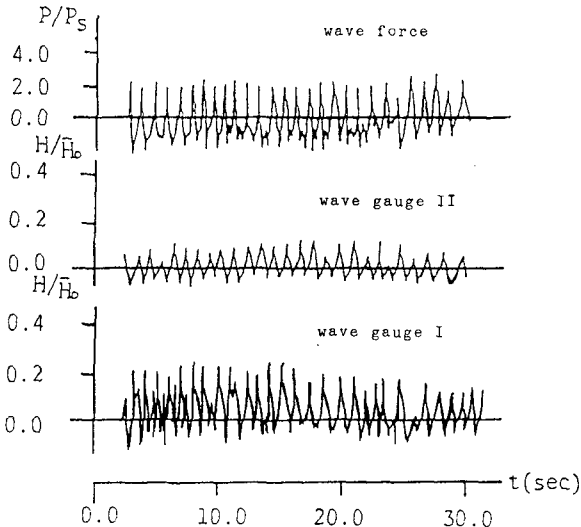


Fig. 4 Profiles of water surface and wave force (in case without surf beat)

3.3) Results of second series of the experiments

Figure 5 shows the profiles of water surfaces, wave pressure and wave forces recorded in second series of the experiments. In this figure, the oscillations with short periods correspond to the elements of irregular waves, which are usually called as individual waves, and the undulating solid curves with long period represent the surf beat. It can be seen, in the figure, that the contribution of the surf beat to the wave pressures or wave forces is so large to compare with one of the individual waves.

To clarify the difference between wave forces in cases with and without bore-like surf beat, the experimental results were analyzed in relation with the coefficient of wave pressure $K_{1/3}$, which corresponds to the ratio of wave pressure to static hydraulic pressure expressed as wH , where w represents unit weight of water and H is the wave height. The experimental results were shown in the Fig. 6. In this figure, it can be seen that the coefficient $K_{1/3}$ may be constant on the axis of wave steepness $K_{1/3}/L$. And in the figure, open circles correspond to the individual wave forces, and filled circles represent the coefficient of the wave forces with bore-like surf beat.

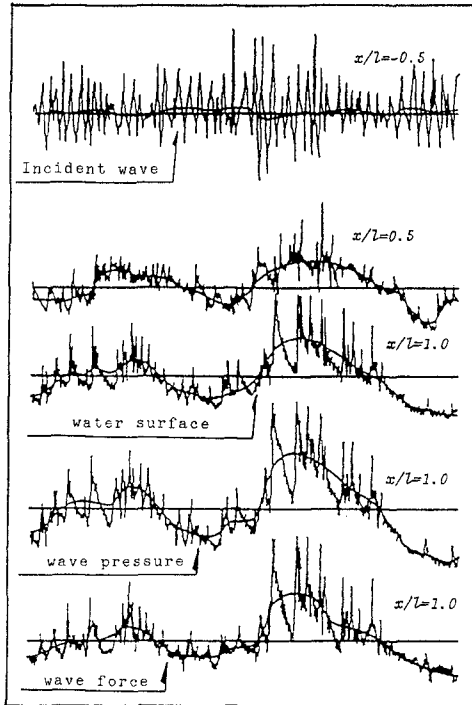


Fig. 5 Profiles of water surfaces, wave pressure and wave force

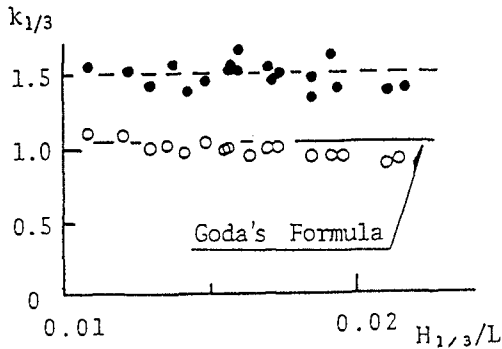
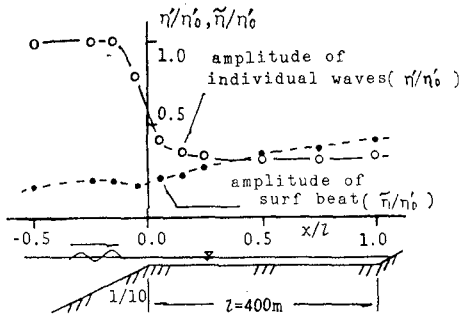


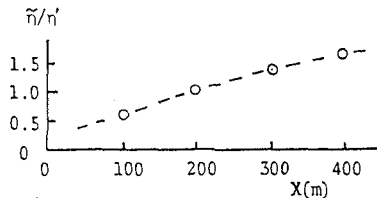
Fig. 6 Coefficient of wave pressure acting on a breakwater (for significant wave)

The results calculated from traditional formula of wave force agree with only that of individual waves, so the traditional wave force formula could not apply to the case with bore-like surf beat. Figure 7 shows the

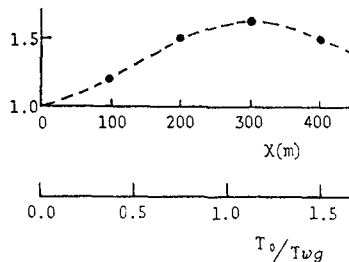
changes of the amplitude of surf beat and the coefficient of wave forces in relation with the width of the reef flat. It can be said, from the fig.7(a) and (b), that the amplitude of the surf beat enlarge with distance from the edge of reef flat. And the other hand, coefficient $K_{1/3}$ become larger with distance X , and take its maximum value at $x=300m$ and then decrease. The reason of this result can be considered as effect of resonant oscillation of water in the reef basin due to incident wave groups.



(a) distribution of amplitude of waves and surf beat



(b) changes of amplitude of surf beat



(c) change of coefficient of wave pressure

Fig. 7 Changes of amplitude of surf beat and wave force coefficient in relation with the width of reef flat
 (η'_0 , η' , $\etã'$ are the root mean square amplitudes of incident wave, individual waves and surf beat on the reef)

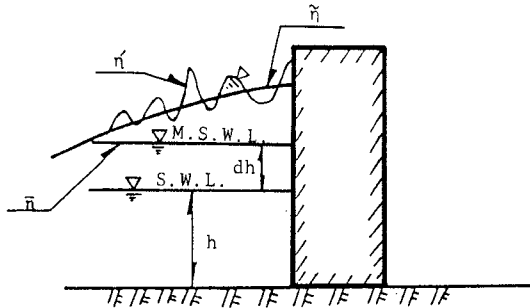
4. Suggestion of a New Pressure Formula

After the experiment, it is found that the water stage in front of the breakwater under existence of bore-like surf beat becomes as Fig. 8(a). Therefore, it can be assumed that the wave pressure distribution on the breakwater as shown in the Fig. 8(b). And, upon this assumption, a new pressure formula taking into account of surf beat have been derived as follows,

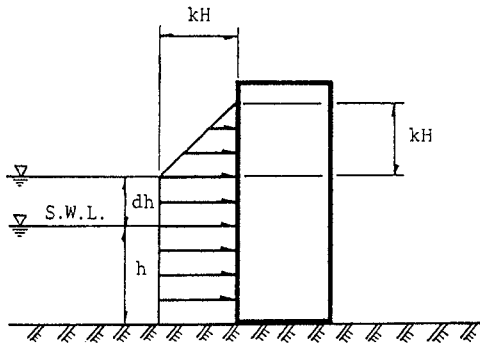
$$P = w A$$

$$A = \frac{1}{2}(KH)^2 + (h+dh)KH \quad \text{--- (1)}$$

where, w is the specific weight of sea water, h is the still water level in front of the breakwater and dh represents the wave set-up on the reef.



(a) sketch of water stage in front of breakwater



(b) distribution of wave pressure

Fig. 8 Definition sketch of wave pressure acting on the vertical breakwater

To test the applicability of newly suggested formula, the wave forces calculated by eq. (1) were compared with experimental results of horizontal wave forces acting on a unit span of the breakwater as in the Figure 9. In the figure, the filled circles represent the wave forces with bore-like surf beat, and the open circles correspond to one of the individual waves only, and it can be seen in this figure that the calculated result by new formula shows good agreement with the experiments under existence of the surf beat,

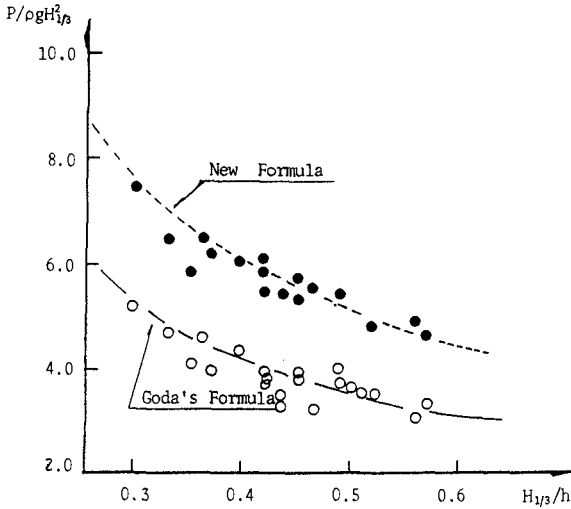


Fig. 9 Wave force distribution in relation with relative water depth $H1/3/h$

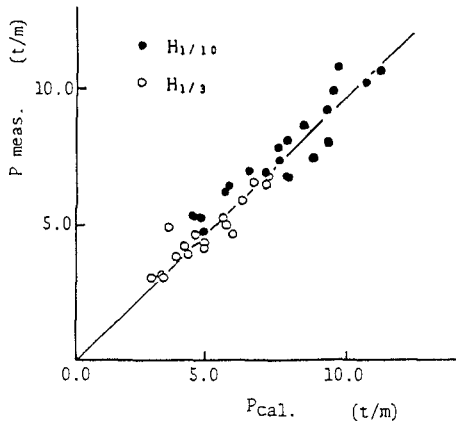


Fig. 10 Comparison of calculated wave forces with results of experiment

whereas the result by the former formula correspond to the wave pressures due to individual waves only. Therefore, the former formula for the wave force can not be applied to a case with the surf beat which has the same order of the wave height as one of individual waves.

Figure 10 shows the comparison of the calculated wave pressures by the equation (1) with experimental ones. Where the representative wave heights of one tenth highest high wave $H1/10$ and significant wave height $H1/3$. Both results from the calculation and the experiment show good agreement with each other. So it can be concluded as the newly suggested wave pressure formula is applicable to the case that the bore-like surf beat exist.

5. Conclusions

Main conclusions of this study are summarized as follows, "Bore-like surf beat" occurs on the reef coast as a result of resonant oscillation of the mean sea-level on the reef flat by incoming wave groups. This "Bore-like surf beat" acts as violent Tsunami, and strongly affects to the wave forces on the breakwater. A new wave pressure formula taking into account of the wave force³ due to the surf beat on the reef is derived and suggested as equation (1).

The new formula is tested by the experiments. The results from this formula show good agreement with the experimental results.

References

- Hino, M., et al. (1988a) :A study on a bore-like surf beat induced by wave groupiness, Proc. 35th Japanese Conf. on Coastal Eng., pp.197-201. (in Japanese)
Nakaza, E., et al. (1988b) :Coastal disasters due to Bore-like surf beat on reef coasts, Proc. 35th Japanese Conf. on Coastal Eng., pp.202-206. (in Japanese)
Nakaza, E., et al. (1988c) :Wave force due to Tsunami-like surf beat, Proc. 35th Japanese Conf. on Coastal Eng., pp.597-601. (in Japanese)
Goda, Y. (1985) : Random seas and design of maritime structures, University of Tokyo Press, p.323.

CHAPTER 134

LOCAL SCOUR AROUND A LARGE CIRCULAR CYLINDER DUE TO WAVE ACTION

Eiichi Saito

Research Engineer, Tech. Res. Inst., Hazama-Gumi Ltd.

Shinji Sato and Tomoya Shibayama

Associate Professor, Yokohama National University
156 Tokiwadai, Hodogaya-ku, Yokohama 240, JAPAN

1. Introduction

In the construction of large-scale maritime structures, the prediction of scouring around the foundation is essential to examine the stability of the structures. The local scour around a large circular cylinder is closely related to problems encountered in the construction of offshore artificial island and large-scale piers and is thus very important from engineering point of view.

The mechanism of local scours at the base of breakwaters as well as small circular cylinders has been investigated mainly by laboratory experiments [*e.g.* Irie and Nadaoka(1984), Bijker and Bruyn (1988)]. The mechanism of sand movement around a large circular cylinder was also investigated experimentally by Katsui and Toue(1988). However, there seems to be no model to predict bottom profile change around large-scale structures, the dimension of which is comparable to the wavelength, since the wave field around them is complicated owing to the presence of diffracted waves.

The aim of the present study is to propose a numerical model to estimate the topographical change around a large circular cylinder installed in the wave field. The validity of the model will be confirmed with laboratory experiments.

2. Experimental Procedures

Experiments were performed in a 9 x 9 m wave basin as shown in Fig. 1. A 2 x 2 m test section enclosed with a wooden frame was installed in the basin. Well-sorted sand of 0.2 mm in median diameter was filled in the test bed on which a circular cylinder of 52.2 cm in diameter was installed. The water depth at the test bed was 16.5cm. A continuous-type bottom profiler and capacitance-type

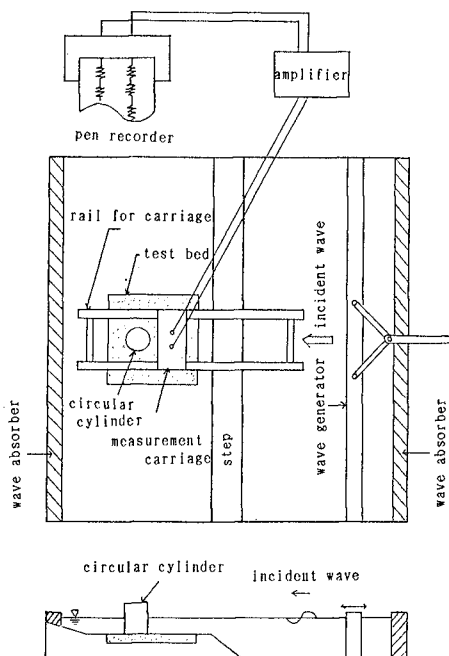


Fig. 1 Experimental Equipment

wave gages were installed on a measurement carriage as shown in Fig. 1. The wave and current field as well as bottom profile change were measured in detail for two monochromatic wave conditions listed in Table 1, where H represents incident wave height and T the wave period.

(1) Distribution of Wave Height

The distribution of wave height was measured systematically at grid points situated with a horizontal spacing of 10 cm. The measurements were carried out from 0 to 1 hour and from 4 to 6 hours upon the initiation of wave action.

(2) Test Bed Topography

The bottom profile in the test bed was measured by using a bottom profiler installed on the measurement carriage. The carriage was allowed to move in

Table 1 Experimental Conditions

case	1	2
T (sec)	0.94	0.94
H (cm)	6.7	7.9
h (cm)	16.5	16.5

parallel to the wave incidence so that the bottom profile along the measuring line was measured. The measuring line interval was set to be 5 cm near the circular cylinder and 10 cm for the other areas. The measurements were carried out at 1, 2, 4 and 6 hours after wave generation. The scouring depth along the cylinder surface was also measured.

(3) Current

The direction and the magnitude of the current developed around the cylinder were measured by tracing the movement of dye particles.

(4) Sand Movement Mechanism

The sand in front of the cylinder was replaced with sand colored with white paint so that the sand movement and suspension were easily observed.

3. Numerical Model

A numerical model was developed for the bottom topography change around a large circular cylinder. The model consisted of three submodels, that is, wave model, current model and sand transport model. In the present study, the model was developed on the assumption that the change of sand surface level was small compared with the initial water depth so that the wave and current field were not changed drastically even after bottom deformation. The present model is therefore applicable only to the sand movement in early stages, where the change in the topography around the circular cylinder was small compared to the water depth.

(1) Wave model

The wave field was evaluated by using the linear diffraction theory presented by McCamy Fuchs(1954). The velocity potential ϕ expressed in the cylindrical coordinate defined in Fig. 2 was given by

$$\phi = -\frac{igH}{2\omega} \frac{\cosh k(h+z)}{\cosh kh} \left[\sum_m \varepsilon_m i^m \left\{ J_m(kr) - \frac{J'_m(kr_0)}{H_m^{(1)}(kr_0)} H_m^{(1)}(kr) \right\} \cos m\theta \right] \quad (1)$$

where ω denotes the angular frequency, k the wave number, h the water depth, r_0 the diameter of the cylinder and $J_m(kr)$ and $H_m^{(1)}(kr)$ are the Bessel and the Hankel function of the first kind respectively. The symbol i represents the imaginary number unit and ε_m is unity for $m = 0$ and 2 for otherwise. Near-bottom velocity and the radiation stress were evaluated analytically by using the theoretical wave field.

(2) Current model

The net movement of sand is influenced by the two current velocities, that is, the depth-integrated current induced by the spatial variation of the radiation stress and the mass transport velocity in the vicinity of the bed. The mass transport velocity $\vec{U}_m = (U_{mr}, U_{m\theta})$ at the edge of the bottom boundary layer was evaluated by the following equation which was converted from the laminar

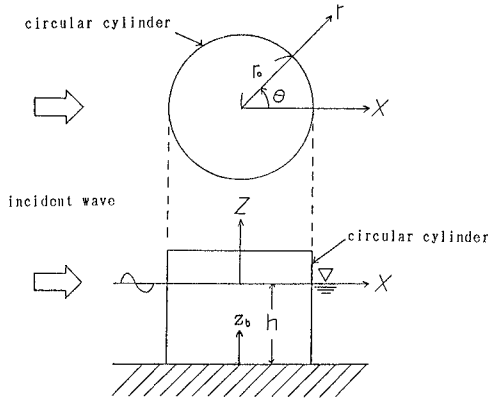


Fig. 2 Definition of Coordinates

solution for compound waves in the Cartesian coordinate presented by Carter et al. (1973) to the cylindrical coordinate (r, θ) :

$$U_{mr} = -\frac{1}{4\omega} [F_5 u_r \frac{\partial u_r^*}{\partial r} + F_6 u_\theta \frac{1}{r} (\frac{\partial u_r}{\partial \theta} - u_\theta)^* + F_7 \frac{u_r}{r} (\frac{\partial u_\theta}{\partial \theta} + u_r)^*] \quad (2)$$

$$U_{m\theta} = -\frac{1}{4\omega} [F_5 \frac{u_\theta}{r} (\frac{\partial u_\theta}{\partial \theta} + u_r)^* + F_6 u_r \frac{\partial u_\theta^*}{\partial r} + F_7 u_\theta \frac{\partial u_r^*}{\partial r}] \quad (3)$$

where u_r and u_θ represents the amplitude of the radial and the tangential components of the orbital velocity and the symbol * denotes complex conjugate. The symbols F_5 , F_6 and F_7 are complex constants such that $F_5 = -3 + 5i$, $F_6 = -1 + 2i$ and $F_7 = -2 + 3i$.

A compound wave field with a complex wave height distribution was observed around the large circular cylinder. The spatial variation of the radiation stress therefore seemed to induce a stationary current field around the cylinder. This stationary current velocity $\vec{U} = (U_r, U_\theta)$ was determined through numerical calculation using depth integrated conservation equation of mass and momentum, expressed by the cylindrical coordinates as follows:

$$\frac{\partial \bar{\zeta}}{\partial t} + \frac{1}{r} \frac{\partial}{\partial r} [r U_r (h + \bar{\zeta})] + \frac{1}{r} \frac{\partial}{\partial \theta} [U_\theta (h + \bar{\zeta})] = 0 \quad (4)$$

$$\frac{\partial U_r}{\partial t} + U_r \frac{\partial U_r}{\partial r} + \frac{U_\theta}{r} \frac{\partial U_r}{\partial \theta} + F_r - M_r + R_r + g \frac{\partial \bar{\zeta}}{\partial r} = 0 \quad (5)$$

$$\frac{\partial U_\theta}{\partial t} + U_r \frac{\partial U_\theta}{\partial r} + \frac{U_\theta}{r} \frac{\partial U_\theta}{\partial \theta} + F_\theta - M_\theta + R_\theta + \frac{g}{r} \frac{\partial \bar{\zeta}}{\partial \theta} = 0 \quad (6)$$

where $\bar{\zeta}$ denotes the mean water level and t the time. The symbols F_r and F_θ

denote the friction term given by the following equation respectively:

$$F_r = \frac{f}{\rho(h + \zeta)} U_r \quad (7)$$

$$F_\theta = \frac{f}{\rho(h + \zeta)} U_\theta \quad (8)$$

where f is the friction coefficient expressed by

$$f = \frac{2}{\pi} \rho C_f u_b \quad (9)$$

where C_f denotes the bottom friction coefficient, u_b the orbital velocity amplitude near the bottom and ρ the density of fluid.

Terms M_r and M_θ represent lateral diffusion expressed by

$$M_r = \frac{1}{r} \frac{\partial}{\partial r} (\varepsilon r \frac{\partial U_r}{\partial r}) + \frac{1}{r^2} (\varepsilon \frac{\partial^2 U_r}{\partial \theta^2}) \quad (10)$$

$$M_\theta = \frac{1}{r} \frac{\partial}{\partial r} (\varepsilon r \frac{\partial U_\theta}{\partial r}) + \frac{1}{r^2} (\varepsilon \frac{\partial^2 U_\theta}{\partial \theta^2}) \quad (11)$$

where ε denotes the diffusion coefficient. The value of ε was assumed to be $100 \text{ cm}^2/\text{s}$ in the present study.

The symbols R_r and R_θ represent the gradient of radiation stress expressed by

$$R_r = \frac{1}{\rho(h + \zeta)} \left(\frac{\partial S_{rr}}{\partial r} + \frac{1}{r} \frac{\partial S_{r\theta}}{\partial \theta} \right) \quad (12)$$

$$R_\theta = \frac{1}{\rho(h + \zeta)} \left(\frac{\partial S_{\theta r}}{\partial r} + \frac{1}{r} \frac{\partial S_{\theta\theta}}{\partial \theta} \right) \quad (13)$$

where S_{rr} , $S_{\theta\theta}$, $S_{r\theta}$ and $S_{\theta r}$ represent components of the radiation stress tensor.

(3) Sand transport model

The sand transport rate was modeled in terms of the bottom shear stress and near-bottom current velocity. The Shields parameter ψ_m was expressed by

$$\psi_m = \frac{1}{2} \frac{f_w u_b^2}{sgd} \quad (14)$$

where f_w denotes the friction coefficient proposed by Jonsson (1966), s ($=1.65$) the specific gravity of sand in water and d the diameter of sand particle. Water particles near the bottom move in general in elliptic orbits under compound wave field and there are many unknown factors involved in the estimation of the friction factor. The friction factor was estimated in the present study by using maximum wave orbital velocity.

Using the mass transport velocity \vec{U}_m , stationary current velocity \vec{U} and the Shields parameter ψ_m , the volumetric net sand transport rate \vec{q} per unit width was assumed to be estimated by the following equation:

$$\vec{q} = A(\psi_m - \psi_c)(\vec{U}_m + \alpha\vec{U})d\frac{1}{1 - \lambda_v} \quad (15)$$

where ψ_c represents the critical Shields parameter for the general movement of sand particles, λ_v the void ratio of sediment and the symbols A and α denote non-dimensional coefficients. The coefficient α is a parameter which represents the ratio of the contribution to \vec{q} of \vec{U} to that of \vec{U}_m . The mass transport velocity \vec{U}_m represents the steady drift velocity at the edge of the bottom boundary layer while the stationary current velocity \vec{U} is depth-integrated velocity calculated assuming that the velocity is uniform over entire water depth. In reality, the current profile is not uniform and therefore the velocity near the bottom is considered to be smaller than that of the averaged velocity. It is thus considered that the influence on the sand movement by the mass transport is greater than that of the stationary current and therefore the value of α is expected to be smaller than unity.

The net sand transport rate was considered to be also affected by local sea bed gradient. The net sand transport rate \vec{Q} was expressed by the following equation by introducing the influence of the sea bed gradient in the same way as proposed by Watanabe et al.(1986):

$$\vec{Q} = \vec{q} - \epsilon_s |\vec{q}| \nabla z_b \quad (16)$$

where z_b denotes the bed level and ϵ_s , a non-dimensional coefficient.

The change of bottom topography was calculated by using the mass conservation equation of the sediment.

$$\frac{\partial z_b}{\partial t} = -\nabla \vec{Q} \quad (17)$$

The numerical calculation was carried out by using a finite difference method with a calculation grid as shown in Fig. 3. Every derivative in the governing equations was replaced with a central difference in the computation.

4. Results

(1) Wave Field

Figure 4 shows the distribution of relative wave height which was the ratio of local wave height to the incident wave height. Figure 4 (a) was measured from 0 to 1 hour after the initiation of wave action and Fig. 4(b) from 4 to 6 hours. The wave field by the linear diffraction theory is shown in Fig. 4(c). No great difference is noticed in Fig.4 (a) and Fig.4 (b), which means that no great

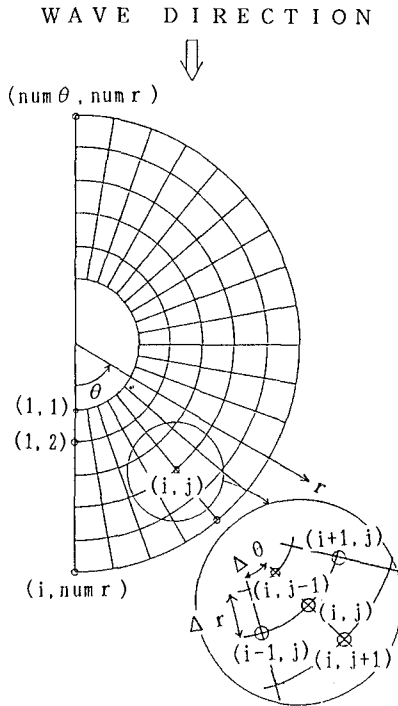


Fig. 3 Calculation Grid

variation in the wave field was developed even when the bed topography varies with time. This implies that the assumption made in the numerical models was almost completely satisfied for the condition of present experiments. The overall agreement between the measurement and the theory supports the validity of the wave model.

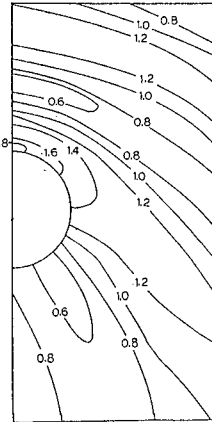
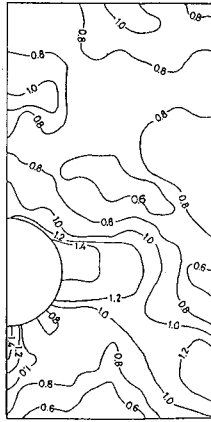
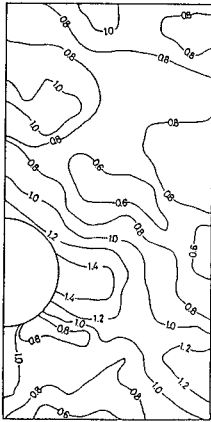
(2) Current Field

Since the current field around the circular cylinder was very complicated, it was very difficult to quantitatively measure the current velocity by tracing injected dye. However, it was observed that there existed a stationary current field as shown in Fig. 5(a). In Fig. 5(a), the large arrow represents the current direction and the arrow given by the continuous line represents the displacement of water particles near the bottom due to wave orbital motion. Figure 5(b) shows the computation of the mass transport velocity and Fig. 5(c) gives the computation of the stationary current velocity. According to these figures, the calculated stationary current velocities agree well with the observed velocity field.

WAVE DIRECTION



CASE 1	
H	= 6.7
T	= 0.94
h	= 16.5



(a) Measured (from 0 to 1 hour after wave action) (b) Measured (from 4 to 6 hours after wave action) (c) Calculation

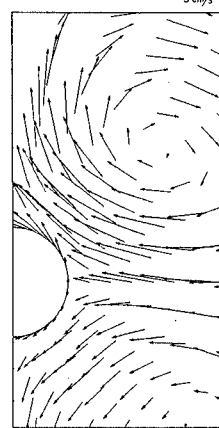
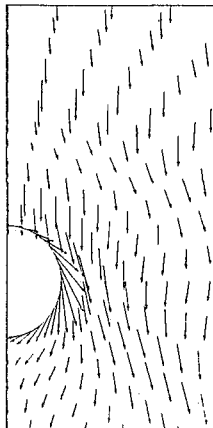
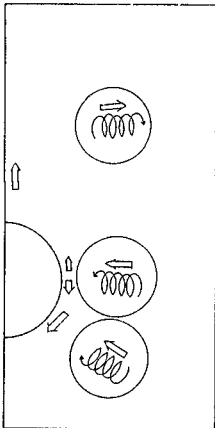
Fig. 4 Distribution of Wave Height

WAVE DIRECTION



H	= 7.9 (m)
T	= 0.94 (s)
h	= 16.5 (cm)

5 cm/s



(a) Measured

(b) Distribution of computed mass transport velocity

(c) Distribution of computed stationary current

Fig. 5 Distribution of Current (Case 2, Waves are incident from the top.)

(3) Test Section Topography

Figure 6 shows a comparison of the calculated bottom topography with the measurement. The hatched areas in the figure indicate the scoured area. Since it took approximately 4 hours for bottom topography to reach equilibrium for the condition shown in this figure, the numerical computation were carried out for 4 hours. The coefficient A was set at 0.07, ϵ_s at 0.03 and the critical Shields parameter ψ_c at 0.06. Figure 6 (a) shows the measurement, Fig. 6(b) the calculation assuming that α be unity and Fig. 6(c) the calculation when α is 0.2.

Since the influence of the stationary current is overestimated in Fig. 6(b), the calculation shows a considerably different topographical variation. Compared Fig. 6(b) and (c) with Fig. 6(a), we can conclude that the numerical model can predict the local scour pattern when α was fixed at 0.2. However, some discrepancies are noticed especially in the area just in front of the circular cylinder. The reasons for the discrepancy will be discussed in the below.

Firstly, there seems to be a problem in the estimation of the Shields parameter. The wave field around the circular cylinder is so complicated that water particles near the bottom move in two-dimensional orbits shaped circle, ellipse and straight line. Therefore, there seems to be inadequacy in estimating the Shields parameter ψ_m and critical Shields parameter ψ_c in an analogy to one dimensional oscillatory flow.

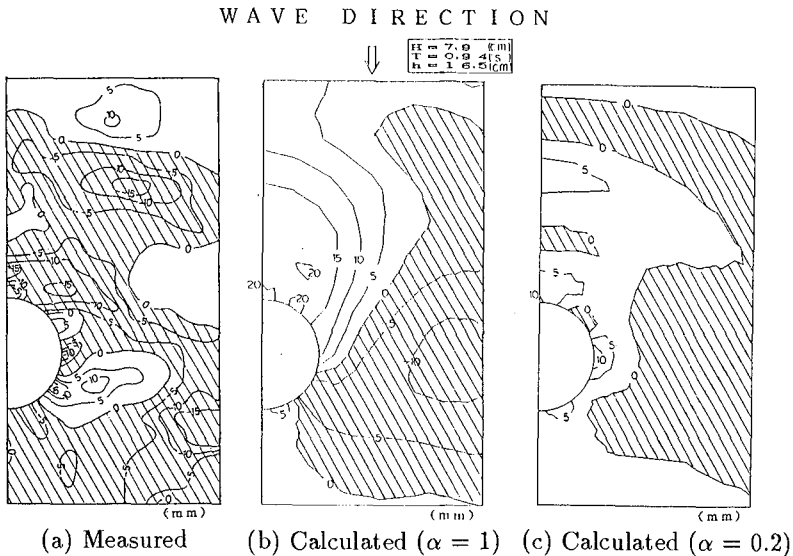


Fig. 6 Bottom Topographies (Case 2, 4 hours after wave action)

Second reason for the discrepancy is due to the use of the linear wave theory. The effect of wave asymmetry was not involved in the model since the near-bottom velocity was estimated by using the linear theory. Remarkable discrepancy is noticed just in front of the cylinder where standing waves were formed. According to Irie and Nadaoka(1984), which investigated the sea bed deformation in front of a breakwater, the direction of sand movement under standing waves was determined by the mass transport velocity and the asymmetry in near-bottom velocity variation. Waves observed in the experiments were relatively high so that the nonlinearity of wave is another factor which should be involved in the model.

5. Concluding remarks

Laboratory experiments were performed in a wave basin to reproduce the local sea bed scour around large-scale maritime structures. Experiments suggested that the mass transport velocity and wave-induced steady currents were essential in modeling sand transport. Based on experimental observations, a numerical model was presented for the local scour around a large circular cylinder. The applicability of the model was confirmed with experiments. Although some discrepancies are still present between experiments and computation, the model seems to provide a basic framework for the local scour around large-scale structures. Future studies are expected on the three-dimensional boundary layer flow as well as on the wave nonlinearity.

6. References

- Bijker, E. W. and C. A. de Bruyn (1988): Erosion around a pile due to current and breaking waves, Proc. 21st ICCE, pp. 1368-1381.
- Carter, T. G., P. L. F. Liu and C. C. Mei(1973): Mass transport by waves and offshore sand bedforms, J. WW, ASCE, No.99, pp. 165-184.
- Irie, I. and K. Nadaoka (1984): Laboratory reproduction of seabed scour in front of breakwaters, Proc. 19th ICCE, pp. 1715-1731.
- Jonsson, I. G. (1966): Wave boundary layers and friction factors, Proc. 10th ICCE, pp. 127-148.
- Katsui, H. and T. Toue (1988): Inception of sand motion around a large obstacle, Proc. 21st ICCE, pp. 1280-1294.
- McCamy, R. C. and R. A. Fuchs (1954): Wave forces on piles, B.E.B. Tech. Memo., No. 69.
- Watanabe, A., K. Maruyama, T. Shimizu and T. Sakakiyama (1986): Numerical prediction model of three-dimensional beach deformation around a structure, Coastal Eng. in Japan, Vol. 29, pp. 179-194.

CHAPTER 135

Stability of Dolosse with Different Waist Thicknesses for Irregular Waves

A H Holtzhausen¹ and J A Zwamborn²

Abstract

Model tests were done to investigate the effect of waist thickness on the stability of dolosse under irregular wave attack. A comprehensive test programme resulted in a better understanding of dolos behaviour under a wide range of different conditions.

Irregular waves with Jonswap and Pierson-Moskowitz spectra were generated using a total of four different peak wave periods. Dolosse with five different waist ratios were tested. All the dolosse had a mass of about 80 g and were placed at a "normal" packing density of $\phi = 1,00$. Tests were done on three different slopes namely 1:1,33, 1:1,5 and 1:2.

The test results showed that the stability of dolosse decreases as the waist ratio is increased. On average, K_D -values for 2 per cent displacement of dolosse with waist ratios of 0,36 0,38, 0,40 and 0,43 were approximately 22, 51, 49 and 69 per cent respectively smaller than the K_D -value of dolosse with a waist ratio of 0,33.

It was found that irregular waves cause more damage than regular waves. In the 2 per cent displacement range, regular waves ($T=1,75$ s) with wave height H , cause the same degree of damage to dolosse with waist ratios of

1 Research Engineer and 2 Programme Manager, Maritime and Hydraulic Structures, Division of Earth, Marine and Atmospheric Science and Technology, CSIR, P O Box 320, Stellenbosch, 7600, South Africa.

0,33, 0,38 and 0,43 as waves with a Jonswap spectrum ($T_p=1,75$ s) with wave heights $H_{mo} \approx 0,9 H$, $H_{mo} \approx 0,8 H$ and $H_{mo} \approx 0,75 H$ respectively. It was also found that the stability factor obtained with the Pierson-Moskowitz Spectrum ($T_p=1,75$ s) is on the average 16 per cent lower than that obtained with the Jonswap Spectrum.

There was a noticeable decrease in stability for shorter wave periods and the shortest wave period ($\xi \approx 3$) produced the lowest stability values.

Dolos stability appeared to decrease as the slope was increased from 1:2 to 1:1,33. This was more pronounced with the $r = 0,33$ dolosse than with the $r = 0,38$ dolosse. The difference in behaviour of these units can be ascribed to differences in their interlocking characteristics.

Introduction

A previous report on the effect of waist thickness on the stability of dolosse (Scholtz and Zwamborn, 1983) contained the results of model tests done with regular waves.

In that report, the results of tests with three different waist-to-height ratios, namely, 0,33, 0,38 and 0,43 were presented. Only regular waves which were produced by a translatory wave board were used. The wave period was kept constant at 1,75 s. The results showed a marked decrease in stability, especially when the waist-to-height ratio was increased to above 0,38.

Although the increased waist-to-height ratio showed a general decrease in stability, it was considered necessary to also test with units having waist-to-height ratios between 0,33 and 0,38 and between 0,38 and 0,43 to confirm this trend. It was also decided to use more realistic irregular waves instead of regular waves for these additional tests.

In addition, the effects of wave period and armour slope on dolos stability were tested to obtain a more comprehensive picture of dolos stability.

Description of Tests

Model layout and Dolos Characteristics

The tests were done in the 127 m long (effective length), 3 m wide and 1,1 m deep wind-wave flume in Stellenbosch.

A total of 538 dolosse were placed in each $750 \times 750 \text{ mm}^2$ test area. Additional 80 g dolosse were placed above and below the 'test area' as shown in Figure 1, but these were not taken into account in assessing damage.

The underlayer consisted of 16,5 g selected stone and was 43 mm thick. The breakwater core was built of loose bricks covered with an approximately 200 mm thick layer of 1 to 5 g gravel.

Test Wave Conditions and Measurements

Waves were generated by Seasim irregular wavemakers placed near to the one end of the flume in 1,0 m deep water. The wavemaker is equipped with a wave absorption control unit which makes it possible to absorb reflections from the breakwater structure, thus minimizing unwanted re-reflections off the wavemaker paddles.

The following wave conditions were used for the tests: Jonswap spectrum with T_p -values of 1,25, 1,5, 1,75 and 2,0 s and Pierson-Moskowitz spectrum with $T_p = 1,75 \text{ s}$.

Waves were measured by means of twin-wire resistance type probes coupled to the CSIR's model hall data acquisition system.

Three probes were positioned in each of the three channels at distances of 5,55, 5,80 and 6,20 m from the model slope. These three sets of three probes each were used to separate the incident from the reflected spectra. A three-point method using a least squares technique for decomposing the measured spectra from three known probe positions, developed by Mansard and Funke (1980), was used.

The wave data calculated from the recordings made during the actual tests at the three probes in each channel (9 probes altogether) were used to calculate the mean incident wave height for each test.

Test Procedures

After the underlayer stones had been smoothed out, the test area was profiled using the standard sounding technique on a 50 mm grid (Zwamborn, 1980). The dolosse were then placed in one operation, from the bottom upwards, and the surface was profiled on the same grid as the underlayer. The profiling of the underlayer

grid as the underlayer. The profiling of the underlayer and the dolosse surface was done for a number of tests only. The mean difference between the two soundings provided the average layer thickness, $t_{n=2}$ while the 'fictitious' porosity, P_f , was calculated using the following two equations:

$$t_n = r_n V^{1/3}$$

$$\text{and } \phi_n = n C_n (1 - P_f/100)$$

where

t = layer thickness

n = number of layers

$r_n = n C_n$ = 'relative' armour thickness

C_n = shape factor

$$= \phi_n/n (1 - P_f/100)$$

P_f = 'fictitious' porosity

Table 1 shows the average values of P_f , and $C_{n=2}$ that were determined for dolosse of five different waist ratios (r).

Waist ratio	$r=0,33$	$r=0,36$	$r=0,38$	$r=0,40$	$r=0,43$
P_f (%)	54,9	52,7	50,5	49,3	47,0
$C_{n=2}$	1,18	1,09	1,05	1,03	1,01

Table 1. Measured values of P_f (%) and $C_{n=2}$

A test series consisted of 60 minutes of wave action for each wave height starting from the smallest wave height and increasing the wave height in steps of about 20 mm until failure occurred or until the biggest wave was reached (normally about 5 to 8 steps).

The return period (55 to 80 minutes) of the input wave sequence used was mostly longer than the actual test period (60 minutes) used, with the result that the wave conditions varied throughout a test. All the repeat tests were started at the same position in the wave sequence, therefore the same section of the wave sequence was used for the different tests. Three 1,8 to 2,9 minute-long wave recordings were made in each test channel during each one-hour test.

Displacement of units were recorded by visual observation after each 60 minute test. Photographs were also taken at the start of a test series and after each 60 minute test. Rocking movements were recorded by

A test series was repeated from 3 to 8 times using the same wave sequence. The sublayer and the dolos cover were replaced after each test series.

Dolosse of different waist-to-height ratios were tested side by side in the flume. To eliminate the effect of small differences in wave conditions in the three channels, the positions of the test dolosse were alternated in the three channels.

Damage Criteria

In the analysis of the test results, the following damage criteria were used:

- (1) displacement, movement of at least h
- (2) continuous rocking or full roll-over (no displacement)
- (3) intermittent rocking (about two-thirds) of the time
- (4) occasional rocking (about one-third of the time)

At least three repeat tests were done for each test condition and the average damage was obtained for the different wave heights from these data.

Test Results and Interpretation

Effect of Irregular Waves

A comparison of the results obtained with regular waves and the results obtained with irregular waves are shown in Figure 2.

The results indicate that dolosse are less stable with irregular waves than with regular waves of height H_{mo} . For the $r = 0,33$, $r = 0,38$ and $r = 0,43$ dolosse, it is found that in the 2 per cent displacement range, regular waves with wave height H cause the same degree of damage as irregular waves with $H_{mo} \approx 0,9 H$, $H_{mo} \approx 0,8 H$ and $H_{mo} \approx 0,75 H$.

Ouellet (1972) concluded from his model test results that "... the use of the significant wave height, $H_{1/3}$ for the design wave height of a rubble-mound breakwater is comparable to a constant periodic wave height ...", which contradicts the above results.

Brorsen *et al.* (1974) concluded from their model test results that irregular waves of H_s cause the same degree of damage as regular waves with the height $H \approx 0,8 H_s$. After checking the results presented by Brorsen, however, it was found that $H_s \approx 0,8 H$ and not

$H \approx 0,8 H_s$ as given in the paper (the same error is carried through in Burcharth *et al.* (1986)). Thus, after making this correction, these results are similar to the above ones.

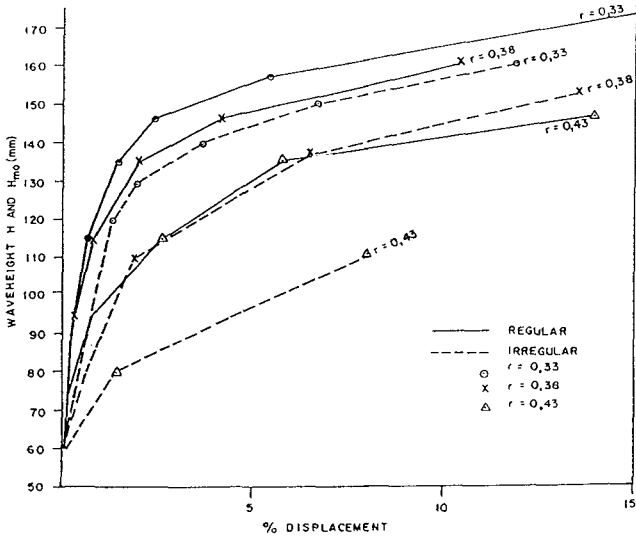


Figure 2. Irregular versus Regular Wave Results for Different Waist Ratios

Effect of Waist-to-Height Ratio

The 'relative' stability factor was used to describe the effect of waist ratio on stability. This is defined as the K_D value for a specific waist ratio divided by the K_D value of a waist ratio of 0,33 i.e. $K_D/K_D(r=0,33)$, where K_D is the Hudson stability coefficient:

$$K_D = \frac{\gamma_s H^3}{W \Delta^3 \cot \alpha}$$

where

W = weight of dolos
 H = wave height

$$\Delta = \frac{\gamma_s}{\gamma} - 1$$

γ = specific density of water
 γ_s = specific density of dolos
 α = breakwater slope angle

Figure 3 shows the relative stability factor against waist ratio for a range of different test conditions including one condition tested by Burchart *et al.* (1986). All the results of the present tests show a very definite trend of decreasing stability with increase in waist thickness. This result is to be expected, considering the reduction of interlocking capability and decrease in porosity (Table 1) for the thicker-waist dolosse.

Surprisingly, the results of Burcharth show no clear influence of waist ratio on stability. Figure 3 shows that Burcharth's results are rather scattered and follow no clear trend with change in waist thickness. The reason for this is probably that the units tested were rather small (30,7 g). Also, the packing density was increased with increasing waist ratios, therefore variation in test results can not be attributed to waist ratio only.

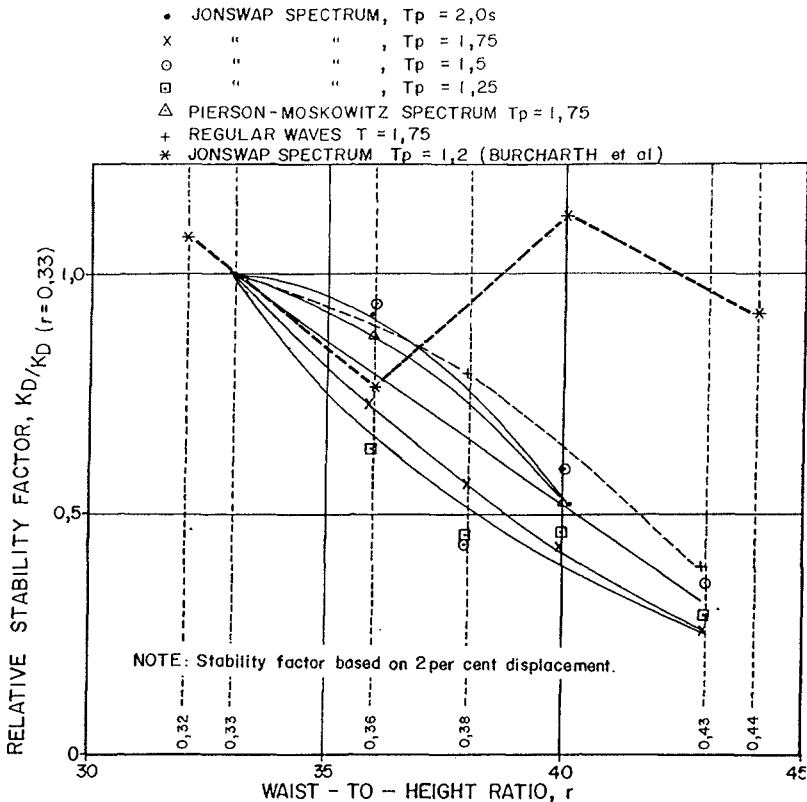


Figure 3. Effect of Waist Ratio on Stability

Effect of Wave-period and Wave Spectrum

The effect of wave period and spectrum shape on stability is shown in Figure 4. There is a noticeable decrease in stability with shorter wave periods except for $T_p = 1,5$ s when K_D is about equal to that for $T_p = 1,75$ s with $r = 0,36$, $r = 0,40$ and $r = 0,43$ dolosse.

- JONSWAP SPECTRUM, $T_p = 2,0$ s
- X JONSWAP SPECTRUM, $T_p = 1,75$ s
- JONSWAP SPECTRUM, $T_p = 1,5$ s
- △ JONSWAP SPECTRUM, $T_p = 1,25$ s
- PIERSON - MOSKOWITZ, $T_p = 1,75$ s
- ▽ REGULAR WAVE, $T = 1,75$ s

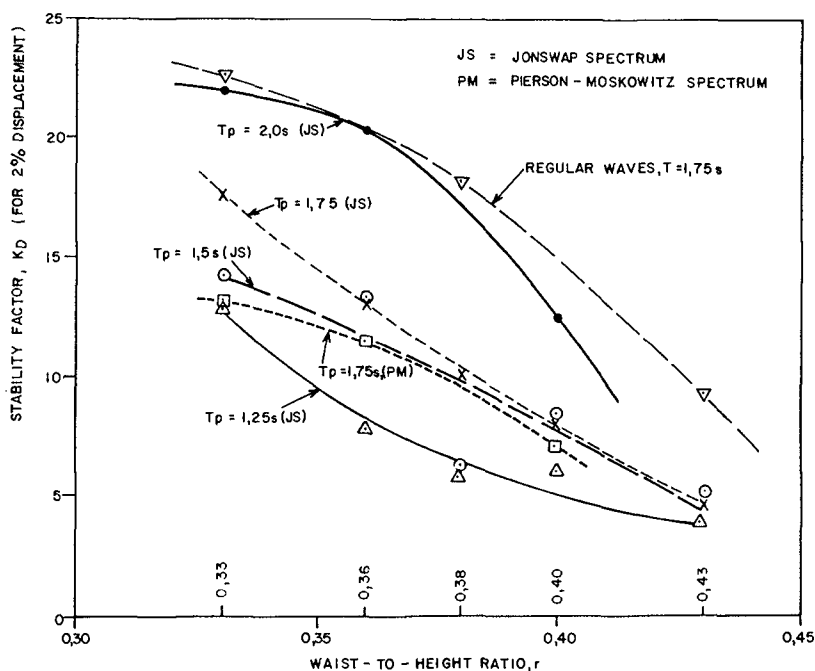


Figure 4. Effect of Wave Period and Spectrum Shape on Stability

For a displacement of 2 per cent for dolosse with $r = 0,33$; $r = 0,36$ and $r = 0,40$ respectively, waves with a Jonswap spectrum were approximately 9 per cent, 6 per cent and 4 per cent larger than waves with a Pierson-Moskowitz spectrum. Therefore the average stability factor obtained with the Pierson-Moskowitz Spectrum, $T_p = 1,75$ s is 16 per cent lower than that obtained with the Jonswap Spectrum, $T_p = 1,75$ s.

Effect of Armour Slope

For comparing the stability of units on different slopes, the stability number $N_s = H_s / (\Delta(W/\gamma_s)^{1/3})$ which equals $(K_D \cot \alpha)^{1/3}$, was used since (unlike K_D) it gives a direct indication of armour weight independent of the slope angle. Another important aspect of stability comparisons between different slopes, is the definition of wave attack. Comparison should be done when the destabilising forces produced by waves on different slopes are the same. Günbak (1979) showed that the Iribarren number $\xi = \tan \alpha / (H/L_0)^{1/2}$ may be used to describe the wave attack on a rubble mound structure. In this formula α is the slope angle, H is the wave height and L_0 is the deep water wave-length.

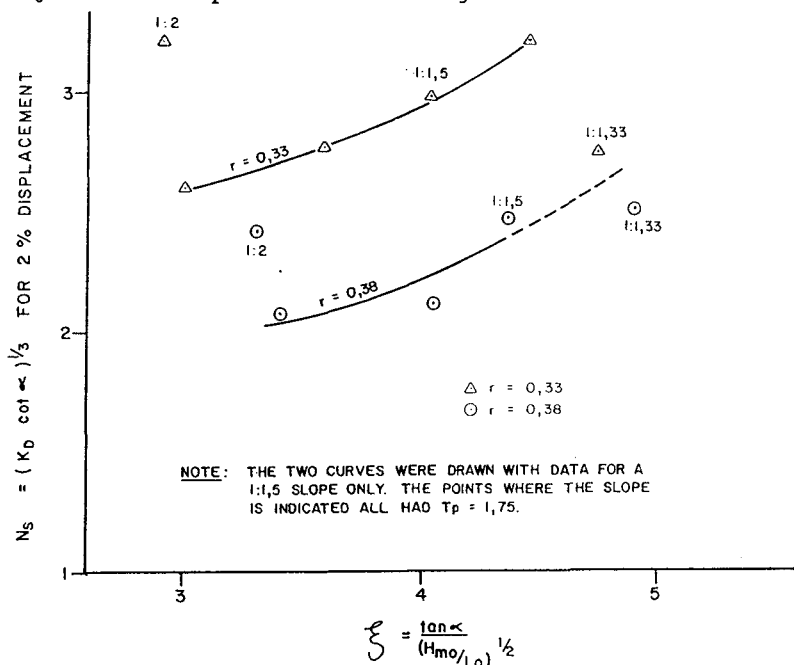


Figure 5. Effect of Armour Slope on Stability

Figure 5 shows the stability (defined by N_s) against the wave attack (defined by ξ) for three different slopes for dolosse with $r = 0,33$ and $r = 0,38$. For calculating ξ , the wave height was taken as H_{m0} just in front of the start of the dolos slope and L_0 was calculated as: $L_0 = (g/2\pi) T_p^2$ where T_p is the peak wave period. The 1:2 and 1:1,33 slopes were tested with

$T_p = 1,75$ s while the 1:1,5 slope was tested with four different peak wave periods.

From Figure 5 it is clear that the stability decreases as the slope is increased from 1:2 to 1:1,33 for both types of dolosse. However, this comparison was done at only one wave period and can therefore not be assumed to apply in general. The decrease in stability was more pronounced for the $r = 0,33$ dolosse than for the $r = 0,38$ dolosse. This seems to indicate that thicker units have better stability (for low displacement values) than more slender units on steep slopes. A possible explanation for this is that steep slopes cause the thicker units to pack close enough to utilize most of their interlocking capacity, while the slender units (with their higher porosity) require some initial settlement before optimum interlocking is achieved.

Design Curves

Based on the present test results, the relationships between the stability factor and the Iribarren number are as shown in Figures 6 and 7. For the range of Iribarren numbers used in the present tests (ξ approximately 3 to 5) the most critical wave conditions for the stability of dolosse have Iribarren numbers of approximately 3.

For the $r = 0,38$ dolosse all the data points (including the 1:1,33 and 1:2,0 slopes) fitted the design curve reasonably well. If the data points for the 1:1,33 and 1:2,0 slopes are included as data for the $r = 0,33$ dolosse, a very bad fit is achieved. These two data points were therefore excluded for the design curve of the $r = 0,33$ dolosse, and this curve is therefore strictly valid only for an armour slope of 1:1,5.

It is clear from the wide spread of data points in Figures 6 and 7 that the two parameters, K_0 and ξ , do not fully describe the stability of dolosse under the various test conditions. However, these design curves can be used as a guide for a first design using Figure 6 for high quality strength-improved dolos projects while Figure 7 should be used for lower quality projects.

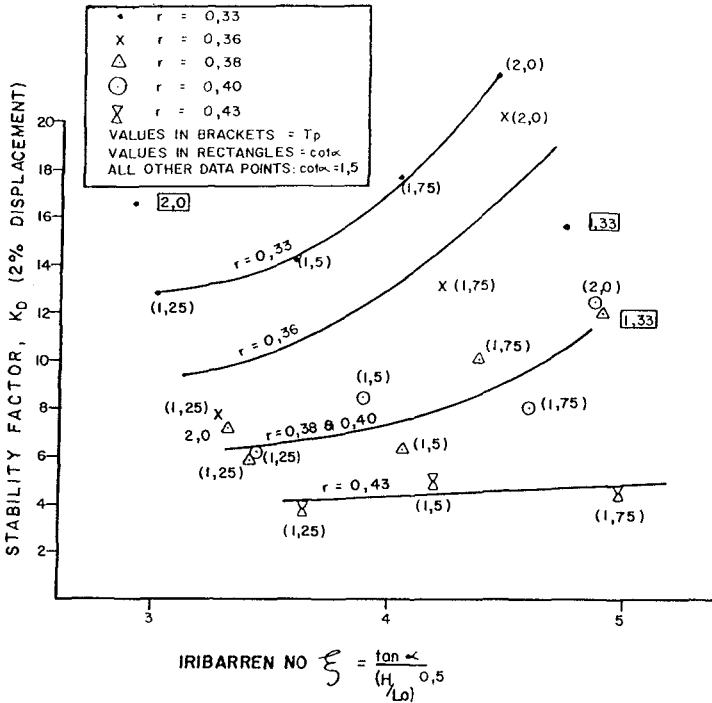


Figure 6. Design Curve for 2 per cent Displacement

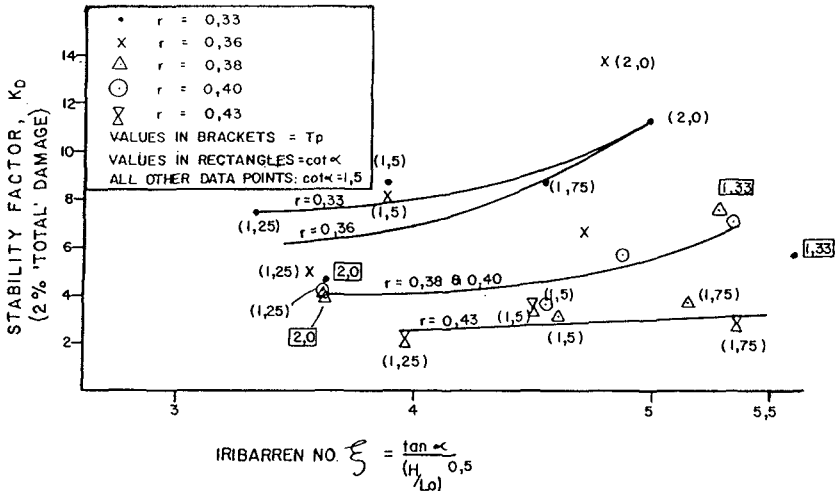


Figure 7. Design Curve for 2 per cent 'Total Damage' (displacement + continuous rocking + intermittent rocking)

Conclusions

Test results showed that the stability of dolosse decreases as the waist-to-height ratio increases. The results also showed that, for 2 per cent displacement, there is a noticeable decrease in stability with shorter wave periods down to $\xi \approx 3$ (minimum ξ value of tests).

It was also found that dolosse are on average 16 per cent less stable with Pierson-Moskowitz Spectra waves than with Jonswap Spectra waves of the same peak period.

It can further be concluded from the test results that irregular waves with a significant wave height equal to the wave height of regular waves, cause significantly more damage than the regular waves. The stability factors for dolosse with $r = 0,33$, $r = 0,38$ and $r = 0,43$, determined with irregular waves are respectively 23, 45 and 55 per cent smaller than the stability factors determined for regular waves. Although regular waves can be used to determine the relative stability of different types of dolos armouring, it is better to use irregular waves in tests where the stability of the armouring for a specific project is to be determined. If only regular waves can be used for these tests, allowance must be made for the expected greater damage by using a regular wave height, $H = 1,1 H_{m0}$ for dolosse with $r = 0,33$, $H = 1,2 H_{m0}$ for dolosse with $r = 0,38$, and $H = 1,3 H_{m0}$ for dolosse with $r = 0,43$.

Tests with different breakwater slopes showed a decrease in stability as the slope was increased from 1:2 to 1:1,33. This decrease was less pronounced for dolosse with $r = 0,38$ than for the $r = 0,33$ dolosse.

Design curves are included in Figures 6 and 7 which show the dolos stability as a function of the Iribarren number and the waist ratio for two different damage levels. The data points in these figures show considerable scatter, indicating that these parameters do not fully describe the stability of the dolos armouring, particularly with regard to armour slope. However, the curves can be used as a guide for a preliminary design, taking into account the above limitations.

References

- BRORSEN, M, BURCHARTH, H F and LARSEN, T (1974). Stability of dolos slopes. Proceedings of 14th ICCE. Copenhagen.
- BURCHARTH, H F and BREJNEGAARD-NIELSEN, T (1986). The influence of waist thickness of dolosse on the hydraulic stability of dolosse armour. Proceedings of 20th ICCE Conference, Vol. II. Taipei, Taiwan.
- GÜNBAK, A R (1979). Rubble mound breakwaters. The Norwegian Institute of Technology. Trondheim, Norway.
- MANSARD, E P D and FUNKE, E R (1980). The measurement of incident and reflected waves in random wave experiments. Proceedings of 15th ICCE. Hawaii.
- OUELLET, Yvon (1972). Effects of irregular wave trains on rubble-mound breakwaters. Journal of the Waterways, Harbors and Coastal Engineering Division. Proceedings of the American Society of Civil Engineers.
- SCHOLTZ, D J P and ZWAMBORN, J A (1983). Effect of the waist thickness on stability of dolosse. CSIR Research Report 556. Stellenbosch.
- ZWAMBORN, J A (1980). Measuring techniques, dolos packing density and effect of relative block density. CSIR Research Report 378. Stellenbosch.
- ZWAMBORN, J A and VAN NIEKERK, M (1982). Additional model tests. Dolos packing density and effect of relative block density.

CHAPTER 136

ESTIMATION OF PEAK WAVE STRESSES IN SLENDER COMPLEX CONCRETE ARMOR UNITS

*Gary L. Howell*¹
*Hans F. Burcharth*²
*Joon P. Rhee*³

1 INTRODUCTION

Recent methods for the structural design of concrete armor units divide the forces into static loads, impact loads, and wave or pulsating loads. Physical model technology is being developed at several laboratories to measure wave loads on model armor units. While this technology represents significant progress, structural designers require a maximum stress value to design armor units. Rubble mound breakwaters are structures with both random loading and random boundary conditions, such that a single set of stress measurements cannot characterize the loading. This paper presents a method to determine a design stress for wave induced loads based on the design wave height, a designer specified exceedance probability, and a site specific parameter, k_s , which can be empirically determined from physical model measurements. The methodology was developed from analysis of many field measurements of wave loads on 38-tonne dolosse armor units at Crescent City, California.

2 PROTOTYPE MEASUREMENTS

Steel bars with strain gages were cast at the shank-fluke interface of the dolosse during construction. The bars were sized and arranged so the strains could be used to estimate the gross structural moments and torque about the shank-fluke section. Strains were sampled and converted to digital data at a 500 Hz rate and later reduced to 50 Hz. Details of the instrumentation can be found in Howell (1986).

The measurements were made during the winters of 1987 and 1988. The experimental design and examples of the prototype data are shown in Howell (1988). The dolos records during storms which occurred March 12-15, November 29-30, and December 1, 5, 6, 1987, and January 9-11, 14-16, 1988 were selected for this analysis. Low wave conditions were represented by data from December 11-14, 1987. The significant wave

¹U S Army Corps of Engineers, Coastal Engineering Research Center, Waterways Experiment Station, Vicksburg, Mississippi 39180-6199 USA

²Department of Civil Engineering, University of Aalborg, Denmark

³U S Army Corps of Engineers, Coastal Engineering Research Center, Waterways Experiment Station, Vicksburg, Mississippi 39180-6199 USA

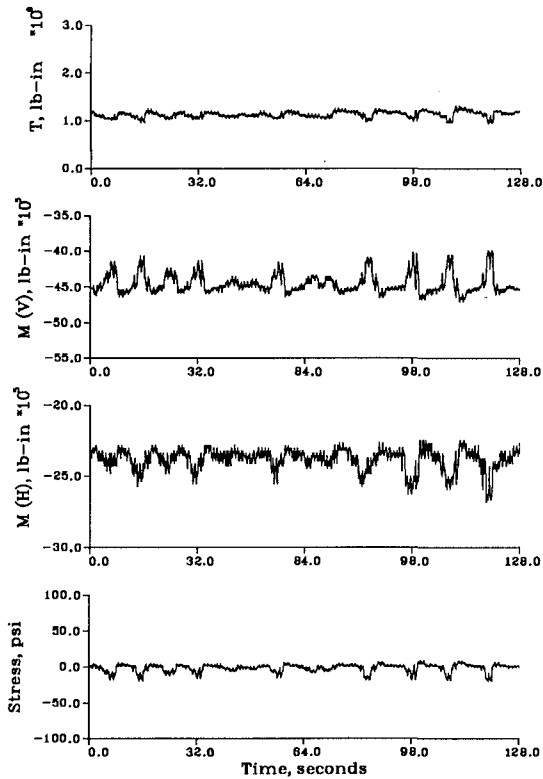


Figure 1: Time Series of Moments and Principal Stress

height for the data set ranged from 0.9 *m*. to 5.0 *m*. and the maximum wave height was 9 *m*. The water depth at the toe of the structure is 10 *m*. with a typical tidal range of 2 *m*. The structure has an average slope of 1:5. More than 1600 records of 30-minute dolosse response were analyzed from 14 dolosse. The sample dolosse were grouped on the top layer from approximately 1 unit length downslope from the mean water line to 3 unit lengths above the mean water line.

3 ANALYSIS

Define σ_1 as the principal tensile stress, at the shank-fluke interface of the dolos armor unit, which can be computed from measurements of moments and torques as shown by Burcharth and Howell (1988). For the wave induced portion of the total load, the required value for design is the maximum principal stress measured from the mean or static stress.

$$\sigma_{max} = Max|\sigma_1 - \sigma_{1,static}|$$

σ_{max} can be interpreted as the maximum tensile stress, due to waves, at any point on the surface of the shank-fluke cross-section. Figure 1 shows example time series of moments, torque and the computed σ_1 . σ_{max} is the maximum of this time series occurring in the half-hour interval. In general σ_{max} will vary over a wide range depending upon breakwater characteristics, dolos boundary conditions, and sea state. The variability due to all but breakwater characteristics was examined statistically.

Consider σ_{max} for all dolosse and all storms grouped into bins of constant $H_{1/10}$. Within each bin, the distribution of σ_{max} was found to be well described by a Rayleigh distribution using the mean σ_{max} , $\bar{\sigma}_{max}$ as the single parameter. Figure 2 shows an exceedance probability distribution plot for measured values together with the Rayleigh exceedance probability for $H_{1/10}$ in the range 3.5 to 4.5 m. Figure 3 shows the range 4.5 to 5.5 m. The distribution of maximum stress for other ranges of wave height were similarly represented by a Rayleigh distribution of $\bar{\sigma}_{max}$.

Figure 4 shows a plot of $\bar{\sigma}_{max}$ computed from measured data vs. the $H_{1/10}$ bin used for the computation. The best fit linear correlation coefficient is 0.976. The best fit linear line passing through the origin has a slope within 10% of the best fit line. Assuming a zero intercept constraint based on physics the slope is defined as k_s , the wave stress constant, such that

$$\bar{\sigma}_{max} = k_s H_{1/10}$$

Note that since both σ and H ideally scale by length, k_s should be model scale invariant. A non-dimensionalized form of k_s can be given by

$$\frac{\bar{\sigma}_{max}}{hg(\rho - \rho_w)} = \frac{k_s H_{1/10}}{h}$$

where h is the dolosse length, ρ is the dolos density, ρ_w is the density of water, and g is the acceleration of gravity.

4 Comparison to Physical Model Measurements

The results from the prototype data indicate that the wave induced stresses for an individual dolos may vary due to many factors. The variation results from the random boundary conditions and random nature of the waves. However, the empirical analysis presented above indicates that for a population of dolosse, the statistical description of the response may be well defined, at least for the case of a site specific prototype breakwater. This possibility has potential for simplifying the use of a hydraulic breakwater model to estimate wave induced stresses on armor units.

Two problems have limited the use of hydraulic models for this task. First the development and verification of a model dolos unit which accurately measures stresses at small scale has required considerable effort due to the very small strains which must be measured. Second, the best method of applying the model scale measurements to the

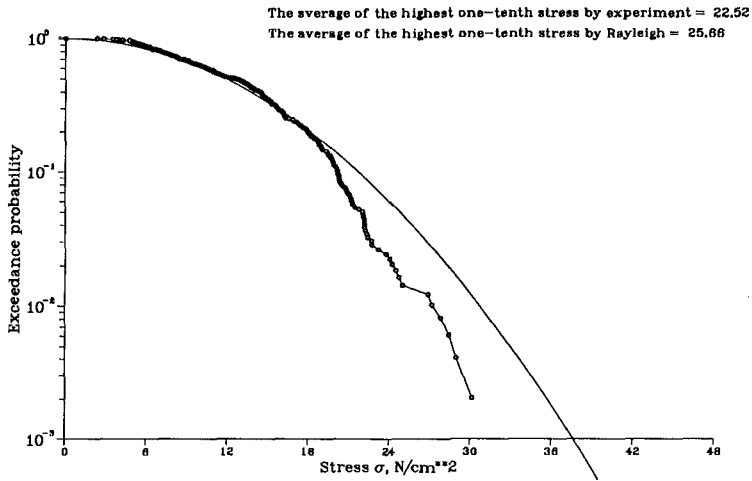


Figure 2: Cumulative Exceedance Probability of σ_{max} for $H_{1/10} = 3.5 - 4.5m$

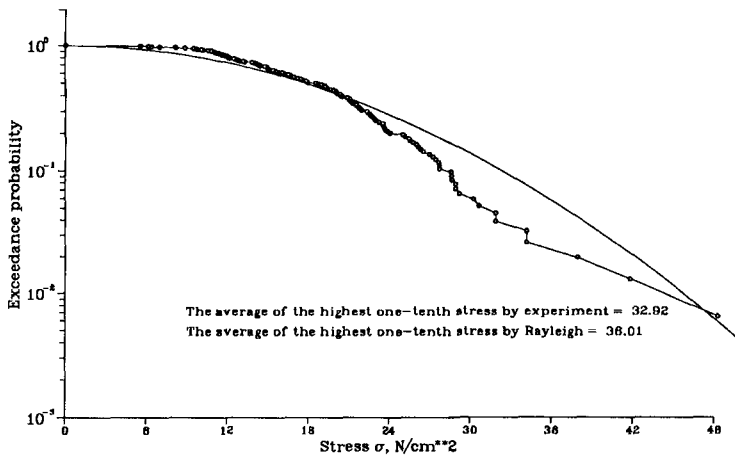


Figure 3: Cumulative Exceedance Probability of σ_{max} for $H_{1/10} = 4.5 - 5.5 m$

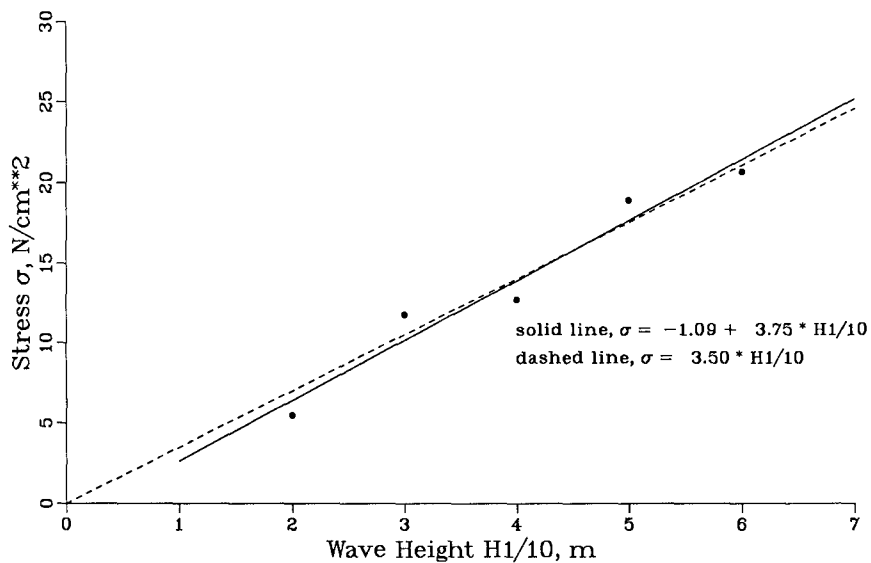


Figure 4: $\bar{\sigma}_{max}$ vs. $H_{1/10}$. The dashed line is the best line through the origin and the solid line is the best fit line.

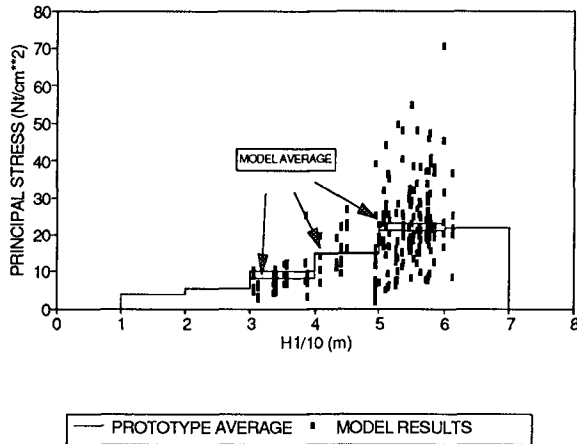


Figure 5: Scatter Plot of σ_{max} from the model test of Crescent City breakwater. The mean values for each bin are shown along with the corresponding prototype values. (Markle, 1990).

prototype has not been determined. Stresses measured for a dolos in the model, may not be applicable to units placed in different positions during prototype construction.

It was therefore proposed that intercomparison of model and prototype be made based on the empirical parameter k_s , rather than deterministic comparison of the stresses from individual units. To test the validity of this approach a physical model of the *as built* Crescent City Breakwater was constructed and tested with instrumented model dolos armor units at CERC by Markle (1990).

The model was exposed to the same storms as used for the above analysis of prototype data. Data from the model were analyzed using the same procedure as described above. Figure 5 shows a scatter plot of σ_{max} from the model along with the $\bar{\sigma}_{max}$ values from the prototype. The $\bar{\sigma}_{max}$ values from the model data exhibit good agreement with the prototype values. Figure 6 shows an exceedance probability distribution plot for measured values together with the Rayleigh exceedance probability for $H_{1/10}$ in the range 5 to 6m. It can be seen that like the prototype, the model data are well described by the Rayleigh distribution.

5 RESULT

These results suggest that a physical model can be used to measure wave induced stresses without considering boundary conditions of units in a deterministic way. Also if the linear relationship between k_s and $H_{1/10}$ is confirmed by additional tests, it may

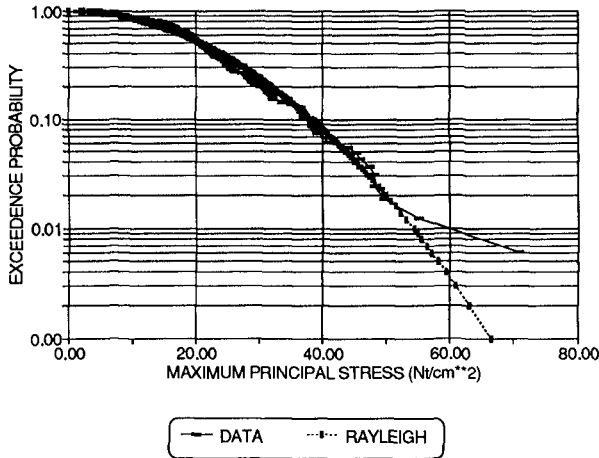


Figure 6: Cumulative Exceedance Probability of σ_{max} from the model tests for $H_{1/10} = 5 - 6 \text{ m}$. (Markle, 1990)

be possible to limit tests in the future to the minimum required to estimate a linear function with zero intercept.

If for a given breakwater model, k_s can be determined by measurements from model dolosse for a range of dolos boundary conditions and wave heights, then a σ_{max} can be determined for the wave load portion by substitution into the Rayleigh p.d.f. to obtain

$$\sigma_{max} = 1.13\sqrt{-\ln P(\sigma_{max})}k_s H_{1/10}$$

where the designer specifies $P(\sigma_{max})$ the probability of exceedance. This σ_{max} can then be combined with the static stress design value for input into the structural design process.

Acknowledgement

The work described in this paper was conducted as part of the Crescent City Prototype Dolosse Study of the Coastal Engineering Research Center, Waterways Experiment Station, US Army Corps of Engineers. Permission to publish was granted by the Chief of Engineers.

References

- Burcharth, H. F. & Howell, G. L. 1988. On Methods of Establishing Design Diagrams for Structural Integrity of Slender Complex Types of Breakwater Armour Units. *Seminaire International Entretien des Infrastructures Maritimes*, Casablanca, Morocco.
- Howell, G. L. 1986. A System for the Measurement of the Structural Response of Dolos Armour Units in the Prototype. *The Dock & Harbour Authority*, **67**, 6-10.
- Howell, G. L. 1988. Measurements of forces on dolos armor units at prototype scale. *Proc., 21st Int. Conf. Coastal Eng.*
- Markle, D.G. 1990. Crescent City Instrumented Model Dolos Study. *Stresses in Concrete Armor Units*, Proceedings of an ASCE seminar, Vicksburg Ms., ASCE.

CHAPTER 137

RESEARCH OF WAVE FORCES OF BREAKWATER IN DEEP WATER AREA

Ho-Shong Hou, Ph. D. , P.E.
Director, Transportation Engineering Dept.
Institute of Transportation
240, Tunhua North Road
Taipei, Taiwan, Rep. of China

ABSTRACT

The design of breakwater in deep water requires a reliable assessment of the forces, it will be subjected to and full understanding of the behaviour of the structure. Wave forces on a vertical wall caisson of composite breakwater vary with the configuration of the rubble mound foundation as well as the condition of incident waves. If the conditions are very unfavorable, powerful impact breaking-wave forces may act on the vertical wall caisson. It is an important subject to clarify the generation conditions of impact breaking wave forces, so that the breakwater under design would not be exposed to a very strong breaking wave force.

The present study points out on the basis of the experimental results for the typical example of slided caisson that careful attention should be paid to the possibility of the generation of impact breaking wave forces in the design of composite breakwater. The generation conditions are investigated by the two dimensional experiments on the variation of wave forces due to the configuration of rubble mound and the three-dimensional experiments on the effect incident wave angle to the breakwater. The impact breaking wave forces are easily be produced on the vertical-wall caisson, where the mound is relatively high and has an appropriately broad crest width.

If the generation of impact breaking wave forces are unavoidable owing to the breakwater configuration, provision of an appropriate wave dissipating work in front of the caisson is recommended to alleviate the method of calculation of design wave forces on the caisson covered with wave dissipating concrete blocks and the wave dissipating caisson with a permeable front wall.

In the study, problems are highlighted with respect to wave climate range that will induce breaking wave pressure, model test is conducted to measure the wave pressure and the sliding effect. Then the current formula for calculated wave pressure is

discussed. The factor of experiment considered in the test flume is depth of composite breakwater, height, width and slope of rubble mound, etc.

1. Introduction

For dealing with the construction problems of the deep water breakwater, as for the caisson-composite type breakwater, the foundation work is the problem as the breakwater goes to deeper due to the limit of operation of diver in the deep water, the pavement of mattress, the leveling of the mound, etc. will cause much problem. Since the body of caisson is larger in the deep water, constructing, tawing and replacing caisson work will be more difficult than those of shallower water part. For flow chart of deep breakwater construction, planning and design of the structure need to be further considered.

For planning aspect, the huge deep breakwater that need to be made sure it is necessary. Since (1) invest benefit: due to expensive cost of engineering fee of deep breakwater, the after construction, its benefit is not larger than the invest cost, then it is unnecessary. (2) alternative plan: due to the elongation of existing breakwater to the deeper position, the construction fee is expected much higher, therefore, to find out the alternative plan such as, to construct one shallow breakwater could be also obtained the same harbor function; or if the breakwater was not prolonged, then to enlarge and repair some wharves could be also reached the same effect, etc. (3) calm wave sheltering area: due to high cost of breakwater, it is naturally to cut down the elongation of breakwater however, the harbor basin need to be calm. Therefore it is necessary to study the relationship between the elongation of breakwater and the calm wave sheltering area of basin. The criteria of the calm basin is necessitated to determine.

2. Test Results and Analyses of Deep Breakwater of Caisson-Composite Type

Around the Taiwan coast, especially the international trade port, breakwater of the caisson-composite type is commonly used. Deep outer breakwaters of the 2nd entrance of Keelung Harbor are tested for impact pressure analyses. The typical design section of -35M deep is shown in Fig.1; while

impact pressure (Fig.2c) is about triple of the normal wave pressure, its period is about 1/7 to 1/20 sec. In addition to the breakwater of 2nd entrance of Keelung Harbor, the varying mound shape, mound height of caisson-composite breakwater are tested and analyzed for further new information.

Fig.3 and Fig.4 are many cases of test results, the results show that, the higher mound of caisson-composite breakwater ($d/h=1/3$), wave pressure increases as the wave height becomes large; therefore the mound height has obvious effect on the wave pressure. The varying transverse width of the mound also shows that wave pressure has the different degree for increasing. Since the test results indicate that the wave pressure is larger as the transverse width of mound is wider, the wave pressure is bigger as the mound height is higher.

Fig.5 shows that the impact wave pressure occurring range of deepwater breakwater has the same tendency as that of shallower depth. That is as d/h smaller (or higher mound), the occurrence of the impact pressure is very often. The case of no wave overtopping is easier to occur than that of wave overtopping. The impact pressure occurring range is indicated by the dot line of Fig.5.

3. Results and Discussion

For caisson-composite breakwater, it is designed that the armour concrete block such as dolos, hollowtripod, etc. to prevent wave acting directly toward the caisson from forming shock pressure (one form of impact pressure). By using porosity of armour concrete block to increase turbulence for dissipating wave energy therefore wave pressure should be minimized. Based on the previous test results, it is considered that in front of composite type, the covering layer of armour unit on the mound could reduce the wave pressure about 60% in the shallower water area. However, reducing of wave pressure depends on water depth, wave condition, mound height, mound slope and mound shape, etc. For the present test results (test section of -35M deep or more) show that the portion of caisson (vertical wall) is subjected to standing wave or part of breaking pattern, the cover layer of armour unit is easily happened that the wave acting on the slope forms the breaking wave and produces shock pressure (strong impact pressure) in a short time, the impact pressure is quite huge. Therefore, the placement of armour concrete unit is inefficient to the wave action and will be a negative effect;

therefore, it is suggested the design section be changed to the section as shown in Fig.6

4. Failure of Deep Water Breakwaters

Failures to deep water breakwaters have occurred over the past decade, are due to the following (main) reasons:

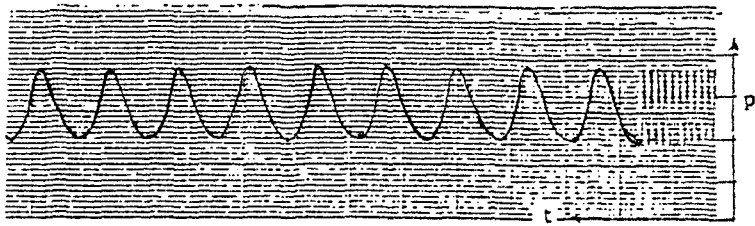
Rubble Mound Type: the increase of depth and related increase of design wave heights led to designs with very steep slopes and protected by concrete armour units of weights and sizes far in excess of previous experience. The strength of these concrete blocks appeared in many cases to be insufficient due to the high peak forces, which occur on the blocks during a storm. The blocks broke and were subsequently easily removed from the slope. The great steepness of the slopes may also have contributed to failure, since the geotechnical stability of the mound becomes critical under wave loading.

Vertical Wall Type: failures to this type of breakwater occurred mainly due to high impact forces of breaking waves at the vertical front, leading to horizontal displacements of the caissons and in some cases to geotechnical instability of the foundation and tilting. The author has been invited in many cases of breakwater failure to investigate the failure and make a design for repairing, e.g. Su Ao Harbor Breakwater and Hualian Harbor Breakwaters in the east coast of Taiwan, R.O.C.

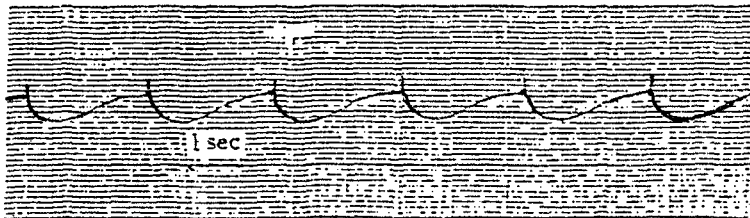
The solution to the problems mentioned above lies primarily in following the proper design procedures, as applied by Hou ('78 '80) throughout its breakwater projects. The main features of this procedure are systematic failure analysis of each design and an integral approach, including hydraulic-, geotechnical- and concrete strength aspects in a balanced way.

5. Conclusion

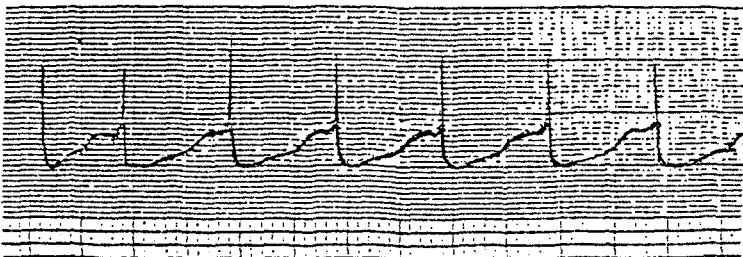
- 1) For the deep water breakwater construction, the field measurement of deep water wave, geological, oceanographic data, foundation and earthquake problem, etc. need to be further studied.
- 2) For the caisson-composite deep breakwater, the higher mound is easily to subject to occur the impact pressure, the lower mound has little such phenomena.



(a) Standing Wave Pressure Record



(b) Weak Impact Pressure Record



(c) Strong Impact Pressure Record

Fig.2 Wave Pressure Pattern

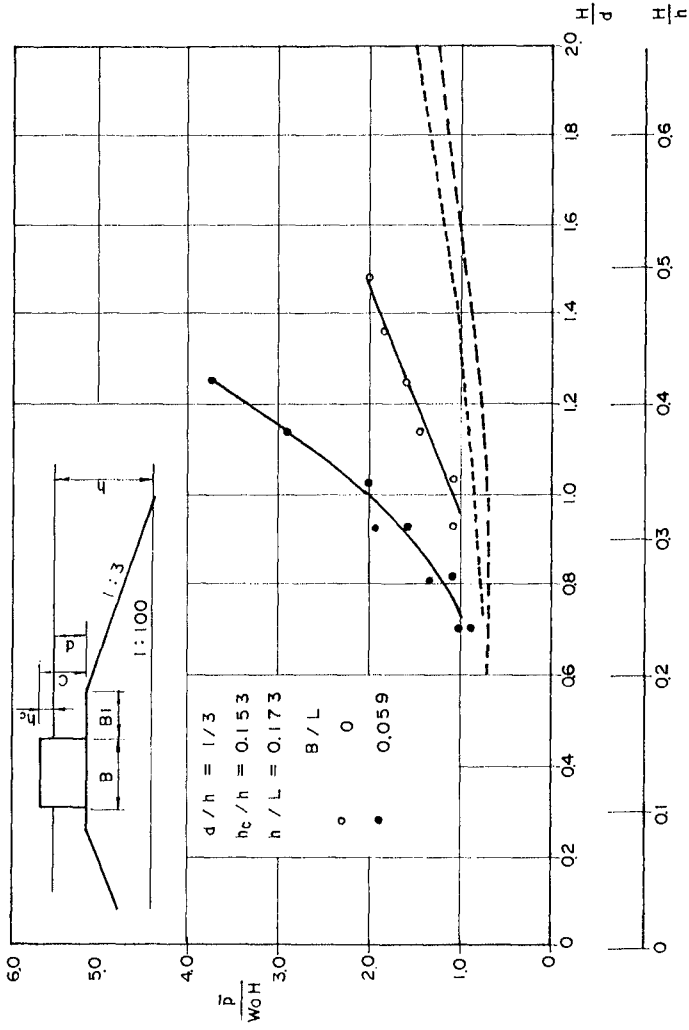


Fig. 3 Mound Shape Affects the Wave Force Diagram

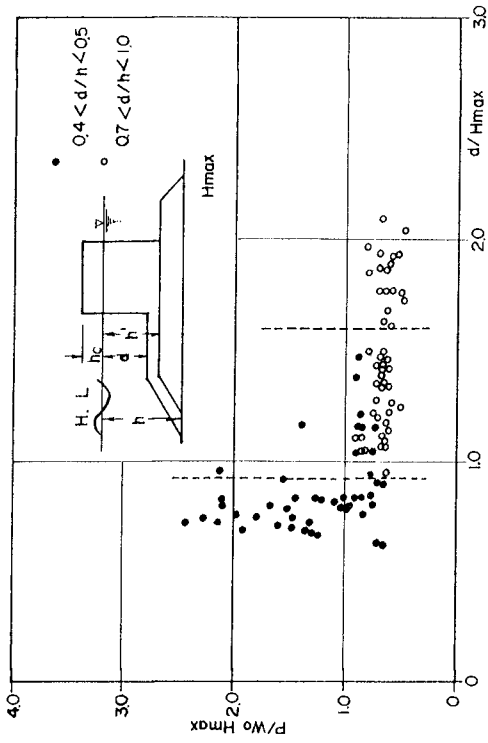


Fig.4 Mound Depth affects the Wave Force Analyses

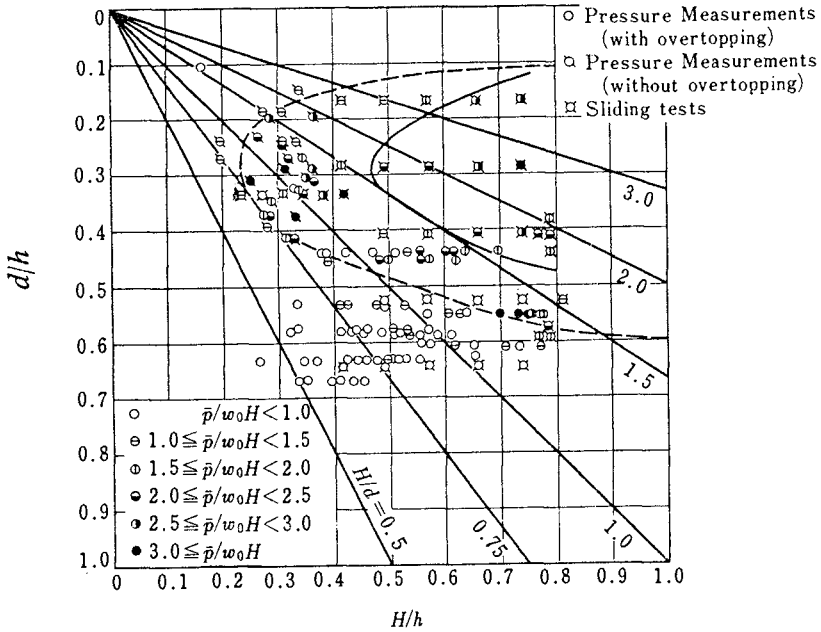


Fig.5 Possible range of the occurrence of impulsive breaking wave pressure

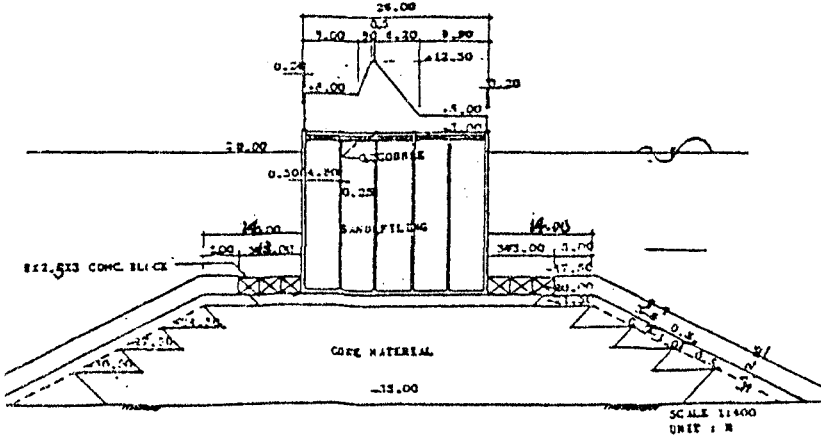


Fig.6 Modified Design Section of Deep Breakwater of 2nd Entrance of Keelung Harbor

References

- 1) "Hydraulic Model Test of Caisson-Composite Breakwater Wave Pressure Distribution of the Bah-Tsu Meng Wharf Area in the Keelung Harbor" by C.T. Kuo, H.S. Hou and C.Y. Chen, Hydraulic experiment research Center, C.E. Dept. Chung-Hsing University, Oct., 1978.
- 2) "Experiment Research of Wave Run-up, Overtopping and Stability of Seawalls around Wai-Muh San Oil Tank" by H.S. Hou, T.F. Lee, L.F. Lin and K.H. Weng, etc. NTU-ina-Tech. Rept. 110, Institute of Naval Architecture, National Taiwan University, April, 1980.
- 3) "Model Experiments of Wave Run-up and Stability of Breakwater Sections in Wai-Muh San Fishery Harbor" by H.S. Hou, T.F. Lee and C.C. Liu, NTU-INA Tech. Rept. 11, Institute of Naval Architecture, National Taiwan University, Jan., 1980.
- 4) "Experimental Research of Wave Run-up, Overtopping and Stability of Seawalls around Hsin-Tah-Power Plant" by H.S. Hou, W.S. Hwang and Y.Y. Hwang, NTU-INA-Tech. Rept. 129, Institute of Naval Architecture, National Taiwan University, June, 1981.
- 5) "Experimental Research Report of 4 Design Sections of the Temporary Quay of the Hua-Lien Harbor" by H.S. Hou, J.F. Tsai and C.C. Chung, etc. NTU-INA-Tech. Rept.155, Institute of Naval Architecture, National Taiwan University, Nov.,1982.
- 6) "Random Seas and Design of Maritime Structures" by Yoshimi Goda, University of Tokyo Press, 1985. Tokyo, Japan.
- 7) "Planning of a Coal Terminal as a Deep Water Port in Taiwan District, R.O.C" by Ho-Shong Hou, June 20-24, 1988, The 9th International Harbour Congress, Antwerp, Belgium.
- 8) "Port Engineering Development in the Deep Water Area of Taiwan District, R.O.C." by Ho-Shong Hou, Oct.24, 1989. The 7th Meeting of Chinese-Dutch Joint Business Council. Howard plaza Hotel, Taipei, Taiwan, R.O.C.

CHAPTER 138

Dynamic Revetments

John P. Ahrens¹

Abstract

The concept of a stone revetment where rock movement is expected is relatively new. For people familiar with gravel and shingle beaches, the idea is an easily accepted extension of the traditional statically stable revetment. However, for engineers familiar with classic breakwater design, the idea that a dynamic structure can provide suitable shoreline protection raises many doubts. Recent research in the Netherlands by van der Meer (1988) and colleagues has gone a long way toward answering difficult questions regarding the development of sound design criteria for dynamic revetments. This paper discusses progress in quantifying the problem and defining solutions. Laboratory model tests were conducted at the Coastal Engineering Research Center (CERC) to confirm and extend Dutch research. These tests are described and important findings presented, including a simple quantitative method to predict the amount of stone required to protect a bulkhead, i.e. critical mass. The method to protect a bulkhead appears to have more general implications which could lead to extensive application to a wide range of shoreline erosion problems. Analysis of data is continuing.

Introduction and Background

The concept of a rubble structure having a dynamic response to wave attack has been around for quite some time. Per Bruun has commented frequently about the high stability of "S" shape profiles of some very old breakwaters in Plymouth, England, and Cherbourg, France (Bruun and Johannesson, 1976). An adaption of the "S" profile is the berm breakwater concept developed by William Baird (see Baird and Hall, (1984) for a discussion of design considerations, or Hall (1987) for background information. The basic strategy is to build an extensive stone berm which can adjust and deform in response to severe wave action. A berm is effective because a large mass of rubble near the water line is capable of

¹Research Oceanographer, U.S. Army Engineer Waterways Experiment Station's Coastal Engineering Research Center, 3909 Halls Ferry Road, Vicksburg, MS 39180-6199

disrupting wave action and dissipating wave energy. Stone size may be smaller than required for traditional armor, and placement does not require special care. The advantages appear to be, berm breakwaters have less expensive construction equipment requirements, are simple to construct, and use smaller stone, which is usually less expensive than conventional heavier armor stone. However, conventional breakwaters have a smaller cross section than berm breakwaters and smaller stone does not always cost less than conventional armor stone, so a berm breakwater is not always cost effective.

The idea of a dynamic revetment seems to be of more recent origin than dynamic breakwaters. van Hijum and Pilarczyk (1982) and Pilarczyk and den Boer (1983) present data and summarize some of the Dutch experience with gravel beaches and cobble-sized revetments. Recently, research has been initiated in England on the response of shingle beaches to wave action (Powell, 1988). Recent research in the Netherlands and England is motivated by a need for fundamental understanding of shingle beaches, how they might be nourished, and if shingle beaches could be used in some situations instead of a traditional statically stable riprap revetment.

With increasing interest in both dynamic breakwaters and revetments, there has been an acknowledgement that not enough was known about the durability of stone. Considerable effort has been directed in the United Kingdom towards understanding rock durability in the marine environment under dynamic conditions, (see e.g. Allsop and Latham, 1987 and Latham and Poole, 1988).

In the United States, Johnson (1987) found that gravel beaches and dumped rubble are frequently cost effective alternatives to using sand for beach nourishment and placed stone for revetments, respectively. Johnson's findings were obtained from extensive experience on Lakes Michigan and Superior where fluctuating water levels created enormous problems for conventional shoreline protection. This experience shows dynamic revetments are not vulnerable to toe scour, overtopping, or flanking. Advantages cited by Johnson for coarse material include a long residence time and an ability to stay in the vicinity of the water line. Other advantages are similar to those noted by Baird and Hall (1984), i.e., ease of placement and lower unit cost.

Comprehensive research efforts conducted recently in the Netherlands resulted in detailed and quantitative findings on dynamic stability (van der Meer, 1988). Findings are based on a very extensive amount of laboratory work and data analysis. One problem in applying van der Meer's results is that his tests were conducted in relatively deep water, and most problems in the United States involving shoreline erosion and protection are in shallow water. One goal of this study is to utilize the Dutch research to the greatest possible extent to help design dynamic revetments.

This paper provides information on laboratory tests conducted to gain familiarity with the concept of dynamic revetments and their use in shallow water. Specifically, this study was initiated to determine how dumped stone might protect a vertical bulkhead.

Test Setup, Conditions and Procedures

The model tests were conducted in CERC's 0.46x0.91x45.73 meter long glass walled wave tank (Figure 1), using an undistorted Froude scale of 1:16 (model : prototype). Irregular waves representing JONSWAP spectra were generated by a hydraulically actuated piston type wave maker. The test sections were placed approximately 35.4 meters from the wave board. Wave data were collected for each run using two Goda Arrays each consisting of three electronically driven resistance-type wave gages. Incident and reflected spectra were resolved using the method of Goda and Suzuki (1976). Wave signal generation and data acquisition were controlled using a DEC MicroVAX I computer. Data analysis was performed on a DEC VAX 11/750.

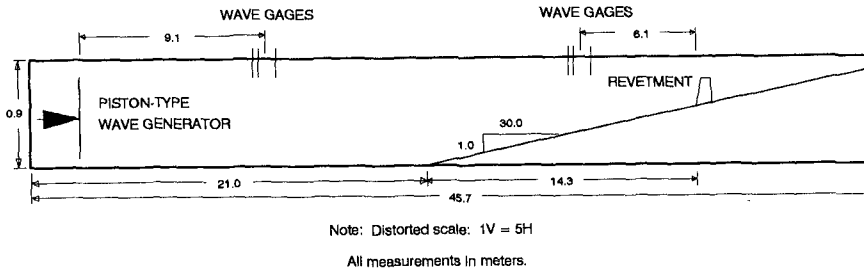


Figure 1. Profile view of wave tank setup.

Figure 2 shows a typical initial and equilibrium profile for a dynamic revetment. All initial profiles, except for Test 4, had a horizontal berm and a seaward face on a slope of 1 on 1, (vertical to horizontal). Test 4 used the equilibrium profile from Test 3 as a starting profile to determine how sensitive the equilibrium profile was to initial conditions. The influence of the initial berm width and berm height above the still water level (SWL) are two of the major variables investigated in this study. One goal of the study was to determine how much stone was required to protect a vertical bulkhead from direct wave attack. The bulkhead was simulated in the model using a plywood board to terminate the rubble on the landward side, located at 0.0 on the horizontal axis in the profile figures. Profiles shown in the figures are the average of five profile surveys along the length of the tank. There was very little across-tank variation in the profile observed during these tests. Surveys were made using a rod attached to a disc with a ball and socket connection. The disc had a diameter of 15 mm.

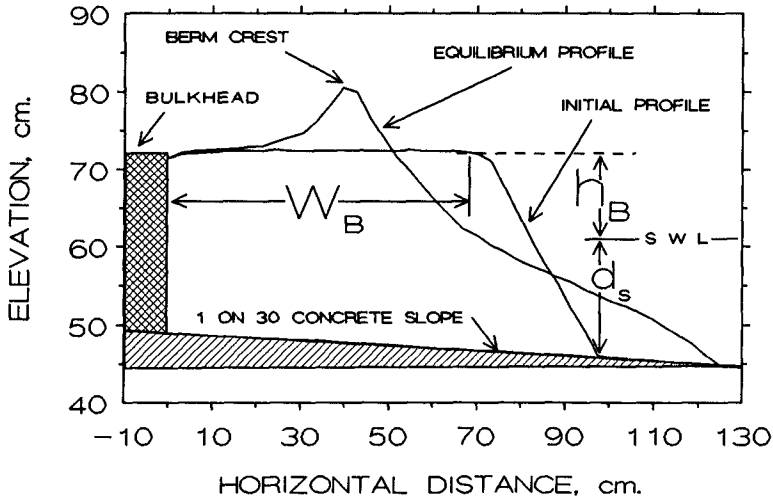


Figure 2a, Typical equilibrium profile.

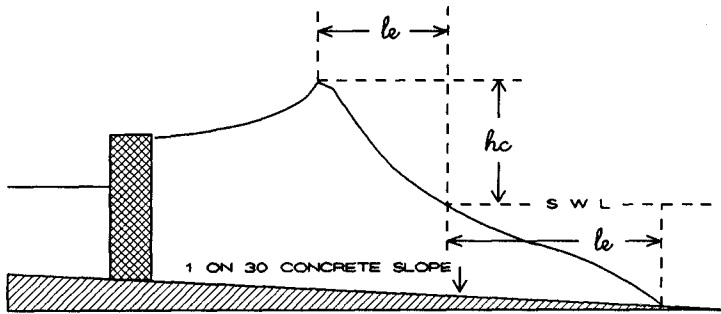


Figure 2b. Definition Sketch

Initial test conditions were first generated to simulate wave action similar to that found on Lake Michigan near a site in Chicago at Devon Avenue. The initial berm width was chosen by substituting these initial test conditions into a simplified version of the Dutch equations (van der Meer, 1988). As testing progressed, more severe wave conditions were run in the wave tank to fully test the range of circumstances for which a dynamic revetment would be suitable. Later tests examined a shorter wave period which may better represent the conditions for a structure on a body of water smaller than Lake Michigan.

Table 1 summarizes the gradations and specific gravity of the stone used in this study. Specifically the stone is a dense limestone.

Cumulative Percent Passing	Tests	Tests
	1-22 Sieve size (mm)	23-26 Sieve size (mm)
2	4.8	3.1
15	5.6	4.3
50	8.1	5.6
85	11.2	7.3
98	12.7	9.3
specific gravity	$\rho(r) = 2.68$	$\rho(r) = 2.72$

Table 1. Characteristics of stone used in this study

Table 2 gives some of the basic data collected during this study. Number of waves is the total number of waves generated during a test based on the period of peak energy density, T_p , of the incident spectrum. T_p and H_{m0} , the incident zero-moment wave height, were measured at Goda Array 2 which is the shallow water array shown in Figure 1. Array 2 depth is the water depth at the middle gage in the three gage array. It was found that the initial profile adjusts rapidly to the incident wave conditions. For tests with $T_p = 2.5$ there was little change in the profile between 3000 and 5000 waves and for tests where $T_p = 1.75$, there was little change between 4245 and 7080 waves.

Berm width, W_B , is the horizontal length of the berm as it was constructed at the beginning of a test. Berm height, h_B , is the average vertical distance from the still water level (SWL) to the almost horizontal berm surface at the beginning of a test. Berm crest height, h_C , and berm crest length, l_B , are the vertical and horizontal distances respectively from the still water line to the conspicuous berm crest formed by the wave runup. Toe water depth, d_s , is the depth at the toe of the revetment at the beginning of a test. Erosion depth, h_e , and erosion length, l_e , are the depth and horizontal distance respectively of the toe of

Test no.	No. Waves N	Array 2				Berm Height Above S.W.L. (cm)	Water Depth At Toe (cm)	Water Depth At Wave Generator (cm)	Revetment Response Category	Berm Crest Height (cm)	Reflection Coeff. Kr
		Hmo (cm)	Tp (sec)	Nominal Depth (cm)	Berm Width (cm)						
1	5000	6.83	2.53	37.19	54.86	10.77	14.81	60.96	I	19.04	0.45
1	3000	6.73	2.51	37.19	54.86	10.77	14.81	60.96	I	18.44	0.45
2	3000	13.31	2.52	37.19	54.86	10.77	14.81	60.96	F	NA	0.36
3	5000	6.92	2.57	34.14	54.86	13.82	11.71	57.91	S	17.07	0.47
3	3000	6.81	2.60	34.14	54.86	13.82	11.77	57.91	S	17.56	0.48
4	3000	13.26	2.52	34.14	54.86	13.82	11.71	57.91	I	21.12	0.36
5	3000	13.03	2.52	34.14	54.86	13.82	11.71	57.91	I	21.61	0.35
6	3000	13.62	2.65	37.19	70.10	11.28	15.30	60.96	I	21.43	0.39
7	5000	7.02	2.50	37.19	70.10	11.28	15.30	60.96	S	19.51	0.46
7	3000	6.86	2.51	37.19	70.10	11.28	15.30	60.96	S	18.50	0.46
8	5000	13.61	2.50	37.19	77.72	11.15	15.58	60.96	I	24.20	0.38
8	3000	14.07	2.64	37.19	77.72	11.15	15.58	60.96	I	23.26	0.39
9	3000	7.07	2.54	37.19	24.38	10.93	13.66	60.96	F	NA	0.49
10	3000	6.90	2.47	34.14	24.38	13.98	10.61	57.91	I	16.73	0.44
11	4286	11.62	1.81	34.14	54.86	14.25	11.51	57.91	S	17.43	0.30
12	4286	11.49	1.85	37.19	54.86	11.20	14.56	60.96	I	17.89	0.28
13	7 143	11.52	1.74	34.14	24.38	13.98	10.61	57.91	I	16.73	0.27
13	4286	11.43	1.76	34.14	24.38	13.98	10.61	57.91	I	16.52	0.28
14	3000	13.46	2.54	43.28	77.72	11.27	15.23	67.06	I	24.05	0.38
15	3000	11.44	1.75	43.28	77.72	11.27	15.23	67.06	I	17.74	0.28
16	3000	13.51	2.56	37.80	92.96	11.24	15.91	67.06	I	24.51	0.38
17	4576	11.45	1.75	34.14	24.38	11.04	13.62	60.96	F	NA	0.32
17	3000	12.07	1.75	34.14	24.38	11.04	13.62	60.96	F	NA	0.32
18	3000	13.44	2.49	34.14	24.38	14.09	10.92	57.91	F	NA	0.37
19	3000	5.56	1.77	34.14	24.38	14.09	10.47	57.91	F	NA	0.35
19	4576	5.61	1.77	34.14	24.38	14.09	10.47	57.91	S	NA	0.34
20	4575	5.71	1.73	37.19	24.38	11.04	13.52	60.96	I	13.69	0.33
20	3000	5.64	1.74	37.19	24.38	11.04	13.52	60.96	I	13.62	0.33
21	3000	13.38	2.49	37.19	24.38	11.04	13.52	60.96	I	13.62	0.33
22	3000	5.75	1.79	37.19	54.86	10.99	14.60	60.96	F	NA	0.42
22	4576	5.65	1.73	37.19	54.86	10.99	14.60	60.96	S	14.48	0.32
23	2 160	12.38	2.51	37.19	54.86	10.63	14.60	60.96	F	NA	0.43
24	3000	6.42	2.52	37.19	54.86	10.63	14.60	60.96	I	20.33	0.50
25	3000	10.97	1.71	37.19	54.86	10.63	14.60	60.96	I	18.99	0.30
25	4576	10.78	1.85	37.19	54.86	10.63	14.60	60.96	I	19.11	0.30
26	3000	5.45	1.72	37.19	54.86	10.63	14.60	60.96	S	14.72	0.37
26	4576	5.37	1.79	37.19	54.86	10.63	14.60	60.96	S	15.79	0.37

Table 2. Basic Data

the revetment from the still water line for the indicated number of waves. Water depth at the wave generator is the depth in the deepest part of the tank (Figure 1). Revetment Response Category (RRC) is a simple evaluation of the performance of the revetment during a test where "F" indicates the revetment failed, "S" indicates the revetment was safe, and "I" indicates an intermediate condition. The RRC and the dimensionless revetment size will be discussed further in the next section. K_r is the reflection coefficient which is defined by Goda and Suzuki (1976) as the square root of the ratio of reflected to incident wave energy.

Critical Mass Analysis

One of the goals of this study was to provide guidance on the quantity of stone, critical mass, necessary to protect a structure, such as a bulkhead, from wave attack. To accomplish this goal, all of the test results were classified into one of three categories. When wave conditions are severe in relation to the quantity of stone in the revetment wave action will erode the rubble, usually by carrying it over the bulkhead, until waves can impact directly against the bulkhead; this category was designated failure, denoted "F" in Table 2 and illustrated by Figure 3a. When the amount of stone in a revetment is large in relation to the wave conditions the development of the berm crest will have enough room so that neither stone or water will be carried over the bulkhead; this category is designated safe, denoted "S" in Table 2, and illustrated by Figure 3b. The third category fell between safe and failure and occurs when the berm crest buildup extends far enough landward to reach the bulkhead and there is at least some overtopping of the bulkhead by both water and stone; this category was designated intermediate, denoted "I" in Table 2, and illustrated by Figure 3c. The ability of a dynamic revetment to protect a bulkhead is a function of the volume of stone per unit length and the incident wave conditions.

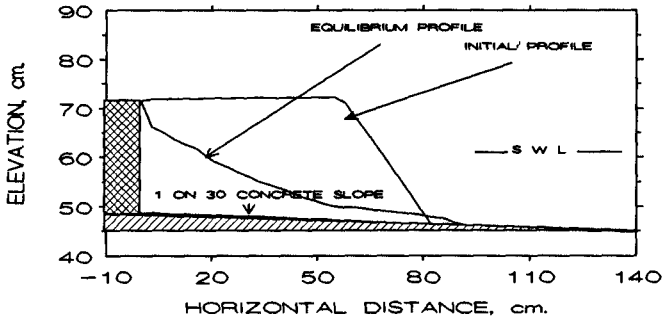
In order to calculate the critical mass it is necessary to estimate three characteristic dimensions of a dynamic revetment, i.e., berm crest height, h_c , berm crest length, l_c , and erosion length, l_e . Regression analysis was employed to determine the following equations which are used to estimate, h_c , l_c , and l_e :

$$h_c/H_{mo} = 0.270*(H_{mo}/L_p)^{-0.645}, R^2 = 0.96 \quad (1)$$

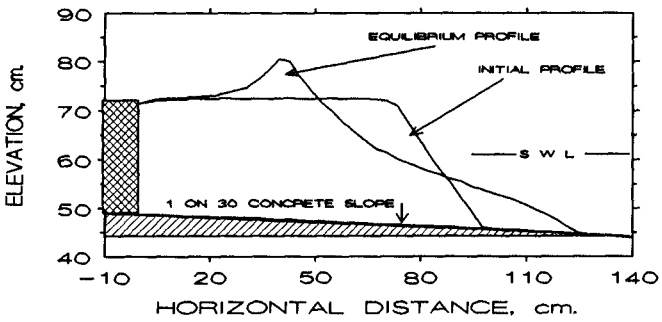
$$l_c/H_{mo} = 0.677*(H_{mo}/L_p)^{-0.521}, R^2 = 0.92 \quad (2)$$

$$l_e/d_s = \exp(2.24*(H_{mo}/L_p)^{0.143}), R^2 = 0.64 \quad (3)$$

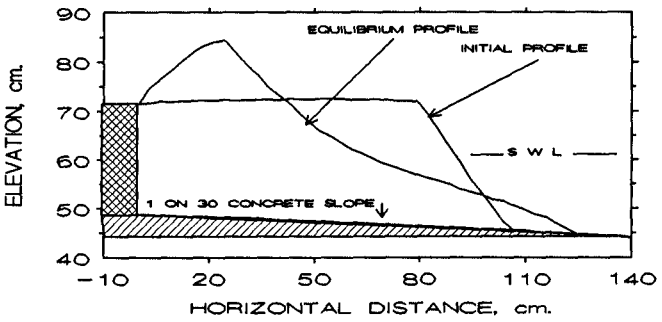
Equations 1, 2, and 3 are based on analysis of Tests 1 through 22. R^2 values give the portion of the variance explained by the regression analysis. Tests 23, 24, 25, and 26 were conducted with somewhat smaller stone (see Table 1) and were withheld from analysis. Figures 4 shows observed data with regression trends for Equations 1, 2, and 3, respectively. Stone sizes are denoted by



3a. FAILURE PROFILE RESPONSE



3b. SAFE PROFILE RESPONSE



3c. INTERMEDIATE PROFILE RESPONSE

Figure 3. Dynamic Revetment Response Categories.

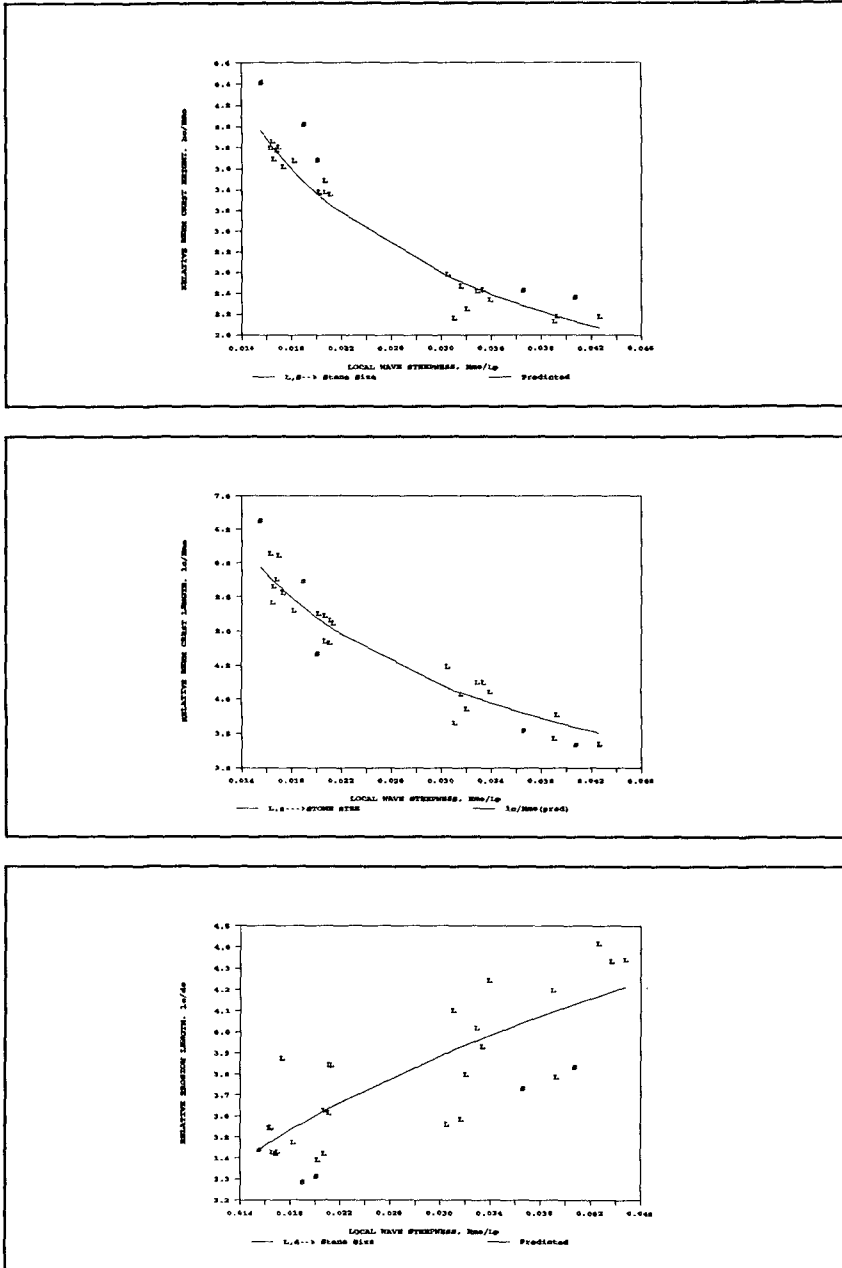


Figure 4, Characteristic dynamic revetment dimensions as a function of local wave steepness.

symbol in these figures so that the suitability of regression curves for the smaller sized stone withheld from analysis can be judged.

To specify the scale of the revetment response to wave attack it is useful to define a scale parameter, $A_s(c_m^3/c_m)$, where

$$A_s = (d_s + h_c) * (l_e + l_c) \tag{4}$$

and where h_c , l_c , and l_e are estimated using Equation 1, 2, and 3, respectively. The water depth at the toe of the revetment d_s is selected based on design considerations. The total volume of the revetment per unit length is denoted $A_t(c_m^3/c_m)$ and includes the void space of about 45 percent. Figure 5 shows the response category versus the ratio of A_t to A_s . For convenience let $A_t'(s) = A_t/A_s$. It can be seen that $A_t'(s)$ is able to properly categorize all tests including those with smaller stone withheld from analysis.

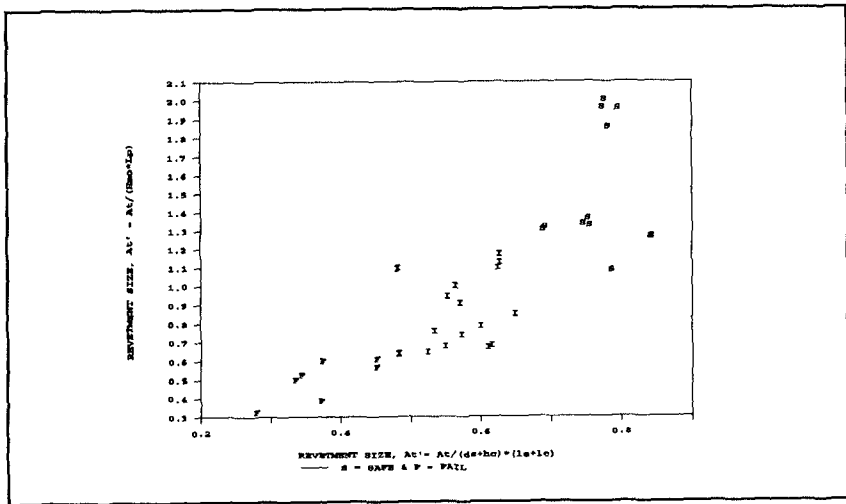


Figure 5, Dynamic revetment response categories as a function of two dimensionless revetment size variables.

A slightly easier but less accurate way to estimate the amount of stone required for a stable dynamic revetment can be obtained using the wave severity parameter, $H_{mo} * L_p$, where L_p is the Airy wave length calculated using d_s and T_p . Let $A_t'(w_s) = A_t / (H_{mo} * L_p)$. In Figure 5 it can be seen that $A_t'(s)$ is somewhat better than $A_t'(w_s)$ at predicting the proper revetment response category. The purpose of considering $A_t'(ws)$ is that it is quite simple and can provide some additional insight. It was found from the study of reef breakwaters that when wave conditions were quite severe in relation to the size of a reef, the reef could not dissipate wave energy effectively. For reefs it was found that for $(A_t / (H_{mo} * L_p)) < 0.5$, energy dissipation was largely a function of the relative size of the structure such that the percent energy dissipation = $(A_t / (H_{mo} * L_p)) * 100$.

From the analysis given above there appears to be at least two ways to interpret the critical mass for a dynamic revetment: (1) It is a supply and demand relation to determine if A_t is large enough to supply the demand, characterized by A_s . (2) It is an energy dissipation relation to determine if there is enough stone A_t available to dissipate the wave energy characterized by $H_{mo} * L_p$.

Wave Reflection and Energy Dissipation

After Coda Suzuki (1976) the reflection coefficient is defined as the square root of the ratio of the reflected wave energy to the total incident wave energy. Wave reflection from dynamic revetments appears to be a function of two variables, wave steepness and relative void size. Reflection coefficients can be predicted with the following equation:

$$K_r = 1 / (1.0 + (C_o * (d_{50} / L_o)^{C_1} * \exp(C_2 / H_{mo} / L_o))) \quad (5)$$

where d_{50} is the median stone size and L_o is the deep water wave length given by, $L_o = (g * (T_p^2)) / 2 * \pi$. The dimensionless regression coefficients are given by,

$$\begin{aligned} C_o &= 23.4 \\ C_1 &= 0.312 \\ C_2 &= -0.00374 \end{aligned}$$

Equation 5 explains about 97 percent of the variance in a sample size of 30, i.e. $R^2 = 0.97$ and $N = 30$. Tests in the failure response category were not included in the above analysis since at failure a substantial part of the reflection is from the vertical bulkhead. Percent of incident wave energy dissipated by a dynamic revetment can be estimated by using Equation 5 and the relation,

$$\%D = (1.0 - (K_r^2)) * 100$$

where %D is the percent energy dissipation. Observed data gives reflection coefficients between 0.27 and 0.50, indicating that dynamic revetments dissipate between 75 and 92 percent of the

incident wave energy. By dissipating over three-quarters of the incident wave energy dynamic revetments would make good wave absorbers.

Summary and Conclusions

A series of laboratory tests were conducted to investigate the response of dynamic revetments to shallow waver wave conditions. No more laboratory tests are planned at this time but data analysis is continuing. Most tests from this study fall into the category "dynamically stable rock slopes" based on the Dutch classification system (van der Meer and Pilarczyk, 1987). For this study, the ratio of the wave height to stone dimension is in the range of roughly 5 to 16. Typically zero-damage on a conventional riprap revetment occurs when the wave is about two and a half times larger than the stone dimension.

It was found the equilibrium dynamic revetment profile was not sensitive to the initial profile. This means that construction costs can be lowered because special care is not required in the placement of the stone. The berm crest is a conspicuous feature of the profile and the crest height is strongly dependent on the product of the zeroth moment wave height and local wave length.

The concept of a critical mass for a dynamic revetment is introduced. Critical mass is the quantity of stone required to protect a unit length of a vertical bulkhead for a given water depth at the toe and given wave conditions. This quantity is found to increase with increasing water depth, and zeroth moment wave height and period of peak energy density. Two methods to calculate the critical mass are introduced and discussed.

Future work includes more analysis and greater familiarity with the extensive Dutch research (van der Meer, 1988). Surprisingly, most of the Dutch laboratory work was conducted in relatively deep water at the toe of the revetment. Part of the effort in this study involves determining to what extent the Dutch findings can be applied to shoreline erosion in the United States. A related study being conducted in England can also provide valuable information to this study (Powell, 1988).

Acknowledgements

The author wishes to thank Mr. Donald L. Ward, Hydraulic Engineer, for contributing valuable insight on the conduct of this study. Mr. Willie Dubose conducted the laboratory work in a careful and professional manner. Mr. John Heggins, Computer Specialist, provided expert assistance in manipulating data files and analyzing the data. Ms. Myra Willis, Secretary, very capably put text, figures, and tables together to produce a paper.

The tests described, unless otherwise noted, were conducted under the Coastal Structures Evaluation and Design program of the

United States Army Corps of Engineers by the Coastal Engineering Research Center. Permission was granted by the Chief of Engineers to publish this information.

References

Allsop, N.W.H. and Latham, J.P., "Rock Armouring to Unconventional Breakwaters: the Design Implications for Rock Durability", Proceedings Workshop on Berm Breakwaters, Ottawa, Canada Sept. 1987, published by ASCE, 1988, D. H. Willis, W. F. Baird, and O. T. Magoon editors.

Baird, W. F. and Hall, K. R., "The Design of Breakwaters Using Quarried Stones," Proceedings 19th Coastal Engineering Conference, Houston, Texas, Sep 1984.

Brunn, P. and Johannesson, P., "Parameters Affecting Stability of Rubble Mounds," ASCE Journal of the Waterways, Harbors, and Coastal Engineering Division, Vol 102, No. WW2, May 1976.

Hall, K. R., "Experimental and Historical Verification of the Performance of Naturally Armouring Breakwaters," Proceedings ASCE Conference on Berm Breakwaters, Ottawa, Canada, Sep 1987.

Hudson, R. Y. and Davidson, D. D., "Reliability of Rubble-Mound Breakwater Stability Models," Proceedings ASCE Symposium on Model Techniques, San Francisco, California, 1975.

Johnson, C. N., "Rubble Beaches Versus Rubble Revetments," Proceedings ASCE Conference on Coastal Sediments' 87, New Orleans, Louisiana, May 1987.

Latham, J. P., and Poole, A. B., "Assessing the Effect of Armourstone Shape and Wear," Proceedings 21st Conference on Coastal Engineering, Malaga, Spain, June 1988.

Pilarczyk, K. W. and den Boer, K., "Stability and Profile Development of Coarse Materials and their Application in Coastal Engineering," Proceedings International Conference on Coastal and Port Engineering in Developing Countries, Colombo, Sri Lanka, Mar 1983, also Delft Hydraulics Laboratory Report 293, Jan 1983.

Powell, K. A., "The Dynamic Response of Shingle Beaches to Random Waves," Proceedings 21st Conference on Coastal Engineering, Malaga, Spain, June 1988.

van der Meer, J. W., and Pilarczyk, K. W., "Dynamic Stability of Rock Slopes and Gravel Beaches," Proceedings 20th Conference on Coastal Engineering, Taipei, Taiwan, Nov 1986, also Delft Hydraulics Communication No. 379, Delft the Netherlands, Mar 1987.

van der Meer, J. W., "Rock Slopes and Gravel Beaches under Wave Attack," PhD Thesis Dept. of Civil Engineering, Delft Technical University, Apr 1988, also Delft Hydraulics Communication No 396, Delft, the Netherlands, Apr 1988.

van Hijum, E., and Pilarczyk, K. W., "Gravel Beaches: Equilibrium Profile and Longshore Transport of Coarse Material under Regular and Irregular Wave Attack," Delft Hydraulics Laboratory Publication No. 274, Delft the Netherlands, July 1982.

CHAPTER 139

STATISTICAL APPROACH OF DURATION OF EXTREME STORMS : CONSEQUENCES ON BREAKWATER DAMAGES

Charles Teisson¹

Abstract

A statistical model of storm duration has been developed and successfully applied to wave records on various French sites. Distribution of storm durations at various significant wave-height levels are fitted to Weibull curves. Extrapolation of these distributions to rarer storm events is presented, and enables the estimation of return period of any storm as a function of the exceeded wave height and the duration of this exceedance.

These results on storm duration have been applied to breakwater design, with the help of laboratory tests displaying the influence of duration on breakwater damages.

1. INTRODUCTION

Actions of waves on natural shores or artificial structures are at first described by the height of incident waves. Observations of phenomena of littoral transport, or damages caused on breakwater also display the importance of duration of the action of this incident wave. This point of view of persistence of sea state is usually disregarded : analysis of waves records is most often carried out without taking interest in information about duration, however implicitly contained in the sampling, equally or irregularly time-spaced.

It is only in the 1970's that the first "mathematical persistence models" were developed, under the impulse of oil industry, for effective planning of offshore activities (HOUMB and VIK, 1975 ; GRAHAM, 1983).

In the same way, we developed a statistical method of analysis of the couple height/duration of storm from available waves record, successfully applied to various French sites, allowing to estimate distribution of storm duration for extreme events (TEISSON, 1984).

¹ Research Engineer

EDF - Laboratoire National d'Hydraulique, 6, quai Watier 78400 Chatou, France.

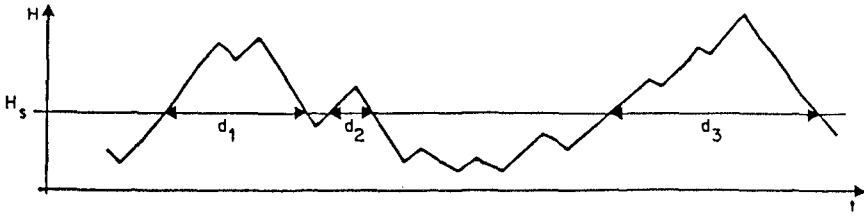


Fig. 1: Definition of the duration of a storm at a selected wave height threshold from waves records

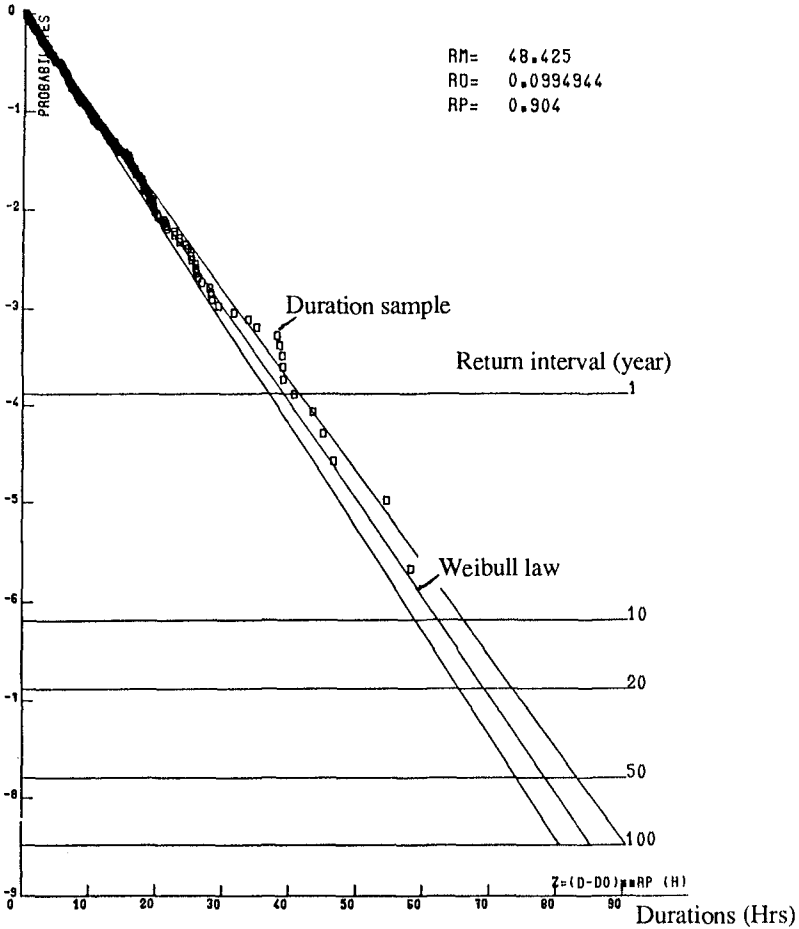


Fig. 2: Statistical adjustment of durations for storms $H_s > 1.50$ m.

These results on storm duration have been applied to breakwater design, in order to judge their influence on the determination of the armour unit size. Previous tests conducted in laboratory enabled to check that storm duration clearly influence the damages : when using stability formulae, as Hudson type, the design wave height producing similar damages lies between $H_{1/10}$ and $H_{1/20}$.

These practical information, combined with the results of the statistical method lead to a more comprehensive use of waves records and a promising approach for breakwater design.

2. THE STATISTICAL METHOD

2.1. Return interval of storm including height and duration

When dealing only with wave height statistics, the definition of storm is reduced to storm peak. We tried to develop a statistical method saving more information and we immediately had to answer some puzzling questions : what is an occurrence of a storm and its duration ? Following LAWSON and YOULL (1977), we defined the occurrence of a storm when wave height passes, in an upward direction, a selected wave height level. The duration of the storm corresponds to the time exceedance of the wave height level, i.e., the duration of the uninterrupted sequence of significant wave height greater than the selected level (fig. 1). Therefore the same storm can be represented by various durations associated to different wave height levels.

For a selected wave height threshold, i.e. $H_{1/3} = 1.5$ m, the set of storm durations observed in the 5 years records was fitted to various distribution laws to estimate the 1 in a year, 1 in 10 years durations ; the best adjustment was obtained for Weibull laws (fig. 2) :

$$P(t) = e^{-\left(\frac{t}{\alpha}\right)^\beta}$$

where $P(t)$ is the probability that a storm duration exceeds t hours, above the selected wave height level of 1.5 m.

The same methodology was reproduced for higher wave height level H , i.e 2 m, 2.5 m, 3 m ..., leading to new values of $P(t)$ at each level. Following the variations of α and β as a function of H enables to extrapolate α and β for extreme H . Thus, on Antifer harbour site :

$$\alpha(H) = 11.4 H^{-0.42}$$

$$\beta(H) = e^{\frac{H - 3.3}{5.4}}$$

Finally this method enables to estimate the distribution of storm duration for extreme events. Returns period R of any storm is thus known not only from the exceeded wave height, but also from the duration of this exceedance (fig.3) :

$$\frac{1}{R} = n(H) \times P(t) \quad (1)$$

where $n(H)$ is the classical distribution of extreme wave height and $P(t)$ is the conditional distribution of the duration, for a given threshold H in wave height. $n(H)$ and $P(t)$ are in general Weibull laws, adjusted by the renewal method developed previously at LNH.

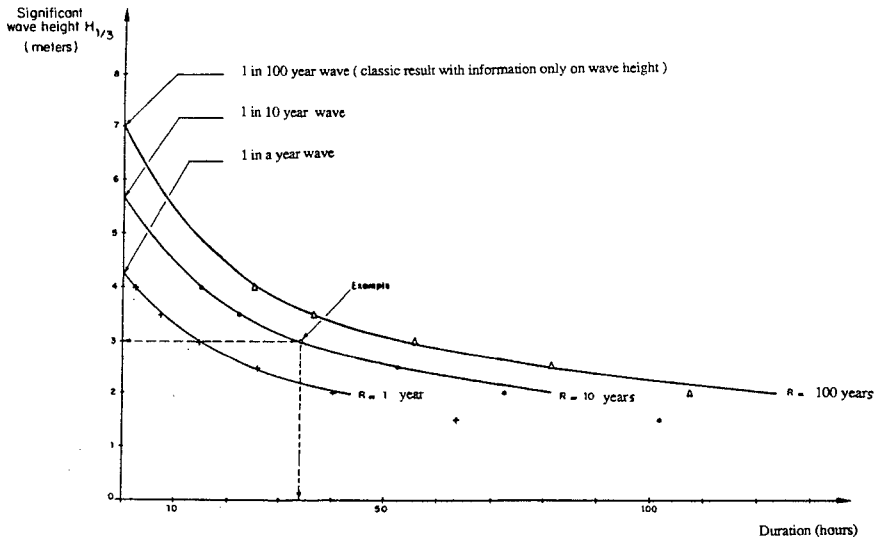


Fig.3: 1 a year, 1 in 10 years, 1 in 100 years storms defined from height and duration parameters
 Ex: A storm with a wave height exceeding 3 m. during 34 hours is a 1 in 10 year storm

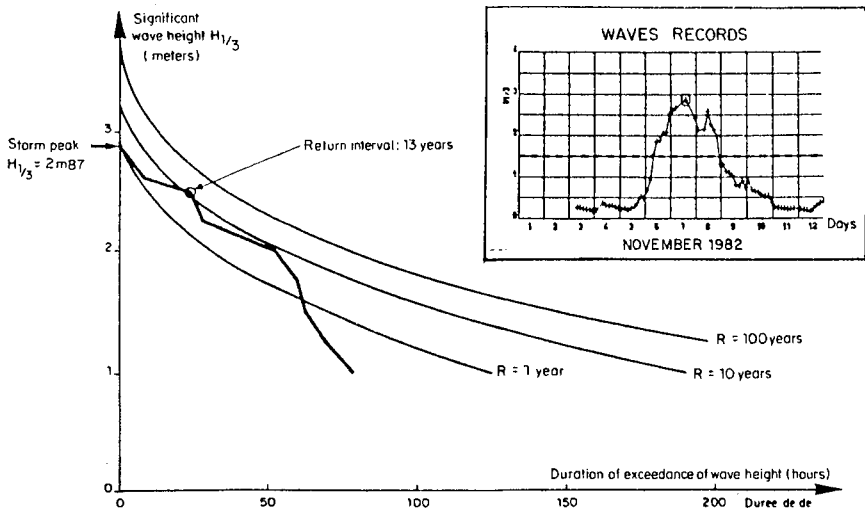


Fig.4: Return interval for the storm of november, 7, 1982 (Marseille site)

2.2. Severity of a storm

As seen above, a storm is a complex event, which cannot be reduced to the maximum wave height reached, or even a duration in hours above a single wave height threshold. In our method, a storm cannot be represented by a single event, and therefore its return interval is not unique. Nevertheless, it is possible to calculate the return interval for various wave height thresholds within the storm from (1), and the greatest return interval will symbolize the "severity" of the storm, and will be selected as the return interval of the storm. This return interval can be visualized by plotting, in the height-duration plan of fig. 3, the various couples wave height-duration of exceedance of any observed storm.

On fig. 4, the storm of november, 7, 1982 in Marseille is plotted in thick line with this value of duration at each level. With classical analysis carried out only on wave height, this storm would be a 1 in a year storm, according to its peak height. Information on duration shows that this storm, at lower height level was a more severe storm, with a return period of 13 years.

3. INFLUENCE OF STORM DURATION ON BREAKWATER DAMAGES

Results on storm duration have been applied to breakwater design, in order to judge their influence on the determination of the armour unit size. Previous tests conducted in a flume (LEPETIT and FEUILLET, 1979) enabled to evaluate the damages as a function of the duration of the action of random waves represented by significant wave height $H_{1/3}$ (fig. 5):

$$D = a H_{1/3}^b t^c \quad (2)$$

D : Cumulative damage at instant t, expressed in number of displaced blocks of the armour ; a, b, c, constants depending on type of blocks (for rubblemound beakwater a = 0.706, b = 3.9, c = 0.37).

A design wave height H_D , producing similar damages in regular waves can be expressed as :

$$H_D = 1.18 H_{1/3} t^{0.095}$$

On fig. 3, for a given return period, R = 10 years for instance, different values of height and durations as design conditions can be selected, leading to damages according to (2) :

1 in 10 year design condition	$H_{1/3}$	1,50m	2m	2,50m	3m	3,50m	4m	4,50m	5m	5,50m
	t (hours)	101,8	72,6	51,02	33,24	22,17	14,89	9,77	5,80	1,83
	H_D (m)	2,36	3,10	3,82	4,50	5,17	5,81	6,42	6,99	7,33

Table 1 : Influence of storm duration in stability formulae - "Equivalent design height H_D "

Duration clearly influence the damages : when using stability formulae, as Hudson type, the design wave height H_D producing similar damages lies between $H_{1/10}$ and $H_{1/20}$, compared with information only on wave height.

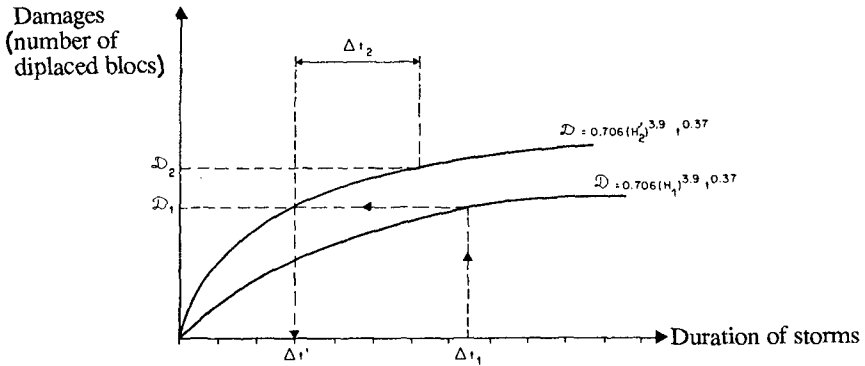


Fig.5: Evolution of damages as a function of duration of storms

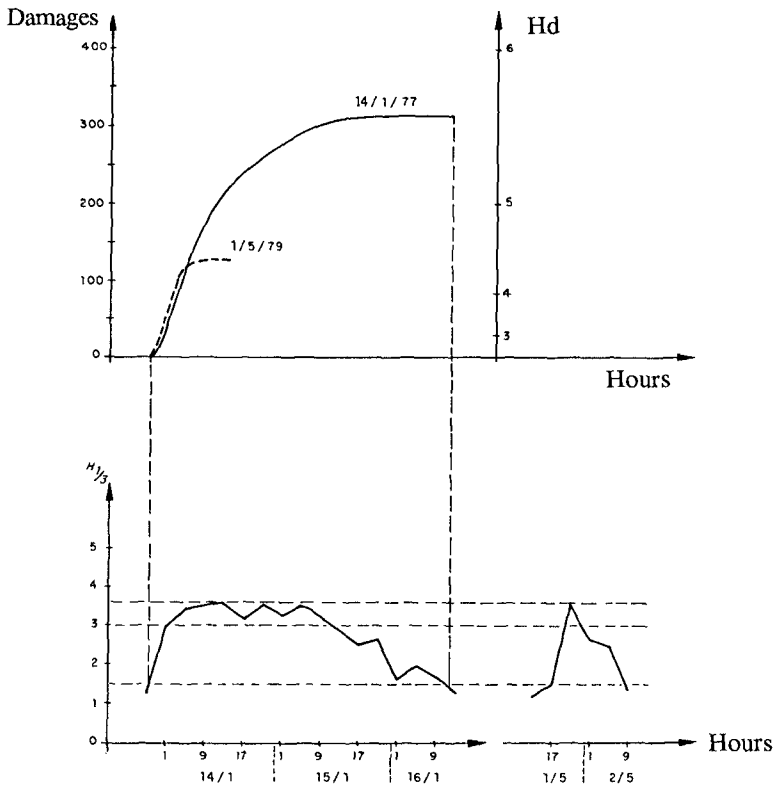


Fig.6: Damages and equivalent dimensional height for storms with same peak height but various durations

Recent developments relate to a better description of sea states, especially storm. The complete information of an occurrence of a storm is tentatively saved : not only the peak height, as in classical long term statistic waves, neither duration at some reference waves level, as stated in the method above, but the complete cycle of waves height growing and then decreasing.

By an integrated theoretical approach from (2), we calculated damage all along the storms. Let us suppose that a storm can be described by a sequence of significant wave height $H_i, i = 1, \dots, n$, the duration of each height being $\Delta t_i, i = 1, \dots, n$. The first wave height reaching the breakwater will produce damages according to (2) :

$$D_1 = 0.706 (H_1)^{3.9} \Delta t^{0.37}$$

The next wave height H_2 , lasting Δt_2 , arrive on a breakwater which has already suffered from damages D_1 . We can calculate the equivalent duration $\Delta t'$ which would have produced similar damages with H_2 (fig. 5) :

$$\Delta t' = \Delta t_1 \left(\frac{H_1}{H_2} \right)^{0.37}$$

Therefore, it looks like if H_2 has played during $\Delta t' + \Delta t_2$, producing damages :

$$D_2 = 0.706 H_2 (\Delta t' + \Delta t_2)^{0.37}$$

Replacing $\Delta t'$, it comes :

$$D_2 = 0.706 \left[\Delta t_1 H_1^{10.54} + \Delta t_2 H_2^{10.54} \right]^{0.37}$$

Reproducing the reasoning step by step, one can write, if we assume that the wave is known in a continuous way :

$$D_{(t)} = 0.706 \left[\int_0^t H_{1/\beta}(\tau)^{10.54} d\tau \right]^{0.37}$$

To see the net influence of duration, this formula has been applied to two storms which appeared in the records, reaching nearly the same peak height of 3.5 m, but with very different durations (fig. 6), the first storm persisting 35 hours above 3 m, the second one only 3 hours. Damages are almost three times greater in the longer storm. Speaking in terms of equivalent design wave height, using $H_D = 1.29 D_{1/3.9}^{1/3.9}$, we found :

$$\begin{aligned} H_D &= 5.63 \text{ m} && \text{for the longest storm} \\ H_D &= 4.46 \text{ m} && \text{for the shortest one} \end{aligned}$$

Reminding that H_D plays at a power 3 in Hudson formula, for instance, the weight of the blocs of the armour layer would be in a factor of 2 between the two storms, if we have to design a breakwater for each of this storm condition. In this particular case, the duration of storm is as important as the reached wave height, for breakwater design.

Fig. 7 exhibits that for a quasi-symmetric storm with respect to duration of growing and decreasing phase, 80 % of damages occur during growing height phase. From another point of view, 80 % of the damages are concentrated near the peak ; this remark pleas for accurate recording of waves height, instead of time step of 4 hours as on fig. 7.

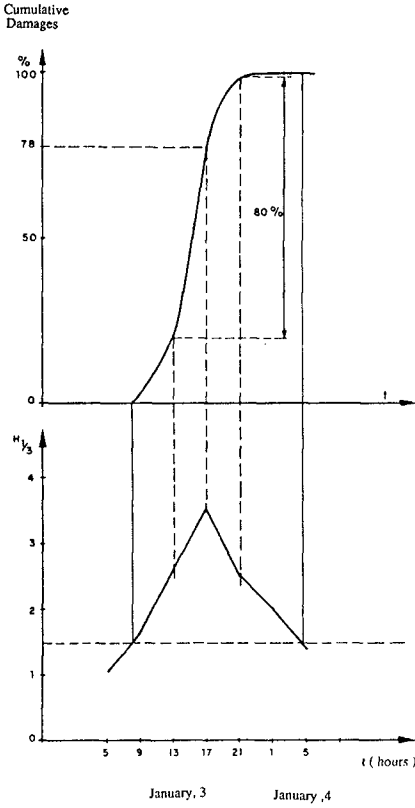


Fig.7: Storm of January, 3 1978
 . Time evolution of cumulative damages
 (in % of the damages at the end of the storm)

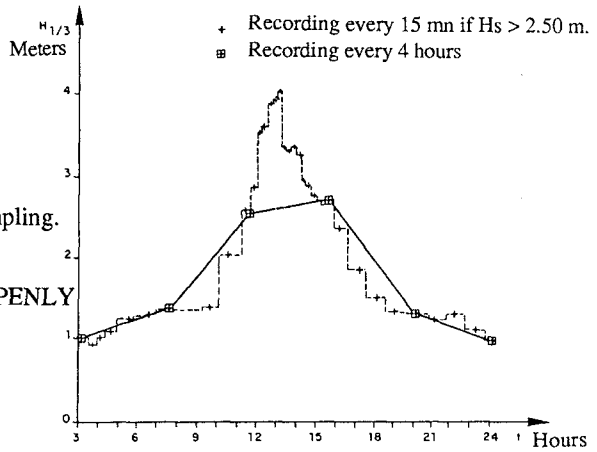


Fig.8: Influence of time sampling.
 Storm of 22 March 1981 at PENLY

4. INFLUENCE OF TIME SAMPLING

Usually wave data acquisition is performed in the following manner : the significant wave height is calculated from records of length 20 minutes, every 4 hours. But what does happen in between ? In fact :

- the persistence of waves at the peak cannot be precised in the range 20 minutes - 4 hours,
- the true peak reached is unknown.

Now these missing information are of major importance. From (2) :

- a storm persisting 4 hours at a given level is 3 times more damageable than a storm of 15 minutes (influence of duration),
- for a given duration, a wave of 6 m is 2 times more damageable than a wave of 5 m (influence of true peak).

What does really happen is shown on fig. 8, on a site where classical records every 4 hours were available, together with another record every 15 minutes in case of storm.

When available, recording every 15 minutes leads to strong influence on design conditions, as a consequence of better description of sea state (TEISSON, 1986). On the same data base, 1 in 10 years extreme significant wave height can be increased by 25 % when changing the time step from 4 hours to 15 minutes.

5. PRACTICAL CONCLUSIONS AND FURTHER DEVELOPMENTS

The synthesis of the theoretical statistical developments and laboratory tests lead to some practical information on storm duration and breakwater damages :

- a storm persisting 4 hours at a wave height level is three times more damageable than a storm persisting only 15 minutes at the same level (influence of storm duration),
- to select $H_{1/3}$ as design wave height in Hudson formulae assumes that the associated storm will last for only 10 minutes : this choice could lead to an under estimation of breakwater design,
- to speak of 1 in 10 years wave estimate has no significance without referring to the time sampling of the records.

On going developments try to treat the waves records, and especially storms, with respect to their specific final aim : each storm is transformed into cumulative potential damages on rubblemound breakwater (see fig. 7). These damages are then expressed in an equivalent dimensional height, by an inverse transformation, which could be extrapolated to extreme event. This theoretical approach, which is now under verification in flume tests, could lead to complete new definitions of design conditions, closer and more adequate for breakwater layout.

All these researches, aiming at a better description of sea state including persistency, may help in a more precise evaluation of design conditions for coastal activities.

ACKNOWLEDGEMENTS

This study was performed as part of a joint research program between EDF-LNH and the French Sea State Secretary.

REFERENCES

GRAHAM C. (1982)

The parameterisation and prediction of wave height and wind speed persistence statistics for oil industry operational planning purposes.
Coast. Eng., 6, 4, 1982, 303-329.

HOUMB O.G. and VIK I. (1975)

Duration of storms in the northern waters . Proc. 3rd Int. Conf. Port and Ocean Engineering under Arctic Conditions (POAC), Fairbank, 1975, pp. 241-261.

LAWSON N.V. and YOULL P.H. (1977)

Storm duration and return interval for waves off the Central N.S.W. Coast.
Proc. 3rd Australian. Conf. on Coastal and Ocean Eng., pp. 123-130.

LEPETIT J.P. and FEUILLET J. (1979)

Study of the stability of a rubble mound breakwater under random waves. Quantification of the effect of duration.
EDF-LNH Report 42/79.15 (in French).

TEISSON Ch. (1984)

Statistical study of the couple height-duration of storm from waves record.
EDF-LNH Report HE/42/84.41 ; 81 p. (in French).

TEISSON Ch. (1986)

New developments of the statistical method for the study of the couple height - duration of storm.
EDF-LNH Report HE/42/86.14 ; 80 p. (in French).

PART IV

The Dutch Coast



CHAPTER 140

COASTAL DEFENCE ALTERNATIVES IN THE NETHERLANDS

The Dutch Coast : Paper No. 1

Cees (C) J.Louisse*) and Ton (A) J. Kuik *)

Abstract

Coastal defence is an important issue in the Netherlands since more than half of its territory is situated below sea-level. Coastal erosion causes a permanent threat for this largely natural system. As a consequence flood-protection of the polderland may not everywhere be sufficiently guaranteed in the future. Besides dune area with valuable interests may be lost. These problems will worsen due to sea-level rise.

In 1987 the minister of public works instructed to perform a study to identify these problems and to develop alternatives for an overall coastal defence strategy in the Netherlands and to determine the effects of implementation of the alternatives over a time interval of several decades. The impacts of 4 alternatives have been determined with a policy analysis model, which has been especially developed for this purpose.

Model calculations indicate that the more (structural) measures for coastal defence are taken the less are the losses of dune area and the higher the costs. As time proceeds (up to 2090) the differences in costs between the alternatives decrease, while losses for some of the alternatives rise highly. Acceleration of sea-level rise results in an increase of costs and losses of dune area. A remarkable increase of impacts shows up when a change in wind climate is introduced.

Introduction

About one third of the Netherlands is situated below sea-level and would be flooded if it was not protected by the coastal defence system. This defence system is composed of three major units: in the south the Delta coast, consisting of (former) delta's and islands; between Hoek van Holland and Den Helder a stretch of coast not interrupted by tidal inlets (the Holland coast) and in the north the Wadden Island coast, consisting of a series of coastal barrier islands with tidal inlets in between (Figure 1). The defence system consists of dunes and dikes protecting the polders, and dams closing off large tributaries (Delta coast). The last have been constructed during the last decades (Delta works). In this period, which ends in 1990, also the defence system of the dunes has been improved. This leads everywhere along the coast to an accepted level of flood-protection. This flood-protection level is expressed as the frequency of exceedance of a storm surge

*) Rijkswaterstaat, Tidal Waters Division, P.O.Box 20907, 2500 EX The Hague, The Netherlands

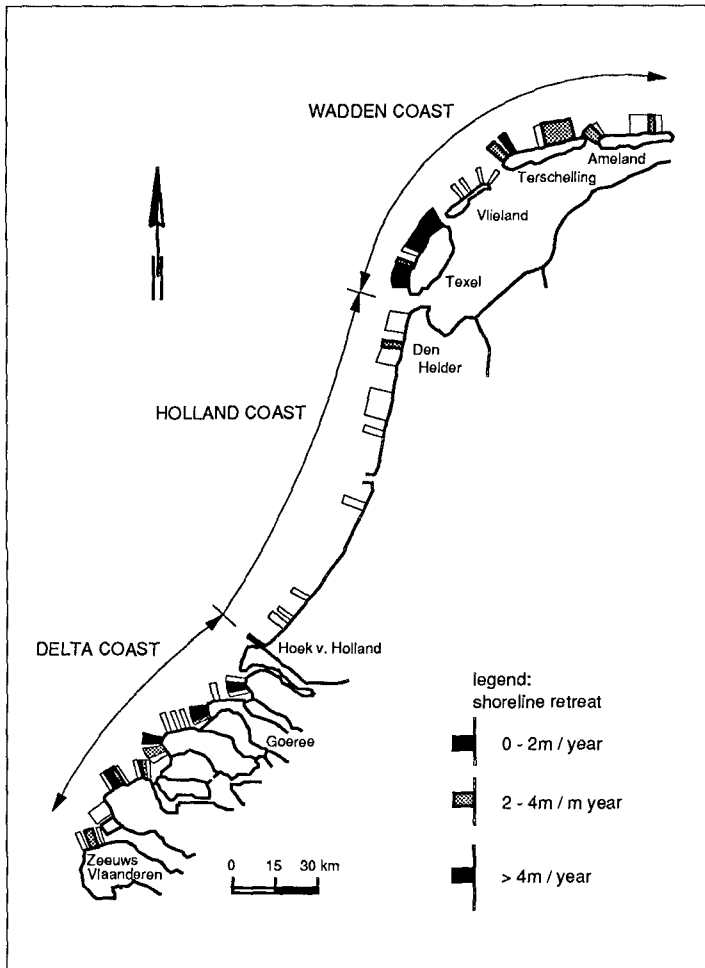


Figure 1. Pattern of erosion and erosion rates along the Dutch coast.

water-level (see Figure 2); dune dimensions are designed in such a way that collapse in these conditions may occur once of a hundred times.

Apart from flood-protection which up till now is the most important function of the dunecoast, the dune area covers a number of communal functions and interests, which also are worthwhile maintaining: drinking water supply, recreation, housing, and such like. Moreover the dune area as a whole is being considered as a very valuable natural landscape. It is one of the largest more or less continuous dune areas of Europe with a specific status of protected nature area.

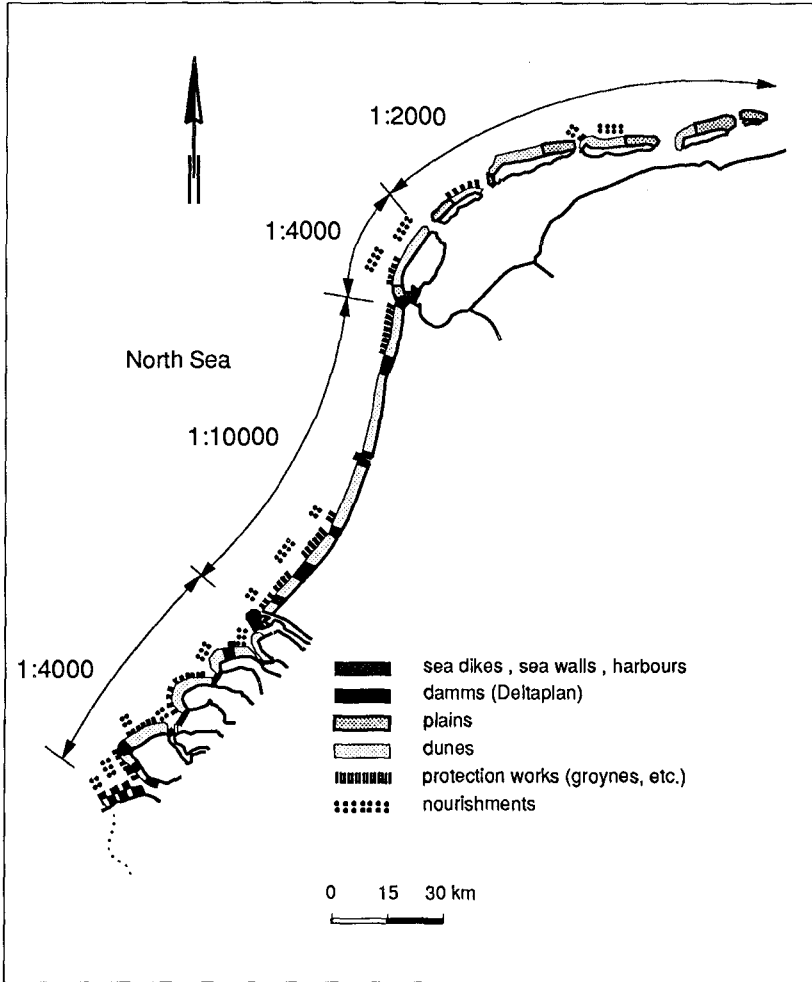


Figure 2. Coastal defence along the Dutch coast and the level of flood-protection along the coast expressed as the frequency of exceedance of a storm surge water-level

However, shoreline retreat due to coastal erosion at various areas along the coast constantly threatens the defensive force of the dunecoast and leads to a loss of valuable dune area. Figure 1 shows the main erosion areas to be situated in Delta and Wadden coast. With the present-day coastal defence policy this process is not being prevented or stopped. The present-day policy is confined to regular maintenance and reinforcement of coastal stretches with a weak defence with sand nourishments. As a consequence at many places shoreline retreat proceeds. Besides, climate changes due to the Greenhouse-effect may worsen or speed up this process.

The major question concerning coastal defence is how to guarantee the level of flood-protection in the future under conditions of continuing shoreline retreat and the threat of an accelerating sea-level rise and climate change. Coastal defence efforts must also as much as possible prevent further loss of dune area and the interests in this area. To investigate precisely the problems of forthcoming coastal erosion under the present-day coastal defence policy and to develop and evaluate new approaches for a coastal defence policy, a policy analysis study of the Dutch coast was performed. In this study three scenarios of sea-level rise are considered: the present-day sea-level rise (20 cm/century), the expected scenario (60 cm/century) and the pessimistic scenario (85 cm/century). The pessimistic scenario also includes a change in wind- and wave-climate (10 % increase of wind force, 10 degrees change of wind direction)

This paper describes the method of the study and presents the results. The study results in a comparison of 4 alternatives for coastal defence.

The policy analysis study has been described in a final report (Rijkswaterstaat, 1989) and in 20 technical documents. Some of these technical studies are presented on this Conference in the session "The Dutch coast". The state-of-the-art of knowledge of coastal development in the Netherlands is described by Zitman et al. (1990), Hoozemans (1990) and Van Vessem et al. (1990). Model analyses and studies on coastal prediction are described by Roelvink et al (1990), Steetzel (1990), Dijkman et al. (1990), Eysink (1990) and Stive et al. (1990). Techniques and strategies for coastal defence are described by Roelse (1990), Van Alphen et al (1990) and Pluym (1990); Terwindt et al. (1990) conclude with a description of implications for future coastal research. Thanks to former and recent coastal research programs like Coastal Genesis and TOW, data and models needed for this study, could be adequately obtained.

Analysis method

The study focuses upon the part of the coast which protects hinterland; dams in the tributaries of the Rhine-Meuse delta are not considered. This part of the coast with a total length of 353 kilometer shows various types of defence against the sea (Figure 2). The dunecoast covers a length of 252 kilometer, 34 kilometer consists of dikes and 27 of other constructions (boulevards, sluices, etc.). The remaining 38 kilometer concern beach plains, located at the extreme ends of the barrier islands of the Wadden coast. These plains do not protect polderland and are merely nature areas.

Since dikes and other constructions are considered as fairly immobile, representing coastal stretches with a fixed coastal defence system at a sufficient level, they are just of marginal importance in this study. From the point of view of flood-protection beach plains are not interesting as well: they do not protect polderland. Concerning nature these plains are most interesting when they can freely develop, thus when coastal management is not too strict. The most interesting part of the coast in this study is therefore the dunecoast.

The main characteristics of the policy analysis study of the dunecoast are on the one hand the sand economy of the coastal morphologic system and on the other the use of the coastal area for communal functions. Both are depicted in the scheme of figure 3. The sand economy describes the movement of sand at large spatial (and temporal) scales and identifies the areas of accretion and erosion and the resulting shoreline movement.

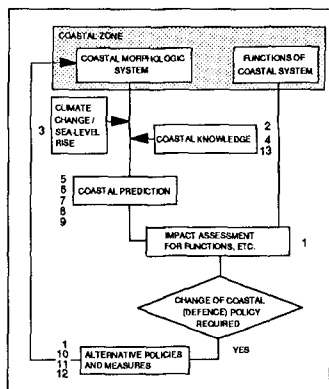


Figure 3. Policy analysis scheme

Evaluation of this shoreline movement (prediction) provides information on future shoreline positions and enables the assessment of the impact on functions of the dunecoast: flood-protection and dune interests. Confronting “autonomous” shoreline behaviour with functions of the dunecoast results in a quantification of the problems, that can be expected when no measures against shoreline retreat are taken (problem analysis).

When this confrontation leads to an undesired number of potential problem’s solutions must be developed. For each problem observed, different solutions can be considered, but this leads to ad hoc approaches. A structural approach was needed and led to a process of development of alternative strategies. These strategies were transferred into a

coherent set of measures for coastal defence along the entire coast: alternatives.

Given the alternative policies, next step in the analysis is to run through the scheme again to evaluate the impacts (benefits and costs) of these alternatives. Now the position of the shoreline as a function of time is not just determined by the prediction of the “autonomous” displacement of the shoreline, but also by shoreline behaviour imposed by the coastal defence alternatives. This identifies the places along the coast where measures are needed. The costs of these measures are computed. Where measures are not necessary, while the shore retreats losses of dune area are calculated.

Both for identification of the problems, and especially for the assessment of the impacts, the need for a policy-analysis model was felt. This model, KUSTBEL, enabled analysis of a variety of alternatives with a high resolution along the coast (1 kilometer) for different scenarios of sea-level rise and met the need for sensitivity-analyses for a number of parameters that greatly influence the final results.

In the scheme of figure 3 the technical studies, that have been performed to support the policy analysis study, are indicated by the numbers, which have been given to the papers in the session “The Dutch coast”.

The main cause of problems: coastal erosion

Shoreline retreat is caused by coastal erosion. Coastal erosion shows up in two ways, which are clearly related to each other: the sudden, fairly local event of storm erosion and the more gradual chronic erosion. In the first case high water level and waves during storm surges can locally result in a sudden loss of sand from the duneface. The storm erosion will result in a structural loss of sand from the coast on a stretch of coast suffering chronic erosion, because the dune sand will (partly) be used to replenish the sand deficit of the shoreface. Accreting coastal stretches may initially show a serious damage due to storm erosion, but this will be followed by a gradual restoration of the original dune profile in course of time.

Although more gradual and global, chronic erosion at the long run is much more threatening for the dunecoast than loss of sand from the dunes due to storm surges. Due to an often very subtle mixture of hydraulic processes residual transport of sand bodies from one place to another takes place and results in accretion at one place and erosion at others. Long-periodic changes in erosional and accretional processes also occur and result in periodic fluctuations of the shoreline with periods of tens of decades (Verhagen, 1988).

Procedure for problem identification

The problems which arise as a consequence of shoreline retreat are twofold: the threat for flood-protection and for loss of valuable dune area. Problems with flood-protection are concentrated on coastal stretches with a relatively narrow dune area; problems concerning loss of valuable dune area mainly concern wide dune areas.

Flood-protection

The entire coastal profile from shoreface to the landward boundary of the dunes is of interest for the safety of land behind the dunecoast; this whole area determines the strength of the coastal defence system. Mostly the main defence is formed by shoreface, beach and the first dune row, the front dune. The strength of this defence-system can be calculated for each profile and compared with the required strength, derived from design instructions (Vellinga, 1986). The strength is expressed as a dune-width, the storm erosion width A in figure 4. A is the distance from the dunefoot to the point O to where, due to the design storm surge sand from the front dune has been removed (see figure 4). This width A is determined by the assumption that the loss of sand from the duneface during a design storm surge equals the amount of sand that (according to the local geometry) can be placed on the profile of beach and upper shoreface (Vellinga, 1986). Besides some additional loss must be anticipated, leading to an increase of A to AT (point P). Connecting all points P along the coast leads to the 'storm erosion-line'. The minimum width in a selected profile must at least equal AT plus a residual width (and height) of the "residual profile". When due to shoreline retreat the front dune has become too narrow to contain AT plus the residual profile, reinforcement of the front

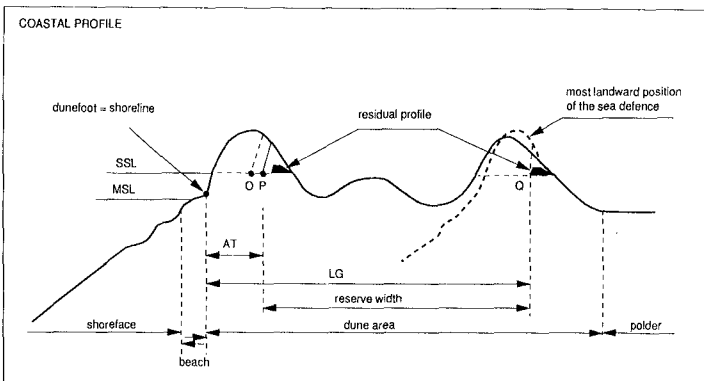


Figure 4 Schematic cross-section of the coastal defence area with definition of the procedure for evaluating problems with flood-protection.

dune is necessary. At present this is often realised by adding sand to the landward side of the front dune, either by activating the natural process of sand blowing or by mechanically replacing sand to the backside. This process results in a narrowing of the dune area. Eventually the dune area may be narrowed to a minimal defence system, consisting of just one row of marginal dunes (AT plus residual profile) at the landward edge of the dune area. Since further landward movement of this row of dunes into the polder is not admitted, potential problems for flood-protection arise when this situation is reached.

In fact at many places along the coast shifting of the defence up to the landward boundary of the dune area is not possible, simply because there is no sufficient volume of sand to contain the residual profile (a height of 2-3 m above the design storm surge level and a width of approximately 25 m). Therefore the ultimate point in the profile to where the backside of the coastal defence (point P) may be retreated is defined as the point (Q) at the landward side of which just the residual profile (related to the local storm surge design level) can be 'constructed' (figure 4). Connecting these points Q along the coast results in a 'most landward residual profile-line', the Q-line. There may be no gaps in this line along the coast. Given this Q-line and the P-line of potential storm erosion damage, the reserve-width for shoreline retreat with respect to flood protection is defined as the distance Q - P. This distance is known for every kilometer of coast.

To evaluate the conditions of flood-protection of the coast it is assumed that the shape of the front dune does not alter in time, even not when the shoreline retreats. When shoreline development as a function of time is known (Stive, et al., 1990), the evolution of the reserve-width due to shoreline development can be identified for every kilometer of coast. Potential flood-protection problems (when the reserve-width equals 0) can now be determined.

Loss of dune area with interests and nature

The economic interests and the nature values of the dune area are presented in table 1. Both economic interests and nature are partitioned to enable a distinction in appraisal within the interests (see table 1). This enabled a more refined analysis. For instance, various levels of appraisal of nature areas are distinguished, so that not just potential

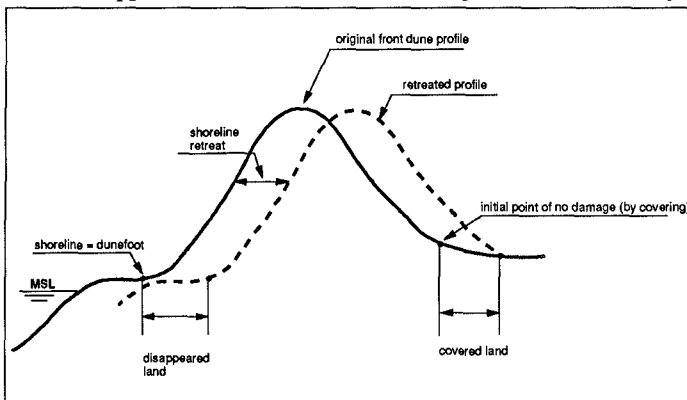


Figure 5. Schematic picture of the effects of shoreline retreat on interests in the dune area.

loss of nature area in general can be determined (which in fact is nearly the entire dune area), but also more specific potential losses of nature values.

Function/ Subfunction	Effects of shoreline retreat		
	Disappearing	Covering	Lowering Ground water table
Nature			
. Wet primary and secondary dunes, moors	+	+	+
. Dry primary dunes	+	+	+
. Dry secondary dunes	+	+	-
. Beach and beach plains	+	-	-
. Remoulde dunes	+	-	-
Water supply			
. Production facilities	+	+	-
. Infiltration infrastructure	+	+	+
. Discharge area	+	-	-
Housing			
. 50% builded	+	+	-
. 10-50% builded	+	+	-
. % builded	+	+	-
Recreation			
. Campings, recreation houses	+	+	-
. Sports-ground	+	+	-
Industrial areas			
. Large plants	+	+	-
. Small facilities	+	+	-
Diverses			
. Infrastructural works (harbours)	+	+	+
. Agricultureal areas	+	+	-
. Military area	+	-	-

Table 1. Sensitiveness of the (sub)functions of the dunes for effects of shoreline retreat (+ = sensitive; - = not sensitive).

Shoreline retreat can threaten the interests of the dune area in different ways. Direct and indirect effects are distinguished. Direct effects of shoreline retreat are directly caused by coastal defence management and concern (see figure 5):

- a loss of land and the interests accommodated on this land due to displacement of the shoreline (**disappearing**).
- due to shoreline retreat the backside of the front dune must be reinforced to keep the front dune at strength; as a consequence interests located at the backside of the front dune will be covered with sand (**covering**). This may lead to a loss for some interests as for instance housing, recreation, etc.
- shoreline retreat leads to a lowering of the groundwater-table. This may cause damage to nature areas and to groundwater-reserves.

Indirect effects of shoreline retreat are caused by the displacement of the front dune due to coastal defence management measures:

- extra blowing of sand caused by damage of the vegetation of the front dune.
- landward shifting of the zone of salt spray.
- inundation of the dune area when a weak front dune collapses.

In the analysis just 'disappearing' and 'covering' are taken into account. For the other effects supporting information for quantification of the impacts lacked, so they were ignored in the analysis.

The front of the area of potential loss is determined by the two lines which indicate the character of the potential loss: the line-of-disappearance and the line-of-covering.

Identification of the potential losses takes place for every kilometer of coast. To obtain a sufficiently refined analysis each unit of one kilometer of coast is split up in crossshore direction in grids with a width of 50 meter. All interests that are found in a grid are identified. This identification is closely related to the way they suffer loss due to shoreline behaviour.

The problems identified

Shoreline retreat may result in a problem concerning flood-protection of the polderland when safety requirements are no longer met. For interests in the dune area a problem has been defined as a situation of loss of area for these interests either due to disappearing or to covering. The analysis for both issues has been performed at each of the 252 cells (of 1 kilometer length) and results in an expression of the length of coast (\approx number of cells) where potentially problems may occur. In figure 6A the length of coast where the flood-protection can not longer be guaranteed is depicted for the whole prediction period and for the three scenario's of sea-level rise. For the present-day value of sea-level rise in the year 2000 already more than 20 kilometer are 'unsafe'; this increases to about 40 kilometer in 2090. For the pessimistic scenario an increase with about a factor 2 must be anticipated. The expected sea-level rise causes intermediate effects.

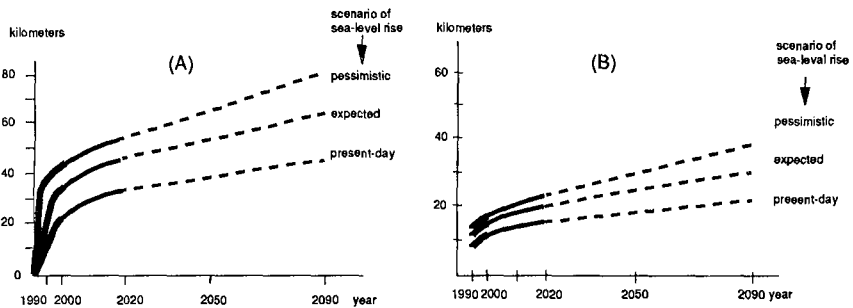


Figure 6. Length of coast where problems for flood-protection (A) and drinking water supply (B) may occur when no measures against shoreline retreat are taken.

The effects of shoreline retreat on the dune area and functions accommodated here can not all be presented here. Just the (potential) loss of area for water supply is shown (figure 6B). In the year 2000 for the present-day value of sea-level rise along about 10 kilometer of coast area for drinking water supply may be lost. In 2090 this is increased to about 15 kilometer. In the pessimistic scenario an increase of about 50 percent may be expected.

Solutions

With the present-day coastal defence policy a gradual increase of places where measures are needed to guarantee safety will occur. Besides due to the absence of a structural approach for protection of dune interests and nature an ever-increasing loss must be anticipated.

A structural approach for coastal defence must mainly be focused on protection of dune interests. Safety of the polderland has already been secured by norms, which vary along the coast (see figure 2). The policy margin here is determined by the distance in cross shore direction along which the defensive front dune can be displaced before the ultimate position has been reached: the reserve width for shoreline retreat (see figure 4). This is also the space within which (extra) protection of dune area and interests can be claimed. The strategies on coastal defence therefore give utterance to the level of protection of the dune area. It will be clear that guarantee of safety against flooding of the low country behind the dunes is a common feature of all strategies. The strategies lead to "alternatives" when they are completed with measures for coastal defence. Four alternatives are distinguished each of which describing the conditions with respect to the initial situation of 1990:

- **Withdrawal W:** admission of further retreat of the shoreline, except for the places where safety can just be guaranteed at the minimum level (norms according to figure 2) and where the reserve width has become zero.
- **Selective erosion control S:** counteract further shoreline retreat at places where dune area with nature and/or functions in this area are threatened; admit shoreline retreat at the other places. Since there is a fair number of interests which all could be separately and in combinations protected, a nearly endless number of alternatives could be defined, which would all fit into Selective erosion control. Just a small selection has been investigated, and the most representative is being presented in this paper. In this alternative the most valuable elements of nature and interests are protected:
 - * Housing: concentrations of houses (villages, residential quarters)
 - * Nature: wet dune, moors, etc.
 - * Drinking water supply: production plants and infiltration works
 - * Recreation: campings and recreation parks
 - * Industries
- **Full erosion control F:** counteract further shoreline retreat everywhere along the coast. Measures for coastal defence for these three alternatives consist of solutions with sand. In this way the natural character of the coast is not irreversibly affected and there is much experience with this type of defence measures (Roelse, 1990). Except for coastal stretches with a tidal gully close to the coast, groynes and pile-rows, which have been frequently applied in the past, are not considered as promising measures. A study on the effectiveness of these measures indicated a low effectivity for coastal defence objectives.

For Full erosion control, for Selective erosion control at those places where interests of the dune area may not be abandoned, and for Withdrawal at those places where the reserve width has become zero, counteraction of shoreline retreat is prescribed. This is realised by beach nourishments. In specific situations reinforcement of the dunes by supply of sand at the landward side of the front dunes is performed.

The fourth alternative is:

- **Seaward expansion E:** seaward expansion of the shoreline at places where the coastal defence is relatively weak with the objective of improving the coastal defence. At those places where seaward expansion measures are not projected, shoreline retreat will be counteracted just like for alternative Full erosion control.

In this alternative structures of hard material, like groins and dams are chosen (Pluijm, 1990). This alternative has just been worked out for the present-day scenario of sea-level rise.

For all alternatives the need for regular maintenance (maintenance of groynes and sea dikes, prevention of sand blowing from the dunefront, etc.) of the coastal defence is discerned. It is clear that the costs for maintenance will differ for the various alternatives: counteracting shoreline retreat will result in a decrease of efforts for maintenance of groynes and other constructions.

Comparison of the alternatives

The various alternatives have different implications for a series of aspects. These aspects are:

- length of coast where measures need to be taken to guarantee safety;
- loss of dune area with economic functions or valuable nature area;
- amount of sand needed for coastal defence;
- costs for coastal defence measures (maintenance and counteraction of shoreline retreat).

The impact of the alternatives on these aspects have been determined. Although regional and local (sectors) variation may be interesting, presentation of the comparison will be focused upon results on a national scale. The present-day scenario of sea-level rise will be discussed first.

Present-day scenario of sea-level rise

In the year 2000 already about 20 km of coast length requires counteraction of shoreline retreat for alternative W (see figure 7). The bars indicate the uncertainties in the estimates due to uncertainties in shoreline predictions and analysis method. The coast length where measures are needed to prevent further shoreline retreat for alternative S is substantially longer than for alternative W: about 60 kilometer. For alternative F and E an increase to about 140 kilometer is observed.

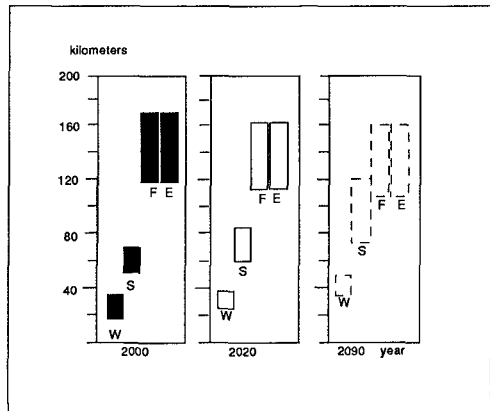


Figure 7. Length of coast where measures against further shoreline retreat must be taken for the 4 alternatives.

As a function of time there is an increase of coast length that needs to be protected for alternatives W and S (Figure 7). For alternatives F and E a slow decrease of this parameter is observed. The explanation for this effect is that the length of coast that suffers erosion has been predicted to be slightly smaller in the far future than in the first decades. This is mainly due to expected favourable periodic behaviour. The increase for the other alternatives has apparently been caused by an increase of coastal places where shoreline retreat leads to 'problems'.

The diagram of the cumulative loss of area shows the same pattern of increase as a function of time for alternatives W and S (Figure 8). For alternative W the loss of dune area amounts to about 3,5 km in 2000 and increases to more than 20 km in 2090. As

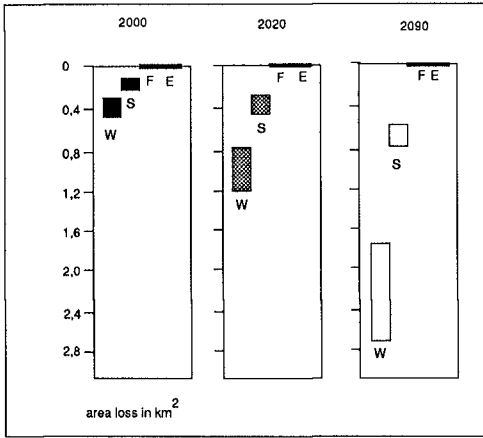


Figure 8. Cumulative loss of dune area for the 4 alternatives

housing about 0.06 km, and for valuable nature about 1.5 km. For alternative S these values respectively amount to: 0.1, 0.02 and 0 km. Obviously these interests are better protected with this alternative. As a function of time an increase comparable to the loss of dune area in general is observed.

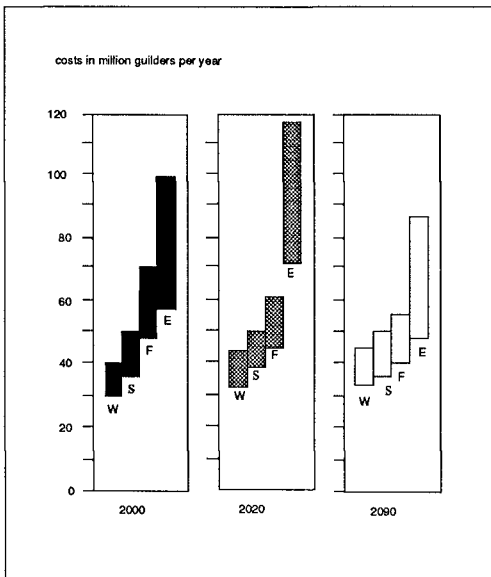


Figure 9. Total costs for coastal defence

could be expected, for alternative S losses of area are considerably smaller: 1,5 km in 2000 rising to about 6 km in 2090. A choice for alternative F or E does not lead to any loss of dune area. Considering the yearly loss of dune area, a decrease as a function of time is observed (W and S). This is caused by the fact that in course of time at an ever increasing length of coast (see Figure 7) further shoreline retreat must be counteracted. At these places further loss of dune area does not occur. The loss of area for economic interests in the dunes is just a fraction of the total loss of dune area. For alternative W the loss for Drinking water supply for the year 2000 is about 0.15 km, for

The costs show a pattern which is more or less in agreement with the coast length where measures against shoreline retreat must be taken (Figure 9). For the year 2000 they rise from about 35 million guilders per year for alternative W to about 60 million guilders per year for alternative F. This rise is caused by the fact that for the consecutive alternatives more sand that erodes from the coast must be replaced. Alternative E is somewhat more costly, about 80 million guilders per year. Here the construction costs have been roughly estimated (large uncertainties). 20 to 25 million guilders of these amounts are allocated for maintenance (higher costs for maintenance for the alternatives where shoreline retreat is less counteracted). In course of time costs for W and S have increased and fro

F and E decreased. Obviously the differences between the costs for the alternatives decrease in course of time. At the longer term F will just be slightly more expensive than W. However, with alternative W a considerable loss of dune area (about 20 km, Figure 8) must be anticipated, while the loss for F is zero.

More severe scenarios of sea-level rise

Acceleration of sea level rise from 20 to 60 cm/century results in an increase of the impacts for the various alternatives. If instead of the present-day scenario the pessimistic scenario (85 cm sea-level rise per century, including a change in wave climate) should be reckoned with, a more severe rise of the impacts must be anticipated. Figure 10 gives an overview of these effects for costs and area loss. For the expected scenario (60 cm/century) costs will increase with 10-20 percent, while losses increase with 20-30 percent. The impacts for a more rapid rate of sea-level rise (pessimistic scenario) are more drastically: 25-35 percent increase of costs and more than 75 percent increase of area loss. Here mainly the effect of a change in wind climate (and as a consequence wave climate) is responsible for the extra increase.

One may conclude that acceleration of sea-level rise and especially climate changes will result in a considerable increase of costs for coastal defence and losses of dune interests.

Expected scenario	increase of costs	increase of area loss
	%	%
Withdrawal	10	20
Selective erosion control	15	30
Full erosion control	20	—
Pessimistic scenario	increase of costs	increase of area loss
	%	%
Withdrawal	25	75
Selective erosion control	35	90
Full erosion control	30	—

Figure 10. Effects of sea level rise

Political choice

In June 1990 the government took the decision on the coastal defence policy for the next 5 years. Erosion will be fully controlled in the near future. This means that yearly on the average 6-10 million cubic meters will be placed upon the coast.

references

- 1.VAN ALPHEN, J.S.L.J., RIBBERINK, J.S., ROELVINK, J.A., LOUISSE, C.J., HALLIE, F.P. (1990).
Offshore sand mining and nearshore profile nourishment.
These conference proceedings, Session The Dutch Coast: Paper No. 11.
- 2.DIJKMAN, M.J., BAKKER, W.T., DE VROEG, J.H. (1990).
Prediction of coastline evolution for specific parts of the Holland coast.
These conference proceedings, Session The Dutch Coast: Paper No. 7.
- 3.EYSINK, W.D. (1990).
Morphologic respons of tidal basins to changes.....
These conference proceedings, Session The Dutch Coast: Paper No. 8.
- 4.HOOZEMANS, F.M.J. (1990).
Long term changes in wind and wave climate on the North sea.
These conference proceedings, Session The Dutch Coast: Paper No. 3.
- 5.PLUIJM, M. (1990).
Seaward coastal defence for the Dutch coast.
These conference proceedings, Session The Dutch Coast: Paper No. 12.
- 6.ROELSE, P. (1990).
Beach and dune nourishments in The Netherlands.
These conference proceedings, Session The Dutch Coast: Paper No. 10.
7. RIJKSWATERSTAAT, (1989)
Coastal defence after 1990, (report in Dutch)
- 8.ROELVINK, J.A., STIVE, M.J.F. (1990).
Sand transport on the shoreface of the Holland coast.
These conference proceedings, Session The Dutch Coast: Paper No. 5.
- 9.STEETZEL, H. (1990).
Cross-shore transport during storm surges.
These conference proceedings, Session The Dutch Coast: Paper No. 6.
- 10.STIVE, M.J.F., ROELVINK, J.A., DE VRIEND, H.J. (1990).
Large scale coastal evolution concept.
These conference proceedings, Session The Dutch Coast: Paper No. 9.
- 11.TERWINDT, J.H.J., BATTJES, J.A. (1990).
(Implications for research on) Large scale coastal behaviour.
These conference proceedings, Session The Dutch Coast: Paper No. 13.
- 11.VAN VESSEM, P., STOLK, A. (1990).
Sand budget of the Dutch coast.
These conference proceedings, Session The Dutch Coast: Paper No. 4.
- 12.VERHAGEN, H.J. (1989)
Sand waves along the Dutch coast. Coastal Engineering, 13, 129-147.
- 13.VELLINGA, P. (1986)
Beach and dune erosion during storm surges, Thesis, DelftHydraulics Communications No. 372.
- 14.WIERSMA, J., ZITMAN, Tj. (1990).
Coastal Genesis I: Geological and historical development of the Dutch coast.

CHAPTER 141

RECONSTRUCTION OF THE HOLOCENE EVOLUTION OF THE DUTCH COAST

The Dutch Coast: Paper No. 2

Tjerk J. Zitman¹, Marcel J.F. Stive¹ and Hans (J.) Wiersma²

Abstract

In 1986 the TOW Coastal Engineering Research Programme was merged with the Coastal Genesis Research Programme. Rijkswaterstaat, the financier and initiator of these programmes, concluded that the growing interest in the longer term development of the coast in relation to sea-level rise and other climatic changes made it necessary to approach the research questions from a wider perspective than just the coastal engineering discipline. Geology, historical geography and physical geography were included as disciplines, and a multidisciplinary approach to a holistic understanding of the Dutch coast was undertaken. The results of the first phase of the Coastal Genesis Programme became available in 1987, comprising a reconstruction of the Holocene evolution of the Dutch coast, and a view on the available knowledge regarding the physical processes responsible for this evolution. A summary of the reported conclusions is given here.

1. Introduction

Since the early 1970's Rijkswaterstaat stimulated Dutch coastal research at Rijkswaterstaat, Delft University of Technology and Delft Hydraulics with the TOW Coastal Research Programme. This programme was mainly devoted to the study of coastal processes from the coastal engineering perspective.

Around 1985, initiated by coastal erosion management questions, an interest grew into larger scale, longer term coastal evolution processes and it was realized that the TOW Programme as such (i.e. focussing on coastal evolution processes of typical time- and length-scales of a year and a kilometer) was too limited in scope. In order to gain an understanding of large-scale, long-term coastal evolution, a variety of geo-morphological processes with a diversity of time- and length-scales needs to be considered, which, in turn, calls for the deployment of many specialisms. This approach has been applied in a new research programme, called Kustgenese (Coastal Genesis). In this programme, the fields of geo-morphology, hydro- and

1 DELFT HYDRAULICS, P.O. Box 152, 8300 AD Emmeloord, The Netherlands

2 Ministry of Transport and Public Works, North Sea Directorate,
P.O. Box 5807, 2280 HV Rijswijk, The Netherlands

morphodynamics, physical and historical geography and geology have been linked in order to study and understand coastal evolution at the scales of interest and, subsequently, to arrive at a (physical-mathematical) tool for coastal erosion and eventually coastal zone management.

The present paper deals with the first phase of the Coastal Genesis Programme, which resulted in a reconstruction of the Holocene evolution of the Dutch coast and a view on the available knowledge regarding the physical processes responsible for this evolution. Based on this, the main research items for the second phase of Coastal Genesis were identified (Terwindt and Battjes, Paper No. 10, these proceedings).

2. Research strategy

The Dutch coast is a complex morphological system with a length-scale of hundreds of kilometers. Since length-scales and time-scales are coupled in the sense that the larger the length-scale, the larger the time-scale (De Vriend, 1988), it immediately follows that in order to unravel this system, a large time-scale has to be considered. Against this background, it was decided to focus the first phase of the Coastal Genesis Programme on the evolution of the entire Dutch coast over the past 5000 years.

In fact, 'typical' time-scales of 100, 1000 and 5000 years were distinguished. For each of these time-scales, a working-group was formed and given the task to identify the physical processes dominating the coastal evolution at the given scale. The fields of geomorphology, hydrodynamics and physical geography took a leading position in the Working Group 100 and the activities in this group were mainly concerned with coastal modelling and gathering field data. Central in the Working Group 1000 were the fields of geology and historical geography and for the Working Group 5000 this position was taken by the field of geology.

The research strategy, applied in each of these working groups, is based on the rationale that the physical processes to be identified, form the link between the external conditions or constraints that influence coastal evolution (wave climate, currents, availability of sediment) and the corresponding morphological response in the coastal zone. In this respect, reconstructions of the external conditions and the actual coastal evolution have been made. These aspects, called Input and Output, respectively, were determined first. The natural link between the Input and the Output is formed by the (geo-)morphological processes and their interactions, shortly denoted as the System. Put together, this approach is called the ISO-method. Correlating the Input and the Output has led to hypotheses regarding the (potential) relevance of various morphological processes which fit in the System. In the description hereafter, the distinction between Input, System and Output is maintained.

3. Output: Reconstruction of the actual coastal evolution

A summary calendar of the Dutch Coastal evolution in the Holocene is given in Table 1. A more detailed description is as follows.

geological time	years BP	years AD	sea level (m)	event in coastol evolution
Pleistocene				
H O L O C E N E	10000			
	Preboreal			
	9000		- 25	8700 BP: Southern North Sea is formed
	Boreal			8300 BP: Connection between southern and northern North Sea
	8000	5500 BC	- 15	7800 BP: Coastline oppr. 25 km west of present locotion
	Atlantic			On average, the coastline retreats and barrier islands are formed in the eastern part of the country
	7000			
	6000			
	5000	3850 BC	- 4.5	5000 BP: Interconnection of borrier islands in the east; formation of old dunes; mouth of river Rhine becomes active; coastline 8 km east of present position and odvncing
	Subboreal			
4000		- 3.0		
3000	1100 BC	- 1.7	3200 BP: Closure of the inlet near Bergen	
2000			Coastal advance comes to an end and retreat begins; the mouth of the river Rhine becomes inactive	
Sublantic				
1000				
0	1987		NAP	+ 500 AD: Break-through of dunes in the south +1100 AD: Break-through of dunes in the north-west 1000-1600 AD: Formation of the young dunes

Table 1 Time table with the main events in the development of the Dutch coast (after Stive, 1987)

At the end of the last Glacial (Pleistocene), some 10,000 years ago, the area presently known as the southern North Sea was completely dry. It took about 2000 years before this area started to flood (Fig. 1). At first, the water came in from the south, through the English Channel. In the meantime, the northern North Sea was formed immediately south of the retreating polar ice. The separation between the southern and northern parts of the North Sea extended from

the present Dutch Wadden island Texel in western direction. It flooded approximately 8300 BP (BP stands for carbon-14 years before present). As the icecaps continued to melt, the sea transgraded. About 7500 BP, the Dutch coastline was situated some 25 kilometers west of its present position and migrated in eastern direction.

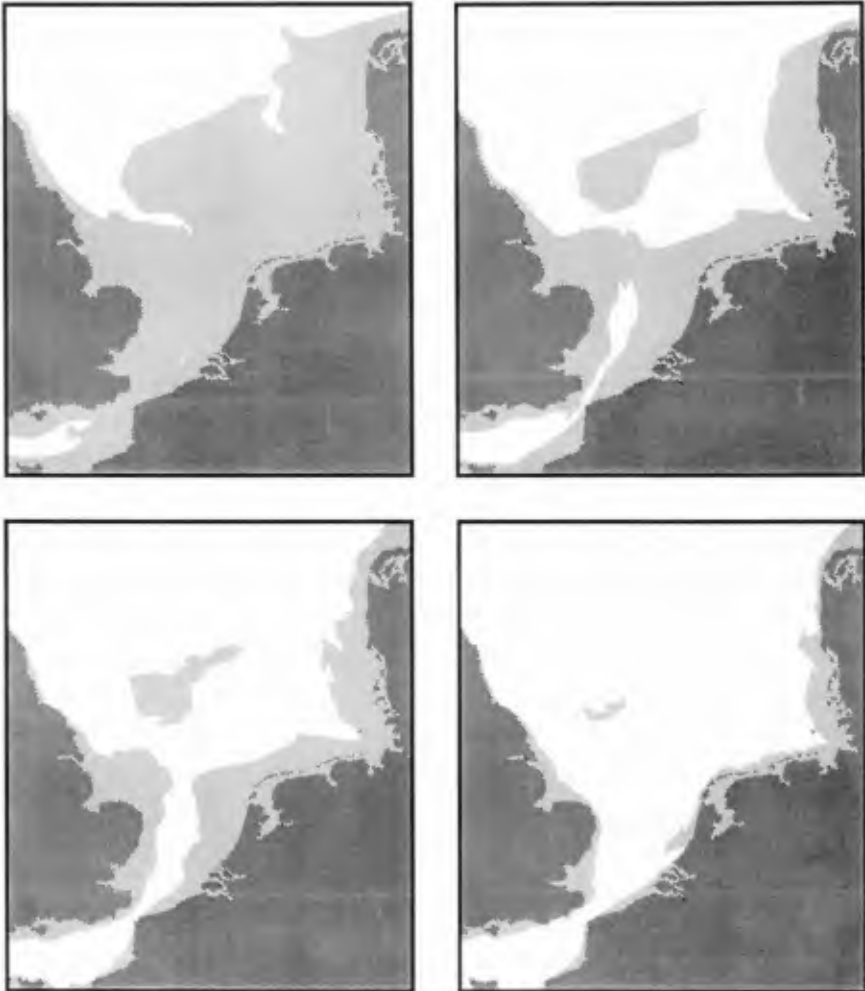


Figure 1 Four stages in the formation of the North Sea (after Zagwijn, 1986) at 9000 BP (a), 8700 BP (b), 8300 BP (c) and 7800 BP (d).

During the first 3000 years since the beginning of the Holocene, the rate of sea-level rise amounted approximately 1 meter/century.

This rate slightly decreased in the following 2000 years. A drastic decrease of this rate occurred around 5000 BP. Within a period of only a few centuries, the rate of sea-level rise almost decimated (Zagwijn, 1986).

These changes in the sea-level rise coincide with and are probably the cause of a turning point in the evolution of the Holland coast (Beets et al., 1990). When the rate of sea-level rise started to decrease significantly, the various tidal inlet systems were suppressed due to siltation processes in the direct vicinity of the main channel systems. As a result, barrier islands were formed originating from the sand reservoirs contained in the underwater deltas (from 7300 BP onwards). Interconnection of these islands took place around 5000 BP and led to a closed coastline at which, during the following 4000 years, the so-called old dunes were formed. In the meantime, the coastline advanced seaward, although the sea-level continued to rise.

The typical shape of a cross-section of these old dunes is low and wide. The amount of sediment contained in these dunes is approx. 62,000 m³ per meter along the coast. The period between 3000 and 1800 BP is characterized by an inversion of the coastline migration. Since that period, the Dutch west-coast has retreated almost continuously and from 1000 to 400 BP the so-called young dunes were formed on top of the old ones. These young dunes are higher than the old dunes, but much narrower. They contain about 14,000 m³ of sediment per meter in long-shore direction.

Before the interconnection of the barrier islands (i.e. before 5000 BP), the area behind these islands flooded with the tide (salt water) and with high river output (fresh water from the Rhine and Meuse). In this wet, brackish environment, peat started to grow and managed to keep pace with the rising sea-level. After the closure of the coastline, the brackish water was entirely replaced by fresh river water. This did not stop the growth of peat but merely caused a change in the type of peat (Van der Valk, 1990).

The retreat of the coastline (from 3000 BP onward) in combination with a continuously rising sea-level caused an increasing number of break-throughs in the dune coast. This initiated a chain of mutually intensifying processes. The first break-throughs caused the drainage of the peat area's behind the dunes. The allied subsidence gave way to extensive flooding and, thus, erosion of the peat. This occurred primarily in the north and in the south-west of the Netherlands and resulted in the Waddensea (north) and the Zeeland estuaries (south-west). The excavation and burning of peat, performed by our ancestors, have intensified this process.

The resulting coastal system has not shown any dramatic changes during the past few centuries. Especially since approximately 1850, the coastline has been intensely regulated by man. The coastal system can roughly be divided into three sub-systems: the estuaries in the south-west (the Delta-coast), the closed dune coast in the west (the Holland coast) and the barrier islands in the north (the Waddensea coast). The estuaries at the Delta-coast have been closed off almost completely after the flooding of 1953. The concave-shaped Holland-coast is slowly eroding at its outer ends, whereas the centre maintains a fairly stable position. However, the shoreface at

the centre of this part of the coast is steepening, so that there is effectively a loss of sediment. The erosion at the northern end of the Holland-coast is related to a vast accretion in the near-by part of the Waddensea, which becomes gradually shallower. These sub-systems of the Dutch coast are indicated in Figure 2.

Human interventions have influenced the coastal evolution since the early middle ages, when the first dykes were built. Especially during the past century this effect is noticeable.

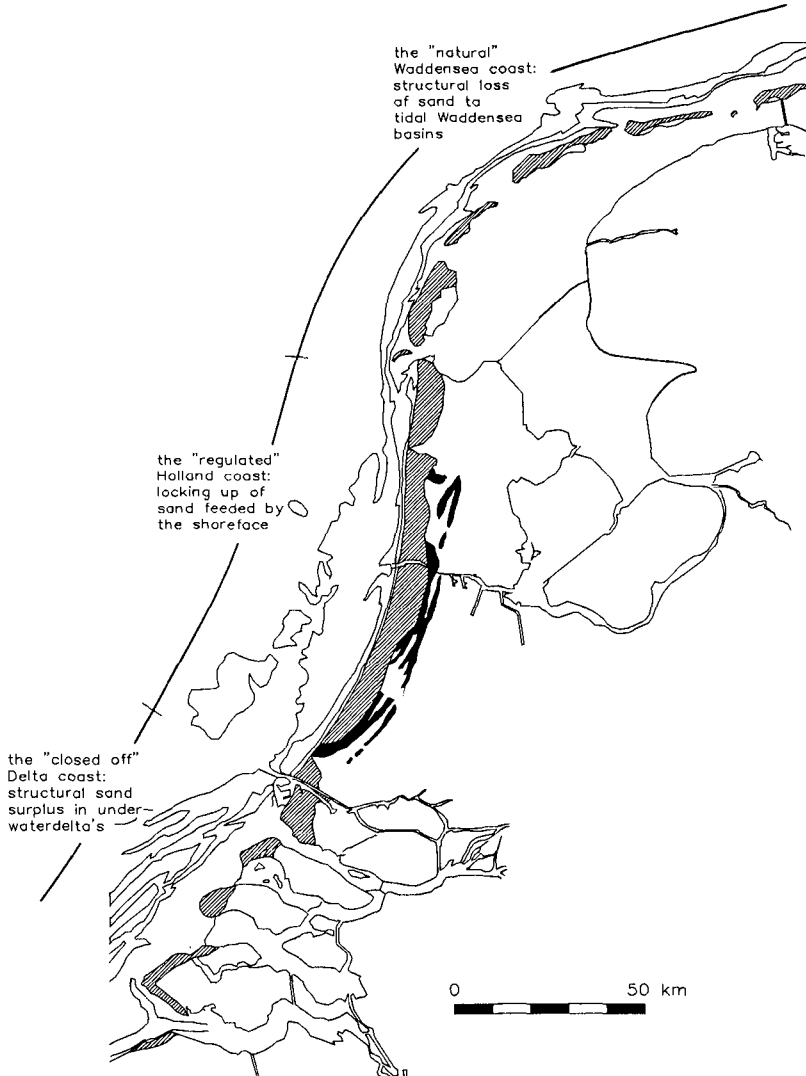


Figure 2 Subsystems of the Dutch Coast

4. Input: Reconstruction of the external conditions

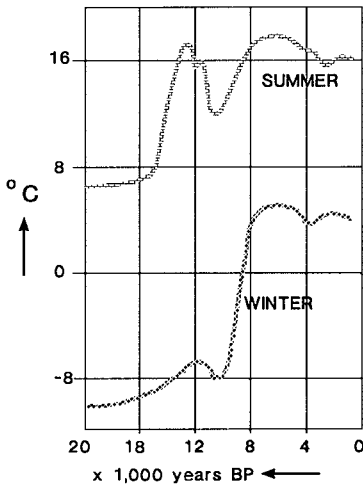


Figure 3 Supposed average summer and winter temperatures (after Lamb, 1982)

The end of the Pleistocene (appr. 10,000 BP) is marked by a sudden (on a geological time-scale) rise in the average winter temperature. Within a period of 2000 years, this temperature rose from appr. -8°C to appr. $+3^{\circ}\text{C}$ (Lamb, 1982; see Fig. 3). This change gave way to the melting of icecaps and, hence, to the formation of the North Sea.

The rise of the sea-level interacts with a number of supposedly important factors in coastal evolution. The horizontal sizes of the sea in combination with the bottom geometry and the water level clearly affects the propagation of the tidal wave and it

has a vast influence on the generation and propagation of wind-waves in the (relatively shallow) coastal area.

The relation between various characteristics of the wind-wave field on the one hand and the sea-level on the other hand has been indicated by Stive (1987; see Fig. 4). Apparently, the significant wave height and the wave period have stabilised after the decrease in the sea-level rise (5000 BP) whereas the wave skewness, an important measure for wave-driven sediment transport, has increased continuously. Furthermore, model computations have been carried out to reconstruct the changes in the tidal conditions due to a rising level of the North Sea (Franken, 1987; see Fig. 5 for an example).

With the rising (average) air temperature, the atmospheric conditions have changed. The dominant wind direction as well as the distribution of the wind speed over time and directions has changed over the years (Kollen, 1987; Hoozemans, Paper No. 3, these proceedings). This has a direct effect on the transport of sediment (aeolic transport), but it has also an indirect effect (wind-induced waves and currents).

5. Input-Output correlation

The purpose of correlating the reconstructed external conditions and the observed coastal evolution is to gain insight in the relevance of processes which determine the large-scale coastal evolution. In the long run, the morphological changes in the coastal zone are obviously determined by the availability of sediment. Hence, it is important to localize the potential sediment sources and sinks. Additionally, the intensity of the mechanisms that transport the sediment to and from these sources and sinks have to be determined.

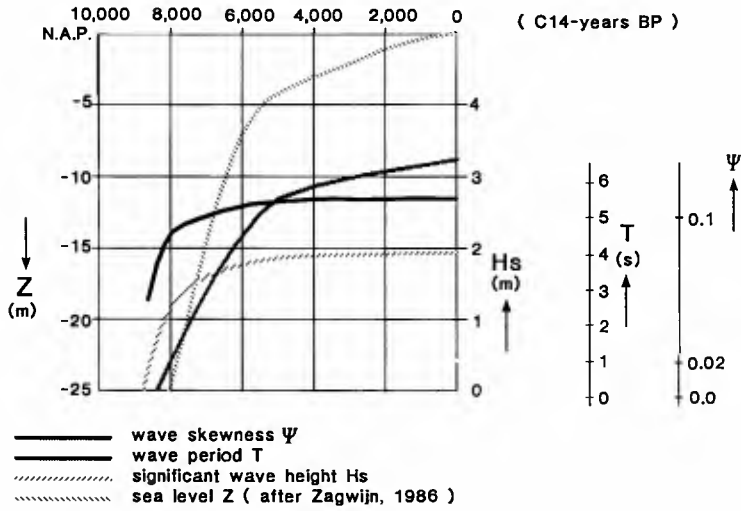


Figure 4 Changes in wave parameters in relation to the sea-level rise (after Stive, 1987).



Figure 5 Iso-amplitude lines and amphidromic points cooresponding to the semi-diurnal tide (after Franken, 1987).

One of these sources or sinks may be formed by a seaward boundary of the coastal system. For example, such a boundary could act as a sink if sediment can only be transported across this boundary in offshore direction. Van Vessem and Stolk (Paper No. 4, these proceedings) have searched for such a boundary, but could not find clear indications for the existence of one.

Tidal basins can act as a sink, for instance if a near equilibrium situation is disturbed by sea-level rise (Eysink, Paper No. 8, these proceedings). These basins appear to strive for an equilibrium ratio of their wet surface and their wet volume. A rising sea-level continuously disturbs this equilibrium in the sense that the basin becomes too deep in relation to its horizontal sizes. This results in accretion inside the basin at the expense of the nearby coastal area.

An important source is formed by sediment contained in river discharge. This way, material is brought into the coastal system at the river mouth and is distributed along the coast by longshore transport mechanisms. Before 5000 BP, the relatively high output of sediment from the rivers Rhine and Scheldt in combination with a transport of sediment from deeper towards the coast, has led to the formation of a delta. Later on, the sediment supply from these rivers decreased and the delta slowly eroded due to gradients in the longshore transport. This erosion process has also acted as a source of sediment.

An important item in the correlation of Input and Output was to gain insight into the relative importance of cross-shore and longshore transport of sediment. A survey has shown that a considerable part of the observed coastal evolution cannot be explained if only longshore transport is taken into account (Zitman, 1987). From this it was concluded that cross-shore transport is at least as important as long-shore transport. However, this survey did not yield any indications regarding the relevance of the involved physical processes. This has been investigated later (Roelvink and Stive, Paper No. 5; Steetzel, Paper No. 6; Stive et al., Paper No. 9; all in these proceedings).

6. Summary of hypotheses

The correlation of the external conditions and the reconstructed (observed) coastal evolution (input and output, respectively) has led to hypotheses regarding the relative importance of physical processes that have played a dominant role in the coastal evolution. This relative importance is dependent on the considered time-scale. Stive (1987) has given an overview of the hypotheses and their relevance in relation to the various time-scales. A summary of this overview is given hereafter.

Exchange of sediment between the nearshore and the inner shelf is a process of which the physics are not fully understood. Nevertheless, it is believed to explain much of the observed coastal evolution. There are no hard indications that there is a seaward boundary to this exchange on a time-scale of 100 years. This cross-shore transport is believed to have provided a considerable part of the material needed in the building up of the coast since the beginning

of the Holocene. Up to 5000 BP this building up kept pace with the rising sea-level. However, at that time the sea-level rise decreased. This, in combination with the earlier described closure of the tidal inlet system on the central Holland coast, yielded a sediment surplus in the nearshore which, eventually, resulted in the formation of barrier islands and the old dunes. Furthermore, cross-shore sediment transport is also believed to have played an important role in the formation of the young dunes, which started approximately 1000 years ago.

In contrast with the cross-shore sediment exchange, there is a good understanding of the physics behind the longshore transport of sediment in the nearshore zone. This type of transport is mainly wave-driven and takes place inside a comparatively narrow band along the coast. In this case, there is a closed system in which the sediment is redistributed along the coast due to gradients in the longshore transport. Examples of this process are the coastal retreat at the outer ends of the Holland coast (time-scale of 100 years) and the interrelation of the coastal advance and the erosion of the Rhine-Scheldt delta (from 5000 BP onwards).

On a time-scale of 1000 years, changes in the sea-level rise appear to be highly correlated with the formation of dunes. However, the understanding of this relation is insufficient to estimate its importance with respect to the observed coastal evolution.

The importance of (changes in) the tidal amplitude is even harder to estimate. The changes themselves can be roughly determined, but the knowledge regarding the physics behind the influence on coastal evolution is insufficient to determine its significance in this respect.

Human interventions in the coastal system are well-known. About 1000 years ago the peat areas behind the dunes were brought under cultivation. This has intensified the process of break-throughs of the dunes, especially in the northern and southern parts of the Dutch coast. This has contributed to the formation of the Wadden Sea (north) and the Zeeland estuaries (south). The effects of human interventions are also noticeable at a shorter time-scale. During the last 100 years, the Dutch coastline has been intensely regulated. Obviously, erosion control measures, the construction of defensive structures as dikes and dams have, at least locally, directed the coastal evolution.

7. Relation with subsequent phases of the coastal genesis programme

The first phase of the Coastal Genesis Project was completed at the end of 1987. It was concerned with a reconstruction of the Holocene evolution of the Dutch coast, the formulation of hypotheses on the physical processes behind this evolution and the, mainly qualitative, testing of these hypotheses. The research activities in this first phase have resulted in an overview of missing knowledge on relevant physical processes. Furthermore, an inventory was made of supplemental historical information required for understanding the observed coastal evolution. Phase I is reported in a main report (Stive, 1987) and five supporting reports (Kollen, 1987; Wind, 1987; Stolk et al. 1987; Keinalda, 1987; Zitman, 1987).

The second phase of the programme is in progress now. It was started around mid 1989 with a consultation of the international scientific world in the form of a Colloquium (Terwindt and Battjes, Paper No. 10, these proceedings). Consensus about the missing knowledge resulting from Phase I and this Colloquium has led to a research strategy for Phase II. Implementation of the gathered knowledge in partly conceptual physical-mathematical models, as well as the verification and testing of these models, is planned to be carried out in a third phase of the programme.

References

- Beets, D.J., Van der Valk, L., Stive, M.J.F. (1990).
Holocene evolution of the coast of Holland.
Manuscript to be submitted.
- De Vriend, H.J. (1988).
Inherent stability of depth-integrated mathematical models of coastal morphology.
Proc. IAHR symp. on math. modelling of sed. transport in the coastal zone, pp. 320-329.
- Eysink, W.D. (1990).
Morphological response of tidal basins to changes; Paper No. 8.
Proc. 22nd Int. Conf. on Coastal Eng., ASCE, New York.
- Franken, A.F. (1987).
Reconstructie van het paleo-getijklimaat in de Noordzee (in Dutch).
Delft Hydraulics report X0029-00.
- Hoozemans, F.M.J. (1990).
Long-term changes in wind and wave climate on the North Sea; Paper No. 3.
Proc. 22nd Int. Conf. on Coastal Eng., ASCE, New York.
- Kollen, J. (1987).
Coastal Genesis report 1: Overzicht van input gegevens (in Dutch).
Rijkswaterstaat, The Hague, The Netherlands, 15 pp.
- Roelvink, J.A., Stive, M.J.F. (1990).
Sand transport on the shoreface of the Holland Coast; Paper No. 5.
Proc. 22nd Int. Conf. on Coastal Eng., ASCE, New York.
- Reinalda, R. (1987).
Coastal Genesis report 4: Samenvatting diverse processtudies (in Dutch).
Rijkswaterstaat, The Hague, The Netherlands, 23 pp.
- Steetzel, H.J. (1990).
Cross-shore transport during storm surges; Paper No. 6.
Proc. 22nd Int. Conf. on Coastal Eng., ASCE, New York.
- Stive, M.J.F. (1987).
Coastal Genesis main report: Vorming en toetsing van hypothesen (in Dutch).
Rijkswaterstaat, The Hague, The Netherlands, 62 pp.

- Stive, M.J.F., Roelvink, J.A., De Vriend, H.J. (1990).
Large scale coastal evolution concept; Paper No. 9.
Proc. 22nd Int. Conf. on Coastal Eng., ASCE, New York.
- Stolk, A., Wiersma, J., Zitman, T.J. (1987).
Coastal Genesis report 3: Literatuurstudei grootschalige processen
(in Dutch).
Rijkswaterstaat, The Hague, The Netherlands, 121 pp.
- Terwindt, J.H.J., Battjes, J.A. (1990).
Research on large-scale coastal behaviour; Paper No. 10.
Proc. 22nd Int. Conf. on Coastal Eng., ASCE, New York.
- Van der Valk, L. (1990).
Holocene sea-level rise and its geological consequences.
Proc. 6th int. IAEG Congress, pp. 249-255.
- Van Vessem, P., Stolk, A. (1990).
Sand budget of the Dutch coast; Paper No. 4.
Proc. 22nd Int. Conf. on Coastal Eng., ASCE, New York.
- Wind, H.G. (1987).
Coastal Genesis report 2: Overzicht van bijdragen uit de taakgroepen
(in Dutch).
Rijkswaterstaat, The Hague, The Netherlands, 20 pp.
- Zagwijn, W.H. (1986).
Geologie van Nederland, deel I: Nederland in het Holoceen (in
Dutch).
Rijks Geologische Dienst Haarlem, staatsuitgeverij.
- Zitman, T.J. (1987).
Coastal Genesis report 5: Analyse van de rol van langstransport bij
de ontwikkeling van de Hollandse kust (in Dutch).
Rijkswaterstaat, The Hague, The Netherlands, 42 pp.

CHAPTER 142

LONG TERM CHANGES IN WIND AND WAVE CLIMATE ON THE NORTH SEA

The Dutch Coast: Paper No. 3

Frank M.J. Hoozemans¹

Introduction

This paper presents the first results of a study on the wind and wave climate along the Dutch coast of the North Sea. The analysis of time series of wind force, wave height, wind direction, etc, identifies the occurrence of long term changes in wind and (wind)wave climate. In the Dutch Coastal Defence Study, the results of these climate analyses were used to develop the so called "unfavourable hydro-meteorological scenario" with which an evaluation was made of the extreme impact of the shore line retreat of the Dutch coast. The wind and wave climate study is part of a project that examines the relation between changes in the regional wind and wave climate and the long term and large scale morphological development of the Dutch coast.

Method

For the study concerning coastal behaviour in relation with climatic changes, continuous time series of meteorologic and oceanographic data are of paramount importance. The available time series of wind waves in the Dutch part of the North Sea, cover a rather short period. To gather information over longer periods supplementary sources have to be found (for the period that wind wave data is lacking). Wind data of light vessels off the Dutch coast confirm to the requirements.

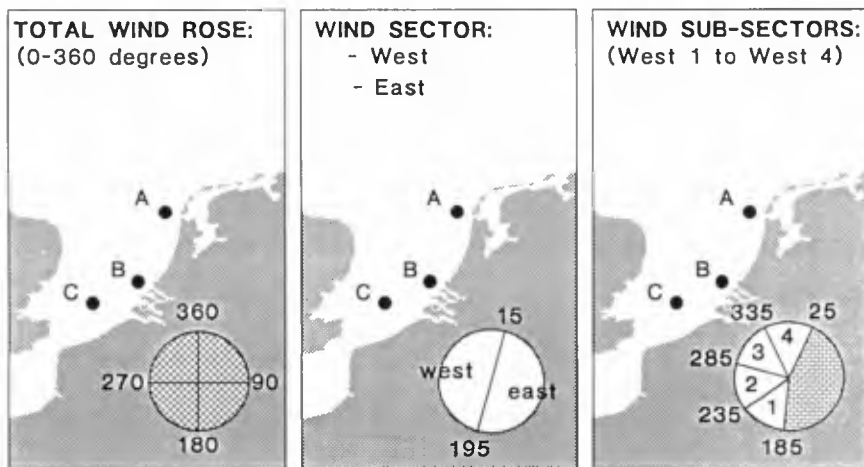
Between 1859 and 1982 various light vessels were stationed off the Dutch coast (Figure 1) to collect meteorological data such as; temperature, wind force and wind direction. As from 1926, the data collected included details of wave conditions and as from 1949 sea-state as well as swell (far field effect) were recorded separately. From that year onwards wave direction, wave period and wave height are available. The climate analysis of this study covers the period 1907-1980 and is in the first part of the project concentrated on wind data.

Analysis of this meteorologic and oceanographic data is concentrated on the time series of mean annual values of wind velocity,

¹ DELFT HYDRAULICS, P.O. Box 152, 8300 AD Emmeloord, The Netherlands

wind percentage and wind direction. Trends in the mean climatologic data indicate long term changes. To identify these trends linear regression techniques were applied. Apart from these trends the time series also seem to contain periodic changes. Since the period of these changes is rather large with respect to the length of the time series, determination of this feature is difficult. Since data of more than one light vessel is available for the same registration period, variations along the coast can be determined. The wind climate analysis is executed for several wind fields (see Figure 1):

1. The total wind rose which covers 360 degrees.
2. A division of the wind rose in two wind sectors WEST and EAST.
3. A subdivision of sector WEST into 4 sub sectors WEST-1 to WEST-4.



- A: Haaks & Texel
 B: Schouwenbank & Goeree
 C: Noordhinder

Figure 1 Wind field division and position light vessels

Results

Wind direction:

Changes in wind and wave climate of sector WEST [195-015°] in the Dutch part of the North Sea do occur. Figure 2 shows the mean annual wind direction measured at three Dutch light vessels of wind sector WEST. The figure shows a backing of the wind for period 1907-1924, a veering of the wind for period 1925-1938 (no high registration density between 1939-1948) and a more or less steady wind direction for the period from 1949 onwards.

Wind velocity:

Analysis of the mean wind velocity shows an increasing wind velocity when period 1907-1940 is compared with period 1950-1980.

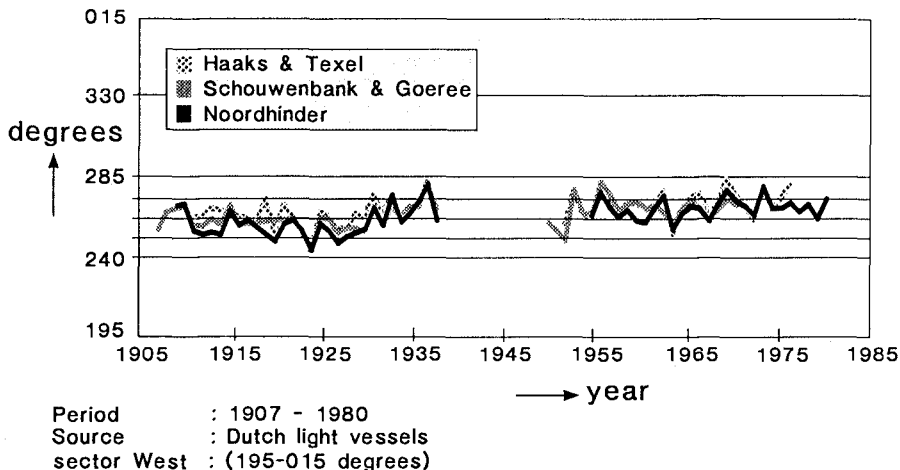


Figure 2 Mean wind direction

Figure 3 shows the mean annual wind velocity measured at three Dutch light vessels supplied with wind data of coast station Den Helder (situated in the north of Holland near light vessels Haaks/ Texel) and a German light vessel/-station Scharhorn and Elbe-1 (situated in the estuary of the river Elbe).

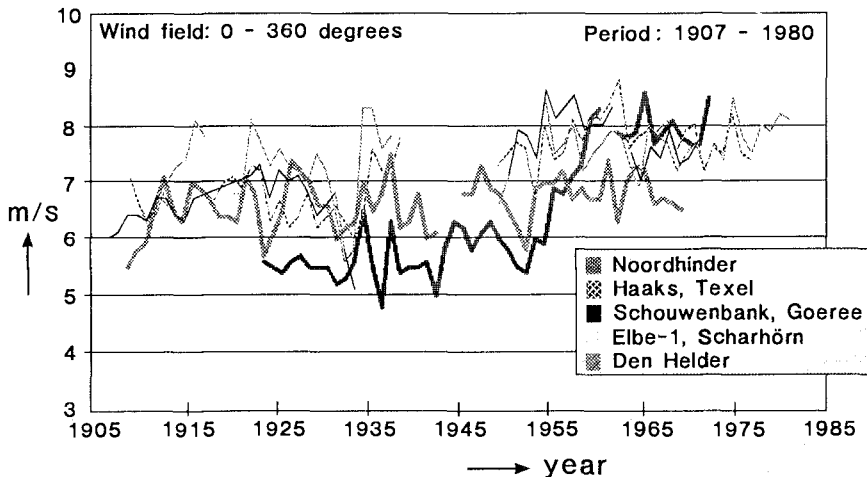


Figure 3 Mean wind velocity

Figure 4 shows the mean annual wind velocity of light vessels Haaks & Texel for the four sub sectors separately. The diagram shows an identical increase in time as figure 3, but far more important are the differences between the sub sectors. Sector West-4 contains

the lowest mean wind vector increase and the three other sub sectors, especially sub sector West-3, contain the highest increase.

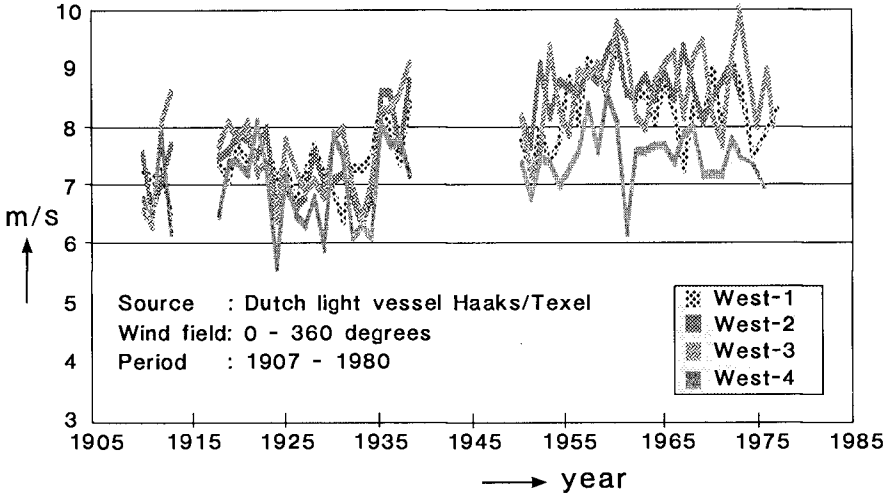
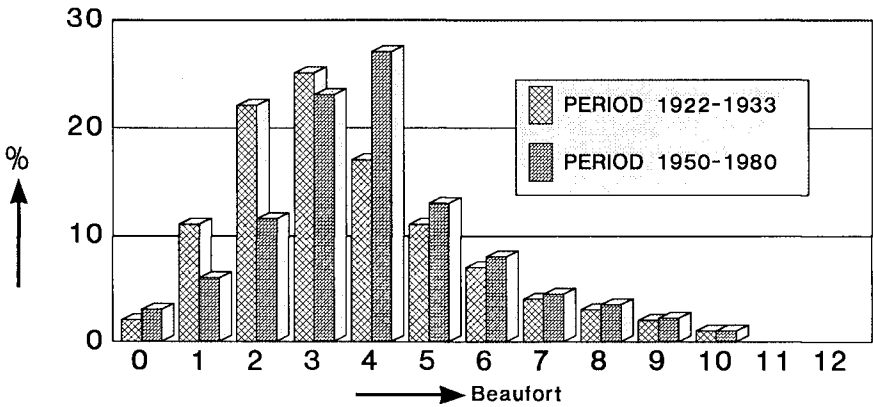


Figure 4 Mean wind velocity

Figure 5 shows the percentage of each Beaufort class of the total wind field for two periods: from 1922 to 1933 and from 1950 to 1980. The histogram shows an increasing force when the two periods are compared. Beaufort class three shows the highest percentage for the period between 1922 and 1933, but this mode has changed into Beaufort class four for the period between 1950 and 1980.



Source : Dutch light vessels
 Wind field: 0 - 360 degrees

Figure 5 Frequency distribution scale numbers of Beaufort

Frequency of wind:

A third wind parameter, the frequency of wind in a sector, shows a decreasing frequency of wind in sector WEST.

Conclusions based on wind analyses:

It can be concluded that the wind climate along the Dutch coast has changed in the period 1960-1980: a veering of the wind direction, an increasing wind velocity and a decreasing wind percentage in sector WEST. Significant spatial differences in wind climate between the several light vessels along the coast could not be found.

Wave height:

Parallel to wind observations, the visual wave height ($H_v \approx H_s$) has been estimated between 1949 and 1982. These observations are less reliable than the time series of wind parameters. Figure 6 shows the mean annual significant wave height measured at three Dutch light vessels. For comparison this figure also shows the series of light vessel Seven Stones (south-west England).

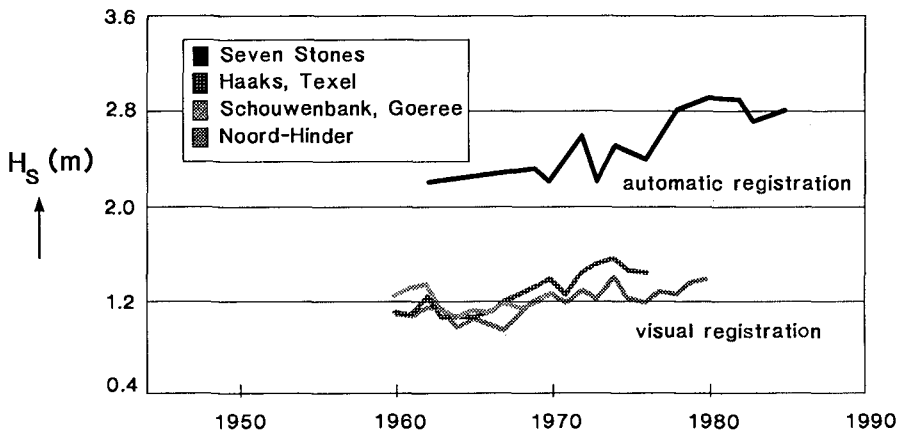


Figure 6 Mean annual significant wave height measured at Dutch and English light vessels

In the Coastal Defence Study the effects of three hydro-meteorologic scenarios have been investigated. The major factor in these scenarios is a sea level rise. The first two scenarios only concern a sea level rise (the present-day sea level rise of 20 cm/century, the expected scenario of 60 cm/century). In the third scenario, which was supposed to present an unfavourable development of hydro-meteorologic conditions, also changes in wind and wave climate were included (a veering of the wind direction of 10° in the most unfavourable direction and an increasing wind velocity of 10%). An indication of the magnitude of these changes expressed in this unfavourable scenario was derived from rough wind data analyses. In the present study the wind parameters are statistically determined. The related values of the wave climate and wave and wind setup are derived by model analysis. Since the Dutch coast is mainly exposed to the west this analysis is focused on the sector West. The results are presented in Figure 7. The values in the centre column present

the mean climate of the period 1907-1980. Column "DEVIATION + 2σ " corresponds to the unfavourable scenario.

PARAMETERS	DEVIATION (-2 σ)	HYDRAULIC SCENARIO	DEVIATION (+2 σ)	DIM
Mean Wind Velocity	6.6	8.0	9.4	m/s
Mean Wind Direction	250	265	281	°
Mean Wave Height	1.0	1.3	1.7	m
Mean Wave Frequency	0.25	0.22	0.19	Hz
Mean Wave Direction	250	265	281	°
Mean Wave Setup	3	10	13	cm
Mean Wind Setup	5	11	21	cm

Figure 7 Effect of variations in westerly winds (195-015 degrees) on hydraulic parameters

Further research

Time series of the above mentioned wind parameters will be used as input variables for wave and transport models. With these models the effect of climatic changes on the hydraulic conditions can be analyzed as well as the impact on the large scale development of the Dutch coast (e.g. coastal erosion or accretion).

There is a relation between the regional climate on the North Sea and the mondial climate of the Northern hemisphere. Changes in the mondial climate have a direct (e.g. displacement of depressions to the north) as well an indirect effect (e.g. far field effect on height of swell). If possible, a simple relation has to be found between the mondial and regional climate in which the far field effect will play an important role.

In the course of time, several authors have given a relation between changes in wind direction, seasonal temperature amplitudes, stability of air masses on sea level, coastal behaviour, etc. The above mentioned meteorologic, oceanographic and morphometric time series will certainly contribute to the knowledge of coastal behaviour as a response to changes in climate.

References

- Hoozemans F.M.J. (1989).
The wind climate along the Dutch coast of the North Sea: period 1907-1980 (in Dutch),
Rijkswaterstaat, Tidal Waters division, GWA0-89.010.
- Hoozemans F.M.J. and Wiersma, J. (1989).
Is mean wave height in the North Sea increasing?
Rijkswaterstaat, Tidal Waters Division, GWA0-89.004.

Carter D.J.T. and Draper, L. (1988).
Has the North Sea become rougher?
Nature Vol. 332, pp. 494.

Louisse C.J. and Kuik, A.J. (1990).
Coastal defence alternatives for the Netherlands.
Proceedings of this conference, session The Dutch Coast,

CHAPTER 143

SAND BUDGET OF THE DUTCH COAST

The Dutch Coast: Paper No. 4

P. van Vessem 1) A. Stolk 1)

1. Introduction

About 255 kilometer (70%) of the Dutch coast is protected against flooding and storm surges by dunes. Another 43 kilometer is defended by dikes with a sandy nearshore. The sand is transported by physical processes in alongshore and onshore-offshore direction. As a result the coast shows continuous alternations. A detailed sand budget is very useful to gain insight into the dynamics of the coast and of different morphological zones. Within the framework of the Coastal Defence Study in the Netherlands recent advances in modelling of large scale coastal development were made (Louisse and Kuik, 1990; Stive, Roelvink and De Vriend, 1990). Verification and calibration of these models is possible by comparing the model results with the sand budget of the coast. According to the Shore Protection Manual (1984) the sediment budget is defined as a sediment transport volume balance for a selected segment of the coast. The elements of the budget are processes that increase (sources) or decrease (sinks) the quantity of sand in a defined control volume. Usually a sand budget analysis is made to calculate an unknown erosion or deposition rate by estimating the different elements of the budget like for instance longshore transport, on- and offshore sand movement and the building or erosion of dunes. The method is clearly described by Bowen and Inman (1966) and Chapman (1981).

The balance itself is defined by Bowen and Inman (1966) and Komar (1983) as the component of the budget that gives the net gain or loss of sand in a control volume. This balance is obtained by monitoring the erosion or deposition rate over a number of years. This paper is concerned with the sand balance of the Dutch coast over the years 1965 - 1986. A method for calculating the balance based on yearly measured profiles is described. Besides the more general results for the Dutch coast a more detailed example of the Schouwen peninsula is given.

1) Rijkswaterstaat, Tidal Waters Division, P.O.Box 20907, 2500 EX The Hague, The Netherlands.

2. Measurements

Along the Dutch coast in the second half of the 19th century a monitoring system was set up to observe the coastal development. Therefore along the whole Dutch North Sea coast poles were placed on the beach at a distance of 1000 m. The line connecting these poles is the reference line for coastal monitoring. The beach poles were placed between the mean high water line and the foot of the dune.

The position of the mean low water line, the mean high water line and location of the foot of the dune is measured yearly with respect to the reference line. In this way a detailed picture of the development of the coastline during the last 100 to 140 years is obtained.

Since 1964 the morphological monitoring is considerably enhanced. A system of about 2000 fixed measuring lines perpendicular to the coastline has been established. The distance between the lines is 200 - 250 meter, less where the coastline is curved.

The height and depth are determined in respect to Dutch Ordnance Datum (NAP) which is about mean sea level. To define the horizontal position in the profiles the original reference line is maintained. Because of the coastline changes since the poles were placed there is no relation between the location of the reference line and the present morphology.

Until 1975 the measurements of the dry part of the profiles were carried out by levelling from the mean low water line to the top of the first dune row. From 1975 onwards the heights are determined by aerialphotography and were extended to at least 200 meter inland from the top of the first dune row.

The measurements of the underwater part of the profiles are carried out by echo-sounding from the low water line to at least 800 m out of the reference line. In several parts of the coast, especially in the Wadden Area the profiles reach much further seaward, up to about 1500 meter.

The survey area includes the first dune row, the beach and the surfzone. Some tidal channels in front of the Delta en Wadden Islands are situated within the reach of the measurements. The tidal deltas and inlets are not included in the data set.

The profiles are measured annually in the non-storm period from April to September and are not equidistant in time. Apart from normal measurement inaccuracy the dataset still contains systematic and random errors due to wrong individual height or depth values or to faults in the distance to the reference line or reference height. To correct for these errors a visual validation is executed by plotting all the yearly profiles of a measuring line together and remove or correct the unreliable values. This procedure can lead to the elimination of yearly profiles or to total elimination of a measuring line from the data set.

In the years before 1975 the levelling was not executed far enough inland to reach a more or less closed boundary in the dunes. The photogrammetrical height measurements do come up to this requirement. For the coast of Holland it was possible to lengthen the earlier profiles by complementary investigations of detailed maps of the dune area (De Ruig, 1987). The dunes in the Wadden Area and the Delta Area are too dynamic to allow such a procedure.

In addition to the yearly measurements every 5 year 2500 m long profiles are measured with an interval of 1000 m along the coast. This has resulted in a dataset of 3 to 4 profiles for each measuring line, what is not yet sufficient for a reliable trend analysis.

3. Method

To make a useful sand balance the following main conditions are specified:

- the relation between the transport processes and the morphological changes must be well connected
- the balance must describe the natural development of the coast (as far as possible on the Dutch coast with dikes, revetments, groynes and harbour moles)
- the control volume only consists of those parts of the nearshore from which the sediment transport is directly related to the safety of the coast.

The first condition means that the changes in volumetric content between predefined upper and lower boundaries must be calculated. Every part of the profile within such a layer accounts for the content (figure 1).

Optionally the upper boundary coincides with the maximum height measured in a yearly profile. This option is used if one wishes to calculate the yearly loss or gain of sediment due to storm surges and eolian sand transport. The other option is to choose a relevant height, for instance mean low-water level.

The lower boundary is formed by the maximum depth within the reach of all measured depths of a specific profile or by an other suitable depth.

It is obvious that the position of the horizontal boundaries determines which of the morphological processes account for the calculated changes.

The already mentioned landward boundary is situated landward of the first dune row. It is preferable that inland of this point the elevation of the profile is more or less constant. In this case there is no net transport through the boundary. Otherwise the transport rate has to be estimated.

All the boundaries are determined for each profile and are time independent, except for the optional "free" upper boundary.

To calculate the volumetric content between two adjacent profiles it is assumed that a profile is representative for the area between the profile and the bisector (figure 1). Given a horizontal distance of less than 200 - 250 m this seems a realistic assumption. Only for small-scale safety problems this assumption must be checked. The first calculated area between two profiles coincides with the lower boundary. This area is multiplied by a given height of 0.1 meter and the procedure is repeated until the upper boundary is reached. The content of the control volume is calculated.

From 1952 onwards beach nourishment projects have been carried out at several locations. Because the sand balance must give insight in the "natural" development of the Dutch coast (second mentioned limiting condition) the calculated contents are corrected with the amount of supplied sand brought into the control volume (Roelse, 1990). There is no correction made for the possible loss of supplied material out of the control volume due to the redistribution of sediment.

Also activities to restore the dune profile after storm surges can influence the amount of sand in the control volume. Other examples of artificial displacement of sand are the building and conservation of elevated beach sections against the dunes to protect recreational facilities on the beach. It is assumed that the involved quantities are small compared with natural sand transport rates. Usually there is only a redistribution of sand within the control volume.

Given the corrected yearly sand content, the net gain or loss of sand in a given period

is calculated by a linear regression analysis.

To gain insight in the annual variations the mean, minimum and maximum value of the difference in sand volumes of the successive years are calculated. Short-term events, such as storm surges, are averaged out.

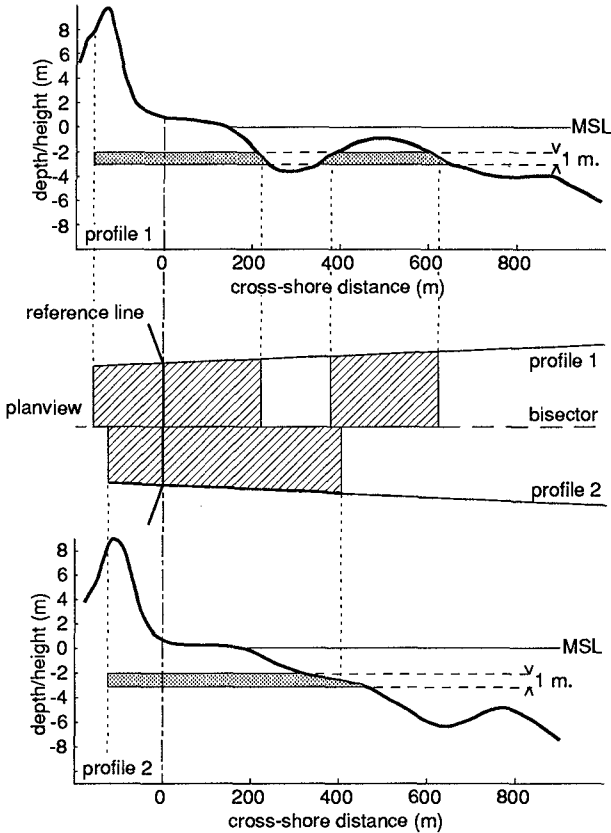


figure 1. Sketch to define the calculation procedure.

4. Results Dutch coast sections

As a first approach the changes in volumetric content of 13 coast sections are calculated. These sections are separated from each other by ebb tidal deltas (Wadden), harbour moles (coast of Holland) and estuaries and tidal basins (Delta). These interruptions are the cause of a more or less independent development of adjacent sections. All sections have specific control volumes from which the balance is calculated.

The length of a section is determined by the first and last measuring line.

The vertical dimension depends, besides on the length of the measured profiles, on the

local morphology. The lower boundary varies from 3 - 10 m along the central parts of the islands and the coast of Holland. The depth of the tidal channels within reach of the measurements varies from 10 - 30 meter. The upper boundary coincides with the maximum height of the profile. This means that sedimentation or erosion in the first dune row are accounted for.

The measurements on the coast of Holland are far enough inland to reach a more or less closed boundary (de Ruig, 1987) The transport rate across the landward boundary in the Wadden and Delta Area are not yet estimated.

It is certain that the lower boundary do not reach the closure depth for cross-shore sand transport at de Dutch coast. This is indicated by the 5 yearly measurements and other, more local, repeated profiling which extended to a greater depth. Roelvink (1990) calculated an onshore transport across the -10 meter line in the order of 10 m³/m/year. This is an important source term in the sand budget.

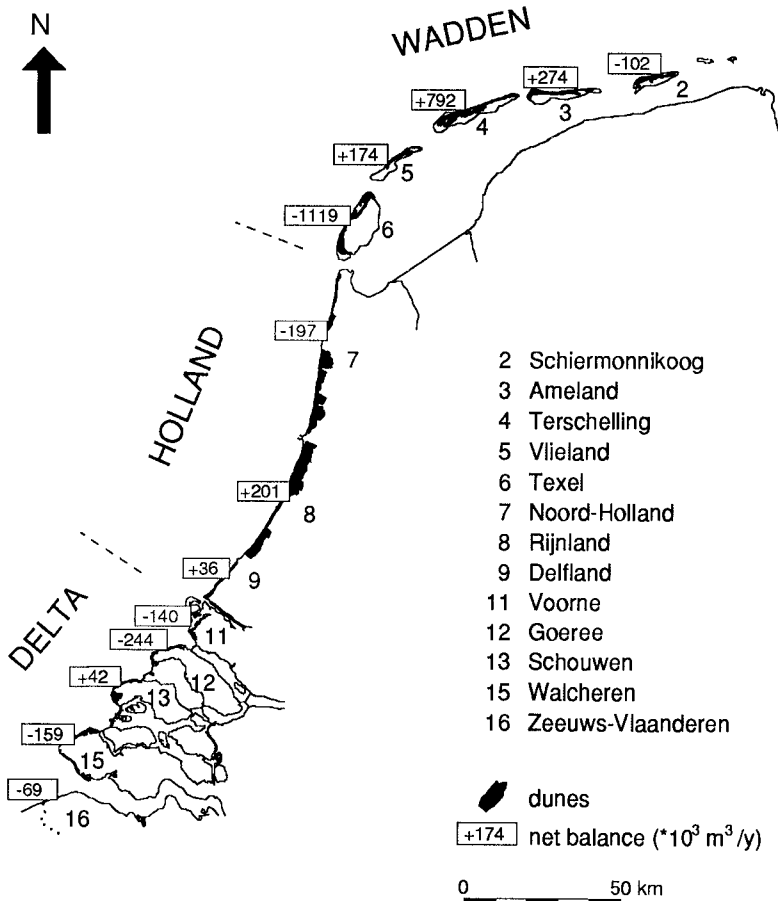


figure 2. Calculated sand balance of the Dutch coast.

Despite of the above mentioned uncertainties the sand balance is calculated (figure 2). The total sum of $-511 \cdot 10^3 \text{ m}^3/\text{y}$ indicates that over the specified period of 20 years and a length of about 302 km the Dutch coast is very slowly eroding ($-2 \text{ m}^3/\text{m}/\text{y}$). On the scale of separate coast sections, 8 - 53 km, the variability is much greater. Trends normalized to coast length of -41 up to $+28 \text{ m}^3/\text{m}/\text{y}$ are calculated (table 1). The difference between the coastal sections are great in respect to the total sum.

The dynamic of a sandy coast is best illustrated by the yearly fluctuations. The mean value varies from 19 to $68 \text{ m}^3/\text{m}/\text{y}$. The minimum and maximum yearly difference amount to respectively 0 and $369 \text{ m}^3/\text{m}/\text{y}$. Due to this large time variability the reliability of the calculated trends depends strongly on the number of validated measured years.

table 1. Calculated sand balance of the Dutch coast.

	period	trend $\text{m}^3/\text{m}/\text{y}$	yearly fluctuations		
			mean $\text{m}^3/\text{m}/\text{y}$	minimum $\text{m}^3/\text{m}/\text{y}$	maximum $\text{m}^3/\text{m}/\text{y}$
Schiermonnikoog	1966-1986	-7.	45.6	9.4	195.5
Ameland	1968-1984	11.	51.7	10.8	226.5
Terschelling	1969-1985	28.	45.9	3.8	146.3
Vlieland	1970-1984	8.	60.5	4.2	171.8
Texel	1965-1986	-41.	44.0	6.7	109.1
Noord-Holland	1965-1984	-4.	19.4	2.1	58.9
Rijnland	1965-1984	4.	33.3	6.2	79.3
Delfland	1965-1984	3.	62.4	0.4	142.2
Voorne	1966-1972	-17.	20.5	7.3	49.9
Goeree	1967-1981	-25.	67.8	1.2	369.4
Schouwen	1968-1983	3.	24.3	0.3	53.0
Walcheren	1969-1986	-6.	21.2	1.4	44.6
Zeeuws-Vlaanderen	1966-1984	-5.	40.2	8.2	150.2

5 Result Schouwen

5.1 Introduction

The peninsula of Schouwen is situated in the Delta Area between the tidal basins "Grevelingen" in the north and "Oosterschelde" in the south (figure 3). The tidal channel "Brouwershavense Gat" in front of the north coast of Schouwen is silting up now, due to the closure of the Grevelingen basin in 1972. A branch of this tidal channel, the "Schaar van Renesse" is situated very close to the coastline (figure 4). In the south the "Westgat" is one of the main tidal channels at the entry of the Oosterschelde. There is another tidal channel, "Krabbengat", around the west coast (figure 4). The tidal range is 2.5 meter.

The human interference with the about 17 km long North Sea coast of Schouwen is restricted to the construction of groyne on the northern part and pile rows on the western

part. Furthermore, there is the usual maintenance of the first dune row like planting of beach grass. The groynes were placed in the middle of the 19th century and were very effective in preventing coastline erosion by the Schaar van Renesse (Verhagen, 1989a). The coastal development in this coastal stretch is not complicated by beach or dune nourishment in the period (1968 - 1983).

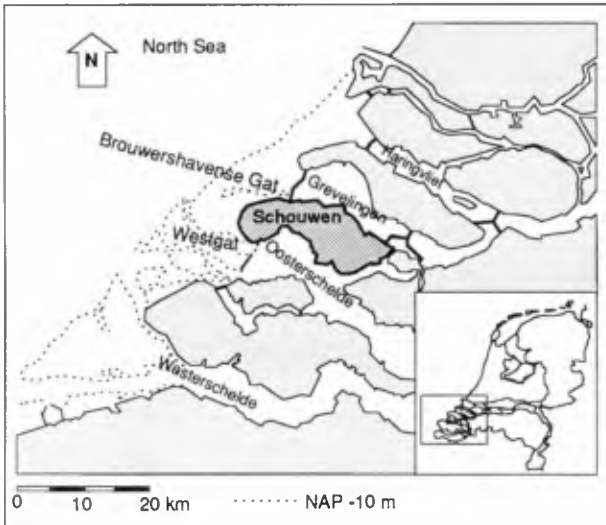


figure 3. The Delta Area with the peninsula of Schouwen.

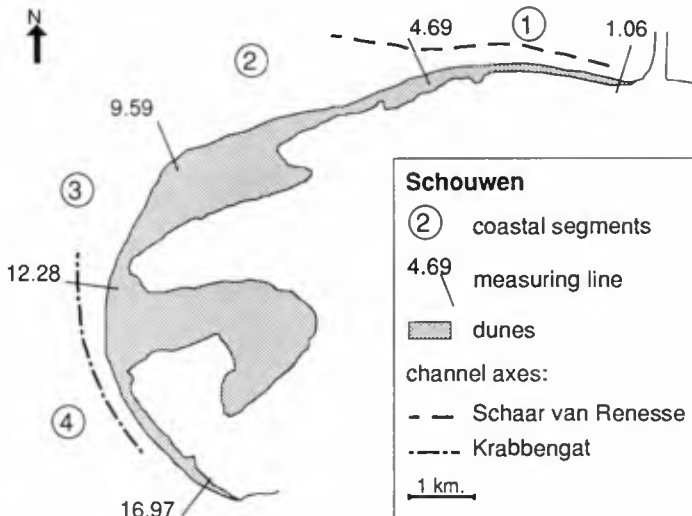


figure 4. Dune coast of Schouwen with channel axes within reach of measurements.

5.2 Profiles

The measuring lines along the part of the coast considered in this case study are numbered from beach pole 1.06 to beach pole 16.97 (figure 4). The numbering of the poles is related to a kilometer scale so the length of coast along the reference line is 15.9 km. In this area 91 measuring lines are situated.

The profile along the coast of Schouwen is not uniform but shows spatial and temporal variations. There is an obvious morphological difference between the northernmost and western coastal stretches, where tidal channels are situated close to the coastline, and the central part where the nearshore profile is more gentle. In the central part the beach is wide and in front of the first dune row some primary dunes have been formed.

There is also a temporal variation in profile morphology. In general the coastal development from 1965 - 1986 does not show a parallel retreat or a parallel progradation over the whole profile.

The coast of Schouwen shows different types of profile development. In a first approximation we divide the profile in an upper part, the dunes, and a lower part, the (upper) shoreface and make a visual estimation of the profile development in three classes; sedimentation, stability and erosion.

A matrix of this kind of two classes gives nine possibilities for profile development. When we group the profiles in the matrix we see that the coast of Schouwen shows all possibilities except a total stable profile (table 2).

table 2. Different classes of profile development, Schouwen.

dunes	(upper) shoreface		
	sedimentation	stable	erosion
sedimentation	4.1 km (25.2%)	0.4 km (2.5%)	1.8 km (11.0%)
stable	3.1 km (19.0%)	-	1.2 km (7.4%)
erosion	1.2 km (7.4%)	1.0 km (6.1%)	3,5 km (21.5%)

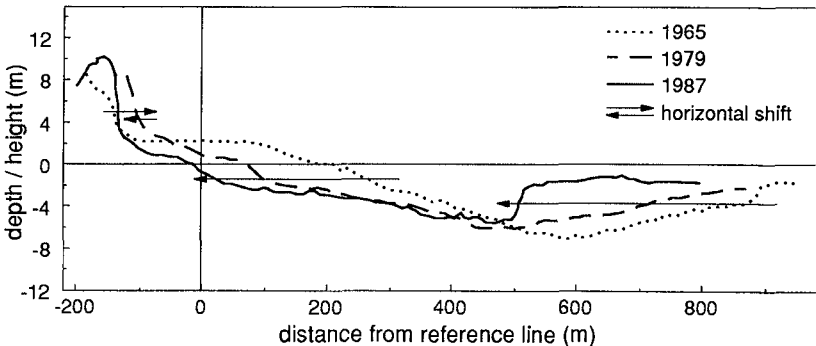


figure 5. Coastal profiles along measuring line 9.59 at Schouwen.

The profiles that show either total sedimentation or total erosion are well represented (25.2 and 21.5% of the coast length). In more than half of the coastal stretch (51.6%) there is a net sedimentation on the shoreface. About forty percent is eroding. In the dunes the classes are more equally represented; 38.7% of the dunes show sedimentation, 35.0% erosion, and 26.4% is stable in the period 1965 - 1986.

An example of profile development is given in figure 5, where some profiles are drawn for measuring line no. 9.59, situated at the very west of the peninsula. This example illustrates the steepening of a dune profile to a certain maximal gradient. The dunefront migrates seaward in the period 1965 - 1979. A landward migration of a small branch of the Krabbengat caused a shifting of the nearshore profile in a landward direction. Therefore the seaward movement of the dune is interrupted and inverted to a landward movement from 1980 onwards because of undermining of the dunefront. Over the period 1965 - 1986 there still is a net sedimentation in the dunes, but when the process goes on the sediment volume in the dunes will soon come down to the value of 1965. On the basis of the different categories of profile development four coastal segments can be distinguished (table 3; figure 4).

table 3. Coastal segments Schouwen.

segment (measuring lines)	profile development
1 (1.06 - 4.69)	stable or eroding dunes and sedimentation in the nearshore
2 (4.69 - 9.59)	sedimentation in the dunes and mainly sedimentation in the nearshore
3 (9.59 - 12.28)	strongly varying profile development in both the dunes and the nearshore
4 (12.28 - 16.97)	mainly erosion in the dunes and nearshore

table 4. Migration mean low-water line (m/y) at Schouwen (+ progradation - recession)

segment	1900-1984 (*1880-1984)	1964-1984
1	+0.17 (*)	+1.70
2	+2.84	+7.76
3	-3.28	+2.79
4	-1.91	-2.29

5.3 Sand balance

The sand balance is calculated for the North Sea coast of Schouwen between measuring line 1.06 and 16.97 as well as for the four segments separately. The landward and seaward boundaries of the control volume are selected according to the procedure described in section 3. So a control volume is defined for which the calculated trends are reliable. The area for which the sand balance is calculated is not uniform in distance to the coastline and in maximum height and depth of the profiles (figure 6). On the landward side always the first dune row is included, except in segment 4. In segment 4 the landward side of the control volume was chosen at the end of the profiles of the first years of the monitoring. These profiles were too short to cover the position of the dune top in later years. So the top of the first dune row moves out of the control volume in this area.

Because of the variation in height of the dunes the maximum height of the control volume varies along the coast. Because of the variation of the seaward boundary along the coast and the variation in local morphology the depth of the seaward boundary is also varying. Figure 7 shows the volumetric contents of the control volume for the period 1968 - 1983. Some years are not included in the calculation, because there were no reliable data for the whole coast of Schouwen. There is a considerable variation in the sand content from year to year, with a minimum of $4 \cdot 10^3$ m³ between 1979 and 1980, and a maximum of $841 \cdot 10^3$ m³ between 1970 and 1971. The fluctuations demonstrate that the coast is highly dynamic and sensitive to changes in e.g. meteorological conditions. Also the fact that the measurements were not carried out with exact twelve month intervals can be of influence.

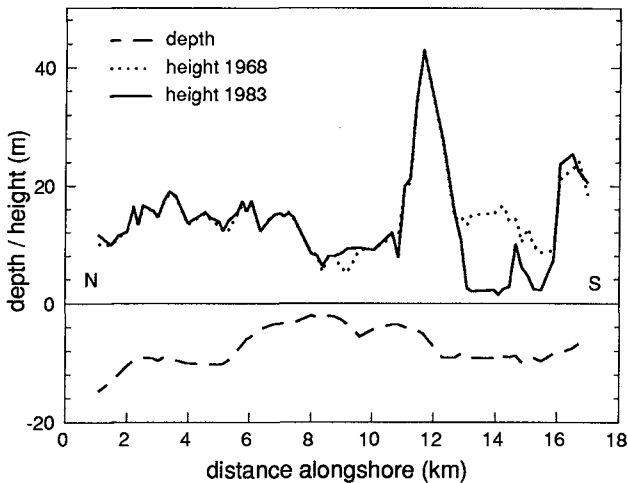


figure 6. Maximum height and depth of control volume of Schouwen.

In the control volume along the coast of Schouwen there is a net gain of $41.7 \cdot 10^3$ m³/year. When we look at the contribution of the various segments to the total amount,

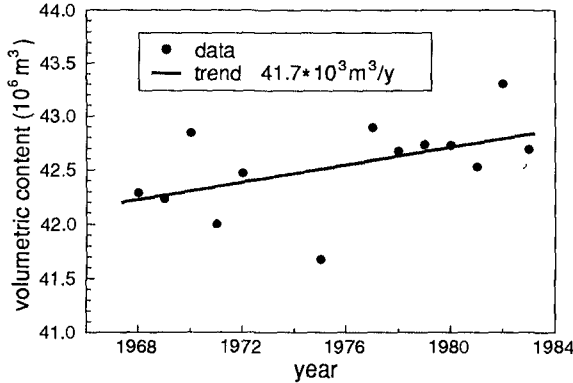


figure 7. Volume change coast of Schouwen; linear trend and yearly fluctuations.

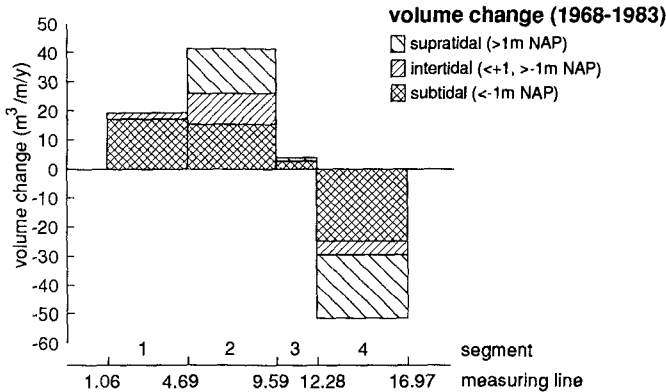


figure 8. Change in volumetric content, Schouwen. For locations see figure 4.

we see that the three northern segments (1,2 and 3) together gain sand to a total of $282 \cdot 10^3 \text{ m}^3/\text{year}$, and the southernmost segment (4) loose sand ($240 \cdot 10^3 \text{ m}^3/\text{year}$). The volume changes normalized to coast length are given in table 5.

The overall impression of the results of the sand balance is not fundamentally different from the one based on shoreline records (table 4); accretion in segments 1, 2 and 3, and erosion in segment 4.

To get an insight in what processes are responsible for the volume changes we divide the control volume in three morphological zones :

- a supratidal zone, which is mainly influenced by storm surges and eolian processes
- an intertidal zone, which is influenced by eolian processes and wave action
- a subtidal zone, which is influenced by wave-, wind- and tide-related processes

The tidal range at Schouwen is 2.5 meter, with MLW at -1.18 m and MHW at +1.35 m NAP. The boundaries of the morphological zones are chosen at -1 m and +1 m NAP. In table 5 the normalized volume changes in the four segments are given, both the total

change and the change in the different morphological zones.

The normalized volume changes are also given in figure 8. This figure clearly shows the contribution of the different morphological zones to the total volume change.

Segment 1 is visually characterized (see section 5.2) by profiles who are stable or eroding in the dunes and gain volume in the nearshore. The sand balance shows the quantitative volume changes. The supratidal zone shows almost no net volume change. In the intertidal zone very little sedimentation took place. For the major part the net sedimentation in segment 1 is due to the sedimentation in the subtidal zone.

table 5. Volume change (m³/m/y) Schouwen.

segment	total	supratidal >+1 m NAP	intertidal -1 to +1 m NAP	subtidal <-1 m NAP
1	+19.2	-0.1	+2.2	+17.1
2	+41.2	+15.3	+10.5	+15.4
3	+4.1	+1.1	+0.2	+2.8
4	-51.4	-21.9	-4.7	-24.8
total	+2.6	-1.6	+2.5	+1.7

The subtidal zone within the control volume reaches depths of 13 meter and includes parts of the Schaar van Renesse. The sedimentation in the tidal channel caused by the decrease of the tidal currents after the closure of the Grevelingen is responsible for the major part of the net sedimentation in this coastal segment.

Segment 2 is characterized by profiles with sedimentation in the dunes and nearshore. The sand balance shows that the contribution of the three morphological zones to the total net sedimentation is quite the same. This means that all kinds of processes are involved with the volume change in this coastal stretch. The depth of the control volume is for the major part between 2 and 5 meter and hardly any influence of the silting up of the tidal channel can be expected here. However, the changed tidal patterns can have influenced the sediment transport pattern e.g. by a relative increase of wave influence. Segment 3 is characterized by its non-uniform profile development in alongshore direction. The depth of the control volume varies from 3.5 to 5.5 meter (locally 9 m). There is no deep tidal channel included. But there is a shallow gully in the subtidal zone in this segment. In the north it migrates landward (see figure 5) and causes erosion in the intertidal and supratidal zone. This is attended by a coastline retreat in this part of the segment. For the segment as a whole the overall coastline development shows progradation, also the overall volume change is positive. The net volume change is positive in all morphological zones (figure 8). Two thirds of the sedimentation takes place in the subtidal zone.

The erosion and sedimentation pattern in this segment can be explained by the lateral migration of the gully, both in an alongshore and crossshore direction. The sandwave that can be seen in the displacement of the mean low water line represents the impact

of this process on the coastline (Verhagen, 1989b).

Segment 4 is characterized by profiles with erosion in the dunes and nearshore. The depth of the control volume is about 9 meter. The landward part of the Krabbengat tidal channel is included in the sand balance. The sand balance shows that the amounts of erosion in the supra- and intertidal zones are about the same. There is less erosion in the intertidal zone. The decrease in volume in the supratidal zone is due to a retreat of the dunefront, rather than a lowering of the dune. As mentioned before the first dune row moves out of the control volume. The decrease of volume in the subtidal zone is due to the landward migration of the Krabbengat tidal channel.

The coast of Schouwen shows a variation in the sand balance in an alongshore direction; negative volume change in the south changing to positive volume change in the north over the period 1968 to 1983.

In every segment the sand balance of the various morphological zones shows the same qualitative trend as the total sand balance for that segment. Their relative contribution to the total sand balance of the segment varies in alongshore direction (figure 8).

Oertel et al. (1989) suggested a classification for volume changes in terms of $m^3/m/month$. According to this classification the coast of Schouwen with a gain of sediment of $2.6 m^3/m/year$ is stable over the period 1968 - 1983.

The length of the coastal stretch (15.9 km) and the long period tend to average out the spatial and temporal variations in erosion and accretion. When we focus on the coastal segments we see that segment 3 is stable, segment 1 has a mild accretion rate, segment 2 has a moderate accretion rate and segment 4 has a strong erosion rate.

However, the classification mentioned is based on data from the microtidal Atlantic and Gulf coasts of the U.S.A. In these areas the sediment transport is concentrated between the upper backshore and the breaking waves at low water, with the foreshore as the major element affecting the volume change (Oertel et al., 1989).

The data from Schouwen shows that the relative small intertidal foreshore is of less influence on the sand balance, especially where tidal channels are close to the coast like in segments 1 and 4. Most of the volume changes occur in the supratidal and subtidal parts of the coast.

It can be concluded that not the normal wave-driven longshore transport is the main process affecting the sand balance of Schouwen, but the eolian- and storm surge related processes (including wave-driven longshore transport at high levels) in the supratidal zone, and the wave- wind- and tide-related processes in the subtidal zone.

6. Conclusions

The results clearly shows the advantage of the horizontal approach in calculating the sand balance for a better understanding of the coastal behaviour. The division of the coast of Schouwen in alongshore segments and cross-shore morphological zones shows how the sand balance is composed and gives insight in the processes that are responsible for the sand transport.

A question is of the dynamic of the Dutch coast is underestimated until now. This can be checked by coastal models with different length and time scales.

On the basis of nine categories of profile development, more or less uniform coastal segments can be distinguished. It is recommended to calculate a separate sand balance for each segment.

Because of the difference in zones where the major net transport take place, it is questionable if the classification as proposed by Oertel et al. (1989) can be used without change for the Dutch coast.

REFERENCES

- BOWEN, A.J. and D.L. INMAN (1966)
Budget of littoral sands in the vicinity of Point Arguello, California. U.S. Army Corps of Engineers CERC Technical Memorandum No.19, 41 pp.
- CHAPMAN, D.M. (1981)
Coastal erosion and the sediment budget, with special reference to the Gold Coast, Australia. Coastal Engineering 4 pp. 207-227.
- KOMAR, P.D. (1983)
Beach processes and erosion - an introduction. In: P.D. Komar (ed.) Handbook of coastal processes and erosion. CRC Press, Boca Raton, pp. 1-20.
- LOUISSE, C.J. and A.J. KUIK (1990)
Coastal defence alternatives for The Netherlands. These conference proceedings, Session The Dutch Coast: Paper No. 1
- OERTEL, G.F., J.C. LUDWICK and D.L.S. OERTEL (1989)
Sand accounting methodology for barrier island sediment budget analysis. Proceedings Coastal Zone 1989, ASCE, Charleston, pp. 43-61.
- ROELSE, P. (1990)
Beach and dune nourishments in The Netherlands. These conference proceedings, Session The Dutch Coast: Paper No. 11
- ROELVINK J.A. and M.J.F. STIVE (1990)
Sandtransport on the shoreface of the Holland coast. These conference proceedings, Session The Dutch Coast: Paper No. 5
- RUIG, J.H.M. de (1987)
The adaptation of a morphological database (JARKUS); A base for a sand balance of the Dutch coast. Notitie GWAO-87.481. Public Work Department, Tidal Waters Division, The Hague, 28 p. (in Dutch).
- STIVE, M.J.F., J.A. ROELVINK and H. de VRIEND (1990)
Large scale coastal evolution concept. These conference proceedings, Session The Dutch Coast: Paper No. 9
- U.S. Army Corps of Engineers (1984)
Shore Protection Manual. U.S. Army Corps of Engineers CERC, Washington, D.C.
- VERHAGEN, H.J. (1989a)
Coastal Defence after 1990 Technical Report 12: Groynes and pile rows. Public Work Department, Tidal Waters Division, 40 p. (in Dutch)
- VERHAGEN, H.J. (1989b)
Sand waves along the Dutch coast. Coastal Engineering 13 pp.129-147.

CHAPTER 144

SAND TRANSPORT ON THE SHOREFACE OF THE HOLLAND COAST

The Dutch Coast: Paper No. 5

J.A. Roelvink¹ and M.J.F. Stive¹

Summary

Yearly averaged transport vectors have been computed along a number of rays, perpendicular to the coast, on the shoreface of the Holland coast. Variation in time and space of wave conditions, tidal flow and long-term average near-bottom flows are considered in fine detail. Special attention is paid to various correlations, both between different velocity components and between velocity and water level, as these correlations play a major role in determining direction and magnitude of net transports. Calibration is performed against both long-term and short-term observations of developments. The resulting transport pattern helps to explain some observed large-scale developments of the Dutch coast.

1. Introduction

The Coastal Genesis Research Programma of Rijkswaterstaat aims to identify geomorphological processes that determine the long-term, large-scale development of the Dutch coast. To this end a collection of interdisciplinary projects has been set up among geologists, geographers and civil engineers of Rijkswaterstaat, National Geology Department, DELFT HYDRAULICS and several universities. In 1988 and 1989 Rijkswaterstaat asked the researchers involved to contribute to supporting studies for a Coastal Defence Study, aiming to develop an overall coastal defence strategy for the Netherlands (Louisse and Kuik, Paper No. 1, these proceedings). The results presented here were generated for this study.

The goal of this study is to provide backing for conceptual large scale evolution models of the Dutch coast, developed in the framework of the Coastal Genesis Programme (see Stive et al, 1990). These models can then be used to improve predictions of the coastal developments, required by the Coastal Management Study. More specifically, this study should provide an estimate of the large-scale net transport pattern on the shoreface, and identify the relative importance of the mechanisms contributing to this pattern.

¹ DELFT HYDRAULICS, P.O. Box 152, 8300 AD Emmeloord, The Netherlands

The general approach followed in this study is, to estimate hydraulic conditions in a number of points, and to analyze the resulting transport vectors in these points. As the interest is focussed on large-scale trends, estimates of the variation of hydraulic conditions along the coast can be based on the data from existing measuring stations. The variation of conditions perpendicular to the coast can be computed (on this large scale) with ray models or empirical formulations. Special care must be given to correlations between variables and non-linear effects; the importance of many of these aspects has been shown, among others, by Roelvink and Stive (1989). As the net transport in the area of interest is generally small compared to the amplitudes of the tidal and orbital contributions, second-order effects are of major importance.

2. Model assumptions

The basic assumptions which are made are, that the deep water (approx. 20 m water depth) wave and current conditions vary slowly along the Holland coast, and that on a longshore scale of tens of kilometres the depth contours are approximately parallel. Under these conditions, the problem is reduced to a one-dimensional problem which is solved for a limited number of cross-shore sections. The spatial resolution is thus limited, in accordance with the large-scale concept that the model is a part of.

In such a large-scale model, the relevant time-scale is at least in the order of years. However, in order to arrive at estimates of yearly-averaged transports, the transport at a given point must be correctly integrated over a number of shorter time-scales: the short-wave time-scale, the wave-group scale, the tidal-scale, the storm-scale and the seasonal variations. The variations on all these time-scales and the interactions between some of them potentially cause net transports. This means that we have to go back some time-scales in order to produce the long-term parameter: 'yearly-averaged transport'.

3. Analysis of relevant interactions

For the computations of sediment transport due to a combination of waves and currents, in both wave- and current direction, one of the few (practically suitable) available formulations is that of Bailard (1981) after the concept by Bagnold (1966). This formulation has proved reasonably accurate in the case of cross-shore transport (Roelvink & Stive, 1988; Ribberink & Al Salem, 1990). It is conceptually simple and is able to combine transport contributions from different directions and on different time-scales.

The formulation describes the transport as a function of the instantaneous near-bottom velocity at a certain reference level:

$$\begin{aligned} \langle \vec{q}_x \rangle = & \frac{c_f}{\Delta g N} \frac{\epsilon_B}{\tan \phi} \left[\langle |\vec{u}|^2 \vec{u}_x \rangle - \frac{\tan \beta_x}{\tan \phi} \langle |\vec{u}|^3 \rangle \right] + \\ & + \frac{c_f}{\Delta g N} \frac{\epsilon_S}{w} \left[\langle |\vec{u}|^3 \vec{u}_x \rangle - \frac{\epsilon_S}{w} \tan \beta_x \langle |\vec{u}|^5 \rangle \right] \end{aligned} \quad (1)$$

$$\begin{aligned} \langle \vec{q}_y \rangle &= \frac{c_f}{\Delta g N} \frac{\epsilon_B}{\tan \phi} \left[\langle |\vec{u}|^2 \vec{u}_y \rangle - \frac{\tan \beta}{\tan \phi} \langle |\vec{u}|^3 \rangle \right] + \\ &+ \frac{c_f}{\Delta g N} \frac{\epsilon_S}{w} \left[\langle |\vec{u}|^3 \vec{u}_y \rangle - \frac{\epsilon_S}{w} \tan \beta_y \langle |\vec{u}|^3 \rangle \right] \end{aligned}$$

where x, y are two arbitrary directions perpendicular to each other, q is the total volume transport, \vec{u} is the instantaneous total velocity vector, c_f a roughness coefficient, Δ the relative density, g the acceleration of gravity, N the fraction of sediment relative to total volume, w the fall velocity, ϵ_B and ϵ_S efficiency factors (calibration constants) and $\tan \beta$ the bottom slope. The $\langle \rangle$ indicate averaging over time, the averaged powers of the velocity are also called 'velocity moments'.

From flume and wave tunnel experiments (Ribberink & Al Salem, 1990) it follows that the term with the power of 3 is the dominant term in the equation. For a first analysis we can therefore use:

$$\langle \vec{q} \rangle = A \langle |\vec{u}|^3 \vec{u} \rangle \quad (2)$$

Now we can estimate the relative importance of contributions to the transport on different time-scales, by decomposing the velocity vector into components which act on the time-scales from short waves to storm periods.

$$\vec{u} = \vec{u}_{nL} + \vec{u}_{nC} + \vec{u}_t + \vec{u}_l + \vec{u}_s \quad (3)$$

where:

$$\vec{u}_{nL} = u_{nL} \begin{bmatrix} 1 \\ 0 \end{bmatrix} = \text{net longshore current,}$$

$$\vec{u}_{nC} = u_{nC} \begin{bmatrix} 1 \\ 0 \end{bmatrix} = \text{net cross-shore current,}$$

$$\vec{u}_t = u_t \begin{bmatrix} 1 \\ 0 \end{bmatrix} = \text{tidal current,}$$

$$\vec{u}_l = u_l \begin{bmatrix} \cos \alpha \\ \sin \alpha_w \end{bmatrix} = \text{long-wave motion,}$$

$$\vec{u}_s = u_s \begin{bmatrix} \cos \alpha \\ \sin \alpha_w \end{bmatrix} = \text{short-wave motion.}$$

All velocities are taken here at a near bottom reference level; the x -direction is taken alongshore, and the y -direction onshore, α_w is the angle between the longshore direction and the direction of wave propagation. Both long waves and short waves are assumed to have the same dominant direction.

The term \vec{u} in equation (2) can be substituted by equation (3); after some simple algebraic manipulations and neglecting what we estimate to be small terms, we then find:

$$\begin{aligned}
 \langle \vec{u} |^2 \vec{u} \rangle = & \langle u_{nL} u_t^2 \rangle \begin{bmatrix} 3 \\ 0 \end{bmatrix} & + & \text{net longshore - tidal current} \\
 & + \langle u_{nC} u_t^2 \rangle \begin{bmatrix} 0 \\ 1 \end{bmatrix} & + & \text{net cross-shore - tidal current} \\
 & + \langle u_{nL} u_s^2 \rangle \begin{bmatrix} \cos 2\alpha + 2 \\ \sin 2\alpha \end{bmatrix} & + & \text{net longshore - short wave} \\
 & + \langle u_{nC} u_s^2 \rangle \begin{bmatrix} \sin 2\alpha \\ 2 - \cos \alpha_w \end{bmatrix} & + & \text{net cross-shore - short wave} \\
 & + \langle u_t^3 \rangle \begin{bmatrix} 1 \\ 0 \end{bmatrix} & + & \text{tidal current asymmetry} \\
 & + \langle u_t u_s^2 \rangle \begin{bmatrix} \cos 2\alpha_w + 2 \\ \sin 2\alpha_w \end{bmatrix} & + & \text{tide - short wave interaction} \\
 & + \langle u_l u_s^2 \rangle \begin{bmatrix} 3 \cos \alpha_w \\ 3 \sin \alpha_w \end{bmatrix} & + & \text{long - short wave interaction} \\
 & + \langle u_s^3 \rangle \begin{bmatrix} \cos \alpha_w \\ \sin \alpha_w \end{bmatrix} & + & \text{short wave asymmetry} \quad (4)
 \end{aligned}$$

The relative importance and some characteristics of these terms are described below.

Net longshore-tidal current interaction

The two components are generally uncorrelated. As the variance of the tidal velocity is relatively high, a small net current can cause significant transport: the tide stirs up sediment which is advected by the net current.

Net cross-shore-tidal current interaction

This term is similar to the previous one. Even though the net cross-shore current may be small, it may give an important contribution in combination with the stirring up due to the tidal velocity.

Net longshore - short wave interaction

The components in this term are highly correlated. Two mechanisms are responsible for this: during storms the wind drives both currents and waves, and, more directly, the waves drive a net longshore current.

An interesting side-effect of the interaction term is, that it is not directed in longshore direction, but has a deviation which for angles $< 90^\circ$ (which is generally the case) is directed onshore.

Net cross-shore - short wave interaction

These components are also highly correlated. During storms, wind- and wave-driven cross-shore currents occur near the bottom, which are generally directed offshore; during calm weather these currents tend to be directed onshore.

Tidal current asymmetry

Along the Holland coast, the tide manifests itself as a northward propagating wave, where the M2 and M4 components are more or

less in phase. This causes an asymmetric velocity; the highest velocity occurs in northward direction. Due to this, the term causes a net northward transport component.

Tide - short wave interaction

The tide and the short waves interact through the water level variation. Two mechanisms play a role. The most important one is, that the water level influences the orbital velocities: the greater the water depth, the smaller the orbital velocity. As the lowest water level occurs during South flowing current, this mechanism causes a net southward effect. On the other hand, a lower water level implies more wave dissipation due to friction and breaking, which reduces the wave height and thus the orbital velocity. This effect reduces the net southward effect somewhat.

Long - short wave interaction

In groupy waves variations in radiation stress occur which drive long waves ('bound long waves', Lonquet-Higgins & Stewart, 1964). Outside the breaker-zone these long waves are generally in counter-phase with the varying wave energy, thus, when the highest waves occur, the long-wave velocity is directed offshore. Due to this, a net offshore interaction term arises (Shi and Larsen, 1984).

Short wave asymmetry

Due to non-linearity, the orbital velocity under short waves is asymmetric in time; the velocities under wave crests are higher than those under the troughs. This leads to a large transport term directed onshore.

4. Model formulation

Based upon the above analysis of the important terms that contribute to the yearly averaged transport, we may conclude that the interaction between the tidal motion and the wave motion is such that we have to take this fully into account. This is done in the following way.

The offshore tidal motion is schematized to a number of 12 steps within a representative tidal cycle; The deep water velocities and water levels at a given location are determined by interpolating tidal coefficients in space between measuring stations. The variation in offshore wave conditions is represented by a climate of 80 combinations of wave heights and directions, each combination with its representative wave period and offshore water level set-up. The deep water wave climate at a given location is also obtained by interpolation in space of measured wave climates, based on 10 years of observations at three measuring stations at 20 m water depth. This leads, for a given location, to 960 sets of deep water boundary conditions.

Each of these boundary conditions is then used in a computation of depth-mean wave and current parameters along a line perpendicular to the depth contours, with the help of one-dimensional models.

From these depth-mean parameters, the near-bottom quasi-steady velocity and the relevant velocity moments due to wave asymmetry and long wave - short wave interactions are computed. These are combined

to yield the total velocity moment vectors which are required by the transport model according to equation (1).

In a number of points along the cross-shore line, the thus computed transport vectors are integrated over all combinations; taking into account the frequency of occurrence of each combination. This then leads to the yearly-averaged transport vector in each point along the line.

In the following, the formulations used to achieve this are summarized.

Cross-shore variation of wave parameters

The wave energy decay model formulated by Battjes & Janssen (1978), with the parametrizations from Battjes & Stive (1985) is used:

$$\left[\begin{array}{l} \frac{\partial}{\partial x} (E C_g \cos \theta_w) = -D \\ \frac{\sin \theta_w}{C} = \frac{\sin \theta_{w,0}}{C_0} \\ \rho g h \frac{\partial \bar{\eta}}{\partial x} = - \frac{\partial}{\partial x} S_{xx} \end{array} \right. \quad (5) \quad (6)$$

Here, E is the wave energy, C_g the group velocity, θ_w the angle of the wave propagation direction to the shore normal, D the dissipation due to bottom friction and breaking, C the phase velocity, ρ the density of water, h the total mean water depth, $\bar{\eta}$ the water level set-up and S_{xx} the radiation stress. The subscript 0 denotes deep-water (most offshore location).

Cross-shore variation of current parameters

For the tidal current, the assumption is used that the along-shore pressure gradient is constant along the cross-shore line, and is compensated by bottom friction. Using the Chézy friction-law, we then find:

$$U_t = U_{t,0} \frac{C_h}{C_{h_0}} \left(\frac{h}{h_0} \right)^{0.5} \quad (7)$$

where $C_h = 18 \log \frac{12 h}{k_s}$ is the Chézy friction coefficient, k_s is the bottom roughness, and \bar{U}_t the depth-mean tidal current.

For the wave-driven longshore current, the cross-shore gradient of the alongshore component of the radiation stress S_{yx} is assumed to be compensated by the bottom shear stress due to current and waves. The radiation stress gradient is modelled according to Dinges et al (1987).

$$- \frac{\partial}{\partial x} S_{yx} = \frac{D}{C} \sin \theta_w \quad (8)$$

and for the bottom shear stress τ_y a linearized form is used:

$$\tau_y = \rho C_f \bar{U}_1 \langle |U_{orb}| \rangle \quad (9)$$

where \bar{U}_1 is the longshore current, $\langle |U_{orb}| \rangle$ the mean value of the absolute magnitude of the orbital velocity and C_f a friction coefficient.

From (8) and (9), \bar{U}_1 can be solved.

Near-bottom quasi-steady velocity

Both the tidal current velocity and the wave-driven longshore current at a reference level near the bottom are derived from the depth-mean velocity by assuming a logarithmic profile.

The wave-driven cross-shore current is computed by the method given in Stive & De Vriend (1987); the formulations will not be repeated here.

An empirically found near-bottom long-term net moment as reported in Borst (1987) was added to the near-bottom velocity components.

Velocity moments of wave motions

The relevant velocity moments due to short wave asymmetry and long wave-short wave interaction can be estimated from the rms wave height, the peak period and the water depth by using the method outlined in Roelvink & Stive (1989). For the short wave asymmetry, the method is based on high order non-linear wave theory; for the long wave effects a simple bound long wave model is used.

Total quasi-steady velocity moments

The near-bottom quasi-steady current and the (also quasi-steady) velocity moments of the wave motions are combined to produce the total quasi-steady velocity moments and moment vectors for the given combination of tidal phase and wave condition. This involves lengthy expressions based on Taylor expansion in two directions, which are given in the original report (Roelvink & Stive, 1989a).

5. Results

Computations with this model were carried out for four rays along the Holland coast. The resulting large-scale transport pattern is shown in Figure 1. The arrows indicating the relative strength of the yearly averaged transport are located at 20 m, 15 m, 10 m and 8 m respectively.

Because of the simplicity of the used models, considerable errors are possible. Therefore, an overall calibration of the transports was performed against observed large-scale phenomena. The observations taken into account are:

- The long-term flattening of the middle shoreface, as evident from a steady shoreward migration of the -10 m depth contour line over the last 90 years.
- The order of magnitude of the net longshore transport in the surfzone as a function of the orientation of the coastline. This has been the subject of much studies based on observed morphologic developments, most recently by Dijkman et al (1990).

- The observed northward migration of the navigation channel off IJmuiden Harbour (see Van Alphen et al, 1990).

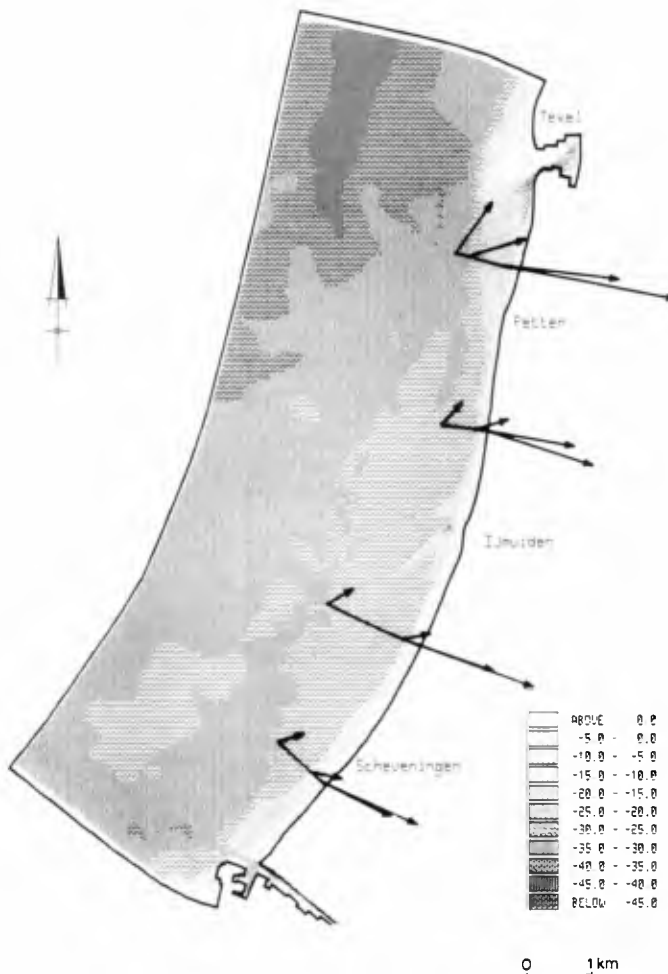


Figure 1 Net transport vectors, uncalibrated

These observations have led to an adjustment of the transport rates; cross-shore transport were reduced by a factor of 2, whereas the longshore transport had to be multiplied by a factor of 2.

Although a factor of 2 in transport formulations is a minor adjustment, the fact that different factors had to be used for long-shore and cross-shore transport is worrying and may be an indication that the transport model, which has proved to perform reasonably for wave-induced transport, does not perform so well in combinations of waves and currents.

The calibrated large-scale transport pattern is shown in Fig. 2. The picture shows a transition from the tide-dominated transport (mainly caused by the coupling of the M2 and M4 components) to wave-dominated transport. Towards the -8 m depth contours, the cross-shore transport increases as a result of increasing wave-induced streaming and short wave asymmetry; the longshore transport also becomes more wave-dominated and shows a clear dependence on the coast orientation.

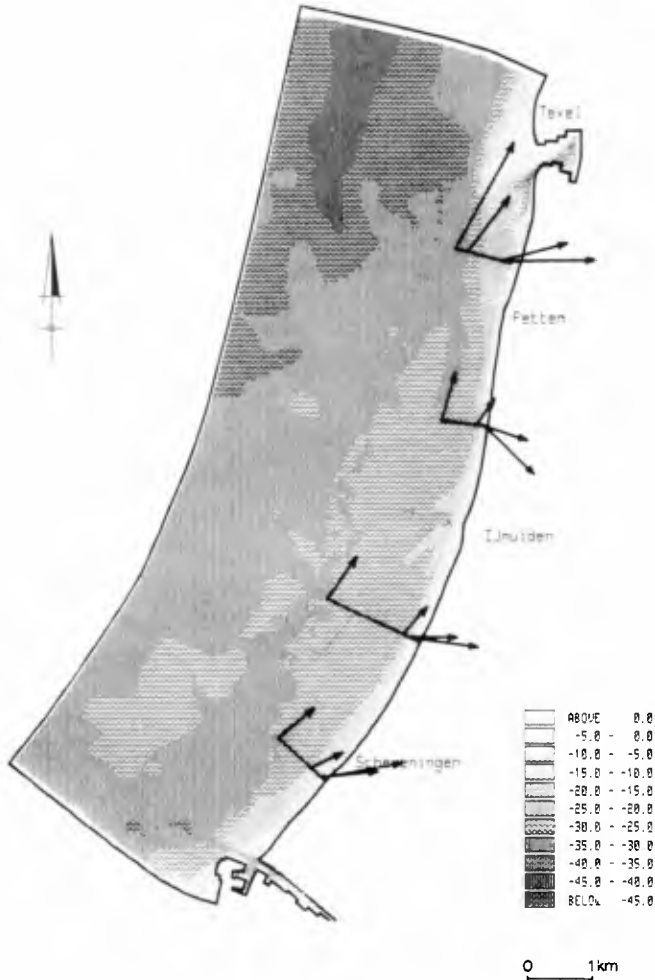


Figure 2 Net transport vectors, calibrated

In Fig. 3a, the variation of the net near-bottom velocity and transport, averaged over all wave conditions, as a function of the tidal phase is given for the most northern ray, at a depth of 18 m;

in Fig. 3b, the same is done at a depth of 10 m. This clearly shows the dominance of the tidal transport in deep water: the transport direction closely follows the tidal velocity; also, the transport increases non-linearly with increasing tidal velocity. At a depth of 10 m, the picture is quite different. The transport has a significant onshore component; also, the dependence of the transport on the tidal velocity is almost linear, which indicates that the waves do most of the stirring of sediment, whereas the tidal velocity merely advects this sediment.

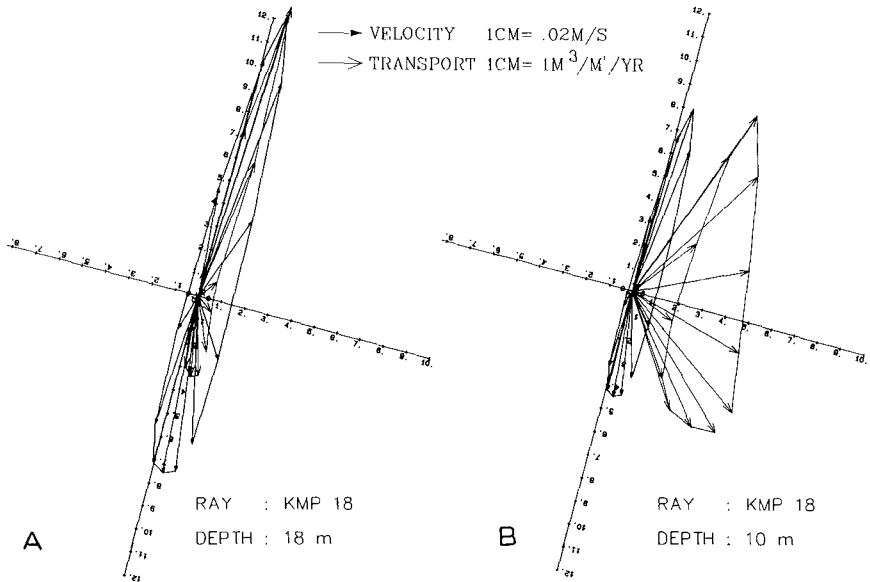


Figure 3 Velocity and transport per tidal phase average over all wave conditions

As an illustration of the variation of the cross-shore transport with water depth, the computed cross-shore transports are plotted against depth in Fig. 4. There is a sharp increase in onshore transport towards the -8 m line. Between approx. 6 m and 10 m water depth, there is a transition from the highly dynamic 'active zone' to the morphologically rather in-active shoreface (see Stive et al, Paper No. 9, these proceedings); therefore, the limit of application of this model also lies somewhere in this transition zone. An important conclusion that can be drawn from Figure 4 is, that for the Holland coast the shoreface acts as a significant source of sand to the 'active zone'.

In Figure 5, the cross-shore transport gradients are shown as a function of depth. These gradients scale directly with the propagation speed of depth contour lines. It follows that the 10 m depth contour moves shoreward at a speed of approx. 2 m per year, which is in accordance with observations.

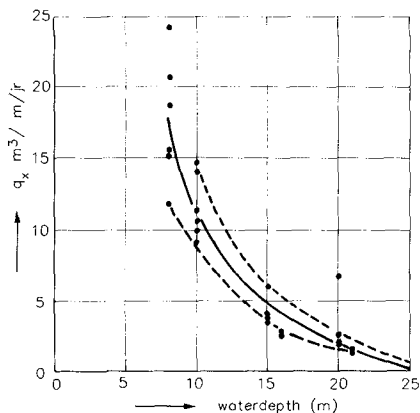


Figure 4 Net cross-shore transport vs. water depth

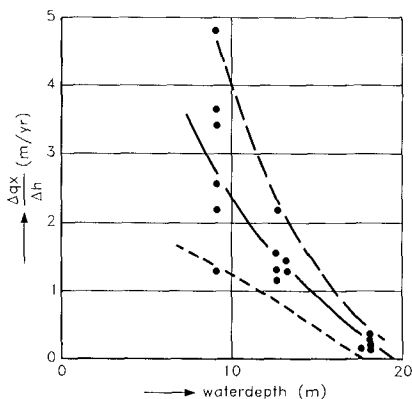


Figure 5 Net cross-shore transport gradient vs. water depth

6. Sensitivity analysis

As the value of a number of coefficients in the model and some hydrodynamic input data was rather uncertain, a sensitivity analysis was carried out in order to estimate the total errors in the computed transport rates. This was done in the following way: for a number of input values, the standard deviation was estimated. The effect on the transport rates was assessed by consecutively adding or subtracting this standard deviation from the expected value of the inputs. The errors in the transport rates due to these errors were then squared and added, and the square root was taken to yield an estimate of the total percentage error. This method is known as the 'mean value' approximation. Here we shall not go into all details of the analysis, but simply present the final result in Fig. 6 for the cross-shore transport, and Fig. 7 for the longshore transport.

The errors in the longshore transport increase in seaward direction, up to around 100%. This is mainly due to the fact, that the net transport rate in deep water is very small compared to the gross transport rates, which increases the sensitivity of the output substantially.

The errors in the cross-shore transport also increase in seaward direction, mainly due to uncertainties in the near-bottom net currents.

7. Discussion

The model presented here has been a useful tool in comparing the relative importance of a number of interacting transport mechanisms on the shoreface. After calibration, a plausible transport pattern emerges which in some aspects helps the understanding of the observed large-scale morphologic developments.

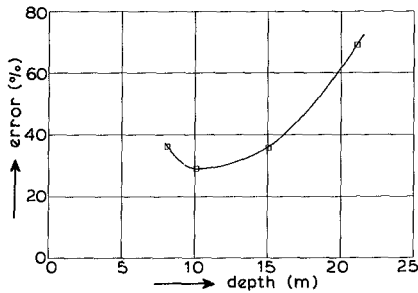


Figure 6 Estimated total error; cross-shore transport

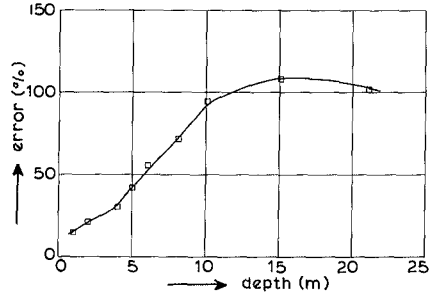


Figure 7 Estimated total error; long-shore transport

However, the model has some serious limitations: many of the processes incorporated in it are crudely schematized, and much about the hydraulic conditions, especially in deeper water, is uncertain.

One might therefore agree that, given these uncertainties, it might be better not to build such a model at all. This is not our opinion; as long as the limitations are stated clearly, models like this are useful tools of analysis and at least provide an educated 'best guess' of what is happening.

References

- Van Alphen, J.S.L.J., C.J. Louisse, F.P. Hallie, J.S. Ribberink and J.A. Roelvink, (1990).
Offshore sand extraction and nearshore profile nourishment. The Dutch coast: Paper No. 12. Proc. 22nd ICCE, Delft, The Netherlands, 1990.
- Bagnold, R.A. (1966).
An approach to the sediment transport problem from general physics. U.S. Geol. Surv. Prof. Pap. 422-I, 1966.
- Bailard, J.A. (1981).
An energetics total load sediment transport model for a plane sloping beach. J. Geophys. Res., Vol. 86, No. C11, pp. 10,938-10,954, 1981.
- Battjes, J.A. and J.P.F.M. Janssen (1978).
Energy loss and set-up due to breaking in random waves. Proc. 16th ICCE, pp. 569-87, 1978.
- Battjes, J.A. and M.J.F. Stive (1985).
Calibration and verification of a dissipation model for random breaking waves. J. Geophys. Res., Vol. 90, pp. 9159-67.
- Borst, J.C. (1987).
Verkennde beschrijving van het stroomklimaat in het kustvak Delfland (in Dutch). Rijkswaterstaat, Nota GWA0-87.477, The Hague, The Netherlands.

- Dingemans, M.W., A.C. Radder, H.J. de Vriend (1987).
Computation of the driving forces of wave-induced currents.
Coastal Eng. 11 (1987) 539-563, Elsevier, Amsterdam, The Netherlands.
- Dijkman, M.J., W.T. Bakker, J.H. de Vroeg (1990).
Prediction of coastline evolution for specific parts of the Holland coast. The Dutch coast: Paper No. 7.
Proc. 22nd ICCE, Delft, The Netherlands, 1990.
- Lonquet-Higgins, M.S. and R.W. Stewart (1964).
Radiation stress in water waves; a physical discussion, with applications.
Deep-Sea Res., 1964, Vol. 11, pp. 529-562, Pergamoma, Great Britain.
- Ribberink, J.S. and A. Al Salem (1990).
Bedforms, sediment concentrations and sediment transport in simulated wave conditions.
Proc. 22nd ICCE, Delft, The Netherlands, 1990.
- Roelvink, J.A. and M.J.F. Stive (1988).
Large-scale tests of cross-shore sediment transport on the upper shoreface.
Symp. Math. Modelling of Sed. Transp. in the Coastal Zone, Copenhagen, 1988.
- Roelvink, J.A. and M.J.F. Stive (1989).
Bar-generating cross-shore flow mechanisms on a beach.
J. Geophys. Res., Vol. 94, C4, pp. 4785-4800, 1989.
- Roelvink, J.A. and M.J.F. Stive (1989a).
Voorspelling ontwikkeling kustlijn 1990-2090, fase 3; deelrapport 3.4: initieel sedimenttransportmodel Hollandse kust.
DELFT HYDRAULICS, report H825, Delft, Sept. 1989 (in Dutch).
- Shi, N.C. and L.H. Larsen (1984).
Reverse sediment transport induced by amplitude-modulated waves.
Mar. Geol., 54: 181-200.
- Stive, M.J.F., J.A. Roelvink and H.J. de Vriend (1990).
Large-scale coastal evolution concept. The Dutch coast: Paper No. 9.
Proc. 22nd ICCE, Delft, The Netherlands, 1990.
- Stive, M.J.F. and H.J. de Vriend (1987).
Quasi-3d current modelling: wave-induced secondary current.
ASCE Specially Conf. "Coastal Hydrodynamics", Delaware, 1987.

CHAPTER 145

CROSS-SHORE TRANSPORT DURING STORM SURGES

The Dutch Coast: Paper No. 6

Henk J. Steetzel¹⁾

Abstract

In order to predict the amount of dune erosion due to a storm surge, a model for cross-shore transport during storm surges has been developed. During a storm with intensive wave breaking, suspended sediment transport is predominant. In the model the nett local transport is computed from the time averaged sediment concentration and the time averaged (secondary) flow profiles. Both profiles are related to the local hydraulic conditions. Finally the computed erosion profile development and the amount of dune erosion are well predicted by the model.

1. Introduction and background

On behalf of the Technical Advisory Committee on Water Retaining Structures (TAW) of the Ministry of Transport and Public Works in the Netherlands, a mathematical model for beach and dune profile changes due to storm surges is being developed. The model, which also predicts the beach profile changes in front of dune revetments (Steetzel, 1987), is to be used as a tool to check the safety of the narrow stretch of sandy beaches and dunes which protect the Dutch population against the sea. It should be used in addition to (or perhaps replace) the model as described by Vellinga (1986).

This paper focusses primarily on the computation of the nett cross-shore transport as incorporated in this model. This transport is based on both time averaged sediment concentrations and time averaged secondary currents.

2. Approach

In order to develop a cross-shore transport model series of investigations in wave flumes have been carried out. These model tests were conducted on different scales reaching from small scale ($n_d = 30$) to full scale ($n_d = 1$). Most investigations concern unprotected dunes, whereas there are only a few tests with dune revetments and three tests with partly protected dunes. Most of those tests were carried out in the large Delta Flume of the DELFT HYDRAULICS.

1) Senior research engineer, DELFT HYDRAULICS, P.O. Box 152, 8300 AD Emmeloord, The Netherlands

The amount of information gathered during those tests varies from only initial and final profile to a (complete) profile development, supplemented with data on wave heights, secondary currents and sediment concentrations. The latter were measured using a transverse suction method (Bosman and Steetzel, 1986). Tests with a lot of data are used for (cross-shore transport) model formulation and calibration. In case of only initial and final profiles the test is used for verification.

The different phases of the dynamical model are obvious. On the initial bottom profile the momentary offshore hydraulic conditions determine the local wave heights by using the wave height decay model ENDEC (Battjes and Janssen, 1978). From this the relevant parameters (e.g. cross-shore secondary current and sediment concentrations) are computed resulting in a local cross-shore transport. This step is illustrated in more detail in the next chapter. Finally the bottom changes are computed through application of the mass balance equation of the sediment. The new bottom profile is computed and the procedure is, for a next time step, started all over again.

3. Model formulation

3.1 Introduction

The fomulation of the cross-shore transport is split up into several different aspects, respectively the principle of cross-shore transport computation in both the general and this specific case, the sediment concentrations, the secondary currents and the nett transport computation. Finally some justification of the presented cross-shore transport computation is given.

3.2 Nett cross-shore transport

In general nett cross-shore transport should be computed from the well-known equation:

$$S_x(x) = \frac{1}{nT} \int_{t=0}^{n.T} \int_{z=-d(x)}^{\eta(x,t)} u_x(x,z,t) \cdot C(x,z,t) \cdot dz \cdot dt \quad [\text{kg/m/s}]$$

in which:

S_x	the nett transport (x-component)	[kg/s]
T^x	the wave period	[s]
u_x	the velocity (x-component)	[m/s]
C^x	the sediment concentration	[kg/m ³]
z	the level above the mean water level	[m]
η	the instantaneous water level	[m]

In case of random breaking waves a proper description of time (t) and place (x,z) variation of both velocity and concentration is not available.

In order to evaluate transport contributions, the transport at a certain level above the bottom can be written as a mean (time averaged) product of velocity and concentration. If both parameters are split up into a mean (overbar) and a fluctuating part (accent), the nett transport can be shown to be composed

of a mean contribution of mean velocity times mean concentration and a, more difficult, correlation component:

$$\left. \begin{aligned} u &= \bar{u} + u' \\ c &= \bar{c} + c' \end{aligned} \right\} \bar{S} = \overline{uC} = \bar{u} \cdot \bar{C} + \overline{u'C'}$$

This correlation component $\overline{u'C'}$ is mainly originated from the asymmetry of the waves.

During a storm surge the transports due to intensive breaking of waves and the local beach slope are dominant above other contributions. Relative to non-breaking waves, breaking waves result in a dramatic increase in turbulence level, and therefor lift sediment into suspension over the whole depth. The concentration fluctuations well above the bed are relatively small and hardly correlated with the velocity fluctuations (DELFT HYDRAULICS, 1989). The contribution of the correlation component will therefor be relatively small. This means that the nett transport can be computed from the mean velocities and the mean sediment concentrations.

3.3 Sediment concentration distribution

The time averaged sediment concentration (the overbar is omitted) can be written as a product of a reference concentration (at the bed level) C_0 and a distribution function $f_c(z)$:

$$C(z) = C_0 \cdot f_c(z) \quad [\text{kg/m}^3]$$

Using the one-dimensional stationary convection-diffusion equation to describe the distribution, the vertical profile of the time mean sediment concentration depends on the vertical distribution of the diffusion (mixing) coefficient $\epsilon(z)$, according to:

$$f_c(z) = \exp \left[-w_s \cdot \int_0^z \frac{dz}{\epsilon(z)} \right] \quad [-]$$

in which w_s stands for the (level independent) sediment fall velocity.

In order to describe the diffusion coefficient distribution $\epsilon(z)$, a great number of measured sediment concentrations were analysed. From each of the 68 used data sets (DELFT HYDRAULICS, 1987) the $\epsilon(z)$ -distribution was computed from the concentration profile using:

$$\epsilon(z) = -w_s \cdot [\partial(\ln C(z))/\partial z]^{-1} \quad [\text{m}^2/\text{s}]$$

The amount of mixing increases with increasing level above the bottom, which is in accordance with results of investigations carried out by other researchers (e.g. v.d. Graaff, 1988; Ras and Amesz, 1989). As a final result for the description of the diffusion profile, $\epsilon(z)$ is modelled as a linear function of the level above the bed, according to:

$$\epsilon(z) = \epsilon_0 + \mu \cdot z \quad [\text{m}^2/\text{s}]$$

in which:

ϵ_0 the reference mixing coefficient [m²/s]
 μ the vertical mixing gradient [m/s]

Both ϵ_0 and μ are functions of the local hydraulic conditions. This linear relationship is also suggested by Songvisessomja et al (1988), who compared different $\epsilon(z)$ -relation, by analysing data from Nielsen (Nielsen, 1984).

The vertical distribution of the mean sediment concentration is now simply described by:

$$C(z) = C_0 \cdot \left[1 + \frac{\mu \cdot z}{\epsilon_0} \right]^{(-w_s/\mu)} \quad [\text{kg/m}^3]$$

in which:

C_0 the reference concentration [kg/m³]
 w_s the fall velocity of the bed material [m/s]

An example of the procedure is presented in Figure 1. The relevant steps are:

- (i) From the measured concentration (\square -symbols the $\epsilon(z)$ -values are estimated (x-symbols);
- (ii) Linear fit of $\epsilon(z)$ -values result in ϵ_0 - en μ -values;
- (iii) Fit of $C(z)$ -values in combination with ϵ_0 and μ result in $C(z)$ -equation and C_0 -value.

As a result of each test both concentration and diffusion distributions are available. The latter will be used as an input for the description of the secondary current (undertow).

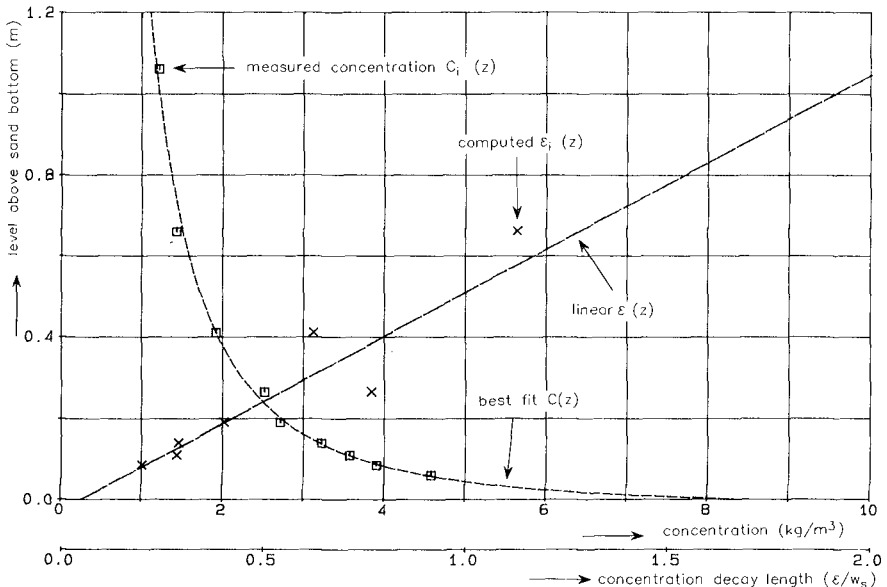


Figure 1 Example of $C(z)$ -fit-procedure (test T1F1)

3.4 Mean velocity distribution

The suspended sediment load is transported by the mean velocity profile, which is present due to the mass transport of the breaking waves above the level of the wave troughs and results in the (compensating) so-called undertow below this level.

The description of this mean velocity profile below the trough level is started with the assumption of a constant vertical gradient in the (time mean) shear stress (Stive and Wind, 1986):

$$\frac{1}{\rho} \cdot \frac{\partial \bar{\tau}}{\partial z} = \frac{\partial}{\partial z} (\epsilon(z) \cdot \frac{\partial u}{\partial z}) = \alpha$$

After integration follows:

$$\alpha = \frac{\bar{\tau}_t - \bar{\tau}_o}{\rho \cdot d_t} \quad [\text{m}^2/\text{s}]$$

in which:

$\bar{\tau}_t$	the mean shear stress at the wave trough level	[N/m ²]
$\bar{\tau}_o$	the mean shear stress at the reference level	[N/m ²]
ρ	the mass density of the fluid	[kg/m ³]
d_t	the vertical distance between reference and wave trough level	[m]

The velocity gradient can be derived from:

$$\frac{\partial u}{\partial z} = \alpha \cdot \frac{z}{\epsilon(z)} + \beta \cdot \frac{1}{\epsilon(z)}$$

in which the integration constant β equals:

$$\beta = \epsilon_o \cdot \frac{\partial u}{\partial z} (z=0) = \frac{1}{\rho} \cdot \bar{\tau}_o \quad [\text{m}^2/\text{s}^2]$$

The final velocity profile can therefore be derived from:

$$u(z) = u_o + \alpha \cdot \int_o^z \frac{z}{\epsilon(z)} dz + \beta \cdot \int_o^z \frac{1}{\epsilon(z)} dz \quad [\text{m/s}]$$

in which u_o stands for the mean velocity at the reference level. This type of equation is also presented by Okayasa et al (1988).

The vertical diffusion (mixing) coefficient is now taken equal to the sediment diffusion coefficient $\epsilon(z)$.

The use of a non-constant but continuous diffusion coefficient distribution in undertow description differs from the approach of several other authors who use two layers of constant diffusion (e.g. de Vriend and Stive 1987).

After some integrations the mean velocity profile can be shown to be described by:

$$u(z) = u_o + K_{lin} \cdot z + K_{log} \cdot \ln[1 + \frac{\mu \cdot z}{\epsilon_o}] \quad [\text{m/s}]$$

$$\text{where: } K_{lin} = \frac{\alpha}{\mu} \quad [1/\text{s}]$$

$$K_{log} = (\beta - \frac{\alpha}{\mu} \cdot \epsilon_o) / \mu \quad [\text{m/s}]$$

The form and magnitude of the velocity distribution below the wave trough depends on the mass flux m and the shear stress at the trough level $\bar{\tau}_t$.

For continuity reasons the mass flux m equals

$$m = \rho \int_{z=0}^{d_t} u(z) dz \quad [\text{kg/m/s}]$$

Both mass flux and shear stress at trough level are based on relations by de Vriend and Stive (1987).

The mean shear stress at the reference level $\bar{\tau}_0$ is related to the mean velocity u_0 at this level.

3.5 Nett local transport computation

The nett transport has to be split up into two parts: the transport below the (mean) trough level and the transport above this level.

In the lower part the nett seaward transport S_1 follows from the integral of the product of mean velocity $u(z)$ and mean concentration $C(z)$, according to:

$$S_1 = \int_{z=0}^{d_t} u(z) \cdot C(z) \cdot dz \quad [\text{kg/m/s}]$$

From the equations for $u(z)$ and $C(z)$ the result of this integral can be shown to be:

$$S_1 = C_0 [u_0 \cdot I_1 + K_{1in} \cdot I_2 + K_{1log} \cdot I_3] \quad [\text{kg/m/s}]$$

with:

$$I_1 = \frac{\epsilon_0}{\mu} \cdot \frac{1}{K_1} \cdot [K_2^{K_1} - 1] \quad [\text{m}]$$

$$I_2 = \frac{\epsilon_0}{\mu} \cdot \frac{1}{K_1} \cdot [K_2^{K_1} (d_t - \frac{\epsilon_0}{\mu} \cdot \frac{K_2}{K_1+1}) + \frac{\epsilon_0}{\mu} \cdot \frac{1}{K_1+1}] \quad [\text{m}^2]$$

$$I_3 = \frac{\epsilon_0}{\mu} \cdot \frac{1}{(K_1)^2} \cdot [K_2^{K_1} (K_1 \ln K_2 - 1) + 1] \quad [\text{m}]$$

and:

$$K_1 = 1 - w_s/\mu \quad [-]$$

$$K_2 = 1 + (\mu/\epsilon_0) \cdot d_t \quad [-]$$

In the upper zone the nett landward transport S_u follows from:

$$S_u = \int_{z=d_t}^{\infty} u(z) \cdot C(z) dz \quad [\text{kg/m/s}]$$

Since vertical gradients in $C(z)$ near the mean water level are rather small this integral can be simplified to:

$$S_u = C_d \cdot \int_{z=d_t}^{\infty} u(z) dz = C_d \cdot m/\rho \quad [\text{kg/m/s}]$$

in which:

C_d the concentration at the mean waterlevel [kg/m³]
 m the mass flux above the wave trough level [kg/m/s]

Finally the total nett transport S_x can be computed from:

$$S_x = S_l + S_u$$

An example of this nett transport computation is shown in Figure 2. The right side of this figure shows the measured and best-fit concentration distribution, whereas the left part shows the measured and best fit nett velocity profile below the wave trough level. Computing nett transport results in a seaward transport of 0.77 m³/m/hr below the trough level, while the landward transport above the trough level amounts 0.33 m³/m/hr. As a consequence the total nett transport is about 0.44 m³/m/hr seaward.

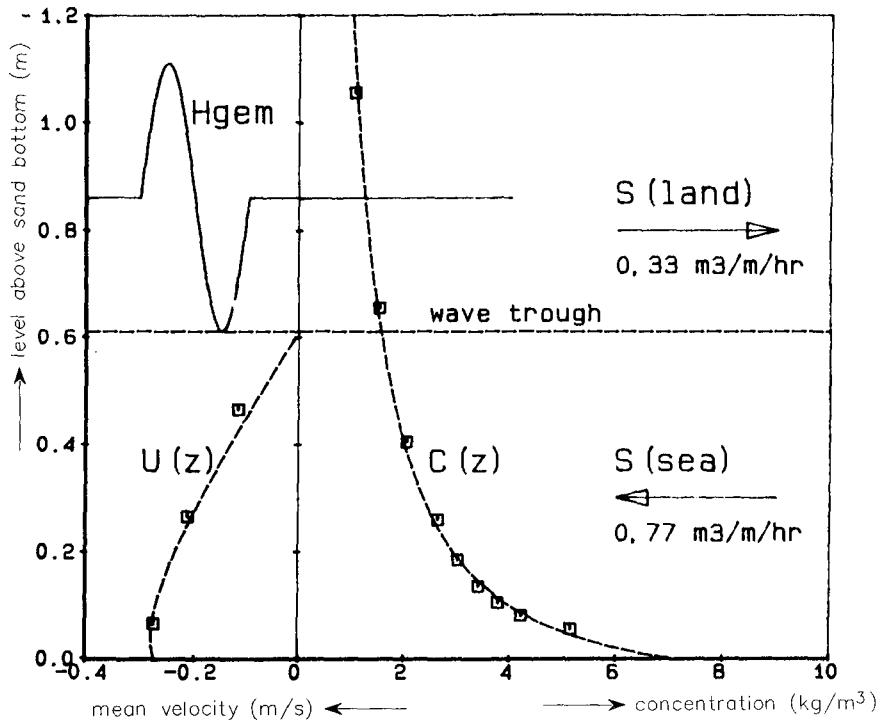


Figure 2 Transport at $x = 181$ m based on velocity profile and concentration profile (test T3I4); Computed transport: $S(\text{net}) = 0.44 \text{ m}^3/\text{m/hr}$

3.6 Justification

In order to give some justification on this method instantaneous transports, computed by integration of the product of $C(z)$ and $U(z)$ over the water depth, are compared with transports computed from frequently measured bottom profiles.

Figure 3 shows the profile development for a partly protected dune due to both 9.5 and 12.5 hrs of wave attack. In this time interval the amount of erosion above and in front of the revetment slowly increases. From this the transport at every position and time can be computed using mass balance equations.

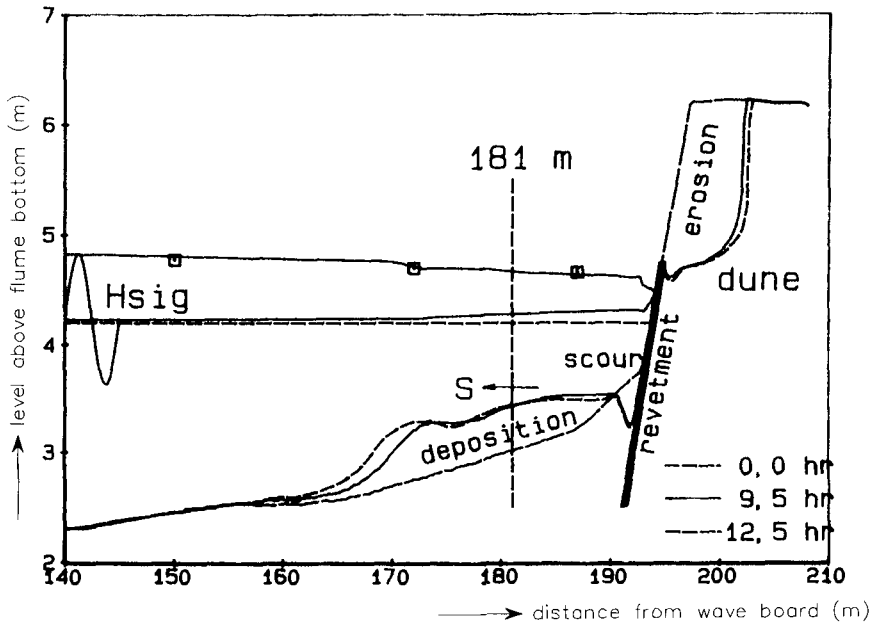


Figure 3 Example of profile development and transport in a large scale model with revetment (test T3I4); Measured transport at $t = 11.25$ hr: $S(\text{net}) = 0.40 \text{ m}^3/\text{m}/\text{hr}$

In this case position and time correspond with the situation from Figure 2 and result in a nett transport of $0.40 \text{ m}^3/\text{m}/\text{hr}$. This "measured" transport deviates only 10% from the former computed transport.

Figure 4 shows a comparison between 22 measured and computed transports. With the dotted line indicating a deviation of 20%, the agreement was concluded to be rather good. It was therefor assumed that the presented method of nett transport computation in case of breaking waves gives a reliable estimate of the actual nett transport.

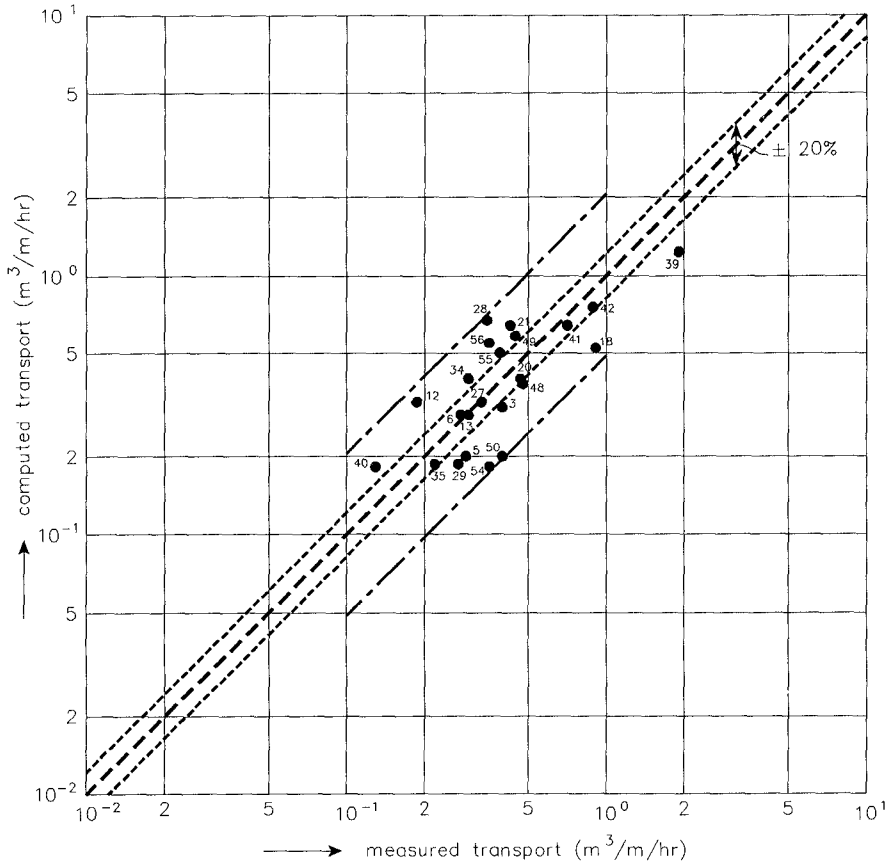


Figure 4 Comparison between measured transports (from profile development) and computed transports (using $C(z)$ and $U(z)$)

4. Model calibration

The calibration of the dynamical model is carried out for the "internal" process parameters, whereas the verification is based on "external" process results, such as profile development and the amount of dune erosion above the maximum surge level.

In this case the transport model is calibrated by the use of approximately 150 simultaneously measured concentration and velocity profiles during storm surge conditions in both small and large scale model tests. For calibration the relevant parameters (e.g. mass flux m and reference concentration C_0) are related to the hydraulic conditions which are computed by the use of results of a calibrated wave decay model.

The reference concentration C_o is related to both the intensity of breaking and the way of breaking (spilling or plunging) according to:

$$C_o = \rho_s \cdot K_c \cdot F_D \cdot [\rho/\bar{\tau}_{cr}]^{3/2} \cdot [F_k(\gamma)]^{3/2} \cdot [Diss/\rho] \quad [kg/m^3]$$

in which:

- K_c a constant [-]
- K_D^C a constant related to the sediment diameter [-]
- F_k^D a function which describes the effect of the kind of breaking [-]
- Diss the dissipation of turbulent kinetic energy [W/m²]

In case of the dissipation term there has been made a distinction between the dissipation source term in the wave energy balance equation and the dissipation of the turbulent kinetic energy Diss. The former is actually a production term of turbulent kinetic energy [Roelvink and Stive, 1989].

In order to take in account the effects of the way the waves are breaking, a relation between the near bottom magnitude of the depth and time mean turbulent energy k_o and the total turbulent energy K is suggested:

$$k_o = K \cdot F_k(\gamma) \quad [m^2/s^2]$$

in which γ is the ratio H_{rms}/d .

Considering a exponential downward decrease in turbulence level and a characteristic penetration depth below the mean water level equal to $\alpha_k \cdot H_{rms}$, this function is:

$$F_k(\gamma) = [\alpha_k \cdot \gamma (\exp(1/\alpha_k \cdot \gamma) - 1)]^{-1} \quad [-]$$

In case of $\alpha_k = 1/2$ this equation can be simplified to:

$$F_k = \begin{cases} 0 & \gamma < 0.33 \\ 0.47(\gamma - 0.33) & \gamma \geq 0.33 \end{cases} \quad [-]$$

In case of spilling breakers, wave breaking does not contribute to the reference concentration.

Figure 5 shows a comparison between measured and computed reference concentrations. With respect to the closed symbols the agreement was concluded to be satisfactory.

5. Model verification

The final verification of the model is done by comparing measured dune erosion quantities with computed profile development for 43 model tests and a small number of prototype data. Figure 6 shows a comparison of measured and computed erosion quantities in a small scale model due to different wave heights, wave periods, water levels and dune heights for constant and varying hydraulic conditions.

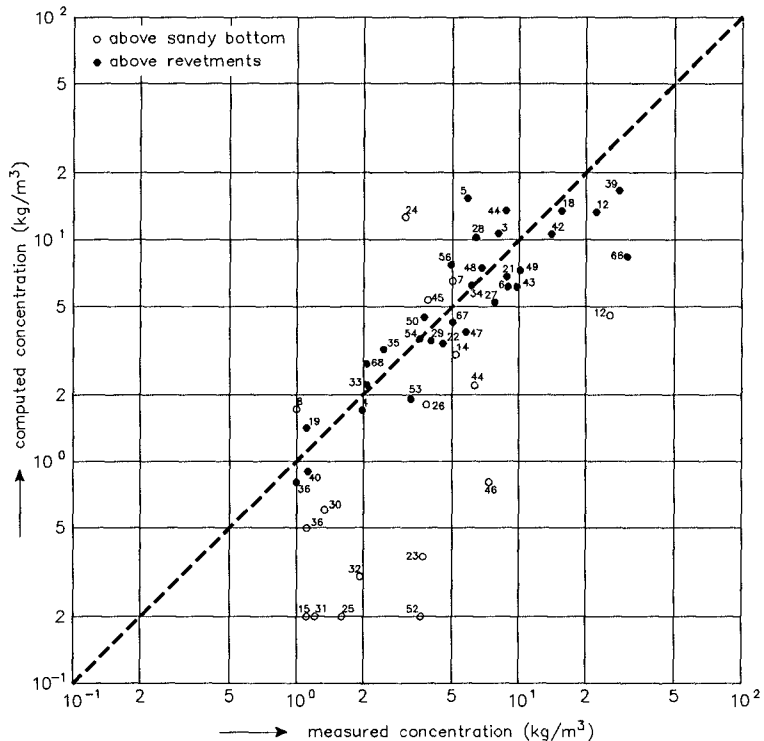


Figure 5 Comparison between measured and computed reference sediment concentrations (open symbols indicate positions above revetment)

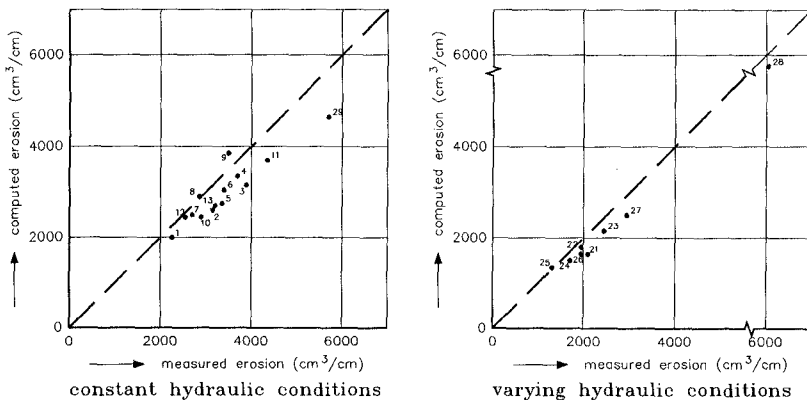


Figure 6 Comparison between measured and computed erosion quantities for constant and varying hydraulic conditions (small scale)

6. Conclusions

During extreme wave attack the suspended transport based on time mean concentrations and velocities is dominant. A predictive model for sediment load and transport due to extreme wave attack is presented which gives a reliable description of the transports and profile development during a storm surge. By the use of this model the amount of erosion for arbitrary coastal profiles, e.g. with bars and tidal gully or with protected dunes (dune revetments) due to arbitrary storm surge conditions can be determined. Finally it should be revealed that in order to increase reliability of the model some further verification and (perhaps) re-calibration for unused data sets will be carried out.

7. Acknowledgement

The present study has been carried out by DELFT HYDRAULICS on behalf of the Technical Advisory Committee on Water Retaining Structures (TAW) of the Ministry of Transport and Public Works in the Netherlands.

References

- Battjes, J.A. and J.P.F.M. Janssen (1978),
Energy loss and set-up due to breaking of random waves.
Proc. 16th Conf. on Coastal Engineering, Vol. I, pp. 569-589.
- Bosman, J.J. and Steetzel (1986),
Time and bed averaged concentrations under waves.
Proc. 20th Conf. on Coastal Engineering, Vol. II, pp. 986-1000.
- DELFT HYDRAULICS (1987),
Systematic research on the effectiveness of dune toe revetments;
large scale model investigations.
Research report H298 part I (in Dutch)
- DELFT HYDRAULICS (1989),
Cross-shore transport due to extreme hydraulic conditions.
Research Report H298 part III (in Dutch).
- Graaff, J. van de (1988),
Sediment concentration due to wave action.
Ph.D. Thesis, Delft Univ. of Technology, Delft, The Netherlands.
- Nielsen, P. (1984),
Field measurements of time averaged suspended sediment concentration
Coastal Engineering, Vol. 8, pp. 51-72.
- Okayasu, A., T. Shibayama and K. Horikawa (1988),
Vertical variation of undertow in the surf zone.
Proc. 21th Conf. on Coastal Engineering, Vol. I, pp. 478-491.
- Ras, S.L. and J.A. Amesz (1989),
Concentration and diffusion coefficient distribution due to irregular and breaking waves.
M.Sc. Thesis, Delft Univ. of Technology, Delft, The Netherlands (in Dutch).

Roelvink, J.A. and M.J.F. Stive (1989),
Bar-generating cross-shore flow mechanism on a beach.
Journal of geophysical research, Vol. 94, No. C4, pp. 4785-4800,
April 1989.

Songvisessomja, S. and N. Samarasinghe (1988),
Profile of suspended sediment due to prototype wave.
Proc. 6th Congress Asian and Pacific Regional Division,
Intern. Ass. for Hydr. Res., pp. 97-104, Japan.

Steetzel, J.H. (1987),
A model for beach and dune profile changes near dune revetments.
Proc. Coastal Sediments '87, ASCE, pp. 87-97.

Stive, M.J.F. and H.G. Wind (1986)
Cross-shore mean flow in the surf zone.
Coastal Engineering, Vol. 10, pp. 325-340.

Vellinga, A.P. (1986)
Beach and dune erosion during storm surges.
Ph.D. Thesis, Delft, Univ. of Technology, Delft, The Netherlands.

Vriend, H.J. de, and M.J.F. Stive (1987),
Quasi-3D modelling of nearshore currents.
Coastal Engineering, Vol. 11, pp. 565-601, Amsterdam.

CHAPTER 146

PREDICTION OF COASTLINE EVOLUTION FOR THE HOLLAND COAST

The Dutch Coast : Paper No. 7

M.J. Dijkman 1), W.T. Bakker 2), J.H. de Vroeg 3)

Abstract

The Coastal Defence Study, as executed in the Netherlands, involved a 100-year prediction for the coastline evolution of specific parts of the Holland coast. In order to create this prediction a mathematical two-line model was used. In this model the effects of wave driven as well as tidal transports are incorporated, also cross-shore transport is implemented. The model is calibrated using sand balances, derived from measurements of coastal profiles. Qualitatively correspondence is reached, but quantitative differences between model and nature remain.

1. Introduction

The mathematical prediction of the coastline evolution of the Holland coast for the Coastal Defence Study is based on a two-line model, as described by Bakker (1968) and in the Manual on Beach Nourishment (Pilarczyk, ed., 1986). The way of prediction is described by Dijkman et al. (1989); the present paper gives a condensed version of this report.

The Holland coast is the central one of the three parts (Rhine/Scheldt estuary, uninterrupted Holland coast,



Figure 1. The Holland coast

- 1) Veldhorstraat 50, 2161 ER Lisse, The Netherlands
- 2) Rijkswaterstaat, Tidal Waters Division, P.O.Box 20907, 2500 EX The Hague, The Netherlands
- 3) Delft Hydraulics, P.O.Box 152, 8300 AD Emmeloord, The Netherlands

Wadden islands), into which the Dutch coast can be divided (see figure 1). Three harbors (Hook of Holland, Scheveningen, and IJmuiden) partition the Holland coast. The harbor moles of Hook of Holland and IJmuiden have a length of 3 km and therefore have a dominating effect on the coastal behavior.

2. The two-line model

The two-line model is based on a schematization of the coastal profile into two zones (see figure 2) :

- the inshore zone: MSL-5m to MSL-1m (MSL-1m represents the average low water level)
- the beach zone : MSL-1m to the local dune top (varying between MSL+10m and MSL+20m)

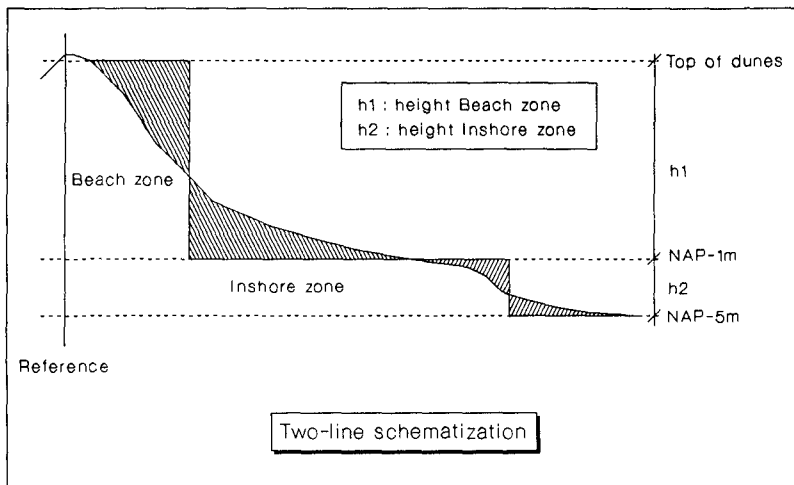


Figure 2. Two-line schematization

The model represents the area up to the depth contour of MSL-5m. This value for the lower boundary of the inshore zone is based more on practical (availability of measurements) than on theoretical considerations. In this zone the effect of the wave driven transport will dominate that of the tidal transport. At the seaside, there will be an interaction with the offshore zone: effects of cross-shore transports as well as tides can be important here. Sand losses due to the sea level rise and to wind transport over the dune tops are not taken into account. The sand quantity in either zone of a specific coastal profile is averaged. Doing so for several profiles, and connecting the so found values results (in plan view) in a couple of lines : the 'beach line' and the 'inshore line'. The mathematical basis of the two-line model consists of an equation of motion and an equation of continuity, this for each zone. The equations of motion consist of two components: the longshore and the cross-shore transports. In the following equations the indices 1 and 2 will be used to refer to the beach zone and the inshore zone respectively.

- Longshore transport:

(eq 2.1a/b)
$$S_i(x, t) = S_{tide, i}(x) + S_{0, i}(x) - s_i(x) \frac{\delta y_i(x, t)}{\delta x}$$

 for $i=1,2$ and with :

- $S_i(x, t)$ (m^3/yr) total longshore transport at location x and at time t .
- $S_{tide, i}(x)$ (m^3/yr) tidal transport at location x . This term has been determined for the present situation near the harbors and is assumed to be constant in time.
- $S_{0, i}(x)$ (m^3/yr) constant component of the wave driven transport at location x . This is the wave driven transport for locations x , where the coastal direction is parallel to the x -axis, and varies only with a gradient in the wave climate along the coast.
- $s_i(x)$ ($m^3/yr/rad$) coastal constant at location x , giving the ratio between a change in coastal direction and the wave driven transport. This constant also varies only with a gradient in the wave climate along the coast.
- $y_i(x, t)$ (m) distance between the x -axis and the beach line ($i=1$) or the inshore line ($i=2$), at location x and at time t .

- Cross-shore transport:

The cross-shore transport is modelled following the principle of the equilibrium coastal profile. According to this principle (under given conditions) an equilibrium profile will be formed in the long run. Applying this principle to the two-line schematization of the coastal profile the equilibrium profile converts into an equilibrium distance between the beach and the inshore line. Any occurring difference between the actual and the equilibrium distance results in a cross-shore sediment transport. The cross-shore transport is furthermore assumed to be proportional to this difference.

In formula: $S_y = s_y \cdot [W - (y_2 - y_1)]$ (eq 2.2)

With:

- S_y (m^2/yr) : cross-shore transport (positive when directed seaward)
- s_y (m/yr) : cross-shore transport constant, determining the timescale at which the equilibrium distance (W) is reached.
- W (m) : equilibrium distance between the schematized beach and inshore line.

• Continuity:

Beach :
$$h_1 \frac{\delta y_1(x, t)}{\delta t} = - \frac{\delta S_1(x, t)}{\delta x} - S_y(x) + p_1(x)$$

Inshore:
$$h_2 \frac{\delta y_2(x, t)}{\delta t} = - \frac{\delta S_2(x, t)}{\delta x} + S_y(x) + p_2(x)$$

(eq 2.3 a/b)

- With : $p_i(x)$ ($m^3/m/yr$) : sediment source in the beach zone ($i=1$) resp. the inshore zone ($i=2$).

Model boundaries

For the model the Holland coast was divided into three areas:

- Callantssoog to IJmuiden
- IJmuiden to Scheveningen
- Scheveningen to Hook Holland

These areas all stretch from one harbor mole to the other, except for the most Northern border. Here the model was limited to Callantssoog, because of the influence of the tidal inlet near Den Helder becoming too strong in the more Northern region.

Model parameters

- Wave climate

The wave climate used is derived from measurements in the period 1978-1984. These measurements lack direct information on the direction of wave propagation, only the wind direction is given. To overcome this problem a correction to the directions has been applied based on the correlation as proposed by Hokke and Roskam (1987), who found this correlation between the wind direction and the wave direction from measurements using Wavec-buoys. The so corrected wave climate significantly differs from the original 'uncorrected' one.

Wave data originating from three different sites (Eierland, IJmuiden and LE Goeree) have been used. A comparison between these three sites gives an impression of the variation of the wave climate along the Holland coast, see figure 3.

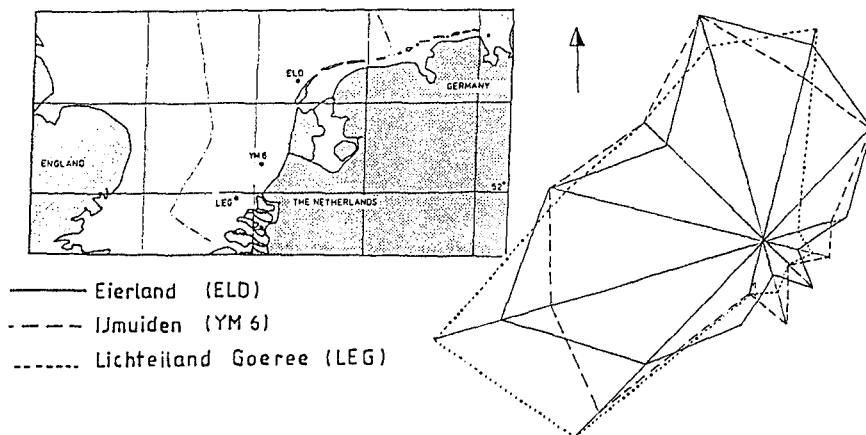


Figure 3. Variation of the wave climate

Furthermore the wave climate as now determined is valid for deep water with a depth of appr. 20-25 m. In order to obtain the required wave climate at shallower water (of appr. 10 m depth) the ENDEC program (ENERgy DECay, Delft Hydraulics, 1988) was

used. This program incorporates the effects of breaking waves, refraction, shoaling, bottom friction and wind.

- Tidal influence

The tidal data have been taken from the HOKU model (Hollandse KUST, which stands for Holland Coast) (Delft Hydraulics, Hartsuiker, 1988). The non-linear relation between tidal velocities and sediment transports has been compensated by using a morphological tide, which is found by multiplying the average tide with a 'tidal factor' (here taken to be 1.1).

In the direct surroundings of the harbors the influence of the tidal effects can be expected to be much more noticeable than at some distance from those harbors. This as a result of the converging/diverging tidal flows, causing sediment transport gradients and accessory erosion/accretion patterns. Qualitatively the formation of an eddy at the leeside of a harbor mole causes a reversal of the longshore transport in this region. For the opposite tide the longshore transport directed to the mole will remain constant until

a much smaller distance from the mole. The resulting effect of a complete tidal sequence will therefore be an accretion at a small distance to the mole, followed by an erosion that at growing distance from the mole becomes less noticeable.

The tidal effects are calculated in the vicinity of the harbors up to the point where the effect of the harbor mole is negligible. In between the harbors a linear interpolation has been used. The tidal velocities at the points in the grid are calculated for an interval of 30 min. (25 in total, covering 12 hours). The probability function for the orbital velocities caused by waves is determined for each grid point. For the fraction of time waves are breaking in this point there is assumed to be no contribution to the tidal transport for that particular combination of waterdepth, wave direction and wave height. Then with the Bijker formula, using both the orbital velocity distributions and the tidal velocities, a resulting tidal sediment transport is calculated. This tidal transport is assumed to be time independent. The results are shown in figure 4.

- Diffraction near the harbors

In the direct vicinity of the harbors the effect of diffracting waves around the harbor moles is an important factor. This effect is implemented in the model, however in a somewhat limited manner: the diffraction and refraction effects have been calculated separately. For the method used see Bakker et al. (1989).

- Coastal constants

These are the constants (constant only in time, but varying along the coast as a result of a variation of the wave conditions along the coast) which determine the longshore wave driven sediment transport ($S_{0,i}$ and s_i in eq 2.1). Calculation of these constants is done using the following assumptions:

- The wave driven longshore transport between two depth contours is proportional to the longshore component of the energy-loss of the driving wave between those depth contours.
- The depth contours are parallel.

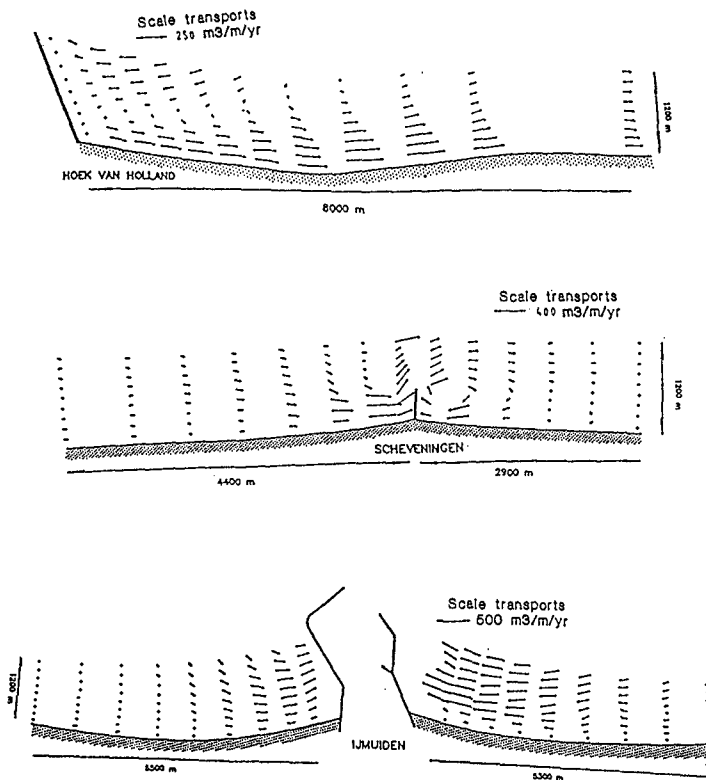


Figure 4. Resulting tidal sediment transports near the harbors. The equation used to calculate the longshore transport is a variation of the CERC formula :

$$s = A * (n_{br} H_{br}^3 c_{br} \sin(\phi_{br}) \cos(\phi_{br})) \quad (eq 3.1)$$

With S : longshore sediment transport (m³/yr)

A : proportionality constant (-)

the wave characteristics at the breaker line:

n (-), H (m), c (m/s), phi (rad)

For a more detailed description of the method used see Svasek (1968), Bakker (1969) and Bakker et al. (1989).

The calculations were performed using the KC program (Kust Constanten, which stands for Coastal Constants, by Casteleyn, 1975) which includes diffraction and refraction effects. In order to compensate for the overestimated diffraction effects, caused by using

monochromatic waves, a reduction factor for the calculated diffraction effect has been applied, this factor is taken to be 0.75. (The difference between the calculated values in the diffraction zone and the value outside this zone is multiplied by the reduction factor). Originally the KC program gives values for the coastal constants for a one-line model, the necessary two line values are derived from the one-line values by assuming a constant ratio between the values for beach and inshore respectively. From calculations a ratio (beach:inshore) of 1:4 was found.

The only remaining unknown in the coastal constants is the proportionality constant A (see eq 3.1). This will be determined in the calibration of the model, just like the cross-shore coastal constants s and W (see eq 2.2).

3. The coastal defence works

There are three different defence methods in use along the Holland coast : groyne, the Hondsbossche Seawall and sand supplies.

The groyne partially block the longshore sediment transport. The effectiveness of the groyne has been roughly estimated by considering the depth to which they reach, in relation to the sediment transport distribution over the depth as found by Bakker (1969). In the model this has been accounted for by using a reduction factor for the coastal constants. Note that this method implies neglecting the impact the groyne may have on the tidal sediment transports : the tidal transports mainly take place at greater depths than the depths to which the groyne reach.

The Hondsbossche Seawall is a rigid seawall, below MSL-1m it is covered by sediment. At both sides of the seawall there are several groyne preventing this area from eroding too severely. In front of the Hondsbossche Seawall the beach zone does not really exist, in the model this has been accounted for by taking the coastal constants in this area equal to zero. In the inshore zone there can be some sediment transport. However, at both sides of the Hondsbossche seawall very strong curves in the coastlines occur, which are not varying too much in time. Therefore the coastal constant s_2 must also be taken equal to zero for this area. This assumption can be backed up by the geological consistency of the bottom material in front of the Hondsbossche Seawall: there are some almost baring clay layers present there (de Mulder, 1983). This implies there can only be a constant transport along the Hondsbossche Seawall: what goes in on one side must go out the other.

The model does not implement the sand supplies, but does take these into account in the calibration of the model, see the next paragraph.

4. Calibration and output

The proportionality constant A, used in the calculation of the coastal constants (see eq 3.1), is used as the instrument to calibrate the model. The calibration is based on the measurements of the coastal profiles of the Dutch Coast on a yearly basis, as stored in the JARKUS database. These measurements are used to create sand balances for the specific parts of the Holland Coast. Some results are shown in figure 5, showing the relative amount of sand (relative to the first year) for three subareas.

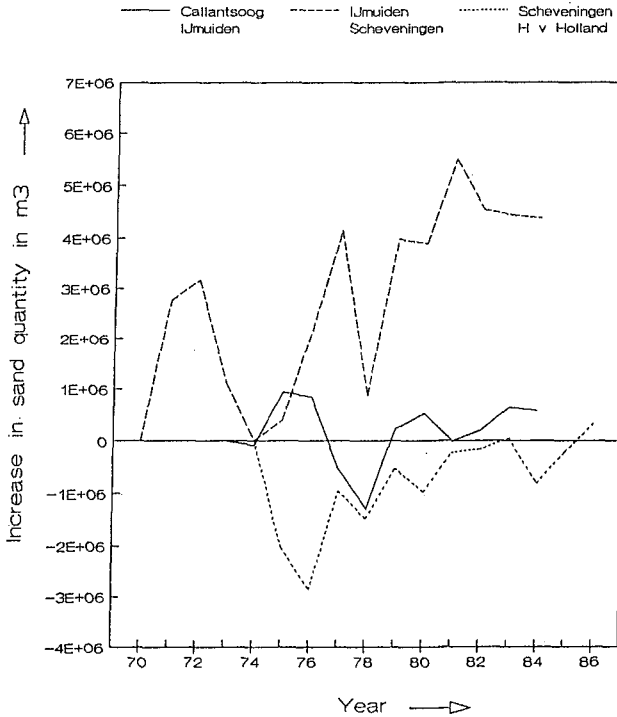


Figure 5. Sand balances for the Holland coast.

By making some assumptions these sand balances can be used to give an idea of the average sediment transports in the considered areas. The necessary assumptions:

- No sand leaking around the harbor mole near Hook of Holland.
- No sand from above the MSL-5m passes from one side of the harbor moles of Scheveeningen and IJmuiden to the other.
- Equally distributed sand supply from deeper water over the MSL-5m line for an area between two harbors.

With these assumptions the following conclusions can be derived:

- Accretion of the area Hook of Holland-IJmuiden of 370103 m³/yr, or 6 m³/m/yr. (=p₂ in eq 2.3).

For the area IJmuiden-Callantssoog this accretion is 40103 m³/yr, or 0.9 m³/m/yr. This value has been neglected (p₂=0 in eq 2.3). This relatively low value (relative to the value in the area Hook of Holland-IJmuiden) can be explained by the increase (going Northward from IJmuiden) of the Northward tidal flow in deeper water, 'consuming' the sediment which would otherwise come to benefit the area above the MSL-5m level.

The onshore transports found here compare reasonably well to those found by Stive (1990). The value Stive proposes, is a bit larger : approximately $10 \text{ m}^3/\text{m}/\text{yr}$, almost constant over the entire Holland coast. However this value is derived for an onshore transport over the MSL-8m line, where in this paper the transport over the MSL-5 line is considered.

- The optimum value for the proportionality constant A is 500, determined for the area Hook of Holland - IJmuiden. This value is about a third of the conventional values! With the proportionality constant A now determined, the longshore transports can be calculated, the results are shown in figure 6.

Again, comparing the so found longshore transports to those found by Stive (1990) a reasonable agreement is found, see Dijkman et al.(1989).

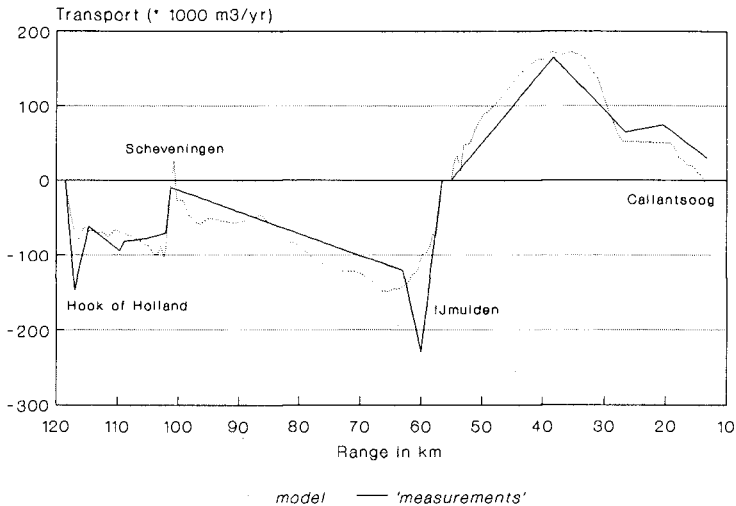


Figure 6. Calibration of the longshore transports.

- The coastal constant for the cross-shore transport, s_y (at a depth of MSL-1m) is found to be in the order of $0.05 \text{ m}/\text{yr}$ (for the region Hook of Holland - Scheveningen) to $0.10 \text{ m}/\text{yr}$ (for Scheveningen-IJmuiden). These results were found by using a value of 280 m for the equilibrium distance between beach and inshore line. In the model a constant value of $0.10 \text{ m}/\text{yr}$ is used.

Other scenarios, for instance large offshore transport caused by rip-currents and tidal currents in the immediate vicinity of the harbor moles, have been elaborated with respect to their consequences for the coastal development. (The report by Dijkman et al. (1989) shows results). However, these scenarios had to be rejected because of the coastal behavior according to these scenarios proved to be unrealistic.

5. Results

Figure 7 shows the calibrated coastal development between 1973 and 1984, for the area Callantsoog to IJmuiden. On the left-hand side one observes the effect of the harbor mole of IJmuiden, and between the ranges 20 to 25 the effect of the Hondsbossche Seawall.

Figure 8 shows predictions found in this way for the years 2020 and 2090.

Finally the same results are presented in a different manner, namely with the reference as the initial situation. Figure 9 shows the development of the beach-line, figure 10 that of the inshore line.

Results for the area IJmuiden to Hook of Holland are not presented here, they can be found in the report by Dijkman et al. (1989).

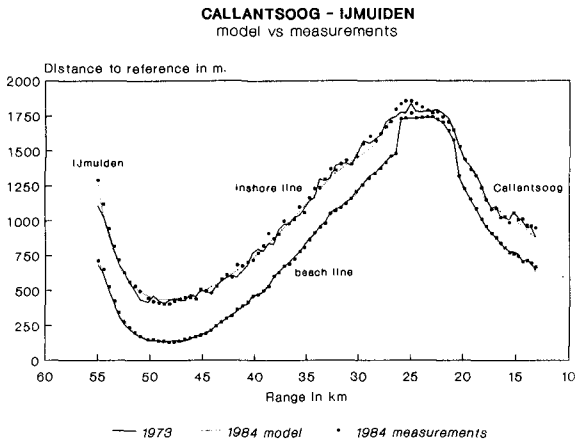


Figure 7.

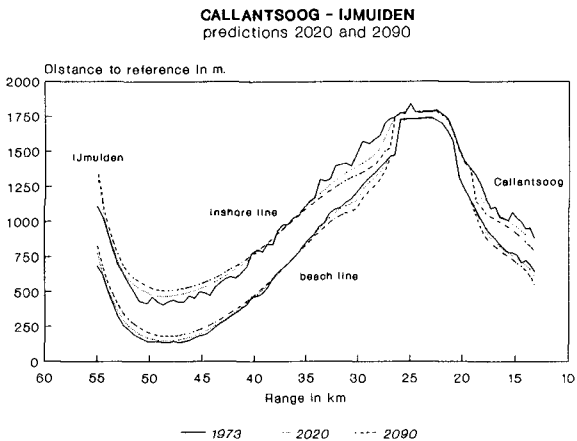


Figure 8.

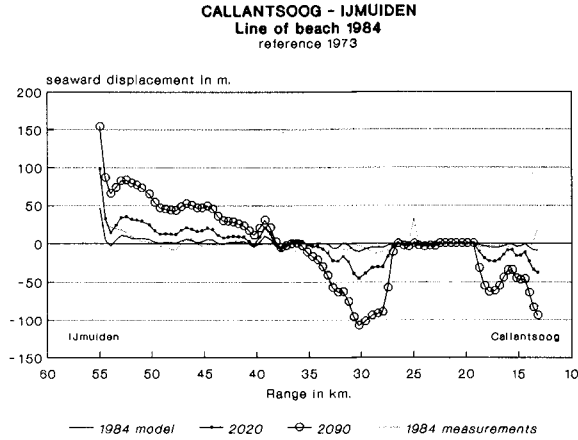


Figure 9.

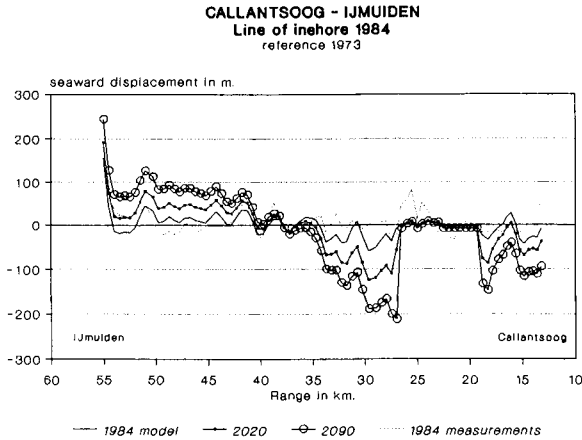


Figure 10.

6. Conclusions

- The results (certainly for an area with harbor moles) strongly depend on the wave climate used (Dijkman et al, 1989). Therefore not only the accuracy, with which the present wave climate is known, but also the accuracy, with which the future wave climate can be predicted highly determines the accuracy of a prediction of the coastline evolution. Accurate wave data (especially concerning wave directions) are vital for accurate coastal prediction.
- The proportionality constant A (giving the ratio between the sediment transport and the longshore component of the wave energy flux, see eq 3.1) found here, is much lower (about a third) than more conventional values.
- The use of the two-line model as an instrument to create a prediction of a coast-line evolution is in creating a qualitative picture giving eroding and accreting areas, but limited in its quantitative accuracy.

References

Bakker, W.T. (1968)

The dynamics of a coast with a groyne system.

Proc. 11th Conf. on Coastal Engng. London.

Bakker, W.T. & J.H. de Vroeg (1987)

Coastal modeling and coastal measurements in the Netherlands.

Proc. Seminar SOGREAH: Prototype measurements to validate numerical models of coastal processes, Grenoble.

Bakker, W.T. (1969)

Calculation of the longshore wave driven transport using the method of parallel depth contours, (in Dutch).

Dutch ministry of public works, report WWK 69-7.

Bakker, W.T., C.v.d.Kerk & J.H. de Vroeg (1989) Determination of coastal constants in mathematical line models.

Second European Workshop on coastal zones as related to physical processes and coastal structures.

Loutraki, Greece.

Bijker, E.W. & J.N.Svasek (1969)

Two methods for determination of morphological changes induced by coastal structures.

22nd .Int. Nav.Congress, Paris, Section II, Item 4.

Casteleyn, J.A. (1975)

Numerical calculations of coastal changes...(in Dutch)

Delft University of technology, technical report 75-1

Dijkman, M.J., W.T. Bakker & J.H. de Vroeg (1989)

Two-line model for the Holland Coast (in Dutch)

Voorspelling ontwikkeling kustlijn 1990-2090,

Fase 3, deelrapport 3.2 (van Technisch rapport 5).

Dutch ministry of public works (Rijkswaterstaat)

Dorrestein, R. (1964)

Wind and wave data of the Netherlands Lightvessels.

Royal Dutch Meteorological Institute, 'Mededelingen', nr.90

Dutch Ministry of Public Works (1989)

Kustverdediging na 1990 (Coastal Defense after 1990).

Hartsuyker, G. (1988)

Tidal flow model for the Holland coast (in dutch).

Delft Hydraulics

Hokke, A.W. & A.P.Roskam (1987)

Measured deep water wave climate (in dutch)

Rijkswaterstaat, Tidal Waters Division, GWAO 87.291.

de Mulder, E.J.F. (1983)

Geological history of the Hondsbossche Seawall (in Dutch)

'vrienden van de Hondsbossche', 3 edition

Rijks geologische dienst

Pilarczyk, K.W. and J.v.Overeem (ed.) (1986)

Manual on Artificial Beach Nourishment

Stive, M.J.F., J.A.Roelvink & H.J.de Vriend (1990)

Large scale coastal evolution concept.

22nd Int.Conf.on Coastal Engng., Delft
De Vroeg, J.H., E.S.P.Smit & W.T.Bakker (1988)
Coastal Genesis.
21st Int.Conf.on Coastal Engng., Malaga

CHAPTER 147

MORPHOLOGIC RESPONSE OF TIDAL BASINS TO CHANGES

The Dutch Coast: Paper No. 8

W.D. Eysink¹

Abstract

This paper is part of a series of papers on a study of the Dutch Coast and describes the method used to determine the sand losses of the North Sea coast to the tidal basins of the Dutch Wadden Sea in the North and the estuaries in the South of The Netherlands. The sand losses can be caused by sea level rise, sand mining, closure works, natural land accretion in the basins or bottom subsidence due to gas extraction. The results of this study were relevant boundary conditions for the study on the behaviour of the North Sea coast in the vicinity of the tidal inlets (paper No. 9 of the Dutch Coast of Stive, Roelvink and De Vriend of these proceedings).

1. Introduction

In the scope of the study on the consequences of sea level rise on the North sea coast of The Netherlands, a practical method has been developed to assess the morphologic response of tidal basins to natural or man-made changes in such a system in terms of sand volumes. This was necessary to quantify the interaction between the North Sea coast and the tidal basins of the Dutch Wadden Sea in the North and the estuaries in the South (Fig. 1).

The hydraulic conditions in tidal basins are important as dominant energy sources causing sediment transports, erosion and sedimentation, and sorting of sediment to size, mineral density and rollability. Together these phenomena form the basis of a very complex geomorphodynamic system in which also flocculation of silt and clay particles and coagulation of those particles by shell fish and diatoms play an important role.

Today it is not possible yet to simulate the above complex processes sufficiently accurate in a numerical model. However, in spite of the complex and dynamic character of these areas, some systems can be recognized in nature if we look in a broad way neglecting details such as migration of channels and shoals. It appears that we can express certain characteristic quantities in empirical relationships which are useful tools for engineers.

¹ DELFT HYDRAULICS, P.O. Box 152, 8300 AD Emmeloord, The Netherlands

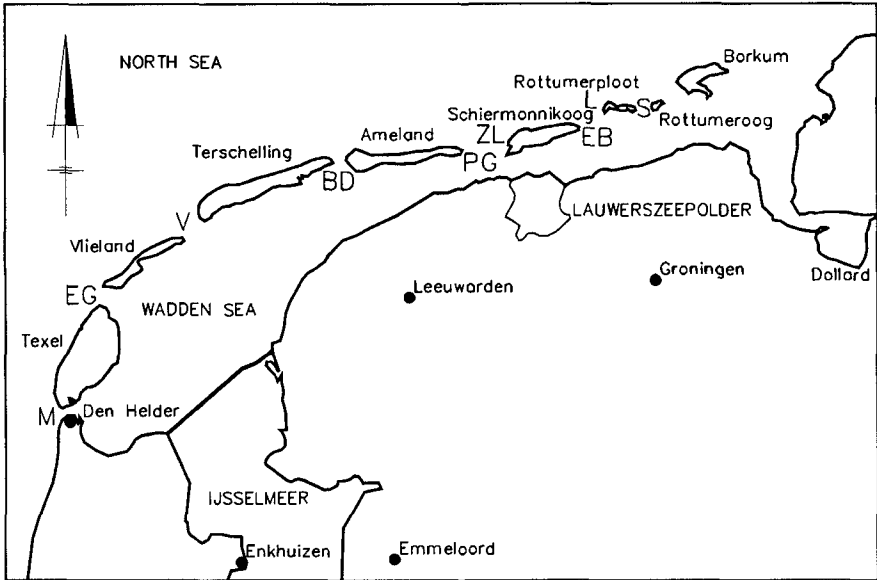


Figure 1a The Dutch Wadden Sea

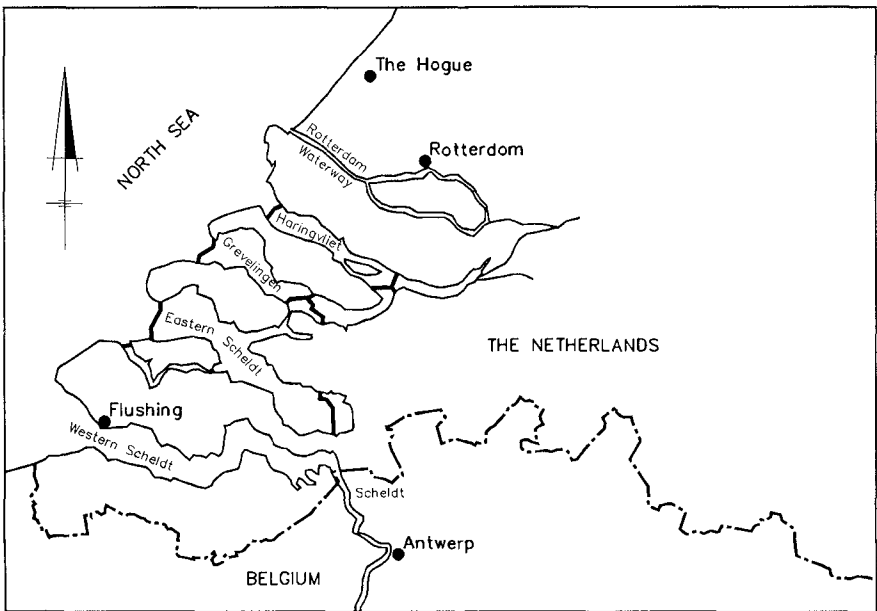


Figure 1b The Dutch Delta Area

2. Morphological relationships

A well known relationship from literature is the relation between the flow area of a tidal inlet and the tidal prism passing that inlet (e.g. O'Brien, 1969 and Bruun and Gerritsen, 1960) or related characteristic quantities such as the mean tidal flow velocity (e.g. Kreeke and Haring, 1979), maximum tidal flow velocity (e.g. De Jong and Gerritsen, 1984) or related shear stress velocities (e.g. Gerritsen and De Jong, 1985).

From data of one tidal channel in the Dutch Wadden Sea presented by De Glopper (1967) it appeared that also along a channel the flow area was related to the tidal volume passing the local cross section. Lateron this was confirmed by extensive investigations of Gerritsen and De Jong (1984, 1985) for various tidal channels in the Dutch Wadden Sea and in the estuaries in the Dutch Delta area in the South.

All results show that a rather good description is presented by the relationship:

$$A_{\text{MSL}} = c_A V^A \quad (1)$$

where:

A_{MSL} = flow area below MSL

c_A = empirical coefficient

V^A = characteristic tidal volume

Also some relation seems to exist between the mean depth of a tidal channel and the tidal volume (Fig. 2). This relationship is less firm and may show deviations due to the occurrence of hard bed layers or man-made bank protections.

Equation (1) does suspect that integration along a channel should result in a relationship for the volume of the entire channel system of a tidal basin. Plotting data of the channel volumes of the different tidal basins of the Dutch Wadden Sea versus their tidal volumes showed such a relation (Fig. 3). A similar relationship was found by plotting channel volumes of the Grevelingen and of various sections of the Eastern Scheldt versus the related tidal volumes (Fig. 4). Data of the Western Scheldt at first glance showed a different picture (Fig. 5). However, the deviation from that of the relationship for the other basins may be explained by the deepening of the River Scheldt and the Western Scheldt in the back of the estuary for a proper access to the Port of Antwerp. In general, the following relationship seems to be valid for the channel volume of a tidal basin or estuary (with minor upland discharge):

$$V_C = c_C V^{3/2} \quad (2)$$

where:

V_C = channel volume below MSL

c_C = empirical coefficient

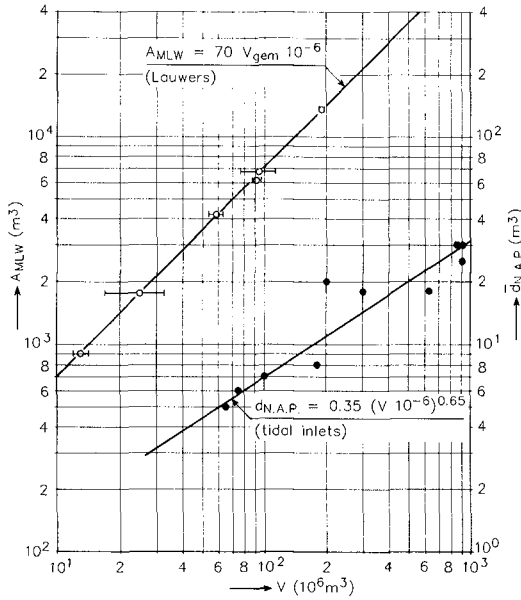


Figure 2 Mean tidal volume versus channel profile and depth

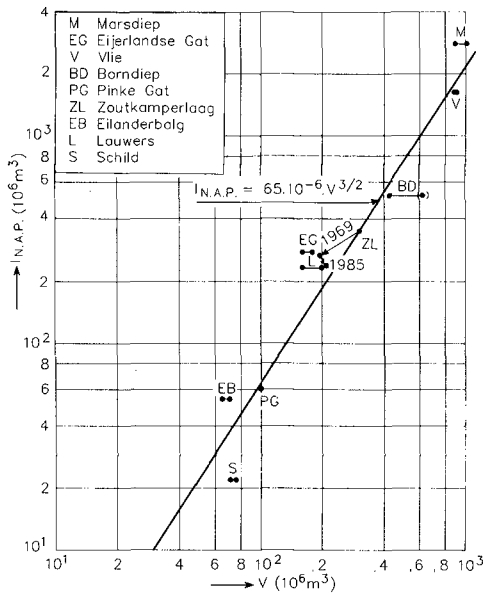


Figure 3 Channel volume versus mean tidal volume tidal basins of the Wadden Sea

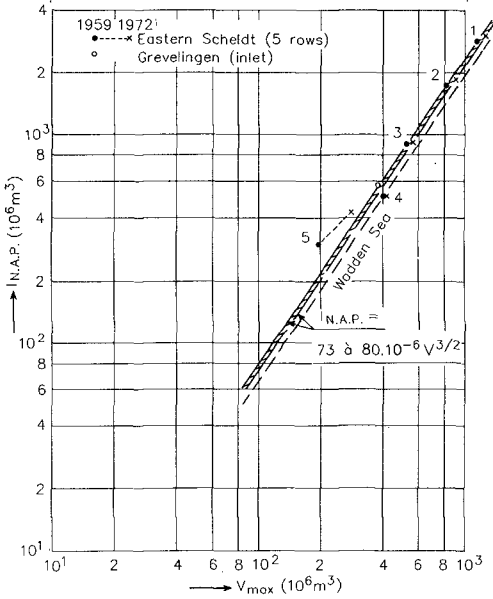


Figure 4 Channel volume - mean tidal volume relation Eastern Scheldt and Grevelingen

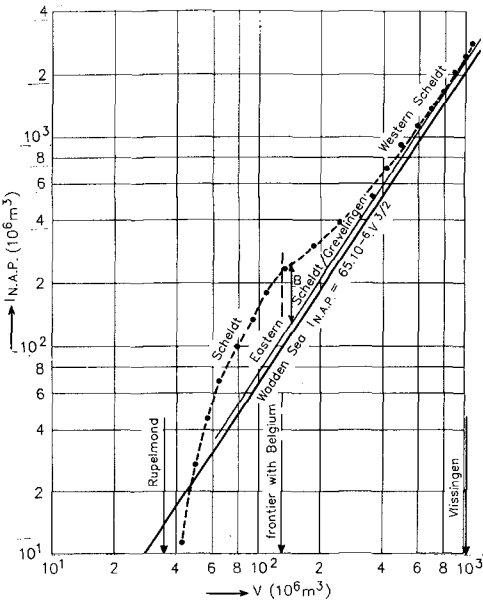


Figure 5 Comparison of channel volume relations Wadden Sea, Eastern Scheldt/Grevelingen and Western Scheldt

Another important relationship is the one for the sand volume stored in the outer deltas in front of tidal inlets which is shown in literature (Bruun, 1978). This relationship is derived for outer deltas in the USA and reads (Fig. 6):

$$V_o = c_o V^{1.23} \quad (3)$$

where:

V_o = sand volume stored in outer delta

c_o = empirical coefficient

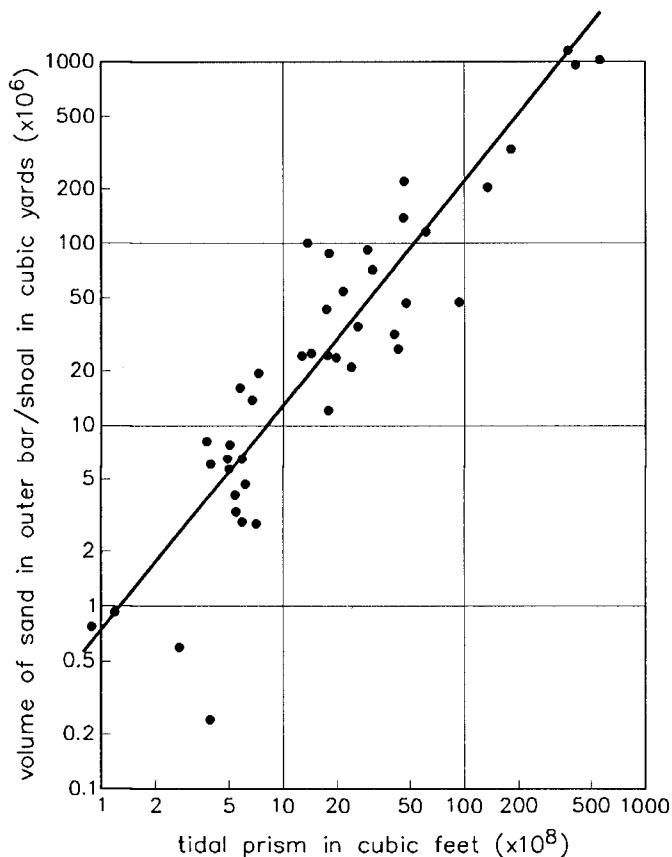
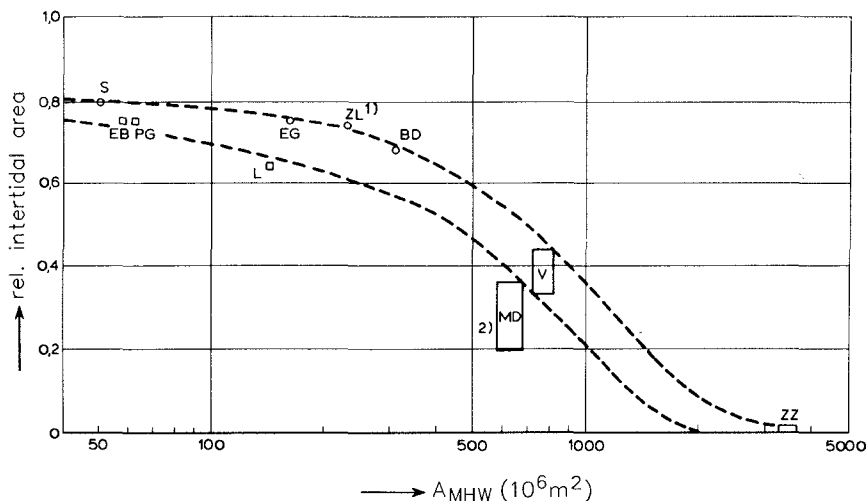


Figure 6 Sand volume outer deltas in America in relation to the mean tidal volume of the inlet

For the time being this relationship has been assumed also valid for the Dutch coast. Its validity will be verified in the near future.

Further, the relative tidal flat area in the Dutch Wadden Sea seems to show a relationship with the size of the basin (Fig. 7).

Also for the estuaries in the South of The Netherlands such a relationship was found which, however, differs from the one for the Wadden Sea. A possible explanation for the trend of the relationships could be the increasing activity of local wind waves in the larger basins (fetch). The difference between the two relationships might be caused by the difference in shape of the basins and the orientation relative to the dominating wind direction. Further investigations on this item may yield a better understanding.



1. Before closure of the Lauwerszee
2. After closure of the Zuiderzee (IJsselmeer); no equilibrium yet?

Figure 7 Relative area of the intertidal zones in the Wadden Sea

Finally, it is believed that the crest level of the tidal flats in between the tidal channels somehow are related to a characteristic tide level (e.g. MSL or MHW), local wave activity and flow conditions. The level is determined by a dynamic balance between sediment transport from the tidal channel to the flats during flood and vice versa during ebb. Also in this respect more investigations could support this hypothesis.

The above relationships are derived for situations where morphology is in a dynamic equilibrium with the hydrodynamic conditions.

3. Application of relationships in coastal engineering

The relationships are very suitable means to determine in what way Nature will respond to changes in the existing dynamic equilibrium. The equations (1) to (3) allow for a quantification of the ultimate change from the disturbed equilibrium to the new equilibrium. The relations of the relative tidal flat area and the height of the tidal flats may be helpful in the interpretation in what way

the developments will occur in combination with knowledge on general sediment transport theories and hydraulics.

For example with Figure 8 it can be demonstrated what will happen in response to closure works. Such works make part of the original basin inactive resulting in a reduction of both the channel volume ΔV and the tidal volume ΔV . The new situation will deviate from the equilibrium lines:

- the remaining channel volume is a m^3 too big, and
- the sand volume of the outer delta has become a volume of $b \ m^3$ too big.

The sand of the outer delta lays on the doorstep of the tidal basin and is readily available for the adaptation of the channels in the basin. The rest ($a-b \ m^3$) has to be supplied from outside.

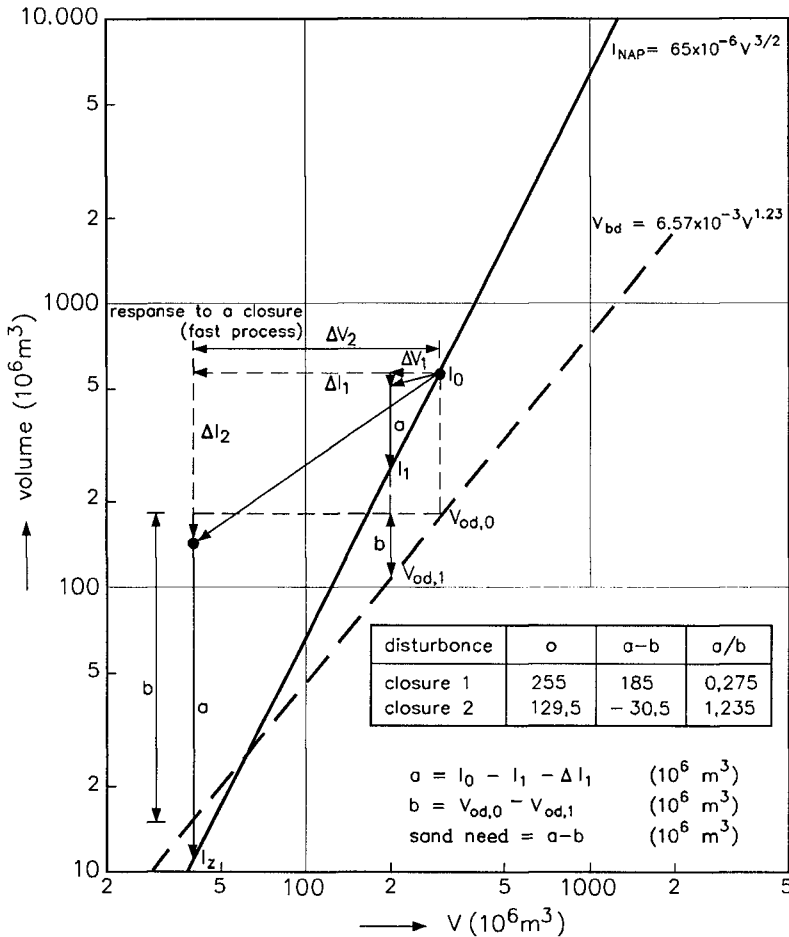


Figure 8 Example of application of morphological relationships

In Figure 9 another example is shown, that is the response of the system to natural accretion of new land mainly by deposition of silt (salt marshes) along the borders of the basin. This is a very slow process causing a gradual reduction of the tidal volume of the basin at a rate ranging from 0.3% in the western Wadden Sea, 0.7% in the more sheltered eastern part of the Dutch Wadden Sea to 0.5% in the sheltered basin of the Dollard (Eysink, 1979). In the same way as before this results in a demand for sand from the outside. The Dutch Wadden Sea reached its greatest extension around the year 1500 and decreased in size ever since due to accretion. Therefore, it is realistic to assume that the adaptation of the channel system and the outer delta keep in pace with the accretion process.

Sand borrowing from the outer delta or the tidal channels of a basin does not effect the tidal volume but only locally the flow velocities. It is obvious that in that case the removed sand will be ultimately replaced by sand from the adjacent North Sea coast or its foreshore.

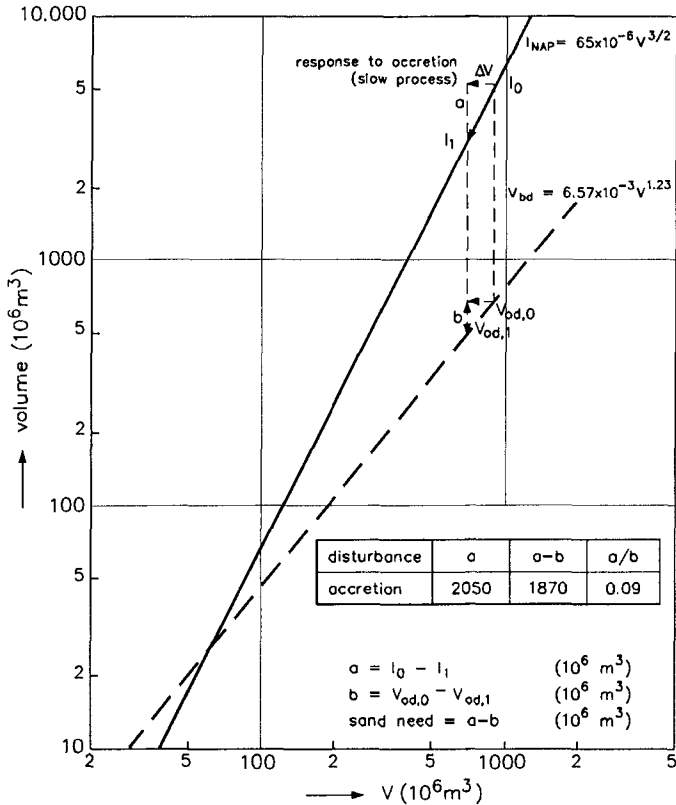


Figure 9 Example of application of morphological relationships

With respect to the effects of increased sea level rise the answers are more difficult to assess. From storage curves of the different basins it follows that, without adaptation of the levels of the tidal flats, the tidal volume will increase and the area of intertidal zones will decrease. The latter effect will be most serious in the Wadden Sea, especially in the western part where the levels of the tidal flats are low (see Table 1). If this scenario is realistic, the channels in the basin will widen and sand will be transported partly to the outer delta, which will extend, and partly will become available for accretion of the North Sea Coast adjacent to the tidal inlet.

Area	losses in km ² /cm SLR
Wadden Sea-East	3.0
Wadden Sea-West	6.0
Eastern Scheldt	0.2
Western Scheldt	0.02

Table 1 Loss of intertidal zone due to increased sea level rise without adaptation of tidal flats

However, an increase of sea level rise also will effect the level of the tidal flats. In a relative sense the disturbance of the characteristic water depth at the flats will be much greater than in the channels. Hence, the sediment transports in the channel will be far less effected than those on the flats. Consequently, it seems realistic to assume that the response of Nature will be the strongest on the tidal flats. If it is assumed that the levels of the tidal flats can follow the extra sea level rise, this implies that the tidal volume of the basin remains unchanged, whereas the volume of the channels increases. Thus, this scenario results in a demand of sand from outside.

There are indications that the response of tidal flat levels to changes in HW is fast and may follow the sea level rise very closely. However, there is no proof that the latter scenario is fully realistic. Anyway, it is a pessimistic scenario for the North Sea Coast.

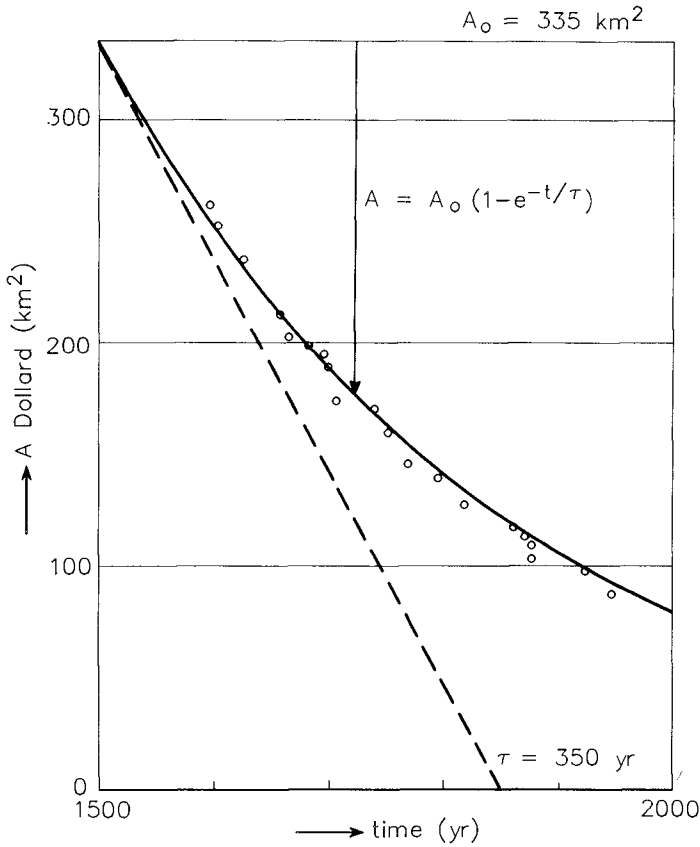
4. Model for adaptation histories

The above mentioned relationships only give an indication of the new equilibrium between morphology and hydrodynamic conditions in case of changes. They don't give any information how the adaptation will take place and what time this will take.

Adaptation processes generally show a logarithmic character; examples of this are found in:

- accretion history of the Dollard (Fig. 10),
- adaptation of the Zoutkamperlaag after the enclosure of the Lauwerszee (Postma and Reenders, 1986),
- infill of sand borrow pits (Kniess, 1976).

This shows that the adaptation history can be described by an expression like:



ca. 1500 largest extension of the Dollard

Figure 10 Accretion of the Dollard

$$X/X_0 = \exp.(-t/\tau) \tag{4}$$

where:

- t = time since disturbance of existing equilibrium,
- X = quantity (depth, area or volume) representing difference from new equilibrium,
- X₀ = initial difference from new equilibrium,
- τ = characteristic time for adaptation equal to:

$$\tau = X_0 / \Delta X_0 \tag{5}$$

where: ΔX₀ = initial rate of adaptation.

The initial disturbance of the system X₀ can be derived via the change in the hydraulic conditions and the morphologic relations.

The initial adaptation rate can be obtained through monitoring or computations with mathematical models. Then the characteristic time τ can be calculated with equation (5) and the adaptation history can be determined by equation (4). This provides a fair indication of reality.

The above approach can not be applied in case of a (sudden) change in sea level rise as this is a process of gradual and continuous growing disturbance of the existing equilibrium. In this case it is not realistic to assume that this will result in an immediate response of the sea bed in a tidal basin. It is more likely that the sea bed will follow with a certain time lag. Based on geological and historical evidence it can be stated that the tidal basins are sedimentation areas. This only can occur if the sediment transport capacities inside the basin are slightly less than outside. This could be explained if it is assumed that the bed of the basin lags slightly behind (below) the actual equilibrium level. This hypothesis is based on the principles of a sand trap. The bed lag causes a small overdepth resulting in a small reduction of flow velocities and sand transport capacities inside the basin. Thus sand is trapped to follow the present sea level rise.

If the sea level suddenly rises faster, more sand has to be trapped. Due to the extra sea level rise the overdepth in the basin initially increases. Consequently, gradually more sand is trapped until the sea bed again rises at the same rate as the sea level.

This process can be calculated in a schematic way by using a fictive overdepth. This quantity can be determined based on the percentage of the annual sand influx that is trapped in the basin and the relation between sand transport and flow velocity. If x percent of the sand is trapped, the fictive overdepth is $l-(1-x)^{1/n}$ percent of the weighted mean depth of the basin if the sand transport is proportional to the flow velocity to the power n . If the annual sand influx of a tidal basin is known, the percentage x can be determined for different rates of sea level rise (sedimentation is equal to the area of the basin times the rate of sea level rise). Next, the adaptation of the bed lag to the increased sea level rise can be calculated numerically (Fig. 11).

5. Conclusions

The above approach with proper interpretations are suitable for practical application in coastal engineering. It can be further developed as a conceptual model for areas like the Wadden Sea by implementing also other relations such as those for the tidal flat areas and heights of tidal flats in relation to characteristic hydraulic parameters.

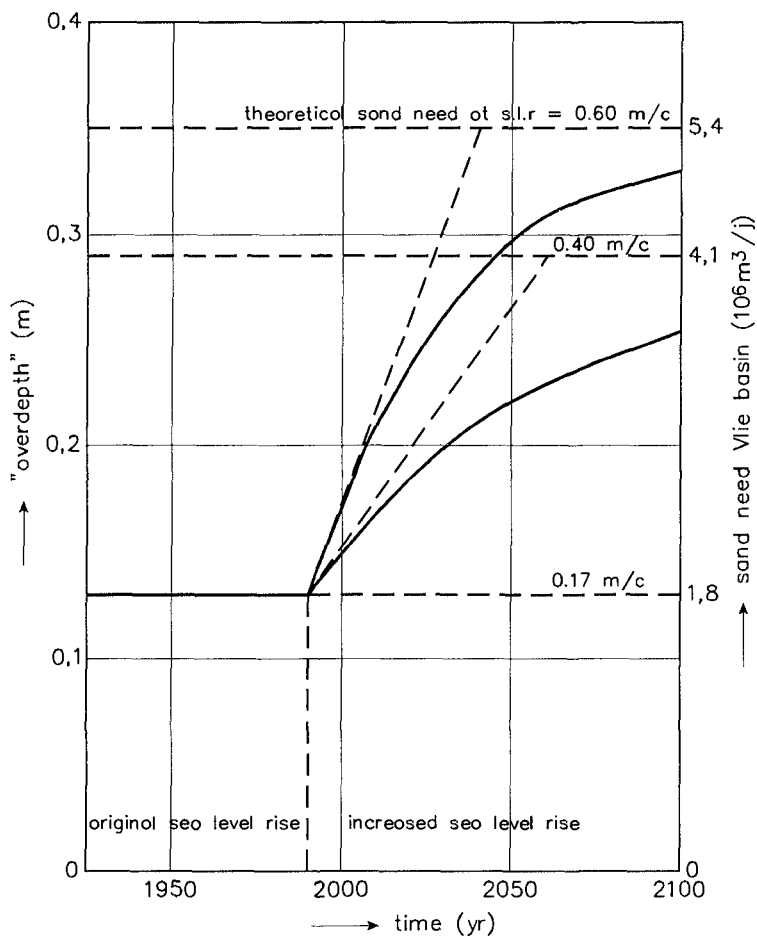


Figure 11 Sand need of the tidal basin of Het Vlie and retardation in the actual deposition rate

References

- Bruun, P. and Gerritsen, F., 1960,
Stability of coastal inlets,
North-Holland Publ. Comp., Amsterdam, 1960.
- Bruun, P., 1978,
Stability of tidal inlets, Theory and engineering,
Elsevier Scient. Publ. Comp., Amsterdam-Oxford-New York, 1978.
- Eysink, W.D., 1979,
Morphology of the Wadden Sea; consequences of sand and shell mining
(in Dutch),
DELFT HYDRAULICS, Report on literature survey R1336, May 1979.

- Gerritsen, F. and Jong, H. de, 1985,
Stability of flow profiles in the Wadden area (in Dutch),
Rijkswaterstaat, Adviesdienst Vlissingen, Nota WWKZ-84, Vol. 6,
December 1985.
- Glopper, R.J. de, 1967,
About the bed composition of the Wadden area (in Dutch),
Series: Van Zee tot Land, 43, 1967, Tjeenk Willink, Zwolle.
- Jong, H. de and Gerritsen, F., 1984,
Stability parameters of Western Scheldt estuary,
Proc. 19th Coastal Eng. Conf., Houston, 1984, ASCE, pp. 3078-3093.
- Kniess, H.G., 1976,
Eiderdam, Wiederauffüllung von Baggerlöchern im Watt,
Mitt. der BAW, Nr. 40, 1976.
- Kreeke, J. and Haring, J., 1979,
Equilibrium flow areas in the Rhine-Meuse Delta,
Coastal Eng. 3, 1979, pp. 97-111,
Elsevier Scient. Publ. Comp., Amsterdam.
- O'Brien, M.P., 1969,
Equilibrium flow areas of inlets on sandy coasts,
J. of Waterways and Harb. Div., ASCE, Vol. 95, No. WW1,
Proc. paper 6405, Febr. 1969. pp. 43-52.
- Postma, J.T. and Reenders, R., 1986,
Morphology and hydraulic consequences of the enclosure of the
Lauwerszee on the basin of the Friese Zeegat and the access channel
to Lauwersoog in particular (in Dutch),
Rijkswaterstaat, Meet- en Adviesdienst, Delfzijl, Nota 84-21, May
1986.

CHAPTER 148

LARGE-SCALE COASTAL EVOLUTION CONCEPT

The Dutch Coast: Paper No. 9

Marcel J.F. Stive¹, Dano (J.)A., Roelvink¹ and Huib J. de Vriend¹

Abstract

Using the coastal evolution of the Netherlands in the Holocene up to the present as an example and a test case, a coastal evolution concept is proposed and materialized with which shoreline position changes for different sea level rise scenarios are predicted. The (more generally applicable) model applies to quasi-uniform coastal stretches. It accounts for morphodynamic processes from the shelf to the first dune-row, and integrates over coastal units of approximately 10 km alongshore length. The added value, compared to earlier published concepts or models, lies in the full inclusion of cross-shore and alongshore processes, and in the distinction between a - with respect to sea level rise - instantaneously responding active zone and a noninstantaneously responding central shoreface zone. Relevant differences have been found to exist between coastal cells on the closed and the interrupted coast. An important conclusion is that the cross-shore effective Bruun-effect is only of limited importance. This is especially true in the case of the interrupted coast. Longshore sand transport gradients are very large there. This is mainly related to the sand demand which is placed on coastal stretches adjacent to estuary mouths of those estuaries which tend to follow the sea level rise.

1. Introduction

Since the early 1970's Rijkswaterstaat stimulated Dutch coastal research with the TOW Coastal Research Programme. The Programme was mainly devoted to the study of coastal processes from the coastal engineering perspective. Around 1985 - initiated by coastal erosion management questions in general and by the anticipated increase in relative sea level rise in particular - an interest grew into larger scale, longer term coastal evolution processes. It was realized that the TOW Programme as such (which focussed on coastal evolution processes of typical time- and space-scales of a year and a kilometer) was too limited in scope. In order to gain an understanding of large-scale, long term coastal evolution, a variety of geo-morphological processes with a diversity of time- and length-scales needs to be considered which,

1 DELFT HYDRAULICS, P.O. Box 152, 8300 AD Emmeloord, The Netherlands

in turn, calls for the deployment of many specialisms. This approach has been applied in a new research programme, called Kustgenese (Coastal Genesis). In this Programme the fields of geomorphology, hydro- and morphodynamics, physical and historical geography and geology have been linked in order to study and understand coastal evolution at the scales of interest and, subsequently, to arrive at a (physical-mathematical) tool for coastal evolution. This has led to Coastal Genesis Phase I in 1987, reporting on the available knowledge of the physical processes responsible for the reconstructed evolution of the Dutch coastal system (for a summary see Zitman et al, Paper No. 2, these proceedings).

The Kustgenese Programme was more or less interrupted for a period of two year to prepare a Coastal Defence Policy Study for the Dutch Government. This study looks into the near (5 years) and far (several decades) future (Louisse and Kuik, Paper No. 1, these proceedings). A main technical item of the study is the prediction of the coastline development, in which one of the topical aspects is the effect of an accelerating rate of eustatic sea level rise due to the greenhouse effect. The look into the far future more or less forced the researchers (drafted from the Kustgenese team and) responsible for the coastline prediction to materialize their concepts of coastal evolution into a predictive, quantitative tool. This has stimulated a coastal modelling approach which considers larger coastal development scales than sofar has been done in the Netherlands. The approach is described below. First however, a concise sketch of the Dutch coastal system and its Holocene evolution is given, with an identification of the relevant processes and external conditions.

2. Recent Holocene evolution of the Dutch coast

The present Dutch coastal system exists of three typical coastal subsystems, which basically differ with respect to the dominance of particular physical processes (see Figure 1). The complexity of the system is due to the fact that these systems place boundary constraints on one another. In the South of the Netherlands the relics of the Rhine-Meuse Delta are located. Centrally, the closed dune system of the Holland coast safeguards in the most literal sense the Randstad, which is the commercial center of the Netherlands. In the North the southend of the Wadden region is found, which extends up to Denmark. A sketch of these subsystems and their evolution is as follows.

The central part of the coast of the Netherlands is called the Holland coast. Geologically speaking it is a recent, closed coastal system, since it was only formed during the Holocene some 5000 years ago. It is expected (Beets et al, 1990) that the Pleistocene based lagoon mouth positioned there, closed itself off during periods of a strongly decreasing rate of sea level rise. Its basic contents are a relatively young (1000 to 1600 A.D.) dune system of variable width, covering an older dune system formed approximately 5000 year ago. By and large the coast has retreated over the last 2000 years, near Rotterdam and Den Helder the most and centrally less and less. Now - mostly due to human regulation - it has come to a standstill centrally and it is retreating under control in the North.

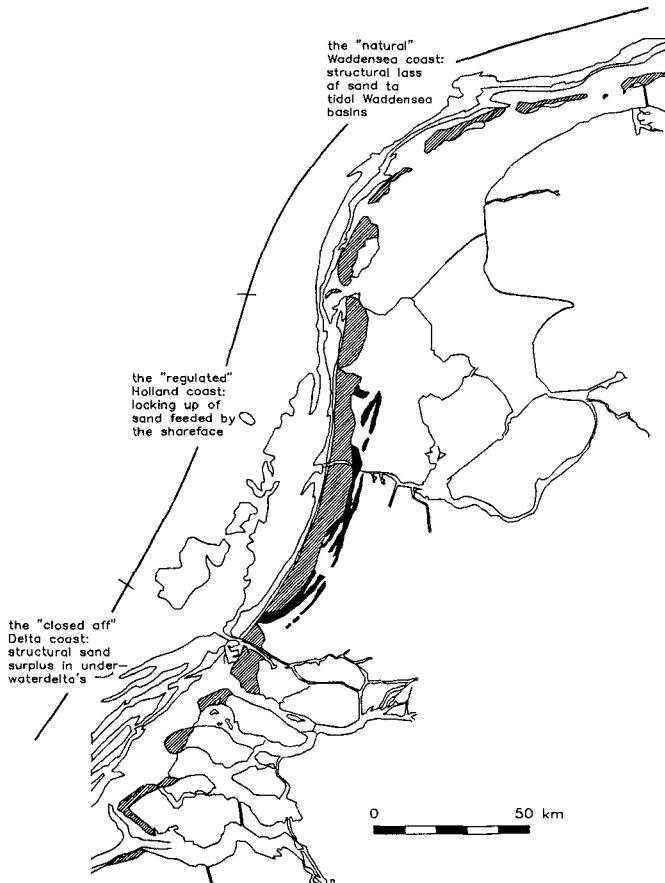


Figure 1 Three subsystems of the coast of the Netherlands

In the South of the Netherlands we find the area which is usually denoted as the Delta-region. It is a region which over the last millennia has experienced considerable variations in opening and closing of the coast, largely related to human agricultural activities. The Delta-works in the region were initiated by the flooding disaster in the region in February 1953. They consist mainly of permanent closure works of the estuary arms, which have the delta now more or less changed into a relic. One of the arms, the Westerscheldt, is still open, being the shipping entrance to Antwerp. The Westerscheldt estuary mouth is a strongly active system of bars and gullies, with important impacts in the form of coastline undulations on the adjacent coastal stretches.

The Dutch Wadden Sea coast consists typically of a system of relatively longstretched barrier islands, with active delta systems. Its present form was more or less reached a thousand years ago, when

important breakthroughs were formed towards the former Almere lagoon in the center of Holland thus creating the Zuiderzee. A characteristic feature of the Wadden Sea region is its continuous sedimentation of the tidal flats in order to keep pace with relative sea level rise, and its siltation along the Wadden shores. These processes are responsible for an important influx of sand, which is basically delivered by the adjacent coastal system. This is the cause of a structural retreat of the Wadden island shores.

By studying the evolution of the Dutch coast over the Holocene up to the present, as was done in Coastal Genesis Phase 1, the following aspects were identified as important for the large scale evolution (see also Zitman et al, Paper No. 2, these proceedings):

- (1) sediment transport in cross-shore direction is at least as important as longshore transport, where the terminology cross-shore refers to the surfzone and the shoreface: in this respect it is emphasized that what counts is the exchange of sediment between shoreface and surfzone (the diabathic exchange) and the exchange of sediment between longshore coastal stretches both in the surfzone and on the shoreface (the parabathic exchange);
- (2) the Subboreal coastal advance (approximately 5000 C14 years BP) and the subsequent formation of the Old Dunes are very likely related to a strong decrease in relative sea level rise (Beets et al, 1990). The physical process responsible for the closing of the coast is similar to that of the behaviour of an underwaterdelta after closure of its tidal basin (Steijn et al, 1989);
- (3) the formation of the Young Dunes along the Holland coast some thousand years ago cannot be explained by longshore motions of sediment alone. The external conditions which may have initiated a diabathic exchange may be those related to relative sea level rise fluctuations;
- (4) tidal basins or estuary mouths bear important effects on adjacent coastal stretches. For instance the Waddensea tidal basins in dynamic equilibrium keeping pace with sea level rise demand high amounts of sediment (Eysink, Paper No. 8, these proceedings), which are eventually delivered by the adjacent North Holland coast and the barrier island coasts.

3. Coastal evolution concept

The need for a longer term prediction has -more so than before- made us aware of the fact that we have to distinguish between coastal evolution concepts or models on a range of scales. Also, there is a relation between the space scale of a coastal feature and the time scale on which its behaviour is manifest. A schematic relation is given in Fig. 2 for the following three spatial and temporal scales of coastal evolution which we have chosen to distinguish:

- (1) Large scale coastal evolution (LSCE) with a morphodynamic length scale of 10 km and a time scale of decades, for which a conceptual model was developed, which is described below. The evolution character in this class can vary between mean trend (e.g. geological processes related), fluctuating (e.g. boundary conditions related) and asymptotic (e.g. morphodynamic constraints related) behaviour. This is typically the sort of model with which longer term predictions can be made, needed for a longterm planning of coastal development both due to large scale natural processes, such as an increasing sea level rise or a changing

- climate, and to large scale human activities, such as an estuary or tidal basin closing;
- (2) Middle scale coastal evolution (MSCE) with a morphodynamic length scale of 1 km and a time scale of years. Important distinctions in this evolution class are cyclic and damping coastline developments. Cyclic developments are for instance due to interactions between geometry and water motions in the low-frequency range, or due to (quasi-)cyclic channel-shoal shift patterns in estuary mouths. Damping developments are mostly due to human interferences like harbour moles, beach nourishments, channel dredging etc. This is typically the sort of model which is used to identify the impact of coastal works on the coastline development;
 - (3) Small scale coastal evolution (SSCE) with a morphodynamic length scale of 100 m and a time scale of storms to seasons. In this class of development it is the local (on the scale of the wave length) variability of topography and hydraulic conditions which interact to result in short-term, often rhythmic, coastline fluctuations. Generally, these fluctuations seem to have little interaction with the longer-term structural coastline evolution. This is typically the sort of model which is used for the more detailed design of coastal defence works.

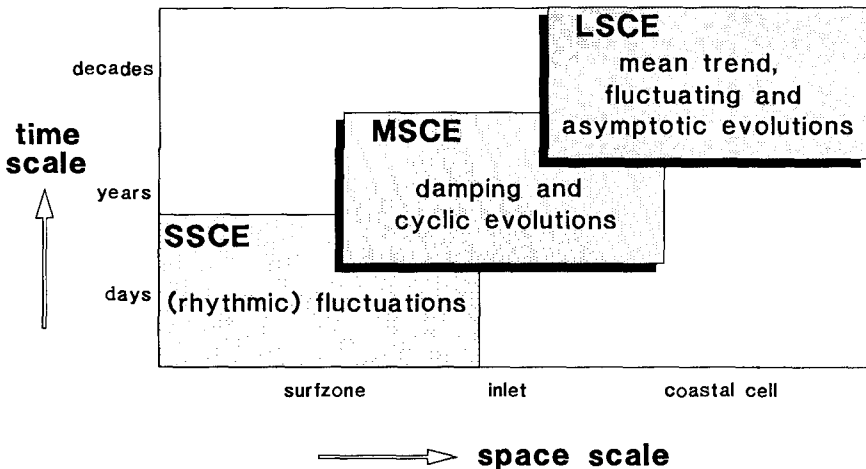


Figure 2 Coastal evolution scales

It is our opinion that the state-of-the-art in deductive modeling (i.e. models deduced from basic physical process knowledge) just about enables us to make predictions of SSCE. While in predictions of MSCE inductive concepts (i.e. model concepts inferred from observed or through analogy expected behaviour) commonly are included, this is certainly the case in predictions of LSCE. We share the viewpoint that the two approaches do not exclude one another, on the contrary: "induction is really the inverse process of deduction" (Jevons, 1958). So, in the following formulation of the large scale coastal evolution concept we try to combine our detailed process knowledge with inductive knowledge.

Our concept is in principle derived for the Dutch coast, but is expected to have some generality for sandy dune coasts and barrier island coasts. The concept further applies to (quasi-)uniform coastal stretches or cells of several km's length, of which it is assumed that the longterm average coastal profile (from the dune to the shelf) and wave, current and sand transport conditions and gradients vary only weakly alongshore. Relatively important interruptions due to river delta's, harbours, shipping channels, headlands, submarine canyons are either point sources or a principal boundary to the cells. Cross-shore three units are distinguished, i.e. the active zone (the upper shoreface, extending from the first dune row to 8 m waterdepth), the middle and lower shoreface (from 8 m to 20 m water depth) and the inner shelf (below 20 m water depth). The waterdepths mentioned are approximate figures for the Holland coast and depend in general largely on the wave climate. We define the important transition of the active zone to the middle shoreface as the level above which profile changes occur as observable from profile measurements over one average year. Alongshore we distinguish two types of coastal cells, i.e. cells on the closed coast and cells on the interrupted coast. The former category is formed by those coastal stretches which develop unaffected by coastal interruptions due to estuary or tidal basin mouths, under offshore hydro-meteo conditions which are relatively slowly varying alongshore. In contrast, the latter category is strongly affected by these interruptions; a tidal basin in dynamic equilibrium keeping pace with the sea level rise, for instance (see Eysink, Paper No. 8, these proceedings), may be the cause of a structurally retreating coastline in adjacent coastal stretches. It is found that alongshore gradients of net sediment transport, wave-induced as well as tidal, may differ by an order of magnitude between these categories. The variety of physical processes which may act on these two categories of coastal cells is summarized in Figures 3 and 4. Also, an indication is given of the relative frequency and intensity of the processes.

The morphodynamic processes are integrated over the three distinguished units, resulting in transport gradients over their control volume, under adoption of the following inductive concepts:

- The active zone has, averaged over the longer term, a steady profile form relative to the position of the mean sea level. This determines the vertical position of the profile. It is noted that this is basically the assumption behind the Bruun-rule. However, here we only adopt this inductive concept to be valid for the active zone, while it is furthermore only one of the factors determining the horizontal position of the active zone and thus of the shoreline. The horizontal position is principally determined by the sediment balance, which takes account of the vertical motion (sea level rise driven), alongshore gradients (wave and current driven) and cross-shore gradients (transport over the "foot" of the active zone and (winddriven) over the first dune row);
- The middle and lower shoreface is a morphodynamically weakly varying zone, where the gross changes over a decade are such that they can be derived from initial sediment transport considerations (Roelvink and Stive, Paper No. 5, these proceedings). This is typically the zone where at the most seaward boundary the transports are tide-dominated and at the shoreward boundary wave-dominated;

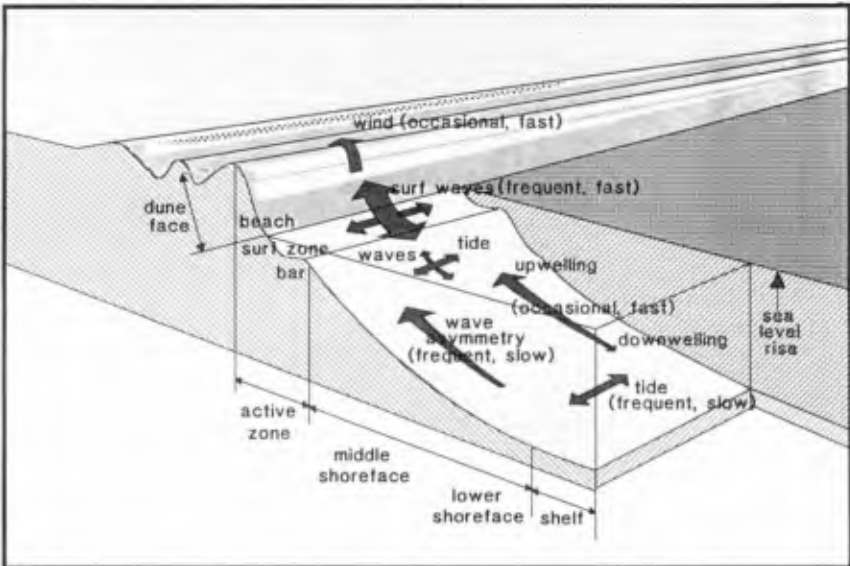


Figure 3 Overview of sediment transport processes in a coastal cell along the closed coast

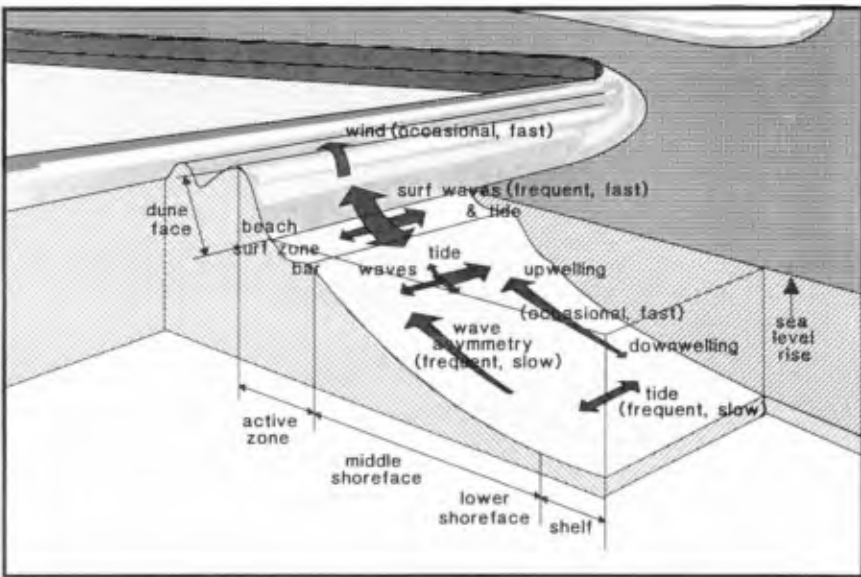


Figure 4 Overview of sediment transport processes in a coastal cell along a coast interrupted by a coastal inlet

- The inner shelf is morphodynamically negligible for the scales under consideration, and is assumed to stay unchanged.

An overview of the general behaviour and possible displacements of the several cross-shore profile zones is given in Table 1.

PROFILE ZONE	BEHAVIOUR AND DISPLACEMENT
Active zone	<ul style="list-style-type: none"> • Yearly averaged, steady profile form • Upward profile displacement with sea level rise • Shoreward horizontal profile displacement due to: <ul style="list-style-type: none"> - upward profile displacement with sea level rise - aeolian transport over first dune row - positive alongshore transport gradient (alongshore loss) - downwelling transport on shoreface • Seaward horizontal profile displacement due to: <ul style="list-style-type: none"> - wave asymmetry and upwelling transport on shoreface - negative alongshore transport gradient (alongshore gain)
Upper shoreface	<ul style="list-style-type: none"> • Inclining or declining depending on: <ul style="list-style-type: none"> - horizontal nearshore zone displacement - declining or inclining shoreface
Central and lower shoreface	<ul style="list-style-type: none"> • Declining (and eroding) in case of: <ul style="list-style-type: none"> - dominance of wave asymmetry and upwelling transport - negative alongshore transport gradient • Inclining (and accreting) in case of: <ul style="list-style-type: none"> - dominance of downwelling transport - positive alongshore transport gradient
Inner shelf	<ul style="list-style-type: none"> • Steady average level with undulations due to: <ul style="list-style-type: none"> - ripples induced by instantaneous currents and waves - megaripples or ridges induced by large scale circulations

Table 1 Large scale evolution of a coastal stretch; general case

Two of the typical evolutions of the cross-shore units that can occur according to the above overview, are actually found on the Holland coast (see Figure 5). On the central part of the Holland coast alongshore net losses in the active zone are small enough that the net shoreface feeding of the active zone (due to wave asymmetry and density flow driven upwelling) can also compensate for the losses due to vertical profile movement with sea level rise and wind induced transport. This causes the active zone to move seaward and the middle shoreface to flatten. As a result, the transition between the active zone and the middle shoreface steepens. On the northern part of the Holland coast alongshore losses in the active zone are

so large that despite compensation due to shoreface feeding appreciable regression occurs. The regression is so strong that the transition between the active zone and the middle shoreface flattens, even though the central shoreface flattens as well. The actual quantitative confirmation of these effects can be found in Knoester (1990), where e.g. long term evolution data (1896-1975) of the -7 m and the -10 m depth contour are presented.

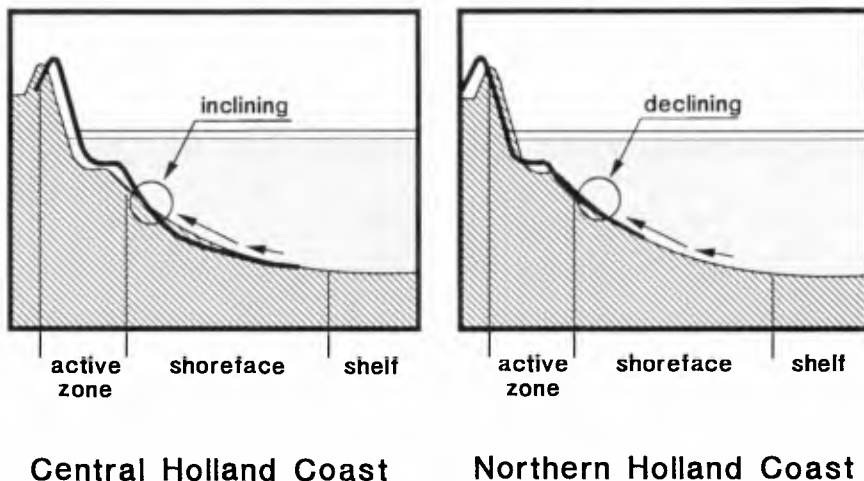


Figure 5 Typical behaviour of the transition between the active zone and the middle shoreface

In accordance with the above concept of LSCE the "present" (i.e. averaged over the last 5 to 10 years) dynamic coastal sediment budget for the whole of the Dutch coastal system has been drawn up (see Figure 6). As explained it is based on a combination of deductive physical process knowledge and inductive concepts, with the latter supported or verified by observations. On the considered time and space scale the dynamics of the model are of a weakly varying character. With hydro-meteo scenarios involving wind, wave, tide, surge level and mean sea level predictions for the next decades as input parameters it was used as a basis for predictions (Louisse and Kuik, Paper No. 1, these proceedings).

Results of the actual coastline predictions are omitted here, since they are not considered to be of interest in this context. One of the most generally interesting results though is the relative importance of the several sources and sinks that contribute to the displacement of the active zone (and therewith of the shoreline). A quantification of the several effects as found for the Holland coast gives the following result:

Effect	Closed coast	interrupted coast
sea level rise direct (Bruun-effect)	15% > 40%	5% > 10%
sea level rise indirect (estuary-pull)	-	55% > 61%
feeding by shoreface	65% > 46%	25% > 20%
dune formation (loss over first dune row)	10% > 7%	5% > 3%
longshore drift (wave-driven)	10% > 7%	10% > 6%

Table 2 Relative importance of absolute contribution to active zone displacement on the Holland coast for a sea level rise of 0.2 m/century > 0.6 m/century (Note: ">" stands for changing to)

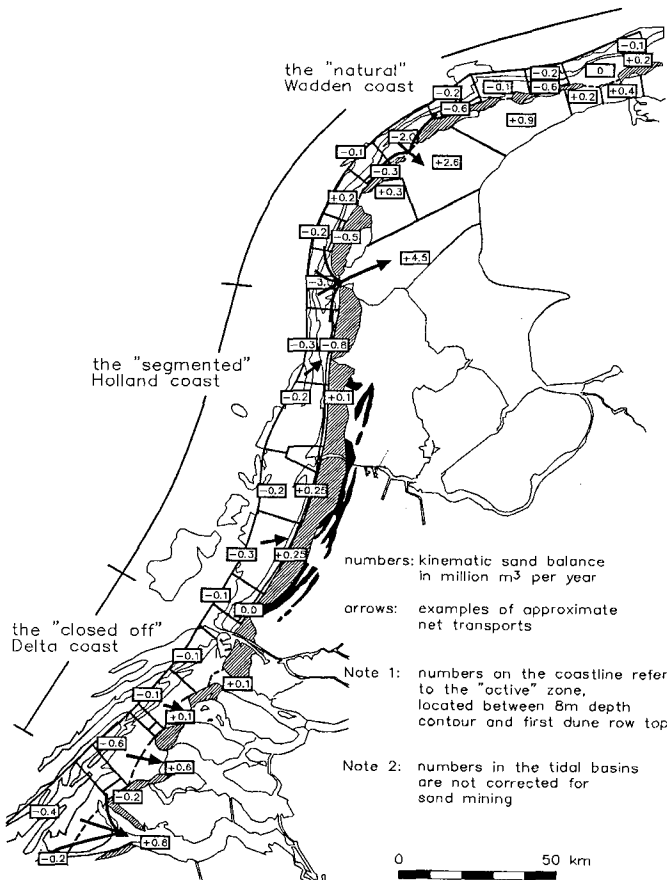


Figure 6 Present sand balance of the Dutch coastal system

From these results, several conclusions may be drawn of which two are mentioned. Firstly, it follows that the Bruun effect is generally of minor importance. Only in the case of a triplication of the present rate of sea level rise on the closed coast sections does it become important. Secondly, wave-driven longshore drift is of minor importance in general. In the following section these conclusions are brought in as contributions to the ongoing discussion of the relevance of sea level rise for coastal erosion.

4. Discussion

The above presented coastal evolution model contains important elements of earlier published work. Without striving for completeness, and certainly not fully aware of all the existing literature in this field, the following categories of references are mentioned. For the "Bruun Rule" aspects reference is made to Bruun (1962), Edelman (1968, 1970) and Dean and Maurmeyer (1983). For the exchange processes between the shoreface and the active zone reference is made to Niedoroda et al (1984) and Wright (1987). For a discussion of coastline recession models and especially the relative importance of cross-shore and longshore effects reference is made to Everts (1985), Pilkey and Davis (1987) and Galvin (1989).

The conceptual model presented here, however, does contain several aspects which make it differ from and more extensive compared to earlier suggested models or concepts in the following sense:

- in cross-shore direction the model includes not only the active zone, which instantaneously follows the relative sea level rise, but also the (central) shoreface which responds non-instantaneously to the relative sea level rise;
- the model takes full account of longshore effects, not only those induced by wave-induced longshore drift variations, but also those induced by coastal inlet systems.

Especially, the quantification of the several effects makes the presented model contribute importantly to the ongoing discussions on the effects of relative sea level rise on coastal recession. From the present application to the Dutch coastal system, it is found that the cross-shore Bruun effect is generally less important than other effects such as shoreface feeding or alongshore effects due to estuary inlets. Since the Dutch coast covers a variety of systems, these conclusions may be of more universal value than the length of the Dutch coast in first instance would seem to justify.

Finally, it needs to be mentioned that the results of these studies enabled the Dutch coastal researchers to identify several research aspects for further study, for instance:

- the morphodynamic behaviour of the shoreface, with specific emphasis on the sediment exchange with the active zone;
- the degree of profile invariance of the active zone relative to mean sea level.

These and other questions are being addressed in the framework of the Coastal Genesis Programme Part II. In this context it is important to point out the following. The resulting coastline development is assumed to be due to a superposition of the abovementioned three scales of evolution. Here, there is a fundamental research

question. This concerns the assumption that smaller scale phenomena are not interacting with or initiators of larger scale phenomena. The degree to which this is indeed true will largely determine the degree of predictability of coastal evolution.

References

- Beets, D.J., Valk, B. van de, and Stive, M.J.F. (1990).
Holocene evolution of the Holland coast.
Manuscript submitted for publication.
- Bruun, P. (1962).
Sea-level rise as a cause of shore erosion.
J. Waterways and Harbors Division, ASCE, Vol. 88, No. WW1, pp. 117-130.
- Dean, R.G. and Maurmeyer, E.M. (1983).
Models for beach profile responses.
In Komar, P.D., ed., Handbook of Coastal Processes and Erosion, Chemical Rubber Company Press, pp. 151-166.
- Edelman, T. (1968).
Dune erosion during storm conditions.
Proc. 11th Int. Conf. on Coastal Eng., ASCE, New York, pp. 719-723.
- Edelman, T. (1970).
Dune erosion during storm conditions.
Proc. 12th Int. Conf. on Coastal Eng., ASCE, New York, pp. 1305-1307.
- Everts, C.H. (1985).
Sea level rise effects on shoreline position.
J. Waterway, Port, Coastal and Ocean Eng., ASCE, Vol. 111, No. 6, pp. 985-999.
- Eysink, W.D. (1990).
Morphologic response of tidal basins to changes. Paper No. 8.
Proc. 22nd Int. Conf. on Coastal Eng., ASCE, New York.
- Galvin, C. (1989).
Beach erosion and beach erosion data.
Paper presented at OAS Seminar on erosion, pollution and recovery of the coastal zone and its resources in Latin America and the Caribbean, Buenos Aires.
- Jevons, W.S. (1958).
The principles of science. A treatise on logic and the scientific method.
Dover Publications, New York, 786 pp.
- Knoester, D. (1990).
Morphology of the Holland coast (in Dutch).
Rijkswaterstaat, Tidal Waters Division, Report GWA0-90.010.
- Louisse, C.J. and Kuik, A.J. (1990).
Coastal defence alternatives in The Netherlands. Paper No. 1.
Proc. 22nd Int. Conf. on Coastal Eng., ASCE, New York.

Niedoroda, A.W., Swift, D.J.P., Hopkins, T.S. and Chen-Mean Ma (1984).

Shoreface morphodynamics on wave-dominated coasts.
Marine Geology, 60, pp. 331-354.

Pilkey, O.H. and Davis, T.W. (1987).

An analysis of coastal recession models: North carolina coast.
Proc. Symposium on Sea-level fluctuation and coastal evolution,
Spec. Publ. No. 41, Soc. of Economic Paleontologists and Mineralogists, pp. 59-68.

Roelvink, J.A. and Stive, M.J.F. (1990).

Sand transport on the shoreface of the Holland coast. Paper No. 5.
Proc. 22nd Int. Conf. on Coastal Eng., ASCE, New York.

Steijn, R.C., Louters, T., Spek, A.J.F. v.d. and De Vriend, H.J. (1989).

Numerical model hindcast of the ebb tidal evolution in front of the Deltaworks.

Proc. Int. Conf. Hydr. and Envir. Mod. Coastal, Estuarine and River Waters, Bradford, England.

Wright, L.D. (1987).

Shelf-surfzone coupling: diabathic shoreface transport.
Coastal Sediments, pp. 25-40.

Zitman, T.J., Stive, M.J.F. and Wiersma, J. (1990).

Reconstruction of the historical development of the Dutch coast.
Paper No.2.

Proc. 22nd Int. Conf. on Coastal Eng., ASCE, New York.

CHAPTER 149

RESEARCH ON LARGE-SCALE COASTAL BEHAVIOUR

The Dutch Coast: Paper No. 10
J.H.J. Terwindt¹, J.A. Battjes²

ABSTRACT

Large scale coastal behaviour (LSCB) regards the development of a certain coastal stretch (order tens of km's) in time (order decades). Knowledge of LSCB is still very limited. Three approaches for analysis of LSCB are distinguished with increasing complexity and necessary level of knowledge, viz. the geostatistical, the phenomenological and the modelling approach. Every approach has serious shortcomings to such an extent that predictions of LSCB are as yet impossible. Nevertheless it is necessary to develop a research strategy which may serve future studies on LSCB.

1. INTRODUCTION

The prediction of the development of sedimentary coasts is still a difficult problem. Coastal changes normally have different spatial and temporal scales and are influenced by developments in adjacent areas in variable degrees.

Policy decisions concerning coastal management, including maintenance of beaches and dunes, require a time span of decades and a space scale of entire coastal units, with lengths up to 10^2 km, say. The changes in underwater topography, shoreline position, beach- and dune profiles on these scales are referred to as "large scale coastal behaviour" (LSCB) in this paper.

¹Dept. of Physical Geography, Utrecht University,
P.O. Box 80.115, 3508 TC Utrecht, The Netherlands

²Dept. of Civil Engineering, Delft University of Technology,
P.O. Box 5048, 2500 GA Delft, The Netherlands

Much of the conventional present-day research related to quantitative modelling of coastal behaviour focusses on relatively small-scale processes such as the wave propagation and decay across the surf zone and the associated velocity field for a single sea state or even a single periodic incident wave. The sediment transport is usually considered locally at the scale of the bottom boundary layer. There is also a tendency of this research to go to even greater resolution both in time (resolving the variations between wave groups or even within individual waves) and in space (horizontally: resolving variations within a wavelength, as in diffraction problems; vertically: resolving variations over the depth, in 2½D or 3D models).

We thus see an increasingly wide gap between the practical needs related to LSCB on the one hand and the focus and trend of ongoing research on the other. This raises serious questions, in particular inasmuch as results of the small-scale approach are not directly transferable to the (much) larger scales.

Research on large scale coastal behaviour (LSCB) is important to determine the long term effects of changing boundary conditions (sealevel rise, wave climate) or of huge interferences by man (closure of tidal inlets, construction of extensive breakwaters, dredging and major beach nourishment operations).

In order to discuss possible LSCB research approaches, a Colloquium was held in Amsterdam on July 10-13, 1989 under auspices of the Royal Dutch Academy of Arts and Sciences. A number of experts was invited to express their views on this subject. This paper deals with some general aspects of LSCB. It also gives an overview of the results of this Colloquium and the plans for Phase II of the Dutch Coastal Genesis Project (see also Zitman et al., 1990), which is an interdisciplinary research project aimed at resolving some LSCB-problems of the Dutch coast.

2. THE PROBLEM OF SCALES

A multitude of processes with a range of time - and space scales has to be considered in coastal morphology problems. Starting at the level of turbulent fluctuations with a time scale of about 1 s, and going up through wind waves, storms or tidal cycles, seasons, years and all the way to durations of several decades (10^{10} s) as required in LSCB, we cover a range of 10^{10} . Likewise, going from the length scale of a sand grain (10^{-1} mm) to that of a stretch of coast of 10^2 km we cover a range of 10^9 .

In general, a hierarchy is present between the (hydrodynamic and morphological) processes at different scales. The larger scale processes only provide (slowly varying) boundary conditions for the smaller-scale ones. Processes of comparable scales interact dynamically. Smaller-scale processes are just noise for the larger scale processes or they may contribute to them in an averaged sense.

One problem arising in this connection is whether LSCB is "just" the net result of small-scale processes or whether autonomous large(r) scale processes are also at work. An example: has the welding of an offshore bar to the coast on a time scale of many years any relationship with the short-term fluctuations of coastal profiles? Or are the latter just noise for the former and may they be omitted in an analysis of large scale behaviour?

The major problem is to specify the process-systems on the meso and large scales. For the small scale the process-systems are much better known because of the wealth of laboratory and field investigations.

3. RESEARCH APPROACHES TO LARGE SCALE COASTAL BEHAVIOUR

The main objective of LSCB research is to identify, analyse and quantify large scale variations in the position of the coastline and the nearshore bottom for purposes of understanding and prediction. Three approaches with increasing complexity and level of knowledge can be distinguished, viz. the statistical, the phenomenological and the modelling approach.

The **geostatistical approach** is purely descriptive. It envisages a paleogeographical reconstruction of the position of the coastline and coastal profiles. Approaching the present time the information density may increase to such an extent (e.g. in the Dutch data set) that statistical analysis becomes possible. Such data sets may be analysed for areas showing similar trends, and for systematic changes in trend over time (fig. 1). This type of descriptive statistical analysis gives insight in the temporal and areal scales of LSCB. It may be used for the extrapolation of the coastal development under the assumption that the past tendencies will proceed in the future (fig. 2). In addition, the data set may provide net sediment budgets over time and area (Van Vessem and Stolk, 1990). The main difficulties in this approach are: inadequate data sets (too short, too small an area), the development of appropriate methods of analysis, and hidden effects of human interferences.

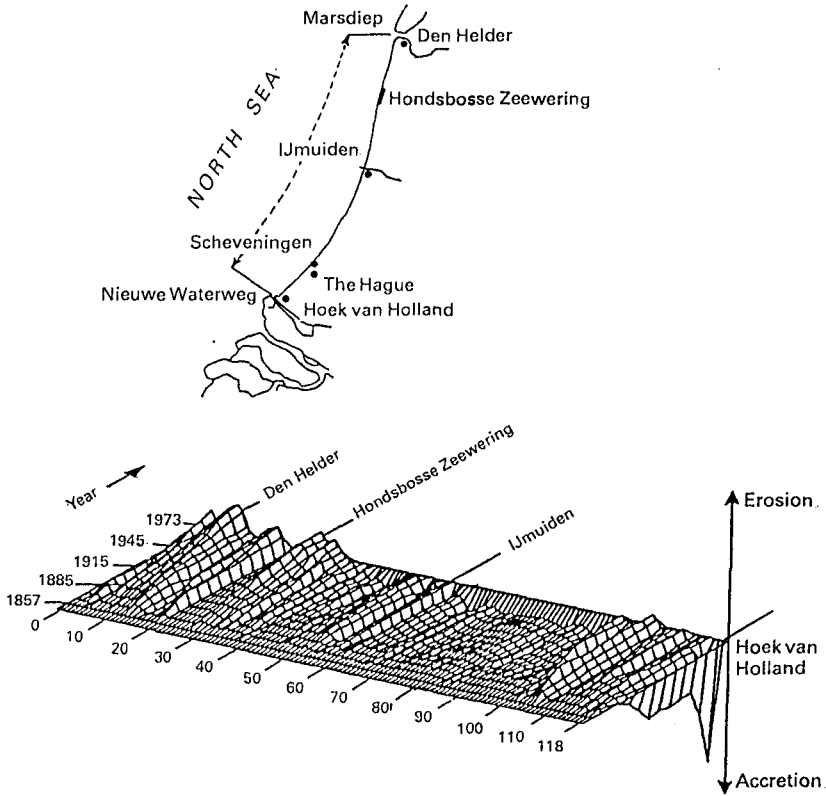


Figure 1 Position of the foot of the dunes along the central part of the Dutch coast as a function of time (1857 as a reference). Note areas showing similar trends in time (e.g. km 65-100; km 8-15 etc.) (after Wiersma 1987).

The **phenomenological approach** tries to find empirical relations for the observed behaviour starting from assumed operating processes. Parameters are selected that are considered relevant to the processes of interest and empirical relations are derived without formulating or using a model for the basic physical processes. For instance, we may try to correlate the Dean and surf-scaling parameters to coastal stages (Wright and Short, 1981). Such parameters include some variables like wave characteristics, slope, sediment size, which are assumed to be of interest for small scale coastal development.

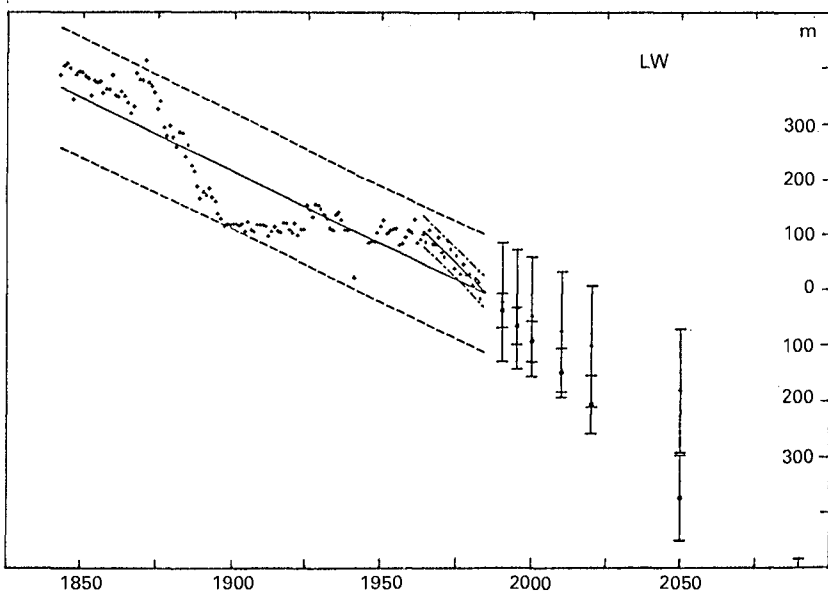


Figure 2 Position of LW-line in time in a line normal to the coast of the island Schouwen. Note the occurrence of a beachwave. The extrapolation of the trend over 150 years is different from that for the last 20 years. If another time interval was chosen, say the last 80 years, another extrapolated trend would have evolved (after Van Vessem, 1988).

Perhaps similar parameters, based on the notion of physical processes, may be developed for large scale coastal behaviour. The main difficulty is the specification of "relevant parameters" for these processes and for the morphological responses. Such parameters are not known for LSCB at the present time.

Another challenging example is the prediction of the dimensions of tidal channel and shoal systems on the basis of equilibrium velocity profile/area considerations (O'Brien, 1931; Bruun, 1978). This approach has recently been extended to non-equilibrium situations, e.g. due to human interference or accelerated sea level rise (Eysink, 1990; Kondo, 1990; Gerritsen et al., 1990; O'Connor et al., 1990).

The **process-modelling approach** starts from the basic driving forces leading to the operative processes assumed to govern LSCB. The process systems may be cast in

a model. The problem is now: can we specify the driving forces, and identify the processes on a level of integration relevant to LSCB? In the most pessimistic view (the "dooms" hypothesis) LSCB is governed by unpredictable inputs fed into a non-linear system, producing a highly unpredictable outcome. In a more optimistic view LSCB is characterized by rather gradual, apparently non-random developments. In this view the underlying process-system may be very complicated and variable but the response viz. the coastal behaviour is rather gradual. Perhaps we may average or simplify the process-system or its response.

The question arises whether existing small scale models can be used for modelling LSCB. During the Colloquium great scepticism was expressed about the possibility to scale up small-scale process models to account for LSCB. The main reasons advanced for this scepticism were: the inadequacy of the present knowledge of small scale processes, especially the sediment transport formulations, and the amplification of errors every time the non-linear mathematical system is integrated to a larger scale.

In this connection it should also be noted that there is a gradual **qualitative** shift in our knowledge as we go from the smaller to the larger scales. The following points are relevant here:

- Residual transports resulting from random advection on the smaller scale can usually be described as diffusion on a larger scale. The Pelnard Considère (1956) approach to the calculation of coastal plan forms is an example where this is utilized. It is deemed likely that the same principle can be extended to other applications.
- Parameterisations of residual effects at each scale require empirical calibration and verification. Small-scale descriptions can be more theoretical, deductive and mechanistic. The larger the scale becomes the more empirical and inductive our knowledge is.
- For empirical investigations relating to small-scale processes, special-purpose, short-term measurements suffice. The empirical input needed in the larger-scale process description calls for more general, continuous monitoring programs.
- The need to go far back into the past to obtain empirical input for LSCB necessitates a multi-disciplinary approach involving not only mechanics but also sedimentology, stratigraphy, geology, climatology and history.

The development of new formulations, appropriate for LSCB, was advocated during the Colloquium. Two ways of arriving at such LSCB-models have been suggested.

The first is to formulate large scale processes, with inclusion of the effects of small scale processes in a parameterized form. The other approach may be the scaling up by filtering the processes at the small scale to arrive at formulations of the larger scale.

As there is so little experience with LSCB-models, several important questions were raised in the Colloquium:

- how to identify processes operating on the larger scales;
- how to cope with catastrophic events like storms which may cause irreversible changes after exceeding threshold values (bifurcation);
- how to introduce the time-sequence of storms. The influence of this parameter is lost in a simple integration over time, although this parameter may be important because of the relatively slow adaption of the coastal morphology;
- how to cope with relaxation times;
- how far is it necessary to solve in detail the small-scale sediment transport problem.

It was generally accepted at the Colloquium that at present long-term prediction of LSCB is impossible. Process-based small-scale simulations remain valuable, not as a predictive tool, but as a research tool, to get a better understanding of the above-mentioned questions.

4. RESEARCH STRATEGIES

The following possible strategy evolved from the discussions during the Colloquium.

1. Make a survey of relevant results of previous studies and reexamine these from the viewpoint of LSCB.
2. Formulate a hypothetical but coherent concept of how the large system works and develop a state-of-the-art model for that. At present such model may be rather rough, but it can serve as a first step (Stive et al., 1990; Roelvink and Stive, 1990). It is expected that different models may evolve for straight coasts and for barrier-island coasts because of the differences in morphology and interaction of the current and wave-system.
3. Make hindcasts of LSCB, on the basis of the aforementioned state-of-the-art model, for field sites for which reliable data are available that can be used for verifications. This may give indications for the potentials and the limitations of the model and it may lead to specific laboratory or field

experiments defined by the applicability of the model.

4. Long-term monitoring programs are indispensable for all LSCB studies. It may be of special interest to select some sites where important coastal engineering works have recently been completed, in order to evaluate the effects of human interference on the coastal system over a long time scale.

The Dutch Coastal Genesis Project Phase I (1985-1989) contains a number of these elements (Zitman et al., 1990). On the basis of the outcomes of Phase I and the discussion at the Colloquium on Large Scale Coastal Behaviour, the following objectives were formulated for the Coastal Genesis Project Phase II (1990-1994).

A distinction is made between the straight central part of the Dutch coast and the intersected barrier island coast in the northern and southern part with their ebb and flood tidal deltas, tidal basins and channel movements affecting coastal developments.

The basic strategies are:

- to continue the paleo-geographic reconstruction of the coastal developments and the statistical analysis of the data on coastline positions and hydro-meteo data in time including geological, sedimentological and historical input;
- to perform theoretical and experimental studies on fundamental gaps in our knowledge (e.g. low-frequency waves, wave-current interactions, bed forms, sand transport with ripples and in sheetflow conditions);
- to conduct some extensive field measurement campaigns in order to increase our understanding of several interacting processes on a natural scale and to provide data for further empirical and modelling studies;
- to explore further the possibilities of morpho-dynamic modelling; this involves:
 - * the development of state-of-the-art models for the straight coast and the barrier islands coast;
 - * the modelling of the behaviour of banks in open sea, shoreface-connected ridges, and breaker bars;
 - * the modelling of the development of channel-shoal system in the ebb tidal deltas and tidal inlets in relation to the morphological developments in the tidal bays;
 - * preliminary efforts to perform reconstruction of past LSCB using existing data on wave and current climate and morphodynamical developments.

It should be noted that the Coastal Genesis Project Phase II incorporates efforts on coastal research of Rijkswaterstaat, Delft Hydraulics, Geological Survey and the Universities of Delft and Utrecht. It is an integrated national research plan.

REFERENCES

- Bruun, P. (1978): Stability of tidal inlets, theory and engineering. Elsevier
- Eysink, W.D. (1990): Morphologic response of tidal basin changes. Paper presented at 22nd Intern. Conf. Coast. Eng. Delft.
- Gerritsen, F. de Jong, H. and Langerak, A. (1990): Cross-sectional stability of estuarine channels in the Netherlands. Paper presented at 22nd Intern. Conf. Coast. Eng. Delft.
- Kondo, H. (1990): Flow area prediction of tidal inlets after sea level rise. Paper presented at 22nd Intern. Conf. Coast. Eng. Delft.
- O'Brien, M.P. (1931): Estuary tidal prisms related to entrance areas. Civil Eng., Vol. 1,8, 738-739.
- O'Connor, B., Nicholson, J. and Rayner, R. (1990): Estuary geometry as a function of tidal range. Paper presented at 22nd Intern. Conf. Coast. Eng. Delft.
- Pelnard Considère, R. (1956): Essai de théorie de l'évolution des formes de rivage et plages de sable et de galets. Journées de l'Hydrolique No. 1: 289-298
- Roelvink, J.A. and Stive, M.J.F. (1990): Sand transport on the shoreface of the Holland coast. Paper presented at 22nd Intern. Conf. Coast. Eng. Delft.
- Stive, M.J.F., Roelvink, J.A. and De Vriend, H.J. (1990): Large scale coastal evolution concept. Paper presented at 22nd Intern. Conf. Coast. Eng. Delft.
- Van Vessem, P. and Stolk, A. (1990): Sand budget of the Dutch coast. Paper presented at 22nd Intern. Conf. Coast. Eng. Delft.
- Van Vessem, P. (1988): A first approach to the prediction of the development of the coast in 1990-2090. Report Rijkswaterstaat GWA0-88.356. 16 pp. (in Dutch).
- Wiersma, J. (1987): Coastal erosion by sealevel rise, methods and models, an overview. Report Rijkswaterstaat GWA0-87.392. 12 pp.
- Wright, L.D. and Short, A.D. (1984): Morphodynamic variability of surf zones and beaches, a synthesis. Mar. Geol. 56, 93-118.
- Zitman, T.J., Stive, M.J.F. and Wiersma, J. (1990): Coastal genesis I: Geological and historical development of the Dutch coast. Paper presented at 22nd Intern. Conf. Coast. Eng. Delft.

CHAPTER 150

BEACH AND DUNE NOURISHMENT IN THE NETHERLANDS

The Dutch Coast: Paper No. 11

Piet Roelse

ABSTRACT

In the Netherlands up to the fifties of this century, dike and groyne building were the most important coastal defence measures. Because of the increased awareness of the importance of the sandy coast the demand for a more environmentally friendly coastal protection measure increased. However, artificial beach nourishment was very expensive. In the past two decades the costs of nourishment have decreased as a result of technical developments in the dredging industry, and erosion control by means of sandfills has become in general cheaper than the construction of groynes and dikes. In that period also large volumes of sand have become available from harbour extension and maintenance dredging. These have been the conditions that led to a new coastal defence method. Up till now nearly 50 beach nourishment projects have been carried out, with a total amount of 60 million m³.

This paper provides a review of the projects carried out in the last 4 decades, with a description of the most important aspects.

1. INTRODUCTION

For centuries severe losses of land occurred along the Dutch coast. Besides local effects such as the shifting of tidal channels and periodical movements of the coastline, the main reasons for the coastal erosion were sea level rise and the effects of decreasing tidal volumes of estuaries. In former days the communal problems caused by coastline withdrawal were small, because of the low economic value of the dune area. The fishing-villages behind the outer dune ridges were simply replaced backwards. Only at some locations where flooding of the land was threatening, people tried to stop the erosion.

In the 19th century the interests in the coastal area increased. Because of the rising value of the land behind the dunes, keeping the land dry became increasingly important. Beach recreation arose, as did settlements for industry and housing. Also the awareness of the natural values and the use as drinking water reservoir increased. All these interests led to the construction of extensive groyne fields in the threatened coastal sections during

the second half of the 19th century and the first half of the 20th century.

Since the main reasons for the erosion were not removed, however, the coastline withdrawal could not be fully stopped by groynes. In spite of successful applications of artificial beach nourishment to compensate beach erosion in the USA and in Germany, and the availability of the dredging equipment in the Netherlands, the long tradition of dike and groyne building resisted a new soft method of coastal defence. Only during the last 20 years is beach and dune nourishment being practiced more and more in the Netherlands as well.

After the severe storm surge of February 1953, which flooded large parts of the Delta area, new safety standards were developed and dikes were heightened. After intensive investigations on dune erosion during storm surges, leading to a guide-book for the testing of dune profiles, it appeared that many dune stretches had to be strengthened as well.

During the last 20 years, the experience with beach and dune nourishment has grown considerably and led in 1987 to the publication of the "Manual on Artificial Beach Nourishment". In 1988 and 1989 this experience was used in the Coastal Defence Study for the Netherlands (Louisse and Kuik, 1990).

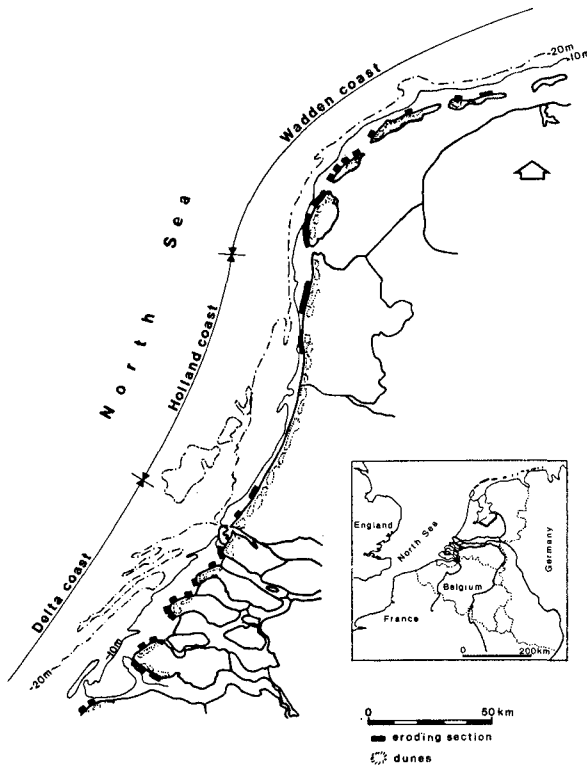


figure 1. The Dutch coast; erosion areas.

2. PROJECTS IN THE PERIOD 1950 - 1989

2.1. Locations, projects

In the Netherlands, 3 coastal types can be distinguished (fig. 1):

- The Wadden coast with several tidal inlets. The coastal profile is rather flat, except in the neighbourhood of the ebb-deltas where deep tidal gullies occur. Some of the Wadden islands are protected with groynes.
- The Holland coast with some harbour entrances. The coastal profile is flat. In general the dune area is wide. At both ends of this coast where the dunes are narrow, the beach is protected by means of groynes.
- The Delta coast where most of the tidal inlets are closed. Although the shoals in the ebb-deltas protect the coast against severe wave attack, the shifting of the deep tidal channels caused much erosion. Along these channels very steep shore faces occur. Because of the narrow dune ridges most of the coastal sections are protected with groynes to reduce the coastline withdrawal.

In figure 1 the eroding coastal sections are marked. Figure 2 gives the situation with the nourishment locations. It is obvious that most of the sand fills are placed in locations with existing groynes. Table 1 gives a list of the projects up to and including 1989. In 1990 sandfill projects are running, at various locations, mainly to restore beaches and dunefaces after a period of storm surges.

In the period 1950 - 1989, the mean yearly amount of sand is 1.5 million m³. However in the fifties and sixties the nourishment efforts were very small. In the period 1970 - 1989 the mean yearly quantity rose to 3.0 million m³. In table 2 the nourishments are classified by volume. It appears that 67% of the projects had a volume less than 1 million m³, whereas only one of the project quantities was greater than 5 million m³ (the dumping of dredged material near Hoek van Holland). In 65% of the years the volume was less than 1 million m³ or there were no projects at all. Four times the yearly volume succeeded 5 million m³.

quantity (10 ⁶ m ⁶)	year		project	
	number	perc.	number	perc.
0	40	100	-	-
>0	28	70	48	100
>1	14	35	16	33
>2	12	30	8	17
>3	7	18	6	13
>4	4	10	1	2
>5	4	10	1	2

table 2. Classification after volume.

2.2. Aims

In the Netherlands the major aims of sand nourishment are:

- Safeguarding the land against flooding.

In the Netherlands the maximum failure frequencies of dikes and dunes have been established at 1/100,000 to 1/20,000 per year, depending on the expected damages.

- Protection of interests in the dunes.

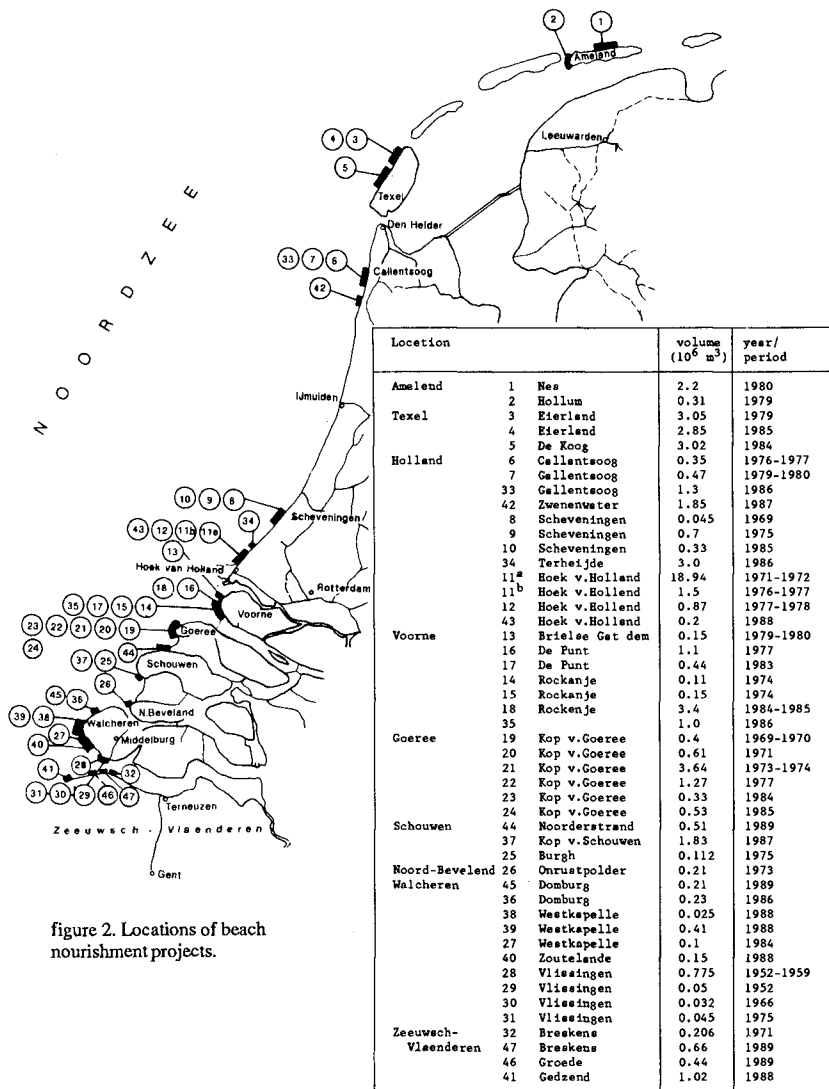


figure 2. Locations of beach nourishment projects.

table 1. Nourishment projects in the Netherlands 1950 - 1989.

Dune areas are valuable from an ecological point of view, but also represent interests for housing, industrial settlements and drinking water reservoirs.

- Prevention of further loss of land.
Each year about 0.3 km² valuable dune area is being lost to the sea. This appears to be small, but most of the erosion takes place in those coastal sections with the narrowest dune ridges.
- Protection of beach recreational interests.
Especially in areas where beaches are bound by dikes or dune foot revetments, beach erosion is detrimental to recreational interests.
- Creation of dump sites for dredged material.

From capital dredging, mainly for harbour extension near Rotterdam, large amounts of sand has become available and much of it has been applied to adjacent coastal sections. From regular maintenance dredging the sand is used for beach replenishment.

Figure 3 shows the yearly amounts of sand with an indication of the aims of the projects. It appears that of many projects the choice for beach replenishment had several reasons. Reviewing the main objective, the total volume can be divided as follows:

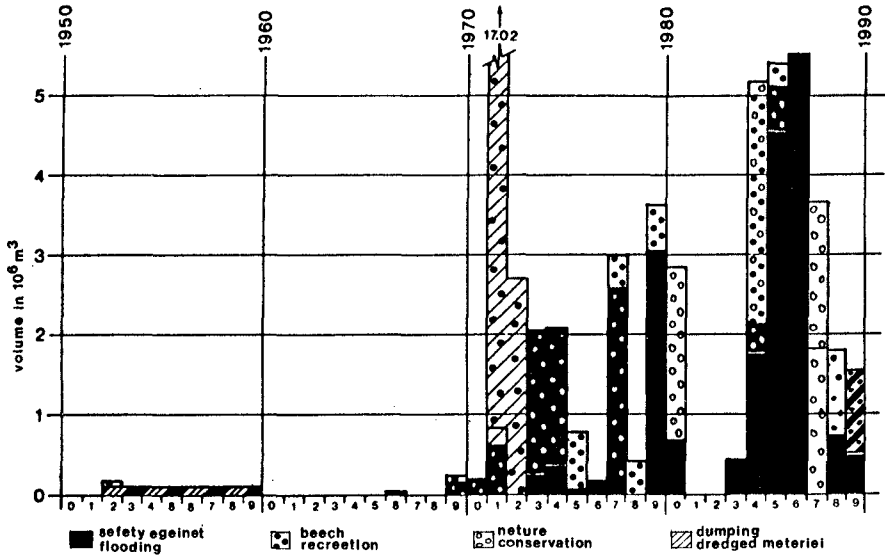


figure 3. Aims of nourishment projects.

Main objective	Volume	
safeguarding the land	24.6 million m ³	(40%)
nature conservation:	12.3 „	(20%)
recreational interests:	5.1 „	(9%)
dumping dredged material:	19.1 „	(31%)
	61.1 million m ³	

The first application of beach nourishment took place on the Walcheren coast in the fifties. Small amounts of sand from maintenance dredging were dumped on the foreshore and the shoreface to safeguard dune and dike revetments after beach erosion. In the period 1969 - 1971, sand fills were placed on the coast of Goeree to strengthen the dunes and to alleviate expected extra erosion after the closure of the tidal inlets. In the years after 1970 large amounts of sand became available from harbour extension works near Rotterdam. In 1971/72 a large part was dumped near Hoek van Holland, creating a recreational and natural area. In the seventies and eighties many nourishment projects have been carried out to strengthen dunes or to maintain their safety-level. Protection of natural values was mainly a secondary goal. Beaches were restored mainly for recreational interests in seaside resorts as Vlissingen, Scheveningen and Hoek van Holland. On the Wadden islands and in the northern part of the Holland coast large amounts of sand have been placed to conserve natural areas.

2.3 Design

In order to define the coastal problem, studies of the morphological processes and of the interests involved have to be carried out. If the problem is considered serious, the appropriate measure can be selected. After making a choice the project design can start.

The design of a nourishment programme mainly depends on the objective(s) and the coastal processes. In addition there are the circumstances for the execution, the aspects of landscape and the costs and benefits. Tools and methods for the design are:

Trend extrapolation. Based on the shoreline movements or lost volumes in the past, by means of curve-fitting an estimation is made of the coastal development in the years after the execution of a sandfill.

Equilibrium coastal profiles/ cross shore transport models. Calculations can be made for short term (dune erosion) and long term (equilibrium profile) profile changes. This is applicable to dune strengthenings and recreational beach nourishments. The effects of massive elements such as a dune foot revetment can also be calculated.

Coastal models. The analytical one-line and two-line models calculate the time dependent wave induced evolution in longshore direction. Two-dimensional coastal models can measure the influence of waves and currents. Presently, however, they are only suited for initial calculations. With both types of models, the influence of groynes and harbour moles can be taken into account.

In the Netherlands, measurements of the shoreline position have been carried out since the middle of the 19th century. Therefore trend extrapolation is the basis of the design of all projects in the coastal area. In the case of dune strengthenings, the dune erosion model (Vellinga, 1986) is used. In general this model is very usable. However the application presents problems in situations with a very steep foreshore or more than one dune ridge and at locations where a dune meets a dike.

Up to now the use of analytical and numerical models for coastline development in longshore direction has not become routine. Because of the complicated morphologic processes in the Dutch situation with tidal inlets and various types of groynes, it is not easy to find the dominant processes and to interpret model results. In most of the cases the sandfills are very long with respect to their width, so longshore deformation is rarely the most important process.

In the last decade the design practice in the Netherlands has been to derive the erosion volume from trend extrapolation and to use the dune erosion model in case of lack of safety. To compensate for dispersion, the volume needed at the seaside of the dune face was added with a certain percentage depending on the local situation. In situations with less tidal influence 25 to 50% was added depending on wave influence and the dimensions of the beach fill. At locations with a steep foreshore sometimes a surplus of 75% was applied. In some cases the choice of the percentage also was based on calculations with coastal models.

In general the textural properties of the borrowed sand were rather similar to those of the native sand. Therefore a fill factor or a renourishment factor based on grain size differences is hardly used.

2.4 Execution, borrowing and transport of sand

Whenever possible the sand was borrowed in the direct neighbourhood of the fill site at a location with a mild current and wave climate. The lowest prices were reached if the sand was pumped directly by the dredger to the shore. In some cases the sand was borrowed from other dredging operations such as harbour extension. In the past decade the possibilities of direct pumping decreased. The main reasons were less capital dredging, the fear for instability of the coastal profile and the prohibition of sand extraction in the closed tidal inlets.

In cases where a shipping channel had to be crossed, where the transport distance was very long or where the sand was borrowed from maintenance dredging, the sand was transported in hoppers. In some projects with small amounts stationary hopper dredgers (hopper volume 500 to 2000 m³) were used in combination with a reclamation dredger near the beach. Generally trailing suction hopper dredgers (hopper volume 1500 to 8000 m³) are used at present. Depending on the draught of the vessel, the depth at the mooring point on the foreshore must be MSL -5 to 12 m. Mostly a combination of a flexible floating pipe and a pipe on the bottom is needed for the transport through the surf zone. In case of a flat shoreface the distance can be so long that an extra source of power is needed (fig.4).

Originally the sand for dune strengthenings often was extracted in the dune area itself and transported by truck (fig.5). This process is not considered as nourishment and therefore is not mentioned in table 1. If the sand came by hopper from elsewhere two main execution methods were used:

-At the back or on the top of the dunes.

With the use of bunds a depot on the beach was made. After some months of desalination the sand was transported by dumping-carts to the fill site.

-At the dune face.

With the use of bunds in 2 or 3 layers the sand was pumped up to a height of about 10 m above MSL.

In the future mining of sand only will be allowed seaward of the MSL - 20 m depth contour to avoid effects on coastal profile stability as much as possible. Exceptions are made for mining in shipping channels and locations where by means of the sand extraction a better morphological situation can be created.



figure 4. Mooring point at the Holland coast.



figure 5. Dune heightening and sand extraction at Walcheren.

2.5 Costs

The price per m^3 depends on many factors, for example: the amount of sand, the circumstances for the dredging operations, the transport distance and labour market tensions. Therefore it is impossible to obtain absolutely comparable data. Nevertheless a relation has been made between the m^3 -price and the quantity of sand, in which the reported project costs have been indexed to a standard price level. Because of the strong labour market tensions, projects in the last 5 years are excluded. Also excluded are projects of which the sand was borrowed from other dredging operations. Figure 6 gives the relation between the sand quantities and the m^3 -prices, indexed to a 1985 price level. The following general conclusions can be made:

- The lowest prices per cubic meter were attained when relatively large amounts were handled, and by operations where the sand was directly spouted to the fill site.
- The most expensive method was that by which the sand was transported by hopper-dredgers and spouted either by the hopper itself or with assistance of a (barge unloading) dredger, or transported further by dump truck.

It should be remarked that before 1985 no big beach nourishment projects were carried out by means of hopper dredgers. Furthermore the equipment used by the hopper dredgers to bring the sand ashore was less developed than at present, so nowadays the price difference between hydraulic transport and water carriage probably will be less.

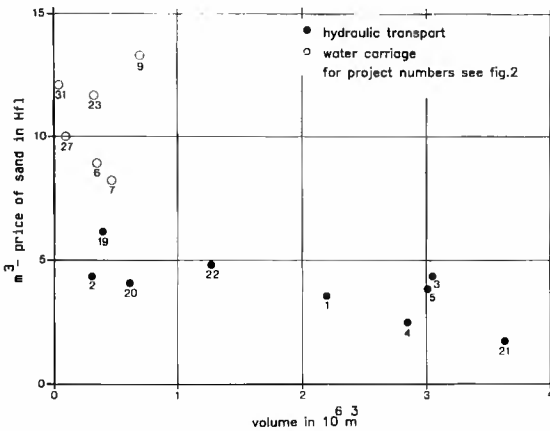
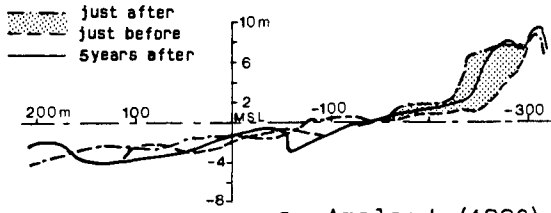
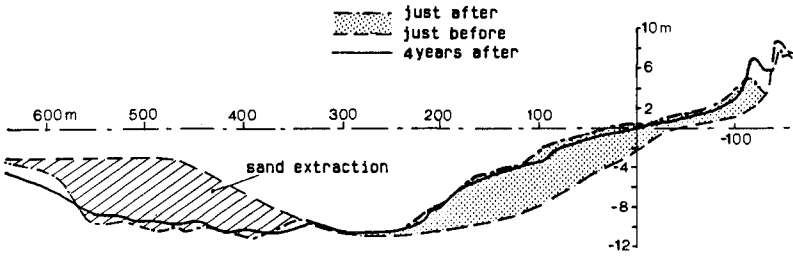


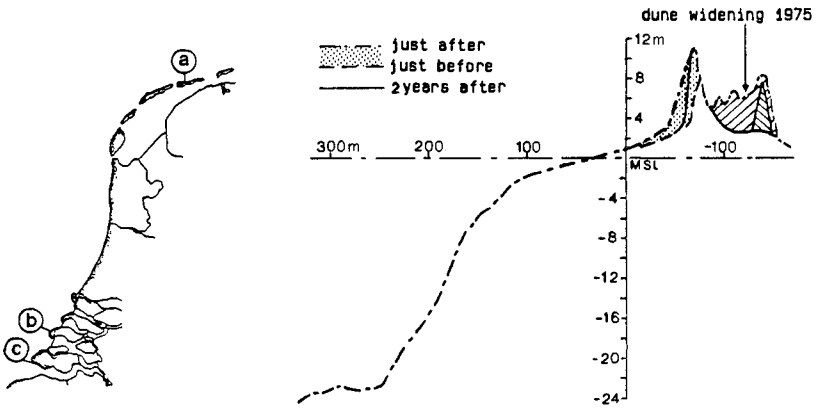
figure 6. Cubic meter price in relation to sand quantity.



a. Ameland (1980)



b. Schouwen (1987)



c. Walcheren (1984)

figure 7. Examples of cross shore profiles.

2.6 Examples

To get an impression of the applied types of sand fills in cross shore direction, in figure 7 profiles at some nourishment locations are shown.

Ameland.

Along the North Sea coast of the Isle of Ameland dune erosion occurred during storm surges. To protect the valuable dune area, in 1980 6 km of the duneface of the outer ridge were restored with 2.2 million m³ of sand. The main objective of this type of fill was to have the optimum protection with the available budget. After nourishing of course the profile was out of balance, so in the following years a natural profile was shaped.

Schouwen.

At the Schouwen coast the shifting of a tidal gully caused severe shoreline withdrawal over many decades. To protect the nature of the area and drinking water reservoir in the dune area, in 1987 in a stretch of 2.3 km the gully was artificially shifted in seaward direction. By a stationary dredger 1.5 million m³ of sand was extracted from the edge of the shoal and pumped through a floating pipe to a pontoon at the shoreface. By means of a booster the shoreface was nourished. The beach was restored by the so-called "rainbow method" (fig.8).



figure 8. Rainbow system at the Schouwen coast.

Walcheren.

Over time the south-western coast of Walcheren was eroded by a shifting tidal channel. Although the erosion of the shoreface nearly stopped, dune erosion went on in spite of a dense groyne field. To maintain a sufficient safety level of the dune ridge, in 1984 a restoration of the back-

shore and the duneface was carried out. Because of the narrow beach and the fear for losses to the very steep shoreface only 0.1 million m³ could be placed. The profile development was as expected and it appears that the required safety level can be maintained by replenishment with intervals of about 5 years.

2.7 Environmental aspects

In general the environmental effects of artificial nourishment in the coastal zone are temporary. In case of sandfills against the duneface, percolation of salt water posed problems to dune vegetation or agriculture at some locations. The effects on the beach fauna were investigated on the Isles of Ameland and Texel (Dankers et al, 1983). It appeared that after 20 months the biomasses returned to a normal level. At the Schouwen coast the influence on the beach was negligible (Adriaanse and Coosen, 1990). In the borrow area there was a temporary influence. Though the benthic community was destroyed, within some months the area was taken over by pioneers and after a year a

community had developed, belonging to the new habitat, that was very similar to the nearby gully. At Schouwen as an effect of the rainbow-system during some months, damage to the dune vegetation could be observed.

3. EFFECTIVENESS OF ARTIFICIAL BEACH NOURISHMENT

3.1 Evaluation.

To inform the Minister of Transport and Public Works about the possibilities of coast line maintenance by means of beach nourishment, 9 representative projects have been selected for an evaluation (Pluym, 1988). Figure 9 shows the locations of these projects. In general the aim of these projects was to compensate erosion, in some cases after a

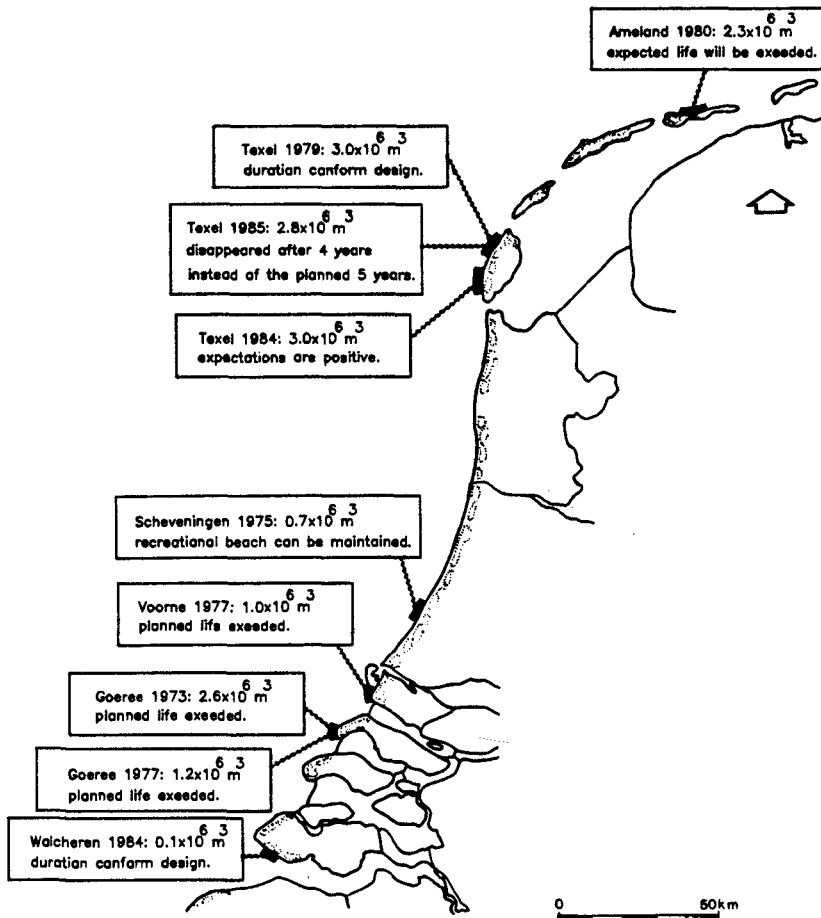


figure 9. Evaluated nourishment projects.

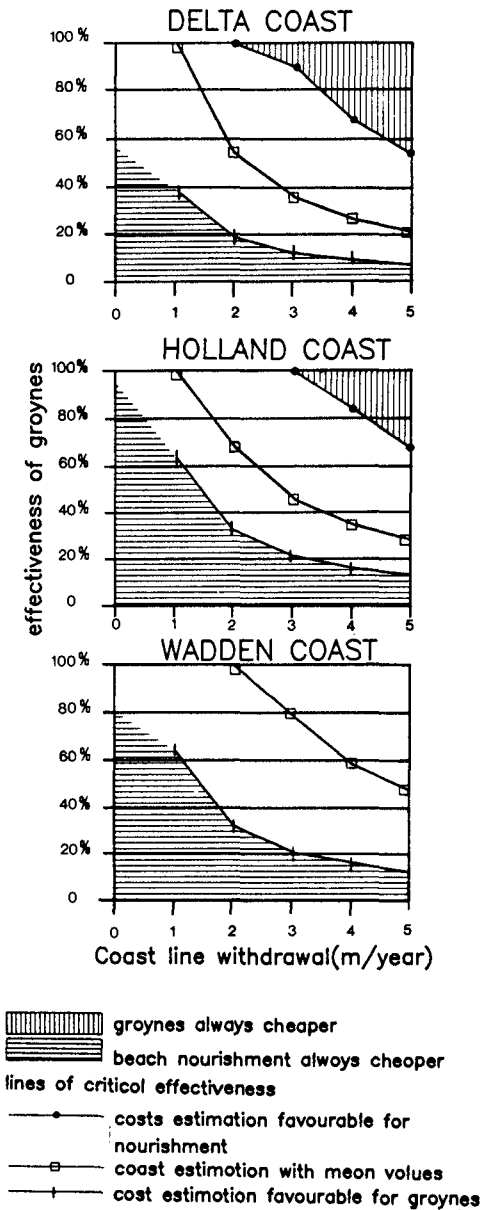


figure 10. Critical effectiveness of groynes.

dune strengthening. One project was carried out in order to create a better recreational beach. The criterium for the evaluation was: Was (or will be) the duration of life of the beach fill as expected?

The main conclusions are:

- 7 of the 9 evaluated projects were succesful and in one case the expectations are positive. Only one project did not meet the expectations. In the tidal inlet north of the island of Texel over a period of 6 years, a large amount of sand was extracted three times. This has likely influenced the behaviour of the 1985 sandfill at the adjacent coastal section. The nourished volume had disappeared after 4 years instead of the planned 5 years.
- It seems possible to design a beach nourishment with a planned duration of life, even in a dynamic coastal situation with a sometimes capricious morphological behaviour.
- Artificial beach nourishment is very effective as a measure for coast line maintenance.

3.2 Relation with groynes

To maintain the present shoreline, sand fills have to be repeated regularly and therefore can be expensive. However, in comparison to the capitalized costs of building and maintenance of groynes, nourishment for the most appears to be cheaper. Furthermore groynes cannot fully stop erosion, so supplementary nourishment is needed. On behalf of the Coastal Defence Study, a costs comparison has been made for several technical solutions for erosion control (Beafort et al, 1989). As an example figure 10

shows the calculated graphs for the 3 coastal types, with the critical effectiveness of new build groynes due to shoreline withdrawal.

The critical effectiveness is defined as the percentage of the erosion that has to be stopped by the groynes to make shoreline maintenance by means of new build groynes and additional nourishment cheaper than shoreline maintenance by nourishment alone. These calculations also have been made for scenario's with maintaining existing groynes and with removing them. Considering the supposed effectiveness of the groynes, the following situations are concluded:

a. Sandy coastline without groynes:

generally, the construction of just groynes is not advisable for reasons of effectiveness and costs;

in the delta area, where landward shifting of tidal channels presents erosion problems, a combination of groynes and nourishment may be cost effective.

b. Sandy coast with groynes:

existing groynes must be maintained for reasons of erosion control;

the costs of nourishing such a coast are relatively low compared to the costs of nourishment in case of removal of the groynes.

The costs of the construction and maintenance of groynes have been derived from prices reported by coastal managers. For future nourishment projects cost estimations have been made. The variable circumstances for dredging operations along the Dutch coast imply various execution methods with different dredging equipment. Therefore the estimated costs per m^3 (on the beach) differ from Hfl 3.00 in case of large amounts and favourable circumstances, to over Hfl 10.00 in case of small amounts and unfavourable conditions. If the sand has to be transported from the beach into the dune area, the extra costs amount from Hfl 4.00 to Hfl 5.50 per m^3 .

REFERENCES

BEAUFORT, G.A., BAARSE, G., PEERBOLTE, E.B., PLUYM, M. AND ROELSE, P. (1989).

Coastal Defence after 1990, Technical Report 11: Beach- and dune nourishment (in Dutch).

Ministry of Transport and Public Works, The Hague.

ADRIAANSE, L.A. AND COOSEN, J. (1990).

Beach and dune nourishment and environmental aspects (in Dutch, in preparation).

DANKERS, N., BINSBERGEN, M. AND ZEGERS, K. (1983).

The effects of beach nourishment on the fauna of the beaches of Texel and Ameland (in Dutch).

Rijks Instituut voor Natuurbeheer, RIN 83/6, Texel.

LOUISSE, C.J. AND KUIK, A.J. (1990).

Coastal defence alternatives in the Netherlands (in Dutch).

Proceedings 22th International Conference Coastal Engineering, ASCE, New York.

RIJKSWATERSTAAT AND DELFT HYDRAULICS (1987).

Manual on Artificial Beach Nourishment.

Centre for civil engineering research, codes and specifications, Gouda.

PLUYM,M.(1988).

Evaluation of beach nourishment (in Dutch).

Rijkswaterstaat, Tidal Waters Division GWWS-87.006, The Hague.

ROELSE,P.(1988).

Beach nourishment as a measure for coastal defence (in Dutch).

i-kwadraad Bouwkunde en civiele techniek, no 8. De Ingenieurspers, Amsterdam.

VELLINGA,P.(1986).

Beach and dune erosion during storm surges.

Doctor Thesis, University of Technology, Delft, The Netherlands.

CHAPTER 151

OFFSHORE SAND EXTRACTION AND NEARSHORE PROFILE NOURISHMENT The Dutch Coast: Paper No. 12

Jos S.L.J. van Alphen 1)
Frank P. Hallie 2)
Jan S. Ribberink 3)
J.A. Roelvink 3)
Cees J. Louisse 4)

Abstract

Because of the increasing need of sand for use on land and coastal protection, offshore sand extraction has become commonplace. On the other hand, the practice of beach nourishment has become a common method to combat beach erosion. Here, economic and other interests may be served by dumping the sand not directly onto the beaches, but nearshore. Within the framework of the Coastal Defence Study for the Dutch coast and the preparation of a Marine Aggregate Extraction Plan model studies were performed in order to obtain indications and quantitative estimates of the morphological effects of offshore sand extraction and nearshore profile nourishment. The major results of the model computations are:

- offshore sand extraction landward of the 16 m isobath may affect the coastline within a century.
- nearshore nourishments landward of the 7 m isobath have positive effects on the coastline.

The model computations could not be validated in the field. Due to the relatively large margins of inaccuracy the political implication of this study is that sand extraction landward of the 20 m. isobath is not licensed.

Introduction

Within the framework of the Coastal Defence Study for the Dutch coast several methods to combat beach erosion have been investigated (Roelse, this volume). One of these methods, and maybe a very promising one, is nearshore profile nourishment. This method consists of the nearshore dumping of sand, say landward of the 10 m. isobath in the breaker zone, followed by onshore transport by the orbital wave motion.

1) Rijkswaterstaat, dir. Noordzee, P.O.Box 5807, 2280 HV Rijswijk, the Netherlands.

2) Rijkswaterstaat, Tidal Waters Division, P.O. Box 20907, 2500 EX Den Haag, the Netherlands.

3) Delft Hydraulics, P.O. Box 152, 8300 AD Emmeloord, the Netherlands.

4) present address: Rijkswaterstaat, Dienst Verkeerskunde, P.O. Box 1031, 3000 BA Rotterdam, the Netherlands.

in the breaker zone, followed by onshore transport by the orbital wave motion. Encouraging field experience with this method has been gained in e.g. Australia (Jackson & Tomlinson, 1990).

For all kinds of nourishments the sand will be extracted offshore. From a coastal zone management point of view offshore sand extraction is an interesting problem. On the one hand sand extraction becomes more expensive with increasing distance offshore (in the Dutch situation several percents of the m³ price per kilometer). On the other hand sand extraction nearshore may induce coastal erosion, because extraction can be considered as withdrawal of sand from the sand budget of the shoreface and adjacent beaches and dunes. In the past the Dutch regulatory authority did not license sand extraction landward of the 20 m. isobath. This policy was based on the idea that wave induced onshore sand transport becomes increasingly important in shallow waters, especially landward of the 20 m. isobath. Results of foreign field studies indicated a similar value (Migniot & Viguier, 1980; C.E.R.C., 1984)

Within the framework of the Coastal Defence Study and the preparation of a Marine Aggregate Extraction Plan for the Dutch part of the North Sea model studies were performed to obtain better and more quantitative estimates of the morphological effects of offshore sand extraction and nearshore nourishments. Various existing modelling techniques for waves, currents, sediment transport and morphology were applied, combined with new knowledge, field data and surveys.

This paper will address the morphological impact of offshore sand extraction and nearshore nourishment, including nourishment with simultaneous extraction. The approach adopted and representative results are presented.

General background

The orientation of the Dutch coastal section considered changes from SW-NE in the southern part to S-N in the northern part (see Table 1). The 20 m. isobath, situated 5 to 15 km. offshore, separates the shelf from the sloping shoreface, on which wave action becomes increasingly important with decreasing waterdepth. Shoreface gradients vary from 1:1000 near the 20 m. isobath to 1:100 near the 10 m. isobath, which is situated about 1 km. offshore. Landward of the 10 m. isobath breaker bars are abundant. Shoreface sediments consist of non-cohesive sands with a median grain size of 0.150-0.300 mm.

Sediment transport on the upper shoreface (breaker or active zone, situated landward of about the 8 m. isobath) is wave dominated due to wave asymmetry, swell action, breaking waves and wave induced currents. On the lower shoreface sediment transport is dominated by tidal currents. They are mainly longshore directed and reach maximum surface velocities of about 1.0 m/s. Tidal action, wind, salinity gradients and waves induce relatively small residual currents. A persistent landward residual bottom current of about 0.03 m/s. exists on the Dutch shoreface (Van der Giessen et al., 1990).

Especially during storm conditions waves act as a stirring mechanism, bringing sand into suspension and ready for transport by currents. Waves approach the coastline predominantly from directions varying from 240 to 360. Year averaged wave height and period are about 1 m. and 5 s. respectively.

Set-up of the study

Although a reasonable qualitative knowledge exists of the dominant physical processes

of sediment transport in the Dutch coastal zone, there is still a considerable lack of:

- quantitative descriptions of these processes
- knowledge of the representative input conditions
- verification and calibration of the existing mathematical models in the field.

Moreover, no general two-dimensional morphodynamic modelling system is available yet in which the sub-models for hydrodynamics and sediment transport are applied in direct interaction with computed changes in sea bed level. Nevertheless, in the present study an attempt was made to estimate and compare morphological effects of different sand extraction and/or near-shore nourishment schemes with relatively simple existing mathematical modelling techniques.

The study focussed on different locations along the Dutch coast (Table 1).

	EXTRACTION			NOURISHMENT			EXTRACTION + NOURISHMENT
LOCATION	S	B		D	N	E	D
ISOBATH (m)	10,	16,	20	3, 5, 7,	10		10+ 5
VOLUME* (10 ⁶ m ³)	0,2	1	10				
(m ³ /m)	100,	500,	2000, 5000	100 , 200			100

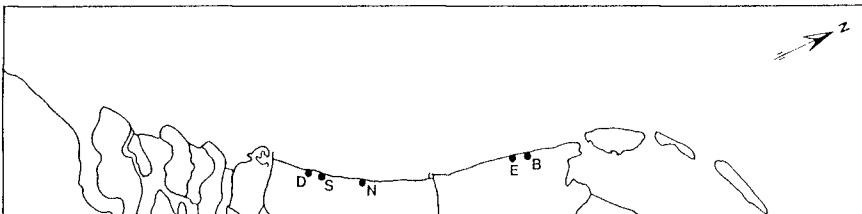


Table 1: extraction and nourishment schemes: locations and variants. S = Scheveningen, D = Delfland, N = Noordwijk, E = Egmond, B = Bergen. *: different volumes of extraction are obtained by different combinations of extraction length (2000 and 5000 m.), width (100, 500 and 1000 m.) and depth (1, 2 and 5 m.).

Different sand extraction schemes between the 10 and 20 m. isobath were analyzed, varying in length, width and extraction depth and, accordingly, in volume (Table 1). Nourishment schemes were assumed between the 3 and 10 m. isobath, varying in width and height. One combined extraction (10 m.) and nourishment (5 m.) simulation was performed.

The morphological processes, as distinguished in the present approach, are outlined in Figure 1.

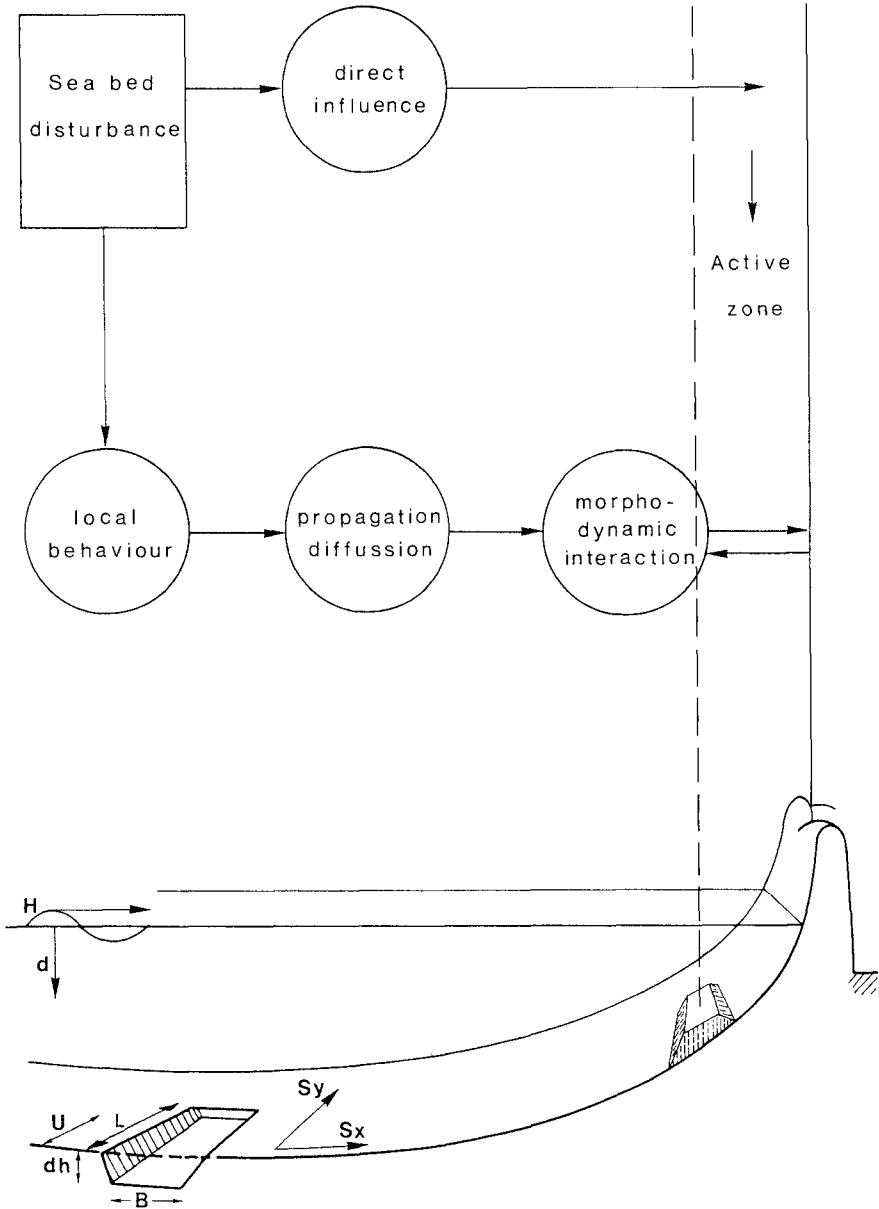


Figure 1: schematization of relevant processes, symbol definition (H = wave height (m), d = water depth (m), dh = depth of extraction (m), B = width of extraction (m), L = length of extraction (m), U = tidal current (m/s), S_x , S_y = cross-shore and along-shore component of sediment transport).

Sand extraction in relatively deep water leads to a local disturbance of the sea bed topography which, under the combined action of waves and currents, can directly affect the hydrodynamics, sediment transport and morphology of the near-shore zone. Moreover, the local sea bed disturbance may lead to erosion of the near-shore zone at a larger time-scale, for example by onshore propagation/diffusion of the extraction pit and/or by acting as a sink for sediment that is eroded from the near-shore zone.

The direct hydrodynamic effects of the different extraction schemes were analyzed by studying:

- the disturbance of the tidal current pattern around the extraction pit (streamline convergence/ divergence), using a two-dimensional (2DH) flow model for depth-averaged currents and water levels.
- the disturbance of the waves (refraction), using a wave field model to obtain the 2DH propagation, refraction and energy dissipation.

The direct and long term morphodynamics of the extraction pits were estimated in longshore and cross-shore direction separately, assuming that this is allowed within certain time limits.

The cross-shore development of the different extraction schemes was computed with a one-dimensional morphodynamic model (CROSTRAN, see Roelvink and Stive, 1988), in which the sediment transport model of Bailard (1981) is adopted. The hydrodynamic input of the transport model is derived from a one-dimensional wave energy decay model in combination with:

- non-linear wave theory for the computation of near-bed velocities (wave asymmetry),
- wave induced net bottom currents (drift currents)
- a persistent onshore directed residual bottom current of 0.03 m/s.

Input conditions were derived from a schematized measured deep water wave climate. The longshore development of the different extraction schemes was estimated with a quasi-2DH morphodynamic model (LOMOR). The sediment transport in longshore direction is dominated by tidal currents. The behaviour of the tidal current along the extraction pit is computed with a simplified steady 2DH flow model. It is assumed that the longshore axis of the pit coincides with the (undisturbed) tidal flow direction and can be considered as symmetry-axis. This model is applied in a quasi-steady way at 10 moments during a characteristic tidal cycle (12h 30 min), using boundary conditions from a calibrated overall 2DH flow model of the area (without seabed disturbance). To be consistent with the cross-shore model the same sediment transport (capacity) formulation, based on the same Bailard model, is used. The sediment stirring effect of waves is incorporated for a selected characteristic wave height-wave period combination ($H_s = 1.5$ m., $T = 6$ s.).

The adjustment of suspended load transport to the changing hydraulic conditions is modelled with a depth-averaged suspended load model, based on Galappatti (1983). Computed local erosion and sedimentation rates are integrated over the tidal cycle. Bed level changes are computed after selecting an appropriate morphological time step. The adjusted sea bed topography is then fed back into the flow model and the computation with the morphological model is repeated. With this technique the long term morphodynamics of the different extraction schemes were estimated for periods up to 40 years.

As a result of the process-schematization and modelling techniques time estimates have

an inaccuracy in the order of a factor 3 to 5.

The nourishment schemes are situated inside the active zone. Here sediment transport is more intense and morphological changes take place on shorter time-scales than on the lower shoreface.

The sediment transport and morphodynamics of the nourishment schemes and nearshore profile were also studied with the above mentioned CROSTRAN model. This model proved to be able to simulate some overall characteristics of the natural nearshore behaviour of e.g. breaker bars (Roelvink and Stive, this volume). Input for this nearshore application were daily averaged values of wave height, wave period and swell characteristics derived from a deep water wave record of 1983. In the computations this time sequence of wave conditions was used as input for 6 consecutive years. The same model was also applied for the combined extraction-nourishment scheme.

Results

The direct effects of extraction on the cross shore distribution of the near bed maximum tidal current velocity is shown in Figure 2a. Only an extreme extraction of 5 m. at a waterdepth of 14 m. ($L = 2000$ m., $W = 1000$ m.) gives a small decrease (about 10 %). On both sides of the extraction pit the width of the affected area is about two times the extraction width. There are no immediate effects landward of the 10 m. isobath.

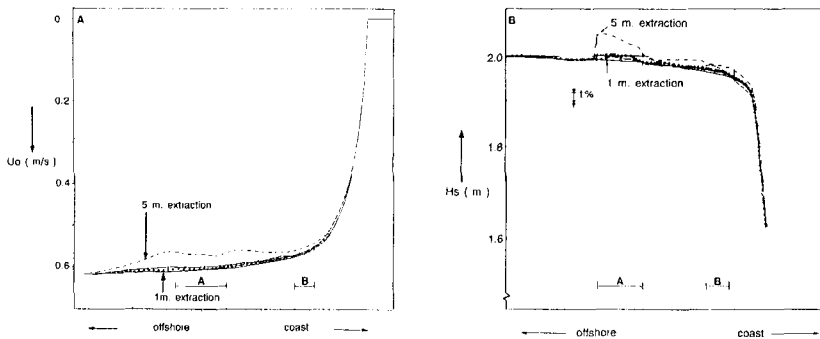


Figure 2a: predicted cross-shore distribution of near bed tidal current velocity and (b) significant wave height. Sand extraction at $d = 14$ m. (A: $W = 1000$ m., $dh = 1$ m. and 5 m.) and at $d = 10$ m. (B: $W = 500$ m., $dh = 1$ m.).

The immediate effect of extraction on the wave climate is local and minor as well. Figure 2b shows that in case of incoming waves ($H = 2$ m., $T = 6$ s.) only an extreme extraction of 5 m. on the 14 m. isobath results in a 1 % increase of the wave height which has disappeared before the 10 m. isobath.

Because of these minor direct changes in hydrodynamics, instantaneous morphological adaptation is negligible as well. Computations on initial transport show that within the affected area vertical sea bed movements are within the order of 0.001 to 0.01 m. per year, which is insignificant compared to the inaccuracy of sounding.

The predicted longterm longshore behaviour of the extraction pit and near bed current

velocity is shown in Figure 3.

In this case the extraction pit is situated on the 16 m. isobath ($L = 2000$ m., $W = 300$ m., $dh = 1$ m., $t = 15$ years). Initially there are gradients in current speed near the head and tail of the pit, but because of the interaction between currents and morphology the steep sea bed slopes become smaller and the gradients in velocity decrease in time. Apart from this diffusive kind of behaviour the pit is relatively stable in time under the given input conditions. Similar results were obtained for other locations and extraction volumes.

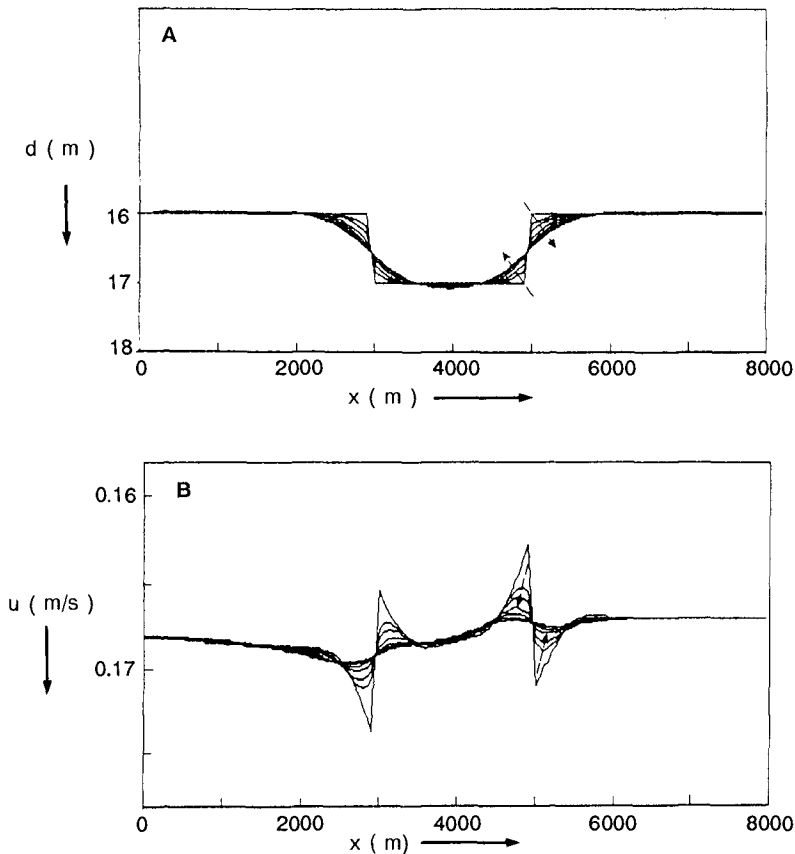


Figure 3a: predicted longshore behaviour of extraction pit and (b) near bed tidal current velocity. $d = 16$ m., $L = 2000$ m., $W = 300$ m., $dh = 1$ m., $t = 15$ years.

The predicted longterm effects in cross-shore direction are shown in Figure 4a and 4b. for extractions on the 20 m. and 16 m. isobath respectively. Extraction on the 20 m. isobath shows almost no cross shore effects, the pit remains stable for at least 40 years.

Extraction on the 16 m. isobath results in a minor change in depth of the pit. In addition, as a result of a small net onshore sediment transport, deposition on the offshore margin and erosion of the landward boundary leads to a onshore migration of the pit with a rate of 1 to 2 m. per year. The gradients in the profile smooth in time.

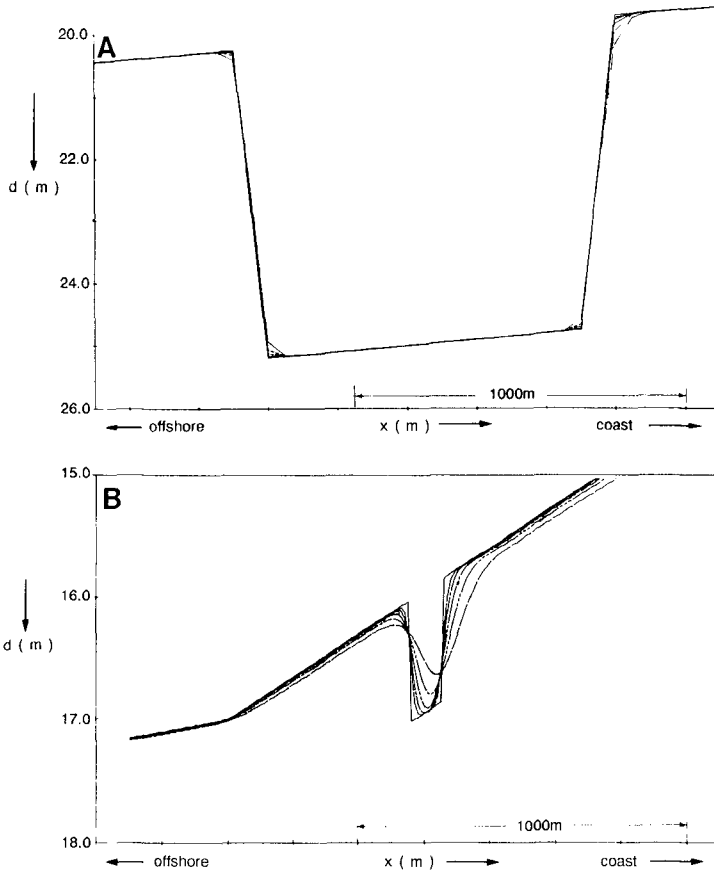


Figure 4a: predicted cross-shore behaviour of extraction pit at $d = 20$ m. ($W = 1000$ m., $dh = 5$ m.) and (b) $d = 16$ m. ($W = 100$ m., $dh = 1$ m.) over a period of 40 years.

According to the CROSTRAN and LOMOR computations the morphological development of the pit mainly occurs at the boundaries of the pit and take place in similar time scales in long and cross-shore direction. This indicates that the separate treatment in long and cross-shore dynamics is justified within the time limits considered (40 years).

By comparing Figure 4a with 4b the increasing importance of wave action with

decreasing waterdepth and distance offshore is illustrated. As a consequence of this phenomenon predicted migration rates of sea bed disturbances speed up rapidly landward of the 16 m. isobath (Figure 5a). Based on these migration rates the necessary time for the head of a given extraction to reach a given isobath was estimated. Figure 5b shows that at Scheveningen the head of an extraction landward of the 14 m. isobath may reach the active zone within a century. It was found that with steeper shoreface slopes the time scale for a sea bed disturbance to reach the active zone decreases. E.g. at Bergen this time scale is twice as small (shoreface slopes between the 10 and 14 m isobath are 0.0016 and 0.0040 for Scheveningen and Bergen respectively).

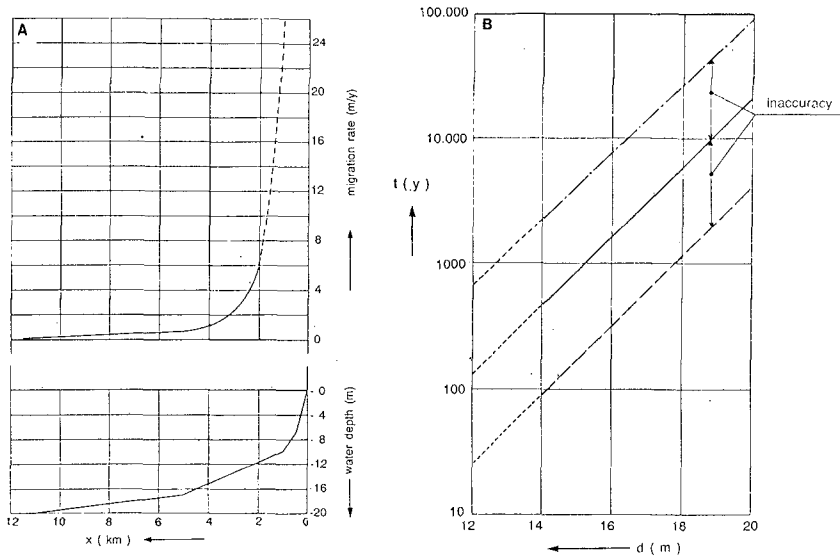


Figure 5a: predicted cross-shore migration rate (m/y) of sea bed disturbance at Scheveningen (S in Table 1) and (b) time necessary to reach the active zone. The dashed lines indicate the margins of inaccuracy.

It should be noted that the time needed for the head of the pit to reach the breaker zone is dependent on the cross shore sand transport rates rather than on the amount of extraction. However when the pit approaches the shore, the amount extracted represents the lack in the sand budget. Then it determines the rate of erosion and the period erosion prevails.

Figure 6 shows the behaviour of a nearshore nourishment of 100 m^3 per m. on the 3, 5 and 7 m. isobath. The thickness of the nourishment is 1 m. As a result of wave induced onshore transport in the landward part and a seaward directed undertow the nourishment volume is divided into an onshore and offshore directed transport in all cases. However when deposited on the 7 m. isobath only a small part of the original volume reaches the beach within 6 years.

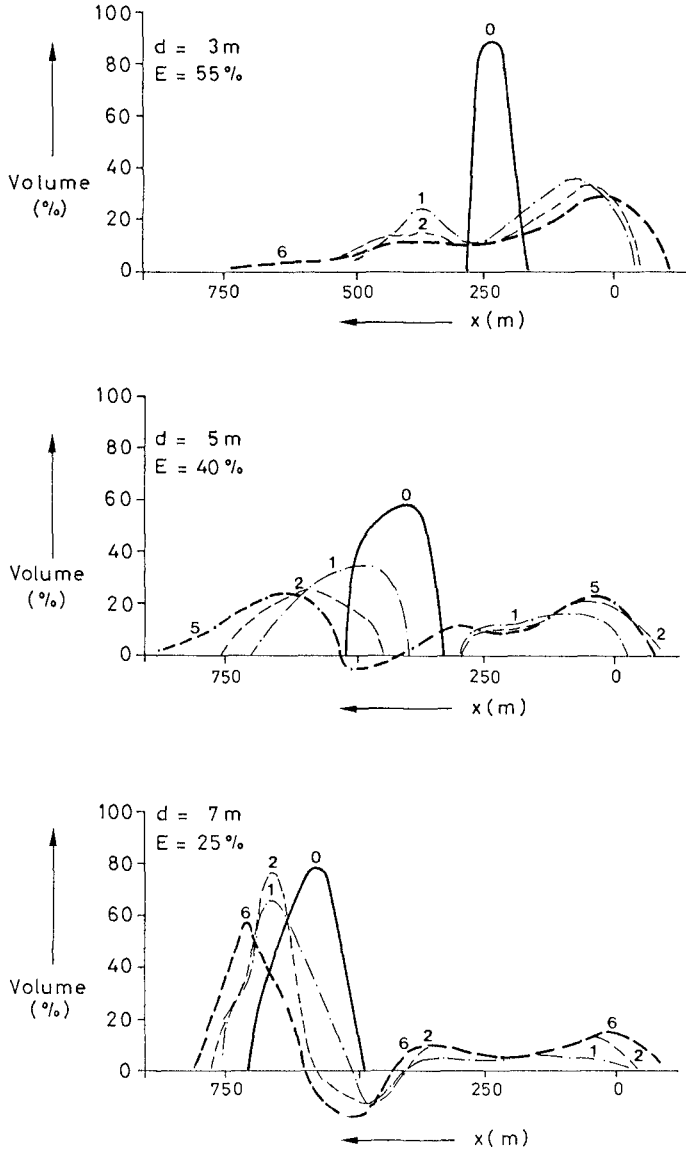


Figure 6: relative volumetric distribution of 100 m³/m profile nourishments at waterdepths of 3, 5 and 7 m. in time. E = Effectivity (see text).

The effectivity of the nearshore nourishment (E) is expressed as the volumetric change of a 300 m. wide zone along a line of reference on the beach, compared to the original volume of the nourishment. It can be seen that the effectivity of nourishments increases in a landward direction: from 25 % of nourishments on the 7 m. isobath towards 55 % of those on the 3 m. isobath. With other words, the seaward loss of the nourishment volume decreases with nourishments in shallower water.

These results hold for the Delfland location but are similar on other locations. It was also found that the relative distribution of the initial volume over the profile is independent on the volume of the nourishment.

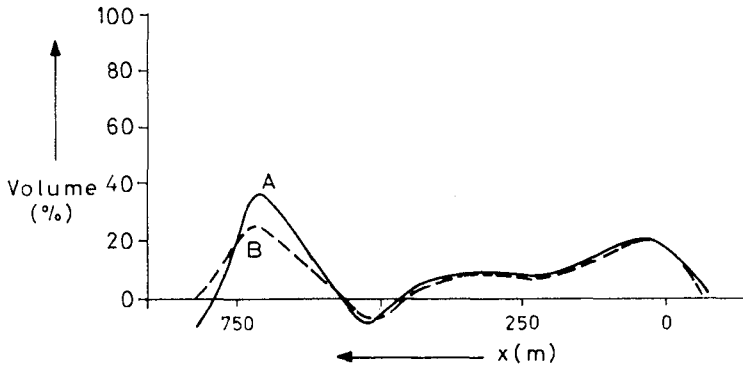


Figure 7: relative volumetric distribution of 100 m³/m. profile nourishment at d = 5 m. after 6 years, with (A) and without (B) simultaneous extraction of 100 m³/m. at d = 10 m.

The effect of extraction during nourishment was studied in a model run with a 100 m³/m. nourishment on the 5 m. isobath and simultaneous extraction of the same amount on the 10 m. isobath. The distribution of the nourishment volume after 6 years with (A) and without (B) extraction is very similar (Figure 7). Only in the most seaward part of the profile with extraction the sea bed is a little lower. It looks as if the sand extraction nearby has no negative effects on the nourishment itself within this period of 6 years. However, the long term studies presented in the former section suggest that on a timescale of decades to centuries detrimental effects may show up in this zone due to the approach of the extraction pit. The lowering of the seabed in the seaward part of the profile may be a signal of this already.

Conclusions

The computations performed showed the following results:

- the direct effects of the studied sand extraction schemes on hydrodynamics (current and wave climate) are very local. On both sides of the extraction pit the affected area has a width that is two times the extraction width.
- on the long term sand extraction landward of the 16 m. isobath may affect the coastline within a
- century by landward migration of the extraction pit, leading to a deficit in the nearshore sand budget.

- nourishments landward of the 7 m. isobath have positive effects on the coastline.
- simultaneous extraction has no significant effects on the nourishment within a period of 6 years, but may have on a larger time scale.

It should be emphasized that the results presented could not be verified in the field. A large scale field experiment like the one reported in Jackson & Tomlinson (this volume) is urgently needed to validate the models and assumptions on which the results are based, and to reduce the margins of inaccuracy.

The political implication of this study is that, from a precautionary point of view, the Dutch regulatory authority will refrain from licensing sand extraction landward of the 20 m. isobath, even if this sand extraction is meant for nourishments (an exception is made for extraction in navigation channels). In addition the Environmental Impact Assessment, prepared for the Dutch Marine Aggregate Extraction Plan, showed that this zone landward of the 20 m. isobath coincides with a area that is very valuable from an environmental point of view (i.e. relatively rich in benthic life and nursery area for several species of commercial fish).

APPENDIX I. References

- Bailard, J. A. (1981). "An energetics total load sediment transport model for a plane sloping beach." *J. Geophys. Res.*, 86(C11).
- Coastal Engineering Research Center (1984). "Shore Protection Manual." Dept. of the Army, US Army Corps of Engineers.
- Galappatti, R. (1983). "A depth-integrated model for suspended sediment transport." *Comm. on Hydraulics*, Dept. of Civ. Eng., Delft University of Technology, The Netherlands.
- Jackson, L. A. and Tomlinson, R. B. (this volume). "Nearshore nourishment: implementation, monitoring and model studies of 1.5 M(3) at Kirra Beach."
- Migniot, C. and Viguier, J. (1980). "Influence de l'extraction en mer des granulats sur l'équilibre du littoral." *La Houille Blanche*, 3, 177-194 (in French, with English abstract).
- Roelse, P. (this volume). "Beach and dune nourishments in The Netherlands."
- Roelvink, J. A. and Stive, M. J. F. (1988). "Large scale tests of cross-shore sediment transport on the upper shoreface." *Proc. Symp. on Math. Modelling of Sed. Transp. in the Coastal Zone*, Copenhagen, Denmark.
- Roelvink, J. A. and Stive, M. J. F. (this volume). "Sand transport on the shoreface of the Holland coast."
- Van der Giessen, A., De Ruijter, W. P. M. and Borst, J. C. (1990). "Three-dimensional current structure in the Dutch coastal zone." *Neth. J. Sea Res.*, 25(1/2), 45-55.

CHAPTER 152

SEAWARD COASTAL DEFENCE FOR THE DUTCH COAST

The Dutch coast : Paper No. 13

Marco Pluijm

1. INTRODUCTION.

The Dutch Delta-works are nearing their completion. Decades of construction of dikes and dunes come to an end. It is obvious that after the completion of these Delta-works, this infrastructure of coastal defence works needs its year to year maintenance as well. Therefore the Dutch Government asked for the so called "Coastal Defence study" and mobilized all the available knowledge with respect to this item, in order to draft a report with which the political decisionmakers could come to the selection of the most suitable maintenance-strategy. Four different possibilities were investigated.

It appeared that the so-called full maintenance strategy will be the most cost effective and profitable solution and was therefore chosen. According to this strategy all retreat of the coastline will always be compensated (in general by beach-nourishment).

However, some parts of the Dutch coast are facing extreme erosion as well as very poor reserves and for those locations the application of a somewhat different approach can be profitable or (in time) even necessary (for instance with respect to sealevel rise). This approach was roughly investigated as the "Seaward Coastal Defence" strategy. According to this strategy additional measures will be taken to influence the morphological system in such a way, that the coastline will not erode any longer, but be kept on its place or even grow in seaward direction. The effectiveness of this approach has to be compared with maintenance by beach-nourishment as such as well as the effects it will have elsewhere on the morphological system.

A pilot-study has been defined at the isle of Texel. The north-point of this island suffers severe erosion. Several beach-nourishments have been carried out here. Unfortunately the effectiveness was not always as planned.

This paper contains a brief description of the seaward strategy as such and more specific the preliminary results of the "Texel" pilot-study as obtained so far. In 1991 the finite conclusions will be available.

Rijkswaterstaat, Tidal Waters Division, P.O.Box 20907, 2500 EX The Hague, The Netherlands

2. SEAWARD COASTAL DEFENCE STRATEGY.

In the Coastal Defence study four strategies have been worked out, respectively retreat (only the real hot spots will be maintained for safety reasons), partially maintenance (also some other uses of the coastal zone can be a reason for maintenance), full maintenance (all retreat of the coastline will always be repaired) and "seaward".

The seaward-strategy aims permanent reinforcement of the weakest, heavy eroding spots along the Dutch coast by "changing" the erosion into a more or less stable situation or even sedimentation. In order to start this process, it is necessary to influence the (large scale) sand-transport phenomena along the Dutch coast. The placement of an initial construction will be the driving force behind this "sand-trapping" process. Because of the difference between the several morphological systems along the Dutch coast, it is not possible to suffice with one solution. Therefore for each of the hot spots specific solutions have been created (tabel 1 and figure 1).

name	aim	construction
Texel	creation of sedimentation along eroding coast. sedimentation, (partially)	large dam, perpendicular to the coastline. In case of to large timescale for natural artificially nourishment to an extended beach.
N.Holland	creation of sedimentation along eroding coast	one or two large dams, perpendicular to the coastline. In case of to large a timescale of sedimentation, artificial placement of sand in the shape of a beach or barrier with a lagoon.
Voordelta	reduction of wave attack	artificial initial raise of sandbanks with ridges of stone or "sand-sausages", stimulation of sand accumulation with artificial seaweed, creation of sand-drift.
Walcheren	prevention of progression erosion by currents	two or more dams to shift currents. Stimulation of sedimentation in an enclosed area.
Cadzand	prevention of negative effects "sandwaves"	sub-merged dams between the groynes. Pending beach.

tabel 1 : possible "seaward" solutions for the Dutch coast

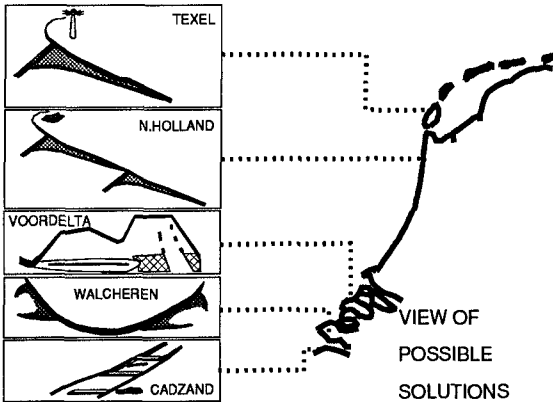


figure 1 : view of possible solutions for seaward defence

These sketches are of an preliminary status. They are based on many assumptions and with respect to several items, further research will be necessary. Therefore Rijkswaterstaat has decided to start a pilot study.

The most likely location for such a study has been found on the heavily eroding northern point of the isle of Texel.

3. THE "TEXEL" PILOT-STUDY.

The pilot-study concerns the hydraulical and morphological background of the erosion at the north part of the isle of Texel, the layout and construction of some solution(s) and determination of its effectiveness from morphological and economical point of view. These solutions have to be compared with the present way of coastline maintenance i.e. beach-nourishments.

3.1 large scale morphological behaviour.

With respect to the large scale sand transport phenomena, the following remarks can be made. Along the Northsea-coast of the isle of Texel sand is transported in northern and southern direction to the Robbengat and the Molengat (fig. 2) due to the combined effect of longshore and tidal currents. This results in a net loss of sand in the direction of the Wadden-sea.

The Delta between the isle's Texel and Vlieland does show a clear system of eb-tidal channels ("Eierlandse Gat"). The system of flood-tidal channels is far less developed. Both types of channels play its role in the transport of sand in the direction of the isle of Vlieland. Some sand is transported directly along the sea-ward boundaries of this delta due to wave-action.

Some sand is trapped into the so called Slufter, an intertidal area behind the dunes just above the center of the island.

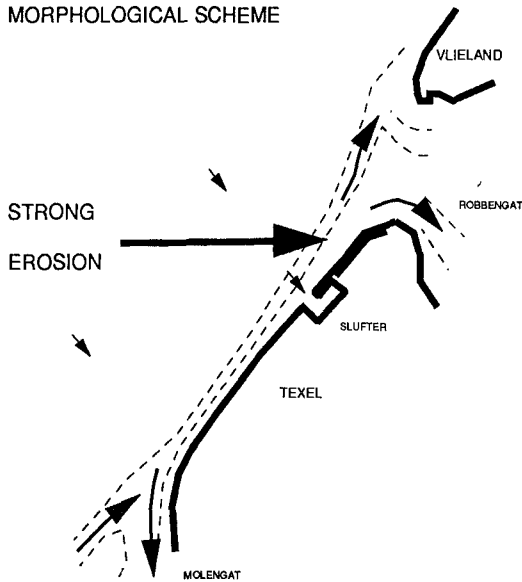


figure 2 : morphological scheme.

From the south the coastline of the island is supplied with sand from the delta between the coast of North-Holland and Texel ("Zeegat van Texel")

Due to cross-shore transport some sand is supplied from deeper water to the coastal zone. This quantity is believed to be of minor importance compared to the mentioned longshore processes.

All this moving sand can not prevent that the entire coastline of the island retreats. In the center of the island this retreat is 1 to 5 meters per year, increasing in northern and southern direction up to 20 meters per year and even more. At some places a retreat of even 30 meters in one year has been occurred.

Predictions have been made, and if nothing would have been done, the coastline north of the Slufter would show an average retreat of 100 to 150 meters for the next ten years (fig. 3).

A retreat like that is absolutely not acceptable for reasons of nature and shipping traffic (a lighthouse is standing close to the edge). Therefore beach nourishments have been carried out.

Upto now in 1979 ($3 \cdot 10^6$ m³) and in 1985 ($2.8 \cdot 10^6$ m³) along this stretch and in 1984 3 billion m³ along the middle of the island. This year the nourishment of 1985 had been disappeared completely. Some parts of the coastline retreated even much further. At present a nourishment is carried out.

The problem with nourishments along this coastline is, that in fact there is not enough

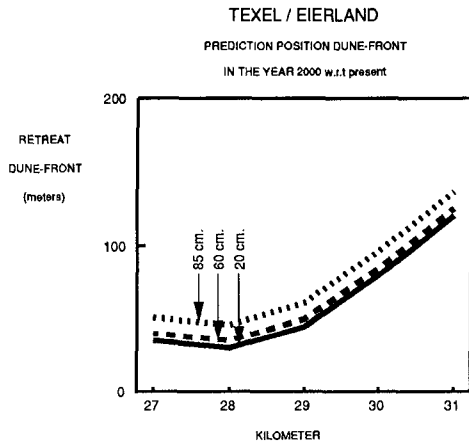


figure 3 : prediction position of dunefront

space to place the sand in such a way that it will not be eroded directly at the toe by tidal currents (fig. 4). From economical point of view, reduction of quantity is therefore needed or the use of coarser material. The latter solution was chosen for the nourishment of this year.

BEACH NOURISHMENT

TEXEL km. 28.4

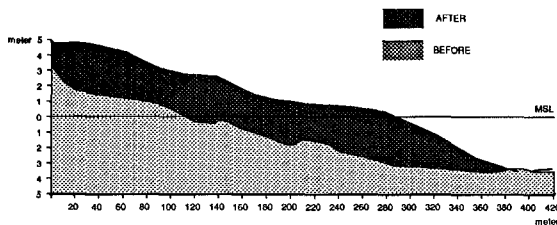


figure 4 : cross-section beach nourishment 1979

3.2 small scale morphological behaviour.

The coastline of Eierland (north of the Slufter) loses a quantity of sand with an average of 400.000 m³ to 500.000 m³ per year (fig. 5). These figures were valid for the “undisturbed” situation, so before the first nourishment had been carried out. Since then these figures have increased (to 600.000 m³ per year) due to the effect mentioned earlier i.e. the lack of space for placing the right quantity of sand without coming under the direct influence of the tidal currents. As stated before, these quantities are average values and will vary from year to year.

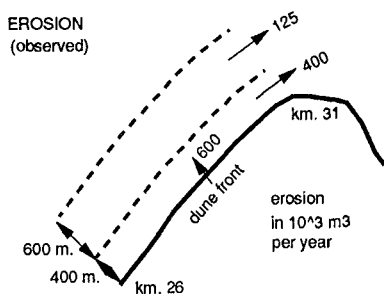


figure 5 : erosion quantities (observed).

These quantities have been established from the yearly soundings of the coastal zone (JarKus = Jaarlijkse Kustmetingen). These soundings have also been used for the analysis of the development of the cross-shore profiles. From this it can be concluded that two different zones can be distinguished. A zone of about 400 meters from the dune-foot with a rapidly changing bottom-topography, followed by a zone of about 600 meters seaward with a rather flat and stable topography.

In the autonomous situation in the first zone the loss of sand amounts approximately 400.000 m^3 per year and in the second zone approx. 125.000 m^3 per year. After the first nourishment the figure for the first zone increased to about 600.000 m^3 per year, whereas in the second seaward zone a sedimentation of about 100.000 m^3 per year was established soon after the works had been completed. However, this was only for a short time. Soon erosion also started here again.

Apart from these figures obtained from measurements, also calculations with relatively simple mathematical models were made on a personal computer. The aim of these calculations was to investigate the different contributions of the transport phenomena with respect to the observed processes.

Calculations were made with respect to wave-height, wave setup, longshore currents and tidal currents, sediment transport (several approaches), dune erosion, etc. It appeared that each of the components could be obtained rather well, compared to the available data. For instance the transport capacities due to the differences in wave setup along this coastline could be checked with tide gauge measurements under storm conditions.

The following contributions to the total erosion due to transport-capacities were calculated (fig. 6) :

- * 60 percent due to waves and currents under normal, "average" conditions;
- * 20 percent due to tidal currents without wave-action;
- * 20 percent due to differences in wave-setup under storm conditions.

This last figure, the 20 percent due to differences in wave-setup under storm conditions, could seem to be of minor importance, but it should be stated that under these circumstances the eroding sand from the dune-front will be transported directly from the coastal zone to elsewhere and does not supply the foreshore. Therefore it will not contribute to the reduction of dune-erosion under these circumstances and will also not be available for the natural restoration processes afterwards.

TRANSPORT PHENOMENA

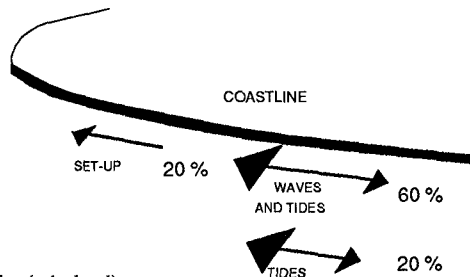


figure 6 : contributions to erosion (calculated).

3.3 next fase of the study.

The first phase of the study was directed to the establishment of the erosion quantities and the phenomena responsible for this erosion. A first order approach appeared so far to be sufficient. This phase has come to an end now.

In the next phase more detailed research will be carried out with respect to those phenomena that appeared to be of vital importance for the development of this coastline. Therefore, a detailed mathematical model shall be made with respect to the tides (currents and elevations) in the whole area. This area includes the tidal-basin, the entire delta's and large parts of the adjacent coastlines (both islands). After tuning this model, different types of solutions to the problem will be brought in. The effect of each of these possibilities to the hydraulics can then be calculated.

From there it will be decided whether further modelling with respect to waves and sandtransport will be necessary. If so, the necessary models shall be build.

3.4 proposed solutions.

One can think of many solutions to this problem. However, it is of utmost importance that the solution chosen, will not have any negative effect elsewhere. Therefore one should be very carefull.

This could lead to the conclusion that for instance a solution with a long, "sand-trapping" dam will not be the answer. In general these harbour-mole like constructions do stimulate sedimentation on one side, but one should be very carefull with the possible

PROPOSED SOLUTION

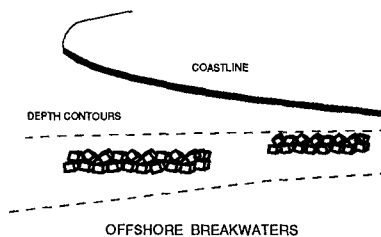


figure 7 : proposed solution

effects due to the erosion on the other side. Especially in a sensitive morphological system like this.

It is more likely that a solution with two or three offshore breakwaters will be much better. Wave-attack on the coastline will be strongly reduced and it must also be possible to influence the tidal current in such a way that its transport capacity in the coastal zone will diminish significantly.

Pleasant features of this solution are the possibility of adaption after construction and the possibility of construction in different phases. So, in its way it is a "flexibel" solution and offers several possibilities of tuning to the morphological system. Along the Channel-coast in the northern part of France such a construction appeared to be very successful.

4. CONCLUSIONS.

- * from now on, the Dutch coast will be kept on its place according to the full-maintenance strategy;
- * the most suitable way to do so, is the placement of beach-nourishments;
- * some places facing extreme erosion and/or very poor reserves a different, seaward strategy can be necessary;
- * according to this strategy, initial measures will be taken to influence the morphological system in such a way, that retreat of the coastline will change into a more or less stable situation or even accretion;
- * one of these places is found on the isle of Texel. A pilot study is carried out;
- * each of the components behind the total erosion process has been established by analysis of measurements and first order approach calculations;
- * 60 percent of the erosion takes place due to average wave and tide conditions, 20 percent due to tides alone and 20 percent due to differences in wave setup under storm conditions;
- * more detailed research will be carried out, to start with a mathematical tidal model for the entire area;
- * the construction of two or three offshore breakwaters looks to be the most promising solution to the problem;
- * in 1991 all finite conclusions and designs will be available.

REFERENCES

RIJKSWATERSTAAT (1989),
Kustverdediging na 1990,
discussienota (in Dutch)

PLUIJM, M. (1989)
Technisch Rapport 20,
Zeevaartse Kustverdediging
(in Dutch)

VAN DER LAAN, A. (1990),
Zeevaartse Kustverdediging Texel,
Thesis Delft University of Technology
(in Dutch).

PART V

Coastal Processes and Sediment Transport



CHAPTER 153

The Effect of a Shore-Parallel Offshore Breakwater on the Beaches at Ocean City, NJ

J. Richard Weggel, F.ASCE (1)

Stewart C. Farrell (2)

Abstract

The design, construction and performance of a shore-parallel nearshore breakwater at Ocean City, NJ (USA) are described. The breakwater, which is connected to a long, high, impermeable groin at 9th Street, was constructed from armor stone removed from the groin when the groin cross-section was lowered. Constructed over a two month period in late 1987 and early 1988, the breakwater caused accretion immediately behind it and erosion along downdrift beaches. A beach fill of 40,000 cu yd of sand was recommended as a part of the original project; however, the beachfill was not placed until the spring of 1990, more than two years after the breakwater/spur was constructed. The project, in the absence of the recommended beach fill, is performing as would be expected. The sand within the groin compartment has been redistributed with a net gain behind the breakwater just downdrift of the 9th Street groin and a loss updrift of the groin at 11th Street.

Introduction

In 1987 the City of Ocean City, New Jersey, commissioned the design of a shore-parallel nearshore breakwater to provide a "sitting beach" in the vicinity of 9th Street in Ocean City. See Figure 1. The design was to be in conformance with an earlier study (Weggel, Douglass & Sorensen, 1988) which recommended that several of the existing rubble-mound groins in Ocean City be lowered so

(1) Professor & Head, Department of Civil & Architectural Engineering Drexel University, Philadelphia, PA 19104, USA.

(2) Director, Coastal Research Center, Stockton State College, Pomona, NJ 08240, USA.

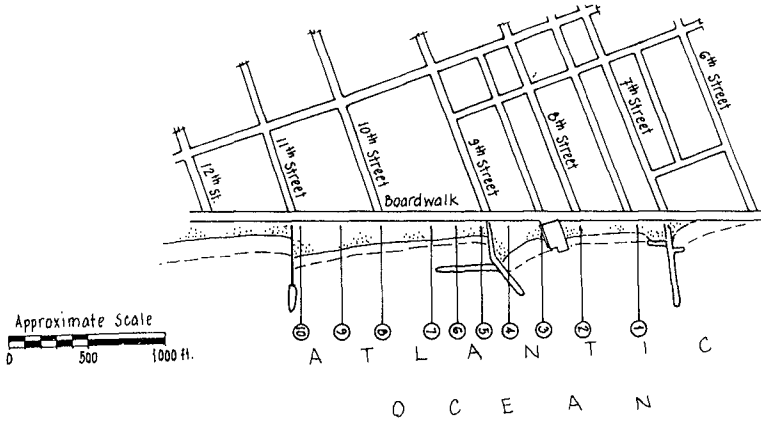


Figure 1 Location Plan, Breakwater/Spur Structure, Ocean City, NJ (USA)

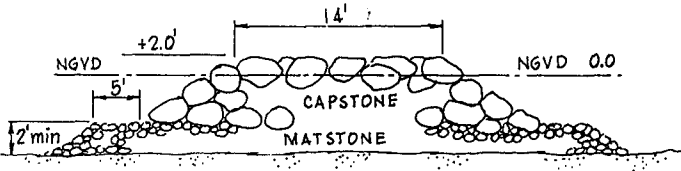


Figure 2 Typical Breakwater/Spur Structure Cross-Section

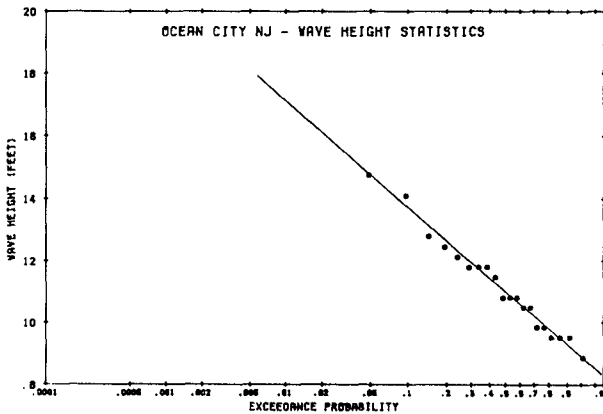


Figure 3 Wave Environment at Ocean City, NJ from WIS Hindcasts (Jensen, 1983)

that sand would be transported over and through them during storms. The resulting breakwater design made use of stone that would become available by lowering the existing groin at 9th Street and by removing a shore-parallel groin stub on the beach face between 9th and 10th Streets. The quantity of stone that would become available by lowering the groin was incorporated into six alternative breakwater designs located in three different water depths with crest elevations of +4 feet (+1.22 m) MLW and +6 feet (1.83 m) MLW. A typical breakwater cross-section is shown in Figure 2. The alternative designs were all connected to the existing 9th Street groin to facilitate construction by land-based equipment. The structure thus formed a shore-parallel groin stub/breakwater rather than a truly detached offshore breakwater. Beach fill was recommended as an integral part of the project. Each alternative was evaluated to estimate its effect on the shoreline.

Design Analyses

The wave environment at Ocean City was determined from the Wave Information Study (WIS) hindcasts of the U.S. Army Corps of Engineers (Jensen, 1983). The 100-year significant wave height at Ocean City is about 17 ft (5.18 m). See Figure 3. Potential net longshore sand transport at the site is generally southward as evidenced by the accumulation of sand along the northerly sides of groins in the area. (About 10 blocks further north the potential net transport is northward because of the proximity of Great Egg Harbor Inlet, the sheltering of the beaches by the inlet's ebb tidal shoal, and a change in shoreline orientation.) Most southward transport takes place during the winter months because of "northeasters" - storms in the North Atlantic that generate winds and waves that approach Ocean City from the northeast. During the summer months, transport is often northward causing some reorientation of the shoreline within groin compartments. Because of the presence of the groins, however, the potential longshore transport is probably never realized. The existing groins are high, long and impermeable and the compartments formed by them are, for the most part, independent cells.

Diffraction analyses for the area behind the breakwater were used to determine if a tombolo would form and the projected shoreline configuration was used to determine how much beach fill was needed. The criterion used to estimate whether a tombolo would form was the location of the $K' = 0.3$ diffraction coefficient line for the range of directions of wave approach at the site. (The breakwater was assumed to be detached with waves propagating around each end and diffraction coefficients were determined

from diffraction diagrams for a semi-infinite breakwater. However, the interaction of the two wave systems coming around each end of the breakwater was not accounted for. Clearly, these assumptions were not met because of the presence of the 9th Street groin at the northerly end of the breakwater.) Incident wave directions at the nearshore site were assumed to range from 15° on either side of a line perpendicular to shore. The breakwater was positioned far enough offshore so that the intersection of the resulting $K' = 0.3$ lines was seaward of the original shoreline location. The post-construction shoreline configuration was estimated from the diffraction analysis. It was judged that the end of the shoreline salient would extend seaward a maximum distance of about 150 ft (45.7 m) from the pre-construction shoreline. The increase in beach area brought about by the breakwater/spur was expected to be about 1,400 sq ft (130 sq m) and, if no sand was to be lost from adjacent beaches, the required volume of fill behind the breakwater was estimated at 40,000 cu yd (30,600 cu m).

The stability of the rubble-mound breakwater/stub was evaluated using the preliminary laboratory test results obtained by Ahrens (1985) for reef-type breakwaters. Ahrens's analysis is for dumped-stone, nearshore breakwaters. He gives the crest height reduction for various levels of wave attack by the equation,

$$\frac{h_c}{h'_c} = \exp(c_0 N_S^* c_1) \quad (1)$$

in which, h_c = the height of the breakwater crest after it has been subjected to wave action, h'_c = the height of the breakwater crest before it has been subjected to wave action, c_0 = a coefficient equal to -0.0000969, and c_1 = a coefficient equal to 3.106. N_S^* = the stability number given by,

$$N_S^* = \frac{\{(H_{mo})^2 L\}^{1/3}}{(W/\tau_r)^{1/3} (\tau_r/\tau_f - 1)} \quad (2)$$

in which, $H_{mo} \approx$ the root-mean-square (rms) wave height at the breakwater, L = the wave length in the water depth at the breakwater, W = the weight of the armor stone, τ_r = the unit weight of the armor stone, and τ_f = the unit weight of the water.

The design significant wave height for the present analysis was 13.6 ft (4.15 m) or an rms height of 9.6 ft (2.9 m). The period was 10 sec. These conditions are

expected to be equalled or exceeded once in 10 years. See Figure 3. The median stone weight available in the existing structure - the material from which the new breakwater was to be built - was about 6 tons (5.45 tonnes). A nearshore breakwater built of 6 ton stone in water 5 feet (1.52 m) deep with a crest elevation of +4 feet (1.22 m) MLW would be reduced in height by no more than 2% by the design wave at the worst stage of the tide (low tide). (Waves at the breakwater were depth limited for many of the design conditions investigated.)

For the above conditions, wave transmission by overtopping can be significant. Ahrens gives the following equation for the wave transmission coefficient.

$$K_T = 1/[1 - (A_T/D_{50}^2)^{0.545} \exp(-6.726 + 3.36 h_c/d_s)] \quad (3)$$

in which, A_T = the area of the breakwater cross-section, d_s = the water depth at the breakwater, and D_{50} = the diameter of the sphere having the same volume as the median stone diameter. For the Ocean City breakwater, $K_T = 0.31$ at low tide. At high tide K_T increases to 0.86. However, some wave transmission by overtopping was deemed necessary to preclude tombolo formation. Based on the design analyses, the alternative selected was a breakwater/spur about 360 feet (109.7 m) long in water about 5 feet (1.52 m) deep, located about 150 feet (45.7 m) seaward of the existing MHW shoreline with a crest elevation 4 feet (1.22 m) above MLW (approximately at MHW). The criteria for selecting this alternative included its ease of construction, the best use of the available stone, the stability of the resulting structure in the selected water depth, and the estimated shoreline location and increased beach area. The estimated volume of beach fill needed for the selected alternative was 40,000 cubic yards (30,600 cubic meters).

Construction

Construction of the breakwater/spur began in October of 1987 and was completed by the end of January 1988. In October and November work was limited to mobilization, site work and lowering the crest elevation of the existing 9th Street groin to obtain stone to construct the breakwater/spur. There was a nine day delay in construction in early December caused by the failure to secure a required permit. Construction of the breakwater/spur itself was completed in December and January. Construction was done using land-based equipment from the tops of the groin and breakwater/spur. The total project cost was \$375,000 of which about \$350,000 was for

breakwater construction including boardwalk removal, lowering the 9th Street groin and breakwater construction. The 9-day construction delay added about \$28,000 to the cost. Beach fill was not placed until spring 1990, more than two years after completion of the breakwater/spur construction. Nourishment sand from the originally proposed source could not be obtained because of pending litigation to determine its ownership. Subsequently, another source was selected. Sand dredged from the navigation channel of Great Egg Harbor Inlet in the fall of 1989 was stockpiled at the north end of Ocean City on the inlet beaches. About 28,000 cu yd (21,400 cu m) of this sand was later trucked to the 9th Street beach and stockpiled north of the groin. In the spring of 1990 some of this sand was moved to the area behind the breakwater/spur. Only about 10,000 cu yd (7,600 cu m) could be placed behind the breakwater because of losses from the stockpile during the preceding winter. Based on a volume of 28,000 cu yd, the cost of obtaining sand for the project was \$7.26/cu yd. About \$2.68 of this cost is associated with trucking the sand from Ocean City's inlet shoreline to the 9th Street area. The rest of the cost (\$4.58/cu yd) is the difference in cost between pumping the sand to Ocean City's inlet beaches and using a hopper dredge with offshore disposal.

Beach Response

The response of beaches in the vicinity of the breakwater/spur was monitored for about 1 1/2 years. Ten profile lines were established; the most northerly profile extends seaward just south of a rubble-mound groin at 7th Street; the most southerly profile extends seaward just north of the groin at 11th Street. See Figure 1. There is also a short timber groin just south of the Music Pier located between 8th and 9th Streets. Thus beaches in the project area are affected by several groins as well as by the breakwater/spur. The lowered portion of the 9th Street groin serves as a control on the amount of sand that enters the compartment between 9th Street and 11th Street. Sand is transported over the groin only during storms and there were only one or two storms during the 1 1/2 year monitoring period during which sand transport over the groin was reported. The compartment between 9th Street and 11th Street is thus practically a closed system, at least for the period of the present analysis. A "pre-construction" survey of the profiles was obtained in November 1987. The first post-construction survey was obtained in January 1988 shortly after construction was completed. Subsequent surveys were obtained monthly during 1988 (except for October) and in January, March and May of 1989. Changes at selected profile lines occurring between November 1987

and January 1988 and February 1988 are shown in Figures 4 through 7. Significant accretion occurred behind the breakwater/spur between November 1987 and February 1988 (Figures 4 & 5). There was little change north of the project while erosion occurred south of the project (Figures 6 & 7). Erosion was greatest adjacent to the 11th Street groin (Profile 10) during this period while intermediate profiles (Profiles 8 and 9) show less erosion. While some erosion at these profiles can be attributed to the normal seasonal profile changes, it appears that the initial accretion behind the breakwater/spur has been at the expense of beaches to the south. A scour hole developed at the southern terminus of the breakwater/spur. The scour hole is shown at Profile 7 in Figure 6. Between March 1988 and August 1988 the profiles north of the site showed some accretion - possibly the normal summer profile recovery after the preceding winter. The profiles through the breakwater showed little change because of sheltering by the breakwater. Following the initial period of accretion, the beach behind the breakwater exhibited little seasonal variation. The scour hole at the terminus of the breakwater filled between March and August 1988 and the profiles south of the project showed accretion - again probably due to the normal summer recovery.

Those beach profiles between the 9th Street and 11th Street groins (Profiles 5 through 10) were subject to detailed analysis to determine how the location of the MSL shoreline and the volume of sand associated with each profile varied with time. (Refer to Figure 1 for the location of the profiles. Also note that the present analysis is for the time period preceding placement of the beach fill in the spring of 1990.) Figures 8 through 11 show the location of the MSL shoreline as a function of time at Profiles 5, 6, 7 and 10, respectively. Profiles 5 and 6 are behind the breakwater; Profile 7 is just south of the southern end of the breakwater and Profile 10 is just north of the 11th Street groin - the most southerly profile within the 9th Street to 11th Street groin compartment. The shoreline at Profile 5 (Figure 8) built out to the breakwater in less than 100 days following the start of breakwater construction. It subsequently receded for a short time but then built out to the breakwater again. The shoreline at Profile 6 (Figure 9) shows similar behavior although it took longer for the shoreline to build. The shoreline at Profile 7 (Figure 10) built out and then receded to about its pre-construction location. Profile 10 (Figure 11) shows significant initial erosion with subsequent recovery and then erosion again. Since this profile is adjacent to the 11th Street groin it shows seasonal accretion and erosion in response to seasonal changes in the direction

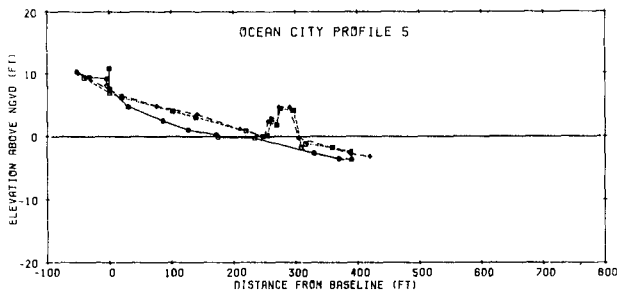


Figure 4 Profile 5 Behind Breakwater/Spur Structure (Solid line = 19 Nov 1987, Long dashes = 22 Jan 1988, Short dashes = 19 Feb 1988)

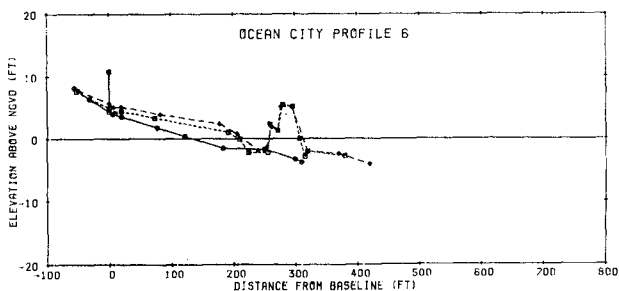


Figure 5 Profile 6 Behind Breakwater/Spur Structure (Solid line = 19 Nov 1987, Long dashes = 22 Jan 1988, Short dashes = 19 Feb 1988)

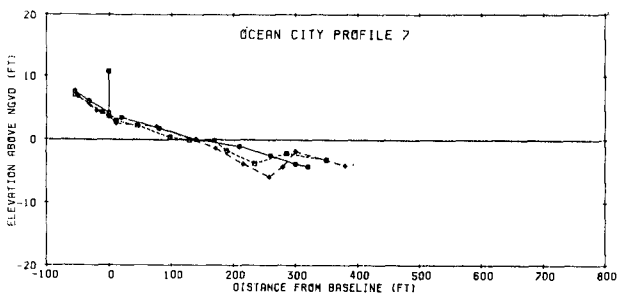


Figure 6 Profile 7, Just South of Breakwater/Spur Structure (Solid line = 19 Nov 1987, Long dashes = 22 Jan 1988, Short dashes = 19 Feb 1988)

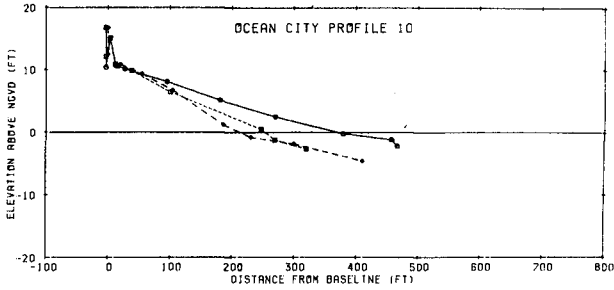


Figure 7 Profile 10 Near 11th Street Groin (Solid line = 19 Nov 1987, Long dashes = 22 Jan 1988, Short dashes = 19 Feb 1988).

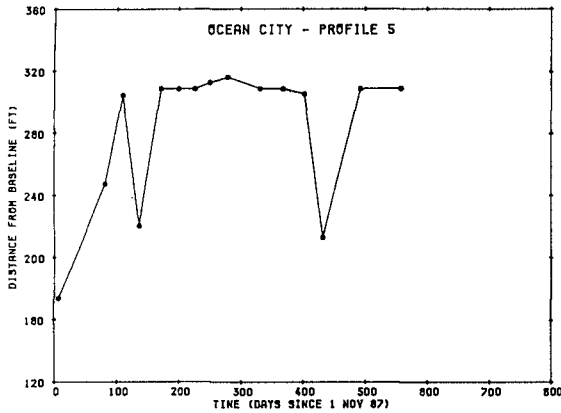


Figure 8 MSL Shoreline Movement at Profile 5

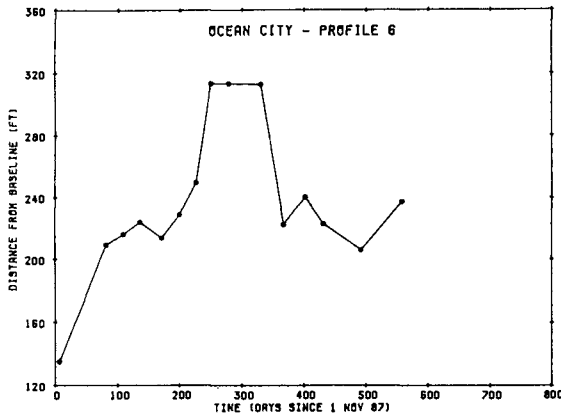


Figure 9 MSL Shoreline Movement at Profile 6

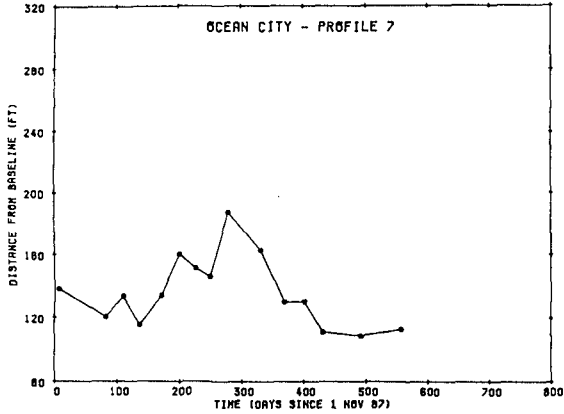


Figure 10 MSL Shoreline Movement at Profile 7

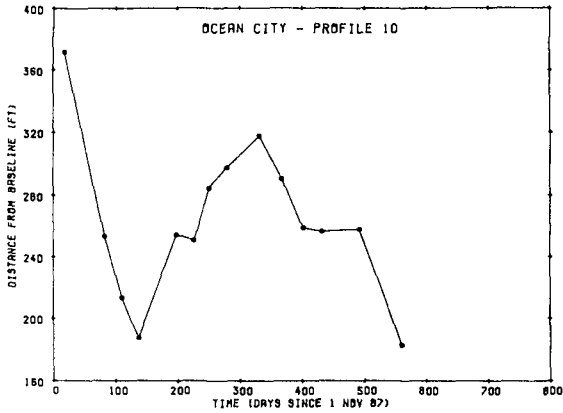


Figure 11 MSL Shoreline Movement at Profile 10

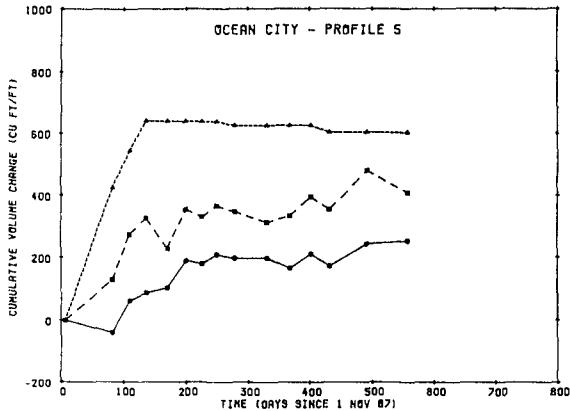


Figure 12 Volume Changes Below Given Contour at Profil 5 (Solid line = MSL, Long dashes = +2 ft Short dashes = +4 ft)

of wave approach. Similar behavior, although less pronounced, was observed at Profiles 8 and 9.

Figures 12 through 15 for profiles 5, 6, 7 and 10 show the cumulative change in volume below the given contour line. The solid lines with circles represents changes occurring below the +4 ft NGVD (National Geodetic Vertical Datum, or mean sea level of 1929) contour line. The long dashes with squares give changes occurring below the +2 ft contour line and the short dashes with triangles are the 0 ft contour (MSL). A positive slope represents accretion while a negative slope represents erosion. A horizontal line indicates no change in the volume of sand below the given contour. Figure 12 indicates that after the initial accretion behind the breakwater at Profile 5 little seasonal change in the volume of sand on the beach occurred. Profile 6 (Figure 13) shows a similar, but more dramatic, initial accretion with little subsequent change. Profile 7 (Figure 14) shows a small seasonal fluctuation with the profiles returning to approximately their initial condition. Profile 10 (Figure 15), however, shows rapid initial loss of sand with a subsequent reduction in the rate of loss followed by another rapid loss. Similar, but less dramatic, losses were recorded at Profiles 8 and 9.

The volume changes at Profile 5 through 10 suggest that the sand accumulation behind the breakwater is at the expense of the beaches to the south. Figure 16 is a sediment budget analysis for the beach cell between the 9th Street and 11th Street groins for the period between 7 November 1987 and 18 February 1988. Figure 16 is a mass curve showing the accretion (positive slope) and erosion (negative slope) as one moves southward along the beach from 9th Street to 11th Street. The figure shows the accretion behind the breakwater between about 0 and 300 ft (91.4 m) along the beach and the erosion along beaches farther to the south. Most of the lines on the curve return to a zero cumulative volume change at 11th Street (1,200 ft or 366 m along the beach) indicating that the volume of sand in the cell was conserved for the period of the analysis. Figure 17 summarizes the sediment budget analysis for the 7 November 1987 to 18 February 1988 time period and shows the location of accretion and erosion areas. The numbers on the figure represent the volume of sand accumulated between the given contour intervals and along the various profiles. (The vertical lines on the figure are at the midpoint between two adjacent profile lines, i.e., the first vertical line parallel with the 9th Street groin is midway between Profiles 5 and 6.)

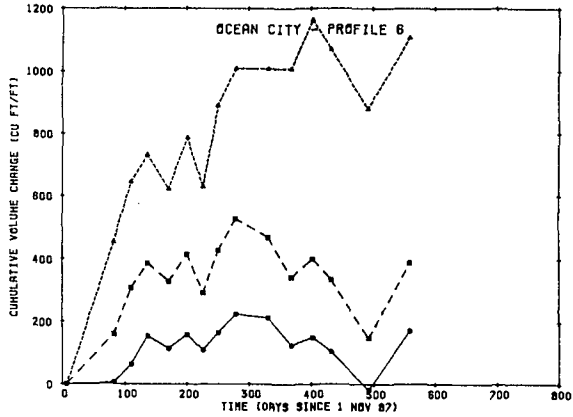


Figure 13 Volume Changes Below Given Contour at Profile 6

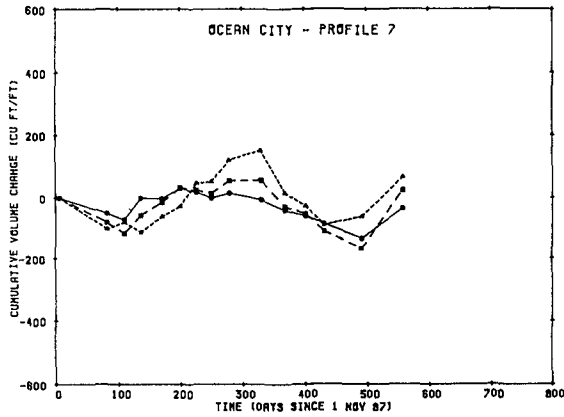


Figure 14 Volume Changes Below Given Contour at Profile 7

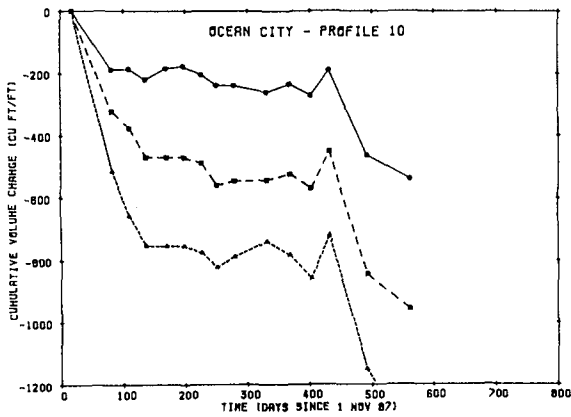


Figure 15 Volume Changes Below Given Contour at Profile 10

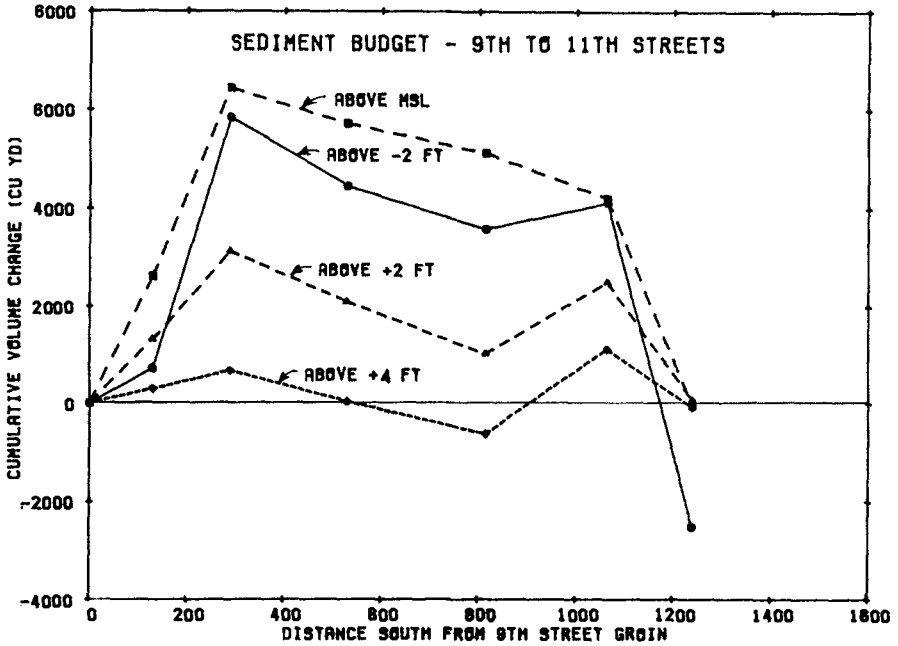


Figure 16 Cumulative Sand Volume Change Along Between 9th Street and 11th Street.

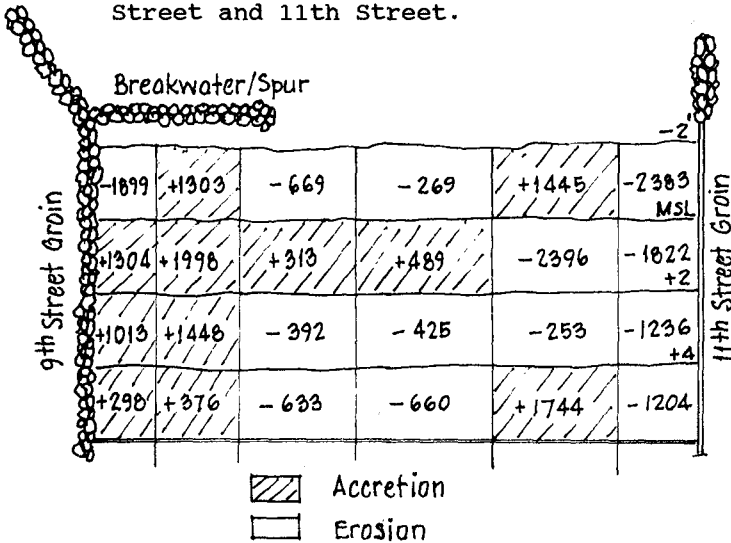


Figure 17 Summary of Sediment Budget Analysis for Area Between 9th Street and 11th Street Groins Showing Spatial Distribution of Accretion and Erosion Areas (Shaded Areas Indicate Accretion, Numbers in Blocks Indicate Volume of Sand Lost [-] or Gained [+])

Conclusions

The breakwater/spur at 9th Street in Ocean City has functioned as expected in the absence of the 40,000 cu yd of beach fill recommended in the original project design. Sand which has accumulated behind the breakwater has been at the expense of beaches farther to the south within the same groin cell. During the period of observation, the beach cell formed by the two long, high, impermeable groins at 9th Street and 11th Street functioned as a closed system. Little sand appears to have entered from the north and little appears to have been lost to the south. The net sand gain or loss in the cell was zero; thus, accretion observed behind the breakwater/spur was balanced by erosion along beaches farther south near 11th Street. Seasonal fluctuations in beach width and volume changes are smaller for the beach behind the breakwater than for adjacent unprotected beaches exposed to direct wave action.

Appendix - References

AHRENS, J. (1985) "Reef Breakwater Characteristics," Draft CERC Technical Report, U.S. Army Coastal Engineering Research Center, WES, Vicksburg, MS, June 1985.

JENSEN, R.E. (1983) "Atlantic Coast Hindcast, Shallow-Water Significant Wave Information," WIS Report 9, U.S. Army Waterways Experiment Station, Vicksburg, MS 39180.

WEGGEL, J.R., S.L. DOUGLASS & R.M. SORENSEN (1988) "An Engineering Study of Ocean City's Beaches, New Jersey, U.S.A.," Proceedings, 21st International Conference on Coastal Engineering, Toromolinos, Spain, 20-25 June 1988.

CHAPTER 154

SHORELINE RESPONSE TO A SINGLE TRANSMISSIVE DETACHED BREAKWATER

Hans Hanson¹ and Nicholas C. Kraus², M.ASCE

ABSTRACT

Criteria are presented for predicting the long-term shoreline response to a single detached breakwater. The criteria, expressed as two algebraic equations, distinguish tombolo formation, salient formation, and limited shoreline response, and were developed by calculation-intensive application of the shoreline change numerical model GENESIS for a large number of wave conditions and structure configurations. A unique feature of the modeling effort is explicit incorporation of wave transmission at the structure. The two other major non-dimensional parameters in the criteria are the length of the structure divided by the average wavelength at the structure and the average deep-water significant wave height divided by the depth at the structure. Prediction of the generalized criteria agree with available field data.

INTRODUCTION

The response of the shoreline and beach to detached breakwaters is difficult to predict. For example, Seiji, Uda, and Tanaka (1987) in a survey of 1552 breakwaters constructed in Japan found that 60 percent produced accretionary developments and 35 percent did not. A frequency diagram for the data set shows shoreline advance ranging from zero to 140 m. Although some empirical guidance is available to design the basic configuration of detached breakwaters, the criteria are crude and based on a few, typically two to four, out of as many as 14 governing variables. A major variable missing in previous work is wave transmission through the breakwater. The objective of the present study is to perform a generalized calibration of the shoreline change numerical model GENESIS against observed field response to a single shore-

(1) Assoc. Prof., Dept. of Water Resources Engrg., Lund Institute of Technol., University of Lund, Box 118, Lund, Sweden S-221 00.

(2) Sr. Res. Sci., Coastal Engrg, Res. Center, U.S. Army Engr. Waterways Experiment Station, 3909 Halls Ferry Road, Vicksburg, MS 39180-6199.

parallel and transmissive detached breakwater for a wide range of structure configurations and wave characteristics.

PROCEDURE

Governing Parameters

By inspection, at least 14 parameters can be identified which control the response of a sandy beach to a single or multiple detached breakwater system (Fig. 1):

$$\text{Beach Resp.} = F[(X, Y, K_T, G), (D, \Delta D, S), (H, T, \theta, \theta_S, \sigma_H, \sigma_\theta, \sigma_T)]$$

or (1)

$$\text{Beach Resp.} = F[(\text{breakwater properties}), (\text{beach properties}), (\text{wave properties})]$$

where X = length of structure segment; Y = distance of segment from original shoreline; K_T = structure segment transmissivity; G = gap distance between segments; D = depth at structure segment; ΔD = variation in depth at the structure, as from the tide; S = sediment availability; H = wave height; T = wave period; θ = predominant wave angle to trend of coast; θ_S = orientation of structure to trend of coast; σ_H = standard deviation (SD) of wave height; σ_θ = SD of wave angle; and σ_T = SD of wave period. In a practical situation, the engineer has control over the first group of parameters only.

In GENESIS, the equilibrium beach profile shape is calculated as $D = A(d_{50}) Y^{2/3}$, where A is an empirical scaling parameter depending on the beach median grain size d_{50} . Once the beach grain size is

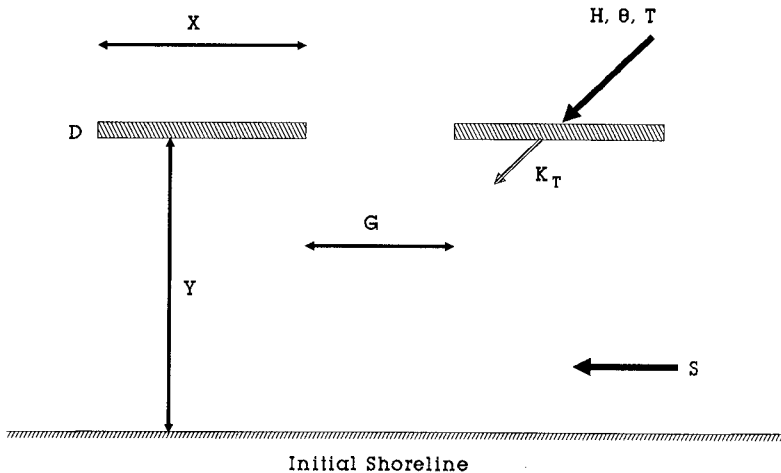


Figure 1. Segmented detached breakwater parameters

specified, D is a function of Y and is not an independent variable. The functioning of all 14 parameters governing long-term shoreline change can be represented in GENESIS.

Numerical Model

GENESIS is a numerical modeling system which calculates wave transformation (refraction, shoaling, diffraction from multiple coastal structures, transmission, and breaking), longshore sand transport rate, and associated shoreline change (Hanson 1989, Hanson and Kraus 1989, 1991). The system is generalized in that it allows representation of a wide variety of user-specified offshore wave inputs, initial beach configuration, boundary conditions, coastal structures (groins, jetties, seawalls, and detached breakwaters), and beach fills.

Several numerical and physical model studies have investigated the response of the shoreline to detached breakwaters. However, these studies did not include wave transmission, referring to wave energy passing through and over a structure, which is present in most projects. This capability is included in Version 2.0 of GENESIS (Hanson and Kraus 1989) and has been tested with excellent results for Holly Beach, Louisiana, with six breakwaters of different construction and transmission (Hanson, Kraus, and Nakashima 1989), as well as for Lorain, Ohio, with three detached breakwaters (Hanson and Kraus 1991).

SENSITIVITY TO GOVERNING PARAMETERS

Prior to the generalized calibration of the modeling system, an investigation of the sensitivity of the shoreline response to variations in the main governing parameters was performed. In all the following simulations, the median sand grain size is 0.2 mm. The empirical predictive formula for the longshore sand transport rate used in GENESIS is:

$$Q = (H^2 C_g)_b (a_1 \sin 2\theta_{bs} - a_2 \cos \theta_{bs} \frac{\partial H}{\partial x})_b \quad (2)$$

in which C_g = wave group speed, b = subscript denoting wave breaking condition, θ_{bs} = angle of breaking waves to the local shoreline. The nondimensional parameters a_1 and a_2 are given by

$$a_1 = \frac{K_1}{16(S - 1)(1 - p)W} \quad (3)$$

and

$$a_2 = \frac{K_2}{8(S - 1)(1 - p)W \tan \beta}$$

in which K_1 and K_2 = empirical coefficients, treated as a calibration parameters, $S = \rho_s/\rho$, ρ_s = density of sand ($2.65 \cdot 10^3 \text{ kg/m}^3$), ρ = density of water ($1.03 \cdot 10^3 \text{ kg/m}^3$), p = porosity of sand (0.4), $\tan \beta$ = average

nearshore bottom slope), W = a numerical factor ($1.416^{5/2}$) used to convert from significant wave height to root-mean-square height.

Effect of variation in wave input mean values

An illustration of the effect of changing wave height is given in Fig. 2. The wave climate was held constant during the simulations with a period of 4 sec and a total simulation time of 100 hrs. The breakwater was 300 m long and placed 300 m offshore in 3 m depth. As expected, shoreline advances with increase in wave height. The maximum shoreline progression varies approximately linearly with wave height, whereas accumulated volume for the greater wave height is an order of magnitude bigger than that for the smaller wave height. This is in part explained by the difference in breaking wave height, but also because the bigger waves are less refracted before breaking, they will break under a bigger angle to the shoreline.

An example of the variation in shoreline response behind a detached breakwater due to changing wave period is given in Fig. 3. The wave climate was otherwise held constant during the simulations with a wave height of 1 m, normally incident wave crests, and a total simulation time of 100 hr. The breakwater configuration was the same as in the previous figure.

Increasing wave period results in greater salient growth behind the structure. The explanation for this is illustrated in Fig. 4, displaying the associated wave height distributions behind the detached breakwater for the three simulations in Fig. 3. The wave height distributions associated with waves entering on either side of the breakwater are shown separately. Longer waves results in a higher

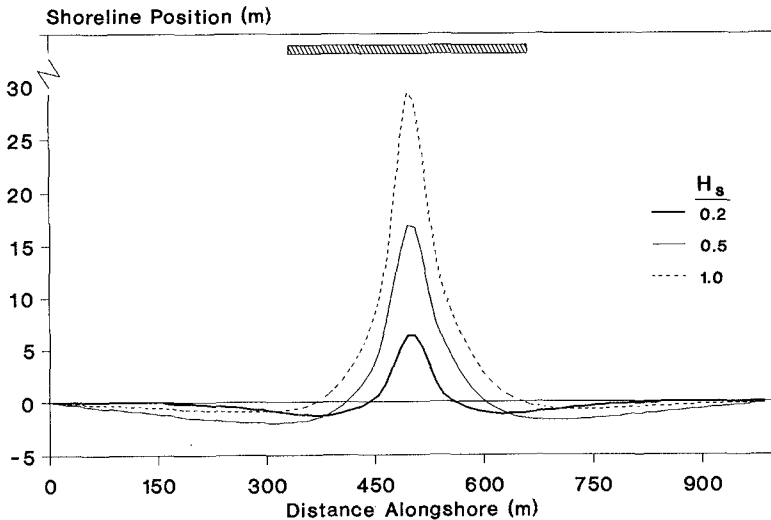


Fig. 2. Influence of varying wave height on shoreline change behind a detached breakwater

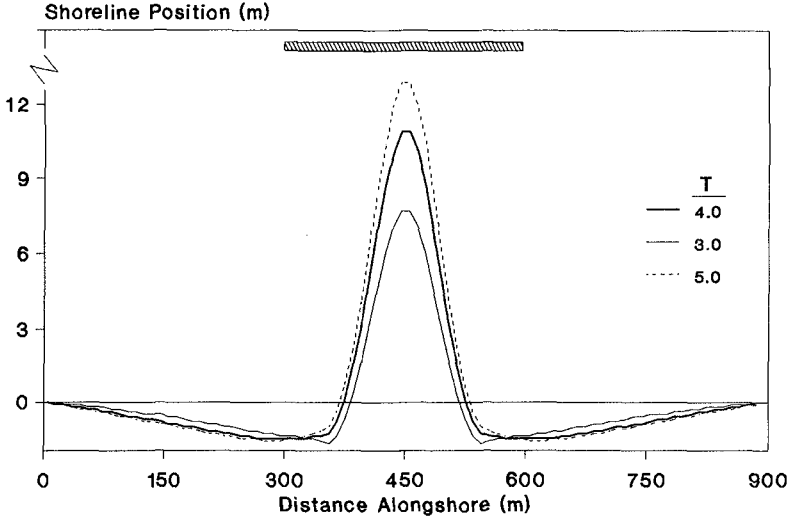


Fig. 3. Influence of varying wave period on shoreline change behind a detached breakwater

shoaling coefficient, causing these waves to break further offshore, resulting in a greater breaking wave height, the offshore wave height being the same.

This means, for the longer waves, that the first term in Eq. 1 (K_1 - term), with a larger H -value, will transport more sand into the area behind the breakwater. Also, the wave height for longer period waves decreases more steeply alongshore behind the structure. This means that the second term in the transport Eq. 1, (K_2 - term), with a higher $\partial H/\partial x$ -value, will also transport more sand into the area behind the breakwater for the longer waves.

Effect of wave variability

In use of the model in a predictive mode, the factors responsible for beach change are not known in detail. The time series of wave height, period, and direction forecast for use in the shoreline change prediction and can be considered as only one of many possible wave climates that might occur. For shoreline response prediction, it is necessary to incorporate wave variability to calculate a probable range of expected shoreline change. The standard deviation is conveniently used as a realistic measure of wave variability and determines the likelihood and magnitude of extreme events (Kraus, Hanson, and Harikai 1984).

Fig. 5 illustrates an example showing accretion behind a 200-m long detached breakwater located in 2 m depth 200 m from the initial straight shoreline. The mean values in deep water characterizing the wave climate are: $T = 4$ sec, $H_s = 1$ m, and $\theta = 0$ deg. The thin solid

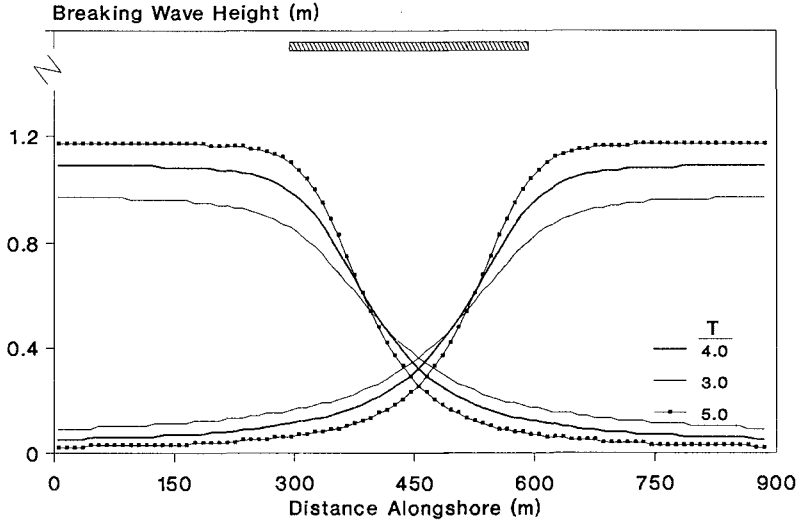


Fig. 4. Influence of varying wave period on wave height distribution behind a detached breakwater

line represents a wave climate with T , H , and θ held constant at their mean values. In the other three simulations, two of the three parameters were held constant while the third was normally distributed with its standard deviation given in the figure as a percentage of the respective mean value.

As seen from the figure, allowing T and H to vary has very little effect on the shoreline response. In contrast, increased variability in the wave direction dramatically increases accumulation behind the structure. The major reason for this is that variation in T and H around their respective mean values merely redistributes the incoming wave energy in time but does not significantly change the total longshore wave energy flux. A deviation in wave direction from normal in any direction, however, increases the longshore component of wave energy flux, which in turn causes more sand to move alongshore. Because of shadowing from the structure, more sand will be transported into than out of the shadow region behind the structure, accounting for the large growth of the salient.

Breakwater Transmissivity

In most cases, detached breakwaters designed for shore protection allow some portion of the incident wave energy to pass through or over the structure because it is economical and often advantageous from the perspective of beach change control to build low or porous structures to allow wave energy to penetrate behind them. Wave transmissivity is difficult to quantify. In order to describe wave transmission in GENESIS, a value of a transmission coefficient K_T must be provided for each detached breakwater (Hanson and Kraus 1989). The transmis-

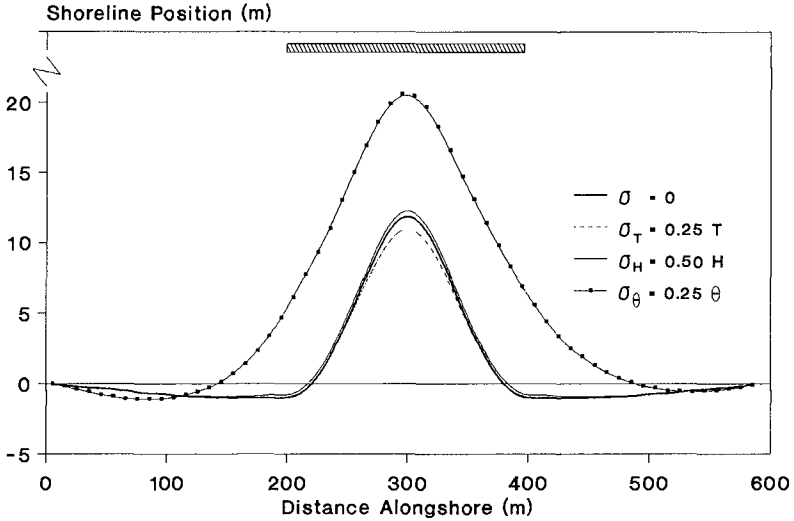


Fig. 5. Influence of wave variability on shoreline change behind a detached breakwater

sion coefficient, defined as the ratio of the height of the incident waves directly shoreward of the breakwater to the height directly seaward of the breakwater, has the range $0 \leq K_T \leq 1$, for which a value of 0 implies no transmission and 1 implies complete transmission.

To investigate the sensitivity of the calculated shoreline response to variations in wave transmission, a series of simulations was made to investigate predicted sand accumulation in the lee of a shore-parallel breakwater, as illustrated in Fig. 6. The breakwater is 200 m long and located 250 m offshore. Incident waves with $T = 6$ sec and $H_s = 1.5$ m propagate with wave crests parallel to the initially straight shoreline. The simulation time was 180 hr.

As expected, the seaward extent of the induced large salient decreases as wave transmission increases, showing that shoreline response is sensitive to breakwater transmissivity. For example, a 20 percent transmissivity reduces the maximum shoreline advance by 36 percent and the accumulated volume by 25 percent. Because of the difficulty of determining the transmissivity for real structures, the value of the parameter is, at present, determined in the shoreline change calibration procedure.

The capability to simulate wave transmission at detached breakwaters and its impact on shoreline change was first tested with excellent results for Holly Beach, Louisiana, a site containing six breakwaters of different construction and transmission characteristics (Hanson, Kraus, and Nakashima 1989). This application also showed that it would

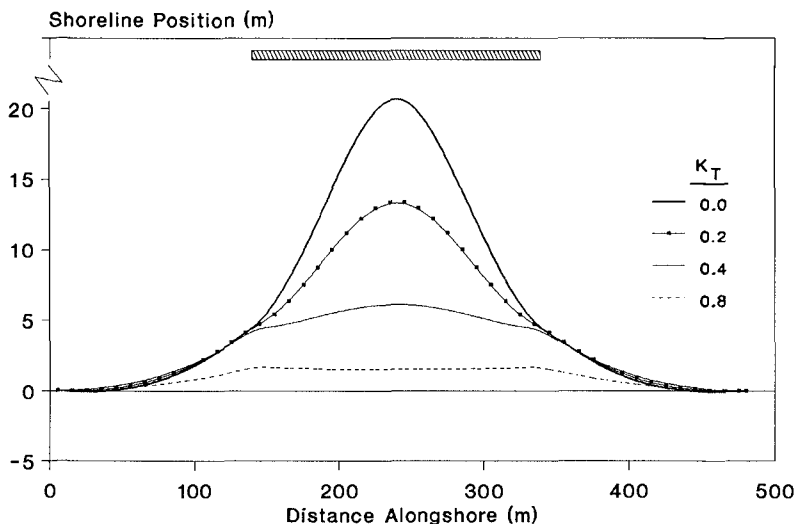


Fig. 6. Shoreline change as a function of transmission (from Hanson et al. 1989)

not be possible to obtain good agreement between field measurements and model predictions if wave transmission were not taken into account.

RESULTS

With an understanding of model capabilities established in the preceding text, we now turn to the problem of developing design curves to predict shoreline response to single, transmissive detached breakwaters. There are two general problems to be addressed. The first is to determine appropriate parameters for distinguishing tombolo development, salient development, or no effective shoreline change (limited or transitory response). The second problem is to develop design curves relating shoreline response to these governing parameters. Here, we present design curves for shoreline response to a single detached breakwater, based on three nondimensional parameters.

Based on field observations and simulation results, shoreline response was classified into three categories as illustrated in Fig. 7:

- * Limited response - maximum accumulation is less than 4 m.
- * Salient development - maximum accumulation is greater than 4 m, but the salient does not reach the breakwater.
- * Tombolo development - salient reaches (touches) the breakwater.

The wave height distribution behind a structure produced by diffraction to a large extent depends on the wavelength L , where the energy of longer waves penetrates further into the shadow region behind the structure. Also, the length of the structure X controls the amount of wave energy reaching the beach. It is therefore likely that

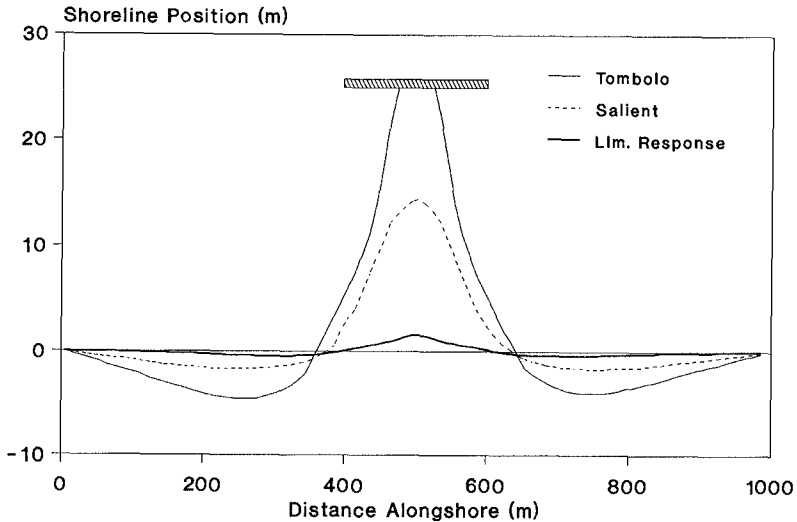


Fig. 7. Possible shoreline response to detached breakwaters

the shoreline response behind a detached breakwater is a function of the ratio X/L . Waves breaking seaward of a detached breakwater have a greater tendency to develop salients and tombolos than waves breaking on the landward side since there is a greater width of longshore transport. The location of the breakwater relative to the breaker line is conveniently expressed through the ratio H_o/D , where H_o and D are the significant deep-water wave height and the water depth at the location of the breakwater. Thus, these two dimensionless parameters were taken as primary variables for examining prototype data and developing design curves. Other parameters were tested and rejected in favor of X/L and H_o/D , based on their performance in distinguishing shoreline response.

Field Data

Most empirical and modeling analyses of shoreline response to detached breakwaters have relied heavily on physical model results, including combined segmented as well as single detached breakwater cases. There are only a few well-documented field examples in the literature for single detached breakwaters, and Table 1 presents conditions at all such sites known to the authors. The values for the transmission coefficient K_T were subjectively estimated on the basis of descriptive classifications ("poor condition," "high and impermeable," etc.) in the project reports.

In the present study, the numerical shoreline change model GENESIS was used to determine the equilibrium shoreline response behind a single shore-parallel detached breakwater. As mentioned previously, the persistence of shoreline response is closely related to the variability in incident wave height, period, and direction. More realistic

Table 1

Project site	Struct. length X	Wave height H_o	Water depth D	Wave-length L	Estim. trans- mission K_T	Observed beach resp.
Nahariyya	180	1.0	3.2	29	0.2	Sal.
Carmel	280	1.0	3.0	29	0.2	Sal.
Tel Baruk	200	1.0	3.0	29	0.2	Sal.
Venice, New	183	1.0	1.8	48	0.1	Tom.
Redington	100	0.8	2.4	20	0.4	Sal.
Santa Monica	610	1.2	7.6	91	0.5	Lim.

simulations of shoreline change are expected by including variability in wave parameters. Seven "standard" yearly wave climates were developed including different means and standard deviations of the wave climate for the simulations, based on review of conditions related to the data in Table 1.

For each of the wave climates a Monte-Carlo simulation technique was applied to input the wave data, with random wave heights generated from a Rayleigh distribution and wave angles and periods specified from normal distributions, resulting in a 1-year wave data set discretized at 12-hr intervals. In these simulations, the mean wave period $T = 2.5, 7,$ and 12 sec with a standard deviation of $T/4$; the significant wave height $H = 0.2, 0.5,$ and 1.0 m; and the mean wave direction was normal to the straight, initial shoreline with a standard deviation of 5 deg. The chosen values encompass conditions along U.S. Atlantic Ocean and Great Lakes beaches. The length of the structure X was varied between 40 and 100 m, with the distance from the initial shoreline Y varying from 16 to 300 m, and with a transmission coefficient of $0.00, 0.20, 0.50,$ and $0.75,$ respectively. The beach median grain size was 0.2 mm in all simulations.

Fig. 8 shows the results of simulations for a single detached breakwater oriented parallel to an initially straight shoreline, for different X/L and H_o/D values. This figure is the main result of this study. Each of the 166 combinations of wave and structure configuration and transmissivity parameter values was run for two years or until a tombolo formed. The different symbols indicate the response type. Situations with short structures in shallow water exposed to high, long-period waves are more likely to produce salients, whereas long structures in deep water exposed to small, short-period waves more often results in a limited shoreline response.

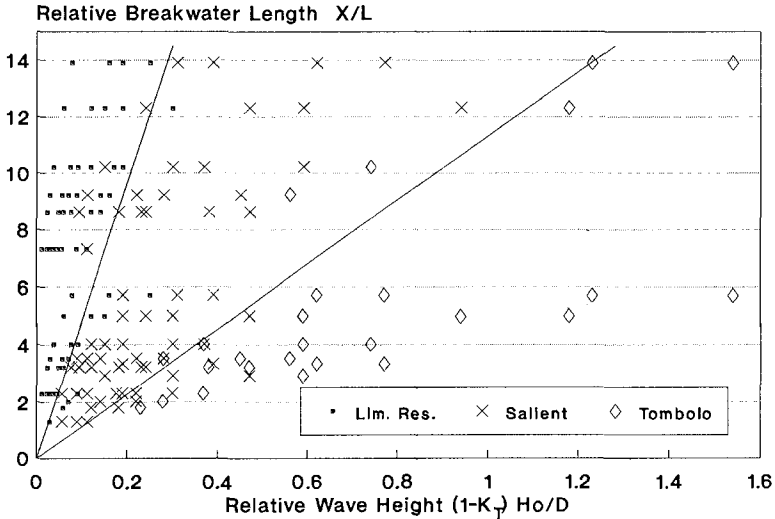


Fig. 8. Calculated shoreline response to a single detached breakwater

Straight lines were drawn to separate the different response types as a function of wave transmissivity. It was found that as breakwater transmissivity increases, shoreline response decreases. Based on these results, the criterion for a salient to form was found to be:

$$\frac{X}{L} \leq 48 (1 - K_T) \frac{H_o}{D} \quad (4)$$

which separates regions of limited shoreline response and clear salient development. Similarly, the criteria for a tombolo to form was found to be:

$$\frac{X}{L} \leq 11 (1 - K_T) \frac{H_o}{D} \quad (5)$$

which separates regions of salient and tombolo formation.

As evidence for the validity of the proposed relationships, the prototype measurements as presented in Table 1 are plotted in Fig. 9. The prototype measurements fit well within the domains of the proposed criteria and provide at least limited validation of the calculated results.

CONCLUSIONS

This paper described a generalized calibration against field measurements of the numerical model GENESIS for simulating shoreline response to detached breakwaters. Three dimensionless parameters, the length of the structure relative to the local wavelength, the deep-water wave

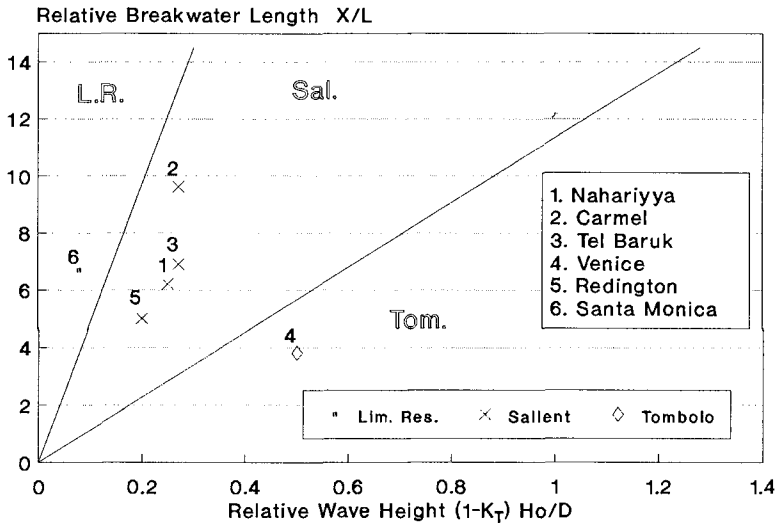


Figure 9. Field measurements and proposed criteria

height relative to the water depth at the structure, and wave transmission through the structure were taken as primary variables in study.

Field measurements and model simulations showed a systematic trend in shoreline response as a function of the three dimensionless variables. In summary, the results indicate that:

- * Holding all other variables constant, as the wavelength (period) increases, shoreline response goes from limited, to salient, to tombolo, because more sand is transported into the shadow zone.
- * Holding all other variables constant, as the length of the structure increases, shoreline response goes from tombolo, to salient, to limited response, because the amount of sand transported into the area behind the structure is distributed over a longer portion of beach.
- * Holding all other variables constant, as the wave height increases, shoreline response goes from limited, to salient, to tombolo, because more sand is transported into the shadow zone.
- * Holding all other variables constant, as the depth at the structure increases, shoreline response goes from tombolo, to salient, to limited response, because a smaller portion of the area behind the structure is located inside the surf zone.
- * Holding all other variables constant, as wave transmissivity increases, shoreline response goes from tombolo, to salient, to limited response because of direct incidence of the transmitted waves, which suppresses protruding features.

* The independent parameters selected (X/L , H_o/D , and K_T) provide effective but preliminary design criteria for distinguishing shoreline response to a single, transmissive detached breakwater.

Although the criteria presented here are based on a most advanced and thorough numerical model study, the results are not intended to replace the judgement of an experienced engineer familiar with a project coast.

ACKNOWLEDGEMENTS

The work carried out by HH was funded through the U.S. Army Research, Development and Standardization Group, UK, under contract DAJA-88-C0015. This support is gratefully acknowledged. The contribution of NCK was supported by the Shoreline and Beach Topography Response Modeling work unit, Shore Protection and Restoration Program, U.S. Army Corps of Engineers. Permission was granted by the Office, Chief of Engineers, to publish this information. We thank Ms. Julie Dean Rosati, Coastal Engineering Research Center, for assistance in obtaining field data, and Dr. Magnus Larson, University of Lund, for helpful discussions.

REFERENCES

- Hanson, H. 1989. GENESIS - A generalized shoreline change numerical model. J. of Coastal Research, Vol. 5(1), 1-27.
- Hanson, H. and Kraus, N. C. 1989. GENESIS: Generalized model for simulating shoreline change. Report 1: Technical Reference, Tech. Rep. CERC-89-19, US Army Engr. Waterways Exp. Station, Coastal Engrg. Research Center, Vicksburg, MS.
- Hanson, H. and Kraus, N. C. 1991. Numerical simulation of shoreline change at Lorain, Ohio. J. of Waterways, Port, Coastal and Ocean Engrg. (in press).
- Hanson, H., Kraus, N. C., and Nakashima, L. D. 1989. Shoreline change behind transmissive detached breakwaters. Proc. Coastal Zone '89, ASCE, 568-582.
- Kraus, N. C., Hanson, H., and Harikai, S. 1984. Shoreline Change at Oarai Beach - Past Present and Future, Proc. 19th Coastal Engrg. Conf., ASCE, 2107-2123.
- Seiji, M., Uda, T., and Tanaka, S. 1987. Statistical study on the effect and stability of detached breakwaters. Coastal Engrg. in Japan, Vol. 30(1), 131-141.

CHAPTER 155

Flow-Fine Sediment Hysteresis in Sediment-Stratified Coastal Waters

Rui G. Costa¹ and Ashish J. Mehta²

Abstract

Hysteresis in the relationship between suspended sediment concentration and the flow velocity is shown to be influenced by sediment-induced flow stratification in high energy coastal environment. A 1-D numerical approach combined with field observation from Hangzhou Bay, China is used to highlight the effects of concentration dependent settling velocity, buoyancy stabilized mass diffusion and bottom sediment fluxes on hysteresis. Typical formulations for the bottom fluxes are believed to have limited utility in high concentration environments.

Introduction

Estuaries and coastal bays have traditionally offered multiple advantages for the development of urban and industrial centers. The rapid development of many of those centers has led to competing demands and technical and ecological problems. Some of the important problems are directly related to sediment dynamics and make the study of the physical mechanisms contributing to sediment transport of fundamental importance in predicting any effects of anthropogenic activities.

The nature and significance of estuarine and coastal sediment transport processes has been investigated by several researchers. Although several procedures have been applied to a variety of estuaries having different geometries and stratification conditions, two transport mechanisms, vertical shear and tidal pumping, have been generally found to be dominant (Dyer, 1989 and Uncles et al., 1984). Transport by vertical shear results from residual gravitational circulation due to salt water penetration. Tidal pumping results from phase differences between cross-sectional area variations and variations of average cross-sectional velocities and concentrations of salt or sediment.

Both transport mechanisms depend on the vertical concentration profiles and, consequently, on the magnitudes of the vertical mass transport fluxes. Such fluxes can be significantly modified if stratified conditions exist in the

¹Research Assistant, Laboratório Nacional de Engenharia Civil, Av. do Brasil, 101, 1799 Lisboa Codex, Portugal; formerly Graduate Assistant, University of Florida, Gainesville, FL, USA.

²Professor, Department of Coastal and Oceanographic Engineering, University of Florida, Gainesville, FL, USA.

water column; moreover, the differences between salt and suspended sediment behaviors suggest the importance of studying sediment-stratified flows and differences relative to salt-stratified flows. Observation of such differences, supported by recent field studies, contradicts the assumption implicit in some early studies that the dominant physical mechanisms transporting salt and sediment landward in an estuary or coastal bay are the same. In the particular case of suspended sediment, which is negatively buoyant, vertical fluxes are strongly dependent on the erosion/resuspension and settling/deposition conditions, thus influencing its response to hydrodynamic forcing. Such influence is expressed by the well known flow-sediment hysteresis which reflects the time-lagged response of sediment to flow variations.

The main purpose of the present investigation was to study the effect of sedimentary processes in the evolution of the vertical concentration profile in a sediment-stratified coastal environment. In particular, the influence of the sediment settling properties, stabilized diffusion parameters and bed properties on the general features of the profile and their effects on the lag phenomena contributing to flow-sediment hysteresis were investigated.

A vertical transport numerical model was used to generate concentration profiles. Measurements of water pressure, velocity and suspended sediment concentration were made in a high-concentration coastal environment (Hangzhou Bay, People's Republic of China). Laboratory tests of local sediment allowed the evaluation of the pertinent physical parameters. The field data were used to test the importance of lagged response of sediment to flow changes and to compare with model results.

Flow-Sediment Hysteresis

It is known that, during decreasing estuarine currents, concentrations are usually higher than during increasing currents. This flow-sediment hysteresis can be decomposed into delays caused by global advective phenomena and those associated with the response of sediment to local flow variations. These last can, in the general case of fine sediment transport, be separated into several parts following Dyer and Evans (1989):

- a) A lag associated with settling, corresponding to the time that a sediment particle in suspension at a certain elevation in the water column takes to reach the bed, once the transport velocity (or $\bar{u}|\bar{u}|$, proportional to the bottom shear stress) has decreased below a minimum value. This settling lag is associated with the settling velocity of the sediment particles and, consequently, depends on the aggregation condition of the sediment and on the concentration dependent settling velocity range;
- b) A lag associated with the diffusion process, corresponding to the time taken by a sediment particle once entrained from the bed, to be diffused to upper layers in the water column. This diffusion lag is associated with the buoyancy stabilization characteristics in the water column and depends on the amount of sediment available for resuspension, as well as on the vertical concentration gradients;
- c) A lag associated with the time difference between the occurrence of a transport velocity (or $\bar{u}|\bar{u}|$) in the water column and the occurrence of higher values of the same parameters causing bed erosion. This threshold

lag is associated with the resistance of the top bed layer to erosion and, particularly, to the critical shear stress for erosion;

- d) A lag associated with bed consolidation, corresponding to the fact that in fine consolidated beds, the bed shear strength increases with bed consolidation time. This effect is called consolidation lag.

Such lag mechanisms can then be superimposed to explain the fact that sediment concentrations usually lag hydrodynamic forcing. In a tidal flow following low water slack, a threshold time lag occurs before sediment resuspension occurs. To this lag a lag associated with particle diffusion to upper layers should be added. Furthermore, once the flow begins to decelerate a certain time is needed for the sediment to settle and thus a settling lag should be included. During slack water a residual sediment concentration may remain in the water column, corresponding to the finer fractions of sediment under the effects of residual turbulence and Brownian motion. Further to these local lag effects any delays caused by advection should also be included.

A rough comparison between the magnitudes of the settling lag and diffusion lag following Dyer (1986), by considering the concept of a time dependent mean height of suspension due to Monin and Yaglom (1971) and typical values of the pertinent physical parameters for cohesive sediment, shows the former to be approximately three times the latter (Costa, 1989). This fact must be taken into account when comparing the behavior of salt and sediment in estuarine flows, since salt is not subject to erosion/deposition.

Field Experiments and Laboratory Tests

In order to investigate fine sediment concentration profile response to currents and waves in a high concentration environment two experiments were carried out in Hangzhou Bay, People's Republic of China, a meso-tidal coastal bay dominated by fine grained sediment (figure 1). Some of the bay's important oceanographic features are presented by Su et al (1988) and Su and Yu (1984), and summarized in the following paragraphs.

Hangzhou Bay, a shallow and relatively flat-bottomed water body, is the outer region of the Qiantang estuary. The rivers upstream of the bay discharge an average water flow of 42 km^3 per year and an average suspended sediment load of $7.9 \times 10^9 \text{ kg}$ per year. Due to the different characteristics of the incoming water relative to the coastal waters, a plume is formed at the mouth. North of Hangzhou Bay lies the mouth of the Chiangjiang River, which has an average annual water flow of 925 km^3 and an annual sediment discharge of $486 \times 10^9 \text{ kg}$. This river is believed to be an important sediment source for Hangzhou Bay, since the mineral composition of both sediments is similar. At the mouth of the Chiangjiang River two plumes are formed (a main plume and a secondary plume directed towards the northern end of Hangzhou Bay), which are believed to contribute to the sediment supply into Hangzhou Bay. The secondary Chiangjiang plume forms with the Qiantang plume a single NE/SW oriented front with high near-bottom sediment concentrations at its landward side. Sediment initially carried by the main Chiangjiang plume also accumulates at the seaward side of the front during winter. Tidal resuspension of sediment along the front, although inhibited by stratification, combined with strong cyclonic along-front surface currents, cause southwestward transport of sediment and accretion, at

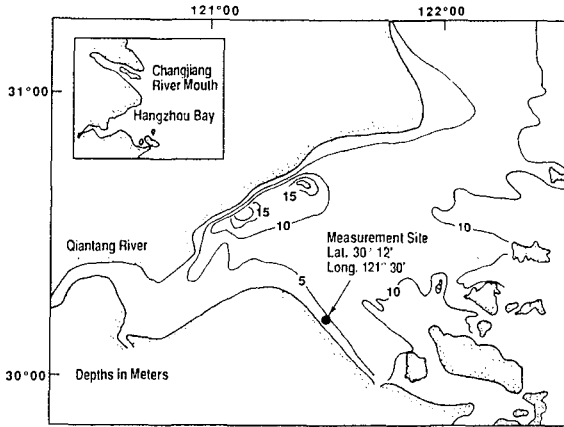


Figure 1: Location of the measurement site in Hangzhou Bay.

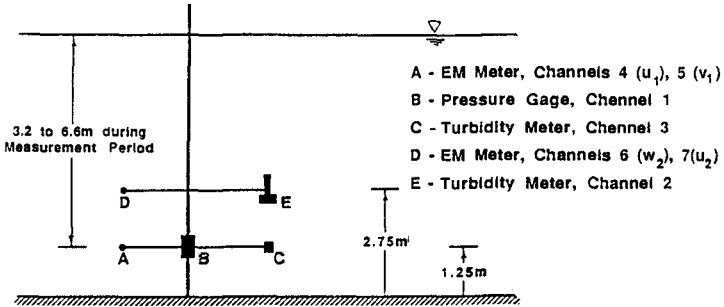


Figure 2: Measurement tower and positions of the equipment used in Hangzhou Bay (deployments C2 and C3).

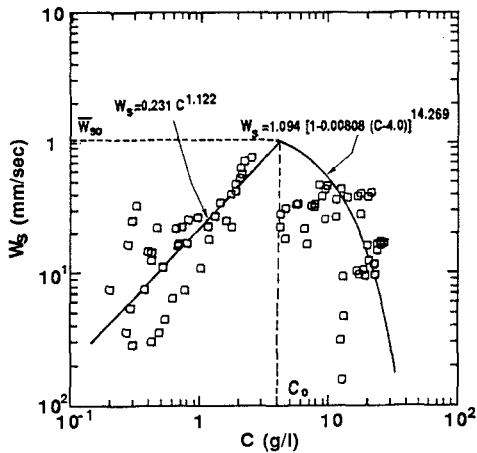


Figure 3: Settling velocity as a function of concentration for Hangzhou Bay sediment.

a rate of about 20 m per year, of the south bank of Hangzhou Bay where the field experiments took place.

The first test was carried out from the 14th to the 16th of May, 1988. The measurement tower (figure 2) consisted of the following: a turbidity meter (Partech SDM16), an electro-magnetic (EM) current meter (Marsh McBirney, model 512) measuring along two horizontal directions (x and y) and a pressure gage to record water surface variation were installed at the lower level. A turbidity meter (Partech TT10 self cleaning unit) and a second EM meter (of the same model) measuring along a horizontal and the vertical direction (x and z) were located at the upper level. The data were sampled at a rate of 4 Hz and recorded with in a data logger. Two experimental phases took place. In the first (deployment C2), six sampling periods of 10 minutes each, separated by 30 minute intervals, were measured; in the second (deployment C3) fifteen sampling periods of 5 minutes each, separated by 60 minute intervals and encompassing a full tidal cycle, were measured. During the study period wave action was generally weak and turbulence in the water column was mainly generated by the tidal current.

A second measurement program took place at the same location from the 4th to the 5th of August, 1989 (deployment C4). In this case the pressure gage and the EM current meter measuring along the x and y directions were located at the upper level, while the second EM meter, measuring along the x and z directions, was located at the lower level. The positions of the turbidity meters remained the same, as in the first field program. Twenty-four data blocks of 5 minutes duration each separated by 60 minute intervals were sampled at 4 Hz.

The field data were processed in order to separate from the records the time-average values and the tidal trends; the remaining portion, generically denoted by e_1 , included a minor wave-induced part \tilde{e} and a turbulent part e' , which were separated using the pressure data through a filtering procedure (Costa, 1989).

In order to characterize the sediment laboratory tests were performed using samples collected at the measurement site. Grain-size test indicated a median floc diameter of 23 μm , while erosion tests, performed in an annular flume, produced values of $M = 2.1 \times 10^{-3} \text{ g}/(\text{cm}^2 \text{ min})$ and of the critical shear strength $\tau_s = 0.05 \text{ N}/\text{m}^2$ for the expression for the erosion rate, $E = M[(\tau_b - \tau_s)/\tau_s]$, where τ_b is the bottom shear stress. Settling velocity tests produced the parameters for settling in the flocculation and hindered settling ranges, as shown in figure 3.

Model Simulations

A numerical model developed by Ross (1988) was used to simulate concentration profile evolution. The model solves a simplified version of the advection-diffusion equation for suspended sediment in the z direction, in the form

$$\frac{\partial C}{\partial t} = \frac{\partial}{\partial z} \left(W_s C + K_z \frac{\partial C}{\partial z} \right) \quad (1)$$

(where C , W_s and K_z are the sediment concentration, the particle settling velocity and the vertical mass diffusivity, respectively), valid for estuarine flows in which the convective vertical velocity is negligibly small and the advective

travel time through the estuary is considerably greater than the characteristic time for sediment settling. In the water column the vertical settling and diffusive fluxes are computed using a finite difference scheme. The settling flux computation includes free settling and the concentration dependent cases of flocculation settling and hindered settling. The neutral mass diffusivities, K_n , are equated to the neutral momentum diffusivities E_n , (using the Prandtl velocity law and assuming a linear shear stress variation) by considering the turbulent Schmidt number (St) to be unity. The mass diffusivity corresponding to the stratified case (K_s) is then obtained through a Munk and Anderson type of damping correction in the form

$$\frac{K_s}{K_n} = (1 + \beta Ri)^{-\alpha} \quad (2)$$

where Ri is the gradient Richardson number and α and β are positive empirical constants.

Appropriate boundary conditions are a no net flux condition at the water surface (the diffusion flux balancing the settling flux) and a bed flux boundary condition. This boundary condition defines a source or sink for the suspended sediment in conditions, respectively, by erosion or deposition. The deposition flux is defined as:

$$F_p = \left(\frac{\tau_b}{\tau_{cd}} - 1 \right) W_s C \quad (3)$$

where τ_b and τ_{cd} are the bottom shear stress and the critical shear stress for deposition, while the erosion flux is defined as

$$F_e = a \exp(-2.33\tau_s) [(\tau_b - \tau_s)/\tau_s] \quad (4)$$

where τ_s and a are the bed shear strength and an empirical erosion parameter, respectively.

Model simulations of the variation of the turbulence-mean value of the sediment concentration (C) with the square of the turbulence-mean horizontal velocity ($\bar{u}|\bar{u}|$) at the elevations corresponding to the measurement positions are shown in figure 4, for the flow conditions during deployment C2. In the figure negative values of \bar{u} denote ebb flow. Agreement between the trends and orders of magnitude of the values of the variables in the simulated loops and the ones measured during the field deployments (figures 5 and 6) is generally observed. For the simulation, the settling parameters determined in the laboratory tests were used, while stabilized diffusivity parameters α and β had the values 2.0 and 1.0, respectively. The bed shear strength and the critical shear stress for deposition, however, had to be assigned values $\tau_s = 15.0 \text{ N/m}^2$, and $\tau_{cd} = 5.0 \text{ N/m}^2$, one order of magnitude higher than those measured in the laboratory.

Sensitivity analysis was performed using the model with adequate variations in the parameters describing the different physical processes. These allowed an evaluation of their effects through the lags involved in sediment response to flow variations. A reference case was computed in which, as occurs in figure 4, C lagged the shear stress in the ebb, while the opposite occurred in the flood. For this simulation the flow conditions, α , β , τ_s and τ_{cd} used for the computation of figure 4 were used while the settling velocities were computed as

$$W_s = 0.406 C^{1.082} \quad (5a)$$

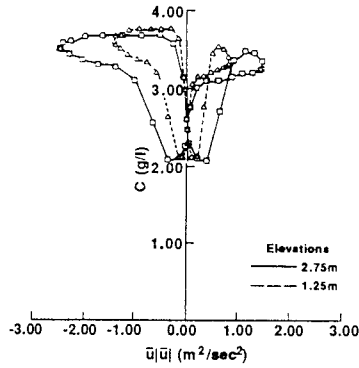


Figure 4: Hysteresis loops simulated using Hangzhou Bay sediment settling properties.

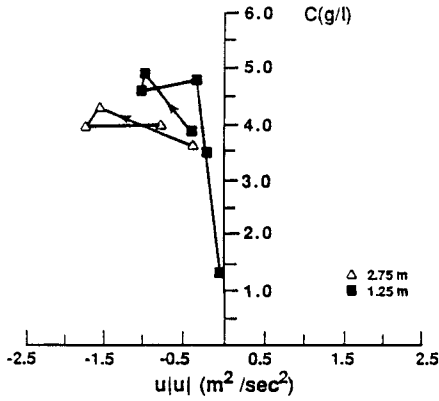


Figure 5: Measured hysteresis loops (deployment C3).

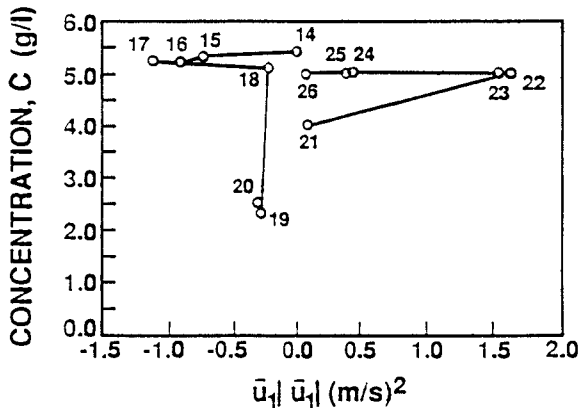


Figure 6: Measured hysteresis loop at the upper position (deployment C4). Numbers next to data points indicate time in hours.

$$W_s = 6.47(1 - 0.00451 C)^{12.067} \quad (5b)$$

in the flocculation settling and hindered settling ranges, respectively.

In figure 7 and 8 plots of C vs. $\bar{u}|\bar{u}|$ and time for the reference simulation are shown, respectively; in figure 7 the elapsed times (in minutes) since the beginning of the simulation (peak flood current) are indicated against the computed points, encompassing a full tidal cycle. The vertical gradient of the net flux (positive values denoting resuspension/diffusion) vs. time is shown in figure 9. From the figure the residual concentration during slack water periods is seen to be almost constant in the water column, suggesting uniform concentration profiles. Comparison of figures 8 and 9 allows the definition of the main periods during which settling and deposition took place. Deposition/settling are clearly dominant around slack water while resuspension/diffusion dominate the subsequent re-entrainment periods. The magnitude of these fluxes, if compared with those occurring during the remaining of the computation period, emphasizes the importance of near-bottom conditions since, clearly, the much higher values of the net flux gradients during deposition and re-entrainment periods are due to these phenomena.

An increase in the stabilization conditions of the water column (parameter β increasing from 1.0 to 2.0) resulting in inhibition of upward mixing showed peak concentrations to increase close to the bed; the ebb maximum concentrations were found to lag the bottom shear stress by an additional 20 min relative to the reference case, which reflects an increase in the diffusion lag. The residual slack water concentrations did not change significantly.

In order to evaluate settling lag effects the settling velocities were decreased by a factor of four, all other parameters remaining the same. An increase in the lag of the concentration relative to the shear stress was observed during ebb, while a similar increase of the lag of the shear stress relative to the concentration during flood was also observed. A decrease in the ebb and flood peak concentrations occurred but, more significantly, a sharp increase occurred in the residual concentration around slack water.

The influence of near bed conditions was investigated by reducing the values of τ_{cd} and τ_s by 4.0 N/m^2 , $\Delta\tau = \tau_s - \tau_{cd}$ remaining constant. Only the lag of the shear stress relative to the concentration in the flood was increased relative to the reference case. Decreasing the critical shear stress for deposition, however, by allowing a shorter period for deposition around slack water, caused higher values of the residual concentration relative to the reference case.

Experimental Results

The time lags in sediment response to flow changes represent a basic manifestation of sediment dynamics in estuaries and coastal bays of which measured flow-sediment hysteresis is an indicator. The net effect of such lags is typically reflected in landward transport of sediment. Figure 5, corresponding to deployment C3, confirms the occurrence of hysteresis. Figure 6, obtained during deployment C4, is of higher clarity. Moreover its similarity with the simulated loop of figure 4 is apparent, despite some differences in the input flow conditions. It should be noted however in figure 6 that, contrary to what happens in the simulated loops, the shear stress lags the concentration in the ebb, while the op-

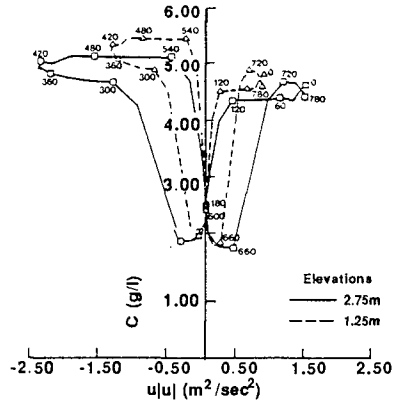


Figure 7: C vs. $\bar{u}|\bar{u}|$ for the simulated reference case.

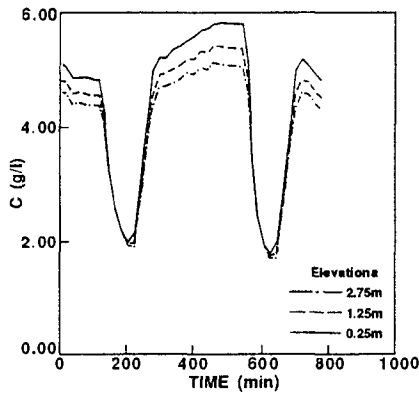


Figure 8: C vs. time for the simulated reference case.

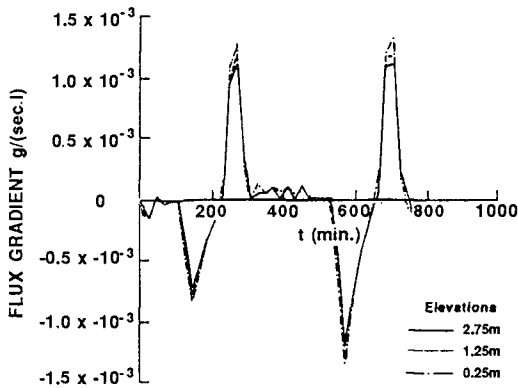


Figure 9: Vertical gradient of the net flux vs. time for the simulated reference case.

posite occurs in the flood. Comparison of figures 6 and 7 also shows agreement between the simulations and the data, and seems to confirm the importance of deposition/settling around slack water and of resuspension/diffusion in periods that follow. Similar conclusions can be drawn by comparing figures 8 and 10.

In order to better assess the role of diffusion in governing hysteresis, the “turbulent” (including wave effects and turbulence) properties of the flow were investigated. Figure 11 shows a plot of the Reynolds stresses at the upper measurement level vs. the mean horizontal velocity \bar{u} , while figure 12 shows the “turbulent” variances which contribute to the turbulent kinetic energy of u (at both levels) vs. \bar{u} . Despite the small number of data points, qualitative hysteresis loops could be drawn, showing higher values of the variables during decelerating flow periods. Since the Reynolds stress at a given elevation can be considered to be an indicator of the bottom shear stress and, consequently related to sediment concentration through erosion/deposition, figure 11 is consistent with the meaning of lagged sediment response to flow variations as an important factor for sediment transport in Hangzhou Bay. Figure 12 provides additional evidence of the same nature since higher turbulent kinetic energy will cause, through increased upward diffusion, higher sediment concentrations during the decelerating periods in the upper layers of the flow.

The mass and momentum diffusivities resulting from the actual field conditions (wave effects and turbulence) were calculated using the difference relations

$$K_s = -\frac{\overline{w'c'}}{\frac{\Delta c}{\Delta z}} \quad (6a)$$

$$E_s = -\frac{\overline{w'u'}}{\frac{\Delta u}{\Delta z}} \quad (6b)$$

which give only rough approximations of the values of the parameters since $\Delta z = 1.5$ m is a rather large value. The mass and momentum diffusivities and the Schmidt numbers using this approach are shown in tables 1 and 2 together with the depth averaged longitudinal velocities computed assuming a logarithmic profile (negative values denoting ebb velocities).

\bar{u}_D (m/sec)	K_s (m ² /sec)
-1.221	3.29×10^{-4}
-1.163	5.60×10^{-5}
-0.861	3.21×10^{-5}
0.416	1.24×10^{-4}
0.762	2.53×10^{-3}
1.137	3.45×10^{-4}
1.336	8.12×10^{-4}
1.454	1.91×10^{-4}

Table 1 – Measured mass diffusivities as a function of depth averaged longitudinal velocities, \bar{u}_D

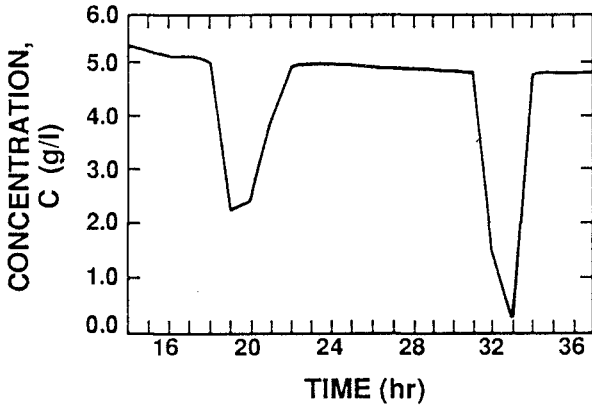


Figure 10: Measured C vs. time for the upper position in deployment C4.

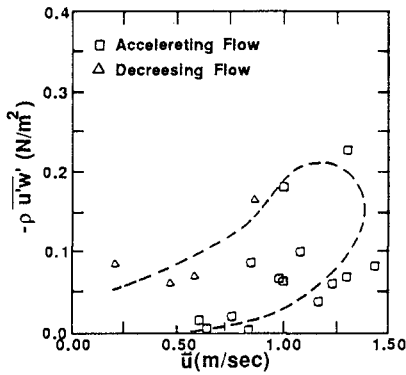


Figure 11: Hysteresis in Reynolds stresses (data from first field test).

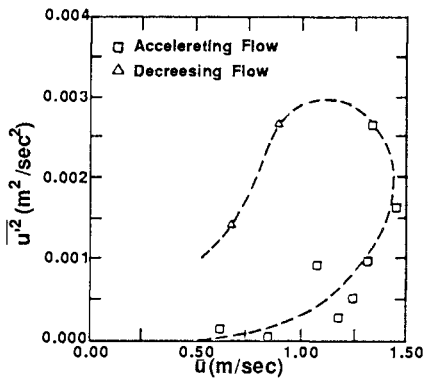


Figure 12: Hysteresis in u variance (data from first field test).

\bar{u}_D (m/sec)	E_s (m ² /sec)	S_t	Ri_f
-1.418	6.81×10^{-4}		
-1.276	4.92×10^{-4}		
-1.260	1.30×10^{-3}		
-1.221	3.08×10^{-4}	0.94	0.090
-1.163	1.37×10^{-4}	2.45	0.042
-0.861	7.71×10^{-5}	2.40	0.277
-0.827	1.36×10^{-3}		
-0.624	7.18×10^{-5}		
-0.603	1.12×10^{-3}		
-0.272	1.53×10^{-2}		
-0.180	2.18×10^{-3}		

Table 2 — \bar{u}_D and measured momentum diffusivities, Schmidt and flux Richardson numbers

The mass diffusivities calculated by the model for values of \bar{u}_D similar to those of table 1 are presented for comparison in table 3. The values of K_s obtained from the data were of order of magnitude of 10^{-3} m²/sec or lower, while the mass diffusivities computed by the model showed, for comparable depth averaged velocities, values of the order 10^{-2} m²/sec, much higher than the former. This fact points to the need for a more accurate description of turbulent diffusion when modeling sediment-stratified flows. The measured values of K_s compare favorably with those used by van Leussen and Winterwerp (1988) (4×10^{-3} and 4×10^{-4} m²/sec for estuaries showing slight and strong stratification conditions, respectively).

\bar{u}_D (m/sec)	K_s (m ² /sec)
-1.278	8.33×10^{-2}
-1.145	8.49×10^{-2}
-0.809	8.62×10^{-2}
0.441	9.33×10^{-2}
0.796	9.20×10^{-2}
1.139	9.06×10^{-2}
1.208	8.79×10^{-2}

Table 3 — \bar{u}_D , and mass diffusivities computed by the model

If time scales for vertical mixing and settling are defined as $T_d = H^2/K_s$ (where H is the water depth) and $T_s = H/W_s$, respectively, their ratio T_s/T_d is the Peclet number for the suspension (Teeter, 1986) and reflects the ratio between the settling lag and the diffusion lag. For typical values of the parameters measured in Hangzhou Bay this ratio is, approximately, equal to seven

and, again, underlines the differences between salt-stratified and sediment-stratified environments. For turbulence under conditions of local equilibrium a flux Richardson number, $Ri_f = Ri/S_i$, represents the efficiency of conversion from turbulent kinetic energy to potential energy (Abraham, 1989); Ri_f also reflects, relative to the gradient Richardson number the difference between mass and momentum diffusivities under stratified conditions. The computed values of Ri_f are presented in table 2.

The difference between the values of the erosion shear strengths τ , used in the simulation and that determined for local sediment (5.0 and 0.05 N/m², respectively) also confirms the need to improve the algorithms currently employed to describe bed fluxes. It is obvious that a simplified erosion/deposition description of the bed phenomena is insufficient to simulate the complex manner in which bottom fine sediment is fluidized and entrained.

Summary

Sediment response to flow variation is time-lagged and is represented by the well-known velocity-concentration hysteresis loop. A numerical model was used to investigate the influence of settling, diffusion and erosion/deposition defining parameters in the hysteresis loops. These parameters were found to affect mainly the time lags between the occurrence of the maximum concentrations and shear stresses, and the slack water residual concentrations.

Field data obtained in a high-concentration coastal environment (Hangzhou Bay, People's Republic of China) showed expected hysteresis and, thereby, highlighted the importance of time-lagged response of sediment to flow variations. Comparison between field data and numerical results showed good qualitative agreement. Comparison between the model computed mass diffusivities and those computed from field data showed the former to be higher than the latter. Moreover the simple erosion/deposition description used in the model required the use of physical parameters which were significantly different from those determined in laboratory experiments performed with local sediment. These facts suggest the need to improve both turbulence modeling and the description of the complex near-bed phenomena which include fluidization, entrainment, settling, bed formation, consolidation and gelling.

Acknowledgement

Support from U.S. Army Engineer Waterways Experiments Station, Vicksburg, MS through contract DACW 39-87-K-0023 is acknowledged.

References

- Abraham, G., "Turbulence and Mixing in Stratified Tidal Flows", *Physical Processes in Estuaries*, W. van Leussen and J. Dronkers, eds., Springer-Verlag, Berlin, 1989.
- Costa, R.C.F.G., "Flow-Fine Sediment Hysteresis in Sediment-Stratified Coastal Waters", *Report UFL/COEL 89/011*, and Oceanographic Engineering Department, University of Florida, Gainesville, FL, U.S.A., 1989.
- Dyer, K.R., *Coastal and Estuarine Sediment Dynamics*, John Wiley and Sons, Chichester, U.K., 1986.

- Dyer, K.R., "Fine Sediment Particle Transport in Estuaries", *Physical Processes in Estuaries*, W. van Leussen and J. Dronkers, eds., Springer-Verlag, Berlin, 1989.
- Dyer, K.R. and Evans, E.M., "Dynamics of Turbidity Maximum in a Homogeneous Tidal Channel", *J. Coastal Res.*, Special Issue No. 5, 1989, pp. 23–30.
- Monin, A.S. and Yaglom, A.M., *Statistical Fluid Mechanics: Mechanics of Turbulence*, M.I.T. Press, Cambridge, Massachusetts, 1971.
- Oduyemi, K.O.K., "Turbulent Transport of Sediment in Estuaries", *Ph.D. Dissertation*, University of Birmingham, Birmingham, U.K., 1986.
- Ross, M.A., "Vertical Structure of Estuarine Fine Sediment Suspensions", *Ph.D. Dissertation*, University of Florida, Gainesville, Florida, U.S.A., 1988.
- Su, J.L.; Wang, K. and Li, Y., "A Plume Front in Hangzhou Bay and its Role in Suspended Sediment Transport", *Second Institute of Oceanography, State Oceanic Administration, Report (in print)*, Hangzhou, Zhejiang, People's Republic of China, 1988.
- Su, J.L. and Xu, W., "Modelling of the Deposition Patterns in Hangzhou Bay", *Proc. XIX Int. Coastal Eng. Conference*, ASCE, New York, U.S.A., 1984, pp. 2181–2191.
- Teeter, A.M., "Vertical Transport in Fine-Grained Suspension and Newly-Deposited Sediment", *Estuarine Cohesive Sediment Dynamics*, A.J. Mehta, ed., Springer-Verlag, Berlin, 1986.
- Uncles, R.J.; Elliot, R.C.A. and Weston, S.A., "Lateral Distributions of Water, Salt and Sediment Transport in a Partly Mixed Estuary", *Proc. XIX Int. Coastal Eng. Conf.*, ASCE, New York, U.S.A., 1984, pp. 3067–3077.
- van Leussen, W. and Winterwerp, J.C., "Laboratory Experiments in the Delft Tidal Flume on the Sedimentation of Fine-Grained Sediments", *Conference on Physics of Shallow Estuaries and Bays*, Pacific Grove, California, 1988.

CHAPTER 156

Nearshore Current Patterns on Barred Beaches

David G. Hazen*, Brian Greenwood†, and Anthony J. Bowen*

INTRODUCTION

The last few years have been marked by a renewed interest in the old concept of undertow, the seaward flow which balances the surface flux of water associated with waves, particularly with breaking waves (Svendsen, 1984; Stive and Wind, 1986; etc.). This is clearly an important current in terms of the sedimentary processes which determine the beach profile. Roelvink and Stive have provided laboratory data that suggests the profile results from a net balance between three main factors; the wave skewness, the undertow, and the beach slope. However, in the field the third dimension, the longshore direction, may play a significant role. Even if the system is assumed uniform alongshore, strong longshore currents certainly influence the mobility of the sediment and may play more complex roles, in generating shear waves for example.

It seems appropriate to represent the system, both on/offshore and alongshore, in one self-consistent model. Recent work has been clearly progressing in this direction (Stive and DeVriend, 1987; Svendsen and Lorenz, 1989). It is therefore also appropriate at this stage to look at existing field data to see how well one can define trends that the modelling results should reproduce.

There are some very clear limitations. In the field it is difficult to describe, in any detail, the longshore variability. Small hydraulic gradients in the alongshore direction may drive longshore currents, rip currents, or some general nearshore circulation associated with larger scale topography. Even in a relatively 2-D situation, it is known that the longshore currents are strongly dependent on the directional distribution of the wave spectrum, a factor which is hard to estimate well, unless the angle of wave approach is large.

The measurements here were taken on a beach at the end of a large bay of restricted width. Large waves can only be generated along the long axis of

* Department of Oceanography, Dalhousie University, Halifax, Nova Scotia B3H 4J1, Canada

† Department of Geography, Scarborough College, University of Toronto, Scarborough, Ontario M1C 1A4, Canada

the system, so that the angles of wave approach relative to the beach tend to be small ($0 - 15^\circ$). Attention is therefore focussed primarily on the on-offshore structure of the flow.

FIELD MEASUREMENTS

The Canadian Coastal Sediment Transport (C-COAST) experiments have taken place over the past three years. These experiments involved the deployment of arrays of up to twenty electromagnetic current meters, ten pressure sensors and an assortment of wave-wires and suspended sediment sensors from the shoreline seawards to a depth of $5 - 7m$. Each of the experiments acquired data during periods of higher wave activity over a period of approximately one month under varying wave conditions. The sites included a two dimensional beach (Queensland, Nova Scotia in 1988), a barred beach with normally incident waves (Bluewater, Ontario in 1987 and 1988) and a multibarred beach with

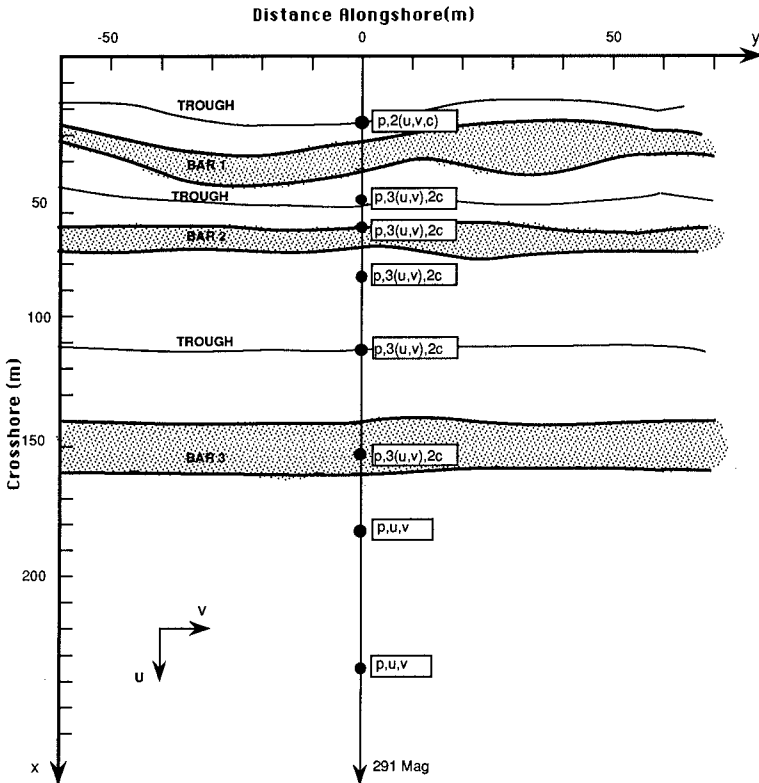


Figure 1. Bluewater 1988 Instrument Schematic showing locations of pressure sensors (p), two component flowmeters (u, v) and optical backscatter suspended sediment concentration sensors (c).

normal or obliquely incident waves (Stanhope Lane, PEI in 1989). The data discussed in this paper will be primarily from the 1988 Bluewater experiment, which took place in May and June of that year.

The data are gathered from a cross-shore array of pressure gauges ('p'), two component flowmeters ('u' and 'v') and optical backscatter suspended sediment concentration sensors ('c'). These instruments were located as shown in Figure 1 with co-ordinate systems as indicated. The sensors were orientated and connected to the hard-wired UDATS data acquisition system (Hazen *et al.*, 1987). Additional sensors were deployed to record wind speed and direction, concentration profiles by acoustic backscatter, depth of sedimentary activity and to collect physical samples of suspended sediment for concentration and grain size measurement.

Detailed analysis of the current data is limited by the number of working flowmeters and the long periods of calm or offshore winds during the study. For these reasons, discussion will concentrate on data collected from flowmeters at 150m on the crest of bar 3 and flowmeters at 55m, just inshore of bar 2 (both at heights of 10 and 25cm above the bed) together with winds from a 10m tower erected adjacent to the beach.

The data base selected for the paper includes the most severe conditions encountered during the experiment (on June 9, 1988) and a period of wave conditions which were more typical of the wave conditions on the lake (June 16). In both cases the incident waves propagate slightly in the y -positive direction, the angle of incidence being $5-10^\circ$ on 9 June, $3-7^\circ$ on the 16th June. In both cases, the longshore current flows in the direction expected.

The conditions on June the 9th are shown in Figure 2 with the wind rising quickly at noon, reaching a steady velocity of about 12 kts. Visual observations included an estimated significant wave height of 0.8m and white capping to the horizon. Observations report short crested waves during the period of active generation. As the wind drops, the waves become longer crested but tend to disappear due to the size of the bay. The mean water level at the shore responds directly to the wind force changing by 20cm in a few hours. The incident wave frequency drops during the maximum of the wind event and then quickly reverts to its previous level. The mean currents track the wind and significant wave heights peaking at 0.3m/s longshore and 0.2m/s cross shore, based on 10 minute averages taken every 30 minutes. The vertical dashed line indicates the start of the data run used in Figures 5 and 7.

Conditions on June 16, however, are more typical of the lower energy events during the study. As shown in Figure 3, the winds averaged around 9 kts. The system responds quite quickly once a threshold wind velocity of 6-7 kts is exceeded with dips in the incident wave frequency, and a rise in the mean water level and mean currents. Again, the vertical dashed line refers to the start of the data run used in Figure 6.

Figure 4 shows the conditions across the surf zone at the peak of the event of 9 June, indicated by the dashed line on Fig. 2. The continuous lines in Figures

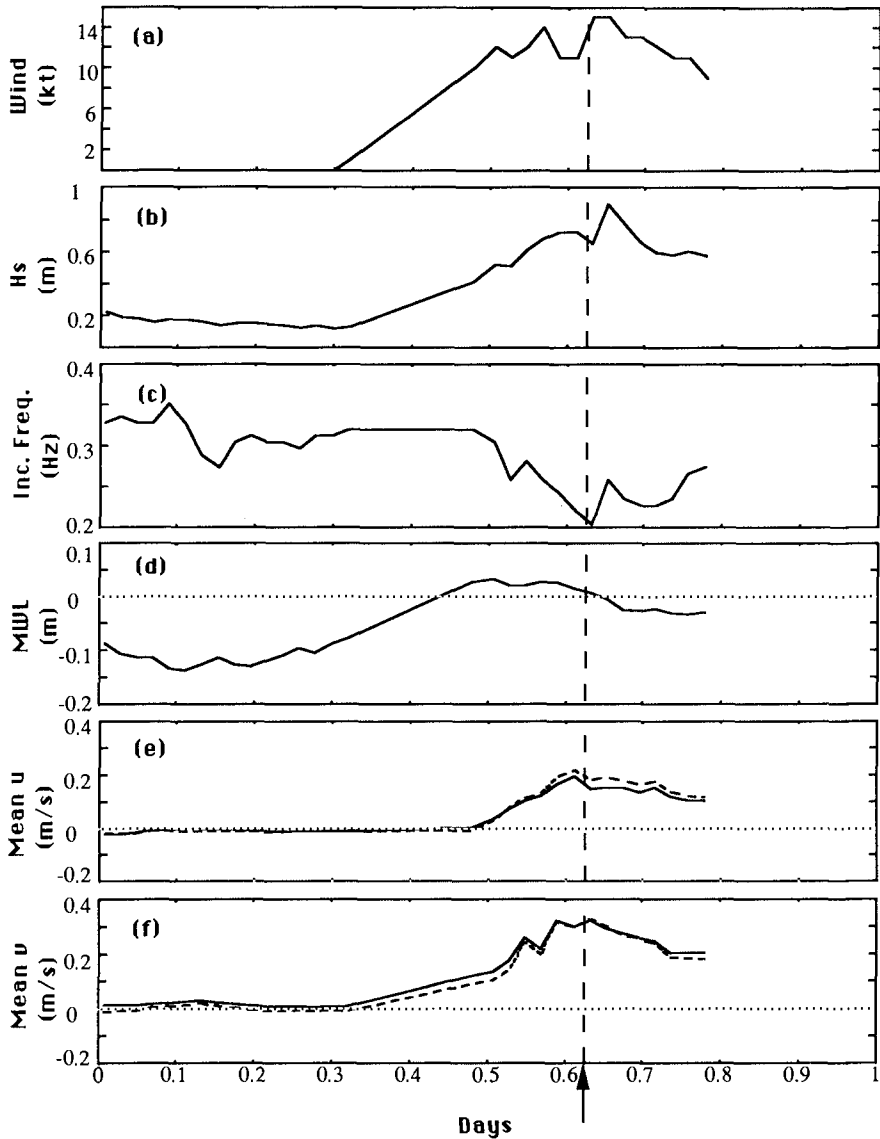


Figure 2. Conditions at Site on June 9, 1988. (a) wind speed, (b) significant wave height, (c) incident wave frequency, (d) mean water level, referenced to an arbitrary datum, (e) mean cross shore flow at 55m station. (Solid line is at 25cm above the bed while dashed line is at 10cm above the bed), (f) mean long shore flow at 55m (solid and dashed lines as in (e)). Vertical dashed line shows the beginning of the time used in Figures 4 and 7.

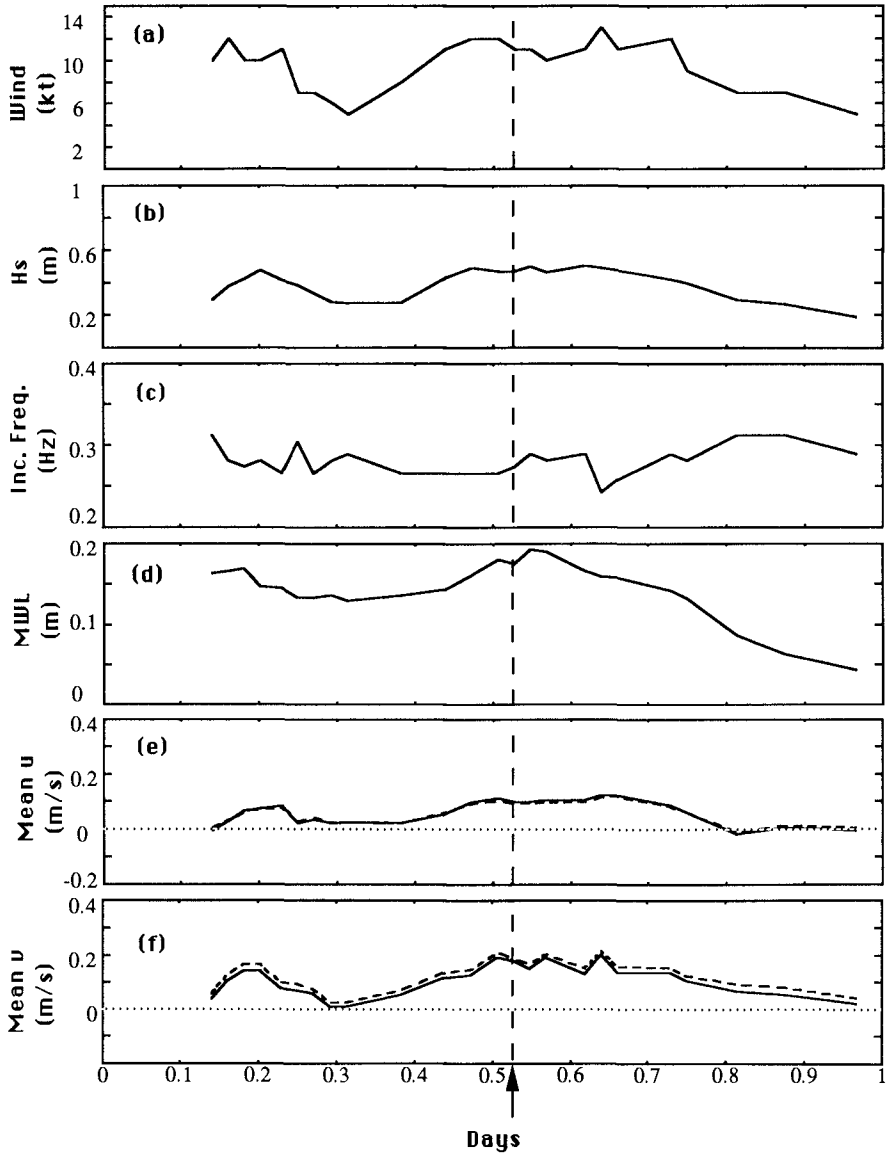


Figure 3. Conditions at Site on June 16, 1988. (a) wind speed, (b) significant wave height, (c) incident wave frequency, (d) mean water level, (e) mean cross-shore flow at 55m, (f) mean long shore flow at 55m. Vertical dashed line shows the beginning of the time period used in Figure 5.

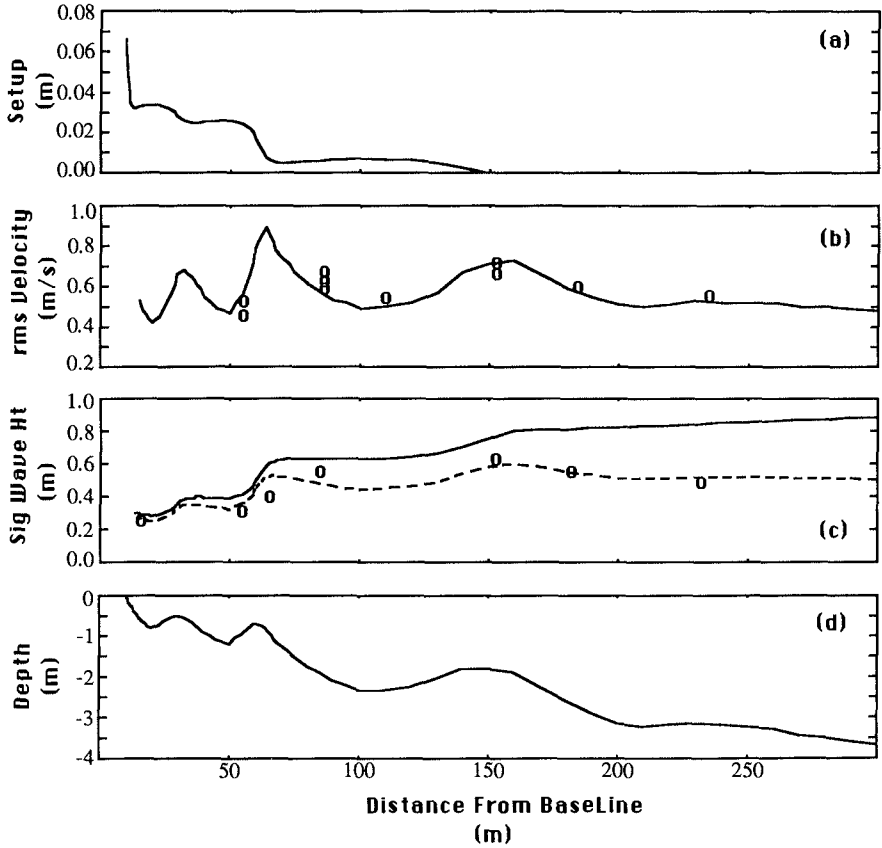


Figure 4. Cross Shore Profiles during June 9, 1988 'P4' data run, beginning at 1540. (a) predicted setup, (b) predicted and measured r.m.s. cross shore velocity, (c) predicted and measured significant wave height (dashed line indicates wave heights "uncorrected" to predict pressure gauge response, (d) measured depths.

4b and 4c show the theoretical distributions of on/offshore velocity, wave height and bottom pressure in the incident wave band, derived from a shoaling model based on Thornton and Guza (1983). The empirical parameters, used in such models are γ a ratio of wave height to water depth, and B a general dissipation constant. The results in Figure 4 are for $\gamma = 0.45$, $B = 1$ typical of values used in modelling wave evolution on open ocean beaches. The superimposed data points are from the flowmeter array (Fig. 4b) and the near-bed pressure gauges (Fig. 4c). The pressure has been expressed in terms of meters of water. Note that the pressure is not hydrostatic, the high wave frequencies found in the lake environment mean that the waves are in intermediate, not shallow, water until

very close to the shore.

The model, and the visual observations made during the field program, show that at the height of the storm there is some breaking on the third bar. Dissipation is generally low in the troughs and high on the inshore bars. Comparison with other model runs shows that the incident waves become saturated in the seaward face of the second bar if the incident waves are larger than about $0.4m$. As can be seen clearly in Figure 4b, the shoaling model predicts significant amplification of the wave orbital velocity over the bars, due to the depth dependent term in the linear theory. Whether this happens in reality is questionable, the model assumes that the rate of change of depth is slow, not a very good assumption even here where the incident frequency is high and the incident waves very short. However, the predicted amplification over bar three is clearly seen in the data. Inshore, the instrumental spacing does not allow a critical test of the model. The crests of the inshore bars were not used as instrument positions due to the very limited water depth above them.

Wave set-up was calculated in the dispersion model, the results shown in Fig. 4a. The predicted set-up is very small, a few centimeters. The general lake set-up (Fig. 2), of the order of $0.2m$ was much more noticeable. Measurements of set-up specifically were obtained by taking the difference between measurements for the inshore pressure gauges (and wave staffs) and the pressure gauge at $230m$. The results were somewhat scattered, the lake level changes being clearly seen at all stations, but the differences did not resolve the wave set-up with any accuracy, they confirmed that the set-up was small.

The model and data comparison for 1240 on the 16th of June, show a very similar picture (Fig. 5). The smaller wave height leads to less energy loss on the third bar, but breaking on the second bar results in a saturation condition and wave conditions inshore are essentially the same.

DISCUSSION

As shown in Figs. 2 and 3, the mean flows, averaged over 29 minutes, increase with increasing wave energy. In Figure 6, the seaward mean flow over the second bar ($55m$) and third bar ($150m$) are shown as a function of the incident wave height. For a significant wave height less than $0.25m$ the waves break only at the shoreline and the mean flows are very weak; if there is any tendency, it appears to be for onshore flow. As wave height increases, the mean flow at both positions increases more or less linearly with increasing waveheight.

Figure 6a shows the theoretical values for the set-up as a function of incident wave height and frequency. The field measurements scatter generally around these lines. The Thornton and Guza dissipation model includes a frequency dependence which results in a functional relationship for set-up which is weakly dependent on f . The set-up value shown is the predicted difference between the level at the third bar and that over the nearshore trough (cf. Figs. 4 and 5). The values reach a maximum, shown by the circles, when the surf zone becomes saturated, inshore from the third bar. Again, this wave height at

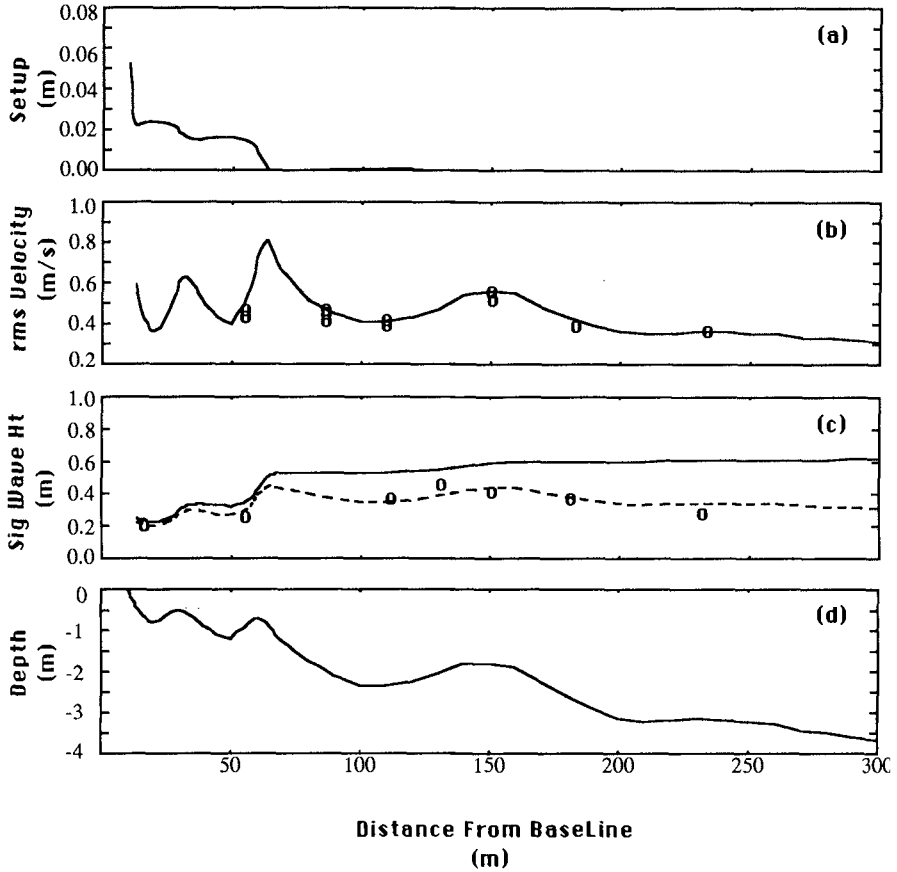


Figure 5. Cross Shore Profiles during June 16, 1988 'M4' data run, beginning at 1240. (a) predicted setup, (b) predicted and measured r.m.s. cross-shore velocity, (c) predicted and measured significant wave height (dashed line is wave height "uncorrected" to predict pressure gauge response), (d) measured depths.

which this occurs is weakly frequency dependent, but is of the order of 1.0m. Any further increase in wave height should merely raise the water level over the whole system, keeping the difference between these specific points constant.

In this particular situation, the set-up is so small that any further increase in set-up does not seriously change the hydrodynamic conditions inshore. The general change in water level due to the large scale wind effects is much more significant. The overall result is that the set-up reaches a definite maximum as should the undertow. Unfortunately, the wave conditions during the six week experiment did not exceed those shown in Fig. 2.

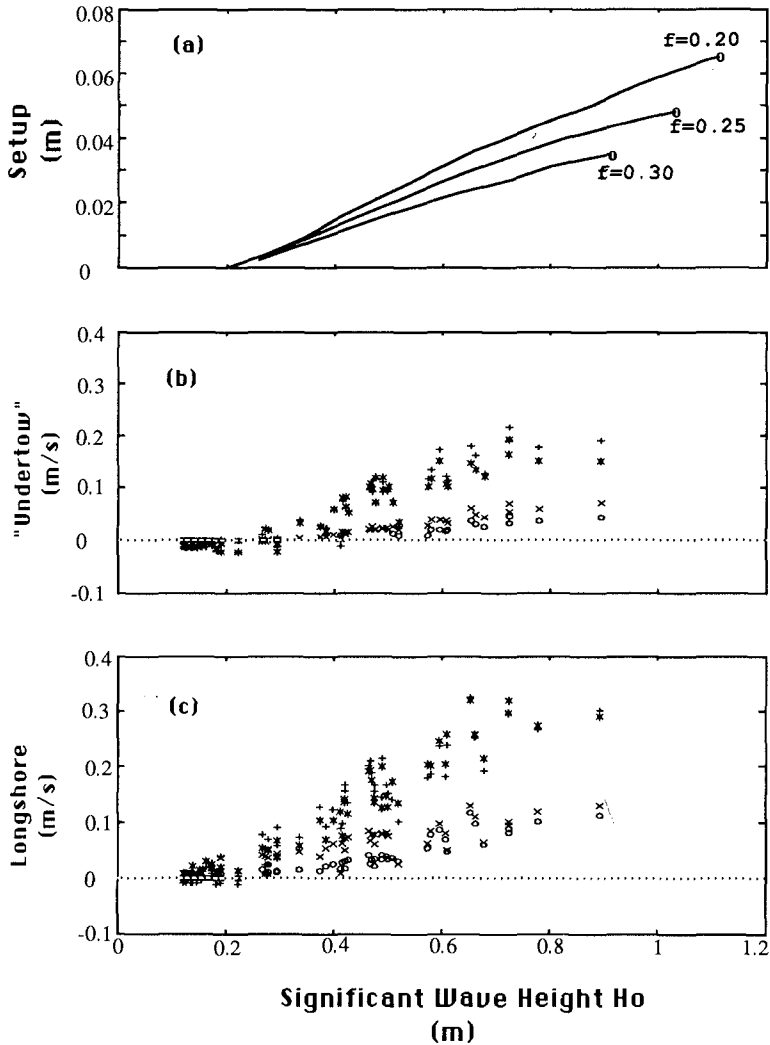


Figure 6. System Response to Various Incident Wave Heights (a) predicted setup at various frequencies (setup defined as (MWL @ 15m) - (MWL @ 150m)) (b) measured mean cross shore flow on June 9 and June 16 (+ = 55m, 10cm; * = 55m, 25cm; o = 150m, 10cm; x = 150m, 25cm), (c) measured mean longshore flow (symbols as in (b)).

The results do however show that the undertow continues to increase even though the wave conditions are *locally* saturated at the point of measurement. This occurs for $H_S \sim 0.5m$ at the 55m station. This is in contrast to the simple

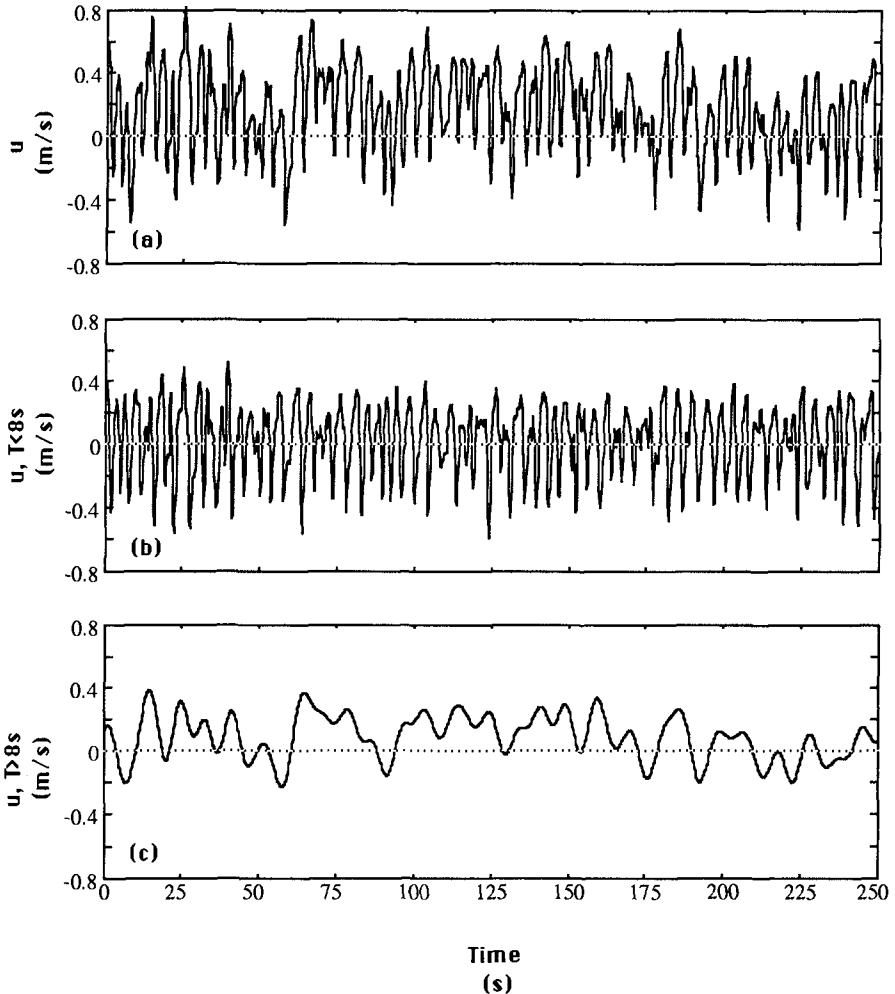


Figure 7. Time Series of Cross Shore Flow at 55m, 10cm height on June 9, 1988 beginning at 1540. (a) Time Series (b) Time series, high-pass filtered at 8 s (0.125 Hz) (c) Time Series, low pass filtered at 8 s (0.125 Hz).

models for plane beaches where the undertow depends primarily on the local conditions.

The discussion has thus far concentrated on the averages taken over a mean length of 29 minutes. This is a compromise between the need to take a reasonable number of points and the need to recognise that conditions at this beach change significantly on timescales of a few hours. However in using values for an analysis of beach equilibrium as in Roelvink and Stive (1989), care has to

be taken to include the motion at all time scales. The time variability seen at the on/offshore flow at the lower flowmeter at 55m is shown in Figure 7a. When this is filtered to separate out the incident waves, using a cut-off frequency of 0.125 Hz, the residual flow is seen (Fig. 7c) as being quite variable on a variety of time scales. While the mean is of over 0.2m/s, pulses in the residual reach 0.4m/s.

CONCLUSIONS

In this rather complex environment, a relatively simple dissipation model based on Thornton and Guza (1983) works reasonably well. Parameter values $\gamma = 0.45$, $B = 1$ suggest that the lake environment is behaving as an ocean environment, although the waves are short and steep there is a full (and rather broad) wave spectrum, tending to be rather short crested during periods of active generation when there are whitecaps to the horizon.

Measurements of the mean flow show a tendency for the flows to be very small during periods of low wave height, increasing approximately linearly with wave height once the waves begin to break on the outer bar. Saturation is predicted, if the motion is primary two-dimensional, for wave conditions slightly more severe than those observed.

The measurements of offshore flow, the undertow, show noticeable variability at all time scales. A factor to be taken into account in any modelling exercise where sediment transport is assumed to be some function of current raised to some power. In general, the wave dissipation over the bars offshore tends to reduce wave activity inshore so that the undertow, the longshore current, and the low frequency oscillations are of the same order of magnitude as the wave orbital velocities.

ACKNOWLEDGEMENTS

The primary funding for the C-COAST experiments came from NSERC (C) Strategic Grants to Greenwood and Bowen and A.E. Hay and Bowen. Additional infrastructure support was obtained from Petro-Canada Ltd. and various branches of the Government of Canada, including the Atmospheric Environment Service, the Atlantic Geoscience Centre, the Marine Environment Data Service, Parks Canada, and the Canadian Coast Guard.

REFERENCES

- Greenwood, B., P.D. Osborne, A.J. Bowen, D.G. Hazen and A.E. Hay. Nearshore sediment flux and bottom boundary dynamics: the Canadian Coastal Sediment Transport Programme (C-COAST). Proc. Twenty-Second Coastal Engineering Conference, ASCE, New York.
- Hazen, D.G., D.A. Huntley and A.J. Bowen, 1987. UDATS: A System for Measuring Nearshore Processes. *Proc. Oceans '87*, IEEE, New York, 993-997.

- Roelvink, J.A. and M.J.F. Stive, 1989. Bar-generating cross-shore flow mechanisms on a beach. *J. Geophys. Res.*, *94*, 4785-4800.
- Stive, M.J.F. and H.G. Wind, 1986. Cross-shore mean flow in the surf zone. *Coastal Engineering*, *10*, 325-340.
- Stive, M.J.F. and H.J. DeVriend, 1987. Onasi 3-D nearshore current modelling: wave-induced secondary currents, in *Proc. of Special Conference on Coastal Hydrodynamics*, ASCE, New York, 356-370.
- Svendsen, I.A., 1984. Mass flux and undertow in a surf zone. *Coastal Engineering*, *8*, 347-365.
- Svendsen, I.A. and R.S. Lorenz, 1988. Three dimensional flow profiles on littoral beaches. *Proc. Twenty-first Coastal Engineering Conference*, ASCE, New York, 705-717.
- Thornton, E.B. and R.T. Guza, 1983. Transformation of wave height distribution. *J. Geophys. Res.*, *88*, 5925-5938.

CHAPTER 157

Berm Erosion due to Long Period Waves

Kazumasa KATOH¹ and Shin-ichi YANAGISHIMA²

Abstract

Breakers in the surf zone are saturated, that is, the wave height at any point is limited by the local water depth. The larger waves in a storm break further offshore making the surf zone wider but leaving the wave height in the inner surf zone the same. Why the beach will erode during the storm? To answer this question, there has recently been considerable interest in the long period waves of one to several minutes in period. The field observation has been carried out for more than one year to acquire the field evidences of berm erosion due to the long period waves. Based on the data obtained, two typical evidences of berm erosion will be shown. A critical level of berm erosion will be discussed, which can be predicted with the mean sea level and the height of long period waves at the shoreline.

1. Introduction

Figure 1 shows the approximate distribution of ocean surface wave energy. The energy in the band of period from 1s to 30s is the largest, which is due to the wind waves. Formerly, the wind waves had been considered to be a main external forces of beach erosion in a storm. The second largest energy is in the band of period from 30s to 5 min. The waves in this frequency band are often called infragravity waves. In this paper, however, they will be referred to as " Long period waves ".

It must be said again that Figure 1 is the approximate

¹Chief of Littoral Drift Lab., Port and Harbour Research Institute, Nagase 3-1-1, Yokosuka Kanagawa, JAPAN

²Littoral Drift Lab., Port and Harbour Research Institute

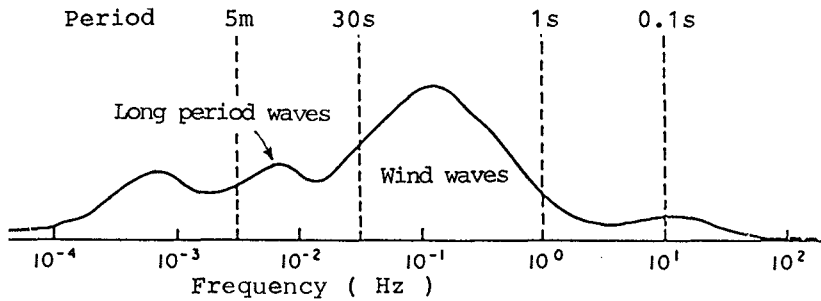


Figure 1 Distribution of ocean surface wave energy

distribution of ocean surface waves, that is to say, in the offshore area. In contrast to the offshore area, for the wave energy in the nearshore, especially in the surf zone, the energy distribution shown in Figure 1 must be modified, since the incident wind waves break and lose their energy in the surf zone. The wave height at any point is limited by the local water depth. The larger waves in a storm break further offshore making the surf zone wider but leaving the wave height in the inner surf zone the same.

On the other hand, the energy in the frequency band of long period waves becomes to be the largest near the shoreline. It has been already known that the amplitude of long period waves at the shoreline becomes larger without breaking in a storm (eg., Bowen and Huntley, 1984).

Therefore, the long period waves of about 1 to several minutes in period have attracted the attentions of researchers as a possible origin of nearshore large scale topographies such as bars. For example, Bowen and Inman (1971) showed theoretically that standing edge waves, which is a kind of the long period waves, can be the origin the formation of crescentic bars. Holman and Bowen (1982) theoretically examined the interaction of two edge waves to predict the three dimensional beach topography such as welded sand bars, and suggested that other three dimensional, complex, rhythmic topographies could also be explained by the same analyses. Katoh (1984) showed with the field data that the two-dimensional multiple longshore bars are formed by the long period standing waves.

Also in the consideration of the mechanism of berm erosion in a storm, it should be very important to take into account not the incident wind waves, but the long period waves, as the external force for the berm erosion. However, we don't have enough field evidences of beach erosion due to the long period waves.

The main purpose of the study is to acquire the field evidences of berm erosion due to the long period waves, and to have a conception for developing a predictive model of abrupt beach erosion in a storm (Katoh et al., 1988).

2. Field observation

The site of field observation is a entirely natural sandy beach, being exposed to the full wave energy of the Pacific Ocean, and is classified as micro-tidal beach with the tide range of about 1.4 meters (see Figure 2). On this beach, Port and Harbour Research Institute has constructed the Hazaki Oceanographical Research Facility (HORF) in 1986 for carrying out the field observation in the surf zone even under sever sea conditions. The research pier is a 427 meters long concrete structures. It is supported by 0.8 meter diameter piles in a single line, at 15 meters interval. The pier deck is 2.5 meters wide and 7 meters above L.W.L. In this facility, the field observation on the relation between the berm erosion and the long period waves had been carried out for more than one year from the 1st of September, 1987 to the 22nd of November, 1988.

Photo. 1 is the side view of the facility, which was taken in a calm wave condition. There is a laboratory at the base of research pier, where two researchers are permanently stationed to measure and observe the many phenomena in the surf zone.

Photo. 2 was taken in a storm condition. Although the facility was isolated in the sea, the two researchers had not any troubles. As a matter of fact, one of them came out from the laboratory to take this picture and went back not by swimming, not by a boat, but on foot with keeping his shoes dry.

Photo. 2 was taken when the crest of the long period waves run up on the beach. After one minute, however, the trough of the long period waves came to the beach and the sandy beach emerged, on which he could go back on foot. Of course, after another one minute the beach was covered with crest again. Then, he had to go bach with quick steps.

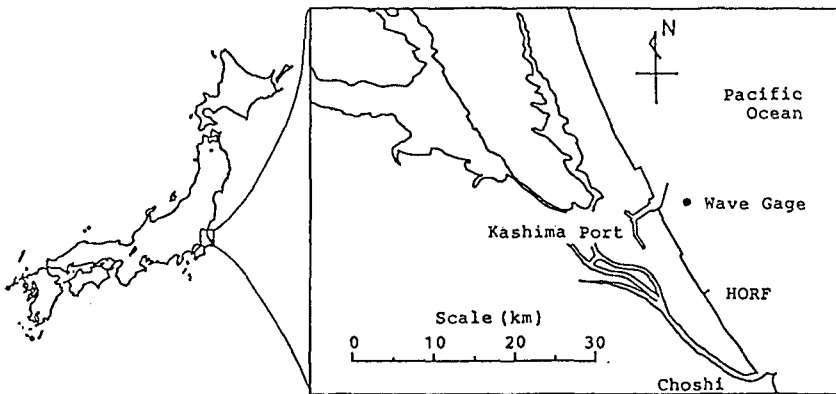


Figure 2 Site of field observation



Photo. 1 Side view of HOLF (in a calm condition)

Under this situation, there was a large wave set-up near the shoreline, which has been discussed by Yanagishima and Katoh (1990).

The field observations conducted in conjunction with this study are as follows;

Survey of beach profile

Beach profile along the research pier was surveyed with



Photo. 2 Isolated HOLF (in a storm)

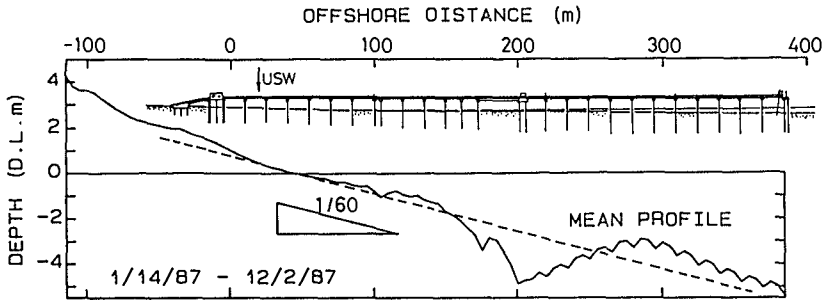


Figure 3 Mean profile and location of observation

a lead from the pier deck. The profile of the backshore and the foreshore was surveyed by using a surveyor's staff and a transit. The cross-shore interval of these measurements was 5 meters. The measurements have been being done, once a day except on Sunday and the national holiday, by the researchers in the HORF. The mean profile during about one year is calculated with these data, and is shown in Figure 3. The foreshore slope is mild, about 1/50 in average, while the mean bottom slope in the surf zone is a little milder, 1/60.

Wave observation near the shoreline

In order to measure the waves near the shoreline, an ultrasonic wave gauge was installed to the pier deck at the reference point of +22m as shown in Figure 3 and 4. The mean grand level at the observation point was 0.3 meter above the datum line. The mean water depth was about 0.4 meter in M.W.L.

The wave measurements were carried out during 20 minutes of every two hours with the sampling time of 0.3 second, which was automatically controlled by using a mini-

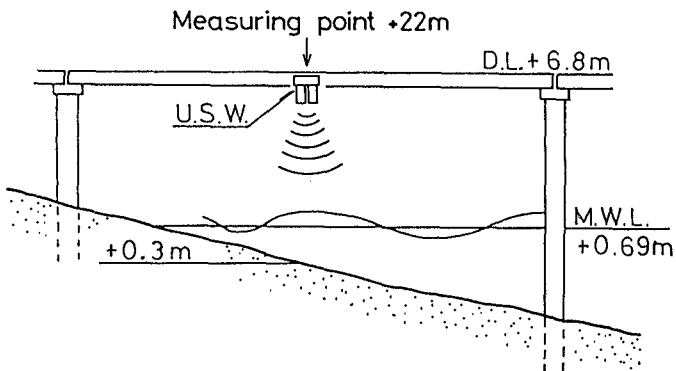


Figure 4 Location of ultrasonic wave gauge

computer in the laboratory at the base of research pier.

By utilizing the wave profile data of 0.3 second interval, the wave heights of incident wind waves and those of long period waves were calculated by the following equations based on the result of spectra analysis;

$$H_s = a \cdot \left[\int_{f_c}^{\infty} S(f) df \right]^{1/2}, \quad (1)$$

$$H_L = a \cdot \left[\int_0^{f_c} S(f) df \right]^{1/2}, \quad (2)$$

where H_s and H_L are the wave heights of the incident wind waves and the long period waves respectively, f is the frequency, $S(f)$ is the spectral energy density, f_c is the threshold frequency of 0.33Hz, and a is the constant coefficient of 4.0.

For trial, to measure the velocity at the same point as that of wave observation, the two-component type electromagnetic current meter was set on the sea bottom. It was, however, impossible to obtain the continuous data for a long time because the current meter was buried under the sea bottom due to the sand accumulation in some time or it caught floatage in another time.

Wave observation in the offshore

The offshore waves have been being measured at the mean water depth of 23.4 meters near the Kashima Port (see Figure 1) during also 20 minutes of every two hours.

3. Evidences of berm erosion

Based on the daily beach profile data for more than one year, the evidences of berm erosion have been abstracted. Those are 28 cases in total. To present the concrete participation of the long period waves in the berm erosion, two typical examples, in which there are large time lags between the occurrence of the maximum peak of wind waves and that of long period waves, will be shown.

Berm erosion due to the typhoon No.8713

The upper in Figure 5 shows the changes of the offshore significant waves during the days when the typhoon No.8713 came to near the observation site in September 1987. The significant wave height in the offshore began to be larger on the 11st of September and was larger than 3 meters on the 14th. It decreased a little in the following two days. During these days, the swell had been arriving with the significant period of 12 to 13 seconds. After that, the waves abruptly increased, being the maximum peak of 5.98 meters in the significant wave height at 16 o'clock on the 17th of September, and gradually decreased from this day on. During the latter period, the wind waves with the

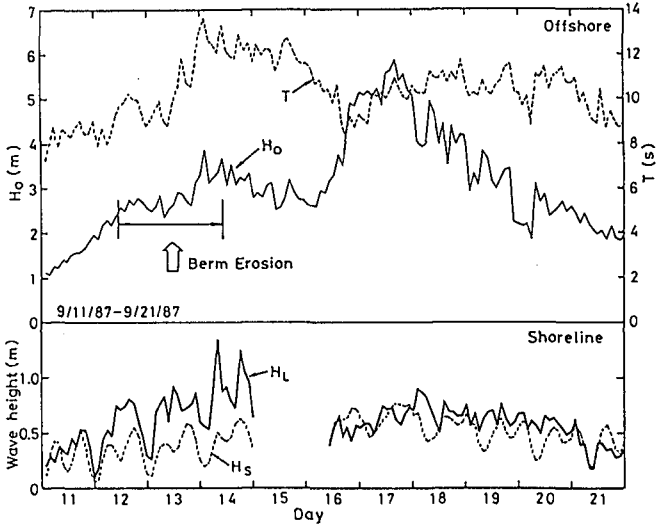


Figure 5 Waves in typhoon No.8713

period of 10 seconds were predominant.

Figure 6 shows the foreshore profiles during the corresponding days. The berm had been formed on the 12th of September, which level was higher than High Water Level. The foreshore profile was not surveyed on 13rd September because it was Sunday unfortunately. We cannot see the berm on the beach profile measured on the 14th of September. This change means that the berm had eroded within two day from the 12th to the 14th of September,

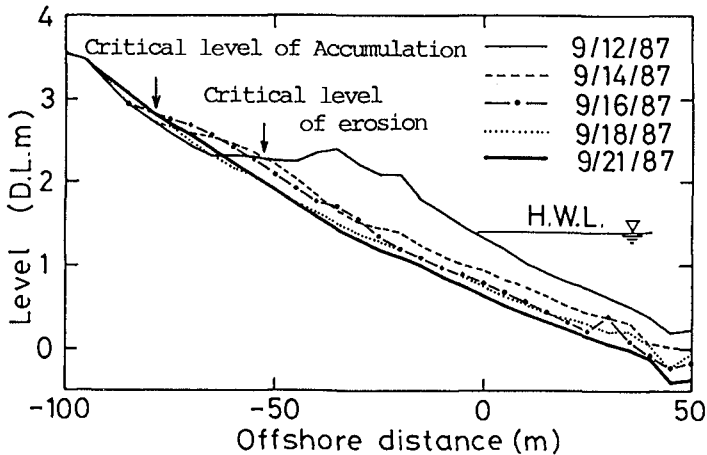


Figure 6 Berm erosion in typhoon No.8713

which is denoted with a blank arrow in Figure 5. It is noticed that the abrupt berm erosion occurred when the swell was coming, being about 4 days before the maximum peak of the offshore waves. When the offshore wave height was maximum, the foreshore also eroded. Its degree, however, was very small as shown in Figure 5. Then, it is rather difficult to obtain the offshore incident waves as the cause of this berm erosion.

The heights of incident waves and the long period waves near the shoreline are shown in the lower in Figure 5. The height of incident waves, H_s , changed periodically, independent on the offshore waves, because the wave height was limited by the shallow water depth which changed with the tide. The detail inspection of Figure 5 reveals that the incident wave height gradually increased with periodical fluctuations during days from the 11st to the 17th of September and also gradually decreased to the end of typhoon. It was due to the sea level rising, including the wave set-up, near the shoreline (Yanagishima and Katoh, 1990). Anyhow, the incident wave heights during the berm erosion were less than 0.5 meter near the shoreline, which was nearly the same values as the incident wave height before the berm erosion, on the 11st of September. Therefore, we cannot decide the incident waves near the shoreline as the cause of berm erosion.

On the other hand, the heights of long period waves, H_L , were nearly 1.0 meter on the 13rd or more on the 14th of September, and were about 0.6 to 0.7 meter when the offshore wave height was maximum on the 17th of September. That is to say, the berm erosion occurred during the days when the heights of long period wave were the largest.

One more notice must be given in Figure 6. There was a interesting paradox that the sand deposited on the greater elevation when the berm eroded, as Bascom (1954) had already pointed out.

Berm erosion due to the typhoon No.8818

The upper in Figure 7 shows the changes of the offshore significant waves during the days when the typhoon No.8818 came to the site in September, 1988. The offshore wave became to be higher since the 14th of September, and had a maximum height on the 16th of September. After that, it decreased with time. The wave period abruptly became to be longer from 6 seconds on the 13rd to 11.9 seconds on the 14th of September. From the 15th on, it fluctuated around 10 seconds.

Figure 8 shows the foreshore profiles during the corresponding days. The berm had been formed on the 13th of September in 1988. Until next day, the 14th of September, this berm had eroded. Since the measurements of beach profile had been carried out just before noon, it can be decided that the initiation of berm erosion occurred before noon on the 14th of September. Also in this case,

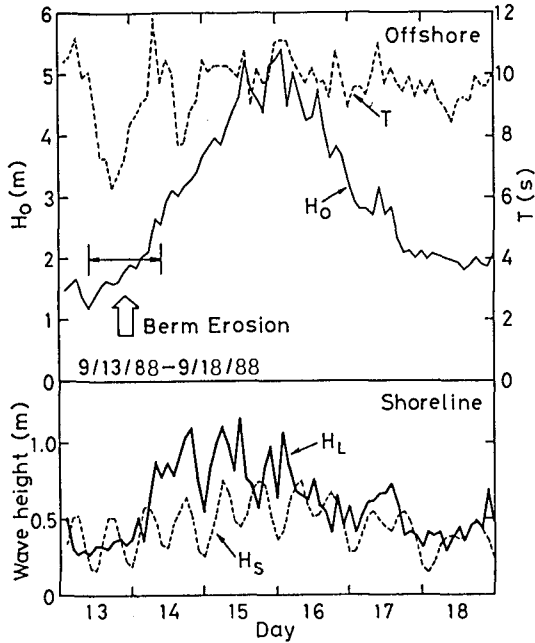


Figure 7 Waves in typhoon No.8818

there was the sand deposition on the greater elevation than the berm crest level. Unfortunately, because it is the national holiday on the 15th of September in Japan, we did not measure the beach profile on that day.

The berm erosion occurred about 3 days ahead of the

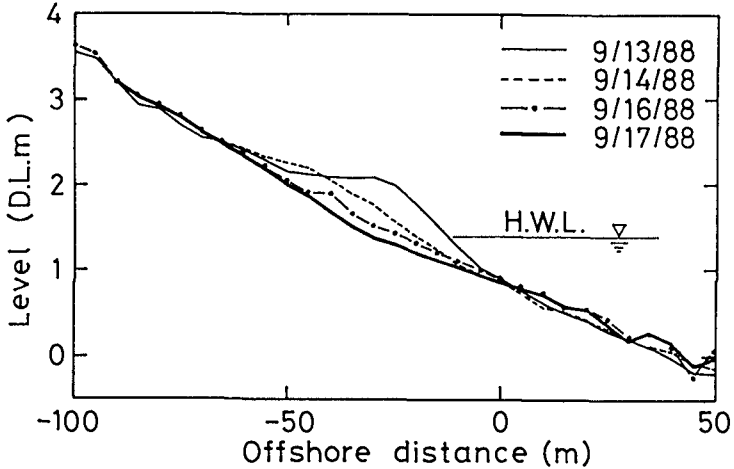


Figure 8 Berm erosion in typhoon No.8818

occurrence of the maximum incident wave height as shown in Figure 7. During the berm erosion, the offshore wave height was less than 2.0 meters. In short, also in this example, it is very hard to explain the berm erosion by taking the offshore incident wave energy into account.

In the lower in Figure 8, the height of incident waves and long period waves near the shoreline are shown. The height of incident waves was less than 0.5 meter during the berm erosion. The height of long period wave became to be larger up to 1 meter in the early morning on the 14th, and was maximum on the 15th of September. Therefore, it can be said that the height of long period waves near the shoreline was large when the berm eroded.

Based on these two examples of berm erosion, we have following tentative conclusions.

- (a) When the berm eroded, the height of offshore wave was small. It was 2 to 4 days before the occurrence of the maximum height of offshore waves. This conclusion can be obtained owing to the time lag between the changes of the incident wave height and the long period waves. In the remaining 26 cases, both the offshore wave height and the height of long period waves near the shoreline were maxima on the same day when the berm eroded.
- (b) When the berm eroded, the height of incident waves near the shoreline were usually less than those of the long period waves. This consideration is supported by all 28 evidences of berm erosion.
- (c) When the berm eroded, the sand accumulated on the greater elevation at the same time. This kind of sand accumulation existed in 23 cases out of 28 evidences of berm erosion.

4. Critical level of berm erosion

It is shown that the waves which have the direct effects on the berm erosion is the long period waves near the shoreline. Then, let's examine the critical level of erosion in the storm, which is shown in Figure 6, in conjunction with the long period waves.

The total wave run-up level on beach will be assumed as

$$R = (\bar{\eta})_0 + R_L + R_s, \quad (3)$$

where R is the total run-up level, $(\bar{\eta})_0$ is the mean sea level, R_L and R_s is the wave run-up due to the long period waves and the incident waves, respectively. These physical values are defined at the shoreline. Since the total wave run-up level is considered to be closely related to the critical level of accumulation, which is also shown in Figure 6, it can be decided in the following manner.

Estimation of mean sea level, $(\bar{\eta})_0$

The mean sea level at the observation point can be calculated by averaging the wave profile data. However, as the observation point was located a little bit offshore side from the shoreline, the calculated mean sea level must be modified to the value at the shoreline. According to the Goda's theory, the rate of wave set-up on this beach increases at the rate of 9% of the decrement in the water depth (Katoh et al., 1989). Then, the mean sea level at the shoreline can be estimated by the following equation:

$$(\bar{\eta})_0 = \bar{\eta}_0 + 0.09h, \tag{4}$$

where $\bar{\eta}_0$ and h are the mean sea level and the actual water depth at the observation point, respectively.

Estimation of run-up due to the long period waves, R_L

The run-up due to the long period wave is considered to be proportional to its wave height at the shoreline as a first approximation, since it is a standing mode. That is to say,

$$R_L = a (H_L)_0, \tag{5}$$

where a is a coefficient and $(H_L)_0$ is the height of long period waves at the shoreline.

In order to have the height of long period waves at the shoreline, we must modify the value of H_L at the observation point. For this purpose, the Goda's (1975) empirical relation between the offshore significant waves and the height of long period waves at any water depth will be introduced.

Based on the wave data measured both in the surf zone and offshore, Goda (1975) obtained the following relation:

$$\frac{\zeta_{rms}}{(\zeta_{rms})_0} = \frac{A}{\left[\frac{H_0}{L_0} \cdot \left(1 + \frac{h}{H_0} \right) \right]^{1/2}}, \tag{6}$$

where ζ_{rms} and $(\zeta_{rms})_0$ are the root-mean-square values of the wave profiles of long period waves and offshore waves, respectively, h is the water depth, L_0 is the significant wave length in deep water, and A is a coefficient which takes a value of 0.04 in the Goda's relation.

By replacing the left term of Eq.(6) with the following relation

$$\frac{\zeta_{rms}}{(\zeta_{rms})_0} = \frac{H_L}{H_0}, \tag{7}$$

the values of Goda's parameter have been calculated and plotted in Figure 9. As seen in Figure 9, almost all data are plotted below the straight line given by Goda. If the Goda's line will be moved parallel downward by employing

the value of 0.023 for A, the relatively good approximation to the data will be obtained.

By taking the Goda's parameter into account, we have the transformation equation as

$$(H_L)_0 = H_L * (1+h/H_0)^{1/2}, \quad (8)$$

being independent of the value of A, where H₀ is the offshore significant wave height.

Estimation of run-up due to the incident waves, R_s

According to the result of field observation conducted by Guza and Thornton (1982), the swash excursions of the long period components increase with the offshore incident wave height, while those of the incident waves is constant, being independent of the offshore wave conditions. Therefore, we can assume the constant value for R_s,

$$R_s = \text{const.} \quad (9)$$

By substituting Eq.(5) and (9) into Eq.(3), we have

$$R = (\bar{\eta})_0 + a(H_L)_0 + \text{const.} \quad (10)$$

In order to assume that the total run-up level is corresponding to the critical level of accumulation, we must give full consideration to the choice of data. The beach profile had been surveyed once a day, while the mean sea level and the height of long period waves had been observed every two hours. Then, after some consideration, it is decided to choose the data set of the mean sea level and the height of long period waves which summation is maximum among 12 sets of data in 24 hours between the successive surveys of profile. Then, in stead of Eq.(10), we can have

$$A_1 - (\bar{\eta})_0 = a(H_L)_0 + \text{const.}, \quad (11)$$

where A₁ is the critical level of accumulation, which value can be obtained by utilizing the beach profile data.

Twenty three sets of data which are estimated with the measured values in the manner described above are plotted in Figure 10. Of course, they are the cases that the sand accumulation have been recognized during the berm erosion. Since the data are plotted close to a solid line which is decided by applying the least squares method to the data,

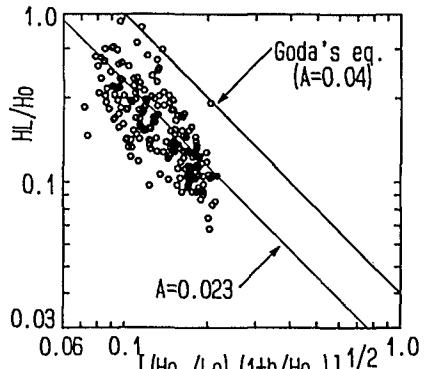


Figure 9 Value of Goda's parameter

we have

$$R = (\bar{\eta})_0 + 0.96(H_L)_0 + 0.31.(m), \quad (12)$$

Please pay attention to the replacement that R has been used in place of A_1 in Eq.(12). Equation (12) means that the total run-up level is the sum of mean sea level which contains the tide level and the sea level rising such as the wave set-up, the height of long period waves near the shoreline, and the constant which is the effect of incident wave run-up.

Figure 11 shows a comparison of the total run-up level with the critical levels of accumulation and erosion. On the abscissa in Figure 11, a symbol R_{max} is used since the largest total run-up level in a day during

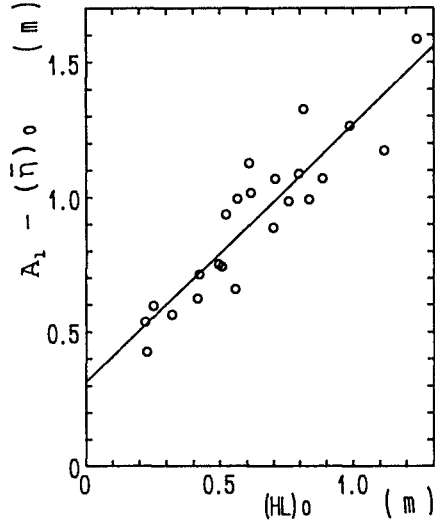


Figure 10 Comparison of wave run-up with the height of long period waves

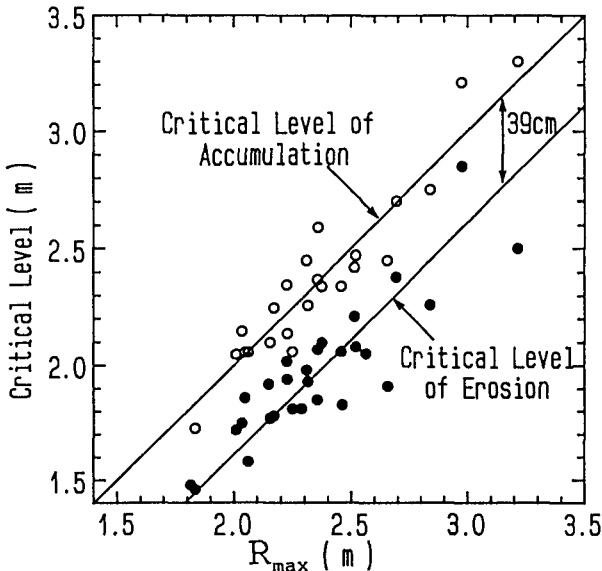


Figure 11 Comparison of critical run-up level of accumulation and erosion with maximum run-up level

the berm erosion has been chosen. The critical levels of accumulation agree well with R_{max} , while those of erosion are about 40 cm lower than R_{max} .

5. Conclusions

The conclusions obtained in this study are as follows:

- (1) When the berm eroded, the height of long period waves near the shoreline was large.
- (2) The paradox that the sand accumulates in the greater level when the berm erodes, which have been already pointed out by Bascom (1954), is confirmed with many evidences of field data.
- (3) The critical levels of accumulation and the erosion depend not on the incident waves, but on the height of long period wave and the mean sea level at the shoreline.

References

- Bascom, W.H. (1954): Characteristics of natural beach, Proc. of 4th ICCE, pp.163-180.
- Bowen, A.J. and D.L. Inman (1971): Edge waves and crescentic bars, J.G.R., Vol.76, No.36, pp.8662-8671.
- Bowen, A.J. and D.A. Huntley (1984): Waves, long waves and nearshore morphology, Marine Geology, Vol.60, pp.1-13.
- Goda, Y. (1975): Deformation of irregular waves due to depth-controlled wave breaking, Rep. of PHRI, Vol.14, No.3, pp.59-106 (in Japanese, see Goda, 1985).
- Goda, Y. (1985): Random seas and design of maritime structures, University of Tokyo Press, 323p.
- Guza, R.T. and E.B. Thornton (1982): Swash oscillation on a natural beach, J.G.R., Vol.87, pp.483-491.
- Holman, R.A. and A.J. Bowen (1982): Bar, bumps, and holes: Models for the generation of complex beach topography, J. Geophys. Res., Vol.87, No. C1, pp.457-468.
- Katoh, K. (1984): Multiple longshore bars formed by long period standing waves, Rep. of Port and Harbour Res. Inst., Vol.23, No.3, pp.3-46.
- Katoh, K. and S. Yanagishima (1988): Predictive model for daily changes of shoreline, Proc. of 21st ICCE, pp.1253-1264.
- Katoh, K. et al. (1989): Wave set-up near the shoreline, -Field observation at HORF-, Rep. of PHRI, Vol.28, No.1, pp.3-41 (in Japanese).
- Yanagishima, S. and K. Katoh (1990): Field observation on wave set-up near the shoreline, Proc. of 22nd ICCE.

CHAPTER 158

A FIELD EXPERIMENT ON BREACH GROWTH IN SAND-DIKES

by

P.J. Visser ^{*}, J.K. Vrijling ^{*} and H.J. Verhagen ^{**}

ABSTRACT

The set-up and results of a field experiment on sand-dike breach erosion are described. It is found that the breaching process for the 2.2 m high sand-dike is similar to that in Visser's (1988) laboratory experiments with a 0.6 m high sand-dike.

Confrontation of Visser's (1988) breach erosion model with the field data shows reasonable agreement for the first stages of the breaching process. As yet the model is not applicable to the final phase of the sand-dike breach erosion. If applied then it would fairly overestimate the breach growth in this final stage.

1. INTRODUCTION

Since dikes have been constructed, in The Netherlands for more than 800 years now, the failure of these high-water defences has been the immediate cause of many inundations. The polder "Alblasserwaard", for instance, has been flooded 33 times since the year 1200. The consequences of a number of these inundations were disastrous, with great losses of human lives, livestock and properties. Curiously the knowledge of the breaching process in dikes is still very limited.

The Technical Advisory Committee on Sea Defences (TAW) in The Netherlands is completing a probabilistic design method for dikes.

* Department of Civil Engineering, Delft University of Technology, P.O. Box 5048, 2600 GA Delft, The Netherlands.

** Road and Hydraulic Engineering Division, Ministry of Transport and Public Works (Rijkswaterstaat), P.O. Box 5044, 2600 GA Delft, The Netherlands.



Fig. 1 Map of The Netherlands showing the locations of the IJsselmeer Dam, the lake IJsselmeer and Cadzand (site of the field experiment). The dark area is land below Mean Sea Level.

This method determines the optimal dike-design as function of the construction costs and the expected damage costs (deaths, loss of property and revenues, repair costs, etc.) due to a failure of the dike.

In order to be able to determine the damage costs, it is necessary to predict the rate of inundation of the polder. This inundation rate is especially governed by the discharge rate through the breach in the dike, which largely depends on the process of breach erosion.

An example illustrating the benefit of a good breach erosion model is the IJsselmeer Dam in The Netherlands (see Fig. 1). This dam, which was completed in 1932, prevents the penetration of storm surges from the North Sea into the lake IJsselmeer and in this way flooding and collapsing of the dikes of the polders around the lake IJsselmeer. The IJsselmeer Dam is a primary dike, the dikes of the polders around the lake IJsselmeer are secondary dikes.

The height and stability of the IJsselmeer Dam do not meet the modern Dutch standards for sea defences. Expensive dike construction works are necessary to meet these requirements.

However, in case of failure of the IJsselmeer Dam it is possible that the dimensions of the breach(es) in the dike remain confined, consequently also the flow rate through the breach(es), such that the water level increase in the lake IJsselmeer remains relatively small and the dikes of the surrounding polders can withstand the higher water level. So it is possibly not necessary to reinforce the IJsselmeer Dam.

The present investigation is part of a project aimed at the development and verification of a mathematical model for breach erosion that describes the breach growth and the discharge rate through the breach in case of a dike-burst.

A first version of the breach erosion model, see Visser (1988), was especially developed for the huge (i.e. about 75 m high) sand-dike of a proposed pumped-storage plant along the Dutch coast.

The heart of the model is a modified Bagnold (1963, 1966) energetics-based sand transport conception combined with a simplified Galappatti and Vreugdenhil (1985) pick up mechanism for the suspended sediment. The model has been tested to three scale experiments in the laboratory giving a good agreement between model predictions and experimental results, see Visser (1988).

Additional experimental data of Dieteren and Pottinga (1988) have also shown good agreement with the model predictions. Dieteren and Pottinga (1988) have also found that the combination of Bagnold's sand transport theory and Galappatti and Vreugdenhil's sand pick up mechanism gives much better results than the erosion functions of Chee (1978) and Mastbergen and Winterwerp (1987) and the sand transport formulas of Engelund and Hansen (1967), Ackers and White (1973) and van Rijn (1984a, 1984b) combined with the Galappatti and Vreugdenhil (1985) sand entrainment formulation.

A field experiment was performed to test the applicability of the model to (sand-)dikes with a height of order of magnitude of 10 m. This paper describes the set-up and results of this experiment, some further work on the model aimed at the present application and the confrontation of the model with the field data.

2. FIELD EXPERIMENT

2.1 Introduction

The field experiment took place on December 13, 1989 in the Zwin Gully near the village of Cadzand, in the south-western part of The Netherlands (see Fig. 1). The experiment was initiated and directed by study group TAW-C and financed by Rijkswaterstaat. De Looff (1990) has reported on the experiment.

2.2 The sand-dike

The Zwin Gully is a tidal inlet connecting the nature reserve "the Zwin" with the North Sea (see Fig. 2). The width of the inlet varies between 50 and 100 m. The bottom of the Zwin Gully is at about 0.3 m above Mean Sea Level.

The sand-dike was constructed, exclusively for the field experiment, with local sand ($D_{50} \approx 0.20$ mm) at low tide. The sand-dam temporarily closed the Zwin Gully, see Fig. 3.

The length of the dike was about 50 m, its cross-section is shown in Fig. 4: outer (seaward) slope is 1:1.25, inner (landward) slope is 1:3, height H_d above the Zwin Gully bottom is 2.2 m and width at the top is about 8 m. A small initial breach, about 0.2 m deep, about 0.5 m wide and about 8 m long was made in the crown of the dike to ensure breaching of the dike near the middle of the Zwin Gully (see Fig. 5).

2.3 Growth of breach width

The sand-dike was constructed at low tide, as described above,



Fig. 2 View of Zwin Gully and distantly natural reserve "the Zwin".



Fig. 3 Photo of sand-dike in Zwin Gully (seaside is to the right, landside is to the left).

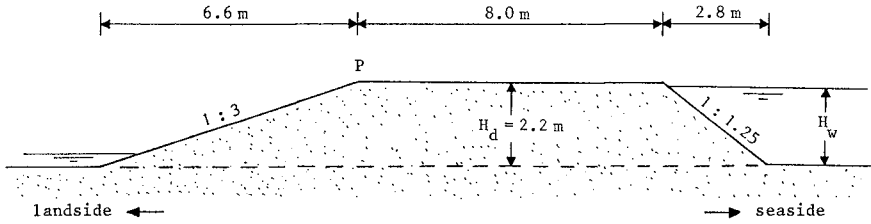


Fig. 4 Cross-section of sand-dike.

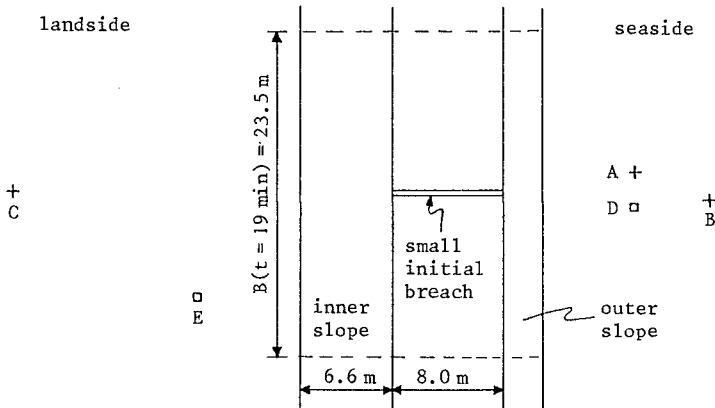


Fig. 5 Plan view of sand-dike and positions of measuring equipment (B = breach width at the top of the dike).

and was breached during (the final phase of) the next rising tide. The flow of water through the small initial breach at high water (at sea) started the breach erosion process. Let us define this point of time as $t = 0$.

The breaching process was both video-taped and photographed. Levelling-staffs in the top of the dike (see one in Fig. 7) provided the proper length-scale for the readings from the video-images and photographs. The main result of these readings, i.e. the increase in time of the breach width at the downstream end of the crown of the dike (point P in Fig. 4) is shown in Fig. 13. Fig. 6 shows the breach at $t \approx 2$ min (minutes), Fig. 7 at $t \approx 10$ min.

2.4 Water level and current velocity measurements

Fig. 5 shows the positions of the points A, B and C where current velocity measurements were made (with Ott propeller current



Fig. 6 Photo of breach at $t \approx 2$ min.



Fig. 7 Photo of breach at $t \approx 10$ min.

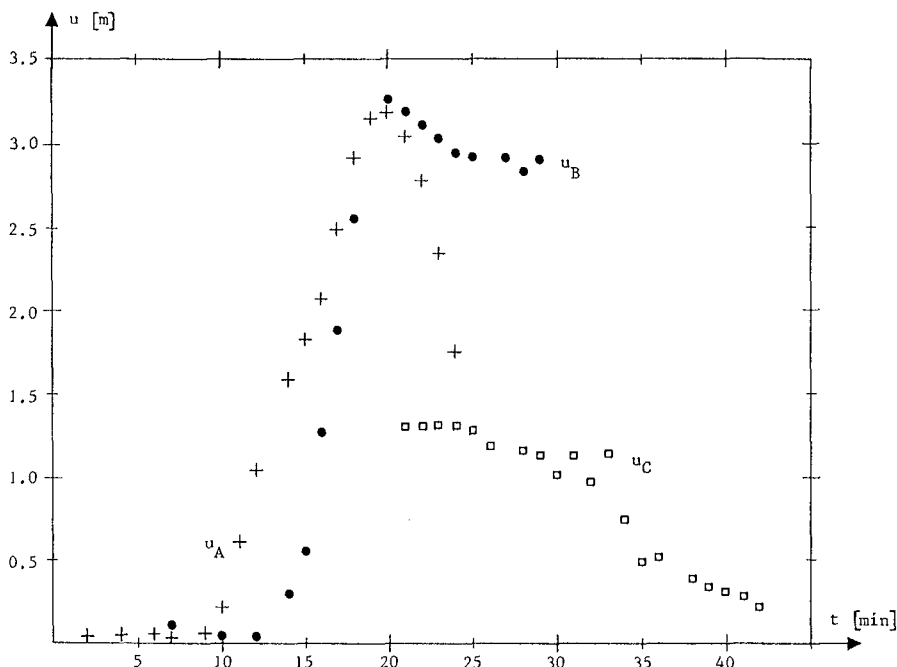


Fig. 8 Measured current velocities in points A, B and C.

meters, in A and C at a level of 0.60 m above the bottom of the Zwin Gully and in B 0.30 m above the bottom). Fig. 5 also gives the positions of the points D and E where water levels were measured (with tide-gauges). Fig. 2 shows the Ott propeller current meter in point C and the tide-gauge in point E. Fig. 3 shows the current velocity meters in the points A and B and the staff-gauge in point D.

The measured current velocities are given in Fig. 8, the observed water levels above MSL + 0.30 m are shown in Fig. 9.

3. BREACH EROSION PROCESS

Both the laboratory experiments, see Visser (1988) and Dieteren and Pottinga (1988), and the present field experiment have indicated that in case of sand-dike breaching, after a small initial gap in the dike top at $t=0$, the following four stages can be distinguished in the breach erosion process (see Fig. 10):

- I. Steepening of the inner slope angle β upto a critical value β_0 for $0 < t < t_0$.
- II. Continuing erosion of the inner slope for $t_0 \leq t \leq t_1$: the width of the top of the dike in the breach gets smaller while

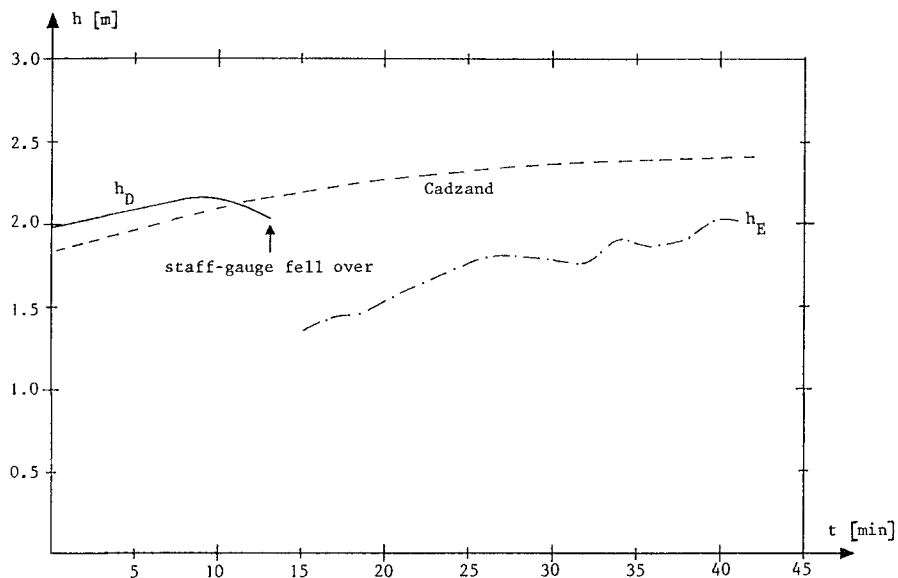


Fig. 9 Measured water levels h above MSL + 0.30 m in points D and E.

β remains equal to β_0 .

III. Lowering of the dike top in the breach and a subsequent increase of the breach width.

IV. Continuation of the breach growth horizontally and in vertical direction (scour hole) after the complete wash-out of the dike in the breach.

Essential for this process of breach erosion is that suspended sediment transport dominates bottom transport, see Visser (1988).

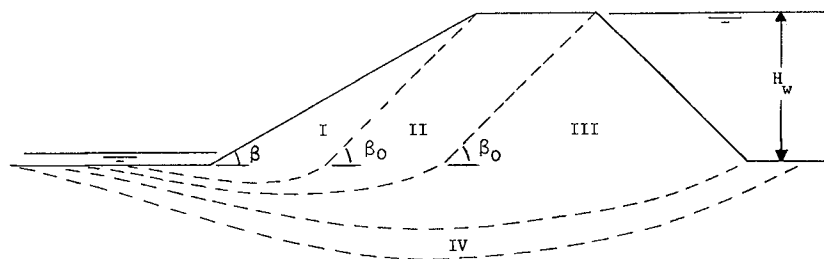


Fig. 10 Four stages in process of breach erosion.

4. MATHEMATICAL MODEL

4.1 Entrainment and transport of sand

The entrainment and subsequent transport of sand in suspension along the inner slope is described by (see Visser, 1988):

$$s(x') = \frac{x'}{L_a} s_s \quad \text{for } 0 \leq x' \leq L_a \quad (1)$$

in which

$$L_a = \frac{q}{w \cos \beta} \quad (2)$$

$$s_s = \frac{0.01 C_f u^4}{(1-p) \Delta g w \cos^2 \beta} \quad (3)$$

where $s(x')$ is the suspended sand transport per unit width along the inner slope (bulk volume transport), s_s is the transport capacity for the suspended sand, x' is the coordinate along the inner slope ($x'=0$ at the top of the dike, see Fig. 11), L_a is the adaptation length, w is the fall velocity of sand in water, C_f is the friction coefficient for the bed (about 0.01), u is the depth-averaged current velocity of the flow on the inner slope with discharge rate q per unit width, p is the bed porosity, $\Delta = (\rho_s - \rho)/\rho$, ρ_s is the sand mass density, ρ is the water mass density, g is the acceleration of gravity and β is the angle of inclination of the inner slope.

Equations (1) and (2) describe the pick up of sediment in suspension for large values of u_*/w (u_* is the bed shear velocity) according to Galappatti and Vreugdenhil (1985). Equation (3) rests on a modified Bagnold (1963, 1966) energetics-based sand transport conception for the suspended sediment load (which dominates bottom load here), see Visser (1988). The factor 0.01 in (3) is also according to Bagnold (1963, 1966). It is assumed that the transport of sand over the top of the dike in the breach is negligible.

4.2 Discharge rate through the breach

The discharge rate q per unit breach width is described by

$$q = m_0 \frac{2}{3} \left(\frac{2}{3} g \right)^{1/2} (H_w - \hat{z})^{3/2} \quad (4)$$

where m_0 is the discharge coefficient (≈ 1.0), H_w is the water level at sea in front of the dike, \hat{z} is the height of the dike top in the breach, both H_w and \hat{z} are measured above $z=0$ (i.e. above the Zwin Gully bottom), see Fig. 11.

It can be concluded from Fig. 9 that for $0 < t < 20$ min: $H_w \approx h_D$ at $t = 10$ min, so $H_w \approx 2.2$ m. For $t > 20$ min: $h_E > (2/3)H_w \approx 1.5$ m, see Fig. 9, so for $t > 20$ min the downstream water dammed up the flow of

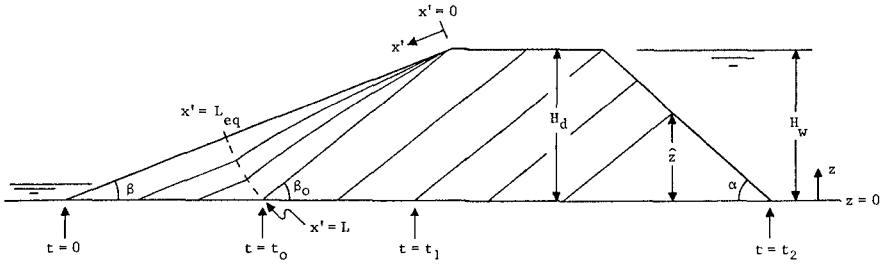


Fig. 11 Erosion of inner slope.

water through the breach. Consequently, equation (4) can be applied for the present field experiment only for $0 < t < 20$ min.

4.3 Breach growth

Fig. 11 shows the process of erosion as discussed by Visser (1988) using theoretical arguments; this process is in agreement with that of Fig. 10 as observed in both the laboratory experiments and the field experiment.

Visser (1988) argues that for $t_0 \leq t < t_2$ the erosion of the inner slope is determined by the erosion at $x' = L_{eq}$ (where the depth-averaged current velocity reaches the equilibrium value for uniform flows), which comes down to the same as the erosion at the toe of the slope (at $x' = L$, L is the length of the inner slope):

$$-L \frac{dz'_b}{dt} = s_L \quad \text{for } t_0 \leq t < t_2 \quad (5)$$

where $z'_b = z'_b(x', t)$ is the position of the sloping bottom in z' -direction and s_L is the sand transport at the toe of the slope.

The current velocity for $x' = L$ can be written as

$$u_L = \left(\frac{g q \sin \beta_0}{C_f} \right)^{1/3} \quad (6)$$

The relation between the decrease dx_c of the width of the crown of the dike and dz'_b , and that between the fall $d\hat{z}$ of the top of the dike and dz'_b , follow both from simple geometrical considerations, see Fig. 12:

$$\frac{dx_c}{dt} = \frac{1}{\sin \beta_0} \frac{dz'_b}{dt} \quad (7)$$

$$\frac{d\hat{z}}{dt} = \frac{\sin \alpha}{\sin(\alpha + \beta_0)} \frac{dz'_b}{dt} \quad (8)$$

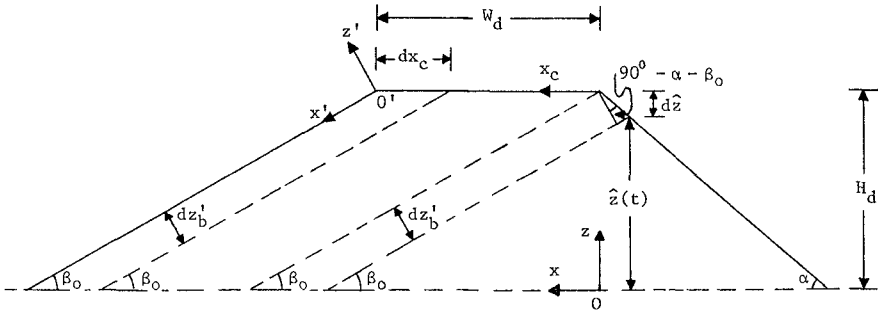


Fig. 12 Decline dx_c of the crown width x_c of the dike and fall $d\hat{z}$ of the top height \hat{z} of the dike, both as function of an erosion dz'_b of the inner slope.

where α is the angle of inclination of the outer slope.

Figures 11 and 12 show the erosion of the inner slope and the breach growth in vertical direction in a 2D-situation. For the 3D-situation Visser (1988) argues that the breach width B at the crown of the dike can be coupled with the breach depth $H_d - \hat{z}$:

$$B = r (H_d - \hat{z}) \quad \text{for } t_0 \leq t < t_2 \tag{9}$$

where H_d is the height of the dike and r is a coefficient with a value of about 3.8 (for sand-dikes).

The effect of the breaching process in horizontal direction on the breach growth in vertical direction is that the latter slows down with a factor f compared with the 2D-situation:

$$f = \frac{b + 2q/u}{2b} \tag{10}$$

where b is the depth-averaged breach width, see Visser (1988).

Substitution of (5), (1) with (2) and (3), (6) and (4) successively into (7) and (8) and taking into account the factor f gives:

$$\frac{dx_c}{dt} = - f k_1 (H_w - \hat{z}_0)^{1/2} \quad \text{for } t_0 \leq t \leq t_1 \tag{11}$$

$$\frac{d\hat{z}}{dt} = - f k_2 (H_w - \hat{z})^{1/2} \quad \text{for } t_1 \leq t < t_2 \tag{12}$$

in which \hat{z}_0 is \hat{z} at $t = t_0$ and where

$$k_1 = \frac{0.0082}{(1-p)\Delta} \left(\frac{m_0}{C_f}\right)^{1/3} (g)^{1/2} \frac{(\sin\beta_0)^{1/3}}{\cos\beta_0} \quad (13)$$

$$k_2 = k_1 \frac{\sin\alpha \sin\beta_0}{\sin(\alpha + \beta_0)} \quad (14)$$

Equations (9), (11) and (12) with (10), (13) and (14) describe the breach erosion for $t_0 \leq t < t_2$. The model is not (yet) valid for $t \geq t_2$, after the complete wash-out of the dike in the breach, since it rests on the erosion process of a (relatively) steep slope.

In principle it is also possible to describe the steepening of the inner slope for $t < t_0$ with the present approach. However, in practise the time period t_0 is very sensitive for the dimensions of the small initial breach.

5. CONFRONTATION OF MODEL WITH FIELD DATA

If $H_w = \text{constant}$, as can be assumed in the present field experiment for $0 < t < 20 \text{ min}$ (see section 4.2), simple analytical solutions for (11) and (9) with (12) result.

Integration of (11) gives with $x_c = 0$ for $t = t_1$:

$$x_c = f k_1 (H_w - \hat{z}_0)(t_1 - t) \quad \text{for } t_0 \leq t \leq t_1 \quad (15)$$

Hence, with $x_c = W_d$ for $t = t_0$, where W_d is the width of the crown of the dike (see Fig. 12):

$$t_1 = t_0 + \frac{W_d}{f k_1 (H_w - \hat{z}_0)} \quad (16)$$

Substitution of the result of the integration of (12), with $\hat{z} = 0$ for $t = t_2$ and $H_d = H_w$, into (9) gives

$$B = r \left[\frac{1}{4} f^2 k_2^2 (t - t_2)^2 + f k_2 (t - t_2) H_w^{1/2} + H_w \right] \quad \text{for } t_1 \leq t < t_2 \quad (17)$$

where

$$t_2 = t_1 + \frac{2}{f k_2} [H_w^{1/2} - (H_w - \hat{z}_0)^{1/2}] \quad (17)$$

The photos and video-images of the breach growth in the field experiment show that: $t_0 \approx 3 \text{ min}$. The results of the computations of t_1 , t_2 and B with $t_0 = 3 \text{ min}$, $H_w - \hat{z}_0 = 0.2 \text{ m}$, $p = 0.4$, $\Delta = 1.65$, $m_0 = 1.0$, $C_f = 0.015$ (see Visser, 1988), $\beta_0 = 32^\circ$ and $\alpha = 39^\circ$ are shown in Fig. 13. Fig. 13 also gives the measured values for B (field experiment). The agreement for $t < t_2$ is good.

The extrapolation in Fig. 13 for $t > t_2$ was done with a constant value for dB/dt , i.e. the value at $t = t_2$.

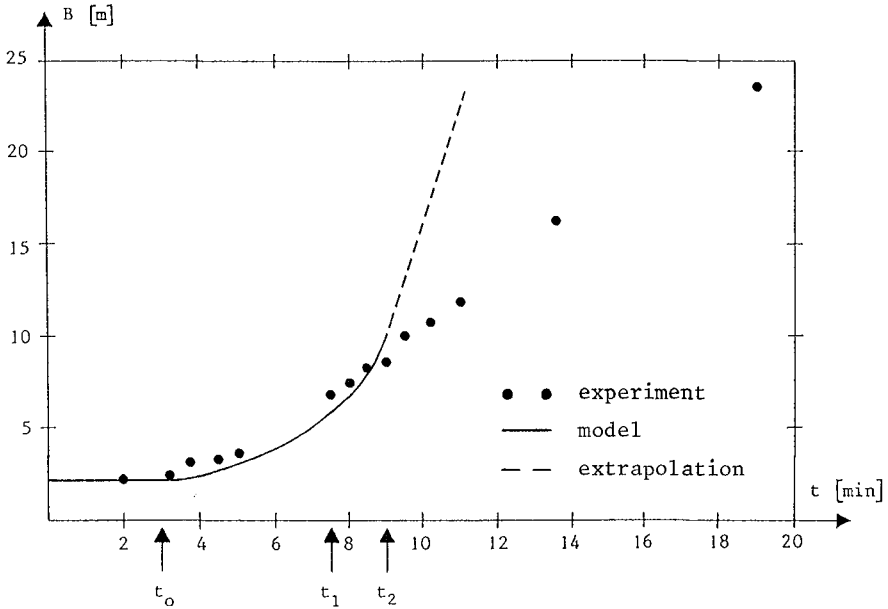


Fig. 13 Comparison of measured and computed development of breach width B at the crown of the dike.

6. DISCUSSION

The agreement between the process of breach erosion in the 0.6 m high laboratory sand-dikes, see Visser (1988), and that in the present 2.2 m high prototype sand-dike gives satisfaction. It means that much of the experimental work on sand-dike breach erosion can be done in the laboratory. This also applies to the comparable process of breach erosion in dunes.

As yet the model is only valid for the breach growth for $t < t_2$, since the model rests on the erosion process of a (relatively) steep slope. The agreement between the model predictions and both the laboratory experiments of Visser (1988) and the present field experiment is quite satisfactory.

The present investigation indicates that extrapolation of the model for $t > t_2$ (in stage IV) gives a significant overestimation of the breach growth. Hence it is meaningless to apply the model in its present state for $t > t_2$. Therefore it can be concluded that further study is necessary to include the process of breach erosion in stage IV in the model.

REFERENCES

- Ackers, P. and White, W., 1973. Sediment transport: new approach and analysis. Journ. Hydraulics Division, ASCE, vol. 99, pp. 2041 - 2060
- Bagnold, R.A., 1963. Mechanics of marine sedimentation. In *The Sea: Ideas and Observations*, vol. 3, Interscience, New York, pp. 507 - 522.
- Bagnold, R.A., 1966. An approach to the sediment transport problem from general physics. Geological Survey Professional Paper 422-I, U.S. Government Printing Office.
- Chee, S.P., 1978. Mobile controls for water resources projects. *Water Resources Bulletin*, American Water Resources Association, vol. 14, pp. 99 - 107.
- Dieteren, J.M.L. and Pottinga, P.H., 1988. Breach development in dike-bursts (in Dutch). Msc-thesis, Hydraulic Eng. Division, Dept. of Civil Eng., Delft Univ. of Techn., Delft, The Netherlands.
- Engelund, F. and Hansen, E., 1967. A monograph on sediment transport. Teknisk Forlag, Copenhagen, Denmark.
- Galappatti, R. and Vreugdenhil, C.B., 1985. A depth-integrated model for suspended sediment transport. *Journ. Hydraulic Res., IAHR*, vol. 23, pp. 359 - 377.
- Looff, A.P. de, 1990. Breach growth in a sand-dike, report on an experiment (in Dutch). Road and Hydraulic Engineering Division, Ministry of Transport and Public Works (Rijkswaterstaat), Rep. no. WBA-R-90.041.
- Mastbergen, D.R. and Winterwerp, J.C., 1987. Flow of sand-water mixtures (in Dutch). Rep. Z46-02, Delft Hydraulics, Delft, The Netherlands.
- Rijn, L.C. van, 1984a. Sediment transport, part I: bed load transport. *Journ. Hydraulic Eng., ASCE*, vol. 110, pp. 1431 - 1456.
- Rijn, L.C. van, 1984b. Sediment transport, part II: suspended load transport. *Journ. Hydraulic Eng., ASCE*, vol. 110, pp. 1613 - 1641.
- Visser, P.J., 1988. A model for breach growth in a dike-burst. *Proc. 21st Int. Conf. Coastal Eng., Malaga, Spain*, pp. 1897 - 1910.

CHAPTER 159

MULTI-SCALE NEARSHORE & BEACH CHANGES

by

R.Ostrowski, Z.Pruszek & R.B.Zeidler¹

ABSTRACT

Empirical orthogonal functions in one- and two-dimensional formulation are employed to identify the variability of longshore and cross-shore features in different scales, ranging from days to years. The prototype topographic data was measured in coastal zones of the Baltic and Black Seas. Conspicuous features such as berms, bars, salients and cusps can be identified through e_{2x} . Temporal variation of cross-shore transport is reflected in e_{2t} and e_{3x} while linkage of e_{3t} to coastal factors remains unspecified.

1 Introduction

Beach transformation processes are usually dealt with in categories of longshore and cross-shore sediment transport. Both modes are discussed in this paper. At the same time one distinguishes different spatial and time scales. For the purposes of this paper, we identify short-term, meso-scale and long-term beach changes. The former include changes ranging from days to weeks, the meso-scale transformation encompassing changes from days to seasons, the seasonal yearly and multi-yearly variation being placed in the category of long-term changes.

We are in possession of a bulk of data for shore transformation along the Polish coast of the south Baltic, the Bulgarian coast of the Black Sea, and some other sites. For illustration, Fig. 1 shows excerpts from bathymetric charts compiled for the years 1967, 1975 and 1987 in the central part of the Polish coastline. It is seen that some parts of the coastal profile undergo very intensive changes while some other display a node-type behaviour with very minor variations. Together with the obvious need for more exploration of coastal processes, that finding has inspired us to undertake the investigation of nearshore and beach changes reflected in this paper.

2 Field Measurements

Field measurements provide the most obvious tool for analysis of nearshore transformation. We have collected data basically at two coastal research stations, one at Lubiatowo on the south Baltic Sea, some 75 km to the west of Gdańsk and the other at Shkorpilovtsi, some 50 km south of Varna, on the Bulgarian Black Sea. The two sites differ in many

¹all Polish Academy of Sciences' Institute of Hydro-Engineering IBW PAN, 80-953 Gdańsk, Kościuska 7, PL

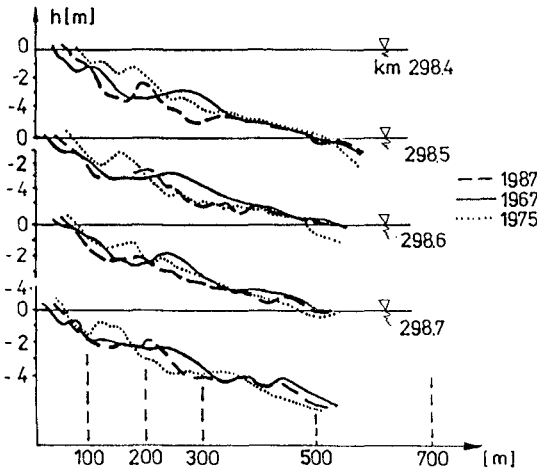


Fig. 1. Examples of shore profiles measured on Polish coast

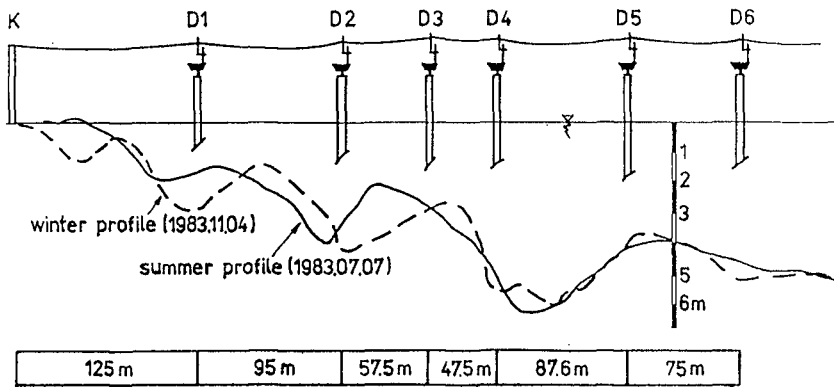


Fig. 2. Shore profile and measuring posts at IBW PAN Station at Lubiatowo (PL)

respects. The coastal zone at Lubiatowo is of dissipation type, with multiple bars, the inclination of bed being about 1%, and the sediment consisting of medium sand having $D_{50} \approx 0.22$ mm. The Bulgarian site is rather reflection type, with average bed slope about 1.5-2%, with one or no bar, its bed consisting of sand with $D_{50} \approx 0.4$ mm.

Fig. 2 depicts typical summer and winter profiles at Lubiatowo while Fig. 4 provides a rough idea of the Shkorpilovtsi environment. Data for short-term and meso-scale changes provided in this paper originate primarily from the Shkorpilovtsi station while the long-term variation is mostly based on measurements at Lubiatowo.

3 Empirical Orthogonal Functions (EOF)

Most of our analysis for bed changes is based on the method of empirical orthogonal functions, see Winant et al. (1975) for reference.

An one-dimensional approach, the variation of depth in time t and across shore, in the

direction x can be given as the following linear series:

$$h_{xt} = \sum_n c_{nt} \cdot e_{nx} \quad (1)$$

in which the index x varies from 1 to n_x , the total number of points along the profile where data is taken, while t is contained between 1 and n_t , the total number of times at which profiles were recorded.

If we require that the orthonormality condition is satisfied as:

$$\sum e_{nx} \cdot e_{mx} = \delta_{nm} = \begin{cases} 1 & m = n \\ 0 & m \neq n \end{cases} \quad (2)$$

then the quantities e_{nx} form a set of normal modes, or eigenfunctions. It is recollected that usual Fourier series also conform to the above condition. The value of EOF consists in the fact that a set of empirical eigenfunctions is selected to fit the data in the least squares sense.

The eigenfunctions e_{nx} are found from the empirical symmetric correlation matrix B having the following elements:

$$b_{ij} = \frac{1}{n_x n_t} \sum_{t=1}^{n_t} h_{it} h_{jt} \quad (3)$$

Any square matrix possesses a set of eigenvalues λ_n being found from the following determinant:

$$\det [B(\lambda)] = 0 \quad (4)$$

and a set of corresponding eigenfunctions, which are found from the following matrix equation:

$$B \cdot e_n = \lambda_n \cdot e_n \quad (5)$$

The coefficients c_{nt} , which may be referred to as a temporal eigenfunctions, are all also orthonormal:

$$\sum_{t=1}^{n_t} c_{nt}^* c_{mt} = \delta_{mn} = \begin{cases} 1 & m = n \\ 0 & m \neq n \end{cases} \quad (6)$$

in which $c_{nt}^* = c_{nt} / \sqrt{\lambda_n n_x n_t}$.

The coefficients c_{nt} are found by analogy from:

$$c_{nt} = \sum_n h_{xt} \cdot e_{nx} \quad (7)$$

For the mean shore profile represented by the first mode ($n = 1$ in Eq. 4) one has

$$h_{xt} = c_{1t} \cdot e_{1x} \approx e_{1x} \cdot (\lambda_1 \cdot n_x)^{\frac{1}{2}} \quad (8)$$

The above one-dimensional description can be expanded to the two dimensions (long-shore and cross-shore), cf. Hsu et al. (1986):

$$h(x, y, t) = \sum_k e_k(x, t) e_k(y, t) \quad (9)$$

The functions $e_k(x, t)$ and $e_k(y, t)$ are given by the following equations:

$$e_k(x, t) = \sum_n (\lambda_n n_x n_t)^{\frac{1}{2}} e_k^n(x) C_{kx}^n(t) \quad (10)$$

$$e_k(y, t) = \sum_m (\lambda_m n_y n_t)^{\frac{1}{2}} e_k^m(y) C_{ky}^m(t) \quad (11)$$

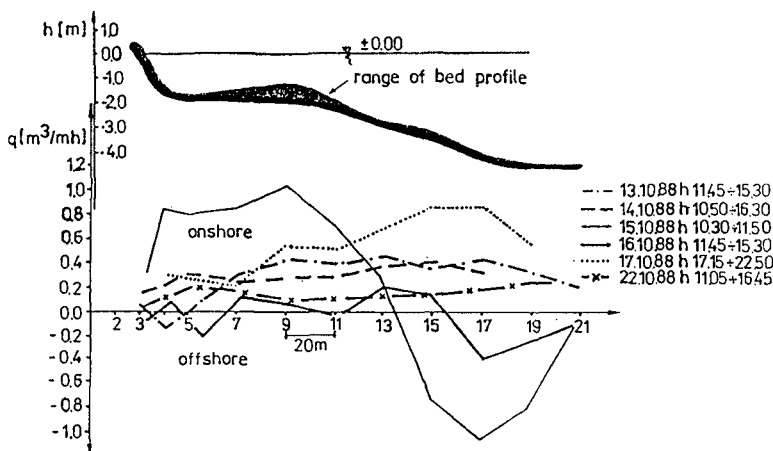


Fig. 3. Short-term bed changes measured at Shkorpilovtsi (Bulgarian Academy of Sciences)

in which:

k = two-dimensional mode of eigenfunction

λ_n, λ_m = eigenvalues for cross-shore and longshore direction, respectively

n_x, n_y, n_t = number of points measured across shore (x axis) and along shore (y axis) and profiles measured in time t , respectively

$e_k^n(x), C_{kx}^n(t)$ = cross-shore (space and time) eigenfunctions

$e_k^m(y), C_{ky}^m(t)$ = longshore (space and time) eigenfunctions.

4 Short-Term Bed Changes

The data for short-term bed changes have been collected at Shkorpilovtsi, where ultrasonic probes of 40-W power and 5° emission angle were deployed across shore in the years 1987 and 1988.

Fig. 3 illustrates the findings, from which it is clear that the most intensive changes occur again in the surf zone stretching between the underwater bar and shoreline. Since the longshore sediment transport did not exist for the particular configuration of shore, the cross-shore transport rates were computed from the continuity equation, as depicted at the bottom of Fig. 3.

The variability of bed prior to during, and after storm can be assessed from Fig. 4. Slow onshore transport is observed before storm. The dramatic changes towards offshore transport at a speed of 0.9 m/h are comparable with the estimates given by Birkenmeier (1984) (1.2 m/h) for waves $H \leq 2$ m and $T \leq 4$ s. During the recovery after storm the onshore transport occurs at a speed of 4 m/day, again somehow comparable with Sunamura (1989) who sites $v \approx 0.5$ m/day for a 1-m underwater bar and $H_b = 0.75 - 1$ m; a quantity which is fifty times smaller than that during the storm!

5 Meso-Scale Changes

5.1 Single-Bar Profile

Multi-yearly measurements of meso-scale variation of shore profiles have been conducted in two regions of single bars and multiple bars. The range of bed changes observed was

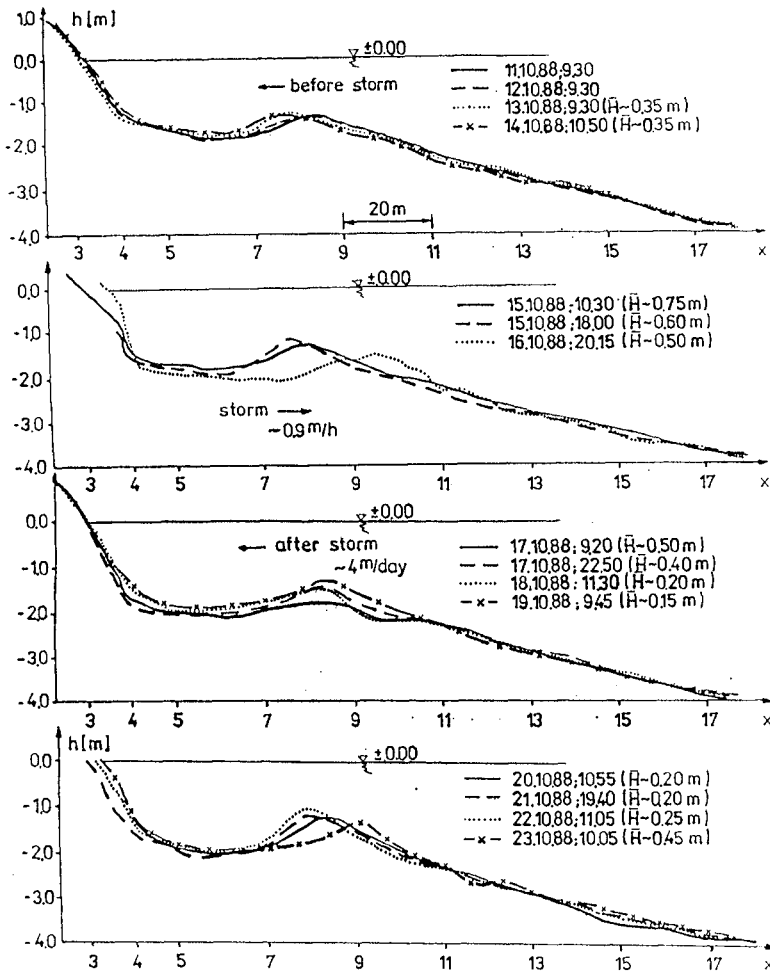


Fig. 4. Single-bar profile transformation in a storm at Shkorpilovtsi

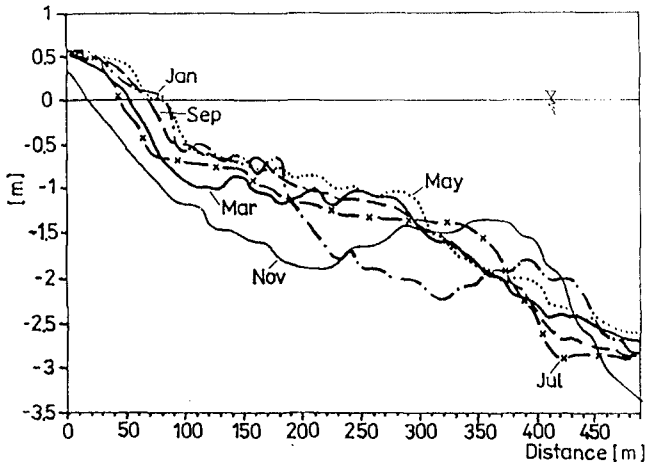


Fig. 5. Mesoscale single-bar profile transformation at Shkorpilovtsi in 1976

about 1 m, which is somewhat visible in Fig. 5 for the Black Sea site of Shkorpilovtsi.

The meso-scale variation on single-bar profile was measured every month from 1973 to 1977.

One-dimensional EOF analysis for the profiles measured every month over the period of one year in the years 1974 and 1976 for the first three eigenfunctions e_{1x} , e_{2x} , e_{3x} has exposed certain relationships between them and pertinent coastal processes. An illustration is provided in Fig. 6. The following findings can be outlined:

- The first eigenfunction e_{1x} describes the average shore profile in which all underwater forms are smoothed out
- The second eigenfunction e_{2x} identifies the location of the underwater bar and berm in the summer (through its maxima). The minimum of the second eigenfunction identifies the location of bar in the winter season
- The third eigenfunction e_{3x} denotes the locations where accretion (maximum) or erosion (minimum) prevails.

The following can be said for the temporal eigenfunctions (the coefficients c_{it} (Fig. 7):

- The first coefficient c_{1t} can be regarded as constant about $c_{1t} \approx \sqrt{n_x \cdot \lambda_1}$, in the range from 9 to 13
- The second temporal eigenfunction c_{2t} depicts the seasonal (yearly) predominance of cross-shore transport direction (offshore or onshore). It is confirmed that the onshore mode prevails in the summer versus the offshore direction in the winter (negative value in the drawing)
- The coefficient c_{3t} is most difficult to identify as it oscillates and varies quite strongly. It can be attributed to the instantaneous predominance of erosion or accretion processes, much as the third eigenfunction e_{3x} . The places where onshore and offshore transport prevails are shown by arrows.

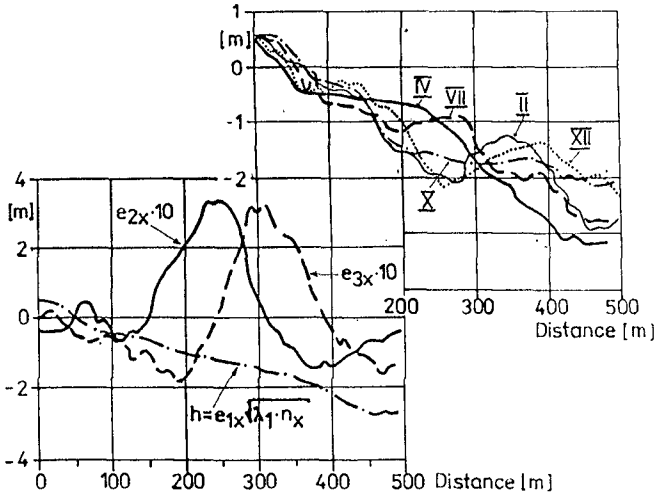


Fig. 6. Mesoscale changes at Shkorpilovtsi in 1974: bed profiles (top) and eigenfunctions (bottom)

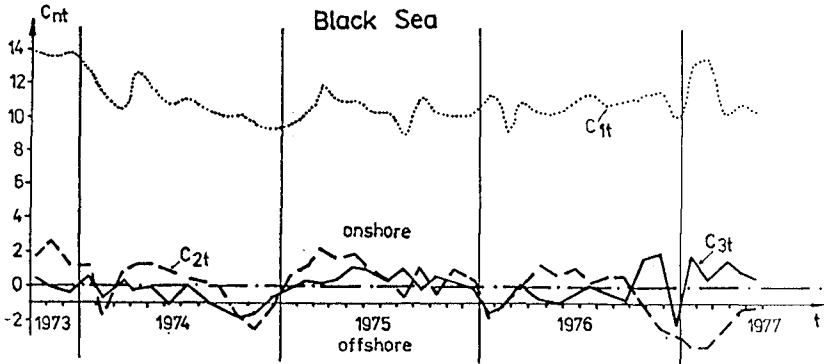


Fig. 7. Coefficients c_{it} at Shkorpilovtsi, 1973 - 1977

5.2 Multiple-Bar Profiles

5.2.1 General Observations

Analysis of the variability of topographical features measured on the multiple-bar profile of the Polish coastline (Lubiatowo) illustrated in Fig. 8 has provided the following findings:

- Seasonal variability of the multiple-bar profile largely depends on the direction of cross-shore transport, the regions of the second and third bars (counted from shoreline) displaying the most intensive bed changes;
- In the summer, the onshore sediment transport prevails, primarily as bedload. This holds particularly for the surf zone, so that the second and third bars and beach are subject to clear transformation;
- If more violent storms appear in the summer, a strong accretion in the central part of underwater profile is noted, particularly about the third bar, which is supplied under these conditions from both land and sea;
- During calm periods most transformations are confined to the zone about shoreline and the shallowest bars.

The variation of shoreline and dune toe, coupled with the above changes in the underwater profile are depicted respectively in Fig. 8 b, c. It is seen that the migration of shoreline exceeds 10 m, the widest beach being exposed in the summer, as anticipated. The variation of the dune toe is generally less pronounced as it is due to extreme storm events, which have not appeared in the period of measurements.

5.2.2 EOF Analysis

The analysis has been based on the measurements performed at Lubiatowo a few times in the period from mid-May to mid-October 1987, in about twenty cross-shore profiles stretching over 700 – 1000 m and spaced from 100 to 200 m. In the one-dimensional representation depicted in Fig. 9 one can see that the first eigenfunction e_{1x} again depicts the average shore profile with characteristic macroforms. The second eigenfunction e_{2x} is attributed to underwater bars, its maximum being associated with clear accretion and its minimum being associated with erosion. The peak of the function e_{2x} is proportional to the intensity of local bed changes. Sharp peaks are localized about crests or troughs while smeared shallow extrema denote local accretion or erosion. The third eigenfunction e_{3x} is correlated with the predominance of offshore or onshore sediment transport. The maximum of e_{3x} can be linked to periodic predominance of onshore transport, while the minimum denotes the offshore mode.

The characteristic features repeat in the cross-shore profiles deployed along shore.

Two-dimensional EOF analysis provides a deeper insight into the coastal phenomena, although very few findings are clear-cut and conclusive.

The prototype results for meso-scale variability measured at Lubiatowo are depicted for the cross-shore eigenfunctions and longshore ones in Figs. 10 and 11, respectively. The following features for the first mode deserve attention:

- The first eigenfunction $e_1^1(x)$ represents the cross-shore profile averaged over the entire area (x, y) ;
- The second eigenfunction $e_2^1(x)$ displays the location of underwater bars representative for the entire area as implied from analysis of the cross-shore profiles measured;

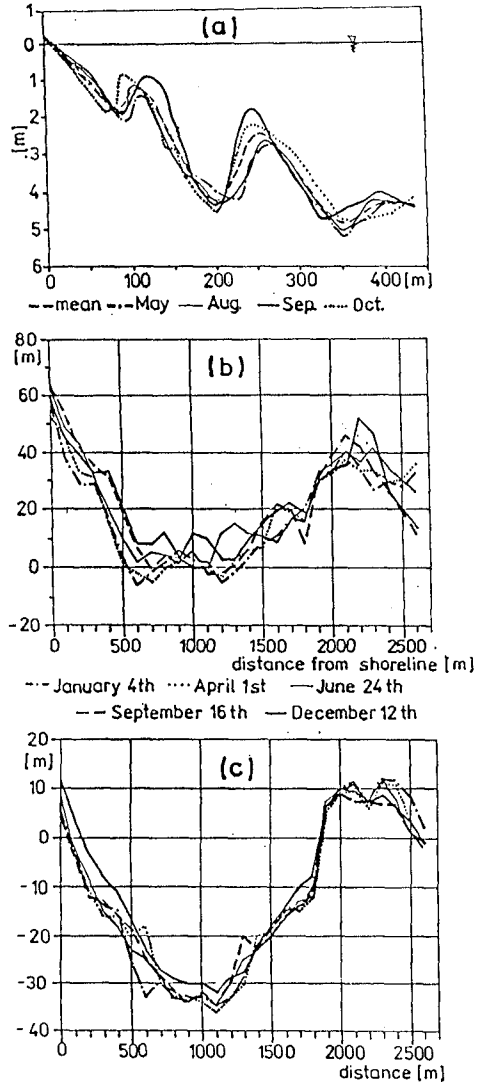


Fig. 8. Mesoscale changes in coastal topography at Lubiato in 1987: (a) bed profile; (b) shoreline; (c) dune toe

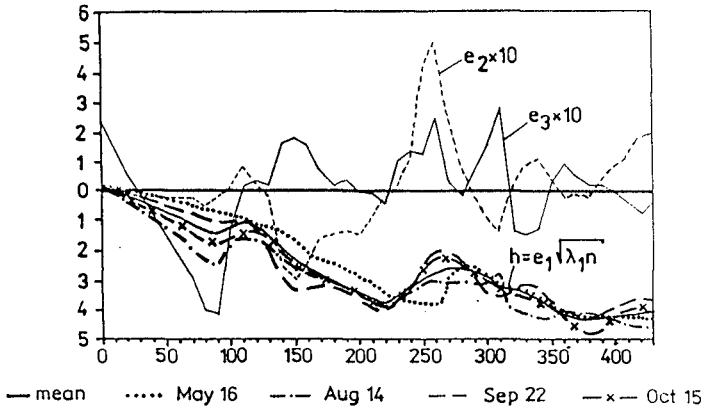


Fig. 9. Bed profiles and eigenfunctions at Lubiatowo in 1987

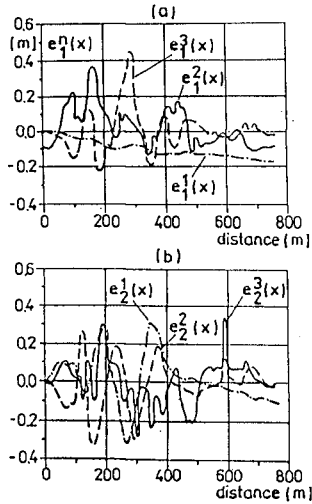


Fig. 10. Cross-shore spatial eigenfunctions (2-D) for modes $k=1$ (a) and $k=2$ (b); Lubiatowo 1987

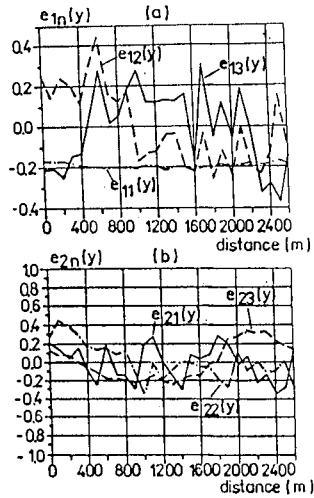


Fig. 11. Longshore spatial eigenfunctions (2-D) for modes $k=1$ (a) and $k=2$ (b); Lubiatowo 1987

- The third eigenfunction $e_1^3(x)$ is linked to locations of predominant erosion or accretion, again averaged over the entire area (x, y) .

It should be noted that the extremum values of the eigenfunctions e_{2x} and e_{3y} appear where the profile changes are maximum.

The findings for the second mode $k=2$, i.e. $e_2^1(x)$, $e_2^2(x)$ and $e_2^3(x)$ have not displayed any clear correlation with profile parameters, as shown in Fig. 10b. It should be stressed that the maximum changes in the function $e_2^3(x)$ are similar to those for $e_1^3(x)$ and appear in the zone of the most intensive profile transformation.

The respective longshore eigenfunctions $e_1^1(y)$, $e_1^2(y)$, $e_1^3(y)$ are illustrated in Fig. 11, for the first mode $k=1$ and second mode $k=2$ respectively, in parts a and b. The first eigenfunction $e_1^1(y)$ again characterizes the average feature, this time the allocation of shoreline. The second longshore eigenfunction $e_1^2(y)$ is difficult to identify. It is not excluded that its existence is associated with longshore forms, but more data is required to confirm this hypothesis. The third longshore eigenfunction $e_1^3(y)$ is associated with longshore changes in cross-shore profiles. The maxima of $e_1^3(y)$ point to the places of prevailing accretion while the minima are linked to erosion.

The longshore EOF for the second mode $k=2$, i.e. $e_2^1(y)$, $e_2^2(y)$, $e_2^3(y)$ do not show any clear correlation whatsoever with the coastal features except for the first function $e_2^1(y)$ which represents the average shape of shoreline (but not its location!).

The temporal eigenfunctions measured at Lubiatowo are depicted in Fig. 12 for cross-shore modes. The following observations can be made:

- The first function $C_{1x}^1(t)$ is constant, which implies that the average profile can be treated as time independent;
- The second function C_{1x}^2 is associated with the net cross-shore sediment transport, or processes of erosion and accretion, in good agreement with Winant et al. (1975) and Hsu et al. (1986);
- The third eigenfunction C_{1x}^3 seems to be uncorrelated with coastal features;

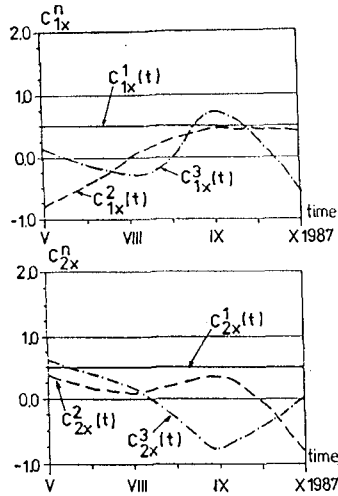


Fig. 12. Cross-shore coefficients c_{it} for modes $k=1$ and $k=2$; Lubiatowo 1987

- The cross-shore characteristics for the second mode $k=2$ do not display any clear-cut regularity or relationship to geometrical and dynamic characteristics.

The geometric and dynamical features of shoreline can be analyzed in terms of one-dimensional EOF. Some findings are illustrated in Fig. 13. For instance, the second eigenfunction e_{2y} indicates the places where the net accretion is the highest (maximum of e_{2y}) or erosion prevails (minimum of e_{2y}) along shore during the entire period of analysis. Oscillations about zero exhibit places of small net variation of shoreline.

The following remarks can be put forth for the temporal eigenfunctions c_{1t} , c_{2t} and c_{3t} (not illustrated):

- c_{1t} is approximately constant
- c_{2t} averaged over all shoreline locations shows a tendency towards accretion or erosion in consecutive time intervals. Positive values of this function point to the seaward advancement of shoreline while negative values indicate the landward retreat.

6 Long-Term Changes

6.1 Single-Bar or Smooth Shore Profiles

Our analysis of long-term single-bar profile changes has been based on multiyearly measurements carried out on the Black Sea coastline in the years 1974 - 1977. Fig. 14 illustrates the results obtained by one-dimensional EOF method. The findings are similar to those obtained for meso-scale changes, but it is because of the addition of multiyearly effects that individual functions are pronounced to a lesser extent. For instance, the average profile $h = c_{1x} \cdot \sqrt{\lambda_1 n_x}$ does not exhibit clear underwater bars and other forms, as they are smoothed out by individual profiles.

6.2 Multiple-Bar Profiles

These changes have been analyzed for the shoreline measured on the Baltic Sea in the years 1983 - 1989. Fig. 15a shows that the shoreline changes in the years 1983 - 1986 were

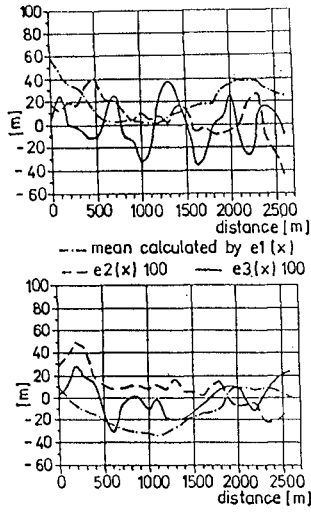


Fig. 13. Longshore empirical eigenfunctions (1-D); Lubiatowo 1987

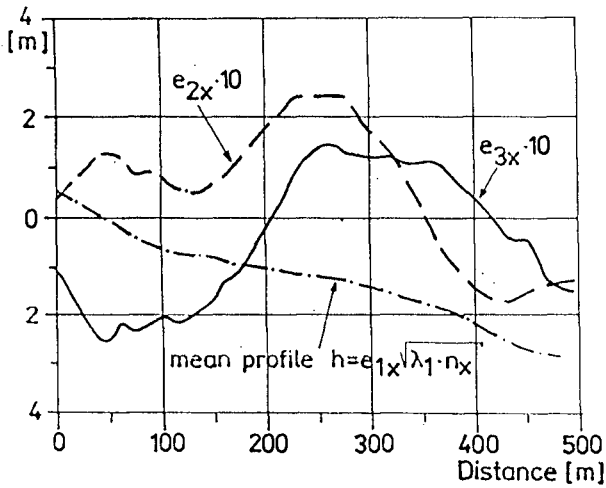


Fig. 14. Long-term variation of single-bar profile at Shkorpilovtsi, 1973 - 1977

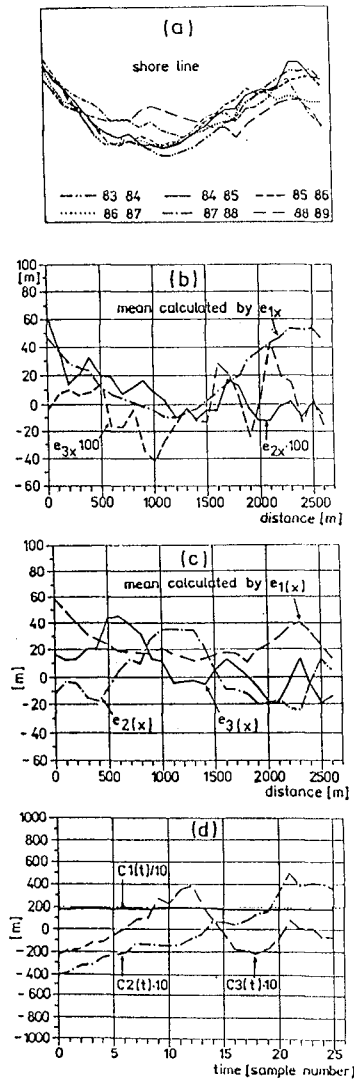


Fig. 15. Long-term variation of shore topography at Lubiatowo: shoreline from 1983 to 1989 (a); longshore EOF (1-D) 1983 - 84 (b); longshore EOF (1-D) 1987 - 89 (c); coefficients c_{it} (d)

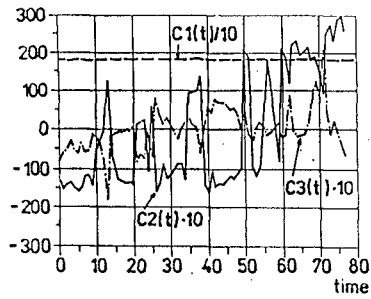
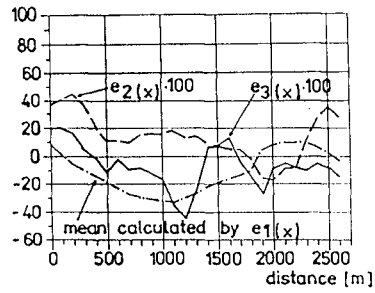


Fig. 16. Longshore empirical eigenfunctions (1-D) at Lubiatowo, for the entire period 1983 - 1989

by far less intensive than those in the years 1987 - 1989. This is also reflected in the second eigenfunction e_{2y} , cf. Fig. 15b vs. Fig. 15c. The coefficients c_{it} are depicted in Fig. 15d.

The interpretation of the eigenfunctions and the temporal coefficients is similar to that provided earlier for the shorter time scales. For comparison, Fig. 16 shows the EOF for the entire period 1983 - 1989.

In order to provide an expanded background for the shoreline changes we analysed the variability of shoreline back to 1890 for the central coastline mentioned in the introduction. Reliable precise bathymetric charts were retrieved for the period from 1967 to date. One interesting feature observed was that in long scales the seabed varied in the vertical range of 1.0 - 2.5 m about both inner and outer bar, although the changes at the outer bar occur in a wider strip. As already mentioned, quasimodes with insignificant changes were observed in between the bars, some 150 - 175 m from shoreline. Beyond the zone of bar migration another node appears 300 - 350 m from shoreline.

7 Conclusions

1. The use of EOF, in 1-D and 2-D formulation, for analysis of bed & shoreline changes in multiple scales, and in different barred environments has confirmed the adequacy of the tool.
2. Some earlier linkage of eigenfunctions to factors of coastal dynamics has been given an extensive experimental support, and some other relationships have been exposed.
3. The following association of eigenfunctions and coastal features have been confirmed:
 - 1st mode e_{1x} → mean profile and/or shoreline
 - 2nd mode e_{2x} → berm/bars and/or salients/cusps, etc.
 - 2nd time f. c_{2t} → temporal predominance of off/onshore transport
 - 3d mode e_{3x} $_{1-bar}$ → intensive bed changes
 - e_{3x} $_{>1bar}$ → predominance of off/onshore transport
 - 3d time f. c_{3t} → difficult to attribute...
4. 2-D EOF sometimes obscures data analysis due to excessive smoothing out, although permits identification of longshore features.
5. Further application of EOF in analysis of scale-model and prototype data is intended.

Acknowledgements

This study has been carried out under the program CPBP 02.12-2.3, which is gratefully acknowledged.

References

- Hsu T.W., Liaw S.R., Wang S.K., Ou S.H. (1986) *Two-dimensional empirical eigenfunction model for the analysis and prediction of beach profile changes*, Proceed. of 20th Coastal Eng. Conf., Taipei
- Winant C.D., Inman D.L., Nordstrom Ch.E. (1975) *Description of seasonal beach changes using empirical eigenfunctions*, Journal of Geoph. Research, Vol. 80, No 15

CHAPTER 160

L a b o r a t o r y S t u d y o n B e a c h P r o c e s s e s d u e t o R a n d o m W a v e s

Ryuichiro Nishi, Michio Sato and Kazuo Nakamura

A b s t r a c t

The beach processes due to regular waves, grouping waves and random waves are studied. The beach models which consist of coarse or fine sand are set to consider bed load and suspended load sediment, respectively. To obtain the equivalent beach topographics between regular wave and random wave conditions, the concept of same energy flux and same representative wave height are applied.

1. P r e f a c e

Natural beach conditions are dominated by random waves and three dimensional sediment transport (Goldsmith, 1982, Nishi, 1989), etc. Much data concerning coastal processes has been collected through experimental and theoretical studies. Regular waves and wave flume have been used mainly in these studies. Recently some reports on beach processes due to random waves have also been published (Dette, 1986, Hsiang, 1976, Irie, 1986, Mimura, 1986, Nishi, 1988, Tsuchiya, 1974).

It is necessary to study beach processes due to random waves in order to correlate knowledge gained from studies under regular wave conditions. It is also important to define regular wave characteristics for coastal and beach process experiments based on the natural random wave record. It seems that the hydraulic model experiment is the first step to correlate the physical phenomena between the numerical and full scale models. The wave irregularity, wave groupiness, the effects of infragravity waves and grain size distribution, as well as the three dimensional sediment transport on beach processes and sea level fluctuation have to be taken into account in the model experiments.

The following points are the results of this laboratory study.

- 1) Development of a measuring system which can simultaneously process numerous topography and wave data.
- 2) The effect of wave irregularity on beach deformation by the

1 Research associate, Dept. of Ocean Civil Engineering, Kagoshima Univ. 1-21-40 Korimoto, Kagoshima-shi, JAPAN

2 Professor, Dept. of Ocean Civil Engineering, Kagoshima Univ.

3 Technical officer, Dept. of Ocean Civil Engineering, Kagoshima Univ

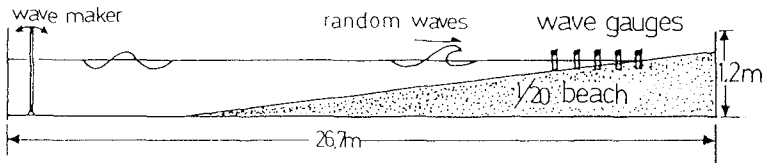


Fig.1 Wave basin.

Table 1 Wave conditions.

Wave type	Case	H1/10	H1/3	Hmean	Period
Experimental series A					
Regular wave	A-1			9.5cm	1.2sec
Grouping wave	A-2			2-13.5cm	1.2sec
Random wave	A-3		13.2cm	9.3cm	1.2sec
Experimental series B					
Regular wave	B-1			4.0cm	1.0sec
Regular wave	B-2			5.0cm	1.0sec
Regular wave	B-3			9.0cm	1.0sec
Regular wave	B-4			12.5cm	1.0sec
Random wave	B-5	9.7cm	7.6cm	4.8cm	1.0sec
Random wave	B-6	13.3cm	10.5cm	6.6cm	1.0sec
Random wave	B-7	15.4cm	12.1cm	7.6cm	1.0sec
Random wave	B-8	18.0cm	14.2cm	8.9cm	1.0sec
Random wave	B-9	23.2cm	18.3cm	11.4cm	1.0sec
Experimental series C					
Regular wave	C-2			8.9cm	1.2sec
Random wave	C-3		7.6cm	4.9cm	1.2sec
Random wave	C-4		11.9cm	7.8cm	1.2sec
random wave	C-5		14.1cm	9.3cm	1.2sec

action of random waves, grouping waves and regular waves on the movable bed beaches which consist of coarse(0.6mm) or fine(0.29mm) sand.

3) The effect of three dimensional sediment transport on beach deformation.

2. Experiments

A wave basin 26.7m long, 14m wide and 1.2m deep, as shown in Fig.1, was used. Two separate 1/20 slope movable bed beaches, which consist of 0.29mm and 0.6mm medium grain size sand, were set to find the effect of suspended sediment and bed load, respectively.

This study was conducted with three experimental series A, B and C. In the first experimental series A, the beach topographies were measured by the bamboo stick system. The beach topographies were measured at 672 evenly spaced points (50cm intervals) by visual measurement at 0.0, 0.5, 1.0, 2.0, 4.0, 8.0, 12.0, 24.0 hours. The incident wave field were measured at the same time. The wave characteristics of random waves, grouping waves and regular waves were chosen to satisfy the same energy wave flux conditions. The schematic graphs of these waves are shown in Fig.2. The BretschneiderMitsuyasu spectrum defined by eq.(1) (Mitsuyasu,1971) was used for generation of random waves in this study.

$$S(f_n) = 0.257 \left(\frac{H_1}{T_1} \right)^2 f_n \exp(-1.03(T_1 f_n)^{-4}) \tag{1}$$

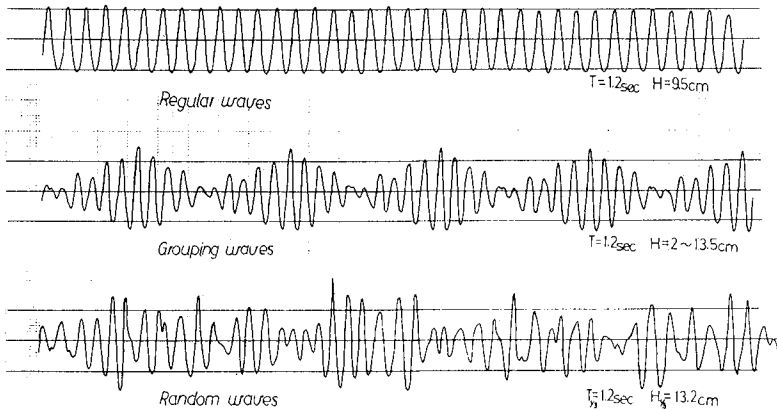


Fig.2 Schematic diagram of waves.

In the second experimental series B, automatic topography measurement system(Fig.3) was used as same as series C. The topographies were measured at 2800 evenly spaced points(30cm intervals) at 0.0 , 0.5, 1.0, 2.0, 4.0, 8.0, 12.0, 24.0hrs. The wave fields were also

measured by 30 wave gauges at the same time. The wave gauges were set in 1.0m spacing parallel to the shore and moved by 0.5m offshore.

The wave characteristics of random waves and regular waves were chosen to satisfy the same characteristic wave heights, viz.

- (i) regular wave height equals maximum wave height
- (ii) regular wave height equals significant wave height
- (iii) regular wave height equals mean wave height

In the third experimental series C, the beach consist of fine (0.29mm) sand were used to investigate the suspended sediment transport. The wave heights were also chosen as those in experimental series B.

The wave conditions are shown in Table 1. The installation of instruments are shown in Fig.5. The nearshore current systems were observed by dye(MnO₄ solution) and tracer(fluorescent light).

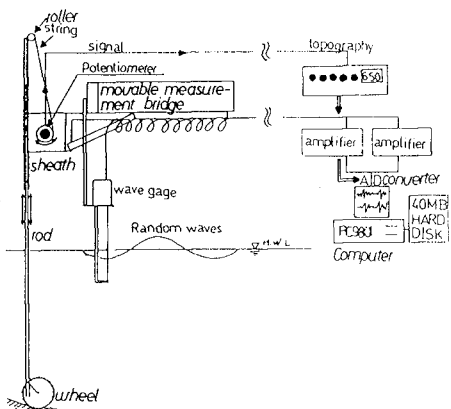


Fig.3 Automatic measurement system for wave and topography.

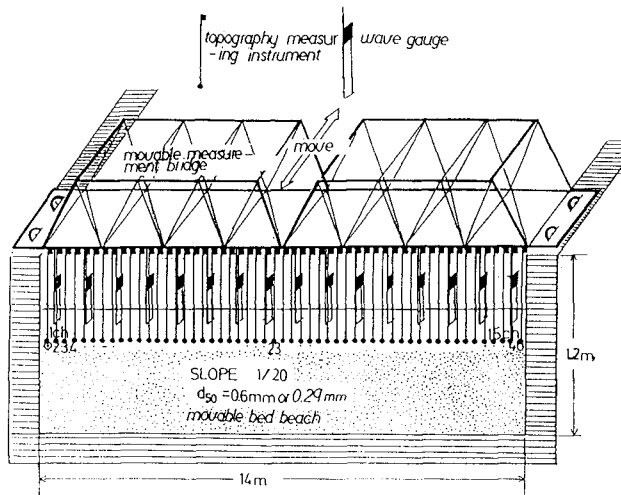


Fig.4 Installation of wave gauges and topography measuring instrument.

3. Results

The purpose of this study is to discover how to correlate knowledge gained under regular wave conditions to that gained under random wave conditions to find a characteristic wave for beach deformation from natural random wave records obtained on the natural beaches.

In regards to the above points, the knowledge which obtained from this study is still limited. This study consists of three experimental series, therefore results are discussed separately. The general results through series A to C are discussed in the final section.

3.1) Experimental Series A.

The purpose of series A is to find "how to obtain the equivalent beach topographies among the action of regular waves, grouping waves and random waves". To obtain the equivalent beach profiles due to each waves, the same energy flux concept was applied. The wave conditions of the three waves were chosen to satisfy the same energy wave flux. This concept is as follows,

$$W_{reg} = \frac{1}{8} \rho g H^2 C_g \tag{2}$$

$$W_{group} = \frac{1}{8T_z} \sum_1^{\infty} \rho g H_n^2 C_{g_n} \tag{3}$$

$$W_{ran} = \frac{1}{8} \sum_1^{\infty} \rho g H_n^3 C_{g_n} \tag{4}$$

$$\begin{aligned}
 &= \sum_1^{\infty} \rho g S(f_n) C_{g_n} \\
 &\quad \text{(deep water wave approximation)} \\
 &= \sum_1^{\infty} 0.78 \rho g S(f_n)/f_n \\
 &= 0.0854 \rho g H_{1.3}^3 \tag{5}
 \end{aligned}$$

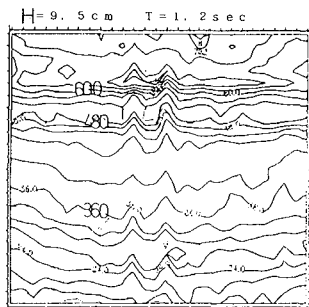
where, W_{reg} , W_{group} , W_{ran} ; the energy flux of regular waves, grouping waves and random waves. The Bretschneider-Mitsuyasu spectrum was applied for $S(f_n)$.

$$S(f_n) = 0.257 \left(\frac{H_{1.3}}{T_{1.3}^2} \right)^2 f_n^{-5} \exp(-1.03(T_{1.3} f_n)^4)$$

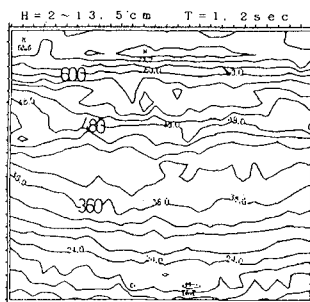
$$C_g = nC = \frac{1}{2} \left(1 + \frac{2kh}{\sinh 2kh} \right) \left(\frac{gT}{2\pi} \tanh \frac{2\pi h}{L} \right)$$

Therefore, this concept can be written as follows.

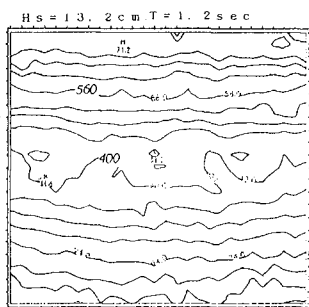
$$W_{reg} = W_{group} = W_{rand} \tag{6}$$



(a) Regular waves



(d) Group waves



(c) Random waves

Fig.5 Beach topographies.

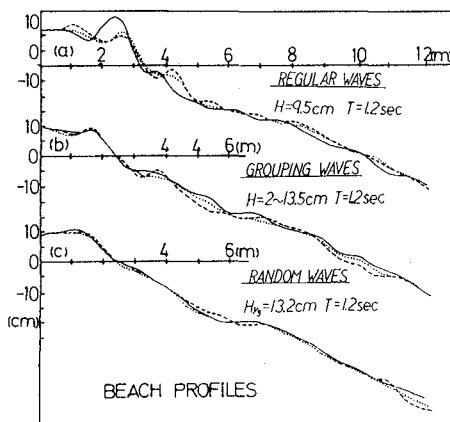


Fig.6 Beach profiles (series A).

Twenty eight on-offshore profiles were measured at 50cm intervals for single measurement of topography. The beach topography caused by random waves is somewhat smooth compared to the other topographies.

The mean profiles are calculated based on these lines and are shown by a solid line in Fig.5. Beach profiles caused by regular waves, grouping waves and random waves do not result in equivalent beach profiles. There are also representative beach profiles under the rip current and mass transport areas, which are shown by a broken line and a dot line respectively. Nearshore circulations are more easily generated by regular waves in the wave basin experiments compared to the wave action of random waves. Related beach profile differences exist between the rip current areas and the mass transport areas.

With regards to the three dimensional sediment transport, the schematic diagrams of sediment drift and hydraulic phenomena in the nearshore zone under regular wave conditions are shown in Fig.7.

Sediment transport is closely related to concave points in the crescentic longshore bar. The floats with fluorescence paint showed zig-zag motion on the crescentic bar due to wave breaking and rip-currents. This movement is related to sediment transport, and suggest that there are cases where the sediment drift direction is not the same as that of corresponding currents. This phenomena could not be generated thoroughly in this case , due to random waves. Some researchers have discussed the relationship between the edge waves and the rhythmic topographies. However, those relationships are not discussed here in detail.

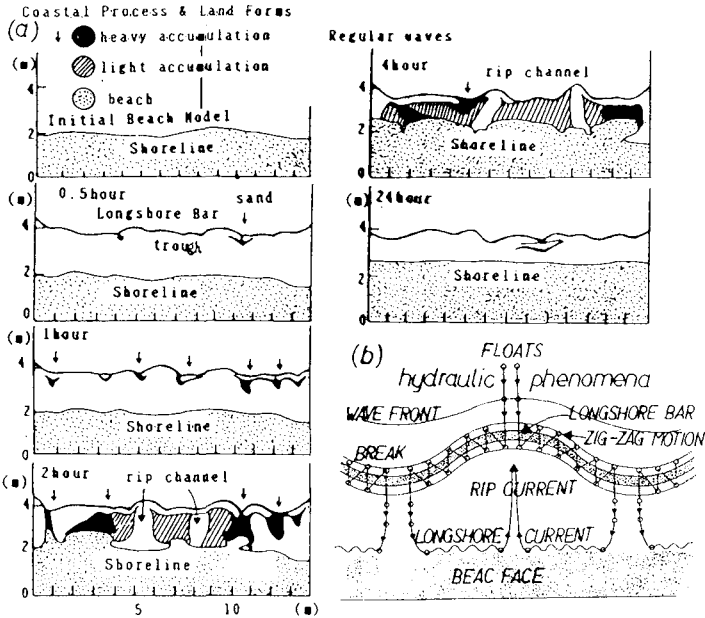


Fig.7 Schematic diagram of
 (a)coastal process and sand drift
 (b)hydraulic phenomena in the nearshore zone.

3.2) Experimental Series B.

The application of the concept of same energy wave flux have been discussed in the previous section. It does not result in equivalent topographies. Therefore, the method of the same representative wave heights was examined here. This concept is based on the statistical analysis of random waves. The three methods for comparison of the topographies due to regular and random waves are employed. The concepts are as follows,

- (i) one-tenth maximum wave height equals regular wave height
- (ii) significant wave height equals regular wave height
- (iii) mean wave height equals regular wave height.

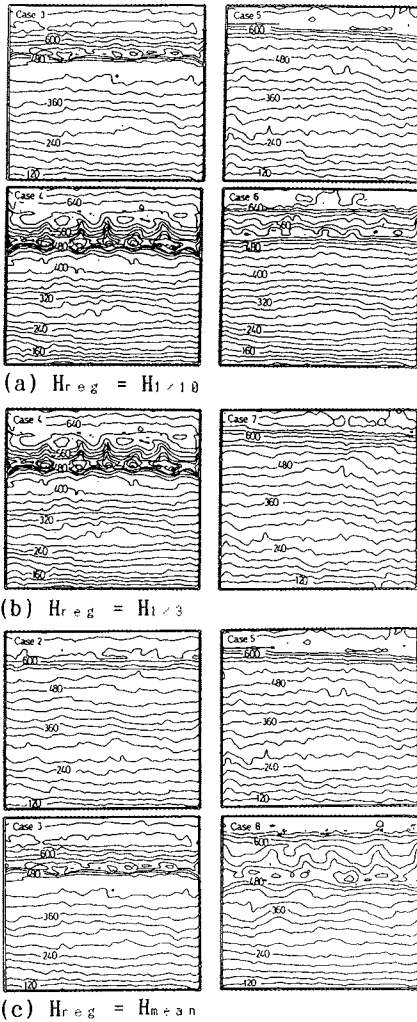


Fig.8 Beach topographies due to regular waves and random waves

The comparison of beach topographies related to the above concept are shown in Fig.12(a), (b), (c). It does not result in the equivalent topographies between the regular wave and random wave cases.

The mean on-offshore sediment transport rate of both cases and the mean beach profiles are shown in Fig.9 and Fig.10, respectively. The onshore beach profile changes due to random wave action are quite large compared to those due to regular waves, since random waves include

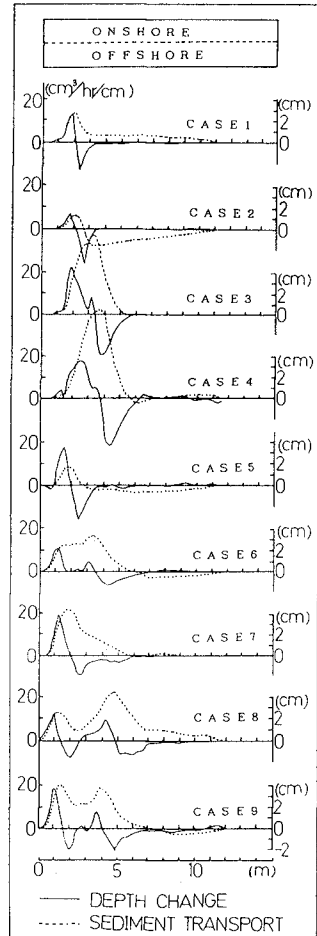


Fig.9 On-offshore sediment transport and distribution of depth change.

many large swash waves. The position of the longshore bar is also farther offshore than in the case of regular waves. Sediment transport due to regular waves is concentrated around the breaking point. The wave breakings of regular wave conditions are generated in a narrow area compared to it of random wave conditions.

3.2.2) Comparison of mean beach profile characteristics

As mentioned in section 3.2, any certain characteristic wave which result equivalent beach topographies as those due to regular waves could not achieved, yet. However, in correlating the knowledge obtained from researches on random waves to that obtained under regular waves, the mean beach profiles are used. The relationships concerning critical water depth for sand movement, shoreline position, berm height, and mean depth change etc. are examined here.

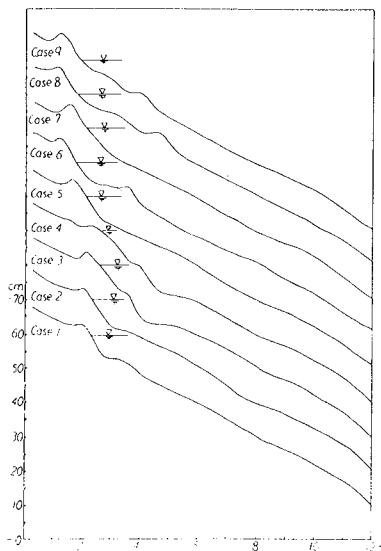


Fig.10 Mean beach profiles (series B).

3.2.2.1) Critical water depth for sand movement.

The critical water depth for sand movement in this study is defined, and shown schematically, in Fig.13. The critical water depth proposed by Tanaka and Sato (eq.(8)) is shown by a solid line in this figure. The critical water depth for sand movement under regular wave conditions is deeper by 2cm than the calculated value, but the tendency is similar to equation (8). The data of the random wave experiment vary widely compared to it due to the regular waves. The data with respect to mean wave are much deeper than equation (8).

$$\left(\frac{H}{H_0}\right)^{-1} \left(\frac{\sinh 2\pi h_i}{L}\right) \left(\frac{H_0}{L_0}\right)^{-1} = 1.770 \left(\frac{L_0}{d}\right)^{1/3} \tag{8}$$

The results using significant waves also have some variance, but they distribute around the calculation and are somewhat shallower than the results of regular waves. Therefore, the significant wave characteristics should be applied for the calculation of critical water depth under random wave action rather than mean wave. This corresponds to the results from a natural beach by Sato et al.

3.2.2.2) Shoreline changes

A time series of shoreline changes from initial position are shown

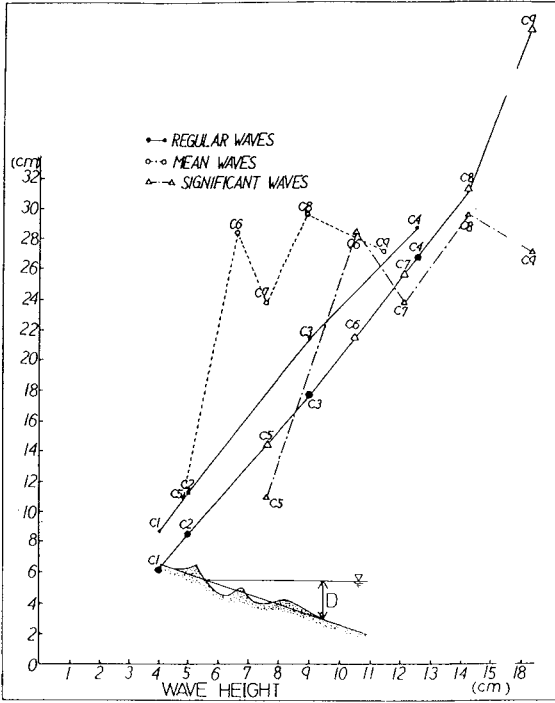


Fig.11 The critical water depth for sediment movement and definition sketch.

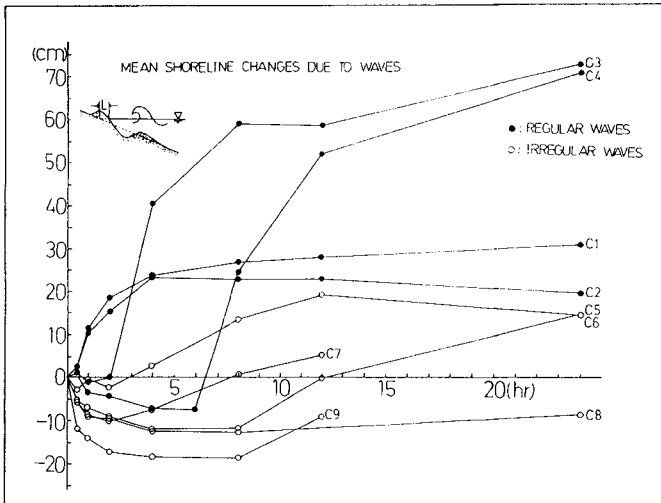


Fig.12 Time series of shoreline changes.

in Fig.14. The shoreline changes due to random waves are smaller than those due to regular waves. The abrupt changes of shoreline position are caused by the welded bar as shown in Fig.8. The shoreline changes at 12 hours are shown in Fig.15. There are some cases where the same representative waves give the contrast topographies between regular waves and random waves .

3.2.2.3) Berm height

Wave run-up contribute to built the berm , this berm height after 12 hours is shown with respect to the wave height in Fig.16. In contrast to shoreline changes, berm heights due to random waves are higher than those due to regular waves. The probability of a large wave run-up in the random waves is higher than that in regular waves, so that random waves result in higher berms.

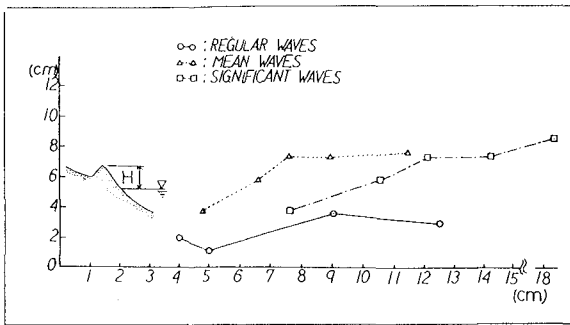


Fig.13 Berm height.

3.2.2.4) Mean depth change

Some researchers have indicated that the topography changes due to random waves are somewhat smaller and smoothed compared to those due to regular waves.

To examine this, two graphs are prepared. One shows the distance from onshore limit of beach deformation to offshore one with respect to wave height. The other shows the sum of depth change, also with respect to wave height. These two graphs are shown in Fig.17 and Fig.18. The distance from onshore limit of beach deformation to offshore one

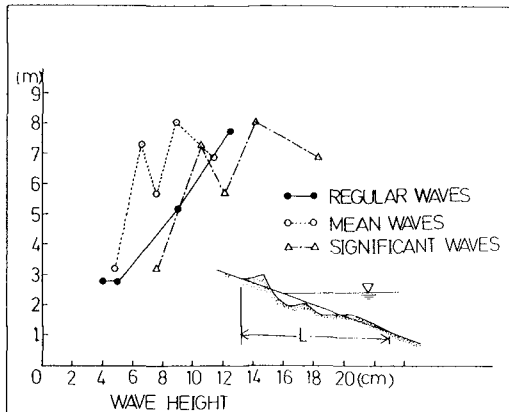


Fig.14 The length of on-offshore depth change limits.

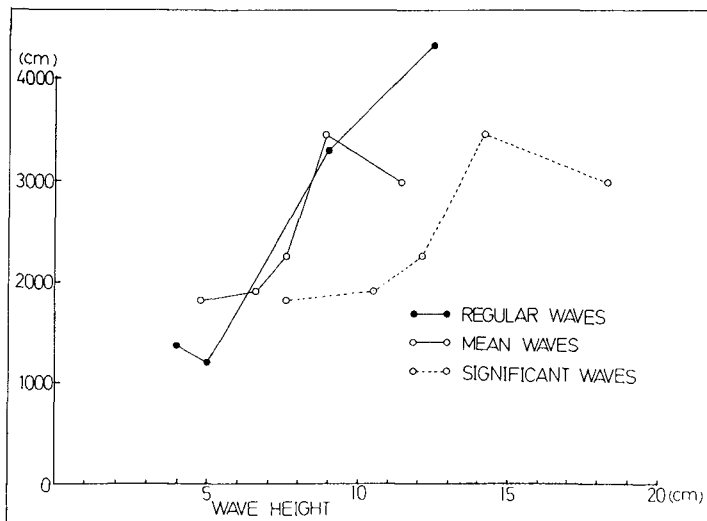


Fig.15 The sum of depth change at 12hours.

caused by regular waves exists between those based on mean and significant waves. The sum of depth changes due to regular waves is nearly equal to those of mean waves and greater than those due to significant waves.

The mean depth change is defined as (sum of depth change) / (length of beach deformation). As a result, mean depth changes due to random waves are smaller than those of regular waves.

3.3) Experimental Series C.

Beach processes were examined by a model consisting of coarse sand (0.6mm) in series A and B. In these experiments, a type III beach (proposed by Horikawa and Sunamura) was not generated. Therefore, a beach model consisting of fine (0.29mm) sand was used to consider the suspended sediment transport and erosion of beach.

3.3.1) comparison based on the same representative wave heights.

Beach topographies based on the same representative wave heights are shown in Fig.19. This seems that the beach topography due to regular waves is characterized by the rhythmic longshore bar, and topography due to random waves is characterized by rhythmic step. These topographies are not similar. Rhythmic topographies are generated in the offshore region on the fine sand beach, but not on the coarse sand beach in this experiments.

3.4) Effect of grain size

The mean beach profiles of fine sand and coarse sand due to same wave conditions are compared and shown in Fig.21. The two upper

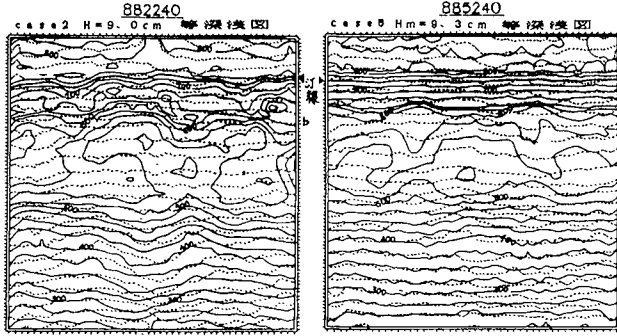


Fig.16 Beach topographies due to regular waves and random waves.
 $H_{reg} = H_{mean}$ (series c)

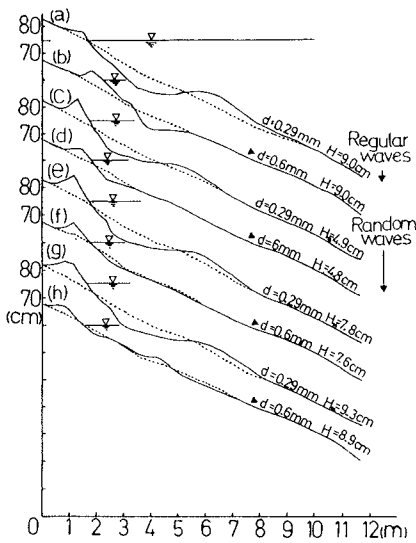


Fig.17 Comparison of profiles of fine sand and coarse sand beaches.

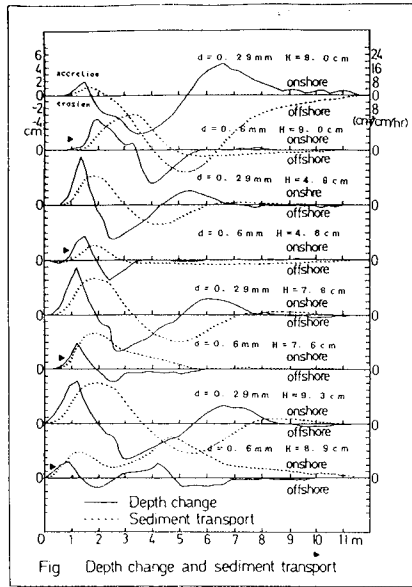


Fig Depth change and sediment transport

profiles resulted from regular waves and the six lower profiles from random waves. The two upper profiles correspond to the lowest two profiles on the basis of same representative wave height (mean wave height). The beach profiles which consist of fine sand, show a larger topographical change.

4. Conclusion

This paper is a basic laboratory study for beach processes due to random waves. However, the main purpose, "obtaining the equivalent topographies for both regular waves and random waves", have not been achieved yet.

The conclusions are;

- (1) The topography measuring instrument system with A/D converter, developed here, can simultaneously collect numerous accurate data.
- (2) Beach topographies due to similar energy flux waves result in different topographies.
- (3) Beach topographies due to the same representative wave height as regular wave height result in different topographies.
- (4) Critical water depth for sediment movement due to random waves can be calculated by using significant wave characteristics.
- (5) There are cases where the direction of sediment drift differ from the corresponding longshore and rip-current directions.
- (6) Rhythmic topographies were observed in the inshore region of coarse and fine sand beaches, and also in the offshore region of fine sand beaches.

References

- (1) Dette, H.H. and K. Ueiczka : Velocity and Sediment Concentration Field Across Surf Zones. 20th Conf. Coastal Engineering, pp.1062-1076, 1986
- (2) Goldsmith, V., D. Bowman, K. Kiley, B. Burdick, Y. Mart and S. Sofer : Morphology and Dynamics of Crescentic Bar Systems, 18th Conf. Coastal Eng., pp.941-953, 1982
- (3) Hsiang Wang and S.S. Liang : Mechanics of Suspended Sediment in Random Waves, JGR., Vol. 80, No. 24. pp3438-3494
- (4) Irie, Y., T. Tsuchiya and A. Watanabe : Beach Profile and Cross-shore Sediment Transport Rate Due To Irregular Waves, 32nd. Japanese Conf. coastal Eng., pp.316-320 (in Japanese)
- (5) Mitsuyasu, H. : Development of Spectrum of Wind Waves(2), 17th Japanese Conf. Coastal Eng., pp.1-7 (in Japanese)
- (6) Mimura, N., Y. Otsuka and A. Watanabe : Laboratory Study on Two-Dimensional Beach Transformation Due to Irregular waves, 20th Conf. Coastal Eng., pp1393-1406
- (7) Nishi, R., M. Sato, K. Nakamura, M. Yaguruma, and K. Matano : Laboratory Study On Beach Processes Due To Regular Waves, Grouping Waves and Random Waves, 34th Japanese Conf. Coastal Eng., pp302-306 (in Japanese)
- (8) Nishi, R. M. Sato. and K. Nakamura : Coastal Processes in Western Coast of Mt. Kaimon, 44th annual Conf. The Japan Society of Civil Engineers, 2. pp.36-39
- (9) Tsuchiya, Y. and K. Inada (1974): Experimental Study on Beach Profile Change Due To Wind Waves—Critical Condition for Bar Formation - 21st Japanese Conf. Coastal Eng., pp.219-224 (in Japanese)

CHAPTER 161

A QUASI-3D MODEL FOR SUSPENDED SEDIMENT TRANSPORT BY CURRENTS AND WAVES.

Irene Katopodi¹ and Jan S. Ribberink²

ABSTRACT

A QUASI-3D model for suspended sediment transport based on an asymptotic solution of the convection-diffusion equation is developed for currents and waves. The influence of waves on the sediment concentration is included through the diffusion analogy and the bed boundary condition. Validity analysis provides conditions that permit the check of the model applicability. The presence of waves enhances the validity area of the model considerably. The model compares favourably with a 3D model and experimental data.

1. INTRODUCTION

In compound mathematical models for coastal morphological problems the suspended sediment transport module forms an essential submodel. For the suspended sediment transport description a wide range of models has been presented in the past (e.g. transport formulas, 3D or 2D horizontal convection-diffusion models).

In this study a quasi-3D formulation is developed based on the analysis of Galappatti and Vreugdenhil (1985) for 2D vertical problems. This quasi-3D modelling technique combines the reduced computational effort of 2DH models with the generality of the 3D models (ie variations in vertical structure of sediment concentration are reproduced and the bed boundary condition is applied as in 3D models). The QUASI-3D model has been recently used for morphological problems of tidal rivers and estuaries (Wang, 1989). The present study is aimed at coastal morphology where wave influence is of importance.

1 Research Assistant, Democritus Univ. of Thrace, Dept. of Civil Eng., 67100 Xanthi, Greece.

2 Researcher, Delft Hydraulics, P.O. Box 152, 8300 AD Emmeloord the Netherlands.

2. BASIC EQUATIONS

The mass balance equation for the suspended sediment when integrated over the wave period (after concentration and velocity components have been split into a wave averaged and an oscillating part) gives rise to wave averaged plus correlation terms. It is assumed that for the correlation terms the Boussinesq assumption holds so they can be connected to the concentration gradients by means of a proper mixing coefficient (diffusion analogy). Then the suspended sediment transport due to current and waves is governed by the wave-averaged convection-diffusion equation:

$$\frac{\partial c}{\partial t} + u \frac{\partial c}{\partial x} + v \frac{\partial c}{\partial y} + (w-w_s) \frac{\partial c}{\partial z} = \frac{\partial}{\partial x}(\epsilon_x \frac{\partial c}{\partial x}) + \frac{\partial}{\partial y}(\epsilon_y \frac{\partial c}{\partial y}) + \frac{\partial}{\partial z}(\epsilon_z \frac{\partial c}{\partial z}) \quad (1)$$

where c, u, v, w are concentration, longitudinal, lateral and vertical velocity components respectively, all averaged over the wave period, sediment fall velocity is w_s and ϵ_x, ϵ_y and ϵ_z are mixing coefficients for the combined action of current and waves.

The convection-diffusion equation has been used to describe the current-waves induced suspended sediment transport before (e.g. van Rijn 1986, van Rijn and Meijer 1988).

Van Rijn (1986), based on measurements of equilibrium concentration profiles, proposed an empirical vertical mixing coefficient for current and waves. According to this empirical approach the influence of waves on the mixing coefficient comes through the following wave quantities: Wave period T , particle size diameter $D_* = D_{50} \{(\rho_s - \rho)/g(\rho\nu^2)\}^{1/3}$, significant wave height H_s , peak value of orbital velocity near the bed \hat{u}_{orb} , a_{br} a breaking coefficient, water depth h and thickness of the near bed mixing layer δ (≈ 3 ripple heights). The influence of the current comes through the current bed shear velocity u_* , the von Karman constant κ , the water depth h and the relative strength of the wave orbital velocity and mean current velocity (van Rijn 1986, van Rijn and Meijer 1988).

The horizontal mixing coefficients are taken constant over the depth. Their magnitude is of the order of $1 \text{ m}^2/\text{s}$ (van Rijn and Meijer, 1988).

To solve equation (1) boundary conditions are needed not only at the vertical boundaries but also at the water surface and at the bottom.

At the water surface the vertical flux is taken to be zero.

The bed boundary is taken at a specified height z_a above the mean bed level (reference level) that here is specified as a small fraction of the depth. At the reference level the concentration is assumed to adapt immediately to equilibrium conditions and is given as function of the local hydraulic and sediment parameters ("concentration" bed boundary condition). Alternatively the concentration gradient at the reference level can be assumed to adapt immediately to equilibrium conditions ("gradient" bed boundary condition). Here the equilibrium concentration (and equilibrium gradient) at the reference level proposed by van Rijn (1986) is used.

3. THE QUASI-3D MODEL

3.1 Derivation

Galappatti and Vreugdenhil (1985) constructed an asymptotic solution of the convection-diffusion equation in 2DV space for current alone under certain assumptions concerning the scales of domain dimensions, time, flow velocities, and horizontal and vertical diffusion.

The same steps are followed here for the solution of the 3D equation (1). The first order solution can be written (see Katopodi and Ribberink, 1988):

$$c(\zeta) = a_{11}(\zeta)\bar{c} + a_{21}(\zeta)\frac{h}{w_s}\frac{\partial\bar{c}}{\partial t} + a_{22}(\zeta)\frac{h\bar{u}}{w_s}\frac{\partial\bar{c}}{\partial x} + a_{22}(\zeta)\frac{h\bar{v}}{w_s}\frac{\partial\bar{c}}{\partial y} - a_{21}(\zeta)\frac{h}{w_s}\frac{\partial}{\partial x}\left(\epsilon_x\frac{\partial\bar{c}}{\partial x}\right) - a_{21}(\zeta)\frac{h}{w_s}\frac{\partial}{\partial y}\left(\epsilon_y\frac{\partial\bar{c}}{\partial y}\right) \quad (2)$$

where \bar{c} is the depth averaged concentration, \bar{u} and \bar{v} depth averaged velocity components, $\zeta = z/h$, h the water depth and $a_{ij}(\zeta)$ profile functions. The profile functions depend only on the explicit knowledge of the vertical mixing coefficient, fall velocity and normalized velocity profile and can be computed in advance.

In the applications that follow the velocity profile is assumed to have the logarithmic shape -an assumption that can hold for boundary layer flows in combination with small wind waves (van Rijn and Meijer, 1988). Nevertheless the method can handle 3D velocity profiles as soon as they are given as similarity series.

The solution (2) and the equations that give the profile functions have been derived with the use of the surface boundary condition and the assumptions that only the zero order concentration terms contribute to the depth averaged concentration and that shape variations of the equilibrium concentration profile can be neglected.

If further the bed boundary condition is used, then from (2) follows ("concentration" condition):

$$\begin{aligned} \bar{c}_e = & \bar{c} + \frac{\gamma_{21}}{\gamma_{11}} \frac{h}{w_s} \frac{\partial \bar{c}}{\partial t} + \frac{\gamma_{22}}{\gamma_{11}} \frac{h\bar{u}}{w_s} \frac{\partial \bar{c}}{\partial x} + \frac{\gamma_{22}}{\gamma_{11}} \frac{h\bar{v}}{w_s} \frac{\partial \bar{c}}{\partial y} - \\ & - \frac{\gamma_{21}}{\gamma_{11}} \frac{h}{w_s} \frac{\partial}{\partial x} \left(\epsilon_x \frac{\partial \bar{c}}{\partial x} \right) - \frac{\gamma_{21}}{\gamma_{11}} \frac{h}{w_s} \frac{\partial}{\partial y} \left(\epsilon_y \frac{\partial \bar{c}}{\partial y} \right) \end{aligned} \quad (3)$$

where $\gamma_{ij} = a_{ij}(0)$ and \bar{c}_e the depth averaged equilibrium concentration.

Equation (3) is a partial differential equation with constant coefficients and \bar{c} as the unknown. The coefficients γ_{11} , γ_{21} , γ_{22} are known in advance. After solving (3) for \bar{c} (with proper initial and boundary conditions), the vertical concentration profile $c(\zeta)$ can be computed from (2). The sediment transport is calculated afterwards.

An equation analogous to (3) can be derived if "gradient" bed boundary condition is used.

The QUASI-3D model (equation 3) was implemented in the SUSTRA 3D/2DV system following the same numerical (finite volume) method (van Rijn and Meijer, 1988).

3.2 Adjustment effects

If horizontal diffusion terms are omitted equation (3) can be written as:

$$\bar{c}_e = \bar{c} + T_A \frac{\partial \bar{c}}{\partial t} + L_x \frac{\partial \bar{c}}{\partial x} + L_y \frac{\partial \bar{c}}{\partial y} \quad (4)$$

with

$$T_A = \frac{\gamma_{21}}{\gamma_{11}} \frac{h}{w_s}, \quad L_x = \frac{\gamma_{22}}{\gamma_{11}} \frac{\bar{u}h}{w_s}, \quad L_y = \frac{\gamma_{22}}{\gamma_{11}} \frac{\bar{v}h}{w_s} \quad (5)$$

Equation (4) describes the adjustment of the depth-averaged concentration to its equilibrium value. The parameters T_A , L_x and L_y represent the characteristic scales in time and space of this adjustment process (adaptation time, adaptation length). The ratios γ_{21}/γ_{11} and γ_{22}/γ_{11} in (5) can be considered as dimensionless adaptation times and lengths.

If the "gradient" bed boundary condition is used only the expressions for dimensionless adaptation time and length change (see Katopodi and Ribberik, 1988).

The adaptation time and lengths as well as the depth averaged equilibrium concentration are determined by the local, instantaneous hydrodynamic conditions and sediment characteristics and can thus be computed in advance before the calculation of \bar{c} .

If adaptation length (time) is smaller than the maximum allowable grid size (time step) of the numerical calculation, the sediment redistribution is not resolved by the grid. Then the concentration can be assumed close to its (local, instantaneous) equilibrium value and a suspended sediment transport formula can be used for the calculation of the bed level changes. If this is not the case, the adaptation phenomena should be taken into account and the concentration can be computed from (3).

The influence of the wave and current parameters that determine the coefficients of equation (4) and consequently the dimensionless adaptation time and length was studied by computing the coefficients for a wide range of these parameters.

The dimensionless adaptation time and adaptation length appeared to be affected most strongly by the parameters w_s/u_* (current mixing) and H_s/h or $H_s/w_s T$ (wave mixing). The combined influence of the two parameters is shown in figure (1). It is shown that the dimensionless adaptation time (and length) show a considerable increase when waves are superimposed to a current. (Compare the curves of $\gamma_{21}/\gamma_{11} = f(w_s/u_*)$ for $H_s/h = 0$ and for $H_s/h = .2$ etc). This increase is more significant when current alone causes negligible suspension adjustment effects ($w_s/u_* > .5$).

The influence of the other parameters \hat{u}_{orb}/w_s , D_* , δ/h , \bar{u}/u_* and z_a/h was found to be considerably smaller.

3.3 Validity conditions

The validity of the model was studied for the case of waves superimposed to a current through comparison with an analytical solution of the convection-diffusion equation, based on an earlier analysis of Wang and Ribberink (1986) for current alone. The results of this analysis are:

The presence of waves leads to a considerable extension of the validity area of the quasi-3D approach. Generally the validity area increases as the suspended load increases (i.e large current velocities, large waves and fine sediment) or for small values of a suspension parameter "modified for the waves", indicated by the analysis:

$$Z_{c,w} = \frac{w_s}{xu_* + .14 \alpha_{br} H_s/T} < .75 \quad (6)$$

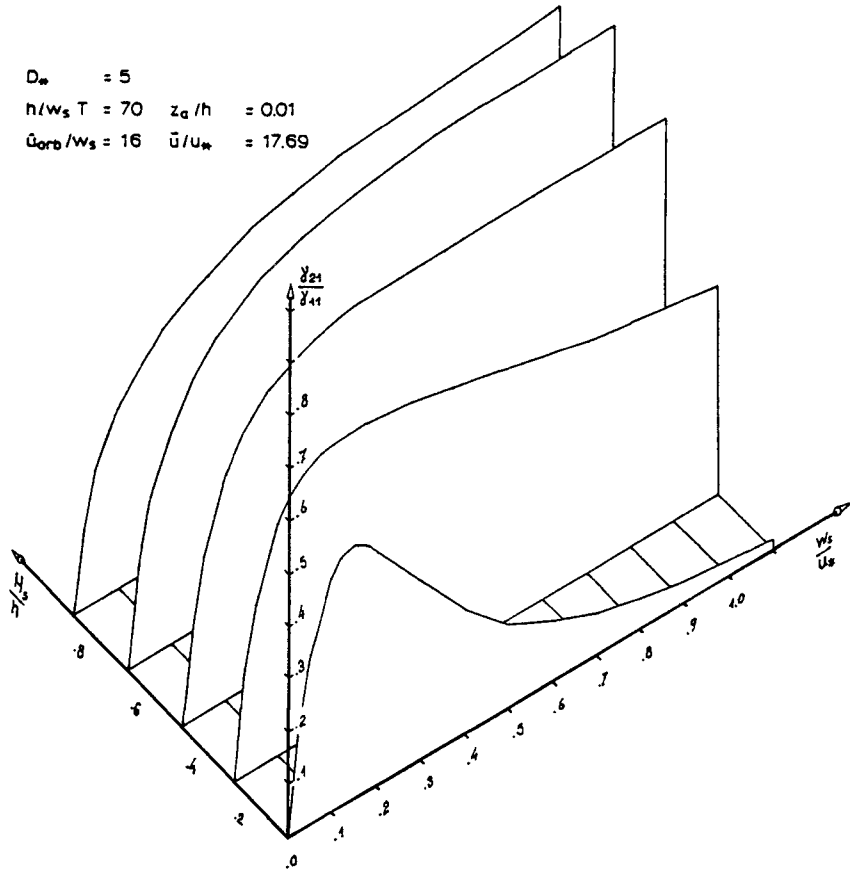


Fig.1 Dimensionless adaptation time as function of (w_s/u_*) and (H_s/h) .

For current only an upper limit holds for the suspension (Rouse) parameter Z_c :

$$Z_c = w_s / (\chi u_*) < 0.75 \quad (7)$$

It is obvious from (6) and (7) that the presence of the waves enhances the model validity area considerably. Of course, the smaller the suspension parameter the better the asymptotic solution.

The assumptions made in order to get the asymptotic solution impose restrictions on the length scale L and time scale T of the particular problem. L and T can be considered as the length scale of changes in hydraulic conditions (e.g bottom shear stress) and time scale of changes in hydraulic conditions (e.g tidal period).

The analysis shows that these changes should be so gradual that the following conditions are fulfilled:

$$L \gg \frac{1}{Z} \frac{u\bar{h}}{w_s} \quad \text{and} \quad T \gg \frac{1}{Z} \frac{h}{w_s} \quad (8)$$

In (8) the suspension parameter Z refers to current or to current and waves (ie Z_c or $Z_{c,w}$)

Comparison of length (and time) scales allowable by (8) for the case of current and current and waves shows that superposition of waves on a current allows the application of the model for less gradual changes in hydraulic conditions than in case of current only and thus enlarges the validity area.

4. RESULTS

4.1 Comparison with a 2DV model

In 2DV plane the problem of suspended sediment transport adjustment in steady uniform flow conditions and zero sediment input at the upstream boundary (similar to fig. 5A) is solved with the asymptotic model and a 2DV numerical model (SUTRENCH, van Rijn, 1986). Several cases with varying current and wave parameters are compared. It should be noted that the chosen problem with a sudden change in bed boundary condition at the upstream boundary (reference concentration goes from zero to equilibrium) is a hard test for the asymptotic model that requires gradually varying conditions.

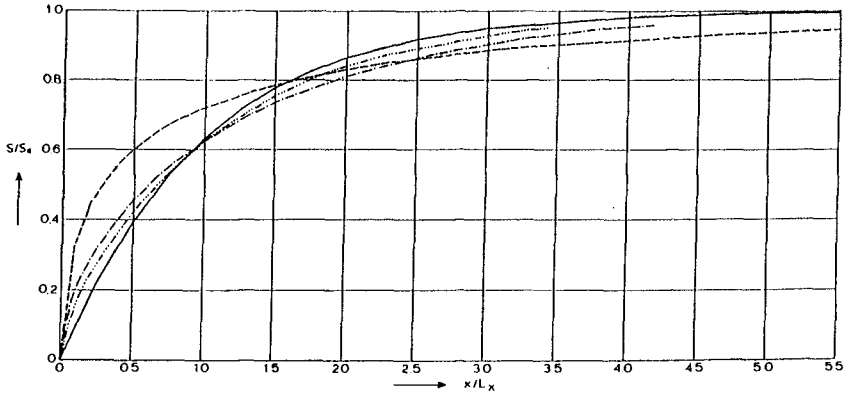
In figure (2) the transport computed with the asymptotic model and SUTRENCH is shown. The x coordinate is divided by the adaptation length so that the QUASI-3D model is represented in all cases by the same line.

For current only (2A) it is evident that the smaller w_s/u_* (or Z_c), the closer the asymptotic model and SUTRENCH are. The agreement is rather good for the last two cases. This confirms the validity analysis (eqn. 7).

In figure (2B), the worse case of fig 2A ($w_s/u_* = .5$) improves more and more as the wave contribution increases.

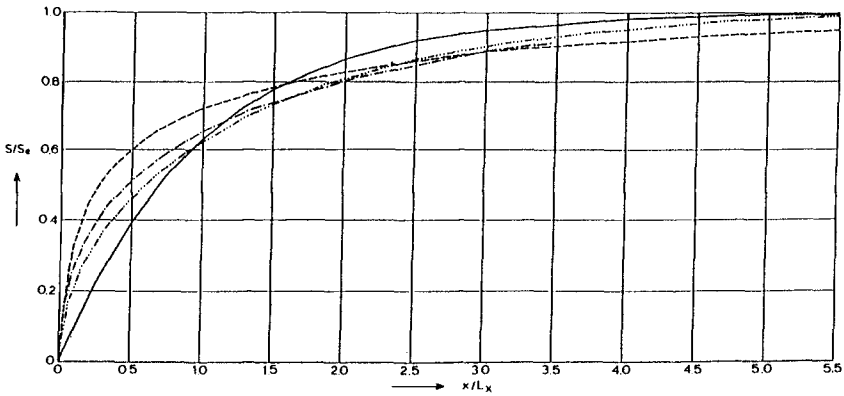
4.2 Comparison with a 3D numerical model

The QUASI-3D model is tested by comparison with a numerical 3D solution (SUSTRA 3D). In figure (3) the non-equilibrium suspended sediment transport computed with the two models is presented for the case of flow around a local construction. The agreement is satisfactory except in the zone behind the dam where the two models use different bed boundary conditions.



SUTRENTCH	H_s/h	\bar{u}_{orb}/w_s	w_s/u_w	γ_{22}/γ_{11}	L_x/h	$L_x/h = (\gamma_{22}/\gamma_{11}) (\bar{u}/u_w) (u_w/w_s)$
-----	0	0	0.5	0.1465	5.184	
-----	0	0	0.2	0.4345	38.443	$z_0/h = 0.01$
-----	0	0	0.1	0.4482	76.296	$\bar{u}/u_w = 1769$

—— asymptotic model (transport zero order) A: CURRENT



SUTRENTCH	H_s/h	\bar{u}_{orb}/w_s	w_s/u_w	γ_{22}/γ_{11}	L_x/h	$L_x/h = (\gamma_{22}/\gamma_{11}) (\bar{u}/u_w) (u_w/w_s)$
-----	0	0	0.5	0.1465	5.184	$D_w = 5$
-----	0.2	34	0.5	0.3276	11.594	$h/w_s T = 30$
-----	0.4	34	0.5	0.4544	16.081	$\delta/h = 0.02$

—— asymptotic model (transport zero order) B: CURRENT AND WAVES

Fig.2 Adaptation of suspended sediment transport.
A: Current only, B: Current and waves

The agreement in the main flow area is depicted more detailed in figure (4 left) where the equilibrium and the non-equilibrium transport along grid line $j=5$ are plotted for the two models. The equilibrium transport, as expected, is exactly the same for both SUSTRA 3D and the QUASI-3D model. The non-equilibrium transport (substantially different than the equilibrium one) as computed with the two models show a very good agreement.

In figure (4 right) the computed non-equilibrium transport along line $j=18$ (much stronger variations) is shown for the two models. In the recirculation zone the difference between the two models becomes considerable.

The necessary computation times of the two models are compared. The QUASI 3D model proved to be 8-10 times faster than SUSTRA 3D.

4.3 EXPERIMENTAL VERIFICATION (CURRENT AND WAVES)

The first order asymptotic model was compared with a laboratory experiment carried out in a mobile bed flume with current and wave conditions and zero sediment transport at the upstream boundary. The experiment was carried out by Galappatti and van Rijn (1984).

Fine sediment particles were entrained by a sediment free flow over a sand bed in the presence of monochromatic waves. The flow and wave conditions were uniform. The velocity profile was logarithmic. The concentration profiles (eight depth points) were measured at six stations along the flume. Upstream the mobile bed, the bed was fixed (experimental set-up in figure 5A).

In figure (5.B) the zero order suspended sediment transport computed with the asymptotic model is plotted against the dimensionless distance along the flume. The results of SUTRENCH (van Rijn, 1986) are also presented. The computed sediment transport is always somewhat smaller than the measured one. The largest deviation is about 20% which can be considered as rather good result.

In figure (6) the concentration profiles computed and measured at the six stations indicated in (5.A) are shown. The agreement again is reasonably good.

In total, the above comparison shows that the QUASI-3D model is able to predict the suspended sediment concentration due to current and waves with a reasonable degree of accuracy against reasonable costs.

Moreover the choice to treat wave mixing in a similar manner to turbulence mixing (diffusion analogy) seems to be justified.

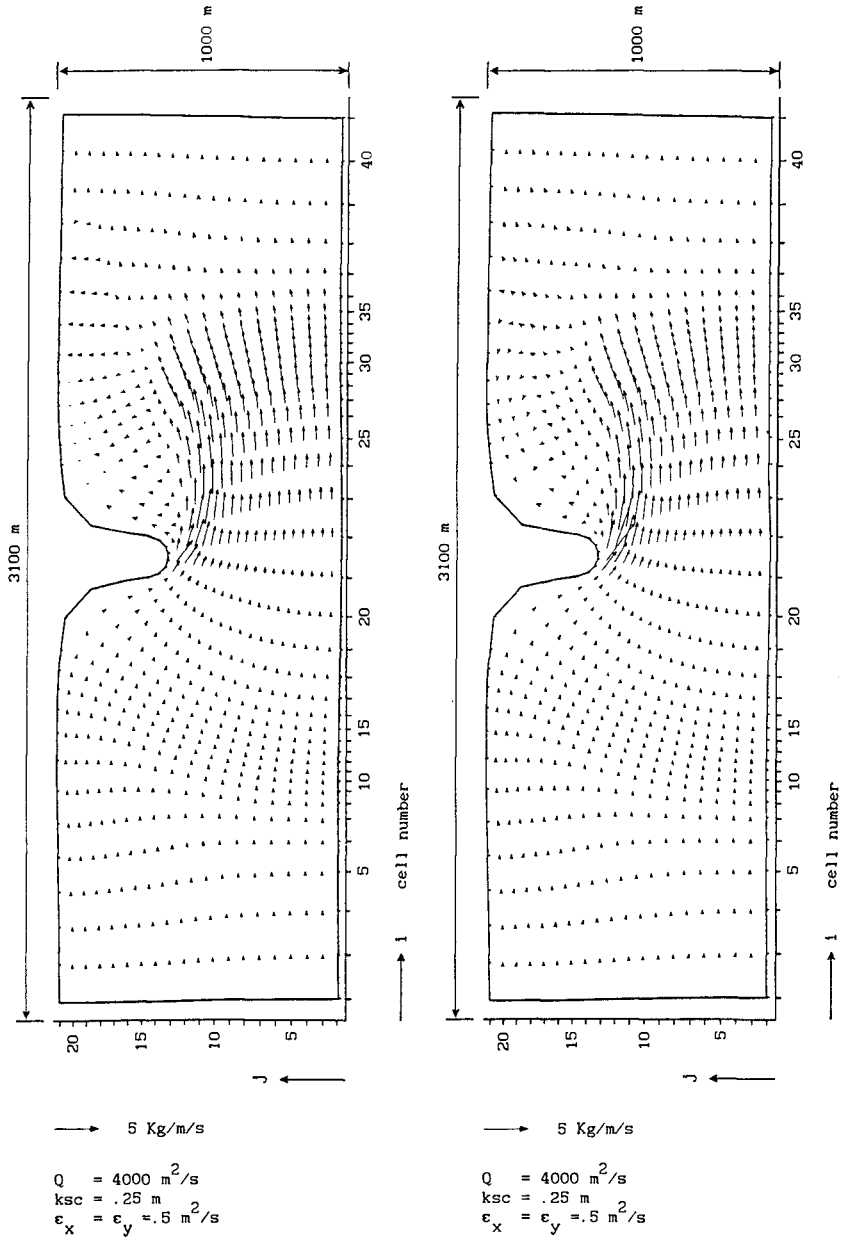


Fig.3 Non-equilibrium transport
 Left: QUASI-3D, Right: 3D

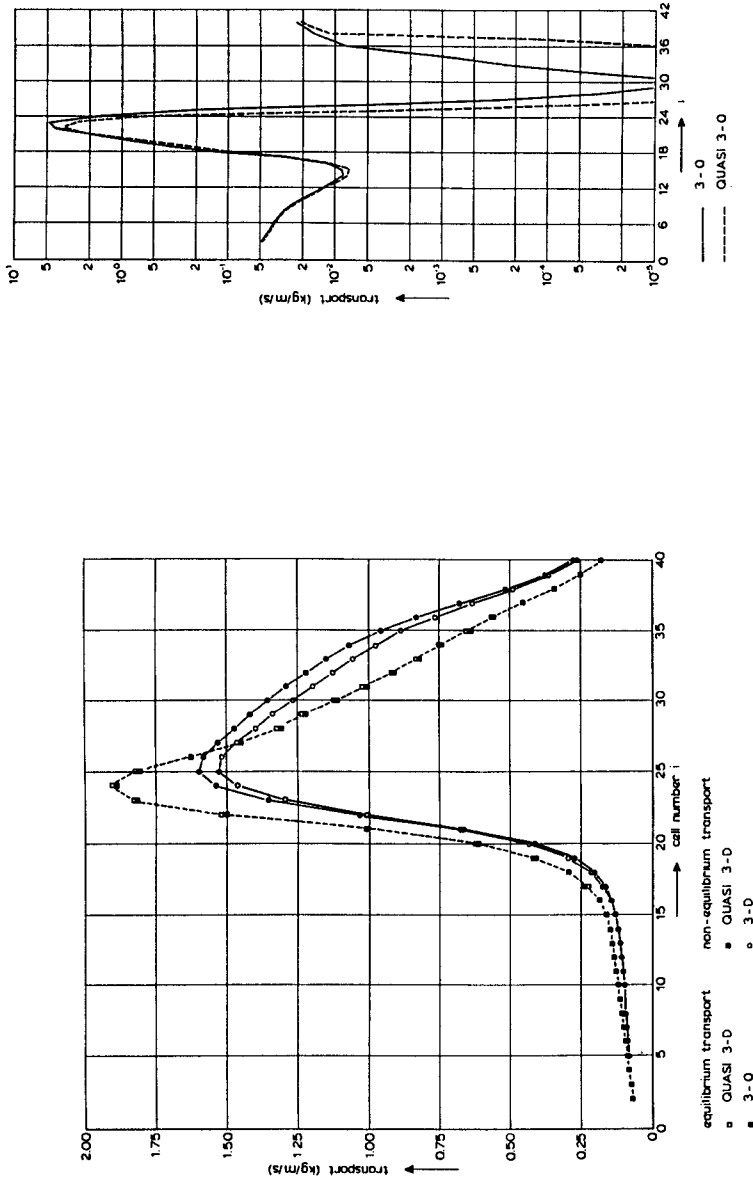
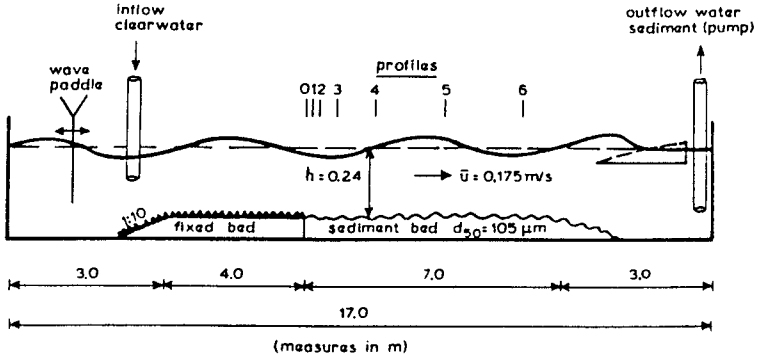
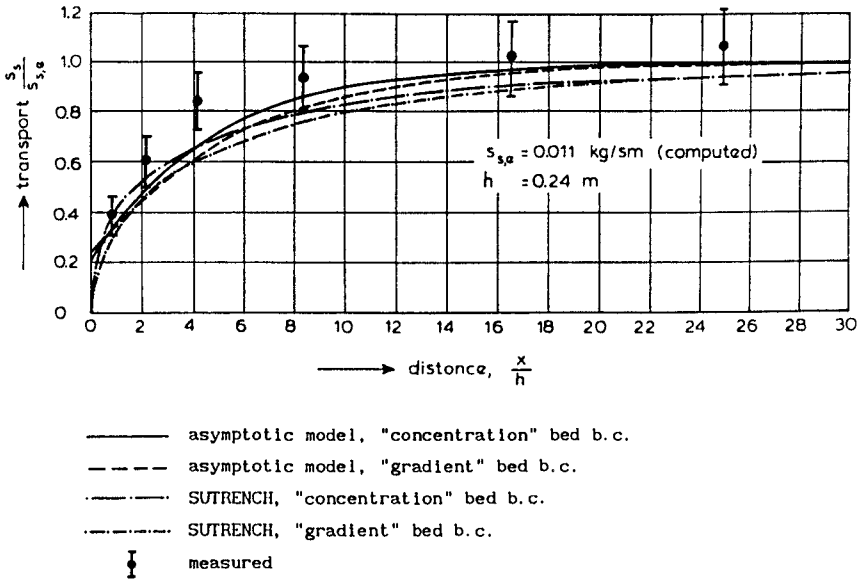


Fig. 4 Left: Equilibrium and non-equilibrium transport along grid line $j=5$
 Right: Non-equilibrium transport along grid line $j=18$



A. EXPERIMENTAL SET-UP



B. SUSPENDED SEDIMENT TRANSPORT

Fig.5 Adaptation of sediment transport in a flume (current and waves).

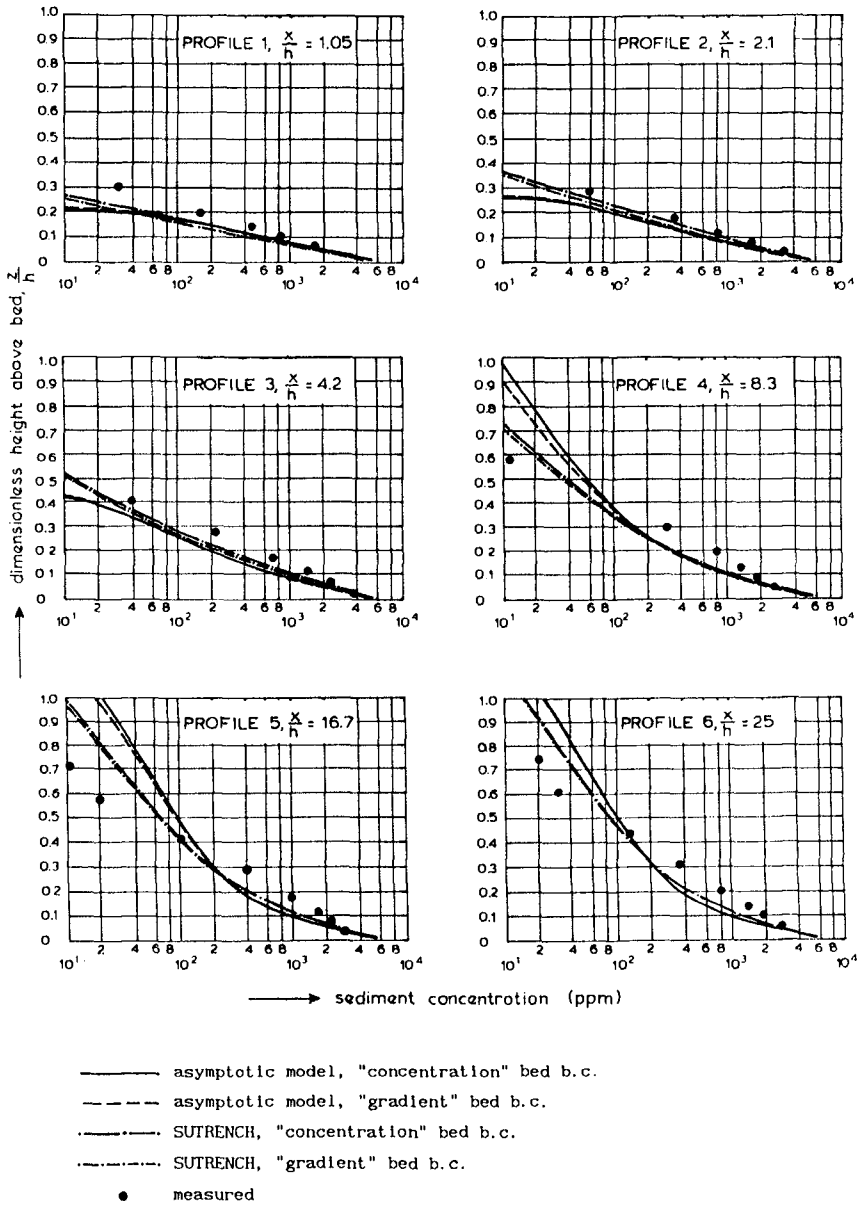


Fig.6 Adaptation of sand concentration profiles in a flume (current and waves).

5. CONCLUSIONS

The QUASI-3D model combines the reduced computational effort of 2DH models with the ability to describe vertical redistribution of suspended sediment concentration while the bed boundary condition is maintained.

The presence of waves leads to a considerable extension of the area of validity of the quasi-3D approach.

The applicability of the model can always be checked beforehand using the validity conditions and this is a big advantage of the model. The validity area indicated by the analysis is in the usual range of many practical (coastal) problems.

As concluded by the the sensitivity analysis superposition of waves on a current appeared to lead to a considerable increase of the importance of the delayed adjustment phenomena.

The numerical as well as the experimental comparison showed that the model behaviour is rather satisfactory.

Introduction of quasi-3D velocities is the next step for the model improvement.

APPENDIX I. REFERENCES

- GALAPPATTI,R. and RIJN,L.C. van, 1984.
Development of concentration profiles in a steady uniform flow with waves and no initial load. Report S 347-I, Delft Hydraulics Laboratory.
- GALAPPATTI,R. and VREUGDENHIL,C.B., 1985.
A depth integrated model for suspended sediment transport. J. Hydr. Res. Vol. 23, No. 4.
- KATOPODI,I. and RIBBERINK,J.S., 1988.
QUASI 3D modelling of suspended sediment transport by currents and waves. Report H 460, Delft Hydraulics.
- RIJN,L.C. van, 1986.
Sedimentation of dredged channels by currents and waves. J. of Waterway Port Coastal and Ocean Eng.,Vol.112, No.5
- RIJN,L.C. van and MEIJER,K., 1988.
Three-dimensional mathematical modelling of suspended sediment transport in currents and waves. IAHR Symposium on mathematical modelling of sediment transport in the coastal zone. Copenhagen, May.
- WANG,Z.B., 1989.
Mathematical modelling of morphological processes in estuaries. Ph.D thesis, Delft Univ. of Technology.
- WANG,Z.B. and RIBBERINK,J.S., 1986.
The validity of a depth integrated model for suspended sediment transport. J. of Hydraulic Research, Vol.24, No.1

CHAPTER 162

Method for Prediction of Bar Formation and Migration

Samuel H. Houston¹ and Robert G. Dean²

Abstract

A computational model based on sediment conservation and transport equations is presented. The bottom shear stress associated with breaking waves is the primary forcing function for the model. A breaking wave model is used to calculate distributions of wave height and mean water level setup across the surf zone and the profile elevations are updated at the end of every time step for each grid across the profile. Examples of the model prediction using large wave tank data are presented. The results of the tests are encouraging for the prediction of bar formation and migration.

Introduction

A significant feature normally found in beach profiles immediately following a storm is the offshore bar, a shore parallel deposition with a scour trough on the landward side. This feature forms as a result of large wave heights, and short wave periods. Once a bar forms, it can dissipate substantial quantities of wave energy thereby reducing the energy reaching the shore and limiting erosion of the berm and dune. After storm water levels and wave conditions have returned to their normal state, the bar usually acts as a significant element in the recovery process of the beach profile. The sediment stored in the bar is available not only to be returned to the beach face during recovery, the bar also can dissipate wave energy during any subsequent storm event. An example of a bar which formed after a storm along the Florida coast in March 1989 and the recovery which occurred during the subsequent months is shown in Fig. 1.

Cross-shore erosion models, such as that developed by Kriebel and Dean (1985), do not typically allow the formation of bars in the profile. They are therefore only capable of predicting berm and dune erosion over time scales on the order of hours to at most days. More recently Larson and Kraus (1989) developed a numerical cross-shore sediment transport model, which is based on extensive correlations of wave, sediment, and profile characteristics. The model was calibrated using large wave tank data and it was compared with profiles predicted by the Kriebel and Dean model for various wave and water level conditions. Larson and Kraus found their model more realistically described the profile at the dune toe when no bar was present in the profile, and because it allowed the formation of bars, there was less erosion of the dune in a case in which

¹Graduate Research Assistant, Coastal and Oceanographic Engineering, University of Florida, Gainesville, Florida 32611 USA

²Graduate Research Professor, Coastal and Oceanographic Engineering, University of Florida, Gainesville, Florida 32611 USA

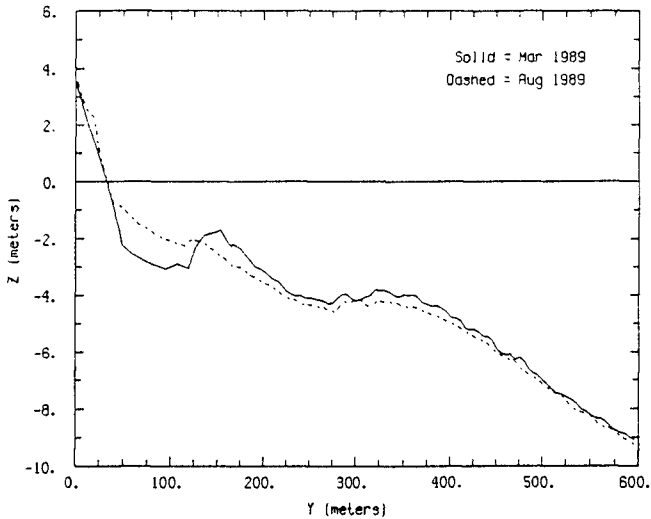


Figure 1: Example of observed barred (March, 1989) and unbarred (August, 1989) beach profiles at Beverly Beach in Flagler County, Florida USA.

offshore bars were present. The size of the model predicted bars and troughs were underestimated and the problem of beach recovery was not included. This paper presents an explicit computational sediment transport model using bottom shear stress parameters to predict the formation and evolution of offshore bars in two-dimensional cross-shore sediment transport processes.

Approach

The development of the berm and offshore bar has been found to be associated with the dimensionless parameter suggested by Dean (1973) and later tested by Wright and Short (1984)

$$H_b/wT \quad (1)$$

where H_b is the breaking wave height, w is the fall velocity of the sediment, and T is the wave period. Wright and Short (1984) found the value of Eq. (1) to be 4.0 ± 1.5 at Eastern Beach in Australia, where offshore bars were present. This dimensionless parameter is important for bar formation because the breaking wave acts to displace sediment shoreward of the breakpoint in the beach profile. Stive and Wind (1986) investigated the mean cross-shore flow in a two-dimensional surf zone and developed an undertow model based on experimental and theoretical considerations. They found the result of the strong spatial decay after breaking was equivalent to a shear stress at the wave trough level, which caused a mean offshore flow in the water near the bottom. Svendsen and Hansen (1988) considered the problem of incorporation of cross-shore circulations into numerical models, which predict wave height and setup. One of the important forcing functions they investigated was the average bottom shear stress, τ_b . They concluded that computed values of τ_b could be included in comprehensive nearshore numerical models.

The approach used in the computational model presented herein to determine the location, volume, and mobility of offshore bars is based on the assumption that transport of sediment across beach profiles is related to the momentum fluxes due to waves. Breaking waves transfer momentum by exert-

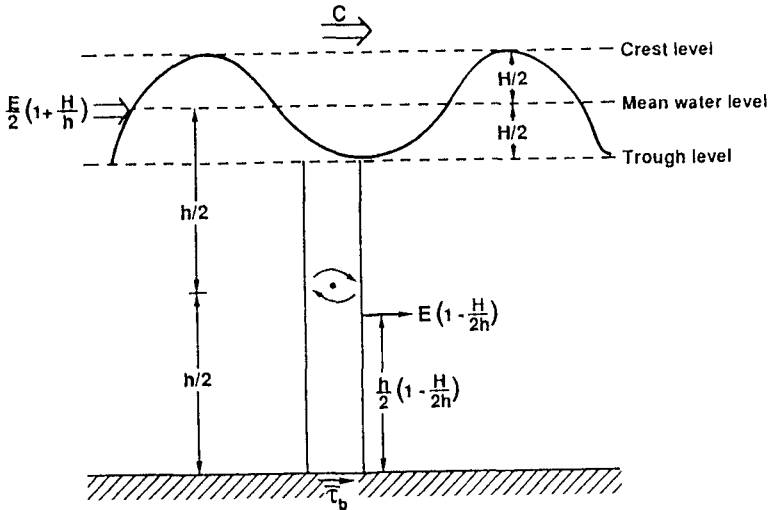


Figure 2: Schematic of the moment due to the wave-related momentum applied to the center of gravity of the water column.

ing a force on the water column directed toward the shore. The momentum force is defined by

$$F = -\frac{\partial S_{yy}}{\partial y} \tag{2}$$

where y is the distance offshore from the shoreline and S_{yy} is the flux in the y -direction of the y -component of momentum due to waves. This momentum is not applied at the centroid of the water column. Instead, the moment of the applied momentum about the center of gravity of the water column, following Boreckci (1982), is

$$M = \frac{Eh}{4} \left(1 + \frac{H^2}{2h^2}\right) \tag{3}$$

where H is the wave height, h is the water depth and $E = (1/8)\rho gH^2$ is the total energy per unit surface area in the wave as determined by linear wave theory. Figure 2 shows a sketch of the water column with the moment due to the applied momentum force. Balancing the moment with the average bottom shear stress leads to

$$\bar{\tau}_b = \frac{2}{h} \frac{\partial M}{\partial y} \tag{4}$$

which is the time-averaged seaward directed bottom shear stress due to the transfer of the wave related moment of momentum. If the applied shear stress is strong enough and the value of Eq. (1) is greater than approximately 4, then a bar would be expected to form in the profile where there was sediment convergence under the breaking wave. A trough would form in the scour region on the shoreward side of the bar, as a result of the turbulence generated by the breaking wave. Once the bar forms, if the wave conditions and water level remain the same, then the breakpoint can move offshore from the bar. This can result in growth and migration of the bar some distance offshore, until there is a balance of transport components, thereby resulting in equilibrium.

Dean (1987) observed that in addition to the tendency for sediment motion due to waves to be offshore, there must be a net “constructive” shoreward force

on the bottom sediment. If not, there would not be an upward slope in the beach profiles in the landward direction. Therefore, the equilibrium profile is the result of a balance between landward forces and seaward forces, including gravity. The average bottom shear stress, which retards the motion of a fluid in unidirectional open channel flow is expressed in terms of a quadratic friction law

$$\bar{\tau}_o = \frac{\rho f}{8} |U|U \quad (5)$$

where f is the Darcy-Weisbach friction factor and U is the velocity of the fluid, and the absolute value ensures the proper direction of the shear stress. It can be shown that whereas simple harmonic bottom velocities result in a zero average bottom shear stress, nonlinear waves cause a shoreward directed average stress. Based on stream function wave theory (Dean, 1974), $\bar{\tau}_o$ can be approximated as

$$\bar{\tau}_o = \frac{\rho f}{8} \frac{0.09 L_o}{d} \frac{H^2}{T^2} \quad (6)$$

where $L_o = gT^2/2\pi$ is the deep water wavelength.

Description of the Computational Model

The computational model used to predict the creation and migration of an offshore bar is based on a sediment continuity and a transport equation. The expression for the conservation of sediment over the profile is

$$\frac{\partial h}{\partial t} = \frac{\partial Q}{\partial y} \quad (7)$$

where h is the water depth, t is time, and Q is the offshore transport. The sediment transport equation used to calculate changes in depth contours is

$$Q = K_1 \bar{\tau}_b + K_2 \bar{\tau}_o + K_3 \frac{\partial h}{\partial y} \quad (8)$$

The forcing functions on the right hand side of this equation include contributions from $\bar{\tau}_b$, the mean bottom shear stress due to nonlinear waves, $\bar{\tau}_o$, and the effect of gravity which is related to the bottom stress, $\partial h/\partial y$. The quantities K_1 , K_2 , and K_3 are transport rate coefficients.

The computational model is an "open-loop" explicit model, which uses finite difference forms of Eqs. (7) and (8) to predict cross-shore sediment transport across a profile. The portion of the profile over which these equations are applied is represented as uniformly spaced offshore grids, although, if desired, smaller grids could be employed in areas of specific interest. Unlike many previous models, this representation allows the model to produce offshore bars, because it does not require monotonic depth increases offshore. The two-dimensional profile for the explicit model begins at the berm or dune and continues offshore to well beyond the maximum breaking depth. The distance offshore can be represented by the contour location, y_i , which is referenced to an arbitrary baseline located landward of the shoreline. To determine the depth at any contour, each elevation contour, h_i , must be considered along with the water level, η_i , which includes tide, storm surge, and wave setup and setdown effects. The total depth at each grid can be represented as $d_i = h_i + \eta_i$.

The continuity equation (Eq. 7) in finite difference form using a space-centered finite difference method, is expressed as

$$\Delta h_i = \frac{\Delta t}{\Delta y} (\overline{Q_{i+1}} - \overline{Q_i}) \quad (9)$$

where $\overline{Q_i}$ represents the time-averaged sediment flux. The terms in the transport equation (Eq. 8) can be considered individually. The most important term for the determination of the location, volume, and mobility of offshore bars is based on the momentum fluxes due to waves. Breaking waves transfer momentum by exerting a force directed toward the shore. By substituting Eq. (3) into Eq. (4), the average moment can be balanced with the average applied shear stress, yielding the following equation:

$$\tau_b = \left(\frac{E}{H} \frac{\partial H}{\partial y} + \frac{E}{2} \frac{\partial h}{\partial y} \right) \left(1 + \frac{H^2}{2h^2} \right) + \frac{E}{2h} \left(\frac{H}{h} \frac{\partial H}{\partial y} - \frac{H^2}{h^2} \frac{\partial h}{\partial y} \right) \quad (10)$$

which can be used to calculate time-averaged moment of momentum induced mean bottom stress acting on the sediment in the bed. expanding this equation and collecting terms leads to the following simplified form of the average bottom shear stress in finite difference form using the total depth, d_i :

$$(\overline{\tau_b})_i = \frac{\rho g}{8} \left[\frac{1}{2} \frac{(H_i)^2}{(d_i)^2} d_i \left(\frac{\partial h}{\partial y} \right)_i + H_i \left(\frac{\partial H}{\partial y} \right)_i \left(1 + \frac{(H_i)^2}{(d_i)^2} \right) \right] \quad (11)$$

Implementation of the Model

The explicit model requires input of a two-dimensional profile with constant offshore grid size, Δy . This input profile (see Fig. 3) must encompass the entire active region from onshore in the dune or berm region to offshore beyond the closure depth. Before transport computations can be made in any time step, the wave height and wave setup model developed by Dally (1980) is implemented. Using this breaking wave model, a realistic calculation of the average bottom shear stress parameters can be made in the explicit model. The instantaneous value of depth, $d_i = h_i + \eta_i$, is found by using the value of wave setup, η_i , determined from the model.

To demonstrate the effects of the average bottom shear stresses, $\overline{\tau_b}$ and $\overline{\tau_o}$, in bar formation and migration, examples of the variations in their values across the profile and in time are presented. The examples used here are from the large wave tank tests documented by Kraus and Larson (1988). It is stressed that in the following, the results are presented for the measured (NOT predicted) profiles. In Case 400 of these tests, the conditions included a breaking wave height of 2.3 m, a wave period of 5.6 s, a constant water level, and a sediment size of 0.22 mm ($w = 0.031 \text{ ms}^{-1}$). Figure 4 shows the values of H/wT across the initial profile (planar with slope 1:15), as well as the values of $\overline{\tau_b}$ and $\overline{\tau_o}$. The maximum value of H/wT (approximately 13, which is much greater than the threshold of 4), located at a distance 30 m offshore, corresponds to the location of the initial break point. The calculated value of $\overline{\tau_b}$ is very small offshore from the breaking wave, but at that point it increases sharply to 700 Nm^{-2} . The average shear stress due to nonlinear waves, which is always negative, has the greatest magnitude at the breakpoint of -3 Nm^{-2} . Toward the shore both values of average bottom shear stress gradually approach zero as the wave

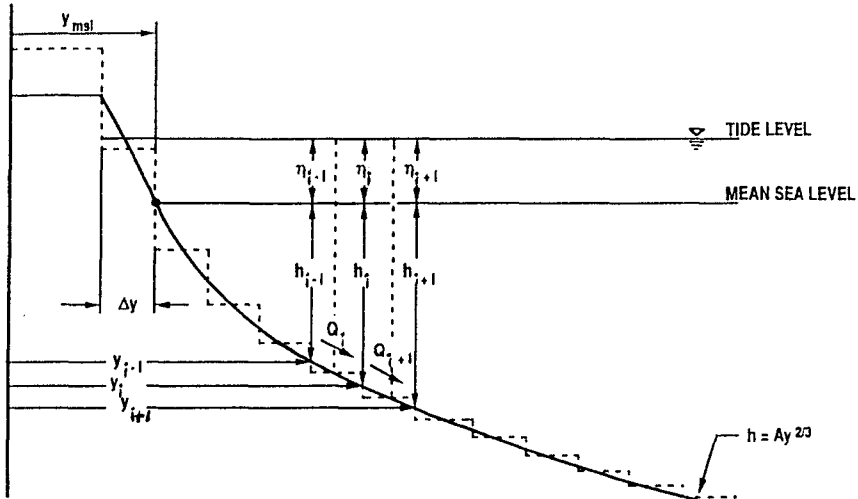


Figure 3: Model representation of beach profile showing depth and transport related to grid definitions; the cross-shore grid elements are of constant length, Δy .

height decreases across the swash zone. One hour later, a bar has formed and the break point has moved offshore to about 37 m, as shown in Fig. 5. The greatest magnitudes of both $\bar{\tau}_b$ and $\bar{\tau}_o$ have also moved offshore with the breaking wave location. After 10 hours Fig. 6 shows the Case 400 bar crest is located at 42 m and the break point is at 48 m, while the largest magnitudes of $\bar{\tau}_b$ and $\bar{\tau}_o$ are both at approximately 45 m.

In the implementation of the predictive model for bar formation and migration, the values of $\bar{\tau}_b$, $\bar{\tau}_o$, and $\partial h / \partial y$ are calculated at each grid point. Because the momentum induced shear stress is based on a local balance, it does not accurately reflect the spreading due to the breaking wave over some distance toward the shore from the breakpoint. In addition, the transport of suspended sediment offshore from the breakpoint must be considered in the computation. The model includes a weighting function which distributes the values of $\bar{\tau}_b$ over adjacent grid cells, with the weights for the onshore values being slightly greater than the offshore portion. The bottom shear stress is lagged using the following expression:

$$\bar{\tau}_{bi} = \sum_{j=-5}^5 W_j \bar{\tau}_{bi+j}$$

Table 1: Lag Weights Used for Prediction of Bar Formation and Migration

i+j	Weight, W_j
i+5	0.01
i+4	0.03
i+3	0.04
i+2	0.05
i+1	0.06
i	0.07
i-1	0.09
i-2	0.10
i-3	0.16
i-4	0.32
i-5	0.07

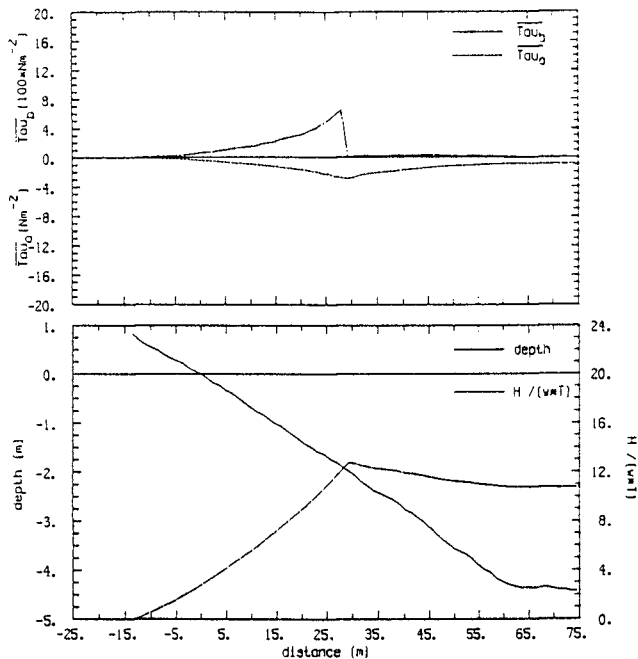


Figure 4: Initial profile and the ratio H/wT for Case 400 shown in lower panel. The upper panel shows the calculated values of $\bar{\tau}_b$ (units = $100 \cdot Nm^{-2}$) and $\bar{\tau}_o$ (units = Nm^{-2}).

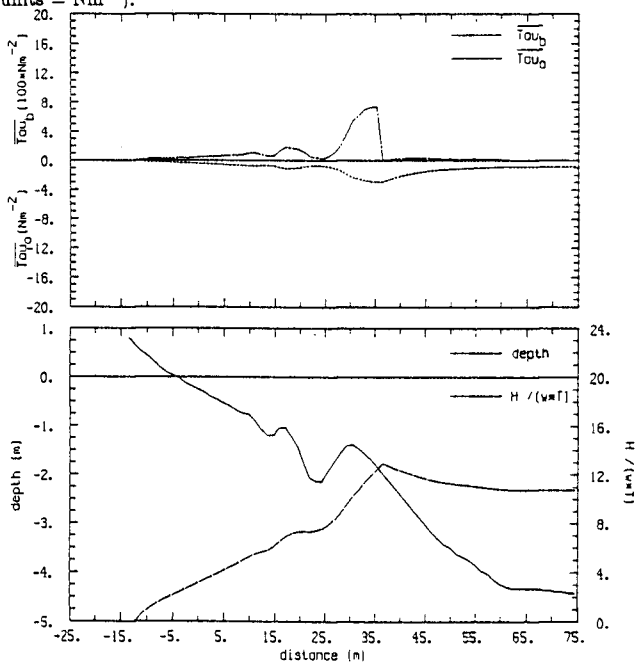


Figure 5: Case 400 at 1 hour.

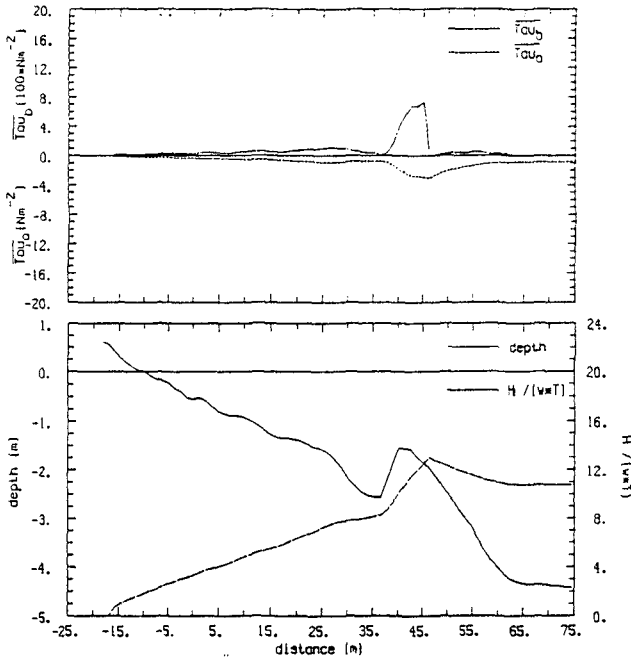


Figure 6: Case 400 at 10 hours.

The volumetric transport over one time step is

$$V_i = \Delta t [K_1(\overline{\tau_b})_i + (0.3(Q_{2p})_i + 0.7(Q_{2n})_i) + K_3(\partial h/\partial y)_i] \quad (12)$$

where Q_{2p} and Q_{2n} are described in the Appendix. When Eq. (12) is input into Eq. (9), the equation for the change of depth at any grid in the profile is

$$\Delta h_i = \frac{V_i - V_{i-1}}{\Delta y} \quad (13)$$

The portion of the profile over which calculations are made is from onshore at the upper limit of the setup to offshore at the index, $imax - 1$, where $imax$ is the total number of grid points in the profile. The two boundary conditions on the model are 1) $V_{is} = 0.0$ where is is the instantaneous upper limit along the profile of the water level setup and 2) $V_{imax-1} = 0.0$. The elevation contours are updated each time step the explicit model is run, and in the next time step the new profile is used as input into the Dally (1980) model to calculate the new wave heights and setup.

Sensitivity Tests

Sensitivity tests were performed on the explicit model to determine which parameters caused significant changes in the prediction of the size and location of offshore bars. In addition, the stability of the model was investigated for various coefficients and different lags of the bottom shear stress parameter. A few examples of these sensitivity tests will be presented here. The first example was a test in which only the average bottom shear stress, $\overline{\tau_b}$, term was used in the transport equation, with the value $K_1 = 2.9 \times 10^{-6} \text{ m}^4(\text{Ns})^{-1}$ and the time step $\Delta t = 360 \text{ s}$. Figure 7 shows that the predicted profile is unstable after 10 times steps when only the parameter $\overline{\tau_b}$ is used in Eq. (13). By simply adding the slope term, $\partial h/\partial y$, to the transport equation with a value for $K_3 = 5.8 \times 10^{-4}$

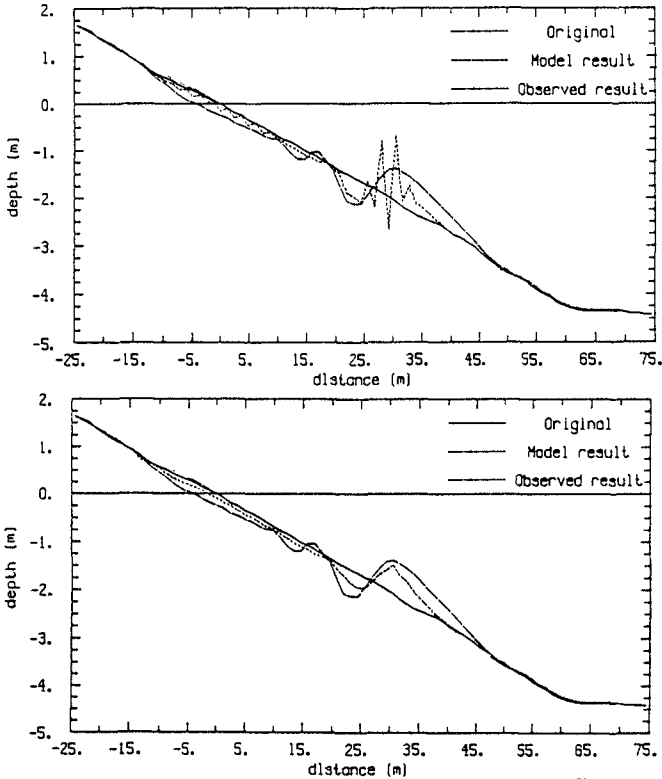


Figure 7: The original, one hour observed, and the model predicted beach profiles after 10 time steps; the upper graph is for the model prediction with $\bar{\tau}_o$ only and in the lower graph both the $\bar{\tau}_o$ and $\partial h/\partial y$ terms are included.

m^2s^{-1} , the model prediction after one hour shown in Fig. 7 now has a stable profile with the bar located accurately, even though its height is smaller than was observed in reality. Figure 8 shows the result of combining only the bottom shear stress due to nonlinear effects, $\bar{\tau}_o$, using $K_2 = 5.8 \times 10^{-5} m^4(Ns)^{-1}$, and the slope term in the transport equation. After 100 time steps, the model produces a stable profile, with sand deposited between 0 m and 15 m offshore.

Results

The predictive offshore bar model was first calibrated using the large wave tank data in Case 400. The simulation of the changes in the bars over time periods longer than the sensitivity tests reported above required that different transport rate parameters be used. The coefficients were established at the values: $K_1 = 2.4 \times 10^{-6} m^4(Ns)^{-1}$, $K_2 = 8.4 \times 10^{-5} m^4(Ns)^{-1}$, and $K_3 = 4.2 \times 10^{-4} m^2s^{-1}$. Using the larger K_i values in these computations was found to be necessary to allow the forcing function, $\bar{\tau}_o$, which produces shoreward sediment motion in the model, to compensate for the increasing magnitude of the slope term, $\partial h/\partial y$, as the bar forms. The time steps were also reduced to $\Delta t = 180$ s, which is half the interval used in the sensitivity tests. This had the result of increasing the stability of the model, which requires very little

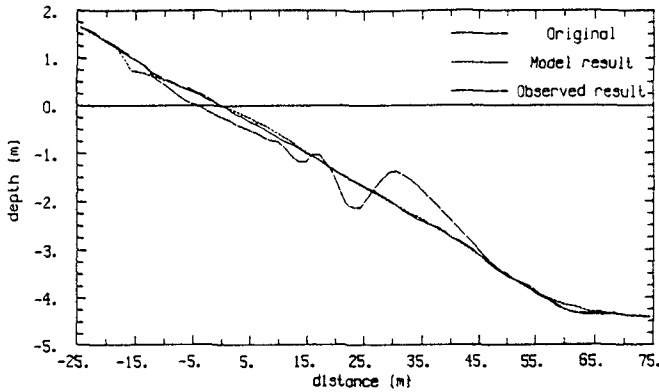


Figure 8: Same as Fig. 7, except here the model is run for 100 time steps and includes only the $\bar{\tau}_o$ and the $\partial h/\partial y$ terms.

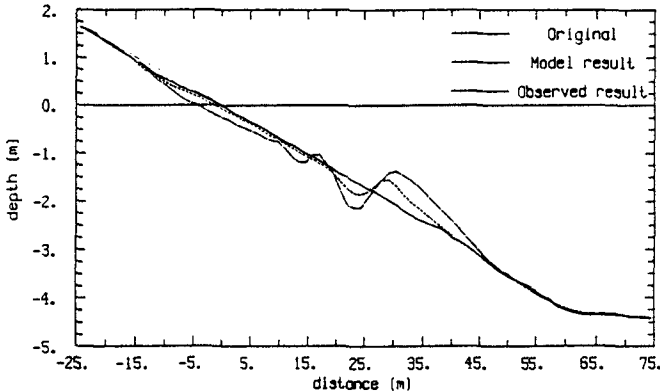


Figure 9: Case 400 profiles initially and one hour observed and predicted.

computational time for the large wave tank beach profiles. The prediction for the first hour shown in Fig. 9 shows the location of the bar agrees very closely with the observed profile, but the size of the predicted bar and trough is nearly half of the actual one hour result. This is an indication of the reduction of the size of the transport rate coefficients. Figure 10 shows the model is simulating the 5 hour profile reasonably well if the size of the bar and its migration offshore are compared with the observed profile. After 300 time steps or 15 hours of simulation, the observed and predicted profiles in Fig. 11 continue to be in good agreement. By the end of 30 hours (Fig. 12), the agreement between the predicted and actual profiles remains quite good. Some of the small differences are likely due to wave reflections in the measured profile.

The model was also run for Case 401, which had nearly the same wave characteristics as Case 400 ($H = 2.0$ m, $T = 5.6$ s), but the sediment size in the large wave tank beach profile was 0.4 mm. The larger sediment size would be expected to result in steeper slopes in the offshore bar, especially on the seaward side of the bar, due to the greater fall velocities associated with sediment having a larger diameter. The profile shown in Fig. 13 after the first 20 time steps of the explicit model run shows very good agreement between the location of the predicted offshore bar when compared with the actual system. Even after five hours (see Fig. 14), the model has predicted correctly the rate of

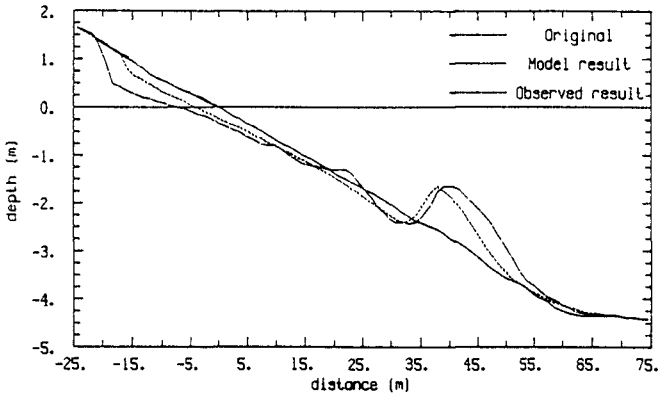


Figure 10: Case 400 profiles initially and 5 hours observed and predicted.

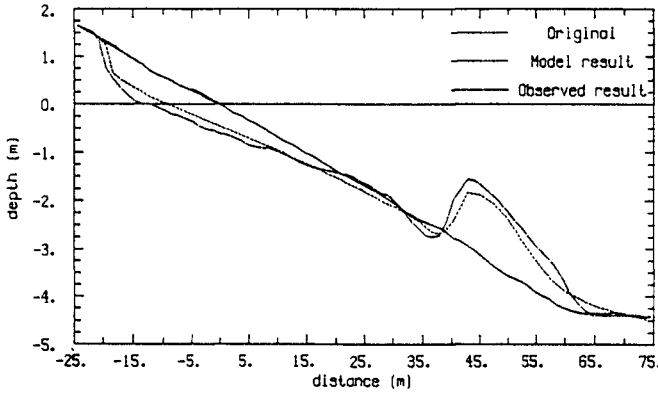


Figure 11: Case 400 profiles initially and 15 hours observed and predicted.

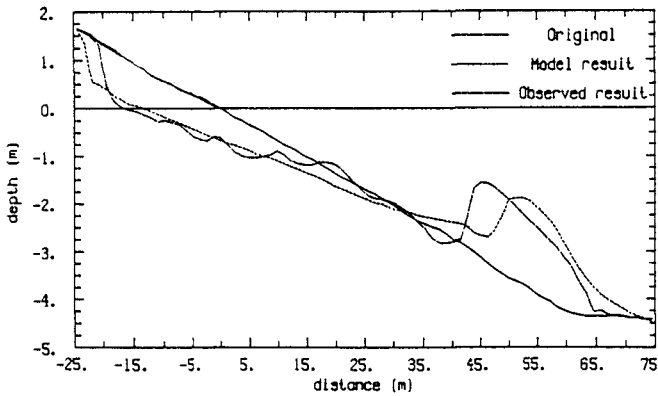


Figure 12: Case 400 profiles initially and 30 hours observed and predicted.

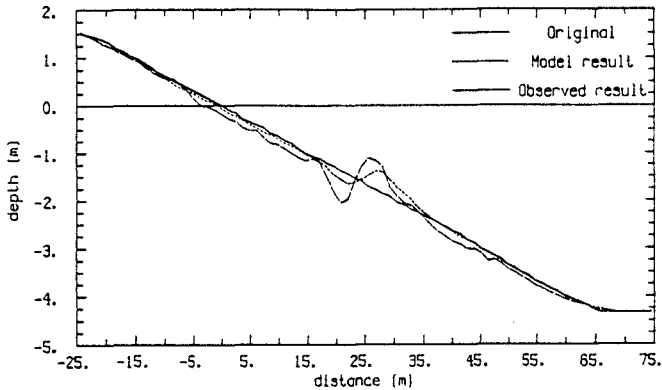


Figure 13: Case 401 profiles initially and one hour observed and predicted.

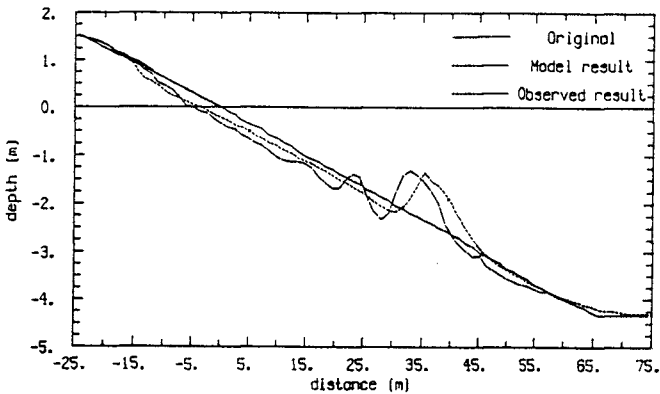


Figure 14: Case 401 profiles initially and 5 hours observed and predicted.

migration of the bar offshore, but the predicted trough is slightly less deep than that of the observed profile. The model is obviously overestimating the amount of movement which occurs in the simulations for longer periods of run times (see Figs. 15 and 16). The effects of the coarser sediment need to be included in a realistic manner to slow the bar migration offshore in the computational model.

Conclusions

An "open-loop" explicit model can be used to determine the location of the formation and subsequent migration of bars. The calculation of average bottom shear stress values based on the use of the moment due to the wave-related momentum applied about the center of gravity of the water appears realistic. The model is based on sediment continuity and transport equations, and the latter equation is used by combining the mean bottom shear stress due to breaking waves, $\bar{\tau}_b$, the mean shear stress due to nonlinear waves, $\bar{\tau}_o$, as well as a slope term, $\partial h / \partial y$. The $\bar{\tau}_b$ term acts to direct sediment offshore from the breakpoint, while the $\bar{\tau}_o$ term produces mostly shoreward sediment motion. The slope term maintains stability in the transport of sediment by acting as a gravity control. The explicit sediment transport model can be applied to beach profiles which have waves breaking over them in such a manner that scouring occurs shoreward of the breakpoint. The prediction of the trough created by the scouring process is accomplished by applying weighting lags to the $\bar{\tau}_b$ values. The coupling of the sediment continuity/transport model with the Daly (1980)

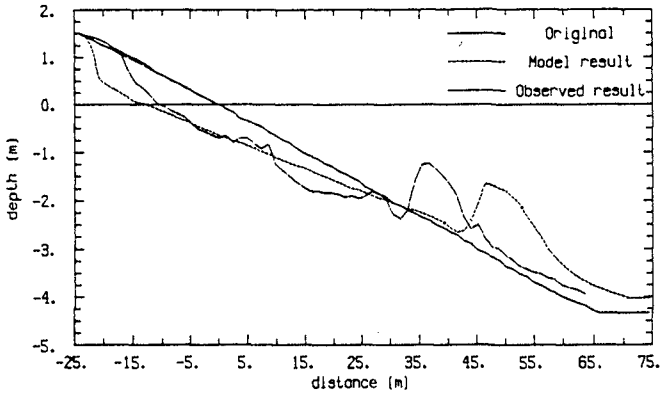


Figure 15: Case 401 profiles initially and 15 hours observed and predicted.

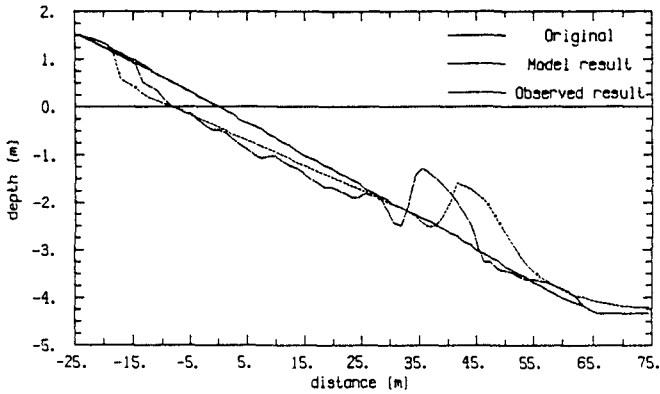


Figure 16: Case 401 profiles initially and 30 hours observed and predicted.

breaking wave model allows the formation and migration of the bar.

Appendix

The value of τ_o is decreased across the profile by including the seaward directed component of bottom shear stress due to nonlinear waves using the expression

$$(Q_{2p})_i = K_2 \left\{ -(\bar{\tau}_o)_i + \frac{2}{3} \omega \delta \sin \phi_i \right\} - \tau_{cr} \tag{14}$$

if $\{ \} \geq \tau_{cr}$; $(Q_{2p})_i = 0.0$ otherwise. The critical bottom shear stress is $\tau_{cr} = \frac{2}{3} \rho g (s-1) \delta \sin \phi_{cr}$, where ϕ_{cr} is the critical slope angle (a function of the sediment diameter) and s is the ratio of mass density of sediment to the mass density

of water. The immersed specific weight of the sediment is ω , δ is the sediment diameter, and ϕ_i is the profile slope. The component of the shear stress directed toward the shore is

$$(Q_{2n})_i = K_2 \left\{ 3(\bar{\tau}_o)_i + \frac{2}{3} \omega \delta \sin \phi_i \right\} + \tau_{cr} \quad (15)$$

if $|\{\} | \geq \tau_{cr}$; $(Q_{2n})_i = 0.0$ otherwise.

Acknowledgements

The financial support provided by the Florida Sea Grant Program for this research is greatly appreciated.

References

- BORECKCI, O.S. (1982).
Distribution of Wave-Induced Momentum Fluxes Over Depth and Applications Within the Surf Zone. Ph. D. Diss., Univ. of Delaware, Newark, DE, USA.
- DALLY, W.R. (1980).
A Numerical Model for Beach Profile Evolution. Unpubl. M.S. Thesis, Univ. of Delaware, Newark, DE, USA.
- DEAN, R.G. (1973).
Heuristic Models of Sand Transport and Beach Profile Evolution. Proc. of Conf. on Eng. Dyn. in Surf Zone, Sydney, AUS, pp 208-214.
- DEAN, R.G. (1974).
Evaluation and Development of Water Wave Theories for Engineering Application. Vols. 1 and 2, Spec. Rep., USAE, CERC, Fort Belvoir, VA, USA.
- DEAN, R.G. (1987).
Additional Sediment Input to the Nearshore Region. Shore and Beach, Vol. 55, No. 3-4, pp 76-81.
- KRAUS, N.C., and LARSON, M. (1988).
Beach Profile Change Measured in the Tank for Large Waves, 1956-1957 and 1962. T.R. CERC-88-6, USACE-WES, CERC, Vicksburg, MS, USA.
- KRIEBEL, D.L., and DEAN, R.G. (1985).
Numerical Simulation of Time-Dependent Beach and Dune Erosion. Coast. Eng., Vol. 9, pp 221-245.
- LARSON, M., and KRAUS, N.C. (1989).
SBEACH: Numerical Model for Simulating Storm-Induced Beach Change, Report 1. T.R. CERC-89-9, USACE-WES, CERC, Vicksburg, MS, USA.
- STIVE, M.J.F., and WIND, H.G. (1986).
Cross-Shore Mean Flow in the Surf Zone. Coast. Eng., Vol. 10, pp 325-340.
- SVENDSEN, I.A., and HANSEN, J.B., (1988).
Cross-Shore Currents in Surf-Zone Modelling. Coast. Eng., Vol. 12, pp 23-42.
- WRIGHT, L.D., and SHORT, A.D. (1984).
Morphodynamic Variability of Surf Zone Beaches: A Synthesis. Mar. Geol., Vol. 56, pp 93-118.

CHAPTER 163

A MICRO-COMPUTER BASED QUASI 3-D SEDIMENT TRANSPORT MODEL

Marie-Hélène G. Briand¹ and J. William Kamphuis²

ABSTRACT

A quasi three-dimensional numerical model for detailed sediment transport calculations on a beach is developed for a micro-computer. It includes a complete description of the wave climate and wave induced currents over the study area. Vertical concentration profiles of suspended sediments, calculated locally to include the effects of shear stress on the bottom and the intensity of turbulence due to breaking waves, are superposed on local velocity profiles to yield sediment transport rates. Sediment transport is calibrated with laboratory experiments performed on a straight sand beach.

INTRODUCTION

In coastal engineering, where hydrodynamics play a major role, the latest numerical models calculating wave-induced currents and sediment transport are usually developed on large, powerful computers because of the problem's complexity. So far, detailed numerical coastal modeling has thus been largely limited to research projects. But recent innovations and rapid developments in the micro-computer industry have transformed the Personal Computer into an essential tool for scientific applications.

The present paper shows an overview of the theory used in the proposed numerical model. Briand (1990)

- ¹ Hydraulics engineer; Lalonde, Girouard, Letendre et Associés, 485 McGill street, 8th floor, Montreal, Canada, H2Y 2H4
- ² Professor, Civil Engineering, Queen's University, Kingston, Ontario, Canada, K7L 3N6

provides a detailed description of the pertinent theory and numerical methods of solution. The numerical model was developed to work efficiently on a micro-computer.

Several aspects of modeling relatively detailed coastal processes are presented with an emphasis on a simple approach to a wide range of applications. The proposed numerical model includes calculations of wave transformation, wave-induced currents and resulting sediment transport in the surf zone. Numerical results of sediment transport are calibrated with laboratory experiments. A practical "quasi" three-dimensional description of nearshore hydrodynamics and its effect on sediment transport is produced.

NUMERICAL MODEL

Wave Transformation

The model requires a discretized representation of the study area bathymetry in the form of a rectangular grid, and offshore wave conditions must be specified for either regular or random wave fields. Calculations start with a complete evaluation of the wave climate over the gridded area: shoaling, refraction, breaking and energy dissipation inside the surf zone are considered.

A Miche type of breaking criterion is used, as suggested by Goda (1970):

$$H_b = 0.17 L_o \left\{ 1 - \exp \left[-1.5 \frac{\pi d}{L_o} \left(1 + 15 m^{4/3} \right) \right] \right\} \quad (1)$$

where:

- H_b is the breaking wave height;
- L_o the deepwater wavelength;
- d the local water depth;
- m the local beach slope.

This breaking criterion was preferred to others because of its relative simplicity and because it fits better the laboratory results presented in this paper.

The principle of conservation of wave energy flux is applied to calculate wave height transformations:

$$\frac{d(Ec)}{ds} = -D \quad (2)$$

- where:
- c_g is the wave group velocity;
 - E is the total wave energy density;
 - s is the distance along the wave path;
 - D is the wave's energy dissipation rate per unit area.

It is possible to include several terms responsible for energy dissipation in Eq. 2, like friction on the bottom or percolation, but the present application considers wave breaking as the main source of dissipation. Outside the surf zone, D is equal to zero.

Energy dissipation in a breaking wave is calculated from the empirical formulation of Dally, Dean and Dalrymple (1984):

$$D = \frac{K}{d} \left[\left(E - E_{st} \right) c_g \right] \quad (3)$$

- where:
- K is an empirical coefficient;
 - E_{st} represents the "stable" energy that a breaking wave strives to attain on a constant depth bottom.

The stable energy is calculated from the stable wave height H_{st} as, suggested by Horikawa and Kuo (1966):

$$H_{st} = \Gamma d \quad (4)$$

Dally *et al* (1984) show that values of $K = 0.15$ and $\Gamma = 0.4$ give good agreement with their laboratory results.

In the wave transformation calculations, a combination of linear and cnoidal wave theories was used for a better description of wave characteristics, especially in shallow water.

In the case of a random wave field, the offshore wave spectrum is divided into several sinusoidal wave components (approximately 40 for the laboratory tests described in the second part of the present paper) with individual periods, heights, angles of approach and probabilities of occurrence. An empirical method is used to relate the components' wave heights and periods, and the probability is determined from the Rayleigh distribution of wave heights. Each regular wave component is shoaled, refracted individually and then dissipated in

the surf zone. Root-mean-square characteristics of the wave climate are calculated for comparison with measurements.

Hydrodynamics Model

For practical reasons, the complete three-dimensional (3-D) equations for hydrodynamics in the nearshore zone are not solved directly on the micro-computer. Instead, a three-step procedure is used. First, a two-dimensional representation of horizontal, time- and depth-averaged velocities and water levels (2-DH model) is developed. The horizontal velocities and local wave characteristics are then used to calculate the local vertical profiles of velocities (2-DV) at each node of the gridded area. Finally, those vertical profiles, calculated from the 2-DH current pattern, are superposed on the horizontal grid to yield what is called a "Quasi 3-D" representation of nearshore hydrodynamics.

Calculation of Velocities and Water Levels

The first step consists of calculating the time- and depth-averaged wave-induced currents \vec{u} and set-up η over the considered area. A steady state solution is obtained using an Alternate Direction Implicit formulation of the two-dimensional, horizontal (2-DH) equations of motion (Eq. 5) and continuity (Eq. 6):

$$\frac{\partial \vec{u}}{\partial t} + \left(\vec{u} \cdot \nabla \right) \vec{u} + g \nabla \eta = \frac{1}{\rho d} \left[\vec{\tau}_\ell - \vec{\tau}_b - \nabla \cdot \vec{S} \right] \quad (5)$$

$$\frac{\partial \eta}{\partial t} = - \nabla \cdot \left(\vec{u} d \right) \quad (6)$$

where the terms in Eq. 5 are respectively: the local acceleration, the non-linear convective acceleration, the hydrostatic pressure force (per unit mass), the lateral mixing shear stress, the bottom friction shear stress, and the gradient of radiation stress tensor.

To reduce instabilities and accelerate numerical computations, 2-DH calculations are performed starting with an approximation of the velocity and set-up solution based on the infinite beach simplification, i.e. variations in the longshore direction are neglected at first. Mean water depths are adjusted by the calculated wave set-up, and the coastline is allowed to shift inland to account for coastal flooding. This preliminary solution

is then introduced as the initial condition for the ADI scheme until a steady state solution is obtained. The result is a two-dimensional, horizontal current description of the study area.

Calculation of Vertical Distributions of Velocities

In the second step of the model, local vertical distributions of horizontal velocities are evaluated using an extension of Svendsen and Hansen's (1988) theoretical development for undertow, where the depth-averaged velocities calculated in step 1 are taken into account. The vertical profile of velocities is developed from a second-order differential equation for vertical momentum balance, Eq. 7, and from the principle of continuity of flow.

$$\frac{\partial}{\partial z} \left[\nu_t \frac{\partial \vec{u}}{\partial z} \right] = \frac{\partial}{\partial x_i} \left[g\eta \right] + \frac{\partial}{\partial z} \left[\vec{\nabla} \cdot \vec{S} \right] \quad (7)$$

- where:
- ν_t is the turbulent eddy viscosity;
 - x_i represents horizontal axes x and y;
 - \vec{S} is the total radiation stress tensor.

The above undertow model considers that the flow occurs in three layers. In the surface layer, between the wave crest and trough, a detailed description of the highly turbulent flow within the breaking wave roller is not necessary. The only information required is the amount of fluid carried by the roller, which is expressed in an empirical formula suggested by Svendsen (1984). A thin bottom boundary layer in which fluid viscosity is considered, includes the effect of bottom friction on the flow and accounts for steady streaming due to the wave oscillatory flow. Lastly, the middle layer flow is governed by the imbalance between the excess momentum flux induced by the breaking wave in the surface layer and the hydrostatic excess pressure created by the local mean water level gradient, or wave set-up.

Calculation of Sediment Transport

Vertical profiles of wave-induced sediment concentrations in the water column are calculated locally to be combined with vertical profiles of velocities from the hydrodynamics model to yield a quasi 3-D sediment transport pattern over the study area.

The vertical profile of sediment concentration is assumed to follow an exponential shape:

$$C(z) = C_A \exp \left(K_e \frac{(z-z_A)}{z_A} \right) \quad (8)$$

with
$$K_e = -\ln \left(C_B/C_A \right) \quad (9)$$

where: - z_A is taken as the bottom boundary layer thickness;
- C_B is the concentration at which the sediment starts moving.

The reference concentration C_A at the upper limit of the bottom boundary layer is estimated from a mobility number made up of two terms representing the individual influences of the local wave-current bottom shear stress and the turbulence created by the breaking wave:

$$C_A = \frac{K_{A1} (\nu_t/d) + K_{A2} (\tau_{wc}/\rho)^{1/2}}{w_f} \quad (10)$$

where: - K_{A1} and K_{A2} are calibration constants;
- τ_{wc} is the waves and currents shear stress;
- w_f is the sediment fall velocity.

The above sediment concentration profiles are multiplied by the local velocity profiles and integrated over the depth to yield the local sediment transport rates, in bed-load and suspended load modes. A "Quasi 3-D" description of sediment transport is obtained which is both practical and easy to solve on a micro-computer.

The above approach has a strong physical basis, and calibration of sediment transport calculations is relatively simple. Once concentration calibration parameters K_{A1} and K_{A2} , in Eq. 10, are determined, all components of sediment transport are also determined since bed-load, suspended load, longshore and cross-shore transport are coupled.

Swash Transport

The wave motion in the swash zone is a time-dependent process that is not described by the above

numerical model. However, the sediment transport contribution from the swash zone is important and must be included in some way for comparison with laboratory results. A global formulation based on the assumption that sediment concentration in the swash zone is caused only by wave energy dissipation, is proposed:

$$Q_{sw} = K_Q \left(S_{sw} \right)^{1/6} \left(L_{sh} \right)^{1/2} \frac{H_{sh}^{7/3}}{w_f} \quad (11)$$

where:

- K_Q is a calibration constant;
- S_{sw} is the swash zone width;
- L_{sh} is the wavelength at the shoreline;
- H_{sh} is the wave height at the shoreline.

Beach Morphology

Finally, each local vertical profile of sediment transport is integrated over the local water depth and included in the equation of conservation of sediment to calculate the beach morphology with time.

LABORATORY EXPERIMENTS

The numerical model was calibrated with results from experiments carried out in the wave basin of the Queen's University Coastal Engineering Laboratory. Only half of the 28 tests performed with various regular and random wave fields and two different sediment sizes were used for the present calibration (Table 1).

Wave heights, longshore currents, alongshore sediment transport rates and their cross-shore distribution were measured on a deformable sand beach. Beach profile evolution in time was monitored in detail. Wave heights and longshore currents were measured at regular intervals at many locations across the surf zone as a barred profile evolved from the initially plane beach. Sediment transport was measured using a series of 7 or 14 sand traps located at the downdrift end of the beach. Kamphuis and Kooistra (1990) provide a complete description of the laboratory set-up and test results.

To calibrate and compare the numerical model results with laboratory measurements performed on a simulated infinitely long beach, the quasi 3-D numerical model was simplified by neglecting all gradients in the alongshore direction.

Table 1. Description of laboratory tests.

Regular Test	T (sec)	H _d (cm)	D ₅₀ (mm)	Random Test	Tp (sec)	Hs _d [*] (cm)
RE	0.92	4.5	.105	IE	0.92	6.3
RF	1.15	4.5	.105	IA	1.15	4.5
RG	1.39	4.5	.105	IF	1.15	6.3
RI	1.38	6.0	.105	IG	1.39	6.3
				II	1.38	7.8
			.180	IJ*	0.92	9.0
			.180	IB	1.15	6.3
RC*	1.15	7.4	.180	IC	1.15	8.8
			.180	ID*	1.15	11.7
			.180	IK*	1.38	8.4

* Subscript "d" indicates depth at the wave generator. In all tests $d = 0.5$ m, except tests marked with a * for which $d = 0.55$ m.

RESULTS AND DISCUSSION

Numerical results for wave heights show very good agreement with measurements both inside and outside the surf zone (Fig.1), even though some regular wave experiments contained important reflection patterns.

Numerical results for longshore velocities agree well in magnitude with experiments but their cross-shore distribution does not always coincide with observations (Fig.2). This is due to the simplistic wave energy dissipation module used in the calculations. A more realistic computation should simulate the exchanges between potential, kinematic and turbulent energies, and account for the formation of a roller.

To compare longshore sediment transport rates, the swash zone contribution was separated from surf zone transport by identifying sediment traps located above mean water level. Surf zone sediment transport rates agree well with the observed results in a calibration that gives 20 times more importance to the turbulent energy dissipation term than to the bottom shear stress term in the sediment concentration calculations (Fig.3). On the other hand, swash transport predictions, based on a simple global formula that accounts only for the total wave energy dissipation on the beach face, do not agree well (Fig.4). It is of interest that the observed swash transport rates for similar wave conditions are higher for the larger sediment size (0.18 mm) than for the

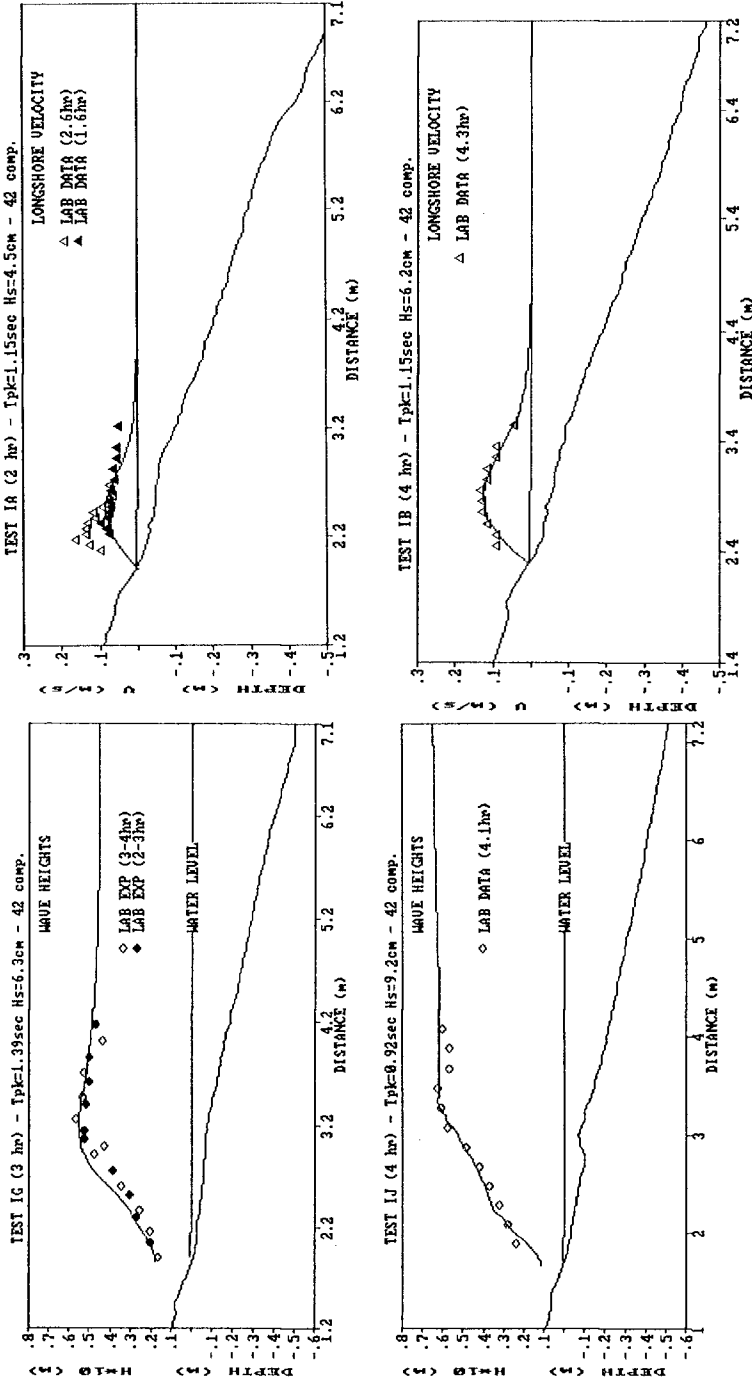


Fig. 1. Calculated and measured wave heights.

Fig. 2. Calculated and measured longshore velocities.

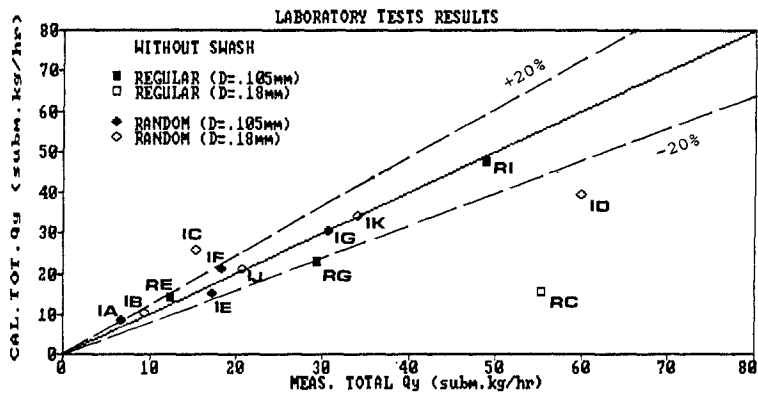


Fig. 3. Global longshore sediment transport results, without swash contribution.

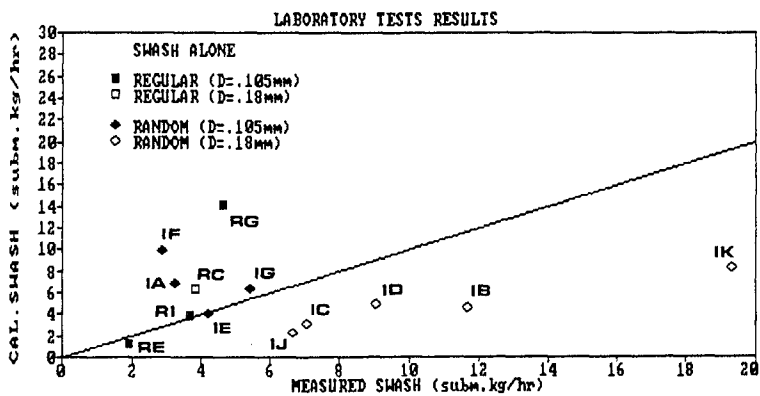


Fig. 4. Global swash transport.

smaller (0.105 mm) sand. From a comparison of calculated and measured swash transport, it is postulated that a bottom shear stress model that accounts for the critical shear stress, based on the Shields curve, would simulate the observed results better.

The calculated cross-shore distributions of long-shore sediment transport agree well with observations (Fig.5); but again, the predicted peak does not always coincide with observations. A better wave energy dissipation model should improve these results.

The numerical model is successful in predicting the proper bar location in all cases, but the observed bars are flatter than in the numerical results, indicating a lack of cross-shore convection in the undertow calculations (Fig.6). This is an effect of the quasi 3-D velocity calculations which could be improved by adding cross-shore convection artificially in the numerical scheme. The fact that swash zone processes are not taken into account in the numerical calculations can also explain the underprediction in offshore sediment transport.

Finally, Figure 7 shows a simulation of a beach profile submitted to the same wave conditions over a long period of time. After 9 hours of constant wave attack, the profile evolution slows down and the only bar transformation that still occurs is a slight accumulation of sediment on the offshore slope. The bar thus slowly moves offshore, as was observed in the laboratory.

CONCLUSIONS

The proposed quasi 3-D numerical model for sediment transport works efficiently on a micro-computer. It is also flexible, as it can account for various natural phenomena (e.g. tides, wind) by simply including additional terms in the momentum equations.

One interesting finding of the present study is that sediment transport in the surf zone is dominated by the influence of the turbulent wave energy dissipation on the sediment suspension process, whereas swash zone transport is clearly driven by the bottom shear stress effect on sediment.

There is one important limitation to the model in its present form: it should not be applied to complex bathymetries since diffraction and wave-current interactions are neglected in calculations, and because of the first approximation approach used in current calculations.

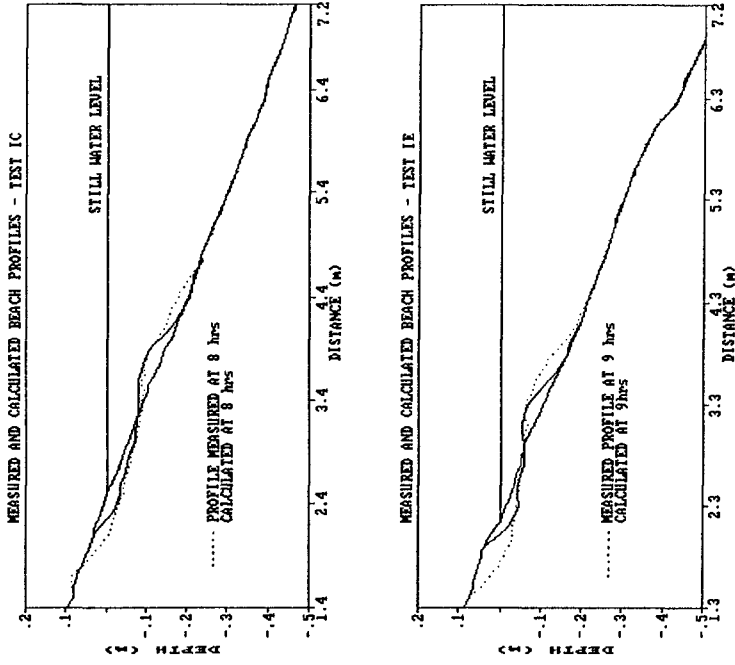


Fig. 6. Calculated and measured beach profiles.

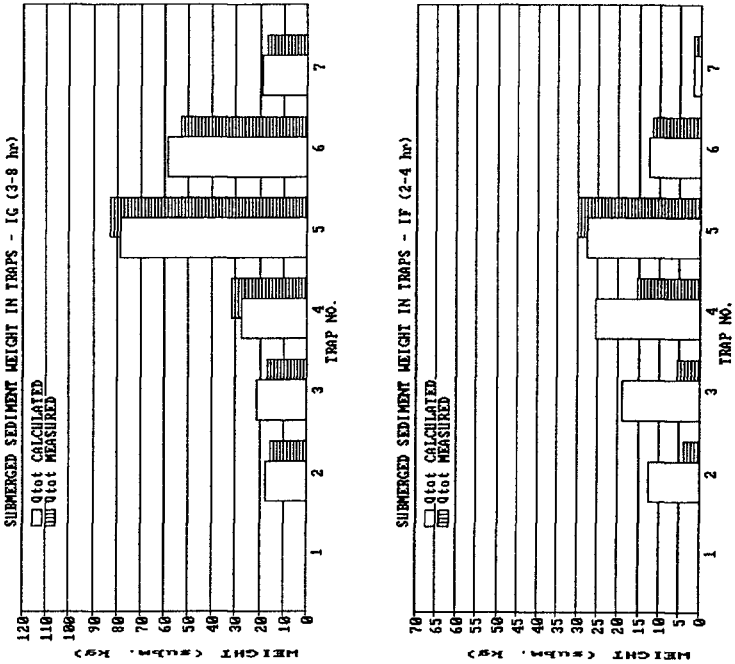


Fig. 5. Calculated and measured cross-shore distributions of longshore transport.

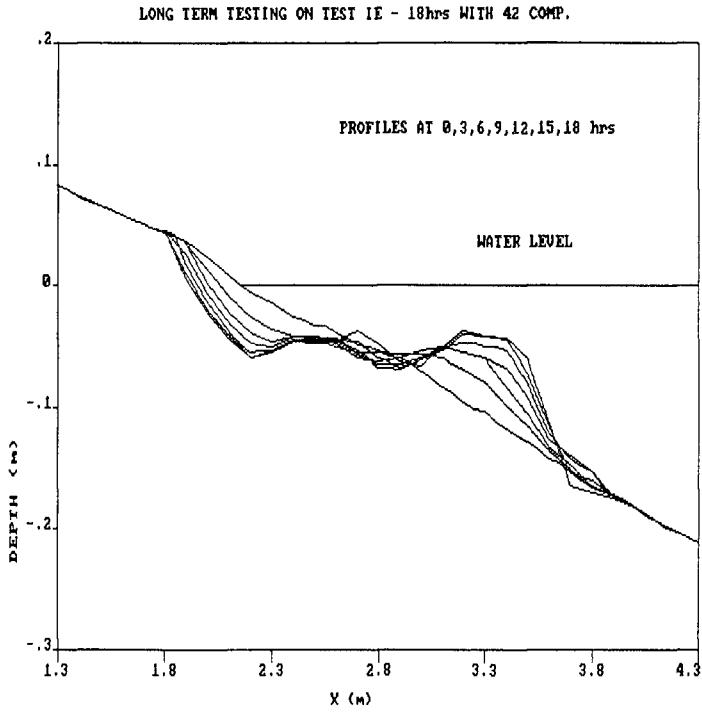


Fig. 7. Long term beach profile evolution.

Further research to improve this model will consider swash zone processes, the energy transition in breaking waves, and calibration with field measurements.

ACKNOWLEDGEMENTS

The authors gratefully recognize the financial support from the National Sciences and Engineering Research Council's Strategic and Operating Grants programs. Ms. Briand was supported from a Senator F. Carrel Award granted by Queen's University, and a Fonds F.C.A.R doctoral scholarship from the Province of Quebec. Travel grants from Queen's School of Graduate Studies and Research and the Department of Civil Engineering to present this paper are also acknowledged.

REFERENCES

- Briand, M.H.G. (1990). A detailed quasi 3-D numerical model for sediment transport processes in the surf zone. Ph.D. thesis, Queen's University, Kingston, Canada, July 1990.
- Dally, W.R., Dean, R.G., and Dalrymple, R.A. (1984). A model for breaker decay on beaches, Proc. 19th Int. Conf. Coast. Eng., ASCE, Vol.1, p.82-98.
- Goda, Y. (1970). A synthesis of breaker indices. Trans. of Japan Soc. of Civ. Eng., Vol.2, No.2, p.227-230.
- Horikawa, K. and Kuo, C.T (1966). A study on wave transformation inside the surf zone. Proc. 10th Int. Conf. Coast. Eng., ASCE, p.217-233.
- Kamphuis, J.W. and Kooistra, J. (1990). Three dimensional mobile bed hydraulic model studies of wave breaking, circulation and sediment transport processes. Proc. of the Canadian Coastal Conference, Kingston, Canada, May 1990, p.363-386.
- Svendsen, I.A., and Hansen, J.B. (1988). Cross-shore currents in surf zone modelling. Coast. Eng., 12, p.23-42.
- Svendsen, I.A. (1984). Mass flux and undertow in a surf zone. Coastal Eng., 8, p.347-365.

SUBJECT INDEX

Page number refers to first page of paper.

- Accretion, 1975, 2580
Advection, 1186
Alaska, 1687
Algorithms, 136, 255, 478, 516
Analytical techniques, 2682
Anemometers, 450, 489, 557
Arctic regions, 1687
Armor units, 1270, 1306, 1334, 1375,
1403, 1417, 1446, 1460, 1538, 1552,
1578, 1620, 1634, 1716, 1730, 1755,
1805, 1819, 2768, 2782, 2796, 3194
Artificial islands, 2768
Assessments, 41
Asymmetry, 396, 637
Atmospheric pressure, 95, 826
Australia, 2241, 2265
- Backwashing, 2360
Bank erosion, 2385
Barges, 1648
Barrier design, 2950
Barrier islands, 783, 3254
Barriers, 1564
Bars, 959, 2101, 2145, 2265
Bars, riverine, 757, 2964
Bathymetry, 597, 1292, 2279, 2416,
2782
Bays, 2047
Beach cusps, 2101
Beach erosion, 95, 570, 1862, 1975,
2010, 2020, 2073, 2173, 2241, 2304,
2360, 2385, 2457, 2471, 2580, 2644,
2710, 2726, 2740, 2782, 2796, 2810,
3063, 3254
Beach nourishment, 783, 1984, 1998,
2020, 2241, 2304, 2394, 2542, 2796,
3183, 3227, 3254
Beaches, 109, 227, 281, 516, 557, 570,
798, 867, 1292, 1702, 2061, 2117,
2159, 2265, 2291, 2443, 2481, 2552,
2566, 2682
Bed load movement, 2332, 2536,
3037
Bed ripples, 661, 2186, 2200
Bed roughness, 450
Bedforms, 2318
Berms, 1730, 2073, 2101, 2304, 3194,
3207, 3222
Blocks, 1606
Boring, 1019
- Boundaries, 2227
Boundary conditions, 1292, 1948
Boundary element method, 840,
1270, 1389, 3140
Boundary layer, 281, 2360
Boundary layer flow, 450, 544, 661,
853, 993
Boundary shear, 2536
Brazil, 3207
Breaking waves, 32, 68, 123, 136, 150,
164, 218, 306, 330, 516, 716, 895,
923, 973, 1019, 1033, 1060, 1362,
1473, 1827, 2145, 2159, 2173
Breakwaters, 136, 164, 306, 1060,
1200, 1270, 1320, 1348, 1362, 1375,
1403, 1473, 1538, 1592, 1620, 1634,
1675, 1702, 1716, 1730, 1755, 1781,
1805, 1827, 1837, 1851, 2020, 2034,
2416, 2603, 2616, 2740, 3194, 3207,
3222, 3239
Bridge foundations, 3268
Bridges, 3268
Building design, 2908
Bulkheads, 1837
Buried pipes, 2508
- Caissons, 1403, 1675, 1827
Channel stabilization, 2922, 2975
Channels, waterways, 2430, 2936,
2975, 3024, 3088, 3126
Characteristics, 82
China, People's Republic of, 82, 2047
Cnoidal waves, 109, 1144
Coastal engineering, 1, 7, 516, 769,
881, 935, 1005, 1513, 1862, 1984,
1998, 2010, 2975, 3112, 3281
Coastal environment, 177, 867, 959,
1088, 1144, 1172, 2047, 2768, 2894,
2908
Coastal management, 7, 41, 1895,
1909, 2589, 2824
Coastal morphology, 1876, 1888,
1948, 1962, 1975, 2589, 2682, 2922,
2950, 2964, 3050, 3171
Coastal processes, 444, 557, 743,
1074, 1876, 1895, 1909, 1935, 1962,
1975, 2061, 2087, 2101, 2117, 2227,
2265, 2332, 2346, 2402, 2443, 2457,
2481, 2522, 2552, 2566, 2589, 2682,
2710, 2810, 3037, 3154

Volume 1, 1-1116 Volume 2, 1117-2172 Volume 3, 2173-3308

- Coastal structures, 371, 743, 757, 923, 1200, 1306, 1375, 1431, 1446, 1460, 1487, 1499, 1524, 1552, 1578, 1592, 1687, 1795, 2457, 2726
- Cohesive sediment, 2984, 3012, 3037
- Computation, 164, 191, 444, 1019, 1060, 1513, 1909, 2255
- Computerized simulation, 1172
- Concrete, 1687, 2768
- Concrete blocks, 1431
- Concrete construction, 1578, 1634, 1755, 1819
- Conferences, 1, 7
- Construction, 1280, 2020, 2950, 3239
- Construction materials, 1648, 3222
- Construction methods, 1648, 1675, 3207
- Contamination, 2894, 3194, 3222
- Control structures, 1060
- Coral reefs, 330
- Coriolis effect, 95
- Critical load, 2671
- Currents, 95, 205, 241, 316, 384, 444, 450, 489, 853, 993, 1074, 1088, 1186, 2131, 2227, 2443, 2495, 2866, 3171
- Cyclones, 358, 2852
- Cylinders, 973, 1280, 1389, 1795
- Cylindrical shells, 1675
- Dam construction, 3050
- Damage, 743, 1446, 1552, 1851, 2416, 2908, 3074
- Damage estimation, 2796
- Damping, 1592
- Data analysis, 345
- Decision making, 1
- Deep water, 623, 1827
- Deltas, 2984
- Design, 136, 597, 923, 1160, 1254, 1320, 1362, 1403, 1417, 1431, 1487, 1524, 1552, 1819, 1827, 1837, 2020, 3102, 3194, 3207, 3239, 3268
- Design criteria, 1634, 3024, 3074
- Design storms, 2304
- Design waves, 18, 647, 1306
- Diffusion, 1186
- Diffusion coefficient, 2998
- Dikes, 895, 1254, 1431, 1487, 1662, 2010, 2087, 2671, 2880, 2998, 3171, 3183
- Dimensions, 959
- Disposal, 2430
- Distribution functions, 18, 345
- Disturbances, 597
- Dolos, 1417, 1805, 1819
- Drag coefficient, 1716, 1769
- Dredge spoil, 1362, 2430, 2824
- Dredging, 2964, 3024, 3088, 3126
- Drift, 3140
- Dunes, 1922, 1984, 2304, 2471
- Dynamic characteristics, 1837
- Dynamic loads, 1755
- Dynamic models, 2265
- Dynamic stability, 1270, 1730
- Dynamic tests, 1755
- Dynamics, 2227, 2346
- Ecology, 2984
- Economics, 2796
- Embankments, 1662, 2754
- Energy dissipation, 123, 1334, 1499, 1620, 2522
- Energy transfer, 123
- Entrainment, 2200
- Environmental effects, 3171
- Environmental impacts, 3024
- Equations of motion, 881, 1513, 3112
- Equilibrium, 2291, 3050, 3063
- Erosion, 935, 1922, 2087, 2998, 3012
- Erosion control, 1662, 2740
- Estimates, 464
- Estuaries, 1962, 2047, 2542, 2866, 2922, 2936, 2950, 2964, 2984, 2998, 3012, 3050, 3154
- Evolution, development, 1876, 1962
- Experimental data, 1242
- Experimentation, 584, 1592
- Extraction procedures, 1998
- Failures, 1755, 2087, 2671
- Failures, investigations, 3222
- Feasibility studies, 1702
- Fences, 2754
- Field investigations, 82, 867, 2047, 2710
- Field tests, 330, 703, 1074, 1702, 2087, 2471, 2644
- Filters, 1524
- Floating bodies, 3140
- Floating structures, 1320, 2740, 2852
- Flood control, 1254, 1862, 1895
- Flood plain insurance, 41
- Flood plain regulation, 2908
- Flooding, 218
- Flow characteristics, 316
- Flow measurement, 489, 503
- Flow profiles, 1922
- Flow visualization, 1033, 2186
- Fluid-structure interaction, 1564
- Flumes, 255, 489, 544, 661, 993, 1046, 1538, 1730, 2536, 2552, 2630

- Forecasting, 986
Foundation construction, 1648
France, 2936, 3088
Frequency analysis, 293, 1102
Friction factor, 420, 637
- Geography, 2589
Geomorphology, 2984
Geotextiles, 1524, 1687
Granular materials, 1524, 2616
Grasses, 1662
Gravity waves, 55, 557, 611
Great Lakes, 2291
Grid systems, 2255
Groins, structures, 783, 2173, 3227, 3254
Groundwater flow, 2644
Gulfs, 986
- Harbors, 597, 1935, 2481, 2894, 3074, 3102, 3154, 3183, 3239
Histograms, 909
History, 1876
Hurricanes, 358
Hydraulic design, 3102
Hydraulic jump, 2880
Hydraulic loading, 1564
Hydraulic models, 267, 371, 1446, 1460, 1538, 2402, 2950, 3207
Hydraulic performance, 1578
Hydraulics, 1033, 1186, 1228, 2880
Hydrodynamics, 68, 123, 241, 1186, 1769, 2213, 2824, 3154
Hydrographic surveys, 3024
Hydrostatics, 1005
- Ice forces, 2768
Image analysis, 1033
Impact, 1473
Implementation, 2241
In situ tests, 2671
Indonesia, 2385
Inertia, 1716, 1769
Information systems, 2589
Inlets, waterways, 2522
Installation, 2852
Instrumentation, 1634
Interactions, 450, 489, 826, 853, 1088, 1200, 1389, 2443, 2696, 3112, 3140
International treaties, 935
Islands, 826, 2010
Italy, 218
- Japan, 18, 623, 769, 1280, 2726, 2754
Jetties, 410
- Kalman filter, 1769
Kinematics, 503, 935, 1513
- Laboratory tests, 255, 420, 503, 661, 1131, 1662, 2471, 2495, 2552, 2668, 2740, 2975
Lagoons, 330, 2880
Land reclamation, 2964
Landfills, 3227
Lasers, 544
Least squares method, 464
Limit design, 358
Littoral currents, 68, 281, 584, 729, 783, 826, 1005, 1118, 1242, 2061, 2173, 2402, 2603
Littoral drift, 783, 2542, 2710, 2880, 3183
Loads, 1606, 1742, 1769
Long waves, 410, 570, 1131, 1144, 1200, 1228, 1270, 1781, 2073
- Maintenance costs, 2010
Mapping, 2279
Marinas, 3239
Marine terminals, 3074, 3207
Mass transport, 544, 2998
Mat foundations, 1687, 2768
Mathematical models, 218, 597, 1060, 1473, 2131, 3126, 3281
Measurement, 584, 909, 1118, 2332, 2668
Methodology, 1592, 2894
Microcomputers, 2159
Mixing, 2346
Mixtures, 2696
Model studies, 2964, 3194
Model tests, 430, 1348, 1606, 1805, 1837, 2782
Model verification, 109, 191, 530, 1564
Modeling, 109, 123, 973, 1131, 1487, 1975, 2213, 2346, 2443, 2566, 2984, 2998
Models, 55, 150, 241, 316, 410, 584, 716, 769, 923, 959, 986, 1922, 1935, 2061, 2087, 2471, 2603
Monitoring, 1564, 3227
Monsoons, 623, 769
Mooring, 3074
Moorings, 1320
Movable bed models, 420, 2372, 2457, 2536, 2566
Mud, 2936, 2975, 2998, 3037
- National Flood Insurance Program, 2908

- Navigation, 2430, 2936, 2975, 3088, 3126
- Nearshore circulation, 150, 241, 267, 316, 444, 729, 783, 826, 1074, 2061, 2241
- Netherlands, 1, 1160, 1254, 1862, 1876, 1888, 1895, 1909, 1935, 1948, 1962, 1984, 1998, 2010, 2984
- New Jersey, 2020
- Nonlinear analysis, 55
- Nonlinear systems, 396
- Nonuniform flow, 281
- North Sea, 1214, 1888, 1948, 2589, 2824, 2838, 3254
- Numerical calculations, 150, 306
- Numerical models, 68, 136, 191, 205, 384, 623, 853, 1088, 1186, 1306, 1320, 1389, 1742, 1795, 2034, 2173, 2186, 2304, 2372, 2430, 2508, 2668, 2824, 2866, 3012, 3024, 3037, 3112, 3140
- Ocean disposal, 2824
- Ocean engineering, 935
- Ocean waves, 82, 384, 410, 503, 557, 623, 703
- Oceanographic surveys, 986
- Offshore structures, 1280
- Oil pipelines, 3171
- Oscillations, 584
- Oscillatory flow, 661, 2186, 2346, 2372, 2495, 2616
- Overtopping, 177, 1348, 1375, 1487
- Overturning tests, 840
- Paddles, 675
- Parameters, 2922
- Peak values, 647
- Performance, 2020, 2768
- Permeability, 1060, 1499, 2616
- Perturbation theory, 478
- Pipelines, 2508
- Planning, 3102
- Plates, 1046, 1228
- Plunging flow, 895, 973
- Policies, 1862
- Pontoons, 2852
- Pore pressure, 1334, 1499
- Porosity, 2616, 2754
- Porous media, 2616
- Porous media flow, 1046
- Ports, 82, 1675, 2975, 2998
- Potential flow, 923
- Predictions, 55, 241, 345, 358, 371, 530, 623, 853, 959, 1446, 1795, 1922, 1935, 1975, 2034, 2145, 2265, 2508, 2603, 3063, 3281
- Pressure distribution, 1606
- Pressure measurement, 1144
- Pressures, 164, 191, 611
- Probabilistic models, 1160
- Probability density functions, 909
- Probability distribution, 371
- Probes, instruments, 2936
- Profile measurement, 2682, 2710
- Profiles, 2566
- Projects, 1984
- Protective structures, 1160, 2810, 3254, 3268
- Prototype tests, 2630
- Prototypes, 2671
- Public opinion, 2394
- Radar, 703, 2279
- Radioactive tracers, 2710
- Random waves, 41, 68, 255, 478, 647, 689, 798, 1102, 1460, 2117
- Reefs, 743, 1375, 1781, 2852
- Reliability analysis, 1403
- Remote sensing, 703
- Repairing, 2416
- Reports, 935
- Research, 729, 935, 1538, 1975, 2471
- Revetments, 1306, 1431, 1524, 1606, 1662, 1837, 2810
- Rheological properties, 2936, 2975
- Rip currents, 729, 959
- Riprap, 2810
- Rock structures, 1306, 1446, 1460
- Roughness, 41
- Rubble-mound breakwaters, 177, 410, 1334, 1417, 1499, 1552, 1578, 1620, 1648, 1805, 1819
- Safety programs, 1254
- Salinity, 2866
- Salt water intrusion, 2866
- Salt water-freshwater interfaces, 2866
- Sand, 1362, 1998, 2087, 2291, 2416
- Sand transport, 1895, 1909, 1948, 1962, 2173, 2213, 2318, 2360, 2495, 2508, 2580, 2668, 2696, 2754, 3154, 3183, 3227
- Sand waves, 2508, 2668
- Scale effect, 973, 1716
- Scale models, 2394, 2457, 3088
- Scour, 2457, 2782, 2950, 3227, 3268
- Scouring, 1795
- Sea floor, 757, 853, 2279, 2508, 2668
- Sea level, 95, 867, 1160, 1862, 1876, 1948, 1962, 2644, 2838, 3063
- Sea state, 345, 358, 464, 478, 647, 675,

- 895, 1851
 Sea walls, 1292, 1742, 2241, 2782, 2810
 Sediment, 2894
 Sediment concentration, 716, 1922, 2047, 2318, 2360, 2630
 Sediment control, 2603
 Sediment transport, 68, 123, 281, 293, 420, 637, 783, 959, 1074, 1795, 1922, 1935, 2087, 2101, 2131, 2145, 2159, 2186, 2200, 2227, 2255, 2291, 2318, 2332, 2346, 2372, 2402, 2430, 2443, 2481, 2495, 2508, 2522, 2536, 2552, 2603, 2630, 2668, 2682, 2710, 2726, 2824, 2880, 3012, 3037, 3102, 3171
 Sedimentation, 2047, 3239
 Sedimentology, 2394
 Sensitivity analysis, 675, 798
 Sensors, 2227, 2279
 Shallow water, 267, 293, 637, 812, 895, 1019, 1088, 1200, 2213, 3126
 Shear flow, 584, 2696
 Shear stress, 637, 993, 2145, 2536
 Shear tests, 2696
 Shear waves, 729, 1242
 Ship motion, 3074, 3088, 3112, 3126
 Shoaling, 55, 109, 267, 396, 430, 530, 1102, 2481
 Shore protection, 1160, 1431, 1592, 1687, 1702, 1837, 1862, 1895, 1935, 1984, 1998, 2010, 2265, 2385, 2542, 2589, 2603, 2796, 2810, 3254
 Shoreline changes, 1292, 1998, 2020, 2034, 2101, 2522, 2566, 2726, 2740, 3281
 Silts, 3088
 Simulation, 255, 267, 420, 464, 675, 798, 812, 1033, 1270, 1606, 2318, 2443, 2726, 3102
 Slope stabilization, 1687, 2768
 Slopes, 293, 306, 371, 544, 570, 1060
 Social aspects, 7
 Solitary wave, 689, 840, 881, 923, 1019, 1033, 1144, 1200, 1270, 1487
 Spain, 826, 3154, 3183
 Spatial data, 812
 Spectral analysis, 32, 703
 Speeches, 1
 Stability, 1306, 1362, 1375, 1403, 1446, 1552, 1716, 1805, 2922
 Standing waves, 1033, 1742
 Static tests, 1755
 Statistical analysis, 516, 909, 2838
 Statistical models, 371, 1851
 Statistics, 18, 358, 812
 Steady flow, 2495
 Steel construction, 2852
 Stochastic models, 516
 Stochastic processes, 255
 Stones, 1837
 Storm surges, 1214, 1564, 1895, 1922, 2304, 2950
 Storms, 18, 218, 227, 358, 743, 1118, 1702, 1851, 2073, 2332, 2372, 2457, 2580, 2671, 2908, 3222
 Stratification, 1186, 2047
 Stratified flow, 3024
 Strength, 2671
 Stress, 1417, 1578, 1819
 Structural design, 1634, 1819
 Structural response, 1634
 Structural stability, 1578, 1578
 Structural strength, 1417
 Surf beat, 32, 743, 1102, 1131, 1781
 Surf zone, 32, 68, 95, 123, 150, 177, 227, 241, 316, 330, 516, 557, 716, 867, 1118, 1348, 2073, 2145, 2402
 Surface waves, 55, 293, 396, 503, 611, 757, 840, 1046, 1228, 3012
 Surfing, 516
 Suspended sediments, 716, 2117, 2131, 2159, 2200, 2227, 2824
 Taiwan, 1675
 Testing, 1592
 Thailand, 986
 Theories, 647, 757
 Thermal stresses, 1755
 Thickness, 1805
 Three-dimensional flow, 2255
 Three-dimensional models, 267, 444, 1005, 1186, 2131, 2159, 2255, 2402, 2481, 2782
 Tidal currents, 909, 1214, 2430, 2964
 Tidal power plants, 3050
 Tidal waters, 1948, 2522, 2838, 2922, 3063
 Tides, 2644, 3050, 3171
 Time dependence, 205, 293
 Time series analysis, 2838
 Time studies, 1102
 Topography, 2101, 2117, 2173, 2213, 2279, 2332, 2481
 Transducers, 1280
 Transformations, 1102
 Transport phenomena, 2998
 Tsunamis, 1172
 Turbulence, 150, 557, 661, 716, 1019
 Turbulent boundary layers, 853
 Two phase flow, 2346, 2372
 Two-dimensional models, 689

- Typhoons, 623, 769
 Undertow, 123, 150, 227, 783, 2061
 Unsteady flow, 993, 2880
 Urban areas, 2394

 Velocity, 191, 227, 503, 557, 909
 Velocity distribution, 661, 2866
 Velocity profile, 281, 450, 993, 2372
 Vertical cylinders, 840, 1769
 Visual perception, 345
 Vortex shedding, 3171
 Vortices, 661, 1019, 1242, 2186, 2200

 Walls, 164
 Waste site cleanup, 2894
 Water depth, 205, 3268
 Water flow, 3063
 Water level fluctuations, 2291, 2838
 Water levels, 826, 1909
 Water quality, 2394
 Water surface, 227, 993, 1144, 1172, 1742
 Water table, 867, 2644
 Water tunnels, 2318
 Water waves, 164, 503, 689, 881, 935, 1389, 1769, 2213, 3140
 Wave action, 41, 191, 205, 895, 1131, 1306, 1730, 1795, 1805, 1819, 1935, 2061, 2073, 2117, 2385, 2542, 2552, 2580, 2630, 2644, 2768, 2908, 3037, 3112, 3194
 Wave attenuation, 330, 420, 1228
 Wave climatology, 986, 1088, 1292, 1888, 2159, 2416, 2542
 Wave crest, 396, 973
 Wave damping, 743, 1046, 1334
 Wave diffraction, 840
 Wave energy, 267, 530, 611, 1118, 1131, 1228, 1242, 1292, 1334, 1375, 1499, 1620, 2522
 Wave equations, 306
 Wave forces, 95, 164, 241, 840, 935, 1005, 1280, 1320, 1334, 1348, 1362, 1389, 1403, 1446, 1473, 1513, 1538, 1606, 1716, 1742, 1781, 1827, 2131, 3126, 3140
 Wave generation, 384, 430, 478, 675, 689, 769, 1172, 1214
 Wave groups, 32, 82, 177, 371, 729, 743, 812, 1131, 1552, 2117
 Wave height, 18, 177, 205, 293, 330, 345, 358, 464, 530, 675, 812, 881, 986, 993, 1102, 1742, 1851, 1888, 2034, 2117, 2145, 2402, 2630
 Wave measurement, 330, 430, 703, 895
 Wave pressure, 1473, 1564, 1620, 1781
 Wave propagation, 32, 306, 316, 384, 410, 420, 530, 544, 611, 689, 703, 798, 812, 881, 1088, 1172, 1214, 1228, 2186, 2213, 3112
 Wave reflection, 109, 136, 306, 570, 757, 923, 1046, 1172, 1460, 1702
 Wave refraction, 109, 205, 384, 530, 1088
 Wave runoff, 41, 68, 191, 371, 557, 570, 867, 895, 1200, 1242, 1270, 1662, 2360, 2471
 Wave spectra, 32, 109, 177, 205, 267, 430, 464, 478, 623, 647, 703, 769, 798, 1102, 1320
 Wave velocity, 396, 853, 2200
 Wavelength, 2034
 Waves, 55, 450, 489, 597, 637, 993, 2318, 2332, 2443, 2495
 Weirs, 1487
 Wetlands, 2542
 Wind direction, 1888
 Wind forces, 95, 218, 444, 1074, 1118, 1888, 2385, 2754
 Wind pressure, 826
 Wind tunnel test, 2754
 Wind velocity, 986
 Wind waves, 32, 218, 611, 1214

AUTHOR INDEX

Page number refers to first page of paper.

- Ahrens, John P., 1837
Alejo, Miguel, 826
Allsop, N. W. H., 1446, 1460
Alonso, Ignacio, 2580
Al-Salem, Abdullah, 2318
Alvarez, Ricardo, 2580
Anastasiou, K., 973
Andrassy, Christopher J., 41
Anglin, C. D., 1634
Anton, Jeffrey P., 757
Araújo, Luiz C., 3171
Asano, Toshiyuki, 2372
- Bailard, James A., 1702
Bakker, K. J., 1524
Bakker, W. T., 1935, 2360
Bakker, Willem T., 2696
Bandeira, Jefferson V., 3171
Basco, David R., 1292
Battjes, J. A., 32, 1975
Bellessort, Bernard, 2394
Bertotti, L., 218
Bezuijen, A., 1431, 1606
Bijker, Romke, 2508
Bjordal, S., 3074
Blázquez, Rafael, 345
Blondeaux, Paolo, 2186
Boczar-Karakiewicz, B., 2213, 2265
Bodge, Kevin R., 2796
Booij, N., 530
Borgman, Leon E., 255
Bosman, D. E., 3239
Bowen, Anthony J., 2061, 2227
Bowers, E. C., 3126
Bradbury, A. P., 1446
Breteler, M. Klein, 1431, 1524
Breteler, Mark Klein, 191
Briand, Marie-Hélène G., 2159
Briggs, Michael J., 267
Broksen, Michael, 3140
Brossard, C., 3088
Bundgaard, Henrik I., 3140
Burcharth, H. F., 1417
Burcharth, Hans F., 1819
Burger, A. M., 1431
Bürger, W. W., 1578
- Caldas, Felipe, 3194
Canestrelli, P., 218
Cavaleri, L., 218
Chandler, Bruce D., 358
Chang, J. J., 1172
Chapalain, G., 2213
- Charulakana, Supot, 986
Chen, W. J., 637
Chiaia, Giancarlo, 1102
Chian, Chimin, 1270
Collado, F., 316
Cooker, M. J., 164, 1473
Costa, Rui G., 2047
Cox, Daniel T., 1306
Craeymeersch, Johan A., 2984
Crapps, David K., 3268
Crowley, J. B., 293, 1074
- Daemrich, K. F., 430
Dally, William R., 516
Dalrymple, Robert A., 675, 729
Damiani, Leonardo, 1102
Davis, A. B., 3227
de Jong, H., 2922
de Kok, J. M., 2824
De Rouck, J., 1755
de Vriend, H. J., 1005
de Vriend, Huib J., 1962
de Vroeg, J. H., 1935
Dean, Robert G., 2145, 2522
Dean, William L., 3268
Dedeyne, R., 1755
Degrieck, J., 1755
Deguchi, Ichiro, 2603
Deigaard, Rolf, 959
Dekker, J., 530
Delouis, A., 3088
den Adel, H., 1524, 1606
den Adel, J. D., 530
Dette, Hans H., 2566
DeVries, Jack, 1702
Diez, J. J., 3154
Dijkman, M. J., 1935
Dijkzeul, Johan C. M., 2255
do Valle, Antonio B., 3171
Dodd, N., 584
Drapeau, G., 2710
- Edge, B. L., 3268
Ekebjærg, Lars C., 1186
Elgar, Steve, 55
Endo, Taiji, 1403
Escobar, V. A., 3154
Eysink, W. D., 1948
- Farrell, Stewart C., 2020
Fassardi, Claudio, 1552
Feral, Alain, 2936
Fernandes, J. L. M., 689

- Fernández, José, 3183
Fisher, J. S., 2471
Fleming, C. A., 2589
Flick, Reinhard E., 557
Fournier, Charles P., 3194
Fowler, Jimmy E., 2457
Fowler, Rachel E., 729
Franken, A. F., 530
Fredsoe, Jørgen, 959
Freilich, M. H., 55
Funke, E. R., 464
- Gadd, P. E., 2768
Gadd, Peter E., 1687
Galichon, P., 3088
Galichon, Pascal, 2936
George, Ronald A., 557
Gerritsen, F., 2922
Gerritsen, Franciscus, 1270
Giménez, Marcos H., 255
Goda, Yoshimi, 18
Gómez Pina, Gregorio, 1592, 3183
González, Angel, 345
González Madrigal, B., 1348
Gordon, A. D., 2880
Götschenberg, A., 430
Gourlay, M. R., 330
Granboulan, J., 3088
Granboulan, Jérôme, 2936
Grassa, José María, 798
Green, Malcolm O., 2200
Greenwood, Brian, 227, 2061, 2227
Griggs, Gary B., 2810
Grilli, Stéphane T., 1200
Grosche, Sven, 895
Grummitt, Alan Albert Campbell, 2852
Grüne, Joachim, 895
Gudmestad, Ove T., 935
Guifen, Wang, 2430
Guza, R. T., 55, 410, 611
Guza, Robert T., 1702
- Haidekker, Mark, 895
Hall, Kevin R., 1620, 1730, 2616
Hallermeier, Robert J., 41
Hallie, Frank P., 1998, 2984
Hamerlynck, Olivier, 2984
Hamm, Luc, 2975
Hansen, Niels-Erik Ottesen, 3024
Hanson, Hans, 2034, 2173
Hara, Masanori, 923
Hardy, T. A., 330
Harkins, Gordon S., 675
Harper, Bruce A., 358
Hatada, Yoshio, 205, 623
- Hattori, Masataro, 396
Hay, Alex E., 2227
Hayashi, Katsuyuki, 177
Hazen, David G., 2061, 2227
Headland, John R., 1320
Herbers, T. H. C., 611
Herbich, John B., 2894
Hino, Mikio, 743, 1781
Hirakuchi, Hiromaru, 703
Hirasawa, Mitsunari, 1280
Holman, Rob, 1118, 1242
Holthuijsen, L. H., 384
Holtzhausen, A. H., 1805
Hoozemans, Frank M. J., 1888
Horikawa, Kiyoshi, 661, 2754
Hotta, Shintaro, 2754
Hou, Ho-Shong, 1827
Houston, Samuel H., 2145
Howd, Peter, 1242
Howd, Peter A., 1118
Howell, Gary L., 1417, 1819
Hudspeth, R. T., 1513
Hudspeth, Robert T., 255, 1552
Hughes, Steven A., 2457
Hunter-Blair, A., 2589
Hwung, H. H., 544
- Ijima, Takeshi, 1228
Ikeda, Syunsuke, 661
Ikeno, Masaaki, 703
Irie, Isao, 2998
Isobe, Masahiko, 123, 136, 647, 1060, 2495
Ito, Kazunori, 812
Iwata, Koichiro, 2740
Izumiya, Takashi, 306
- Jackson, L. A., 2241, 2265
Jasińska, Ewa, 2866
Jeng, Dong-Sheng, 1742
Jensen, John, 2671
Jensen, Jürgen, 2838
Jensen, Ole Juul, 1538, 3074, 3102, 3222
Jones, J. Sterling, 3268
Jongeling, Tom, 1564
Jonsson, Ivar G., 1131, 1389
Juhl, Jørgen, 1538
- Kadono, Takashi, 1280
Kai, Yen, 2964
Kajima, Ryoichi, 1716
Kamphuis, J. W., 2710
Kamphuis, J. William, 2159, 2402
Kang, Hong-Yoon, 371
Kao, Joseph S., 1730

- Kapp, J. F., 3239
Kardana, 2385
Katoh, Kazumasa, 95, 2073
Katopodi, Irene, 2131
Katsuragawa, Tetsuyuki, 396
Kawata, Yoshiaki, 281, 2332
Kim, Ga-Ya, 2603
Kirby, James T., 109, 757, 1702
Kitou, N., 1005
Klatter, Leo, 1564, 2950
Klomp, Wim H. G., 2696
Kloos, M., 3239
Klopman, Gert, 478
Kluger, J. W. J., 2416
Kobayashi, Nobuhisa, 1306
Kobune, Koji, 18
Kojima, Haruyuki, 1228
Komaguchi, Tomoaki, 769
Komar, Paul, 1242
Komar, Paul D., 1118
Kondo, Hideo, 3063
Kondo, Kosuke, 2481
Konter, Jan, 1564, 2950
Kraus, Nicholas C., 2034, 2173
Kriebel, David L., 2304
Kubota, Susumu, 570
Kuik, Ton (A) J., 1862
Kunz, H., 3254
Kuo, C. T., 637
Kuo, Shih-Duenn, 1675
Kyriacou, Andreas G., 993
- Langerak, A., 2922
Larson, Magnus, 2173
Latham, J. -P., 1446
Laubscher, W. I., 3227
Laustrup, Chr., 2671
Lean, G. H., 3126
Lee, J. J., 1172
Leendertse, Jan J., 444, 2255
Leidersdorf, C. B., 2768
Leidersdorf, Craig B., 1687
Leitão, J. M., 689
Lemos, M., 316
Lin, C., 544
Lin, D. T., 1046
Lionello, P., 218
Liu, Shiao-Kung, 444
Liu, Shu-xue, 82
Long, B., 2710
Losada, Miguel A., 675
Louisse, Cees (C) J., 1862
Louisse, Cees J., 1998
Louters, Teunis, 2984
Lundgren, J., 3074
- McDougal, W. G., 1417
McDougal, William G., 1687
McLaren, P., 2589
Madsen, H. Toxvig, 2671
Madsen, Ole S., 420
Madsen, Per A., 3112
Manoha, Bruno, 2542
Mansard, E. P. D., 464
Martinez, Javier, 345
Martínez, Jesús, 2580
Mase, Hajime, 177
Mathisen, Paul P., 420
Matsumi, Yoshiharu, 1648
Medina, Josep R., 255, 1552
Mehta, Ashish J., 2047
Melo, Eloi, 410
Migniot, Claude, 2975
Mitsunobu, Norihiko, 2668
Mizuguchi, Masaru, 570
Mizumura, Kazumasa, 1403
Mizuno, Yuzo, 1280, 1362
Møller, Jacob Steen, 3024
Monadier, P., 3088
Moutzouris, C. I., 2552
Mügge, Hans-Eckart, 2838
Mulder, Herman P. J., 3012
Mulder, Jan P. M., 2984
Muñoz, Angel, 3183
Murakami, Kazuo, 2998
Murakami, Noritaka, 2740
Murray, Malcolm, 3207
- Nadaoka, Kazuo, 2346
Nagai, Yutaka, 1280
Nairn, Robert B., 68
Nakamura, Kazuo, 2117
Nakaza, Eizo, 743, 1781
Nelson, R. C., 330
Nicholson, John, 3050
Nielsen, Peter, 867
Niemeyer, H. D., 530, 783, 2360
Nishi, Ryuichiro, 2117
Nishimura, Hitoshi, 1033
Nnadi, Fidelia N., 2536
Nodani, Hitoshi, 2481
Nosek, Kevin B., 41
- Obana, E., 716
Ochi, Michel K., 909
O'Connor, Brian, 3050
Ohnaka, Susumu, 2443
Ohyama, Takumi, 840
Okayasu, Akio, 123
Okuno, Masakazu, 3037
Olivares Prud'Homme, J., 1348
Oltman-Shay, J., 584
Oltman-Shay, Joan, 1118, 1242

- Osborne, Philip D., 227, 2227
 Ostrowski, R., 2101
 Oumeraci, H., 1334, 1578
 Overton, M. F., 2471
 Özhan, Erdal, 1487
- Partenscky, H. W., 1334, 1578
 Peregrine, D. H., 164, 1019, 1473
 Petrillo, Antonio, 1102
 Pfaff, W. M., 3227
 Philipse, Leo, 1662
 Pilarczyk, K. W., 1431
 Pilarczyk, Krystian W., 1375
 Pluijm, Marco, 2010
 Postma, Renske, 2984
 Poulsen, L., 2671
 Prins, J. E., 7
 Prüser, H. -H., 1088
 Pruszek, Z., 2101
 Putrevu, Uday, 241
- Raichlen, Fredric, 1144
 Ramsden, Jerald D., 1144
 Rasmussen, Erland B., 1186
 Rayner, Ralph, 3050
 Refaat, Hossam El-din A. A., 281
 Retief, G. de F., 3239
 Rhee, Joon P., 1819
 Ribberink, Jan S., 1998, 2131, 2318
 Ridge, A. B., 3239
 Rivero, F., 316
 Roelse, Piet, 1984
 Roelvink, Dano (J) A., 1962
 Roelvink, J. A., 1909, 1998
 Roelvink, J. A. (Dano), 68
 Rogers, Spencer M., Jr., 2908
 Rojanakamthorn, Somchai, 1060
 Romafczyk, W., 1769
 Rosengaus, M. Michel, 420
 Rouch, Franck, 2394
 Ryu, Cheong-Ro, 371
- Saito, Eiichi, 1795
 Sakai, T., 716
 Sakakiyama, Tsutomu, 1716
 Sánchez-Arcilla, A., 316
 Sánchez-Carratalá, Carlos R., 255
 Sand, Stig E., 3102
 Sato, Michio, 2117, 2644
 Sato, Shinji, 1795, 2668, 3037
 Sawaragi, Toru, 2603
 Sayao, Otavio J., 3194, 3207
 Schäffer, Hemming A., 1131
 Schönfeld, Wolfgang, 2838
 Schoonees, J. S., 2416, 3227
 Scott, Katherine, 2810
- Scott, R. D., 1634
 Seiffert, Jan Willem, 1662
 Shibayama, Tomoya, 1795, 3037
 Shih, Robert W. K., 1499
 Shimizu, Takuzo, 2481
 Shimoda, Naokatsu, 2740
 Shiraishi, Naofumi, 769, 1403
 Silvester, Richard, 2726
 Simons, Richard R., 993
 Skjelbreia, James E., 503
 Skourup, Jesper, 1389
 Sleath, J. F. A., 450
 Smallman, Jane V., 597
 Smith, Gregory M., 2616
 Smith, Jane M., 267
 Sobey, Rodney J., 358
 Sobierajski, E., 1769
 Son, Huynh-Thanh, 853
 Sørensen, Ole R., 3112
 Sørensen, Torben, 3222
 Southgate, Howard N., 68
 Spanhoff, R., 2824
 Sparboom, Uwe, 895
 Spencer, J. M. A., 3126
 Staub, Carsten, 2508
 Steetzel, Henk J., 1922
 Stive, M. J. F., 1909
 Stive, Marcel J. F., 1876, 1962
 Stockberger, M. Todd, 2291
 Stolk, A., 1895
 Stone, A. L., 2471
 Struik, P., 1254
 Suriamihardja, Dadang Ahmad, 150
 Svendsen, Ib A., 241, 1200
 Swan, Christopher, 489
 Swart, D. H., 293, 1074, 3227
 Syamsudin, 2385
- Tada, Y., 716
 Taerwe, L., 1755
 Tait, James F., 2810
 Takewaka, Satoshi, 1033
 Takezawa, Mitsuo, 570
 Tanaka, Mitsuhiro, 881
 Teisson, Charles, 1851, 2542
 Tejedor, Begoña, 826
 Tejedor, Luis, 826
 Teles da Silva, A. F., 1019
 Temperville, André, 853
 Terwindt, J. H. J., 1975
 Thomsen, J., 3074
 Thornton, E. B., 584
 Tokikawa, Kazuo, 1280
 Tolman, H. L., 384
 Tolman, Hendrik L., 1214
 Tomlinson, R. B., 2241

- Tørum, Alf, 503, 935
 Toue, Takao, 2566, 2782
 Toumazis, A. D., 973
 Townend, I. H., 2589
 Tozer, Nigel P., 597
 Tsai, Ching-Piao, 1742
 Tsuchiya, Yoshito, 150, 281, 769,
 2332, 2726
 Tsukayama, S., 743, 1781
 Tsuruya, Hiroichi, 2998
 Tuah, Hang, 255
 Turcke, D. J., 1634
 Twu, S. W., 1046
- Udink, Connie, 3012
 Ukai, Akiyuki, 812
 Uliczka, Klemens, 2630
 Umezawa, Nobutoshi, 1362
- Valdés Fernández de Alarcón, J. M.,
 1592
 Vallianos, Limberios, 1320
 van Alphen, Jos S. L. J., 1998
 Van Beurden, I. J. C. A., 1160
 Van Damme, L., 1755
 van de Graaff, Jan, 2682
 van der Burg, G., 2279
 van der Meer, Jentsje W., 191, 1375
 van Halsema, D., 2279
 van Heuvel, Tj., 2824
 van Kesteren, Walther G. M., 2696
 van Leeuwen, P. J., 32
 Van Leeuwen, Peter Jan, 478
 van Vessem, P., 1895
 Verhagen, H. J., 2087
 Vested, Hans Jacob, 1186
 Viggosson, G., 3074
 Viguier, Jacques, 2936
 Vincent, Christopher E., 2200
 Visser, P. J., 2087
 Vittori, Giovanna, 2186
 Vogel, J. A., 530
 Vogelzang, J., 2279
- von Amsberg, Claus, 1
 Vrijling, J. K., 1160, 2087
 Vrouwenvelder, A. W. C. M., 1254
- Walker, James R., 1144
 Wang, Hsiang, 2566, 2782
 Watanabe, Akira, 123, 136, 1060,
 2443, 2495
 Weesakul, Sutat, 986
 Weggel, J. Richard, 2020
 Wensink, G. J., 2279
 Wiersma, Hans (J.), 1876
 Wilde, P., 1769
 Wilson, Kenneth C., 2536
 Wind, H. G., 3281
 Work, Paul A., 2522
 Wouters, J., 1606
 Wurjanto, Andojo, 1306
- Yagi, Hiroshi, 2346
 Yalçmer, Ahmet Cevdet, 1487
 Yamaguchi, Masataka, 205, 623
 Yamamoto, Masato, 1403
 Yamashita, Takao, 150, 177, 2726
 Yanagishima, Shin-ichi, 95, 2073
 Yanase, Tomoyuki, 1362
 Yano, Kenji, 1362
 Yasuda, Takashi, 812, 923
 Yixin, Yan, 2964
 Yoshida, Akinori, 1228
 Yoshioka, Hiroshi, 2332
 Young, I. R., 330
 Yu, Xiping, 136
 Yu, Yu-xiu, 82
 Yu, Z., 2360
- Zeidler, R. B., 2101
 Zhou, Liu, 1417
 Zielke, W., 1088
 Zitman, Tjerk J., 1876
 Zude, Cao, 2430
 Zwamborn, J. A., 1805, 2416
 Zyserman, Julio, 959

CHAPTER 164

DECOUPLED NUMERICAL MODEL OF THREE-DIMENSIONAL BEACH CHANGE

Magnus Larson¹, Nicholas C. Kraus², M. ASCE, and Hans Hanson³

ABSTRACT

This paper describes a numerical model of three-dimensional beach change as produced by breaking waves and wave-induced currents. Cross-shore lines spaced at intervals alongshore form the basic calculation element, and cross-shore and longshore transport rates are calculated independently on the lines. Transport rates are coupled indirectly through the mass conservation equation and a contouring routine that determines local depth contour orientation for calculating wave transformation. The model has reduced calculation time compared to fully gridded hydrodynamic and beach change models, yet allows representation of complex boundary conditions, coastal structures, and movement of longshore bars and berms. Results of two test series are presented, one for the movement and protective functioning of a linear mound constructed of dredged material, and the other for impoundment at a jetty.

INTRODUCTION

The goal of beach change numerical modeling is to describe the three-dimensional (3D) evolution of nearshore bottom topography resulting from spatial and temporal differences in sand transport. For practical use, five model capabilities were considered to be essential: (1) accurate and reliable beach change simulation compatible with input data routinely available at engineering projects; (2) representation of sand transport and beach change on temporal and spatial scales of engineering interest; (3) representation of general boundary conditions and coastal structure configurations; (4) calculation robustness, meaning that uncertainties typically present at projects do not produce

(1) Assist. Prof., (3) Assoc. Prof., Dept. of Water Resources Engrg., Institute of Technol., Univ. of Lund, Box 118, Lund, Sweden S-221 00.
(2) Sr. Res. Sci., Coastal Engrg, Res. Center, U.S. Army Engr. Waterways Experiment Station, 3909 Halls Ferry Road, Vicksburg, MS 39180-6199.

aberrant model predictions; and (5) economical execution time. The second capability implies that both short-term processes (e.g., storm-induced beach erosion/recovery, and cyclical daily and seasonal change in the beach profile shape and position) and long-term processes (e.g., accretion and erosion at shore-normal structures) are simulated, including approach to an equilibrium bottom configuration under constant forcing and boundary conditions. A model having these capabilities is now under development, and this paper introduces the model and representative initial test results.

Model Architecture

To develop a 3D bathymetric change numerical model with the aforementioned five capabilities for wide-application use, the model architecture was founded on two design concepts. The first concept was to combine essential features of two previous successful beach change models, SBEACH for calculating storm-induced beach erosion and recovery (Larson et al. 1988, Larson and Kraus 1989, Larson et al. 1990) and GENESIS for calculating long-term change in shoreline position (Hanson 1989, Hanson and Kraus 1989). The 3D modeling system also allows extension of capabilities of the two models that is not possible within the limits of the individual models. The second design concept was to treat lines running across the shore as the basic calculation element. Waves, longshore current, and longshore and cross-shore transport rates are calculated independently on the cross-shore lines, thereby decoupling the transport rate calculation along the beach. Neighboring areas of the beach interact through a local contouring routine that calculates the beach orientation at each grid point on the cross-shore lines and through the sand mass conservation equation, from which the change in bathymetry is obtained from the transport rates.

The resultant model, called 3DBEACH for 3-dimensional Decoupled model of BEAch CHange, is significantly more efficient than "point models" that require computation-intensive and sophisticated 2D gridded hydrodynamic wave and current models, yet it gives stable, equilibrium beach profile shapes that are difficult to attain in point models. Despite the simplification introduced by the decoupling approach, the model has substantial generality in representation of profile shape, such as multiple bars and troughs, than allowed in "line models" that require monotonically increasing depth with distance offshore.

By decoupling cross-shore and longshore transport processes, execution time is minimized, allowing the model to be applied either on the local or regional level and for long simulation times. The local validity of the cross-shore line as the basic calculation element restricts model applications to situations with mild bottom slopes alongshore; also, partially enclosed embayments where the shoreline intersects a cross-shore line more than once cannot be represented. Thus, 3DBEACH is targeted toward the open coast, and local bathymetric disturbances such as rip currents and rip channels are not represented directly.

Model Structure

3DBEACH consists of six calculation modules that function semi-independently, allowing modification of any module without affecting or requiring detailed knowledge of the other modules. Principal quantities calculated by the respective modules are: (1) wave height, wave angle, mean water level, and runup; (2) longshore current; (3) cross-shore sand transport rate; (4) longshore sand transport rate; (5) bottom contour orientation; and (6) bottom topography change.

Fig. 1 is a schematic of a 3DBEACH calculation grid. A Cartesian coordinate system is placed on the project coast with the x-axis pointing offshore and the y-axis following the trend of the shoreline. Cross-shore lines are placed along the coast with an interval Δy , and grid points on the line are spaced Δx apart. Typically, Δy is much larger than Δx under the assumption that the beach slope changes much more gently alongshore than across-shore. Fine grid spacing across-shore (typically 1 to 5 m) is needed to describe dominant morphological profile features such as bars, troughs, berms, and rapid change occurring during storms, whereas a coarse spacing alongshore (typically 25 to 100 m) is compatible with more gradual beach change produced by gradients in longshore sand transport. A time step in the range of 5 to 40 min is used in the model, with a typical value of 20 min. Short descriptions of the six calculation modules follow.

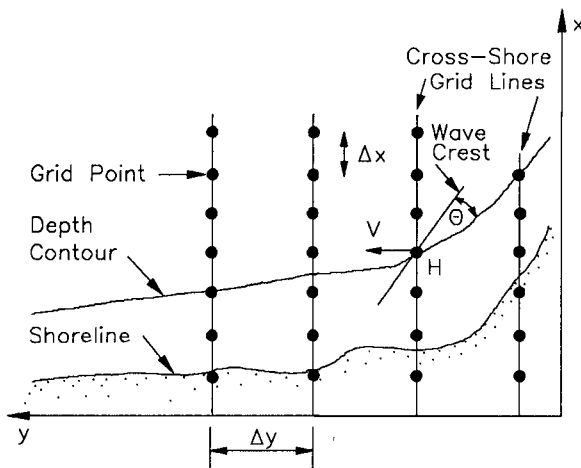


Fig. 1. Schematic of a 3DBEACH calculation grid

(1) Wave module. The wave module calculates the wave height H and other wave-related quantities, such as wave angle θ and wave- and wind-induced setup, at grid points on each profile line (Kraus and Larson 1990). Cell opening (wetting) and closing (drying) occurs according to the wave and wind conditions, and tide level. Assuming locally plane and parallel depth contours the wave height is determined by linear

wave theory in regions of nonbreaking and by the Dally et al. (1985) model where waves break. Either regular or random wave height can be specified. The module reproduced wave breaking and reformation over bar and trough profiles measured in a large wave tank (Kajima et al. 1982), as well as wave height and setup in laboratory experiments with a plane beach and oblique wave incidence (Visser 1982). The wave module only requires input time series of wave height, period, and direction (and wind speed and direction if wind is important).

(2) Longshore current module. The longshore current V is calculated at grid points on each cross-shore line as in the model NMLONG (Kraus and Larson 1990, Larson and Kraus 1991b). NMLONG was developed to calculate the longshore current over a multiple bar and trough profile produced by oblique wave incidence and wind, and it contains linear or nonlinear bottom friction as options, and lateral mixing. The model was verified using two field data sets (Kraus and Sasaki 1979, Thornton and Guza 1986) and one laboratory data set (Visser 1982), and default values of empirical parameters are provided. The longshore current is used to calculate the longshore sand transport rate.

(3) Cross-shore transport module. The net cross-shore sand transport rate on each cross-shore line is calculated as in SBEACH (Larson and Kraus 1989). The profile is divided into four zones of different wave and transport properties, with the magnitude of the transport mainly governed by energy dissipation in the surf zone. SBEACH has been verified with data both from large wave tank experiments and the field (Larson and Kraus 1989, 1991a, Larson et al. 1990). The calculation procedure can generate bars and berms, but at present it is restricted to cross-shore transport related to breaking waves. The wave module supplies the main input to this module, which also requires an initial profile shape and sediment grain size.

(4) Longshore transport module. A local transport rate formula proposed by Kraus et al. (1988) based on field measurements is used, in which the needed longshore current velocity and wave height are obtained from modules (1) and (2). Inputs are supplied by the wave and longshore current modules. This module contains an empirical transport rate parameter that must be determined in calibration.

(5) Contour module. The orientation of depth contours is required to define a local wave angle to determine the magnitude and direction of the longshore transport. The contour orientation at each grid point is obtained by approximating the local bathymetry with a plane. The calculation requires depths from neighboring cross-shore lines and provides indirect interaction among the lines.

(6) Bottom change module. Changes in the bottom topography are obtained from the mass conservation equation after the cross-shore and longshore transport rates have been calculated at each grid point for the particular time step.

MODEL TESTS

Results of two of many model test series are described. The objective of these initial "proof of concept" tests was demonstration of correct qualitative behavior for simulating realistic project conditions. One series focused on the response of a subaqueous mound of dredged material and the feedback to the waves, current, and beach from the mound. The other series focused on impoundment at a jetty or groin. In the simulations, if a random wave input time series was used, the wave height and/or angle were uniformly distributed over a given interval. The longshore grid spacing varied between 20 and 50 m, and the cross-shore spacing varied between 2 and 5 m, depending on the test. The time step was fixed at 20 min.

Placed Mound (Silver Strand, Calif.)

Simulation conditions pertain to a Corps of Engineers project at Silver Strand Beach, California, located south of San Diego Harbor (see Junke et al. 1989). In December 1988, approximately 80,000 cu m of sand with median diameter 0.18 mm were dredged from the harbor entrance channel and placed offshore of Silver Strand in the form of a short linear mound on the existing bottom of 0.25-mm sand. The mound was intended to break higher, potentially erosive waves, as well as nourish the beach by onshore migration. The mound was initially 381 m long and 76 m wide, extending from about 225 m to 450 m from the shoreline (between bottom contours of 4.5 and 9 m), and with an average relief of 2.1 m at its crest. The bathymetry was surveyed periodically for two years on seven profile lines spaced at 76-m intervals, five lines on the feature and two to the south (historic direction of littoral movement alongshore). The bathymetry shortly after construction of the feature was completed is shown in Fig. 2. This configuration served as the initial condition for this model test series.

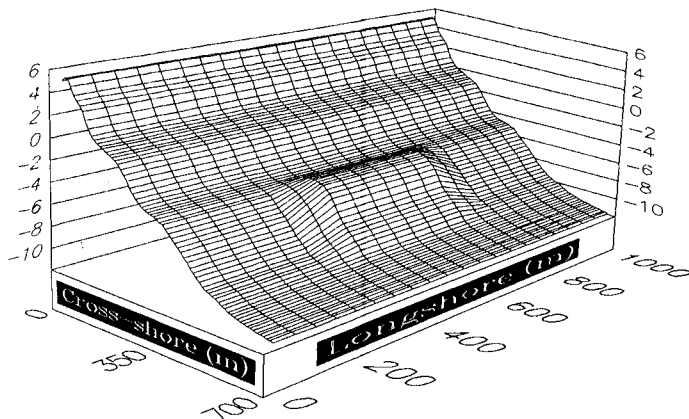


Fig. 2. Initial bathymetry for offshore mound test series

Four tests distinguished by input wave conditions are presented: (1) moderately erosional waves; (2) storm with shore-normal approach; (3) storm with oblique approach; and (4) accretionary waves. A semi-diurnal tide with amplitude of 0.56 m (mean amplitude for Silver Strand) was applied in all tests, and calculations were carried out for simulated times of 3 to 10 days. A pinned-beach boundary condition (Hanson and Kraus 1989) was specified at both sides of the grid, whereby sand could freely enter and leave the calculation domain from the lateral boundaries. The cross-shore lines ended in a depth of 11.4 m, necessary to ensure that negligible transport occurred at the seaward boundary, even under storm waves. The net direction of transport as erosive (offshore directed) or accretionary (onshore directed) is determined in the model according to the criterion used in SBEACH (Larson et al. 1988, Larson and Kraus 1990) that has subsequently been further verified with a large field data set (Kraus et al. 1991).

Test 1: Moderately erosive waves. Fig. 3 displays simulation results after exposure of the coast to moderately erosional waves for 10 days. The deepwater wave height H_0 randomly varied between 1 and 2 m, the wave period T was 12 sec, and the incident deepwater wave angle θ_0 randomly varied between -10 and $+10$ deg. Because of their relatively small height, the waves passed over the mound with little change and broke further inshore. The waves gradually removed material from the foreshore and deposited it shoreward of the mound to produce an almost uniform longshore bar. This storm bar has distinct depressions resulting from refraction at the ends of the mound. Mound end effects also produce depressions on the foreshore.

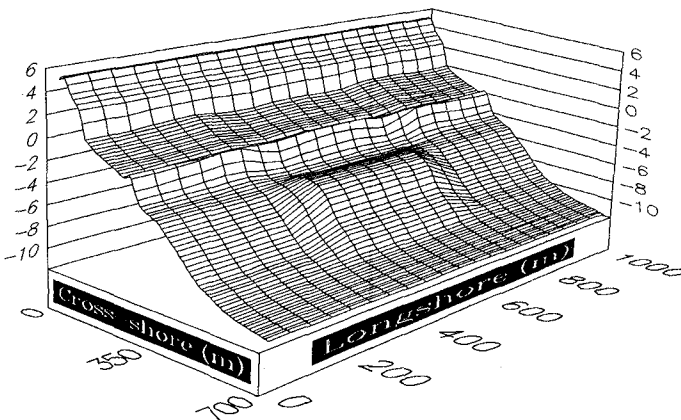


Fig. 3. Bar formation and beach erosion by moderately erosive waves

Test 2: Strong storm, normal wave incidence. It is of considerable interest to quantitatively evaluate the protection afforded by a mound to the beach in its lee. Thus, simulations were conducted for a 3-day

storm with H_0 randomly varying between 4 and 6 m and $T = 12$ sec, with the waves incident normal to the mound. Fig. 4 shows the bathymetry at the end of the storm, in which a pronounced and curved longshore bar is seen. The shape of the mound significantly changed because the waves breaking on its seaward side moved material from the mound offshore to form part of the bar. At the sides of the mound the bar lies closer to shore because material forming it had to be taken from the inner surf zone, whereas the mound supplied sand to the erosive waves breaking directly seaward of it. The mound therefore protected the beach and surf zone directly shoreward of it, both satisfying the demand for sand by the breaking waves in development of the storm bar and by causing additional wave breaking. The sand supplied by the mound replaced that taken from the surf zone in the regions on the sides of the mound, as seen by the more seaward movement of contour lines on the unprotected sides. The beach face does not show significant change alongshore, because erosion on the foreshore is strongly controlled by water level, and not depth-limited breaking waves. The complete symmetry of the calculation with respect to a shore-normal line at the center of the mound is an indication of the stability of the calculation.

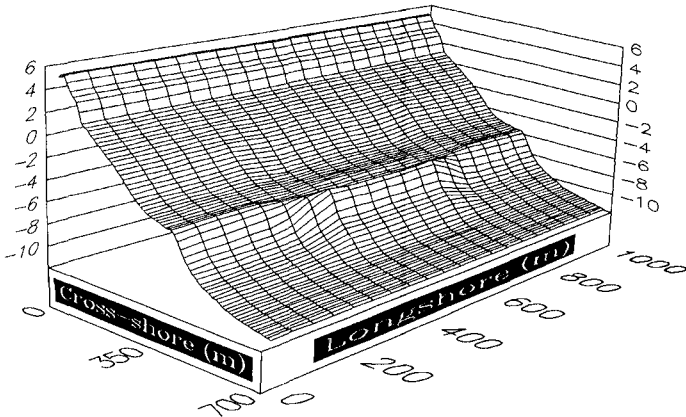


Fig. 4. Bathymetric change for a storm, normally incident waves

Test 3: Strong storm, oblique wave incidence. The previous test, a strong storm, was repeated, but with θ_0 varying between 0 and 20 deg to introduce net longshore transport. Fig. 5 shows that the bathymetric response is no longer symmetric as in Test 2. Because of wave refraction, the longshore sand transport rate was reduced at the downdrift end of the mound; a local depth maximum appeared downdrift of the mound, further modifying the wave transformation. The present test produced satisfactory results; however, in related tests examining sensitivity to incident wave angle, if a large oblique angle was maintained for a long time interval, the greatly changing bathymetry induced numerically-generated rhythmic features. In such extreme cases,

decoupling of the cross-shore lines was not satisfactory because the longshore depth gradients were not small.

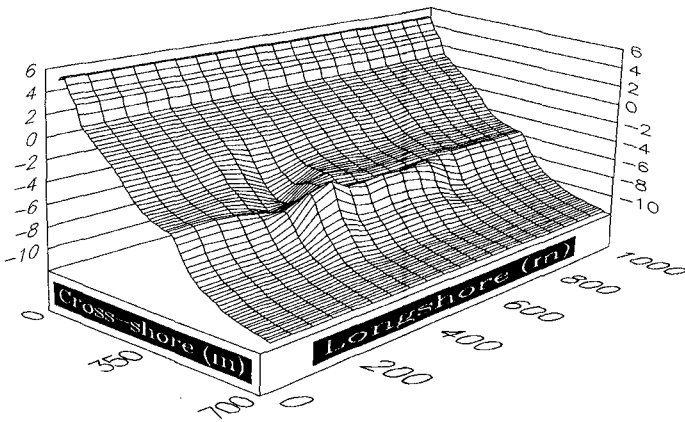


Fig. 5. Bathymetric change for a storm, obliquely incident waves

Test 4: Accretionary waves. Simulations with low waves were conducted to calculate the response of the beach and mound to accretionary forcing conditions. Such conditions occur in the summer (in the northern hemisphere) and after storms, when low waves of long period typically arrive. Fig. 6 shows the results of one such test performed with H_0 varying between 0.6 and 0.8 m, $T = 14$ sec, and the θ_0 varying between 0 and 20 deg. The waves were run for 10 days. The mound shape was only slightly altered by the low waves which passed over it and travelled shoreward to break in shallower water. A distinct berm formed on the foreshore that is not uniform alongshore due to refraction of the incident waves at the mound.

Impoundment at Jetty

This test series examined model predictions for impoundment at a jetty or groin. Two tests are described which exercised the "groin boundary condition," one without bypassing and the other including bypassing. Mildly erosional monochromatic waves were applied ($H_0 = 2$ m, $T = 8$ sec, $\theta_0 = 20$ deg). Similar calculations performed with random waves did not change the essential features of the bathymetric response, randomness only acting to produce a smoother topography. Fig. 7 shows the initial bathymetry for the groin test series, consisting of a groin situated on a plane-sloping profile joining an equilibrium ($x^{2/3}$) profile at the still-water shoreline. The tide was semidiurnal with an amplitude of 0.5 m, and the area was exposed to 3 days of wave action.

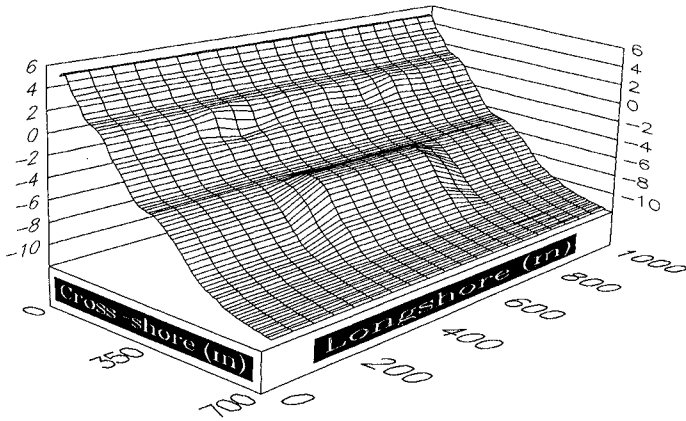


Fig. 6. Bathymetric change for accretionary waves

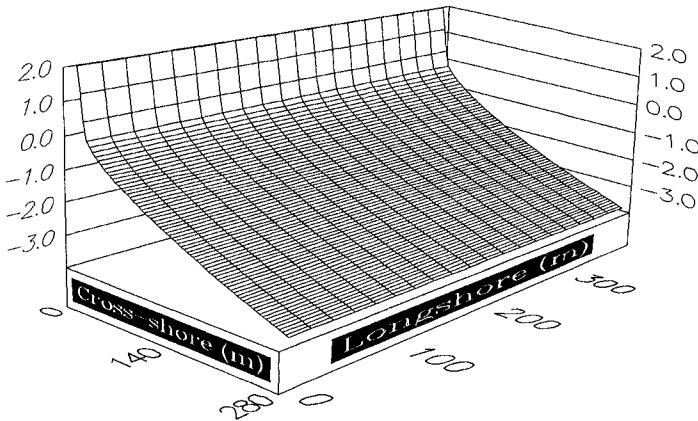


Fig. 7. Initial bathymetry for jetty test series

Infinitely long jetty. Fig. 8 shows impoundment by a long jetty (long with respect to the width of the surf zone) located on the right side of the grid. The jetty acts to completely block sand moving toward it. A longshore bar formed with its crest curving offshore with approach toward the jetty from the updrift coast. A plateau more gently sloping than the initial beach formed in the vicinity of the jetty; its buildup continued to the high-tide water level if the simulation was run for a very long time. The time scale of the beach response here and in other tests is controlled by empirical coefficients that enter as factors in the cross-shore and longshore transport rate predictive

relations. These two coefficients must be determined by model calibration at the project site.

Bypassing at jetty. For this test the jetty was terminated at the initial 2-m depth contour. The incident waves broke at approximately this depth, but the changing tide moved the break point seaward and shoreward of this contour. The longshore sand transport rate tailed off seaward of the break point in accordance with the tail in the longshore current. Sand that was transported alongshore seaward of the tip of the jetty was allowed to pass the jetty as an implementation of a simple boundary condition representing bypassing. As shown in Fig. 9, for these conditions, the bar was almost straight alongshore because the jetty did not extend to where the bar developed. The jetty still impounded sand and a gently sloping plateau developed near it, but the plateau extended only to the end of the structure.

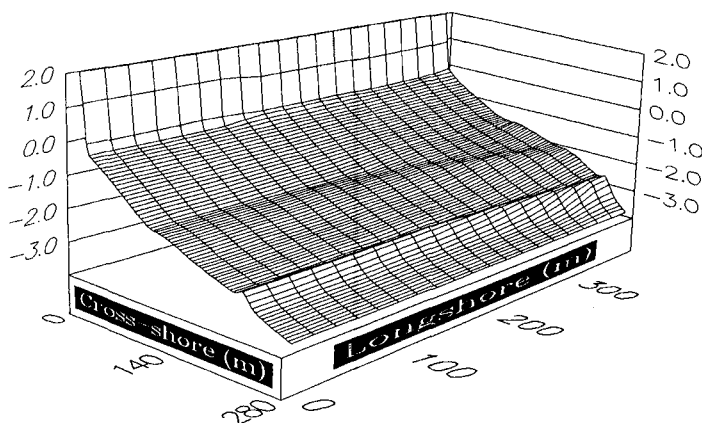


Fig. 8. Impoundment at a long jetty (no bypassing)

Additional simulations were carried out for a long jetty, encompassing 10 days of wave action ($H_0 = 1$ m, $T = 8$ sec, $\theta_0 = 20$ deg), which illustrates the equilibrium properties of 3DBEACH. Fig. 10 shows the time evolution of the profile line located closest to the groin and how the sand build-up occurs along the groin. The accumulation of sand on the updrift side of the groin will continue as long as the waves have a predominant direction. However, as the beach contours adjust towards a position where they are parallel to the incident wave crests, the sand transport decreases and the rate of accumulation becomes smaller. Thus, the model correctly describes the equilibrium characteristics of a beach with groins observed in the laboratory and field.

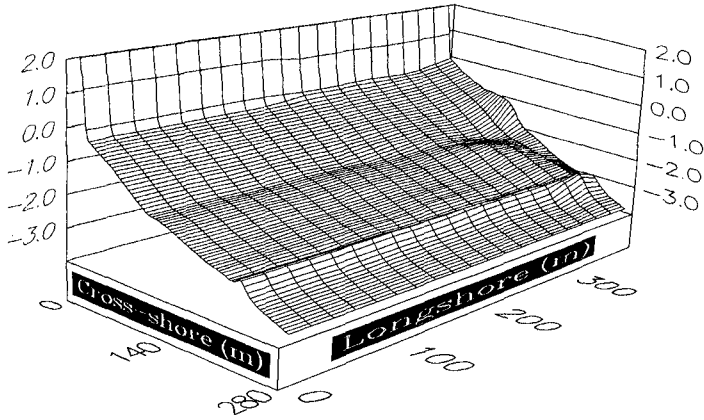


Fig. 9. Impoundment at a jetty with bypassing

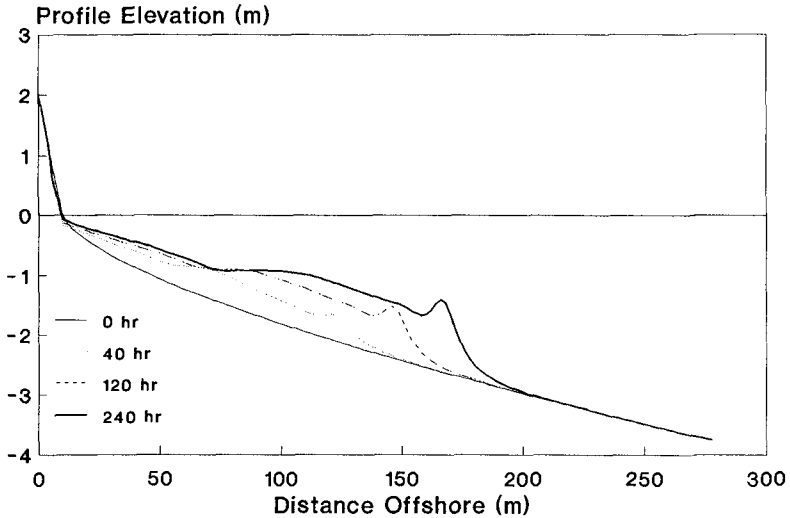


Fig. 10. Profile evolution immediately updrift an infinitely long jetty

CONCLUDING DISCUSSION

This paper described initial tests of a new class of numerical model of three-dimensional beach change. The distinguishing characteristic of the model is decoupling of wave, current, and sediment transport processes on cross-shore lines spanning the nearshore. The decoupling

approximation reduces calculation time significantly over beach change models using full two-dimensional wave and current calculation schemes, yet still describes morphologic nearshore profile features of engineering interest. The model is expected to be valid if longshore bathymetry gradients are small and significantly less than cross-shore gradients.

The model presently describes sediment transport and beach change in and around the surf zone as produced by breaking waves. Because the model calculates process-driven sediment transport rates and uses the mass conservation equation to determine beach change, inclusion of non-breaking wave sediment transport generating mechanisms is possible and will be incorporated in the next phase of the study.

The tests series demonstrated that the model can describe changes in large-scale morphologic features such as breakpoint bars, berms, and plateaus formed near structures. Important features of the model are a stable approach to an equilibrium bottom configuration under steady waves and ease of implementing boundary conditions. Without possessing a regular approach to equilibrium, both the time scale and reliability of model predictions would be ambiguous. Such properties were well studied in the beach change modeling technology underlying 3DBEACH (Kraus and Larson 1988, Hanson and Kraus 1989, Larson and Kraus 1989).

ACKNOWLEDGEMENTS

The work carried out by ML and HH was funded through the U.S. Army Research, Development and Standardization Group, UK, under contract DAJA-88-C0015. This support is gratefully acknowledged. The contribution of NCK was performed as part of the activities of the Calculation of Boundary Properties (Noncohesive Sediments) work unit of the Dredging Research Program, US Army Corps of Engineers. Permission was granted by the Chief of Engineers to publish this information.

REFERENCES

- Dally, W. R., Dean, R. G., and Dalrymple, R. A. 1985. "Wave height variation across beaches of arbitrary profile," J. Geophys. Res., 90 (C6), pp 11917-11927.
- Hanson, H. 1989. "GENESIS - A generalized shoreline change numerical model," J. Coastal Res., Vol 5 (1), pp 1-27.
- Hanson, H. and Kraus, N. C. 1989. "GENESIS: Generalized model for simulating shoreline change. Report 1: Technical reference," Tech. Rep. CERC-89-19, Coastal Engrg. Res. Center, U.S. Army Engr. Waterways Expt. Station, Vicksburg, MS.
- Junke, L., Mitchell, T., and Piszker, M. J. 1989. "Construction and monitoring of nearshore disposal of dredged material at Silver Strand State Park, San Diego, California," Proc. 22nd Annual Dredging Seminar, Texas Engrg. Expt. Station, CDS Rep. No. 317, pp 203-217.
- Kajima, R., Saito, S., Shimizu, T., Maruyama, K., Hasegawa, H., and Sakakiyama, T. 1983. "Sand transport experiments performed by using a large water wave tank," Data Rep. No. 4-1, Central Res. Institute for Electric Power Industry (in Japanese).

- Kraus, N. C., Gingerich, K. J., and Rosati, J. D. 1988. "Toward an improved empirical formula for longshore sand transport," Proc. 21st Coastal Engrg. Conf., ASCE, pp 1182-1196.
- Kraus, N. C., Kriebel, D. L., and Larson, M. 1991. "Evaluation of beach erosion and accretion predictors," Proc. Coastal Sediments '91, ASCE.
- Kraus, N. C. and Larson, M. 1990. "NMLONG: Numerical model for simulating the longshore current," Tech. Rep., Coastal Engrg. Res. Center, U.S. Army Engr. Waterways Expt. Station, Vicksburg, MS, (in prep.).
- Kraus, N. C. and Sasaki, T. O. 1979. "Influence of wave angle and lateral mixing on the longshore current," Marine Science Communications, Vol 5 (2), pp 91-126.
- Larson, M. and Kraus, N. C. 1989. "SBEACH: Numerical model for simulating storm-induced beach change. Report 1: Theory and model foundation," Tech. Rep. CERC-89-9, Coastal Engrg Res. Center, U.S. Army Engr. Waterways Expt. Station, Vicksburg, MS.
- Larson, M. and Kraus, N. C. 1991a. "Mathematical modeling of the fate of beach fill," Coastal Engrg., Special Issue on Beach Fill, (in press).
- Larson, M. and Kraus, N. C. 1991b. "Numerical model of longshore current for bar and trough beaches," J. Waterway, Port, Coastal, and Ocean Engrg., ASCE, (in press).
- Larson, M., Kraus, N. C., and Byrnes M. R. 1990. "SBEACH: Numerical model for simulating storm-induced beach change. Report 2: Numerical formulation and model test," Tech. Rep. CERC-89-9, Coastal Engrg. Res. Center, U.S. Army Engr. Waterways Expt. Station, Vicksburg, MS.
- Larson, M., Kraus, N. C., and Sunamura, T. 1988. "Beach profile change: Morphology, transport rate, and numerical simulation," Proc. 21st Coastal Engrg. Conf., ASCE, pp 1295-1309.
- Thornton, E. B. and Guza, R. T. 1986. "Surf zone longshore currents and random waves: Field data and models," J. Phys. Oceanography, Vol 16, pp 1165-1178.
- Visser, P. J. 1982. "The proper longshore current in a wave basin," Rep. No. 82-1, Dept. of Civil Engrg., Delft Univ. of Techn., Delft.

CHAPTER 165

OSCILLATORY FLOW AND SEDIMENT MOTION OVER A RIPPLED BED

Paolo Blondeaux¹ & Giovanna Vittori²

Abstract

Experimental visualizations have been performed of the oscillatory flow and of the sediment motion produced by a sea wave propagating over a rippled bed. In particular the dynamics of the vortex structures generated by flow separation at the ripple crest is investigated along with the mechanism through which sediments are lifted up from the bed and carried in suspension. A numerical model is formulated and the results obtained are successfully compared with the experimental data.

Introduction

Field observations seem to indicate that the main contribution to the total load in the nearshore region is due to the suspended load (Sleath, 1984). It is thus clear that an important aspect controlling sediment transport in the coastal area is the mechanism through which sediment grains are lifted and maintained in suspension. The latter mechanism is largely affected by the bottom profile which may exhibit a regular pattern of sandy waves (ripples). Indeed it was recognized as early as Ayrton (1910) that the formation of sand ripples on the sea bottom is connected with the existence of vortices shed at the crests of the ripples in alternate directions every half wave cycle and that these vortex structures play a crucial role in sediment transport. Experimental evidence (Nielsen, 1979; Sunamura, 1980) suggests that in a wave cycle two distinct mechanisms operate. The first mechanism is the trapping of sediments in the vortex structures which are generated by flow separation at the ripple crests. When flow reverses and the vortex structures are no longer reinforced but simply convected by the local velocity, the second mechanism operates: sediments are carried into suspension far from the point where they were picked up. Finally sediments are slowly released along the ripple profile when vortices decay because of viscous effects.

A model able to transform these qualitative observations into quantitative results has not been formulated yet.

¹ Associate Professor, Hydraulic Institute, University of Genoa, Via Montallegro, 1, 16145 Genova, Italy.

² Researcher, National Research Council, Via Opera Pia 11, 16145 Genoa, Italy, also Hydraulic Institute, University of Genoa.

Some attempts have been made to determine the oscillatory flow over a rippled bed as a first step towards the prediction of the sediment motion (Sleath, 1973; Sato et al., 1984; Longuet-Higgins, 1981). Numerical approaches have been used to solve momentum and continuity equations. Sleath (1973) and Sato et al. (1984) made use of finite difference schemes. Longuet-Higgins (1981) used a discrete vortex method. Even though some information on vorticity dynamics has been gained, the above methods present some drawbacks. The finite difference approaches fail when applied to conditions characterized by the relatively large values of the Reynolds number characteristic of the flow at the bottom of gravity waves. In fact a large number of grid points would be necessary in order to describe both the irrotational part of the flow and the boundary layer adjacent to the bottom; consequently an extremely large amount of CPU time would be required. The main drawback of a discrete vortex method is that it is essentially inviscid. In other words it is assumed that viscous boundary layers remain thin and passive at all times except at singular geometrical points where they separate and generate a vortex sheet. Whence if applied to the oscillatory flow over a rippled bed, a discrete vortex method fails to provide quantitative results when the boundary layer thickness is of the same order of magnitude as the ripple height and when flow separation is induced along the flat portion of the ripple profile by pressure gradients. Moreover, to the authors' knowledge no attempt has been made in the past to formulate a model able to predict sediment motion.

In the present contribution we study the oscillatory flow over a rippled bed solving the vorticity equation and Poisson equation (which relates vorticity and stream function) by means of a new numerical approach based on spectral methods and finite difference approximations. The proposed numerical approach makes it possible to obtain detailed quantitative results for values of the parameters of physical relevance using a limited amount of CPU time. Using the computed flow field we then formulate a numerical model which provides a description of the dynamics of sediment grains in suspension. The numerical results are also compared with experimental visualizations described in the first part of the present contribution.

Experimental Visualizations

In order to obtain new information on the sediment motion produced by an oscillatory flow over a rippled bed, experimental visualizations have been performed.

The experimental apparatus consists of a duct 290 cm long with a rectangular section, the width and the height of which are equal to 46 cm and 63 cm respectively. The duct is filled with water and the lower part of it is covered with sand. The fluid motion is produced by two pistons located at the ends of the duct and driven by a pneumatic motor. The amplitude and the period of the piston oscillations can be continuously varied by means of an electronic device.

Sediments in suspension are visualized using a sheet of light produced by a 2 kw lamp and an appropriate system of lenses. Sediment motion is then filmed by a standard video camera and recorded using a video tape recorder. Then a sequence of images of sediment trajectories during the flow cycle is digitalized and transferred onto the computer HP 9000. Each image is computer-analysed and different shades of grey are assigned to different light intensities. This type of procedure allows

qualitative information on sediment concentration to be gained. Moreover, looking at a sequence of images, it is also possible to obtain the trajectories of the clouds of sediments picked up and carried in suspension by the vortex structures characteristic of the flow field in the presence of ripples.

An example of the results obtained is shown in plate 1. Fluid oscillations are characterized by an amplitude S equal to 8 cm and a period T equal to 2 s. Quartz sand is used with a relative density ρ_s/ρ equal to 2.65 and a mean diameter d equal to 0.28 mm.

In photo a the flow is directed from the right to the left and the fluid velocity is maximum. The combined action of the attached boundary layer along the stoss side of the ripple and of the vortex structure generated by flow separation at the ripple crest creates a cloud of sediment just above the lee side of the ripple where a recirculating cell of fluid is located. After $T/10$ (photo b) the flow decelerates, the vortex structure strengthens and the size of recirculating cell increases. Sediments tend to be piled up at the ripple crest by the action of the vortex.

$T/10$ later (photo c) the flow goes into reverse and the vortex has almost reached its maximum strength. A lot of sediments are carried in suspension far from the bottom leaving the ripple profile at the crest. Now (photo d) the flow has reversed its direction and the main vortex structure is no longer reinforced but simply convected from the left to the right by the action of the local velocity. Sediments are carried in the same direction. Most of them tend to move close to the bottom but still a relevant part remains in suspension.

After $T/10$ (photo e) the strength of the main vortex structure decays because of viscous effects. Gravity effects tend to prevail over drag forces and sediments are slowly released along the bed profile, only few of them being in suspension. In the meantime a new vortex structure is generated by flow separation at the ripple crest and a new cloud of sediment is formed along the lee side of the ripple. Photo f, which was taken $T/2$ after photo a, shows a flow field and a sediment concentration distribution which are the mirror image of those shown in photo a. Then the sediment time development repeats similarly during the second half of the cycle.

Similar results have been obtained for different values of the parameters even though quantitative differences have been detected. In plates 2 and 3 sediment distribution is shown for T equal to 2 s, d equal to 0.28 mm and S equal to 7 cm and 10 cm respectively. It can easily be observed that in the former case less sediment is moved by the oscillatory flow and that the larger part moves close to the bottom, few sediments being picked up from the bed and carried in suspension far from the ripple profile.

The Numerical Model

Let us consider the oscillatory flow over a rippled bed and introduce a cartesian coordinate system (x^*, y^*) with the x^* -axis lying on the bottom and the y^* -axis directed upwards. Let us assume the bed profile to be described by the following equations

$$y^* = \frac{h^*}{2} \cos(k^* \xi^*) \quad x^* = \xi^* - \frac{h^*}{2} \sin(k^* \xi^*) \quad (1)$$

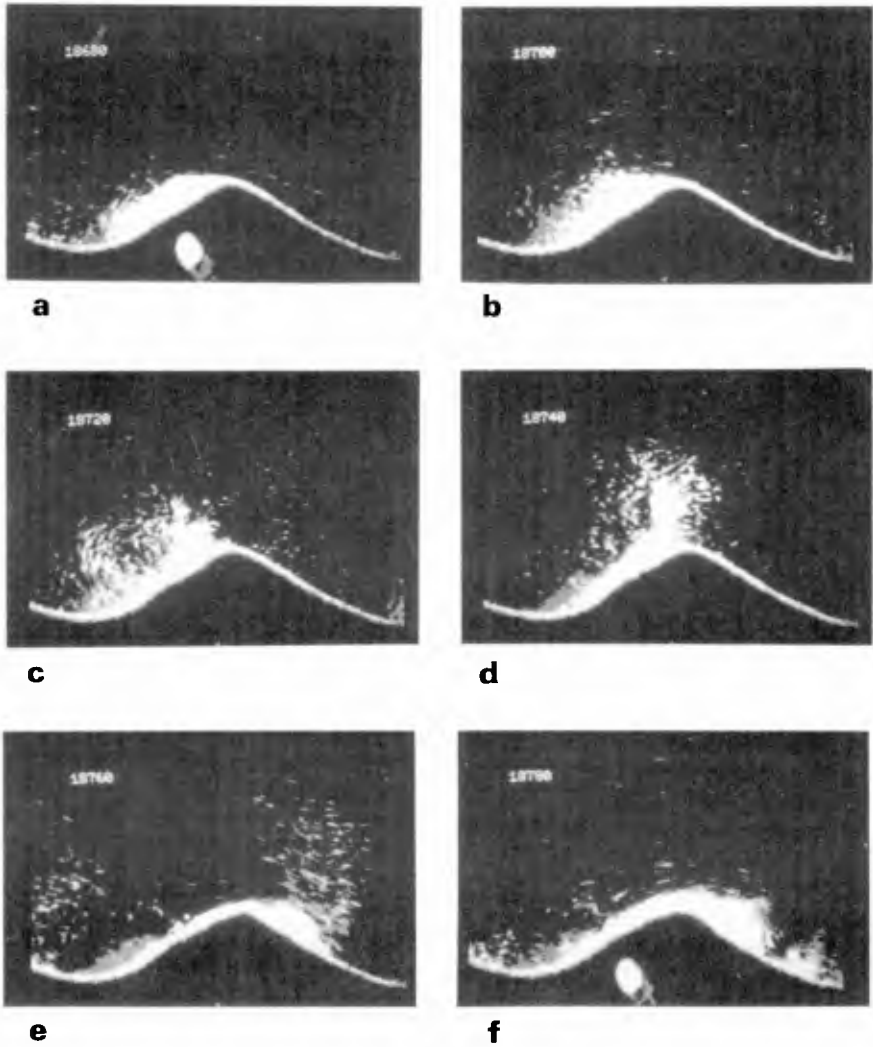


Plate 1 Experimental visualization of sediment motion over ripples in an oscillatory flow.

($S = 8$ cm, $T = 2$ s, $\rho_s/\rho = 2.65$, $d = 0.28$ mm.)

(a) $t^*/T^* = 3/4$; (b) $t^*/T^* = 17/20$; (c) $t^*/T^* = 19/20$; (d) $t^*/T^* = 21/20$;
 (e) $t^*/T^* = 23/20$; (f) $t^*/T^* = 5/4$.

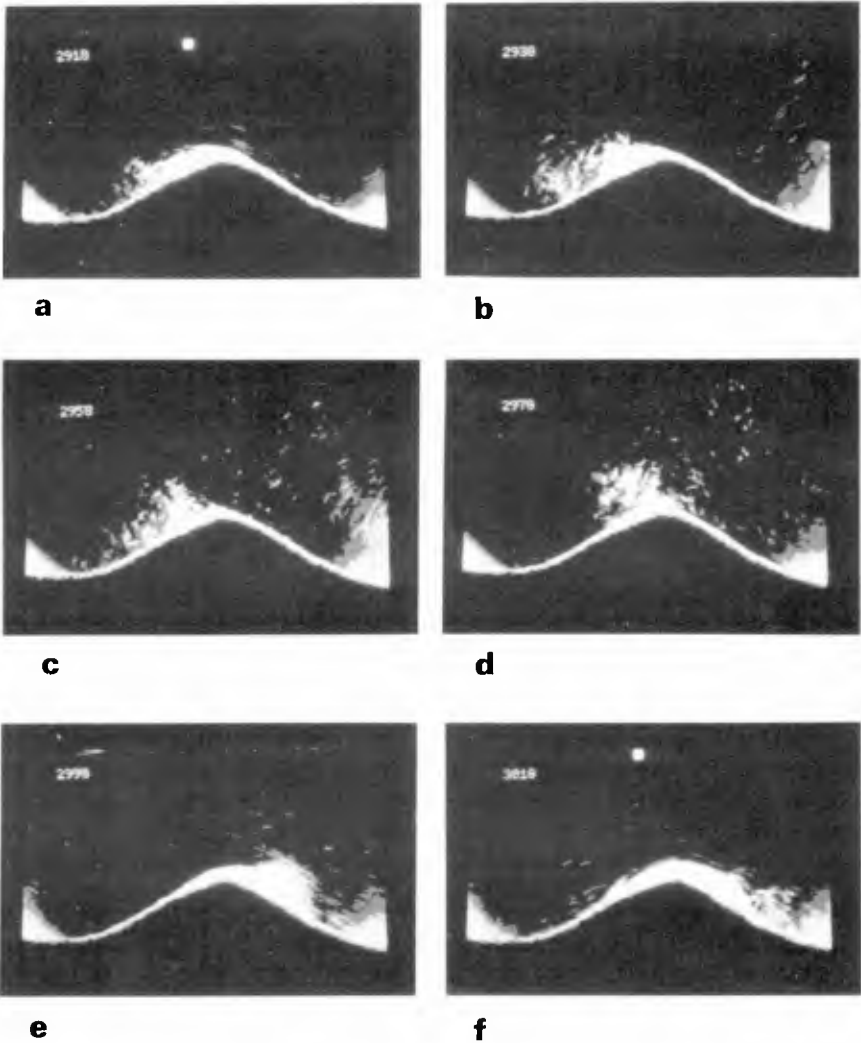


Plate 2 Experimental visualization of sediment motion over ripples in an oscillatory flow.

($S = 7$ cm, $T = 2$ s, $\rho_s/\rho = 2.65$, $d = 0.28$ mm.)

(a) $t^*/T^* = 3/4$; (b) $t^*/T^* = 17/20$; (c) $t^*/T^* = 19/20$; (d) $t^*/T^* = 21/20$;
 (e) $t^*/T^* = 23/20$; (f) $t^*/T^* = 5/4$.

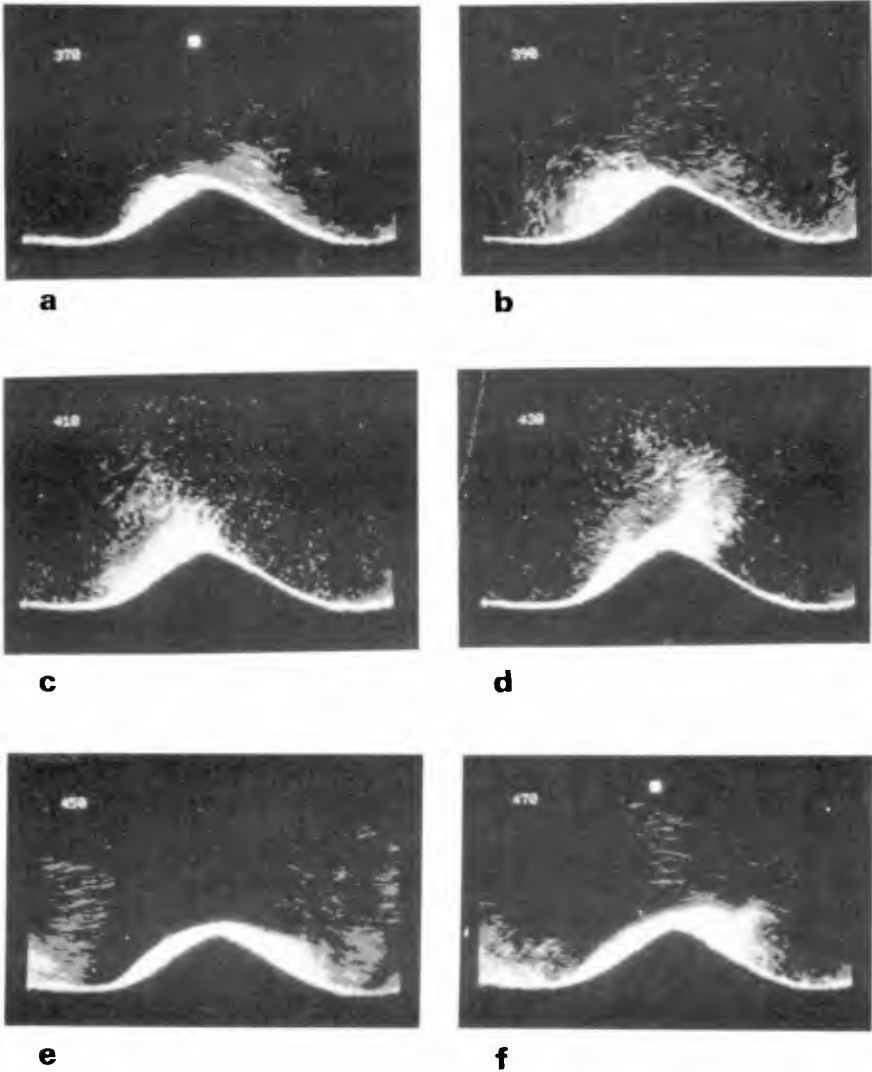


Plate 3 Experimental visualization of sediment motion over ripples in an oscillatory flow.

($S = 10$ cm, $T = 2$ s, $\rho_s/\rho = 2.65$, $d = 0.28$ mm.)

(a) $t^*/T^* = 3/4$; (b) $t^*/T^* = 17/20$; (c) $t^*/T^* = 19/20$; (d) $t^*/T^* = 21/20$;

(e) $t^*/T^* = 23/20$; (f) $t^*/T^* = 5/4$.

where $k^* = 2\pi/l^*$ is the wavenumber characteristic of the ripple, h^* , l^* its height and wavelength and ξ^* a dummy variable. As observed in real ripples the bed profile (1) exhibits crests sharper than the troughs. Moreover a comparison between experimental profiles and relationships (1) performed by Sleath (1984) shows good agreement. Assuming the flow to be two-dimensional, the differential problem governing the flow field is posed by the vorticity equation along with the Poisson equation which relates the vorticity ω^* with the stream function ψ^* and boundary conditions which force no-slip at the bottom and the matching of the flow in the bottom boundary layer with the outer irrotational flow. The latter can be assumed to be:

$$(u^*, v^*) = (U_o^* \sin 2\pi t^*/T^*, 0) \quad (2)$$

where u^* , v^* are the velocity components in the x^* and y^* directions, U_o^* and T^* the amplitude and the period of the velocity oscillations far from the bottom and t^* is time.

In order to solve the problem it is useful to introduce a new orthogonal coordinate system (ξ^*, η^*) defined by the following relationships (Sleath, 1973)

$$\xi^* = x^* + \frac{h^*}{2} e^{-k^* \eta^*} \sin(k^* \xi^*) \quad \eta^* = y^* + \frac{h^*}{2} e^{-k^* \eta^*} \cos(k^* \xi^*) \quad (3)$$

which maps the bottom profile into the line $\eta^* = 0$. Introducing the following dimensionless variables

$$t = t^* 2\pi/T^* \quad (\xi, \eta) = (\xi^*, \eta^*)/\delta^* \quad \omega = \omega^* \delta^*/U_o^* \quad \psi = \psi^*/U_o^* \delta^* \quad (4)$$

where $\delta^* = \sqrt{vT^*/\pi}$, the governing differential problem reads

$$\frac{\partial \omega}{\partial t} + \frac{R_\delta}{2J} \left[\frac{\partial \psi}{\partial \eta} \frac{\partial \omega}{\partial \xi} - \frac{\partial \psi}{\partial \xi} \frac{\partial \omega}{\partial \eta} \right] = \frac{1}{2J} \left[\frac{\partial^2 \omega}{\partial \xi^2} + \frac{\partial^2 \omega}{\partial \eta^2} \right] \quad (5)$$

$$\frac{\partial^2 \psi}{\partial \xi^2} + \frac{\partial^2 \psi}{\partial \eta^2} = -J \omega \quad (6)$$

$$\frac{\partial \psi}{\partial \xi} = \frac{\partial \psi}{\partial \eta} = 0 \quad \text{at } \eta = 0 \quad (7)$$

$$\frac{\partial \psi}{\partial \xi} \rightarrow 0 \quad \frac{\partial \psi}{\partial \eta} \rightarrow \sin t \quad \text{for } \eta \rightarrow \infty \quad (8)$$

In the equations above R_δ is the flow Reynolds number defined as $U_o^* \delta^*/\nu$ and J is the Jacobian of transformation (3). The problem is solved numerically by following a procedure which makes use of spectral methods and finite difference approximations. First of all we consider the values assumed within a ripple wavelength l by the stream function $\psi(\xi, \eta, t)$ and the vorticity $\omega(\xi, \eta, t)$ on a regular grid along the ξ -direction. Then the discrete Fourier coefficients are introduced (Orzag, 1971)

$$\psi\left(\frac{j l}{N}, \eta, t\right) = \sum_{n=0}^{N-1} \Psi_n(\eta, t) e^{i 2\pi n \frac{j}{N}}$$

$$j = 1, 2, \dots, N \quad (9)$$

$$\omega\left(\frac{j l}{N}, \eta, t\right) = \sum_{n=0}^{N-1} \Omega_n(\eta, t) e^{i 2 \pi n \frac{j}{N}}$$

Making use of (9), the problem posed by (5)-(8) is transformed into a time dependent boundary value problem in the variable η which is amenable to a classic computational approach. The solution starts with the establishment of initial conditions for the complex fields Ψ_n, Ω_n which are assumed to vanish. Then the computational cycle begins by the implementation of finite difference equations analogous to the partial differential equations for the discrete Fourier coefficients. A balance between computational costs and the attainment of accurate results made it advisable to use a first order forward scheme to approximate time derivatives and a second order central scheme to approximate spatial derivatives (Roache, 1972). It is worthwhile pointing out that a further variable $\tilde{\eta}$ was defined [$\tilde{\eta} = \ln((\eta + b)/b)$] in order to stretch the region near the bottom where the gradients of the dependent variables are larger. The value of 'b' was suitably chosen on the basis of numerical experiments. With these approximations, Ω_n inside the computational domain at a new time level is determined explicitly starting from the knowledge of Ω_n and Ψ_n at the previous time level. These updated values of Ω_n make the solution of the Poisson equation for Ψ_n possible. Indeed the implementation of a finite difference equation analogous to the Poisson equation leads to a tridiagonal system for the values assumed by Ψ_n on a regular grid along the $\tilde{\eta}$ direction. The latter system can be solved by standard methods. The last step in the computational cycle consists in calculating Ω_n on the boundary of the domain. This step is accomplished by forcing vanishing values of Ω_n far from the ripple and computing Ω_n at $\eta = 0$ according to the first order scheme suggested by Thom (1928). The above numerical procedure makes it possible to use up to 256 Fourier components and 256 grid points in the $\tilde{\eta}$ direction with a limited amount of CPU time.

Once the flow field is known, a picture of the motion of sediment grains in suspension is obtained releasing sand particles near the bottom and computing their trajectories taking into account the action of their weight, drag and lift forces. Flow acceleration effects have been ignored since the values of the Keulegan-Carpenter number characteristic of sediments are usually very large for sand at the bottom of sea waves.

It is easy to see that the equations governing the motion of a single sediment particle are

$$\begin{aligned} \frac{d \xi_p}{d t} &= \frac{v_{p \xi} R_b}{\sqrt{J} 2} & \frac{d \eta_p}{d t} &= \frac{v_{p \eta} R_b}{b e^{\eta p} \sqrt{J} 2} \\ \frac{d v_{p \xi}}{d t} &= \frac{R_b^2}{2 s R_d} \left[\frac{0.5 h k e^{-h \eta} \sin k \xi}{\sqrt{J} F_d^2} + \frac{3}{4} \left| \underline{v}_f + \underline{v}_p \right| \left(C_D (v_{f \xi} - v_{p \xi}) - C_L (v_{f \eta} - v_{p \eta}) \right) \right] \\ \frac{d v_{p \eta}}{d t} &= \frac{R_b^2}{2 s R_d} \left[\frac{1 - 0.5 h k e^{-k \eta} \cos k \xi}{\sqrt{J} F_d^2} + \frac{3}{4} \left| \underline{v}_f - \underline{v}_p \right| \left(C_D (v_{f \eta} - v_{p \eta}) + C_L (v_{f \xi} - v_{p \xi}) \right) \right] \end{aligned}$$

where the subscripts f and p refer to fluid and particles respectively and an underline denotes a vector.

R_d , F_d and s are the Reynolds number, the Froude number of the sediments and the ratio between sediment and fluid density respectively

$$R_d = \frac{U_o * d^*}{\nu} \quad F_d = \frac{U_o^*}{\sqrt{(s-1)gd^*}} \quad s = \frac{\rho_s}{\rho}$$

Finally it should be pointed out that the drag coefficient C_D has been computed by means of the relationship holding for the steady flow in terms of the instantaneous Reynolds number of the relative motion fluid-particle and that the ratio C_L/C_D has been assumed constant along the bottom and exponentially decaying with the distance of the particle from the ripple profile.

These approximations are likely to be very poor for large concentrations of suspended sediments; however we feel that the gross features of particle dynamics are likely to be well reproduced for low concentrations.

In figure 1 regions of clockwise and counter-clockwise vorticity are shown for $R_\delta = 100$, $k = 0.19$, $h/l = 0.15$.

The flow far from the bottom starts from rest and behaves like $\sin(t)$. It appears that clockwise vorticity is generated along the bed profile and particularly near the crest of the ripple during the first part of the cycle. By increasing t , the boundary layer thickens in the downstream side of the ripple till flow separates and vorticity of the opposite sign is generated at the bottom. Then the roll up of clockwise vorticity generates vortex structures (see figure 1_a). When the flow goes into reverse (see figure 1_b), the main vortex structure induces flow separation along the lee side of the ripple and the generation of a free shear layer characterized by vorticity of the opposite sign. In the second half of the cycle the main vortex structure is no longer reinforced but simply convected away by the local velocity.

The free shear layer originates a new vortex which couples with the previous one forming a vortex pair which travels along the bed profile moving with its self-induced velocity (see figures 1_c, 1_d). Then further counter-clockwise vorticity is shed from the ripple crest and when the flow is about to reverse its direction again, a new vortex structure is present near the crest (see figure 1_d) and the phenomenon is repeated similarly. Similar results are obtained for values of the parameters of physical relevance.

As regards the trajectories of sediment grains released near the bottom, the experimental observations are found again. Indeed looking at figure 2 where sediments in suspension are drawn for $R_\delta = 50$, $R_d = 27.5$, $F_d = 2.5$, $s = 2.65$ at different times during the cycle, it can be seen that for $t = 5.25$, when the flow is almost maximum and its direction is from right to left, a cloud of sediment is present just above the lee side of the ripple. The numerical results, in accordance with experimental findings, show that the vortex structure generated by flow separation tends to pile up sediments near the ripple crest and to carry some of them in suspension far from the ripple profile. When flow reverses, sediments are carried from left to right. Both numerical results and experimental visualizations indicate that most sediments move close to the bottom even though a relevant part is in suspension. Thus the results depicted in figure 2 show that many of the sediments rolling and sliding along the ripple profile are trapped by the new vortex forming along the lee side of the ripple. On the other hand, the sediments in suspension are

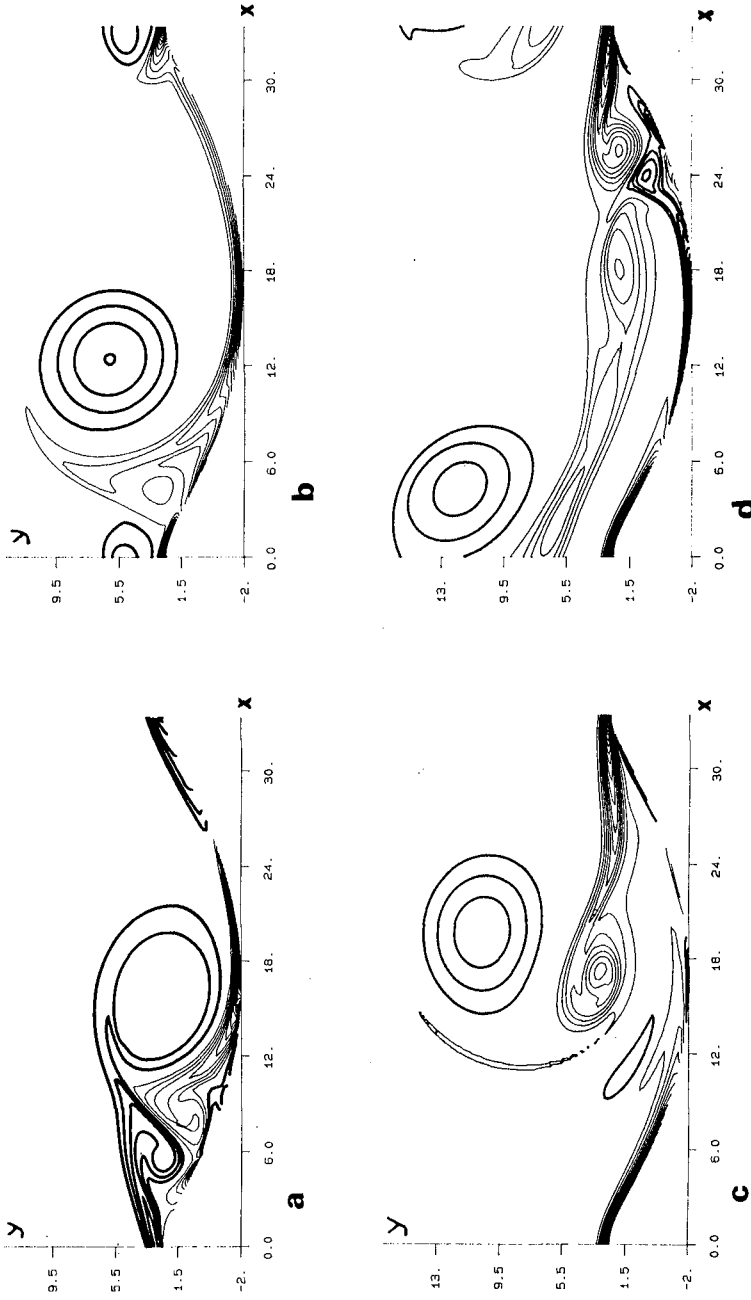


Figure 1 - Vorticity contours: $\Delta\omega = 0.15$ (— clockwise vorticity, --- counter clockwise vorticity) $R_\delta = 100$, $k = 0.19$, $h/l = 0.15$, (a) $t = 3\pi/4$; (b) $t = \pi$; (c) $t = 5\pi/4$; (d) $t = 3\pi/2$.

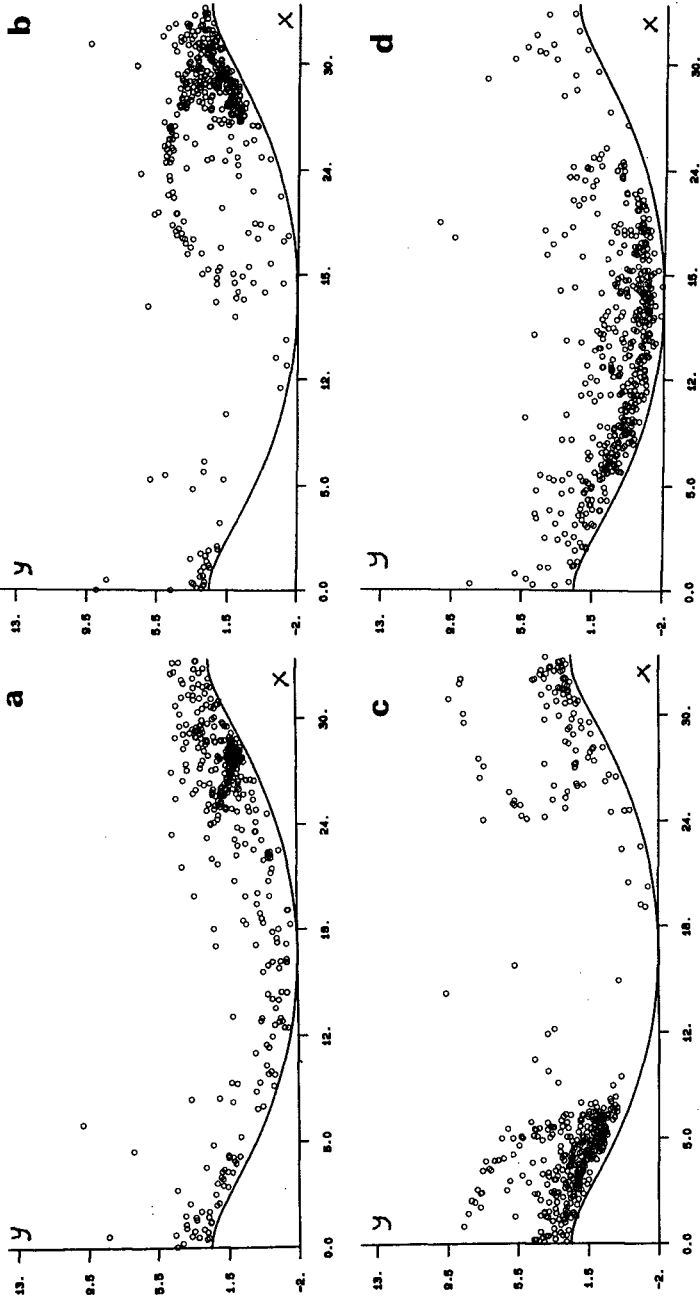


Figure 2 - Sediment particles: $R_b = 50$, $R_d = 27.5$, $F_d = 2.5$, $s = 2.65$, (a) $t = 5.25$; (b) $t = 7.0$; (c) $t = 8.05$; (d) $t = 8.95$.

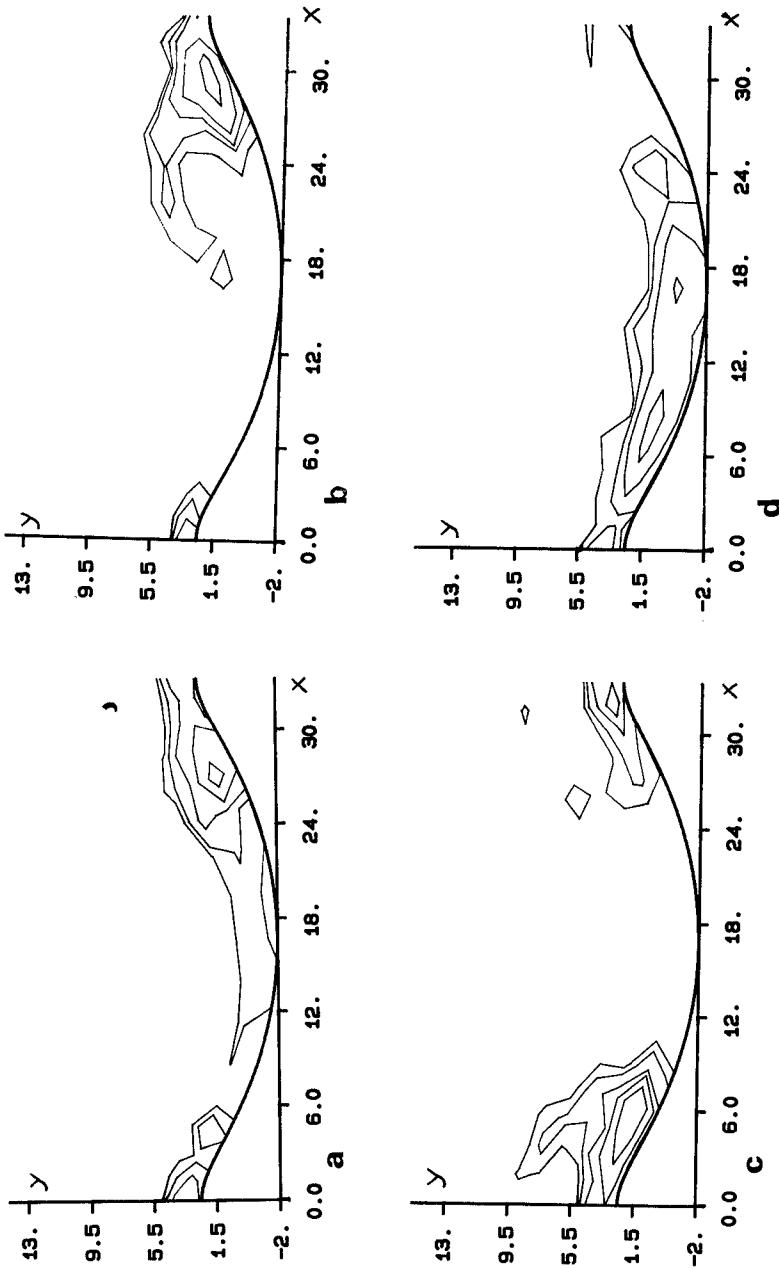


Figure 3 - Particle density (c, 2c, 4c, 8c,...); $R_b = 50$, $R_d = 27.5$, $F_d = 2.5$, $s = 2.65$,
 (a) $t = 5.25$; (b) $t = 5.95$; (c) $t = 7.0$; (d) $t = 8.05$.

slowly released along the ripple profile since the strength of the old vortex decays because viscous effects and gravity effects prevail over drag forces. When the irrotational flow reaches its maximum in the opposite direction a new group of sediment particles is piled up at the crest of the ripple and in the next cycle the phenomenon is repeated similarly.

A rough idea of the time development of concentration over a rippled bed during a wave cycle can be gained from the numerical results by looking at the regions characterized by the same particle density. Because the number of particles moved in the numerical model is arbitrary, only relative information is obtained (see figure 3).

Clouds of sediments can be identified, which have the same dynamics as those visualized in the experiments, for the sake of brevity we will not describe the results obtained for different values of R_s , R_d , F_d , but we only state that the present model can be used to investigate the influence of the parameters on flow time development and sediment dynamics. Moreover asymmetric ripples can be obtained by slightly modifying relationships (3) and asymmetric flow forcing can also be considered.

The qualitative agreement between experimental visualization and the numerical model is encouraging for the development of the work. Information on the tendency of sediments to move onshore or offshore depending on wave and sediment characteristics can be gained.

This work has been partially supported by the Italian Ministry of Education and partially by the National Research Council (CNR) under contract "Piano finalizzato: Sistemi informatici e calcolo parallelo - Sottoprogetto calcolo scientifico per grandi sistemi" N° 8903344.

References

- Ayrton H., "The origin and growth of ripple mark" Proc. Roy. Soc. A84, 285 - 310, 1910.
- Longuet-Higgins M.S., "Oscillating flow over steep sand ripples" J. Fluid Mech. 107, 1 - 35, 1981.
- Nielsen P., "Some basic concepts of wave sediment transport" Inst. Hydrodynamics and Hydraulic Engineering. Tech. Univ. of Denmark, paper n. 20, 1979.
- Sato S., Mimura N., Watanabe A., "Oscillatory boundary layer flow over a ripple bed", XIX ICCE, Houston, 2293 - 2309, 1984.
- Sleath J.F.A., "A numerical study of the influence of bottom roughness on mass transport by water waves" Proc. Int. Conf. Num. Methods in Fluids Dynamics. Southampton, U.K., 1973.
- Sleath J.F.A., "Sea bed mechanics", Wiley Ocean Engineering Series. Mc. Cornick E., 1984.

Sunamura T., "A Laboratory study of offshore transport of sediment and a model for eroding beaches", XIII ICCE, 1051 - 1070, 1980.

Thom A., "An investigation of fluid flow in two-dimensions", Aerospace Research Center, R. and M., N.1194 U.K.

CHAPTER 166

Wave Entrainment of Sand from a Rippled Bed

Malcolm O. Green¹ and Christopher E. Vincent²

Abstract

Wave-orbital velocities at 20 cm above the bed and continuous vertical profiles of near-bed suspended-sediment concentration were measured seaward of the surfzone over a rippled bed. Sand was intermittently entrained from the bed and ejected upwards in discrete clouds. The typical sequence of events in the entrainment cycle, with sand being rolled up in a thin near-bed layer and ejected into the flow on alternating wave strokes, is attributed to the action of vortices shed from the bed ripples by the reversing flow. The orderly cycle of events causes a time-domain correlation between the wave fluctuations of velocity and concentration, and the resulting sediment flux is comparable in size, and at some elevations directed opposite to, the mean sediment flux.

Introduction

Time-averaged horizontal suspended-sediment flux in a combined wave and current flow may comprise two terms: a "mean" term, which is readily understood, and a "correlation" term, which arises from correlation in time of the wave fluctuations in suspended-sediment concentration and horizontal velocity (e.g., Jaffe et al., 1984; Vincent and Green, 1990). The latter component of the total flux is analogous to the vertical turbulent flux of horizontal momentum that occurs in the benthic boundary layer. In the case of the boundary layer, sublayer bursting drives the momentum flux; in the

¹Bullard Laboratories, Department of Earth Sciences, University of Cambridge, Cambridge, CB3 0EZ, England.

²School of Environmental Sciences, University of East Anglia, Norwich, NR4 7TJ, England.

case of the sediment transport, the correlation flux is driven by the orderly process of flow separation and vortex-shedding associated with reversing flows over ripples.

The process of vortex shedding from rippled beds by reversing flows has been studied using flow visualization techniques in the laboratory (e.g., Bijker et al., 1976; Honji et al., 1980); Eulerian measurements of the resulting suspended-sediment concentrations and fluid velocities have been made in the laboratory by several workers (e.g., Homma et al., 1965; Nakato et al., 1977; Sleath, 1982); and theoretical models of the velocity and suspended-sediment fields have been developed (e.g., Tunstall and Inman, 1975; Nielsen, 1984). Although rippled beds are virtually ubiquitous in nature, and vortex shedding has been invoked to explain the cause of measured correlation fluxes that were a significant fraction of the total flux (e.g., Vincent and Green, 1990), there have been few descriptions of the process in the field from either a Lagrangian or Eulerian point of view.

Our objective is to describe field observations of the cycle of vortex-entrainment and ejection into the flow of sand by waves from a rippled bed. Vincent and Green (1990) used part of the same data set in an analysis of the time-averaged suspension profile and of the distribution of the two components of the total sediment flux close to the bed. In that analysis, we hypothesized that vortex-shedding was the underlying cause of the measured correlation fluxes. Our objective here is to describe in more detail, using wave-by-wave and statistical analyses, the temporal variability of the entrainment process and the vertical and temporal structure of the individual clouds of suspended sediment.

Data

The data are from an experiment conducted over a rippled sand bed in 1.7 ± 0.2 m water depth seaward of the surfzone on the North Norfolk coast of England. The modal grain size of the bed sediment was 0.023 cm, which is a fine to medium noncohesive sand, and bed ripples were a few centimeters high by several tens of centimeters long. The ripple dimensions were not measured, however Vincent and Green (1990) estimated, using Grant and Madsen's (1982) model, that the ripple height was ~ 3 cm.

Continuous profiles of suspended-sediment concentration from 48 cm above the bed down to the bed level were obtained every 0.58 s using an acoustic

backscatter sensor (ABS). The ABS emitted 2.8-MHz acoustic pulses and the backscattered acoustic pressure was sampled at 13 μ s intervals, which provided a vertical resolution of 1 cm. A calibration equation was applied to convert the measurements of backscattered pressure into estimates of suspended-sediment concentration. The particular calibration equation used was based on the grainsize distribution of the bed sediment, thus we make an implicit assumption that the suspended-sand population is the same as the bed-sediment population.

Simultaneous measurements of horizontal current velocity at 20 cm above the bed were obtained with an electromagnetic current meter. In this analysis, we use one record, termed run 2046, of 12-min duration, which consists of 1250 measurements of velocity and concentration at 1-cm intervals above the bed. The wave period during the deployment was \sim 6 s, and the significant on-offshore velocity was 60 cm/s, which was superimposed on an alongshore current of 15 cm/s.

The ABS was positioned 2 m seaward of the current meter, thus a correction had to be made to align the velocity and concentration time series. This is required in order to compute cross-correlation functions and ultimately to estimate correlation sediment fluxes. In order to align the two series, the phase spectrum, $\phi_{U_w C_z}(\omega)$, was examined, where U_w is on-offshore zero-mean velocity (which is taken to be the wave-orbital velocity) and C_z is concentration at an elevation z above the bed. If the estimated phase function approximates a straight line through the origin (i.e., 0 or 360 degrees):

$$\phi_{U_w C_z}(\omega) = -d\omega$$

then this indicates a delay or constant offset of $d \cdot \Delta t$ seconds between U_w and C_z where $-d$ is the slope of the phase function and Δt is the sampling interval (Chatfield, 1980). Shown in Figure 1a are the phase spectra for U_w crossed with concentration at 5 levels.

Each phase spectrum falls off at a rate that indicates a constant offset of $2\Delta t$ between the velocity and concentration series. The velocity series was thus shifted forward by $2\Delta t$ relative to the concentration series, and the phase spectra were recomputed. The rolloff is thus removed from the phase function (Figure 1b). This shift is applied throughout this analysis; note that an identical offset was indicated by consideration of the average phase speed of the waves and the measured separation of the sensors.

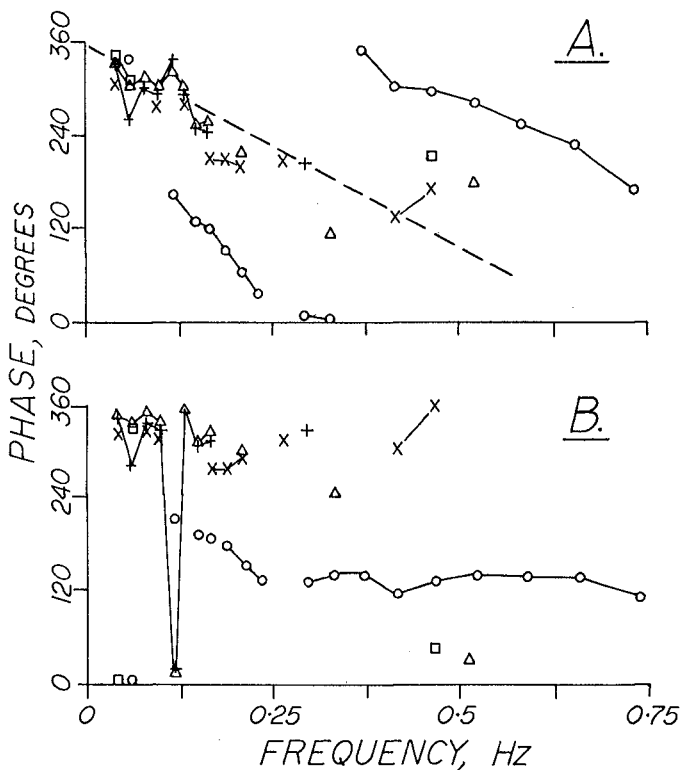


Figure 1. (a) Phase spectra $\phi_{U_w C_z}(\omega)$. All spectra appear to roll off at a constant rate indicated by the dashed line, the slope of which is consistent with a constant offset of $2\Delta t$ between the velocity and concentration series. (Note that only the statistically significant estimates of phase are shown. $o = U_w$ vs. C_2 , $\square = U_w$ vs. C_3 , $\Delta = U_w$ vs. C_5 , $+$ = U_w vs. C_{10} , $x = U_w$ vs. C_{20} .) (b) The same spectra as in (a) but with the velocity series shifted forward in time by $2\Delta t$.

Description of Time Series

Shown in Figure 2 are time series of U_w measured at $z = 20$ cm and concentration measured at 5 elevations above the bed. The elevations are shown normalized by the ripple height of 3 cm, i.e. $z^* = z/\eta$, where η is the wave-ripple height.

Sand was intermittently entrained from the bed and ejected upwards into the water column. Although the intermittency appeared to be related to the waves, not every wave initiated a suspension event. The intermittency leads to unacceptably large amounts of leakage when computing energy spectra, thus we avoid frequency-domain analyses of the data and instead use wave-by-wave and other statistical methods.

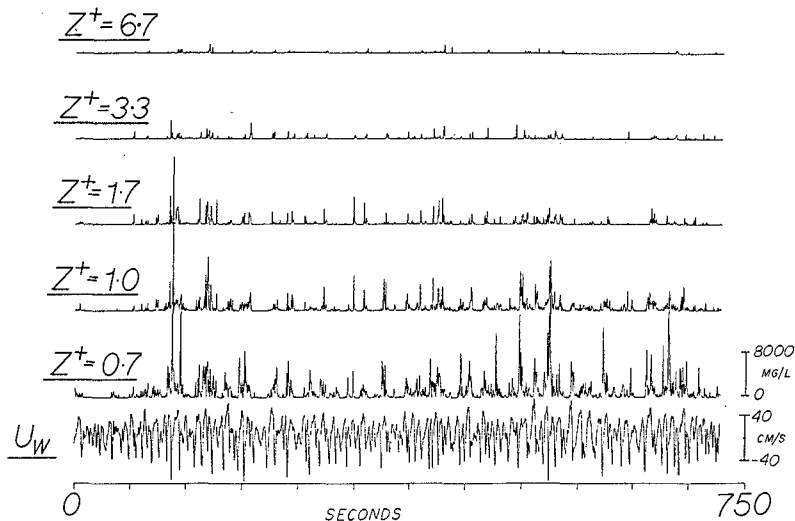


Figure 2. Time series of wave-orbital velocity (U_w) and concentration at 5 elevations above the bed. Elevation is nondimensionalized by the ripple height (3 cm).

Wave-By-Wave Analyses

The shapes of individual sediment clouds are shown in Figure 3 for two elevations above the bed. For these plots, zero-downcrossings of on-offshore velocity were used to identify 123 individual waves in the 12-min record, but waves were selected for analysis only if the concentration at $z = 1$ cm, which was the lowest usable bin, exceeded a certain threshold value. In this way, 26 well-developed sediment pulses were chosen for display. Also shown are the corresponding cycles of zero-mean velocity (U_w) measured at $z = 20$ cm. Note that a lot of the "noise" in the plots is due to the fact that wave periods varied from wave to wave and so the effective resolution also varies from wave to wave.

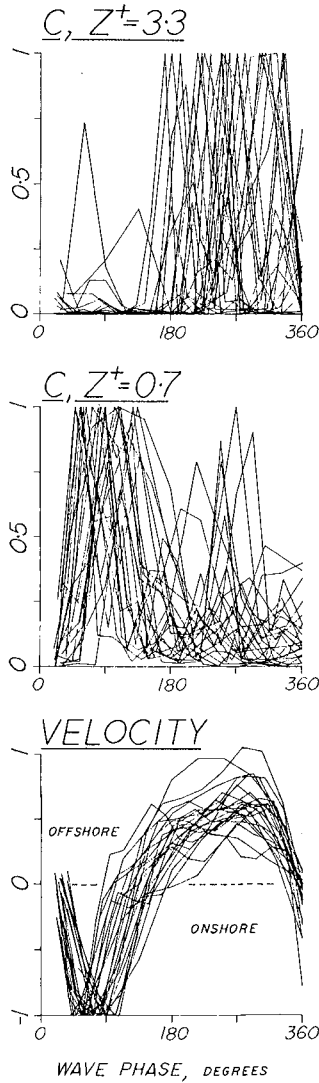


Figure 3. Wave cycles of zero-mean velocity and concentration at $z^+ = 0.7$ and $z^+ = 3.3$. The horizontal axes are wave phase in degrees, with zero phase defined as the instant of velocity zero-downcrossing. Each cycle of velocity has been nondimensionalized by the maximum onshore velocity that occurred in the cycle. Each cycle of concentration has been nondimensionalized by the maximum concentration that occurred in the cycle.

The wave-orbital velocities were skewed onshore: note that in any one cycle the onshore stroke was usually the stronger of the two, and the offshore velocities typically persist for longer than half of the wave period (Figure 3). At $z^+ = 0.7$, there are often two peaks in the concentration cycle. The first, which occurs while the orbital velocity is directed onshore, is stronger, and corresponds to the initiation of a sediment pulse at the bed. The second, which occurs while the orbital velocity is directed offshore, is weaker and corresponds to the advection back through the beam of the sediment pulse generated on the previous shoreward stroke. This second pulse is weaker since sand has settled back to the bed since the pulse was generated half a wave period previously.

At $z^+ = 3.3$ the picture is quite different: the water column is clear whilst the orbital velocity is directed onshore, and the sediment cloud only arrives at this elevation after the orbital velocity has reversed. Thus, ejection from the bed of the sediment cloud that is initiated during the onshore wave stroke only occurs after the flow has reversed.

Cross-Correlation Analyses

Cross-correlation functions were computed to investigate the phasing of the peak concentration in the sediment cloud with the peak orbital velocity.

At $z^+ = 0.7$, the peak suspension is exactly coincident with the peak onshore orbital velocity (Figure 4). In a fully rough turbulent flow, the peak bed shear stress leads the orbital velocity by approximately 10° , however the sampling rate was insufficient to resolve any such lead of the concentration over the velocity. We conclude then that, within the resolution of the data, the peak concentration very close to the bed was exactly in phase with the peak bed shear stress and that there was therefore a causal relationship between the two.

For $z^+ > 1.0$, the results of the cross-correlation analyses show that the peak concentration occurs during the offshore wave stroke and furthermore that the cloud arrives slightly earlier at higher elevations. This result is consistent with the horizontal advection of the cloud from a distant source - if the clouds were propagating upwards from the bed directly underneath the sensor then they would arrive earlier at lower elevations (e.g., Hanes and Huntley, 1986). Thus, the clouds arriving on the offshore wave stroke above the ripple tops have been released from distant (shoreward) parts of the bed.

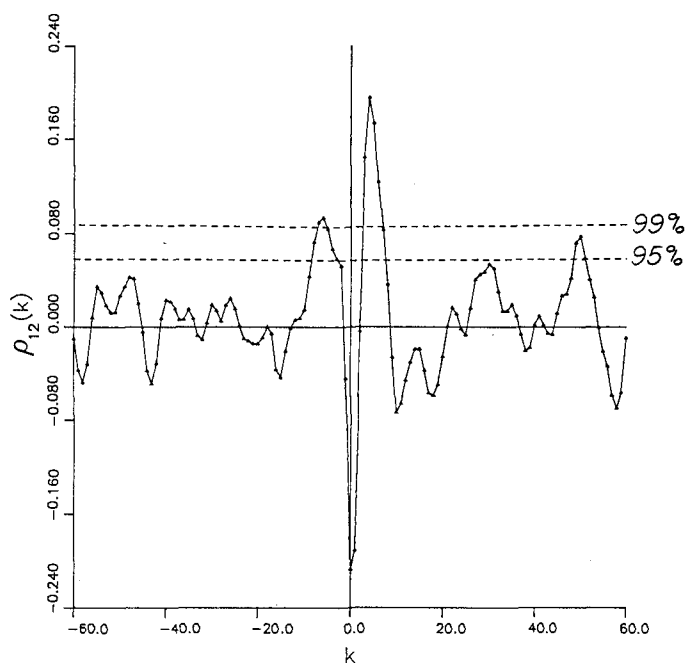


Figure 4. Cross-correlation function, ρ_w versus C at $z^+ = 0.7$. The peak concentration occurs at the same time as the peak onshore orbital velocity.

The field observations so far described are consistent with a vortex model of sediment entrainment in which sediment clouds are initiated at the bed and ejected into the flow on alternating wave strokes (e.g., Sleath, 1982). The roll-up of the cloud during the onshore wave stroke was restricted to $z < \eta$ (i.e. $z^+ < 1$): since flow visualization experiments have demonstrated that the vortex fills the ripple trough (e.g., Honji et al., 1980), it seems feasible that the ABS was looking down into a ripple trough.

Magnitude of Events

The fact that peak bed shear stress is synchronous with peak concentration in the vortex points the way to predicting the size of the sediment clouds that are ejected from the bed when the orbital velocity reverses. For this, we draw from well-known time-averaged theory in which the suspended-sediment reference concentration close to the bed is hypothesized to be a function of the skin friction that is in excess of critical stress:

$$C = \gamma_0 C_b S^n / X, \quad S = (|\tau'| - \tau_{cr}) / \tau_{cr} \quad (1)$$

(Smith, 1977). In equation (1), C is the time-averaged reference concentration which is specified at the top of the bedload layer; S is the time-averaged skin friction, τ' , in excess of the critical stress, τ_{cr} ; C_b is the bed sediment concentration; γ_0 is an empirical constant, $O(10^{-4})$. Smith and McLean (1977) used $X = (1 + \gamma_0 S)$ and proposed $n = 1$, although others have used different values for n (e.g., Shi et al., 1985). We hypothesize that, by analogy, the peak concentration in the vortex is related to the peak excess skin friction.

To evaluate the model, we replace C in equation (1) with \bar{C} the peak concentration in the vortex (i.e. from the region $z^+ < 1$), and S by $\bar{S} = (|\tau'_{cw}| - \tau_{cr}) / \tau_{cr}$, where τ'_{cw} is the total maximum skin friction, which is the sum of the maximum wave-induced and time-averaged components. τ'_{cw} was calculated by a combined-flow boundary layer model using the maximum observed half-cycle velocity and observed zero-downcrossing wave period. The roughness length was taken as proportional to the grain size of the bed sediment, thus these estimates are meant to represent the skin friction. The critical stress applicable to fully rough turbulent flow was found from a classical Shields curve, which has been shown to apply to rippled beds in combined wave and current flow provided the grain texture is used to scale the hydraulic roughness (Larsen et al., 1981). Finally, since the observed values for \bar{S} are $O(10^2)$ or less, X in equation (1) is set to 1.

Shown as the crosses in Figure 5 are the observed values of \bar{C} plotted against \bar{S} for the shoreward-directed cycle of 103 waves in which critical stress was exceeded. The line in the figure is the fit of the model to the data, which yielded an r^2 of 0.73, which is significant at the 95% level. The best-fit exponent, n , was 1.33 ± 0.23 at the 95% level, which is similar to Smith's proposed value of 1 for the time-averaged case. The corresponding value for γ_0 was 0.91×10^{-4} with a lower bound of 0.59×10^{-4} and an upper bound of 1.40×10^{-4} at the 95% confidence level.

Also shown in Figure 5 are 13 data points from offshore-directed wave strokes in which vortices were initiated at the bed. These points cluster around the model fit derived from the onshore data. This result is

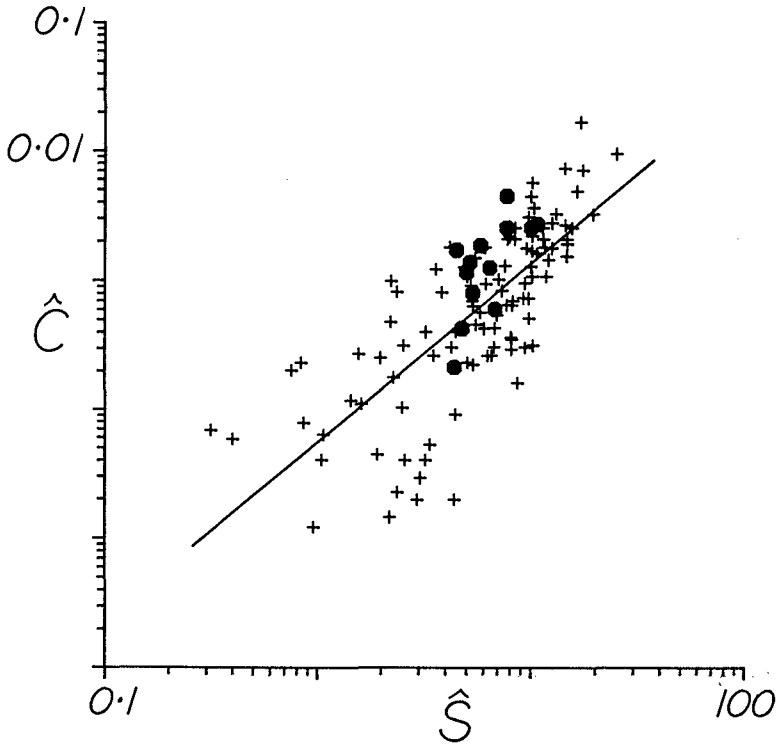


Figure 5. Fit of equation (1) to data. The crosses represent peak concentration in the vortex generated on the onshore wave stroke and the filled circles represent peak concentration generated on the offshore wave stroke.

counter to Bijker et al.'s (1976) and Hanes and Huntley's (1986) suggestions that the local acceleration governs the size of the sediment cloud generated at the bed and ejected into the flow. If this were the case, the data from the two half-cycles, which exhibit markedly different accelerations on account of the wave skewness, would not cluster in this way.

Sleath (1982) suggested a mechanism that accounts for a link between bed shear stress and concentration in the vortex: he showed that the vortex is fed by a thin bedload layer that cascades over the ripple crest and into the developing vortex; equation (1) can be used to predict the size of the sediment cloud that is ejected into the flow when the orbital velocity reverses.

Discussion

Vincent and Green (1990) showed that the correlation flux for run 2046 contributed a significant fraction of the total flux, and was sufficient close to the bed to cause reversals in the direction of the total flux (Figure 6). The size of the correlation term is dependent on the phasing of the sediment cloud relative to the wave-orbital velocity: the magnitude of the correlation varies with elevation above the bed, becoming smaller at higher elevations as the sediment clouds disperse and lose their wave-scale structure. The sign of the correlation term also changes: below an elevation approximately equal to the ripple height, the peak suspension is in phase with the onshore motion in the potential-flow region of the wave, and above this elevation the onshore motion and suspension are $\sim 180^\circ$ out of phase.

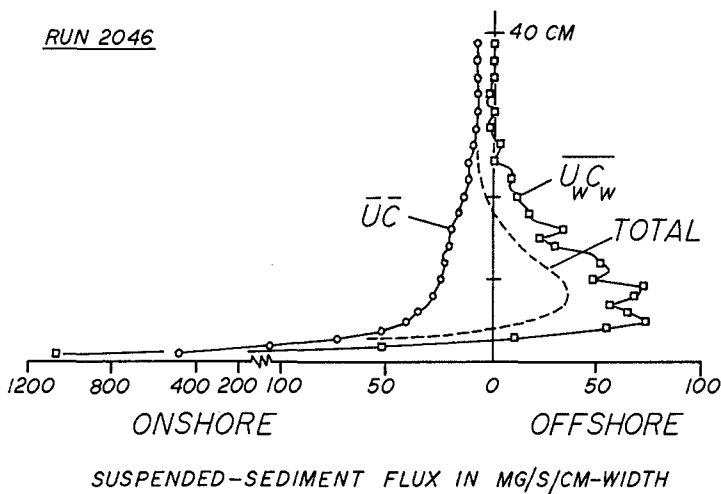


Figure 6. Vertical profiles of cross-shore suspended-sediment flux, run 2046. \overline{UC} is the mean cross-shore flux, where \overline{U} is the mean velocity and \overline{C} is the mean concentration. $\overline{UC_w}$ is the correlation flux, where U_w and C_w are the wave (i.e. zero-mean) fluctuations in velocity and concentration respectively (see Vincent and Green, 1990, for details of how the flux profiles were estimated).

Since the bed shear stress controls the size of the sediment cloud ejected from the bed when the flow reverses, the vertically-integrated correlation flux above the level of the ripple crests will be opposed to the direction of wave skewness (assuming the mean current is negligible). Furthermore, since the vertically integrated flux below the ripple crest depends upon the characteristics of the vortices and the vortices are distributed periodically in space, then there exists the possibility of a periodic divergence in sediment flux close to the bed which could govern the bedform migration and modify the net flux close to the bed.

Conclusions

The periodic vortex entrainment and release of sand from a rippled bed causes a flux of sediment that may be comparable in magnitude and opposite in sign to the mean suspended-sediment flux. Transport predictions based on the time-averaged distributions of velocity and sediment concentration will neglect this component of the sediment flux and may therefore be in serious error.

Contribution ES1768, Department of Earth Sciences,
University of Cambridge.

REFERENCES

- Bijker, E.W., E. van Hijum and P. Vellinga, 1976. Sand transport by waves. Proc. 15th Int. Conf. Coastal Eng., pp. 1149-1167.
- Chatfield, C., 1980. The Analysis of Time Series: An Introduction. 2nd Edition, Chapman and Hall, London, 268 pp.
- Grant, W.D. and O.S. Madsen, 1982. Movable bed roughness in unsteady oscillatory flow. J. Geophys. Res., 87(C1): 469-481.
- Hanes, D.M. and D.A. Huntley, 1986. Continuous measurements of suspended sand concentration in a wave-dominated nearshore environment. Cont. Shelf Res., 6(4): 585-596.
- Hom-ma, M., K. Horikawa and R. Kajima, 1965. A study on suspended sediment due to wave action. Coastal Eng. Japan, 8: 85-103.
- Honji, H., A. Kaneko and N. Matsunaga, 1980. Flows above oscillatory ripples. Sedimentology, 27: 225-229.

- Jaffe, B.E., R.W. Sternberg and A.H. Sallenger, 1984. The role of suspended sediment in shore-normal beach profile changes. Proc. 19th Int. Conf. Coastal Eng., Houston, pp. 1983-1996.
- Larsen, L.H., R.W. Sternberg, N.C. Shi, M.A.H. Marsden and L. Thomas, 1981. Field investigations of the threshold of grain motion by ocean waves and currents. Mar. Geol., 42: 105-132.
- Nakato, T., F.A. Locher, J.R. Glover and J.F. Kennedy, 1977. Wave entrainment of sediment from rippled beds. J. Wat. Port Coastal and Ocean Div., ASCE, 103(WW1): 83-99.
- Nielsen, P., 1984. On the motion of suspended sand particles. J. Geophys. Res., 89(C1): 616-626.
- Shi, N.C., L.H. Larsen and J.P. Downing, 1985. Predicting suspended sediment concentration on continental shelves. Mar. Geol., 62: 255-275.
- Sleath, J.F.A., 1982. The suspension of sand by waves. J. Hydr. Res., 20(5): 439-452.
- Smith, J.D., 1977. Modeling sediment transport on continental shelves. In: E.D. Goldberg, I.N. McCave, J.J. O'Brien and J.H. Steele (Eds.), The Sea, Volume 6, Wiley-Interscience, New York, pp. 539-577.
- Smith, J.D. and S.R. McLean, 1977. Spatially averaged flow over a wavy surface. J. Geophys. Res., 82: 1735-1746, 1977.
- Tunstall, E.B. and D.L. Inman, 1975. Vortex generation by oscillatory flow over rippled surfaces. J. Geophys. Res., 80(24): 3475-3484.
- Vincent, C.E. and M.O. Green, 1990. Field measurements of the suspended sand concentration profiles and of the resuspension coefficient γ_0 over a rippled bed. J. Geophys. Res., 95: 11,591-11,601.

MODELLING OF MULTICOMPONENT SANDY BEDS EVOLUTION
UNDER SHALLOW WATER WAVES

G. Chapalain¹ and B. Boczar-Karakiewicz²

ABSTRACT

A study of hydrodynamics and multicomponent sedimentary processes associated to unbroken water waves propagating in coastal areas is presented. For the specific case in which the waves are normally incident, weakly non-linear and dispersive, and the foreshore profile displayed a gentle slope, a model of wave-induced heterogeneous sand transport and resulting topographical and granulometric changes is developed. The general conclusion of this study is that the model presented describes some of the observed features of the sedimentology of longshore bars systems.

INTRODUCTION

Coexistence of several classes of sediments of varying sizes is a striking characteristic of coastal environments. This is due to the fact that the vectors for the sediment, i.e. rivers, transport granulates of various sizes. Coastal hydrodynamic forces subsequently redistribute the sediment within the medium. In the foreshore areas where sandbar systems develop, descriptive investigations (Sitarz, 1963; Davis and McGreary, 1965; Fox et al., 1966; Bajorunas and Duane, 1967; Mothersill, 1969; Saylor and Hands, 1970; Long et al., 1984; Forbes et al., 1986) have shown a high correlation between granulometry and bathymetry (Figures 1-2). The majority of observations reveals a localization of coarse fractions ($0 < \phi < 2$) in the troughs and fine grain fractions ($2 < \phi < 3$) at the crests. Moreover, the majority of observations shows that better sorted sediments are located at the crests and poorly sorted sediments are located in the troughs.

Various mechanisms have been invoked to account of the development of nearshore multiple longshore sand bars. These have included standing waves (Carter et al., 1973), edge-waves (Bowen and Inman, 1971), undertow and rip-cell circulation (Dyhr-Nielsen and Sorensen, 1970) and the non-linear interaction of higher harmonics in a regular incident wavetrain during shoaling (Boczar-Karakiewicz et al., 1981).

In the present paper, we focusse on the outer part of gently sloping profiles and therefore concentrate on the last mechanism which involves the non-linear evolution of progressive waves as they approach the shore. To proceed in an idealized way a two dimensional situation wherein a deepwater plane periodic wavetrain impinges on the shore is considered. It is assumed that the activity of edge-waves and breaking waves is reduced or confined close to the shore.

The model is composed of four constituents, describing processes involved in the mechanism of wave-bed interactions: (1) the surface hydrodynamics, (2) the near-bed boundary layer flow, (3) the sediment transport, and (4) the evolution of the bottom topography and composition. All four modules are linked together in a two-step morphological time-loop. In the first step, the fluid flow and the heterogeneous sediment flux are calculated over a bed configuration which is instantaneously fixed. In the second step, the temporal evolution of the seabed is calculated while keeping all variables describing the fluid and sediment flow constant. The two-step approximation is justified by observations in laboratory and in natural coastal environments (Boczar-Karakiewicz et al., 1987; Boczar-Karakiewicz and Davidson-Arnott, 1987)

¹ Institut de Mécanique de Grenoble, BP53X, 38041 Grenoble, France

² INRS-Océanologie, Université du Québec, 310 ave. des Ursulines, Rimouski, PQ, Canada

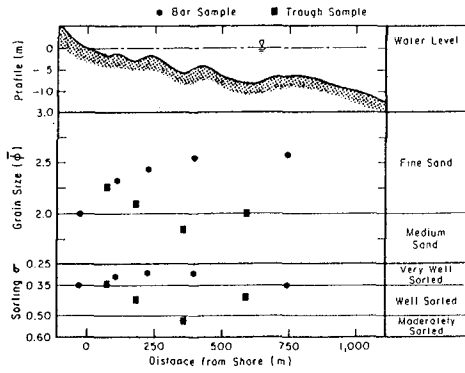


Figure 1. Measurements of mean value $\bar{\phi}$ and of the sorting σ across bar systems in Great Lakes (Saylor and Hands, 1970).

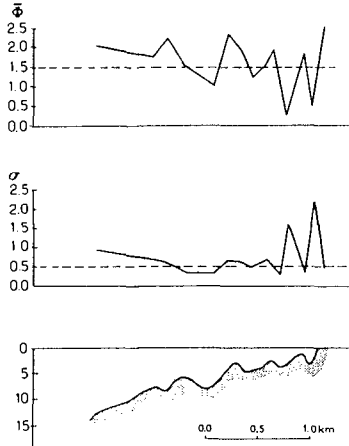


Figure 2. Spatial structures of the mean value $\bar{\phi}$ and of the sorting σ across a bar system on the north shore of the St Lawrence estuary (Long et al., 1984).

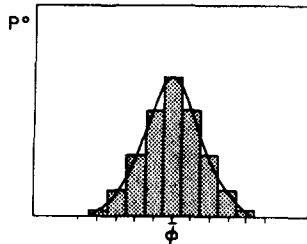


Figure 3. Initial granulometric distribution.

WAVE FIELD DESCRIPTION

The incident regular two-dimensional wavetrain is characterized by an amplitude a and a wavelength L . It propagates in a domain described by a coordinate system (x, z) . The undisturbed water level is at $z = 0$ and $h(x)$ is the water depth at point x . The vertical deviation from equilibrium of the free surface at point x at time t is $\xi(x,t)$ and $q(x,t)$ is the depth-averaged horizontal velocity. All physical variables are non-dimensionalized and scaled:

$$h = \frac{\bar{h}}{H}, \quad x = \frac{\bar{x}}{H}, \quad t = \frac{\bar{t}}{\sqrt{H/g}}, \quad \xi = \frac{\bar{\xi}}{\alpha H}, \quad q = \frac{\bar{q}}{\alpha \sqrt{gH}} \tag{1}$$

where H represents a characteristic depth, g is the acceleration due to gravity, $\alpha = a/H$ is a relative wave amplitude parameter.

The Boussinesq set of equations describing the shallow water wave is modified by a dissipative term induced by the bottom shear stress of the underlying turbulent boundary layer:

$$q_t + \xi_x + \alpha q q_x = \frac{h^2}{3} q_{xx} + h h_x q_{xt} + \frac{1}{2} h h_{xx} q_t + \frac{R}{h} q \tag{2}$$

$$\xi_t + [(\alpha \xi + h) q]_x = 0 \tag{3}$$

In the derivation of the dissipative term $(R/h)q$ it has been assumed that friction is linear, where the constant $R = 3/4 \pi f_w \alpha q_{max}$ is expressed by constant flow and friction parameters: the depth-averaged maximum velocity q_{max} at $x = 0$, and Jonsson's (1978) friction coefficient f_w

$$\left\{ \begin{array}{ll} f_w = \frac{0.0605}{\text{Log}^2 \frac{27\delta_1}{k_b}} & k_b/a_b < 1 \\ f_w = 0.24 & k_b/a_b > 1 \end{array} \right. \tag{4}$$

where δ_1 , k_b and a_b are respectively the Jonsson's length, the roughness height and half of the near-bed orbital excursion (see Grant and Madsen, 1982).

Following Lau and Barcelona (1972) and Boczar-Karakiewicz et al (1987) we are seeking for a solution of (2) and (3) where the free surface elevation ξ is presented by a simple modal decomposition

$$\xi = \xi(x,X,t) = \sum_{j=1}^2 a_j(X) \exp [i (k'_j x - \omega_j t)] + c.c. \tag{5}$$

The first-order amplitudes a_j in (5) are taken to vary on the scale of wavelengths, and therefore depend on X which is a horizontal length-scale measured in wavelength L (i.e. $X = \bar{x}/L = \beta x$ where $\beta = H/L$ is the aspect ratio for the motion assumed to be of the order of α). In equation (5) c.c. stands for the complex conjugate of the quantity just preceding it. A similar representation is postulated for q .

In (5) ω_1 is the frequency of the postulated incoming wavetrain, and $\omega_2 = 2\omega_1$ is its second harmonic, k'_1 and k'_2 are wave numbers associated with ω_1 and ω_2 respectively.

It is further assumed that the principal features of the bottom variation are gradual, and therefore, it also may be taken that h is a function $h(X)$ (i.e. $h(X) = 1 + O(\alpha)f(X)$ where f is an $O(1)$ function) of the long variable, only.

The dispersion relation results from linear theory (first-order) and reads

$$k_j'^2 = k_j^2 + i \frac{R \omega_j}{1 - \frac{\omega_j^2}{3}} \quad (6)$$

where k_j denotes the first-order wave numbers obtained when friction is ignored.

The amplitudes ξ_j , and consequently of the depth-averaged velocities q result from solvability conditions for the second-order approximation (Lau and Barcilon, 1972)

$$\begin{cases} a_1 X + H_1(X) a_1 + S_1(X) \exp\left(\frac{\Delta k^I X}{\beta}\right) \exp\left(-i \frac{\Delta k^R X}{\beta}\right) a_1 a_2^* = 0 \\ a_2 X + H_2(X) a_2 + S_2(X) \exp\left(\frac{\Delta k^I X}{\beta}\right) \exp\left(i \frac{\Delta k^R X}{\beta}\right) a_2^* = 0 \end{cases} \quad (7)$$

where * denotes complex conjugation, $\Delta k' = \Delta k^I + i \Delta k^R = k_2' - 2k_1'$, H_1 , H_2 , S_1 and S_2 are known functions of X .

As shown in (6) and (7), the essential modifications induced by a linear friction term appear in the first-order dispersion relation (6). The non-linear equations (7) for the amplitudes a_j ($j = 1, 2$) remain identical when compared to the frictionless model (see Lau and Barcilon, 1972; Boczar-Karakiewicz et al., 1987), except that in all coefficients the frictionless wave-number k_j has to be replaced by k_j' .

For a chosen frequency ω_1 of the incident wave the set of equations (7) has to be completed by the initial values at $X = 0$:

$$a_1(0) = 1; \quad a_2(0) = 0 \quad (8)$$

reflecting the assumption that the incoming regime is composed of a single-frequency wavetrain.

The coupled system of non-linear evolution equations (7) supplemented by (8) are solved numerically using a stable and accurate fourth-order Runge-Kutta method.

WAVE-INDUCED NEAR-BED BOUNDARY LAYER PROCESSES

The governing equations for the near-bottom flow with suspended sediment are simplified by several assumptions. It is assumed that

- the suspended sediment concentration is sufficiently low to neglect particle interactions, but high enough to represent the mixture as a continuum,
- the fluid is newtonian,
- the inertia of the particles is assumed to be small and thus the sediment velocity is equal to the fluid velocity minus the particle fall velocity.

Completing the previous assumptions by Boussinesq's formulation of the Reynolds shear stress and the turbulent mass flux, the sediment-laden flow may be approximately described by the following system of equations

$$\frac{\partial u}{\partial t} = -\frac{1}{\rho_f} \frac{\partial p}{\partial x} + \frac{\partial}{\partial z} \left(\nu_t \frac{\partial u}{\partial z} \right) \quad (9)$$

$$\frac{\partial c(K)}{\partial t} = w_f(K) \frac{\partial c(K)}{\partial z} + \frac{\partial}{\partial z} \left(\gamma_t(K) \frac{\partial c(K)}{\partial z} \right) \quad (10)$$

$$\rho = \rho_s C + (1-C) \rho_f, \quad C = \sum_{K=1}^{KM} c(K) \quad (11)$$

where u denotes the horizontal fluid velocity inside the boundary layer, p is the pressure, $c(K)$ is the volumetric concentration of suspended sediment of class K , KM is the number of classes, ρ is the density of the fluid-sediment mixture with ρ_f and $\rho_s (= 2.65)$ denoting respectively the fluid and sediment density, ν_t and $\gamma_t(K)$ are respectively the eddy viscosity and diffusivity of sediment of class K and $w_f(K)$ is the sediment fall velocity which can be determined as a function of the radius $r(K)$ of the sediment particles of class K by the Gibbs et al.'s (1971)

$$w_f(K) = \frac{-3\mu_f + \sqrt{9\mu_f^2 + g r(K)^2 \rho_f (\rho_s - \rho_f) (0.015476 + 0.19841 \cdot r(K))}}{\rho_f (0.011607 + 0.14881 r(K))} \quad (12)$$

(Notice that all the physical quantities are expressed in c.g.s. units and μ_f is the fluid dynamic viscosity).

The closure of the set of equations (9), (10), and (11) can be achieved at different levels of sophistication. For example a local "quasi-equilibrium" second-order closure is achieved by adding analytical expressions for the eddy viscosity ν_t and for the eddy diffusivity γ_t and two transport equations for the turbulent macroscale Λ and the turbulent kinetic energy q^2 (Sheng and Villaret, 1989).

Boundary conditions at the upper and lower limit of the boundary layer must be satisfied.

At the upper limit of the boundary layer it is required

(i) the mean horizontal velocities u to match the free stream velocity U_b (at $z = -h$) of the main water body,

$$u = U_b = \frac{\alpha}{2} \left\{ \sum_{j=1}^2 \left(1 - \frac{\beta^2 h^2 k_j^2}{6} \right) \left(-\frac{\omega_j}{k_j} \right) a_j(X) \exp \left[i(k_j x - \omega_j t) \right] + c.c. \right\} \quad (13)$$

(ii) the vanishing of all turbulence-related characteristics and suspended sediment concentration.

At the lower limit of the boundary layer it is required

(i) to provide a near-bed mean velocity condition,

(ii) to provide a turbulent macroscale length model,

(iii) the vanishing of the turbulent energy flux,

(iv) to estimate the near-bed flux of sediment particles into the suspension. Numerous fluorescent or radioactive tracer measurements have revealed the existence of mixture in the topmost sediments. Conceptually, this mixing layer lends support to the idea of modelling the bottom by a juxtaposition of elementary boxes, whose vertical dimension will henceforth be related to the depth of the shifted sand. This thickness is correlated with the local hydrodynamic conditions and therefore the characteristics of boxes should vary in space. Given the limitations of the global modelling procedure, however, it will be assumed that the number of particles contained in an elementary box remains constant. In an erosion zone the problem arises of replacing the sediment removed from the control volume. One possibility consists of refilling with underlying sediment of the initial composition. This procedure, however, tends to drive the granulometric distribution back to the initial distribution, which ought in principle to be "forgotten" as the calculation proceeds, i.e. with increasing time. There is another alternative for the approach of equilibrium. Replacement can be achieved with sediment whose characteristics are identical with those calculated at the current time step, i.e. with a number of particles slightly smaller to the INP (hereinafter referred to as INP) in each box. In the initial stage, i.e. on an undeformed bed, it is assumed that the spatial composition of the sediment substrate is uniform throughout. The population of each class present is taken to be represented by a normal distribution. It will be denoted $P^0(K)$, where K designates the class. This weight frequency distribution is characterized by its mean value ϕ^0 and its standard deviation σ^0 . The number of classes is fixed at nine with a ϕ -interval equal to $1/2$ (Figure 3). This distribution law was

selected because it represents the granulometric response to random hydrodynamic processes. The Initial Number of Particles in each class is then given by

$$N^0(K) = INP \cdot P^0(K) \quad (15)$$

The consequence of the superficial mixed layer concept on the near-bed flux of sediment particles into the suspension is an hypothesis of independence between the different fractions during the process of extraction and suspension of particles from the bed. Consequently, the near-bed sediment flux for each class K can be modelled by the Svendsen's (1977) pick-up function characterized by two peaks located at the free velocity reverses (i.e., phases when the vortices are released in the bottom boundary layer) and expressed as

$$p(K,t) = p_d(K) + \frac{p_d(K)}{1+\mu} \sum_{n=1}^m \frac{2(m!)^2}{(m+n)! (m-n)!} \left\{ \cos n(\omega t - \varphi^+) + \mu \cos n(\omega t - \varphi^-) \right\} \quad (14)$$

where the parameter $\mu = (U_b^-)^2 / [U_b^+]^2$ allows an account of non-linearities of the wave field. In (14) m is a parameter controlling the skewness of the peaks, superscripts $+$ and $-$ refer to the phases (φ^+ , φ^-) of the velocity reverse following respectively the maximum and the minimum outer flow velocity; the quantity denoted by $p_o(K)$ is equal to $\bar{C}_0(K) \cdot w_f(K)$ where $\bar{C}_0(K)$ is the mean bottom concentration is given by Nielsen (1979) as

$$\bar{C}_0(K) = 0.028 \left(\psi'(K) - \psi'_c(K) \right) \frac{2}{\pi} - \arccos \left(\frac{\psi'_c(K)}{\psi'(K)} \right)^{1/2} \quad (15)$$

with $\psi'(K)$ and $\psi'_c(K)$ are respectively Madsen and Grant's (1976) wave-extended Shields parameter and its critical value (Figure 4).

Conclusions resulting from numerical experiments using the coupled local "quasi-equilibrium" second-order turbulent closure model in single class version justify a simplification of the modelling procedure for a flow with a low sediment concentration (Chapalain, 1988; Boczar-Karakiewicz et al., 1988). In this procedure, the flow dynamics and the sediment concentrations are modelled separately. In pursuit of our goal consisting in studying heterogeneous sediment transport under wavetrains (i.e. in a two-dimensional configuration), a simple modelling which capture the main features of the flow is preferable to more complicated numerical solutions like this one mentioned above. To proceed in this way, we decide to test the capacity of a first-order decoupled model consisting in a constant (in time and space) effective eddy viscosity model.

The hydrodynamics of the wave-induced boundary layer flow is now described by an analytical approach using the following Reynolds averaged momentum equation

$$\frac{\partial u}{\partial t} + u \frac{\partial u}{\partial x} - \frac{\partial u}{\partial \eta} \int_0^\eta \frac{\partial u}{\partial x} d\eta = \frac{\partial U_b}{\partial t} + U_b \frac{\partial U_b}{\partial x} + \frac{1}{l^2} \left[v_t \frac{\partial u}{\partial \eta} \right] \quad (16)$$

where $\eta = z/l$ and l is a characteristic length scale of the boundary layer.

The required effective eddy-viscosity closure is obtained by applying following model

$$v_t = [U] \cdot [L] \quad (17)$$

where $[U]$ and $[L]$ are characteristic scales for the velocity and turbulent eddies respectively.

The velocity scale $[U]$ is estimated by the friction velocity

$$u^* = \sqrt{\frac{\tau_{bm}}{\rho}} \quad (18)$$

where τ_{bm} denotes the maximum bottom stress and the length scale $[L]$ in (17) is assumed to be the ripple height (Nielsen et al., 1982).

A classical perturbation analysis provides explicit expressions for the first- and second-order horizontal mean velocity. Both expressions are defined in Appendix.

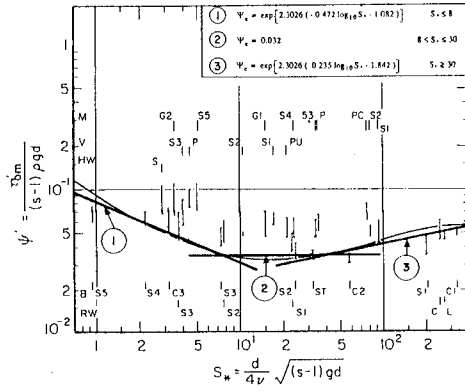


Figure 4. Madsen and Grant's wave extended Shields (1976) diagram.

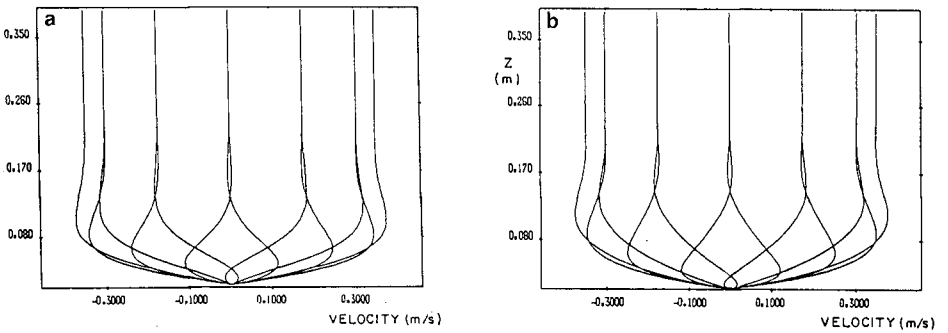


Figure 5. Mean velocity profiles calculated by the constant, time-independent eddy viscosity model [a], by the second-order turbulence closure model [b].

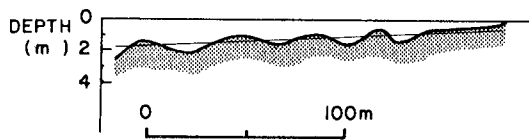


Figure 6. Observed bathymetric profile of Wasaga Beach.

The predicted velocity profiles for an oscillatory flow whose maximum velocity U_0 and period are 0.35m/s and 10s respectively are shown in Figure 5 for every 30° of the wave-cycle. Comparison with results of the second-order turbulent closure model shows a satisfactory agreement.

A simple analytical model can now be derived for prediction of sediment concentration for each independent class in the wave-induced near-bed boundary layer flow.

The time-periodic and modally decomposed (Nielsen, 1979) sediment concentration c ,

$$c(K) = \sum_n^n c_n(K) \exp(in\omega t) \quad (19)$$

is assumed to satisfy the advective-diffusive equation (10) and the above boundary conditions.

Following the original solution of Nielsen (1979) the spatial and temporal sediment concentration is described by an explicit analytical expression $c(K, X, z, t)$ (defined in the Appendix). In this expression the eddy diffusivity $\gamma_t(K)$ is assumed proportional to the eddy viscosity ν_t and dependent on the particle size according to Van de Graaff and Roelvink's (1984) relationship involving the fall velocity of the form

$$\gamma_t(K) = \frac{1}{1 + 23 \cdot w_f(K)} \quad (20)$$

SEDIMENT TRANSPORT RATE AND RELATED SEABED RESPONSE

The wave-induced, time-averaged flux of sediment of class K is estimated by the product of the instantaneous sediment concentration and the sediment velocity vector

$$Q_J(K) = \frac{1}{T} \int_0^T \int_0^\delta u(X, z, t) c(K, X, z, t) dz dt \quad (21)$$

where subscript J denotes the box index resulting from the spatial discretization (i.e. $X = J \Delta X$)

In order to analyse the quantitative contributions of time-independent and time-dependent flow velocities and concentrations to the sediment flux Q , the product u.c. in (21) will be formally decomposed

$$u(X, z, t) \cdot c(X, z, t) = \left\{ \alpha u^{(1)}(X, z, t) + \alpha^2 \beta [u_s(X, z) + u_p^{(2)}(X, z, t)] \right\} \cdot [\bar{C}(X, z) + c(X, z, t)] \quad (22)$$

where $u^{(1)}$ and $u_p^{(2)}$ denotes the first and second-order periodic velocity components, u_s is the time-averaged velocity, \bar{C} denotes the mean concentration and c is the instantaneous concentration.

In the following we are separating the local sediment flux into two components

$$Q_J(K) = Q_{m_J}(K) + Q_{n_J}(K) \quad (23)$$

where $Q_{m_J}(K)$ denotes the contribution of time-independent quantities and $Q_{n_J}(K)$ the contribution of time-dependent quantities.

The component $Q_{m_J}(K)$ is

$$Q_{m_J}(K) = \frac{S_J(K)}{T} \int_0^\delta \bar{C}(K, X, z) \cdot u_s(X, z) dz \quad (24)$$

where $S_J(K)$ controls the threshold of sediment movement and defined by

$$S_J(K) = \begin{cases} 0 & \text{if } \psi'(K) < \psi'_c(K) \\ 1 & \text{if } \psi'(K) > \psi'_c(K) \end{cases} \quad (25)$$

Choosing now for the mean sediment concentration in (24) the following expression (Rouse, 1937)

$$\bar{C}(K, X, z) = \bar{C}_0(K, X) \exp(-D(K) z) \quad (26)$$

with $D(K) = w_f(K) / \gamma_s(K)$

and substituting in (24) the mass transport velocity defined in Appendix, the component $Q_{mj}(K)$ may also be expressed by an explicit formula given in Appendix.

Proceeding now in a similar way with time-dependant quantities in (22) the component $Q_{nj}(K)$ may also be made explicit and the related expression is given in Appendix.

The "effective" sediment transport rate is obtained by weighting this latter quantity by the composition of the sediment substrate. Finally, the notion of "numerical" sediment rate is introduced for each class, such that

$$N_J^T(K) \simeq Q_J^T(K) \cdot P_J^T(K) / (4\pi r(K))^3 \quad (27)$$

The spatio-temporal evolution of the granulometric distributions is described by the continuity relation for each class of sediment. This procedure allows the calculation of the number of particles of each class present in the box J after exposure for a time ΔT to the ambient hydrodynamic conditions, i.e.

$$N_J^{T+\Delta T}(K) = N_J^T(K) + (N_{J,f}^T(K) - N_{J+1}^T(K)) \quad (28)$$

The new updated local distribution for the different sediment classes is determined by

$$P_J^{T+\Delta T}(K) = \frac{N_J^{T+\Delta T}(K)}{\sum_{K=1}^{KM} N_J^{T+\Delta T}(K)} \quad (29)$$

The total instantaneous sediment transport rate is the sum of the individual transport rates corresponding to each class:

$$Q_J^T = \sum_{K=1}^{KM} Q_J^T(K) \quad (30)$$

The overall variation in depth is calculated using an equation of conservation of matter expressed in the form

$$h_J^{T+\Delta T} \simeq h_J^T - \Delta T \cdot [Q_{J-1}^T - Q_{J+1}^T] / (\Delta X \cdot C_p) \quad (31)$$

where C_p is the concentration of the compact bed arbitrary taken equal to 0.74 like for the idealized rhomboedric arrangement.

APPLICATION

In order to contain the high costs of computation, the application of multicomponent modelling will be limited to the case of Wasage Beach located along the shore of Georgian Bay in Lake Huron. On account of its location in a narrow bay this area is hydrodynamically very well-controlled with waves whose period and height are respectively about 5s and 1m propagating exclusively from the north. The bathymetric profile illustrated in Figure 6 is characterized by a mean slope of 0.5% modulated by four bars. The granulometric analysis leads to consider a mean sediment grain diameter equal to 0.35mm. Even though local measurements of the granulometric distribution are not available on this profile, as an approximation one will apply here the synthetic results of Saylor and Hands (1970) pertaining to Great Lakes (Figure 1).

The initial granulometric curve has an average value of $\bar{\phi}^0 = 1.5$ (corresponding to a sediment of mean diameter equal to 0.35 mm) and a root mean square deviation $\sigma^0 = 0.5$. The main parameters associated to this initial distribution are listed in Table 1.

In order to facilitate the comparison with the single class modelling, the results from the single class version will be placed beside those of the multiclass model.

The sediment transport rate distribution across the foreshore zone is shown in Figure 7-I. It displays slightly lower transport rates magnitude than for the single class case (Figure 7-II). The horizontal gradients are very close in both cases. For this reason, a very similar bathymetric response is obtained, generated on a characteristic time scale of the deformation that closely resembles that obtained in the single case version.

Figure 8 illustrates the spatial structure of the mean value and the root mean square deviation of the granulometric curve. Comparison of these results with the associated topography reveals:

(i) a drift of the the granulometric curve towards fine sediments at the crest and towards coarse sediments in the troughs (Figure 8a). The simulation is in agreement with the observations described in the introduction (Figures 1-2). Characteristic granulometric curves for crests and troughs are shown in Figure 9 (curves B and C, respectively).

(ii) degradation of the sorting at the crests combined with an improvement in the troughs (Figure 8b). This specific result is contradiction with all the observations, apart from some (outer zone) of those of Long et al. (1984) (Figure 2)

CONCLUSION

Multicomponent simulation is an attempt to provide as realistic as possible a model for problems of sedimentation. From a quantitative point of view, this approach, although highly simplified, allows an appreciation of the impact of a fairly actual granulometric distribution on the transport of sediment across the foreshore profile. The global effect (i.e. on sediment transport rates and seabed response) proves insignificant on account of the crudeness of the modelling. The second, more novel, point which concerns the simulation of the spatial adjustment of the granulometric characteristics across the profile, shows that the model gives correct representation of what happens in nature as to the confinement of fine fractions at the crests of the bars and coarse fractions in the troughs between the bars. About the sorting of sediment classes, however, the model results are in contradiction with the main body of available in situ measurements. This discrepancy may suggest that there are many difficulties remaining and related to additional effects like for example wave breaking, reflected or trapped waves. Nevertheless, further effort to verify the basis of multiclass geomorphological modelling should be devoted to collect more data in laboratory and in the field in order to clarify the pattern of the sorting of sediment distributions across the bar systems.

APPENDIX: WAVE-INDUCED VELOCITIES, SEDIMENT CONCENTRATION AND RELATED SEDIMENT TRANSPORT RATES IN THE NEAR-BED BOUNDARY LAYER

Substituting a perturbation series for u

$$u = \alpha u^{(1)} + \alpha^2 u^{(2)} + \dots$$

into the Reynolds equation (16), the first-order oscillatory velocity component is

$$u = \alpha u^{(1)} = \alpha \operatorname{Re} \sum_{j=1}^2 U_j \exp [-(1+i) \eta_j] \quad (32)$$

$$\text{where } \eta_j = z / l_j = z / \sqrt{\frac{2\nu_t}{\omega_j}}$$

On account of the smallness of the imaginary part of the wave number k_j^I in geophysical conditions (Chapalain, 1988) the second-order steady velocity identified to the mass transport

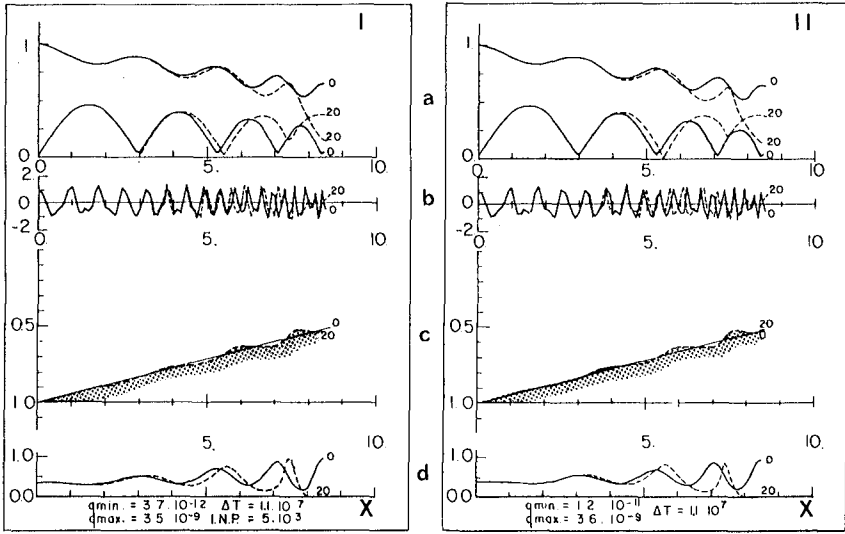


Figure 7. Multiclass model run (I) for Wasaga Beach, compared with single class model (II). (a) Two first harmonic component amplitudes non-dimensionalized by the wave amplitude. (b) Free surface elevation at a given time non-dimensionalized by the wave amplitude. (c) Near-shore topography non-dimensionalized by the incident water depth. (d) Total sediment transport rate Q . The horizontal distance X is measured in incident wavelengths.

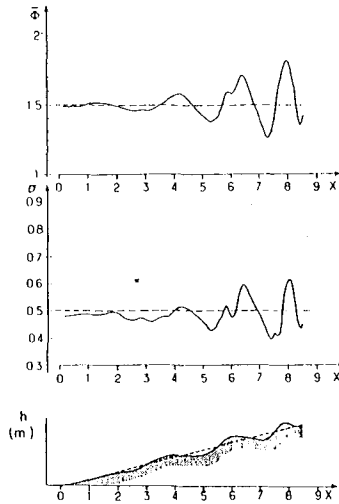


Figure 8. Calculated spatial structures of the mean value $\bar{\phi}$ and of the sorting σ across Wasaga Beach foreshore profile.

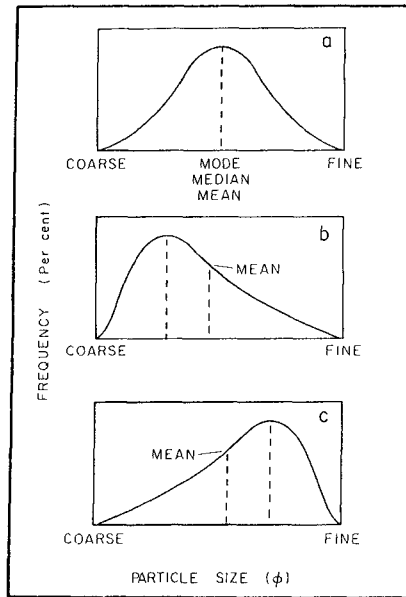


Figure 9. Typical granulometric distributions (A: initial normal distribution, B: characteristic distribution for troughs, C: characteristic distribution for the crests).

ϕ (K)	d (mm)	W_f (m/s)	ψ_c' (K)	p^o (K)
-0.5	1.4	0.207	0.0367	0.00013383
0.0	1.0	0.153	0.0324	0.00443186
0.5	0.7	0.110	0.0320	0.05399113
1.0	0.5	0.0763	0.0320	0.24197145
1.5	0.35	0.0509	0.0338	0.39894347
2.0	0.25	0.0325	0.0432	0.24197145
2.5	0.177	0.0197	0.0552	0.05399113
3.0	0.125	0.01136	0.0705	0.00443186
3.5	0.088	0.00620	0.0901	0.00013383

Table 1. General Characteristics of sediment particles making up the multiclass substrate at Wasaga Beach in the numerical simulation.

velocity (Longuet-Higgins, 1953) may be approximated by

$$u_s = \frac{\alpha^2 \beta}{4} \sum_{j=1}^2 \left[1 - \frac{1}{6} \beta^2 k_j^R n^2 \right] \frac{\omega_j}{k_j^R} |a_j|^2 \exp\left(\frac{2k_j^I}{\beta}\right) H_j^I(\eta_j) \quad (33)$$

$$\text{where } H_j^I = -8 \exp(-\eta_j) \cos \eta_j + 3 \exp(-2\eta_j) + 5 \quad (34)$$

For convenience we omit to specify the sediment class index K in the following expressions. The expression for spatial and temporal evolution of the suspended sediment concentration is

$$c(X, z, t) = \sum_{n=0}^{\infty} \frac{\bar{C}_0}{1+\mu} \cdot \frac{a'_n}{\alpha_n} \left(\exp(-i n \Phi^+) + \mu \exp(-i n \Phi^-) \right) \exp\left(-\frac{w_f}{\gamma_t} \alpha_n z\right) \exp(in\omega_1 t) \quad (35)$$

$$\text{where } a'_n = \frac{2 (m!)^2}{(m+n)! (m-n)!}$$

$$\text{and } \alpha_n = \frac{1}{2} + \sqrt{\frac{1}{4} + i \frac{n\omega\gamma_t}{w_f}}$$

The time-independent sediment transport rate Q_m is

$$Q_m(X) = \frac{1}{4} \alpha^2 \beta \bar{C}_0(X) \sum_{j=1}^2 \frac{-8\delta_j}{(D\delta_j-1)^2 + 1} \left[\exp(D\delta_j-1)\eta_{sj} \left((D\delta_j-1) \cos \eta_{sj} + \sin \eta_{sj} \right) + 1 \right] \\ + \frac{3\delta_j}{D\delta_j-2} \exp[(D\delta_j-2)\eta_{sj}] + \frac{5}{D} \exp[-D\eta_{sj}] \quad (36)$$

The time-dependent sediment contribution Q_n in an integral form is

$$Q_n(X) = \frac{\delta}{2} \operatorname{Re} \left\{ \sum_{j=1}^2 \frac{\bar{C}_0}{(1+\mu)\alpha_j} U_j a'_j \left(\exp(-i j \Phi^+) + \mu \exp(-i j \Phi^-) \right) \int_0^{\delta} \exp\left(-\frac{w_f \alpha_j z}{\gamma_t}\right) (1 - \exp(-(1-i)\beta_j z)) dz \right\} \quad (37)$$

where $\eta_{sj} = \delta/\delta_j$

This expression can be made explicit after some tedious algebra (Chapalain, 1988).

REFERENCES

- Bajorunas, L. and Duane, D.B. (1967) Shifting offshore bars and harbor shoaling. *J. Geophys. Res.*, Vol 72, (24), 6195-6205.
- Boczkar-Karakiewicz, B., Paplinska, B. and Winiecki, J. (1981) Formation of sandbars by surface waves in shallow water. Laboratory experiments. *Rozprawy Hydrotechniczne*, Vol 41, 11-25.
- Boczkar-Karakiewicz, B., Bona, J.L. and Cohen, D.L. (1987) Interaction of shallow water wave and bottom topographies. in: *Dynamical Problems in Continuum Physics*. Springer Verlag, Vol.4, 131-176.
- Boczkar-Karakiewicz, B., Chapalain, G. and Temperville A. (1988) Sand bars formation by waves in coastal zones. *Proc. of the 2nd International Symposium on Water Wave Research*, Hannover, 89-102.
- Boczkar-Karakiewicz, B. and Davidson-Arnott, R.G.D (1988) Near-shore bar formation by non-linear wave processes-a comparison of model results and field data. *Marine Geology*, Vol.77, 287-304.

- Bowen, A.J. and Inman, D.L. (1971) Edge waves and crescentic bars. *J. Geophys. Res.*, Vol.76, 8662-8671.
- Carter, T.G., Liu, P.L.F. and Mei, C.C. (1973) Mass transport by waves and offshore sand bedforms. *J. Waterways, Harbour, Coastal Eng.*, Vol.99, 165-184.
- Chapalain, G. (1988) Etude hydrodynamique et sédimentaire des environnements littoraux dominés par la houle. Thèse de Doctorat de l'Université Joseph Fourier-Grenoble I.
- Davis, R.A. and McGreary, F.R. (1965) Stability in nearshore bottom topography and sediment distribution, southeastern lake Michigan. Pub. N° 13, Great Lakes Research Division. 222-231, 1965.
- Dyhr-Nielsen, M. and Sorensen, T. (1970) Some sand transport phenomena on coasts with bars. *Proc. of the 12th International Conference on Coastal Engineering*, 855-863.
- Forbes, D.L., Frobels, D., Heffler, D.E., Dickie K. and Shiels C. (1986) Surficial geology, sediment mobility, and transport processes in the coastal zone at two sites in the southern Gulf of St Lawrence: Pte Sapin (N.B.) and Stanhope Lane (P.E.I). C2S2 Report 20.
- Fox, W.T., Ladd, J.W. and Martin, M.K. (1966) A profile of the four moment measures perpendicular to a shore line, south haven, Michigan. *J. sedimentary Petrology*, Vol. 36, (4), 1126 - 1130.
- Gibbs, D., Matthews, M.D. and Link, D.A. (1971) The relationship between sphere size and settling velocity. *J. Sedimentary Petrology*, Vol.41, 1, 7-78.
- Graaff, J. van de and Roelvink, J.A., (1984) Grading effects in concentration measurements. *Proc. of the 19th Conference on Coastal Engineering*, 1618-1634.
- Grant, W.D. and Madsen, O.S. (1982) Movable bed roughness in unsteady oscillatory flow. *J. Geophys. Res.*, Vol. 87, C1, 469-481.
- Jonsson, I.G. (1978) A new approach to oscillatory rough turbulent boundary layers. Technical University of Denmark, Inst. of Hydrodynamics and Hydraulic Engineering. Ser. Pap. 17, p.87, 1978. (Also published in *Ocean Eng.*, 7, 109-152, 1980).
- Lau, J. and Barcelon V. (1972) Harmonic generation of shallow water waves over topography. *J. Phys. Oceanography*, 2, 405-410.
- Long, B.F., Boczar-Karakiewicz, B. and Drapeau, G. (1984) Transport sédimentaire dans un système de barres d'avant-côte. Abstract book, C0411, 27ème International Geology Congress, Moscow.
- Longuet-Higgins, M.S. (1953) Mass transport in water waves. *Phil. Trans. Roy. Soc. Lond.*, A, 245, 535-591.
- Madsen, O.S. and Grant, W.D. (1976) Quantitative description of sediment transport by waves. *Proc. of the 19th Conference on Coastal Engineering*, 1093-1112.
- Mothersill, J.S. (1969) A grain size analysis of longshore - bars throughs , lake superior, Ontario. *J. Sedimentary Petrology*, Vol. 39, (4), 1317-1324.
- Nielsen, P. (1979) Some basic concepts of wave sediment transport. Technical University of Denmark, Inst. of Hydrodynamics and Hydraulic Engineering, Ser. Pap. 20, p. 160.
- Nielsen, P., Green, M.O. and Coffey, F.C. (1982) Suspended sediment under waves. Coastal Studies Unit Technical Report 82/6.
- Rouse, H. (1937) Modern concepts of mechanics of turbulence. *Trans. Am. Soc. Civ. Eng.*, Vol.102, 463-543.
- Saylor, J.H. and Hands, E.B. (1970) Properties of lonshore bars in the Great Lakes. *Proc. of the 12th International Conference on Coastal Engineering*, 839-853.
- Sheng, Y.P. and Villaret, C. (1989) Modeling the effects of suspended sediment stratification on bottom exchange processes. *J. Geophys. Res.*, Vol.94, C10, 14429-14444.
- Sitarz, J.A. (1963) Contribution à l'étude de l'évolution des plages à partir de la connaissance des profils d'équilibre. Travaux du C.R.E.O., Tome V, Fasc. II, III, IV.
- Svendsen, I.A. (1977) A model of sediment motion under waves. Internal Research Note, Technical University of Denmark, Inst. of Hydrodynamics and Hydraulic Engineering.

CHAPTER 168

NEARSHORE SEDIMENT FLUX AND BOTTOM BOUNDARY DYNAMICS THE CANADIAN COASTAL SEDIMENT TRANSPORT PROGRAMME (C-COAST)

Brian Greenwood¹, Philip D. Osborne¹
Anthony J. Bowen², David G. Hazen²
Alex E. Hay³

ABSTRACT

The Canadian Coastal Sediment Transport Programme (C-COAST) is designed to increase our knowledge of the dynamics of non-cohesive shorefaces through field measurement of sediment transport and the response of the bottom boundary under combined waves and currents. Suspended sediment concentrations are measured using Optical Backscatterance Suspended Solids Sensors (OBS-1P - D & A Associates) and a new multi-frequency, Remote Acoustic Sediment Transport system (RASTRAN). Near-bed velocities are measured using electromagnetic and electroacoustic flowmeters; cross-products of velocity and concentration provide estimates of sediment flux. The bottom boundary response is determined at the roughness (bedform) scale using a High Resolution Remote Tracking Sonar (HRRTS II) and at the shoreface scale using Depth-of-Activity rods and standard survey. Suspended sediment flux is extremely episodic, responding to individual waves, wave groups and low frequency motions, including mean flows. A significant time-dependent transport is revealed in the vertical structure. Net transport includes contributions from wind waves, low frequency waves and mean flows. A sediment transport balance controlling local slopes can therefore be achieved by spatial and/or temporal divergence of these components. Reservations must exist with respect to transport models which use depth and/or time averaged terms and which fail to recognize the distinct components of fluid motion contributing to the total sediment transport.

-
1. Scarborough College Coastal Research Group, University of Toronto, Scarborough, Ont., Canada, M1C 1A4.
 2. Dept. of Oceanography, Dalhousie University, Halifax, N.S., Canada, B3H 4J1.
 3. Dept. of Physics, Memorial University of Newfoundland, St. John's, Nfld., Canada, A1B 3X7.

INTRODUCTION

Perhaps the most intransigent problem restricting our understanding of coastal behaviour is the relationship between local sediment flux rates, sediment flux divergence and the response of the bottom boundary. Laboratory experimentation has been extensive and a number of parameterizations of the system have been proposed; however, they fail when applied to the prototype (see Seymour and Castel, 1989). Existing physically-based theory (e.g. Bowen, 1980a, Bailard, 1981) provide useful qualitative predictions, but include time and depth-averaged terms which remain questionable (Bowen, 1980b; Bailard, 1987). Few field data exist which have the necessary temporal and spatial resolution for evaluating either existing sediment transport theory or the underlying assumptions. A requirement in the testing of existing models and in the generation of new models is adequate field measurement of sediment transport and bottom boundary response. The Canadian Coastal Sediment Transport Programme (C-COAST) is a joint University venture, which has evolved from the Canadian Coastal Sediment Study (C²S² - Willis, 1987), and is designed specifically to measure sediment transport and the concurrent response of the bottom boundary under combined waves and currents on the shoreface. The overall objectives are to: (i) investigate the spatial and temporal behaviour of near-bed suspended sediment concentrations; (ii) compute suspended sediment fluxes and relate them to both the forcing agents and to the bottom boundary responses; (iii) investigate the mechanisms controlling the directions and rates of suspended sediment flux; (iv) understand the nature of cross-shore and alongshore sediment fluxes on barred and non-barred shorefaces. In this paper we summarize the methodologies adopted, focus on mechanisms for cross-shore suspended sediment flux and suggest implications for existing models of sediment transport and beach equilibrium.

EXPERIMENTAL DESIGN

In Phase I of the programme, four field experiments have been completed at: (i) Bluewater Beach, a single barred (1987) or double barred (1988) shoreface with a slope of 0.014 in medium-to-fine sands in Nottawasaga Bay, in the Canadian Great Lakes. (ii) Queensland Beach, Nova Scotia, a non-barred shoreface in medium sands, with a slope of 0.03-0.10 and a spring tide range of 2 m on the Eastern Seaboard of Canada. (iii) Stanhope Lane Beach, Prince Edward Island, a triple barred shoreface in medium-to-fine sands, with a micro-tidal regime in the Southern Gulf of St. Lawrence, Canada.

SEDIMENT FLUX DETERMINATION

Direct measurement of sediment flux in the field is still difficult and a wide range of techniques have been tried (for reviews of philosophy and methodology see Greenwood et al., 1979; Huntley, 1982; Horikawa, 1988; Basinski, 1989; Seymour, 1989). No reliable bedload sensor exists; however, development of reliable, high frequency response, optical and acoustic sediment concentration sensors provide, together with reliable velocity sensors, measurements of suspended sediment flux. The cross-product of velocity and sediment concentration vectors determined from "collocated" sensors is an approximation of the "instantaneous" sediment transport rate, assuming that the sediment moves at the same speed as the fluid. Time-averaging this product gives the "net" sediment transport rate. Assuming also that values of velocity and concentration are both composed of a steady (\bar{u}, \bar{c}) and an unsteady (u', c') part, then the "net" transport is:

$$\begin{aligned} \langle uc \rangle &= \langle (u + u')(c + c') \rangle \\ &= \bar{u}\bar{c} + \langle \bar{u}c' \rangle + \langle u'\bar{c} \rangle + \langle u'c' \rangle \end{aligned}$$

Since $\langle \bar{u}c' \rangle$ and $\langle u'\bar{c} \rangle$ must tend to zero then:

$$\langle uc \rangle = \bar{u}\bar{c} + \langle u'c' \rangle$$

where $\bar{u}\bar{c}$ is the "mean" transport and $\langle u'c' \rangle$ is the "flux coupling" induced by correlations between velocity and concentration (Jaffe et al., 1985). The latter can most conveniently be computed from the co-spectrum (Huntley and Hanes, 1987), which also reveals the relative importance of differing frequencies to the rate and direction of this "oscillatory" transport. Integration of the cospectrum (or part thereof) gives the "net oscillatory" (or part thereof) transport.

Such computations, however, depend upon accurate high resolution (temporal and spatial) measurements of the velocity and concentration vectors. Figure 1 illustrates a typical monitoring station used in the C-COAST programme. It consists of "collocated" vertical arrays of current and concentration sensors, together with a wave sensor, either a pressure sensor or a continuous resistance staff (see Greenwood et al., 1990 for details) and an underwater digitization and transmission system (UDATS; Hazen et al., 1988).

The structure of the local suspended sediment profile has been determined most usually from point measurements using Optical Backscatterance Suspended Solids Sensors (OBS-1P - see Downing et al., 1981; D & A, 1989). Quasi-

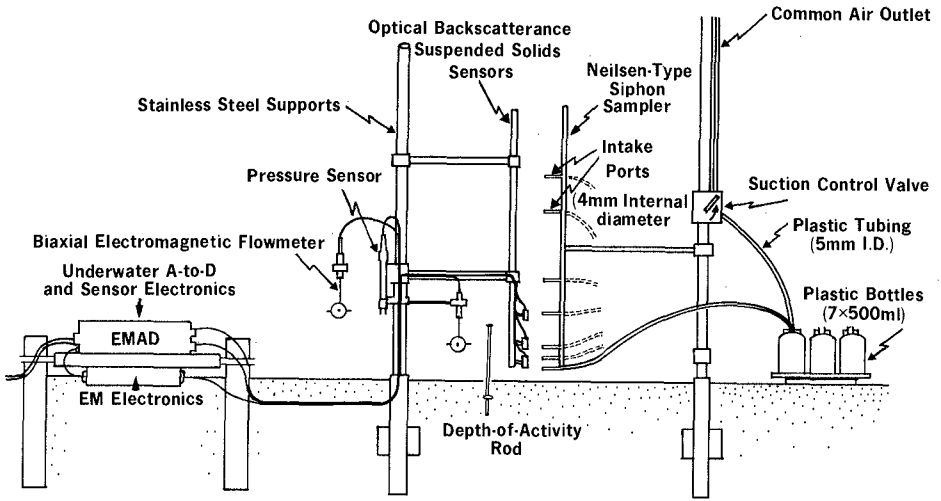


Figure 1. Typical sensor deployment configuration; note that neither RASTRAN nor HRRTS II are depicted.

continuous concentration profiles (2 cm resolution) is also possible using a new multifrequency (1, 2.5, 5 MHz) Remote Acoustic Sediment Transport system (RASTRAN, Hay et al., 1988). Direct multiple point measurements of sediment concentration are obtained using a modified Neilsen-type hydraulic sampler (Neilsen, 1984). Extensive calibrations of the optical and acoustic suspended sediment sensors have been undertaken and cross-calibrations between the two have been made in the laboratory and in the field (Figure 2 - see Greenwood et al., 1990 for details).

BOTTOM BOUNDARY DYNAMICS

The response of the bottom boundary to sediment transport has traditionally been determined at large scales using standard Survey Techniques and Depth-of-Activity Rods measured by SCUBA divers (Greenwood and Hale, 1980; Greenwood, 1987). Such techniques are restricted by environmental constraints to pre- and post-storm measurements; spatial and temporal resolution is, therefore, limited to time-averaged values and gross morphological shifts. In the C-COAST experiments, bed elevation changes have been monitored locally on a continuing basis using acoustic imaging. RASTRAN is capable of determining bottom elevations continuously to within a few centimeters, while a new High Resolution Remote Tracking Sonar (HRRTS II - see Greenwood et al.,

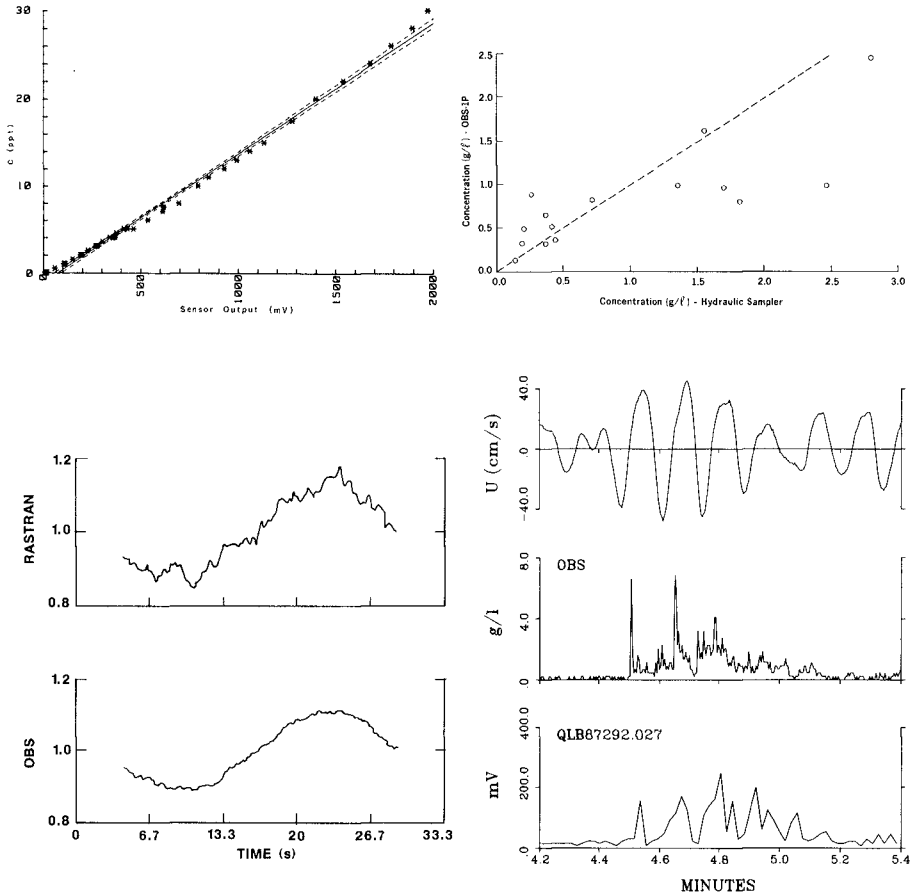


Figure 2 Optical and acoustic measurements of concentration: (a) calibration curve for the OBS-1P including the 95 % confidence band; (b) comparison between time-averaged concentrations using the OBS-1P and a Neilsen-type sampler; the 1:1 line is shown; (c) optical and acoustic signals from the same sediment concentrations generated in a suspended sediment jet - signals have been normalized with respect to the means; (d) field response of the OBS-1P (middle) and RASTRAN (bottom) to the same re-suspension event and the near-bed velocity field (top). Note: the uncalibrated RASTRAN signal was sampled at 0.8 Hz, whereas the OBS and velocity data were acquired at 4 Hz.

1985; Greenwood and Richards, 1991) can resolve bed elevations on a continuous basis to the order of less than one centimeter. Also the local bottom roughness (bedforms - Figure 3) can be measured over several meters with HRRTS II which uses a 5 MHz transducer, with a beam width of 0.72 degrees (nominal), a 30 s pulse length, a repetition rate of 20 Hz and , and which is driven mechanically along a track mounted on the bed.

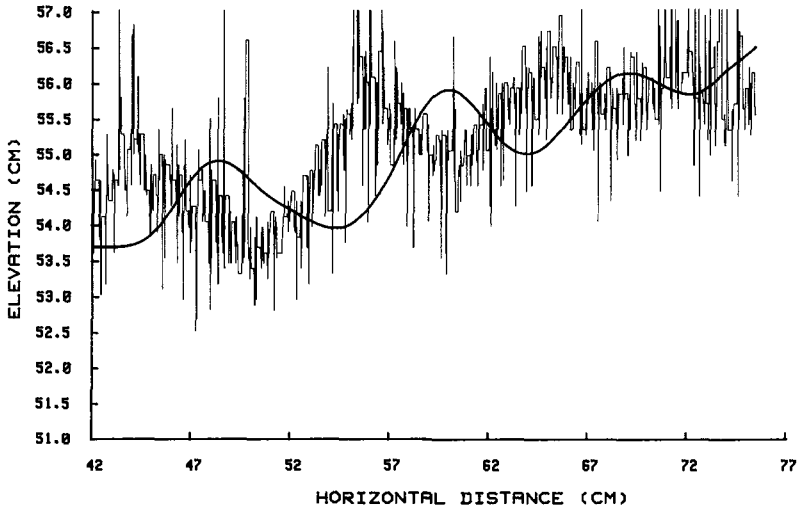


FIGURE 3 Acoustic signature of the bottom boundary using HRRTS II: shown are an unfiltered signal sampled at 8 Hz and a filtered spatial series; note the phase shift associated with the six pole recursive digital filter. Asymmetric ripples with heights of 0.5-1.5 cm and spacings of 9-11 cm existed at this time; considerable sediment re-suspension creates much of the noise.

SEDIMENT RE-SUSPENSION

Sediment re-suspension is an extremely episodic process even under breaking waves; however, contrary to expectations, the suspended sediment concentrations do not exhibit strong spectral signatures typical of the major forcing function (near-bed velocity (stress) - Figure 4). Spectral peaks at the frequency of the primary wave and the first harmonic may be seen under shoaling waves and indicate a dependency upon stresses generated during both onshore and offshore half-wave cycles; this pattern disappears with increasing elevation. A large low frequency peak is present in this example. Under breaking waves, the high frequency peaks disappear and spectral density increases rapidly with decreasing frequency.

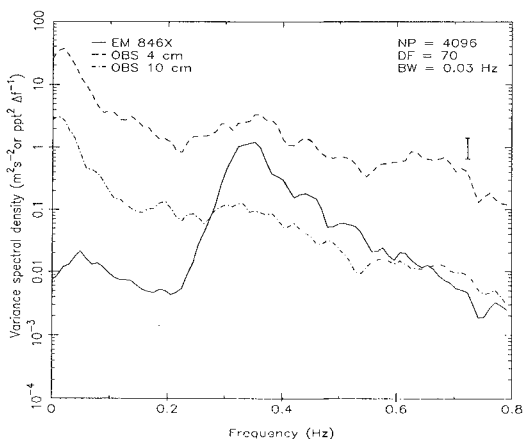


FIGURE 4 Spectra of cross-shore velocity (EM846X) and sediment concentration (OBS) at 4 and 10 cm elevation; the vertical bar indicates the 95% confidence limits, NP = sample size, DF = degrees of freedom BW = bandwidth.

A more appropriate expression of the dynamics of sediment suspension is achieved with time series (Figure 5):

(i) sediment concentrations respond to both individual wave cycles and, more importantly, to wave groups. As a group of large waves pass re-suspension occurs as a cumulative increase and then decrease in concentration lasting for several tens of seconds; fluctuations associated with individual wave cycles are superimposed. Spatially coherent re-suspension events can be identified as wave groups propagate across the nearshore, and even within surf zones dominated by spilling breakers. Since wave groupiness is ubiquitous in both wind forced wave fields (e.g. Great Lakes) and swell (e.g. East Coast) it plays an extremely important role in sediment transport.

(ii) small asymmetries in the near-bed velocity field associated with non-linear wind waves can induce significantly larger asymmetries in transport. Figure 5 illustrates the larger landward transports induced by wind waves shoaling over the lakeward slope of a bar.

(iii) concentrations decrease rapidly away from the bed in general (Figure 6), with maxima measured at 0.04 m elevation only rarely exceeding 10-15 g/l, even under spilling breakers. While time-averaged values decay exponentially with height (Osborne, 1990), this is not a good reflection of the transport process. Concentration gradients over the lowest 0.20 m vary within wave cycles

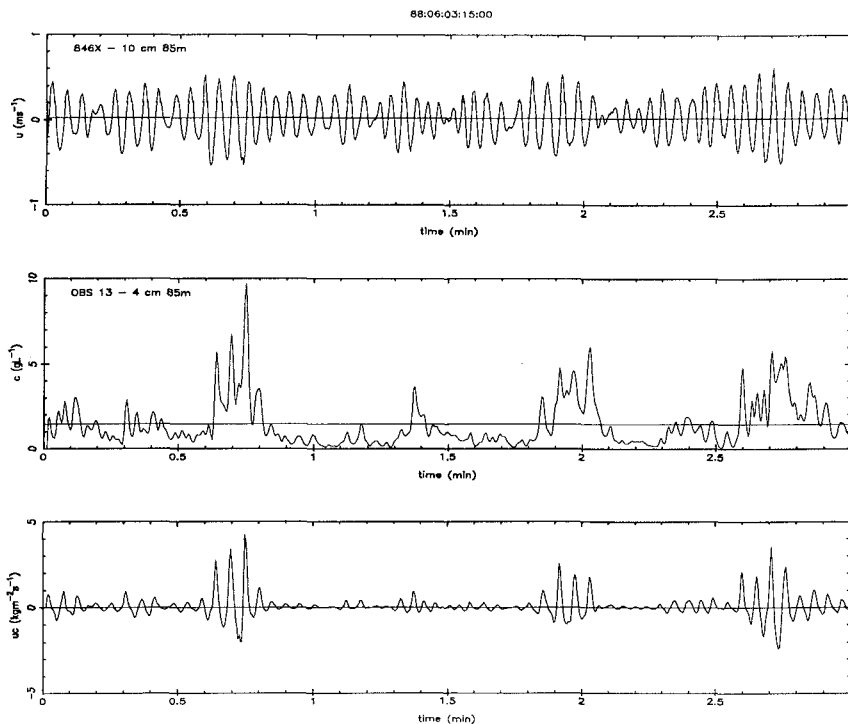


FIGURE 5 Time series of cross-shore velocity (u), sediment concentration (c) and sediment flux (uc) at one elevation, 85 m offshore in 1.8 m of water.

from large decay rates (6C), to near-uniformity (6N) and occasionally inversions with height (6F). This variation results from both the varying intensity of turbulence from one half wave cycle to the next as a wave group passes and the vertical propagation of separation vortices shed from rippled beds. The latter are common even in the surf zone, under flow conditions well above the threshold established by laboratory experiments for flat bed (Ollerhead and Greenwood, 1990).

(iv) phase lags between the near-bed maximum velocity and maximum sediment concentration are common and increase with increasing elevation above the bed. The lag does decrease with increasing velocity, as might be expected (Osborne, 1990).

(v) complex interactions involved in natural sediment re-suspension prevent identification of simple thresholds (velocity or acceleration) for the initiation of suspension. No simple functional relationships can be established between concentration increases and increases in the forcing function, even allowing for phase lags.

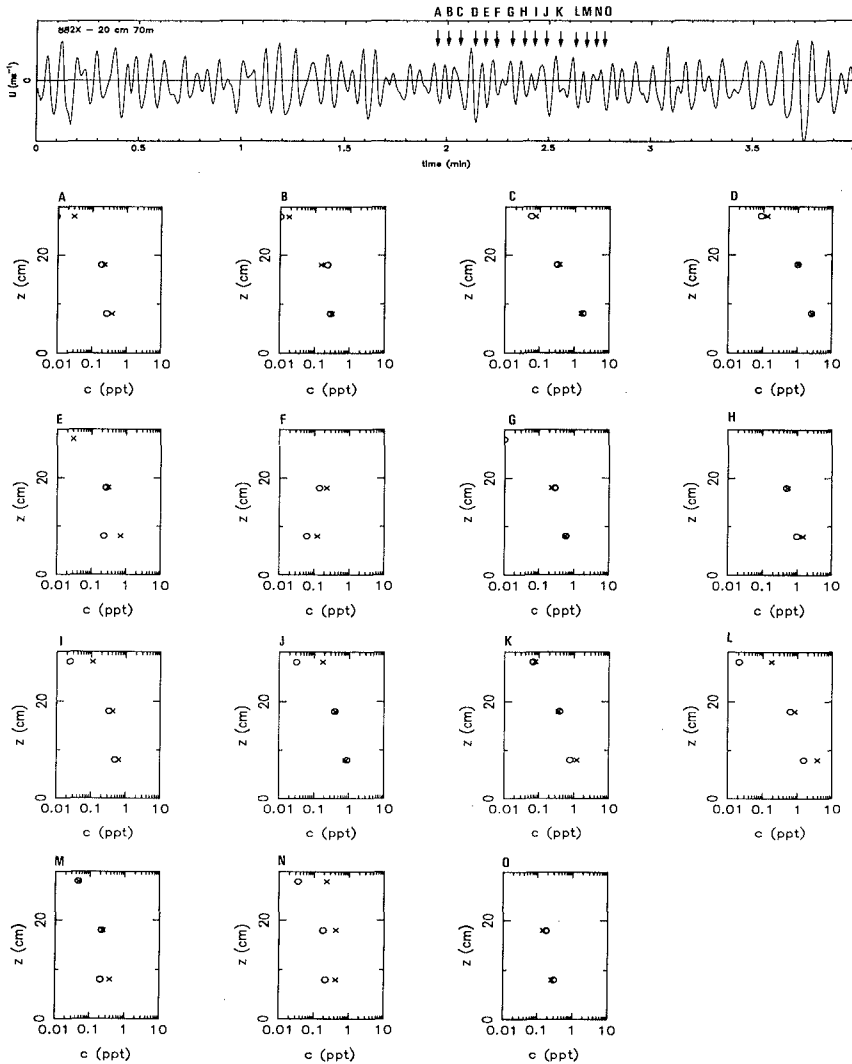


FIGURE 6 Time series of suspended sediment concentrations averaged over each half-wave cycle and at several elevations; crosses indicate the onshore phase of motion, the circles the offshore phase. The arrows indicate the fifteen wave cycles analysed.

The episodic, time-dependent nature of sediment re-suspension clearly influences both the directions and rates of transport at any particular elevation above the bed (Figure 5). Phase lags may cause actual reversals of

net transport within a short distance of the bed. Furthermore, the direction and rates of sediment transport reflect contributions from both oscillatory components of fluid motion and mean flows. Estimates of the oscillatory components can be determined from the co-spectrum (Figure 7). Note in this example: (a) large onshore transports at wind wave frequencies (all elevations); (b) at low frequencies transport is offshore near the bed and onshore higher in the water column. Contributions to the net transports from both "oscillatory" and "mean" components have been computed for a range of wave, current and bedform conditions (Osborne, 1990; Osborne et al., 1990) and it is clear that these contributions vary both with time and over space (with respect to distance above the bed and distance offshore). Figure 8 illustrates an example of the variations across shore in the transport contributions with respect to height above the bed for both non-breaking and occasionally spilling conditions on a non-barred marine beach. Under non-breaking waves, only a small amount of net transport was occurring; this was close to the bed and landward under wind wave asymmetries. Net oscillatory transport is generally landward under near-breaking waves while the mean transport is offshore at all levels. It is clear that the "oscillatory" and "mean" transport components can operate in different directions and at similar rates, such that large volumes of sediment may be transported but the net transport may be close to zero. This suggests the possibility of a locally balanced sediment transport system producing steady state slopes, even under high waves and large suspended loads.

DISCUSSION AND CONCLUSIONS

Both the OBS-1P and RASTRAN give coherent signals from sands suspended by waves and currents. Laboratory cross-calibrations and field comparisons of the time-averaged OBS-1P signals and hydraulic sampling of sediment concentrations supports the contention that both optical and acoustic sensors record sediment concentrations accurately. The acoustic system has the added capability of recording "continuous" vertical profiles and the advantage of being non-intrusive.

Suspended sediment transport is neither continuous nor a simple diffusive process under the combined flows (oscillatory and quasi-steady) of the shoreface. Rather it is extremely episodic and not always coherently related to single incident waves cycles, even under wave breaking. A strong association exists with the velocity structure (and stresses) induced by wave groups. The latter is true for environments with local wind-waves as

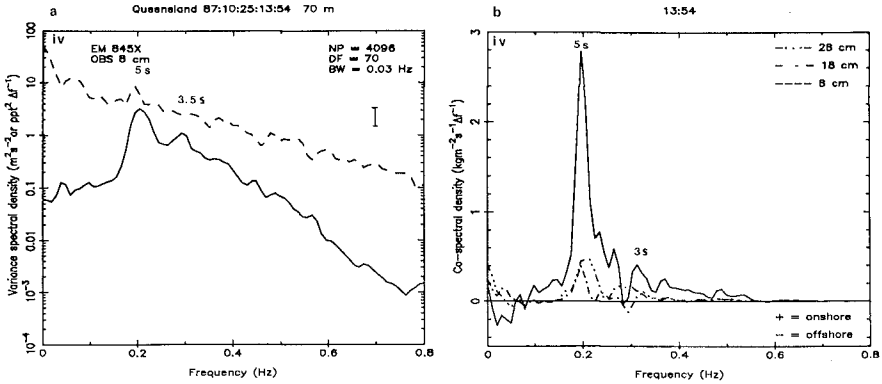


Figure 7 Velocity and concentration spectra (a) and associated cospectra (b) for transport 70 m offshore on a planar beach under near-breaking and spilling breakers. Note: the spectral estimates use 4096 values (17 minutes) with 70 degrees of freedom and a bandwidth of 0.03 Hz; the 95% confidence band for the spectral estimates is shown by the vertical bar.

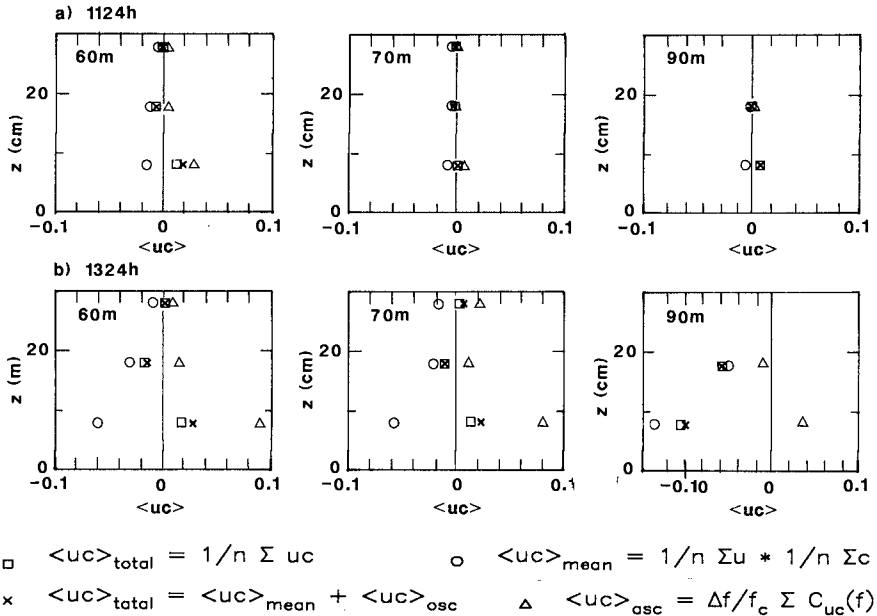


Figure 8 Vertical structure of net suspended sediment transport across shore on a non-barred shoreface, Queensland Beach: (a) shoaling waves; (b) near-breaking (90, 70 m) and occasionally spilling waves (60 m).

Sediment re-suspension also exhibits a strong time-dependency; significant phase lags exist between near-bed velocity (stress) and sediment concentration at any given elevation. Furthermore, vertical gradients in sediment concentration are variable at the wave cycle scale. Although time-averaged profiles of sediment concentration can be described by an exponential decay function, "instantaneous" profiles may show extremely large gradients or near uniformity in the near-bed water column during suspension events; "concentration inversions" are not uncommon. This temporal dependency with elevation clearly controls both sediment transport rates and directions at any specific elevation.

The bed geometry (bedforms) has a large influence on the vertical gradients in the sediment concentration. Sediment re-suspension is characterized by the vertical propagation of coherent turbulent vortices resulting from flow separation over rippled beds, which persist even under spilling breakers.

Present predictive models for cross-shore sediment transport fail to incorporate the effects of wave groupiness or the vortex-shedding effects of bed forms and inadequately model the depth and time dependant character of the system. Furthermore, the strong frequency dependence of suspension transport and the relative contributions to the total transport from wind waves, low frequency waves and mean flows have still to be effectively addressed.

ACKNOWLEDGEMENTS

The Canadian Coastal Sediment Transport Programme (C-COAST) is supported through Strategic Grants awarded by the Natural Sciences and Engineering Research Council of Canada to B. Greenwood, A.J. Bowen and A.E. Hay; P.D.O. was supported by a Post-graduate Fellowship from the same body. We would like to acknowledge the technical assistance of R. Brander, A. Hincenbergs, R. Richards, and K. Weiser (Scarborough College), J. Doering, K. Lewis and S. McLean (Dalhousie University) and E. Colbourne, R. Dittman, L. Huang and J. Sheng (Memorial University).

REFERENCES

- Bailard, J.A., 1981. An energetics total load sediment transport model for a plane sloping beach. *J. Geophys. Res.*, 86:10,938-10,954.
- Bailard, J.A., 1987. Surf zone wave velocity moments. In: *Coastal Hydrodynamics*, R.A. Dalrymple (ed.), ASCE, New York, p. 328-342.

- Basinski, T.**, 1989. Field studies on sand movement in the coastal zone. Polska Akademia Nauk, Instytut Budownictwa Wodnego, W Gdansk, 298 pp.
- Bowen, A.J.**, 1980a. Simple models of nearshore sedimentation: beach profiles and longshore bars. In: The Coastline of Canada, S.B. McCann(ed.), Geol. Surv. Canada, Paper 80-10: 1-11.
- Bowen, A.J.**, 1980b. Nearshore velocity measurements and beach equilibrium. Proc. Canadian Coastal Conference, Burlington, Ont., ACROSES, Natl. Res. Council. Canada, Ottawa, p.21-30.
- D & A Instruments**, 1989. Optical methods for measuring turbidity and suspended particles in water: some notes for users of OBS Sensors. Technote (3/89), 9 pp.
- Downing, J.P., Sternberg, R.W. and Lister, C.R.B.**, 1981. New instrumentation for the investigation of suspended sediment processes in the shallow marine environment. Marine Geol., 42: 19-34.
- Greenwood, B.**, 1987. Sediment balance and bar morphodynamics in a multiple bar system: Georgian Bay, Canada. International Geomorphology 1986, edited by V. Gardiner, John Wiley & Sons Ltd., Chichester, p.1119-1143.
- Greenwood, B., Hale, P.B. and Mittler, P.R.**, 1979. Sediment flux determination in the nearshore zone: prototype measurements. Workshop on Instrumentation for Currents and Sediments in the Nearshore Zone. ACROSES, Natl. Res. Council. Canada, Ottawa, p. 99-120.
- Greenwood, B. and Hale, P.B.**, 1980. Depth-of-Activity, sediment flux and morphological change in a barred nearshore environment. In: S.B. McCann (Editor), The Coastline of Canada: Littoral Processes and Shore Morphology. Geol. Surv. Canada, Pap. 80-10: 89-109.
- Greenwood, B., Dingler, R.J., Sherman, D.J., Anima, R.J. and Bauer, B.O.**, 1985. Monitoring bedforms under waves using high resolution remote tracking sonars. Canadian Coastal Conference 1985, NRCC, Ottawa, p.143-148.
- Greenwood, B., Osborne, P.D., Bowen, A.J., Hazen, D.G and Hay, A.E.**, 1990. C-COAST: The Canadian Coastal Sediment Transport Programme - Suspended sediment transport under waves and currents. Proc. Canadian Coastal Conference, Kingston, Ont., ACOS, Natl. Res. Council. Canada, Ottawa, p.319-336.
- Greenwood, B. and Richards, R.**, 1991. Acoustic imaging of the bottom boundary geometry and dynamics: a High Resolution Remote Tracking Sonar. Marine Geol. (in prep.).
- Hay, A.E., Huang, L., Colbourne, E.B., Sheng, J. and Bowen, A.J.**, 1988. A high speed multi-channel data acquisition system for remote acoustic sediment transport studies. Oceans '88, IEEE, p. 413-418.

- Hazen, D.G., Huntley, D.A. and Bowen, A.J.** 1988. UDATS: a system for measuring nearshore processes. Oceans '87, IEEE, p. 993-997.
- Huntley, D.A.**, 1982. In situ sediment monitoring techniques, a survey of the state of the art in U.S.A. Canadian Coastal Sediment Study, Natl. Res. Council. Canada, Rept. No. C2S2-1,35 pp.
- Huntley, D.A. and Hanes, D.**, 1987. Direct measurement of suspended sediment transport. Coastal Sediments '87, Proc. Speciality Conf. Advances in Understanding Coastal Sediment Processes, ASCE, New York, NY, p. 738-755.
- Horikawa, K.** (ed.), 1988. Nearshore Dynamics and Coastal Processes: Theory, Measurement and Predictive Models. University of Tokyo Press, Tokyo, 522 pp.
- Jaffe, B.E., Sternberg, R.W. and Sallenger, A.H.**, 1985. The role of suspended sediment in shore-normal beach profile changes. Proc. 19th Coastal Eng. Conf., ASCE, New York, N.Y., p. 1983-1996.
- Neilsen, P.**, 1984. Field measurements of time-averaged suspended sediment concentrations under waves. Coastal Engineering, 8: 51-72.
- Ollerhead, J.W. and Greenwood, B.**, 1990. Bedform geometry and dynamics in the upper shoreface, Bluewater Beach, Ontario, Canada. Proc. Canadian Coastal Conf., Kingston, Ont., ACOS, Natl. Res. Council. Canada, Ottawa, p. 337-348.
- Osborne, P.D.**, 1990. Suspended sediment transport on barred and non-barred beaches. Unpubl. Ph.D. Thesis, University of Toronto, 196 pp.
- Osborne, P.D., Greenwood, B. and Bowen, A.J.**, 1990. Cross-shore suspended sediment transport: the role of wind waves, low frequency waves and mean flows. Proc., Canadian Coastal Conf., Kingston, Ont., ACOS, Natl. Res. Council. Canada, Ottawa, p. 349-361.
- Seymour, R.J. (ed.)**, 1989. Nearshore Sediment Transport. Plenum Press, New York, 418 pp.
- Seymour, R.J. and Castel, D.**, 1989. Validation of cross-shore transport formulations. Proc. 21st Coastal Eng. Conf., Malaga, ASCE, New York, p. 1676-1687.
- Willis, D.H.**, 1987. The Canadian Coastal Sediment Study: An Overview. Coastal Sediments '87, Proc. Speciality Conf. Advances in Understanding Coastal Sediment Processes, ASCE, New York, NY, p. 682-693.

CHAPTER 169

NEARSHORE NOURISHMENT IMPLEMENTATION, MONITORING & MODEL STUDIES OF 1.5M³ AT KIRRA BEACH

L.A. Jackson¹ & R.B. Tomlinson²

1.0 INTRODUCTION

Whilst the Gold Coast beaches are generally in long term equilibrium, the southern Gold Coast beaches have suffered serious erosion (approximately 7M m³) since construction in 1962-1964 of the Tweed River training walls, to the south (updrift) of the Gold Coast (Fig. 1).

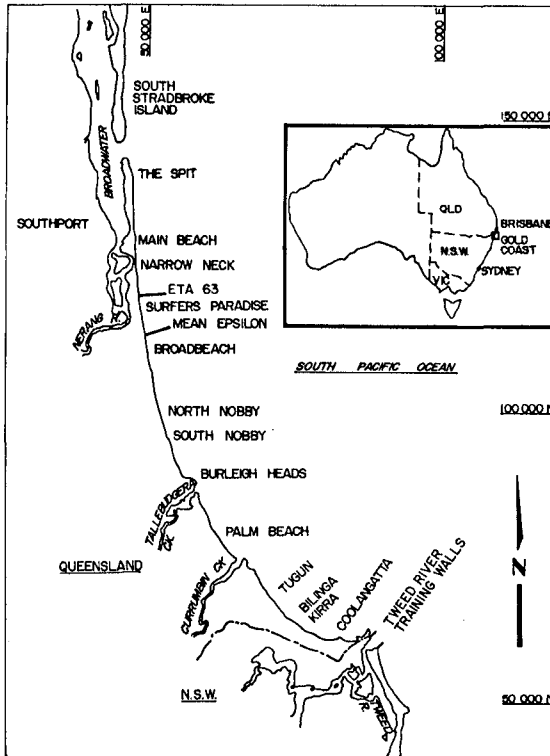


Figure 1.

1 Supervising Engineer, Special Projects, Gold Coast City Council, Qld, Australia.

2 Engineer, Water Research Laboratory, Univ. of New South Wales, Manly Vale, NSW, Australia.

Erosion first became evident in the late 1960's and since this time, various restoration works have been implemented:-

- 1972 Kirra Point groyne to stabilise Coolangatta beach.
- 1974 Kirra Beach nourished ($0.8M m^3$) and Miles Street groyne constructed to entrap a beach at South Kirra Surf Life Saving Club.
- 1983 Investigation into sand transport around Tweed River walls/delta commenced and various options considered due to further erosion as 1974 nourishment was inadequate to cope with ongoing erosion.
- 1985 A 300m section at North Kirra Surf Life Saving Club nourished ($0.315M m^3$) and stabilised by a sand-filled groyne.

The 1985 works (Ref. Jackson 1985) were implemented as an interim measure to restore the eroded public beach at the North Kirra Surf Life Saving Club whilst investigations into the sand transport and losses were continued. This nourishment utilised the offshore sand reserves and the work included nearshore and deposition at North Kirra as well as other Gold Coast beaches to evaluate the behaviour of nearshore nourishment (approximately 50% of the cost of pumping onshore). Observation of the natural storm bars which form approximately 500m offshore in 6-8m water depth showed that these natural bars dissipate the storm wave energy and in subsequent milder conditions move back onshore (Ref. Boczar-Karakiewicz & Jackson 1990). The nearshore nourishment trials, whilst limited, indicated that as expected, sand deposited shoreward of 9m water depth generally moved shoreward.

The erosion at the unnourished sections of Kirra continued and further works were planned for winter 1988, again using the offshore sand reserves. Further sand sampling showed adequate sand of suitable quality seaward of the 20m water depth.

As it was considered that nearshore nourishment would be the likely method chosen analytical studies were undertaken by the Water Research Laboratory for the Gold Coast City Council. This was to give a qualitative assessment of the impact on coastal processes of the dredging and nearshore nourishment at various depths and to examine the applicability of the modelling techniques for predicting future nearshore nourishment behaviour and options.

2.0 MODEL STUDIES

2.1 Wave Refraction Studies

Forward ray wave refraction computer modelling techniques were employed to examine the sensitivity of the shoreline wave climate to offshore dredging. The criterion for assessing the impact on the shoreline wave climate was the change in calculated refraction coefficients and wave angles from the initial bathymetric conditions to the post-nourishment condition.

In general, the study demonstrated that dredging in areas seaward of the 20m depth contour is not likely to have any significant effect on shoreline conditions. This was not a totally unexpected result as both the dredged area and the nourishment bar approximately follow the bottom contours.

Typical results for waves approaching from the dominant wave direction are shown in Figure 2.1. Three dredging and placement options were considered and the results expressed in terms of the average change in refraction coefficient K_R and the change in wave angle for sections of coast in the study area. The results showed changes in the wave climate, although these were generally within the order of accuracy of the technique. The study showed that dredging in depths greater than 20m would have negligible effect on the shoreline wave climate. This result was expected as the dredging operation was contour parallel. Placement of material on the nourishment bar resulted in some significant localised changes, but these were more a function of the irregularity in the schematised disposal pattern introduced by the model formulation.

2.2 Sediment Transport Predictions

The monitoring of a previous small scale nourishment at Kirra in 1985 indicated that although there was a rapid smoothing of the individual dump mounds, the deeper sections (to R.L. -10m) of the bar were slow to respond to gross sediment transport forces. The purpose of this study was to attempt to predict the rate of migration shoreward of a nourished bar as a whole in various conditions using a coastal sediment transport model.

The criteria for selection of a model was that it should be cost effective, user friendly and have been originally developed as an interpretive tool. The model chosen was that developed by Perlin and Dean (1983) and subsequently updated by Scheffner and Rosati (1987). This is a shoreline evolution model in which the beach profile is schematised into N contour levels. There are a number of severe limitations, but nevertheless it can assist in assessing sediment transport in some locations.

offshore bars to be modelled correctly. Furthermore, the profile must be schematised to a limited number of stepped changes, for computational reasons.

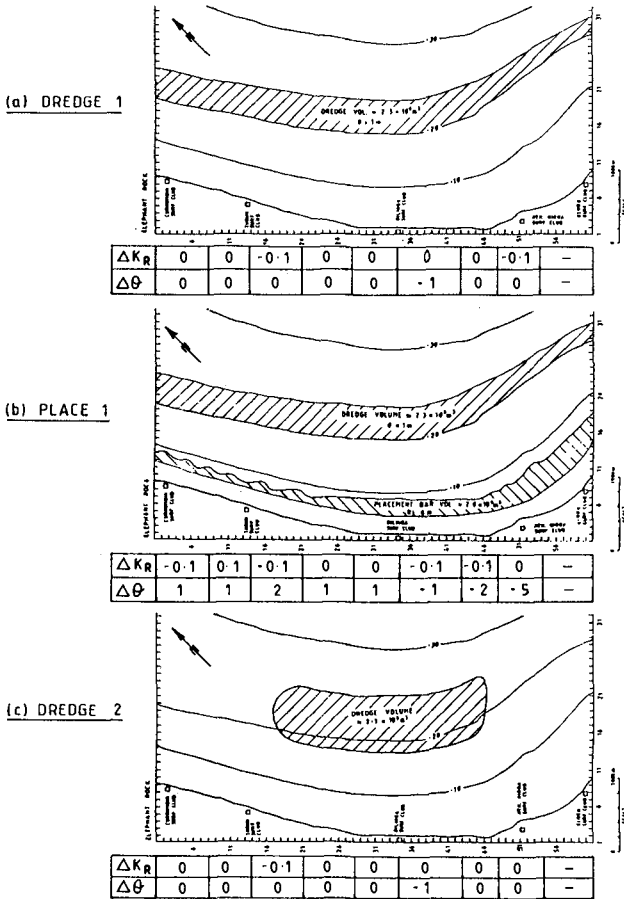
Profiles of a different shape can be modelled by inputting horizontal contour adjustment distances which represent the difference between the equilibrium profile and the actual profile. Dumped dredge material can only be modelled correctly if the seabed continues to slope down in the offshore direction. An additional limitation is that the model boundaries are fixed; that is, there can be no allowance for longshore transport into or out of the area modelled. The onshore-offshore transport rate is proportional to the bed steepness relative to the equilibrium profile steepness and hence is sensitive to the method of placement of the nourishment.

2.2.1 Schematic Models of Kirra

A preliminary assessment of whether this model could be used to predict the response of Kirra beach to dumping of dredged material offshore has been carried out. This was done using schematic beach profiles referred to an equilibrium profile chosen to represent the typical pre-nourished Kirra beach profile as shown in Figure 2.2. Three idealised cases have been examined in this preliminary assessment. They are:

- 1) Equilibrium beach profiles with dredge material dumped in a V-shaped mound, in 5 to 11m water depth.
- 2) Equilibrium beach profiles with material added uniformly along the shore to simulate as closely as possible an offshore bar in 3 to 7m water depth.
- 3) Equilibrium beach profiles with material added uniformly along the shore to simulate as closely as possible an offshore bar in 3 to 7m water depth and dredge dumped material in 6 to 10m water depth.

The equilibrium profile used a Dean coefficient, A , of 0.15 and a grain size of 0.2mm. The beach slope was set to 0.05 up to a berm level of 3m. The computational grid consisted of up to 39 alongshore grid cells at 50m spacing.



NOTE $\Delta K_R = (K_R(\text{initial}) - K_R(x))$ $\Delta \theta = (\theta_{\text{initial}} - \theta(x))$ (degrees)

OFFSHORE WAVE DIRECTION: S.E.
 OFFSHORE WAVE PERIOD: 14 secs.

Figure 2.1 Change in Shoreline Wave Climate

The Perlin and Dean model is based on the equilibrium beach profile concept. The seabed depth is assumed to increase monotonically in the offshore direction. The relationship used is the Dean equilibrium profile given by

$$h = Ay^{2/3}$$

where n is the water depth, y is the distance offshore and A is a coefficient. This profile does not allow

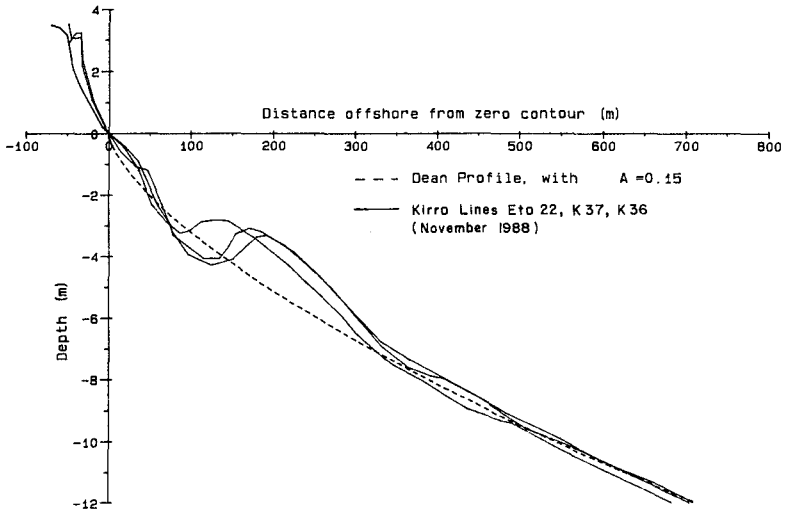
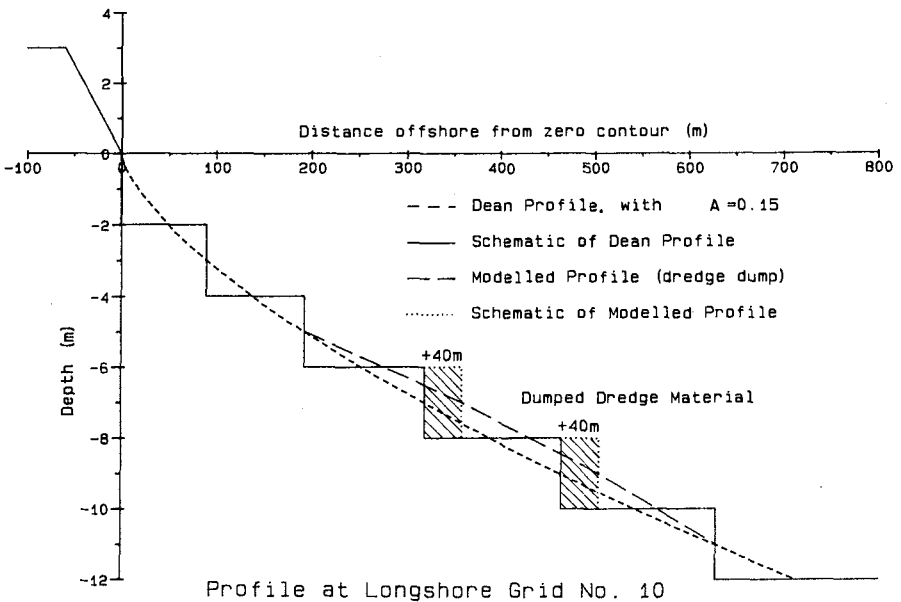


Figure 2.2 Equilibrium Profile Based on Typical Kirra Profiles

1. The rapid smoothing of the individual dredge dumps shown by the survey data was examined by simulating each dump as a V-shaped deposit. This was done by moving the R.L. -7 and R.L. -9m contours offshore as shown in Figure 2.3.



Profile at Longshore Grid No. 10
Figure 2.3 Schematic Profile of Individual Dredge Dumps

Running the model with an average annual wave climate caused the V-shaped contours to be smoothed out very rapidly even when the wave climate was mild. Figure 2.4 shows the initial and final contours for the case of a model run for one year using synthesised wave data.

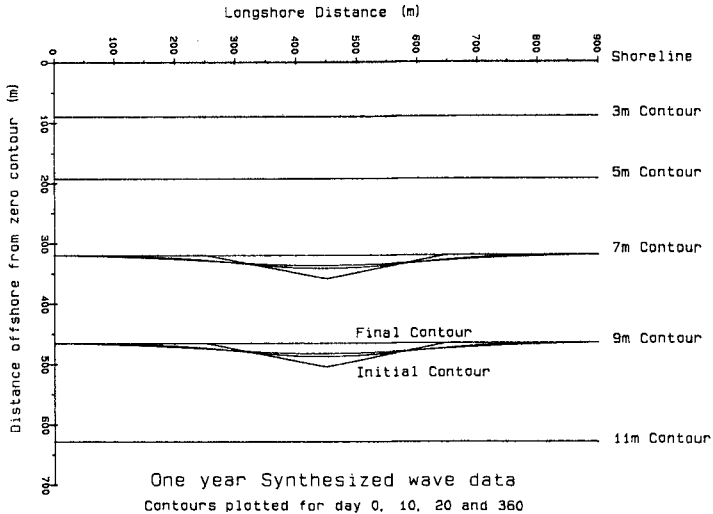


Figure 2.4 Individual Dredge Pump Response

2. Material was then added to the model to simulate as closely as possible a real offshore storm bar. Surveyed beach profile data from Kirra was used for this purpose. Since the offshore depths must increase monotonically with offshore distance, a true bar could not be modelled. However the contours between R.L. 0 to R.L. -7m were adjusted either onshore or offshore by up to 65m to schematically represent the bar.

The model was run for a period of one year using the synthesised annual wave climate. This resulted in rapid changes to the nearshore areas, but no significant change to contours beyond R.L. -4m. There was no suggestion that with this wave climate the profile as a whole would move towards an equilibrium profile.

3. Having established that the response time was slow for this case, material was added to the storm bar profile to simulate the nourishment bar as shown in Figure 2.5. The equilibrium profile contours were adjusted onshore and offshore by up to 95m to schematise the nourished profile. The model was run using the synthesised wave data as well as specific storm data. The length of the idealised shoreline was varied to test the sensitivity of the model to the chosen grid spacing.

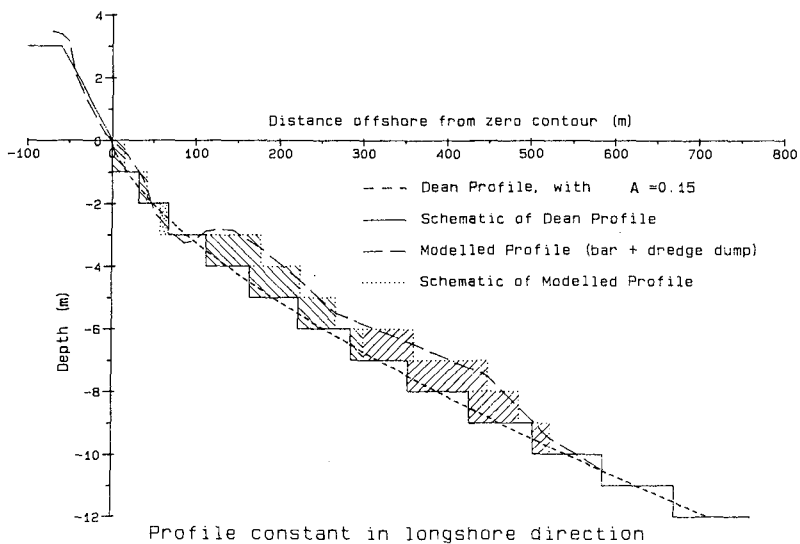


Figure 2.5 Schematic Profile of Nourished Profile

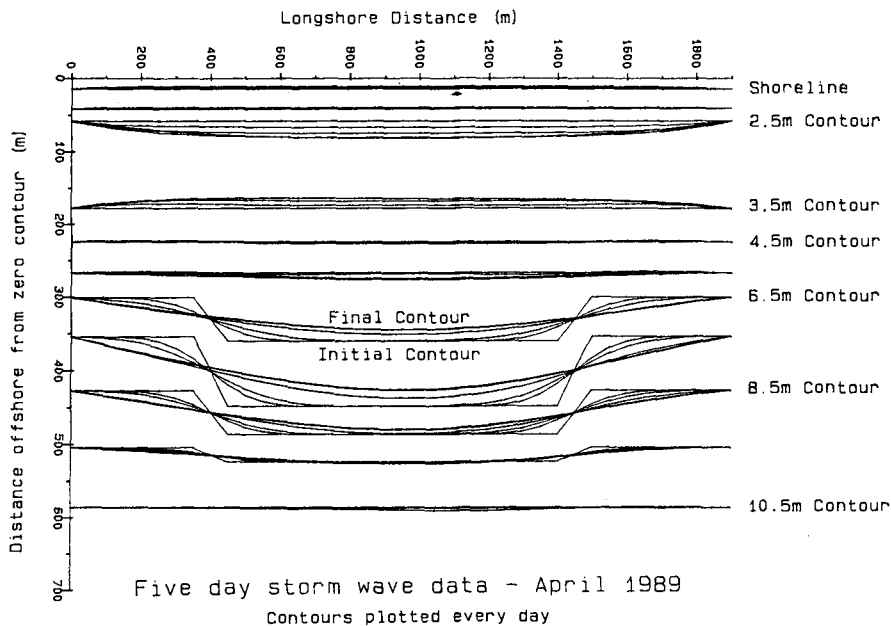


Figure 2.6 Idealised Nourished Bar Response

The results shown in Figure 2.6 were for a storm which occurred in April 1989 some five months after the nourishment. The significant wave height was 5 to 6m for

two to three days with wave periods of up to 12 seconds. A section of coastline was idealised as being a straight beach, and a uniformly placed nourishment was as shown by the initial conditions given in Figure 2.6.

The results of this run showed predominantly longshore transport to the north as was expected, given the SSE wave approach direction. It was found that of the material added to represent the nourishment, less than 10% was transported out of the control area. The survey results for the whole of the beach profile suggest that around 30% of the deposition was transported out of the region during the four months between surveys.

3.0 TENDER EVALUATION

Investigations had shown the whole active profile out to approximately R.L. -10m, to be depleted in the area to be nourished. The required quantity in this area was estimated to be approximately 1.5M m³. The tender documents specified nourishment of the whole profile from the beach to R.L. -10m as the preferred option. However, a range of options of nourishment locations was included. The tender prices were:

- a) Nearshore nourishment only: \$2.3M (WestHam Dredging)
R.L. -6 to -10m)
- b) Profile nourishment : \$6.8M
- c) Onshore nourishment only : \$8.3M

It was decided to accept the tender of WestHam Dredging Pty. Ltd. to carry out nearshore nourishment only (Fig. 3.1).

4.0 IMPLEMENTATION

The sand was dredged from seaward of R.L. -20 some 1,500m offshore and deposited between R.L. -6 to 10.5m using the trailing suction hopper dredge "W.H. Resolution" with bottom opening hopper gates to discharge the material. As stand-down conditions applied for H(sig) greater than 1.9m, and to evaluate the behaviour of the nourished bar, a wave rider buoy with a real time analysis system installed on both the dredge and in Council's offices.

The deposition operations involved grounding the bow of the dredge as far shoreward as possible in the deposition area (shoreward of the R.L. -10m contour) and moving shoreward as the load was dumped. This method resulted

in discrete mounds being left on the seabed with a crest level of approximately R.L. -6m. In order to verify quantities and the dredging/deposition location, two Council inspectors were stationed on board the dredge.

To optimise deposition placements, the contractor carried out daily surveys over the deposition area using a 43' survey vessel, which provided updated soundings daily to the dredge. The location of each load deposited was also plotted by the Council inspectors on board to verify acceptability of each load location and to provide details of areas filled to the dredge Captain.

Council also carried out regular surveys from the beach to R.L. -12m prior to and during the project. In order to be able to distinguish between individual mounds in the deposition area, these surveys were carried out approximately shore parallel at 10m max. spacing.

Unfortunately, the works were curtailed some 4,000m³ short of the 1.5M m³ due to heavy sea conditions and storm conditions were experienced repeatedly for over a year afterwards (Fig. 4.1). This severely restricted accurate surveys of the post-nourishment behaviour and data available for analysis. Despite the storm wave conditions which caused considerable erosion elsewhere and accelerated erosion of the depleted area to the north (downdrift) of the nourishment, significant onshore translation and accretion at the toe of the boulder wall has been measured as a result of the increased offshore wave breaking, decay and refraction over the artificial bar zone. Accretion to form a narrow beach in front of the boulder walls occurred between storms in most of the area nourished (Fig. 4.2).

As the erosion to the north threatened private foreshore properties (the nearshore nourishment was mainly seaward of foreshore fronted by public park), considerable public pressure from the affected residents resulted, and the Queensland Government implemented a scheme to fully restore the southern Gold Coast beaches.

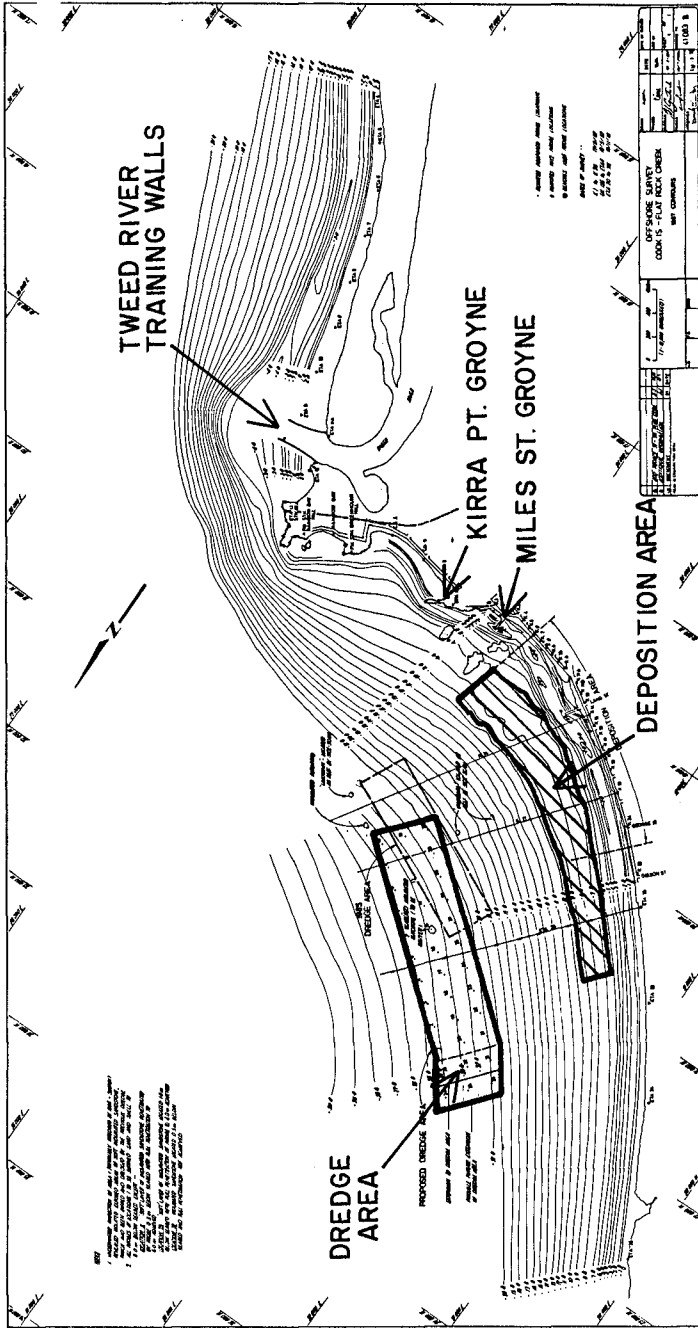


Figure 3.1 Plan of Kirra Nourishment Project (1988)

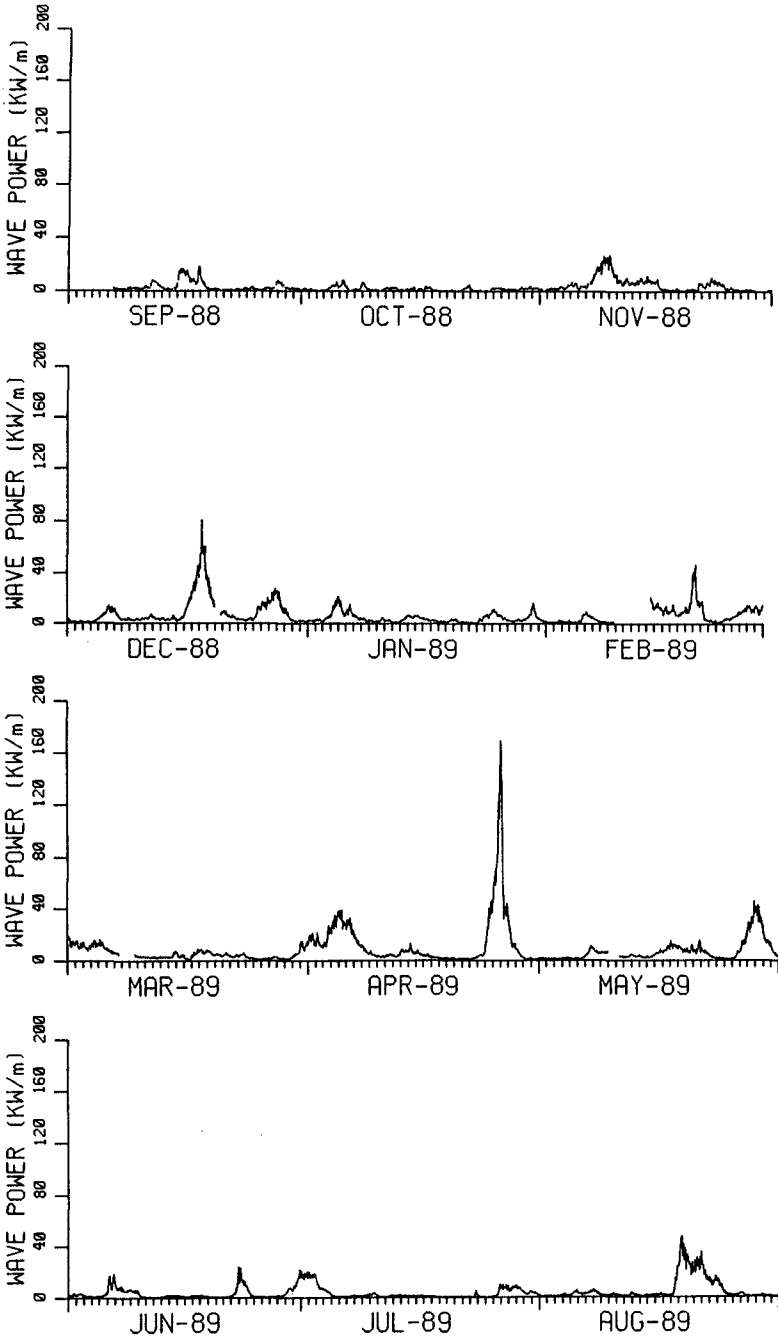


Figure 4.1 Kirra Waverider Buoy Records

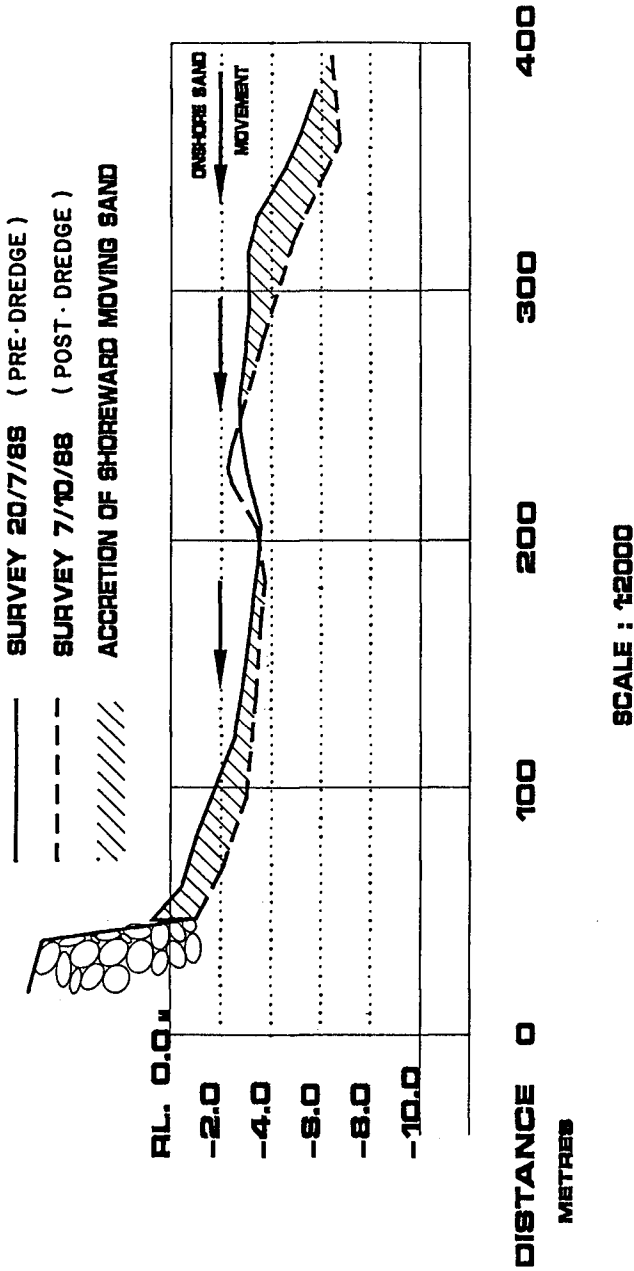


Figure 4.2 Post Nourishment Profile (Typical)

5.0 CONCLUSION

Despite adverse conditions, the works carried out in 1988 appear, as predicted by the model investigations, to have been effective in protecting the foreshore and allowing accretion of a usable beach. The adverse weather conditions and the further works of $3.6M m^3$ implemented in November 1989 limited the survey data which could be collected and analysed. The results of the 1988 works are to be further analysed in conjunction with the 1989/90 works which included $400,000m^3$ nearshore nourishment.

References

Boczar-Karakiewicz, B. and Jackson L.A. (1990) "Effect of Nearshore Bars on the Protection of the Upper Beach, Gold Coast, Australia", Proceedings, 22nd Int. Conference on Coastal Engineering, Netherlands, 1990.

Jackson, L.A. (1985) "North Kirra Beach Restoration Project", Proceedings, 7th Australian Conference in Coastal & Ocean Engineer, Christchurch, N.Z., 1985.

Perlin, M. and Dean, R.G. (1983) A Numerical Model to Simulate Sediment Transport in the Vicinity of Coastal Structures. U.S. Army Corps. of Engineers, Coastal Engineering Research Centre, Miscellaneous Report No. 83-10.

Schneffner, N.W. and Rosati, Julie Dean (1987) A User's Guide to the N-Line Model : A Numerical Model to simulate Sediment Transport in the Vicinity of Coastal Structures. U.S. Army Corps. of Engineers, Coastal Engineering Research Centre, Instruction Report No. CERC-87-4.

CHAPTER 170

A New Approach to 3D Flow and Transport-Modeling

Johan C.M. Dijkzeul¹
Jan J. Leendertse²

Abstract

In recent years two-dimensional numerical models have been applied successfully not only to large scale tidal computations, but also to small scale detailed flow computations (Bosselaar et al., 1987, Leendertse et al., 1989). However the application of three-dimensional models for fine-grid computations is very limited due to the very high requirements for computer times, caused by the explicit numerical algorithms which are being used. This problem is now alleviated by use of an alternating direction implicit computation method for three-dimensional flow- and transport-modeling. With this method, presented in this paper, the effective computation time is about an order of magnitude smaller then with previous models with similar accuracy.

Introduction

Two- and three-dimensional numerical models are used more and more for fine grid computations. At the 20th I.C.C.E., Taiwan, 1986, small scale applications were presented of fine grid two-dimensional models for the Delta-project in the Dutch Eastern Scheldt estuary. In this case, flow patterns near the construction sites of the storm surge barrier and compartmentation dams at different stages have been computed (Bosselaar et al., 1986, Klatter et al., 1986).

The gridsizes in these models varied from 400 m. down to

¹Projectadvisor, Icim bv, P.O. Box 5809, 2280 HV Rijswijk, The Netherlands

²Manager, TRI-FLOW COMP Inc., 2672 Bayshore Av., Ventura, CA 93001, U.S.A.

10 m. In Figure 1 an example is given of a flow pattern in a two-dimensional model for the northern channel Hammen in the Eastern Scheldt estuary.

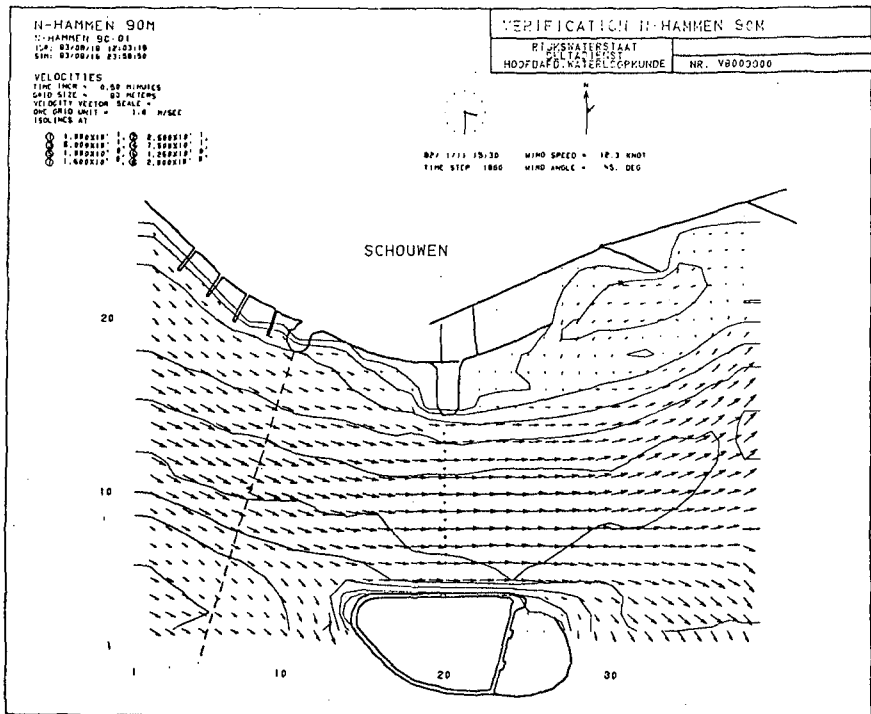


Figure 1.: Flow-pattern in the two-dimensional model of the Hammen

The results were used for example for stability-analysis of the bed protection by mattresses and the computation of sand losses. Therefore, velocities and shear stresses in the bottom layer were needed. The possibility of using three-dimensional models was investigated and 3D-computations were made with the available explicit 3D-code, developed by Leendertse and Liu (1973, 1987) (see Figure 2).

These 3D-computations appeared to be feasible but the computer-time needed was very large. This can be understood from table 1.

The gridsize in the 2D-model was 45 m., but for the comparison a gridsize of 90 m for the 2D- and 3D-models has been used. The 2D-modelling system WAQUA (Stelling, 1983) is using an implicit ADI-type of scheme, so a

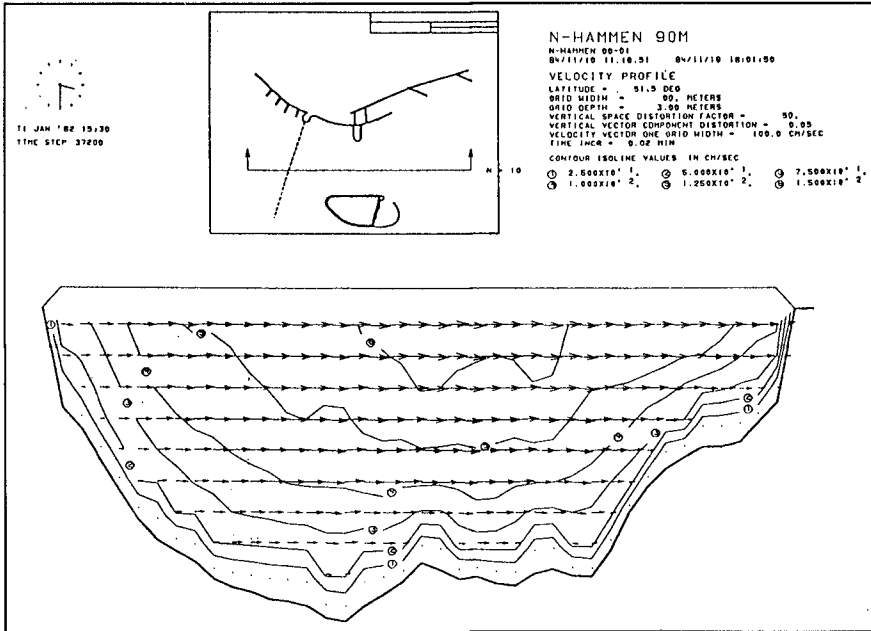


Figure 2.: Flow-pattern in a cross-section of the three-dimensional model of the Hammen

model characteristics	2-dimensional model	3-dimensional model
gridsize (m)	90	90
timestep (s)	60	1.5
method	implicit ADI	explicit
number of layers	1	10

Table 1: characteristics of the 2D- and 3D-model Hammen

stability requirement is absent and timesteps of 0.5 to 1 minute are possible. The explicit 3D-scheme however, needs a timestep of 1.5 second for stability reasons. The 3D-model has 10 layers and a lot of CPU-time is needed for a computation.

It should be emphasized that for accurate flow-computations the approximation of the advection-terms in the momentum equations is very important. An inaccurate time- and space discretisation will introduce numerical (eddy-) viscosity or will make the scheme first order accurate (Stelling, 1983) and details in computed

velocity distributions will be lost. Only fourth order dissipation is introduced by the approximations in the schemes for the advection terms.

For successful investigations and detailed 3-dimensional flow-computations with numerical models an implicit 3D-scheme is required and the computation method used has to meet the following requirements:

- The computation method must be stable,
- The algorithm must have an accuracy of at least second order,
- Numerical (eddy-) viscosity must be absent,
- The computation method must allow for large timesteps and must be efficient.

Computation method

The requirements above are met by the two-dimensional system WAQUA and also by the extension in the 3D-algorithm, which will be explained briefly in the next sections. For more details about the equations, the finite difference approximations and the solution technique the reader is referred to (Leendertse, 1989).

In this three-dimensional system also an alternating direction implicit computation method is used. The variables in the three-dimensional field are solved by successive solution of sets of equations that are described in vertical planes. With the use of special advection term approximations, the three-dimensional problem is broken down in a sequence of two-dimensional problems, which in turn can be reduced to the solution of sets of one-dimensional problems.

The most important aspects of this three-dimensional solution technique are:

- The use of horizontal momentum and continuity equations for the different layers in the model,
- The use of an ADI-type of scheme on a horizontal and vertical staggered grid,
- The use of asymmetrical higher order advection term approximations developed for the cross-advection terms in a two-dimensional model by Stelling (1983),
- The hydrostatic pressure assumption,
- A second order accuracy of the solution method with fourth order dissipation,
- An unconditional stability of the computation,
- A limitation of the timestep by requirements for accuracy only.

For the one layer case, this 3D-method reduces to the original two-dimensional scheme, except for some minor details.

Flow-computation

The solution of the finite difference equations for each stage in the ADI-method are solved iteratively. In general, iterations are required only for the expressions for the advection term coefficients and for the upstream gradients in the advection terms in case the local flow direction is different from the dominant flow direction.

In the first half-time-step (stage 1) of the multistep operation, the horizontal V-velocities in the vertical planes in Y-direction are computed first. The coordinate system used is X and Y for the horizontal and Z for the vertical direction with velocities U, V and W respectively.

For each column the momentum equations for the V-velocities are implicitly coupled in the vertical by the approximation of WV_{zz} , resulting in a three-diagonal system of equations for V which can be solved very economic way.

In the vertical plane the implicit horizontal coupling in Y-direction, due to the upwind-differencing for the gradients V_y in the advection term VV_y , can be solved with 2 iterations in opposite Y-directions using just computed values of V during the ongoing iterations.

Also the implicit horizontal coupling in X-direction due to the upwind-differencing for the gradients V_x in the advection term UV_x can be solved with 2 iterations over the planes in opposite X-directions using just computed values of V in the planes during the ongoing iterations.

The solution of the horizontal velocities U, the vertical velocities W and the waterlevels in the other equations in stage 1 is more complicated. The velocities U are coupled in the vertical by the approximation of WU_{zz} in the U-momentum equations and in the horizontal by the approximation of the continuity equation. This coupling is solved as follows: substitution of the discretized U-momentum equations in the continuity equation and summation over the vertical results in a three-diagonal system of equations for the waterlevels to be solved. With the new waterlevels U and W can be solved respectively with the U-momentum and the continuity equations. Iterations are needed for the nonlinearities in the continuity equation.

The second half-time-step (stage 2) follows the same pattern described above for the first stage, but now first the U-velocities are computed implicitly with the U-momentum equations, followed by the implicit computation of V and the waterlevels with help of the V-

momentum and continuity equations.

The combination of both upwind- and central differencing alternatively in the 2-step scheme results in a second order accurate approximation in time and space of the horizontal advection terms with fourth order dissipation. If the advection is expressed upstream, and the coefficients of the nonlinear terms are constant during the timestep, the above presented computation method can be proven to be unconditionally stable.

Transport-computation

Not only the fluid flow is important in three-dimensional modeling. Dissolved substances, salinity distributions and sediment distributions need also to be computed simultaneously with the water motions. For accurate computations of transport and concentrations of dissolved matter in fine-grid models of for example estuaries, an accurate flow-computation is essential.

Experiments have shown (Ridderinkhof, 1990) that for small gridsizes advection is dominant for the dispersion of constituents. With an accurate transport-scheme also stratified flow or transport of sediments can be computed.

For this, a new numerical transport-scheme has been developed, is based on the principles explained above in the scheme for flow computation and is using the same asymmetrical approximations for the advection. The computation method is conservative, second order accurate and shows very limited spatial oscillations near steep fronts, due to the higher order of approximations.

Results

An example of both flow- and transport computation is the dispersion due to wind of a pollutant flowing into lake IJssel from the river IJssel in the Netherlands.

The different flow-directions in top- and bottom-layer caused by wind, results in quite different results in concentrations, compared to the results obtained with a two-dimensional model.

The first application of this new approach has been a management type of model of a closed-off estuary, lake IJssel. A wind driven circulation was generated by a south-easterly wind of about 11.3 m/s. An inflow into

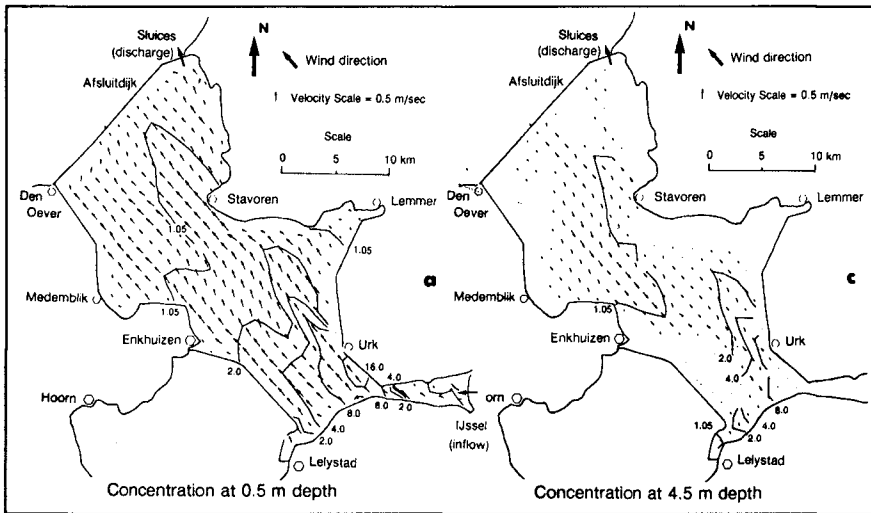


Figure 3.: Computed concentrations and velocities 72 hours after start of computation at 0.5 m depth (a) and 4.5 m depth (c)

the lake from the river IJssel of 500 m³/s was assumed with a concentration of 50 gr/m³ for a limited period to simulate a spill. The outflow at discharge sluices in the north was also set to 500 m³/s.

The lake was represented by a grid of 36 x 21 points in the horizontal plane. The gridsize was 1200 m, the vertical representation was made by five layers of 1 m, and the bottom layer was taken at 1.5 m. The timestep was 7.5 minutes.

Even with the limited depth the concentration distributions at the surface and near the bottom are quite different as is shown in Figure 3. Particularly during the first few days, considerable differences in concentrations over the vertical exist in the southern part of the lake as is shown in the timehistories of the concentrations in Figure 4.

Developments

The above presented computation method for flow- and transport computation is now being used by the Dutch Rijkswaterstaat and by Delft Hydraulics.

Further developments with this scheme are:

- The incorporation of (curvilinear-) transformations

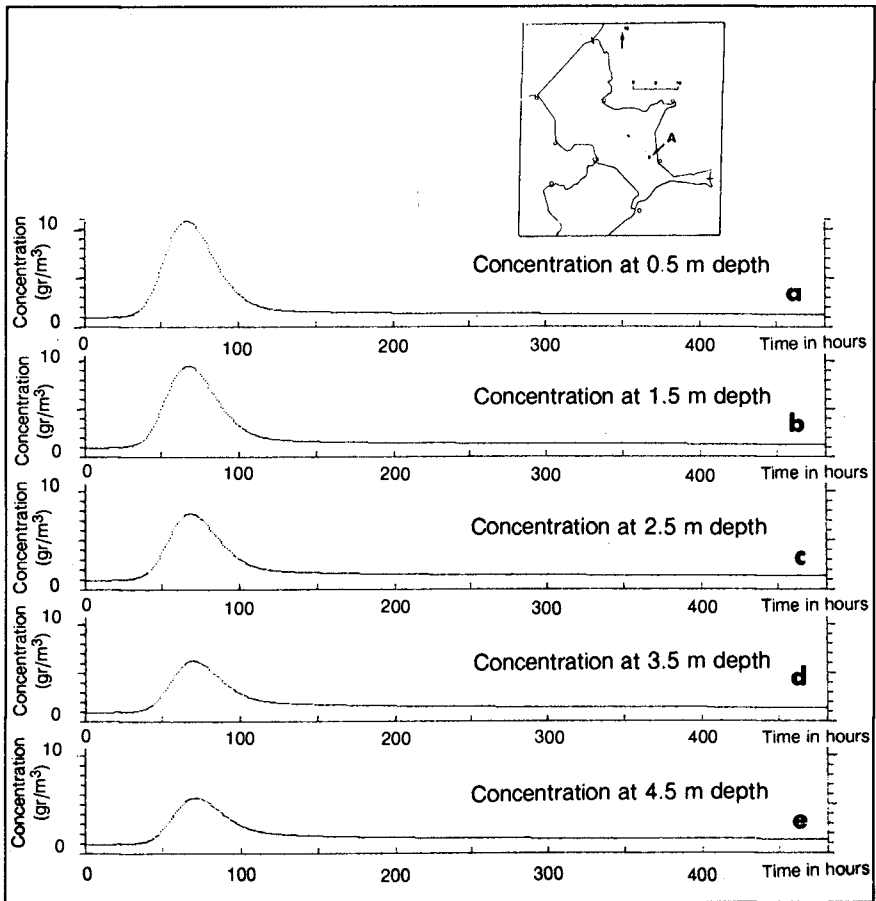


Figure 4.: Computed time-series of the concentration at station A at 0.5 m depth (a), 1.5 m depth (b), 2.5 m depth (c), 3.5 m depth (d), and 4.5 m depth (e) (timestep=7.5 min.)

in the horizontal direction and (σ -) transformations in the vertical direction (de Vriend, 1990),

- The use of a higher order approximation for the advection in the vertical with a different computation method,
- The incorporation of a turbulent energy (K-epsilon) model for vertical diffusion,
- The incorporation of vertical field accelerations for near field computations.

Conclusions

With the presented (ADI) computation method, implicit three-dimensional flow- and transport-computations can be made which are stable and second order accurate.

Large timesteps can be used, compared to explicit codes for small-scale and fine-grid applications, therefor the algorithm is effective in CPU-demand.

Acknowledgements

This study was performed for the Dutch Ministry of Transport and Public Works, Rijkswaterstaat, Tidal Waters Division.

References

- Bosselaar, G.J., Thabet, R.A.H., van Roermund, A.J.G.M. and Bijlsma, L., (1986), "Simulation of sandfill building stages with numerical flow models". Proc. 20th ICCE, Taipei, pp.1003-1015.
- Bosselaar, G.J. and Dijkzeul, J.C.M., (1987), "Two-Dimensional Numerical Flow Models, Built and Used by Civil Engineers". Proc. ASCE '87 National Conference on Hydraulic Engineering, Colorado Springs, pp.740-745
- Klatte, H.E., Dijkzeul, J.C.M., Hartsuiker, G. and Bijlsma, L., (1986), "Flow Computations nearby a Storm Surge Barrier under Construction with Two-Dimensional Numerical Models". Proc. 20th ICCE, Taipei, pp.1943-1957.
- Leendertse, J.J., Liu, S-K., (1973), "A Three-Dimensional Model for Estuaries and Coastal Seas: Volume I, Principles of Computation". Report R-1417-OWRR, Rand Corporation, Santa Monica.
- Leendertse, J.J., Liu, S-K., (1987), "Modeling the Alaskan Continental Shelf Waters". Report R-3567-NOAA/RC, Rand Corporation, Santa Monica.
- Leendertse, J.J., (1989), "A New Approach to Three-Dimensional Free-Surface Flow Modeling". Report R-3712-NETH/RC, Rand Corporation, Santa Monica.
- Leendertse, J.J., Roos, A. and Dijkzeul, J.C.M., (1989), "Nesting of Two-dimensional Models for Tidal Flow Computations". Report WD-4260-NETH/RC, Rand Corporation, Santa Monica.

Stelling, G.S., (1983), "On the construction of computational methods for shallow water flow problems". Ph. D. Thesis, Delft.

Ridderinkhof, H., (1990), "Residual Currents and Mixing in the Wadden Sea". Ph. D. Thesis, Utrecht.

Vriend, H.J. de, Kitou, N., (1990, this proceedings), "Incorporation of wave effects in a 3D hydrostatic mean current model". Proc. 22nd ICCE, Delft.

CHAPTER 171

The Analysis and Role of Bars on the Protection of a Beach System Gold Coast, Queensland, Australia

B. Boczar-Karakiewicz¹ and L.A. Jackson²

Abstract

Gold Coast beach profile changes have been analysed using a dynamical model describing wave-bed interactions. The model explains the formation and dynamics of prominent longshore bars which are characteristic features of the studied nearshore. Model predictions are compared with field observations and measurements in several locations. Obtained results justify protection measures (eg. nourishment of offshore bars) applied in the study area by the Gold Coast City Council.

1. Introduction

According to observations over a period of the last 100 years, the beach system in the Gold Coast (Fig.1) area is extremely dynamic. At times of severe storm and cyclones events, the beaches are exposed to

high energy waves up to 8.5 m with corresponding wave periods of 14.0 secs. The amplitudes of highest waves observed in this region over to 12.0 m and the largest wave periods are of 17-18 secs (McGrath and Robinson 1973, Gold Coast City Council 1990).

In those conditions, the beaches are eroded but subsequently restored under mild weather conditions and swell waves. After the worst recorded erosion in 1967, the recovery of the

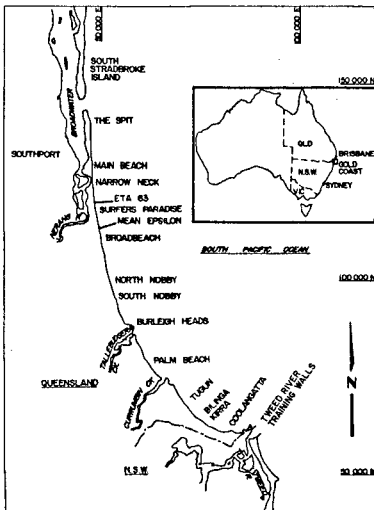


Figure 1. Location map

¹Professor, INRS-Océanologie, Rimouski (Québec) Canada, G5L 3A1

²Engineer, Gold Coast City Council, QLD 4217, Australia

upper beach took a period of some 18 months. With a frequency of major storm and cyclone events lower than 1/18 month, the beach system may recover under conditions that a natural buffer zone comprising the dunes is conserved, and that the sediment supply from the local Tweed River compensates losses of sediment due to the wave-induced longshore transport (Jackson, Smith and Piggot 1988). However, the conservation of a sufficiently large natural dune system has been difficult given the rapid expansion of the recreational usage of the Gold Coast area (Smith and Jackson 1990). Additionally, the construction and subsequent extension of the training walls of the Tweed River (1910 and 1964, respectively) have significantly modified the local sediment supply. The extension of the walls caused an approximated deficit of sediment of some 250,000 m³/yr. Therefore, in recent years quite severe effects of erosion were observed mainly in the southern part of the Gold Coast propelling gradually downdrift to central beaches.

To date some 9 M m³ of beach nourishment has been carried out but protection of the beach and foreshore development requires more beach nourishment to compensate intrusion into the active beach zone by past developments (Chapman 1980, Smith and Jackson 1990). Nourishment has been placed onshore, nearshore and a combination of both. The cost and efficiency of nourishment varies considerably with the location of placement. As nearshore nourishment is generally considerably less expensive in the Gold Coast case, research has been carried out on the behaviour of natural and artificial (nourished) nearshore bars.

To better understand the natural beach system and the effect of natural and artificial bars on the protection of the upper beach, a model has been developed. An analysis of beach equilibrium is presented and based on observations and mathematical modelling of large scale sand bars which are prominent features of the Gold Coast nearshore. Aerial photography shows evidence of offshore sand bars in the entire nearshore of the Gold Coast area. The geometry of bars, their appearance and stability varies in different parts of the coast. Generally they are strongly related to the incidence of predominant storm waves and swell. Typically, the outer shore-parallel bar lies in a water depth of 6-10 m and at distances of 400-500 m from the mean position of the shoreline.

The Gold Coast beach system is extremely mobile with changes occurring in several very different time scales: incident wave trains are changing during normal weather conditions in several tens of hours, the weather over a few days, the climate over years, sediment supply over decades and the shape of the seabed in days to several months.

Observations and measurements show, however, that the complex beach system periodically reaches some kind of dynamical equilibrium which in turn is controlled only by two main factors. These factors are the incident waves and the shape of the underlying seabed from its deepwater end (extending to some 20-25 m of water depth) up to the visible beach (Smith and Jackson 1990).

The incident wave and seabed parameters are the only free parameters in the dynamical model applied in the presented analysis. Model predictions have been compared with observations and resulting conclusions justify the use of nearshore nourishment as a protection measure applied in the study area by the Gold Coast City Council.

2. The model

The model has four constituent processes describing wave-bed interactions, namely (1) the hydrodynamics of the main water body, (2) the near-bed boundary-layer flow, (3) the sediment transport, and (4) the evolution of the bed topography. These four modules are linked together and the resulting model is discretized for numerical integration. The integration procedure consists of a two-step time loop. In the first step, the fluid flow and the sediment flux are calculated over a bed configuration which is instantaneously fixed. In the second step, the temporal evolution of the seabed is calculated while keeping all variables describing the fluid and sediment flow constant. This two-step approximation is justified both on mathematical grounds, and by observations in the laboratory and natural coastal environments which indicates significant changes in bed topography are only observed over a period of many thousands of wave periods. A time-scale is quite long when compared to rapid changes in the fluid flow that can occur during one wave period (Boczar-Karakiewicz *et al.* 1987, Boczar-Karakiewicz and Davidson-Arnott 1987).

The first model constituent describes surface-wave motion in a typical nearshore setting in which the wavelength λ of a peak-period storm wave is large, compared with local water depth h . Following Keller (1988), the recent surface wave description has been derived directly from Euler equations and continuity for a fluid flow bounded by a free surface at $\bar{z} = \zeta(\bar{x}, \bar{t})$, and by a fixed bed at $\bar{z} = -\bar{h}(\bar{x})$. Application of Keller's approach allows us to solve the earlier defined problem of wave propagation in three spatial dimensions in a curvilinear coordinate system (x, z) , where x , is the path of the wave ray (Boczar-Karakiewicz *et al.* 1990).

At the present stage of modelling, it is assumed that the incident waves and the nearshore bathymetry do not vary appreciably in the longshore direction so that both the wave and bed motion are two-dimensional as indicated in Figure 2.

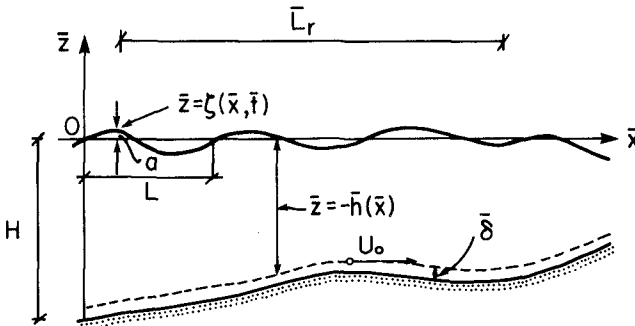


Figure 2. Notation scheme

In this idealized version of the bed-fluid system, it is assumed that the incident wave propagates shoreward from the deep water end of the nearshore and that the incoming wave train is of constant amplitude and frequency. The horizontal coordinate, in Figure 2, is $\bar{x} = 0$ at the deep end of the nearshore where $\bar{z} = -H$, \bar{z} is the vertical coordinate with $\bar{z} = 0$ at the undisturbed, free water surface. The surface wave is assumed to be progressive in the whole spatial domain and the free surface elevation ζ is expanded into a power series and modally decomposed,

$$\zeta = \zeta(x, X, t) = \sum_{j=1}^2 a_j(X) \exp(ik_j x - i\omega_j t) + c.c., \quad (1)$$

In equation (1), X is an independent, horizontal variable defined by $X = B \cdot x$. The small parameter β ($\beta \leq 0.1$) is evaluated from incident water depth H , and wave length λ , thus $\beta = H/\lambda$. The notation c.c. stands for the complex conjugate of the quantity just preceding it, so in this case,

$$c.c. = \sum_{j=1}^2 a_j^*(X) \exp(i\omega_j t - ik_j x).$$

In equation (1), ω_1 is the frequency of the postulated incoming wave train and $\omega_2 = 2\omega_1$ is its second harmonic, k_1 and k_2 are wave numbers associated with ω_1 and ω_2 , respectively. The complex, first order amplitudes a_1 and a_2 are taken to vary on the scale of wave lengths, and therefore, are dependent only on the variable X . The symbol a_j^* denotes the complex conjugate of a_j . In equation (1), dimensional variables have been nondimensionalized and scaled according to the scheme,

$$(h, x, z) = \frac{1}{H} \bar{h}, \bar{x}, \bar{z}, t = (g/H)^{1/2} \bar{t}, \zeta = \frac{1}{\alpha H} \bar{\zeta}, \quad (2)$$

where H denotes a characteristic water depth (e.g. depth at the deep water end), g is the magnitude of acceleration due to gravity, and $\alpha = a/H$, where a denotes the wave amplitude. A similar representation to equation (1) is postulated for the velocity potential ϕ . Assuming the principal features of the bottom variation to be gradual, it may also be taken that h is a function $h(X)$ of the variable X , only.

Requirements that ζ and ϕ are to satisfy Euler equations and continuity, in conjunction with the above hypotheses yield the linear dispersion relation from which k_1 and k_2 are determined,

$$k_j \tanh k_j h = \omega_j^2, \quad j = 1, 2. \quad (3)$$

Solvability conditions for the second order solutions provide a coupled pair of nonlinear ordinary differential equations for the complex amplitudes a_1 and a_1^* ,

$$\frac{da_1}{dx} = -\frac{1}{2C_1} \frac{dC_1}{dx} a_1 - \frac{1}{2} i \frac{\alpha}{\beta} a_1^* a_2 \exp(-i \frac{\Delta k}{\beta} x) \frac{B_1}{C_1} \tag{4}$$

$$\frac{da_2}{dx} = -\frac{1}{2C_2} \frac{dC_2}{dx} a_2 - \frac{1}{2} i \frac{\alpha}{\beta} a_2^2 \exp(i \frac{\Delta k}{\beta} x) \frac{B_2}{C_2}$$

where functional coefficients B_j ($j = 1,2$) depend on ω_j , k_j and X . The symbols C_j and dC_j/dX in (4) denote the group velocity and its spatial derivative given in the present approximation by following expressions,

$$C_j = \frac{1}{2} \frac{1}{\omega_j k_j} [\omega_j^2 - h(\omega_j^4 - k_j^2)]; \quad j = 1, 2, \tag{5}$$

$$\frac{dC_j}{dx} = \frac{k_j^2 - \omega_j^2}{k_j} \frac{\omega_j (h\omega_j^2 - 1)}{\omega_j^2 (h\omega_j^2 - 1) - hk_j^2} \cdot \frac{dh}{dx}, \quad j = 1, 2,$$

and $\Delta k = 2k_1 - k_2$ denotes the difference of wave numbers of the two modal wave components in equation (1).

As shown by Keller (1988), equations (4) are coupled transport equations. The linear dispersion relation, equation (3) and the transport equations (4) constitute the first component of the model. These equations, when supplemented with boundary conditions for α , ω_1 , a_1 and a_1^* at $X = 0$, provide an approximate description of the evolution of the waveform ζ and associated velocity field over a given bed configuration h .

The derivation of the second and third model constituents in which the boundary layer flow and resulting sediment flux are evaluated have been presented in earlier work (Boczar-Karakiewicz and Bona 1986, Chapalain and Boczar-Karakiewicz 1989, Boczar-Karakiewicz *et al.* 1987).

The fourth model constituent relates through continuity the differential of the sediment flux $\partial Q/\partial X$ to the desired temporal evolution of the seabed topography h , thus,

$$\frac{\partial h}{\partial \tau} = \chi \frac{\partial Q}{\partial X} \tag{6}$$

where τ is the time scale of bed deformation and χ denotes the threshold constant. Equation (6) has to be supplemented by sediment parameters (grain diameter, fall velocity, etc.) required in the second, third and fourth model constituents.

Eventually, the coupled system of equations (4),(5) and (6) supplemented by boundary conditions specifying the incident wave parameters (α , ω_1 , a_1 , a_1^*), the initial bed topography h' at $\tau = 0$, and

sediment characteristics, constitutes the dynamic description for wave-bottom interactions.

Results of a typical numerical experiment with a set of incident and initial data for waves of $T = 17$ s and a uniform sloping bed ($\tan \phi = 0.0125$) are presented in Figures 4a-d. At the chosen incident water depth $H = 18$ m the incident wave is assumed to "feel" the presence of a shallow seabed ($\beta = H/\lambda = 0.1$). The incident wave parameter $\alpha = a/H = 0.1$. Selected wave and bed data characterize an extreme cyclonic event in the central region of the Gold Coast area (Broadbeach, see Figure 1 for location).

The instantaneous wave profile ζ over the final bed profile (at $t = 6 \Delta\tau$) is shown in Figure 3a. The harmonic amplitudes $|a_1|$ and $|a_2|$ of the two modal components of the interface ζ are presented in Figure 3b and the relative phases between a_1 and a_2 , $\psi = k_1 - 2k_2 + \arg a_2 - 2 \arg a_1$, are shown in Figure 3c. The initial and final state of the bed topography is shown in Figure 3d (at $t = 0$ and $t = 6 \Delta\tau$, respectively) and $\Delta\tau$ denotes the time step in this experiment.

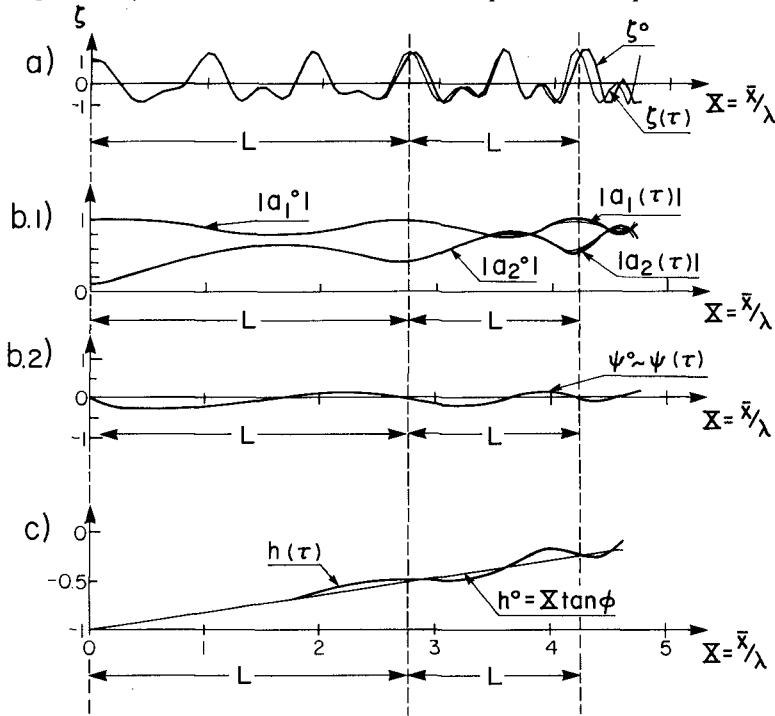


Figure 3. Model predictions of bar formation by cyclonic waves ($T = 17$ s): a) the surface wave profile ζ° , (over h°) and $\zeta(\tau)$ (over $h(\tau)$); b) the Fourier decomposition of ζ into two modal components; c) the initial state h° , and final state $h(\tau)$ of the seabed. The symbol L denotes the repetition length.

The most important aspect of the evolution of the surface wave, which is seen transparently in the evolution of the free surface ζ , is the slow oscillation of the first and second harmonics that is superimposed upon the mean increase in the energy of the second harmonic due to shoaling.

According to the model, energy is exchanged between the modal wave components in a nearly periodic fashion. The horizontal distance between two successive minima of the second harmonic amplitude $|a_2|$ is referred to as the local repetition length L . Such an energy transfer towards higher harmonics has been observed in both laboratory experiments with regular waves (Boczar-Karakiewicz *et al.* 1987) and in spectra of wind waves propagating in a nearshore (Boczar-Karakiewicz and Davidson-Arnott 1987). The repetition length L , which is typically several times the length associated to the surface wave, is also a characteristic length scale in the pattern of the associated velocity field and, consequently, the same scale is induced in the sediment flux pattern Q . The continuity described by equation (6) relates the divergence of the spatially oscillating sediment flux Q , with instantaneous, temporal changes in the bed configuration $h(X)$. Thus, the repetition length L determines the spacing of the sand bars that evolve from the initially featureless bed topography as shown in Figure 3d, (erosion occurs, forming the troughs of the sand bars where $\delta Q/\delta X$ is negative, while sand bar crests are formed where $\delta Q/\delta X$ is positive).

Dynamic equilibrium in a beach system : predictions and comparisons

Formation of sand bars by cyclonic waves simulated on the model and presented in Figure 3 indicate that pronounced changes in the bathymetry may be considered in a zone confined between the isobath of -10 m up to the shoreline. The following experiments are restricted to this narrower part of the nearshore and attention will be focused on time scales of the wave-bed interaction process. Results presented in Figure 3 show two very different time scales considered in the model : the time scale of the surface wave parametrized by its wave period T , and the time scale of bed evolution τ introduced in equation (6). The later can be made explicit by using the parameters of incident waves,

$$\tau = \alpha^5 \beta^{-2} \frac{\bar{f}}{T} \quad (7)$$

and by assuming that sediment concentration and the boundary layer thickness both depend upon the wave amplitude (Boczar-Karakiewicz and Bona 1986). In the following we will investigate the time scale τ carrying out a series of numerical experiments simulating a sequence of wave-bed interaction events typical for the Gold Coast beach system.

The first experiment (Figure 4a) reproduces the event of extreme cyclonic waves ($T = 17$ s, $\alpha = 0.2$; $\beta = 0.5$) resulting in the formation of a two-bar system h . The experiment is initialized now at the water depth of $H = 10$ m from an initial state $h' = X \tan \phi$. The final state h is established after a time $t = 6 \Delta\tau$ (where $\Delta\tau$ denotes the time step

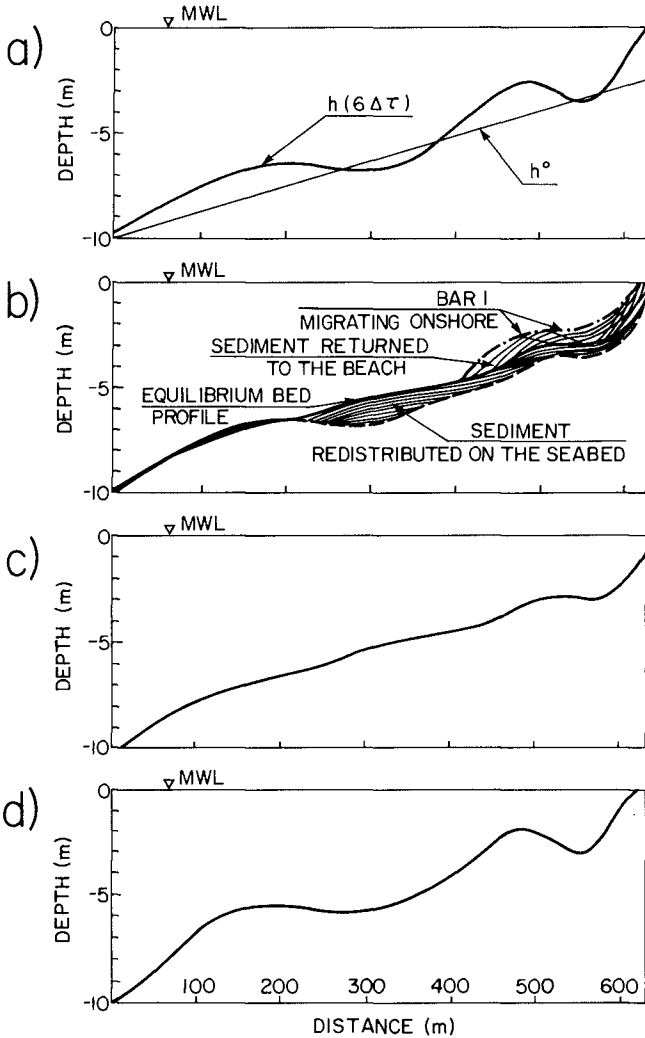


Figure 4. Model predictions of a full cycle of beach transformation: a) formation of a two-bar profile by cyclonic waves ($T = 17$ s) from an initial uniform slope h° ; b) stages of formation of the equilibrium profile by moderate storm waves ($T = 10$ s); c) final equilibrium state; d) reformation of bars by cyclonic waves ($T = 17$ s) from equilibrium state shown in c.

in the present experiment). The second numerical experiment (Figure 4b) simulates moderate storm wave activity ($T = 10$ s, $\alpha = 0.1$, $\beta = 0.1$) which interacts with the seabed which initial state h' that has been formed by cyclonic waves in the previous experiment. Broken lines in Figure 4b represent consecutive stages of the seabed evolution into its final state h of dynamical equilibrium which has been reached after a time $t = 12 \Delta\tau$, (where $\Delta\tau$, denotes the time step in experiment 4b). In the equilibrium state, the seabed remains constant under the action of a wave train of constant parameters. In this state, the offshore bar (bar 1 in Figure 4) is flattened; the trough between bar 1 and bar 2 is filled up with sediment and bar 2 is shifted shorewards. The area between the initial post-cyclonic bed profile and the final equilibrium profile in Figure 4b provides an estimate of sediment volume redistributed on the seabed and of the volume moved onshore, toward the beach. Figure 4c shows again the state of beach equilibrium which constitutes the initial state h' for a following simulation of a cyclonic event under extreme waves ($T = 17$ s, $\alpha = 0.2$, $\beta = 0.05$) presented in Figure 4c. After a time $t = 6 \Delta\tau$, a final state of two bars, denoted by h , is reestablished. Comparisons of h in Figure 4d and 5a shows a close similarity. The final state in Figure 4d terminates a full cycle of nearshore transformation simulated by the sequence of experiments shown in Figure 4b-4d.

The cycle of beach transformation is shown in a three-dimensional version in Figure 5. The initial bar formation (Figure 5a) is followed by two successive stages of profile recovery (Figure 5b) which are terminated by the equilibrium stage (Figure 5c). The stability of the equilibrium state is shown in Figure 5d under moderate storm waves ($T = \text{const}$, $a = \text{const}$). Eventually the reformation of the two-bar post-cyclonic bed profile is shown in Figure 5e.

Time scales in Figures 4 and 5 will now be calibrated using equation (7) and observations from the Gold Coast nearshore. Observations report a typical period of beach recovery under moderate storm conditions in a period of 18 months (Jackson, Smith and Piggot 1988) that provides an estimate of the time step $\Delta\tau$, in the corresponding numerical experiment (Figure 4b), $\Delta\tau = 45$ days. Given the ratio of α and β^{-1} for cyclonic and moderate waves being of the order of 2, the estimate for the time step $\Delta\tau$ in experiment 4a and 4b equals $\Delta\tau = 0.35$ day. Consequently, the period of cyclonic activity forming the two-bar system (Figure 4a and 4d) is approximately equal to two days. Comparisons of model predictions in which the earlier calibrated time scales were used are presented for two sites in the Gold Coast area in Figures 6 and 7. The location of bar crests, their number and dynamics under both extreme and moderate waves is in a quite satisfactory agreement with observations. However, the amplitude of the predicted offshore bar (bar 1) is generally lower than indicated by observations. The latter is maybe not surprising given the extreme simplicity of the model and the extreme complexity of the prototype nearshore.

The post-cyclone seabed profile for the southern part of the Gold Coast area (Kirra, see Figure 1 for location) is presented in Figure 8b. Predictions show that in case of a gradually decreasing mean slope gradient given by observations (Figure 8a) the mean position of the shoreline shifts into the shoreward direction. It may be inferred that

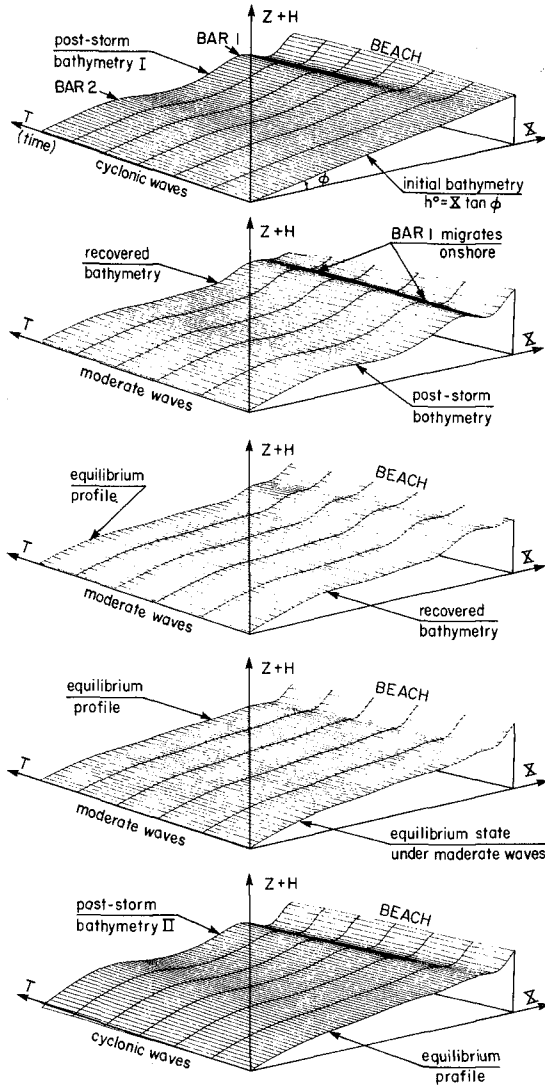


Figure 5. A three-dimensional presentation of model predictions of the cycle of beach transformation : a) formation of post-storm bathymetry by cyclonic waves ($T = 17$ s); b) beach recovery by moderate waves ($T = 10$ s); c) formation of equilibrium by moderate waves ($T = 10$ s); d) equilibrium state under moderate waves ($T = 10$ s); e) bar reformation by cyclonic waves ($t = 17$ s).

observed changes in the nearshore topography are at least partially caused by the deficit of sediment supply in this location, subsequent of the extension of the Tweed River training walls.

3. Conclusions and protection measures for the Gold Coast beach system

The wave-bed interaction model applied in the present paper simulates correctly a typical observed cycle of beach erosion and recovery in the Gold Coast nearshore caused by extreme cyclonic events and followed by periods of moderate storm activity (Figures 4 and 5). Predictions and observations show that beach erosion occurs during a couple of days of an extreme cyclonic event (see Figures 4a and 4d, Figures 5a and 5e) in association with a formation of a prominent two-bar system in the area of the nearshore, limited approximately by a water depth of 10 m. Beach recovery and formation of a nearly uniform featureless equilibrium bed profile has been shown to result from moderate storm wave activity (see Figures 4b-c, Figures 5b-d) during a period of several months.

The simulation of a transformation cycle from post-cyclonic bars into an equilibrium bed profile provides an estimate of sediment volume redistributed over the nearshore and returned to the beach (Figure 4b).

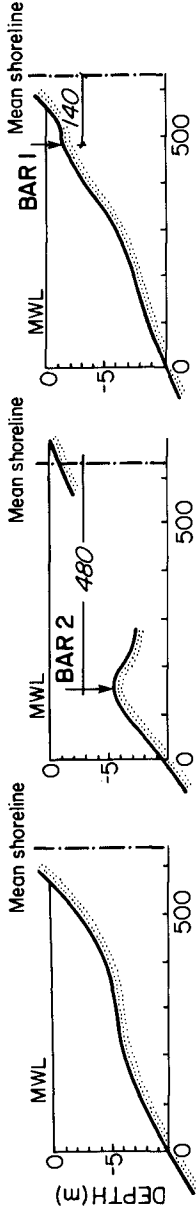
The transformation of the post-cyclonic barred nearshore into recovered equilibrium is shown to be reached when assuming a non-deficit sediment supply and a fully dissipative beach system. The latter requires a conservation of a buffer zone which temporary allows erosion during extreme weather events. The presented beach transformation cycle requires a sufficiently long period of moderate storm-wave activity between two successive extreme storm events (of the order of 18 months, see Figure 5b-c).

In presented calculations, extreme cyclonic waves (characterized by peak periods of 17 secs) were simulated by a regular wave train with a period $t = 17$ s, and a wave amplitude of $a = 2$ m at the incident water depth $H = 19$ m. Moderate wave activity was simulated with an incident wave train of a wave period $T = 10$ s and an amplitude $a = 1.0$ m at the incident water depth $H = 10$ m. Model predictions compared with observations in two chosen locations of the central Gold Coast area have shown a satisfactory agreement for both the pre- and post-cyclonic bars (see Figures 6 and 7).

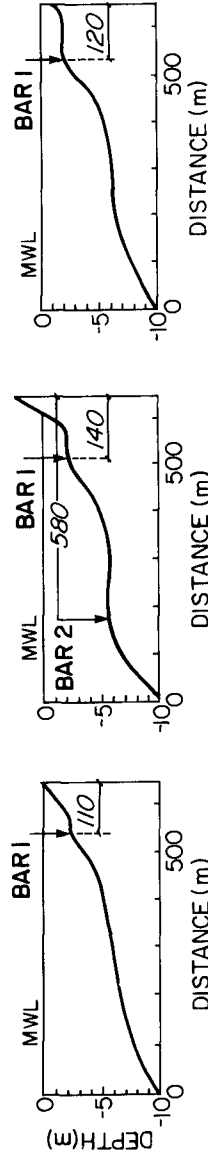
Presented results compared with available observations suggest beach protection measures in the Gold Coast area, which would compensate progressing erosion resulting from a deficit in sediment supply and from development pressures.

Suggested method of beach nourishment consists of the formation of a post-cyclonic profile, i.e. in placing sediment pumped from offshore in the location of the two offshore bars. The volume of the placed sediment will compensate the local deficit in the sediment supply, will be partially redistributed over the active nearshore and be partially returned to the beach after several months of moderate wave activity. The reconstruction of bars by beach nourishment will additionally provide protection to the beach due to energy dissipation caused by a multiple offshore breaking of the incident wave. However, according to presented results, sediment for nourishing the nearshore

[i] MEASURED BATHYMETRIES (1967-68)



[ii] MODEL PREDICTIONS



a) PRE-STORM PROFILES b) POST-STORM PROFILES c) RECOVERED PROFILES

Figure 6. Comparison of measured and predicted bathymetries at Surfers Paradise for a) pre-storm conditions; b) post-storm conditions; and for c) beach recovery.

PRE-STORM

POST-STORM

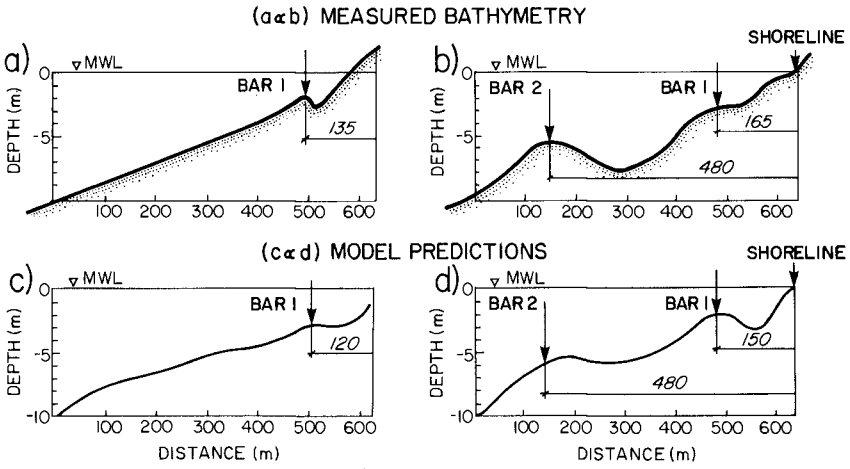


Figure 7. Comparison of model predictions with measured bathymetries : pre- and post-storm bathymetries at Broadbeach.

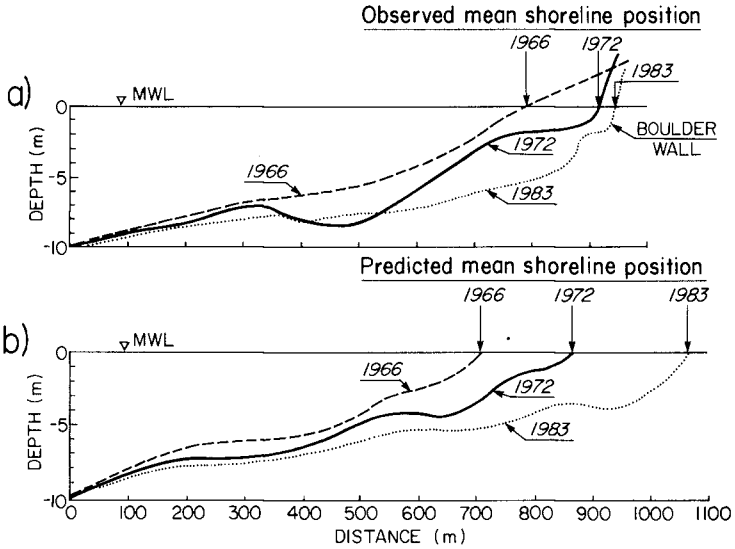


Figure 8. Observed (a) and predicted (b) shoreline recession due to changes in the mean slope of the underwater beach at Kirra.

should be removed from areas lying deeper than the isobath -20 m which constitutes the outer limit of the active nearshore for extreme cyclonic waves.

Results of model simulation in the area of Kirra (Figure 8) indicate that construction of seawalls is only a temporary measure of protection. The constantly decreasing mean nearshore slope of the seabed in this region due to acute sediment deficit results in a constant shoreward shift of the mean shoreline position. The latter causes slumping of seawalls which themselves have a negative effect on nearshore stability associated with strong wave reflection.

Acknowledgements

Support for this project was provided by the Ministry of Fisheries and Oceans (Government of Canada) and by the Natural Sciences and Engineering Research Council of Canada (Grant no A2621). Both authors also acknowledge the Gold Coast City Council, QLD, Australia, for releasing survey data for this publication.

References

- Boczar-Karakiewicz, B. and J.L. Bona. 1986. Scale effects in modelling sand bar formation in coastal regions by progressive surface waves. Symposium '86. Int. Ass. Hydr. Res. (IAHR), Toronto, Proceedings : 49-61 (ed. A.S. Yalin).
- Boczar-Karakiewicz, B., J.L. Bona and D.L. Cohen. 1987. Interaction of shallow-water waves and bottom topography. *In* : Dyn. Problems Cont. Physics, Springer-Verlag, 4 : 131-175.
- Boczar-Karakiweicz, B. and R.D.L. Davidson-Arnott. 1987. Nearshore bar formation by non-linear wave processes - A comparison of model results and field data. *Mar. Geol.*, 77 : 287-304.
- Boczar-Karakiewicz, B., A. Létourneau, Y. Gratton and B. Pelchat. 1990. Oblique incident waves in a shore-parallel bar system. *Can. Coastal Conf.*, Kingston, (ed. M. Davies). : Proceedings : 99-109.
- Chapalain, G. and B. Boczar-Karakiewicz. 1989. Longshore bar formation in coastal wave-dominated areas. XXIII Congress of Int. Ass. Hydr. Res., Ottawa, Proc., Tech. Session C : C531-C538.
- Chapman, D.M. 1980. Beach nourishment as a management technique. Proc. 17th Int. Coast. Eng. Conf., Sydney : 86-92.
- Gold Coast City Council, 1990, Coastal Engineering Works, Internal Report
- Jackson, L.A., A.W. Smith and T. Piggot. 1988. Data for coastal management in a beach zone. *Coast. Zone Manag.* 88 Workshop, Lismore. Proceedings : 102-110.
- McGrath, B.L. and D.C. Patterson. 1972. Wave climate at Gold Coast, Qld, Australia. *Inst. Eng. Aust.*, 8 Div. Tech. Papers 13 (5) : 1-17.
- Smith, A.W. and L.A. Jackson. 1990. The siting of beach nourishment placements. *Shore and Beach*, 58 (1) : 17-24.

CHAPTER 172

SEA BOTTOM TOPOGRAPHY WITH IMAGING RADAR

J. Vogelzang¹, G.J. Wensink², D. van Halsema³
and G. van der Burg⁴

ABSTRACT

Mapping sea bottom topography with imaging radars or optical sensors can add valuable information to traditional bathymetric surveys. This paper describes a series of (already performed or planned) experiments in which the Dutch Bottom Topography Group is involved. It is shown how radar and optical imagery can be used to map the sea floor.

1. INTRODUCTION

The first observation of sea bottom topography with imaging radar (Side Looking Airborne Radar, SLAR or Synthetic Aperture Radar, SAR) was made in 1969 by de Loor and his co-workers (de Loor and Brunsveld van Hulten, 1978 ; de Loor, 1981). At that time it was not understood why sea bottom topography could be visible on radar images: since sea water is almost a perfect conductor at radar frequencies, the penetration length is a fraction of the radar wave length (which was about 1 cm in these observations). Therefore the radar beam never penetrates to the bottom.

¹ Rijkswaterstaat, Tidal Waters Division, PO Box 20907,
2500 EX The Hague, The Netherlands.

² Delft Hydraulics, PO Box 152, 8300 AD Emmeloord, The
Netherlands.

³ Physics and Electronics Laboratory TNO, PO Box 96864,
2597 JG The Hague, The Netherlands.

⁴ National Aerospace Laboratory NLR, PO Box 153,
8300 AD Emmeloord, The Netherlands.

The phenomenon received little attention until SEASAT was launched in 1978. This satellite carried among other sensors a L-band SAR. With this instrument dramatic images of sea bottom topography in the Southern Bight of the North Sea and the English Channel (Alpers and Hennings, 1984), and the Nantucket Shoals (Shuchman, Lyzenga and Meadows, 1985) were obtained. All SEASAT images revealing bottom related structures are reviewed by Kasischke et al. (1983). Also internal waves (Rufenach and Smith, 1985) and ship wakes (Vesecky and Stewart, 1982) were clearly visible on SEASAT images.

The SEASAT mission has provoked much interest, both from the experimental and the theoretical side. It has stimulated further experimental research (McLeish et al., 1981; Valenzuela et al., 1985, Apel et al., 1985, Chubb et al., 1989). It was also found that bottom topography is visible in the optical range (Kasischke and Tanis, 1986; Hennings, Doerffer and Alpers, 1988).

From these studies it appeared that sea bottom topography can be visible with imaging radar in shallow seas (maximum depth about 50 m) with (tidal) currents of 0.5 m/s or more at a wind speed between 2 and 10 m/s.

In this paper the research activities in the Netherlands are described. In section 2 the imaging mechanism is described. Section 3 is devoted to past and future experimental campaigns. In section 4 the conclusions are stated.

2. IMAGING MECHANISM

Several theories have been proposed to describe the imaging mechanism. It is now generally accepted that the mechanism consists of three steps:

- (1) Interaction between (tidal) flow and bottom topography produces modulations in the surface current velocity.
- (2) Modulations in the surface current cause spatial variations in the wind generated spectrum of water waves.
- (3) Variations in the wave spectrum are visible as modulations in the radar backscatter.

Models of this kind have been proposed by Alpers and Hennings (1984), Shuchman, Lyzenga and Meadows (1985), Holliday, St-Cyr and Woods (1986) and by van Gastel (1987). Internal waves also cause variations in the surface current, so the second and third step of this mechanism can be used to describe their signature on radar images. The mechanism also applies to other regions than the microwave part of the electromagnetic spectrum.

The first step is usually described using the continuity equations (mass conservation)

$$U_{per} = C_{per}/h \quad , \quad (1a)$$

$$U_{par} = C_{par} \quad , \quad (1b)$$

where U_{per} stand for the component of the surface current perpendicular to the (elongated) sand bank or sand wave, U_{par} for the parallel component and h for the depth, C_{per} and C_{par} being constants. Equations (1a) and (1b) are in general valid for the depth averaged current velocity, but not for the surface current velocity which also is influenced by the wind. A better description of the surface current field can be obtained from a (quasi) three-dimensional flow model.

The second step, the wave current interaction or hydrodynamic modulation, is described by the Action Balance Equation. This is a transport equation with a source term describing the combined effect of wind input, dissipation and non-linear wave-wave interactions. The precise form of this term is not well known. Therefore most authors use simple relaxation forms for the source term, which is either linear (Alpers and Hennings, 1984 ; Holliday, St-Cyr and Woods, 1986 ; Hennings, 1990) or quadratic (Shuchman, Lyzenga and Meadows, 1985) in the action spectrum. Van Gastel (1987) includes the effects of wind input, dissipation and non-linear interactions in a rigorous way.

The scattering of radar from the ocean surface is usually described with first-order Bragg scattering. In this approach, the radar cross section of the sea is proportional to the spectral density at the so called Bragg wave number k_B , given by

$$k_B = 2k \sin(\theta) \quad , \quad (2)$$

where k is the wave number of the incident radiation and θ the angle of incidence.

Vogelzang (1989) has compared these models by solving the action balance equation numerically, showing that these models give almost the same results. At high radar frequencies (X-band) and at wind speeds exceeding 5 m/s or more, the effect of advection can be neglected as in the original model of Alpers and Hennings (1984). In this case, the radar cross section is proportional to the gradient of the surface current, or, using the continuity equations (1a) and (1b), to the bottom slope.

At L-band, the simple relaxation models predict modulations of the order of 10 per cent, in agreement with the experimental data. At X-band, however, these models underestimate the modulation by an order of magnitude. By including non-linear interactions (van Gastel, 1987) or other scattering mechanisms than first-order Bragg (Holliday, St-Cyr and Woods, 1986) the modulation is increased to its correct value.

3. EXPERIMENTS

In this section the research activities of the Dutch Bottom Topography Group will be described. The group is formed by representatives from Rijkswaterstaat, Delft Hydraulics, Physics and Electronics Laboratory TNO and National Aerospace Laboratory NLR. International cooperation has been established with institutes from Germany, the United Kingdom and the United States of America.

3.1 DDSLAR

A first experiment was performed on January 19, 1988 using the Dutch Digital SLAR (DDSLAR) to investigate the possibilities and limitations of mapping sea bottom topography with imaging radar for cartographic purposes. The experiment was performed in a test area 30 km off the Dutch coast (see figure 1). The bottom topography in this area is dominated by sand waves with a height between 2 and 6 m and a crest-to-crest distance of typically 500 m at a mean depth of about 22 m.

This area was chosen for the following reasons :

- (1) the bottom topography is simple and quasi one-dimensional.
- (2) the access time to the test area is short.
- (3) it is close to the Measuring Platform Noordwijk (MPN), an oceanic research platform that is part of the North Sea Monitoring Network.
- (4) the area has been studied in earlier experiments.

The test area has been recorded with the Dutch Digital SLAR, an airborne X-band HH polarized SLAR system operated by the National Aerospace Laboratory NLR. With this system and the processing facilities available at NLR it is possible to obtain both geometrically and radiometrically correct images. During the experiment the current velocity profile was measured from two ships near the centre of the test area. The position of one of these ships was recorded using HYPERFIX with a precision of 1.5 m. Therefore the image of this ship could be used as a position fix, and the position in the radar image could be determined with an

error of two pixel sizes (30 m) at most. An ordinary bathymetric map of the test area has been digitized.



Figure 1. The test area off the Dutch coast.

During the experiment, the wind speed varied between 7 and 8 m/s, while the surface current during the radar overflights was between 0.6 and 0.8 m/s. Under these circumstances one expects that the bottom slope is visible on the radar images. Figure 2 shows a radar image, a simulated radar image using the model of Alpers and Hennings (1984) and the bathymetry of the test area. The radar image is rather noisy due to the low sensitivity of the DDSLAR.

Figure 3 shows the correlation between the intensity and the bottom slope, which should have a minimum at $j = 0$ if the radar cross section is proportional to the bottom slope (note that the constant of proportionality is negative).

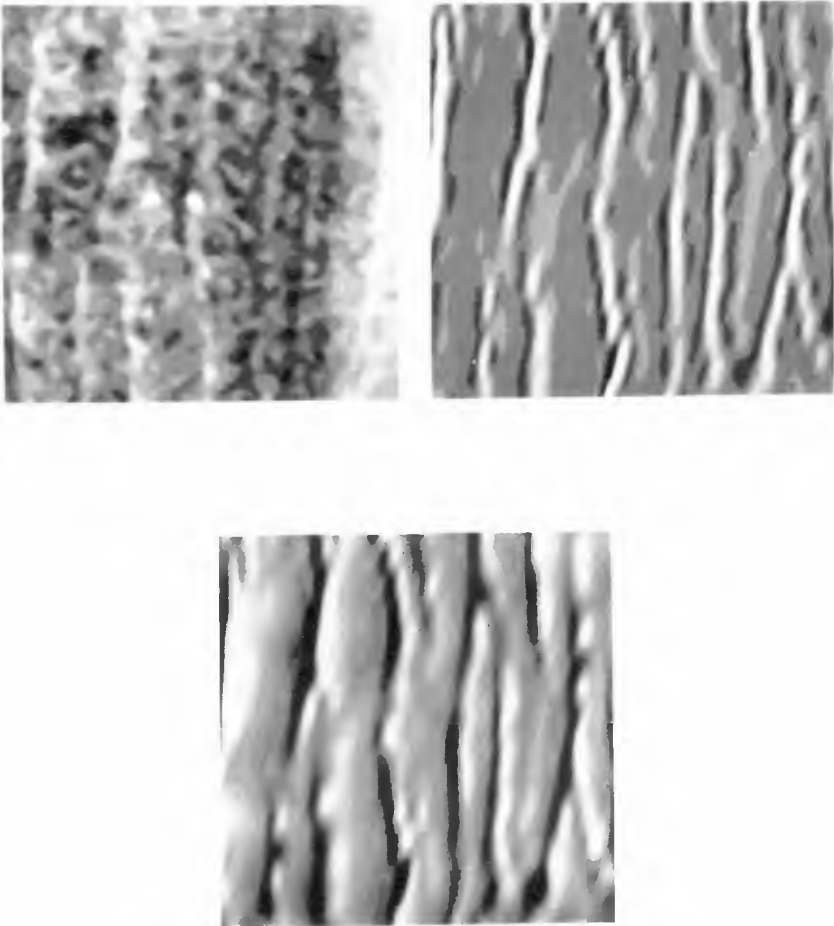


Figure 2. Radar image (upper left), simulated image (upper right) and bathymetry (lower).

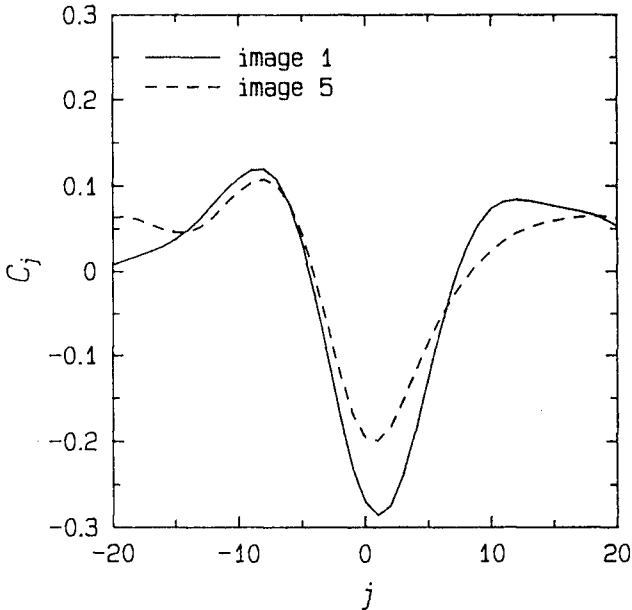


Figure 3. Correlation between intensity and bottom slope for two of the radar images recorded during the experiment

From this experiment the following conclusions were drawn :

- (1) At wind speeds of 5 m/s or more, X-band radar imagery shows the bottom slope, as predicted by simple relaxation models. The sand waves in the test area have an asymmetric profile, with the steeper slopes directed to the NorthEast. Therefore the steeper slopes are visible as a pattern of bright or dark lines, depending on the direction of the tidal current, while the gentle slopes act as a background.
 - (2) The positional accuracy in radar images can be about two pixel sizes. For most radar systems this is of the order of 20 m.
 - (3) The sensitivity of the radar system is a crucial parameter for mapping bottom topography.
- More information can be found in the final report of this project (Vogelzang et al., 1989).

3.2 JPL-SAR

On August 16, 1989, the test area was recorded with the airborne P-, L- and C-band polarimetric SAR of NASA/JPL, to study the effect of radar wave length and polarization. The sand waves are clearly visible on the P- and L-band images, but not on the C-band image. This is due to the low sensitivity of the C-band SAR. These images are now under study. They will be compared with predictions of a one-dimensional model for the imaging mechanism. The surface current field in this model is generated by a detailed quasi three-dimensional flow model of the test area. The flow model includes the effect of the wind on the surface current. The action balance equation will be solved in one dimension using existing simple expressions for the source term. The radar cross section will be evaluated using a two-scale scattering model. Such a scattering model includes the effect of longer waves by integrating the first-order Bragg scattering over the tilt caused by longer waves.

3.3 Future research

The test area will be studied with the C-band SAR carried by the first European Remote Sensing satellite (ERS-1). Wind and wave data will be collected at MPN, while the surface current will be hindcasted using the quasi three-dimensional flow model. Since the ERS-1 will make images of the test area at different points in the tidal cycle and under different wind conditions, these images can be used to fix the optimum hydro-meteorological conditions for mapping sea bottom topography with imaging radar. Also the dynamical behavior of the bottom topography can be studied, since the ERS-1 mission extends over a longer period.

In collaboration with the Universities of Hamburg and Kiel (Germany) and the University of North Wales (UK) the bottom topography in the same test area will be studied using both microwave and optical sensors. The goal of this research, sponsored by the Commission of European Communities (CEC) in the framework of the Marine Science and Technology (MAST) program, is to establish how remote sensing methods can be used as input in morphodynamic models which are currently being developed. To achieve this goal, a large experiment is planned for April 1991. The model for the imaging mechanism will be extended to two dimensions. To compare the experimental results with the bathymetry, a precise bathymetric survey with a multi-beam echo sounder will be held in the test area after the experiment.

The models developed during these experiments can be tested in a region with a more complicated bottom topography during the SIR-C/X-SAR mission with multi-polarization L-, C- and X-band SAR. A preparatory flight with the airborne P-, L- and C-band SAR of NASA/JPL is planned for 1991.

The final goal of this research is to obtain information about the bathymetry from microwave (and optical) imagery, using data-assimilation techniques as indicated in figure 4. Starting with an initial guess or an old bathymetric map, the radar image can be calculated. The simulated image is compared with the observed image. By changing the input-bathymetry, the simulated image is matched to the observed image. When both images match, the input-bathymetry equals the actual bathymetry. The next MAST program would be suited for investigating this possibility.

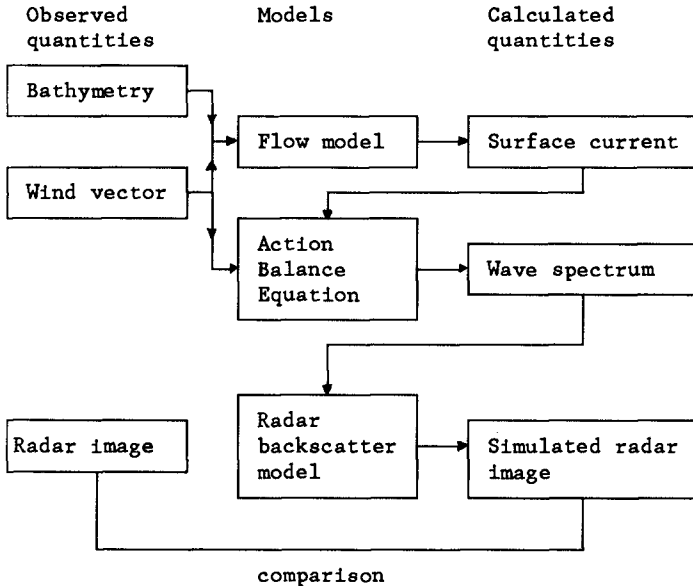


Figure 4. Modelling.

4. CONCLUSIONS

Under favorable conditions (low wind speed and strong tidal current) sea bottom topography in shallow seas can be mapped with imaging radar. At wind speeds of 5 m/s or more, X-band radar imagery reveals the region with large bottom slopes. The horizontal accuracy can be of the order of two pixel sizes, which corresponds to about 20 m for existing systems.

If the processes involved in the imaging mechanism are well modelled, data-assimilation techniques can be applied to obtain bathymetric information from radar images.

It is not expected that remote sensing methods will replace traditional bathymetric surveys. However, remote sensing methods give an overview over large areas at low costs. This information can be used for validating and steering morphodynamic models and optimizing bathymetric surveys.

ACKNOWLEDGEMENTS

Part of this work has been financially supported by the Netherlands Remote Sensing Board (BCRS) as a part of the National Remote Sensing Program (NRSP).

The project in the framework of the Marine Science and Technology Program (MAST) is supported by the Commission of European Communities, Directorate General XII (Science, Research and Development).

The authors wish to thank W. Alpers (University of Hamburg), I. Hennings (University of Kiel), J. Matthews (University of North Wales) J. Klein (Jet Propulsion Laboratory) and G.P. de Loor for their fruitful collaboration.

RÉFERENCES

- ALPERS, W. and HENNINGS, I., 1984,
A theory of the imaging of underwater bottom topography by real and synthetic aperture radar.
Journal of Geophysical Research, 89 C, 10529-10546.
- APEL, J.R. et al. (SARSEX EXPERIMENTAL TEAM), 1985,
SARSEX interim report.
JHU/APL STD-R-1200.
The John Hopkins University/Applied Physics Laboratory, Laurel, Maryland, USA.
- CHUBB, S.R., VALENZUELA, G.R. and GREENBERG, D.A., 1989,
Radar surface signatures based on the two-dimensional tidal circulation of Phelps Bank, Nantucket Shoals, MA.
Proc. IGARSS '89 Symposium, Vancouver, Canada, July 10 - 14, 1989. pp 2700 - 2702.
- HENNINGS, I., DOERFFER, R. and ALPERS, W., 1988,
Comparison of submarine relief features on a radar satellite image and on a Skylab satellite photograph.
International Journal of Remote Sensing, 9, 45 - 67.
- HENNINGS, I., 1990,
Radar imaging of submarine sand waves in tidal channels.
Journal of Geophysical Research, 95 C, 9713 - 9721.
- KASISCHKE, E.S., SHUCHMAN, R.A., LYZENGA, D.R. and MEADOWS, G.A., 1983,
Detection of bottom features on SEASAT Synthetic Aperture Radar imagery.
Photogrammetric Engineering and Remote Sensing, 49, 1341 - 1353.
- KASISCHKE, E.S. and TANIS, F.J., 1986,
Detection of bottom-related surface patterns on visible spectrum imagery.
Proceedings IGARSS '86 Symposium, Zurich, 8 - 11 Sept 1986. Ref. ESA SP-254, pp 1301 - 1306.
- DE LOOR, G.P. and BRUNSVELD VAN HULTEN, H.W., 1978,
Microwave measurements over the North Sea.
Boundary Layer Meteorology, 13, 113 - 131.

- DE LOOR, G.P., 1981,
The observation of tidal patterns, currents and bathymetry with SLAR imagery of the sea.
IEEE Journal of Oceanic Engineering, OE-6, 124-129.
- McLEISH, W., SWIFT, D.J.P., LONG, R.B., ROSS, D. and MERRILL, G., 1981,
Ocean surface patterns above sea-floor bedforms as recorded by radar, Southern Bight of the North Sea.
Marine Geology, 43, M1 - M8.
- RUFENACH, C. and SMITH, C., 1985,
Observation of internal waves in LANDSAT and SEASAT satellite imagery.
International Journal of Remote Sensing, 6, 1201-1207.
- SHUCHMAN, R.A., LYZENGA, D.R. and MEADOWS, G.A., 1985,
Synthetic Aperture Radar imaging of ocean-bottom topography via tidal-current interactions : theory and observations.
International Journal of Remote Sensing, 6, 1179-1200.
- VALENZUELA, G.R., PLANT, W.J., SCHULER, D.L., CHEN, D.T. and KELLER, W.C., 1985,
Microwave probing of shallow water bottom topography in the Nantucket Shoals.
Journal of Geophysical Research, 90 C, 4931 - 4942.
- VESECKY, J.F. and STEWART, R.H., 1982,
The observation of Ocean surface phenomena using imagery from the SEASAT Synthetic Aperture Radar : an assessment.
Journal of Geophysical Research, 87 C, 3397 - 3430.
- VOGELZANG, J., 1989,
The mapping of bottom topography with imaging radar. A comparison of the hydrodynamic modulation in some existing models.
International Journal of Remote Sensing, 9, 1503-1518.
- VOGELZANG, J., WENSINK, G.J., DE LOOR, G.P., PETERS, H.C., POUWELS, H. and VAN GEIN, W.A., 1989,
Sea bottom topography with X-band SLAR.
Netherlands Remote Sensing Board report BCRS-89-25, Rijkswaterstaat, Survey Department, Delft, The Netherlands.

CHAPTER 173

APPLICATION OF EQUILIBRIUM BEACH CONCEPTS TO SANDY GREAT LAKES PROFILES

M. Todd Stockberger*
(Associate Member ASCE)
William L. Wood**
(Member ASCE)

ABSTRACT

This study was designed to evaluate the equilibrium beach concept for conditions of "rapidly" varying water level, experienced on the North American Great Lakes. It was determined that the mathematical expression $h(x) = Ax^{2/3}$ is appropriate for describing sandy beach and nearshore profiles of the Great Lakes. In addition, a correlation was found between lake-level change and the shape factor A, that indicates a phase lag in beach and nearshore response to "rapidly" changing water level. Results from this study also raise some questions about the reliability of determining the shape factor A directly from sediment size. Reliability in the determination of A may be related to the stability shape of the profile relative to its equilibrium shape.

INTRODUCTION

During the past two and one half decades many researchers (Bruun, 1962; Edelman, 1968, 1972; Swart, 1974, 1976; Le Mehaute and Soldate, 1980; Kriebel and Dean, 1985; Hands, 1979, 1980, 1984; Weishar and Wood, 1983; Wood and Weishar, 1984) have investigated the response of the beach and nearshore to changes in water level. Concern has

* Research Engineer, Black & Veatch, P.O. Box 8405, Kansas City, MO 64114

** Associate Professor of Ocean Engineering and Director, Great Lakes Coastal Research Laboratory, School of Civil Engineering, Purdue University, West Lafayette, IN 47907

primarily been with rising water level since it is recognized as being a major contributor to the cause of increased shore erosion. While the focus of research has been on increases in water level and the corresponding shore response, there has been little similar research concerning rapidly changing or decreasing water level and the resulting effects on the beach and nearshore.

Recently, efforts have been made to apply the equilibrium beach concept to a variety of coasts, including the Great Lakes (Hands, 1979, 1980, 1984; Dean, 1977; Hughes, 1978). Dean (1977) proposed that nearshore profiles assumed a form consistent with $h(x) = Ax^{2/3}$, where h is the depth, x is the distance offshore, and A is a parameter dependent upon sediment characteristics of the profile being examined. Hands (1984) extended this formulation to the Great Lakes and hypothesized that the effects caused by rising lake level would simply be reversed by falling levels.

It appears reasonable to base a predictive model for Great Lakes beach profile response on the equilibrium beach concept. However, it must be shown that the nearshore profiles of the Great Lakes respond on a time scale similar to that of lake-level change. If the nearshore does not respond on a time scale similar to that of lake-level, serious limitations would be imposed on the ability of the equilibrium beach concept to predict nearshore response.

DATA COLLECTION AND ANALYSIS

The data used for this research consists of two series of nearshore profiles collected along the southeastern shore of Lake Michigan (see inset Figure 1). The first series consists of beach and nearshore profiles taken at 6 locations downdrift of the Michigan City, Indiana Harbor ("MTB" series, Figure 1). A total of 42 profiles were collected during the years 1975 through 1978, 1981, 1983, and 1985. Sediment samples were taken at the time of profiling for each line at water's edge and at the 1, 2, 3, 4, 5, 6, and 7 meter isobaths. The second series consists of beach and nearshore profiles taken at 6 locations updrift of the Michigan City Harbor ("SR" series, Figure 1). A total of 57 profiles were collected during the years 1966 through 1973, 1980, and 1988. Sediment data was also collected for this series for the years 1966 through 1973 (Hawley and Judge, 1969); however, these data were not available for analysis.

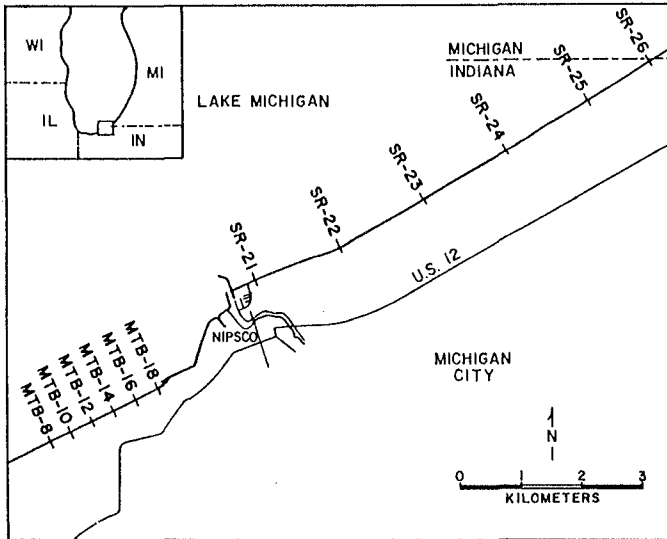


Figure 1 Study Area

Analysis of the Profile Form: $h(x) = Ax^m$

In order to determine whether the equilibrium profile form $h(x) = Ax^m$ is appropriate in describing Lake Michigan profiles, each profile was fit (using the method of least squares) from water's edge to closure depth. This analysis was used to obtain the distribution of the values of the exponent m and coefficient A . If the distributions of both m and A are found to be similar to those found by Dean (1977) and Hughes (1978), it can be concluded that an equation of the form $h(x) = Ax^{2/3}$ is valid for describing the profiles examined. If dissimilar distributions are found, then either a different exponent or a new equation describing the profile form can be established.

Analysis of Coefficient A and Mean Sediment Size

Dean (1977), Hughes (1978), and Moore (1982) showed that a relationship seems to exist between mean sediment size and the shape factor A . Therefore, it is reasonable to analyze the data in such a manner as to determine if this relationship holds true for Lake Michigan profiles. The measured profiles are separated into three sections (Figure 2). The first section consists of that part of the

profile extending from water's edge to the point of inflection within the trough of the inner bar. The second section consists of that part of the profile lakeward of the inner bar trough and extending to the point of inflection within the trough of the outer bar. The third section consists of that part of the profile lakeward of the outer bar trough and extends beyond the depth of closure. Although the second slope break occurs at a point coincident with the trough of the outer bar, the outer section of the profile is actually initiated just lakeward of the outer bar. By using the section of the profile which is initiated just past the outer bar, any numerical ambiguity associated with the trough is avoided. The difference in the value of A was calculated for the outer section using both locations for section initiation and the error was found to be on the order of a few tenths of a percent.

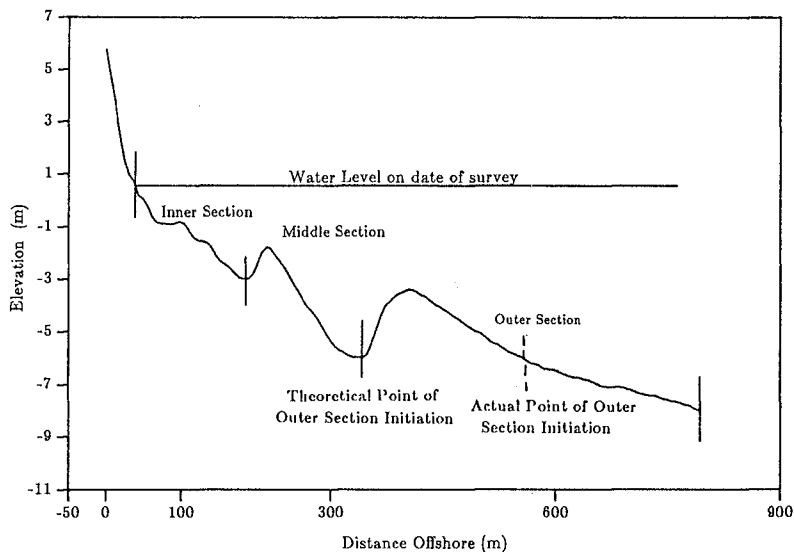


Figure 2 Nearshore Profile Sections

The first, or inner, section of the profile ranges in depth from water's edge to approximately the 1 to 1.5 meter isobath; therefore, the mean grain size at the 1 meter isobath and at water's edge were averaged to characterize the mean grain size of the inner section. The second, or middle, section of the profile ranges from approximately the 1 to 1.5 meter isobath to approximately the 2.5 to 3

meter isobath; therefore, the mean grain size at the 2 and 3 meter isobaths were averaged to characterize the middle section. The third, or outer, section of the profile ranges from approximately the 2.5 to 3 meter isobath to approximately the 7.5 meter isobath. The mean grain size of the 3, 4, 5, 6, and 7 meter isobaths were averaged to characterize the mean grain size of this section. The A value of each section of each profile is plotted against its characteristic mean sediment size. A comparison is then made with the findings of Moore (1982) to determine if his empirically determined curve is valid for the Great Lakes.

The Effect of Water Level Change on Shape Factor A

On the Great Lakes water level changes on a much shorter time scale and a much larger vertical scale than on ocean coasts. The rate of mean still water level change on the Great Lakes is of the order of 10's of centimeters per year. In order to determine whether Great Lakes profiles respond on a time scale similar to that of water level change, the average value of A for all profiles, for each survey period and with each of the two series considered separately, are plotted against time. If the profiles respond on a time scale slower than that of water level, the mean A values will be seen to vary in correspondence with the water level. If the profiles respond on a similar time scale, the mean A values will remain relatively constant.

RESULTS

Nearshore Profile Form

The values of the exponent m and coefficient A were determined for all 99 profiles used in the study. Figure 3(a) shows the distribution of exponent m for all profiles. This distribution compares favorably to the distribution of m values found by combining the results of Dean (1977) and Hughes (1978). The mean m value for Lake Michigan profiles is 0.632 which is in agreement with the values found by Dean, 0.66, and by Hughes, 0.671.

The results of this analysis support Dean's finding that a value of m equal to $2/3$ is appropriate in describing nearshore profiles. Figure 3(b) shows the distribution of the coefficient A for all profiles. This distribution also compares well to the distribution found by combining the results of Dean (1977) and Hughes (1978). Owing to the

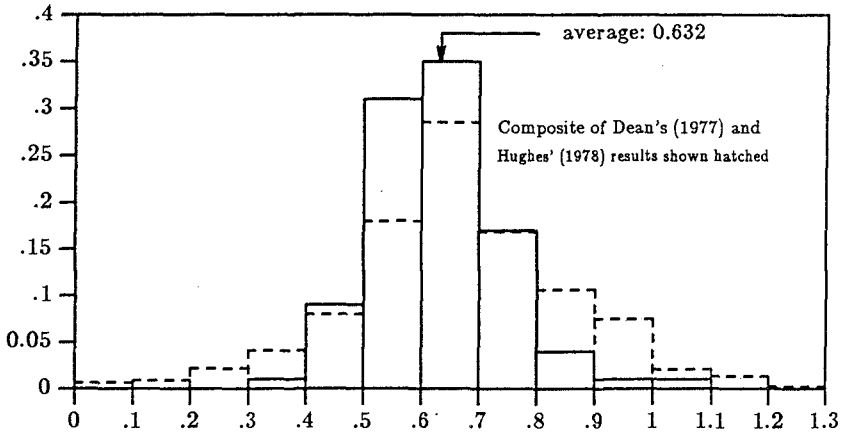


Figure 3. Frequency Distributions of: a) exponent m, and b) coefficient A

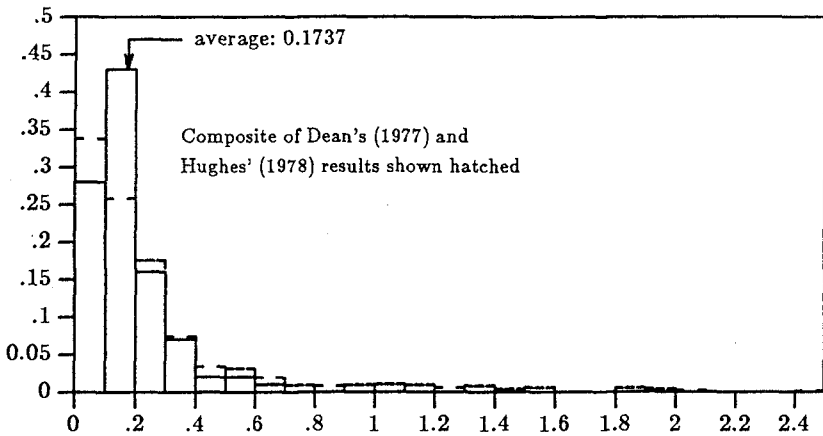


Figure 3. continued

similarity between the distributions of m and A for Lake Michigan profiles and the distributions found by Dean and Hughes, it appears that the nearshore profiles of Lake Michigan can, in general, be described by the equation $h(x) = Ax^{2/3}$.

Variation of Shape Factor A with Mean Grain Size

Figure 4 shows the joint distribution of coefficient A and grain size for the Lake Michigan profiles plotted with a set of curves developed by Moore (1982). Each of the three sections of the nearshore profiles were examined individually to evaluate any relationships that may exist between A and grain size. In general, the majority of data points lie within the range of expected values. The data for the inner sections of the profiles show the most variability in mean sediment size and the best correlation with Moore's curves. Both the middle and outer sections exhibit very little variation in mean grain size, thus, the data points for these sections result in nearly vertical distributions in A (Figure 4).

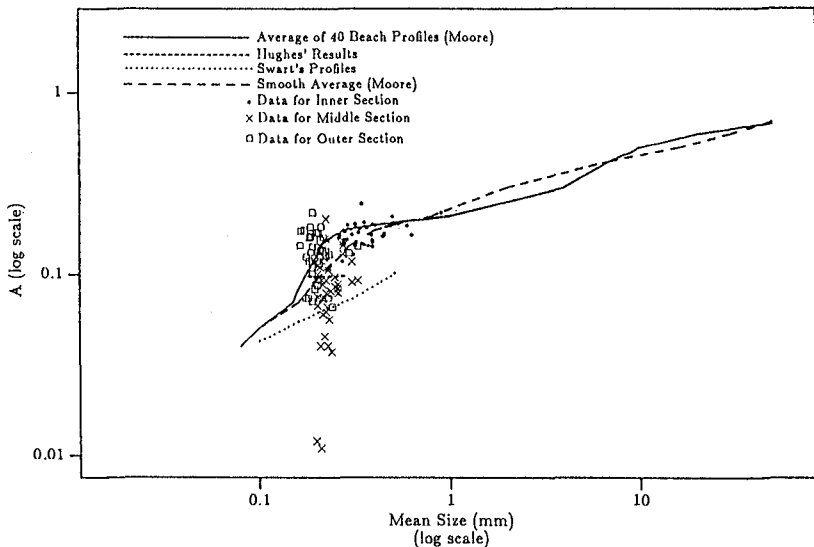


Figure 4. Distribution of A versus Grain Size for the Inner, Middle, Outer Sections of the Profiles.

The data for the inner sections of the nearshore profiles have been plotted separately on the set of curves

developed by Moore (Figure 5). The data for the inner section lie primarily between the curve representing Moore's averaged data and the "smooth curve" developed by Moore. In order to better evaluate the relationship between the calculated values of A and the curves developed by Moore (1982), a statistical analysis was performed (Table 1). The results of this analysis show that a correlation between the A data of this study and the curves developed by Moore does not exist. This result raises questions concerning the relationship between sediment size and the shape factor A.

The Effect of Water Level Change on Shape Factor A

In order to evaluate whether the nearshore profiles of the Great Lakes respond on a time scale similar to that of water level change, the average values of A for each year were plotted against time. Figure 6 shows the mean value of A for the inner sections of the SR series plotted against time, with changes in water level superimposed.

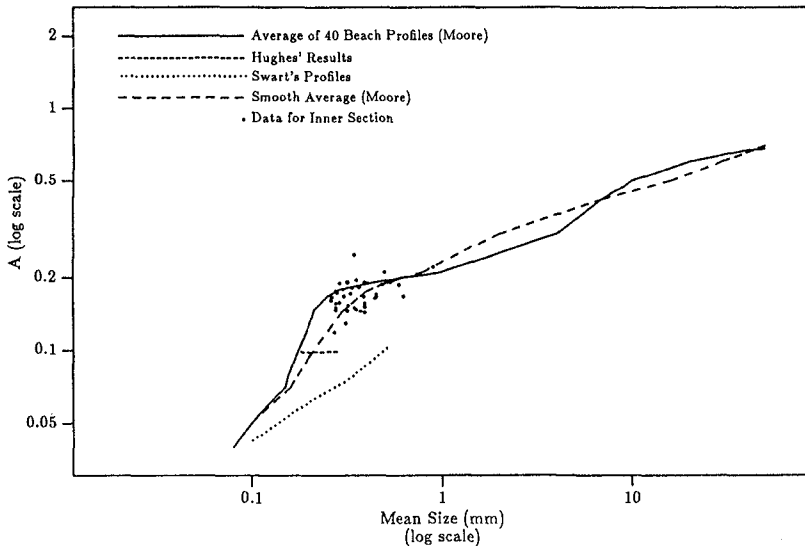


Figure 5. Distribution of A versus Grain Size for the Inner Sections Only

The horizontal hash marks show the respective limits of the coefficient A for plus and minus one standard deviation. The coefficient of determination, r^2 , (where r is the correlation coefficient) was calculated for all lines and all sections except for the outer section of the SR lines.

It could be seen from graphical analysis of this outer section that the plot of mean A values with time was essentially a horizontal line, thus showing no correlation with water level change. The coefficient of determination, r^2 , represents the amount of variation in the mean values of A that can be predicted or accounted for by water level change. Table 2 shows the values of the correlation coefficient and the coefficient of determination for the analyzed sections.

For Comparison to Moore's Data Curve				
Section	error	rms error	r	r^2
Inner	-0.000 9	0.023	0.32	0.1
Middle	-0.061	0.076	---	---
Outer	0.003	0.050	---	---
For Comparison to the Smooth Curve				
Section	error	rms error	r	r^2
Inner	0.0185	0.030	0.36	0.13
Middle	-0.011	0.050	---	---
Outer	0.0023	0.034	---	---

Table 1. Statistical Results for Sediment Size versus Coefficient A Data Comparison to Moore's Curves

Examination of Table 2 indicates that A value variations within the inner section of the profile correlate well with water level change. However, A value variation within the middle and outer sections of the profiles show no correlation with water level. To better illustrate the correlation between water level change and shape factor A for the inner section, demeaned values of A and demeaned values of the water level elevation are plotted against each other (Figure 7). The parallel trend illustrated in Figure 7 supports the argument that profile change is lagging water level change. The estimated lag time is not easily discernible from the data, but is of the order of years.

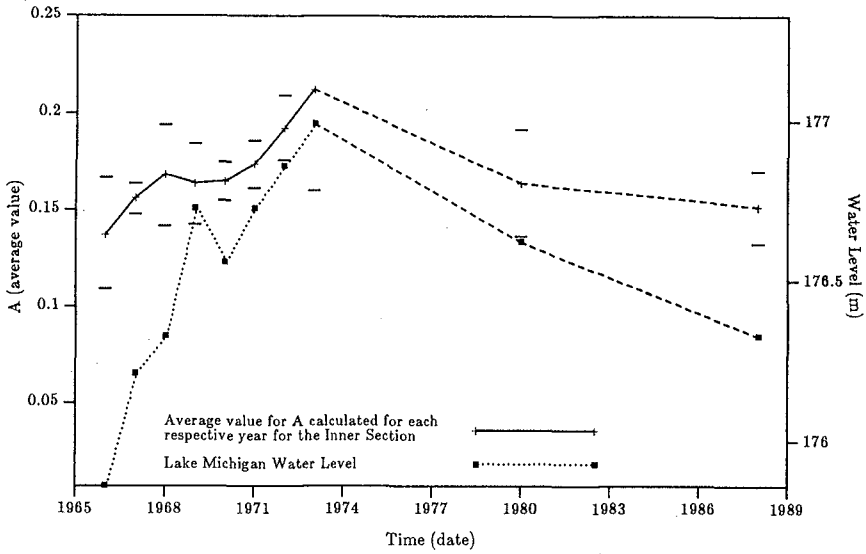


Figure 6. Time Variation of Mean A Values and Water Level for the Inner Sections of the SR Profiles

Section	r	r ²
Results for SR profiles		
Inner	0.865	0.75
Middle	0.325	0.11
Results for MTB profiles		
Inner	0.76	0.58
Middle	0.046	0.00
Outer	-0.438	0.19

Table 2. Correlation Statistics for A Versus Water Level

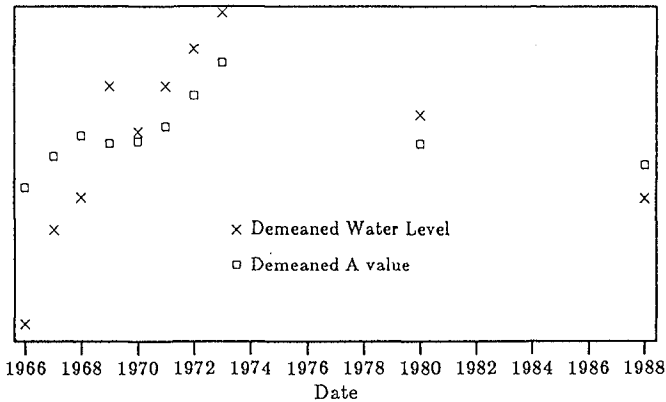


Figure 7. Demeaned A Values and Water Level Plotted Against Time for the Inner Sections of the SR Profiles

DISCUSSION AND CONCLUSIONS

Discussion

The equilibrium beach concept is based essentially on two premises. The first is that the form or shape of the nearshore profile is known, the second is that the nearshore profile responds on a time scale similar to that of water level change. The results of this study have shown that the nearshore profile form found by Dean (1977), $h(x) = Ax^{2/3}$, is appropriate for use in describing the "average" or characteristic nearshore profile found on the Great Lakes. However, the results have also shown that nearshore profiles respond on a much longer time scale than that of mean annual water level change. These results indicate that the equilibrium beach concept should not be used to predict nearshore response to short term water level changes on the Great Lakes. However, use of this concept may be appropriate for prediction of changes in the nearshore due to changes in water level which occur over a relatively long period of time (order of years). These results are similar to those found by Hands (1980). Hands concluded that response of nearshore profiles on the Great Lakes appeared to be "out-of-phase" or lagging behind that of water level change. In addition, Hands concluded that the lag between profile response and water level change was on the order of a few years.

The effect of falling water level on the nearshore profiles could not be determined due to the slower than

expected response of the profiles to water level change. Since questions still exist as to the applicability of the equilibrium beach concept to falling water level, it is strongly suggested that this concept not be applied under conditions of falling water level.

Results of this investigation fail to support the argument that the shape factor A is dependent on mean sediment size. Although some paired data grouped around the curves developed by Moore (1982), there were not significant relationships supported by statistical analysis. This result is contrary to the findings of Dean (1977), Hughes (1978), and Moore (1982).

It is important to note that the parameters m and A are interdependent and that the effect of setting m to a constant is to force the values of A into a much tighter distribution about the mean, thus reducing the amount of information that can be gained by examining the joint distribution. Perhaps the restricted application of the equilibrium profile equation $h(x) = Ax^{2/3}$ is not appropriate. It is recommended that determination of both variables should be carried out in a statistical context.

Conclusions

The following conclusions were reached as a result of this study.

1. The equilibrium profile form determined by Dean (1977), $h(x) = Ax^{2/3}$, is adequate for use in describing the "characteristic" nearshore profiles found on the Great Lakes.
2. The equilibrium beach concept should not be used to predict nearshore profile changes for short periods of time. However, the equilibrium beach concept may be adequate for use in predicting changes to the nearshore due to water level changes which occur over a long period of time.
3. The shape factor A does not appear to be well correlated with mean sediment size.

LIST OF REFERENCES

Bruun, P. (1962). Sea-Level Rise as a Cause of Shore Erosion, *Jour. of the Waterways and Harbors Division*, ASCE, 88(WW1), 117-130.

- Edelman, T. (1972). Dune Erosion During Storm Conditions, *Proc. 13th Conf. Coast Eng.*, Vancouver, 1305-1312.
- Hands, E.B. (1979). Changes in Rates of Shore Retreat, Lake Michigan, 1967-76, *CERC Technical Paper No. 79-4*.
- Hands, E.B. (1980). Prediction of Shore Retreat and Nearshore Profile Adjustment To Rising Water Levels on the Great Lakes, *Technical Paper No. 80-7*.
- Hands, E.B. (1984). The Great Lakes as a Test Model for Profile Response to Sea Level Changes, *Misc. Paper CERC-84-14*.
- Hawley, E.F., and Judge, C.W. (1969). Characteristics of Lake Michigan Bottom Profiles and Sediments from Lakeside, Michigan to Gary, Indiana, *Proc. 12th Conf. Great Lakes Res.*, Int. Assoc. Great Lakes Res., 198-209.
- Hughes S.A., (1978). The Variation of Beach Profiles when Approximated by a Theoretical Curve, M.S. Thesis, Univ. Florida.
- Kriebel, D.L., and Dean, R.G. (1985). Numerical Simulation of Time-Dependent Beach and Dune Erosion, *Coastal Eng.*, 9, 221-245.
- Le Mehaute, B. and Soldate, M. (1980). A Numerical Model for Predicting Shoreline Changes, *CERC Misc. Report No. 80-6*.
- Moore, B. (1982). Beach Profile Evolution in Response to Changes in Water Level and Wave Height, M.S. Thesis, Univ. Delaware.
- Swart, D.H. (1974). Offshore Sediment Transport and Equilibrium Beach Profiles, Publ. No. 131, Delft Hydraulics Lab., Delft Univ. Technol.
- Swart, D.H. (1976). Predictive Equations Regarding Coastal Transports, *Proc. 15th Conf. Coast. Eng.*, Honolulu, 1113-1132.
- Weisher, L.L., and Wood, W.L. (1983). An Evaluation of Offshore and Beach Changes on a Tideless Coast, *J. Sed. Petrology*, 54, 847-858.
- Wood, W.L., and Weishar, L.L. (1984). Beach Response to Long Period Lake-Level Variation, *Proc. 19th Conf. Coast. Eng.*, ASCE, Houston, 1571-1583.

CHAPTER 174

ADVANCES IN NUMERICAL MODELING OF DUNE EROSION

David L. Kriebel¹

INTRODUCTION

Estimating dune erosion during severe storm events continues to be a major coastal engineering problem. In the United States, for example, numerous state and federal regulatory programs now require an estimate of the erosion caused by the 100-year hurricane or extratropical storm. In addition, most beach replenishment projects include storm protection berm and dune systems that must be sized to survive some design storm event.

Given these requirements, methods of predicting dune erosion must continue to evolve and improve. Before the early 1980's, most dune erosion methods were based on geometrical arguments. Since then, however, the two most widely-used methods for predicting dune erosion in the United States have been the empirical model of Vellinga (1983, 1986), based on extensive large wave tank tests, and the numerical model of Kriebel and Dean (1985), based on a finite-difference solution of simplified governing equations. A recent model by Larson and Kraus (1989) is also being used by the Corps of Engineers and is based on governing equations similar to those used in the Kriebel and Dean model. These models have been successful largely because of their simplicity in describing the macroscopic cross-shore profile changes without considering details of surf zone hydrodynamics or sediment transport.

For widespread application in the U.S., however, it is generally recognized that neither the Vellinga model nor the Kriebel and Dean model are sufficiently general to accommodate all beach profile, storm surge, and wave conditions of interest. The most critical limitation on both models is that they have been developed for the case of high dunes that extend infinitely landward and which

¹Assistant Professor, Ocean Engineering Program
U.S. Naval Academy, Annapolis, Maryland 21402 U.S.A.

are not overtopped by storm surge or wave uprush. In the U.S., however, most coastal locations do not have such massive frontal dunes. Dune erosion models must, instead, be capable of simulating profiles with low dunes that may be overtopped, narrow dunes that may be eroded completely, multiple dune ridges that may erode sequentially, or dunes that are backed by shore protection structures.

In this paper, revisions to the Kriebel and Dean model are reviewed that remove some of the previous limitations. These modifications, primarily in the onshore boundary region, enable more realistic simulation of a variety of beach and storm conditions while retaining the general simplicity of the original model.

BACKGROUND

The original Kriebel and Dean erosion model predicts the time-dependent evolution of beach and dune profiles based on time-histories of storm surge and wave height, as described by Kriebel and Dean (1984, 1985). This model is based on Dean's (1977) equilibrium profile theory, in which the profile form that will ultimately be attained if water level and wave conditions are held constant indefinitely is of the form

$$h = A x^{2/3} \quad (1)$$

where h is the water depth at a distance x from the shoreline. This form is consistent with the uniform dissipation of wave energy per unit volume in the surf zone based on shallow water spilling breaker assumptions. The parameter, A , is related theoretically to a value of the energy dissipation per unit volume, D_E , which must occur everywhere across the profile when the system is in equilibrium. Dean (1977, 1987), Moore (1982) and others have then related A empirically to the median sand grain size.

The time-dependent profile response is then simulated by solving two simplified governing equations in finite-difference form. These are the continuity equation

$$\frac{dx}{dt} = - \frac{dQ}{dh} \quad (2)$$

and a simplified expression for the net sediment transport rate at any location in the surf zone

$$Q = K (D - D_E) \quad (3)$$

based on the difference between the energy dissipation at any location, D , and the equilibrium value, D_E .

Based on shallow water spilling breaker assumptions, the energy dissipation per unit volume is given by

$$D = \frac{1}{h} \frac{dF}{dx} = \frac{5}{16} \rho g^{3/2} k^2 h^{1/2} \frac{dh}{dx} \quad (4)$$

where k is the ratio of the breaking wave height to the water depth, assumed to be 0.78. Based on equation (4), energy dissipation is a function only of the local water depth in the surf zone such that the sediment transport rate across the surf zone is dictated only by the shape of the profile relative to its equilibrium shape for a given water level.

The rate parameter, K , in equation (3) is the only free parameter in the governing equations and is used to calibrate the model. In the recent model by Larson and Kraus, equations (1) and (3) are modified to also include a gravity driven slope-dependent term, at the expense of introducing an additional parameter which then must be empirically determined. In the original model by Kriebel and Dean (1984, 1985), the value of K was adopted from a previous study by Moore (1982). An initial verification was then carried out in a simulation of erosion during Hurricane Eloise. In this case, one representative or average profile was used for the initial condition and computed erosion volumes were found to agree reasonably well with county-wide average erosion values. Steepening of the dune during erosion was not simulated, however, so that predicted recession of specific dune elevation contours did not agree closely with observed values.

In a subsequent study, Kriebel (1986) performed a more detailed calibration and verification of the model using several measured profiles from the Hurricane Eloise data set. In that study, one profile was selected and used to calibrate the numerical model. This profile, denoted R-41, was previously used by Hughes and Chiu (1981) to verify a small-scale physical model for dune erosion. This profile was also used by Vellinga (1986) to verify the Dutch dune erosion model for hurricane conditions. As a result, this profile has become a sort of calibration standard. From this, a value of the transport parameter, K , was found to be about $0.0045 \text{ ft}^4/\text{lb}$ ($8.75 \times 10^{-6} \text{ m}^4/\text{N}$). This is larger than the value originally adopted from Moore (1982) but it provided results that were accurate to within about 25% when 20 other Hurricane Eloise profiles were simulated in detail. A comparison of the calibrated numerical model and the measured post-storm profile is shown in Figure 1.

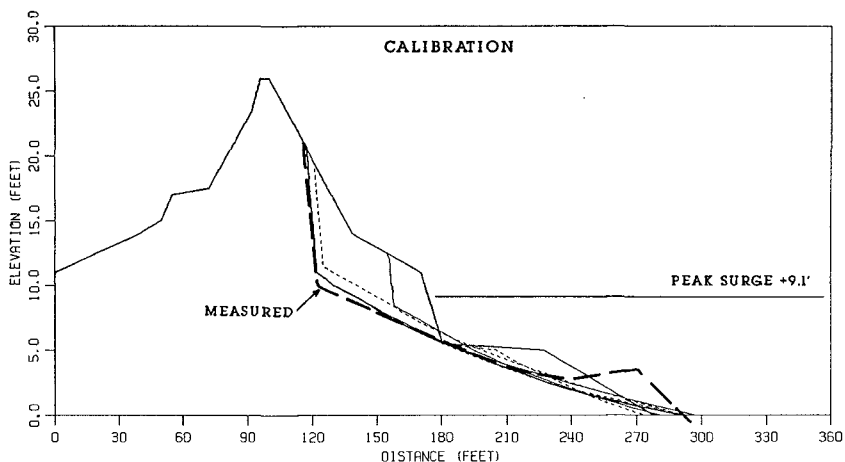


Figure 1. Example of predicted profile response for calibration profile R-41 from Hurricane Eloise data set.

MODEL REVISIONS

The revised numerical model uses the same governing equations to describe onshore-offshore transport and to solve for profile changes. The major revisions are in the initial profile description and in the onshore boundary conditions. In the original model, wave runup was not simulated and the entire dune face was required to erode while maintaining its initial slope. In the revised model, provisions for realistic wave runup limit are included along with a new method for estimating sediment transport rates on the beach face. This allows formation of a dune scarp along with flattened post-storm beach face slope.

Initial Profile Form

As shown in Figure 1, the initial profile is no longer limited to the two idealized forms used in the original model. Previously, the profile was defined only by the position of the dune crest, the slope of the dune face, the position of the berm, and the slope of the beach face. Dunes were assumed to be of infinite width which extended landward indefinitely at the elevation of the dune crest. In the revised model, the initial profile closely simulates a measured profile. Dunes of finite width may be simulated by specifying both a landward and a seaward position of each elevation contour to define the dune width at each elevation.

For narrow dunes, each elevation contour can then erode only until it reaches the landward contour location. Once erosion reaches this position at each elevation, no sand remains at or above that contour and the upper limit of the active profile is then taken at the next lower elevation contour. This routine also enables simulation of vertical and sloping seawalls when the wall location is used as the landward limit of each elevation contour. In these cases, once the eroding contour reaches the wall location, the upper limit of the active profile is again transferred to the next lower contour.

Runup Limit

Provisions are then made for input of a realistic runup limit to describe the upper limit of the active swash zone and to fix the transition from a flattened post-storm beach face to a near-vertical erosion scarp. This does not represent the true wave runup limit since runup for some waves in a random sea may reach above this elevation on the dune scarp. In some erosion models, such as the Dutch method of Vellinga (1983), the dune scarp is fixed at the peak storm surge level. This may be a good approximation in areas of high dunes where large amounts of sand are fed to the beach face by dune undermining and slumping. Most post-storm conditions in the U.S., however, show a distinct erosion scarp at an elevation above the peak surge level.

A more realistic upper limit on the eroded profile may be established from local field observations of previous storm events. For example, in the Hurricane Eloise data, the elevation of the dune scarp is about 2 feet (0.6 m) above the estimated peak still water level. This is below the elevation of debris lines surveyed after the storm and illustrates that the dune scarp usually forms below the maximum wave runup elevation.

For more general application, the elevation of the erosion scarp may be estimated by any of the available methods of predicting wave runup. One effective method is to estimate this elevation according to the Hunt formula

$$R = m_* (H_{rms} L_o)^{1/2} \quad (5)$$

where the deep water rms wave height is used along with an estimate of the equilibrium post-storm beach slope, m_* , to be discussed. Since the swash is saturated during severe storms, use of higher wave height descriptions, such as the significant wave height, seem to overestimate the dune scarp elevation. The above method seems to predict runup elevations that correspond closely with observed dune scarp locations and is of a comparable level of simplicity as the rest of the numerical model.

Post-Storm Beach and Dune Slopes

Methods are also required to describe the post-storm slopes of the beach face and dune face. The Vellinga model fixes the dune scarp at the peak surge level and assumes a 1:1 slope for the eroding dune face. This has recently been adopted in a similar erosion model for the National Flood Insurance Program described by Hallermeier and Rhodes (1988). This method works well for dune erosion in large wave tank tests but does not work as well for field conditions where a flattened post-storm beach face is usually evident below the dune scarp at an elevation above the peak surge level. In addition, most natural dunes are vegetated and display near-vertical post-storm slopes.

In the present model, any realistic post-storm dune scarp slope may be specified. For simulation of large wave tank tests, a slope of 1:1 is appropriate; however, for field conditions, slopes of 5 vertical to 1 horizontal are more reasonable. For the beach face slope, observations in the area of interest are usually the best guide when available. Lacking these, predictions can be made based on the observations of Sunamura (1984) where the beach slope was found to vary with sediment and wave conditions as

$$m_* = 0.12((gd_{50})^{1/2}T/H_{rms})^{1/2} \quad (6)$$

It is found that offshore rms wave height works well in equation (6). However, Sunamura does not specify which wave height should be used in random waves and equation (6) was developed using observed breaker heights.

Sediment Transport on Beach Face

A major problem encountered in all numerical models of cross-shore beach response is that no simple descriptions are available of sediment transport rates in the swash region. This problem is symptomatic of a more fundamental problem: the lack of valid wave transformation models that describe wave conditions in the swash zone. As a result, existing numerical models for cross-shore transport must include ad hoc treatments of the sediment transport rate on the active beach face.

In the original model, sediment transport rates were calculated only in regions of finite water depth. The energy dissipation and the sediment transport rates were calculated by equations (3) and (4) for all points in the surf zone up to the last submerged depth. At this point, the transport value was determined and the transport distribution was then assumed to decrease linearly to zero at the runup limit. This leads, however, to uniform retreat of the beach face from equation (2) since the gradient in transport is the same at all elevations.

In the revised model, a simple algorithm is used to provide an estimate of sediment transport rates on the beach face based on geometrical arguments. Water level and wave conditions are established at each time step and two reference elevations are located. The depth h_* is first established at the transition depth where the equilibrium profile, with an $Ax^{2/3}$ form, is tangent to the equilibrium beach slope, m_* . The elevation h_u is then defined at the upper limit of the active profile, either at the runup limit or at the crest of the remnant dune if the dune is overtopped. Based on equation (3), the transport rate Q_* is then determined at the transition depth h_* . The volume of sand that must be eroded from the beach face between the elevation contours h_* and h_u over one time step is then $V_* = Q_* \Delta t$.

An estimate is then made of the potential eroded volume, V_p , between h_* and h_u . This so-called potential erosion prism is depicted in Figure 2 for three basic cases: two for beach face rotation and one for beach face translation. In Case I, the equilibrium slope is steeper than the existing slope. The erosion prism is then defined by passing the equilibrium slope through the runup limit, h_u , so that contours near h_* have the greatest erosion potential. In Case II, the equilibrium slope is milder than the existing slope. The erosion prism is defined by passing the slope m_* through the transition depth h_* so that contours near h_u have the greatest erosion potential. In Case III, the existing slope is in equilibrium. All elevation contours have the same erosion potential and the erosion prism is then defined by translating the beach slope landward until V_p equals V_* .

In general, the potential volume V_p defined in Cases I and II does not equal the demand volume V_* . When the potential volume is too large, only the fraction V_*/V_p is actually eroded over the time step. When the potential volume is too small, the additional volume must then be supplied by translating the equilibrium slope m_* landward. In this way combinations of Cases I and III and Cases II and III are used to obtain the final potential volume V_p .

The estimated distribution of sediment transport on the beach face is finally established according to the fraction of the potential volume that may be eroded from above each elevation contour. Denoting the potential volume above contour n as V_n , the transport rate at elevation contour n is estimated as

$$Q_n = Q_* (V_n/V_p) \quad (7)$$

For the cases depicted in Figure 2, this gives the transport distributions depicted in Figure 3.

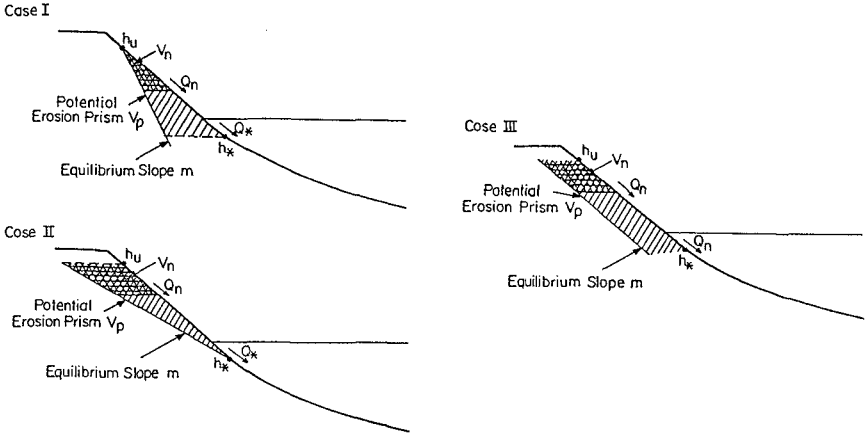


Figure 2. Illustration of potential erosion prism for fundamental cases of beach face rotation and translation.

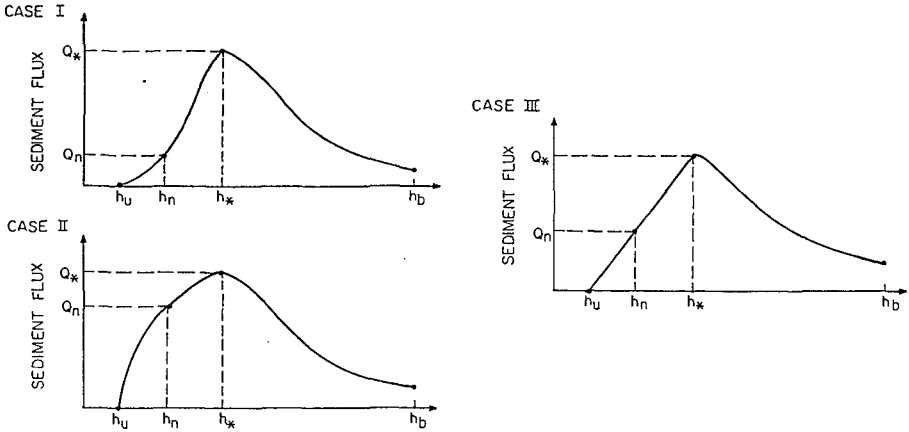


Figure 3. Illustration of sediment transport distributions for example cases shown in Figure 2.

For Case I, the beach slope steepens since the transport distribution is concave with the largest gradients near h_* . For Case II, the beach face must flatten since the transport distribution is convex with the largest gradients near the runup limit h_u . For Case III, the beach face maintains its initial slope as it erodes since the transport distribution is linear with uniform gradients at all elevations. With this method, the beach face evolves toward the specified equilibrium slope while the submerged profile evolves toward the $Ax^{2/3}$ form. An example of the computed slope evolution is shown in Figure 4 for one of Saville's (1957) large wave tank tests. In this case, the equilibrium slope is steeper than the original 1:15 slope and slope steepening is simulated by the above method.

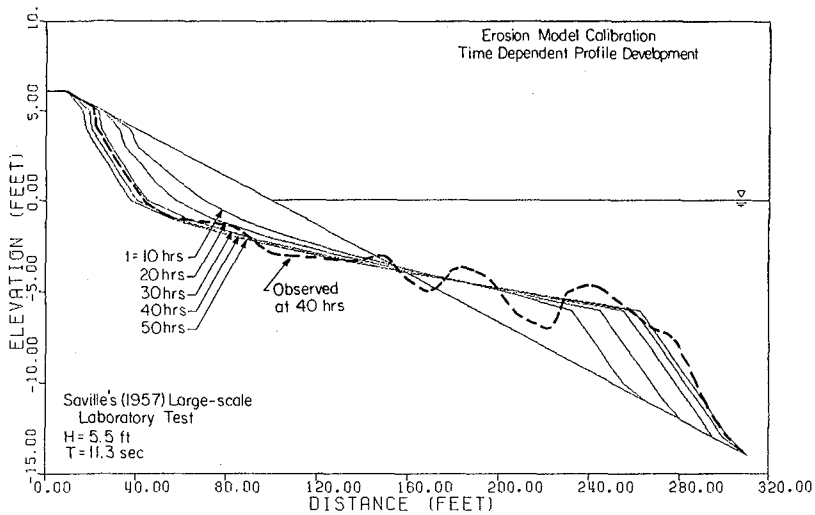


Figure 4. Example of slope steepening introduced by the potential erosion prism method.

Examples of Model Application

In order to validate the revised model, several large wave tank results of dune erosion using random waves were simulated. These included tests described by Vellinga (1986) as well as tests described by Dette and Uliczka (1987). In each case, the initial profile form, water level, wave conditions, and sand grain size were obtained from the references cited. The A parameter for the equilibrium profile form was obtained from Dean (1987) based on the median grain size. The equilibrium beach slope, m_* , was estimated using equation (6). A post-storm dune slope of 1:1 was assumed and the elevation of the

dune scarp was estimated from equation (5). The offshore breaking depth, forming the offshore limit to sediment deposition, was adopted as 1.06 times the rms wave height, in accordance with observations by Vellinga (1983).

One example of these simulations is shown in Figure 5. Numerical results are shown for simulation times of 0.1, 0.3, 1, 3, 6, and 10 hours while the measured profile obtained after 10 hours in the Delta Flume is also shown. For this case, the dune scarp elevation and horizontal location are slightly underpredicted but, in general, the scarp formation and the eroded volume are predicted to within about 10% from their measured values. Similar results were then obtained from the other tests with numerical results generally being within about 10 to 20 percent of the measured values.

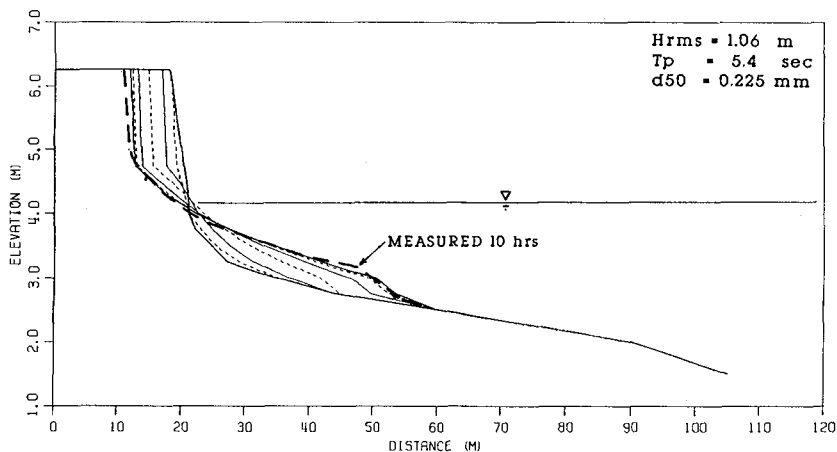


Figure 5. Comparison of erosion simulation to measured profile response for test #2 of Vellinga (1986).

A similar comparison is shown in Figure 6 for the case of a sand beach backed by a sloping dike tested by Dette (personal communication). The predicted profiles are shown at times of 0.25, 0.5, 1.25, 2.75, and 4.0 hours and are compared to the measured profile after about 3 hours. In this case, the final profile form at the base of the dike is predicted reasonably well. Once the upper contours eroded back to the wall location, the upper limit of the active profile is transferred to the next lower contours and it is found that these erode faster for a time until they approach equilibrium.

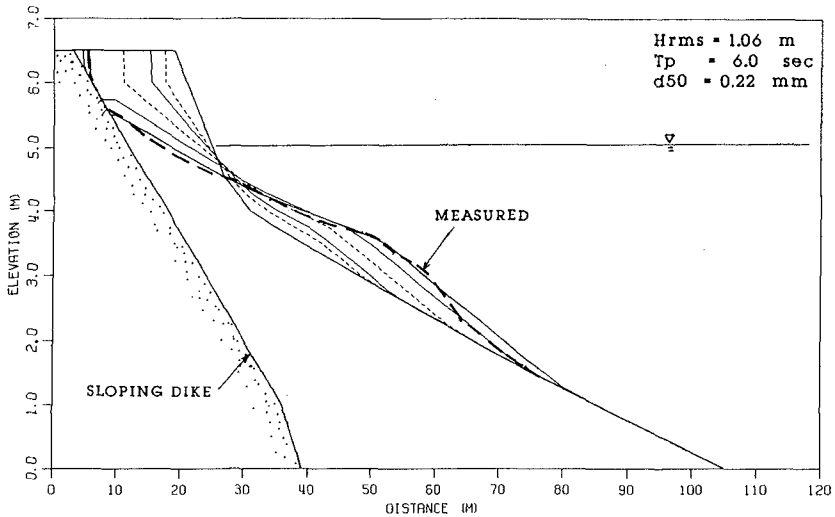


Figure 6. Example of profile backed by seawall tested by Dette (personal communication).

In Figure 7, field conditions documenting the complete erosion of a narrow dune are simulated, based on data presented by Chiu and Dean (1986) for Hurricane Frederic on the Alabama coast. This storm was similar to Hurricane Eloise in that the storm duration was very short. However, Hurricane Frederic was more severe in that the peak surge elevation was higher and since the storm struck an area with relatively low dunes that were overtopped. As shown in Figure 7, the numerical model predicts the formation of a dune scarp for the first profile, 3.2 hours before the peak surge. On the next profile, 1.6 hours before the peak surge, wave runup overtopped the remnant dune. On the third profile, at the time of the peak surge, the dune was submerged and was then quickly flattened afterward.

At present, the numerical model simulates only off-shore transport at the crest of the remnant dune and does not simulate landward transport of sand due to overwash. Trial calculations with an upper boundary condition that includes overwash transport gave a faster planing of the remnant dune crest and results that agree more closely with the measured profile. However, more accurate data is needed to verify this algorithm. With the present approximation, reasonably realistic estimates of the time at which the dune is breached can be obtained.

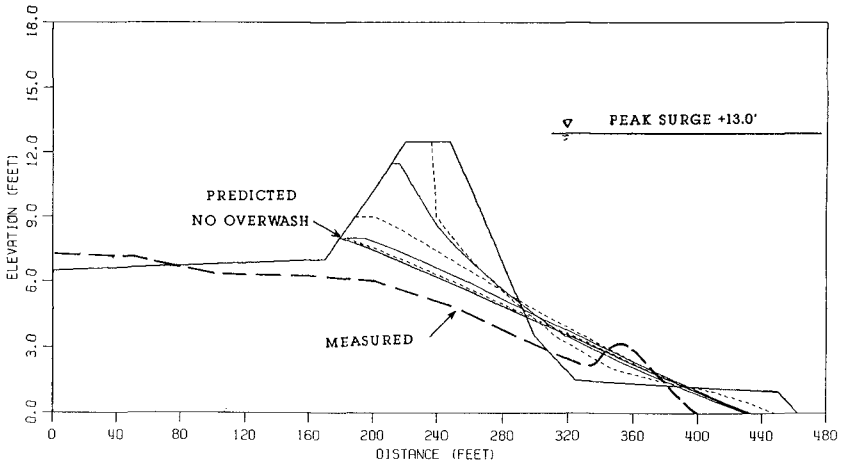


Figure 7. Example of erosion of narrow dune during Hurricane Frederic as reported by Chiu and Dean (1986).

As a final example, Figure 9 shows results from the simulation of a long-duration winter storm from the coast of New Jersey. In this case, data were provided to the author by Jeff Gebert of the Philadelphia District of the Corps of Engineers. A total of 17 profiles were measured out to a depth of about 10 meters 1 to 2 days before the storm and were then remeasured just 3 to 4 days after the storm. Wave and water level conditions were both measured during the duration of the storm. This data set probably constitutes the most well documented storm erosion case on the U.S. East coast.

This condition is also interesting since: (1) the median grain size (from the beach face) is much larger than any other condition previously simulated, (2) the storm lasted for more than 2 days but included a peak surge elevation of only 6.1 feet (1.86 meters), and (3) the eroded volumes are very large, on the order of 1100 ft³/ft (100 m³/m). Results in Figure 9 are shown since they represent examples of model under and overprediction, in this case occurring on adjacent profiles located just 175 meters apart. Some post-storm recovery had occurred by the time of the post-storm survey and the presence of beach cusps may explain some of the differences observed on the beach face in the two profiles. These cases demonstrate, however, that the numerical model gives reasonable results for long-duration storm events.

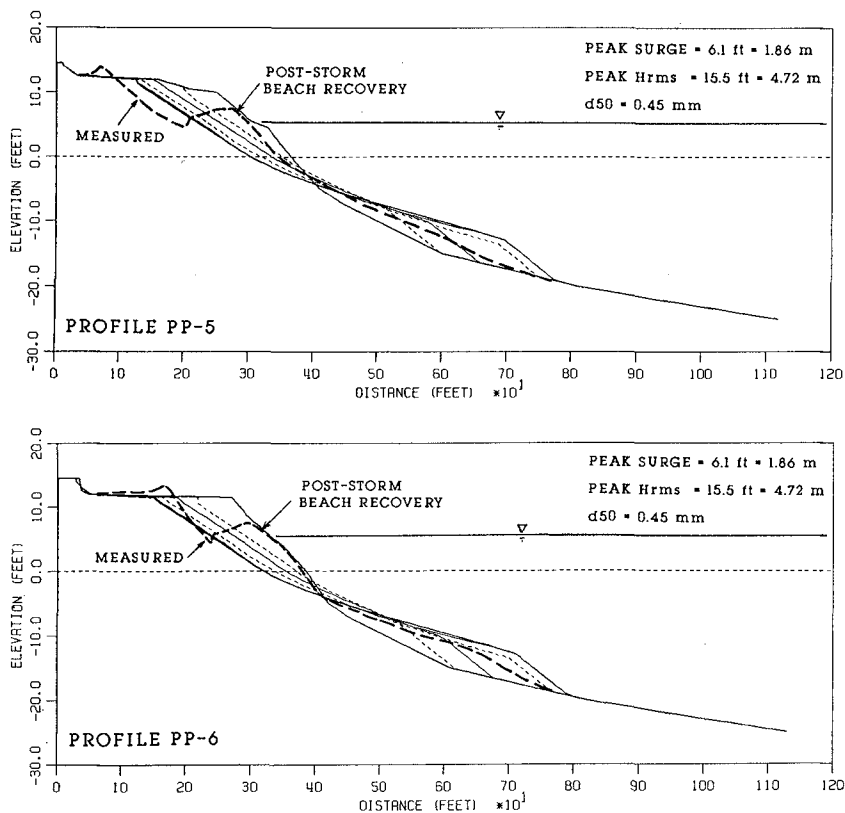


Figure 9. Examples of storm simulation for March 1984 storm at Pt. Pleasant, New Jersey.

CONCLUSIONS

Numerical algorithms may be readily developed to handle most dune erosion conditions to a first level of approximation which retains an overall level of simplicity in terms of required parameters and numerical code. For example, a simple method has been presented for estimating sediment transport rates on the beach face. Such numerical algorithms may then be incorporated into other macroscopic profile response models to enhance their applicability to a broad range of dune geometries. However, other more physically-based methods of predicting wave transformation and sediment transport on the beach face are needed, along with new lab and field data for model verification.

REFERENCES

- Ghiu, T.Y. and Dean, R.G., 1986, "Additional Comparisons Between Computed and Measured Erosion by Hurricanes," Beaches and Shores Resource Center, Florida State Univ.
- Dean, R.G., 1987, "Coastal Sediment Processes: Toward Engineering Solutions," Coastal sediments '87.
- Dean, R.G., 1977, "Equilibrium Beach Profiles: U.S. Atlantic and Gulf Coasts," Univ. of Delaware, Ocean Engr. Rpt. No 12.
- Detle, H.H., and Uliczka, K., 1987, "Prototype Investigation of Time-dependent Dune Recession and Beach Erosion," Coastal Sediments '87.
- Hallermeier, R. and Rhodes, P., 1988, "Generic Treatment of Dune Erosion for 100-Year Event, 21st IGGE, Malaga.
- Hughes, S.A., and Ghiu, T.Y., 1981, "Beach and Dune Erosion During Severe Storms," Univ. of Florida, COEL Rpt. 43.
- Kriebel, D.L., 1986, "Verification Study of a Dune Erosion Model," Shore and Beach, Vol. 54, No. 3.
- Kriebel, D.L., and Dean, R.G., 1985, "Numerical Simulation of Time-Dependent Beach and Dune Erosion," Coastal Engineering, Vol. 9.
- Kriebel, D.L., and Dean, R.G., 1984, "Beach and Dune Response to Severe Storms," 19th ICCE, Houston.
- Larson, M., and Kraus, N.G., 1989, "SBEACH: Numerical Model to Simulate Storm-Induced Beach Change," Army Corps of Engr., Waterway Expt. Sta., Tech. Rpt. GERG-89-9.
- Moore, B., 1982, "Beach Profile Evolution in Response to Changes in Water Level and Wave Height," M.S. Thesis, University of Delaware.
- Saville, T., 1957, "Scale Effects in Two-Dimensional Beach Studies," Trans. 7th Mtg. IAHR, Lisbon.
- Sunamura, T., 1984, "Quantitative Predictions of Beach-Face Slopes," Geol. Soc. of America Bulletin, Vol. 95.
- Vellinga, P., 1986, "Beach and Dune Erosion During Storm Surges," Erosion During Storm Surges,' Delft Hydraulics Lab., Publ. No. 372.
- Vellinga, P., 1983, "Predictive Computational Model for Beach and Dune Erosion During Storm Surges," Coastal Structures '83.

CHAPTER 175

BEDFORMS, SEDIMENT CONCENTRATIONS AND SEDIMENT TRANSPORT IN SIMULATED WAVE CONDITIONS

Jan S. Ribberink¹⁾ and Abdullah Al-Salem²⁾

Abstract

Two series of experiments were conducted in a new Large Oscillating Water Tunnel of Delft Hydraulics with the main objectives to study the behaviour of bedforms and the transport of sand in controlled wave conditions simulated at full scale (1:1). The main results are:

- i) Bedform dimensions are strongly influenced by the type of oscillatory flow. The transition from rippled bed to plane bed conditions - as predicted by Nielsen's (1979) empirical relations - was not observed for sinusoidal waves but did occur for (ir)regular asymmetric waves.
- ii) The net sediment transports as measured during (ir)regular asymmetric wave experiments in plane or almost plane bed (sheet flow) conditions show a consistent linear relation with the third-order moment of the velocity $\langle U^3 \rangle$ and show a good agreement (within a factor 2) with the energetics total load sediment transport model of Bailard (1981). A calibrated formula of the form $q_s = A \cdot \langle U^3 \rangle$ shows a reasonable agreement (within a factor 1.5-3) with available existing datasets over a wide range of measured values (factor 1000).

Introduction

For the transport of sediment in the marine coastal environment the complex interactions between the wave and sea bed itself (bedforms, sediment stirring) play a key role. After several years of experimental research in a small oscillating water tunnel, recently a new large oscillating water tunnel was constructed at DELFT HYDRAULICS with the aim to extend the research to full scale (1:1) conditions.

Sediment transport under the influence of waves and current is generally divided into transport as carried by the current and transport as carried by waves. By splitting up of the horizontal velocity U

-
- 1) Senior research officer, DELFT HYDRAULICS, PO Box 152, 8300 AD Emmeloord, The Netherlands
 - 2) Kuwait Institute for Scientific Research, presently: Guest Researcher, DELFT HYDRAULICS, PO Box 152, 8300 AD, Emmeloord, The Netherlands

and the sediment concentration C at a certain level in a time-averaged component and a fluctuating component due to the waves, the horizontal sediment flux at that level ϕ_{cw} can be split up in a current-related part ϕ_c and a wave-related part ϕ_w , as follows. For a colinear situation (i.e. current and wave propagation have the same or opposite direction):

$$U = U_0 + \tilde{U}$$

$$C = C_0 + \tilde{C}$$

$$\begin{aligned} \phi_{cw} = \langle UC \rangle &= \phi_c + \phi_w \\ &= \langle U_0 C_0 \rangle + \langle \tilde{U} \tilde{C} \rangle \end{aligned}$$

Much of the research on sediment transport in the past has been concentrated on the transport component as carried by the current (often dominant in longshore direction). The waves are treated as an additional stirring mechanism for the sand. The sediment transport component as carried by the waves (e.g. due to wave asymmetry outside the surfzone) is much less understood, which is probably caused by the complex character of this type of sediment transport which is governed by the intra-wave processes taking place in a relatively thin layer (millimeters to centimeters) near the sea bed. Nevertheless, the wave-carried transport is of great importance for especially the transport in cross-shore direction. For example, wave asymmetry (leading to relatively high orbital velocities in the direction of the wave propagation and relatively low orbital velocities in the opposite direction) is generally held responsible for the onshore motion of sand on the upper shoreface and for example for the onshore motion of offshore bars.

The experimental research programme around the new tunnel was therefore started with the objectives: i) to obtain a better understanding of the wave-carried sediment transport and ii) to verify and improve existing concepts for the description of this type of sediment transport.

Large Oscillating Water Tunnel

A general outline of the new tunnel is given in Figure 1. The horizontal test section has an approximate length of 15 m, an inner width of 0.3 m and an inner height of 1.1 meter. The complete test section can be provided with a sand bed with a layer thickness of 0.3 meter, leaving 0.8 m height for the oscillatory flow above the bed. A desired oscillatory water motion (regular or irregular) can be imposed by a computer controlled hard driving system, which consists of a hydraulic servo-cylinder moving a steel piston in one of the cylindrical risers. The other cylindrical riser is open to the atmosphere. The maximum amplitude of the piston is 0.75 m which coincides with a maximum semi-exursion length of water particles in the test section of app. 1.75 meter.

Figure 2 shows the working regime of the new tunnel in terms of period and maximum velocity amplitude of the oscillatory flow, in comparison with the small tunnel of DELFT HYDRAULICS and the existing large tunnels at SCRIPPS (USA) and ISVA (TU Copenhagen). The main feature of the new tunnel is that it has the possibility of

controlled simulation in the relevant velocity/period regime (scale 1:1). A desired regular and irregular oscillatory flow can be produced in the test section with a limited deformation. Figure 2 shows that the tunnel covers the bedform regimes from initiation of motion to sheet flow ($D_{50} = 0.2 \text{ mm}$).

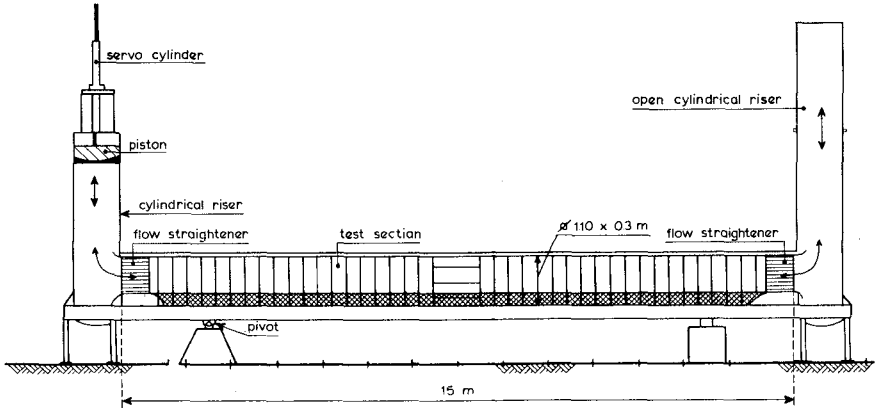


Figure 1 Large Oscillating Water Tunnel

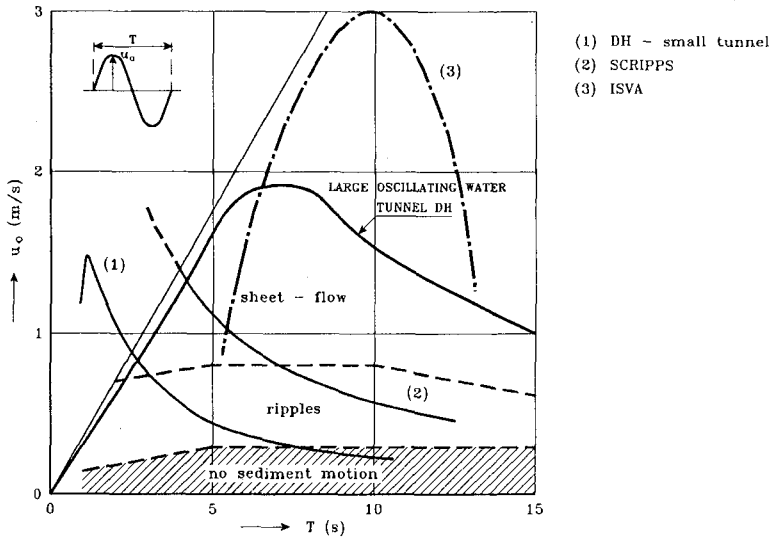


Figure 2 Velocity-amplitude and period regime

Set-up of experiments

Because bedforms are essential features for the sediment transport process, a first set (series A) of experiments was focussed on

bedform behaviour under the influence of regular sinusoidal oscillations, covering the major part of the tunnel's working regime. Twenty-nine tests were conducted with periods 4-10 s and velocity amplitudes 0.3-1.5 m/s using quartz sand with $D_{50} = 0.21$ mm. The main objectives of this first series were: i) to compare the observed bedforms (dimensions, transition to sheet flow) with existing datasets and empirical formulations (tunnel validation) and, ii) to study the bedform behaviour in the still very unknown high velocity ($U > 1$ m/s) and large period ($T > 5$ s) regimes.

A second set of experiments (series B) was focussed on the net sediment transport as induced by wave asymmetry. Only a limited set of data is available on this type of transport especially in the high velocity regime (Horikawa et al, 1982 and Sawamoto & Yamashita, 1986). A series of 12 experiments were carried out in the large tunnel with irregular (exps. 1-6) and regular (exps. 7-12) asymmetric oscillatory flow in which the net sediment transport, bed form dimensions and time-averaged suspended concentration profiles were measured. The experimental conditions are summarized in Table 1 (U_{rms} = root mean square value of the measured velocity in the tunnel, $T_{(peak)}$ = (peak) period of the oscillatory flow).

exp.	U_{rms} m/s	$T_{(peak)}$ s	(ir)regular -
1	0.48	6.5	irregular JONSWAP 2nd order Stokes
2	0.32		
3	0.43		
4	0.48	9.1	
5	0.33		
6	0.44		
7	0.50	6.5	regular 2nd order Stokes
8	0.70		
9	0.92		
10	0.54	9.1	
11	0.70		
12	0.97		

Table 1 Experimental conditions series B (wave-asymmetry)

The irregular wave experiments are based on a JONSWAP spectrum for the water surface elevation in combination with a second-order Stokes wave theory (Liu and Dingemans, 1989). The 2nd-order theory is also applied for the regular wave experiments. Figure 3 shows an example of a time series of the applied non-linear (asymmetric) velocity signal in comparison with the linear (symmetric) signal. The degree of asymmetry, expressed in (significant) crest velocity U divided by the sum of (significant) crest and trough velocity ($U_c + U_t$), was kept constant (0.62-0.65).

Two different oscillation (spectral peak) periods were used (6.5 and 9.1 s) for similar velocity time series in order to study the validity of a quasi-steady approach for the description of the sediment transport.

A laser-doppler system is used for the measurement of the horizontal velocity variation outside the boundary layer (20 cm above the sand bed). The net sediment transport rate in the middle of the test section (not disturbed by boundary effects at the two ends of the test section) is determined with a mass-conservation technique. The measured bed-level change along the test section and the collected sand volume in two sand traps at both ends of the test section during a certain time interval (5 - 50 min) are used for the integration of the sediment continuity equation, yielding the distribution of the net transport rate along the test section. By repeating each experiment 5-8 times the net transport rate could be determined with an error of approximately 10-15%. Totally 93 tests were carried out in the above mentioned 12 different conditions.

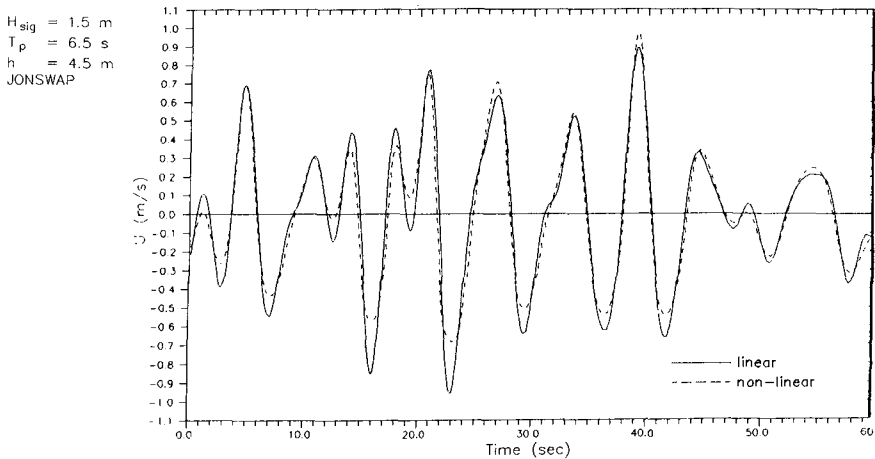
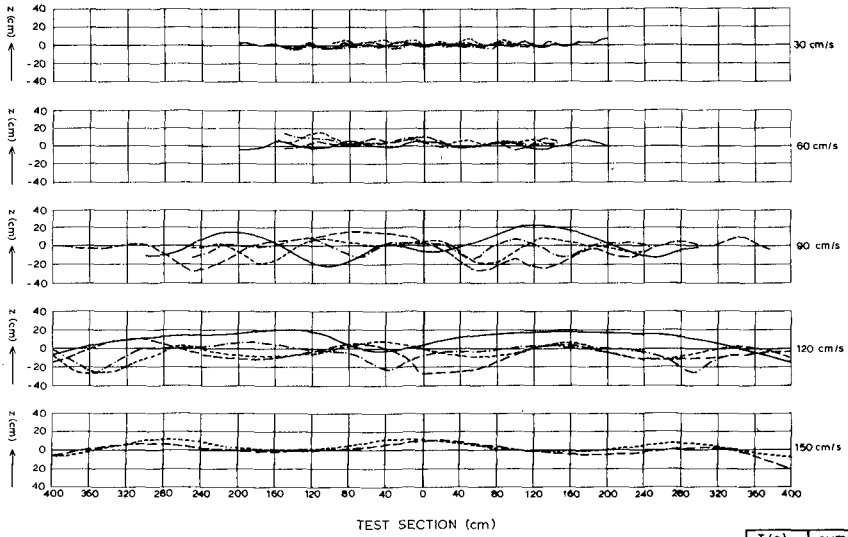


Figure 3 Irregular asymmetric velocity signal

The data analysis was concentrated on the bedform behaviour and the sediment transport rate. For information about the measured suspended concentration profiles (time-averaged), reference is made to Ribberink and Al-Salem (1989, 1990).

Bedforms

Figure 4 gives an impression of the bedform behaviour in the test section (central 8 m) for different velocity amplitudes and periods (series A: regular sinusoidal oscillations). The bedform length and height increase for increasing velocity amplitude and period. Very large bedforms developed in the high velocity/period regime ($U > 0.9 \text{ m/s}$) which, although considerably larger than generally observed in small wave flumes, show a clear consistency with results from other wave tunnels and flumes in the world (see Fig. 5, $X_2 = D_{50}/\Delta g T^2$).



T (s)	symbol
4	---
6	---
8	---
10	---

Figure 4 Bed geometry, regular sinusoidal flow (series A)

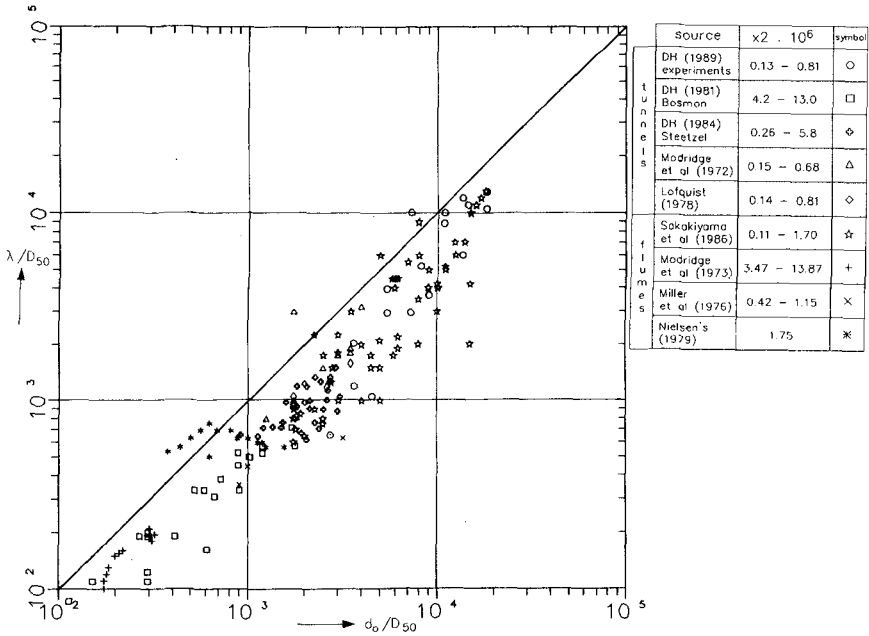


Figure 5 Ripple length as a function of orbital excursion length

It is shown that the measured dimensionless bedform length λ is roughly a linear function of the dimensionless total orbital excursion length d_o of water particles near the bed ($\lambda \approx 0.5 \cdot d_o$).

The new tunnel observations (DH, 1989) show a good agreement with the measurements conducted by Sakakiyama et al (1986) in the large Japanese CRIEPI wave flume (field scale).

The transition to sheet flow conditions in the high-velocity regime did not coincide with the transition to plane bed conditions. For example, for $\hat{U} = 1.5$ m/s large bedforms could be observed with a length $\lambda \approx 0.5 \cdot d_o$, with sheet flow taking place in a thin layer (appr. 0.5 cm) along the bedforms and without vortex generation in the bedform troughs (no flow separation on the bedform crests).

This behaviour is also shown in Figure 6A in which the measured bedform lengths are compared with Nielsen's (1979) empirical formulations (laboratory and field conditions).

In Figure 6: $\hat{x} = 0.5 \cdot d_o$ and $\hat{U}^2/\Delta g D_{50}$ is the mobility number with $\Delta = (\rho_s - \rho)/\rho$, ρ_s = density of sediment, ρ = density of water and g = gravity acceleration.

Although the transition to sheet flow indeed took place for mobility numbers $> 100-200$, the (dimensionless) bedform length measured in the tunnel but also in the CRIEPI flume did not show the expected decrease.

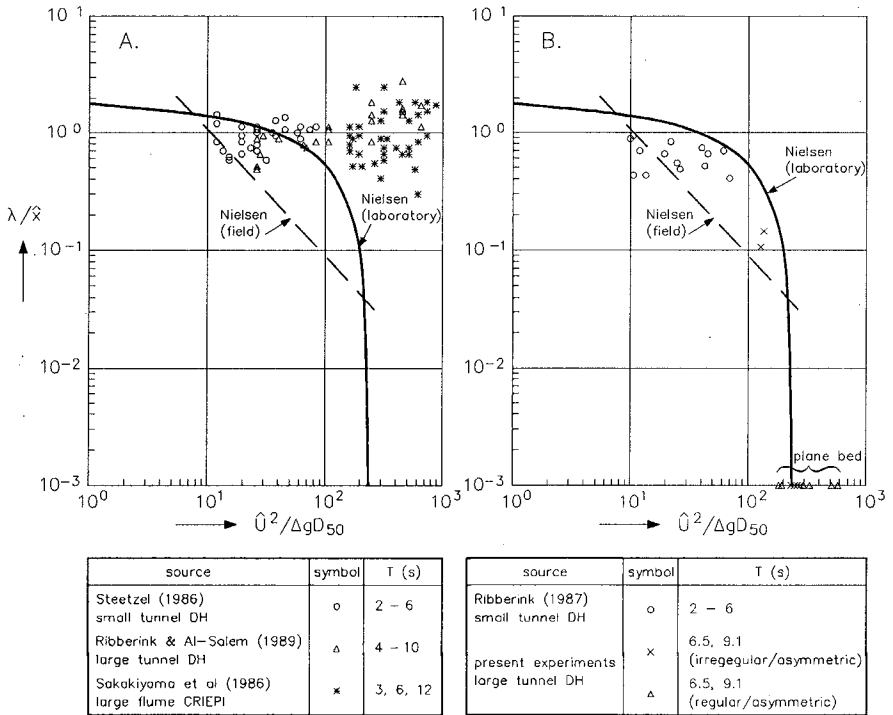


Fig. 6 Dimensionless ripple length as a function of mobility number

However, the situation changed in case the oscillatory flow becomes asymmetric (experimental series B) as shown in Figure 6B. Only the experiments 2 and 5 showed the presence of small two-dimensional rolling grain ripples, during the other 10 experiments the bed was plane and sheet flow was present. Now the reduction in ripple length roughly coincides with Nielsen's relations.

Similar results were obtained for the measured ripple height. For more details, see Ribberink and Al-Salem (1990).

Sediment transport induced by wave asymmetry

For the modelling of sediment transport as carried by waves several approaches exist varying from relatively simple to very sophisticated (research) formulations. In the most simple approach the instantaneous transport during the wave cycle is directly related to the instantaneous horizontal velocity above the wave boundary layer near the sea bed. It is assumed that (time) phase lags between transport rate, sediment concentration and bed-shear stress and between bed-shear stress and velocity above the boundary layer can be neglected (quasi-steadiness). A general notation for this kind of transport concept is:

$$q_s(t) = A|U(t)^{(n-1)}|U(t) \quad (1)$$

in which $q_s(t)$ = transport rate during the wave cycle expressed in volume per unit width and time, $U(t)$ = horizontal velocity during the wave-cycle above the wave boundary layer, n = power and A = factor depending on several parameters such as grain size and friction factor.

Madsen & Grant (1976) base their transport description on the transport formula for uni-directional steady flow of Einstein-Brown, yielding $n = 6$.

Bailard (1981) proposes formulations for bed-load and suspended transport based on energy considerations of Bagnold, yielding $n = 3$ for bed-load transport and $n = 4$ for suspended transport.

For plane bed conditions also more sophisticated model concepts exist in which the detailed behaviour of sediment concentration and water/grain velocities during the wave cycle (also vertical structure) is described. For example, a wave-boundary layer flow model is used in combination with a convection-diffusion model (see Fredsøe et al, 1985). The above-mentioned phase lag effects are taken into account and for example, the delayed response of suspended particles to the varying (unsteady) flow conditions is modelled. Although even more extensive modelling efforts are carried out (see e.g. Bakker and van Kesteren, 1987), a general problem is the lack of detailed measurements for the verification of the various concepts. Observations and measurements are often done in small laboratory flumes and tunnels in which the orbital velocities and wave periods are generally far below their natural values.

During all tunnel experiments in series B: i) the bed was plane or almost plane (rolling grain ripples in expts. 2 and 5), ii) a uniform (net) transport distribution could be realized in the central 8 meters of the test section, and iii) a net 'onshore' transport was measured. The latter agrees qualitatively with the power-law formulation eq. (1) (power $n > 1$) in combination with a velocity signal $U(t)$ based on 2nd-order Stokes wave theory.

The validity of the power law approach was verified by testing the relation between the measured net transport rates $\langle q_s \rangle$ and the velocity moments $\langle |U^{n-1}|U \rangle$ with $n = 3, 4$ and 6 (see Fig. 7). Hereto, the horizontal velocity signal, as measured (lda) during the complete experimental duration, was substituted into the power-law formulation and averaged over this duration. It is shown in Figure 7 that a clear correlation exists between the velocity moments and the net transport rate and that the power $n = 3$ yields the best results (i.e. dashed and solid line almost coincide).

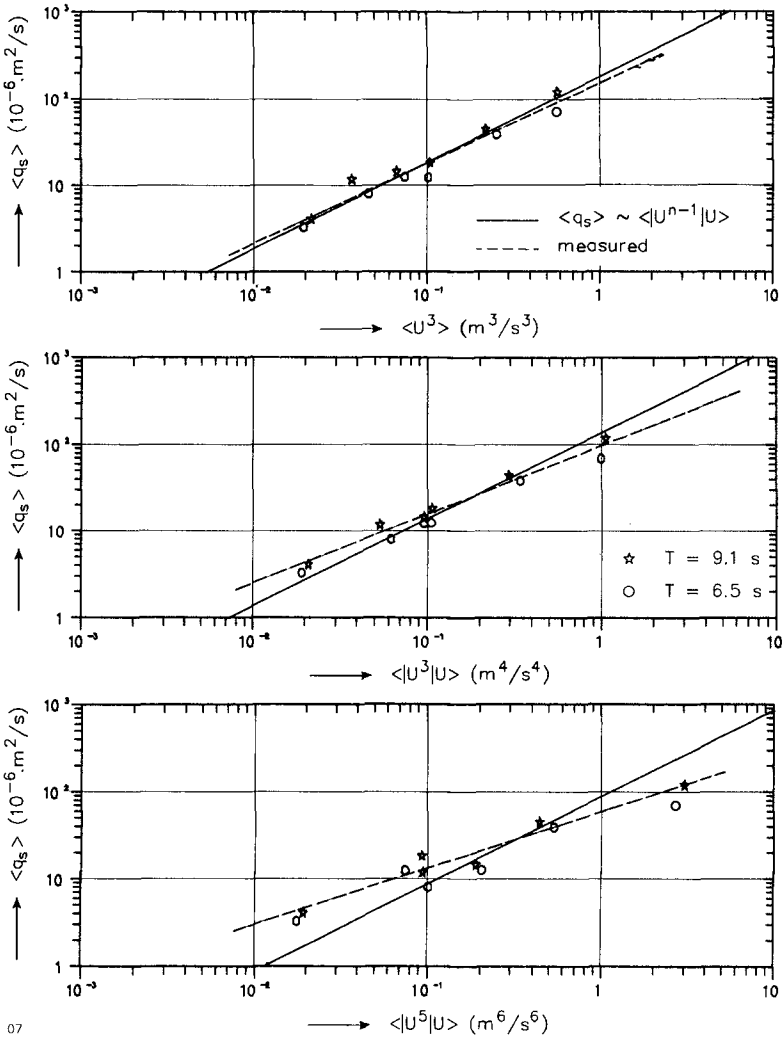


Figure 7 Net transport rate as a function of velocity moments

The experiments with regular and irregular oscillatory flow seem to follow the same line, which confirms the quasi-steady approach of the power-law description. Nevertheless, a wave period influence is present (see Fig. 8) as for the experiments with $T = 9.1$ s the measured net transport rates are systematically higher (20-60%) than for the experiments with $T = 6.5$ s. This indicates that phase-lag effects (or acceleration/inertia effects) are present and should be taken into account for more accurate transport modelling.

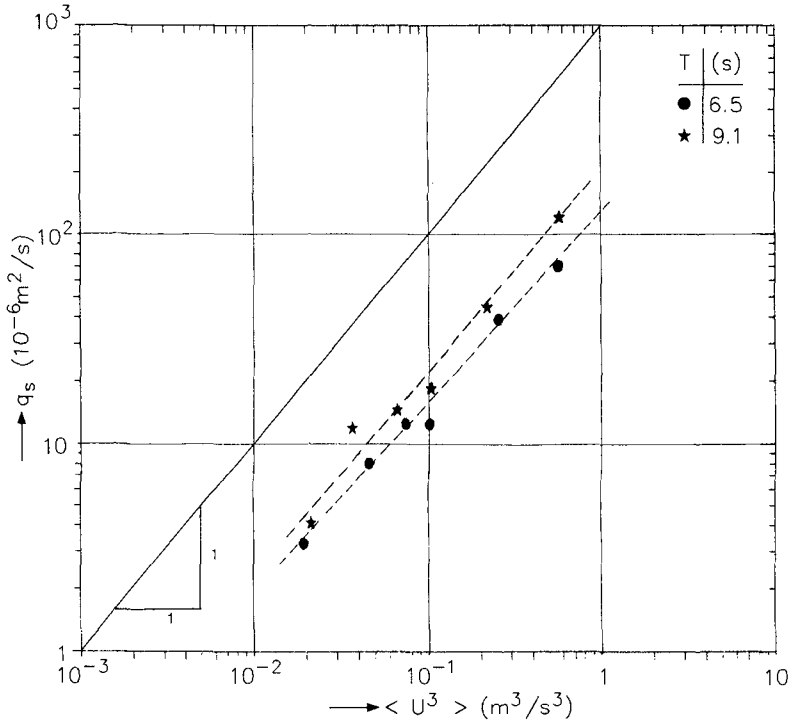


Figure 8 Period influence

In Figure 9 the formulas of Bailard (1981) and Madsen & Grant (1976) are verified in an absolute way by comparing computed net transport rates with the measurements. It is shown that the formula of Bailard (1981) can produce the measured transport rates within inaccuracy limits of a factor 2. The Madsen & Grant formula not only has the wrong power $n (= 6)$ but also clearly overpredicts the transport rate in the high-velocity regime.

Remark: In both formulae the friction factor formulation of Jonsson (1980) was used with roughness height $k_s = D_{50}$ and the significant water particle semi-excursion length (x_s^{sig} for the tests with irregular waves). The Bailard formula was applied with bed-load efficiency factor $\epsilon_b = 0.1$ and suspended-load efficiency factor $\epsilon_s = 0.02$ as suggested by Bailard.

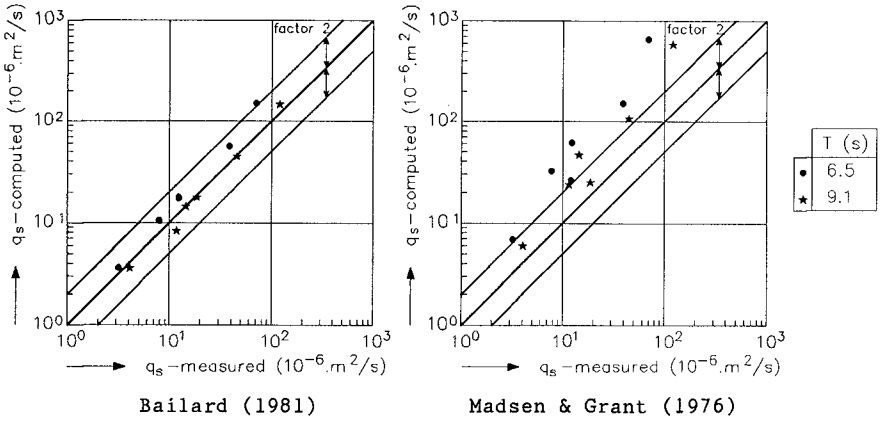


Figure 9 Verification of transport formulae of Bailard (1981) and Madsen & Grant (1976)

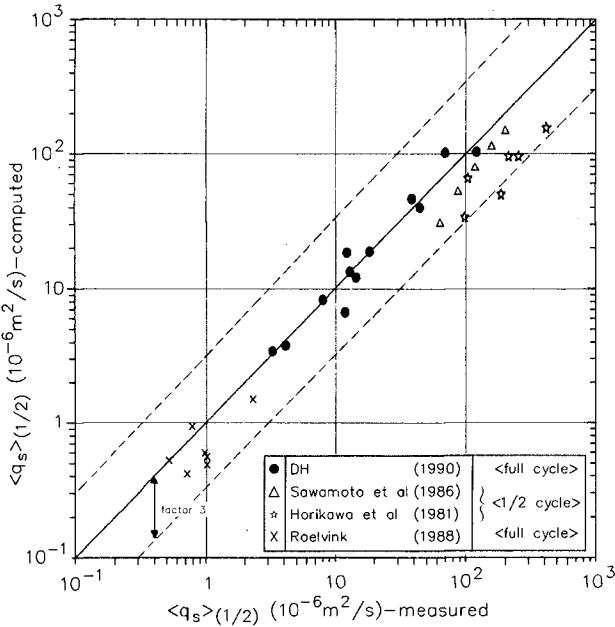


Figure 10 Comparison with other measurements ($D_{50} \approx 0.2 \text{ mm}$)

In Fig. 10 a comparison is made between the present measurements and other available datasets. The measurements of Horikawa et al (1982) and Sawamoto & Yamashita (1986) were carried out in tunnels in the sheet flow regime using almost the same sand as during the present experiments ($D_{50} = 0.2 \text{ mm}$). However, sinusoidal oscillations

were applied (Horikawa: $T = 2-6$ s and Sawamoto: 3.1 s) and the transport per half wave cycle ($\langle q_s \rangle_{1/2}$) was measured. The measurements of Roelvink and Stive (1988) were carried out in the large wave flume of DELFT HYDRAULICS (DELTA flume) using the same sand as used for the present tests. A net (onshore directed) transport $\langle q_s \rangle$ (due to wave asymmetry) was measured in case of irregular waves ($T_{\text{peak}} = 5.1, 6.1$ s, $U_{\text{rms}} \approx 0.3$ m/s). The inter-comparison of the different data sets is made through the power-law formulation₃(1), as calibrated with the new tunnel data (factor $A = 0.18 \cdot 10^{-3}$ s²/m and $n = 3$) and applied to the other datasets. A reasonable agreement is obtained (within a factor 1.5-3) over a wide range (factor 1000) of measured values. Although the data of Horikawa and Sawamoto are systematically underpredicted by the calibrated formula (effect of wave period, 1/2 cycle transport?), the validity of the power $n = 3$ is clearly confirmed (see slope of the data points in Fig. 10).

Conclusions

Two series of experiments were conducted in a new Large Oscillating Water Tunnel of Delft Hydraulics with the objectives to verify and develop (existing) relationships for sediment transport carried by waves, for suspended sediment concentrations and for bedform dimensions in controlled full-scale (1:1) conditions. Series A was conducted with regular sinusoidal waves, series B with regular and irregular asymmetric waves.

Bedforms

For regular sinusoidal waves the observed ripples:

- i) were considerably larger in the high velocity regime (sheet flow) than as predicted by the empirical relations of Nielsen (1979) and did not show the expected transition to plane bed,
- ii) had dimensions (height/length) which were linearly correlated with the orbital excursion length and showed a clear consistency and agreement with existing datasets including the large wave flume measurements of Sakakiyama et al (1986).

For (ir)regular/asymmetric waves the expected transition to plane bed conditions (sheet flow) did occur and agreed well with the relations of Nielsen (1979).

Sediment transport

The net sediment transports as measured during the regular and irregular asymmetric wave experiments in plane or almost plane bed (sheet flow) conditions showed:

- i) a consistent linear relation with the third-order moment of the velocity $\langle U^3 \rangle$,
- ii) a systematic (20-60%) wave-period influence (phase-lag effects),
- iii) a much better agreement with the energetics total load sediment transport formula of Bailard (1981) (within a factor 2) than with the bed-load formula of Madsen & Grant (1976).

A formula of the form $q_s = A \cdot \langle U^3 \rangle$, calibrated with the new experimental data ($A = 0.18 \cdot 10^{-3}$ s²/m), showed a reasonable agreement (within a factor 1.5-3) with the small number of existing datasets (Horikawa et al, 1982, Sawamoto & Yamashita, 1986 and Roelvink,

1988, all: $D_{50} \approx 0.2$ mm) over a wide range of measured values (factor 1000).

Acknowledgements

The measurements were carried out by Mr. T. van Maar of DELFT HYDRAULICS. The necessary software for the generation of the desired oscillatory flow in the water tunnel was developed by Mr. G. Klopman and Mr. L. Verhage. The authors appreciate the comments of Prof. E.W. Bijker as given during the research work. The work was funded in the framework of the 'Coastal Genesis' Research Programme of the Ministry of Transport and Public Works (Rijkswaterstaat).

References

Bailard, J.A.

An energetics total load sediment transport model for a plane sloping beach.

Journ. of Geoph. Res. Vol. 86, no. C11, pp. 10938-10954, 1981.

Bakker, W.T. and van Kesteren, W.G.M.

The dynamics of oscillating sheet flow.

Proc. 20th Int. Coast. Eng. Conf., Taipeh, Vol. 2, 1986.

Fredsøe, J., Anderssen, O.H. and Steen Silberg.

Distribution of suspended sediment in large waves.

Journ. of Waterw., Port, Coast and Ocean Eng., Vol. 111, no. 6, 1985.

Horikawa, K., Watanabe, A. and Katori, S.

Sediment transport under sheet flow condition.

Proc. 18th Int. Coast. Eng. Conf., ASCE, 1982.

Jonsson, I.G.

A new approach to oscillatory rough, turbulent boundary layers.

Ocean Eng., Vol. 7, pp. 109-152, 1980.

Liu, P.L.F. and Dingemans, M.W.

Derivation of the third-order evolution equations for weakly non-linear water waves propagating over uneven bottoms.

Wave motion 11, pp. 41-64, Elseviers Science Publishers B.V., 1989.

Madsen, O.S. and Grant, W.D.

Sediment transport in the coastal environment.

M.I.T. Ralph M. Parsons Lab., Report 209, 1976.

Nielsen, P.

Some basic concepts of sediment transport.

Techn. Univ. of Denmark, Series Paper No. 20, 1979.

Ribberink, J.S. and Al-Salem, A.

Bedforms, near-bed sediment concentrations and sedimenttransport in simulated regular wave conditions.

DELFT HYDRAULICS, Report H840 Part 3, November 1989.

Ribberink, J.S. and Al-Salem, A.

Bedforms, near-bed sediment concentrations and sedimenttransport in simulated asymmetric wave conditions.

DELFT HYDRAULICS, Report in preparation, 1990.

Roelvink, J.A. and Stive, M.J.T.

Large scale tests of cross-shore sedimenttransport on the upper shoreface.

Symp.: Mathematical modelling of sed. trsp. in the coast. zone, Copenhagen, 1988.

Sakakiyama, T.

Sand ripples generated by prototype waves in a large wave flume.

CRIEPI report E385007, Civ. Eng. Lab., Central Res. Inst. of Electric Power Industry, 1986.

Sawamoto, M. and Yamashita, T.

Sedimenttransport rate due to wave action.

Journ. Hydrosience and Hydr. Eng. 4(1), pp. 1-15, 1986.

CHAPTER 176

THE IN SITU MEASUREMENTS OF SEDIMENT TRANSPORT AND BOTTOM TOPOGRAPHY CHANGES

by

Yoshiaki KAWATA¹ M.ASCE, Hiroshi YOSHIOKA²
and Yoshito TSUCHIYA³ M.ASCE

Abstract

In order to get the data about bed-load transport rate and bottom topography changes under storm wave conditions, field equipments were newly developed and tested at the T-shaped Observation Pier(TOP) on the Ogata coast facing the Japan Sea. The surf sled with a pressure sensor can precisely detect the spatial water depth changes along the survey lines. Based on the compiled data, the 3D bottom topography changes for a winter season connect with the appearance of a dip and shoal system on the Ogata coast. The bed-load sampler has also developed to operate in rough sea state in a plane bed conditions. The data were well fitted with the law of cross-shore bed-load transport proposed by Kawata(1989a).

1. INTRODUCTION

A meaningful field study of nearshore sediment dynamics requires the in situ measurement of sediment transport and bottom topography changes. The validity of various proposed sediment transport relationships by waves has not been evaluated in the field. For lack of extensive 3D bottom topography data under severe wave conditions, the reliability of any analytical and numerical prediction methods of beach processes is still ambiguous. Recent field observations such as NSTS program(Seymour, 1987), C²S²(Willis,1987) and Duck85(Mason et al.

¹Associate Professor, Disaster Prevention Research Institute,
Kyoto University, Goka-sho, Uji, Kyoto, 611 Japan

²Instructor

³Professor

1987) had been carried out but no one did not directly measure these variables. In our field study, simultaneous measurements were also made of waves, water particle motion and nearshore currents at various locations along the T-shaped Observation Pier(TOP) in the surf zone.

In the field, the rate of sediment transport normal to the beach has been measured with a newly developed bed-load trap in a series of field experiments conducted at the TOP. The law of sediment transport formulated by Kawata(1989a) can be verified with the field and experimental data. At the same time, a sounding method in rough sea state around the TOP has been also developed to discuss the beach processes on the Ogata coast.

2. PROCEDURE

The field experiments were conducted in the three winter seasons in 1988,1989 and 1990, the periods that encompass the more intense wave activity on the Ogata coast which is a straight sandy beach of 20km long facing the Japan Sea as shown in Fig.1. The TOP extends 250m offshore and parallels the shore for 100m at the offshore end. Usually, seven ultrasonic type wave gauges (aerial emission type) and one 2D and two 3D ultrasonic type current meters are installed for routine observation. In addition, intensive observation uses extra two 3D ultrasonic type current meters whose spacing is 1m in the vertical direction and ten capacitance

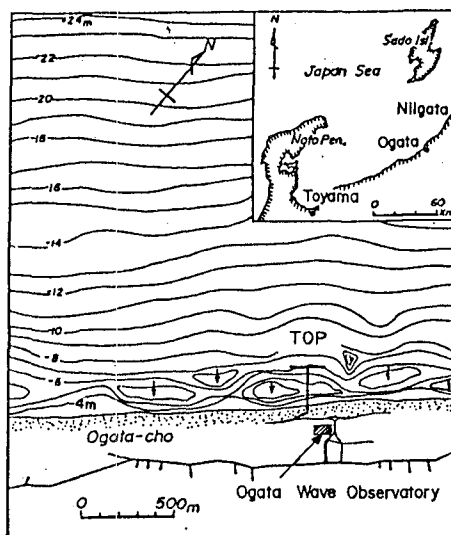


Fig.1 Locations of the Ogata coasts and T-shaped Observation Pier(TOP)

type wave gauges as shown in Fig.2. A wave-rider buoy is anchored at the 3km offshore. The buoy is on a production of the pier axis(almost NW direction) so that in the case of normal incident waves, wave transformation can be analyzed accurately. The nearshore zone in which the water depth is more than about 4m has a very mild slope of around 1/120. At the offshore end of the pier, the water depth is about 6m. All data are gathered and compiled at Ogata Wave Observatory.

2.1 Bed-load trap

The unique design of a bed-load trap has been evolved over several years. Some operation and setting problems had been solved one by one with some ideas. The trap can operate under moderate to severe wave conditions because it is installed by using the local scour around the trap itself. Photo 1 shows the shape, attached equipments and size. Before the setting of the trap on the sea bottom, the sand bed condition is confirmed to be the plane bed with a measuring comb of 1.8m long with 61 stings which are coated with the grease as shown in Photo 2. The small scale bottom undulations in the cross-shore direction can be measured.

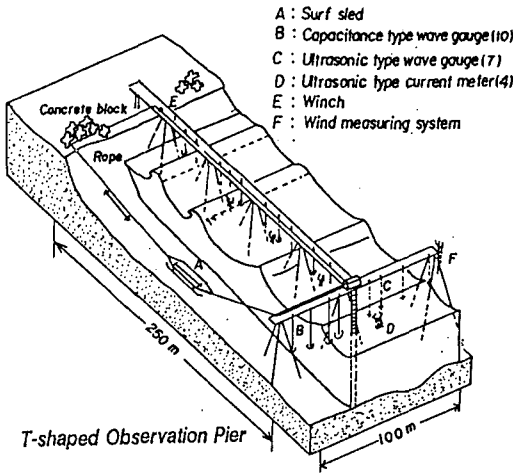


Fig.2 TOP and setting of surf sled, wave gauges, current meters and other equipments

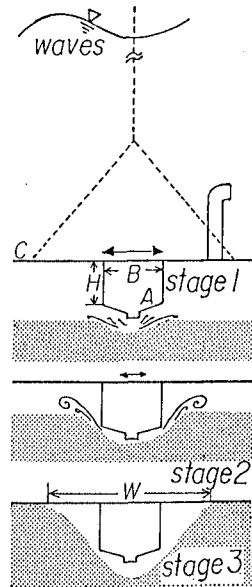
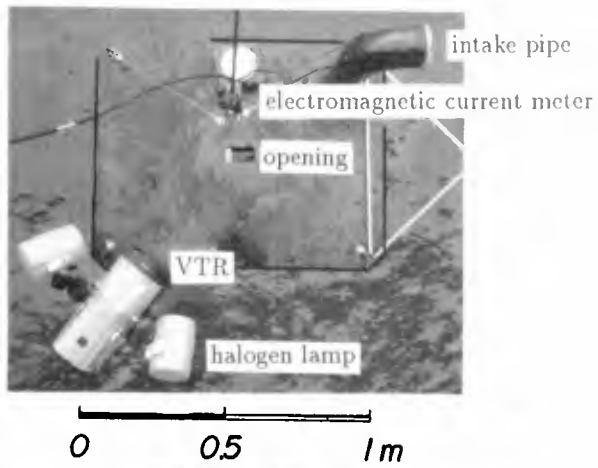


Fig.3 Procedure of setting of bed-load trap using local scouring



(a) Plane view



(b) Side view

Photo 1 Bed-load trap

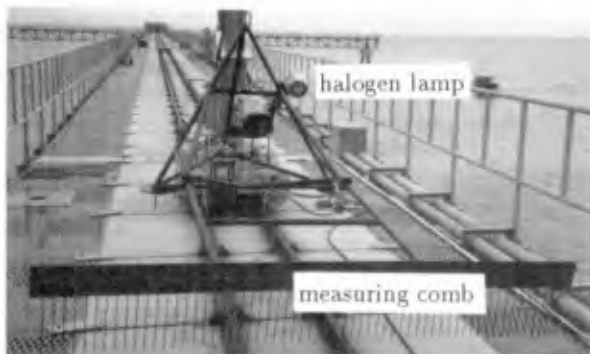


Photo 2 Measuring apparatus of small scale bottom undulations

Usually, at the breaker zone the plane bed condition is observed.

Fig.3 shows the setting process of the trap. Firstly, the opening(10cmx5cm) on the top steel plate of the trap is capped with a small cover which is fixed on the trap with an adhesive tape. This cover can be easily removed from the deck of the pier by pulling a fine string. Secondly, the trap is taken down into the sea by a crane and the air inside the trap is released through the intake pipe. Thirdly, the trap is touched on the bottom. The next moment local scouring around the trap advances. At the stage 3 in Fig.3, the trap is gradually stabilized in accordance with the development of the local scouring. The measurement of the bed-load transport starts in a moment when the string removes the cover from the opening of the trap. A compact videocassette recorder and two components electromagnetic current meter (the probe is set at the height of 17.3cm from the top plate of the trap) were equipped on the trap.

The net onshore (or offshore)bed-load transport rate can be just trapped through the opening on the plate. The inflow and outflow of sea water through the opening connected with a pipe as shown in Photo 1 keeps the one-way bed-load measurement. This system surely corresponds to the periodic changes of flow direction of water particle motion.

2.2 Surf sled

A surf sled (1.5m long, 0.7m wide, 40kg in weight) with a semiconductor pressure transducer has been also developed as shown in Photo 3. The sled can be operated in the cross-shore direction by two winches and roop rope system. The A-D converted data are compiled in the datalogger in a watertight stainless housing. With the sled the beach profiles were measured at longshore intervals of 5m. The sampling interval is 2.5s and average moving speed of the sled is 19.4cm/s. The overall error of the sounding keeps less than 5cm in any sea state. Preliminary tests show that low pass filter of 0.03Hz is adequate to eliminate the effect of incoming waves.



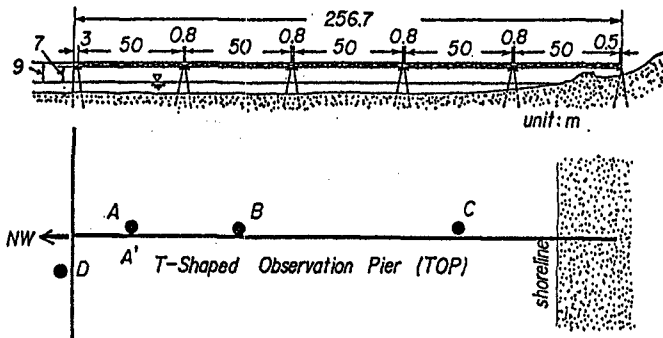
Photo 3 Surf sled

3. FIELD MEASUREMENTS

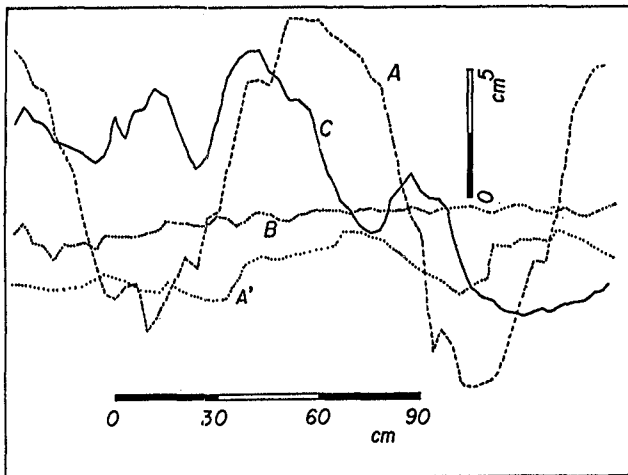
3.1 Bed-load transport

Fig.4 shows the sea bottom conditions at some measuring sites. In the surf zone on the Ogata coast, the rippled bed is usually observed and at the breaker zone, a plane bed condition is formed.

Fig.5 shows the cumulative curves of sediment on the bed and in the trap at site B. The mean diameters of the bed and of trapped sediment are 0.25mm and 0.3mm respectively. It was found that the relatively coarse part of the bed sediment moves as bed-load and therefore the standard deviation of the trapped sediment is smaller than that of the bed one.



(a) Measuring site around the pier



(b) Bottom conditions

Fig.4 Small scale bottom topography

Table 1 lists the results of observations on onshore sediment transport rate. These data are plotted in Fig.6 in which q_* ($=q/u_*d$) is dimensionless sediment transport rate and τ_* is dimensionless tractive force (the Shields number). In the arrangement, some unknown variables were estimated with the small amplitude wave theory and the friction factors introduced by Jonsson (1966). The visual observation with a VTR shows that bed-load movement on the plate of the trap was very smooth and made a parallel stripe pattern of accumulated sediment on the plate of the trap in the cross-shore direction. When the direction of water particle motion changes to offshore, the discharge from the opening through the pipe can blow off sediment which usually falls into the trap as offshore sediment transport rate. Therefore, it was confirmed that the trap efficiency of onshore sand transport is very high. The solid line in the figure shows the theoretical relationship of cross-shore sediment transport rate given by Kawata (1989a) as follows:

The theoretical reduction for cross-shore sediment transport is based on the momentum conservation of a cloud of saltating sand particles on a sloping beach.

(a) In the case of onshore sediment transport

$$\begin{aligned}
 q_{*u} = & a_1 [1 + e + (1 - e) \sqrt{\sin \theta} / (\sqrt{3}/2 A_r \sqrt{C_D \tau_*}) \\
 & - \{1 - e + (1 + e) \sqrt{\sin \theta} / (\sqrt{3}/2 A_r \sqrt{C_D \tau_*})\}^2 \\
 & + 8(1 - e) \cos^2 \theta / (3 \lambda C_D A_r^2 \tau_*^2)^{1/2}] (\tau_* - \tau_{*c}) \quad \text{--- (1)}
 \end{aligned}$$

(b) In the case of offshore sediment transport

$$\begin{aligned}
 q_{*d} = & a_1 [1 + e - ((1 - e)^2 + 8 \cos^2 (1 - e - 2e \lambda \tan \theta) \\
 & / (3 \lambda C_D A_r^2 \tau_*^2)^{1/2}] (\tau_* - \tau_{*c}) \quad \text{--- (2)}
 \end{aligned}$$

$$a_1 = (e/1 - 1) \tan \beta_m (1 + \rho/\sigma) A_r / \sqrt{\cos \theta}$$

$$\tau_{*c} = \tau_{*o} \{ \cos \theta \pm (\sigma/\rho) / (\sigma/\rho - 1) (\sin \theta / \tan \varphi) \}$$

Table 1 Results of field observation on onshore bed-load transport rate

No.	H _{1/3} (m)	T _{1/3} (s)	H _m (m)	T _m (s)	u _{1/3} (cm/s)	u _m * (cm/s)	t (s)	q** (cm ³ /cm/s)
1	1.38	5.41	0.88	4.51	-	-	658	9.48x10 ⁻³
2	1.71	6.00	1.00	4.86	-	-	1583	69.8
3	0.94	4.65	0.63	3.97	58.5 (47.7)	34.6 (27.6)	1476	0.952
4	1.09	4.48	0.71	3.71	47.7 (52.5)	27.3 (37.5)	1554	2.18
5	1.00	4.43	0.68	3.87	-	-	1440	0.466
6	1.13	4.47	0.76	4.20	65.8 (52.0)	40.2 (30.2)	4967	1.03
7	0.88	4.82	0.61	4.07	50.3 (56.8)	26.5 (33.2)	1477	2.82
8	0.93	4.40	0.67	4.27	58.5 (64.0)	26.9 (46.0)	2398	7.36
9	1.10	4.98	0.75	4.38	41.7 (62.3)	23.7 (39.6)	1410	2.26
10	1.04	4.66	0.75	4.45	46.0 (64.0)	23.9 (44.3)	1366	1.73
11	1.59	4.94	1.07	4.93	72.6 (81.2)	43.9 (51.6)	1800	7.84
12	3.04	8.80	1.78	6.20	-	-	4360	36.8
13	1.98	4.40	1.26	3.00	-	-	4500	14.8

* Parenthesis means offshore direction.

** Substance volume (porosity is assumed to be 0.4)

in which θ :beach slope, e :rebound coefficient of sand particle , C_D :drag coefficient, $A_r=8.5$, $\lambda/4$:ratio of height to length of a saltating sand particle, σ and ρ :densities of sand and fluid respectively, φ :angle of repose, τ_* :the Shields number and suffix u , d and c :upward slope, downward slope and critical condition respectively.

Typical variables are shown in Fig.6, in which the experiments of saltation of a sand particle were done in a water stream. In the horizontal bed, Eqs.(1) and (2) completely coincide. It should be noted that the trend of the field data calculated with mean wave height and period as well as experimental data in a plane bed condition is in reasonable agreement with the theory. However, arrangement with characteristics of significant waves is not adequate.

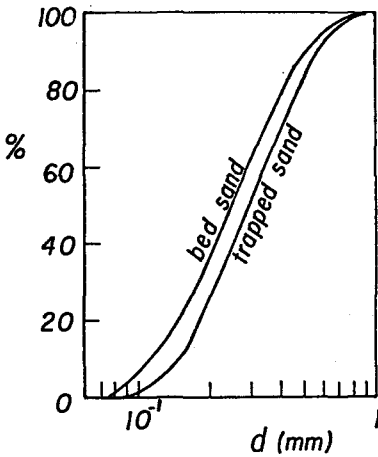


Fig.5 Sieve analysis of sediment

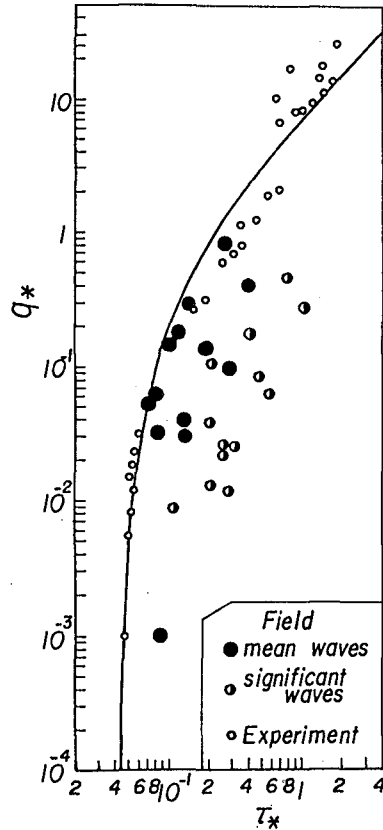


Fig.6 Relationship between the Shields number and dimensionless onshore sediment transport rate

3.2 Bottom topography changes

(1) Wave characteristics

The intensive observation was conducted from November 28 to December 7, 1987. In this period, some storms came on the Ogata coast. Fig.7 shows the time series of wave climate recorded by a wave-rider buoy, a capacitance type wave gauge at the east end of the pier. The wave directions were analyzed with the linear array of four capacitance type wave gauges at the offshore end. The water depth of about 6m at the offshore end of the pier controls the maximum wave height. The tidal range is less 40cm. Usually, low pressures move eastwards in the midst of the Japan Sea in winter season, so that wave directions change from west to east at the offshore. However, in the records of the wave directions at the pier, they are not widely distributed but have a sharp peak around 90° (This means that wave angles at the pier are perpendicular to the beach) as shown in Fig.8. In the peak, wind waves from WNW to NW and swell waves from NW to NNW are included. This results reveals that the longshore sediment transport in the coast is small in spite of a straight sandy beach.

(2) Erosion and deposition area

Fig.9 shows the bottom topography on December 9 and 10, 1987 and March 13, 1988 in which D and S depict dip and shoal respectively. Over this period, waves are usually very small, so that it is assumed that the bottom topography is not remarkably changed in other seasons except by typhoon. Firstly, it was pointed out from Fig.9(a) that the contour lines in the shallow area which is less than 4m are parallel each other, two shoals are appeared at the both offshore ends of the pier and a dip with the maximum water depth of 5.2m expands to the central zone of the pier. In Fig.9(b), it was found that the distance of two shoals becomes short and the dip further extends to west direction(upper side of the figure). In general, water depth around the pier increased after winter season. This is partly due to forced offshore sediment transport. The armour unit mounted in the foreshore reflects the incoming waves and makes this coast an wave energy reflected beach defined by Short(1979).

The erosion and deposition diagram as shown in Fig.10 was made from the bottom topography changes between two observation date. In the figure, a hatched line is a boundary between erosion and deposition areas. As the characteristics of bottom topography change, the areas of erosion and deposition are not uniformly distributed in the cross-shore direction. Moreover, the positions of dips and shoals are almost fixed around the pier. Fig.11 shows the depth sounding chart in July 1986 and 1987 around the pier and Fig.12 reveals the pattern of dip and shoal in another place on the Ogata coast(kawata, 1989b). The distribution

pattern of dip and shoal was not changed annually, so that this system is stable and crescentic bars are formed on the Ogata coast. As before mentioned, there are two dominant wave directions on the Ogata coast. Their breaking points are usually a little different in the offshore direction, i.e., the fully-developed wind waves break relatively offshore in comparison with the breaking of the swell waves. Moreover, their incoming angles are slightly different. This characteristics may introduce the typical crescentic bar systems.

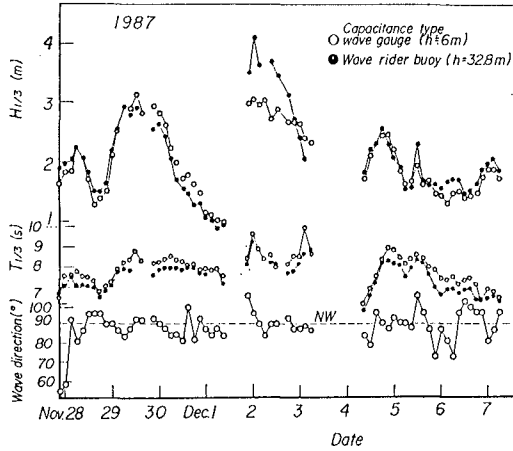


Fig.7 Changes of significant wave height and period and wave direction

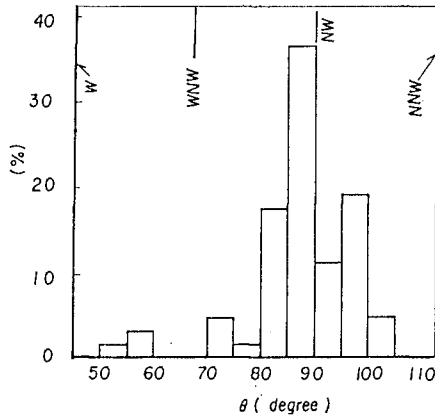
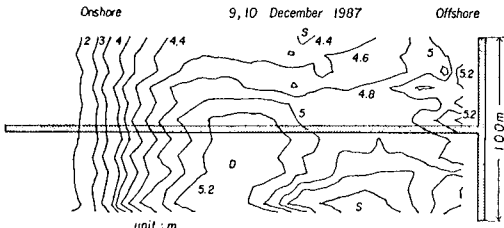
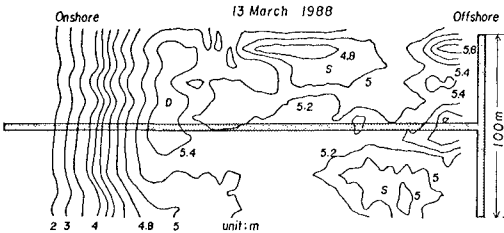


Fig.8 Histogram of incident wave angles at the offshore end of the TOP



(a) 9 and 10 December 1987



(b) 13 March 1988

Fig.9 bottom topography around the TOP

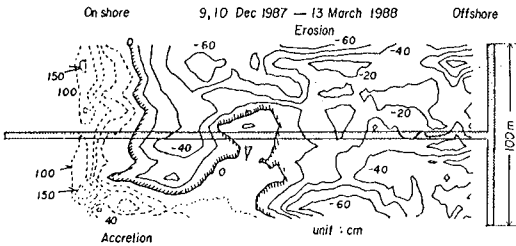


Fig.10 Deposition and erosion diagram

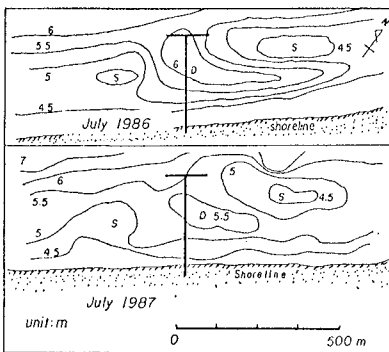


Fig.11 Depth sounding charts in Summer

(3) Beach profile changes

Along the pier the depth sounding with a lead has been conducted every week. The sounding interval in the cross-shore and longshore directions is 1.25m. The width of the pier is 4m so that we have two set of data along the pier in the cross-shore direction. The discrepancy of the mean beach profiles is very small so that the west side data were used in the analysis. The temporal difference from the mean beach profile are shown in Fig.13 in which black and grey areas show erosion and accretion from the mean beach profile respectively. In early winter, the offshore area beyond $x=70\text{m}$ was eroded, but this tendency was gradually eliminated and finally the deposition area was appeared. As shown in Fig.9,

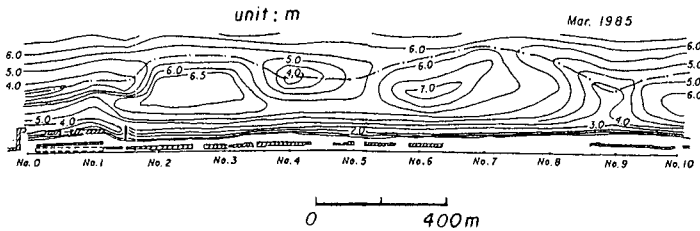


Fig.12 Typical bottom topography changes on the Ogata coast

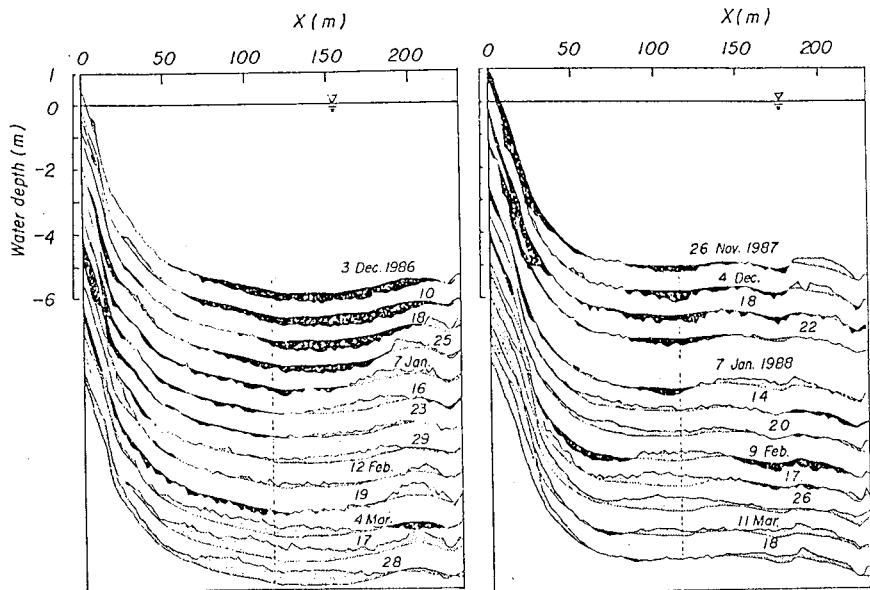


Fig.13 Beach profile changes in winter

this area is a "battle" zone of accretion and deposition areas. It is explained that westward longshore sediment transport may contribute the deposition in this area in winter season. From the data of the ultrasonic type current meter, strong undertow was observed around this place so that local changes of bottom topography may largely depend on the 3D nearshore current system.

4. CONCLUSIONS

A new type bed-load trap has been developed with two ideas. The principles are as follows: local scouring around the trap stabilizes the trap itself and an intake pipe keeps the onshore or offshore sediment transport rate in the trap. The effectiveness of the trap was certified with VTR analysis under sheet flow conditions. The field data as well as experimental one on a plane bed confirmed the validity of the law of cross-shore sediment transport proposed by Kawata(1989).

A surf sled is also applicable to the measurement of bottom topography changes under rough sea state. The accurate sounding data can reveal the beach processes on the Ogata coast. This sandy straight beach has a series of crescentic bars which correspond to the dip and shoal system in the longshore direction. Under small longshore transport rate due to almost normal incoming waves, their positions are annually stable. The slight discrepancy of incoming wave angles between fully- developed wind waves and swell ones makes the direction of sediment transport complex and may lead to formation of the crescentic bar systems.

REFERENCES

- Jonsson, I. G. (1966): Wave boundary layer and friction factor, Proc. 10th ICCE, pp. 127-148.
- Kawata, Y. (1989a): The law of cross-shore sediment transport, Proc. Coastal Engineering, JSCE, Vol. 36, pp. 289-293.
- Kawata, Y. (1989b): Methodology of beach erosion control and its application, Coastal Engineering in Japan, Vol. 32, No. 1, pp. 113-132
- Mason C., W. A. Birkemeier and P.A. Howd (1987): Overview of DUCK85 near-shore processes experiment, Coastal Sediments '87, pp. 818-833.
- Seymour, R. J. (1987): An assessment of NSTS, Coastal Sediments '87, pp. 642-651.
- Short, A. D. (1979): Three-dimensional beach-stage model, J. Geology, Vol. 87, pp. 553-571.
- Willis, D. H. (1987): The Canadian coastal sediment study: an overview, Coastal Sediments '87, pp. 682-693.

CHAPTER 177

Single-phase fluid modelling of sheet-flow toward the development of "numerical mobile bed"

by

Kazuo NADAOKA ¹⁾ and Hiroshi YAGI ²⁾

ABSTRACT

As a first step to develop "numerical mobile bed" as a promising tool for the study of sheet-flow problem, a computational scheme based on a single-phase fluid model has been constructed by formulating the vertical transport of mass and momentum within the sheet-flow layer. The numerical results have shown the satisfactory agreements with the experimental results in velocity profile, sediment transport rate, and others. Further the difference in the period of oscillation was found to have appreciable influence on the temporal evolution of the sheet-flow thickness, indicating the importance of unsteadiness in the sheet-flow dynamics.

1. Introduction

The sheet-flow is a mode of sediment transport in the condition of large bottom shear stress and has quite important role in nearshore sedimentary process because of its large transport rate. For the sheet-flow study, however, the efficiency of conventional approaches for sediment transport study, i.e., laboratory experiments and field measurements are limited because of the similitude problem for laboratory wave-flume experiments and the lack of measuring devices in field measurements. The use of U-shaped tank to generate oscillatory flow with large velocity amplitude is one of possible ways to avoid

1) Associate Professor, Department of Civil Engineering, Tokyo Institute of Technology, Tokyo 152, Japan.

2) Research Associate, Department of Civil Engineering, Tokyo Institute of Technology, Tokyo 152, Japan.

the similitude problem in the wave tank experiments (Horikawa et al. 1982, Sawamoto & Yamashita 1987). However, such simplification of the flow field from the original wave field into a pure sinusoidal oscillatory flow field may yield significant difference in the dynamics of the sediment movements in the sheet-flow layer, as demonstrated theoretically by Nadaoka et al. (1988, 1990).

As a promising tool to overcome these difficulties, the authors emphasize the need to develop the "numerical mobile bed (NMB)", corresponding to the recent idea of the "numerical wave tank" or "numerical wind tunnel". The benefits of NMB are quite obvious; i.e., it makes possible to simulate the sheet-flow under arbitrary wave conditions, and in the NMB we can easily see its internal structure.

Although two-phase fluid modelling is most desirable for the development of NMB, there exist no reliable constitutive equations to express the momentum transport through the sediment collision process, which is one of most essential processes in the sheet-flow dynamics. Hence in the present study, as a first step toward the development of NMB, a computational scheme based on a single-phase fluid concept has been constructed by modelling the vertical transport of mass and momentum within the sheet-flow layer.

2. Formulation and modelling of sheet-flow phenomenon

(1) Basic equations

For the "numerical wave tank" and "numerical wind tunnel", there exist definite basic equations, i.e., Laplace's equation and the Navier-Stokes equation, respectively. For the "numerical mobile bed (NMB)", however, the basic equation to describe the dynamical process of sediment-fluid mixture has not yet been well established in the form having universal applicability. This is mainly attributable to the fact that there exist no reliable ways to formulate the vertical transport of mass and momentum in the sheet-flow layer. Especially for the modelling of sheet-flow as two-phase fluid we have no constitutive equation to evaluate the momentum exchange through sediment collision described as follows, although the basic equations can be easily expressed in the two-phase forms as shown by, e.g., Kobayashi and Seo(1985).

Since the pioneering work by Bagnold(1954), many studies have been made for the additional shear stress attributable to the presence of solid particles, which is so-called "grain stress". According to Bagnold(1954), the flow regime of particle-laden two-phase flow can be divided into "grain-inertia region", "macro-viscous region", and "intermediate region" between them.

Estimates of order of magnitude can show that the sheet-flow in usual condition falls into the viscous or intermediate regions (e.g., Bakker and Kesteren, 1986). As the experimental formula of the grain stress, τ_g , for these regions, Bagnold(1954) suggested the following expression.

$$\tau_g = 2.25\lambda^{1.5}\mu_0 \frac{\partial u}{\partial z} , \quad (1)$$

where λ is the linear concentration, μ_0 is the viscosity of intergranular fluid and $\partial u/\partial z$ is the rate of shearing. More recently Ahilan & Sleath (1987) arranged the experimental data by Savage and McKoewn (1983) and obtained the following formula of τ_g for the use in their numerical computation of oscillatory sheet-flow.

$$\tau_g = 1.2\lambda^2\mu_0 \frac{\partial u}{\partial z} . \quad (2)$$

However, for the viscous region, the actual mixed shear stress cannot legitimately be split into grain and fluid elements as described by Bagnold(1954). This is reflected in the fact that these experimental formulae have the forms with linear dependence on the fluid viscosity μ_0 ; hence τ_g becomes zero as $\mu_0 \rightarrow 0$. Therefore these experimental formulae cannot be used for the expression of the shear stress due to the grain-grain interaction in the two-phase formulation.

Considering such state of the limited knowledge on the constitutive equations at present, we have adopted a single-phase fluid formulation as one of realistic approaches. In this formulation, the equations of motion can be express as

$$\frac{Du}{Dt} = -\frac{1}{\rho} \frac{\partial p}{\partial x} + \frac{1}{\rho} \left[\frac{\partial}{\partial x} \left(\mu_e \frac{\partial u}{\partial x} \right) + \frac{\partial}{\partial z} \left(\mu_e \frac{\partial u}{\partial z} \right) \right] + \frac{\partial}{\partial x} \left(\Omega_x \frac{\partial u}{\partial x} \right) + \frac{\partial}{\partial z} \left(\Omega_z \frac{\partial u}{\partial z} \right), \quad (3)$$

$$\frac{Dw}{Dt} = -\frac{1}{\rho} \frac{\partial p}{\partial z} + \frac{1}{\rho} \left[\frac{\partial}{\partial x} \left(\mu_e \frac{\partial w}{\partial x} \right) + \frac{\partial}{\partial z} \left(\mu_e \frac{\partial w}{\partial z} \right) \right] + \frac{\partial}{\partial x} \left(\Omega_x \frac{\partial w}{\partial x} \right) + \frac{\partial}{\partial z} \left(\Omega_z \frac{\partial w}{\partial z} \right), \quad (4)$$

where u and w are horizontal and vertical components of composite velocity of the sediment-fluid mixture, p is the pressure, ρ is the density of the mixture, Ω_x and Ω_z are x and z components of eddy viscosity, and μ_e is an equivalent viscosity to represent sediment collision effect. In order to obtain a closed system of the basic equations, we need further the continuity equation(5) and mass conservation equation(6) for the sediments.

$$\frac{\partial u}{\partial x} + \frac{\partial w}{\partial z} = 0, \quad (5)$$

$$\frac{\partial c}{\partial t} + \frac{\partial}{\partial x}(cu) + \frac{\partial}{\partial z}\{c(w-w_f)\} = \frac{\partial}{\partial x}\left[K_x \frac{\partial c}{\partial x}\right] + \frac{\partial}{\partial z}\left[K_z \frac{\partial c}{\partial z}\right], \quad (6)$$

in which c is the volumetric concentration of sediments, K_x and K_z are their horizontal and vertical diffusion coefficients, and w_f is the settling velocity of the sediment particles.

(2) Modelling of mass and momentum diffusivities and fall velocity of sediments

The accuracy of the present numerical model entirely depends on the way to specify the diffusion coefficients, μ_e , Ω_x , Ω_y , K_x , K_z and the settling velocity w_f . Unfortunately, however, there exist no established methods for the modelling of these quantities. Hence, in the present study, we have introduced tentative modellings of these factors as described in what follows.

a) Vertical diffusion coefficients of momentum

The factors governing the physical process of momentum exchange within the sheet-flow layer are

- 1) Momentum exchange through the sediment collision,
- 2) Viscous stress within the intergranular fluid,
- 3) Reynolds stress in the intergranular fluid.

Among these, in the present model, 1) and 2) are incorporated by an effective viscosity μ_e varying with sediment concentration c . The functional dependence of μ_e on c is assumed to be formulated as eq.(7) after Eilers (1941).

$$\frac{\mu_e}{\mu_0} = \left[1 + \frac{1.25c}{1-c/c_{\max}}\right]^2. \quad (7)$$

In this formula, as c becomes the maximum possible concentration c_{\max} , μ_e attains infinitely large value. This behavior of $\mu_e(c)$ near c_{\max} is consistent with the fact that the particles with the concentration of c_{\max} remain at rest. Although Eilers specified c_{\max} to be 0.74, the concentration c for the real sand particles in the sheet-flow layer can attain 0.65 at most. Hence, in the present model, c_{\max} is assumed to be 0.65. Furthermore, in order to avoid the infinitely large number to appear in the numerical calculation when c becomes c_{\max} , eq.(7) has been slightly modified as eq.(8) for the use in the present numerical simulation.

$$\frac{\mu_e}{\mu_0} = \left[1 + \frac{1.25c}{1-0.95(c/c_{\max})} \right]^2 \quad (8)$$

Reynolds stress within the intergranular fluid is another important factor for momentum transfer in the sheet-flow layer and it may be formulated most simply through a mixing length theory such as

$$\Omega_z = l^2 \left| \frac{\partial u}{\partial z} \right| \quad (9)$$

However, there arises a difficulty in the way to define the mixing length for the fluid domain with "fuzzy" boundary such as sheet-flow layer. Namely, for the sheet-flow with a typical vertical profile of the sediment concentration c as shown in Fig.1, the vertical location of the boundary can not be prescribed definitely. Hence, in the present study, a tentative new model of the mixing length has been introduced by considering a physical aspect of the eddy structure in the sheet-flow layer. Namely, within the sheet-flow layer, the eddy scale is not prescribed with the local concentration $c(z)$, but is considered to be governed by the overall feature of $c(z)$ profile. On the other hand, far above the sheet-flow layer, the layer acts as if it is a fixed boundary for the eddy structure. Hence at the far field above the sheet-flow layer, the mixing length should be almost coincide with that for the rigid boundary.

As one of possible models being consistent with these consideration, a new mixing model defined by equation (10) have been introduced, which is shown schematically by the solid curve for the mixing length $l(z)$ in Fig.1.

$$l(z) = \kappa \int_{-\infty}^z \frac{c_{\max} - c(\zeta)}{c_{\max}} d\zeta, \quad (10)$$

where κ is the Karman constant (=0.4).

b) Vertical diffusion coefficients and fall velocity of sediments

Another important factor to be modeled is the vertical mass transport of the sediments in the sheet-flow layer. This is considered to be governed by the following three factors.

- 1) Particle collisions,
- 2) Turbulence of interstitial fluid,
- 3) Particle settling.

Among these, the former two factors have been estimated by a similar diffusion model with a mixing length.

$$K_z = (\beta d + \alpha l)^2 \left| \frac{\partial u}{\partial z} \right| + K_0, \quad (11)$$

in which the scale of mixing is assumed to be the sum of those proportional to the particle diameter, d , and to the turbulent mixing length, l . The former scale is introduced by considering that the minimum mixing scale should be governed by the sediment diameter. The values of α and β were determined as 0.35 and 1.7 respectively so that the calculated c-profiles fit the experimental results by Horikawa et al. (1982) as well as possible. K_0 is a coefficient introduced to stabilize the numerical calculation, and was set to be $5\nu_0$ by trial and error, where ν_0 is the kinematic viscosity of the intergranular fluid. The particle settling velocity, w_f , varies with the sediment concentration, c , because of the hindered effect by particle collision. This dependence of w_f on c has been proposed by several researchers to be expressed as

$$\frac{w_f}{w_{f0}} = \left(1 - \frac{c}{c_{\max}} \right)^n, \quad (12)$$

where w_{f0} is the settling velocity in the still water. Although the exponent n in this equation has been reported to have several values by the experiments, the optimal value of n for complex unsteady flow conditions such as sheet-flow can not be specified. Hence, in the present study, the value of n was set simply to be one.

(4) Boundary conditions

At the left and right boundaries of the computational domain, the periodic conditions are used for u and c . At the upper boundary, on the other hand, the conditions

$$u=U_0, \quad cw_f + K_z \frac{\partial c}{\partial z} = 0, \quad (13)$$

are imposed, where U_0 is the sinusoidally oscillating velocity at the outer edge of the sheet-flow layer. Hence the horizontal pressure gradient can be given by U_0 as

$$\frac{\partial p}{\partial x} = -\rho_0 \frac{\partial U_0}{\partial t}. \quad (14)$$

where ρ_0 is the density of the pure fluid.

At the lower edge of the sheet-flow layer, the following simple rest condition is imposed, because for

unsteady two-phase flows there exist no reasonable condition such as the yielding stress for static problems.

$$u=0 \quad \text{for } c > 0.999c_{\max}, \quad (15)$$

where the coefficient of 0.999 is a factor to allow the computational error in c so that it does not yield any unrealistic influence on the rest condition.

3. Computational results and discussion

(1) Comparison of calculated values with experimental data

To confirm the validity of the present model, it has been applied to an oscillating sheet-flow problem, for which several experimental results are available for the comparison. Figure 2 is an example showing the vertical profiles of the sediment concentration c , horizontal velocity u and sediment flux q with the experimental data by Horikawa et al.(1982), and demonstrates that the present model can simulate the overall feature of these profiles and their time evolution.

Figure 3(a) shows the phase-variation of the sheet-flow depth h , representing that the present numerical model can give almost the same magnitude of variation of h within a half-cycle, as compared with the experimental results. However, the large difference in h between the acceleration and deceleration phases as seen in the experimental result cannot be reproduced by the present model. This is due to the fact that the characteristic difference of turbulent flow structure between at acceleration and deceleration phases cannot be represented by the zero-equation turbulence closure such as the mixing length model, which we have adopted for the present formulation

Figure 3(b) shows the phase-variation within a half cycle of the instantaneous sediment transport rate Φ defined as eq.(16).

$$\Phi(t) = \frac{1}{w_{F0}d} \int_{-\infty}^{\infty} q(z, t) dz. \quad (16)$$

There arises appreciable discrepancy between the calculated and measured values around the peak and decelerating phases. This is mainly attributable to the fact that the magnitude of the experimental velocity exhibits smaller values at the deceleration phases as shown in Fig.2.

(2) Dependence on Shields parameter

Figures 4(a) and (b) represent the dependence of the phase-variation of h and the nondimensional sand transport rate averaged over a half cycle, Φ , on the Shields parameter, ψ_m defined as eq.(17). The figures indicate that as the Shields parameter increases, the phase-variation patterns of h and Φ become skewed shapes having their peak behind the phase of $\pi/2$.

$$\psi_m = \frac{1}{2} \frac{u_{*m}^2}{sgd}, \quad (17)$$

where u_{*m} is the maximum friction velocity, s is the specific gravity of sediments in fluid and g is the gravitational acceleration.

Figure 5 shows the relation between $\bar{\Phi}$ and u_{*m}/w_f . The full line in the figure represents the experimental formula by Sawamoto & Yamashita(1987) obtained by reexamining the formula by Madsen & Grant(1976) with their own experimental data. Comparison with this experimental line indicates that the present model can estimate the mean transport rate with acceptable magnitude, though its dependence on u_{*m}/w_f is slightly weaker than that of the experimental formula.

(3) Effect of unsteadiness

The conventional ways to estimate the sediment transport rate is based on the assumption of quasisteadiness of the sediment transport process. For example, Madsen & Grant (1976) derived a formula to estimate $\bar{\Phi}$ by assuming that the instantaneous transport rate $\Phi(t)$ can be evaluated by Brown's formula(1950) for the unidirectional steady flow. In order to investigate the validity of this assumption, the effect of the unsteadiness of the sheet-flow phenomenon has been examined.

The dashed-line in Fig.3(b) indicates the instantaneous sand transport rate calculated by the Brown's formula under the assumption of such quasisteadiness. The quasisteady value of Φ is found to exhibit rapid increase and decrease pattern around its peak phase as compared with the experimental and present computational results. This fact strongly suggests that the unsteadiness has quite important role in the sheet-flow dynamics, hence it is indispensable factor for the sheet-flow modelling.

In order to investigate this point more clearly, the calculations have been executed for various values of the oscillating period T with the same Shields parameter ψ_m . Figure 6 shows the phase-variation of the sheet-flow depth h for the three periods indicated. It is found that as the period decreases the relative magnitude of h -

variation within the a half cycle also decreases, and the depth value attains its peak at more later phase. This is closely correlated with the fact that as the oscillating period becomes shorter, the sediment pick-up and successive settling process cannot catch up with the phase-variation of the flow field without any phase lag. Existence of such strong dependence of the sheet-flow evolution on the oscillating period T indicates that we should treat the sheet-flow phenomena as a nonstationary process for its modelling.

4. Conclusions

Although the present model is still rather simple and primitive in contrast with our final goal to develop the "numerical mobile bed", the present model can estimate the essential feature of sheet-flow dynamics, such as temporal evolution of sheet-flow profiles and their overall dependence on the Shields parameter. Further the difference in the period of oscillation was found to have appreciable influence on the temporal evolution of the sheet-flow thickness, indicating the importance of unsteadiness in the sheet-flow dynamics.

References

- Ahilan, R.V. and Sleath, J.F.A. (1987): Sediment transport in oscillatory flow over flat bed, *J. of Hydraulic Eng.*, Vol.113, No.3, pp.308-322.
- Bagnold, R.A. (1954): Experiments on a gravity-free dispersion of large solid spheres in a Newtonian fluid under shear. *Proc. R. Soc. Lond.* A225, 49-63
- Bakker, W.T. and van Kesteren, W. G. M. (1986): The dynamics of oscillatory sheet flow, *Proc. of 20th Int. Conf. on Coastal Eng.*, ASCE, pp. 940-954.
- Brown, C.B. (1950): Sediment Transportation, In: Rouse H., Ed., *Engineering Hydraulics*, John Wiley and Sons, Inc., N.Y., 1039pp.
- Eilers, H. (1941): Die Viskosität von Emulsionen hochviskoser Stoffe als Funktion der Konzentrationen, *Kolloid, Z.*, 97, pp. 317-321.
- Horikawa, K., Watanabe, A. and Katori, S. (1982): Sediment transport under sheet flow condition, *Proc. of 18th Int. Conf. on Coastal Eng.*, ASCE, pp.1335-1352.
- Kobayashi, N. and Seo, S.N. (1985): Fluid and sediment interaction over a plane bed, *J. of Hydraulic Eng.*, ASCE, pp.903-921.
- Madsen, O.S. and Grant, W.D. (1976): Sediment transport in the coastal environment, Rept. No. 209, Dept., Civil Eng., MIT.
- Nadaoka, K. Ueno, S. and Yagi, H. (1988): A theoretical analysis of sheet flow under wave motion, 35th Japanese

Conf. on Coastal Eng., pp. 292-296, (in Japanese).
 Nadaoka, K. Yagi, H. and Ueno, S. (1990): A weighted residual analysis of sheet-flow under wave motion, (in preparation).
 Sawamoto, M. and Yamashita, T. (1987): Sediment transport in sheet flow regime, Coastal Sediments '87, ASCE, pp. 415-423.

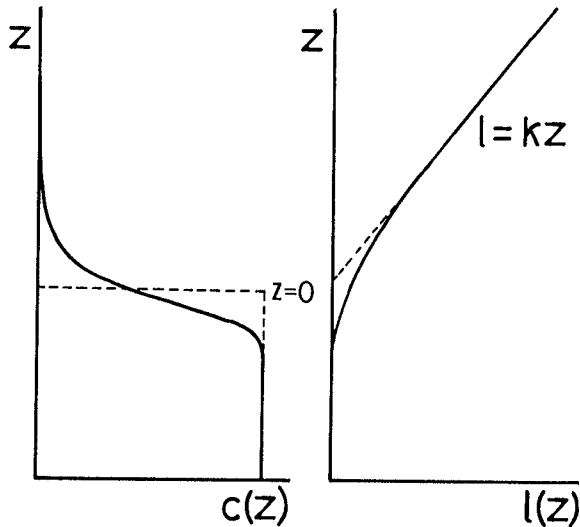


Figure 1 Conceptual illustration of the mixing length $l(z)$ corresponding to a c -profile.

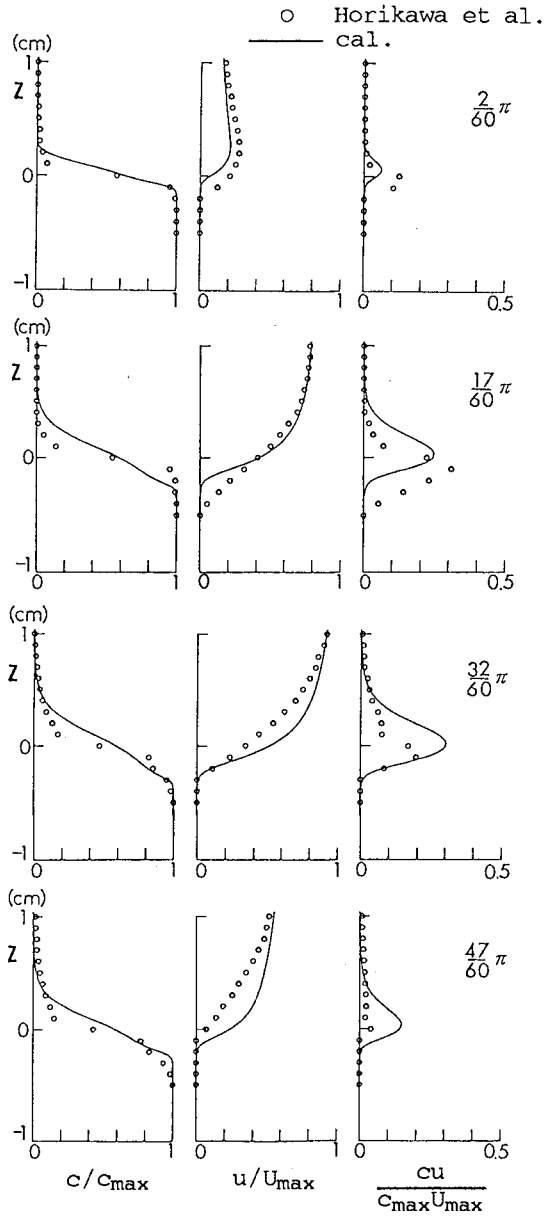


Figure 2 Vertical profiles of c , u , and q at various phases.
($T = 3.6s$, $U_{\max} = 126cm/s$ and $d = 0.02cm$.)

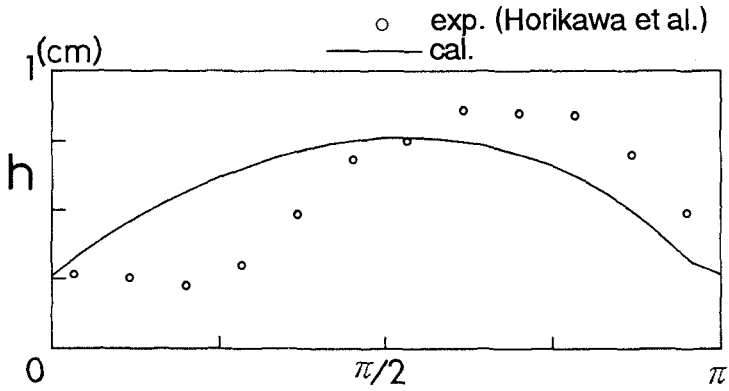


Figure 3(a) Phase-variation of the sheet-flow depth, h .

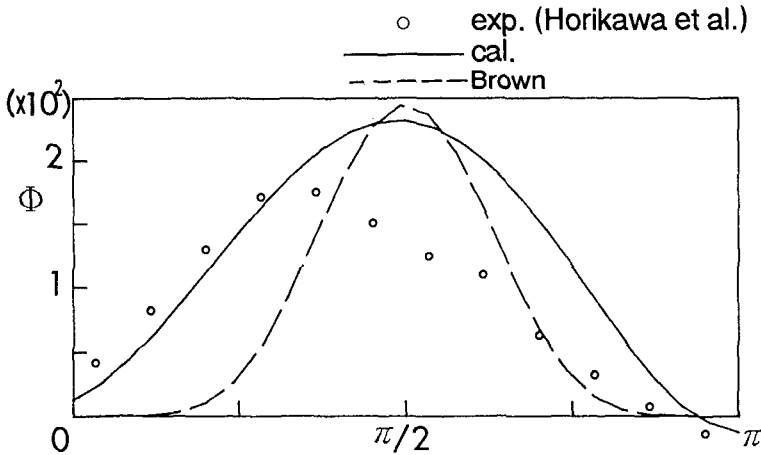


Figure 3(b) Phase-variation of the nondimensional sediment transport rate, Φ
 ($T = 3.6s$, $U_{max} = 126cm/s$ and $d = 0.02cm$)

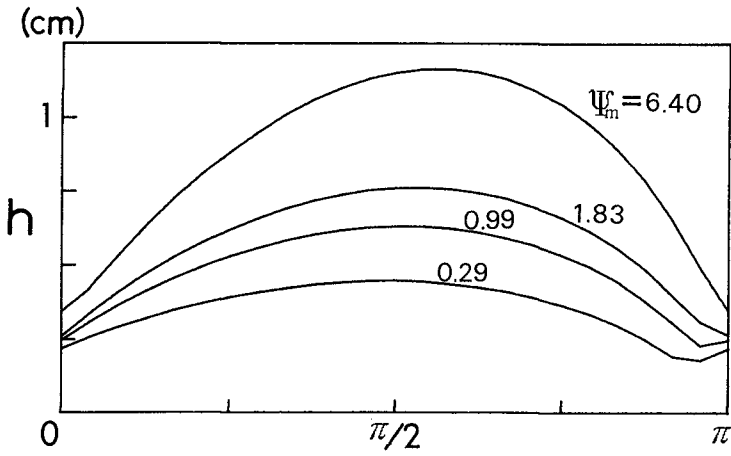


Figure 4(a) Dependence of the phase-variation of h on ψ_m .

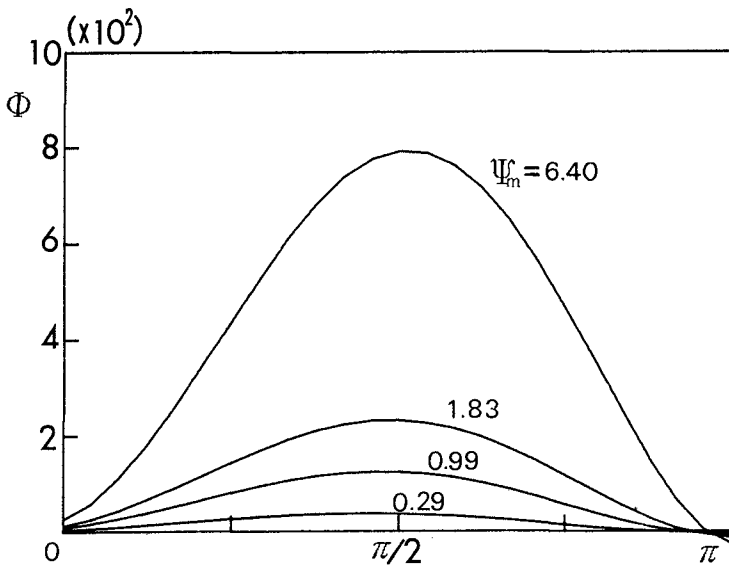


Figure 4(b) Dependence of the phase-variation of Φ on ψ_m .

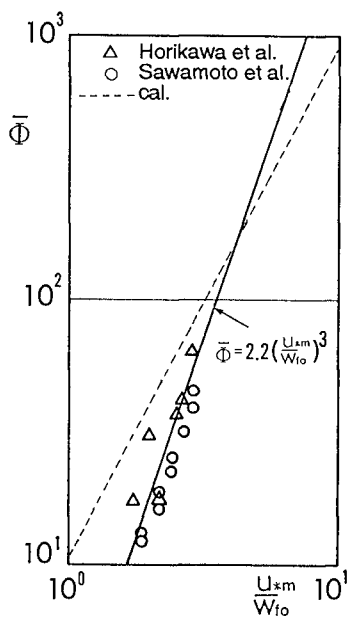


Figure 5 Relation between $\bar{\Phi}$ and u_{*m}/w_{f0} .

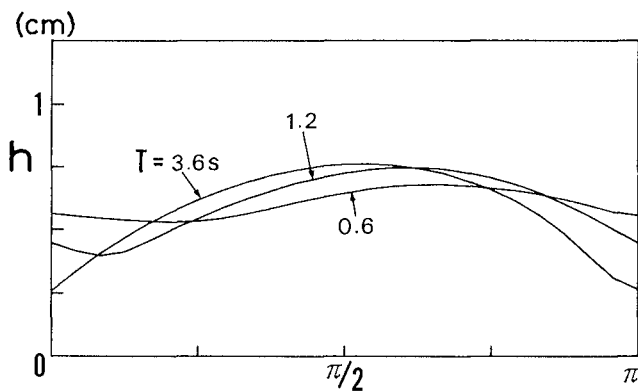


Figure 6 Dependence of the phase-variation of h on T .

CHAPTER 178

SITE INVESTIGATION ON SAND CONCENTRATION IN THE SHEET- FLOW LAYER

Z. YU¹, H.D. NIEMEYER² and W.T. BAKKER³

ABSTRACT

Field measurements of sand concentration in the sheetflow layer have been carried out in the swash zone on a beach on the island of Norderney. Simultaneous registration of both sediment concentration at three levels and the velocity of wave induced water movement in the boundary layer gives an impression of the phenomenon sheetflow for prototype conditions.

1 INTRODUCTION

The development of sheetflow due to oscillating water movement for laboratory conditions was already reported 35 years ago by MANOHAR (1955). HORIKAWA et al. (1982) measured the vertical distribution of sand concentration and orbital velocities in the sheetflow layer in a wave tunnel. Meanwhile the observation of sheetflow in the

¹ Coastal Research Station, Norderney/East Frisia;
now: Rotterdam Public Works (IUW), Rotterdam, The
Netherlands

² Coastal Research Station (Forschungsstelle Küste)
Norderney/East Frisia, F. R. o. Germany

³ Ministry of Public Works (Rijkswaterstaat)/Delft
University of Technology (TU Delft) The Hague/Delft, The
Netherlands
now: University of Hawaii, Honolulu/USA

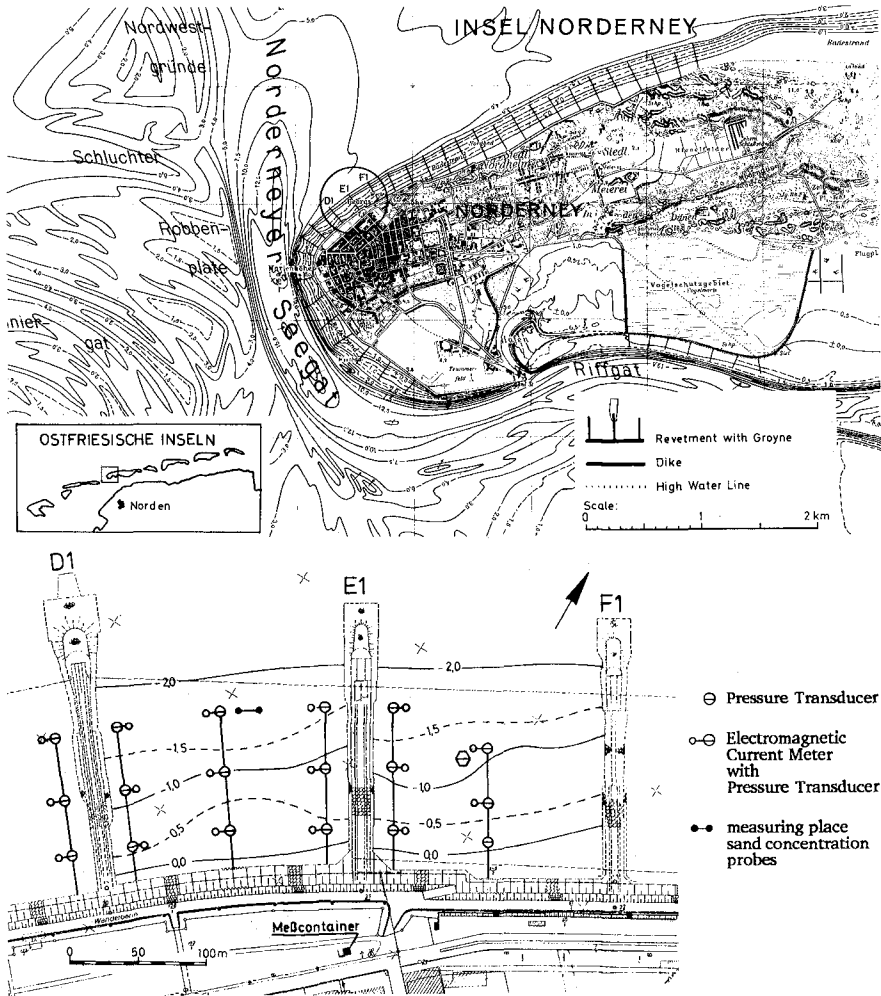


Fig. 1: Measuring site of the Forschungsstelle Küste at Norderney

prototype has also been mentioned and recently numerous theoretical studies and laboratory experiments have paid attention to the subject of sheetflow (BAKKER et. al 1989).

Under the umbrella of a Dutch-German cooperation site investigations on sheetflow has been started on the East Frisian island of Norderney, East Frisia, F.R. of Germany. Purposes of this study have been:

- a. to obtain measured prototype data of sheetflow, which can provide some pictures of the reality of sheetflow,
- b. to gain experience for future large scale field measurements.

2 MEASURING SITE AND INSTRUMENTATION

The measurements have been carried out in the measuring array (Fig. 1) of the Coastal Research Station Norderney (CRS), where a matrix of wave and current meters is installed on the beach (NIEMEYER 1991). Additionally electrical resistance probes for measurements of sand concentration are used during the experiments, which have originally been developed and manufactured by DELFT HYDRAULICS for laboratory investigations. Due to limited financial resources only three probes have been available for this pilot study.

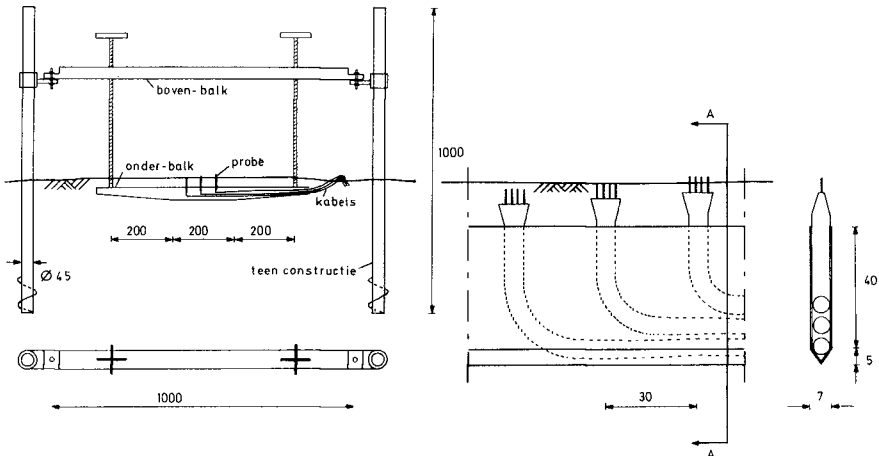


Fig. 2: Measuring set-up, right: front- and top-view of the set-up, left: detail position of probes on the lower bar of the frame

In the first stage of the study trials have been carried out to get a suitable frame construction (Fig. 2). The basic conception, which had been developed at Delft University of Technology had to be improved step by step due to prototype experience. Design and manufacturing was carried out at the Coastal Research Station. This construction meets the following requirements:

- a: limited disturbance of water and sediment movements which should be unaffected in the area around the probes,

b: flexible, exact adjustable vertical level for each probe.

This instrumentation was already described by BAKKER et al. (1989).

3 CALIBRATION

The probes had only been used at DELFT HYDRAULICS for freshwater. For prototype measurements in salt water it was therefore necessary to adapt their measuring range and to carry out a corresponding calibration. Its final goal is to get a general function

$$U = f(\text{field parameters}) \quad (1)$$

where U is the output of the probe [V].

The calibration procedure was carried out in consideration of the following four parameters with respect to the output signal of the probes:

1. characteristics of sediment particles
2. sand concentration
3. temperature
4. salinity

The first parameter was taken into account by using sand from the measuring site. This allows the simplification of formula (1) to

$$U = f(c, S, T) \quad (2)$$

with c: volumic sand concentration [%]
 S: salinity [ppt]
 T: temperature [°C].

A suitable experiment set-up was installed in the soil mechanics laboratory of the CRS. Sand-water mixtures with variable 'composition' (c, S, T,) were created by use of a mixer to simulate conditions according to prototype boundary conditions:

- uniform suspension in the entire water column for sand concentrations from 0 to 45 %
- variation of salinity between 20 and 35 ppt
- controlled water temperature for a range of 2 - 20 °C

The treatment of calibration data was done by multiple regression analysis. As a result the following calibration function was established:

$$U = \sum_{j=1}^3 \sum_{i=1}^3 a_{ij} x_i^{b_{ij}} x_j^{b_{ji}} \quad (3)$$

where: a_{ij} , b_{ij} , b_{ji} are constants derived from the regression-analysis and

$$x_1 = 1 - c$$

$$x_2 = S$$

$$x_3 = T$$

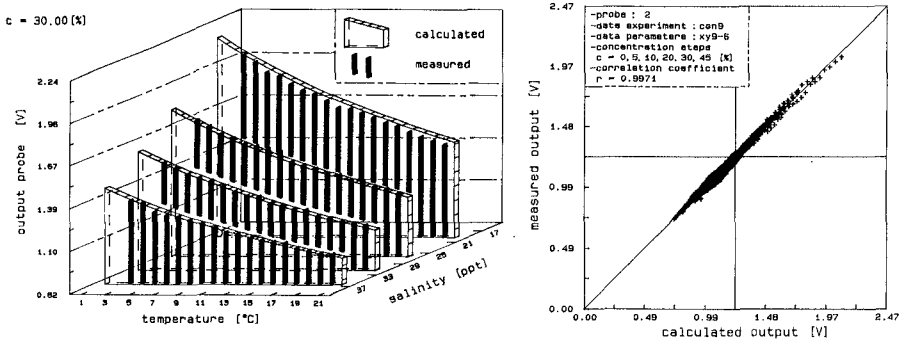


Fig. 3: left: Fitting of calibration function to data for variations of temperature and salinity, right: Fitting of calibration function for variations in sand concentration

Scatter diagrams for calibration data in comparison to the calibration function for variations of sand concentration, salinity and temperature demonstrate its applicability and soundness (Fig. 3).

4 EXECUTION OF FIELD MEASUREMENTS AND DATA ANALYSIS

The installation of the probes with the frame (Fig. 1 and 2) took always place at low tide close to one current meter of the existing measuring array (NIEMEYER 1991). The probes had a cable connection to a data acquisition system which was established in a container close to the beach (Fig. 1). For the performance of the system two cooperating crews are acting: one at the measuring site and the other one in the container.

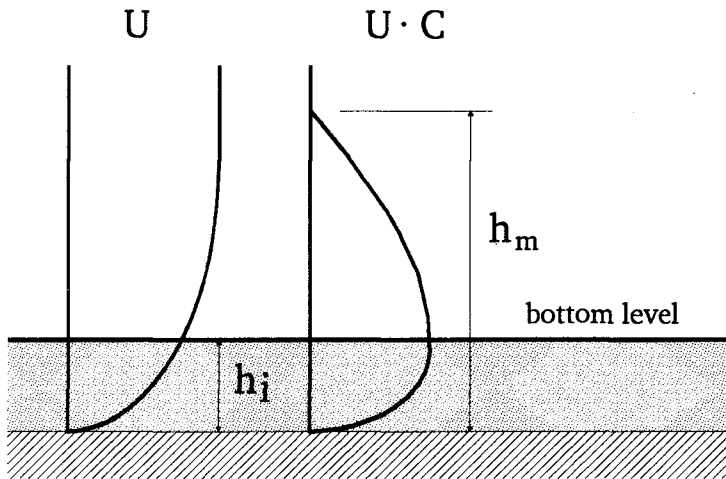


Fig. 4: Definition of intrusion depth and thickness of moving layer

The measuring procedure was started, when the sea bed near the probes was covered by water of the rising tide. It is very important to ensure that the probes 'stay' in the moving layer (definition: Fig. 4). The crew in the container acts therefore as steering group. By observation of the measuring signals on a strip chart recorder the current position of the probes and necessary readjustments could be evaluated:

- the probe is in water ($c = 0$)
- the probe is in sand ($c = c_0$, c_0 : maximum concentration)
- in the moving layer ($0 < c < c_0$, variable in time)

The measuring strategy is to keep the lowest probe at the level where sand particles will just move or not. This is necessary for the estimation of the intrusion depth h_i and guarantees that the two higher placed probes will catch the moving layer. If a readjustment of the probes is required due to erosion or sedimentation, orders will be given from the container crew by radio to the beach crew in order to follow the moving layer by heightening or lowering the frame. The measurements could be continued in this manner until rising water level and increasing wave heights force the crew to leave the beach.

Additionally temperature T and salinity S are measured in order to establish proper data sets. For this case function (3) may be reduced to

$$g(c) = 0 \quad (4)$$

which allows the derivation of c by iteration.

5 RESULTS OF THE MEASUREMENTS

Several measurements have been performed in the swash zone on the beach of Norderney. As the electromagnetic current meters must keep within a certain distance from the sea bed, velocity registrations show many disturbances at begin of each time series, because the sensor head is not continuously covered by water. If the sensor head falls dry, it measures wind speed. Data of one time series will be discussed here concerning the following aspects:

- concentration in the moving layer h_m ,
- intrusion depth of the sheetflow h_i ,
- local morphological change during the measurement.

Additional boundary conditions of the measuring set-up and initial beach geometry are:

- height of current meter sensor head above sea bed:
70 mm
- beach slope: $\sim 1 / 60$
- vertical difference between probe levels:
3 mm between 1 (highest) and 2 (center);
2 mm between 2 and 3 (lowest)

Measured concentrations at three levels and the cross- and longshore components of wave induced currents are plotted in Fig. 5. At the beginning (mark A) probe 3 is just at the lower boundary of the moving layer (level of the intrusion depth) and probe 1 is above the sea bed. It only measures sand concentrations, if high velocities occur. The intrusion depth h_i of the sheetflow should be about 2 mm and the total moving layer h_m might have a thickness of nearly 7 mm at mark A and B. The current meter is from time to time exposed to air, especially in the final stage of backwashes. Between the marks C and D a layer with a thickness of 2 mm or more is eroded, but is afterwards again restored by sedimentation.

The continuation of this registration is shown in Fig. 6: At mark E there is an intrusion depth of less than 2 mm and a moving layer of about 4 mm. Responding to large velocities as well higher concentrations occur as the layer thickness increases (mark F: $h_i \sim 3$ mm, $h_m \sim 8$ mm). Noteworthy is also the rapid change of onshore-offshore current directions. This specific feature of wave induced currents in the swash zone is totally different from the orbital motions which are reproduced in wave tunnels in order to generate sheetflow conditions there, as e. g. done by HORIKAWA et al. (1982) or BAKKER et al. (1988).

The maximum intrusion depth occurs often in coincidence with flow direction changes (long backwash followed by large uprush) which is obviously the case at mark F and again at mark G. At mark F both probe 2 and 3 are still covered with sand ($c=c_0$). But then both are subsequently eroded and the resedimentation is only sufficient to recover probe 3 which is finally eroded at mark G. This resulting step by step erosion does occur in the final stage of long backwash movements with increasing offshore directed velocities. Even the comparable high onshore directed velocities of the uprush do not have the same effectiveness with respect to resedimentation, as the uprush duration is remarkably lesser than that of the backwash.

This causes a continuous erosion during the first stage of the rising tide. At the measuring point an erosion of about 5 mm has taken place some 30 minutes after the start of the registration. During the following 10 minutes a layer of another 4 mm sand has additionally been washed away. As documented in Fig. 7 the erosion process could even accelerate: the frame is lowered at mark H to a level which is 4 mm lower than before. But within less than three minutes this layer is again eroded (mark I).

Another 10 minutes later the probes are already 24 mm lower than at the beginning (Fig. 8). This tendency remains stable for the whole measuring period: After an hour plus a few minutes a total erosion of about 55 mm has taken place.

With respect to the development of sheetflow conditions it seems noteworthy that a thickness of 2 mm does often occur and in some cases (e. g. mark F; Fig. 6) a thickness of 5 mm with concentrations of more than 5 mm. This is about twenty times of mean local sediment diameter.

Field Measurement of Sand Concentration in Sheetflow Layer

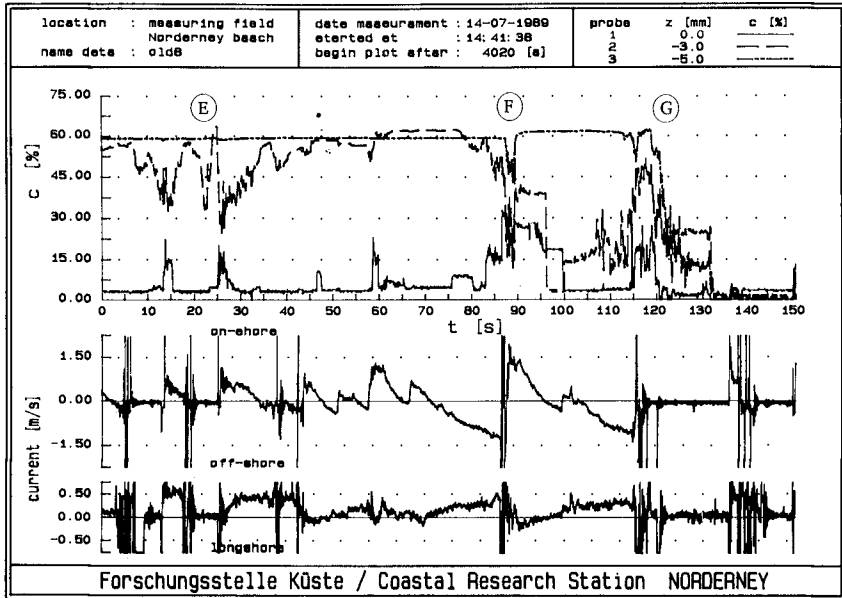
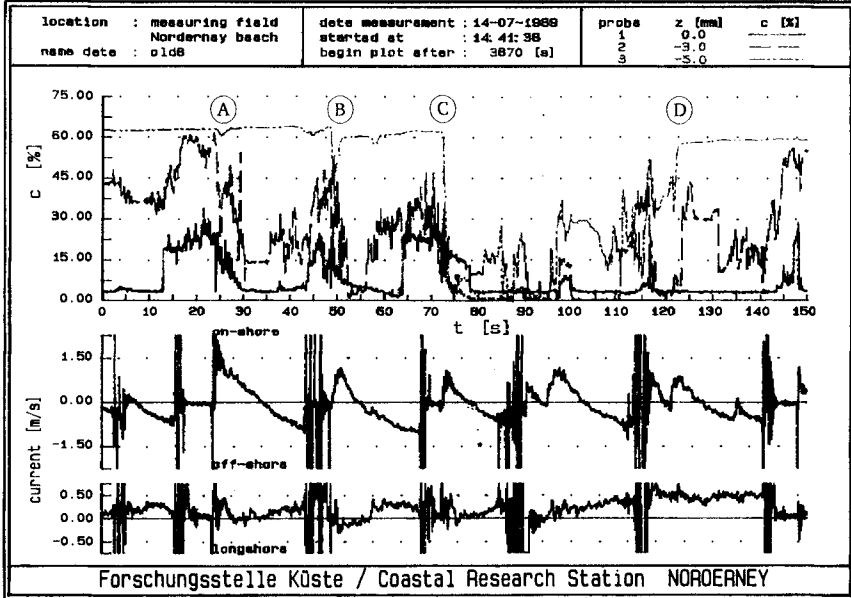


Fig. 5+6: Time series of sand concentration on three levels with cross-shore and longshore current components. - Example 1+2

Field Measurement of Sand Concentration in Sheetflow Layer

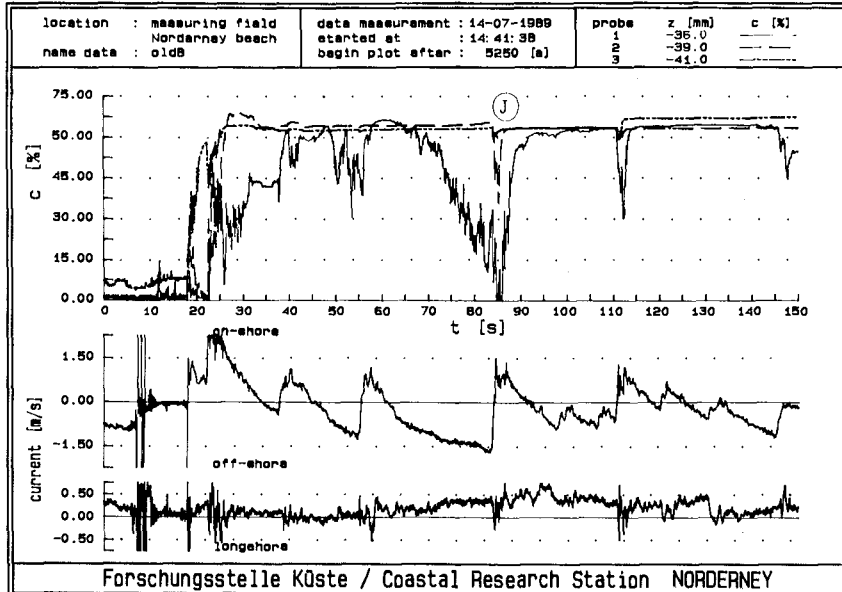
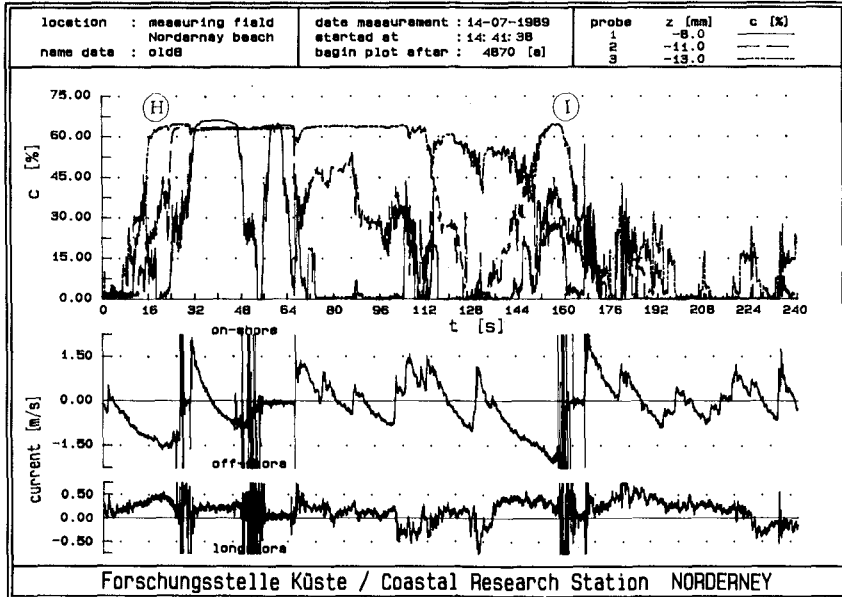


Fig. 7+8: Time series of sand concentration on three levels with cross-shore and longshore current components. - Example 3+4

6 CONCLUSIONS

6.1 INSTRUMENTATION

1. The measuring set-up is suitable (up to a water depth of about 1 m) for sheetflow measurements in the swash zone. However for measurements in the surf zone the system must be remote controlled in order to adjust the position of the probes with respect to bottom level fluctuations.
2. Measurements with three probes provide a quite good impression of the reality of sheetflow in field. Detailed studies will require more probes, because the large vertical gradients in sheetflow demand for distances of not more than 1 mm. In order to overcover the moving layer h_m with an expected maximum thickness of about 8 mm a measuring height of 10 mm is recommended.
3. The distance of the current meter of 70 to 100 mm to the sea bed causes disturbances due to measurements of wind speed when it falls dry. A lower position might effect scouring, especially for the occurrence of high velocities and intensive sediment transport. The use of a finer shaped current meter might reduce this handicap.

6.2 Sheetflow and Beach Erosion

1. The measured maximal intusion depth h_i of sheetflow is about 2 to 5 mm and the maximal moving layer h_m is about 8 mm.
2. A moving layer can be observed if the near bottom velocity in the boundary layer exceeds a value of about 1.3 m/s. This takes mostly place in the final stage of the backwash.
3. At the measuring point a 55 mm thick sand layer was eroded within an hour and an average erosion rate of 1.5 mm/min does occur during the last 30 minutes of the measurement.
4. There is a certain correlation between erosion and backwash with long periods.

ACKNOWLEDGEMENTS

The authors wishes to thank their colleagues of the Coastal Research Station for the support they got, especially Messrs. Brandt, Gerrelts, Glaser and Meemken. Mr. Groeneveld (Delft University of Technology) had constructed the initial version of the frame.

REFERENCES

- BAKKER, W.T., VAN KESTEREN, W.G.M. & YU, Z.H. (1989):** Grain-Grain interaction in oscilating sheetflow. Proc. 21st Int. Conf. o. Coast. Eng. Costa del Sol - Malaga, ASCE, New York
- BASINSKI, T. (1989):** Field studies on sand movement in the coastal zone. Prace Instytutu Budownictwa Wodnego PAN, Nr 16 (Institute of Hydroengineering-Polish Academy of Sciences, Gdansk)
- HORIKAWA, K., WATANABE, A. & KATORI, S. (1983):** Sediment transport under sheetflow condition. Proc. 18th. Int. Conf. o. Coast. Eng. Capetown, ASCE, New York
- MANOHAR, M. (1955):** Mechanics of bottom sediment movement due to wave action. U.S. Army, Corps of Engineers, Beach Erosion Board, Tech. Memo. No.75
- NIEMEYER, H.D. (1991):** Field measurements and analysis of wave induced nearshore currents. Proc. 22nd Int. Conf. o. Coast. Eng. Delft, ASCE, New York

CHAPTER 179

Two-Phase Flow Model on Oscillatory Sheet-Flow

Toshiyuki Asano

1. INTRODUCTION

Under stormy waves on a sandy beach, a flat movable bed may appear when ripples have been washed out. Studies of the sheet flow have recently received much attention because a large amount of sand is transported under such conditions. However, most of the existing studies on the sediment transport are dealing with the phenomena under small tractive forces because this is easily reproduced in a small wave tank. Until now, very little understanding has been obtained on the sheet flow phenomena.

The first systematic study on the sheet flow is likely the work of Horikawa et al.(1982). They measured the sediment transport velocity and sediment concentration in an oscillatory flume. The reported velocity and concentration profiles were different from existing results obtained under the condition of small amount of sediment movement. Yamashita et al.(1985) and Ahilan-Sleath(1987) performed similar experiments with light artificial particles as the sediment. These experiments have increased the understanding of sheet flows. However, difficulties in the measuring densely mixed sediment-fluid flow prevent investigating the detailed structures of the flow. In addition, the limited size of the experimental flume may cause several problems in generating idealistic conditions.

Since a numerical model has an advantage of being free from the restrictions imposed on the experiment, several models on the sheet flow have recently been proposed. Ahilan-Sleath modelled sediment-fluid mixture flow as a mono-phase flow with varying density in time and depth. Since this model ignores the sediment-fluid interaction, the accuracy is likely to decrease as the sediment concentration becomes higher.

Associate Professor, Department of Ocean Civil Engineering, Kagoshima University, 1-21-40, Kourimoto, Kagoshima, 890, JAPAN

The present paper develops a numerical model to analyze the oscillatory sheet flow. The mathematical formulation based on fluid-sediment two phase flow is performed by expanding models from a unidirectional flow (Bogardi(1974), Kobayashi-Seo(1985)) into an oscillatory flow. The developed model predicts the velocity field, properties of friction and sediment transport rate. The model is shown to describe existing experimental data for oscillatory sheet flow.

2. SOLID - FLUID MIXTURE MODEL FOR OSCILLATORY SHEET FLOW

(1) Basic assumptions and mathematical formulation

The mathematical model derived herein is based on a continuum assumption for fluid and a uniform cohesionless sediment mixture. The analysis is performed for the case of two dimensional oscillatory flow over a plane bed. Molecular diffusion and viscous stresses are assumed to be negligible compared with those due to turbulence.

The continuity equation for the fluid phase is

$$\frac{\partial}{\partial t}\rho(1 - c) + \frac{\partial}{\partial x_j}\rho(1 - c)u_j = 0 \tag{1}$$

in which ρ : fluid density, c : volumetric concentration of sediment, and u_j : fluid velocity in the x_j direction. The continuity equation for the sediment phase is

$$\frac{\partial}{\partial t}\rho_s c + \frac{\partial}{\partial x_j}\rho_s c u_{s,j} = 0 \tag{2}$$

in which ρ_s : density of sediment, and $u_{s,j}$: sediment particle velocity in the x_j direction.

The momentum equation for the fluid phase is described by

$$\frac{\partial}{\partial t}\rho(1 - c)u_i + \frac{\partial}{\partial x_j}\rho(1 - c)u_i u_j = -(1 - c)\frac{\partial p}{\partial x_i} - \rho(1 - c)g\delta_{i2} - f_i \tag{3}$$

in which p : pressure, g : gravitational acceleration, δ_{ij} : Kronecker delta, and f_i : x_i component of interaction force per unit volume between the sediment and fluid.

The momentum equation for the sediment phase is expressed by

$$\frac{\partial}{\partial t}\rho_s c u_{s,i} + \frac{\partial}{\partial x_j}\rho_s c u_{s,i} u_{s,j} = -c\frac{\partial p}{\partial x_i} + \frac{\partial \gamma_{ij}}{\partial x_j} - \rho_s c g \delta_{i2} + f_i \tag{4}$$

in which γ_{ij} : intergranular stress tensor.

(2) Simplification of the equations

In the following analysis, the x-axis is taken in the horizontal direction, and the z-axis is taken upward from the origin placed at the top of the immovable

layer where the sediment transport velocity is always zero. The velocity component in the x and z directions is given by u and w , respectively. The equation for the mean quantities can be derived by first decomposing the instantaneous quantities in Eqs.(1) ~ (4) into the steady, oscillatory and turbulent components, and then averaging the resultant equations with respect to time. Some simplifications are made by assuming $u \gg w$, $u_s \gg w_s$, and $uc'w' \gg c'u'w'$. For example, a fluid shear stress term which arises in the x -momentum equation is given by

$$\tau/\rho = -\{(1-c)\overline{u'w'} - c\overline{u'w'}\} \quad (5)$$

The turbulent eddy viscosity K_v and the turbulent diffusion coefficient K_c are introduced to represent the turbulent correlation terms by the mean quantities as shown by

$$\overline{c'w'} \simeq \overline{c'w'_s} = -K_c \frac{\partial c}{\partial z} \quad (6)$$

$$\overline{u'_s w'_s} \simeq \overline{u'w'} = -K_v \frac{\partial u}{\partial z} \quad (7)$$

Assuming that proximity effects among the sediment particles may be ignored and that the added mass force acting on a sediment particle is negligible as compared with the drag force, the interaction force between the sediment and fluid may be expressed as the sum of the buoyancy and drag force.

$$f_i = \rho c g \delta_{i2} + \frac{\rho}{2} C_D \left(\frac{\pi d^2}{4} \right) \frac{c}{\pi d^3 / 6} u_{i,r} \sqrt{u_r^2 + w_r^2} \quad (8)$$

in which $u_r = u - u_s$ and $w_r = w - w_s$ denote the relative velocities between the fluid and sediment and C_D is the drag coefficient. The interaction force in the x -direction is approximated by

$$f_x = \frac{\rho}{2} C_D \left(\frac{\pi d^2}{4} \right) \frac{c}{\pi d^3 / 6} |u_r| u_r \quad (9)$$

Rubey's formula is used to estimate the drag coefficient.

$$C_D = 24/Re + 2 \quad (10)$$

in which the Reynolds number is defined as $Re = u_r d / \nu$.

Although the intergranular stress resulted from the momentum transfer from solid to solid is not well understood yet even for steady flows, the constitutive equation of Savage-McKeown(1983) is adopted here as

$$\gamma_{xz}/\rho = 1.2\lambda^2 \nu \partial u_s / \partial z \quad (11)$$

in which λ : the linear concentration related to c and to the maximum possible static concentration of uniform spheres c_{max} .

$$\lambda = 1/[c_{max}/c]^{1/3} - 1] \quad (12)$$

The following dimensionless variables are introduced,

$$\begin{aligned}
 u &= \bar{u}u_0, \quad u_s = \bar{u}_s u_0, \quad u_r = \bar{u}_r u_0, \quad w = w_{f_0} \bar{w} / \sqrt{R}, \\
 w_s &= w_{f_0} \bar{w}_s / \sqrt{R}, \quad x = \frac{g\xi}{\omega^2}, \quad z = \sqrt{\nu/\omega} \zeta, \\
 t &= \tau/\omega, \quad p = \rho \left(\frac{g}{\omega}\right) u_0 \bar{p}, \quad K_c = \sqrt{\nu/\omega} u_0 \bar{K}_c, \\
 K_v &= \sqrt{\nu/\omega} u_0 \bar{K}_v, \quad \sqrt{R} = u_0 / \sqrt{\nu\omega}
 \end{aligned}
 \tag{13}$$

in which u_0 : free stream velocity amplitude, w_{f_0} : settling velocity of a single sediment particle in pure water, ν : kinematic viscosity of the fluid, and ω : angular frequency of the oscillatory flow. The dimensionless form of the continuity equation for the sediment phase is obtained from Eq.(2) as follows

$$\frac{\partial c}{\partial \tau} = -\frac{w_{f_0}}{u_0} \frac{\partial}{\partial \zeta} (c\bar{w}_s) + \sqrt{R} \frac{\partial}{\partial \zeta} \left\{ \bar{K}_c \frac{\partial c}{\partial \zeta} \right\}
 \tag{14}$$

The dimensionless equation for the fluid phase momentum in the x-direction is given by

$$\begin{aligned}
 &\frac{\partial}{\partial \tau} \{c^* \bar{u}\} + \frac{w_{f_0}}{u_0} \frac{\partial}{\partial \zeta} \{c^* \bar{u} \bar{w}\} = \\
 &\sqrt{R} \frac{\partial}{\partial \zeta} \left\{ \bar{K}_v c^* \frac{\partial \bar{u}}{\partial \zeta} - \bar{K}_c \bar{u} \frac{\partial c}{\partial \zeta} \right\} - c^* \frac{\partial \bar{p}}{\partial \xi} - \frac{3}{4} R \left(\frac{u_0 d}{\nu}\right)^{-1} C_{Dc} \left| \bar{u}_r \right| \bar{u}_r
 \end{aligned}
 \tag{15}$$

in which $c_* = 1 - c$.

The dimensionless equation for the sediment phase momentum in the x-direction is

$$\begin{aligned}
 &\frac{\partial}{\partial \tau} \{c \bar{u}_s\} + \frac{w_{f_0}}{u_0} \frac{\partial}{\partial \zeta} \{c \bar{u}_s \bar{w}_s\} = \\
 &\sqrt{R} \frac{\partial}{\partial \zeta} \left\{ \bar{K}_v c \frac{\partial \bar{u}_s}{\partial \zeta} + \bar{K}_c \bar{u}_s \frac{\partial c}{\partial \zeta} \right\} - \frac{1}{s} c \frac{\partial \bar{p}}{\partial \xi} + \frac{1.2}{s} \frac{\partial}{\partial \zeta} \left(\lambda^2 \frac{\partial \bar{u}_s}{\partial \zeta} \right) \\
 &\quad + \frac{1}{s} \frac{3}{4} R \left(\frac{u_0 d}{\nu}\right)^{-1} C_{Ds} c \left| \bar{u}_r \right| \bar{u}_r
 \end{aligned}
 \tag{16}$$

in which $s = \rho_s/\rho$ denotes the specific density of the sediment. Adding Eq.(1) to Eq.(2) yields the following relation

$$(1 - c) \bar{w} + c \bar{w}_s = 0
 \tag{17}$$

From the vertical momentum equation for the fluid phase given by Eq.(4), an equation for the pressure would be derived. From the corresponding equation for the sediment phase given by Eq.(5), an equation describing the relationship between the intergranular stress term $\partial \gamma_{zz} / \partial z$ and the fluid-sediment interaction term f_z would be derived. Since these equations are related to u, u_s, w, w_s, p and c in a highly non-linear fashion, the simultaneous differential equations

are difficult to solve even numerically. Therefore, according to experimental results on the settling velocity in dense fluid-sediment mixture by Richardson et al.(1979), the vertical sediment velocity is assumed to be given by

$$w_s = w_{f_0}[1 - (c/c_{max})]^n \quad (18)$$

in which n is an experimental variable, which is taken to be 2.3 in this study. The velocity for the fluid phase w can be calculated from Eq.(17) with estimated w_s . The pressure is assumed constant throughout the boundary layer.

The parameters involved in Eqs.(14), (15) and (16) are as follows:

$$s = \frac{\rho_s}{\rho}, \quad R = \frac{u_0^2}{\omega\nu}, \quad \frac{u_0^2}{gd}, \quad \frac{u_0 d}{\nu} \quad (19)$$

The variable of w_{f_0}/u_0 in Eqs.(14), (15) and (16) is also expressed by the above parameters if w_{f_0} is given by Rubey's formula.

The sediment transport field is conventionally divided into the following two regions: the bed load region where the sediment concentration is high and the particles are mainly supported by the intergranular stress, and the suspended load region where the sediment concentration is small and the particles are mainly supported by the fluid turbulent stress. According to the experiment of Wilson(1984), the thickness of bed load region, z_G , is given by

$$z_G = 10(\theta - \theta_{cr})d \quad (20)$$

in which θ is the Shields number and θ_{cr} is the critical Shields number. The thickness of the suspended load region, z_s , is assumed to be equal to the turbulent oscillatory boundary layer for fixed beds. That is,

$$z_s = \kappa u_* / \omega \quad (21)$$

in which κ : Karman constant, and u_* : friction velocity.

In the bed load region, the mixing length may be governed by the distance among the sediment particles d/λ ; whereas, in the suspended load region, the mixing length may be assumed to be the mixing length for the pure fluid flow with modifications of flow stratification. The turbulent eddy viscosity K_v may be expressed as follows

$$K_v = \kappa u_*(t)\beta(d/\lambda) : z < z_G/2$$

$$K_v = \frac{\kappa u_*(t)(z - z_G/2)}{1 + 4.7(z/L)} + \kappa u_*(t)\beta(d/\lambda) \Big|_{z=z_G/2} : z \geq z_G/2 \quad (22)$$

in which \hat{u}_* : amplitude of the friction velocity, β : constant (here assumed to be 10), and L : Monin-Obukhov length written by

$$L = \hat{u}_*^3 / (\kappa g(s-1)w_{f_0}c) \quad (23)$$

According to the model of Brevik(1981), K_v is assumed to be constant for $z \geq z_G + \Delta$, in which Δ is given by

$$\Delta = 0.036\{2d(u_0/\omega)^3\}^{1/4} \tag{24}$$

Fig. 1 shows an example of the profile of the turbulent eddy viscosity.

The friction velocity amplitude \hat{u}_* is estimated using the roughness height k_b based on the formula of Grant-Madsen(1982). Since the efficiency of the turbulent transfer for mass is generally different from that for momentum, K_c is not really the same as K_v . However, for lack of reliable data for oscillatory flow, K_c is assumed herein to be the same as K_v .

The boundary conditions for \bar{u} and \bar{u}_s are given as follows

$$\bar{u} = \bar{u}_s = 0, \quad \partial\bar{u}_s/\partial\zeta = 0 \quad : \zeta = 0$$

$$\partial\bar{u}/\partial\zeta = 0 \quad : \zeta = \bar{\delta} \tag{25}$$

Near the immovable layer where c is nearly equal to c_{max} , the intergranular stress in the vertical direction is assumed to equal the submerged weight of the sediment above it as hypothesised by Bagnold to avoid divergence of the calculated results.

$$|\partial\bar{u}_s/\partial z| \leq (s-1)g \tan \phi \int_z^\infty c dz / (1.2\lambda^2\nu) \tag{26}$$

The boundary conditions for the sediment concentration are given by

$$c = c_{max} \quad : \zeta = 0$$

$$-(w_{f_0}/u_0) \frac{1}{\sqrt{R}} c \bar{w}_s + \bar{K}_c \frac{\partial c}{\partial \zeta} = 0 \quad : \zeta = \bar{\delta} \tag{27}$$

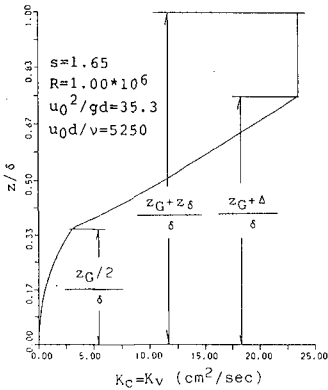


Fig. 1
Profile of turbulent eddy
viscosity K_v

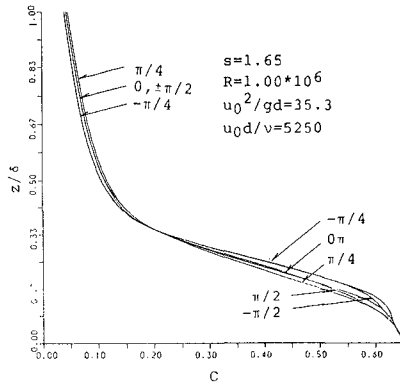


Fig. 2
Profiles of sediment con-
centration c

The basic equations for the numerical calculation have been obtained as Eqs.(14),(15),(16). These equations were discretized by a Crank-Nicolson implicit scheme. The number of the vertical grids was 140, and the time increment was $1/5000$ of an oscillatory period. The calculation was continued until the calculated results in successive cycles converged. It was found that most of the deviation from the converged solution disappeared typically after half a period.

3. CALCULATED RESULTS

The profiles of the sediment concentration c shown in Fig.2 indicate that the concentration decreases gradually from c_{max} in the region $z/\delta \leq 0.2$, exponentially for $z/\delta \geq 0.2$.

Fig.3 shows the profiles of the fluid velocity u and the sediment transport velocity u_s . The sediment transport velocity u_s is found to be nearly zero close to the immovable layer around $z/\delta \leq 1/6$ because the intergranular stress term becomes very large in this region. The fluid motion is also suppressed due to the drag resistance between the fluid and sediment. In the region $1/6 \leq z/\delta \leq 1/3$, a phase precedence over the free stream velocity is observed. In the region $z/\delta \geq 1/3$, $|u|$ is always larger than $|u_s|$ in the accelerating phase, and smaller in the decelerating phase. This property is caused by the difference of the inertia between the sediment and fluid particles.

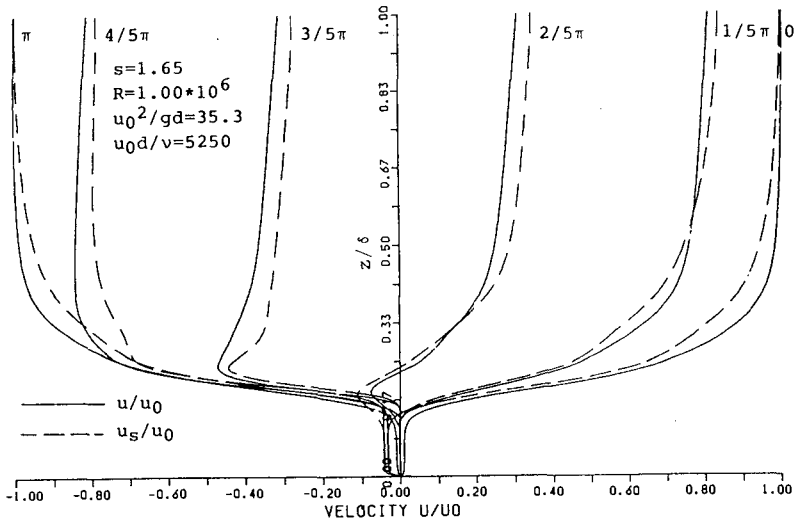


Fig. 3 Profiles of horizontal fluid velocity u (solid line) and sediment transport velocity u_s (dotted line)

The phase variation of the concentration is depicted in Fig. 4. The phase variations of the fluid velocity are given in Fig. 5. The results at $z/\delta = 0.1$ and 0.15 near the immovable layer show peculiar variations which are similar to the variations of the pressure gradient $-\partial p/\partial x$. The fluid flow around this level resembles a seepage flow because the concentration there is close to the maximum packing concentration. At $z/\delta = 0.2$, u and u_s increase gradually up to the maximum, then decrease suddenly. This result can be related to the temporal variation of the concentration.

Fig.6 is a semi-log plot of the horizontal fluid velocities at the phase = 0π for various values of the specific density s . The velocity profiles can be approximated by log-linear lines over a wide range. The intersection, z_0 , of the z -axis with the extended log-linear line, which corresponds to the roughness

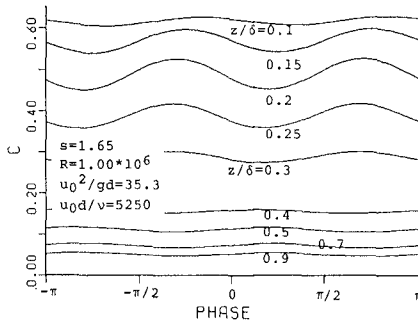


Fig. 4 Phase variation of sediment concentration

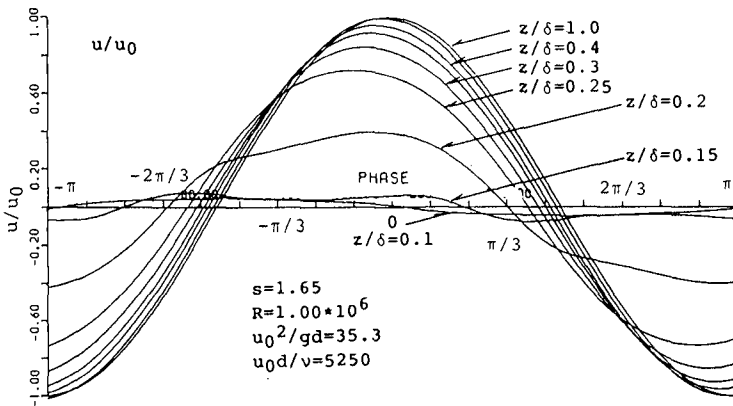


Fig. 5 Phase variation of horizontal fluid velocity

height, decreases with the increase of s . The gradient, α , of the log-linear line decreases slightly with the increase of s . The log-linear part of the velocity distribution is described by

$$u/u_0 = \alpha \ln(z/z_0) \tag{28}$$

Fig.7 (a) and (b) show the variations of z_0/d and α with the specific gravity s , respectively. The figures show that both z_0 and α increase with a decrease of s . These result seems to be reasonable because the decrease of s results in more intensive movement of the sediment. However, it is noted that the results do not approach the values for fixed beds, $z_0/d = 1/15$ and $\alpha = \sqrt{f/2}/\kappa$, even when s becomes large. That is because the present model assumes the fluid-sediment mixture flow as a continuum, consequently it is not applicable to flow conditions when only a few layers of sediment particles move.

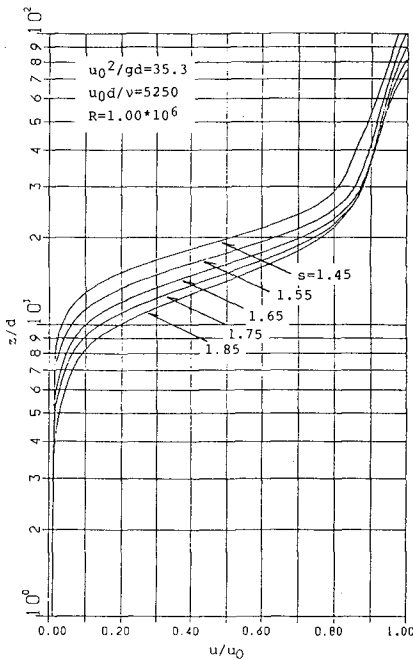


Fig. 6 Semi-log plot of fluid velocity

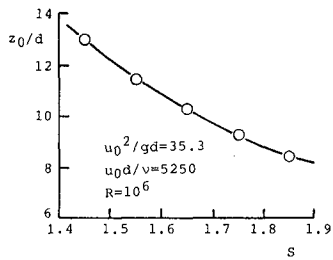


Fig. 7 (a)

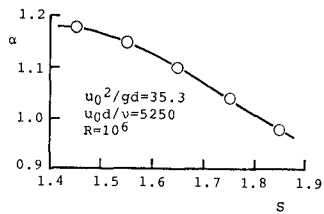


Fig. 7 (b)

Variation of z_0/d and α with specific gravity s

4. COMPARISON WITH EXISTING EXPERIMENTAL DATA

Three sets of data of Ahilan-Sleath(1987), Horikawa et al.(1982) and Yamashita et al.(1985) are used to examine the validity of the present model. All three experiments were carried out in oscillatory tunnels. Horikawa et al. used fine sand, whereas the others used light plastic particles. The experimental conditions are summarized in Tabel-1.

First, comparisons on the sediment transport velocity at phase = 0π between the measurements of Ahilan-Sleath and the predicted results are made as shown in Fig.8. The results of cases (a) and (b) were obtained using nylon particles with a small specific density ($s=1.137$), while case(c) uses particles of slightly higher density($s = 1.44$). The calculated velocity for case (c) becomes very small in the region $z \leq 3$ cm. Considering that the location of the immovable layer may not be easily determined in the experiment, the plotted data points are shifted upward by 3cm for this case.

Table 1 Test condition of existing data

		s	T (sec)	u_0 (cm/sec)	d (cm)	R (*10 ⁵)	$\frac{u_0^2}{gd}$	$\frac{u_0 d}{\nu}$	$\frac{u_0^2}{(s-1)gd}$
Ahilan-Sleath (1987)	Test-2	1.137	3.67	45.0	0.40	1.18	5.17	1800	37.7
	Test-5	1.137	3.59	31.5	0.40	0.57	2.53	1260	18.5
	Test-9	1.44	4.86	122.0	0.43	11.5	38.0	5246	86.3
Horikawa et al. (1982)	Case 1-1	2.66	3.60	127.0	0.02	9.24	823	254	496.0
Yamashita et al. (1985)	Case-2	1.58	3.10	80.6	0.50	3.21	13.3	4030	22.9

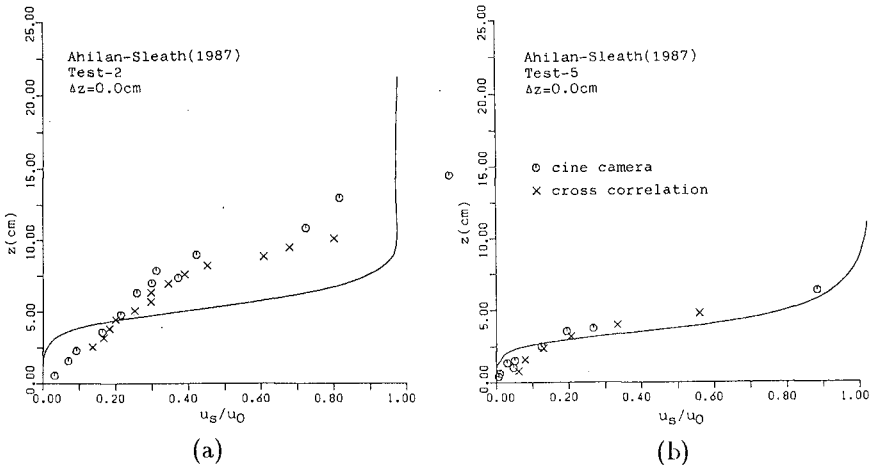


Fig. 8 Comparison between Ahilan-Sleath(1987)'s data and predicted results on sediment transport velocity

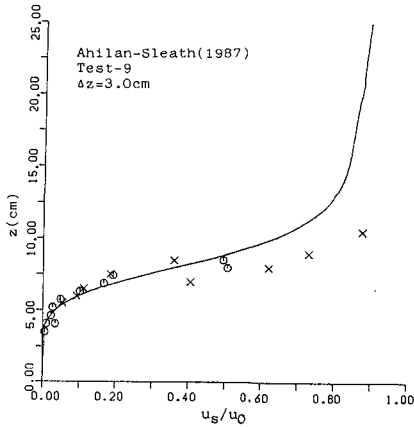


Fig. 8 (c) (conti.)

Finally, the data of Horikawa et al are examined. The predicted results do not agree well with this data set, because the measured values of u_s and c vary only in a thin region close to the immovable layer. The cause of the discrepancy, which is not obvious however, might be due to the very fine sand particles they used as the sediment.

5. CONCLUSIONS

A mathematical model is developed to describe the flow field under oscillatory sheet flow. The model is based on the conservation of mass and momentum for the fluid and sediment. In order to simplify the model, certain assumptions on the settling velocity, turbulent stress and intergranular stress are introduced. The trend of the calculated results on the concentration, the fluid velocity and the sediment transport velocity are examined. Finally, comparisons with available data are made. The conclusions obtained herein are as follows:

- (1) In the high concentration region close to the immovable layer, the sediment transport velocity approaches zero due to the intergranular stress, and consequently the fluid velocity becomes small in this region due to the fluid-sediment drag resistance. The phase variation of the velocity in this region is similar to that of a seepage flow. In the low concentration region, the sediment transport velocity becomes smaller than the fluid velocity during the accelerating phase and larger during the decelerating phase.
- (2) The changes of the fluid velocity profiles can be described by the gradient and z -intersection of the logarithmic distribution. These two parameters can be described by the four dimensionless parameters involved in the present model.
- (3) The present model is capable of predicting most of the experimental data considered here.

Second, the data of Yamashita et al. on the fluid velocity and sediment transport velocity are compared. The compared results are shown in Fig.9 for different phases. Although small discrepancies are found, the predicted results are consistent with the following experimental properties: the heights where the velocity starts to increase from 0, the phase precedence of the velocity variation from the free stream velocity, and the decrease of the sediment transport velocity relative to the fluid velocity during the accelerating phase.

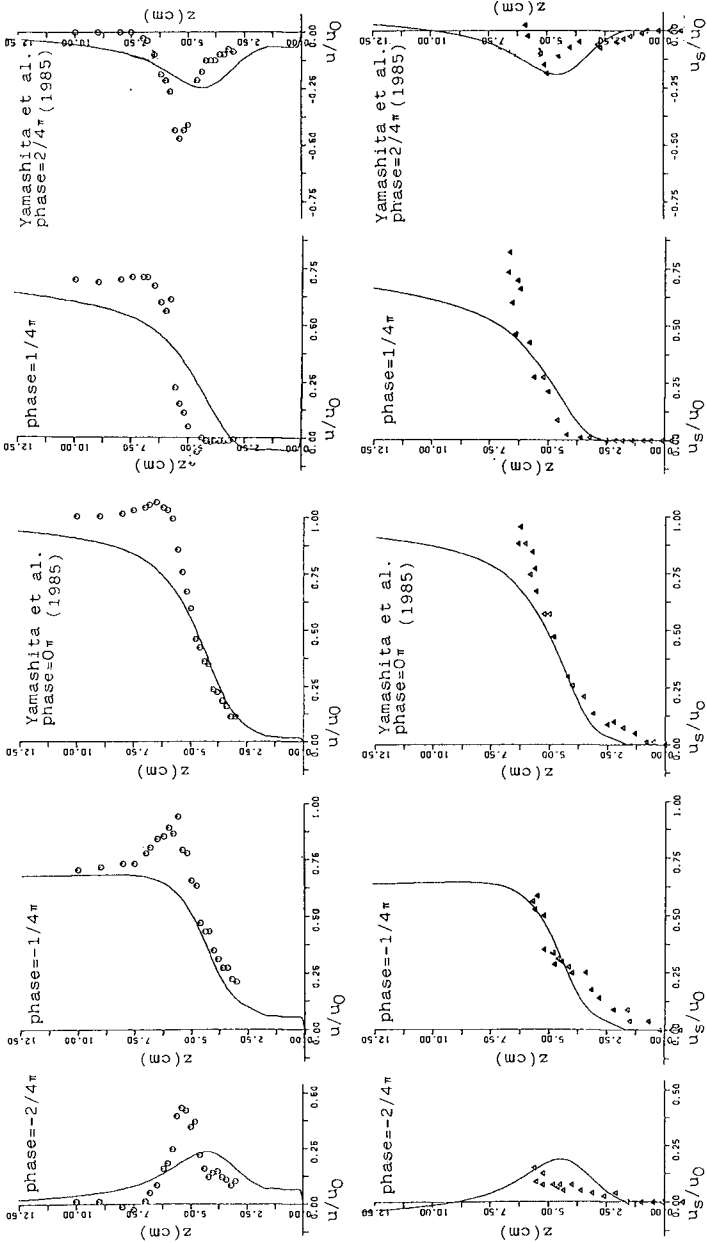


Fig. 9 Comparison between Yamashita et al. (1985)'s data and predicted results on fluid velocity (the upper row) and sediment transport velocity (the lower row).

The present model has tentatively adopted the empirical relationship for the intergranular stress which was originally obtained for a unidirectional flow. There remains the future work of re-examining the assumed distributions for the turbulent eddy viscosity and turbulent diffusion coefficient. Studies on the basic mechanisms involved in a sediment laden oscillatory flow is essential to improve the model accuracy, and accumulation of reliable experimental data is also needed.

ACKNOWLEDGMENTS

Part of this study was carried out at the Institute of Hydrodynamics and Hydraulic Engineering (ISVA), Technical University of Denmark. The staff at ISVA are appreciated for their useful comments and their helpfulness. The author would also like to thank Prof. N. Kobayashi, Delaware University, for constructive comments, and Prof. J. F. A. Sleath, Cambridge University, for sending his useful data.

REFERENCES

- Ahilan R. V. and J. F. A. Sleath** : Sediment transport in oscillatory flow over flat beds, *J. of Hydraulic Engrg.* , Vol. 113, NO.3 ,pp.308-322,1987.
- Asano T.** : Energy dissipation in oscillatory flow over plane movable beds, Progress Report No.68, Inst. of Hydrodyn. and Hydraulic Eng., Technical University of Denmark, pp.3-14, 1988.
- Bagnold, R. A.** : Experiments on a gravity free dispersion of large solid spheres in a Newtonian fluid under shear, *Proc. of Royal Soc.* , A225, pp.49-63, 1954.
- Bakker, W. T. and W. G. M. van Kesteren** : The dynamics of oscillatory sheetflow, *Proc. of 20th ICCE*, pp.940-954, 1986.
- Bogardi, J.** : Sediment Transport in Alluvial Streams, Akademiai Kiado, Budapest, Hungary, p.826, 1974.
- Brevik I.** : Oscillatory rough turbulent boundary layers : *Proc. of ASCE, WW3, Vol.107, AUG.*, pp.175-190, 1981.
- Grant, W. D. and O. S. Madsen** : Movable bed roughness in unsteady oscillatory flow, *J. of Geophy. Res.* , Vol. 87, No. c1, pp.469-481, 1982.
- Hanes, D. M. and A. J. Bowen** : A granular-fluid model for study intense bed-load transport, *J. of Geophys. Res.*, Vol.90, No.C5, pp.9149-9158.
- Horikawa, K., A. Watanabe and S. Katori** : Sediment transport under sheet flow condition, *Proc. of 18th ICCE*, pp.1335-1352, 1982.
- Kobayashi N. and S. N. Seo** : Fluid and sediment interaction over a plane bed, *J. of Hydraulic Engrg., ASCE*, pp.903-921, 1985.
- Richardson J. F. and M. A. daS Jeronimo** : Velocity-voidage relations for sedimentation and fluidization, *Chem. Eng. Sci.*, Vol.34, pp.1419-1422, 1979.
- Savage, S. B. and S. McKeown** : Shear stresses developed during rapid shear of concentrated suspensions of large spherical particles between concentric cylinders , *J. Fluid Mech*, Vol. 127, pp. 453-472, 1983.
- Wilson K. C.** : Analysis of contact-load distribution and application to deposit limit in horizontal pipes, *J. of Pipelines*, Vol.4, pp. 171-176, 1984.
- Yamashita T., M. Sawamoto, H. Takeda and G. Yokomori** : A study on oscillatory flow and sediment transport at sheet flow condition, *Proc. of Japanese Conf. on Coastal Eng., JSCE*, pp.297-301, 1985(in Japanese).

CHAPTER 180

Abrasion at the Tanah Lot Temple - Bali - Indonesia, and Its Counter Measures

Syamsudin and Kardana *)

1. INTRODUCTION

Tanah Lot Temple is situated in Tabanan Regency - Bali, on the coast of the Indonesian Ocean. Due to continuous wave attack, wind force, and weathering of the rock bank where the Temple stands, abrasion has occurred which is more and more threatening the existence of the Temple. Considering that Tanah Lot Temple is a sacred place for the Hindu Balinese people and a place of high cultural value, and also an important tourism, steps to save the Temple are imperative. The Central as well as the Regional Authorities, and also the Balinese community are very much interested in the effort to keep the Temple intact.

Measures have been undertaken to protect both the sea-side and land-side banks of the Temple rock bank. This paper only discusses counter measures of the sea-side bank of the Temple.

2. SITUATION AND CONDITION

Tanah Lot Temple is located on a small island with an area of about 1000 m². The Temple was established in the 16th century. Because of lack of information, we don't know precisely whether the temple was built on the island separated from or connected with the land. If the temple was built unseparable with the land and the separation with the land such a present condition is resulted from abrasion processes, it was truly remarkable work. Eventhough man at that time did not recognize sophisticated technology, they were able to locate the temple on the more stable area than of already eroded by wave and weather. Therefore, they are forced to wait for the tide to flow out, which lasts for a relatively short time only, to make their offerings. If there is a great number of templegoers, making the offering meets with difficulties. Not only because

*) Institute of Hydraulic Engineering, Ir. H. Juanda 193, Bandung, Indonesia.

of the tide, but also of the relatively small area of the Temple, and the narrow access path which is used by the people both coming to and leaving the temple. Figure 1.a shows the situation of Tanah Lot Temple and figure 1.b shows coastal cross-section at the location of the temple. It can be shown from the figure the island where the temple is located rest on a reef flat that relatively solid. The temple is located around 30 m from the reef and 100 m from the land. At low tide the reef flat appears above low water level (LWL), while at high-tide the depth is about 2 m. Therefore, visitors are only able to reach the temple at low-tide. The outer reef is an area where its depth is relatively hard to be measured since the area is the location of breaker-zone. Water depth in front of reef-edge that can be sounded is about 150 m from reef-edge with depth of about 30 m. The depth at outer reef as read in the figure is based on linear approximation, with zero references = LWL. The condition of the Temple is critical, particularly at the southern corner where there is a hollow as shown on figure 1.c which might cause the Temple to collapse.

The process of abrasion of Tanah Lot can be explained as follows :

- a. The sea-waves break on the rock bank at the front part of the Temple. The wave energy erodes the bank and the bottom of the coast. Measurements reveal that the waves reach a height (H) of 2 to 3 M, with a wave period (T) ranging from 5 to 10 seconds.
- b. The mass of water flowing landward through the right and left banks of the Temple at high speed in conjunction with the incoming waves have created cracks/hollows in the bottom will take the bank stability at the upper part.
- c. The cracks resulting from geologic process and cavities made by sea-animals have agravated the abrasion process.

3. PLAN OF COUNTER MEASURES

Protection of Tanah Lot Temple to be carried out using landward revetment that indirectly attacked by waves. Landward revetment consists of pillars and concrete flat as a buffer of sectors that possibly broken. The buffer pillar and concrete flat are modified in such a way so that look natural according to original temple bank condition. As stated in the introduction, the protection of the temple in the land direction could not be explained in detail since this protection is ba-

sically structural engineering and arsitecture not aspects of coastal engineering protection.

Protection of Tanah Lot Temple on the sea-side covers:

- Constructing a structures to protect the sea-side bank,
- Installing wave breaker in front of the sea-side of the island,
- Placing of stones and concrete blocks between the wave breaker and Temple bank.

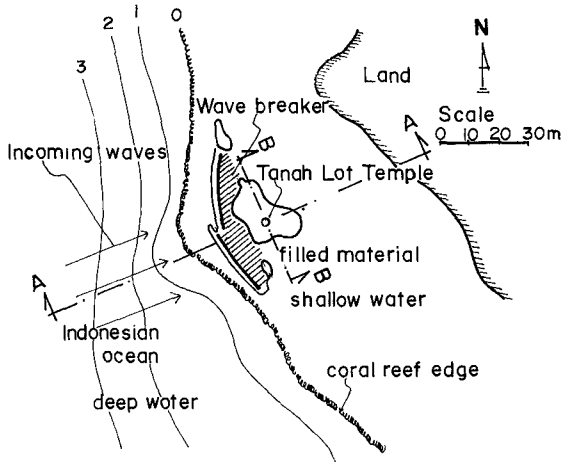


Fig. 1.a. Situation of Tanah Lot Temple

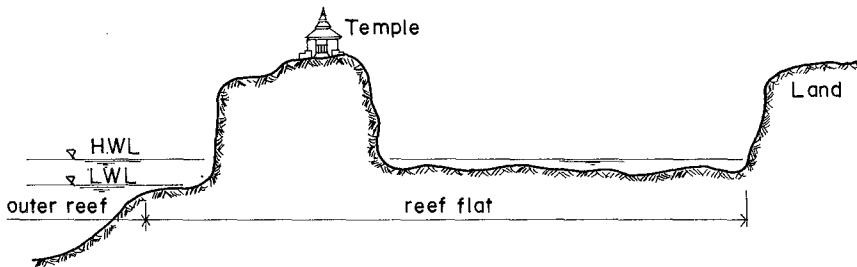


Fig. 1.b. Cross section of the beach (A - A)

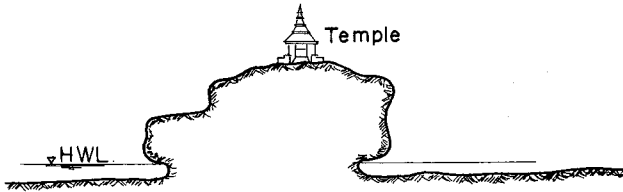


Fig. 1.c. Longitudinal section of the beach (B - B)

3.1. Information from the Public

From discussions, interviews and exchanges of ideas with the community the following were obtained :

- 1) The space both on the land-side and sea-side is not permitted to be closed.
- 2) To facilitate the offerings especially at times when there is a great number of temple-goers, the community propose :
 - to extend the area of the Temple grounds
 - to make different paths for going to and from the Temple.
- 3) For aesthetic, it is proposed to execute the coping of the problem with the assistance of an art so that the result could be natural and harmonious in line with the environmental condition.

3.2. Protection of the Sea Side Bank

Seaward revetment consists of lean concrete casted and joined with original temple bank, the thickness of lean concrete is 1.50 m. The use of lean concrete not only to strengthen but also to enlarge the area of temple and to construct road for outway from the temple. Originally the entrance and outway of the temple are in one channel and narrow make the visitors and pilgrimage have dif-

difficulty doing praying. However, after two-way road already constructed, the difficulty can be overcome. Like landward revetment, lean concrete also has been modified so that look natural.

3.3. Wave Breaker

Many alternatives in planning for wave breaker has been made such as by constructing seawall and concrete wall. However, because of difficulty in the implementation, the choice is by using wave breaker type rubble structure from tetrapod, and the weight of each unit of tetrapod is calculated on the basis of the design wave height $H = 3.0$ m. To place the tetrapods, heavy equipment is needed or a helicopter.

By the Hudson 1) formula,

$$W = \frac{W_r \cdot H^3}{K_d (S_r - 1)^3 \cotg \phi}$$

the weight of each tetrapod for various slopes ($\cotg \phi$) is :

$\cotg \phi$	Body (kg)	Head (kg)
1,5	2,490	3,950
2,0	1,900	2,450
3,0	1,250	2,250

3.4. Filled Material

Filled material is placed behind wave breaker, casted after wave breaker has been carried out. On the lower layer, it consists of graded stones with diameter between 0,1 and 0,4 m filled with concrete block and the thickness of the blocks are 0,50 m. By using layer cap made from concrete blocks, the area of the temple seaward become larger. It can be used at low-tide while at high-tide overtopping as a result of wave breaking continually occurs. In addition to enlarge the area, the main purpose of filled material is to stabilize wave breaker and to support wave attenuation. From field inspection, it is obvious that after setting filled material waves that attack the wall is relatively high. It results from watermass entering tetrapod arrangement. After casting of

filled material wave attenuation works well.

4. TECHNICAL EXECUTION

Since field situations are hard and narrow while local road is impossible to be passed by heavy vehicles the tetrapods are transported by helicopter, which has a maximum capacity of 2.0 tons. For this reason, it has been decided to use tetrapods with a maximum weight of 1.9 tons. In the execution, the helicopter will be able to place the tetrapods only 20 m at the nearest from the temple bank. The crest of the breakwater will be as high as the highest water level (HWL). The wave breaker will be ± 125 m in length, and the number of tetrapods to be placed 2,800. It has been explained in Chapter 3.1 that there will be an opening in the middle of the breakwater. Filled material will be placed behind the breakwater. The bottom part consists of an arrangement of stones and the surface of a concrete plate 0.5 m in thickness. Overlaying the concrete plate will be modified concrete blocks to produce a natural view. In the first stage of implementation, ten tetrapods which are placed separately move toward the temple bank because the bottom of beach is relatively slippery. However, after it was constructed in one unit type, the tetrapod arrangements are able to stand against waves. Until now part of body is relatively stable while in head sectors are estimated to transform to get its stability.

5. MONITORING RESULT

5.1. Change in Wave Characteristics

After the tetrapods have been placed, the waves will not directly hit the temple bank but break on the tetrapod arrangement. As the tetrapod arrangement has holes in it, breaking of the waves will be different from that on a massive surface. Fig. 2a shows the condition of the waves before construction of wave breaker. Waves break directly on the bank of the temple.

Fig. 2b shows the wave condition after construction of wave breaker. From Fig. 2b it is obvious that the tetrapod arrangement dampens the waves well. From point of view of protection, wave breaker already worked well while from the type of wave breaking, wave breaker have changed the original form.

Considering that one of the attractive features of Tanah Lot Temple is the beautiful wave - breaking against the rock, dampening of the waves might

reduce the attraction of the Temple. In order to produce a wave condition similar to the original one it seems that the tetrapod arrangement has to be cast to become a massive unit. Fig. 2c, shows the estimated wave condition after the tetrapods are casted. Casting can be done after the tetrapod arrangement has become stable.

5.2. Condition of tetrapod arrangement

The monitoring result reveals that the body part of the tetrapod arrangement, which currently has side slopes of 1 : 1.5, is relatively stable. The head part (ends of the tetrapod arrangement) with side slopes of 1 : 2, however, is not yet stable. Calculation in Chapter 3.1 turns out that for a tetrapod weighing 2,244kg and a wave height of 3 m, the side slopes are 1 : 3. A tetrapod arrangement with a weight of ± 1.9 tons is estimated to still undergo changes in its stabilization process.

6. CONCLUSIONS AND RECOMMENDATION

1. The tetrapod arrangement serving as a wave breaker is functioning well. However, if one desires a protective structure with a natural look, this break water should be modified.
2. It is estimated that the tetrapod arrangement will still be modified, especially the head parts, in view of the stability process.
3. Damping of the waves is successful, but it probably reduces the attraction of Tanah Lot Temple in terms of breaking of the waves. It is suggested to create a massive tetrapod arrangement in order that the breakers will be as beautiful as before.

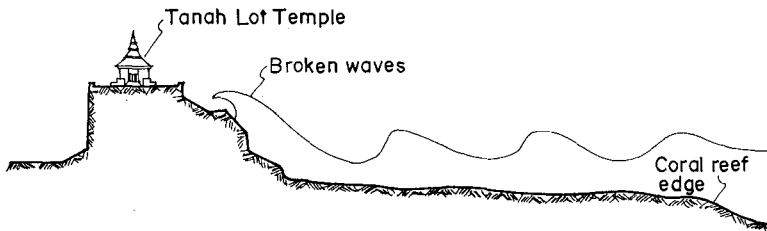


Fig. 2a. Wave condition before construction of wave breakers.

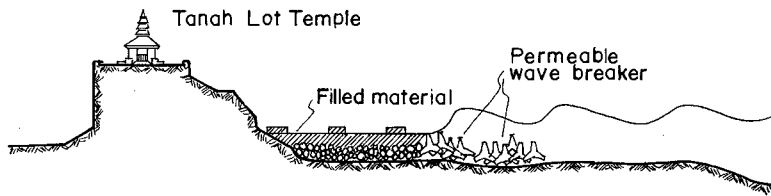


Fig. 2b. Wave condition after construction of permeable wave breaker.

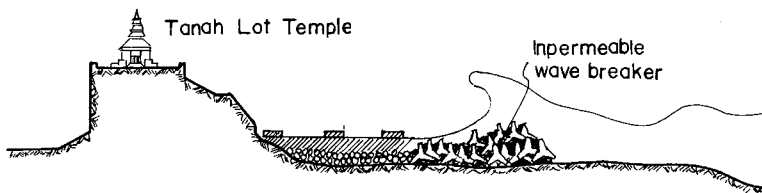


Fig. 2c. Estimated wave condition after construction of impermeable wave breaker.

7. ACKNOWLEDGEMENT

This study was performed under the budget from the Institute of Hydraulic Engineering, Ministry of Public Works Indonesia. Permission was granted by the Director of the Institute of Hydraulic Engineering to publish this information.

REFERENCES

1. Coastal Engineering Research Center, US Army Corps of Engineers, Shore Protection Manual, Volume I, II, 1984
2. Pusat Litbang Pengairan, Laporan Hasil Peninjauan ke Pura Tanah Lot dan Uluwatu, 1986 (Institute of Hydraulic Engineering, Report on Survey of Tanah Lot and Uluwatu, 1986)
3. Pusat Litbang Pengairan, Rencana Penanggulangan Pura Tanah Lot, Pebruari 1987 (Institute of Hydraulic Engineering, Plan of Safeguarding Tanah Lot Temple, February 1987)

CHAPTER 181

MAN-MADE BEACHES MORE THAN 20 YEARS ON

FRANCK ROUCH¹
BERNARD BELLESSORT²

Abstract

This article is an overview of the behaviour of artificial beaches based more particularly on three important examples designed by SOGREAH: La Croisette (Cannes), Larvotto (Monaco), Prado (Marseille).

The main conclusions are:

- . a man-made beach in an urban area is generally very well received by the general public,
- . the general behaviour of beaches has proved to be satisfactory and as forecast on the basis of sedimentological scale model studies from the following points of view: stability, water quality, safety, maintenance.

1. Introduction

When SOGREAH was called upon in 1960 to study the possibilities of widening the Croisette beaches in Cannes, this proved to be the first man-made beach ever built. With the rapid growth of tourism since that time, SOGREAH has designed throughout the world more than 60 beaches out of which about a half have actually been built. It is interesting to make a hindsight assessment of the various man-made beaches.

With focusing on three important examples designed by SOGREAH: la Croisette (Cannes), Larvotto (Monaco), Prado (Marseille).

¹ PROJECT ENGINEER SOGREAH, 6 rue de Lorraine,
38130 Echirolles, France
² Ph. D. Oceanology. Senior Engineer SOGREAH

2. Characteristics of artificial beaches

a) La Croisette (Cannes)

As a matter of fact, the idea of developing a new beach in front of the shoreline of La Croisette Promenade originated in the need for the town of Cannes to widen the Promenade in order to extend the vehicle traffic and to improve the area reserved for the pedestrians along the shoreline.

Widening directly the Promenade in accordance with the needs would have involved of setting the small beach that existed partially along the Promenade at the time. So, SOGREAH proposed to build a new beach before widening the Promenade. The new shoreline was not parallel to the natural shoreline. It is the reason with the new beach is divided in three parts by groins. The main characteristics of the beach are:

- . widening of the natural beach by 20 m over a distance of 1040 m,
- . deposition of 125.000 m³ of sand with a mean diameter of 0.8 mm,
- . three 60 m stabilisation groynes,
- . expected equilibrium slope: 6.5%,
- . construction over a period of 2 years (1962-1964).

b) Larvotto (Monaco)

Larvotto is doubly an artificial beach:

- . first, this beach was built on a quite rocky coast,
- . secondly, the material used to built the beach was fully artificial: crashed dolomite limestone.

This project presented three difficulties:

- . coastline quite rocky and bottoms slope very steep,
- . wave climate very high ($H_{1:10}$: 8 m),
- . any natural sand available.

Main characteristics of the new beach are:

- . length: 400 m,
- . construction of an underwater platform levelled at -2.5 m,
- . deposition of 80,000 m³ of 3-8 mm gravel on the platform,
- . protection with three 80-100 m long breakwaters spaced 80 m apart in water 6-10 m deep and connected to the shore by groynes,
- . construction took place from 1965 to 1967.

c) ___ Prado (Marseille)

The scheme involved the development of 33 hectares of reclaimed area in the sea and the building of new beaches totalising an area of 9 hectares with a total length of 2800 m and an average width about 50 m.

The renourishment material used was 3-8 mm diameter gravel (150,000 m³).

Protection is provided by three breakwaters, 150-220 m long and in water 4 m deep, connected to the shore.

3. Changes in beaches since their constructiona) ___ Renourishment material. Prado beach:

Precise monitoring was carried out at the Prado beach and after 15 years, the following conclusions could be reached:

- the gravel (hard limestone) is worn and rounded only in an area of the beach that is subject to wave action,
- the average diameters have decreased from 5.5 mm to 3.2 mm (in the area subject to wave action), but wear has stabilised with time. There is no noticeable difference between samples taken between 12 and 15 years after completion,

- the larger the particles, the greater the wear,
- from the methodological point of view, the Los Angeles test appears to provide significant results concerning particle wear. The experimental conditions were:
 - . Los Angeles machine,
 - . 20 kg of gravel + 40 l of sea water,
 - . rotation speed: 30 rpm,
 - . number of rotations: 30 000.
- . La Croisette beach:

No change at all in grain size for the sand.
- . Larvotto beach:

No measurement data are available but visual observations lead to similar conclusions from the qualitative point of view.

b) Behaviour of beaches

In the three cases, and as confirmed by the slight amount of consolidation carried out (see 3.3), the artificial beaches have behaved in a highly satisfactory manner and, generally, speaking, as forecast, particularly with regard to:

- . slopes: of the order of 10% with gravels (Larvotto and Prado, protected by breakwaters) and coarse sand (Croisette, with no protection),
- . no major loss offshore,
- . shoreline: as forecast and stable (within the usual known limits of change).

However, the following points must be underlined:

- . At Cannes, there is a discrepancy between plan view of the promenade and that of the beach because the groynes are not long or high enough (for environmental needs). So, it must be accepted some littoral drift from East to West. Every year before the summer season, some sand (about 2 000 m³) has to be redistributed from the western part of the beach to the eastern part in order to balance its width.
- . In the three cases, a ridge is formed on the upper part of the beach, mainly in winter, accompanied by a steeper beach profile. This makes it necessary to rework the profile at the start of the summer period.
- . At Larvotto, during severe storms, beach material is thrown together with sea water to the back of the beach where shops and costly equipments are located. Protective boarding is needed in winter. This is removed during the summer.
- . The beach slopes of the order of 10% appear to be steep for bathers and, in particular, for children.

In the three cases, the renourishment required for correct beach maintenance has been limited and has been quite acceptable from both the technical and financial viewpoints:

- . Cannes:
 - Initial renourishment: 125 000 m³
 - Maintenance (over 20 years): 5 000 m³

- . Larvotto:
 - Initial renourishment: 80 000 m³
 - Maintenance (over 23 years): 5 000 m³

- . Prado:
 - Initial renourishment: 150 000 m³
 - Maintenance: none to date

To interpret these satisfactory results, the following points need to be taken into account:

- . the absence of any tide,
- . the large particle size of the material, which favours stability,
- . the protective and stabilisation structures (groynes, brakwaters) built near the beaches.

This being so, these are highly instructive examples of how artificial beach projects should be designed to ensure reliable use.

4. Water quality

In the three cases, treatment work was carried out in parallel with the construction of the beaches. Water quality monitoring shows that, in general, the water is of class A (good quality) or B (moderate quality), and thus poses no problems for bathers.

For example at Cannes, the water is 70% class A and 26% class B. Exceptionally, polluted water has occurred, but this was the result of very heavy rains. In one case, the pollution was due to a burst pipe.

The water at Larvotto is of good quality, but there are temporary problems of pollution in certain places around the central landfill platform. As at Cannes, there is a correlation between pollution and rainfall.

Measurements taken at Prado beach (1988) show that the water is of good quality. Measurements at different times of the day show that use of the beach by bathers does not notably affect the water quality.

5. Operating problems

Problems of beach operation are not connected with the fact that they are artificial but with their used and more particularly with access and parking facilities.

Maintenance of gravel beaches has proved to be easy with screening machines.

At 8-10%, the beach slopes, which are connected with the particle size of the material used, have appeared to be just acceptable for bathers and particularly for children.

The use of consolidation material with the same particle size as the gravel (3-8 mm) does not appear to be an inconvenience for bathers (the limit of discomfort appears to begin around 5 mm).

6. Conclusions

In conclusion, as these three exemples of most important artificial beaches along the French Mediterranean coast show, it is of a great importance to carry out proper design studies before construction of artificial beaches. In this way, the beach is assured of a long lasting stability of the beach with minimal maintenance at litte or no cost.

CHAPTER 182

Littoral Transport Rate

J. William Kamphuis¹ M. ASCE

Abstract

This paper describes a study of littoral sediment transport rate based on three-dimensional hydraulic model experiments performed with regular and irregular waves. Deep water wave conditions, wave heights through the surf zone, wave breaking angles, longshore current velocity distribution and the bed load and suspended load sediment transport distributions were measured simultaneously to form a coherent data set. An expression is developed linking sediment transport rate to wave steepness, beach slope, relative grain size and breaking angle. The expression compares well with published field data.

1. Introduction

This paper describes the continuation of research on alongshore sediment transport described in Kamphuis and Readshaw (1978), Kamphuis and Sayao (1980) and Kamphuis et al. (1986). A new set of three dimensional mobile bed hydraulic beach model results is used; a summary of the tests is shown in Table 1; the experimental layout is shown in Figure 1 and more detail about the tests may be found in Kamphuis and Kooistra (1990).

2. General Description of the Tests

The section of the wave basin used was 23.4 m long by 10.0 m wide. An initial plane sand beach slope of 1:10 was prepared for each test. The depth of water in Table 1 was measured at the toe of the sloping beach.

Constant regular and irregular wave climates were generated for approximately 7 hours; the irregular waves consisted of a Jonswap spectrum with $\gamma = 2.3$ and the random wave signal typically repeated itself after 200

¹Professor, Queen's University, Department of Civil Engineering, Kingston, Ontario K7L 3N6 CANADA

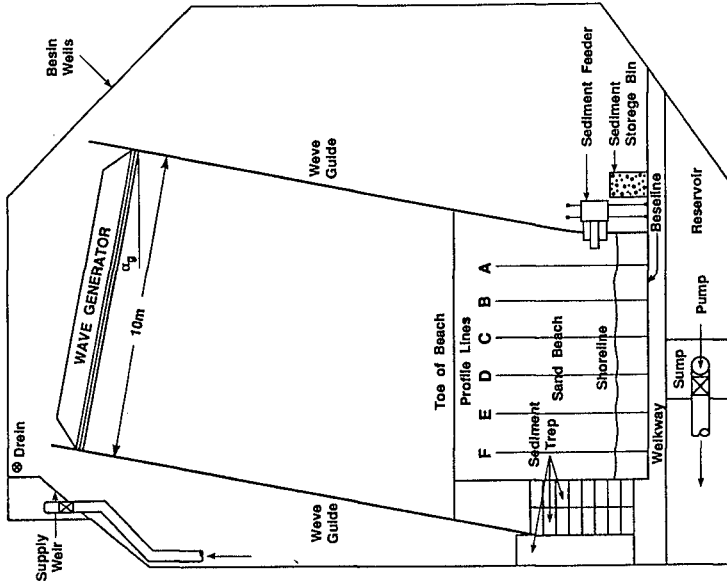


FIGURE 1 WAVE BASIN

TABLE 1
SUMMARY OF 3-0 TESTS

Test	Hs (m)	Tp (sec)	Generated Wave d (m)	Wave Type	Groupiness Factor	Incident Angle	Grain Size (mm)
IA	.045	1.15	.50	irr	.8	10	.105
IB	.063	1.15	.55	irr	.8	10	.18
IG	.088	1.15	.55	irr	.8	10	.18
IO	.117	1.15	.55	irr	.8	10	.18
IE	.063	0.92	.50	irr	.8	10	.105
IF	.063	1.15	.50	irr	.8	10	.105
IG	.063	1.39	.50	irr	.8	10	.105
IJ	.078	1.38	.50	irr	.8	10	.105
IK	.084	1.38	.55	irr	.8	10	.18
IL	.122	1.15	.55	irr	.8	20	.18
IM	.094	1.15	.55	irr	.8	20	.18
IN	.063	1.15	.55	irr	.8	20	.18
IO	.063	1.15	.55	irr	.8	30	.18
*IP	.080	1.15	.55	irr	.8	30	.18
*IQ	.124	1.15	.55	irr	.8	30	.18
*IR	.084	1.15	.55	irr	.2	30	.18
*IS	.084	1.15	.55	irr	1.4	30	.18
*IT	.127	1.00	.55	irr	.8	40	.18
*IU	.139	1.50	.55	irr	.8	40	.18
*IV	.094	1.20	.55	irr	.8	40	.18
RG	.074	1.15	.55	reg		10	.18
RE	.045	0.92	.50	reg		10	.105
RG	.045	1.39	.50	reg		10	.105
RI	.060	1.38	.50	reg		10	.105
RM	.084	1.15	.55	reg		20	.18
*RP	.051	1.15	.55	reg		30	.18
RT	.132	1.00	.55	reg		40	.18

* VI0E0

waves. Each test was divided into one hour segments. Wave heights, wave angles, longshore current velocity distributions, sediment transport rates and distributions, and beach profiles were measured in an hourly cycle.

Waves were measured at a sampling rate of 10 HZ, offshore and at 15 locations, 0.2 m apart from offshore of the breaker, through the surf zone, into the swash zone. Breaking wave angles were measured for eight of the tests using an overhead video camera (Table 1).

Alongshore current velocities were measured at 0.1 metre intervals across the surf zone using a ducted mini-impeller flow meter.

A sediment trap was located at the downdrift end of the beach but within the lines of the wave guides. It was designed to separate bedload from suspended load and to measure their distributions across the swash and surf zone (Figures 2 and 3). Each trap box extended from above the swash zone to well offshore of the breakpoint and was sub-divided into a number of compartments permit measurement of the distribution of sediment transport across the surf zone.

Templates supporting the trap covers were vertically adjustable to ensure the top of the trap matched the beach profile near the trap. The covers contained slots which extended the full length of the boxes from above the swash zone to offshore of the breakpoint. The slot width (in the sediment transport direction) over the updrift box was adjustable so only bedload was trapped. Any sediment transported past this slot was considered to be suspended load and was trapped through much wider slots over the downdrift boxes.

Sediment was supplied at the updrift end of the beach by a feeder at a rate comparable to the sediment transport rate along the beach. Beach profile measurements and observations of the waves breaking along the beach verified that the beach contours were maintained reasonably parallel by this procedure.

Beach profiles were recorded at the beginning of each test and at the end of each one hour segment using an automatic bed profiler. Profiles were measured at one metre intervals alongshore; depths were recorded at .01 metre intervals offshore. Only the centre 5 m section of the model beach was profiled, resulting in 6 profiles for each one hour segment.

More detail about the experimental procedure may be found in the Kamphuis and Kooistra (1990) and Kamphuis (1991).

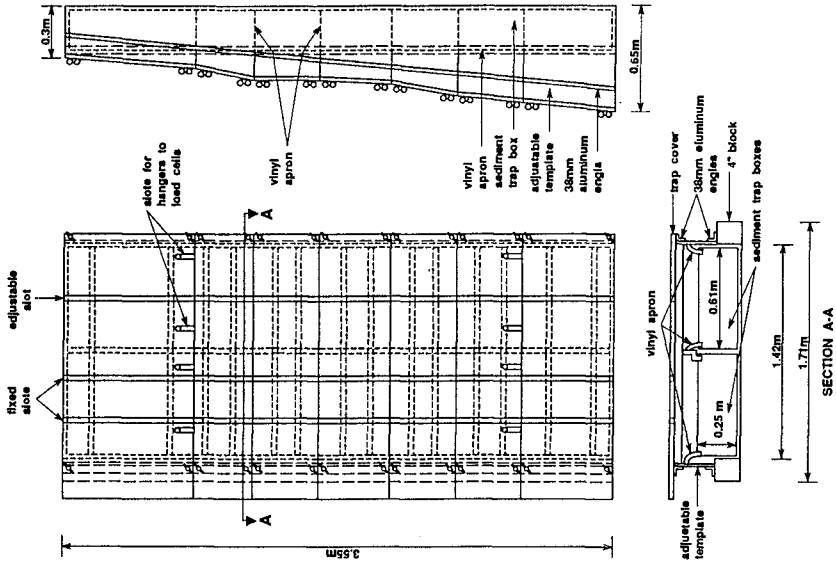


FIGURE 3 SEDIMENT TRAP COVERS AND DETAILS

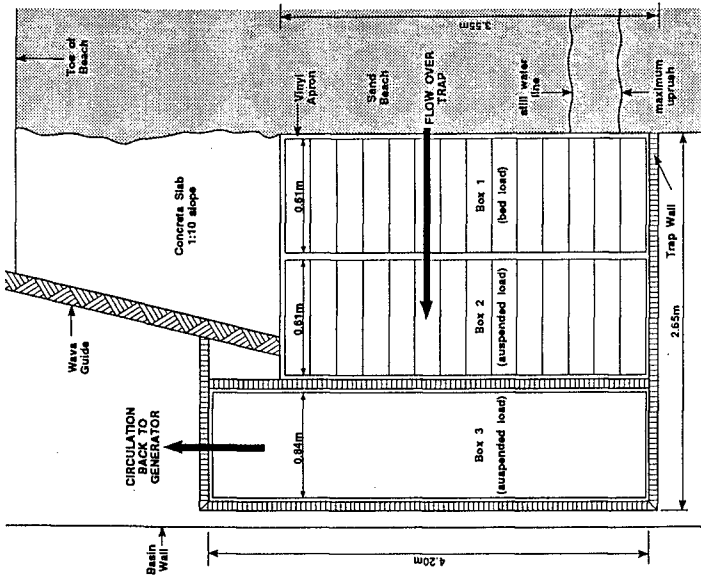


FIGURE 2 SEDIMENT TRAP LAYOUT

3. The Data Analysis

3.1 WAVES

For the irregular waves, the wave period was determined from the peak of the offshore wave spectrum. Significant and rms wave heights were determined at each probe position using a zero crossing analysis. For every hour of the test, wave heights were plotted against probe position as shown in Figure 4. The magnitude and location of the breaking wave height, H_b and X_b respectively, were thus defined and the corresponding values of breaking depth (δ_b) and the distance from the still water line to the breakpoint (λ_b) were determined from the measured beach profiles. The wave transformation for these tests is discussed in Kamphuis (1990); the wave breaking in Kamphuis (1990a).

3.2 SEDIMENT TRANSPORT

The immersed mass of sediment trapped as bedload, suspended load and total load was measured every 15 minutes and plotted as a function of time as shown in Figure 5. For each one hour segment of the test, the slope of the curve was calculated to determine the sediment transport rate, Q , in kg/s. After approximately three hours of testing, the sediment transport rate approached a steady-state as the beach profile approached equilibrium. At this stage in the test, the trap boxes were pumped completely empty of all sediment and the distribution of sediment transport was measured over the next 3 or 4 hours under equilibrium conditions. A typical plot of the sediment transport distribution is shown in Figure 6.

4. Results

4.1 DIMENSIONAL ANALYSIS

Dimensional analysis for bulk sediment transport rate in the turbulent breaking zone leads to:

$$\frac{Q}{\rho H^3/T} = K \left(\frac{H}{L_0}\right)^a m_b^b \left(\frac{H}{D_{50}}\right)^c \sin^d 2\alpha_b \quad (1)$$

as demonstrated in Kamphuis (1991). Here a, b, c and d are exponents. Sediment transport is thus a function of wave steepness, beach slope, relative grain size and wave angle and since bulk sediment transport rate is normally assumed to be closely related to alongshore wave thrust, the wave angle term used was $(\sin 2\alpha_b)$.

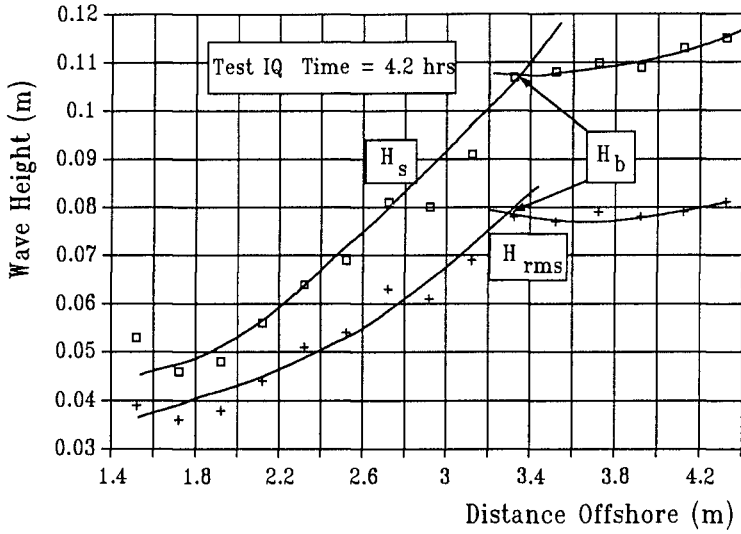


FIGURE 4 BREAKER HEIGHT AND LOCATION

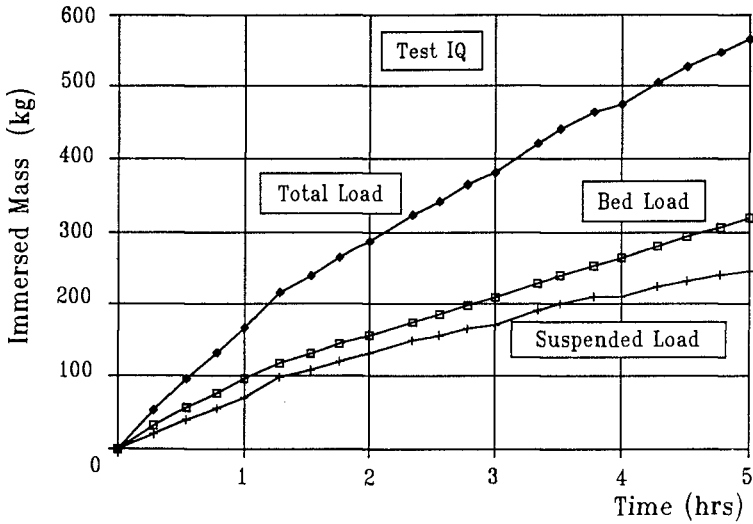


FIGURE 5 MEASURED SEDIMENT TRANSPORT

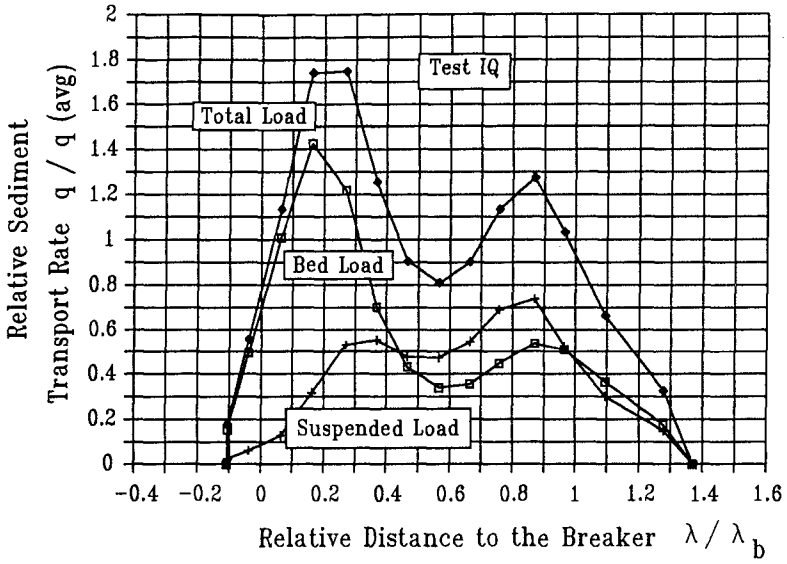


FIGURE 6 SEDIMENT TRANSPORT DISTRIBUTION

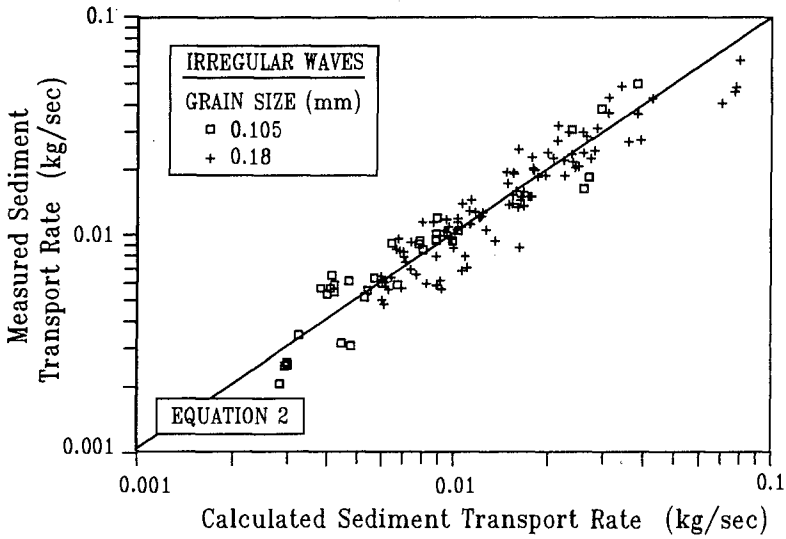


FIGURE 7 IRREGULAR WAVE TESTS

4.2 IRREGULAR WAVE TESTS

Figure 7 shows how:

$$\frac{Q}{\rho H_{sb}^3 / T_p} = 1.3 \times 10^{-3} \left(\frac{H_{sb}}{L_{op}} \right)^{-1.25} m_b^{0.75} \left(\frac{H_{sb}}{D_{50}} \right)^{0.25} \sin^{0.6}(2\alpha_b) \quad (2)$$

fits the experimental data for the irregular waves well. Here H_{sb} is the breaking significant wave height, T_p is the peak period of the offshore wave spectrum and L_{op} is the deepwater wave length corresponding to the peak wave period. It is seen that there is no systematic difference between the tests with the two different grain sizes. The standard error of estimate, $s(y/x)$, is 0.10 log cycles, i.e. 95% of the points lie within a factor of ± 1.6 times Equation 2.

Sensitivity analysis on the exponents of Equation 2 shows that the actual exponents could vary over the following ranges without materially affecting the result:

$$\begin{aligned} -1.15 < a < -1.30 & ; 0.6 < b < 0.85 \\ 0.15 < c < 0.30 & ; 0.55 < d < 0.6 \end{aligned}$$

A similar analysis using H_{rms} resulted in:

$$\frac{Q}{\rho H_{rms}^3 / T_p} = 2.6 \times 10^{-3} \left(\frac{H_{rms}}{L_{op}} \right)^{-1.25} m_b^{0.75} \left(\frac{H_{rms}}{D_{50}} \right)^{0.25} \sin^{0.6}(2\alpha_b) \quad (3)$$

with $s(y/x)$ the same as for Equation 2.

Inspection of Equations 2 and 3 shows that Q varies with H^2 . If the wave height distribution at breaking approximates a Rayleigh distribution, one would expect the constant in Equation 6 to be twice that in Equation 2. Since this is indeed the case, it would indicate that for bulk sediment transport calculations, a Rayleigh distribution may be assumed for breaking wave heights.

4.3 REGULAR WAVES

Figure 8 shows that if H and T are substituted for H_{rms} and T_p in Equation 6, the regular waves line up exactly with the irregular wave results. Earlier regular wave results obtained by Readshaw (1978) for much larger grain size ($D_{50} = 0.56$ mm) also fit the relationship well. This would indicate that the sediment transport process is indeed closely related to wave energy and that the diameter effect is well simulated by Equation 1.

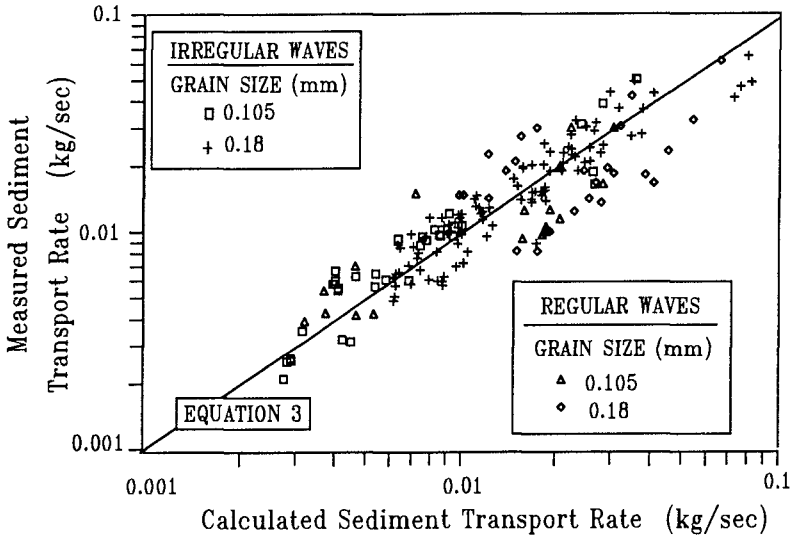


FIGURE 8 REGULAR AND IRREGULAR WAVES

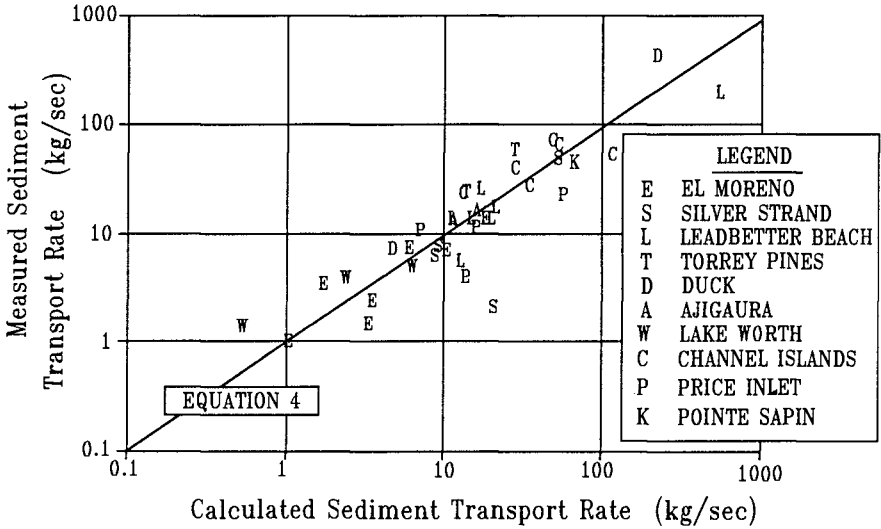


FIGURE 9 FIELD DATA USED

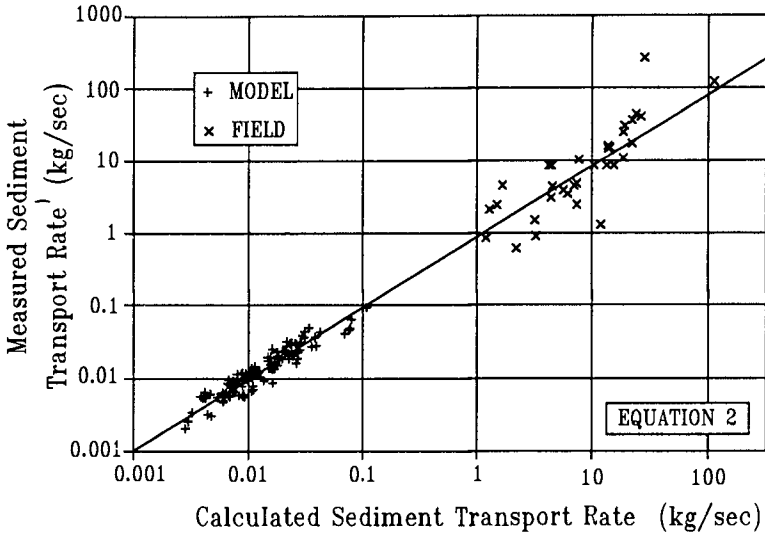


FIGURE 10 MODEL AND FIELD DATA WITH EQUATION 2

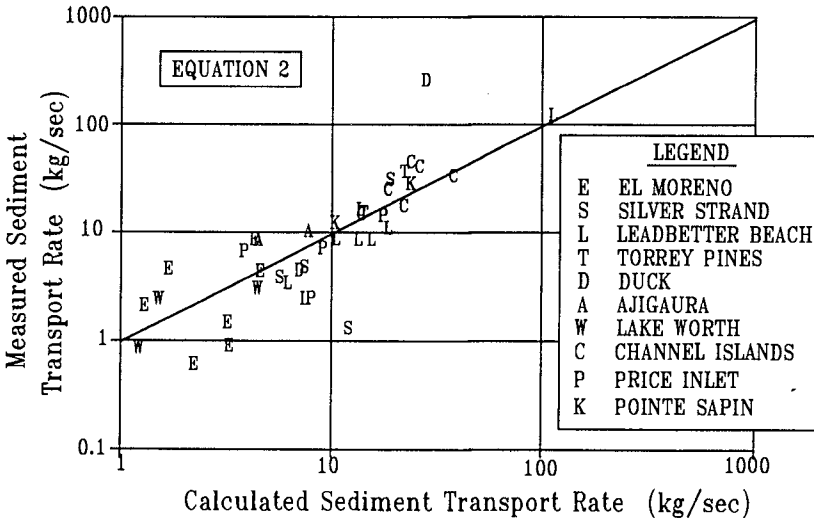


FIGURE 11 FIELD DATA ONLY WITH EQUATION 2

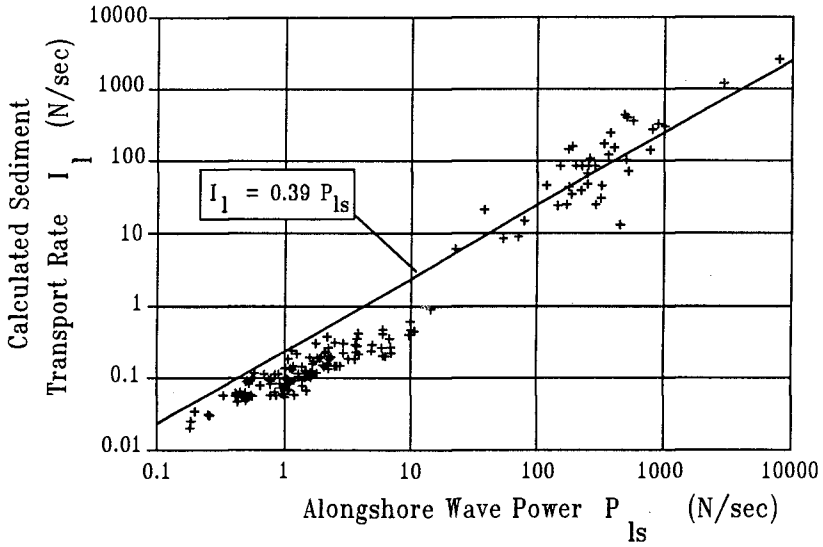


FIGURE 12 CERC EXPRESSION

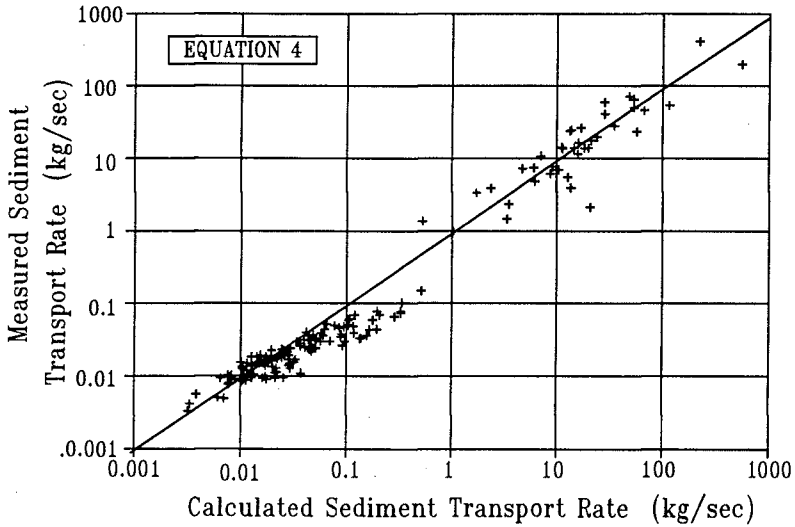


FIGURE 13 MODEL AND FIELD DATA WITH EQUATION 4

4.4 FIELD DATA

The extensive field data set described by Kamphuis et al (1986) is used in the present study. Kamphuis et al (1986) derived a sediment transport expression, based on these field data:

$$\frac{Q}{\rho H_{sb}^3 T_p} = 0.6 \times 10^{-3} \left(\frac{H_{sb}}{L_{op}} \right)^{0.5} m_b^{1.0} \left(\frac{H_{sb}}{D_{50}} \right)^{1.0} \sin(2\alpha_b) \quad (4)$$

The field data and their fit to Equation 4 are shown in Figure 9.

Figure 10 shows how Equation 2 fits the irregular wave data and the field data. For the complete data set in Figure 10, $s(y/x)$ is 0.18 log cycles. Figure 11 shows how Equation 2 fits through the field data alone; $s(y/x) = 0.33$. Clearly Equation 2 represents field conditions as well as model conditions.

To fill the gap between the model and field data, the gravel beach tests of Van Hijum and Pilarczyk (1982) were investigated and Equation 2 appears to be completely robust covering model and field beaches of sand and gravel.

4.5 EARLIER EXPRESSIONS

Figure 12 demonstrates how the well-known CERC expression (Shore Protection Manual - 1984) fits the irregular waves and field data set. It is clear that the CERC expression over-estimates sediment transport for the model tests, particularly for the larger incident wave angles. $s(y/x)$ is 0.60 log cycles for the complete data set and 0.35 for the field data only. If the constant in the CERC expression is changed from 0.39 to 0.12 (the line of best fit), $s(y/x)$ is 0.30 for the complete set and 0.49 for the field data alone.

The same data set is plotted with Equation 4 in Figure 13. It is seen that this expression fits the data better than the CERC expression; $s(y/x) = 0.27$ for the complete data set and 0.29 for the field data alone.

5. Discussion of Results

Equations 2 and 3 may be reduced to the form:

$$Q = K \rho (g/2\pi)^{1.25} H^2 T^{1.5} m^{0.75} D^{-.25} \sin^{0.6}(2\alpha_b) \quad (5)$$

It is seen that the sediment transport rate is proportional to H^2 . This exponent of H is smaller than for Equation 4 and the CERC expression. This smaller sensitivity to wave height, corrects a criticism often levelled at the earlier expressions, i.e. that they overpredict sediment transport at high wave heights.

The present expressions are more sensitive to wave period than the earlier expressions.

Sediment transport rate increases with beach slope, a phenomenon noted during the Pointe Sapin field study (Kamphuis et al - 1986). It also shows some inverse variation with grain size. This is as might be expected intuitively, but the small exponent explains the fact that for many years, sediment transport rate expressions have ignored grain size at no great peril.

Sediment transport rate varies with $\sin 2\alpha b$ to a power smaller than 1. It is clear that $\sin 2\alpha b$ overestimates the sediment transport at higher incident angles (Figures 12 and 13). Part of the reason is wave-current interaction as discussed by Kraus and Sasaki (1979) and Liu and Dalrymple (1978). But this does not account for all of the observed decrease in sediment transport with wave angle, relative to an expression with $\sin 2\alpha b$. The present $\sin^{0.6}(2\alpha b)$ is a much more severe wave angle effect than the results given for mean values of longshore currents by Kraus and Sasaki.

8. Conclusions

A bulk sediment transport expression has been presented, based on an extensive, coherent set of laboratory experimental data. The expression correctly predicts sediment transport over a wide range of grain sizes and for field data presented in the literature.

Sediment transport rate is found to be proportional to wave energy since regular wave data and irregular wave data using Hrms form one population.

Sediment transport rate is proportional to H^2 , which results in a smaller transport during major storms, as compared to earlier expressions.

Sediment transport rate is a function of beach slope and depends only slightly on grain size. The commonly used wave angle term $\sin 2\alpha b$ over-predicts sediment transport rate.

References

- Kamphuis, J.W. (1990), "Wave Transformation", Accepted for publication by Coastal Engineering.
- Kamphuis, J.W. (1990a), "Incipient Wave Breaking", Accepted for publication by Coastal Engineering.
- Kamphuis, J.W. (1991), "Alongshore Sediment Transport Rate", Submitted to Journal of Waterway, Port, Coastal and Ocean Engineering, (ASCE).
- Kamphuis, J.W., Davies, M.H., Nairn, R.B. and Sayao, O.J. (1986), "Calculation of Littoral Sand Transport Rate", Coastal Engineering, Vol. 10, pp. 1-21.
- Kamphuis, J.W. and Readshaw, J.S. (1978), "A Model Study of Alongshore Sediment Transport Rate", Proceedings 16th International Conference on Coastal Engineering, Hamburg, pp. 1656-1674.
- Kamphuis, J.W. and Kooistra, J. (1990), "Three-Dimensional Mobile Bed Hydraulic Model Studies of Wave Breaking, Circulation and Sediment Transport Processes", Proceedings Canadian Coastal Conference '90, Kingston, Ontario, National Research Council of Canada, Associate Committee on Shorelines (ACOS), pp. 363-386.
- Kooistra, J. and Kamphuis J.W. (1984), "Scale Effects in Alongshore Sediment Transport Rates", Canadian Coastal Sediment Study Report No. C2S2-13, National Research Council of Canada, Ottawa, 104 pp.
- Kraus, N.C., Isobe, M., Igarashi, H., Sasaki, T. and Horikawa, K. (1982), "Field Experiments on Longshore Sand Transport in the Surf Zone", Proceedings 18th International Conference on Coastal Engineering, Capetown, pp. 969-988.
- Kraus, N.C., and Sasaki, T.O. (1979), "Effects of Wave Angle and Lateral Mixing on the Longshore Current", Coastal Engineering in Japan, Vol. 22, 1979, pp. 59-74.
- Liu, P.L.-F. and Dalrymple, R.A. (1978), "Bottom Frictional Stresses and Longshore Currents due to waves with Large Angles of Incidence", Journal of Marine Research, Vol. 36, pp. 357-375.
- Readshaw, J.S. (1979), "A Model Study of Alongshore Sediment Transport", M.Sc. Thesis, Queen's University, Kingston, 163 pp.
- Shore Protection Manual, (1984), 4th edition, Coastal Engineering Research Center, U.S. Army Corps Engineers, Vicksburg.
- Van Hijum, E. and Pilarczyk, K.W. (1982), "Equilibrium Profile and Longshore Transport of Coarse Material under Regular and Irregular Wave Attack", Delft Hydraulics Laboratory Publication 274, 107 pp.

Acknowledgements

Financial support for this study was provided by a Strategic Grant (OCEANS) from the Natural Sciences and Engineering Research Council (NSERC).

CHAPTER 183

Causes of Damage to Saldanha Sand Breakwater

J S Schoonees*, J W J Kluger*** and J A Zwamborn*

1. Abstract

The Port of Saldanha, situated 120 km north-west of Cape Town, South Africa, is protected from the dominant south-south-westerly swell conditions by a sand breakwater which is presently eroding. This paper summarises the results of the monitoring of the breakwater, which consisted of aerial and beach photographs as well as hydrographic surveys. Another part of the investigation was to examine the reasons for the erosion (found by the monitoring to be increasing) on the basis of the prevailing environmental conditions such as wind, waves and currents. To do this the wind and nearshore wave climates were determined. Subsequently, the optimum alignment of the sand breakwater was calculated by three different methods. The equilibrium slope of the breakwater, which was also determined, indicated that the design slope was too steep. Of the remedial measures considered, namely, the use of sand or rock, the latter was chosen.

2. Introduction

The Port of Saldanha, situated some 120 km north-west of Cape Town on the South African west coast was constructed mainly for the export of iron ore. Shelter from the swell conditions that occur there was obtained by building a sand (or spending beach) breakwater between Hoedjiespunt on the mainland and Marcus Island (Figure 1). Zwemmer and Van't Hoff (1982) describe the design and construction of the breakwater in detail.

About 20 million m³ of sand was used for the construction of the 1,9 km long breakwater. Some difficulty was encountered in obtaining this quantity. It was also found that rock protection (as a spur before placing sand) was necessary in order to build the breakwater. This resulted in a sand breakwater with some rock protection, mainly above the low-water mark. See Zwemmer and Van't Hoff (1982) for details.

* CSIR, P O Box 320, Stellenbosch, 7600, South Africa.

** J W J Kluger passed away in 1988. His contribution is gratefully acknowledged.

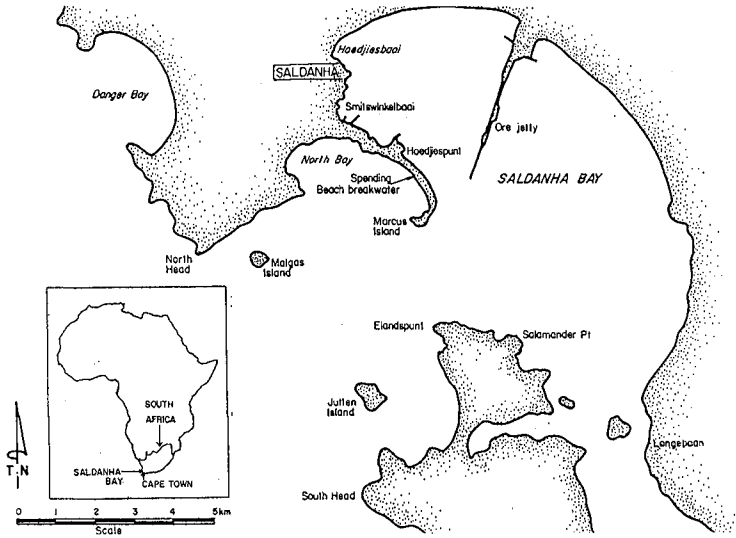


FIGURE 1 : LOCALITY MAP

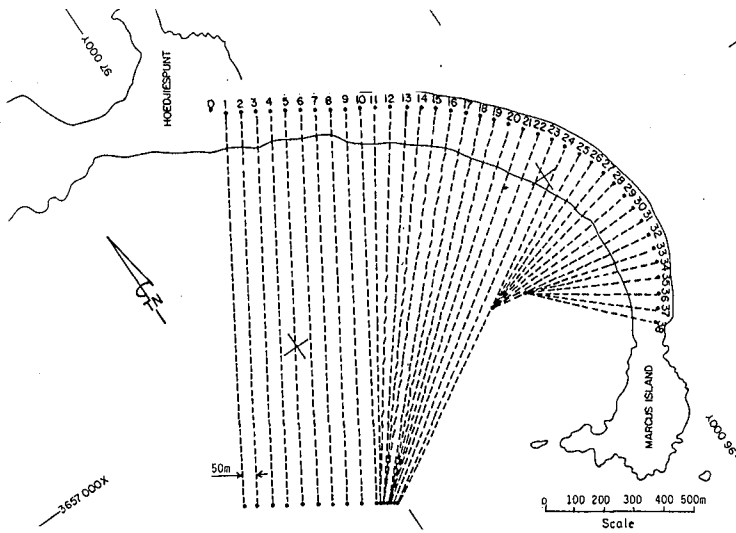


FIGURE 4 : POSITION OF THE SURVEY LINES

A preliminary study of the stability of the sand breakwater (CSIR, 1985) was commissioned by the then South African Transport Services (now Portnet). This study, by using the then available hydrographic and beach survey data, concluded that sand is eroded steadily from the breakwater at a rate of approximately 50 000 m³/year. Based on a recommendation of this study, a detailed investigation (CSIR, 1988) was undertaken to establish the reason(s) for this erosion on the basis of the prevailing environmental conditions such as wind, waves and currents. It was further recommended that the breakwater be monitored on a regular basis.

CSIR (1988), of which this paper is basically a summary, deals with the photographic and hydrographic monitoring of the breakwater, the effect of wind, the wave climate, the optimum alignment of the breakwater and the equilibrium slope of the breakwater as well as possible remedial measures.

3. Monitoring of the Breakwater

3.1 General

The monitoring consisted of low-altitude aerial photography, beach photography and beach and hydrographic surveys.

3.2 Aerial Photography

The aim of the aerial photography, conducted at roughly three-monthly intervals and taken at low water, was to establish whether overall changes of the breakwater, and especially the erosion areas detected previously in the rock protection placed during construction, had taken place.

Figure 2 is an example of a photomosaic compiled from such photographs.

The aerial photography showed that no drastic change of the erosion areas occurred and that the overall appearance of the breakwater has virtually stayed the same during the period August 1985 to November 1986.

3.3 Beach Photography

The main purpose of the close-up beach photographs was to provide an indication of the movement of stone and of possible degradation of the stone of the rock protection itself.

An aluminium tripod, giving a camera elevation of 3 m above ground level, was used to photograph the beach. One leg of the tripod consisted of a ladder which provided access for the photographer to the top of the tripod (Figure 3). At each position of the tripod, a horizontal area of 4,2 m × 4,2 m was photographed. Thus, by moving the tripod 4 m along a selected line after taking each photograph, a continuous strip of the beach 4,2 m wide and as long as required, could be photographed.

Seven beach photography areas were chosen, namely, survey lines 2, 4, 9, 15, 21, 27 and 37. See Figure 4 for the positions of these survey lines and Figure 5 for an example of such photographs.



FIGURE 2 : AERIAL PHOTOMOZAIC TAKEN ON 26 JUNE 1986



FIGURE 3 : TRIPOD USED FOR THE BEACH PHOTOGRAPHY

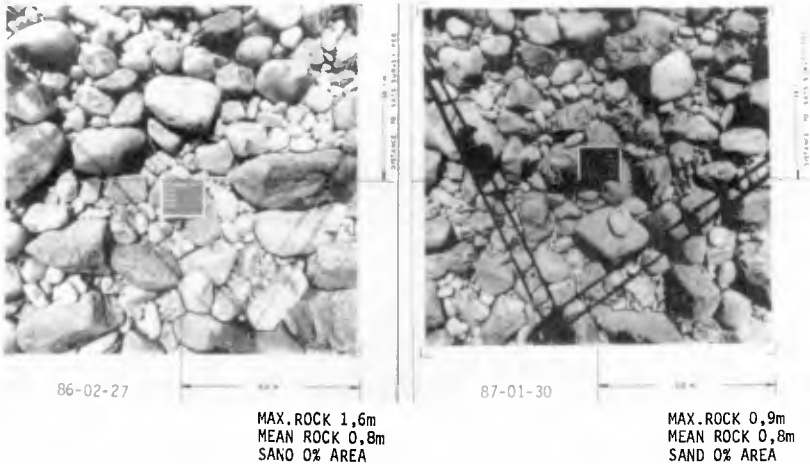


FIGURE 5 : AN EXAMPLE OF THE BEACH PHOTOGRAPHY ON SURVEY LINE 15

No measurable stone degradation could be detected on the beach photographs taken during the 11-month recording period. These photographs, however, indicated that stones up to 1,5 m in size (approximately 3 t) moved on the beach slope below +4 m CD (CD = chart datum which is 0,90 m below mean sea level (MSL)). The most severe movement took place between survey stations 3 and 9 and stations 27 to 37.

3.4 Beach and Hydrographic Surveys

Hydrographic surveys were done by measuring nearshore profiles along survey lines (Figure 4) with an echosounder mounted on a boat. Depths up to about -20 m CD were recorded. The beach profiles were surveyed on the beach along the same survey lines by using a theodolite and a staff.

Figure 6 shows a fair chart of one of the surveys. Note that there is a gap between the beach and hydrographic surveys. This, is unfortunately, in the area where most of the seabed changes occur. This is due to the restriction imposed by the draught of the available survey vessel as well as by the rough wave conditions normally encountered at the breakwater.

Volume differences between surveys were calculated (in the gap between beach and hydrographic surveys, linear interpolation was used). The following table summarises these volume changes:

Date	Volume difference ¹ (m ³)	Period (months)	Calculated rate (m ³ /year)
27-06-78			
	-43 500	3,75	-139 300
20-10-78			
	-93 400	6,25	-179 400
26-04-79			
	+168 800	7,00	+289 400
28-11-79			
	-271 700	35,00	-93 200
29-10-82			
14-11-84			
	-362 600	17,75	-245 100
07-05-86			

¹ + means accretion

- means erosion

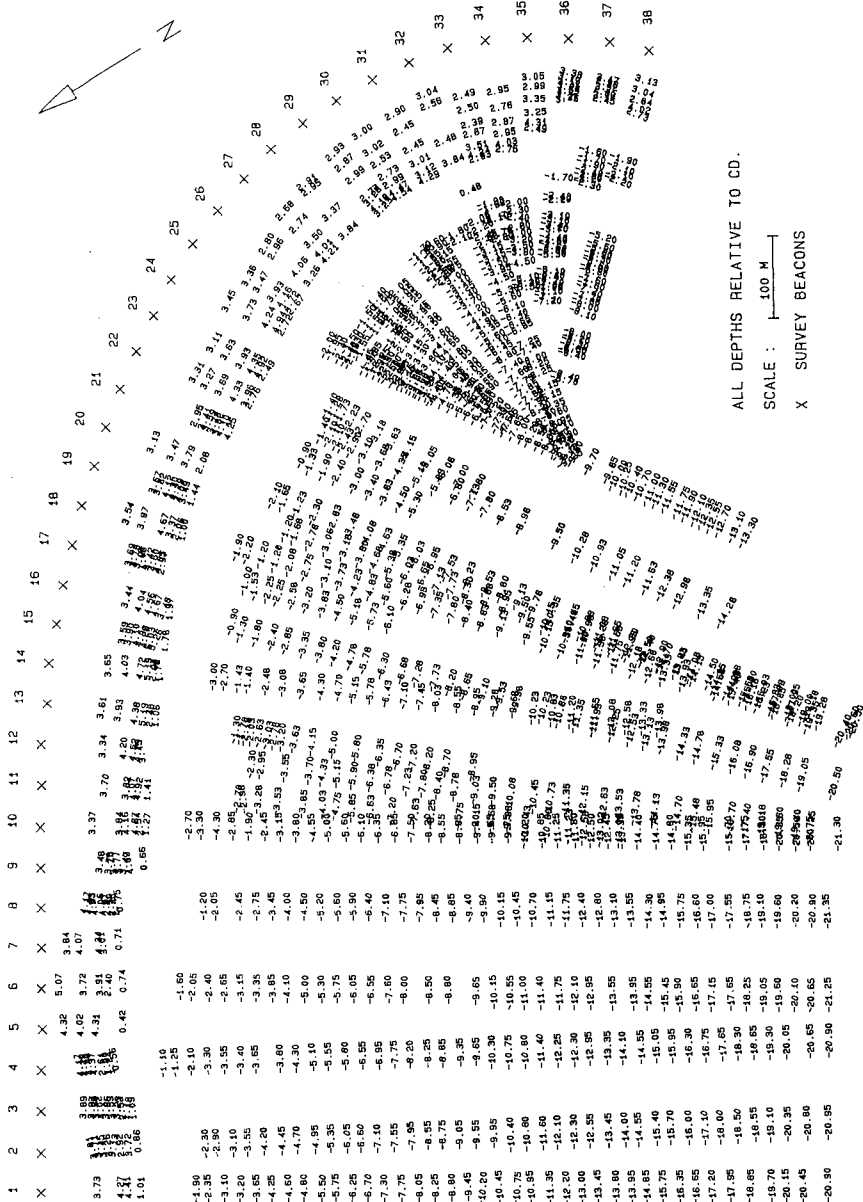


FIGURE 6 : HYDROGRAPHIC SURVEY OF 86-05-07

From this table it is clear that considerable volume changes (erosion and accretion) occurred. Statistical comparison of the last erosion rate, of -245 100 m³/year, with the previous rates indicates (at a 90 % confidence level) that the erosion rate increased significantly during the period November 1984 to May 1986. Although this rate is small in comparison with the total volume of sand placed to form the breakwater, this loss of sand may endanger the breakwater. It is, therefore, important to monitor the breakwater in future to establish whether this tendency continues. If so, it is important that remedial measures be undertaken.

Every effort should be made to minimise the gap between the future hydrographic and beach surveys because some of the large variation in the volume differences between surveys and possibly the accretion, can be attributed to this.

The beach profiles showed either erosion or remained basically stable. The most severe beach erosion occurred at profiles 2 and 36.

4. Wind

Based on hourly wind recordings over a 3-year period at nearby Elandspunt (see Figure 1 for the position of Elandspunt), the dominant wind directions were found to be SSW, SW, S and NNE. Calms occur on average 6,9 % of the time.

It was found that, because of the very limited availability of sand on the breakwater owing to stone and vegetation cover and because of short wind fetch lengths for the major wind directions, the effect of wind on the breakwater is negligible.

5. Wave Climate

For sediment transport computations, simultaneous recordings of wave height, wave period and wave direction are necessary. The only wave data sources that met this requirement, namely, clinometer (graded telescope) and VOS data (estimates from voluntary observing ships), were compared with other available measurements of wave characteristics (Waverider records). The clinometer data were found to be the better data source. Deep-sea clinometer wave directions were accepted unaltered while clinometer wave period and deep-sea wave heights were adjusted by means of exceedance curves to give 'equivalent' Waverider periods and deep-sea wave heights.

Figure 7 gives the details of the deep-sea wave climate. Combinations of deep-sea wave directions from SSE, S, SSW...NW and peak wave periods between 6,2 s and 23,8 s were compiled to serve as input for a wave refraction study.

This study was to transfer the deep-sea wave climate to shallow water at the spending beach breakwater. For this purpose extensive coverage of the irregular bathymetry of the area at and surrounding the spending beach breakwater was obtained from hydrographic maps. The bathymetry was then

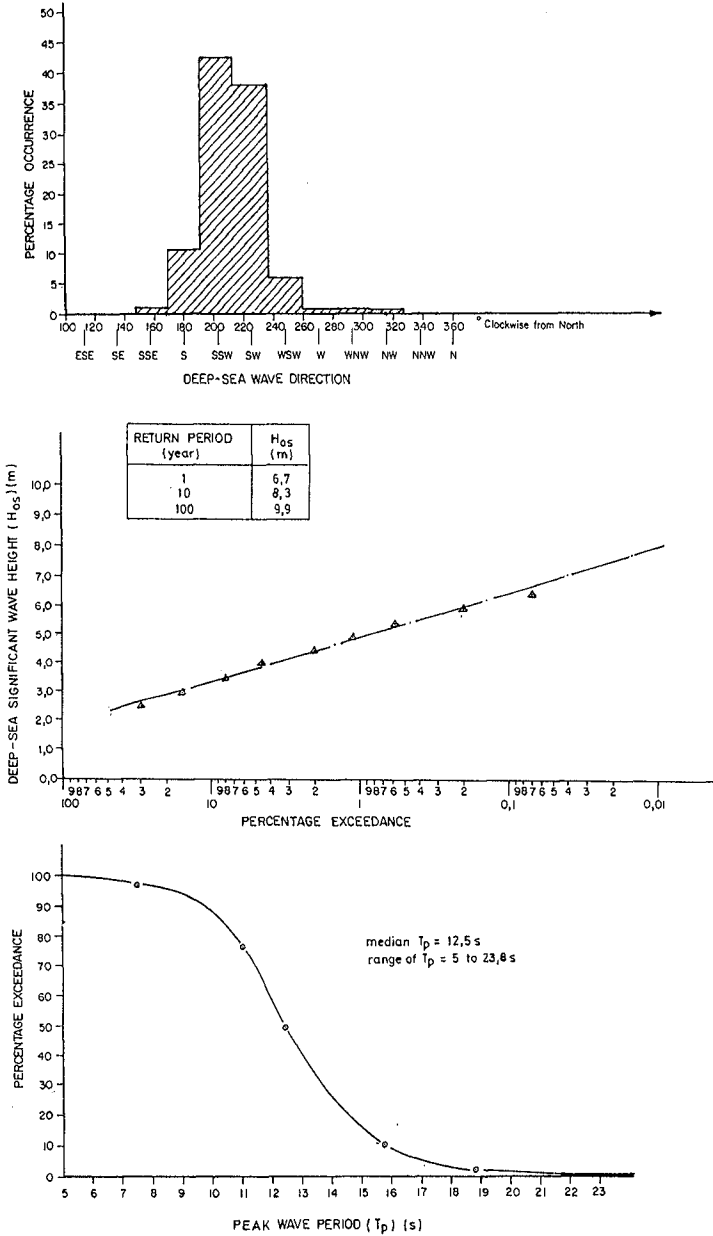


FIGURE 7 : DEEP-SEA WAVE CHARACTERISTICS

represented in eighteen model grids in which the grid squares became progressively smaller from deep to shallow water.

Refraction and shoaling of each of 37 recorded deep-sea wave conditions were done. Figure 8 shows a refraction diagram. For each deep-sea wave direction/wave period combination, the nearshore wave characteristics at the 3 m (to MSL) contour were compiled every 200 m along the breakwater.

6. Optimum Alignment of the Breakwater

6.1 General

The optimum alignment of the breakwater was calculated in two ways (Methods 1 and 2). A third and empirical method (Method 3) was used to check the results of Methods 1 and 2.

6.2 Method 1

The optimum alignment of the breakwater was calculated by determining at different points along the breakwater, what the alignment of the breakwater should be for each wave condition in order to make the longshore sediment transport potential due to obliquely incident waves zero. A weighted mean alignment of the breakwater at the different points was then computed. This is similar to the way in which the alignment of the breakwater was initially determined (Zwemmer and Van't Hoff, 1982).

The approach of Shore Protection Manual formula for longshore sediment transport given in US Army Corps of Engineers (1984) was applied. This formula is valid for non-cohesive sediment of grain sizes between 160 μm and 1 mm. Although it does not contain sediment grain size, it has been shown by Swart (1976) and Bruno *et al.* (1981) that the 'constant' in the formula is actually a function of the grain size. Therefore, although the breakwater consists predominantly of sand (but covered by a stone capping at and above the water line), the form of the formula can be regarded as being the same for coarser material even though the 'constant' will change. Therefore, if the wave incidence angle is zero, no longshore transport will occur, irrespective of the grain size.

The weighted mean values were used to plot, in Figure 9, the general alignment of the breakwater if it is to be left alone as well as the realignment needed for reconstruction.

The alignment calculated by Method 1 neglects the effects of secondary flows due to diffraction-type currents. This shortcoming is eliminated in Method 2.

6.3 Method 2

The basic procedure followed was the same as in the first method, except that the longshore current velocity in the middle of the surf zone, due to obliquely incident waves and a longshore variation in breaker wave height was set to zero and the corresponding orientation of the breakwater calculated. Because the longshore sediment transport is a function of the longshore current

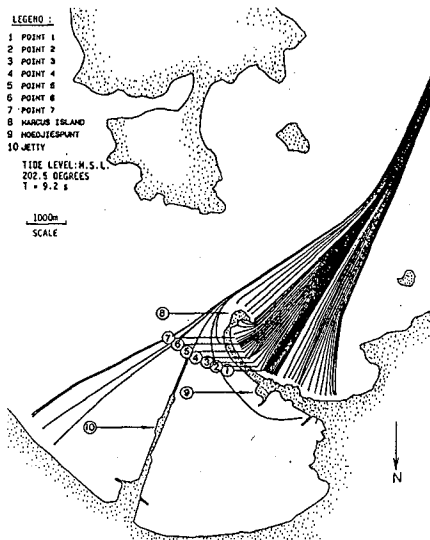


FIGURE 8 : WAVE REFRACTION DIAGRAM

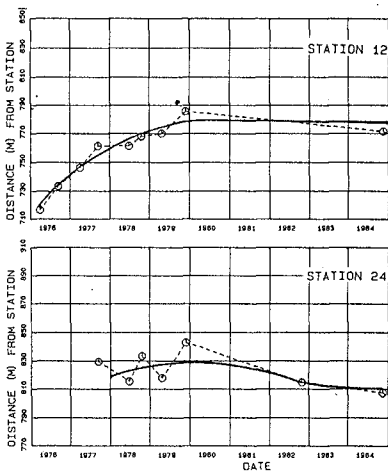


FIGURE 10 : EQUILIBRIUM TREND IN THE MOVEMENT OF THE -14m CD CONTOUR

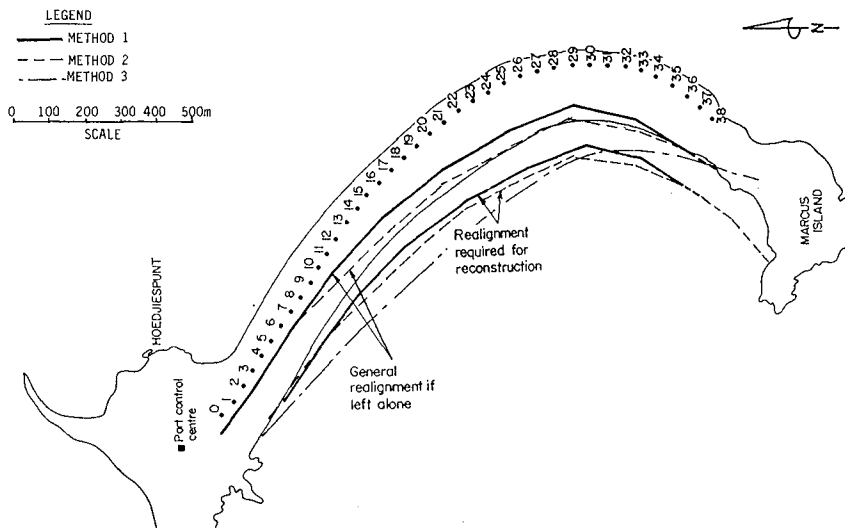


FIGURE 9 : OPTIMUM ALIGNMENT OF THE BREAKWATER

velocity, this means that the longshore transport will be zero if no longshore current is generated. Again, a weighted mean alignment was computed along the breakwater (at 21 points, 100 m apart).

A formula by Komar (1975) for the determination of the longshore current velocity (v) distribution across the surf zone due to obliquely incident waves and a longshore variation in breaker heights, was applied in the same way as in Schoonees (1986) to calculate the wave incidence angle at which $v = 0$ in the middle of the surf zone.

The results of this method are also illustrated in Figure 9.

6.4 Method 3

Building on the earlier work of amongst others, Yasso (1965), Silvester (1970) and Silvester and Ho (1972), Hsu *et al.* (1989) proposed new relationships to determine the equilibrium planform of bays.

The weighted mean wave approach angle at Marcus Island was calculated in order to apply the method. Figure 9 shows the predicted planform of the breakwater according to Method 3.

6.5 Discussion

Although the results of the first two methods differ somewhat, as can be expected, the same conclusions can be drawn from them. These are:

- (i) It is not feasible to realign the breakwater considering the volume of material (approximately 500 000 m³) that will be required. Furthermore, no suitable (medium to coarse) sand is available.
- (ii) If the breakwater is left indefinitely to realign itself, it may be in danger of eventually being breached.

The equilibrium planform of the breakwater according to Method 3 agrees reasonably well with the planform of the breakwater needed for reconstruction obtained from the other two methods.

7. Equilibrium Slope of the Breakwater

7.1 Method

The equilibrium beach and nearshore profile at a specific position along the breakwater was determined in the following way from the surveys available at the time of the analysis:

A series of plots of distance of the contour from the survey station versus time for different depths (+4 m, +2 m, 0 m,... -20 m CD) were drawn. An example of such a plot is included as Figure 10.

These plots were used to deduce the long-term (equilibrium) trend in the movement of the specific contour (Figure 10). In other words, the equilibrium distance of the specific contour from the station was obtained. By

plotting the depths of the contours versus these equilibrium distances, an equilibrium beach and nearshore profile was acquired.

Equilibrium profiles were determined opposite survey stations 2, 12 and 24 (see Figure 4 for the positions of these stations). These positions were chosen to be representative of the breakwater. The profiles are plotted in Figure 11.

7.2 Results

The predicted equilibrium slope at the three stations is virtually identical ($1/45$) and considerably flatter than the design slope of $1/35$. This explains why erosion occurs above approximately -4 m CD and accretion below this level.

Therefore, while the breakwater is realigning itself alongshore, sediment is being steadily moved in an offshore direction from the breakwater. Thus when the breakwater has reached its optimum alignment, it will recede slowly as a whole and may in time be in danger of being breached.

8. Remedial Measures

Using sand as a solution was not considered feasible for the following reasons:

- (i) A large volume (approximately $500\,000\text{ m}^3$) of sand would be needed for realignment. In addition, regular maintenance of the breakwater requiring about $50\,000\text{ m}^3/\text{year}$ of suitable sand (medium to coarse) would be needed.
- (ii) Suitable sand is not readily available. All available sources were utilised during the construction of the breakwater.
- (iii) Some sort of expensive toe protection at about -14 m CD is most probably necessary to prevent excessive sand losses to deep water.

It was therefore recommended that a suitable rock protection be provided along the spending beach breakwater.

Before rock can be placed as protection, the erosion areas (Figure 2) should be filled up with sand. This should be followed by a geo-textile on the sandy areas and a layer of 0.5 m of well-graded filter stone (2 kg to 5 kg) over the whole area to be treated. Rock protection using stone between 1 t and 6 t should be placed as conceptually shown in Figure 12. The foundation of geo-textile and filter stone should extend beyond the toe of the rock armouring to provide scour protection. About $50\,000\text{ m}^3$ of rock will be needed for the erosion areas and approximately $150\,000\text{ m}^3$ for the entire sand breakwater.

It was recommended to check and optimise the design of the rock armouring in a model study using random waves. Flume tests to this effect were subsequently carried out (CSIR, 1989). The results of this investigation, however, fall outside the scope of this paper.

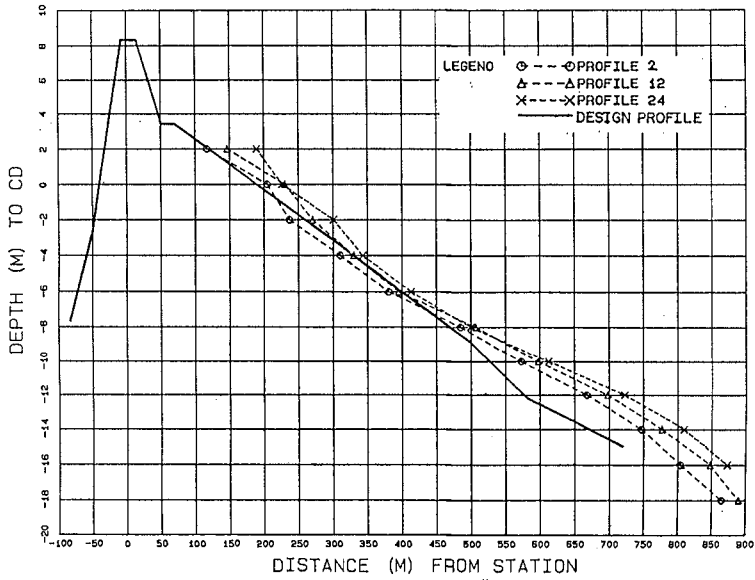


FIGURE 11 : EQUILIBRIUM PROFILES

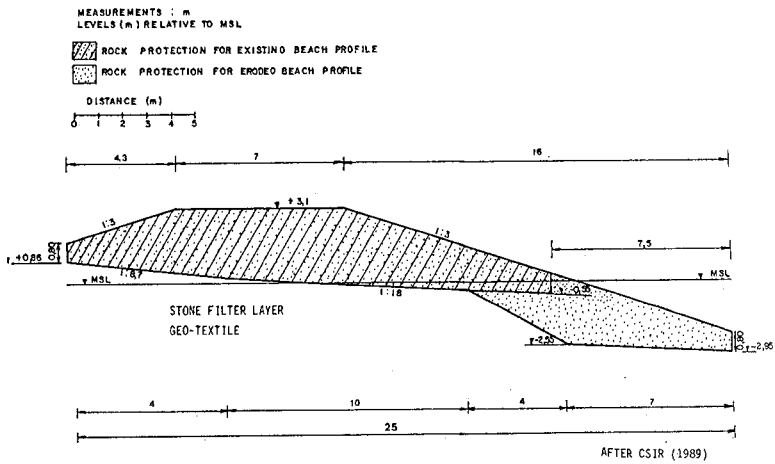


FIGURE 12 : CONCEPTUAL LAYOUT OF ROCK PROTECTION

It was also recommended that a hydrographic survey together with aerial photography be conducted annually and that beach profiles and beach photography be done more often to monitor the breakwater and the erosion areas. Particular attention should be given to obtain nearshore profile data in the surf zone.

References

- Bruno, R O, Dean, R G, Gable, C G and Walton, T L (1981). Longshore sand transport study at Channel Islands Harbor, California. *Technical Paper* No. 81-2, Coastal Engineering Research Center, US Army, Corps of Engineers, Fort Belvoir, Virginia, USA.
- CSIR (1985). A study of the stability of Saldanha spending beach breakwater. *CSIR Report C/SEA 8507*, National Research Institute for Oceanology, Stellenbosch, South Africa.
- CSIR (1989). Saldanha spending beach breakwater: model study of rock protection. *CSIR Report EMA-C 89120*, EMATEK, Stellenbosch, South Africa.
- Hsu, J R C, Silvester, R and Xia, Y-M (1989). Static equilibrium bays: new relationships. *ASCE, J. Waterway, Port, Coastal and Ocean Engineering*, Volume 115(3): 285-298.
- Komar, P D (1975). Nearshore currents: generation by obliquely incident waves and longshore variations in breaker height. *Proc. Symposium on Nearshore Sediment Dynamics* (Hail, J R and Carr, D (eds)), p 17-45, Wiley, London.
- Schoonees, J S (1986). Breaker wave characteristics and longshore sediment transport along a bay. *CSIR Research Report 570*, National Research Institute for Oceanology, Stellenbosch, South Africa.
- Silvester, R (1970). Growth of crenulate shaped bays to equilibrium. *ASCE, Journal of Waterways and Harbors Division*, Volume 96 (WW2): 275-287.
- Swart, D H (1976). Predictive equations regarding coastal transports. *15 International Conference on Coastal Engineering*, ASCE, Volume 2: 1113-1132, Honolulu, Hawaii, USA.
- US Army Corps of Engineers (1984). *Shore Protection Manual*, Volumes I and II. Coastal Engineering Research Center, Fort Belvoir, Virginia, USA.
- Yasso, W E (1965). Plan geometry of headland bay beaches. *Journal of Geology*, Volume 73: 702-714.
- Zwemmer, D and Van't Hoff, J (1982). Spending beach breakwater at Saldanha Bay. *18 International Conference on Coastal Engineering*, ASCE, Volume 2: 1248-1267, Cape Town.

Acknowledgement

The permission granted by Portnet to publish this paper is gratefully acknowledged.

CHAPTER 184

Numerical Modeling of the Dredged Spoil Disposal

Cao Zude¹ Wang Guifen²

Abstract

To calculate the sediment movement under waves and currents, a simulating system called CW system has been developed by the authors. It can determine the effect of the dredged spoil disposal.

1 Introduction

Under the interaction of the wind wave and the tidal current some fluid mud and sediment suspension caused by dredged spoil disposal transport and flow complicatedly. Its propotion varies with the hydragraphic conditions.

We have measured the movement of the fluid mud by using "Neutron activation" and have developed a series of 2-dimensional and 3-dimensional numerical models to simulate the movement of suspended load, the fluid mud and their transformation by using the moving ADI method (Chen and Cao, 1990)

By field data, spoil materials were casted into the sea area, 70~90% of which were fluid mud on the bottom and 10~30% suspended load.

The fluid mud flows along the bottom by gravity, wave and current. The suspended load moves with water. Both fluid mud and suspension deposit by and by. Some times in case of strong

1. Associate research fellow of coastal and estuary engineering, Tianjin Research Institute of Water Transport Engineering, Xingang, Tanggu, Tianjin, P.O.300456, China

2. Engineer of coastal and Estuary Engineering. Tianjin Research Institute of Water Transport Engineering, Xingang, Tanggu, Tianjin, P.O.300456, China

wind-wave the fluid mud becomes suspended. When the sea is calm the suspended load turns into the fluid mud.

The process is shown in Fig.1 as follows.

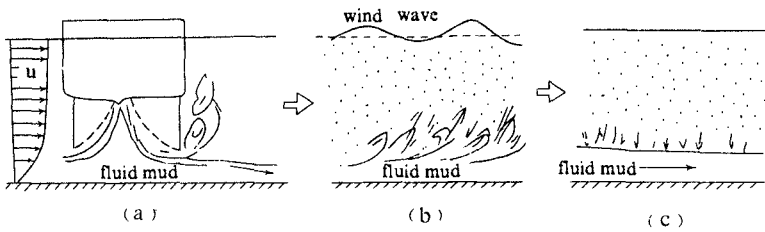


Fig. 1 Movement of dredged materials

Numerical modelling of the processes are shown in the Fig.1 of appendices.

2 Basic differential equations

2-1 Tidal current

2-1-1 Two dimensional equations (Cao et al.,1989)

In case of no wind

$$\frac{\partial \zeta}{\partial t} + \frac{\partial}{\partial x} (uh) + \frac{\partial}{\partial y} (vh) = 0$$

$$\frac{\partial u}{\partial t} + u \frac{\partial u}{\partial x} + v \frac{\partial u}{\partial y} + g \frac{\partial \zeta}{\partial x} + \frac{g u \sqrt{u^2 + v^2}}{c^2 h} - fv = A \Delta u$$

$$\frac{\partial v}{\partial t} + v \frac{\partial v}{\partial y} + u \frac{\partial v}{\partial x} + g \frac{\partial \zeta}{\partial y} + \frac{g v \sqrt{u^2 + v^2}}{c^2 h} + fu = A \Delta v$$

In case of wind-wave

$$\frac{\partial \zeta}{\partial t} + \frac{\partial}{\partial x} (uh) + \frac{\partial}{\partial y} (vh) = 0$$

$$\frac{\partial u}{\partial t} + u \frac{\partial u}{\partial x} + v \frac{\partial u}{\partial y} + g \frac{\partial \zeta}{\partial x} - fv - \frac{c_s \rho_a}{h \rho} |W - U| (\omega_x - u)$$

$$+ \frac{1}{h} \frac{\tau_x}{\rho} + \frac{1}{\rho h} \left(\frac{\partial s_{xx}}{\partial x} + \frac{\partial s_{xy}}{\partial y} \right) = A \Delta u$$

$$\frac{\partial v}{\partial t} + u \frac{\partial v}{\partial x} + v \frac{\partial v}{\partial y} + g \frac{\partial \zeta}{\partial x} + f u - \frac{c_s \rho_a}{\rho h} |W - U| (\omega_y - v) \\ + \frac{\tau_y}{\rho h} + \frac{1}{\rho h} \left(\frac{\partial s_{yx}}{\partial x} + \frac{\partial s_{yy}}{\partial y} \right) = A \Delta v$$

2-1-2 Three dimensional equations (Cao et al., 1988)

$$\frac{\partial \zeta_k}{\partial t} - \frac{\partial \zeta_{k-1}}{\partial t} + \frac{\partial (u_k h_k)}{\partial x} + \frac{\partial (v_k h_k)}{\partial y} = 0$$

$$\frac{\partial h_k}{\partial t} = - \frac{\partial u_k h_k}{\partial x} - \frac{\partial v_k h_k}{\partial y}$$

$$\frac{\partial u_k}{\partial t} + u_k \frac{\partial u_k}{\partial x} + v_k \frac{\partial u_k}{\partial y} + \omega_k \frac{\partial u_k}{\partial z} + g \frac{\partial (\zeta_k - \zeta_{k-1})}{\partial x} - f v_k + \frac{1}{\rho h_k}$$

$$\times (\tau_{xk-1} - \tau_{xk}) = A_x \Delta u_k$$

$$\frac{\partial v_k}{\partial t} + u_k \frac{\partial v_k}{\partial x} + v_k \frac{\partial v_k}{\partial y} + \omega_k \frac{\partial v_k}{\partial z} + g \frac{\partial (\zeta_k - \zeta_{k-1})}{\partial y} + f u_k$$

$$+ \frac{1}{\rho h_k} (\tau_{yk-1} - \tau_{yk}) = A_y \Delta v_k$$

2-2 Wave

The wave forecast and refraction are used in the CW system

2-3 The dispersion equations of suspended load

In case of 2-D (Cao et al., 1989)

$$\frac{\partial}{\partial t} (sh) + \frac{\partial}{\partial x} (suh) + \frac{\partial}{\partial y} (svh) + F_s = \frac{\partial}{\partial x} \left(D_x h \frac{\partial s}{\partial y} \right)$$

$$+ \frac{\partial}{\partial y} \left(D_y h \frac{\partial s}{\partial x} \right)$$

In case of 3-D (Cao et al., 1988)

$$\frac{\partial}{\partial t} (S_k h_k) + \frac{\partial}{\partial x} (u_k S_k h_k) + \frac{\partial}{\partial y} (v_k S_k h_k) + (\omega - \omega_s) \times$$

$$s \left| \frac{z_k}{z_{k-1}} - \varepsilon_z \frac{\partial s}{\partial z} \right| \frac{z_k}{z_{k-1}} = \frac{\partial}{\partial x} (k_x h_k \frac{\partial S_k}{\partial x}) + \frac{\partial}{\partial y} (k_y h_k \frac{\partial S_k}{\partial y})$$

2-4 The fluid mud movement equations. (Cao et al., 1988, 1989).

$$\frac{\partial h_m}{\partial t} + \frac{\partial}{\partial x} (u_m h_m) + \frac{\partial}{\partial y} (v_m h_m) + F_s + F_b + F_c = 0$$

$$\frac{\partial u_m}{\partial t} + u_m \frac{\partial u_m}{\partial x} + v_m \frac{\partial u_m}{\partial y} + g \frac{\rho}{\rho_m} \frac{\partial \zeta}{\partial x} + g \frac{\Delta \rho}{\rho_m} \frac{\partial \zeta_m}{\partial x} +$$

$$\frac{1}{\rho_m h_m} (\tau_{bx} + \tau_{Bx} - \tau_x) = D_m \Delta u_m$$

$$\frac{\partial v_m}{\partial t} + u_m \frac{\partial v_m}{\partial x} + v_m \frac{\partial v_m}{\partial y} + g \frac{\rho}{\rho_m} \frac{\partial \zeta}{\partial y} + g \frac{\Delta \rho}{\rho_m} \frac{\partial \zeta_m}{\partial y} +$$

$$\frac{1}{\rho_m h_m} (\tau_{by} + \tau_{By} - \tau_y) = D_m \Delta v_m$$

2-5 Morphology

$$\frac{\partial \zeta_b}{\partial t} = F_s / \gamma_c$$

where ζ is the vertical displacement between the water level and the still water level; u, v, w are respectively component velocities in x, y and z directions; h —the water depth; f —Coriolis acceleration; H —the wave height; L —the wave length; C —the wave velocity; S —the concentration of suspended load; F_s —the Function of siltation and deposition; S_{xx}, S_{xy}, S_{yx} and S_{yy} —the radiational stress; τ_b —the shear stress on bottom; τ_ω —the shear stress on surface by wind; τ_B —Bingham stress; and footnote "K"—the K-layer on 3-D; footnote "m"—fluid mud; footnote "b"—sea bottom.

These differential equations mentioned above can be solved by the determined boundary conditions and initial conditions.

3 Applications (for example)

3-1 Computational regions

Based on these differential equations mentioned above the simulating system called CW system has been developed by the writers in Tianjin Research Institute of Water Transport Engineering, China.

The CW System has been used to study the effects of the dredged spoil disposal on the environment and siltation in Tianjin Port.

As there is lack of boundary condition required in numerical simulations in Tianjin Port Area, 4 calculational regions with different ranges are set up by using the method of nesting small model in a large one. Bohai Sea is the first calculational region; Bohaiwan Bay—the second; The Tianjin Harbour Area—the third and the spoil ground—the fourth. These four regions are nested with each other.

The calculated results of the former regions provide the boundary conditions for the latter. The open boundary conditions of the first region are controlled by M_2 , S_2 , K_1 , O_1 component tides.

Table 1 characteristics of calculation regions

no.	1	2	3	4
name	Bohai Sea	Bohai Bay	north part of Bohai Bay	dredged spoil ground
area(km ²)	168,000	10,800	5,400	25
simulation method	moving ADI method	moving ADI method	moving ADI method	explicit method
dimension	2	2	2	3
space step				
Δx (m)	10,000	5,000	500	500
Δy (m)	10,000	5,000	500	500
Δz (m)				2
time step (s)	1,800	900	90	90

As contracted by the storage capacity, two dimensional modellings are used for the former three regions by means of "moving ADI method". and three dimensional modelling is used for the fourth region with explicit method. The "moving ADI method"

not only remains ADI method's characteristics but also has following advantages—fast in convergence; high in stability; simple in calculation and convenient in programming (Wang, 1989).

The pictures of four calculational regions mentioned above are shown in Fig.2 and the technical functions of these regions are listed in table 1.

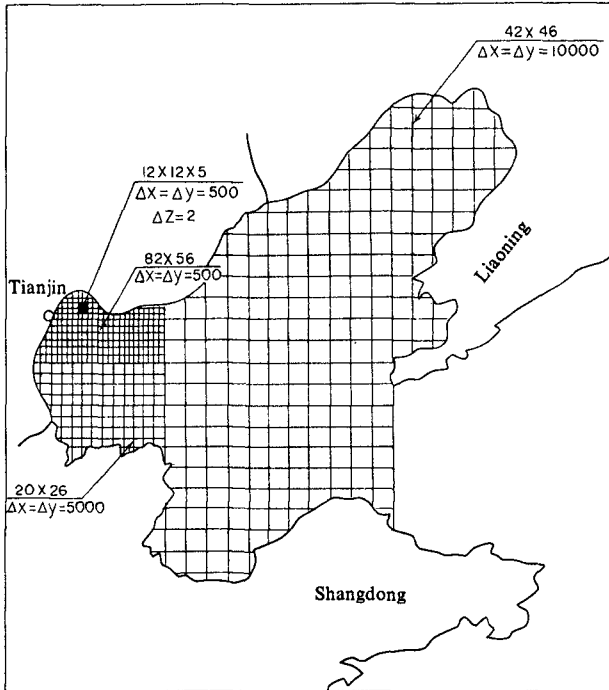


Fig. 2 Diagram of each calculation network

3-2 Verification

Five aspects are verified for these numerical modelling. The computational results agree well with the field data as follows.

3-2-1 Water level

The water level process at the center of spoil ground in spring tide on Aug. 1st 1988 is shown in Fig 3.

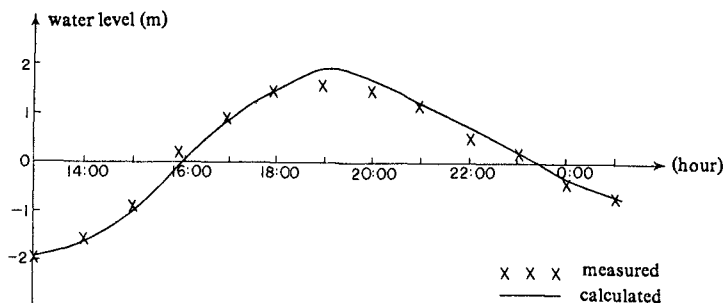


Fig. 3 Verification of water level process of spoil ground

3-2-2 Velocity

The velocity processes of five stations on the spoil ground during spring tide on Aug. 1st of 1988 are shown in Fig.4.

The velocity processes of the four stations in both side of the channel during spring tide on Aug.1st , 1988 are shown in Fig. 5

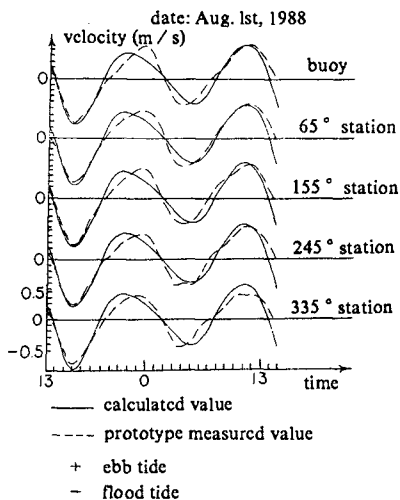


Fig. 4 Verification of current velocity process of spoil ground

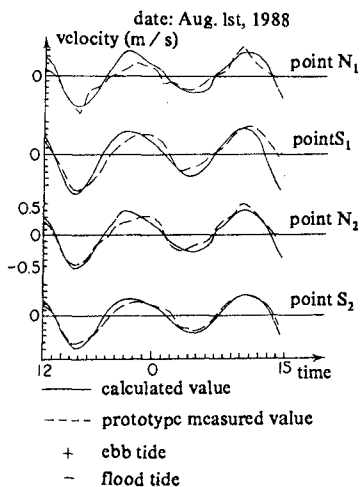


Fig. 5 Verification of current velocity of measuring stations to the south and north of the channel

The velocity distributions of velocity on the Aug. 1st 1988 in the center of the spoil ground at different time are shown in Fig. 6.

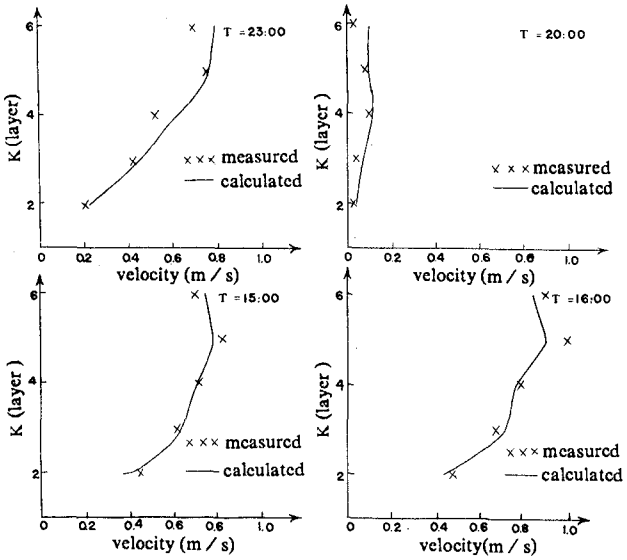


Fig. 6 Vertical distribution of current velocity of spoil ground

3-2-3 Tracing floats

Tracing floats from the center of the spoil ground at the flood tide and ebb tide are shown in Fig.7.

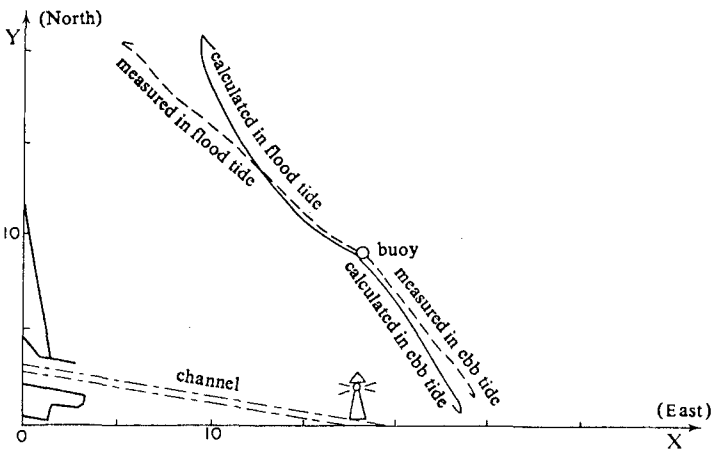


Fig. 7 Diagram of flow tracks of flood tide and ebb tide

3-2-4 Concentration of suspended load

The vertical distributions of concentration of suspended load in the center of the spoil ground at different time are shown in Fig. 8.

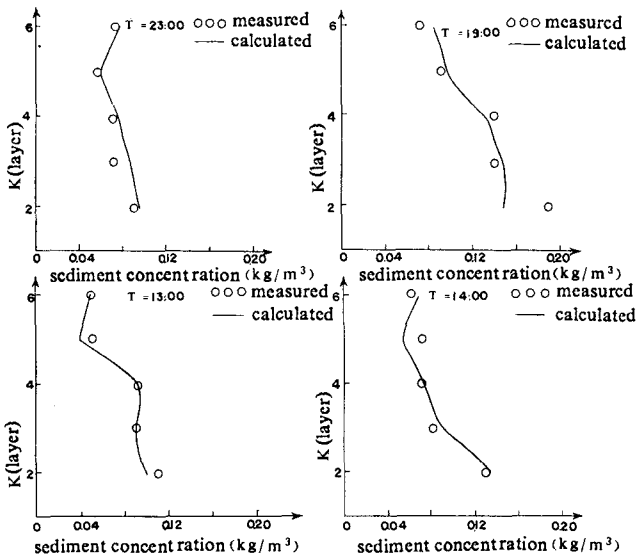


Fig. 8 Verification of vertical distribution of suspended sediment concentration at different times

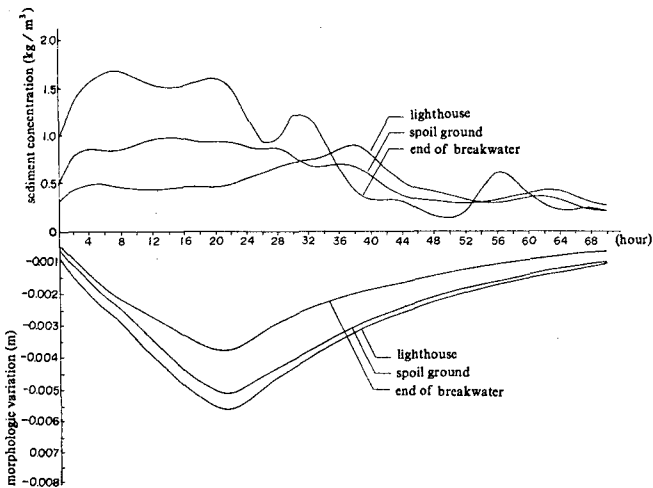


Fig. 9 Process curves of sediment concentration and morphologic erosion

3-2-5 Morphologic processes.

Sediment concentration and morphologic variation of 3 locations (the entrance of Tianjin port, near the lighthouse and the center of spoil ground) under the action of the northeast gale are shown in Fig 9.

The simulated results are in good agreement with the measured in field.

3-3 Simulation of dredged materials

The dredged materials are disposed to the spoil ground with the self-propelled trailing suction hopper dredger as follows:

1. Disposing one boat of spoil materials;
2. Disposing a boat of spoil materials continuously at the interval of every two hours a week.
3. Simulating the effects of wind-wave process on the movement of spoil materials. The following simulated results are obtained:

The variation suspension and fluid mud under the effect of the northeast gale are shown in Fig 2 and 3 of appendices.

It is inticated from Fig 2~3 of appendices that the dredged materials on the existed spoil ground have no direct effect on the siltation of Tianjin Port.

4 Conclutions

By comparing the simulated value and the field data we believe the CW system is an effective tool to study the movement of the spoil disposal

Reference

- (1)Cao Zude, Wang Guifen, Zhang Yingping, 1988, Three Dimensional Numerical Modelling of Tidal Current and its Applications, Rep. of TRIWTE No. 8811.
- (2) Cao Zude, Wang Guifen, Xu Hongming, Zhang Yinping, 1989, Numerical Simulation of Spoil Disposal on the Spoil Ground, Rep. of TRIWTE No. 8909.
- (3) Chen Shengliang, Cao Zude, 1990, Effect of Dredged Spoil Materials on Siltation of Tianjin Port, Rep of TRIWTE No. 8912,
- (4)Wan Guifen, 1989, A New Calculation Method—Moving ADI Method, Rep of TRIWTE No. 8911.

Appendices

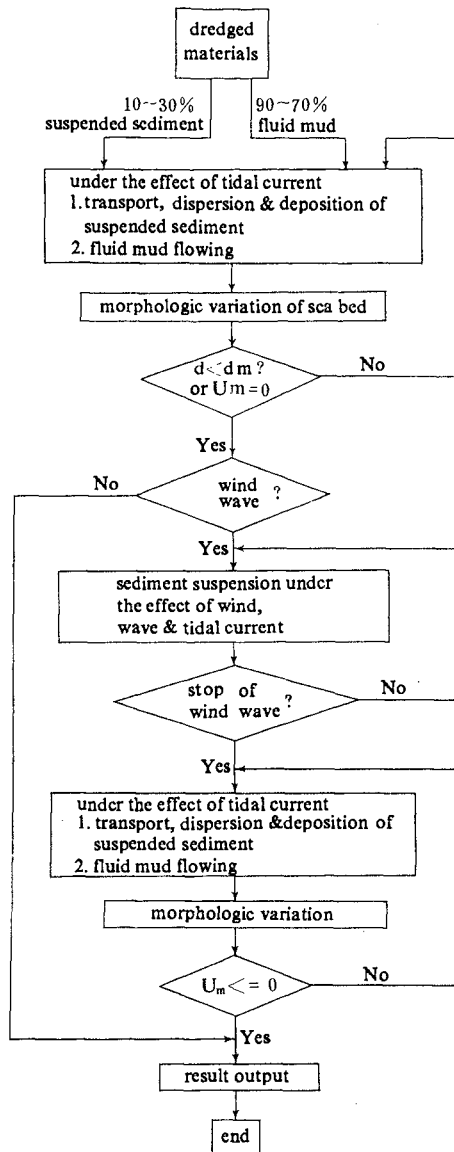


Fig. 1 Diagram of numerical model of dredged materials

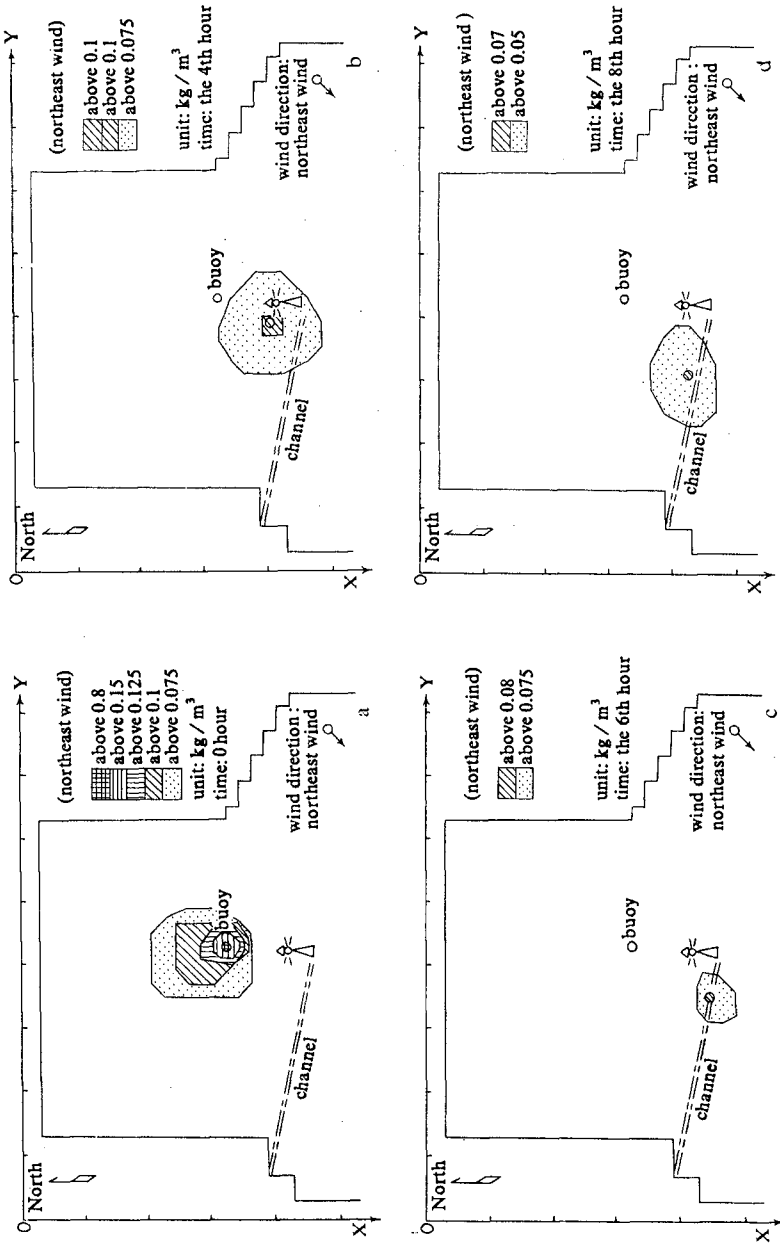


Fig. 2 Diagram of suspended sediment distribution processes under the effect of northeast wind

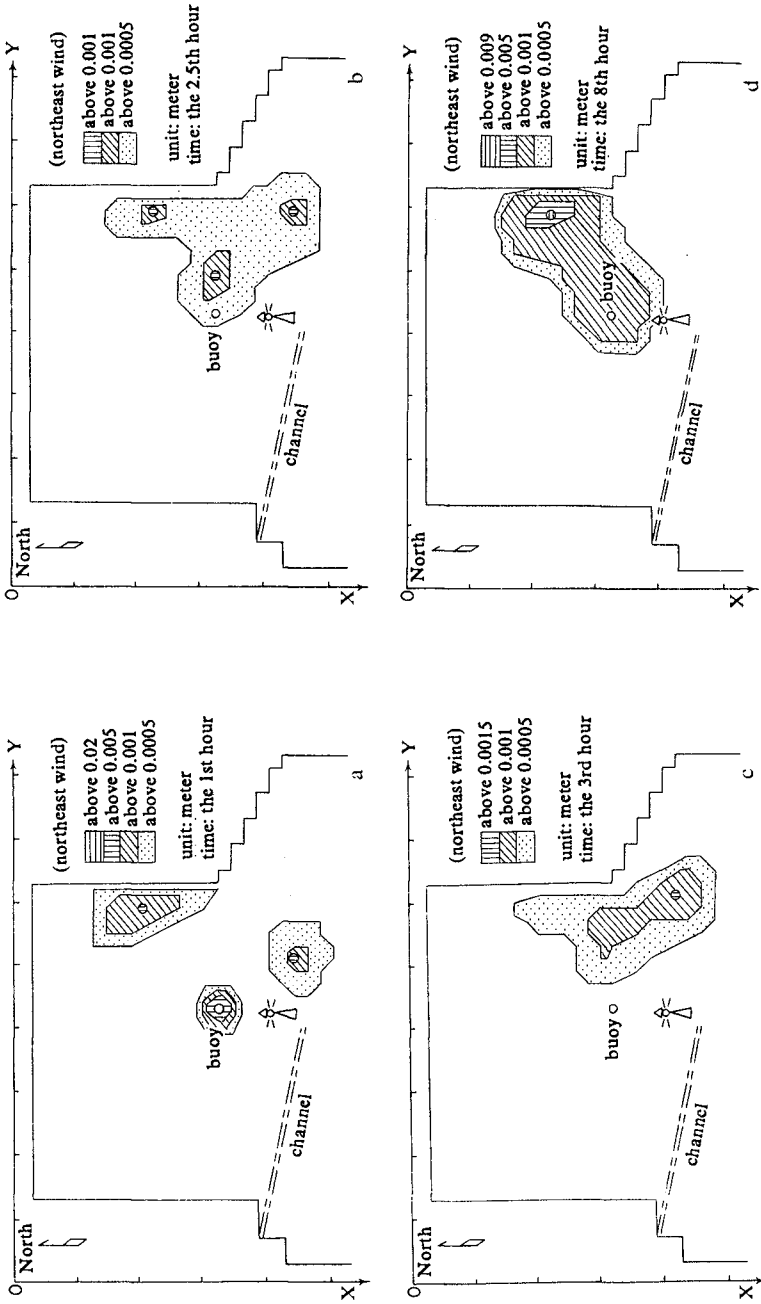


Fig. 3 Diagram of fluid mud distribution processes due to northeast wind

CHAPTER 185

MODELING OF WAVE-CURRENT INTERACTION AND BEACH CHANGE

Susumu OHNAKA* and Akira WATANABE**

ABSTRACT

This paper presents a mathematical model of waves, currents and beach change with wave-current interaction. The wave model is based on the time-dependent mild-slope equations extended to a wave-current coexisting field, and is applicable to the computation of wave deformation due to combined effects of shoaling, refraction, diffraction, reflection, breaking and currents. Some examples of numerical computation are shown, and effects of the wave-current interaction on the nearshore waves, currents and beach evolution is discussed. In addition, a simple treatment of obliquely incident wave condition as well as improvement of sediment transport rate formulas are presented.

1. INTRODUCTION

Not a few mathematical models of nearshore processes have recently been developed and applied to the prediction of nearshore waves, currents and beach evolution. In most models, however, effects of the interaction between waves and currents are neglected. In actuality nearshore waves induce currents through radiation stresses, and resultant currents conversely affect the wave field; namely, the wave-current interaction always takes place to a greater or less extent. Under certain conditions, it will become very important to take the interaction effects into consideration for an accurate prediction of nearshore waves and currents as well as resultant sediment

* Research Engineer, Technical Research Institute, Toa Corporation, 1-3, Anzencho, Tsurumi-ku, Yokohama, 230 Japan

** Professor, Department of Civil Engineering, Univ. of Tokyo, Hongo-7, Bunkyo-ku, Tokyo, 113 Japan

transport and beach change.

In order to incorporate the wave-current interaction into nearshore process models, the wave deformation due to currents should be included in the computation of waves. For a wave field coexisting with a varying current in the water of non-uniform depth, a few kinds of wave models have been proposed (Booij, 1981; Liu, 1983; Kirby, 1984). These models are based on elliptic-type partial differential equations, which are in general rather difficult to solve numerically. Hence these equations are sometimes approximated by parabolic equations, but then they become inapplicable to a wave field including significant reflection from structures. On the other hand, Ohnaka et al. (1988) have proposed another kind of numerical computation model for a nearshore wave field with a varying current and depth. Their model employs time-dependent mild-slope equations, and is applicable to the computation of wave deformation due to combined effects of shoaling, refraction, diffraction, reflection and breaking as well as wave-current interaction.

In the present study, this wave model is utilized as a part of a mathematical model of nearshore processes, and the effects of the wave-current interaction on the nearshore waves, currents and beach change are discussed on the basis of the results of numerical computation for two typical cases. Treatment of obliquely incident waves and improvement of sediment transport formulas are also presented.

2. BASIC EQUATIONS AND METHODS IN THE MODEL

2.1 Wave Computation

Ohnaka et al. (1988) have proposed time-dependent mild-slope equations for a wave-current coexisting field, which are applicable to the computation of wave deformation due to combined effects of the shoaling, refraction, diffraction, reflection and breaking as well as the wave-current interaction. The equations have been derived by separating the mild-slope equation for waves coexisting with a current proposed by Kirby (1984) into the following two equations expresses in terms of the water surface elevation ζ and the depth-integrated flow rate vector Q :

$$m \cdot (\partial \zeta / \partial t) + \nabla \cdot (U \zeta) + \nabla \cdot (n Q) = 0 \quad (1)$$

$$\partial Q / \partial t + \omega C^2 \nabla (\zeta / \sigma) + f_b Q = 0 \quad (2)$$

$$m = 1 + (\sigma / \omega)(n - 1), \quad n = C_s / C \quad (3)$$

where t is the time, ∇ is the horizontal gradient operator, C and C_g are the phase and group velocity vectors and U is the ambient current velocity vector. The last term in Eq. (2) is the energy dissipation term, where f_D is the energy dissipation coefficient to be defined later; this term has been added in order to deal with the wave decay and recovery after breaking. The apparent angular frequency ω is defined by the following dispersion relation for a wave-current coexisting field:

$$\omega = \sigma + k \cdot U, \quad \sigma = g k \tanh k h \quad (4)$$

where σ is the intrinsic angular frequency, k is the wave number vector, h is the water depth, and g is the acceleration due to gravity. If the ambient current velocity vector U is set to be zero, Eqs. (1) and (2) reduce to the original time-dependent mild-slope equations proposed by Watanabe and Maruyama (1986).

We need a value of the wave angle at every point to solve the above dispersion relation, Eq. (4). Since this wave model is based on the time-dependent equations, we can calculate the wave angle from values of ζ and Q which have already been computed in the previous cycle over one wave period.

To determine the location of wave breaking, we adopted the breaker index for compound waves proposed by Watanabe et al. (1984), which is given by the ratio of the orbital velocity at the wave crest to the phase velocity as a function of the deepwater wave steepness and the local bottom slope. This breaker index will be applicable to the wave-current coexisting field by using values relative to the current for both the orbital velocity and the phase velocity.

As for the energy dissipation coefficient f_D , Eq. (5) proposed by Watanabe and Dibajnia (1988), which can express not only the wave decay but also the wave recovery in the surf zone.

$$f_D = \alpha_D \tan \beta \sqrt{\frac{g}{h}} \sqrt{\frac{Q_m - Q_r}{Q_r - Q_s}} \quad (5)$$

where $\tan \beta$ is a representative bottom slope around a breaking point, α_D is a nondimensional coefficient whose value is 2.5, Q_m is the amplitude of Q , Q_s is the flow rate amplitude of breaking waves on a uniform slope, and Q_r is that of recovering waves in a constant depth region. The quantities Q_s and Q_r are expressed as

$$Q_s = \gamma_s c n, \quad Q_r = \gamma_r c h \quad (6)$$

According to experimental data, the coefficients γ_s and γ_r are given by

$$\gamma_s = 0.4(0.57 + 5.3 \tan \beta), \quad \gamma_r = 0.4(a/h)_b \quad (7)$$

where $(a/h)_b$ is the ratio of the wave amplitude to the water depth at a breaking point.

It has been demonstrated by Ohnaka et al. (1988) that the above breaker index and the energy dissipation factor are applicable to the computation of cross-shore distribution of wave height in a wave-current coexisting field with sufficient accuracy.

2.2 Current Computation

The current field is calculated by commonly used depth-average equations of the mean flow as follows:

$$\frac{\partial \bar{\zeta}}{\partial t} + \frac{\partial U(h + \bar{\zeta})}{\partial x} + \frac{\partial V(h + \bar{\zeta})}{\partial y} = 0 \quad (8)$$

$$\frac{\partial U}{\partial t} + U \frac{\partial U}{\partial x} + V \frac{\partial U}{\partial y} + g \frac{\partial \bar{\zeta}}{\partial x} + R_x + F_x - M_x = 0 \quad (9)$$

$$\frac{\partial V}{\partial t} + U \frac{\partial V}{\partial x} + V \frac{\partial V}{\partial y} + g \frac{\partial \bar{\zeta}}{\partial y} + R_y + F_y - M_y = 0 \quad (10)$$

where (x, y) are Cartesian coordinates in a horizontal plane, (U, V) are the corresponding velocity components of the mean flow, $\bar{\zeta}$ is the elevation of the mean water surface measured from the still water level, (R_x, R_y) are the radiation stress terms, (F_x, F_y) are the bottom friction terms, and (M_x, M_y) are the lateral mixing terms.

In order to treat the wave-current interaction, alternate computations of waves and of currents are necessary. An efficient iteration scheme is required so as to obtain the convergence of solutions in a computation time as short as possible. For this, no-current condition is assumed in the first step of wave computation as shown in Fig. 1. Then reduced values of radiation stresses R_1' are used in the first cycle of current computation, because if the actual values of radiation stresses R_1 calculated from the wave solutions are adopted, a large number of iterations are required to attain the convergence. Waves in the next step are calculated using the resultant reduced current velocity U_1 . The reduction rate of radiation stresses is

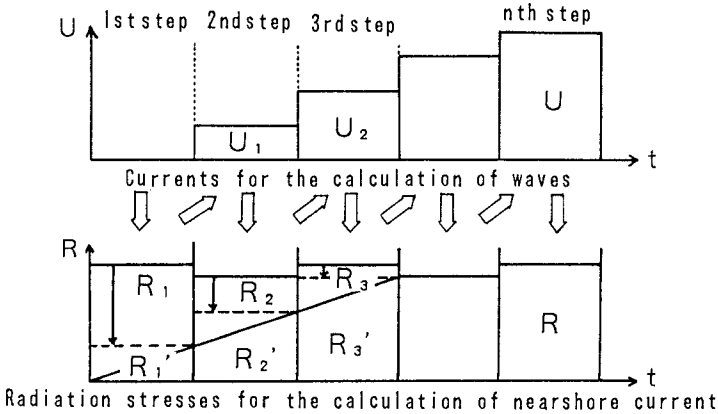


Fig. 1 Iteration of computations for waves and currents.

gradually decreased for every step, and finally full values of the radiation stresses and resultant currents are adopted for the calculation of currents and of waves, respectively.

2.3 IMPROVEMENT OF FORMULAS FOR SEDIMENT TRANSPORT RATES

Watanabe et al. (1986) proposed formulas for sediment transport rates under combined action of waves and currents on the basis of the power model concept. In their formulas the sediment transport rates are treated as summation of those due to waves q_w and due to currents q_c , which are expressed, respectively, by

$$q_w = A_w (\tau_b - \tau_{cr}) F \hat{u}_b / (\rho g) \tag{11}$$

$$q_c = A_c (\tau_b - \tau_{cr}) U / (\rho g) \tag{12}$$

where A_w and A_c are nondimensional coefficients, values of which should be empirically determined, τ_b is the maximum value of the bottom shear stress in a wave-current coexisting system, τ_{cr} is the critical shear stress for the onset of general movement of sediment grains, \hat{u}_b is the amplitude of the near-bottom wave orbital velocity vector, ρ is the density of water, and F_D is the net transport direction function. The bottom shear stress τ_b for a wave-current coexisting system is evaluated by the friction law proposed by Tanaka and Shuto (1981). Since this friction law is based on the bottom boundary layer theory, its applicability to the surf zone, where turbulence due to wave breaking is

predominant, is questionable. In the present model, therefore, the effects of the breaker-induced turbulence are incorporated in addition to the bottom shear stress as sediment-entraining forces in the surf zone. Namely the improved formulas for sediment transport rates are expressed as follows:

$$q_w = \{A_w(\tau_b - \tau_{cr}) + A_{wb}\tau_t\} F_D \hat{u}_b / (\rho g) \quad (13)$$

$$q_c = \{A_c(\tau_b - \tau_{cr}) + A_{cb}\tau_t\} U / (\rho g) \quad (14)$$

where τ_t is the breaker-induced turbulent stress, and A_{wb} and A_{cb} are nondimensional coefficients. The magnitude of τ_t is evaluated from the rate of energy dissipation by the following formula based on a dimensional analysis and experimental data:

$$\tau_t = \rho^{1/3} (n f_D E)^{2/3} \quad (15)$$

where $n f_D E$ is the breaker-induced energy dissipation rate per unit area and time.

To examine the applicability of these formulas, numerical computation has been conducted for the cross-shore sediment transport rates on a beach with initially uniform slope of 1/20. Figure 2 shows the comparisons between the computation and measurements of cross-shore distributions of the transport rates. The upper figure is for the case of offshore transport, while the lower is for that of onshore transport. The dash-dot lines

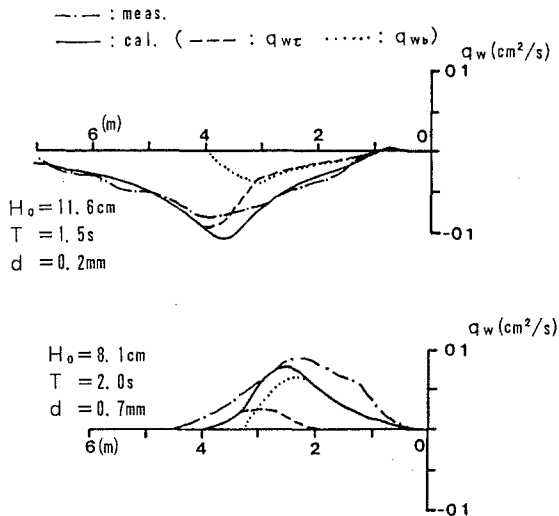


Fig. 2 Cross-shore distributions of transport rates.

show the measured transport rates and solid lines indicate the calculated ones. The component due to the bottom shear stress q_{wt} and that due to the breaker-induced stress q_{wb} are shown by the dash and the dot lines, respectively. Computed transport rates agree fairly well with the measured ones.

The change in local bottom elevation, z_b is calculated from the spatial distribution of the sediment transport rates by solving the following equation for the conservation of sediment volume:

$$\frac{\partial z_b}{\partial t} = - \frac{\partial q_x'}{\partial x} - \frac{\partial q_y'}{\partial y} \quad (16)$$

$$q = q_w + q_c = (q_x, q_y)$$

where (q_x', q_y') are the components of the transport rates in the x- and y-directions corrected in order to include the bottom slope effect, and are given by

$$q_x' = q_x - \varepsilon_s |q_x| \frac{\partial z_b}{\partial t}, \quad q_y' = q_y - \varepsilon_s |q_y| \frac{\partial z_b}{\partial t} \quad (17)$$

where ε_s is the dimensionless coefficient of the order of unity.

3. NUMERICAL COMPUTATION METHOD FOR WAVES

Equations (1) and (2) are solved by using a finite difference method. For the discretization of the convection term due to mean flow in Eq. (1), the Alternating Direction Explicit (A. D. E.) scheme is adopted in order to solve explicitly without numerical diffusion as follows:

$$\left(\frac{\partial (U \zeta)}{\partial x} \right)_{\text{point}=i} = \frac{U_{i+1/2} \zeta_{i+1/2}^{j+1/2} - U_{i-1/2} \zeta_{i-1/2}^{j+1/2}}{\Delta x} \quad (18)$$

$$\zeta_{i+1/2}^{j+1/2} = 0.5(\zeta_i^j + \zeta_{i+1}^j), \quad \zeta_{i-1/2}^{j+1/2} = 0.5(\zeta_i^j + \zeta_{i-1}^j)$$

Namely, as for ζ at a point (i-1) which is needed for the discretization of the convection term at a point (i), its values at a time-step (j) are successively replaced with values at a time-step (j+1) calculated just before.

Now let us consider boundary conditions in the wave computation. The boundary conditions must be imposed on all the boundaries surrounding the computation region: namely, the offshore open boundary, shoreline boundary,

and two side boundaries.

Waves on the offshore open boundary are expressed as the superposition of the incident waves ζ_I and the outgoing waves ζ_R as shown in Eq. (19).

$$\begin{aligned}\zeta'(x_0, y_0) &= \zeta_I'(x_0, y_0) + \zeta_R'(x_0, y_0) \\ \zeta_I'(x_0, y_0) &= a_I \sin(k x_0 \cos \theta_I + k y_0 \sin \theta_I - \sigma t) \\ \zeta_R'(x_0, y_0) &= \zeta'^{-\tau}(x_0, y_0) \\ &\quad - a_I \sin \{ (k(x_0 + \Delta x) \cos \theta_I + k y_0 \sin \theta_I - \sigma(t - \tau))\}\end{aligned}\tag{19}$$

where a_I is the incident wave amplitude, Δx is the grid length normal to the boundary, and the subscript 0 denotes quantities at the boundary. The time shift τ is defined by

$$\tau = \Delta x \cos \theta_n / C\tag{20}$$

where θ_n is the direction angle of the outgoing wave component measured from the normal line to the boundary.

The shoreline is treated as a moving boundary to include the change in its location caused by the change in the mean water elevation due to wave setup, and ζ is kept equal to 0 on this moving shoreline boundary.

In case of obliquely incident waves, one of the side boundaries becomes an incident boundary, while the other becomes an open boundary. For the open side boundary, the value of ζ at a point (x_0, y_0) on the boundary at time t is set equal to the one at an adjacent inner point $(x_0, y_0 - \Delta y)$ at time $t - \tau$ as follows:

$$\zeta'(x_0, y_0) = \zeta'^{-\tau}(x_0, y_0 - \Delta y)\tag{21}$$

The time shift τ is defined by

$$\tau = \Delta y \sin \theta / (C + U \cos \theta + V \sin \theta)\tag{22}$$

where θ is the wave direction angle measured from the x -axis.

On the other hand, ζ on the incident side boundary is expressed as follows:

$$\zeta'(x_0, y_0) = a(x_0) \sin \left(\int_0^{x_0} k \cos \theta dx + k \sin \theta y_0 - \sigma t \right)\tag{23}$$

In this equation, however, the wave amplitude $a(x_0)$ is unknown because it changes towards the onshore direction owing to the shoaling, refraction, breaking, etc. The problem is how to determine $a(x_0)$ along the boundary.

In the present study we propose a simple and practical computation method, in which the wave amplitude $a(x_0)$ on the boundary is calculated from the quantities in the inner region by assuming the local wave periodicity in the alongshore direction. For this, an imaginary computation region is attached to the incident side boundary of the actual computation region as shown in Fig. 3. Assuming shore-parallel straight bottom contours in this region, we obtain Eq. (24).

$$L_y = L/\sin\theta = \text{const.} \tag{24}$$

where L_y is the wavelength in the alongshore direction. If the width of the imaginary region is set equal to L_y , waves change periodically in the alongshore direction, and consequently the following relation holds:

$$\zeta_{1,j} = \zeta_{N_y,j} \tag{25}$$

where $\zeta_{1,j}$ is the water surface elevation on the lower boundary, and $\zeta_{N_y,j}$ on the upper boundary of this imaginary region. Using this condition, we can calculate ζ and Q in the imaginary region without specifying any values on the side boundaries.

Figures 4 and 5 are the results of numerical computation in imaginary regions for cases of constant depth and of uniform slope, respectively. Waves come into the region with an incident angle of 60 degrees. The width equal to L_y has been divided into 15 grids. The left and the right figures respectively show the distributions of the normalized wave height and of the phase. These results are quite satisfactory and indicate the validity of this treatment.

The values of $\zeta_{N_y,j}$ thus obtained are given along the incident side boundaries in the computation for the actual region. Figure 6 is an example of the wave field computed for the case of obliquely incident waves. The

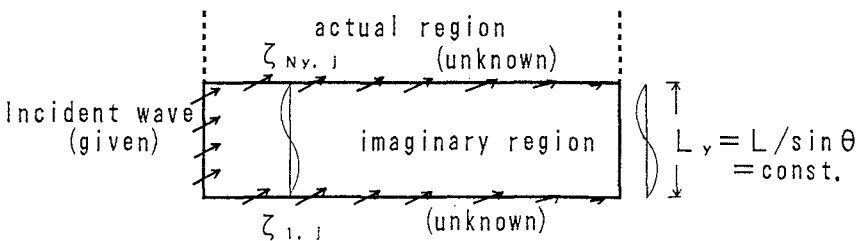


Fig. 3 Imaginary region.

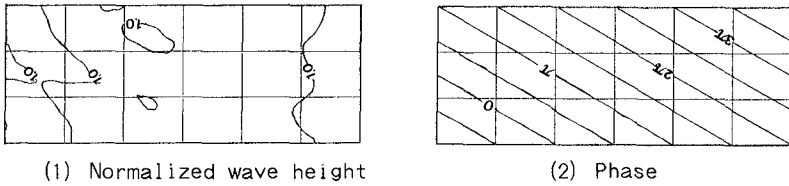


Fig. 4 Waves in the imaginary region for the case of constant depth.

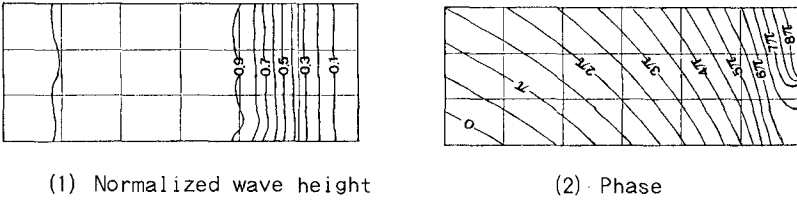


Fig. 5 Waves in the imaginary region for the case of uniform slope.

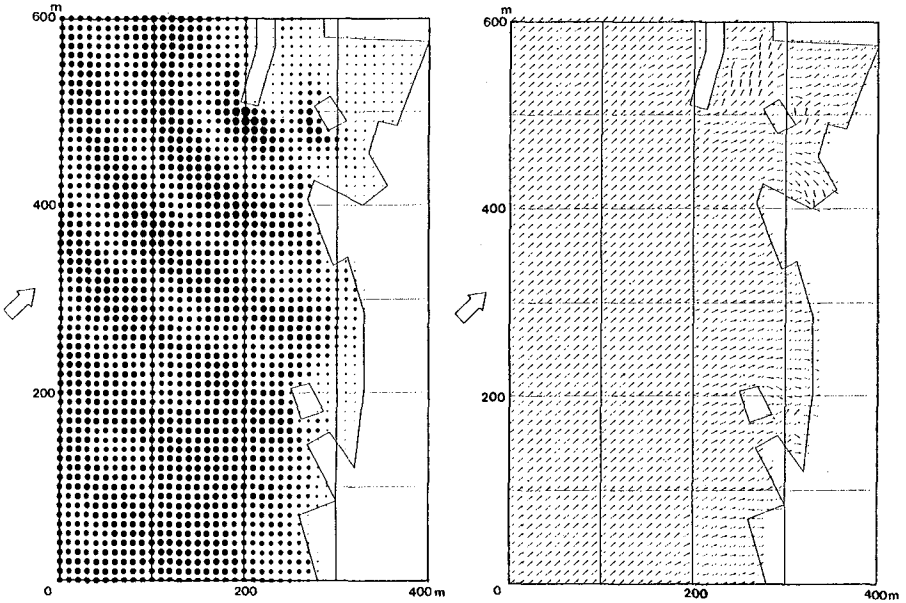


Fig. 6 Computed wave field for obliquely incident waves.

left and the right figures show the distributions of the wave height and the wave angle, respectively. As indicated in these results, incident waves come into theregion across not only the offshore boundary but also the lower side boundary.

4. EXAMPLES OF APPLICATION OF THE MODEL

The present numerical model has been applied to the computations of waves, currents and beach change for two typical cases involving the wave-current interaction.

The first case is for a region around detached breakwaters on a beach with initially uniform slope of $1/25$. The incident wave height is 2.5 m, the period is 8 s and the incident direction is normal to the shoreline. It is difficult at the present stage to evaluate proper values of the coefficients in the sediment transport rate formulas because of insufficient experimental and field data. Values of $A_w=0.15$, $A_c=0.50$, $A_{wb}=0.03$, and $A_{cb}=0.10$ has been adopted in this computation according to some experimental results. The grid size is $\Delta x=\Delta y=2.5$ m for the calculation of wave field and $\Delta x=\Delta y=5.0$ m for the calculation of nearshore current and beach change. Iteration in the calculation of waves and currents to include the wave-current interaction has been conducted nine times, and in the first four iteration steps values of the radiation stresses has been increased gradually by 25% for each step.

Figure 7 shows the wave height distribution, where the upper half gives the result computed with the wave-current interaction, and the lower half without the interaction. The differences of the wave height in the surf zone and of the breaker line are clearly observed. The distribution of the wave direction is shown in Fig. 8. Refraction due to nearshore current is observed when the wave-current interaction is considered. The distribution of nearshore currents is presented in Fig. 9, where reduction of the current intensity due to interaction and the shoreline change induced by the wave setup are well recognized. The distribution of the mean water elevation is presented in Fig. 10. Significant wave setup variation near the shoreline without the wave-current iteration is smoothed out when the interaction is considered. Figure 11 is the resultant beach topography, in which significant effects of the wave-current interaction appear near the shoreline.

The second case is for a region around a rip channel as shown in Fig. 12. Figure 13 shows the normalized wave height distribution. The difference of the

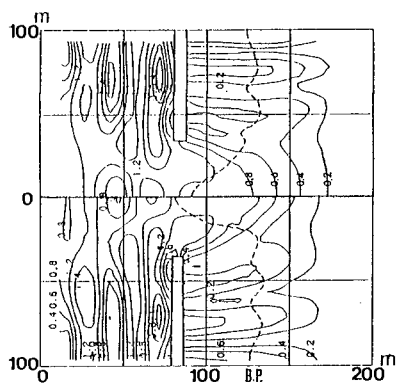


Fig. 7 Distribution of normalized wave height.

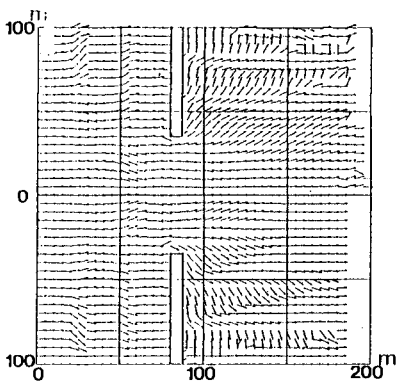


Fig. 8 Distribution of wave direction.

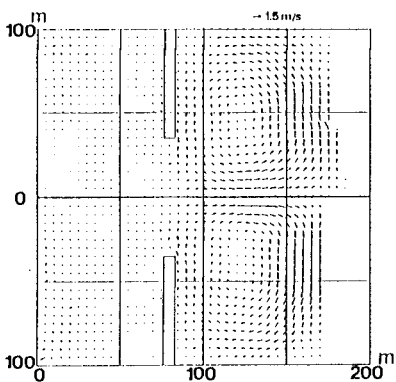


Fig. 9 Distribution of nearshore current.

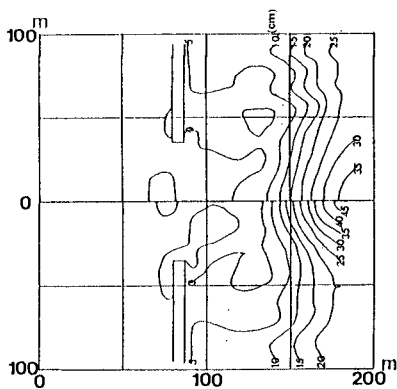


Fig. 10 Distribution of mean water elevation.

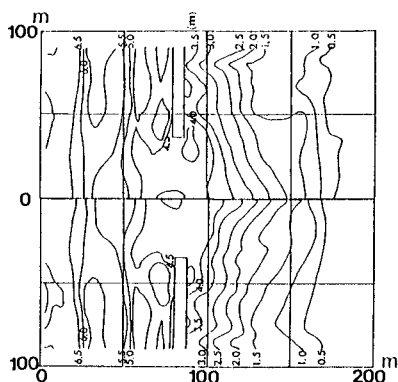


Fig. 11 Distribution of bottom topography.

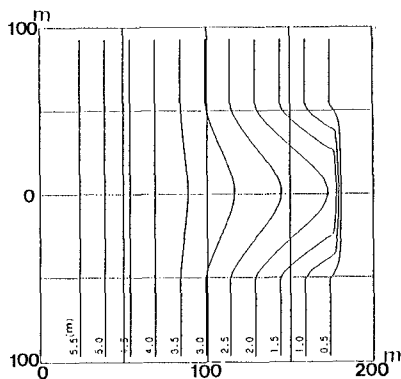


Fig. 12 Initial bottom topography around a rip channel.

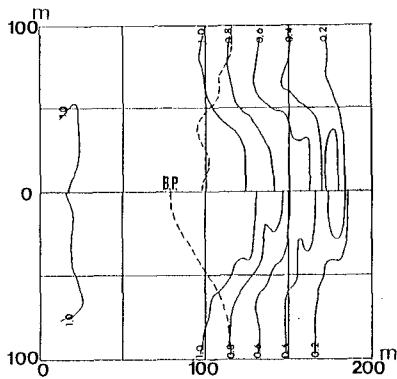


Fig. 13 Distribution of normalized wave height.

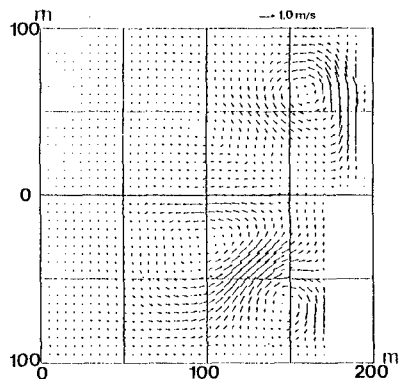


Fig. 14 Distribution of nearshore current.

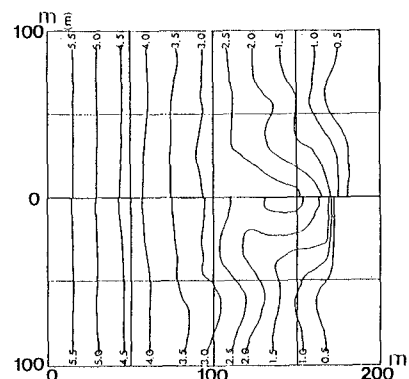


Fig. 15 Distribution of Bottom topography.

breaker lines is clearly seen. The distribution of nearshore currents is presented in Fig. 14. The computation region is extended along the shoreline by the wave setup and in this expanded region a strong longshore current is observed. Rip current velocity is considerably reduced when the wave-current interaction is included. Figure 15 shows the resultant beach topography. In this case the sand transport due to waves has been ignored in order to emphasize the difference induced by the currents with and without the wave-current interaction. It is seen that the beach topography change is reduced when the wave-current interaction is considered.

5. CONCLUSIONS

A numerical computation model for nearshore waves, currents and beach change with wave-current interaction was presented, and the influences of the wave-current interaction were examined. It was shown that the wave-current interaction affected the wave field, current field and beach change in the nearshore zone. A treatment of the side boundary condition for the case of obliquely incident waves and improvement of sediment transport rate formulas were also presented, and their validity was demonstrated.

REFERENCES

- Booij, N. (1981): Gravity waves on water with non-uniform depth and current, Communications on Hydraulics, No.81-1, Dept. of Civil Eng., Delft Univ. of Tech., 131p.
- Kirby, J.T. (1984): A note on linear surface wave-current interaction over slowly varying topography, J.Geophys. Res., Vol. 89, No. C1, pp.745-747.
- Liu, P.L.F. (1983): Wave-current interaction on slowly varying topography, J. Geophys. Res., Vol. 88, No. C7, pp.4421-4426.
- Ohnaka, S and A Watanabe(1988): Numerical modeling of wave deformation with a current, Proc. 21st Coastal Eng. Conf., ASCE, pp.393-407.
- Tanaka, M.and N Shuto(1981): Friction coefficient for a wave-current coexistent system, Coastal Eng. in Japan, Vol.24, pp.105-128.
- Watanabe, A., T. Hara and K. Horikawa(1984): Study on breaking condition for compound wave trains, Coastal Eng. in Japan, Vol. 27, pp.71-82.
- Watanabe, A. and K.Maruyama(1986): Numerical modeling of nearshore wave field under combined refraction, diffraction and breaking, Coastal Eng. in Japan, Vol. 29, pp.19-39.
- Watanabe, A., K. Maruyama, T. Shimizu and T. Sakakiyama(1986): Numerical prediction model of three-dimensional beach deformation around a structure, Coastal Eng. in Japan, Vol. 29, pp.179-194.
- Watanabe, A. and M. Dibajnia(1988): A numerical model of wave deformation in surf zone, Proc. 21st Coastal Eng. Conf., ASCE, pp.578-587.

CHAPTER 186

VALIDATION OF MOVABLE-BED MODELING GUIDANCE

Steven A. Hughes¹ and Jimmy E. Fowler¹

Abstract

A 1-to-7.5 scale (midscale) movable-bed physical model was used to validate model scaling criteria selected as most appropriate for turbulence-dominated, erosion of sediment by waves. Two-dimensional flume tests successfully reproduced profile evolution observed in prototype-scale wave flume tests conducted in Germany under both regular and irregular wave conditions. For the case of regular waves, a sloping concrete revetment was exposed, thus validating the scaling guidance for use in studying scour at coastal structures. Comparisons between regular wave and irregular wave profile evolution indicated that best correspondence is achieved when the significant wave height equals the monochromatic wave height, although irregular wave profile evolution takes about twice as long.

Introduction

Physical models at reduced scale offer an alternative for examining coastal phenomena that are beyond analytical approaches. However, engineers must temper their enthusiasm for physical models by remembering the model's usefulness is directly related to the ability to understand the inherent lab and scale effects; and, when possible, to correct for these effects in the design and conduct of experiments.

Similitude relationships for modeling hydrodynamic phenomena are well established and thoroughly tested against prototype-scale data. Scaling effects in movable-bed models are not as well understood and are difficult to quantify.

A multitude of scaling relationships for modeling coastal sedimentary processes has been proposed over the years (see Hudson et al. 1979, and Kamphuis 1982 for overviews and lists of references). Hudson et al. (1979) give the basic philosophy for movable-bed scale modeling as fully understanding the physical processes involved and ensuring that the relative magnitudes of all dominant processes are the same in model and prototype. They also state, "This is an impossible task for movable-bed models . . ." because of the complications of the fluid-sediment interactions, and thus it is necessary to attempt to reproduce the dominant process "... with the anticipation that other forces are small."

¹Research Hydraulic Engineers, US Army Engineer Waterways Experiment Station, Coastal Engineering Research Center, 3909 Halls Ferry Road, Vicksburg, MS 39180-6199

Similar views are held by Dean (1985), who lists two major requirements in proper physical modeling of sand transport processes: (a) knowledge of the character of the dominant forces and (b) an understanding of the dominant response mechanisms of the sediment.

In the absence of fundamental knowledge of the dominant processes and associated sediment response necessary to develop scale relationships, movable-bed scale models can be used to investigate the effects of certain parameters in systematic ways to establish general behavior patterns (Gourlay 1980). Alternately, the researcher can abandon the idea of reproducing the dominant physical processes and instead attempt to maintain similitude of important observed engineering characteristics such as beach profile shape or longshore transport rates (Hudson et al. 1979).

Regardless of the approach taken to develop scaling relationships for movable-bed models, the nearly unanimous opinion among researchers is that it is important to verify the scaling laws by reproducing prototype-scale events. Preferably, the scale model should be validated using field data, but often this is not practical, and large-scale laboratory results must suffice. Only after validation can credence be given to the model results, and then only for situations which seem to be governed by the same processes that were assumed dominant in the validation.

The purpose of the research described herein was to verify previously suggested movable-bed scaling criteria for modeling turbulent wave-induced scour phenomena in small-scale movable-bed physical models. This verification involved model replication of the spatial and temporal evolution of a beach fronting a sloping revetment as observed in a prototype-scale flume experiment conducted using monochromatic waves. Because the sloping concrete revetment became exposed during the course of the experiment, the structural influence on the profile evolution made this case particularly germane to the study of scour at structures.

Further validation of the movable-bed scaling criteria was achieved by midscale model reproduction of profile evolution caused by irregular waves in the prototype-scale flume. In this case, no structure was exposed to complicate the profile evolution.

Selected Scaling Guidance

Generally, movable-bed modeling criteria can be divided into two broad categories based on the transport mechanism: bed shear-stress-dominated transport, and turbulence-dominated transport. The present research focussed on the latter case.

Historical Perspective

Many investigators have expressed opinions regarding the important physical parameters and scaling requirements to be considered in formulating guidance for movable-bed models of coastal sedimentary processes. Perhaps the most relevant requirement for modeling coastal scour, as well as nearshore beach dynamics, is to attain similarity of the equilibrium beach profile between prototype and model, particularly in the surf zone. Parameters that appear to correspond to features of the equilibrium profile are similarity candidates for developing scaling criteria.

In the nearshore region, turbulent water motions play a greater role in mobilizing and transporting sediment; and in this region there is increasing evidence that the

dimensionless fall speed parameter, given as:

$$\frac{H}{wT} \quad (1)$$

where H = wave height, T = wave period, and w = vertical fall speed of the sediment, should be similar in both prototype and model.

The use of the fall speed parameter to characterize nearshore processes began in the late 1960's, and it was popularized by Dean (1973) when he incorporated it into an expression for distinguishing between swell and storm profiles. One physical interpretation of the parameter was given by Gourlay (1968) who pointed out that H/w represented "... the time taken for a sand particle to fall a distance equal to the wave height." If this time is large compared with the wave period, he reasoned the particle would remain in suspension and move as suspended load. Conversely, if the time is equal to or less than the wave period, then the sediment will move primarily as bed load. Hughes and Fowler (1990) summarize several of the research efforts that have led to acceptance of the fall speed parameter for describing certain aspects of nearshore sediment processes.

Dalrymple and Thompson (1976) were among the first to propose movable-bed modeling criteria that maintained similarity between prototype and model values of the fall speed parameter. Kamphuis (1982) concluded that preservation of the fall speed parameter eliminates most of the scale effects associated with attempting to geometrically scale the grain size diameter of quartz sand. Vellinga (1982) and Hughes (1983) proposed different distorted model relationships; however, the undistorted versions were identical and conformed to that recommended by Dalrymple and Thompson (1976).

Dean (1985) reviewed previous movable-bed modeling criteria and considered the dominant physical mechanisms involved in surf zone sediment transport. He argued that the Shield's criterion need not be met in the surf zone because turbulence, not bed shear, is the dominant cause of sediment mobilization; and therefore, bed shear is not an important consideration above Reynold's numbers constituting the fully rough range. Dean made specific recommendations for successful modeling of surf zone processes:

- a. Undistorted model (equal horizontal and vertical length scales).
- b. Hydrodynamics scaled according to Froude similarity.
- c. Similarity of the fall speed parameter between prototype and model.
- d. Model is large enough to preclude significant viscous, surface tension, and cohesive sediment effects so that the character of the wave breaking is properly simulated.

Dean (1985) argued that, in an undistorted model, the fall trajectory of a suspended particle must be geometrically similar to the equivalent prototype trajectory and fall with a time proportional to the prototype fall time. This is accomplished by ensuring similarity of the fall speed parameter between the prototype and the undistorted model.

The scaling recommendations of Dean (1985) were specifically tested in undistorted, erosive movable-bed models by Kriebel, Dally, and Dean (1986) and by Vellinga (1986). Both studies documented success in reproducing prototype-scale profile development. Other acceptance of the scaling criteria is discussed in Hughes and Fowler (1990).

In conclusion, efforts aimed at reproducing surf zone profile response in small-scale movable-bed models during erosive conditions have converged on scaling criteria that preserves the parameter H/wT between prototype and geometrically undistorted model, with the hydrodynamics (waves primarily) being scaled by the Froude criterion. As Dean (1985) discussed, the model law preserves similarity in wave form, sediment fall path, wave-induced velocities, break point, breaker type, and wave decay (provided the model is large enough to preclude viscous and surface tension effects.) The bottom shear stress will not be correctly scaled using the fall speed parameter criteria because the bottom boundary layer and ripple formations are not reproduced. This will result in noticeable scale effects when wave breaking turbulence is **not** dominant in the domain being modeled.

Scale Relationships

The selected scaling guidance consists of simultaneously satisfying two scaling criteria in an undistorted movable-bed model. The first is the well-known Froude criterion for the hydrodynamics that results in the relationship

$$N_t = \sqrt{N_\ell} \quad (2)$$

where N represents the prototype-to-model ratio of the subscribed parameter, t is time, and ℓ is length. In deriving Equation 2, the gravity scale, N_g , was set equal to unity.

The second criterion requires maintaining similarity of the fall speed parameter between prototype and model, i.e.,

$$\frac{H_p}{w_p T_p} = \frac{H_m}{w_m T_m} \quad (3)$$

where the subscripts p and m represent prototype and model, respectively. Rearranging Equation 3 and expressing it in terms of scale ratios yields

$$N_H = N_w N_T \quad (4)$$

Recognizing in an undistorted model that $N_H = N_\ell$ and that the wave period will scale the same as the hydrodynamic time scale, the combination of Equations 2 and 4 results in the unique scaling relationships satisfying both criteria:

$$N_t = N_w = \sqrt{N_\ell} \quad (5)$$

Xie's Scaling Guidance

As mentioned, various parameters other than the fall speed parameter have been suggested for use in characterizing sediment transport processes. Xie (1981) conducted numerous small-scale movable-bed model tests to examine the scouring of bed material adjacent to a vertical seawall subjected to nonbreaking waves. After testing several parameters, including the fall speed parameter, Xie presented a criterion for distinguishing between the two scour patterns that depends on the grain size of the bed material and on the wave conditions. The criterion is based on the parameter

$$\frac{U_{max} - U_*}{w} \quad (6)$$

where U_{max} = horizontal component of the maximum orbital water particle velocity near the bed, U_* = critical velocity for incipient motion of the sediment, and w = sediment fall speed. High values of the parameter imply movement by suspension (turbulence-dominated), and low values correspond to bed-load-dominant conditions.

Xie (1981) suggested that similarity of the parameter given by Equation 6 should be maintained between prototype and model, but noted that this would be difficult at times because of the dependence of both U_* and w on grain size.

The scaling criterion derived from maintaining similarity of Xie's parameter in an undistorted Froude model requires that:

$$\left(\frac{U_{max} - U_*}{w}\right)_p = \left(\frac{U_{max} - U_*}{w}\right)_m \quad (7)$$

Rearranging Equation 7, using the notation for scale ratios, and noting that, in an undistorted Froude model, the scale for the water velocity will be the same as the time scale, Equation 7 becomes

$$N_* N_t = N_w = \sqrt{N_t} \quad (8)$$

where

$$N_* = \frac{\left(1 - \frac{U_*}{U_{max}}\right)_p}{\left(1 - \frac{U_*}{U_{max}}\right)_m} \quad (9)$$

In essence, the scaling guidance given by Equation 8 is a more generalized version of the guidance determined with the fall speed parameter (Equation 5). Equation 8 agrees with that given by Equation 5 if the scale ratio N_* is equal to unity.

Examining Equation 9, there are two conditions by which N_* could approach unity. The first is if $U_{max} \gg U_*$ in both the prototype and model. This would be representative of highly turbulent conditions, such as exist in the surf zone during energetic wave conditions; and in the limit it corresponds somewhat to the physical description given by Gourlay (1968) and Dean (1973) for a suspended grain falling through the water column under the influence of horizontal currents.

The other conditions leading to unit value for N_* is if the ratio U_*/U_{max} is kept similar between prototype and model. In general the investigator will be unable to satisfy both the fall speed scale and the grain size scale necessary to meet this condition. Even if possible, the scaling would be valid for only one specific hydrodynamic condition because U_{max} depends on wave period and wave height, whereas U_* is independent of wave height. This would hamper investigations using irregular waves, as well as studies in which numerous regular wave periods were of interest.

Applicability of Selected Scaling Criteria

The selected movable-bed scaling criteria given by Equation 5 are for undistorted Froude models where the sediment size is selected so that the fall speed parameter is held constant between prototype and model. Past experience with these and similar scaling criteria, coupled with the assumptions used in formulating the guidance, restricts application of this type of physical modeling to coastal sediment problems and processes that are chiefly erosional in nature, with the erosion occurring in an energetic, turbulence-dominated region such as the surf zone. Typically, the scaling is intended

to replicate the short-term response of the sea bed to storm-induced waves. Examples of situations that may be candidates for modeling with the selected criteria include: beach and dune profile response to storm events, initial beach-fill adjustment to larger waves, beach-fill response to storm events, and storm-related short-term scour at the toes of structures.

Validation

All tests described in this paper were conducted in a 1.8-m-wide wave tank at the Coastal Engineering Research Center (CERC) during 1988–1989. Hughes and Fowler (1990) provide details on laboratory setup, experimental procedures, and detailed results.

Regular Wave Validation With Revetment

Movable-bed physical model tests conducted by H. Dette and K. Uliczka at the Großer Wellenkanal (GWK) facility in Hannover, Federal Republic of Germany (Dette and Uliczka 1987; Uliczka and Dette 1987; Uliczka and Dette 1988) served as the prototype-scale target conditions for reproduction at midscale. In the prototype experiments, sand with a median diameter of 0.33 mm was placed in front of a concrete structure with a slope of 1 on 4. The sand was molded to the same initial slope as the concrete structure shown by the long-dash line in Figure 1. Subsequent exposure of the solid revetment during testing makes this regular-wave case particularly useful for validation of movable-bed scaling guidance intended for modeling of scour processes.

The fall speed scaling relations of Equation 5 were used to determine the movable-bed model parameters. Fine quartz sand having a median diameter of 0.13 mm and specific gravity of 2.65 was used to simulate the 0.33-mm median-diameter prototype sand. The Froude scaling criterion was used to determine model wave period and the time scale for morphological development. Table 1 gives prototype and model experimental values and sediment fall speeds used to calculate the undistorted length scale ratio of 7.5 (prototype) to 1 (model).

Table 1: Prototype and Model Experiment Parameters

Parameter	Prototype	Model
Sediment Median Diameter	0.33 mm	0.13 mm
Mean Sediment Fall Speed	4.47 cm/s	1.64 cm/s
Wave Period	6.0 s	2.2 s
Wave Height	1.5 m	0.20 m
Water Depth	5.0 m	0.67 m
Horizontal Berm Width	11.0 m	1.47 m
Berm Thickness	2.67 m	0.36 m

The validation testing consisted of reproducing the experiment procedure used in the GWK during the prototype tests. Representative profile comparisons between

prototype and model after equal numbers of waves (Froude scale for morphological development) are given in Figure 1. In these plots the model results have been scaled up to prototype dimensions using the length scale ratio of 7.5.

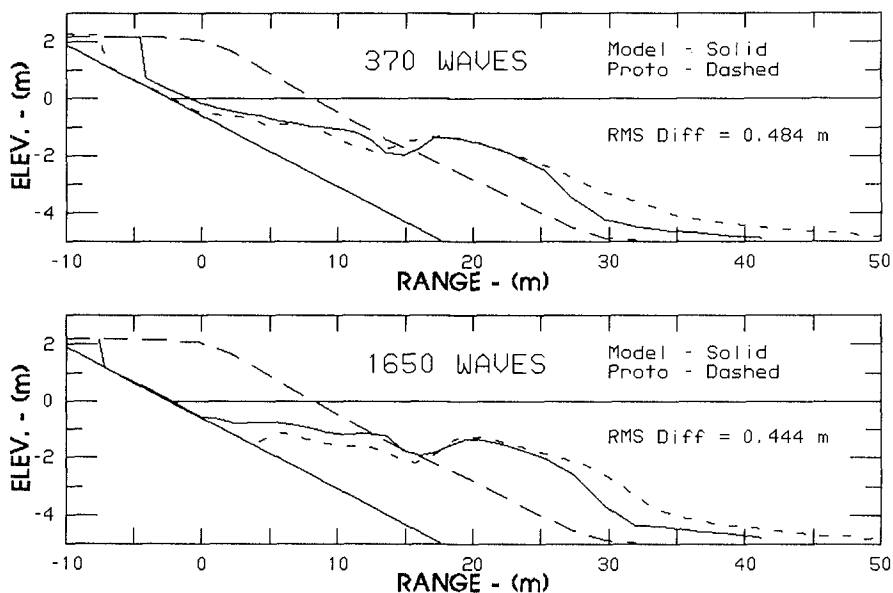


Figure 1: Prototype-Model Comparison, Regular Waves (RMS = root-mean-squared)

The profile comparison after 370 waves is relatively good, particularly in the surf zone and in the vicinity of the bar. The berm in the model was not eroded as much as in the prototype, and not as much sediment was moved to the region seaward of the breakpoint bar. An RMS (root-mean-squared) variation between profiles was calculated to be 0.49 m.

The center-line profile after 1,650 waves (Figure 1) represents the equilibrium condition for this test, and the comparison produced an RMS variation of 0.44 m. The model did not succeed in eroding the final portion of the berm on the upper portion of the revetment, and the model did not succeed in moving enough sediment to seaward of the breakpoint bar. Consequently, the scouring in the surf zone was not as severe as evidenced in the prototype.

The observed difference between prototype and model in the region offshore of the bar is most likely a result of the scaling relationship selected. This scaling relationship works best for regions dominated by turbulence-induced sediment transport. Because the model sand grains are not scaled according to the geometric length scale, they undergo a transition from suspended mode to bed-load mode of transport before this transition occurs in the equivalent prototype flow regime. With the selected scaling criteria, the bed-load mode of transport is not properly scaled in the model; consequently the model sand grains are at rest under scaled conditions that still result in offshore sediment transport in the prototype.

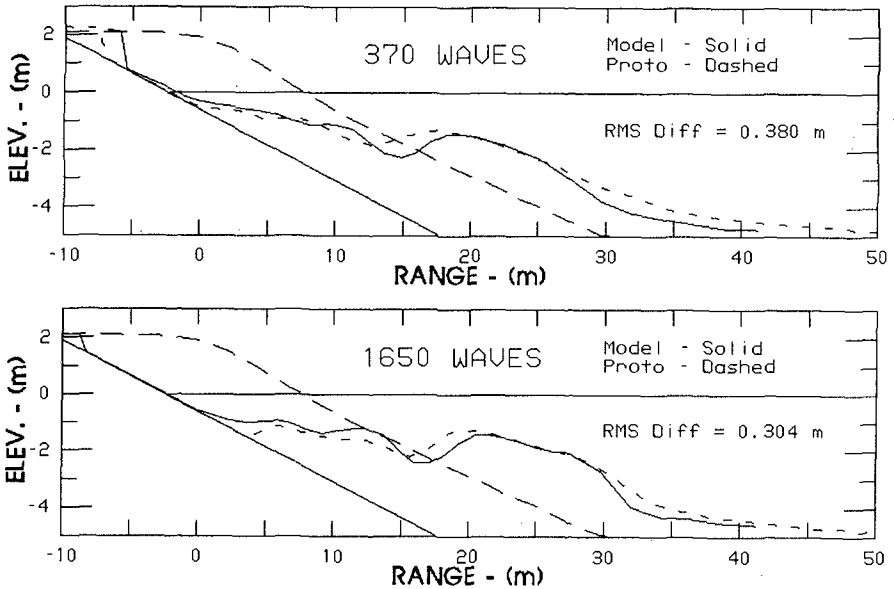


Figure 2: Prototype-Model Comparison, Waves Increased 10%

Figure 2 compares the prototype results to profiles obtained at midscale with the wave heights increased by 10% over the properly scaled value. As seen in Figure 2, better correspondence between prototype and model profiles resulted. The increased wave-induced water velocities in the offshore region appear to have transported sediment in the model to a greater offshore depth that more closely corresponds to the prototype. This increased *sediment demand* was met by the removal of more sand in the nearshore region; consequently, better profile reproduction, both in the final equilibrium and in the developmental stages, was achieved.

Table 2 gives values of Xie's parameter calculated at different water depths in the offshore region for the prototype (*Proto*), the basic validation model test (*Base*), and the model test with wave height increased by ten percent (*+10%*). Model values were calculated using the model depth equivalent to the prototype depth listed in the table. Columns 5 and 6 in Table 2 present the ratio of Xie's parameter in the prototype to that of the model. For the *Base* test, this ratio was always greater than one, approaching unity as the depth decreases. However, the ratio for the *+10%* test was nearer to unity over the range of offshore depths, and appears to be a reasonable compromise over the extent of the offshore portion of the profile.

The better comparison to prototype shown by the *+10%* test suggests a modification to the selected modeling criteria that includes a procedure for adjusting the scaled model wave height in such a manner as to achieve better similarity of Xie's parameter in the offshore regions of the modeled regime. This adjustment is dependent upon the wave period and should probably be limited to the more dynamically active portion of the offshore profile rather than being extended to full depth of closure.

Table 2: Prototype and Model Values of Xie's Parameter

Prototype Depth (m)	$(U_{max} - U_*)/w$			Ratio of Xie's Parameter	
	Proto.	Base	+10%	Proto/Base	Proto/+10%
5.0	20.86	18.15	20.42	1.15	1.02
4.5	23.57	20.84	23.33	1.13	1.01
4.0	26.83	24.09	26.83	1.11	1.00
3.5	30.89	28.09	31.19	1.10	0.99
3.0	36.12	33.33	36.80	1.08	0.98
2.5	42.23	39.42	43.36	1.07	0.97
2.0	51.83	48.97	53.67	1.06	0.97

Irregular Wave Validation Without Revetment

Prototype tests were also conducted in the Großer Wellenkanal using irregular waves that conformed to a JONSWAP spectrum. In these tests additional sand was added in front of the revetment so that the structure would not be exposed during profile development. The significant wave height and peak spectral period had the same prototype values as given in Table 1 for the regular wave tests. This prototype condition was reproduced as an additional midscale validation test. Every attempt was made to recreate the experiment in the same manner as it was conducted in the GWK. Representative profile comparisons between prototype and model after equal numbers of waves (Froude scale for morphological development) are given in Figure 3.

Reproduction of the irregular-wave prototype-scale flume experiment was considered to be very successful as indicated by the RMS differences shown in Figure 3. This further validates the selected movable-bed modeling guidance as being appropriate for energetic regimes of sediment transport. It is significant that close reproduction was obtained over the entire extent of the profile using properly scaled irregular waves. Recall from previously presented results that the regular wave tests suggested augmentation of the model wave height to provide a better correspondence of the Xie parameter between model and prototype. Because this was not required for the case of irregular waves, it is tentatively concluded that the natural variations within the irregular wave field were sufficient to assure correct redistribution of sediment over the entire extent of the modeled profile.

Irregular Wave Equivalence

Much of the established design guidance for sediment transport has been derived in part from laboratory tests conducted with movable-bed models using uniform, regular wave trains. For engineering design based on this guidance, the irregular wave condition which exists in nature is commonly represented by a single statistical wave height parameter that is taken as being equivalent to the regular wave height in the design formulae. Therefore, it is important to determine which irregular parameter best matches the regular wave parameter used to establish the design guidance.

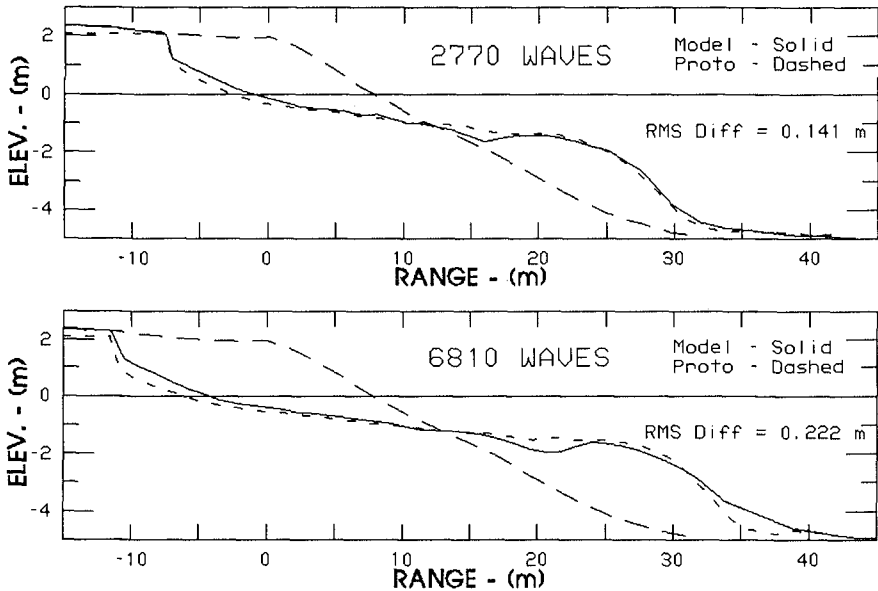


Figure 3: Prototype-Model Comparison, Irregular Waves

Midscale tests employing irregular waves were conducted using the initial revetment configuration shown in Figure 1. In one test the significant wave height was chosen so that the energy present in the irregular wave train was equivalent to the energy of the regular waves used in the validation test. This resulted in a value of $H_{1/3}$ about 41% greater than the regular wave height (H_{mono}). In the other test, $H_{1/3}$ was set equal to H_{mono} .

Irregular Wave Energy Equal to Monochromatic Wave Energy

The purpose of this test was to examine whether equivalent energy levels are necessary to obtain similar profile development between model regular and irregular wave physical model tests. Figure 4 compares the irregular wave case (solid line) with the regular wave test (dashed line). The irregular waves resulted in greater erosion of the berm area and also resulted in movement of the sediment farther offshore than in the regular wave case. The comparison after 1,650 waves also reveals a significantly different profile in the region of wave breaking and seaward of breaking.

Irregular $H_{1/3}$ Equal to Monochromatic Wave Height

Figure 5 compares regular-wave profiles with corresponding profiles from the irregular test with $H_{1/3} = H_{mono}$ after approximately the same number of waves (equal elapsed time of wave action).

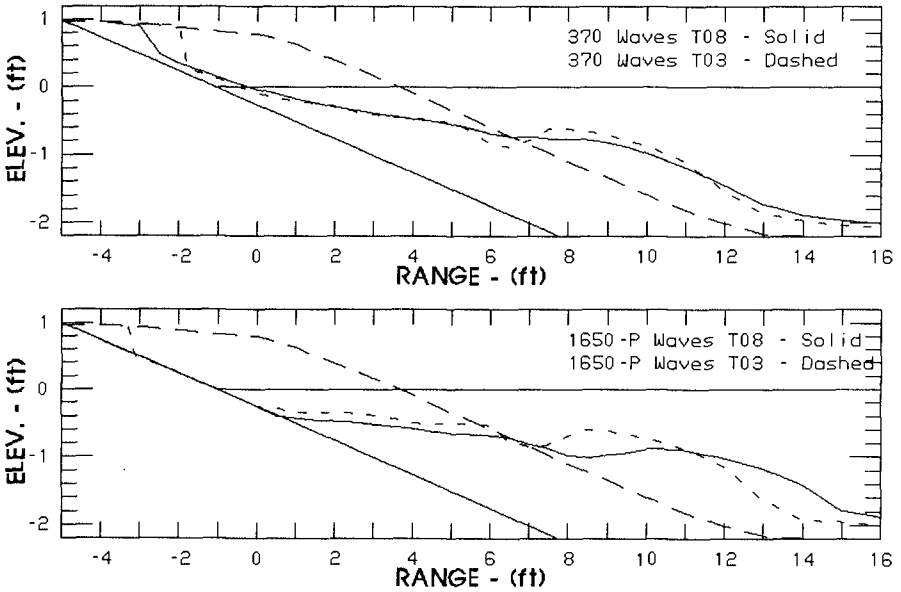


Figure 4: Irregular Wave Comparison, $H_{1/3}$ Equals 141% H_{mono}

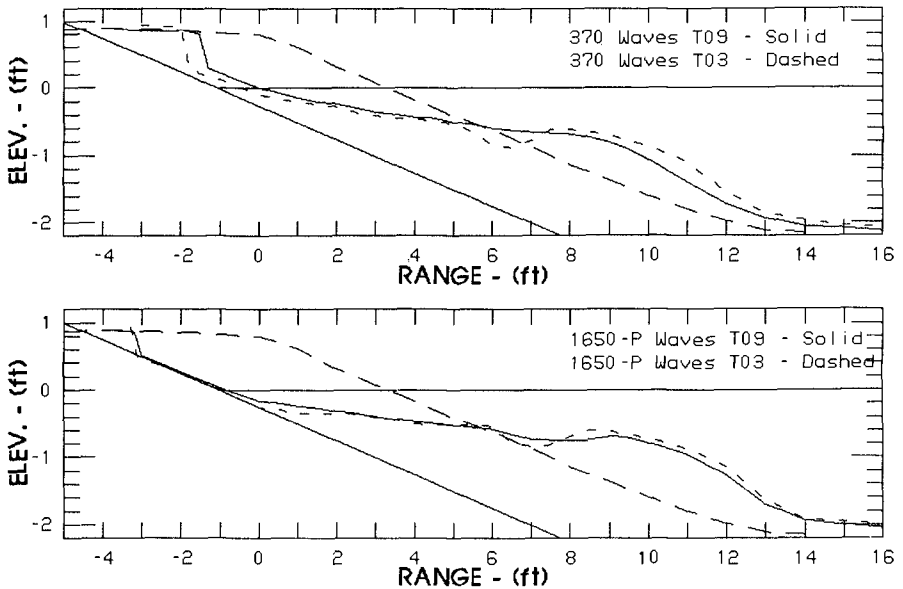


Figure 5: Irregular Wave Comparison, $H_{1/3}$ Equals H_{mono}

Generally, the irregular wave condition (solid line) produced similar erosional history as the regular wave case (dashed line), but at a slower rate. After the initial adjustment, evolution of the profile under irregular wave action was less than in the regular wave case, with the most noticeable region of difference being the berm recession. This observation follows the same trend as reported by Mimura, Otsuka, and Watanabe (1986) and Uliczka and Dette (1987). The irregular wave-induced profile reached a near-equilibrium state after 1,650 waves, which corresponds to the same response of the profile under regular wave action. The good comparison shown in Figure 5 indicates that best equivalence between regular and irregular waves is found when $H_{1/3} = H_{mono}$.

The time lag in profile development under irregular waves was estimated by comparing irregular and regular wave profile that had been shifted in time. Figure 6 shows irregular wave profiles (solid) compared to regular wave profiles (dashed) that developed in about half the time. The good comparison qualitatively supports morphological development taking approximately twice as long if equivalent irregular waves are used instead of regular waves.

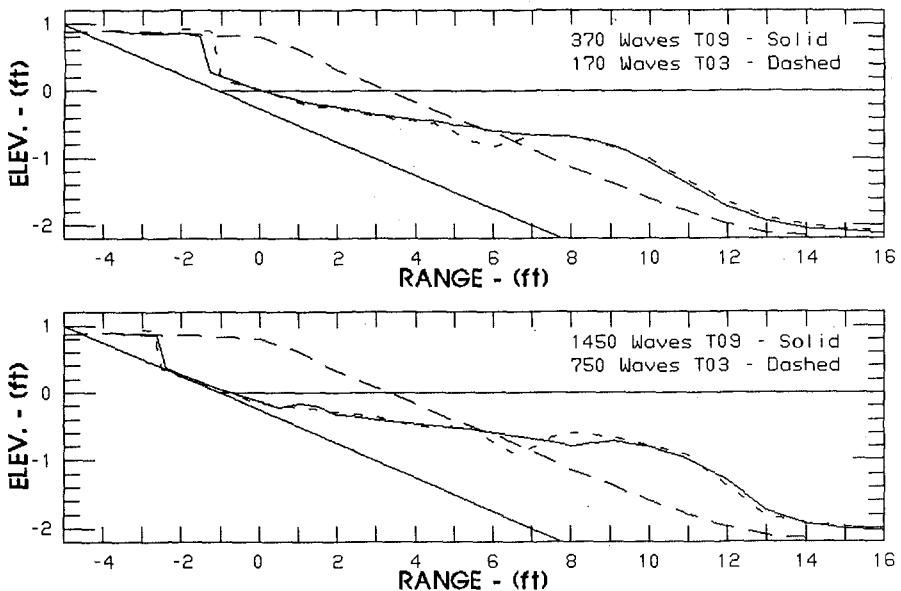


Figure 6: Time-Shifted Irregular Wave Comparison, $H_{1/3}$ Equals H_{mono}

Conclusions

Prototype-scale experiments conducted in the Großer Wellenkanal were reproduced at a prototype-to-model scale of $7\frac{1}{2} : 1$ using both regular and irregular wave trains. The testing procedures were designed to duplicate those used in the GWK tests. Conclusions resulting from the midscale tests are listed below:

- a. Mid-scale test results support preservation of the dimensionless fall speed parameter in an undistorted Froude model as a viable method of scaling models intended to replicate wave erosion under turbulence-dominated situations.
- b. For tests involving regular waves, model designers should consider augmenting the Froude-scaled experimental wave height to provide better prototype-to-model correspondence of the Xie parameter in the offshore region. This correspondence should be limited to the more active portions of the offshore and need not extend out to closure depth.
- c. Tests conducted using irregular waves do not require the augmentation described in (b) above.
- d. Comparable profile development can be achieved between regular and irregular wave models when the irregular significant wave height, $H_{1/3}$, is equal to the regular wave height. Profile development will take approximately twice as long in the irregular wave model.

Acknowledgements

The authors gratefully acknowledge the cooperation of Dr. H. Dette, Technical University of Braunschweig, and Dr. K. Uliczka, Bundesanstalt für Wasserbau (formerly University of Hannover), in making their results from the Großer Wellenkanal available for this study.

This study was performed under the work unit *Scour at Coastal Structures* of the Coastal Shore Protection and Restoration Program of the U.S. Army Corps of Engineers, Waterways Experiment Station, CERC. Permission was granted by the Chief of Engineers to publish this information.

References

- Dalrymple, R. A., and Thompson, W. W. 1976. "Study of Equilibrium Beach Profiles," *Proceedings of the 15th Coastal Engineering Conference*, American Society of Civil Engineers, Vol 2, pp 1277-1296.
- Dean, R. G. 1973. "Heuristic Models of Sand Transport in the Surf Zone," *Proceedings of the Conference on Engineering Dynamics in the Surf Zone*, Sydney, Australia, pp 208-214.
- Dean, R. G. 1985. "Physical Modeling of Littoral Processes," in *Physical Modelling in Coastal Engineering*, R. A. Dalrymple, Ed., A. A. Balkema, Rotterdam, The Netherlands, pp 119-139.
- Dette, H. H., and Uliczka, K. 1987. "Prototype Investigation on Time-Dependent Dune Recession and Beach Erosion," *Proceedings of Coastal Sediments '87*, American Society of Civil Engineers, Vol 2, pp 1430-1444.
- Gourlay, M. R. 1968. "Beach and Dune Erosion Tests," unpublished report, Delft Hydraulic Laboratory, The Netherlands.
- Gourlay, M. R. 1980. "Beaches: Profiles, Processes and Permeability," *Proceedings of the 17th Coastal Engineering Conference*, American Society of Civil Engineers, Vol 2, pp 1320-1339.

- Hudson, R. Y. , Herrmann, F. A., Sager, R. A., Whalin, R. W., Keulegan, G. H., Chatham, C. E., and Hales, L. Z. 1979. "Coastal Hydraulic Models," Special Report No. 5, US Army Engineer Waterways Experiment Station, Vicksburg, MS.
- Hughes, S. A. 1983. "Movable-Bed Modeling Law for Coastal Dune Erosion," *Journal of Waterway, Port, Coastal, and Ocean Engineering Division*, Vol 109, No. 2, pp 164-179.
- Hughes, S. A., and Fowler, J. E. 1990. "Midscale Physical Model Validation for Scour at Coastal Structures," *Technical Report CERC-90-8*, US Army Engineer Waterways Experiment Station, Vicksburg, MS.
- Kamphuis, J. W. 1982. "Coastal Mobile Bed Modelling from a 1982 Perspective," C. E. Research Report No. 76, Queen's Univeristy, Kingston, Ontario.
- Kriebel, D. L., Dally, W. R., and Dean, R. G. 1986. "Undistorted Froude Model for Surf Zone Sediment Transport," *Proceedings of the 20th Coastal Engineering Conference*, American Society of Civil Engineers, Vol 2, pp 1296-1310.
- Mimura, N., Otsuka, Y., and Watanabe, A. 1986. "Laboratory Study on Two-Dimensional Beach Transformation Due to Irregular Waves," *Proceedings of the 20th Coastal Engineering Conference*, American Society of Civil Engineers, Vol 2, pp 1393- 1406.
- Uliczka, K., and Dette, H. H. 1987. "Prototype Investigation on Time-Dependent Dune Recession and Beach Erosion," *Proceedings of Coastal Sediments '87*, American Society of Civil Engineers, Vol 2, pp 1430-1444.
- Uliczka, K., and Dette, H. H. 1988. "About the Influence of Erosion Volume on Cross-Shore Sediment Movement at Prototype Scale," *Proceedings of the 21st Coastal Engineering Conference*, American Society of Civil Engineers, Vol 2, pp 1721-1735.
- Vellinga, P. 1982. "Beach and Dune Erosion During Storm Surges," *Coastal Engineering*, Vol 6, No. 4, pp 361-387.
- Vellinga, P. 1986. "Beach and Dune Erosion During Storm Surges," Ph.D. Dissertation, Communication No. 372, Delft Hydraulics Laboratory, Delft, The Netherlands.
- Xie, S.-L. 1981. "Scouring Patterns in Front of Vertical Breakwaters and Their Influences on the Stability of the Foundations of the Breakwaters," Department of Civil Engineering, Delft University of Technology, Delft, The Netherlands.

CHAPTER 187

Large Scale Laboratory Tests of Dune Erosion

M. F. Overton, Associate Member ASCE¹
J. S. Fisher, Member ASCE²
A. L. Stone, Associate Member ASCE³

Introduction

An ongoing research program at North Carolina State University (NCSU) has investigated the viability of a mechanics based swash induced dune erosion model. Early work includes both small scale laboratory and field experiments. The overall objective of the experiments was to determine the relationship between the swash characteristics and dune erosion under a variety of conditions. A linear relationship between the specific swash force (per unit width of the dune) as defined by the bore depth and velocity, and the specific volume eroded has been documented for an individual swash (in the lab), Overton et al. (1988) and for a series of swash events (in the field) Fisher et al. (1987). Problems of scale, dune material and manner of construction in the field led to a series of experiments in the large wave tank at Oregon State University (OSU). The objective of the OSU tests was to investigate the relationship between the swash force and the volume eroded for two prototype scale dunes of different sand grain size.

¹ Associate Professor of Civil Engineering, PO Box 7908, North Carolina State University, Raleigh, N.C. 27695

² Professor of Civil Engineering, PO Box, 7908, North Carolina State University, Raleigh, N.C. 27695

³ Engineer, Hazen and Sawyer, 4000 WestChase Blvd., Suite 550, Raleigh, N.C. 27607

Experimental Design and Setup

The experiments were designed to simulate dune erosion under storm conditions at prototype scale. The experimental design and procedure summarized in the following are described in detail in Stone (1989). The OSU wave tank has a length of 104 m, a width of 3.7 m and a height of 4.6 m and is equipped with a programmable wave generator. The permanent bottom of the flume is flat with a 3.6 m step at one end. In order to accommodate the beach and dune requirements, the tank was modified in two ways. One, a beach with a 1:10 slope was installed. Two, side walls were constructed at the location of the dune to increase the height of the tank to 2.5 m. This would allow for the dune to be built with a height of approximately 2 meters.

Two dunes were constructed on the step portion of the tank as shown schematically in Figure 1. The economics of testing dictated that the dunes were built during the initial tank modification and setup phase of the experiments. Therefore, two dunes were built with a depth along the length of the tank of approximately 4 m with a plywood barrier placed at point B to separate the two. Similar material, fine sands, with median sand grain sizes, d_{50} , of 0.32 mm and 0.23 mm were used for construction. This material was locally available river sand. Dunes were constructed by placing sand in the

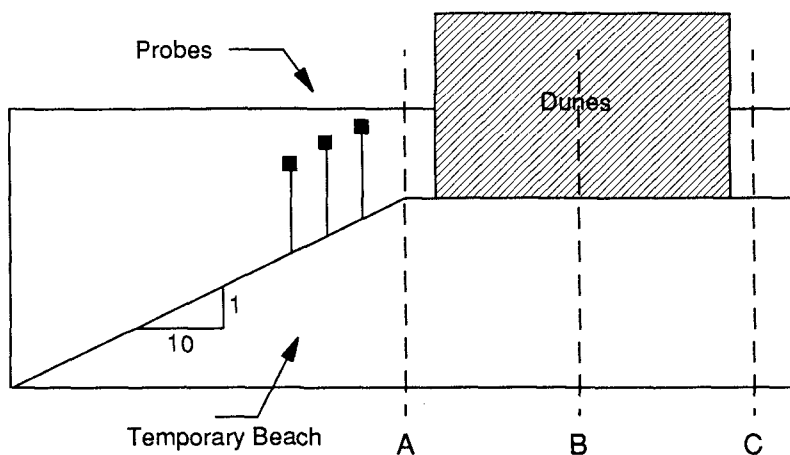


Figure 1. Schematic of the experimental setup.

flume with the aid of a Bobcat front-end loader. Sand was added to the flume in 30 cm layers. A vibrating compactor was then used to consolidate the material. The compactor was run across the top of the dune at least twice for each layer. This procedure was repeated until the dunes were approximately 1.5 m high.

Swash data was collected by three capacitance type wave gages placed on the beach in front of the dune. The probe closest to the dune was set 2.5 m away so that as the dune began to erode and collapse the dune material would not bury the probe. Bore depth was determined from the record at this probe. The subsequent probes, intended for use in determining the velocity of the leading edge of the bore, were placed 1 m apart, Figure 1.

Dune position was documented by a 35 mm camera before, during and after each experiment. Each photograph of the dune included the profile of the dune face and a 60 cm by 60 cm standard grid to determine scale. Specific volume eroded for a given event is defined as the difference in area between the original dune position and subsequent position at the defined interval of time.

Each experiment proceeded as follows. The pre-test beach and dune profile was surveyed. Instrumentation was calibrated and synchronized. Pre-test dune position was documented on film. Waves were generated which eroded the dune face. The experiment continued until sufficient erosion was recorded, at which time the wave generator was shut down. Post-test profiles and position of the dune were then determined.

Eleven experiments were successfully conducted. The conditions of each test are given in Table 1. Five of the tests were on dune one ($d_{50} = 0.32$) and six on dune two ($d_{50} = 0.23$). The wave height and the wave period were held constant for the duration of an individual test, however, the beach slope and distance from the dune altered with the subsequent erosion and adjustment of the beach. The test wave heights ranged from 0.46 m to 1.02 m while the wave period ranged from 5 secs to 10 secs. Four tests, numbers 6, 8, 7 and 9, conducted on dune two, had the same wave conditions in order to look at the repeatability of results. With each test, the horizontal distance from the mean water level and the dune changed as the dune eroded, however the tank was filled several times to bring the water level back within range. This distance varied between approximately 0.9 m and 3.0 m.

Test #	Wave Period (secs)	Wave Height (m)	Beach Slope	Distance from Dune (m)	Grain Size (mm)
1	7.0	0.86	0.18	2.18	0.32
2	7.0	0.61	0.10	0.92	0.32
3	10.0	0.46	0.12	1.92	0.32
4	5.0	0.91	0.12	2.32	0.32
5	7.0	0.91	0.12	0.98	0.32
6	7.0	0.61	0.10	2.03	0.23
7	10.0	0.46	0.13	2.50	0.23
8	7.0	0.61	0.14	2.48	0.23
9	10.0	0.46	0.19	2.88	0.23
10	7.0	1.02	0.18	3.15	0.23
11	7.0	0.46	0.14	3.11	0.23

Table 1. Test conditions.

Data Reduction

The experimental data were analyzed for two parameters, specific swash force and specific volume of dune eroded. Earlier work, both small scale laboratory and field work, indicates that a linear relationship exists between these two factors, (Fisher, 1987 and Overton, 1988). Specific swash force is quantified as

$$SF = \rho v^2 d \quad (1)$$

where ρ is the density of the water, v is the leading edge velocity of the swash and d is the depth of swash immediately after impact with the dune. These data were determined from the records of the three capacitance swash gages placed on the beach in front of the dune. A sample of this data is shown in Figure 2. For each time history for an individual swash the following characteristics are observed. One, a dramatic increase in the water depth marks the time that the swash hits the probe. The rule of thumb used was if the depth increased 3 cm in 0.1 seconds it was assumed that a swash was on the beach. Because the probes were buried in the beach approximately 30 cm, the background reading in the absence of a swash indicates the moisture in the sand. Two, the depth of the swash increases and then levels off. This plateau is taken to be the maximum depth of the swash before the backwash moves down the beach and interferes with the signal. Three, there is a subsequent rapid increase and decay in the depth which signifies the

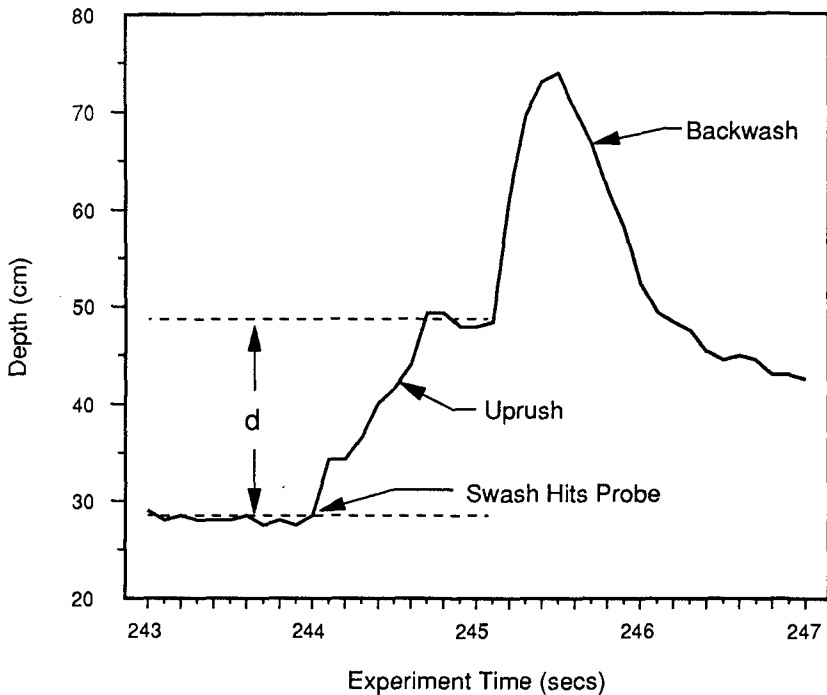


Figure 2. Swash depth versus time at the dune.

passing of the backwash. The depth of swash required in computing the specific force is the difference between the background depth and the depth of the plateau before backwash, Figure 2.

The velocity of the leading edge of the swash is determined by identifying the time at which the bore hits the first and last probes on the beach. An example of this data is given in Figure 3. The characteristic shape of each depth time history is above. The feature required for the determination of velocity is the time the bore hits the probe. From this, the velocity is calculated based on the distance traveled between two swash probes (2 m) and the time of travel, dt .

The force for each bore was calculated using Equation 1. While quantifying the force for an individual bore is possible, it was not always possible to measure the amount eroded due to that loading. Therefore, the summation of the force in a given interval of time versus the volume of dune eroded in the same time

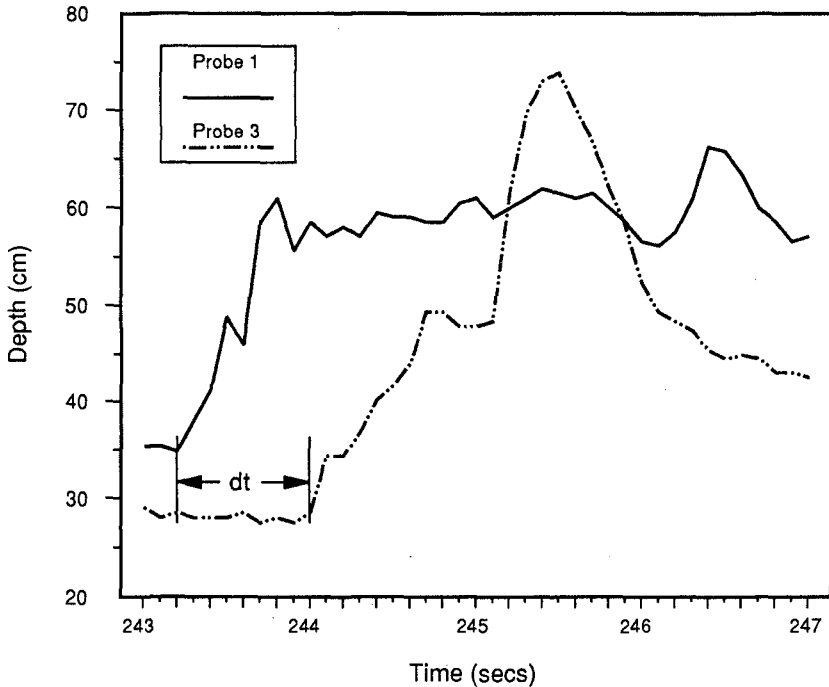


Figure 3. Depth versus time at two probes placed 1 m apart.

interval becomes the quantity evaluated. The duration of an experiment is the time between the first swash that hit the dune and the last slide taken to document the position of the dune.

Specific volume eroded was determined from the before and after profiles of the dune face as recorded on 35 mm film. Pre-test profiles were shot to record the initial dune face position. Then, during the test, photos were shot at a minimum of three minute intervals for the duration of the test. The time of the shot was recorded either in the field book or on the photo by the data back on the camera. This enabled not only before and after quantification of the dune position but the progressive erosion as well. In order to differentiate between beach erosion and dune erosion, the initial face of the dune was used to define the seaward extent of the dune. Regardless of the orientation of the material as the dune failed and the beach readjusted, the volume lost from the dune was determined as material lost landward of the original dune face. Obviously, the numerical value

of the volume eroded could vary with the interpretation of the differentiation of dune and beach material.

In order to quantify the data, the black and white 35 mm film was developed and mounted as slides. These slides were projected and the dune image traced in order to digitize volumes. The reference grid included in each frame was used to determine the scale. The original plan was to record the erosion by photography on both sides of the flume; however, due to equipment malfunction a complete set of data on one side of the flume only was available. Therefore, the numbers used in the analysis represent one side of the dune and the assumption is that the erosion was uniform across the dune face.

Results

The results of the experiments, as quantified by specific force and erosion, are given in Table 2.

TEST NUMBER	SWASH FORCE (kN/m)	VOLUME ERODED (m ³ /m)
1	90.6	0.20
2	195.5	0.39
3	101.3	0.05
4	133.0	0.16
5	233.6	0.54
6	158.4	0.25
7	50.0	0.10
8	187.8	0.29
9	54.0	0.08
10	258.0	0.37
11	93.0	0.23

Table 2. Specific swash force and volume eroded.

The data were analyzed with three objectives in mind. One, were the experiments valid with respect to reproducibility? Two, would the linear relationship established in the earlier work hold up for prototype wave and dune conditions? Three, would grain size effect this relationship?

In order to examine the first question, two experiments were conducted with identical offshore wave conditions. Experiments 6 and 8 were conducted with a 7 second period and a wave height of 0.61 meters. Results from these tests presented in Table 2 indicate that conditions in experiment 8 netted a higher force and a correspondingly higher volume eroded than in experiment 6. This can be accounted for by the duration of the experiment. Experiment 8 was approximately 200 seconds longer than experiment 6. Given the wave period, this represents approximately 28 additional swashes that attacked the dune. Using intermediate photography, it was possible to analyze experiments 6 and 8 at durations of 499 and 509 seconds, respectively. Therefore, the specific force and the specific volume eroded for these intervals were 126.4 kN/m and 123.5 kN/m and 0.190 m³/m and 0.184 m³/m, respectively, representing a 4% difference in results. Likewise for experiments 7 and 9, in which in which the measurable difference between experimental results is a specific force of 4 kN/m and a specific volume eroded of 0.02 m³/m. It is felt that these measures indicate the reproducibility of the experimental conditions and results.

The linearity of the relationship is examined by plotting and analyzing the data. The data were first analyzed as two distinct sets, characterized by sand grain size. Separately, the hypothesis of a linear relationship holds as these data fit with r squared values of 0.74 and 0.86 for sand grain size 0.32 and 0.23 respectively. Given this, the question was asked if the data could support the conclusion that these two lines (relationships) were unique, i.e., that based on these tests that sand grain size had a significant impact on the results. In order to answer this question a test for parallelism was performed. It was hypothesized that the relationships were parallel (and thus the same). Statistically, this hypothesis could not be rejected. This indicated that the data did not support the hypothesis that the force erosion relationship could be distinguished by sand grain size. Thus, Figure 4 presents the data and the line which best fits the data presented as a single dataset. Forcing the line through the origin (no force, no erosion), the slope of the best fit line is 0.00174. This correlates with an r squared value of 0.78.

Conclusions

The results from the large scale laboratory experiments at OSU support the hypothesis that the volume

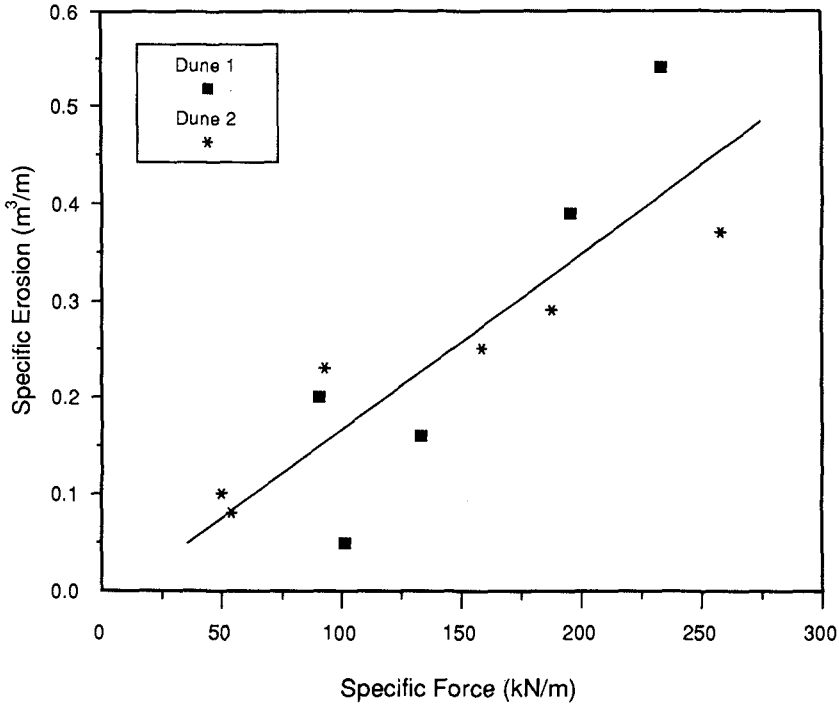


Figure 4. Specific force versus specific volume eroded.

of dune eroded during swash attack is linearly related to the summation of the swash force during that event.

However, the investigation into the effect of sand grain size is incomplete based on these experiments. While the data do not show that sand grain size is important, several aspects of the experiments which could influence this should be kept in mind. One, this conclusion is based on a limited number of experiments: a dataset of five for dune one and a dataset of six for dune two. Perhaps a more significant factor is that while the sands were distinguished by different d_{50} 's, they both could be classified as fine sands. Thus, the effect of sand grain size on the force erosion relationship cannot be determined at this level.

References

Fisher, J. S., et al., "Field Measurements of Dune Erosion", Proceedings of the 20th Conference on Coastal Engineering, Taipei, Taiwan, 1987, pp.1107-115.

Overton, M. F. et al., "Laboratory Investigation of Dune Erosion", Journal of Waterway, Port, Coastal and Ocean Engineering, ASCE, Vol. 114, No. 3, May 1988, p. 367-373.

Stone, A. L., "Analysis of the Effect of Grain Size on the Stability of Sand Dunes", MS Thesis, Department of Civil Engineering, North Carolina State University, Raleigh, North Carolina, 1989.

CHAPTER 188

PRACTICAL APPLICATION OF THE THREE-DIMENSIONAL BEACH EVOLUTION MODEL

Takuzo Shimizu¹, Hitoshi Nodani² and Kosuke Kondo³

ABSTRACT

The long-term bottom topography changes around the entrance of a fishery harbour were simulated by using the three-dimensional beach evolution model. The practical applicability of the model was demonstrated through comparisons with the actual topographical changes. And the equilibrium state of beach evolution due to construction of a coastal structure could be also predicted by repeating the calculation of the wave and current field and that of the bottom topography change.

1. INTRODUCTION

In constructing a harbour on a sandy coast, it is necessary to give careful consideration not only to countermeasures against sand deposition at the entrance of or inside the harbour, but also to the effects on the neighbouring beaches. So, the beach evolution due to construction of a coastal structure must be predicted in order to design a suitable layout plan of breakwaters.

In recent years, a numerical simulation model of beach evolution, so-called a three-dimensional beach evolution model, has been rapidly developed and applied to many practical problems in Japan, since Watanabe et al.(1986) proposed a model and confirmed its validity on the basis of laboratory experimental data. However, quantitative verification of its applicability to the actual field has not been thoroughly discussed.

In this study, we aimed to discuss quantitatively, through comparisons with field data, the applicability of the model to the long-term topographical changes around Iioika Fishery Harbour, Chiba, Japan.

¹Senior Engineer, Design and Engineering Department,

²Engineer, Design and Engineering Department,

³Divisional Manager, Research and Development Department, Penta-Ocean Construction Co.,Ltd. 2-2-8 Koraku, Bunkyo-ku, Tokyo 112, Japan.

2. OUTLINE OF THE MODEL

The numerical simulation model used in this study is fundamentally similar to the model proposed by Watanabe et al. (1986). Figure 1 shows the calculation flow of the model. The total model consists of three submodels for calculation of waves, nearshore currents and beach changes. At the first step, the wave field is computed under a certain incident wave condition and the initial bottom topography in the study area. Next, the nearshore current field is computed from the spatial distribution of radiation stresses which is estimated by using the results of the wave field computation. Finally, the sediment transport rates are computed at the local points from the wave-current conditions calculated in advance, and then the three-dimensional bottom topography change is computed by solving the equation of sediment mass conservation.

The incident wave conditions change daily and the change in bottom topography produce changes in the nearshore waves and currents. So, the short time-interval iterations are needed in the computations of waves, currents and topography changes. In practice, the iterations using daily wave conditions are not possible, because the computation time of each model is not sufficiently short. But only one step of the iteration is useful to predict the tendency of the spatial distribution of bottom topography change under a representative wave condition. This way of application of the model is effective to discuss relatively the merits or demerits of layout of breakwaters.

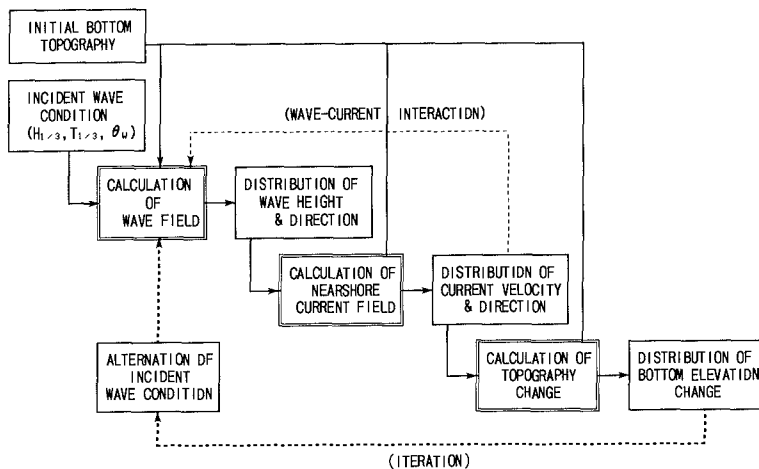


Fig.1 Flow chart of computation

On the other hand, in order to quantitatively predict the long-term beach evolution due to construction of the coastal structures, the interaction between the wave and current field and the bottom topography change cannot be ignored and several iterations are needed. So, we attempted to reduce the number of iterations by using a simply modelled series of wave conditions.

Table 1 shows the calculation methods of waves, currents and beach changes. The wave field is computed using the energy flux equation as described with the directional wave spectrum presented by Karlsson(1969). The wave heights in the surf zone are estimated by the model of random wave breaking proposed by Goda(1975). This equation is applicable only for wave shoaling and refraction, and is not for wave diffraction in a strict sense. Recently, more accurate equations for combined refraction and diffraction such as the mild-slope equation and its approximate parabolic-type equations are often adopted. Watanabe and Maruyama(1986) also presented the time-dependent mild-slope equations. These are applicable to calculate all kinds of wave transformation including wave breaking as well as shoaling, refraction and diffraction. But the applicability of the computation models based on these equations are generally restricted to the linear regular wave. The reason for using the method based on the energy flux equation is because treatment of random waves is important for practical applications and because the computing time of the actual random wave field in a wide region is relatively short.

In computing the nearshore current field, the spatial distributions of radiation stresses were estimated as regular waves; the wave energy and the principal direction at the local point were estimated from the directional wave spectrum calculated in the wave field computation, and the group velocity and the wave celerity were estimated by using the significant wave period.

As the momentum exchange coefficient, the expression proposed by Longuet-Higgins(1970) was adopted. The mixing length is generally set to be the distance from the shoreline, but in this study, it was set to be the shortest length either from the breakwater or from the shoreline. Then, the nearshore current field including circulation near the breakwater could be reproduced better.

In calculating bottom elevation change, we employed the formula of local sediment transport rate in a wave-current coexistent field proposed by Watanabe et al.(1986). This model is simple and practical. The sediment transport rate is divided into the transport due

to mean currents and that due to waves. The cross-shore sediment transport rate due to waves is assumed to be important to the short-term beach deformation, and not so important to the long-term change. In many cases, sediment transport due to nearshore currents is the dominant feature of long-term change caused by construction of a coastal structure. So, in this study, only the sediment transport due to nearshore currents were taken into account. The local sediment transport rates were evaluated using the quantities corresponding to the significant wave and the principal direction.

Table 1 Calculation methods of three submodels

CALCULATION OF WAVE FIELD
(REFRACTION) Wave energy flux equation (Karlsson, 1969) (BREAKING) Goda's model (1975) (DIFFRACTION) Energy flux transmitted from the breakwater is zero
CALCULATION OF NEARSHORE CURRENT FIELD
Vertically integrated equations of mean momentum and of continuity
CALCULATION OF BOTTOM ELEVATION CHANGE
Equation of sediment mass conservation [Local sediment transport rate formula proposed by Watanabe et al. (1986)] Sediment transport due to mean currents q_c : $q_c = A_c (\tau - \tau_c) u_c / \rho g$ where A_c : a non-dimensional coefficient, τ : the maximum value of the bottom shear stress in a wave and current coexistent field, τ_c : the critical shear stress for the onset of sediment movement, u_c : the mean current velocity.

3. PRACTICAL APPLICATION OF THE MODEL

3.1 TOPOGRAPHY CHANGES AROUND IIOKA FISHERY HARBOUR

Figure 2 shows the location map of Iioka Fishery Harbour. Iioka Fishery Harbour faces directly to the Pacific Ocean and is located at the northeastern end of the Kujyukuri Coast. This coast is one of the most famous sandy beaches with the continuous coastline of 55km and bounded at both ends by eroding sea cliffs. The northern sea cliff, Byobugaura, stretches northeastward 10km long and is bordered immediately on the north by Iioka Fishery Harbour. And the Byobugaura Cliff has supplied considerable amounts of sediment to the Kujyukuri Coast.

Judging from an aerial photograph taken in February of 1986 shown in Photo 1, it was a little stormy day with the significant wave height of about 2m. Looking at the crestlines of waves, we will find that the incident wave attacks the harbour much obliquely and then the longshore drift to the southwest is predominant.

As Iioka Fishery Harbour is located at the passing point of longshore drift from the Byobugaura Cliff to the Kujyukuri Coast, a large portion of longshore sand drift has been obstructed by the harbour. Consequently, not only harbour shoaling but also beach erosion of the neighbouring beaches have occurred.

Figure 3 shows the bottom topography change around the harbour during approximately one and half years from June of 1986 to November of 1987. The upper figure shows the comparison of bottom contours and the lower shows the distribution of depth changes. Considerable accretion took place along the breakwater on the updrift side of the harbour, especially around the entrance. On the other hand, erosion took place on the downdrift side. The mechanism of these beach deformations can be explained by the following two kinds of nearshore currents. One is the longshore current developing westward on the eastern side of the harbour, and another is the clock-wise nearshore circulation in the sheltered area of the breakwater on the western side. This is a typical case of beach deformation in constructing a structure on a sandy coast with considerable amounts of longshore drift.

3.2 VERIFICATION OF THE WAVE AND CURRENT COMPUTATIONS

In order to verify the wave and current field computations, the field observation was carried out around Iioka Fishery Harbour over a period of approximately one month from September to November in



Fig.2 Location map of investigation site

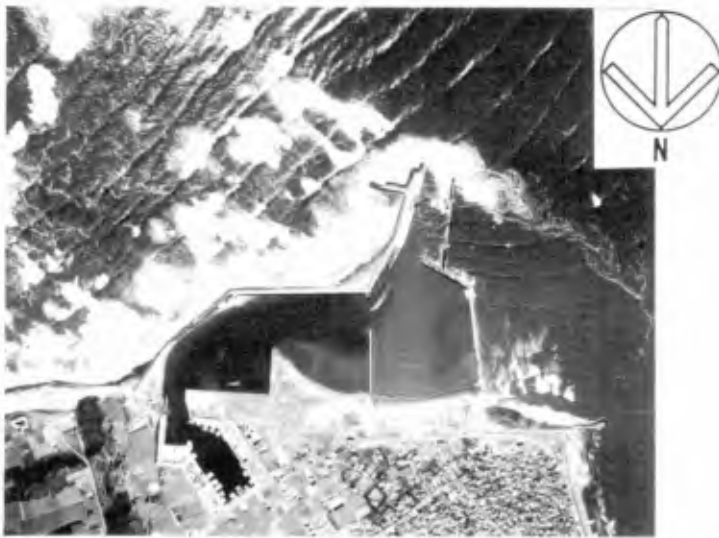


Photo 1 Aerial photograph (February, 1986)

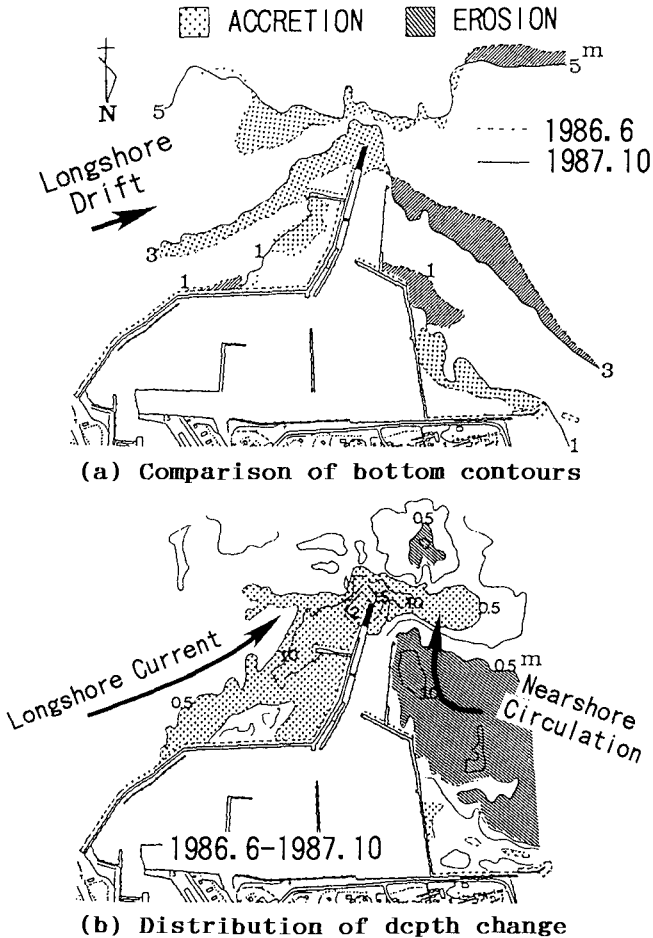


Fig.3 Bottom topography change around lioka Fishery Harbour(1986.6-1987.10)

1987. Figure 4 shows the measuring points around the harbour where wave directions and nearshore currents were observed using electro-magnetic current meters. Incident wave conditions such as wave heights, periods and directions were also measured using a combination of an ultra-sonic wave gauge and an electro-magnetic current meter at a water depth of 15m offshore in front of the harbour. During the observation, storm waves greater than 2m in significant wave height were frequently encountered. Therefore, we could collect much data on the large waves caused by typhoons.

Figure 4 also shows the computation area which is about 4km long in the alongshore direction and about 6km long in cross-shore direction. Three cases of wave height conditions were treated, that is, the significant wave height of 2m with its period of 8s, 3m with 10s and 4m with 12s. With respect to these three cases of wave height conditions, three wave directions of ESE, SE and SSE were considered. And totally nine cases of computations were performed. According to these nine cases of calculations, measured data of wave directions and mean currents were divided into nine classes in total. And the mean values of wave directions and mean currents at each point in every class were regarded as the measured values and compared with the results of the computations.

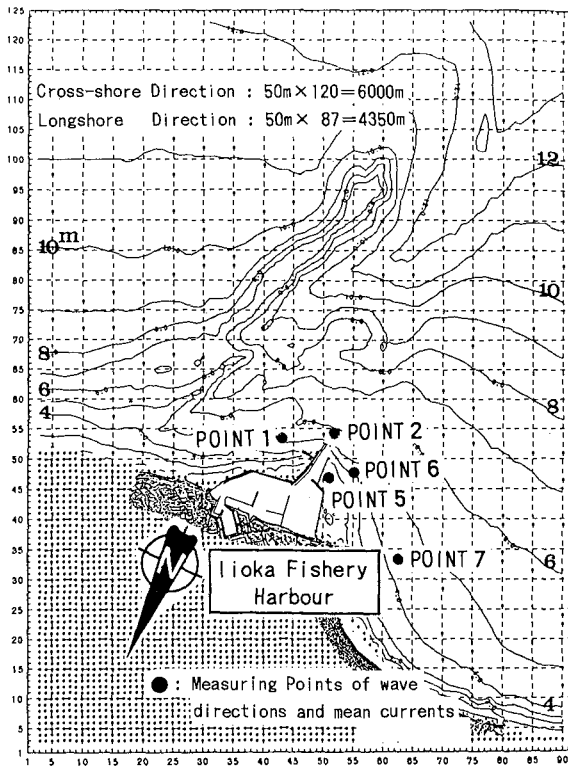


Fig.4 Location of the current meters and the area of numerical simulation

Figure 5 shows comparisons between the measured and the computed principal wave directions. As the wave propagating directions are scarcely affected by the incident wave periods in the range of 8 to 12 seconds, the results of computations of 3m in wave height with 10 seconds in wave period were used. The computed results show fairly good agreement with the observed.

Figure 6 shows the examples of the nearshore current computations under the wave direction of ESE. The measured vectors are also shown in this figure and expressed by bold arrows in the different scale from the calculated vectors. The longshore current develops westward along the eastern breakwater and passes the entrance of the harbour quickly. And the clock-wise circulation occurs remarkably around the western side of the harbour entrance. The observed dominant current pattern is reproduced satisfactorily by the numerical simulation.

Figure 7 shows comparisons between measured and computed absolute values and directions of mean current vectors. The computed results are compared with only reliable data which satisfy such conditions that the current velocity is beyond 5 cm/s and the current direction is stable. There exists a little disagreement between the measured and the calculated. However, in spite of assuming the quasi-stationary wave and current field and neglecting the wave-current interaction, the computed results agree well with the measurements, especially at the POINT 2 in front of the harbour entrance.

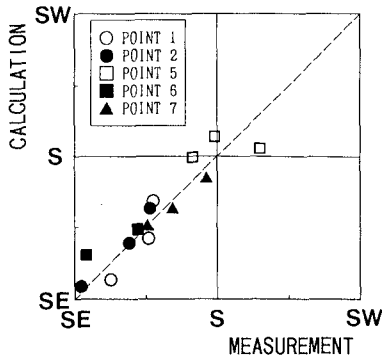


Fig.5 Comparison between the measured and the calculated principal wave direction

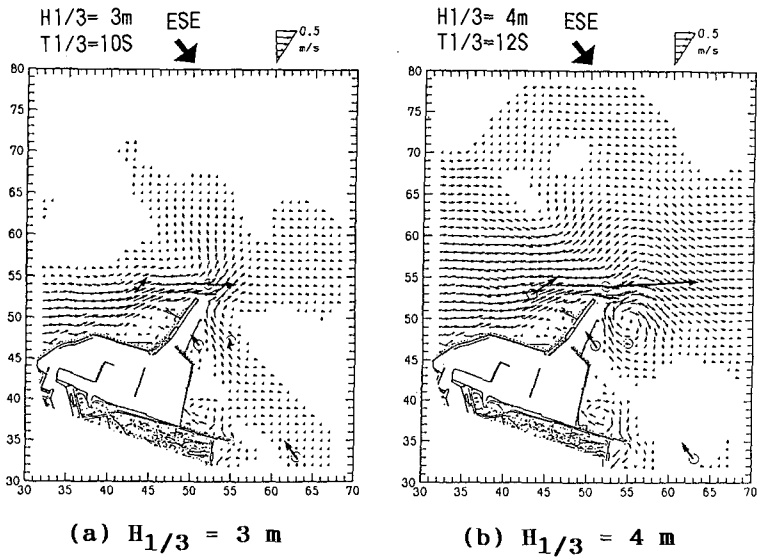


Fig. 6 Distribution of the calculated nearshore current field and the measured current vectors

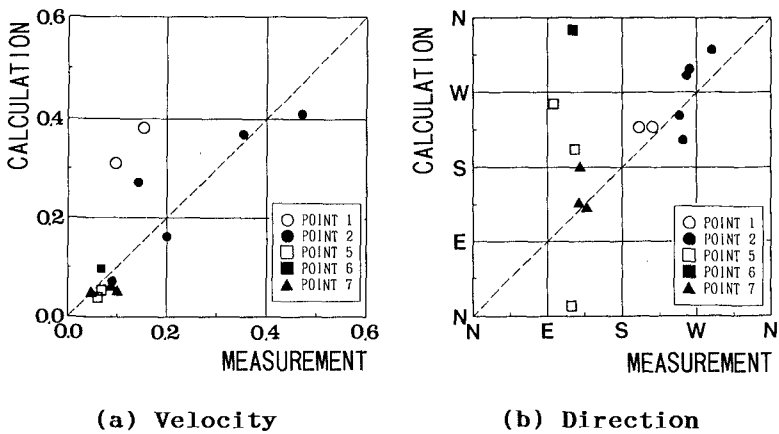


Fig. 7 Comparison between the measured and the calculated velocities and directions of the nearshore current

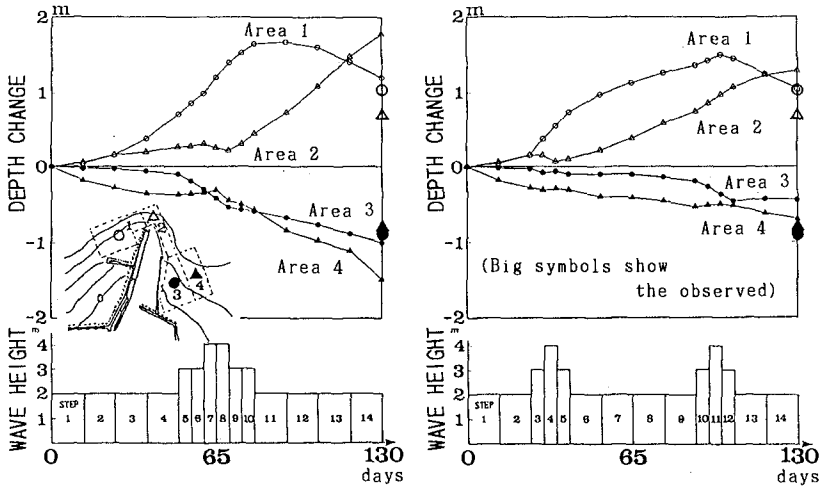
3.3 REPRODUCTION OF THE LONG-TERM BEACH EVOLUTION

We tried to reproduce quantitatively the long-term topography changes around Ilioka Fishery Harbour during approximately one and half years shown in Figure 3. The numerical simulation was performed by repeating the calculation of the wave-current field and that of the beach changes alternatively. In order to shorten the computation time, we attempted to use the three modelled wave conditions. These have one, two, or four series of severe waves for the investigation period of one and half years (peak significant wave height is 4m). The occurrence frequency of severe waves was determined on the basis of the observed wave climate data, and each modelled wave condition has the same occurrence frequency in total. The wave conditions with the significant wave height below 2m were not taken into account, because the longshore current could not reach the entrance of the harbour and little accretion took place under such a calm wave condition.

Figure 8 shows the calculated time series of mean depth variations in the four areas around the harbour entrance. In every case, the calculated depth variations after one and half years (130 days of severe waves) show accretion of about 1.0m in Area 1 and 2, and erosion of about 0.5m in Area 3 and 4. These results agreed quantitatively with the actual topographical changes.

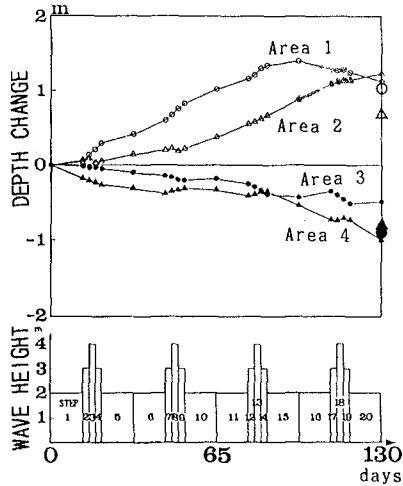
Investigating more precisely the results of case 2, in Area 1 along the breakwater on the updrift side, rapid accretion takes place during the first severe wave series. And the depth change reaches an equilibrium state after the first severe wave series. In Area 2 at the harbour entrance, rapid accretion takes place after accretion advanced in Area 1, and the depth change then reaches an equilibrium after the second severe wave series. On the other hand, in case 1, an equilibrium state is not reached in Area 2 after only one series of severe waves.

Figure 9 shows comparisons between the measured and the computed bottom elevation changes. Big symbols indicate the average in each area and small symbols indicate the values at each calculation grid. Although there exist a little disagreement at the local points, the averaged value of calculation in each area shows good agreement with that of observation. In spite of greatly simplifying the wave conditions, it is found that the long-term beach evolution around the harbour entrance and its consequent bottom topography change can be reasonably simulated by using a model with two or more series of severe waves.



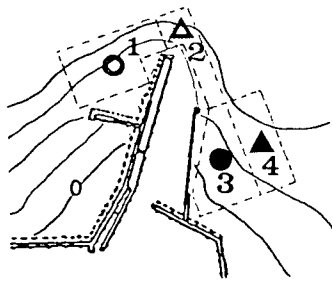
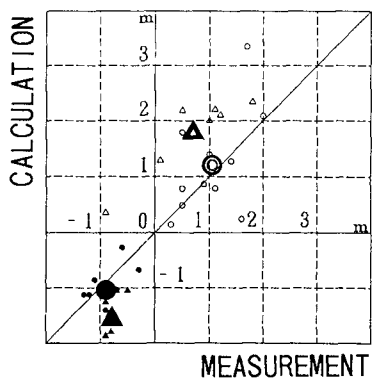
(a) Case 1

(b) Case 2

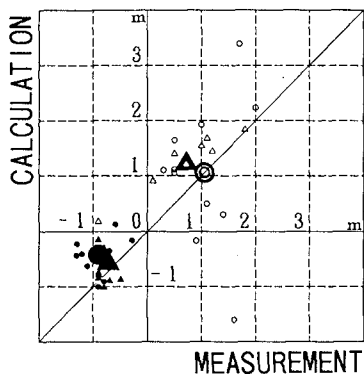


(c) Case 3

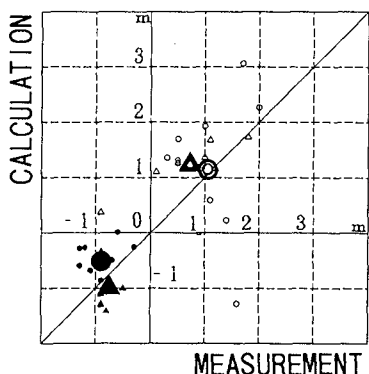
Fig. 8 Comparison between the measured and the calculated bottom elevation changes



(a) Case 1



(b) Case 2



(c) Case 3

Fig.9 Calculated time series of depth changes in the four areas around the harbour

4. CONCLUSIONS

The bottom topography change around a fishery harbour during one and half years were simulated by using the three-dimensional beach evolution model under the simplified wave condition. It is concluded that the model has the required accuracy for practical use and that the equilibrium state of topography change can be also predicted.

ACKNOWLEDGMENTS

We would like to express our thanks to Dr. Yamamoto of National Research Institute of Fisheries Engineering and Mr. Nishi of the Japanese Institute of Technology on Fishing Ports and Communities (now, Fisheries Agency) for their advice and useful discussion.

REFERENCES

- Goda, Y. (1985): Irregular wave deformation in the surf zone, Coastal Eng. in Japan, Vol.18, pp.13-26.
- Karlsson, T. (1969): Refraction of continuous ocean wave spectra, Proc. ASCE, Vol.95, No. WW4, pp.437-448.
- Longuet-Higgins, M.S. (1970): Longshore currents generated by obliquely incident sea waves, Jour. of Geophys. Res., Vol.75, No.33, pp.6778-6789.
- Watanabe, A., K. Maruyama, T. Shimizu and T. Sakakiyama (1986): Numerical prediction model of three-dimensional beach deformation around a structure, Coastal Eng. in Japan, Vol.29, pp.179-194.
- Watanabe, A. and K. Maruyama (1986): Numerical modeling of nearshore wave field under combined refraction, diffraction and breaking, Coastal Eng. in Japan, Vol.29, pp.19-40.

CHAPTER 189

SAND TRANSPORT RATE UNDER WAVE-CURRENT ACTION

Akira Watanabe¹ and Masahiko Isobe²

Abstract

Laboratory experiments were conducted to obtain data on sand transport processes and transport rates under combined action of waves and currents using an oscillatory-steady flow tank. The sand transport processes were classified into seven types. Four kinds of non-dimensional flow power parameters were defined, and their linear relations with the non-dimensional net transport rates were found for all the transport types.

1. Introduction

Considerable efforts have been devoted in recent years to developing mathematical models of beach evolution, which will be generally classified into three groups: "shoreline change models (e.g. Hanson et al., 1989)", "beach profile change models (e.g. Larson et al., 1989; Watanabe & Dibajnia, 1989), and "beach topography change models (e.g. Watanabe et al., 1986; Vriend & Ribberink, 1989)". Topography change models generally require formulas for estimating local sediment transport rates under combined action of waves and currents. The model developed by Watanabe et al. (1986) employs simple but useful sediment transport formulas based on the power (or energetics) model concept, and has been applied to various engineering practice in Japan (e.g. Shimizu et al., 1990). However we have not yet established highly-reliable formulas to be built in topography change models for accurately evaluating net rates of sediment transport under general conditions of waves and currents.

Purposes of the present study are to obtain fundamental experimental data on net rates of sand transport due to combined action of waves (oscillatory flow) and currents (steady flow) under a simplified condition where the directions of oscillatory and steady flows are parallel, and to investigate relations between the

¹ Professor, Dept. of Civil Eng., Univ. of Tokyo, Bunkyo-ku, Tokyo, 113 Japan.

² Associate Professor, ditto.

net transport rates and relevant hydraulic parameters on the basis of the power model concept.

2. Experimental Procedure and Results

2.1 Experimental procedure

The experiments were conducted using an oscillatory-steady flow tank, in which a steady flow was superimposed in parallel on an oscillatory flow with an arbitrary time variation of velocity as shown in Fig. 1. The time histories of the oscillatory flow velocity were sinusoidal in some cases, but in most case they were non-sinusoidal and asymmetric between positive and negative velocities as illustrated in the figure. The test section was 2 m in length, 24 cm in width and 31 cm in height.

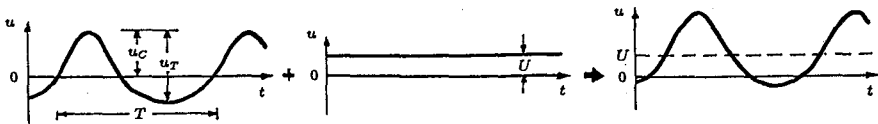


Fig. 1 Definition sketch for combined-oscillatory-steady flow.

The oscillatory flow conditions were changed for the period, $T = 3$ and 6 s, the total amplitude of velocity u_T from 54 to 86 cm/s, and the velocity asymmetry defined by the ratio of the positive (or onshore) velocity amplitude u_C to the total amplitude u_T , for $u_C/u_T = 0.5$ (sinusoidal oscillation), and for 0.6 and 0.7 . The steady flow velocity U was also changed between -30 cm/s and $+25$ cm/s.

Two kinds of sand with the median diameter $D = 0.18$ and 0.87 mm were used. For each condition, 1) first the sand bed was made even, 2) next oscillatory-steady flow was generated for a time duration of $600T$, 3) then bottom profiles in dynamical equilibrium were measured, 4) again the same flow was generated for a period of 10 to 60 s, and 5) lastly final bed profiles and volumes of the sand trapped at both ends of the test section were measured. Bed profiles were measured along ten cross-shore lines with electric resistance-type bed profilers. Net rate of sand transport was evaluated at the mid-cross-section of the test section from the bed profile changes and trapped sand volumes.

Sand ripples were formed in all the cases; two-dimensional ripples with long parallel crests in relatively weak flows and three-dimensional ripples with ladder-shaped short crests in intensive flows. The sand movement was recorded on a VTR. For all the flow conditions, the velocity was measured with an LDV above a fixed flat bed. The velocities measured at an elevation 10 cm above the bed will be used in the following data analysis.

2.2 Net transport rate and sand movement types

Let us define a non-dimensional net sand transport rate Φ by

$$\Phi = \frac{(1 - \epsilon_v) q_{net}}{w_0 D} \tag{1}$$

where q_{net} is the volumetric net transport rate per unit width per unit time, and ϵ_v , w_0 and D are the porosity, fall velocity and median diameter of the sand, respectively. For the fine sand ($D = 0.18$ mm), $\epsilon_v = 0.44$ and $w_0 = 2.1$ cm/s, whereas for the coarse sand ($D = 0.87$ mm), $\epsilon_v = 0.47$ and $w_0 = 8.2$ cm/s. The direction of the net transport is taken positively into that of the positive (onshore) velocity.

Figure 2 shows the relations between the non-dimensional transport rate Φ and the steady flow velocity U for each oscillatory flow condition for the fine sand. It is seen that the net transport rates are mostly negative, which corresponds to the offshore transport. For example, for the oscillatory flow condition indicated by the inverted triangle symbols, the net transport rates took the largest negative magnitude when there was no steady flow, decreasing in magnitude with the increase in the steady flow velocity U , either positive or negative, and it became positive only for the large positive U .

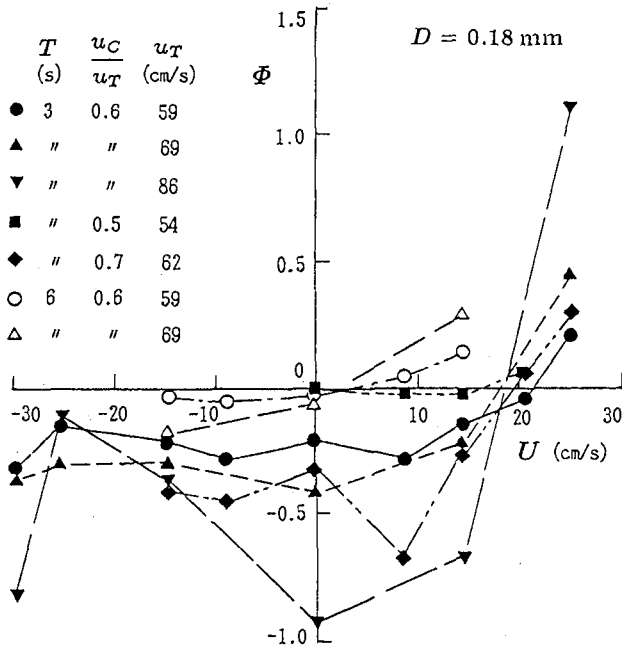


Fig. 2 Non-dimensional net transport rate Φ vs. steady flow velocity U for fine sand.

The relations between Φ and U for the coarse sand are shown in Figure 3. For the coarse sand, the net transport rates Φ are mostly positive, namely the onshore transport was predominant even for the negative steady flow velocity U with moderate magnitude.

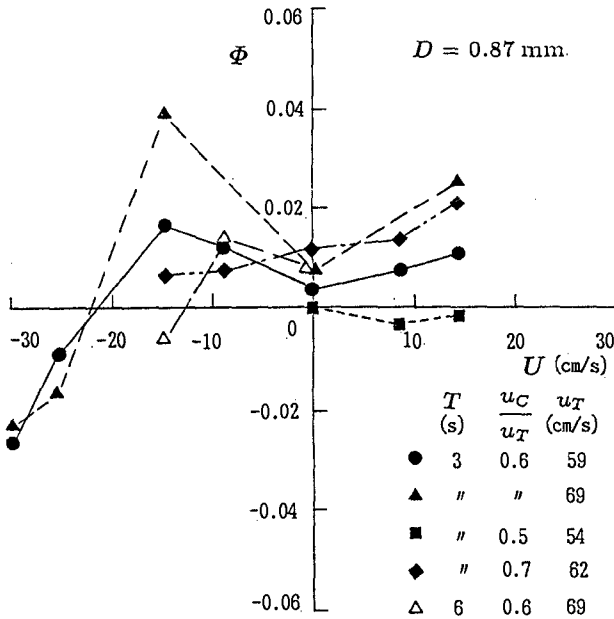


Fig. 3 Non-dimensional net transport rate Φ vs. steady flow velocity U for coarse sand.

These figures indicate that the dependency of the net transport rate on the steady flow velocity and on the oscillatory flow conditions is not simple or monotonic at all. Their interrelations appear too complicated to express by a single general formula.

Now, according to the observation of sand movement in the experiments, it has been concluded that the sand transport processes in the present experiments will be classified into the following seven types.

The first four types are for the fine sand. The sand transport process of **Type I** was observed when $T = 3$ s and $|U| < 20$ cm/s. For this type, the sand was set in suspension by lee-vortices formed during positive velocity, and was transported into the offshore direction during negative velocity, whereas the sand suspended during negative velocity was transported shoreward during positive velocity. Because of the asymmetric velocity change, the net transport was into the offshore (negative) direction (see Fig. 4). **Type II** appeared for the cases of

strong onshore steady flow ($T = 3\text{ s}$, $U > 20\text{ cm/s}$), and **Type III** took place for those of strong offshore flow ($T = 3\text{ s}$, $U < 20\text{ cm/s}$). For **Type II**, the sand suspended during the large onshore flow velocity was transported into the shoreward direction (Fig. 5), whereas for **Type III**, the suspended sand was transported into the offshore direction (Fig. 6). **Type IV** was observed when $T = 6\text{ s}$, namely, the oscillatory flow was of relatively long period. For this type, the sand was suspended up to an elevation higher than in the previous types, and was transported mainly by the steady flow. Hence the direction of the net transport agreed with that of the steady flow (Fig. 7).

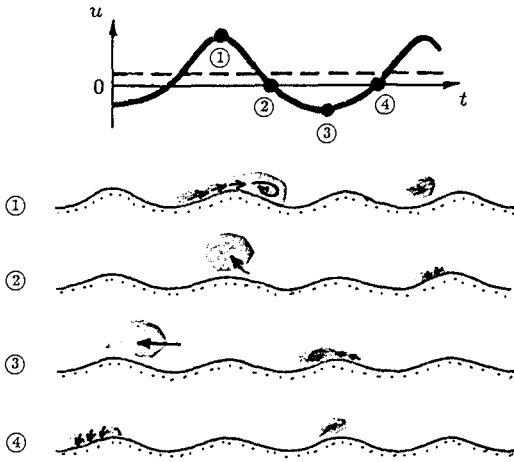


Fig. 4 Transport process of Type I.

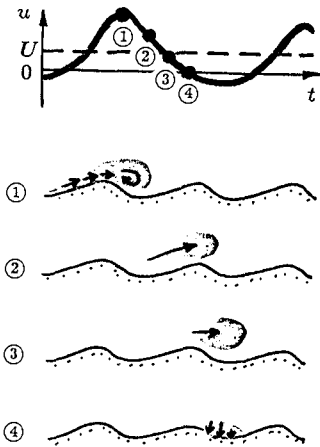


Fig. 5 Transport process of Type II.

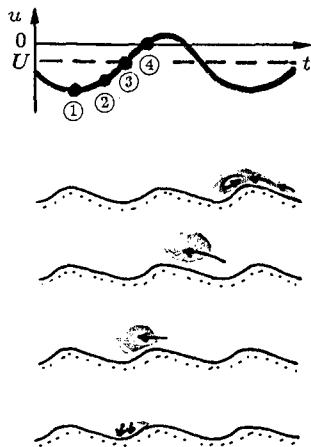


Fig. 6 Transport process of Type III.

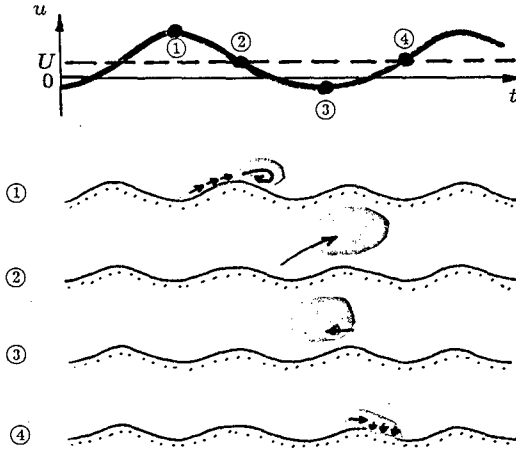


Fig. 7 Sand transport process of Type IV.

The remaining three types are for the coarse sand. **Type V** occurred when $U \geq 0$. For this type, bedload transport was predominant, and the sand was transported into the onshore direction by both the oscillatory flow and the steady flow (Fig. 8). **Type VI** took place when the steady flow was strong and in the offshore direction ($U < -20$ cm/s). Again bedload transport was predominant, and the sand was transported into the offshore direction by the very strong offshore flow (Fig. 9). The last type, **Type VII**, appeared when -20 cm/s $< U < 0$. For this type, the sand suspended during negative velocity as well as bedload during positive velocity contributed to the onshore net transport (Fig. 10).

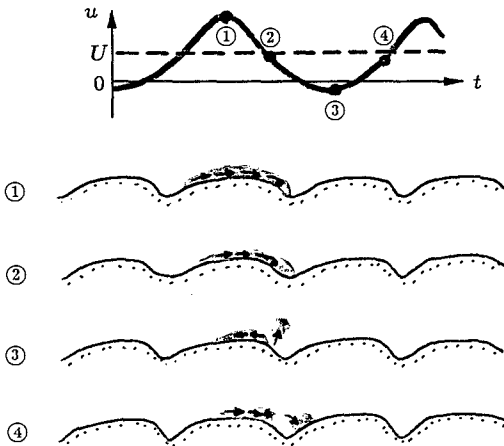


Fig. 8 Sand transport process of Type V.

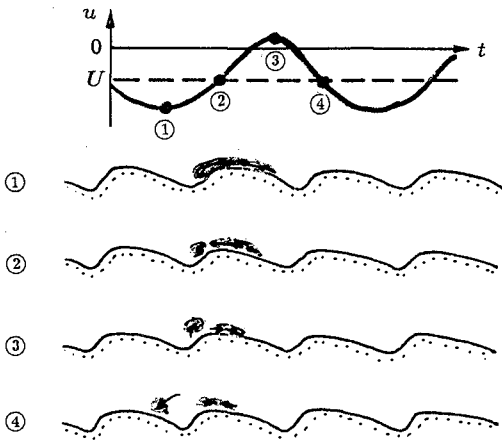


Fig. 9 Sand transport process of Type VI.

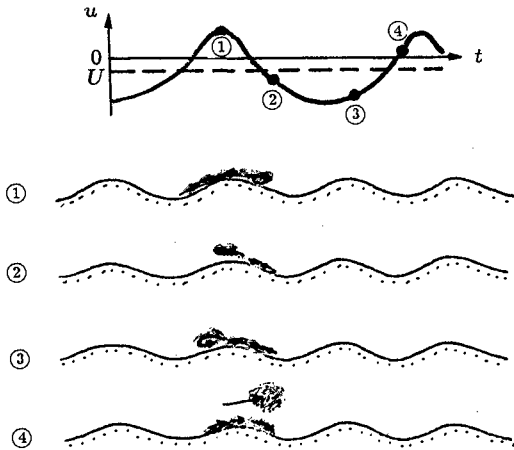


Fig. 10 Sand transport process of Type VII.

3. Net Transport Rate and Flow Power

We will now attempt to relate the net transport rate with the flow condition for each type applying the power model concept. For this let us first define the excursion lengths d_{0+} and d_{0-} and the Shields numbers Ψ_+ and Ψ_- for the positive velocity period T_+ and the negative velocity period T_- , respectively, (see Fig. 11) by

$$d_{0+} = \int_{T_+} u dt, \quad d_{0-} = - \int_{T_-} u dt \tag{2}$$

$$\Psi_+ = \frac{f_{cw+} u_C^2}{2sgD}, \quad \Psi_- = \frac{f_{cw-} (u_T - u_C)^2}{2sgD} \tag{3}$$

where s ($= \rho_s/\rho - 1$) is the immersed specific gravity of the sand, and f_{cw+} and f_{cw-} are the friction factors in a coexistent wave-current field and are determined from the hypothetical sinusoidal oscillation velocities and the steady flow velocity (Fig. 11) with the frictional law proposed by Tanaka and Shuto (1981). The median diameter D of the sand grains was used as the equivalent roughness k_s ($= 30z_0$) in spite of the presence of sand ripples.

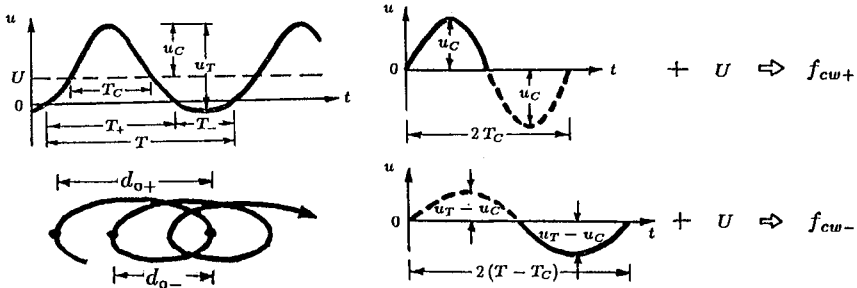


Fig. 11 Definition sketch for computing excursion lengths and Shields numbers.

With the consideration of the transport processes for the above seven types, let us further define four kinds of non-dimensional flow powers, P_I , P_{II} , P_{III} and P_{IV} , and examine their correlations with the non-dimensional transport rate Φ .

a) Type I

On the basis of the power model concept, we assume that the immersed-weight of the sand set in suspension per unit horizontal area during the positive velocity period T_+ is proportional to the excess shear stress $(\tau_+ - \tau_c)$ times (T_+/T) , where $\tau_+ = \rho s g D \Psi_+$ is the amplitude of the bed shear stress during T_+ , and τ_c the critical shear stress for the onset of the general movement. We further assume that the offshore displacement of this suspended sand during T_- is proportional to the excursion length d_{0-} . Then the resultant offshore transport rate q_- averaged over the period T is to be proportional to a kind of flow power $(\tau_+ - \tau_c) (T_+/T) (d_{0-}/T)$. In a similar way, the onshore transport rate q_+ will be in proportion to $(\tau_- - \tau_c) (T_-/T) (d_{0+}/T)$, and then the net transport rate q_{net} will be given by the difference between q_+ and q_- .

Hence if we define a non-dimensional flow power P_I by

$$P_I = (\Psi_- - \Psi_C) \frac{T_-}{T} \frac{d_{0+}}{w_0 T} - (\Psi_+ - \Psi_C) \frac{T_+}{T} \frac{d_{0-}}{w_0 T} \tag{4}$$

where Ψ_C is the critical Shields number, then we can expect the non-dimensional net transport rate Φ to be proportional to P_I .

Figure 12 shows the relation between Φ and P_I for Type I. Since this type includes the transport of the fine sand only, the critical Shields number Ψ_C was set as equal to 0.11 (see Watanabe et al., 1981). Although the scatter of the plotted data is not small, it is clear that Φ and P_I have a positive correlation, which is expressed approximately by the following linear relation:

$$\Phi = 1.5 P_I \tag{5}$$

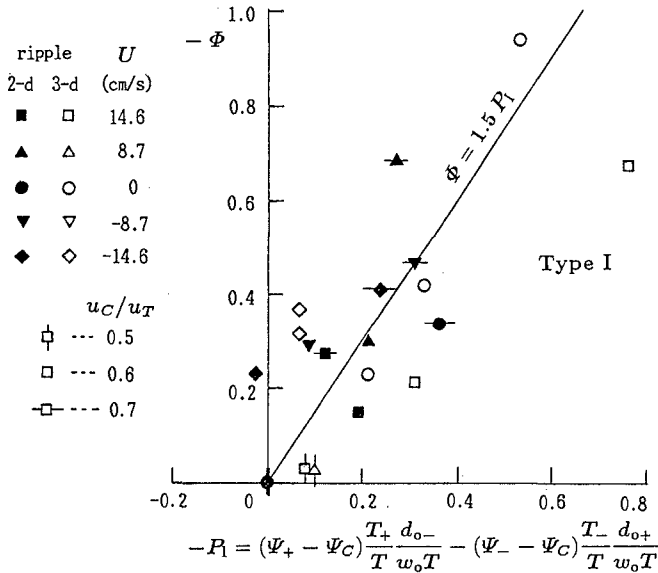


Fig. 12 Net transport rate Φ vs. flow power P_I (Type I).

b) Types II, III, V and VI

In the transport processes of these four types, just contrary to Type I, the sand set in motion by the onshore flow was transported into the onshore direction, and the one agitated by the offshore flow was carried toward the offshore. Hence we define a non-dimensional flow power P_{II} by

$$P_{II} = (\Psi_+ - \Psi_C) \frac{T_+}{T} \frac{d_{0+}}{w_0 T} - (\Psi_- - \Psi_C) \frac{T_-}{T} \frac{d_{0-}}{w_0 T} \tag{6}$$

According to Watanabe et al. (1981), a value of Ψ_C for the coarse sand (Types V and VI) should be about 0.06, but it was changed to 0.04, because noticeable sand movement was observed even when $\Psi_C < 0.06$ in the experiments.

The results shown in Fig. 13 indicate that, although the data for Type II show much scatter and are deviated from those for the other types, an overall relation is expressed fairly well by

$$\Phi = 0.15 P_{II} \tag{7}$$

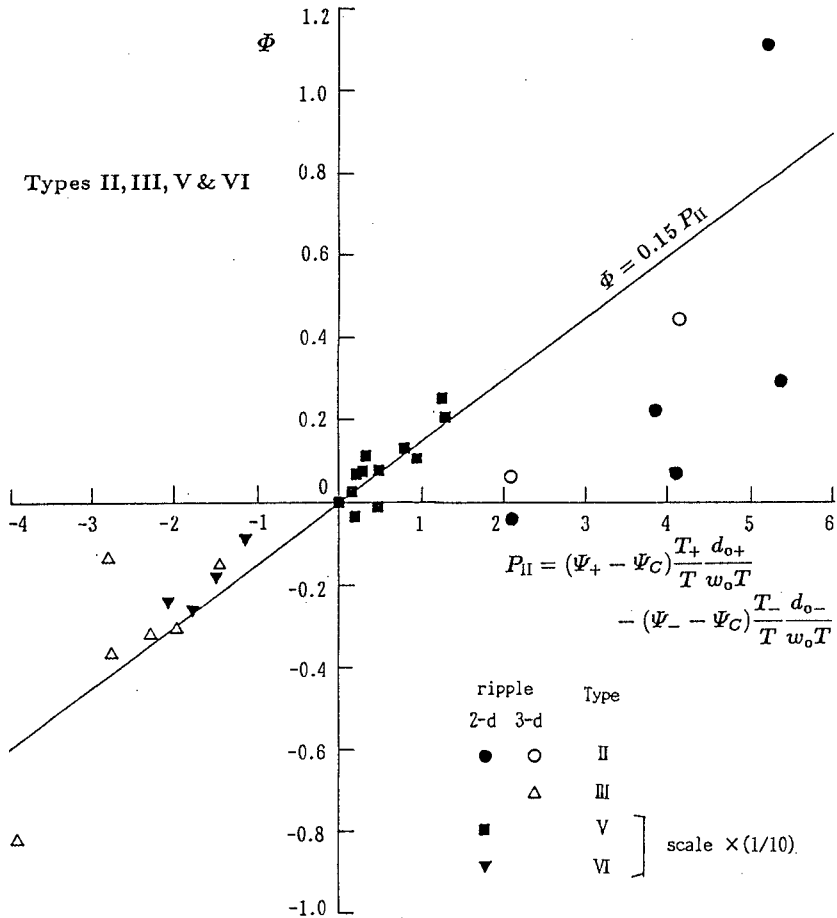


Fig. 13 Net transport rate Φ vs. flow power P_{II} (Types II, III, IV & V).

c) Type VII

For this type, both the bedload during the positive velocity period and the sand suspended during the negative velocity period contributed to the onshore net transport. Therefore the combination of the onshore components of P_I and P_{II} will be appropriate as an effective flow power P_{III} for Type VII, which is defined by

$$P_{III} = (\Psi_- - \Psi_C) \frac{T_-}{T} \frac{d_{0+}}{w_0 T} + 0.1 (\Psi_+ - \Psi_C) \frac{T_+}{T} \frac{d_{0+}}{w_0 T} \quad (8)$$

where the factor of 0.1 in the second term was determined by considering the proportionality coefficients in Eqs. 5 and 7.

Figure 14 shows the relation of Φ with P_{III} , which is well approximated by

$$\Phi = 2.7 P_{III} \quad (9)$$

It should be noted that the sand ripples were two-dimensional in all the cases of this type.

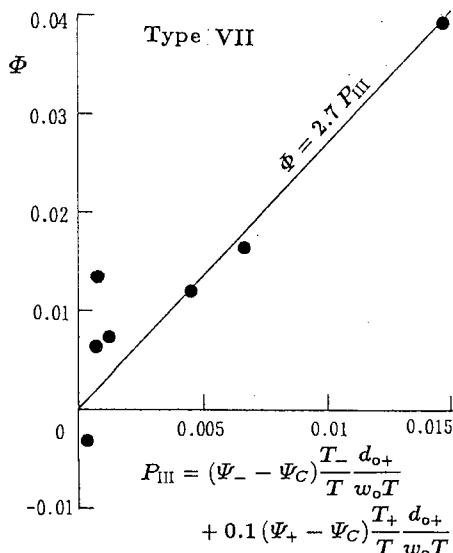


Fig. 14 Net transport rate Φ vs. flow power P_{III} (Type VII).

d) Type IV

For this type, the suspended sand was transported mainly by the steady flow, and the direction of the net transport changed with that of the steady flow. (The sand ripples were three-dimensional.) Hence the net transport rate will be given by the summation of the component due to the steady flow and that due to the oscillatory flow as in the transport rate formula proposed by Watanabe et al. (1986). Let us therefore define a non-dimensional flow power P_{IV} for this type by

$$P_{IV} = (\bar{\Psi}_C - \Psi_C) \frac{6U - u_T/2}{w_0} \quad (10)$$

where $\bar{\Psi}_C$ is the representative time-mean Shields number defined by

$$\bar{\Psi}_C = \frac{\Psi_+ T_+ + \Psi_- T_-}{T} \quad (11)$$

The relation between Φ and P_{IV} for this type is shown in Fig. 15, and is approximately expressed by

$$\Phi = 0.08 P_{IV} \quad (12)$$

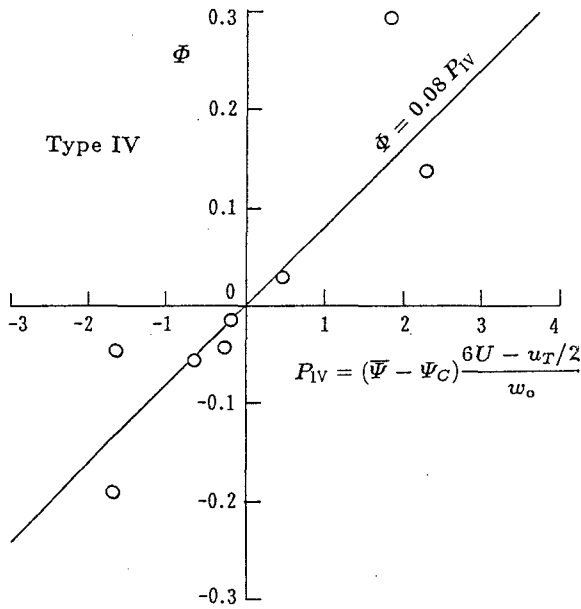


Fig. 15 Net transport rate Φ vs. flow power P_{IV} (Type IV).

4. Concluding Remarks

Experimental data were obtained on the net sand transport rate in combined-parallel-oscillatory-steady flows. The sand transport processes in the experiments were classified into seven types. Considering typical features of the transport process of each type, we defined four kinds of non-dimensional flow power, and found that the net transport rates under combined action of waves (oscillatory flow) and currents (steady flow) were well correlated to the relevant flow powers. It should be mentioned that the relations between the non-dimensional net transport rates and flow powers obtained in this study don't involve explicitly the size and shape of sand ripples in spite of their presence.

The formulas presented in this paper cannot be directly built in mathematical models; we need to accumulate more experimental data and to study more detailed sand transport processes. However these results would provide us yet with very useful information such as for the establishment of generalized sediment transport rate formulas, and for the development of numerical simulation models of sand grain motion over a rippled bed under waves and currents, on which our group is now working.

This paper is a part of the outcomes of our study supported by National Science Foundation of the Ministry of Education, Science and Culture, to which we would like to express our thanks. We also appreciate the efforts of Mr. M. Sakinada in conducting the experiments.

REFERENCES

Hanson, H., M.B. Gravens and N.C. Kraus (1989): Prototype applications of a generalized shoreline change numerical model, *Proc. 21st ICCE*, ASCE, pp. 1265-1279.

Larson, M., N.C. Kraus and T. Sunamura (1989): Beach profile change: morphology, transport rate and numerical simulation, *Proc. 21st ICCE*, ASCE, pp. 1295-1309.

Shimizu, T., H. Nodani and K. Kondo (1990): Practical application of the three-dimensional beach evolution model, *Abstracts, 22nd ICCE*, pp. 407-408.

Tanaka, H. and N. Shuto (1981): Friction coefficient for a wave-current co-existent system, *Coastal Eng. in Japan*, JSCE, Vol. 24, pp. 105-128.

Vriend, H. J. de and J.S. Ribberink (1989): A quasi-3D mathematical model of coastal morphology, *Proc. 21st ICCE*, ASCE, pp. 1689-1703.

Watanabe, A., Y. Riho and K. Horikawa (1981): Beach profile and on-offshore sediment transport, *Proc. 17th ICCE*, ASCE, pp. 1106-1121.

Watanabe, A., K. Maruyama, T. Shimizu and T. Sakakiyama (1986): Numerical prediction model of three-dimensional beach deformation around a structure, *Coastal Eng. in Japan*, JSCE, Vol. 29, pp. 179-194.

Watanabe, A. and M. Dibajnia (1989): Numerical modeling of nearshore waves, cross-shore sediment transport and beach profile change, *Proc. IAHR Symp. on Mathematical Modelling of Sediment Transport In the Coastal Zone*, pp. 166-174.

CHAPTER 190
DYNAMIC NUMERICAL MODELS FOR SAND WAVES
AND PIPELINE SELF-BURIAL

by

Carsten Staub ¹⁾ and Romke Bijker ²⁾

ABSTRACT

Two independent numerical models for prediction of sand wave heights and migration rates and for calculation of pipeline/cable seabed interaction have been developed. Both models are fully dynamic and respond to detailed and comprehensive input describing environmental conditions, seabed and soil characteristics and pipe/cable data. The models are based on state-of-the-art knowledge and include theoretical developments, model tests, field data and advanced sediment transport formulations. The models have been validated and calibrated against field data of sand waves and buried pipelines.

1. SAND WAVE MODEL

1.1 Introduction

Erodible sea beds will not usually remain plane when exposed to changing environmental conditions. A variety of different bed forms may emerge and continuously modify and adjust in response to varying wave/current conditions. The bed forms and their response to environmental conditions are also highly dependent on the bed material. Dimensions of wave/current generated bed forms observed in the offshore environment vary considerably from small ripples of a few centimetres height to the large tidal banks of heights up to 50 metres and many kilometres long.

1) Carsten Staub, M.Sc., Chief Engineer, Subsea Technology Division, Danish Hydraulic Institute, Agern Allé 5, DK-2970 Hørsholm, Denmark.

2) Romke Bijker, M.Sc., Manager, Offshore Section, Delft Hydraulics, Voorsterweg 28, P.O. Box 152, NL-8300 AD Emmeloord, The Netherlands.

The most important bed form in relation to marine pipelines is the offshore sand wave. Sand waves can at the same time be large enough and migrate fast enough to cause bed level changes, which are significant compared with the diameter of the pipeline. Furthermore, the sand wave is a widespread form which is observed in a large number of tidal areas but may also occur in deep water where density differences are responsible for relatively high current velocities near the bed.

1.2 Description of the model

The numerical model for sand waves is based on state-of-the-art theories for sand waves and for sediment transport in combinations of current and waves.

Basic theory

Deigaard and Fredsøe (1986) combined a theory for fully developed sand dunes in rivers by Fredsøe (1982) with a detailed model for sediment transport in current and waves developed by Fredsøe et al. (1985). The result was a calculation model for equilibrium sand waves in an offshore environment with waves and a unidirectional current perpendicular to the sand wave front.

This model was taken as a basis in the development of the present sand wave model.

The basic elements of the theory are:

- continuity equation for sediment
- constant form sand waves assumed
- sediment transport model
- description of deposition "downstream" of sand wave crest.

The equations to determine migration rate and height of equilibrium sand waves thus become (see e.g. Deigaard and Fredsøe, 1986)

$$a = - \frac{1}{1-n} \frac{dq}{dD} \quad (1)$$

$$A = \frac{q_D}{(1-n)a} \quad (2)$$

$$q_D = q_B + q_S (1 - \exp(-6A/L_S)) \quad (3)$$

The following notation is used:

- a : Sand wave migration rate
- A : Sand wave height
- q_D : The part of the sediment transport which is deposited downstream of the sand wave crest
- n : Porosity of the sea bed
- D : Water depth at sand wave crest
- q : Total sediment transport rate at sand wave crest
- q_B : Bed transport rate at sand wave crest
- q_S : Suspended transport rate at sand wave crest
- L_S : Length scale for the lag of the suspended sediment

The length scale of the lag of the suspended sediment, L_S , can be estimated from the concentration profile as:

$$L_S = \frac{U_C \cdot y_C}{w_s} \quad (4)$$

where y_C is the height of the centroid of the concentration profile above sand wave crest level, U_C is the flow velocity at the height, y_C , and w_s is the settling velocity of the suspended sediment.

A key assumption for the prediction of sand wave height is that the deposition of sediment at the front, and thus the migration rate of the sand wave, can be calculated directly on the basis of the sediment transport at the crest of the sand wave. The basis for this assumption is that flow separation occurs at the (instantaneous) sand wave front, leading to a vanishing sediment transport capacity in the separation zone. Thereby all the bed load and some of the suspended load which passes the sand wave crest will be deposited downstream of the crest. The deposition rate described by (3) assumes that the separation zone has a length of 6 times the sand wave height. Note that (3) has been slightly modified compared with the corresponding expression by Deigaard and Fredsøe (1986).

The model of Deigaard and Fredsøe (1986) has been extended to include:

- non-equilibrium sand waves
- arbitrary angles between waves and currents and sand waves (including reversing tidal currents)

- effects of short-crested sand waves
- effects of high water waves
- effects of wave generated ripples

The extensions are further described below.

Sand_wave_length

The sand wave length, λ , is in the model determined by a purely empirical relation

$$\lambda = 64A \quad (5)$$

The factor 64 was determined from field observations with significant variation in length/height ratio.

In pure steady current experiments show that the bed shear stress after a step attains a local maximum 16 times the step height downstream of the step indicating that for situations with dominant bed load transport the dune length would be 16 times the dune height. Presence of suspended load would cause the dunes to become longer but for the current and depth conditions prevailing in offshore areas this effect would be very limited.

There is presently no satisfactory explanation of why offshore sand waves are approx. 4 times longer than dunes of the same height in rivers.

Effect_of_high_waves

Flow separation downstream of the sand wave crest is essential for the formation of sand waves. Deigaard and Fredsøe (1986) described briefly the separation suppression effect of relatively high water waves. When waves are present together with a current, the tendency towards separation of the mean current is reduced. A crude criterion for suppression of flow separation was taken to be that the oscillating part of the shear velocity, U_{fw} , associated with the wave motion is larger than 7 times the shear velocity, U_{fo} , characterizing the mean current in the wave boundary layer.

In the present model the above criterion has been applied to form a correction factor by which the equilibrium sand wave height is reduced to zero (smoothly) when U_{fw} exceeds 7 times U_{fo} . The effect of waves on flow separation has been described in more details recently by Deigaard (1990).

Non-equilibrium sand waves

The wave and current conditions are normally highly variable, and it is therefore of interest to predict the behaviour of sand waves that are not in equilibrium under the actual hydraulic conditions. The adaptation time of a sand wave will depend on the sediment transport rate and on the volumes of the equilibrium versus the actual sand waves, i.e. the amount of sediment that has to be shifted in order to form the equilibrium sand wave.

Fredsøe (1979) and (1981) presented a model for the change of dune dimensions subject to a change in hydraulic conditions. The rate of change in dune height is found assuming a given shear stress distribution evaluated on the basis of an idealized triangular dune shape. A simple expression for the rate of change of dune height is readily derived from Fredsøe's formulas

$$\frac{dA}{dt} = \frac{a}{\lambda} (A_{eq} - A) \quad (6)$$

where

- A : Actual sand wave height
- A_{eq} : Instantaneous equilibrium sand wave height
- a_{eq} : Actual sand wave migration rate
- λ : Actual sand wave length
- t : Time

The above equation (6) has been applied in the present model to calculate the transient behaviour of the sand waves.

Directions of waves and current

The Sand Wave Model has been developed to deal with arbitrary directions of both waves and currents relative to the direction of the sand wave crest. The migration rate of a sand wave is calculated in a direction perpendicular to the sand wave crest. When the direction of the total sediment transport forms an oblique angle with the sand wave crest, only the sediment transport component perpendicular to the crest is taken into account in the calculation of sand wave migration and development.

It is assumed that long-crested sand waves will not affect the direction of a current approaching at an oblique angle i.e. streamline refraction has not been taken into account in the model.

Tidal flow conditions with reversing flow direction characterize many sand wave areas. A reversing tidal current may significantly change the shape of the sand wave crest region during a tidal cycle and thereby affect the migration and development of the sand wave. No effects of the sand wave profile shape have, however, been included in the model.

Effect of short-crested sand waves

Field data show some systematic differences in sand wave morphology from one area to another. One of the most pronounced is the difference in relative crest length. The present model is not able to explain this difference, but the effect of short-crestedness on sand wave development has been included in the model in a simplified way as described in the following:

If the sand wave crest lengths are not large compared to the sand wave length then the three-dimensional structure of the bed will result in a three-dimensional flow pattern. There will be a decrease in the water discharge over the crest peaks. The decrease is partly due to the energy loss in the separated flow downstream of the crest and partly due to the decreased water depth at the crest of the sand wave.

Fredsøe (1989) calculated analytically the equilibrium height of sand waves as a function of their length/width ratio, λ/w . He assumed a double periodic bed topography, did not include wave effects and found that a short crested sand wave will have a larger equilibrium height, A_{3D} , than the height, A_{2D} , of a sand wave with infinitely long crest.

$$A_{3D} = A_{2D} (1 + (\lambda/w)^2) \quad (7)$$

Eq. (7) has been included in the present sand wave model as a correction applied to the equilibrium sand wave height.

Effect of wave generated ripples

The detailed sediment transport model originally developed by Fredsøe et al. (1985) is applied as an important submodule for the Sand Wave Model. This transport model was developed for plane sea bed conditions i.e. without wave generated ripples. This situation will occur during storm conditions which are very important in relation to

sand wave development and migration. More calm wave conditions where ripples are present are, however, also important. The sediment transport module has therefore been further developed to handle both situations without and with wave generated ripples. The modifications to the sediment transport model include descriptions of the processes involved as and are briefly outlined as follows:

- estimates of ripple dimensions as function of wave-current conditions.
- estimates of contribution to eddy viscosity due to ripples.
- estimate of mean concentration at the level of the ripple crests.
- estimate of the roughness due to the influence of ripples on the current.

The ripple dimensions, the eddy viscosity and the mean concentration are calculated from empirical formulas presented by Nielsen (1979). The ripple roughness is calculated by a formula of Raudkivi (1988).

1.3 Example of calculation

In a simulation of sand wave development the equilibrium sand wave height is first calculated i.e. the height that would exist after a long time with the same wave/current conditions. Sand waves will form for a certain range of current velocities and the height may theoretically be up to about 30 percent of the mean water depth. Wave action generally tend to increase the sand wave height (except when they totally dominate the current) and particularly when the waves travel perpendicular to the sand wave crests.

Fig. 1 shows part of the input and the output time series for a 10 days Sand Wave Model simulation. The example which is taken from a location in the Southern North Sea illustrates the effect a stormy period has on sand wave development and migration in an area dominated by tidal currents. Directions of waves and currents which are also part of the input are not shown in this figure.

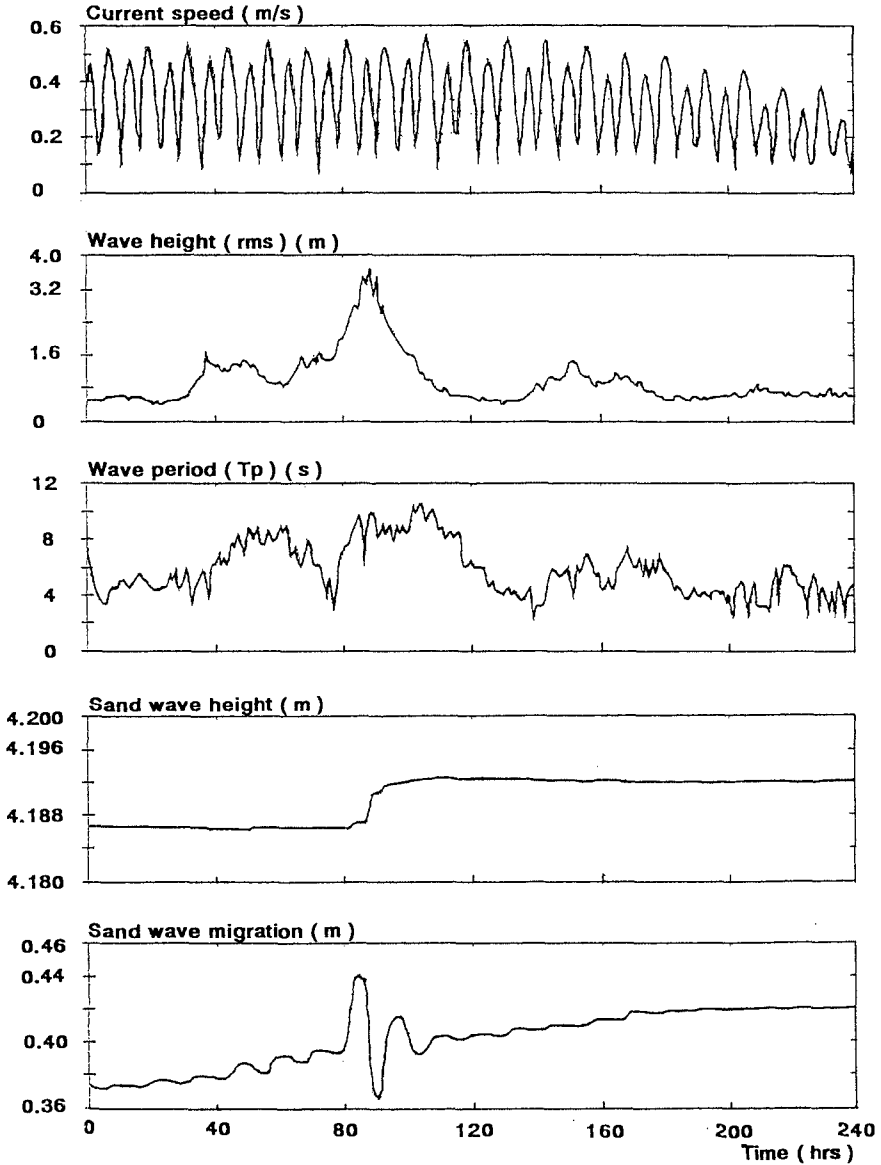


Fig. 1 Sand wave development and migration during a 10 days period with a storm. Example from Southern North Sea. Water depth: 35 m, Sediment: $d_{50}=0.35$ mm.

2. SELF-BURIAL MODEL

2.1 Introduction

Self-burial of submarine pipelines has been subject to study since 1978. At that time, a sudden, and unexpected, self-burial of a just-laid pipeline triggered extensive research programs.

The Dutch authorities almost immediately recognized the potential of self-burial as a cost-effective burial method and approved a large number of pipelines to become self-buried. As result of this attitude, significant experience with self-burial of submarine pipelines has been gained. Fig. 2 shows the self-buried pipelines in the Dutch sector. However, a reliable method to predict the self-burial of submarine pipelines did not yet exist.

The aim of the present development has been to achieve a model which is able to predict the self-burial behaviour of submarine pipelines as a function of environmental conditions (waves and currents), seabed and sediment characteristics and pipeline dimensions.

2.2 Description of the model

The concept of the Self-Burial Model is based on the observation of two dominant erosion processes under and around the pipeline: tunnel erosion and leeside erosion.

Tunnel erosion is a short term process with a time scale of the order of hours or days. After initiation of scour through seabed irregularities or vigorous water movements, a tunnel will be eroded under the pipeline.

Leeside erosion is an erosion process with a time scale of the order of weeks or months. It affects a much larger area of the seabed than tunnel erosion. A pipe protruding from the seabed disturbs the flow causing turbulence on the leeside of the pipe and thus increases the capacity for sediment transport. When the flow reverses, the leeside erosion now takes place at the other side of the pipe and some backfilling occurs at the upstream side. During a tidal cycle, however, the leeside erosion generally dominates over this backfilling effect. As a consequence the leeside erosion lowers the seabed near the pipe and at a certain moment the pipe will again be exposed to tunnel erosion.

Both tunnel and leeside erosion have been clearly observed in large scale two dimensional flume tests (scale 1:1 to 1:2).

Small scale flume tests and field data confirmed the existence of the third process which determines the actual burial of the pipeline: the natural backfilling.

As the local seabed around the pipe and the pipe itself sink relative to the original seabed, the capacity of the upstream eroded hole to capture sediment increases, so that backfilling becomes more and more dominating over leeside erosion.

The environmental conditions (waves and currents) determine to a large extent the equilibrium position of the pipe. In fact, each set of environmental conditions result in a different equilibrium position. It means that for instance a storm may trigger further lowering of the pipe after a period of stable pipeline position.

2.3 Calibration of the model

The model is primarily based on flume tests and numerical models of the two-dimensional situation of the behaviour of a cross-section of the pipeline. As a consequence, the pipeline diameter and the pipeline configuration (plain or fitted with piggy-back or spoiler) are in fact the only pipe related parameters taken into consideration in the formulations. Pipeline stiffness and weight are not (yet) explicit input parameters.

The calibration of the model has therefore been very important. Fortunately a relatively large number of pipelines in the Dutch sector of the continental shelf have self-buried and regular surveys showing the lowering process were available.

The shortcomings of a 2D model concept has been compensated by extensive calibration of the model against actual field (3D) survey data.

Actual waverider buoy measurements covering the survey periods of the calibration pipelines have been used to ensure correct representation of the wave conditions. The importance of this is clearly demonstrated in Figure 3. It shows the measured and the computed position of pipe and seabed of the Mobil P6AB pipeline. The effect of storms is evident after approximately 90 and 160 days.

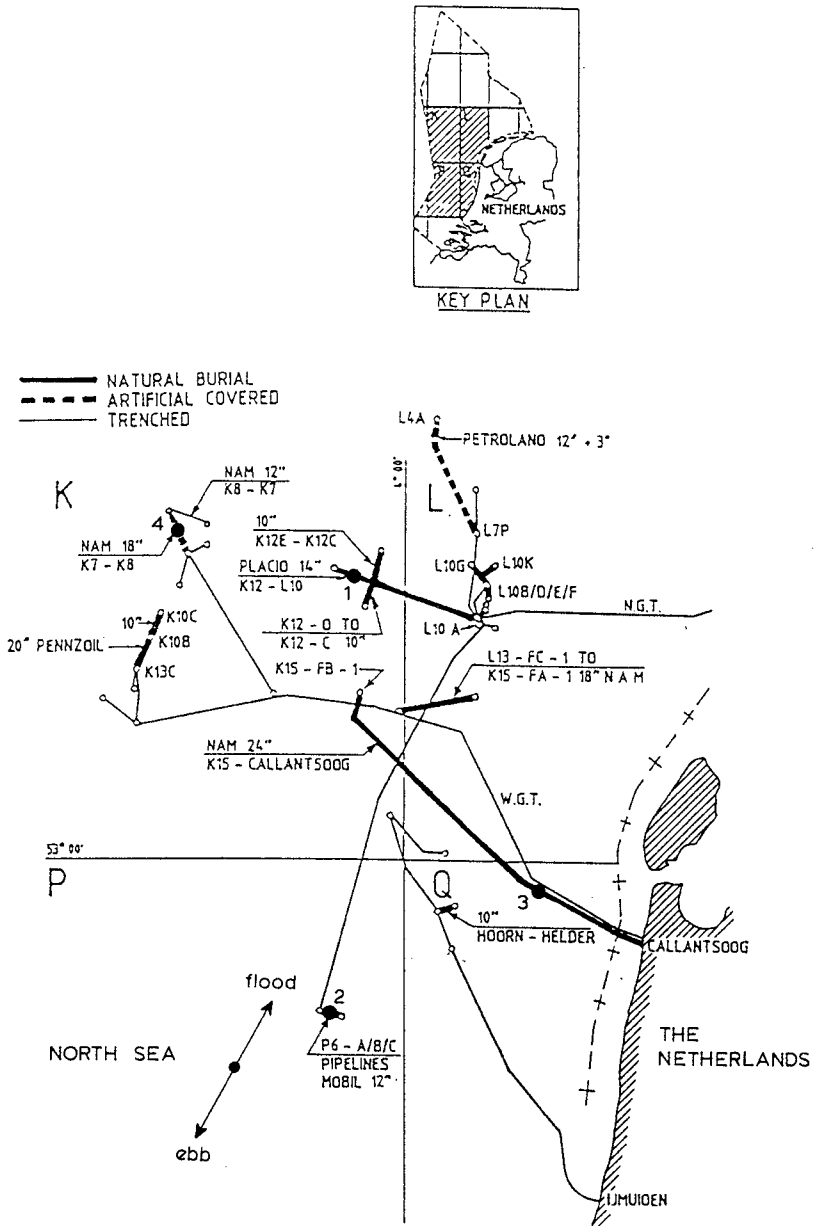


Fig. 2 Pipeline locations in North Sea.

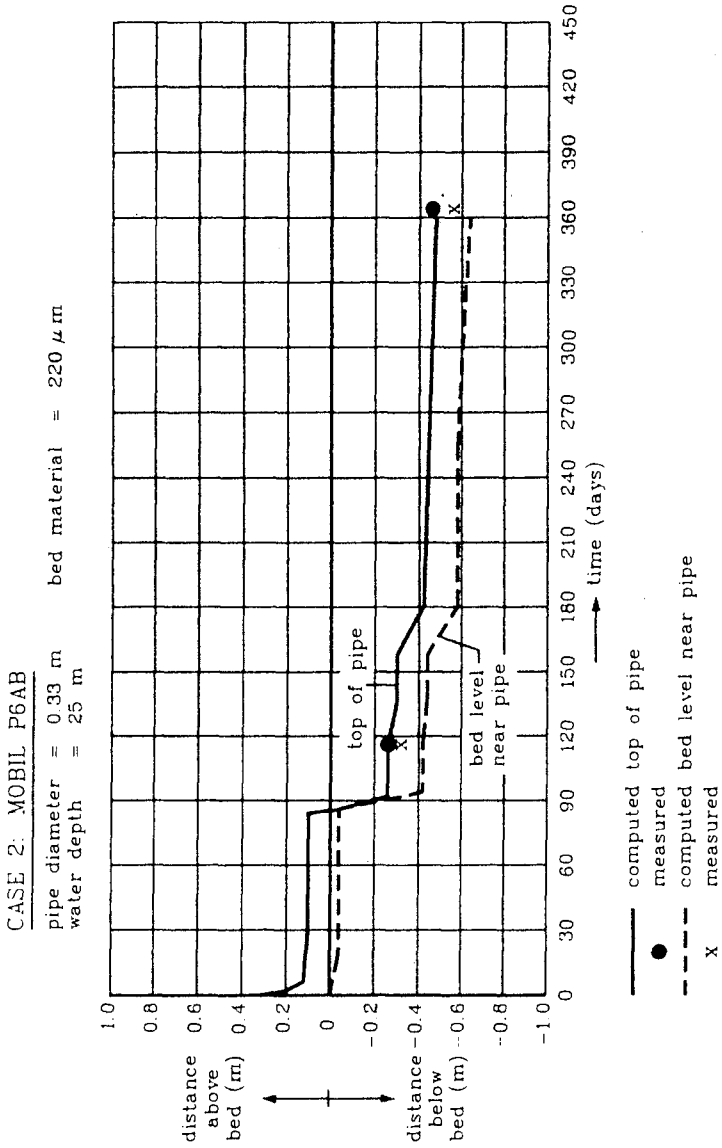


Fig. 3 Computed and measured pipe position of CASE 2: MOBIL P6AB

3. CONCLUSIONS

Two independent PC based computer models have been developed. Both models require comprehensive environmental input data in the form of time series of wave/current data. By the new developments existing theoretical models have been integrated to useful tools that are operational in engineering practice.

The Sand Wave Model:

- the model has been developed from existing theoretical models.
- modifications and extensions of the existing theory has been made with respect to:
 - . non-equilibrium sand waves
 - . varying directions of waves and currents
 - . effects of short-crested sand waves
 - . effects of high water waves
 - . effects of wave generated ripples.
- the model does not include the presence of any structure.
- future extensions of the existing model should focus on including the observed natural variability of sand waves.

The Self-Burial Model:

- the Self-Burial Model integrates the effects of the physical processes of tunnel erosion, leeside erosion, pipe lowering and backfilling.
- the model has been based on flume tests and numerical models.
- effects of pipeline stiffness is not included directly in the (2D) model but enters through extensive calibration against actual (3D) pipelines.
- future extensions of the existing model should focus on modelling of the development of free spans and pipe lowering in the scour holes.

4. ACKNOWLEDGEMENTS

The authors wish to thank Professor E.W. Bijker and Professor J. Fredsøe who both acted as scientific specialist consultants for the project team.

5. REFERENCES

- R. Deigaard: "Flow separation in combined waves and current". Progress Report no. 71, Institute of Hydrodynamics and Hydraulic Engineering, Technical University of Denmark, pp. 13-22, 1990.
- R. Deigaard and Fredsøe J.: "Offshore sand waves". 20th Int. Coastal Eng. Conf., Taipei, Taiwan, pp. 1047-1061, 1986.
- Fredsøe J.: "Unsteady flow in straight alluvial streams: modification of individual dunes". J. Fluid Mech., Vol. 91, pp. 497-512, 1979.
- Fredsøe J.: "Unsteady flow in straight alluvial streams, part 2: Transition from Dunes to Plane Bed". J. Fluid Mech., Vol. 102, 1981.
- Fredsøe J.: "Shape and dimensions of stationary dunes in rivers". J. Hydr. Div., ASCE, Vol. 108, No. Hy 8, 1982.
- Fredsøe J.: "Height of 3-dimensional dunes". Progress Report no. 69, Institute of Hydrodynamics and Hydraulic Engineering, Technical University of Denmark, pp. 3-8, 1989.
- Fredsøe J., Andersen O.H. and Silberg, S.: "Distribution of suspended sediment in large waves". J. Waterway, Port, Coastal and Ocean Engineering, ASCE, Vol. 111, No. 6, 1985.
- Nielsen P.: "Some basic concepts of wave sediment transport". Series Paper 20, Institute of Hydrodynamics and Hydraulic Engineering, Technical University of Denmark, 160 p., 1979.
- Raudkivi, A.J.: "The roughness height under waves". J. Hydr. Res., Vol. 26, No. 5, 1988.

CHAPTER 191

Even/Odd Analysis of Shoreline Changes Adjacent to Florida's Tidal Inlets

Paul A. Work¹ and Robert G. Dean²

Abstract

Measured shoreline changes up- and downdrift of several tidal inlets on the eastern coast of Florida are decomposed into even and odd components. The odd component of shoreline change is compared to both analytical and numerical predictions of shoreline response to a shore-normal littoral barrier. A best-fit iterative scheme is used for application of the analytical solution. The numerical solution improves upon the analytical approach by accounting for refraction, diffraction, and wave energy dissipation on the ebb tidal shoal. Predicted and measured changes agree reasonably well for several cases, and future refinements and improved long-term wave data are expected to allow more accurate prediction of smaller-scale features.

Introduction

Formation of a tidal inlet, whether resulting from natural events or human activity, often leads to large-scale, long-term shoreline changes, as the inlet represents an interruption of longshore sediment transport. This is particularly true where the inlet is stabilized by training structures, as is common along the eastern coast of Florida. The wave climate that provides the energy to mobilize the sediment is in turn altered by the evolving beach-inlet system. The resulting situation is often a complex wave field where wave breaking, diffraction, and refraction due to both tidal currents and time-varying bathymetry are all important.

A shore-normal littoral barrier placed along a coast having a strongly dominant direction associated with its longshore sediment transport will typically lead to the familiar result of accretion updrift and erosion downdrift of the barrier. In the field, other processes often complicate the picture. For this reason, a method is presented by which the "shoreline signature" of an inlet may be decomposed for study. The method has been applied to a number of tidal inlets along Florida's eastern coast, and analytical and numerical simulations of shoreline change have been generated for comparison. Figure 1 shows the locations of the tidal inlets addressed in this paper.

¹Graduate Research Assistant, Coastal and Oceanographic Engineering, University of Florida, Gainesville, Florida 32611 USA

²Graduate Research Professor, Coastal and Oceanographic Engineering, University of Florida, Gainesville, Florida 32611 USA

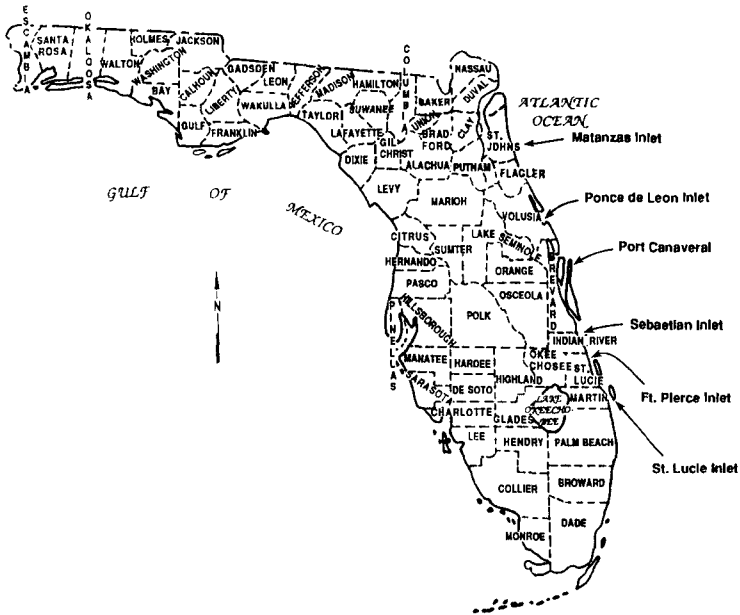


Figure 1: Locations of tidal inlets studied.

Several goals of the study were defined: to investigate and interpret shoreline changes at tidal inlets, examine the effectiveness of methods for prediction of these changes, and suggest improvements to these methods. The focus throughout the study was on changes directly attributable to the presence of the inlet.

Analytical Solution

A method by which shoreline response to a shore-normal littoral barrier may be predicted was proposed by Pelnard-Considère (1956). It is assumed that all offshore contours behave similarly, reducing the problem to the description of the position of one contour, typically the shoreline (hence the term “one-line model”). The x -axis is placed along the shoreline and the y -axis directed offshore. The coordinate system origin is at the point where the initial shoreline and the littoral barrier intersect.

Assuming that the wave crests are nearly shore-parallel, a sediment continuity equation may be combined with a dynamic sediment transport equation and linearized to show that the problem is governed by the heat, or diffusion equation (Pelnard-Considère, 1956):

$$\frac{\partial y}{\partial t} = G \frac{\partial^2 y}{\partial x^2} \quad (1)$$

where G is a diffusivity parameter containing, most importantly, the breaking wave height:

$$G = \frac{KH_b^{5/2}\sqrt{g/\kappa}}{8(s-1)(1-p)(h_*+B)} \quad (2)$$

where

- K = Dimensionless transport coefficient of order 1
- H_b = Wave height at breaking
- g = Acceleration of gravity
- $\kappa = H_b/h_b$ (Spilling breaker assumption)
- h_b = Water depth at breaking
- s = Sediment specific gravity
- p = Sediment porosity
- h_* = Maximum depth of sediment motion, or depth of closure
- B = Berm height

Note that G has units of length squared per unit time.

A solution to Equation 1 requires application of appropriate boundary conditions, and an initial condition:

$$y(\pm\infty, t) = 0, \quad \text{for all } t \quad (3)$$

$$y(x, 0) = 0, \quad |x| < \infty \quad (4)$$

specifying no change in the far-field and a shoreline that is initially straight. The boundary condition at the barrier consists of two parts, the second part being invoked subsequent to the initiation of sediment bypassing around the tip of the littoral barrier:

$$\left. \frac{\partial y}{\partial x} \right|_{x=0} = \tan \theta_b \quad 0 < t < t_{bp} \quad (5)$$

$$y(0, t) = \pm l \quad t \geq t_{bp} \quad (6)$$

where θ_b is the angle (measured counter-clockwise) between the shore-normal and the wave ray at breaking, and l denotes the length of the littoral barrier. The positive sign in Equation 6 corresponds to the updrift side of the barrier. The first part of this boundary condition forces the shoreline at the structure to parallel the wave crests, resulting in zero longshore transport past the structure. The second part (which is approximate) fixes the shoreline to the end of the barrier.

The time of bypassing, t_{bp} , may be expressed in terms of known quantities:

$$t_{bp} = \frac{\pi}{G} \frac{l^2}{4 \tan^2 \theta_b} \quad (7)$$

The solution to this problem is given by Equations 8 and 9. The solution is presented here only for $x > 0$, but it is noted that the solution is anti-symmetric about the y -axis, i.e. $y(-x, t) = -y(x, t)$.

$$y(x, t) = \frac{-\tan \theta_b}{\sqrt{\pi}} \left[\sqrt{4Gt} \exp\left(-\frac{x^2}{4Gt}\right) - x\sqrt{\pi} \operatorname{erfc}\left(\frac{x}{\sqrt{4Gt}}\right) \right] \quad \text{for } t < t_{bp} \quad (8)$$

and

$$y(x, t) = -\frac{\tan \theta_b}{|\tan \theta_b|} \operatorname{erfc} \left(\frac{x}{\sqrt{4Gt}} \right) \quad \text{for } t \geq t_{bp} \quad (9)$$

where erfc denotes the complimentary error function. The solution given by Equations 8 and 9 will be applied for the prediction of shoreline changes at a tidal inlet by assuming that the inlet itself has negligible width. Several additional assumptions have been invoked to achieve this result: the littoral barrier is assumed impermeable, the shoreline is homogeneous, and the wave climate does not vary in the x -direction or in time. Also note that sediment is conserved; all sediment bypassing the structure reaches the downdrift shore. These assumptions are not well-suited to all field sites, suggesting that attempts be made to relax some of them. One approach is described below.

Even/Odd Decomposition of Measured Shoreline Changes

At this point it is appropriate to consider the measured shoreline changes to which predictions will be compared. Digitized historical charts and surveys were obtained from the Department of Natural Resources, State of Florida (Foster and Savage, 1989; Savage and Foster, 1989). Using the coordinate system of the previous section, surveys from different dates were compared to determine a net shoreline change "function", $y_N(x)$. An attempt was made to select a first survey corresponding to the time at which the inlet was constructed or stabilized. The second (later) survey was chosen to place it before any beach nourishment or sand bypassing projects, but long enough after inlet construction that long-term shoreline changes dominated over seasonal changes.

It was decided to divide the shoreline change function, $y_N(x)$, into even (symmetric about the y -axis) and odd (anti-symmetric) components. This can be done easily for any function, with the two components given as follows (Berek and Dean, 1982; Dean and Pope, 1987):

$$y_E(x) = \frac{y_N(x) + y_N(-x)}{2} \quad (10)$$

$$y_O(x) = \frac{y_N(x) - y_N(-x)}{2} \quad (11)$$

The justification for this approach becomes evident when one considers the contributions to shoreline change at a tidal inlet. The interruption of longshore sediment transport should, according to the analytical solution of the previous section, contribute only an odd component. Storms and sea level rise will tend to exert similar influences on both sides of the domain, leading to an even component. Refraction and diffraction effects will vary, possibly contributing to both even and odd components.

It can easily be demonstrated that sand bypassing will add a "negative" odd component; i.e. an odd component that reduces the offset created by the presence of a littoral barrier, and that beach nourishment will tend to contribute to both even and odd components. The effects of factors leading to the presence of an even component are often difficult to predict, and most would exist even without the presence of the inlet. The primary influence of the inlet is a blockage of longshore sediment transport, so it was decided to compare predicted shoreline

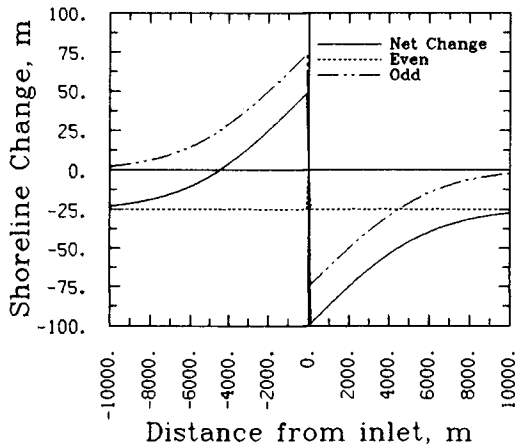


Figure 2: Analytical solution with superimposed uniform background erosion of 25 m in 75 years. $l=75$ m, $H_b=0.5$ m, and $\theta_b=1^\circ$. All shoreline change plots are oriented to place the ocean at top.

changes to the odd component of measured shoreline changes.

A simple, illustrative example is helpful. If a uniform background erosion is superimposed upon the analytical solution of the previous section, the result shown in Figure 2 is obtained. Note that for this case, decomposition into even and odd components simply returns the initial constituents, since the analytical solution is odd and the background erosion even. Also note that any loss or gain of sediment within the domain is revealed by the integral of the even component, as the integral of the odd component is zero.

Best-Fit Analytical Solution

Application of the analytical solution requires confident estimates of several parameters, including wave height and direction at breaking, and the length of the jetty. The jetty length may seem to be well known, but three factors complicate selection of a value for this parameter: structure permeability, physical modifications which take place during the time period of interest, and the fact that portions of the active, updrift profile extend beyond the jetty tip well before the shoreline reaches the jetty tip. These factors suggest the use of an "effective" jetty length. Lacking long-term values for the parameters, a best-fit technique was developed to compare the analytical solution to the odd component of measured shoreline change.

An iterative scheme was developed to find parameters that minimized the mean square difference, or error, between the analytical solution and the odd component of measured shoreline change. This error is defined as follows:

$$\epsilon^2 = \frac{1}{N} \sum_{i=1}^N [y_A(x_i, t) - y_O(x_i)]^2 \quad (12)$$

where x_i denotes the longshore coordinate of the i th point, $y_O(x_i)$ the value of the odd component at that point, $y_A(x_i, t)$ the analytical solution, and N the number of data points available.

The best fit will exist when the derivative of ϵ^2 with respect to each parameter is zero. Initially, only the pre-bypassing portion of the analytical solution, which has no dependence on jetty length, was used. The two parameters allowed to vary were the diffusivity, G (containing the wave height at breaking), and the tangent of the wave angle at breaking, $\tan \theta_b$. Figure 3 gives contours of equal values of ϵ , plotted against G and $\tan \theta_b$, for Ft. Pierce Inlet. This inlet was constructed in 1921, but the first of the two surveys used to determine the odd component of shoreline change is from 1928. For cases such as this, the analytical solution used in the best-fit procedure is defined as the difference between the solution at the time of the second survey (t_{end} , 46 years for this case) and the solution at the time of the first survey (t_{start} , 7 years here). All times are thus referenced to the construction of the inlet.

The best-fit methodology was then extended to include both parts of the analytical solution (pre- and post-bypassing) and thus allow for the variation of jetty length, l . This then accommodates three scenarios, depending on whether the surveys are dated before or after initiation of bypassing. Note that if both surveys are pre-bypassing, jetty length cannot be inferred, since the pre-bypassing solution has no dependence on jetty length. Similarly, if both surveys are post-bypassing, wave direction is indeterminable. Only if the first survey is pre-bypassing and the ending survey post-bypassing can wave height, direction, and jetty length all be determined. This last scenario occurred for only one case, that of Ft. Pierce Inlet. For each of the other cases, the pre-bypassing solution provided the best fit. Figure 4 compares the measured odd component for Ft. Pierce Inlet to the two best-fit solutions; Figure 5 illustrates the error surface when the full analytical solution is allowed. This error surface depends on three variables, and is therefore four-dimensional. The jetty length has been "frozen" at its best-fit value for illustration. Note that the full solution for this case provides a very good fit, but the associated wave angle (8.4 degrees) appears unreasonably large for a long-term average.

The error surface that results when the full analytical solution is used (Figure 5) should have at least three relative minima: one corresponding to the case where both surveys predate bypassing; one where the surveys lie to either side of the time of bypassing; and one where both surveys post-date initiation of bypassing. Recall that the time of bypassing depends on G , $\tan \theta_b$, and l , so varying any of these parameters changes the time of bypassing. One could allow any number of the available parameters to vary, but it was felt that the three chosen contained the most uncertainty.

Numerical Model

A numerical model was developed to investigate the effects of wave refraction due to both bathymetry and tidal currents, diffraction of energy into the "shadow zone" in the lee of the downdrift jetty, and the sheltering effect of an ebb tidal

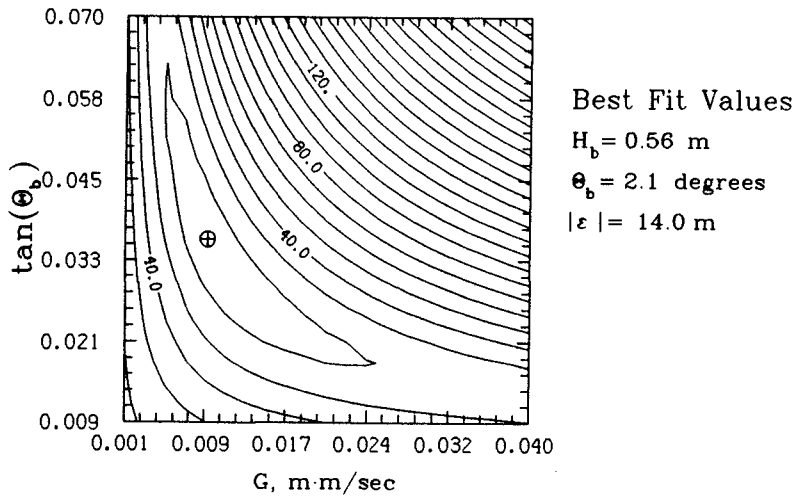


Figure 3: Contours of equal error, $|\varepsilon|$, for Ft. Pierce Inlet, 1928-1967. Pre-bypassing solution only.

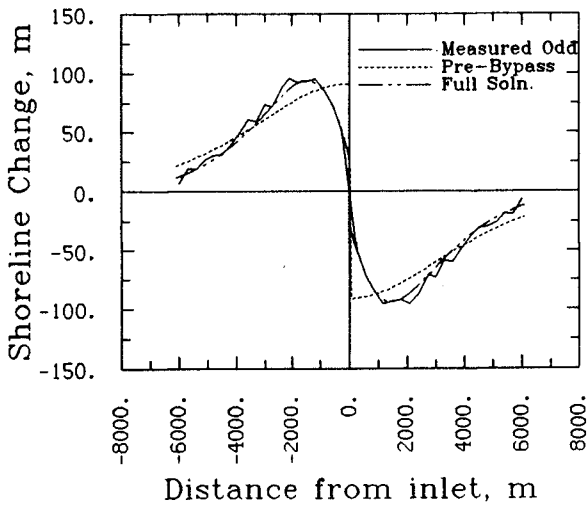


Figure 4: Measured odd component and the two best-fit solutions for Ft. Pierce Inlet, 1928-1967.

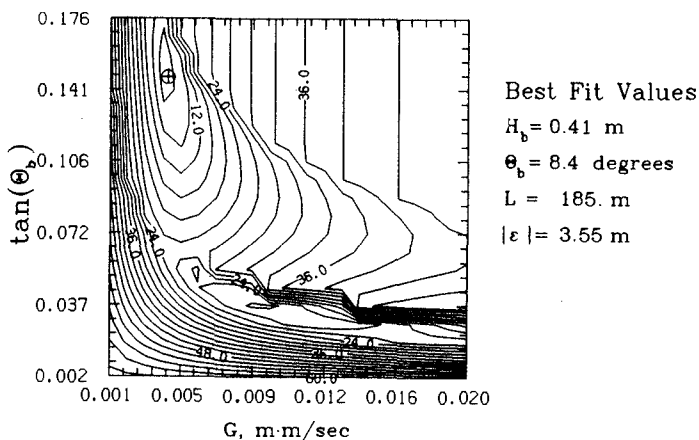


Figure 5: Error surface for Ft. Pierce Inlet, 1928-1967. Full analytical solution.

shoal.

The model includes a two-dimensional finite-difference wave propagation routine, providing the nearshore wave climate for computation of shoreline change by a one-line finite-difference model. The primary advantage of this method over the analytical solution is that spatial and temporal variability in the nearshore wave climate can be accommodated. The governing equation and boundary conditions for the sediment model remain unchanged.

Wave conditions at the offshore boundary are specified and the bathymetry and tidal currents approximated analytically. The dispersion relationship including the effects of currents is given in terms of an intrinsic wave frequency, σ :

$$\sigma^2 = gk \tanh kh \quad (13)$$

where

$$\begin{aligned} \sigma &= \omega - \vec{k} \cdot \vec{u} \\ \omega &= \text{absolute frequency} = 2\pi/T \\ T &= \text{wave period} \\ \vec{u} &= \text{mean current vector} \\ \vec{k} &= \text{wavenumber vector} \\ h &= \text{water depth} \end{aligned}$$

Irrotationality of the wavenumber vector specifies wave direction:

$$\nabla \times \vec{k} = 0 \quad (14)$$

and conservation of wave action is applied to solve for wave height:

$$\nabla \cdot \left[\frac{E}{\sigma} (\vec{u} + \vec{C}_g) \right] = 0 \quad (15)$$

where

$$E = \text{Wave energy density} = \rho g H^2 / 8$$

$$\vec{C}_g = \text{wave group velocity vector}$$

Starting at the offshore boundary, Equations 13, 14, and 15 were applied iteratively at each grid point to solve for wavenumber vector, \vec{k} , and wave height, H . To account for wave energy dissipation across a shoal or other bathymetric feature, the wave height was checked at each point and truncated to 78% of the water depth if it exceeded this height. Diffraction of wave energy into the sheltered area behind the jetty was included through application of the method of Perlin and Dean (1985).

The best-fit analytical solution was used to determine the offshore wave climate for the numerical model. The best-fit wave direction and height were transformed offshore using Snell's Law and conservation of wave energy flux. For each inlet studied, the analytical and numerical predictions of shoreline change differ little. The primary factor accounting for this is that the wave climate used as input to the numerical model represents a long-term average, with a relatively small wave height, and the direction deviates little from shore-normal. Thus wave energy dissipation on the shoal (where one is present) and wave diffraction are thought to be under-predicted in the numerical model.

Sensitivity tests indicate that moderate tidal currents have little effect on the results. This appears reasonable, since the modelled domain typically extends up to 10 km to either side of the inlet, well outside the zone of strong tidal influence.

Results

Shoreline changes at each of the tidal inlets along the eastern coast of Florida for which data were available were studied by the techniques described above. As might be expected, the analytical and numerical predictive methods appear to be best suited to inlets that are stabilized at the time of construction by relatively impermeable jetty structures.

Figure 6 shows the odd component of measured shoreline change, the best-fit analytical solution, and the numerical simulation for Ft. Pierce Inlet. The pre-bypassing best-fit solution is used here, as the full solution yielded unreasonable wave parameters. Agreement is fairly good except near the inlet, suggesting for this case that the initial accretion/erosion immediately adjacent to the inlet is underestimated. Reversals in the direction of longshore sediment transport could also contribute to this feature. Note that the predictions do not include any of the small-scale deviations seen in the measured odd component. The models tend to smooth out any irregularities in the shoreline, given sufficient time.

Results for St. Lucie Inlet, which was constructed in 1892, are presented in Figure 7. The inlet was initially stabilized only on its north side, the south jetty being added in 1982. The shape of the solutions match the measured odd component well, despite the fact that several of the assumptions implicit in the solutions (impermeable structures on both sides of the inlet, homogeneous shoreline, no temporal variation in wave climate) are not well-satisfied at this inlet. As with each of the inlets discussed here, the net longshore transport of sediment is directed to the south, but reversals are common in the summer season.

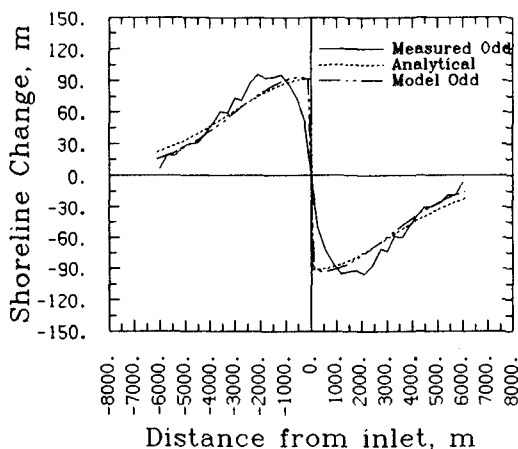


Figure 6: Measured odd component and predictions of shoreline change for Ft. Pierce Inlet, 1928–1967 (inlet constructed 1921). $H_b = 0.56$ m, $\theta_b = 2.1$ degrees.

Figure 8 presents results for Sebastian Inlet. This inlet was constructed in 1924, but closed naturally in 1941–42. It was then re-opened in 1948 and has remained open to date. The results shown in Figure 8 neglect the closure of the inlet from 1942–1948. The magnitude of the shoreline change for this case is smaller, so small-scale deviations from the predicted changes are more evident.

Figure 9 provides results for Port Canaveral, constructed in 1951. Agreement between the measured and predicted changes is not as good here, and it is seen that there is a spike in the measured odd component for $x = \pm 4000$ m. Inspection of only the odd component of measured change does not allow determination of whether this feature is accretional or erosional. Inspection of the net shoreline change for this case reveals that this is an accretional feature on the updrift side of the inlet. Natural or man-made shoreline features can often introduce shoreline inhomogeneities that do not satisfy the assumptions of the methods used here. One possible future improvement to the numerical shoreline change model would be to account for inhomogeneities by allowing the diffusivity parameter, G , to vary along the domain.

Shoreline changes at inlets not well-suited to the assumptions implicit in the predictive methods presented here must often receive careful consideration for thorough understanding. Figure 10 shows the net shoreline change, and its even and odd components for Ponce de Leon Inlet, 1952–1973. This is a natural inlet that was stabilized by jetties in 1971, the northern jetty incorporating a weir in order to facilitate sand bypassing to the southern shore. The weir was closed in 1984 to reduce erosion on the northern side. The erosion on the updrift side (north; left in Figure 10) is evident in the figure, as is a very large accretional zone immediately downdrift of the inlet. This accretion is due primarily to the configuration of the downdrift jetty; as built, it formed a “pocket” that tended to trap material.

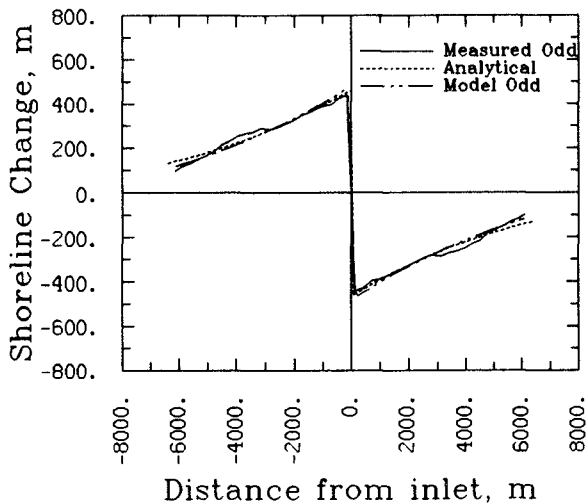


Figure 7: Measured odd component and predictions of shoreline change for St. Lucie Inlet, 1883-1967 (inlet constructed 1892). $H_b = 0.62$ m, $\theta_b = 4.4$ degrees.

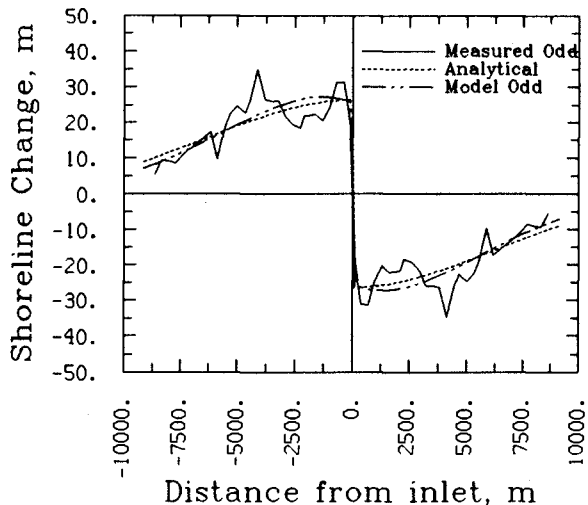


Figure 8: Measured odd component and predictions of shoreline change for Sebastian Inlet, 1946-1970 (inlet constructed 1924). $H_b = 0.75$ m, $\theta_b = 0.8$ degrees.

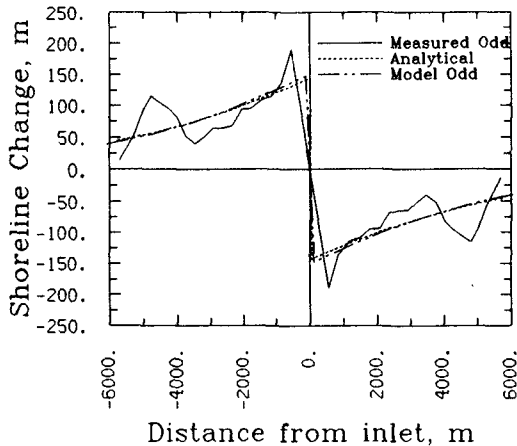


Figure 9: Measured odd component and predictions of shoreline change for Port Canaveral, 1951-1970 (inlet constructed 1951). $H_b = 1.07$ m, $\theta_b = 1.4$ degrees.

Another case of interest is that of a natural, unstabilized tidal inlet. Figure 11 provides the shoreline change components for Matanzas Inlet, 1923-1986. The position of the downdrift boundary of this inlet is partially restrained by a bridge abutment, and the downdrift shore is now heavily armored, but there are no jetty structures. Note that the even component of shoreline change indicates a slight gain of sediment within the domain, and the expected pattern of accretion updrift and erosion downdrift is present. Another future goal is to be able to accurately predict both bypassing rates and shoreline changes at an unstabilized tidal inlet.

Conclusions

Computation of shoreline changes at many of Florida's tidal inlets and decomposition of these signals into even and odd components reveals a fairly consistent updrift offset pattern, particularly at entrances that have been stabilized on both updrift and downdrift sides. Several inlets deviate from this trend, but the reasons are usually evident upon consideration of the history of the area.

The best-fit analytical solution developed matches the odd function well at several inlets showing a significant updrift offset, although it is not capable of predicting the small-scale features seen in the field. Reasonable values for the long-term wave climate are generated using the pre-bypassing analytical solution. Lack of reliable, long-term, directional wave data hinders complete assessment of results and remains a limitation to improved modelling efforts.

Refinement of the numerical model will be necessary to predict the small-scale features seen in the field. The wave transformation model could be improved by using higher-order wave theory, including wave-current interaction, providing a more sophisticated method for computation of tidal currents, and improving the wave breaking computations. Directional wave data would allow simulation of

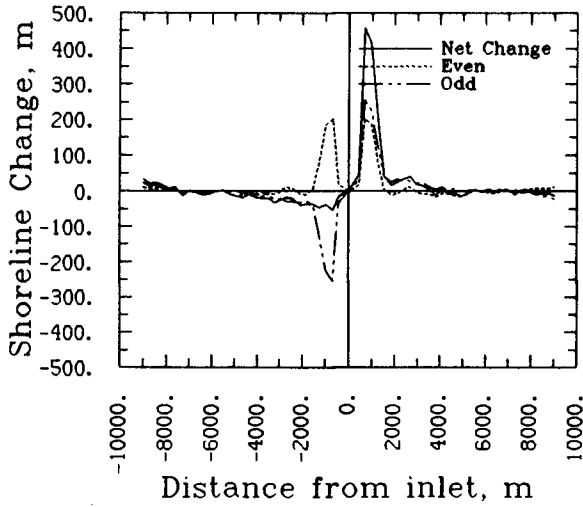


Figure 10: Net, even, and odd components of measured shoreline change for Ponce de Leon Inlet, 1952-1973.

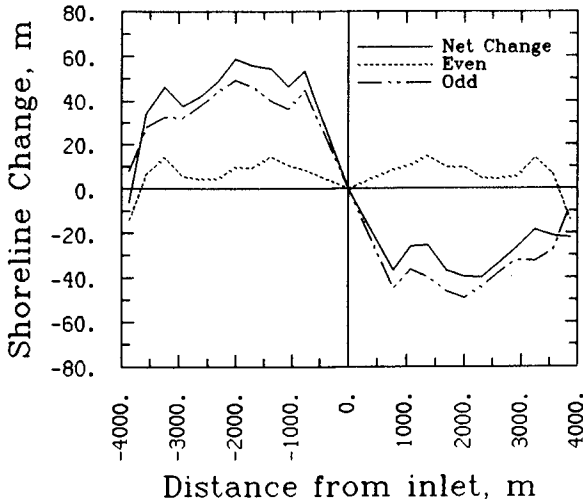


Figure 11: Net, even, and odd components of measured shoreline change for Matanzas Inlet, 1923-1986.

the longshore sediment transport reversals known to occur at many of Florida's inlets. The sediment transport model could be refined to account for the inhomogeneous nature of the shoreline in both the longshore and cross-shore directions.

The problems of interpretation and prediction of shoreline evolution adjacent to tidal inlets remains of both considerable interest and difficulty. Further refinement of the methods applied to date should lead to improved predictive ability.

Acknowledgement

Support provided by the Florida Sea Grant College Program of the National Oceanic and Atmospheric Administration under Project R/C-S-22 is hereby gratefully acknowledged.

References

- BEREK, E.P., and DEAN, R.G. (1982).
Field Investigation of Longshore Transport Distribution. Proc. 18th Coastal Engineering Conference, ASCE, pp. 1620-1639.
- DEAN, J.L., and POPE, J. (1987).
The Redington Shores Breakwater Project: Initial Response. Proc. Coastal Sediments '87, ASCE, pp. 1369-1384.
- FOSTER, E.M., and SAVAGE, R.J. (1989)
Methods of Historical Shoreline Analysis. Proc. Coastal Zone '89, Sixth Symposium on Coastal and Ocean Management, Charleston, S.C. Vol. 5, pp. 4420-4433.
- PELNARD-CONSIDÈRE, R. (1956).
Essai de Théorie de l'Evolution des Forms de Rivages en Plage de Sable et de Galets. 4th Journées de l'Hydraulique, les Energies de la Mer, Question III, Rapport No. 1, pp. 289-298.
- PERLIN, M., and DEAN, R.G. (1985).
3-D Model of Bathymetric Response to Structures. Journal of Waterway, Port, Coastal, and Ocean Engineering, ASCE, Vol. 111, No. 2, pp. 153-170.
- SAVAGE, R.J., and FOSTER, E.M. (1989)
Historical Shoreline Changes in Southeast Florida. Proc. Coastal Zone '89, Sixth Symposium on Coastal and Ocean Management, Charleston, S.C. Vol. 5, pp. 4406-4419.

CHAPTER 192

Behaviour Of Mobile Beds At High Shear Stress

Kenneth C. Wilson¹ and Fidelia N. Nnadi²

Introduction

Beds of granular material show various types of behaviour as the dimensionless shear stress or Shields ordinate, Y , is increased. This quantity is defined as $\tau/\rho g(S-1)d$, where τ is boundary shear stress, ρ is fluid density, g is gravitational acceleration, S is the ratio of solids density to fluid density and d is particle diameter. No movement occurs until Y exceeds a critical value. As Y is increased beyond the critical sand waves form, first increasing and then decreasing in steepness with successive increases in Y . Finally, in the high-shear-stress region, say $Y \geq 0.8$, the bed becomes plane (or exhibits antidunes in cases of critical or supercritical free-surface flow). This high-stress condition, sometimes called the upper plane-bed region, may be encountered for rivers in flood, large flows in estuaries, and closures or breaches of cofferdams or dykes. Because of the very high rates of sediment transport this type of flow has a disproportionate effect on both natural topographic features and engineering works. It is not easy to investigate this behaviour by traditional flume experiments, but the use of enclosed pressurised conducts can eliminate many of the experimental difficulties (Wilson, 1966).

Analysis

At high shear stress the bed load moves in a near-bed zone (the shear layer or sheet-flow layer), with thickness δ_s . Within this layer, the grains comprising the bed load (also called the contact load) are supported by intergranular contacts, which may be either continuous or sporadic. For this type of motion Bagnold (1956)

¹ Professor, Department of Civil Engineering, Queen's University, Kingston, Ontario, Canada K7L 3N6

² Grad. Student, Department of Civil Engineering, Queen's Univ., Kingston, Ontario, Canada K7L 3N6

demonstrated the existence of both an intergranular normal stress, σ_s , and an intergranular component of shear stress, τ_s . The latter is equal to $\sigma_s \tan \phi'$, where ϕ' is the dynamic equivalent of the friction angle used in soil mechanics. At the bottom of the shear layer all of the applied shear stress τ is resisted by the intergranular shear stress, which must equal $\tan \phi'$ times the normal intergranular stress at that location. This normal stress equals the submerged weight of the contact-load solids in the shear layer, which can be written $\rho g(S-1)\bar{C} \delta_s$ where \bar{C} is the average volumetric concentration of bed-load solids within this layer. Rearrangement gives

$$\delta_s = \tau / [\rho g(S-1)\bar{C} \tan \phi'] \quad (1)$$

showing that δ_s/d equals $Y/(\bar{C} \tan \phi')$. It was suggested earlier (Wilson, 1989) that for typical values of \bar{C} and $\tan \phi'$ this relation gives δ_s/d as roughly $10Y$. More recent analysis of concentration-profile data obtained in Saskatchewan (Daniel, 1965; Shook and Daniel, 1965) indicates that a value of $7.5 Y$ is better, i.e.

$$\delta_s/d \approx 7.5 Y \quad (2)$$

Previous analysis of the velocity distribution within the shear layer (Wilson, 1984, 1989) had demonstrated that the ratio of local velocity to shear velocity (U/U_*) can be expressed in terms of the relative height within the shear layer, y/δ_s . Thus at the top of the shear layer, where $y/\delta_s = 1.0$, the ratio U/U_* has a specific value which can be used as a match point for the logarithmic profile of the velocity in the main flow above the shear layer. On this basis the ratio of mean velocity to shear velocity can be calculated, leading to the overall friction relation. This analysis indicated that mobile beds at high shear stress are neither smooth boundaries nor rough ones, but obey their own frictional law analogous to the other cases but with characteristic length proportional to δ_s .

When this law is compared with the rough-boundary equation it is found that the roughness k equivalent to the mobile-bed friction law is about $0.5 \delta_s$, i.e. the value of k/d is not constant (as for the rough boundary law) but increases approximately linearly with Y . This conclusion was verified (Wilson, 1989) using the results of closed-conduct experiments carried out with sand (relative density $S = 2.67$) and nylon ($S = 1.14$). These are shown on Fig. 1, together with results of a more recent research program using particles of Bakelite ($S = 1.56$). The plot covers a considerable range of both variables, and although some scatter is present, the general increase of k/d with Y is very clear.

Up to this point it had been assumed in the analysis that the boundary shear stress τ was applied to all levels of the shear layer, i.e. the variation of total shear stress with height was ignored. However, for some of the experiments δ_s occupies a sizable fraction of the waterway height, implying a significant variation of τ within the shear layer. This variation depends directly on the ratio δ_s/R , (R is hydraulic radius). As the friction factor itself depends on R/k , and k is proportional to δ_s , no additional parameters were required for the analysis with variable τ , and the algorithm was re-written to incorporate this case.

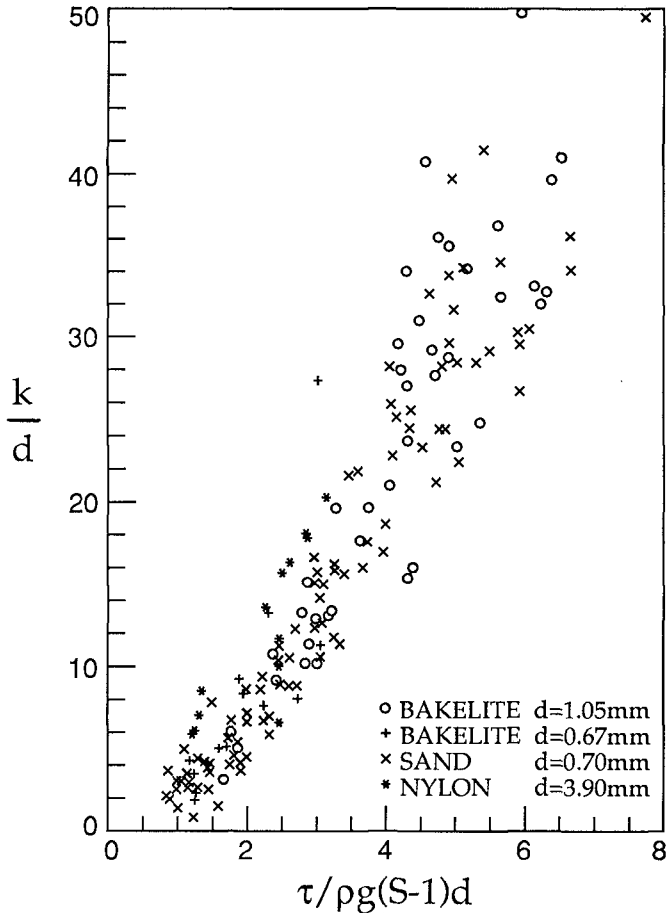


Fig. 1 Plot of Effective Roughness Ratio

By use of Eq. 1 it is readily seen that the ratio R/δ_s depends only on $(S-1)/i$, i.e.

$$\frac{R}{\delta_s} = \frac{(S-1)}{i} (\bar{c} \tan \phi') \approx 0.13 \frac{(S-1)}{i} \tag{3}$$

For constant τ , it was predicted that a plot of the velocity ratio \bar{U}/U_* versus the logarithm of $(S-1)/i$ should form a straight line. These axes can also be used to show the new calculations for variable τ . The resulting curve is plotted on Fig. 2, together with points for the data sets mentioned above.

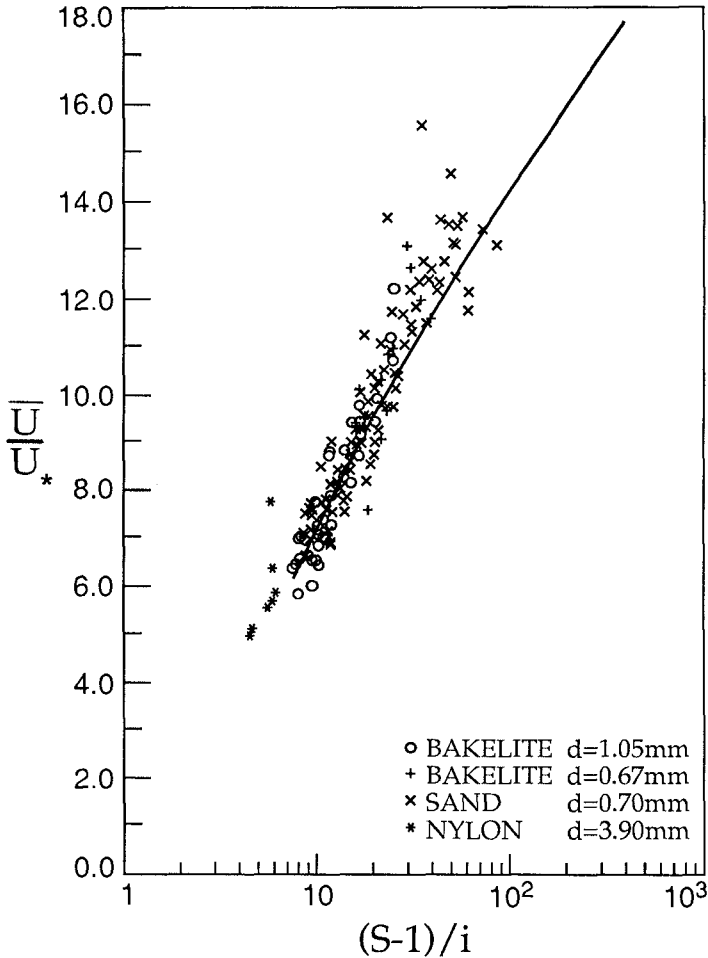


Fig. 2 Velocity-Ratio Plot

It is most encouraging to see the agreement between theory and experiment which is displayed on Fig. 2. From a practical point of view, however, the curve shown on this figure is not convenient to use, and it is preferable to approximate it by a simpler function such as a power law. If necessary, the curve can be divided into several regions, and a separate approximating power law found for each region.

In applying this approximating technique, it was found that a single power law was adequate to cover a broad range of conditions of practical interest i.e. subcritical flow with particles having S of 2.6 or more. For these conditions the approximating function was found to be

$$\frac{\bar{U}}{U_*} = 9.55 \left[\frac{(S-1)}{i} \right]^{0.11} \quad (4)$$

or

$$\bar{U} = 9.55 (S-1)^{0.11} i^{0.39} \sqrt{(gR)} \quad (5)$$

This equation can also be re-written to give the Darcy-Weisbach friction factor, i.e.

$$f = 0.088 \left[\frac{i}{(S-1)} \right]^{0.22} \quad (6)$$

The form of the approximating function given by Eq. 5 may be considered as a replacement for the Manning formula, for use with mobile beds at high shear stress ($Y \geq 0.8$). As friction does not depend on particle diameter for this type of behaviour, this equation involves no roughness coefficient (such as n in the Manning formula) and thus is exceptionally simple to apply. This point can best be illustrated by an example. Consider the flow over a mobile bed in an estuary, with R of 6 m, and mean velocity of 4 m/s. With $(S-1)$ taken as 1.65, Eq. 5 is readily solved for i , which is found to be approximately 5×10^{-4} . The shear stress τ , i.e. $\rho g R i$, is about 30 Pa, and Y is 1.8, verifying that the flow is in the appropriate range. The thickness of the shear layer δ_s will be about 14mm and U_* about 0.17 m/s.

The values of τ (and U_*) found above can themselves be used to estimate the transport rates of bed-load and suspended load. This matter has been analysed by Wilson and Pugh (1988), who noted that the suspended load occurs as an addition to the bed-load particles considered previously. This addition can have only a secondary effect on the thickness of the sheet-flow layer that

contains the bed load, and the same applies to the velocity at the top of this layer. Hence it is expected that suspended load will have, at most, a minor influence on the numerical coefficients of Eqs. 4 to 6.

Conclusion

Experimental evidence from flows in pressurised conduits has provided striking verification of the predictions from the analysis. Both analysis and experiment show that mobile-boundary flows at high shear stress do not obey the rough-wall friction law, (as had been imagined for many years). Instead, they follow their own law, with frictional length scale proportional to the shear stress itself. In this case equations based on rough-wall friction, such as the Manning formula, do not apply and the friction factor depends on the ratio $i/(S-1)$. A power-law approximation to this function gives a simple friction equation which can replace the Manning formula for high-shear-stress mobile-boundary flow.

References

- BAGNOLD, R.A. (1956). The flow of cohesionless grains in fluids. Phil. Trans. Roy. Soc. London, Ser. A. Vol. 249, 235-297.
- DANIEL, S.M. (1965). Flow of suspensions in a rectangular channel. Ph.D. Thesis, University of Saskatchewan, Saskatoon, Saskatchewan, Canada.
- SHOOK, C.A. and DANIEL, S.M. (1965). Flow of suspensions of solids in pipelines, Part I. Flow with a stable stationary deposit. Canad. J. Chem. Engrg. April, pp. 56-61
- WILSON, K.C. (1966). Bed-load transport at high shear stress. J. Hydr. Div., ASCE, 92(6), 49-59.
- WILSON, K.C. (1984). Analysis of contact-load distribution and application to deposition limit in horizontal pipes. J. Pipelines, 4(3), 171-176.
- WILSON, K.C., and PUGH, F.J. (1988). Dispersive-force basis for concentration profiles. J. Hydr. Engrg., ASCE, 114(7), 806-810.
- WILSON, K.C. (1989). Mobile-bed friction at high shear stress. J. Hydr. Engrg., ASCE, 115(6), 825-830.

CHAPTER 193

TO RETREAT IN ORDER TO BETTER FIGHT : LITTORAL PROTECTION OF SHINGLE BEACHES IN THE NORTH OF FRANCE

Bruno Manoha¹ and Charles Teisson²

Abstract

Rather than endeavouring to protect a shoreline under severe waves attack, on the northern coast of FRANCE, a new solution a retreat landwards up to 800 m. With a slight retreat (180m), the orientation of the new shoreline is drawn according to the dominating wave climate and enables the stabilization of the beach. A larger retreat (800 m) could allow the re-estuarisation of a valley. These solutions are tested on a physical movable bed model.

1. INTRODUCTION

Several parts of littoral in the North of France, constituted of chalky cliffs and shingle beaches are suffering today severe erosion, due to past human action : extraction of shingle for industrial purpose, construction of seawards harbour breakwaters interrupting littoral transport.

Previous responses of coastal engineers to this problem have been to construct classical seawalls or groynes, with unequal issue, problems usually shifting downcoast. Today, on the most critical site, annual shingle renourishment is employed : this is a soft, but onerous method, with bleak outlook, as the renourishment disappears downcoast in winter, during storms.

This most exposed site lies at the outlet of a valley, a 1 km indentation between the cliffs, with the beach lined landwards by a sea front road (fig. 1). Rather than protecting at any cost the present shore, with ineffective long term perspective, a new solution considers a retreat of the shore line in the valley. This draw back could be realized in two ways :

- either a slight retreat at the entrance of the valley,
- or even a re-estuarisation of the valley, with the sea entering landwards up to 800 meters.

¹ Head of Maritime Group

² Research Engineer,

EDF - Laboratoire National d'Hydraulique, 6, quai Watier 78400 Chatou FRANCE.

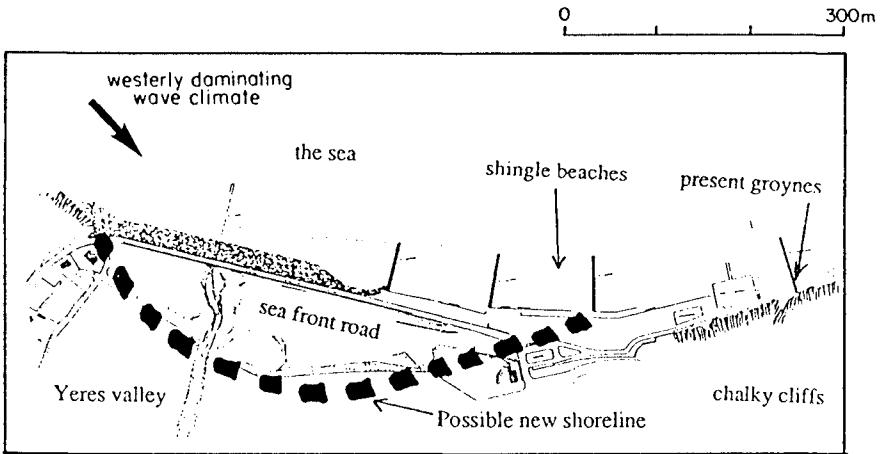
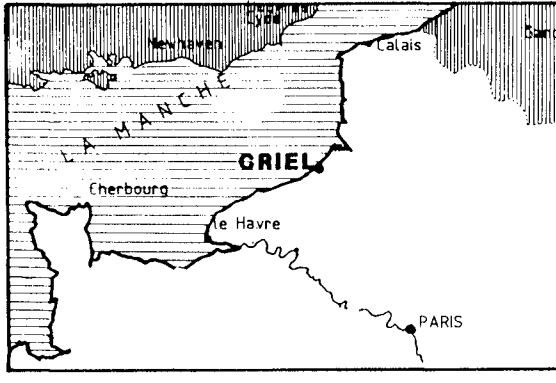


Fig 1 : Map of the site

Beyond the response to present problem, this approach integrates long term tendencies, as the annual recession of 0.20 m of surrounding cliffs exposing seawards the present sea front road, and possible sea level surelevation due to greenhouse effects.

This innovative solution, with strong local impact - destruction of the sea front road, partial intrusion of the sea in the valley - is tested and optimized on a physical movable bed model.

2. SEDIMENTOLOGICAL BACKGROUND

As a general manner, shingle beaches differ from sandy beaches by a steeper equilibrium slope and their mode of transport restricted to the swash zone, landward of the breaker line (MUIR WOOD, 1970).

In the North of France, likewise, shingles created from the cliff erosion lay down at the foot of the cliffs along the 140 km of the littoral and build up as a beach 20 to 30 meters wide, with an equilibrium slope of 10 %. Due to the westerly dominating wave climate, it exists an easterly littoral transport of 20 000 m³ per year. As the annual production of shingle from cliff erosion is also 20 000 m³, the sedimentary budget was well balanced in the past.

But, since the beginning of this century, various coastal developments as harbours breakwaters have deeply disturbed this natural transit, causing the breaking up of the shingle line into accumulation of dead stocks to the west of the breakwaters and its disappearance on the eastern parts. Quarrying of shingle for industrial purpose has also contributed to weaken the shingle line : half of the 5 millions m³ of the stock existing at the beginning of the century has disappeared in that manner.

In some areas, as Criel sur Mer, one of the most critical site, the annual easterly departure of shingle reaches, in spite of existing groynes, is 15 000 m³ per year, while the natural transit, cut down to 1000 m³ per year, can not feed the beach in a satisfactory way.

Therefore, since the last ten years, artificial shingle renourishment has relieved the nature, supplying the beach by lorries on an amount of 10 to 15 000 m³ per year in an attempt to fill up the deficit. This is a soft but onerous method, with ineffective long term perspective, as the renourishment disappears downcoast in winter, during storms.

Innovative planning policies, to save the beach while reducing drastically renourishment budget required to be tested on a physical movable bed model (TEISSON and al, 1989).

3. THE PHYSICAL MODEL

Bathymetry and shoreline have been represented in a 28 x 33 m tank, at an undistorted scale of 1/150.

Shingle of 30 mm mean diameter (D_{50}) is satisfactorily represented by bakelite of 1.5 mm, a lightened artificial material. After preliminary test with uniform granulometry, extended granulometry measured in the prototype (5-50 mm) has been set up in the model in order to reproduce the effects of sorting.

Sand is also simulated by another artificial material ; at the present time this sand is passing in front of the site ; it is expected to deposit in the future in the new sheltered area. The tank is fitted out with a mobile random wave generator, and tide generator. Measurements are carried out by digital waves gauges and limnimeters and by an automatic bottom probe sensor for bottom evolution.

Calibration of the model has been performed in two steps :

- to seek for the sedimentological time scale from the situation in the past, i.e. a stable beach with a littoral transport of 20 000 m³/year,
- to verify and reproduce present erosion problems.

For that purpose, random waves from various directions respecting wave climate, tide level with associated storm surges, are reproduced in the tank, in order to simulate evolutions up to 15 years in the future with the new lay out.

4. TESTS AND RESULTS OF PLANNING POLICIES

4.1. Bounded shore line retreat

The purpose of the planning policies is to adapt the beach line with the present situation, characterized by a very weak natural sediment supply. The idea is therefore to destroy the sea front road, badly orientated and to draw a new shore line well adapted to the westerly dominating wave climate.

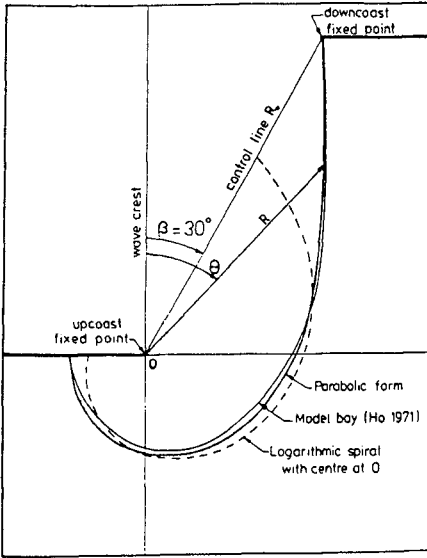
We extended for shingle beaches the concept of static equilibrium bay, developed by SILVESTER in the 70's for sandy beaches, using the latest results of HSU et al. (1989). In stable condition, the tangential section downcoast is parallel to waves crests approaching the coast from offshore ; the incoming waves will refract and diffract into the bay and break simultaneously, arriving more normal to the coast along the whole peripheries (fig. 2).

These results have been used to define theoretically a so called logarithmic spiral beach shape in the valley (fig. 3). Tests on the physical movable bed model have enabled to optimize the maximum indentation in the valley to 180 m, bounded by a sea wall. The part of the beach sheltered in the valley, with an initial replenishment of 40 000 m³ of shingle is fully stable (fig. 4) : vertical cross sections of the beach after 6 and 12 years (fig. 5) show very little evolution. Sand, presently passing in front of the site, tends to deposit at the toe of the shingle beach. Annual renourishment could be carried back to 2500 m³, six times less than now, devoted to the eastern part of the beach below the cliffs, protected by a lengthened easterly groyne.

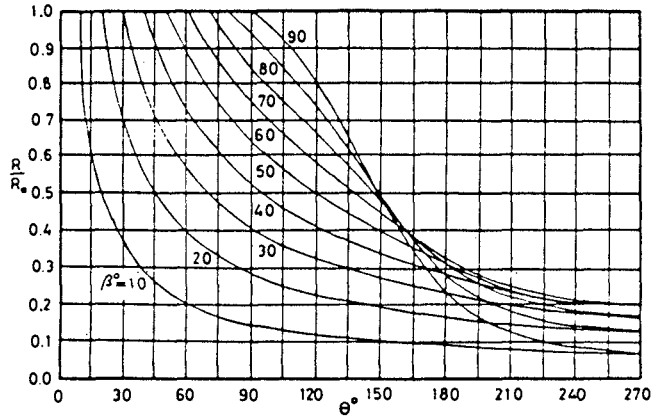
4.2. Estuarization of the valley

This most ambitious project (fig. 6), after destruction of the sea front road leaves the sea to intrude the valley ; topography of this flat valley lies 1 meter below the highest tide level. At the beginning of the century, during a major storm, the sea invaded the valley 2 km landwards. Nowadays, estuarization would be limited to 800 m by a sea wall, to protect the city.

One of the main point of interrogation is the behavior of the soft, water saturated meadows under the waves attacks : new equilibrium slope, transition time. This aspect cannot be reproduced on the physical model, in the absence of similitude laws. An expertise has therefore been conducted from geological surveys (fig. 7), to deliver a first shape of this estuary (LAFOND, 1990). This high perched estuary, with a small tidal prism, has been set up on the physical model. Waves will diffract and vanish behind the western chalky cliff (fig. 8) : erosion of the meadows by waves would be limited to the first 300 meters. Upstream, topography of the valley would remain unchanged, forming a high marsh, irregularly flooded, only for the 10 % highest tides. Downstream, consolidated soil below the present road and shingle beach would act as a barrier and limit the thickness of the eroded layer to 4 or 5 meters. Behaviour of shingle and sand has been surveyed over 15 years : littoral transport appears too weak to form a westerly spit. Superficial deposits of sand are noticeable at the mouth of the estuary.



Definition Sketch for Bay in Static Equilibrium



R/R_0 versus θ for varying β

Fig.2: Characteristics of bays in static equilibrium (from HSU and al, 1989)

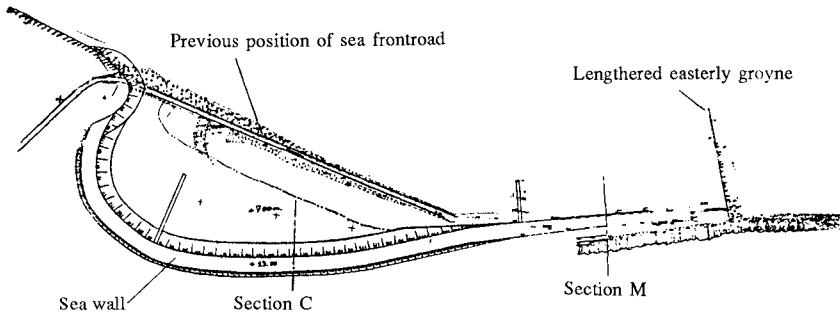


Fig.3: Layout of the shoreline retreat. "Logarithmic spiral" beach shape after optimization test.
Position of section C and M on Fig.5

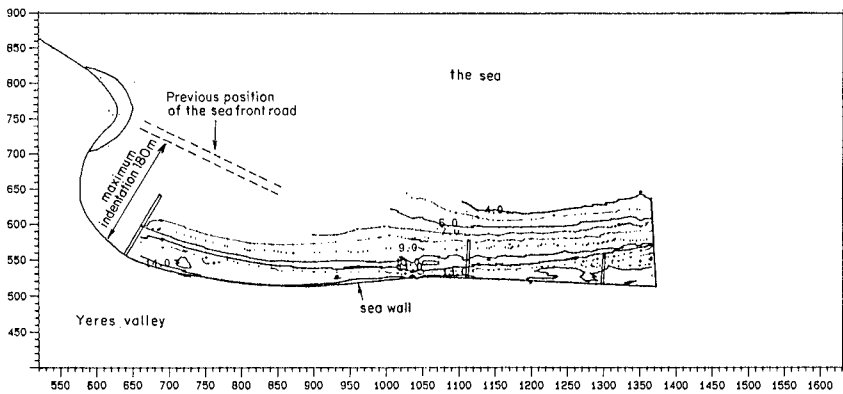


Fig.4: Shore line retreat. New bathymetry of the shingle beach after 6 years. Automatic data acquisition with the bottom probe sensor on the physical movable bed model.

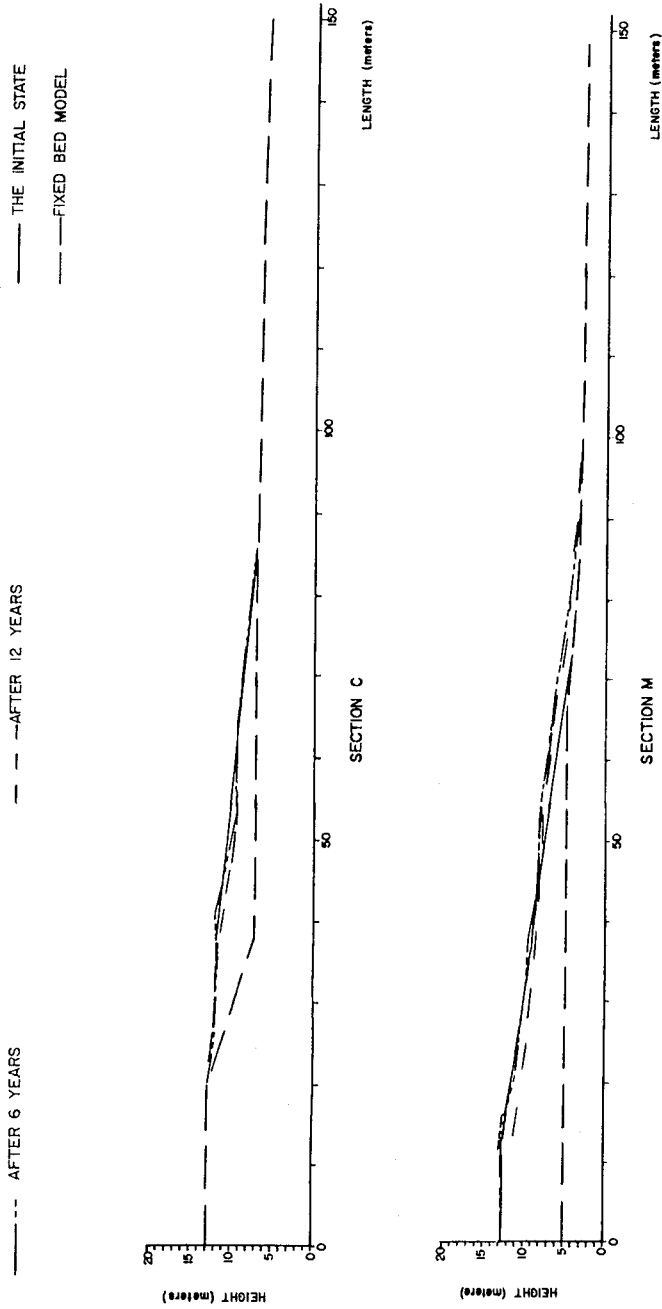


Fig.5: Evolution of typical vertical cross section of the beach after 6 and 12 years on the model

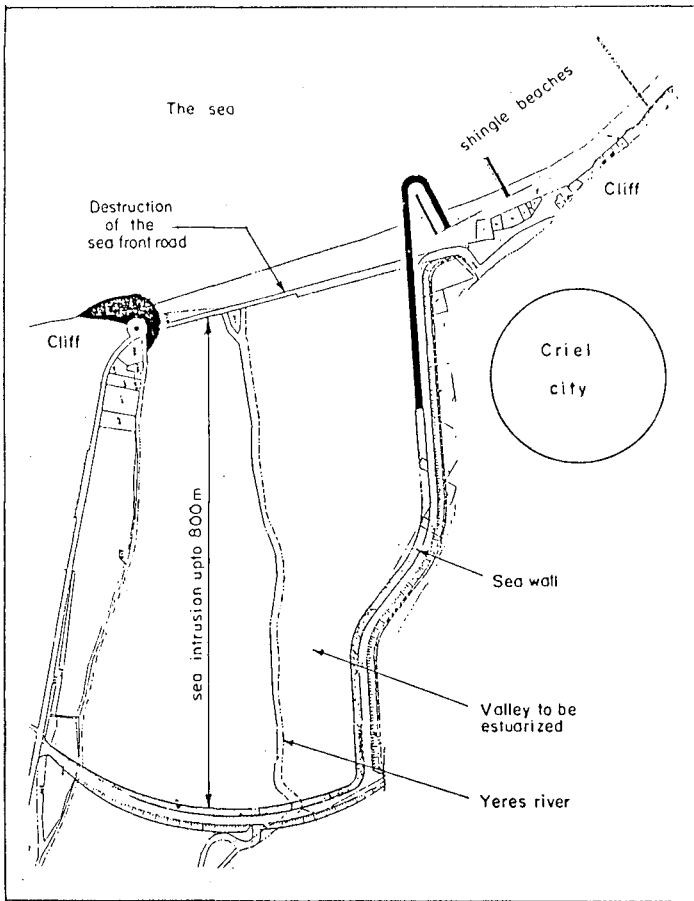


Fig. 6 Estuarisation planning

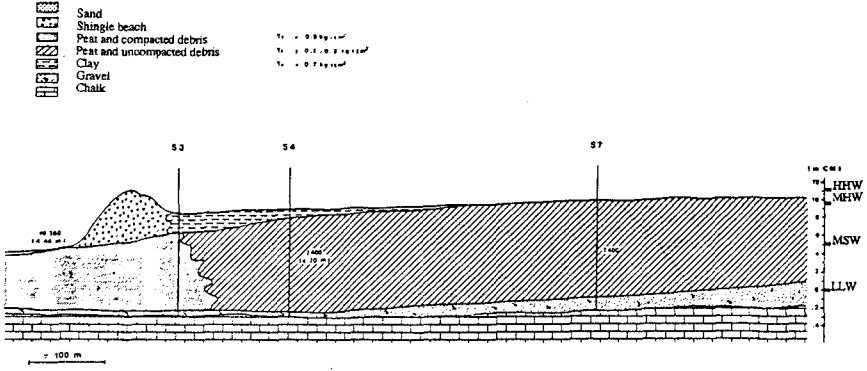


Fig. 7: Longitudinal section of alluvial forms in the valley

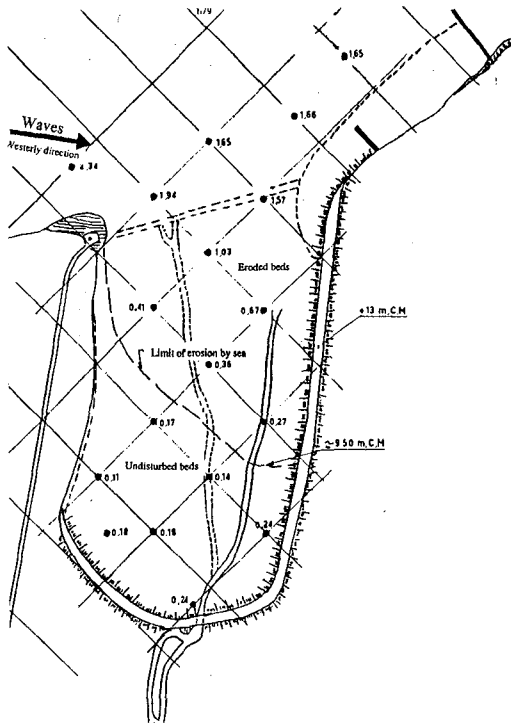


Fig. 8: Agitation survey (in meters) in the physical model in the case of estuarisation. Storm conditions, highest high water level.

5. CONCLUSIONS

Thus, littoral protection of this site reflects the evolution in coastal engineering state of mind : from hard solutions as groynes, then soft approach as beach nourishment, and finally a retreat to build up a new equilibrium shore line.

This new shore line, rather than fighting endless against the sea, is well adapted to the depletion of littoral transport and waves attack.

This approach as a retreat appears valuable when no worthwhile patrimony has to be safeguarded landwards.

6. ACKNOWLEDGEMENTS

This study has been granted by the Conseil Général de Seine-Maritime under the control of Direction Départementale de l'Équipement de Seine-Maritime.

REFERENCES

LAFOND L.R. (1990)

Mechanical and sedimentological properties of the filling up of the Yeres Valley, Criel - Consequences on re estuarisation - Association Rivages - Feb. 1990 (in French)

MUIR WOOD, A.M. (1970)

Characteristics of shingle beaches : the solution to some practical problems. Proc. of the 12th Coastal Engineering Conf., 1970, pp. 1059-1076.

HSU, J.R.C., SILVESTER R. and XIA, Y.M. (1989)

Generalities on static equilibrium bays. Coastal Engineering, 12, 1989, pp. 353-369.

TEISSON ch., BOBIN C., GUIPPE C. (1989)

Protection against the sea of the shingle beach of Criel : study of planning policies on a

CHAPTER 194

Experimental Results on the Sediment Grain Threshold under Short-Wave Action

C.I.Moutzouris¹

Abstract

Results on the conditions of initiation of first sediment movement on a flat bed under the action of monochromatic short waves are presented in this paper from a laboratory study. The results indicate the existence of a correlation between the Ursell number and the parameter a . The correlation is of the $a = \lambda U^n$ type. The values of n and λ , as defined from the experiments, were not unique and were different from the values found in an earlier study by Sunamura. Therefore it was considered necessary to cross-check the values of n using data from real-world beaches.

Introduction

The Laboratory of Harbour Works, National Technical University of Athens, is conducting a research programme on the sediment distribution on the bed of real-world beaches under the action of waves. The beaches from which field data are collected are located along the coastline of Greece, which is an almost tideless environment. This means that the collected data are free of tidal effects, which may influence the results considerably. Other specific features of the beaches are as follows: slopes are, generally speaking, steeper than in many other parts of the world, and sedimentary environments are of the mixed type as far as grain size is concerned.

A rather important conclusion derived from the programme is that grain size changes considerably in the cross-shore direction of beaches. Grain size distribution is found to be related to the wave energy level. Consequently, grain size-related parameters, which are known to influence nearshore processes significantly, are found to change in the cross-shore direction. Results from the

¹ Director, Laboratory of Harbour Works, National Technical University of Athens, Patission 42, 10682 Athens, Greece

programme have been reported in a series of past papers (Moutzouris,1989,Moutzouris and Kypraios 1987,etc.).

In almost all cases, it was found that cross-shore changes mainly occur in a zone extending from the line of maximum wave run-up to a critical depth d_c . In the zone seawards of d_c , changes become almost insignificant (see Fig.1). d_c is believed to depend upon the previous sea state, the prevailing sediment size and the bed topography. From one point of view, d_c could be equivalent to the "closure depth" of van de Graaff, in which the profile of a beach becomes insensitive to changes. From another point of view, d_c could be related to the critical depth of initiation of grain movement under wave action.

In the present paper, an attempt is made to investigate whether a correlation exists between d_c and the critical depth of initiation of grain movement. Results from the laboratory are presented on the sediment grain threshold and field data are also used.

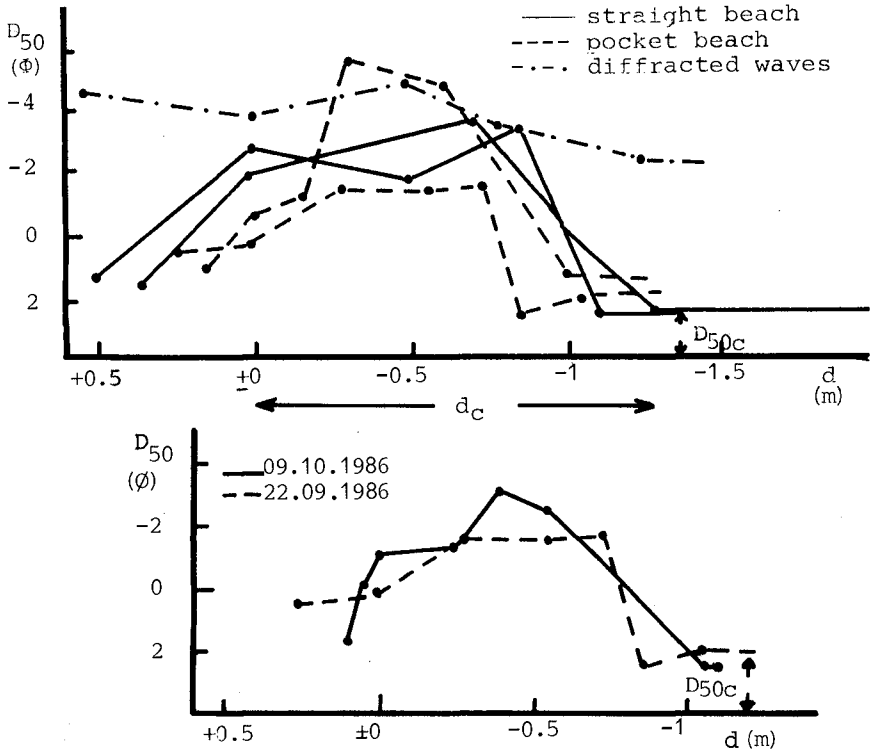


Fig.1.-Cross-shore distribution of sediment grain size (D_{50} is the median grain diameter)

Methodology and Experimental Apparatus

A number of beaches were selected along the coastline of eastern Attica, Greece. The beaches were surveyed four times a year, namely in spring, summer, autumn and winter. Sediment samples from the sea bed were collected along transect lines on each beach. The cross-shore distributions of grain size on these beaches were computed. The critical depth d_c in each case and the corresponding median diameter D_{50c} of grains were then evaluated. d_c and D_{50c} are defined in Fig.1.

A first attempt to compare the above values of d_c found on the beaches to the depth of initiation of sediment movements d_s , as computed from various existing empirical formulae, did not lead to any decisive conclusion. One major reason for this is believed to be the lack of adequate knowledge of the wave disturbance, which had caused the sediment distributions found on the beaches.

It was thus considered necessary to define precisely the critical values of wave height, wave period and the water depth at which initiation of the first movement of grains of diameter D_{50c} occurs on the sea bed. For this purpose, experiments were conducted in a concrete wave flume with a glass sidewall, 27m long, 1.50m deep, and 60cm wide. At one end of the flume, a piston wave-maker created monochromatic waves and at the other end, an absorbing mildly sloping beach was installed. An aluminium tray 1.00m long and 60cm wide was placed on the bottom of the flume. The bed material used consisted of natural sediment grains obtained from a single sieve fraction, in order to obtain the same diameter as the median diameter D_{50c} in nature. A sediment layer consisting of beach material several millimeters thick was placed on the tray. The surface of the sediment was smoothed and waves were then allowed to act on the sediment grains. In each experiment, the grain diameter was kept constant and the wave-induced bed shear stress τ was progressively increased. Starting at a value of $\tau=0$ and increasing τ , the layer initially stayed at rest. After τ reached a critical value τ_c , the first grain movement was observed and then bed load transport started occurring. Five kinds of well-sorted sediment of a constant density (2.6) but different diameter were used in the experiments. All diameters tested had been found in nature to be D_{50c} and are presented in Fig.2. Numerous water depths were tested. The experiments are described by Loisidou (1989).

Experimental results

Various dimensionless parameters were computed using the data obtained from the experiments. Among others, the Hallermeier parameter F , which indicates the intensity

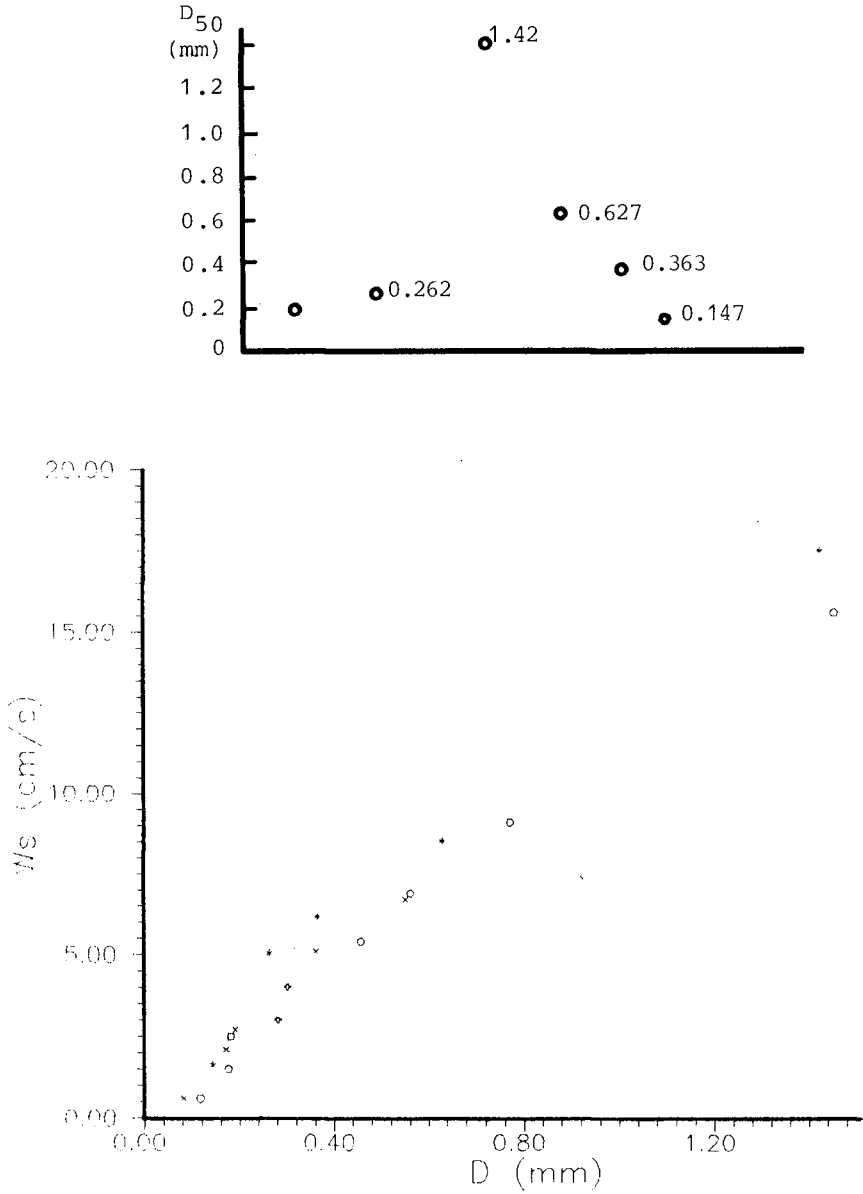


Fig.2.- Sediment grains used in the experiments (w_s is the settling velocity)

of sediment movement, the Shields parameter Ψ , the Ursell number U , which represents the skewness of the water particle velocity profile, the Reynolds number R , the Dean number and finally the parameter a , which is defined by equation(2). It was found that the best correlation existed between the Ursell number and the parameter a , defined as follows:

$$(1) \quad U = \frac{HL^2}{d^3}$$

$$(2) \quad a = \frac{u_m^2}{\gamma'_s g (D_{50} A_0)^{1/2}}$$

$$\gamma'_s = \frac{\rho_s - \rho_w}{\rho_w}$$

where H and L the wave height and length, respectively, d is the corresponding water depth, g is the gravitational acceleration, D_{50} is the diameter of the grains tested, γ'_s is the specific gravity of immersed sediment, and ρ_s and ρ_w are the densities of sediment and water, respectively. A_0 and u_m are respectively the near-bottom orbital diameter and velocity of water particles, as computed using the Airy theory. All wave-related parameters in equations (1) and (2), namely H, L, u_m and A_0 , represent values at the moment of occurrence of initiation of first grain movement.

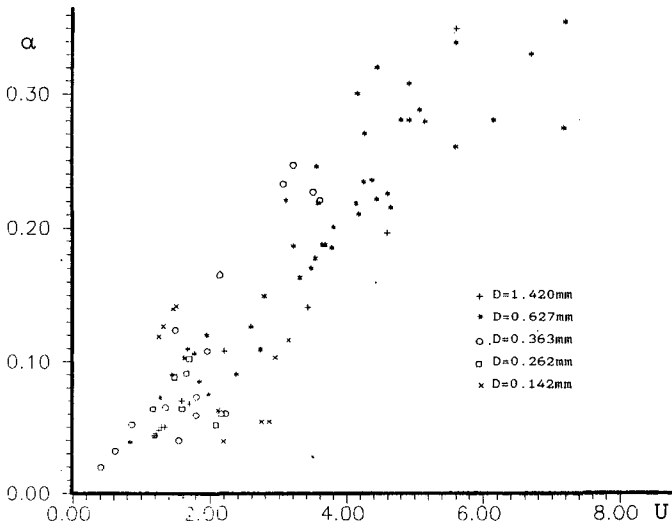


Fig.3.-Dimensionless parameter a versus U
(from laboratory measurements)

A plot of the correlation obtained is shown in Fig.3. The correlation is of the following type:

$$(3) \quad a = \lambda U^n$$

where λ and n are constant. The lefthand of equation (3) is similar to Shield's relative stress. The correlation obtained shows a scatter, which does not allow a unique set of (λ, n) values to be defined from the experiments. The following ranges of values emerge instead, as is also shown in Fig.4:

$$(4') \quad \begin{array}{lll} \lambda = 0.04 & \text{to} & 0.075 \\ n = 0.6 & \text{to} & 1 \end{array}$$

The best fitting curve is the one with:

$$(4) \quad \lambda = 0.05 \quad \text{and} \quad n = 1$$

The above correlation between a and U is not surprising. In a previous similar experimental study by Sunamura (1980), a qualitatively similar relationship was derived for a flat bed with:

$$(5) \quad \lambda = 0.1 \quad \text{to} \quad 0.2 \quad \text{and} \quad n = 0.25$$

The considerable quantitative differences between equations (4') and (5) may partly be attributed to the different initial conditions in the two studies. The conditions examined by Sunamura were as follows

$$2 < U < 300$$

which were different to the ones in the present study, namely:

$$0.5 < U < 8$$

The ranges of values tested in the two studies are shown in Fig.5. The relationship derived by Sunamura is compared to the present one in Fig.4.

According to the Komar and Miller (1975) laboratory results for sediment threshold on a flat bed with monochromatic waves:

$$\lambda = 0.21 \quad \text{and} \quad n = 0 \quad (D < 0.5\text{mm})$$

which means that initial sediment movement is independent of the skewness of the water particle velocity profile. These values were derived from the best fit to their data. It is believed (Drake et al., 1985) that lower values of λ should be expected, when the characteristics of the largest waves in a spectrum are used.

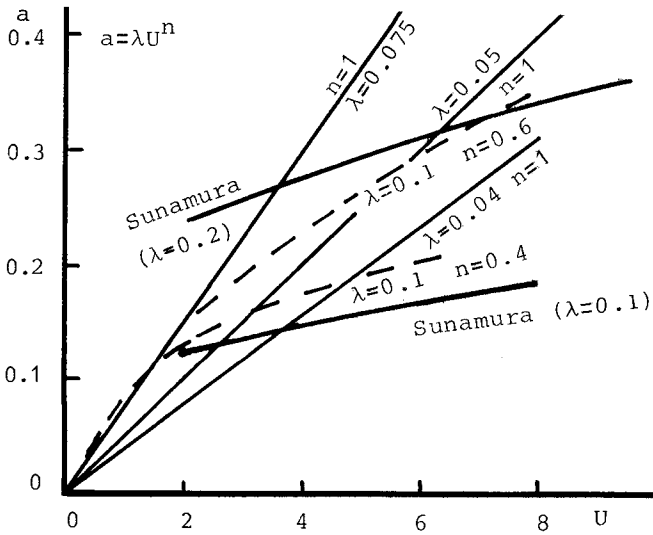


Fig.4.-Equation (4') compared to experimental results

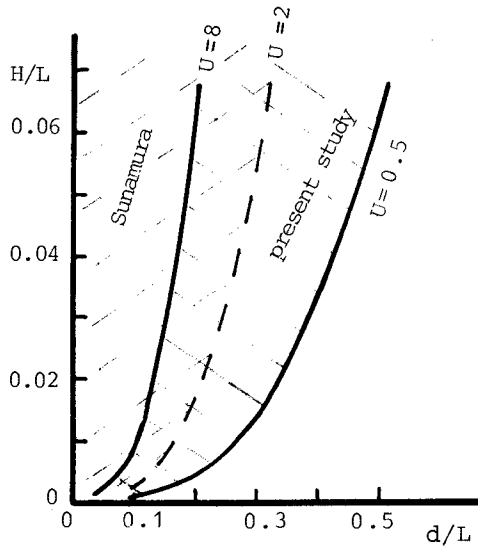


Fig.5.-Range of conditions tested in the present study and in the study of Sunamura

As a result of the above uncertainties and contradicting values of λ and n , it appeared useful to verify the values of λ and n using data from field measurements.

Field Results

Combining equations (1),(2) and (3) and rearranging leads to the following equation:

$$(6) \quad F_w = \frac{1}{\lambda} F_b$$

with

$$(7) \quad F_b = \frac{\pi}{2} \frac{\rho_w}{\rho_s - \rho_w} \left(\frac{d}{D_{50}} \right)^{0.5}$$

$$(8) \quad F_w = \left(\frac{H}{L} \right)^{n-1.5} \left(\frac{d}{L} \right)^{0.5-3n} f$$

with

$$f = \cosh kd (\sinh kd)^{0.5}$$

where k is the wave number. F_b is a function of the sediment parameters and the bed morphology whereas F_w is function of the local wave parameters only. Both F_b and F_w change in the cross-shore direction of a beach. Equation (6) indicates that grain movement occurs when a certain number of wave, bed and sediment-related parameters combine in a way to satisfy the criterion indicated by this equation. Initiation of grain movement occurs when F_b/λ becomes larger than F_w .

It now seems appropriate to look closer at both functions F_b and F_w and how they change in the cross-shore direction. Equation (7) may be written as:

$$(9) \quad F_b = C \left(\frac{d}{D_{50}} \right)^{0.5}$$

with

$$C = \frac{\pi}{2} \frac{\rho_w}{\rho_s - \rho_w}$$

Sediments usually found on beaches have a value of $\rho_s=2.4$ to 2.6. In a previous paper (Moutzouris,1988), it was reported that ρ_s does not seem to change considerably across-shore (see Fig.6).

It therefore seems reasonable to assume that for the beaches examined, C is almost constant in the cross-shore direction with values in the following range:

$$(10) \quad C = 1.02 \text{ to } 1.15$$

The cross-shore distribution of $(d/D_{50})^{0.5}$ is now examined using field data. Typical cross-shore profiles of d and D_{50} are shown in Fig.7. The local depth normalized by the corresponding median diameter for a number of cases is shown in Fig.8.

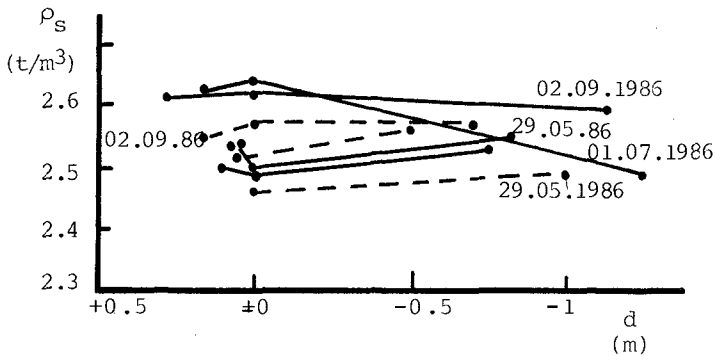


Fig.6.-Cross-shore distribution of ρ_s

The envelope of all cross-shore distributions found on the beaches studied is shown in Fig.9, which is also the envelope of F_b if a multiplication factor of 1.02 to 1.05 is applied. It is seen that F_b was never found to be larger than, say, 110 (see equations 9 and 10). In most cases F_b was smaller than, say, 80. A rather important conclusion is that F_b is very much dependent on the cross-shore distribution of D_{50} .

The cross-shore change of F_w is now computed using the Airy theory. Values of n introduced in equation (8) range from 0.25 to 1. F_w is computed for wave steepnesses $\gamma_0 (=H_0/L_0)$ in deep water ranging from 1 to 4%. The energy flux conservation principle is applied. The results are shown in Fig.10.

From the analysis it was found that F_b and F_w change in the cross-shore direction of a beach. In deeper water F_w is always larger than F_b/λ , which means that no sediment movement occurs. The criterion of sediment movement is satisfied in the zone of shallow water. The depth of first grain movement depends upon the bed form, the cross-shore distribution of sediment grain sizes and the wave characteristics. The data from the beaches did not lead to any clear conclusion concerning the values of n . It seems that n depends upon the conditions prevailing on each beach.

It was then decided to adopt the values of n and λ from the best fitting curve to the laboratory results. Equations(3) and (4) were used to compute the depths of initiation of sediment movement d_s for the beaches where depths d_s had been defined, as mentioned earlier. Depths d_s were then compared to d_s . This second attempt again did not lead to any conclusion, which means that d_c was not found related to d_s .

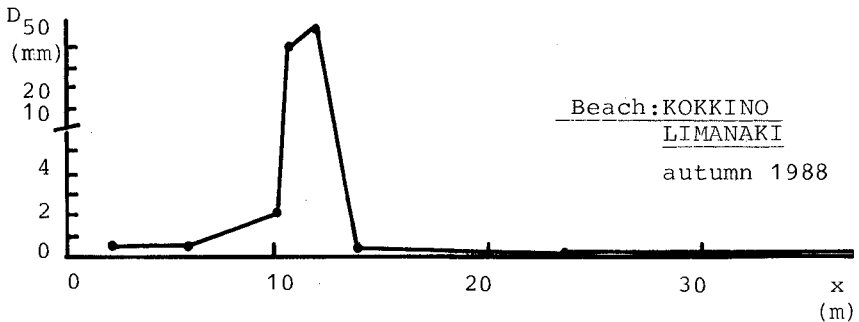
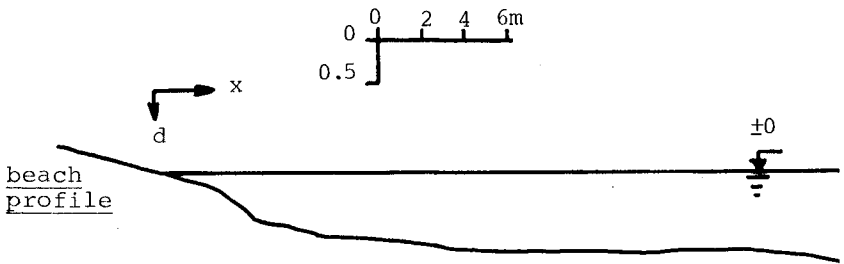
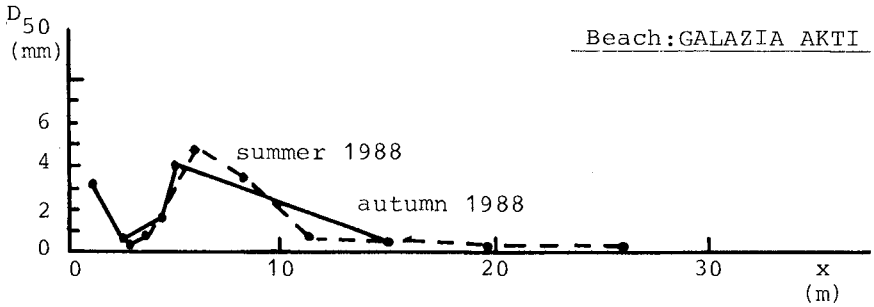
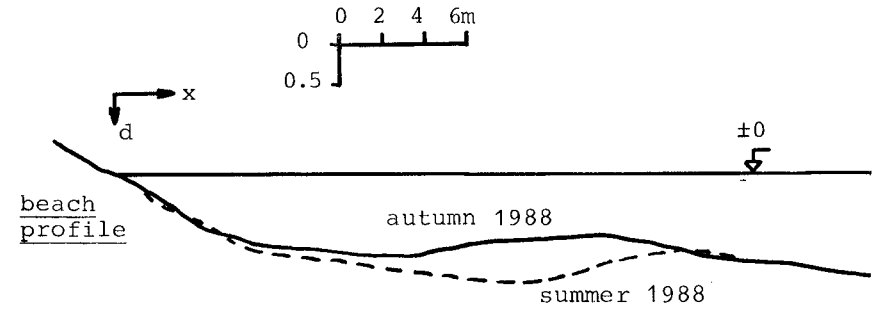
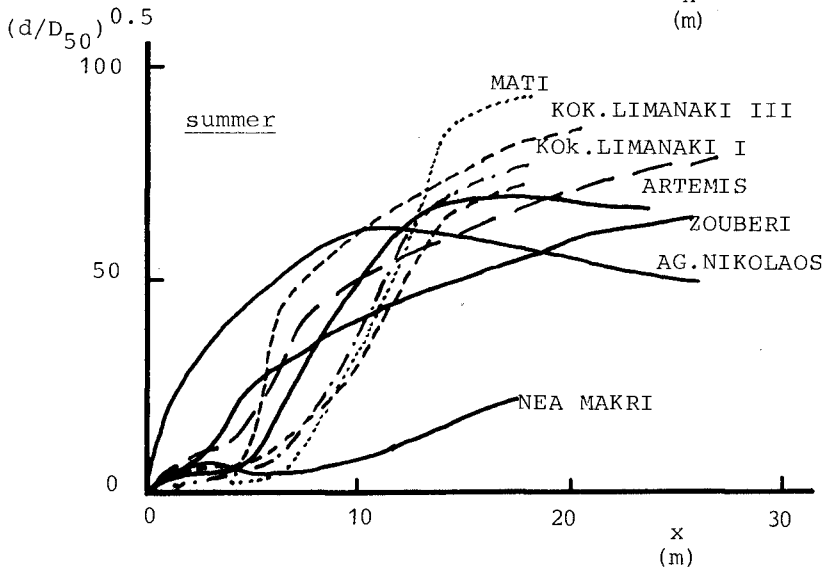
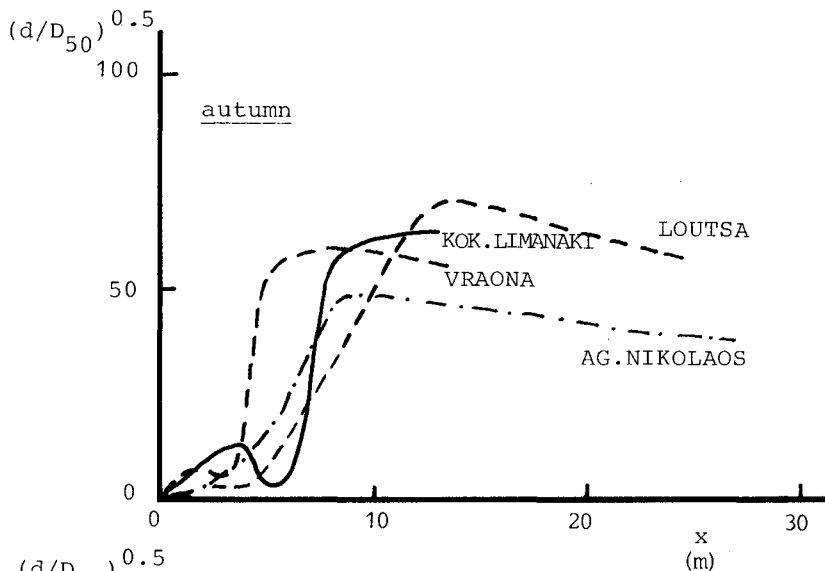


Fig.7.-Typical cross-shore distributions of water depth and grain median diameter on Greek beaches



(continued)

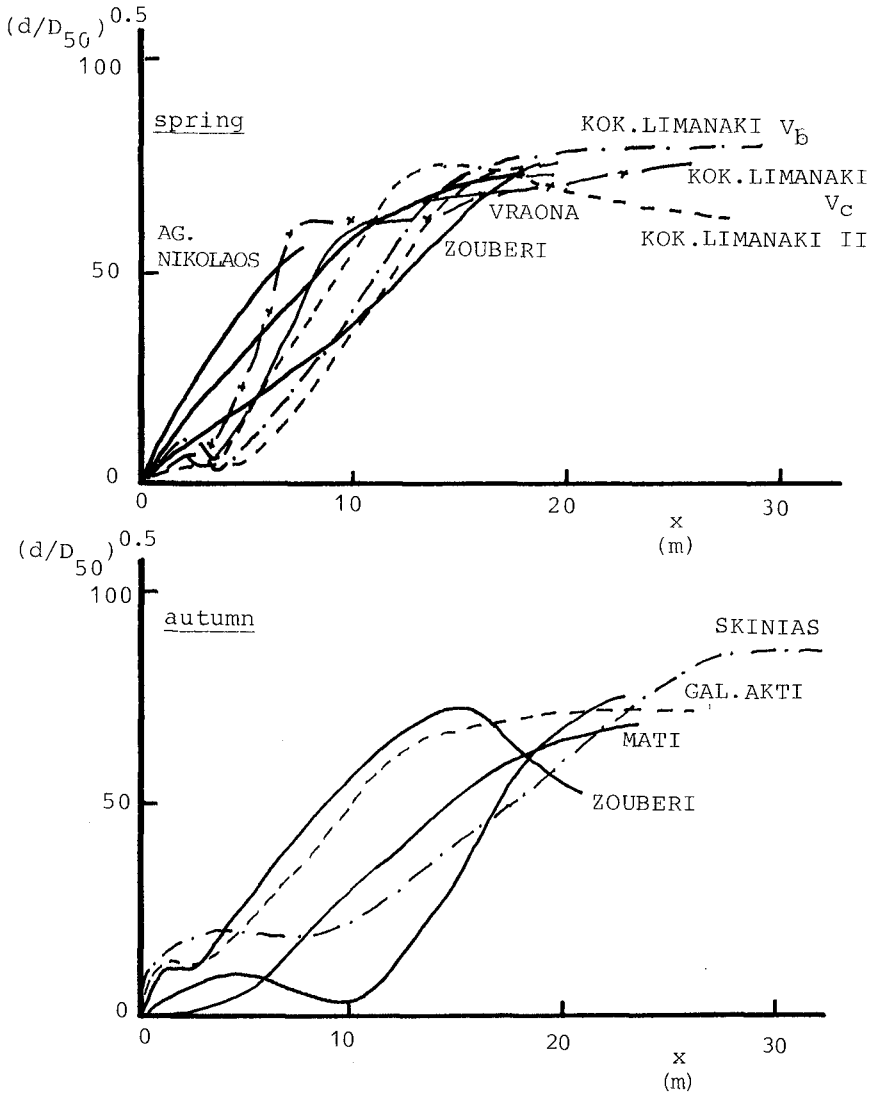


Fig.8.-Typical cross-shore distributions of the parameter $(d/D_{50})^{0.5}$

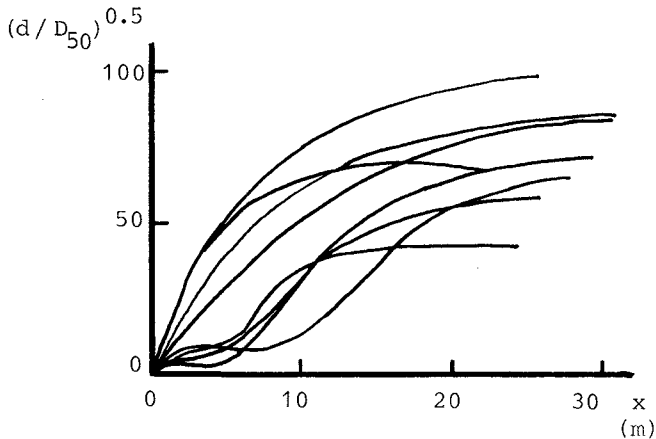


Fig.9.-Envelope of cross-shore distributions of $(d/D_{50})^{0.5}$

Discussion

The results from laboratory measurements on the conditions of initiation of sediment movement under the action of monochromatic short waves confirm the existence of a correlation between the Ursell number U and the parameter a , as defined by equation (2). The coefficients of the correlation n and λ were not found to be unique and are different from the values found in an earlier study. A first explanation could be that the values of U tested in the two studies were different. The use of data from various beaches did not help to a better definition of the correlation coefficients.

The depth of initiation of sediment movement was not found to be correlated to the depth of stabilisation of grain size on a beach.

References

- Drake, D.E., Cacchione, D.A., and Karl, H.A., 1985, "Bottom currents and sediment transport on San Pedro Shelf, California", *Jour. Sedim. Petr.*, vol.55, No.1, pp.0015-0028.
- Komar, P.D., and Miller, M.C., 1975, "The initiation of oscillatory ripple marks and the development of plane bed at high shear stresses under waves", *Jour. Sedim. Petr.*, vol.45, pp.697-703.
- Loisidou, P., 1989, "Experimental study of the initiation of sediment grain movement under the wave action", Diploma Thesis, Nat. Techn. Univ. of Athens, Lab. Harbour Works.

Moutzouris, C.I., 1989, "Longshore sediment transport rate vs. cross-shore distribution of sediment grain sizes", Proc. 21 ICCE, ASCE, Malaga, Chapter 145, 1959-1973.

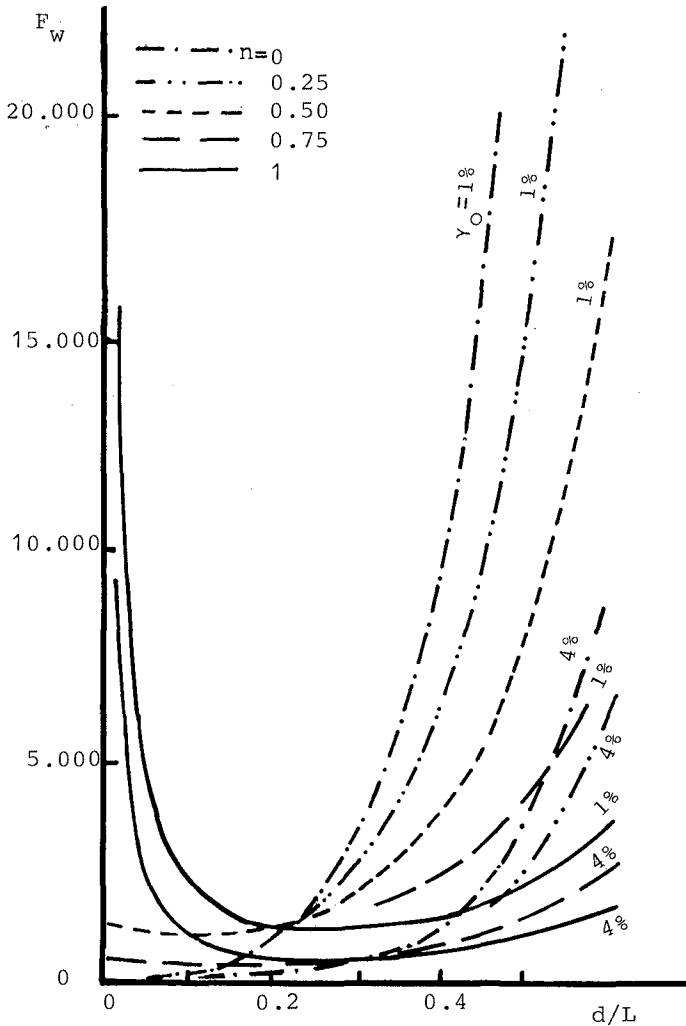


Fig.10.-Cross-shore distribution of the function F_b

Moutzouris, C.I., and Kypraios, N., 1987, "Temporal and spatial grain size distribution of sediment in a tideless pocket beach", Proc. Coastal Sediments '87, Vol. II, 1909-1924.

Sunamura, T., 1980, "A laboratory study of offshore transport of sediment and a model for eroding beaches", Proc. 17 ICCE Sydney, Vol. II, 1051-1070.

CHAPTER 195

Movable Bed Modeling Criteria For Beach Profile Response

Hsiang Wang,¹ Takao Toue,² and Hans H. Dette³

Introduction

Modeling coastal phenomena using movable bed means is a complicated problem with no general solution at present. Most modeling laws that are realizable in the laboratory usually only apply to certain restricted conditions. This paper, like many others, elects to deal with a restricted case, here, the two dimensional beach profile changes under the influence of wave action.

Numerous papers have been written on this subject. A general review can be found in Hudson et.al. (1979), LeMenhaute (1990) and Wang (1985). Those of particular relevance to the present study are briefly reviewed here. Noda (1978) examined several theoretical scaling laws but recommended a completely empirical model Law based on similarity of equilibrium profiles in the breaker zone. His model involves three scaling parameters, the sediment diameter ratio, the vertical and horizontal length scales. Vellinga (1982) and Graaff (1977) conducted a comprehensive laboratory study by using different scales in attempting to duplicate the beach and dune erosion of the Dutch's coast. Vellinga also settled on a pair of empirical relationships. The geometrical scale relationship bears certain resemblance to the Noda's with an additional fall velocity scale incorporated into it. A morphological time scale is also added. Both Noda's and Vellinga's laws require that the wave steepness and the Froude number be preserved. Hughes (1983) presented a model based upon preserving the Froude number and a non-dimensional fall velocity parameter. Hughes' model allows for wave distortion. There are similarities as well as very settled differences among the three modeling laws. All these modeling laws compared well with its own data set. Inter comparisons in most cases were not successful.

Kamphis (1974) using an entirely different approach listed four different non-dimensional parameters as requirement for complete similarity. Realizing that preserving all of them in the model is impractical, he proposed a set of four different modeling laws requiring preservation one or more non-dimensional parameters but not all of them. Each modeling law is suitable for a specific range of environmental conditions. There was no comparison with Laboratory data reported. Table 1 summarized the modeling laws by these authors.

¹Department of Coastal and Oceanographic Engineering, University of Florida, Gainesville, Florida 32611 U.S.A.

²Coastal and Hydraulic Section, Taisei Research Center, Taisei Corporation, 344-1 Nazemachi, Totsuka-ku, Yokohama, Kanagawa 245, Japan

³Leichtweiß-Institut für Wasserbau Technische Universität Braunschweig Beethovenstrasse 51a, 33 Braunschweig, Federal Republic of Germany

Table 1 Existing Beach Profile Modeling Laws

<u>Author</u>	<u>Requirement</u>	<u>Modeling Law</u>
Noda (1978)	$(\frac{H_a}{L_o})_p = (\frac{H_a}{L_o})_m$	$N_D = (N_\delta)^{0.55}$
	$F_p = F_m$	$N_\delta = (N_\lambda)^{0.76}$
Vellinga (1982)	$(\frac{H_a}{L_o})_p = (\frac{H_a}{L_o})_m$	$N_T = N_t = (N_\delta)^{\frac{1}{2}}$
	$F_p = F_m$	$N_\delta = (N_W)^{0.44} (N_\lambda)^{0.78}$
Hughes (1983)	$F_p = F_m$	$N_T = N_t = N_\lambda / (N_\delta)^{\frac{1}{2}}$
	$(\frac{H}{TW})_p = (\frac{H}{TW})_m$	$N_\delta = (N_W N_\lambda)^{\frac{2}{3}}$
Kamphis (1974)	$(N_{R*}) = 1$	
	$(N_{F*})_p = 1$	
	$\frac{(N_{\rho*})}{N_\rho} = 1$	
	$\frac{N_a}{N_D} = 1$	

δ : Vertical Scale; λ : Horizontal Scale; D : Sand Size;
 T : Fluid Motion Time Scale; t : Morphological Time Scale;
 W : Fall Velocity.

Judging from the argument used by the authors and the evidence provided by them, the modeling laws by the first three authors are clearly based on suspended-load dominated case. Kamphis' model did not specify the mode of transport. From the selection of the parameters, it appeared that the resulting modeling laws should be more pertinent to bed-load dominated cases.

In the first three modeling laws, Noda's and Vellinga's are undistorted but Hughes' is distorted. This needs some clarification. In the modeling law itself, the vertical and horizontal scales are all distorted as can be seen from Table 1. The distortion or non-distortion originates from the requirement. Noda and Vellinga both require the wave steepness to be preserved, thus, the wave form should be undistorted. Hughes' model, on the other hand, preserves non-dimensional fall velocity, thus, permits wave form distortion. If one insists upon a consistent undistorted model (wave form treated as a geometrical scale) by letting $N_\delta = N_\lambda = 1$, then Noda's model reduces to $N_D = N_\delta^{0.55}$ and Vellinga's and Hughes' models yield identical results in both morphological scale and fall velocity scale:

$$N_T = N_t = N_\delta^{\frac{1}{2}}$$

$$N_W = N_\delta^{\frac{1}{2}}$$

This is of great comfort that all the model laws are somewhat consistent at undistorted scale except none of the authors actually intended to propose $N_\delta = N_\lambda = 1$ as quite evident from the formulas they presented.

Modeling Law By Inspectional Method

So far all the above modeling laws were derived from dimensional analysis of physical quantities. A slightly different approach is taken here by the inspection of the basic governing equation. The two-dimensional sediment conservation equation states that

$$\frac{\partial h}{\partial t} = \frac{\partial q}{\partial x} \quad (1)$$

where h is the bottom elevation, q is the volumetric sediment transport rate in the x direction; t is time and x is on-off shore direction. This equation can be non-dimensionalized as follows:

$$\frac{\partial \bar{h}}{\partial \bar{t}} = \frac{q_n t_n}{\delta \lambda} \frac{\partial \bar{q}}{\partial \bar{x}} \quad (2)$$

where the overbar refers to non-dimensional quantities and q_n , t_n , δ and λ represent, respectively, the reference values of sediment transport rate, the morphological time scale, vertical geometrical scale and horizontal geometrical scale. To maintain similitude between the model and prototypes requires

$$\frac{N_q N_t}{N_\delta N_\lambda} = 1 \quad (3)$$

where N refers to the ratio of prototype to model.

Suspended Load Transport

The suspended load transport rate can be expressed by depth averaged properties:

$$q_s = hVc \quad (4)$$

where h is equal to depth; V is equal to mean transport velocity and c is equal to depth-averaged mean sediment concentration. The suspended sediment concentration is directly proportional to the ratio of stirring power due to turbulence and the settling power due to gravity and can be expressed as (Hattori and Karvamata, 1980):

$$c \propto \frac{\rho u'}{(\rho_s - \rho)W} \propto \frac{u'}{SW} \quad (5)$$

where u' is the turbulent intensity, W is the particle settling velocity and S is the submerged specific weight. Thorton (1978) suggested that the ratio of turbulent velocity and wave induced velocity is a function of surf zone parameter, ξ , i.e.,

$$\frac{u'}{u} = f(\xi) \quad (6)$$

The surf zone parameter is defined as $Tan \beta / \sqrt{H_o/L_o}$ with $Tan \beta$ the beach slope, H_o and L_o , the deepwater wave height and length, respectively. Physically, this equation states that if the surf zone property is similar, the turbulence intensity should be proportional to the mean velocity scale, a plausible assumption. Since in a wave field u is proportional to H/T , substituting Eqs. (5) and (6) into Eq. (4) and then combining it with Eq. (3) leads to

$$\frac{N_o N_{f(\xi)} N_t N_H}{N_\lambda N_W N_T N_S} = 1 \quad (7)$$

If we let $N_{f(\xi)} = 1$, or $\xi_p = \xi_m$, we require

$$[g^{1/2} T \cdot Tan \beta / H_\delta^{1/2}]_p = [g^{1/2} T \cdot Tan \beta / H_\delta^{1/2}]_m \quad (8)$$

which when expressed in basic scaling quantities becomes:

$$N_T = N_\lambda / N_\delta^{1/2} \quad (9)$$

Here the wave height is treated as a vertical scale parameter. In Froude-number similitude, the horizontal velocity is scaled in accordance with $N_\delta^{1/2}$, i.e.,

$$N_F = \frac{N_V(\text{horizontal})}{(N_g N_\delta)^{1/2}} = 1 \quad (10)$$

or

$$N_V(\text{horizontal}) = N_\delta^{1/2} \quad (11)$$

Thus, Eq. (9), in essence, is the scale ratio of horizontal distance to horizontal velocity in a distorted model. Now, substituting Eq. (9) into Eqs. (7) and (4) and letting $N_{f(\xi)} = 1$, we obtain a pair of model laws as follows:

$$N_q = \frac{(N_\delta)^3}{N_s N_W N_\lambda} \quad (12)$$

$$N_t = \frac{N_s N_W N_\lambda^2}{(N_\delta)^2} \quad (13)$$

Morphological Time Scale and Field Evidence

Equations (12) and (13) essentially form the proposed modeling laws with the basic modeling requirement that the surf zone parameter be matched. One of the important but also more difficult aspects of beach profile modeling law is the determination of morphological time scale. Two different hypotheses are tested here. First, if we assume that the number of incoming waves per unit time is preserved for the similitude of erosion rate, then,

$$N_t = N_T = \frac{N_\lambda}{N_\delta^{1/2}} \quad (14)$$

Substituting the above equation into (13), one obtains

$$N_\delta = (N_s N_W)^{2/3} N_\lambda^{2/3} \quad (15)$$

This equation when expressed in dimensional form becomes:

$$h = \alpha_1 \left(\frac{SW}{g^{1/2}} \right)^{2/3} x^{2/3} \quad (16)$$

with α_1 , a constant of proportionality. This equation is similar to Dean's empirical equilibrium profile which was deduced from field data provided the scale parameter "A" in Dean's equation equals to $\alpha_1 \left(\frac{SW}{g^{1/2}} \right)^{2/3}$.

Second, if we assume that instead of preserving the number of waves, the trajectory of a fallen particle be preserved in the erosion rate, then the morphological time scale becomes

$$N_t = \frac{N_\delta}{N_{v(\text{horizontal})}} = N_\delta^{1/2} \quad (17)$$

Again substituting the above equation into Eq. (13) results in

$$N_\delta = (N_s N_w)^{2/5} (N_\lambda)^{4/5} \quad (18)$$

The dimensional counter part is:

$$h = \alpha_2 \left(\frac{SW}{g^{1/2}} \right)^{0.4} X^{0.8} \quad (19)$$

This is very close to the empirical equilibrium profile form proposed by Vellinga (1982) which was derived from field data along the Dutch coast.

Laboratory Data

As was shown, the proposed modeling laws are consistent with field data even though the morphological time scale remains somewhat unclear. In this section, laboratory experiments were compared. We put our emphases on inter comparisons among data sets from different laboratories and on the morphological time scale. We shall refer to Eqs. (14) and (15) as model "A" and Eqs. (17) and (18) as model "B".

The selected data sets used in the inter-comparisons are listed in Table 2, with the key parameters associated with each experiment. Here, Saville's experiment is treated as the reference and the vertical scales of the other tests are all referred to it. Figure 1 shows the comparison between Saville and Kriebel. According to the proposed modeling law, the model has no geometrical distortion by either Law "A" or Law "B", i.e., $N_\delta = N_\lambda = 9.6$ from both "A" and "B". The comparison is good except in the foreshore where the mode of transport in the small scale (may be even in the large scale) can no longer be considered as suspended-load dominated. Since there is no geometrical distortion, Law "A" and Law "B" yield the same morphological time scale as they should. Hughes and Fowler (1990) recently presented the results of a mid-scale experiment intended to duplicate the large scale experiment of Dette and Uliczka (1986). The model was also geometrically undistorted and the comparisons were judged to be excellent. Both sets of data support the modeling law but are not able to differentiate Law "A" from Law "B".

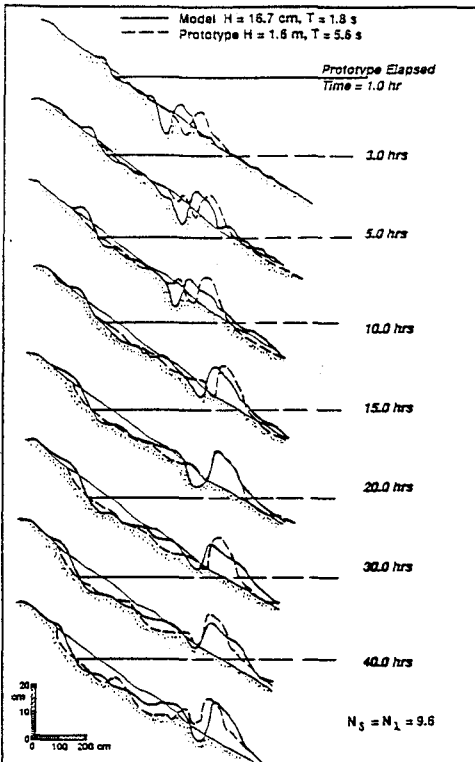


Figure 1: Comparison between Saville and Kriebel (from Kriebel, et.al. 1986).

Table 2 Selected Data Sets

Origin	Profile (Slope)	H(m)	T (sec)	Wo(cm/s)	N _f (est.)	ξ _T
CERC (Saville)	$\frac{1}{18}$	1.28-1.72	5.8-11.3	5.57	1	0.37
Delft (Graaff, Vellinga)	Composite	0.05-2	0.98-7.6	0.6-2.5	0.36 to 34	
Germany G W K Flume	Composite $\frac{1}{4}$	1.50 0.15 1.50 0.15	6 1.9 6 1.9	4.0 4.0 4.0 4.0	1.1 11 1.1 11	0.30 ² 0.30 ² 1.53 1.53
U. Florida Kriebel et.al. Barnett Toue ¹ Hughes	$\frac{1}{18}$, and $h = AX^{\frac{1}{2}}$ $h = AX^{\frac{1}{2}}$ $h = AX^{\frac{1}{2}}$ Composite	0.085-0.175 0.04-0.12 0.03-0.11 0.10	1.8-3.67 1.3-1.8 1.74 1.07	1.8 1.7 1.7 1.3	9.6 14-43 16-57 17	0.35
Field data Dean Vellinga	$y = AX^{\frac{1}{2}}$ $y = 20.39W^{0.44}X^{0.78}$					

¹ 3D test

² estimate base on average slope between shoreline and breaker bar

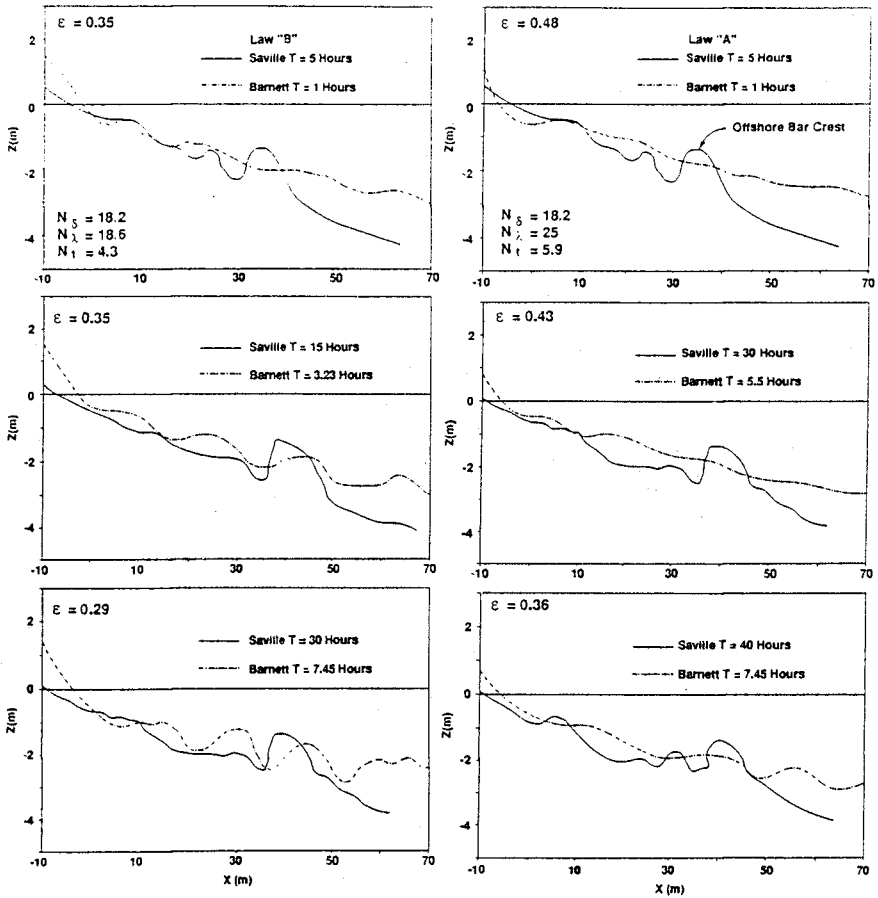


Figure 2: Comparisons between Saville's and Barnett's results.

The second comparison is between Saville's and Barnett's experimental results. Barnett's experiments were not intended for verification of modeling laws; rather were designed for testing the effects of seawalls on the fronting beaches. However, his bench mark cases of beaches without seawalls could be used for the present purpose. As stated earlier, the initial condition in Saville's tests was a beach of uniform slope of 1 to 15. The initial condition in Barnett's tests, on the other hand, was a beach of equilibrium shape in accordance with $h = AX^{\frac{2}{3}}$, with $A = 0.075m^{\frac{1}{3}}$. Since the surf zone parameter is defined with single beach slope value, we define here an equivalent slope as the mean slope value within the surf zone:

$$\bar{m} = \frac{\int_0^{X_b} m dx}{X_b} \tag{20}$$

where m is local slope and X_b is the surf zone width. Assuming $H_b = 0.8h_b$

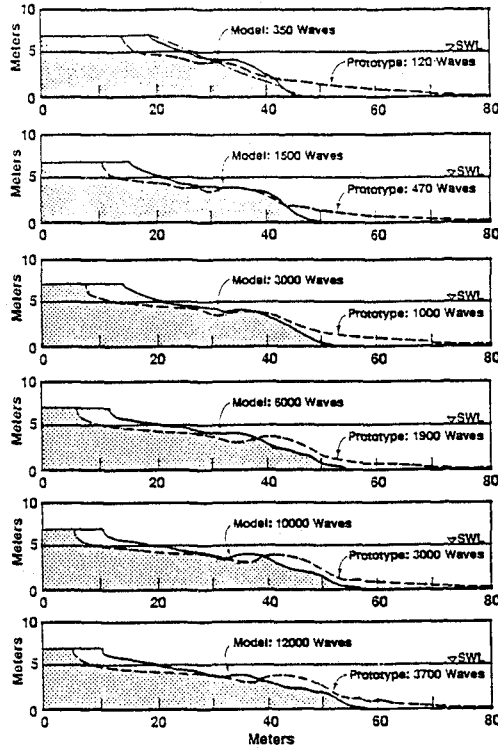


Figure 3: Comparisons between GWK and $\frac{1}{10}$ Scale Model with $N_f = N_\lambda = 10$ and $N_t = 1$ (from Dette and Uliczka, 1986).

and $h_b = 0.075x_b^{\frac{2}{3}}$, the \bar{m} value is found to be equal to 0.06 or 1 to 16.7, which is very close to 1 to 15 used in Saville's tests. Barnett tested three wave conditions; the one suitable for comparison was with $H_o = 8.8\text{cm}$ and $T = 1.3\text{ sec}$. For this case, the corresponding ξ is 0.33, very close to Saville's value of 0.37. The comparisons are shown in Figure 2. It should be noted here that the morphological time scale could only be preserved approximately as profiles were measured at discrete time intervals selected at the convenience of the investigators in the respective experiments. This is also the case for other comparisons reported here after. To evaluate the goodness of the comparison, the RMS values of the profile elevation differences were computed from the shoreline to the crest of offshore bar (see Figure 2), by the following equation

$$\epsilon = \left[\frac{1}{n} \sum_{i=1}^n (h_i^S - h_i^B)^2 \right]^{\frac{1}{2}} \quad (21)$$

where h^S and h^B are profile elevations of Saville and Barnett, respectively. These values are also given in Figure 2. From these values, it can be seen that Law "B" performs better than Law "A". Also, as time progresses, the modeling law becomes better as the influence of initial condition becomes less.

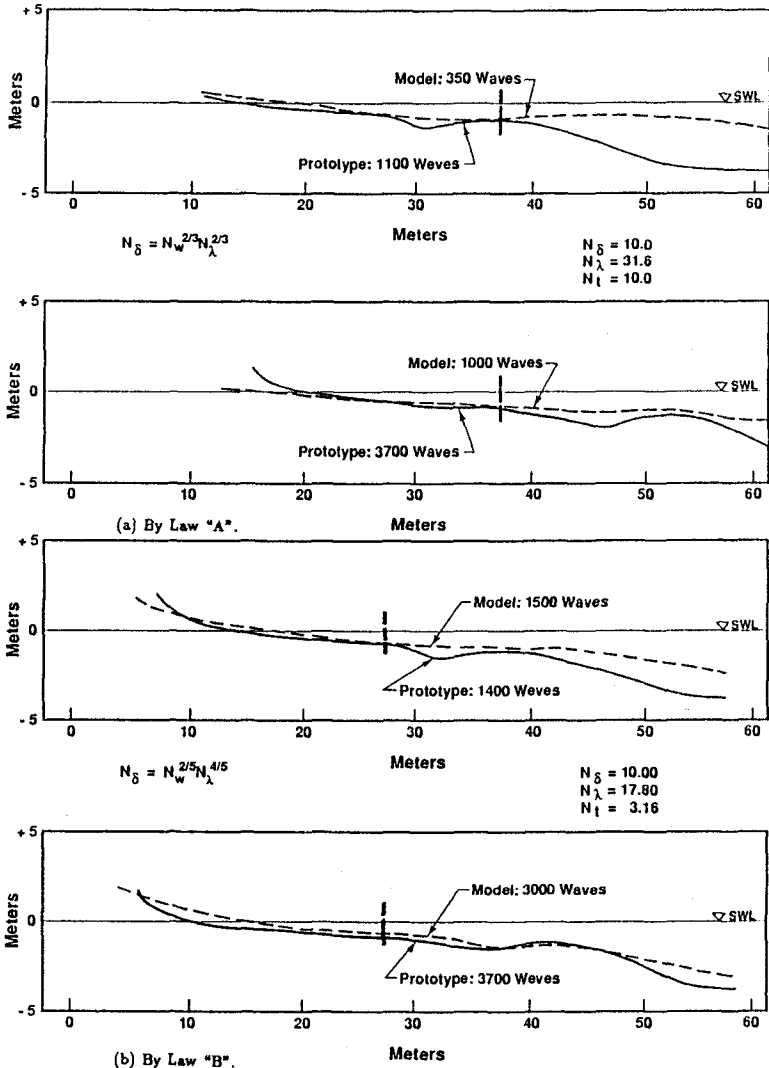


Figure 4: Comparisons Between GWK and $\frac{1}{10}$ Model Using Proposed Modeling Law.

Detle and Uliczka (1986) performed small scale tests treating results from large wave channel (GWK) as prototype. The small scale tests were conducted using same size sand as the prototype at an undistorted geometrical scale of 1:10. Straight comparisons with $N_\delta = N_\lambda = 10$ and $N_t = N_T$ or $N_t = 1$ were unsuccessful. Figure 3, for instance, shows their comparisons with $N_t = 1$ (which is the better of the two time scales according to the authors). The data are replotted in Figure 4 according to the proposed modeling laws. The comparisons are much more favorable, particularly with Law "B". Therefore, the experiment although has the appearance of an undistorted model is actu-

ally highly distorted according to the proposed modeling laws (a horizontal to vertical distortion of 3.2 or 1.8 depending on whether Law "A" or Law "B" is adopted). The reason for this high distortion is because the size of sand is the same in the model and prototype. Since the fall velocity ratio is now unity, the geometrical scale has to be highly distorted to compensate for the fall velocity effect.

The results of the last two cases seemed to suggest that preservation of wave form and/or initial beach geometry are not essential, though might be desirable. The following case further reinforces this observation.

The GWK test and Kriebel's test have very different initial geometry and different H_o/L_o values. However, the ξ value of GWK's composite slope test matches well with the Kriebel's and the fall velocity ratio of the two tests lead to small geometrical scaling distortion according to the proposed laws. All these are favorable conditions to test the proposed modeling laws. The various scale ratio between these two experiments are summarized as follows:

$N_{(H_o/L_o)}$	N_ξ	N_δ	N_W	$N_\lambda(Law A)$	$N_\lambda(Law B)$
0.81	0.86	9	2.22	12	10.5

The ratio is defined as GWK/Kriebel; the initial geometry of GWK is $\frac{1}{4}$ followed by $\frac{1}{20}$ slopes whereas the initial geometry of Kriebel is $\frac{1}{15}$ uniform slope. The comparisons are given in Figure 5. Again like the previous cases Law "B" performs better than Law "A". When time progresses, the effects of the initial condition gradually disappear and the agreement becomes better.

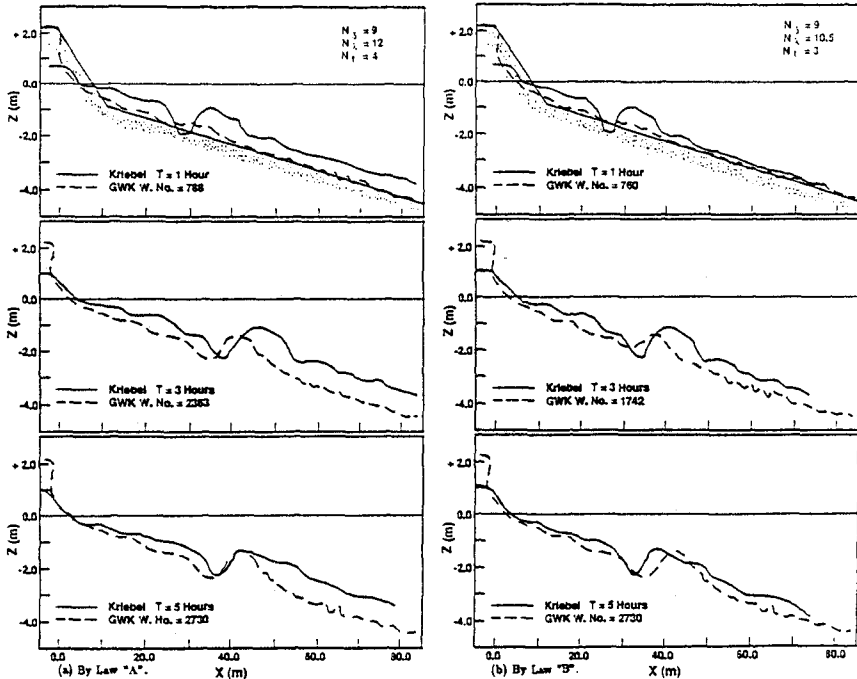


Figure 5: Comparisons of GWK and Kriebel.

Graaff (1977) and Vellinga (1982) used different vertical scales and sediment sizes in their experiments. Realizing that the surf zone in the model will be compressed, they purposely distorted their initial beach profiles in the model in accordance with a hypothetical profile representing the prototype Dutch coast condition. This, however, makes it difficult to compare their results with others and even among themselves. Table 3 summarizes their test conditions and scaling requirement according to Law "A" and Law "B". The N_H values in the first column are in reference to prototype scale. For the convenience of inter-comparisons we designate the case $N_H = 26$, $D_{50} = 225$ as the reference, thus, all the corresponding scale values are unity for this case. Two major difficulties arose; the surf zone parameters are difficult to determine because of the distortion and the composite nature of the profiles; secondly, the N_T values used in the tests do not match those required by the current modeling laws. Here, we simply selected cases (indicated by underline in Table 3) that the actual N_T values approximately meet the requirement and ignored the surf zone parameter criterion completely. Thus, the comparisons could only be viewed as qualitative. Figure 6 shows the results. Law "B" seemed to yield acceptable results considering the crude nature of the comparisons.

Toue's (1989) experiment is the only 3-dimensional laboratory test available. His results revealed a number of points worth mentioning. 1). He separated the suspended-load and bed-load dominated cases. 2). For suspended-load dominated cases, his results compared well with the 2-dimensional counterpart carried out by Barnett for natural beaches but less desirable for beaches with seawall backings. 3). For bed-load dominated cases, the modeling law given above failed to produce reasonable results.

About the Scale Parameter in Equilibrium Profile

The concept of Equilibrium profile has gained wide acceptance. The correct functional form of the scale parameter "A" remains unsettled. Moore (1982) first proposed "A" to be a function of particle size "D" with a dimension of $M^{\frac{1}{2}}$.

Table 3 Test Conditions and Modeling Laws of Graaff and Vellinga

N_H	$D_{50}\mu m$	Law A				Law B				$N_T(\text{actual})$
		N_δ	N_λ	N_T	N_t	N_δ	N_λ	N_T	N_t	
26	225	1	1	1	1	1	1	1	1	1.00
	150	1	0.52	0.52	0.52	1	0.72	0.72	1	1.00
	130	1	0.40	0.40	0.40	1	0.63	0.63	1	1.00
	95	1	0.24	0.24	0.24	1	0.49	0.49	1	1.00
47	225	<u>1.79</u>	2.4	1.79	1.79	<u>1.79</u>	2.07	1.55	1.33	1.33
	150	<u>1.79</u>	1.24	0.92	0.92	<u>1.79</u>	1.49	1.11	1.33	1.33
	130	1.79	0.95	0.71	0.71	1.79	1.31	0.98	1.33	1.33
	95	1.79	0.57	0.43	0.43	1.79	1.01	0.75	1.33	1.33
84	225	3.2	5.70	3.18	3.18	3.2	4.28	2.39	1.79	1.79
	150	<u>3.2</u>	3.00	1.68	1.68	<u>3.2</u>	3.01	1.72	1.79	1.79
	130	3.2	2.30	1.28	1.28	<u>3.2</u>	2.71	1.51	1.79	1.79
	95	3.2	1.37	0.77	0.77	3.2	2.09	1.17	1.79	1.79

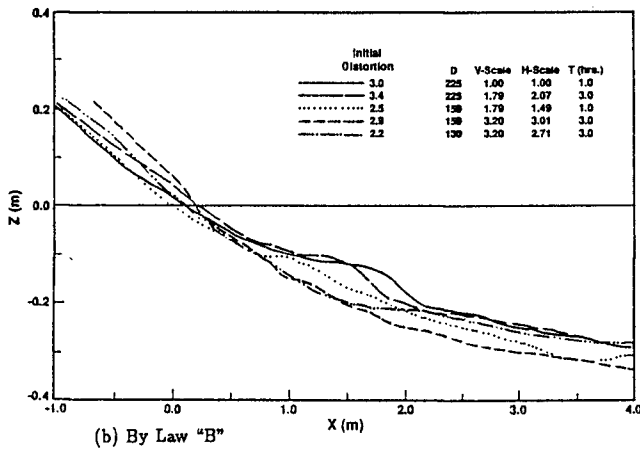
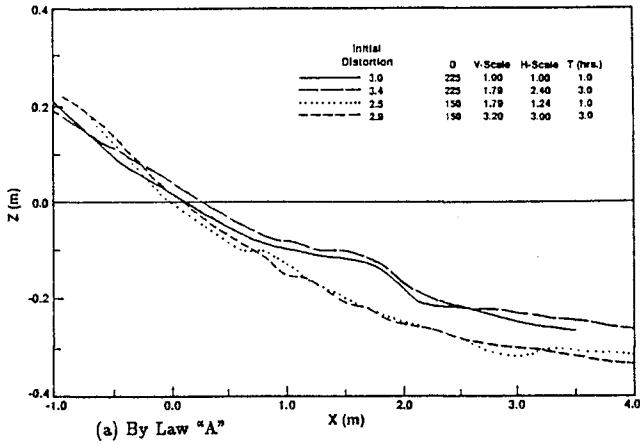


Figure 6: Comparisons of Graaff Results at Different Model Scales.

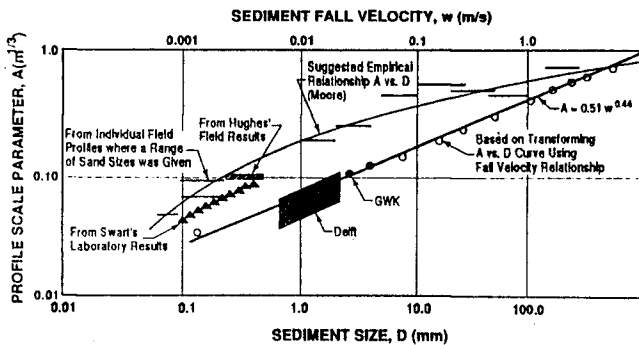


Figure 7: Profile Scale Parameter vs Sediment Fall Velocity Parameter.

Vellinga (1982), through empirical data fitting, proposed a dimensional coefficient $A = 0.39 W^{0.44}$. Based upon the analysis presented in the paper, the correct form of A should be $\alpha \left(\frac{SW}{g^{\frac{1}{2}}} \right)^n$ where α is now a non-dimensional coefficient. The value of n should be either equal to 0.67 or 0.4 depending upon which law is adopted. Dean (1990) re-plotted the A values as a function of W as shown in Figure 7. The results of GWK tests and all the Delft data are also added to the figure. The best fit is found to be $A = 0.51 W^{0.44}$. This relationship is very close to Vellinga's empirical formula as well as to the analytical form of law "B". This presents another favorable evidence that law "B" might be a better choice.

Bed Load Transport

Various formulas have been proposed for bed load transport; practically all of them relate bed load transport to the Shields parameter. Therefore, they will lead to the same modeling requirement by matching model Shields parameter to that of the prototype. The scaling of the transport rate and the relationship of morphological time are different for different transport equations. Table 4 summarizes the results based on different transport equations. We note here that the third row in Table 4 is consistent with the "best model" referred by Kamphuis (1974). By leaving f as an independent parameter allows greater flexibility in selecting scales and material.

Table 4 Bed Load Transport Scaling Law

Transport Equation	Modeling Requirement*	N_q	N_t
$q_b = w D^2 (\varphi - \varphi_c)^n$	$N_D = N_s N_f N_\delta$	$\frac{(N_\delta)^{\frac{3}{2}}}{N_\lambda} N_s N_f$	$\frac{(N_\lambda)^2}{N_s N_f (N_\delta)^{\frac{3}{2}}}$
$q_b = W D \varphi^3$	$N_D = N_s N_f N_\delta$	$N_w N_s N_f N_\delta$	$\frac{N_\lambda}{N_s N_f N_w}$
$q_b = (sg D^3)^{\frac{1}{2}} (\varphi - \varphi_c)^n$	$N_D = N_s N_f N_\delta$	$N_s (N_f)^{\frac{3}{2}} (N_\delta)^{\frac{3}{2}}$	$\frac{N_\lambda}{N_s (N_f)^{\frac{3}{2}} N_\delta^{\frac{3}{2}}}$

Symbols

w : Wave Frequency	s : Specific Weight of Submerged Sand
φ : Shields Parameter	φ_c : Critical Shields Parameter
f : Friction Factor	*Assuming $\varphi \gg \varphi_c$.

Conclusions

The advantage of the proposed modeling criteria over those presented by previous investigators is its ease to implement in ordinary laboratory facilities. It is restricted to cases that either bed load or suspended load dominates. Also, only the gross effect of transport and profile changes are modeled without concern whether the detailed flow pattern or the sediment motion is accurately portrayed.

For suspended load dominated case, the proposed modeling law is in consonance with the equilibrium beach profile concept. The surf zone parameter appears to be the most important similarity criterion that should be matched between the prototype and the model. In general, the modeling law leads to geometrical distortion. The degree of distortion is affected mainly by the sediment fall velocity ratio. Two different hypothesis of morphological time scale are tested. It appears that the preservation of particle trajectory lead to the correct morphological time scale. Laboratory results from various sources seem to support the proposed modeling law. For bed load dominated case, laboratory information is not available. Further investigation is suggested.

Finally, the scale limitations are such that the laboratory flow field should

maintain turbulent boundary layer (Jonsson's flow regime criteria, for instance, 1966) and the mode of sediment should be correct (Shibayama and Horikawa's sediment transport classification, for instance, 1980). It is always prudent to verify the flow and the mode of transport prior to data collection.

References

- Barnett, M.R., (1987) "Laboratory Study of the Effects of a Vertical Seawall on Beach Profile Responses" UFL/COEL-87/005, University of Florida, Gainesville, FL., pp.129
- Dean, R.G., (1990) personal communication.
- Detle, H.H. and Uliczka, K., (1986) "Prototype and Model Evolution of Beach Profile", Proc. Symposium on Scale Effects in Modeling Sediment Transport Phenomena, Toronto, Canada.
- Graaff, J. Vande., (1977) "Dune Erosion During a Storm Surge", Journal Coastal Eng., Vol. 1, pp. 99-134.
- Hattori, M., (1980) "Onshore-Offshore Transport and Beach Profile Changes", Proc. 17th Conf. on Coastal Eng., ASCE, New York, New York, Vol. 2, pp. 1175-1193.
- Hudson, R., Herrmann, F., Sager, R., Whalin, R., Keulegan, G., Chatham, C. and Hales, L., (1979) "Coastal Hydraulic Models", SR-5, U. S. Army, Corps of Engineers, Coastal Research Center.
- Hughes, S.A., (1983) "Movable-Bed Modeling Law For Coastal Dune Erosion", J. WPCOE, ASCE, New York, New York, 109 (2), pp. 161-179.
- Hughes, S.A. and Fowler, J.E., (1990) "Validation of Movable-Bed Modeling Guidance", Abstract, 22nd Coastal Engineering Conference, ASCE.
- Kamphis, J.W., (1974) "Practical Scaling of Coastal Models", Proc. 14th Conf. of Coastal Engineering, ASCE, New York, New York, 2086-2101.
- Kriebel, D.L., Dally, W.R. and Dean, R.G., (1986) "Beach Profile Response Following Severe Erosion Events", UF/COEL-86/016, Coastal and Oceanographic Engineering Department, University of Florida, Gainesville, FL., pp.
- LeMenhaute, B., (1990) "Similitude", Chapter 29, The Sea, Vol. 9, Ocean Engineering Science, Ed. LeMenhaute, B. and D. M. Hanes, J. Wiley and Sons, NY, pp. 955-980.
- Moore, B.D., (1982) "Beach Profile Evolution in Response to Changes in Water Level and Wave Height", M.S. Thesis, University of Delaware, Newark, DE., 1982, pp. 164.
- Noda, E.K., (1978) "Scale Relations for Equilibrium Profiles", Proc. 16th Coastal Engineering Conference, ASCE, Vol. 2, pp. 1531-1541.
- Saville, T., (1957) "Scale Effects in Two-Dimensional Beach Studies", Int. Assoc. of Hydraulic Research, 1957.
- Thorton, E.B., (1978) "Review of Status to Energetics and Momentum Fluxes in the Surf Zone: Field Data", Proc. on Coastal Sediment Transport, DEL-SG-15-78, Uni. Delaware, Newark, DE. 63-77.
- Toue, T., (1989) "Effects of Seawalls on the Adjacent Beach", UFL/COEL-89/015, Coastal and Oceanographic Engineering Department, University of Florida, Gainesville, FL., pp. 129.
- Vellinga, P., (1982) "Beach and Dune Erosion During Storm Surges", Journal Coastal Eng., Vol. 6, pp. 361-389.
- Wang, H., (1985) "A Note on Beach Profile Scale Modelling", Sonderdruck, aus Heft 88 (1985) der Mitteilungen der Leichtweiss -Instituts für Wasserbau, der Technischen Universität Braunschweig, pp. 356-398.

CHAPTER 196

STORM EROSION ON A SANDY BEACH

Jesús Martínez *
Ricardo Alvarez *
Ignacio Alonso *

Abstract

Present paper describes the different behaviour of the foreshore of a sandy beach faced with stormy events. Two storms have been selected, since they present a fairly distinct wave approaching direction between them, according with wave forecast maps.

For the first stormy situation waves came for west, and the effect was an accretion on the north end of the beach while an important erosion happened on the south side. With regard to the second storm in which waves came from northwest, an erosive trend was observed all along the beach.

Sandy movements are quantified as net volume changes as well as by means of the erosion and accretion percentages, defined from the sedimentary variability indice.

Description of the beach under study

The beach under study has a total length of 3000 m., is located in the north coast of the Island of Gran Canaria (Spain), and is sheltered from the prevailing northeastern wind and swell. (Fig. 1)

According with Larson's (1988) definition of the backshore and the foreshore, in certain areas the width of the foreshore can reach 100 m. and that of the backshore 50 m. The submerged beach is partially broken up by a fragmented rocky bar that emerges at low tide and affects the larger part of the beach.

* Department of Física, University of Las Palmas de G. C. Apartado 550, Las Palmas, Spain.

This beach is divided into two principal sub-environments, according with the beach stages proposed by Short (1978): Las Canteras North between ranges 10 to 16, and Las Canteras South between ranges 1 to 8. The former behaves as a reflective beach while the latter one as a dissipative beach. There is an small central sector called "Short Beach" between ranges 8 to 10 which is studied separately due to its peculiarity, since it is considered an small pocket beach 90 metres long that is in the middle of a much larger pocket beach. (Fig. 2).

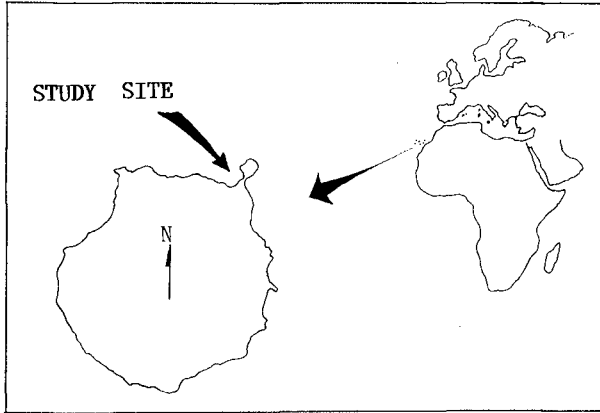


Figure 1. Location map of the beach under study.

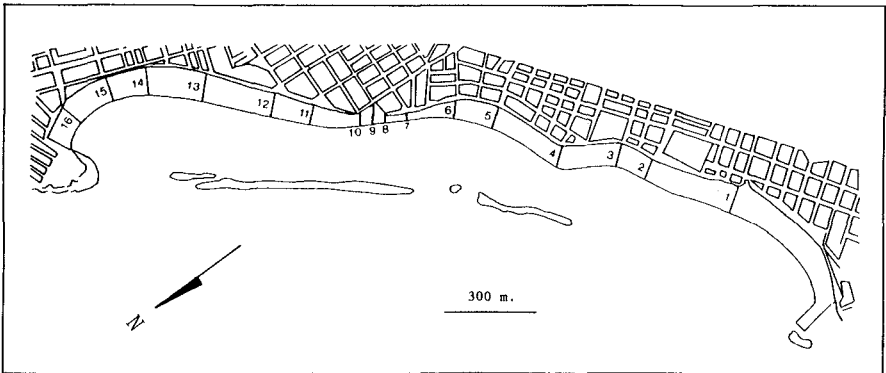


Figure 2. Sketch of Las Canteras beach showing position of the different rangelines and the rocky bar.

If the whole beach is considered, the major accretions take place during the summer period, when the prevailing swell is coming from northeast. The major erosions show up during the fall-winter period, coinciding with the seasonal northwestern storms.

Methodology

Profile data

Sixteen rangelines across the beach have been surveyed between June 26, 1987 and July 24, 1990, approximately at monthly intervals. Surveys were always carried out at low tide using a leveling method, down to about 1 to 1.5 metres below MSL (Martínez et al, 1990).

With regard to the first stormy event, the survey of December 7, 1987 was carried out almost at the end of the storm, but the previous survey was carried out just a month before. In the second situation, an extra survey was carried out just at the end of the storm, only four days after the previous survey which was almost at the beginning of the higher waves.

Sedimentary accretions and erosions on the foreshore were calculated according with Kriebel et al (1986).

Storm characteristics

Two stormy situations have been selected:

- First one between December 2 and 9, 1987.
- Second one between December 26, 1989, and January the second, 1990, although the strongest point took place on December 29 and 30.

First stormy situation corresponded to an strong Atlantic squall centered westward Portugal, that produced barometric lows of 1006 mb. over the Canary Islands, and winds up to 75 km/h where registered. To estimate the approaching wave direction, wave forecast maps were employed. It can be seen the sea coming from west. (Fig. 3).

Significant wave heights higher than 4 metres, and maximum heights around 7.5 metres were recorded by means of a wave gauge placed 1800 metres offshore the beach. (Fig. 4).

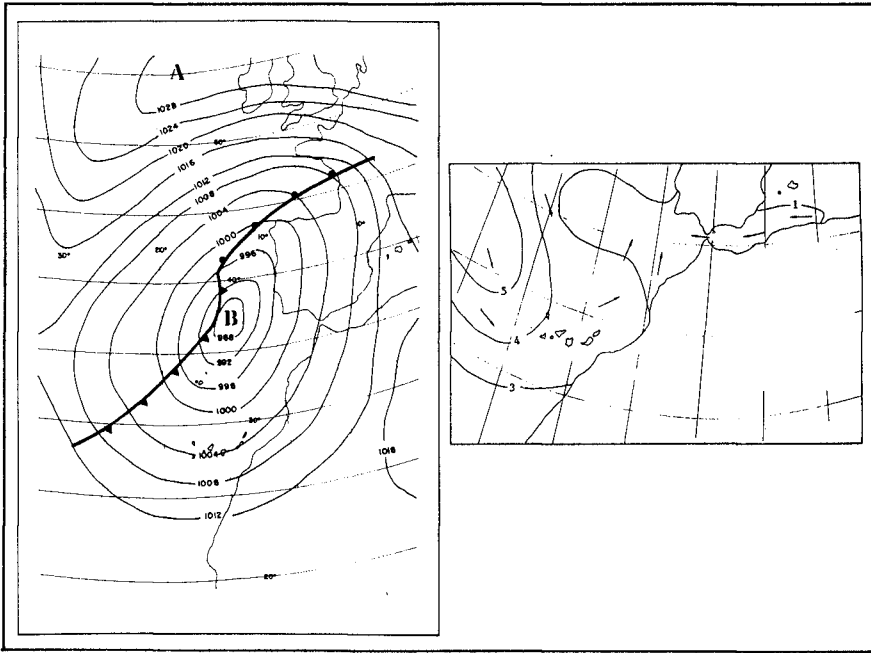


Figure 3. Weather chart and wave forecast map corresponding to December 3, 1987.

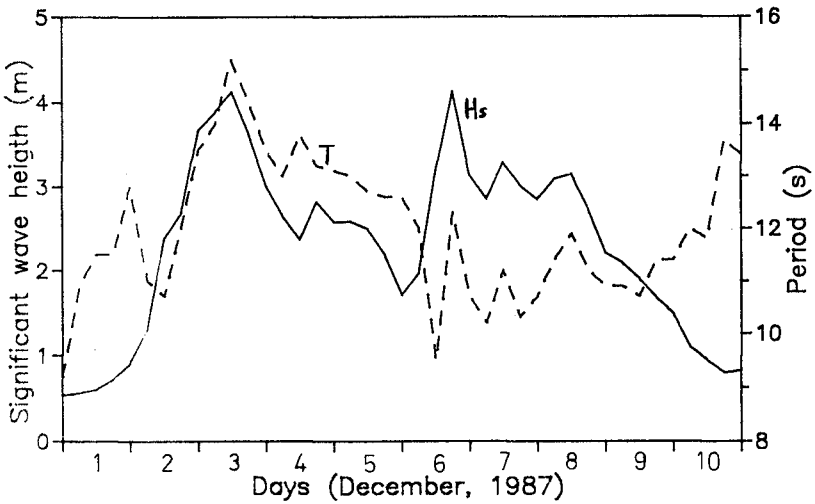


Figure 4. Evolution of significant wave height (H_s) and period (T) during the first storm.

The second storm was due to another squall centered northeast Canary Islands, that produced barometric pressures of 1000 mb and winds up to 100 km/h in the Canary Islands area.

Unfortunately, the wave gauge was out of service, so wave characteristics were estimated from the wave forecast maps provided by the National Meteorological Service. As a result, mean wave heights up to 4 to 5 metres coming from northwest were predicted. (Figure 5).

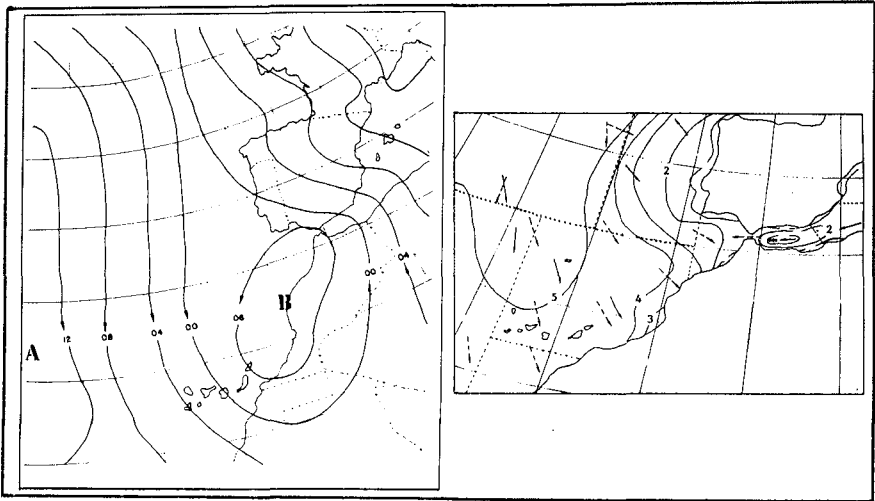


Figure 5. Weather chart and wave forecast map corresponding to December 30, 1989.

New parameters

To analyze the morphological evolution of the beach with regard to these situations, the sedimentary variability indice was employed, defined as the change of mean height between highest accretion to lowest erosion and vice versa, which happen on the beach surface within a sedimentary cycle.

This indice is obtained dividing the net losses or accumulations of sand, in cubic metres, by the delimited surface. Starting from this indice, the erosion and accretion percentages are obtained.

The erosion percentage is defined as the percentage of decrease of the sedimentary variability indice between two surveys, within an erosive period.

On the other hand, the accretion percentage is the percentage of increase of the indice between two surveys, but in this case, within an accretionary subcycle.

Both percentages are good to evaluate the relative magnitude of the erosive / accumulative processes in a given period, within the relative erosive / accretive subcycles. It is necessary to take into account that an accumulative process may happen within a general erosive trend, and vice versa.

Discussion and Conclusions

In relation to the first stormy situation, we estimate sedimentary losses of about 2000 cubic metres on a 21 metre wide foreshore strip, all along the beach. (Table 1).

Date	Whole Beach	Las Canteras North (Profs.10-16)	Short Beach (Profs.8-10)	Las Canteras South (Profs. 1-8)
Nov.7-Dec.7 1987	-1944 (-4.2)	2088 (10.5)	-406 (-21.1)	-3677 (-14.4)
Dec.29,1989 -Jan.2,1990	-5988 (-12.6)	-3806 (-19.1)	-96 (-5)	-2077 (-8.1)

Table 1. Sedimentary losses and accumulations in m³ for both storms, only in a 21 metres wide foreshore strip. Data in brackets are the average heigth changes in cm. on the same area.

These losses assume an erosion percentage of 15.5 % of a sedimentary variability indice of 0.27 m., corresponding to the erosive subcycle.

The above-mentioned erosion percentage has a low value in relation to the others of the same sub-cycle. These others reach up to 41.4 % at monthly intervals, out of significant stormy situations. (Table 2).

Date	1		2		3		4	
	E.P.	A.P.	E.P.	A.P.	E.P.	A.P.	E.P.	A.P.
7-28, 1987							3.2	
9- 9, 1987	38.5		92.2				2.6	
10-10, 1987	41.4			8.3			53.9	
11- 7, 1987	4.6		16.1				5.2	
12- 7, 1987 *	15.5			61.8	55.7		35.1	
1-20, 1988		19.1	47.6		18.0			40.2
2-20, 1988		2.2	1.3		14.3			4.1
3-19, 1988		13.0		15.8		1.2		9.1
5- 2, 1988		0.8		12.7	13.2		2.6	
6- 1, 1988		2.7	38.3			20.0		14.8
7- 1, 1988		51.9		96.9		43.2		20.2
7-31, 1988	20.3		7.6			7.8	19.1	
8-29, 1988	13.1		19.9			8.2	3.1	
9-29, 1988		43.7		17.8		20.8		36.4
10-24, 1988	32.3			5.6	1.9		49.2	
11- 8, 1988	62.8		95.9		19.6		36.8	
11-24, 1988		16.2		12.7	6.2			5.8
12-24, 1988		57.7		12.6	22.9			67.4
1-23, 1989	10.3			3.1		12.4	20.5	
2-21, 1989	32.7		4.5		12.3		39.3	
3-23, 1989	35.8		16.4		8.1		27.4	
4-22, 1989		1.2		1.8	41.4			2.9
5-22, 1989		51.7		23.7		33.2		59.3
6-19, 1989		40.5		28.8		27.8		37.8
7-21, 1989	13.6		20.4			8.5	4.6	
9-15, 1989		20.2		58.6		30.5	19.8	
10-17, 1989	66.6		73.1		35.5		43.9	
10-27, 1989	4.7			18.5		1.4	24.8	
11-28, 1989	28.7		45.4		8.3		6.9	
12-29, 1989		52.6		61.4	51.3			47.4
1- 2, 1990 *	24.1		25.0		6.3		22.0	
1-27, 1990		35.4		27.3		17.8		46.5
2-27, 1990	46.0		49.2			49.8	48.4	
3-28, 1990		39.7		38.6	10.3			43.5
4-25, 1990		0.3	5.9			1.4		10.3
6-22, 1990		24.4		24.1		19.1		22.7
7-24, 1990		17.7		28.7		22.2		

Table 2. Values of erosion percentages (E.P.) and accretion percentages (A.P.) on Las Canteras Beach. Column 1 is the whole beach and columns 2, 3 and 4 are the different sectors (Las Canteras North, Short Beach and Las Canteras South respectively). Dates of studied storms are highlighted with *. Erosive and accretive subcycles are separated with horizontal lines.

There was a distinctly different behaviour in the two main sectors of the beach: while a significant erosion took place in Las Canteras South, an important accretion happened in Las Canteras North.

In Las Canteras South, the storm caused an erosion percentage of 35.1 %, of a sedimentary variability indice of 0.41 m. corresponding to the erosive subcycle. That is to say, the foreshore had a mean drop of 0.14 m.

On the other hand, las Canteras North had an accretion percentage of 61.8 % of a sedimentary variability indice of 0.17 metres calculated for the accretionary subcycle. This represents a mean accumulation of 10 cm. for the foreshore along this sector.

This tilt was due to the strong westerly waves, and explains the low erosion percentage for the whole beach, since sedimentary losses and accumulations become balanced between the two main sectors of the beach.

However, it is necessary to take into account that the above-mentioned sandy movements, might be not only due to the storm, but also to other less important sedimentary processes that happened during the 25 previous days to the storm, and that could be responsible for the softening of the final erosion.

If the whole sedimentary cycle is considered, the most important erosion percentages are not precisely related to this significant storm, which was the most energetic one. In the specific case of Las Canteras South, mean sedimentary losses larger than those measured during the storm, were calculated for the pre-stormy period.

An explanation for this fact can be based on by considering that a beach, immediately after having reached its maximum accretion, is very susceptible to suffer great sand losses due to slight increases in waves energy. In this case, these situations happen with the first sporadic manifestations of northwestern swell and with the fall of the dominant northeastern winds.

In relation with the second stormy situation, we estimate sedimentary losses of nearly 6000 cubic meters in only 4 days for the same foreshore strip defined for the previous case, all along the beach. This amount of eroded sediments involves a decrease of 12.6 cm. all along the beach (see Table 1). The calculated sedimentary variability indice was 0.52 m., and the relative erosion percentage was 24.1 % within an accumulative subcycle (see Table 2).

Although the whole beach was eroded, the average decrease was around 8.1 cm. in Las Canteras South and 19.1 cm. in Las Canteras North. The respective erosion percentages were 22 % and 25 %, and the sedimentary variability indice was 0.37 m. for the northern sector and 0.76 m. for the southern sector, but in both cases within accumulative subcycles.

In this case there were no tilt, but the greatest erosion took place where the accumulation was previously produced.

The difference in the behaviour of the beach, in view of the two stormy situations analyzed, can be explained due to the different characteristics of the storms, specially as for the waves approaching direction. In the first situation waves were coming from west while in the second one were approaching from northwest.

References

- Kriebel, D.L., Dally, W.R., and Dean, R.G., 1986. "Beach profile response following severe storm events," UFL/COEL-86/016, Coastal and Oceanographic Engineering Department, University of Florida.
- Larson, M., 1988. "Quantification of beach profile change," Report No. 1008, Department of Water Resources Engineering, Lund University.
- Martínez, J., Alvarez, R., Alonso, I., and Del Rosario, M.D., "Analysis of sedimentary processes on Las Canteras Beach (Las Palmas, Spain) for its planning and management," Eng. Geol. (in press).
- Short, A.D., 1978. "Wave power and beach stages: a global model," Proc. 16th Coastal Engineering Conference, ASCE, Hamburg, West Germany.

CHAPTER 197

A REGIONAL STUDY OF COASTAL MORPHOLOGY

I H Townend¹, C A Fleming¹, P McLaren² and A Hunter-Blair³

ABSTRACT

In 1987 Anglian Water (now the National Rivers Authority, Anglian Region) initiated a coastal management study covering 750 km of coastline, the largest and most comprehensive study of its kind in the UK. Stage I involved the selection of the best technical approach to the problem. In Stage II the successful consultants adopted a philosophy of maximising the use of existing data sources through a geographic information system (GIS) incorporating a database and powerful enquiry facilities. In all 19 main variables were included in the GIS database, each with complex data structures in order to provide a comprehensive description of any particular variable. The main variables were selected on the basis that they either provided information on the direct influences or responses of the coast or on their implications with respect to any protection strategy that may be implemented.

Analysis of the data through the GIS led to a number of significant findings with respect to dominant processes on the coast. This work also highlighted the areas in which further data collection and study would be beneficial to formulating the most appropriate long term management strategy. As a result Stage III of the study has been initiated in order to develop a better understanding of the physical processes responsible for the mechanisms identified.

INTRODUCTION

In 1953 a major storm surge in the southern part of the North Sea caused severe flooding in south east England, leading to the loss of some 200 lives, as well as domestic livestock, wildlife and devastating damage to property and agricultural land. As a result there was a major reconstruction of the sea defences along the east coast of England. These defences have been maintained, extended and rebuilt during the ensuing years, but the time has now come to

¹Sir William Halcrow & Partners Ltd, Swindon, UK; ²GeoSea Consulting Ltd, Cambridge, UK; ³National Rivers Authority (Anglian Region), Peterborough, UK.

re-think the sea defence system as a whole and make some major reinvestments. Overall there are some 300 km of first line sea defences and it has been estimated that it will cost £130 m over the next 10 years to bring these defences up to standard.

Anglian Water, realising the problems that must be faced in the future, and being responsible for one the longest and most vulnerable coastlines in Britain stretching from the estuaries of the Humber to the Thames, commissioned a study of the foreshore, which would help them to establish a coastal management strategy based on sound scientific principles. Thus the Anglian Sea Defence Management Study emerged and is one of the most extensive studies of coastline properties and processes to have been carried out in the UK.

The general terms of reference for the investigations were to provide an understanding of the mechanisms causing changes in foreshore levels along the Anglian Coast and this is the focus of this paper. For completeness a brief outline is given of the study as a whole, together with some indication of the form of the management strategy.

THE STUDY

Study Area

Anglian Water's sea defences run from Canvey Island on the Thames to Trent Falls on the Humber Estuary. Given that the objective of the study was to establish management procedures based on a sound regional understanding, it was felt necessary to extend the northern boundary of the study area to incorporate the Holderness coast. This thereby includes an important sediment source for the East coast. In contrast the Kent coast, on the south side of the Thames Estuary, was not considered to interact significantly with the regime along the Essex coast and was not therefore included. The extent of the study area is shown in Figure 1.

Stage I

The first stage was a form of competition, where three consultants were invited by the Authority to present their approach to the problem. In effect they were asked the question "If this was your problem, what would you do about it?" The winning proposal focused on making maximum use of existing data sources to develop an integrated management strategy for the whole coastline.

Stage II

The rationale of the approach adopted was to extract a coherent picture from the wide range of information that was already available. This philosophy was adopted because it was felt that over such a large and diverse area, any attempt to apply numerical models to examine processes and coastal genesis would inevitably be constrained by limited knowledge of the governing mechanisms. The

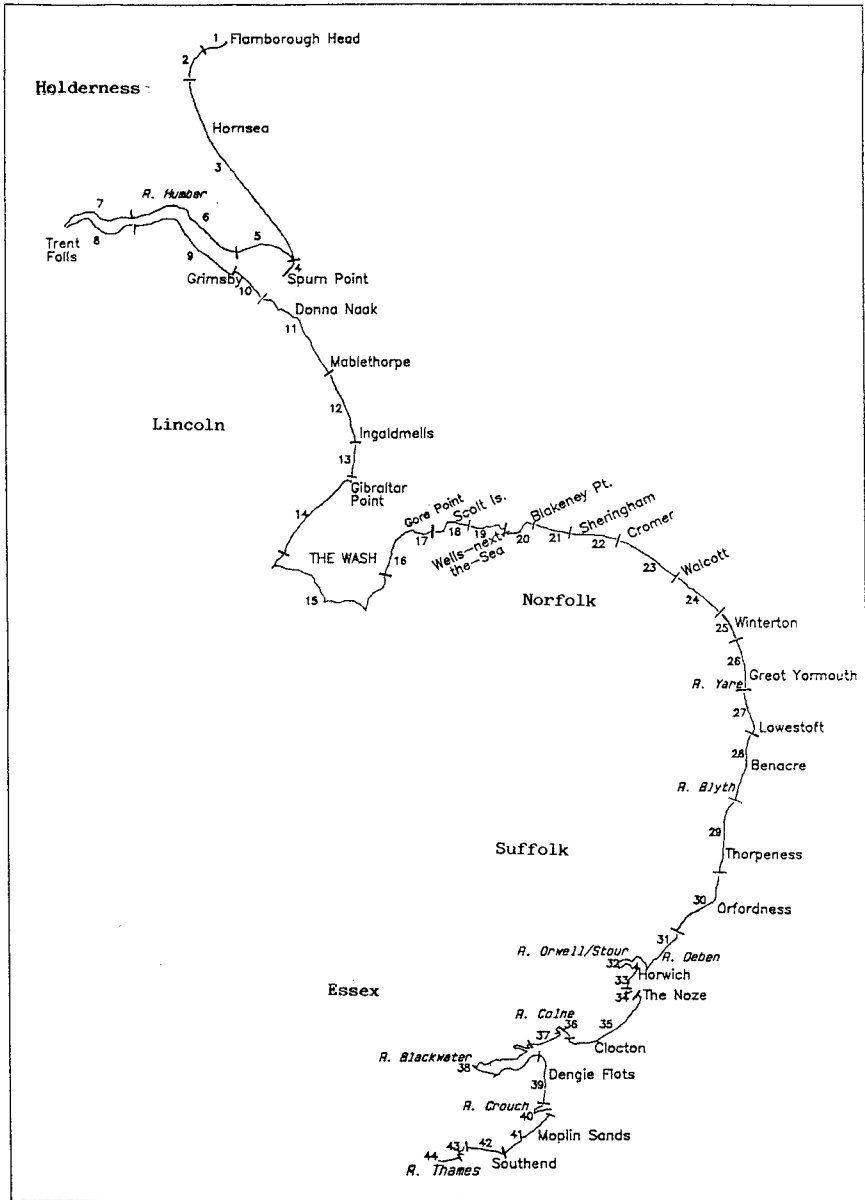


Figure 1: Study Area with Coastal Units

prime objective was therefore to structure the data in such a way that it could be rapidly manipulated. A thorough analysis of existing sources of information could then be made, to both gain insights and focus the objectives of future field work and numerical model studies.

As the first stage a referral database was established. This database essentially provides a listing of relevant references and data sources. It includes entries for reports, papers and relevant literature, as well as details of the type, extent and holder for the various sources of measured data that were identified. The database was set up using Ashton Tate's 'dBASE III' software using two separate record structures; one for references and the other for environmental data. Searches can be constructed in several ways, to give either comprehensive listings (eg all references for the Lincoln region), or much more specific responses (eg the data on waves collected during 1982 in the Norfolk region).

It was recognised from the outset that a number of important variables could not be adequately defined by simply using existing sources. As a consequence six supplementary studies were undertaken, with the objective of providing additional data and/or some further understanding. These studies provided:

- a definition of the wave climate offshore and at approximately 10 km intervals along the coast;
- an understanding of the coupling between the residual flow regime in the southern North Sea and local wind effects, in determining nearshore current residuals;
- detailed analysis results of beach profiles taken over the last 10 to 25 years;
- a description of extreme sea levels around the coast;
- a quantification of sea level rise, tectonic movement and subsidence in a geological setting;
- a summary of recent literature on the subject of coastal processes relevant to the Anglian coast.

After being screened and compiled into the desired format, all the various data were entered into a database capable of storing the geographical location of the data. The system is based on a geographical information system (GIS) and has a database which is able to handle not only single attributes but also attributes which themselves have complex data structures. Configured for this particular application the system is referred to as the 'Coastal Management Database' (CMD) and was used to meet the following objectives:

- to map relevant variables for the entire coastal region;
- to use the graphical output of the system to present each variable or combination of variables on a series of maps;
- to assess the inter-relationships among variables and their contribution to coastal erosion;

- to produce interpretive maps which form the basis of a coastal management policy.

The variables included in the database, were selected on the basis that they either provide information on the direct influences and responses of the coast (eg waves, coastal morphology, rate of retreat, etc) or on their implications with respect to the impact of the erosion and any defence strategy that may be implemented (eg present coastal works, SSSIs, land use, etc).

The development and application of the GIS is described more fully by Fleming and Townend (1989) and Townend (1990).

DISCUSSION OF RESULTS

A detailed examination and intercomparison of data sets has led to a number of general conclusions with respect to governing processes. These were used with more localised interpretations to assess coastal regimes and to establish a series of coastal units (Townend and McLaren, 1989).

For the purposes of this study the coastal zone is defined as made up of five parts; hinterland, backshore, foreshore, nearshore and offshore (Figure 3). The hinterland is landward and includes any cliff or dune system, the backshore (if it is present) extends to high water, between high and low water is classed as the foreshore, from low water out to an approximate limit of storm erosion (d_L) is taken as the nearshore, and from there on out is the offshore.

Governing Processes

The data interpretation is wide ranging and a number of key insights have been found. In many cases these were established as a result of the contrasts existing along the coast. A necessary qualification is therefore that if there is no contrast in a particular variable on the coastline, then the associated understanding may not have been picked up. Sea level rise is one such possibility, where an appreciation was derived by testing the data against an accepted "rule", rather than a direct correlation of cause and effect. Furthermore associations were only sought as a first step in seeking to develop a better understanding of the underlying physical processes.

i) Coastal Retreat/Advance Classification

An examination of long term estimates of coastal retreat and advance (established using historic Ordnance Survey maps) reveals that a very large proportion of the Anglian coast is retreating. Recent beach profile data, although more variable, reveal consistent trends.

The long term retreat data were used to develop a retreat/advance classification system which characterises the different types of

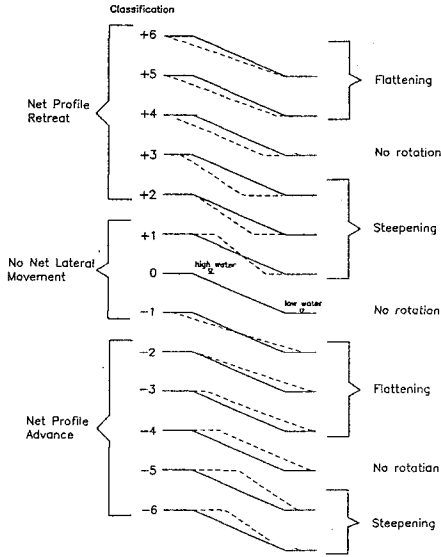


Figure 2: Retreat/Advance Classification

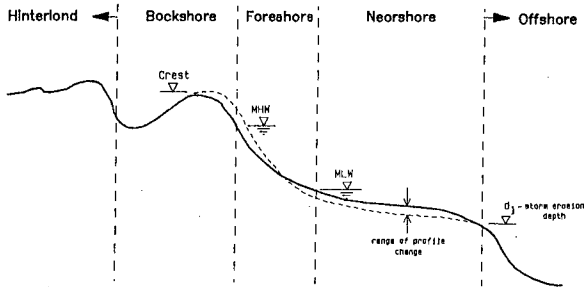


Figure 3: Coastal Zone Definition

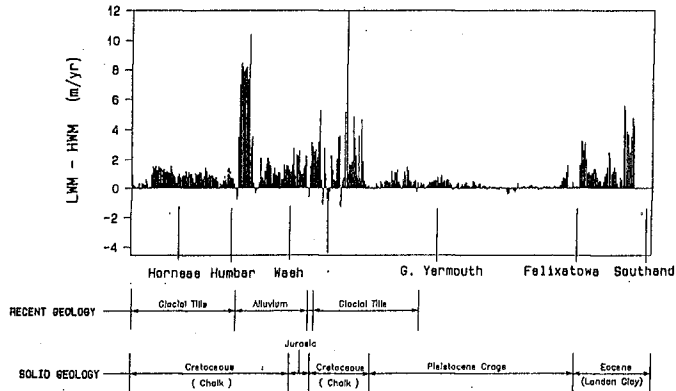


Figure 4: Differential Beach Retreat

beach movement. Rates of retreat at high and low water are combined to define horizontal and rotational movements of the foreshore. In all 13 combinations have been defined and these are illustrated in Figure 2. The results for the Anglian coast, excluding the Humber, the Wash and the Essex rivers, reveal that some 70% of the coast has been subject to retreat, with 15% advancing and 15% showing no horizontal movement (Table 1). The problem of erosion on the Anglian coast is therefore clearly a substantial one.

The coastal retreat/advance classification also highlights one other characteristic that has been found to be particularly significant on the Anglian coast. Classification types +1, +2 and +3, totalling 67%, represent types of retreat in which the beach is steepening and types -5 and -6, totalling 11%, describe types of advance, again where the beach is steepening. Thus beaches appear to be steepening (to a varying extent) for 78% of the total shoreline. This is therefore an ongoing mechanism, which is of prime importance where coastal works are sited at the top of the beach.

Table 1 : Summary of Retreat/Advance Classification Data

	Net Profile Retreat		No Net Movement		Net Profile Advance	
	Type	%	Type	%	Type	%
Steepening	+2	15.1			-6	1.9
	+3	41.4	+1	10.8	-5	9.1
No Rotation	+4	10.2	0	3.2	-4	2.4
Flattening	+5	3.8	-1	0.3	-3	1.3
	+6	0.0			-2	0.5

Note: results exclude the Humber, the Wash and the Essex Rivers

In addition to providing a broad overall summary of the retreat data, the retreat/advance classification also provided extremely useful information for the interpretation task. There is considerable variation of classification type along the coast and this variation is often quite rapid. In some cases the fact that the mode of retreat did not change helped to define the limits of a coastal unit. Elsewhere it was the consistent way in which classification type changed along the shore which helped to identify particular features.

ii) Geological Setting

The retreat/advance classification provides a clear indication of the extent of the beach steepening phenomenon. Beach steepening is not however, happening uniformly along the coast (Figure 4). Indeed on

the coast between Great Yarmouth and Harwich it is hardly happening at all, despite the fact that the rate of retreat is comparable with other areas. What is striking is the marked change at either end of this particular length, which appears to correlate with the change in geology. To the north and south the coast comprises tills, alluvium and clays and is therefore essentially cohesive. In contrast the intermediate length is composed of Pleistocene Crags which makes it a predominantly non-cohesive shore.

Examining the geology set against the retreat rate, reveals that beach steepening is remarkably consistent along the till cliff frontages of Holderness, whereas the more complex stratigraphy of the North Norfolk cliffs results in more variable rates. This variability increases substantially in low-lying areas such as the barrier beach system from Weybourne to the Wash, where there are marked changes in the sediments which provide the geological setting. Interestingly, the Lincoln and Clacton coasts have very similar retreat characteristics and both comprise sand veneer beaches overlaying a clay bed, suggesting that there is much in common in the way these two areas behave. This all emphasises the importance of the nearshore geology.

One further association that has been noted is the increase in nearshore width in areas with the highest rate of beach steepening. Figure 5 shows the two data sets at approximately a 10 km resolution, and the correlation is clear. Examining the data at a finer resolution (eg 1 km) the correlation is less obvious because the beach steepening in areas with high nearshore widths is very erratic. Thus high values of beach steepening occur when the nearshore width is high, but the converse does not necessarily hold.

This is fortuitous because it provides a setting in which steepening can take place. The corollary must be that there is a threshold at which steepening no longer takes place (possibly because retreat increases to a point where the additional sediment supply becomes sufficient to protect the resultant, much narrower beach).

The geological setting has been found to induce beach steepening. The physical explanation is less clear. It has been postulated that this is a consequence of increased downcutting towards low water on cohesive shores, where the erosion process is irreversible (once a clay surface is eroded the fines are rapidly washed away). It may also reflect a changing tidal regime as a consequence of sea level rise.

iii) Coastal Orientation

A surprising feature of the coastal retreat data is an apparent rhythmic variation along the shore. Further analysis revealed that there is indeed a cyclic variation along the entire coast with a periodicity of between 3 and 6 kilometres.

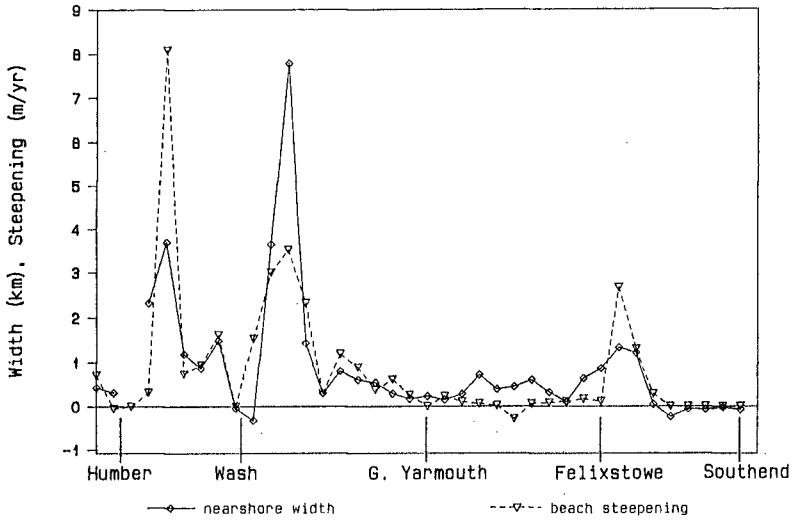


Figure 5: Comparison of Nearshore Width with Beach Steepening

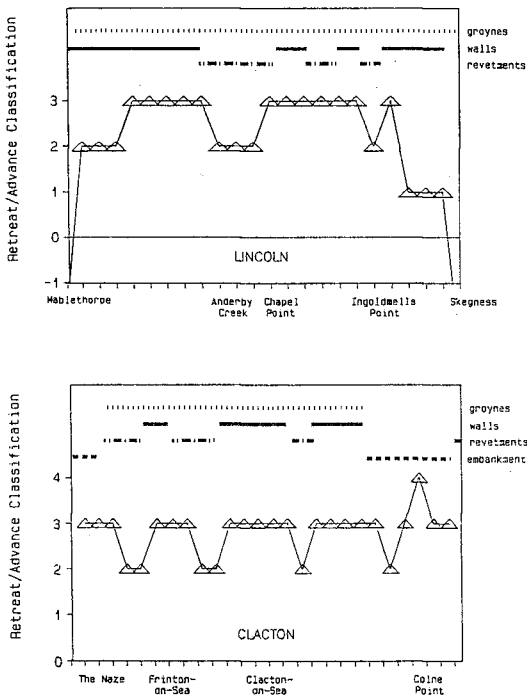


Figure 6: Influence of Coastal Structures on Mode of Retreat

In the search for an association with this rhythmic variation, coastal orientation was examined. The data was prepared by taking off the bearing of the normal to the coast at one kilometre intervals, using the latest edition of the 1:50,000 OS retreat revealed no obvious association. However by deriving the rate of change of orientation along the coast a good match was found. Maximum retreat occurs within embayments and minimum retreat or accretion takes place on bulging shores. This is indicative of a natural instability where erosion at one point produces an exaggerated response which is then countered by an under-response on the adjacent shoreline.

There are two types of feature which can cause a reversal of this relationship. The first is the presence of structures which can force a localised reversal on the natural perturbation (eg the accretion updrift and erosion downdrift of an outfall), or exaggerate the perturbation (eg where a coastline is over-constrained by a seawall). The second variation occurs at natural features such as nesses, spits and points which involve major changes in coastal orientation. Again these can be explained in terms of the interaction of cyclic perturbations on a line which changes direction.

The exciting mechanism for the perturbations is unclear, as is the reason for the variation in the periodicity on different lengths of coast. The understanding of this phenomenon is at a very preliminary stage. Its presence on the whole of the Anglian coast is seen as particularly significant and may well be of major importance for a proper understanding of the morphological genesis of the coast. Given the interaction with structures that has been noted, such an understanding will also aid the proper planning of coastal works.

iv) Tides and Waves

No correlation could be established between the wave energy incident on the shore and the long term retreat. Furthermore only on the Lincoln coast and from Blakeney Point to Gore Point is the potential of alongshore littoral drift clearly uni-directional. Elsewhere the variations are such that the direction of net drift can reverse from year to year.

The presence of beach steepening on both accreting and retreating features, together with the fact that rates vary significantly with the presence of channels in the nearshore seabed, suggests tidal currents (and most likely tidal residuals) play a dominant role over much of the coast from Flamborough to the Thames. Much local evidence and data for individual lengths of coast supports this finding.

A study of beach volume changes around the coast indicated that growth and depletion of the beach on a given stretch of coast shows more coherence in time than it does alongshore. This therefore suggests that major beach volume changes are due to onshore/offshore movement.

These various findings lead to the conclusion that waves are significant for moving material locally and over short time-scales. However, the major movement of material and consequently the long term geomorphological development for the majority of the coast is tidally dominated. This movement is back and forth in the nearshore, interacting with the foreshore by onshore/offshore movement. The material supplied to the beach is then moved by alongshore wave activity, the significance of which will vary according to the amount of material available for movement on the beach and the consistency of the drift direction. For example when beach levels are low on the Lincoln coast (such that the clay layer is exposed) there is little drift despite the high drift potential. In contrast when beaches are full, the groynes play an important role in reducing alongshore movement. Alternatively on the beach between Great Yarmouth and Lowestoft, the drift direction is highly variable such that the movement on the beach due to alongshore wave energy is back and forth. (Note: the strong interaction with the nearshore on this frontage results in a net southerly drift for the system as a whole).

v) Sea Level Rise

It might be argued that rises in mean sea level, and hence the levels on the beach swept by the tide, has induced the observed coastal retreat. However, an examination of potential retreat due to sea level rise based on the "Bruun rule" (Bruun,1962), shows that generally this is less than the rate actually experienced. This suggests that the retreat is not due to sea level rise alone. Indeed, work on the Dengie Flats has shown that although the margins are eroding, the main body of the marsh is accreting at a rate in excess of the rise in sea level (Reed 1988).

vi) Coastal Structures

The retreat/advance classification data was used to evaluate the influence of coastal structures on the extent and type of movement which is occurring. The deductions that have been made took advantage of the similarities between the Lincoln and Clacton coasts and the Holderness and North Norfolk cliffs. Certain other data sets, such as the actual rates of retreat and the description of backshore widths led to further amplification of the conclusions.

- a) Where there are no structures on an open cliff coast, then the cohesive shoreline is retreating and steepening, whereas the non-cohesive shore is retreating uniformly (no steepening).
- b) On cohesive shores which supply material to the coastal system (Holderness, North Norfolk), the type of structure has no discernible effect on the type of erosion taking place, but does locally slow the rate of retreat.

- c) On cohesive shores which receive sediment from other sources (Lincoln, Clacton) then the type of erosion is dependent on both the type of structure and the presence or absence of a backshore. Where there is no backshore then all structures result in beach steepening. In contrast where there is a backshore, then walls were found to induce retreat and steepening (similar to cliff coastlines) whereas lengths with revetments or embankments exhibit only steepening (no significant movement of the high water mark); the latter not necessarily being a consequence of the structures presence. This correlation is illustrated for the Lincoln and Clacton coastlines in Figure 6.

vii) Offshore Banks

A study of the offshore zone has suggested that the region can be divided up into a number of areas based on the different type of bank systems which are present. The most significant areas with respect to the Anglian coast are the Great Yarmouth banks and the series of linear banks further to the north-east.

The linear bank system may well derive from the Anglian coast via the nearshore banks at Great Yarmouth (Townend and McLaren, 1990). It is postulated that material is in circulation off Great Yarmouth, where the amount of sediment being moved is substantially greater than the present supply from the north at Winterton and south at Benacre. This circulation cell initiates new banks in the vicinity of North Cross Sands and Winterton Overfalls (to the northeast of Great Yarmouth), which evolve as linear banks moving offshore in a north-easterly direction. By examining sea level rise and historic shoreline positions it has been estimated that the supply from the coast would have been sufficient to progressively develop the bank system over the last 7-8,000 years.

Changes in Time

Not only the coast itself, but the processes which influence the coast are changing with time. Indeed the conclusions with respect to a number of the governing mechanisms described above suggest that the coast is not in dynamic equilibrium with the environment. Rather the changes taking place are altering the shore from flat and low-lying, characteristic of a low energy dissipative shore, towards a much steeper, high energy reflective shore. This change is on a geological timescale and seems to be a consequence of the initial setting of the coast, prior to, and during the Flandrian transgression.

The Anglian coast is all to the south of what was once the main sea basin which now forms the northern North Sea. It sits alongside the ridge which divides the northern and southern basins of the North Sea, and the southern basin itself. The latter developed as a tidal river estuary and only following the rise in sea level and coalition

with the northern basin could it be considered as a sea basin. Thus the coastal setting is one of a shoreline on the edge of a newly formed sea basin and still adjusting to this much more dynamic environment.

CONCLUSION

There have been a number of aspects to the Stage II studies which have each seen significant advances. The first is the development of a methodology which allows the data (either raw or in some summary format) to be freely explored. This has involved the use of a sophisticated database and much has been learned about both the limitations and potential of mapping analysis. The application of this approach has led to an extensive interpretation of the coast both on a regional and a local scale. With the understanding that this has provided, there are a number of implications for the efficient and cost-effective management of the coast. These include:

- Beaches on cohesive shores are generally steepening, although this may also be a consequence of the geological setting.
- The rate of retreat exhibits a cyclic variation along the coast and this is related to the rate at which the coast changes its orientation.
- Tidal influence has been found to play a major role in the long term development of the coast.
- Retreat rates were found to be in excess of that which could be attributed to sea level rise.
- The type of structures found on the shoreline influence both the rate and type of erosion which takes place.
- The bank system off the North Norfolk coast has an important interaction with the coast.

These findings are all important for the proper management and, where appropriate, design of works, in the coastal zone. A more localised interpretation was developed in order to divide the coast up into a series of coastal units. These are not necessarily independent units but are based on the presence of coherent characteristics within the unit (Figure 1).

The basis of the short term management strategy, developed following the Stage II studies, has been described by Fleming and Townend (1989). The context of this development in terms of the overall formulation of a management framework is considered by Townend (1989, 1990).

In view of the substantial nature of some of the insights derived, a number of further investigations have been initiated as Stage III of the study. This comprises a wide range of tasks aimed at filling in data gaps, developing a better understanding of the coastal mechanisms identified, and refining the "management system" as a fully operational tool for coastal managers. There are essentially four aspects to the work; field measurements, detailed studies, preparation of monitoring guidelines and further development of the GIS based management system (Townend and Fleming, 1990). It is anticipated that these studies will lead to specific recommendations for future sea defence works, and provide a coherent framework for the long term management of this coast.

ACKNOWLEDGEMENTS

This work was funded by Anglian Water and is now the responsibility of the National Rivers Authority, Anglian Region. Their support and permission to publish this paper is gratefully acknowledged.

REFERENCES

- Bruun P M, 1962, J Waterway Harbour Div. ASCE. 88, 117-130
- Fleming C A, Townend I H, 1989, ASCE Coastal Zone '89 Proc.
- Townend I H, 1990, EGIS '90 Proc.
- Townend I H, McLaren P, 1989, Anglian Coastal Management Atlas, Sir William Halcrow & Partners.
- Reed D J, 1988, Estuarine, Coastal and Shelf Science, 26, 67-79.
- Townend I H, 1989, PIANC (UK) Gustav Willems Prize
- Townend I H, 1990, Int Symp "Littoral 1990", Eurocoast Assoc.
- Townend I H, Fleming C A, 1990, 1990 Flood Plain Management Conf, Canada.
- Townend I H, McLaren P, 1990, The Relationship Between Bank Development and Coastal Response for East Anglia, UK. In Press.

CHAPTER 198

FUNCTION OF DETACHED BREAKWATER TO CONTROL LONGSHORE SEDIMENT TRANSPORT

Toru Sawaragi¹, Iehiro Deguchi² and Ga-Ya Kim³

ABSTRACT

The function of offshore detached breakwater of controlling longshore current and resulting sediment transport under oblique wave incidence is examined mainly through experiments. Although the offshore detached breakwater can effectively reduce incident wave energy, it has little influence on longshore current. More than 50% of the volume of sediment transported in the longshore direction on the natural beach is trapped behind the breakwater. The total longshore sediment transport rate around the breakwater can be predicted more precisely by integrating the local longshore sediment transport rate estimated from the flux model than by the empirical formula of Savage type.

INTRODUCTION

Various coastal structures have been used to construct protective works against beach erosion. Among them, offshore detached breakwaters are the most popular structures in Japan. This is because they can effectively reduce and absorb incident wave energy. A crown height of the offshore detached breakwater in Japan is usually determined to be one half of the design wave height higher than the high water level. So, the offshore detached breakwater often detracts from natural coastal views and prevents effective utilization of coastal regions. Strongly diffracted waves by the offshore detached breakwater also creates concavoconvex shoreline.

¹ Professor and ² Associate Professor, Dept. of Civil Engineering, Osaka University, Yamada-oka 2-1, Suita-city, Osaka 565, Japan

³ Head Researcher, Municipal Administration Research Inst., Pusan city, Korea

Recently, there is increased concern with preservation of coastal environments and easy access to the shoreline. To cope with these requirements, another coastal protection works such as sea dikes of gentle slope, artificial reef with a submerged breakwater, head-land defence works and so on have been newly planned and constructed in Japan. However, all offshore detached breakwaters cannot be replaced by these new structures. The applicability of these engineering works depends on the causes and local situations of potential disasters together with the ability of these structures to control sediment movement.

As regards the offshore detached breakwater, it became possible to predict wave deformation behind it by some numerical procedures (for examples, Ohnaka, et al., 1988) and the authors have already developed numerical model for predicting wave-induced current behind it (Sawaragi et al., 1981). Formations of salient or tombolo behind the offshore detached breakwater have also been investigated by many researchers. However, until now, only a few studies have been carried out about the wave-induced current and sediment movement around the offshore detached breakwater under the condition of oblique wave incidence.

On the other hand, a suitable plane-arrangement of coastal protective works against beach erosion caused by longshore sediment transport can be effectively determined by predicting the shoreline deformation based on the so-called one-line theory. In such cases, it is very important to know how the offshore detached breakwater affects the longshore sediment movement on a natural beach.

The aim of this study is to investigate the function of the offshore detached breakwater of controlling obliquely incident waves, longshore current and resulting longshore sediment transport by conducting 3-D experiments.

EXPERIMENT

Method of experiment:

Experiments were carried out in a wave basin of 20m long, 10m wide and 0.6m deep. A model beach of the slope of 1/10 whose contour lines made an angle of 30° to the wave generator was constructed in the basin as shown in Fig.1. The experimental wave height and period were 6.5cm and 1sec. In this study, effects of the offshore detached breakwaters on waves, wave-induced current and longshore sediment transport caused by this

wave arc investigated. The dimensions of the model offshore detached breakwater are summarized in Table 1. The wave height, water depth and direction at the breaking point on the natural beach were 7.7cm, 7.5cm and 18°.

In this paper, the following notations and coordinate system are used: x axis is taken offshore from the initial shoreline and y axis is in the direction of longshore. X_b is the width of the breaker zone and X_{off} is the distance between the initial shoreline and the breakwater, l is the length of the breakwater, B is the opening between breakwaters when they are constructed as a pair, and L_0 is the wave length in deep water.

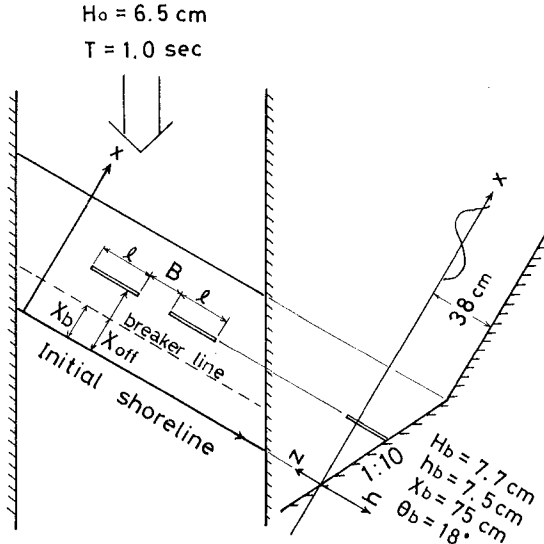


Fig.1 Wave basin and coordinate system

Table 1 Experimental conditions

[Fixed bed experiment]		[Movable bed experiment]		
X_{off}/X_b		X_{off}/X_b	l/L_0	B/l
l/L_0	0.57, 0.86, 1.7	0.86	0.5	---
B/l	0.25, 0.5, 1.0	0.86	1.0	---
		1.70	0.5	---
		1.70	1.0	---
		0.86	1.0	1.0
		0.86	1.0	0.5
		1.70	1.0	1.0
		1.70	1.0	0.5

Through the whole movable bed experiments, sand of median grain size of 0.05cm was used to make a movable bottom. Distributions of wave heights and directions, velocity of wave-induced current and topographic change around the breakwater were measured at time intervals determined in advance.

Data analysis:

Based on the measured change in the water depth, $\Delta h(x,y,t_k)$, longshore distributions of total longshore sediment transport rate, $Q_{ye}(y)$, was evaluated to investigate the effect of offshore detached breakwater on the longshore sediment transport. The water depth was measured at grid points set at the distance $\Delta x=12.5\text{cm}$ and $\Delta y=25\text{cm}$ in the wave basin. The change in the water depth, $\Delta h(x,y,t_k)$, is defined as a difference of water depths measured at time $t=t_{k+1}$ and $t=t_k$

$$\Delta h(x,y,t_{k+1})=h(x,y,t_{k+1})-h(x,y,t_k). \quad (1)$$

A continuity equation of the total longshore sediment transport, $Q_y(y,t)$, is expressed as follows:

$$\frac{\partial A(y,t)}{\partial t} = \frac{1}{(1-\lambda)} \frac{\partial Q_y(y,t)}{\partial y} \quad (2)$$

where $A(y,t)$ is the sectional area shown in Fig.2 and is defined as

$$A(y,t) = \int h(x,y,t) dx \quad (3)$$

The total longshore sediment transport rate in the experiment is calculated by transforming Eq.(2) into the following difference form and is represented by $Q_{ye}(y,t)$.

$$Q_{ye}(j,t_{k+1}) = \frac{\Delta y}{\Delta t} (1-\lambda) \sum [A(j,t_k) - A(j,t_{k+1})] + Q_{ye}(j-1,t_{k+1}) \quad (4)$$

where j indicates the j -th grid point along the shoreline and $y=j*\Delta y$.

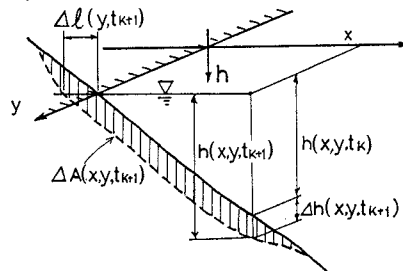


Fig.2 Definition sketch of Δh , ΔA and Δl

An eigenfunction analysis becomes a great help to understand the mode and characteristics of sediment movement around the breakwater (for example, Deguehi et al., 1986). In this study, measured changes in water depth $\Delta h(x, y, t_k)$ are expanded into the products of longshore and cross-shore eigenfunctions $C_i(y) \cdot E_i(x)$.

$$\Delta h(x, y, t_k) = \sum_{i=1}^{\infty} C_i(y) \cdot E_i(x) \quad (5)$$

WAVE HEIGHT AROUND BREAKWATER

Figure 3 illustrates comparisons of measured wave heights along the line of $x/X_b=0.28$, i.e., near the shoreline behind the offshore detached breakwaters of different lengths ($X_{off}/X_b=0.57, 0.86$ and 1.7). A vertical axis is the ratio of measured wave height, H , around the breakwater and that measured on the natural beach, H_n , at the same point.

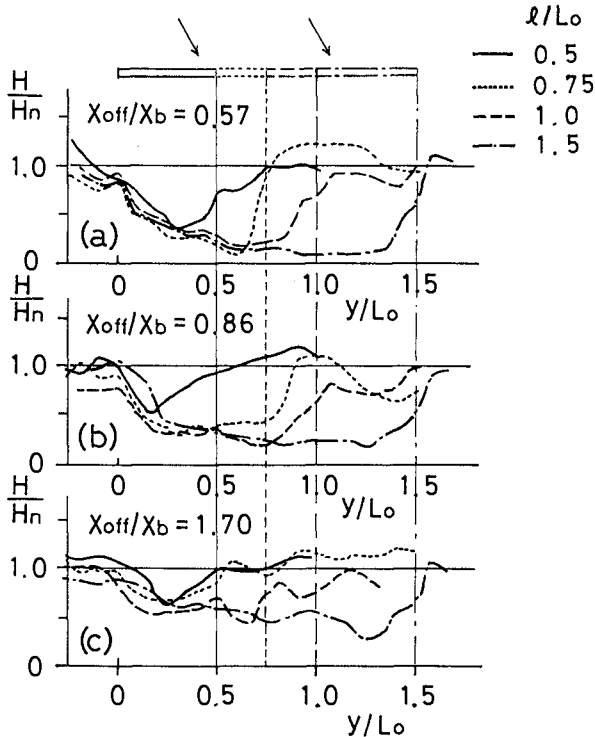


Fig.3 Wave height distribution behind breakwater ((a): $X_{off}/X_b=0.57$, (b): $X_{off}/X_b=0.86$, (e): $X_{off}/x_b=1.7$)

Solid, dotted, broken and chainlines in these figures are the wave height around the breakwaters whose lengths l correspond to $l/L_0=0.5, 0.75, 1.0$ and 1.5 , respectively.

As the distance between the line of $x/X_b=0.28$ and the breakwater increased, that is in the case where the breakwater was constructed outside the breaker zone, the longshore distribution of wave height approaches uniform due to the interaction of two diffracted waves from both sides of the breakwater.

An attenuation of wave height behind the breakwater also becomes less significant because the wave height at the depth along $x/X_b=0.28$ is depth-limited. Naturally, the longer the breakwater, the larger attenuation of wave height took place. However, when the length of the breakwater is larger than the incident wave length, the maximum attenuation behind the breakwater is almost the same.

WAVE-INDUCED CURRENT AROUND BREAKWATER

It is well known that wave-induced current behind the breakwater caused by the normally incident waves is featured by the formation of a pair of circulation cells. However, under conditions of oblique wave incidence, as were the cases of our experiments, longshore current flowed behind the breakwater smoothly as can be seen from Fig.4.

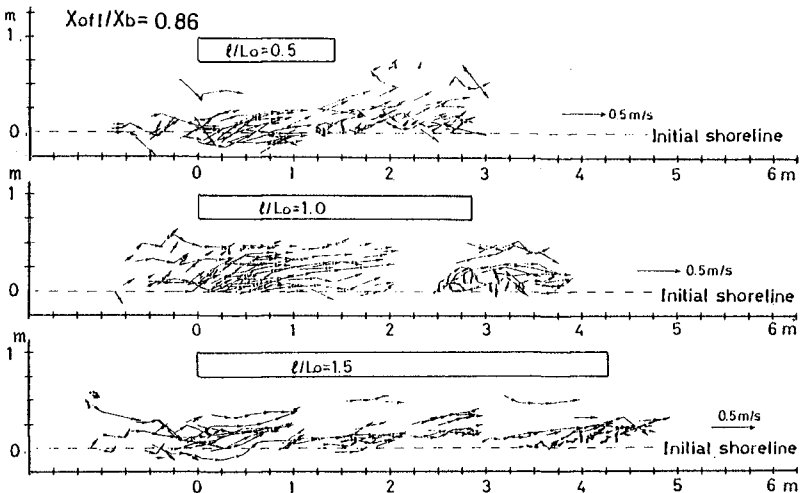


Fig.4 Flow pattern of wave-induced current ($X_{off}/X_b=0.86$)
 ((a): $l/L_0=0.5$, (b): $l/L_0=1.0$, (c): $l/L_0=1.5$)

Figure 4 is the flow patterns of wave-induced current around the breakwater of various length. Arrows in the figures are the velocity vectors obtained by tracing floats in the experiments.

Although wave heights decrease to a great extent behind the breakwater, these wave field have little influence on the longshore current behind the breakwater.

TOPOGRAPHIC CHANGE AROUND BREAKWATER

Figure 5 shows three examples of the topographic changes took place around the breakwaters during 1hr after wave generation. Figures (a) and (b) are the cases of the single breakwater constructed within and outside of the breaker zone. Figure (c) is the case of a pair of breakwaters constructed outside the breaker zone.

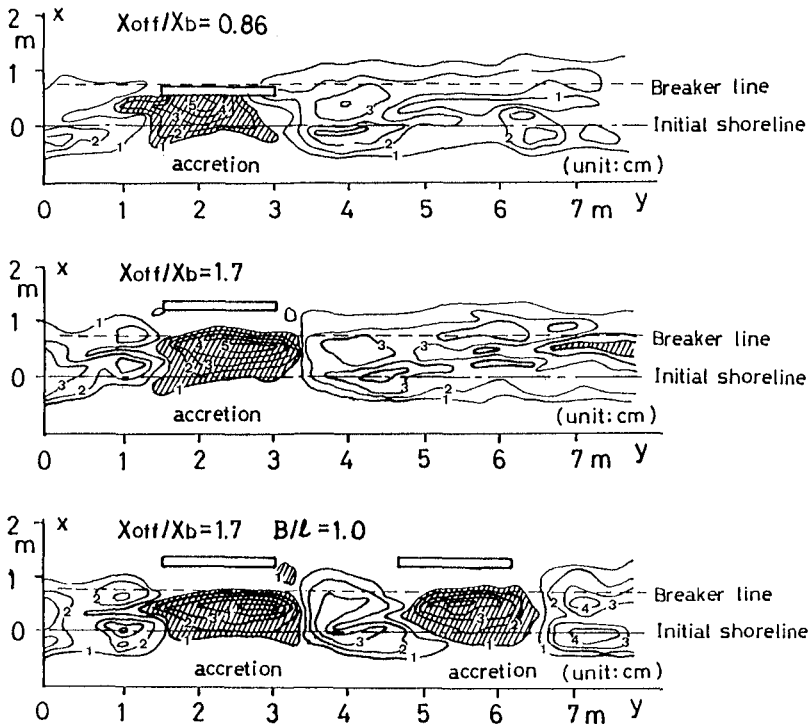


Fig.5 Topographic change around breakwater ($l/L_o = 1.0$)
 ((a): $X_{off}/X_b = 0.86$, (b): $X_{off}/X_b = 1.7$ and
 (c): $X_{off}/X_b = 1.7$, $B/l = 1.0$)

In the figure accreted regions are shown by the hatched area. A significant deposition took place behind the breakwater in every cases.

To discuss the function of the offshore detached breakwater of controlling sediment transport, it is necessary to examine where did these deposited sand come from, ie, from the upstream side, downstream side or from the offshore. The authors investigated this point by analyzing the topographic change, $\Delta h(x,y)$, at a measuring grid point (x,y) in two different ways. One is to examine the distribution of the total longshore sediment transport rate, $Q_{ye}(y)$, and the other is the empirical eigenfunction analysis.

EFFECT OF BREAKWATER ON CONTROLLING LONGSHORE SEDIMENT TRANSPORT

Total longshore sediment transport rate:

Solid line in Fig.6 shows some examples of estimated longshore distribution of the total longshore sediment transport rate, $Q_{ye}(y)$, calculated from Eq.(4).

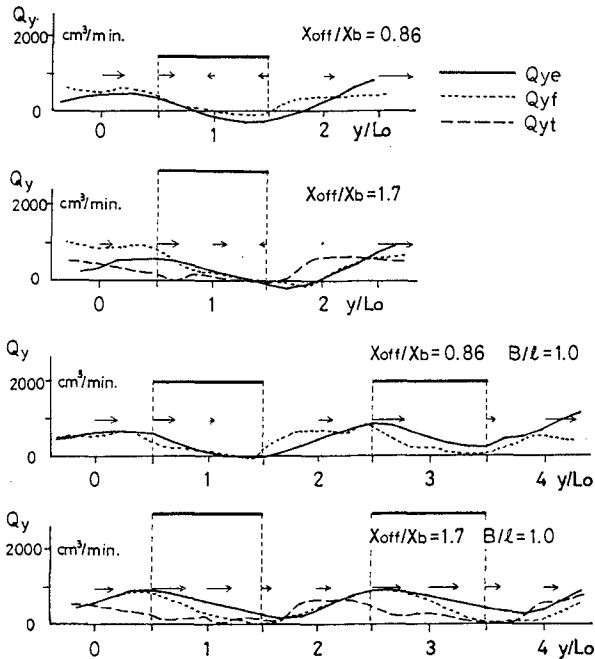


Fig.6 Total longshore sediment transport rate around breakwater ((a): $X_{\text{off}}/X_b = 0.86$, (b): $X_{\text{off}}/X_b = 1.7$, (c): $X_{\text{off}}/X_b = 0.86$, $B/l = 1.0$, $X_{\text{off}}/X_b = 1.7$, $B/l = 1.0$)

When the single breakwater was constructed within the breaker zone, the value of Q_{ye} becomes negative in the lee-side of the breakwater which means that sediment was transported in the opposite direction of the longshore current in this region. On the other hand, when a pair of breakwaters was constructed, no significant negative value of Q_{ye} appears regardless of its position.

Cross-shore and longshore eigenfunction:

Figures 7 illustrates examples of the longshore and cross-shore eigenfunctions with the maximum eigenvalue. The ratio of these maximum eigenvalues to the traces are more than 60%.

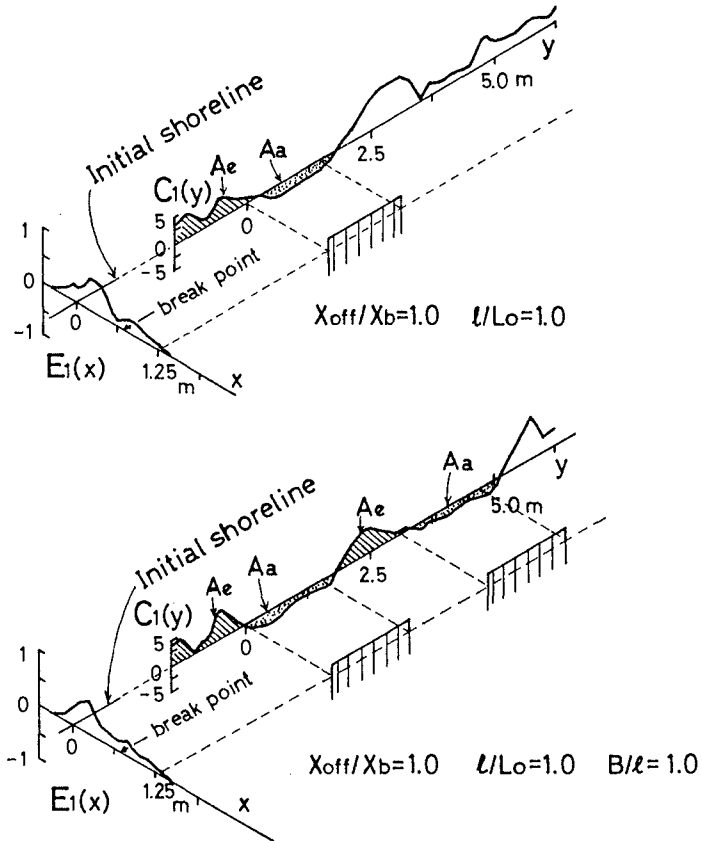


Fig.7 Cross-shore and long-shore eigenfunctions correspond to the largest eigenvalue($X_{off}/X_b=1.0$)
 ((a): $l/L_o=1.0$, (b): $l/L_o=1.0, B/l=1.0$)

Figure(a) is the case where the single breakwater was set at $x/X_b=1.7$. Figure(b) is the result of the case where a pair of breakwaters was constructed at the same location. As can be seen from these figures, $E1(i)$ is positive throughout the whole region and $C1(y)$ indicates both positive and negative values along the longshore direction. Especially, behind the breakwater, the value of $C1(y)$ is negative. Therefore, it can be judged that the pattern of the topographic change represented by the product $C1(y)*E1(x)$ was caused by the longshore sediment transport.

Ability of breakwater to trap sediment:

The ratio of the volume of deposited sediment behind the breakwater and the volume of eroded sediment in the upstream side of the breakwater is also estimated by the ratio of the area of hatched region A_e and the area of dotted region A_a . If A_a is greater than A_e , more sediment transported from the upstream side of the breakwater was deposited behind the breakwater. This means that the sediment in the downstream side of the breakwater was transported in the opposite direction of longshore current by the diffracted waves. If A_a is smaller than A_e , a part of sediment transported from the upstream side of the breakwater in the longshore direction was transported to the lee-side through behind the breakwater.

Figure 8 shows the ratio of A_a/A_e of the whole cases carried out in the experiments. Open circles are the cases of single breakwater and the breakwater of upstream side. Closed circles are the results of the lee-ward breakwater.

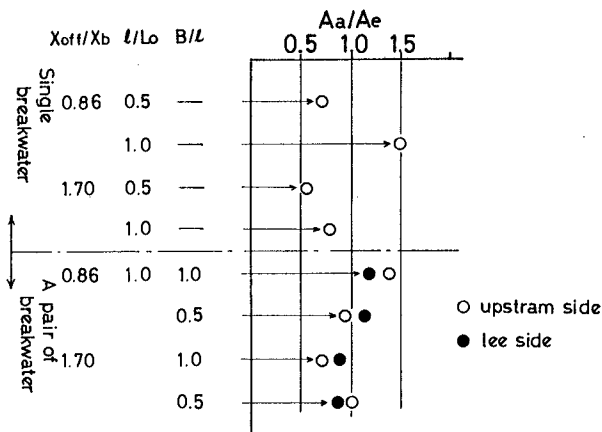


Fig.8 Ratio of A_a/A_e

In the case of $X_{off}/X_b=0.86$ and $l/L_o=1.0$, the ratio of A_a/A_c becomes almost 1.5. In this case, the sediment in both upstream-side and lee-side of the breakwater was transported behind the breakwater and settled down there. The same conclusion has already been derived from the analysis of the distribution of Q_{ye} .

When the length of the breakwater is 1/2 of the incident wave length, 60 to 70% of the amount of the sediment transported in the longshore direction is trapped behind the breakwater and the rest is flow through behind the breakwater to the leeward. Furthermore, the each breakwater constructed as a pair has a high efficiency to trap sediment behind them when compared to the single breakwater of the same dimension.

Relation between ΔA and Δl :

Figure 9 shows the relation between the change in sectional area ΔA and the shoreline displacements Δl . It is found that relatively high correlation exists between ΔA and Δl regardless of the location and dimension of the breakwater.

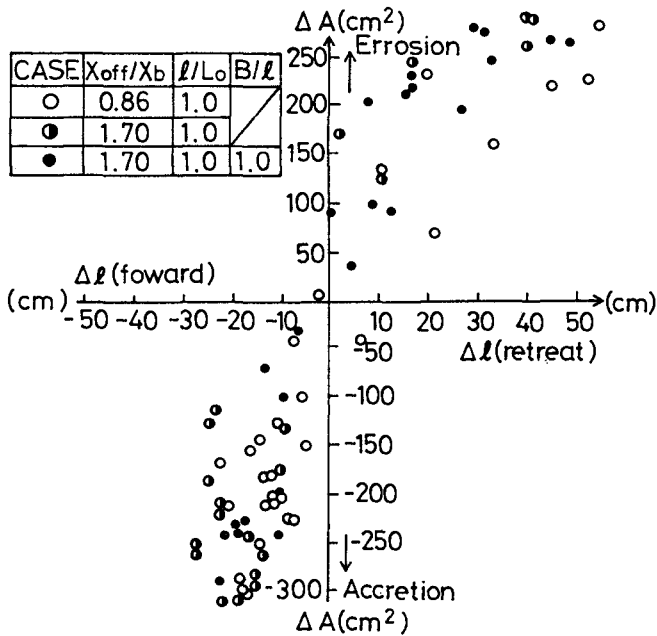


Fig.9 Relation between ΔA and Δl around breakwater

From these results, a so-called one-line theory can be applied for the prediction of shoreline change which

will take place around the offshore detached breakwaters provided that the longshore distribution of total longshore sediment transport rate can be given.

ESTIMATION OF TOTAL LONGSHORE SEDIMENT TRANSPORT RATE AROUND THE BREAKWATER

The total longshore sediment transport rate is generally estimated by the following empirical formula of Savage type.

$$Q_y = \alpha (ECg)_b \sin(2\theta_b) \quad (5)$$

where $(ECg)_b = (\rho g H^2 C_g)_b / 8$ is the incident energy flux at wave breaking point, θ_b is the wave breaking angle and α is the empirical coefficient. According to Eq.(5), Q_y is directly related to the wave conditions at breaking point. Therefore, the total longshore sediment transport rate around the structures constructed in the breaker zone can not be predicted by this kind of formula.

There also remains another problems in the expression of Q_y because the direction of the longshore sediment transport is uniquely determined by the wave breaking angle. It seems reasonable to assume that the longshore current play a more important role in the longshore sediment transport than the wave breaking angle does.

We can also estimate the total longshore sediment transport rate by integrating local longshore sediment transport rate, q_y . Some formulas for predicting the local longshore sediment transport rate have already been proposed. In this study, the value of q_y is estimated from the flux model (Sawaragi et al., 1985). The wave field and the velocity of wave-induced current were obtained by the numerical simulation based on the unsteady linear mild slope equations (Ohnaka et al., 1988) and depth and time averaged basic equations of wave-induced current (Sawaragi et al., 1981).

In Fig.6, the total longshore sediment transport rate, Q_{yf} , calculated by integrating the local longshore sediment transport rate are shown by the dotted line. Broken lines in the figure are the total longshore sediment transport rate, Q_{yt} , calculated from the empirical formula of the form of Eq.(5). The value of Q_{yt} can be estimated only in the cases where the breakwater were constructed outside the breaker zone. In the calculation of Q_{yt} , simulated results of wave height, water depth and direction at the wave breaking point were used and the value of α was tentatively determined to be 1.

As can be seen from Fig.6, there is a large discrepancy between Q_{ye} and Q_{yt} . On the other hand, Q_{yf} calculated by integrating local longshore sediment transport rate gives more accurate estimation of the total longshore sediment transport rate, Q_{ye} , estimated from the topographic change.

CONCLUSIONS

1. Waves behind the offshore detached breakwater under the obliquely incident waves attenuate significantly as is the case of normal wave incidence. However, these wave fields have little influence on the longshore current behind the breakwater. Longshore current flowed smoothly behind the breakwater. No circulation cell of wave-induced current appeared.

2. In spite of the flow pattern of longshore current, a large amount of sediment transported in the longshore direction is trapped behind the offshore detached breakwater. The pair of offshore detached breakwaters has higher efficiency to trap sediment transported in the longshore direction than the single breakwater does.

3. The total longshore sediment transport rate behind the offshore detached breakwater can be predicted more precisely by integrating the local longshore sediment transport rate estimated from the flux model than by the so called Savage type formula.

Reference

- Deguehi, I. and T.Sawaragi, 1986. Beach fill at two coasts of different configurations, Proc. 20th Coastal Eng. Conf. ASCE, pp.1032-1046.
- Ohnaka, S., A.Watanabe and M.Isobe, 1988. Numerical modeling of wave transformation with a current, Proc. 21st Coastal Eng. Conf., pp.393-407.
- Sawaragi, T., I.Deguehi and Y.Izumi, 1981. Behaviors of wave-induced current behind offshore breakwaters and submerged breakwaters, Proc. 28th Japanese Conf. on Coastal Eng., pp.310-314 (in Japanese).

CHAPTER 199

OSCILLATORY FLOW INVESTIGATIONS IN POROUS MEDIA

Gregory M. Smith¹ and Kevin R. Hall²

INTRODUCTION

A series of experiments has been conducted at the Coastal Engineering Laboratory of Queen's University in order to investigate the characteristics of accelerating flow through porous media. The nature of the steady flow law in coarse granular material has been reasonably well defined from a large number of previous studies. Variations on this steady flow law have been applied to the case of oscillatory flow, in numerical models of forces in breakwaters for example, with the explicit assumption that the steady law is applicable to the unsteady case. Few experimental investigations have been conducted to verify this assumption. Hence the present study was designed specifically to test the applicability of the steady flow law (Forchheimer's equation) to oscillatory flow.

EXPERIMENTAL PROCEDURE

Parameters relevant to this study include the grain size and porosity of the test sample (and shape), bulk or macroscopic velocity of flow through the sample and the pressure loss associated with the flow. A test programme was established to measure these quantities for both steady unidirectional and oscillatory flows.

Tests were conducted in an oscillating water tunnel (Figs 1,2). A test section of porous material was installed in the centre of the measuring section. Both unidirectional and oscillatory flows could be generated within the tunnel. The

¹ Graduate student, Queen's University, Kingston Ont. Canada.

² Assist. Prof. of Civil Engineering, Queen's University, Kingston, Ont. Canada K7L 3N6.

test section had a height of 85cm, width of 45cm and the length varied according to the test material.

Tests were made on three different types of materials: 75 mm diameter plastic spheres, 42 mm spheres (golf balls) and one sample of rock ($M_{50}=1.43$ kg; $D_{50}=100$ mm). Each type of sphere was tested at high and low porosities (cubic and rhombohedral packings, respectively). The effect of the dimples on the golf balls was not considered in the analysis. The use of these different sizes of spheres allowed an illustration of the wall effect of the tunnel on the measurements. In situ porosity measurements were made on all samples.

Head losses across the test section were measured with four pressure transducers (Data Instruments AB/99; 0 to 6 psi), installed in the centre of the sample; two near the upstream end and two near the downstream end. Samples were measured at 10 Hz for all tests; this provided adequate resolution of the pressure traces while minimizing the storage space required. Sampling was controlled by a Zenith 386 microcomputer.

The transducers were calibrated over their full range in a 4.5 metre high water column periodically during the test programme but it was found that no significant changes occurred to their calibration curves. For tests on the spheres, the transducers were mounted inside of the spheres for placement in the test section (Figure 3). This allowed for measurement without interference with the flow. For the test on the rock sample the transducers were set in the voids and rocks were placed around them so as to hold them securely and prevent movement. During the first test series, the 75mm spheres in rhombohedral packing, two transducers were installed side by side, but facing opposite directions at both the upstream and downstream ends of the section. This was to compare measurements of the transducers themselves and to test if orientation altered the readings. Orientation made no difference and both sets of transducers provided identical readings. Subsequent tests were made with two sets of transducers located at two elevations within the section to investigate any differences due to possible flow variations. The majority of tests showed no difference in these readings. Where differences did occur, the readings were averaged; no attempt was made to include effects of non-uniformities in flow or pressure readings.

Velocity measurements were made using a laser doppler anemometer (LDA). This consisted of a DISA 15 mW helium-neon laser, photomultiplier and a frequency tracker. Only the amplifier component of the tracker was used; since no frequency shifting was employed the tracker was not adequate to measure small and reversing flows generated for the experiments. Instead, the photomultiplier signal was sampled directly by a VAXstation 3200 mini computer, via an analogue to digital converter. The photomultiplier outputs

a voltage signal, the frequency of which is directly proportional to the velocity of flow. After this signal was acquired (and time stamped), its peak (Doppler) frequency was determined by power spectrum analysis software. Velocities were computed by the relation

$$V = \frac{\lambda}{2 \sin \frac{\theta}{2}} \times f_D$$

where V = velocity of flow
 λ = wavelength of laser light = 632.8 nm
 θ = beam intersection angle
 f_D = Doppler (signal) frequency.

For each flow condition tested, velocities were measured at several locations across the tunnel section in order to determine the average velocity. The velocity distribution was not uniform, varying typically +/- 10% from the mean from top to bottom and inside to outside walls of the tunnel. Measurements were taken at only one position along the length of the tunnel, that being approximately 2.1 metres upstream of the upstream end of the test section. This was due to space restrictions for location of the laser equipment. As it was only the "bulk" or average velocity that was required, this was considered adequate since the flow rate at any given instant in time must be constant along the length of the tunnel. No effects of the non-uniformity of the velocity profile were considered and only (spatial) average velocities and hydraulic gradients were compared.

A concern of velocity values derived from bulk discharge measurements is that higher discharge rates occur near the walls of the permeameter. This causes the "bulk" velocity value to be higher than that actually flowing through the centre of the section. Direct measurement of velocities near the centre of the tunnel should minimize this error. Ideally the velocity measurements should be made adjacent to the test section but it was found that large fluctuations occur in that area due to rapid expansions and contractions from the pore exits and entrances. Without the use of a frequency shifter and a two component LDA it was not possible to obtain reasonable measurements in that location.

Steady flows in the tunnel were generated with a constant speed pump. The flow rate was varied by means of two valves which controlled the amount of water directed into the measuring portion of the tunnel. Water prevented from entering the test section was recirculated into a stilling basin behind the tunnel. Flow rates tested in these experiments ranged from approximately 1.5 cm/sec to 30 cm/sec.

Oscillatory flows were generated by means of a piston driven by a variable speed motor. The stroke length of the piston was also variable. Tests were conducted with stroke lengths of 2.5 cm, 5.0 cm and 10.0 cm for each sample, and periods ranging from 3 seconds to 12 seconds. These values represented the widest ranges that could be tested without damaging the test sections, although the piston is capable of operating over greater ranges.

The porosity of each sample tested was measured by sealing off the test section from the rest of the tunnel and adding measured amounts of water. The volume of water added indicated the volume of voids in the section. The section was sealed using metal plates fitted with a rubber gasket around the edges, which could then be expanded outward by tightening a series of screws, thereby providing a tight seal around the edges of the tunnel. However, initial measurements revealed significant leakage from the lower corners of the plates as well as through the false floor inside the tunnel (although no water leaked out of the tunnel itself). Further attempts to seal these areas were only partially successful at preventing leakage as the head of water in the section increased. To further reduce leakage secondary partial barriers were installed in the tunnel, adjacent to the metal plates and the space between was filled with water to the same elevation as that within the section. This was found to adequately minimize any leakage.

Water was added to the section by buckets, each bucket containing a known volume, and the water level in the section was measured after each bucket was added. This provided a means to determine if any leakage had occurred (fig 4). For the sections with spheres in rhombohedral packing, no half spheres were used around the edges so the porosity was much higher in that region. In order to calculate the porosity of the section proper, the volume of these extra voids was calculated and subtracted from the volume of water added. Porosity values for the five test sections are listed in the table below.

The values for the spheres differ slightly from the theoretical values which can be calculated precisely. These differences arise from the fact that the packing arrangements were not perfect, since the spheres did not fit exactly into the tunnel section; there were always some small gaps here and there that caused the porosity to be somewhat higher than that for perfect packing.

No attempt was made to make highly accurate measurement of the porosity in this study. Previous work has shown that permeability is highly sensitive to porosity while accurate measurements of porosity are very difficult to make owing to factors such as surface adsorption and air entrapment in the voids. This has been discussed by Dudgeon (1968). On the other hand, the goal of such research is to provide a method of predicting the hydraulic performance of coarse granular structures where porosities can not be accurately estimated. Porosities were measured in this study only to provide some comparison to other work, rather than to define the exact form of their relationship to the

hydraulic conductivity of the sample.

RESULTS

The Forchheimer equation can be linearized if written as

$$\frac{S}{V} = a + bV$$

where S = hydraulic gradient
 V = macro. velocity
 a,b = coefficients

The coefficients a and b can be found by regression analysis. Steady flow data for each test is plotted on figure 5 and the associated a and b values are:

	a (sec/m)	b (sec/m) ²	porosity
75mm spheres			
Rhombohedral:	0.32	12.0	0.32
Cubic:	0.06	2.60	0.52
44mm spheres			
Rhombohedral:	0.38	26.1	0.30
Cubic:	0.06	5.92	0.52
Rock:	0.06	3.25	0.49

It is evident that geometrically similar packing arrangements display similar values of the intercept a, indicating similar permeability coefficients as defined by Ward (1964) but the slope b is steeper by a factor of two for the smaller 42mm spheres. The length of the test section was 15 diameters for both the large and small spheres, hence the amount of surface area of each sample was of similar magnitude (within 10%). Evidently, using material that is large compared to the tunnel dimension will lead to underestimation of the energy losses. The 42mm spheres correspond to the general rule of maximum grain size to container dimension of 1/10 as proposed by Rose and Rizk (1949). The data for the rock sample falls close to the cubic arrangement of the 75mm spheres, ie. offering the least resistance.

Results from the oscillatory tests are presented in phase averaged form. Typical phase averaged curves for velocity and hydraulic gradient are shown in figure 6. When this data is plotted in the form of figure 5 above, it becomes apparent that the points do not all follow the steady flow curves

(figure 7). Also, the traces for increasing velocity are slightly different than those for decreasing velocity and the differences increase as acceleration increases. There also seems to be a general trend that the magnitude of these differences increases as the period decreases, which supports the findings of den Adel (1987), who concluded that inertial effects are most dominant at smaller periods, especially at periods less than 1 second.

Figure 8 shows values of S/V vs. V for two periods (5 and 10 seconds) for the 42mm spheres in cubic packing, along with the steady flow regression line. The steady flow line passes through the lower curve for both data sets. As is the trend with all results, the upper ends of the oscillatory curves follow the steady flow regression lines. At smaller velocities, however, significant deviations occur as the accelerations increase. These deviations are larger for smaller periods with the associated higher mean velocities, ie. with higher magnitudes of acceleration. Den Adel (1987, 1990 pers. comm.) has shown that such deviations can arise from a phase shift between the velocity and hydraulic gradient. The occurrence of an added mass effect may also cause part of this deviation, as proposed by Hannoura and McCorquodale (1978) and Abdel-Gawad and McCorquodale (1985).

Similar effects are evident in figure 9, which shows data for various piston stroke lengths. The period of oscillation was constant at 8 seconds and stroke lengths of 25, 50 and 100mm were tested. Shorter stroke lengths produce smaller flow velocities and therefore smaller accelerations.

Results presented herein are preliminary in nature and more detailed data analysis is in progress. Specifically, the effect of phase shifts between velocity and hydraulic gradient and the presence of added mass effects will be given further consideration. At the present time, the data suggests that the steady coefficients in the Forchheimer equation describe oscillatory conditions reasonably well where the velocities are maximum and accelerations minimum. At higher accelerations, differences between steady and oscillatory curves can be significant.

REFERENCES

- Abdel-Gawad, S.M. and McCorquodale, J.A. (1985): "Rapidly Accelerated Flow Past Multiple Obstructions", Proc. 21st IAHR Congress, Melbourne, pp. 92-95.
- den Adel, H. (1987): "Cyclic Permeability of Granular Material", Delft Soil Mechanics report no. CO-272550/35 (in Dutch).
- Dudgeon, C.R., (1968): "Relationship between Porosity and Permeability of Coarse Granular Materials", Proc. Conf. on Hydraulics and Fluid Mechanics, IEA., pp. 76-80.

Hannoura, A.A. and McCorquodale, J.A. (1978): "Virtual Mass of Coarse Granular Media", J. Waterway, Port, Coastal and Ocean Div., ASCE, Vol. 104, No. WW2 (May), pp. 191-200.

Ward, J.C. (1964): "Turbulent Flow in Porous Media", J. Hydraulics Div., ASCE, Vol. 90, No. HY5, pp. 1-12.

Rose, H.E. and Rizk, A., (1949): "Further Researches in Fluid Flow through Beds of Granular Material", Proc. I, Mech. Eng. Vol. 160, pp. 493-511.

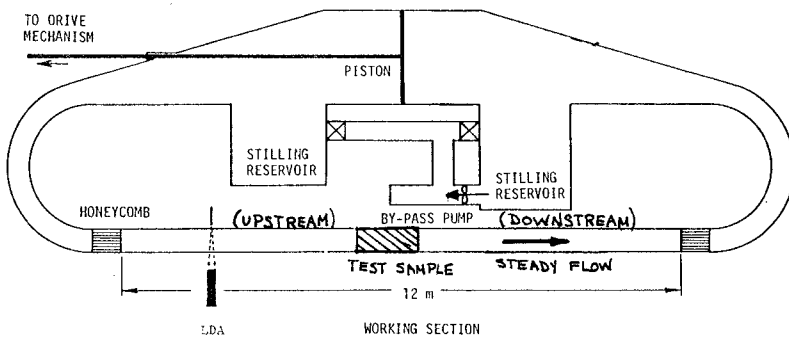


Figure 1



Figure 2

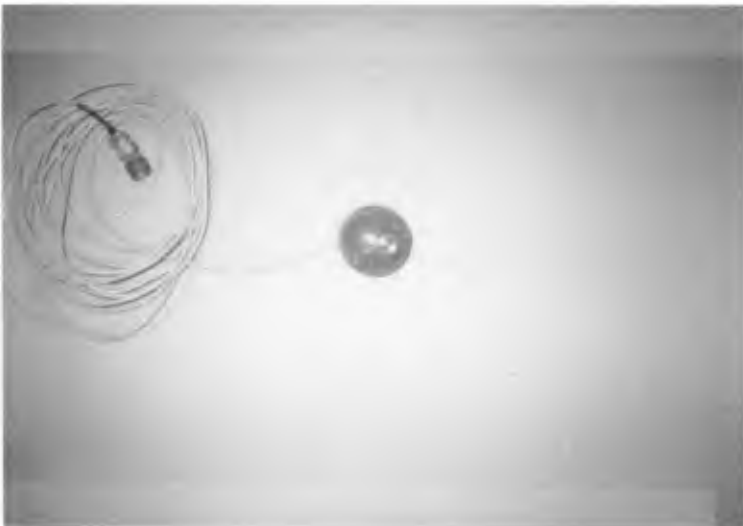


Figure 3

POROSITY MEASUREMENT

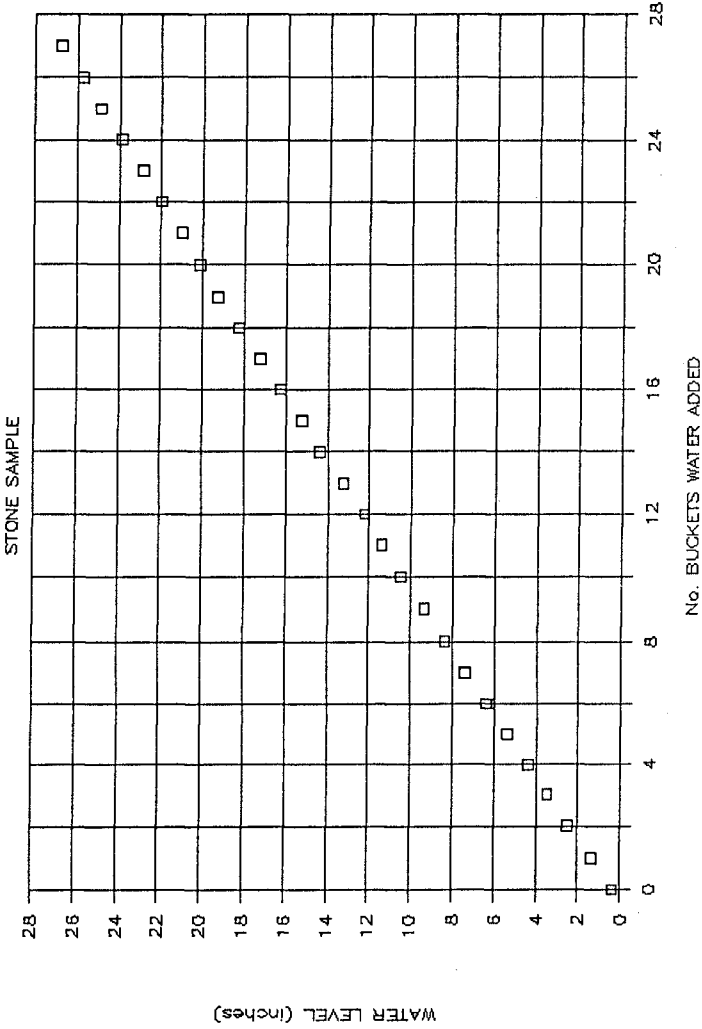


Figure 4

STEADY FLOW TEST RESULTS

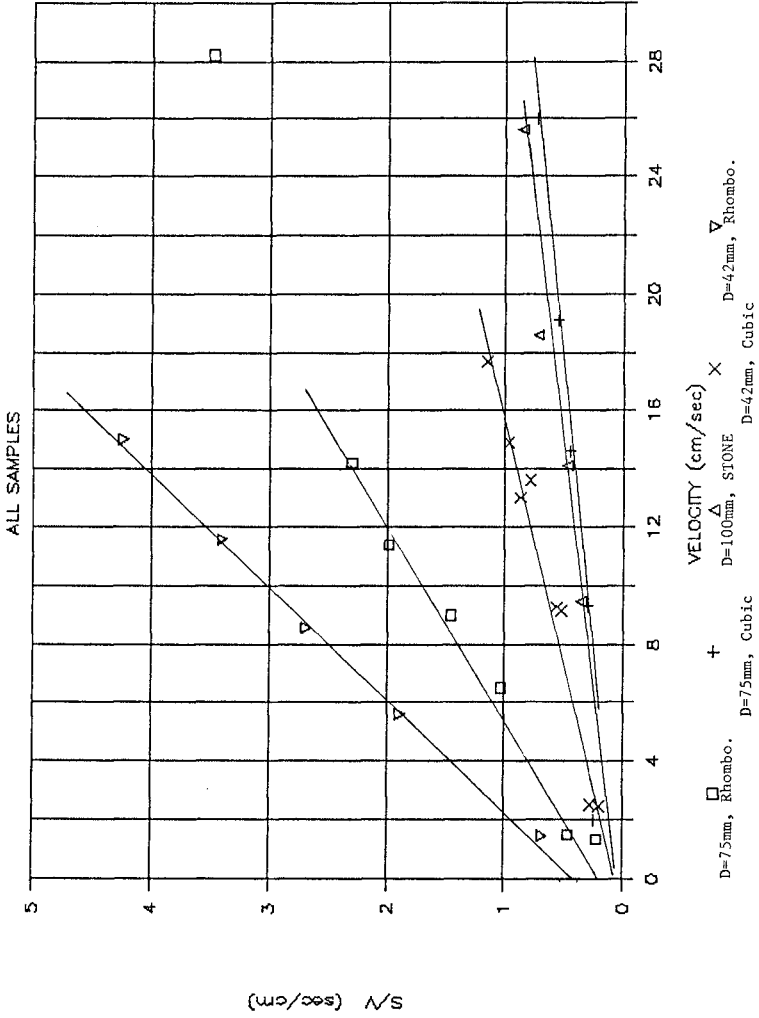


Figure 5

SPACE & PHASE AVG. V & S

D=42mm, T=10 SEC, STROKE=100mm CUBIC

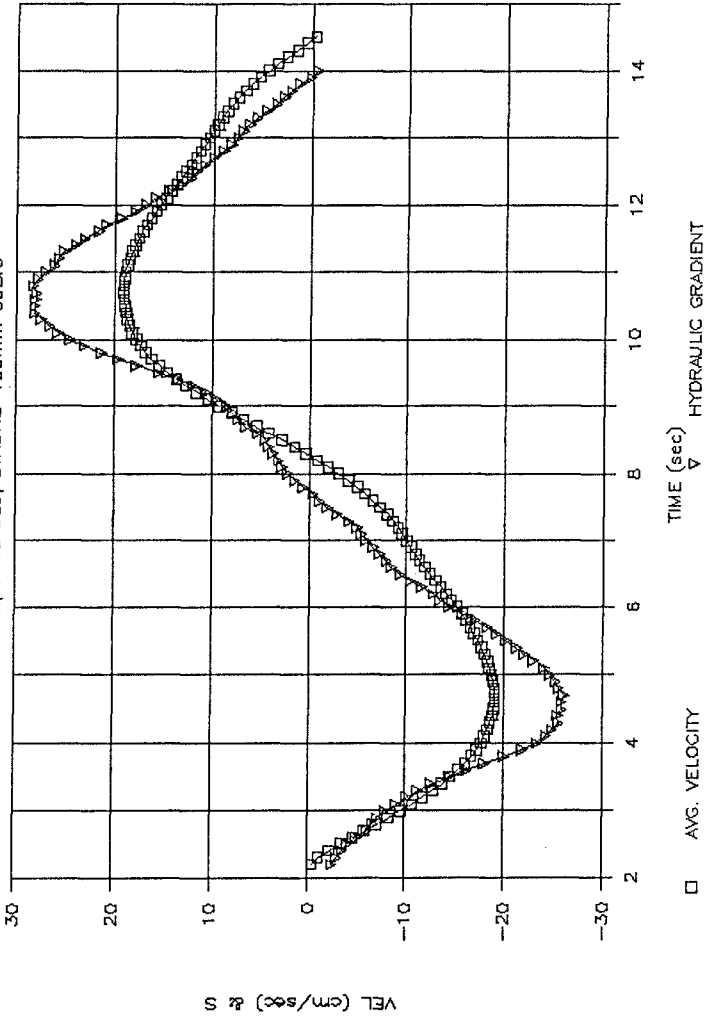


Figure 6

OSCILLATORY TEST SERIES QAI

D=4.2mm, T=1.0 SEC, STROKE=100mm, CUBIC

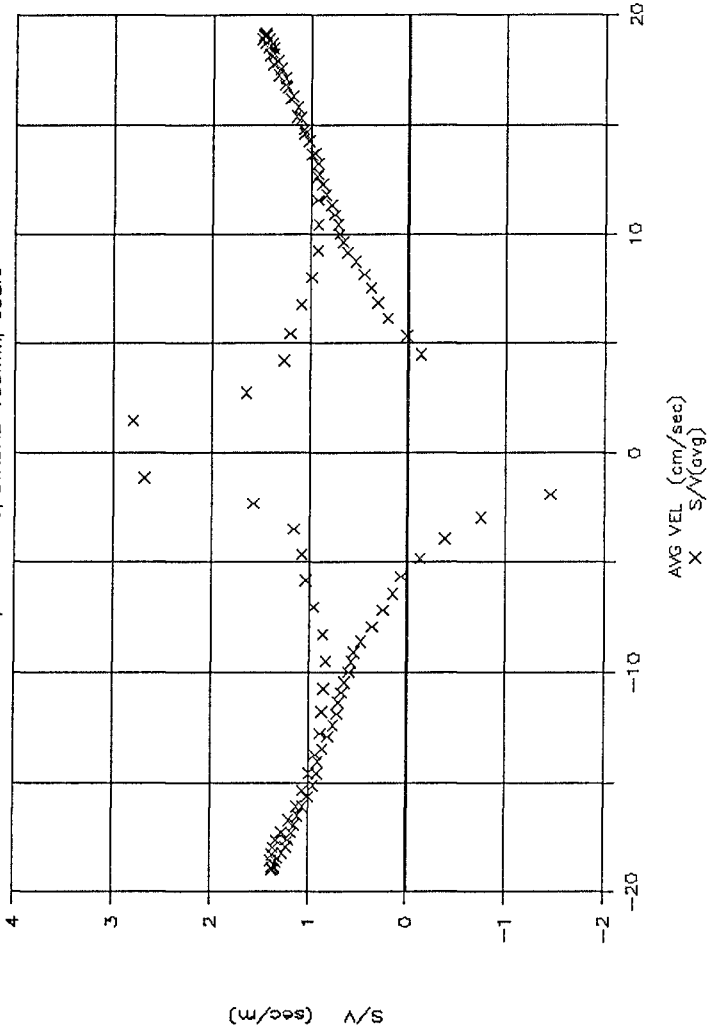


Figure 7

Period Influence

STROKE = 50mm, D=4.4mm, CUBIC PACKING

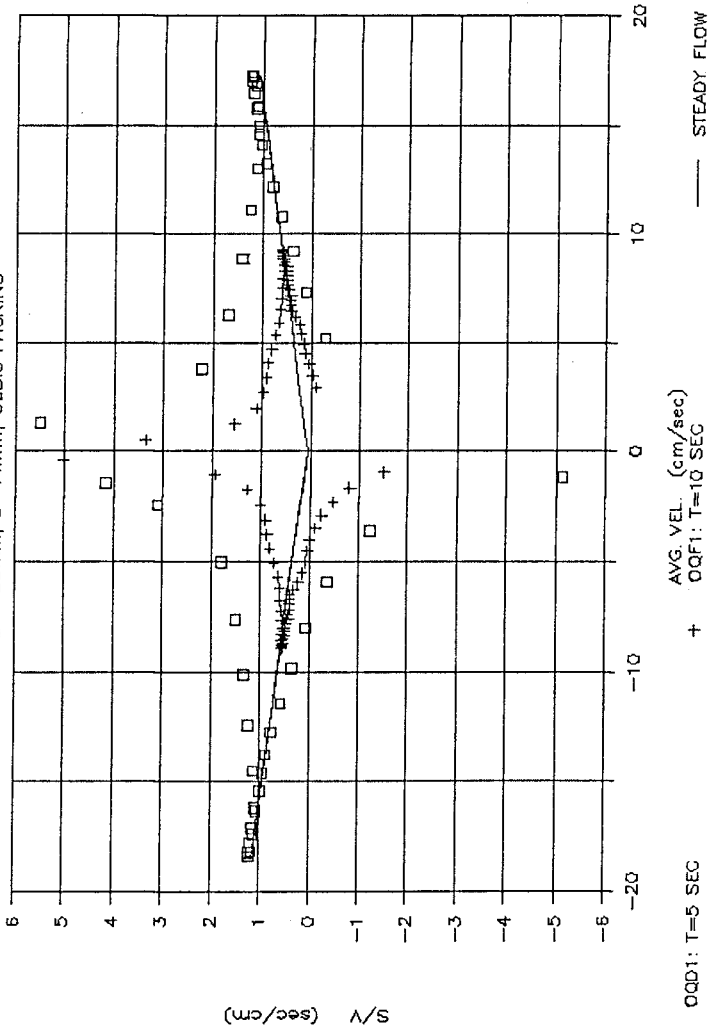


Figure 8

Stroke Influence

T=8 SEC, D=42mm, CUBIC PACKING

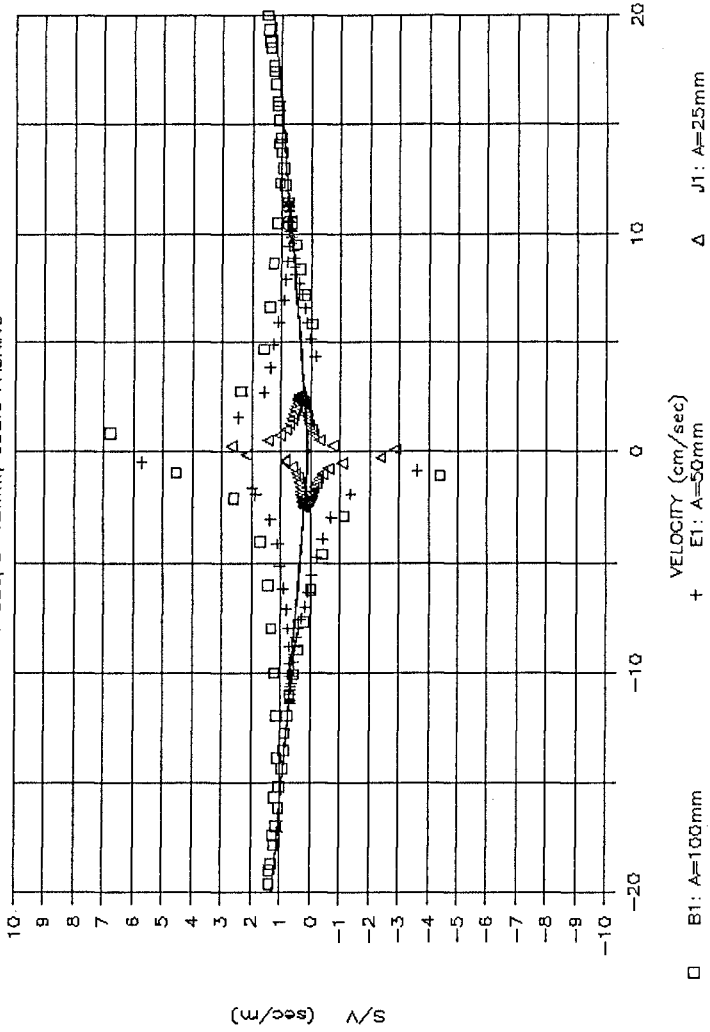


Figure 9

CHAPTER 200

INSTANTANEOUS SEDIMENT CONCENTRATION DUE TO WAVE ACTION AT PROTOTYPE SCALE

Klemens Uliczka*

1. INTRODUCTION

At sandy coasts the sediment transport due to wave action can cause beach erosion and loss of protecting dunes. In order to calculate the wave-induced sediment transport the physical parameter of wave height, wave-induced current, instantaneous sediment concentration and bottom elevation have to be known or measured. The following study was concerned with field measurements and extreme conditions (wave-induced sheet-flow transport), which were simulated at prototype scale in the Large Wave Flume (GWK) in Hannover.

2. MEASURING EQUIPMENT

From first investigations in the year 1987 with respect on wave-induced sediment concentration at velocities in the range up to 1.2 m/s followed the development of an electro-resistance- type-sediment-concentration-probe (ERSC) for prototype conditions. The idea arose from the small scale probe ERSC, used at wave tunnel experiments by HORIKAWA et al. (1982). The electric system enables the measurement of the bottom ($c/c' = 1.0$) and nearbottom concentrations at ripple as well as sheet-flow conditions.

The aim of the test series was, to get experience with the system. The probe ist still in development at the Leichtweiss-Institute in Braunschweig, and it has to be

*Research Engineer, Dr.-Ing., Bundesanstalt für Wasserbau
-Aussenstelle Küste-, Wedeler Landstrasse 157,
D-2000 Hamburg 56, Fed. Rep. of Germany

solved some structural problems. It will be presented, that the ERSC-probe is in principle prepared for measurements and that the results warranted the continuing development of the probe.

2.1 ERSC-PROBE IN FIELD TESTS

Since the GWK could be used only for a limited time for experiments with sand bottom, a prototype of the ERSC-probe, developed at the Leichtweiss-Institute of the Technical University of Braunschweig, was tested under field conditions at the island Norderney in the German Bight. The ERSC-probe had 6 electrodes in steps of 1 cm, connected to WHEATSTONE-half-bridges.

The ERSC-probe was positioned in the middle of an groyne field in the north-west part of the island. The water depth during the measurements was about 1.0 m, and the wave height about 0.5 m. The water temperature was $T_w = 9^\circ\text{C}$. The sand near the test section had the mean diameter D_{50} of 220 μm and the geometric standard deviation was $\sigma_g = 1.43$.

The probe was installed after calibration under field conditions in the breaker zone during ebb tide, so that all electrodes were covered by sand. The assumption, that due to wave action the electrodes will be exposed, was verified by the electric signals. The reflection of waves from the groynes strongly influenced the measurements as seen from the current-vector during 40 s in Fig. 1. The wave-induced orbital velocity in on- and offshore direction could not be defined.

The time sequence of a measurement over 40 s is shown in Fig. 2. The upper part of Fig. 2 shows the measured wave induced velocity with a maximum of 1.38 m/s, registered about 0.1 m above the bottom. Below are plotted the signals of 4 ERSC-electrodes, calculated from the extreme values of clear water and packed sand.

The correlation of the sediment concentration with the wave induced velocity is very difficult and the result cannot be used for basic research because of the current vector (see Fig. 1).

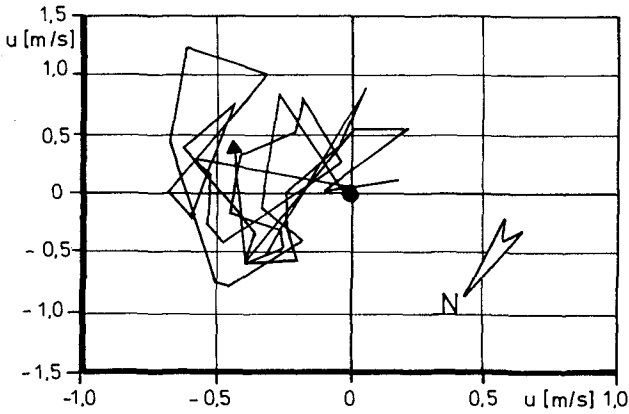


Figure 1. Current vector during 40 s of the measurement at the island Norderney

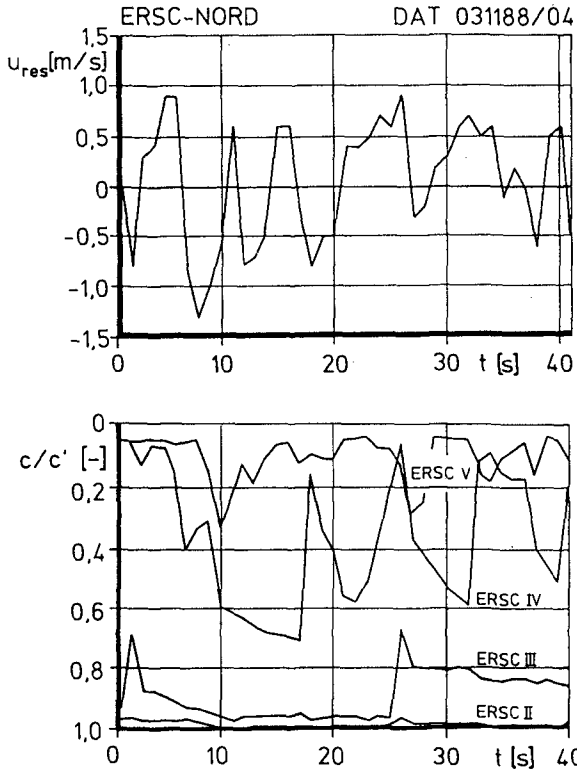


Figure 2. Time sequence during 40 s of the measurement at the island Norderney

Fig. 3 illustrates the variety of the vertical sediment concentration distribution during 40 s. The distance between the electrodes was 1 cm. The distribution between the measured values was plotted linear.

At the beginning of the measurement all wires were covered by sand and at the end the probe registered clear water, so that for the analysis the calibration values could be taken directly from the measurement. But, changing water temperature and conductivity has to be compensated in further developments. Scours due to vertical supports were assumed, but could not be observed visually.

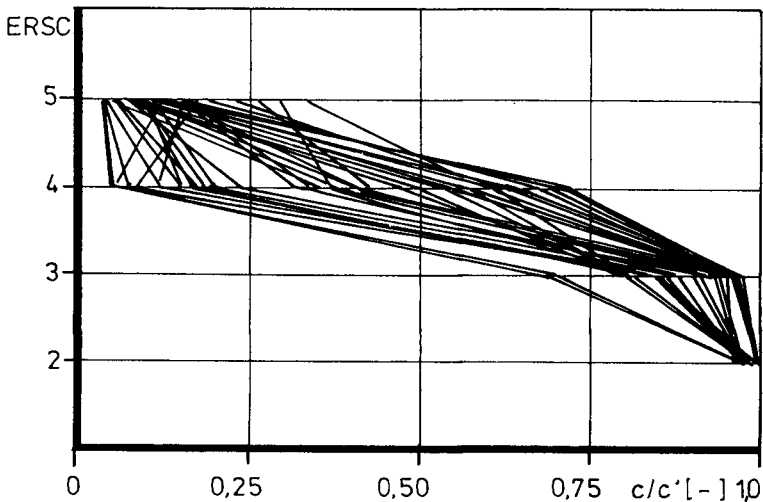


Figure 3. Sediment concentration distribution during 40 s of the measurement at the island Norderney

The results presented demonstrate the problems with information gathering particularly on sediment concentration in the surf zone which can be used for basic research. The necessity of instantaneous data on wave induced sediment concentration and the possibility to simulate high orbital velocities in the GWK in Hannover led to further investigations on the development of the ERSC-Probe.

2.2 THE ERSC-GWK-PROBE

The ERSC-GWK-probe (GWK: Large Wave Flume in Hannover) was developed at the Leichtweiss-Institute for large scale conditions. It recorded the instantaneous sediment concentration in the range of 7 cm (in steps of 1 cm) over the bed, and was steered by optical sensors, so that it should follow the bottom elevation as it changed due to hydraulic conditions.

The change of water temperature and conductivity was compensated with electrodes about 0.5 m above the bottom shielded against suspended material. These wires were connected parallel to the measuring electrodes within the WHEATSTONE-half-bridges. Consequently, only the sediment concentration was registered inside the electric field, of which 90 % were measured with a radius of 2.2 mm around each electrode. Starting from the principle, that an electric resistance has to be linear, the probe was calibrated for both extreme boundary conditions: clear water ($c/c'=0$) and wave-induced packed sand ($c/c'=1$). The scattering of both of these values yielded a measure of the accuracy.

The diameter of the wires was reduced from 1 mm (Norderney-probe) to 0.8 mm and the horizontal distance of the lateral supports was 8 cm. The measuring section of 1 cm length on each wire was placed in the middle between the vertical supports. Fig. 4 shows a sketch of the ERSC-GWK-probe.

Two optical sensors, one in vertical, the other in horizontal direction at the tip of one support recorded the distance of the lowest ERSC-wire to the sand bed. The sensitivity of the optical sensors was tuned in the laboratory in such a way, that the vertical sensor had all the time to register sediment concentration greater than about 1,000 g/l. The horizontal sensor had to measure clear water. The distance between both sensors was 1 cm. The hydraulic power steering, by means of on/off connections, should keep the probe near the bottom, so that the lowest wire, ERSC I, should register the near bottom concentration.

Under prototype conditions in the GWK the sensitivity of the optical sensors had to be tuned new before each test series. Therefore a constant distance was not kept for all test series. As the sensitivity was to less,

the lowest wires were covered by sand.
 The time-analysis of the vertical movements yielded the order of magnitude of the bottom elevation changes even during a single wave.

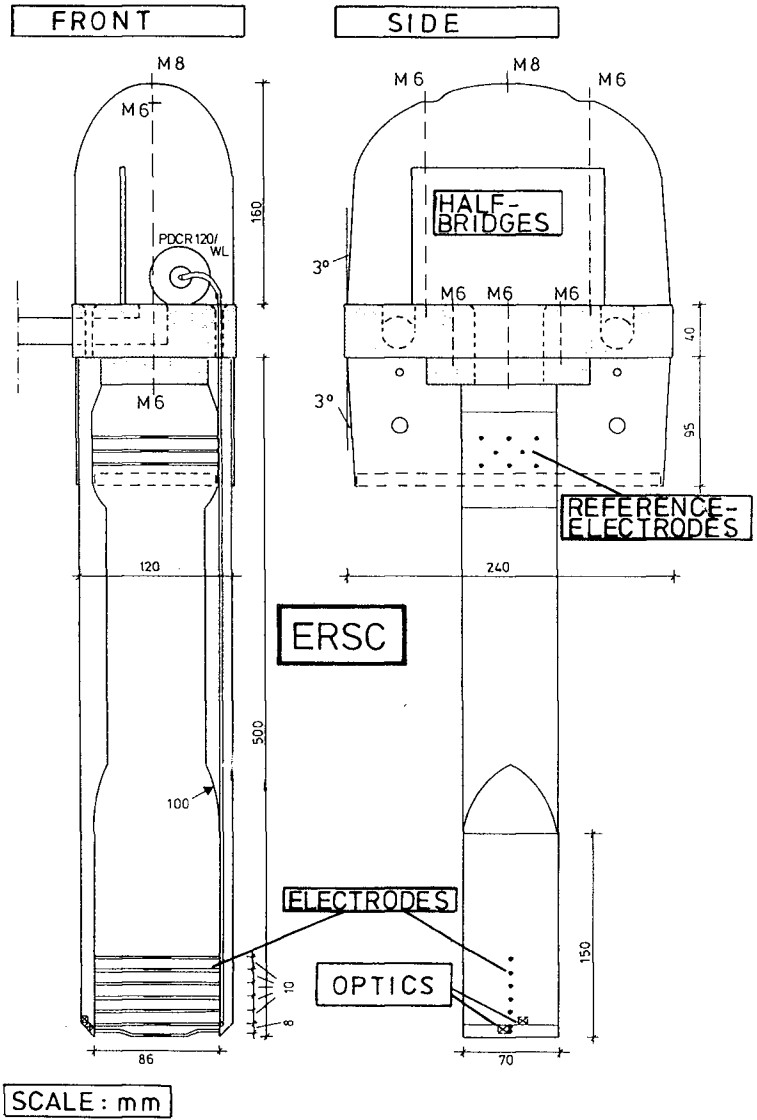


Figure 4. Sketch of the ERSC-GWK-probe

3. INVESTIGATION IN PROTOTYPE SCALE

3.1 TEST SECTION IN THE GWK

The investigations in August and September 1989 were carried out in the GWK in Hannover, in which waves of the size up to 1.8 m were generated.

A sand bed of 0.5 m thickness was installed in the flume extending 40 m in both directions of the test section (110 m from the wave generator). The transition to the concrete of the wave flume floor was at an initial slope of 1 to 40 (Fig. 5).

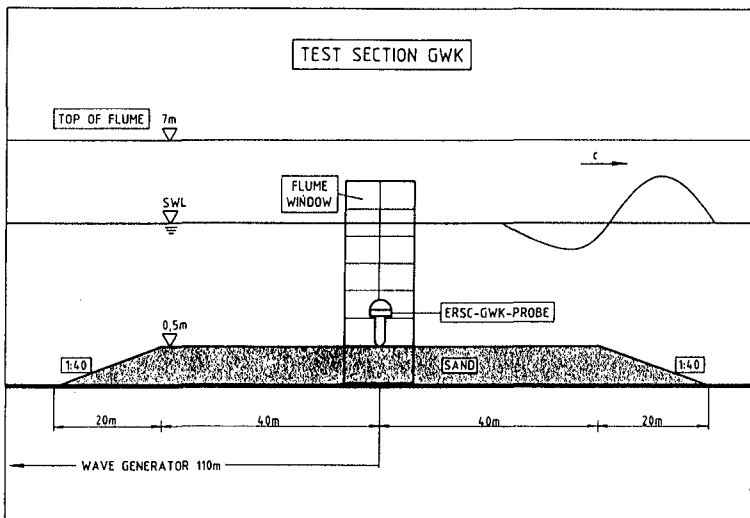


Figure 5. Test section in the GWK (not scaled)

3.2 USED SAND

About 250 m³ of sand was used, originating from the west coast of the island Norderney. It had the following parameters:

$$D_{50} = 220 \mu\text{m}, \sigma_g = 1.48, w = 0.0284 \text{ m/s}$$

where σ_g is the geometric standard deviation and w the mean fall velocity of sand at 18 °C.

The wave-induced packed sand below water had the mean dry density of 1708 g/l. With this value the relative concentration was calculated in g/l. The band width of error from five density samples was about ± 1 %.

3.3 CALIBRATION

The ERSC-Probe was calibrated for the limiting conditions: clear water and wave-induced packed sand. The signals from the ERSC-Probe were registered before each test series first in clear water. Then the probe was covered with sand and consolidated by 100 monochromatic waves of 0.3 m wave height. This procedure was repeated three times and results were compared.

The mean scatter from one calibration of ERSC II, III and IV yielded 0.5 % for the water and 2.6 % for the sand in terms of the full measuring-range of each electrode.

The mean standard deviation of the water values yielded 21 mV (mean value: 171 mV; deviation: 12 %), the standard deviation of the sand values yielded 97 mV (mean value: 6111 mV; deviation: 2 %).

Since at times at control after an experiment the water value changed from test to test, the assumption was made, that the thin wires were deformed by larger shells or stones, enclosed in the natural sand. Therefore only a limited number of tests could be analysed for sediment concentration, those for which also the limiting conditions were registered and the band width of error could be decreased.

3.4 ANALYSIS OF TIME SEQUENCES

The analysis of orbital velocity, near-bottom sediment concentration and bottom elevation was aimed at the interaction during single waves as well as a sequence of waves.

The experiments were run with monochromatic waves as well as wave-spectra. The water depth was varied from $d = 4.5$ m to $d = 3.5$ m above the horizontal sand bottom. The oscillating velocity 0.1 m above the initial sand bed was measured up to $u_{max} = 1.3$ m/s. In the following some selected results are presented.

Fig. 6 illustrates a 20 s sequence of waves showing instantaneous wave height, orbital velocity and sediment concentration from the test at the GWK.

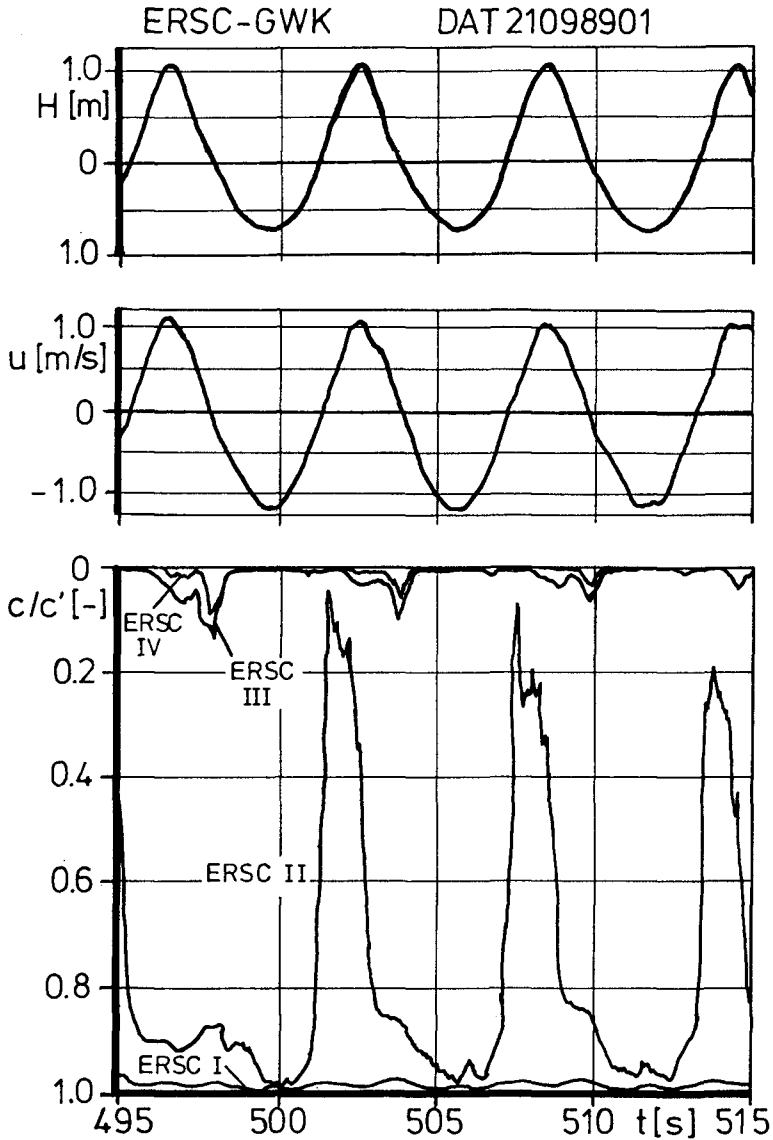


Figure 6. Wave sequence of the ERSC-GWK-probe at large scale conditions (21.09.89/01, 495 s to 515 s)

The ERSC-GWK-probe shows concentration signals from 4 electrodes ranging from high concentration near the bottom electrode and clear water ($c/c'=0$) at the electrode 4 cm above. The wave conditions were:

Monochromatic waves, $H = 1.8$ m, $T = 6$ s, $d = 4.5$ m

at water temperature $T_w = 19.1$ °C.

The results illustrate the highly time-dependent sediment concentration about 1 cm above the sand bed (from $c/c'=0.05$ to 0.95) and the phase-shift between the concentration maxima at different levels (about 2.5 s) as well as orbital velocity 10 cm above the bed

($u_{max} = 1.25$ m/s at wave trough).

The orbital velocities measured were in the range of sheet-flow-conditions indicated for the sand used and an horizontal bed. The actual bed showed formations with mean λ / d -values of about 0.05 ($\lambda = 0.1$ m, $d = 1.9$ m). This could be the reason why the sediment concentration has not the same phase as the oscillating velocity.

The wave conditions for the measurement, shown in Fig. 7, were:

Monochromatic waves, $H = 1.15$ m, $T = 6$ s, $d = 4.0$ m

The maximum orbital velocity was recorded at $u_{max} = 1.0$ m/s and $T_w = 19.2$ °C.

Noticeable during this sequence was the stepwise up and down movement of the probe. From observations at the window of the flume the position of the probe before test run was on the face (Luff) of a flat dune ($\lambda = 0.14$ m, $d = 1.1$ m); additionally sheet-flow conditions were possible (ALLEN, 1984). The upwards movement of about 1 mm was recorded 0.7 s after the start of the return current at $u_{mean} = 0.5$ m/s. The downwards movements were in the range of 1 to 4 mm, mean value 2.4 mm, at return current of $u_{mean} = 0.9$ m/s, at $t_{mean} = 1.7$ s after the maximum velocity below the wave trough.

The maximum of the sediment concentration was measured about 0.5 s after the wave crest, about 0.4 s after the maximum of orbital velocity. A phase shift between the recorded signals of the three wires is not indicated at every wave.

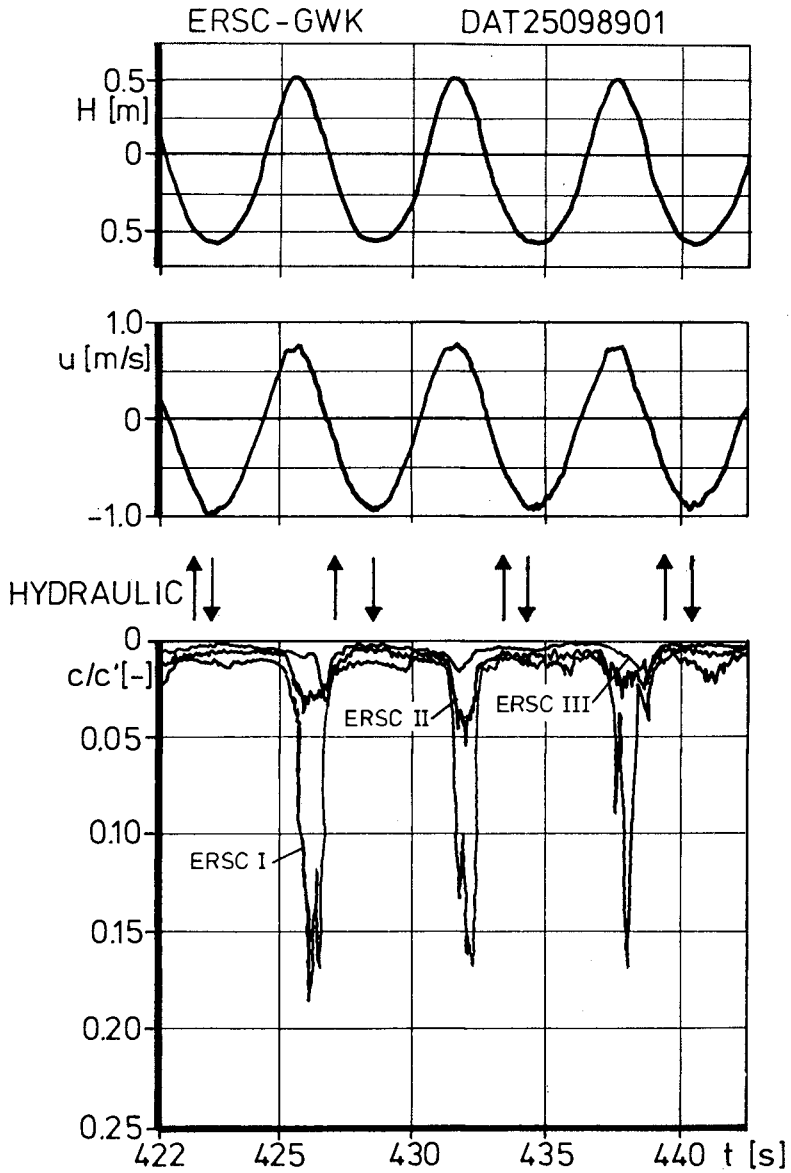


Figure 7. Wave sequence of the ERSC-GWK-probe at large scale conditions (25.09.89/01, 422 s to 442 s)

3.5 SINGLE WAVE ANALYSIS

One single wave will be presented from the monochromatic wave series. The wave was divided in 9 steps, corresponded with $\pi/4$.

Fig. 8 shows the phase dependent sediment transport after about 0.8 s due to:

Monochromatic waves, $H = 1.8 \text{ m}$, $T = 6 \text{ s}$, $d = 4.5 \text{ m}$.

At the right top corner the instantaneous phase - here phase 1 - was plotted. Below from left the measured orbital velocity, the sediment concentration and the calculated sediment transport is shown. The minus values of the orbital velocity stand for return current below the wave trough.

The near bottom orbital velocity was calculated from a simple parabolic distribution from the lowest current meter down to the instantaneous bed. The instantaneous sediment transport was calculated from the time dependent orbital velocity times the instantaneous sediment concentration.

Fig. 9 demonstrates the phase dependent sediment transport during this single wave.

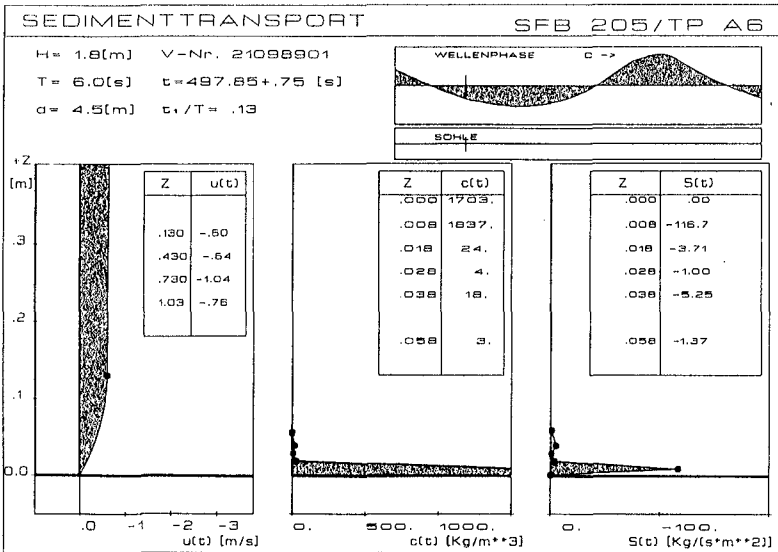


Figure 8. Example of phase dependent sediment transport after about 0.8 s ($H = 1.8 \text{ m}$, $T = 6 \text{ s}$, $d = 4.5 \text{ m}$)

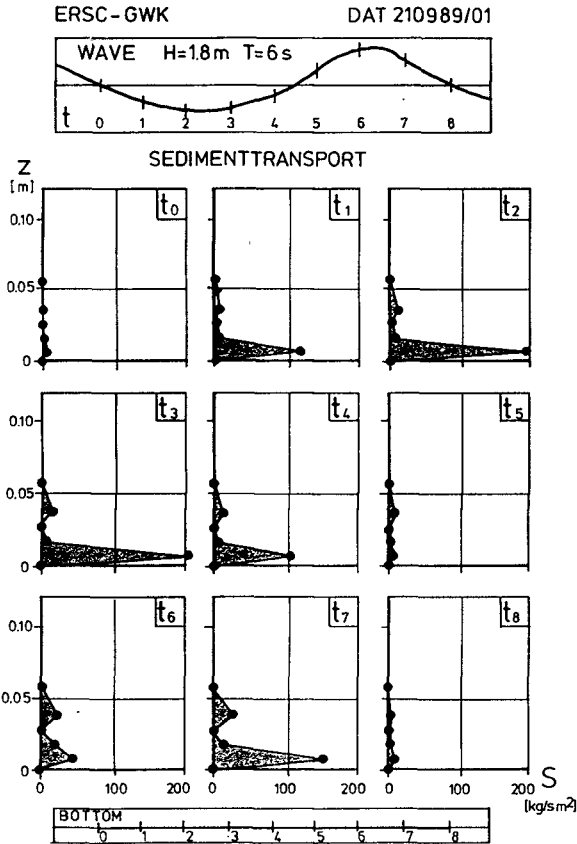


Figure 9. Phase dependent sediment transport due to wave action (Monochromatic waves, $H=1.8\text{ m}$, $T=6\text{ s}$, $d=4.5\text{ m}$)

During this wave no vertical movement of the ERSC-probe was recorded. The maximum sediment transport rate was calculated to about $200\text{ kg/s}\cdot\text{m}^2$ at phase no.3, 2.2 s after wave start. About 10 cm above the bed the orbital velocity was 1 m/s . These should be sheet-flow-conditions.

It is open to discussion, whether the very high sediment transport was affected by sheet-flow or resulted from the multiplication of the sediment concentration with the assumed parabolic distribution of the velocity. After 0.8 s , phase no.4, the velocity as well as the sediment transport was reduced to half.

The zigzag distribution above ERSC III points to sediment transport in clouds and whirls.

4. CONCLUSIONS

Experiments were run in the Large Wave Flume (GWK) in Hannover with the aim of obtaining data on wave-induced instantaneous sediment concentrations. The measurements were made with an electro-resistance-type-sediment-concentration-probe (ERSC-GWK-probe). The data presented illustrate features of time dependent sediment concentrations under waves, particularly the instantaneous values and their phase dependency. Likewise problems which arose during the calibration, the measurement as well as the analysis have been indicated. The results were sufficiently encouraging and warranted the continuing development of the ERSC-probe as a means of measurement of instantaneous sediment concentrations under wave actions. The probe is still under development at the Leichtweiss-Institute in Braunschweig.

5. ACKNOWLEDGEMENTS

The investigations were carried out as part of basic research in connection with prototype experiments on dune and beach erosion at the GWK within the research project "A6" of the "Sonderforschungsbereich 205" : "Interaction between foreshore and coastal structures". The funding by the German Research Foundation ("Deutsche Forschungsgemeinschaft") is gratefully acknowledged. The ERSC-probes were developed at the Leichtweiss-Institute of the Technical University of Braunschweig. The author like to express his sincere thanks also to Professor Dr.-Ing. E.h. A.J. RAUDKIVI, University of Auckland, and Dr.-Ing. H.-H. DETTE, Leichtweiss-Institute for their generous support and their stimulating remarks during the preparations of the investigations.

6. REFERENCES

- ALLEN, J.R.L. (1984). Sedimentary Structures: Their Character and Physical Basis, Vol. 1., Developments in Sedimentology, Elsevier Scientific Publishing Company.
- HORIKAWA, K. et al. (1982). Sediment Transport under Sheet Flow Condition. Proc. 18th Int. Conf. on Coastal Engineering, Kapstadt.

CHAPTER 201

UNDERGROUND WATER TABLE AND BEACH FACE EROSION

MICHIO SATO¹

Abstract

Numerical results show that the beach face of a tidal beach could be considered erosive due to the action of the surface flow formed by the escape of groundwater unless the action of moderate accretive waves, and that the effect will be intensified when the mean level of water table is higher than the mean sea level. Experimental results show that waves act to conceal the effect on the whole. These results suggest that the action of accretive waves are indispensable to maintain a tidal beach in an equilibrium condition. They also suggest that the cause of erosions of Surigahama beach and Iso beach was accumulative workings of the surface flow and insufficient wave action for the restoration during high tides.

Introduction

Field measurements of underground water table at Surigahama beach and Iso beach of Japan showed that the mean level of the watertable was higher than the mean sea level, and suggested that beach face erosion of the beaches was caused by the surface flow on the beach formed by the efflux of underground water. Another feature common to the beaches was that waves acting on these beaches are small all year around.

Previous researchers have considered about the effects of watertable and tidal cycle on changes in equilibrium beaches. Emery and Foster (1948), and

¹Professor, Department of Ocean Civil Engineering, Kagoshima University, 1-21-40 Korimoto, Kagoshimashi, 890 JAPAN

Grant (1948) found that groundwater escaping to the surface of the foreshore during a low tide contribute to the sorting through elutriating silt from the beach, and the running water cut small streams known as rill marks. They also noted that the water enhances erosion of beach face through not only increasing velocity and depth of backwash flow by adding to the backwash but dilating the sand. And conversely, during a high tide, a low water table may result in pronounced aggradation of the foreshore (Grant,1948). Therefore, we may expect that eroded beach face during a low tide will restore during a high tide in usual states unless erosive storm waves act.

Minute changes in foreshore during tidal cycles were discussed by Duncan (1964), Otvos (1965), Strahler (1966), Schwartz (1969) and Hurrison (1969) based on their own field observation.

In this study, a little different situation in that mean level of water table is higher than mean sea level is considered in association with erosions of beach face at Surigahama beach and Iso beach. Firstly, the erosions of foreshore at Surigahama and Iso beach are outlined. Then, thin flow on a beach face, formed by the efflux of underground water from the beach face, and beach materials which were washed away are discussed based on a numerical model. Lastly, the role of waves in the profile change of a beach where there is an inclined water table is considered based on some experimental results.

Field Measurements

Surigahama beach is famous for natural sandsteam baths and is one of the main features of a well-known hot spring town, Ibusuki. The beach is a small part of the Ibusuki coast, and is located on Kagoshima bay, Kagoshima Prefecture, Japan (Figure 1).

In 1951, a big typhoon struck the coast and caused heavy erosion. The shoreline is said to have retreated up to one hundred meters. Although most parts of the coast gradually recovered beaches from the erosion, the Surigahama beach did not restore at all.

As the beach is one of the important tourist attractions, many different measures, such as seawalls, jetties, detached breakwater and the like, have been tried to preserve the small beach area since 1950's (Figure 2). The beach is now surrounded by concrete structures.

According to Sunamura (1980), $C=18$ defined by the following relationship demarcates erosion and accretion of natural beaches.

$$\frac{H_0}{L_0} = C(\tan\beta)^{-0.27} \left(\frac{D}{L_0}\right)^{0.67} \quad (1)$$

where H_0 is deep water wave height, L_0 is deep water wave length, $\tan\beta$ is average nearshore bottom slope to a depth of 20m.

Long term measured wave data was not available. But, waves had been hindcasted for the period from 1971 to 1975. And we conducted wave measurement for 16 days using three capacitance type wave gauges in 1978 (Figure 3). These results showed that 80 percents of the significant wave heights were smaller than 0.2m and 80 percent of the wave periods were between 2 and 4 seconds. They also showed that the probability of wave heights exceeding 1m is one percent. On the otherhand, the erosive wave height is estimated to be over 1.2m from the above relationship. Therefore, this beach may be taken to

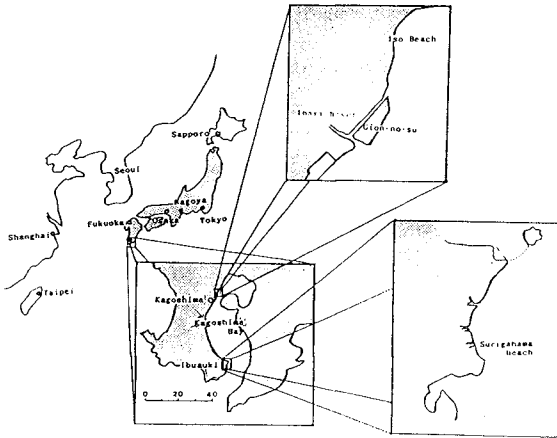


Figure 1. Location Map

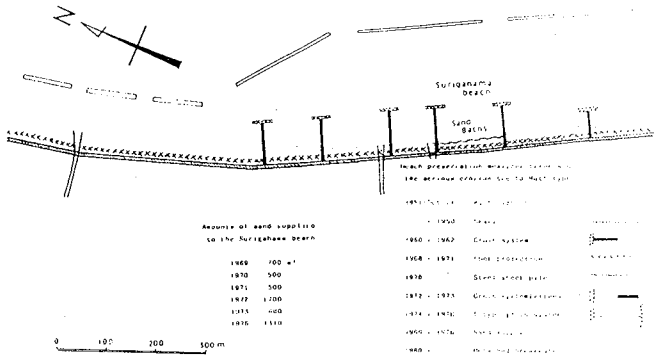


Figure 2. Measures taken since Ruth typhoon

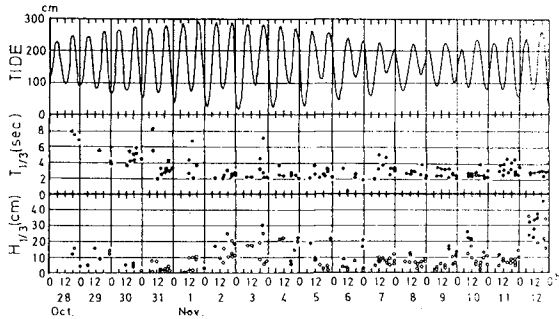


Figure 3. Results of wave measurements

be accretive. However, in spite of the great effort for many years to preserve the beach, it still needs artificial nourishment work.

A condition unique to the beach is the existence of hot springs underneath it. Besides, the range of spring tide is about 2.8m. Paying attention to these facts, we conducted a field measurement of the watertable under the beach.

In order to measure the level of water table, 18 pipes 3m long were driven into the sand. The inside diameter of each pipe was 40 mm. All of the measurements were repeated at half-hour intervals during the period between 9 and 13 of December, 1981.

Figure 4 is the contours of mean level of the water table and shows that the mean level of the water table is higher than the mean sea level. Figure 5 shows the water table at low tide. As the tide falls, underground water began to seep to the foreshore surface and cut meandering channels as shown in Figure 6. The temperature of underground water measured at the same time varied from 40 degree C to 80 degree C according to the tide. The high temperature reduces viscosity of the water and increases the permeability up to the double of the value under normal condition.

Iso beach is a similar example in that the mean water table is higher than the mean sea level. This is due to the topographical reason that there is a hilly area close to the beach (Figure 7). The beach is located about forty kilometers north from Surigahama beach and also on Kagoshima bay.

It had been nourished with the sediments supplied from the Inari river several kilometers south of the beach until the land between the river and the beach was reclaimed. The reclaimed land began to block the longshore sediment transport from the river to the beach, as did the highly developed waves from the south. Since the reclamation, Iso beach has been nourished artificially by supplying sand. Waves acting on this beach are smaller than the ones acting on Surigahama beach on the average throughout the year.

Measurements of the profile changes of the water table transverse to the shore line in respond to the changing tide level were made at one hour interval in September, 1982. We can see that the mean level of the water table is higher than the mean sea level from the results shown in Figure 8.

From the above mentioned observations, it is necessary for us to take the effects of difference between mean water table and mean sea level on beach face erosion into account so that we could plan more effective measures for the situation under consideration.

Numerical model

Though coastal aquifers often contain two fluids, freshwater and saltwater, for simplicity we consider only single fluid. Assuming two dimensional motion of underground water, the following equations were used for the analysis of the water table.

$$k \left(\frac{\partial^2 h}{\partial x^2} + \frac{\partial^2 h}{\partial y^2} \right) = S_s \frac{\partial h}{\partial t} \quad (2)$$

$$h = y + \frac{p}{\rho g} \quad (3)$$

Figure 4. Contours of mean level of groundwater table

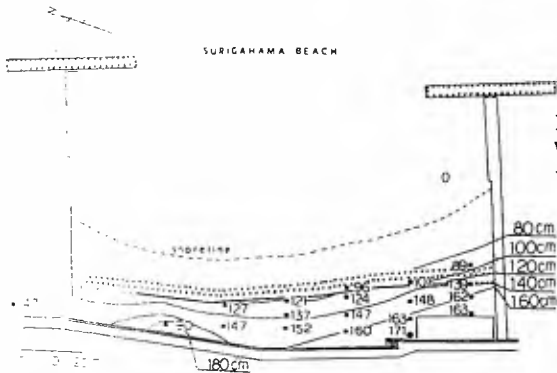
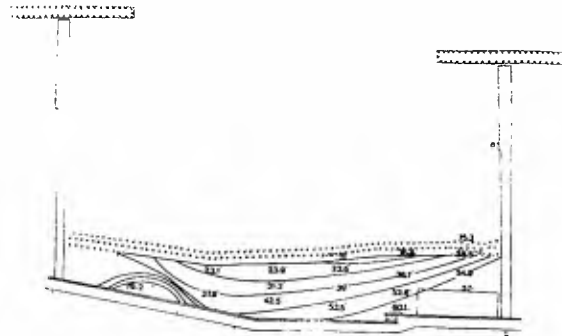
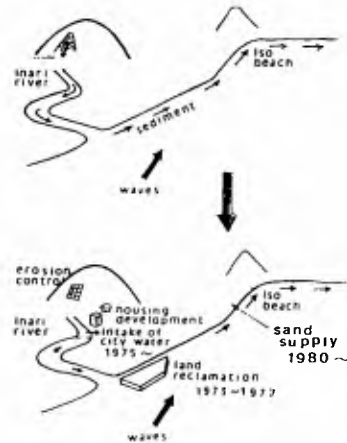


Figure 5. Contours of Water table at low tide

Figure 6. Beach face cut by surface flows



Figure 7. Changes of the area around Iso beach



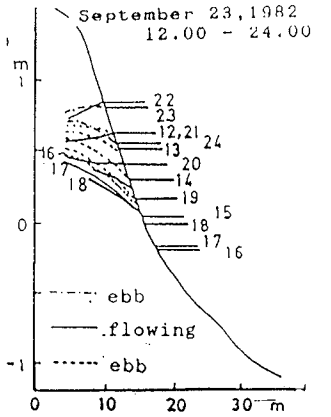
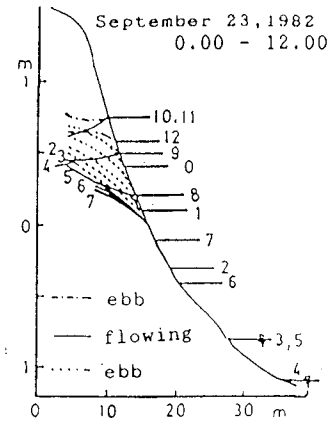


Figure 8. Measurements of water table at Iso beach
H = 13.5 m

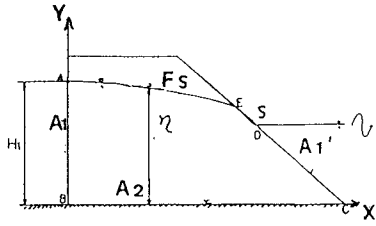


Figure 9. Definition sketch

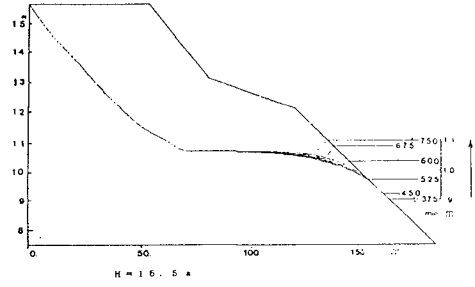
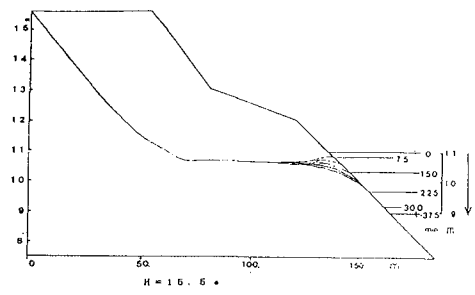


Figure 10. Numerical results of water table
H = 16.5 m

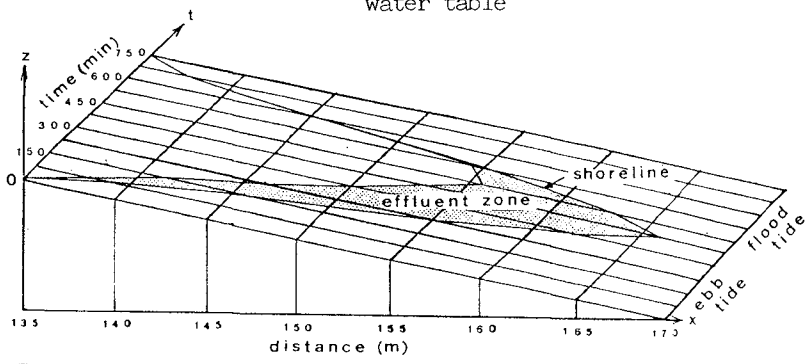


Figure 11. Tide cycle change of effluent zone

$$u = -\frac{\partial h}{\partial x}, \quad v = -\frac{\partial h}{\partial y} \quad (4)$$

where S_s is specific storage, h is the elevation of water table from the sea level, and k is the coefficient of permeability. The positive x-axis and y-axis point seaward and upward respectively.

Initial conditions are specified by prescribed functions for water table and head as

$$h(x, y, 0) = h_0(x, y) \quad (5)$$

$$\eta(x, t) = \eta_0(x) \quad (6)$$

The boundary condition on the left boundary A1 is

$$h(x, y, t) = H = \text{constant} \quad (7)$$

and on the boundary A1'

$$h(x, y, t) = H(t) \quad (8)$$

where $H(t)$ is the sea water level and assumed to vary sinusodally with the period of 12.5 hours and the amplitude of 1 meter.

On the bottom of the aquifer, the boundary condition for a prescribed flux is given by

$$k \left(\frac{\partial h}{\partial x} l_x + \frac{\partial h}{\partial y} l_y \right) = -V \quad (9)$$

where V is the velocity of drain from the bottom and taken positive downward, (l_x, l_y) is a unit vector normal to the boundary. In the following model, we put V equal to zero. On the free surface, two conditions must be satisfied

$$\eta(x, t) = h(x, y, t) \quad (10)$$

$$k \left(\frac{\partial h}{\partial x} l_x + \frac{\partial h}{\partial y} l_y \right) = S_y \frac{\partial h}{\partial t} \quad (11)$$

where S_y is the storage coefficient. The boundary condition for the seepage surface, along S , is

$$h = y \quad (12)$$

Introducing the variational principles, the functional χ of a minimizing function h is

$$\chi(h) = \int_R \left[\frac{k}{2} \left\{ \left(\frac{\partial h}{\partial x} \right)^2 + \left(\frac{\partial h}{\partial y} \right)^2 \right\} + S_s \frac{\partial h}{\partial t} \right] dR + \int_{A_2} V h dA_2 + \int_{F_s} S_y \frac{\partial h}{\partial t} l_y h dF_s \quad (13)$$

The finite element method based on the Rayleigh-Ritz method was used to obtain the head h from equation (13). The temporal change of the watertable h was obtained by using finite difference method.

The computation program was checked by comparing with an existing theoretical result and an experimental result obtained by the equipment described later.

As any detailed data on the aquifer were not available, we adjusted parameters so that the computation results satisfied the data of the elevation of ground water obtained from two wells, an old well about 140m from the beach and an observational well on the beach.

The results of the profile of the water table are shown in Figure 10. From this result we can see the temporal variation of the effluent zone as shown in Figure 11. The efflux from the beach face forms a thin surface flow. We attempted to investigate the natures of the flow two dimensionally neglecting the three dimensional characters for simplicity. The surface flow was analysed based on equation(14), and the depth averaged mean velocity was obtained. The derivation of the equation is given in Appendix.

$$\frac{dd}{dx} = \frac{i - \frac{q^2}{c^2 d^3} + \frac{H w_b}{q} - \frac{q w_b}{g d^2}}{1 - \frac{q^2}{g d^3}} \quad (14)$$

where i is the slope of the beach, d is the depth of the surface flow, w_b is the velocity of the efflux at the beach face, H is the elevation of the free surface of the flow measured from a datum, c is Chezy constant, g is the acceleration of gravity, and $q = \int_0^x w_b dx$. In this equation, the positive x-axis points downstream along the beach surface.

The results are shown in Figure 13. The calculated depth increases approximately linearly to the downstream of the flow and the maximum depth at the downstream end is small and less than 1cm. The calculated velocity of the flow is shown in Figure 14. The result shows that the velocity is about 14cm/sec and almost constant from the upper end to the downstream end except the flow after 150 minutes from the highest tide. The efflux from the beach face increases the depth. However, it does not accelerate the flow in this case.

When the velocity exceeds a threshold of sediment movement, the beach materials are washed away by the flow from the beach face. And this threshold was estimated to be 1.74cm/sec. Therefore, the whole flow has enough intensity to erode the beach face.

In order to contrast these results with the case in which there is no difference between the mean level of water table and mean sea level, similar computations were made. The results are shown in Figures 15, 16 and 17. In this case, the area of the effluent zone becomes a little smaller. However, these results show that the beach face will be eroded by the flow formed on it even if mean level of water is equal to mean sea level. And, in order for a tidal beach to be maintained in a equilibrium condition, the action of the changing tide must be canceled, or the beach must be restored during high tide, by the action of waves.

Figure 18 is the measured results of the effluent zone. This shows that the upper limit of the effluent zone does not become lower in comparison with the numerical result. And the length becomes double of the calculated value. We are not certain about the reason of this discrepancy. In any case, this result

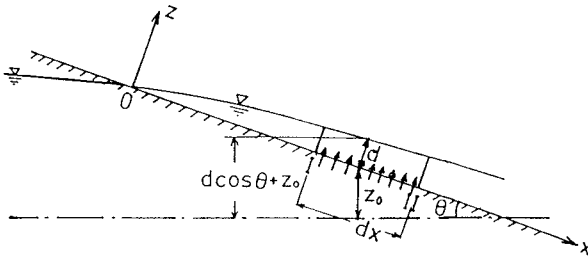


Figure 12. Definition sketch of surface flow

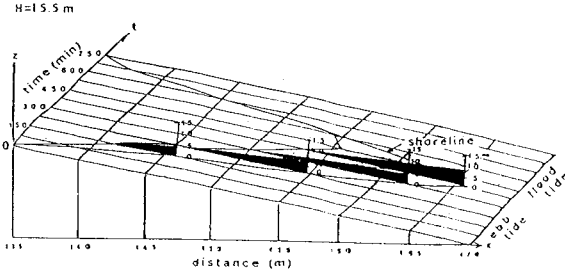


Figure 13. Change of thickness of surface flow

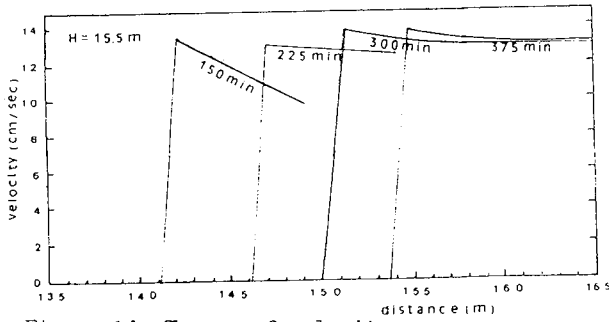


Figure 14. Change of velocity

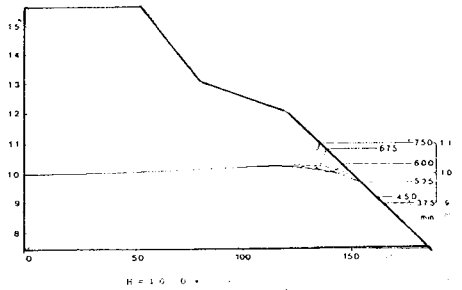


Figure 15. Numerical Result of water table

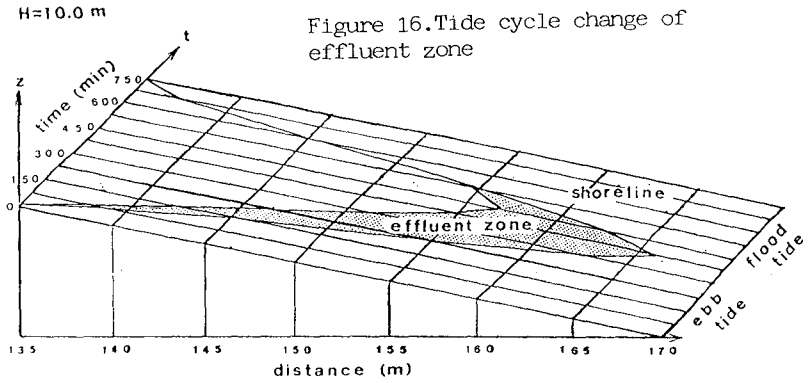


Figure 17. Change of thickness of surface flow and the velocity

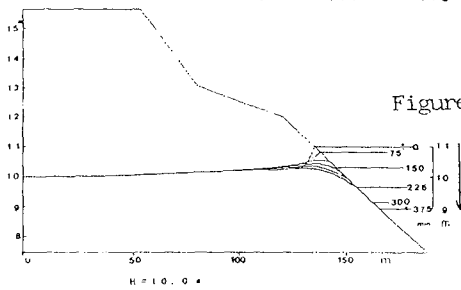
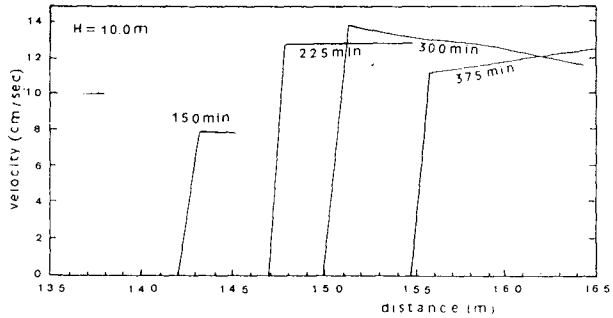
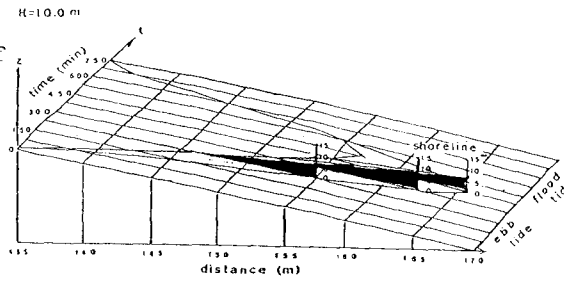


Figure 15. Numerical result of water table

shows that the erosion due to the surface flow will be enhanced as the mean level of landward water table becomes higher than sea level.

Experiments

In order to investigate two dimensional beach profile change due to waves under the situation where there is an inclined water table, some experimental studies were carried out. The main purpose of these experiments was to know the roles of waves acting on a tidal beach rather than to do model experiments of a special beach.

A wave channel of 13 m long, 0.4m wide and 0.4m deep was used (Figure 19). Three types of model beach with 1/10 slope were installed at the end of the channel. The grain sizes of the beaches were 0.2mm, 0.7mm and 0.7mm+0.2mm (2cm thick) respectively. The water level behind the beach model was adjusted to be +20cm, 10cm, 0cm, -10cm, -20cm higher than the sea level. Water levels were measured by using 10 manometers which were connected with the bottom of the model beach through porous stones. Beach profiles were measured at 0.5, 1, 2, 4 and 8 hours after waves began to act. Final beach profiles for all runs are shown in Figure 20. Solid line and dashed line inside the beach denote water tables under the action of waves and without it respectively. We expected a little different beach profile changes for a different condition of water table even if the wave conditions were the same, considering the importance of the water table characteristics pointed out by Harrison (1969) as that no laboratory experiment on beach formation would adequately model a natural beach unless provisions for simulation of them were included. Results did not show a remarkable difference of beach profile change due to the existence of the gradient of the watertable. Waves have a tendency to reduce the gradient of water table when the water level behind the beach is higher than the sea level, and this will weaken the efflux of the groundwater from the beach face. This is due to the effect of wave setup and infiltration of swash. When the water level behind the beach is lower than the sea level, the gradient becomes steeper and this will increase the subtraction of water from the backwash. However, these effects were too small to result in a remarkable difference of the beach profile change and waves acting on the beach concealed the effects as far as our experimental results were concerned.

Conclusion

Numerical model showed that tidal beaches could be considered to be erosive due to the flow formed on the beach surface whether or not the mean level of water table was higher than mean sea level without waves. When the mean level of water table is high, the effect will be intensified. However, when waves act on a beach, it is deduced from the experiments that waves act to conceal the effect on the whole. Therefore, moderate accretive waves are indispensable to preserve a beach in an equilibrium condition.

Judging from these results, the erosion of Surigahama and Iso beaches may be concluded to be caused by accumulative workings of surface flow. The surface flow is formed on the beach face by the efflux of underground water which washes the beach materials away, and small waves are insufficient for the recovery. Therefore, measures for beach erosion due to heavy wave attacks, some of which

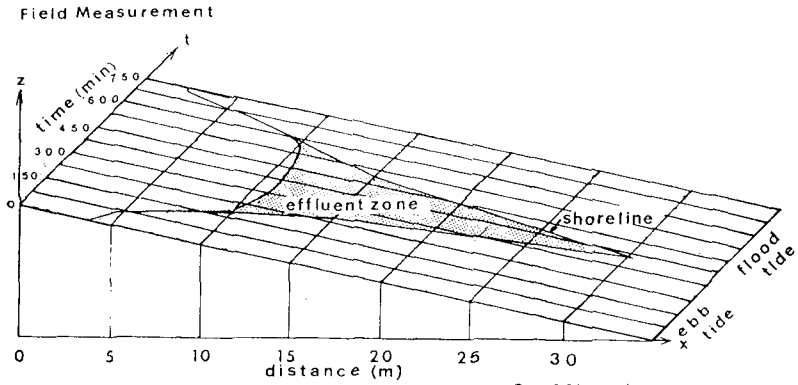


Figure 18. Measured tide cycle change of effluent zone

Figure 19. Experimental equipment

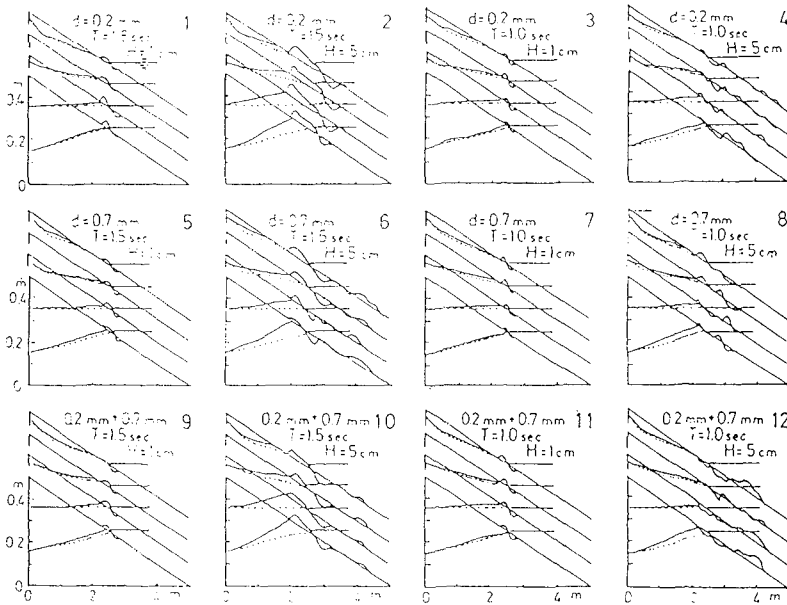
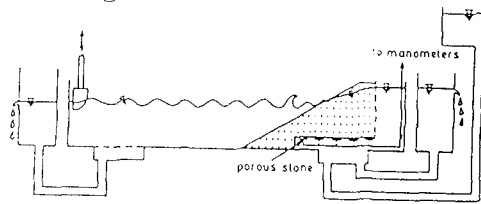


Figure 20. Experimental results of beach profile change

have been adopted at Surigahama beach, will not be effective for the cases considered.

Acknowledgements

The author would like to express his thanks to Mr. K. Nishihara and Mr.K.Byoga, who were students of Kagoshima University, for their assistance in computation and field experiments in the course of the study.

References

- Duncan, J.R.,1964. The effects of water table and tide cycle on swash-backwash sediment distribution and beach profile development, *Mar.Geol.*,2:186-197
- Emery, K.O. and J.F.Foster.,1948. Water table in beaches, *J.Mar.Res.*,7(3): 644-654
- Grant, U.S.,1948. Influence of the water table on beach aggradation and degradation, *J. Mar. Res.*,7(3): 655-660
- Harrison,W.,1969. Empirical equations for foreshore changes over a tidal cycle, *Mar.Geol.*,7:529-551
- Otvos, E.G.,1965. Sedimentation-erosion cycles of single tidal periods on Long Island Sound Beaches, *J. Sedimentary Petrology*,35(3):604-609
- Schwartz, M.L.,1967. Littoral zone tidal-cycle sedimentation, *J.Sedimentary Petrology*,37(2):677-709
- Strahler, A.N.,1966. Tidal cycle of change in an equilibrium beach, Sandy Hook, New Jersey, *J.of Geology*,74: 247-268
- Sunamura, T.,1980. Parameters for delimiting erosion and accretion of natural beaches. Annual Report, Inst. Geosci., Univ.Tukuba,6: 51-54

Appendix

Multiplying velocity component v_i ($i = 1, 2, 3$) and Reynolds equation for each component for incompressive steady flow and adding them, following expression is obtained.

$$v_i \frac{\partial E}{\partial x_j} = v_i \frac{\partial \tau_{ij}}{\partial x_j} \quad (A1)$$

$$E = \frac{\rho}{2} \overline{q^2} + \rho \Omega + p, \quad \overline{q^2} = \sum_{i=1}^3 v_i^2 \quad (A2)$$

where τ_{ij} is Reynolds stress tensor, p is pressure and Ω is given by (see Figure 12)

$$\Omega = g(Z_0 + Z \cos \theta), \quad Z_0 = (x_0 - x) \sin \theta \quad (A3)$$

Integrating equation (A1) from section I to section II, using Divergence Theorem and adopting conventional assumptions for slowly varied one dimensional flow, we obtain the following equation.

$$\int \int_S E v_n dS = - \int \int \int_V (-\rho \overline{u'v'}) \frac{\partial u}{\partial z} dV \quad (A4)$$

where S and V denote the surface area and the volume of the domain of the integration, respectively. Using w_b , left-hand side of this equation becomes

$$\int_0^{d_1} Eudz - \int_0^{d_1} Eudz - E_b w_b dx$$

On the other hand, using mean-value theorem for integral, right-hand side becomes

$$\left\{ \int \int_A (-\rho \overline{u'v'}) \frac{\partial u}{\partial z} dA \right\}_{x+\theta dx} dx, \quad (0 < \theta < 1)$$

where A denotes the area of the cross-section of the flow. Assuming that the depth is small compared with the width, we consider unit width of the flow. Substituting above expressions into equation (A4) and dividing it by dx , the following equation is obtained in the limit of $dx \rightarrow 0$.

$$\frac{d}{dx} \int_0^d Eudz = E_b w_b - \int_0^d (-\rho \overline{u'v'}) \frac{\partial u}{\partial z} dz \tag{A5}$$

As $p = \rho g(d - z) \cos \theta$, $E_b w_b$ in the right-hand side becomes as follows

$$E_b w_b = \rho g(d \cos \theta + z_0) w_b$$

And left-hand side may be written as follows

$$\frac{d}{dx} \left\{ \alpha \frac{\rho}{2} q v^2 + \rho g(d \cos \theta + z_0) \right\}$$

where

$$q = \int_0^d u dz = vd, \quad \alpha = \frac{1}{qv^2} \int_0^d u^3 dz$$

Putting the head loss of the flow H_l as

$$\frac{dH_l}{dx} = \frac{1}{\rho g q} \int_0^d (-\rho \overline{u'v'}) \frac{\partial u}{\partial z} dz = f' \frac{1}{d} \frac{v^2}{2g}$$

We obtain the following expression for equation (A5).

$$\frac{d}{dx} \left(\frac{\alpha v^2}{2g} \right) = \frac{H w_b}{q} - f' \frac{1}{d} \frac{v^2}{2g} \tag{A6}$$

where $H = d \cos \theta + z_0$. From this equation, the following flow equation is obtained

$$\frac{dd}{dx} = \frac{\sin \theta - \frac{f' q^2}{2g d^3} + \frac{H w_b}{q} - \frac{q w_b}{g d^2}}{\cos \theta - \frac{q^2}{g d^3}} \tag{A7}$$

When we put $\cos \theta \approx 1$ and $\sin \theta \approx \tan \theta \approx i$ and use $\frac{2g}{f'}$ for friction factor f' , we obtain equation (14).

CHAPTER 202

A NUMERICAL MODEL FOR SAND TRANSPORT UNDER COMPOUND WAVES

Shinji Sato

Associate Professor, Civil Eng. Dept., Yokohama National Univ.
Tokiwadai, Hodogaya-ku, Yokohama 240, JAPAN

Norihiko Mitsunobu

Shizuoka Prefectural Government

1. INTRODUCTION

In order to understand sediment transport around various maritime structures, it is essential to elucidate the mechanism of sand transport under compound waves. Although numerous studies have been carried out on sand transport, most of them have been concentrated to the sand movement mechanism under one-component wave. Laboratory experiments and numerical modeling of sand movement under compound waves are required for better understanding sand transport due to three-dimensional waves.

The objectives of the present study are to describe sand transport mechanism under three-dimensional compound waves through laboratory experiments and to develop a numerical model to estimate the net sand transport rate under compound waves. As a simple example of compound wave field, we selected the wave field in front of a breakwater with obliquely incident waves. This is because under such conditions the water particle near the bottom moves in various orbits, from linear to elliptic or circular orbit, so that they cover a wide range of conditions encountered in general compound wave conditions.

2. EXPERIMENTS

Experiments were performed in a 9m by 9m wave basin. A breakwater model was installed in the wave basin obliquely to the direction of wave incidence as shown in Fig. 1. The angle α between the breakwater and the incident wave was varied to 30, 45 and 60 degrees. All the bed in the wave basin was fixed except in a tray

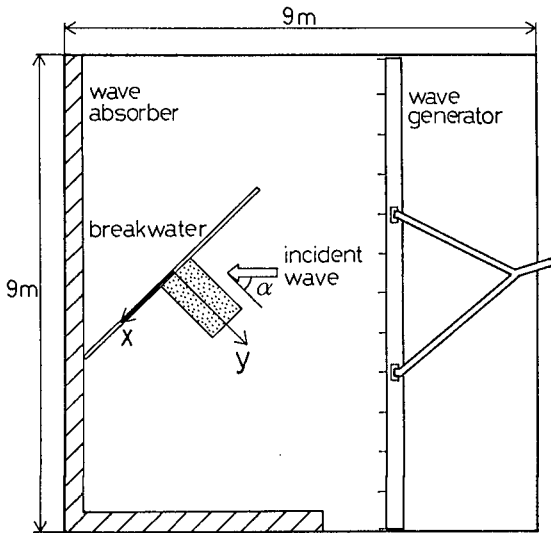


Fig. 1 Experimental setup.

installed in front of the breakwater. The tray was 120cm long, 40cm wide and 2cm deep. Well-sorted sand of median diameter $D = 0.16\text{mm}$ was filled in the tray to make an initially flat test bed. The depth in the wave basin was changed from 12 to 16cm. The period of incident waves was varied in a range from 0.65 to 1.41s. Thirty three runs of experiments were carried out for the condition of perfect reflection by changing the incident wave height so that experiments covered a wide range of conditions from weak sand movement to vigorous sand movement.

The reflection coefficient r of the breakwater was adjusted by changing the height of the top of the breakwater. Seventeen runs of experiments were performed for the condition of partial reflection by using a submerged breakwater model. The total number of experimental runs was 50.

The distribution of wave height was measured by capacitance-type wave gages. The variation of near-bottom velocities was measured by using a two-component electro-magnetic current meter. The sensor of the current meter shaped a cylinder of 1cm in diameter. The data were recorded on a magnetic tape through a personal computer system.

The development of sand ripples and the change of bottom profile in the test bed was measured in detail by vertically inserting a transparent film coated with grease oil. The sand surface level as well as the sand ripple geometry were evaluated from the trace of sand particles attached to the transparent film.

The test bed was divided into twelve parts and the sand in each part was collected separately after each run of experiments. The volume of sand was measured by using a mess-cylinder. The sand was repeatedly thrusted by a stick until it reached densely packed condition. The distribution of net sand transport rates in x (parallel to the breakwater) and y (perpendicular to the breakwater) directions were evaluated from the amount of the collected sand.

3. RESULTS OF EXPERIMENTS

3.1 Wave field and near-bottom velocities in front of a breakwater

Figure 2 shows an example of wave height distribution, bottom profile and net sand transport rates measured in front of a breakwater. The wave field was found to be calculated in a good accuracy by a third-order nonlinear wave theory (solid line) derived by Hsu *et al.* (1978). The net sand transport rate q_x parallel to the breakwater was found to be positive at nodes and negative at loops, which was also the case in most of the experimental runs.

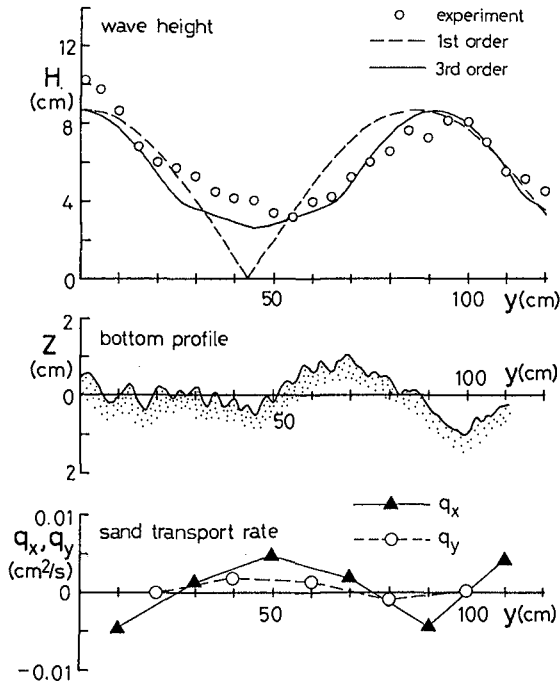


Fig. 2 Distributions of wave height, bottom profiles and net sand transport rates.

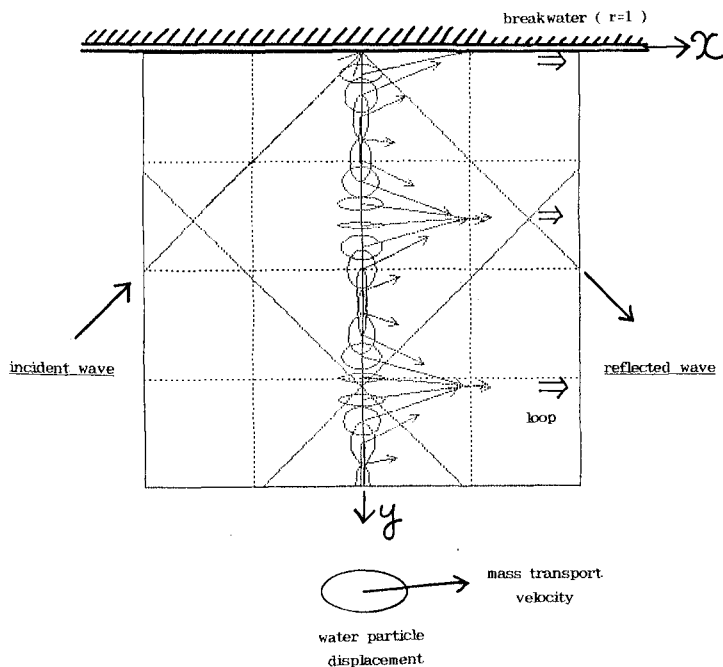


Fig. 3 Near-bottom velocity field in front of a breakwater.

Figure 3 shows the orbital motion due to waves as well as mass transport velocity in front of the breakwater with perfect reflection. The water particle near the bottom moves in circular, elliptic and linear orbit dependent on the distance from the breakwater. The nonlinear theory predicts that the wave orbital velocity becomes asymmetric in such a way that the velocity under wave crest is larger than that under wave trough. Measurements with an electro-magnetic current meter and dye injection supported the validity of the third-order wave theory in the estimation of the wave induced orbital velocity and the mass transport velocity.

3.2 Sand ripple geometry

Figure 4 shows sand ripple pattern observed in front of a breakwater. Three types of sand ripples were observed, that is, two-dimensional (2-D) ripples parallel to the breakwater, brick pattern ripples and 2-D ripples perpendicular to the breakwater.

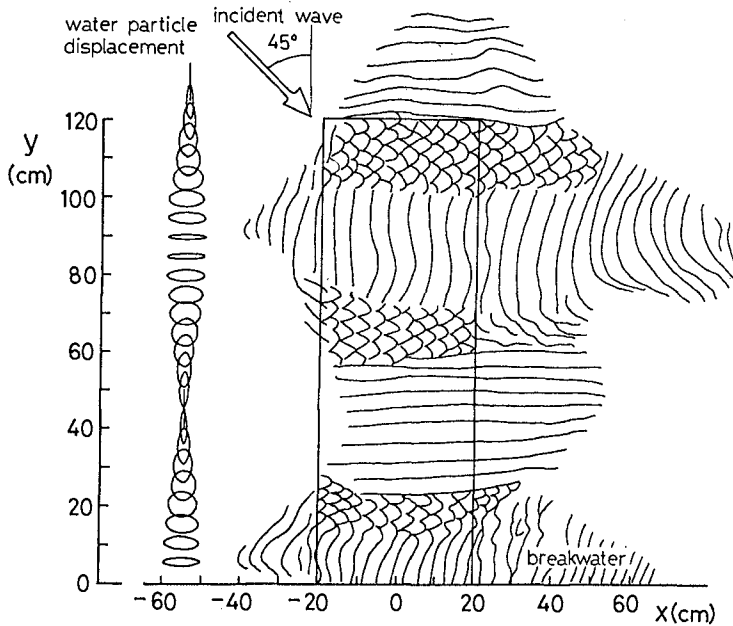


Fig. 4 Sand ripple pattern observed in front of a breakwater.

Figure 5 shows the classification of ripple patterns in terms of the Shields parameter Ψ and d_{oy}/d_{ox} , where d_{ox} and d_{oy} are diameters of water particle displacement in x and y directions. The Shields parameter was expressed by

$$\Psi = \frac{f_w u_m^2}{2sgD} \quad (1)$$

where $s(=1.65)$ was the specific gravity of sand particle in water, g the gravity acceleration, f_w the friction factor and u_m the maximum velocity near the bottom. The friction factor was estimated by using Jonsson's formula in terms of the maximum velocity and the diameter of near-bottom water particle displacement. The roughness element was assumed to be the diameter of the sand particle.

It was found that brick pattern ripples developed in the range

$$0.5 < d_{oy}/d_{ox} < 2 \quad (2)$$

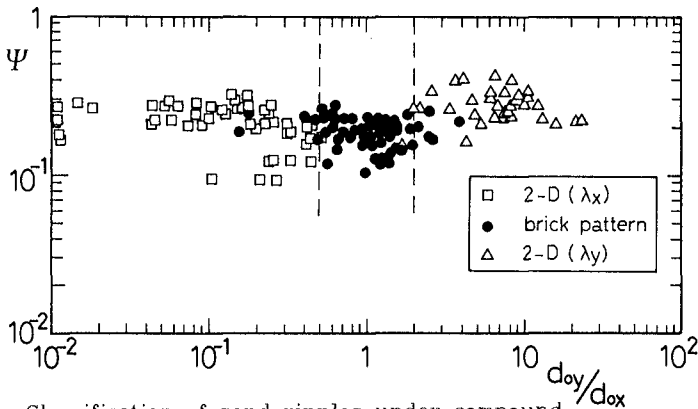


Fig. 5 Classification of sand ripples under compound waves.

and two-dimensional ripples developed for

$$d_{oy} / d_{ox} < 0.5 \text{ and } d_{oy} / d_{ox} > 2 \quad (3)$$

It was also found that the wavelength and wave height of sand ripples were able to be evaluated in terms of d_{ox} , d_{oy} and Ψ . The wavelengths λ_x and λ_y of sand ripples were found to be estimated by

$$\begin{aligned} \lambda_x &= 0.6 d_{ox} \\ \lambda_y &= 0.6 d_{oy} \end{aligned} \quad (4)$$

for both 2-D and brick pattern ripples. The ripple wave steepness was predicted by

$$\eta / \lambda = 0.15 \quad (5)$$

for 2-D ripples and

$$\eta / \lambda = 0.11 \quad (6)$$

for brick pattern ripples. These equations will be used in the numerical model to estimate sand ripple geometry.

3.3 Sand movement mechanism

Significant sand suspension was observed in most of experimental runs. The suspended sand concentration was observed to be determined by the asymmetry in the near-bottom velocity variation. The concentration was high under wave crests and low under wave trough since the velocity magnitude under wave crests was larger than that under wave trough in nonlinear wave field. The net direction of sand transport was determined by the balance between the transport due to the asymmetry in velocity variation and that due to the mass transport velocity.

Sand suspension was not significant in the area where brick pattern ripples were developed. The reason for this was considered that the maximum velocity was in general small over brick pattern ripples and that a strong vortex which contains a large amount of sand was not developed efficiently on the lee side of brick pattern ripples.

4. NUMERICAL MODEL

4.1 Sand entrainment at the ripple crest

In order to estimate the sand transport rate under compound waves, a numerical model was developed which evaluated the net sand transport rate above rippled bed by using near-bottom velocities calculated by the nonlinear wave theory. The outline of the model is schematically shown in Fig. 6.

Nielsen (1986) proposed on the basis of laboratory experiments a relation between the temporally-averaged sand concentration C_o at the bottom and the Shields parameter by

$$C_o = 0.005 \Psi_r^3 \tag{7}$$

where Ψ_r was the Shields parameter corrected by the flow acceleration at the ripple crest defined by

$$\Psi_r = \Psi / (1 - \pi \eta / \lambda)^2 \tag{8}$$

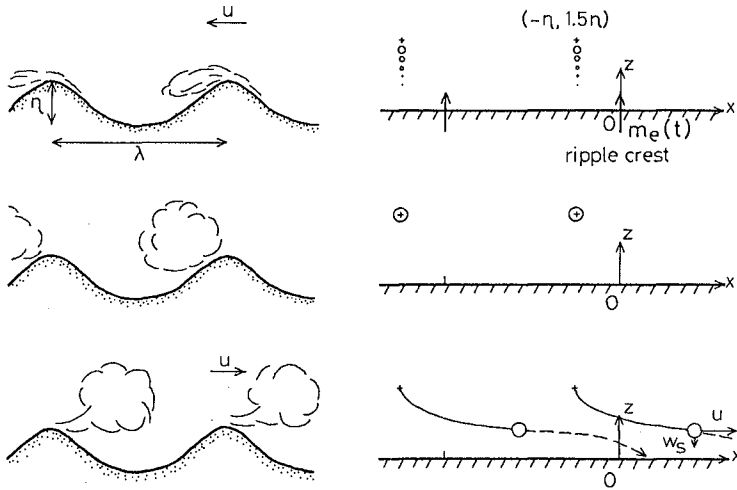


Fig. 6 Schematic diagram of the numerical model.

The rate $m_e(t)$ of the sand entrainment at ripple crests was assumed to be proportional to the third power of the instantaneous Shields parameter $\Psi_r(t)$ as,

$$m_e(t) = \alpha_c \Psi_r(t)^3 w_s \lambda \quad (9)$$

where w_s denotes the settling velocity of sand particles, λ the wavelength of ripples, α_c a nondimensional constant and $\Psi_r(t)$ was instantaneous Shields parameter at ripple crest defined by

$$\Psi_r(t) = \frac{f_w u(t)^2}{2sgD(1-\pi\eta/\lambda)^2} \quad (10)$$

The value of α_c was determined so that the entrainment during a period be the same as that estimated from the suspended sand concentration above rippled beds. According to Eq.(7) the amount M_s of sand entrained during one wave period over one wavelength of ripples was estimated by

$$M_s = 0.005 \Psi_r^3 w_s T \lambda \quad (11)$$

By assuming that the velocity variation is sinusoidal as a first approximation and that the total amount of entrainment was prescribed by Eq.(11), we can evaluate α_c in Eq.(9) as 0.016.

The numerical calculation was proceeded with a time step of $\Delta t = T/40$. On the rippled bed, sand was carried on the upstream slope of ripple crest and was thrown at the ripple crest into suspension. In order to simplify the complicated mechanics of sand movement on the ripple slope, an assumption was made in the present model that all the sand was entrained at the ripple crest. The amount m_s of sand entrained during each time step was given by

$$m_s = m_e(t) \Delta t \quad (12)$$

4.2 Transport of suspended sand particles

The entrained sand was assumed to be trapped in the vortex on the lee side of ripple crest and be transported after the flow direction changed. The movement of suspended sand cloud was numerically traced on the assumption that each sand cloud was transported with the same speed as the near-bottom water particle velocity due to wave orbital motion plus the Eulerian mass transport velocity. Net sand transport rates were evaluated from the settling position of the each sand cloud.

4.3 Application to the compound wave field

When we apply the model to compound wave fields, an assumption is needed on the position of suspended sand cloud formation. Figure 7 shows an example of water particle displacement at a node of obliquely incident standing waves. The water particle displacement

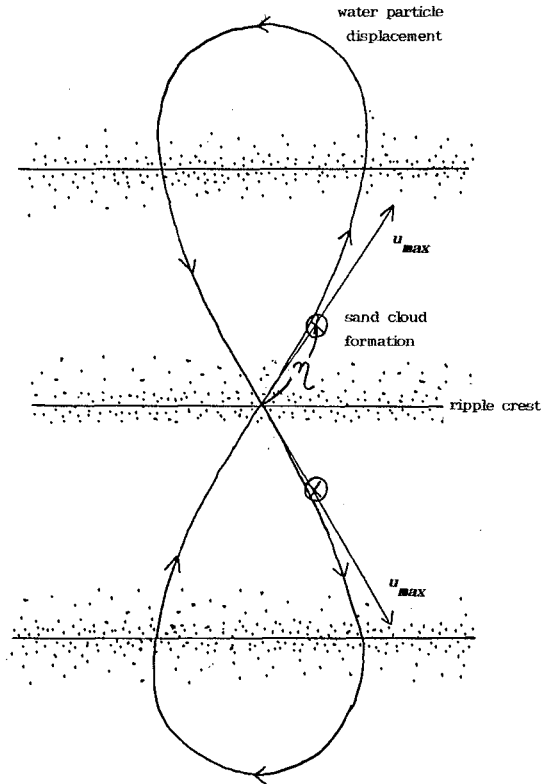


Fig. 7 Example of water particle displacement near the bottom.

was calculated by using the third order nonlinear theory. The figure illustrates that water particles near the bottom move in an 8-shaped orbit so that the velocity component v in the y direction is positive when the velocity is maximum. As sand moved most vigorously when the velocity was maximum, the most appropriate position would be the position on the lee side of ripple crest in the direction of the maximum velocity. The transport of sand cloud was calculated in the same manner as in the one-dimensional case.

4.4 Comparison with experiments

The applicability of the numerical model was examined by calculating the net sand transport rate under the following three-conditions; a finite-amplitude progressive wave, a standing wave and the compound wave field in front of a breakwater with oblique incidence.

Sato and Horikawa (1986) carried out movable bed experiments in an oscillatory flow tunnel and measured net sand transport rates over sand ripples for the condition of asymmetric oscillatory flows. Velocity histories of the oscillatory flows were simulated by using the fifth-order Stokes and the third-order cnoidal wave theory. Figure 8 shows a comparison between net sand transport rates $|\Phi_c|$ calculated by the numerical model and those $|\Phi_m|$ measured by Sato and Horikawa (1986) for the condition of asymmetric oscillatory flows. It was confirmed that the present model was able to estimate the net sand transport rate for asymmetric oscillatory flows observed in shallow water progressive waves.

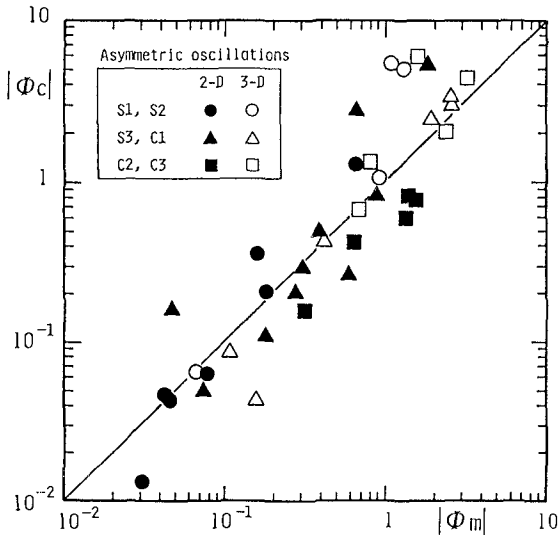


Fig. 8 Comparison of net sand transport rate for asymmetric oscillatory flows.

Irie and Nadaoka (1984) classified the seabed scour pattern under standing waves into two types. They defined L-type movement in which bed materials move from nodes to loops and N-type movement in which bed materials move from loops to nodes. Based on laboratory experiments, they concluded that the occurrence of the two types depended on the Ursell number of the incident wave and the ratio of near-bottom velocity amplitude to the settling velocity of sand particles.

The present model was applied to the condition of standing wave with normal incidence. The condition of calculation was varied systematically in a range with the water depth 8-30cm, the incident wave height 2-10cm, the wave period 0.8-2s and the sediment

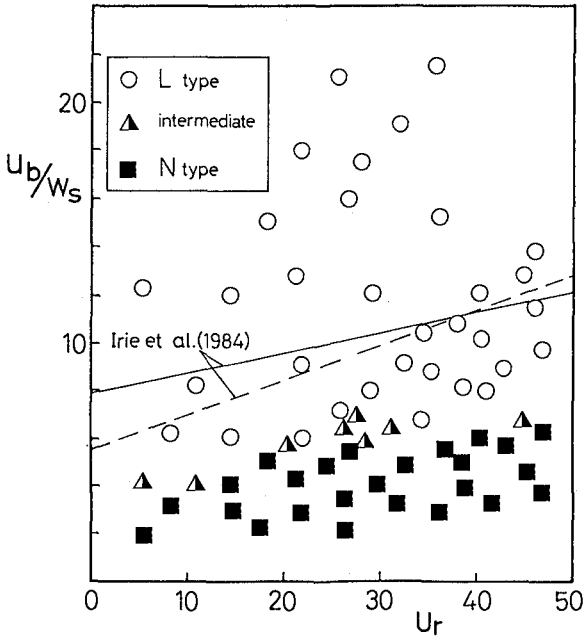


Fig. 9 Classification of sea bed scour under standing wave.

diameter 0.1-0.5mm. Figure 9 shows the occurrence of N- and L-type movement in the numerical calculation. The symbol \circ indicates the L-type movement and \blacksquare indicates the N-type movement. The solid line indicates the criterion empirically proposed by Irie and Nadaoka (1984) on the basis of laboratory movable bed condition and the broken line indicates that judged from the movement of sand particles distributed on a fixed bed. Although the model tends to produce L-type movement even for smaller values of u_b/w_s , the numerical model reproduces the tendency that the bed type changes from N-type to L-type with the increase of u_b/w_s .

Figure 10 shows a comparison of net sand transport rates under compound waves. The agreement between the experimental data and the calculation supports the applicability of the present model to the sand transport under compound waves.

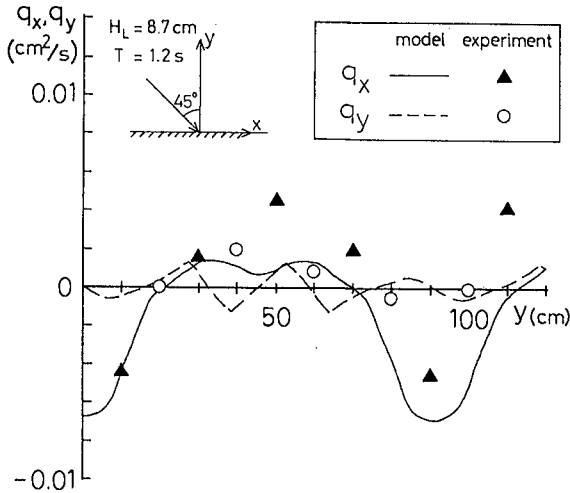


Fig. 10 Comparison of net sand transport rate for obliquely incident waves.

5. CONCLUSIONS

Characteristics of sand movement under compound waves were described through laboratory experiments. A numerical model of sand transport due to compound waves was presented which involved the process of sand suspension above rippled beds. The applicability of the model to a variety of conditions was confirmed with experimental data. As the model requires only the velocity variation near the bottom, it will be easy to apply the model to three-dimensional directional waves.

6. REFERENCES

- Hsu, J. R. C., Y. Tsuchiya and R. Silvester (1979): Third-order approximation to short-crested waves, *J. Fluid Mech.*, Vol. 90, pp. 179-196.
- Sato, S. and K. Horikawa (1986): Laboratory study on sand transport over ripples due to asymmetric oscillatory flows, *Proc. 20th Conf. on Coastal Eng.*, pp. 1481-1495.
- Irie, I. and K. Nadaoka (1984): Laboratory reproduction of seabed scour in front of breakwaters, *Proc. 19th Conf. on Coastal Eng.*, pp. 1715-1731.
- Hsu, J. R. C., R. Silvester and Y. Tsuchiya (1980): Boundary-layer

velocities and mass transport in short-crested waves, *J. Fluid Mech.*, Vol.99, part 2, pp.321-342.

Nielsen, P. (1986): Suspended sediment concentrations under waves, *Coastal Eng.*, Vol.10, pp.23-31.

Silvester, R. (1986): The influence of oblique reflection on breakwaters, *Proc. 20th Conf. on Coastal Eng.*, pp. 2253-2267.

CHAPTER 203

Dike Failure Calculation Model Based on In Situ Tests.

Chr. Laustrup M.Sc.¹
H. Toxvig Madsen M.Sc.²
John Jensen M.Sc.²
L. Poulsen M.Sc.³

Abstract

A method has been developed to determine the strength of a dike expressed as the mean return period for the critical load.

The method is based on tests carried out on prototype dikes.

1. Introduction.

As severe storms in 1981, 1984 and 1985 caused a number of dike failures, the Danish Government decided to lay down guidelines for future economic compensation in the event of major flooding.

These guidelines were based on a study dealing primarily with the following subjects:

- a) Mathematical simulation of historic storms to generate statistics of extreme water levels at any point along the 7,000 km Danish coastline, see figure 1.
- b) Establishing a data bank with information about buildings in low-lying areas and the construction details of the 350 km dikes of varying quality.
- c) Developing a method for the evaluation of dike strength in terms of return period of failure.

This paper summarizes the work of item c.

1) Chief engineer 2) Senior engineer 3) Project engineer
Danish Coast Authority, P.O. Box 100, 7620 Lemvig,
Denmark.

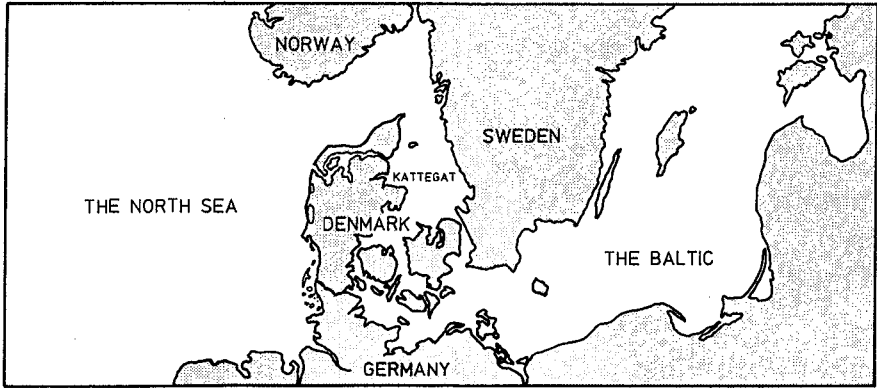


Figure 1. Waters Around Denmark.

2. Basic Description of the Method.

A diagram illustrating the dike strength calculation method is shown in figure 2. As can be seen, the calculation starts with a certain water level in deep water outside the specific dike. Using this water level and corresponding waves we then calculate whether this situation causes front or back slope failure of the dike.

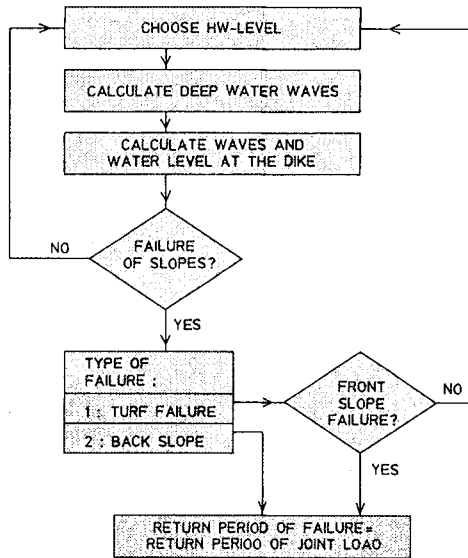


Figure 2. Calculation Diagram.

If the dike does not fail the calculation is repeated using a higher water level. This process continues until we find the lowest water level at which the dike fails.

The mean return period for this combination of water level and waves is determined and used as an expression of the dike strength.

The different steps in the calculation diagram are treated below.

3. Local Extreme Water Level Statistics.

Extreme water level statistics were calculated using a truncated Weibull-distribution to describe the size-distribution, and the Poisson-distribution to describe the arrival-process.

The statistics were prepared using partial series of either recorded or calculated extreme water levels. Reliable recorded water levels are always preferable to calculated water levels. Unfortunately, reliable recorded water levels are relatively scarce in Denmark.

Therefore all major storms in the Kattegat and in the Baltic Sea from 1965 to 1984 were simulated mathematically by The Danish Hydraulic Institute.

The recorded and calculated water levels during these storms were stored in a data base. This makes it possible to calculate extreme water level statistics for any location on the Danish coastline.

4. Duration of High Water Level.

The typical duration of the water level above a certain value was determined in order to be able to determine the number of waves causing erosion of the dike core, see section 9.

Naturally there are large variations in the water level curves around the maximum value. Therefore a number of water level curves for different storms and localities were incorporated by plotting the maximum water levels at the same point.

On the basis of these curves a connection was established between the difference in water level between a given level and the maximum value, and the duration of this water level interval.

5. Estimation of Storm Waves.

The waves were generally estimated by using the procedure described in The Shore Protection Manual (1984). The fetch used was calculated as the average value of the fetches in the 90° angle evenly distributed around the direction perpendicular to the coastline.

In cases where there are large shallow sea areas in front of the dike the storm waves were estimated according to the procedures outlined by Siefert (1974).

6. Simultaneous Onshore Waves and High Water Level.

On many Danish coasts high water level situations can arise without simultaneous onshore waves.

However, clearly the most dangerous situation is a combination of high water level and onshore waves.

The conditional probability $P(\text{onshore waves} \mid \text{water level} > \eta)$ was estimated by considering the storms used in the mathematical simulation mentioned in section 3.

The number of storms where the wind direction at the time of maximum water level was within the 90° sector around the perpendicular to the coast was enumerated. This figure, divided by the total number of storms, is used for the conditional probability $P(\text{onshore waves} \mid \text{water level} > \eta)$.

7. Waves and Water Level at the Dike.

The water level and waves at the dike can be calculated on the basis of the water level and waves in deep water.

The calculation is based on successive breaking and shoaling of the waves, with specific criteria for the transition between these phases.

The breaking criterion is defined according to Goda (1985) as

$$\frac{H_B}{L_0} = 0.17 \left\{ 1 - \exp \left[- \frac{1.5 \pi h}{L_0} (1 + 15 \tan^{4/3}(\varphi)) \right] \right\} \quad (1)$$

where H_B is the wave height at breaking, L_0 is the wave length in deep water, h is the water depth and $\tan(\varphi)$ is the bottom slope.

Using small amplitude wave theory the governing equations are

$$\frac{db}{dx} = -\frac{3}{16} \cdot \frac{1}{h} \cdot \frac{d(H^2)}{dx} \quad (2)$$

$$\frac{dE_f}{dx} = \begin{cases} 0 & \text{no breaking} \\ -E_{f,B}/l_{DISS} & \text{breaking} \end{cases} \quad (3)$$

where b is the wave setup, x is a horizontal distance increasing onshore, h is the local water depth, H is the local wave height, E_f is the energy flux, $E_{f,B}$ is the energy flux at the point of breaking, and l_{DISS} is the dissipation distance.

l_{DISS} is a fixed value at a given point of breaking. l_{DISS} is chosen so the local ratio of wave height to depth, H/h , decreases monotonically. The following expression is used for l_{DISS}

$$l_{DISS} = \frac{2}{5} \cdot h_B \left(1 + \frac{3}{8} \left(\frac{H_B}{h_B}\right)^2\right) \cdot \tan^{-1}(\psi) \quad (4)$$

where B denotes the point of breaking.

The transition from wave breaking to shoaling is governed by the criterion given by Deigaard et al. (1986).

$$\frac{H}{h} = 0.5 \quad (5)$$

The surf zone calculations are carried out using a PC-programme.

8. Strength of a Turf Revetment.

For dikes covered with turf, a front slope failure starts with failure of the turf and continues with erosion of the dike core, see section 9.

Methods to predict failure of the turf slope and erosion of the dike core are not known to the authors. Therefore such methods had to be developed.

A series of tests were carried out to find the resistance of turf as a function of the dry weight of grass roots per m^2 and the particle velocity in the breaking wave. The tests were carried out on prototype dikes.

Wave breaking was simulated with a water jet from a 4" pipe. A total of 16 tests were carried out on turf of 4 different qualities. These tests indicate that there is a certain critical particle velocity of the breaking

wave which initiates damage to the turf. Figure 3 shows the test results from one site. Each test with a certain water velocity was repeated four times.

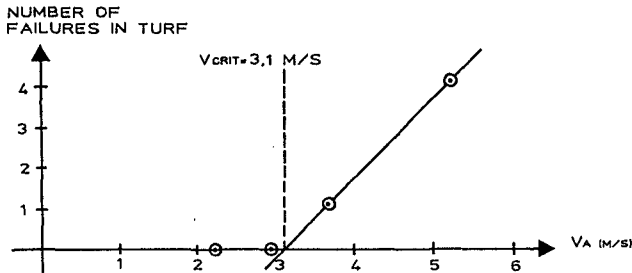


Figure 3. Example of Test Results.

In figure 4 the critical velocities found are plotted as a function of the dry weight of the grass roots in the turf.

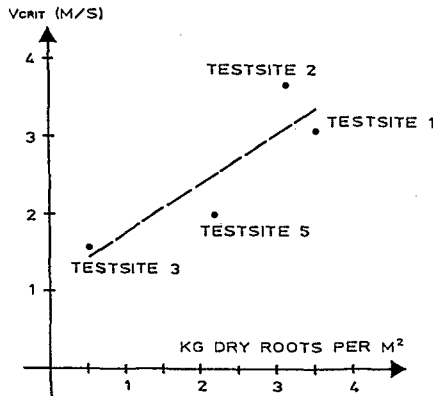


Figure 4. Critical Velocity as a Function of Dry Weight of Grass Roots in the Turf.

For dike slopes covered with turf and steeper than 1:6 it is assumed that the slope fails when the velocity in the plunging breaker exceeds the critical velocity for the turf.

The impact velocity V_A is calculated assuming that the plunging breaker falls from a height of $0.78 \cdot H_B$ above the mean water level. H_B is the wave height at breaking.

$$V_A = \sqrt{g(h_B + 1.56 H_B)} \quad (6)$$

where g is the acceleration of gravity and h_b is water depth at breaking.

The wave is assumed to hit the slope at the intersection between the slope and the mean water level.

9. Erosion of the Core Material.

In this study, front slope failure is defined as the situation where the front slope turf has failed and the erosion of the dike fill has reached the back slope, see figure 5.

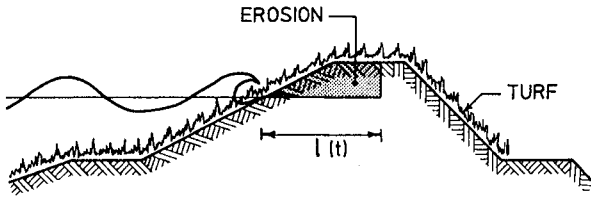


Figure 5. Model of Front Slope Failure.

The horizontal erosion l is described by the following expression

$$l(t) = k_c \cdot k_e \cdot V_A \cdot \frac{t}{T} \quad (7)$$

where t is time, k_c is a calibration constant, k_e is a core material constant, V_A is the impact velocity and T is the wave period.

The core material constant was determined for different core materials. The method used was repeated flushing with a well-defined velocity.

Figure 6 shows a typical set of test results. As can be seen, the erosion depth is roughly proportional to the number of jets.

The following material constants k_e have been determined from the tests

Sand, small amount of silt (10%)	$1.35 \cdot 10^{-3}$ sec/jet
Sand, large amount of silt (17%)	$0.89 \cdot 10^{-3}$ sec/jet
Clay with sand (60%)	$0.059 \cdot 10^{-3}$ sec/jet

The equation for horizontal erosion was calibrated on real front slope failures recorded at the Rejsby dike after a severe storm in 1976. In figure 7 the horizontal erosion for each failure is plotted as a function of the time the water level remained above the bottom of the indentation.

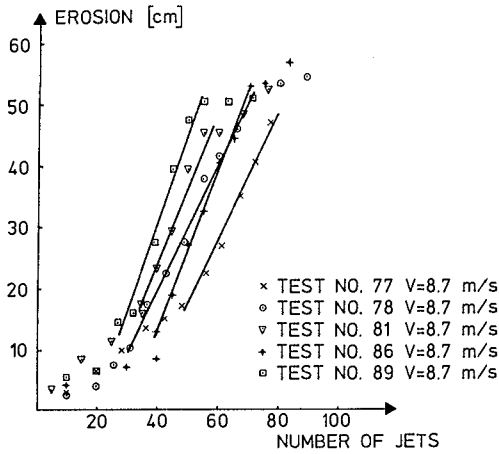


Figure 6. Results from Simulation Tests with Core Erosion.

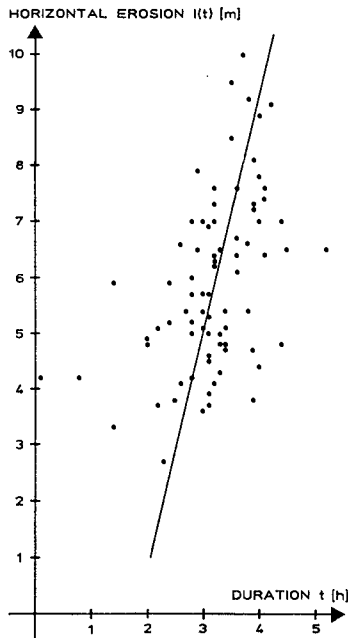


Figure 7. Horizontal Erosion and Duration of High Water Level for Real Dike Failures.

The calibration factor k_c in equation (7) was determined from figure 7.

10. Wave Overtopping.

The run-up level Z_{PCT} exceeded by a certain percentage of the waves can be determined by using the formula

$$Z_{PCT} = 0.77 \sqrt{2 - \log(PCT)} \cdot 0.7 \cdot T \sqrt{gH_0'} \tan(\varphi) \quad (8)$$

given in Technical Advisory Committee (1974). PCT is the percentage of the waves, T is the average wave period, H_0' is the equivalent wave height in deep water and φ is the bottom slope angle.

In dimensioning the Danish Wadden Sea dikes 2% was used in the formula as the critical overtopping percentage for back slope failure.

This percentage was considered too conservative for this study. Records show that overtopping in excess of 50% can occur without dike failure.

Therefore the critical overtopping percentages shown in table 1 have been used in this study.

Overtopping percentages	Dike surface		
	Unprotected	Turf, sandy	Turf, clayey
Slope:			
1:1.5	2%	10%	10%
1:2	2%	20%	50%
1:3	2%	30%	90%

Table 1. Critical Overtopping Percentages.

11. Geotechnical Failure of the Back Slope.

The risk of back slope failure has also been examined using geotechnical calculations.

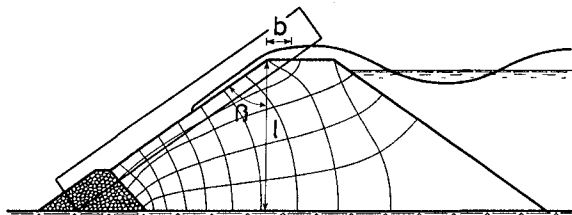


Figure 8. Geotechnical Description of Back Slope Failure.

Assuming stability in the box indicated in figure 8, and assuming completely cohesive soil, the critical cohesion C_{crit} along the failure line can be described by the following equation

$$C_{crit} = [b (\gamma_w + \gamma_m) + \frac{A_{o1}}{l} \cdot \gamma_w] \cos^2 \beta \quad (9)$$

where b , l and β are defined in figure 8, γ_w is the specific gravity of water, γ_m is the specific gravity of saturated fill and A_{o1} is the cross section area of the overtopping water.

This critical cohesion is compared to the shear strength in the back slope determined by vane tests. The vane test results are reduced to between $1/3$ and $1/4$ due to fractures in the soil.

Equation (9) has been confirmed by full-scale tests on two dikes. One test resulted in back slope failure and one test gave no failure. Both results were in accordance with the formula. The tests showed that relatively low levels of overtopping result in complete saturation of the soil.

The main drawback of this geotechnical method in evaluating the stability of the back slope is the large number of vane tests required.

12. Calculation of Dike Strength.

A dike fails either when the water level reaches the top of the dike or when a combination of high water level and onshore waves causes front or back slope failure.

The shorter of the mean return periods for these two events is used as an expression of the dike strength.

The mean return period for the situation where the water level reaches the top of the dike is calculated using the water level statistics for the particular location.

The situation with onshore waves has a mean return period which can be calculated using the value for the conditional probability $P(\text{onshore waves} | \text{water level} > \eta)$ determined in section 6.

13. Conclusions.

A usable method has been developed to calculate the strength of dikes of varying quality. The method is based on results from rather simple tests on prototype dikes. The test results have been calibrated using re-

sults from real failures recorded at a Danish dike following a severe storm.

The model has been used to calculate the strength of about 30 Danish dikes. The results are consistent with the known lifetime of the dikes and the storms they have withstood without damage.

References.

Deigaard, R. Fredsoe, J. and Hedegaard, I.B. "Mathematical Model for Littoral Drift", Journal of Waterway, Port, Coastal and Ocean Engineering, Vol. 112, No. 3, May 1986.

Goda, Y. "Random Seas and Design of Maritime Structures", University of Tokyo Press, Japan, 1985.

"Shore Protection Manual", Coastal Engineering Research Center, Waterways Experiment Station, Corps of Engineers, Vicksburg, 1984.

Siefert, W. "Über den Seegang in Flachwassergebieten", Leichtweiss-Institut für Wasserbau der Technischen Universität Braunschweig, Mitteilungen, Heft 40, 1974.

Technical Advisory Committee "Wave Run-up and Overtopping", Government publishing office, The Hague, 1974.

CHAPTER 204

HOW TO ANALYSE BEACH PROFILE MEASUREMENTS ?

Jan van de Graaff ^{*})

1 INTRODUCTION

A manager of a sandy coastal area is by virtue of his or her profession interested in the behaviour of that coastal area. Is the coast eroding, accreting or, by chance, stable? And, if the coast is not stable: what are the erosion or accreting rates?

It is almost trivial to mention that the basic information can be acquired with a measuring program.

In collecting data almost always a more or less 'natural' evolution can be noticed. One starts often collecting data which can be simply acquired. E.g. aerial photographs or surveys of the position of the waterline only.

A next step in a 'natural' evolution consists often of more extended measurements. E.g. entire cross-sections are measured on a regular basis. These extended measurements are often necessary to really understand what happens with the coast. That doesn't mean, however, that the former, simple, measurements become useless. A special treatment is necessary to 'couple' the results of the simple measurements to the results of the extended measurements. If that is possible indeed, mostly a data set holding over a longer period can be acquired.

If, after a couple of years, a series of measurements is available, the question arises: how to analyse the data in order to get a clear insight in the behaviour of the coast?

In this contribution mainly two topics are discussed:

- analysis of entire beach profiles
- coupling procedures of 'simple' measurements to 'extended' measurements.

^{*}) Senior scientific officer
Delft University of Technology
the Netherlands

2 BEHAVIOUR OF A STRETCH OF COAST

Fig. 1 shows in plan view a piece of a sandy coast. The coastal zone manager likes to know 'the' behaviour of stretch AB of the coast. Many coastal zone managers pay their attention often mainly to the behaviour as a function of time of the position of the waterline or line DD'. Line DD' is the so-called dune foot line; generally the transition between the beach and the mainland. Fig. 2 shows schematically what can occur as a function of time with the position of point P (see Fig. 1) with respect to an arbitrary reference line. The three possibilities, accreting, stable and eroding can simply be discerned. We will confine ourselves further (mainly) to the eroding case.

To quantify reliably the rate of the average yearly retreat (that is in the simplified case of Fig. 2 the slope of the fitted line through the measuring points), is just a very important topic. These erosion-numbers are important, for instance, to predict the position of the coastline in near future.

Often a coastal zone manager is almost forced (e.g. by 'society') to combat the erosion. Counter-measures have to be taken to stop the erosion or to overcome the detrimental effects of the erosion. Planning and designing the appropriate counter-measures is only possible if one 'understands' what the real reasons are of the underlying erosion problem. It is self-evident that sediment transports are the basic reason of any coastal erosion problem.

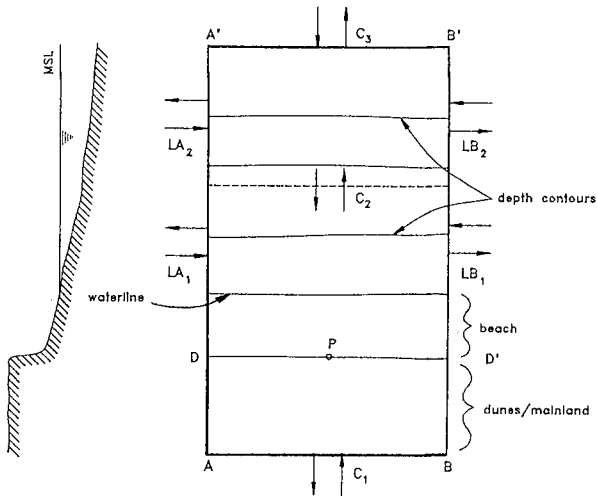


Fig. 1 Coastal processes in stretch of coast

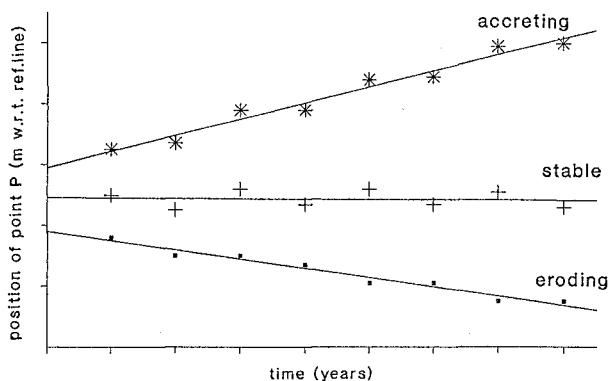


Fig. 2 Behaviour of coast as a function of time

In Fig. 1 some sediment transport vectors have been indicated; the magnitude of these vectors 'steer' the sand volume in the area AA' B' BA. A decrease of the volume of sand in that area is in principle the real reason of the erosion problem. So generally (gradients in) longshore transports and/or cross-shore sediment transports are the reason of the erosion problem.

In Fig. 1 the longshore transports have been split up in two components (LA_1 and LA_2 through section AA'; through section BB' similar). If desired, a further splitting up of the longshore transport in more vectors can be considered. (Or only one vector can be taken into account.)

Let us consider a time period of one year. In order to quantify the variation of the volume of sand in that year in the area AA' B' BA one has to calculate the yearly net transport of the contributions LA_1 , LA_2 , C_3 , LB_2 , LB_1 and C_1 . However, due to very inaccurate sediment transport formulae and due to the often highly varying boundary conditions (like wave height, wave direction and tidal current velocities), it is in fact almost impossible to quantify the several yearly contributions properly.

In some classes of coastal erosion problems this calculation-first-method is in fact the only possibility to tackle the problem. In many other classes of problems, however, the 'field' shows already clearly the coastal behaviour (often an unacceptable erosion). A proper analysis of that behaviour may yield 'true' volume variation figures. Sediment transport calculations can be carried out next. If these calculations yield eventually similar results as the 'true' volume variations, the

sediment transport calculation method can be used to predict (or better: to estimate) the behaviour of the coast in (near) future. E.g. changes in the coastline position due to expected changing boundary conditions can be estimated in this manner. Or, in cases without changing boundary conditions, the results of sediment transport calculations can be used as a more or less sophisticated extrapolation method. Most likely the calculated sediment transport rates depend for example on the actual position of the coastline; changing positions yield so different transports.

Artificial beach nourishments are nowadays increasingly considered and increasingly used as a fair method to solve erosion problems. [See e.g. Manual on Artificial Beach Nourishment (1987).] Also for the design of an artificial beach nourishment scheme a proper insight in the actual loss of sand out of the problem area is desired.

In conclusion it can be stated that it is essential to quantify the sediment volume (and its variation with time) in areas like area AA' B' BA in Fig. 1. In the next Section it will turn out that the selection of the proper boundaries of area AA' B' BA is in fact a difficult and also tricky task.

3 QUANTIFICATION OF VOLUME VARIATIONS

Whether a certain stretch of coast is considered or only a single cross-section, is not principally different. In the latter case the stretch of coast has (accidentally) a length of 1 m only!

Let us next consider a set of yearly measured cross-shore beach profiles. Let us assume that a set of 20 yearly measurements is available. Fig. 3 shows, as an example, the shape of the cross-sections for three distinct profiles from the series; the 17 other profiles have been left out to avoid confusion.

The aim of the analysis is to quantify (the trends in) the variations in the volume of sand in the cross-section. Cross-shore profiles can, however, be extended indefinitely. As well from a practical point of view as from a coastal morphological point of view, the length of cross-shore profile measurements must, however, be limited. A requirement for the length, covered by measurements, is that the so-called closure-points (depths) are included by the measurements.

In a beach profile in fact two closure-points can be discerned; a landward- and a seaward closure-point. The landward (seaward) closure-point in the profile is the

position in the beach profile where landward (seaward) of that position apparently no systematic profile variations do occur. All systematic profile variations (losses and gains) take place consequently between the landward- and seaward closure-points (the so-called control area).

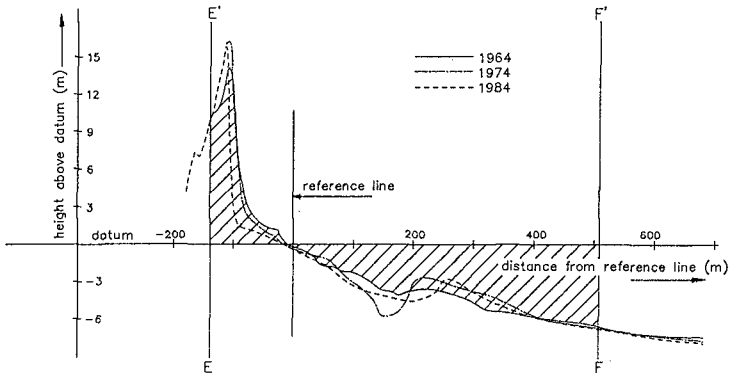


Fig. 3 Beach profile measurements in several years

Although this definition seems sound, in practice the relevant time- and length scales of the problem have also to be taken into consideration.

The loss of sand out of the control area through a chosen landward closure-position of say $1 \text{ m}^3/(\text{m year})$ due to landward directed winds, might be very important if the formation of dunes on a geological time-scale is considered. If, in contrast, the erosion problem in the lee-area of a newly built harbour is considered, the same loss of $1 \text{ m}^3/(\text{m year})$ plays most likely a minor role only.

In the present paper only classes of problems are considered where losses or gains (if any) out of the control area of orders of magnitude of $1 \text{ m}^3/(\text{m year})$ are negligible small.

If the series of profiles (represented by Fig. 3) are analysed, the choice of the landward closure-position is next relatively simple to make. By visual inspection the selection of line E'E seems to be a good choice. All profile fluctuations take apparently place seaward from line E'E.

The choice of the seaward closure-position (F'F) is far more difficult. In the example case of Fig. 3 the measurements have been extended over a distance of almost 1000 m. That seems rather long. However, even a visual inspection yet of the measured profiles, points already to noticeable fluctuations at the very seaward end of the profiles. That complicates much the selection of a

reliable (so covering all relevant volume fluctuations) seaward closure-position.

Requirements for the selection of a single standard point as the seaward closure-position cannot be given. A procedure is, however, proposed which meets the proper selection problem to some extent. The analysis of the results of the proposed procedure will furthermore enlarge the insight in the morphological processes which apparently take place.

In the procedure as proposed the position of the seaward closure-position (in Fig. 3 the line F'F) is systematically varied. With the selected (fixed) landward- and (varied) seaward closure-position, the 'volume' of sand in the profile as has been indicated in Fig. 3, is calculated for each profile of the long-continued series of yearly measurements. In Fig. 3 the 'datum' level (e.g. mean sea level; MSL) is selected as reference level. The volume per running m of 'sand' above datum is considered as positive; the volume of 'water' below datum as negative.

In Fig. 4 the thus calculated volumes per running m have been plotted as a function of time. (Fig. 4 holds for the case that the position of F'F is selected at 510 m from the reference line; see Fig. 3.)

Although some scatter does occur, a distinct trend can be noticed in Fig. 4. If a linear trend line is fitted through the calculated volumes from the profile measurements (e.g. with a least square method), apparently an average yearly loss of sand occurs between the limits E'E and F'F of approximately $25 \text{ m}^3/\text{m}$. [According to Fig. 4 the resulting 'wet' volume (so negative values) of the profiles increases, so a loss of sand is found indeed; on an average of $25 \text{ m}^3/(\text{m year})$.]

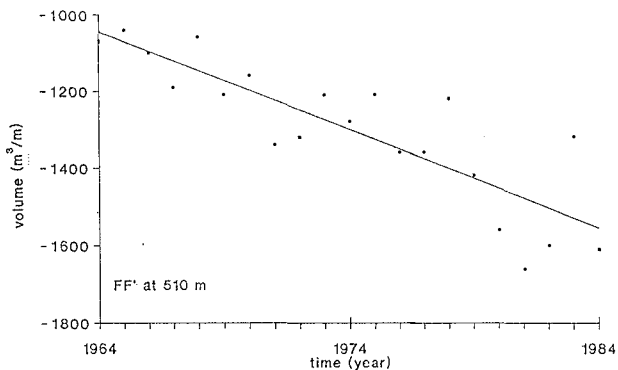


Fig. 4 Volume as a function of time

The standard deviation of the differences of the individual points of Fig. 4 with the fitted line is about $100 \text{ m}^3/\text{m}$. Real fluctuations in the volume of sand in the profile, but also measuring errors, contribute to that seemingly rather high value. A standard deviation in the volume of $100 \text{ m}^3/\text{m}$ over 650 m of the profile (distance between E'E and F'F) yields a standard deviation per measuring point of about 0.15 m . That value is, however, a quite usual figure for the standard deviation of even the measuring errors only of this type of profile measurements. So $100 \text{ m}^3/\text{m}$ is not unacceptable large.

Whether it is allowed to represent the results like in Fig. 4 by a simple straight line, has to be investigated from case to case. In some cases for example also periodic fluctuations with a period of several years can be discerned.

The result of Fig. 4 [loss of $25 \text{ m}^3/(\text{m year})$] holds for the selected position of F'F. By varying the position of F'F different yearly losses (or gains) are found. Next a plot of the average yearly variation as a function of the position of F'F can be made. Fig. 5 shows four typical results of real Dutch cases. Fig. 6 shows the locations along the Dutch coast. All results are based on at least 20 yearly profile measurements (period: 1964 - present).

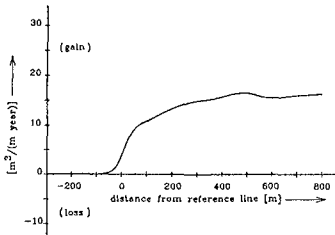


Fig. 5a Case 5a

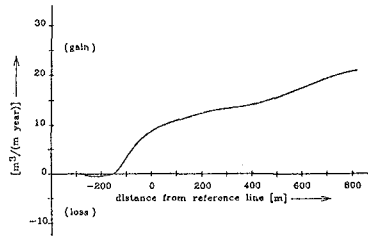


Fig. 5b Case 5b

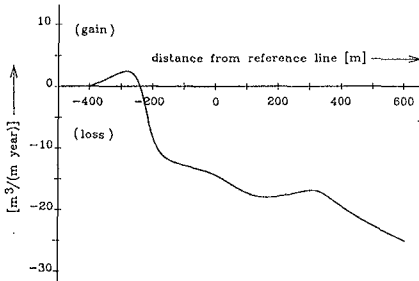


Fig. 5c Case 5c

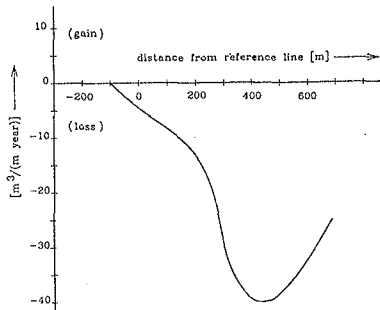


Fig. 5d Case 5d

Fig. 5a (an accreting case) is the easiest one to handle. It is apparently possible to select a proper (according to the definition) seaward closure-point. The horizontal course of the line seaward of say 500 m from the reference line means that from that position no additional losses or gains do occur. A slightly wrong selected seaward closure-position will not yield fundamentally different results. From Fig. 5a an indeed total gain of about $15 \text{ m}^3/(\text{m year})$ can be determined.

Fig. 5b (also an accreting case) is more difficult to handle. Apparently seaward from say 500 m from the reference line, still relatively large profile fluctuations do occur; resulting in an ever increasing yearly accreting volume for the profile the farther the seaward 'closure-position' is selected. In fact a real closure-position is not yet reached with the present length of the profile measurements. Consequently the total (in this case) gain of sand in the profile cannot be determined. The description of 'the' behaviour of the beach profile as a function of time remains still open.

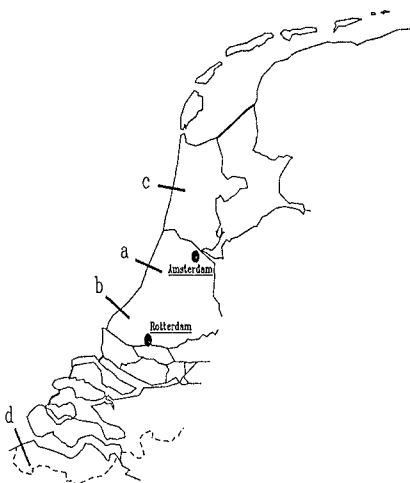


Fig. 6 Location of profiles along coast

Fig. 5c (an overall eroding case) shows a remarkable pattern. Starting from the landward closure-position (-400 m) and looking in seaward direction, first a small gain is noticed. (Apparently some sand is accumulated in the dunes seaward of the landward closure-position.) Further seaward an ever increasing erosion appears. Between -150 m and 300 m from the reference line the yearly rate of erosion does not change very much; however, seaward of 300 m the total

average yearly erosion is ever increasing. Apparently due to additional losses in that area. Also in this case a description of 'the' behaviour of the beach profile is in fact impossible.

In Fig. 5d an ever increasing yearly erosion takes place up to 450 m from the reference line (average yearly erosion $40 \text{ m}^3/\text{m}$). Seaward of 450 m accumulation of sand does occur, resulting in an ever decreasing erosion figure. At the end of the measurements (approximately at 700 m from the reference line) the total erosion yields still yet approximately $23 \text{ m}^3/(\text{m year})$.

Also in the case of Fig. 5d 'the' behaviour of the profile depends largely on the distance over which the profile fluctuations are considered.

4 DISCUSSION QUANTIFICATION OF VOLUME VARIATIONS

About 2000 cross-shore profiles are measured along the Dutch coast yearly. In most of these cases it is rather easy to find a reliable seaward closure-position; in many cases directly; in some other cases by some acceptable slight extrapolation. The cases of Fig. 5a up to 5d are in this respect by no means fully representative to the total Dutch situation. There remain, however, many cases where it is, notwithstanding the distance of often 800 m from the waterline over which profile measurements have been carried out, very difficult to determine the behaviour of the profile properly.

The question arises whether that is a real problem or in fact some kind of an artificial problem. If for instance in all cases a distance of up to say 600 m seaward of the reference line is considered, the gains or losses in just that zone can be calculated and can be taken as a basis for further considerations. It is of course next possible to calculate transport vectors holding especially for that part of the profile. In that case, however, an essential contribution to the sand-volume balance is then due to cross-shore transports through the vertical at 600 m from the reference line. (Cf. vector C_3 in Fig. 1.) Since the reliable computation of cross-shore sediment transports is often considered as far more difficult than the computation of longshore transports [see Van de Graaff (1988)], extra complicating elements are introduced in the entire analysis of the coastal behaviour. To analyse cases where real seaward closure-points are found, is far easier. Also in these cases cross-shore transports play their role in the behaviour of the coast, but they can, at least in first instance, be considered as a redistribution factor only. By cross-shore sediment transport processes, volumes of sand are redistributed over the active part of

the profile; the real gains or losses are then mainly due to (gradients) in longshore sediment transport rates.

In conclusion it can be stated that seaward closure-points are extremely important in coastal morphology studies. Along the Dutch coast these seaward closure-points are sometimes apparently situated beyond the limits of the standard yearly measurements. (Sometimes beyond approximately 800 m from the position of the waterline.) If 'new' standard measuring programmes are planned, it is recommended to extend the measurements beyond the seaward closure-point.

5 MEASUREMENTS OF CHARACTERISTIC DEPTH CONTOURS

Often series of measurements of only some characteristic depth contours are longer lasting than series of regularly measured entire beach profiles.

In the Netherlands, for instance, over approximately 140 years results are available of yearly measurements of the position of the MLW -, the MHW - and the Dune Foot line for each kilometer of the Dutch coastline. (Systematic entire profile measurements for each 200 - 250 m along the coast are available in the Netherlands over 'only' 25 years; for some portions of the coast longer lasting series.)

This long lasting series can in principle serve as a very valuable data base.

A plot of e.g. the MHW -line in a cross-section as a function of time, shows often a lot of scatter (in the Netherlands these plots are therefore often indicated with 'lightening-plots'). With filter-techniques often clear trends can be derived of such long series of measurements; sometimes even clear long-periodic fluctuations can be noticed in the plots.

For many phenomenological studies these measurements are very valuable. The coastline behaviour from the past to present can be described with the help of these measurements. The measurements can also be fruitfully used to predict the position of the coastline in (near) future. (Some extrapolation is probably allowed.) From the results even time-average yearly erosion - or accreting rates can be derived. However, these rates are expressed in m/year.

As has been discussed in Section 2 the real reason of coastline development with time is due to variations of sediment transports along the coast and sediment transports in the cross-shore direction. And to understand what really happens, insight in these actual sediment

transports is necessary. A time-average coastline recession rate of say x m/year is in reality associated with a loss of sand out of the beach profile of y $\text{m}^3/(\text{m year})$. The latter value is next directly associated with (gradients in) sediment transport rates. [Also eventually expressed in $\text{m}^3/(\text{m year})$.]

Consequently the use of long lasting series of measurements of the position of a few depth contours only in sediment transport studies, calls for conversion factors. (E.g. what is the relationship between x and y as mentioned in the preceding paragraph?)

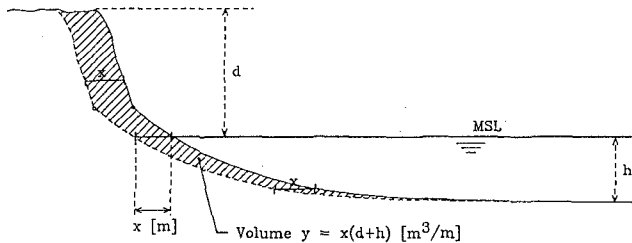


Fig. 7 Eroding beach profile behaviour

Fig. 7 shows a rather simple model to derive a conversion factor. In the sketch of Fig. 7 it is assumed that the shape of the active profile remains constant. A yearly retreat of the 'coastline' with x m means that all depth contours in the active part of the profile will retreat with the same x m. If this model is true y and x are related as follows:

$$y = x (d + h) \quad (1)$$

where: y : average yearly loss/gain of volume of sand in the beach profile [$\text{m}^3/(\text{m year})$]
 x : average yearly erosion/accretion of the 'coastline' (e.g. average position of MLW- and MHW line) [m/year]
 d : height of dunes/mainland above MSL [m]
 h : depth of seaward closure-point below MSL [m]

An arbitrary selection of 23 cases has been made, more or less regularly divided along the Dutch coast. Only 14 cases have been ultimately used in the further analysis. In these 14 cases the time-averaged yearly losses or gains exceed $10 \text{ m}^3/(\text{m year})$. (If the yearly losses or gains are too small the accuracy of the conversion factors to be derived, becomes too low.)

The series of measurements of entire beach profiles have been used (more than 20 yearly measurements). Of these profiles also the average position of the MLW- and MHW line (so say the coastline) has been determined.

Two methods to check Eq. (1) have been used.

In Method I plots have been made of the average position of the MLW- and MHW line in every year versus the volume of sand in every year. (To determine the volume of sand in the beach profiles the entire measured profiles have been used. According to Fig. 5 it is not quite sure that the relevant volume is covered entirely in all cases.) The trend line through the more than 20 yearly measurements has next been calculated. The slope of that trend line yields an estimate of the ratio y/x , so an estimate of a proper conversion factor. In Fig. 8a that conversion factor is compared with the height $(d + h)$. [The magnitude $(d + h)$ has been measured from profile measurements.] It is remarkable that the conversion factor as calculated with Method I is in all cases smaller than $(d + h)$. The 4 cases with time-average yearly losses/gains which are larger than $30 \text{ m}^3/(\text{m year})$ score relatively better than the other cases.

In 4 cases it was clear (from figures like Fig. 5) that the real control area is not covered by the measurements and that y is consequently underestimated. That could be a reason of the low conversion factors as derived in comparison with the height $(d + h)$ in these cases. (In 8 cases of Fig. 8a the proper control area was covered by the measurements.)

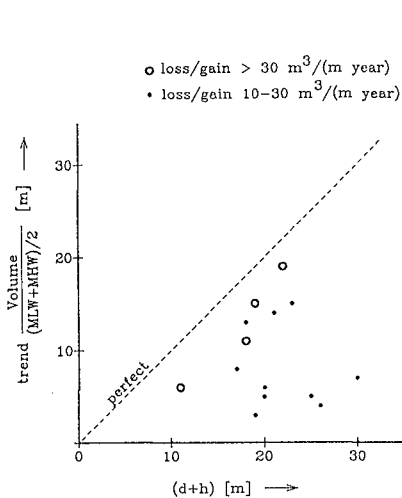


Fig. 8a

Conversion factor versus $(d + h)$

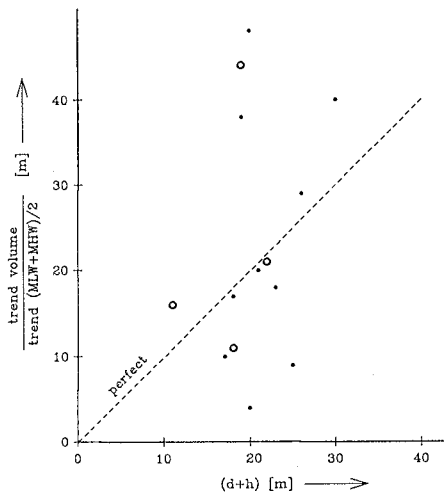


Fig. 8b

In Method II first linear trend lines have been determined in plots showing the volume as a function of time as well as in plots showing the average position of the MLW- and MHW lines. Next the two resulting trends have been divided, yielding an other estimate for a conversion factor. Fig. 8b shows the comparison between this conversion factor and the height ($d + h$). A great deal of scatter can be noticed. Under-estimations as well as over-predictions can be observed in this comparison.

6 DISCUSSION MEASUREMENTS CHARACTERISTIC DEPTH CONTOURS

The Method I and Method II to calculate a conversion factor, yield different results. (Method I is felt to be slightly 'better' than Method II.) In both cases, however, large differences do exist from the simple model according to Fig. 7. That means in fact that, based on the results of this research, a single simple conversion factor does not exist. So it is still difficult to couple series of measurements of a few characteristic depth contours to series of measurements of entire profiles. It is not excluded, however, that with longer joint series (longer than say 20 - 25 years) a more conclusive result will be obtained.

If the results of Fig. 8a are considered as 'true', the basic idea of Fig. 7 (a constant shape of the profile) does apparently not hold. Due to the general under-estimation two hypotheses can be considered to 'explain' the behaviour, viz.:

- a) systematic flattening of the entire profile
- b) (temporarily) steepening of the profile

Re a)

If the beach profile flattens systematically the (e.g.) regression of the MLW- and MHW lines is faster than the deeper depth contours. The associated volume loss out of the profile is consequently less than expected from Fig. 7.

Re b)

In a structural eroding beach profile the erosion of the dunes or mainland occurs mostly more or less shock-wise. Under usual conditions the erosion of the beach and foreshore takes already gradually place, but the dunes or mainland are not reached by the water and waves. The erosion of the dunes 'waits' for rather rare more severe conditions. The profile adjustments in the dunes 'necessary' according to the model of Fig. 7, can only occur during a storm (surge). Especially if rather short series are considered (however, is 20 - 25 years short?), it is not excluded that the necessary adaptations in the dunes or mainland have not yet been finished due to lack

of stormy weather. Due to the storm (surge) the volume of sand in the profile will not change in principle, but the position of the MLW- and MHW lines will do.

7 CONCLUSIONS

- Systematic measurements of entire beach profiles are indispensable in analysing the behaviour of coasts (coastlines).
- Insight in systematic volume changes in profiles (losses/gains) is an important analysing goal of profile measurements.
- Even very good (rather long lasting) series of entire profile measurements (like in the Netherlands) cannot always be analysed straightforwardly.
- The length over which the measurements extend in seaward direction calls for special attention (often too short).
- 'New' series of systematic measurements should be analysed as soon as possible in order to check whether the measurements fulfil the requirements. (The set-up of the measurements have to be adapted possibly.)
- With a restricted number of arbitrarily selected beach profiles along the Dutch coast as basis, it turned out to be very difficult to determine a simple conversion factor to couple series of measurements of a few characteristic depth contours and series of measurements of entire beach profiles.

ACKNOWLEDGEMENTS

The data of entire beach profile measurements as used in the present study, have been provided by the Tidal Waters Division of Rijkswaterstaat.

Results of the MSc.-thesis of Mr. B. P. van den Bunt have been used to prepare the present paper.

REFERENCES

- Graaff, J. van de, (1988)
Results of recent experiments on sediment transport by waves and currents.
2nd International Symposium on Wave Research and Coastal Engineering.
October 1988, Hannover, Germany.
- Manual on Artificial Beach Nourishment (1987)
CUR/Rijkswaterstaat/Delft Hydraulics Report 130.
ISBN 90 212 6078 6, Gouda, the Netherlands.

CHAPTER 205

GRAIN-FLUID INTERACTION IN COUETTE FLOW

by

Willem T. Bakker ¹, Walther G.M. van Kesteren ² and Wim H.G. Klomp ²

1. ABSTRACT.

This paper is a continuation of the papers of Bakker & Van Kesteren (1986) and Bakker et al. (1988). In this paper the results are presented of ring shear tests on mixture of oil and spheres with the same density (880 kg/m³). In order to study in detail the behaviour of a sand water mixture at high concentrations in a Couette like shearflow in the viscous regime the grain diameter and viscosity are enlarged by a factor 100: respectively 15 mm and 10⁻⁴ m²/s. The test are executed in the so called grain carousel with shear rates up to 75 s⁻¹ (Bagnoldnumber N=240). The experimental set up is such that only constant volume test could be performed.

The test results indicate that at concentration below 30% (vol.) no dispersive stresses are generated. At higher concentrations the generated dispersive stresses increases with concentration and shearrate. From videofilms it was observed that the grains are moving in layers with only small mutual exchange (grainswop).

2. SCOPE OF PAPER.

This paper reports on a continuation of a study on the bottom-boundary layer in oscillatory flow. This series started with a paper of Bakker (1974) on suspended sediment in a horizontally uniform oscillating flow. After considering the near bottom velocity field more into detail (Bakker and Van Doorn, 1978; Bakker and Van Kesteren, 1984) the study proceeded with a closer investigation of the sand transport mechanism at the bottom under sheetflow conditions (Bakker and Van Kesteren, 1986, 1987; Bakker, Van Kesteren and Yu, 1988).

¹) Visiting Professor, University of Hawaii, Dept. Ocean Engng., Holmes Hall 403, 2540 Dole Street, Honolulu, Hawaii 96822, USA.

²) Delft Hydraulics, P.O. box 177, 2600 MH Delft, The Netherlands.

In the last-mentioned paper experiments in a grain Carrousel and measurements in nature were mentioned. The present paper gives more data and some analysis concerning the Carrousel measurements. New prototype data, measured with the Harp during the Lohengrin project are reported on in the subsequent paper (Yu, Niemeyer and Bakker).

In a reliable mathematical model on sheetflow as well the shear stresses between shearing layers of grains as well as the normal stresses should be well reproduced.

With the theory of Bagnold (1954,1956) and a simple analytical model it is possible to reproduce concentration profiles and intrusion depth in sheetflow reasonable well, however, velocity profiles and shear stress distribution found in this way are based upon too primitive assumptions and thus do not match nature very well (Bakker and Van Kesteren, 1986, fig.6 and 7).

Furthermore, Bagnold's theory is designed for stationary flow.

In a numerical model (Bakker and Van Kesteren (1986)), in which layers of grains (with a rigid rectangular structure) are sliding over each other, it was not possible to reproduce Bagnold's dispersive stress in the case of a Couette shearflow at constant volume. Because the model is based on viscous motion, squeezing pressures found when the grains move to each other are cancelled by equal tensile forces when the grains move from each other.

Thus the questions arise:

- a. if rigid layers are shearing over each other, will there be dispersive stress?
- b. which are the stresses, when two grains from different layers nearly touch each other?
- c. is it reasonable to schematize a Couette flow of grains with a layer model?
- d. under which circumstances will dispersive stress be created?

This leads to the following aims of the experiments planned:

- insight in the physical background of the Bagnold stresses;
- visualisation of the grain motion during grain-grain interaction.

3. EXPERIMENTAL SET-UP.

A ring shear apparatus ("Carrousel") has been developed (fig.1, Bakker and Van Kesteren, 1986). Detailed description of experiments accuracy and calibration has been given by Klomp (1990).

Between two plan-parallel rings placed in a circular flume (diameter in the center 1.13 m; internal width 0.07 m) a Couette like shear flow of a mixture of polypropene spheres (diameter $D=14$ mm; Young's modulus 1300 N/mm²), immersed in oil (medical oil Shell code M.W.O.95 or V7047) with the same density (oil: 889 kg/m³; spheres: 860 ± 30 kg/m³) is generated by rotating the upper ring, where the lower ring is fixed. The level of the upper ring is adjustable. Both rings have a spacing in the circular flume of 1 mm on both sides.

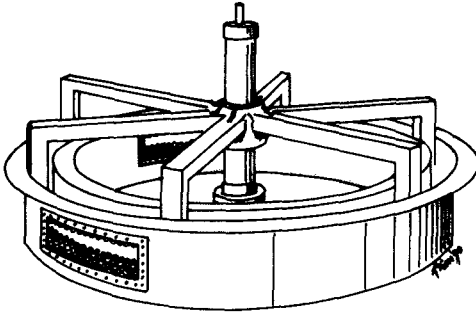


Fig.1 Carousel.

The viscosity of the oil is 10^{-4} m²/s at a temperature of 20° Celsius. It has been chosen in this way, that the shear Reynold's number (see ch.7 eq.2) in the tests was of the same order of magnitude as occurs in oscillating sheetflow in the prototype. The bottom ring rests on three supports (under a mutual angle of 120° with respect to the center of the flume), provided with strain gauges, which all measure normal force, where one of those measures the tangential force. The other

two supports are provided with a skirt-like construction to prevent transducing of any shear stress. After mounting a static and dynamic calibration with and without oil was performed. Elaborate accuracy analysis with respect to the gap width between the rings is given in Klomp (1990) and Bakker et al.(1990).

On upper- and lower ring each 4 rows of 199 hemi-spheres are glued in a regular pattern. For visual observation, three glass windows with a length of 29 cm each were made in the carousel. Sampling occurs with a frequency between 60 and 540 per second, depending on the experiment.

4. EXPERIMENTS.

Five series of experiments have been carried out:

- NO: no interjacent spheres;
- SOME: half a row of interjacent spheres (100 spheres)
- 1LR: (about) one layer of interjacent spheres (510 spheres)
- 3LR: three to five layers of interjacent spheres (3641 spheres).
- VIS: Visual observations, using ca. 3600 grains

Going from series NO to series 3LR the probability of dispersive stress increases, which forms the motivation of these succession of series of tests.

The experiments are determined by the distance between the rings and the turning period of the upper ring. The following table 1 gives the schedule. The table consists of combinations of 2 columns indicating resp. the variables "height between rings" (h) and "revolution period" (T). The mean velocity gradient or shearrate S is given by:

$$S = 2 \frac{\pi R}{T h} ; R = (\text{central}) \text{ radius ring} = 565 \text{ mm} \quad (1)$$

Table 1. Experiments carried out.

Series:	height between rings [mm]	revolution period [sec]
NO	14.9	20 ?
	16 17 18 20 25 50	3 4 5 7 10 20
SOME	25 35 50	3 5 10 20
1LR	35 50 65	3 5 10 20
3LR	51	20
	53	7 10 20
	55	4 5 7 10 20
	60 65 75	3 4 5 7 10 20
VIS	48	5 10.3
	60	4 7.8
	78	2.7 9.5

For each of the indicated heights of the rings tests have been carried out for all of the revolution periods, mentioned on the same line.

Other combinations, which could be imagined have not been carried out because of practical disadvantages: too large forces on the gauges or the destruction (loosening) of the hemispheres on upper and lower ring. The blanks in table 1 show the limits of the possibilities because of blocking.

For instance: during the firstmentioned experiment (of series NO) the distance between upper and lower ring has been reduced as much as possible, up to 14.9 mm. Although according to the schedule still a gap width of 0.9 mm should exist, accuracy analysis made clear, that the utmost extruberance of the upper ring could easily "hit" the utmost extruberance of the lower ring. The experiment had to be stopped soon, in order to avoid destruction, and therefore the revolution period has not been measured accurately.

Mind, that it was possible to carry out experiments with $h=25$ mm (less than $2D$, where D is the grain diameter) in the series SOME; however, this was not the case in the series 1LR, although technically all spheres used in series 1LR could find a place in one layer.

Using a distance between the rings of $3.6 D$ (51 mm) during the series 3LR, it was only possible to measure with a slow revolution period of 20 sec. Here the allowable forces on the measuring system were used as criterion.

During the visual tests the force measuring device was blocked and the allowable torque on the Carrousel (with respect to the motor) could be used as criterion, which gives the opportunity to reduce the distance to $3.44 D$ (48 mm).

With respect to the series VIS (table 1), as well as in series 3LR the grains have been dumped randomly in the Carrousel. Paradoxally, this gave less blocking than an initially arranged order of the grains in a similar way as the one of the hemispheres on both rings. In the arranged order the initial spacing was rather large, which gave freedom for disorder.

Apart from the measurements, photographs in a succession of 0.04 seconds were made from series SOME, and video-films from series VIS. These photographs were analyzed by Bakker, Van Kesteren and Yu (1988; ch.3). The analysis of the video's will be treated in ch.6.

5. GEOMETRIC CONSIDERATIONS.

If it is assumed that in 3 adjacent grainlayers resp. 5, 4 and 5 rows of loose spheres are stacked (in closest packing) in the Carrousel. and the layers would be perfectly flat, only 3548 grains could be stacked. However, when the layers show a certain "waviness" (wave length 2 grain diameters; amplitude 1.5 mm), all 3641 grains can be stored. This waviness occurs anyway, as the lowest loose grains will partly be situated in the hole between 4 hemi-spheres, partly will have their center point in the cross-section perpendicular to the flume through the center of the hemispheres. This gives a variation in height of the center points of those loose spheres (with respect to the lower ring) between 7.83 and 12.12 mm. Thus $4 \times 10 = 40$ mm is considered the minimum distance for storing the grains in the Carrousel (conc.=62.7%).

When the distance between 2 layers of grains becomes more than 12 mm, theoretically those layers should have the probability to slide with respect to each other. Thus a slide plane can occur when the distance between the rings exceeds 42 mm (conc.59.7%).

The effect of the waviness of the layers on the shearing resistance is not quite clear. As the undulating layers can reshape each other during the shearing process, the effect will be less than the one of a fixed roughness. Still, the extra 2 mm allowing for shearing anyway will be a minimum. The minimal distance between the rings when 3 layers of 5 rows in simple cubic piling turn around in the Carrousel becomes 48 mm (conc.=52.2%). This asks for a distance of $2(D+10)$ mm (the center of the grains of the lowest layer are 10 mm above the lower ring, as in the former case). If all layers are fully occupied, 3801 grains are needed, i.e. more than available. Mind, that 48 mm was the minimum distance for which the uperring of the Carrousel was able to rotate in test VIS.

6. VISUAL OBSERVATIONS; GRAIN SWOPS.

From Bakker, Van Kesteren and Yu (1988), ch.3, especially the theoretical and phenomenological aspects of the "centering effect", mentioned in that paper should be remembered (photo 4 a,b,c of that paper).

When there is enough space between the various loose spheres in the same row (in series SOME somewhat more than a grain diameter) the grains move to a central position between the rings and turn around in a stable position, having half the velocity of the upper ring. Furthermore these rotate around their axis.

When the distance between the rings increases or the velocity decreases the effect becomes less distinct (photo 4a of Bakker, Van Kesteren and Yu (1988)); then doublets of spheres can be formed, which can tumble around as a unit (Vand, 1948; Batchelor and Green, (1972)).

During the series LLR (about one layer loose grains) the centering effect turned out to be not large enough to enable a small distance between the rings. A single grain blocking between the hemi-spheres of upper or lower ring could disturb already the order, after which total blocking was just a matter of time.

During experiments in the series VIS carried out with a height between the rings of 60 mm or less, 3 layers were to be distinguished; in the other 2 experiments ($h=78$ mm) 5 layers were observed. In fig.2 the horizontal and vertical velocities of the centers of the visible spheres are shown for the test with a height of 48 mm and a revolution time of 5 s ($S=14.8$ s⁻¹). The vertical coordinate is the position of the spheres with respect to the fixed bottom ring. The velocities are obtained from the digitized videofilm.

The figure shows clearly that the grains move in layers: the vertical position of the centers of the grains is concentrated at three different (grainlayer) levels. Also it must be concluded that the

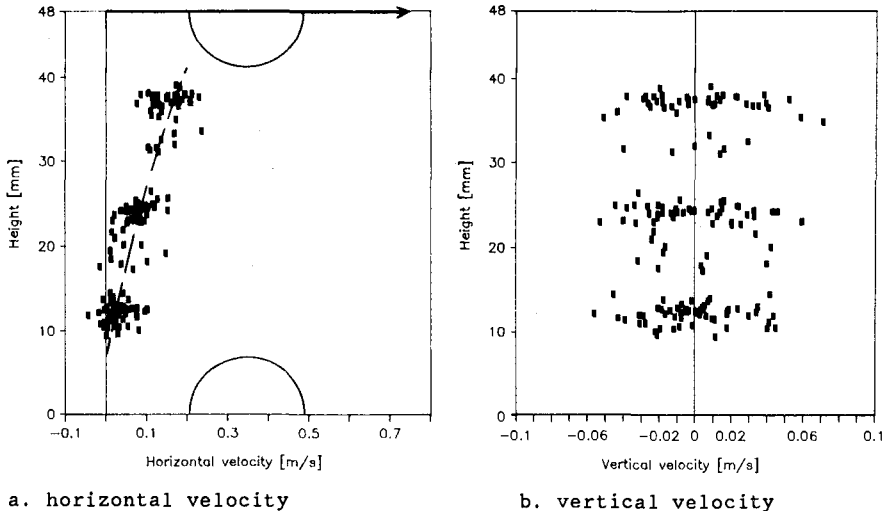


Fig.2 Grain velocities testserie VIS (height $h=48$ mm, period 5 s)

velocity gradient is not constant over the height: in the lower half the velocity gradient is about half the installed velocity gradient. In the upper half of the Carrousel concentration is less than in the lower half, notwithstanding the fact, that the grains are as an average very slightly buoyant and concentrate on the upper part in the starting position. Apparently, the same shear stress can be transmitted with high velocity gradient and low concentration as well as with low velocity gradient and high concentration. Although only some tests have yet have been elaborated in the present way, it is the impression that relative low concentrations occurred on the topside of the Carrousel in all tests. Reason for deviation from symmetry can be: the walls, remaining at rest or relatively large shear stresses near the top ring during the initiation of motion.

A certain grain, emerging in a certain layer on the lefthand side of one of the windows, was followed with the eye until it disappeared on the right hand side. It was registered, whether this grain was at that moment in the original layer, or one or two layers higher/lower. Fig. 3 shows the probability of grain swop in various tests; on the first line for the tests where the grains divided themselves in 3 layers, on the second one for the tests, where 5 layers could be observed. Vertically the various layers are indicated; horizontally the percentage of observed grains, found in this layer at the end of the observation time. With an arrow the layer is indicated, in which the grains emerged on the lefthand side of the window. These observations have been elaborated in the following way. Call a "grain encounter" the event, that two grains of adjacent layers "meet" each other, i.e. (nearly) come into contact with each other.

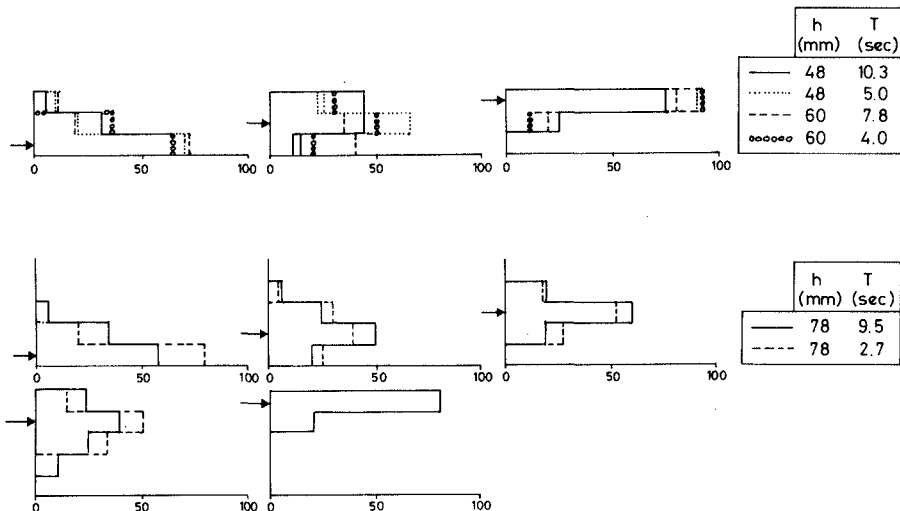


Fig.3 Probability of grain swop in various tests

The number of grain encounters during the observation time (the time during which the grain is visible in the window) can be calculated from the (expectation of the) increment in velocity of a higher layer compared to the one of the adjacent lower layer. It also depends on the distance between the grains in one layer, which can be approximated as $(1 + 1/\lambda)D$ (λ =linear concentration according to Bagnold (1954)) and of the length of the observation time, which is smaller for the higher layers than for the lower layers. Thus is found (Bakker,1989) that the number of grain encounters during the observation period equals $\lambda L/\{(\lambda+1)kD\}$, where L is the length of the window (29 cm) and k the number of the layer (counting from downwards to upwards).

During each encounter the two grains involved can either remain in the layer in which they are, either exchange position. This last event will be called a "grain swop". Let p be the probability of a grain swop per encounter. For the upper or lowest layer thus the probability Pr that a grain still is in the same layer in which it started equals:

$$Pr = (1 - p) \lambda L/\{(\lambda+1)kD\} \tag{2}$$

This under the assumption, that the probability can be neglected, that a grain returns to its former layer after swopping to another layer.

If a layer is enclosed by two adjacent moving layers grain swop can occur to two sides and "1-p" in (2) should be replaced by "1-2p".

From the results, depicted in fig. 3, with the aid of (2) the probability p of a grain swop per encounter has been calculated as function of the linear concentration λ and the shear Reynolds number Re_s , where Re_s is defined as:

$$Re_s = r^2 S/\nu \tag{3}$$

Here S is the velocity gradient, ν the kinematic viscosity and r the radius of the grain (i.e.D/2).

Fig. 4 shows the result with its confidence limits. The probability of grain swops tends to decrease with increasing velocity gradient and increasing concentration.

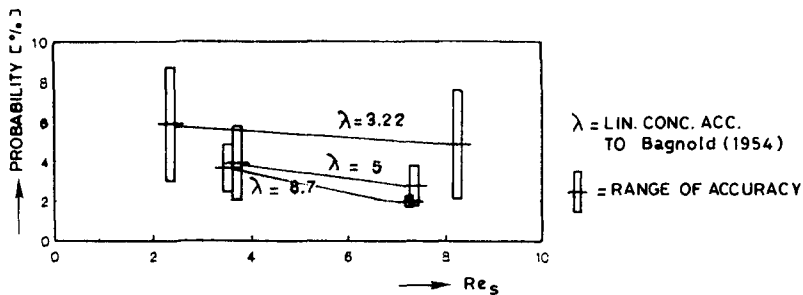


Fig.4 Probability of grain swop as function of λ and Re_s

Bakker (1989) calculated the increase in shear stress caused by momentum transfer from one layer to another. Only the direct transfer - a grain with its momentum comes suddenly in the next layer - has been calculated (the effect of the whole process of blocking and collision, during which a grain could transfer as well the momentum of other grains in its layer to the adjacent layer has not been taken into account). It was found, that the increase of viscosity, caused by this process is proportional to Re_s and p ; for the present tests this increase only amounts to 10 % of the viscosity of the oil.

7. PREVIEW OF THE RESULTS OF THE MEASUREMENTS.

The measured normal forces on the bottom ring in the tests NO showed the occurrence of a propagating pressure wave in phase with the revolution of the upper ring. In the shear force data these fluctuations were absent. Putting separating screens in the space of the carousel below the lower ring, in order to attenuate these waves, gave some improvement, but not enough.

Using Fourier analysis, the signal with the revolution period has been filtered away and a mean normal pressure time series during a period of encounter between two hemispheres of resp. upper and lower ring could be determined. The result, a nearly symmetrical curve with its confidence limits, is shown in fig.5.

Fig 6 shows the tension/pressure in one pressure gauge as function of time in the case of nearly-touching (the first-mentioned experiment of series NO; see table 1 and text ch.6). A very large pressure peak is followed by a small peak of tension. Cavitation could be the cause.

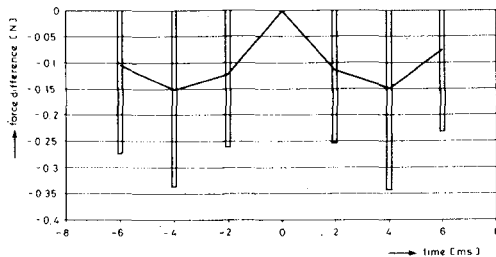


Fig.5 Course of pressure during encounter of hemi-spheres (height=16 mm)

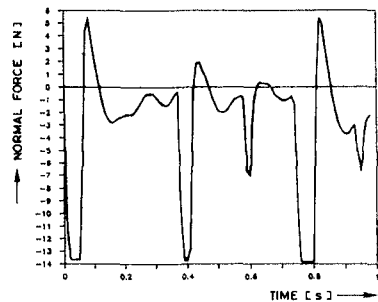


Fig.6 Tensile force in test NO (nearly touching hemi-spheres).

8. ELABORATION OF THE MEASUREMENTS.

By averaging over an integer number of revolutions, summation over the number of supports (i.e. 3) and by division over the area of the lower ring (0.23 m²) the normal forces are converted into pressures (or tractions). The shear stress can be found by direct division by the area of the lower ring.

Data will be presented as function of the shear Reynolds number (eq.(3)) and in the dimensionless Bagnold parameters N and G^2 , defined by:

$$N = 4 \sqrt{\lambda} \cdot Re_s \quad (4)$$

$$G^2 = \tau/\tau_0 \quad \text{or } p/p_0 \quad \text{with } \tau_0 = p_0 = \rho \cdot v^2 \cdot \lambda/D^2 \quad (5)$$

Here S is the velocity gradient, ν the kinematic viscosity, ρ the common specific density of grains and fluid, r the radius of the grain and τ_0 (p_0) is a reference shear stress (pressure). Mind that G^2 according to Bagnold entails one of two variables; it is rather a dimensionless way of presenting τ and p than a variable. Furthermore λ is the linear concentration ϵ/r , where ϵ is half the smallest distance between two adjacent grains.

It thus may be found from:

$$\lambda = \{(c_{\max}/c)^{1/3} - 1\}^{-1} \quad (6)$$

where c_{\max} is the maximum concentration.

Presenting the data on the way of Bagnold thus has no other meaning than presenting the shear stress (c.q. normal stress) versus the velocity gradient at a certain, by Bagnold described dimensionless way. If one wants to compare with Bagnold's results, it should be kept in mind, that Bagnold starts from the conception, that shear stress can be divided into shear stress, acting on the fluid and shear stress acting on the grains, where the present idea is: an integral shear stress, acting on the fluid only and transmitted via the fluid on the grains. It must be kept in mind, that the "correction" of the shear stress for fluid shear stress is not applied in this paper.

9. PRESENTATION OF RESULTS.

Shear stress:

A plot of the shear stress according to Bagnold (G^2 versus N) of the NO-series (fig 7) shows, that the slope of the line follows Bagnold's theory; however, the shear stress is an order 2 lower than Bagnold predicts. Similar results were found in the series SOME (shown in Klomp, 1990 and Bakker et al., 1990) and 1LR (fig.8) apart from one

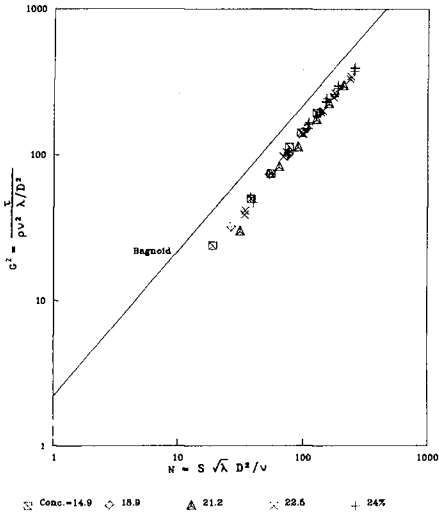


Fig.7 Shear stress as function of velocity gradient; series NO

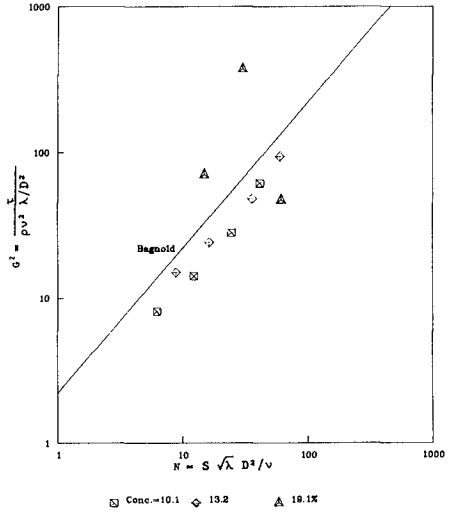


Fig.8 Shear stress as function of velocity gradient; 1LR

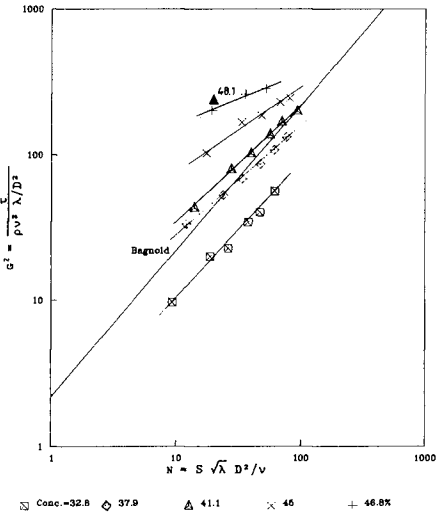


Fig.9 Shear stress as function of velocity gradient; 3LR.

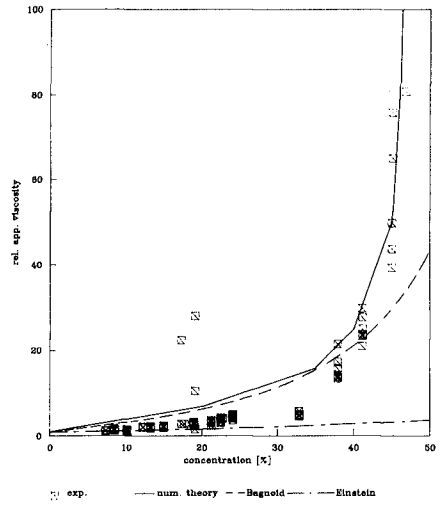


Fig.10 Relative apparent viscosity vs. concentration.

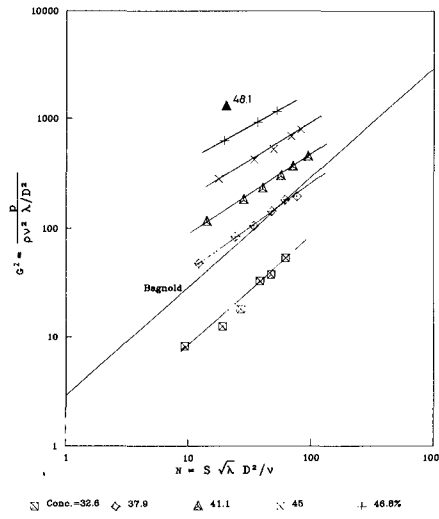
test with smallest distance between the rings in series SOME and two tests with the same conditions in series 1LR, giving a shear stress being orders higher, which can be attributed to blocking.

In series 3LR (fig 9) each concentration gives a different line in the Bagnold graph, being especially for higher concentrations somewhat flatter than the Bagnold line. For high concentration the shear stress is orders of magnitude larger than Bagnold predicts, probably due to the boundary condition of no dilatation and the rigid boundary of hemispheres at the rings in the present tests. Mind (fig.8) that given a relatively high concentration (17.4% in series SOME, 19.1 % in series 1LR) no blocking occurred at relatively high velocity gradient.

In fig.10 the relative apparent viscosity (determined from the experiments) as function of concentration is compared with the theory of Bagnold, Einstein and the numerical theory (Bakker and Van Kesteren 1986). For high concentrations the numerical theory predicts quite well the increase of the apparent viscosity with increasing concentration. The blocking during the series SOME and 1LR appear clearly in this figure.

Normal stress:

In the series NO,SOME and 1LR under some circumstances traction forces on the lower ring are registered instead of pressure, as Bagnold predicts. This makes a presentation impossible according to the Bagnold way, implying a logarithmic plot of the pressure. For



series 3LR, always pressure forces are found; the Bagnold plot of this series is given in fig. 11. Linear plots of fig.11 (Klomp, 1990; Bakker et al.1990) show dispersive pressure and shear stress build up, approximately linear with the velocity gradient. However, the linear relation has a zero-shift: one gets the impression that in the "soil mechanics region" (neglegible motion, non-neglegible strains and stress field) shear stresses and pressures build up, which are enhanced during the motion in the viscous region. The relation between shearstress and normal stress is depicted in fig.12 including the stress points, determined by extrapolation, corresponding to a zero velocity gradient. It appears that the results for different concentrations together form a single unique relation similar to failure envelopes in soil-

Fig.11 Normal stress as function of velocity gradient; 3LR.

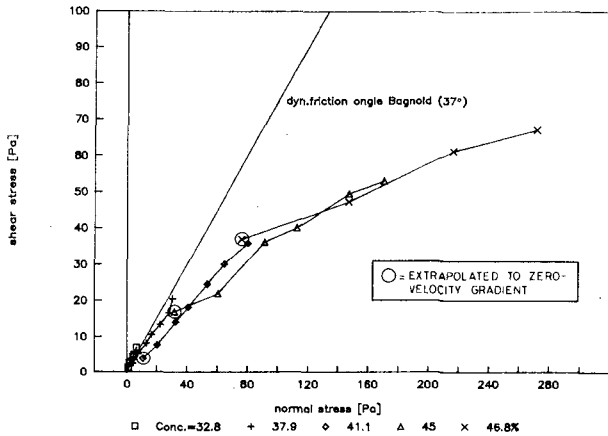


Fig.12 Shear stress vs. normal stress

mechanics. From this relation it can be concluded that the same stress point (shear stress - normal stress) can occur at a high velocity gradient and low concentration or at a low velocity gradient and high concentration.

10. CONCLUSIONS.

- a. Dispersive stresses are found in the grain carousel, when the concentrations exceed 30%.
- b. Probably because of the rigid boundaries (fixed hemispheres, no dilatancy allowed) the dispersive stresses in these cases are (especially at high concentrations) much higher than those found by Bagnold.

A much stronger relation between dispersive stress and concentration was found than according to Bagnold's theory.

- c. Most probable reason of this dispersive stress is blocking (although no straight-forward theory can yet be given concerning the mechanism).

In the case that no blocking occurs (series NO and the most experiments of series SOME and 1LR) only for small shear Reynolds number a minimal dispersive pressure is found; for larger shear Reynolds number even traction forces between the layers are measured.

If no blocking occurs, the shear stress found is about 2/3 of the value predicted by Bagnold.

- d. The grains in a high-concentrated mixture move generally in layers. Only a small percentage of grain swops occur.
- e. When the grain motion is not blocked (exp. series NO, SOME and 1LR) the spheres tend to move in a central position between the rings. This can be explained by the centering force acting on grains, moving between two plates (Bakker et al., 1988).

REFERENCES.

- Bagnold, R.A., Experiments on a gravity-free dispersion of large solid spheres in a Newtonian fluid under shear, Proc. Royal Society, Vol.225, A, p.49 (1954)
- Bagnold, R.A., The flow of cohesionless grains in fluids, Proc. Royal Soc. Vol.249, A964, p.235; Dec.18 (1956)
- Bakker, W.T., Sand concentration in an oscillatory flow, Proc. 14th Conf. on Coastal Engng., Copenhagen (1974)
- Bakker, W.T. and Th.van Doorn, Near bottom velocities in waves with a current, Proc. 16th Int. Conf. on Coastal Engng., Hamburg; pp.1394-1414 (1978) (also: Publication 208, Delft Hydraulics Laboratory)
- Bakker, W.T. and W.G.M. van Kesteren, Near-bottom velocities in waves with a current; analytical and numerical computations, Proc. 19th Int. Conf. on Coastal Engng., Houston (1984)
- Bakker, W.T. and W.G.M. van Kesteren, The dynamics of oscillating sheetflow, Proc. 20th Int. Conf. on Coastal Engng., Taipei (1986)
- Bakker, W.T. and W.G.M. van Kesteren, Oscillating sheetflow in the turbulent boundary layer, "Mechanics of sediment transport in fluvial and marine environments", Euromech 215; St.Marguerite Ligure (1987)
- Bakker, W.T., W.G.M. van Kesteren and Z.H.Yu, Grain-grain interaction in oscillating sheetflow, Proc. 21st Int. Conf. on Coastal Engng., Malaga (1988)
- Bakker, W.T., Grain-swop, Private communication KKI 63 to van Kesteren (in dutch)
- Bakker, W.T., W.G.M. van Kesteren and W.H.G. Klomp, Grain-fluid interaction in Couette flow, Publication J345 Delft Hydraulics Laboratory (1990).
- Batchelor, G.K. and J.T.Green, The hydrodynamic interaction of two small freely-moving spheres in a linear flow field, J.Fluid Mech. 56,part 2, 375-400 (1972)
- Klomp, W.H.G., Korrel-korrel-Interacties; verslag experimentele studie (grain-grain interactions: report of an experimental study; in dutch), Delft University of Technology; Dept. for Civil Engng., Coastal Engng. Group (Jan. 1990)
- Vand, V., Viscosity of solutions and suspensions I,II,III. J.Phys.Colloid Chem.52, 277-321 (1948)
- Yu,Z.H., H.D.Niemeyer and W.T.Bakker, Site investigation on sand concentration in the sheetflow layer, Proc. 22st Int. Conf. on Coastal Engng., Delft (1990)

CHAPTER 206

EVALUATION OF RADIOACTIVE SAND TRACERS TO MEASURE LONGSHORE SEDIMENT TRANSPORT RATES

G. Drapeau¹, B. Long¹ and J.W. Kamphuis²

ABSTRACT

This paper analyzes and compares radioactive sand tracer experiments with beach profile measurements and calculations of littoral sand transport rates performed at Pointe Sapin, N.B. in the Gulf of St. Lawrence, Canada. The three methods give comparable results. In theory, all sediment tracers should be dealt with the same way, but in practice the nature of the tracers has to be taken into account. Tracers do fulfill the purpose for which they are used and they can solve sediment transport problems when used with knowledge and care. The wide variation among littoral sediment transport formulas should not be attributed to the lack of accuracy of tracer experiments but rather to the fact that expressions are over-simplistic and important factors such as the influence of beach slope and grain size are not taken into account.

1. INTRODUCTION

The determination of alongshore sediment transport rate remains one of the fundamental problems of coastal engineering. The Canadian Coastal Sediment Study (C²S²) brought together oceanographic, geological, and engineering researchers in Canada to study coastal processes and improve the knowledge of sand transport on beaches (Willis, 1987). One of the main achievements of (C²S²) has been to coordinate different experiments at two sites in the Gulf of St. Lawrence: Pointe Sapin, N.B. and Stanhope Lane, P.E.I. The purpose of this paper is on the one hand to analyze and compare radioactive sand tracer experiments with beach profile measurements and calculations of littoral sand transport rates performed at Pointe Sapin and on the

1 INRS-Océanologie,
Université du Québec,
Rimouski, Qc,
CANADA G5L 3A1

2 Dept. Civil Engineering
Queen's University
Kingston, Ont.
CANADA K7L 3N6

other hand to compare these results with sand tracer experiments carried out elsewhere.

As the sediment tracer measurements are compared with other measurements and calculations of sediment transport carried out simultaneously at the same site, it permits verification of the capabilities as well as the limitations of the sediment tracer technology. Sediment tracer results have been one of the main sources of information to develop littoral transport formulas. The behavior of tracer particles in the longshore sediment transport system has been examined by Madsen (1987) who points out that sediment tracer experiments must meet many assumptions to sustain the theory on which the sediment tracer technology is based and he concludes that in his opinion whether or not the longshore sediment transport system invalidates the assumptions behind the use of tracer methodologies is not yet resolved.

In this study the spatial integration of radioactive tracers is used to determine sediment transport rates. The basic assumption behind the use of tracers is that advection, the downstream transport of sediments associated with the flow in the transport system, dominates diffusion and dispersion. The use of tracers to measure longshore transport of sand in the surf zone is based on the principle of continuity described by a continuity equation such as:

$$Q = V_a b \quad (1)$$

where V_a is the mass velocity of the tracer and b is the thickness of the mobile sediment layer.

Inherent to the use of tracers is the problem of defining to what extent the observed movement of tracer grains is representative of the movement of sediment within which the tracer grains have been injected. There are two premises: one is that the trajectory of tracer grains is the same as that of the sediment in which they are injected, and the other is that the depth of mixing of the tracer is representative of the thickness of the mobile sediment layer.

The centroid of all tracer grains detected during a given survey is used to determine the mass velocity (V_a) of the tracer which is obtained by dividing the distance the centroid of the tracer cloud has moved between two surveys by the time elapsed between these two surveys. Tracers with the same grain size and density as the parent sediment are assumed to follow similar paths. The depth of mixing of tracer grains is more difficult to assess because sediment tracers are usually deposited at the water-sediment interface and their mixing within

the sediment mobile layer is not instantaneous. The thickness of the moving sediment layer was estimated using an analytical solution developed by Sauzay (1967). Cores of the beach were also taken during the tracer experiment. The distribution of tracer within the cores shows different patterns depending on location and time, but a parabolic distribution is found in many cases that confirms Alquier's experimental verification (Alquier et al. 1970) of Sauzay's model as well as the theoretical tracer distribution, based on "waiting time considerations", developed by Galvin (1987).

In theory, all sediment tracers should be dealt with the same way, but in practice the nature of the tracers has to be taken into account. The time scale and the space scale of luminescent tracers and radioactive tracers differ by one order of magnitude. Luminescent tracer experiments are measured in terms of hours and tens of meters, while radioactive tracer experiments last many days and cover hundred of meters. These large differences imply that the results are interpreted differently.

2. EXPERIMENTAL SETTING

2.1 Location of study area

Two sites were selected in the Gulf of St. Lawrence for the Canadian Coastal Sediment Study; one was located at Pointe Sapin, N.B. and was occupied during the fall of 1983 and the other was located at Stanhope, P.E.I. and occupied during the fall of 1984. The present paper is dealing with the Pointe Sapin experiment (Fig. 1).

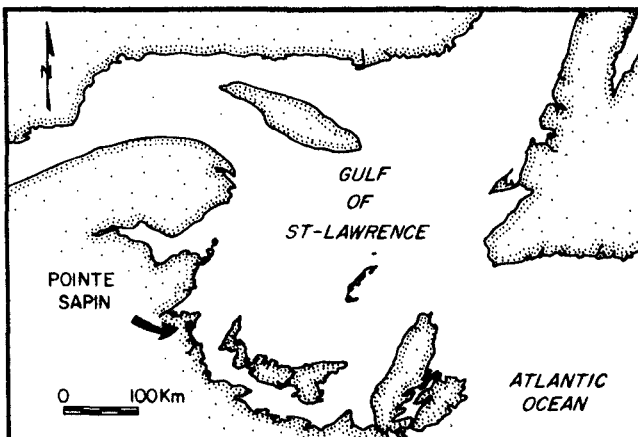


Figure 1. Location of study area.

Pointe Sapin is a small fishing harbor on the coast of New Brunswick in the Gulf of St. Lawrence. The location of this site is such that it is exposed to long fetches exclusively from the north-east. The Pointe Sapin site is then subjected to an almost unidirectional alongshore sediment transport, which is an advantage for studying the transport of sediments. Furthermore, the littoral sediment drift is terminating in a sand trap, a detached breakwater designed to keep Pointe Sapin Harbor entrance open (Fig. 2-A).

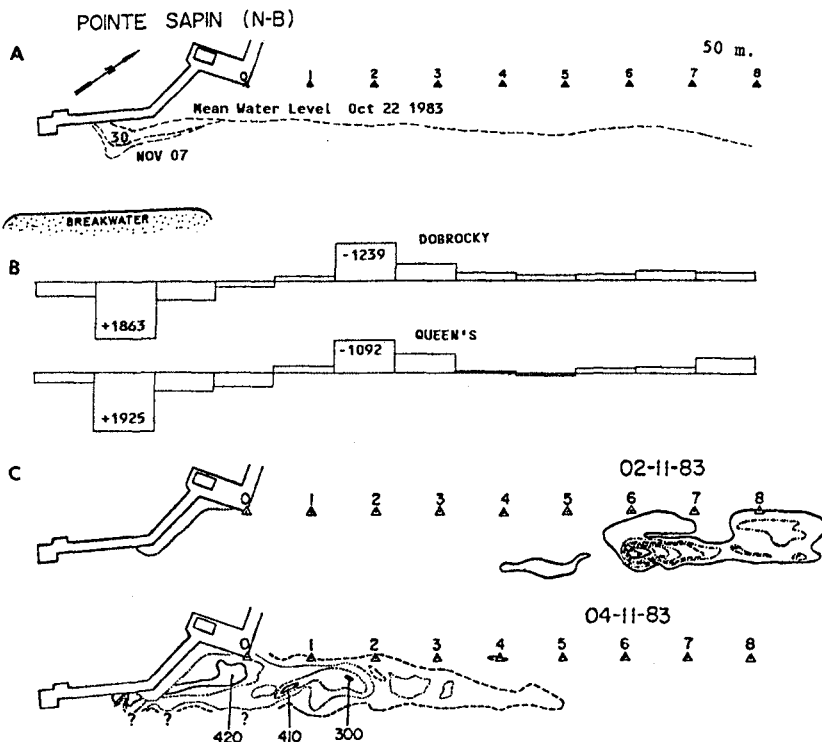


Figure 2. A) General setting. B) Measured (Dobrocky) and calculated (Queen's) transport rates. C) Sediment tracer distribution before and after Nov 4 storm.

2.2 Field measurement program

The Canadian Coastal Sediment Study measured: 1) directional waves at 4 km and 750 m. offshore 2) cur-

rents at 1100 m. and 700 m. offshore and in the surf zone, 3) beach profiles, 4) volumetric sand transport at the trap, 5) suspended sediment concentration, and 6) dispersion of radioactive tagged sand.

2.3 Sand trap at Pointe Sapin

The study site at Pointe-Sapin benefits from a detached breakwater that serves as a sediment trap filling up on a yearly basis. Figure 2-A shows the evolution of the sand trap that had been dredged in September 1983, prior to the field operations, and then partially filled during the field study, mostly during the passage of two north-easterly storms over the area (October 25th and November 4th, 1983).

2.4 November 4th storm

Two north-easterly storms developed during the field experiment; one on October 25th and the other on November 4th. The results from the present study are centered on November 4th storm. Periods of dominant waves varied from about 3 seconds during calmer conditions, up to nearly 10 seconds for the two storm events. Immediately prior to the Nov. 4th storm, the wave period gradually increased, as typical of a developing local storm system. Because of the geometry of the coastline and the adjacent islands, the wave field did not shift in direction significantly as the storm front passed. This is largely due to the narrow window through which waves may pass to impinge onto Pointe Sapin. During the November 4th storm, significant wave height exceeded 1.25 m, propagating towards 272-273 degrees TN with periods of 8.5 seconds, growing to 9.8 seconds near the end of the storm (Aubrey and Spencer, 1984).

3. RESULTS

3.1 Volume measurements of erosion and sedimentation

Beach and bathymetric profiles of the sand trap and the adjacent beach and nearshore zone were measured regularly and also after each storm by the Dobrocky-Seatech group (Gillie, 1984). Consecutive sets of profiles were compared to determine the volumes of erosion and sedimentation. A complete survey was carried out before (Oct. 30th) and after (Nov. 7th) the November 4th storm. The erosion and sedimentation of the beach and sand trap resulting from that storm are shown in Fig. 2-B.

3.2 Tracer measurements

The radioactive element used for the sediment tracer study was gold¹⁹⁸ (2.7-day half-life) incorporated in glass grounded to the size of the beach sediment. One kilogram of sediment tracer was injected on November 1st at the location of marker #6 as shown in Fig. 2-C (Long, 1984). Twelve surveys of the radioactive tracer were carried out during the nine following days (Table 1). The distribution of tracers before (03 Nov. 15:00 hrs) and at the end of the storm (04 Nov. 15:00 hrs) is shown in Fig. 2-C.

Table 1

Tracer Experiment Parameters

Time (hrs)	Q (m ³ /hr)	b (cm)	X (m)	Y (m)
12.00	0.00	0.00	500.00	33.000
34.00	-0.06	2.10	502.07	33.250
40.00	-0.88	7.00	504.01	34.250
59.00	-0.98	11.80	508.10	32.650
63.00	-2.66	9.30	511.74	37.050
84.00	271.53	50.80	244.49	25.000
87.00	143.67	55.60	218.65	21.920
107.00	23.00	48.10	226.72	35.000
132.00	31.41	45.20	151.00	31.900
156.00	-7.77	23.80	170.56	32.920
179.00	1.50	9.50	243.92	32.720
208.00	-0.05	5.30	166.97	34.150

Time = time in hours starting at 00:00 hrs 01/11/83

Q = sediment transport rate

b = depth of mixing of tracer

X = longshore coordinate of tracer cloud centroid

Y = crossshore coordinate of tracer cloud centroid

3.3 Calculations of erosion and sedimentation

Kamphuis *et al.* (1986) developed a model based on the wave energy flux to calculate littoral sand transport rates. This model was used at Pointe Sapin to calculate sand transport rates as well as erosion and sedimentation in the study area for the November 4th storm (Kooistra and Kamphuis, 1984). The results are shown in Fig. 2-B and in Fig. 3.

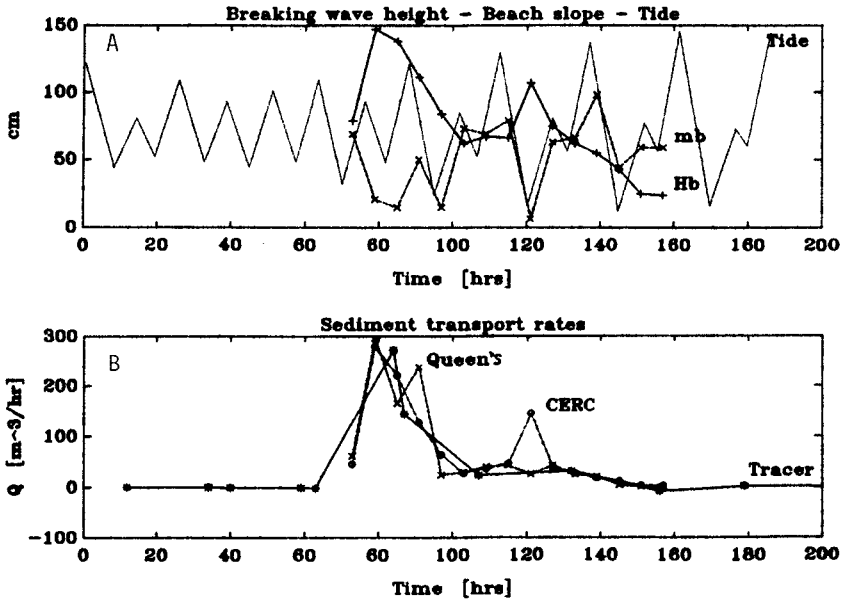


Figure 3. Time series starting at 00:00 hrs Nov. 1st 1983.
 A) Tide height (Tide [cm]), Beach slope (mb [x1000])
 Breaking wave height (Hb [cm]).
 B) sediment transport rates.

4. DISCUSSION AND CONCLUSIONS

4.1 Coherence of Pointe Sapin results

Estimates of total volume of sediments transported during the November 4th storm are shown in Tab. 2.

Table 2

Transport using volume method	5200 m ³
Transport using tracer method	
30 m. wide beach	5300 m ³
40 m. wide beach	7100 m ³
Calculated transport:	6070 m ³

These results outline the good agreement between the three methods used at Pointe Sapin. As explained above,

the Pointe Sapin site is particularly appropriate to perform comparative studies because uniform conditions are maintained during storm events. Time series of littoral drift estimates based on: a) 12-hourly tracer surveys, b) 6-hourly calculations based on Queen's model (Kooistra and Kamphuis, 1984), c) 12-hourly calculations based on CERC formula are compared in Fig. 3-B, using wave height, tide and beach slope of Fig. 3-A. These time series show that the tracer method estimates concur with the littoral drift calculations. It is worth noticing that although the tracer method calculations for littoral drift are based on a spatial integration, they are nonetheless sensitive to short-time variations of the wave climate. Fig. 3-B also shows that the CERC formula is directly linked to the wave climate exclusively, while the Queen's formula also incorporates the beach slope. This is the reason why at hour 120 in Fig. 3-B the CERC formula shows a peak which is reflected neither by the Queen's estimate nor by the tracer measurements.

4.2 Comparison with other studies

Extensive field experiments on longshore sand transport in the surf zone have been carried out in Japan. The results of these experiments were synthesized by Kraus *et al.* (1982). Eight sand tracer experiments were performed in energetic surf zones on natural beaches and on beaches near structures to measure short-term longshore sand transport rates. Tracers of up to four distinct colors were used to better outline the distributions of the longshore sand advection velocity and transport rate.

The transport rate of sediments is related to the fluid energy dissipation on the shore. Kraus *et al.* (1982) obtain the relationship:

$$Q = 0.024H_b^2V \quad (2)$$

where Q is the volumetric transport rate, H_b the wave height at breaking and V the average longshore current, assuming a beach slope of 1/50 and a breaking index of 0.8. This equation is plotted in Fig. 4 as well as the results from the Japanese tracer program. It can be seen that the equation is a good descriptor of the Japanese tracer data from which it is derived. Tracer results from Pointe Sapin are shown on the same figure. The energy dissipation levels are comparable for the two sets of data but the corresponding transport rates are one order of magnitude larger in the case of Pointe Sapin.

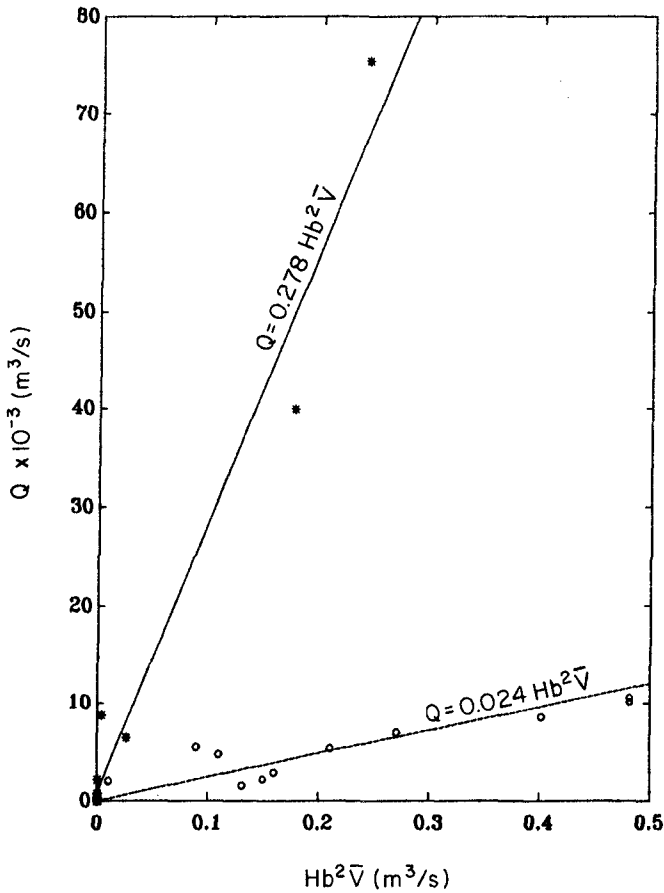


Figure 4. Volumetric transport rate.
 O = Kraus et al. 1982 data.
 * = This study.

Kraus et al. (1982) arrive at that definition of equation 2 using two other equations derived empirically from their field measurements:

$$V_a = 0.014V \quad (3)$$

$$b = 0.027H_b \quad (4)$$

where V_a is the tracer cloud centroid advection velocity, b the depth of tracer mixing and the other parameters are the same as Eq. 2.

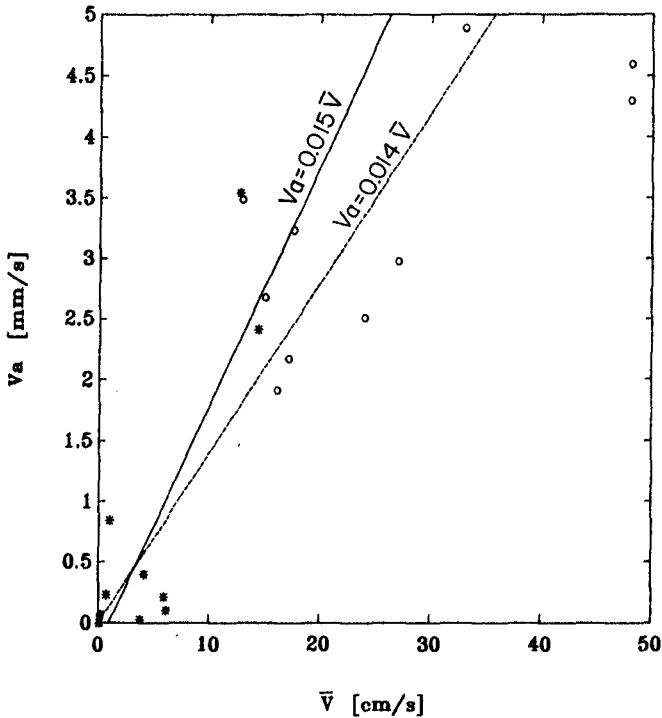


Figure 5. Sand advection velocity.

O = Kraus et al. 1982 data.

* = This study.

Equation 3 establishes a relationship between the mean longshore current (\bar{V}) and the sand advection velocity (V_a). The results from the Japanese program and those from Pointe Sapin are plotted on the same diagram in Fig. 5. In this case the results from Pointe Sapin and those from Kraus *et al.* (1982) concur, which implies that for comparable conditions the advection of sand in the longshore transport process is essentially the same be it on Japan beaches or in the Gulf of St. Lawrence.

Equation 4 which correlates the depth of tracer mixing to the wave height is plotted in Fig. 6. Here again the results from Pointe Sapin are one order of magnitude larger than those from Japan beaches. It indicates that transport rates obtained for the present study are different from those obtained by Kraus *et al.* (1982) for comparable energy conditions because esti-

mates of thicknesses of the mobile sediment traction layer are different.

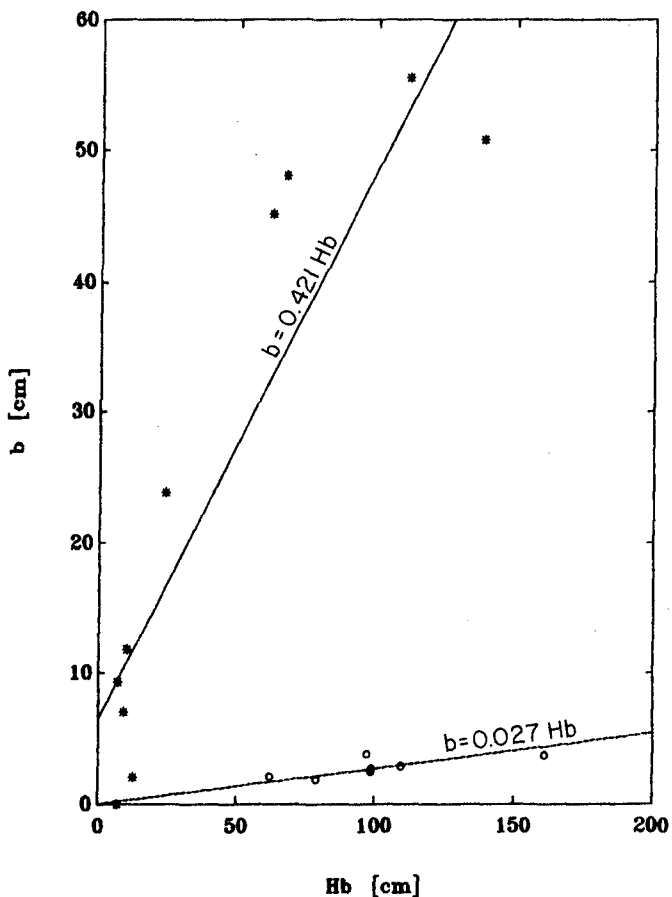


Figure 6. Depth of mixing.
 O = Kraus et al. 1982 data.
 * = This study.

The thickness of the mobile layer is determined indirectly when radioactive tracers are used. It is based on the evaluation of the diminution of tracer signal as a function of depth of burial into the sediment (Sauzay, 1967). With luminescent tracers the thickness of the mobile layer is determined by coring the sediment and sampling at different intervals. Kraus (1985) has examined the vertical mixing of luminescent tracer within the sand of the surf zone for the eight

Japanese experiments referred above. He takes the thickness of the mobile layer to be the depth where 80 percent of the total tracer included in the core is reached. The results of Kraus *et al.* (1982) plotted in Fig. 4, 5 and 6 are based on that premise.

Galvin (1987) has reviewed the problem of vertical distribution of sand tracers in the littoral zone. He approached the problem using a stratigraphic as well as a hydraulic analogy and developed the concept of waiting time. This concept explains, from theoretical considerations, how a given quantity of tracer grains evolves as a function of time as well as a function of distance from the tracer source. These results show that the depth of mixing and also the distribution of tracer change as time passes after the initial tracer release. This is particularly relevant when radioactive tracer experiments are compared with luminescent tracer experiments. Luminescent tracer experiments last less than a day and cover a few tens of meters. By contrast radioactive tracer experiments last for many days and cover hundred of square meters.

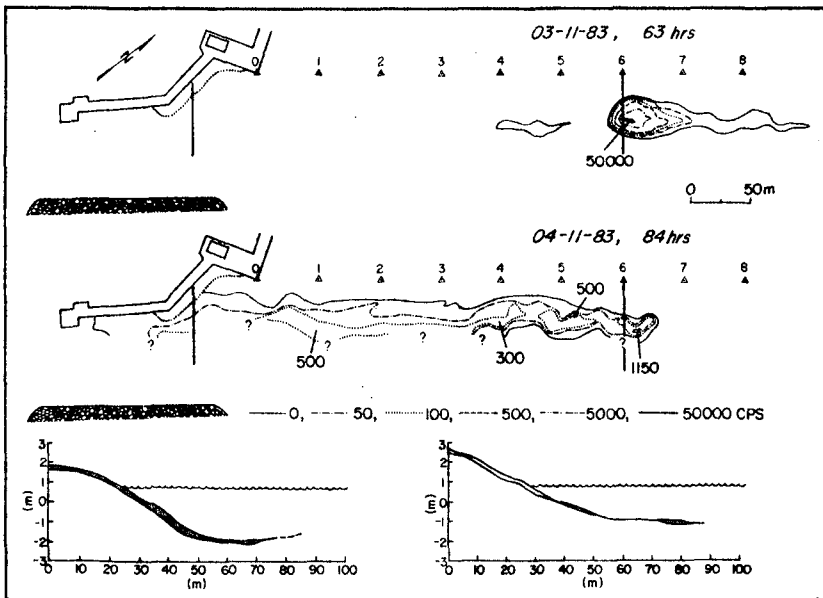


Figure 7. Distribution of tracer cloud before the November 4th storm (03/11/83 63 hrs) and after the storm (04/11/83 84 hrs) Beach profiles surveyed on Oct. 30 and Nov. 7, at station #6 and at the wharf, are shown on the lower portion of the figure. Sedimentation is identified by gray tone.

It is not surprising then that the estimates for the depths of mixing are not the same. If one refers to Galvin's (1987) Fig. 5, it can be seen that if radioactive and luminescent tracer experiments were performed at the same site they would produce different results, the radioactive tracer experiment yielding deeper mixing depths because it lasts longer and covers a larger area.

Data from Tab. 1 show that the depth of mixing during the first 40 hours of the Pointe Sapin experiment is comparable with what was measured on Japanese beaches. The values obtained for the depth of tracer mixing at Pointe Sapin are verified by comparing depth estimates of tracer mixing with beach profile measurements. Beach profiles across the tracer clouds are shown in Fig. 7. Profiles surveyed before and after the Nov. 4th storm are drawn on that figure. Erosion is dominant along profile #6 while sedimentation is prevails along the beach profile extending between the wharf and the detached breakwater. The thicknesses of erosion and sedimentation obtained by comparing beach profiles are in agreement with the depths of mixing estimates shown in Tab. 1.

Conclusions that can be drawn from this study are: 1) tracers do fulfill the purpose for which they are used and they can solve sediment transport problems when used with knowledge and care; 2) the wide variation among littoral sediment transport formulas should not be attributed to the lack of accuracy of tracer experiments but rather to the fact that expressions are oversimplistic and important factors such as the influence of beach slope and grain size are not taken into account.

5. ACKNOWLEDGMENTS

The research presented in this paper was sponsored by the National Research Council and the National Sciences and Engineering Council of Canada.

6. REFERENCES

- ALQUIER, M., COURTOIS, G., GRUAT, G. AND SAUZAY, G. 1970. La notion de bon mélange dans l'emploi de traceurs. La Houille Blanche:25 (7):643-650.
- AUBREY, D.G. and SPENCER, W.D., 1984. Inner shelf sand transport wave measurements, Pointe Sapin, N.B., Canada. Canadian Coastal Sediment Study Rep. C2S2-5.

GILLIE, R.D. 1984. Evaluations of measurement techniques. Canadian Coastal Sediment Study Rep. C2S2-9.

GALVIN, C. 1987. Vertical profile of littoral sand tracers from a distribution of waiting times. Coastal Sediments'87 (N. Kraus ed.), ASCE p.436-451.

KAMPHUIS, J.W., DAVIES, M.H., NAIRN, R.B. and SAYAO, O.J. 1986. Calculation of littoral sand transport rate. Coastal Engineering, 10:1-21.

KOOISTRA, J. and KAMPHUIS, J.W. 1984. Scale effects in alongshore sediment transport rates. Canadian Coastal Sediment Study Rep. C2S2-13.

KRAUS, N.C., ISOBE, M., IGARASHI, H., SASAKI, T.O., and HORIKAWA, K. 1982. Field experiments on longshore sand transport in the surf zone. Proc. 18th Coastal Engineering Conf. (B.L. Edge, ed.) A.S.C.E. p. 969-988.

KRAUS, N.C., 1985. Field experiments on vertical mixing of sand in the surf zone. Jour. Sedimentary Petrology, 25:3-14.

LONG, B.F. 1984. Evaluations of measurement techniques. Canadian Coastal Sediment Study Rep. C2S2-9.

MADSEN, O.S. 1987. Use of tracers in sediment transport studies. Proc. Coastal Sediments'87, (N. Kraus ed.) ASCE p.424-435.

SAUZAY, G. 1967. Méthode de bilan des taux de comptage d'indicateurs radioactifs pour la détermination de débit de charriage de lits sableux. Thèse doctorale, Toulouse, 162 p.

WILLIS, D.H. 1987. The Canadian Coastal Sediment Study: an overview. Coastal Sediments'87 (N. Kraus ed.), ASCE p.682-690.

PART VI

Coastal Estuarine and Environmental Problems



CHAPTER 207

Beach Erosion Due to Large Coastal Structure and Its Control

Yoshito Tsuchiya¹, Member ASCE, Takao Yamashita² and Richard Silvester³,
Member ASCE

1. Introduction

Beach erosion has recently been recongnized as accelerating due to the influence of coastal structures. This tendency is especially severe in Japan where coastal structures are over abundant. Blockage of the longshore sediment transport and changes in the wave field are the most common causes of structure induced beach erosion. In this paper, these are indentified as the first and second causes of erosion. Examples of such beach erosion in Japan are provided.

In order to explain the two common erosion causes and beach erosion control, results of numerical simulations of shoreline change by a coastal structure and nearshore currents due to wave fields changed are also shown. In the numerical simulation, a countermeasure for beach erosion which is caused by changing of nearshore currents by the coastal sturcture is proposed.

The scenario for the beach erosion can be easily described by Figure 1. In this figure beach erosion due to the first erosion cause, the blockage of longshore sediment transport, is shown in (a) which explains the continuous erosion extending downstream in longshore sediment transport. Beach erosion due to the second erosion cause, the change of nearshore currents by the coastal structure, is shown in (b) which describes ersoion taking place within a limited area. Due to both the first and second erosion causes, beach erosion generally takes place. Beach erosion control should be considered by taking into account these erosion processes, and more strictly speaking for the beach erosion the sandy beach being eroded must be stabilized. For this purpose a dynamical background for the formation of stable

¹Professor, Disaster Prevention Research Institute(DPRI), Kyoto University, Uji, Kyoto 611, Japan.

²Instructor, DPRI, Kyoto University, Uji, Kyoto 611, Japan.

³Honarary Research Fellow, The University of Western Australia, Nedlands, WA 6009, Australia.

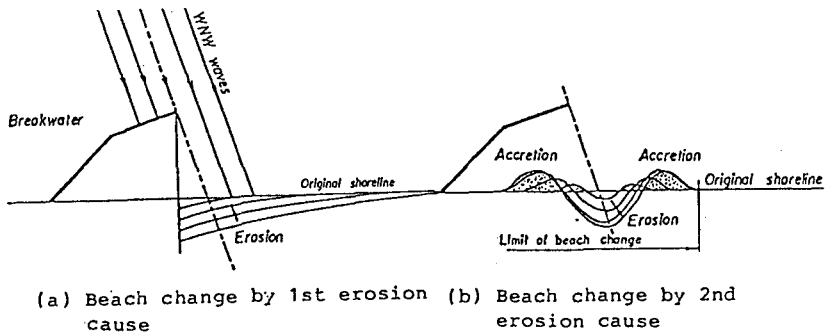


Figure 1 Shoreline changes by two common beach erosion causes.

sandy beaches has to be established. Applying our recent theory of nonuniform longshore sediment transport along the sandy beach, a theory of the formation of stable sandy beaches was recently established by Tsuchiya and Refaat(1990). The theoretical result is very briefly introduced, and then a methodology for the structure induced beach erosion is proposed with a special reference to the Ogata coast facing the Japan Sea.

2. Beach Change by Large Coastal Structure

In order to describe beach changes such as changes in shoreline and bottom topography, an example of the Ogata coast beach erosion is shown in Figure 2. The Naoetsu Harbour shown in this figure has recently been enlarged. NW or WNW and N or NNE waves are predominant to the coast, the former waves are 8 to 10 sec in wave period with a very high wave height, and the later ones are 12 to 14 sec with a small wave height. The predominant direction of longshore sediment is therefore mostly easterly and sometimes changed. In the area just upstream the Naoetsu Harbour, the Seki river is flowing into the area to supply sediment which is the main sediment sources for the coast. The harbour breakwaters were constructed on the right side of the river mouth. Since no longshore sediment can be transported downstream, severe beach erosion has then taken place, and it has recently been accelerated by extending the breakwaters.

Changes in shoreline due to the construction of the breakwaters are shown in Figure 3 where the origin of the distance is taken at Gotsu and the harbour is located

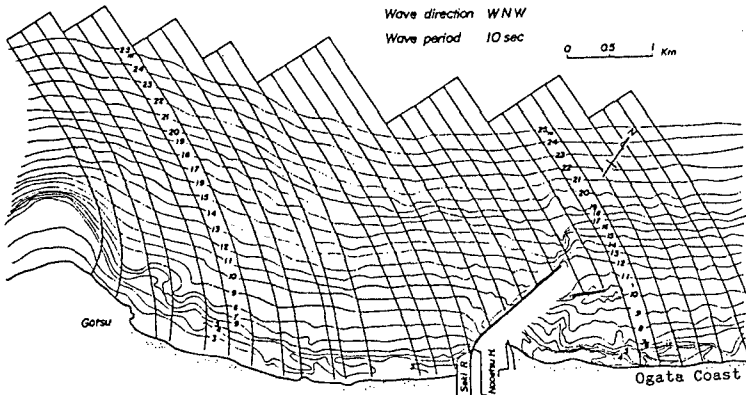
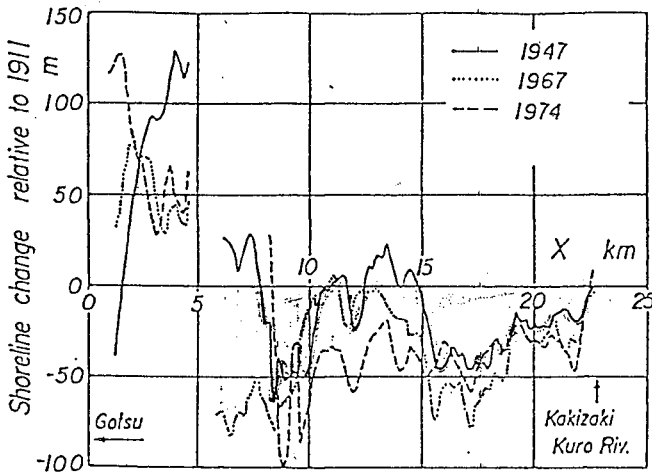


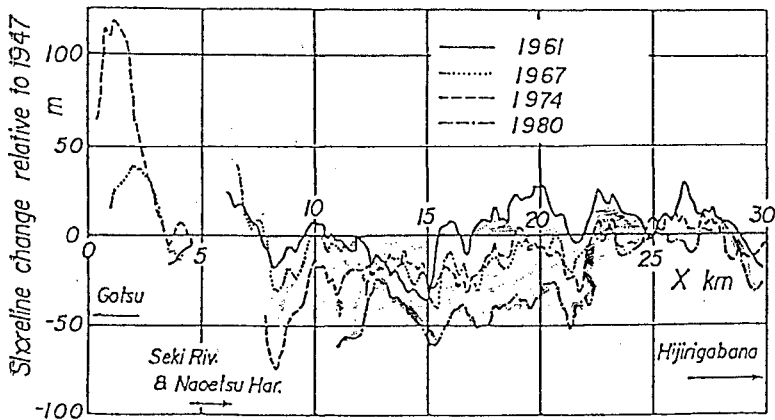
Figure 2 Locations of Ogata coast and Naoetsu Harbour, and refraction diagram of WNW waves with a period of 10sec.

around 4 to 7km. In reference to the shoreline positions in 1911 and 1947 the shoreline changes are shown in (a) and (b) of the figure, respectively. It should be understood that the beach erosion has advanced greatly and the erosion waves have been propagated in the easterly direction, showing some undulations in the waves. To the contrary on the west side, sediment deposition has recently taken place due to the effect of waves reflected by the breakwaters.

To prevent beach erosion, sea dikes were first constructed, but beach erosion had advanced and sandy beaches no longer existed. Secondly, offshore breakwaters were constructed and a great number of concrete units were used. However, the beach erosion have been still in progress and accelerated by structure reflected waves. The water depths have deepened in front of sea dikes and offshore breakwaters. As seen in Figure 4, concrete unit weight to be used increased with an increase in water depth in front of the structures. In advance of beach change beach profiles become generally steep. An example of beach profile change is shown in Figure 5 where the beach profiles measured in 1968, 1972 and 1976 are compared. At that time in 1968 the coast was so-called wave energy dissipative beach, but gradually changing beach profiles more steep they have already become so-called wave energy reflective beach. Catastrophic beach change has therefore sometimes taken place in the coast. This may mean that nature intends to recover the beach profiles to her native ones. It can therefore be concluded from these cases that more natural sandy beaches must be



(a) Shoreline change from 1911 to 1974



(b) Shoreline change from 1947 to 1980

Figure 3 Changes in shoreline due to construction of breakwaters of Naoetsu Harbour.

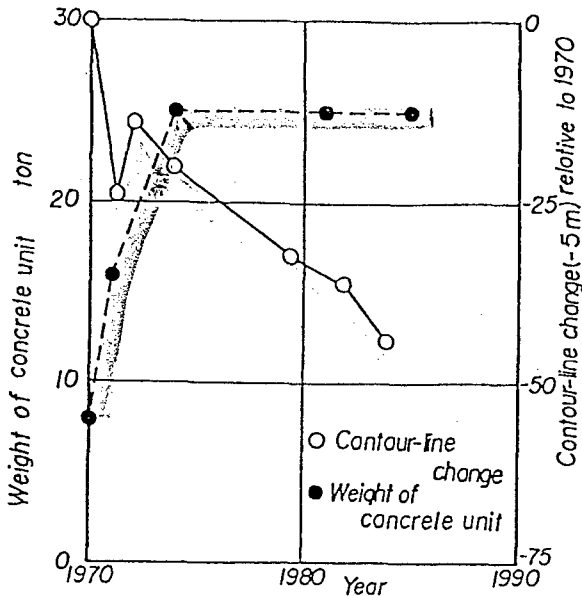


Figure 4 Changes in concrete unit weight used and contour-line of water depth of 5m.

recovered for erosion control (Tsuchiya, 1987).

3. Numerical Simulations of Changes in Shoreline and Nearshore Currents and Their Control

By use of one line models for shoreline change, calculation was made to predict changes in shoreline in a model condition. One of the numerical results of shoreline change by the breakwaters is shown in Figure 6 where the incident wave conditions being 4 m in wave height, 7 sec in wave period and 10 degrees in wave direction from the north are given. It can be easily understood by the time sequence in shoreline change that the shoreline change occurs continuously to extend in the downstream direction, and that as shown in Figure 2 beach change severely takes place in the area where the two common causes for beach erosion exist.

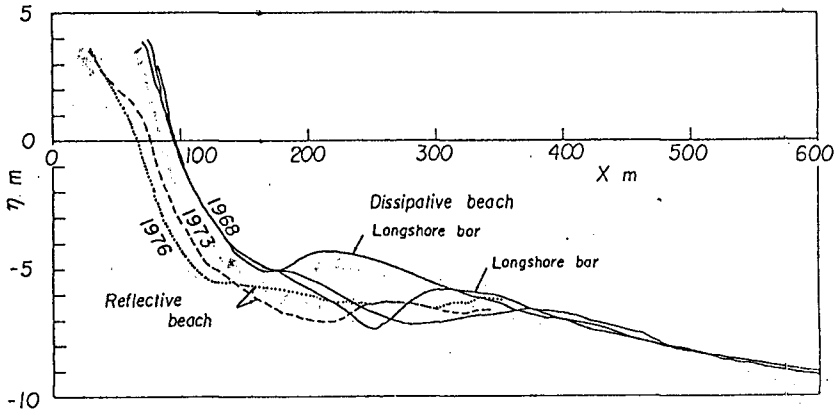


Figure 5 Changes in beach profiles at Ogata coast.

As discussed in Figure 2, the breakwaters generally induce change in the nearshore currents. By use of a nearshore current model numerical calculations were made to find changes in wave field in the area where breakwaters exist and in the

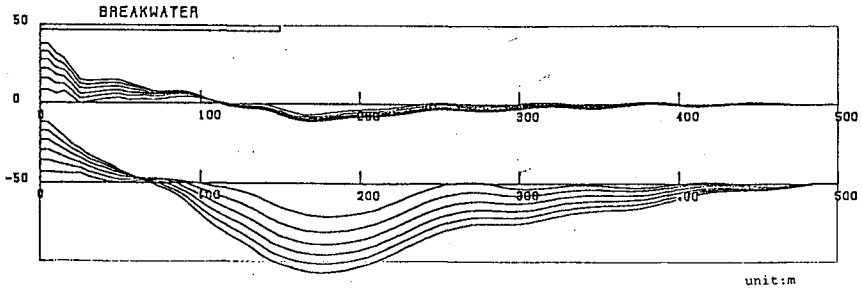


Figure 6 Numerical result of shoreline change due to blockage of longshore sediment transport.

structure induced nearshore currents. Figure 7 shows an example of the numerical calculations where the incident wave conditions being 4 m in wave height, 7 sec in wave period and normal wave incidence were given. In the numerical simulations the

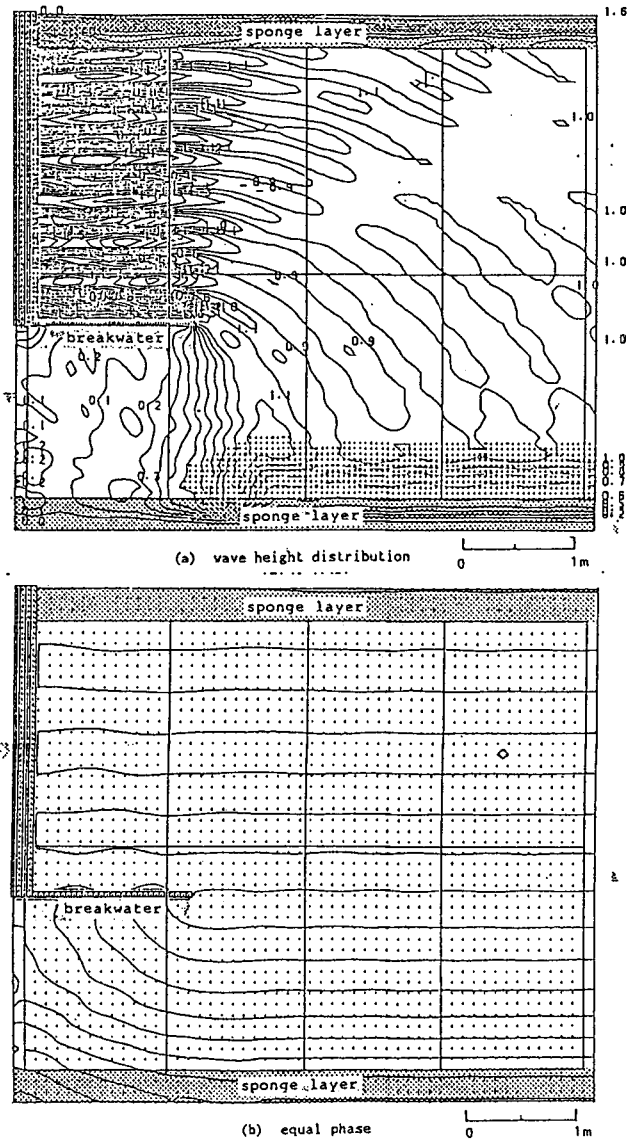


Figure 7 Numerical result of wave field in the area where a breakwater exists.

so-called sponge layer was employed both in the offshore and shoreline areas. The upper figure shows the wave height distribution and the lower figure does the equi-phase lines. Using this wave field nearshore currents were calculated as shown in Figure 8. It is clearly shown that there clearly exist a couple of nearshore

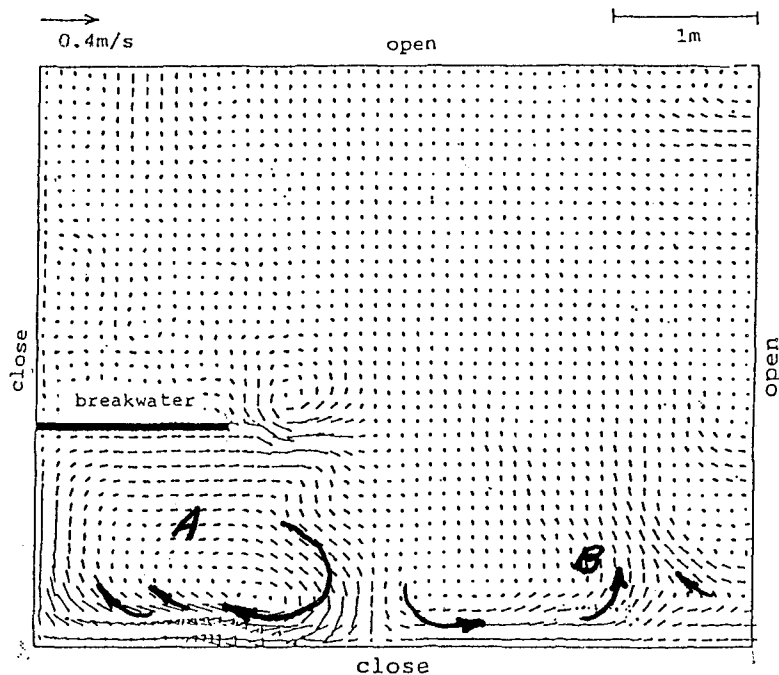


Figure 8 Numerical result of nearshore currents in the area where a breakwater exists.

circulations, which are shown by A and B exist in the area behind the breakwaters. In order to control beach erosion caused by the changing wave field, these circulation must be reduced. Numerical consideration was made of changing nearshore currents by a small groin. Figure 9 shows the wave field in the case where a small groin is constructed in the nearshore circulation A. Using this wave field nearshore circulation was calculated as shown in Figure 10. It is concluded that the groin is

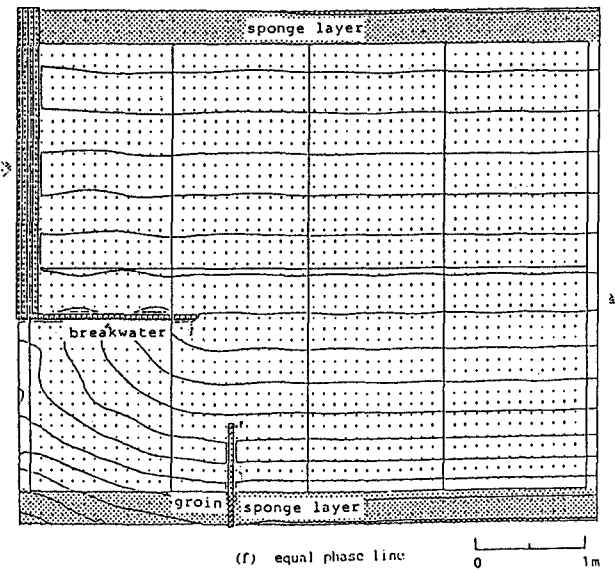
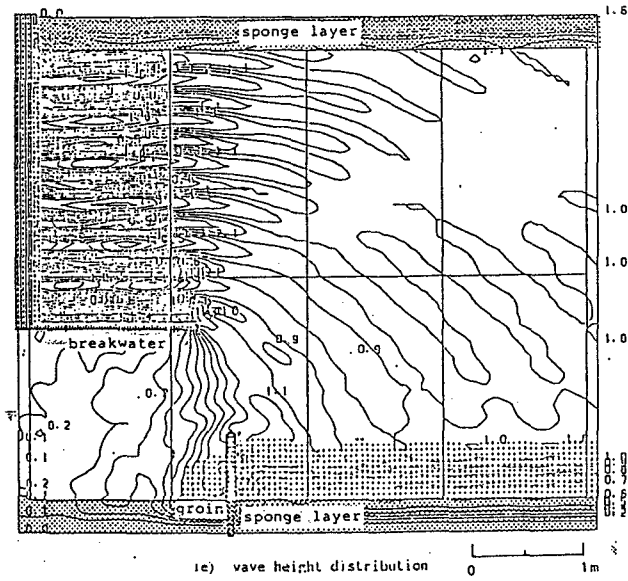


Figure 9 Numerical result of wave field in the area where a breakwater and groin exist.

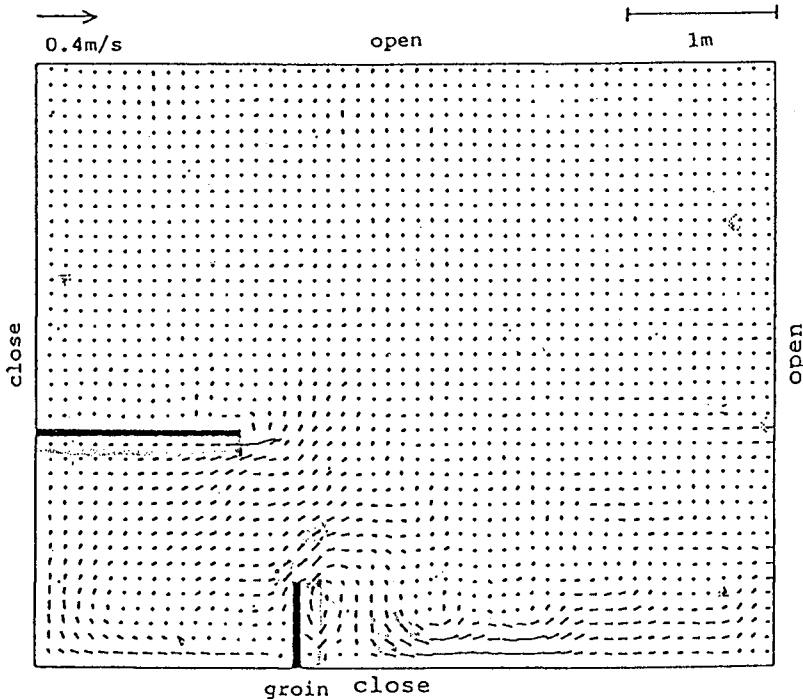


Figure 10 Numerical result of nearshore currents in the area where a breakwater and groin exist.

very effective to reduce the nearshore circulations. In the construction of offshore structures such as breakwaters, the beach erosion due to the change in wave field may be controlled by constructing a small groin in the area behind the breakwater.

4. The Formation of Stable Sandy Beaches

The authors have demonstrated that, as schematically shown in Figure 11 there exist static and dynamic equilibrium sandy beaches which are sometimes identified as static and dynamic stable ones (Tsuchiya, Silvester and Shibano, 1979 and Silvester, Tsuchiya and Shibano, 1982). The static stable beach and its application to beach erosion control was first proposed by Silvester(1956). He proposed the geometry of stable beaches as shown in Figure 12 where the solid curve

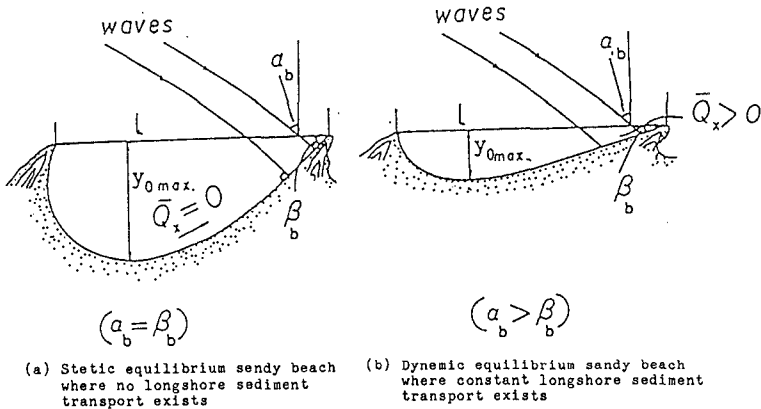


Figure 11 Schematic diagram of static and dynamic stable beaches.

indicates his empirical formula for static sandy beach and the values shown are field data of stable sandy beaches such as those in the Amanohashidate beach and others (Tsuchiya, Silvester and Shibano, 1979). Recently a theory of the formation of stable sandy beaches was proposed by Tsuchiya and Refaat (1990) by applying the non-equilibrium longshore sediment transport and equation of continuity of beach change. It was concluded by the theory that the stable sandy beaches can be formed by the upstream and downstream boundary conditions in the formation of sandy beaches. The existence of the stable sandy beaches was qualified and theoretical configuration of the stable sandy beaches were also obtained. Figure 12 shows an example of the theoretical configurations of dynamic stable beach which are compared with those of sandy beaches formed between two groins at the Amanohashidate Beach where a sediment amount of about 4,000 m³ is bypassed annually. It is therefore noted that, based on this theoretical background stable sandy beaches can be formed by two headlands for beach erosion control.

5. Application of the Headland Control Methodology to Ogata Coast

As already described in Section 2, the Ogata coast has being eroded severely

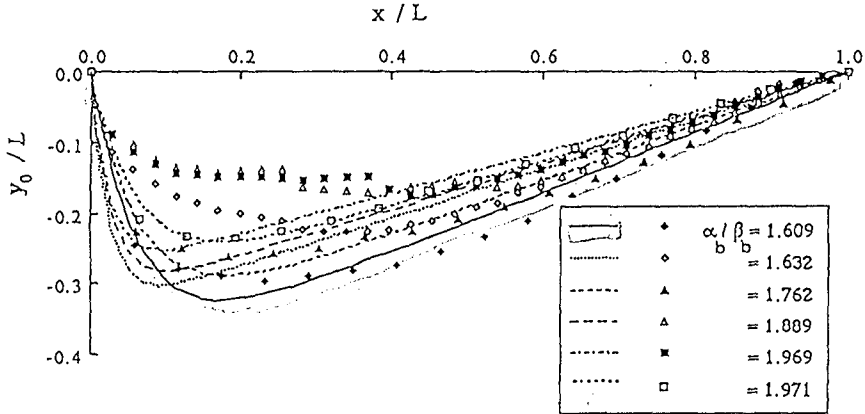


Figure 12 Comparison between theoretical and measured configurations of dynamic stable beaches.

following the construction of the breakwaters of Naoetsu Harbour. Numerous methods of beach erosion control by coastal structures have been implemented including sea dikes and offshore breakwaters. The reflection of incident waves due to such structures, as already shown in Figure 5, can transform a dissipative sandy beach with a longshore bar, into a reflective beach without a longshore bar, thus accelerating the erosion process (Tsuchiya, 1987). This particular situation may be labeled as a third main cause of structure induced shoreline erosion.

Sandy beaches are thought to possess a stable configuration based on the properties of the predominant waves and beach sediments. This stable configuration is frequently altered by man's interaction, from its normal dissipative beach state to a reflective one, and erosion will proceed only until its normal dissipative state recovers. The three previously described main beach erosion causes are harnessed by the previously mentioned headland control, thus providing the necessary influence to restore and retain the dissipative beach form. Based on the theoretical background of the formation and existence of static and dynamic stable sandy beaches, the headland control methodology can be applied for beach erosion control at the Ogata coast. In order to examine the principal methodology of erosion control mentioned above, numerical and physical simulations of the beach change were carried out. By use of

the results of these investigations, the proposed erosion control method is shown in Figure 13 as a series of dissipative sandy beaches to be formed by man-made

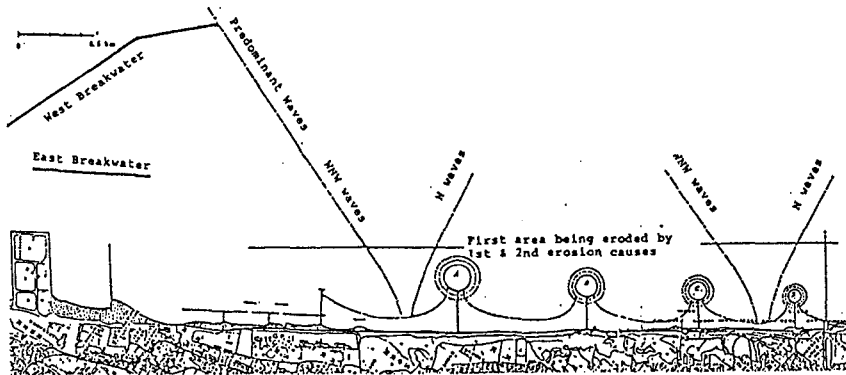


Figure 13 The proposed beach erosion control for Ogata coast by headland control methodology.

headlands. In this proposal, due to the economical sense in the construction, the man-made headlands are constructed slightly offshore the breaker depth and the water depth at which the headlands are constructed decreases in the downstream direction. The dimensions of the headlands and their spacings, as shown in the figure, are decided according to the first and second beach erosion causes. At the downstream end their dimensions become small, as shown in Figure 14, their influence must be vanished to reach the natural situation. Additionally a sediment amount of about $5,000 \text{ m}^3$ per year may be bypassed. The headlands are of T-shaped groin type with a mild offshore face. A couple of these are now under construction.

6. Conclusion

In this paper, structure induced beach erosion causes were classified into the first and second, and their erosion processes were examined with a special reference to the Ogata coast facing the Japan Sea and by numerical simulations of shoreline and nearshore currents. In the headland control methodology, the theoretical background of the formation and existence of stable sandy beaches was very briefly described based on our current investigation.

Based on the theoretical background of the existence of stable sandy beaches, a series of stable, dissipative sandy beaches were proposed and they are to be formed by the headland control methodology.

References

Silvester, R.: Headland defense of coasts, Proc. 15th ICCE, ASCE, 1972, pp. 1394-1406.

Silvester, R., Y. Tsuchiya and T. Shibano: Zeta bays, pocket beaches and headland control, Proc. 17th ICCE, ASCE, 1980, pp. 1306-1319.

Tsuchiya, Y., R. Silvester and T. Shibano: Beach erosion control by headland control methodology, Proc. 26th Japanese Conf. Coastal Engg., JSCE, 1979, pp. 191-194(in Japanese).

Tsuchiya, Y.: Beach erosion control, Proc. JSCE, No. 387/II-8, 1987, pp. 11-23(in Japanese).

Tsuchiya, Y. and H.E.A.A. Refaat: A theory of the formation of stable sandy beaches, Jour. Water Way., Port , Coastal & Ocean Engg., ASCE, 1990(in review).

CHAPTER 208

BEACH EROSION CONTROL BY SUBMERGED FLOATING STRUCTURE

Naokatsu SHIMODA¹
Noritaka MURAKAMI²
and
Koichiro IWATA³

ABSTRACT

This paper is to investigate experimentally the beach erosion control function of a submerged tension-moored breakwater. Two- and three-dimensional laboratory experiments are performed.

The single-peaked, double-peaked and triple-peaked cusped spits are formed by placing the submerged tension-moored breakwater on an accreted-type or intermediate-type beach. When the submerged tension-moored breakwater is placed on an eroded-type beach, the shoreline denudation is stopped and the shoreline is restored to the original location.

The submerged tension-moored breakwater is concluded to be possibly one of effective measure works against beach erosion in an inner gulf area in which huge waves do not attack.

1. INTRODUCTION

So far, a semi-submerged bottom-seated offshore breakwater made with natural stones and concrete armour units

- 1 B.Eng., Vice-Head, General Technical Research Lab., Gikenkogyo Co.Ltd., Hachioji, Tokyo, Japan
- 2 B.Eng., Graduate student, Dept.of Geotechnical Eng., Nagoya Univ., Nagoya, Aichi 464, Japan
- 3 M.ASCE, D.Eng., Professor, Dept.of Civil Eng., Nagoya Univ., Nagoya, Aichi 464, Japan

have been constructed to protect beaches from severe erosion as well as to prevent the coastal zone from wave-caused disasters. The offshore breakwater has been verified to be an effective measure against beach erosion as well as an useful disaster prevention work, and Japanese coasts have been protected by many numbers of this kind of offshore breakwater.

Very recently, however, the bottom-seated offshore breakwater made with concrete armour units is pointed out to have some demerits such as (1) poor sea water exchange between the onshore and offshore side of the breakwater, (2) destruction of beautiful scenery and (3) bad barrier for marine sports. Therefore, research and development of new type of beach erosion control works is strongly requested in relation to re-development of urban water front in the bay area in which huge waves do not attack.

The artificial reef work utilizing a submerged sea-dike made with natural rocks are under construction, in some Japanese coasts, as a new measure work against beach erosion. All the measure works against beach erosion which have been put into practical use utilize bottom-seated structures. Another possible choice instead of the bottom-seated structure will be a moored-type structure. However, very few researches regarding the measure work using moored structures have been conducted.

With this background in mind, this paper deals with a submerged tension-moored breakwater from the view point of (1) good sea water exchange between onshore and offshore side of breakwater, (2) no destruction beautiful scenery and (3) no bad barrier for marine sports and discusses the beach erosion control function by means of two- and three-dimensional laboratory experiments.

2. TWO-DIMENSIONAL LABORATORY EXPERIMENT

1) Equipment and procedure

A wave tank in 1m width, 1.5m height and 50m length at Gikenkogyo Co.Ltd. was used to discuss 2-dimensional beach deformation. Experimental waves were all regular ones and their wave steepness (H_o/L_o : H_o ; deep water wave height, L_o ; deep water wavelength) were 0.01, 0.03 and 0.06, which were selected so as to produce the accreted-type, intermediate-type and eroded-type beaches without structures (Horikawa and Sunamura (1974)). Bed material was fine sand of 0.38mm medium diameter (d_{50}) and the initial bottom slope ($\tan\theta$) was 1/10. The floating breakwater was fixed to the bottom with tension using 4 stainless wires of 3mm diameter. The initial mooring force (F_o) of one wire was about 7.2kg. The dimension of model breakwater was 10cm in height (D), 30cm in width (B) and 99cm in length (A). The schematic illustration of experimental set-up is given in Fig.1.

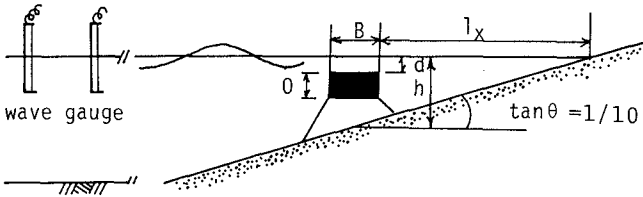


Fig.1 Schematic illustration of experimental set-up

The waves were generated for about 4 hours until the beach approached to an equilibrium state. The beach profiles at 0.5, 1, 2,3 and 4 hours from the initiation of wave generation were measured carefully with point gauges. The incident and partial standing wave in front of the breakwater were measured with capacitance-type wave gauges. Experiments were carried out, changing the location and submerged depth of the breakwater. Table-1 shows experimental conditions and total experimental runs were 32.

Table-1 Experimental condition

T(s)	Ho/Lo	d/h	lx/L	D/h	d50/Ho
1.0	0.007	0	0.63	0.286	0.0039
1.8	0.019	0.288	}	}	0.0040
		0.330			0.0081
		0.358			0.0111

2) Dimensional analysis

The equilibrium beach profile is mainly dominated by the following dimensionless 6 parameters, due to a dimensional analysis;

$$\left(\frac{H_o}{L_o}, \frac{D}{h}, \frac{d}{h}, \frac{l_x}{L}, \frac{d_{50}}{H_o}, \frac{F_o}{\rho g d^2} \right) \text{ ----- (1)}$$

where, h is the stillwater depth at breakwater, d the submerged water depth, l_x the offshore distance of breakwater from shoreline, g the gravitational acceleration and ρ the fluid density.

There are so many leading factors, but the laboratory experiments are limited. Therefore, the effect of l_x/L and d/h to beach deformation are mainly discussed here.

3) Result and discussion

Experiments showed, as a general feature, that the change of bottom configuration mainly takes place in shallower water depth than the setting location of the breakwater and the magnitude of bottom configuration change becomes smaller with increasing l_x/L and with decreasing D/h .

Figures 2 and 3 show some examples of bottom configuration change taken place by placing the breakwater. The bottom configuration shown in Figs.2 and 3 correspond to the equilibrium state beach. Figure 2(a) shows that the beach without the breakwater is eroded by the wave whoes

steepness is 0.06 ($H_o/L_o=0.06$). However, by placing the submerged tension-moored breakwater, the eroded beach was changed to the uneroded-type or a little accreted-type beach, as shown in Fig.2(b) and (c). The reason of this is that the steep incident wave is broken by the breakwater and the attenuated wave encouraged onshore sediment transport. On the other hand, in case of the accreted-type or intermediate-type beach, the bottom configuration change by the breakwater is not drastical. The intermediate-type and accreted-type beaches were never changed to the eroded-type beach by the breakwater. As shown in Fig.3, the intermediate-type beach was still intermediate-type ones even by placing the breakwater.

The bottom configuration is closely correlated with six dimensionless parameters as shown by Eq.(1). Among them, D/h , d/h and l_x/L were found to be significantly important parameters. With increasing of D/h and decreasing of d/h , the wave breaking-caused vortex and incident wave attenuation become larger, which bring larger change of bottom configuration. In the experiments, large change of bottom configuration was observed to take place under the conditions of $0.33 \leq D/h \leq 0.83$ and,

$$d/h=0 \text{ and } 0.63 \leq l_x/L \leq 2.5 ; \quad 0 \leq d/h \leq 0.33 \text{ and } 0.63 \leq l_x/L \leq 2.2$$

(for eroded-type beach)

$$d/h=0 \text{ and } 0.63 \leq l_x/L \leq 2.5 ; \quad 0 \leq d/h \leq 0.33 \text{ and } 0.63 \leq l_x/L \leq 0.9$$

(for intermediate-type beach)

The bottom around the submerged tension-moored breakwater was scoured in case that the clearance between the breakwater's bottom and beach was less than the breaker height. Material on onshore-bed of the breakwater is

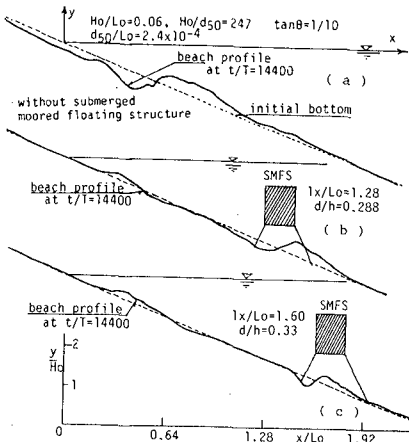


Fig.2 Bottom configuration change (eroded-type beach)

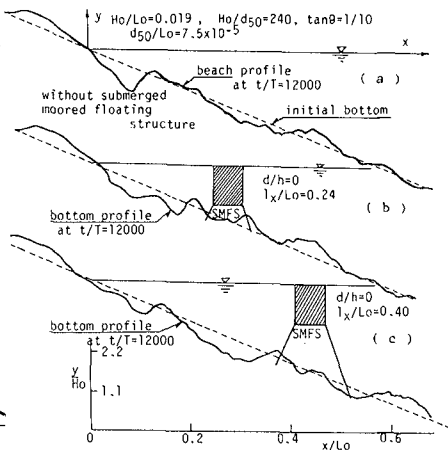


Fig.3 Bottom configuration change (intermediate-type beach)

suspended by wave breaking-caused vortex and is washed away mainly toward offshore ward by the return flow. This scouring was clearly observed in case of the eroded-type and intermediate-type beaches. The maximum scoured depth Δh is closely related to l_x and d , and the dimensionless maximum scoured depth $\Delta h/H_0$ is less than 0.65, as shown in Fig.4.

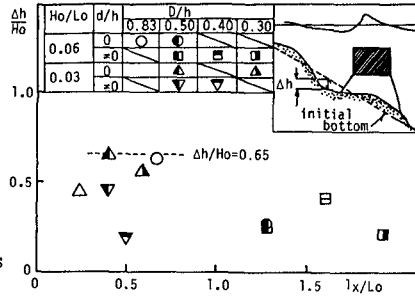


Fig.4 Nondimensional maximum scouring depth $\Delta h/H_0$

3. THREE-DIMENSIONAL LABORATORY EXPERIMENT

1) Equipment and procedure

A wave basin in 10m width, 0.65m height and 30m length at Nagoya University was used to investigate the combined effect of the transmitted and diffracted waves to beach profile. Three plywood breakwaters whose dimensions are $D=10\text{cm}$, $B=30\text{cm}$ and $A=130\text{cm}$, $D=10\text{cm}$, $B=30\text{cm}$ and $A=65\text{cm}$, and $D=5\text{cm}$, $B=30\text{cm}$ and $A=130\text{cm}$ were employed, and they were fixed to the beach with tension by stainless wires of 0.3cm diameter. The bed material and initial bottom slope were quite the same as those of two-dimensional experiments. The stillwater depth at wave paddle was 40cm. Experimental waves were all regular ones and they were generated for about 6 - 12 hours until the beach approached to an equilibrium state. The incident wave was measured with capacitance-type wave gauges. Water particle velocities at bottom around the breakwater were measured with electro-magnetic velocimeters to study the wave-induced current. Particle velocities at 20 different locations were collected. Figure 5 illustrates an outline of experimental set-up. Experimental condition is given in Table-2. The total experimental run was 48.

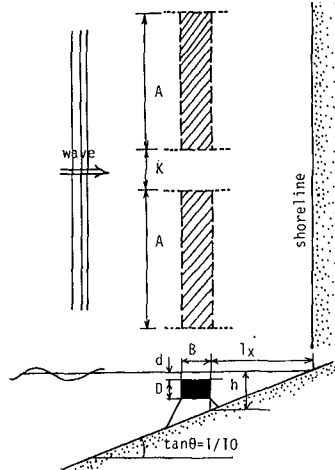


Fig.5 Sketch of experimental set-up

2) Dimensional analysis

The equilibrium beach profile is largely dominated by the following 8 parameters, due to a dimensional

analysis,

Table-2 Experimental condition

$$\left(\frac{H_o}{L_o}, \frac{D}{h}, \frac{d}{h}, \frac{l_x}{L}, \frac{d_{50}}{H_o}, \frac{A}{l_x}, \frac{F_o}{\rho g d^2}, \frac{K}{A} \right)$$

Ho/Lo	d/h	lx/L	0/h	d50/Ho	A/L	K/A
0.007	0	0.63	0.415	0.0040	0.22	0.25
0.030	0.10	}	0.500	0.0081	}	0.50
0.060	0.25		0.588	0.0111		1.00
		0.33	1.65	0.833	1.09	

--- (2)

where, K is the gap between two breakwaters as shown in Fig.5. When one breakwater is placed, the term K/A is neglected. The initial mooring force (Fo) was about 10kg for all experimental runs, although Fo differed a little from 10kg depending on experimental conditions. There are many leading factors which dominate the bottom configuration change. However, since the laboratory experiment runs are limited like two-dimensional ones, the effect of D/h, d/h, lx/L A/lx and K/A to beach deformation are mainly discussed hereafter.

3) Result and discussion

3-1) Case of one submerged tension-moored breakwater

A) Intermediate-type and accreted-type beaches

Beach morphology was found, as a general feature, to be largely changed by nondimensional quantities relating to a setting location and dimension of the breakwater such as D/h, d/h, lx/L and A/lx.

The cusped spit is generally formed by placing the breakwater on the intermediate-type and accreted-type beaches. Laboratory experiments revealed that the cusped spit is classified into three types such as the single-peaked, double-peaked and triple-peaked cusped spits, as shown in Fig.6. In Fig.6, Lc is the wavelength at the depth of h=40cm in front of the 1/10 bottom slope(tanθ), and the bottom contour is depicted with lcm depth interval. The beach morphology is an equilibrium state one.

The tombolo is well known to be formed by the bottom-seated structure. However, tombolo was not formed in our experiments. This is due to the reason that the incident wave breaks at the breakwater and the overtopped breaking wave suspends onshore-side sediment and stops the growth of the cusped spit. This is a remarkable feature of the submerged tension-moored breakwater, which quite differs from the bottom-seated offshore breakwater made with concrete armour units whose crown height is higher than the water level.

Fig.6(a) is one example of the single-peaked cusped spit in case of d/h=0. The shoreline behind the breakwater is seen to advance offshore-ward. The diffracted wave dominates over the transmitted wave in this case, and then

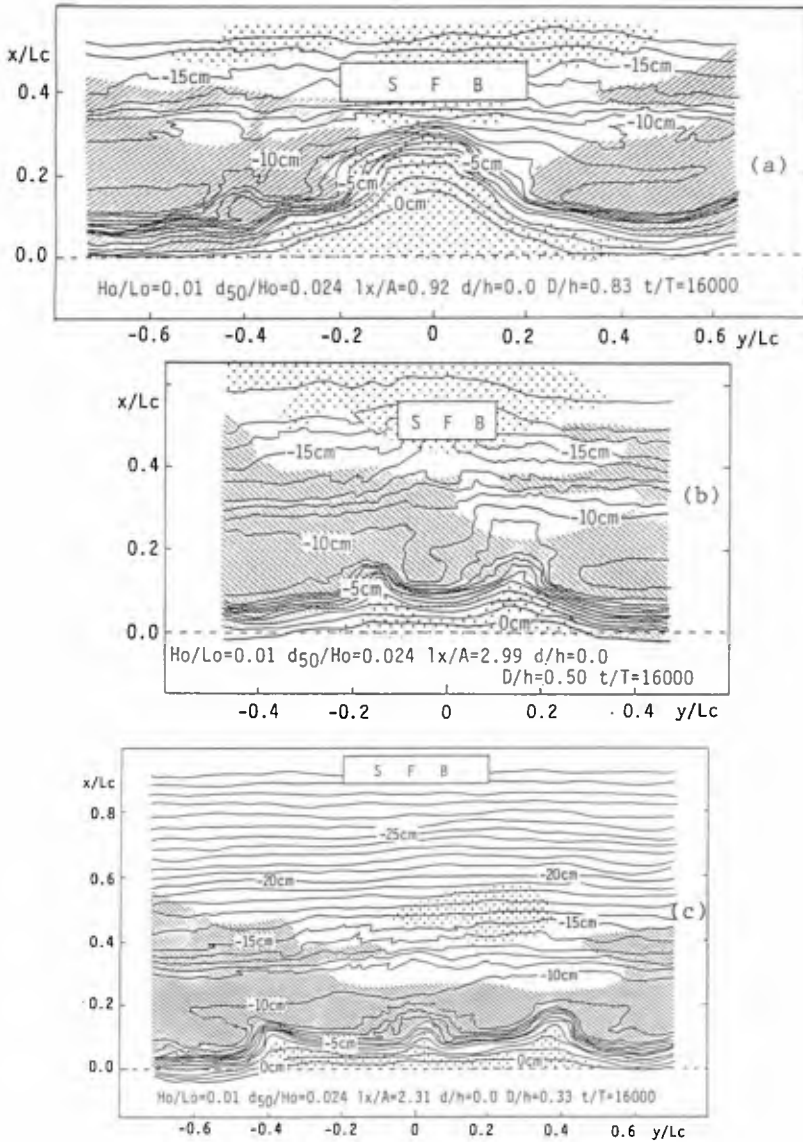


Fig.6 Examples of single-peaked, double-peaked and triple-peaked cusped spits formed by the submerged tension-moored breakwater placed on accreted-type beach (▨; erosion, ▤; accretion)

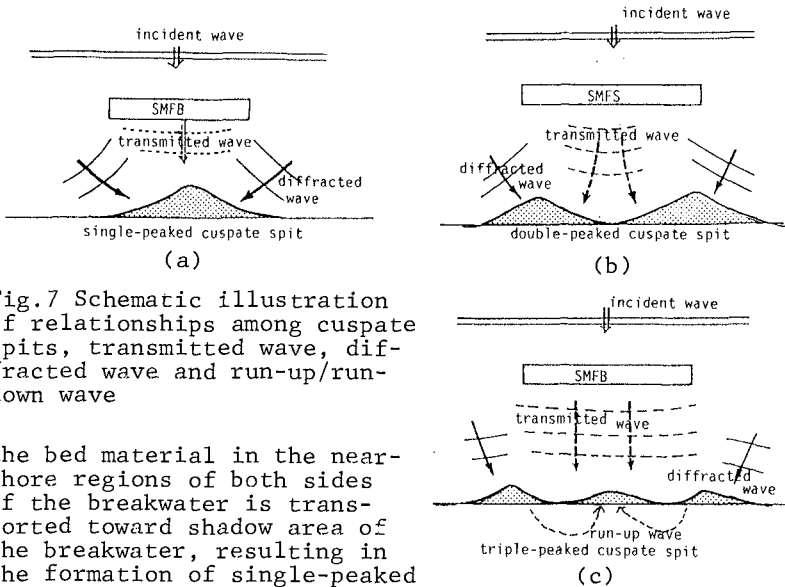


Fig.7 Schematic illustration of relationships among cusped spits, transmitted wave, diffracted wave and run-up/run-down wave

the bed material in the near-shore regions of both sides of the breakwater is transported toward shadow area of the breakwater, resulting in the formation of single-peaked cusped spit, as shown in Fig.6 (a) and Fig.7(a).

Fig.6(b) is one example of the double-peaked cusped spit. Two peaks are formed behind the breakwater due to the combined effect of the transmitted and diffracted waves. With decreasing of D/h and A/lx , the triple-peaked cusped spit is apt to be formed behind the breakwater. The amount of sediment accumulation around the shoreline is much less than that of the single-peaked and double-peaked cusped spits. The mechanism of forming the triple-peaked cusped spit is different from those of the other cusped spits. As shown schematically in Fig.7(c), the run-up waves obliquely climbed on dry bed run down concentratedly to the same region corresponding to the trough area of double-peaked cusped spit. The frequency of occurrence of the triple-peaked cusped spit was very low in the experiments.

The cusped spit shapes formed by the submerged tension-moored breakwater are very close to those formed by bottom-seated breakwaters made with concrete armour units and natural stones. However, the leading physical parameter which dominates the shapes is different between the two types of structures. lx/A (offshore distance/breakwater width) is the leading parameter in case of the bottom-seated breakwater, and the shoreline shape is classified by lx/A (Shinoda and Ikeda (1972)). However, in case the submerged tension-moored breakwater, D/h and d/h as well as lx/A change largely the morphology of the beach.

Figs.8(a),(b) and (c) show examples of change of equilibrium bottom configuration due to change of D/d and d/h .

Figure 8(a) shows the single-peaked cusped spit in case of $d/h=0$. Only by increasing d/h from 0 to 0.17 with the other quantities fixed, the double-cusped spit is formed as shown in Fig.8(b). This is due to the reason that the transmitted wave becomes larger with increasing d/h and then the transmitted and diffracted waves contribute a lot to beach deformation. d/h is an important parameter relating to the magnitude of wave breaking, as the magnitude of breaking wave-caused vortex tends to be smaller with increasing of d/h . Therefore, the local scouring around the

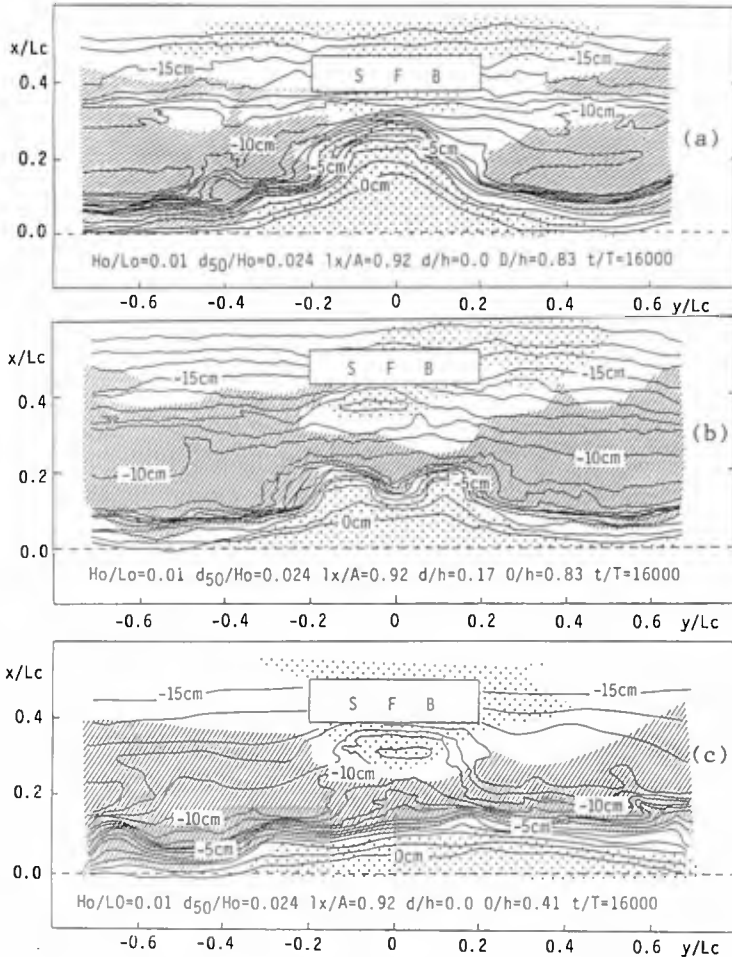


Fig.8 Effects of D/h and d/h to beach deformation (//////; erosion,; accretion)

diminishes generally with increasing of d/h , especially on eroded-type beach.

The dimensionless parameter D/h is more important than d/h , since D/h controls largely the diffracted and transmitted wave height. That is, increasing of D/h enlarges the diffracted wave height and diminishes the transmitted wave height. As shown in Figs.8(a) and (c), decreasing of D/h from 0.83 to 0.41 clearly diminishes the amount of sediment accumulation around the shoreline. This reason is that the diffracted wave in case of $D/h=0.41$ becomes smaller than the case of $D/h=0.83$ and becomes less effective to accumulate the sediment around the shoreline.

The other dimensionless quantities such as $d50/H_0$ and lx/L are also important parameters which deform the beach. However, their effects to beach deformation cannot be discussed here in details due to the limited laboratory experiments.

B) Eroded-type beach

In case of the eroded-type beach, the cusped spit was not formed in the experiments. In the experiments, it was observed that the shoreline erosion (shoreline denudation) is stopped in the shadow area behind the breakwater, by placing the submerged tension-moored breakwater.

Fig.9 shows one example of change of beach configuration by placing the breakwater on eroded-type beach. The cross-sectional change at the section B located at x/Lc at $y/Lc=-0.9$ is very little, as in Fig.9(c). However, beach profile at section A located at $y/Lc=0$ (centerline) shows clearly that the shoreline denudation is stopped and the shoreline advances to the initial position.

Thus, it is clear that the submerged tension-moored breakwater has high function of protection of beaches from erosion in the shadow area of the breakwater. However, it should be noted that onshore-side bottom in front of the

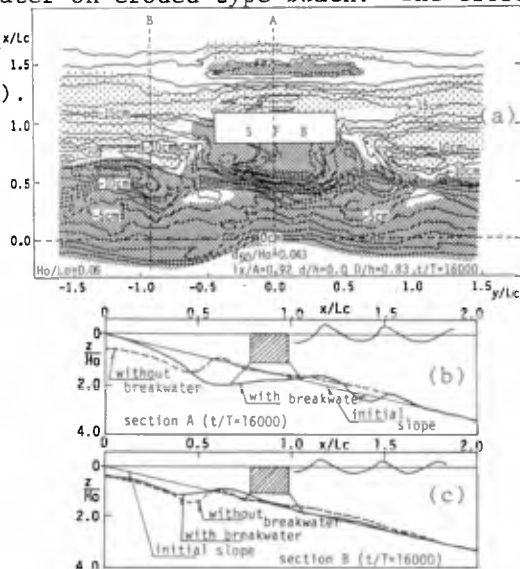


Fig.9 One example of placing breakwater on eroded-type beach (//; erosion, . . . ; accretion)

breakwater is eroded by breaking wave-caused vortex, as shown in Figs.9 (a) and (b).

(C) Local scouring around the breakwater

The onshore-side bottom beneath the breakwater is always scoured on the eroded-type beach and sometimes scoured on the accreted-type and intermediate-type beaches. The maximum dimensionless scouring depth $\Delta h/H_0$ obtained in the experiments is shown in Fig.10. $\Delta h/H_0$ is seen to vary with d/h , D/h and lx/L_0 . The maximum value of $\Delta h/H_0$ is 1.1, which is larger than that of two-dimensional experiments. This may be caused by following reason. The moored structure in three-dimensional experiments has six-degree-freedom motions, different from three-degree-freedom motions in two-dimensional experiments, and a lot of desiment are suspended and transported to both on-offshore and alongshore directions.

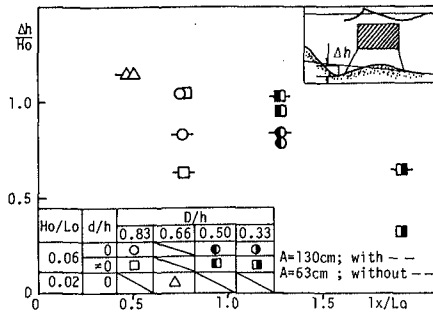


Fig.10 Dimensionless maximum scouring depth $\Delta h/H_0$

(D) Range forming cusped spits

Drift and transportation of bed materials is largely controlled by the wave-induced current. In case of bottom-seated breakwater made with concrete armour units, a pair of current cells is known to be formed behind the breakwater.

On the other hand, the current cell was not formed clearly in case of the submerged tension-moored breakwater. The gap between breakwater's bottom and seabed weakens forming the wave-induced current cells and encourage the return flow toward offshore, although the diffracted wave dominates over the transmitted wave with increasing of D/h and decreasing of lx/A and d/h . Figure 11 shows one example of velocity vectors of the wave-induced current, in which left-half of the breakwater is shown because velocity vectors in right-half is almost equal to the left-half. Figure 11 shows no clear current cell, although the return flow is observed.

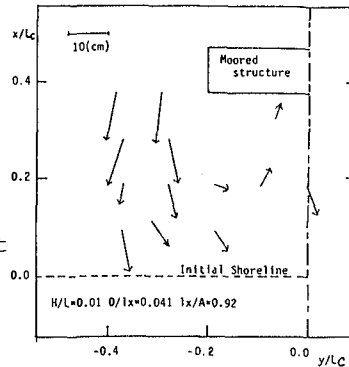


Fig.11 One example of velocity vectors of wave induced current

As already mentioned, three types of cusped spits are

formed on the accreted-type and intermediate-type beaches. The outline of range in which three kinds of cusped spits take place in case of $d/h=0$ is shown in Fig.12, in which experimental results for bottom-seated breakwater made with concrete armour units are shown simultaneously (● and ■).

From Fig.12, it is seen that double- and triple-peaked cusped spits are formed in the limited ranges of $D/A=0.3 - 0.7$ and $(lx/A)(h/L) \leq 0.27$. On the other hand, the single-peaked cusped spit is shaped under wider range of D/h and $(lx/A)(h/L)$ than those of the double-peaked and triple-peaked cusped spits.

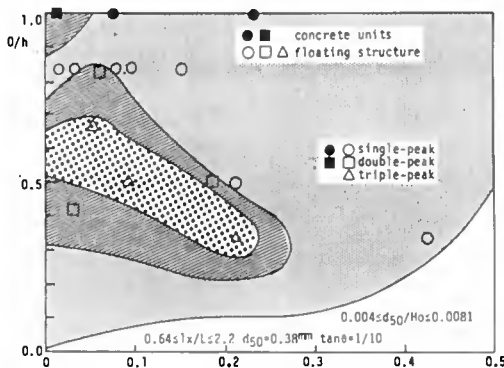


Fig.12 Range which cusped spits are formed. ($\tan\theta=1/10$, $d/h=0$, $0.64 \leq lx/L \leq 2.2$ and $0.004 \leq d50/Ho \leq 0.0081$)

3-2) Case of two submerged tension-moored breakwaters

When the natural beach is an accreted-type and intermediate-type beach, cusped spits are formed by two submerged tension-moored breakwaters. The magnitude of the cusped spits depends on K/A as well as D/h , lx/A and lx/L . Figures 13(a), (b) and (c) show examples of cusped spits. It was found that the magnitude of the cusped spit decreased with decreasing of relative gap between two breakwaters (K/A), as shown in Fig.13. Each shape of two cusped spits formed behind the breakwater in case of $K/A=1.0$ is very similar to that formed in the case of one breakwater. This would imply that when K/A is larger than 1, the coupling effect of two breakwaters to beach deformation is vanished and each breakwater deforms independently the beach.

When two breakwaters were placed on the eroded-type beach, the shoreline denudation behind the breakwaters was stopped, as shown in Fig.14. Therefore, summarizing the above-mentioned, the submerged tension-moored breakwater is concluded to have a function of protecting beaches from erosion.

4. CONCLUDING REMARKS

In this paper, beach deformation by the submerged tension-moored breakwater is discussed experimentally.

The experiments have revealed that the single-peaked,

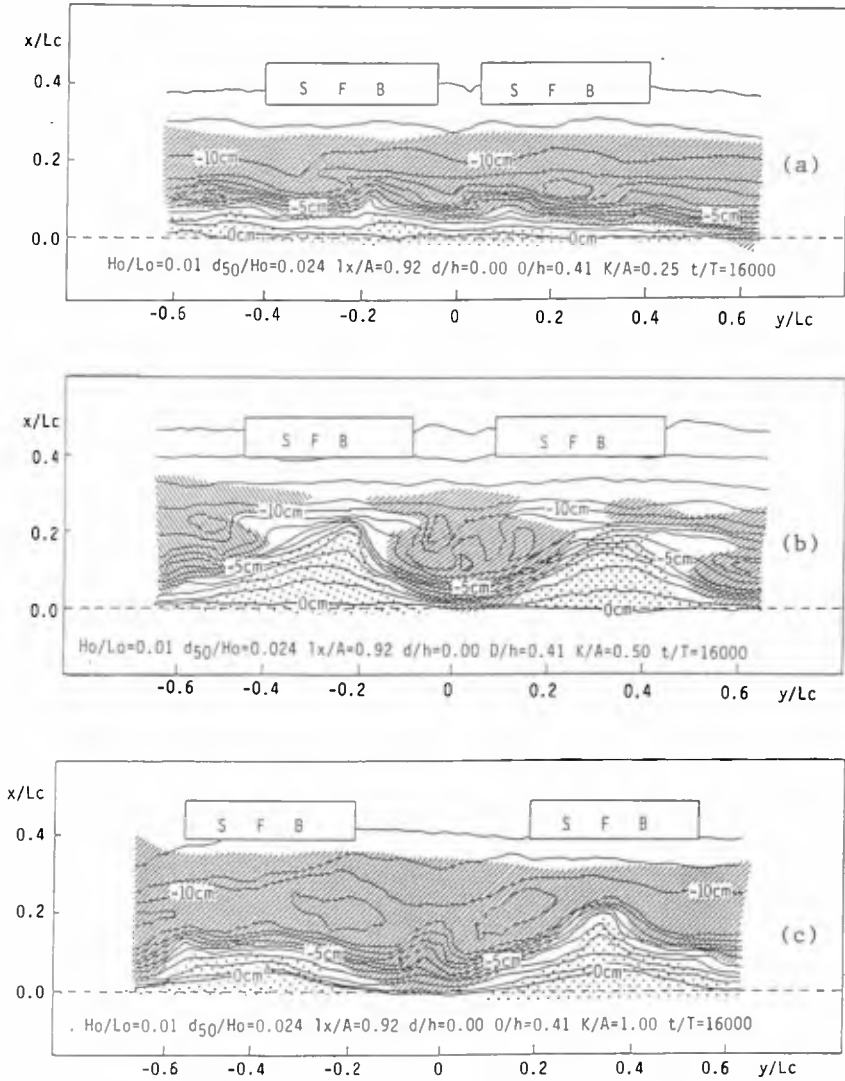


Fig.13 Some examples of beach deformation by two breakwaters placed on the accreted-type beach

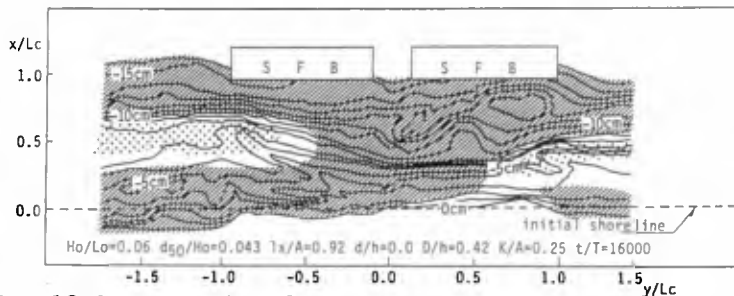


Fig. 13 One example of beach deformation by two submerged tension-moored breakwaters on eroded-type beach

double-peaked and triple-peaked cusped spits are formed behind the submerged tension-moored breakwater on the accreted-type and intermediate-type beaches. The magnitude of these kinds of cusped spits are largely controlled by the location and dimension of breakwater.

In the case that the submerged tension-moored breakwater is placed on the eroded-type beach, the shoreline denudation behind the breakwater is stopped.

Therefore, it is said that the submerged tension-moored breakwater has a high function of beach erosion control and is possibly one of the useful measures against beach erosion in an inner gulf area in which huge waves do not hit.

In this paper, the relationship between beach deformation and motions of breakwater is not discussed. The present authors are going to investigate this problem.

REFERENCES

- 1) Horikawa, K., Sunamura, T. and Y. Kondo (1974): Experimental study on two-dimensional beach deformation due to waves, Proc. 21st Japanese Conf. on Coastal Eng., pp.193 - 200.
- 2) Shinoda, K. and S. Ikeda (1972): Characteristics of beach deformation by offshore breakwaters, Proc. 13rd Japanese Conf. on Coastal Eng., pp.146 - 150.

CHAPTER 209

FUNCTION OF SAND FENCE PLACED IN FRONT OF EMBANKMENT

Shintaro Hotta¹ and Kiyoshi Horikawa²

ABSTRACT

In order to find the optimum sand fence porosity and the best position for placing a sand fence in front of an embankment, a series of experiments were conducted in a large wind tunnel. The results obtained were that a fence with 40 % or 50 % porosity should be placed at a distance between 15 H and 20 H in front of the embankment, where H is the fence height.

I INTRODUCTION

Sand fence are often employed to control wind-blown sand. However, the characteristics of sand fences are not well understood. The reasons why the characteristics of sand fences have not yet been entirely clarified are that (1) the air flow around the fences is governed by the Navier-Stokes equations and the equations are difficult to solve in practical problems, and (2) the mechanisms that govern the air flow near the sand surface and the interaction with the surface itself, which is constantly changing due to accumulation or erosion, are not clear. Therefore, the function of sand fences has mainly been studied through experiments performed in the field or the wind tunnels. Recently Hotta et al. (1987) made a comprehensive literature survey on the function of sand fences. The review summarized the operational characteristics of sand fences and provided specific guidelines for their use.

Recently in Japan, expressways have been constructed along the coastline. Also, to protect conservation

1 Dr. Eng., Professor, Dept. of Civil Engineering, College of science and Technology, Nihon University, Kanda-surugadai 1-8-14 Chiyoda-ku, Tokyo 101 Japan

2 Dr. Eng., Professor, Dept. of Foundation Engineering, Saitama University, Shimo-okubo 255, Urawa, Saitama Pref. 338 Japan

forests or residential and cultivated land from coastal disasters such as tsunami, storm surge or contamination by wind blown sand, embankments are often constructed along sandy beaches. Wind-blown sand often intrudes beyond these embankments and contaminates conservation forests and residential and cultivated land. Sometimes wind-blown sand accumulating on the expressways will prevent vehicles from passing. Sand fences are often placed in front of the embankments to interrupt the wind-blown sand. In order to find the optimum fence porosity and the best position for the fence in front of the embankment, a series of experiments were conducted in a large wind tunnel. The purpose of this paper is to describe the results of the experiments. Because of the space limitation, results obtained from a mobile sand bed experiment will be described. A description of results concerned the wind flow field will defer to a future paper.

11 EXPERIMENTAL FACILITY AND PROCEDURES

2.1 Experimental Facility

Experiments were carried out using a blow-off type wind tunnel with a cross-section that was 1.1 m high and 1.0 m wide, and with a length of 20 m belonging to the Central Research Institute of Electric Power Industry. The experimental section was located at a segment of the tunnel from 14 m to 18 m from the upstream end. On the top of the tunnel in the segment, a 4-cm wide groove wide was cut along the center line in the direction of the wind. Small rails were laid along to the groove with a spacing of 20 cm for carrying an anemometer array and a profile indicator for measuring changes in the sand surface elevation.

Wind speed was measured with an array of hot-film anemometers consisting of fifteen anemometers. An amplifier unit of anemometer equips A-D converter itself and changes data into RS232C signal. Data were transferred to a personal computer and recorded on a floppy disk. The sampling frequency was 10 Hz.

For visualizing flow patterns around the fence, a smoke tube with a 5-mm diameter having a funnelled-shaped mouth with 1-mm diameter was employed.

In order to measure changes in the sand surface elevation, a profile indicator developed especially for this study and modified from the indicator commonly employed in sounding the sea bottom topography in wave tank experiments was used. The output from the indicator was recorded with an open-reel type digital data recorder, simultaneously monitoring the signal with a chart recorder.

The sand used in the mobile-bed experiment was taken from a natural beach having a median diameter of 0.3 mm and a uniformity coefficient of approximately 1.7. The uniformity coefficient is defined as d_{60}/d_{10} where d is the grain size and the subscript denotes the cumulative percentage. More information on the sand characteristics are given in Horikawa et al. (1983).

2.2 Model Fences

The model fences employed in the experiments were slat-type fences made of small pieces of wood. Each slat had a thickness of 2 mm. The porosity of the fence, which is defined as the ratio of space area to total projected area, was changing by varying the width of the slats while keeping a constant gap of 2 mm between the slats, i.e., widths of 2 mm, 3 mm, 5 mm, 8 mm and 18 mm gave 50 %, 40 %, 28.5 % (hereafter this porosity is referred to as 30 % for convenience), 20 %, and 10 % fence porosity. The slats were glued to horizontal slide bars that were 5 mm in width. Therefore, porosity of 10, 20, 30, 40 and 50 % correspond to 9, 18, 25, 36 and 44 %, respectively if definition is strictly followed. The height of the fence was 9 cm on the fixed-bed experiments for measuring the wind speed field. The height of the fence on the mobile sand experiments was 12 cm, but the

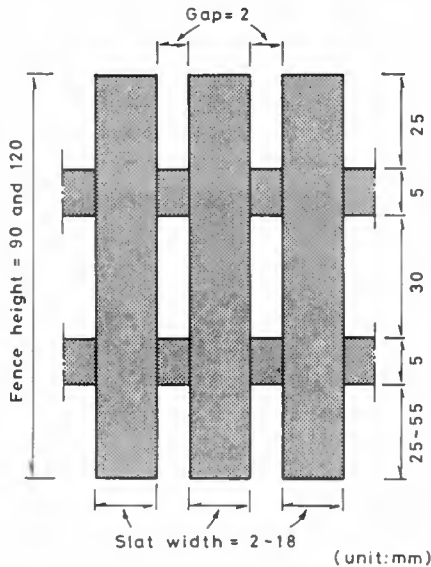


Fig. 1 Dimensions of the model fence.

lower 3-cm part of the fence was buried in sand implying a 9-cm effective height as in the fixed-bed experiments. Figure 1 shows the dimensions of the model fence.

2.3 Experimental Procedures

At first, the flow patterns were observed by using smoke tubes and the wind speed field was measured by an anemometer array on the fixed surface glued sand grains, which were used in a mobile bed experiment. After completing the experiments with the fixed sand surface, the bed was replaced by a mobile bed. Then, experiments on a mobile sand bed were carried out in the order as follows:

- (1) Experiments for fences with 0, 10, 20, 30, 40 and 50 % porosity on a flat bed without an embankment.
- (2) Experiment for an embankment without fences.
- (3) Experiment for fences with 20, 30, 40 and 50 % porosity with an embankment, varying a fence position at 5 H, 10 H, 15 H and 20 H in front of embankment.

The sand surface change was measured by the profile indicator. The measurements of sand surface elevation were made a time interval of 10 min and the experiment duration was 60 to 90 min, depending on the specific run.

In the mobile bed experiments, the vertical distribution of the wind speed was measured at the elevation 10, 20, 35 and 50 cm at a location of 14 m from the upstream end on the tunnel.

Figure 2 shows the model beach and locations of fence placed.

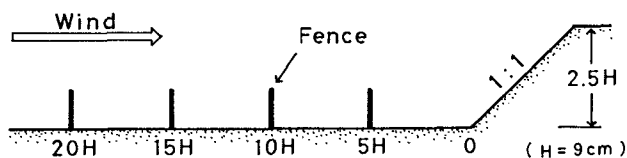


Fig. 2 Model beach and employed location of the fence.

III RESULTS AND DISCUSSION

3.1 Vertical Distribution of Wind Speed on the Fixed Sand Surface

Figure 3 shows an example of the vertical distribution of the wind speed on the fixed sand surface measured without a fence and an embankment. A logarithmic velocity distribution provided a satisfactory description. Attempts were made to keep a constant wind speed of 9.8 m/sec at the reference point throughout the experiments. However, some experimental errors occurred. The shear velocities calculated from the measured vertical distri-

bution in the runs ranged from 41 to 45 cm/sec with an average value of 43 cm/sec, which gave a wind speed of 9.8 m/sec at the reference point.

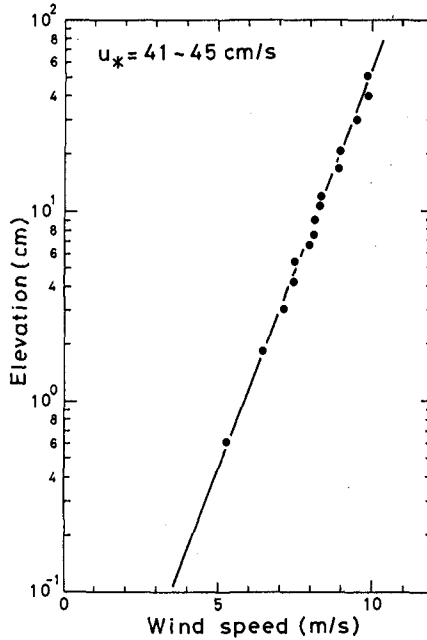


Fig. 3 Vertical distribution of wind speed on a fixed bed.

3.2 Sand Trapping Efficiency of Porous Fences

Figure 4 shows the time evolution of the sand accumulation around porous fence. For the 60 % fence, no experiment was conducted because it was inferred from the wind reduction conditions around the fence that the sand trapping ability would be low. In Fig. 4, the undulation of initial sand surface is vertically exaggerated since the horizontal distance is reduced by 1/14.5 compared to the vertical distance (figures are drawn at a scale of 1/1.1 in the vertical direction and 1/16 in the horizontal direction).

The time evolution of the sand accumulation is quite different depending on the fence porosity. Sand is mainly accumulated in front of the fence for the 0, 10, 20 and 30 % porosity fence. In contrast, sand is accumulating at a high rate behind the 40 and 50 % porosity fence. Sand was rapidly accumulating during the early stage of the experiments but with time elapsed the rate

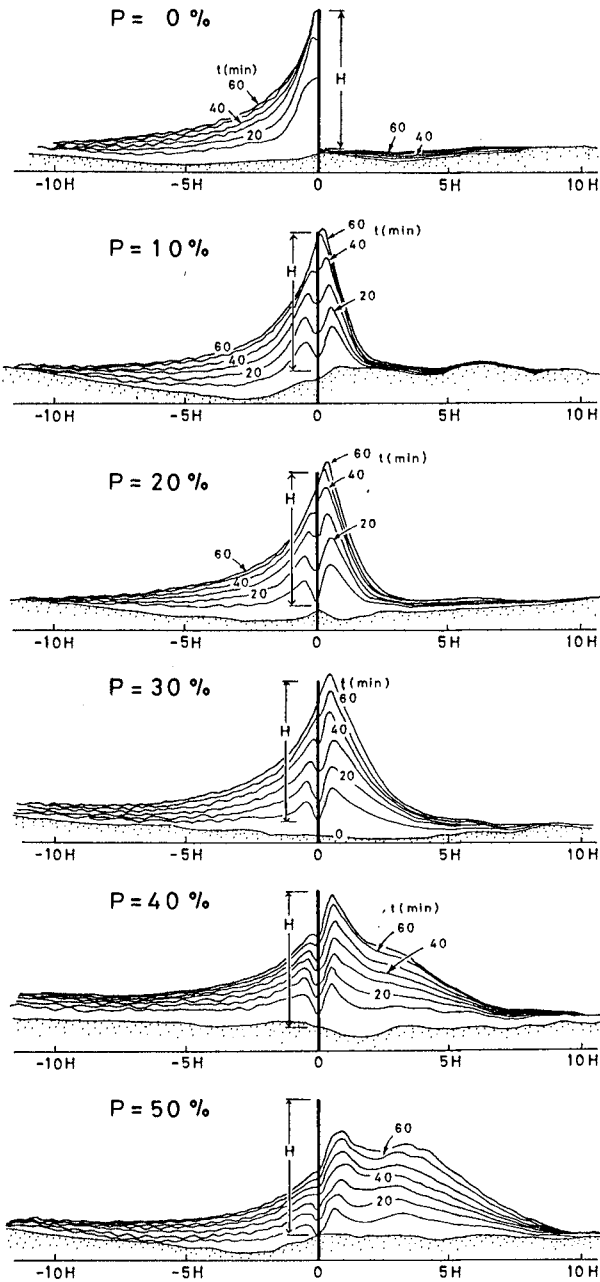


Fig. 4 Time evolution of the sand accumulation.

of accumulation was reduced. The small depression in the sand surface at the fence position caused by local scour due to the accelerating wind passing through the fence gaps, and the scour disappeared when the fence was buried to about 80 % of its height as seen for the 10, 20 and 30 % porosity fences. Also, the rate of sand accumulation rate became considerably smaller when a fence was buried at this stage of the experiment. That is, the sand fence practically loses its sand trapping function when the fence is buried to about 80 % of its height.

A lowering of the sand surface was observed at the downwind area from a distance around 15 H behind fence, although no figure are shown here. This is probably due to the fact that sand is not conserved for this region. The fence trapped sand coming from the updrift side and the amount of sand flowing into the area was smaller than the amount flowing out from the area. As a result, the sand surface in the area was lowered.

A dune was formed immediately behind the fence and Figure 5 shows the growth of the dune crest taking the initial sand surface as the zero elevation. Figure 5 shows that among the five porous fences tested the fence porosity for which the dune crest grew most rapidly was 20 %.

As seen from Fig. 4, almost all of the sand accumulated in a region defined by a distance of 10 H in front and behind the fence. Figure 6 shows the accumulated sand volume with elapsed time. The sand volume was determined as the cross-sectional area measured on the

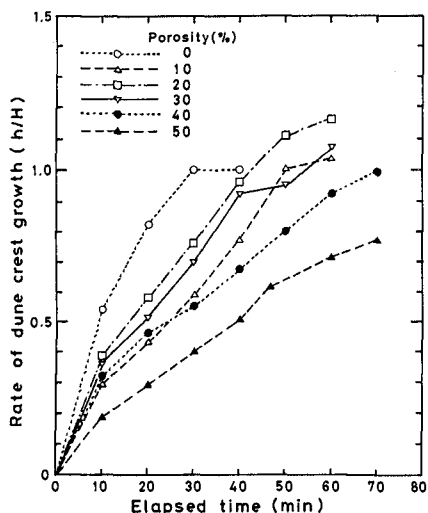


Fig. 5 Dune crest growth rate with elapsed time for different fence porosity

distorted figures as described before. The ordinate gives the distorted area. Figure 6 shows that for a fence porosity of 40 % a large amount of sand accumulates rapidly. Thus, with respect to the fence porosity. The porosity of 40 % may be considered to be the optimum fence porosity. Fences with 20 % and 30 % porosity trapped nearly equivalent volumes of sand, although the shape of the sand accumulation was different.

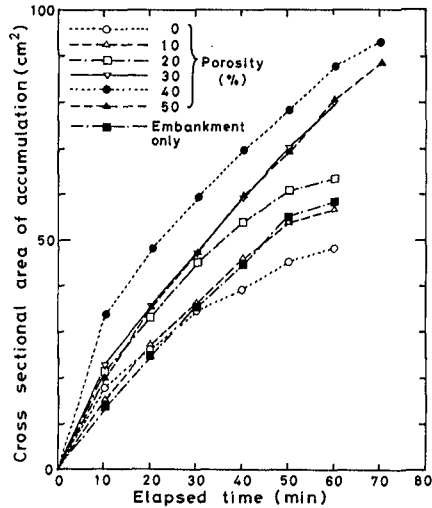


Fig. 6 The time evolution of the sand accumulation for different fence porosity.

3.3 Sand Accumulation in front of an Embankment

Figure 7 shows the time evolution of the sand accumulation in front of the embankment. Sand is mainly accumulated in a region extending from the foot of the embankment to a location 10 H in front of the embankment.

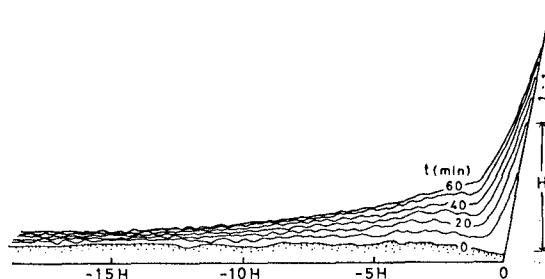


Fig. 7 Sand accumulation in front of an embankment.

The sand accumulation in this region is almost equivalent to the 10 % porosity fence (see Fig. 6). From the experimental results it may be concluded that a 40 % or 50 % porosity fence should be placed at locations ranging from 15 H to 20 H in front of the embankment if rapid sand accumulation is expected in front of the embankment. Otherwise, for low rate of sand accumulation a low porosity fence (10 % or 20 %) should be placed in front of the embankment.

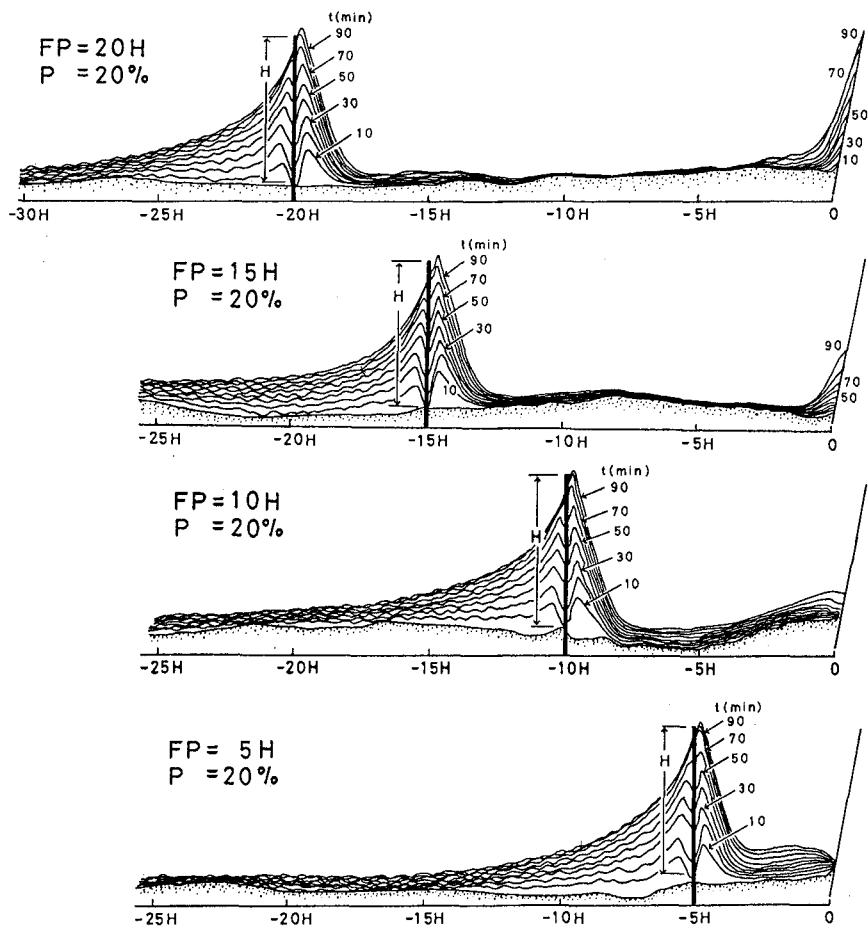


Fig. 8(a) The time evolution of the sand accumulation around fence placed in front of an embankment ($P=20\%$).

3.4 Sand Accumulation in front of an Embankment with a Fence

Figure 8 shows the time evolution of the sand accumulation for the 20, 30, 40 and 50 % porosity fences placed at the locations 5 H, 10 H, 15 H and 20 H in front of the embankment. It is difficult to determine the optimum location from these figures. Figure 9 displays a comparison of the cross-sectional area of accumulated sand in the region extending from 10 H in front of the fence to the foot of the embankment. The cross-sectional area was measured with a planimeter on the distorted figures (the ordinate is given as the distorted

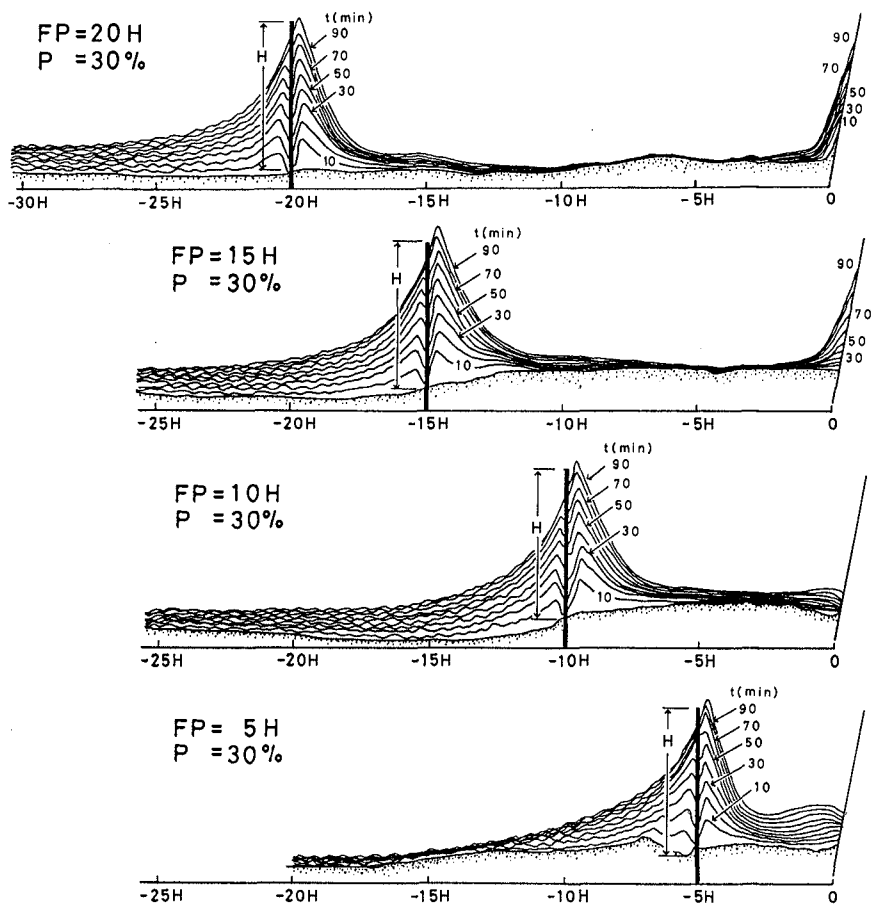


Fig. 8(b) The time evolution of the sand accumulation around fence placed in front of an embankment ($P=30\%$).

area). In Fig. 9, there is a tendency that the sand accumulation was the largest when the fence was placed at a location of $15H$, although a fair amount of scatter in the data is seen.

3.5 Sand Weight Transported beyond the Embankment

Figure 10 shows a comparison among different porosity of the sand weight transported beyond the embankment for the 90-min experiment duration. The amount of sand transported beyond the embankment was different during each stage of the experiment depending on the conditions in front of embankment. However, the fences with 20 %

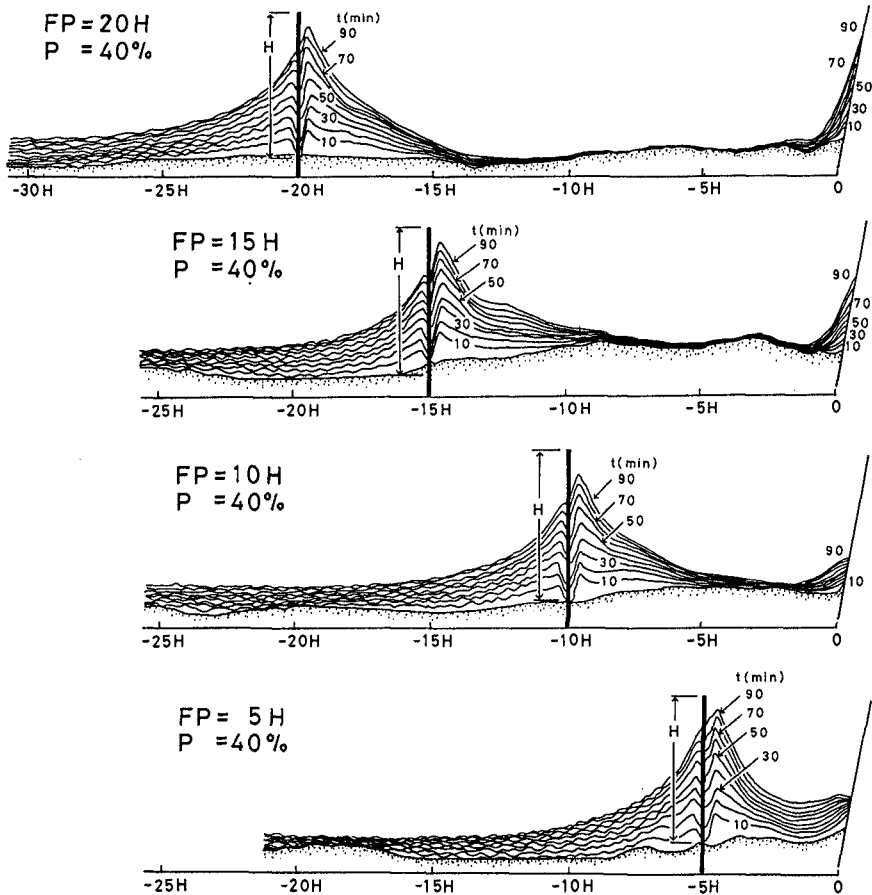


Fig. 8(c) The time evolution of the sand accumulation around fence placed in front of an embankment ($P=40\%$).

and 30 % porosity were completely buried at every location during the entire experiment and the fence with 40 % and 50 % porosity were buried to more than 60 % of its height. If it is assumed that the fences have lost their sand trapping function at this stage, the transported sand weight shown in Fig. 10 may be used as an index to determine a suitable location for the fence. The amount of sand transported was small when fences with 40 % and 50 % porosity were placed at locations of 15 H or 20 H in front of the embankment. This is an important conclusion for the present research work.

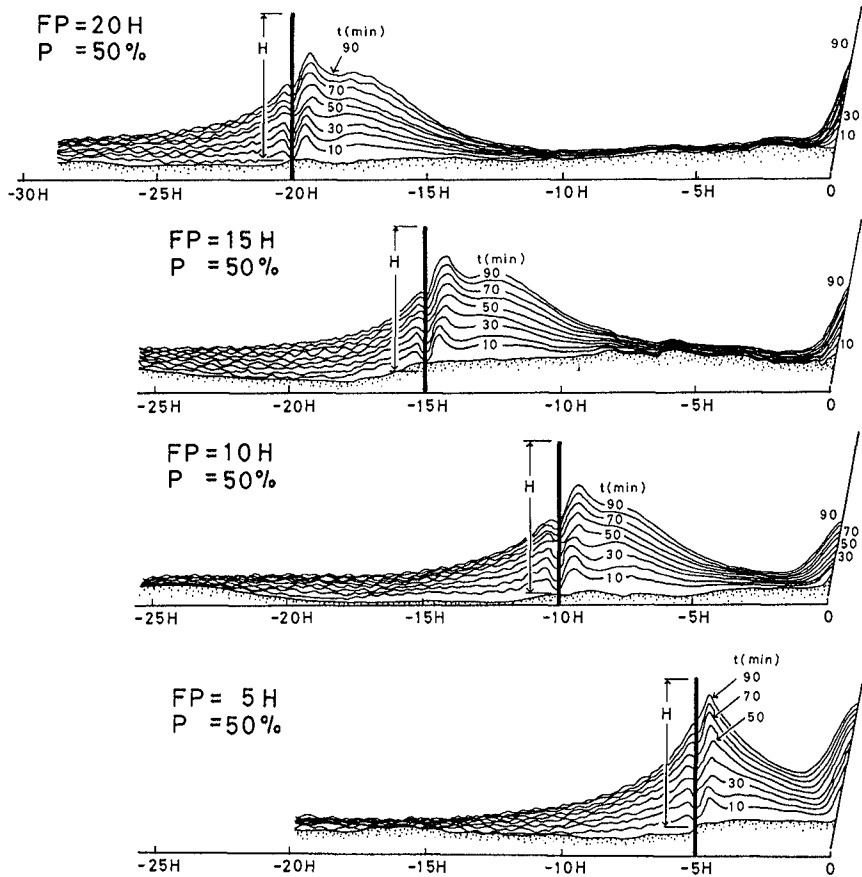


Fig. 8(d) The time evolution of the sand accumulation around fence placed in front of an embankment ($P=50\%$).

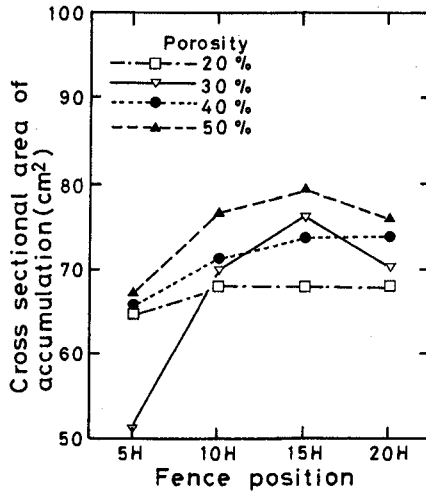


Fig. 9 Cross-sectional area of accumulated sand as a function of fence porosity and position.

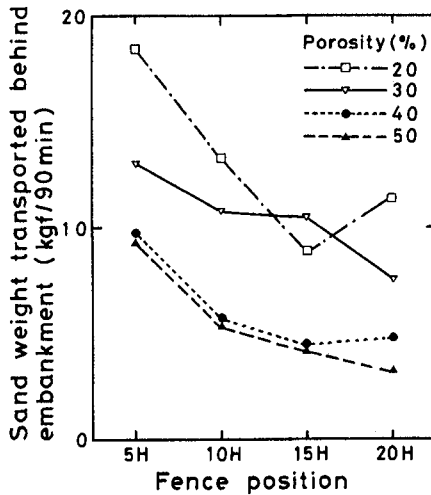


Fig. 10 Sand weight transported beyond embankment as a function of fence porosity and position.

IV CONCLUSIONS

The results obtained in this study may be summarized as follows:

1. The fence porosity for which sand accumulated most rapidly in large quantities was 40 %.
2. The fence porosity which produced the most rapid dune

crest growth was 20 %.

3. The fences lost their sand trapping function if they were buried to 80 % of their height.
4. Sand accumulated in a region extending from 10 H in front of the fence to the foot of the embankment, and the maximum accumulation occurred when the fence was placed 15 H in front of the embankment.
5. The amount of sand transported beyond the embankment was small when the 40 % and 50 % porosity fences were placed at a distance of 15 H or 20 H in front of the embankment.

Based on the above observations, the overall conclusion of this study is that, for controlling wind-blown sand in front of the embankment, a fence with 40 % or 50% porosity should be placed at a distance between 15 H to 20 H in front of the embankment.

Finally, some comments regarding the experiments should be given. This experiment was a distorted model experiment where the wind speed and sand employed were prototype-scale. The fence height was about 1/10 of a prototype-size fence which commonly has a height of 1 m (about 3 ft). Scale effects are anticipated during the experiments, although it is not possible to evaluate how the scale effects influenced the results. The wind speed employed in this experiment was of moderate strength commonly encountered on natural beaches. Sand accumulations characteristics around fences are different depending on the wind speed, especially for wind speed over 15 m/sec, requiring further studies in future. The wind blowing in the field is irregular in time and space. These facts must be kept in mind when the results obtained in this study are applied to field condition.

ACKNOWLEDGEMENTS

The authors would like to thank the Central Research Institute of Electric Power Industry, for permission to use the wind tunnel. A portion of this study was supported by the General Individual Research Grant, Nihon University Research Grants for 1989, and the Grant-in-Aid for Scientific Research (No. 63550381) from the Ministry of Education, Science and Culture of Japanese Government.

REFERENCES

- Horikawa, K., S. Hotta, S. Kubota and S. Katori (1983): On the sand transport rate by wind on a beach, Coastal Engineering in Japan, Vol. 26, JSCE, pp. 101-120.
- Hotta, S., N.C. Kraus and K. Horikawa (1987): Function of sand fences in controlling wind-blown sand, Proc. Coastal Sediments '87, ASCE, pp. 772-787.

CHAPTER 210

RECENT PERFORMANCE OF LINKED CONCRETE MAT ARMOR UNDER WAVE AND ICE IMPACT

P.E. Gadd, M. ASCE and C.B. Leidersdorf, M. ASCE¹

INTRODUCTION

Concrete mat slope armor has been used for many years to provide slope protection in mild inland and coastal wave environments. Presently, flexible block revetments are gaining popularity for application in moderate wave climates where more conventional types of slope protection are uneconomical or unavailable. European investigators have undertaken design and model testing of placed (non-linked) concrete block revetment systems (Burger, et al., 1990, for example). Systems requiring physical linkage of adjacent blocks have been designed and deployed as well (Hayley, et al., 1987; Leidersdorf, et al., 1988; Munday and Bricker, 1987).

Previous authors have described linked concrete mat systems in detail and suggest its promise for both Arctic and non-Arctic applications (Hayley, et al., 1987; Leidersdorf, et al., 1988; Munday and Bricker, 1987). The objective of this paper is to describe the results of on-going performance monitoring of linked concrete mat systems deployed upon a man-made island in the rigorous Arctic offshore environment. We wish to place particular emphasis upon recent observations that indicate performance limitations of existing concrete mat technology when subjected to the combined effects of severe Arctic wave and ice impacts at offshore deepwater sites.

LINKED CONCRETE MAT ARMOR

Concrete mat slope protection has been advanced by numerous investigators as an alternative to more conventional discrete-unit slope armor. Principal advantages to the concrete mat alternative are related to enhanced stability of light-weight armor units (by

(1) Principals, Coastal Frontiers Corporation, P.O. Box 515,
Altadena, California 91003, USA

virtue of physical linkage), ability to accommodate changes in subgrade without loss of underlying gravel fill, and suitability for quick and economical modular placement. In addition, Arctic applications require ease of removal (for short-lived oil exploration structures) and resistance to ice abrasion and impact.

As indicated above, several large oil industry projects in Arctic Alaska that utilized the linked concrete mat concept have been described previously. The mat system under study is composed of individual blocks having plan dimensions of 1.2 m square. Block thickness can vary with application but has typically measured 0.23 m. Block linkage is provided by galvanized shackles and chain segments.

PERFORMANCE MONITORING OBSERVATIONS AT NORTHSTAR ISLAND

Northstar Island was constructed at an unprotected offshore location having a water depth of 13.7 m located approximately 25 km northwest of Prudhoe Bay, Alaska. This island has provided a unique setting in which environmental influences on the slope protection system have been carefully monitored annually since the completion of construction in 1985. The design of Northstar Island has been described previously (Hayley, *et al.*, 1987; Leidersdorf, *et al.*, 1988), and is summarized in Figure 1.

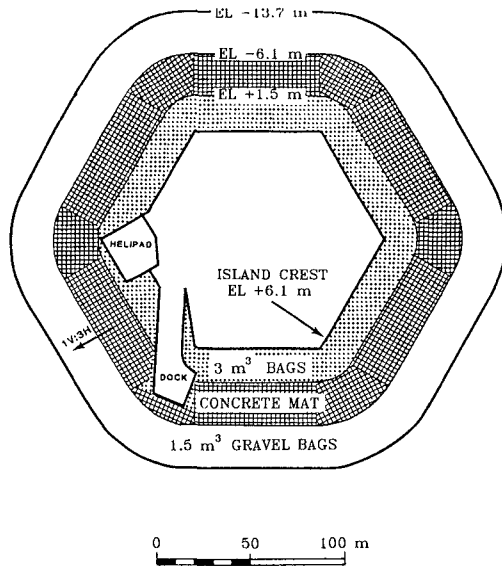


FIGURE 1: NORTHSTAR ISLAND DESIGN

The slope armor system is composed of linked concrete mat in the zone of primary wave and ice impact (El. +1.5 m to -6.1 m, MLLW)

placed upon a slope of 1 (vertical) on 3 (horizontal). On the slopes up-slope and down-slope from the concrete mat, large (1.5 to 3.0 m³ capacity) gravel-filled fabric bags are placed. The overlapped placement configuration of the gravel bags on the upper slope of the island reduces wave run-up elevation.

Northstar Island is an oil exploration island having an intended design life of three years. The design storm event was expected to be accompanied by storm surge of 1.0 m and to exhibit a significant wave height of 3.7 m, and a significant wave period of 9.6 sec.

Prior to the construction of Northstar Island, shallow water installations of linked concrete mat slope armor in the Arctic in water depths of 2-4 m met with success. Owing to the mild wave and ice conditions at these locations, significant damage has not been noted to date. At Northstar Island, however, degradation of the mat revetment has been noteworthy, related to the alternating impacts of large storm waves and massive ice features.

In the 1987-1988 period, the performance of the mat system degraded following significant damage imposed by multiple episodes of large wave and ice impact. The discussions in this paper seek to describe the damage that has occurred on Northstar Island since its construction in 1985 and to offer insights that will improve the existing state of engineering knowledge concerning deployment of linked concrete mat slope protection in the Arctic offshore.

WAVE-INDUCED CONCRETE MAT DAMAGE

Effects of Angle of Wave Incidence

During a strong northwest storm accompanied by wave heights in the three to four meter range that occurred in late September 1986, significant uplift and undulation of the concrete mat at Northstar Island first occurred. It was clearly noted, however, that the extent of mat uplift was not uniform around the island circumference. Photo 1 is presented to show the condition of the island sector that received the incoming wave impact at a normal (i.e. wave ray approach = 90° from waterline) angle of incidence. The undeformed nature of this slope suggests that mat uplift did not occur along this island sector.

Conversely, along the sides of the island which experienced wave passage at highly oblique angles of incidence, mat uplift and the resulting mat undulation was severe, as shown in Photo 2. Wave-induced mat instability was noted along the island slopes on the lee side of the island as well, where wave crests did not detach from the island slopes, but proceeded along the slopes at angles of incidence greater than 45°.



PHOTO 1: POST-STORM CONDITION, NORMAL ANGLE OF WAVE INCIDENCE



PHOTO 2: POST-STORM CONDITION, OBLIQUE ANGLE OF WAVE INCIDENCE

We believe that the reasons for the destabilizing effect of oblique wave passage over the concrete mat at Northstar Island is based both on hydrodynamic effects that impose negative wave pressures on the mat, and as a consequence of asymmetrical mat linkage tension imposed during the construction process. The

hydrodynamic effects that produce greater wave uplift for oblique angles of wave attack (relative to normal incidence) have been noted by researchers utilizing three-dimensional physical model studies at Delft Hydraulics, The Netherlands (Bezuijen, A., and A.M. Burger, personal communication).

Asymmetric block linkage tension within the mat was caused as a result of the construction process, undertaken during August-September, 1985. In placing the mat upon the island slopes, narrow mat segments were used incorporating 22 blocks in the upslope-downslope direction by two blocks across. As the placement crane lowered the mat to its above-water anchorage position and boomed the mat offshore, high tension was achieved in the upslope-downslope mat direction. Successive mat sections were placed closely side-to-side to allow divers to easily connect the mat beneath the water. Consequently, substantial slack resulted in the side-to-side block linkage. The resulting lack of side-to-side restraint in the mats surrounding the island promotes mat instability in response to oblique wave attack. Conversely, the lack of alongslope linkage tension would seem not to affect mat stability given a normal angle of wave incidence where side-to-side restraint would be less important. This indeed appears to be the case, given the visual observations of the effects of wave-induced uplift at Northstar Island.

Effects of Island Subsidence

Northstar Island is composed of approximately 800,000 m³ of terrestrial gravel that was trucked to the offshore island site in winter over a floating ice road. Such an Arctic gravel placement project undertaken in winter typically results in the dumping of gravel having a temperature of -20° to -40° C. into ocean water exhibiting a temperature of -2° C. As a result, ice forms in the interstitial spaces within the gravel fill. With time, summer thawing and long-term creep of the ice within the fill can result in island subsidence. Such subsidence has been noted continuously at Northstar Island within the 1985-1989 inspection period. Figure 2 shows the nature of the subsidence as evidenced at several benchmarks located on the island. The rate of subsidence is generally noted to be 10 cm annually, yielding a total subsidence of about 40-50 cm since the conclusion of construction in 1985.

The effect of island fill consolidation results in the inward relative motion of the individual concrete blocks within the mat surrounding the island. This subtle effect leads to a gradual decrease in the space that exists between adjacent blocks. As the block spacing decreases, relief of hydraulic pressures that build within the fill during the alternating action of wave run-up and wave run-down becomes increasingly more difficult to accomplish.

Originally, the design of Northstar Island specified a block spacing of 5.0 to 6.4 cm, yielding a "percent open area" (the area of open space within the mat relative to the total area) of 19%.

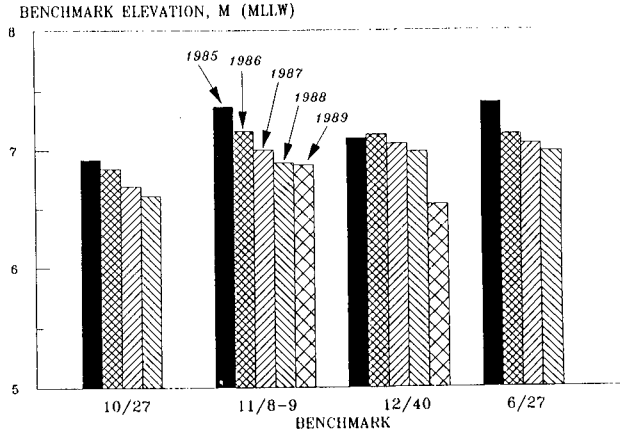


FIGURE 2: NORTHSTAR ISLAND SUBSIDENCE, 1985 - 1989

As a result of island subsidence/fill consolidation and a block fabrication process that yielded slightly oversized blocks, the existing "percent open area" is now estimated to be 11%, based on recent measurements of block spacing. This reduction in block open area will yield a propensity for mat uplift at lower wave height thresholds and also for greater vertical block uplift when wave-induced uplift does occur.

Effect of Mat Underlayer

A durable and permeable mat underlayer is important for the successful deployment of concrete mat armor over the granular fill material commonly used in the Alaskan Arctic offshore. At Northstar Island, a highly permeable non-woven polyester filter fabric was used for this three year design life application. The characteristics of the fabric are summarized as follows:

Fabric Weight = 510 gm/m^3
 Tensile Strength = 525 N/cm
 Permeability = 0.65 cm/sec .

In addition, the fabric readily sinks in seawater--an important detail that greatly aids the construction effort.

Successive mat uplift events can cause abrasion and parting of the underlying fabric, allowing the loss of gravel fill beneath the mat. Given the abrasive nature of concrete block slope armor relative to the underlying filter fabric, it is apparent that mat

uplift must be eliminated if long-term survival of the fabric is to occur.

Inspection of the concrete armor at Northstar Island following large storm events indicates that uplift pressures beneath the filter fabric have been excessive. This has become evident at areas where gravel fill, completely encased in filter fabric, has been forced through block spaces to form outward pockets of gravel on the upper surface of the mat. An instance of this occurrence is shown in Photo 3.

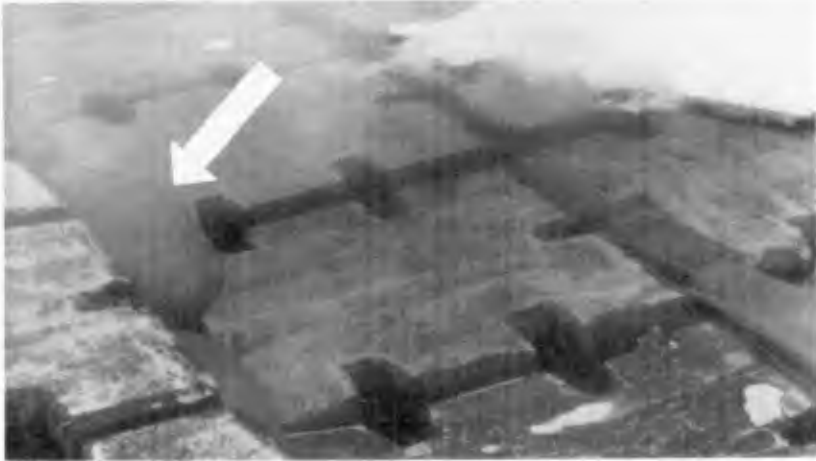


PHOTO 3: FILTER FABRIC AND GRAVEL PROTRUSION BETWEEN BLOCK SPACES

Once these gravel bulges formed, ice or wave motion causes failure of the fabric pocket leading to filter fabric voids. Initially, the localized and infrequent nature of this occurrence did not render it of serious concern to the integrity of the slope protection system. However, the filter fabric shortcomings related to permeability were clearly indicated.

Repeated instances of wave-induced mat uplift at Northstar Island resulted in filter fabric abrasion and parting that caused loss of gravel fill beneath the mat. Major damage to the filter fabric in this regard occurred during the November 1987 storm event, when large waves and multi-year ice impacts heavily damaged the eastern side of Northstar Island. Repeated profiling of the island slope (as shown in Figure 3) shows the effect of the 1987 storm, and indicates the large volume of gravel lost from beneath the concrete mat due to filter fabric voids.

The damage sustained by the filter fabric at Northstar Island indicates that a more durable and permeable filter medium is vital

in promoting improved performance of concrete block slope armor. Stronger, more permeable filter fabrics do exist in the geotextile industry and should be carefully considered for Arctic offshore applications.

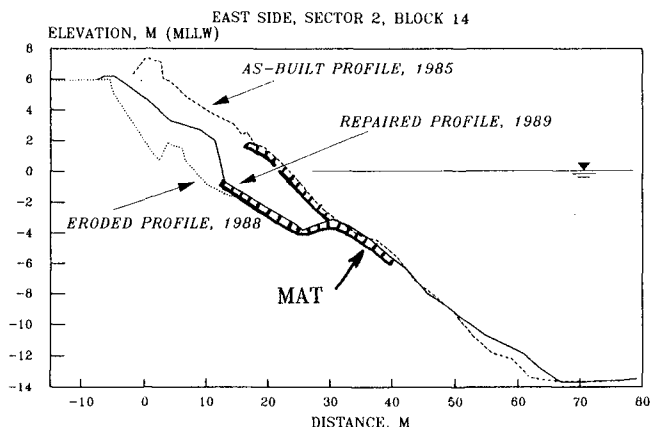


FIGURE 3: TYPICAL PROFILE CHANGES, EAST SIDE, 1985 -1989

For long-lived offshore production facilities, consideration has been given to the use of small quarrystone or concrete rubble as underlayer for concrete mat armor. The concrete alternative can be unreinforced and cast in shapes of the required size in a conventional concrete stamping procedure. These durable underlayers would benefit from their high permeability and abrasion resistance relative to fabric alternatives. Important issues related to construction placement and the effect on concrete block support must be resolved to render these materials viable for use as an underlayer/filtration medium.

ICE-INDUCED CONCRETE MAT DAMAGE

The concrete blocks used at Northstar Island were constructed at Prudhoe Bay, Alaska, using a highly mechanized "dry cast" block fabrication technique. The concrete mix exhibited low water:cement ratio ($w/c = 0.32$), high cement content (392 kg/m^3), air entrainment (5-7%), and use of fly ash pozzalon (10% by weight). The resulting concrete product exhibited an average compressive strength of 55 MPa (8,000 psi). By contrast, the expected compressive strength of ice impacting this site is 2.8 MPa.

Despite the high strength characteristics indicated, isolated instances of concrete block breakage were noted during the summer

of 1986, the year following island construction. Samples of broken concrete blocks were tested at that time to determine the characteristics of the failed blocks. Test results indicated that the broken blocks were not atypically weak blocks, but exhibited the same high compressive strength characteristics that were noted during the block fabrication period.

In November 1987, a high-energy easterly storm occurred along the northern coast of Alaska for a period of 14 days. The storm was accompanied by alternating periods of ice-free water (leading to large wave generation) and the incursion of large ice floes (leading to damaging ice impacts). Erosion of nearby islands protected solely by gravel bags was excessive during this storm period.

Damage to the slope protection at Northstar Island during this storm included major displacement of the concrete mat in response to wave-induced uplift and ice impact, breakage of concrete blocks due to direct ice impact and/or inter-block collision induced by ice impact, loss of underlying gravel fill material through filter fabric tears and voids induced by storm-related processes, and failure of steel chain/shackle linkages caused by ice impact forces.

During July of the following summer, large-scale damage to the concrete blocks occurred on the east and north sides of Northstar



PHOTO 4: BLOCK BREAKAGE CAUSED BY ICE IMPACT

Island as a result of the collision of massive ice features with the island during the open-water season. The nature of the damage included block breakage (as had been noted in rare instances in 1986), mat displacement caused by impacts of large ice features, and surface abrasion of the mat armor by ice impact.

Concrete mat breakage has proven to be impressive at Northstar Island, primarily affecting blocks located above an elevation of -3.7 m (MLLW). Block breakage has occurred, in which cracks propagate through the block without substantial loss of concrete volume. In addition, blocks have been stripped of concrete cover, leaving only the steel reinforcement where the concrete mass had once been. Photo 4 is presented to show an example of excessive block damage of this type.

When the slopes of Northstar Island were pristine and free from irregularities and undulations, the early winter ice would collide with the concrete and form ice piles that would build seaward from the waterline. These ice piles would form a barrier providing protection from the larger ice features that might impact the island later in the freeze-up period. Later, following the storm damage of September 1986, undulations in the concrete mat slope caused by wave-induced mat uplift, generated irregularities within the mat surface upon which incoming ice forces could act. As a result, deformation and displacement of the concrete mat armor occurred as large ice features collided with the irregular island slopes. With time, therefore, the ability of the island slopes to safely withstand large ice impacts degraded. Damaging mat displacements during both winter and summer were noted. Photo 5 shows the results to a particularly forceful ice collision with the north slope of Northstar Island during late July 1988. The nature of the concrete mat damage that occurred as a result of this incident is shown in Photo 6, following the natural ablation of the ice that caused the damage.

Figure 4 is presented to illustrate the sequence of the damage experienced as a joint result of both wave and ice processes at Northstar Island. Initially, wave-induced mat uplift occurred that led to deformation and undulation of the pristine "as-built" island slope. Subsequent to this event, incoming ice features, which had previously been ineffective in displacing the uniformly smooth mat, were capable of imparting force to the various mat irregularities, thereby inducing significant mat displacements. Such displacements further permitted filter fabric degradation and loss of underlying fill material. Therefore, elimination of concrete block uplift is of ultimate importance--to prevent abrasion of the underlying filter medium and subsequent loss of gravel fill, and to prevent the development of slope irregularities and deformations that allow large ice features to impart significant damage and displacement to the slope armor.



PHOTO 5: BLOCK DISPLACEMENT BY LARGE ICE IMPACT, AUGUST 1988



PHOTO 6: MAT DAMAGE OF PHOTO 4 FOLLOWING ICE REMOVAL, JULY 1989

CONCLUSIONS AND RECOMMENDATIONS

Recent experience at Northstar Island has allowed an evaluation of linked concrete mat performance when subjected to the harsh wave and ice environment of the Alaskan Arctic offshore. Observations

have been made that could not be observed accurately in any other method of investigation. While performing as an oil exploration island, Northstar Island has also performed as a prototype laboratory in which the interaction of Arctic ice forces, three-dimensional wave impact, and the linked concrete slope

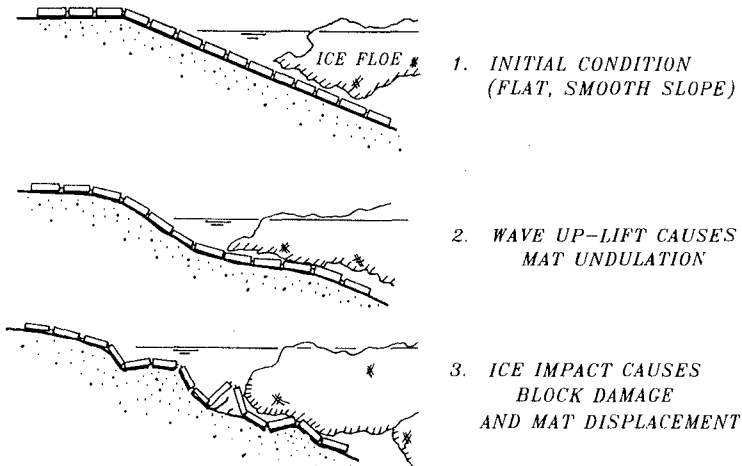


FIGURE 4: NORTHSTAR ISLAND MAT DAMAGE SEQUENCE, 1985 - 1989

protection system could be observed. The valuable lessons learned from this experience are ongoing. To date the following conclusions are worthy of note:

- o Oblique Wave Impact: Wave impact arriving at high angles of wave incidence to the slope effectively induce mat uplift more readily than the same wave conditions arriving at a normal incident angle. This is due both to hydrodynamic effects yielding higher negative wave pressures from oblique wave attack, and also to the lack of side-to-side tension in the linkages of the Northstar Island mat system.
- o Reduction of Mat "Open Area": The void space within the mat system ("open area") allows relief of hydraulic pressures that are created within the island fill during periods of wave run-up. This "open area" must be sufficient to allow adequate hydraulic relief initially, and must be maintained with time if mat performance is to continually achieve the design intent. One factor that has caused a reduction in the "open area" at Northstar Island is island subsidence. Due principally to

thermal effects within the gravel fill, the elevation of the island has decreased approximately 40-50 cm since 1985. This subtle effect has contributed to a decrease in the "percent open area" of the mat from the designed value of 19% to the present (summer 1990) measured value of 11%.

- o Underlayer Characteristics: Important factors related to the proper performance of an underlayer for the concrete mat are high permeability and durability. While the filter fabric selected for use at Northstar Island exhibited excellent performance in both of these areas relative to other fabrics, it is clear that improvement of underlayer performance is vital to future concrete mat installations in this environment. Should fabric permeability be lacking leading to creation of excessive uplift pressures beneath the fabric, mat uplift may occur. Once the concrete blocks uplift periodically in response to wave passage, failure of the fabric through block abrasion will follow. Fabric voids caused by mat abrasion will lead to loss of gravel fill from beneath the fabric and subsequent slope deformations. For long-lived offshore structures, concrete or quarystone rubble may provide more suitable underlayer characteristics for concrete block revetments. An expensive alternative to a highly permeable underlayer is the utilization of heavier concrete blocks that can adequately withstand the wave-induced uplift pressures.
- o Side Slope Configuration: Improvements in linked concrete mat performance will result from consideration of slope alterations that include the incorporation of milder slopes and/or horizontal benches having a width of perhaps 10-20 meters in the zone of wave impact. Previous physical modelling efforts (Potter, et al., 1983) have noted that such slopes reduce block uplift, lower wave run-up, reduce ice impact forces, and improve overall block stability against wave impact relative to the straight smooth 1 (vertical) on 3 (horizontal) slopes utilized on Northstar Island. In addition, the inclusion of a flat bench of significant width near the waterline will provide a safety buffer to restrict any damage that may occur to areas of the slope that are distant from the island work surface.

REFERENCES

- Burger, A.M., M.K. Breteler, L. Banach, A. Bezuijen, and K.W. Pilarczyk, 1990: "Analytical Design Method for Relatively Closed Block Revetments Block Revetments". Journal of Waterway, Port, Coastal, and Ocean Engineering, American Society of Civil Engineers, Vol. 116, No. 5, p. 525-543.
- Hayley, D.W., P.E. Gadd, and D.E. Horn, 1987: "Advances in Design and Construction of Slope Protection for Gravel Islands". Proceedings, POAC '87, Fairbanks, Alaska.

Leidersdorf, C.B., R.E. Potter, B.C. Gerwick, and Y.Y. Hsu, 1982: "Modular Slope Protection for the Arctic Environment". Proceedings, 14th Annual Offshore Technology Conference, Houston, Texas, p. 689-704.

Leidersdorf, C.B., R.E. Potter, and C.J. Sonu, 1984: "Study of Slope Protection Works for the Arctic Ocean". Proceedings, 31st Conference, Japan Society of Civil Engineering, p. 552-556.

Leidersdorf, C.B., P.E. Gadd, and W.G. McDougal, 1988: "Articulated Concrete Mat Slope Protection". Proceedings, 21st Coastal Engineering Conference, Malaga, Spain, p. 2400-2415.

Munday, J. and W. Bricker, 1987: "Endicott Slope Protection--Design and Construction". Proceedings, 6th International Symposium on Offshore Mechanics and Arctic Engineering (OMAE '87), Houston, Texas, p. 47-54.

CHAPTER 211

THREE DIMENSIONAL EFFECTS OF SEAWALL ON THE ADJACENT BEACH

Takao Toue¹
Hsiang Wang²

ABSTRACT

The effects of seawall on the adjacent beach is examined by the three dimensional physical model test. The experiment results are analyzed by means of the volumetric change analysis and the shoreline change analysis. The results show that the groin effects are dominant but they are localized within a region spanning three or four times of seawall length for the cases tested

1. Introduction

Beach erosion is found along many portion of the coast of the world. The cause of the erosion could be sea level rise, reduction in sediment supply, interruption of the littoral drift by structures. There are several conventional engineering solutions to combat such erosion. Those are (1) coastal structure such as groins, seawalls, breakwater and coastal dike, and (2) non structural solutions, such as beach nourishments. Among them, seawalls might be the most efficient and direct method to protect the up-land property provided that they are designed adequately.

Recently, the adverse effects of seawalls on their fronting and adjacent beaches have great attention and raised criticism about the use of seawalls in the coastal area. The most often alleged effects are (1) offshore profile slope steepening, (2) intensified local

¹Research Engineer, Technical Research Center, Taisei Corporation, 344-1 Naze, Yokohama Kanagawa, 245, Japan

²Chairman and Professor of Coastal and Oceanographic Eng., Dep. University of Florida, Gainesville, Florida, 32611, U.S.A

scour, (3) transport of sand to a substantial distance offshore, (4) adverse down drift erosion and (5) delay post-storm recovery (Dean, 1986). Although numerous examples can be found from articles in newspaper or popular magazine reporting the adverse effects of seawall, reliable and scientific based document is actually scarce. Moreover, the conclusion derived from the few technical reports on the adverse effects of seawalls remains controversial. Considering the merits of seawall altogether as means of coastal protection without firmly establishing their effects might be irrational. Therefore, there is a need to examine the effects of seawall carefully and to quantify them if possible. Also, by examining the cause and effects of seawall might lead more rational design in the future. The main objectives of the present study is to attempt to quantify the three dimensional effects on beach changes. In order to gain a fundamental understanding it was decided to conduct three dimensional model tests in the laboratory environment.

2. Possible Mechanisms of Seawall Effects

The effects of seawall are not well understood, but several possible mechanisms can be deduced from our general knowledge in coastal engineering. These are illustrated in Fig. 1 and also described below.

(1) flanking effects; Flanking due to wave refraction and diffraction is expected to occur on the corners of the seawall to cause local erosion.

(2) cross wave effects; During storm surge period, the water depth in front of seawall is likely to be larger than that along beach and wave reflection will occur as shown in Fig. 1(b). Consequently, the longshore current together with more reflected wave energy trapped in the trough will remove sand in front of seawall and transport them to down drift location.

(3) groin effects; If the shoreline retreat due to littoral drift, the seawall will eventually protrude seaward and act like a groin. Although this groin effect does not remove sand from the system it inverse downdrift erosion pressure.

(4) sand supply cut off; Seawall prevents sand from being added to the littoral system, which again adds erosional stress downdrift and could result in lower bar profile in front of seawall during the storm surge period.

3. Model Test Apparatus and Test Condition

The model test is carried out in the wave basin of the Coastal and Oceanographic Engineering Department, University of Florida. The dimension of the basin is

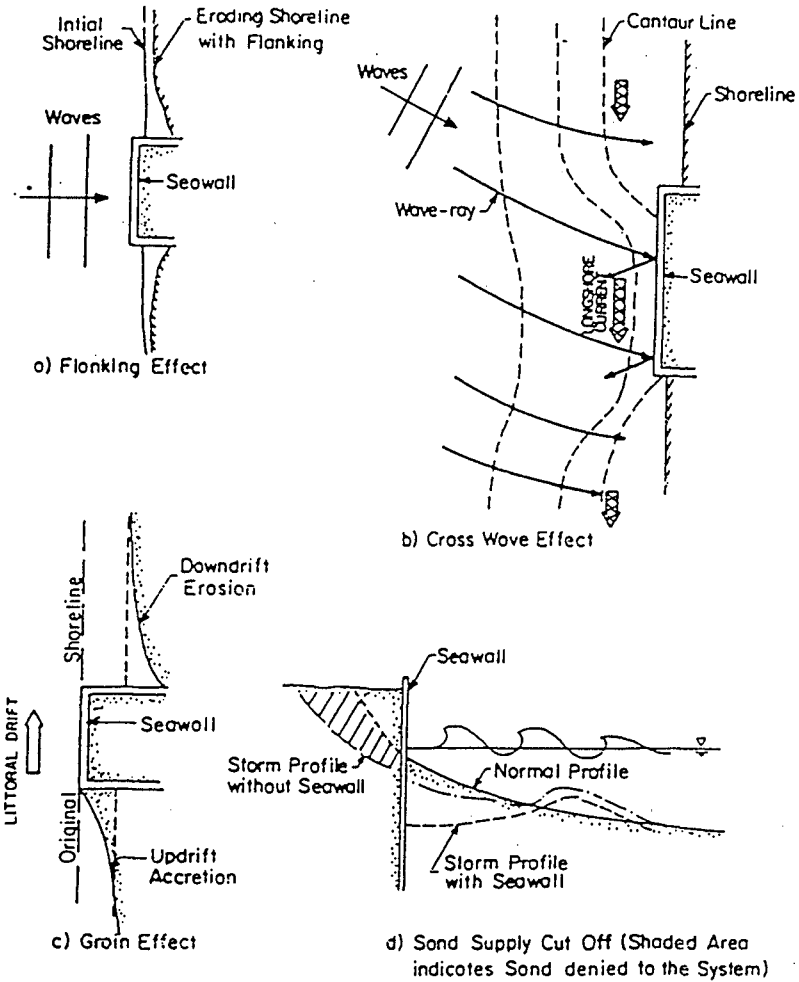


Fig. 1 Possible Mechanisms of Effects of Seawall

approximately 28m x 28 m and 1m deep. The beach and seawall system used in the experiments is shown in Fig. 2. The beach is composed of 125 tons of well sorted

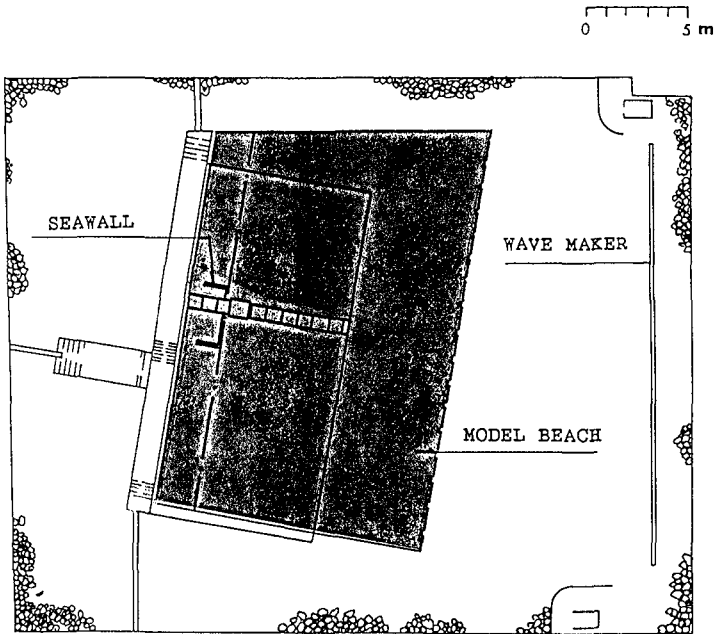


Fig. 2 Model Test Apparatus

quarts sand. Both side of the beach are constrained by wooden template cut into a design beach profile shape. This design allows wave induced long-shore current to circulate unimpeded through the backside of beach. The beach profile is shaped in accordance with the concept of equilibrium beach profile (Dean 1977). The length of seawall is 3.0m and with 1.0m return walls on each side to prevent flanking. The height of seawall is 45 cm which is sufficient to prevent wave over topping. The toe of the seawall is located at 45 cm above the basin bottom which corresponds to the mean water level in the present test configurations.

The beach was subjected to the test wave condition for a designated duration. During test period, profile measurements were carried out at regular intervals. A total of 21 profiles were surveyed at equal spacing of 75 cm. Surveys were conducted at 0, 1, 2, and 4 hrs. Wave height was 11 cm and wave period was 1.74 s. The test conditions are summarized in Table 1.

Table 1 Test Condition

Case	wave height (cm)	wave period (sec)	water depth (cm)	wave angle (°)	seawall	elapsed time (hour)
Case1	11.0	1.74	45.0	0	no	4.0
Case2	11.0	1.74	45.0	0	yes	4.0
Case3	11.0	1.74	45.0	5	no	4.0
Case4	11.0	1.74	45.0	5	yes	4.0
Case5	11.0	1.74	45.0	10	no	12.0
Case6	11.0	1.74	45.0	10	yes	5.0

4. Volume Change Analysis

The coordinate system in this study is shown in Fig. 3.

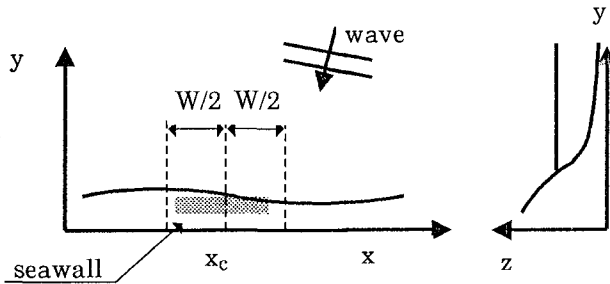


Fig. 3 Coordinate System

Based on the coordinate system, the rate of volumetric change in a local control area centered around the seawall, $v_1(t)$ is defined as

$$v_1(t) = \int_{x_c - W/2}^{x_c + W/2} \int_0^{y_0} \frac{\partial z}{\partial t} dy dx, \tag{1}$$

where z =profile elevation, x =shore-parallel axis, y =shore-perpendicular axis, x_c is the location of the center of seawall, y_0 = measurement length, W is the width of control area and t is time. .

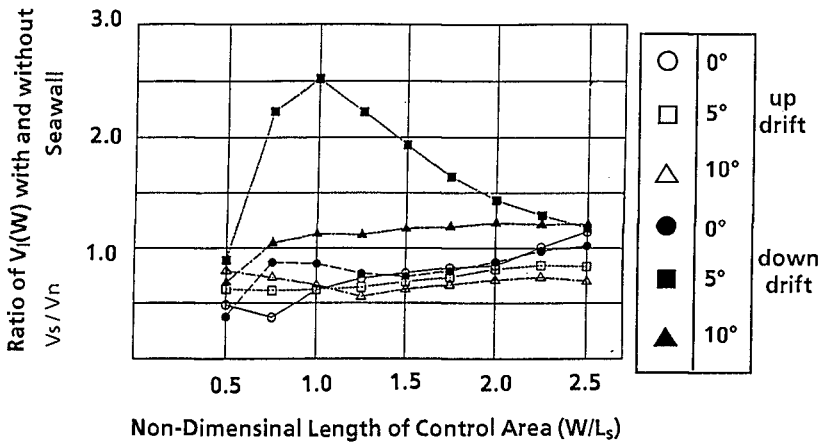
The ratio of the volumetric change, with(v_s) and without(v_n) is plotted against the non - dimensional control width(W/L_s) where L_s is the length of seawall in Fig. 4. If the ratio is larger than 1.0, the rate of erosion is larger with seawall than without seawall and vice versa.

In Fig.4(a), the ratio of v_s and v_n is plotted for the updrift and down drift region separately. In the updrift region, v_s/v_n is always less than 1 irrespective the width of the control region and the wave angles. Thus, in the case of normal incident wave, this value less than one because more sand is retained by the seawall in the backshore than the additional material being eroded in front of seawall, when compared with the natural beach case. For cases with oblique waves on the other hands, sand is retained in the updrift due to groin effect. They also make this ratio less than unity. On the down drift side, the situation is different, As expected, under normal incident waves v_s/v_n is less than 1.0 much the same as the updrift side. Under oblique waves, v_s/v_n is less than 1 when $W/L_s = 0.5$, or when the control region coincides with seawall length much the same as the two dimensional model test case by Barnett (1988). Apparently, even under oblique wave, the material retained from the scouring trough in front of seawall. However, when W/L_s become larger than 0.5, v_s/v_n also become larger than 1.0. The presence of seawall now interrupt the normal longshore transport and cause down drift erosion to be greater than the natural beach condition.

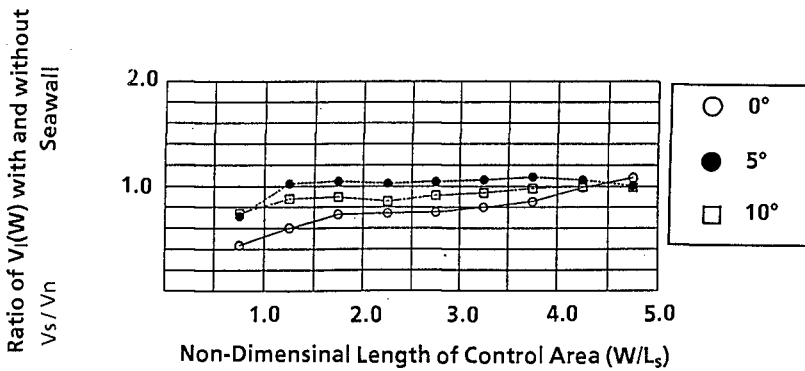
Finally, in Fig. 4(b) the ratio of total volumetric change including both updrift and down drift region are given. It can be seen that when $W/L_s < 1.25$, $v_s/v_n < 1.0$. When $W/L_s > 1.25$, the ratio of v_s/v_n become constant and approaches 1 as it should do when W/L_s becomes large. Therefore, the effects of seawall appears to be quite localized, certainly within 3 to 4 times of seawall length for the cases tested.

5. SHORELINE CHANGES

Fig. 5 shows general view of bathymetric change of four hours elapsed time for all cases tested. It can be seen that for the natural beach under normal incident waves the shoreline almost uniformly recessed. As wave angle is larger, the recession of the shoreline becomes



a) Ratio of Volumetric Change with and without Seawall Up-Drift ,Down Drift Separately



b) Ratio of Volumetric Change with and without Seawall

Fig. 4 Volumetric Change in Local Control Area

larger. For the seawall backed beach under normal incident waves, the shoreline also uniformly recessed, but under oblique waves, the recession of the shorelines of down-drift side is larger than that of natural beach, and that of up-drift side are smaller. The scour hole can be seen in front of seawall and the contour lines in front of seawall protrude shore ward there.

Shoreline changes are examined by means of Empirical Eigenfunction (EEF) analysis. For a multi variate function such as the three dimensional contour line represented by $h(x,y,t)$ there are several possible combinations of eigenfunction representation such as

$$h(x,y,t) = \sum_m w_m c_m(t) e_m(x) f_m(y), \quad (2)$$

$$h(x,y,t) = \sum_m w_m c_m(t) e_m(x,y), \quad (3)$$

$$h(x,y,t) = \sum_m w_m c_m(x,t_0) e_m(y,t_0), \quad (4)$$

where w_m is the weighting function, c_m, e_m, f_m are eigen vectors and m is the mode. These combination are, however, not independent of each other. The hope is to have the right choice such that most of the variance in the data set will be accounted for in fewest terms. Unfortunately, at present, there is no criterion for making such a choice and one has to rely on intuition and trial and error. After a number of preliminary tests, it is decided to use the distance from a baseline to shoreline, $d(x,t)$, as the dependent variable. Thus, we assume that this distance can be represented by the linear sum of spatial eigenfunction, $S_m(x)$, and temporal eigenfunction $T_m(t)$, of the following form:

$$\begin{aligned} D(x,t) &= d(x,t) - d(x,t_0) \\ &= \sum_{m=1}^{\infty} w_m S_m(x,t_0) T_m(t), \end{aligned} \quad (5)$$

where $D(x,t)$ is the difference between the distance of the shoreline at time t and that of the initial shoreline, and t_0 is the initial time.

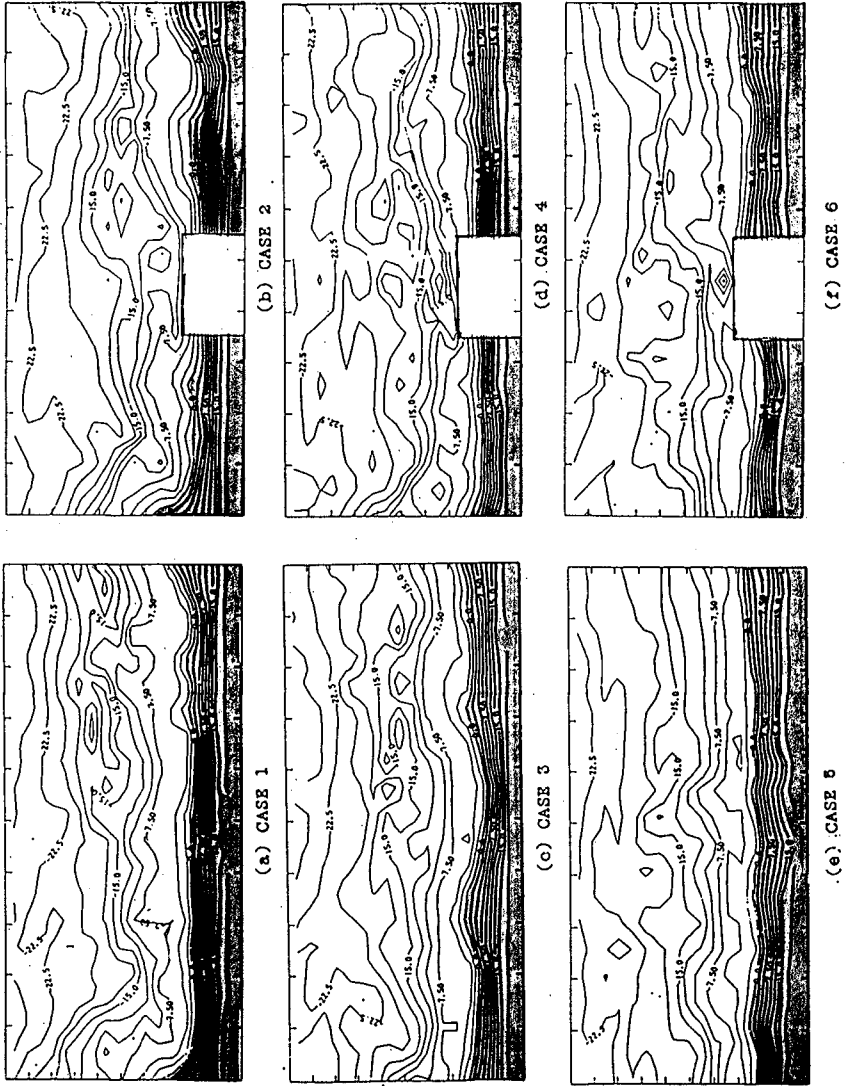


Fig. 5 Contour Maps for Four Hours Elapsed Time

In applying the procedure outlined here to the present experiment data set, a number of problems are identified that require special attention:

(1) Owing to the existence of offshore shoals and bars, $d(x,t)$ has, at times, multi-values. Care must be exercised to select the depth contour that is physically meaningful. (2) In EEF analysis, the contour lines near it are clearly not continuous. In such case, the contour lines are divided into segmented continuous lines and EEF analysis is performed to each line individually.

Fig. 6 shows the results of EEF analysis for all cases. In all the cases tested, the first eigen vector appears to account for more than 90% of the variance. Therefore, there is no surprising that the real shoreline changes is similar to the first spatial eigen vector. For cases of erosional waves with normal incident angle, ideally the shoreline would recede uniformly as there should be no longshore component of sediment transport. By examining Fig. 6 for the case of no seawall, the first spatial eigen vector is almost a parallel line with the exception near the edge where the three dimensional effects come into play. For the case with seawall, the first spatial eigen vector is almost a parallel line. The flanking effects, if any, is not visible. The temporal vectors are almost identical for both cases.

Under oblique waves, for the case of no seawall, the first spatial eigen vector exhibits a rhythmic features in addition to a uniform recession. The first temporal vectors appear to be similar to the case of normal incident waves. With presence of seawall, the rhythmic features on the updrift sides becomes more pronounced. Again, the temporal vectors possess similar characteristics as the previous cases. Now, as the wave angle increases (to 10 degree), this rhythmic features diminishes in amplitude. The groin effects becomes more evident that results in severe down-drift erosion immediately in the shadow of the seawall.

6 Correlation between Shoreline Changes and Volumetric Change

The correlation between shoreline changes and volumetric changes are examined here. The one-line theory for shoreline change is based on the following continuity equation of sediment flux:

$$\frac{1}{h} \frac{\partial S}{\partial x} + \frac{\partial d_s}{\partial t} + p = 0, \quad (6)$$

where d_s denotes shoreline change, S is the longshore sediment transport, h is the water depth at a closure point, p is the sink/source of sediment. Eq.(8) can be written in this finite difference form neglecting the term, p ,

$$\Delta d_s = -\frac{1}{h} \frac{\Delta t}{\Delta x} \Delta S = -\frac{1}{h} \Delta V, \quad (7)$$

where ΔV is the volumetric change per unit length along shore.

The value of h is usually treated as a constant. Therefore, according to one-line model the shoreline changes, Δd , has a linear relation to the cross-sectional volumetric changes. Fig. 7 shows the comparison of the calculated shoreline changes based on Eq (7) to the measured shoreline changes. As can be seen, agreement are good for beach with no seawall. The agreement actually becomes better as the test duration increases. This is because the profile gradually reaches the new equilibrium configurations. For beaches with seawall the agreement is poor at the initial stage but improved progressively as the duration of test becomes longer. Obviously, during the early stage of profile adjustment, the main mode of sediment transport is in the cross-shore direction. The one-line model which assumes no profile adjustment between time steps cannot be applied. As time elapses the profile becomes stabilized and longshore transport takes over as the main mode of sediment transport. The presence of seawall will create profile disturbance in both up-wave and down wave directions away from the seawall as can be seen in Fig 7. However, as time progress, the disturbance, instead of spreading further, actually, tends to diminish and the beach will revert back to the natural state of no seawall with the exception of the very localized effects just adjacent to the seawall.

7. Concluding remarks

To examine the effects of seawall, volumetric change analysis and shoreline changes analysis were employed. In volumetric change analysis, it was found that under normal incident wave, the rate of volumetric erosion as well as the total eroded volume in front of seawall was smaller than that of natural beach. For oblique waves, due to groin effects the erosion of down drift side is severe, but the effects were found to be localized within a region spanning 3 to 4 times of seawall length of fronting beach centered around seawall.

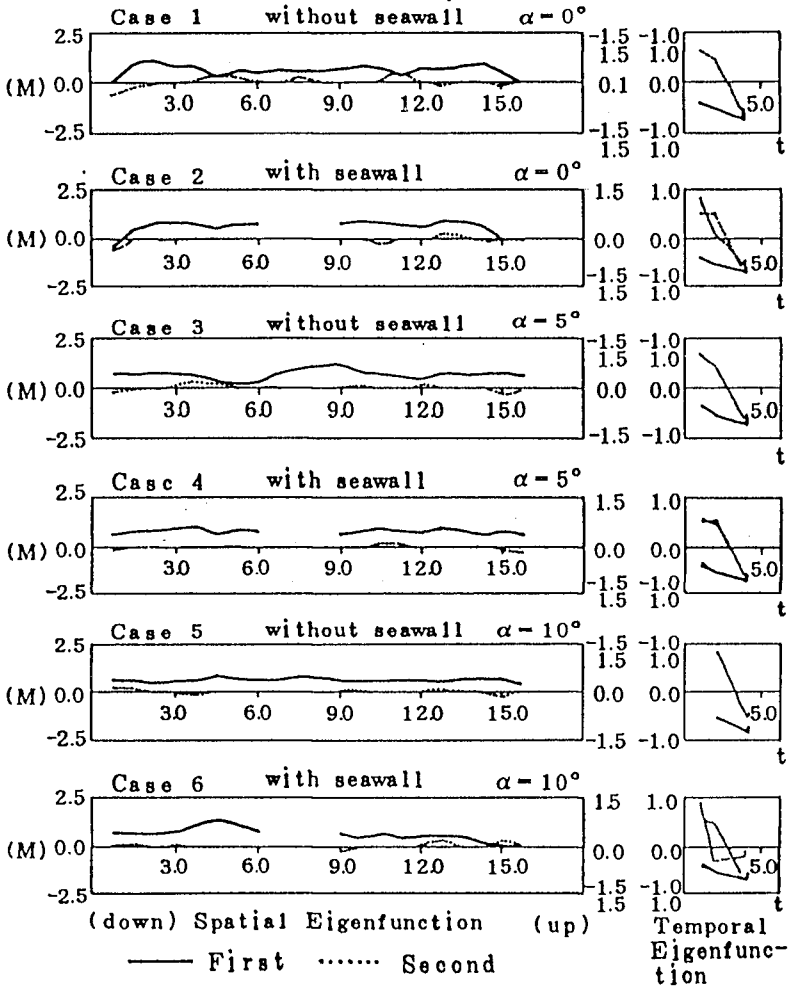


Fig. 6 Spatial and Temporal Eigenfunction

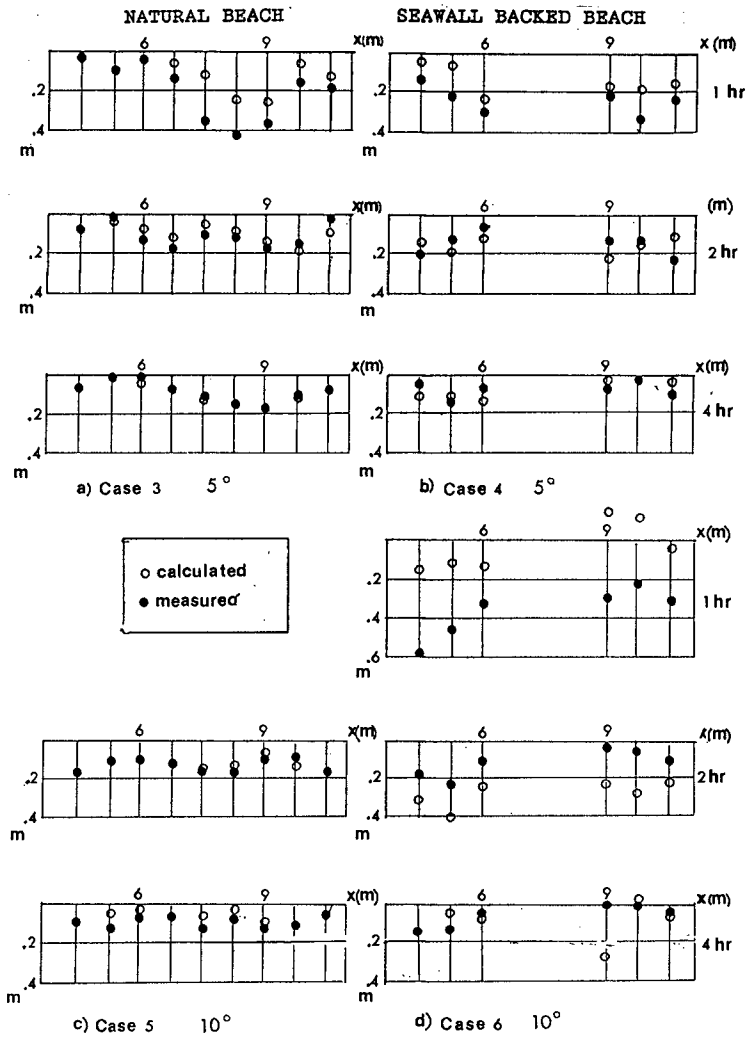


Fig. 7 Comparison of Shoreline Changes Calculated and Measured

In shoreline change analysis, empirical eigen function were utilized. EEF was applied to the shoreline changes. The first spatial eigen function accounted for 90 % of the variance of shoreline data. Under normal incident wave, the spatial eigenfunction manifested a uniform recession and was very similar for a natural beach and seawall backed beach. Under oblique wave, the local effects of increased down drift erosion and decreased updrift erosion were evident.

The validity of one-line model for seawall backed beach was examined. Comparison between the measured shoreline and calculated shoreline supported the validity of one-line model for natural beach , but for seawalled beach especially at the initial stage of profile evolution while shoreline changes were dominated by on/off shore transport, one-line model was not valid well.

reference

Barnett M.R., " Laboratory Study of the effects of a Vertical Seawall o Beach Profile Response,' UFL/COEL - 87/005, University of Florida, Gainesville, Florida, 1987.

Dean R.G. "Equilibrium Beach Profiles:U.S. Atlantic and Gulf Coast," Ocean Engineering Report No.12, Department of Civil Engineering, University of Delaware, New Wark, Delaware,1977.

Dean , R. G., " Coastal Armoring Effets," Abstract of the 20th Conf. of Coastal Engineering 1986.

CHAPTER 212

PREDICTING DAMAGE BENEFITS OF SHORE PROTECTION PROJECTS

Kevin R. Bodge, Ph.D.¹

ABSTRACT

A numerical simulation method is described to estimate damage and associated benefits to oceanfront (and "backrow") properties without-, with- and adjacent to shore protection project areas. Damage to structures, land, and structure contents is described -- as is the effect of shoreline armoring. Input data include property attributes and estimates of beach recession for various intensity storms. Projects are described by their geometry, life expectancy, construction intervals, and effect upon the chronic and storm-induced recession. Projects can include nourishment, armoring, or other types which have a quantifiable effect upon chronic and storm-induced recession. Damage is computed based upon (1) the encroachment of the eroded bluffline to the property by chronic (historical) erosion stress and by storms, and (2) functions which depend upon structure type or land use. Spatial and temporal resolution is adaptable to the user's needs.

1. INTRODUCTION

Shore protection projects such as beach nourishment, dune enhancement, and shoreline armoring decrease the potential damage to upland properties associated with chronic annual erosion and episodic storm events. These effects are central to the benefit/cost and cost-sharing analyses necessary for most shore protection projects. While a basic approach to predicting shorefront damage generally exists, actual methodologies are not standardized and vary greatly in their level of sophistication.

¹Senior Engineer, Olsen Associates, Inc., 4438 Hershel St., Jacksonville, Florida 32210 U.S.A.

This paper presents a rational, automated technique to predict shorefront damage due to combined chronic and episodic storm-related beach erosion. Damage due to flooding and wind are excluded. The technique utilizes input data which are fairly readily obtainable. Damage to any particular property is predicted as a function of the property's structural, siting, and beach-profile characteristics. Individual rows of property (shorefront, second row, third row, etc.) can be separately evaluated. Both existing and simulated post-project conditions can be evaluated in a year-by-year, property-by-property approach with various levels of temporal and spatial resolution, as desired. The effects of a project both inside and outside the project area can be investigated. The results can be used directly in a benefit/ cost analysis or can be used to develop a project's cost-sharing formulae. Additionally, the technique complies with current U.S. Federal guidelines regarding prediction of storm damage benefits of coastal works (U.S. Army, 1989).

2.0 OVERVIEW OF METHOD

The technique requires that shorefront properties be grouped into contiguous, self-similar parcels. Data which describe physical and economic attributes of the property within each parcel are tabulated (Section 3.2). The recession due to various return-level storm events is then predicted for each property parcel through a dune-erosion (or similar) model (Section 3.3).

Damages to property are calculated by "tracking" changes of a reference location on the beach. This, in turn, allows one to track changes in the setback distance between the property and the reference location. This reference location is typically the vegetation line, dune crest or bluff escarpment -- and is hereafter referred to as the "bluffline". Changes in the bluffline location may be the result of (i) chronic (historical) erosion stress, (ii) storm induced erosion, and/or (iii) a shore protection project.

The method by which property damage is computed is identical for with- and without-project conditions. The effect of a shore protection project is accounted for by changes in bluffline location and storm recession estimates. Damage benefits of a shore protection project are simply the difference between the damages computed for with- and without-project conditions.

The actual damage prediction algorithm is in the form of a numerical simulation. Input to the simulation includes two data files: The "property" data base in-

cludes economic values and various physical characteristics of each of the property parcels along the study area. The "erosion" data base includes estimates of dune recession expected for various-intensity storm events for each of the property parcels. Output from the simulation includes, for each time step, the cumulative damage to structures and the loss in land value at each of the property parcels.

3.0 PREPARING INPUT DATA

3.1 Parcel Division

The shorefront properties are first grouped into contiguous parcels self-similar in (1) beach profile characteristics, (2) property depth, (3) structural set-back, (4) structure size and construction-type, and (5) historical shoreline erosion rate. If cost-sharing estimates are of interest, then the use or function of the properties within each parcel should also be similar. That is, publicly-owned properties should be isolated from privately-owned properties; commercial properties should be isolated from residential properties, etc.

The shore-parallel length of each parcel is not particularly important. It is only important that the properties within each parcel are self-similar, and that the parcels are not so long that they obscure potential project boundaries.

It is convenient to establish an artificial baseline along the shorefront's bluffline by which the endpoints of each parcel can be referenced. A baseline with 1000-ft or 200-m station intervals drawn upon aerial photographs or plat maps is usually appropriate.

3.2 Property Data Base (Input)

For each property parcel, the following items are identified (see Figure 1):

- (1) location along a shore-parallel baseline, Y_1 & Y_2 ;
- (2) structure value, V_S ;
- (3) land value, V_L ;
- (4) average set-back distance of the structures from the initial (year-zero) bluffline, S ;
- (5) average footprint (depth) of the structures, F ;
- (6) lot depth, L ;
- (7) structure type (piles, slab-on-grade, etc), S_t
- (8) historical bluff or dune erosion rate, dx/dt ; and
- (9) an index number identifying the appropriate storm recession data which apply to the parcel (see Section 3.3).

These data (for each parcel) are entered to a data file. Items 1 through 7 are developed through aerial photography, ground truthing, and appraisal or tax records. Item 8 is developed through historical shoreline analysis. Item 9 is described below.

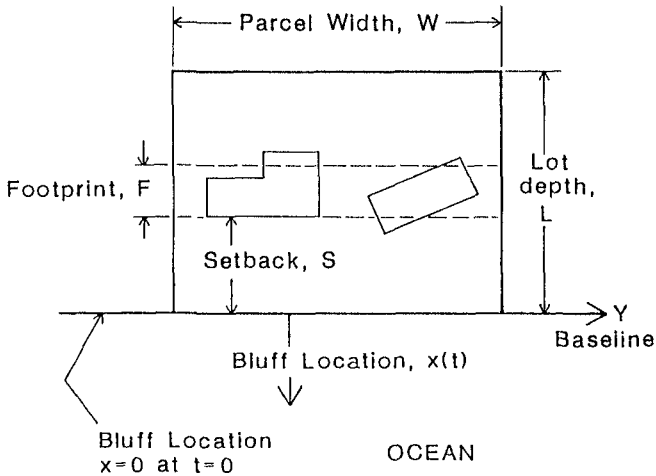


Figure 1: Attributes of an oceanfront property parcel.

3.3 Storm Recession Data Base (Input)

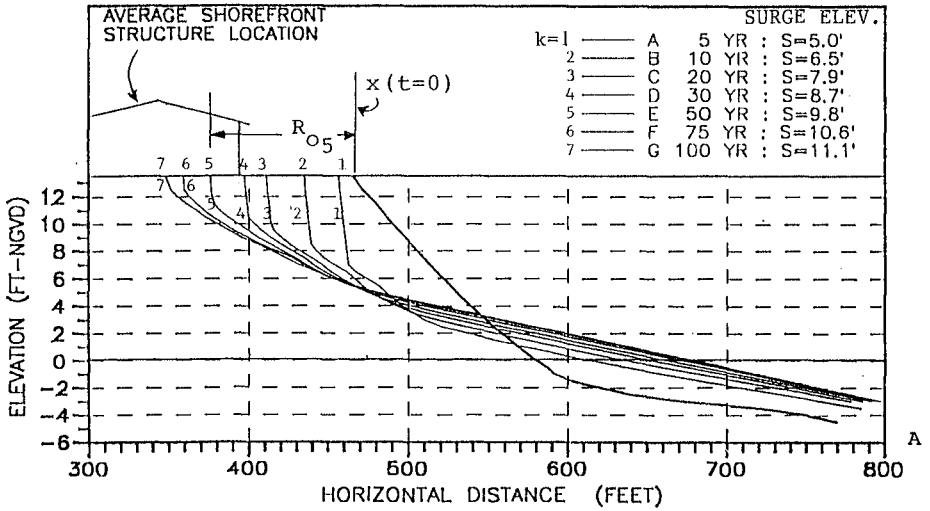
For several representative beach profiles along the study area, the recession of the existing (year-zero) bluffline is predicted for K storms of various return-period intensity using a dune erosion model. This is done for both existing (no-project) conditions and simulated post-project conditions. In this way, a pair of storm recession estimates is computed for each representative beach profile which includes

- * without-project conditions, R_{0k} , and
- * with-project conditions, R_{pk} .

(See Figure 2). The subscript k refers to various return period storm intensities; e.g., $k=1$ is a 5-yr event, $k=2$ is a 10-yr event, etc. Generally, $K=5$ to 10.

An identifying index number is assigned to each pair of storm recession estimates. One of these index numbers is then assigned to each property parcel (item 9, above) to describe the storm recession for that parcel. For quasi-uniform alongshore conditions, a single profile (or single pair of storm recession estimates) will usually characterize several adjacent parcels.

COMPOSITE PROFILE 51-90 : WITHOUT PROJECT



COMPOSITE PROFILE 51-90 : 75 FOOT PROJECT

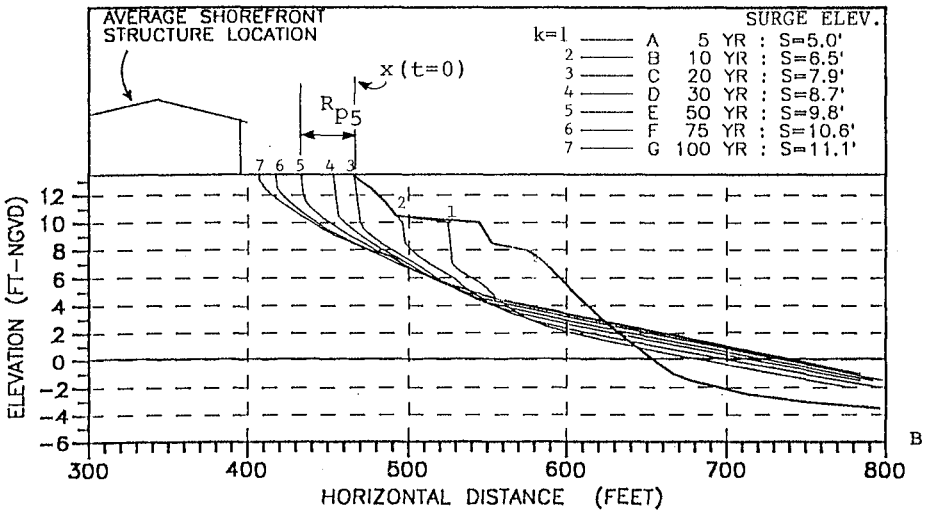


Figure 2: Storm recession for (a) without- and (b) with-project conditions. The recession R for storm k=5 is indicated for both.

4.0 COMPUTING EROSION DAMAGE AND BENEFITS

4.1 Tracking Non-Armored Bluffline Location

Chronic (Historical) Erosion Stress - For each time step Δt (usually one year), the present position of the bluffline $x(t)$ for each parcel is updated based upon historical trends or current project conditions. In the absence of an active beach nourishment project (or shoreline armor), the bluffline position x at time t is

$$x(t) = x(t_r) + (t-t_r-z) \frac{dx}{dt} \quad \text{for } (t-t_r) > z \quad (1)$$

where $x(t_r)$ is the bluffline location at the time of the most recent nourishment t_r , z is the project life, and $(t-t_r) > z$. If there have been no nourishments, then $t_r=t_0$ (where t_0 is the initial time $t=0$), and $z=0$.

In the presence of an active beach nourishment project, the bluffline position is computed as a function of the project's life z and initial equilibrium berm width W :

$$x(t) = x(t_r) + (1 - (t-t_r)/z) W \quad \text{for } (t-t_r) \leq z \quad (2)$$

where t_r is the time of the last nourishment, and where $(t-t_r) \leq z$. If $(t-t_r) > z$, then the project is not "active" and Equation 1 applies. (If the beach is historically accretive such that $dx/dt > 0$, then the value $(dx/dt)\Delta t$ can be added to the right hand side of Eq. 2. However, it is unusual that a shore protection project would be built upon an historically accretive beach.)

For parcels downdrift or adjacent to an active nourishment project, historically erosive shoreline change rates (dx/dt) are set to zero to conservatively simulate the effects of beach fill "feeding". Alternately, an alongshore diffusion model could be used to modify the dx/dt values adjacent to a project (Dean, 1988; Phlegar and Dean, 1989).

Storm Erosion - In the absence of an active beach nourishment project (or shoreline armor), the bluffline location resulting from a given storm is the superposition of the current [no-storm] bluffline location, $x(t)$, and the storm's recession estimate R_{Ok} :

$$x_k(t) = x(t) + R_{Ok} \quad \text{for } (t-t_r) > z \quad (3)$$

where R_{Ok} is the computed "no-project" recession for storm k . If $(t-t_r) \leq z$, then a project is "active" and Equation 3 is replaced by Equation 4, below.

In the presence of an "active" beach nourishment project, the bluffline location resulting from a given storm is the superposition of the [no-storm] bluffline location prior to the nourishment, $x(t_r)$, and the storm recession R -- where R is the given storm's recession estimate tempered by the project's status. During the first year of an "active" project, R is simply the storm recession computed for full-project conditions; $R=R_{pk}$. As the project approaches the end of its life, R approaches the storm recession computed for no-project conditions; $R=R_{ok}$. Between these limits, the storm recession is computed linearly. That is,

$$x_k(t) = x(t_r) + (1-(t-t_r))R_{pk} + (t-t_r)R_{ok} \quad (4)$$

for $(t-t_r) \leq z$

Note that Eqs. 3 and 4 implicitly assume that the recession for various storm events is independent of the current bluffline location. For real beaches, this is not true unless the beach and dune profile remains geometrically similar as the shoreline chronically retreats or advances each year. However, this assumption eliminates the time-consuming task of re-computing the storm erosion for each chronic change of the bluffline location.

4.2 Tracking Armored Bluffline Location

Chronic Erosion Stress - For parcels which are predominantly armored, the chronic erosion rate of the bluffline, dx/dt , is equal to zero in Eq. 1 -- until the armor is estimated to fail due to chronic erosion stress.

The year at which existing armor might fail can be estimated in several ways; e.g.,

1.) The chronic erosion rate can be transformed to a volumetric rate -- and the impact of this cumulative volumetric loss to the armor's toe stability can be projected to a year of catastrophic failure.

2.) The return-period of the storm surge which will result in a wave height significantly exceeding the armor's design condition can be computed. This return-period can then be conservatively assigned as the armor's ultimate life. (This simplistically assumes that the catastrophic storm which will destroy the armor is certain to occur at least within the storm's return period interval.)

The results of both techniques should be computed and compared in order to guide selection of a reasonable life-span of the armor.

Subsequent to armor failure, the bluffline location is assumed to rapidly retreat to the location of the bluffline at the adjacent parcels. A simple geometric simulation of this is to set the armored parcel's post-failure erosion rate to:

$$dx/dt = \frac{1}{2} (x(t-\Delta t) - x(t)) \quad (5)$$

where $x(t-\Delta t)$ is the bluffline location at the armored parcel's previous time step, and $x(t)$ is the average current location of the bluffline at the immediately adjacent parcels. This implies that the "bulge" in the shoreline left by the failed armor will only be $1/2^n$ of its initial size at n -years after the failure. That is, the shoreline at the previously armored parcel will be within 12.5% of the neighboring shorelines after 3 years, and within 3% after 5 years, etc.

Storm Erosion - At armored properties, storm recession is generally zero for storms less severe than that storm which is estimated to cause armor failure. The severity of this catastrophic storm can be estimated by: (1) examining the extent of toe scour predicted at the armor's toe for various storms, or (2) back-calculating the storm surge (and its frequency) which would produce waves significantly beyond the armor's design condition. Both techniques require one to consider both no-project and with-project conditions. For storms more severe than that which is estimated to cause armor failure, the recession can be computed by simply ignoring the armor - or preferably, by failing the armor during the storm event.

4.3 Damage Computation for Structures

The damage to shorefront structures due to both chronic (historical) erosion stress and storm-induced erosion is a function of the bluffline's location relative to the structures' set-back S and the structures' footprint F . That is,

$$\begin{aligned} d_s(t) &= f\{ -(S+x(t))/F \} \cdot V_s \\ &= f\{u\} \cdot V_s \end{aligned} \quad (6)$$

where $d_s(t)$ is the dollar damage to structures at year t due to chronic erosion stress, and where $x(t)$ is given by Eq. 1 or 2.

Likewise,

$$\begin{aligned} \hat{d}_{sk}(t) &= f\{ -(S+x_k(t))/F \} \cdot V_s \\ &= f\{\hat{u}\} \cdot V_s \end{aligned} \quad (7)$$

where $\hat{d}_{sk}(t)$ is the the dollar damage to structures in year t due to storm k , and where $x_k(t)$ is given by Eq. 3 or 4.

The nature of the function $f(u)$ or $f(\hat{u})$ in Eqs. 6 and 7 is determined by the structure type. The following are suggested examples. In each, u and \hat{u} are interchangeable.

For slab-on-grade foundations:

$$f(u) = \begin{cases} 0 & \text{for } u < 0 \\ 2u + 0.1 & \text{for } 0.45 \geq u \geq 0 \\ 1.0 & \text{for } u > 0.6 \end{cases} \quad (8)$$

such that the structure is 100% damaged if the bluffline or storm recession extends through 45% of the structure's footprint. Some damage (10%) occurs when the bluffline or storm recession reaches the seaward face of the structure.

For some spread-footer or non-engineered pile foundations:

$$f(u) = \begin{cases} 0 & \text{for } u < 0 \\ u & \text{for } 1.0 \geq u \geq 0 \\ 1.0 & \text{for } u > 1.0 \end{cases} \quad (9)$$

in which case the structure is 100% damage when the bluffline or storm recession extends to the landward edge of the footprint.

For engineered structures on piles or substantial spread-footers:

$$f(u) = \begin{cases} 0 & \text{for } u < 0 \\ 2/3 u & \text{for } 1.5 \geq u \geq 0 \\ 1.0 & \text{for } u > 1.0 \end{cases} \quad (10)$$

such that 100% damage occurs only when the bluffline or storm recession extends 50% of the structure's footprint beyond its landward edge.

While the damage caused by chronic erosion in a single year is simply that of Eq. 6, the damage expected in a single year due to storms is determined by the storms' probabilities of occurrence. That is, the probabilistic -- or expected -- storm damage in each year is the weighted sum of the damage estimated for each of the K storm events considered. This is estimated by:

$$E[\hat{d}_s] = \hat{d}_s = p_1 \frac{\hat{d}_{s1}}{2} + \sum_{k=2}^K (p_{k-1} - p_k) \frac{\hat{d}_{sk-1} + \hat{d}_{sk}}{2} \quad (11)$$

Maximum Damage Limit - Maximum limits should be placed on structure damage. For example, it is convenient to assume that a structure will be demolished or relocated (and removed from analysis) if its cumulative damage exceeds some multiplier of its original value (say, 1.5) -- or if the probabilistic damage in a single year exceeds, say, 50%.

Additionally, structures can be demolished or relocated when the bluffline location $x(t)$ reaches a critical distance from the structure's seaward edge. Criteria vary locally. For example, in North Carolina (USA), the rule is 10 ft (3 m) plus 5.0 times the average annual erosion rate. The cost of relocation or demolition can be included in the analysis at the appropriate year.

4.3 Computing Damage to Structure Contents (Furnishings)

If damages to contents are to be considered, it is imperative to identify only those damages associated with erosion or with the flooding which may be prevented by the project under consideration (if any). Contents damage due to chronic (historical) erosion is assumed to be zero (because it is assumed that the owner will have plenty of time to remove the contents before chronic erosion causes damage). However, storm erosion may cause damage to contents due to its unexpected nature.

For storms which are not anticipated to cause flooding beyond that prevented by the shore protection project (if any), contents damage is conservatively assumed to occur at half the magnitude of the structure's damage function. (For example, if 40% of the structure value is lost, 20% of the contents value is lost. The other 80% is assumed to be salvageable.) For storms which cause flooding beyond that prevented by the project, no contents damage is calculated. This conservatively assumes that all contents damage is due to flooding and none is due to erosion.

The value of a structure's contents is assumed to be a fraction, c , of the structure's value, V_s . The fraction c depends upon the structure's use. From insurance underwriters,

Single- & Multi-Family Residences:	$c = 0.55$
Restaurants:	$c = 0.35$
Hotels & Motels:	$c = 0.25$

Concisely, the damage to contents for storm k in year t is:

$$d_{ck}(t) = \begin{cases} f\{\hat{u}\} \cdot c \cdot V_s & \text{for storms w/o flooding} \\ 0 & \text{for storms w/ flooding} \end{cases} \quad (12)$$

where $f\{ \}$ is from Eq. (7), or as from Eqs. (8), (9), or (10). The probabilistic contents damage in each year is found as through Eq. 11, above.

4.4 Computing Damage to Land

Loss of coastal land value may be due to (1) chronic erosion and/or (2) acute storm impacts. To ensure conservative valuation (and to avoid potential "double-counting") the author accounts only for the former. This implicitly assumes that land lost to a storm recovers 100% (minus any chronic year-to-year losses).

Generally, loss of land value at time t is expressed as:

$$d_L(t) = g\{ -x(t)/L \} \cdot V_L \quad (13)$$

where g is a function of the eroded bluffline location $x(t)$ relative to the lot depth L , and V_L is the original (non-eroded) land value. The function $g\{ \}$ can vary; i.e.,

1.) Land value is lost linearly with erosion:

$$g\{ -x(t)/L \} = \begin{matrix} -x(t)/L & \text{for } -x(t)/L \leq 1 \\ 1.0 & \text{for } -x(t)/L > 1 \end{matrix} \quad (14)$$

This is identical to assuming that land is valued uniformly.

2.) Land value is lost in proportion to erosion, but the lot is completely de-valued when the erosion reaches a certain fraction, a , of the total lot depth L :

$$g\{ -x(t)/L \} = \begin{matrix} -1/a x(t)/L & \text{for } -x(t)/L \leq a \\ 1.0 & \text{for } -x(t)/L > a \end{matrix} \quad (15)$$

where, for example, $a = 2/3$.

3.) Land value is lost in proportion to erosion, but the lot is completely de-valued when some "minimum" lot depth L_{\min} is left:

$$g\{ -x(t)/L \} = \begin{matrix} x(t)/(L_{\min} - L) & \text{for } -x(t) \leq L - L_{\min} \\ 1.0 & \text{for } -x(t) > L - L_{\min} \end{matrix} \quad (16)$$

4.5 Cumulative and Present-Worth Damage & Benefits

The predicted damage which occurs over the time step t at time t is the sum of (1) the probabilistic storm damage d at time t (Eq. 11), and (2) the increase in damage due to chronic erosion between time t and the previous time step, i.e., from $d(t-\Delta t)$ to $d(t)$.

For example, structure damage over the time step Δt at time t is

$$D_S(t) = \hat{d}_S + [d_S(t) - d_S(t-\Delta t)] \quad (17)$$

The present worth (P.W.) of this damage is

$$DPW_S(t) = D_S(t) * (1+i)^{-t} \quad (18)$$

The cumulative structure damage at year t is simply

$$\int_0^t D_S(t) dt$$

and the P.W. equivalent is simply $\int_0^t DPW_S(t) dt$.

Project benefits are simply the difference in damage computed for without- and with-project conditions. This can be calculated on, for example, a year-by-year basis (Eqns. 17 & 18), or on a cumulative basis.

4.0 DISCUSSION

The simulation technique and algorithms described above feature useful flexibility, some features of which are highlighted below.

Sensitivity of Damage Functions - The damage functions for structures, $f\{\}$, and land, $g\{\}$, are defined functions -- and can be easily modified for sensitivity tests without altering the rest of the simulation code. While damage functions are suggested herein for various structures and land conditions, others can be easily created and tested as appropriate to the study area.

Project Simulation - Virtually any traditional shore protection project can be analyzed by the technique. The parameters which describe the project's effects appear in three controlled groups: (1) project characteristics (i.e., boundaries, life, width (if applicable), construction interval/timing, and storm intensity up to which flooding is prevented (if any); (2) chronic erosion rates (dx/dt), and (3) storm recession data.

"Backrow" Properties - Properties two, three, or more "rows" from the oceanfront can be explored by creating additional property data bases. For these, the structural set-back distance is the total distance from the structure's seaward face to the bluffline, as usual. Land loss is computed by accounting for the "margin" of land, M , between the subject property and the bluffline. Equation 13 then becomes:

$$d_L(t) = g\{ -(M + x(t)) / L \} \cdot V_L \quad (19)$$

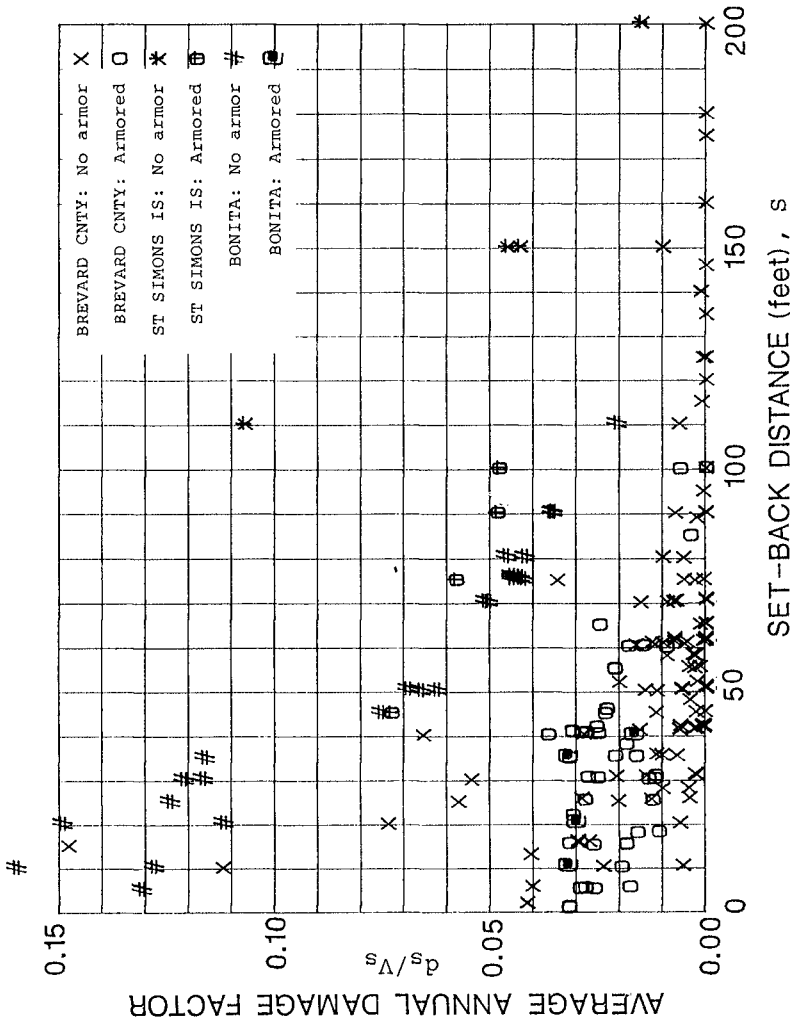


Figure 3: Average expected storm damage to structures (normalized by structure value).

such that loss of land value does not occur until the recession extends through the margin and into the "backrow" lot.

Simplification of Damage Functions - Damage to a property is a function of many parameters: e.g., set-back, width, storm frequencies, beach profile, storms, chronic erosion rates, structure type, local armoring, etc. Because each is of similar importance, attempts to express an average damage multiplier as a function of only one or two of these parameters is not advised. As an example, Figure 3 depicts the annual probabilistic (expected) storm damage vs. the local set-back distance for (i) 179 property parcels along a 40-mile segment of Brevard County, Florida, (ii) 21 parcels along a 3-mile segment of Bonita Beach, Florida, and (iii) seven parcels along a 2-mile segment of St. Simons Island, Georgia. While a general envelope is suggested, a simple relationship is not discernable. Inclusion of one or two additional parameters does not significantly improve the correlation (Bodge, in review).

REFERENCES

- Bodge, K. R., in review. "Damage Benefits and Cost Sharing for Shore Protection Projects," J. Shore & Beach, ASBPA.
- Dean, R. G., 1988. "Realistic Economic Benefits from Beach Nourishment," ASCE, Proc., 21st Int. Conf. on Coastal Eng.
- Phlegar, W. S. and R. G. Dean, 1989. "Beach Nourishment Performance Predictability," Fla. Shore & Beach Preservation Assn. (FSBPA), Proc., Beach Preservation Tech. '89, Tallahassee, FL 32301.
- U.S. Army, 1989. "Water Resources Policies and Authorities; Federal Participation in Shore Protection," Dept. of the Army, Office of the Chief of Engineers, E.R. 1165-2-130; Washington, DC 20314-1000.

CHAPTER 213

THE IMPACTS OF SHORELINE PROTECTION STRUCTURES ON BEACHES ALONG MONTEREY BAY, CALIFORNIA

Gary B. Griggs*
James F. Tait*
Katherine Scott*

Abstract

As a result of severe coastal storm damage in recent years along the California coast and the continuation of development and redevelopment in hazard prone oceanfront areas, large numbers of coastal protection structures have been built. This same trend has been observed on the Atlantic and Gulf coasts as well. At present, fully 12%, or 130 miles of California's 1100 miles of shoreline have been armored. As the number of structures and their coastal frontage has increased, concern along the California coast and elsewhere has arisen in regard to the impacts of these protective structures on the adjacent beaches. Three Atlantic coast states (Maine, New Jersey, and North Carolina) have responded to this concern by establishing state-level policy which prohibits construction of any new "hard" protective structures.

Although considerable laboratory scale research has been carried out on this problem, field work has been extremely limited. A study along the central California coast was initiated in order to resolve some of the most critical questions regarding the impacts of protection structures on beaches. Based on 4 years of precise, biweekly, shore-based surveys in the vicinity of different types of seawalls along the shoreline of northern Monterey Bay along the central California coast, some consistent beach changes have been documented. All of the changes observed to date have been seasonal and are best developed in the fall and winter months during the transition from summer swell to winter storm conditions. The effects or changes documented include:

(1) Loss of summer berm sooner in front of seawalls and revetments

* Earth Sciences Board, University of California, Santa Cruz, Ca. 95064

relative to adjacent unprotected beaches with the onset of winter storm waves.

(2) No significant or consistent differences in the beach profiles at the contact between a vertical impermeable seawall and a permeable revetment despite the apparent differences in permeability and reflectivity.

(3) A lack of significant difference in matured winter profiles seaward of seawalls or revetments relative to adjacent unprotected beaches.

(4) Accelerated berm retreat and beach scour up to 150 m downcoast from seawalls due to a combination of end reflection and upcoast sand impoundment.

(5) Late spring/summer berm rebuilding independent of any protective structure, resulting in a continuous, uniform alongshore berm crest well seaward of the seawall.

Introduction

Much attention of coastal planners is focussed on the impacts of seawalls and revetments on beaches. A body of opinion exists that such impacts are adverse and promote erosion. Pilkey (1981) has asserted that building a seawall dooms the beach in front of it. Other researchers deny this, asserting that such claims are not based on an understanding of coastal processes (Dean, 1988). One reason for recent focus on seawalls is the increased development along our coastlines with a simultaneous increase in demand for coastal protection. Unfortunately, our knowledge of the long- and short-term effects of seawalls on beaches is limited. Planners and decision-makers are becoming more hesitant about granting permits or authorizing funding for such structures while the issue of impacts remains unresolved. One of the principal complaints of the decision-making community is that not only are they being told one thing by some scientists and something else by others, but they are frequently being told different things at different times by the same scientists.

Central to this dilemma is the lack of sufficient field data with which to resolve the claims. Most of our ideas are based on theoretical or laboratory models which have their own limitations. The coastal environment is extremely complex and does not readily lend itself to reductionism. In order to be manageable, mathematical models rely on a number of simplifying assumptions. In the study of seawalls and revetments, such assumptions as infinite length and perfect wave reflection have been used (e.g., Jones, 1975). Similarly, hydraulic models used by engineers (e.g., movable bed experiments conducted in wave tanks or basins) have serious problems with sediment and wave

scale. Even when near-prototype scale wave basins are employed, the waves used are usually monochromatic, or at best unidirectional spectra and three-dimensional processes are not accounted for; in general, reality is oversimplified. Furthermore, the results of such modeling are frequently not checked in the field.

For the most part, the lack of field results is a direct outcome of the large expense in both time and money that such studies require. A number of very good reviews of the seawall problem are now available. Dean (1986) and Everts (1985) have authored speculative synopses which are both comprehensive and well reasoned. Kraus (1988) has reviewed the literature concerning laboratory, field, and theoretical studies and provides an excellent critique. In October, 1986, Griggs and Tait (1988) began a study of beach response to four seawalls along northern Monterey Bay, California (Figure 1). Objectives included:

- (1) How do beaches backed by seawalls change seasonally in response to changing wave climate compared to adjacent beaches without seawalls?
- (2) What bearing does seawall design have on beach response?
- (3) Does the position of the seawall on the beach profile (i.e. farther seaward relative to another structure) exert any effect on seasonal beach changes?
- (4) Do seawalls exert alongshore control on beach development, cross-shore control, or both?

Four monitoring sites were initially selected with the objectives of observing different types of protective structures at different locations on the beach profile. Both vertical impermeable seawalls and sloping permeable revetments were monitored. These structures varied in their location from being placed at the base of the seacliff to as far as 75 m seaward on the beach profile. Precise biweekly shore normal surveys were carried out between October 1986 and May 1989. In addition, more frequent winter surveys were carried out at one site during the winter of 1989-1990. Profiles extended either from the seawall or back of the berm offshore as far as feasible using a field assistant in a wet suit (typically to 100 to 150 m offshore to depths of -1 or -2 m MSL).

The profile lines were spaced at 30 m intervals alongshore at locations where seawalls abutted unprotected beaches. A Leitz EDM and pole mounted prism reflector were used for surveys. Approximately 2000 individual profile lines have been surveyed.

The coast of California forms a marked contrast to the Atlantic and Gulf coasts of the United States where other researchers have

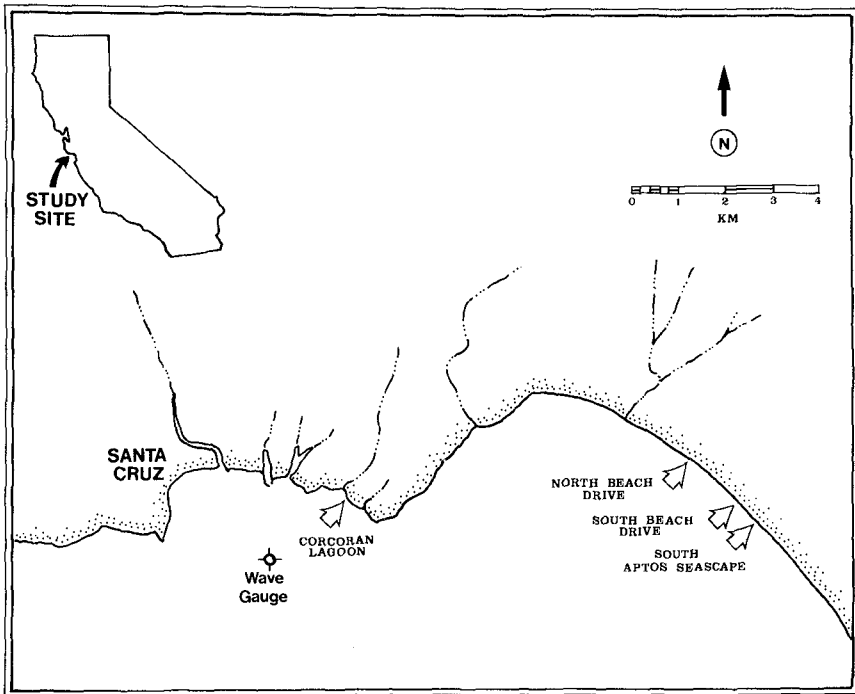


Figure 1. Location map of study area in Monterey Bay, California

carried out some post-hurricane seawall monitoring. The study area in Monterey Bay is fronted by a broad equilibrium beach (Figure 2) which, while undergoing seasonal variations in width, is not undergoing net erosion. The Atlantic and Gulf coasts are typically fronted by barrier islands which are migrating landward in response to sea level rise, and are also subject to hurricane overwash and breaching. Seawalls along these coasts attempt to fix the position of the shoreline on a coast which is otherwise retreating. The long term effects thus appear to be quite different due to basic difference in geomorphic and tectonic setting than the coastline of California.

Beach Response

Beach response is the morphological transformation of a beach due to gradients in sediment transport. Field studies show the response of a beach in front of a seawall to storm waves to be quite variable. The following beach responses have been observed at seawalls (Figures 3 and 4):



Figure 2. South Aptos Seascape site where beach in front of and up and downcoast from concrete seawall were monitored.

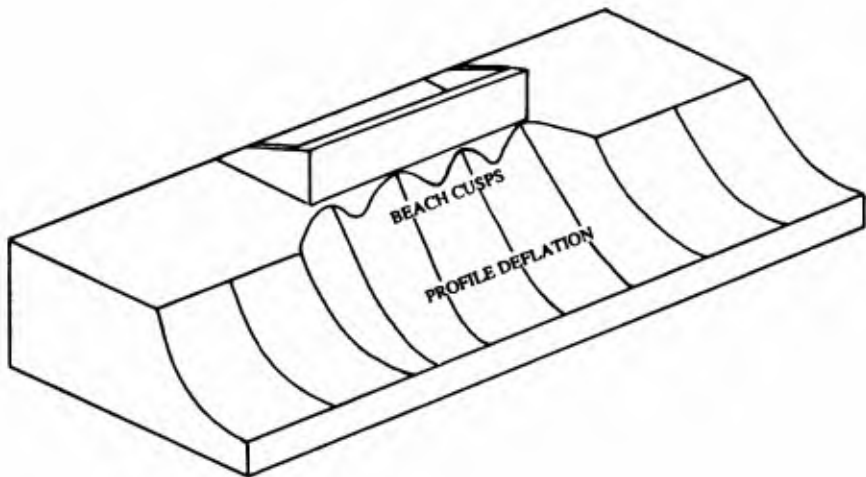


Figure 3. Types of beach response observed by Griggs and Tait (1988) before berm retreats past seawall.

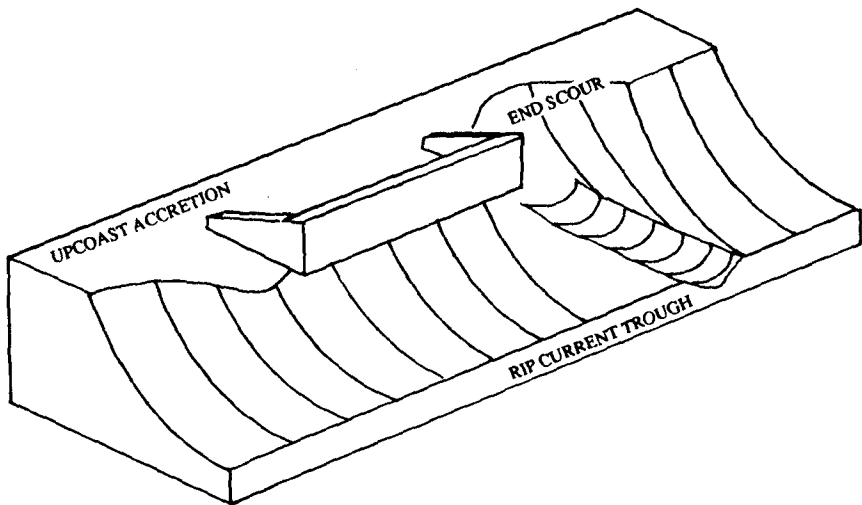


Figure 4. Types of beach response observed by Griggs and Tait (1988) after berm retreats past seawall.

- Scour Trough- a linear trough or depression fronting a seawall
- Deflated Profile- the lowering or erosion of the beach face
- Beach Cusps- crescentic or semi-circular embayments on the beach face
- Rip Current Trough- a trough or embayment crossing through the surf zone
- End Scour- erosion of the unprotected beach adjacent to the end of a seawall
- Upcoast Sand Accretion- the impoundment of sand on the upcoast or updrift end of a structure

Many of the types of beach response can be divided into two broad categories: "frontal effects" and "end effects". Scour trough, deflated profile, and cusping are all examples of "frontal effects". End scour, sometimes referred to as "flanking", and upcoast sand accretion are examples of "end effects". Rip current embayments appear to be a more complicated case, affecting both the profile in front of the wall and the profile alongside the wall. Any of the above may occur as a response to wave-seawall interaction. Or, beach response at a seawall may be indistinguishable from that on neighboring beaches which have not been modified by structures.

Results

A number of consistent beach changes related to the presence of seawalls and revetments have been recognized during the

course of four years of surveying. These are discussed below in a chronological fashion.

(1) **SUMMER BEACH CONDITIONS:** At the start of each new season of monitoring (early fall) the beach at each of the monitoring sites had accreted to the point where the berm was well seaward of the seawall and there was no wave-seawall interaction. The summer berm was continuous alongshore with no deflection or difference in the vicinity of the seawall. Thus, although the summer berm varied somewhat each year in both its seaward extent and height, the beach/seawall system retained no memory of the previous winter conditions.

(2) **EROSION OR RETREAT OF SUMMER BERM:** During the transition from summer to winter (dissipative to reflective) beach state, the berm is usually cut back sooner in front of the seawalls monitored relative to the adjacent unprotected control beaches. Thus a flatter winter profile is attained sooner in front of the seawalls in contrast to the adjacent beach which will still have a relict summer berm. The difference in elevation between the beach in front of the seawall and the adjacent berm may vary from a few tens of centimeters to over a meter and the berm offset may be up to 12 m (Figure 5). The timing and extent of this premature berm erosion is controlled by the width of the initial summer berm fronting the seawall and the winter wave climate. The berm is typically lost first from those walls which are farthest seaward on the beach profile.



Figure 5. Example of winter berm erosion in front of rip-rap prior to berm removal on adjacent unprotected beach.

It is believed that this premature berm removal is due to wave reflection from the seawalls and revetments at high tide. Waves which overtop a berm of an unmodified beach will expend their energy over the width of the berm, depositing whatever sediment they carry. Waves colliding with a seawall before their energy is spent will be partially reflected and are still capable of scour. An issue of some controversy along the California coast is whether permeable revetments produce less reflection and beach scour and are, therefore, preferable to impermeable seawalls. Although several sites were studied where vertical impermeable concrete seawalls abut sloping permeable revetments, there was no consistent difference in the beach profiles at these sites over three years of monitoring (Figure 6) indicating that under the wave conditions experienced, that the difference in apparent permeability was not a significant factor affecting berm erosion.

(3) WINTER OR STORM PROFILE: As winter waves continued to erode both the seawall backed beach and the unprotected beach, the berm on the unprotected beach retreated until it was landward of the seawall (Figure 7). Once this winter state had been reached there was no significant difference in the profiles between the protected and the unprotected beaches (Figure 8).

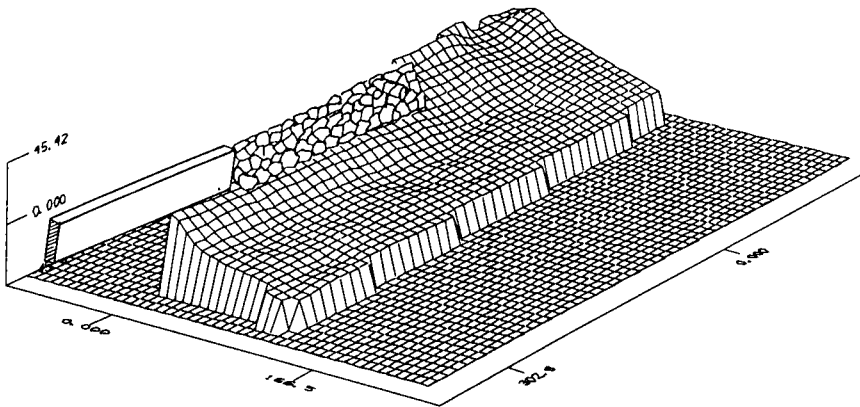


Figure 6. Uniform winter beach conditions at contact between permeable revetment and impermeable seawall.



Figure 7. Early winter conditions. Berm has retreated behind revetment leaving uniform planar beach in front of revetment and control beach.

There has been considerable controversy in recent years regarding whether or not seawalls are responsible for beach scour. In 4 years of surveying (3 years of biweekly surveying and a year of storm surveying) we have never observed a scour trough directly fronting any of the seawalls studied. Relative to some of the more severe coastal storms of the past decade, however, the winter wave conditions during the four years of monitoring have been only of moderate height (maximum significant wave heights in the range of about 1.5 to 2 m).

(4) END EFFECTS OF SEAWALLS: Direct wave reflection from the end sections of seawalls was commonly observed. As a result of this increased wave energy at the downcoast or downdrift ends of seawalls, an arcuate zone of localized scour typically developed in the winter months which extended downcoast from 50 to 150 m (Figure 9). The downcoast extent of this impact depended upon wave height and wave period or the arrival of the next wave uprush which tended to override and dissipate the reflected wave. Additional factors which appeared to influence this end effect were the end geometry and permeability of the structure, the angle of wave approach, and tidal stage. The extent of end scour was consistently greater at a structure which offered the greatest angle to the incoming wave and which had the most reflective surface.

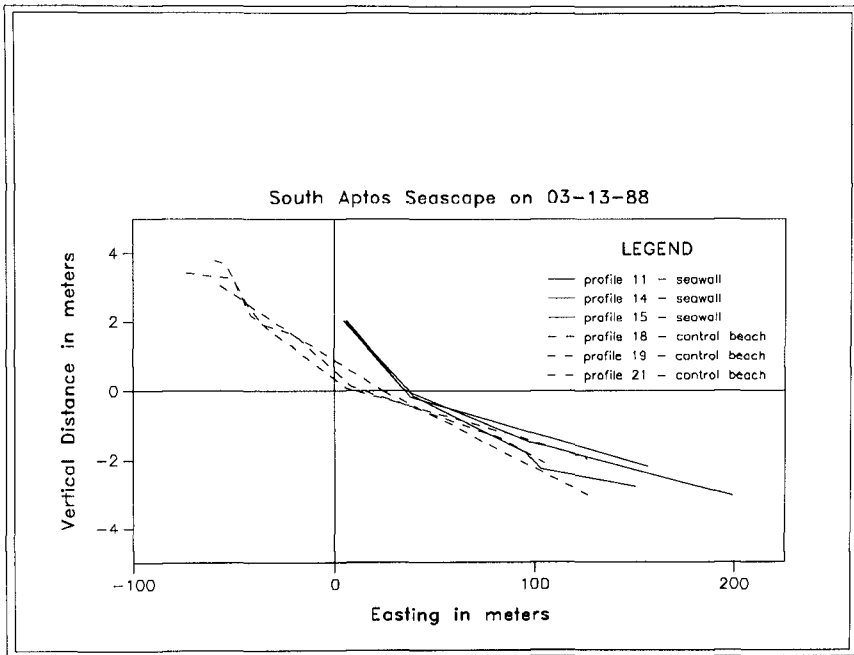


Figure 8. Winter profiles at Aptos Seascape site showing similarity in beach fronting seawall (profiles 11-15) and control beach (profiles 18-21).

Upcoast sand accretion counteracted the modest increased scour at the downcoast end of the structures. The significance of this groin effect or upcoast accretion is dependent upon the location of the seawall on the beach profile and the winter position of the berm crest relative to the seawall.

(5) RECONSTRUCTION OF SUMMER BERM: With the change from winter to spring and summer wave conditions, the berms in the study area began to rebuild during May and June, a process which continued into July and August. Sequential biweekly surveys of this accretionary phase indicate that the berm on the unprotected beach advances seaward until it reaches the seawall, and then the berm in front of both seawall and adjacent beach advance together (Figure 10). Thus, while the winter erosional phase of the seasonal beach cycle was influenced to some degree by the presence of the seawall, this was not the case for the summer accretionary or rebuilding phase. At the end of this reconstruction phase a uniform alongshore berm crest exists well seaward of the seawalls.



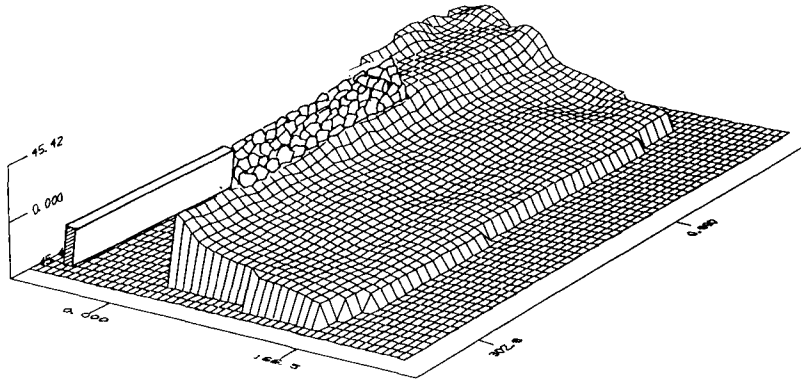
Figure 9. Localized scour adjacent to downcoast end of seawall.

Discussion

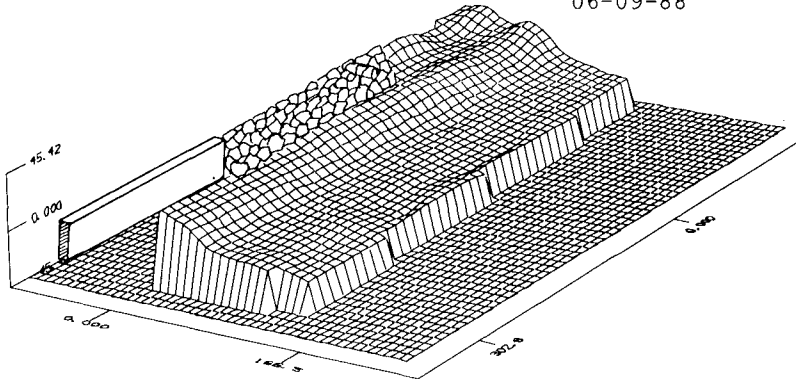
Overall, relatively little field research has been conducted on the problem of beach-seawall interactions. The few studies to date indicate that beach response can be variable with a number of processes at work and with the factors controlling the type and magnitude of beach response interdependent (Tait and Griggs, 1990). Kriebel et al (1986), for example, noted the presence of a scour trough in front of a vertical impermeable seawall during hurricane conditions. In this study, on the other hand, we never encountered a trough in front of any of the seawalls or revetments monitored, but instead observed a more rapid retreat of the summer berm. We have observed downdrift scour, yet Kriebel et al (1986) observed no flanking in a downdrift area where it was expected. Both of these studies, however, found that beach recovery was approximately as rapid in front of seawalls as it was on adjacent natural beaches.

Beach response to seawalls appears to be variable because of the number of factors involved; furthermore, these factors are interrelated, and each factor influences other controlling factors. Attempts to assess the potential impacts of a seawall on a beach should be site specific. The following basic controls appear to be important in governing seawall-beach interactions (Tait and Griggs, 1990):

South Beach Drive - 04-26-88



06-09-88



08-18-88

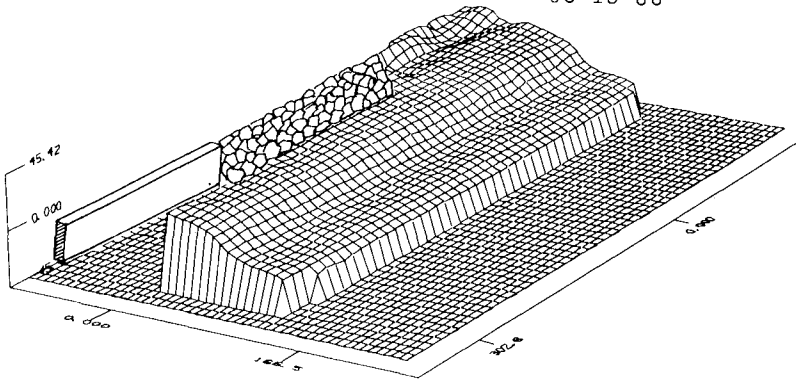


Figure 10. Spring/summer berm reconstruction with no seawall effect.

- (1) Longterm shoreline trends
- (2) Position of seawall on the beach profile
- (3) Coastal Geomorphology
- (4) Sediment supply/beach width
- (5) Offshore gradient/width of surf zone
- (6) Wave energy and exposure
- (7) Seawall design (height, permeability, slope)
- (8) Length of seawall

More studies are needed, particularly on the Atlantic and Gulf coasts where the beach/seawall controversy has reached a peak. Most of the processes and controls involved in beach/seawall interaction have not been measured in the field. Measurements of parameters such as suspended sediment concentration, sediment transport, nearshore current fields, and beach water table levels in the vicinity of seawalls are necessary before beach/seawall interactions can be predicted with any confidence. Kraus (1988) makes some excellent suggestions for future seawall studies and monitoring programs. To underscore the speculative nature of the processes currently being associated with beach/seawall interactions, Dean (1986) points out that a rational argument, based on momentum flux considerations, can be advanced to show that increased wave reflection at a seawall actually reduces sediment transport.

Acknowledgements

This research was made possible through funding from the Engineering Performance of Coastal Structures research unit of the Army Corps of Engineers Coastal Engineering Research Center, Waterways Experiment Station in Vicksburg, Mississippi.

References

- Dean, R. G. ,1986, "Coastal Armoring: Effects, Principles and Mitigation", *Proceedings of 20th Coastal Engineering Conference*, American Society of Civil Engineers, pp.1843-1857.
- Dean, R. G., 1988, In: " Eroding Shorelines Impose Costly Choices," *Geotimes*, V.33 (No.5), pp.9-13.
- Everts, C. H. ,1985, "Effects of Small Protective Devices on Beaches," *California's Battered Coast: Proceedings from a Conference on Coastal Erosion*, California Coastal Commission, pp.127-137.
- Griggs, G. B. and Tait, J. F. ,1988, "The Effects of Coastal Protection Structures on Beaches Along Northern Monterey Bay, California" *Journal of Coastal Research*, Special Issue No. 4: pp.93-111.

Jones, D. F., 1975, *The Effect of Vertical Seawalls on Longshore Currents*, Unpublished Ph.D. Thesis, Department of Coastal and Oceanographic Engineering, Univ. of Florida, Gainesville, FL, 118 p.

Kraus, N. C., 1988, "The Effects of Seawalls on the Beach: a Literature Review", *Proceedings of Coastal Sediments '87*, American Society of Civil Engineers, pp. 945-960.

Kriebel, D. L., Dally, W. R., and Dean, R. G., 1986, *Beach profile response following severe erosion events*, Coastal and Oceanographic Engineering Department, UF/COEL-86/016, University of Florida, Gainesville, FL.

Pilkey, O. H., 1981, "Geologists, Engineers, and a Rising Sea Level", *Northeastern Geology*, V. 3, Nos. 3/4, pp. 150-158.

Tait, J.F., and Griggs, G.B., 1990. "Beach Response to the Presence of a Seawall". *Shore and Beach*, V.58, No. 2, pp.11-28.

CHAPTER 214

Fate of dredged material dumped off the Dutch shore

R. Spanhoff, Tj. van Heuvel, and J.M. de Kok ¹

Abstract

In the North Sea off the Dutch shore annually tens of millions cubic meters dredged material are dumped. Recent progress in assessing and predicting the fate thereof is described. Field studies and modelling activities are both required in the considered relatively complex situations.

Introduction

At several places along the Dutch shore harbours and their entrance channels have to be regularly dredged. Tens of millions cubic meters of dredged material are involved per annum. Notably the silt fraction therein attracts more and more attention in recent years because of its potential to transport and accumulate adsorbed contaminants. Therefore, the fate in the marine environment of dumped cohesive sediments is studied. Two locations are considered here, namely the dump site for the Scheveningen harbour near The Hague, respectively the site for the Rotterdam harbour region.

The latter dump site, called Loswal Noord, is of special interest because of the relatively large quantities of material dumped there, at present circa 15 million m³ per annum. In the last ten years or so this site has been the subject of field studies, on the one hand to monitor the impact of the dumping on the development of the region, and on the other hand since the dumped amount should provide a noticeable signal in the sediment transport along the Dutch shore. In studying this signal tools can be developed to predict the transport and fate of fine sediments entering the marine environment at specific places. The strongest tool would be a sediment-transport model with a prognostic capacity. We are working towards

¹Project engineers, Tidal Waters Division, Rijkswaterstaat
P.O. Box 20907, 2500 EX The Hague, The Netherlands

such a model for the considered region. A proper dumping management would greatly benefit from such a tool which helps in deciding where to dump how much of a specific material.

History

The western part of Holland, which lies below sea level in the Rhine-Meuse-Scheldt delta, has been created over centuries in a continuous struggle of man with water. One has not only changed the shore line, but also the outflow routes of the mentioned rivers. For instance, the Nieuwe Waterweg, the canal to the original Rotterdam harbours, was constructed in the previous century in traversing the dunes, a natural protection against the sea. With the more recent completion of the so-called Delta Works, in which among others several river arms in this delta were closed in order to prevent a repetition of the 1953 inundation of the area, the Nieuwe Waterweg became the most important outlet of the river Rhine. The run-off through the Waterweg is regulated to a large extent, with a (tidally averaged) value in the order of $1500 \text{ m}^3/\text{s}$ during most of the year.

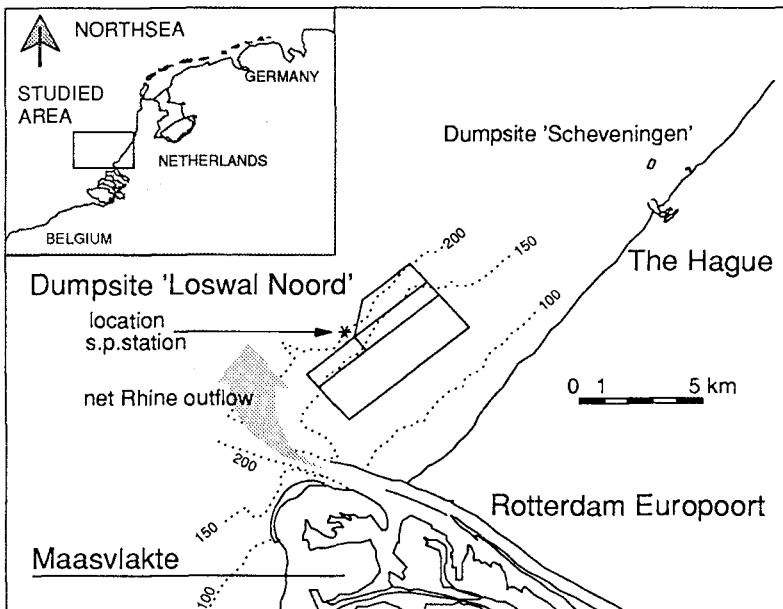


Figure 1. Studied area off the Dutch shore with two dump sites. The man-made Maasvlakte, the residual Rhine outflow and some depth contours (cm) are indicated

Another major man-made change in the present study area depicted in figure 1 was the construction in the beginning of the sixties of the extensive Europoort Harbour region and of the land acclimation Maasvlakte. Since then the need for dredging has increased significantly. The initial capital dredging concerned mainly sand. The later maintenance dredging, that turned out to be required permanently, involves mostly mud and fine sand (ratio circa 1:2 by weight). These materials are dumped on the Loswal Noord (see fig. 1) since 1961, annually on the average circa 20 million m^3 . Polluted muds from the Rotterdam harbours are stored on land since 1982 (order 1 million m^3 per year).

The actual spots of the Loswal Noord to be used have gradually shifted towards its more northern sections, because of the induced rise of the sea bottom and of the larger draughts of more modern hopper dredgers. The area was selected according to the best available knowledge of that time, among others balancing the extra costs of a larger distance from the harbour with the possible risk of a return of the dumped material to the sites to be dredged. For instance, the long-term residual currents are known to be directed to the North along the Dutch shore, so it is likely that sediments are transported in the same direction.

Area description

The sea bottom in the present study area is relatively flat outside the dump site, as can be seen in figure 2, with typical values in the range 10 - 20 m below mean sea level. A circa 25 m deep gully into Europoort harbour leads far to the open sea. Horizontal maximum tidal velocities are of the order of 1 m/s, and the tidal range is circa 1.8 m. Prevailing winds come from the Southwest thus lining up with the local shore line.

The fresh-water discharge of the Rhine through the Nieuwe Waterweg (the northern branch of the canal shown in fig. 1) is relatively large with a typical value of 1500 m^3/s . Fourfold values may occur during large river run-offs. Mixing of fresh and salt water in the tidally influenced region of the Waterweg is limited leading to stratified water masses entering the North Sea. Within a radius of 10 km around the mouth of the Nieuwe Waterweg mostly a strong and stable density stratification exists, leading to totally different residual current patterns in upper and lower layers.

The outflowing river water in the upper layer, influenced by Coriolis forces takes its way to the Northeast (fig. 1) together with the fluvial sediments suspended in it. The sediments originating from the dump site Loswal Noord are confined to the lower layers, where residual currents are determined by the large density gradients of

the outflow plume, ranging until 30 km off coast. Up to ten km around the entrance of the Nieuwe Waterweg residual bottom currents are directed towards the outflow point and have magnitudes of 10-20 cm/s or more. More to the North, where the influence of the upper layer is larger, there is a tendency to follow the large-scale residual current pattern, that is directed to the North-east but cross-shore, southeastward components still amount 2-3 cm/s.

The resulting horizontal and vertical density gradients strongly influence the water and sediment transports along the Dutch shore, up to the Wadden Sea (Van Alphen et al. 1988). For instance, relatively high suspended-sediment concentrations result (see fig. 4) because of the rather permanent landward residual current near the bottom, where the sediments prefer to reside.

Investigations

Several activities have accompanied the use of the dump site Loswal Noord. They ranged from routine measurements with an operational purpose, such as echo soundings to check navigational depths, till scientific attempts to give a firmer basis for the chosen dump location. Emphasis was on field studies with an occasional laboratory experiment. Since a few years we have incorporated numerical modelling in our program as well, since we think that an integration of experimental and theoretical approaches is required to make progress. In the following some of the activities and their results are discussed.

Mass balance

The changes in the bottom topography at the Loswal Noord as a consequence of the dumpings there, were regularly monitored.

Every two years a finely-spaced depth sounding program was performed, with cross-shore sections 250 m apart. An example of the results is shown in fig. 2 in a three-dimensional presentation.

In addition, every two or three years bottom-sampling campaigns were held, often with a relatively narrow grid size of 1x1 km². Thus, the mud content in the upper bottom layer could be determined.

From an analysis of the various depth-sounding charts of the region the amounts of material stored there can be determined. They were compared with the amounts dumped, for which a book keeping is available (see figure 3). For instance, for the period 1968-1986 in total 119 million m³ was stored, from the 291 million m³ dumped. Accounting for the estimated fractions of mud, sand and water in the hopper and at the site, respectively, a net loss of mud from the site is calculated. We have calculated the values

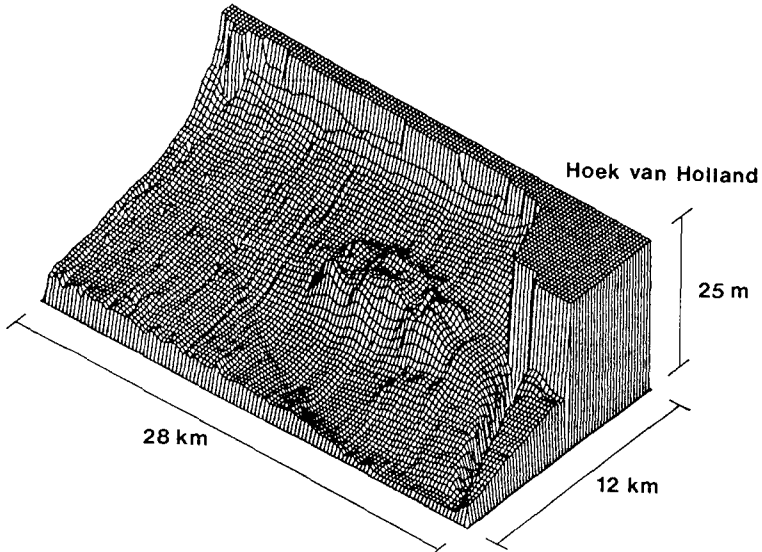


Figure 2. Three-dimensional presentation of the sea bottom echosounded in 1979, seen from the West

for the various considered time frames assuming constant loss rates therein. These are plotted in fig. 3 as well; the average value amounts circa 80 kg/s. Some 80 per cent of the dumped mud leaves the site. Since the beginning of the eighties this value tends to decrease to about 50 per cent; by dumping into deeper waters the mud probably has a better chance to settle permanently there. The sand fraction of the dumped material turns out to be stored rather permanently at the site, albeit that some 30 per cent migrates to its surroundings.

Hydrodynamics and sediment transport

Salinity and current profiles were regularly measured during 13 hours (covering a full tidal cycle) with ships at specific positions. Various stations in the area have been visited over the years. Clear vertical and horizontal gradients were observed, see e.g. figure 4. The relatively small survey vessels could operate at moderate wind conditions only. In a few cases moored self-recording current meters have been deployed that could measure during storm periods as well.

From these survey vessels in many cases sediment-concentration profiles were measured also, with in-situ optical turbidity sensors as well as by water sampling and subsequent filtering and determining the sediment's weight.

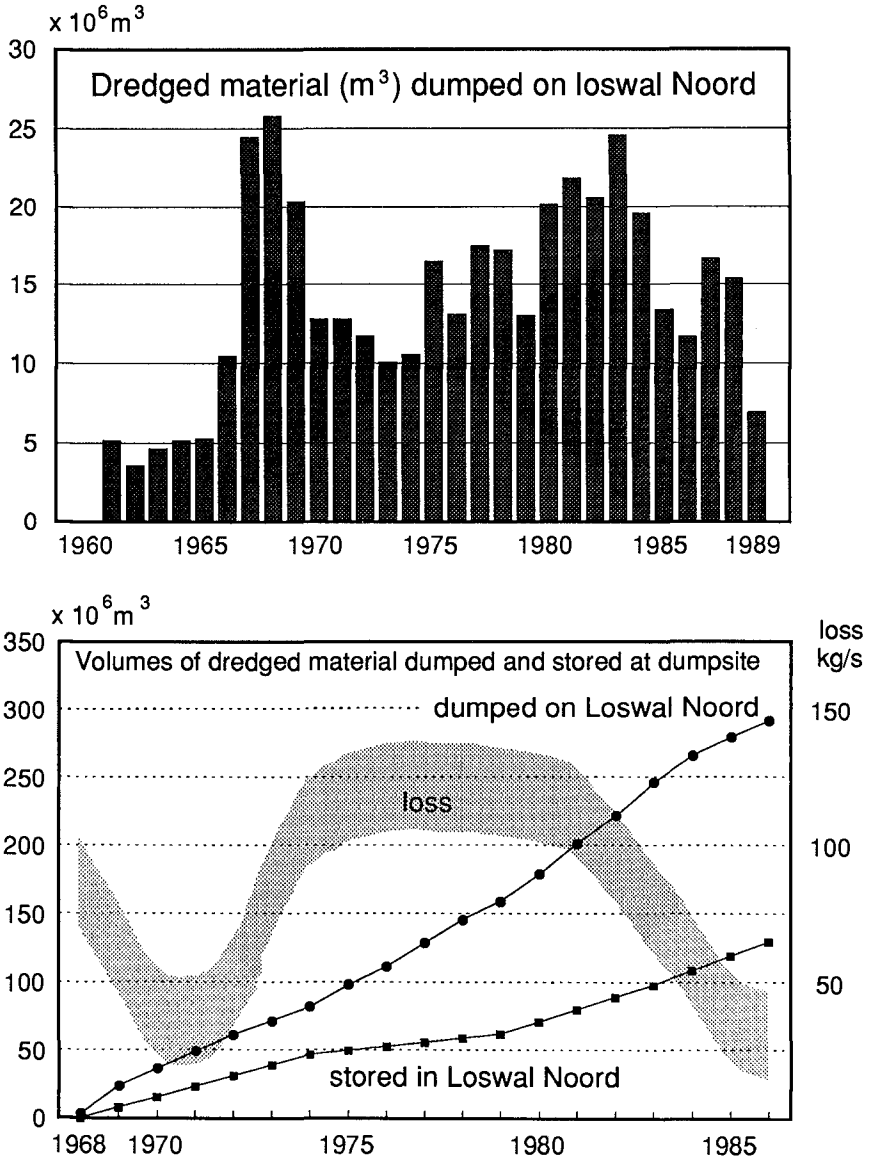


Figure 3. Top : Amounts of material dumped annually at the Loswal Noord
 Bottom: Cumulative amounts dumped and stored materials and the calculated loss per second

Combining the current and concentration profiles as measured over a tidal cycle provides indications of the rates of suspended-sediment transport in the area. These rates were much lower than expected when assuming a constant emission from the dump site, suggesting that special conditions such as storms or phenomena that escape detection play a dominant role. Current data under storm conditions were scarce while sediment-concentration information was lacking completely. Therefore, instruments were developed under contract for Rijkswaterstaat to fill these gaps, the so-called semi-permanent stations.

The chosen set-up consists of a complete package of sensors, batteries and electronics to be installed at the sea bottom in up to 25-m deep water that can measure and register the data autonomously for one or two months, thus also under storms, according to a preset program. The measuring intervals are chosen in a compromise between total operation time (data-storage capacity, power) and the frequencies of the phenomena of interest. At present, recordings are made every one to five minutes.

The sensors are mounted on one or two poles and are situated between 15 and 100 cm above the sea bottom, in

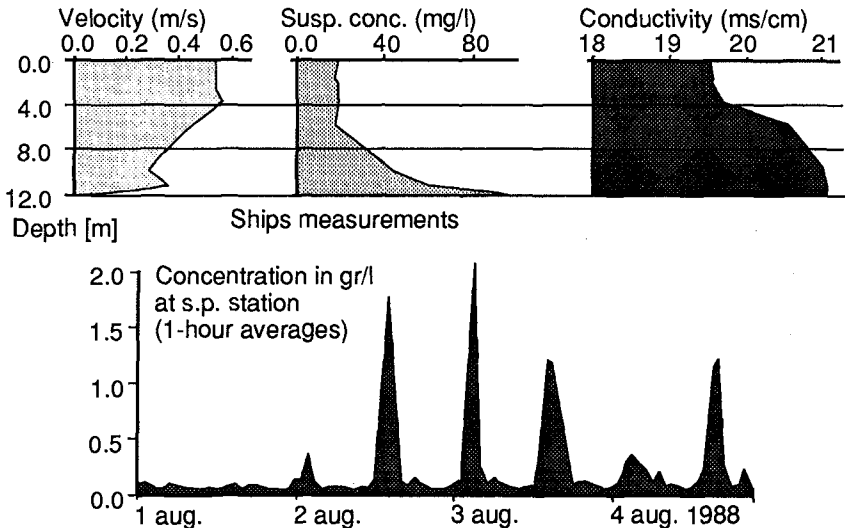


Figure 4. Current, sediment-concentration and conductivity profiles measured from ships (top)
Near-bottom sediment concentrations measured at the semi-permanent station (bottom)

practice. In general two optical (infrared) concentration probes are combined with one electromagnetic current sensor, but other configurations including more types of probes are possible. The equipment is brought into position by a diver at relatively calm weather conditions at the turn of the tide. The electronics and batteries are placed in a hole in a concrete foundation stone in the sea bottom to protect them against possible damage from the rather intense fishery in the area. Sometimes a sensor pole is overturned or even lost.

The equipment now has reached an operational stage, and it will be used almost continuously. Several weeks of data have been obtained in 1988 and 1989 with prototype versions. A result of a measured (time-filtered) sediment-concentration recording is presented in figure 4.

Description of the paths and fate of dumped materials

As a prerequisite for the best judgement of the costs and possible effects on the coastal-water system of the dumping of dredged materials, a description of the paths and fate of the latter is needed. A general insight in the existing situation has been required with the above field investigations, but predictions of the consequences of changes in the dumping scenario's, such as the use of alternative dump sites, have a qualitative nature only. For more stringent predictions more powerful tools such as models with some prognostic capability are required. The degree of sophistication of the tools to be used, and thus in practice among others the amount of physics incorporated in the model, depends on the acceptable uncertainty margins in the required predictions.

Important processes with respect to cohesive-sediment transport take place near the bottom. This follows not only from the increased values there of the measured concentration profiles but also from the observation of (temporary) sedimentation areas. Thus processes as settling, sedimentation and erosion may be important. Furthermore, the salinity and current profiles in the study area of fig. 1 display strong vertical gradients, with different residual currents for the top and bottom layers of the water, respectively. Therefore a full 3D description of water and sediment transport is appropriate in this case, including some of the mentioned processes of the latter.

As an example figure 5 is discussed. It was prepared as a 'first-order (3D) sediment transport model' at a time (1986) we did not have a hydrodynamic 3D model of the region. In this approach emphasis on the near-bottom suspended-sediment transports was put by considering current measurements made at circa 1 m above the bottom: a large collection of ships measurements in the area was normalized to mean-tide conditions and arranged according

to a standard time (high tide in Hook of Holland) with respect to the tidal phase. Thus it was possible to calculate at every time step for every place in the field the current vector by linearly interpolating between values observed at neighbouring stations. The sediment transport at 1 m above the bottom was simulated by considering the net displacements (in a large number of time steps) over a full tidal cycle of a large number of particles in the varying current field. The particles were moving with the water when the local current exceeded some critical value, and they returned (instantaneously) to the bottom as soon as the current was less than another fixed value, thus accounting for sedimentation and erosion.

A fair picture emerged of the transport directions from the Loswal Noord and Schevevingen dump sites. It should

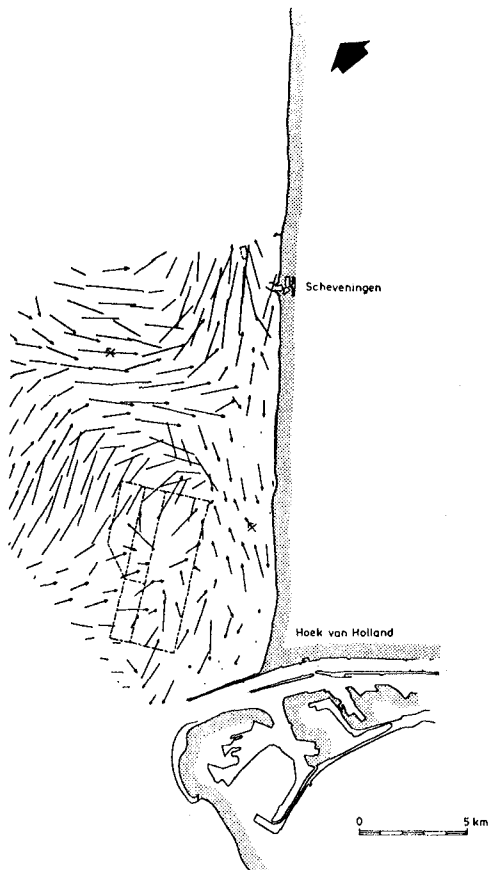


Figure 5. Residual near-bottom displacements of sediment particles calculated with measured current data

be noted that this picture applies to fair-weather conditions only because of the used current data (see above). Still, the picture is probably valid more generally, since it agrees quite well with the mud-content pattern in the bottom as deduced from the bottom samplings, see figure 6. The latter for instance also suggests a return flow along the shore to the South of mud dumped at the Loswal Noord.

3D sediment-transport model

As a further step towards a prognostic capacity a numerical 3D sediment-transport model was developed. It combines a hydrodynamic model with a sediment-transport part. The hydrodynamic-model equations are the momentum and mass balance equations, with hydrostatic and Boussinesq

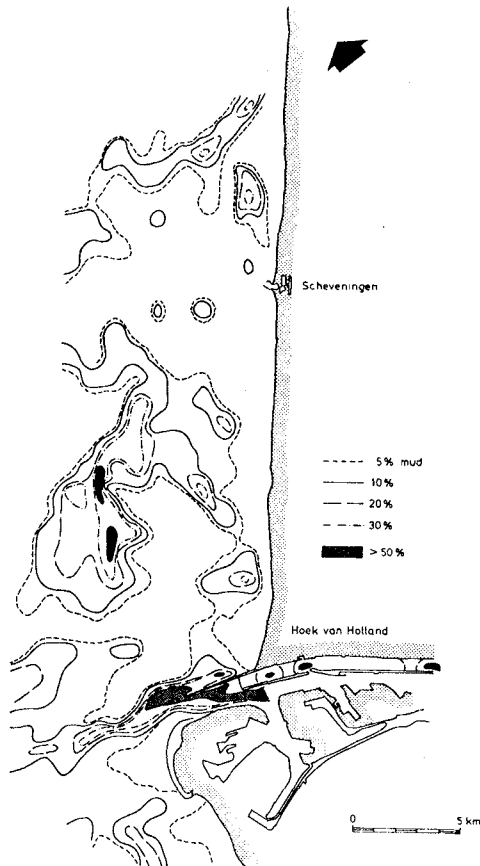


Figure 6. Mud contents (5%,10%,20%,30%,>50% contours) in samples of the upper bottom layer

assumptions, integrated over the layer depth in order to assure mass conservation. An explicit leapfrog difference scheme is used on a space staggered grid (Leendertse 1973).

The lower layers have a uniform, small depth for good near bottom resolution of the model with a horizontally uniform numerical error. Since layers are not horizontal anymore, both vertical and horizontal density gradients are represented in the momentum equations.

For salinity a separate advection-diffusion equation is solved and coupled to the momentum equations via the density gradients. Also the vertical turbulent exchange of momentum and mass is influenced by the vertical density gradients via the turbulent diffusion coefficients.

Sediment concentrations are computed with an advection-diffusion equation, with a fall velocity superimposed on the vertical velocity field, and an extra bottom layer for sedimentation and resuspension, depending on bottom shear stresses. No consolidation is taken into account yet.

In order to obtain a good reproduction of point releases a highly accurate finite difference method has been developed, with the possibility of representation of subgrid-scale details like first and second mass moments and cross moments. In de Kok (1989,1991) more details are given.

The modelled area was a coastal strip of 15 x 56 km, on a grid with a horizontal mesh width of 1 km, and a vertical mesh width of 1 m at the bottom until 10 m for the surface layer, depending on the depth. There were everywhere 5 layers. Time step size was 60 s for the hydrodynamic part and 500 s for the sediment transport part.

Boundary conditions were obtained via a series of coarser nested 2-DH models, beginning with a Continental Shelf model, then a North Sea model, then a Southern Bight model and finally a two layer coastal model.

Values for bottom roughness, eddy viscosity and eddy diffusivity were calibrated with observational data of velocity and salinity. Special attention had the maximum flood velocities, and the annual means of salinity and velocity in certain cross sections.

Computations were done for several wind and salinity conditions, and for several sediment grain sizes.

The transport of fine sediments from various sources, such as an individual dump release at a specific place, can be calculated for chosen environmental conditions. Various scenario's including the present situation can thus be simulated.

In the calculated (Lagrangian) velocity field for particles near the bottom an anticyclonic gyre in the residual currents around the present dumping site is emanant (see figure 7). It corresponds nicely with the transport

directions suggested independently by the mud contents in the bottom (see above), thus an appreciable return flow to the harbour mouth is likely. Furthermore a direct residual current to the mouth from the western part of the dump site is predicted, also in accordance with the mud chart. The latter current is induced by density differences. The former gyre is located in the lee of the relatively strong flood current of the land acclamation Maasvlakte extending into sea, and it is probably largely caused by it, as well as by the bottom topography around the dump site. Sediment concentrations calculated near the bottom with the 3D model confirm the above trends of a return flow (see figure 8).

Discussion

A large number of variables determines the hydrodynamics in the area of fig. 1, such as the tide, the wind which induces among others strong circulation currents and waves, swell, the only partially mixed variable Rhine outflow with its strong density gradients and induced residual currents, etcetera. Thus the hydrodynamics are hard to measure and to model. This holds even stronger for the sediment transport, being not only determined to a large extent by the hydrodynamics but also being subject to often poorly understood processes in flocculation, settling, sedimentation, consolidation and erosion. Thus at present, and in the near future, any sediment-transport model in the considered region has to be a mix of deterministic physics, parameterized formulations and empirical phenomenology.

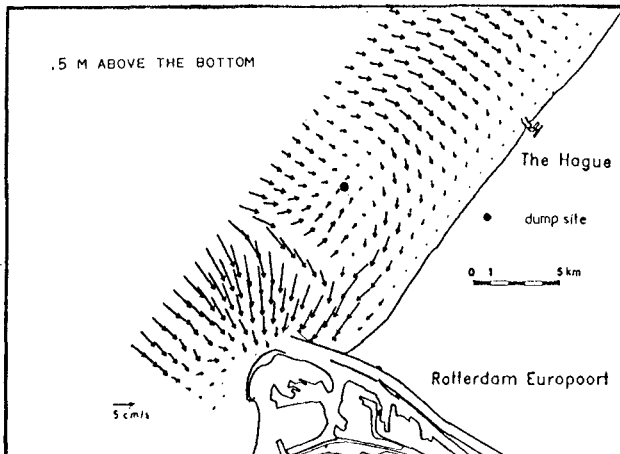


Figure 7. Near-bottom Lagrangian residual currents calculated with the 3D model

This is reflected in our program in which we combine field studies and numerical modelling. Proces-related field studies give clues of what proces should be included in the model and how. In turn, various processes, e.g. taken from the literature, can relatively easily be incorporated in the model that can predict in a kind of sensitivity analysis what the consequences in the field would be and where they should be clearly detectable. Thus the (expensive) field program can be directed. For instance, at present we assume that the dumped material is spreading below the hopper dredger over the bottom and that the transport of the major part of the finer fractions is governed quickly by the water movement there. This hypothesis is hard to verify directly in the field but it can be tested indirectly with the registrations of our sediment platforms at the bottom when combined with model calculations. Other points thus to be addressed are the hypotheses that spring tides have a dominant effect because the stronger currents only then exceed the critical erosion velocities at many places, respectively that storms influence the sediment transports not only by induced currents but also by their waves that help in faster eroding the bottom. If so, the present relatively simple parametric formulation of the latter effect in our model then will be verified. With the approach sketched we anticipate a constant improvement of the quality of our model predictions. In the mean time the model is used as a tool to analyse the present situation, with respect to return flow etcetera,

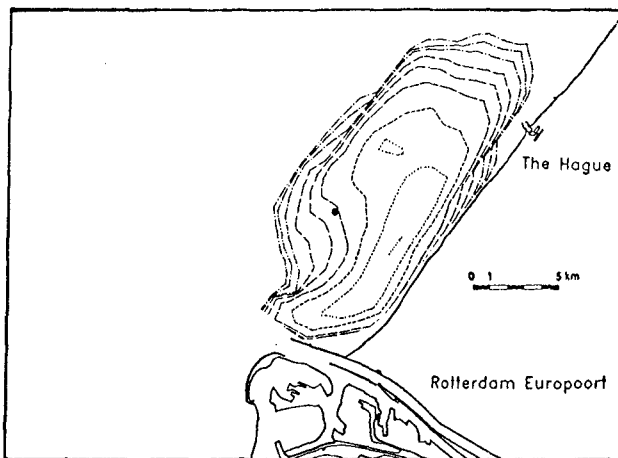


Figure 8. Calculated near-bottom sediment concentrations (arb. units) five days after a release at the indicated dump site. Note the high near-shore concentrations extending southwards

and to develop alternatives in terms of dump sites, for instance.

One of the questions to be addressed is how much the sediment concentrations in the Dutch coastal zone, and thus e.g. in the Wadden Sea, are affected by the dumping. This problem is relevant, since the amounts of mud disposed of are comparable with those transported in a 20-km wide zone along the Dutch shore (Van Alphen 1990). To answer this question, the present detailed analysis of the area of fig. 1 is required. Namely, the amounts of fine sediment returning to the harbour region that are dredged several times do not contribute to those concentrations. Furthermore, the presently dumped sediments originate from the sea and thus are artificially trapped by the man-made constructions in the area. Viewed on a large scale the dumping in first order simply compensates for this effect, but by injecting the material at one specific site local changes in the coastal zone may be induced, with some bearing on the large-scale sediment distributions. The problem can be tackled by nesting the present model, once validated, in a larger model for the whole of the Dutch coastal zone.

Conclusion

Field studies and model results suggest a relatively strong return flow of mud dumped at the present dump site Loswal Noord, largely due to an observed gyre in the residual currents and to density differences. In combining field studies, with innovative equipment, and modelling activities a promising program towards a more quantitative assessment is performed.

References

- Van Alphen, J.S.L.J., de Ruijter W.P.M., and Borst J.C. Outflow and 3D spreading of Rhine water in the Netherlands coastal zone. In *Physical Processes in Estuaries*. J. Dronkers and W. van Leussen (eds.). Springer Verlag 1988. pp. 70-92
- Van Alphen J.S.L.J. A mud balance for Belgian-Dutch coastal waters between 1969 and 1986. *Neth. J. Sea Res.* 25, 1990, pp. 19-30
- De Kok J.M. A 3-D silt transport model with subgrid-scale resolution. *Proc. 6th Int. Conf. Num. Methods in Laminar and Turbulent Flow*. Swansea, 1989. C. Taylor (ed.) Pineridge Press
- De Kok J.M. A 3-D finite difference model for the computation of near field and far field of transported matter near a river mouth. Submitted to *Continental Shelf Research*, 1990
- Leendertse J.J., Alexander R.C., Liu S.K. A three dimensional model for estuaries and coastal seas. Vol I. R-1417-OWRR. The Rand Corporation 1973.

CHAPTER 215

DEVELOPMENT OF WATER LEVEL CHANGES IN THE GERMAN BIGHT, AN ANALYSIS BASED ON SINGLE VALUE TIME SERIES

Jürgen Jensen*, Hans-Eckart Mügge**
and Wolfgang Schönfeld***

Abstract

Time series of semidiurnal single values of Tidal High Water and Tidal Low Water and their occurrence times from certain tide gauges in the German Bight were evaluated. Detailed analyses were performed to detect distinct periodicities and changes in the trends not only of water levels but also of the occurrence times by means of mathematical-statistical methods.

Introduction

The eustatic variations of the global sea level are strongly influenced by worldwide changes in climate. There is no longer any doubt that the "greenhouse effect" and other human activities have a definite impact on our climate. In many parts of the world changes and accelerations in sea level rise have been detected, such as the east coast of the USA, the Gulf of Mexico, and the Bay of Bengal. In the North Sea, and even in the German Bight, an enhanced rise of the sea level will also lead to far-reaching alterations. In this context not only changes in mean sea level are important, especially alterations in Tidal High Water (THW), Tidal Low Water (TLW) and Tidal Range (TR) will play a decisive role. Changes in tidal dynamics of the flat coastal regions affect erosion, endangering of storm surges, changes in ground water level, and shipping.

In the project "Water Level Changes in the German Bight", the evaluation of time series of semidiurnal THW and TLW shows rises of THW up to 6 mm/year for cer-

*Senior Research Engineer, Dr.-Ing.,

Research Engineer, Dipl.-Ing., *Dipl.-Oceanogr.

BUNDESANSTALT FÜR WASSERBAU - AUSSENSTELLE KÜSTE; F.R.G.

tain sites on the German coastline, whereas the TLW decreases (Jensen et.al.,1988). This leads to the assumption, that during the last three decades a change in the tidal dynamics of the German North Sea coast may have taken place (Führböter, 1986, Siefert, 1984).

The Data

In order to achieve satisfactory results in determination of long term (secular) changes in water level and tidal dynamics, the analysis must be based not only on comparatively prolonged series of observations or records, but also on data which are highly accurate.

The database of the present examination consists of more than 500000 single values of semidiurnal THW and TLW. The data were recorded at 12 sites in the German Bight (Fig.1).

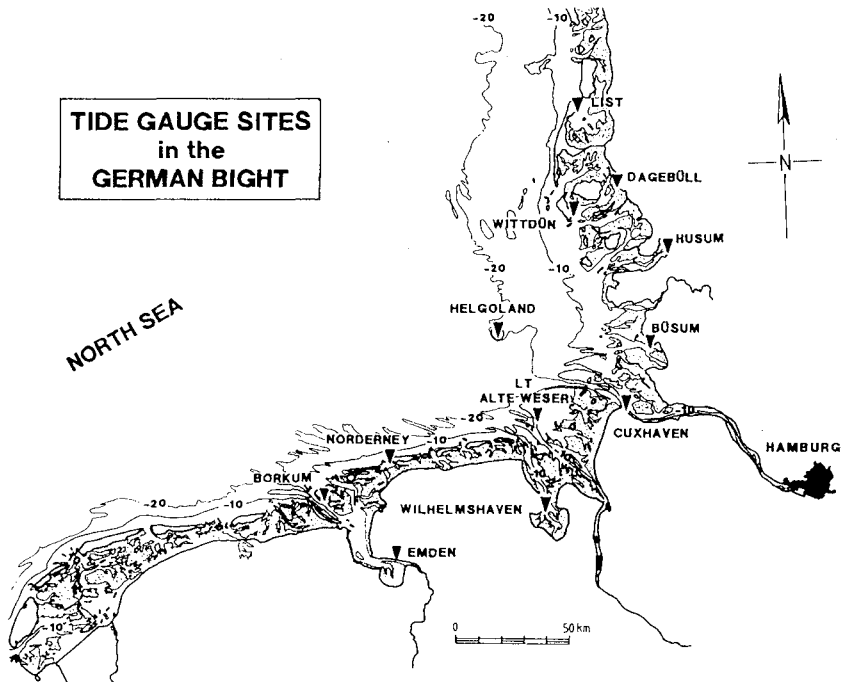


Fig. 1: Tide gauge sites in the German Bight.

The tide gauges are located in the south eastern part of the North Sea. The sites are on islands (Borkum, Norderney, LT Alte Weser, Helgoland, Wittdün/Amrum, and List/Sylt), in tidal estuaries (Emden, Wilhelmshaven, and Cuxhaven), and in small harbours (Büsum, Husum, and Dagebüll). The area includes most of the wadden sea. Big parts of the coastal region are below the sea level. The whole coastline is protected with dykes. The oldest continuous tide gauge recordings considered here had been performed in 1843 at Cuxhaven.

The time series of the tide gauges had to be as long as possible and should not much be influenced by antropogenic or morphologic factors. The data had been carefully checked and adjusted to a unique reference level. Changes in the location and vertical alterations of the tide gauges also had been taken into account. Gaps in the older parts of the time series had to be closed with the aid of linear regression and double-sum-analysis.

Linear Trends

The linear trends are determined with the aid of least square methods, as $H(t) = H_0 + S_T * t$. S_T denotes the average rise or fall of THW, TLW, TR, or Mean Sea Level (MSL) within the time period examined. The trends can be expressed either in mm/year or, as some authors do, formally extrapolated to a century and expressed in cm/100 years as secular trends (Führböter and Jensen, 1985).

In the German Bight a rise of the THW of 20 - 30 cm per century, i.e. 2-3 mm/year, has been observed since the beginning of regular water level observations in the middle of the last century (Rhode, 1977). Pirazzoli (1989) anticipated a rise of MSL in the North Sea of 1 - 1.5 mm/year. Woodworth (1987) estimated a global eustatic rise of 1 - 2 mm/year based on U.K. tide gauge data. In the current project, linear regressions show an increase of THW up to 6 mm/year at some tide gauges on the German North Sea coast. The TLW remains constant or decreases with maximum rates of 4 mm/year at certain tide gauges.

Table 1 shows spatial averaged trends of THW, TLW, TR, and MSL and their standard deviations over different time periods of the last 100, 50, 25, and 19 years (\approx period of the nodal tide). The mean trends are obtained by computing linear trends for each tide gauge separately and then taking spatial mean values.

TIME SERIES	LINEAR TRENDS $S_T \pm \sigma$ [mm/YEAR] MEAN VALUES GERMAN BIGHT			
	Tidal Low Water	Tidal High Water	Tidal Range	Mean Sea Level
1890-1989 (100 Years)	0.0 \pm 0.7	2.5 \pm 1.0	2.6 \pm 1.0	1.2 \pm 0.6
1940-1989 (50 Years)	-0.7 \pm 0.6	3.3 \pm 0.8	3.9 \pm 0.8	1.2 \pm 0.6
1965-1989 (25 Years)	-0.2 \pm 0.6	4.0 \pm 0.6	4.2 \pm 0.5	2.1 \pm 0.6
1971-1989 (19 Years \approx nodal tide)	4.0 \pm 0.6	6.7 \pm 0.7	2.6 \pm 0.5	5.3 \pm 0.6

Table 1: Mean trends over different time periods
(S_T : regression coefficient,
 σ : standard deviation)

The increase of the trends in THW can clearly be seen, the trends of TLW are much smaller, at some tide gauges TLW even is decreasing. Due to this development the trends of TR increase faster and those of MSL rise much slower than the trends of THW. Conspicuous alterations have taken place in the last decades. Compared with the longer trends, the trends from 1971 to 1989 reveal the first time an increase of TLW. So the rise of TR becomes smaller and therefore the MSL increases much faster during this period of time.

The alterations of the trends of THW and TLW at the tide gauge Cuxhaven from 1890 to 1987 are shown in Fig.2. The trends are computed within 25-year time-windows and the value is expressed in cm/100 years. The

trend is plotted at the end of the 25-year period. Negative values indicate decreasing water levels within the 25-year period. The differences to the 25-year trends in table 1 arise from the different time periods. In table 1 only data until 1987 are considered.

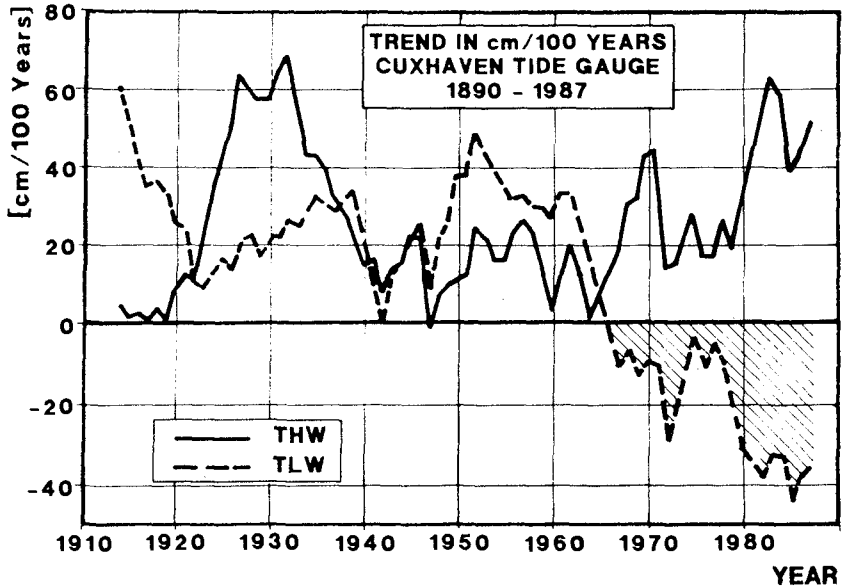


Fig. 2: Alterations of the trends of THW and TLW at the tide gauge Cuxhaven from 1890 to 1987, computed with 25-year time-windows.

The trends reveal strong temporal variations. In the middle of this century (the trend within the time period from 1941 to 1965 is plotted in 1965) the trend of THW clearly is rising and the trend of TLW is decreasing (negative values since 1965). Hence an increased rise of TR took place. The rise of the TR is of great importance for the tidal dynamics. Enhancement of tidal energy will lead to increased current velocities and sediment transports. This has great impact on the morphological structure of the coastal regions.

Frequency Analysis - Fast Fourier Transform

The corrected time series of tide gauge observations were transformed from periodic functions of time into the frequency domain using the Fast Fourier Transform.

Fig. 3 shows as a result of the FFT the frequency distribution of THW at the tide gauge Cuxhaven. The amplitudes of the frequencies for 1, 14, and 28 days as well as for 1 year are clearly seen. Furthermore some longperiodic oscillations of 4.2, 6.2, 7.8, 13.3, and 18.6 years can be recognized.

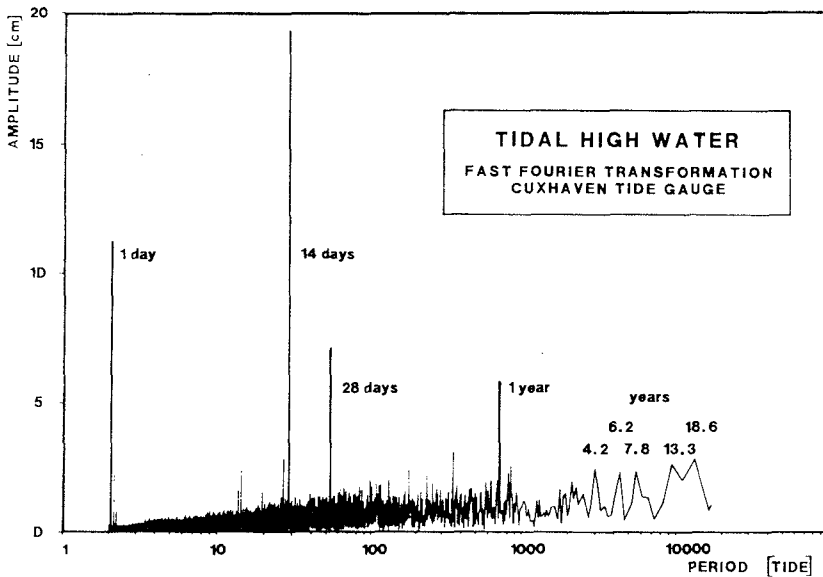


Fig. 3: Frequency distribution of THW at tide gauge Cuxhaven for the years 1894 to 1986.

The periods up to 1 year and the 18.6 year period obviously are of astronomical origin. The origin of higher amplitudes in periods between 3 and 13.3 years are at present not clear. Meteorological or hydrological cycles may play a role (eg. a supposed 6 to 7 year meteorological cycle).

Fig. 4 shows the frequency distribution of the TR at the same tide gauge. Here the 18.6 year period (nodal tide) with an amplitude of 4 cm, this is a range of 8

cm, can clearly be seen. At other gauge sites the range of this partial tide amounts up to 12 cm.

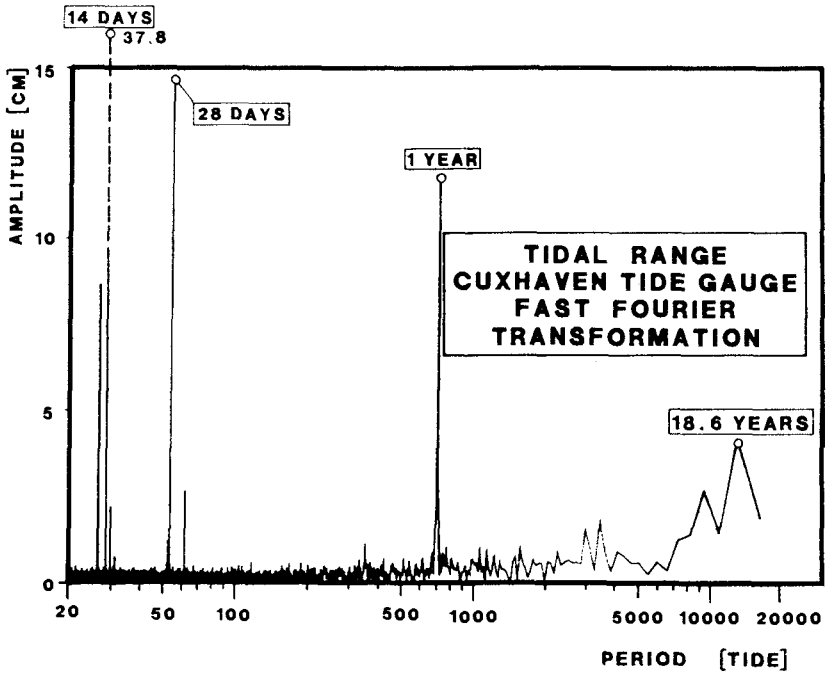


Fig. 4: Frequency distribution of the TR at tide gauge Cuxhaven.

Filtering

With the "Inverse Fast Fourier Transform", a retransformation of the frequency spectrum can be performed. By omitting distinct frequencies one gets digitally filtered time series.

A retransformation of THW and TLW at tide gauge Cuxhaven was performed with a low-pass-filter, all periods shorter than 2.7 years have been omitted. So long periodic oscillations can be recognized and analyzed. Fig. 5 shows an increase of the amplitudes of long periodic oscillations in the last decades.

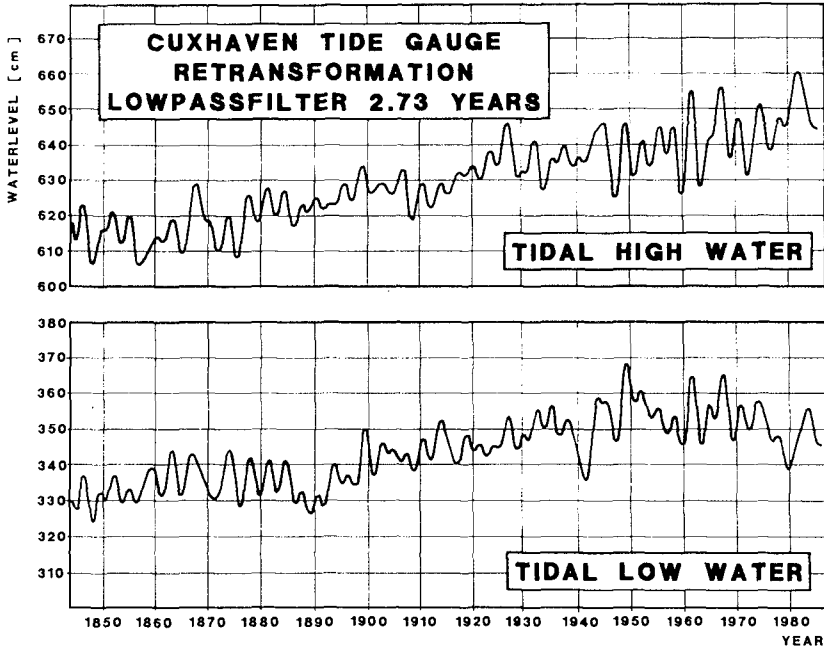


Fig. 5: Retransformation of THW and TLW at tide gauge Cuxhaven (from 1843 to 1986).

In another application of the inverse FFT, first distinct periods of TR time series have been filtered out and then the other components were superposed.

Fig. 6 shows the oscillations of the TR with periods of 13.3, 18.6, and greater 23.3 years. The upper curve is the sum of these oscillations with periods greater than 13.3 years. The curves for 13.3, 18.6, and greater 23 years all have a maximum approximately at the same time, so the curve of the sum of these components has an extraordinarily maximum at the beginning of the eighties. The 13.3 year cycle cannot yet be explained.

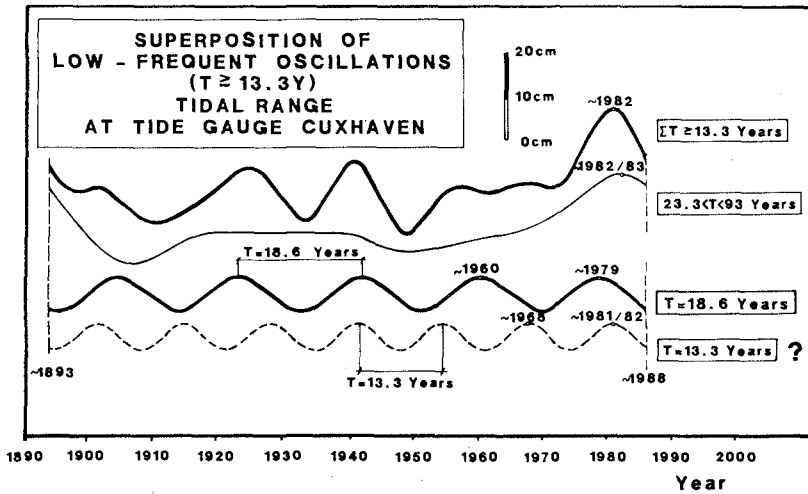


Fig. 6: Superposition of periods > 13.3 years

Nodal Tide

The nodal tide arises from the relative movement of moon and earth to each other. The lunar and the earth's orbit are inclined with an angle of $5^{\circ}9'$. The point of intersection of the lunar orbit and the ecliptic changes its position within a period of 18.6 years. Due to this, the declination of the moon varies between 18.5° and 28.5° around the equator.

From a viewpoint on the earth this effect is depicted in Fig. 7. At the minimum declination, the tide generating force of the nodal tide has a maximum. The last minimum declination was in 1979.

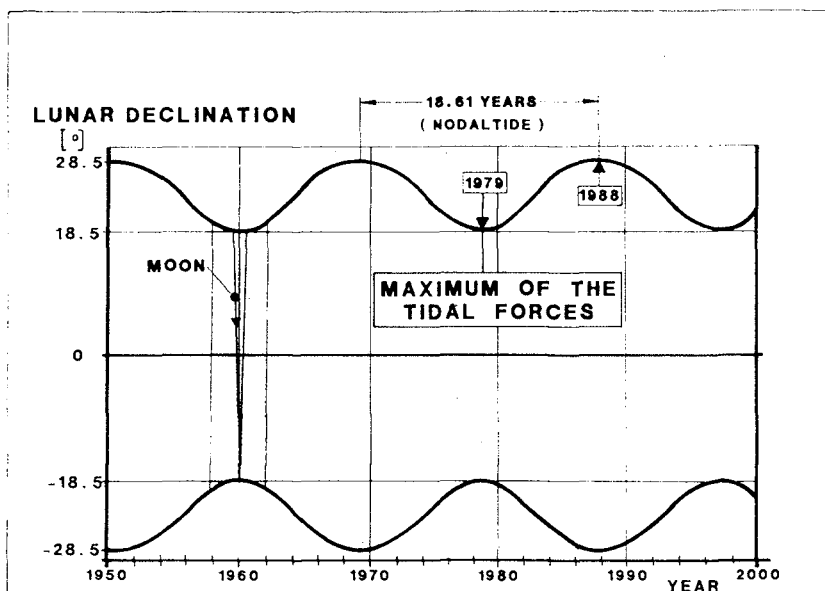


Fig. 7: Declination of the moon

The nodal tide effect is mainly detectable in the TR. In the time series of THW and TLW this signal is considerably weaker. At the tide gauges in the German Bight the contribution of the nodal tide on the TR is about 7 cm. Other investigations reveal the TR at the dutch tide gauge at Vlissingen a portion of ≈ 12 cm and at certain english tide gauges more then 16 cm (Woodworth et al., 1990).

Occurrence times of THW and TLW

The previous investigations considered only the variations of water levels and TR. Water level changes, however, also cause temporal changes in the tidal dynamics. The investigations of tidal dynamics include the time series of the occurrence times of semidiurnal THW and TLW.

The tidal regime of the North Sea is dominated by the semidiurnal M₂-tide. The tidal wave from the Atlantic Ocean enters the North Sea through the entrance to the north and through the English Channel. First the tide

propagates counterclockwise along the english coastline southward and turns east near the dutch coast. In the German Bight the tide turns northward and leaves the North Sea along the norwegian coastline. Therefore the time of occurrence of THW and TLW at the North Sea coastline takes place in a definite sequence. Temporal alterations of the tidal regime will change the time when THW or TLW occur at certain tide gauge sites.

The tide in the North Sea is not directly determined by the astronomical potential, it depends on the tidal wave of the Atlantic Ocean. Nevertheless there is a relation of the position of the moon and the occurrence time of semidiurnal THW and TLW in the North Sea. Therefore the time of transition of the moon through the Greenwich meridian is chosen as a reference time. This reference time only depends on astronomical factors. The investigations of temporal variations are based on the time difference between occurrence of THW and TLW at several tide gauges in the German Bight and the transition of the moon through the Greenwich meridian. The data are not affected by vertical movements, eustatic effects or changes in reference levels.

Table 2 shows the averaged time differences between the occurrence of THW and TLW and the transition of the moon through the Greenwich meridian for selected tide gauges in the German Bight. The differences are averaged over a period of 34 years from 1954 to 1987. At tide gauge Norderney eg. the THW occurs in 1987 approximately 17 min earlier than in 1954 with respect to the transition of the moon through the Greenwich meridian.

GAUGE SITE	MEAN TIME DIFFERENCE		ALTERATION WITHIN 34 YEARS	
	$\Delta t(\text{THW})$ [min]	$\Delta t(\text{TLW})$ [min]	$T_T \pm \sigma$ $T_T(\text{THW})$ [min/34a]	$T_T \pm \sigma$ $T_T(\text{TLW})$ [min/34a]
NORDERNEY	613	253	-17±1.2	-21±0.7
HELGOLAND	637	297	- 7±1.2	- 3±0.7
WILHELMSHAVEN	711	334	-25±1.2	-26±0.7
CUXHAVEN	716	378	- 9±1.2	-12±0.7
HUSUM	764	406	-15±1.3	- 8±0.8
LIST	802	425	- 6±1.4	- 8±0.6

Table 2: Mean time difference between the occurrence of THW and TLW and reference time

The development of the time difference at tide gauge Wilhelmshaven from 1936 to 1987 is depicted in Fig. 8 . Generally the time differences reveal a negative trend. Since the beginning of the sixties an enhanced reduction of the time differences can be detected. Presumable this is due to construction works in the Jade Waterway.

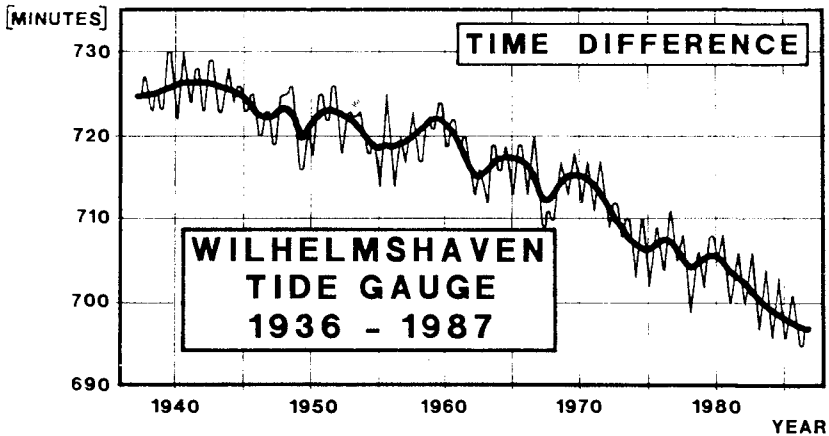


Fig. 8: Development of mean time difference between the occurrence of THW at tide gauge Wilhelmshaven and reference time.

At all tide gauges considered here, the time differences of occurrence of THW and TLW and reference time has been reduced in the last decades. So it can be resumed, that also changes in tidal dynamics have taken place in the German Bight.

Conclusions

These evaluations reveal, that there is no uniform trend in the tidal regime of the German Bight. The secular rise strongly depends on the location of the tidal gauge and on the period of time considered. One obtains different results depending upon whether the MSL (predominantly used parameter) or THW and TLW are computed. Based on the historical development of MSL in the German Bight, no extraordinary rise can be detected when taking time periods of more than 25 years into account. Only computations of trends over shorter periods reveal an enhanced increase of the MSL in the German Bight. As mentioned above, more interesting developments have occurred with respect to the extreme values of the tidal regime. The rise of THW compared with constant or decreasing TLW leads to an enhanced increase of the TR. The rise of the TR is of great importance for the tidal dynamics. Enhancement of tidal energy will lead to increased current velocities and sediment transports. This has great impact on the morphological structure of the coastal regions and is of high importance for coastal engineering purposes.

The evaluations of occurrence times lead to the assumption, that the propagation velocity of the tidal wave has increased in the last decades.

More insight into the development of tidal phenomena in the German Bight may also be gained when taking meteorological time series into account.

Acknowledgement

The research project "Water Level Changes in the German Bight" of the KFKI (Kuratorium für Forschung im Küsteningenieurwesen - Committee for Research in Coastal Engineering) is sponsored by the BMFT (Bundesminister für Forschung und Technologie - Federal Ministry for Research and Technologie) under MTK 0388.

References

FÜHRBÖTER, A.: Veränderungen des Säkularanstiegs an der deutschen Nordseeküste. Wasser und Boden, Heft 9, 1986

FÜHRBÖTER, A. and JENSEN, J.: Longterm Changes of Tidal Regime in the German Bight (North Sea). Proc. of the Fourth Symposium on Coastal and Ocean Management, COASTAL ZONE '85, Vol II, Baltimore, U.S.A., 1985

JENSEN, J.: Änderungen der mittleren Tidewasserstände an der Nordseeküste. Mitt. d. Leichtweiß-Inst. der TU Braunschweig, Heft 83, 1984

JENSEN, J., MÜGGE, H.-E., and VISSCHER, G.: Untersuchungen zur Wasserstandsentwicklung in der Deutschen Bucht. Die Küste, H.47, 1988.

PIRAZZOLI, P.A.: Recent Sea-Level Changes in the North Atlantic. in: D.B. Scott et al. (eds.), Late Quaternary Sea-Level Correlation and Applications, 1989

RHODE, H.: Sturmfluthöhen und säkularer Wasserstandsanstieg an der deutschen Nordseeküste. Die Küste, H.30, 1977.

SIEFERT, W.: Long term tidal changes along the south-eastern North Sea coast. Annales Geophysicae, Section 2, 4, 1984.

WOODWORTH, P.L.: Trends in the U.K. mean sea level. Marine Geodesy, 11, 1987.

WOODWORTH, P.L., SHAW, S.M., and BLACKMAN, D.L.: Secular Trends in Mean Tidal Range Around the British Isles and Along the Adjacent European Coastline, (unpublished manuscript), 1990.

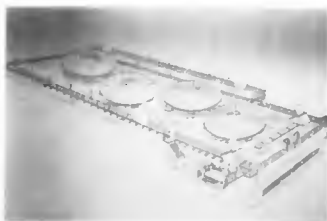
CHAPTER 216

DAY VISITOR PONTOON GREAT BARRIER REEF, AUSTRALIA

ALAN ALBERT CAMPBELL GRUMMITT
B.E., M.I.E.(Aust.), MICE., M.ASCE.

1.0 ABSTRACT

This paper describes the structural and environmental aspects considered in the installation of a 45 metre x 16 metre steel pontoon equipped as a day visitor centre and installed at Wistari Reef, a southern section of the Great Barrier Reef, Australia.



In order to achieve environmental acceptability, any floating facility has to be structurally adequate and moored in such a way to withstand the most serious cyclonic weather without breaking free and damaging the reef.

The paper details the process of studying the reef environment, analyzing the structure, and obtaining the prerequisite approvals. It then discusses the actual installation of the pontoon and details ongoing monitoring requirements imposed by the Great Barrier Reef Marine Park Authority.

Managing Director, Cullen Grummitt & Roe Pty Ltd,
Consulting Engineers, 126 Wickham Street, Fortitude
Valley, Qld, 4006, Australia

2.0 INTRODUCTION

The Great Barrier Reef is a natural Coral Reef formation stretching from the northern tip of Eastern Australia parallel to the eastern coastline to its southern extremity near Bundaberg in Queensland, covering a distance of some 1850 km.

The reef is recognised as one of the wonders of the world, and is of major significance in both World Heritage terms and for its commercial value as a tourist destination.

It is protected by Federal and State Government legislation to ensure that any activity within its boundaries is environmentally acceptable.

Our client, P & O Resorts Pty Ltd, leases and operates a world famous Barrier Reef tourist resort at Heron Island on the Great Barrier Reef located some 88 km off the Queensland coast and almost on the Tropic of Capricorn.



The island is a renowned dive site to natural corals, has prolific bird life and is a major turtle nesting area.



P & O Resorts Pty Ltd purchased the nearly completed pontoon and thus commenced the task of modifying the pontoon for the exposed location proposed on the southern end of the Great Barrier Reef and obtaining the necessary statutory approvals for its installation.

As part of the statutory requirements a public environmental report was prepared and subjected to public scrutiny. The proposal was then modified to accommodate the requirements of the public and of the authorities and the pontoon was finally installed at the reef. The company agreed that it would obtain a Lloyd's classification on the reef pontoon and mooring system to satisfy the Marine Park Authorities requirements. In order to achieve this a full structural analysis of the pontoon, its mooring system and anchor components had to be completed and full detailed calculations submitted to Lloyd's register of shipping to obtain the necessary approvals. In addition many of the major components of the structure and in particular the mooring system including anchor chains, shackles and fasteners all had to be load tested and certified.

The Great Barrier Reef, and the pontoon installation, came ultimately under the control and standards of five bureaucracies and two permanent tenants on Heron Island. Finally the Lloyd's Register of Shipping certification had to be obtained for both the pontoon and its anchoring system.

It is fair to state that the frustrations, difficulties and, at times sheer pettiness and pedantic approach of some of these groups was certainly well beyond any expectations. By contrast some of the parties and bureaucrats were extremely helpful in the process.

3.0 ENVIRONMENTAL CONSIDERATIONS

Included in the environmental consideration of the site were:-

- (a) Existing Environment
 - . Physical
 - . Biological
 - . Socio Economic
- (b) Environmental Impacts
 - . During installation
 - . During operation
- (c) Control of Impacts
- (d) Monitoring of Impacts
- (e) Existing Environment

3.1 Existing Environment

The site initially chosen for the pontoon installation was on a reef shelf on the North Western end of Masthead Island and the Public Environment Report concentrated its attention to this preferred site. Seven alternatives were also considered in the P.E.R. and in the final result, it was not Masthead Island, but Wistari Reef, one of the seven alternatives for which approval was received.

Masthead Island is a typical tropical coral cay.

One of the major attractions of the Masthead site was the proximity of the island itself, affording visitors the opportunity to spend part of their day excursion on a typical tropical island paradise.

Regrettably, the approved site at Wistari reef does not have any island and guests are able to be taken ashore to reef walk only during low tides.

In the study of the existing environment, each of:

- . physical
 - . biological
 - . socio economics
- was addressed

Physical:-

The P.E.R. contained a complete description of the physical environment of Masthead.

The pontoon was to be moored in approximately 8 - 9m of water, with the underwater observatory looking onto a large (c. 4m diameter) living Porites coral bommie. This bommie, composed of two main colonies, rises to about 5m below the surface. Beyond this bommie the staghorn corals thin and the relatively flat substrate is covered by numerous small coral colonies dispersed in an otherwise sandy area.

In the original proposal, the human waste generated on the pontoon by 100 day visitors was to be treated in a twin three stage Microphor MC300 treatment system.

The effluent from the system is guaranteed within the following limits:-

- 100 guests per day maximum
- 4200 litres/day of diluted effluent
- 26 dumps each of 1.1 minutes each day
- 145 litres/minute dump
- less than 15mg/litre suspended solids
- better than 10mg/litre B.O.D
- Nitrate-Nitrogen 0.13mg/litre
- Soluble phosphates: Phosphate-phosphorus
2.14mg/litre
- Particulate phosphates: Phosphate-phosphorus
1.42mg/litre

The effluent standards were generally accepted as high, and quite suitable for the operation. The one reservation was that the treatment process did not remove nitrates and phosphates.

The presence of nitrates and phosphates in reef waters is undesirable as they can accumulate and act as nutrients for the growth of algae which in turn kills live coral. An extensive study was therefore undertaken to investigate the risk of such a nutrient build up.

Numerical simulations of hydrodynamic and advection/dispersion were completed to assess the potential contamination of reefs by sewerage effluent proposed to be discharged from the pontoon.

The models indicated that in one particular combination of spring tides and light onshore winds, retention of material around the reef chain was significant for several days.

In view of this perceived risk of nutrient accumulation during the combination of spring tides and light onshore winds, the decision was taken not to discharge the effluent into the sea but to take the treated effluent ashore for alternative disposal.

Other aspects of the physical environment impacts addressed included:-

- . Solid Waste Management
- . Disposal of shower water
- . Disposal of dish washing water
- . Disposal of deck washing
- . Fuel spill prevention
- . Disposal of food scraps
- . Effect of antifouling paint

Biological:-

The biological environment identified:-

- . terrestrial insects, birds and plants;
- . turtles;
- . sessile benthic (corals, algae and other);
- . fish.

Plants:

Plant species were predominantly *Pisonia* forest, fringed with *Casuarina* and *Pandanus* trees and grasses. A total of 41 plant species was identified.

Birds:

Masthead Island is a principal rookery for White-capped Noddies, a major rookery for the Wedge-tailed Shearwater, Silver Gulls, Crested Terns and Bridled Terns, and additionally supports colonies of Reef Heron, Roseate Tern, Black-naped Tern, Lesser-crested Tern, Sooty Oyster-catchers and Ospreys (Environment Science and Services, 1984).

Turtles:

The World Conference on Sea Turtle Conservation, held in Washington D.C., U.S.A. in November 1979 identified the Capricorn-Bunker Group as being of world significance for sea turtle conservation, being one of the eleven most important green turtle breeding areas and one of the worlds three major loggerhead turtle breeding areas. Masthead Reef, like other reefs in the region, supports resident populations of immature and adult green, loggerhead and hawksbill turtles throughout the year.

Coral:

A coral comparison for some of the alternate sites investigated shows the following results:-

Reef	Algae	Diversity	Size	Aesthetics
Erskine	1.38	1.88	1.38	2.13
Heron	0.63	2.17	1.80	2.74
Masthead	1.17	2.46	2.00	3.00
Polmaise	3.25	1.88	1.38	2.75
Wilson Is.	0.70	2.50	2.10	3.70
Wistari	0.59	2.55	1.90	2.79

Values given are means for the cover of each category where cover is marked on a scale 0 (0%) to 6 (76%-100%).

It can be seen from the table that the site finally chosen - Wistari Reef - was inferior in coral in all categories except diversity to the preferred site at Masthead.

This aspect was regarded as unfortunate, given that the prime attraction for visitors to a coral reef is the coral itself.

The figures, however do refer to average coral over the reef area, and the local site finally selected at Wistari Reef contains very attractive and impressive coral colonies and is not regarded as locally inferior to the local coral at the preferred Masthead site.

In order to minimize impact of the pontoon and its anchorage system on the coral, yet place the pontoon as close as possible to attractive coral colonies for viewing both by snorkeling and from the underwater observatory, a detailed site search was carried out in company with a marine biologist. The search was done from helicopter boats and finally in the water using scuba and snorkeling equipment. Once the actual site was selected, the pontoon shadow was pegged on the sea bed, as was the actual position of each anchor and anchor chain.

A detailed coral and fish survey of the site was completed.



General Comments on Fishes

Fish communities observed over the duration of the survey (12 - 14 December 1988), appeared typical of similar reefs in terms of species, composition, and numbers of individuals, with respect to the two principle habitat types encountered. Associated with the major inshore bommies, staghorn thickets and to a lesser extent the scattered hard coral patches, there was a much more diverse assemblage of fishes. Families Apogonidae, Chaetodontidae (eg. Cheetodon spp.), Haemulidae (Plectorinchus sp.), Labridae (eg. Thalassoma spp.) Pomacentridae and, Serranidae (eg. Epinephelus spp., Plectropomus maculatus) were visually dominant.

Dolphins, green turtles and game fish (probably long-tail tuna, Thunnus tongol) were seen from the dive boat when on station over the survey site.

Socio Economic

The examination of socio economic effects considered:-

- . existing private use of the area;
- . existing commercial tourist oriented use;
- . tourist impact on the local community in Gladstone, the adjacent mainland city;
- . impact on the central Queensland tourist trade.

The studies concluded that the facility would provide a positive socio economic effect on the area; that it would not intrude unduly on the existing private use and that the extensive international advertising, conducted by a major tour operator (P&O) would bring more positive impact to the only existing operator that the negative effect resulting from increased competition.

3.2 Environmental Impacts

Environmental impacts were divided into two categories:-

- . impacts during installation; and
- . impacts during operation.

Impacts during installation included:-

- . Towing to site and associated risks;
- . Accidental grounding of pontoon or tug;
- . Disturbance of Benthos and Substratum;
- . Disturbance to Marine Life.

To minimize accidents in the towing and installation phase, the operation was planned to occur, and did in fact occur, during very calm clear weather. Visibility both above and below water was excellent.

Some coral transplanting occurred before the anchors were laid to ensure minimum disturbance to coral by either physical damage or as a result of shading from the pontoon. All coral transplanting was done by qualified marine biologists under the direct supervision of an officer of the National Parks and Wildlife Service.

Impacts during operation included:-

- . Shading of coral;
- . Damage from mooring chain movement;
- . Damage from snorkeling, coral viewing, reef walking;
- . Collecting;
- . Disposal of wash water;
- . Effects of fish feeding.

Impacts during operation have been minimized by a number of operational procedures, limitations imposed both by the operator and the authorities and general care and attention to detail.

For example:-

- . sewerage effluent and all solid waste is taken ashore for disposal;
- . all coral in shade footprint has been transplanted;
- . coral in the anchor and anchor chain corridors have been transplanted;
- . an extensive educational program, and trained guides and observers ensure snorkeling, coral viewing and reef walking are confined to specific areas and paths, collecting is prohibited etc;
- . environmentally unacceptable antifouling paint is not used;
- . fish feeding occurs by releasing the food well below surface level to prevent the attraction of seagulls.
- . the pontoon is moved to a cyclone mooring whenever a cyclone alert reaches predetermined levels;
- . procedures and precautions are in hand for accidents such as fuel spills, equipment failure, fire, collision, explosion, weather, etc.

4.0 STRUCTURE

As previously mentioned, the pontoon structure and its anchoring system had to be checked for acceptability at the exposed location and in order to gain Lloyds Classification.

The pontoon itself consists basically of a rectangle fabricated from 1.5m diameter x 8mm wall thickness steel tube, strengthened by 8mm plate stiffener frames at 1.2m centres throughout. One end transverse compartment consists of a steel underwater observation chamber for viewing of the adjacent coral and fish.

Two basic design weather conditions were considered:-

- (a) Cyclonic winds combined with current and impulsive wave forces; and
- (b) Breaking - wave forces.

To establish significant wave heights, two techniques were used.

Firstly, use was made of cyclonic wave hindcasts for the Masthead Reef vicinity carried out by Dr Mike Gourlay of the University of Queensland and Mr Charles McMonagle.

Cyclone	Date	Time	H_s	Tav.	T_p	Dir.
Dinah	27/1/67	02.15	4.32	7.46	7.17	339
Fiona	21/2/71	23.30	2.52	5.46	5.96	314
Daisy	9/2/72	15.00	5.07	7.96	8.46	355
Emily	1/4/72	03.00	3.51	6.53	7.14	329
Zoe	9/3/74	13.00	2.41	5.25	5.56	327
David	19/1/76	14.00	2.84	5.58	5.61	294
David	19/1/76	21.00	2.86	6.05	7.11	287
Beth	21/2/76	13.30	2.36	5.13	5.54	314
Simon	25/2/80	07.30	3.72	6.33	7.05	185??

Where: H_s = significant wave height (metres).
 Tav = Average wave period (seconds).
 T_p = Peak energy wave period (seconds).

In addition, the design storm surge at the site was calculated as 3.3m.

Secondly, the traditional methods of wave forecasting, based on:-

- . wind velocity,
- . wind duration, and
- . fetch distance

were used.

For non cyclonic waves, the US Army Coastal Engineering Research Centre "Shore Protection Manual" was used.

For cyclonic waves, Design Wave Characteristics for Tropical Cyclones in the Australian Region by R L Nelson was the text. Analysis based on these texts, and cross checked against hindcasting by Gourlay/McMonagle led to design criteria of:-

	<u>Non Cyclonic</u>	<u>Cyclonic</u>
Wind Speed	75 knots	110 knots
Wave Height	7.3 metres	9.0 metres
Wave Period	11.1 seconds	12.5 seconds

All forces have been applied in three directions viz:-

- (a) Abeam;
- (b) Fore and Aft; and
- (c) Shoulders/Quarters.

The hull structure has been analyzed in two wave support conditions viz:-

- (a) spanning between wave crests at extreme ends; and
- (b) straddling a single central wave crest and unsupported each end.

Early analysis of the pontoon and mooring system showed that the hull and mooring system were competent to withstand all applied force combinations except that of a wave breaking on the beam. The forces from a breaking wave or cyclonic winds on parts of the superstructure elements would certainly be destructive. The mooring system is such as to restrain the pontoon on all four corners.



To take best advantage of the coral and local currents for boat activities, the pontoon is moored with its long axis NE - SW and its short axis SE - NW. This places the major beam directly into the NW, the direction from which maximum waves are generated. In all other directions, the site is protected by reefs and islands.

On the Wistari Reef site, it therefore became necessary to install a cyclone mooring in adjacent deep water outside the breaking wave zone in the wave climate profile anticipated, and to plan to move the weather conditions in the region are predicted to exceed preset values. These predictions are provided by the Australian Bureau of Meteorology Cyclone Strike Probability Service, in the form of a percentage probability that wind speeds will exceed preset values within the coming 36 hours.

This service commences at a time when the probability of winds in excess of a predetermined velocity at the site within 36 hours is 1%. The three hourly updates then continue until the probability no longer exists.

If...

- . the probability of winds exceeding 50 knots exceeds 70%,
 - . the cyclone path is adverse, and
 - . the maximum wind speed in the cyclone exceeds 70 knots,
- the TOW decision is taken.

5.0 INSTALLATION

In preparation for the installation of the pontoon the immediate footprint of the pontoon together with a strip 4 metres wide around each side of the pontoon, the position of the anchors, the alignment of the anchor chains together with a strip 2 metres each side of the anchor chains, were all cleared of live coral by transplantation. Much of the coral transplanted was able to be moved by hand by the marine biologists working with scuba gear. For the larger pieces, airbags were used as lifting devices and large coral sections were gently prized away from the surrounding sand bed, lifted by airbag and shifted from the anchoring position to a temporary site some distance away. After the installation these large coral pieces were returned to the south east corner of the pontoon where they added to the existing coral to form an enhanced coral garden immediately visible to the underwater observatory.

The need for careful planning, attention to the detail of how the pontoon was to be received, taken over from the tug, attached to the anchors and finally secured in position, and the need for skilled seamanship to prevent grounding of the tug and/or the pontoon were all prerequisites.

By the afternoon of Easter Saturday 1989 the pontoon was secured in its final operation position and preparation began to make it ready to receive its first visitors. Some time later the cyclone anchorage was installed using similar techniques so as to avoid damage to any of the adjacent coral.

After all systems had been checked the first paying guests arrived at the pontoon on the high speed passenger catamaran Reef Adventure II on the 30th of April 1989. Since then the pontoon has been operating successfully as a commercial venture and a large number of day visitors has had the opportunity to enjoy the beauty of Australia's Great Barrier Reef.

6.0 INSERVICE MONITORING

As part of the approval process a condition imposed on the installation of the pontoon by the Great Barrier Reef Marine Park Authority following the completion of the preliminary site selection and site environmental study, was that a baseline study be established at the site and that an ongoing environmental monitoring programme be introduced in order to assess, over time, the effect which the pontoon had on the environment. The baseline study conducted by approved marine biologists was such as to produce a complete coral map of the area and a complete fish survey of the area.



In addition two remote sites were selected as control sites to monitor variations which were independent of the pontoon itself. These two sites were located, permanently marked, and were also accurately mapped for both coral and fish populations.

As part of the baseline study each outcrop of coral was tagged and catalogued. Additionally each outcrop was photographed to show its position relative to the pontoon and anchor lines and as a series of closeups using a one metre square grid to provide a scale. The grid was fitted with a photographic standard colour spectrum enabling accurate colour correction.

A balanced three factor analysis of variance performed on the resulting data for total percentage cover indicated that:-

1. there was no significant difference between the pontoon and control sites;
2. there was a significant difference between zones (footprint, north anchor line, east anchor line, etc.);
3. there was a significant difference between strata; and
4. samples within strata were not significantly different.

An Anova table was generated. Cochran's homogeneity of variance test was applied prior to analysis of variance: data was analysed untransformed.

Data pertaining to percent cover by species was collated in readiness for similar analyses based on sampling over time. This will provide an indicator of change-over-time in community structure.

At the time of preparation of this paper one subsequent site study has been completed and the data obtained from this study has been compared against the baseline data. To date no significant variation from the baseline state has been determined and no remedial works or procedures have been found to be necessary. Already some of the acropora which had suffered minor damage is showing remarkably good recovery and regrowth.

So the final word is the area is alive and well, and the facility and Heron Island well worth a visit.



APPENDIX - BIBLIOGRAPHY

Some 31 references were used in the environmental studies alone. Many of these were papers reporting specific environmental studies of particular elements of the ecosystem. Additional references for the mooring and structural analyses were:-

Dexter P.E. and Watson K.B. - "A Climatology of Extreme Wave Heights in the Australian Tropics." Australian Meteorological Magazine Vol. 24 No. 2, June 1976, pp 59 to 72.

Nelson R.C. - "Design Wave Characteristics for Tropical Cyclones in the Australian Region." Civil Engineering Transactions, I.E.Aust., Vol. CE14, No. 1, April 1972, pp 37 to 41.

Quinn A.D. - "Design and Construction of Ports and Marine Structures New York" McGraw-Hill, 1961.

Remery, G.F.M. and Van Oortmerssen G. - "The Mean Wave, Wind and Current Forces on Offshore Structures and Their Role in the Design of Mooring Systems." Proceeding Fifth Annual Offshore Technology Conference, Houston, Texas, 1973, Paper Number OTC 1741, pp 1169 to 1184.

U.S. Army Corps of Engineers - "Shore Protection Manual" Coastal Engineering Research Centre, Washington D.C., 1975.

SALT INTRUSION IN TIDELESS ESTUARIES

Ewa JASIŃSKA¹

ABSTRACT

The data of several field measurements performed in different types of estuaries along the Polish Baltic Coast are presented here. The results of measurement showed how unsteady and changeable the flow conditions and the motion of salt water in tideless estuaries are. The salinity and velocity distributions in the tested estuaries demonstrate that the change of current direction occurs at different depth and different times. It has been stated that the dynamics of the flow in tideless estuaries is similar to that of the tidal estuaries. A method of determination of longitudinal dispersion coefficient for tideless estuary is presented. The results from calculations for tidless estuary using a threedimensional estuary model previously developed for tidal estuaries are presented.

1 INTRODUCTION

Most rivers enter the sea at the place where there is enough tidal rise and fall to modify flow near their mouths. The area where there is an interaction between river and sea waters is called an estuary. This paper deals with a penetration of salt waters into tideless estuaries which are typical of the Southern Baltic Coast.

Distributions of salinity and velocity in tideless estuaries are primary determined by variation of water level at both extremes of the estuary, flow rate, density of fresh and salt water and the geometry and bathymetry of water bodies. They are also affected by wind and wave and sometimes by the Coriolis force. The interaction of fresh and salt water in estuaries provides a circulation of water and transport typical of each estuary. The circulation and transport in estuarine waters are generally turbulent and time-dependent and often have threedimensional character. The relation between magnitudes of barotropic and baroclinic horizontal pressure gradients has a vital importance to the flow characteristic. The prediction of changes in salinity distribution in each estuary, caused by changes of some above mentioned parameters is a problem that often arises. The forecast requires the recognition of the physical processes and forces taking place in the estuary.

Some results of testing relevant physical processes by field measurements and numerical simulations in estuaries along the Polish Baltic Coast are presented in

¹ Ph.D., Institute of Hydroengineering Polish Academy of Sciences, Kościarska 7, 80-953 Gdańsk, Poland

this paper. To describe the above mentioned processes field measurements were conducted in the following estuaries: Odra, Łeba, Łupawa, Piaśnica and Wisła (Fig. 1).

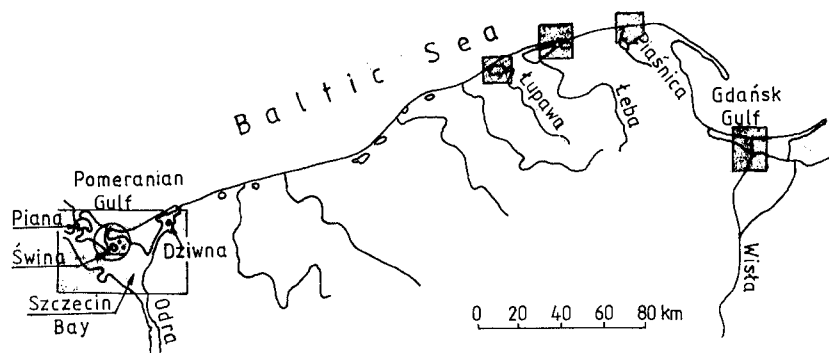


Fig. 1 Estuaries along the Polish Baltic Coast

It is proved that a profound knowledge of the hydrodynamic conditions and the character of motion of salt water in the estuaries are very important to water quality observation in these areas. A method of determination of the longitudinal dispersion coefficient for a tideless estuary and some results of calculations using a three-dimensional baroclinic model adapted for the Odra estuary are also presented in the following sections.

2 CHARACTER OF FLOW AND SALT INTRUSION

The problem of intrusion of salt waters and character of flow was tested by the Institute of Hydroengineering in Gdańsk. It was done for several different types of estuaries along the Polish Baltic Coast. In this paper as the example is presented the data for two estuaries: Odra and Łupawa, whose size and topography are quite different. The Odra estuary (Fig. 1) is a very complex system in the western part of the Polish Baltic Coast. The river Odra flows into the sea through Szczecin Bay and three straits: Piana, Świna and Dziwna. The straits connecting the Szczecin Bay with Pomeranian Gulf, part of the Baltic Sea. The total area of Szczecin Bay together with the straits is 910 km². The area of the bay is 686.9 km² and the length of its coast line is about 243 km. The greatest extension of the bay along the east-west axis is around 50 km, the smallest width 7.8 km. Depths are small, except in the central part, where the depth reaches 6 m. Through the bay runs the navigational channel from Szczecin to the Baltic Sea which has a mean depth of 10 m and is 250 m wide (Jasińska et al. 1988).

The water exchange between the bay and the sea through the straits varies from one to another and depends on the water level differences on the ends of straits and meteorological conditions. The water levels in Pomeranian Gulf are mainly caused

by storm surge and in extreme situations they changed in range + 1.96 m and - 1.34 m. The tide range in the Baltic Sea in this region is around 0.04 m and is negligible. The velocities of the water rise may reach 0.20 m/h and about 1 m within 10 – 12 hours. Water levels in the Szczecin Bay oscillated from + 1.29 m to - 0.72 m. Average water level in the Szczecin Bay is a little bigger than in the Pomeranian Gulf.

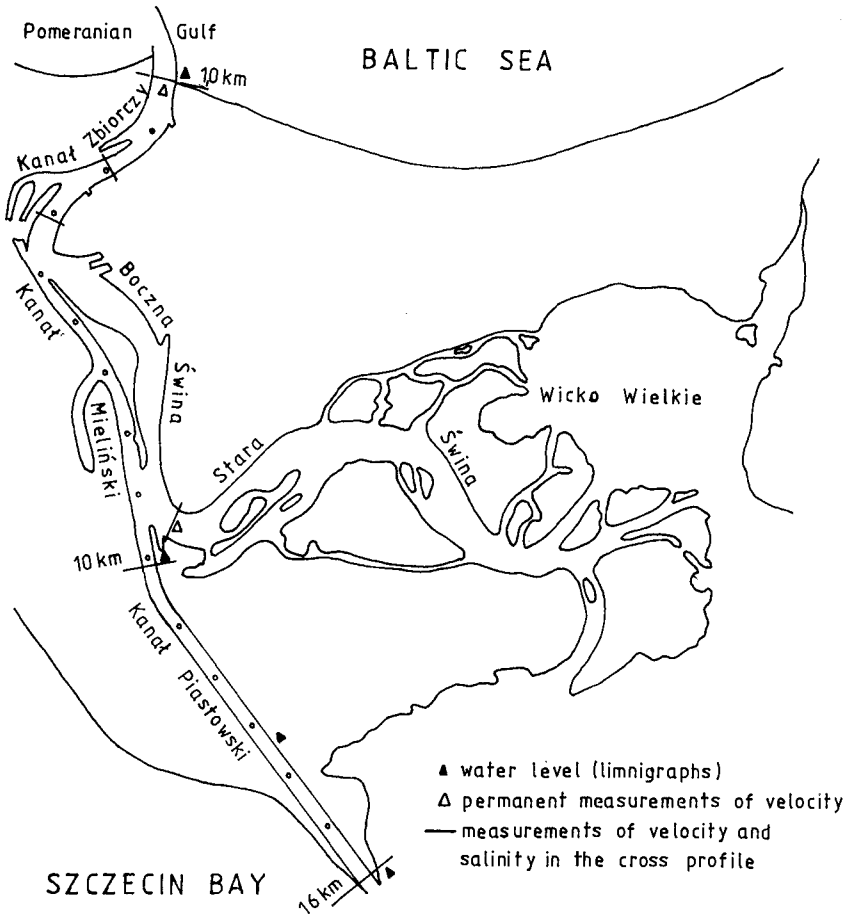


Fig. 2 The Świna Strait

The Świna Strait (Fig. 2), the main connection of the Szczecin Bay with the sea, consists of natural canals and man-made canals. Its length is 16.3 km and water areas are 13.2 km². Particular part of Świna Strait are of the following depths: Kanal

Zbiorczy (KZ) 15 – 17 m (at some places up to 21 m), Kanał Mieliński (KM) 10 – 12 m, Kanał Piastowski (KP) 10 m and Boczna Świna and Stara Świna 5 – 6 m.

The field measurements mainly concerned the water level and the distributions of velocity and salinity in so many points as possible. Very interesting results were obtained from continuous registration of velocity and water level during a longer period of time. In the analysis of the measurement data (Jasińska 1987) cyclic changes of the directions and values of currents and the distributions of salinity were noticed. Small changes of the water level and of its slope (Δh) caused a considerable oscillation of the value and direction of the velocity and in the distribution of salinity (Fig. 3).

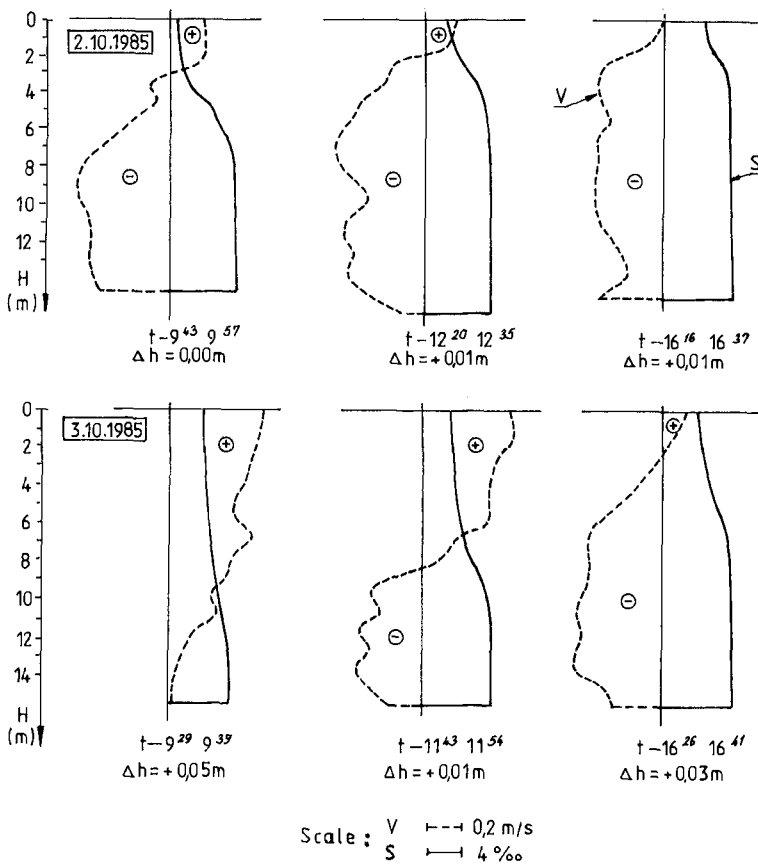


Fig. 3 Distributions of salinity and velocity at the small Δh in the Świna Strait

The strong inflow changed the conditions of flow and salt water filled the whole Świna Strait (Fig. 4) and also the part of Szczecin Bay within a short time.

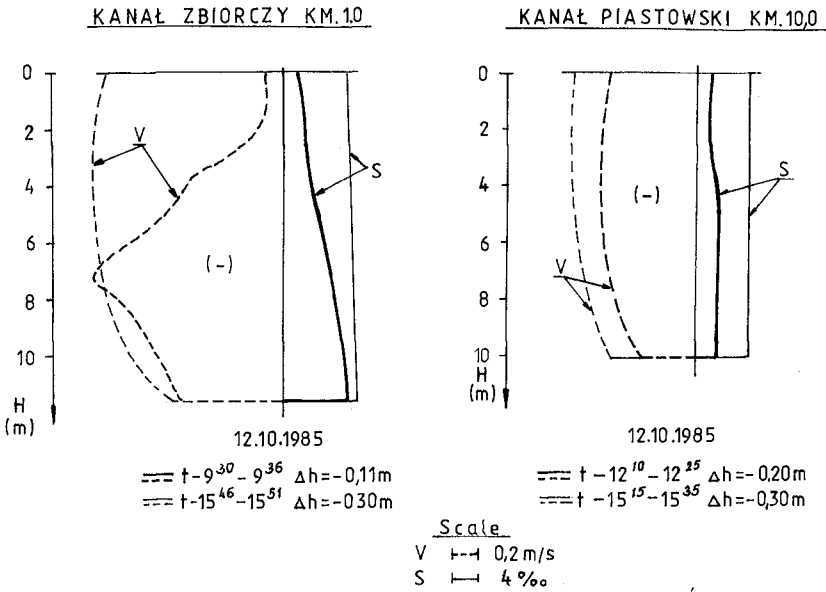


Fig. 4 Distributions of salinity and velocity at strong inflow in the Świna Strait

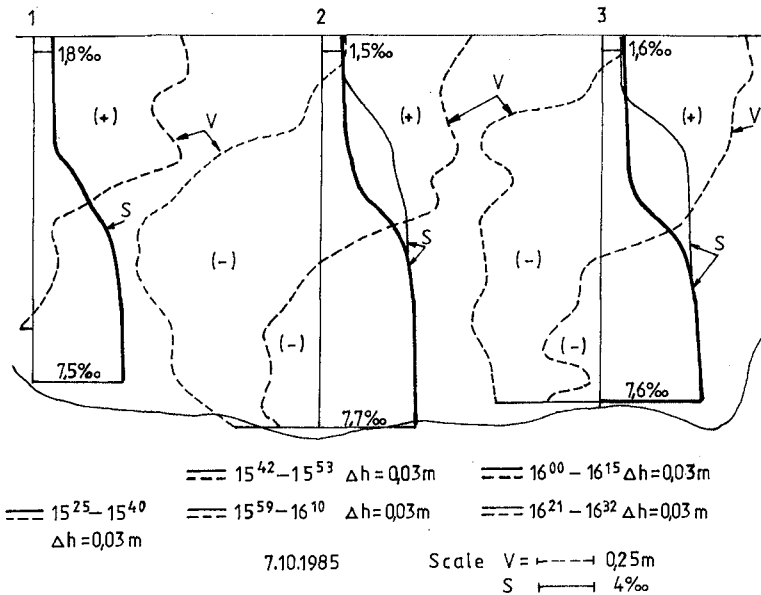


Fig. 5 Example of dynamic changes of flows and water salinity in cross-section, KZ - 1.00 km

Dynamic changes of flows are reflected in changes of water salinity (Fig. 5). As a result of a systematic increase of slope the salt water was gradually displaced out of the surface layers. Between 16.00 and 16.30 a sudden change in water salinity as well as in velocity was recorded within a few minutes. Measurements were taken directly succeeding one another and in vertical 3 an increase in the thickness of the salty layer from 5 m to 10 m (from the bottom) was recorded. The difference of water level between the two end of estuary changed from 0.0 m to 0.05 m and it was a typical example of salinity and velocity distributions under conditions of twodirectional flow of unsteady character.

When the water level difference between the sea and the bay under calm weather conditions is smaller than about 0.05 m the baroclinic pressure gradient has the main effect on the current causing two layer stratified flow. When the differences (Δh) are bigger than ± 0.05 m there is an outflow or inflow, when the differences are between $+ 0.05$ m and -0.05 m may take place outflow, inflow or twodirectional flow.

Sometimes fronts between the salt Baltic and the brackish bay water in horizontal and vertical plane appear. As a result of the intensive turbulence after inflow the salinity gradients in the vertical plane quickly disappear.

The Lupawa estuary is located in the middle part of the Polish Baltic Coast. In the lower part of the Lupawa river (Fig. 6) there is a shallow lake Gardno. The two km long section of the river joins the lake with the sea. Between the bridge (500 m from the mouth) and the sea there is a fish harbour Rowy. The river in this part is a harbour chanel with concrete walls on both sides. There is continuous dredging work in this region because of the strong sedimentation in the river mouth. The depths are 1.5 m to 2.0 m and the average width is 20 m.

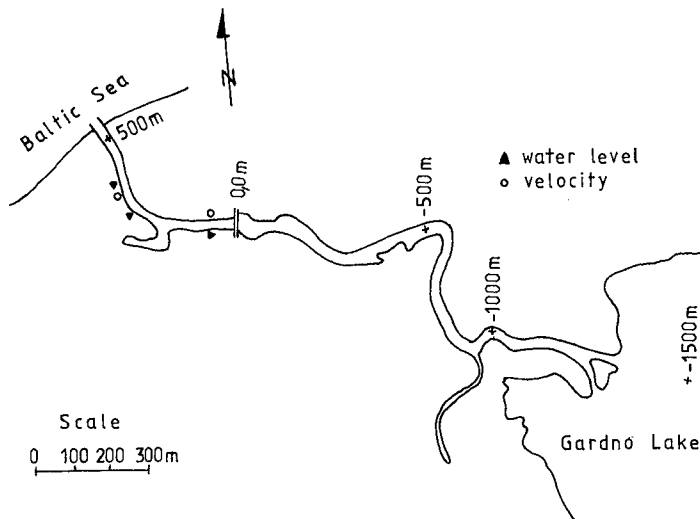


Fig. 6 The Lupawa estuary

The measurements were carried out in May 1989 in the area between the lake and the sea. In Fig. 6 there are shown profiles and verticals where the measurements

were performed. The water levels in the lower part of the Łupawa during the measurements and in the period before were slightly changeable but had an oscillating character. The periods of oscillation were from a few minutes to several hours. The water level difference between the bridge and the sea were very small from + 0.12 m to - 0.03 m but most of them were close to zero. In May and particularly at the time of expedition winds were weak but changeable in their directions.

In spite of such small variations of water level and weak winds very substantial changes of flow conditions with strong inflows of salt waters into Łupawa estuary were noticeable. The flows were noticed in the whole profile towards the sea or towards the Gardno lake. The two-direction flows with a wedge of salt water were observed too. The existence of homogenous fresh or salt water in the whole profile was noticed. There were also completely or partially mixed waters with stratification. The salinity of the water in the Łupawa estuary changed from 0.8‰ to 9.2‰ (Jasińska 1990).

As an example of the penetration of salt water into the Łupawa estuary the situation observed on May, 15th is presented (Fig. 7 and Fig. 8). At the almost zero gradient of the barotropic pressure there was a typical baroclinic inflow. At 8 o'clock in the morning there was a beginning of a set of measurements in the profiles and verticals. The measurements were started in profile 400 m towards the bridge, the velocities were small up to + 0.10 m/s, the salinity of water was about 1.2‰ in the whole area (Fig. 7). The wind was from NE with the velocity from zero to 2 m/s. Because of the observed change of flow conditions at 9.40 a set of continuous measurements was begun. It was made in profile 230 m in the vertical near the west pier.

During the first period only the salinity and water temperature were measured because the velocities were close to zero. The time of measurements in the whole vertical ($H = 1.90$ m) every 0.20 m was about three minutes. The inflow with the salinity changing at the bottom from 1.2‰ to 9‰ (Fig. 8) was registered. The conditions were changing very quickly and the whole process lasted to 11 o'clock. The velocities increased up to - 0.15 m/s at the bottom, but at the surface they were still close to zero. The water slope was almost constant close to zero and all the time was towards the sea. It appears from the continuous registration at profile 310 m that the direction of the flow was changed and it took place at 9.40 and again at 12.40 and the velocities were about - 0.10 m/s.

After 11 o'clock there was a gradual decrease in salinity in profile 230 m. The velocities there were close to zero. At 11.10 a new set of measurements was begun in the longitudinal profile in the Łupawa in order to define the range of inflow. The salt water filled the whole cross section of the Łupawa up to the profile 310 m (Fig. 7), further the salinity gradually decreased in the surface layer but at the bottom it was still about 9‰ in the distance - 100 m (above the bridge). The velocities changed from - 0.20 m/s near the sea to zero in the region of the profile 60 m. They were two-directional above the bridge. The water slopes were still very small.

The similar situations repeated a few times during the measurements. These results confirmed the intrusion of salt water into the tideless estuaries in spite of small variations of water level in the sea.

On basis of the results of field measurements the classification of the tested estuaries was performed. The estuaries are classified according to two basic quantities:

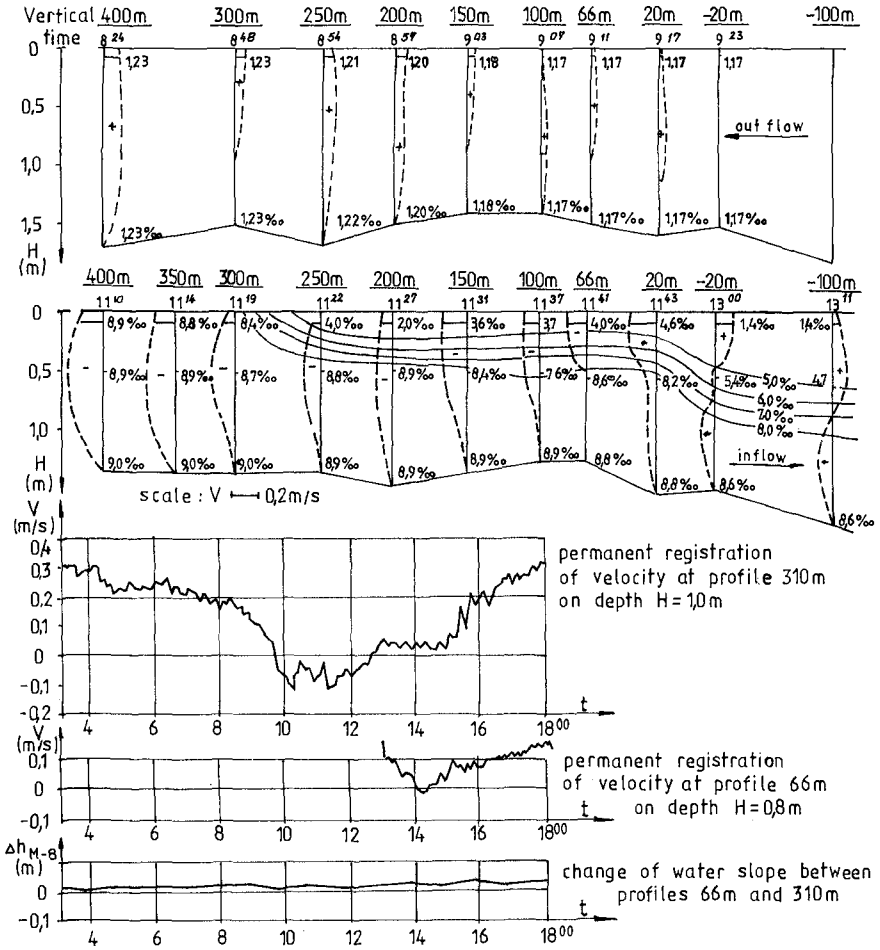


Fig. 7 The change of conditions of flow and salinity in the Lupawa - 15.05.1989

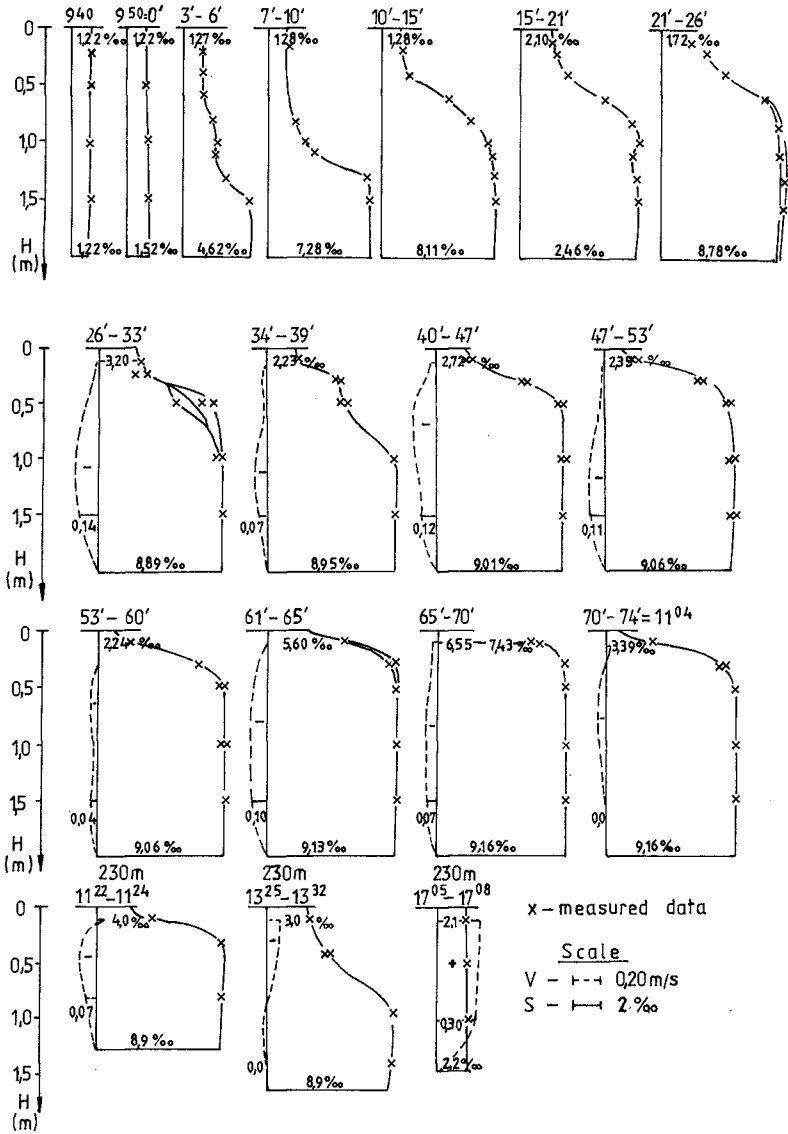


Fig. 8 The baroclinic inflow of salt water into the Lupawa - 15.05.1989

topography and structure of salinity. The estuaries along the Polish Baltic Coast are well or partially mixed and also temporary highly stratified with a salt wedge. The type of an estuary may change when there are changes in the river flow or in the dynamics of the inflow of the salt water.

3 RESULTS OF NUMERICAL SIMULATION

Parallely to the field measurements theoretical analysis and calculation based on one- two- and three- dimensional numerical models were carried out. First results were obtained from the onedimensional model. For this calculation it was necessary to determine the longitudinal dispersion coefficient. A method of determination of the longitudinal dispersion coefficient for a tideless estuary (Jasińska 1983) has been based on the Ippen and Harleman's (1961) approach made for a tidal estuary. The analysis of the field data has exposed a new dimensionless parameter L_u

$$L_u = \frac{D_o}{v_f Z}$$

where: L_u - the Estuary Number, D_o - the dispersion coefficient at $x = 0$, v_f - the fresh water velocity, Z - the distance in the seaward direction, where the salinity is equal S_o - sea water salinity. During an analysis of the field data it was found that the Estuary Number maybe correlated with the dimensionless values \bar{S}/S_o , v_f/v_s and Z/D charakterizing the estuary and its processes, where \bar{S} - instantaneous salinity averaged over the cross-section, v_s - the salt water velocity, D - the depth in $x = 0$. The correlations (Fig. 9 and Fig. 10) were established for the conditions of tideless estuaries along the South Baltic basing on the results from the field measurements of Leba and Dziwna. The effect of estuary depths, fresh water flow rate and changes in salt water in the flow into the estuary on the dispersion coefficient may be described from these correlations.

The complexity of the hydrodynamic regime and their threedimensional characteristics require the use of a threedimensional model in order to get better results. For the Odra estuary a threedimensional baroclinic model of high resolution in the vertical and horizontal plane (Duwe et al 1983, Pfeiffer and Duwe 1987) has been used for the simulation of hydrodynamic conditions and the movement of salt water. The adaptation and verification of this model were done for the Odra estuary (Jasińska and Nöhren 1988) using the data of the above mentioned measurement. The calculations were done in cooperation with the Institute of Oceanography Hamburg University. This model takes into account the horizontal momentum equations, the continuity equation, the transport of salinity and an equation of state. Hydrostatic equilibrium, kinematic boundary conditions at the free surface and Newton-Taylor bulk - formulas for wind stress and bottom friction are applied additionally. Detailed description of the model and its numerical scheme were done by Duwe et al. (1983).

The area of the model extends over the straits of Piana, Świna and Dziwna, the Szczecin Bay and the Odra to Gozdowice. The horizontal grid size of the rectangular net is 250 m as the main waterway through Szczecin Bay is 200 m to 300 m wide. In the vertical there are eight layers with a thickness of 2 m each. The time step is chosen to be 600 s, which is sufficient to resolve the dominant oscillations.

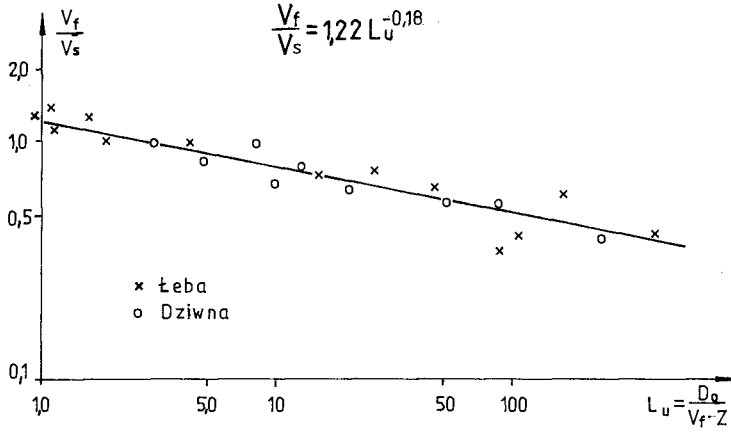


Fig. 9 Velocity distribution vs L_u

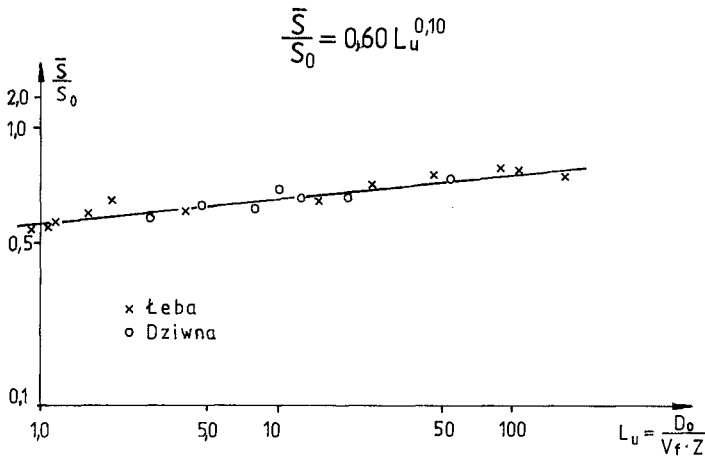


Fig. 10 Concentration vs L_u

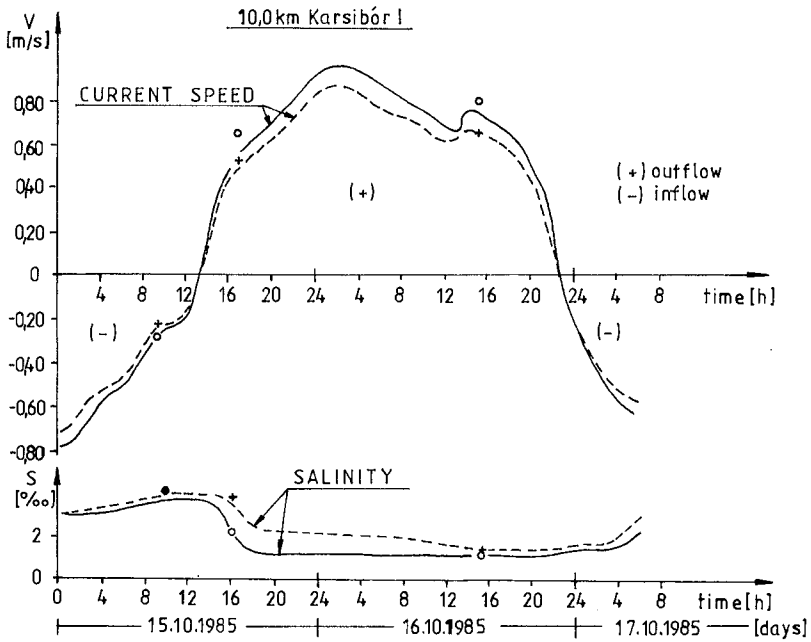
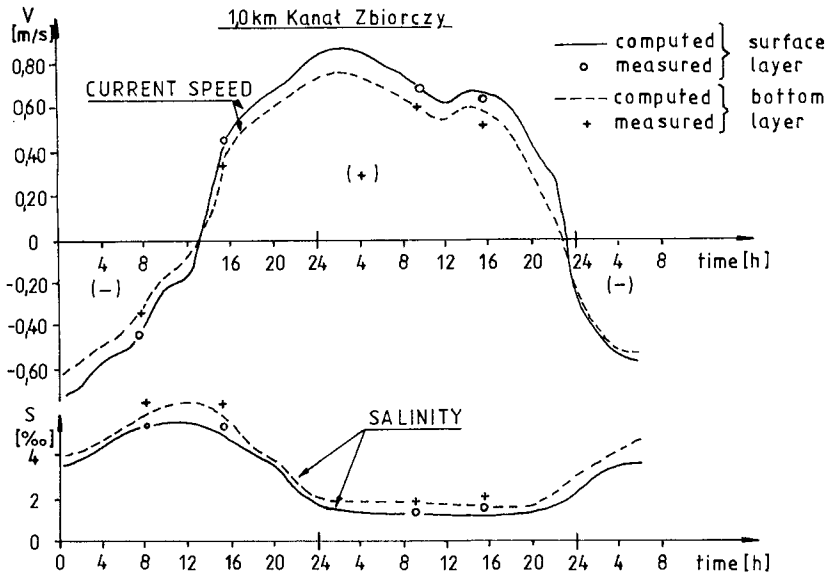


Fig. 11 Changes of salinity and velocity at points KZ - 1 km and KP - 10 km

As a boundary conditions water level elevations and time dependent vertical salinity distributions were given at the boundary to the Baltic Sea (the mouth of Piana, Świna and Dziwna). At the landward open boundary the Odra discharge in Gozdowice was given. For the wind field, the data set was taken from the measurements in Świnoujście and was assumed to be uniform in space.

The comparison of the computation with the measurement data showed a good accordance, some results are present in Fig. 11. In the figure time series of velocity and salinity in the surface and bottom layers for the points Kanal Zbiorczy - 1.0 km and Karsibór 1 - 10 km are shown. The difference between measured and computed results is small. The measured velocities, their values and directions, are correctly reproduced by the computation. The agreement between measured and computed values for the salinity is also very good. There is a very well reproduced change of salinity in the vertical as well as in longitudinal direction.

Summarizing the results of calibration and verification it can be concluded that generally the flow phenomena and the motion of salt water in the Odra estuary are well reproduced by this model. The results will be applied to determination of boundary conditions for more detailed model of the subarea of the Odra estuary which is now being made in the Institute of Hydroengineering in Gdańsk. In future the model will be improved by additional data from field measurement and numerical studies in order to get a better insight into the dynamics of estuaries along the Polish Baltic Coast and possibility of forecast.

4 CONCLUSIONS

The above described study increased considerably the knowledge of the circulation and the transport processes in the tideless estuaries along the Polish Baltic Coast. It has been stated that the dynamics of the flow in tideless estuaries is similar to that of the tidal estuaries. In spite of very small changes in the gradients of barotropic pressure and of weak wind there are significant changes in the flow conditions. The intrusion of marine waters appeared not only at a storm surge but also during calm weather conditions. During calm weather a weak balance of the barotropic and baroclinic pressure gradients is present which yields changeable inflow and outflow conditions. Under these conditions the intrusion of salt water in the tested estuaries is probably caused by the change of pressure conditions above the Baltic Sea. It is very difficult to define and predict the flow conditions when the water slope is small what happens very often. Under such conditions there may be an outflow, inflow or two-directional flow.

The continuous measurement showed how unsteady the flow conditions are. The velocity and salinity distributions in the tested estuaries demonstrate that the change of current direction occurs at different depth and different times, thus there is a need of threedimensional numerical modelling. The applied threedimensional numerical model reproduces the flow phenomena and the motion of salt water in the Odra estuary very well.

The model can be advised for design and exploitational purposes as well as for the analysis of transport problems. It is planned to develop a separate section model for the Świna Strait with the boundary conditions obtained from the whole Odra estuary model which has been already verified.

REFERENCES

- Duwe K.C., Hewer R.R., Backhans J.O., 1983. *Results of a semi-implicit two step method for the simulation of markedly nonlinear flows in coastal seas.* Continental Shelf Research Vol. 2, No. 4, pp. 255-274.
- Ippen A.T., Harleman D.R.F. 1961. *One dimensional analysis of salinity intrusion in estuaries.* Technical Bulletin 5., Committee on Tidal Hydraulic, Corps Eng. U.S. Army.
- Jasińska E. 1983. *On longitudinal dispersion coefficient for tideless estuary.* Hydrotechnical Trans. Vol. 49, pp. 35-44.
- Jasińska E. 1987. *Distribution of currents and salinity in the Świna Strait,* Hydrotechnical Trans. Vol. 49, pp. 185-196.
- Jasińska E., Nöhren J. 1988. *Adaptation and verification of a highresolving three-dimensional baroclinic numerical model of the Odra Estuary.* Proc. of the 3rd German-Polish seminar (in print).
- Jasińska E., Robakiewicz W., Walkowiak A. 1988. *Hydrodynamics of Zalew Szczeciński and adjacent Straits.* Hydrotechnical Trans. vol. 50, pp. 96-106.
- Jasińska E. 1990. *The structure of flows and salinity of waters into the Lupawa estuary.* Unpublished data material of IBW PAN Gdańsk.
- Pfeiffer K.D., Duwe K.C. 1987. *The brackish water zone of the Elbe estuary; Measurement and model results.* Hydrotechnical Trans. vol. 49, pp. 197-215.

CHAPTER 218

COASTAL LAGOON ENTRANCE DYNAMICS

A D GORDON¹

1. INTRODUCTION

The coastline of New South Wales (NSW), Australia features numerous lakes and lagoons. The ocean entrances of the lakes tend to be continuously open to the sea. The lagoons, however, experience only intermittent periods of ocean influence following breakouts across the beach. Although the lagoons and their catchments vary markedly in size and overall geometry their hydraulic behaviour is remarkably similar. This is particularly true of their entrance dynamics.

The lagoons, which are the subject of this paper, were formed during the Holocene sea level rise in embayments where the onshore movement of sand impounded small estuaries behind the coastal sand barriers (Roy 1984). They are generally 1 to 2m deep, have a water surface area of between 3 and 300 ha and are located in catchments ranging in size from 5 to 40 km².

The main lagoon water body is generally located immediately landward of the ocean beach and foredune system. It can become connected to the sea if the sand barrier is breached by natural or mechanical means. Following barrier breaching the lagoon becomes tidal

¹Manager, Manly Hydraulics Laboratory, Public Works Department, NSW, Sydney, Australia.

until, after a time, the entrance is resealed with a sand plug transported into the mouth by the interaction of ocean tide and wave processes.

Because there has been a history of building waterfront housing on the shorelines of these lagoons, social pressures have developed for the control of both lagoon water quality and of the low lying land around the lagoon.

These issues can be related to the lagoon water balance and entrance behaviour. The more frequently the entrance is open to the sea, the better the water quality and the lower the frequency of high flood levels. The desire for lagoon management has in turn generated a need to develop a better understanding of the processes governing entrance dynamics and lagoon water level behaviour.

2. FIELD STUDIES

Studies of both the lagoon water balance and the entrance behaviour were commenced in the mid 1970's on a small lagoon at Dee Why, a northern beach suburb of Sydney (Gordon 1981). This lagoon has a water surface area of 25 ha and a catchment area of 5 sq km. The catchment is undulating sandstone country, much of which has been developed for residential and commercial purposes. During the studies twenty-five lagoon breakouts and closures were observed, of which five were studied in detail. Information on the lagoon water balance was based on water level data obtained from an automatic water level recorder, a network of rainfall gauges in the catchment and a study of the phreatic line through the dune barrier and beach.

In the mid to late 1980's these studies were extended to a lagoon at Narrabeen, 3km north of Dee Why (Kulmar et al, 1989). Narrabeen Lagoon has a surface area of 250 ha and a catchment of 55 sq km. The catchment is principally sandstone country however only some 30 per cent of the catchment has been developed, the remainder is natural bushland. Between 1984 and 1988 twenty-one breakouts and closures were observed at Narrabeen. Nine of these events were studies of which three of the

breakouts and four of the closures were examined in detail. Lagoon water levels were continuously recorded through the study period by an automatic water level gauge. Rainfall records were available for the catchment from a network of gauges. In addition, weekly photographs of the entrance configuration were taken from a nearby headland which overlooks the entrance.

More recently, information has become available for a larger lagoon (Aber and Downey, 1989). This lagoon is Lake Wollumboola, on the South Coast of New South Wales some 130 km south of Sydney. It has a surface area of 650 ha and its catchment consists of sandy barrier deposits backed by clay slopes. The catchment is mainly natural bushland.

3. MODEL STUDIES

During the late 1970's a three dimensional moving bed model of a lagoon entrance was constructed at Manly Hydraulics Laboratory using fine beach sand ($D_{50} = 0.16\text{mm}$) placed in a 3m x 4m x 0.3m model basin. An entrance sand plug was established and then the water level raised on the lagoon side until overtopping occurred. The "breakout" channel development observed in the model displayed similar characteristics to that observed at the prototype lagoon entrances, however, difficulty was experienced in appropriate selection of model scales to achieve simultude throughout the entire breakout sequence.

4. LAGOON WATER BALANCE

There are two distinct water balance regimes for the coastal lagoons. The first is the tidally dominated condition; entrance open (Figure 1(a)). The second regime is governed by the balance of inflows and outflows which occurs when the entrance is closed (Figure 1(b)).

4.1 Entrance Open

With the the entrance open the lagoon water level behaviour is determined by the tidal forcing at the

ocean entrance and by the occasional flood (fresh water) event. The tidal phase lag and head loss through the entrance channel combine to superelevate the mean daily water surface of the lagoon (see Figure 2).

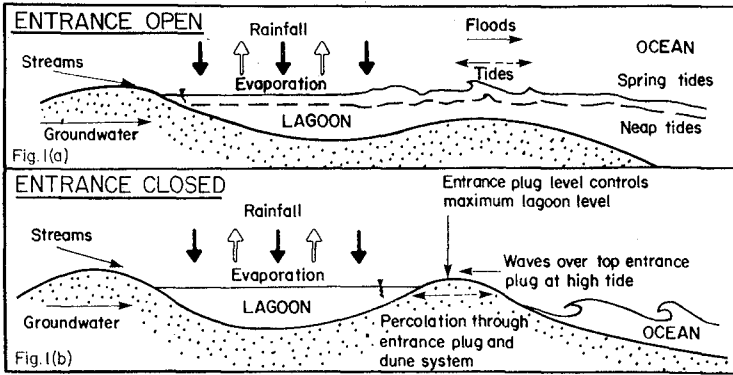


Figure 1 Lagoon Water Balance

The superelevation varies over 28 days from a high during the spring to a low during the neap tide cycles; this spring tide pump-up effect is a subtle but important factor in the ecology and sediment process of the lagoon. During the spring tide period the superelevation typically is of the order of 0.4m while during the neaps it is 0.2m.

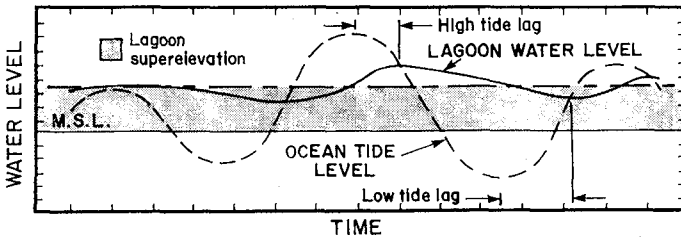


Figure 2 Lagoon Tidal Superelevation

Other factors such as ocean storm events producing storm surge at the entrance and wave setup in the surf zone adjacent to the entrance, can also superelevate the mean water level for a period of days. For the NSW lagoons this can produce an increase of some 0.3m in excess of the tidally induced superelevation.

In addition, there appears to be evidence of a weak seasonal periodicity in superelevation. This is thought to be caused by seasonal variations in mean air pressure due to the northward shift of the low pressure belt during winter and to seasonal changes in the ratio of onshore/offshore winds.

4.2 Entrance Closed

With the entrance closed the mean lagoon water level is dictated by the inflows - stream, groundwater and direct rainfall on the lagoon's water surface; and the outflows - evaporation and percolation through the sand barrier to the ocean (Figure 1(b)). During the period immediately following closure wave overtopping of the entrance sand bar can also provide a short term inflow mechanism. These factors generally produce lagoon water level between 0.8m and 1.4m above mean sea level, with the entrance closed.

Percolation losses through the barrier sand deposit, including the entrance bar is a function of the lagoon water level and the tailwater conditions on the ocean side of the sand barrier. This latter factor is determined by the ocean tide, wave run up and wave set up on the beach. The combined effect of these factors produces an effective tailwater level which is generally elevated between 0.5 and 1.6m above MSL (Figure 3).

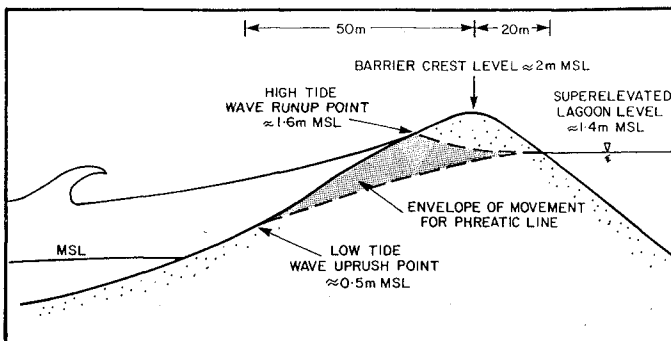


Figure 3 Phreatic Surface

5. ENTRANCE BREAKOUT

Two types of breakout have been observed: mechanical opening using earth moving equipment; and natural breakout. This paper concentrates on the latter mechanism.

Natural breakout is associated with lagoon overtopping of the entrance barrier as a result of rainfall runoff from the catchment. Ocean wave action tends to close rather than open an entrance (Gordon 1981).

For the natural breakout case, three distinct stages have been identified (Figure 4):

- * the initiation channel stage (IC), Froude No. <1
- * the weir/hydraulic jump stage (WHJ), Froude No. >1
- * the river flow stage (RF), Froude No. <1

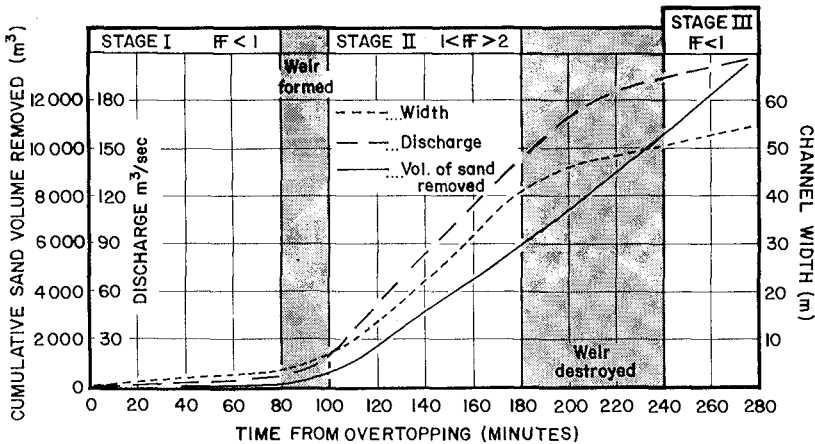


Figure 4 Three Staged Behaviour of Breakout

5.1 The Initiation Channel

At first bar overtopping occurs as a thin sheet. This flow only extends a short distance downslope on the ocean side of the barrier before it is absorbed into the beach. Gradually as overtopping increases a preferred scour channel develops from the crest, down the slope towards the ocean. Once the channel becomes

established bed slope adjustment takes place from the downstream end (Gordon 1981).

In the early part of this first stage the scour rate is low because threshold conditions are only marginally exceeded. As the stage develops however bed ripples, and then small dunes, develop and the Froude No. of the flow approaches unity. The formation of a sand delta at the channel discharge point in the swash zone of the beach, and bank collapses, can result in local slope flattening which produces choking of the channel. At this stage of the breakout flood tide and/or wave conditions may seal the initiation channel causing the breakout to fail, particularly if the runoff from the catchment reduces. If, on the other hand, runoff continues, the scour channel will develop.

For the two lagoons where this process has been repeatedly observed, Dee Why and Narrabeen, the initiation stage generally takes between 80 and 100 minutes. The factors which control time for this stage include: rate of rise of lagoon water level, the differential head between the lagoon and the ocean water level, porosity of beach, width and cross-sectional shape of the barrier at the entrance and the wave conditions. Towards the end of the IC stage the channel width is generally 1 to 2m, the flow depth is 0.2 to 0.25m and the velocity 1.4 to 1.5m/sec.

5.2 The Weir/Hydraulic Jump

Stage two develops quite rapidly. A semi circular weir forms in the sand at the upstream end of the channel, the flow becomes supercritical on the crest and a plunge pool and a series of undulating hydraulic jumps develops downstream. The unsteady downstream flow conditions caused by the undulating jumps initiates a series of bedforms which progressively become steps in the channel (Figure 5). The flow accelerates on the downstream face of these steps and a standing roll wave develops at their base. Bed scour is most pronounced on the downstream face of the steps and hence they are translated up the channel towards the plunge pool. As each step arrives at the plunge pool there is a sudden increase in weir face erosion and hence the weir is

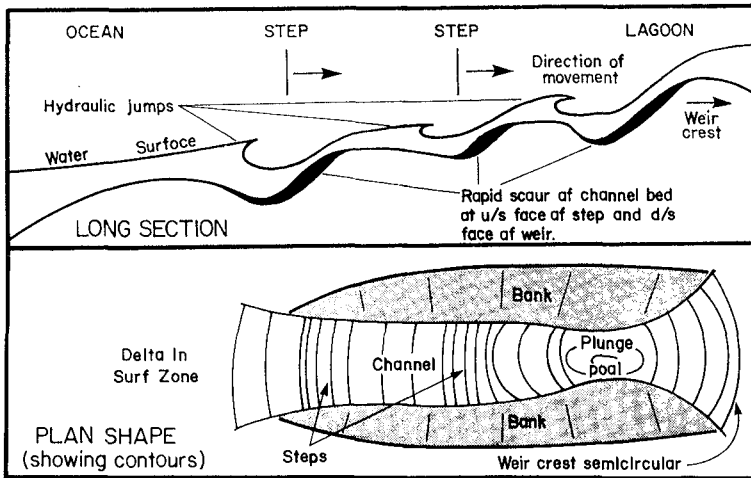


Figure 5 Breakout Channel Geometry

translated further inland. The channel then re-adjusts and a new step forms at the downstream end. Hence channel bed slope adjustment translates upstream from the downstream end.

An interesting feature of the weir geometry is that it is determined by the minimum specific energy condition, that is it forms an efficient dam spillway crest shape (Gordon, 1981). Discharge can be approximated using the weir formula:

$$Q = 3.97LH^{3/2}$$

Where H is the lagoon water level height above the crest and L is the length of the crest.

The principal factors which determine the duration of the WJH stage include: lagoon water level; ocean water level; and the width and cross-sectional geometry of the barrier. Wave action has little impact during the WHJ stage. The outflow is sufficiently energetic that it dominates the normal nearshore surf zone processes.

Velocities in the channel are in the range 3 to 4 m/s with peak short term velocities of 6 m/s. The Froude

No. is generally between 1.2 and 1.8; hence the undulating jump formation. The stage usually lasts between 100 and 140 minutes. Figure 6(a) which is based on data gathered for the WHJ stage of the three lagoons studied, summarises the development in mean channel width downstream of the plunge pool while Figure 6(b) presents the cumulative volume of sand removed over time.

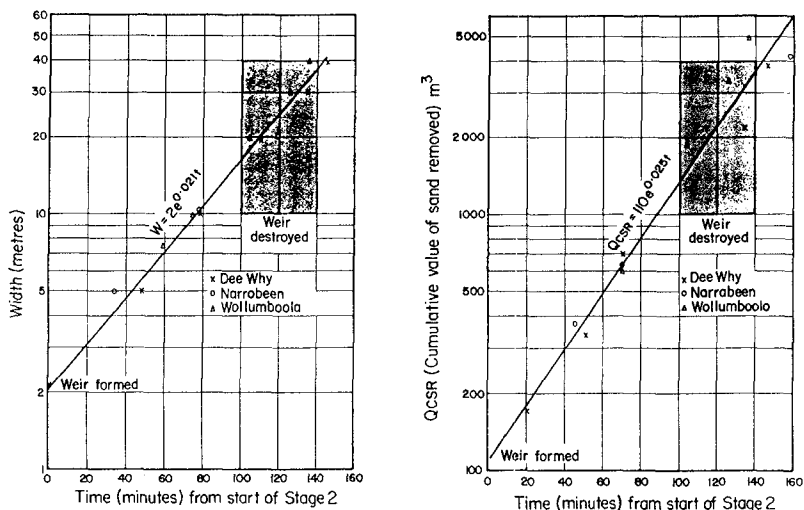


Figure 6 Channel Characteristics, WHJ Stage

5.3 River Flow Stage

The final stage is reached approximately 180 to 240 minutes after overtopping first commences. The weir feature completes its upstream translation through the barrier and disappears. The Froude No. reduces to below unity and a steadier flow regime is established. However, scour of the channel continues for as long as threshold conditions are exceeded. The larger the lagoon and/or the runoff event the greater the final channel width. Of the three stages, this is the only one whose duration is in part dependent on the lagoon and catchment size. As the head level difference between the lagoon and the ocean decreases, the discharge reduces. Within a matter of hours the lagoon becomes tidally dominated and the entrance starts to infill.

5.4 Breakout Sediment Transport

Different approaches are required for the three stages. The IC stage is mainly bedload dominated, transport capacity is rapidly achieved, however, percolation losses into the adjacent beach berm and intermittent bank slumping are important considerations.

Stream flow during the WHJ stage is highly energetic with Froude Nos. from 1.5 up to 2 and is therefore outside the domain of most existing theories. Visser (1988) has developed an interesting approach for dike-burst. Based on a modified Bagnold (1966) formulation, the Visser approach includes an expression for calculation of the progressive sediment load uptake in a channel. The approach can be summarised as:

$$S(x) = \frac{x}{l_a} S_s \quad \text{where } S(x) \text{ is the sediment load transport and } x \text{ is the distance down the slope}$$

$$l_a = \frac{q}{w \cos \beta} \quad \begin{array}{l} \text{where } q \text{ is the discharge per unit width} \\ w \text{ is the fall velocity} \\ \beta \text{ is the slope angle} \end{array}$$

$$S_s = \frac{e C_f u^4}{(1-p)\Delta g w \cos^2 \beta}$$

where e is the efficiency factor

C_f is the bedform drag

u is the depth averaged velocity

p is the porosity

Δ is $(\rho_s - \rho) / \rho$

g is gravity

While the Visser formulation is conceptually attractive, it is highly sensitive to the value of stream velocity. Unfortunately, this variable is the most difficult to measure during the energetic WHJ stage. Coupled with the need to determine relevant values for C_f and e , the velocity sensitivity has to date hampered evaluation of the Visser approach. Further, it is felt that the differences in channel slope (Visser case $\beta = 14^\circ$, Lagoon case $\beta = 1.5^\circ$) and

hence velocities (Visser case $u = 20$ m/s, Lagoon case $u = 4$ m/s) and bedform size (Lagoon channel bedform height ≈ 0.5 depth) requires some modifications of Visser's assumptions to adapt the approach to the WHJ stage.

Sediment transport during the RF stage can be satisfactorily assessed using a traditional approach such as that of Ackers and White (1973).

6. ENTRANCE CLOSURE

Infilling of the entrance channel commences on the first flood tide following breakout. Initially infilling is rapid (Figure 7). During flood tides the wave stirring in the surf zone adjacent to the entrance entrains sediment which is then available to be transported into the entrance by the tide and deposited in the entrance channel. In addition, wave obliquity on the beach face at the entrance combined with wave overwash into the channel across the beach, erodes material from the beach berm and deposits it along the channel edge.

On the ebb tide, however, as the impact of wave stirring on re-entrainment of the sediment in the entrance is limited to the downstream region of the mouth, the outflowing water is unable to achieve a

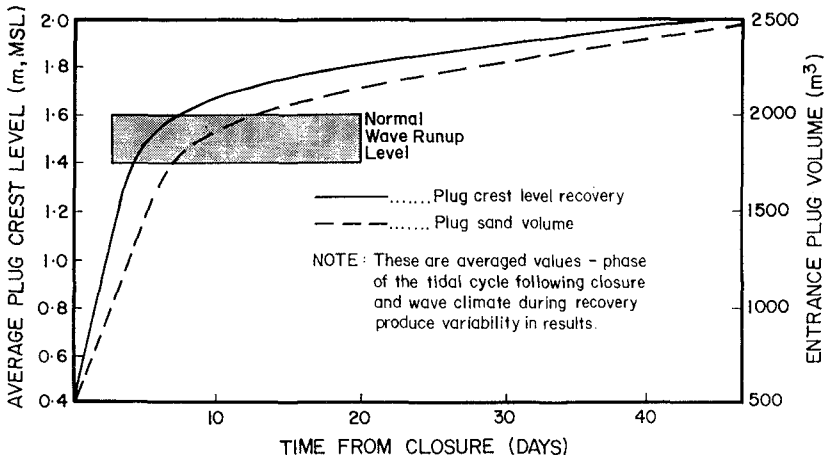


Figure 7 Entrance Plug Re-establishment

matching removal of sand. Thus, there is a net imbalance favouring flood tide transport of sediment into the lagoon. Progressively an hydraulic choke which limits the tidal prism, develops in the entrance.

The flood tide imbalance is exacerbated by the asymmetry of the flood and ebb tidal flows. Flood tides produce relatively high velocities near the peak flow of the tide as compared with the ebb tide which generates longer lasting but lower flow conditions (Kulmar et al, 1989). The relationship between flow velocity and sediment transport being highly non-linear, the flood tide produces a greater transport of sediment than the ebb. Hence the channel trends towards closure under normal oceanographic and meteorological conditions.

As the entrance choke develops, the channel starts to meander across the beach berm. The wave obliquity prevailing at the time causes the channel to be deflected in a down drift direction. The slope of the channel reduces as the meander length increases. This in turn reduces tidal velocities hence entrance shoaling is accelerated.

Because of the relative sensitivity of the entrance behaviour to the prevailing wave and tidal conditions, daily changes in entrance geometry are often significant. These changes are so rapid that to date, numerical simulation of entrance behaviour has not proved a practical proposition for anything other than a short period of time. Winton and Mehta (1981) have developed a numerical model, based on the Bruun approach (1978), which can however be usefully applied to predict the rapid lagoon closure situation associated with storm wave events.

Modelling of entrance behaviour for those lagoons which experience extended periods of opening is further complicated by freshwater flood events; storm surge events; and by the spring/neap pump-up effect. Intermittent freshwater floods produce entrance scour which reverses the normal closure trend. A storm surge and/or wave setup event initially produces a net inflow of water and sediment into the lagoon. However, on the

falling stage it can also result in entrance scour as the lagoon level returns to normal. The spring tide pump-up phenomenon produces a similar effect.

The time a lagoon is open is dependent on the the tidal prism of the lagoon and the gross sediment transport environment of the adjacent beach. At Dee Why the average time the lagoon was open was found to be 17.5 days (Gordon, 1981). While at the larger Narrabeen lagoon the average time was 89.2 days (Kulmar et al, 1989). The sensitivity of entrances to the variable oceanographic and meteorological conditions can be illustrated by examining the standard deviations and range of the times for which the entrances are open. For Dee Why the standard deviation was found to be 13 days and the range was 2 to 44 days. At Narrabeen the standard deviation was 122 days and the range was 5 to 365+ days.

With the channel in a choked condition, closure can occur quite suddenly; commonly over one tidal cycle. Closure is normally associated with any one, or any combination of the following: a flood tide, a storm surge event, elevated wave energy conditions, the spring tidal cycle and low rainfall in the catchment. Once the entrance is closed, the plug rapidly develops over a period of 10 days after which the crest height is at an elevation of 1.4 to 1.6m above sea level; the normal elevation of wave uprush (see Figure 7). After this initial rapid build up the rate of plug development substantially reduces. Aeolian processes take over as the dominant formation mechanism, assisted at times by wave uprush during spring tides and/or storm waves. The plug gradually assumes the geometry of the surrounding beach berm with its crest level at an elevation of between 2 and 3m above mean sea level.

7. DISCUSSION

Investigations to date have concentrated on developing an overall conceptual understanding of lagoon water level behaviour and entrance dynamics. Further studies are planned to examine breakout sediment transport in more detail.

8. REFERENCES

Ackers, P. and White, W.R. (1973) "Sediment Transport : New Approach and Analysis". Journal of the Hydraulics Division Vol. 99 No. HY11, November pp 2041-2060.

Aber, D. and Downey, J. (1989) "Scour Mechanism At Lake Openings On Sandy Coasts". Proceedings 9th Australian Conference on Coastal and Ocean Engineering, Adelaide, Institution of Engineers Australian Publication no. 89/20, pp 93097.

Bagnold, R.A. (1966) "An Approach To The Sediment Transport Problem From General Physics". Geological Survey Professional Paper 422-I, U.S. Government Printing Office, Washington.

Bruun, P. (1978) "Stability Of Tidal Inlets: Theory and Engineering". Elsevier Scientific Publications, Amsterdam.

Gordon, A.D. (1981) "The Behaviour Of Lagoon Inlets". Proceedings of 5th Australian Conference on Coastal and Ocean Engineering, Perth, Institution of Engineers Australian Publication No. 81/16, pp 54-58.

Kulmar, M.A., Hurst, A.M. and Gordon, A.D. (1989) "Narrabeen Lagoon Entrance Study". Manly Hydraulics Laboratory Report 552, Sydney August, 105p.

Roy, P.S. (1984) "New South Wales Estuaries: Their Origin and Evolution". In Thom, B.G., (ed), Coastal Geomorphology in Australia, Academic Press, Sydney, pp 99-120.

Visser, P.J. (1988) "A Model for Breach Growth In a Dike-Burst". Proceedings 21st International Conference on Coastal Engineering, Malaga, pp 1897-1910.

Winton, T.C. and Mehta, A.J. (1981) "Dynamic Model For Closure Of Small Inlets Due To Storm Induced Littoral Drift". Proceedings IAHR Conference, India.

CHAPTER 219

Extent of Contaminated Marine Sediments and Cleanup Methodology

John B. Herbich, Ph.D., P.E.¹

Abstract

The problem of contaminated marine sediments has emerged as an environmental issue of national importance. Harbor areas in particular have been found to contain high levels of contaminants in bottom sediments due to wastes from municipal, industrial and riverine sources. The paper examines the extent and significance of marine sediment contamination in the United States; reviews the state-of-the-art of contaminated sediment cleanup and identifies research and development needs.

Introduction

Contamination of marine sediment in all areas of the world, particularly in the shallow water areas, poses a potential threat to marine resources and human health. Improving the capability to assess, manage and remediate these contaminated sediments is critical not only to the well-being of the marine environment but as well as to its use for navigation, commerce, fishing, and recreation.

This paper concentrates on the problem of contaminated marine sediments in U.S. waters which has emerged as an environmental issue of national importance. The summary is based on the results of the study conducted by a Committee on Contaminated Marine Sediments of the Marine Board, Commission on Engineering and Technical Systems, National Research Council. Members of the Committee were: Kenneth S. Kamlet (Chairman), A.T. Kearney, Inc., Williams J.

¹Director, Center for Dredging Studies, Holder of W. H. Bauer Professorship, Civil Engineering Department, Texas A&M University, College Station, TX 77843-3136, USA.

Adams, Monsanto Company, A. Karim Ahmed, Environ Corporation, Henry J. Bokuniewicz, State University of New York, Thomas A. Grigalunas, University of Rhode Island, John B. Herbich, Texas A&M University, Robert J. Huggett, College of William and Mary, Howard L. Sanders, Woods Hole Oceanographic Institution, and James M. Thornton, Department of Ecology, State of Washington. Charles A. Bookman is the Director of the Marine Board.

The expertise of the members of the Committee spanned the fields of aquatic toxicology, dredging technology, resource economics, sediment dynamics and transport, benthic ecology, environmental law and public policy.

The nature of the problem has resulted from using coastal waters, intentionally or unintentionally, for waste disposal for many decades. Confined or partly confined areas where low wave and current energies are present (such as harbors) contain high levels of contaminants in bottom sediments due to wastes from urban, industrial and riverine sources. Such areas where flushing action is unlikely (except during hurricanes) have accumulated contaminants which may now be buried by fine sediment deposits of recent years that contain no, or low levels of contaminants.

Legislative authority for the management of contaminated marine sediments falls largely under three statutes: the Comprehensive Environmental Response, Compensation, and Liability Act of 1980 (CERCLA), the Marine Protection, Research, and Sanctuaries Act (MPRSA), and the Clean Water Act (CWA). The Comprehensive Environmental Response Compensation and Liability Act of 1980, as amended by the Superfund Amendments and Reauthorization Act (SARA) of 1986, is aimed at the cleanup and remediation of inactive or abandoned hazardous waste sites, regardless of location. Superfund sites are currently ranked by the Environmental Protection Agency (EPA) based on the hazard they may pose to human health and the environment via releases to groundwater, surface water, and air. Underwater accumulations of hazardous wastes in marine environments are unlikely to threaten human health except by way of food chain exposure, which is not currently addressed in EPA's hazard-ranking process. Under the 1986 Superfund amendments, however, EPA was required to modify its Hazard Ranking System to address "the damage to natural resources which may affect the human food chain and which is associated with any release (or a hazardous substance)" S(Section 105(a)(2)).

Meanwhile, the Clean Water Act of 1970, as amended by the Water Quality Act of 1987, gives EPA lead responsibility for safeguarding the quality of U.S. coastal and inland waters. This includes regulating the disposal of dredged and fill materials (shared with the U.S. Army Corps of Engineers, under Section 404), and removing in-place toxic pollutants in harbors and navigable waterways (under Section 115). The 1987 amendments added new authorities requiring EPA to study and conduct projects relating to the removal of toxic pollutants from Great Lakes Bottom sediments (Section 118(c)(3)); and to identify and implement individual control strategies to reduce toxic pollutant inputs into contaminated waterway segments (Section 304(1)).

In response to Title II of the Marine Protection, Research, and Sanctuaries Act of 1972 (PL 92-532) and the National Ocean Pollution Planning Act, the National Oceanic and Atmospheric Administration (NOAA) Office of Marine Pollution Assessment conducts comprehensive interdisciplinary assessments of the effects of human activities on estuarine and coastal environments. Among these assessment activities is the National Status and Trends Program (NST), which attempts to create, maintain, and assess a long-term record of contaminant concentrations and biological responses to contamination in the coastal and estuarine waters of the United States. This assessment provides some insight into the extent of contamination nationally.

As a result of legislative responsibility and programmatic interests, a wide variety of federal agencies have shown active interest in this subject. EPA's responsibilities under Superfund and the CWA are the source of its interests in water quality concerns and remediation of uncontrolled hazardous waste sites. The U.S. Army Corps of Engineers (COE) is involved because of its responsibility to dredge and maintain navigable rivers and harbors. The COE also assists in the design and implementation of remedial cleanup actions under Superfund. NOAA has responsibility for assessing the potential threat of Superfund sites to coastal marine resources as a natural resource trustee as well as under its NS&T program. The U.S. Fish and Wildlife Service has legal authority for various endangered coastal species, food chain relationships, and habitat considerations, all of which are potentially impacted by contaminated sediments. The Navy has had experience in assessing contaminated sediments and now must grapple with such problems in locating and maintaining homeports for Navy vessels.

Procedure

There are many definitions of contamination of sediments. The Committee defined the contaminated sediments for the purpose of the study as follows:

"Contaminated sediments are those that contain chemical substances at concentrations which pose a known or suspected environmental or human health threat."

A symposium and a workshop was organized to examine the extent of contamination nationwide, the methods for classification of sediment contamination, risks to human health and the ecosystem, sediment re-suspension and contaminant mobilization, remedial strategies and technologies for handling contaminated sediments. In addition, five case studies were examined of the different ways in which a variety of sediment contamination problems are being handled. They include the PCB problem in New Bedford Harbor, Massachusetts; PCBs in the upper Hudson River, New York; kepone contamination of the James River, Virginia; the variety of chemicals contaminating Commencement Bay, Washington; and the Navy Homeport Project in Everett Bay, Washington.

The main purposes of the study included a) examination of the extent and significance of marine sediment contamination, b) a review of the state-of-the-art of contaminated sediment removal and remediation technology, c) identification and appraisal of alternative sediment management strategies, and d) identification of research and development needs and issues for future technical assessments (Marine Board, 1989).

Extent of Contamination

Many contaminated marine sediments are found along all coasts of the contiguous U.S., both in local "hot spots" and distributed over large areas. There is a wide variety of contaminants including: heavy metals, polychlorinated biphenols (PCBs), DDT, and polynuclear aromatic hydrocarbons (PAHs). At present, there are no generally accepted sampling techniques or testing protocols.

Classification Methodologies for Determining Sediment Contamination

There have been some research efforts in classifying the extent of contamination and some States have collected data for special purposes. No uniform

methods have been adopted by various State of Federal agencies.

A variety of classification methods are available:

- a) Sediment bioassays - sediment toxicity on a crustacean, infaunal bivalve and infaunal polychaetes. Essentially marine life is subjected to various levels of toxicity and their survival noted.
- b) Sediment quality triad:
 - 1) contamination quantified by chemical analysis,
 - 2) toxicity determined by laboratory bioassays, and
 - 3) benthos community structure determined by taxonomic analysis of biofauna.
- c) Apparent effects threshold technique equilibrium partitioning (AET) - A tool for deriving sediment quality values for a range of biological indicators to assess contaminated sediments. The AET is the contaminant concentration in sediment above which adverse effects are always expected for a particular biological indicator.

Recommendations

To ensure that decision making is informed and scientifically based, continued research and use of assessment methodologies should provide information to determine:

- a range of concentrations of chemicals in sediments that will result in biological effects, and
- whether in-place sediments are causing biological impacts.

A tiered approach to the assessment of contaminated sediments should be used. The approach would progress from relatively easy and less expensive (but perhaps less definitive) tests to more sensitive methods as needed.

Contaminated Sediment Management Strategies

Although the dredged material management strategy developed by the Corps of Engineers may be relevant to severely contaminated sediments, it is important from a management standpoint to differentiate them from less contaminated sediments. In particular, most

highly sophisticated remedial technologies (i.e, those involving treatment or destruction of associated contaminants) are likely to be cost-effective only in small areas and for sediments with relatively high contamination levels. Sediment contamination problems often involve large volumes of sediment with relatively low contamination levels. As a result, some highly sophisticated technologies may be inapplicable or inefficient for remediating contaminated sediments.

"No action" may be the preferred alternative in cases in which the remedy may be worse than the disease - e.g., where dredging or stabilizing contaminated sediments results in more biological damage than leaving the material in place. Contaminants generally accumulate in depositional zones, and, if the source is controlled, new clean sediments will deposit and cap the contaminated material over time. In effect, no action alternatives in such cases may result in natural capping.

1. No action may be an acceptable option if the contamination degrades or is buried by natural deposition of clean sediment in a short period of time.

2. In-place capping may be a useful option if the sediments are not in a navigation channel or if groundwater is not flowing through the site.

3. Removal and subaqueous burial off-site may be a viable option, although the experience with this technique is limited to relatively shallow water (less than 100 ft).

4. Incineration seems to be viable only for sites with relatively small amounts of sediments containing high concentrations of combustible contaminants.

5. Other techniques to assist in remediation of contaminated sediment may be appropriate in special cases. Examples include a variety of sediment stabilization or solidification techniques, and biological and/or chemical treatment.

Recommendations

- Additional evaluation should be conducted to determine the applicability of the Corps of Engineers' dredged material management strategy to more severely contaminated sediments.

- No action should always be considered as an alternative strategy for minimizing biological damage. In using the no-action strategy as a form of natural capping of contaminated material, consideration should be given to the length of time it takes for contaminants to be isolated from the food chain.

Remedial Technologies

From a remediation standpoint, the most important factors are likely to be a definition of the clean-up target, technical and cost feasibility, natural recovery estimates, and ability to distinguish and/or control continuing sources of contaminants.

Dredging technology exists that is capable of greatly reducing turbidity and resuspension in connection with dredging of bottom sediments in most applications (Herbich and Brahme, 1990).

The selection of proper dredging equipment is important to achieve an efficient removal of contaminated sediments, and to prevent additional contamination generated during dredging. The selection depends on a number of factors:

- 1) characteristics of sediments,
- 2) quantity of sediments to be removed,
- 3) degree of contamination,
- 4) toxicity of contaminants,
- 5) location,
- 6) environmental conditions at the site (waves, currents, tides, etc.),
- 7) distance to the disposal site,
- 8) type of disposal, and
- 9) availability of particular equipment.

Since conventional type of dredges designed for removal of large volumes of sediment are generally not suitable for small operations to remove pockets of contaminated sediments, special purpose dredges have been developed to dredge contaminated sediments while minimizing sediment resuspension and contaminant release. The specialty dredges may be placed in three categories:

1. mechanical - watertight clamshell,
2. mechanical-hydraulic - Mud Cat, remotely controlled Mud Cat, and clean-up system,
3. hydraulic - Refresher, waterless, matchbox, and wide sweeper, cutterless dredge, and
4. pneumatic - Pneuma and Oozer.

Watertight clamshell. A watertight clamshell was developed in Japan (Figure 1) and evaluated by the U.S. Army Engineer Waterways Experiment Station (Hayes et al., 1988). Experiments indicated that the watertight bucket significantly reduced water column turbidity.

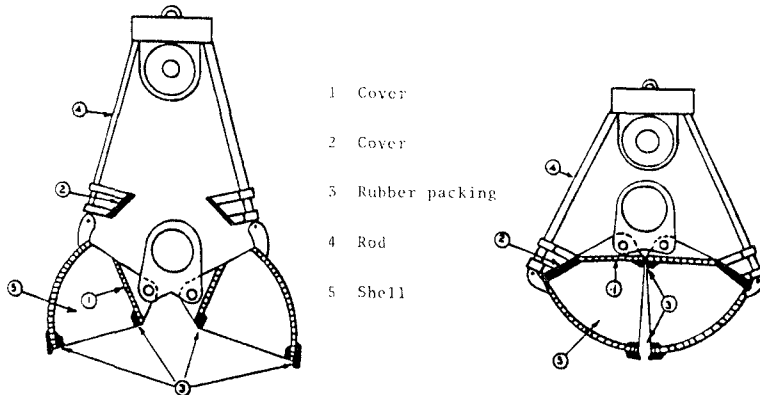


Figure 1. Open and closed positions of the watertight clamshell bucket

Mud Cat. The Mud Cat has a horizontal cutter-head equipped with knives and spiral augers that cut the material and move it laterally toward the center of the augers where it is picked up by the suction. The dredge can remove sediments in a 2.6-m width and in water depths up to 4.9 m. The dredge operates on anchor cables, and the manufacturer claims that it leaves the bottom of the dredged area flat. By covering the cutter-auger combination with a retractable mud shield the amount of turbidity generated by Mud Cat's operation can be minimized.

Remotely-controlled Mud Cat. A remotely-controlled unit has been developed in which the control cab is located on land and is remotely connected to the Mud Cat by an umbilical cord. This allows safe dredging of hazardous or toxic materials. The remote control provides the shore-based dredge master with a variable traversing winch control, a variable auger control, a variable dredge pump speed control, and a manually-controlled emergency shut down.

The "Clean-up" System. The clean-up head consists of a shielded auger that collects sediment as the dredge swings back and forth and guides it toward the suction of a centrifugal pump. The auger is shielded and a moveable wing covers the sediment as it is being collected by the auger. An underwater TV camera and sonar devices indicate the topography of the bottom (Figure 2). Fairly large volumes have been excavated by "Clean-up" dredges in soft muds and sand containing various contaminants such as mercury, cadmium, PCBs, oily and organic substances (Sato, 1984).

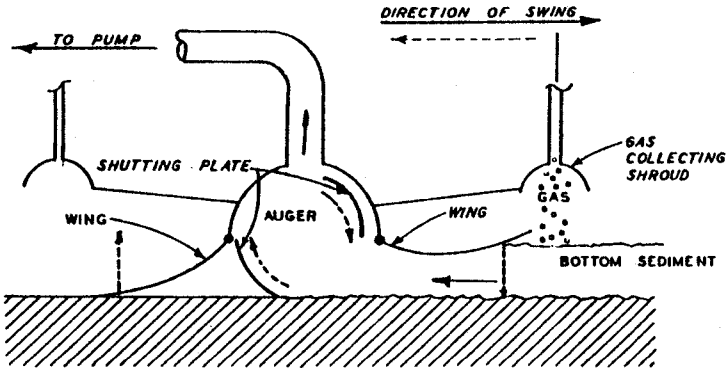


Figure 2. The "Clean-up" system (Sato, 1984)

Refresher. The material being dredged is confined by a specially-designed flexible enclosure that completely covers the cutter, preventing escape of sediments to the outside of the immediate dredging area (Figure 3). The working open section is always on the swing side of the cutterhead. A gas removal system is also installed and can be activated as needed to prevent gas moving up the suction pipe. The flexible enclosure of the cutterhead is automatically adjusted to bottom contours (Figure 4) (Shinsha, 1988).

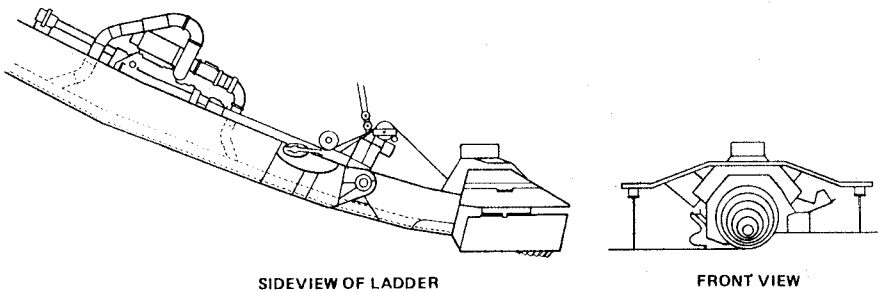


Figure 3. "Refresher" dredge (Shinsha, 1988)

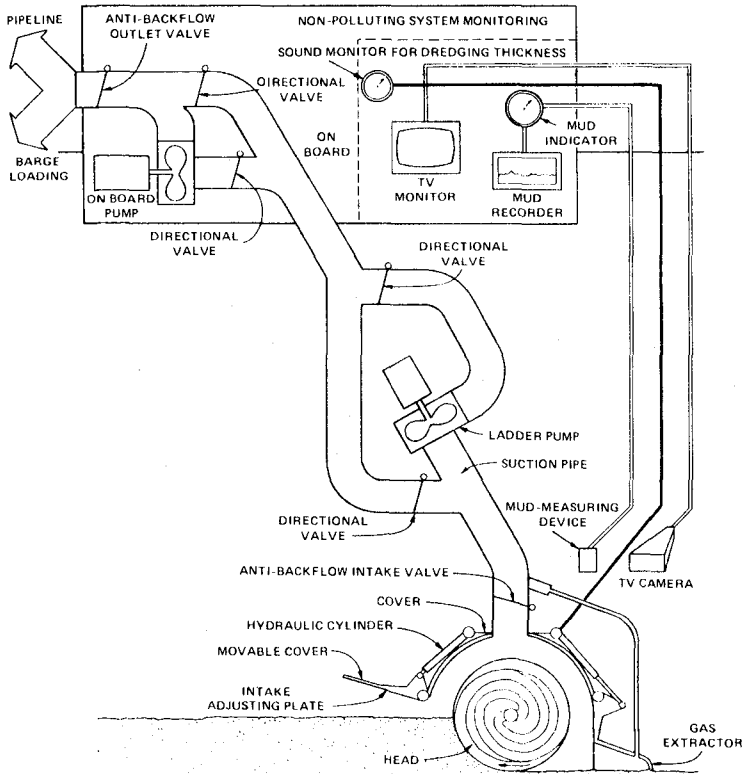


Figure 4. Description of a "Refresher" dredge (Shinsha, 1988)

Matchbox dredge. A special suction head was developed by a dredging contractor in the Netherlands to replace the traditional cutterhead (d'Angremond et al., 1984). The main design points are as follows:

1. A large plate covers the top of the dredge head to avoid inflow of water and escape of gas bubbles.
2. Adjustable angle between the drag head and the ladder to create an optimum position of the drag head independent of the dredging depth.
3. There are openings on both sides of the drag head to improve dredging efficiency. During swinging action the leeward side is closed to prevent water inflow.
4. Dimensions of the head must be carefully designed for the average flow rate and swing rate.

A direct comparison between a Matchbox suction head, a conventional cutterhead and a clamshell was made by the Waterways Experiment Station in Calumet Harbor (Hayes et al., 1988). The Calumet Harbor demonstration indicated that the clamshell dredge generated the largest suspended sediment plume affecting the entire water column. The cutterhead slightly outperformed the Matchbox dredge in this field experiment.

Pneuma pump. The Pneuma pump is a compressed-air-driven, displacement-type pump with several major components (Herbich, 1975). The pump body, the largest of these components in dimensions and weight, incorporates three large cylindrical pressure vessels, each having a material intake on the bottom and an air port and discharge outlet on top. Each intake and discharge outlet is fitted with a check valve, allowing flow in one direction only. Pipes leading from the three discharge outlets join in a single discharge directly above the pressure vessels. Different types of attachments may be fitted on the intakes for removal of varying types of bottom material. Pneuma pump was evaluated by the U.S. Army Engineer Waterways Experiment Station (Richardson et al., 1982).

Oozer dredge. The Oozer pump was developed by Toyo Construction, Japan. The pump operates in a manner similar to that of the Pneuma pump system; however, there are two cylinders (instead of three) and a vacuum is applied during the cylinder-filling stage when the hydrostatic pressure is not sufficient to rapidly fill the cylinders. The pump is usually mounted at the end of a ladder and equipped with special suction heads and cutter units depending on the type of material being dredged. The conditions around the dredging system, such as thickness, bottom elevation after dredging, and amount of resuspension, are monitored by high-frequency acoustic sensors and an underwater television camera. A large Oozer pump has a dredging capacity ranging from 300 to 500 m³/hr. During one dredging operation, suspended solids levels within 3 m of the dredging head were all within background concentrations of less than 6 mg/liter.

Recommendations

• Source control measures must be considered in all cases, including no action. Federal and state regulatory agencies requiring remedial action should implement source control measures as a component of remedial action when applicable and appropriate. Use of financial incentives through strict liability for assessment cost, remedial actions, and damages also may

play an important role in source control, provided that trustees make aggressive efforts to hold responsible parties liable for releases into the environment.

- Aggressive technology and information transfer mechanisms are needed to ensure that knowledge gained and lessons learned from all remedial actions are available and accessible to managers confronting new remediation problems at federal, regional and local levels. Knowledge gained should be systematically compiled in guidance documents. Lessons learned regarding the feasibility of sophisticated remedial technologies under varying conditions of contamination severity and extent should be documented and made widely available to facilitate future decision making. Lastly, experience gained through the use of screening procedures at large sites should be distilled and generalized into routine methodologies for economically assessing smaller sites.

- When possible, remediation projects should be designed to take advantage of existing navigational dredging activities that may already be authorized in conjunction with the Clean Water Act, Section 115 or Section 10/404.

- Research and development should be encouraged by the federal government to develop technology and equipment for efficiently removing contaminated sediments and to make it available in the United States. Foreign technologies should continue to be examined relative to their appropriateness in this country. Efforts to conduct and fund research and development as a partnership between government and industry should be encouraged.

- Although capping might not, in the strictest terms, be considered a remedial technology, it should not be ignored because it can play a valuable role in remediating contaminated sites.

- Monitoring programs should be well-focused on testing forecasts made during design of the remediation plan. To the extent possible, monitoring should be extended to remove uncertainties in the basic understanding of contaminated sediment behavior. For example, monitoring of capped areas might focus on changes of cap thickness, erosion around boundaries, and leakage of contaminant through the cap.

Remediation and Source Control: Economic Considerations

Remedial actions are costly and become more expensive as additional levels of clean-up or treatment are pursued. The role of tradeoffs between possible technologies at and among sites must be considered, given the scarcity of funds to clean up contaminated sites and the potentially great number of sites.

The use of the benefit-cost analysis as part of the remedial action decision process would provide perspective on the issues involved. It would place investments in this area on the same footing as other public investments. However, difficulty in quantifying benefits from remedial actions in monetary terms makes reliance on benefit-cost analysis infeasible in a number of cases. Nonetheless, in light of the high cost of remedial actions, it is important that implicit (if not explicit) consideration be given to potential benefits before remedial actions are undertaken.

Removal of contaminated sediments can be very expensive, varying widely from several hundred thousand dollars to tens of millions of dollars. Data on 15 clean-up sites indicate that total clean-up costs can reach \$500,000 to \$1,000,000 per acre* (U.S. Congress Office of Technology Assessment, 1988). This compares with an average unit cost of navigation dredging of \$1 to \$2 per cubic yard of sediment dredged. The average unit cost of all dredging, both government and private, is estimated in 1988 at \$1.67 per cubic yard of material dredged. On site incineration, one of the remedial measures proposed at various sites, is also very expensive. The estimates quoted are from \$186 to \$750 per cubic yard.

Recommendations

- In view of the high cost of remedial actions in most cases, greater use should be made of benefit-cost comparisons over ecologically relevant time periods in order to place investments in this area on the same economic footing as investments in other public projects.

- Cost-effectiveness analysis of alternative remedial actions should consider both short- and long-term costs. Comparisons at and among sites should be based on costs estimated using a consistent approach.

- In evaluating the degree of remediation to be conducted at a site, it should be recognized that incremental costs typically will increase rapidly as additional levels of clean-up are sought.

- The decision as to whether or not remedial actions are undertaken should be based on a balanced

*For purposes of comparison, assume that a one-acre clean-up involved removing overburden to a depth of one yard, or a total of 43,560 yds³ of contaminated material. In that event, total clean-up costs would range from \$11.50 to \$23.00 per yd³.

comparison of the anticipated environmental and public health benefits of actions with their costs, including possible environmental and health risks.

Clearly infeasible options should be eliminated at the outset, before alternative remedial actions are considered in depth.

References

d'Angremond, K., A.J. de Jong, C.P. de Waard. 1984. Dredging of polluted sediment in the first petroleum harbor, Rotterdam. Proc. 3rd U.S.-the Netherlands meeting on Dredging and Related Technology. Fort Belvoir, VA: U.S. Army Engineer Water Resources Support Center.

Hayes, D.F., T.N. McLellan and C.L. Truitt. 1988. Demonstration of innovative and conventional dredging equipment at Calumet Harbor, Illinois. MP EL-88-1. Vicksburg, MS: U.S. Army Engineer Waterways Experiment Station.

Herbich, J.B. 1975. Coastal and Deep Ocean Dredging. Houston, TX: Gulf Publishing Company.

Herbich, J.B. and S.B. Brahme. 1990. A literature review and technical evaluation of sediment resuspension during dredging. Vicksburg, MS: U.S. Army Engineer Waterways Experiment Station (in press).

Marine Board, 1989. Contaminated marine sediments - assessment and remediation. Washington, DC: National Research Council, National Academy Press.

Pequegnat, W.E. 1987. Relationship between dredged material and toxicity. Terra et Aqua, 34.

Richardson, T.W., J.E. Hite, R.A. Shafer and J.D. Ethridge. 1982. Pumping performance and turbidity generation of model 600/100 Pneuma pump. TR HL-82-8, Vicksburg, MS: U.S. Army Engineer Waterways Experiment Station.

Sato, E. 1984. Bottom sediment dredge CLEAN UP. Principles and results, management of bottom sediments containing toxic substances. Proc. 8th U.S./Japan Experts Meeting, T.R. Patin, ed. Vicksburg, MS: U.S. Army Engineer Waterways Experiment Station, pp. 403-418.

Shinsha, H. 1988. Personal communication, Refresher dredge, Japan: Technical and Research Institute, Pentacocean Construction Company, Ltd.

U.S. Congress Office of Technology Assessment. 1988. Are we cleaning up? 10 Superfund case studies. Special Report OTA-ITE-362. Washington, DC: U.S. Government Printing Office.

CHAPTER 220

DESIGNING FOR STORM AND WAVE DAMAGE IN COASTAL BUILDINGS

Spencer M. Rogers, Jr.*

1. INTRODUCTION

Gulf Shores is a small town on the Gulf of Mexico near Mobile, Alabama (Figure 1). The area is geologically part of a wide peninsula extending from the eastern side of Mobile Bay. Several brackish water lakes along the peninsula create barrier island-like features along the Gulf shoreline. Gulf Shores, like many other beach communities, gradually evolved from fishing shacks and modest beach cottages into a resort community of primarily single-family residences and second homes. By 1979, the national boom in beach resort development was beginning and several motels and condominiums had been completed, others planned.



2. NATIONAL FLOOD INSURANCE PROGRAM

The NFIP evolved from the National Insurance Act of 1968. The act was intended to reduce public disaster relief expenditures in river basins and to limit private flood losses, particularly in areas where such losses were severe or reoccurring. With the incentive of making federally subsidized flood insurance available to anyone in the community, local governments were encouraged to adopt and enforce certain floodplain management regulations in identified flood prone areas. The program

* Coastal Engineer, Dept. of Civil Engineering, N. C. State University and Sea Grant Marine Advisory Service, P.O. Box 130, Kure Beach, NC 28449.

received minimal interest until legislative changes in 1973 required flood insurance for any loan that is supervised, regulated or insured by a federal agency. For identified flood-prone areas, it was a simple amendment: no insurance, no bank loan. Interest in the program skyrocketed. Owners and lenders have grown to appreciate the financial protection provided by the insurance.

Floodplain management regulations evolved from the most common Riverine protection scheme: Elevate the building higher than the water so it does not get wet. The NFIP modeling and mapping of the predicted 100-year flood level, having a 1 percent chance of occurrence in any given year, has been completed in most flood prone areas. In exchange for flood insurance availability, most local governments have willingly established local ordinances requiring lowest floor elevations to be above predicted levels. Similar methods have been adopted in coastal areas even though the cause of the 100-year flood is usually a hurricane, another severe coastal storm, or in some Pacific areas, a tsunami.

Coastal flood maps denote ground elevations below the 100-year flood elevation as A-zones and prone to flooding (NFIP, 1988). Higher elevations are mapped as B-and C-zones. B-zones are flooded on an average of once in 100 to 500 years. C-zones are above the predicted 500-year flood area. Within the A-zone, the minimum floor elevation may be reached by any normal construction method, including the placement of fill.

The most significant accommodation for coastal flooding is the additional identification of "coastal high hazard" or "velocity" zones, which are denoted on the maps as V-zones. The V-zone designation attempts to define an area subject to waves 3 feet or higher during the 100-year storm. A wave threshold of 3 feet was adopted after a Corps of Engineers study estimated that it was a reasonable design limit for typical wood frame construction (Corps of Engineers, 1975). Initially, the same still water elevations were applied in the V-zone as in the adjacent A-zone. But in the V-zone, a piling foundation was required and building on fill was not allowed. The floor elevation in the V-zone was redefined as the bottom of the floor joists, in effect raising the finished floor elevation about 1 foot higher than in the A-zone. Insurance rates were higher in the V-zone.

3. CONSTRUCTION REGULATIONS

Like many resort communities, Gulf Shores developed with little or no regulation of building construction standards, even after its incorporation in 1956. Adoption of the NFIP standards was one of the first

significant regulatory changes. The first flood hazard boundary maps were published by NFIP in 1971 (NFIP). Based on those maps, minimum floor elevation standards were adopted throughout the town as part of an updated zoning ordinance in April 1972 (Alabama Development Office). The adjacent unincorporated areas of Baldwin County adopted similar elevation and construction requirements that were effective May 1973 (Baldwin County Commission). In both areas, the minimum floor elevation requirement was set at +11.5 feet NGVD (3.5 M) based on the predicted 100-year storm surge elevation. Piling foundations were required in the V-zone. In the A-zone owners of most new buildings voluntarily chose to elevate on piling foundations. This was probably to gain underhouse parking and to lower the cost over bringing in large amounts of fill.

4. HURRICANE FREDRIC

In September of 1979, Hurricane Fredric made landfall across Dauphin Island on the west side of Mobile Bay, approximately 30 miles west of the center of Gulf Shores (COE, 1981). On the Saffir/Simpson hurricane scale of 1 to 5, Hurricane Fredric was ranked as a high category 3, a major hurricane. Damage to Alabama, Mississippi and Florida was severe and widespread. The worst damage was within Gulf Shores and along Dauphin Island. The Corps of Engineers and the U.S. Geological Survey have estimated still-water elevation rose to +11.4 feet NGVD (3.5M) within the town limits. The storm surge was essentially identical to the predicted elevation on which the original construction standards were based.

One of the previously identified weaknesses of NFIP coastal flood regulations was the use of a still-water elevation to set minimum floor elevations. The minimum levels are appropriate for riverine floods, but in coastal flooding, wave damage at elevations above the recorded still-water elevation was being substantially underestimated. Even small breaking waves can generate extremely high forces on a building. Waves are often the worst cause of major structural damage in coastal floods. Before the storm, a National Academy of Science committee recommended a methodology to add wave heights to the NFIP storm surge model (National Academy of Science, 1977). After Fredric, Gulf Shores became the first community in the nation to have its flood maps revised to include wave height elevations.

Using the same storm surge elevation and applying linear wave theory, the minimum floor elevations were raised to include depth limited waves over the existing ground elevations. The lower the ground elevation, the deeper the water and the bigger the wave. Unfortunately,

the model can be substantially distorted by small sand dunes and other erodible topographic features which may be altered during a severe storm. Since the topography of Gulf Shores had already been flattened by waves during Fredric, it offered the ideal site to use the new wave model. The original still-water elevations were increased to include wave heights based on the post-Fredric ground elevations. The first flood maps to include wave heights were released April 1980 (NFIP). Significant revisions were published again in April 1981 (NFIP).

About the same time, NFIP developed a different storm surge model to predict still-water elevations specifically for flood insurance mapping purposes (Tetra Tech, 1981). The new model replaced previous models that were developed and prepared by the National Weather Service and the Corps of Engineers for other purposes, primarily life safety and evacuation. In January 1985 new flood maps were released based on the revised storm surge model and incorporating the same wave height methods applied previously. The elevation standards were reset significantly lower than any of the previous elevation requirements.

A variety of factors make Gulf Shores an ideal site for a case study of the flood regulations. Most importantly, Fredric's peak still-water elevations appear to have been extremely close to the previously predicted 100-year flood elevation. A wealth of post-storm damage data was accumulated by the Corps of Engineers and others. The topographic features that can distort the wave height predictions in most other areas were all flattened by Fredric's waves, making the post-storm wave predictions more accurate than is normally possible. The pre-storm construction was not designed for wave heights since those maps were released after the storm. However, since the predicted still-water elevation equaled the recorded elevation, the later maps should closely estimate the actual elevation of peak wave damage during Fredric. Therefore, the more recent maps should reflect relatively higher damage levels where higher waves are predicted.

If elevation requirements are an effective method of reducing damage to buildings, then there should be a difference between the damage to buildings pre-dating the 1971 flood map and the newer elevated buildings built before Fredric. The benefits of the construction standards should be most apparent in areas where the predicted still-water elevation reasonably reflected the actual conditions during Fredric.

5. METHODS

A study area was selected that was entirely within the 1985

corporate limits of Gulf Shores extending inland 1000 to 2500 feet (300 to 800 M) landward from the Gulf. After the low sand dune was flattened during Fredric, the ground elevations rose gradually inland from the Gulf. Post-storm surveys indicate that the entire study area was flooded during Fredric (U.S.G.S., 1980). The Disaster Report was the primary source of building damage data (COE, 1981). The Corps compared post-storm aerial photographs taken one day after Fredric by the Florida Department of Transportation and with aerial photos taken in March 1979 six months before the storm. The destroyed buildings were marked with a symbol on the post-storm photos. The Corps data was augmented when necessary by careful inspection of the original post-storm aerial photos or with ground inspections and ground photography made 10 days after the storm by the author.

The age of each building in the study area was determined by overlaying the Corps damage photos with transparencies of U.S.G.S. aerial photos taken in May 1972. The photos were taken around the time of the adoption of the minimum elevation requirements in Gulf Shores and Baldwin County. Buildings in existence in 1972 were coded as "old," pre-dating the elevation requirements. Buildings only appearing in the more recent photos were coded as "new", constructed after the minimum elevation requirements were implemented.

A scale-corrected, transparency of each flood map was produced, delineating the elevation zones within the study area. The transparencies were overlaid on the damage sheets previously coded by age. The buildings in each zone were tabulated. It was noted whether the building survived or was destroyed, and whether it was old or new. Any building located in more than one zone was considered to be in the higher of the two risk zones. Also, the distance between the seaward end of each building and the waterline position mapped by the Corps was measured.

To assess the effects of the elevation requirements, it is desirable to remove as much of the wind damage as possible. Wind damage can be extensive in areas with weak construction standards and sustained winds over 100 mph. Damage patterns are usually distinct. Partial damage to a roof, wall or foundation may leave the building beyond salvage, but large, visible remnants usually remain. Even small waves can create forces several orders of magnitude higher than design wind forces. Wave damage often leaves little debris nearby. It is not uncommon to find only a few leaning pilings. Most destroyed buildings in Gulf Shores appeared to be caused by water damage. Where the photography indicated extreme wind damage, buildings were considered to have "survived" for the purposes of this study even though it may have been a total insurance loss.

The majority of buildings in the study area were single-family residences. Piling-supported houses frequently had underhouse enclosures for parking, storage and finished living areas. The lower enclosures usually had "breakaway" walls. In principle, little or no damage should occur to the rest of the building when the lower walls fail. In such cases, destruction of the underhouse improvements did not affect the classification of "survived" for the rest of the piling-supported building. Buildings that floated away from their foundations were considered destroyed even though the buildings were intact and potentially salvageable. Roughly 5 percent of the buildings in the study area were larger, commercial motel and condominium buildings. Most were constructed on much heavier and deeper piling foundations. When these larger buildings lacked adequate floor elevation, the first floor rooms were frequently gutted by waves but remained structurally sound with the upper floors intact. Since the lower non-bearing walls were never intended to be breakaway, the buildings were considered destroyed even if the upper floors remained.

6. RESULTS

A typical shoreline cross section showing the required elevations of the various flood maps is shown in figure 2. Minimum elevations in the V-zones have been labeled 1 foot higher than mapped to account for the different definition of lowest floor elevation (bottom of the joists). In 1971 there were only two zones both very close to Fredric's surge elevation. In 1980 six different elevation zones were identified. In 1981 many buildings in the middle zones were reclassified into less restrictive elevations. No reason for the rapid restudy was provided. The 1985 maps, implementing the newer storm surge model, significantly lowered the predicted surge elevation therefore dropping the wave height elevation compared to all

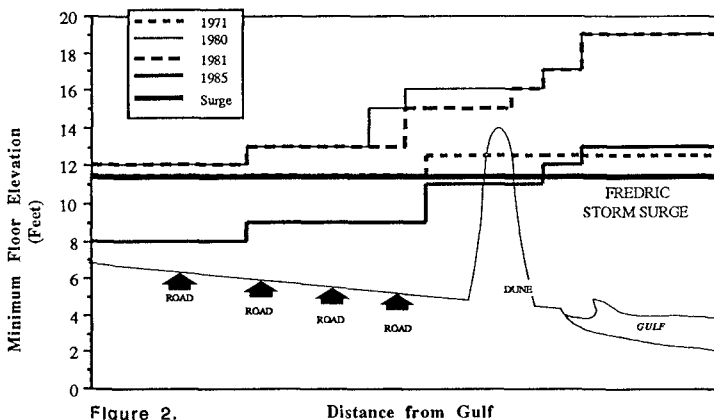


Figure 2.

Distance from Gulf

previous maps. The most seaward zone in the 1980, 1981 and 1985 maps was located seaward of the mean high water line and contained no buildings. Only one new building was located in the next most seaward zone and its results cannot be considered statistically significant.

Of the 1056 buildings in the study area 377 (36 percent) were destroyed. Of the total, 777 were old, 279 new. New buildings constructed on pilings and meeting the minimum elevation standards performed slightly better than earlier designs: 32 percent of the new buildings destroyed vs. 37 percent of the old. Clearly the loss of 32 percent of the buildings in a design storm indicates significant problems with the standards. Figure 3a displays the damage distribution based on the 1971 maps. In the A-zone there was a 10 percentage point reduction of damage in new buildings over old, but 13 percent of the new buildings were still destroyed in the area where the original standards should have performed best. New buildings in the V-zone were more frequently damaged than the old. Although a modest improvement can be seen in the A-zone, the standards resulted in no improvement in the original V-zone.

Damage Distribution by Flood Map

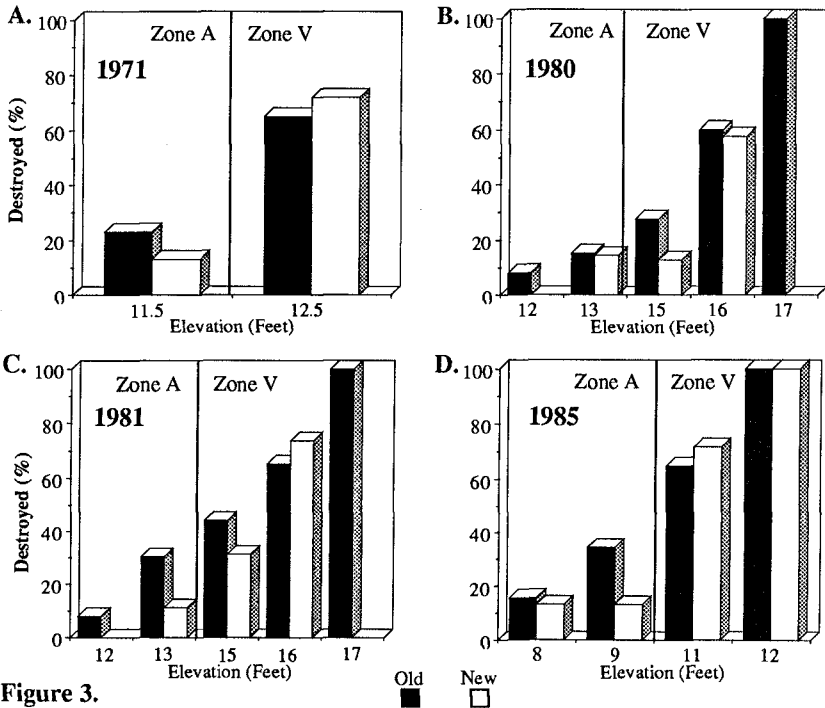


Figure 3.

The wave height predictions included in the 1980 and 1981 maps (figures 3b & 3c) were used as a hindcast of actual wave heights in the hurricane. Increasing levels of damage to both old and new buildings occurred as the predicted elevations increasingly exceeded the original standard. Improved survival of new buildings can be observed in the three most landward zones (elevation 12, 13 & 15), but no improvement in the most seaward zone with a significant sample size (el. 16). No new buildings were destroyed in the most landward zone compared with losses of 8 percent of the old buildings in the same areas. Damage to new buildings rose to unacceptable levels in all zones farther seaward (14 and 11 percent at el. 13). Every old building in the most seaward, developed zone (el. 17) was destroyed.

The 1985 maps show similar damage trends but cannot be considered a wave hindcast since the revised storm surge prediction is 3.5 feet (0.9 M) lower than the predicted still water elevation used in all earlier maps and measured after Fredric (figure 3d). After the addition of wave heights, the minimum elevation standards in 1985 were lowered 4 to 7 feet (1.2 to 2.1 M) below the 1980-81 maps and 0.5 to 4 feet (0.2 to 1.2 M) below the standards adopted with the 1971 maps.

One week before Fredric, the Alabama Coastal Area Board voted to establish a statewide, gulf-front construction setback line (Hegenbarth, 1985). The Town of Gulf Shores eventually adopted a setback ordinance requiring all new construction to be located more than 40 feet landward of the pre-Fredric dune crest, except in the central, commercial district where the setback for larger buildings was reduced to five feet landward of the crest. The regulation took effect in March 1981.

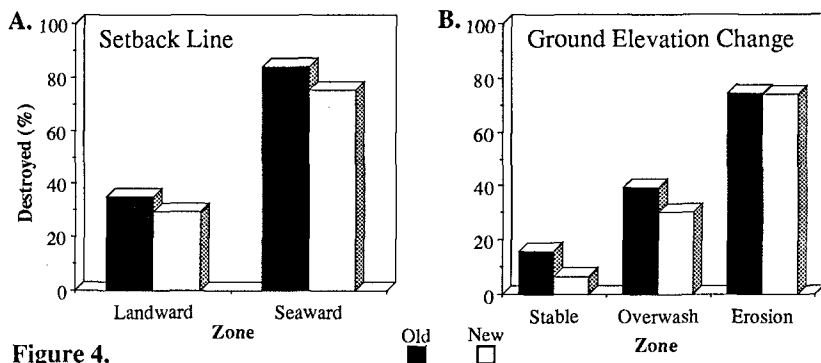


Figure 4.

The study analyzed what the effect of the setback would have been if it had been enforced for all earlier construction. A pre-development setback would have relocated or reduced in size less than 5 percent of

the buildings in the study area. But it would have included many of the largest motels and condominiums. Eleven percent of the damaged buildings were seaward of the setback. Eighty-four percent of those old buildings and 75 percent of the new buildings were destroyed (Figure 4a). Although an earlier implementation of the setback would appear to have reduced damage levels, the setback without other construction regulations farther landward would not have reduced damage to acceptably low levels in the community. Even if the most seaward buildings had been constructed a few feet farther inland, most would still have been damaged. Eighty-nine percent of the damaged buildings were landward of the setback. If an even more restrictive setback had been established along to the north side of the Gulf-front road, prohibiting up to three rows of single-family houses, 39 percent of the destroyed buildings would have been even farther inland.

The influence of ground elevation changes was also measured. The Corps of Engineers (1981) reported erosion occurred 300 feet landward of the post-storm waterline. Overwash deposition was mapped from post-storm photography and appeared to correlate with wave damage to low elevation buildings. On average the overwash penetrated 700 feet (210 M) inland of the waterline. In figure 4b there are similar percentage point improvements in stable ground and overwash but much higher overall levels in overwash. In the erosion area approximately 75 percent of both the old and new buildings were destroyed.

Buildings in the study area were sorted by distance from the waterline and grouped in increments of 100 feet (30 M). The results are displayed in Figure 5. The most dependable points are more than 100 feet and less than 900 feet. Outside that range there were too few buildings for reliable results.

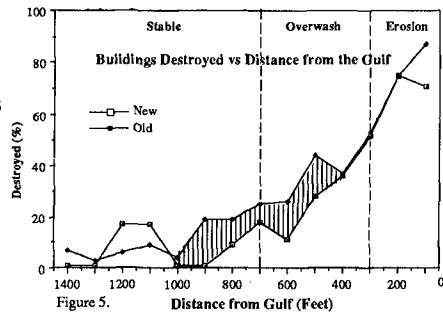


Figure 5.

When the average hazard zone distances are added to the graph, the benefits and limitations of the NFIP construction regulations become more apparent. The effect of the regulations is revealed as the shaded difference between the two lines. The reliable points in the stable but flooded zone show significantly lower damage levels for new NFIP standard buildings than for pre-NFIP buildings. Throughout most of the overwash zone, the damage rates of new buildings show a similar relative improvement as in the stable zone, averaging 13 percentage points better than the older ones. However, the overall likelihood of damage in both

groups increases moving seaward, from an overall average of 22 percent to 37 percent. The steep trend of higher losses closer to the ocean is continued through the erosion zone. All groups closer than 400 feet to the waterline showed remarkably consistent damage levels in old and new buildings.

7. DISCUSSION

The construction standards based on the 1971 maps reduced losses during Hurricane Fredric. The shaded area in figure 5 represents the benefits of the NFIP standards. The survival of 19 buildings out of the 279 constructed between 1972 and 1979 appears to be attributed to the regulations, preventing damage in 7 percent of new construction (Photo 1). If equally effective regulations had been implemented for the 777 older buildings in the study area, about 72 buildings could have been saved by the construction standards as adopted from the 1971 maps.



Photo 1. Typical buildings elevated to meet construction standards. Note foundation of demolished building in foreground.

For design storm conditions, unacceptable levels of damage were allowed by the regulations. Eighty-nine new buildings (32 percent) were destroyed during Fredric. The initial maps show the improvement occurred only in the original A-zone (Figure 3a). The V-zone revealed higher damages in new buildings than in old, the opposite of the desired effect. The addition of wave heights in the 1980 and 1981 maps was an obvious and necessary improvement. The V-zone construction standards specify minimum floor elevations for piling construction but do not address piling embedment. Field inspections indicated that local practice prior to the storm provided 3 to 10 feet (1-3 M) of embedment below existing grade, consistently too little to survive in the erosion zone (photo 2). At its best the A/V zone designations still used by NFIP can address wave height



Photo 2. Undermined foundation of "new" building in erosion zone.

variations and floor elevations but are not suited to address erosion or foundation embedment requirements. The most likely benefit of the wave height additions will be improved survival in the overwash (wave) area in figure 4b and 5 as well as photo 3.



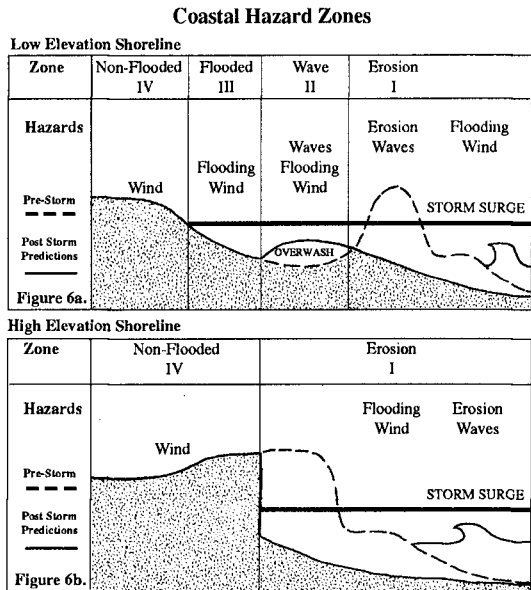
Photo 3. Wave damage to "old" building in the overwash zone. Originally and presently an A-zone, but a V-zone in 1980-1.

Construction setback lines could have reduced the number of damaged buildings but not enough to be the sole method of damage prevention in extreme, but relatively rare storms such as Fredric. Adequate construction standards are necessary to adequately control

building damage on low elevation shorelines that are expected to be overtopped by waves like Gulf Shores. Setbacks appear more likely to be successful if properly applied along high elevation shorelines or if used to control damage caused by long-term erosion.

More realistic coastal hazard zones have been previously suggested in the literature. The Model Minimum Hurricane Resistant Standards for the Texas Gulf Coast (Texas Coastal and Marine Council, 1978) proposed the use of hazard zones for scour, battering by debris, flooding, and wind. The results of this study suggest slightly different designations. On low elevation shorelines where inland flooding is likely, the threats to buildings can be separated into four zones: I) erosion, II) waves (overwash), III) flooded (without waves) and IV) wind (without flooding) as in figure 6a.

High velocity winds can be expected in the entire coastal area, all four zones. Flooding takes place in the three most seaward zones, comparable to the present NFIP flood maps. In the two most seaward zones wave heights must be addressed as well as some foundation considerations for overwash deposition, similar to present V-zones standards. The most seaward zone by definition receives all of the erosion as well as the worst of the previous hazards. Foundation embedment is a critical design consideration that is not adequately addressed in NFIP standards.



On high elevation shorelines the hazard zones can be further simplified. The eroded dune or bluff defines both the limit of erosion and all flooded areas. Zone II and III cannot occur. The erosion of zone I is bounded by the high winds without flooding of zone IV (figure 6b).

It should be noted that this study only addressed the effect of a single, but very severe, short-duration storm. The construction standards

in this study have been in place for only seven years, too short a period to be significantly affected by the long-term erosion in Gulf Shores. In areas of significant long-term erosion it seems prudent to expect the zones to move landward with the erosion rate over the lifetime of any new building constructed. Additional approaches like setbacks or erosion control projects may be required to adequately protect buildings.

5. CONCLUSIONS

The NFIP building construction standards in Gulf Shores significantly reduced damage in buildings constructed between 1972 and 1979. However damage levels were far too high to be considered successful in meeting the reasonable damage-reduction goals in design storm conditions. Damage patterns indicate that wave height considerations in 1980 and 1981 were an appropriate improvement that should reduce damage to buildings constructed after the storm but prior to the 1985. Due to the large drop in the predicted storm surge, buildings constructed to the minimum standards after 1985 can expect higher levels of damage than 1971-1985 buildings if a storm of equal severity occurs. In such a storm, post-1985 buildings are likely to receive damage at levels similar to the unregulated, (old) buildings.

The original construction standards proved to be totally ineffective in areas that experienced erosion. Appropriate foundation penetration standards must be established if damage to small buildings is to be reduced to acceptable levels in 100-year design conditions along the coast.

The identification of more realistic hazard zones is already technically feasible. A variety of existing two-dimensional, dune erosion models can be used to define the erosion zone when the dune is not overtopped (figure 6b). The models are less precise in predicting overtopping and overwash but are still useful when applied with sufficient engineering judgment. Additional considerations for long-term erosion are necessary for buildings to avoid storm damage over a normal useful life.

REFERENCES

Alabama Development Office, Zoning Ordinance for Gulf Shores, Alabama, Article 8, 2nd Revised Edition, April 1972.

Baldwin County Commission, Land Management of Flood Prone Areas in Baldwin County, Alabama, Adopted May 1973.

Hegenbarth, Jane L., Gulf Shores, Alabama from 1979 to 1984: It's Redevelopment and Growth Following Hurricane Fredric, University of North Carolina, Chapel Hill, Report 85-09, June 1985.

National Academy of Sciences, Methodology for Calculating Wave Action Effects Associated with Storm Surges, Washington, DC, 1977.

National Flood Insurance Program, Flood Insurance Rate Map, Baldwin County, Alabama, Community Number 15000, April 15, 1980.
_____, April 1, 1981.

NFIP, Flood Insurance Rate Map, Gulf Shores, Community Number 015005, January 15, 1971.
_____, April 15, 1980.
_____, April 1, 1981.
_____, January 3, 1985.

NFIP, Flood Plain Management Standards, 44 CFR, Parts 59, 60, 61, 62, 65, 70, and 72. Federal Register, Vol. 53, No. 88, May 6, 1988.

Shows, Warren E., University of South Florida, Dept. of Economics, The Economic Impact of Florida's Coastal Setback Line: A Study of Bay County, Florida, September 1976.

Tetra Tech, NFIP Coastal Flooding Storm Surge Model, National Flood Insurance Program, 1981.

Texas Coastal & Marine Council, Model Minimum Hurricane Resistant Building Standards for the Texas Gulf Coast, 1978.

_____, Galveston District, Guidelines for Identifying Coastal High Hazard Zones, June 1975.

U.S. Army Corps of Engineers, Mobile District, Hurricane Fredric: Post Disaster Report, 30 August - 14 September, 1979, February 1981.

U.S. Geological Survey, Hurricane Fredric Tidal Floods of September 12 - 13, 1979, Coast, Gulf Shores Quadrangle, Alabama, 1980.

CHAPTER 221

CROSS-SECTIONAL STABILITY OF ESTUARY CHANNELS IN THE NETHERLANDS

BY

F. Gerritsen¹, H. de Jong², A. Langerak³

ABSTRACT

In this paper, stability characteristics of tidal channels of the Western Scheldt and of the Wadden Sea are compared.

The Western Scheldt is a major estuary in the southern part of the country and is the only remaining open sea-arm in that area after construction of the Delta Project. The Wadden Sea is situated in the northern part of the country and the inlets form the connection between the North Sea and the Wadden Sea.

Stability parameters used for the comparison are the maximum discharge, Q_{max} , the Flood Volume FV (of Tidal Prism) and the mean tidal velocity.

It appears that linear trends can be established between the cross-section and the various stability parameters, for each of the two systems, but that the regression relationship is not the same.

Attempts have been made to develop a universal relationship by introducing a dimensionless stability parameter, in which the dominating hydraulic characteristics are combined. The results are interesting but further research is required to refine this method. The established morphological relationships can be used to predict the changes in channel equilibrium when external changes in the estuary system are introduced. For the Western Scheldt the one-dimensional numerical tidal model IMPLIC will be combined with distinct morphological relationships for the estuary to be used as a predictive tool for the new equilibrium situation created by dredging works.

1 Professor of Ocean Engineering, University of Hawaii, Honolulu

2 Researcher, Rijkswaterstaat, Tidal Waters Division, Middelburg

3 Project Engineer, Rijkswaterstaat, Tidal Waters Division, Middelburg,
The Netherlands

1. Introduction

During recent years the interest in morphological behavior of estuarine channels has significantly increased. There is a distinct need to predict the morphological changes in a system after man-made works have been carried out. Among the latter are the dredging of navigation channels and the construction of guide dams to maintain channel depth. Another important reason for the rising interest is the prediction of the effect of sea level rise on the estuarine system on a longer time scale.

Examples of man-made interventions in The Netherlands are the development of the New Waterway leading to the Port of Rotterdam, the dredging operations in the Western Scheldt and the construction of coastal protection works in and near the Texel Inlet (see Figure 1).

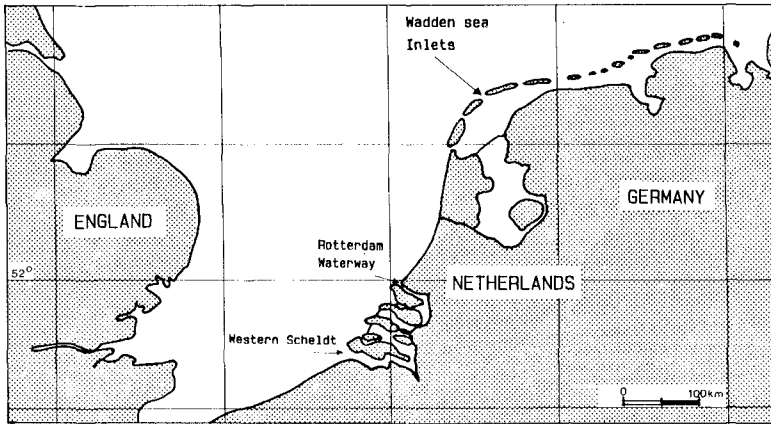


Figure 1. Inlets on the Dutch coast.

The study of morphological behaviour of hydraulic systems such as estuary channels and tidal inlets can follow two different lines of approach. In the first the governing hydraulic equations are combined with equations for the movement of sediment and for the conservation of the mass of sediment. Up to present this avenue has not led to satisfactory results mainly because of uncertainties in the transport equation for the sediments. The second approach is to combine hydraulic calculations with appropriate morphological relationships between channel dimensions and tidal flow.

Detailed studies of the Western Scheldt as a whole and of the Wadden inlet systems (including the channels in the flood tidal delta) have shown that a number of morphological relationships are well defined and consistent so that they can be used as predictive tools to predict future equilibrium. A combination of these relationship (one of them) with a tidal numerical model is seen to be of great significance for future morphological studies.

The objective of this study is to compare cross-sectional stability criteria for the Western Scheldt Estuary and the Wadden Inlets. As stability parameters we will use the

maximum discharge (Q_{max}), the flood volume (FV), the stability shearstress s and the mean tidal velocity, v . In addition a dimensionless stability parameter will be introduced to account for the influence of different hydraulic characteristics on the stability relationship. Finally the one-dimensional numerical model IMPLIC will be used in combination with distinct stability relationship as a predictive tool for morphological development.

2. Regression Analysis

In this section regression relationships for the selected parameters will be discussed for both the Western Scheldt and the Wadden Inlets and conclusions will be drawn regarding the usefulness of these parameters as stability indicators.

Western Scheldt

In previous studies (Gerritsen and De Jong, 1984,1985) it has been suggested that the maximum discharge Q_{max} may well be related to the cross-sectional profile A_c^1 , which is the cross-section of the channel below the tide level, at which the maximum discharge occurs.

In this paper characteristic tidal parameters are related to the mean tide. Although in some cases the mean springtide condition may be a better criterion for stability analysis (because bedforming conditions are likely to be associated with springtide) for our study area this difference appears not to be significant. The relevant stability relationships for the Western Scheldt are shown in Figures 2 to 5 (incl.).

The Western Scheldt is a well mixed estuary; the contributing river Scheldt originates in the southern part of Belgium with a mean discharge of $105 \text{ m}^3/\text{s}$, which is small compared to the maximum tidal discharges in various locations along the estuary itself. Although the river discharge is small, it creates a density gradient along the estuary and has a minor effect on the vertical velocity distribution. However, in the stability analysis no significant influence has been detected from the river discharge or density gradient.

Figures 2 to 4 show the various transects across the Western Scheldt, numbered 1 through 13 (location 13 at the mouth). The dots in the graphs numbered 1-13, correspond with the transects shown in the Figures.

Figure 2 shows the regression between Q_{max} and A_c^1 for flood flow. The dotted line represents the computed regression relationship. For the calculation of this line the cross-sections 12 and 13, which show a somewhat deviating behaviour, have been excluded. This deviating behaviour is also visible in other graphs (see Figures 3 and 4) and can be explained by the effect of wave action on the stability relationships. The presence of waves affects the shearstress near the bottom and thereby affects the stability relationship.

The remaining cross-sections 1 through 11 are grouped around the mean regression line, but some distinct deviations are also noticeable, such as for cross-sections 7 and 11. In these locations the estuary is narrower than would be expected from the overall trend due to bank stabilization works and the profiles are consequently somewhat deeper and

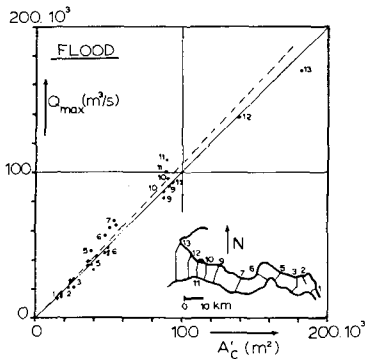


Figure 2. Regression between Q_{max} and A_c^1 for cross-sections in the Western Scheldt (flood conditions, mean tide).

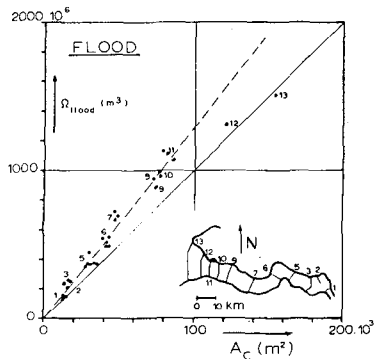


Figure 3. Regression between Ω and A_c for cross-sections in the Western Scheldt (flood conditions, mean tide).

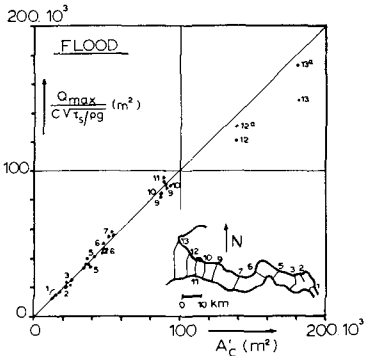


Figure 4. Regression between $\frac{Q_{max}}{C \sqrt{\tau_s / \rho g}}$ and A_c^1 for cross-sections in the Western Scheldt and constant value of τ_s related to mean tide (flood conditions).

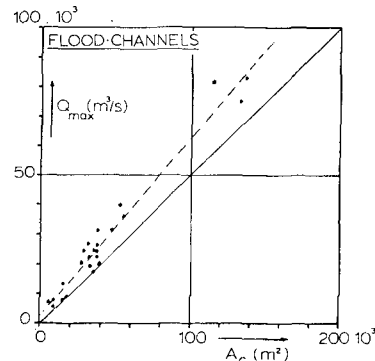


Figure 5. Regression between Q_{max} and A_c for flood channels in the Western Scheldt (mean tide).

the velocities somewhat higher than in the other profiles, for which the width is not controlled.

The relationship between Flood Volume FV (Tidel Prisma) and cross-sectional area A_c (taken below M.S.L.) is shown in Figure 3.

Cross-sections 12 and 13 again deviate from the regression curve (because of wave action), but the profiles 7 and 11 now fall into place. The correlation coefficient is slightly higher than for the relationship between Q_{max} and A_c^1 .

The third regression relationship of interest is that between $\frac{Q_{max}}{C \sqrt{\tau_s / \rho g}}$ and A_c^1 , in which τ_s represents the stability shear converted to mean tide conditions) and C is Chézy coefficient. The mean fluid density is ρ and the acceleration of gravity is denoted by g .

In this analysis the stability shear stress τ_s selected in such way that the regression line makes an angle of 45 with both axis. The two transects 12 and 13 again show a deviating behaviour.

Corrections for the influence of waves can be made by considering the effect of waves on the sediment transport by currents. For this correction use is made of the Bijker

formulation (Bijker, 1967) and the method for this is discussed in Gerritsen and De Jong, 1984. This correction changes the points 12 and 13 to 12a and 13a, which is a significant improvement in the overall relationship.

An estuary like the Western Scheldt is characterized by the existence of flood and ebb channels, in which the flood respectively the ebb dominates.

Figure 5 shows the relationship between Q_{\max} and A_c for the typical flood channels. It appears that a high correlation occurs, but it is also evident that the slope of the line is somewhat steeper than in the similar relationship of Figure 2.

A steeper line indicates that maximum velocities (average over profile) are higher for the channels than for the entire cross-section between banks, which is to be expected.

Wadden Inlets

The Wadden Inlets connect the North Sea with a shallow inland sea, called the Wadden Sea (fig. 6). In the early part of this century the Wadden Sea was in open connection with a large but shallow sea, the Zuiderzee, between Noord-Holland and Friesland and the other eastern provinces. The construction of the Zuiderzee enclosing dam, which was accomplished between 1928 and 1932, affected a significant change in the tidal characteristics and flow conditions of the remaining Wadden Sea. The body of water south of the dam is now called IJssel Lake. A small amount of fresh water is discharged from the lake into the Wadden Sea through sluices in the dam. The effect of this freshwater flow on the larger discharge rates in the Wadden Inlets is considered negligible.

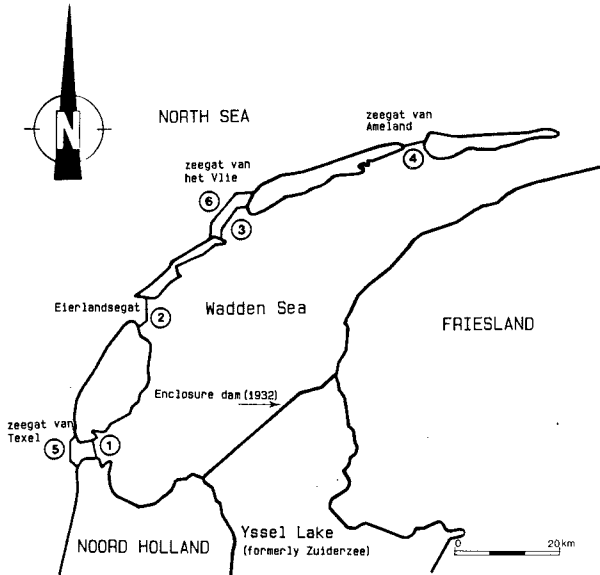


Figure 6. Dutch Wadden Sea (Western part) and Tidal Inlets.

One of the consequences of the closing has been a significant increase in Q_{\max} in the Texel Inlet (cross-sections 1 and 5, Figure 6), which resulted in a strong morphological adjustment (first a reduction followed by an enlargement) of the channel cross-section. Although some parts of the Wadden Sea itself may not have reached a new equilibrium it is found that the Wadden Inlets have reached a condition with a new equilibrium.

In the following some of the prevalent stability relationships will be discussed.

Figure 7 shows the relationship (regression) for all the inlet cross-sections shown in Figure 6. Again we will notice that cross-sections 5 and 6, which are exposed to the open North Sea and are affected by wave action, show a deviating behaviour. The regression line for sections 1-4 shows a high correlation

($r = 0.960$). It is to be noted that the cross-sections 1 through 4 have widely different cross-sections and depths. The Q_{\max}/A_c^1 value (which represents

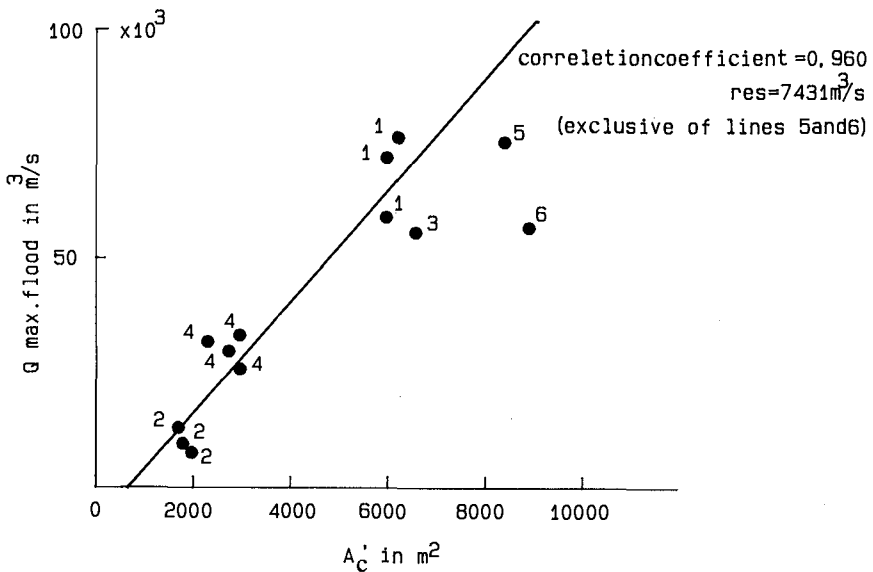


Figure 7. Regression between Q_{\max} and A_c^1 for Wadden Inlets (flood conditions, mean tide).

the average maximum velocity) is not the same for all profiles but increases with the size of cross-section. The regression line consequently does not pass through zero, which is an important characteristic of this relationship.

Figure 8 shows the regression between the flood volume (FV) and the area A_c . The solid line represents the calculated regression line for all sections, exclusive 5 and 6 (which are affected by wave action), whereas the dashed line represents the corresponding line for the Western Scheldt cross-sections (excluding profiles 12 and 13). It appears that the values for the Eyerlandse Gat, E, (section 2) somewhat deviate from the line, but that the other inlets fit the general relationship well.

It is to be noted that the Eyerlandse Gat is a relatively shallow part of the Wadden Sea

in which the depth of the major channels is much less than that of the other parts. The above suggests that a smaller depth corresponds to a lower maximum velocity, which would plot the points for cross-section E (or 2) below the average regression line.

A comparison between the solid and the dotted line shows that the trends for the two systems, the Western Scheldt and the Wadden Inlets, are somewhat different. The suspected effect of velocity on the plottings in Figure 8 is proven by plotting the value of the tide average velocity against the hydraulic radius R (Figure 9). In the data points information for the Wadden Inlets as well as for the Western Scheldt is included. The trend is clear and convincing: the hydraulic radius (or depth) plays a significant role on the velocity, which translates into effects on Q_{max} and FV as well. The data points of the Eyerlandse Gat (E) now fit well in the overall relationship of Figure 9, as do the values for the Western Scheldt (W).

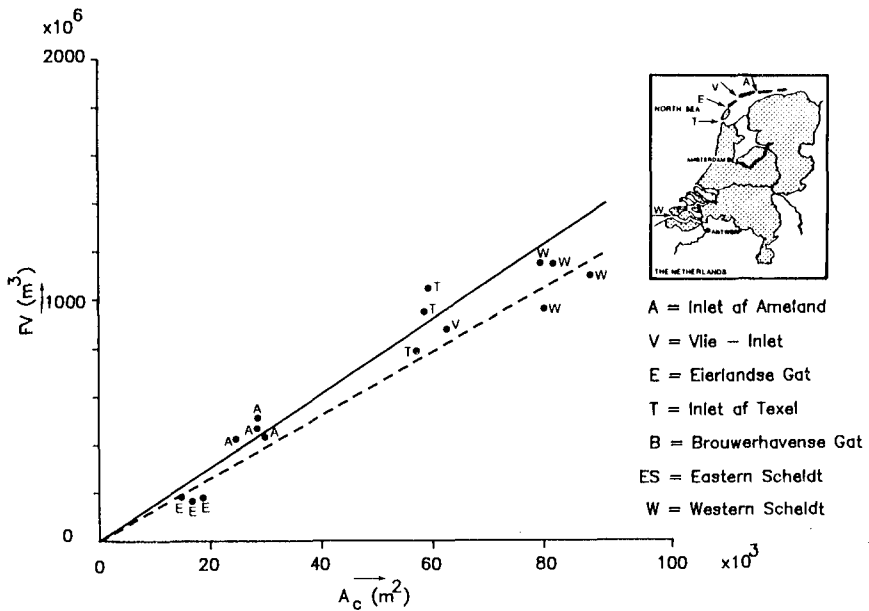


Figure 8. Regression between FV (Ω) and A_c for Wadden Inlets and compared with relationship for Western Scheldt.

It may be concluded that the difference in hydraulic radius (or depth) is one of the principal reasons why regression relationships show deviating trends.

Figure 9 presents important information to calculate and predict the expected behaviour. The relationship between A and Ω (FV) may be adjusted by the dependency on R

(or h). Using the data of Figure 8 we may express that relationship between \bar{v} and R by:

$$\bar{v} = \alpha R^\beta \tag{4}$$

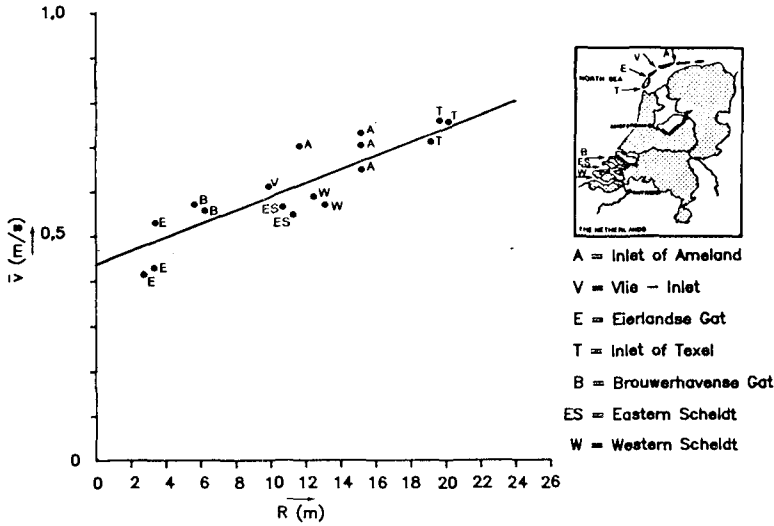


Figure 9. Relationship between v and R for Dutch inlets.

Figure 9 provides the data to calculate the values of α and β : $\alpha = 0.353$ and $\beta = 0.25$
 From the relationship between v and Ω or (FV)

$$v = \frac{2 \Omega}{A_c T} = \alpha R^\beta \tag{2}$$

$$A_c = \frac{2 \Omega}{T \alpha R^\beta}$$

Substituting the experimental values of α and β , and taking a semi-diurnal tide, we have:

$$A_c = 1.269 \times 10^{-4} \frac{\Omega}{R^{0.25}} \tag{3}$$

This relation shows an influence of R on the dependency between A_c and Ω
 In a relatively wide and shallow estuary the hydraulic radius R is almost equal to the mean depth h; equation (3) then develops into:

$$A_c = 1.269 \times 10^{-4} \frac{\Omega}{h^{0.25}} \tag{4a}$$

For relatively deep channels R is retained. Writing $R = \frac{A}{P}$ where p is the wetted perimeter, equation (3) develops into

$$A_c = (7.64 \times 10^{-4}) p^{0.2} \Omega^{0.8} \quad (4b)$$

In shallow channels $p \approx b$, so that

$$A_c = (7.64 \times 10^{-4}) b^{0.2} \Omega^{0.8} \quad (4c)$$

which equation reminds us of the early O'Brien equation with power 0.85.

The equations 4a through 4c express the influence of the form of the cross-section (wide and shallow versus deep and narrow) on the relationship between A_c and Ω .

In the Western Scheldt overall depths in the various channels vary between 9 and 11 m, thus the effect of depth on the relationship between A_c and Ω will be small.

Exceptions are Transects 7 and 11, where the mean depth is over 15 m and for which a small deviation from the overall trend can be expected.

3. Dimensionless stability parameter

A philosophical discussion on stability problems in tidal inlets and estuaries reveals that hydraulic and sedimentological characteristics play a role in the total stability equation (see Bruun and Gerritsen, 1959, Bruun, 1978).

The following parameters may be considered:

Hydraulic Characteristics

Mean tidal velocity, \bar{v}

Hydraulic radius, (or average depth) R

Bottom roughness, k

Chezy coefficient, C

Wave action, H_s

Density of water (sea and estuary), ρ

Sedimentological characteristics

Diameter bottom material, D_{50} and D_{90} .

Density of sediment, ρ_s

Concentration of sediment, \bar{c}

Littoral drift, M

Unfortunately field data do usually not contain a significant range of the various parameters which allow the determination of the influence of these various parameters on the stability problem.

The inlets and estuary under consideration all have for instance a large $\frac{Q_{max}}{M}$ ratio, meaning that tidal flow by passing, if it occurs, is prevalent. The one exception may be the Eyerlandse Gat which has a smaller tidal prism.

With these large tidal flows it is thus expected that the rate of littoral drift does not significantly affect the stability relationships. If water density differences are neglected and the effect of wave action is eliminated (by excluding the profiles exposed to strong wave action) the following parameters remain as essential to the problem:

Relationship between Q_{max} and gross rate littoral drift, M

Diameters of bottom material D_{50} , D_{90}

Chezy coefficient C

Relative density of sediment $\Delta = \frac{\rho_s - \rho}{\rho}$

Ripple effect on sediment (μ)

Depth of channel (h)

It is of interest to formulate a dimensionless parameter, in which the above characteristics are grouped together, either directly or indirectly.

One approach is to consider the similarity between the natural conditions and those in a hydraulic model with movable bed. The design of a movable bed model is based on the condition that the transport scale (the ratio in which sediments in the field and in the model are transported) must be invariant. Only then will a movable bed model give a correct representation of the field conditions to be simulated. In a tidal inlet or estuary channel stability is associated with the condition that

$$\frac{\partial q_s}{\partial s} = 0 \quad (5)$$

Only then a stable cross-section can be expected. This condition represents a self similarity condition comparable to the one for a moveable bed model.

In order to determine what type of relationship provides such (self) similarity a distinction is made between two conditions: one in which the bedload transport dominates and another one, in which the sediment transport in suspension provides the larger portion of the sediment transport. We will consider bed load predominance here. If bedload may be obtained from Bijker (1967) he finds that for the invariance of the transport scale the following condition must be met:

$$n_v = \left(\frac{n_D n_A}{n_\mu} \right)^{1/2} n_c \quad (6)$$

in which scale relationships are identified by n and

$$\frac{V}{\left(\frac{\Delta D}{\mu} \right)^{1/2} C} = \text{const.} \quad (7)$$

The velocity V in the above expression refers to the time averaged velocity v , as well as to the maximum velocity V_{\max} . The value of the constant will consequently differ for these two characteristic velocities.

In the present analysis we will use the value and the corresponding constant we identify with A_1 :

$$\frac{\bar{v}}{\left(\frac{\Delta D}{\mu} \right)^{1/2} C} = A_1 \quad (8)$$

In the above expressions 6 - 8, C represents the Chezy coefficient and μ the ripple coefficient, which expresses the ratio between the bottom shear stress acting on the grain and the total bottom shear stress in the channel where is calculated from

$$\mu = \left(\frac{C_{D90}}{C} \right)^{3/2} \quad (9)$$

in which C_{D90} represents the Chezy coefficient corresponding to the grain size D_{90} .

Using data from the Western Scheldt the values of A_1 have been calculated and are plotted against A_c in Figure 10. The average value of the calculated data points is $A_1 = 0.37$.

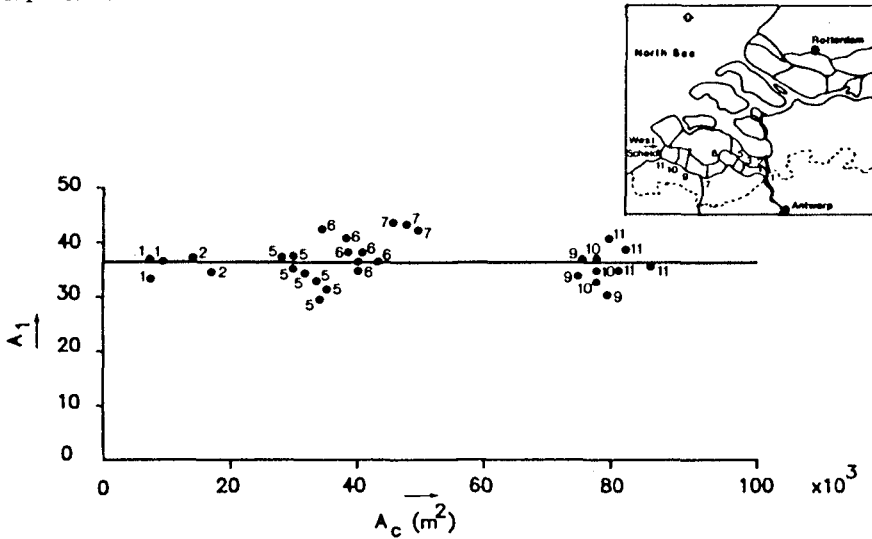


Figure 10. Dimensionless parameter A_1 versus cross-section A_c for Western Scheldt.

In a similar way values of A_1 are calculated for the Wadden Inlets and for the channel system inside the Vlie Inlet. Values of A_1 for the Wadden Inlets were respectively:

- All inlets (incl. 5, 6) $A_1 = 0.43$
- Channels $A_1 = 0.40$

It is concluded that with the present formulation the objective of finding a universal constant that fits all data is not met.

However, a certain amount of precaution is warranted. The determination of the values of A_1 includes the use of hydraulic parameters (μ and C) which have values, that may deviate from the calculated ones, because of lack of precise formulation for the values of these parameters.

It may also be true that the conditions that underlie the basis for A_1 (predominant bedload transport) are not as they were assumed and that suspended transport plays a more dominant role in the process than assumed.

Further analysis will be required to clarify this uncertainty.

It is of interest to confront the condition expressed in equation (7) with the validity of the assumption that the stability shear stress may constitute a stability parameter.

Equation 7 may be converted to:

$$\frac{\mu \tau_s}{(\rho_s - \rho) g D_{50}} = \text{const.} = A_2 \tag{10}$$

It is concluded that a constant value of s is not in agreement with a constant value of $A2$, but that the stability condition requires

$$\frac{\tau_s}{(\rho_s - \rho)g D_{50}/\mu} = \text{const.} \quad (11)$$

4. Computer Simulation

The use of morphological stability relationships in computer simulation of these processes is based on the use of an appropriate numerical model (for hydraulic calculations) and an additional morphological submodel to be incorporated in the numerical scheme.

In the Western Scheldt the numerical hydraulic model IMPLIC, which is a one-dimensional tidal model, provides an efficient basis for the calculations.

In order to find out whether or not the present schematization for the IMPLIC model is accurate enough to allow formulation of stability relationships, model data have been used to verify the possible use of stability relationships in the model. Figure 11 shows the present channel system of the Western Scheldt and Figure 12 the corresponding set of interconnected channels that form the IMPLIC model.

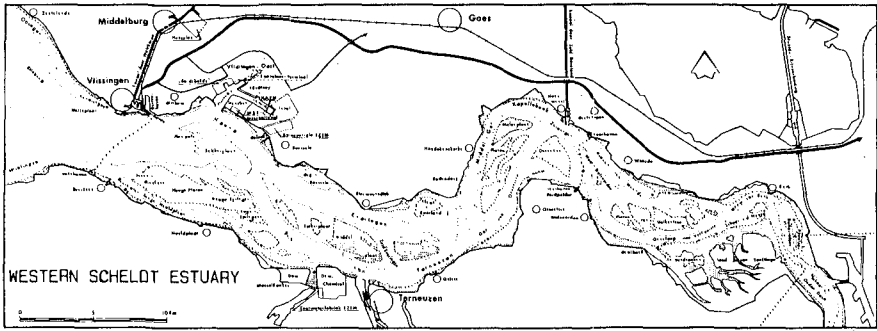


Figure 11. Western Scheldt Estuary.

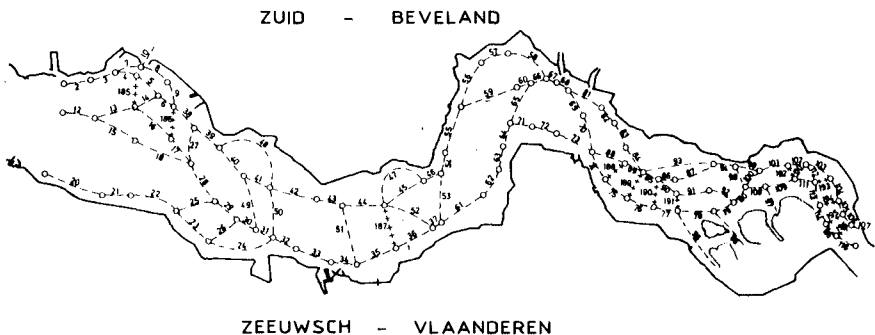


Figure 12. Schematization of Western Scheldt for IMPLIC model.

It appears that the schematization of the model is accurate enough to allow the establishment of morphological relationships from the model data.

That the present model has the capabilities to be used in conjunction with predescribed stability relationship to calculate stability conditions after technical changes have been made in the system.

The procedures of computation are in an iterative mode. After a change has been made in the system, (which is in equilibrium) tidal calculations are made with IMPLICIT to determine the changes in discharge. In general the system will be out of equilibrium after the change is made and will turn back to a new equilibrium. An example is the deepening of a navigational channel by dredging, which has been the case in the Western Scheldt.

Suppose the increase in cross-section from a dredging operation equals ΔA . Depending on the extent of the dredging operation tidal velocities in the system will change (usually decrease) after the dredging and the system will develop into a new equilibrium. In the computations cross-sections are adjusted gradually until a new equilibrium stage is obtained, in which the morphological parameter which is selected for the computations, corresponds with the adjusted cross-section.

Morphological adjustment usually develops in an exponential way as a function of time. This corresponds with the assumption

$$\frac{\partial A}{\partial t} = -\lambda \Delta A = -\lambda (A - A_0) \quad (12)$$

in which A_0 represents the equilibrium cross-section and λ a time scale factor. If A_i is the initial cross-section immediately after dredging integration gives

$$\frac{A - A_0}{A_i - A_0} = e^{-\lambda t} \quad (13)$$

The coefficient determines the time scale of the process. An estimate for the value of λ can be obtained from the gradient of sediment transport that has been induced into the system.

The continuity equation for sediment transport can be written in the form

$$\frac{\partial A}{\partial t} + \frac{\partial \bar{Q}_s}{\partial s} = 0 \quad (14)$$

In which \bar{Q}_s is the mean rate of sediment transport through the cross-section over a tidal cycle.

Using equation 12 thus leads to:

$$\frac{\partial A}{\partial t} = -\frac{\partial \bar{Q}_s}{\partial s} = -\lambda (A - A_0) \quad (15)$$

$$\lambda = \frac{\partial \bar{Q}_s}{\partial s} / A - A_0 \quad (16)$$

$$\lambda_i = \left(\frac{\partial \bar{Q}_s}{\partial s} \right)_i / A_i - A_0 \quad (17)$$

Where the index i denotes the initial condition after dredging.

The value $\partial \bar{Q}_s / \partial s$ can be calculated using an appropriate formulation for sediment transport from which λ can be calculated.

5. Conclusions and recommendations

1. Both for the Western Scheldt Estuary and for the Wadden Inlets morphological relationships have been established that provide a valuable tool for morphodynamic analysis.
2. Morphological relationships can be established for entire cross-sections, but also for separate flood or ebb channels, if the corresponding flood flow or ebb flow is taken as the relevant parameter.
3. The hydraulic radius or mean depth appears to be a significant scaling parameter in comparing large and small tidal inlets. The established relationship between v and R can be used to modify the relationship between A_c and v , taking the effect of depth into account.
4. The introduction of a dimensionless parameter is intended to make morphological relationships independent of grain size, material density mean depth and channel roughness.
A first approach is promising but needs further work.
5. Morphological relationships can be used in combination of a numerical tidal model. The model IMPLIC has been selected to be used for the Western Scheldt.

6. Selected References

1. Bruun, P. and F. Gerritsen (1960): 'Stability of Coastal Inlets'. Elsevier Scientific Publishing Co., Amsterdam, Oxford, New York.
2. Bruun, P. (1978). 'Stability of Tidal Inlets, Theory and Engineering'. Elsevier Scientific Publishing Co., Amsterdam, Oxford, New York.
3. Bijker, E.W. (1976): 'Some Considerations About Scales for Coastal Models with Movable Bed'. Doctoral Dissertation, Delft Technological University.
4. De Jong, H. and F. Gerritsen (1984): 'Stability Parameters of the Western Scheldt Estuary'. I.C.C.E., 1984, Houston.
5. Gerritsen, F. and H. de Jong (1985): 'Stabiliteit van doorstroomprofielen in het Waddengebied'. Rijkswaterstaat, The Netherlands, Nota WWKZ-84.V016.
6. Kreeke, J. v.d. and J.A.C. Haring (1979): 'Equilibrium Flow Areas in the Rhine-Meuse Delta'. Coastal Engineering, 3, 97-111. Elsevier Scientific Publishing Co., Amsterdam.

CHAPTER 222

Variations in rheological properties of muds in the Gironde estuary

Pascal Galichon*, Alain Feral**,
Jérôme Granboulan**, Jacques Viguier*

ABSTRACT

In numerous navigation channels, the bed consists of muds. The navigability threshold adopted by many ports is currently that which corresponds to a specific gravity of 1.2. This virtual standard does not fully take into account the rheological characteristics of the muds, which may differ from one site to another.

Investigations were carried out to determine the rheological properties of the Gironde estuary muds. Analyses were carried out in the laboratory on samples taken from different sites and on different dates and in situ, using the SR 10 probe developed by SOGREAH and ultrasonic sedimentometric probe developed by the Bordeaux Port Authority. The results demonstrated the occurrence of major spatial and temporal variations.

The two principal phenomena revealed by the research were that with the same dry sediment content:

- . muds were less rigid at the front of the maximum turbidity zone than at the back, by a factor of about 1.6 to 2.5,
- . the greater the annual flood, the lower the rigidity.

A proper understanding of the spatial and temporal variations of rigidity is therefore essential to determine and adjust the navigability threshold.

* SOGREAH Consulting Engineers, 6 Rue de Lorraine, 38130 Echirolles, France

** Port Autonome de Bordeaux, Quai de Bacalan, 33000 Bordeaux, France

INTRODUCTION

The beds of navigation channels consist of muds. Today, the nautical depth is considered to be the depth of water between the unconfined surface and a given level of density (or specific gravity) referred to as the nautical bottom.

A specific gravity value of 1.2, which corresponds to a dry sediment density of around 300 g/l, is currently adopted as navigability threshold by ports such as Rotterdam, Zeebrugge, Nantes-Saint-Nazaire and Bordeaux. However, the establishment of this virtual standard does not fully take into account the rheological behaviour of the muds. With the same concentration levels, muds at different sites may have widely varying rigidity values. Thus, defining the notion of navigability threshold on the basis of a rigidity criterion rather than specific gravity could in some cases result in an increase in the nautical depth.

In order to examine whether this type of procedure would be possible, the Bordeaux Port Authority commissioned SOGREAH to compare the rheological characteristics of muds from the Gironde with those from other ports where the navigability threshold is based on a specific gravity value of 1.2 and where rheological measurements were available. The study consisted of three parts: preliminary investigations, in situ measurements and additional rheological analyses.

1. PRELIMINARY INVESTIGATIONS

Preliminary investigations involved comparing the rheological curves for Gironde mud obtained in the laboratory and dating from before March 1987 with similar curves for muds from the Loire and Mahury.

The same rheological analysis methodology has been used at the Laboratoire Central d'Hydraulique de France and at SOGREAH for nearly 30 years. It enables a comparison to be made between different investigations. Here, the initial rigidity is defined as the torque required to set in motion a rotor immersed in the mud.

This rigidity varies with the dry sediment concentration, following a relation of the type: $\tau_y = aT_z^b$, in which τ_y is the initial rigidity and T_z is the concentration. Two different domains - liquid and plastic - may be defined, where a and b are different (fig. 1). These are separated by what is referred to as critical values, namely critical initial rigidity and critical dry

sediment concentration. Determination of these values enables a comparison to be made between muds from different sites.

Figure 2 shows the critical dry sedimentation concentration for different sites. It appears that mud from the Gironde passes from a liquid to a plastic state at higher concentrations (340-620 g/l) than muds from the other sites considered (250-350 g/l).

Figure 3 shows that the initial rigidity for a dry sediment concentration of 300 g/l is less in the Gironde estuary than at the other sites. Seen from another point of view, the initial rigidity of muds from the Gironde at 350 g/l corresponds to that found for concentrations of 300 g/l (i.e. a specific gravity of the order of 1.2) from the other sites.

However, there was a certain spread of the results (figure 4) showing that the trend observed would have to be confirmed by other investigations, namely in situ measurements and additional rheological analyses.

2. IN SITU MEASUREMENTS

The aim of the in situ measurements was:

- . to establish an approach for in situ rheological characteristics variations in relation to density,
- . to make comparisons with the measurements carried out in other ports.

2.1. CONDITIONS AND MEANS EMPLOYED

The SD 105 ultrasonic densitometric probe, belonging to the Bordeaux Port Authority and the SR 10 probe were mounted on the same structure (fig. 5). This was done in such a way as to ensure that the two probes, separated horizontally by about 20 cm, should remain at the same level as they descended vertically. In this way it was possible to measure, in situ and applied to the same mud, the pair of values for the density (ultrasonic probe) and a rheological characteristic of the mud (SR 10 probe).

2.1.1 PRINCIPLE OF THE SR 10 RHEOLOGICAL PROBE

The probe comprises a cylindrical body, at the end of which a cone rotates at a constant speed (240 rpm). The electrical intensity required to maintain a constant rotating speed is measured. It is then correlated, after laboratory calibration, in relation to the initial rigidity.

2.1.2 SR 10 PROBE LABORATORY CALIBRATION

Two measurements are made for single mud sample:

- . on the one hand the initial rigidity using a Brookfield viscometer,
- . on the other hand measurement of the electrical intensity using the SR 10 probe.

In this way an initial rigidity-intensity pair is obtained for each sample.

The probe calibration curve is established on the basis of all the pairs (initial rigidity, intensity) obtained using samples of varying concentration.

Figure 6 illustrates the various values obtained on different sites. The low dispersion of values should be noted, and a standard calibration curve may be used for an initial approach, regardless of the site.

Due to the lack of a specific calibration curve, the standard calibration curve was adopted for this investigation.

In this way, it is possible to establish a correspondence between an intensity obtained by the SR 10 probe and a single initial rigidity, which we shall refer to as the "associated initial rigidity".

2.1.3 SD 105 PROBE PRINCIPLE

The SD 105 probe measures attenuation of ultrasonic sound attributable to the mud passing between the transmitter and the receiver. This is proportional to the concentration. Laboratory calibration using Gironde mud made it possible to establish the mud concentration. It should be noted that the probe was used here for vertical measurements, but a version does exist which may be pulled behind a ship. This latter makes it possible to make horizontal density measurements in navigation channels.

2.2 MEASUREMENTS CARRIED OUT

2.2.1 METHODOLOGY

Three vertical investigations were carried out on three different sites, with the probes mounted on the same structure. Subsequently a single vertical investigation was carried out on one site, with the probes separated.

During each of the vertical investigations, pauses in the descent were made. At each pause, a pair of SD 105 attenuation (concentration) and SR 10 intensity (associated initial density) values was noted. Fig. 7 shows an example of a recording.

2.2.2 MEASUREMENT RESULTS

Sites 1, 2 and 3

Figure 8 shows the concentration and associated initial rigidity variations in the axis of the channel, on the basis of the measurements made for the first three sites.

It would appear that in the area of site 3, the furthest downstream, one pass was filled by density currents coming from upstream. In the light of measurements made elsewhere, the slope of approximately 0.4% between sites 1 and 2 appears to be sufficient to produce a flow of this type carrying with it a higher proportion of sandy matter. In addition the vertical rigidity and density gradients show that, in all probability, the uppermost layer on site 3, over approximately 30 cm, is a recent arrival which has not yet had the time to solidify.

Site 4

On this site the two probes were separated.

As is shown in figure 7, the two probes detected a superficial layer, about 20 cm thick, with a higher density and rigidity than the layer immediately below. The measurements, carried out at the end of the ebb-tide, indicate a contribution from upstream, which supports the previous hypothesis concerning flow from upstream to downstream and in addition the possible existence of a negative density and rigidity gradient (but certainly only temporarily).

2.3 COMPARISON WITH MEASUREMENTS MADE ON THE GIRONDE IN OCTOBER 1984

The circumstances of the two missions, both in terms of space and time, are very different; the two sites are situated about 30 kilometres apart and the first investigations were carried out in the autumn, the second in the spring. However it should be noted, as G. Allen showed (1972), that sites may correspond to the respective positions of the maximum turbidity zone, which is located further downstream in March than in October.

Figure 9 makes it possible to compare the results of the two investigations: it appears that the majority of the points correspond to the range of values noted during the last mission. (The 1984 values nevertheless appear slightly lower, as a whole, than in 1987).

2.4 COMPARISON WITH MEASUREMENTS CARRIED OUT ON OTHER SITES

Comparison with measurements carried out on the Seine and the Loire (cf figure 10) show that in two cases Gironde mud appears in situ to be less rigid than that from other estuaries. For example a concentration of 300 g/l in the Loire corresponds to an associated initial rigidity of 15 N/m², which would correspond to a 350 g/l concentration in the Gironde.

Consequently, after taking account of the in situ measurements, it appears that in comparison with the other ports and taking account of the hydro-sedimentary conditions encountered during the different investigations, the Gironde muds are less rigid in situ. Consequently this result would justify admitting a navigability threshold situated at a higher density than 1.2. However, to be sure that such steps may be taken, it seems appropriate to acquire increased knowledge on spatio-temporal variability of rigidity levels in situ, for the comparison of different analyses of mud samples collected at different places and times show that significant variations may occur. During this assignment, samples were taken for analysis. The mud proved to be more rigid than that studied previously. It was then decided to carry out rheological analyses on samples in order to show up any spatio-temporal variations in rigidity.

3. SPATIO-TEMPORAL RIGIDITY VARIATION

These analyses were carried out on 10 samples taken between March 1987 and April 1988. They concluded that in general, mud from 1987 was more rigid than that from 1984. In an attempt to explain the cause of initial

rigidity value dispersion, the 300 g/l rigidities were entered in a graph. This was done for all the samples collected in the Gironde, whose date and place of collection was known. The position of the maximum turbidity zone, as observed by G. Allen in 1970-71 (figure 11) was also entered on the same graph.

It should be noted that movement of the mud zone may vary in time. It depends on variations in river flow.

It has been established that in general mud collected to the rear of the mud zone, in relation to the direction in which it is moving, appears more rigid than mud collected to the front of the zone. The ratio varies between 1.6 and 2.5. It seems probable that the age of the mud partly explains the phenomenon, but there may exist other factors such as grain sizes or changes in the mineral composition.

3.1 VARIATION IN RIGIDITY WITH RIVER FLOW

In addition, taking the samples collected between March and April and tracing the 300 g/l initial rigidity variations in relation to river flow in February (the month in 1984, '87 and 88 when flow was highest - cf. figure 12), it is clear that at PK 72 (the only PK for which measurements are available for three different years) the 300 g/l initial rigidity drops at the same time as the flow.

A relation of this sort deserves confirmation on the basis of other measurements.

The high rigidity values observed in 1987 seem to be accounted for by the absence of significant flood flow that year, and inversely, the low values obtained in 1984, in particular in May, seem to be attributable to the heavy flooding in February 1984.

4. CONCLUSIONS

The results of the 1987 measurements did not confirm that Gironde mud is systematically less rigid than that from the other sites. Because of this, in the present state of information, no decision can be reached with respect to the systematic adoption of a navigability threshold corresponding to a specific gravity of more than 1.2. However, it is likely that this would be possible in certain cases.

Indeed, the study showed that at a given spot, the rheological properties of the Gironde muds appear to be in relation to the hydrosedimentary conditions (and more particularly the river discharge).

In particular, it would appear that the rigidity of a mud is lower when the deposit is the result of suspended sediment introduced recently into the estuary. In the lower reaches of the river, fluid mud generally forms after the initial floods. Consequently, under these circumstances, the rigidity of the mud in the downstream reaches of the estuary is lower than that at other sites. Hence, a navigability threshold corresponding to a specific gravity higher than 1.2 could be considered.

Far more data is available for the Gironde than for the other sites. More information, obtained under varying hydrosedimentary conditions, will be needed for these sites before statistically valid comparisons can be made.

REFERENCES

G.P. Allen: Etude des processus sédimentaires dans l'estuaire de la Gironde. Doctoral thesis, University of Bordeaux I, 1972.

J. Grandboulan and M. Chaumet-Lagrange: Un nouvel instrument pour optimiser l'entretien des chenaux d'accès portuaires: la sonde sédimentométrique à ultrasons. Revue Technique des Phares et Balises N° 71, 1986.

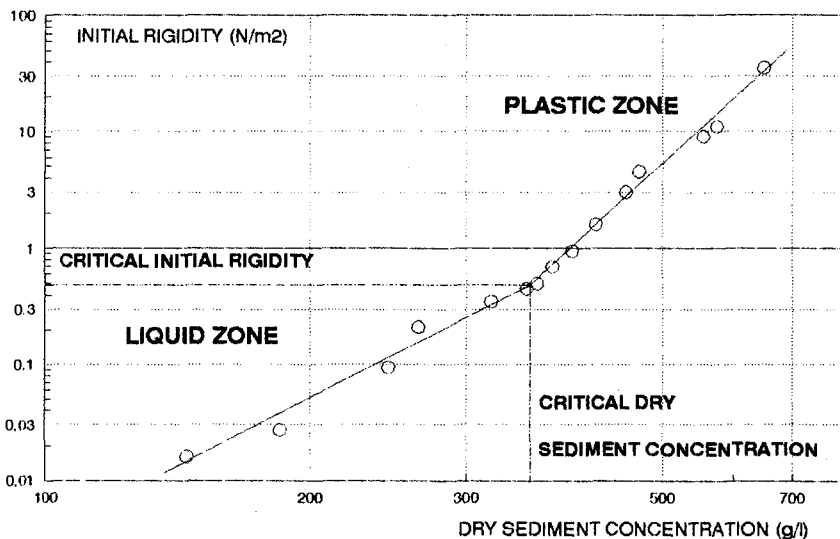


FIG 1: INITIAL RIGIDITY IN RELATION TO THE DRY SEDIMENT CONCENTRATION

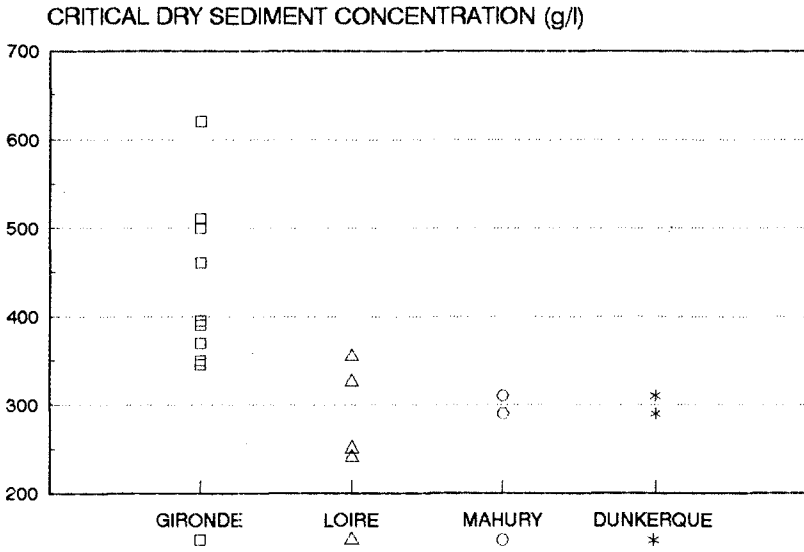


fig 2: CRITICAL DRY SEDIMENT CONCENTRATION FOR DIFFERENT SITES

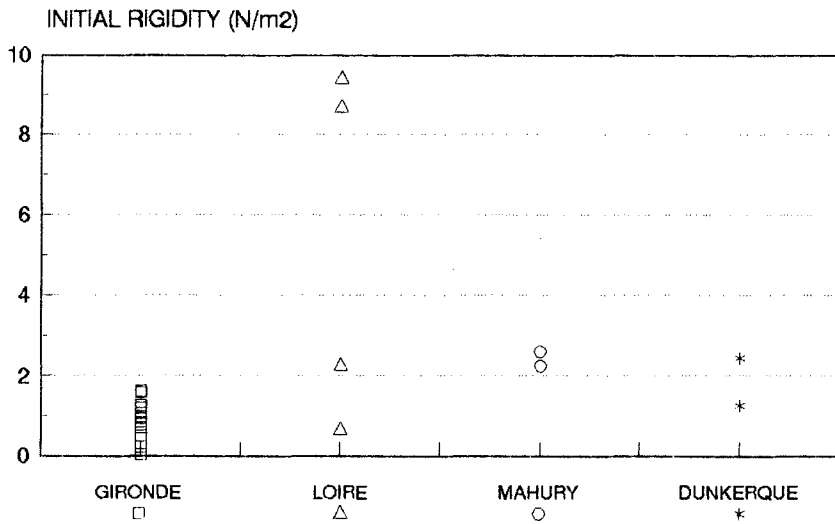


FIG 3: INITIAL RIGIDITY FOR DIFFERENT SITES FOR A DRY SEDIMENT CONCENTRATION OF 300 g/l

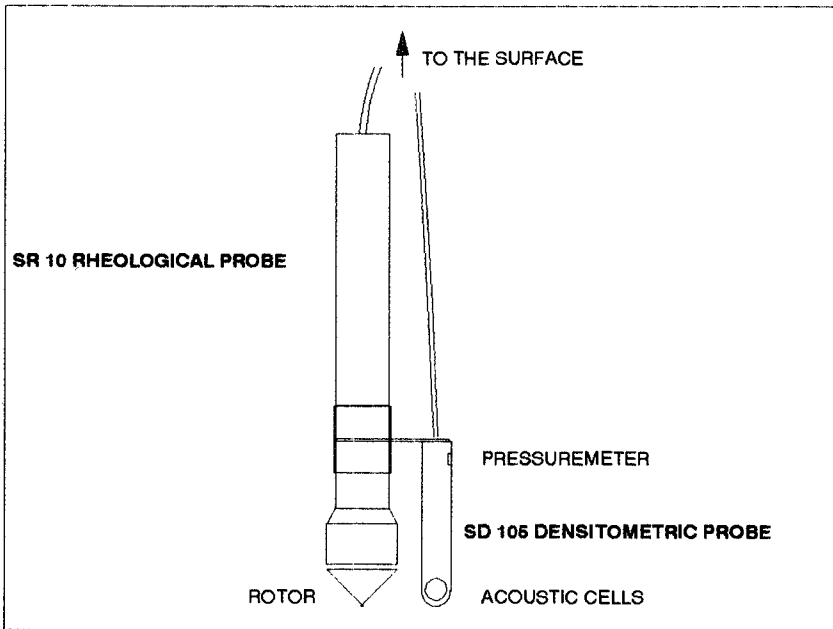
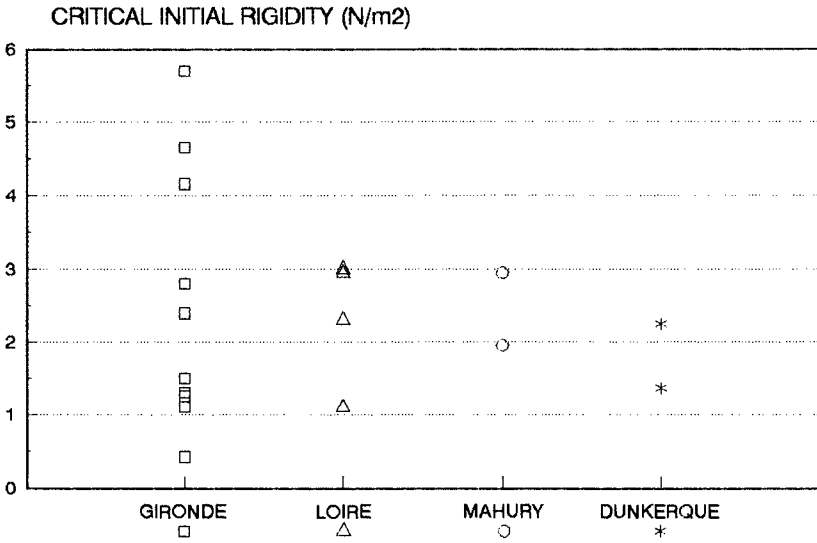


FIG 5: SCHEME OF THE COUPLING OF THE DENSITOMETRIC AND RHEOLOGICAL PROBES

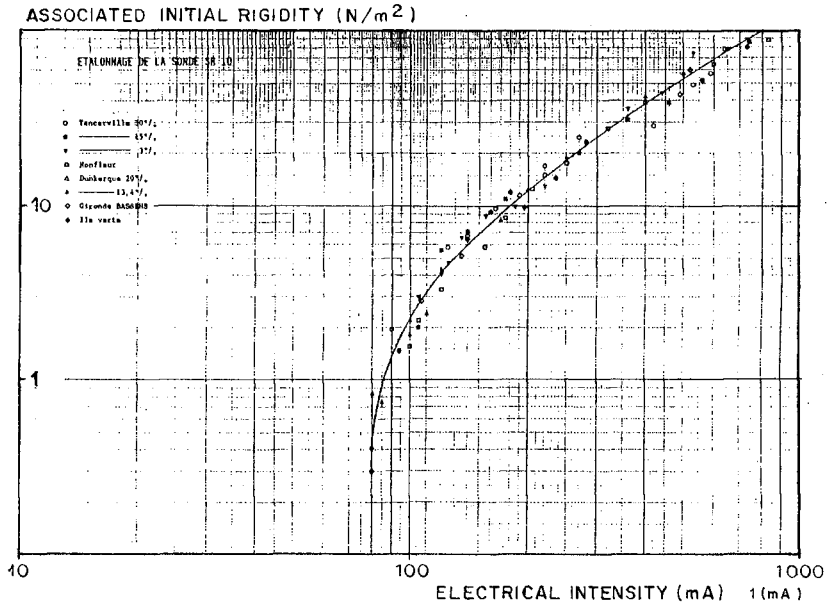


Fig. 6 - SR 10 RHEOLOGICAL PROBE CALIBRATION

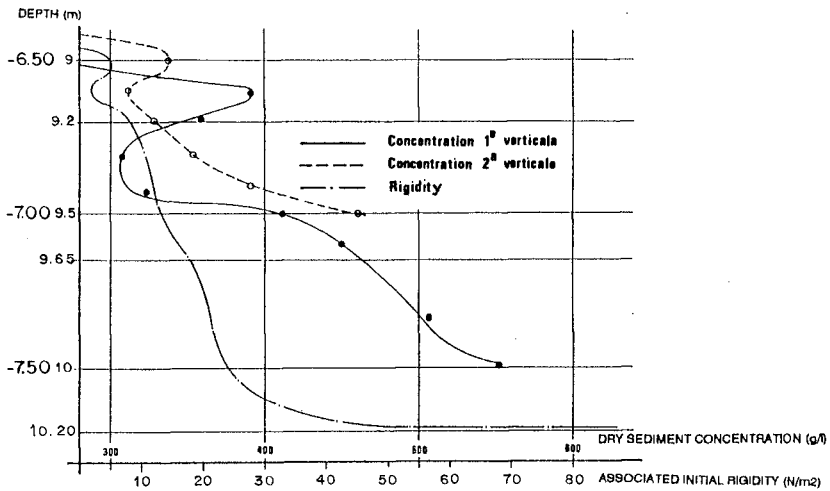


Fig. 7- VARIATION OF THE CONCENTRATION AND THE RIGIDITY WITH THE DEPTH (SD 105 AND SR 10 SEPARATED)

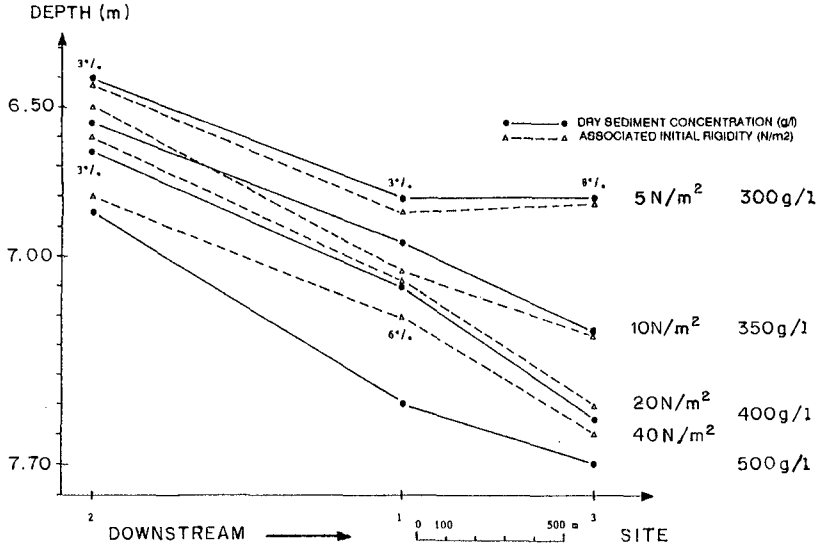


Fig.8 - SPATIAL VARIATION OF DRY SEDIMENT CONCENTRATION AND ASSOCIATED INITIAL RIGIDITY

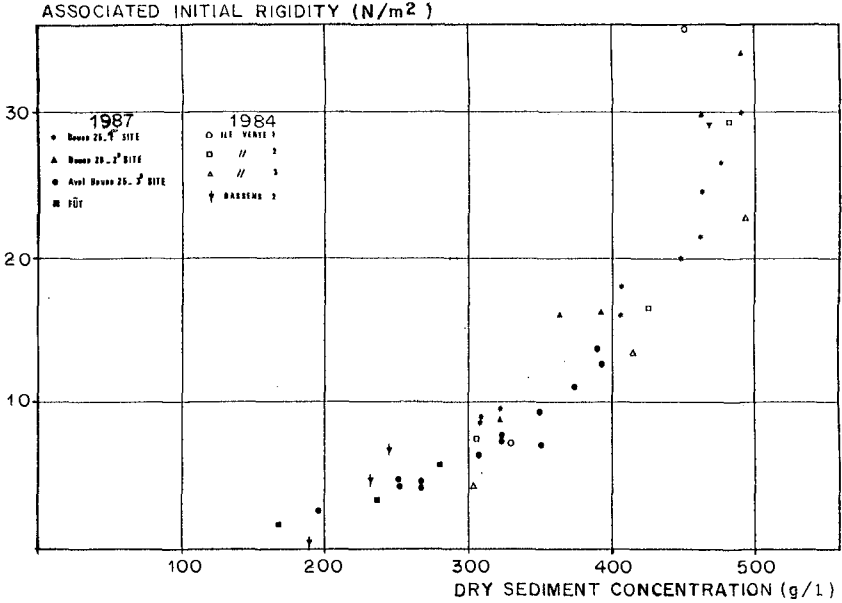


Fig. 9 - RELATION BETWEEN DRY SEDIMENT CONCENTRATION AND ASSOCIATED INITIAL RIGIDITY IN SITU FOR GIRONDE

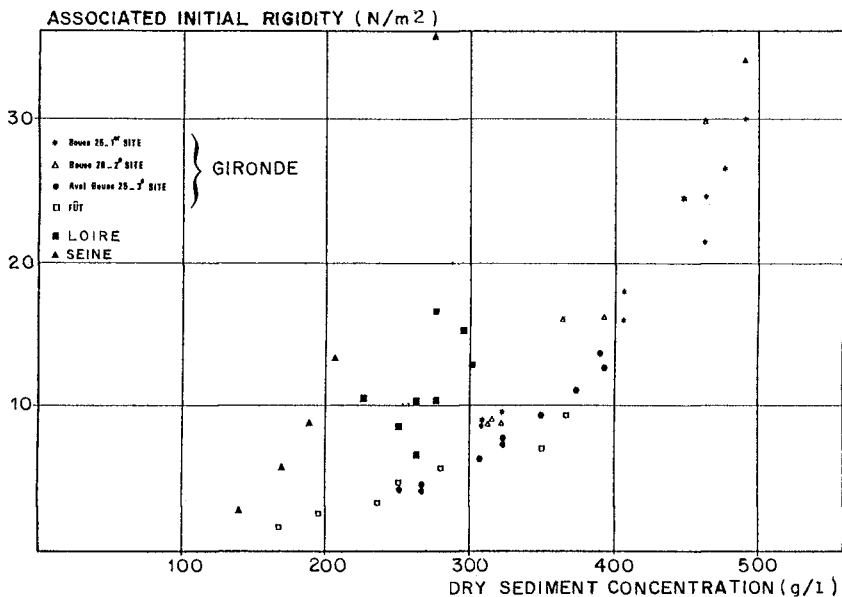


Fig. 10- RELATION BETWEEN DRY SEDIMENT CONCENTRATION AND ASSOCIATED INITIAL RIGIDITY IN SITU FOR DIFFERENT SITES

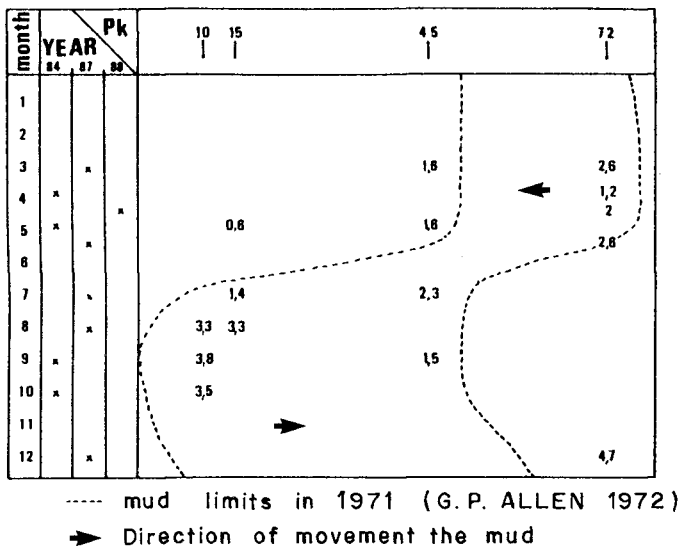


Fig. 11- Initial rigidity variations at concentration of 300g/l (Pa)

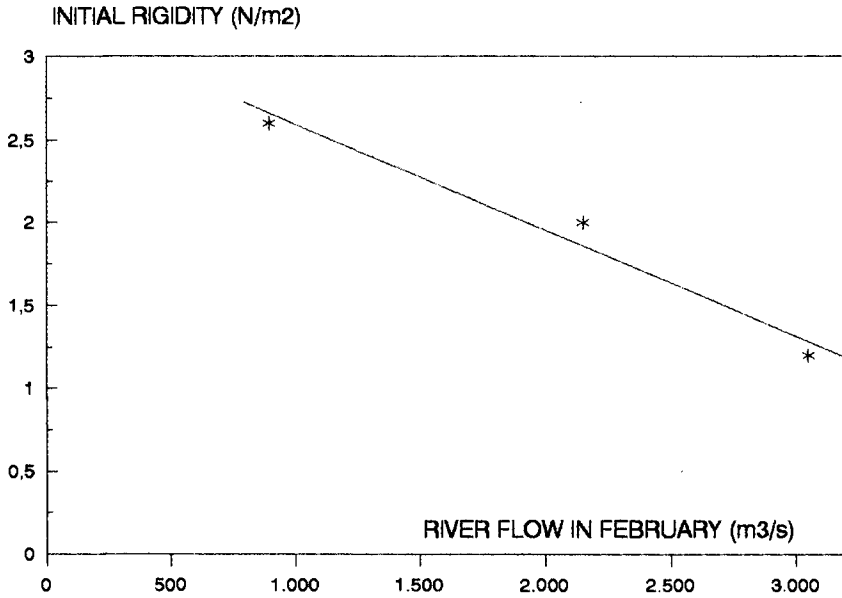


FIG 12: VARIATION AT Pk 72 OF THE INITIAL RIGIDITY FOR A DRY SEDIMENT CONCENTRATION OF 300 g/l IN RELATION TO THE RIVER FLOW IN FEBRUARY (annual maximum)

CHAPTER 223

Hydraulic Aspects of the construction of the Eastern Scheldt Storm Surge Barrier

Jan Konter¹ and Leo Klatter²

1. Abstract

The paper gives an overview of the results of the evaluation studies of the hydraulic aspects of the construction of the Eastern Scheldt Storm Surge Barrier. Subjects discussed are: methods used, design philosophy, results of flow modelling, stability of rubble stone structures, local scour and morphology.

2. Introduction

The Eastern Scheldt Storm-Surge-Barrier has been built across the three main tidal channels in the mouth of the Eastern Scheldt, from North to South respectively Hammen, Schaar and Roompot (see figure 1).

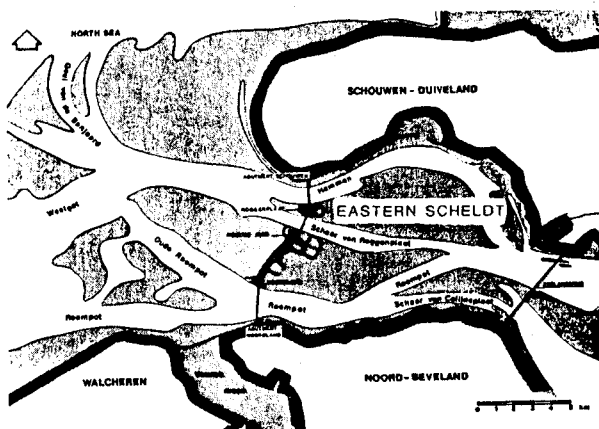


Figure 1: Location of the Storm-Surge-Barrier in the mouth of the Eastern Scheldt

^{1,2} Rijkswaterstaat, Construction Division, Hydraulic Branch, P.O. Box 20.000, 3502 LA Utrecht

The three barrier sections are interconnected by dams, that have been constructed upon the shallow tidal flats between the main channels. The construction of the barrier took place in the original channels, without a building pit. This construction method was chosen to minimize the effect of the construction activities on the tidal movements. To enable such a construction method, prefabricated elements were used when and where possible. The original seabed served as a foundation. After soil improvement and compaction the sand-bed was covered with large prefabricated mattresses 41 m wide and 200 m long. Upon the filter mattresses the piers were placed (see figure 2).

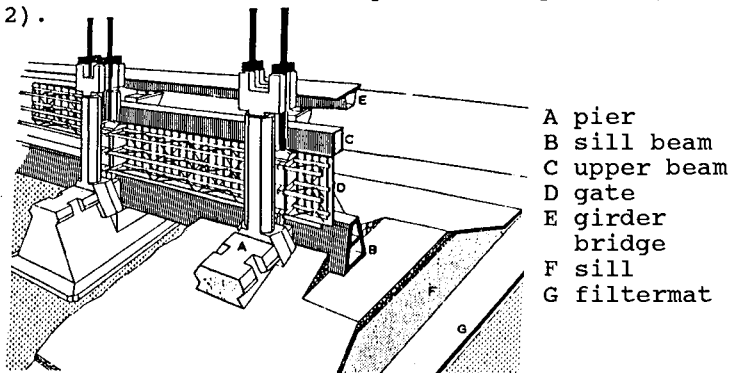


Figure 2: Elements of the Eastern Scheldt Barrier

The piers were packed by a rubble sill, that was built up in layers. A concrete sill beam and upper beam frame the actual flow opening, which can be closed by a gate. This gate is operated by hydraulic cylinders which were placed on top of the piers. The entire structure was assembled under open sea conditions. The construction activities took place simultaneously in the three channels.

The type of the structure, as well as the construction method inflicted a number of hydraulic problems that had to be solved:

- flow problems
- stability of rubble stone and bottom protection
- local scour at the borders of the bottom protection
- morphology of the mouth of the Eastern Scheldt
- environmental aspects.

3. Set up of the Investigation

The construction of the Barrier often resulted in conflicting interests, e.g.

- the time schedule of the work favoured finishing one channel after another, but this was unacceptable for morphological reasons.
- Closing already installed gates, created favourable working conditions in the vicinity of the Barrier, but closing of some gates may create problems at locations where the gates were not closed, with the stability of stones and bottom protection. The complete closure of one channel was also not allowed for morphological and environmental reasons.

This indicates that numerous possible geometries of the Barrier under construction were possible, each with its own complex flow pattern. Therefore a flexible prediction system for the flow conditions was necessary. This could be accomplished by choosing a selected number of hydraulic parameters as "load" parameters and to relate the "strength" of the item considered (e.g. stability of stones) to the selected "load" parameter. The selected hydraulic parameters fulfill two important criteria:

1. It can be predicted with reasonable accuracy
2. It governs the process to the hydraulic problem.
In other words there must be an unique relation between this hydraulic parameter and the strength.

In table 1 some examples are given of the flow parameters that were used as "governing hydraulic parameters" for the hydraulic problems encountered.

aspect	hydraulic parameter
environmental aspects	tidal difference γ
morphology at the mouth of the Eastern Scheldt	Δh_s
stability of rubble sill: - during construction - at final situation	q/A Δh
hydrodynamic loads on the large structural elements (piers, sill beams, upper beams, gates) during positioning	q/A
stability of bed protection	Δh
scour	Q

Table 1

To represent the flow conditions in the vicinity of the Barrier the following basic hydraulic parameters were selected

- Q = discharge through a main channel (m^3/s)
 Δh = head difference over the Barrier (m)

- Δh_s = difference in water level between two main channels (m)
- q/A = average velocity at the axis of the Barrier, defined as discharge per barrier section divided by the wet cross section (m^3/s)
- Y = tidal difference in Yerseke (selected harbour in the Eastern Scheldt).

With this approach the flow parameters that had to be predicted (Q , Δh , Δh_s , q/A and Y), depended only on the global geometry of the Barrier under construction (expressed as μA).

Details of the flow pattern are not important for the behaviour of these parameters. In general these parameters can be predicted by a one dimensional flow model, eventually combined with a resistance model to get q/A (See figure 3).

The prediction of the wave characteristics can be done in the same way with a wave model. Basic flow parameters and wave characteristics are the boundary conditions for the structure and the input for eventually necessary three-dimensional scale models.

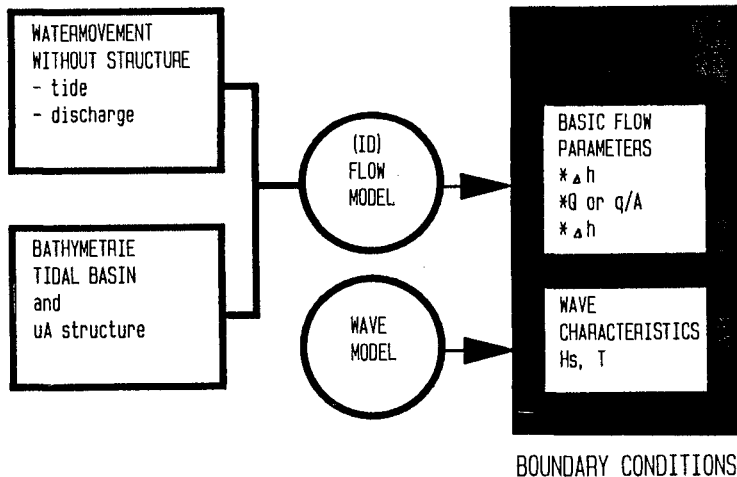


Figure 3: determination of boundary conditions

The next step is to find the "load-strength" relations, or the relation between the basic flow parameters and the design problems. It is strongly recommended to select a model that can express the strength in the same way as the loads (See figure 4) for example:

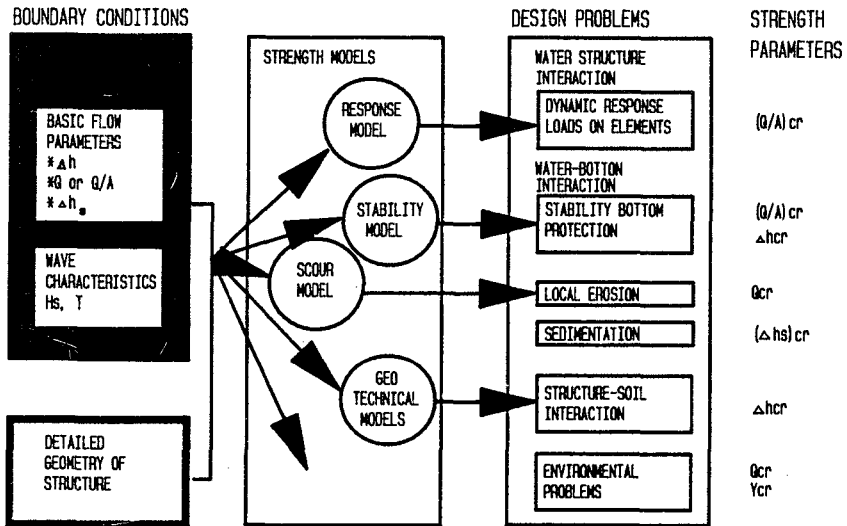


Figure 4: "load-strength" relations

Δh_{cr} and $(q/A)_{cr}$ are for example the critical values of Δh and Q/A at which the strength is not enough anymore (movement of stones, or to much erosion, etc.). In this way insight can be obtained in the interaction between the different hydraulic aspects, and with this insight the optimal solution for the conflicting hydraulic problems can be found. Beside this, expressing the loads and strength in the same parameter is necessary for probabilistic calculations.

It is noticed that as input for the strength models the detailed geometry of the structure is necessary. Therefore a three-dimensional model is necessary, in which the geometry of the structure can be reproduced correctly. The most reliable way to study the "load-strength" relation is the use of physical scale models. Also for the Eastern-Scheldt Barrier studies, a lot of attempts were made to find the "load-strength" relation by mathematical models. A reliable mathematical model for the complex three-dimensional interaction between structure-structure element bottom and water movement needs still a lot of effort and time before the same accuracy can be reached as a physical (scale) model. The mathematical model, gave more insight in the "black-box" of the physical scale model, but for most of the design purposes of the Barrier the results of the scale models were used.

A combination of relatively simple 1D or 2D-mathematical

models (finding the boundary conditions or "loads") and 3D scale models (finding the "load-strength" relations) proved to be the optimum tool.

4. Results

The approach described in section 2 proved to be very successful. The selected governing parameters made an integration of all items possible, and in most cases an optimal solution could be found between the conflicting interests.

A continuous evaluation of field experience during the construction period served as a check on the relations that were used. By means of the experience gained, the reliability of the predictions could be improved significantly.

After completion on the Barrier, it was decided to perform evaluation studies on the main hydraulic aspects of the construction (flow modelling, stability of rubble stone and bottom protection, local scour and morphology). In this evaluation study was looked at the accuracy of the used models, not from a scientific point of view, but as a design tool.

4.1 flow modelling (Klatter et al, 1986, 1989)

A comparison between (tidal) scale models and numerical models showed that overall tidal models can be safely substituted by numerical models, either one - or two dimensional (vertically averaged). The choice between one dimensional and two dimensional depends on the geometry of the estuary and type and extend of the results that are needed, e.g.

- a one dimensional model can predict Q , Δh , Δh_s and Y
- a two dimensional model can also predict the horizontal velocity distribution.

A detailed scale model is strictly needed if three-dimensional phenomena play a significant role. For large structures, such as the Eastern-Scheldt Barrier, the combination of a numerical model and detailed scale models will provide an optimal design tool.

The correct reproduction of the hydraulic characteristics of the Barrier was vitally important for the application of all models, both numerical and scale models. The hydraulic characteristics of the Barrier could be simulated correctly in a two-dimensional (depth-average) numerical model by using the discharge coefficients, determined from flume tests on representative sections of the structure.

For use in a one-dimensional numerical model, an overall

discharge coefficient had to be used. This discharge coefficient must be determined from either a scale model of the entire structure or through a two-dimensional numerical model combined with flume tests.

Verification of the models was of major importance, since the basic design parameters (Q , Δh) were determined with these models. The verification procedure was set up in such a way that each step in the forecast procedure was checked systematically. In this way not only the final results of the forecast system (predicted design parameters) were evaluated, but also the models as individual elements in the forecast system.

In this paper only a summary of the results of the verifications is presented for the following items:

- discharge in the main channel Q
- head difference over the Barrier Δh .

Discharge in the main channel Q

The measured discharges were compared with hindcast of the tidal motion during the respective day of measurements. The results of this comparison were used to determine the need of a re-calibration of the 1D-model, especially for the discharge coefficients of the barrier.

The experience gained by the verification was that, as the construction of the Barrier progressed, the discharge characteristics of the Barrier more and more dominated the tidal flow in the estuary. The influence of the overall discharge coefficient became more important than the schematization of the Eastern Scheldt itself. Additionally a verification was performed of the predicted design values of the discharge at maximum (ebb/flood) flow Q_{max} . This was done by transforming the measured Q_{max} to the corresponding value at average tidal conditions. The results of the verifications, both for design values and hindcast of the discharge at maximum flow are summarized in table 2.

Table 2 gives the average and standard deviation of the difference between measurement and forecast (in %)

relative deviation	design values Q_{max}				hindcast Q_{max}			
	max. ebb		max. flood		max. ebb		max. flood	
	mean	σ	mean	σ	mean	σ	mean	σ
[%]								
Roompot	-1.5	6.2	4.1	4.8	1.5	5.4	3.1	4.7
Schaar	-5.3	10.2	2.5	11.3	-2.7	3.9	4.4	5.0
Hammen	2.6	9.6	3.8	5.6	-2.4	6.4	-2.4	3.3
Total	-1.6	8.9	3.5	7.5	-2.1	5.1	1.7	5.2
Overall	mean=0.9% σ = 8.5%				mean=-0.2% σ = 5.4%			

Table 2: Results of verification Q_{max} 1D-model IMPLIC

The conclusions from the results presented in Table 2 are:

- The model errors mostly had a random character.
- The errors in the hindcasts were less than in the design values.
- The accuracy of the initial calibration of 10% (maximum error) had also been achieved with the hindcast ($2 \sigma \approx 10\%$).

In figure 5 the predicted design values of the mean velocity between two piers Q/A have been plotted against the measured values. In this figure low velocities corresponded to early construction stages and high velocities to later stages. The overall error in the Q/A forecast proved to be 12.4% (σ/μ), against 15% that was assessed before hand.

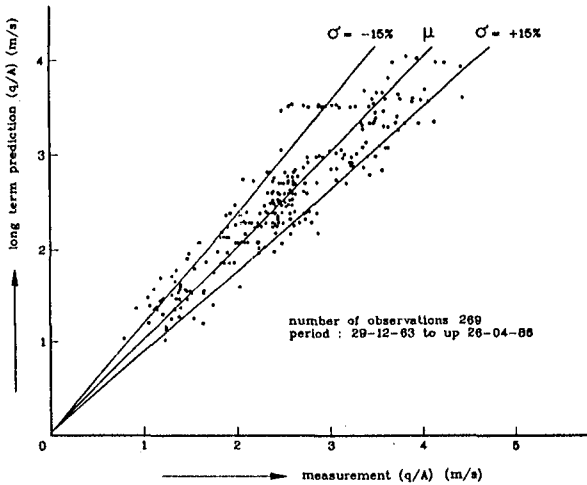


Figure 5: Results of the verification of the velocity forecasts at the location of the barrier.

Head difference across the Barrier Δh

The use of the parameter Δh depended strongly on the narrowing of the channel, and thus of the construction stage of the Barrier. Δh increased from less than 0.2 m in early construction stages to over 1.0 m in the later stages (overage tide conditions).

The accuracy, in which this parameter could be predicted turned out to be 10% to 20% (narrowing of the channel with more than 75%). Once experience was gained with a specific geometry of the barrier re-calibration diminished the errors in Δh computation with 5% to 10%.

4.2 Stability of rubble sill and bottom protection

Prediction of the stability of the rubble sill and several types of bottom protections at structures like the Storm-Surge-Barrier is only possible in a scale model based on Froudes law of similarity (see De Groot et al, 1984 and Konter et al, 1988).

The scale rules for a stability model are rather simple. The geometry of the structure and the dimensions of the bottom protection must be reproduced on the same linear length scale. Beside this the density and shape of the stones or blocks in the model must be the same as in nature. It can be shown that also stiffness and water-permeability can be reproduced correctly.

In general, it proved to be possible to build in all the relevant strength properties of stones and other types of bottom protections in a Froude model. With such a model the "load-strength" relation can be determined very well. However, a close interaction between modeler, designer and contractor during the whole test-program proved to be important.

The influences of changes in geometry, changes in the stone-size during construction, inaccuracies in the layer thickness due to the construction method must be investigated. Also the bed-roughness of the subsoil may have a great influence on the stability, especially in case of a filter layer directly laying on a (smooth) geotextile. All these aspects have to be incorporated in the test-program.

A result of a test series is given in figure 6.

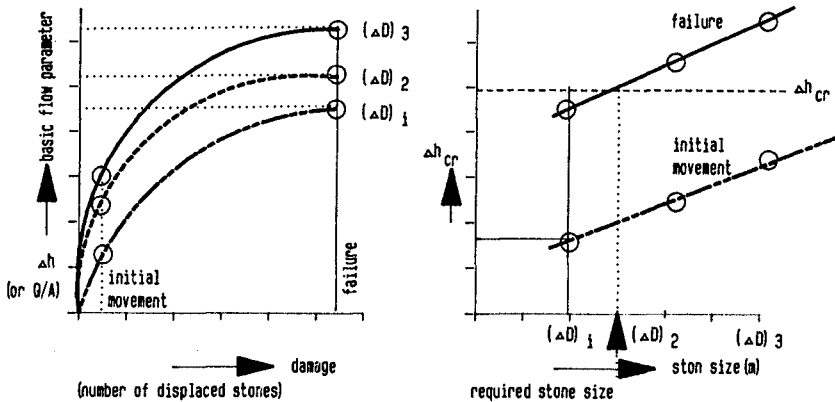


Figure 6a: Test result

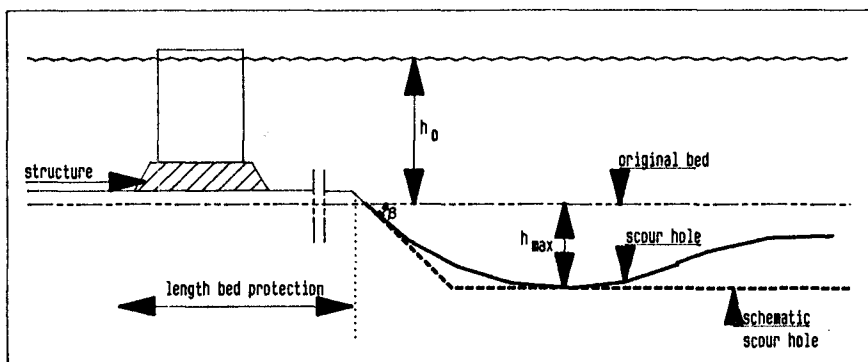
Figure 6b: Design graphs

Figure 6a gives the relation between basic flow parameter and the number of displaced stones, for three different stone sizes. It is recommended to test the whole range of the flow parameter because in some cases, unexpected changes occurred in the vertical flow pattern and therefore also in the relation between flow parameter and damage. The damage is also a function of the exposure time. A representative exposure time for extreme conditions has to be defined. With this exposure time figure 6a gives for each tested stone-size the critical value of the flow parameter for initial movement and failure, which can be plotted in figure 6b. The require stone size can be found, comparing figure 6b with the boundary conditions.

For the Eastern-Scheldt Barrier tests had been done in scale models with length scales varying between $N_L=80$ and $N_L=13$. Also a test in nature with coloured stones placed on the bottom protection has been carried out. The results of these tests, were in agreement with each other, if taken into account all the aspects (different exposure time, stone size diameter, geometry).

4.3. Local scour (Konter et al, 1986)

A method has been developed to predict the scour development in time, during the several construction stages of the Barrier. This method is based on a systematic investigation, which has resulted in the following empirical relations (see figure 7).



$$t_1 = \frac{330 \cdot \Delta^{1.7} \cdot h_0^2}{(\alpha U - U_{cr})^{4.3}} \quad (1) \quad \text{and} \quad \frac{h_{max}}{h_0} = \frac{t}{t_1}^p \quad (2)$$

Figure 7: Empirical relations for local scour

in which:

- Δ = relative density of the bed material under water (-)
- t = time (hours)
- t_1 = time in which $h_{\max} = h_0$ (hours)
- U = current velocity (= Q/A_{total} or q/A) m/s
- U_{cr} = critical velocity for initiation of bottom material m/s
- α = geometry parameter, depending on the geometry of the structure (construction stage)
- p = coefficient (in two dimensional flow conditions $p=0.4$) in three dimensional flow conditions p = varying between 0.2 and 0.6 depending on the water-depth.

The time scale of the scouring phenomenon can be deduced from relation (2).

$$n_t = n_1^2 \cdot n_{\Delta}^{1.7} \cdot n_{(\alpha U - U_{\text{cr}})}^{-4.3}$$

The values of α and p are the same in model and nature. For a particular construction stage $h_{\max}(t)$ can be measured in a scale model, in which the geometry is represented on length scale. The values of α and p can be determined with this model tests and the relations mentioned above.

In nature the values of α , U , U_{cr} and Δ are known, so the time scale is known, and the development in time can be determined. The influence of unsteady flow and upstream sand transport can be introduced (see Konter et al, 1986).

Relation (2) indicates that the erosion capacity depends mainly on the scour rate parameter αU . It proved to be important to investigate the value of αU for each specific construction stage

Figure 8 gives a direct insight in the construction stages with maximum erosion. The maximum scour rate occurs downstream the part of the Barrier at which the sill beams have not yet been placed. Downstream the already placed sill beams αU has a lower value, which can be seen in figure 8, when placing the sill beams in one channel is completed. The translation of αU to $h_{\max}(t)$ can be made using the relations mentioned above.

It has been proved by the scour development in nature (see Konter et al, 1986) that there is a reasonable similarity between model and nature for construction stages with αU values greater than 3.0. For situations with αU -values lower than 3.0 the scour development is

strongly depending on the (often) uncertain amounts of cohesive parts in the bottom material and the upstream sand transport. In such situations the prediction method can only give an upper limit of the scour development in time 0.3 m in a month).

The model tests can also give insight in the steepness of the upstream slopes for a specific geometry (construction stage).

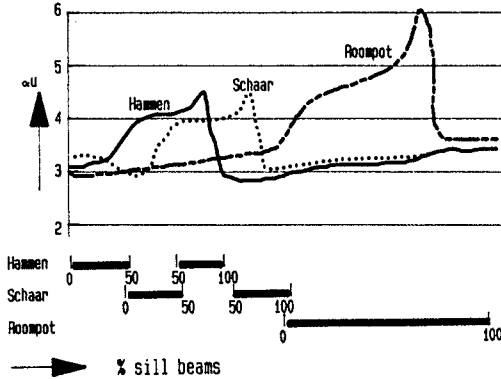


Figure 8: The values of αU (flood) during placing of the the sill beams

It showed that vortices with vertical axes cause very steep slopes (in model) and therefore relatively dangerous for the geo-technical stability of the bottom protection. These dangerous geometries configuration with (partly closed gates in a channel) were avoided and therefore no evaluation in nature was possible.

The method mentioned can also be applied for situations without a bottom protection, and gives a very accurate prediction of the time development of local scour (high values of αU).

4.4 Morphology (Bliek et al, 1986)

During the construction of the Barrier, the three main channels were unequally constricted. This might cause water-level differences between the main channels, with increasing flow velocities and therefore unacceptable developments in the morphology. Even short cut channels could be initiated or deepened. One of the dangers of short cut channels is the progressive erosion that might occur.

- the initial increase of flow velocities could result in erosion on the shoal
- the deepening of the shoal due to erosion could reduce its flow resistance and cause an extra increase in velocities, with an increase erosion rate and so on

- finally, there may be a significant change in the main channel system in the mouth of the estuary, with its influence on the design parameters (Q and Δh) of the channels
- change in the design parameters have its influence on the other hydraulic aspects (stability bottom protection, scour).

Short cut channels cannot be compared with main tidal channels where, in general, an increase in flow velocities, will cause a widening of the profile and a reduction of the flow until a new equilibrium is reached. The approach to study the effects of short cut channels is presented in fig. 9.

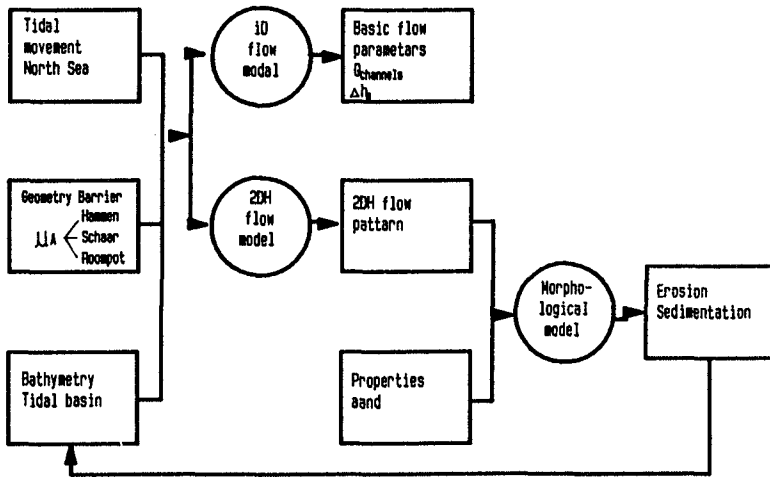


Figure 9: Set up morphological investigation

- investigation of the change of the governing load parameters Δh_s for the different geometries of the Barrier by means of a 1D-model, from which the critical construction stages can be derived
- calculation of the flow pattern for a selected number of critical construction stages by a 2DH-model
- quantifying the erosion under extreme conditions and what's most important the consequences of an extreme erosion on the basic flow parameters (that means other hydraulic aspects).

This approach proved to be very successful, also because the used mathematical models appeared to be applicable and reliable.

5. Conclusions

- * For large hydraulic structures a combination of scale models and numerical models will provide optimal results, in general:
 - 1D or 2DH numerical models to predict the boundary conditions
 - 3D scale models to find the "load-strength" relations.
- * To ensure optimal use of hydraulic research results, a careful selection of "governing" hydraulic parameters is very important. Both the "loads" and the "strength" have to be expressed in these parameters.
- * A scale model based on Froudes law on similarity can solve almost all hydraulic problems at hydraulic structures. In general a correct reproduction of the flow pattern is more important than a correct reproduction of all the stability parameters.

REFERENCES

- Bliek, A.J., Klatter, H.E., Konter, J.L.M. and Van der Meulen, T. (1986).
Short Cut Channels in Tidal Estuaries, Proceedings 3rd International Symposium on River Sedimentation, Mississippi, 1986.
- De Groot, M.B. and Konter, J.L.M. (1984).
Prediction of Mattress Stability in Turbulent Flow, Proceeding IAHR Symposium on Scale Effects in Modelling Hydraulic Structures, Esslingen, 1984.
- Klatter, H.E., Dijkzeul, J.C.M., Hartsuiker, G. and Bijlsma, L. (1986).
Flow Computations Nearby a Storm-Surge-Barrier Under Construction with Two-Dimensional Numerical Models. Proceedings 20th ICCE, Taiwan, 1986.
- Klatter, H.E., Dijkzeul, J.C.M., Hartsuiker, G. and Thabet, R.A.H., (1989).
Storm-Surge-Barrier Eastern Scheldt, evaluation of the Water Movement Studies for Design and Construction of the Barrier.
Report, Delft Hydraulics, code Z88, 1989
- Konter, J.L.M. and Van der Meulen, T. (1986).
Influence of Upstream Sediment Transport on Local Scour. Proceedings IAHR Symposium on Scale Effects in Modelling Sediment Transport Phenomena, Toronto 1986.

CHAPTER 224

INVESTIGATION ON IMPROVEMENT OF YANGTZE ESTUARY

Yen Kai & Yan Yixin

Abstract

The improvement of the Yangtze Estuary has attracted much attention in China. The fluvial processes of the estuary are rather complicated. The frequent move of sandbanks in the estuarine channels and the bar forming at the mouth give much trouble to navigation.

Investigation on the guiding principles and schemes for the improvement of the Estuary has been carried out since 1958. Comprehensive field survey, laboratory experiments and numerical modeling as well as planning work have been done in the past 30 years with some preliminary achievement. A scale model study with horizontal scale 1:1600 and vertical scale 1:120 was conducted by the Nanjing Hydraulic Research Institute.

Introduction

The Yangtze River is the largest river in China, with a total length of 6300 km and a catchment basin of 1,800,000 km². The 145 km stretch from Xuliujing to the sea forms the estuary. As a result of interaction of river flow and tidal current, the estuary is splitted into several channels. It is bifurcated by the Chongming Island into North and South Branches. The former undergoes serious accretion and the latter is now the main passage for runoff and navigation. The South Branch is further divided into North and South Waterways by Changxing and Hengsha Islands. Finally the South Waterway is again bifurcated into the North and South Channels(Fig.1).

Yen Kai, Professor and Honorary President, Hohai University, Nanjing 210024, China
Yan Yixin, Associate Professor of the same university

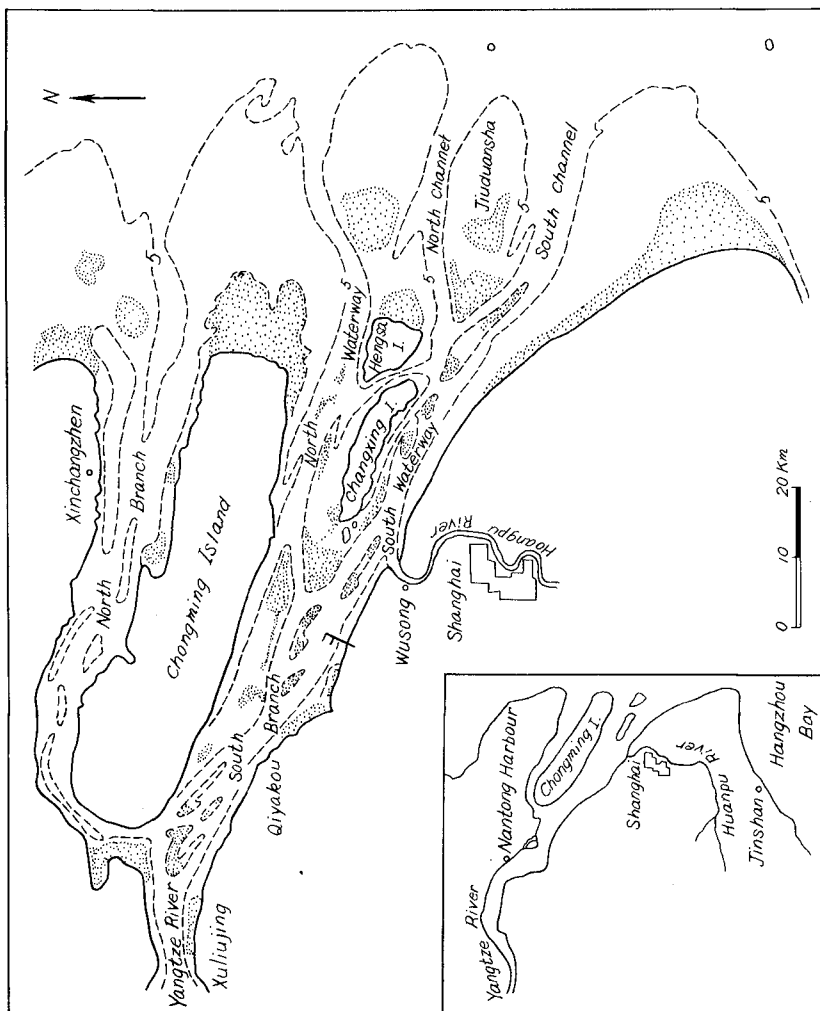


Fig.1 The Yangtze River Estuary

As the Yangtze Estuary, serving as a vital passage for foreign trade and the gateway of the largest port of China, Shanghai, has a great value in the development of China's national economy, its comprehensive improvement has attracted much attention in China.

Hydrological Features of the Estuary

Both the river runoff and the tidal flow play important role in moulding the estuary. The yearly mean total runoff amounts to $925 \times 10^9 \text{ m}^3$ with an average discharge of $29,300 \text{ m}^3/\text{s}$. The max. discharge is $92,600 \text{ m}^3/\text{s}$ and the min. is $4620 \text{ m}^3/\text{s}$. The tide in the estuary is semidiurnal tide, with a mean tidal range at the mouth of 2.66 m, a max. of 4.62 m and a min. of 0.17 m. The intensity of tidal current varies with seasons, generally it is high in the flood season. For example, in the flood season, at the mouth of South Channel the average current velocities during flood and ebb tide are respectively 0.91 m/s and 1.13 m/s, the respective max. values are 1.64 m/s and 1.88 m/s. The tidal current could reach as far as 300 km from the mouth and the effect of tidal action could be felt at the Datung Station, some 640 km from the mouth in the low water season with strong tide.

The total silt load is on the average $486 \times 10^6 \text{ t}$ per year, with a mean silt concentration of 0.54 kg/m^3 , being high in the flood season, attaining 1.00 kg/m^3 , and low in dry season, amounting to 0.10 kg/m^3 .

The salinity at the mouth of the estuary is on the average 16%. It varies with seasons, reaching 20% in dry season and 10% in flood season. The estuary belongs to the partly mixing type, but during the flood season with high river runoff it may be changed into a weak mixing type and in dry season into well mixed type.

Morphological Characteristics of the Estuary

The mouth of the Yangtze Estuary was located about 200 km inland of its present position some 3000 years ago and the land of Shanghai and Chongming Island were formed by the alluvial deposition during the last thousand years. Under the action of Coriolis force the ebb current is deflected to the right bank of the channel and the flood current to left. This gives rise to a divergence of ebb and flood currents in the channel, causing deposition of sediment in the slack water zone between the two currents paths. As the process of deposition goes on shoals are formed which in the course of time may be developed into islands, such as the Chongming Island and the Hengsha Island. Take the Chongming Island for example, it divides the estuary into two branches.

More or less influenced by the Coriolis force the main ebb current enters the South Branch and in the North Branch the flood current predominates. The flood current in the North Branch, being close to the north bank, causes bank erosion with consequent accretion at the south bank, i.e. the north waterfront of the Chongming Island. As to the South Branch, the erosion of the south bank has been long since checked by the construction of bank protection works, thus aggravated the erosion of the north bank, i.e. the south waterfront of the Chongming Island. There is, therefore, a tendency of gradual shifting of islands or sandbanks to the north in the Yangtze Estuary, which may eventually result in their attachment to the north bank.

As the South Branch is now the main passage for runoff and navigation, it has called much of our attention. One important feature of the South Branch is the periodic shifting of the bifurcation point of the North and South Waterways, the range of shifting may attain 20 km or more. Such shifting has in turn influence on the fluvial processes of the two Waterways, causing frequent move of sandbanks in the channels. The cause of shifting is rather complicated. One important point is that, when the main current takes one of the Waterways, say the North Waterway, then more sediment, particularly the bed load, is also carried into this Waterway, causing accretion, reduction of channel capacity and increase in flow resistance. The main current is thereby obstructed and gradually turned into the South Waterway. In the meantime, due to the encroachment of the bifurcation point, it shifts gradually downstream, twisting the channel leading to the North Waterway, thus further increases its flow resistance and reduces its discharge capacity. When the flow in the South Waterway is increased to such an extent that its channel capacity is not sufficient to take over the increased ebb flow, a new channel leading to the North Waterway will eventually be cut through the sandbanks upstream of the bifurcation point, and a new bifurcation point is thus formed. The old bifurcation point is then gradually abandoned. A similar cycle of such change will occur when the main ebb flow turns from the South Waterway to the North Waterway. Nevertheless, a relative stable condition could occur when the ebb flow is approximately equally divided into the two Waterways.

As a partly mixing type, the Yangtze Estuary shows its typical salinity distribution as shown in Fig.2. It can be seen that there is a longitudinal salinity gradient which affects the ebb and flood currents and sediment movement. In the course of a tidal period

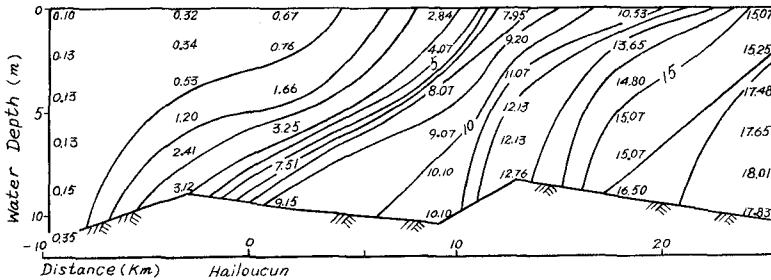


Fig. 2 Salinity Distribution in South Channel
Dec. 23-24, 1963 Tidal Range 2.77 m
Discharge 15000 m³/s Salinity in %.

when the ebb flow turns into the flood flow, we can find a stagnation point somewhere near the river bottom where the net velocity is zero. Around stagnation point there is a stagnation zone where deposition of sediment most likely to take place. The settling of suspended sediment here is further facilitated by the flocculation process caused by the mixing of river runoff with sea water. As a result bars are formed at the mouths of the North Waterway, the North Channel and the South Channel, which extend for a distance of 10 to 20 km or more.

As a rule, deposition on the bars takes place during the flood season and in the dry season the bars are subjected to erosion.

Guiding Principles and Schemes for the Improvement of the Estuary

The improvement of the Yangtze Estuary is chiefly aimed at navigation, with due consideration of the benefits of land reclamation, irrigation and drainage of the adjacent land, water supply, flood protection, tourism industry and environment protection. The South Branch, being the main waterway connecting the inland and ocean navigation, in its natural state is insufficient to answer the growing demand of water transportation. The length of the stretch of the South Branch from Xuliujing to Wusongkou, the confluence of Huangpu River to the Yangtze Estuary, is 69 km. As we know, most of the quays of the port of Shanghai are situated along the banks of the Huangpu River. The upper reach of this 69 km river stretch, from Xuliujing to Qiyakou, for a distance of 35 km is called Baimousa stretch, and lies between the two "nodal points". We take Xuliujing and Qiyakou as "nodal point" or sub-nodal point", because the channel here is relatively stable and is contracted to only about 5 km

and 9 km in width respectively. The Baimousa stretch is splitted by the Baimou Sandbank into a north channel and a south channel, the latter is now the main navigation waterway having a water depth of 10 m except at the upper end, where auxiliary dredging is needed to increase the depth required for navigation.

The lower reach of the 69 km river stretch from Qiyakou to Wusongkou is 34 km long and is called Three-Bank stretch, because there are three sandbanks, viz. the Central Sandbank, the Biandan Sandbank and the Liuhe Sandbank in the estuary, which are very unstable. The width of Three-Bank stretch increases from 9 km at Qiyakou to 17 km at Wusongkou, which leads to the formation of shoals here and there in the estuary, among which the three sandbanks are the most prominent ones. The bifurcation point of North and South Waterway lies in this stretch, shifting up and downstream for a distance of ca. 20 km in a period of some 30 years, as mentioned before. The unstable channel condition and the shoals in the channel give much trouble to navigation, although a water depth of 10 m can be maintained for the most part of this river stretch.

Based on the results of investigation, the guiding principles and schemes for the improvement of the Yangtze Estuary may be summarized as follows:

1. Regulation of Upper Reach of South Branch

For the regulation of the upper reach of the South Branch, i.e. the Baimousa river stretch, it is important to protect the two "nodal points" at Xuliujing and Qiyakou. The Xuliujing "nodal point" has the function of stabilizing the direction of main current and refraining shoals upstream from moving downstream into this river stretch. The Qiyakou "sub-nodal point" exercises similar function to the lower reach of the South Branch, which is important for the creation of stable channels.

The existing north and south channels of the Baimousa river stretch will be maintained, but the direction of flow and the river discharges into these two channels have to be readjusted by the construction of regulation work in combination with land reclamation as shown in Fig.3.

2. Regulation of Lower Reach of South Branch

In order to maintain a stable deep channel in this river stretch it is necessary to contract the channel, stabilize the bifurcation point of the North and

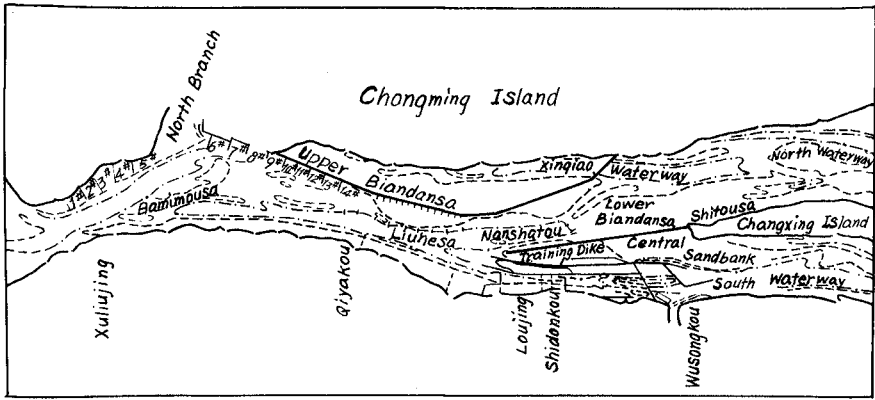


Fig.3 The South Branch of Yangtze Estuary

South Waterways and adjust the discharges into the two Waterways. After analysing the morphological changes in the past it is found that in 1971 when the bifurcation point was situated at a location about 10 km upstream of the Shitousa on the Central Sandbank the channel was relatively stable as shown in Fig.4. So this point may be taken as the project bifurcation point. At present the bifurcation point is several km upstream of the project point and is shifting downstream at a rate of 1 km per year. It is therefore advisable to stabilize the bifurcation point in time to avoid the difficulties incurred when it moves too far downstream.

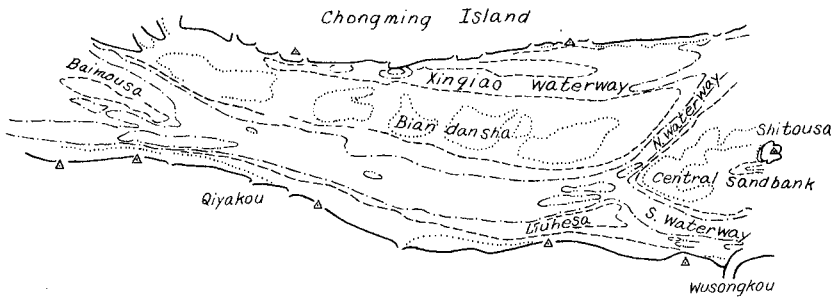


Fig.4 South Branch in 1971

Once the bifurcation point is stabilized, it is still necessary to take measure to control the flow condition so as to approximately equally divide the ebb discharge into the North and South Waterways. Such a discharge distribution is favorable to the maintenance of stable channel condition for both Waterways, each of which is important to navigation. Because the South Waterway is at present the main waterway for seagoing vessels and quite a few important enterprises are situated on its south bank, while the North Waterway is indispensable for the navigation of the Chongming Island and is also a prospective deep outlet channel to the sea.

The waterway channels should be contracted. Studies have been made for the layout and orientation of the channel regulation lines, beyond these lines land reclamation and construction works are prohibited. Some of the branch channel cutting through the sandbanks should be dammed up to reduce the random flow over them.

The stabilization of the Biandan Sandbank is of particular importance to the regulation of the lower reach. The regulation of the upper reach and the stabilization of the bifurcation point of the North and South Waterways are favourable to the stabilization of this sandbank. But due to the existence of the Xinqiao Waterway on the north side of the sandbank there is still random discharge over the latter, affecting its stability. Therefore training work has to be constructed on the south side of the sandbank to cut off the random discharge and to stabilize its south boundary.

The regulation work will be carried out in stages. As the first stage, the work for the stabilization of the bifurcation point should be built in the coming few years. Several schemes have been investigated, and the one comprising a training dike connecting Nanshatou to the Shitousa on the Central Sandbank has been selected (Fig.3). Besides stabilizing the bifurcation point at the project location, it has also the function of refraining the shoals upstream from moving into the river stretch Luoqing-Shidankou and confining the ebb flow into this river stretch, both are favorable to the maintenance of a stable and deep water channel. This is important because the Baoshan Iron and Steel Work, a key enterprise, as well as the prospective deep water berths of the Port of Shanghai are located on south bank of this river stretch. Moreover, the dike will check the flow over the sandbank and prevent the formation of new cut off channel, which would endanger the stabilization of the bifurcation point.

For preliminary study a scale model has been constructed in the Nanjing Hydraulic Research Institute.

Owing to the immense extent of the estuary, a highly distorted model was built with a horizontal scale 1:1600 and a vertical scale 1:120. The model has an overall length of 120 m and a maximum width of 32.6 m. The upper end of the model was connected to an arbitrary meandering channel stretch, 200 m long, representing the waterway upstream of the estuary. Two different tide generating devices, consisting of a tidal chamber and a tail water gate, are installed at the lower end (Fig.5). From the test results it can be seen that, with the construction

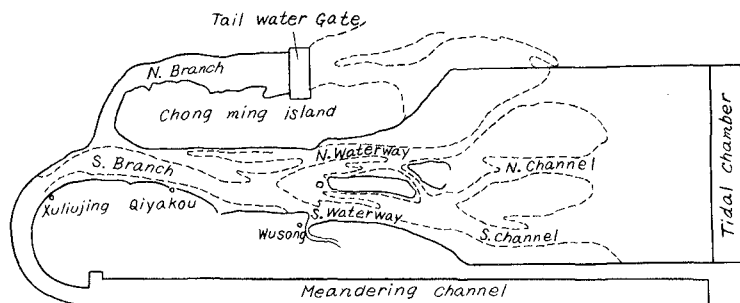


Fig.5 Model Layout of Yangtze Estuary

of the training dike, the ebb velocity flanking the south bank of the south channel is increased, which is favorable to the maintenance of deep water in front of the Baoshan Iron and Steel Work and the project new berths of Shanghai Port, while the current velocities at Qiyakou, Wusongkou and other places in the North and South Waterway are practically unchanged, showing the regulation work will not exercise notable influence on the flow regime upstream and downstream. This means that the training dike as the first stage of the work of regulation can well coordinate with the successive stages of regulation to be followed. The model was essentially a fixed bed model, but some tests were conducted with partly movable bed to observe the fluvial processes of the lower reach of the South Branch. Only fresh water tests were performed, the facilities and techniques for conducting experiments with salt water are now in preparation.

3. Improvement of Outlet Channels to the Sea

As mentioned before, bars are formed at the mouth of the North Waterway, the North Channel and the South Channel, the water depth over the bars is generally 6.0 - 6.5 m. After dredging a water depth of 7 m is now maintained over the bar of the North Channel. Vessels with draft of 9.5 m could enter the estuary by saving the tide.

In the near future it has been proposed to increase the depth to 7.5 m. In prospect, a deep outlet channel of 9.5 m is considered appropriate. Of the three possible outlets, the bar of the North Waterway is shortest and that of the South Channel is longest. To acquire a deep outlet channel dredging alone is impracticable. At present, the yearly maintenance dredging for a 7 m outlet channel is as high as $14 \times 10^6 \text{ m}^3$, that of a 9.5 m channel would evidently many-fold of this. Training work has to be carried out, supplemented by dredging and land reclamation. Other possible solutions have been proposed, such as the creation of a by-pass outlet channel beyond the influence of bar-forming.

4. Improvement of the North Branch

The North Branch is now under the process of gradual accretion. The sea water intrusion caused by flood tide carries part of the sediment and salt water upstream along the channel and turns them into the South Branch, which is unfavourable to the improvement of the latter as well as to the North Branch itself. In order to reduce the sea water intrusion and to maintain a relatively stable channel in the North Branch, regulation work is also necessary. One way is to confine the North Branch by contraction work or in combination with land reclamation. An alternative is to dam up or partly enclose the North Branch. Feasibility study has to be made to make the final decision.

Conclusions

The improvement of the Yangtze Estuary is a rather complicated problem. Although comprehensive field investigation, laboratory experiment and numerical modeling, as well as planning work have been carried out in the past 30 years, yet still much remains to be done. The compilation of basic data, particularly at the mouth, should attract much of our attention. The study of fluvial processes should be continued with the aim to find out the optimal scheme and layout of the works of regulation. For this, movable bed model tests with salt water installation should be conducted.

References

- Huang Shen et al. (1980).
Analysis of Siltation at Mouth Bar of the Yangtze River Estuary, Proc. of the First International Symposium on River Sedimentation 1980, 447 - 456.

Shi Liren et al. (1986).

Diffusion and Transport of Seaward Sediment from the Chongming (Yangtze) Estuary, Proc. of the Third International Symposium on River Sedimentation 1986, 602 - 611.

Zhu Yuan-sheng (1985).

Model Study on the Schemes for the Regulation of the South Branch of the Yangtze Estuary, Model Test Report, Nanjing Hydraulic Research Institute, 1985 (in Chinese).

CHAPTER 225

CONSOLIDATION AND RHEOLOGICAL PROPERTIES OF MUD DEPOSITS

Claude MIGNIOT and Luc HAMM (1)

Abstract

The temporal evolution of consolidation and associated rheological properties of mud deposits has been studied by means of laboratory experiments for more than 40 sites throughout the world.

Standard procedures have been used for all these experiments.

The present paper describes the experimental procedures and gives a summary of the results obtained.

1. Introduction

Typical engineering studies involving mud carried out for 30 years by SOGREAH(Grenoble) and Laboratoire Central d'Hydraulique de France (Maisons-Alfort) have covered the main fields of port and coastal engineering, namely:

- Maintenance of depths in harbour basins, navigation channels and water intakes,
- Navigation in muddy waters(Brossard et al.,1990),
- Evolution of waste disposal sites.

In order to adequately describe the mechanical properties of mud deposits, standard laboratory experiment procedures have been developed and applied.

Two basic parameters are measured to characterize these properties:

- The dry sediment density $T_s(z,t)$ in kg/m^3 or g/l
- The yield value $\tau_y(T_s)$ in N/m^2

with z : depth in the deposit and t :time

(1) SOGREAH Consulting Engineers,
6 rue de Lorraine 38130 Echirolles France -

2. Consolidation experiments

2.1 Description of the procedure

These experiments are carried out in settling tubes 0.10m in diameter. Mud samples are diluted in pure or salt water to obtain an homogeneous fluid mud with an initial dry sediment density (Tsi) varying between 5 and 300 g/l and an initial height (Hi) varying between 0.25 and 3m. The temperature is kept around 20°C. The evolution of the mean dry sediment density is monitored by measuring the position of the water-mud interface.

The density profile over the depth is measured at different time intervals with a gamma-ray source and a detector(non-destructive measurement).The duration of the test is usually 100 days.

2.2 Evolution of the mean dry sediment density

The mean dry sediment density is deduced from the position of the water-mud interface by the relationship:

$$Tsm(t) = Tsi * [H(t) / Hi] \quad (1)$$

Results are plotted on a semi-log diagram. Typical results are presented hereafter(fig 1).

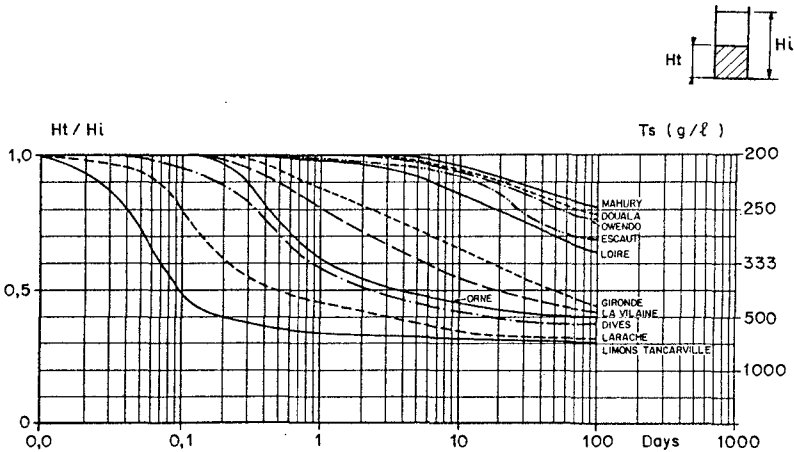


Figure 1. Consolidation tests - typical results

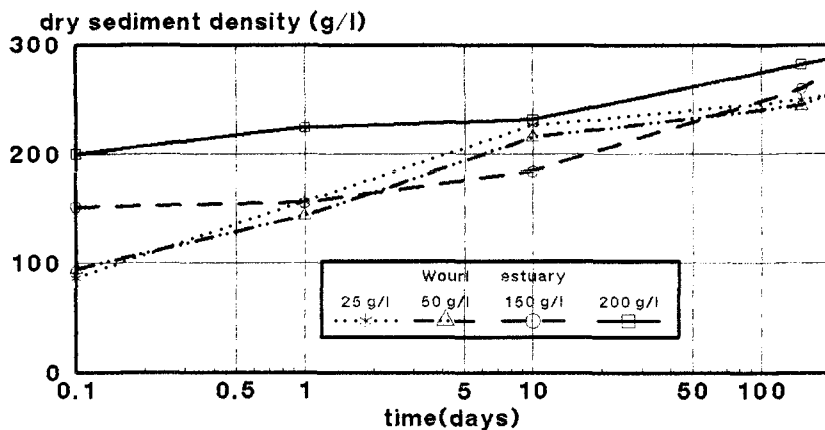


Figure 2. Consolidation tests:Wouri estuary
Influence of the initial dry sediment density

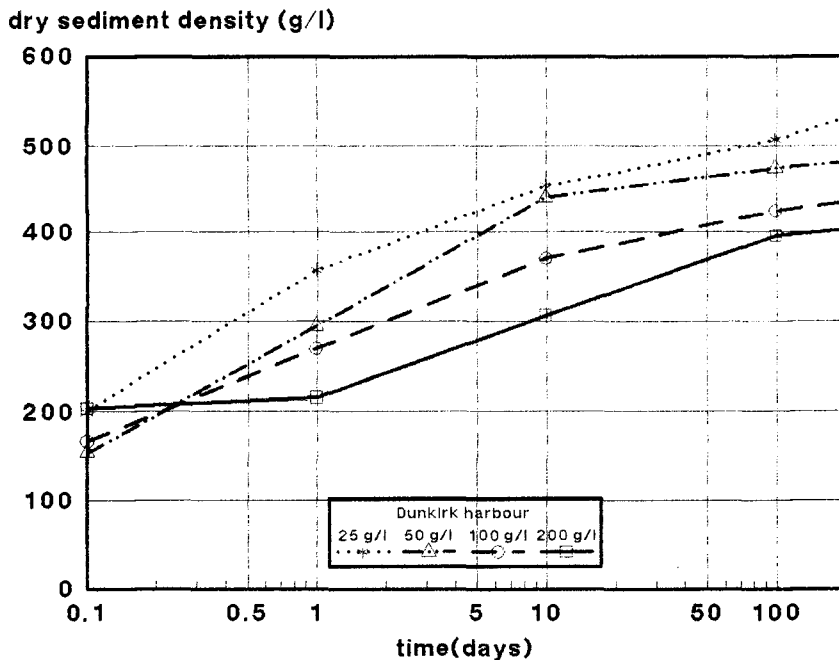


Figure 3. Consolidation tests:Dunkirk harbour
Influence of the initial dry sediment density

After 100 days the consolidation process has reached its final state in a few cases. Equatorial muds (Mahury, Douala, Owendo) with high kaolinite contents and a very fine particle size have a very low rate of consolidation and have not reached their final state. European estuarine muds (Loire, Escaut, Gironde, Orne, Dives) are made of a mixture of several clay minerals (illite, smectite, kaolinite, chlorite) and include quartz, feldspar and a variable proportion of silt. In these cases, the consolidation is a function of composition.

The comparison of results with the same initial height but different initial dry sediment densities shows the greater the initial density, the greater the final density. A typical result is shown on fig 2 (Wouri estuary, Cameroon). In a few cases, when a small proportion of sand is included in the mud, the opposite trend is observed as shown on fig 3 (Dunkirk harbour, France, 5% of sand). This is due to the segregation of sand particles, which form thin drained beds increasing the final density.

The comparison of results with the same initial dry density but different initial deposit heights shows that the final density is not too influenced by this parameter when it varies between 0.25 and 3 m. Typical results are shown on fig 4.

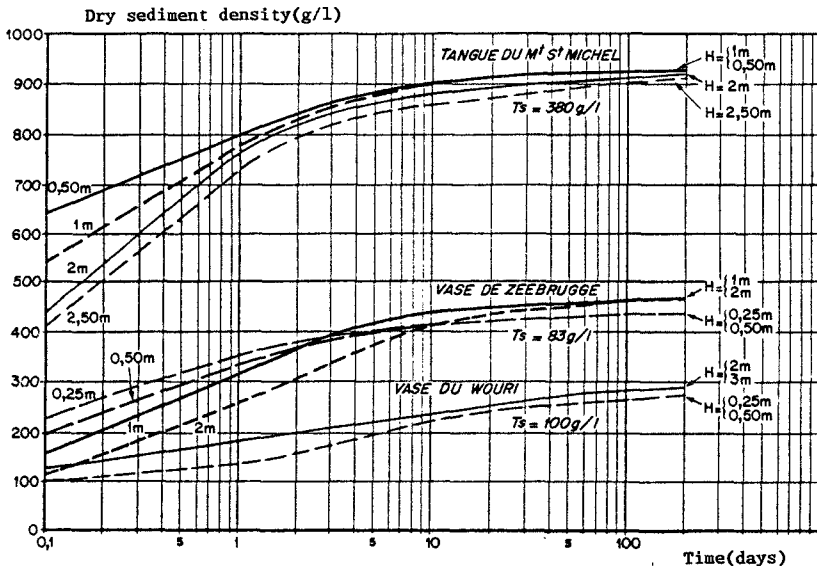


Figure 4. Consolidation tests: influence of the initial height of deposit

2.3 Evolution of the vertical profile

During the consolidation test, a vertical gradient appears and increases with time. Figure 5 shows a typical result in the Gironde estuary. Study of the influence of the initial deposit height shows that the gradient increases when the height decreases (fig 6). These results can be applied to increase the stability of waste disposal sites by depositing thin layers and letting them consolidate a few days in between.

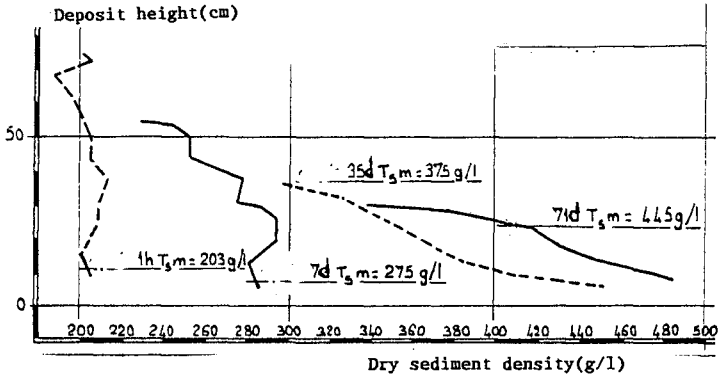


Figure 5. Consolidation tests: Gironde estuary
Vertical profiles at different time intervals
($T_{si} = 200 \text{ g/l}$; $H_i = 0.75 \text{ m}$)

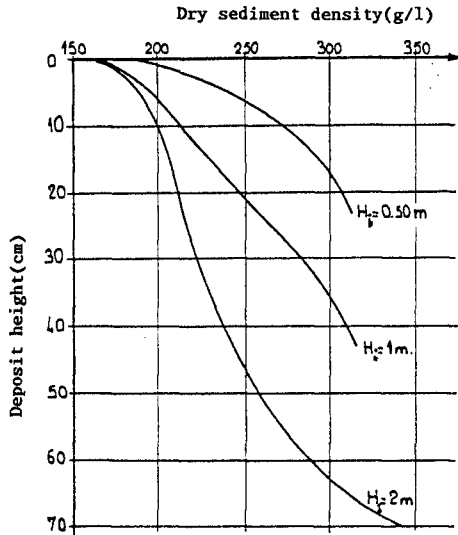


Figure 6. Consolidation tests: Loire estuary
Vertical profiles after 6 days ($T_{si} = 100 \text{ g/l}$)
Influence of the initial deposit height

3. Rheological measurements

3.1 Purpose of the measurements

Knowledge of the dry sediment density of a mud deposit is not enough to characterize its mechanical properties in the presence of hydrodynamic forces. Flume tests have given evidence that the erodability of cohesive sediments is primarily a function of their rheological properties, which are not simply related to the dry density.

The complexity of natural sediments precludes a fundamental interpretation of their rheology. That is why a simple and standard procedure has been used in order to obtain good comparative results and be able to develop empirical relationships to be applied in engineering projects.

3.2 Description of the procedure

The measurements are made with a BROOKFIELD LVT viscometer using 4 rotating cylinders with the following dimensions:

	1	2	3	4
diameter(mm)	18.84	10.25	5.88	3.20
length (mm)	65.10	53.95	42.86	31.01
range of use (N/m ²)	< 1.	1.to 4.	4.to 10.	>10.

The speed range varies between 0.3 and 60 rpm and the temperature is usually kept at 20°C.

The yield value is determined with the following procedure:

- Strong homogenization of the mud,
- Introduction of the rotating cylinder,
- Keeping at rest during 2 to 5 min in order to avoid thixotropy on one side and consolidation on the other.
- Starting with the lowest speed of 0.3 rpm.

The yield value (τ_y) is defined as the peak value of the recorded shear stress as illustrated by figure 7. In some cases, rheograms are determined by increasing the speed.

3.3 Typical results

Measurements are carried out with the same mud and different dry sediment densities. Results are plotted on a log-log diagram as illustrated by figure 8. These results show that in many cases, two domains can be observed. At low concentrations the mud sample looks fluid. When the concentration increases, the mud becomes plastic and the yield value increases dramatically.

For such a fluid mud, the relationship between the yield value and the dry density is usually of the form:

$$\tau_y = C_1 \quad Ts^3 \quad (2)$$

For a plastic mud, this relationship becomes:

$$\tau_y = C_2 \quad Ts^6 \quad (3)$$

C_1 and C_2 are parameters depending on the site studied. The limit between the two domains usually lies within 1 to 3 N/m².

4. Applications

The above measurement data are usually used for particular engineering projects including desk studies, mathematical simulation of mud transport or physical scale models. Two more general applications can be noted: The first deals with navigation in muddy waters where it is necessary to define the nautical depth in the turbidity maximum of many estuaries. Galichon et al (1990) describe in detail the use of the yield value to define the nautical depth in the Gironde estuary.

A second application is the investigation of relationship between the critical shear stress for erosion (τ_{ce}) under a steady current and the yield value. First results from small-scale flume tests have shown that such a relationship can be written as:

$$\tau_{ce} = 0.17 \sqrt{\tau_y} \quad \text{for fluid mud}$$

$$\tau_{ce} = 0.10 \tau_y \quad \text{for plastic mud}$$

References

- . Brossard C. Delouis A, Galichon P., Granboulan J, Monadier P. (1990)
"Navigability of mud silted channels - scale model experiments"
Abstracts of 22nd ICCE, Delft, 95-96
- . Galichon P., Feral A, Granboulan J, Viguiier J (1990)
"Rheological properties of muds in the Gironde Estuary spatio - temporal variations in rigidity"
Abstracts of 22nd ICCE, Delft, 369-370
- . Migniot C (1968) :
"Etude des propriétés physiques de différents sédiments très fins et de leur comportement sous les actions hydrodynamiques"
La Houille Blanche, 7, 591-620
- . Migniot C (1989) :
"Tassement et rheologie des vases"
Part 1 : La Houille Blanche, 1, 11-29
Part 2 : La Houille Blanche, 2, 95-111

CHAPTER 226

INTEGRATED COASTAL RESEARCH IN THE SW NETHERLANDS

Jan P.M. Mulder¹, Teunis Louters², Frank P. Hallie², Renske Postma³,
Johan A.Craeymeersch⁴ and Olivier Hamerlynck⁵

ABSTRACT

The geomorphological and ecological response of the ebb tidal deltas of the SW Netherlands to implementation of the Delta Project during the last decades, has been the subject of an integrated research project. General observed geomorphological trends are: erosion of the delta fronts and of the relic tidal bars in the landward parts of the deltas, and sedimentation in the tidal channels and in longshore bars at the edges of the deltas. Ecologically, a general trend towards richer benthic fauna communities is observable. The integrated approach in coastal research combining geomorphological analysis of field data with numerical modelling, and integrating hydraulic, geomorphological, sedimentological and biological data, has appeared very promising. Progress in this field would be stimulated by further research of the driving processes in the interaction of hydrodynamics - sediment - biota. The level of detail (spatial and temporal) in geomorphological contributions to such research will have to be much higher than usual in current coastal morphological studies.

¹ Rijkswaterstaat Tidal Waters Division, P.O. Box 8039, 4330 EA Middelburg, The Netherlands

² Rijkswaterstaat Tidal Waters Division, P.O. Box 20907, 2500 EX The Hague, The Netherlands

³ Rijksuniversiteit Utrecht, Department of Physical Geography, P.O. Box 80115, 3508 TC Utrecht, The Netherlands; present address: Rijkswaterstaat Directorate Zeeland, P.O. Box 5014, 4330 KA Middelburg, The Netherlands

⁴ Delta Institute of Hydrobiological Research, Vierstraat 28, 4401 EA Yerseke, the Netherlands

⁵ Rijksuniversiteit Gent, Institute of Zoology, Marine Biology Section, Ledeganckstraat 35, B-9000 Gent, Belgium

1. IMPACT OF DELTA PROJECT ON EBB TIDAL DELTAS OF THE SW NETHERLANDS

Implementation of the Delta Project in the SW Netherlands has induced major changes. The closure of the Haringvliet and Grevelingen estuaries in 1970 and 1971 respectively, and the completion of the Oosterschelde storm surge barrier in 1986, have initiated a dramatic change in hydraulic conditions and the geomorphology of the former ebb tidal deltas. The changes in physical boundary conditions affect the total ecosystem of the coastal area and entail consequences for various human activities. This environmental impact creates a challenge to integrated water- and coastal management (Hallie et al., 1990).

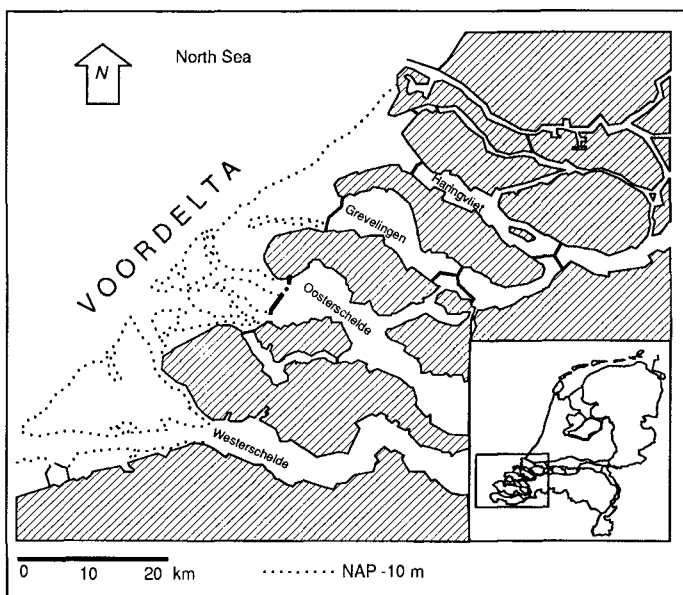


Fig. 1 Study area: the Voordelta

2. INTEGRATED RESEARCH PROJECT

The developments of the former ebb tidal deltas of the Grevelingen, Haringvliet and Oosterschelde - area known as the Voordelta (Fig. 1) have been the subject of an integrated research project, aimed at

- describing the recent developments and present situation of both geomorphology and ecology; and
- predicting on an intermediate time scale (1990 - 2010), the change in geomorphology and possible shift in ecological functioning of this area.

The results are being used as basic information to develop an integrated policy plan during 1990.

This paper summarizes the general results of the research project.

Specific results have been described in more detail by Kohsiek (1988), Steijn et al. (1989), Mulder (1989), Hallie et al. (1990), Louters et al. (1990), Postma et al. (1990), Craeymeersch et al. (1990) and Hamerlynck et al. (1990).

3. PHYSICAL CHARACTERISTICS OF THE STUDY AREA VOORDELTA

The actual geomorphology of the Voordelta is characterised by interlinked (former) ebb tidal deltas extending 10 - 15 km seaward from the coastline. The delta fronts are marked approximately by the depth contour of -10 mNAP [NAP= mean sea level as defined for Amsterdam]. Maximum depths of tidal channels range from -23 mNAP at the Oosterschelde -, through -14 mNAP at the Grevelingen -, to -10 mNAP at the Haringvliet ebb tidal delta. Maximum heights of longshore - and tidal bars range between -1 and +1mNAP. The mean grain size in the area varies from 150 - 350 micron.

The dominant tidal currents run parallel to the coast: northward during flood, southward during ebb. The semi-diurnal vertical tide has a mean range of ca. 2.6 m and can be classified as mesotidal. Maximum current velocities at the Oosterschelde ebb tidal delta, still with a substantial east - west component to and fro the basin, presently amount 1 - 1.2 m/s; at the Grevelingen - and Haringvliet ebb tidal deltas maximum velocities range from .40 - .60 m/s. These values imply the significant velocity reductions that have occurred due to the construction of dams: the Oosterschelde storm surge barrier (1986) induced a reduction of ca. 30%, closure of Haringvliet and Grevelingen (1970/71) reductions of 45 - 80% (Kohsiek,1988).

For the prevailing winds (southwest to northwest), the wave climate is characterised by a significant wave height (H_s) of 1.2 m (Louters et al., 1990).

4. INTEGRATED APPROACH

The Voordelta research project has been characterised by an integrated approach at two levels (Fig. 2).

At the level of geomorphological research an integration took place of results from field data analyses and from numerical modelling. Ecological research was based on an integrated analysis of hydraulic, geomorphological, sedimentological and biological data.

4.1 Geomorphological research

Echo sounding maps of the study area have been recorded almost yearly since the early 60's. These soundings have provided the basic data for geomorphological research.

First a qualitative analysis has been performed comparing different sounding maps. Then, after preparing 200*200 m and 100*100 m grid squares with interpolated depth values, changes in sediment volume

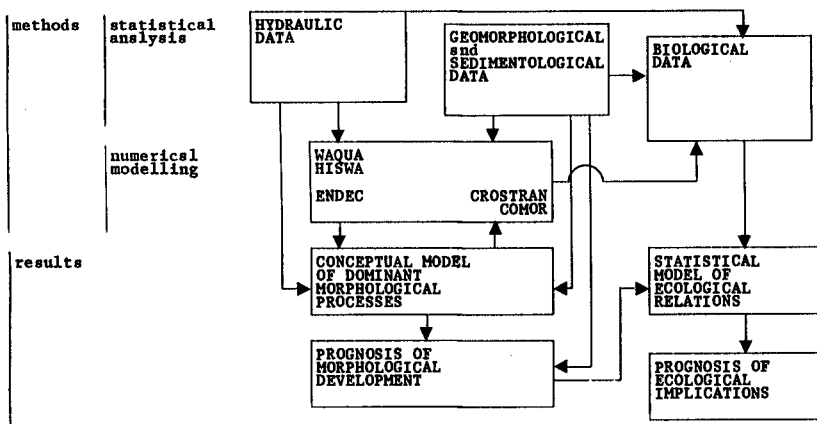


Fig. 2 Schematic representation of the integrated approach both in geomorphological and in ecological research

of the ebb tidal deltas and specific sub units have been quantified. Trends in these changes have been analysed statistically. Parallel to the analysis of bathymetric data, numerical modelling has been applied to study the dominant processes: a 1D model of CROSS-shore TRANSPORT (CROSTRAN) to investigate the adaptation of the cross shore profile (Stive, 1986) and a 2DH model of COastal MORphology (COMOR) to study the spatial interaction between tide- and wave induced currents and sediment transports (de Vriend and Ribberink, 1988; Steijn et al., 1989). Integrating results from bathymetric analyses and numerical modelling a conceptual model of the dominant processes and actual sediment transport patterns has been defined (Louters et al., 1990).

A prognosis of geomorphological developments on an intermediate timescale has been based on a procedure during which the following activities have been executed in an iterative way (Postma et al., 1990):

After defining a conceptual model of dominant processes, specific geomorphological units have been defined (e.g. the delta front and individual shoals and channels, or parts of these). Each unit definition, preferably was based on explicit geomorphological and process characteristics. Successively, each unit has been described by certain geomorphological parameters and the trend of each parameter since 1970, has been extrapolated towards the year 2010. Extrapolation mostly occurred according to an exponential function, fitted for the observed trends over the period 1970 - 1987. In each case the prognosis has been tested to be consistent with predicted developments of other units and with the earlier defined conceptual model. Finally, a check has been performed on the total sediment balances of the areas.

4.2 Ecological research

The ecological impact of the change in physical boundary conditions has been studied mainly on developments in benthic fauna.

The study has concentrated on macrozoobenthos, representing a vital link at the base level of the food chain in the marine ecosystem. Macrozoobenthos are animals of sizes over 1 mm, living in the toplayer (ca. 10-20 cm) of the sediment. Main representatives are worms (Polychaeta), small shrimps (Crustacea), shellfish (Bivalva) and echinoderms (Echinodermata).

Beside macrozoobenthos, attention has been paid to epibenthos (animals living on top of the sediment surface or in permanent contact with it: demersal fishes like flat-fish, cod and gobies, and adult shrimps, crabs and starfish) and on hyperbenthos (animals living in the lower parts of the water column, dependent on the vicinity of the sediment surface: macrozoobenthos larvae, mysids, eggs and larval stages of fish).

Basic data for the macrozoobenthos research were provided by an inventory sampling campaign during 1984, 1985 and 1986 covering a total of 457 locations scattered randomly over the Voordelta, including the ebb tidal delta of the Westerschelde (Fig. 1). During 1987 and 1988 monthly sampling was performed at a total of 150 sites in two key areas on the Grevelingen - and Oosterschelde ebb tidal delta respectively.

At each location have been determined from direct sampling: macrozoobenthos biomass and species composition, soil parameters (silt content, median grainsize, sorting) and water depth. Other hydraulic parameters (maximum current velocity, wave heights, near bottom orbital velocity) have been derived indirectly from numerical modelling. Water quality parameters (salinity, chlorophyll-a and suspended matter) were determined from data supplied by a campaign of water quality sampling at 60 locations, executed with monthly intervals during 1986.

All macrobenthos samples taken in autumn were classified according to macrobenthic species composition by a statistical classification program. Then, canonical correspondence analysis and multiple discriminant analysis were applied to correlate the animal assemblages to abiotic environmental variables (Craeymeersch et al., 1990; van der Meer, 1988).

Epibenthos and hyperbenthos data were sampled in the Grevelingen and Oosterschelde key areas during campaigns of 1987 and 1988. Sampling was performed with a specially constructed 'hyperbenthos sledge' (Hamerlynck and Mees, 1990). Statistical analysis has been applied to investigate correlations with abiotic variables.

An indicative prognosis of a future shift in ecological functioning of the Voordelta has been based on the statistical relations derived for the study area.

5. GENERAL RESULTS

5.1 Geomorphological development

Sediment balances of the Haringvliet and Grevelingen ebb tidal deltas indicate a mean yearly sedimentation surplus of respectively circa 3 and 2 million cubic meters since 1972. Between 10 and 30 percent of this surplus has been estimated to be marine mud, deposited mainly in former ebb tidal channels. A major part of the sedimentation surplus most probably is due to a net northward longshore sediment transport from the south (Louters et al., 1990). A continuing sedimentation in the relic tidal channels (Fig. 3) is a typical phenomenon of the geomorphological changes in the study area.

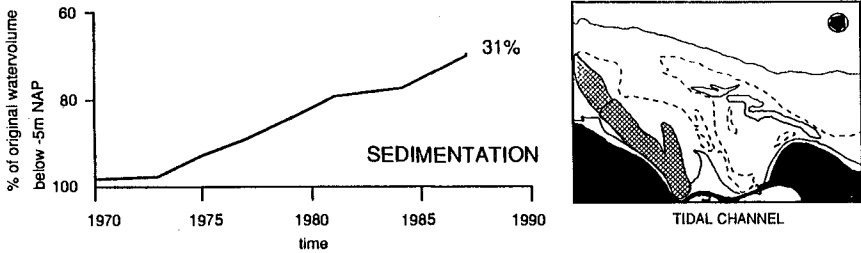


Fig. 3 Sedimentation in the the former main tidal channel of the Grevelingen ebb tidal delta since 1970

Typical erosive areas are the delta front, indicated by a continuing landward shift of the -5 mNAP depth contour, and the relic tidal bars in the landward parts of the deltas (Fig. 4).

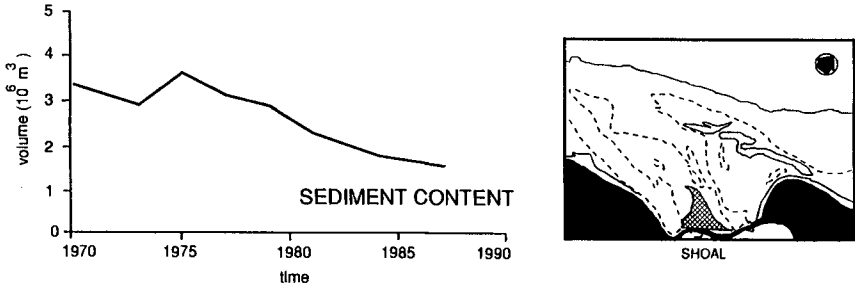


Fig. 4 Erosion of the main relic tidal bar in the landward part of the Grevelingen ebb tidal delta since 1970

The most striking phenomenon however is the development of large long shore bars at the edges of the Haringvliet and Grevelingen ebb tidal deltas (Fig. 5). The sedimentation trend at these bars is continuing but the growth rate is stagnating at a height around mean sea level. This stage had been reached circa 1980. From then on the

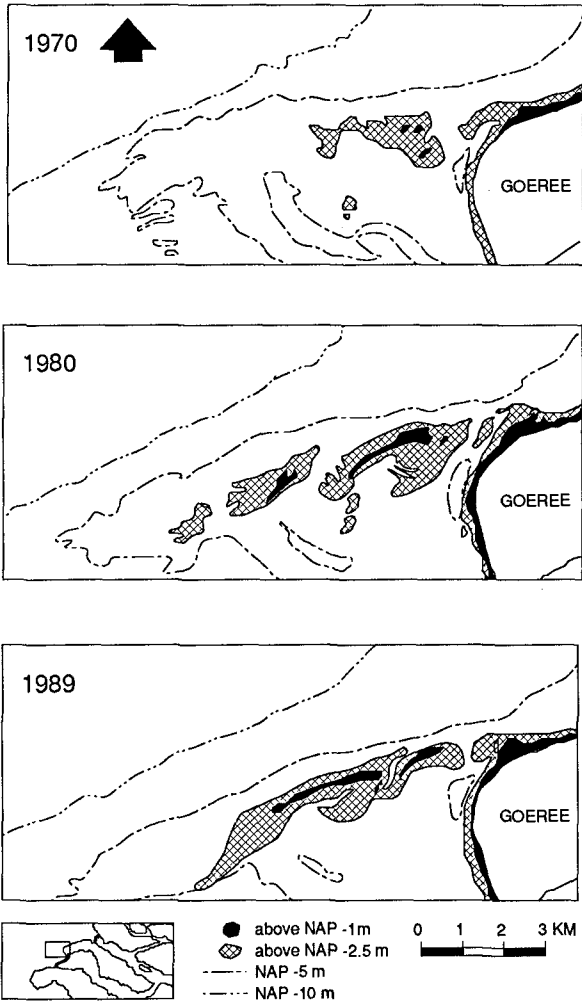


Fig. 5 Development of longshore bars at the edge of the Grevelingen ebb tidal delta since 1970

longshore bars are only showing a tendency towards a continuing shift in landward direction (Kohsiek, 1988; Louters et al., 1990). The total geomorphological change apparently is to a large extent due to a local redistribution of sediments.

The first observations of the Oosterschelde ebb tidal delta after completion of the storm surge barrier in 1986, indicate a tendency of changes similar to the changes of the Haringvliet and Grevelingen deltas: erosion of the delta front and tidal bars in the landward

parts of the ebb tidal delta, and sedimentation of the channels. However, until now no indication has been derived of developing long shore bars.

Among the driving forces of the geomorphological changes observed at the Haringvliet and Grevelingen ebb tidal deltas, a prominent one is represented by the asymmetrical wave orbital motion, inducing upslope sediment transport responsible for the initial development of long shore bars (Stive, 1986; Kohsiek, 1988). At later stages this bar development is depending on the equilibrium of four different mechanisms (Kohsiek, 1988): (-) a decrease in upslope sediment transport by the mentioned force due to an increase of the time mean of seaward flow under breaking waves; (-) a wave driven landward sediment transport over the crest of the longshore bars during storms, especially from the northwest; (-) a residual tide induced seaward sediment transport over the crest of the longshore bars; and (-) a wave induced longshore sediment transport during low water on the seaward side of the longshore bars. Since the prevailing winds are from westerly directions the residual longshore sediment transport is to the northeast.

Analyses of COMOR model results largely have confirmed this picture (Steijn et al., 1989). The mentioned mechanisms represent the main components of the conceptual model of dominant processes, as defined for the area (Louters et al., 1991).

The prognosis of future geomorphological changes (see e.g. Fig. 6) indicates that on an intermediate timescale (1990 - 2010), the generally observed trends will continue. The rate of change however, will reduce due to the assumption of exponentially decreasing process velocities. It then appears that, on an intermediate timescale, nor the available space between neighbouring geomorphological units, nor the spatial interaction between driving processes does impose definite limits to the development of any defined unit or to the activity of any presently acting process.

On longer time scales the geomorphological developments are less certain, as these are influenced by uncertainties in e.g. the effects of an increased sea level rise or a change in the net northward longshore sediment transport to the study area (Louters et al., 1991).

5.2 Ecological development

The intermediate position of the Voordelta on the ecological gradient estuary - open sea, becomes apparent from its macrozoobenthos characteristics; both its diversity and its total biomass. In the Voordelta a total of 150 different species of macrozoobenthos have been observed, with a mean total biomass of ca. 20 gADW/m² (ADW= Ash free Dry Weight i.e. the weight of biologically active parts). A total number of species which is significantly lower than generally observed in the North Sea, but higher than in the estuaries of the SW Netherlands. On the other hand the mean total biomass observed in the Voordelta appears approximately twice as high as in the open North Sea, but twice as

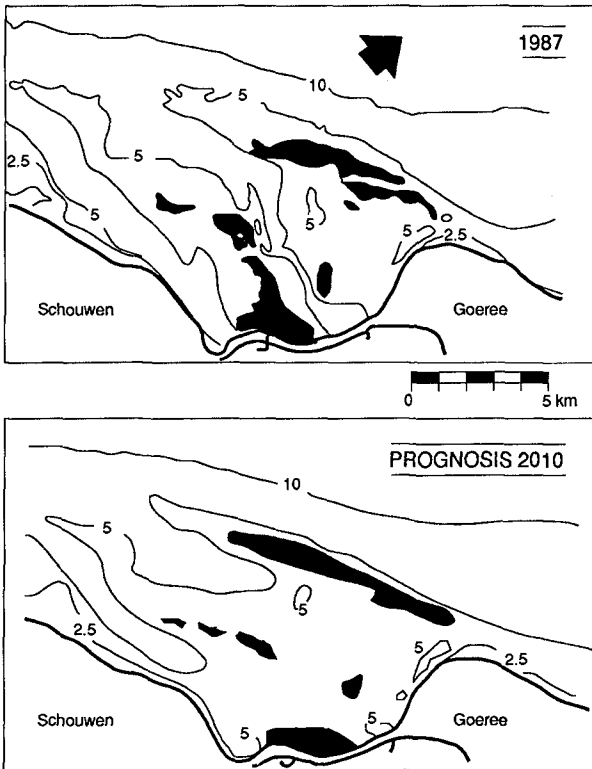


Fig. 6 Actual (1987) and predicted (2010) geomorphology of the Grevelingen ebb tidal delta. Indicated in black are the sandy shoals (above -2.5 mNAP).

low as in e.g. the Oosterschelde estuary.

Epibenthos observations showed a total of 48 different species, of which 40 species of fish.

Statistical analysis has demonstrated that the total Voordelta (including the Westerschelde ebb tidal delta) may be characterised by 6 different communities of macrozoobenthos, of which 4 communities occur in the key areas at the Grevelingen and Oosterschelde ebb tidal deltas. Each macrozoobenthos community has its own typical species composition, density (individuals/m²) and total biomass (Fig. 7).

The spatial distribution appears significantly correlated with sediment composition (especially mud content) and with water depth (Fig. 8) (Craeymeersch et al., 1990).

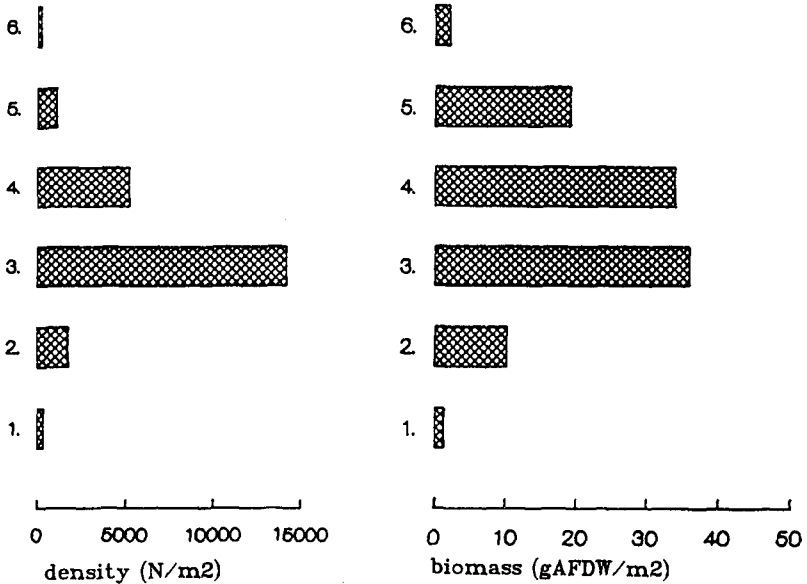


Fig.7 Characteristics of the six typical macrozoobenthos communities of the Voordelta

Spatial differences may be quite large. This is illustrated e.g. by observations of both hyperbenthos and macrozoobenthos. The Oosterschelde ebb tidal delta appears much poorer in this benthic fauna than the Grevelingen ebb tidal delta: the densities are about half, the total biomass about one third to one half of the Grevelingen values (Hamerlynck and Craeymeersch, 1990; Hamerlynck and Mees, 1990).

This difference is directly related to the changes in physical boundary conditions as induced by the Delta Project (see section 3). The Oosterschelde, which has remained partly open, only has known a relative small reduction in hydraulic energy conditions (current velocities ca. -30%); the hydrodynamic climate of the Grevelingen ebb tidal delta however, has become drastically calmer after closure of the estuary. This has induced large scale sedimentation of fine sediments especially in the tidal channels (see 5.1). Together with mud and silt sedimentation, organic material is deposited and several suspended juvenile stages of marine organisms are imported. Thus creating a very rich benthic fauna in this area (Hamerlynck and Craeymeersch, 1990).

The prognosis of future ecological changes indicates that, consistently with the expected, relatively small change in geomorphological characteristics for the next 10 - 30 years, also ecological changes most probably will be only gradual.

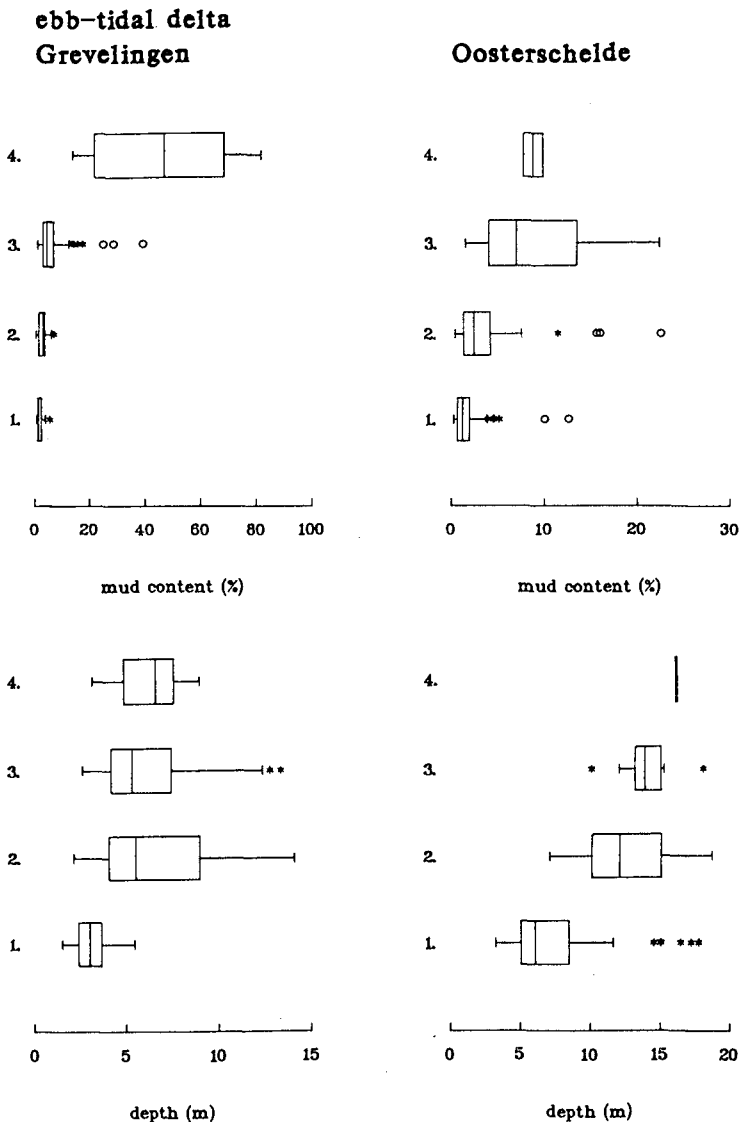


Fig. 8 Distributions of mud content and depth over the four typical macrozoobenthos communities of the Grevelingen - and Oosterschelde ebb tidal deltas, indicated by box-and-whisker plots. The median is marked by the central vertical line. The right and left edges of the box divide the distributions at the 25% and 75% level. The end of the whiskers denote the minimum and maximum values, unless there are outside values denoted by stars and circles.

6. CONSEQUENCES FOR WATER AND COASTAL MANAGEMENT

The observed and predicted changes in geomorphology and ecology of the Voordelta affect a series of (potential) human activities in the area. The main implications concern the following interests, each illustrated by an example (Hallie et al., 1990):

- shore protection; longshore bars and sand banks are reducing direct wave attacks on beaches and dunes, especially during storms. The resulting reduction in dune erosion has been calculated to amount locally 15 -25 percent.
- natural environment and landscape; the relative abundance of food, the extent of intertidal sand bars and shallow waters with a relatively mild hydraulic climate provide favourite conditions to several bird species and (potentially) to seals.
- recreational uses; enlargement of beaches has a positive, mud deposition around low water slack a negative effect on beach recreation. Shipping and surfing is stimulated by the attractive morphological variation and hydraulic conditions in the Voordelta.
- fisheries; the shallow, protected conditions make the area a potential nursery for some commercially interesting fish species (plaice, sole). Potentials for shellfish culture might develop.
- shipping; silting up of tidal channels and migrating sand bars affect shipping traffic towards local harbours.
- sand mining; the growth of sand bars near shore, provides a relatively cheap source of sands for several purposes (e.g. beach nourishments or land fills).

Obviously many of these interests are conflicting, at least potentially.

7. DISCUSSION, CONCLUSIONS AND RECOMMENDATIONS

Benthic fauna appears to be significantly correlated to abiotic variables. The distribution of macrozoobenthos of the Grevelingen area shows the highest correlation with mud content of the sediment top layer; on the other hand, macrobenthos of the Oosterschelde ebb tidal delta with water depth (Craeymeersch et al., 1990; also see Fig. 8). This illustrates that the established statistical correlations do not necessarily represent causal relationships. Possibly the variable water depth on the Oosterschelde ebb tidal delta, is a 'derived variable' from the driving variable current velocity.

In fact the ignorance of causal relationships between environmental variables and benthic fauna, poses a sincere problem once a prognosis of future developments is required. The statistical relation established for an open estuary (e.g. the Oosterschelde) does not necessarily have to be valid after the estuary has been closed (e.g. the Grevelingen).

This stresses the need of specific research of the driving processes in the relation between hydrodynamics - sediment (morphology and composition) - biota.

In this type of research, the level of detail (spatial and temporal)

in the geomorphological contributions, will have to be much higher than usual in current coastal morphological studies: for example, the need for hydrodynamic information near bottom, close to the benthos sampling locations, will eventually lead to hydrodynamical modelling at grid sizes of say 50 m or less. Another example is supplied by the statistical analyses of macrozoobenthos (Craeymeersch et al., 1990). As shown by the Grevelingen area (Fig. 8), 3 out of 4 macrozoobenthos communities (and among them the richest community) are correlated with mud contents between 2 and 10%. This indicates that in future research of this type, and in comparable environments, the distribution of mud content of the sediment has to be established at intervals between 2 - 5% ! These examples reveal the shortcomings of the applied integrated approach, and at the same time indicate possible ways of future progress in this field.

In general it may be concluded that the integrated geomorphological - ecological approach in coastal research as presented in this study, has appeared to be promising. The approach seems indispensable in view of the development of integrated coastal zone management.

ACKNOWLEDGEMENTS

By order of the Ministry of Transport and Public Works (Rijkswaterstaat) the present investigations have been carried out within the framework of a major multidisciplinary research project. Conducted by Rijkswaterstaat Tidal Waters Division, the following research institutes have participated: Rijksuniversiteit Utrecht Department of Physical Geography, Delft Hydraulics, Delta Institute of Hydrobiological Research and Rijksuniversiteit Gent, Institute of Zoology, Marine Biology Section.

REFERENCES

- Craeymeersch, J.A., van der Meer, J., Heip, C. and Smaal, A. (1990). Macrozoobenthos - environment relationships in a coastal subtidal community. In: Proc. ECSA-20., Hull, England, 1990. Int. Symp. Series, Olsen & Olsen Fredenborg, Denmark (in prep.).
- De Vriend, H.J. and Ribberink, J.S., (1988). A quasi-3D mathematical model of coastal morphology. Proc. 21st I.C.C.E. Malaga
- Hallie, F.P., Louters, T., Mulder, J.P.M., Postma, R., (1990). Geomorphological and ecological changes in the littoral zone of the south-west Netherlands; Consequences for integrated coastal zone management. In: R.E. Qu elennec, E. Ercolani, G. Michon (Editors), Symp. 1st EUROCOAST, Littoral 1990, Marseille, pp. 330-334.
- Hamerlynck, O., Mees, J., Vyver, P. van de, Landschoote, E. van,

- Hostens, K. and Cattrijsse, A., (1990).
Eindverslag Hyperbenthosonderzoek Voordelta. Internal Reports Marine Biology Section Rijksuniversiteit Gent - DIHO
- Hamerlynck, O. and Craeymeersch, J.A., (1990).
Het bodemleven in de Voordelta, In: De veranderende Delta. Proc. Symp. 60 jarig KNNV afd. Voorne, Brielle oct. 1990, p.p. 27-37
- Hamerlynck, O. and Mees, J. (1990).
Temporal and spatial structure in the hyperbenthic community of a shallow coastal area and its relation to environmental variables. *Oceanologica Acta* (in press)
- Kohsiek, L.H.M. (1988).
Reworking of former ebb tidal deltas into large longshore bars following the artificial closure of tidal inlets in the southwest of the Netherlands. In: P.L. de Boer et al. (eds.), *Tide Influenced Sedimentary Environments and Facies*, 113-122, D. Reidel Publ. Comp.
- Louters, T., Mulder, J.P.M., Postma, R. and Hallie, F., (1990).
Changes in coastal morphological processes due to the closure of tidal inlets in the SW Netherlands. *Journal of Coastal Research* (submitted)
- Meer, J. van der, (1988).
Exploring macrobenthos - environment relationships by multiple discriminant analysis. Note GWAO 89.319 Rijkswaterstaat Tidal Waters Division The Hague
- Mulder, J.P.M., (1989).
The changing tidal landscape in the Delta area of the SW Netherlands. In: Hooghart, J.C. and Posthumus, C.W.S. (eds.) *Hydro-ecological relations in the Delta waters of the south-west Netherlands*. Proc. and Information no.41 TNO Comm. Hydr. Res., The Hague: 71-88
- Postma, R., Mulder, J.P.M., Louters, T., Hallie, F.P., (1990).
Coastal geomorphological response to the closing of the Grevelingen tidal basin, S.W. Netherlands. In: Proc. ECSA-20., Hull, England, 1990. Int. Symp. Series, Olsen & Olsen Fredenborg, Denmark (in prep.).
- Steijn, R.C., Louters, T., Van der Spek, A.J.F., De Vriend, H.J., (1989).
Numerical modelling hindcast of the ebb-tidal delta evolution in front of the deltaworks. In: R.A.Falconer, P.Goodwin and R.G.S. Matthew (Editors), *Hydraulic and Environmental Modelling of Coastal, Estuarine and River Waters*, Int. Conf. Bradford, England, Chapter 23: pp. 255-264.
- Stive, M.J.F., (1986).
A model for cross-shore sediment transport. Proc. 20th I.C.C.E., Taipei, pp. 1551-1564.

CHAPTER 227

Numerical Simulations of Mud Transport by a Multi-Layered Nested Grid Model

Hiroichi Tsuruya¹
Kazuo Murakami¹
Isao Irie²

Abstract

A multi-layered model is developed for the prediction of mud transport in an estuary and ports to take into account the effects of submerged dikes and to reproduce the vertical distribution of suspended mud concentrations. A most remarkable result in the field observation in Kumamoto Port was the effect of a submerged dike on reducing the amount of deposition rate within the test trench.

It is predicted from the calculation that submerged dikes 1 m in height from the bottom will prevent siltation in the access channel and anchorages of Kumamoto Port by about 30% of the total deposition without submerged dikes.

1. Introduction

Extensive field measurements have been carried out in Kumamoto Port which is under construction to obtain detailed information on siltation mechanisms. Measured deposition rates within three trenches were used to calibrate the present model.

A nested grid model is adopted to treat the composite mesh arrangement of rough and fine meshes because the dimension of the trenches is so small, *i.e.*, 70m×50m in area.

The calculation is conducted with the supercomputer NEC SX-1E of the Port and Harbour Research Institute.

¹Port and Harbour Research Institute, Ministry of Transport, 1-1, Nagase 3 Chome, Yokosuka, 239 Japan.

²Kyushu University, Dept. of Civil Engineering, 6-10-1, Hakozaki, Higashi-ku, Fukuoka, 812 Japan.

2. Mathematical Modeling of Mud Transport

For the treatment of the detailed configuration of the sea bed and construction such as submerged dikes, we adopted the multi-layered model with nested grid for the calculation of mud transport (Tsuruya et al., 1990). The present model consists of several horizontal layers as shown in Figure 1.

The water depth is vertically divided into seven layers as shown in Figure 2.

Tidal currents are calculated by a set of known equations: (1) continuity equations, and (2) equations of motion. Mud is transported in suspension and this process can be represented by diffusion equations.

Random wave deformations by refraction, wave breaking, diffraction, reflection are considered. Wave damping due to interaction between surface waves and a mud bed is also considered (Tsuruya et al., 1987b).

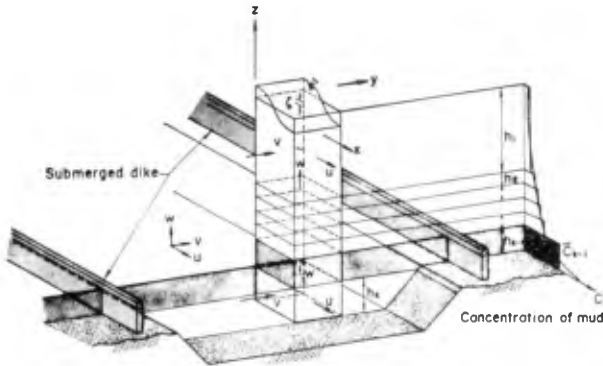


Figure 1. Multi-Layered Level Model

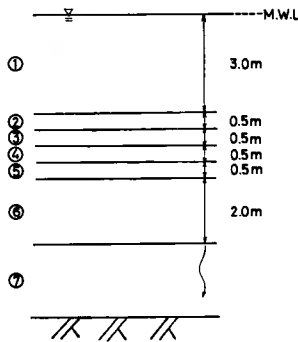


Figure 2. Division of Water Depth into Seven Layers

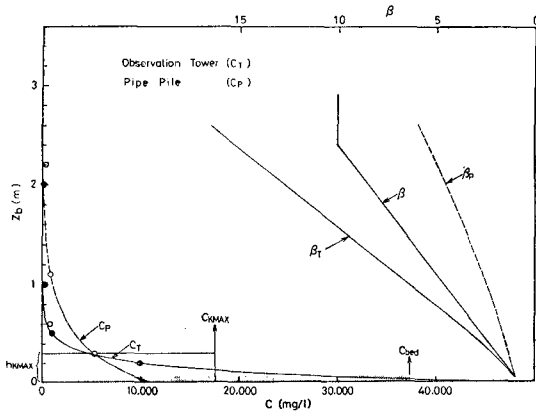


Figure 3. Vertical Distribution of SS and β

Erosion and Deposition

The rate of erosion of mud has been formulated by Partheniades (1965) as

$$E = M \left(\frac{\tau_b}{\tau_c} - 1 \right), \tag{1}$$

where τ_b (Pa) is the shear stress at the bottom by the combined action of waves and currents, τ_c (Pa) the critical shear stress for erosion, and M ($\text{kg/m}^2/\text{min}$) is the constant. The bottom shear stress τ_b is given by Tanaka and Shuto (1981).

Deposition rate D is estimated by a similar consideration by Sheng and Lick (1979) as

$$\begin{aligned} D &= w_s C_{bed} \\ &= \beta w_s C_{KMAX}, \end{aligned} \tag{2}$$

where w_s is the settling velocity, C_{bed} the concentration of mud at the bed, and β is the correction factor to estimate C_{bed} from the calculated mean concentration of the bottom layer (C_{KMAX}). The correction factor β is introduced to estimate the concentration near the bottom from the calculated mean concentration C_{KMAX} at the bottom layer. The factor β may depend on the wave conditions, turbulence, the type of bed materials, and the thickness of the bottom layer. We now estimate the value of β from the field observation data. Figure 3 shows the typical distributions of SS observed at the observation tower and the pipe pile on August 31st, 1987. Plotted data are the average values of SS measured by water samplers.

Fitted curves are exponential functions and the concentration at the bed is assumed to be the average value

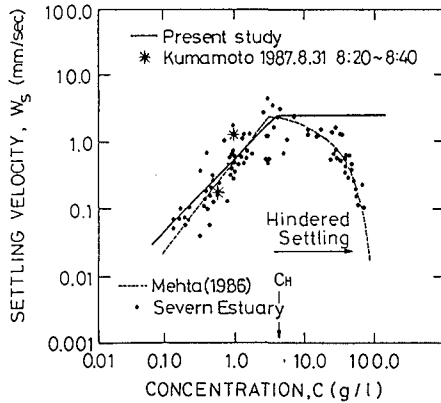


Figure 4. Relation between Settling Velocity and Concentration of Mud

from the bed to the height of 5 cm. Estimated value of β for each observation station are also shown in the figure as a function of the thickness of the bottom layer. We assume that the value of β is given by the average value obtained at the observation station and the pipe pile, and β is constant if the thickness of the bottom layer is larger than 2.4 m. The thick solid line in Figure 3 shows the functional relationship between the thickness of the bottom layer and β , given by the following expression as

$$\begin{aligned} & 1.0, (z_b \leq 0.05\text{m}) \\ \beta &= 3.9z_b + 0.805, (0.05 < z_b \leq 2.4\text{m}) \\ & 10.0, (z_b > 2.4\text{m}) \end{aligned} \quad (3)$$

where z_b is the height from the bed and equal to the thickness of the bottom layer h_{KMAX} .

Settling Velocity

The settling velocity w_s for mud depends on the concentration. As the concentration increases, a probability of collision between mud particles increases and the settling velocity increases. Above some specific concentration, the settling velocity begins to decrease because of the hindered settling.

The relationship between the settling velocity w_s and mud concentration C is schematically shown in Figure 4. The broken line in the figure is given by Mehta (1986).

In the present model, hindered settling is not effectively applied because the erosion rate in this region will not be appropriately represented by Eq.(1). For the modeling of the process, more detailed research

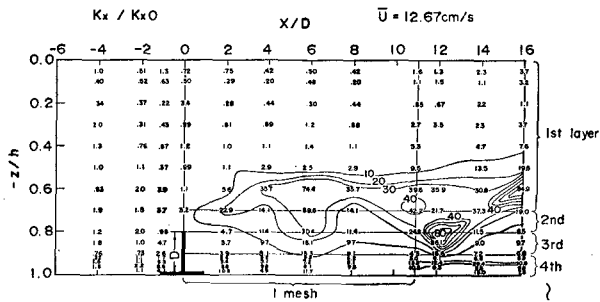


Figure 5. Rate of Increase in Horizontal Diffusion Coefficient

is required. Here we assumed that the settling velocity is constant for the concentration greater than the critical value C_H . Two asterisks in the figure are obtained by solving the diffusion equation in which the convection and diffusion terms are neglected.

Diffusion Coefficients behind Submerged Dikes

Turbulence intensity in the region behind a submerged dike increases considerably. Vertical and horizontal diffusion coefficients also increase when compared with cases without submerged dikes. The rate of increase in the diffusion coefficients with and without submerged dikes is investigated experimentally (Tsuruya et al., 1987a).

If the velocity is larger than the reference velocity U_{ref} , horizontal and vertical diffusion coefficients are increased according to the following expression as

$$\frac{K_H}{K_{H_0}} = \left[\frac{U_m}{U_{ref}} (K_H' - 1.0) + 1.0 \right], \tag{4}$$

where K_H is the diffusion coefficient behind a submerged dike, K_{H_0} the diffusion coefficient without a submerged dike, U_m the mean velocity in the second layer, U_{ref} the reference velocity ($=25\text{cm/s}$), and K_H' is the rate of increase in the diffusion coefficient which is given by the experiment. An example of the increase in the horizontal diffusion coefficient is represented in Figure 5.

3. Field Observations at Kumamoto Port

Kumamoto Port is under construction as a new commercial port at a site off-Kumamoto City in Ariake Bay.

Figure 6 shows the final plan of Kumamoto Port. The observation tower and the pipe pile which are shown by open circles were built at 4 m and 2 m depth, respec-

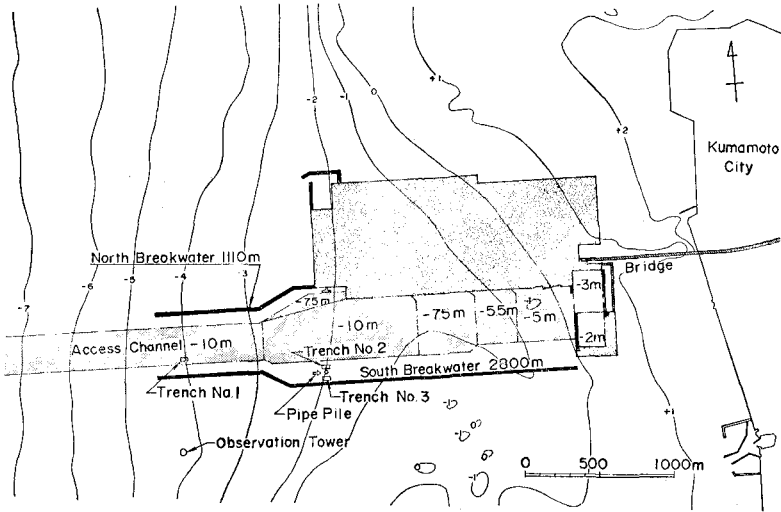


Figure 6. Plan of Kumamoto Port and Field Observation Site

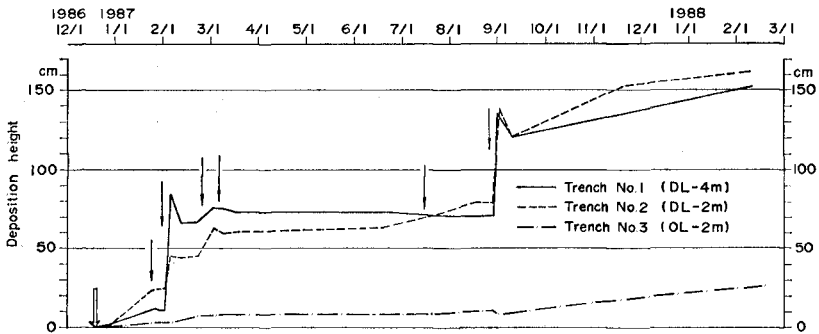


Figure 7. Time Variation of Deposition Heights at the Center of Three Trenches

tively, below the LWL to measure tides, waves, winds and turbidity of sea water.

Three trenches are constructed to investigate the relationship between the amount of sediment deposition and external forces such as waves and currents. The effect of a submerged dike to reduce the amount of deposition is also tested. Three trenches are shown in Figure 6. Trench No.1 is located at 4 m depth below LWL, and trenches No.2 and 3 are located at 2 m depth below LWL. Trench No.3 is surrounded by a submerged dike of 1m in height. On the other hand, trench No.2 is surrounded

by no facility. The dimension of the trenches is 70m×50m in area. Trenches No.2 and No.3 are located 100 m apart from each other. The depth of the trenches is 2 m from the bed level and the side slope is 20 %.

Siltation Rate in Trenches

Figure 7 shows the time variation of deposition heights at the center of each trench. In the figure, six arrows show the onset of large waves. The leftmost arrow shows the start of the observation. It is found from the figure that the severe and sudden deposition occurred at

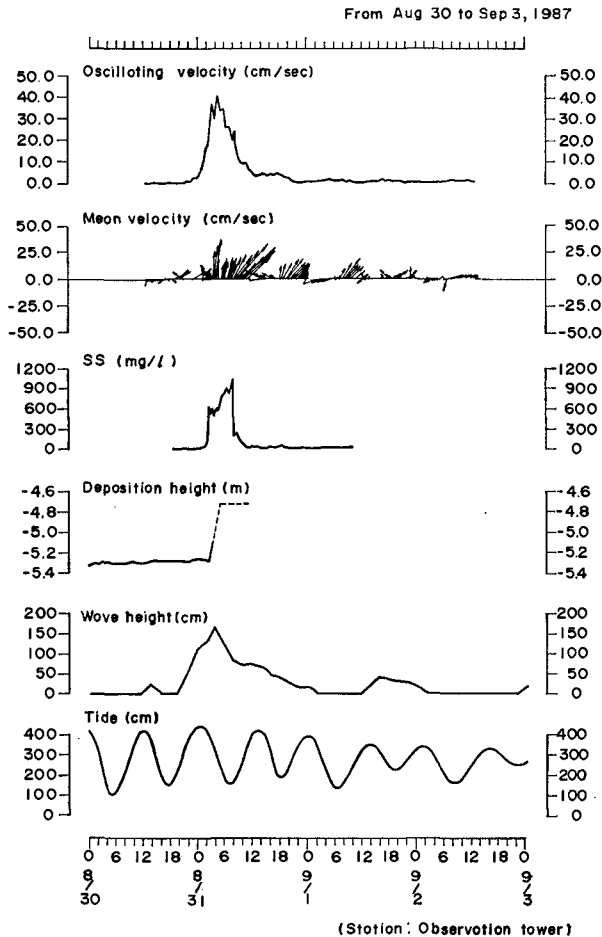


Figure 8. Example of Measured Time Series Data from Aug. 30 to Sept. 3, 1987 at Observation tower

trenches No.1 and No.2 during rough seas on February 3rd, 1987 and on August 31st, 1987. On the other hand, the deposition at trench No.3 was small. It is considered that the submerged dike has a considerable effect on reducing the deposition of mud. During gentle and calm seas, a small amount of deposition occurred in three trenches. This fact means that the tidal current has little effect on the deposition. Around the submerged dike, no extreme erosion and deposition could be observed.

The simultaneous measurements of tides, currents, turbidity, and bottom levels were carried out. Figure 8 shows the measured time series data of the oscillatory current velocity, averaged current vector, turbidity concentration, deposition height in trench No.1, wave height, and tidal level at the observation tower from August 30th to September 2nd, 1987. From the figure, it is found that there is a strong correlation between the oscillatory current velocity and the turbidity concentration. Moreover, increase of the bottom level starts when wave height is large and tidal level is low. It is suspected that the bottom sediments around Kumamoto Port are eroded mainly by wind waves. Also, the bottom sediments were eroded by stormy waves when the tidal level was low.

4. Calibration

Figure 7 shows the abrupt deposition occurred on February 6th and September 1st. We adopt the deposition on September 1st as the representative case for the

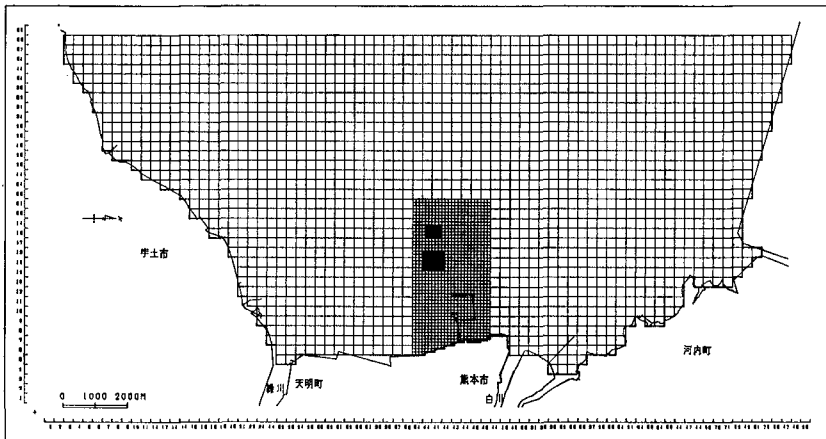


Figure 9. Mesh Map for the First Area

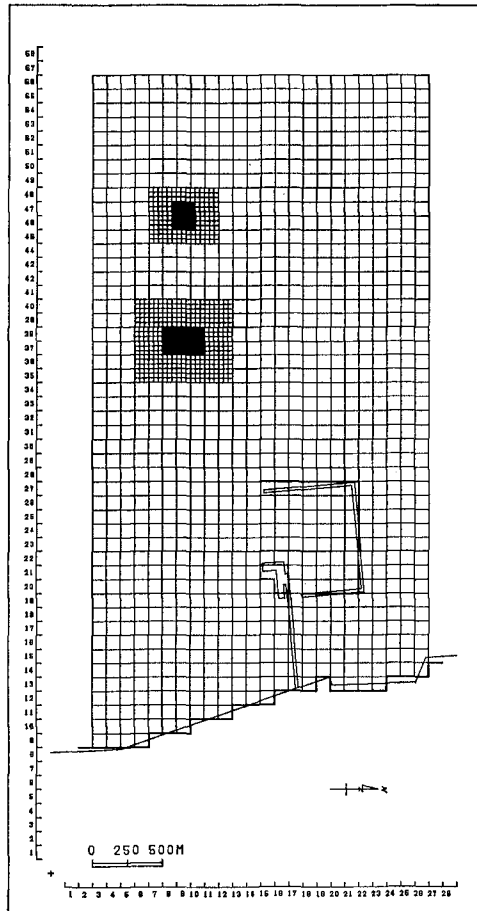


Figure 10. Mesh Map for the Second Area

calibration. Part of port facilities had been constructed at that time. The "Kumamoto Port Ohashi" bridge with a length of 872m, connecting the offshore port and the city, a wharf with a length of 300 m, and part of the revetment for a reclaimed land were completed.

The area for calculation is divided into five areas from the first to the fifth. Mesh sizes are 300m, 100m, and 100/3m for each area from the first to the third, respectively. For the fourth and the fifth area, the mesh size is 100/9m. Arrangement of the mesh for the first area is presented in Figure 9. Magnified meshes for the second area are shown in Figure 10. The third area is separated into two parts. Within them, there

exist the fourth and the fifth area. They are shown in Figure 10 as the solid rectangles because the mesh size is so fine (11.1m). The fourth area (the lower solid rectangle) includes No.2 and No.3 trenches. The present nested grid model can treat the composite mesh arrangement of rough and fine meshes. Therefore, calculation, which included the small area with special interest, can be efficiently conducted.

The predicted wave damping ratio of the pipe pile to the observation tower by the multi-layered viscous fluid model (Tsuruya et al., 1987b) was 0.56. This value agreed closely with the observation when wave heights are large, i.e., from 2:00 to 6:00 a.m., August 31st. In the calculation, the depth of the mud layer and water content are set to at 10 cm and 200 %, respectively.

From Figure 8, wave conditions are decided to be as follows: $H_{1/3} = 1.25$ m, $T_{1/3} = 4$ s, direction of the wave is WSW and their duration is 6 hours. When waves are large, the tidal level is low. Therefore waves are operated from 15:00 to 21:00 in the calculation as shown in Figure 11. Only tidal current is calculated from 0:00 to 15:00. Calculations of erosion, diffusion, and settlement are conducted from 15:00 to 27:00. All the calculations are finished at time 27:00.

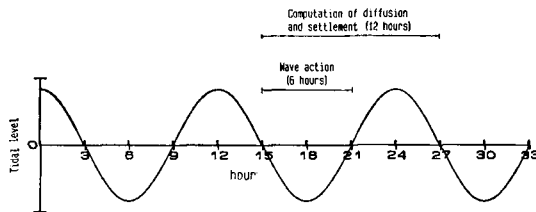


Figure 11. Time Table of Calculation

Tidal Currents

An example of the calculated tidal current distribution is shown in Figure 12. Velocities in the second area where the mesh is three times smaller than that of the first area are expressed together with the velocities for the first area.

Measured deposition heights during rough seas from August 31st to September 1st within three trenches are listed in Table 1 together with the water content.

In the calculation of erosion, the critical shear stress τ_e was set at 0.1 (Pa) after Murakami et al. (1989) and the constant M was varied until the reasonable deposition heights are obtained. The calculated deposition heights are listed in Table 2. The upper row

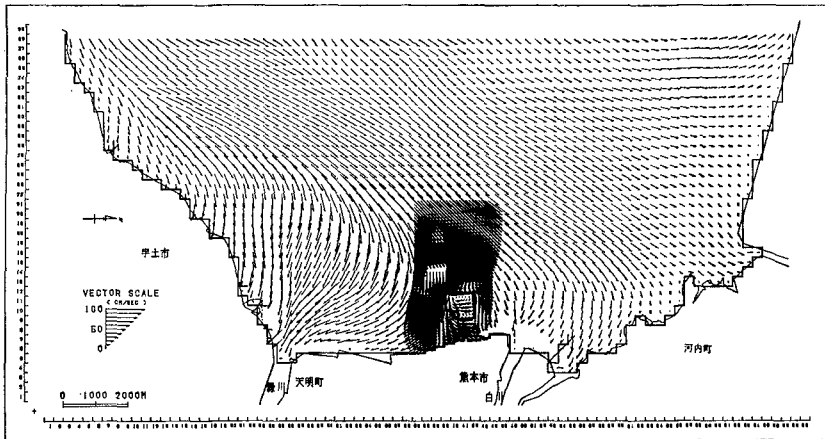


Figure 12. Calculated Velocity Distribution for the First Layer at the Maximum Flood Tide

Table 1. Deposition Heights and Water Contents within Three Trenches (Aug. 29 - Sept. 2, 1987)

	Trench No. 1	Trench No. 2	Trench No. 3
Deposition Height (cm)	63	60	-2
Water Content (%)	231	189	192

Table 2. Calculated Result of Deposition Heights

	Trench No. 1	Trench No. 2	Trench No. 3
Deposition (cm)	63.4	39.8	4.0
Deposition + Mass Transport (cm)	74.6	53.4	4.0

shows the contribution from deposition only and the lower one shows the total amount by both deposition and mass transport of the mud layer due to wave action. Comparing with Table 1, the calculated total deposition heights agree with the measured one. The value of M thus estimated $1.2 \text{ kg/m}^2/\text{min}$. According to van Leussen and

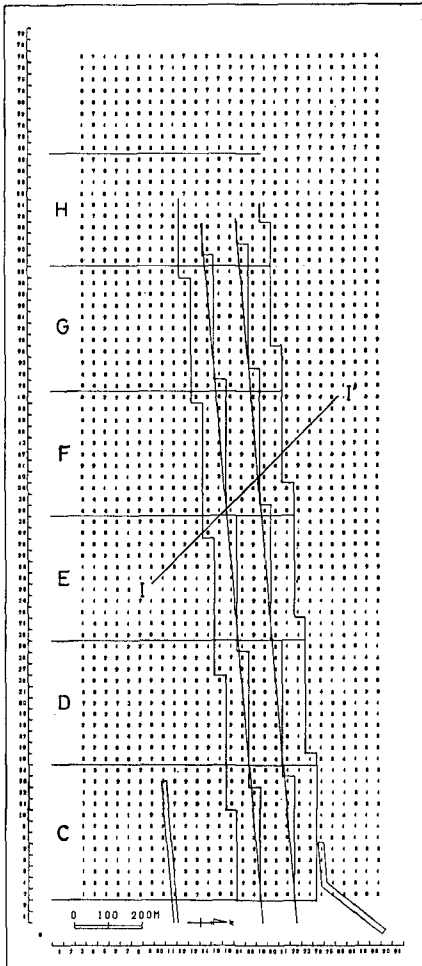


Figure 13. Access Channel

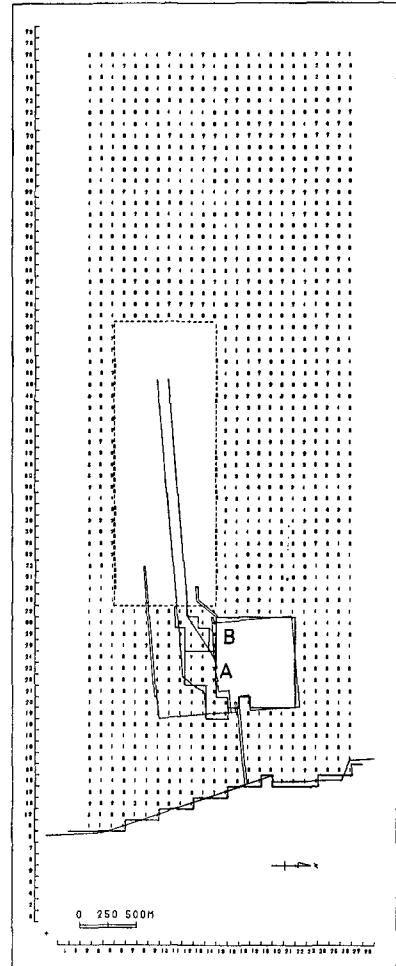


Figure 14. Anchorage

Dronkers (1988), the range of M is $0.006-0.24 \text{ kg/m}^2/\text{min}$. We have a larger value of M for the present model than usual. However, as the model does not include every process in the field, we must finally calibrate the calculated value with the field data. Therefore, we concluded that the present model could reproduce the deposition heights in the field.

5. Application to Future Plan of Kumamoto Port

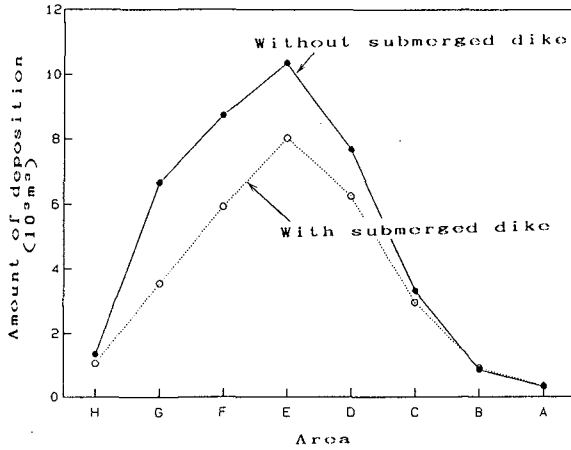


Figure 15. Amount of Deposition in Each Area

We show only the tentative plan that will be completed within a couple of years (Figures 13 and 14). In Figure 13, the access channel is 100m wide and 4.5m depth, and is shown as the inner parallel lines. The outer lines parallel to the access channel are submerged dikes which are 2,000m in length and 1m in height from the bottom. The calculated deposition heights inside the access channel are added together to get the volume of deposition for each area as shown in Figures 13 and 14. It is assumed that the water content of the deposited mud is 200%. The amount of deposition in each area is shown in Figure 15. The maximum deposition occurs at area E. The reducing effect of deposition by submerged dikes is about 23% for area E and 47% for area G. The calculated volume includes mass transport by waves. The amount of decrease in the volume of deposition owing to the submerged dike is about 30%.

6. Conclusions

Three-dimensional multi-layered level model with nested grid is developed for the calculation of siltation. After the calibration of deposition heights within three trenches, calculation for the future plan of Kumamoto Port is conducted. The amount of decrease in the volume of deposition due to submerged dikes was 30%.

Acknowledgements

We would like to express our appreciation to the Ministry of Transport and the Fourth District Port Construction Bureau for their support of the siltation research work project and for providing the field data.

We also thank Mr. Cao Zude, Chief Engineer of the Tianjin Research Institute of Water Transport Engineering, for analyzing the field data. Also, thanks are due to Mr. Hiroshi Yoshinaga, the member of Hydrodynamics Laboratory of the PHRI, for his assistance in typing the manuscript.

References

- Mehta, A. J. (1986): Characterization of cohesive sediment properties and transport processes in estuaries, in Mehta A. J. (Ed), *Estuarine Cohesive Sediment Dynamics*, Lec. Notes Coastal Estuarine Stud. 14, pp.290-325.
- Murakami, K., F. Sukanuma and H. Sasaki (1989): Experimental investigation on erosion and deposition of fine cohesive sediments in an annular rotating channel, Report of the Port and Harbour Research Institute, Vol.28, No.1, pp.43-76 (in Japanese).
- Partheniades, E. (1965): Erosion and deposition of cohesive soils, *Proc. ASCE*, Vol.91, No.HY1, pp.105-139.
- Sheng, Y. P. and W. Lick (1979): The transport and resuspension of sediments in a shallow lake, *J. Geophys. Res.*, Vol.84, No.C4, pp.1809-1826.
- Tanaka, H. and N. Shuto (1981): Friction coefficient for a wave-current coexistent system, *Coastal Engineering in Japan*, Vol.24, pp.105-128.
- Tsuruya, H., Y. Matsunobu, T. Korezumi and S. Yanagishima (1987a): Measurements of turbulent flow downstream of a submerged structure, Report of the Port and Harbour Research Institute, Vol.26, No.2, pp.127-169 (in Japanese).
- Tsuruya, H., S. Nakano and J. Takahama (1987b): Interactions between surface waves and a multi-layered mud bed, Report of the Port and Harbour Research Institute, Vol.26, No.5, pp.137-173.
- Tsuruya, H., K. Murakami and I. Irie (1990): Mathematical modeling of Mud Transport in Ports with a Multi-Layered Model -Application to Kumamoto Port-, Report of the Port and Harbour Research Institute, Vol.29, No.1, pp.3-51.
- van Leussen, W. and J. Dronkers (1988): Physical Processes in estuaries: An introduction, in Dronkers, J. and W. van Leussen (eds), *Physical processes in estuaries*, Springer-Verlag, pp.1-18.

CHAPTER 228

Modelling of cohesive sediment transport.
A case study: the Western Scheldt Estuary

Herman P.J. Mulder¹ and Connie Udink¹

Abstract

A depth-averaged numerical model for the erosion, sedimentation and transport of cohesive sediment is applied to a mesotidal estuary. The transport model is coupled to a hydrodynamic and a wave model. First results are presented as part of the aim to predict year-averaged quantities. Comparisons with measured data of net sedimentation and suspended concentration are made. As the bed of the estuary consists mainly of non-cohesive sediments, the erosion formula is adapted to account for the local (non-)cohesive fraction in the bed. The effect of the spatial variation in this property of the bed is significant. Furthermore the influence of surface waves is investigated and showed to be of great importance in a qualitative and quantitative sense. The model can take into account the dumping of dredged material and gives reasonable results in case of the spreading and sedimentation of mud from one source, as shown by a simulation of the transport of fluvial mud.

Introduction

In the Western Scheldt Estuary (figure 1) in the south-western part of the Netherlands the input of severely contaminated fine sediments from the river Scheldt causes a considerable environmental problem. Especially in sedimentation dominated areas, like the great marsh land in the eastern part of the estuary, these sediments with cohesive properties accumulate in the bottom influencing the environment for many years to come. There is a need for models capable of simulating these processes and predicting the consequences of measures to reduce the pollution. Such models must

¹Rijkswaterstaat, Tidal Waters Division, P.O. Box 207, 9750 AE, Haren, The Netherlands

undoubtedly include the transport of cohesive sediments.

In the estuary the main channels are dredged frequently because of the shipping to the harbour of Antwerp up the river in Belgium. Also harbours along the estuary are regularly dredged. These activities involve not only high costs but also environmental problems in case the dredged material contains polluted sediments. A model for predicting the fate of dumped sediments is a powerful tool for decisions about the assessment of dump sites.

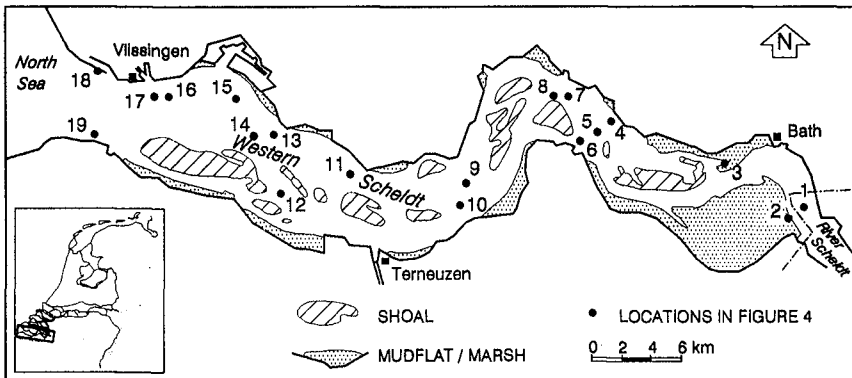


Figure 1. The Western Scheldt Estuary.

This paper presents some results of the numerical modelling of the transport of cohesive sediment or mud - here defined as the anorganic fraction finer than 63 micron - related to the problems in the Western Scheldt Estuary. The model involves hydrodynamics, surface waves and sediment transport. Descriptions of and experiences with models for estuaries (e.g. Hayter (1983), Sheng (1986), O'Connor and Nicholson (1988), Fritsch et al (1989)) showed that strongly empirical relations have to be used and that the incorporation of all relevant processes as well as the schematization of hydraulic and meteorological conditions form an enormous task. Therefore some processes are neglected in the present model while others are investigated, viz. the importance of the local mud fraction and the role of surface waves. Our final aim is a predictive model for long term behaviour of the cohesive sediment. Especially the spreading of fluvial mud is of interest and a simulation is presented.

Model description

Because of the considerable morphological variety in the lateral direction of the estuary (see figure 1) and the fact that the estuary is well mixed, two-dimensional

horizontal (depth-averaged) models are used: a hydrodynamic model, a surface wave model and a sediment transport model.

The hydrodynamic model (WAQUA) calculates the water flows, water levels and densities on a time scale much smaller than the tidal period (Stelling, 1983). Calibration of the model was carried out by others (Dekker, 1985). Wind induced currents appeared to be very small and are not taken into account in the calculations. Also the wind generated water level rise is neglected. The tidal range in the estuary varies between 3 and 4 m, while the average depth is 10 m. The simulation was carried out for a tidal cycle of 24.5 hrs of a semi-diurnal tide with a tidal range 5 % higher than the long term mean value. The grid is rectilinear and the element size is 400*400 m. The bottom schematization of the hydrodynamic model was used as input for both the wave model and the transport model, via different interface programs.

The wave model (HISWA) is suitable for shallow water waves and produces stationary wave fields. It solves a spectral action balance and takes into account the generation, dissipation, refraction and diffraction of waves (Booij et al, 1985). To restrict the computational costs a limited number of boundary conditions is used. As input for the wave calculation the mean values of wind speed (1983-1987) are used in four dominating wind directions: 220° (wind speed 10.3 m/s), 250° (9.7 m/s), 280° (9.3 m/s) and 310° (9.6 m/s; North=0°=360°), respectively representing 16%, 12%, 9% and 7% of time within a sector of 30°. The remaining 56% of time fair weather conditions are assumed. Because the model is stationary, an interpolation is performed between the calculated wave heights and wave periods at four different tidal stages: LW slack, maximum flood current, HW slack and maximum ebb current. The interpolated values are used to determine the orbital velocity and consequently the bottom shear stress component due to waves. Verification of the model at 6 locations throughout the estuary showed a systematic overestimation of the long term mean wave height of about 30% by the model. However, the available observations were made visually and exclude rough weather conditions. Therefore the wave model results are satisfying.

The dynamic model for the cohesive sediment transport, based on the program package DELWAQ (Delft Hydraulics, 1990), incorporates advection, diffusion and bottom exchange by sedimentation and erosion. The model solves the finite volume advection-diffusion equation with sink and source terms on the same grid as WAQUA. The tidal cycle can be repeated until a dynamic equilibrium is reached. The dispersion coefficients were chosen constant and equal in both horizontal directions. Although the bottom exchange processes are extremely complex and

influenced by physical, chemical and biological factors for practical reasons we adopted well-known empirical expressions for sedimentation (Krone, 1962) and erosion (Partheniades, 1962), in which the bottom exchange rates both linearly depend on the bottom shear stress with critical shear stresses of 0.2 and 0.4 Pa respectively. A constant settling velocity of 2 mm/s was used, based on indications from field measurements. The bottom shear stress can have three components: (i) the depth-averaged current velocity, assuming a logarithmic profile, (ii) the orbital velocity and (iii) the horizontal density gradient. The influence of the waves is restricted to the shear stress in the bottom exchange terms. The third component is omitted in this paper because of the relatively small effect on the presented results. The wave and current bottom shear stresses, τ_{bw} and τ_{bc} respectively are combined according $\tau_{bw} + \alpha_w \tau_{bc}$, in which α_w is a reduction factor related to the wave-current interaction (van Rijn and Meijer, 1986). The model takes into account one homogeneous bottom layer with a space and time dependent thickness although consolidation is neglected. In order to use the model to determine optimal dump sites for dredged material a special subgrid scale dumping routine is incorporated (van Heuvel, 1988). At first the dumped mud undergoes the process of transport on a detailed scale governed by the flow velocity and the slope of the bottom at the dump location. Then the location and the thickness of the layer after complete sedimentation in the neighbouring grid elements is determined by the dumping routine. Subsequently resuspension and transport can proceed under the proper hydrodynamic circumstances. Although simulations of the dumping and spreading of dredged material have been made the results could not be verified and are subject of further study.

Results

The results presented here concern the cohesive sediment transport only. A study of two influencing factors, the local mud fraction and the waves respectively, is performed. These factors are presumed to be very important for a reliable model result. Furthermore an application to the spreading of polluted mud from the river is made. Some verification of the model is made by comparison with measurements of net sedimentation and (suspended) concentrations. It is assumed that morphological changes in the estuary can be neglected.

The influence of a local mud fraction

The mud fraction in the bottom of the estuary shows a strong spatial variation (figure 2). In the channels

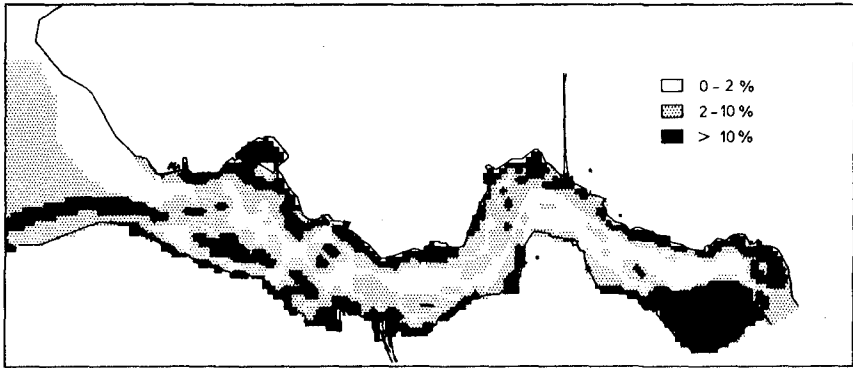


Figure 2. Silt content in the top layer (0 - 10 cm) of the bed (1980-1985).

the mud fraction is very low (<0.02) while the average fraction is about 0.15. This is partly the result of a morphodynamic process and it questions the applicability of a sediment transport model without the influence of the non-cohesive material. Because of the supposed effect on the availability of mud during erosion or resuspension, this influence is taken into account by putting the mud fraction $f_e(x,y)$ in the formula for the erosion rate E [$\text{kg}/\text{m}^2/\text{s}$]:

$$E(x,y,t) = f_e(x,y) M (\tau_b(x,y,t)/\tau_{ce} - 1) \quad \text{if } \tau_b > \tau_{ce}$$

$$E(x,y,t) = 0 \quad \text{if } \tau_b \leq \tau_{ce}$$

in which M [$\text{kg}/\text{m}^2/\text{s}$] is the erosion constant, τ_b the bottom shear stress and τ_{ce} the critical shear stress for erosion. Two calculations are made representing two extreme cases: (i) assuming a bed of pure mud, i.e. $f_e(x,y) = 1$ (with $M = 5 \cdot 10^{-5}$) and (ii) using values of $f_e(x,y)$ for each grid cell obtained from the measurements (with $M = 7 \cdot 10^{-4}$). For each case the value of M is found by calibration to obtain suspension concentrations of the same order of magnitude as the measured values in order to make a meaningful qualitative comparison. In both cases the bottom layer thickness is not a limiting factor and only fair weather conditions are applied. It appears that the tide-averaged sedimentation, see figure 3, and concentration, did not show important differences on a large scale. However in the channels with very low mud

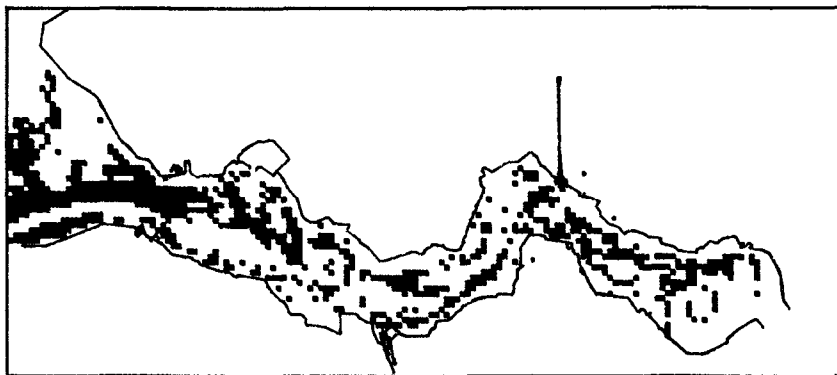


Figure 3. Non-corresponding areas (black) of erosion or sedimentation for case 1 and 2.

fraction the sedimentation pattern can differ importantly, while the tide-averaged concentration in some areas can differ more than 30% (after correction for systematic difference). Comparison of the calculated and measured concentrations, corrected with respect to tidal and seasonal effects, at 19 locations, mainly located in the channels, shows reasonable agreement in both cases (see figure 4). Case 2 seems to be better than case 1 at locations 1-8. For one particular location with a water depth of 10 m and a low mud fraction the comparison of the time series is displayed in figure 5. Apart from a systematic deviation between the three time series, there are the following differences: a quick increase of concentration in case 1 directly after LW slack, which is absent in case 2. So the availability of mud in the bed influences the time series strongly. From the measured values it seems that in reality the availability of mud is high directly after slack tide, while afterwards it is low (other measurements show a similar pattern). This qualitative disagreement with the model is likely to be caused by the spatial variation in the presence of mud in both horizontal and vertical direction. Hence a more sophisticated model, including a sand transport model to account for fractional sorting in the bed, could be more appropriate. Due to tidal dynamics and the very small thickness of the active mud layer (in the order of 1 mm) consolidation may be excluded in case of sandy channels.

A consequence of the results above is that a spatial variation in other erosive bed properties, like biological activity or the composition of the mud, could have a similar impact.

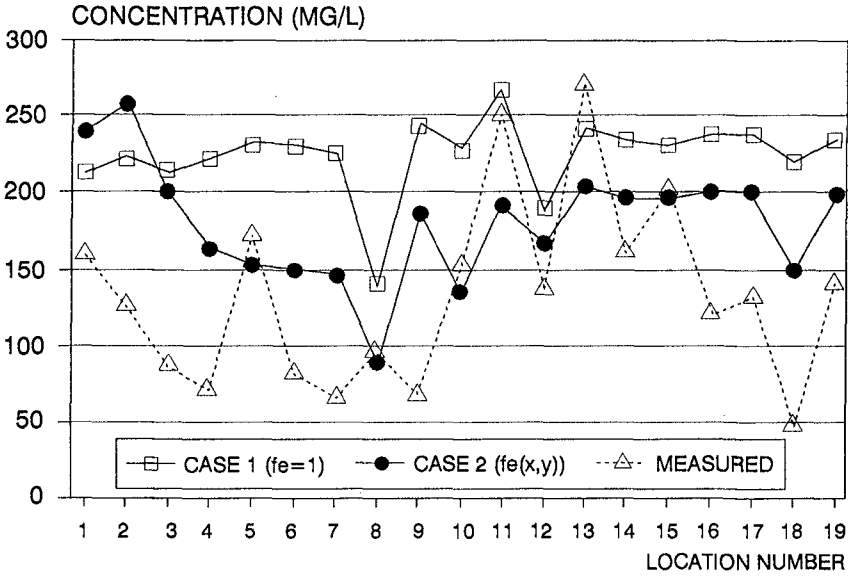


Figure 4. Measured and calculated (case 1 and 2) tide-averaged concentration at 19 locations (see figure 1).

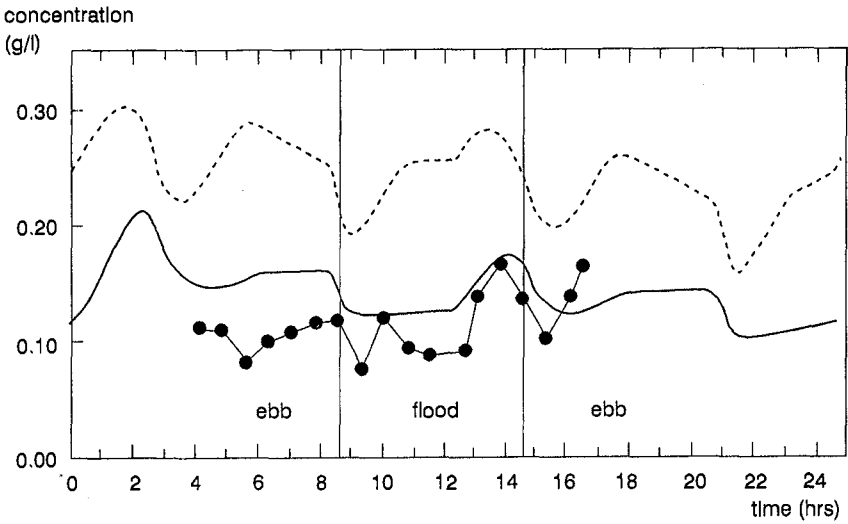


Figure 5. Calculated concentrations for case 1 (dashed) and case 2 (solid) and measured values (dots).

The influence of waves

From observations in several estuaries, the Eastern Scheldt e.g., it is clear that rough weather conditions lead to a resuspension of material in the intertidal zone of shoals and marshes and consequently to a transverse transport to the channels. During fair weather conditions this process is reversed resulting in a dynamic equilibrium on a time-scale of years. To verify this process and to examine the importance of it, some calculations are made assuming that the imposed tidal and wave conditions are representative for a yearly averaged situation. Figure 6 shows the tide-average sedimentation for the 4 different wind directions and the fair weather condition (current only). The area of the estuary between Vlissingen and the Belgian border is divided into five morphological units: tidal channels, shoals, i.e. the ones surrounded by channels, flats, i.e. muddy or sandy flats near the embankment, marshes and harbours. The differences between the wind directions is significant as well as the difference with currents only. In the simulation the superimposed waves cause extra transport from the shoals (more eroded with respect to currents only) and the marshes (more eroded) to the channels (less eroded). Whereas one part of the flats is more eroded, the other part, partly because of the sheltered position, shows more sedimentation leading to an overall increase of sedimentation on the flats. Because the channels form the interface between the other four units the increase in sedimentation of the flats and the harbours can be explained by the increase in concentration in the channels caused by extra erosion of shoals, marshes and some flats. Qualitatively this is in good agreement with observations. However, this result can be affected by some important limitations of the model, namely (i) the absence of water level set-up during storm events, by which more sedimentation can take place on marshes and flats, and (ii) the rough schematization of the marshes and harbours.

In a qualitative sense the yearly averaged sedimentation of the five morphological units (current+waves in figure 6), which is assumed equal to the tide-averaged value of the five schematized meteorological conditions combined by means of the percentage of occurrence, is in agreement with measured data. However, in a quantitative sense there is a disagreement of one order of magnitude, or even more in areas with a low mud fraction (channels 6%, shoals 7%). In areas with a high mud fraction (marshes and harbours up to 80%) the agreement is better. It should be noticed that the model was not calibrated again in the case of waves, which led to an important overestimation, and that the reliability of the measurement is not known. Nevertheless the result indicates that the

bottom exchange of mud is more easily simulated for sedimentation dominated regions than for erosion dominated ones, where bottom properties are more important.

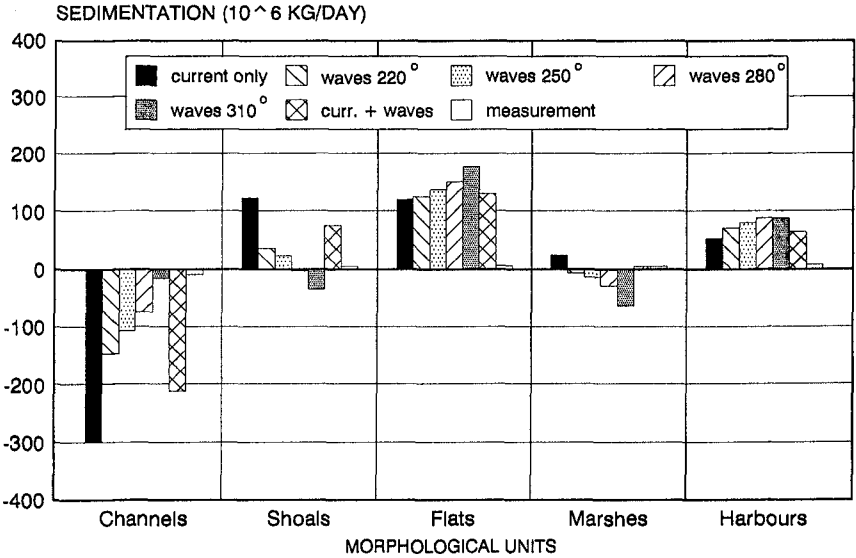


Figure 6. Tide-averaged sedimentation/erosion for each morphological unit calculated with and without wave influence (for 4 different wind directions and in total) and according to measurements.

The spreading of fluvial mud

One of our main purposes is the application of the model to the transport of the polluted fluvial mud. The fluvial and marine mud fraction can be distinguished by means of an analysis of carbon isotopes. Measurements of bottom level change (1980-1985) in combination with the observed mud fraction and correction for dredging and dumping quantities are used to estimate the year-averaged sedimentation or erosion. Verifying this with estimations of the river input has led to the fluvial mud sedimentation given in figure 7a, where the sedimentation of each grid element is related to the total input.

In the simulation only mud input from the river was allowed and the bottom layer started with zero-thickness. The result, see figure 7b, applies only to fair weather conditions and is presented in the same way as the measurements because of different the river inputs ($15 \cdot 10^5$ against $23 \cdot 10^5$ kg/day).

In both the simulation and the measurement the main

part of the river mud is deposited in the eastern part of the estuary. Areas with pronounced sedimentation are reproduced satisfactorily, although the agreement on a detailed scale can be poor.

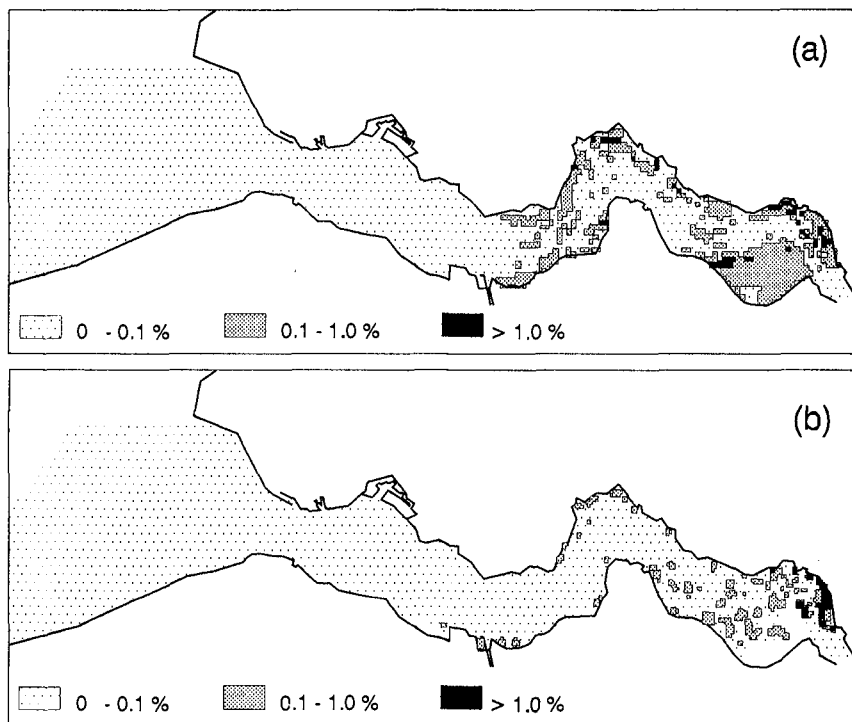


Figure 7. Measured (a) and calculated (b) fluvial mud sedimentation (relative to total river input).

Conclusions

First results of a numerical model, existing of a hydrodynamic, wave and sediment transport model, applied to the Western Scheldt Estuary are presented. Boundary conditions are roughly schematized in aiming at simulations of year-averaged quantities. Dumping of dredged material is modelled but needs verification. With the model the influence of the non-cohesive material in the bottom and the influence of surface waves is investigated. The results show that the spatial variation in erosive properties of the bed and the availability of mud have an important influence on the space and time depen-

dent distribution of concentration and sedimentation. The influence of waves according to the model is significant and qualitatively in reasonable agreement with reality. Waves redistribute the sediment from the wave-attacked shallow areas of shoals, flats and marshes to the deeper parts of channels and harbours and to the sheltered parts of flats. Spreading and sedimentation of the polluted fluvial mud can be simulated satisfactorily. It is believed that sedimentation can be modelled more easily than erosion, due to the strong influence on erosion of the usually poorly-known bed properties. For the present this justifies the use of the erosion constant as a tuning parameter.

References

- Booij, N., Holthuijsen, L.H. en Herbers, T.H.C. (1985), "The shallow water wave hindcast model HISWA - Part I: physical and numerical background", Rep. No. 6-85, Dep. of Civil Engineering, Delft University of Technology, Delft.
- Dekker, L. (1985), "Presentation of calculation results of the extended two-dimensional hydrodynamic model (400 m-grid) of the Western Scheldt", Report WWKZ-85.V002, Rijkswaterstaat, Vlissingen (in Dutch).
- Delft Hydraulics (1990), "DELWAQ Technical Reference Manual - Version 3.0", Delft Hydraulics Laboratory, Delft, January 1990.
- Fritsch, D., Teisson, Ch. and Manoha, B. (1989), "Long term simulation of suspended sediment transport. Application to the Loire estuary", in Proceedings of the XXIII IAHR Congress, Ottawa, Canada, 21-25 August 1989, pp C277-C284.
- Hayter, E.J. (1983), "Prediction of cohesive sediment movement in estuarial waters", Ph. D. Dissertation, University of Florida, Gainesville, Florida.
- Heuvel, Tj. van (1988), "Spread of dredged material during the release from a dredger", Report GWAO-88.034, Rijkswaterstaat, Tidal Waters Division, The Hague (in Dutch).
- Krone, R.B. (1962), "Flume Studies of the Transport of Sediment in Estuarial Shoaling Process", Hyd. Eng. Lab., University of California, Berkeley.
- O'Connor, B.A. and Nicholson J. (1988), "Mud Transport Modelling", in Dronkers, J. and Leussen, W. van (eds.), "Physical Processes in Estuaries", Springer Verlag, Berlin, pp 532-544.
- Partheniades, E. (1962), "A Study of Erosion and Deposition of Cohesive Soils in Salt Water", Ph.D. Dissertation, University of Berkeley, California.

- Rijn, L.C. van and Meijer, K. (1986), "Three-dimensional modelling of suspended sediment transport for current and waves, SUTRENCH-3D model", report H461/Q250/Q422, Delft Hydraulics Laboratory, Delft.
- Sheng, Y.P. (1986), "Modeling bottom boundary layer and cohesive sediment dynamics in estuarine and coastal waters", in Mehta, A.J. (ed.), "Estuarine Cohesive Sediment Dynamics", Springer Verlag, New York, Chapter XVII, pp 360-400.
- Stelling, G.S. (1983), "On the construction of computational methods for shallow water flow problems", Ph.D. Dissertation, Delft University of Technology, Delft.

CHAPTER 229

THE GREAT BELT LINK HOW TO ACHIEVE ZERO ENVIRONMENTAL IMPACT ON THE BALTIC SEA

Jacob Steen Møller¹ and Niels-Erik Ottesen Hansen²

Abstract

The Great Belt Link crosses the Great Belt (Denmark) which is the major strait connecting the Baltic Sea with the North Sea. A law passed by the Danish Parliament imposes an environmental design criteria of 'zero far field effect' on the Link. This paper describes how the challenge of zero effect is met by compensation dredging. The compensation dredging is designed by the use of highly sophisticated numerical models.

Introduction

The Great Belt is a channel approximately 18 km wide that divides Denmark into Jutland and Funen to the west and Zealand to the east. It is the largest of the three channels linking the Baltic to the Kattegat and North Sea (Figure 1). A major construction project (The Great Belt Link) is now underway to build a rail and road link across the strait and thus replace the busy cross-Belt ferry routes. The strategic location of the link and environmental concern about potential interference in the exchange of water between the Baltic and Kattegat have led to a comprehensive environmental plan.

¹ Ph.D., Head of Coastal and Environmental Division, Danish Hydraulic Institute, Agern Allé 5, DK-2970 Hørsholm, Denmark

² Ph.D., Director, LICEngineering A/S, Ehlersvej 24, DK-2900 Hellerup

The 'Zero Blocking Solution'

In general not much attention is given to the impact of bridges or causeways on the surrounding flow. However, the peculiar hydrography of the Danish Straits

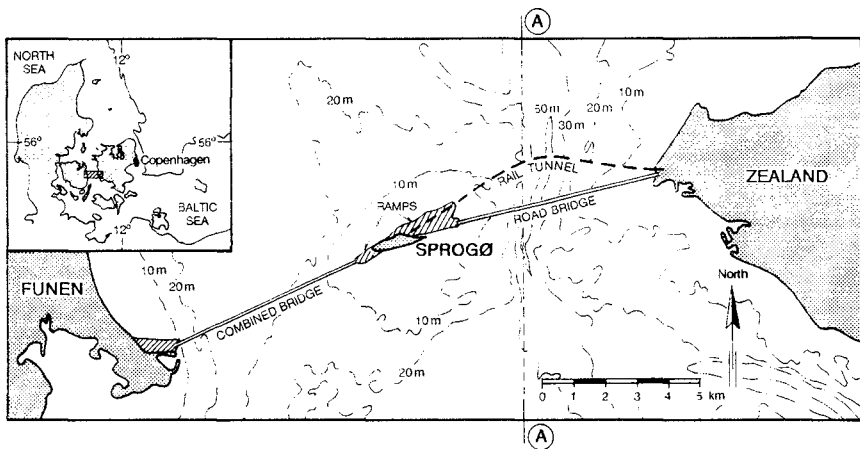


Fig. 1. The Great Belt Link

with a distinct layered flow, results in a flow with a very small hydraulic resistance. Therefore the total resistance may be sensitive to small changes in geometry. For instance, the hydraulic head difference between the Kattegat and the Baltic is normally only 0.2-0.6 m over a length of 300 km with a flow rate of 100,000 m³/s. Further, bridges built in the Straits will have to be designed for heavy ship impact and for ice loads which make the bridge abutments large, leading to increased blocking.

Most of the hydraulic loss in the Great Belt takes place through 4-5 narrows where the current becomes strong. The fixed link across the Great Belt will span the most constricted narrow of the Great Belt. Since a large part of the salt influx to the Baltic (60-70%) passes through this narrow, concern has been expressed that the construction of causeways, tunnels and bridges may exert a large flow resistance.

It is likely that the consequent reduction in the water exchange would significantly alter the hydrography and environment of the Baltic. A review of the hydrography of the Great Belt is given by Farmer and Møller (1990). To avoid such a change it has been specified in Paragraph 5 of the Danish law for contracting the link that "The work is to be carried out ... in such a way that the water flow through the Great Belt shall remain unchanged ... for the sake of the environment of the Baltic Sea". This somewhat unprecise design criterion has been interpreted by the authors to be understood as: "- The water discharge (m^3/s) through the Belt must not be changed by the crossing.

- The salt balance (kg salt/s) for the Baltic must not be changed by the crossing."

This so called "Zero Blocking Solution" ensures that no environmental impact on the Baltic, be it hydrographical or biological, will originate in the construction of the link.

It is cheaper to build causeways than heavy duty structures like suspension bridges or immersed tunnels. Therefore there is an economical demand for letting part of the Great Belt Link consist of causeways. This contradicts environmental interest which dictates as small a blocking of the flow as possible. A suitable compromise has been reached where causeways are only built in areas of water depth less than 6 metres and the blockage of these causeways and bridge piers has been compensated for by dredging.

Several proposals for compensation dredgings have been made. In the end it turned out that it would be most favourable to place the dredging on the reef East of Sprogø Island, Figure 2. This location was chosen because of high hydraulic efficiency of dredging and because materials from the area can be used for construction of causeways etc.

Designing the Compensation Dredging

The problem arises, how to determine the size and location of the compensation dredging. This engineering design work is carried out according to the following principle.

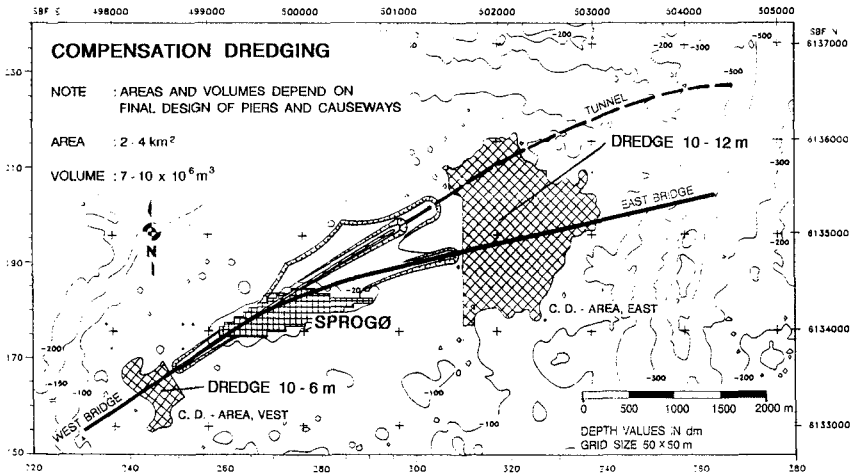
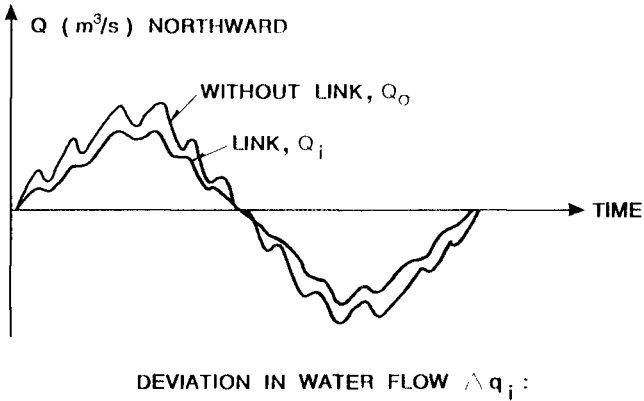


Fig. 2. Typical Compensation Dredging

Given the boundary condition for the flow through the Great Belt the surface current is calculated as it is without the Link, and as it will be with the Link. By calculating the deviation in surface water flow, we have defined a measure of deviation from the zero solution. This measure will depend on the geometry of the Link; large piers and long causeways will increase the deviation, see Figure 3.

Now for a given design of the Link we can introduce a dredging scheme and calculate the resulting deviation caused by the combined Link and dredging. If, for instance, the area to be dredged is kept constant the only parameter determining the efficiency of the dredging is the dredging elevation. By repeating the calculation of deviation for different dredging elevations the deviation is minimized, see Figure 4. The zero solution is reached for minimum deviation.

PRINCIPLE



$$\Delta q_i = \int_T |Q_o - Q_i| dt / \int_T |Q_o| dt$$

Fig. 3. Definition of Deviation in Water Flow

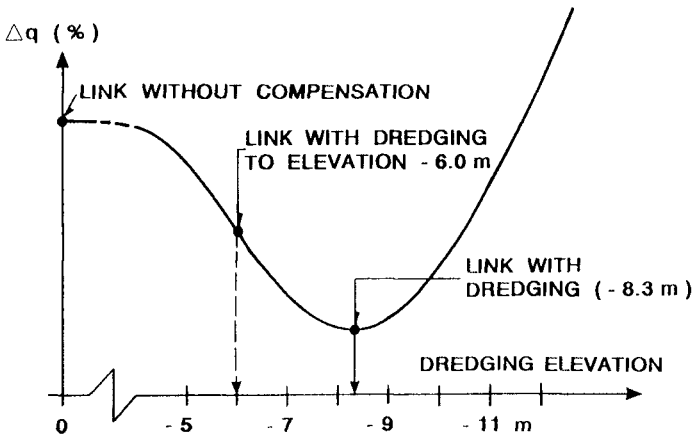


Fig. 4. Water Flow Deviation as a Function of Compensation Dredging Elevation

As demonstrated above not only the surface water flow but also the bottom water flow and the mixing must be kept unchanged by the Link. This is ensured by the use of a verified two layer numerical model.

Numerical Modelling

A comprehensive modelling and field study aimed at designing and controlling the compensation dredging has been carried out. For modelling the hydraulic effects the System 22 two layer numerical model developed by DHI is used, see e.g. Abbott (1979). The model is forced by meteorological data and measured water levels and interface levels at the model boundaries. Results are verified using field data from what is believed to be the most complete field data programme ever dedicated to numerical model verification. The verification includes the model's capability to describe the undisturbed flow field, the effect of ramps, piers and dredging all under baroclinic sub-critical as well as supercritical condition. The model area is shown in Figure 5.

The system 22 is a numerical modelling system for the simulation of two-layer stratified flows in two horizontal dimensions. The system computes the surface levels, interface levels and flows in both layers. The mixing between the layers is described in terms of entrainment between the layers. Entrainment rates are determined on the basis of turbulence production for each layer. (Bo Pedersen, 1986).

The equations solved by S22 are those of conservation of mass and momentum. The equations include the effects of:

- Non linear convective and cross momentum terms
- Coriolis forces
- Wind shear stress
- Bed shear stress
- Interfacial shear stress
- Flow resistance due to bridge piers
- Interfacial mixing
- Turbulent momentum dispersion
- Horizontal density gradients.

The Link and the Compensation Dredging are included in model by corresponding changes in model topography. Bridge piers are included by subgrid scaling methods, see Figure 6.

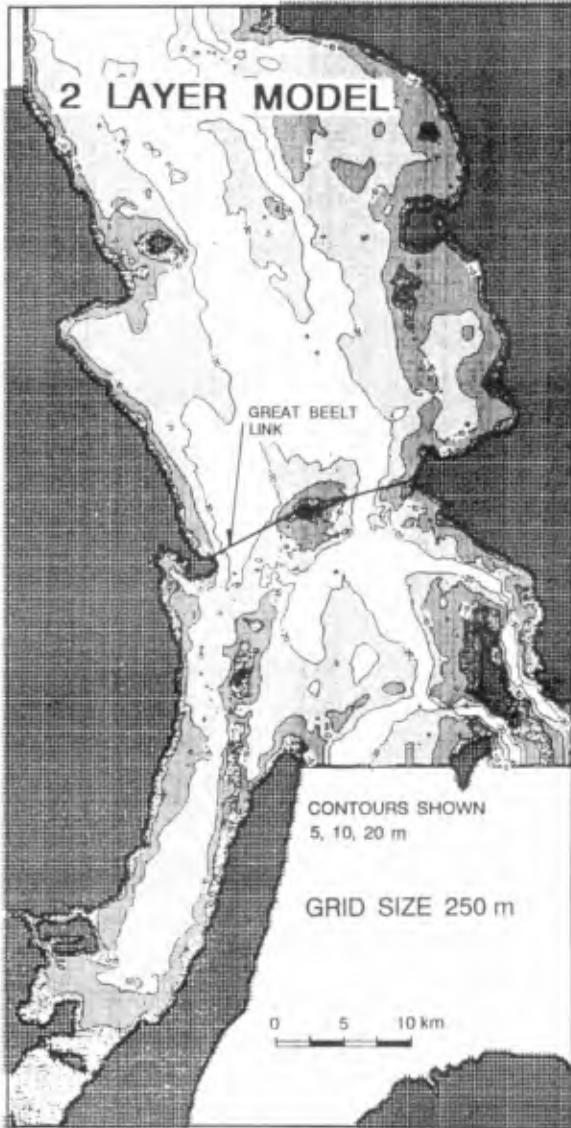
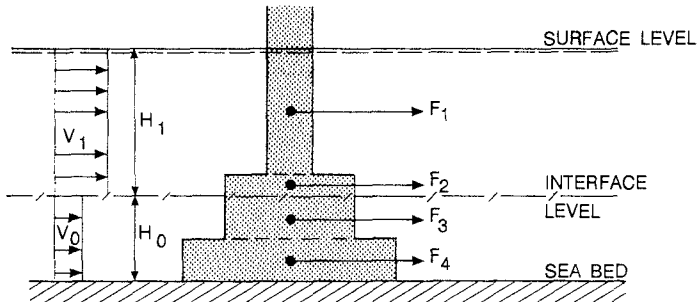


Fig. 5. Model Topography

DRAG FORCE ON BRIDGE PIER IN TWO LAYER FLOW.



DRAG FORCE IS CALCULATED FOR EACH SEGMENT OF THE PIER.

FORCE IS MODELLED AS "SUB-GRID" FRICTION TERM IN NUMERICAL MODEL S22.

Fig. 6. Subgrid Scaling of Flow Resistance due to Bridge Piers

Model Verification

The method needs verification; will the model describe:

1. The flow in nature ?
2. The effect of the link and dredging ?

These two questions are answered by comparing the model with field observations before beginning the dredging, and after 2/3 of the dredging is completed.

In practice model boundary data and verification data are assembled by a field monitoring programme. Simulations are carried out using measured boundary data. Modelled data are compared with measured data to check the performance of the model. Moreover a feedback mechanism is employed. If the results of the model verification show that the compensation dredging needs adjustment this may be done following the '2/3 through' verification of the hydraulic effect of the dredging.

A thorough description of the verification method is given by Farmer and Møller (1990).

Preliminary results of the verification have shown good agreement between modelled and measured data. Figures 7, 8 and 9.

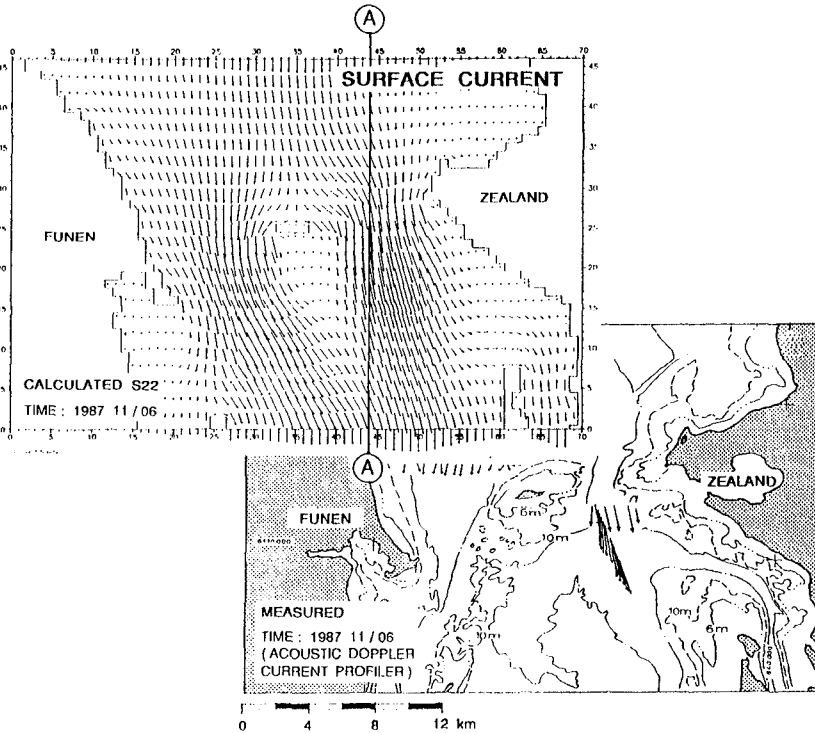


Fig. 7. Measured and Calculated Current Vectors. (Current Vectors in 500 m grid). Section A-A is shown on Figure 1. Synoptic Data from Nov. 6 1987. Measured Data from a Vessel Mounted Acoustic Doppler Profiler (ADCP) Operated by Danish Hydraulic Institute.

An interesting feature of the model is its capability to describe weak internal hydraulic jumps (hydraulically controlled flow), see Figure 8. The presence of hydraulic control has a dramatic influence on the interface position; this is seen both on Figures 8 and 9.

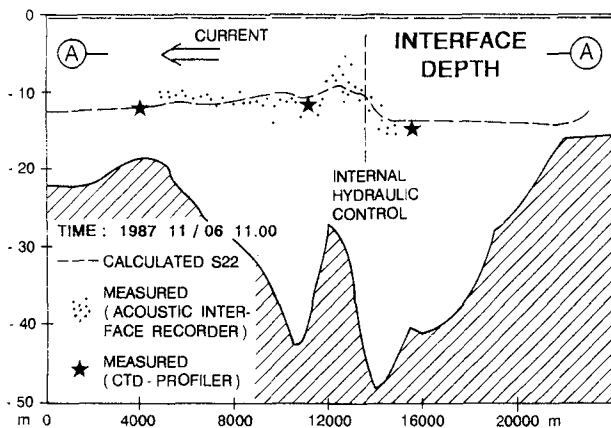


Fig. 8. Measured and Calculated Density Interface. Section A-A is shown in Figure 1. Measured Interface Based on Vessel Mounted Acoustic Interface Recorder developed by Danish Hydraulic Institute and on Conventional CTD-Instrument

Sensitivity Analysis

Based on a sensitivity analysis, where the compensation dredging design has been determined with varying model and boundary data input it is possible to evaluate the uncertainty of the zero solution dredging volume.

The uncertainty of the determined zero solution dredging volume has been found to be less than 10% of the total dredged volume. Given this uncertainty it is possible to evaluate the potential effects on the Baltic Sea due to uncertainty in the compensation dredging design.

In Farmer and Møller (1990) is described a model for the salinity and layering of the Baltic Sea. The LIC-Baltic-model developed by LIC-engineering A/S. By using the resistance of the Great Belt as input data the LIC-Baltic-model calculates the salinity and interface positions in the Baltic Sea. In Table 1 are shown the effects on the Baltic Sea due to various Link designs.

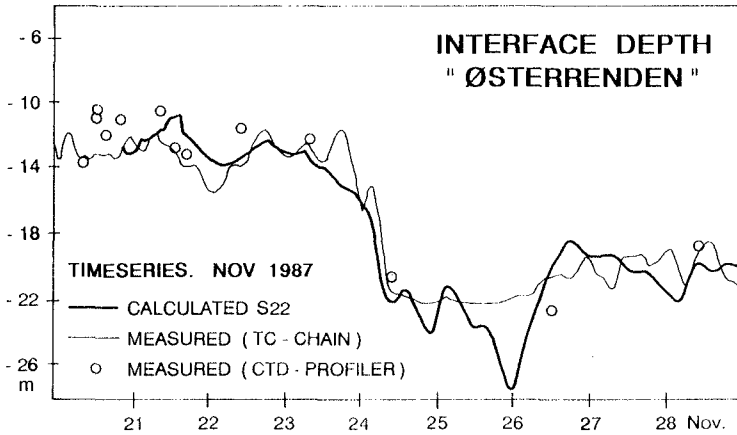


Fig. 9. Time Series of Measured and Calculated Density Interface at Measurement Station 'Østerrenden' shown in Figure 8. Note the Rapid Change in Position on Nov. 24. This Change is Associated with the Occurrence of Internal Hydraulic Control of the Two Layer Flow.

It is seen that when the zero blocking solution is exactly reached then by definition no changes will occur in the Baltic.

If the maximum expected uncertainty of the dredging amount is assumed then the effect of the Link measured as change in the Baltic salinity, is reduced by a factor of 10 compared with the case of the Link without dredging. In other words: Even if the maximum error in determining the dredging is assumed then the change in the Baltic salinity will be less than 10% of the change without compensation dredging.

Case	k	S	Y
	‰	o/oo	m
Undisturbed Storebælt	0.0	7.00	71.0
Link without dredging	+5.0	6.79	71.7
Link with correct dredging (by defin.)	0.0	7.00	71.0
Link with maximum overcompensation due to uncertainty	-0.5	7.02	70.9
Link with maximum undercompensation due to uncertainty	+0.5	6.98	71.1

Table 1 Calculated Change in Total Resistance, k, through the Model Area, see Figure 5. Surface Layer Mean Salinity of the Baltic, S, and Depth to Primary Interface in the Baltic, y.

Conclusions

The Great Belt Link project has initiated remarkable technical developments within hydraulics and environmental protection in association with major marine construction works.

The Great Belt Link project has introduced the concept of 'zero solution' meaning that any potential far field effect on the marine environment shall be compensated in such a way that no effects will occur. This policy is carried out in the Great Belt Link project by carefully compensating the hydraulic effect of the Link by dredging.

The dredging is designed by the use of advanced numerical models. These models are verified by comparison with field data from the Great Belt area.

Acknowledgements

The environmental studies presented here are sponsored by the Great Belt Link Ltd. Further information can be obtained from the Great Belt Link Ltd., Vester Søgade 10, DK-1601 Copenhagen V, Denmark.

References

Abbott, M.B. (1979). 'Computational Hydraulics. Elements of the Theory of Free Surface Flows'. Pitman Adv. Publish. Program. London.

Bo Pedersen, F. (1986). 'Environmental Hydraulics: Stratified Flows'. Springer Verlag.

Farmer, D. and J.S. Møller (1990). 'Measurements and Modelling in the Great Belt' in 'The Physical Oceanography of Sea Straits'. L. Pratt (ed.), NATO ARW series.

CHAPTER 230

MUD TRANSPORT RATE IN MUD LAYER DUE TO WAVE ACTION

Tomoya Shibayama¹

Masakazu Okuno²

and

Shinji Sato³

ABSTRACT

In order to calculate mud transport rate, two forms of transport should be considered, which are (1) mud mass transport in mud layer, and (2) suspended mud transport in water layer. The first type of transport (mass transport in mud layer) is greater than the second one in quantity under soft mud or fluid mud condition, therefore the first type of transport is mainly considered. The previously proposed methods to calculate the first type of transport are summarized and discussed. Then a new transport model called visco-elastic-plastic model is derived and some of the results of the model are shown. The model is based on the assumption that the fluid mud layer can be assumed to be visco-elastic fluid and when the magnitude of stress in mud layer exceeds the value of yield stress, the mud layer is modeled as visco-plastic fluid. Results of the new numerical model are compared with laboratory results and some discussions are given.

1. INTRODUCTION

In coastal environment, a part of bottom surface is covered with soft mud. In estuaries, in river mouth area of large rivers

1 Associate Professor, Asian Institute of Technology, G.P.O. Box 2754, Bangkok 10501 Thailand

2 Engineer, Yokohama City Government

3 Associate Professor, Civil Engineering Department, Yokohama National University, Yokohama 240 Japan

such as Yangtze river in China or Ganges river in Bangladesh, or in large bay areas, most of the coastal bottom surface is covered with soft mud. In these areas, when surface water waves travel onto a bottom of soft mud, inter-surface wave between water layer and mud layer is generated. In the interface, fluid mud layer with high water content is formed under stormy conditions. The inter-surface wave causes mass transport in mud layer. This type of mud mass transport as well as suspended mud transport in water layer is considered to be the main mechanisms to transport mud in coastal environment. The former (mass transport in mud layer) is larger than the latter in quantity under many conditions of soft mud and therefore it is important. Behavior of suspended mud is also important when we analyze coastal environment problems or the effect of construction works to the environment.

As stated in the previous part of this paper, the mechanism of mud transport can be classified into two types which are (1) mud mass transport in mud layer, and (2) suspended mud transport in water layer. In the followings, the first transport type will be discussed mainly because the first one is greater than the second one in quantity.

Before we start to talk about mud behavior, mud characteristics should be considered. Otsubo and Muraoka (1986) classified mud into two groups according to their characteristics of settling form, flow curve (shear rate - shear stress curve) and resuspension behavior under unidirectional flow. The main factor to control these characteristics is the nature of cation attached to particle surface. The first group is represented by Kaolinite with Al^{3+} , Ca^{2+} or H^+ , and the second group by Bentonite which consist of Na^+ Montmorillonite. The first group forms apparent mid-surface between water layer and mud layer when mud particles settle down and it has yield value in flow curve. The second group does not form mid-surface and does not have yield value. Shibayama et al. (1986) suggested that both suspended load and mass transport in mud layer should be considered for the first group and suspended load alone should be considered for the second group. It is also suggested by Shibayama et al. (1986) that in the coastal environment, since the salinity of sea water supplies enough number of cation, major part of mud behaves like the first group. Therefore if we consider mud behavior in the coastal environment, we only consider the first group.

Figure 1 shows the diagram of a model for mud transport due to waves. In the figure, it is stated that mud behavior or mud transport rate is governed by mud characteristics and wave conditions. In order to calculate transport rate, mass transport in mud layer and suspended mud transport should be evaluated. The

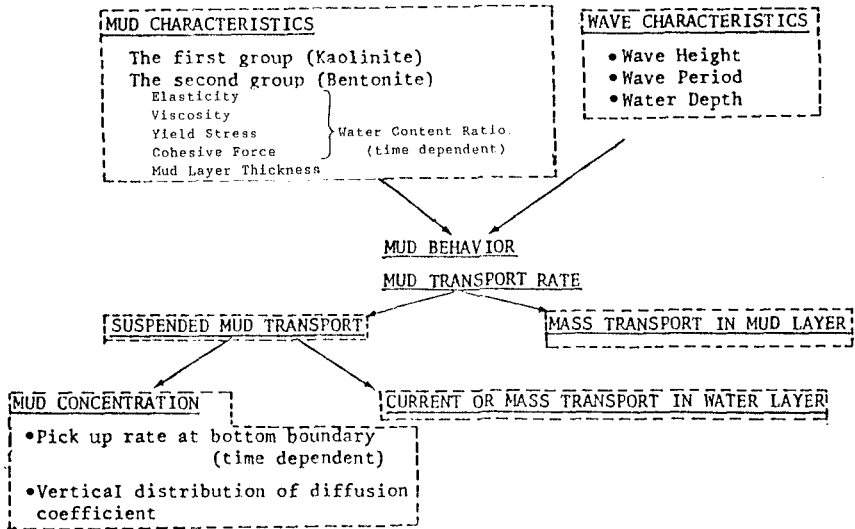


Figure 1: A diagram to evaluate mud transport rate.

suspended transport rate can be evaluated by the information of mud concentration distribution and current or mass transport in water layer. In the followings, mud mass transport in mud layer will be discussed.

2. GENERAL REVIEW OF PREVIOUS STUDIES

The study on the behavior of cohesive bed materials under wave action was started by Gade (1958). He treated mud as viscous fluid and estimated theoretically the decay rate of water surface waves propagating over mud bottom, under the assumption of long waves. Dalrymple and Liu (1978) derived "complete model" which models water layer and mud layer as viscous fluid. They also used boundary layer approximation and obtained an analytical solution of velocity field of mud layer. Recently, Hsiao and Shemdin (1980) and Mcpherson (1980) treated mud layer as visco-elastic fluid. The above four studies were carried out mainly to get the decay rate of water waves which travels over soft mud bottom.

In these five years, several attempts were carried out to estimate mud mass transport rate in mud layer. Nagai et al. (1984) performed experiments using wave flume and gave some qualitative descriptions for mud mass transport. Shibayama et al. (1986) used analytic solution of velocity field which was derived by Dalrymple and Liu (1978) using boundary-layer approximation and got formula to

calculate mass transport velocity. Mehta and Maa (1986) formulated multi-layered model with the assumption of visco-elastic fluid property and the results were compared with experiments. Tsuruya et al. (1986) extended the model of Dalrymple and Liu (1978) from Newtonian viscous fluid to Bingham fluid by using a technique of multi-layer model. They divided mud layer into several layers and applied different value of viscosity according to the velocity gradient in each layer. They also calculated mud mass transport rate. However, these two studies, Shibayama et al. and Tsuruya et al., calculated Lagrangean component of transport rate only, excluding Eulerian component. Shibayama et al. (1989) formulated visco-elastic model and calculated both Lagrangean and Eulerian components of mud mass transport velocity. Then they compared the model result of mass transport with the laboratory results and got good agreements.

3. THEORETICAL FORMULATION OF MUD BEHAVIOR

Dalrymple and Liu (1978) formulated two-layer viscous fluid model. In both water layer and mud layer, the Navier-Stokes equation with neglecting non-linear terms was given. For horizontal direction,

$$\frac{\partial u_j}{\partial t} = -\frac{1}{\rho_j} \frac{\partial p_j}{\partial x} + \nu_{ej} \left(\frac{\partial^2 u_j}{\partial x^2} + \frac{\partial^2 u_j}{\partial z^2} \right) \quad (1)$$

and for vertical direction,

$$\frac{\partial w_j}{\partial t} = -\frac{1}{\rho_j} \frac{\partial p_j}{\partial z} + \nu_{ej} \left(\frac{\partial^2 w_j}{\partial x^2} + \frac{\partial^2 w_j}{\partial z^2} \right) \quad (2)$$

The mass continuity equation is

$$\frac{\partial u_j}{\partial x} + \frac{\partial w_j}{\partial z} = 0 \quad (3)$$

Tsuruya et al. (1986) divided mud layer into n layers in order to incorporate the effect on non-Newtonian viscous fluid (multi-layer viscous fluid model). In each layer, the governing equations are given by (1), (2), and (3). Here we assume the solution as (in j -th layer)

$$u_j = \hat{u}_j e^{i(kx - \omega t)}, \quad w_j = \hat{w}_j e^{i(kx - \omega t)}, \quad p_j = \hat{p}_j e^{i(kx - \omega t)}, \quad \eta_j = \hat{\eta}_j e^{i(kx - \omega t)} \quad (4)$$

In mud layer, Mcpherson (1980) treated ν_{ej} as complex function. In j -th layer,

$$\nu_{ej} = \nu_j + i \frac{G_j}{\rho_j \sigma} \quad (5)$$

where G_j is elasticity, ρ_j is density, σ is radian frequency. Here the real part gives viscous effect and the imaginary part gives elastic effect. Shibayama et al. (1989a) incorporated the function (5) into equations (1) to (3), and determine the unsolved unknowns by using the following boundary conditions (which is the same as Tsuruya et al., 1986, for viscous fluid),

In water surface ($z = \eta_1 + h_1$)

$$\frac{\partial \eta_1}{\partial t} = w_1 \quad (6)$$

$$p_1 - 2\rho_1\nu_1 \frac{\partial w_1}{\partial z} = 0 \quad (7)$$

$$\rho_1\nu_1 \left(\frac{\partial u_1}{\partial z} + \frac{\partial w_1}{\partial x} \right) = 0 \quad (8)$$

In inter-surface ($z = -\sum_{i=2}^j h_i, z=0$)

$$\frac{\partial \eta_{j+1}}{\partial t} = w_j \quad (9)$$

$$u_j = u_{j+1} \quad (10)$$

$$w_j = w_{j+1} \quad (11)$$

$$p_j - 2\rho_j\nu_{ej} \frac{\partial w_j}{\partial z} - \rho_j g \eta_j = p_{j+1} - 2\rho_{j+1}\nu_{e(j+1)} \frac{\partial w_{j+1}}{\partial z} - \rho_{j+1} g \eta_{j+1} \quad (12)$$

$$\rho_j\nu_{ej} \left(\frac{\partial u_j}{\partial z} + \frac{\partial w_j}{\partial x} \right) = \rho_{j+1}\nu_{e(j+1)} \left(\frac{\partial u_{j+1}}{\partial z} + \frac{\partial w_{j+1}}{\partial x} \right) \quad (13)$$

In the bottom ($z = -\sum_{i=2}^n h_i$)

$$u_n = 0 \quad (14)$$

$$w_n = 0 \quad (15)$$

By using above conditions, simultaneous equations are obtained. Then we can calculate unknowns numerically by using computer.

In order to calculate, we have to give the values of elasticity and plasticity. A diagram to give viscosity is given by Tsuruya et al. (1987) as a function of water content ratio and velocity gradient. The way to give the value G , the elasticity is not yet established. However Shibayama et al. (1989b) used oscillating type viscous meter which is shown in Figure 2 and got the value of elasticity and viscosity simultaneously. Figure 3 shows some of the results of measured elasticity.

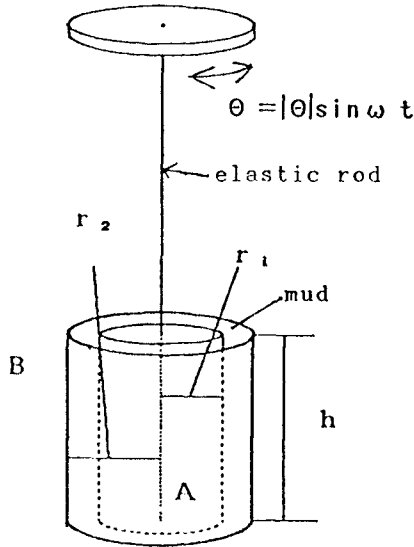


Figure 2: Apparatus of oscillating type visco-elastic meter.

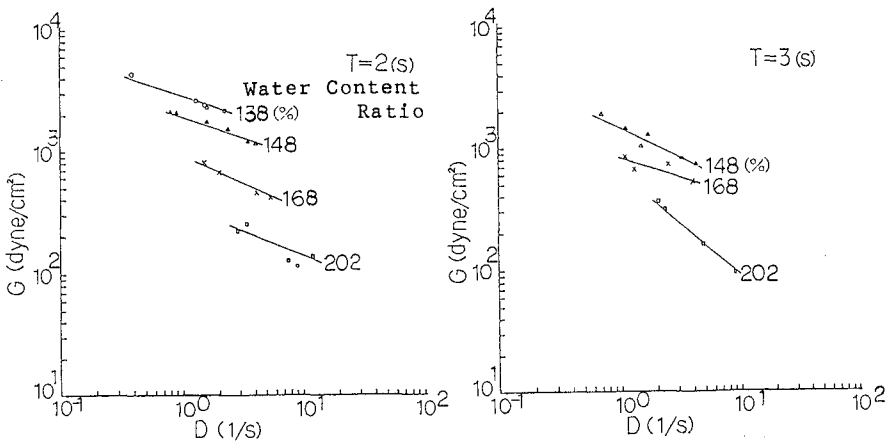


Figure 3: Measured results of mud elasticity.

Here we formulate a model called visco-elastic-plastic model. In the model, we calculate magnitude of shear stress in mud layer by using the visco-elastic multi-layer model (Shibayama et al., 1989a). If the magnitude of stress exceeds the yield value of mud, the layer (in multi-layered mud layer) is assumed to be visco-plastic layer. In the visco-plastic layer, the value of elasticity, G , is given as 0 and instead of elastic term, a fixed value of yield stress is incorporated into governing equations and boundary conditions. In the real calculations, the following false elasticity G_y is used in order to left the effect of yield stress to the momentum conservation equation (Equation 1 and 2) in the visco-plastic assumption. The G_y is given as follows.

$$G_y = \frac{\tau_{y2} \sigma}{\left(\frac{\partial u_j}{\partial z} + \frac{\partial w_j}{\partial x}\right)_i} \quad (16)$$

Figure 4 shows the flow curve of Kaolinite mud which was given by Otsubo and Muraoka (1986) based on their measured results by using rotating type viscosity meter. In the figure, we will use τ_{y2} as the yield stress of the mud, that is the boundary between visco-elastic model and visco-plastic model.

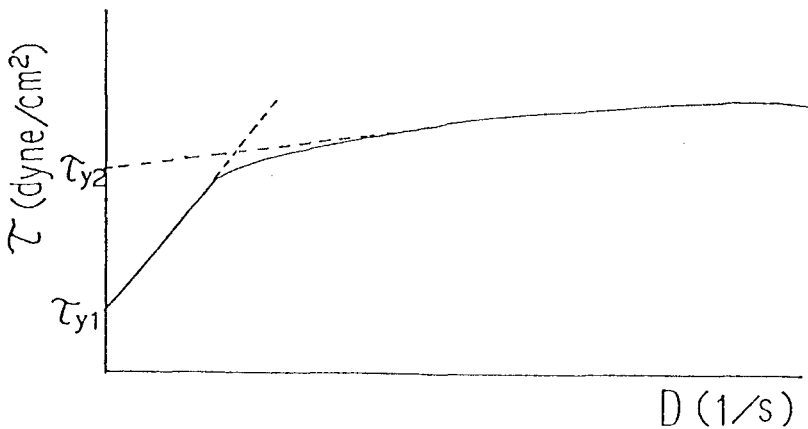


Figure 4: Flow curve for Kaolinite mud. (Otsubo and Muraoka, 1985)

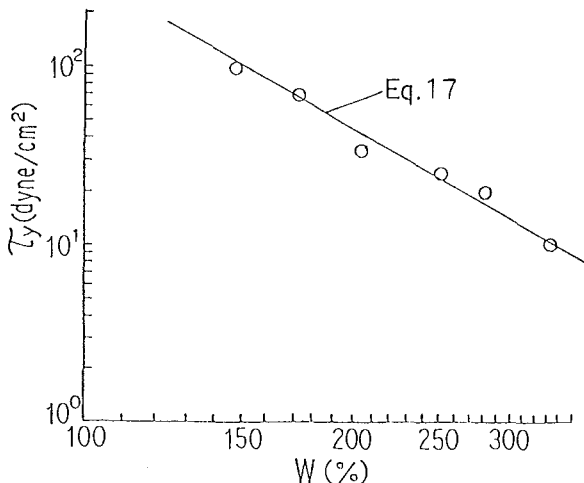


Figure 5: The relationship between the yield stress and the water content ratio. (Data from Otsubo and Muraoka, 1986)

Figure 5 shows the relation between water content ratio and the yield stress. The data for the yield stress is taken from the measured results of Otsubo and Muraoka (1986). From the figure, we will use the following formula for the yield stress based on the regression analysis.

$$\tau_y = 1.47 \times 10^8 \times W^{-2.83} \quad (\text{dyne/cm}^2) \quad (17)$$

Figure 6 shows some of the representative results of numerical model. In the figures, the following natures of mud layer are indicated. (1) All layers are modeled as visco-plastic, (2) upper layers are modeled as visco-plastic and lower layers are modeled as visco-elastic, (3) middle layers are visco-plastic and lower and upper layers are visco-elastic, (4) all layers are modeled as visco-elastic.

4. MUD MASS TRANSPORT RATE IN MUD LAYER

By using the above described method, we can evaluate the velocity field in both water layer and mud layer. The Lagrangean component of mass transport rate is given by ($\overline{\quad}$ gives time average over one wave period)

$$U_L = \overline{\frac{\partial u}{\partial x} \int_0^t u dt} + \overline{\frac{\partial u}{\partial z} \int_0^t w dt} \quad (18)$$

The Eulerian component of mass transport velocity is given by the

Period: T (s) Wave Height: H (cm)
 Water Depth: h (cm) Mud Depth: d (cm)

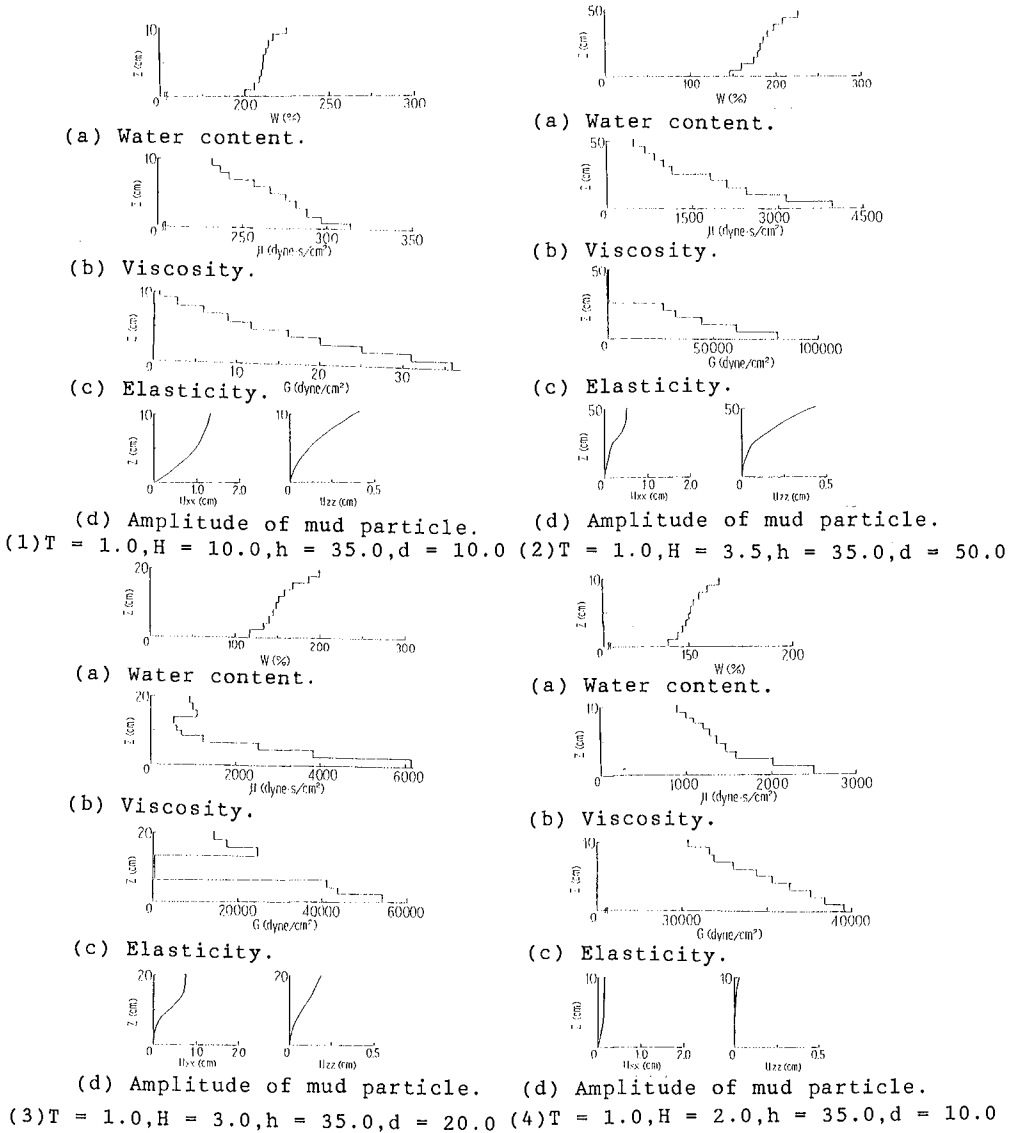


Figure 6: Results of numerical model.

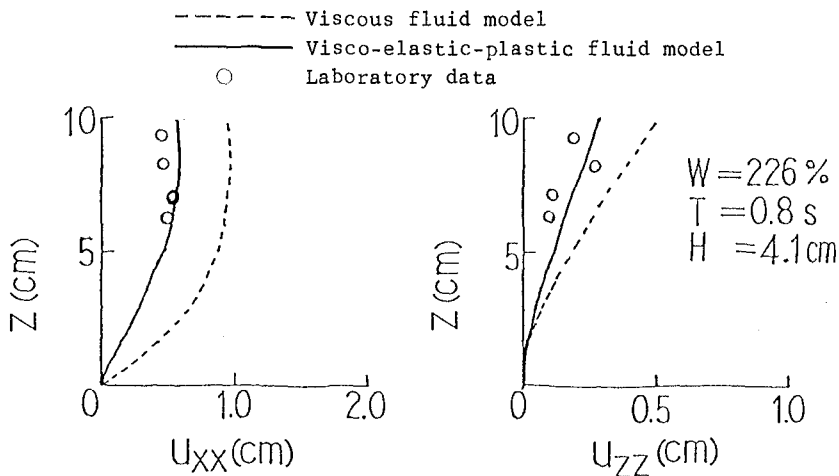


Figure 7: Comparison between laboratory data of mud particle excursion amplitude and visco-elastic-plastic model or viscous fluid model.

following momentum-conservation equation.

$$\overline{(uw)}_j - \overline{(uw)}_\infty = \nu_j \frac{dU_{Fj}}{dz} \quad (19)$$

where ∞ indicates the location of outer edge of boundary layer. The sum of Lagrangean and Eulerian components of mass transport velocity gives the total mass transport velocity.

Shibayama et al. (1989a) performed laboratory experiments in a wave flume. A number of tracers were inserted into the mud layer, and from the movement of tracers mud mass transport rate was quantitatively obtained. Figure 7 shows the comparison of laboratory results of mud particle excursion amplitude and calculated results by using visco-elastic-plastic model and viscous fluid model. It can be seen that the agreement of laboratory data and the visco-elastic-plastic model is better than that of viscous fluid model.

In Figure 8, the comparisons between the visco-elastic-plastic model and laboratory data are shown. The distributions of amplitude of vertical and horizontal excursion amplitude and mass transport velocity are shown in the figure. It can be observed that a good agreement is seen between laboratory results and model calculations.

5. CONCLUSIONS

A numerical model has been developed and used to predict mud mass transport rate in mud layer under the effect of water surface waves. In the model, the water layer was modeled as viscous fluid and the mud layer is modeled as visco-elastic or visco-plastic fluid. It was concluded that the present numerical model based on the assumption of visco-elastic or visco-plastic mud layer is useful to predict mud transport rate due to wave action.

————— Visco-elastic-plastic fluid model
 ○ Laboratory data

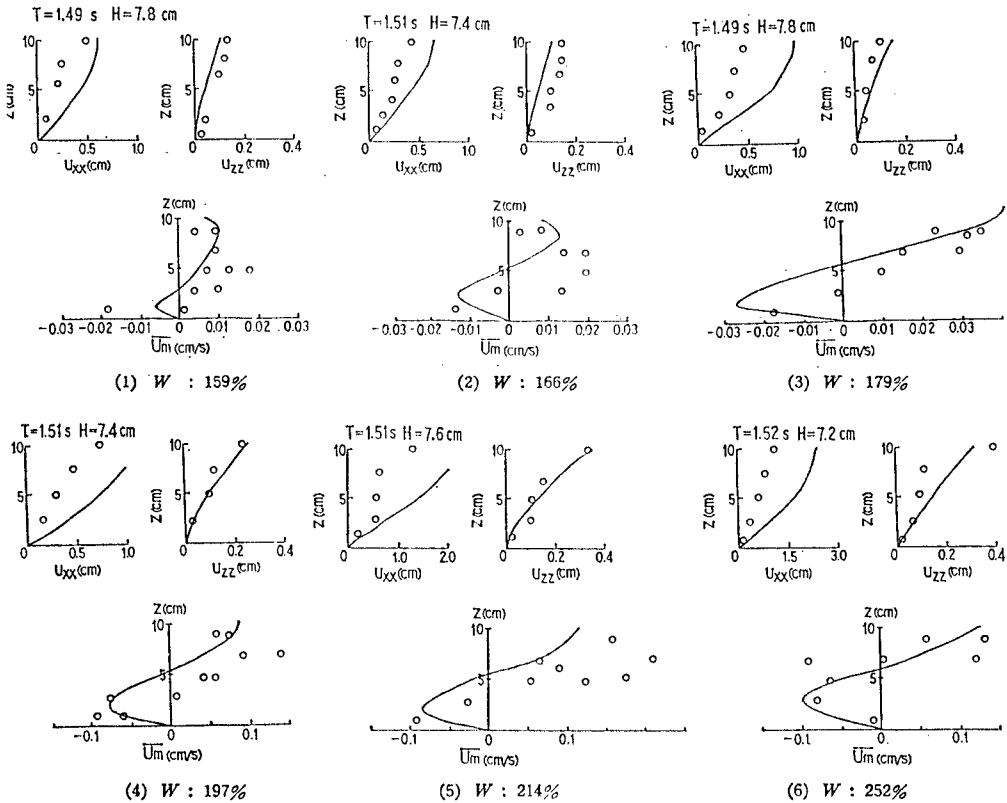


Figure 8: Comparison of Visco-elastic-plastic model and laboratory data.

W : water content ratio(%), \bar{U}_m : mass transport velocity
 u_{xx} : amplitude of horizontal excursion
 u_{zz} : amplitude of vertical excursion
 water depth: 35cm, mud layer thickness: 10cm

ACKNOWLEDGEMENT

The present research was financially supported by the grant in aid for scientific research (No. 63750519), Japanese Ministry of Education, Science and Culture and the research fund from Penta-Ocean Construction Co., Ltd..

REFERENCES

- (1) Dalrymple, A.R. and Liu, P.L.F., 1976. Waves over soft muds: a two-layer fluid model. *Jour. of Physical Oceanography*, 8: 1121-1131.
- (2) Gade, H.G., 1958. Effect of nonrigid, impermeable bottom on plane surface waves in shallow water. *Jour. of Marine Research*, 16-2: 62-82.
- (3) Hsiao, S.V. and Shemdin, O.H., 1980. Interaction of ocean waves with a soft bottom. *Jour. of Physical Oceanography*, 10: 1121-1131.
- (4) Mehta, A.J. and Maa, P-Y., 1986. Waves over mud: Modeling erosion. *Proc. of Third International Symposium on River Sedimentation*, : 588-601.
- (5) Mcpherson, H., 1980. The attenuation of waves over a non-rigid bed. *JFM*, 97-4: 721-742.
- (6) Nagai, T., Yamamoto, T. and Figuerou, L., 1984. A laboratory experiment on the interactions between water waves and soft clay beds, *Coastal Eng. in Japan*, 27: 279-292.
- (7) Otsubo, K. and Muraoka, K., 1985. Physical properties and critical shear stress of cohesive bottom sediments, *Proc. JSCE*, 363, 225-234.
- (8) Shibayama, T., Takikawa, H. and Horikawa, K., 1986. Mud mass transport due to waves. *Coastal Eng. in Japan*, 29: 151-161.
- (9) Shibayama, T., Aoki, T. and Sato, S., 1989. Mud mass transport rate due to waves: A visco-elastic model, *Proc. of 23rd IAHR*, B567-B574.
- (10) Shibayama, T., Aoki, T. and Sato, S., 1989b. Mud mass transport rate due to waves: A visco-elastic-plastic model, *Proc. of Japanese Coastal Eng. Conference*, 36, 334-338 (in Japanese).

(11)Tsuruya, K., Nakano, S. and Takahama, J., 1986. Interaction between waves and mud. Proc. of Japanese Conf. on Coastal Engineering, 33, 317-321 (in Japanese).

(12)Tsuruya, K. and Nakano, S., 1987. Interactive effects between surface waves and a muddy bottom. Proc. of Coastal Sediments,1:50-62.

CHAPTER 231

Estuary Geometry as a Function of Tidal Range

Brian O'Connor¹, John Nicholson² and Ralph Rayner³

Abstract

The tidal characteristics, and consequently the morphology, of an estuary can be altered substantially by engineering works. A method is suggested for estimating the magnitude and the time-scale of the resulting morphological changes. This method is then applied to the Welsh River Usk which will be affected by the construction of a planned tidal power barrage across the nearby Severn Estuary.

Introduction

Engineering works in an estuary, such as dredging, training walls, reclamation, storm surge barriers and tidal power barrages, can cause a marked change in the upstream tidal characteristics. This, in turn, can lead to changes in the geometry of the estuary and any sub-estuaries, provided that there are sources of mobile sediment. As these alterations have an impact on such factors as navigation and land drainage, there is a need to predict their magnitude and time-scale.

A method of predicting the new equilibrium shape of a disturbed estuary system containing fine sediment and the time needed to attain this shape is outlined herein. The proposed method is then applied to a real situation, namely the River Usk which is located in South Wales and is a tributary of the River Severn. The latter is the site of a planned tidal power barrage which will reduce the existing 12m spring tidal range to just over 4m.

¹Head, ²Research Associate, Department of Civil Engineering, University of Liverpool, P.O. Box 147, Liverpool L69 3BX, England.

³Director, Wimpey Environmental Ltd., Hargreaves Road, Groundwell Industrial Estate, Swindon SN2 5AZ, England.

Method

Two possible methods of determining the new geometry of a disturbed estuary are the detailed approach and the regime approach. The first method involves the use of two-dimensional, or even three-dimensional, numerical models of tidal motion and sediment transport. The second method, on the other hand, involves a simple one-dimensional tidal model in combination with empirical expressions which relate the flow field to the estuary geometry. The advantage of the detailed approach is the high level of accuracy but this is offset by appreciable running costs; the opposite holds true for the regime approach. Because of its simplicity and ease of operation, the regime approach is the basis for the proposed method.

The first empirical expression of the regime approach relates the estuary cross-sectional area to the tidal prism. If it is assumed that the tidal discharge at a given cross-section varies sinusoidally with time, then

$$P = \int_0^{T/2} Q_{MAX} \sin(2\pi t/T_T) dt$$

$$= Q_{MAX} T_T / \pi \quad \dots(1)$$

where P = tidal prism (m^3); Q_{MAX} = maximum discharge during a tidal period (m^3/s); t = time (s); T_T = tidal period (s). In addition,

$$Q_{MAX} = A_{MWL} U_{MAX} \quad \dots(2)$$

where A_{MWL} = cross-sectional area below mean water level (m^2); U_{MAX} = maximum cross-sectionally-averaged flow velocity during a tidal period (m/s). Hence, combining Eqs. 1 and 2 yields

$$A_{MWL} = (\pi / (U_{MAX} T_T)) P \quad \dots(3)$$

However, field studies (Bruun, 1967) have established that U_{MAX} is approximately constant along the length of a stable estuary, in which case Eq. 3 reduces to

$$A_{MWL} = a.P \quad \dots(4)$$

where a is a constant. In practice, work carried out by O'Brien (1931), and later modified by Jarrett (1976), indicated that for a stable estuary

$$A_{MWL} = a(P_s)^b \quad \dots(5)$$

where b is a constant; P_s = spring tidal prism (m^3).

The second empirical expression relates the centreline depth

at mean water level of a cross-section, H_{MWL} , to the spring tidal prism. In a study of North American inlets, Vincent and Corson (1981) found that H_{MWL} is directly related to A_{MWL} . Hence, from this information and from Eq. 5, it follows that

$$H_{MWL} = H_{MWL}(P_s) \quad \dots(6)$$

Also in a study of North American inlets, Bruun (1978) concluded that the mean water level width of a cross-section, W_{MWL} , is a function of H_{MWL} . This function, in combination with Eq. 6, therefore, yields the third empirical expression

$$W_{MWL} = W_{MWL}(P_s) \quad \dots(7)$$

It can also be shown that, under idealised flow conditions, W_{MWL} varies exponentially with distance downstream of the head of the estuary. Details are given in Appendix 1.

The fourth and final empirical expression concerns the shape of a cross-section, an idealised version of which is shown in Fig. 1. The cross-sectional shape is described by the relationship

$$W/W_{MWL} = (H/H_{MWL})^S \quad \dots(8)$$

where W = cross-sectional width (m) at any elevation H (m); S = side slope at the mean water level. It is argued that S is a function of the local sediment type which, in turn, is a function of the local flow conditions as represented by P_s . This line of reasoning leads to

$$S = S(P_s) \quad \dots(9)$$

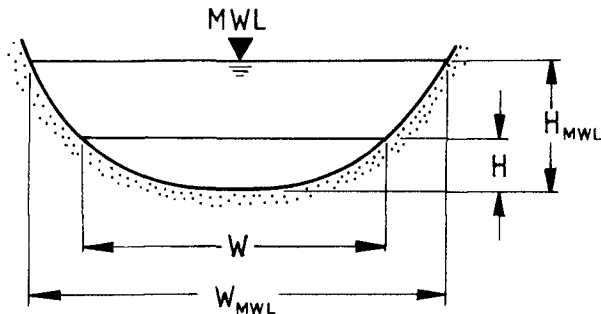


Figure 1. Cross-Sectional Shape

The determination of the new estuary geometry is carried out using Eqs. 5 to 9 in conjunction with a one-dimensional tidal model. The sequence of operations is shown in Fig. 2. First of all, the tidal model is run for the original estuary geometry and the original hydrodynamic boundary conditions, the aim being to establish the exact form of the empirical relationships (Eqs. 5, 6, 7 and 9). The resulting $P_s - A_{MWL}$ relationship (Eq. 5) is then compared with the Jarrett version of this curve in order to check that the estuary was originally in a state of equilibrium. Assuming this to be so, the tidal model is then run again but this time for the original estuary geometry and the new hydrodynamic boundary conditions. This yields a new set of P_s values for various locations along the length of the estuary. Eqs. 5 to 9 are then used to give a first estimate for the new estuary geometry. The latter half of the above cycle of operations is then repeated until the $P_s - A_{MWL}$ relationship converges to the version associated with a stable estuary.

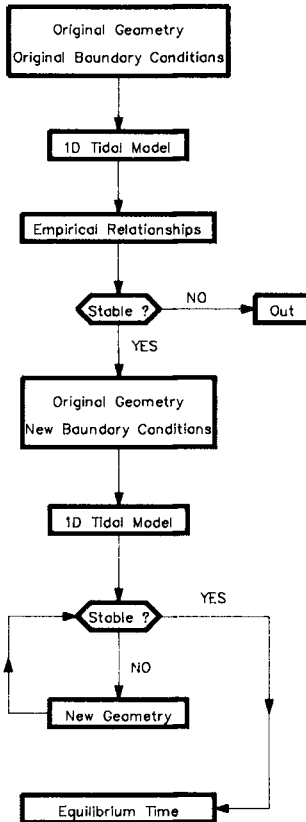


Figure 2. Sequence of Operations

The method used to compute the time taken by a disturbed estuary to attain a new state of equilibrium requires, firstly, that a relationship be established between mean sediment concentration and tidal range. This can only be done using available field data and makes it possible to derive the quantity of sediment carried into the estuary by any flood tide occurring during the lunar tidal cycle. Then, if an assumption is made regarding the fraction of the suspended sediment load deposited per tidal period, the rate of change in the estuary capacity immediately after the estuary is disturbed can be computed. Next, it is assumed that the rate of change of the estuary capacity varies exponentially with time until nominal equilibrium has been attained; a typical value for the latter is 95 per cent, say, of the capacity change. Finally, knowing the total quantity of siltation (from the difference between the original and the new estuary geometries), integration of the area under the curve describing the rate of change of the estuary capacity with time yields a solution for the total time required to reach equilibrium. Full details are given in Appendix 2.

Application

The proposed method of establishing the new equilibrium shape of a disturbed estuary was applied to the River Usk. This river, the location of which is shown in Fig. 3, discharges into the Severn Estuary and it is planned that a tidal power barrage be built across the latter. The River Usk is approximately 120 km long, of which the lower 27 km are tidal, and it has a mean spring tidal range at its mouth of just over 12 m. After construction of the barrage, the mean spring tidal range will be reduced to 4.3 m.

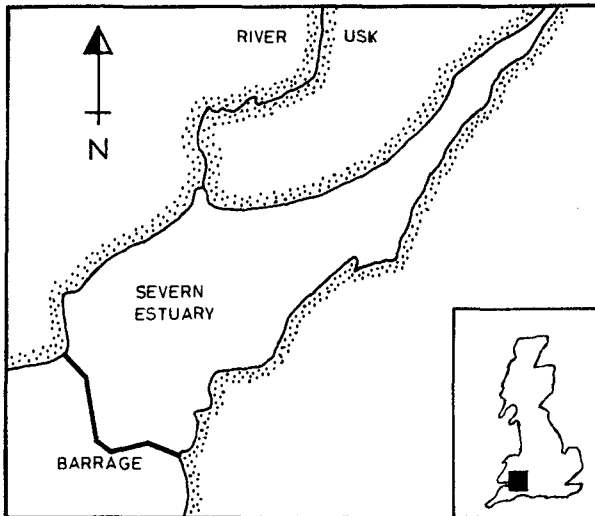


Figure 3. Location of the River Usk

The new estuary geometry was determined as described in Fig. 2. Following the running of a one-dimensional tidal model for the pre-barrage layout and hydrodynamic boundary conditions, the resulting relationships between P_s and A_{MWL} , H_{MWL} , W_{MWL} and S are as shown in Figs. 4 to 7 respectively. As can be seen, there is a strong correlation between the spring tidal prism and the first three variables but the situation is less clear for the fourth variable, S .

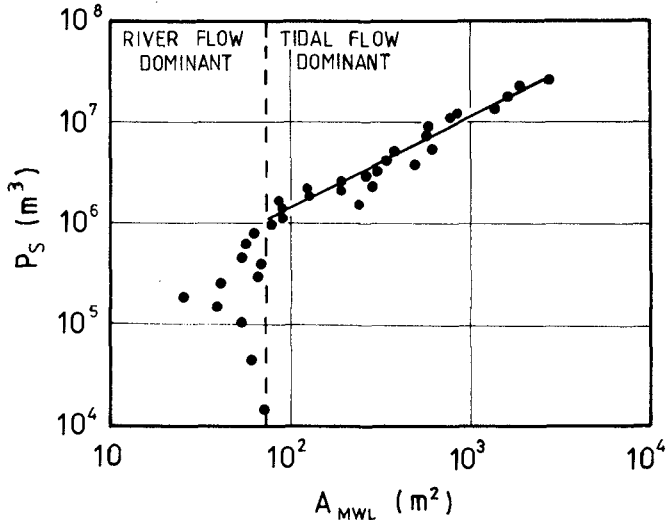


Figure 4. P_s versus A_{MWL}

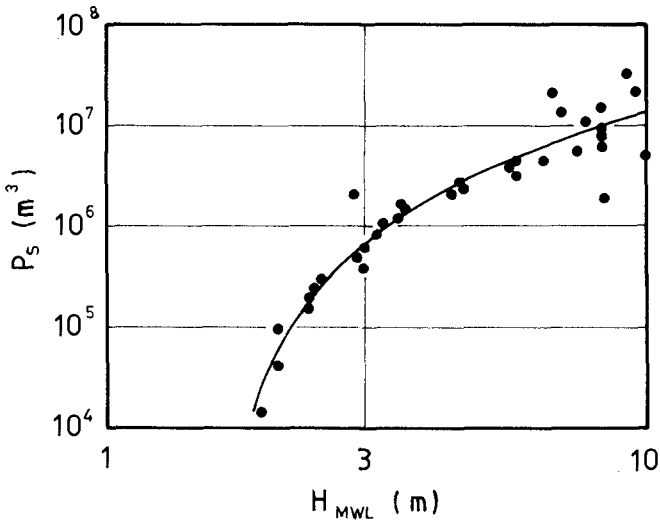


Figure 5. P_s versus H_{MWL}

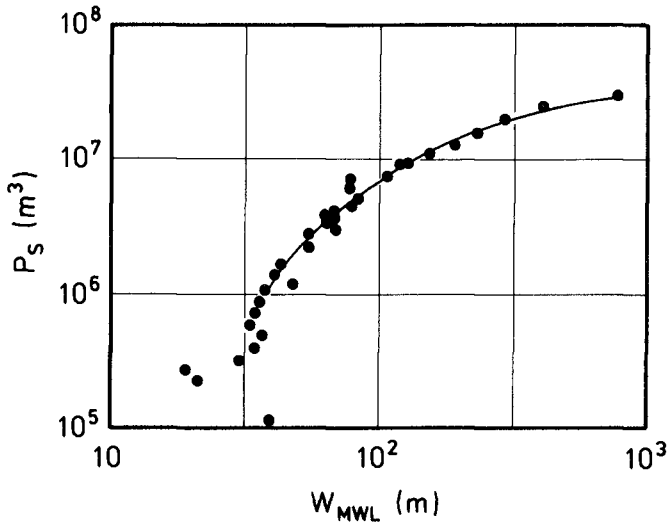


Figure 6. P_s versus W_{MWL}

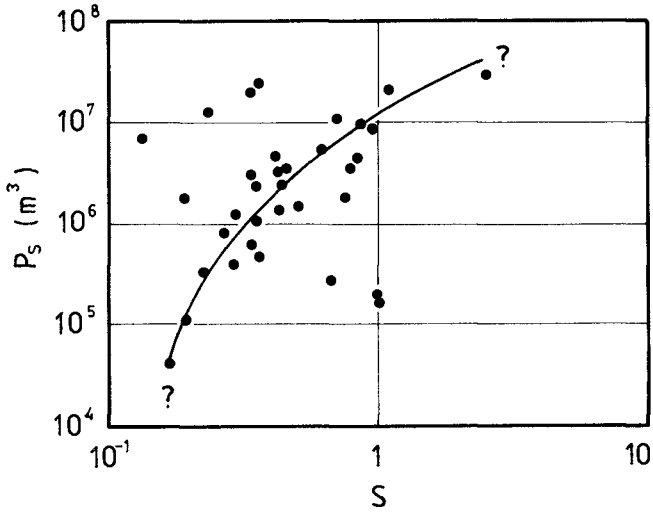


Figure 7. P_s versus S

The stability of the existing layout was then checked by comparing the form of the $P_s - A_{MWL}$ curve with that obtained by Jarrett (1976) for stable estuaries. This comparison is contained in Fig. 8 which shows a close measure of agreement between the two curves. It was concluded, therefore, that the existing layout of the River Usk is in a state of equilibrium.

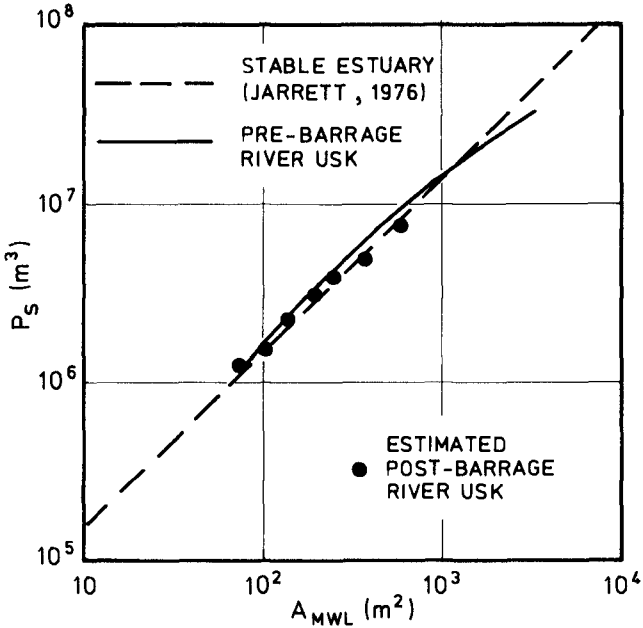


Figure 8. P_s versus A_{MWL}

The one-dimensional tidal model was then run again, this time for the pre-barrage estuary geometry but the post-barrage hydraulic boundary conditions. This yielded a first estimate for the new estuary geometry which, following one more circuit of the tidal model computational loop (see Fig. 2), resulted in a $P_s - A_{MWL}$ curve which closely matched that of Jarrett; the comparison is included in Fig. 8. The model output produced at this point, therefore, was considered to be an acceptable estimate for the final equilibrium geometry of the post-barrage estuary. An example of the pre-barrage and post-barrage shapes of a typical cross-section is shown in Fig. 9.

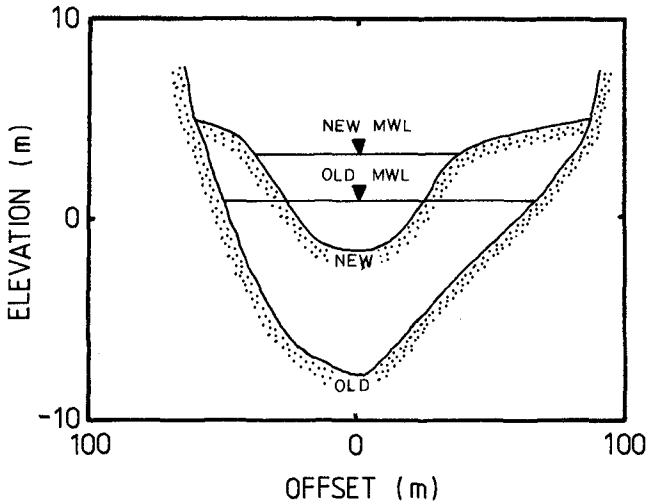


Figure 9. Typical Old and New Cross-Sections

The time required to attain a new state of equilibrium was computed as described in Appendix 2. Values adopted for the relevant independent variables were as follows:

$$\begin{aligned}
 F_E &= 0.95 & R_N &= 2.8 \text{ m} & \rho_D &= 1100 \text{ kg/m}^3 \\
 P_N &= 8 \cdot 10^6 \text{ m}^3 & R_s &= 4.3 \text{ m} \\
 P_s &= 12 \cdot 10^6 \text{ m}^3 & V_{TOT} &= 6.3 \cdot 10^6 \text{ m}^3
 \end{aligned}$$

where F_E = fraction of equilibrium attained; P_N = neap tidal prism at the estuary mouth (m^3); R_N and R_s = neap and spring tidal ranges at the estuary mouth (m) respectively; V_{TOT} = total estuary capacity change (m^3); ρ_D = dry density of the bed material (kg/m^3). The results of this exercise are set out in Fig. 10, the estuary-mean spring tidal concentration, C_s , and the fraction of the sediment load deposited, F_D , being treated as variables. If best estimates of 0.5 g/l and 0.10 are adopted for C_s and F_D respectively, then the computed equilibrium time, T_E is approximately 180 years.

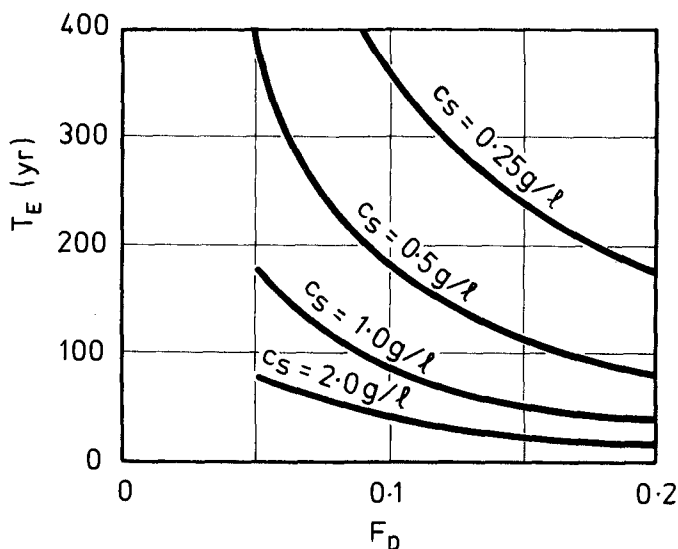


Figure 10. T_E versus F_D

Conclusions

The suggested method for estimating the new morphology and the equilibrium time of a disturbed estuary has been applied to a real situation. The indications are that the suggested method can be operated without undue difficulty and that it yields meaningful results. It is necessary, however, that the method be checked against a situation for which both pre-disturbance and post-disturbance information is available.

Acknowledgements

The authors wish to thank Drs. R. Harpin and C. Whitlow of Sir W. Halcrow and Partners, Swindon, England for making available the output from a one-dimensional tidal model of the River Usk.

References

- Bruun, P., "Tidal Inlets Housekeeping", Proc. ASCE, Vol. 93, No. HY5, Sept. 1967, pp. 167-184.
- Bruun, P., Stability of Tidal Inlets : Theory and Engineering, Elsevier Scientific Publishing Co., Amsterdam, Netherlands, 1978.
- Jarrett, J.T., "Tidal Prism - Inlet Area Relationship", US Department of the Army, Corps of Engineers, General Investigation of Tidal Inlets, GITI Report 3, 1976.

McDowell, D.M. and O'Connor, B.A., Hydraulic Behaviour of Estuaries, MacMillan Press Ltd., London, 1977.

O'Brien, M.P., "Estuary Tidal Prism related to Entrance Areas", Civil Engineering, Vol. 1, No. 8, 1931, pp. 738-739.

Vincent, C.L. and Corson, W.D., "Geometry of Tidal Inlets : Empirical Equations", Proc. ASCE, Vol. 107, No. WW1, Feb. 1981, pp. 1-9.

Symbols

a,b = constants;
 A = cross-sectional area (m²);
 C = estuary-mean concentration (g/l);
 F = fraction;
 H = depth (m);
 P = tidal prism (m³);
 Q = discharge (m³/s);
 R = tidal range (m);
 S = side slope;
 t = time (s);
 T = period (s);
 U = flow velocity (m/s);
 V = volume (m³);
 W = width (m);
 ρ = density (kg/m³).

Subscripts:

D - dry;
 E - equilibrium;
 MAX - maximum;
 MWL - mean water level;
 N - neap;
 S - spring;
 T - tidal;
 TOT - total.

Appendix 1 : Variation of W_{MWL} along the Length of the Estuary

Conservation of fluid mass, assuming a sinusoidal variation of tidal discharge with time, requires that

$$\partial Q_{MAX} / \partial x + W_{MWL} (\partial \eta / \partial t)_{MWL} = 0 \quad \dots(1.1)$$

where x = distance downstream of the head of the estuary (m); η = elevation of the water surface above some arbitrary datum (m); the other symbols are as defined in the text. However,

$$Q_{MAX} = A_{MWL} V_{MAX} \quad \dots(1.2)$$

where

$$A_{MWL} \approx H_{MWL} W_{MWL}/2 \quad \dots(1.3)$$

Hence, combining the above equations gives

$$\partial(H_{MWL} W_{MWL} V_{MAX})/\partial x + 2 W_{MWL} (\partial\eta/\partial t)_{MWL} = 0 \quad \dots(1.4)$$

If it is also assumed that H_{MWL} , V_{MAX} and $(\partial\eta/\partial t)_{MWL}$ are independent of x , then integrating the above equation with respect to x yields

$$W_{MWL} = (W_{MWL})_0 \exp(\alpha x) \quad \dots(1.5)$$

where $(W_{MWL})_0$ = mean water level width of a cross-section at the head of the estuary and α is a constant. Eq. 1.5 is the well known exponential shape of an 'ideal' estuary (McDowell and O'Connor, 1977).

Appendix 2 : Derivation of the Time to attain Equilibrium

Assume, for simplicity, that there is a linear relationship between suspended sediment concentration and tidal range, so that

$$C = \beta R \quad \dots(2.1)$$

where C = estuary-mean concentration (g/l); R = tidal range (m); β is a constant. Then, because R varies sinusoidally with time,

$$C = \beta((R_N + R_s)/2 + (R_s - R_N) \sin(2\pi t/T_L)/2) \quad \dots(2.2)$$

where R_N and R_s are the neap and spring tidal ranges, respectively, at the estuary mouth (m); t = time (s); T_L = lunar period (s). In addition,

$$P = (P_N + P_s)/2 + (P_s - P_N) \sin(2\pi t/T_L)/2 \quad \dots(2.3)$$

where P , P_N and P_s are the typical, neap and spring tidal prisms, respectively, at the estuary mouth (m^3). Furthermore, by definition,

$$M = (1/T_L) \int_0^{T_L} C P dt \quad \dots(2.4)$$

where M = mass of sediment entering the estuary per tidal period averaged over a lunar cycle (kg). Hence, combining Eqs. 2.1 to 2.4 yields

$$M = \beta((P_N + P_s)(R_N + R_s)/4 + (P_s - P_N)(R_s - R_N)/8) \quad \dots(2.5)$$

Next, the initial change in the estuary capacity per tidal period averaged over a lunar cycle, V_o , can be described by

$$V_o = D/\rho_D \quad \dots(2.6)$$

where D = deposition per tidal period averaged over a lunar cycle (kg); ρ_D = dry bed density (kg/m³). However,

$$D = F_D \cdot M \quad \dots(2.7)$$

where F_D = fraction of sediment load deposited and

$$\rho_D = \rho_s(\rho_B - \rho_F)/(\rho_s - \rho_F) \quad \dots(2.8)$$

where ρ_B = bulk bed density (kg/m³); ρ_F = fluid density (kg/m³); ρ_s = sediment density (kg/m³). Hence, combining Eqs. 2.5 to 2.8 results in an expression for V_o containing variables the values of which are known or can be estimated.

Assume that the variation of the capacity change with time is of the form

$$N = \exp(\gamma(1 - V/V_o)) - 1 \quad \dots(2.9)$$

where N = number of tidal periods; V = typical value of V_o (m³); γ is a constant. However, at equilibrium, Eq. 2.9 becomes

$$N_E = \exp(\gamma(1 - V_E/V_o)) - 1 \quad \dots(2.10)$$

where N_E and V_E are the equilibrium values of N and V , respectively. In addition, it is assumed that

$$V_E = (1 - F_E) V_o \quad \dots(2.11)$$

where F_E = nominal fraction of equilibrium attained. Combining Eqs. 2.9 to 2.11 then gives

$$V = V_o(1 - F_E \ln(1 + N)/\ln(1 + N_E)) \quad \dots(2.12)$$

However, by definition,

$$V_{TOT} = \int_0^{N_E} V \, dN \quad \dots(2.13)$$

where V_{TOT} = total change in the estuary capacity (m³). Hence, from Eqs. 2.12 and 2.13

$$V_{TOT} = V_o F_E N_E / \ln(1 + N_E) - V_o(F_E - N_E + F_E N_E) \quad \dots(2.14)$$

Eq. 2.14 is solved by trial and error for N_E , F_E being known or estimated, V_o being obtained from Eqs. 2.5 to 2.8 and V_{TOT} being derived from the known change in the estuary geometry.

CHAPTER 232

Flow Area Prediction of Tidal Inlets After Sea Level Rise

Hideo Kondo*

Abstract

An approach to predict flow area of constricted tidal inlets due to a mean sea level rise is developed. Increase of bay surface area is found to be the most dominant factor to increase the flow area due to SLR. A case study is conducted for an entrance channel of Lake Noto in the Okhotsk coast.

1 INTRODUCTION

The trend of excessive sea level rise (SLR) has brought several crucial problems to coastal engineers, above all the beach erosion due to it. Studies until now have been restricted to the problems at an open coast affected by waves and the resulting sediments (e.g. Bruun (1983), Everts (1985), Dean(1987)).

The problem at a shore along a tidal inlet is somewhat complex. The tidal amplitude in an inlet does not always coincide with that at sea, since the former is dominated essentially by the tidal discharge through the constricted entrance between sea and inlet. This means the effect of SLR on the flow area is a key problem to be solved in advance of estimating the inlet level rise. A change of the flow affects navigation, water quality, maintenance of coastal facilities, etc. besides beach erosion.

In the present study a prediction approach is proposed for the equilibrium flow area of tidal inlets after SLR in coasts with littoral drift.

.....
* Professor, Department Civil Engineering & Architecture,
Muroan Institute of Technology, Muroran, 050 Japan.

2 EQUILIBRIUM FLOW AREA OF TIDAL INLETS

The minimum flow area of a stable or equilibrium tidal inlet (see Fig. 1) A_e has long been extensively studied by many researchers such as O'Brien (1931), Bruun (1958), Shigemura (1974) and Jarrett (1976). In 1975 the writer had proposed a relationship between the flow area A_e and the tidal prism P of inlet as in the following.

$$P / A_e = K_s \sqrt{a_s g} \cdot T \dots\dots\dots (1)$$

where a_s is the amplitude of tide at sea, T is the predominant tidal period and g is the gravitational acceleration. K_s is a dimensionless coefficient depending mainly on the littoral drift at sea M_l and entrance configuration. Eq. 1 had been deduced from an analysis of the maximum tidal current velocity of inlet and the data of P and A_e about inlets in US and Japan as shown in Fig. 2.

K_s had been given as;

$$\left. \begin{aligned} K_s &= 0.22, & \text{for } M_l/Q_m > 300 \\ &= 0.15, & \text{for } M_l/Q_m < 30 \end{aligned} \right\} \dots\dots\dots (2)$$

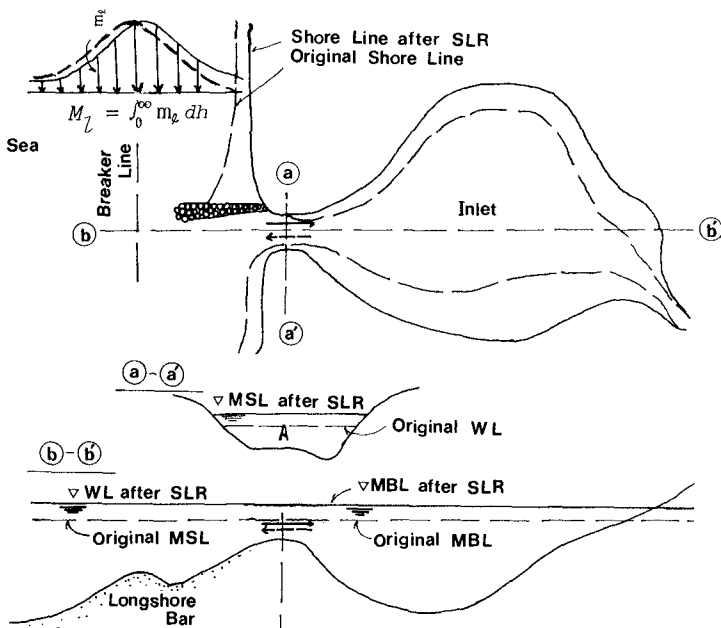


Fig. 1 Sketch of Tidal Inlet before and after SLR

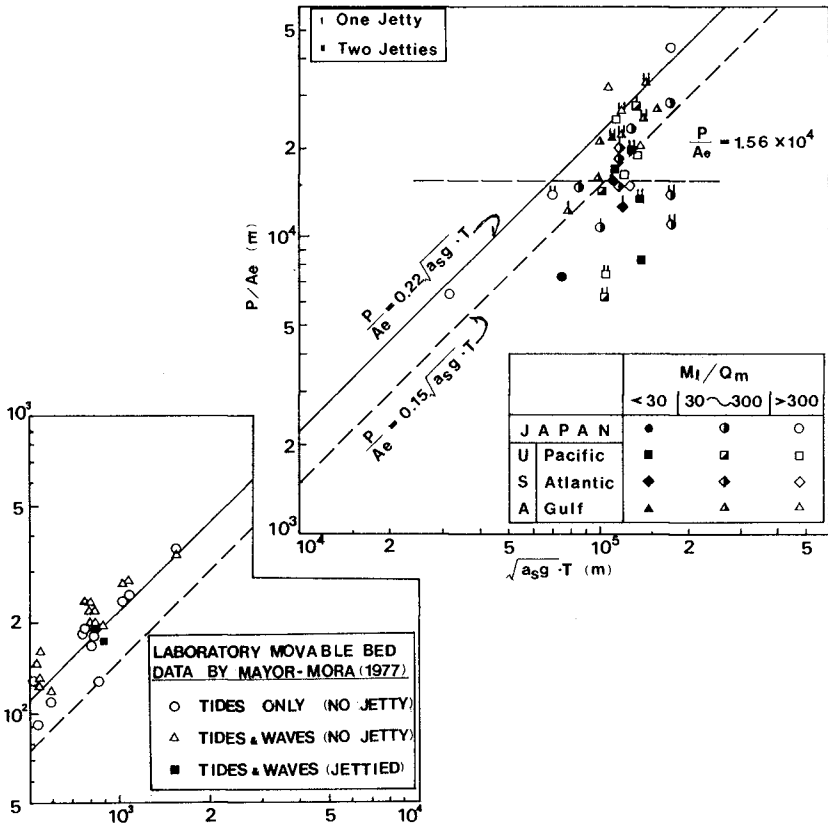


Fig. 2 P/A_e versus $\sqrt{a_s g} T$ and M_l/Q_m for Prototype and Model Tidal Inlets

In Fig.2, computational results for the movable bed laboratory data by Mayor-Mora (1973) are added. They fit well with Eq.1.

In order to determine effect of M_L on Ae , K_s must be determined more quantitatively. A dimensionless parameter $P / (Ae \sqrt{\alpha_s g T})$ is plotted against M_L / Q_m as Fig. 3.

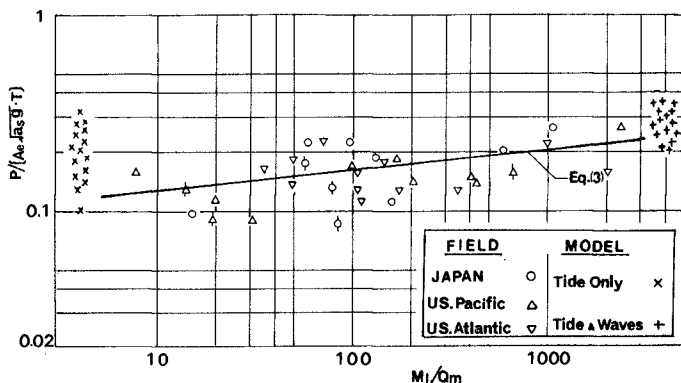


Fig. 3 $P / [Ae \sqrt{\alpha_s g T}]$ versus M_L / Q_m

The solid line drawn as an average in the figure brings a relationship as in the following :

$$P / (Ae \sqrt{\alpha_s g T}) = 0.1 [M_L / Q_m]^{0.1} \dots\dots\dots (3)$$

As far as a simple harmonic tides concerned, P is expressed

$$P = Q_m T / \pi = Ae U T / \pi \dots\dots\dots (4)$$

From Eqs. 3 and 4, Ae is derived as,

$$Ae = 1.02 Q_m^{1.1} \alpha_s^{-0.5} M_L^{-0.1} \dots\dots\dots (5)$$

a simplified analytical solution of the peak current velocity U and the tidal amplitude at bay a_b is (Kondo,1972),

$$U = \frac{1}{p} \sqrt{\frac{1}{2} [- \{ (\frac{\alpha}{\sigma^2}) - 1 \}^2 + \sqrt{ \{ (\frac{\alpha}{\sigma^2}) - 1 \}^4 + 4 \cdot (\frac{\beta p}{\sigma^2})^2 }]} \dots\dots\dots (6)$$

$$a_b = \alpha_s (\frac{\alpha}{\sigma^2}) \sqrt{\frac{1}{2} [\{ (\frac{\alpha}{\sigma^2}) - 1 \}^2 + \sqrt{ \{ (\frac{\alpha}{\sigma^2}) - 1 \}^4 + 4 \cdot (\frac{\beta p}{\sigma^2})^2 }]} \dots\dots\dots (7)$$

where

$$\alpha = Ag/lS \dots\dots (8) \quad n_p = n \sqrt{1 + (\int_0^L R^{4/3} / 2gl n^2)} \dots\dots (10)$$

$$\beta = \alpha_s g \sigma / l \dots\dots (9) \quad p = 4\pi n_p^2 g T \dots\dots\dots (11)$$

and l is channel length $\sigma = 2\pi/T$ and n is Manning roughness coefficient of it.

3 PREDICTION PROCEDURE

By making use of Eq. 4 we can estimate A_e after SLR with the procedure as shown in Fig. 4. Several cautions in the course of calculating procedure are:

- (1) Make use of a dominant simple harmonic tide to compute tidal discharge Q_m and P employing an analytical approach.
- (2) Initial value of bay surface area s and A inlet flow area are those at the MWL simply raised by $\bar{\eta}_s$ from the original one and neglecting effect of the other factors.
- (3) Neglect effect of SLR on M_l itself, as we have presently no substantial knowledge about it. The distribution of m_l only shifts due to SLR.
- (4) Due to the fact of (3), increment of trapped littoral drift by SLR ΔM_t may be evaluated as,

$$\Delta M_t = \int_h^{h+\bar{\eta}_s} m_l dh \dots (12)$$

referring to Fig. 1.

Thus the effective littoral drift rate M_l' is given as,

$$M_l' = M_l - \Delta M_t \dots\dots (13)$$

4 TREND OF CHANGE OF FLOW AREA

From Eq.4 the rate of change of the flow area is

$$\frac{\Delta A_e}{A_e} = 1.1 \left(\frac{\Delta Q_m}{Q_m} \right) - 0.5 \left(\frac{\Delta \alpha_s}{\alpha_s} \right) - 0.1 \left(\frac{\Delta M_l}{M_l} \right) \dots\dots\dots (14)$$

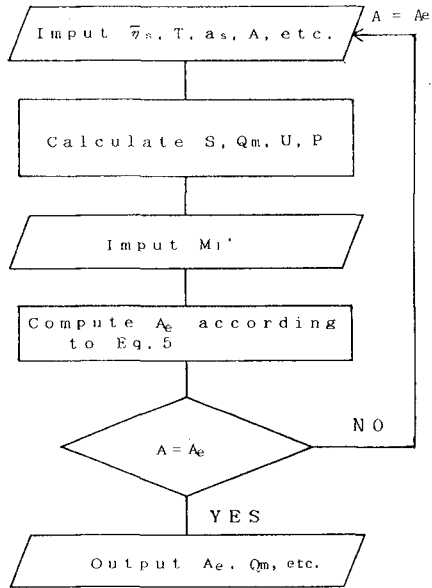


Fig. 4 Procedure to Estimate A_e after Sea Level Rise

This means the effect of change of discharge is much larger on the change of flow area. The discharge is approximated for common tidal entrances as,

$$Q_m = \alpha_s \sigma S \dots\dots\dots (15)$$

since they satisfy the following condition in Eq. 6,

$$\frac{\alpha}{\sigma^2} \gg \sqrt{\frac{Bp}{\sigma^2}} \gg 1 \dots\dots\dots (16)$$

Thus for those inlets, Eq.14 becomes

$$\frac{\Delta Ae}{Ae} = 1.1 \left(\frac{\Delta S}{S}\right) - 1.1 \left(\frac{\Delta T}{T}\right) + 0.6 \left(\frac{\Delta \alpha_s}{\alpha_s}\right) - 0.1 \left(\frac{\Delta M_L}{M_L}\right) \dots (17)$$

Applying the procedure above mentioned, it is found that the rate of variation of the flow area to SLR, $\Delta Ae/Ae$ behaves roughly as shown in Fig. 5 provided sea tide unchanged with SLR. Remarkable change of Ae which refers to $(\Delta Ae/Ae) > 0.5$ occurs for inlets of $\Delta S/S$ is larger than 0.4 due to SLR. It is deduced that those tidal entrances of inlet with low and flat beaches will suffer scouring troubles.

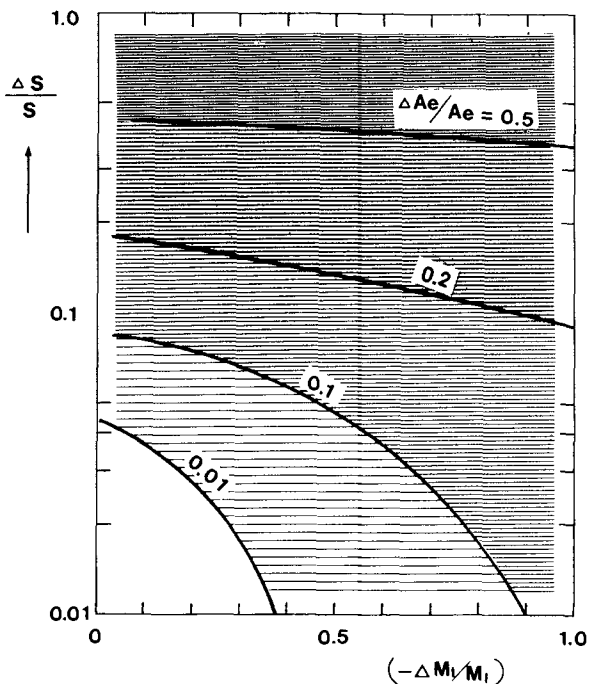


Fig. 5 Trend of Change of Stable Flow Area

4 A CASE STUDY

Lake Notoro in the Okhotsk coast, Japan has the surface area of 58 km^2 of an elliptic form. It had a shallow natural entrance with width of 100 m and the mean depth of 2 m below MWL as shown in Fig. 6. An analytical computation by Kondo (1978) had shown that the depth bringing the maximum tidal current was about 4 m for the width of 150 m . Since the entrance had had the depth less than 2 m , the flushing power of tidal current had been decreased with shoaling of the depth due to the drift sand by storm waves. An artificial entrance channel had been cut with a sheet piled side wall at the spring of 1974. After 16 years had passed, the entrance is 200 m wide between two side walls and protected with two long jetties (Kondo et.al, 1988) as shown with the broken line in the figure.

Estimation of A_e after SLR, has been performed for the present condition, and for the cases of $\bar{\eta}_s$ up to 2 m , according to the procedure explained in Chapter 3.

Computational conditions in the present case are;

- (1) Sea tide ; $T = 8.9410^4 \text{ (sec)}$, $a_s = 0.3 \text{ (m)}$
- (2) Channel ; $B = 200 \text{ (m)}$, $l = 200 \text{ (m)}$
 $n = 0.02$, $f_c = 1.5$

Estimation of A_e for case of each $\bar{\eta}_s$ is performed with the aid of topographical maps. M_l at the coast approximated to be about $100,000 \text{ m}^3$. At the present case which the entrance being protected with breakwaters as shown in the figure, the effective littoral drift rate M_l' is estimated to be $50,000 \text{ m}^3$. And it is assumed to decrease linearly with the value of $\bar{\eta}_s$.

A summary of the result is shown in Fig. 7. The bed scouring depth reaches approximately to 0.6 m for case of $\bar{\eta}_s = 1.5 \text{ m}$, and to 1 m for $\bar{\eta}_s = 2 \text{ m}$. The scouring depth become considerably large with the SLR value.

5 CONCLUSION

A sea level rise gives incidentally an excess tidal discharge and a decrease of effective littoral drift for inlets on sandy coasts. The flow area increases with increase of SLR from the present approach. Thus an entrance with vertical side wall will probably suffer severe bottom scouring trouble at inlets with ample low and flat shores.

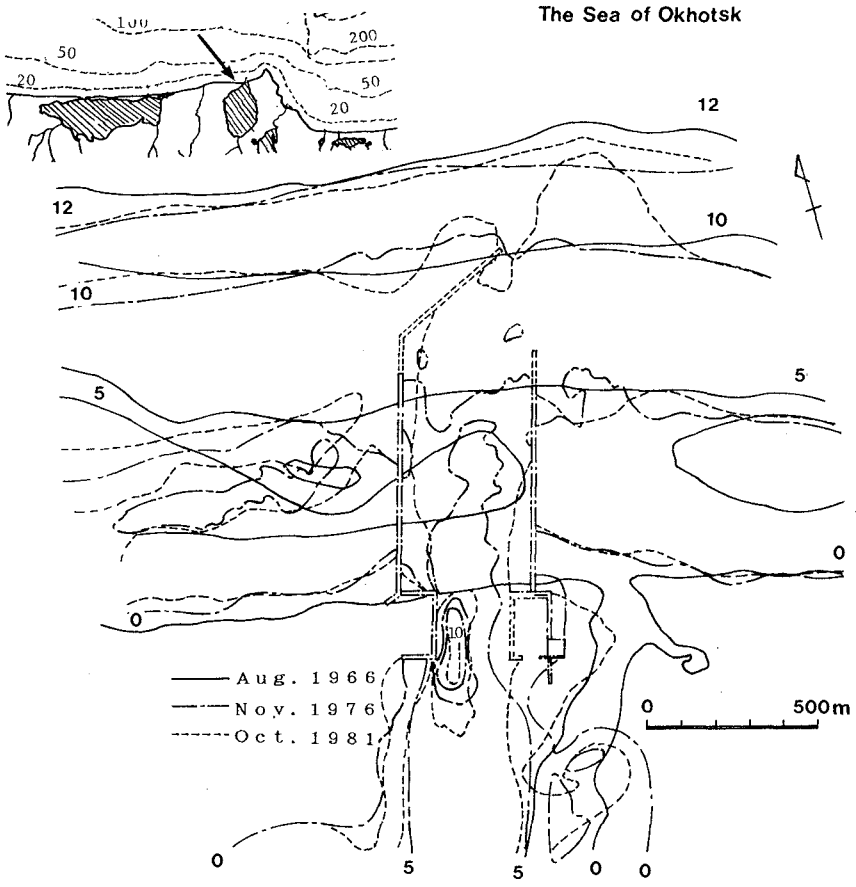


Fig. 6 Change of Under Water Topography around Entrance of Lake Notoro

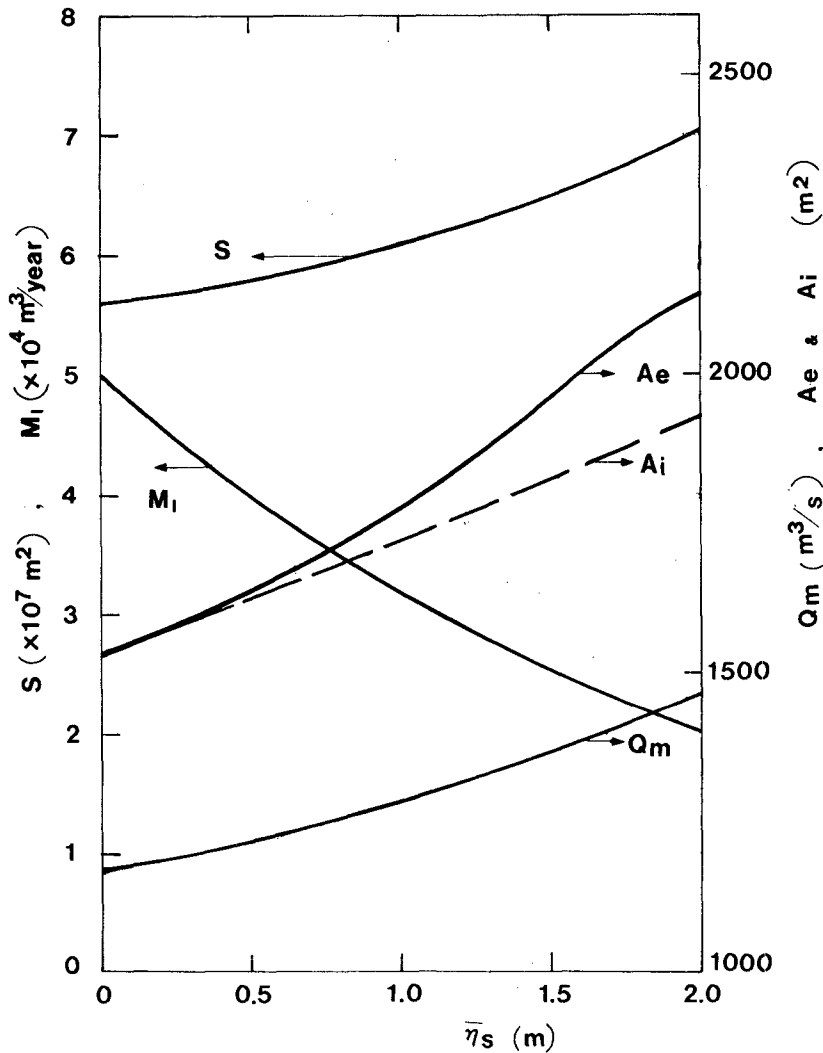


Fig. 7 Result of Prediction of Flow Area for Lake Notoro Entrance due to Sea Level Rise

REFERENCES

- Bruun, Per. (1983): Review of conditions for use of Bruun Rule for erosion, *Coastal Engineering*, 7, 117-133.
- Dean, R. G. (1987): Additional sediment input to the nearshore region, *Shore & Beach*, Jul.-Oct., 76-81.
- Everts, C. H. (1985): Sea level rise effects on shoreline position, *Proc. ASCE*, Vol.111, WW6, 985-999.
- Jarrett, J.T. (1975): Tidal prism-inlet area relationship, GITI Rept. 3, U.S Army Corps of Engineers.
- Johnson, J.W.(1973): Characteristics and behavior of Pacific coast tidal inlets, *Proc. of ASCE*, WW3, 325-339.
- Kondo, H. (1975): Depth of maximum velocity and minimum flow area of tidal entrances, *Coastal Engineering in Japan*, JSCE, 18, 167-183.
- Kondo, H. (1978): Design procedure of artificial channels for tidal entrances, *Coastal Engineering in Japan*, JSCE, 21, 191-199.
- Kondo, H., N. Nitta and S. Touma. (1988): Tidal in the Okhotsk coast, Japan, *Proc. of 9th Int. Symp. on Ice*, IAHR, 2, 103-111.
- Mayor-Mora, R.E. (1973): Hydraulics of tidal inlets on sandy coast, *Hydraulic Eng. Lab., College of Engrg., Univ. of California, Berkeley*, HEL 24-16, 241p.
- O'Brien, M.P. (1931): Estuary tidal prisms related to entrance area, *Civil Engineering*, Vol.1, No.8, 731-739.
- O'Brien, M.P. (1967): Equilibrium flow area of tidal inlets on sandy coast, *Proc. of 10th Conf. on Coastal Eng., ASCE*, 676-686.
- Shigemura, T. (1976): Characteristics of tidal inlets on the Pacific Coast of Japan, *Proc. of 15th Coastal Eng. Conf., Vol. IV, ASCE*, 1666-1679.

PART VII

Ship Motions



CHAPTER 233

CRITERIA FOR SHIP MOVEMENTS IN HARBOURS

Ole Juul Jensen M.Sc.¹
G. Viggosson, M.Sc.²
J. Thomsen, M.Sc.³
S. Bjordal, M.Sc.⁴
J. Lundgren, Dr. Tech.⁵

Abstract

Knowledge of ship behaviour at berth is of fundamental importance for the design of harbours and marine terminals. To develop more precise data on acceptable ship movements than available in the literature, a joint research project was undertaken in cooperation between governmental and research institutions in the Nordic countries: Denmark, Faroe Islands, Iceland, Norway and Sweden. The purpose of the project was to establish criteria for acceptable ship movements in harbours for working and for safe mooring conditions.

Introduction

Modern maritime transport requires minimum time for loading and unloading in ports and at marine terminal. This requirement is in some ports restricted by ship movements at quay (operational conditions). If the ship movements are too large, damage to the ships and port installations may occur (safe mooring conditions).

¹Head of Dept., Danish Hydraulic Institute, Agern Allé 5, DK-2970 Hørsholm, Denmark (in cooperation with the Danish State Ports Authority).

²Head of Dept., Iceland Harbour Authorities, Hafnam lastofnun Ríkisins, Seljavegi 32, Reykjavik, Iceland.

³Former Head of Dept., Faroe Island Harbour Authorities.

⁴Head of Section, Norwegian Hydrotechnical Laboratory, Klæbuveien 153, N-7032 Trondheim/NTH, Norway (in cooperation with the Norwegian Coast Directorate).

⁵SSPA Marine Research Consulting, Chalmers Tvärgata 10, S-400 22 Göteborg, Sweden.

In recent years, changes in cargo-handling methods have resulted in changes of both ships and port installations. All these changes have large economic consequences, and the requirements to fast loading/unloading operations without delays due to ship movements are increasing. The above mentioned changes involve for example the containerization of general cargo and changes of methods of handling fish in fishing ports. The latter is of great importance in the Nordic countries which all have large fishing fleets.

As the new techniques are often more sensitive and vulnerable to ship movements than the conventional methods previously used, it is mandatory for cost benefit analyses of new ports or analysis of existing installations that pertinent criteria for acceptable ship movements be established for use in conjunction with the most modern investigation methods for determining ship movements at quay.

The present paper describes the methods applied and the results leading to recommendations for criteria for acceptable ship movements in harbours.

Aims and Objectives

The purpose of the project has been to determine criteria for acceptable movements of moored vessels in relation to:

- Efficiency of loading/unloading operations (denoted as working conditions)
- Safe stay at berth (denoted as safe mooring conditions).

The project has primarily concentrated on assessment of criteria for fishing vessels, ferries, coasters (freighters) and container vessels. The project involved the following four phases:

- Literature study.
- Pre-study to identify ports with ship movement problems that could be selected for prototype measurements of ship movements etc.
- Prototype measurements of ship movements and simultaneous interviews with captains and port personnel.
- Supplementary studies comprising interview with port masters and operators etc., and comparison with results from existing hydraulic investigations of the same ports. In two occasions, studies of container operations were also performed.

The prototype measurements of ship movements have been made in Denmark, Faroe Islands, Iceland, Norway and Sweden.

The supplementary study had the purpose of extracting as much information as possible from previous model studies from researchers, planners, port engineers and port users in the Nordic countries. By these interviews, critical situations have been described and compared with already existing knowledge of ship movements or wave agitation in the ports in question. In this way, it has in a number of cases been possible to procure more data on criteria for acceptable conditions in ports than obtained from the field measurements.

Fig. 1 shows the locations of prototype measurements and other studies in the five countries.

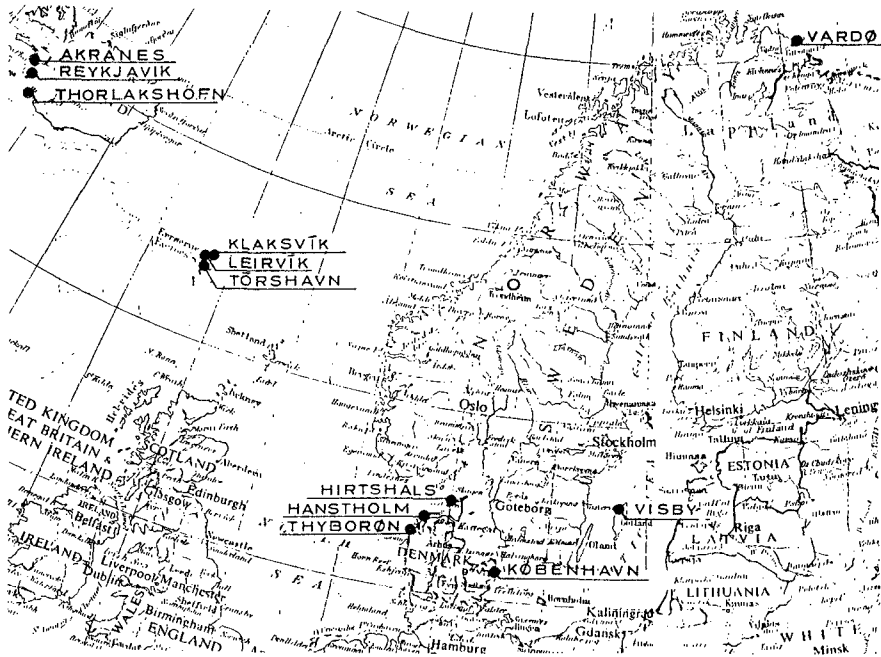


Figure 1. Locations of prototype measurements and other studies.

General on Ship Movements at Berth

The movements of a moored ship at berth can be described by the three translatory movements: surge, sway and heave, and the three movements of rotation: pitch, roll and yaw. The movements are defined in Fig. 2.

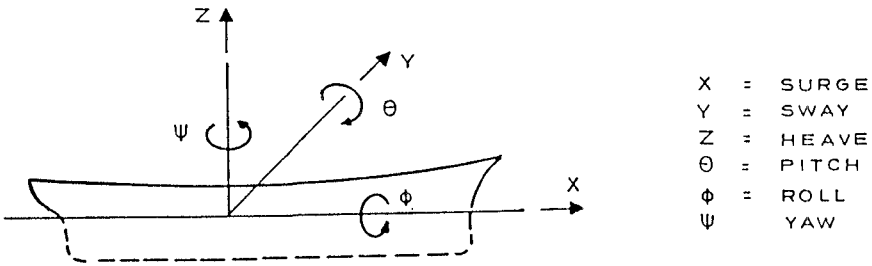


Figure 2. Definition of ship movements.

The movements of rotation, i.e. pitch, roll and yaw, are almost independent of the mooring system. They depend on the resonance period of the ship, the wave spectrum, the berth angle relative to the waves, the reflection pattern for the waves and the type of berth.

The translatory movements of a moored ship depend upon the type of ship, the mooring and fender system (geometry and stiffnesses), the type of berth, and the wave conditions (spectrum, direction of berth relative to the waves).

Typically, the natural periods of motion of the planar motions of a moored ship are for large vessels almost one order to magnitude larger than rotational movements, i.e. approximately 100 s to be compared with 10 s.

The various types of ship movements may, when they become excessive, cause different kinds of damages. Large surge movements may as an example cause breaking of mooring lines and collision with other ships aft or for. Yaw and sway movements may also cause breaking of mooring lines, but also in many cases damage to quay and fenders or to the ship itself.

It is, however, important to notice that ship movements are only one of several parameters influencing the conditions (ease and speed) of loading and unloading operations and safe stay at berth for a moored ship. Of major importance is also:

- Loading/unloading equipment and the level of skill and experience of the personnel,
- Type of goods to be handled,
- Type of vessel,
- Waiting time due to lacking capacity or efficiency at the quay front or for transport in the port,
- Wind,
- Snow, ice,
- Rain,
- Light.

The acceptable movements of a ship in a certain port are dependent on a number of factors:

- Local conditions,
- Loading/unloading methods, i.e. cranes on ship or quay, other devices for bulk or liquid products or Ro-Ro type operations,
- Movement pattern of the vessel, i.e. acceptable movement depends on not only the magnitude of movements but also on their composition,
- Mooring and fender system.

Possibility for Escape and Alternative Ports

Another very important factor to be considered for the safety of harbours is whether it is possible for a vessel experiencing excessive movements to leave the port and survive the storm either at sea or in an alternative harbour. In some ports, the manoeuvring conditions in the harbour entrance are so difficult that ships cannot enter or leave the port once a storm has reached the site. In such a port, the aspect of safe mooring at berth becomes even more important as the vessels have no other choice but to stay in the port.

Summary of Harbour Problems

The following Fig. 3 schematically presents an impression of the parameters which influence and might cause problems for mooring of vessels in a port.

Field Measurements

The measurements included ship movements, mooring forces, wind, waves off the port and inside the port and, in one occasion, fender deflections. The field measurements of ship movements were carried out with two different types of equipment developed in Iceland/Faroe Islands and Norway, respectively. Figs. 4 and 5 show the principles of the two different measuring systems. The Icelandic instrumentation was a further development of the Norwegian type to allow for measuring larger movements.

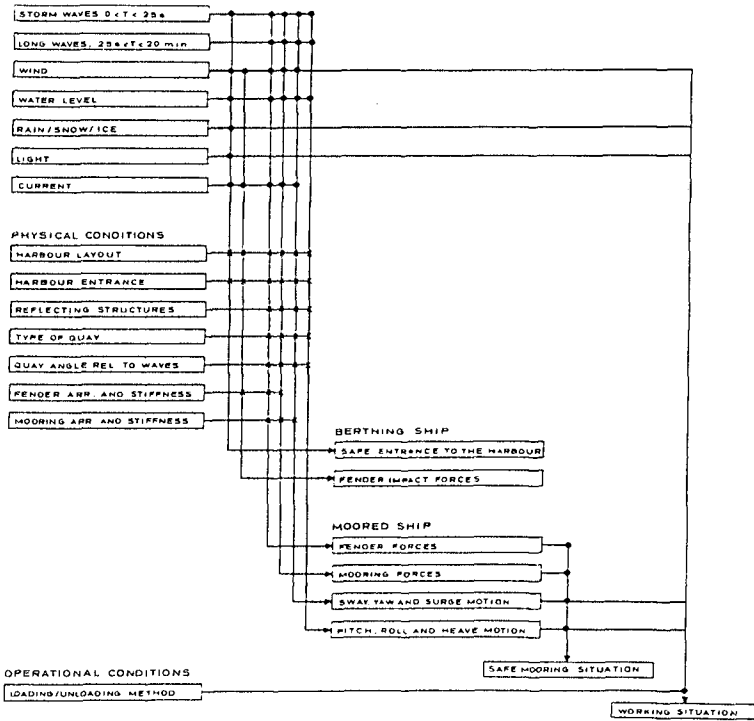
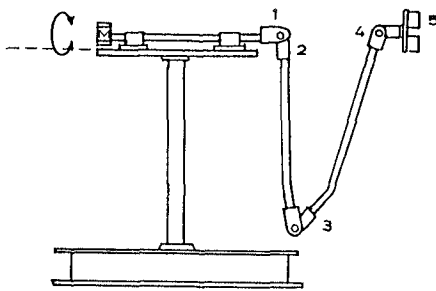


Figure 3. Parameters of importance for the conditions for a moored vessel.



- M: ROTATION (Pitch movement)
- 1: Angle in the horizontal plane
- 2: Angle in the vertical plane
- 3: Angle in the vertical plane
- 4: Angle in the vertical plane
- 5: Angle in the horizontal plane

Figure 4. Principle of Norwegian instrument.

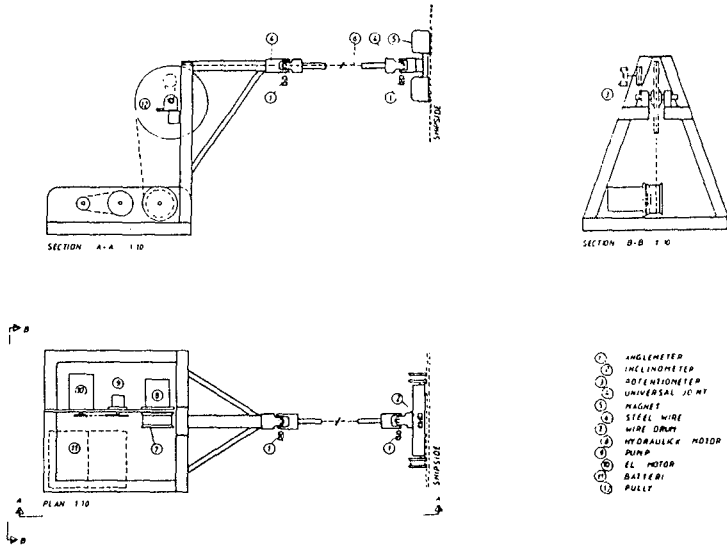


Figure 5. Principle of Islandic instrument.

The measurements were analysed to determine representative parameters, such as:

- T^S : the significant period determined by Z-crossing
 T^m : the mean period determined by Z-crossing
 T_{mo2}^m : a characteristic period determined through spectral analysis. $T_{mo2}^m = 2\pi\sqrt{m_0/m_2}$
 T_P : the peak period determined through spectral analysis
 H_s : a significant value determined as the average of the highest third
 H^m : the mean value determined by Z-crossing
 H^{max} : the maximum value determined by Z-crossing
 H_o : 4 x the maximum-value determined through spectral analysis $H_o = 4\sqrt{m_0}$
 H_{rms} : 4 x the rms-value determined by Z-crossing.

Questionnaire

A questionnaire was used in parallel with the measurements in order to quantify the results of the measurements. However, the questionnaire was also used in situations where measurements did not take place. This was done in order to obtain more data and to obtain a more complete knowledge of conditions in certain ports.

The questionnaire contained four main items:

- Information on harbour, quay, ship (incl. moorings etc.),
- Evaluation by ship personnel of the situation during the measurements,
- Evaluation by ship personnel of whether it is necessary to interrupt the operations,
- Evaluation by ship personnel of critical mooring situations.

Results of Field Measurements

A total of 117 measurement sequences were carried out with 11 in Denmark (Hirtshals and Hanstholm), 22 at the Faroe Islands (Torshavn, Lervik and Klaksvik), 24 in Iceland (Reykjavik, Thorlakshöfn and Akranes), 43 in Sweden (Visby) and 17 in Norway (Vardö).

The measurements were carried out on different types of vessels: large passenger and car ferries, cargo vessels, trawlers, smaller fishing vessels and container vessels. In national reports, more detailed information on the ships, i.e. type and size of ships, loading/unloading equipment, mooring arrangement, etc., are presented.

Fig. 6 shows as an example results of measurements on a 27.4 m long vessel in Torshavn, Faroe Islands.

Fig. 7 shows the analyses of the same data.

In Fig. 8, results from nearly all the measurements of ship movements have been related to the length of the ship. It has been distinguished whether it was possible to load/unload or whether the movements were excessive for operations, but still allowed the ship to stay at berth.

Supplementary Investigations

Supplementary investigations were carried out including studies of the actual conditions in ports and harbours in which hydraulic model tests had been undertaken within the last 10-15 years using irregular natural waves for testing.

Fig. 9 shows an example from Visby in Sweden comparing field measurements of ship movements, mooring forces and wave disturbance with the results of hydraulic model tests of ship movements made at DHI.

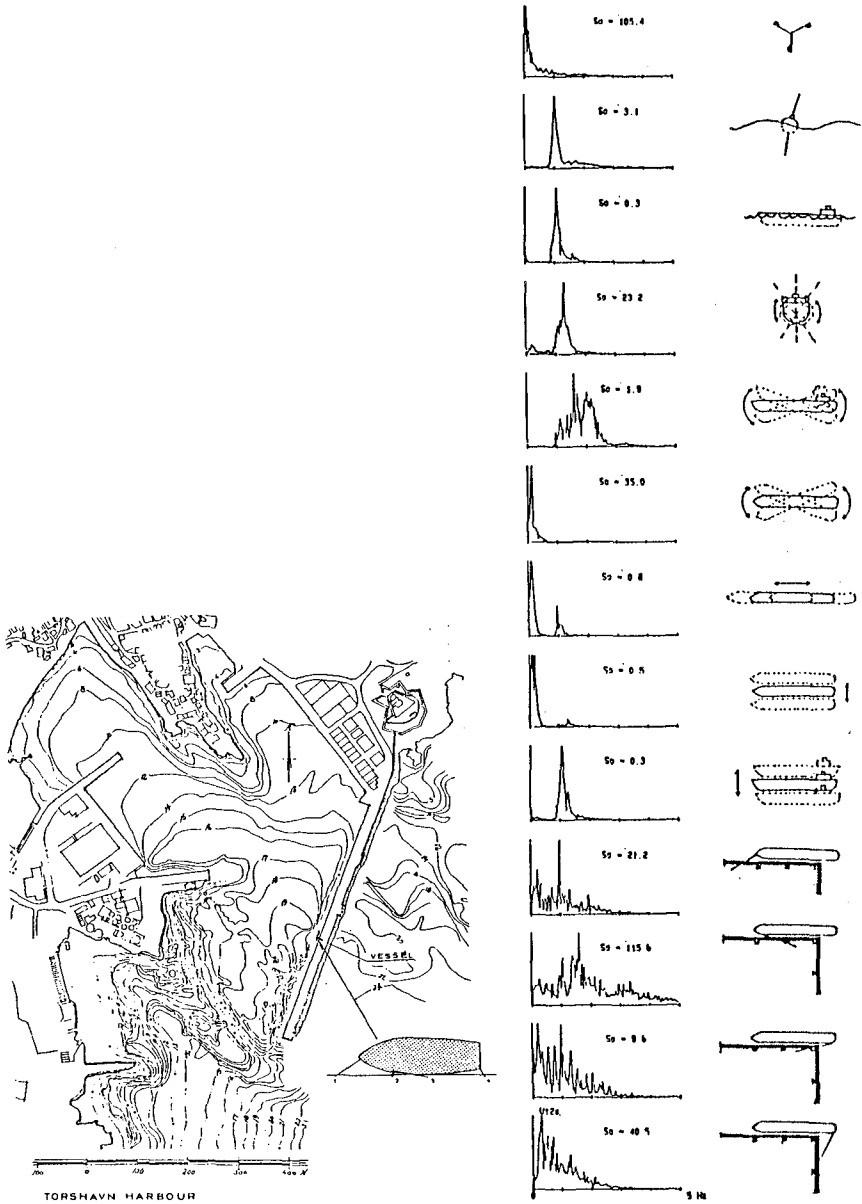


Figure 6. Example of field measurements in Torshavn, Faroe Islands.

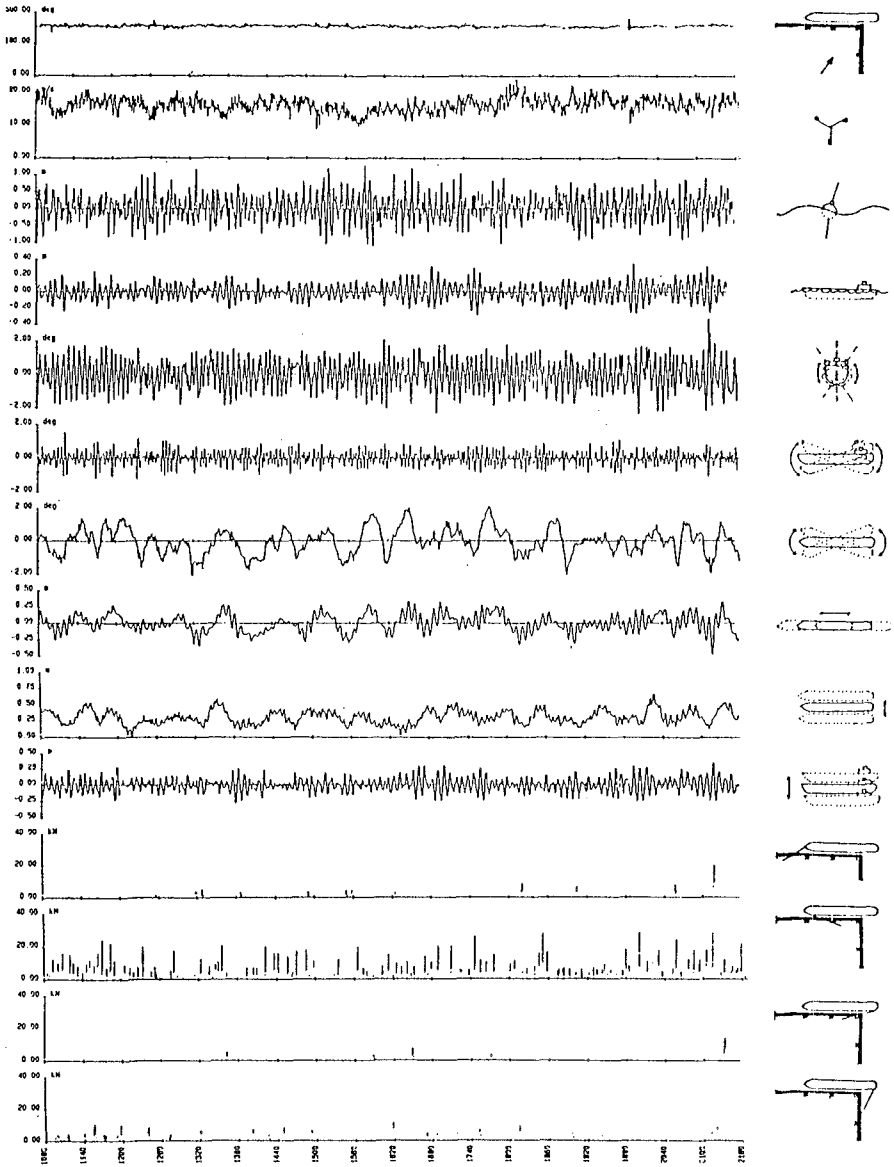


Figure 7. Results of field measurements in Torshavn, Faroe Islands.

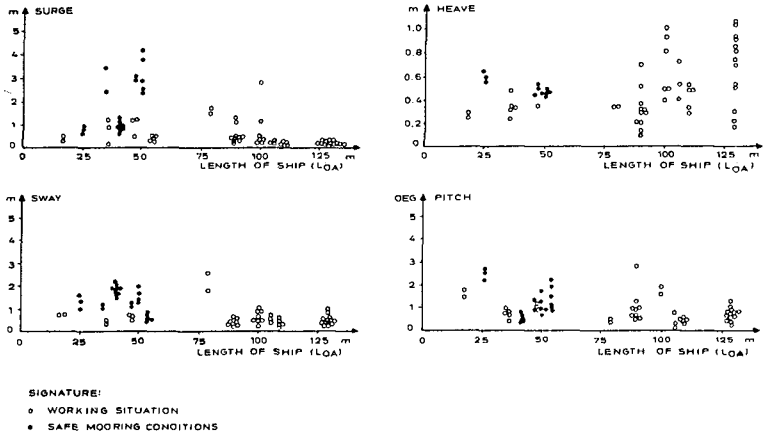


Figure 8. Ship movements in relation to the length of the ship.

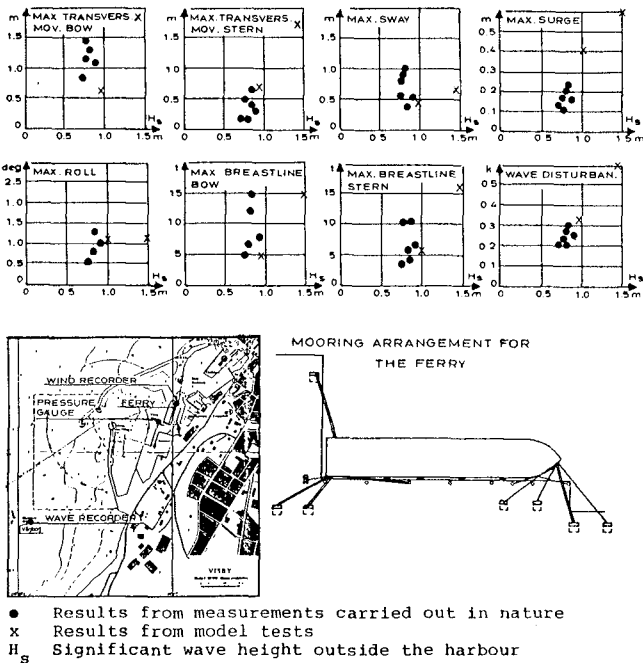


Figure 9. Example from Visby (Sweden).

It appears that there is a reasonable agreement between the field and model measurements. The differences found is believed to be caused by uncertainty about the stiffness and pretensioning of the mooring lines in nature.

Criteria for Acceptable Ship Movements

The following definitions have been adopted:

Interrupted Working Situation:

This situation is characterised by movements causing an interruption or a substantial reduction of the effectiveness of the loading/unloading operations. For this critical movement, analysis of the frequency of occurrence were undertaken. The results depend to a certain extent upon type of vessel and loading/unloading operations.

The investigations carried out have shown that on the average, a harbour in which operations have to be stopped for a total of up to 1 week/year may normally be regarded as having acceptable conditions for loading/unloading operations.

Safe Stay at Berth:

This condition is limited by the largest movements for which no damage occurs to vessel or quay, provided that the vessel is reasonably well moored and the quay is well equipped with fenders.

For acceptable condition in a harbour, attempts should be made to keep the frequency of occurrence of this situation less than once a year.

Criteria for Ship Movements

Tables 1 and 2 present the main results of the joint Nordic project in terms of criteria for acceptable ship movements for the working situation as well as for safe mooring conditions at berth.

The criteria for safe mooring conditions at berth are also given as critical velocities, as the velocity and the mass of the vessel are important parameters which determine the dynamic forces which may cause damage to the quay and/or the vessel.

Type of vessel	Surge (m)	Sway (m)	Heave (m)	Yaw (deg)	Pitch (deg)	Roll (deg)
<u>Fishing vessels</u> ¹⁾						
(L _{oa} = 25-60 m)						
LO-LO	1.0-1.5	1.0-1.5	0.4-0.6	3-5	4	3-5
Elevator crane	0.15	0.15				1.5
Suction pump	2.0-3.0	1.5-2.0				
<u>Freighters, Coasters</u> ¹⁾						
(L _{oa} = 60-130 m)						
Crane on the vess.	1.0-2.0	1.2-1.5	0.6-1.0	1-3	1-2	2-3
Crane on the quay	1.0-2.0	1.2-1.5	0.8-1.2	2-4	1-2	3-5
<u>Ferries</u> ²⁾						
(L _{oa} = 100-150 m)						
		0.8	1.0	1.0	1.0	2.0
<u>Container Vessels</u> ¹⁾						
(L _{oa} = 100-200 m)						
90-100% efficiency	0.6-1.0	0.6-0.8	0.6-0.9	0.5	1.5	3.0
50% efficiency	2.0	2.0	1.2	1.5	2.5	6.0

1) Frequency of these movements should be less than 1 week/year (2% of time)

2) Frequency of these movements should be less than 3 hours/year (0.03% of time).

Table 1. Criteria for ship movements (loading/unloading operations). The movements are maximum peak-peak.

Type of vessel	Surge (m)	Sway (m)	Heave (m)	Yaw (deg)	Pitch (deg)	Roll (deg)
<u>Fishing vessels</u>						
(L _{oa} = 25-60 m)						
Movement	1.2-1.5	1.0-2.0	0.6-1.0	6	4	8
<u>Freighters, Coasters</u>						
(L _{oa} = 60-120 m)						
Movement	1.0-2.0	1.5-2.0	1.0-1.5	3-5	2-3	6
<u>Velocity</u>						
Size of vessel						
about 1000 DWT	0.6 m/s	0.6 m/s		2.0 deg/s	2.0 deg/s	
about 2000 DWT	0.4 m/s	0.4 m/s		1.5 deg/s	1.5 deg/s	
about 5000 DWT	0.3 m/s	0.3 m/s		1.0 deg/s	1.0 deg/s	

Table 2. Criteria for vessel movements for safe mooring conditions at berth. The movements are peak-peak values. For the berth to be acceptable, the frequency of these movements should be less than 3 hours/year.

Criteria for Wave Height

Wave height criteria for safe mooring conditions at berth were also established. Table 3 presents the main result.

Ship type	L_{oa} (m)	H_s (m)
Open boats	5-12	0.20
Other boats	5-12	0.30
Small fishing vessels	15-30	0.30
Coasters (<2,000 DWT)		0.45

H_s is the significant wave height equal to the mean value of the highest one-third of the waves in a wave train. This criterion is valid only if wind waves are causing the disturbance. In harbours where seiching/long periodic waves are significant, the indicated wave height cannot be regarded as a criterion for acceptable conditions.

Table 3. Wave height criteria for safe mooring conditions.

Further Studies

PIANC decided upon review of the study report of the Nordic Research Project to set-up a new international working group for the study of Criteria for Ship Movements in Harbours and related problems. The group is chaired by the first author of this paper and three of the authors are members of the PIANC Working Group. Contributions and suggestions from firms, institutions and individuals on the subject of Ship Movements will be graciously acknowledged.

References

1. Viggosson, G. Field Observations of Ship Behaviour at Berth, Advances in Berthing and Mooring of Ships and Offshore Structures, 1988 NATO ASI Series E, Applied Sciences - Vol. 146.
2. Icelandic Harbour Authority (IHA), 1986.
Danish Hydraulic Institute, 1986.
Landsverkfrøðingurin, 1986, Faroe Islands.
Kystdirektoratet, 1986, Norway.
SSPA Maritime Research and Consulting, 1986, Sweden.
Skibsbevegelser i havner (Ship Movements in Harbours), NET-Project.

NOTE: Five national reports available.

1006/2/OJJ/YBR/PA13

CHAPTER 234

NAVIGABILITY IN CHANNELS SUBJECT TO SILTATION

PHYSICAL SCALE MODEL EXPERIMENTS

C. BROSSARD 1, A. DELOUIS 2, P. GALICHON 3, J. GRANBOULAN 4,
P. MONADIER 5

ABSTRACT

The paper gives a brief description of the studies carried out in France during the last years, especially on scale models, in order to improve the knowledge of the behaviour of ships progressing in approach channels subject to siltation.

1 - INTRODUCTION

The French Ministry of the Sea and three French port authorities - Port Authority of Nantes - Saint-Nazaire, Port Authority of Bordeaux and the Maritime Service in French Guiana - have been working together over the past few years on studies with two main aims :

- to allow ships to use port approach channels subject to siltation, taking full advantage of potential while at the same time ensuring excellent navigability conditions,

- to ensure that technical conditions and maintenance dredging programmes are correctly adapted to the real requirements of port operations.

1 - Director of Approaches and Marine Environment, Port Authority of Nantes - Saint-Nazaire - Centre des Salorges - 18, Quai Ernest Renaud - B.P. 2199 - 44031 NANTES CEDEX 04 FRANCE

2 - Head of the Maritime Subdivision in French Guiana - Port of Degrad-des-Cannes - B.P. 338 - 97306 CAYENNE CEDEX FRANCE

3 - Head of Laboratory Division, SOGREA Consulting Engineers - B.P. 172 X - 38042 GRENOBLE CEDEX FRANCE

4 - Director of Development Works and Environment - Port Authority of Bordeaux - Palais de la Bourse - 2, Place Gabriel - 33075 BORDEAUX CEDEX FRANCE

5 - Head of Central Technical Department for Sea Ports and Inland Waterways - 2, Boulevard Gambetta - B.P. 53 - 60321 COMPIEGNE CEDEX FRANCE

These works cover three aspects :

- development of devices and methods for measuring the physical and chemical characteristics of fluid muds, such as the JTD 3 gamma densimetric probe (CEA - ORIS) working at fixed point, the JTT 4 gamma densimetric probe (CEA - ORIS) and the SD 105 ultrasonic densimetric probe (Port Authority of Bordeaux) working continuously and the SR 10 rheological probe (LCHF - SOGREAH), which are now fully operational, (ref. 1, C. BROSSARD and al, 1990, and ref. 2, C. MIGNIOT, 1984),
- physical scale model studies of the behaviour of ships in channels subject to siltation,
- observations and measurements taken from ships navigating in such areas.

This paper gives a brief summary of the exploratory work carried out by the Laboratoire Central d'Hydraulique de France (LCHF) in 1986 and then deals essentially with the systematic scale model tests carried out by SOGREAH in 1989.

2 - EXPLORATORY STAGE (ref. 3, LCHF, 1986)

This included :

- a preliminary bibliographical search that illustrated the interest of the study, but which also revealed that very few results were available from laboratory or in situ observations,
- theoretical considerations on the dimensional approach to ship displacement in clear water, the rheological problems connected with mud characteristics, the similitude applicable to scale model tests and the manoeuvrability of a ship moving over muddy beds,
- qualitative tests at a scale of the order of 1/100, enabling the measurement technology to be finalised and initial information to be obtained, giving an idea of the behaviour of a ship sailing over muddy beds.

3 - SIMULATION METHODS USED IN THE SYSTEMATIC TESTS (ref. 4, SOGREAH 1990)

This section deals successively with the problems of similitudes and scales, the experimental apparatus and the modelling of the mud.

3.1 - Similitudes and scales

Dimensional analysis of the factors constituting resistance to progress and ship behaviour led to the definition of dimensionless numbers enabling an accurate representation of the various phenomena involved.

Perfect modelling is impossible, as this would involve keeping many dimensionless parameters. Given the nature of the problem, the following choices were made :

- compliance with the Froude number and Froude densimetric number, which involves a velocity scale equal to the square root of the length scale and a mud density gradient increased in reverse proportion to the geometric scale,

- compliance with the ratio of inertia forces to rigidity forces and the ratio of densimetric forces to rigidity forces, which involves reducing the rigidity in the ratio of the geometric scales.

In contrast, neither the Reynolds numbers for water and for the mud medium nor the Grashov number (damping of internal waves) are retained. The medium in the model is therefore too viscous and forces are overevaluated.

The scales adopted after choosing the similitude rules and taking into consideration three geometric scales (1/100, 1/70 and 1/55) to represent different analysis situations are defined in the tables of figure 1.

Nature	Scale	Values		
Length	1/n	1/100	1/70	1/55
Area	1/n ²	1/10 ⁴	1/4 900	1/3025
Volume	1/n ³	1/10 ⁶	1/343 000	1/166 375
Speed	1/√n	1/10	1/8.37	1/7.41
Rigidity	1/n	1/100	1/70	1/55
Density	1	1	1	1
Theoretical tractive force	1/n ³	1/10 ⁶	1/343 000	1/166 375
Practical tractive force	-	1/3.310 ⁵	1/130 000	1/65 000
Power	1/n ^{3.5}	1/10 ⁷	1/2.87 10 ⁶	1/1.23 10 ⁶

1.1 - Chosen scales

Model		1/100	1/70	1/55
Speed	0.2 m/s	3.88 kn	3.25 kn	2.87 kn
	0.3 m/s	5.82 kn	4.87 kn	4.31 kn
	0.4 m/s	7.76 kn	6.50 kn	5.77 kn
	0.5 m/s	9.70 kn	8.12 kn	7.21 kn
	0.6 m/s	11.6 kn	9.71 kn	8.65 kn
Draught	15.6 cm	15.6 cm	10.9 m	8.58 m
	12.2 cm	12.2 cm	7.8 m	6.16 m

1.2 - Correspondences with full - scale speeds and draughts

Fig. 1 - Scales chosen for the tests and correspondences with some full scale parameters

3.2 - Experimental apparatus

The tests were run in the looped wave flume at SOGREAH in Grenoble. This flume is 50 m long and 3.2 m wide. It has a trolley that runs on rails, used for pulling the model and taking measurements (fig. 2)

The model used was that of a tanker of classic type, 2.56 m long, representing :

- at scale 1/100, a ship of the same type with a displacement of 120 000 t,
- at scale 1/70, a 25 000 - 30 000 t bulk carrier with a high block coefficient,
- at scale 1/55, a ship of the type calling in at French Guiana.

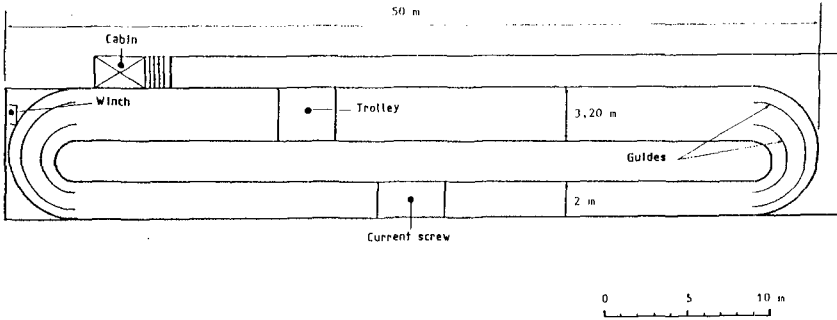


Fig. 2 - Plan of the looped flume

The model was equipped with sensors for measuring squat, trim and tractive force.

Four parameters were thus recorded simultaneously : foreward squat, trim, tractive force and speed (fig. 3).

The mud concentration was determined using an ultrasonic probe developed during the first stage of the study. Via two sensors, this measures the acoustic power transmitted through a layer of mud after direct immersion in the medium under study.

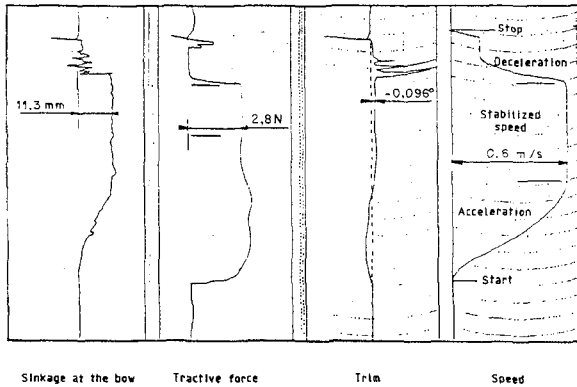


Fig. 3 - Examples of recordings

3.3 - Modelling of mud

In order to comply with the chosen rules of similitude, the mud had to be represented by a mixture which, at equal concentration, would have a rigidity value in proportion to the geometric scale, i.e. 1/100 for the basic configuration, and density gradients in similitude with those obtained in reality.

Following a review of the characteristics of mud deposits in the Loire, Gironde and Mahury (French Guiana), showing the variation of initial rigidity as a function of concentration and the density gradients in the deposits, it was decided to carry out tests with the following, in order to cover the entire range of possible situations :

- two types of mud : high rigidity and low rigidity,
- three concentration gradients as a function of depth : high, intermediate and low.

The techniques used to model the mud have allowed to respect, from the point of view of rheology and from the point of view of the density gradients, the conditions of similitude previously considered.

Figure 4 shows the gradients obtained on the model, for the mud of high rigidity, in conformity with those observed in situ and allowing profiles to be accurately repeated.

4 - TESTS IN CLEAR WATER

The aims of the tests carried out in clear water were :

- to check that the model behaved in conformity with the prototype,
- to gather information for comparing the results obtained with muddy beds.

4.1 - Programme of tests

The programme comprised 29 tests with :

- draughts of 15.6 cm and 11.2 cm with the ship at rest,
- speeds varying from 0.2 m/s to 0.6 m/s,
- under-keel clearances at rest varying from 8 cm to 0.5 cm.

The tests with large under-keel clearances at rest (6 and 8 cm) were carried out in order to appreciate the effect of reducing this parameter on the behaviour of the ship.

4.2 - Squat

The measurements were compared with the theoretical results obtained by applying the Barrass formula (1977) (ref. 5, L. Ribadeau-Dumas, 1982). The mean deviations observed were :

- 0.054 cm with a draught of 15.6 cm,
- 0.032 cm with a draught of 11.2 cm

i.e. about 0.3 % of the draught considered, which is less than the accuracy of the sensors.

4.3 - Trim

In the absence of known formulae, the measurements were compared only with the results of observations taken in the Netherlands Ship Model Basin (NSMB) and published by R. Sellmeijer and G. van Oortmerssen (ref. 6, 1983).

It appears that the results concur well for the narrow interval than can actually be plotted.

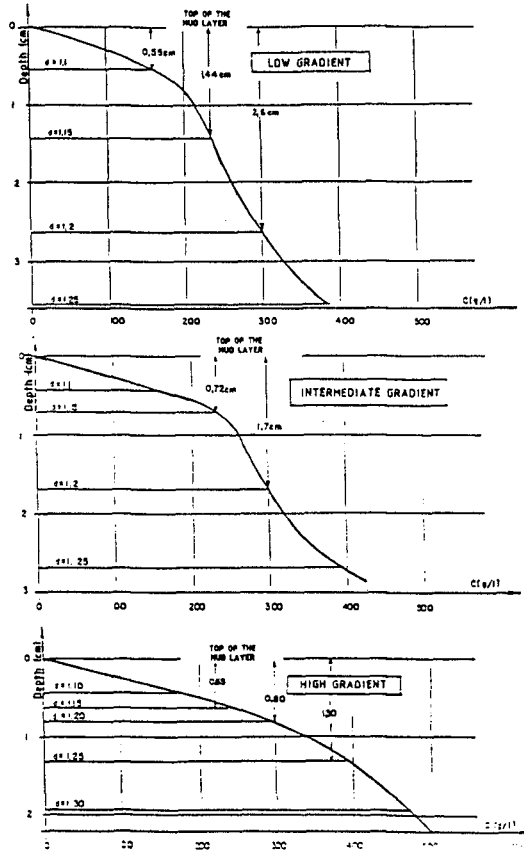


Fig. 4 - Density gradients on the model - Mud of high rigidity

4.4 - Tractive forces

4.4.1 - With the Froude similitude and a geometric scale of 1/100, the forces are theoretically in the scale of $1/10^6$ but on the model the viscous forces are actually increased owing to the fact that the Reynolds similitude is not respected, thus leading to a higher resistance than in reality.

Comparison of the in situ and model results indicates that the forces on the model are about three times too great with respect to the Froude similitude, which leads to the practical values shown on the table of figure 1.1, for example $1/3.3 \times 10^5$ for scale 1/100.

4.4.2 - The tests led to four types of conclusions :

- Forces increase when the under-keel clearance falls and forces are greater with a draught of 15.6 cm than with one of 11.2 cm.

- The difference between the tractive forces obtained for these two draughts is on average 5-10 % greater than could be expected from an increase in force based simply on the variation in hull area (+ 19 %).

- For both draughts, the force increases in an almost linear fashion as a function of the Froude number.

- A comparison of the forces measured on the model and those computed for the model shows that, overall, the forces measured are greater than those computed, though the differences are slight in the case of the lowest forces, increasing progressively with them. Given the lack of theoretical knowledge, uncertainties over the measurements, the methodology chosen and the aims pursued, it was considered that the model and sensors were adequate.

5 - TESTS WITH MUDDY BED AND NO CURRENTS

5.1 - Test programme

A programme of 99 tests was carried out.

The test or navigation conditions were characterised by five parameters, two linked to the mud :

- concentration-rigidity relation (type of mud used),
- concentration gradient of the mud deposit,

and three linked to the ship :

- draught at rest,
- under-keel clearance,
- speed.

5.2 - Squat

When the ship is above the top of the mud, the squat measured is of the same order of magnitude as with clear water when the keel is close to a hard bed, but when the keel is in the mud, the squat values differ according to navigation conditions.

- The type of mud has little effect on the squat values obtained.

- The draught has little effect on the squat values obtained, but, as in clear water, the squat values observed with a draught of 11.2 cm are very slightly higher than those obtained with a draught of 15.6 cm.

- Generally speaking, the greater the mud density gradient, the more the squat decreases algebraically.

- When the ship's keel is in the mud, the squat may be considered as the resultant of the hydrodynamic force connected with the speed and of the hydrostatic thrust.

. The observations made on the model at low speed, especially in the case of low and intermediate gradients, can be explained in this way.

. In the case of high gradients, in contrast, the ship is lifted more, as her trim is then positive, and this tends to cause the ship to climb on the top of the mud, all the more so as the speed increases.

. At high speeds (0.4 and 0.6 m/s), in the case of low gradients, there is an increase of the squat in comparison with the values obtained when the ship is above the mud.

- Considering the position of the keel when the vessel is at rest in comparison with density level 1.2, the squat values observed are greater than those obtained with clear water (with respect to the solid bed), even with under-keel clearances of the order of 10 % of the draught with low gradients and speeds of 0.4 to 0.6 m/s.

- The squat values vary in proportion to the square of the speed (fig. 5) :

. With low gradients, the squat values obtained in the presence of mud are higher than those observed in clear water, from about 0.5 m/s upwards.

. Independently of the density gradient, the positive squat values obtained with the under-keel clearances considered (vessel at rest) only appear with speeds above about 0.3 m/s.

All these various observations show that the density level is not, in fact, the only parameter to be taken into account, but that the density gradient is also an important factor.

5.3 - Trim

As far as manoeuvrability is concerned, a variation in trim is significant as soon as it corresponds to a difference of about 30 cm between fore and aft draught, i.e. an angle of the order of 0.068° . This phenomenon is significant especially in the case of a ship with a negative trim.

- The trim values obtained are very low with a mud of low rigidity, so that the effect of the other parameters may be examined only with rigid mud.

- Trim values increase with gradient, keeping the same speeds and under-keel clearances relative to the top of the mud, and, when the under-keel clearance decreases, the higher the gradient, the earlier the transition from a negative to a positive value.

- In the case of high gradients, the trim values remain lower for a draught of 11.2 cm than those observed, with the same under-keel clearance, for a ship with a draught of 15.6 cm.

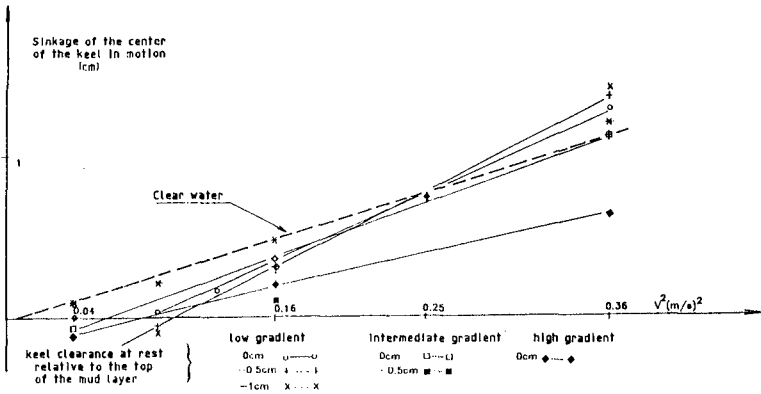


Fig. 5 - Tests with mud bottom and without current - Variation of the value of the squat with the speed - Mud of high rigidity - Draught 15.6 cm

- Generally, the trim changes from a negative value to a positive value as the hull penetrates the mud. The lower the speed, the earlier the transition to a positive value.

- The trim varies in proportion to the square of the speed (fig. 6) :

. with the same under-keel clearance and the keel in the mud, the greater the speed, the more the trim decreases, to the extent where it may become negative ;

. the variation in trim resulting from an increase in speed is, however, less in the presence of mud than with clear water.

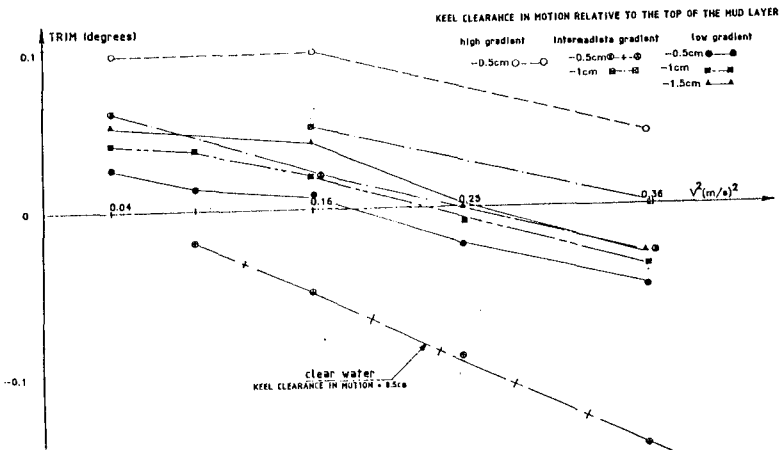


Fig. 6 - Tests with mud bottom and without current - Variation of the value of the trim with the speed - Mud of high rigidity - Draught 15.6 cm

5.4 - Tractive forces

Given scale effects, the forces involved should be mainly considered as relative.

Generally speaking, so long as the keel of the moving vessel is well above the top of the mud, forces are of the same order of magnitude as those observed in clear water. As the ship penetrates the mud, forces increase rapidly, but in a different way, however, depending on navigation conditions. In certain cases, a local maximum is observed when the ship's keel is just above the top of the mud.

- The effect of mud rigidity is felt particularly at low speed. The higher the speed and the less sinkage in the mud, the greater the relative proportion of the tractive force linked to the rigidity value. In areas where there may be differences in mud rigidity, this should be taken into especial account during periods of low-speed navigation and even more so during manoeuvring as, depending on the rigidity of the mud, the forces required may be very different.

- Low density gradients appear more favourable (less force with the same under-keel clearance during motion) than high gradients, considering the top of the mud as reference level. In contrast, low gradients appear less favourable if the 1.2 density level is taken as reference, because in this case and with the range of under-keel clearances used in the tests, the gentler the gradient, the greater the force appears to be with the same under-keel clearance.

- Tractive forces are generally higher with a draught of 15.6 cm than with one of 11.2 cm, and they vary in a relatively similar way depending on the under-keel clearance as the ship advances. The relative differences are of the order of 28 % for a speed of 0.4 m/s and 20 % for one of 0.6 m/s.

- Three types of variation in force may be distinguished, depending on the under-keel clearance during motion with respect to the top of the mud (fig. 7) :

. A variation as in clear water, when the ship's keel is distinctly above the top of the mud.

. A slight variation, when the ship's keel is close to the top of the mud. This type of change does not occur systematically.

. A very rapid increase with the sinkage of the ship in the mud. The speed at which this occurs increases with the gradient.

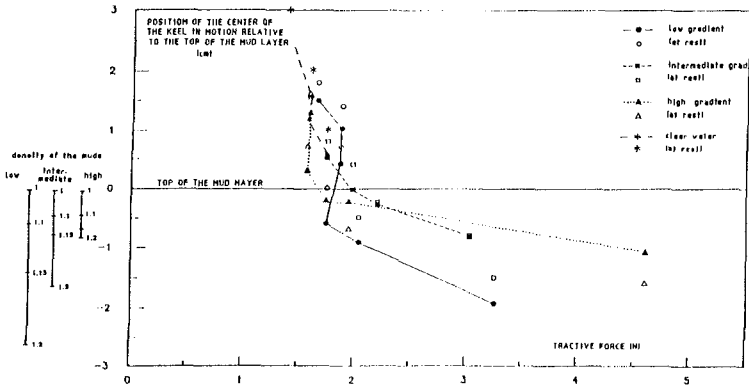


Fig. 7 - Tests with mud bottom and without current - Variation of the value of the tractive force - Mud of high rigidity - Draught 15.6 cm, $v = 0.4$ m/s

- An initial approximation of the variation in tractive force as a function of velocity may be written as follows (fig. 8) :

$$F = F^0 + k V^2$$

The values of F^0 and k depend on the under-keel clearance during motion relative to the top of the mud, the density gradient and the type of mud.

. The value of F^0 is nil when the keel is above the top of the mud and rises to 1.4 N for a high sinkage of the keel in the mud, with a rigid mud and a high density gradient.

. The values of k are higher by 20-50 % than that noted for clear water (10.5 N/m^2), depending on the type of mud deposit.

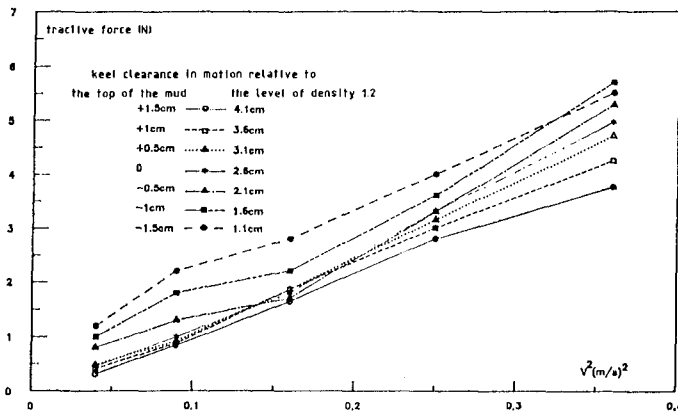


Fig. 8 - Tests with mud bottom and without current - Variation of the value of the tractive force with the speed - Mud of high rigidity - Low gradient - Draught 15.6 cm

5.5 - Internal waves

Internal waves were analysed on the basis of photographs taken through the flume observation window.

Internal waves are not visible with the most rigid mud, irrespective of speed, nor with the least rigid mud, with a speed of 0.2 m/s, but they appear with the least rigid mud and speeds of 0.4 and 0.6 m/s.

They generally occur in the form of a double-bump undulation above the top of the mud at rest, the first bump being less pronounced than the second one. The main characteristics are as follows :

- Distance between the two bumps, parallel to the keel centre line, of the order of 1 m, with the total wave length being of the order of 2 m.

- Wave crest making an angle of 30-50° with the centre line of the ship.

- Wave propagation speed perpendicular to the wave crest between 0.4 and 0.6 m/s.

- The amplitude of the internal wave depends little on the draught of the ship and on the density gradient. It increases with speed and reaches a maximum of 4-5 cm when the ship's keel during motion is close to the top of the mud and reaches a more or less constant value of 1.5-2 cm when the keel sinkage in the mud is of the order of 1 cm.

These observations concur, for the most part, with those published by R. Sellmeijer and G. van Oortmerssen (ref. 6).

6 - TESTS WITH CURRENTS

In order to assess the impact of a current on navigation in silted channels, some tests were also carried out with current in clear water and with muddy beds, using a ship with a draught of 15.6 cm.

The current speeds are denoted as positive when currents run in the same direction as the ship's motion, and negative in the opposite direction.

6.1 - Tests in clear water

Two series of three tests each have been performed, with an under-keel clearance of 1.6 cm (10 % of draught) at rest, with ship speeds in relation to the bed of 0.3 m/s and 0.4 m/s. Each series consisted of three tests : no current, a current of + 0.1 m/s and one of - 0.1 m/s.

The values obtained show that the results should be compared with those obtained under no-current conditions and with the same surface speed (i.e. in relation to the water).

With a current, squat is about 25 % greater and trim identical, irrespective of the current direction in relation to the ship's motion.

With the same surface speed, the tractive force is about 30 % greater than that observed in the absence of current when the current is in the same direction as the ship's motion and about 5 % less when it is in the opposite direction.

6.2 - Tests with muddy bed

Two series of three tests each were carried out, with the most rigid mud.

With the same surface speed and a muddy bed :

- squat decreases with a counter-current and is practically nil in the opposite situation,
- tractive forces are, as in clear water, slightly higher with a current.

With the same speed relative to the bottom and in the presence of a current, the tractive force is greater than in the absence of a current when it runs opposite to the direction of the ship's motion and is lower in the opposite situation. An initial approximation of the force may be obtained by considering that, with a given bottom speed and current, the force is close to that measured in the absence of a current considering the ship's speed to be equal to the bottom speed plus the current velocity.

7 - TENTATIVE APPLICATION OF TEST RESULTS TO REAL CASES

The study was completed by an attempt, suggested by ship's captains, to examine how the results obtained during the tests could be applied to real situations, in the form of nomographs.

The nomographs are formed by superimposing two families of curves (fig. 9).

- The first one, deduced from the tests, is taken from a set of ten figures corresponding to the ten categories of tests carried out (fixed rigidity, gradient and draught at rest). For known underkeel clearances at rest, this gives the force-speed curves (F-V), which can be transposed to real situations by applying the scales given in fig. 1.1.

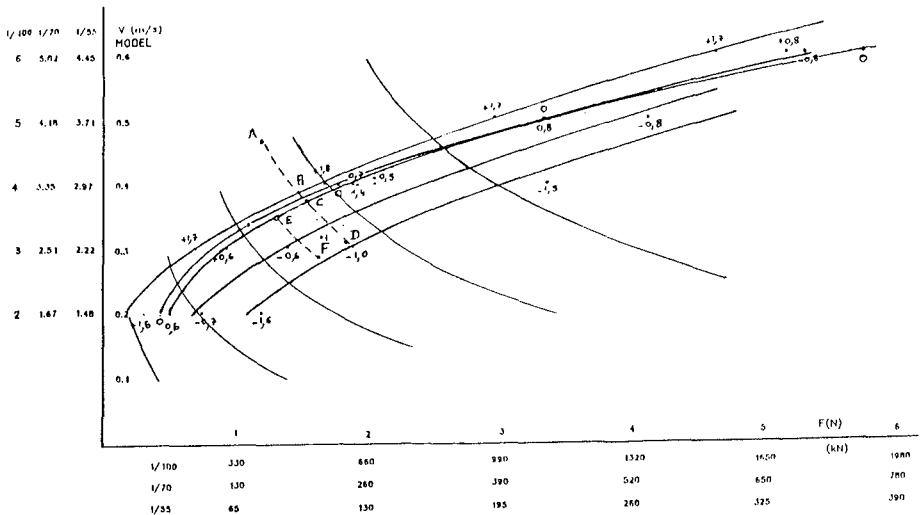


Fig. 9 - Diagram giving the conditions of navigation - Mud of high rigidity - Low gradient - Draught 15.6 cm

- The second family of curves represents the characteristics of the ships. Isopower curves are defined in the plane F, V by the relation :

$$P = F V$$

with the curves being calibrated by the approximately verified relation for unconfined waters :

$$P = k V^3$$

in which k is a coefficient depending on the characteristics of the ship. A set of three figures represents the isopower curves of the three ships considered.

The ship's operating curve is represented schematically on these nomographs by successions of displacements along the isopower curves when the engine power can be maintained and along the curves of constant under-keel clearance at rest relative to the top of the mud when the engine power is reduced.

Three practical cases have been examined, concerning the ports of Nantes - Saint-Nazaire, Bordeaux and French Guiana.

8 - CONCLUSIONS

The scale model experiments enabled substantial progress to be made in understanding the behaviour of ships sailing in channels subject to siltation. The nature of the phenomena observed and the orders of magnitude of the parameters for characterising these phenomena were acknowledged to be quite valid by the mariners and pilots involved in the study.

The first attempts made to establish nomographs defining navigation conditions in real situations are encouraging, but they must of course be treated with great caution. Precise measurements under real navigation conditions should constitute the next stage of study, enabling the theoretical nomographs derived from the scale model studies to be adjusted to real navigation conditions.

REFERENCES

- 1 - C. BROSSARD, M. GALLENNE, M. CAILLOT, J. GRANBOULAN, C. MIGNIOT, P. MONADIER and J. ROUDIER - Sécurité de la navigation dans les chenaux envasés. Report for the 27th PIANC Congress, Section II, Subject 1, May 1990
- 2 - C. MIGNIOT - Mesures des caractéristiques mécaniques des vases déposées dans les chenaux de navigation - Société Hydrotechnique de France, XVIIIème journées de l'Hydraulique, Question n° 1, Report n° 13, September 1984
- 3 - Navigabilité dans les chenaux envasés - Report on the first stage of the study - LCHF, August 1986
- 4 - Navigabilité dans les chenaux envasés - Report on the second stage of the study - SOGREA, February 1990
- 5 - L. RIBADEAU-DUMAS - Le surenforcement des navires dû à leur mouvement - Revue Technique des Phares et Balises - n° 53, 1982
- 6 - R. SELLMEIJER and G. VAN OOTMERSSSEN - The effect of mud on tanker manoeuvres. The Royal Institution of Naval Architects - Paper n° 71, Spring meetings, 1983

CHAPTER 235

INTEGRATION OF MARINE SIMULATION IN HARBOUR DESIGN

Stig E. Sand ¹

Ole Juul Jensen ²

Abstract

The strong increase in the capabilities and efficiency of modern marine simulators are briefly outlined as the background for demonstrating the advantages of a much closer coordination of hydraulic and maritime oriented design work in relation to harbour planning and alteration. The interaction of the two disciplines and the implications on the final configuration of two different harbours are described.

Introduction

In the design of a harbour the two dominating engineering disciplines are hydraulic engineering and naval architecture. Just the fact that two different disciplines are involved brings about the inevitable risk of lack of coordination, which in turn may be the explanation for several far from well functioning harbours in the past.

Traditionally, the hydraulic engineer conducts environmental investigations, basic lay-out studies, sediment transport assessments, down time analyses, etc. Some of the key activities herein are numerical wave and current computations, wave disturbance model testing and stability tests of breakwaters.

In the design of a new harbour the naval architects have typically been consulted (separately) on assessment of space requirements, dredging limits, approach, berthing and departing strategy for a given class of ships, which are planned to call on the harbour. The most important tools in manoeuvring studies have traditionally been Planar Motion Mechanism (PMM) tests or free sailing model tests in combination with theoretical considerations. However, these tools cannot fully account for the great complexity and the large number of parameters inherent in the design of an optimal harbour from a maritime point of view. The development of computer based marine simulators has clearly filled a gap in this sense by increasing the number of combined

¹General Manager, Simulation of Marine Operations, Danish Maritime Institute, 99, Hjørtekaersvej, DK-2800 Lyngby, Denmark.

²Head, Ports and Marine Structures Division, Danish Hydraulic Institute, 5, Agern Alle, DK-2970 Hørsholm, Denmark

variables that can realistically be taken into account in the design process. One of the important additional capabilities of a simulator is the provision of the man-machine interaction. Furthermore, the unique flexibility of a marine simulator as regards description of environmental conditions, harbour lay-out, ship characteristics, etc. is the key to a closer coordination of hydraulic and naval architectural tasks in the design process.

As the background for a call for further integration of marine simulator services in the design of harbours the subsequent sections briefly outline the traditional hydraulic and maritime areas of work and examples of the benefits of integration.

Typical Hydraulic Investigations

The design of a harbour requires the definition of a long list of design parameters which relate to amongst other hydrographic conditions and various criteria for the different installations and structures. The hydraulic investigations for a harbour typically comprise:

- i) Definition of wind, water level, tide, wave parameters and statistics. These can be established by various methods ranging from analysis of existing data, performance of measurement programmes to different types of computations and modelling. The definition of design water levels, e.g. in hurricanes, may require mathematical modelling with the most advanced models available for computation of the highly complex influence of winds and barometric pressure on the flow (currents) and water level. The definition of offshore waves and the transformation of waves to the nearshore zone of the harbour also requires numerical modelling using the most advanced models for definition of the wave climate and related nearshore design waves.
- ii) The layout and general arrangement of a harbour is often determined by a combination of numerical and physical models using as input the above defined wave and water level statistics. It is further of importance for the interpretation of any model investigation, numerical or physical, that pertinent criteria are available for the harbour. Such criteria are related to wave disturbance, ship movements and mooring forces.
- iii) Equally important to the layout is the verification of the long term stability of the protecting structures. Such investigations are still today mainly carried out in physical models.
- iv) For almost any harbour on sandy beaches aspects of scour and sedimentation as well as the effect in general on the coastal morphology requires often detailed investigations. Such investigations are mostly performed by means of numerical models.

Typical Maritime Investigations

As mentioned earlier naval architects have traditionally been consulted on ship manoeuvring performance and the implications on operational strategies as well as on physical boundaries such as turning basins, entrance channel, etc. Because of the considerable difficulties inherent in assessing manoeuvring performance under specific environmental conditions, physical restraints, human (navigator, pilot) interaction, etc. a large part of the considerations in the past have been based on simplified rules of thumb. These are typically associated with the standard manoeuvres, e.g. turning circle, zig-zag, stopping, etc.

For illustrative purposes consider the determination of the diameter of a planned turning basin. Often it may be chosen to be equal to the tactical diameter of the ship(s). If tugs are available the diameter may alternatively be determined as 1.2 - 1.5 times the length of the ship(s) as a general rule of thumb. Similarly, the use of duc d'albe's or manoeuvring by means of the ship's anchor may be based on generalized rules.

In contrast to these simple rules it is worth recalling that manoeuvring performance is composed of the interaction between:

- hull
- propeller(s)
- thruster(s)
- rudder(s)

which, as described above, should be considered under environmental conditions such as:

- wind field, lee effects and gusts
- current conditions, incl. shear current
- wave action
- water depth variations (bathymetry)
- bank proximity

It is rather obvious that general considerations as opposed to a true representation of the complexity indicated above may have implications on the serviability and in turn the economics of the harbour.

It is therefore comprehensible that a reliable description of all the elements and their interaction together with an important feature such as real time man-in-the-loop operations are what make today's marine simulators attractive.

Marine Simulators

As an example of a marine simulator the one at DMI is described. DMI is a full member of the International Marine Simulator Forum (IMSF).

The mathematical models represented in the marine simulator cover all vessel characteristics and environmental elements so that design and training tasks related to ship manoeuvring, navigation, dredging, harbour lay-out, offshore operations, etc. can be undertaken.

The simulator was originally developed for two basic purposes, viz. training of navigators and evaluation of manoeuvring performance. However, as clear needs were identified for a more sophisticated simulator it was developed to encompass shallow water effects, limited channel boundaries (bank effects), ship-ship interactions, complex wind and current patterns, etc. DMI is presently developing its fifth generation simulator which amongst other includes first and second order wave effects in six degrees of freedom.

The present software consists of more than 30.000 Fortran statements organized in a general purpose computer. The latter communicates with three graphic computers and in turn three projectors for illustration of the view from the actual ship's bridge on a 6,6 m x 1,5 m screen. The computer is also connected to the ship's instruments such as machinery telegraph, rudder, thruster command, etc. One PC screen shows the actual speed, draught, underkeel clearance, wind, wave and current information as well as machinery characteristics and fender or tug forces. Another PC shows a "radar" picture in the form of a plane "birds-eye-view". Fig. 1 illustrates the DMI simulator.

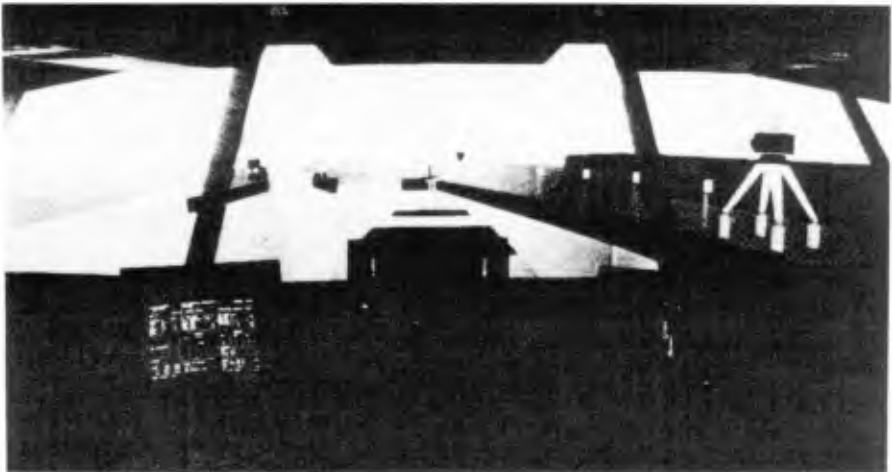


Fig. 1 Illustration of the DMI simulator with instrument screen, steering stand, radar picture and visual screen in the background.

As regards the subjects discussed in section 2 and 3 in relation to the design of harbours the strong points of the simulator is:

- accurate hydrodynamic modelling of vessels
- space and time varying currents
- space and time varying winds including gusts

- wave spectrum modelling
- representation of actual bathymetry
- three-dimensional graphics of harbour
- real time man-in-the-loop operations.

in combination with high flexibility such that any of the items above can be easily changed in the search for optimal solutions.

To this end it should be mentioned that also fast-time simulations are available. These do not include a man-in-the-loop, but instead a deterministic rule bound autopilot. The advantage is, however, that a fast screening of various alternative solutions can be performed. A few of the most promising solutions can then be tested in real-time.

Examples of Integrated Designs

The first example of a harbour which has been subject to combined hydraulic design studies and maritime simulations is shown in Fig. 2. The harbour, which is located in the Far East, was planned at a rather open stretch of coast with considerable influence from wind, waves and current.

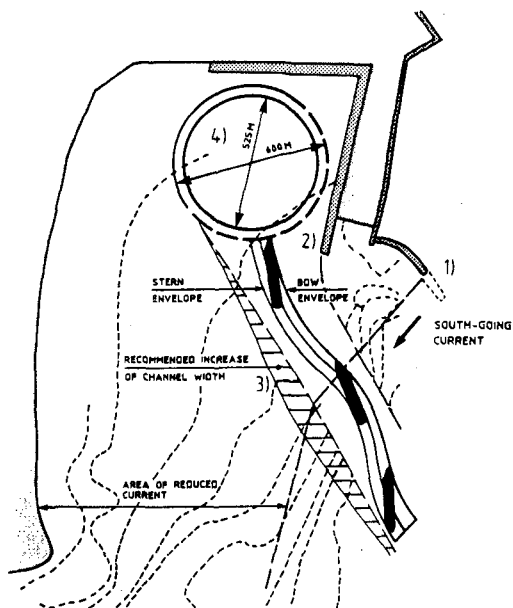


Fig. 2 Far East harbour.

The hydraulic investigations involved field measurements of waves and physical modelling of wave disturbance and currents. The wave disturbance study comprised a number of layouts and lengths of the main breakwater. It was found that the waves breaking over the shoal immediately to the west of the entrance channel caused considerable seiching in the channel and cross-currents in a certain area. These currents were expected to significantly affect the manoeuvring in the entrance channel.

The subsequent maritime investigations in the DMI simulator were based on the following plans:

- approach from north inside outer reef
- approach channel of width X m
- breakwater of length Y m
- turning basin of diameter Z m

After a series of simulations with amongst other a 130,000 DWT bulk carrier in loaded and in ballast conditions the maritime considerations led to the following solutions:

- a) The approach from north was too difficult in strong south-going current, because of the rather sharp starboard turn into the entrance channel. A better and cheaper solution was to dredge a channel through the outer reef. A much more appropriate alignment of the vessel when still in deep water had the advantage that the width of the approach channel could be reduced.
- b) Due to the shear current produced by the breakwater 1) in Fig. 2 the vessel had a tendency to turn starboard with the risk of colliding with the end of the quay 2). It was therefore recommended to lengthen the breakwater in order to separate the shear current zone and the deceleration area. Furthermore, the entrance channel 3) should be widened a bit to allow the vessel to keep away from the north bank and the quay.
- c) A detailed study of simulated tug boat and winch assisted manoeuvres led to a reduction of the turning basin 4) by about 75 m. The associated savings in dredging were not least important.

From the investigations and the results obtained, this example shows that simulations have a clear influence on the traditional hydraulic design objects and vice versa. The advantage of a coordinated work in the design phase is obvious. Site reports indicate that the harbour operates very well even in rather strong wind and current.

The second example focus on the design of a breakwater in a small ferry and fishing harbour, cf. Fig. 3, in the Faroe Islands.

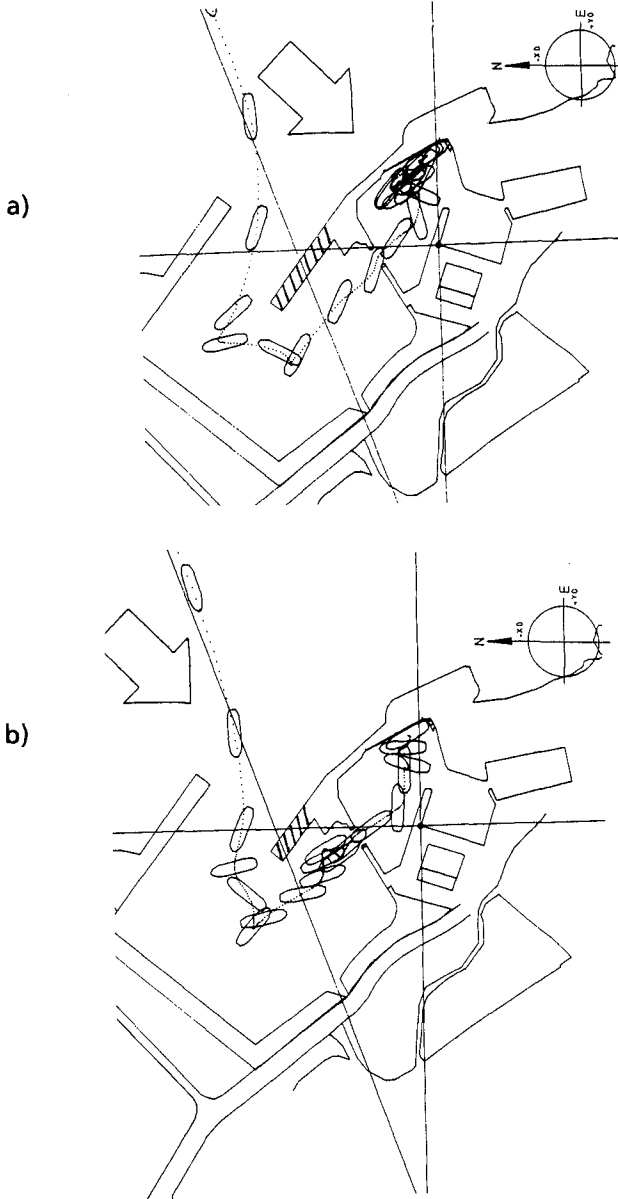


Fig. 3 Harbour in the Faroe Island with
a) rather long 70 m outer breakwater and,
b) a short 40 m breakwater.

The harbour is located in a fiord open in both ends to the Atlantic Ocean. The wave climate is very rough with yearly waves of about, $H_s = 4.0$ m, and extreme waves exceeding $H_s = 6.0$ m. The conditions are further aggravated by the wave periods associated with these waves. For $H_s = 4.0$ m the peak period is in the order of 13-16 s, while in the extreme events the peak period approaches 20 s. The harbour has until recently been characterized by very unacceptable wave disturbances due to resonance oscillations. The size of the basin corresponds to natural periods of 12-14 s waves, which are very frequent in the North Atlantic and in the fiords of the Faroe Islands. Therefore the harbour authorities decided to change the layout of the harbour. Very detailed studies have been performed in physical models including alternative solutions with a new outer harbour in front of the existing harbour. This solution, however, requires the construction of breakwater in water depths up to between 25 m and 35 m and it was consequently given up due to excessive construction costs.

An alternative solution was developed. This solution appearing in Fig. 3 involved construction of a new outer harbour with absorbing rubble-slopes on all boundaries by blasting into the rocky shore. This solution had the advantage that all the stones blasted in the new outer harbour basin could be used for construction of a new reclamation with a berm breakwater as seaward protection. In this way both the quarry-run and the gradation of larger stones were used in an optimum manner.

Physical model tests at DHI showed that the length of the breakwater had the most significant influence on the wave disturbance in the harbour. Lengths from 0 to 100 m were studied.

Having investigated the length of the breakwater from a wave disturbance point of view the aim of DMI's manoeuvring simulations was to test the operational conditions.

First the new 38 m ferry calling on this harbour was mathematically modelled. It was planned to be fitted with two astern propellers, two astern rudders and a bow thruster. Three alternative harbour lay-outs were modelled with all associated land contours, marks, buoys, leading lines, bathymetry, currents (time varying), wind (incl. lee effects) and fenders. A total of 89 simulations were carried out. About one third of these concentrated on the length of the breakwater at the entrance.

Compared to the hydraulic investigations it appeared clearly that the length of the breakwater should be rather short, i.e. not exceeding 60-70 m. Especially in north-easterly winds the manoeuvres were rather complicated. A port or starboard turn was necessary in the outer basin as a part of the preparatory alignment before entering the narrow inner harbour, cf. Fig. 3a). Although an increasing length of the breakwater provided better lee for wind and waves the necessary manoeuvres became increasingly difficult. Compared to a shorter breakwater e.g. Fig. 3b) the one shown in Fig. 3a) causes the ship to

initiate the starboard turn earlier and it forces the ship towards the north-west boundary of the basin with the risk of grounding. The latter implies that there is a longer distance for the ship to pass with low speed in order to reach the inner harbour.

As in the preceding example the optimal solution was again a balance between the hydraulic design aspects and the maritime requirements, described above, thus leading to a final length of the breakwater of about 70 m.

Conclusions

A modern marine simulator provides several very important features which form the basis for further integration in the design process of harbours - some of these are:

- quantification of complex ship-environment and man-machine interactions in real time.
- large flexibility and hence an ideal forum for discussion among harbour authorities, consultants and navigators/pilots, of alternative solutions.
- low cost investigations as future harbour alterations, training of crews, call of larger ships, etc. can easily be studied once the graphics of the basic harbour, bathymetry, etc. are established.

The examples discussed in the preceding section clearly illustrate the advantages of carrying out combined hydraulic and maritime investigations as a careful balance of requirements have to be achieved. This is shown schematically in Fig. 4 in which a hydraulic and a maritime organization are illustrated by DHI and DML, respectively.

Marine simulators represent still a rather new technology, which, however, undoubtedly will be generally accepted as an important tool for developing safe, cost effective and well functioning harbours and waterways. The (fast-time) screening facility of simulator and the interaction with the hydraulic aspects clearly call for simulations at the design stage and not only for verification or testing of decided solutions. Fig. 4 indicates the principle in such an interaction, which is claimed here to result in a harbour where all parties - authorities, consultants, navigators, and pilots - their requirements and views have been taken seriously into account.

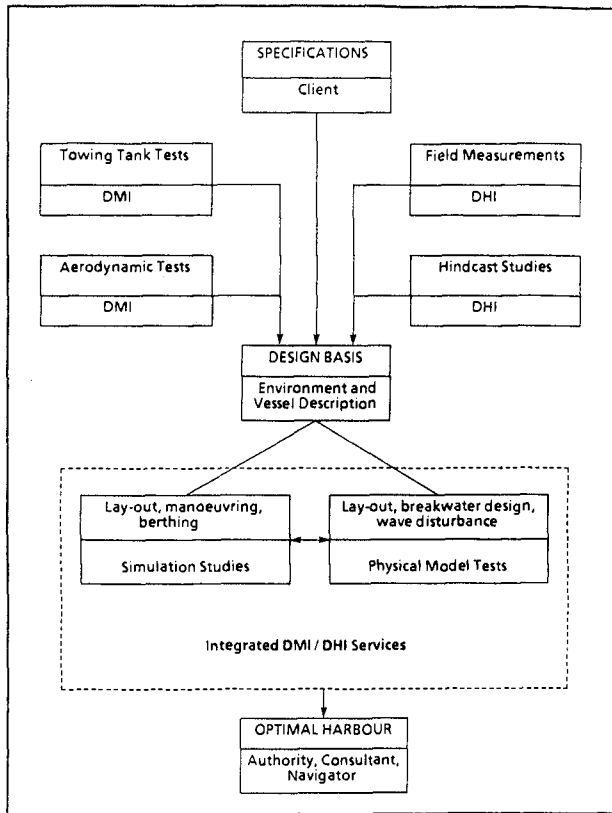


Fig. 4 Illustration of the integration of hydraulic and maritime services in optimal harbour design.

APPENDIX:

References

Chislett, M.S. and Wied, S. (1985).

A note on the mathematical modelling of ship manoeuvring in relation to a nautical environment with particular reference to currents.

Proc. Int. Conf. Numerical and Hydraulic Modelling of Ports and Harbours, BHRA, 119-129.

Chislett, M.S., Sand, S.E., Tersløv, O. and Wied, S. (1989).

Use of manoeuvring simulator as a design and test tool for ship control systems.

Proc. Conf. Expert Systems and Signal Processing in Marine Automation, CAMS '89, Control Applications in Marine systems, Techn. Univ. of Denmark.

CHAPTER 236

EXTENSION OF THE BOUSSINESQ EQUATIONS TO INCLUDE WAVE PROPAGATION IN DEEPER WATER AND WAVE-SHIP INTERACTION IN SHALLOW WATER.

Per A. Madsen¹ and Ole R. Sørensen²

1. INTRODUCTION

Mathematical short wave models based on the Boussinesq equations have been shown to be capable of reproducing the combined effects of most of the wave phenomena of interest to the coastal engineer for a relatively low cost. Today, the following phenomena can be taken into account in the most advanced numerical wave models:

- Shoaling, refraction, diffraction
- Partial reflection from breakwaters
- Irregular wave trains
- Directional wave input
- Wave-wave and wave-current interaction.

In this presentation the standard Boussinesq equations will be extended for two different purposes:

- To simulate irregular wave propagation from deep to shallow water
- To simulate wave-ship interaction in shallow water.

Section 2 will cover the first topic. The depth limitation of the standard forms of the Boussinesq equations will be discussed. It is shown that the worst form of the equations breaks down for depth to deep water wave length ratios (h/L_0) larger than 0.12 while the best forms are limited to say 0.22, corre-

¹ Chief Engineer, Danish Hydraulic Institute,
Agern Allé 5, DK-2970 Hoersholm, Denmark

² M.Sc., Ph.D., Danish Hydraulic Institute, as above

sponding to a 5% celerity error. In order to improve these limitations a new form of the Boussinesq equations is presented. With the new equations it is possible to simulate the evolution of irregular wave trains propagating from deep water to shallow water. In deep water, the new equations become effectively linear and phase celerities agree with Stokes first-order theory. In more shallow water, the new equations converge towards the standard equations which are known to provide good results for waves up to at least 75% of their breaking height. The combination of a linear wave model in deep water and a non-linear wave model in shallow water is justified by the fact that waves which are non-breaking in shallow water will be only weakly non-linear in deeper water. More details can be found in Madsen et al. (1990).

In the second part of this paper (Section 3) a new solution method for calculating wave-ship interaction in shallow water is presented. The ship motion is represented by six degrees of freedom and roll and pitch angles are assumed to be small, while there is only physical limitations on the other four displacements of the ship. The model which is still under development has the potential of solving the following types of wave-ship interaction problems:

- a) Wave induced motion of ships moored in harbours or at unprotected installations, e.g. at single point moorings
- b) Wave generation and wave resistance due to ships sailing in calm water or in wave fields.

A general outline of the principles used in the development is given in Section 3 while details concerning theoretical formulations and numerical solution procedures can be found in Madsen (1990).

2. IMPROVEMENT OF THE DEPTH-LIMITATION OF THE BOUSSINESQ EQUATIONS

As discussed by McCowan (1987) a variety of different forms of the Boussinesq equations exists. Firstly the dependent variables can be chosen in different ways, and typical velocity variables are the surface velocity, the bottom velocity, the depth-averaged velocity or the depth-integrated velocity. Secondly the dispersive terms can be manipulated by invoking the long wave equation as a first approximation.

A natural starting point for the derivation of the different forms of Boussinesq equations is the depth-integrated continuity equation and the Bernoulli equation for the surface velocity (see e.g. Witting, 1984). In order to close the equations, a relation between the depth-averaged velocity and the surface velocity is necessary. The classical way to do this is to apply Taylor expansion about the bottom and to express the horizontal velocity in terms of the bottom velocity (see Svendsen, 1974 or Witting, 1984). As shown by Madsen et al. (1990) three different forms of the Boussinesq equations can be derived in this way.

The first form is expressed in terms of the bottom velocity, U_b :

$$S_t + h U_{b_x} - \frac{1}{6} h^3 U_{b_{xxx}} = 0 \quad (1)$$

$$U_{b_t} + gS_x - \frac{1}{2} h^2 U_{b_{xxt}} = 0$$

where S is the surface elevation and h the still water depth.

The second form is expressed in terms of the surface velocity, U_s :

$$S_t + h U_{s_x} + \frac{1}{3} h^3 U_{s_{xxx}} = 0 \quad (2)$$

$$U_{s_t} + gS_x = 0$$

The third form is expressed in terms of the depth-averaged velocity, \bar{U} :

$$S_t + h \bar{U}_x = 0 \quad (3)$$

$$\bar{U}_t + gS_x - \frac{1}{3} h^2 \bar{U}_{xxt} = 0$$

In principle, this is the form used by Abbott et al. (1984) and suggested by Whitham (1973).

The dispersion relation corresponding to a specific form of the equations can be obtained by considering solutions of constant form. It turns out that the resulting phase celerities can be expressed by

$$\frac{c^2}{gh} = \frac{1 + Bk^2h^2}{1 + (B + \frac{1}{3})k^2h^2} \quad (4)$$

where

$$B = \begin{cases} 1/6 & \text{for Eq. (1)} \\ -1/3 & \text{for Eq. (2)} \\ 0 & \text{for Eq. (3)} \end{cases}$$

Notice that each form of the equations leads to a different celerity expression, but for small wave numbers all the derived expressions converge towards the Stokes first-order theory for waves on arbitrary depth, which for this purpose will be considered as the exact solution. As the wave number increases, the various celerity expressions become more and more inaccurate relative to the Stokes theory.

The percentage errors of the phase celerities are shown in FIG 1 as a function of h/L_0 : Firstly, Eq. (1) appears to have the poorest phase properties, and for $h/L_0 > 0.12$ solutions to the dispersion relation cannot be found. As remarked by McCowan (1987), this corresponds to the depth limitation for cnoidal wave theory. Secondly, Eq. (3) has the best phase properties of the standard Boussinesq equations. This is the form recommended by Whitham (1973) and applied by most of the existing numerical models today. The absolute water depth limit beyond which solutions to the dispersion relation cannot be found is $h/L_0 = 0.48$. However, in order to restrict phase errors to, say, 5% the practical upper limit for h/L_0 reduces to 0.22,

which corresponds to the water depth limit determined numerically by McCowan (1981).

For many applications, a less restrictive water depth limitation is desirable. This requirement of an improved linear dispersion property in deeper water was addressed by Witting (1984), who presented a new set of equations valid for a single horizontal dimension. As shown by Madsen et al. (1990) the linear reduction of Witting's equations leads to a phase celerity on the form of Eq. (4) with $B = 1/15$. This leads to a significant improvement of the depth-limitation, and for h/L_0 as large as 0.50 celerity errors are still restricted to approximately 5% (FIG 1).

The group velocities corresponding to the various forms of the Boussinesq equations can easily be derived from Eq. (4), which yields

$$c_g = c \left[1 + \frac{Bk^2 h^2}{1 + Bk^2 h^2} - \frac{(B + \frac{1}{3})k^2 h^2}{1 + (B + \frac{1}{3})k^2 h^2} \right] \quad (5)$$

The percentage errors compared to Stokes first-order theory are shown in FIG 2. The errors are surprisingly large even for relatively shallow water. By restricting the percentage errors to, say, 6% the practical water depth limitations become

$$h/L_0 = \begin{cases} 0.055 & \text{for } B = -1/3 \\ 0.12 & \text{for } B = 1/6 \\ 0.13 & \text{for } B = 0 \\ 0.32 & \text{for } B = 1/15 \end{cases}$$

Again Witting's method is superior to the standard forms of the Boussinesq equations. Unfortunately, it turns out to be very difficult to generalize Witting's approach to two horizontal dimensions. Instead we have formulated a new set of Boussinesq equations which meet the following requirements:

- a) The equations should be expressed in two-horizontal dimensions in terms of the surface elevation and the depth-integrated velocity components.

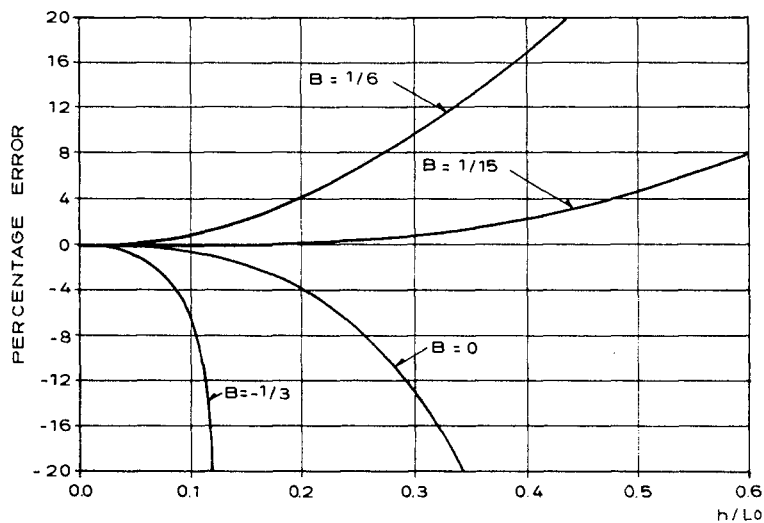


Fig. 1 Percentage error of the phase celerity.

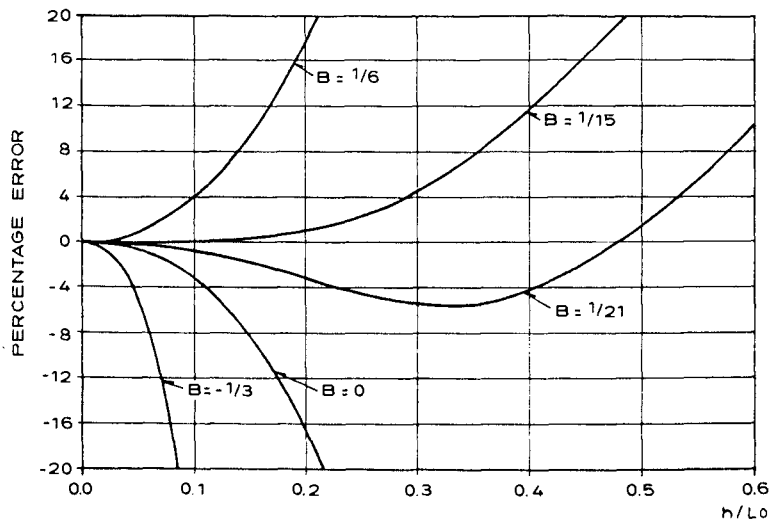


Fig. 2 Percentage error of the group velocity.

- b) The resulting linear dispersion characteristics should follow Eq. (4) where the coefficient B can be chosen explicitly to improve accuracy in deeper water.

The following equations meet these requirements:

$$S_t + P_x + Q_y = 0 \quad (6a)$$

$$P_t + \left(\frac{P^2}{d}\right)_x + \left(\frac{PQ}{d}\right)_y + gdS_x - (B+\frac{1}{3}) h^2 (P_{xxt} + Q_{xyt}) - Bgh^3 (S_{xxx} + S_{xyy}) = 0 \quad (6b)$$

$$Q_t + \left(\frac{Q^2}{d}\right)_y + \left(\frac{PQ}{d}\right)_x + gdS_y - (B+\frac{1}{3}) h^2 (Q_{yyt} + P_{xyt}) - Bgh^3 (S_{yyy} + S_{yxx}) = 0 \quad (6c)$$

where d is the total water depth, h is the still water depth, and P and Q are the depth-integrated velocity components (m^2/s). Notice that in extremely shallow water, where the long wave equations are valid as a first approximation, the new equations will converge towards the standard Boussinesq equations.

FIG 3 shows the effect of applying the new equations. The bichromatic wave considered is comprised by a 2.5 s wave ($h/L_0 = 0.43$) and a 3.0 s wave ($h/L_0 = 0.30$) each having an amplitude of 0.05 m. In the standard model (i.e. with $B = 0$) the group celerity errors are -90% for the 2.5 s wave and -44% for the 3.0 s wave. Hence, especially the 2.5 s wave is slowed down so much that the resulting time series taken at a position only 12 m down the channel almost looks like a monochromatic wave, at least until the 2.5 s wave eventually reaches the point and re-establishes the bichromatic wave pattern. In the new model with the coefficient $B = 1/21$, the wave train travels down the channel almost undisturbed.

More details, especially concerning the numerical solution procedure, are given by Madsen et al. (1990).

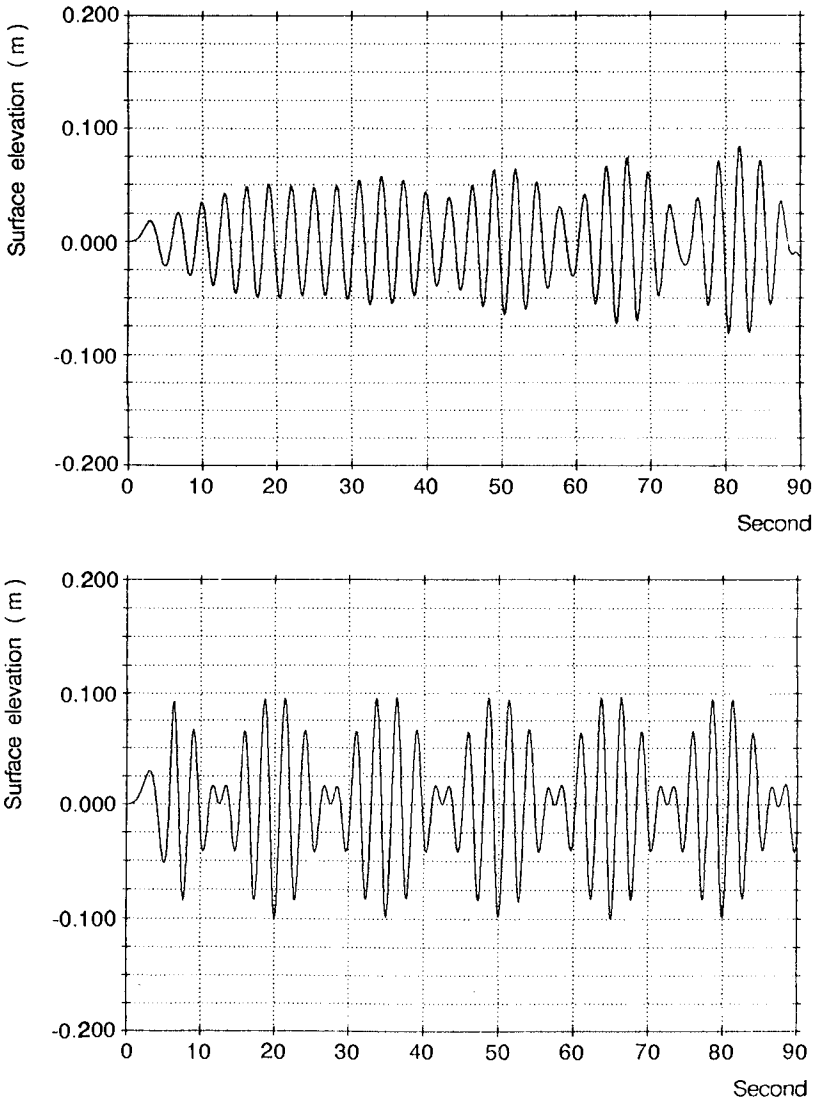


Fig. 3 Bichromatic wave test
a) Standard Boussinesq model (i.e. $B = 0$)
b) New model ($B = 1/21$)

3. SIMULATION OF WAVE-SHIP INTERACTION IN SHALLOW WATER

The second topic in this paper represents a natural step forward in the development of the Boussinesq type models by including the interaction between waves and moored or sailing ships in shallow water. Details concerning the theoretical formulations and the numerical solution procedure will not be given here but can be found in Madsen (1990). Instead a general outline of the general principles will be given below.

Depth-integrated flow equations in the time-domain are formulated to describe the free surface flow beside the ship as well as the pressurized flow under the ship. A slot-technique is used to combine the two flow regimes into a single set of equations expressed in terms of the depth-integrated velocity components and the local pressure height. This technique is similar to the one used by Preissmann and Cunge (1961) for modelling pressurized flow in conduits. The excess pressure, depth-averaged over the underkeel clearance, is used to determine the hydrodynamic forces and moments on the ship. This approximation is valid in shallow water and especially if the underkeel clearance is small. The local wave generation due to the moving ship is taken into account by distributing sources on the ship hull and including the effect in the continuity equation. The ship motion is represented by six degrees of freedom using one coordinate system, which is fixed relative to the moving ship and one, which is fixed relative to the surrounding bathymetry. Both systems are rectangular but the grid spacing can be different. First of all, the ship is described in the ship coordinate system by defining two-dimensional maps of ship draft and ship slot factors. A slot factor of 0.01 will indicate solid ship body, while a factor of 1.0 indicates an open water point. Normal vectors defining the ship elements will be determined in each ship grid point. When the ship moves around in the harbour coordinate system, the ship slot factors in this system will change from time step to time step indicating the new position of the ship. A simple interpolation routine is used to determine the successive ship configurations in the harbour coordinate system during the motion. This requires the roll and pitch angles to be small, while there is only physical limitations on the other four displacements of the ship.

The depth-integrated formulation makes the model very efficient and even though it is solved directly in the time-domain the computer economy is quite reasonable: The speed of the model is approximately 1200-1500 points/s on an IBM 4381 depending on the ratio of ship points to clear water points. A typical grid size will be from 1 to 5 m, depending on the beam of the ship, and a typical time step will be 0.1 to 0.2 s.

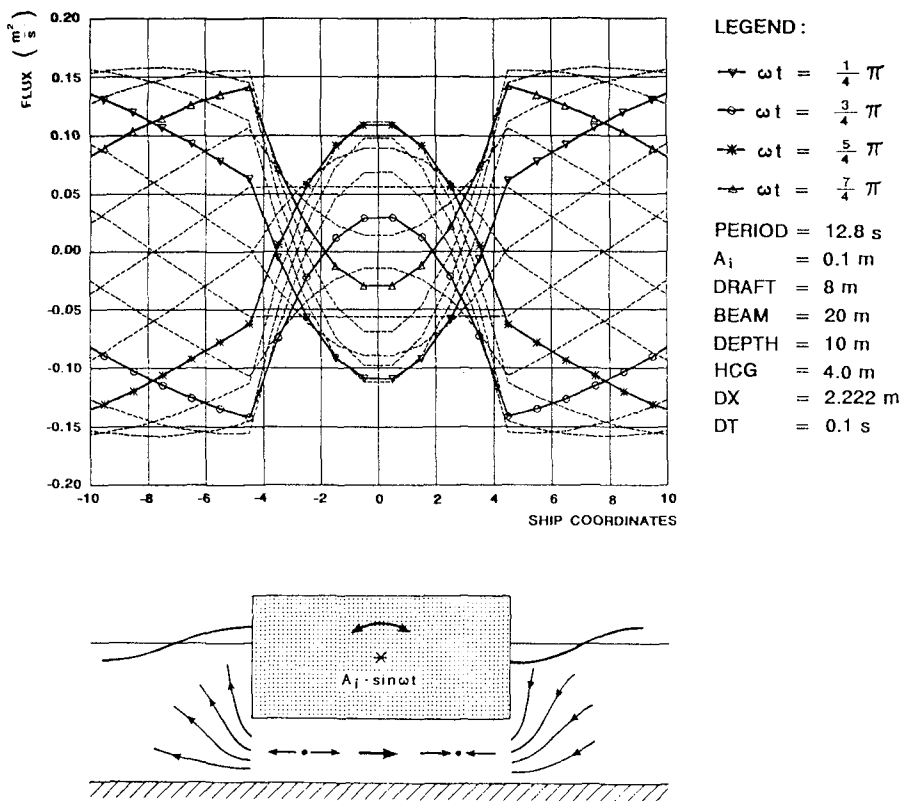


Fig. 4 Forced roll motion: Flux envelope.

One of the key problems in the model development has been the internal wave generation due to the motion of the ship. The resulting pressure and velocity distribution on the ship hull has to be accurate in order to take added mass and wave damping effects proper into account. In order to test this the forced

harmonic motion of a box shaped ship has been considered. Simple analytical solutions for this problem were derived by Svendsen & Madsen (1981) and Madsen et al. (1980) and they concluded that

- a) The forced sway motion leads to a linear pressure distribution and a constant flux distribution in space.
- b) The forced heave motion leads to a parabolic pressure distribution and a linear flux distribution in space.
- c) The forced roll motion leads to a cubic pressure distribution and a parabolic flux distribution in space.

The internal wave generation in the Boussinesq model has been verified against these analytical distributions. As an example the simulated flux envelope for forced roll motion is shown in FIG 4 comprising of sixteen instantaneous line plots covering one period in the forced motion.

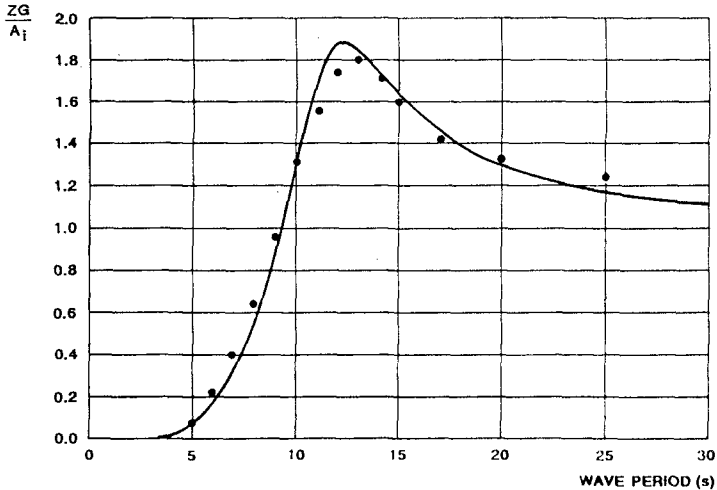


Fig. 5 Response curve for wave induced heave.
 Draft = 8.0 m, Beam = 20 m, Depth = 10 m.
 - Theory by Svendsen & Madsen (1981)
 • Boussinesq model.

An example of wave induced motion of a moored ship is shown in Fig. 5 where the response curve for heave motion has been compared with the analytical solution by Svendsen and Madsen (1981).

Finally, Figs, 6, 7 and 8 show examples of perspective plots of the wave field surrounding a moored ship (Fig. 6), the wave field generated by yaw extinction (Fig. 7) and the wave field generated by a sailing ship which is accelerating from rest to a maximum speed of 20 knots in 14 m of water depth.

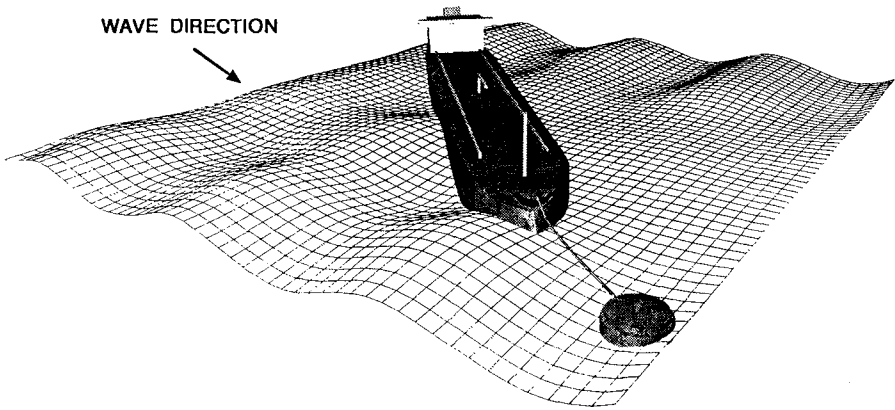


Fig. 6 Moored ship in cross waves.

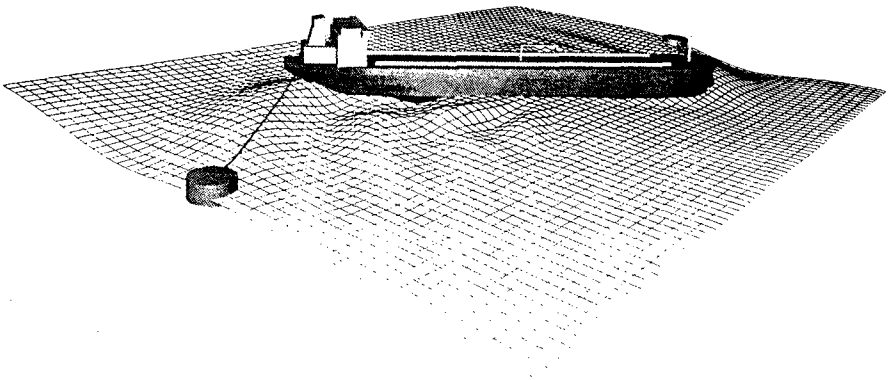


Fig. 7 Yaw Extinction test.

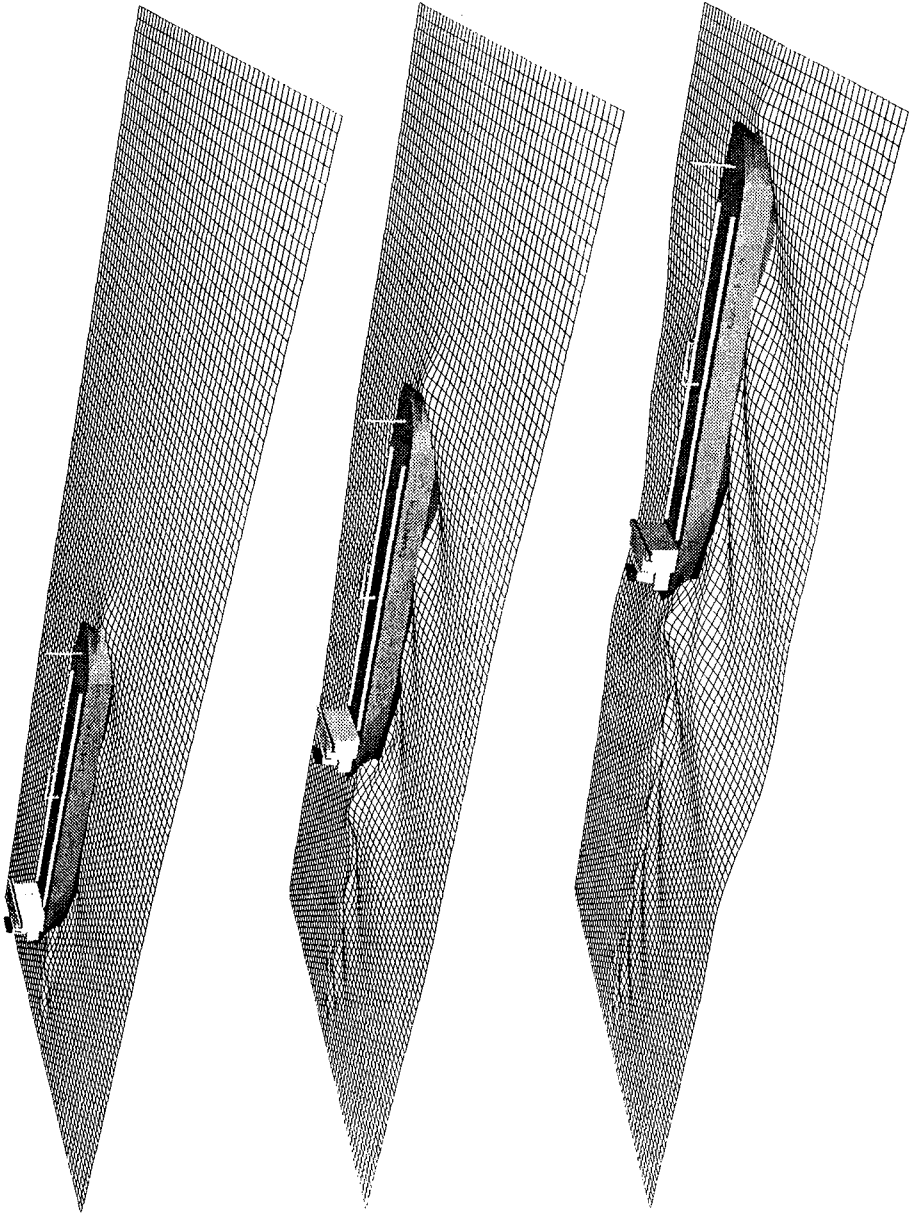


Fig. 8 Sailing ship in calm water.

REFERENCES

- Abbott, M.B., McCowan, A.D. and Warren, I.R. (1984). **Accuracy of short-wave numerical models.** Journal of Hydraulic Engineering, 110, No. 10, 1287-1301, ASCE, ISSN.
- McCowan, A.D. (1981). **Developments in numerical short wave modelling.** Proc. 5th Australian Conf. on Coastal and Ocean Eng., Perth 1981.
- McCowan, A.D. (1987). **The range of application of Boussinesq type numerical short wave models.** Proc. 22nd IAHR Congress, Lausanne.
- Madsen, P.A., Svendsen, I.A. and Michaelsen, C. (1980). **Some recent results for wave induced motions of a ship in shallow water.** Proc. 17th Coastal Engineering Conference, Sydney, 12-28 March 1980.
- Madsen, P.A., Murray, R. and Soerensen, O.R. (1990). **A new form of the Boussinesq equations with improved linear dispersion characteristics.** Submitted to Journal of Coastal Engineering.
- Madsen, P.A. (1990). **A depth-integrated formulation of wave-ship interaction in shallow water, Part 1 : Derivation, Part 2 : Validation.** In preparation for Journal of Ocean Engineering.
- Preissmann, A. and Cunge, J.A. (1961). **Calcul des intumescences sur machines électroniques.** Proc. 9th Congress, IAHR, Dubrovnik 1961, 656-664.
- Svendsen, I.A. (1974). **Cnoidal waves over a gently sloping bottom.** ISVA, series paper 6, Tech. Univ. of Denmark, Lyngby.
- Svendsen, I.A. and Madsen, P.A. (1981). **The dynamics of wave induced ship motions in shallow water.** Ocean Engineering, 8, No. 5, 443-479, Pergamon Press Ltd.
- Whitman, G.B. (1973). **Linear and nonlinear waves.** John Wiley & Sons, New York.
- Witting, J.M. (1984). **A unified model for the evolution of nonlinear water waves.** J. Computational Physics 56, pp. 203-236.

CHAPTER 237

Safe Underkeel Allowances for Vessels in Navigation Channels

J M A Spencer, E C Bowers and G H Lean¹

Abstract

This paper describes methods used at Hydraulics Research to evaluate risks of ships grounding in navigation channels due to wave induced vertical motion. Risk assessments are then used as an aid to optimising channel depths with a view to minimising dredging. A mathematical model of ship response in waves in shallow water is presented and two case studies are considered to show how methods may be applied.

1. Introduction

Modern deep draught ships require long deeply dredged navigation channels for access to many ports. In many cases these are exposed to waves, and it is then necessary to ensure that sufficient allowance is made for vertical movement of any ship using the channel to prevent it damaging itself by bed contact (see Van Wyk and Zwamborn, 1988, for example).

At the same time, it is important not to design too deep a channel: each extra metre dredged in a channel 12 km long and 200m wide (Port Qasim, Pakistan) requires removal of at least an extra 2.4 million m³ of material. This sort of amount of dredging represents a considerable capital expenditure for any port, and more maintenance dredging may be necessitated to maintain the deeper channel as well - thus adding to the expense.

It is therefore important to design channels to be of optimum depth: deep enough for groundings to be acceptably infrequent, usable in most wave conditions at the site and all at minimum cost. Finding such an optimum channel depth is thus an integral part of port design.

Deciding on depths to which channels should be dredged is an area in which empirical procedures are commonly used: a 'marine expert' is engaged to give his advice based on past experience but

¹ Hydraulics Research, Wallingford, Oxon, OX10 8BA, UK

the complexity of ship response in waves makes this a difficult judgement to make with precision. It seems probable that some navigation channels are overdredged due to unnecessarily cautious expert advice, while others suffer excessive downtime because a little too much emphasis was put on saving construction costs. Where such subjective decisions have to be made, departures from the optimum are inevitable.

Physical models using radio-controlled ships underway in random or irregular waves can and should be used as design tools to assist in obtaining an optimum channel. They are the most reliable method for predicting vessel vertical motion, and thus form a reliable basis for assessing bed contact risks. But comprehensive physical model test programmes are expensive and time consuming because of the large number of variables involved: wave direction, wave spectrum, underkeel allowance, vessel type and speed being just some of the major parameters. The cost and time factors have dissuaded many port designers from using model tests in many cases and particularly at early stages in design when little money may be available to develop a fledgling project.

Mathematical models promise to overcome the drawbacks of using physical models in feasibility studies and of over-reliance on expert opinion. Because of this, mathematical models will be of increasing importance in the field in years to come. By making accurate estimates of vessel vertical response, a good mathematical model enables good quantitative estimates of the risk of a vessel grounding in a channel to be made; objectivity can thus be added to necessarily subjective expert opinions, and margins of error in design will be reduced. A mathematical model has the advantage over a physical model of being much quicker and cheaper to use. It therefore has applications in feasibility studies where large numbers of test conditions need to be examined in a short time. Having proved the feasibility of a particular project the physical model should be used to examine critical cases, etc in order to further reduce margins of error.

This paper describes a mathematical model of ship response in waves, called UNDERKEEL. The model has been developed at Hydraulics Research (HR) specifically for coastal engineering applications, and its use for assessing dredged depth requirements in navigation channels is described here. Two case studies will be examined: one considers VLCC safety in the Dover Strait, and another considers the use of the access channel to Port Qasim (Pakistan) by PANAMAX container vessels.

2. Description of the Ship Response Model

UNDERKEEL is a frequency domain model of ship response to waves using calculations of water flow derived from linear potential theory. It being linear, superposition principles are

applicable to its output and it can readily be used to compute ship response spectra for any given multi-directional wave spectrum.

The model is intended for use on ships in unprotected channels or moored at open quays; it is not appropriate to problems involving vessels close to wave reflecting obstacles like quay walls and canal banks. It does, however, model moving ship responses to waves as well as stationary ones.

UNDERKEEL has been developed specifically for coastal engineering applications in which the underkeel clearance between vessel hull and seabed is small compared to the vessel beam. Boundary element type models of ship response, commonly used in deep water applications, often have difficulty simulating flows in narrow gaps, and are thus not ideal for coastal usages. The difficulty is overcome in UNDERKEEL by using a semi-analytical approximate treatment of flow in the underkeel region. This gives an accurate model of ship response in shallow water, and has the further advantage of producing a model that is both quick to set up for a new ship and to run.

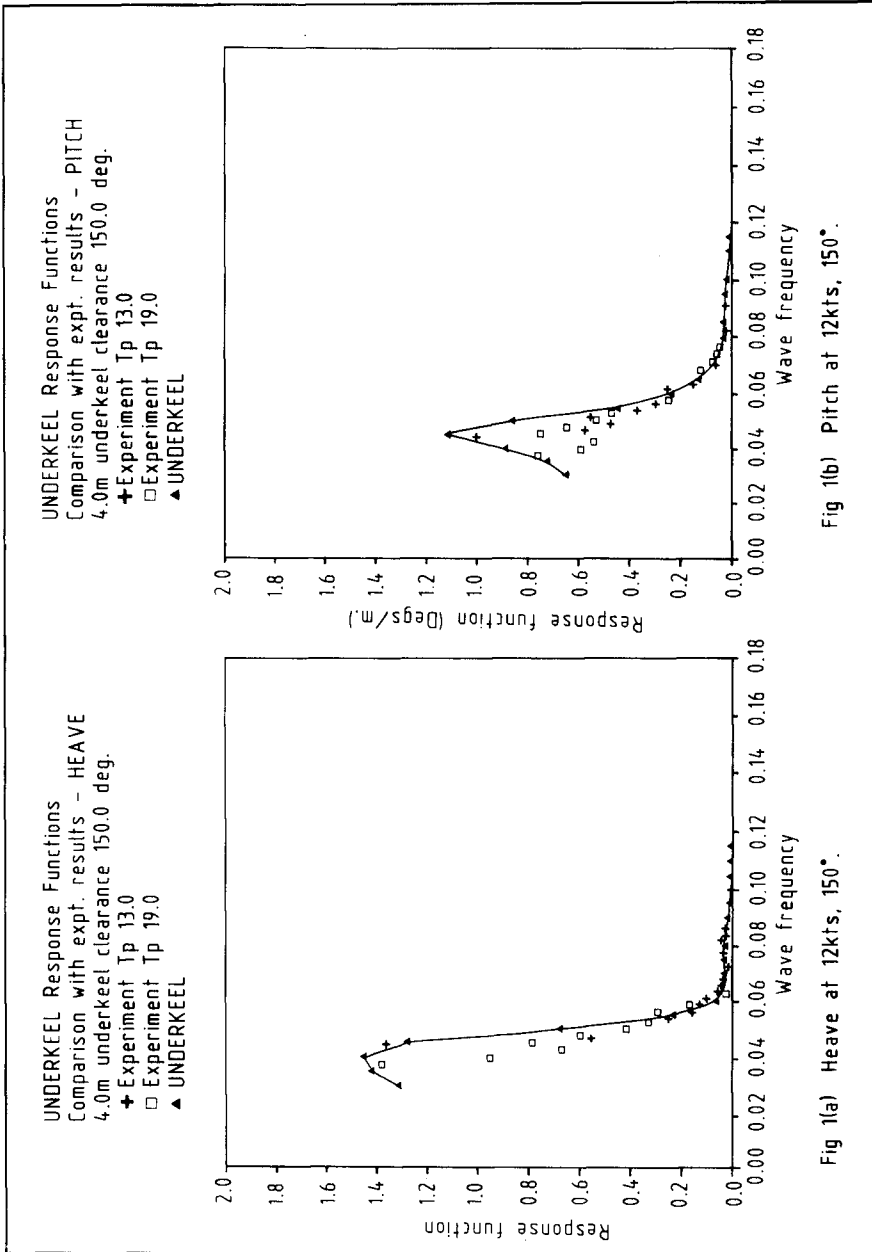
Standard output from the model is in the form of response functions: amplitudes of ship motion in response to unit amplitude regular waves of specified frequency and direction of propagation. Both horizontal ship movements (surge, sway, yaw) and vertical movements (heave, roll, pitch) can be simulated. As the vertical motions affect bed contact risks, this paper will focus on them although coupling between the various movements is taken into account.

There is a difficulty modelling roll response using any model, like UNDERKEEL, based on potential theory. The problem arises because most of roll damping in nature is due to eddy shedding and other viscous effects that are not present in the model. Adopting a conservative philosophy, we neglect all forms of viscous and eddy shedding roll damping in UNDERKEEL and include only the wave making damping predicted by potential theory; this course of action can be anticipated to lead to over-prediction of roll in nearly all circumstances.

But roll is often not a significant determinant of grounding risks. Most harbour entrance channels are aligned roughly perpendicular to the coastline and approximately colinearly with dominant directions of wave propagation after wave refraction is taken into account. Head and stern seas do not excite roll in ships. Thus, in these channels roll can be anticipated not to contribute to grounding risks.

2.1 Comparison with Experimental Results

Response functions calculated using UNDERKEEL may be compared



with physical model results. One such set of comparisons is shown in figure 1 for a VLCC sailing at 12 knots. Experimental results were obtained using a 1:100 scale model (radio controlled) of a 330m long, 22m draught VLCC. Details of the experiments are given by Bowers (1989).

The experimental results in figure 1 are for long crested random waves approaching the bow at an angle of 30°. Spectral peak periods are at 13s (significant wave height 5.0m representing storm conditions) and at 19.0s (significant wave height 1.5m representing swell conditions). It can be seen that response functions derived from the two different experimental spectra are similar despite the differing wave heights involved. This similarity of response is good evidence that heave and pitch response is linear which justifies the assumption of linearity made in UNDERKEEL. Comparison between UNDERKEEL and the experimental results show good correlation.

The full physical model programme involved testing the VLCC with a range of underkeel clearances. UNDERKEEL was found to predict the trends in the results very well as the following table shows (% changes in response are presented in going from a 4m to a 6m underkeel clearance).

Wave condition	Sea direction	% change in standard deviation response	
		Physical model	Mathematical model
$T_p = 19s$	Stern sea	-5	-5
$H_s = 1.5m$	Head sea	+33	+33
$T_p = 14.5s$	Stern sea	-16	-9
$H_s = 2.8m$	Head sea	+38	+24
$T_p = 13s$	Stern sea	-11	-5
$H_s = 5.0m$	Head sea	+25	+33
$T_p = 11s$	Stern sea	-12	-4
$H_s = 4.8m$	Head sea	+31	+40

2.2 Comparison with Boundary Element Model

Comparisons have also been made between responses computed using UNDERKEEL and NMI-WAVE developed by Standing (1978), a more conventional boundary element model of a type often used in offshore work. Figure 2 shows a comparison for heave and pitch. Responses in this case are computed for a 320m long hull with a 60m beam and 24m draught. No physical model data is available for comparison. Response functions are plotted as a function of wave direction for a fixed $0.06 H_z$ wave frequency. The hull was stationary. Underkeel clearance was 20% of draught.

UNDERKEEL agrees well with NMI-WAVE but UNDERKEEL requires a great deal less computer time and resources to run; the exact

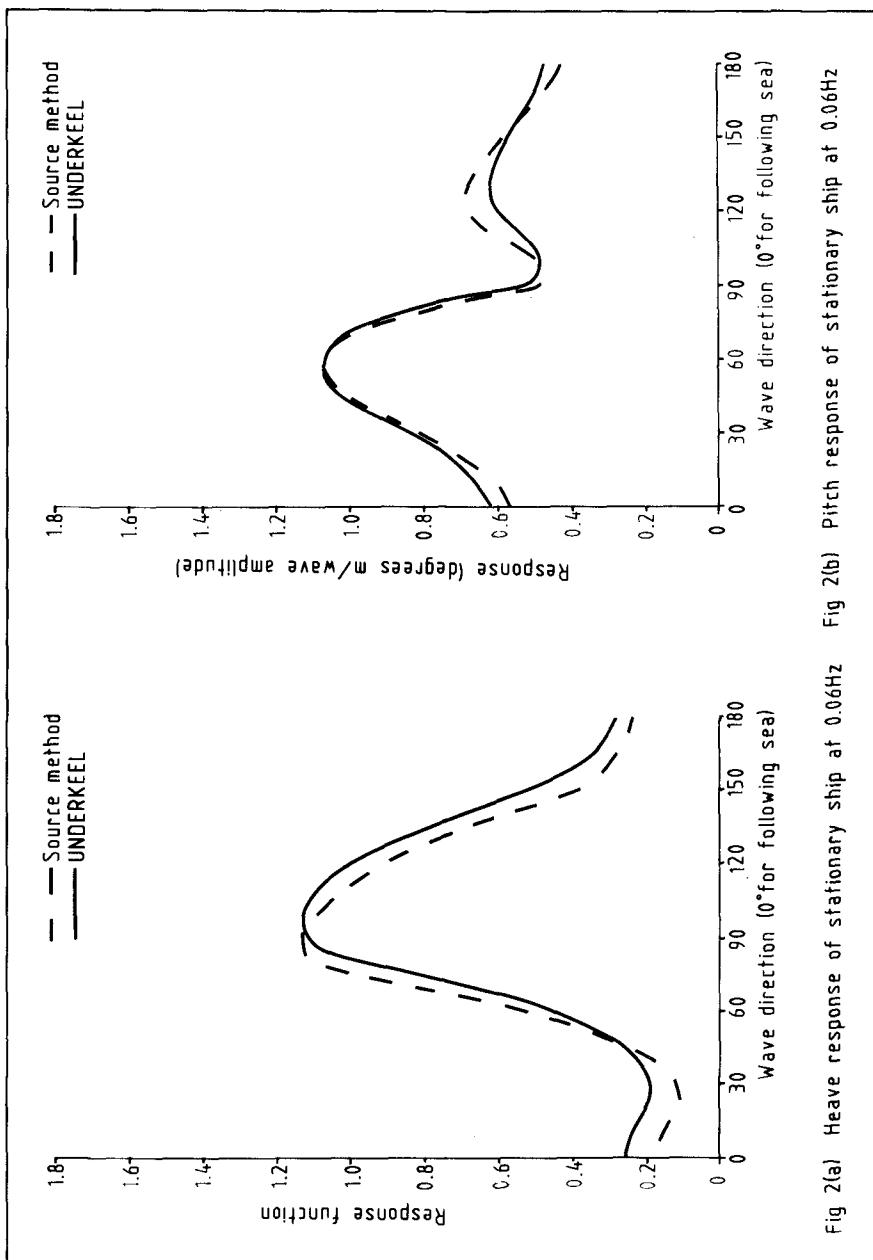


Fig 2(a) Heave response of stationary ship at 0.06Hz Fig 2(b) Pitch response of stationary ship at 0.06Hz

difference will depend on the application, but ten times the speed of calculation should be easily achievable in practice. Perhaps more important, there are similar differences in ease and speed of setting up data describing any ship for calculation. UNDERKEEL is also more easily applicable in the limit of very small underkeel clearances.

3. Grounding Risk Calculations

Given a response function for the vertical motion of a point on a ship hull, $R(f,\theta)$, which is a function of wave frequency and direction, and which may be obtained using UNDERKEEL, and given also a directional wave spectrum, $S(f,\theta)$, (directions taken relative to the ship) then the spectrum $S_V(f)$ of vertical movement of the point may be computed:

$$S_V(f) = \int_{\theta=0}^{360} R^2(f,\theta) \cdot S(f,\theta) d\theta \quad (1)$$

The root mean square vertical movement amplitude, σ , is calculable from the response spectrum:

$$\sigma = m_0^{1/2} = \left(\int_{f=0}^{\infty} S_V(f) df \right)^{1/2} \quad (2)$$

The second spectral moment of response is:

$$m_2 = \int_{f=0}^{\infty} \int_{\theta=0}^{360} \frac{R^2(f,\theta)}{T_e^2(f,\theta)} S(f,\theta) d\theta df \quad (3)$$

Here, T_e is the ship's response period which contains a Doppler shift due to forward motion. This makes T_e different from the wave period $T = 1/f$.

$$T_e = \frac{\lambda T}{\lambda - TU \cos\theta} \quad (4)$$

where

λ = wavelength

U = ship speed

The zero up-crossing period of vessel motion - the average period between successive upwards movements through its equilibrium position - is defined as:

$$T_0 = \left(\frac{m_0}{m_2} \right)^{1/2} \quad (5)$$

The Gumbel probability distribution was found in experiments

(Bowers, 1989) to define the risk, of points at the bow and stern of the vessel, moving down from its mean position more than a distance d in a stationary sea state producing a root mean square vertical movement σ ,

$$p(\sigma, d) = 1 - \exp \left[- \frac{t}{T_0} \exp \left(- \frac{d^2}{2\sigma^2} \right) \right] \quad (6)$$

Here, t is the length of time the vessel is in a channel section,

$$t = \frac{\text{channel section length}}{\text{vessel speed}}$$

Such a distribution can be expected if the vessel response is linear, which appears to be the case for heave and pitch.

In general, and in the two applications that follow, navigation channels are aligned such that the vessels using them do not experience particularly beamy seas. In these cases rolling is not sufficient to cause quarter points on the keel to experience the largest downward movements. Therefore, we assume points on the vessel at the bow and stern experience the largest vertical movements. The probability p defined by equation (6) is simply the risk of grounding of a given point on the vessel if the mean underkeel clearance, when underway, is equal to d . We make the further assumption that risks at the bow (p_b) and stern (p_s) are independent (they typically have different average movements and periods) leading to a conservative estimate of the total risk of grounding (p_t)

$$p_t = p_b(\sigma_b, d) + p_s(\sigma_s, d) - p_b(\sigma_b, d) p_s(\sigma_s, d) \quad (7)$$

Thus, using UNDERKEEL we can calculate the risk of grounding in waves with a directional spectrum $S(f, \theta)$ using equations (1) to (7).

For determining design criteria for channels, figures such as the expected number of groundings in a year's (or century's) operation are required. This would depend on the volume of traffic through the port and on average bed contact risk to vessels in all wave conditions.

This average risk is found by weighting risks in different wave conditions according to the likelihood of those wave conditions occurring and then summing. In outline, wave prediction in a typical ship response application would involve parameterisation of offshore wave spectra. Using significant wave height, H_s , and mean wave direction, $\bar{\theta}$; a probability function (eg Weibull) is fitted to parameterised offshore wave data. A number of offshore wave spectra describing wave conditions of specified

return period from different directional sectors are constructed and then refracted inshore to positions along the navigation channel by mathematical modelling. Ship responses can then be computed in these inshore waves.

If $p_t(H_s, \bar{\theta}, d)$ is the risk of grounding in the channel in wave conditions with an offshore significant wave height H_s and mean direction $\bar{\theta}$, and $f(H_s, \bar{\theta})$ is the probability density function for those wave conditions, then the average risk of grounding in a transit through the channel with an underkeel clearance d is:

$$P(d) = \int_{\bar{\theta}=0}^{360} \int_{H_s=0}^{\infty} p_t(H_s, \bar{\theta}, d) \cdot f(H_s, \bar{\theta}) dH_s d\bar{\theta} \quad (8)$$

In the applications that follow two approaches to the calculation of safe underkeel allowances are used. In one approach the requirement is assumed to exist that safe passage must be possible in all weather. Having (subjectively) decided on an acceptable risk (P_{acc}) of grounding, equation (8) can be used to find the underkeel allowance (d) for vessel motion in waves that produces that risk

$$P(d) = P_{acc}$$

In an alternative approach a limit can be placed on the wave conditions in which it is safe to transit the channel. This limit must, of course, lead to an acceptable level of channel downtime. In this case the underkeel allowance (d) has to be chosen to satisfy

$$\int_{\bar{\theta}=0}^{360} \int_{H_s=0}^x p_t(H_s, \bar{\theta}, d) f(H_s, \bar{\theta}) dH_s d\bar{\theta} + \int_{\bar{\theta}=0}^{360} \int_{H_s=x}^{\infty} p_t(x, \bar{\theta}, d) f(H_s, \bar{\theta}) dH_s d\bar{\theta} = P_{acc} \quad (9)$$

In the above, the limiting H_s value is x and if the wave height exceeds x when a vessel arrives, passage is assumed to take place after waiting for the wave height to drop to the acceptable level.

In both the "all weather" and "weather window" approaches it is also important to ensure that individual risks to a vessel, as defined by (6) and (7) are acceptable in extreme conditions, eg the 100 year storm for an "all weather" channel and limiting conditions in the case of "weather windows".

4. Case Study I - Dover Strait

The Dover Strait is not a harbour navigation channel, but it poses similar problems for the transit of Very Large Crude Carriers (VLCCs) with draughts of up to 22m carrying oil to Rotterdam. On this north east (NE) bound route charted depths (at lowest astronomical tide) of 27.5m occur in known sand wave areas with a large uncertainty in seabed level.

The planning guide for the NE route (Deep Draught Planning Guide 1985) makes no use of the tide to aid passage (the passage takes about six hours in normal weather so delays due to fog could result in a vessel experiencing low water) and no particular restrictions are placed on weather conditions during passage. This guide recommends an underkeel allowance of 5.7m for a 22m draught VLCC in the central region of the Strait. Given all the factors to be taken into account: vessel movement in waves, vessel squat, negative tidal surges, seabed level uncertainties, the quoted allowances are not obviously safe. As a result the UK Department of Transport approached Hydraulics Research (HR) with a view to independently establishing safe allowances within the Strait. The work at HR involved both mathematical modelling (to predict wave climates and vessel response using UNDERKEEL) and physical modelling (to verify UNDERKEEL).

For wave prediction purposes the deep water NE bound route was divided into eight sections. In each section, storms with return periods of 3, 10, 30 and 100 years from all relevant directional sectors were predicted. Corresponding wave spectra were obtained taking into account local wave generation by winds and refraction around the many sand banks. Similarly, spectra were obtained for swell waves after taking into account refraction. The model used to make these predictions made use of extensive wind records after calibration against measured data from the Sandettie WSW buoy and the Dyck and Varne light vessels. The comparison between measurements and hindcasts from the prediction model showed good correlation provided wave refraction was taken into account.

It was then necessary to obtain ship responses. This was a two stage process. The first stage was done entirely by mathematical modelling using UNDERKEEL in the manner described earlier in this report. Grounding risks were estimated on the basis of these results and critical parameters identified.

In stage two physical model tests were performed to calibrate UNDERKEEL (see section 2.1 of this paper). This calibration showed good correlation between the physical model and UNDERKEEL and it was deemed better to base our definitive risk calculations on calibrated UNDERKEEL responses rather than on purely physical model results. This avoided a very large physical model test programme.

All risk calculations we did were based on a typical VLCC hull form: sensitivity tests carried out with UNDERKEEL having already been carried out in stage one of the study to quantify the effects of varying hull dimensions, ship speed and underkeel clearances.

A feature of the Dover Strait is that depth uncertainties are a greater factor in risk assessment there than they are likely to be in a normal navigation channel. They arise from several causes. Surveying inaccuracies, which are likely to be greater in the open sea. Bed mobility - at certain places sand waves and dunes encroach into the deep water channel, and these constantly move around. Storm surges can reduce grounding risks because those storms causing the greatest vessel movement in the Dover Strait will tend to raise water levels. However, some storms (producing little vessel movement in the Strait) can cause a negative surge and such surges could occur at the same time as swell in the Strait.

We had to modify equation (8) to take account of all these possible depth uncertainties by introducing a probability density function, $g(x)$, expressing the likelihood of depth variations. The probability calculation became:

$$P(d) = \int_{\bar{\theta}=0}^{360} \int_{H_s=0}^{\infty} \int_{x=-\infty}^{\infty} p_t(H_s, \bar{\theta}, d+x) f(H_s, \bar{\theta}) g(x) d\bar{\theta} dH_s dx \quad (10)$$

Using this probability calculation and ship responses from the calibrated model, and adding an allowance for vessel squat and trim underway, the following acceptably safe allowances were obtained:

<u>NE vessel route</u>	<u>HR allowance</u>	<u>Planning Guide</u> (Neth. Navy)
West of the Strait	6.2m	6.5m
	9.5m	6.5m
Central part of Strait	5.7m	5.7m
	5.3m	5.7m
	6.4m	5.7m
East of the Strait	6.4m	6.5m

On the whole, the HR results agree well with the Dutch allowances for the NE bound route. Only in two sections (one west of the Strait and one in the central part of the Strait) does HR suggest a larger allowance. In these sections tankers are exposed to quartering seas, which UNDERKEEL and physical model tests agree

are prone to cause particularly large pitch responses as well as rolling. However, these sections are deep enough not to affect vessel safety.

5. Case Study II - Port Qasim

Port Qasim is a developing port in Pakistan on the Indus Delta. Its approach is by a 12km long outer navigation channel with, until recently, a maintained depth (after allowing for siltation) of 12.4m CD through an offshore sand bar. This outer channel has experienced severe sedimentation problems due to combined wave and current action. Wave heights along the outer channel have been monitored using waverider buoys. Although primarily for sedimentation study purposes, this supply of high quality, frequently sampled wave data from several points along the channel was also of immense help in predicting waves at the site for use in estimating safe underkeel allowances.

In 1987, Port Qasim Authority (PQA) proposed a container facility at the port for handling PANAMAX vessels of up to 12m draught. Such ships would obviously require deepening of the approach channel, particularly for service during the months of the south west (SW) monsoon (May-September) when significant wave heights at the Fairway Buoy can reach over 3.5m which, with spectral peak periods of 13 seconds, will cause considerable vertical vessel movement. The question was how much deeper should the channel be? Hydraulics Research was commissioned to investigate.

Offshore wave predictions were based on visual observations of wave heights and directions by shipping in the Arabian Sea. This was necessary because waveriders do not record wave direction. Predicted wave spectra were then refracted inshore. The waverider records then formed an excellent check on the accuracy of these offshore predictions and the resulting refraction process after allowing for bottom friction. Bottom friction was found to be a significant factor in attenuating inshore wave energy. The calibration against measured data resulted in friction factors that were in the expected range (0.01 to 0.04). Good correlation was achieved between measured and predicted wave spectra at various points along the channel showing that wave height variation along the channel was well predicted.

Having predicted wave conditions, grounding risk calculations were as described in section 3 of this paper. To date, no physical model tests have been authorised for this study so responses are based solely on UNDERKEEL. The hull form used represented a third generation container vessel 207m long sailing at 11 knots. Sensitivity tests were performed to check the effects of underkeel clearance and of vessel speed and dimensions (including testing a 280m long, fourth generation hull, which proved far less vertically mobile than the much shorter version).

Our standard case was chosen for being the one that moved most in Port Qasim wave conditions.

Calculations indicated that, after taking into account allowances for vessel squat, set-down and vertical motion in waves, the maintained depth of the approach channel would need to be increased by at least 4.6m to allow acceptably risk-free all weather operation at high tide in June and July, at the peak of the monsoon. Dredging could be minimised by only deepening the more exposed outer 8km length of the approach channel but it was anticipated the costs involved would still make the scheme unviable.

Instead, the adoption of weather windows was suggested. PQA already had much successful experience of operating waverider buoys, and this experience could be utilised in monitoring wave heights at the seaward end of the channel (which is not visible from the port itself). The following table shows the percentage of time month by month we estimated the channel would be usable if a weather window were introduced for various underkeel allowances for vessel motion in waves (2m was available at high tide in the channel with a declared depth of 12.4m CD after allowing for vessel squat and trim).

Month	u/k allowance for vessel movement in waves (metres)				
	1	2	3	4	5
April	97	100	100	100	100
May	83	96	100	100	100
June	0	2	34	73	89
July	0	0	14	52	83
August	13	33	60	85	100
September	77	91	99	100	100

Thus, deepening the channel by 3m to give an underkeel allowance of 5m (instead of deepening by 4.6m for all weather operations) and using a weather window controlled by a standard waverider would allow almost uninterrupted port operations throughout the year except in June and July. In those months three to five days of disruption of container traffic is expected. This might be more acceptable than the cost of dredging and maintaining an all weather channel.

Also, one effect of deepening the channel would be to change wave refraction patterns; in general, a deeper channel would be expected to refract more waves away from itself, resulting in a calmer sea with less grounding risk and less channel downtime. In practice then, the 83% expected utilisation in July is probably an underestimate.

A further possibility, and one we recommend to PQA, is to measure wave direction as well as height at the channel entrance.

This can be done using a directional wave buoy. Vessel response is very sensitive to wave direction, so fairly high waves from some sectors generate less response than lower waves from other directions. This sensitivity can beneficially be built into weather windows. By allowing operation in higher waves from less sensitive directions, we estimate June-July channel usage can be greatly improved. For example, with just a 3m underkeel allowance and a directional weather window, the channel would be usable 58% of the time in June and July instead of an average usage of 24% for the two months with non-directional wave monitoring.

6. References

- BOWERS, E C (1989). Safe underkeel allowances for vessels in restricted depths. Recent Advances in Hydraulic Physical Modelling, Lisbon, Portugal. NATO ASI Series E Vol 165, Kluwer Academic Publishers.
- Deep Draught Planning Guide. Greenwich Buoy to Europoort for vessels with a draught between 20.7m and 22.0m. Second edition (1985). Published by the Hydrographer fo the Royal Netherlands Navy.
- STANDING, R G (1978). Applications of wave diffraction theory. Int J Num Meth in Engrg, Vol 13, p49.
- VAN WYK, A C and ZWAMBORN, J A (1988). Wave induced ship motions in harbour approach channels. Proceedings of 21st ICCE, Malaga, Spain.

CHAPTER 238

NUMERICAL MODEL OF THE NONLINEAR INTERACTION OF WAVES AND FLOATING BODIES

Michael Brorsen ¹ Henrik I. Bundgaard ²

Abstract

A numerical model for the computation of the nonlinear interaction of water waves and floating large-volume bodies is described. The model works in the time domain and is based on the boundary element method (BEM) with internal generation of the incident waves and absorption of all outgoing waves (internally generated as well as reflected). This procedure makes it possible to simulate long time series of nonlinear wave forces even in case of irregular waves. Drift forces are extracted from the time series by filtering. Steady and slowly varying drift forces are computed in 2D and first order wave forces are computed in 3D.

Introduction

The need for an accurate description of the interaction of nonlinear water waves with floating large-volume bodies has been increasing during the last decade. The forces acting on a floating body are generally divided into three components:

- forces at wave frequencies.
- low-frequency forces caused by e.g. wave groups.
- steady components of the forces.

In most (if not all) commercial models today the wave-body interaction is based on linear theory in the frequency domain. This approach leads normally to accurate estimates of the forces at wave frequencies. The estimates of the two nonlinear components of the forces are, however, usually less accurate and only available up to second order.

Especially the low-frequency force is difficult to estimate from the linear theory. See e.g. Standing (1981). These forces are denoted slowly varying drift forces in this paper.

¹University of Aalborg, Sohngaardsholmsvej 57, DK-9000 Aalborg, Denmark

²Danish Hydraulic Institute, Agern Alle 5, DK-2970 Hørsholm, Denmark

All nonlinear effects which can be described by potential theory can be taken into account by the approach presented here. This is achieved by the fulfilment of the nonlinear boundary conditions at the free surface and integration of the nonlinear pressure forces up to the free surface.

Isaacson (1982) applied a very similar approach, but it was not possible to simulate long time series. Scattered waves were reflected back into the domain from that part of the boundary, where the incident waves were generated. In order to avoid this problem either a very long computational domain or a spatially periodic boundary condition has been applied.

The application of a long domain is very costly as it generates a large system of equations and the spatially periodic boundary condition is only an approximation in most cases with a body of arbitrary shape.

If the incident waves are generated inside the computational domain all waves reaching the domain boundaries are per definition outgoing waves. At the open boundaries these waves can be absorbed and the wave field inside the domain is not corrupted by scattered waves reflected at the boundaries. This approach was introduced for the BEM method by Brorsen and Larsen (1987) and it makes it possible to simulate time series as long as necessary to determine the slowly varying drift forces as well as the steady drift force.

It should be stressed that this approach is applicable in both 2D and 3D models.

The 2D version of the model is used to calculate the drift forces on a rectangular body in case of regular waves and beating waves.

The 1. order wave forces on a barge are calculated by the 3D version of the model.

Theoretical formulation

Fluid flow

Irrotational flow of an incompressible and inviscid fluid is considered. Therefore a velocity potential φ exists, giving the fluid velocity \vec{v} as

$$\vec{v} = \nabla\varphi \quad (1)$$

The incident waves are generated by a vertical source distribution situated between the floating body and the open boundary of the domain.

The time varying volume flux density of the source distribution is denoted q^* , and the velocity potential φ must satisfy the Poisson equation

$$\nabla^2\varphi = q^*(\vec{\zeta}, t) \quad (2)$$

where $\vec{\zeta}$ is the position vector of the source and t is the time.

Brorsen and Larsen (1987) has described how q^* should be varied in space and time in order to generate a specified incident wave field.

On the free surface the nonlinear kinematic and dynamic boundary conditions are fulfilled, i. e.

$$\frac{\partial \varphi}{\partial n} \cdot \frac{1}{\cos \beta} = \frac{\partial \eta}{\partial t} \quad \text{at } z = \eta \tag{3}$$

$$\frac{\partial \varphi}{\partial t} + gz + \frac{1}{2} (\nabla \varphi)^2 = 0 \quad \text{at } z = \eta \tag{4}$$

where β is the angle between the outward normal to the free surface and the vertical direction, g is the gravitational acceleration, z is the level of the point.

On the sea bed the no flow condition is used,

$$v_n = \frac{\partial \varphi}{\partial n} = 0 \quad \text{at } z = -h \tag{5}$$

On the surface of the floating body it is assumed that the body and the fluid have the same velocity component in the direction of the normal to the body, i.e.

$$\frac{\partial \varphi}{\partial n} = \vec{v}_b \cdot \vec{n} \quad \text{on } S_b \tag{6}$$

where \vec{v}_b is the velocity of a point on the surface of the body and S_b denotes the instantaneous wetted surface of the body.

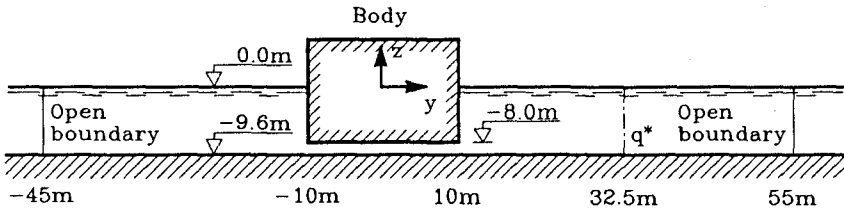


Figure 1. Sketch of 2D wave channel and floating body. Still water.

The domain is enclosed by vertical open boundaries, see Fig 1., where all outgoing waves are absorbed. The absorption is modelled with the radiation condition:

$$\frac{\partial \varphi}{\partial t} = -c \frac{\partial \varphi}{\partial n} \tag{7}$$

where c is the phase velocity. The radiation condition is nonreflecting in case of waves of constant form propagating out of the domain. This boundary condition is, however, found to be adequate also in case of beating waves provided that the wave periods do not deviate substantially from each other, i.e. the rate of change in form is rather small.

The forces from the fluid on the body is found by integration,

$$\vec{F}_p = \int_{S_b} p \vec{n} dS \tag{8}$$

where S_b denotes the instantaneous wetted surface of the body and p the pressure. The pressure is obtained from the nonlinear Bernoulli's equation:

$$\frac{\partial \varphi}{\partial t} + gz + \frac{1}{2} (\nabla \varphi)^2 + \frac{p}{\rho} = 0 \tag{9}$$

where ρ is the density of the fluid.

We need to calculate the pressure at points moving with the velocity \vec{v}_{point} . In that case, see e.g. Brorsen (1989), equation (9) reads:

$$p = -\rho gz + \rho \frac{d\varphi}{dt} + \rho \vec{v}_{point} \cdot \nabla \varphi - \frac{1}{2} \rho (\nabla \varphi)^2 \tag{10}$$

The boundary value problem is transformed into an integral equation by the application of Green's 2. identity.

Thus the potential at point P positioned at \vec{x} is given by

$$\alpha \cdot \varphi(\vec{x}) = \int_S \left(\varphi(\vec{\xi}) \frac{\partial G(\vec{x}, \vec{\xi})}{\partial n} - G(\vec{x}, \vec{\xi}) \frac{\partial \varphi(\vec{\xi})}{\partial n} \right) dS + \int_A q^*(\vec{\zeta}, t) G(\vec{x}, \vec{\xi}) dA \tag{11}$$

where S is the boundary of the domain A , $\vec{\xi}$ denotes the position vector of a point on the boundary, $G(\vec{x}, \vec{\xi})$ is a Green function and α is a constant.

In case of constant water depth and \vec{x} is situated on the boundary of the domain, we use the following Green function:

$$\text{2D model : } \alpha = \pi \text{ and } G(\vec{x}, \vec{\xi}) = \ln |\vec{\xi} - \vec{x}| + \ln |\vec{\xi} - \vec{x}_r|$$

$$\text{3D model : } \alpha = -2\pi \text{ and } G(\vec{x}, \vec{\xi}) = \frac{1}{|\vec{\xi} - \vec{x}|} + \frac{1}{|\vec{\xi} - \vec{x}_r|}$$

where \vec{x}_r is the position vector of the point which is the reflection of point P into the sea bed.

Motions of the body

In 3D the body has the 6 degrees of freedom shown in Fig. 2. Only 3 degrees of freedom are present in 2D, namely sway, heave, and roll.

The motions of the body are found from the equations of motion expressed in a coordinate system with origo at the center of gravity (CG) and fixed to the body, i.e.:

$$\sum \vec{F}_{external} = m(\vec{v}_G + \vec{\omega} \times \vec{v}_G) \tag{12}$$

$$\sum \vec{M}_{external} = \bar{I} \frac{d\vec{\omega}}{dt} + \vec{\omega} \times (\bar{I} \vec{\omega}) \tag{13}$$

where \vec{v}_G is the velocity of CG and $\vec{\omega}$ is the angular velocity of the body. \bar{I} is the matrix of moment of inertia and m the mass of the body. $\vec{F}_{external}$ and $\vec{M}_{external}$ denote external force and moment with respect to CG, respectively.

The external forces are pressure forces from the fluid, see equation (8), and e.g. forces from moorings, fenders and wind.

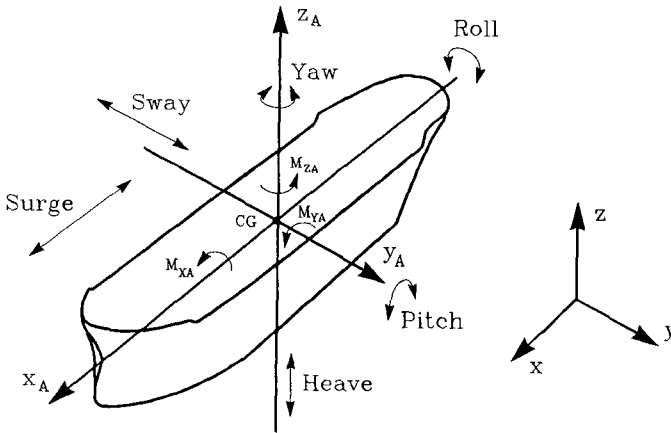


Figure 2. Definition sketch of surge, heave, roll, sway, pitch and yaw.

Numerical formulation

A time-stepping technique is used, where the flow problem is solved at each time level. Time-dependent terms are discretized as finite differences, and time step k is indicated with k as a superscript, i.e. φ^k denotes the velocity potential at the time $t = k\Delta t$, where Δt is the time step.

The boundary is discretized into N linear (in 2D) or plane (in 3D) elements and the variables φ , $\partial\varphi/\partial n$, p and η are calculated at points situated at the centroid (the node) of each element. It is, furthermore, assumed that the variables are constant over each element.

The pressure force on the body is calculated by the discretized version of equation (8), i.e.

$$\vec{F}_p = \sum_{j=1}^N p_j \vec{n}_j dA \tag{14}$$

where index j refers to a element on the body, p is the pressure at node j and \vec{n} is the unit, outward normal to the body.

Note that equation (14) is exact if the pressure distribution over each element is linear.

It is now assumed that the flow, the velocity of the body and the position of the boundary are known at time step k . The unknown shape of the boundary at

time step $k + 1$ is estimated by a linear extrapolation, see Isaacson (1982). The first estimate of the flow at time step $k + 1$ is found by application of equation (11) at each node. This gives N equations, which can be solved together with the discretized boundary conditions, see Brorsen and Larsen (1987). After the solution φ^{k+1} and $(\partial\varphi/\partial n)^{k+1}$ are known at all nodes. The pressure $p^{k+\frac{1}{2}}$ and the elevation η^{k+1} are known at the nodes on the body and the free surface, respectively.

When the values of $p^{k+\frac{1}{2}}$ are known, updated values of forces and moments from the fluid are calculated. This leads to the calculation of improved estimates of the position and velocity of the body by use of the discretized versions of equation (12) and (13).

Hereafter the free surface is updated according to the η^{k+1} -values, and the N equations are set up and solved once more. In this study only insignificant changes were observed if the procedure was repeated a 3. time.

In all simulations the fluid is at rest at time $t = 0$.

Numerical example, 2D

The objective of this section is to show that it is possible to calculate the nonlinear wave forces on both fixed and floating bodies so accurately that the drift forces can be obtained by filtering of the raw force time series.

Rectangular body exposed to nonlinear regular waves

In this example a rectangular body with beam $b = 20$ m and draft $d = 8.0$ m is exposed to regular waves generated at $y = 32.5$ m.

The drift forces on both a fixed body and a freely floating body are calculated.

The incident wave height H is varied between 0.2 m and 0.9 m and the applied wave period is constant $T = 8.0$ sec corresponding to a 1. order wave length $L = 69.8$ m.

The water depth is 9.6 m and the two open boundaries are radiation boundaries. See Fig. 1. The boundary is discretized into 41 elements, where the element length near the open boundaries is 5.0 m decreasing to 2.0 m on the body. The time step is $\Delta t = 0.5$ sec corresponding to only 16 steps per wave period.

The steady drift force on the body is calculated by a low pass filtering of the total lateral force found by equation (14). The numerical results are in Fig. 3 compared with the theoretical second order drift force derived by Longuet-Higgins (1977):

$$F_{drift} = \frac{1}{16} \rho g \left(1 + \frac{2kh}{\sinh 2kh} \right) (H_i^2 + H_r^2 - H_t^2) \quad (15)$$

where $k = 2\pi/L$ and H_i, H_r, H_t are the incident, reflected, and transmitted wave heights, respectively.

H_r and H_t are estimated by Fourier analysis, and it is found that the numerical damping is insignificant, i.e. $H_i^2 \approx H_r^2 + H_t^2$.

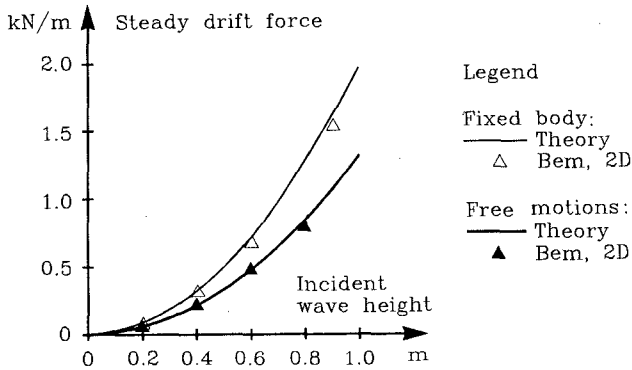


Figure 3. Comparison of calculated and theoretical steady drift force, 2D model.

From Fig. 3 is seen that the agreement between the numerical results and the theoretical solutions are excellent even though a steady drift force is only a few percent of the amplitude of the total lateral force (0.6% if $H_i = 0.20$ m in case of fixed body). Note that the floating body is more transparent to the waves than the fixed body.

Rectangular body exposed to a pair of nonlinear, beating waves

The mean drift force and the slowly varying drift force on a fixed body are calculated.

The domain and the body are the same as described in the preceding example. The two beating waves have each a wave height of 0.4 m and the periods are 8 and 10 sec, respectively. This gives a wave group period of 80 sec and the length between the nodes of the group is 302 m. The corresponding slowly varying drift force has a period of 40 sec.

In case of beating waves one must be careful to generate the correct bounded long wave in order to avoid spurious free long waves, see Stig Sand (1982). In this study this is done by including the velocities corresponding to the bounded long wave when the source distribution is calculated.

Initially it was checked that the correct bounded long wave (amplitude and phase) was created and that only insignificant reflection took place at the radiation boundary. This was done by calculation of the beating waves in a domain without the body. The bounded wave amplitude and phase were found by filtering of the elevation time series at several stations. Excellent agreement was found with the theoretical results, probably because the phase velocities of the short and long waves do not deviate to much in case of shallow water.

Note, however, that in a deep water situation, the larger deviations in phase velocities are expected to create a significant reflection on the radiation boundary. This will result in both wrong amplitude and phase of the long wave.

The slowly varying drift force on the body and the corresponding surface elevation 1.5 m upstream of the body are shown in Fig. 4. This drift force is found by application of a filter with a cut-off frequency of 0.04 Hz .

The mean value of the drift force is calculated to -0.59 kN/m . Note that the mean value of the drift force only deviates 2% from the theoretical value, -0.60 kN/m , which is the sum of the steady drift forces corresponding to the individual regular waves.

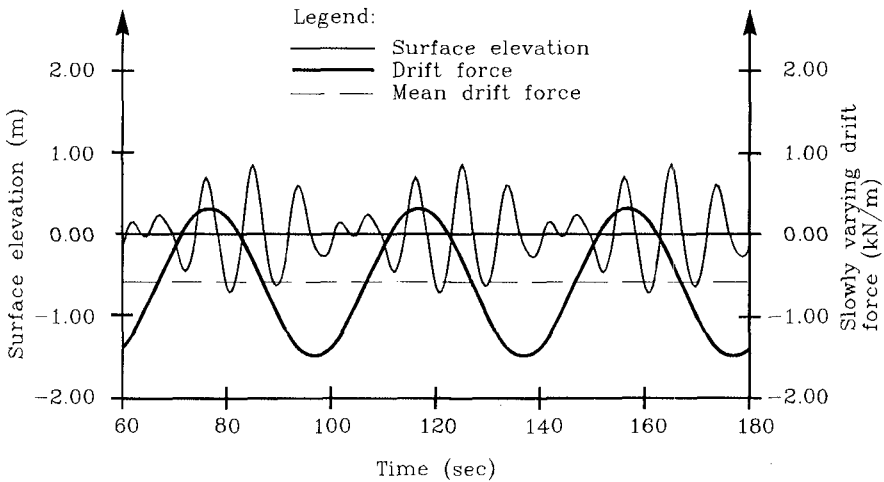


Figure 4. Slowly varying drift force on a fixed body. 2D model.

From Fig.4 is seen that the maximum drift force (negative) appears later than the maximum elevations in the wave group.

According to Newman's approximation the maximum drift force (negative) should appear at the same time as the max. elevations in the wave group. However, when the effect of the surface gradient of the bounded long wave is taken into account, it must be expected that the maximum drift force appears later than the maximum surface elevations and increase in magnitude.

The amplitude of the slowly varying drift force is seen to be approx. 30% bigger than the corresponding value according to Newman's approximation, which in this case is equal to the mean drift force.

A full verification of the computed results, e.g. by comparing the result with results from a theoretical 2. order model, see Faltinsen (1979), has not been made so far.

Linear 3D-Model (BEMSHIP)

At the Danish Hydraulic Institute a 3D model has been developed. This model calculates the motions in six degrees of freedom of a floating body. So far this model is based on the linearized equations, but non-linear mooring forces and fender forces can easily be included.

3D ship movements calculated by BEMSHIP are in the following compared to some test values, see Östergaard (1987).

The 'ship' selected is a rectangular barge representative for a vessel frequently used by the offshore industry as a lay barge or crane vessel. The main particulars for the barge are listed in Table No. 1 below.

Length	(m)	150
Beam	(m)	50
Draft	(m ³)	10
Displaced volume	(m)	73750
C.G. above base	(m)	10
Transverse gyradius	(m)	20
Longitudinal gyradius	(m)	39
Vertical gyradius	(m)	39
Natural heave period	(sec)	10.4
Natural pitch period	(sec)	12.1
Natural roll period	(sec)	9.4

Table 1. Particulars of rectangular barge.

The discretization of the barge can be seen in Fig. 5.

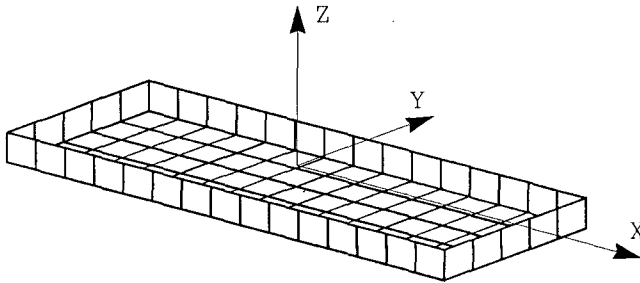
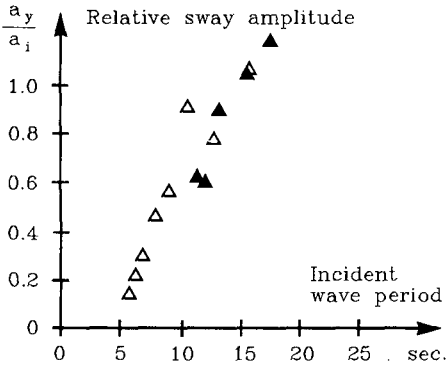


Figure 5. Sketch of wetted surface of the barge. xy -plane situated in SWL.

In the following calculations the barge is floating freely in all six degrees of freedom and it is exposed to regular, linear beam waves. The incident waves are generated within the calculation domain.

The sway, heave and roll motion transfer functions are plotted in Fig. 6-8, where they are compared to the experimental values obtained by Östergaard.



Legend:
 Δ Experiment
 \blacktriangle Bemship

Figure 6. Comparison of calculated and experimental sway motions of the barge in beam waves. a_y and a_i are the amplitude of sway and the incident wave, respectively.

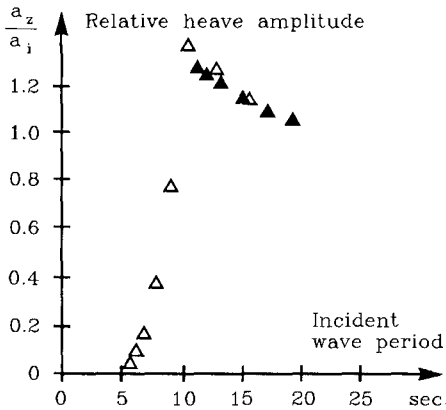


Figure 7. Comparison of calculated and experimental heave motions of the barge in beam waves. a_z and a_i are the amplitude of heave and the incident wave, respectively.

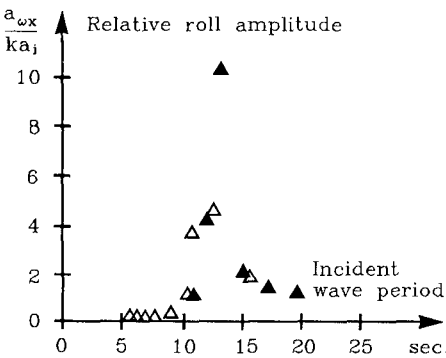
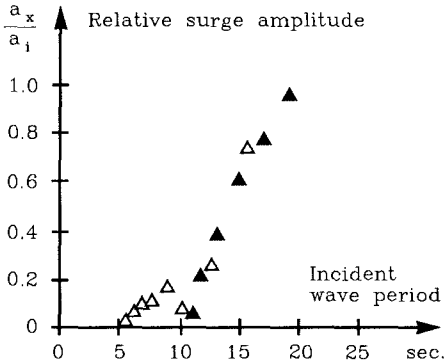


Figure 8. Comparison of calculations and experimental roll motions of the barge in beam waves. a_{wx} and a_i are the amplitude of roll and the incident wave, respectively, k is the wave number $k = 2\pi/L$.

The barge is again floating freely, but is now exposed to regular, linear head waves.

The surge, heave and pitch motion transfer functions are plotted in Fig. 9-11, where they again are compared to the experimental values obtained by Östergaard.



Legend:

- \triangle Experiment
- \blacktriangle Bemship

Figure 9. Comparison of calculated and experimental surge motions of the barge in head waves. a_x and a_i are the amplitude of surge and the incident wave, respectively.

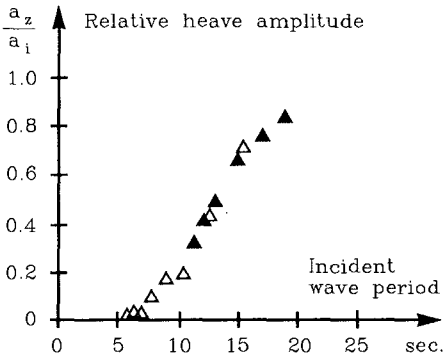


Figure 10. Comparison of calculated and experimental heave motions of the barge in head waves. a_z and a_i are the amplitude of heave and the incident wave, respectively.

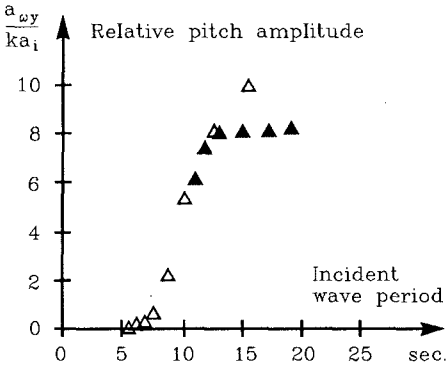


Figure 11. Comparison of calculated and experimental pitch motions of the barge in head waves. a_{wy} and a_i are the amplitude of pitch and the incident wave, respectively, k is the wave number $k = 2\pi/L$.

When looking at the calculated and experimental measured barge motions in Figs. 6-11, a good agreement is found despite the rather low spatial resolution ($10 \cdot 10 \text{ m}^2$) of the body. Wave periods lower than 11 sec. are not used, as a spatial resolution of at least 16-18 elements per wave length is needed.

Conclusion

A new approach to the calculation of nonlinear drift forces on large bodies is reported. The numerical model is working in the time domain and the drift forces are calculated by filtering of long time series of the nonlinear lateral wave force acting on the body.

The nonlinear 2D version of the model is used to calculate steady drift forces as well as slowly varying drift forces.

Excellent agreement is found between the numerical results and the corresponding analytical solutions when the steady drift force (regular waves) and the mean drift force (beating waves) are considered.

In case of beating waves the preliminary results indicates that the amplitude of the slowly varying drift force may be somewhat underestimated by Newman's approximation.

An improved modelling of the absorption of the wave energy at the open boundaries is, however, probably required if the forces corresponding to deep water, irregular waves are to be calculated satisfactorily.

The linear version of the 3D model BEMSHIP is shown to yield good estimates of the motions of a freely floating barge exposed to head or beam waves.

References

- Brorsen, M., 1989. *Numerical Model of the Nonlinear Interaction of Waves and Fixed Bodies*. Proceedings, IAHR XXIII Congress, Ottawa, Canada.
- Brorsen, M. and Larsen, J., 1987. *Source Generation of Nonlinear Gravity Waves with the Boundary Integral Equation Method*. Coastal Eng. 11 : 93-113.
- Faltinsen, O. M. and Løken, A. E., 1979. *Slow drift oscillations of a ship in irregular waves*. Applied Ocean Research, Vol. 1, No. 1 : 3-13.
- Isaacson, M. de St. Q., 1982. *Nonlinear Wave Effects on Fixed and Floating Bodies*. J. Fluid Mech. 120 : 267-281.
- Longuet-Higgins, M.S., 1977. *The mean forces exerted by waves on floating or submerged bodies with the applications to sand bars and wave power machines*. Proc. R. Soc. Lond. A : 463-480.
- Standing, R.G., Dacunha, N.M.C and Matten, R.B., 1981. *Slowly-Varying Second-Order Wave Forces: Theory and Experiment*. NMI report R138, National Maritime Institute, UK.
- Östergaard, C. and Schellin, T. E., 1987. *Comparison of Experimental and Theoretical Wave Motions on Floating and Compliant Structures*. Applied Ocean Research, Vol. 9, No. 4 : 192-213.

PART VIII

Case Studies



CHAPTER 239

RIA DE FOZ: WORKS BEHAVIOUR

DIEZ, J.J. Catedrático de Oceanografía en la E.T.S.I. Caminos C. P. Universidad Politécnica de Madrid
ESCOBAR, V.A. Ingeniero de Caminos C. y P. Responsable de proyectos en el Centro de Estudios de Puertos y Costas C.E.D.E.X. Madrid.

INTRODUCTION

When, in the previous Conference, a paper was presented and published (1) aboarding the problems and solutions in a ria of the West End of the Spanish Cantabrian coast, the works of the solution project had just been finished (JUN 1988), so that very few data had been obtained about their behaviour. Additionally, the systematic survey of the dynamics in the ria had been initiated but not finished, not even in the field data collecting, therefore the hydrodynamic and morphodynamic model obtained to implement the project, having explained rather satisfactory all the known coastal and estuary process and changes, only was a qualitative approximation. Nevertheless it was in agreement with a very complete methodology of coastal processes analysis (2) and good enough to justify some singular circumstances: one of them refers to the increasing sandy filling of the ria what, like in all Cantabrian ones and probably like in many other bights -glaciars, like in New England, U.S.A., and Scotland, or structural, like in the rest of the Cantabrian and Bretagne (France),- has been principally filled with littoral materials, without any significant contribution of the respective rivers, whichever its size; other one, to the spit nature and genesis of the barriers of all the Cantabrian rias; they have been generated by the longshore transport through a "negative geometric singularity" (3) more than by onshore-offshore equilibrium and, consequently the migration of the tidal inlets is downdrift, but respect to the local drift, though it could appear to be updrift.

As the rias practically are the only shelter areas in the Spanish Cantabrian coast, the harbours have been initially established in them and even one or more small fishing harbours remain in each of them at present, so that the sandy filling processes, together with the increasing size and draught of the ships has become a meaningful problem in them. In the case of the Foz ria the problem had become even more acute because

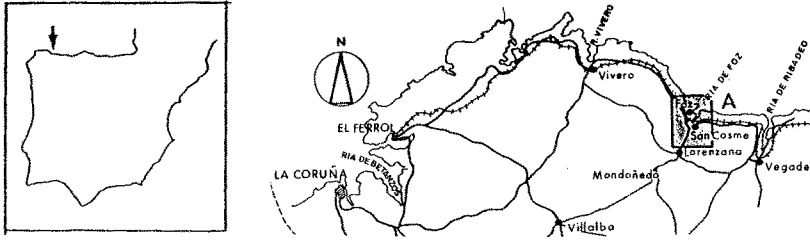


Fig. 1
Location

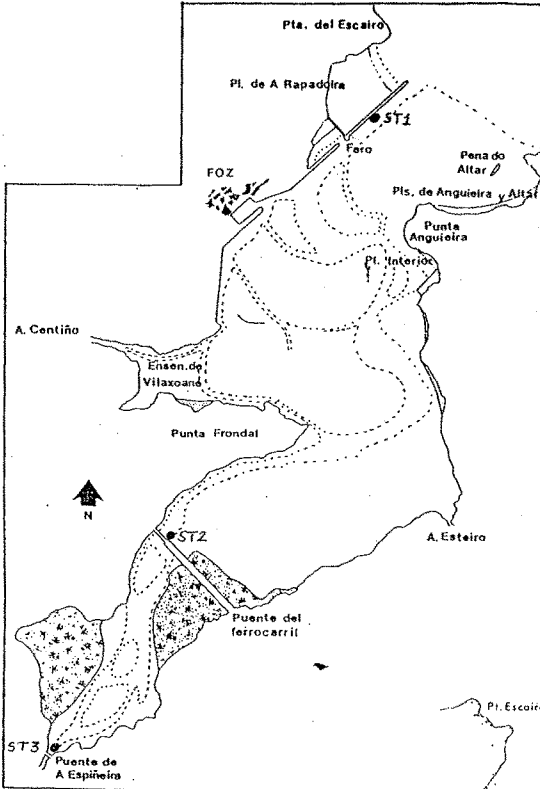
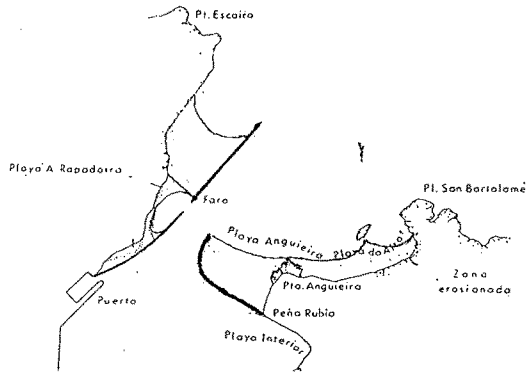


Fig. 2
designed project



it affected extremely the stability of the channel entrance, so that a jetty had to be constructed, but, being a unique jetty facing the spit end, when it was extended landward at the other side of the gorge, the fast erosion of the spit (just in the winter of 1977-78) was induced, the problem has both extended to the beaches around, which have begun to suffer erosion, and accentuated in the ria, which has increased several times the rate of filling.

The project, described two years ago, tried to be a solution for both aspects of the problem: the regeneration and protection of the beaches and the lessening of the process of filling of the interior of the ria, but subordinating the later to the former.

The aim of this paper is to analyze the data obtained since then to check the initial hypothesis and the behaviour of the works.

2. DESCRIPTION OF THE WORKS

The construction of the project defined two different kind of works: one of them, the basic one, was the artificial nourishment of the eroded beaches and spit up to about 275.000 m³, the minimum volume was supposed to guarantee the posterior stability of the system; the other, the construction of a jetty to support the spit-sand and to lead the interior channel, this jetty might, likely have not been necessary if the nourishment had been developed during the summer and accomplished in a short term; nevertheless this last condition would have been very unlikely to happen.

The sands for the designed nourishment had to be obtained exclusively from the interior of the ria, from a delimited area, which was supposed to have been overfilled since the erosion of the spit-barrier and whose sands were not only compatible but equal to the remaining sands of the beaches; our previous sedimentological surveys show the identity not only in the grain-size distribution but in the minerals content too. and it had been projected to be laid down adequately distributed along all the eroded area to obtain the best effect, taking into account the direction of the local transport (westward) and trying to minimize it. The bulk of sand was determined from the designed final form of the beaches and barrier so that the sand had to be laid rather homogeneously down, half about along the beaches (Altar and Anquieira) to partially replenish them, and half about in the spit, to regenerate it.

The jetty was designed shorter than the supposed necessary one to keep the channel clean, trying more to behave like a hook-groin than to constitute a real jetty, and being only the initial stretch of the final

likely necessary complet jetty, whose seaward stretch was not considered at that moment nor was designed. A mere arc of circle, ending the designed jetty was considered enough to behave like a suport-groin. The first strait section was designed aproximately parallel to the longshore transport from the Angueira point towards the channel; and it was short designed too, leaving so a wider than the adequate gorge for the channel. Two kind of reasons have imposed this design: the first and principal one was that no sufficient previous research had been developed to accurately determine the most convenient width for the channel (distance between jetties). The second one was derived from the different but convergent responsibilities of several administrative authorities; Coastal authorities (central) has the responsibility of shore protection, had assumed the regeneration of the beaches and financed the project and other studies in the ria; harbour (authonomic) authority has the responsibility of the harbour facilities; and township (local) authority was afraid that the project could affect the opposite beach of the "Rapadoira". Being urgent the regeneration of the beaches, this solution was assumed to guarantee none administrative delay was going to be produced. And, at the same time, it compatibilized its efficiency with a minor foreseeable destruction when the posterior extention and adaptation of the jetty ought to be decided, once the most adequate width between jetties could be defined for the outlet.

During constructions (September 86-June 88), coastal authorities decided to enlarge the hook stretch of the jetty 30 meters aproximately and to increase the volume of nourishment up to 350.000 m³; some differences between the project bathymetry (Aug. 1985) and the one for planning work (Nov 86) seemed to justify the last decission, supposing mistake in the former.

Nearly all the sands obtained from the interior of the ria have been pumped down by the jetty and, later, distributed on land by means of dumpers, bulldozers, etc. The accretion of the upper part of the beaches seemed to be minor than the theoretically pumped sand; so the constructor decided to take the sands of the tidal plane (fig 3). They supposed that part of the pumped sand was moved by water. The authors of this paper claimed against this practice without any possitive result.

3. SURVEYS AND MONITORING.

A complete series of compaigns of observation has been developed since August-86 to Spring-89 as surveying the dynamics of the ria, but the analysis of

some of the data has not been completed yet.

On other hand, a monitoring program of cross profiles has been developed during and after the construction of the works. Related to the first program, the maritim weather of this area permits to stablish four annual seasons but the storms are randomly distributed along winter and springtime, in such a way that spring equinox happens at the end of the stormy period and the fall-equinox happens before it begins; therefore the two annual survey compaigns have been developed around equinoccial terms, just before and during the spring and fall tides, which happen here in the later relative maxima immediately anterior to every equinoccial date; just before every maximum, a minimum of the astronomical tide happens, so that the largest and the smallest annual tides have been surveyed with this schedule. The data obtained in every campaign have been the following:

- a. Flood and ebb currents (maximum and minimum) have been measured in different cross-sections of the interior channels and in the gorge, and in several pints of each cross-sections.
- b. Tide levels have been continuously registred in two meaningfull points of the inner part of the ria and in a third one close to the gorge of the inlet (formerly in the closest basin of the harbour and lately by the Rapadoira jetty); the two former points are respectively around the middle and the end of the ria and coincident with two narrowness caused by embankments and bridges built for railway and the highway crossing the ria.
- c. the bathymetries of both the inner and outer (here not always extended under low tide) areas of the ria and the long cross-profiles in front of the beaches, have been as accurately surveyed as possible every season and compared to the previous references.
- d. Sedimentological analysis including organic material containt, percentage of carbonats and grain size distribution have been surveyed in all the shoals and beaches.

Besides: 1. Once and for all a more complete sedimentological survey, including mineralogical analysis has been done afecting to the ria and the rest of the shore between the rias of Vivero and Ribadeo. 2. An ecological survey, completed with a more ambitious research (4) have been developed before the construction (1984-1986), but no posterior observation could be done because of the lack of financial support. 3. And a very frequent survey of the beaches and spit cross-profiles has been developed by the coastal authorities as a monitoring work during the priod of construction (1986-88) though unfortunately these profiles were short, not having been extented farer

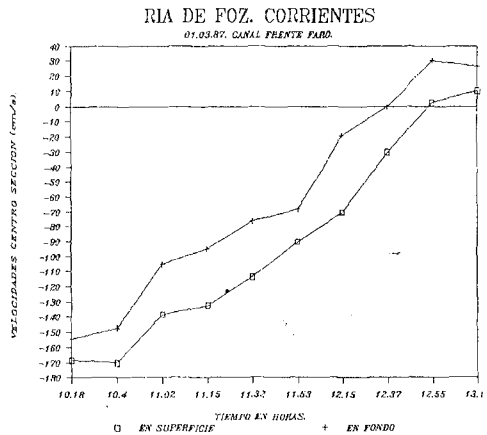
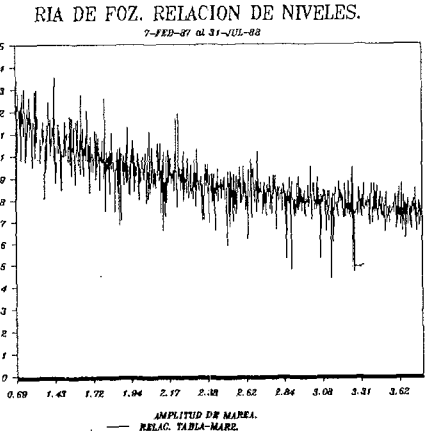
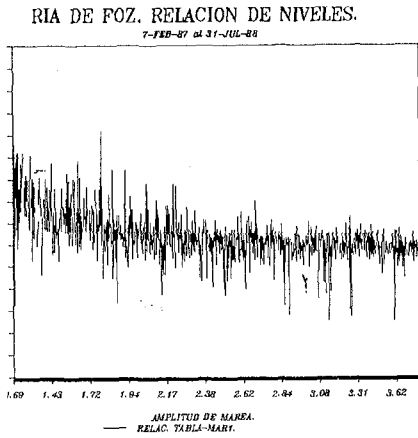
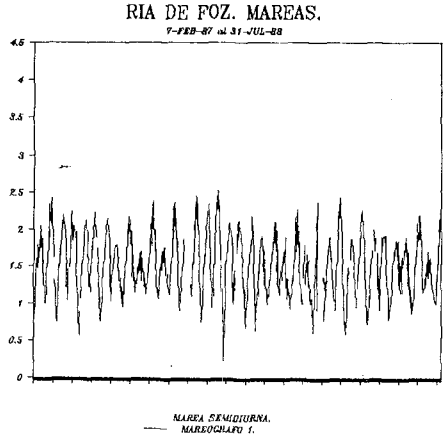
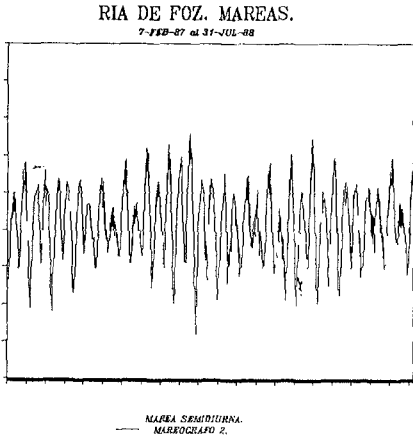


Fig. 3, 4, 5, 6 y 7
Tides and currents

than the low see level.

For this paper not all these data were equally outstanding and, unfortunately, not all the relevant ones could be completely analysed. On the other hand study of littoral dynamics developed for the project and described in (1) has been assumed in the following discussion as related to the winds, wind-waves and littoral transport. But some few considerations must be done:

a) Wave regimes estimated from the visual observations seem to be only roughly accurate and has some unacceptable distribution of the calms. b) Hindcasting wave regimes seem to be much more accurate but their use in estimating the littoral transport appears very problematic here because of the extreme high power of the storms (at least using the C.E.R.C. formule). It has been realized that above a certain value of the wave energy (or height) the estimated longshore transport rate became roughly high, as under a certain value they are too low. c). In any case, the littoral drift is much less than the potential littoral transport because of the lack of materials and the steepness of the platform. d) Whatever the estimation method the net littoral transport and drift are eastward seaside in front of the mouth headlands (Escairo and San Bartolome points), but both of them are westward in front of the Altar and Angueira beaches, landside between the points, over all with high tide levels of the sea. And the mouth is extremely short and narrow to permit an accurate reflection-refraction-diffraction model.

3.1 Tides

Between March and July 1987 a mareograph was located in the harbour of Foz. Continuous data was registered in this point, being the most relevant results these that follow: The maximum amplitude registered was 3.9 m. faced to 3.67 m. in the same date, calculated by the Tables of Tides published by the "Centro Hidrografico Nacional" related to Gijon harbour and corrected to Foz.

The maxima negative differences (bigger in the mareograph than in the Tables) and positive are shown in the next table:

	MAX. DAILY DIFFERENCE		MAX. MONTHLY AMPLITUDE
	+ DIF	-DIF GAUGE	TABLE GIJON
March	0.33	-0.42 3.9	3.83
April	0.26	-0.44 3.65	3.64
May	0.14	-0.43 3.5	3.58
June	0.18	-0.42 3.5	3.47
July	0.09	-0.31 3.7	3.62

An estadistical analysis of the data shows that the probability of a tide-amplitude differing of the one calculated by the Tables in less than 10 cm. is about 65 %, between 10 and 20 cm. 21 % and more than 20 cm. 14 % being the difference bigger than 30 cm only in 4 % of the tides. Considering a posible measuring error of about 10 cm. (the mareograph is graphic), the correlation between the meassures and the Table calculations can be defined as good. The observed differences can be attributed to the meteorological tide and the interferences principally caused by the flow of the river Masma. A maximum of about 50-60 cm. has been estimated for the meteorological tide. The two other mareographs mentioned in a paragraph above were located in two sections in the inner part of the ria (in the railway and the highway bridges), both were registrering tide-levels between February 1987 and July 1988. figs 3,4

The relationships between tide amplitudes in gauges 1 and 2 are very stable when the amplitude in the mouth of the ria is higher than 1.75 m. and do not vary too much with minor amplitudes, this relationship is not bigger than 1 in any case. However, between the gauge 2 and 3 (or the tables) the mentioned relationship is higher than 1 for amplitudes minor than 1.75 m. in the exterior, that means that there is a noticeable steepness of the tide in some special cases (Mehta, Mc. Manus). The tidal prism is in these circunstances bigger than the one calculated without any level-gradient along the ria. The opposite occurs when the amplitudes are bigger; so the tidal prism is more delimited than the prism calculated in previous phases of the study, (aproximately 15 % bigger for little amplitudes and 10 % minor for the higher ones).

3.2 Currents

Since 1986 some campaigns has been made; currents has been measured in several points of the ria, especially in the gorge cross-section, in the railway and highway bridges, and in the main ebb-channel. The velocities in the gorge have had a maximum of about 170 cm/s in ebb equinoctial tide and a minimum of 75 cm/s in neap tide. After the construction of the jetty the velocities have increased in about 30 cm/s for the maxima and 10 cm/s for the minima. The other sections have practicaly maintained the maxima and minima after the contructions (60 cm/s and 30 cm/s respectively for the highway and, 50 cm/s 30 for the railway).

3.3 Several bathymetries of the ria were used: 1967, March 1985, September 1986, March 1987, September 1987, September 1988 (partial) and September 1989 (partial).

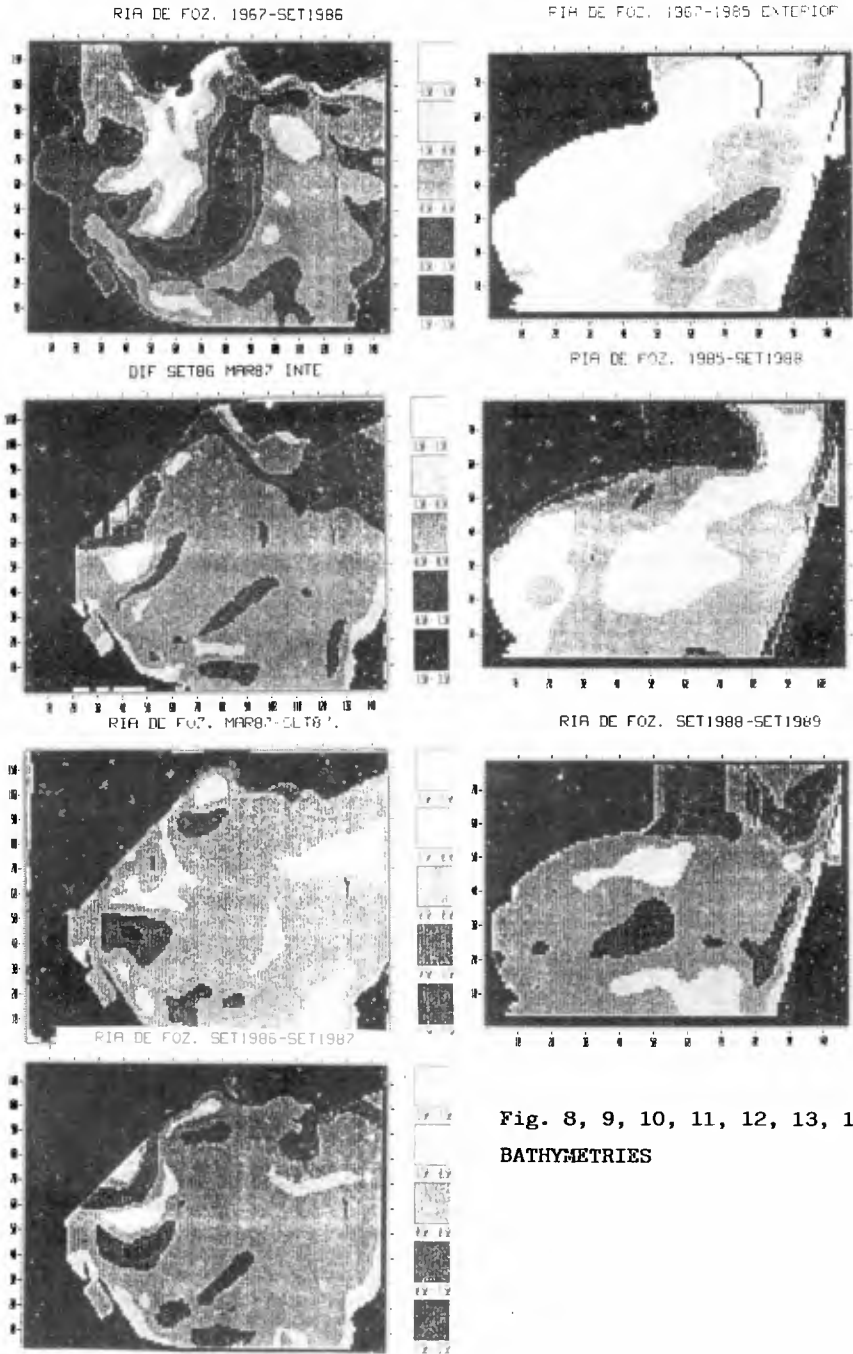


Fig. 8, 9, 10, 11, 12, 13, 14
BATHYMETRIES

in the inner part of the ria and: 1967, August 1985, September 1988 and September 1989. From 1985 to 1989 in the outer part, 22 cross profiles has been taken 17 times.

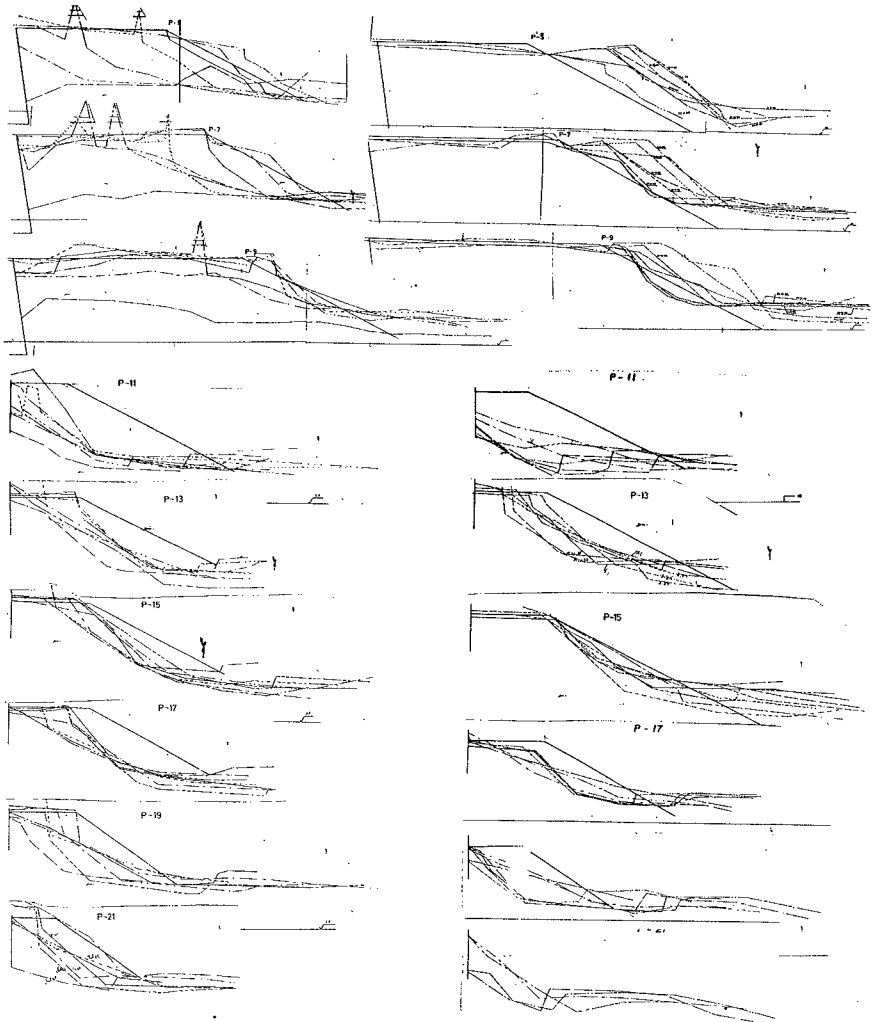
Comparing the inner bathymetries (figs 8-11) it may be noticed that the rate of filling of this area has increased after the erosion of the old natural spit (barrier); during the construction a local reduction of sand is noticeable, undoubtedly related to the sand dredged for nourishment. After the construction of the artificial barrier the rate of filling is unnoticeable from the bathymetries and may be estimated in about 12.000 m³/year, locally by the end of the jetty, part of the filling seems to have passed in front of the end of the jetty and the rest through it because its impermeability has not been appropriately got. Comparative analysis as a calcul permit estimate in about 10.000 m³/yr and in about 80.000 m³/yr the rates of filling respetively before and after the destruction of the natural barrier in March 1978.

Comparing quantitatively outer bathymetries (figs 12-14) it may be shown: 1. A strong erosion has been produced from 1967 to 1985 (it has been visually observed that the process began after 1978), of at least 420.000 m³. 2. The bathimetrie of the project (Aug. 1985) was allright, the difference of 75.000 m³ mentionedd before likely being product of the erosion. 3. The rate of erosion after desapearing the natural barrier was about 67.000 m³/year, consistent to the anterior datum; and before 1978 the rate of accretion of the outer part of the ria was of about 37.000 m³/yr.

During the period of erosion not less than 135.000 m³ have been dredged from the inner part of the ria, in agreement with all the bathymetries, but the bathymetry of March 1985 (5).

The analysis of the profiles fig (15-16) shows that a permanent, or quasi-permanent, tranport of sand from the eastbound westward nas been happening along all period of monitoring. A continuous erosion was detected from August 1985 to May 1987, when the jetty began to behave as a barrier, and a continuous accretion may be noticed later.

3.4 The mineralogical analysis of the samples of the banks from the interior of the ria are completely similar to the samples of the beaches around the ria. Only the samples from the beaches westward of the Fazouro ria show a meaning difference. It means a general littoral transport eastward, some kind of sink in front of Fazouro mouth and a unique origine for all sands of the beaches and the ria banks. In its turn the ecological study shows: a) The maritime origin of all the materials (sands) of the banks and its recent



- 21 JULIO 1987
- 31 JULIO 1987
- 7 AGOSTO 1987
- 30 SEPTIEMBRE 1987
- 31 OCTUBRE 1987
- 29 JUNIO 1988
- 1 AGOSTO 1988
- 28 SEPTIEMBRE 1988
- 23 NOVIEMBRE 1988
- 23 NOVIEMBRE 1988
- 10 FEBRERO 1989
- 7 ABRIL 1989
- 19 JULIO 1989

Fig. 15 y 16
Profiles.

increasing. b) The reduction of the land materials at the marshes of the inner ends of the different lobes of the ria.

4. DISCUSSION AND CONCLUSIONS

Tides in the ria of Foz have an acceptable correlation with the tides of Gijon harbour, but some differences are very noticeable, over all by the effect of the storm surges (frequently up to 50 cm) and by the steepness in the interior basin of the ria (weaker the tides, more meanings the local differences the water level). These discord may explain the disagreement of some bathymetry (5) analyzed above.

Inlet currents have increased a little bit after the construction of the jetty because of the small increasing of the tidal prism and mostly because the better estabilization of the channel. Nevertheless, currents still are less than admisible what, together with the sediments laid backside by the jetty end, show that the aim of designing a short barrier was got, but that the cleaning capability of the currents has improved also.

As it has previously said, nearly all the sands obtained from the interior of the ria have been pumped by the jetty and later distributed by land means. But the periodic visual observations of the works permit to question the accuracy of the nourishment operations: an overview to the bulk of the materials accumulated in front of the jetty supports that the real nourished volume was rather minor than the bulk theoretically pumped; and the way in which sand was fetched up to the berm (upper part) of the Angueira and, over all, Altar beaches to get the designed profiles, that nearly all of sand was obtained from the tidal plain in frot of both beaches; so it would be happening that very few sand from outside of the beach system was actually being used in the regeneration of the berms and that most of it was merely transported from the lower to the upper part of the emerged profile during low tide (that is to say, from the emerged tidal plain towards the permanent berm), it would be like trying to accelerate the natural process of nourishment of these beaches, which had been foreseen in the project to happen when the jetty had been finished and the spit rebuilt. Nevertheless the rate of fetching up sand was undoubtely excesive because an immediate strong and very noticeable steepness of the berm profile was produced after every high tide; the sand so applied obviously formed already part of the beach and, consequently, it was put immediately back in the tidal platform by the onshore-offshore dynamics. Some of the
in this paper in

observations described and analysed in this paper in the previous items permit to support this explanation which is particularly consistent with the different bathymetries of the ria: March 87, Sept 87 and Sept 88 in the inner part, showing the effects of the extraction and Aug 85, Sept 88 (showing the effects of the dragging from the tidal plain) and Sept 89 (showing the deferred consequences) of the outer part of it.

The immediate answer of the system shows an insufficient volume of nourishment: the tombolo and most of berm in Altar and Anguleira beaches, just where the sand was brought from the tidal plain vanished. The slow recovery up to the natural rebuilt of the tombolo was favoured by the delay of the storms in the 1988-1989 winter. Nevertheless, the insufficiency of sands permitted the new disappearance of the tombolo (Feb-Mar 89). As a consequence, in both occasions part of the mobilized sand has been transported westward, and it has passed to the backside of the jetty, laying aside just by it, approximately in a volume of 12.000 m³/yr, and, in both occasions it happened in a very short time (Mar-May) following the disappearance of the tombolo; in May the new natural accretion from the seaside permitted the regeneration of the tombolo and the restabilization of the system.

All these processes could be continuously followed by visual observations, besides the monitoring here shown. And they are consistent with the continuous westward potential transport and with the necessity of a certain minimum threshold of sand to set firmly the tombolo; also with the hypotheses of the project that this is necessary to estabilize the system and to reduce at a minimum the sand entering and filling the ria.

The winter 1989-1990 was anomalously quite in storms and the natural nourishment permitted the tombolo to remain all the year: it was enough to permit a beautiful recovery of all the beaches (fig 19) in the summer of 1990. What shows that, in any case, the natural nourishment exceeds the volume entering into the ria, and it is consistent with the rough calculs from bathimetries. As a consequence the volume of sand overpassing and laying aside by the jetty in this year (1990) was unnoticeable (less than 5000 m³/yr roughly).

From the ecological point of view, the fishing had vanished from the ria since the erosion of the natural barrier in 1978. Though many opinions supposed this phenomenon to be caused by washing aggregates of a next quarry, in the memorandum of the project was assumed to be caused by the biotopic changes so suddently produced, in such a way that regenerating the barrier, a recuperation of the catch could be expected. In fact fishing has been recovered in the inner part of the ria since 1989, and specially since 1990, when the



Fig. 17
1.978



Fig. 18
1.985

Fig. 19 1.990



the ria since 1989, and specially since 1990, when the movements of sands in the outer part of the ria have begun to be reduced.

Consequently with all these analysis and discussion several conclusions may be established.

1. The natural barrier had been generated as a spit, that is to say, as a consequence of a longshore littoral drift, instead as a bar, consequence of the onshore-offshore equilibrium. The question was not obvious because the general net littoral transport in all Spanish Cantabrian coast is eastward, but it is in agreement with the remake of the project about the permanent westward local littoral drift in the outer basin of the ria. And the conclusion is not trivial because most of the barriers of the Cantabrian rias and other analogous estuaries and bights behave in the same way; also because it shows that many tidal inlets, if not all of them, described as "updrift" migrating inlets, really migrate "downdrift", taking into account the local nearshore drift and not the direction of the net littoral transport along a more general and extensive coastal stretch. In this case, the headlands of Escario and St. Bartolome and the bathymetry of the Gulf of Masma may justify, as it was exposed in the project (1) this local change on the transport direction. But in many inlets, their ebb-shoals may be cause enough to produce an analogous change. In the ria of Foz, the role of the shoals at both sides of the Rapadoira jetty may explain the unsuitability of some numerical models to explain the actual permanent westward transport along the Altar and Angueira beaches; that is likely right because this area was not taken into account in the refraction model.

2. Nevertheless the littoral transport off-shore of both the Peña do Altar, and the Rapadoira jetty is dominantly eastward, justifying the submerged spit starting in the end of the Rapadoira beach eastward; this spit is noticeable in the bathymetry of Sept 88, when the channel was very dangerous at strong low tides, but it nearly disappeared in Sept 89. It may be explained by the process of recovery of the tidal plain after the undue (wrongful) extraction to nourish the berm; and may be noticed comparing both bathymetries each other and with the design's (figs 13-14).

3. Also the real volume of sand obtained from the inner part of the ria likely was less than projected having been substituted by the sand previously accumulated on the tidal plain of the outer part of the ria, but not accrued from the pumped sands. That explain the immediate erosion of Altar and Angueira beaches just after the construction of the designed profiles, and the differed partial recovery of the profiles once the tidal plain was reacrued from both the berm and the

submerged spit.

4. The behaviours of the artificial barrier has been successful in spite of the defects of construction: it has permitted the natural renourishment of the beaches and, secondary improved the conditions of the harbour channel. Nevertheless this improving situation must be considered only transitory because an increasing of the outer ebb-shoals must be expected. Therefore the complementary actions foreseen in the project must be put forward.

4.bis. It has also been successful decreasing the filling rate of the inner basin of the ria, from about 70.000 m³/yr to about 12.000 m³/yr as a maximum (or transitory) and likely to less than 5.000 m³/yr. But the present situation of the ria corresponds to a very high degree of filling.

5. The behaviour of the ria as a sink of sands has been checked, so that the beaches seaward of it obviously suffer now a deficit of material. Therefore dredging the ria to nourish this beaches and to increase its tidal prism up to at least the bulk of filling since 1978 seems to be previous to the construction of the eastern jetty of the inlet.

BIBLIOGRAPHY

1. Díez J., Escobar V.,- Ria de Foz solution for a harbour and coastal problem. Proceedings of the XXI Conf. on Coastal Engineering. N.York 1988 pp 2896-2907
2. Díez J. Methodology for the final determination of the parameters for planning and design of coastal works. Short course XXI Conf. on Coastal Eng. 1988
3. Suarez P. Clasificación Genética de Formas Costeras Simples. Unpublished. Notes for a course. Escuela de Caminos Universidad Politécnica. Madrid
4. Junov J. Estudio de Macrofauna Intermareal de Sustrato Blando de la Ria de Foz. Ph D. Theses. Alacala de Henares (Madrid) 1988.
5. Lechuza A. Estudios varios sobre la ria de Foz. Batimetría 1985.



Fig. 20

Taking sand from the tidal plane.

ACKNOWLEDGEMENTS

The study of the ria and the project have been financed by the General Direction of Ports and Coast of the Ministry of Public Works. The monitoring of profiles has been developed by the Service of Coast of Lugo. The rest of the monitoring works has been financed by the author. The topographers J.M. Olmo and Isabel Olmo, the civil Engineers J.M. Perez-Pozuelo and J.M. Silvestre and different students sporadically as a crew have decisively to the long development of the surveys.

CHAPTER 240

EMERGENCY SITUATION IN THE SHORELINE REACH OF AN OFFSHORE OILFIELD PIPELINE AND REMEDIAL MEASURES

Jefferson V. Bandeira¹ Luiz C. Araújo² and Antonio B. do Valle²

Abstract

This paper describes the critical situation experienced in the northeast coast of Brazil by an oil and a gas pipeline, in their shoreline reach, due to the growth of a spit, and the remedial measures adopted, which avoided an environmental and economical disaster.

Introduction

For the exploitation of the offshore gas and oil fields of "Agulha" and "Ubarana", in the coast of Rio Grande do Norte State in Brazil (Fig. 1), PETROBRÁS, the Brazilian Petroleum Company, has installed a group of six steel pipelines linking the offshore to the mainland facilities.

The region is a flat sand beach, with a mean slope 1/1360 between 0 and -10m depth contour, in a coast with an E-W alignment (Fig. 2) and subjected to the action of waves coming from the NE quadrant and winds blowing from N to SE. The currents outside the breaker zone, with velocities up to 0,5m/s, have a westward resultant and are also influenced by the tide which is semi-diurnal and has amplitudes ranging from 1.0 to 3.1m (INPH 1981) (Moreira et al. 1987). In consequence, there is a westwards littoral drift which promotes the growth of spits in the region (Fig. 3).

¹Engineer, Environmental Engineering Division-CDTN/CNEN
P.O. Box 1941 - 30161 - Belo Horizonte, MG, Brazil

²Engineer, RPNS/PETROBRÁS
Rua Interventor Mario Câmara, 2783 - 59070 Natal, RN,
Brazil



Figure 1. Situation Map

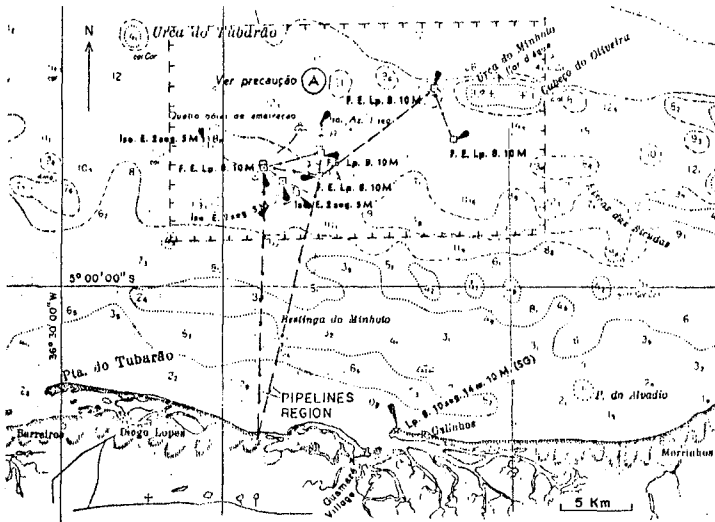


Figure 2. Key Map (Guamaré Coast)



Figure 3. Galinhos Spit

The bottom is active with respect to sediment movement down to depths of 12 to 13m, as observed comparing successive bathymetric surveys made in the pipelines region, which also revealed the existence of sand banks (Fig. 4).

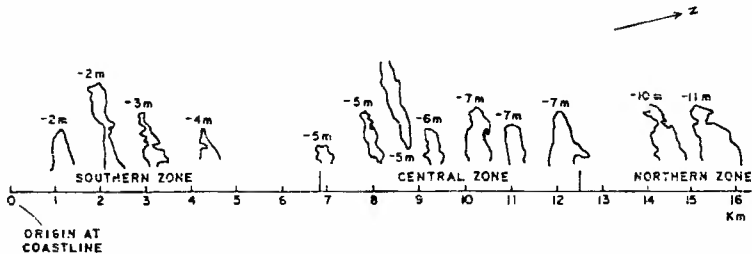


Figure 4. Sand Banks in the Coastal Region of Guamaré

When the pipelines were buried, the shoreline presented no problems. Nevertheless, there existed eastwards a spit, almost parallel to the shoreline, originating in a nearshore island situated in front of Guamaré village. With the growth of this spit (Fig. 5), which defines, between it and the mainland, a double-entrance estuary, the pipelines region, in the shoreline, was submitted to a tidal current that eroded severely the seabottom under the two western pipelines, due to a narrowing of the tidal channel right in their placement, leaving in suspension an extension of about 40m of both lines (Fig. 6, 7, 8 and 9). One of them is a gas and the other an oil pipeline, both with an outside diameter of 0.66m and lined with a concrete coating, 7.6cm thick.



Figure 5. Spit at the Pipelines Region
Date: 03/16/88 Hour: 15:30 W.L.= +3.1m (H.W.)



Figure 6. Undermined Pipelines
Date: 03/02/88 Hour: 10:24 W.L.= +0.7m



Figure 7. Gas Pipeline
Date: 03/02/88 Hour: 09:08 W.L.= +0.9m (ebb tide)



Figure 8. Gas Pipeline
Date: 03/02/88 Hour: 09:10 W.L. = +0.9m (ebb tide)

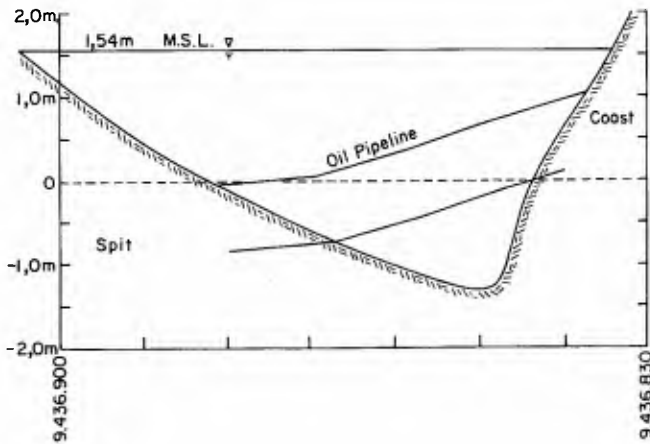


Figure 9. Channel Cross Section at Oil Pipeline Placement. Date: March 1988

Statement of the Problem

The influence of the strong crossing tidal currents, with measured values of 2.5 knots (1.3m/s), could produce rupture of the pipelines through a vortex shedding, prompt to happen for conditions nearly those the pipelines were subjected, as pointed out in a simulation study (Carvalho 1988):

a) the oil pipeline was in a situation dangerously close to resonance conditions because: for a free length of the order of 50m its natural frequency of vibration would coincide with the vortex frequency caused by a current of 2.8 knots (1.4m/s) flowing in its surroundings. Indeed, the extremities of the suspended portion of the oil pipeline had already presented deep fissures in the concrete lining;

b) the gas pipeline, lighter than the oil pipeline and with a higher natural frequency would be in resonance for a free length of 70m and then it was in a situation of lesser risk than the oil pipeline.

The real free length of both pipelines were greater than the measured ones, as the pipelines would find effective support, only some metres inside the margins of the channel.

Remedial Measures

In order to cope with this situation, three alternatives were considered as remedial measures (Bandeira 1988) (Santos 1988):

I - burying the two pipelines deeper underneath the eroded bed;

II - holding the suspended portion of the pipelines by means of piles until, due to the westwards displacement of the spit extremity, the channel sections in the pipelines region might be naturally shoaled;

III - closing the tidal channel entrance by construction of two sand dikes, the first (E dike) as near as possible the region where the tidal waves, entering the channel at both entrances meet each other, and the second (W dike) in the western entrance, where the pipelines cross the shoreline.

Considerations about the Remedial Measures

The first remedial measure considered was abandoned due to the risks of rupture of the pipelines, during the process of burying, as they were already dangerously stressed and submitted to the action of strong crossing tidal currents.

The second one could avoid the imminent vortex shedding by diminishing the free length of the pipelines, but still the pipelines would be submitted to the strong crossing tidal currents until the channel sections in

the pipelines region might be naturally shoaled. But this natural shoaling could not be assured and then, another intervention could be required.

Solution Adopted and Further Reaction of the Coastline

Having in mind the possible drawbacks of the first two considered remedial measures, PETROBRAS has decided to implement the third one, which seemed the most convenient and proved to be successful.

For the construction of the sand dikes, PETROBRAS made use of two bulldozers which piled sand in the two sides of the dike sections, and plastic bags filled with sand. Shortly before the low water of a neap tide, the plastic bags were placed in the deepest part of the channel section and, after that, the bulldozers, simultaneously from both sides, pushed the piled sand over the section, completing the closure.

The E dike (Fig. 10 and 11) was built on March 22, 1988 and the W dike (Fig. 12) three days after. There was a strong sediment deposition westwards of the western dike as expected (Fig. 12, 13 and 14) and on March, 1989, a rupture in the spit portion between the two dikes occurred during an equinoctial tide and is presently being monitored.

The E dike was not constructed in the region where the tidal waves, entering the channel by both entrance, meet each other (mangrove region in Figure 10)



Figure 10. East Dike and Mangrove Region
Date: 04/07/88 Hour: 08:25 W.L. = +2.2m

but, for environmental reasons and ease of construction it was situated at the narrowest section of the channel, near the mangrove region and west of it, as indicated in Figure 5, which was taken at the high water of a spring tide. In this way there was an increase in the tidal prism flowing through the eastern entrance.



Figure 11. East Dike (Closer View)
Date: 04/07/88 Hour: 14:23 W.L. = +0.8m



Figure 12. West Dike (13 Days After Closure)
Date: 04/07/88 Hour: 14:27 W.L. = +0.8m



Figure 13. West Dike (10 Months After Closure)
Date: 01/25/89 Hour: 13:50 W.L.= + 1.1m



Figure 14. West Dike (27.6 Months After Closure)
Date: 06/14/90 Hour: 14:00 W.L.= +0,6m

Then, when the rupture of the spit occurred (Fig. 15 and 16), PETROBRAS decided to open the E dike in order to re-establish the original tidal circulation in the mangrove area and in the eastern entrance (e.g. a decrease in the tidal prism flowing through this entrance). This action caused a correspondent increase in the tidal volume flowing through the new western entrance.



Figure 15. Disrupted Spit with the E Dike Opened
Date: 12/27/89 Hour: 9:55 W.L.= +0.7m



Figure 16. New Western Entrance
Date: 12/27/89 Hour: 10:00 W.L.= +0.7m

This new western entrance has now a greater tidal volume flowing through it than the original one (which is estimated in $425,000\text{m}^3$ relatively to the average tide amplitude), when the extremity of the spit was situated in the same region as the entrance. Now, there is a contribution of the tidal prism western of the mouth (in the channel between this mouth and the W dike) which is estimated in $326,000\text{m}^3$, giving a total tidal prism of the order of $751,000\text{m}^3$. This increased tidal volume flowing through the mouth added to the fact that now the flood flow branches E and W after crossing the mouth and the ebb flow coming from these two directions converges upon the entrance, may have an influence in the rate of advance of the mouth to W, compared to the velocity of migration of the spit when its extremity occupied the same region of the present mouth, from which there is no record.

Presently the mouth is situated about 1920m east of the section of the W dike, and its migration to W due to the unidirectional littoral drift is being monitored. In Figure 17, the contours of the two margins relatively to the MSL, are pictured for four surveys made in the interval February - May 1990. Geometrical calculations considering the portions of the shoreline contours limited by horizontal lines passing by A and B (E side) and C and D (W side), indicated an average rate of migration of the mouth to W:

$$V = 10.5\text{m/month (E side)}$$

and

$$V = 24.9\text{m/month (W side)}$$

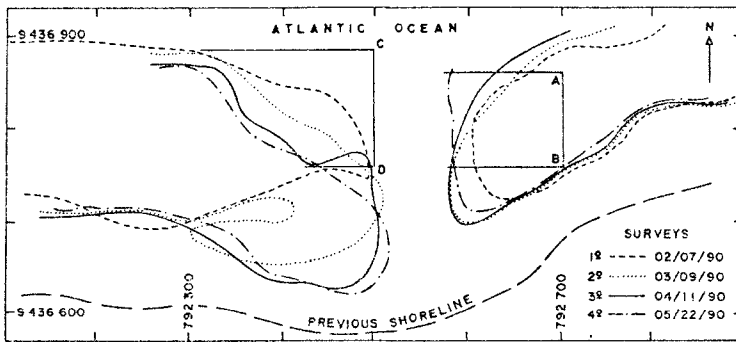


Figure 17. Surveys in the New Western Entrance

Conservatively assuming the rate of migration to W of the W side of the mouth as constant, in $1920 / (24.9 * 12) = 6.4$ years the problem could happen again, unless some preventive measures are taken, such as: to bury the pipelines deeper underneath the level of the eroded bed, before they are exposed to the strong crossing tidal currents again. In this way the spit can migrate freely, and it will not be necessary to construct dikes and alter the tidal circulation in the mangrove area.

The monitoring of the migration of the entrance will be continued at four months interval.

A great deal of information on the features of this unstable coast has been gained by the study of this emergency situation.

References

- Bandeira, J.V. (1988). "Observations about the undermining of an oil and a gas pipeline from the fields of Ubãrana and Agulha, in the shoreline region, in Guamaré-RN, and suggestions for remedial measures". Technical Report. DERL.CN-008/88. Environ. Engrg. Div. NUCLEBRAS/CDTN. Belo Horizonte, MG, Brazil (in Portuguese).
- Carvalho, M.A.G. (1988). "Report about the present situation of the oil pipeline - 026" - PUB-2/ECUB - and the gas pipeline - 026" - PUB-3/ECUB - in the shoreline region of Guamaré-RN". Technical Report. PETROBRAS, Rio de Janeiro, RJ, Brazil (in Portuguese).
- INPH (1981). "Investigations and definitions of the studies for the design of an outfall for the effluents to be discharged in the ocean at Macau-RN". Technical Report. 163/81. INPH/PORTOBRAS, Rio de Janeiro, RJ, Brazil (in Portuguese).
- Moreira, R.M., Bandeira, J.V., Salim, L.H., Pinto, A.M. F., and Condessa, M.L.M.B. (1987). "Study for the discharge of the effluents from the Guamaré oil facilities by means of an oceanic outfall". Technical Report. DERL. CN-008/87. Environ. Engrg. Div. NUCLEBRAS/CDTN, Belo Horizonte, MG, Brazil (in Portuguese).
- Santos, J.A. (1988). "Technical opinion about the present situation of the pipelines that arrive at the breaker zone in the littoral near Guamaré-RN". Technical Report. 18/88. INPH/PORTOBRAS, Rio de Janeiro, RJ, Brazil (in Portuguese).

CHAPTER 241

SAND BYPASSING TO "PLAYA DE CASTILLA" (HUELVA SPAIN)

José Fernández (1)
Gregorio Gómez Pina (2)
Angel Muñoz (3)

Abstract

The "Sand bypassing to Playa de Castilla" project consists of a sand bypassing from the zone behind Huelva Harbour dike to "Playa de Castilla" beach, situated in the downdrift direction of littoral transport.

The objective of this project is to artificially nourish a 25 Km eroded beach ("Playa de Castilla") as well as to check some coastal engineering theories.

The total volume of sand has been transferred to the updrift extreme of the beach, forming a 2 Km protrusion. The high rate of littoral transport guaranties its quick distribution along the whole beach, following the downdrift direction.

Introduction

The "Sand bypassing to Playa de Castilla" is a recently finished work in the Southwest Coast of Spain (Province of Huelva) (Refer.1).

-
- (1) Head of "Demarcación de Costas de Canarias"
(M.O.P.U., Ministry of Public Works).
P.O. Box 2235 35008 LAS PALMAS DE G.C. (SPAIN)
 - (2) Coastal Project Manager. Dirección General de
Puertos y Costas (M.O.P.U.) 28071 MADRID (SPAIN)
 - (3) Head of "Servicio de Costas de Alicante" (M.O.P.U.)
Plaza de la Montañeta, 9 03001 ALICANTE (SPAIN)

The Southwest coast of Spain, between the Guadiana and the Guadalquivir rivers, was created by the large sand sediment supplies coming from those rivers during the last thousand years.



Fig.1.- Situation

This portion of the coastline has been exposed to the oblique incidence of predominant swell.

There are several coastal formations that indicate very clearly the net result direction of littoral transport.

In fact, one can find some important sandy spits along Huelva coastline, like "El Rompido", "Punta Umbría" and "Doñana", all of them associated with wide tidal marshes systems.

This kind of formations provides an idea of the

strength of the littoral processes in the Huelva coastline.

As indicated in the scheme, there is a very clear littoral drift direction from West to East along the whole coastline.

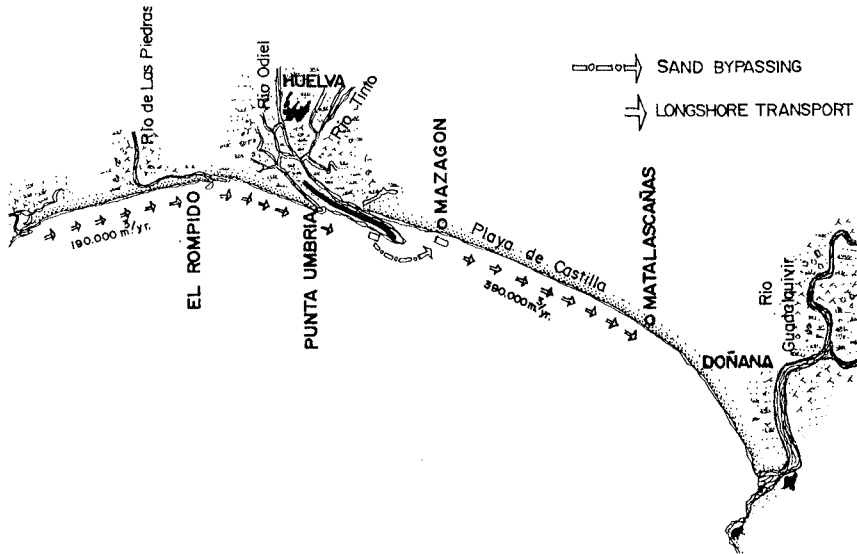


Fig.2.- Huelva Coastline Scheme

Figure 2 shows the coastline is divided into two parts by the Tinto-Odiel Estuary, also called "Ria de Huelva".

The tidal flow along this Estuary has almost acted as an integral barrier to the longshore sand transport.

The rates of the net result for littoral drift are evaluated around 190,000 m³/yr. on the west side (between the Gadiana river and the Tinto-Odiel Estuary), and around 390,000 m³/yr. on the east side (from Tinto-Odiel to Guadalquivir river).

Up to a few hundred years ago, the volume of sand brought to the coast, mainly by the Gadiana river, was enough to determine its progressive shape, but now there is an important shortage of sediment supplies, and this is due to several causes:

- Climatic variations (less rain)

- Physical factors (smoother river profiles)
- Human actions (constructions of dams, littoral barriers, etc...)

So the Huelva coastline is, at present, strongly recessive, and specially on its eastern side.

Firstly, because the coastal alignment makes it more exposed to the oblique incident waves attack.

And secondly, because the natural barrier effect due to the Tinto-Odiel Estuary has been recently reinforced by the construction of the sand contention dike for Huelva Harbour.

Description of the Sand Bypassing Project

The "Playa de Castilla" beach, that extends for 25 Km between Mazagón and Matalascañas tourist resorts, is situated on this part of the coast.

Field data obtained during the last 30 years indicate that the coastline recession has reached a mean of 1.5 m/year.

Through the sand bypassing project, an artificial nourishment of that eroded beach was carried out nearly a year ago.

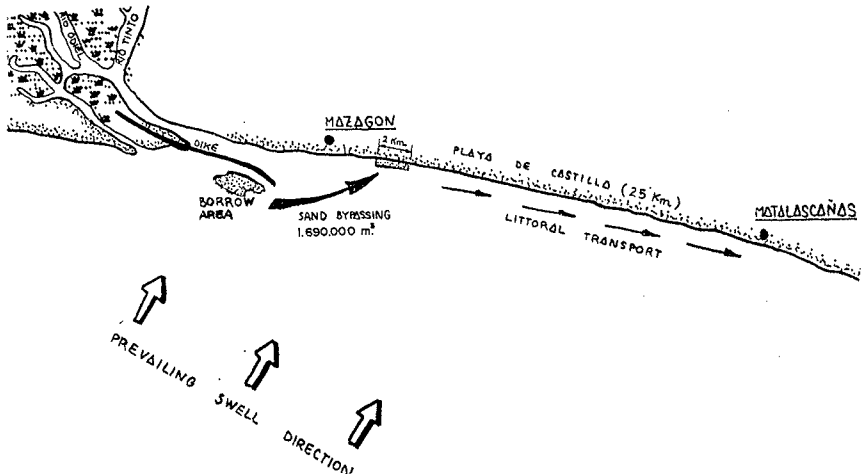


Fig.3.- Sand Bypassing Scheme

The work consisted of a sand bypassing from the zone behind Huelva Harbour dike to the "Playa de Castilla", situated on the other side of the Tinto-Odiel Estuary.

As mentioned before, the increasing of the barrier effect of the Tinto-Odiel Estuary (that it is due to the construction of the sand contention dike) has produced a large sand accumulation on the beach formed on its west side.

Figure 4 shows the sand contention dike for Huelva Harbour. The photograph was taken in 1.985, a few years after the construction of the dike. As one can see, there is a large sand accumulation in the beach formed on the updrift side of the dike:



Fig.4.- Beach Behind the Sand Contention Dike (Huelva Harbour)

The volume of sand moved from the accumulative area to the eroded beach was 1,690,000 m³, and the cost was \$5,800,000, what means \$3.4 per m³.

The sand was dredged by a trailing suction hopper dredger, then transported to the fill zone, that is situated out of the dike's shadow area, and pumped to the beach through a 2 Km long steel submerged pipeline.

The nourishment length is 25 Km.

The total volume of sand was transferred to the updrift extreme of the beach, forming a protruding area of about 2 Km length by 115 m width (Fig.5):



Fig.5.- Aerial View of the Protruding Area

The high rate of littoral transport guaranties the nourishment of the whole beach by the borrowed sand, that it is moved along it following the downdrift direction.

The chosen system to keep the beach stable was a "complete artificial nourishment", without any other kind of works and constructions.

This system implies that only periodic beach filling has to be carried out.

Another system could have been to built groynes, detached breakwaters, etc..., together with the beach nourishment.

Using this system it would not be necessary to make regular filling, but the coastline would have too many groynes and other hard coastal constructions.

It is hoped that the right decision was made regarding the system chosen, as the preliminary studies have indicated it was cheaper, more effective and clearly softer alternative.

It has been calculated that a sand bypassing like this would be needed every 4-5 years. However, more precise data will be available once the field investigation is finished.

Some of the First Results

In order to show the beach behaviour in the protruding area, in the next figures we can see some of the first data and results obtained after the sand bypassing works.

Several samples of the native sand were taken along many profiles of the beach, each one from a certain depth. As it is shown, the expected sand sorting along the beach profile is clearly indicated by the native sand lines.

Characteristics samples of borrowed sand were taken on the dredger during the works.

As one can see in Fig.6, the borrowed sand is coarser than the native sand.

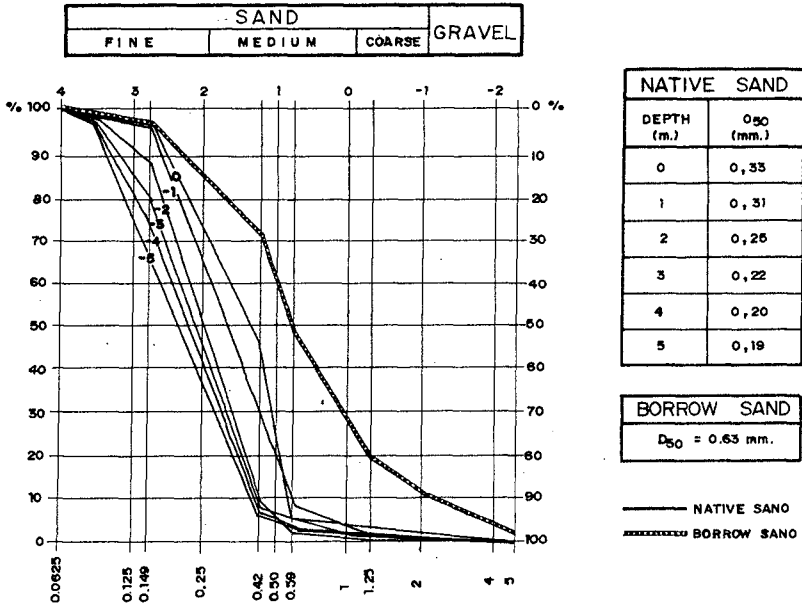


Fig.6.- Native and Borrow Sand

Fig.7 shows the evolution of the bathimetric line +2m:

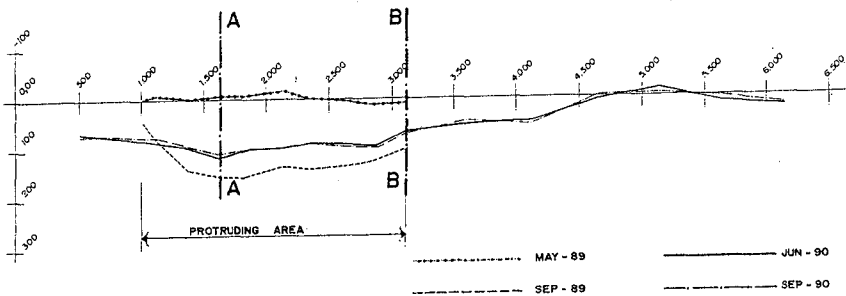


Fig.7 Evolution of Bathimetric Line +2 m

Fig.8 indicates the evolution of the bathimetric line 0 m:

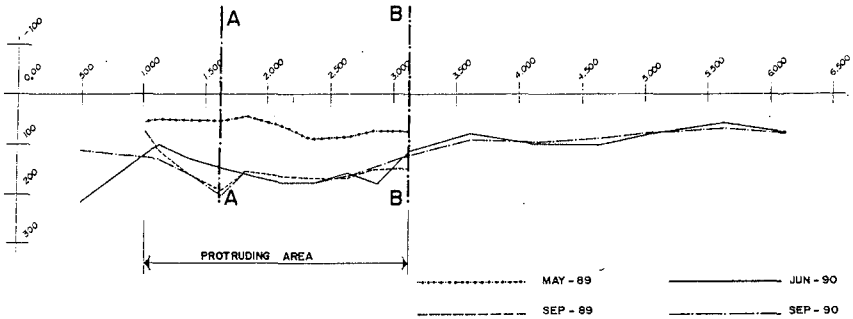


Fig.8.- Evolution of Bathimetric Line 0 m

As was expected, the recession of bathimetric +2 m in the protruding area after the sand fill, is clearer than the recession of bathimetric 0 m.

As is indicated the recession in the protruding area is made in benefit of the downdrift beach.

Fig.9 shows the beach transect AA in the middle of the protruding area:

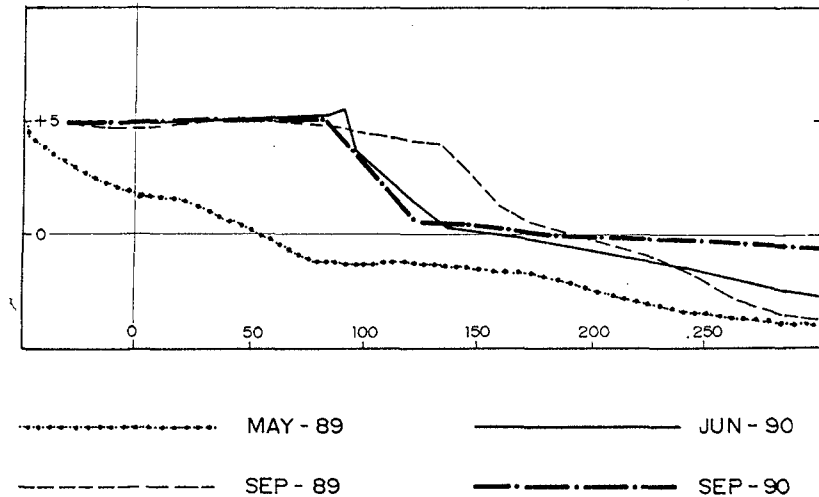


Fig.9.- Cross Section of the Beach in Transect AA

Fig.10 shows the beach transect BB at the downdrift extreme of the protruding area:

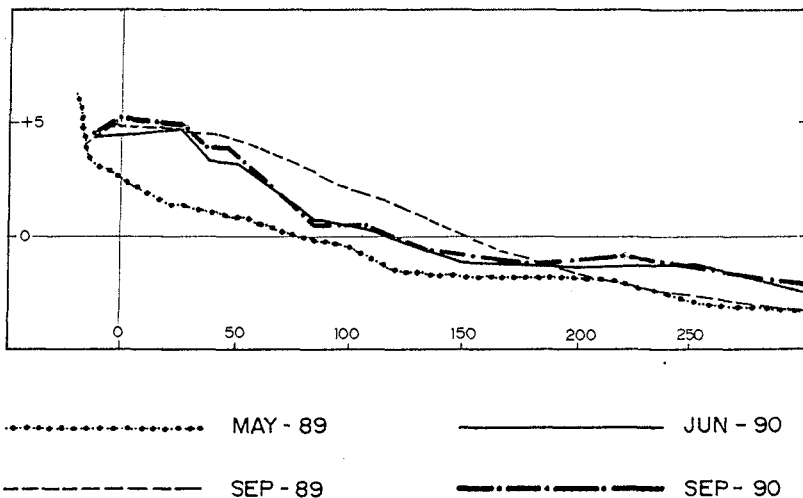


Fig.10.- Cross Section of the Beach in Transect BB

As one can see, the evolution of the beach shape after the sand fill seems to follow the behaviour described by Hallermeier.

Field Measurement Program

After having finished the works a field measurement program is being carried out in order to obtain the needed data to check different coastal engineering theories related to sediment transport, shaping of active profiles, planform of beach fill, sediment sorting and distribution, etc...

The main objective of this checking of theories is to obtain applicable results for beach improvement policy, particularly in the Huelva coastline.

The scheduled field measurement program has only recently started. Therefore, any kinds of results or conclusions would not be able to be presented at this point.

Interesting results are expected in the space of one year, in time to present them at the 23rd ICCE in Venice.

The main parameters that are being taken are:

Daily:

- * Visual observations: Two measurements.
 - Wave direction in shallow water.
 - Breaking width.
 - Wave period and wave height within the surf zone.
- * Wave recording by a buoy gauge.

Monthly:

- * Beach transects each 500 m along "Playa de Castilla" beach.
- * Sand samples at different depths in each transect.
- * Sand analysis.

Since the results of the definitive current field measurement program are not available, conclusions about the scheduled checking of some coastal engineering theories cannot be presented.

However, visual observations of the beach platform evolution, have so far indicated a positive benefit of the downdrift adjacent coastline, which was the main goal.

Acknowledgements

We would like to thank Mr. F. Palao, General Director of Ports and Coasts, and Mr. F. Osorio, Director of Coasts, for their interest shown in this study and also for their anticipated support for future investigations.

References

- 1.- FERNANDEZ, J. "Proyecto de Traspase de arenas a la Playa de Castilla" (Huelva, 1.987).

CHAPTER 242

BERM BREAKWATER CONTAMINATION STUDY SERGIPE MARINE TERMINAL, BRAZIL

Charles P. Fournier ¹, Otavio J. Sayao ¹, M.ASCE and Felipe Caldas ².

ABSTRACT

A physical modelling programme was undertaken to investigate the contamination of a berm breakwater armour stone layer with fines. For construction purposes, it became necessary to significantly increase the berm breakwater core crest width (construction roadway) beyond the design value. Thus, contamination of the armour material by fines, much beyond the specified tolerance, immediately adjacent to the core section resulted. As the original design did not consider the influence of this contamination on the armouring stability, the present modelling study was carried out, in response to the above construction limitation. The implications of a contaminated berm armour section was investigated. The results showed that for a high crested breakwater structure, the contamination of the armouring close to the core did not influence the breakwater stability and, profile reshaping was virtually the same for the contaminated and the original structure. This is due to the fact that the contaminated section was not placed in the active berm area. However, for a low crested structure, the contaminated section was less stable than the uncontaminated counterpart, due to the increased volume of water which overtopped the structure resulting in back slope instability.

1.0 INTRODUCTION

The berm breakwater under investigation is presently under construction for the Sergipe Marine Terminal in Brazil (see Figure 1). The terminal (Terminal Portuário de Sergipe, TPS) consists of a 2.4 km long trestle way connecting the berthing pier to shore. The pier is protected from wave attack by an offshore berm breakwater 543 m long, located in about 10 m depth at low water (see Figure 2).

The alternative design for the berm breakwater was developed by Construtora Norberto Odebrecht S.A. (CNO) in 1988 (Sayao and Hall, 1988). The final design specified an 11 m berm width and a 4 m core crest width both at 0.75 m above the Design High Water Level (see Figure 3). The contractor, CNO, was interested in constructing the structure by widening the core crest to 8 m, resulting in contamination of 4 m of armour material adjacent to the core. The

¹ Atria Engineering Hydraulics Inc., Ottawa, Ontario, Canada.

² Construtora Norberto Odebrecht S.A., Salvador, Bahia, Brazil.

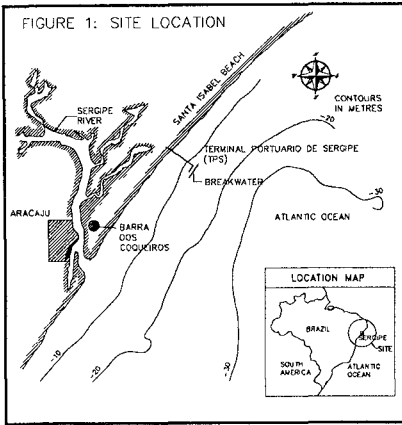


Figure 1 - Site Location

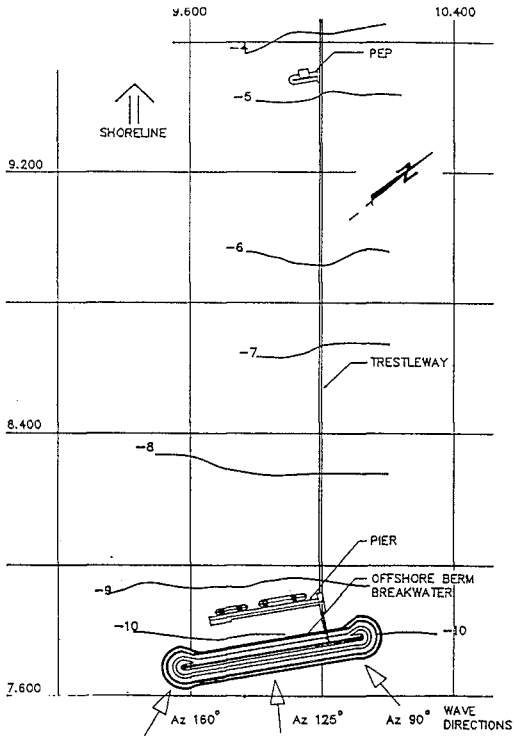
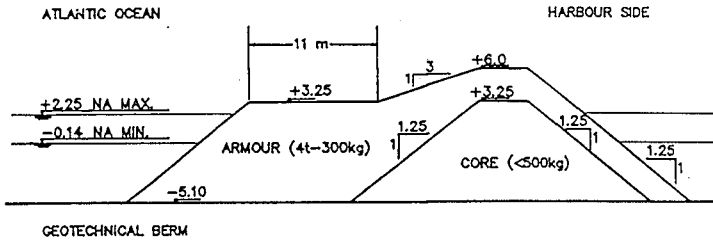


Figure 2 - Structure Layout



TRUNK CROSS-SECTION

Figure 3 - Original Berm Cross Section

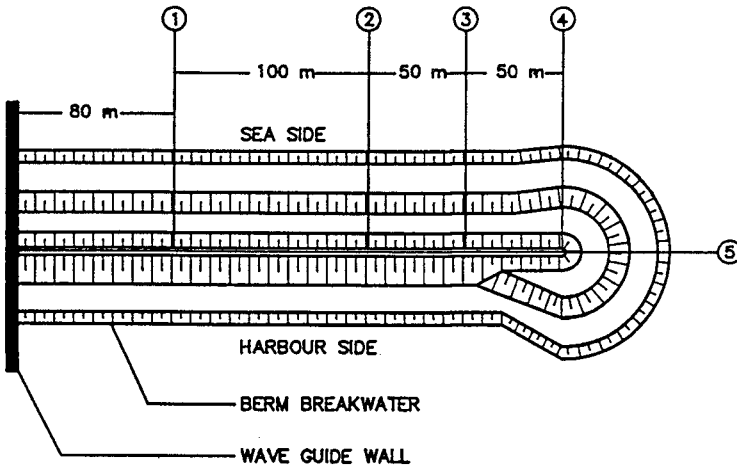


Figure 4 - Queen's University Model Layout Profile Reshaping Measurement Lines

berm breakwater stability depends on a porous berm of armour stones to dissipate wave energy. It is, therefore, essential that the expected prototype armour stone gradation and structure cross-section geometry be modelled correctly. The original design did not consider a contaminated section during the modelling programme. Thus, a physical modelling programme was undertaken at the National Research Council Canada (NRC) Hydraulics Laboratory to investigate the contamination of a berm breakwater armour stone layer with fines adjacent to the core crest. The purpose of the testing programme was to compare profile reshaping which occurred in the original (uncontaminated) design tests to those with a high percentage of fines (contamination) adjacent to the core.

2.0 MODEL STUDIES

This paper draws on information obtained from three separate model studies undertaken over the past couple of years (for details, see Murray and Sayao, 1990). The first, the original berm breakwater design conducted at Queen's University (Sayao and Hall, 1988), is referred to as the Queen's 3D tests. The second model study was dedicated to the investigation of armour contamination by fines and is the subject of the present paper. This model study is referred to as the NRC 2D tests. Finally, a redesign of the structure was carried out for geotechnical reasons (Murray and Sayao, 1990) and is referred to as the NRC 3D tests.

Queen's University 3D Design Model Tests (Queen's 3D tests)

The design of the berm breakwater for Sergipe Marine Terminal was achieved by means of a series of three dimensional hydraulic model studies at a geometric scale of 1:35. The tests were undertaken in a wave basin at the Queen's University Coastal Engineering Laboratory in Kingston, Canada. The modelling programme consisted of a total of 24 tests, all conducted using irregular waves. Variables in the test included design water levels, wave direction, geometry of the structure and the occurrence of single and multiple design storms (Sayao and Hall, 1988). Profile reshaping measurements were taken after each storm at the 5 locations shown in Figure 4.

NRC 2D Contamination Model Tests (NRC 2D tests)

A berm breakwater contamination study was conducted at the National Research Council Canada with the aid of two-dimensional physical hydraulic model tests at a geometric scale of 1:42.5 (Atria, 1989). The purpose of the testing programme was to assess the influence of a contaminated armour layer on structural stability by comparing the contaminated profile reshaping results with the ones obtained for the original design section. The design storm and prototype armour stone gradation for the present study were virtually the same as the Queen's 3D tests described above (for comparative purposes).

NRC 3D Redesign Model Tests (NRC 3D tests)

In November 1989, CNO commissioned the coastal engineering redesign of the offshore breakwater, due to the weak bearing capacity of the sub-soil (Atria, 1990). The redesign breakwater was a low crested structure which allowed overtopping. The objective of the design process was to achieve a modified berm breakwater structure founded on soft clays ensuring its safe performance for both the geotechnical and the hydraulic aspects of the site.

The 3D physical model studies carried out for the redesign of the breakwater were undertaken in the National Research Council

Hydraulics Laboratory at a geometric scale of 1:35. The modelling programme consisted of hydraulic stability tests which lead to the development of the breakwater redesign for the TPS. Included in this modelling programme was a series of tests to assess the influence of the contaminated armour material immediately adjacent to the core. In fact, the approach to modelling contamination during this series of tests was conceptually identical to that used previously in the NRC 2D contamination tests discussed here.

INPH Design Storm

Details of the environmental conditions which were utilized throughout the course of the design and modelling programme are given in Sayao and Hall (1988) and Atria (1990). However, a brief review of the specific storm used for the NRC 2D tests is presented.

This design storm utilized in all three model studies was developed at the Instituto Nacional de Pesquisas Hidroviárias (INPH) in Rio de Janeiro for the original conventional breakwater design (Murray and Sayao, 1990). The individual wave train characteristics were based on prototype measurements. Table 1 illustrates the 12 segments of the INPH design storm representative of the 100 year return event (Hidroservice, 1987). Irregular waves were used throughout the course of the NRC 2D modelling programme and the influence of different sequences of water levels were considered analogous to the Queen's 3D tests. The peak significant wave height of the design storm was 4.0 m.

The maximum design high water level was specified as elevation +2.5 m above chart datum. The design low water level was specified as -0.15 m below chart datum. To achieve a comparison with the Queen's 3D tests, a low water, high water storm sequence was necessary to reproduce the test conditions in the Queen's 3D tests (Sayao and Hall, 1988).

TABLE 1: INPH DESIGN STORM

Segment	Duration (hrs)	Cumulative Duration (hrs)	Significant Wave Ht. (metres)	Peak Wave Period (sec)
1	3	3	2.5	9.3
2	3	6	3.0	9.3
3	3	9	3.5	9.3
4	3	12	4.0	9.3
5	3	15	2.5	11.5
6	3	18	3.0	11.5
7	3	21	3.5	11.5
8	3	24	4.0	11.5
9	3	27	2.5	14.3
10	3	30	3.0	14.3
11	3	33	3.5	14.3
12	3	36	4.0	14.3

Armour Stone

The model stones used for the berm armour at the Queen's 3D tests were not available for the NRC 2D tests. Thus, the geometric scale of 1:42.5 was chosen such that the armour stone distribution of the berm armour material matched (reasonably well) the armour stone distribution from the Queen's 3D tests. Figure 5 shows the comparison of the armour stone distributions for both the 2D contamination study and the original Queen's 3D tests. At this

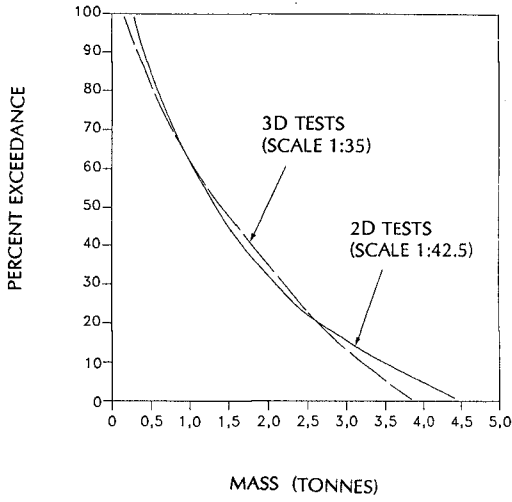


Figure 5 - Berm Armour Stone Gradation Curves

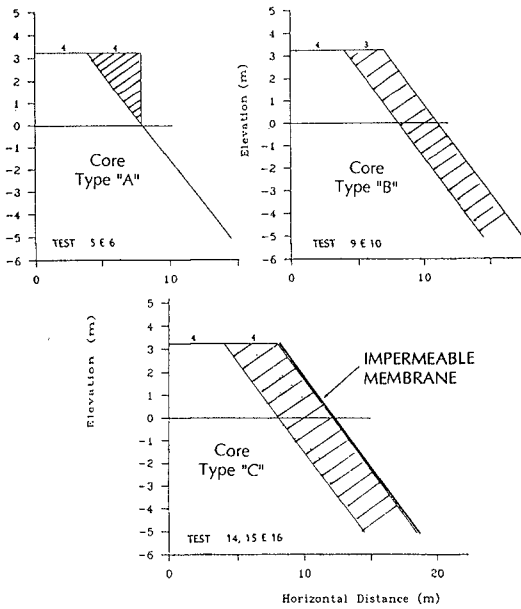


Figure 6 - Contamination Core Types

scale, the Reynolds number in the armour layer is maintained at a value exceeding 5×10^4 , which is sufficient to minimize scale effects resulting from the inability to simultaneously model both Reynolds and Froude criteria (Dai and Kamel, 1969, U.S. Army Corps of Engineers, 1984). As can be seen from Figure 5, the armour stone gradation ranged from 300 kg to 4 tonnes. This resulted in the determination of the following parameters:

$$\frac{D_{60}}{D_{10}} = 1.65; \frac{D_{85}}{D_{15}} = 1.86; \frac{H_s}{\Delta D_{n50}} = 3.1$$

where D_{85} , D_{60} , D_{n50} , D_{15} and D_{10} are the armour stone diameters exceeded by 15%, 40%, 50%, 85% and 90% of the armour stone distribution respectively, H_s is the (maximum) significant wave height and Δ is the submerged relative density of the armour stone.

3.0 INFLUENCE OF ARMOUR STONE CONTAMINATION

The approach adopted for the contamination study (NRC 2D tests) was to compare the reshaping characteristics of the contaminated structure versus the uncontaminated breakwater cross section. For this, profiles 1 and 2 from the Queen's Tests (see Figure 4) were used for comparative purposes. Firstly, a calibration procedure was necessary to ensure that the reshaping of the NRC 2D structure was (practically) identical to that of the Queen's 3D structure. That is, the reshaped profile after the design storm in the NRC 2D tests should be comparable to the reshaped profile after the same design storm from the Queen's 3D tests. This calibration technique therefore addresses the issue of the 2D versus 3D modelling effects, i.e. the 2D berm width is not the same as the 3D berm width to achieve the same profile reshaping. Having achieved an acceptable calibration, contamination of the breakwater was considered by comparison of contaminated versus uncontaminated reshaped profiles.

Simulation of Contamination

The simulation of contamination immediately adjacent to the core crest was achieved by constructing (in the model) various core extensions as shown in Figure 6. Core type "A" perhaps represented a physically realistic geometry of a contaminated armour layer given a construction roadway extension of 4 m over already placed armour. Core type "B" adopted a narrower contaminated section than core type "A" with a more extensive degree of contamination over the front slope. Finally, Core type "C", considered a worst case scenario for the simulation of contamination in the physical model study. This section utilized an additional 4 m of core material extended to the base of the structure over the entire front slope of the core. Furthermore, an impermeable membrane was placed over the entire front slope of the (new) core to eliminate any permeability effects into the core.

Summary of NRC 2D Tests and Results

A summary of the 2D tests conducted at the National Research Council Canada to study the contamination of a berm armour layer is given in Table 2.

TABLE 2: TEST SUMMARY - NRC 2D CONTAMINATION STUDY

Test No.	Berm	Berm Width	Water Level	Core Type	Purpose
1	1	11.0	LW	"U"	calibration to 3D model
2	1	(11.0)	HW	"U"	calibration to 3D model
3	2	8.0	LW	"U"	calibration to 3D model
4	2	(8.0)	HW	"U"	calibration to 3D model
5	3	8.0	LW	"A"	assess contamination type "A"
6	3	(8.0)	HW	"A"	assess contamination type "A"
7	4	9.0	LW	"U"	calibration to 3D model
8	4	(9.0)	HW	"U"	calibration to 3D model
9	5	9.0	LW	"B"	assess contamination type "B"
10	5	(9.0)	HW	"B"	assess contamination type "B"
11	5	(9.0)	HW	"B"	assess contamination type "B"
12	6	8.0	LW	"UI"	calibration to 3D model
13	6	(8.0)	HW	"UI"	calibration to 3D model
14	7	8.0	LW	"C"	assess contamination type "C"
15	7	(8.0)	HW	"C"	assess contamination type "C"
16	7	(8.0)	LW	"C"	assess contamination type "C"
17	7	(8.0)	HHW	"C"	assess contamination type "C"

Legend: "U" - Uncontaminated Core
 "UI" - Uncontaminated with Impermeable Membrane over Core
 () - reshaped profile from previous test
 "A" - Core Type "A" LW - low water level
 "B" - Core Type "B" LW - low water level
 "C" - Core Type "C" HW - high water level
 HHW - high water + 1 m

Calibration of 2D Contamination Tests

The calibration phase of the modelling programme consisted of modelling in the 2D flume various berm widths until the reshaped profile from the 2D tests matched those from the Queen's 3D tests. It is important to note that the same prototype armour stone distribution and design storm (wave climate) was utilized in both model studies, and therefore a 2D berm width existed which produced the same reshaped profile as in the 3D tests.

Tests 1 and 2 (low water, high water storm sequence) started with an 11 m berm width identical to the Queen's 3D tests. As expected, the berm reshaped less in the 2D testing than measured in the 3D Queen's tests. For tests 3 and 4, an 8 m berm width was used which yielded a reshaped profile very similar to that obtained in the 3D Queen's test. Tests 5 and 6 tested the same structure with contamination defined by core type "A".

Tests 7 and 8 tested a 9 m berm width which reshaped somewhat less than the 3D tests. Comparison of tests 7 and 8 results with the Queen's reshaped profile after low and high water respectively showed inadequate agreement in 2D versus 3D reshaped profiles, particularly after the high water test. It was therefore concluded that a 9 m berm in the 2D tests had more reserve capacity than the 11 m berm in the Queen's 3D tests. Nevertheless, contamination tests using core type "B" were conducted for comparative purposes between an uncontaminated structure with a contaminated structure (tests 7 with 9, 8 with 10). Although not shown in this paper, the profile reshaping for contaminated versus uncontaminated sections was (practically) identical. These tests provided a preliminary indication that contamination of the berm armour stone adjacent to the core did not influence the reshaping of the structure.

Due to the inability to model permeability in the core, it was decided to proceed testing (subsequent to test 11) with an impermeable membrane over the outer edge of the core and/or contaminated section. This effectively eliminated any debate with respect to the correct scaling of flow through the core since flow was not permitted, and thus it was guaranteed that the contamination had a maximum impact on stability.

Tests 12 and 13 represented the "calibrated test section" in that the profile reshaping after low water (test 12) and high water (test 13) were very similar to the Queen's 3D tests. Figures 7 and 8 illustrate the 2D versus 3D comparison of reshaped profiles after low water (test 12) and high water (test 13) respectively. A comparison of tests 12 and 13 results with the Queen's reshaped profiles showed acceptable agreement which lead to the conclusion that an 8 m berm width in the 2D model was equivalent to an 11 m berm width in the 3D model from a stability (reshaped profile) point of view, and for the tests boundary conditions.

Contaminated versus Uncontaminated Profile Reshaping

Having achieved a reasonable calibration of the 2D reshaped profile to that of the 3D Queen's tests, i.e., having considered the 2D versus 3D modelling effects, a valid assessment of contamination was achieved. Tests 14 and 15 were conducted using the same structure geometry as tests 12 and 13 with the contaminated core type "C" as shown in Figure 6. A comparison of low water and high water uncontaminated versus contaminated profile reshaping (test 12 with 14 and 13 with 15) are shown in Figures 9 and 10 respectively. It can be seen from these figures that very similar reshaped profiles resulted in both the uncontaminated and contaminated test sections, particularly at the water line. Some additional onshore transport of material towards the berm crest is visible for the contaminated section which is not an unrealistic result. Therefore, the results of the study indicate that contamination of the armour material immediately adjacent to the core as shown in core type "C" (Figure 6) does not significantly affect profile reshaping for the given structure and wave climate.

NRC 3D Contamination Tests

As mentioned in Section 2.0, a redesign of the breakwater was required due to geotechnical restrictions. To meet these restrictions, a low crested structure was adopted (crest 1.5 m above high water) which utilized heavier armour material (ranging from 1 to 4 tonnes) in the berm and conventionally placed armour stone over the core crest and backslope. During the course of the modelling programme, contaminated structures were tested using the core type "C" shown in Figure 6. For the redesigned structure, very little profile reshaping occurred for either the uncontaminated or contaminated structures. Figure 11 shows a typical plot of profile reshaping of the contaminated structure after a low water, high water and a second high water storm sequence. However, the contamination had a pronounced effect on the stability of the crest and backslope stones. Localized zones of damage were quite apparent (by eye) on the crest and backslope of the contaminated structure which were not present during testing of the identical uncontaminated structure. The displacement of crest and backslope stones occurred for a direction of wave attack perpendicular to the structure centerline. The effect of varying direction of wave attack was not considered during the contamination component of the structure redesign because the contamination option for construction was immediately ruled out.

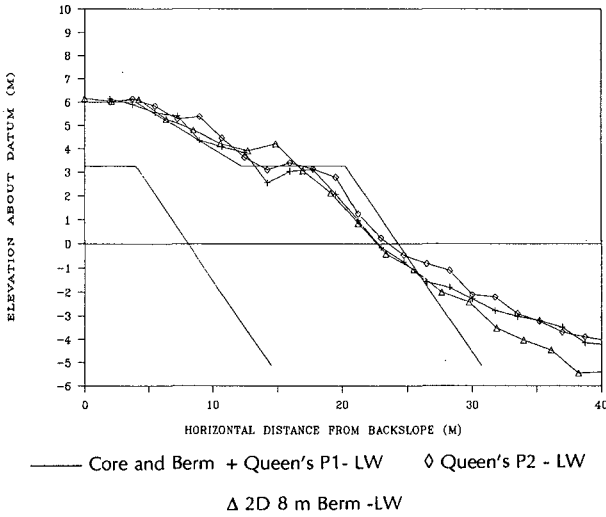


Figure 7 - 3D versus 2D Reshaping (Low Water)

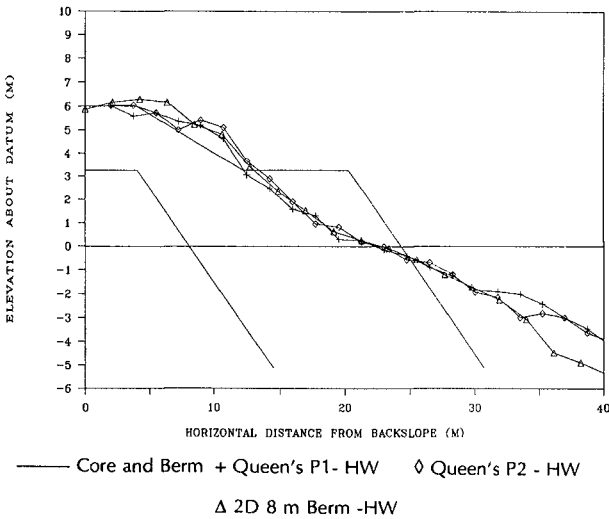


Figure 8 - 3D versus 2D Reshaping (High Water)

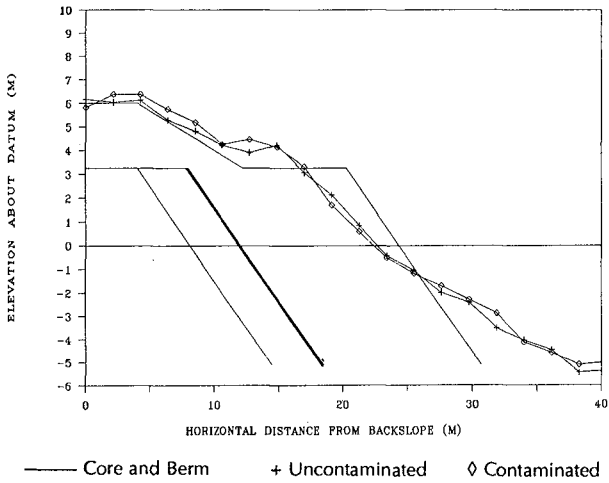


Figure 9 - Contaminated versus Uncontaminated Reshaping (Low Water)

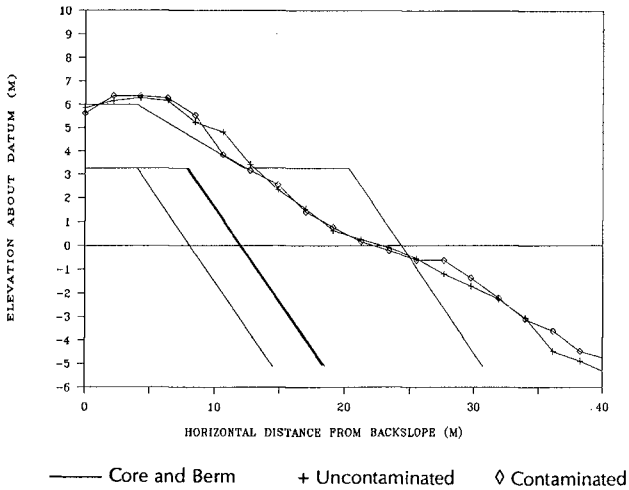


Figure 10 - Contaminated versus Uncontaminated Reshaping (High Water)

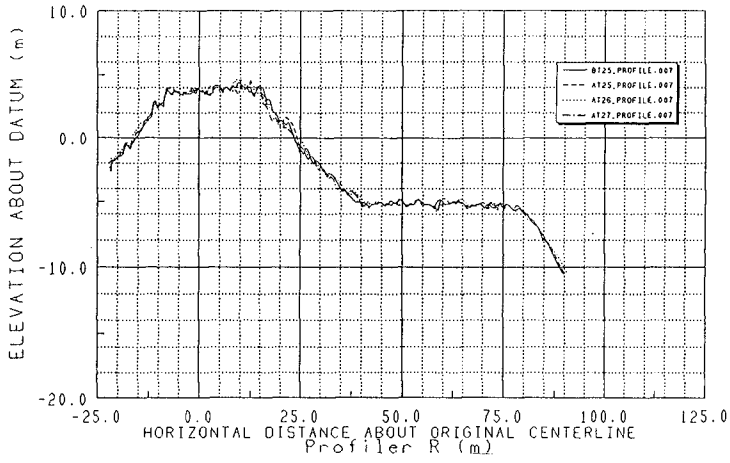


Figure 11 - Reshaping of Contaminated Redesign Structure (3D)

4.0 CONCLUSIONS

The results of the present study showed that for a high crested breakwater structure where overtopping is minimum, increasing the core dimensions to facilitate construction resulting in the contamination of the armouring close to the core did not influence the breakwater stability. In this case, profile reshaping was virtually the same for the contaminated and the original (uncontaminated) structure. This was due to the fact that the contaminated section was not placed in the active berm area. However, for a low crested structure where overtopping is significant, increasing the core dimensions to facilitate construction could have a significant effect on the stability of the crest and backslope stones. During tests of this nature, the contaminated section was less stable than the uncontaminated counterpart, due to the increased volume of water which overtopped the structure resulting in back slope instability.

If the construction methodology is changed after any breakwater design, rather than investigating the increase of core width and the contamination of the adjacent armouring, an alternative armouring design could be considered. This may consist of a heavier gradation resulting in a reduced berm width and an increased core width, thus making effective use of quarry materials.

It should be realized that this study was site specific and thus more research is required to determine the permissible dimensions of core and armour extremities.

REFERENCES

- ATRIA ENGINEERING HYDRAULICS INC., 1990. Hydraulic Model Studies and Redesign of the Offshore Breakwater for Terminal Portuário de Sergipe. Final report submitted to Construtora Norberto Odebrecht S.A., May.
- ATRIA ENGINEERING HYDRAULICS INC., 1989. Estudo do Alargamento da Pista de Rolamento e sua Influência na Estabilidade da Berma do Quebramar do Terminal Portuário de Sergipe. Final report submitted to Construtora Norberto Odebrecht S.A., August.
- DAI, Y.B. and KAMEL, A.M., 1969. Scale Effects Tests for Rubblemound Breakwaters. U.S. Army Corps Waterways Experiment Station, Report H-69-2.
- HIDROSERVICE, 1987. Final Design, Terminal Portuário de Sergipe. São Paulo, Brazil.
- MURRAY, M. and SAYAO, O.J., 1990. Offshore breakwater for the Sergipe Marine Terminal, Brazil. Proc. 22nd Int'l Conf. on Coastal Engineering, Delft, The Netherlands.
- SAYAO, O.J. and HALL, K.R., 1988. Berm Breakwater Design for the Sergipe Offshore Terminal, Brazil. Final report prepared by F.J. Reinders and Associates, submitted to Construtora Norberto Odebrecht S.A., March.
- U.S. ARMY CORPS of ENGINEERS, 1984. Shore Protection Manual, 4th Edition, Coastal Engineering Research Center.

ACKNOWLEDGEMENTS

Appreciation is extended to Petróleo Brasileiro S.A. (Petrobrás) and Construtora Norberto Odebrecht S.A. for permission to publish this paper.

CHAPTER 243

OFFSHORE BREAKWATER FOR THE SERGIPE MARINE TERMINAL, BRAZIL

MALCOLM MURRAY¹, MICE and OTAVIO J. SAYAO², M.ASCE

ABSTRACT

This paper describes the development of an alternative design for the offshore breakwater of the Sergipe Marine Terminal (Terminal Portuário de Sergipe, TPS), in northeast Brazil. Earlier alternative designs for the breakwater are presented and the chosen solution, a berm breakwater design, is described. Details of the hydraulic model testing carried out during the designing stages are given and the construction methods are explained together with a brief overview of construction controls and organization. In order to accommodate the unfavourable subsoil conditions which were found to be worse than initially expected, a redesign of the offshore breakwater was carried out. The new redesign is presently under construction. The TPS breakwater is the first berm type structure to be constructed in Brazil and one of the few in the world to be constructed over a soft marine clay layer.

1. INTRODUCTION

The growing industrialization of the state of Sergipe led to the need for the construction of a port to handle solid and liquid bulk cargo near the industrial pole to be established to the north of Aracaju, the state capital. Engineering feasibility studies (e.g. Sondotécnica, 1978) comparing an estuarine port on the Sergipe River and an offshore terminal located 17 km north of the river led to the adoption of the latter. With a total forecast investment of US\$ 110 million, the implementation of the new port was started in 1986 and is due to be concluded in 1991.

A contract was signed between Petróleo Brasileiro S.A. (Petrobrás) and Construtora Norberto Odebrecht S.A. in March 1987 for the construction of the marine civil works. Figure 1 shows the TPS location and layout. The terminal consists of a pier located in 10 m of water (below chart datum), connected to the port area by an access bridge 2,400 m long and protected by a breakwater 543 m long. The 332 m quay is designed for two 15,000 DWT vessels.

¹ Senior Manager; CONTRUTORA NORBERTO ODEBRECHT S.A., Alameda das Espatódias 915, Caminho das Árvores, Salvador, Bahia, CEP 41827, Brazil.

² Principal; ATRIA ENGINEERING HYDRAULICS INC., 8 Stavebank Rd. N., Suite 301, Mississauga, Ontario, L5G 2T4, Canada.

The sea bed at the breakwater site consists of a 4 m layer of fine sand overlaying an extremely soft layer of marine clay about 8 m thick which in turn overlays another sand layer (Figure 2).

2. TENDER DESIGN AND ALTERNATIVE SOLUTIONS

Figure 3 shows the tender design (Hidroservice, 1987), a conventional design adapted to the unfavourable subsoil conditions (Lundgren and Jacobsen, 1987). It involved placing of eight grades of stones during 17 distinct construction phases. These included the placing of a sand layer within the geotechnical berm. Construction of the geotechnical berm is done with floating plant while the superstructure of the breakwater is constructed by land-based equipment using the access trestle.

According to the tender planning, within the contractual period of 24 months construction would proceed with the use of marine equipment such as split barges and floating cranes, as well as land-based equipment. Even though the tender design was subsequently trimmed by the client, it would still involve the use of marine equipment during the winter of 1989. Thus, alternative solutions were sought which would simplify construction, also by maintaining marine operations within the summer months only. A number of structural and mixed solutions were developed in-house by CNO. Here, the structural solutions would require extremely heavy elements to resist hydraulic impacts of the order of 100 t/m (Danish Hydraulics Institute, 1987).

The classic solutions of substituting the marine clay by sand drains to accelerate the dissipation of pore pressures were already eliminated by the client on economical grounds. The alternative solution chosen and developed was a berm breakwater (Figure 3). It consisted of a geotechnical berm designed to distribute loads over the subsoil (as in the tender design) and a hydraulic berm to dissipate wave energy. Table 1 summarizes the comparison between the conventional tendered design and the alternative berm design.

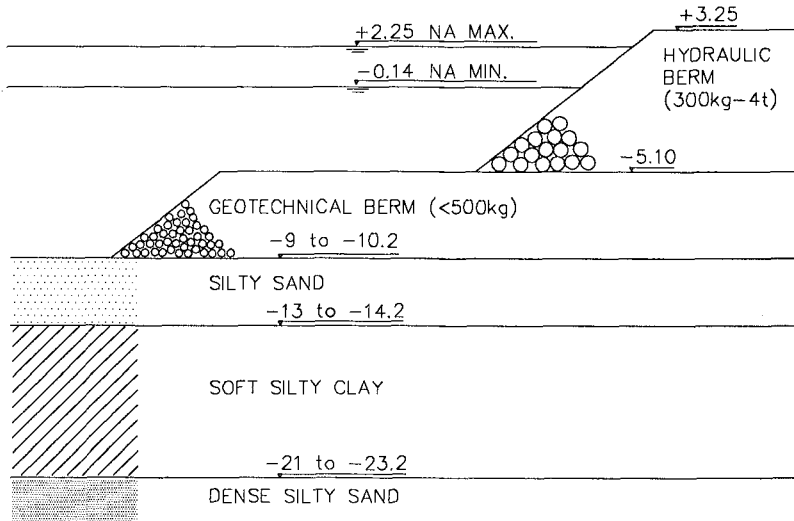
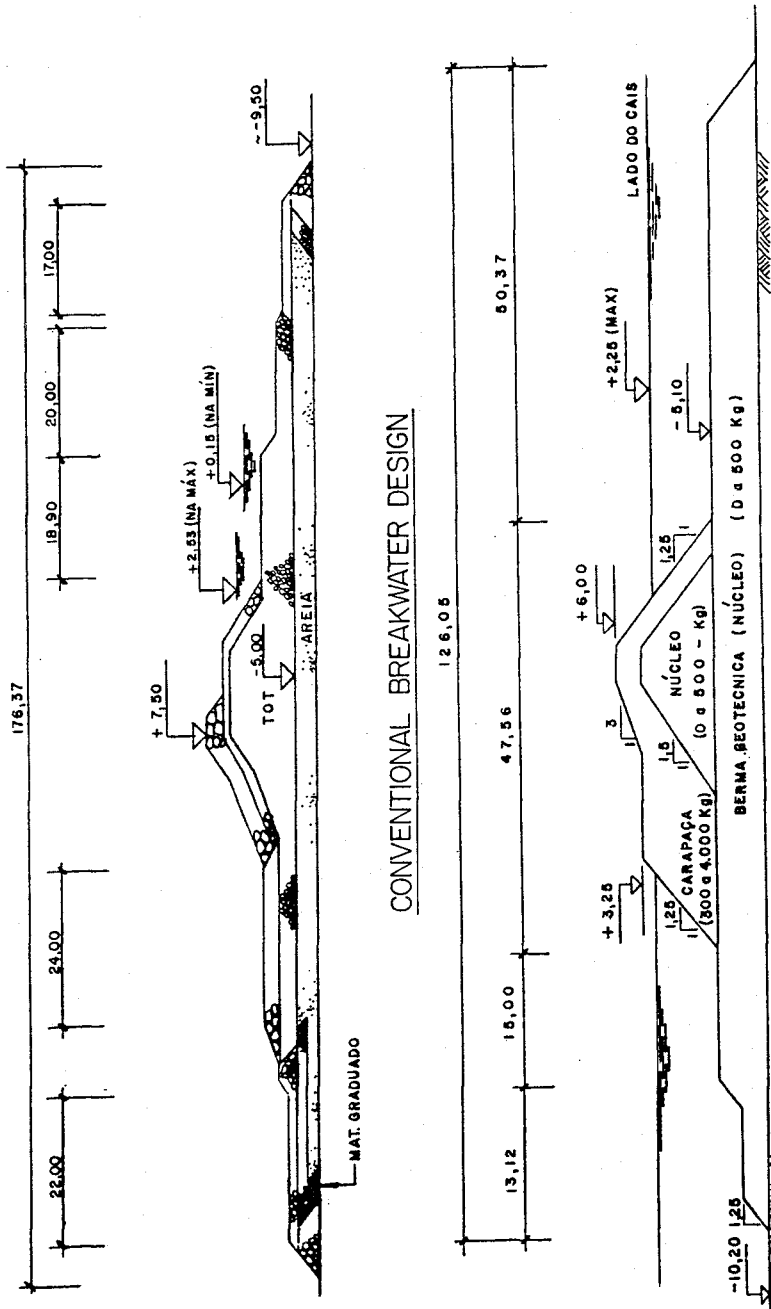


FIGURE 2: TYPICAL SOIL PROFILE



ALTERNATIVE BERM BREAKWATER DESIGN

FIGURE 3: TPS BREAKWATER ALTERNATIVES

3. BERM BREAKWATER SOLUTION

DESIGN CONCEPT

The design concept for the offshore breakwater, known as berm breakwater, has been reported in a number of references (Willis et al., 1987; Foster and Hall, 1987; Van der Meer, 1988). Figure 4 shows examples of recent berm breakwater projects. The features and advantages of this type of structures can be summarized as follows:

- The main armour can be constructed using lighter stones than those required for a comparable design using a conventional double layer armour.
- The structure can be constructed using relatively simple procedures which allow the relaxation of tolerances leading to better control during construction.
- The berm structure exhibits greater stability than a conventional double layer armour breakwater for a number of reasons. The berm has a high bulk porosity which allows the waves to propagate into it, dissipating their energy over a large volume. This does not occur in a conventional design since the flow into the filter and core layers is restricted due to reduced permeability, causing energy reflection and consequent instability of the armour due to down-rush.
- The berm breakwater also increases its stability as a result of wave action which tends to move stones about in the outer layers of armour. This leads to stabilized slopes of about 1:5 inclination as well as consolidation of the mound due to interlocking between the stones. As a result a stable profile is developed which is very resilient to wave action.

The adopted berm breakwater design is shown in Figures 3 and 5. The final structure dimensions was designed after carrying out hydraulic tests and geotechnical stability analyses.

Core is composed of stones in the range of 0 to 500 kg while armour stones range from 300 kg to 4,000 kg. With this simplified design, consisting of only two types of stones, the construction period was reduced from 24 to 15 months.

Table 1 Breakwater Design Quantities

Item	Unit	Conventional	Berm
Sand fill	m ³	344,000	0
Rock quantities	m ³	735,000	587,000
No. of material grades	-	8	2
No. of construction phases	-	17	4
Width of geotechnical berm	m	169	123
Acceptable percentage of damage	%	4	0
Maximum settlement	cm	150	120

Figure 3 shows cross-sections of both alternatives.

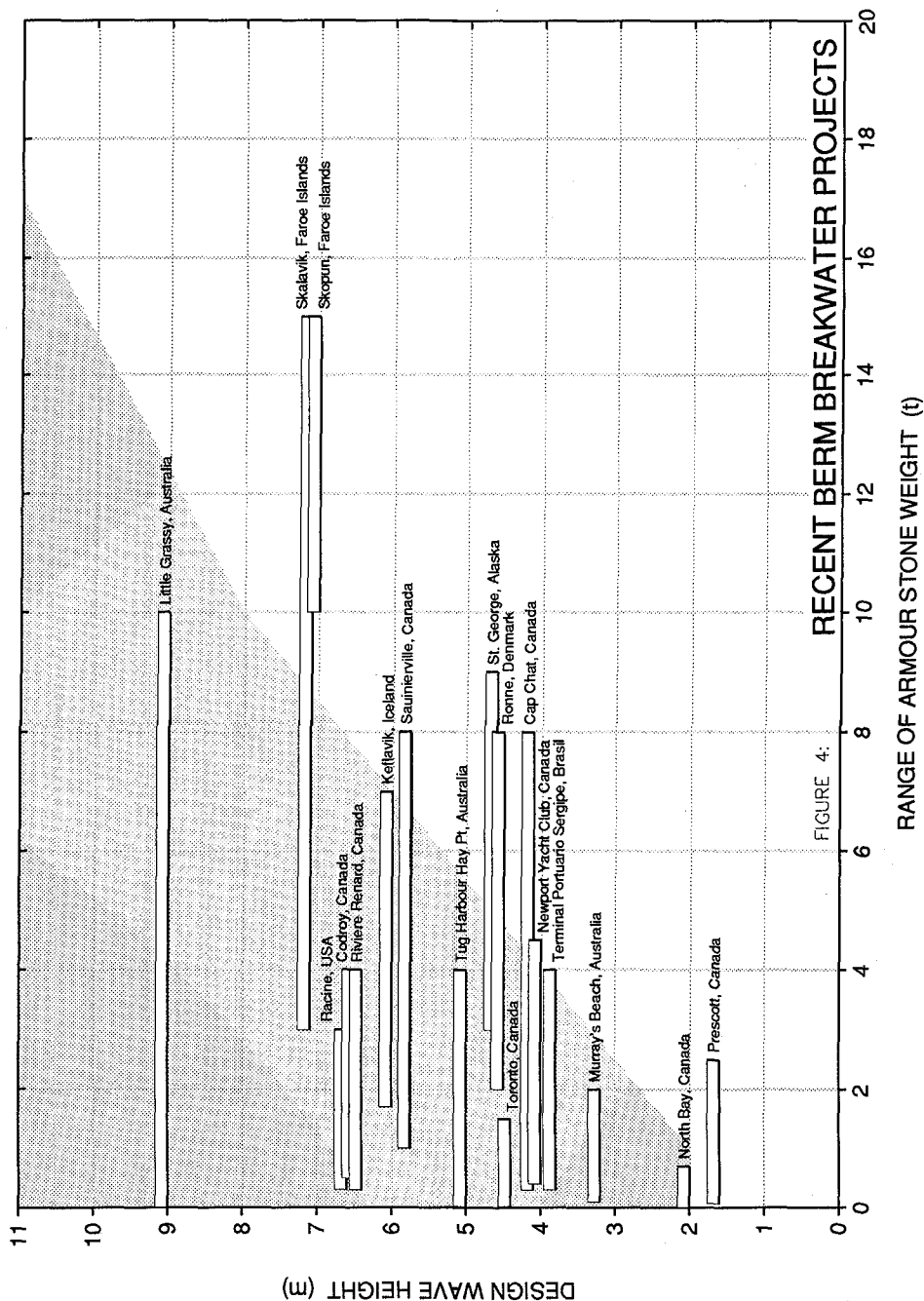


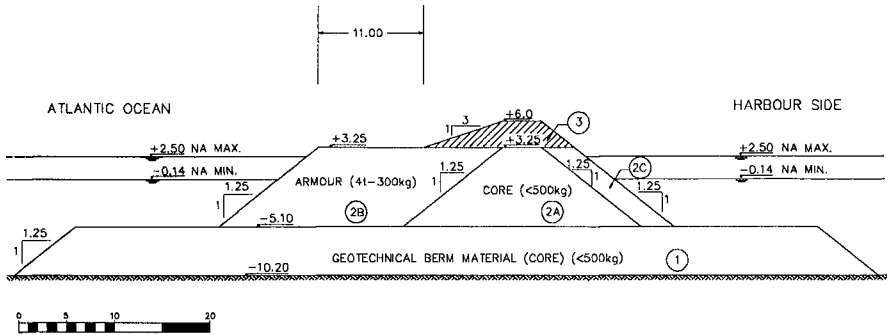
FIGURE 4:

RECENT BERM BREAKWATER PROJECTS

RANGE OF ARMOUR STONE WEIGHT (t)

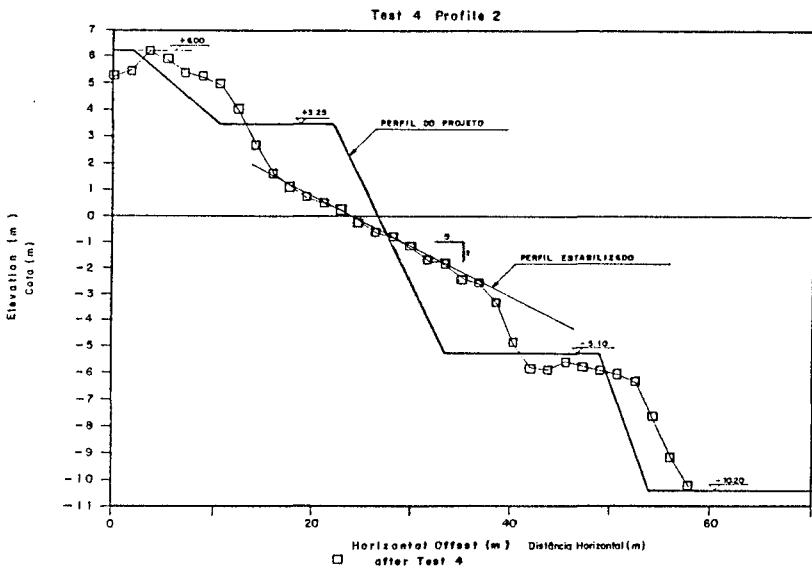
FIGURE 5: CONSTRUCTION PHASES

CONSTRUTORA NORBERTO ODEBRECHT S.A.
 TERMINAL PORTUARIO DE SERGIPE
 BARRA DOS COQUEIROS



- NOTES: 1 - ○ CIRCLED NUMBERS REFER TO CONSTRUCTION PHASES.
 2 - AT THE BREAKWATER HEAD THE BERM WIDTH IS 13m.
 3 - ALL DIMENSIONS ARE IN METRES.
 4 - ELEVATIONS IN METRES AND REFERED TO DATUM (N.R. OF DHN.)

FIGURE 6: TYPICAL MODEL PROFILE RESHAPING
 ARACAJU BREAKWATER STUDY



HYDRAULIC MODEL TESTING

The berm design was model tested at the Coastal Engineering Laboratory, Queen's University, Canada (Murray, 1989; Sayao and Hall, 1988). The model structure was subjected to a wide range of wave conditions including two different design storms (DS1 and INPH, see Table 2). Testing was undertaken using the notion of a design storm which had wave characteristics during the peak segment of the storm corresponding to the 100 year wave event. Waves from 2 directions, orthogonal and 35° oblique attack, were tested with both high and low water levels. A summary of the design parameters is given in Table 3.

The structure was also tested to assess its performance when subjected to multiple consecutive design storms. The most intensive testing involved subjecting the breakwater to three consecutive design storms undertaken at low water, high-water and low-water respectively or to the following sequence: 100 years storm at low water; two consecutive 100 year storms at high water; 24 hours (prototype) of waves having a height equal to the 100 year height. The final design was successful in surviving these events, both along the trunk and at the heads of the structure. Figure 6 shows a typical profile development after physical model testing (Murray, 1989).

4. CONSTRUCTION

TEMPORARY LOADING FACILITY

One of the first activities to be carried out during the construction phase of the project was the construction of the temporary loading facility (Porto de Embarque Provisório, PEP) which was accomplished during the winter of 1988 (Figure 7). This facility was constructed alongside the access trestle, at 800 m from its abutment, in 5 m of water at low tide. Its breakwater was designed for waves with a recurrence period of 5 years and a significant wave height of 3.2 m. The PEP layout and a typical cross-section of the temporary breakwater are shown in Figure 8.

Table 3: Summary of Design Parameters

• Deepwater Design Wave	≈ 6.0 m
• Highest Recorded H_s at the Structure	3.0 m
• Mean Water Depth at Structure	11.5 m
• Tidal Range at Structure	≈ 2.5 m
• Foundation Conditions	poor (soft clay)
• Design Wave at Structure	4.0 m
• Design Wave Periods (T_p)	6.5; 8; 10 s
• Dimensionless Wave Height ($H_s/AD_{0.50}$)	≈ 3
• Dimensionless Wave Period ($\sqrt{g/D_{0.50}}T_p$)	22; 27; 34
• Length of Structure	543 m
• Berm Width	11.0/13.0 m
• Crest Height	+ 6.0 m
• Berm Armouring Gradation	300 kg - 4t
• Mean Stone Weight (W_{50})	1.5 t



FIGURE 7 PEP Photograph (Jan 89)

Table 2 Design Storms used for Physical Modelling**Design Storm 1 (DS1)**

Segment	Duration (h)	Cummulative Duration (h)	Significant Wave Height (m)	Peak Wave Period (s)
1	3	3	2.0	8.0
2	3	6	2.5	8.0
3	3	9	3.0	10.0
4	3	12	3.4	10.0
5	3	15	3.8	12.0
6	3	18	3.4	10.0
7	3	21	3.0	10.0
8	3	24	2.5	8.0

Design Storm 2 (INPH)

Segment	Duration (h)	Cummulative Duration (h)	Significant Wave Height (m)	Peak Wave Period (s)
1	3	3	2.5	9.3
2	3	6	3.0	9.3
3	3	9	3.5	9.3
4	3	12	4.0	9.3
5	3	15	2.5	11.5
6	3	18	3.0	11.5
7	3	21	3.5	11.5
8	3	24	4.0	11.5
9	3	27	2.5	14.3
10	3	30	3.0	14.3
11	3	33	3.5	14.3
12	3	36	4.0	14.3

Design Storm 3 (DS3)

Segment	Duration (h)	Cummulative Duration (h)	Significant Wave Height (m)	Peak Wave Period (s)
1	3	3	2.5	8.0
2	3	6	3.0	10.0
3	3	9	3.5	10.0
4	3	12	3.5	12.0
5	3	15	4.0	12.0
6	3	18	4.0	14.0
7	3	21	3.5	12.0
8	3	24	3.5	10.0

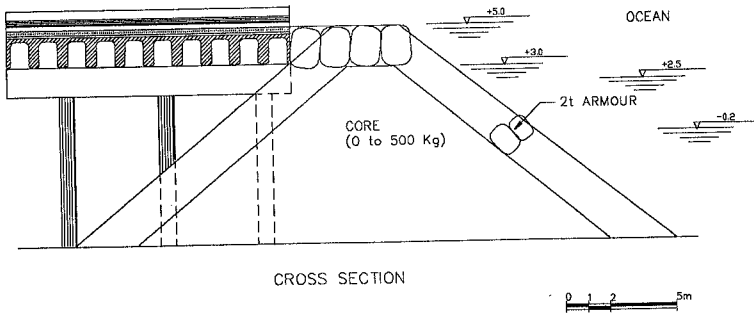
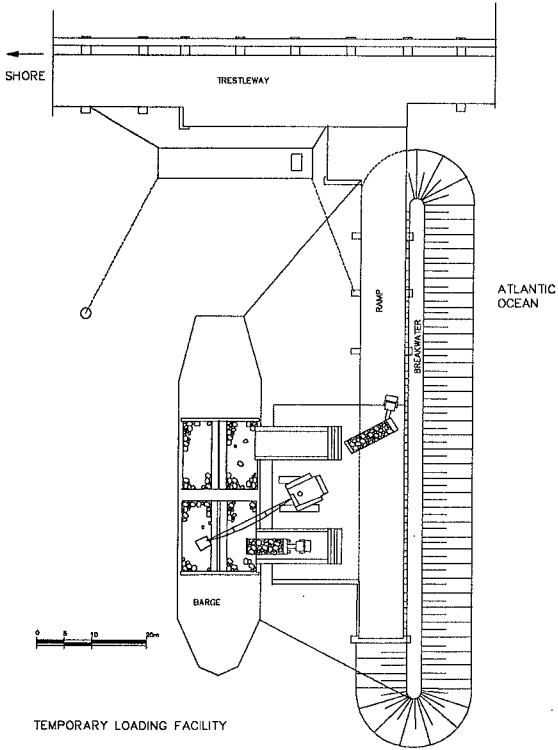


FIGURE 8: PEP PLAN AND CROSS SECTION

QUARRY

The quarry is situated 73 km from the terminal site. Rock extraction is obtained by conventional methods with bench heights of 10 m. The rock is gneiss and granite of sound quality. Fines are separated at the quarry by a simple grizzly operation and transported to the site by 40 t lorries. A buffer stock pile is maintained at the terminal site to smooth out loading peaks. With the berm design and a suitable blasting pattern it was found possible to utilize nearly all of the quarry production, with the obvious exception of the fines and overburden material.

CONSTRUCTION SEQUENCE

The first main construction activity to be carried out in October 1988, following the winter season was to place the stones of the geotechnical berm. This task involved dumping 340,000 m³ over an area of 124 m by 669 m, with a depth of water over the berm of 5.10 m.

Dumping was to be carried out in the open sea under waves and littoral currents. In order to conclude the operation in five months before the winter of 1989, weekly productions of 30,000 t would be necessary. After examining various solutions, including the use of locally available split barges, it was decided to charter a side dumping vessel of 1,100 t capacity which loaded down stone carpets on the sea bed in areas of approximately 30 m by 60 m and 0.30 m thickness. As this vessel was equipped with a dynamic positioning system, Schottel driven screws and bow thrusters, it was possible to achieve tolerances on the geotechnical berm construction of plus or minus 0.30 m vertically and plus or minus 1.0 m horizontally, leading to a substantial reduction of wastage. Figure 9 shows the phases of marine construction. The land based construction sequence is shown in Figures 5 and 9. It consists of dumping of the core and placing the armour stone by a combination of lorry tipping and skips handled by cranes. Production during these phases was expected to be about 40,000 m³ per month.

CONSTRUCTION ORGANIZATION AND CONTROL

Construction falls under the responsibility of a Construction Manager reporting to the Contract Manager, while design coordination and macro-planning are the responsibility of a specialized Engineer Manager. In order to maximise production, double shifts have been worked, with Saturday nights off and Sundays reserved for equipment maintenance. Quality control is carried out by members of the contractors staff, with a Quality Control Manager reporting directly to the Contract Manager as well as liaising with the client's supervisory staff.

Control of breakwater construction includes periodic checking of project geometry and construction tolerances, rock quality, and gradation curves for core and berm armour materials. It should be mentioned here that the design gradation curves were based on pilot curves prepared after experimental blasting had been carried out on opening up of the quarry, with the intention of optimizing quarry production.

During the design stage several experimental methods for gradation control were tried, including curves based on computer analysis of photographs of rock samples (Maerz et al., 1987). In most cases, however, gradation curves are carried out simply by weighing randomly chosen samples and ensuring that the measured curve falls within the specified gradation tolerance intervals.

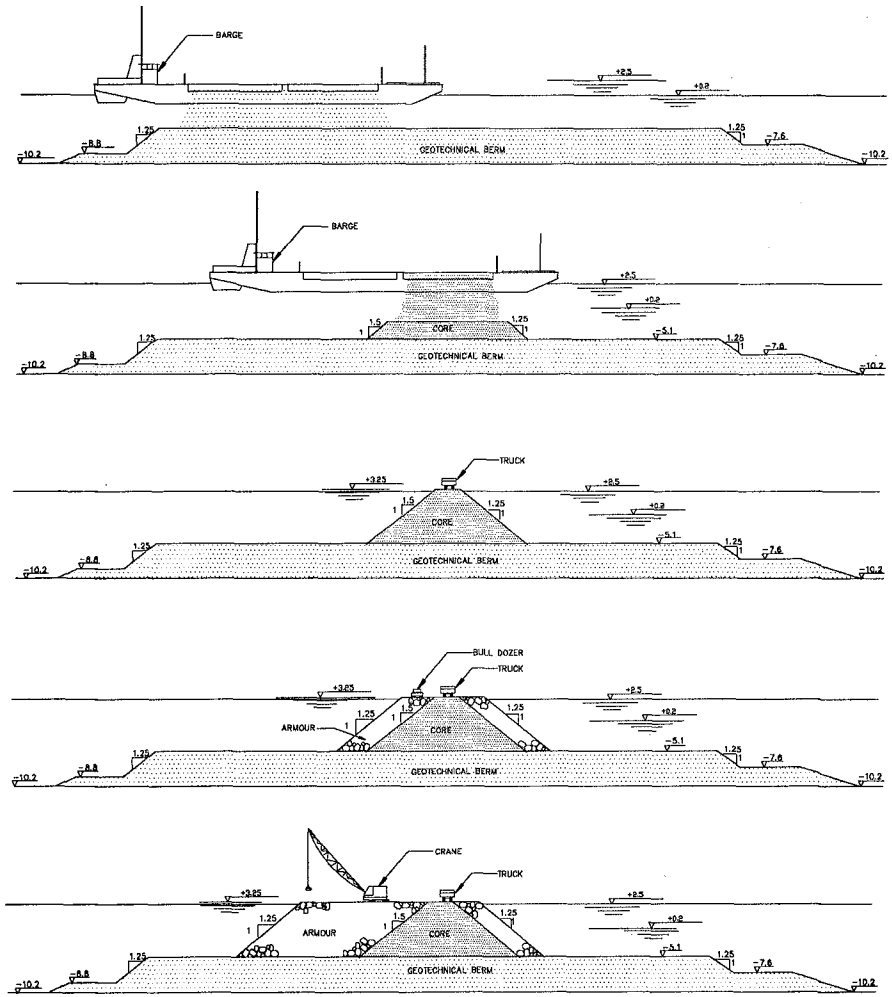
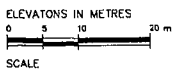


FIGURE 9: CONSTRUCTION SEQUENCE



5. REDESIGN

While under construction, evidence that the soft clay layers were much weaker than expected was obtained through subsidence of the breakwater foundation. Subsequently, the breakwater project was reviewed to adapt to the new soils situation. Both hydraulic and geotechnical engineering redesigns were carried out (Atria, 1990a; Geoprojetos, 1990). In order to decrease the loading on the subsoil the hydraulic design has evolved to a low crested berm design, overtopping being reduced by a suitable increase in the hydraulic berm width as indicated in Figures 10 and 11.

The wave climate for the TPS used in the CNO original design (Sayao and Hall, 1988) was the same as given in Hidroservice (1986). Site measurements of the wave climate are still underway. Since more data are collected near the study site, more work has been carried out to examine the given design wave climate (Atria, 1990b). Even though there is evidence that the wave climate for the TPS has changed since Hidroservice (1986) work, the decision was made by Petrobrás to redesign the breakwater structure for the same wave climate as used in the original design.

Physical model studies for the redesign of the breakwater were carried out in the National Research Council Hydraulics Laboratory (NRC), Ottawa, Canada. The modelling programme included hydraulic stability tests for the breakwater structure as well as wave agitation measurements in the lee of the breakwater. Several model structures were tested under 2 different design storms (INPH and DS3, see Table 2), leading to the development of the breakwater redesign for the TPS. A typical section of the final redesign is shown in Figure 10 and a comparison with the original berm design is shown in Figure 11.

The rubble-mound redesign structure consists of an outer berm placed at a slope of 1:3 (due to geotechnical constraints), extending from the geotechnical berm elevation to the crest elevation. The berm armouring material consists of stones weighing between 1 and 4 tonnes; crest and backslope are armoured with stones of 4 to 8 tonnes, providing for protection against wave overtopping. A description of the model testing programme and test results leading to the final redesign of the TPS offshore breakwater are given in Atria (1990a).

In order to avoid the need to contaminate the hydraulic berm by the widening of the temporary access road, it has been decided to advance the cranes over the berm on a system of leap-frogging girders. Contamination of the armouring due to fines is discussed in Fournier et al., (1990).

6. CONCLUSION

The design phases for the offshore breakwater of the Sergipe Marine Terminal were presented. The TPS breakwater is one of the few in the world to be constructed over a soft marine clay layer and to accommodate for unfavourable subsoil conditions an extensive redesign was carried out. The new redesign is presently under construction.

The advantages of the adaptation of the tender breakwater design from a contractors point of view can be summarised as follows: elimination of the sand layer in the geotechnical berm, reduction of rock quantities, reduction of the number of stone gradations, simplification of the construction methods, execution of the marine phases during the summer months only and finally, reduction of the overall construction period.

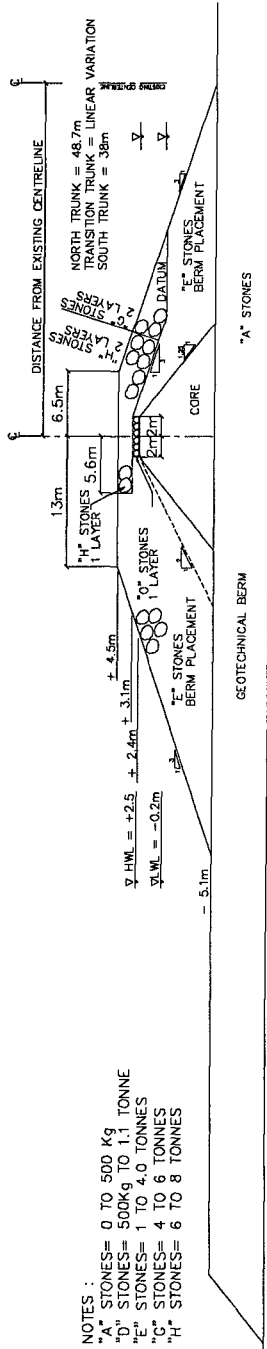


FIGURE 10: TYPICAL SECTION THROUGH SUPERSTRUCTURE TRUNK

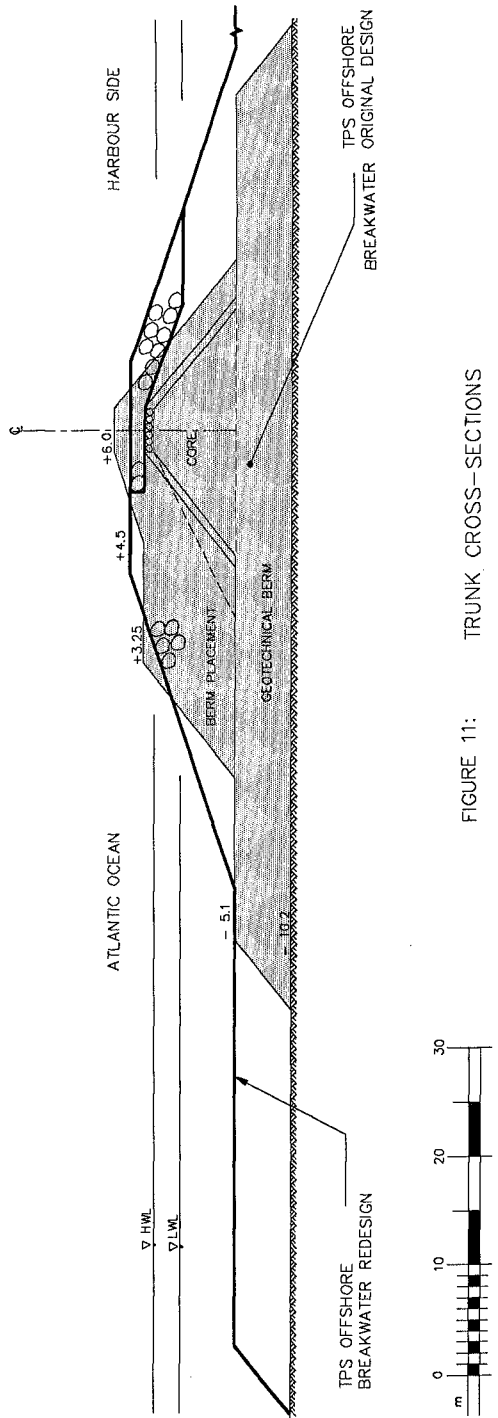
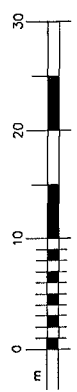


FIGURE 11: TRUNK CROSS-SECTIONS



There is also the philosophical aspect that for the conventional design a certain percentage of damage of the armour layers is acceptable, whereas the berm design does not suffer 'damage' for the design conditions, thus eliminating the need for maintenance.

REFERENCES

- Atria Engineering Hydraulics Inc. (1990a). "Hydraulic model studies and redesign of the offshore breakwater for Terminal Portuário de Sergipe". Final Report for Construtora Norberto Odebrecht S.A., May, 115p.
- Atria Engineering Hydraulics Inc. (1990b). "Estudo do clima de ondas no Terminal Portuário de Sergipe". Unpublished Report for Construtora Norberto Odebrecht S.A., May.
- Danish Hydraulics Institute (1987). "Sergipe terminal, alternative breakwater, phase I, conceptual design". Report for Construtora Norberto Odebrecht S.A., in association with Portconsult, Consulting Engineers A/S, Copenhagen, Denmark, April.
- Foster D.N. and Hall N.R. (1987). "Natural armoured rubble-mound structures". Proc. 2nd Int. Conf. on Coastal and Port Engrg. in Developing Countries, Beijing, China, Vol. 1, p.587-601.
- Fournier C.P.; O.J. Sayao and F. Caldas (1990). "Berm breakwater contamination study, Sergipe marine terminal, Brazil. Proc. 22nd Int. Conf. on Coastal Engrg., Delft, The Netherlands, ASCE.
- Geoprojetos Engenharia Ltda. (1990). "Apresentação da versão 6 do reprojeto do quebra-mar". Report R.220990-137-17 for Construtora Norberto Odebrecht S.A., March.
- Hidroservice Engenharia de Projetos S.A. (1986). "Terminal Portuário de Sergipe, projeto básico, memorial descritivo". Report HE-1072-R02-0785 for the Governo do Estado de Sergipe, Instituto de Economia e Pesquisas-INEP, July.
- Hidroservice Engenharia de Projetos S.A. (1987). "Terminal Portuário de Sergipe, final design". São Paulo, Brazil.
- Lundgren H. and Lindhardt Jacobsen H.C. (1987). "Breakwaters on weak soils". Proc. 2nd Int. Conference on Coastal and Port Engrg. in Developing Countries, Beijing, China, Vol. 1, pp. 779-793.
- Maerz, N.H. et al. (1987). "Measurement of rock fragmentation by digital photoanalysis". Proc., International Society for Rock Mechanics, A.A. Balkema, Rotterdam, pp. 687-692.
- Murray, M. (1989). "Projeto e construção do quebra-mar offshore do Terminal Portuário de Sergipe". Presented in the IV Encontro de Engenharia Portuária, Santos, São Paulo, August/September.
- Sayao O.J. and Hall, K.R. (1988). "Berm breakwater design for the Sergipe offshore terminal, Brazil". Unpublished Report to Construtora Norberto Odebrecht S.A. by F.J. Reinders and Associates, May, 140p.
- Sondotécnica S.A. (1978). "Estudo da viabilidade técnico-econômica e ante projeto para a implantação de um terminal fluvial ou marítimo de graneis sólidos e líquidos no Estado de Sergipe". Final report, 1st. phase, Rio.
- Van der Meer, J.W. (1988). "Rock, slopes and gravel beaches under wave attack". Delft Hydraulics Communication No. 396.
- Willis, D.H.; W.F. Baird and Magoon, T.O. (1987). "Berm breakwaters: unconventional rubble-mound breakwaters". Proc., ASCE workshop held at the Hydraulics Laboratory, National Research Council of Canada, Ottawa, September, 284p.

ACKNOWLEDGEMENTS

Thanks are due to Petrobrás - Petróleo Brasileiro S.A. and Construtora Norberto Odebrecht S.A. for authorizing and motivating the preparation of this paper, respectively. Also, the authors would like to thank Dr. Kevin R. Hall, Queen's University, for supervision of hydraulic model testing. The tender design was developed by Hidroservice Engenharia de Projetos Ltda., Brazil. The alternative berm design was carried out by Dolfim Engenharia S.A., Brazil and F.J. Reinders and Associates, Canada. Placing of the geotechnical berm was accomplished by ACZ Marine

CHAPTER 244

ST. PAUL BREAKWATER, PHASE 1

The Project, the Failure and the Subsequent Investigations

Torben Sørensen¹ and Ole Juul Jensen²

Abstract

The St. Paul Phase 1 berm breakwater was destroyed by two storms within approximately two months of its completion. Investigations made after the failure demonstrate that the cause of the failure was that the breakwater was built from material that was vastly undersized as compared to the recommended minimum rock gradation, and heavily contaminated by fines and overburden from the quarry.

Original Design and Hydraulic Studies

In 1982, the City of St. Paul, Alaska commissioned an American consulting engineering firm (the Consultant) to design a fishing harbour on St. Paul Island, one of the Pribilof Islands in the Bering Sea approximately 450 km north of the Aleutian Islands. The Consultant subcontracted the Danish Hydraulic Institute (DHI) to perform scale model tests and other hydraulic studies to support the design of the project. These studies resulted in the recommendation of a conventional rubble-mound breakwater to be constructed from locally available quarry rock material.

Construction and Revised Design

Construction of the breakwater started early May 1984 under the supervision of the Consultant. Soon after commencement of construction, it became clear that the contractor was unable to produce the stones required for the breakwater armour as designed.

¹ Director and ² Head, Ports and Marine Structures Division, Danish Hydraulic Institute, Agern Allé 5, DK-2970 Hørsholm, Denmark.

On the basis of detailed information of quarry yield reported to have been obtained DHI, in response to an inquiry from the Consultant, suggested consideration of a berm type breakwater, including suggestions for a trunk cross-section that might be used with the available stone sizes.

On 20 July 1984, DHI was authorized to perform a model test programme to be executed during the first two weeks of August 1984. This is to be seen on the background that Phase 1 of the breakwater, i.e. the first approximately 900 ft of a 2050 ft long breakwater, should be completed before the start of the winter, presumably before November 1984. The revised breakwater design (Fig. 1) involved only two stone gradations, called A and B-stones. The A-stones, also called the "1-8 t" gradation, were the armouring with a prescribed minimum gradation curve and the B-stones were 0 to 0.5 t quarry run. DHI's final report of September 1984 states the following with respect to the A-stones: "It is recommended that the coarse "1-8 t" gradation used in the tests is made a minimum requirement for construction, understood so that the material built into the breakwater should at no point have a gradation curve below (with smaller stones) than the "1-8" t stones".

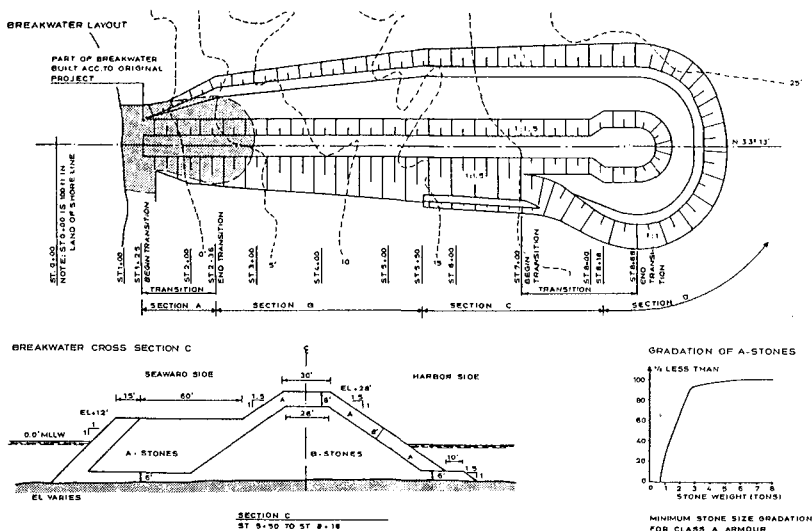


Figure 1. Plan and Cross-Section of St. Paul Breakwater Redesign, Phase 1.

Due to the planned interruption of construction during the winter 1984/85, a temporary protection of the outer end of the Phase 1 breakwater was required.

Having been informed that large armour stones were not available for the temporary breakwater head, DHI suggested the use of a berm type roundhead as a temporary protection using the same "1-8 t" A-stones as used on the trunk of the breakwater. However, DHI cautioned the Consultant that "it is expected that the provisional roundhead will suffer severe damage in the coming winter, but that the damage will not hamper the progression of construction work on Stage II in the spring of 1985, since the stones displaced from the roundhead will be deposited on the harbour side where the inner breakwater is to be constructed. It is thus expected that the stones can be directly incorporated in the inner breakwater" (which formed part of the envisaged construction under Phase 2 of the project). For reasons of time and costs, no three-dimensional model tests with the temporary breakwater head were made prior to construction.

During construction, the Consultant's "Construction Manager" on the site repeatedly complained that the contractor was deviating from the specifications using too small stones and stone material mixed with overburden and fines. However, neither the Consultant nor the contractor apparently ever made any measurements by weighing or by any other means to determine the actual gradation of material being placed in the breakwater profile. At least, no such measurements were ever presented or found during the subsequent litigation. Similarly, it appears that none of the undersized rocks was ever removed from the breakwater.

The Breakwater Failure

The Phase 1 breakwater was completed 2 October 1984 and was severely damaged during two storms in November and December the same year. At the end of the December storm, the length of intact crest of the breakwater was reduced from its original approximately 800 ft to less than 300 ft (Fig. 2).

Various surveys of the A-stone gradations used for construction were made after the damage. Fig. 3 shows the results of all of these surveys. It appears clearly from the various surveys that the average weight of the A-stones used for construction was generally very much smaller than what was recommended by DHI.

Model Tests

During "discovery" under the subsequent litigation, model tests were made both by DHI (defendant) and by ARCTEC for plaintiffs (the Consultant and its insurance company). These tests were three-dimensional model

tests with a structure modelled in compliance with DHI's recommendations regarding profiles and stone material. The wave conditions used in these tests represented those of the two storms that destroyed the breakwater built at St. Paul and were determined by numerical hindcasting made in-house by DHI and by OCTI on behalf of plaintiffs.

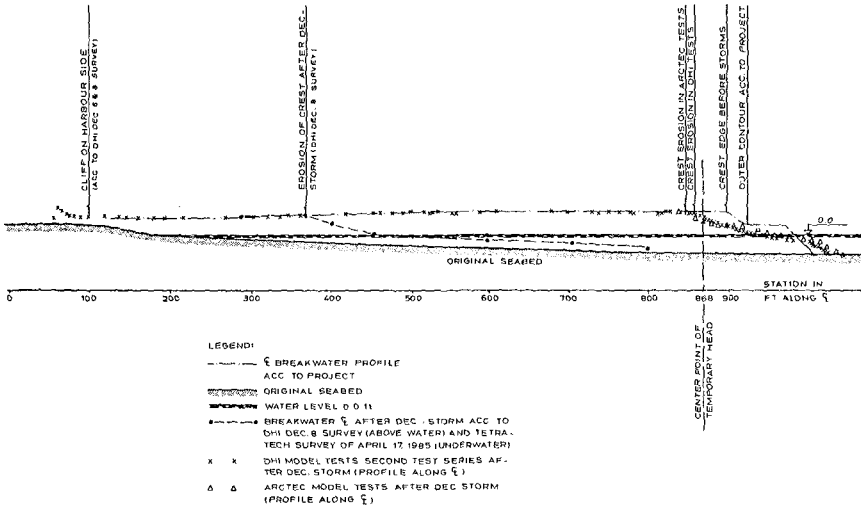


Figure 2. Comparison of Model Test Results and In-Situ Damage.

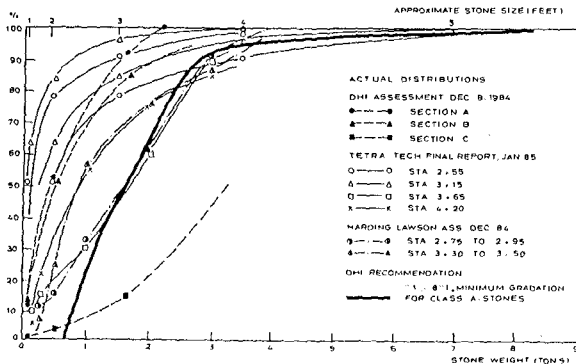


Figure 3. Estimates of A-Stone Gradations As-Built.

In spite of a number of differences between the two sets of model tests, both in the hindcast wave conditions and in the physical modelling, the results of the two sets of tests were remarkably similar. In both tests, the damage observed in the models had no resemblance whatsoever to that experienced in nature. In the models, the damage was limited to the temporary breakwater head proper and fell well within what was predicted in DHI's final report of September 1984, whereas in the nature the breakwater had suffered virtually total destruction (Fig. 2), chiefly through the process of crest erosion caused by excessive overtopping.

In both sets of model tests, overtopping was insignificant and did not at any point cause damage to the crest of the breakwater. This is in sharp contrast to what was observed in nature where photographs taken during the storms show violent overtopping, and photos taken after the storms show extensive damage in the form of crest erosion over the entire outer portion of the breakwater.

The difference in overtopping between models and nature is entirely consistent with the assumption that the rocks used for construction were much smaller (and contaminated with fines and overburden) than corresponding to those used in the model tests and recommended by DHI. This assumption is also supported by numerous photographs taken during and immediately after construction.

Conclusion

DHI considers the identical results of the two sets of model tests as conclusive engineering proof that the St. Paul Phase 1 breakwater was built from stones that were generally very much smaller than those recommended by DHI. Smaller stones combined with extensive contamination with fine material would cause both highly accelerated erosion from the end and drastically increased overtopping resulting in heavy damage to the crest and the rear side - i.e. exactly those processes that destroyed the breakwater in nature as seen from the surveys and the photographs.

CHAPTER 245

The Durban Beach Restoration Scheme after 30 years

W I Laubscher*, D H Swart*, J S Schoonees*, W M Pfaff** and A B Davis**

1. Abstract

The harbour breakwaters at Durban in conjunction with the dredging of the harbour entrance cut off the sediment supply to the important bathing beaches of the city, necessitating a beach restoration scheme. This paper reviews this scheme. Before 1977, the measures to restore the beaches included an underwater mound, beachfill and rock groynes. After 1977 and following a previous review, it was recommended not to complete the mound, to place initial beachfill, regularly nourish the beaches and to build low-level groynes. Implementation started with a sand pumping scheme and 600 000 m³ of beachfill followed by the building of three multi-functional pier/groynes. Monitoring of the beach restoration scheme enabled valuable experience to be gained on aspects such as the loss rate of sand from the beaches, beach profile and scour levels alongside the pier/groynes and on the determination of a potential erosion line and building control zone. This paper concludes with some important lessons learned from the scheme.

2. Introduction

Durban, situated on the South African East Coast, is one of the oldest South African harbour cities and a popular holiday resort renowned for its golden beaches and subtropical climate. Since construction of the harbour started in 1857, the natural northbound littoral drift was cut off from the bathing beaches in the Durban Bight north of the harbour entrance. Figure 1 shows the position of the harbour and the beaches along the Durban Bight.

The state of the beaches deteriorated progressively over the years and this led to the local council, the Durban Corporation, to consider and implement measures to prevent the increasing erosion. Beach replenishment in the form of various sand pumping schemes had been implemented over the years and two rubble-mound groynes, known as the Paterson groynes, were constructed in a critical area to retain longshore sediment transport. However,

* CSIR, P O Box 320, Stellenbosch, 7600, South Africa.

** The City Engineer's Department, P O Box 680, Durban, 4000, South Africa.

these measures did not cope sufficiently with the erosion problem and the Durban Corporation was forced to take further action.

The Council for Scientific and Industrial Research (now CSIR) became involved in 1957 when it was contracted by the Durban Corporation and the then South African Railways and Harbours (now Portnet) to investigate the whole beach erosion problem and to devise a strategy for beach improvement and restoration. The investigation consisted of field studies to collect environmental data (e.g. on wave and current characteristics, sedimentological and morphological conditions) and various model studies to investigate the effect of present and proposed structures on the sediment movement around the harbour entrance and the beaches to the north. This extensive investigation was undertaken over a period of 20 years during which numerous reports were published regarding the results of the different investigations. All the work done over this period was summarised in a *status quo* report (CSIR, 1976) which also described various alternative schemes to improve the condition of the beaches and presented proposals for prototype monitoring.

After an intensive review of the information contained in the *status quo* report an amended beach management strategy was proposed in 1977. This strategy was published in CSIR (1977). The Durban Corporation accepted the strategy outlined in this report and in 1980 embarked on an extensive restoration and replenishment scheme for the beaches south of Somtseu Road (Figure 1). The CSIR was again involved in the implementation of the scheme through model studies of proposed structures and through prototype monitoring. At present the CSIR is involved in the scheme as specialist advisor on beach improvement and management by means of interpretation of the monitoring data. A second *status quo* report compiled in 1989 (CSIR, 1989), summarised all work done and the conclusions reached over the years and also made recommendations for further work.

The beach improvement scheme over the last 30 years can therefore be divided into two distinct periods, namely, (1) the original beach restoration scheme implemented before 1977, and (2) following the intensive review in 1977, the new restoration and management strategy after 1977. The purpose of this paper is to review the beach restoration and management scheme and to share with others some of the important lessons learned over a period of 30 years.

3. Beach Restoration Before 1977

3.1 Strategy

The original beach restoration strategy proposed in the early 1960s, was based on various model studies and prototype monitoring and consisted of:

- (i) Construction of an offshore underwater mound designed to reduce storm-wave energy in order to reduce longshore sediment transport along the beaches.
- (ii) Provision of an initial beachfill to restore the beaches along the sediment starved section of the Bight.

- (iii) A renourishment scheme to replenish material as compensation for the natural losses from the Bight. (These natural losses were calculated then to be about 70 000 m³/year (CSIR, 1963, 1974 and 1976) and it was therefore recommended that this volume of material be placed annually on the beaches).
- (iv) Replacement of the old dilapidated Paterson groynes by a number of groynes to retain sediment transported along the Bight.

3.2 Implementation

Implementation of the above-mentioned strategy started in 1966 and was initially centred around the construction of the underwater mound. The position of the mound is shown in Figure 1. The mound was constructed by placing dredged sand on the line indicated on Figure 1 according to a design profile. It was found that the mound naturally reached a stable profile such that the ratio of the height of the mound to the original water depth was approximately 0,4. An effort was also made to place an initial fill on the southern Bight beaches. Replenishment of the beaches was done through a simple sand pumping scheme which delivered sand at two locations immediately north of the northern harbour breakwater. However, construction of the proposed new groynes to replace the Paterson groynes were then not attempted due to concentration on the mound construction.

In 1976, after 20 years of involvement in the project, the CSIR compiled an overview of all the work done up to that point. Conclusions were drawn from all the information available and recommendations were made concerning future work with respect to beach improvement and management. These can be summarised as follows (see Figure 1 for the different locations referred to):

- (i) Due to progressive lengthening of the harbour breakwaters, the northward directed longshore transport was cut off at the harbour entrance. This, together with the focusing effect of the old dredger spoil dump situated offshore from the harbour entrance, led to the coastline in the Bight realigning itself to a new long-term equilibrium shape which was more concave than that which existed before harbour construction.
- (ii) Development between Somtseu Road and West Street encroached into the dynamic beach area and was, therefore, subjected to extensive storm erosion.
- (iii) The beaches between Mgeni River mouth and Somtseu Road appeared to be in a state of long-term equilibrium while the beaches south of Somtseu Road were subjected to gradual long-term erosion at a rate of 70 000 m³.
- (iv) The underwater mound, which had by 1976 not been completed to the design dimensions, offers some protection against extreme conditions in the area north of Somtseu Road, while little or no protection is provided in the area south of Somtseu Road.
- (v) The underwater mound could be extended in a northerly direction which would provide better protection for the area immediately south of the Mgeni River. This would result in a reduction of the loss rate from the beaches in the

Bight. However, this would mean that erosion of the beaches immediately north of the Mgeni River mouth would increase with an amount equal to the reduction in the Bight loss rate.

The above conclusions indicated that beach restoration and improvement should be concentrated on the Bight beaches south of Somtseu Road. It was recommended that, should additional protection against storm erosion be required, the underwater mound should be extended to the north and completed to its design dimensions. Additional erosion north of the Mgeni River would then have had to be accepted. An estimated 2,5 million m³ of sand would have been required to complete the mound. It was further advised that a sufficiently wide buffer be provided along the beaches south of Somtseu Road and that an estimated 200 000 m³ of sand would be needed for this purpose. A combined beachfill and low-level groyne scheme was considered the most feasible alternative of the possible beach restoration schemes. However, it was necessary for the Durban Corporation to define their specific requirements for the Bight area and to decide on the level of improvement necessary to meet these. Besides the restoration measures, it was recommended that some prototype monitoring be carried out to gain more knowledge of the complex system and to ensure optimization of the improvement measures.

4. Beach Restoration After 1977

4.1 Strategy

Shortly after the appearance of the 1976 *status quo* report, the conclusions and recommendations of which were summarised in the previous paragraph, an extensive re-evaluation of the functioning and effectiveness of the underwater mound was carried out. The results indicated that the mound was not as effective as was first thought and that the actual loss rate from the Bight was higher than estimated previously. A detailed report (CSIR, 1977) addressed the problem of how the Bight beaches should be managed and outlined firm recommendations and guidelines for a beach restoration scheme. These recommendations, which built on but superseded previous recommendations, can be summarised as follows:

- (i) The mound should not be completed to its design dimensions.
- (ii) A control zone, where building should not be permitted due to potential erosion, should be established 40 m landwards of the 1977 high-water line.
- (iii) An initial fill should be placed in the area south of where the Paterson groynes then were, so as to provide sufficient buffer width.
- (iv) Renourishment should be carried out to compensate for the loss rate from the Bight, the rate of which at the time had been determined to be between 70 000 m³/yr and 90 000 m³/yr. Renourishment of 60 000 m³/yr on the Addington and South Beaches and another 30 000 m³/yr on the North Beach was recommended, assuming that compatible borrow material was available.
- (v) The Paterson groynes, being dilapidated and of a high level design, should be replaced with new low-level groynes.

These firm proposals were accepted by the Durban Corporation and they embarked on the implementation of the revised scheme in 1978/79.

4.2 Implementation

The implementation of the proposals started in 1978/79 with the design of a sand pumping scheme to deliver replenishment material along the eroding beaches (Barnett, 1982).

The scheme consisted of a hopper station (into which sand is delivered from a dredger) with four booster pump stations and a number of outlets along the pipeline. To allow for losses, the required replenishment rate was calculated to be 100 000 m³/yr. The system was designed with a capacity of being able to pump 4 000 m³ of sand per day (2 dredger loads) on anticipation of dredgers working 100 days per year. The overall limiting factor on the operational capacity of the scheme was, at that time, the supply of dredger sand for pumping on the beaches which was made available from the harbour authorities (Portnet) routine dredging operations. However, a supplementary agreement between the Durban Corporation and Portnet now provides for the charter hire of the dredger when necessary to win sand solely for the purpose of supplying the sand pumping scheme. With good co-operation between Portnet and the Durban Corporation, the replenishment scheme has, over the last few years, been operated at approximately 230 000 m³/yr, thus achieving some beach-building as well.

In 1982 an initial bulk placement of 600 000 m³ was carried out on Addington and South beaches (between Survey Stations 13 and 16 - Figures 1 and 2) in addition to the renourishment scheme.

A further component of the restoration scheme consisted of the replacement of the old Paterson groynes by two low-level groynes. The position of the groynes are shown on Figure 2. The basic design concept for the new structures was that of a low-level groyne which allows sand to pass over it once the design beach profile, and therefore the desired beach width, have been attained. Both the feasibility study and the subsequent design and construct contract were awarded to a contractor who came forward with several alternative designs based on performance requirements laid down by the Durban Corporation. The resulting design was that of a combined pier/groyne structure, the pier consisting of a deck and two rows of piles with the groyne comprising rock placed between the piles to form a low-level obstruction. The hydraulic design of these two new groynes was carried out by the CSIR on the basis of small-scale physical model tests. Construction of the piers, known as the North Beach Pier and the Bay of Plenty Pier respectively, started in September 1983 and both piers were completed in June 1985. Removal of the Paterson groynes followed and was completed by October 1985.

In 1987 the Durban Corporation decided to construct a third pier/groyne, named the Dairy Beach Pier, with a design similar to of the older two piers (see Figure 2 for the location).

This pier was needed to provide a usable recreation beach adjacent to West Street jetty (Figure 2) in an area where encroachment into the dynamic

beach area had occurred (Section 3.2). Again the CSIR was involved in supplying design information such as the design beach profile, permeability of the rock core, predicted scour adjacent to the pier and orientation of the pier. Construction of the pier has since been completed.

Both during and following the implementation of the above measures, the initial field studies were continued and expanded into an extensive ongoing prototype monitoring programme which includes:

- (i) Beach and bathymetric surveys (see Figure 2 for an example as well as for the position of the survey sections).
- (ii) Sedimentological surveys and computation of volumes of sand lost and gained from the beaches as well as the volumes of sand pumped onto the beaches. In total, 1 175 000 m³ of sand has been placed on the beaches between 1984 and 1988.
- (iii) Monitoring of the nearshore wave climate by means of Waverider and clinometer measurements. The median peak wave period was found to be about 10 s within a range from 5 s to 15 s. At the Waverider position (landwards of the mound in about 13 m of water (to mean sea level)) the 1 in 1 year and 1 in 100 year significant wave heights were found to be respectively 3,6 m and 5,3 m. The mean spring tidal range is 1,72 m.
- (iv) Monitoring the profile behaviour adjacent to the new piers to determine the extent of scour. Because of the large rocks used for the cores of the pier/groynes, the permeability of the structures was found to be too high. Grouting was carried out to rectify this. Generally speaking, it was found that the beach profile (sand) levels on the updrift side of the pier/groyne were about 1 m to 1,5 m and on the downdrift side, approximately 2 m below the rock level in the core. The scour alongside the structures was found to exceed the design values considerably. This is presently the subject of a detailed investigation.

The monitored data provide valuable information on the physical processes in the Durban Bight. The following work resulted directly from the analysis and interpretation of the monitored data:

- (i) A computer data bank was developed where all monitored data are stored. Reports on the interpretation and analysis of these data are published annually.
- (ii) A representative nearshore wave climate for the Central Beaches was determined from the wave measurements.
- (iii) The functioning of the North Beach and Bay of Plenty piers continue to be closely monitored, especially with respect to scour adjacent to the seaward ends. Estimates of the expected scour were calculated for the piers and are updated as more information becomes available. Design parameters for the new Dairy Beach Pier were also determined through these analyses.
- (iv) The average loss rate from the Bight was further revised through a detailed study which included theoretical and empirical calculations and which

used as input wave data from voluntary observing ships, dredging data from Cave Rock Bight (the harbour sand trap - see Figure 2) and beach surveys. The dredger records cover a 60-year period - see Campbell *et al.* (1985). A combined estimate of the loss rate, based on the theoretical and empirical results, was made. It was found to be about 200 000 m³/yr with a corresponding replenishment rate of 210 000 m³/yr to cater for additional losses caused by a steepening of beach profiles as a result of a seaward advancement of the shoreline. Long-term changes in the deep-sea wave climate, especially the wave direction, caused the loss rate to vary significantly over time.

(v) The long-term stability (over a 15-year period) of the Bight beaches was determined using the beach surveys since 1973. This study indicated as had been stated previously, that the beaches between the Mgeni River and Somtseu Road are in equilibrium. Figure 3 shows the variation in the shoreline position at Section 14 over time. It is clear from this and other similar figures that the beaches south of Somtseu Road are at present in the best state since 1973.

(vi) A new potential erosion line for the Bight was determined through a combined numerical and empirical method. A building control zone for the Bight has also been defined. It was found that by specifying the potential erosion line as simply a fixed distance behind the median position of a certain beach profile level (for example +1 m to mean sea level) can be misleading if the slope of the lower limit beach profile is rather flat. Figure 4, taken from CSIR (1990), illustrates this point.

It can therefore be stated that all the measures which were proposed in the 1977 beach restoration and management strategy have been carried out to the substantial benefit of the bathers in the Durban Bight.

5. Conclusions

5.1 General

Following a 30-year period during which various different beach improvement and restoration methods and schemes were proposed and some also implemented, the beaches in the Durban Bight are at present in a better state than at any time since 1959. The combination of experience gained over the years, valuable information gained from prototype monitoring, theoretical and empirical studies, construction of hard structures and the implementation of a sound beach management policy have lead to the present good state of the beaches. The wealth of information which has over the years become available on the specific problem experienced in Durban can now be applied to similar situations elsewhere.

It is anticipated that pressure will increase for further development along the Bight beaches as a result of an increasing demand for recreational facilities.

5.2 Lessons Learned

The following lessons have been learned:

- (i) The initial position of the dredger spoil dump caused wave focusing on the beach, which aggravated the erosion due to the harbour cutting off the sand supply.
- (ii) The loss rate of sand from the beach was found to vary significantly with the deep-sea wave climate, especially with the wave direction.
- (iii) The height of the underwater mound stabilised naturally at about 0,4 times the original water depth. With this equilibrium crest level, the mound offered only limited protection from wave action to the beaches.
- (iv) Development in the dynamic beach zone should be avoided and must be controlled by designating a potential erosion line and a building control zone where strict controls of development proposals have to be done.
- (v) Specifying the potential erosion line as a fixed distance behind the median position of a certain beach profile level can be misleading if the slope of the lower-limit beach profile is rather flat.
- (vi) The pier/groyne combination provides a multi-functional structure. Sand levels on the beach on the updrift side adjacent to the structure are generally about 1 m to 1,5 m, and approximately 2 m on the downdrift side, below the rock core level. The permeability of the rock core and the scour alongside the piles are very important design considerations.

References

- Barnett, K A (1982). Durban beaches reclamation: practical aspect. *18 International Conference on Coastal Engineering*, ASCE, Volume 3:1970-1991, Cape Town, South Africa.
- Campbell, N P, Macleod, D C and Swart, D H (1985). Bypassing and beach nourishment scheme at Durban. 26 PIANC, Section II, Subject 3:7-18, Brussels, Belgium.
- CSIR (1963). Fifth report on Durban harbour siltation and beach erosion: hydraulic model investigation. *CSIR Report CMEG 537*, Pretoria, South Africa.
- CSIR (1974). An appraisal of the Durban beaches, nearshore areas and underwater mound from 1958 to February 1974. *CSIR Report C/SEA 75/2*, Stellenbosch, South Africa.
- CSIR (1976). *Status quo* of the Durban Beach protection investigation. *CSIR Report C/SEA 7607*, Stellenbosch, South Africa.
- CSIR (1977). Management of the beaches in the Durban Bight, Volumes 1 and 2. *CSIR Report C/SEA 7622*, Stellenbosch, South Africa.
- CSIR (1989). *Status quo* report on the Durban Beach Monitoring Programme. *CSIR Report EMA-C 89145*, Stellenbosch, South Africa.

CSIR (1990). Setback analysis for the Durban Bight and Glen Ashley Beach. *CSIR Report*, Stellenbosch, South Africa, (in prep.).

Acknowledgement

Permission by the Durban Corporation to publish this paper is gratefully acknowledged.

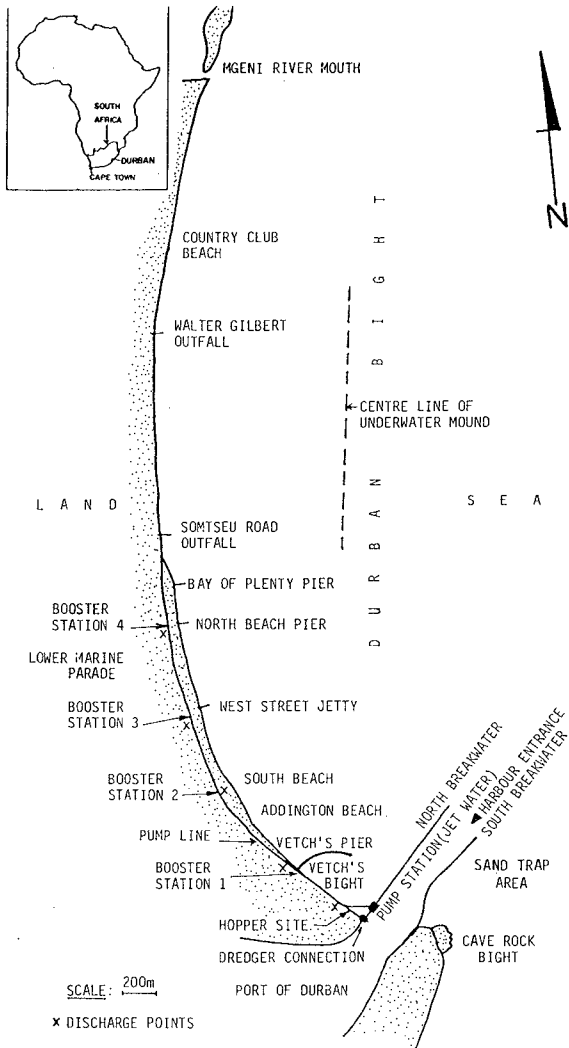


FIGURE 1 : LOCATION MAP

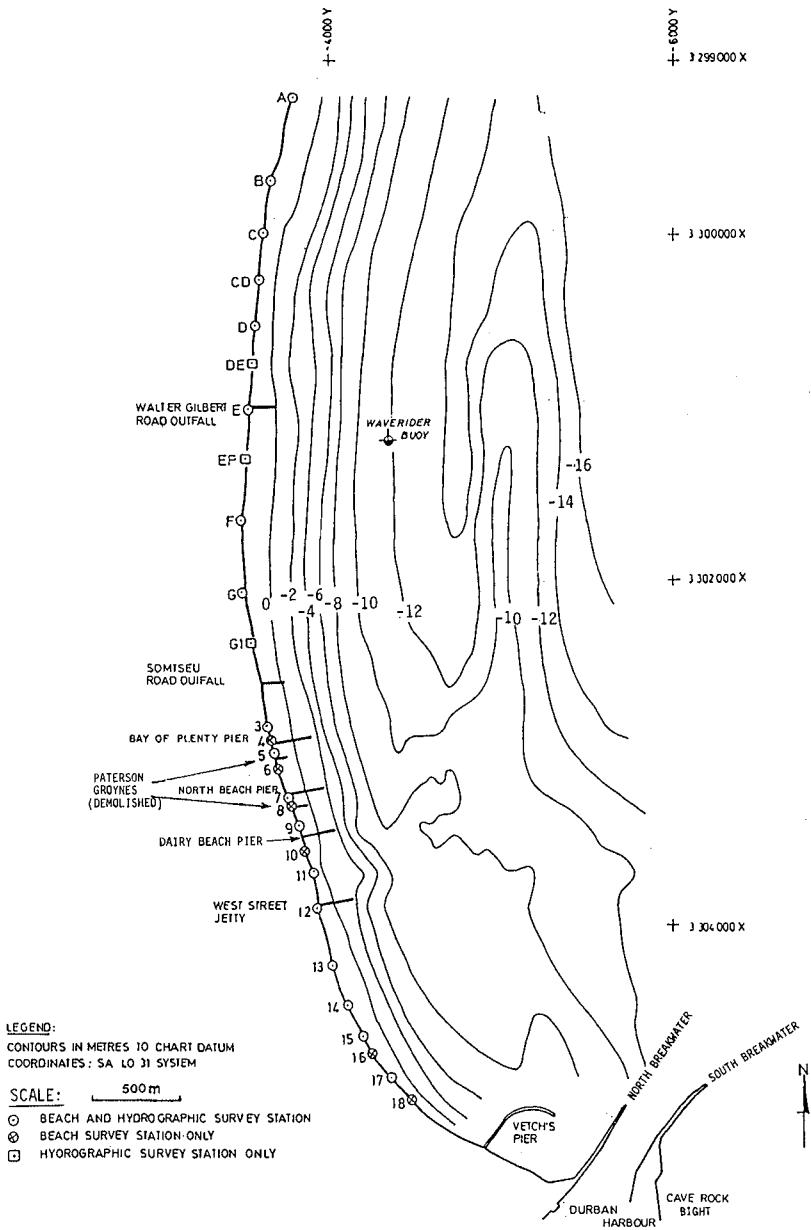


FIGURE 2 : BATHYMETRY OF THE DURBAN BIGHT

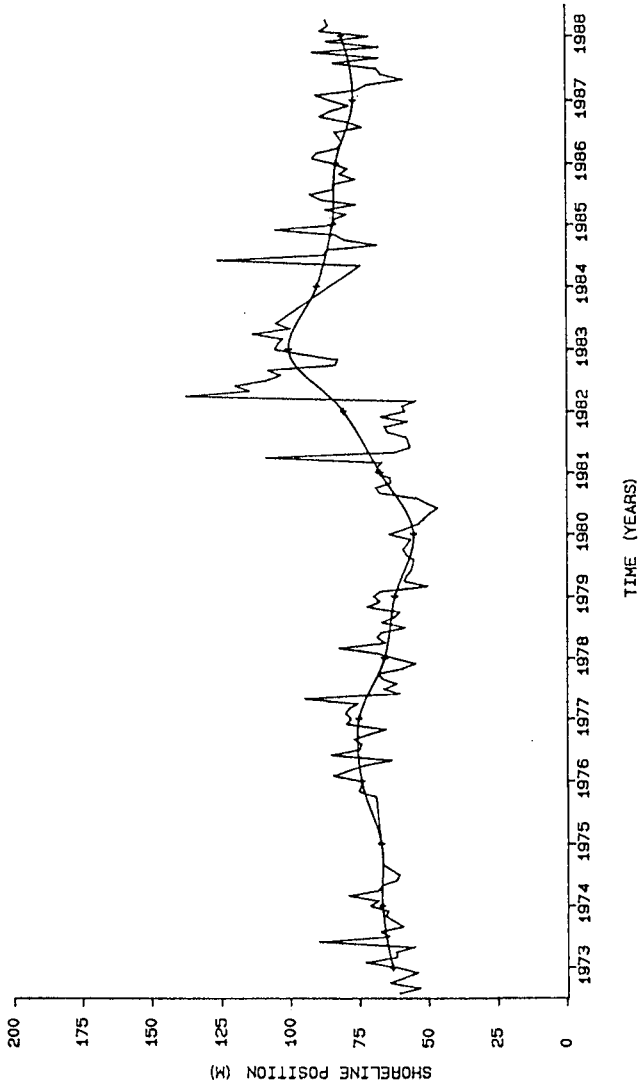
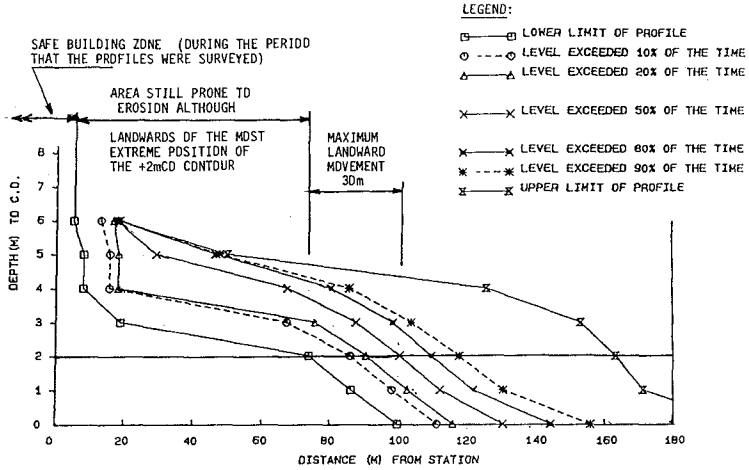
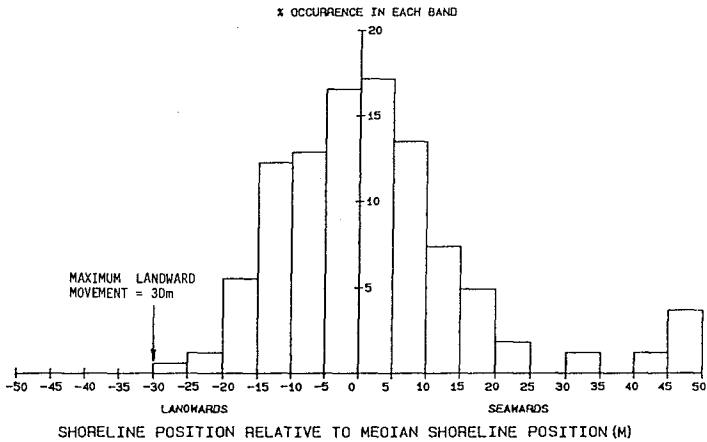


FIGURE 3 : VARIATION IN THE POSITION OF THE +1m CD CONTOUR



A. PROFILE ENVELOPE



B. RESPONSE HISTOGRAM AT +2M CD

FIGURE 4 : BEACH PROFILE RESPONSE AND EROSION SETBACK LINE AT SECTION A

CHAPTER 246

DESIGN AND CONSTRUCTION OF PLEASURE CRAFT HARBOUR - CLUB MYKONOS LANGEBAAN

Bosman D E*, Retief G de F*, Kapp J F* Kloos M*
Ridge A B†

1. ABSTRACT

A description of the pre-design investigation, design and construction of a pleasure craft harbour is given. The influence of the breakwaters on the sedimentation pattern in the direct vicinity of the harbour during construction and after completion of the harbour is described. Adaption of the design of some of the harbour components due to unforeseen circumstances revealed during the construction period is also discussed.

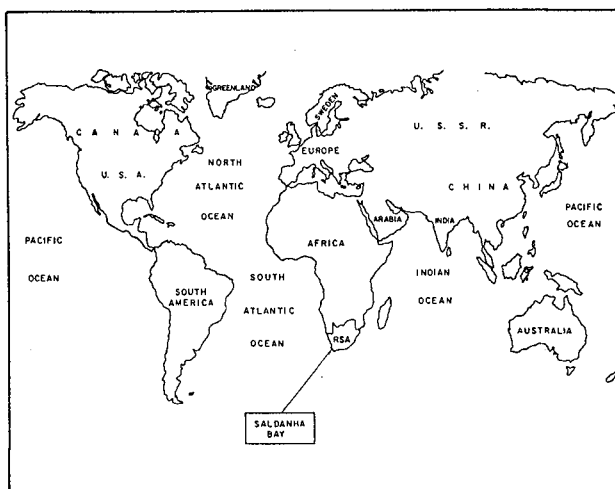


FIGURE 1 : LOCALITY MAP OF CLUB MYKONOS LANGEBAAN SMALL CRAFT HARBOUR AT SALDANHA BAY

2. INTRODUCTION

The Club Mykonos Langebaan Pleasure Craft Harbour Development is situated to the east of and in line with the entrance to Saldanha Bay on the West Coast of South Africa.

* Kapp Prestedge Retief, Consulting Coastal & Environmental Engineers, P O Box 523, Stellenbosch 7600, South Africa

+ Geustyn Forsyth & Joubert Inc, Consulting Civil and Structural Engineers, P O Box 413, Stellenbosch 7600, South Africa.

In view of the similarity in climate and scenery of the South African West Coast and that of the Greek Island settlements in the Aegean Sea, the architectural and aesthetic model of the development was drawn from the latter - therefore the Greek name: Club Mykonos Langebaan.

It is the first privately owned pleasure craft harbour on the open coast of South Africa and forms the nucleus of an ultimately planned 100 million US Dollar private resort. The development includes a commercial centre (restaurants and shops), accommodation (single residential, timeshare, share block and sectional title), recreational, hotel and conference facilities. Figure 2 illustrates the proposed ultimate project.



FIGURE 2 : ILLUSTRATION OF ULTIMATE SCHEME

The harbour works were completed in 14 months during 1988/89 at a cost of about 4 million US Dollars. Figure 3 presents the layout and components of the harbour.

The harbour can accommodate yachts with draft up to 3 m and provides floating walk-on moorings for about 130 vessels. A boat ramp, launching jetty, fuelling and sewage pump-out facilities are also provided.

The basin size is approximately 4 ha of which a part had to be dredged to the required depth. Spoil from dredging has been used to create approximately 1,4 ha reclaimed land adjacent to the harbour basin.

The size of the harbour was determined mainly by the size of the land development from which the funds for it had to be generated. The layout of the harbour breakwaters was designed such that the harbour could be expanded towards the south if required in future.

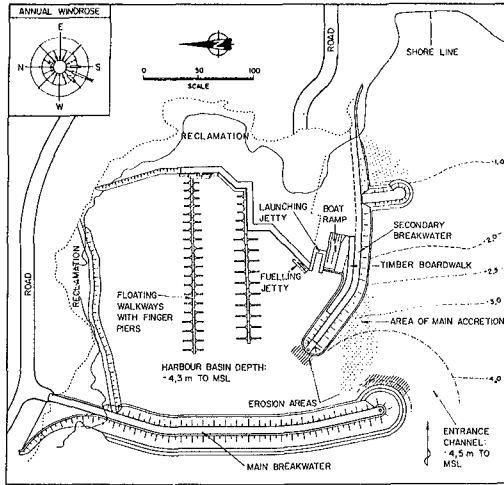


FIGURE 3 : HARBOUR LAYOUT AND COMPONENTS

For marketing reasons and since the harbour forms the nucleus of the development, creating a focal attraction point and therefore increases the market value of the adjacent land, it had to be completed before the land development.

To minimize time for which bridging capital had to be provided (i.e. the time during which expenditure exceeds income), selling of accommodation units on land had to commence soon after expenditure on construction of the harbour had started. This requirement from the developer's side necessitated a fast track programme for the design and construction of the harbour. The predesign investigations and design were done in about 4 months followed by a two months tender and contract adjudication period. The contract was completed in 14 months.

3. ENVIRONMENTAL CONDITIONS

Figure 4 indicates the location of the development in Saldanha Bay as well as the macro scale bathymetry, wind and wave conditions. The wind direction is predominantly from the South-Southwest sector.

The spring tidal range at the site is about 1,5 m.

Waves that directly penetrate Saldanha Bay in the direction of the pleasure craft harbour are reduced in height due to refraction to about 60% of their deepsea height. The 1:10 year deepsea significant wave height in the area is about 7 m which will therefore reduce to a significant wave height of 4,2 m at the harbour site. Peak wave periods vary between 11s and 13s.

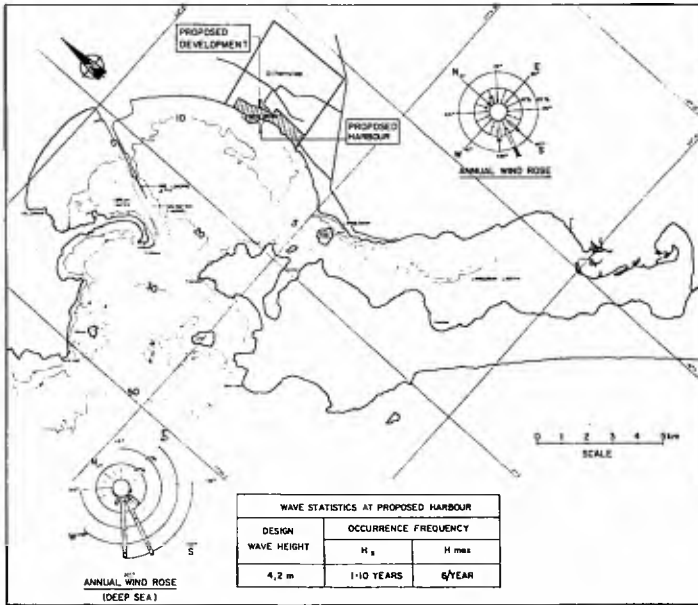


FIGURE 4 : ENVIRONMENTAL CONDITIONS

Figure 5 indicates the wave crest patterns in Saldanha Bay which is practically unidirection at the harbour site. Because of the latter, negligible longshore sediment transport due to wave action was expected. Tidal currents are reasonably high in the entrance to Langebaan lagoon (maximum of about 0,5 m/s) however the tidal current velocities at the Mykonos harbour site are very small.

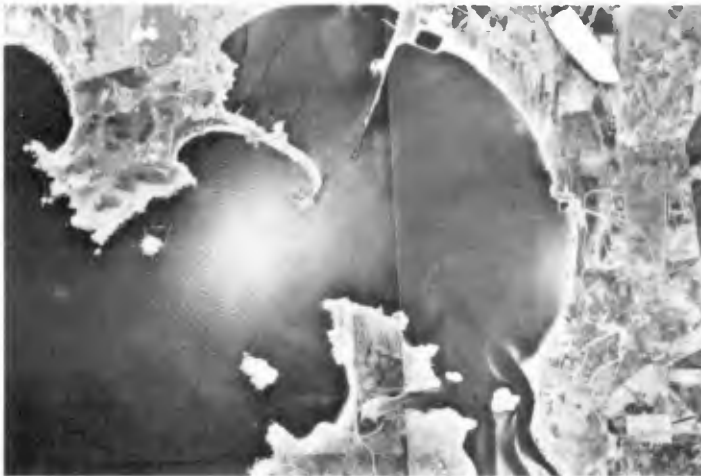


FIGURE 5 : WAVE REFRACTION PATTERNS IN SALDANHA BAY

The sediment on the seabed in the vicinity of Mykonos harbour is fine (D50 = 140 micron) and sediment movement due to wind-driven currents is possible.

Figure 6 indicates the hydrographic survey of the harbour site. Water jet probings were also done to establish rock depths. From the latter the landward limit of the harbour mooring area (after sand dredging) was derived.

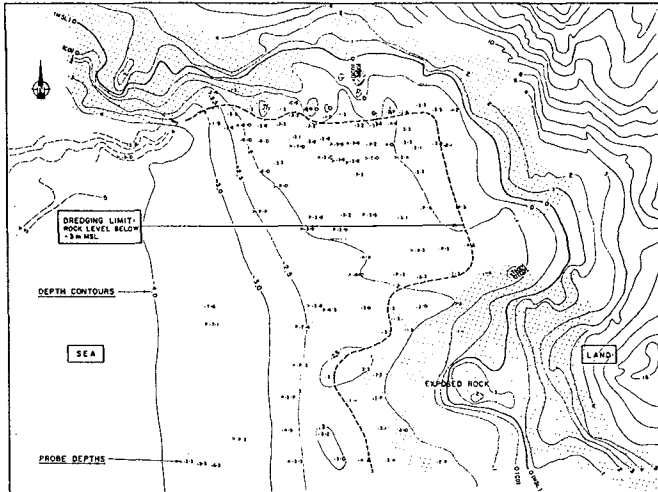


FIGURE 6 : HYDROGRAPHIC SURVEY OF HARBOUR SITE

Good quality granite rock was available from an existing quarry about 2 km from the harbour site.

4. DESIGN AND CONSTRUCTION OF HARBOUR

4.1 Breakwaters

4.1.1 Layout of Breakwaters:

A survey of existing yacht population on the South African coastline indicated the distribution of sizes as indicated in Table 4.1 below. The required mooring water depth for these sizes are also indicated in Table 4.1.

**TABLE 4.1 : LENGTH DISTRIBUTION OF YACHTS AND
REQUIRED MOORING WATER DEPTH**

Length	Percentage Distribution %	Required Mooring Depth below Mean Sea Level m
Up to 8 m	17	2,9
8 m - 11 m	40	3,9
11 m - 15 m	37	4,2
Longer than 15 m	6	

Based on the above boat size distribution, provision was made for 180 moorings of the walk-on floating jetty type anchored to concrete piles.

The following facilities were also needed:

Boat launching jetty

Boat ramp

Fuelling and sewage pump-out jetty

To provide for the above needs, a water area (including access channel and fairways) of about 4 ha was required.

The required water area together with the following factors determined the basic breakwater layout:

- o Landward limit of mooring area that could be dredged to the required depths as determined from the rock depth survey.
- o Required minimum depth at harbour entrance = 4,5 m below Mean Sea Level and entrance width of 45 m.
- o Provision for expansion of harbour towards the south.

The Phase I breakwater layout as optimised by means of three-dimensional hydraulic model tests together with a possible layout of an extended harbour (Phase II) is illustrated in Figure 7.

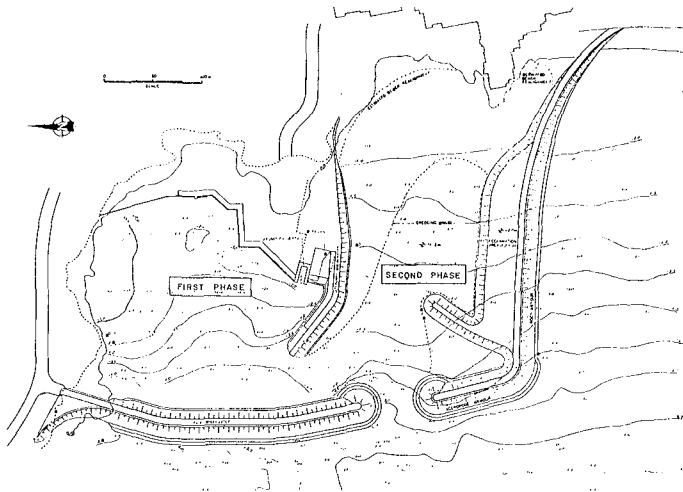


FIGURE 7 : BREAKWATER LAYOUT, PHASE I, WITH POSSIBLE EXTENSIONS, PHASE II

4.1.2 Main Breakwater:

The design conditions for the main breakwater were:

- Design water depth = 5,4 m
- Design wave height = 4,2 m (breaking wave)

The occurrence frequency of a significant wave of 4,2 m is 1:10 years, however considering the maximum wave in the wave spectra, breaking waves can occur approximately 6 times per year at the location of the main breakwater.

- Wave period = 11s to 13s.

Two basic alternative breakwater designs for the main breakwater (as indicated in Figure 8) were included in the tender to establish the cheapest solution. Stability tests on these were done in both two- and three-dimensional model tests.

The two alternatives were (refer Figure 8):

Alternative 1 : Berm type breakwater

Alternative 2a: Conventional rubble mound protected with Dolos armour units

Alternative 2b: Conventional rubble mound protected with Accropode units

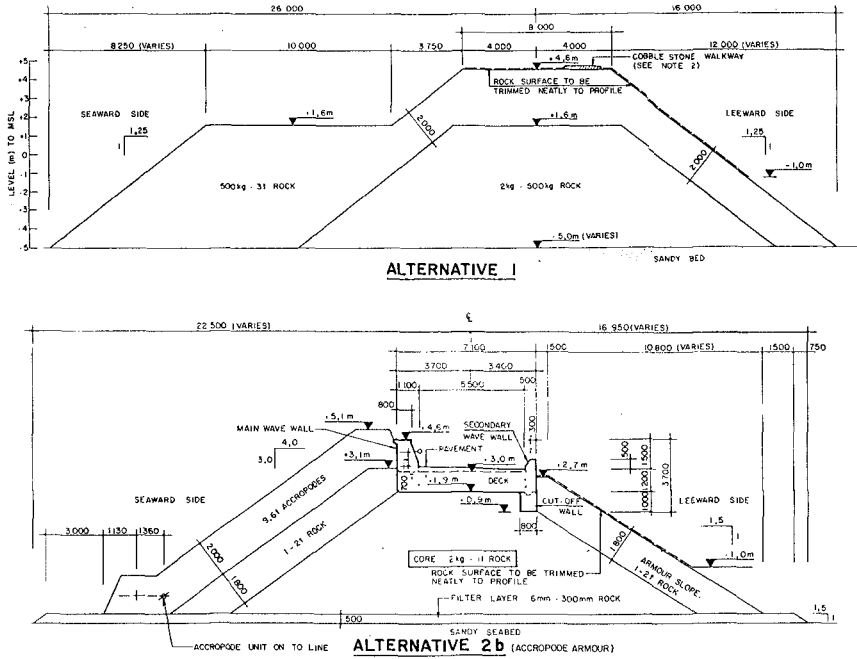


FIGURE 8 : ALTERNATIVE BREAKWATER DESIGNS

Alternative 2b protected with 9.6 t Accropodes was finally selected based on both cost and stability considerations. This design was also checked by Sogreah who holds the patent rights on the Accropode units. Although Alternative 1 proved to be the cheapest, it was not chosen because of the remote possibility of crest damage under extreme storm events. The latter problem could not be investigated in more depth due to the limited time available for the design period.

Some of the characteristics of the finally selected main breakwater design (Alternative 2b) are:

- o The crest level at +5,1 m above Mean Sea Level allowed some overtopping and the leeward armour slope is thus protected by means of a secondary wave wall.
- o The main breakwater comprises of 45 000 cub metres of rock, 1 400 Accropodes and 3 000 cub. metres of concrete capping and wave walls.

The main works on the main breakwater were completed in 5 months. It was subjected to breaking waves (i.e. the design wave height) for a number of times during the construction period. The wave action during one of these occasions are shown in Figure 9.



FIGURE 9 : BREAKING WAVES ON MAIN BREAKWATER DURING CONSTRUCTION

A precast and placed cut-off wall designed to be finally part of the concrete capping, rendered significant protection to the structure against breaking wave attack during the vulnerable construction stages. Figure 10 shows the effectiveness of the cut-off wall protecting the vulnerable crest during construction against breaching. The completed main breakwater with concrete capping, wave walls and Accropode protection is shown in Figure 11.



FIGURE 10 : ILLUSTRATION OF PROTECTION PROVIDED BY CUT-OFF WALL DURING CONSTRUCTION



FIGURE 11 : COMPLETED HARBOUR WITH MAIN BREAKWATER ON LEFT SIDE

4.1.3 Secondary Breakwater:

The secondary breakwater is also of the conventional rubble mound type with 1 to 3 t primary armour on the seaward side (see Figure 12).

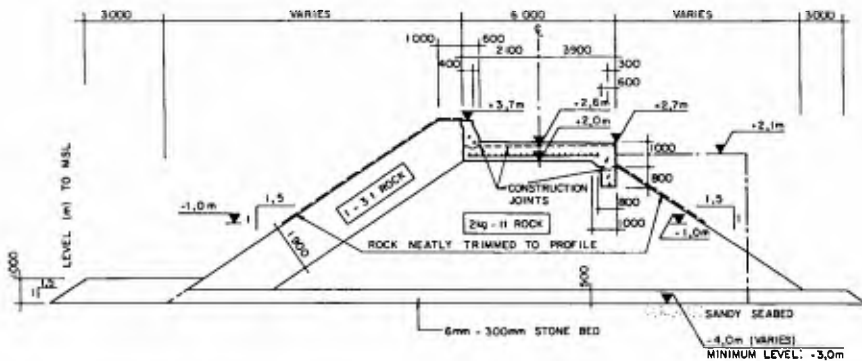


FIGURE 12 : SECTION THROUGH SECONDARY BREAKWATER

At commencement of construction of this breakwater it was found that the construction level (i.e. level at crest of rubble core at which the crane and trucks operated) had to be raised from the designed +1,4 m to +2,0 m above Mean Sea Level due to excessive damage experienced at the construction face.

Due to sediment accretion at the position of the secondary breakwater from the original -2,5 m contour and deeper (refer Section 4.1.4), the breakwater had to be founded on a higher level than the original seabed level. To prevent future undermining of the breakwater due to possible scour, a special toe protection on the seaward side was provided (see Figure 12).

The end of the breakwater comprises a 12 m caisson section built up of concrete box units filled with concrete after placement. The units were founded on a 1,3 m thick stone bed based at a dredged level of -5,8 m. The concrete box units were placed on aligned and levelled concrete pads with the void between the rubble foundation and concrete boxes being filled by tremie concrete contained in a filter cloth bag as shown in Figure 13.

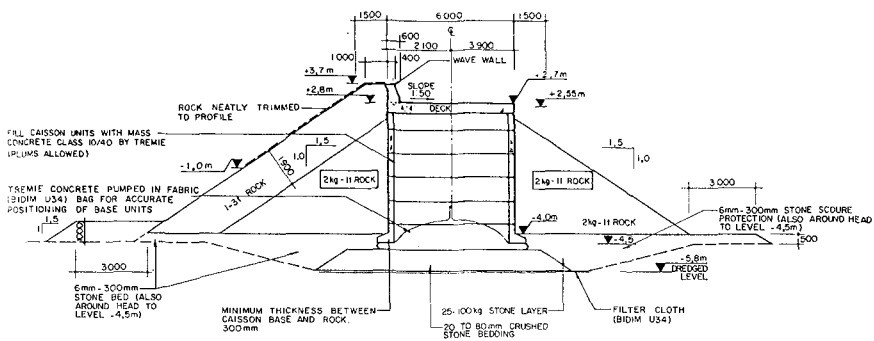


FIGURE 13 : CROSS SECTION THROUGH SECONDARY BREAKWATER CAISSON END

4.1.4 Local Sediment Accretion and Erosion Patterns during and after Construction of Breakwaters:

The main breakwater was constructed first to provide protection to construction operations of other components in its lee. The construction progress (in months) of the breakwaters is indicated in Figure 14; the main breakwater was completed in 4 months after which construction of the secondary breakwater commenced.

Construction of the secondary breakwater was delayed when about half of its length was constructed (at month 7 of breakwater construction - Figure 14) due to a significant amount of sediment accretion encountered at the construction face. An attempt to remove the sediment by grab crane so that the breakwater could be founded on the original seabed level was not successful since accretion took place at the same rate as removal.

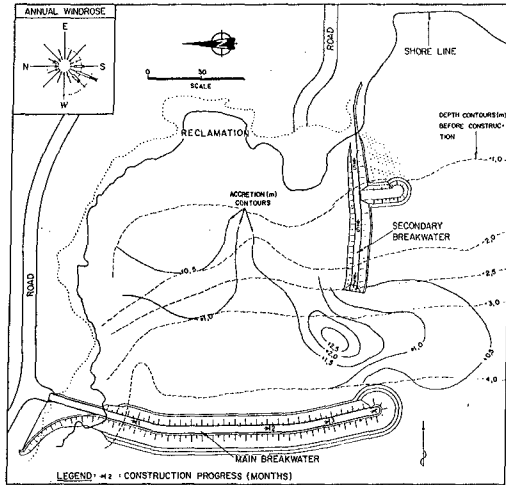


FIGURE 14 : CONSTRUCTION PROGRESS AND SEDIMENT ACCRETION DURING CONSTRUCTION

A hydrographic survey of the harbour area during this stage of construction indicated sand accretion that took place during construction as shown in Figure 14. Current measurements in the prototype during this stage indicated a rip current along the seaward side of the secondary breakwater causing sediment accretion in the area of the construction face.

Based on current measurements in the 3-D model of the harbour, it was decided to build a spur breakwater as indicated in Figure 14 to deviate the rip current so that the sediment accretion problem in the construction area as well as in the harbour mouth area could be limited.

The sediment accretion/erosion pattern 12 months after completion of the breakwaters is indicated in Figure 15. Erosion areas occurred at the end of both main and secondary breakwaters. Accretion occurred in the lee of the spur breakwater as well as in the harbour mouth area. The latter will necessitate periodic maintenance dredging estimated at about 15 000 m³/year.

4.2 Reclamation and Revetment

The reclaimed area (1,3 ha) as shown in Figure 3, was formed from 43 000 cub metres sand dredged from the harbour basin. The reclaimed area is edged with stone revetment at a 1:1,5 slope to reduce undesirable wave reflection. Where required, timber boardwalks mounted on concrete columns were provided for public access to the water's edges. Vertical guides fitted to these columns restrain the floating jetties installed next to the boardwalk. Figure 16 illustrates the revetment, boardwalk and floating walkways.

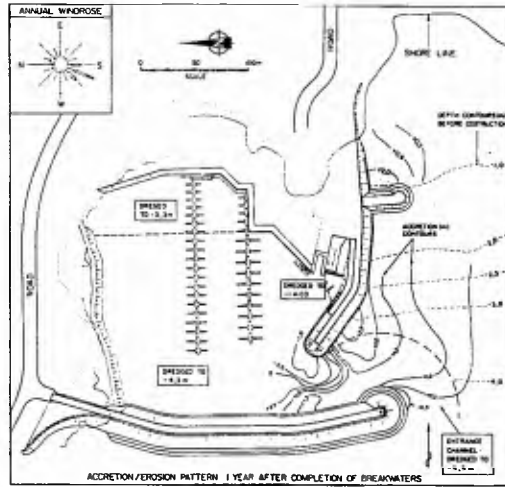


FIGURE 15 : SEDIMENT ACCRETION/EROSION AFTER CONSTRUCTION



FIGURE 16 : REVTMENT, BOARDWALK AND FLOATING WALKWAY

To prevent settlement of buildings founded on the reclaimed area, steep foundations of the buildings were founded on gravel piles (520 mm diameter; 19 mm stone; hammer compacted and spaced at 2 m intervals).

The timber boardwalk deck was constructed of untreated hardwood (Keruing) fixed with hot-dipped galvanized bolts and brass screws.

4.3 Floating Jetties

A floating walk-on jetty system comprised steelframed timber decking on polyethylene floats held by concrete gravity piles, was provided for boat moorings. The floats under the walkways were filled with polyurethane foam. The steel is protected after sandblasting with two zinc-rich base coats followed by two coats of polyachrothane paint. The floating jetty system is illustrated in Figure 17.



FIGURE 17 : FLOATING JETTY SYSTEM

Due to shallow rock substrata, concrete gravity anchor piles for the jetties had to be used. Three precast concrete rings, placed concentrically and the spaces between filled in situ, with tremie concrete, formed the gravity footing for the anchor piles (see Figure 18).

4.4 Launching Jetty, Boat Ramp

The yacht launching facility consists of two piers providing access for a mobile straddle carrier capable of launching yachts with a dry mass of up to 20 t. The two vertical walled parallel piers are constructed from precast concrete blocks on a rubble foundation.

A boat ramp is provided to enable the launching of motor boats on trailers with sufficient width to launch two craft simultaneously. The boat ramp consists of precast slabs on rubble fill below Mean Sea Level and in situ cast slabs above this level. The boat ramp slope is 1:8 and terminates at 2 m below Mean Sea Level.

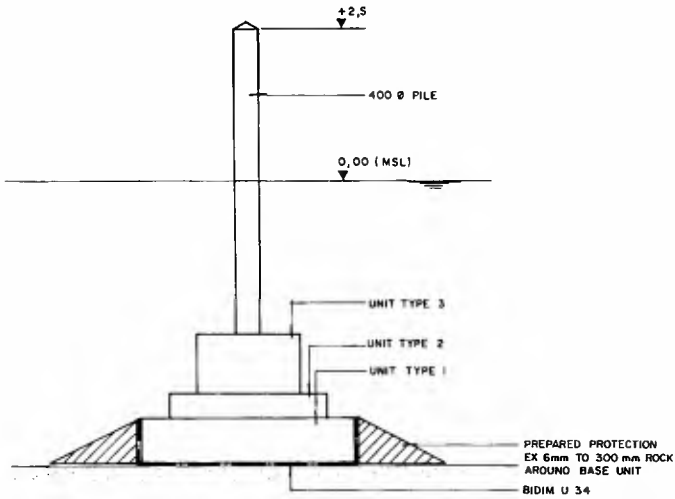


FIGURE 18 : CONCRETE ANCHOR PILES FOR FLOATING JETTIES

Figure 19 shows the launching facility, boat ramp and fuelling/sewage pump-out jettie.



FIGURE 19 : LAUNCHING FACILITY, BOAT RAMP AND FUELLING JETTY

5. ACKNOWLEDGEMENTS

The authors would like to acknowledge the co-operation of the Client (Club Mykonos Langebaan Ltd) and the Contractor (Marine Civil (Pty) Ltd) during the execution of the project. This made it possible to successfully complete the project from design commissioning to completion of the works in 20 months.

CHAPTER 247

ARTIFICIAL BEACH NOURISHMENT ON NORDERNEY, A CASE STUDY

H. KUNZ

Coastal Research Station/NLWA-Forschungsstelle Küste
Norderney, Federal Republic of Germany

ABSTRACT

Norderney is one of the East Frisian Barrier Islands that extend along the western part of the German North Sea coastline (Fig. 1). Severe dune erosion jeopardized the health resort settlement on the west end of Norderney and necessitated the construction of solid coastal protection structures since 1857. These structures were successful in stopping the migration of the inlet and in preventing further dune erosion; but they were not able to maintain stable beaches. To protect the existing structures against damage artificial beach restoration was initiated on Norderney in 1951. Since then five further beach fills were necessary to affect an active protection by shifting the zone of wave attack seawards. The scouring from the groyne fields had been monitored. Based on these data the sand budget has been investigated. It has been proved, that on Norderney beach nourishment is an appropriate solution to protect the existing structures from failure during severe storm-floods. If we want to lower the amount of losses, we have to nourish the beach not higher than necessary to achieve the protection goals. Above a 'critical beach profile' in certain areas losses of nourished material increase considerably with height. Especially for the Norderney-case we should develop a 'low-cost-technique' for a 'low-rate-beach-nourishment'.

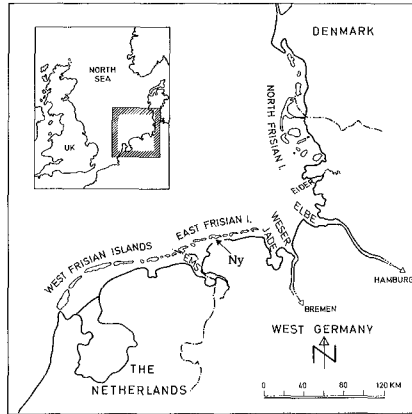


Fig. 1: Location map of the German North Sea Coast with Norderney-island (Ny)

INTRODUCTION

Like the other East Frisian Islands, the barrier-island of Norderney is formed by the coincidence of current, surf, wind (LÜDERS 1953). The migration of the islands has been well documented for the last three hundred years (FORSCHUNGSSTELLE 1964). During the two centuries, 1850 ago, the situation between Norderney and the island to its west had changed from two hydraulically equivalent inlets, separated by a small middle island, into a single inlet. This inlet shifted to the east, eroding the core of the west end of Norderney (HOMER 1964, LUCK 1975). In accordance with the changed hydraulic conditions the offshore sandbars were forced seawards and therefore the west end of Norderney was no longer sufficiently supplied with sand. The development can be explained by the connection between the tidal inlet and the tidal prism; the eastward migration of the affiliated catchment area located on the tidal flat has to be considered (O'BRIEN 1969, FITZGERALD et al. 1984a/b, BRUUN 1978, LUCK 1976).

In 1857, people started to construct a combined system of shore-parallel structures and groynes on Norderney to prevent further erosion. It was necessary to extend the groynes into deep water to a depth of almost twenty meters to prevent the ongoing shifting of the inlet channel. During one century the system of protective structures was extended to a length of six kilometers. Descriptions are given by FÜLSCHER (1905), BACKHAUS (1938), PEPER (1956), KUNZ (1987). The development of the city of Norderney into a seaside health resort provided economical justification for the investment.

Even the shoreparallel structures were successful in preventing further dune erosion and the groynes were able to keep away the strong tidal currents from the core of the island, they could not stop the scouring from the beach. As the beach level progressively fell, the toe-protection of seawalls and groynes had to be extended and strengthened several times. Because of World War II the structures were not well maintained during the nineteen-forties. The classical approach of toe protection had been reviewed by a special task group. As an alternative they recommended a restoration of the beach (ARBEITSGRUPPE NORDERNEY 1952). Thus the first artificial beach nourishment in EUROPE was implemented on Norderney in 1951/52. For the same reason five further beach fills were necessary up to now. This paper focuses on the development of the sand volume in groyne fields that ensure the safety of the structures. Results of volumetric calculations based on field data shall be presented and the question shall be discussed what we might learn from a feed-back to the monitored information concerning the technique of beach restoration on Norderney.

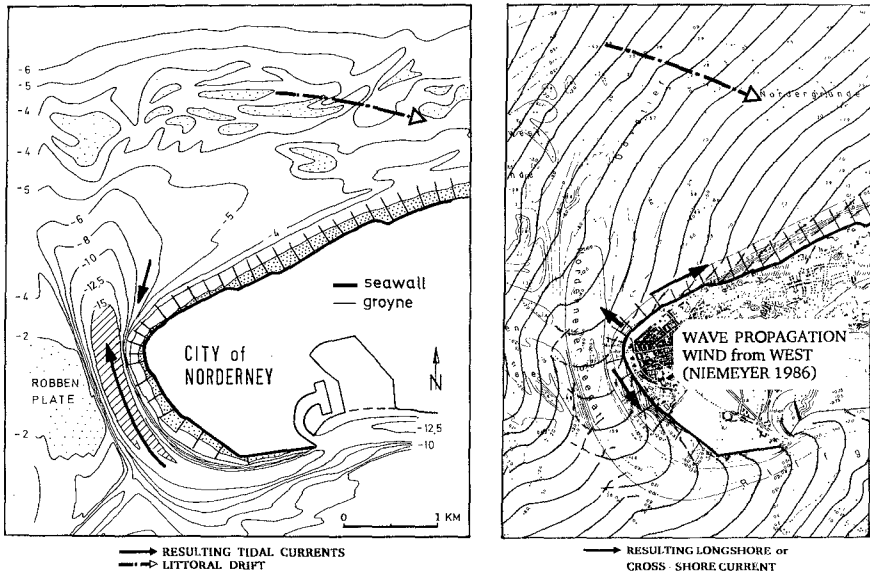


Fig. 2: Depth-contourlines, resulting currents and littoral drift (left); Wave propagation, resulting wave-induced currents (right) - Western spit of Norderney

BEACH RESTORATION SINCE 1951/52

The western spit of Norderney is displayed on Fig. 2. The left picture shows the depth-contour lines. The crescent shaped reefbow is dotted. The net littoral drift runs within the reef-bow from West to East. From time to time bars merge with the island, but only far from the western spit. For this reason there is barely sand naturally supplied to the western area. The hedged part of the tidal channel is more than fifteen meters deep. The groynes facing this part of the inlet are essential to govern the strong tidal currents. The MTR of 2,40 m leads to velocities of more than 1,50 m/s. There is a strong wave action predominantly from the west to northwest sector. An example for the wave propagation is shown in the right hand picture. The resultant longshore currents run bidirectional from an area located near the very western part. We address it as 'area of divergence'. This is the stretch where we have to face the greatest losses of sand and the strongest wave attack. Breaking waves generate high velocities in the groyne fields (NIEMEYER, 1990). The groynes which cover the easterly beach part as well as the other groynes, diminish the effects of longshore currents in the nearshore area. They are less effective the higher the water level is. The highest water level measured during storm flood (HHW) is three meters above MHW-level.

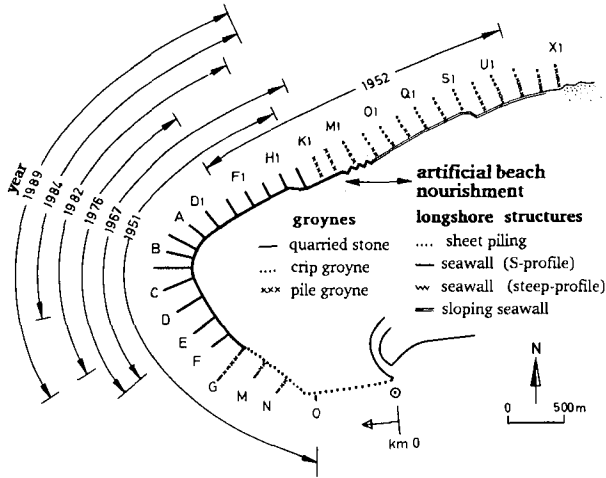


Fig. 3: Combined Protection System on Norderney-island

The combined protection system on Norderney is described by Fig. 3. Only the first artificial beach nourishment in 1951/52 covered the whole stretch.

The Fig. 4 gives some information on nourished volumes, on grain size and on literature. For the first nourishment the sand had been dredged from the tidal flat, where only fine material with a medium d_{50} of about 0,1 mm

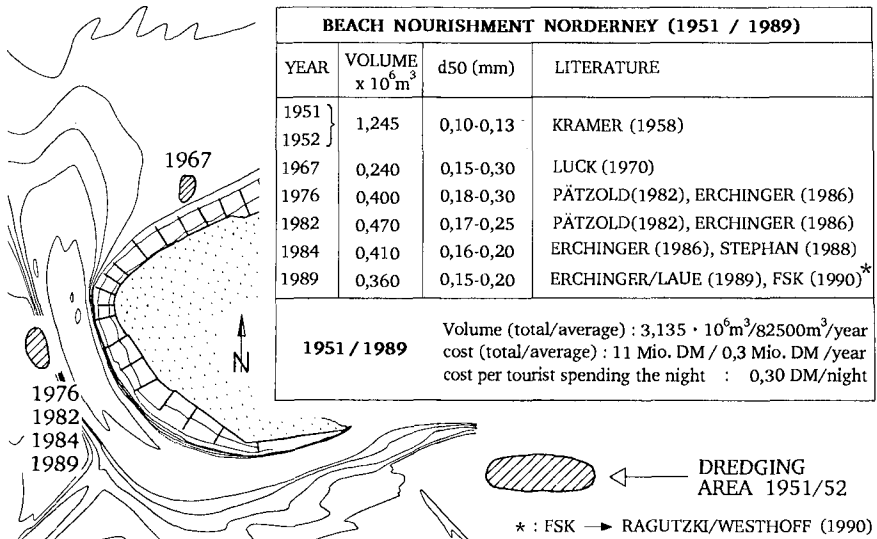


Fig. 4: Beach nourishments on Norderney (1951 to 1989)

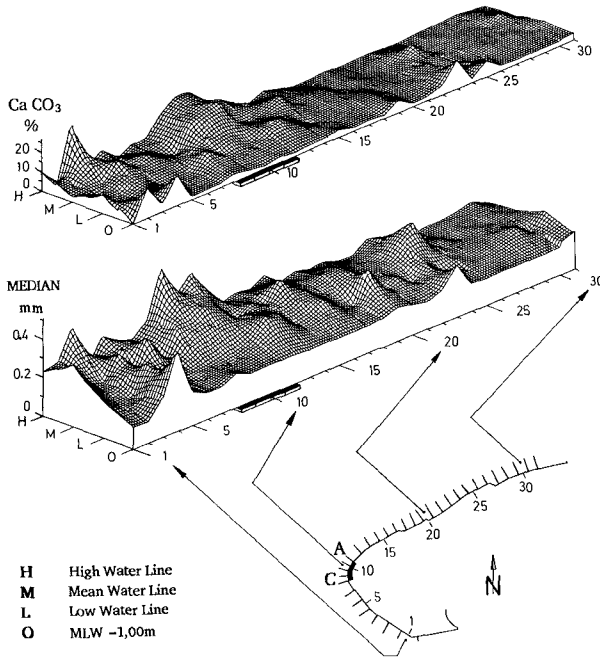


Fig. 5: Shell material and grain size in the groyne-fields of Norderney, Sept. 1987 - WESTHOFF (1990)

is available (KRAMER 1960, 1972). In 1967 the dredging of a relatively small amount of material with a medium d_{50} of about 0,25 mm was accomplished from a foreshore area (LUCK 1970). Since 1976, when the technique was available to cross the deep channel by submerged pipe-line, the sand was taken from an ebb shoal across the inlet. The material was less coarse, especially in 1989 with a medium d_{50} of about 0,17 mm (RAGUTZKI/WESTHOFF 1990). Since 1951 an average volume of 82500 m³ per year had been nourished.

The grain-size of the sand in the groyne-fields varies quite a bit. Fig. 5 pictures the situation in Sept. 1987. The convergence area (C-A) is marked by the solid line. The effects of sorting are obvious. The coarse material contains relatively more parts of broken shells, indicated by CaCO₃ (WESTHOFF 1990).

VOLUMETRIC CALCULATIONS AND LOSSES (1951 TO 1990)

As mentioned before, the paper is restricted to volumes to give an idea of the losses out of the vulnerable part of the groyne fields with time. The calculation focuses on the beach area where we definitely do need beach restoration for the purpose of securing groynes and shoreparallel

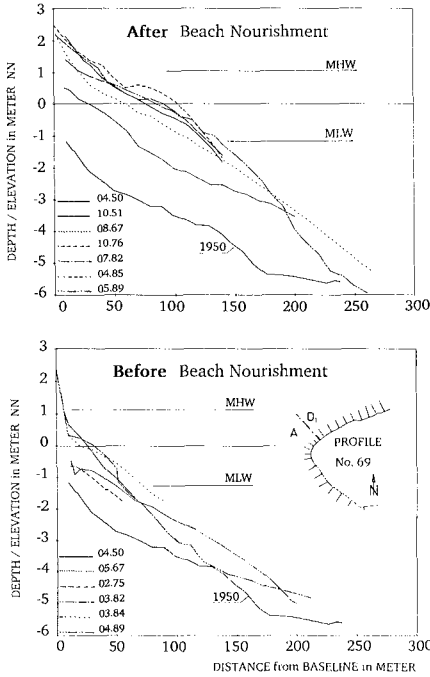


Fig. 6: Beach-Profiles in the groyne-field (A-D₁)

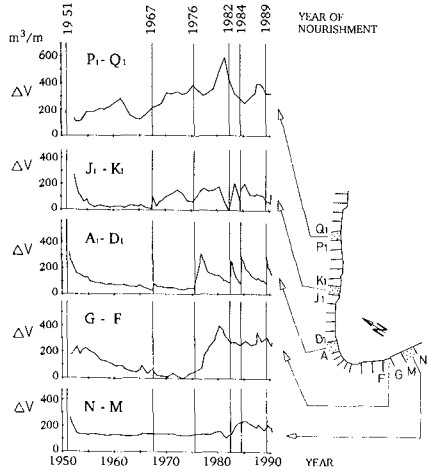


Fig. 7: Volumes above the 1950-Reference-Profile and the NN -1,50 m -level (ΔV) of five selected groyne-fields - Western spit of Norderney, 1951 to 1990

structures against failure during storm floods. To meet this target the volume calculation can be restricted to the beach part above NN -1,50 m - level, that's about MLW. This practical engineering approach is appropriate. There will be no discussion on the complicated cross- and longshore processes within enlarged boundaries.

An example for the monitored beach profiles is mapped on Fig. 6. Since the preliminary aim of the survey has been to monitor the vulnerable part of the seawall - and groyne - system, only some of the profiles extend deeper than MLW (STEPHAN 1988). The lowest profile is that of 1950, just before the first beach-restoration. We use the 1950-profile, specifically for each groyne field, as a 'reference profile' for the volumetric calculation. A restored beach would at least reach this profile if we would'nt nourish. From the lower picture we can see that the beach nourishments started off from different heights. The upper one depicts the different profiles just after the beach restoration. If we would plot the shape of the groyne into the picture, it almost would envelope the highest profiles (type of low lying groynes).

In the following, the volume-data always will be addressed as ΔV with unit cubic-meter per meter shoreline

(m^3/m). The accuracy of the volume calculations has errors within the range of $\pm 7,5\%$. The used field data for the profiles have been provided by STAIK (agency for island and coastal protection, Norden) and FORSCHUNGSSTELLE KÜSTE (research station, Norderney).

We can not expect to define a groyne-field that provides representative conditions for the whole six-kilometer stretch. The development of the volume (ΔV) over time is to be seen from Fig. 7. The field A-D₁, discussed above, is placed almost in the middle. Since it is located near the 'divergence area', each beach-nourishment indicated by the vertical solid lines, is to be recognized clearly. The deviation from the rectangular line in 1976 is an exception: the profiles after the nourishment had been monitored six month later. With greater distance from the 'divergence-area' the ΔV -graph is less immediate determined by the nourishment. The picture for the groyne-field P₁-Q₁ shows effects of sand supply from the reef-bow-bars that merged further to the East. The picture for groyne-field N-M displays an almost constant ΔV -curve, whereas the nearby-lying groyne-field G-F is obviously impacted by sand arriving from nourished parts. In general it seems to be justified to distinguish the period before 1976 with relatively moderate beach-volumes and the time after 1976 with comparably higher rates of beach nourishments. The 1967-restoration was weak and had almost no impact on the ΔV -curves. This contrast to data published by ERCHINGER (1986) can be explained by different boundaries fixed for the volumetric calculations.

1951 to 1976 is the only long-time period we can look at. The beach-nourishment of 1967 can be neglected, since it had almost no effect, that would interfere. Fig. 8 indicates how the volume (ΔV) of the divergence-area A-C decreases rapidly after the 1951-beach-nourishment. The curve does not seem to follow a kind of exponential-function (AUSSCHUSS KÜSTENSCHUTZWERKE 1977, 1988, FÜHRBÖTER et al. 1976, PÄTZOLD 1982). There are ups and downs in the ΔV -graph that might be caused by storm-surges. To prove this expectation, the storm-surge-duration and the number

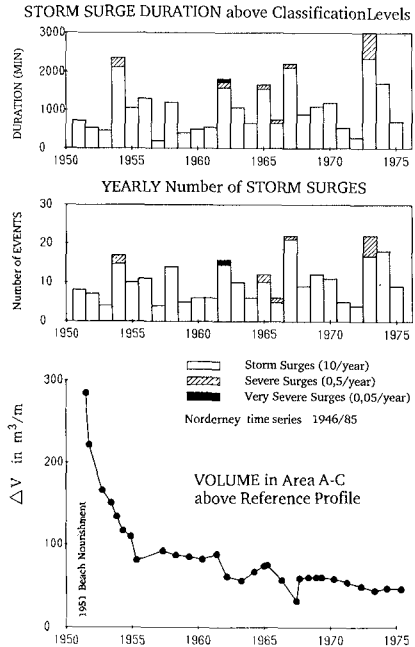


Fig. 8: Storm Duration, Number of Storm Surges, Volumes in area (A-C)

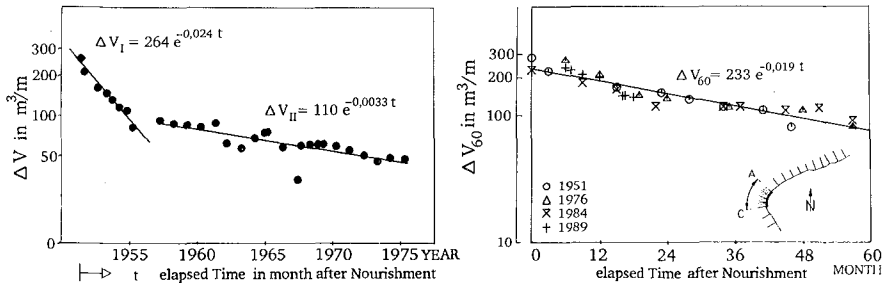


Fig. 9: Volume (ΔV) plotted over time and approximation by exponential functions. Left: 1951 to 1976. Right: periods after the nourishments of 1951, 1976, 1984, 1989

of storm-surges per year are plotted above. If we look at it carefully, we hardly will find a significant correlation; investigations on a much smaller time-scale are needed, if we want to describe the impact of storm-surge and wave action on profiles and on volumes (HOMEIER 1975). However, if we calculate and integrate wave-energy over time, we can get a relationship to the losses (PÄTZOLD 1982).

Plotting the volume ΔV against time in a semi-logarithmic scale, we come up with the results shown in Fig. 9. The elapsed time after beach-nourishment (first volumetric data) is indicated by 't'. Left hand again we have the period from 1951 to 1976. We have to distinguish at least two periods if we want to approximate by e-functions: a first one over 5 years from 1951 to 1956 and a second one for the following years. The two solid lines give the approximations (ΔV_I and ΔV_{II}). The exponent of the e-functions lead to 'half-times' of 6 years, respectively 37 years. After these time periods we have lost 50% of the nourished volumes through the fixed boundaries: in cross-shore-direction into deeper parts of the beach and in long-shore-direction across the groynes.

For a time-period of 60 months we adjusted data of different nourishment-periods to a fixed scale representing the average conditions of the used periods. The results can not be compared directly with those published by PÄTZOLD (1982). The data from the 1982 beach-nourishment have been skipped; there are only two years to the nourishment and the losses are not well documented. Instead of this, the much better data from the 1989-nourishment have been used; the ΔV -function seems to behave quite similar to that one after 1982. The weak 1967-nourishment had only little impact on the ΔV -curve, as mentioned earlier. Again, the linear approximation is given in the semi-logarithmic scale. The exponent stays for a 'half-time' of 29 months. There is a substantial scattering but taking into account the different conditions (nourished material, profiles, tides, waves) we should not expect more.

From Fig. 9 we learn, that we can't describe properly the volume ΔV over the whole time-period by only one exponential function: If we use several different e-functions, the 'half-time (t_h)' of those would increase with the elapsed time (t). This leads to the non-exponential approximation as shown in the upper part of Fig. 10. The exponent of ΔV_{III} is a function of the elapsed time (t) after beach-nourishment: $t_h(\Delta V_{III})$. From this we come to the 'half-period' as function of 't' - shown below. The e-functions, as described before, are plotted into the distinguished time-periods for comparison-purpose: for the first 60 months this is $t_h(\Delta V_I)$ and $t_h(\Delta V_{60})$; the graph $t_h(\Delta V_{II})$ is representative for the time beyond the 60 months. Again, the graphs highlight that we face substantial errors, if we extrapolate a constant 'half-time' - for example from the fixed time boundaries in Fig. 10 (dotted vertical line).

We can convert the elapsed time into volume ΔV and come up with a curve as shown in Fig. 11. On the vertical axis again the 'half period t_h ' in months; on the horizontal axis the volume ΔV . We can take this volume as nourished volume above the reference profile, landwards the fixed NN -1,50 m boundary. The curve (1) points out, how sensitive the 'half-period' reacts on the volume placed above the reference

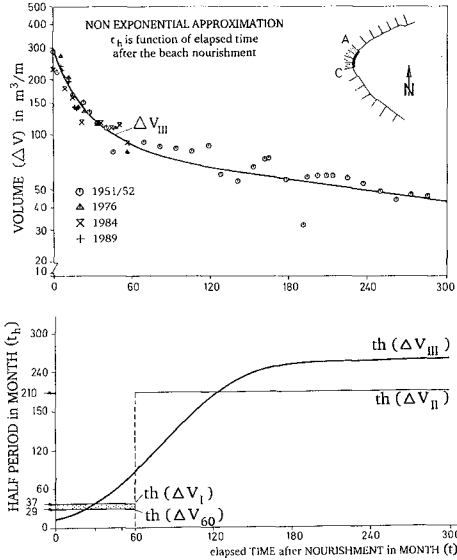


Fig. 10: Non exponential Approximation for ΔV versus time in semi-logarithmic scale (ΔV_{III}) Half-Period as function of elapsed time $t_h(\Delta V_{III})$ - Norderney (A-C)

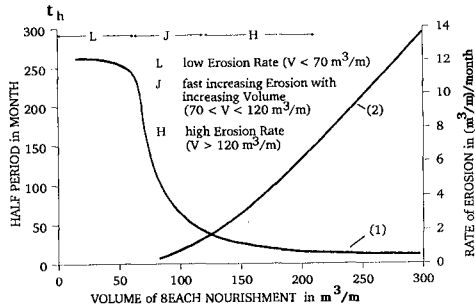


Fig. 11: Half Period and Rate of Erosion as function of nourished Volumes - Norderney, divergence-area (A-C)

profile. The rate of erosion (2) increases with decreasing half-period.

We draw as results:

If possible, we should nourish the divergent area, which determines the beach restoration-procedure, not more than 70 m³/m. In other words: we should stay in the 'L-area'. If we exceed out of the L-area the 'half time' decreases substantially with volume. This area is indicated as J. Beyond 120 m³/m the half-time gets almost constant; losses increase linear with volume.

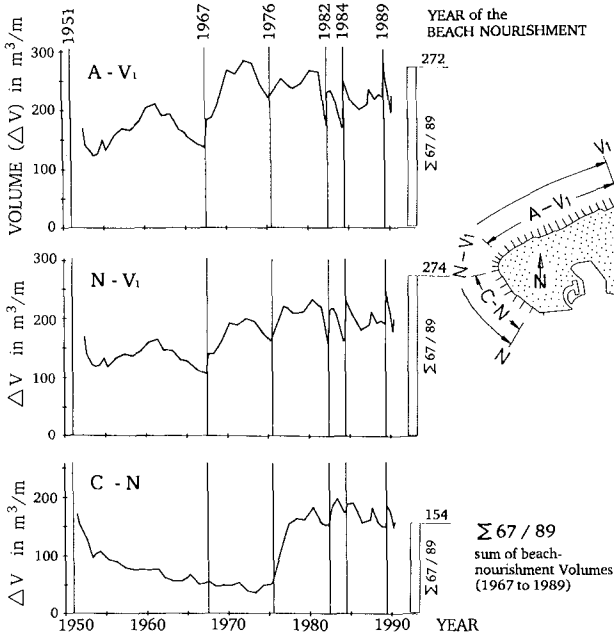


Fig. 12: Volumes (ΔV) - Norderney 1951 to 1990

Figure. 12 leads back from the 'convergence area' to the whole armoured stretch, to get an idea, how the volumes of groyne-fields on both sides of the 'convergence-area' change and how they benefit from the losses out of that area. The upper curve indicates the volume in m³/m in area 'A-V₁'. We use the same seaward boundary conditions as described earlier. The graph on the bottom is for the area 'C-N'. The curve in the middle stands for the whole stretch - that is 'N-V₁'. The beam on the right side of each picture indicates the total volume of sand in m³/m placed into the groyne fields after the first beach nourishment. If we compare the sum of nourished volumes (Σ67/89) with the difference between the 'actual ΔV' and the 'ΔV before the 1967-nourishment' we can conclude, that

almost none of the material is left. The upper picture indicates, that from 1968 to 1973 substantial sand supply must have been provided by sandbars that arrived at the beach eastwards of the groyne-fields. To address the impact of beach nourishment on the ΔV it is favorable to brake the time into two distinct periods: one 'from 1951 to 1976' and another one 'from 1976 to 1990'. Comparing the areas it is obvious, that since 1976 the average volume-level is significant higher than it had been before. With the effort of beach nourishment every 2 to 6 years a kind of volume-equilibrium is obtained, that seems to range on a higher level than needed. This encourages to look into the addressed problems, to answer the question whether we can go along with a lower volume-level, which would us enable to decrease beach nourishment-volumes substantially.

FINAL REMARKS AND CONCLUSION

The western spit of Norderney is endangered because: there is a natural tendency of the inlet to shift eastwards to the island, there is a negative sand budget, there are storm surges up to more than 3 meters above MHW-level and strong wave-induced currents.

To protect Norderney, a combined system has been established since 1857. It consists of three components
shoreparallel structures
groynes with two different purposes
groynes to keep away the strong tidal currents from the core of the island
groynes to stabilize the beaches
artificial beach nourishment.

By storm surges in combination with waves the beach-profiles on Norderney are lowered, especially in front of the shoreparallel structures and groynes. Artificial beach nourishment is an appropriate solution to protect the existing structures against damage.

To achieve the protection goals we must ensure, that the beach area above MLW-level is considerably higher than the 'natural beach' would be without beach-restoration. Calculations of the beach volumes above the dynamic natural equilibrium profiles (approximated by 'reference profiles') on a long term time-period (1951 to 1990) led to relationships between the losses of nourished sand and beach volume. Above a 'critical beach profile' the losses of fulfilled material increase considerably with height (divergence area). The losses over a long time period can be calculated by an exponential function, if we use an exponent that itself depends on volume, respectively time. The function represents the average conditions that be-

sides the volume-parameter have an impact on the losses; different diameter and shape of the nourished sand and the initial profiles of the beach restoration as well as wave-energy lead to random scattering or temporary to different tendencies compared to the approximation-function. However, if we look at a long term time scale the losses out of the most vulnerable part of the Norderney-protection-system mainly depend on the calculated volumes within the fixed boundaries. If we want to lower the amount of losses, we should nourish the beach not higher than necessary to achieve the protection goals.

The efficiency of the groyne in the 'extended divergence area' against wave-induced longshore currents seems to account for one of the major reasons of this result.

We should try to approximate the natural beach slopes; however it seems to be essential that we nourish sand not finer than the natural beach.

It appears advantageous to nourish only the area from which the longshore currents are bidirectional (area of divergence) with a limited extension to the East. From the nourished area sand will be moved naturally to both directions (feeder beach).

We should try to get experience with a deposit of sand in the foreshore-area of the easterly part of the 'extended divergence area' in combination with lower beach profiles in the area above MLW-level.

We have to look after a 'low-cost-technique' for a 'low-rate-beach-nourishment' on Norderney (KRAMER 1960). The comparison of low- and high-rate beach-nourishments will bring us to the cost-benefit-optimum.

Since the beach restoration on Norderney is part of the 'Coastline Defence System', the costs are paid by Federal and State. The enhancement of the recreational features of the beach is a welcome side-effect. Because Norderney is a highly frequented recreational beach area, there is an immediate demand for beach restoration after severe storm floods. However, we have learned that there can be a substantial amount of natural beach replenishment. There may be major savings in the cost of beach nourishment by postponing the decision on the design and quantity of sand to be placed on the beach, until the major quantity of the natural replenishment has occurred.

ACKNOWLEDGEMENT

This study is part of an interdisciplinary research-programme sponsored by the GERMAN FEDERAL MINISTRY FOR SCIENCE AND TECHNOLOGY (BMFT). The author is grateful for the support he got from his colleagues at the COASTAL RESEARCH STATION, NORDERNEY.

REFERENCE

- ARBEITSGRUPPE NORDERNEY (1952):** Gutachtliche Stellungnahme des Küstenausschusses Nord- und Ostsee ...; Die Küste, vol. 1, March 1952, pp.27-42
- AUSSCHUSS KÜSTENSCHUTZWERKE der HTG und DGEg (1977,1981):** Empfehlungen für Strandauffüllungen als Küstenschutz; Naßbaggerberichte vol. 5, 1977 and Die Küste, vol. 36, 1981.
- BACKHAUS, H., (1938):** Die Entwicklung der ostfriesischen Inseln in geschichtlicher, geomorphologischer, hydro-mechanischer und seebautechnischer Hinsicht; Dissertation University of Berlin
- BRUN, P. (1978):** Stability of Tidal Inlets; Elsevier Scientific Publishing Company
- ERCHINGER, H.-F., (1986):** Strandaufspülungen als aktiver Küstenschutz vor Schutzwerken und Dünen auf Norderney und Langeoog; Die Küste, vol. 43, pp. 181-204.
- ERCHINGER; H.-F.; M. LAUE (1989):** Sechste Strandaufspülung mit besonderer Berücksichtigung der Sandentnahme und Transporttechniken; report STAIK, Norden.
- FITZGERALD, D.M., S. Penland, and D. NUMMEDAL, (1984a):** Changes in Tidal Inlet Geometry due to Backbarrier Filling - East Frisian Islands, West Germany; Shore and Beach, vol. 52, no. 4, pp. 3-8.
- FITZGERALD, D.M., S. Penland, and D. NUMMEDAL, (1984b):** Sedimentation Processes along the East Frisian Islands, West Germany; Proc. 19th ICCE, vol. 3, pp. 3051-3066.
- FORSCHUNGSSTELLE FÜR INSEL UND KÜSTENSCHUTZ , Norderney (1964):** Niedersächsische Küste, Historische Karte Nr. 5, 1:50000.
- FÜHRBÖTER, A. et al. (1976):** Beurteilungen der Sandaufspülungen 1972 und Empfehlungen für die künftige Stranderhaltung am Weststrand der Insel Sylt; Die Küste, vol. 29, pp. 23-95
- FÜLSCHER, (1905):** Über Schutzbauten zur Erhaltung der Ost- und Nordfriesischen Inseln; Zeitschrift für Bauwesen, vol. 1905
- HOMEIER, H. (1964):** Beiheft zur Historischen Karte Nr. 5; report Forschungsstelle für Insel und Küstenschutz, Norderney
- HOMEIER, H. (1975):** Die Auswirkungen schwerer Sturmtiden auf die ostfriesischen Inselstrände und Randdünen; Jbr. Forschungsstelle für Insel und Küstenschutz, vol. 29, pp 107-122
- Kramer, J. (1958):** Künstliche Wiederherstellung von Stränden unter besonderer Berücksichtigung der Strandaufspülung Norderney 1951/52; Jbr. Forschungsstelle für Insel und Küstenschutz, vol. 9, pp. 53-92

- KRAMER, J. (1960):** Beach-Rehabilitation by use of Beach Fills and further Plans for the protection of the Island of Norderney; Proc. 7th ICCE, vol. 2, pp. 847-859.
- KRAMER, J., (1972):** Artificial Beach Nourishment on the German North Sea Coast; Proc. 13th ICCE, vol. 2, pp. 1465-1483.
- KUNZ, H. (1987):** History of Seawalls and Revetments on the Island of Norderney; Coastal Sediments '87, proc. vol. 1, pp. 974-989.
- LUCK, G., (1970):** Die zweite Strandaufspülung von Norderney; Jbr. 1968, Forschungsstelle für Insel und Küstenschutz, vol. 20, pp. 7-34.
- LUCK, G., (1975):** Der Einfluss der ostfriesischen Inseln auf die morphologischen Vorgänge im Bereich der Seegaten und ihrer Einzugsgebiete; Mitteilungen des Leichtweiss - Institut für Wasserbau, University of Braunschweig, vol. 47, pp. 1-122.
- LUCK, G., (1976):** Inlet changes of the East Frisian Islands; Proc. 15th ICCE, vol. 2, pp. 1938-1957.
- LÜDERS, K., (1953):** Die Entstehung der Ostfriesischen Inseln und der Einfluß auf den geologischen Aufbau der Ostfriesischen Küste; Probleme der Küstenforschung im südlichen Nordseegebiet, vol. 5.
- NIEMEYER, H. (1986):** Ausbreitung und Dämpfung des Seegangs im See- und Wattengebiet von Norderney; Jbr. 1985, Forschungsstelle Küste, vol. 38, pp. 49-95.
- NIEMEYER; H. (1990):** Field measurements and analysis of wave induced nearshore currents; 22nd ICCE, to be published
- O'BRIAN, M.P., (1969):** Equilibrium Flow Areas of Inlets on Sandy Coasts; Journal of the Waterways and Harbors Division, vol. 95, pp. 43-52.
- PÄTZOLD, U. (1982):** Bilanz und Verformung aufgespülter Sandstrände; Jbr. Forschungsstelle für Insel und Küstenschutz, vol. 32, pp. 41-53.
- PEPER, G. (1956):** Entstehung und Entwicklung der Insel-schutzwerke auf Norderney mit besonderer Berücksichtigung der Bauten der letzten Jahre; Neues Archiv für Niedersachsen, Bd. 8, vol. 3.
- RAGUTZKI, G.; T. WESTHOFF (1990):** Vierter Zwischenbericht zu Sedimentologischen Untersuchungen für das Forschungsvorhaben Wechselwirkungen zwischen Küstenbauwerken und mariner Umwelt; report Forschungsstelle Küste, Norderney.
- STEPHAN; H.-J. (1988):** Fünf Strandauffüllungen vor Norderney - Ergebnisse morphologischer Untersuchungen; report Forschungsstelle Küste, Norderney.
- WESTHOFF, T. (1990):** Sedimentologische Untersuchungen zur Klärung von Transportvorgängen im Bereich sandiger Küsten am Beispiel Norderney; dissertation University of Münster (in preparation).

CHAPTER 248

DESIGN AND INSTALLATION OF SCOUR PROTECTION FOR THE ACOSTA BRIDGE

Billy L. Edge¹, David K. Crapps²,
J. Sterling Jones³ and William L. Dean⁴

ABSTRACT

The Acosta Bridge is located in a bend at a natural constriction of the tidally influenced St. Johns River. This natural constriction has resulted over time in scour of the river bottom resulting in present water depths up to 80 feet. The Acosta Bridge is presently being replaced with a new bridge. The existing bridge is located immediately adjacent to a railroad bridge and both bridges are on caisson foundations. Divers have reported that penetration of the foundations for one of these existing bridges is as little as two feet. Construction of the replacement bridge will increase the scour potential. Therefore, scour protection had to be provided not only for the replacement bridge but the two existing bridges. The scour protection for the existing bridges was completed in 1990. The replacement bridge is under construction and scour protection is being installed as the piers are constructed.

INTRODUCTION

The Acosta Bridge, as shown in Figure 1, is located in a bend of the St. Johns River at a natural constriction of the flow. This natural constriction has resulted in scour of the river bottom which is considerably deeper than at other sites in this part of the river. Another important aspect is the proximity of the existing Acosta Bridge piers to the piers of the railroad bridge. It is obvious that the proximity of the two sets of bridge piers in this tidal area creates local scour beyond that which would normally be encountered were there only one set of bridge piers. The bridge piers in the center of the river of the existing Acosta and railroad bridges and the new Acosta bridge are shown in Figure 2. It is noted that the bottom topography and the bend in the river causes the stream flow to be helical and therefore it is difficult to define the flows in this part of the river accurately.

The St. Johns River is very flat and the tidal prism extends over 100 miles upstream from the

¹Edge & Associates, Inc., Charleston, SC 29401

²Schmertmann & Crapps, Inc., Gainesville, FL 32606

³Federal Highway Administration, McLean, VA 22101

⁴Kisinger Campo & Associates Corp., Jacksonville, FL 32207

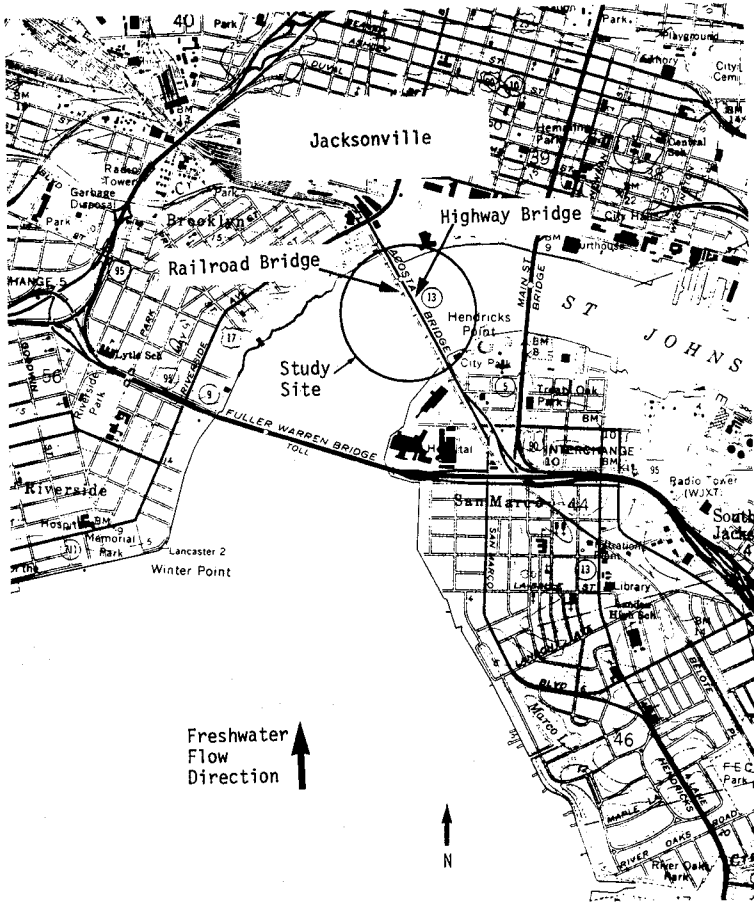


Figure 1. Location of the Acosta Bridge

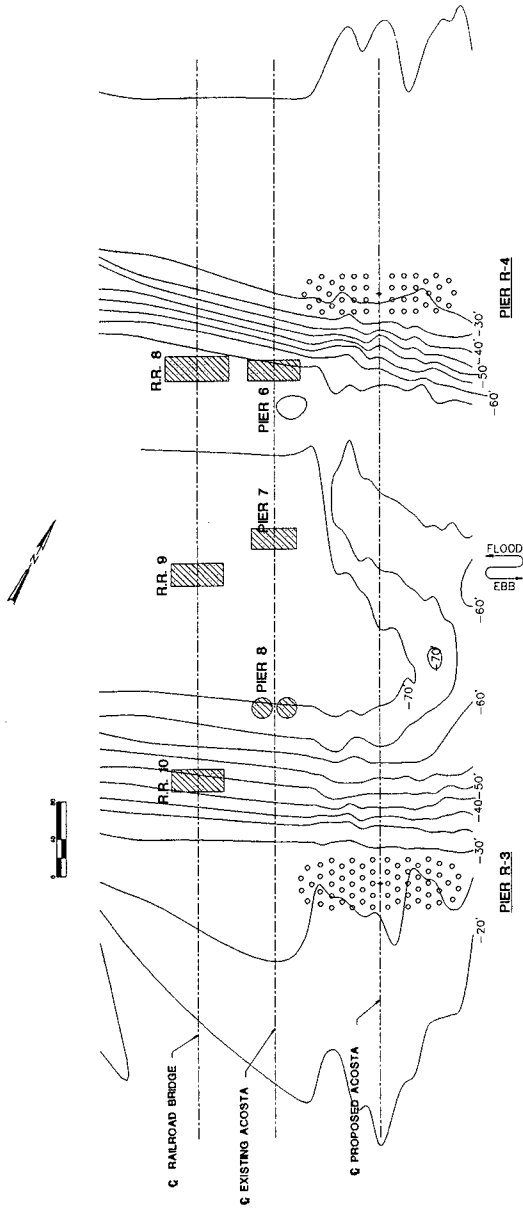


Figure 2. Plan View of the Acosta and Railroad Bridge Piers

bridges. The most severe storm conditions of record were during Hurricane Dora in September 1964. At that time there was an estimated flow of approximately 244,000 cfs downstream and 204,000 cfs upstream with a maximum stage at about elevation 5.2 MSL. The adjacent stream banks are at about elevation 6 MSL.

In the shallow water area of the site there is a sand layer varying in thickness from about 2 to 10 feet. This thin upper sand layer is highly erodable. The sand layer is underlain by a layer of lime rock varying in thickness from about 10 to 20 feet. Below the lime rock is marl that extends to great depth below the bottom of the channel. The marl erodes more easily than the lime rock. When the marl erodes it eventually leaves an overhang of lime rock which subsequently falls to reform a smooth channel slope. Figure 3 shows a survey that was made in 1924 and a recent survey of the area made in 1986. This figure shows that there has been approximately 20 feet of scour during this 62 year period. The largest amounts of scour occurred in the deeper parts of the river cross section. It also appears that geomorphologically the channel is migrating to outside of the bend in the river at the site. Similar scour has been observed at other bridges in the area.

ANALYSIS OF SCOUR

The scour which occurs in this part of the river can be considered as the cumulative effect of general scour and local scour. "General scour" results from a net reduction in the cross-sectional area of the river when additional bridge piers are added. The addition of obstructions or piers in this case results in an increase in the velocity of flow. This increased velocity in turn causes scour. The general trend is for erosion to continue until a stable channel is established. General scour usually increases with an increase in water depth according to Christensen and Bush (1971).

To determine general scour the procedure referenced in Christensen and Bush (1971) was followed. Dr. Christensen used this approach to provide the necessary general scour coefficient for the Acosta Bridge site which is shown in Figure 4. The existing Acosta Bridge as well as the range of pier widths considered during the preliminary design phase are also shown in Figure 4. To obtain the ultimate general scour the following relationship was used:

$$d_{gs} = c_{gs} (d^2)$$

where d_{gs} = depth of ultimate general scour in feet
 c_{gs} = coefficient of ultimate general scour from
 Figure 4
 d = water depth in feet

The construction of additional piers in the river for the new Acosta Bridge will create general scour that will adversely impact the existing Acosta and railroad bridges unless proper precautions are taken. This is particularly true for the deep water piers located in the marl (Acosta Bridge Piers 6, 7, and 8 and railroad piers 8, 9 and 10). Assuming that the total sum of pier widths added is about 200 ft, the general scour coefficient from Figure 4 is .0028. For different water depths, Table 1 summarizes the estimated general ultimate scour, estimated scour after three years (the time expected for construction of the new bridge and removal of the old bridge) and the minimum present footing depth below the river bottom.

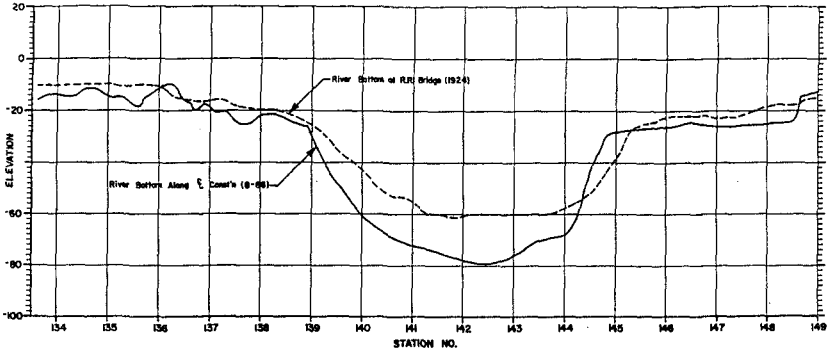


Figure 3. Profiles Across the St. Johns River in 1924 and 1986 at the Acosta Bridge

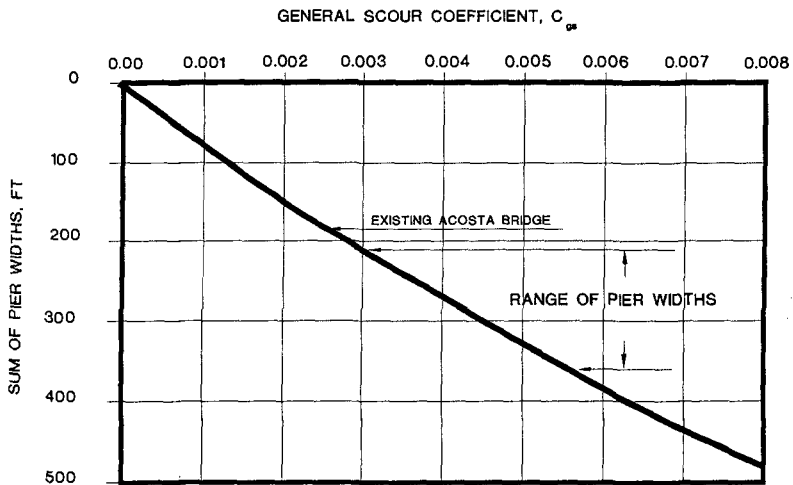


Figure 4. General Scour Coefficient for Acosta Bridge Site on St. Johns River

TABLE 1
SCOUR SUMMARY FOR DEEPWATER PIERS IN MARL

Pier #	Average Width ft	Shape ft	Original Water Depth ft	Actual Scour ft	Estimated Ultimate Scour ft	Estimated Time To Ultimate Scour years
6	12.0	circular	54.2	15.8	31.2	32,700
7	12.0	circular	60.0	26.0	32.8	330
8	12.0	circular	52.2	16.6	30.7	14,600
9 (RR)	17.8	rectangular	61.5	23.3	55.5	448,100

The table shows that the estimated scour after three years is below the foundations for the Acosta piers 6 and 7 and railroad pier 9. These data predict likely pier failure for both bridges due to general scour alone if steps are not taken to protect the deep water piers. Similarly it can be shown that the construction of new foundations for the replacement bridge will cause local scour and most likely cause pier failure for both bridges if adequate steps are not taken for protection.

Addition of bridge piers in the cross-section creates a local obstruction to flow as well. The flow divides in front of the pier and the velocity increases as it flows around the pier. A system of vortices develop around the pier which are generally described as a horse-shoe vortex (Breusers, Nicollet and Shen, 1977). The combination of increased velocity plus the vortices form to create an environment for scour in the vicinity of the pier which is commonly termed "local scour". The local scour depth and the width to the affected area increases both with the width of the pier and with the depth of the water. It has been determined that the shape of the pier is also very important in determining the depth and extent of the local scour. Likewise the presence of other piers or structures have a very important role in local scour.

The total amount of scour is the sum of the general scour and local scour. In this analysis it was assumed that general scour is complete and that the local scour is superimposed for the ultimate conditions.

To determine local scour several procedures were considered. One procedure used a complete set of velocity profiles taken in 1962. These raw data taken by the USGS at the Main Street Bridge were analyzed to develop a velocity profile at the Acosta Bridge site. The Main Street Bridge is approximately one-half mile downstream from the Acosta Bridge. Based on all the analyses it was decided that the maximum flow during the 100-year storm would have an average velocity of 6.2 fps on both flood and ebb conditions.

Initially, it was decided that stone riprap should be used for general and local scour protection. The method of Isbash as reported in Bruesser, Nicollet and Shen (1977), Blodgett and McCaughy (1983) and ASCE (1975) was used to calculate the minimum stone size. The formula was originally proposed by Isbash in 1936 for the construction of dams by dropping rock into a flowing stream. The size of the stone was then modified to take into account the slope of the bank and the curvature of the channel. The Isbash equation is frequently given in the following form:

$$W = \frac{4.1 \times 10^{-5} G_s V^6}{(G_s - 1)^2 \cos^3 \phi}$$

in which W = the weight of the stone in pounds
 G_s = the specific gravity of the stone
 V = velocity
 ϕ = angle of the bank

Typical results with this approach yielded stone size for general scour protection on the flat slopes of 0.4 feet in diameter. On the steeper slope of 1.3h:1v, the required stone diameter increased to 1.5 ft. For local scour, required stone sizes varied from 1.2 ft in water depths of 30 ft to 4.5 ft in water depths of 80 ft. Considering a minimum protection of two layers of stone plus bedding stone the thickness of the bottom scour protection is such that in itself it will cause an increase in the general scour and possibly increase flooding in Jacksonville during design conditions.

PHYSICAL MODEL

Since there was not time to develop a full three dimensional tidal model a unidirectional movable bed model was done for this project by the Federal Highway Administration. The purpose of the model was to develop further confidence in the analytical results and to further understand the interrelationship of the pier structures on the local scour. Undistorted wooden scale models of the pier configurations were placed in a sump filled with sand within the flume. The model scale was restricted by the size of the flume. The scale of 1:50 was based on a maximum flume flow depth of about 1.25 ft and a river depth of 70 ft. The actual bathymetry in the river was not reproduced in the model. The appropriate model ratios are listed below:

<u>Parameter</u>	<u>Ratio</u>
length	50:1
velocity	7.1:1
unit flow	354:1
riprap size	50:1

Since the flume was only 6 ft wide the full river could not be modeled at any given time. The available sand at the laboratory was used as the movable bed material. However, no specific specifications were given to the sand to insure that it would quantitatively model the depth, time rate or extent of scour. The approach to the sump in the flume was plywood with sand glued to the surface to provide continuity of bottom roughness. There was no mechanism for recirculating sand therefore the bed shear stress, t_o , was kept near the critical shear stress value, t_c . For higher values of shear stress, sand would wash out of the sump. With an upstream supply of sand, the scour holes would fill as fast as scouring occurred once equilibrium was reached. The flow rate used in the experiments was determined from the minimum flow at which sand particles began to move under the maximum depth of flow. After the threshold flow was determined a pier was placed into the sand and the time for full development of the scour hole was measured.

Flow in the flume was unidirectional unlike the flow in the prototype. The model bridge piers

were therefore placed so that the flow traveled in the tidal flood direction. The bridge piers were also altered so they could be aligned with a flow approach direction of 15 degrees from normal to account for the bend in the St. Johns River at this location. Results from the model gave upstream and adjacent velocity profiles as well as the extent of scour. Results from these model tests showed that generally the maximum velocity by the bridge piers was approximately 1.4 times the approach velocity. The hydraulic model study also concluded that stone riprap with 1.5 ft diameter and a specific gravity of 2.65 would be satisfactory with a stability factor of 1.2 for local scour protection.

DESIGN

Since the St. Johns River is tidal at the Acosta site, scour protection design had to consider both upstream and downstream bridge piers. Initially riprap protection from general scour and local scour was considered. The size of stone was calculated using an approach velocity of 6.2 fps for the design conditions of a 100 year storm. These calculations indicated a stone size of approximately 4.0 feet. The steep side slopes of the channel which approached 1:1 would require even larger stone. The stone would need to be placed upon an appropriate filter which would be difficult to install considering the deep water, high currents, poor visibility and limited bridge clearance at the site.

Because of the large sizes of stone required for traditional riprap protection around the bridge piers it was decided that an alternative form of construction should be considered. The selected alternative was gabion wire baskets. These baskets when tied together form a blanket which holds smaller stone in place and which can have a filter integral to the installation. Individual gabion baskets can be wired together into large units to be placed on the bottom. These units can then in turn be laced (wired) to other units to create a continuous layer of protection across the bottom in the areas where local scour protection is required.

The final gabion design was developed based on Agostini et al. (1985). The structure included two layers of 9 inch mattresses. The baskets were filled with stone with the following gradation:

<u>Weight</u>	<u>% Finer Than</u>
11 lb	100
6.2 lb	50
1.3 lb	0

Filter fabric was in the bottom of the upper mattress layer. The layout for the existing Acosta and railroad bridges is shown in Figure 5. This layout will be connected to and become part of the scour protection for the new Acosta Bridge which is under construction. To minimize the effects of corrosion the wire mesh baskets were first galvanized and then coated with PVC. All tie wire was also galvanized and coated with PVC.

Two other bridges have also used similar techniques as alternatives to armor stone. The most recent was the Kalamazoo River Bridge in Michigan (personal communication with David Parsh of C-Way Construction, 1989). A very similar project was completed at the Vendee Bridge which crosses Loire River in Nantes, France. Although the conditions were not tidal on the Loire River, the combination of general and local scour posed a serious threat to the safety of the bridge (Officine MacCaferri S.p.A., 1983). Soon after construction was completed in 1982 a 100-year flood occurred on the Loire River and the scour protection performed satisfactorily.

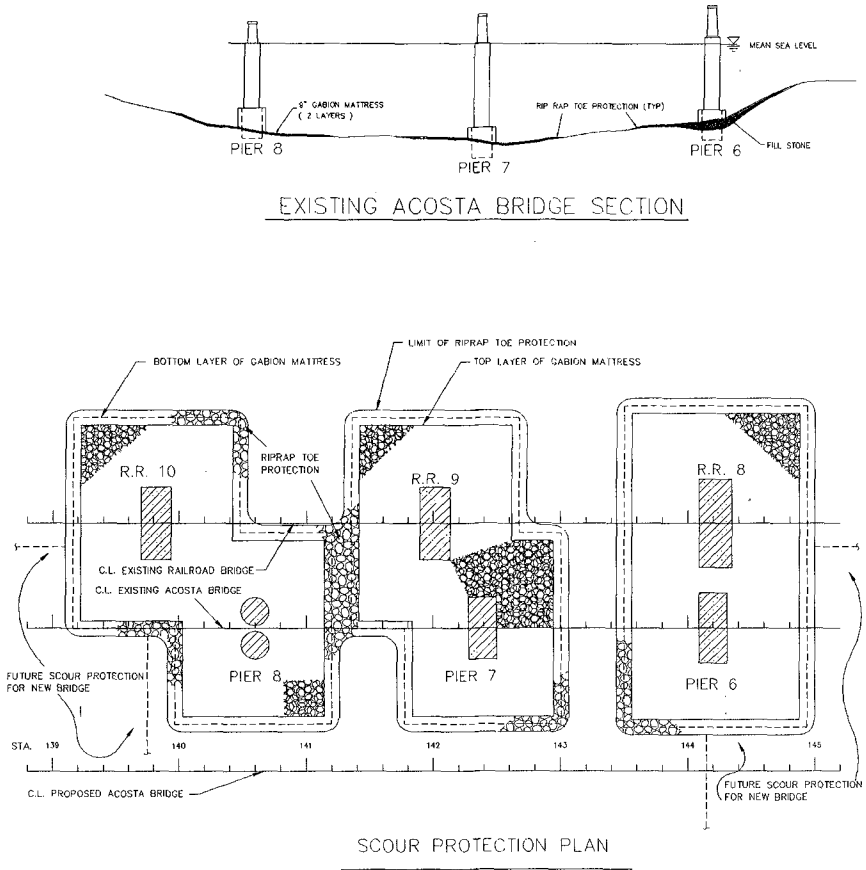


Figure 5. Plan of Scour Protection for Existing Acosta and Railroad Bridges

CONSTRUCTION

The individual mattresses of 6 feet by 18 feet were laced together on land and filled with stone on a barge before being placed. Special placement barges were fabricated by the Contractor to handle large sections of mattresses placed together to form a single unit 18 feet by 36 feet. Figure 6 shows the mattresses on the support barge and Figure 7 shows the special placement barge and the 18 ft by 36 ft unit being transferred from the support barge to the special placement barge. Note that the placement barge had to be partly submerged to maneuver and place the mattress assembly beneath the low railroad bridge. This was accomplished by transferring the assembly from the crane to the placement barge which was then winched by anchor cables to the proper location. In order to secure an adequate foundation for the mattresses side scan sonar and detailed bathymetric surveys were made to identify areas which were too steep to support the mattresses, to identify debris on the bottom which would have to be removed and to identify other obstructions which the mattresses would have to accommodate through construction or modification of design. In areas that were too steep for the mattresses to lay properly, stone fill was added to bring the slope up to at least 1v:1.5h and generally 1v:2.0h. Placement of the mattress assemblies and subsequent lacing underwater was made doubly difficult by the high tidal currents which although generally less than 2 feet per second occasionally exceeded 4 feet per second and the turbid water which limited visibility to a maximum of 4 feet and generally 12 inches with occasions of zero visibility. The placement was completed in August 1990 in time for construction of the new bridge piers.

SUMMARY

Scour protection was designed and installation completed for two existing bridges on the St. Johns River. Scour protection was designed to accommodate a 100 year design storm with a flood elevation of approximately 6.0 feet. This is the largest known tidal deep water installation for this type of protection. Coordination of the design and execution of the construction in adverse conditions was a challenge to all concerned.

REFERENCES

- Agostini, R., A. Conte, G. Malaguti and A. Papetti, "Flexible Linings in Reno Mattress and Gabions for Canals and Canalized Water Courses", MacCafferri Gabions, Inc., Williamsport, MD, 1985.
- ASCE, **Sedimentation**, edited by Vito A. Vanoni, Manuals and Reports on Engineering Practice -- No. 54, New York, 1975.
- Blodgett, J.C. and C.E. McConaughy, "Rock Riprap Design for Protection of Stream Channels near highway Structures: Volume 2 -- Evaluation of Riprap Design Procedures," Water Resources Investigations Report No. 86-4128, U.S. Geological Survey, 1986.
- Breusers, H.N.C., Nicollet, G., Shen, H.W., "Local Scour Around Cylindrical Piers", **Journal of Hydraulic Research**, No. 3, IAHR, 1977.
- Christensen, B.A. and Bush, P.W., "Statistically Based Determination of Depth and Width Ratios

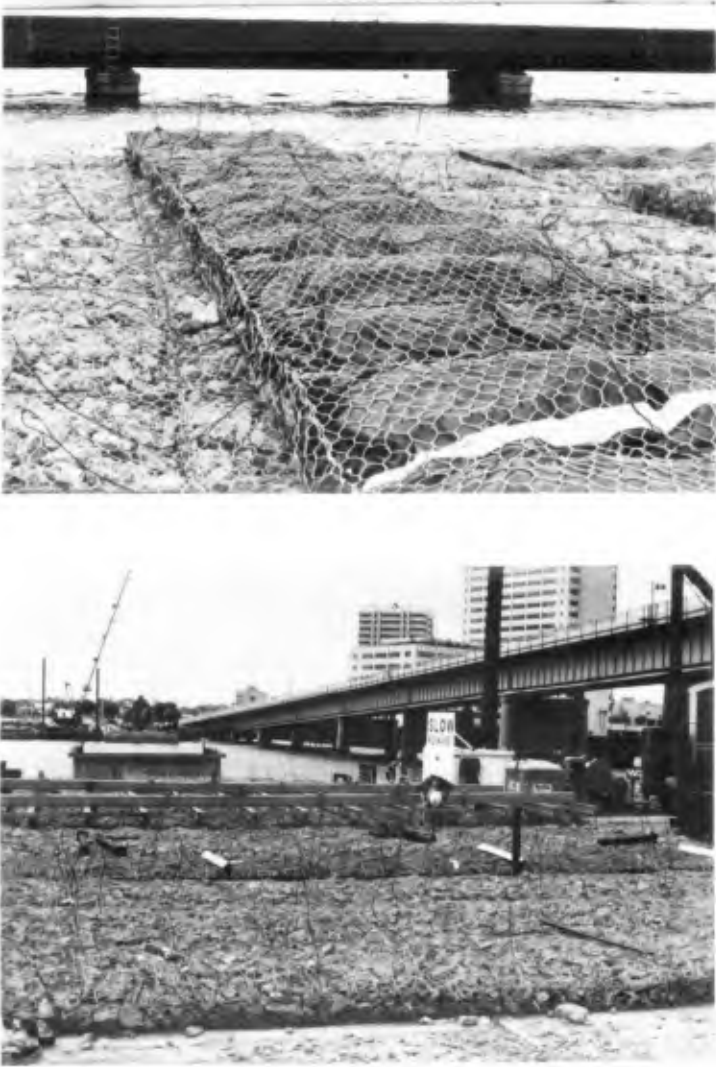


Figure 6. Gabion Mattresses on Supply Barge

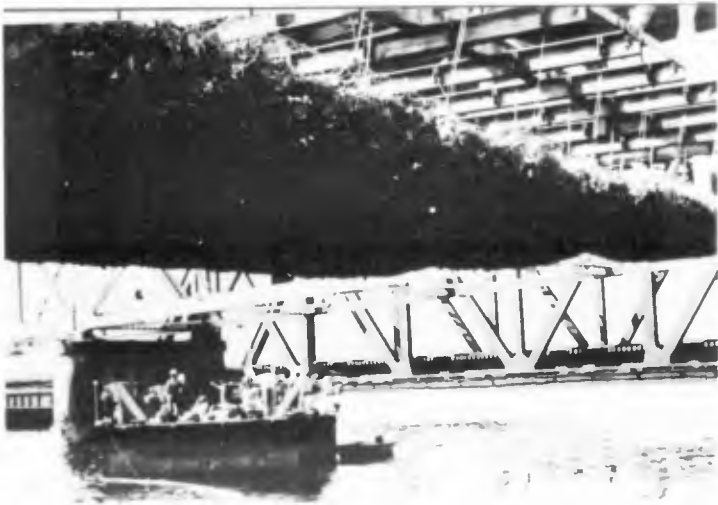


Figure 7. Mattress Assembly Being Lowered by Crane to Special Placement Barge. Note the Low Clearance of the Railroad Bridge in the Background.

in Alluvial Water Courses", **Proceedings of the First International Symposium on Stochastic Hydraulics**, Pittsburgh, ASCE, 1971.

GKY and Associates, Inc., "Lab Report for the Acosta Bridge Scour Study", Prepared for the Federal Highway Administration, McLean, VA, 1988.

Officine MacCafferri S.p.A., "Protection of the Foundations of the Vendee Bridges Crossing The Loire River - Nantes", Brochure Published by MacCafferri Gabions, Inc., Williamsport, MD, 1983.

CHAPTER 249

Influence functions

H.G. Wind¹

Abstract

Influence functions combine part of the strong body of coastal engineering knowledge, the one-line theory, with the most reliable sources of data: position of the shoreline and geological information about the evolution of the shoreline. Influence functions yield a model of the shoreline erosion or -accretion, which is based upon the characteristic length $\sqrt{4at}$. This model can be used to reproduce the present shoreline and predict the changes of the shoreline after human interference. Examples are given of the Petrace delta in Italy and the port construction near the Kelantan Delta in Malaysia.

1. Introduction

Engineers must provide reliable answers based upon unreliable data. Coastal engineers are no exception to this rule. At the start of a project they are faced with scanty wave data, unreliably or lacking bathymetric data and hardly any information on sediment yield of rivers. They have knowledge about the processes which take care of the longshore distribution of sediment. Clients however often have restricted time and money for the required advice. On these cross-roads the influence functions were born.

The first step on the mathematical modeling of curved shorelines has been made by Pelnard Considère (1956). He showed that the shoreline evolution could be described by the diffusion equation. This theme has been elaborated by various investigators e.g. Walton (1979), Grym (1960,1964) and Bakker and Edelman (1964).

¹Professor of civil engineering, University of Twente, P.O. Box 217, 7500 AE Enschede, The Netherlands, Scientific advisor of Delft Hydraulics.

The application of the diffusion equation in engineering practice is often hampered by the fact that at the initial stage of the project the wave data is not available and in a later stage of the project that both wave data and sediment transport formulae appear to be somewhat unreliable. In the present study therefore a slightly different approach has been taken. A framework of analysis has been set up in which various sources of geological and geophysical information can be combined in the morphological study.

In chapter 2 the theory behind the diffusion equation is explained. Influence functions and some applications are worked out in chapter 3. A large scale study, dealing with the Kelantan delta, is presented in chapter 4, followed by a summary and conclusions.

2. Theory

Consider a stretch of beach as shown in Figure 1.

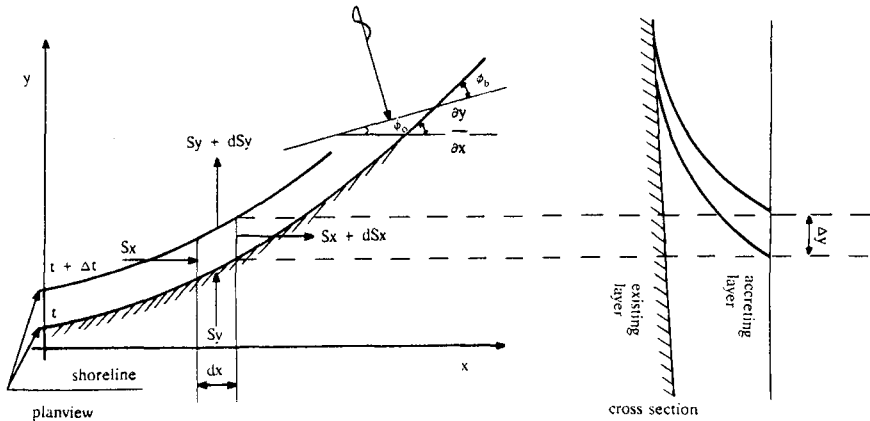


Figure 1: Definitions

It will be assumed that the time scale of changes in the beach profile in the direction normal to the shore is either much shorter or much longer than the time scale of changes in the direction parallel to the coast. This allows for the approximation of a parallel displacement of the beach profile. Furthermore it will be assumed that in all profiles similar sediment transport processes are taking place. Along the beach this leads to parallel depth contours allowing for simple refraction computations. The erosion or accretion depth h is assumed to be constant along the beach. The continuity equation for the sediment transport S then reads:

$$\frac{\partial S_x}{\partial x} + \frac{\partial S_y}{\partial y} + h \frac{\partial y}{\partial t} = 0 \quad 2.1$$

In this study only sedimenttransport induced by wave driven longshore currents will be regarded. The effects of tidal currents on the sediment transport will be ignored. A similar restriction can be found in the work of M. Blosset (1935), where he presents the original conclusions, which form the basis of the famous 1956 Pelnard Considère study. The conclusions of Blosset were obtained from the morphological model studies of the port of Abidjan in Delft Hydraulics.

An important parameter in wave driven longshore transport is the angle ϕ_b between the wavecrest at the breakerline and the local depth contour (see Figure 1). The angle ϕ_b can be expressed in terms of the angle ϕ_o , (angle between the wavecrest and the positive x-axis) and $\partial y/\partial x$, (the angle between the shoreline and the positive x-axis) by:

$$\phi_b = \phi_o - \partial y/\partial x \quad 2.2$$

In the present study it will be assumed that ϕ_o and $\partial y/\partial x$ are sufficient small, such that the longshore transport S may assumed to be equal to S_x and that S_y can be neglected ($S_y \ll S_x \approx S$). In the discussion in chapter 5 this point will be taken up again.

Noting that with the chain rule $\partial S/\partial x$ can be expressed as $\partial S/\partial \phi_b = \partial S/\partial \phi_b \cdot \partial \phi_b/\partial x$ it follows from formulae 2.1 and 2.2 that:

$$a \frac{\partial^2 y}{\partial x^2} - \frac{\partial y}{\partial t} = 0 \quad 2.3$$

in wich




$$a = \frac{1}{h} \frac{\partial S}{\partial \phi_b} \quad 2.4$$

3. Influence functions and applications

3.1 Influence functions

Pelnard Considère (1956) has presented solutions of the diffusion equation 2.3 for the accretion near a breakwater and sediment passing a breakwater. Furthermore Pelnard Considère obtained a solution describing the behaviour of

a replenishment. These solutions are reproduced in Table 1 (see also Bakker, 1964).

	accretion near breakwater river delta 	sediment passing a breakwater 	sand replenishments 	definitions
y	$\text{tg } \phi \sqrt{\frac{4at}{\pi}} F(u)$	L G(u)	$\frac{1}{\sqrt{\pi}} \frac{Q}{\sqrt{4at}} H(u)$	$F(u) = e^{-u^2} \cdot u \sqrt{\pi} G(u)$
$\frac{\partial y}{\partial x}$	$\text{tg } \phi G(u)$	$\frac{2}{\sqrt{\pi}} \frac{L}{\sqrt{4at}} H(u)$	$\frac{2}{\sqrt{\pi}} Q u H(u)$	$G(u) = 1 - \frac{2}{\sqrt{\pi}} \int_0^u e^{-u^2} du$
$\frac{\partial y}{\partial t}$	$\text{tg } \phi \frac{1}{2t} \sqrt{\frac{4at}{\pi}} H(u)$	$\frac{1}{\sqrt{\pi}} \frac{L}{t} u H(u)$	$\frac{1}{\sqrt{\pi}} \frac{Q}{\sqrt{4at}} \frac{1}{t} (-\frac{1}{2} u^2) H(u)$	$H(u) = e^{-u^2}$

Boundary conditions $x = 0 \quad S = \text{constant}$ $x = 0 \quad S = 0$ $x = 0 \quad S = \text{constant}$
 $x = \infty \quad S = 0$ $x = \infty \quad S = \text{constant}$ $x = \infty \quad S = \text{constant}$

Table 1: Influence functions

As shown in Table 1 the solutions of the diffusion equation can be regarded as representing the influence in longshore direction of sources and sinks on respectively the shoreline displacements y, shoreline rotation $\partial y/\partial x$ and rate of displacement of the shoreline $\partial y/\partial t$.

It will be shown that complex morphological systems can rather simply be expressed in terms of influence functions. This expression can then be used to obtain an estimate of the parameter $\sqrt{4at}$, describing the shape of the shoreline, based upon a characteristic dimension of the existing shoreline.

The approach is based upon the property of the linear diffusion equation, that the superposition of two solutions of the diffusion equation forms a new solution of the diffusion equation. However this is only true if the boundary conditions for both initial solutions are also satisfied by the superposed solution.

3.2 The riverdelta consisting of one river

The evolution of a river delta, dominated by wave driven longshore transport, can according to the solutions given in Table 1, be described by

$$y = \text{tg } \phi \sqrt{\frac{4at}{\pi}} F(u) \tag{3.2.1}$$

where ϕ is the angle between the incoming averaged wave field and the shoreline. The influence of the individual source on the displacement y of the shoreline at a distance x can be expressed in dimensionless terms, by

rearranging 3.2.1, dividing by the distance x and noting that $u = x / \sqrt{4at}$.

$$\frac{y}{x \operatorname{tg} \phi} = \frac{1}{\sqrt{\pi}} \frac{1}{u} F(u) \tag{3.2.2}$$

The expression 3.2.2 is shown in Figure 2.

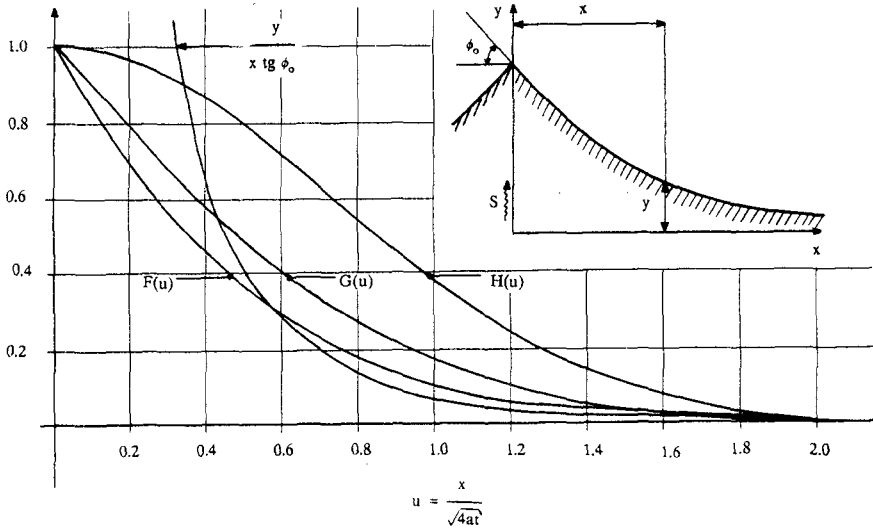


Figure 2: Influence functions

As can be seen from Figure 2 the influence of the source on the shoreline displacement is reduced to 10% of the displacement at the source at a distance of about $0,85 \sqrt{4at}$. It is interesting to note that a similar influence on $\partial y / \partial x$, represented by $G(u)$ in Figure 1, extends upto $1,2 \sqrt{4at}$.

3.3 The riverdelta consisting of two rivers

3.3.1 Introduction

The second example is related to a coastal plain near Gioia Tauro in the South of Italy. This coastal plain is formed by two rivers: the Petrace and the Mesima. The Petrace and the Mesima will be represent by two sources with a sediment yield of $\gamma Q \text{ m}^3/\text{yr}$ and $Q \text{ m}^3/\text{yr}$ respectively.

3.3.2 Determination of the value of $\sqrt{4at}$ if the baseline is known.

The evolution of the riverdelta due to a single source is

described by 3.3.1. In case of two sources the contributions of the two rivers will be linearly superposed. The width of the delta respectively at the Petrace ($x = 0$) and the Mesima ($x = L$) becomes in that case respectively

$$y(0,t) = \operatorname{tg} \phi \sqrt{\frac{4at}{\pi}} \{ 1 + \gamma F(u_1) \} \quad 3.3.1$$

$$y(L,t) = \operatorname{tg} \phi \sqrt{\frac{4at}{\pi}} \{ \gamma + F(u_1) \} \quad 3.3.2$$

$$\text{where } u_1 = \frac{L}{\sqrt{4at}} \quad 3.3.3$$

and L is the distance in meters between both rivers.

From a map the angle ϕ_0 between the shoreline at the mouth of the Mesima with a line parallel to the baseline can be obtained. This angle ϕ_0 is formed by superposition of the angle ϕ in absence of the Petrace and the value of $\partial y/\partial x$ at the Mesima due to the Petrace alone or

$$\operatorname{tg} \phi_0 = \{ 1 + \gamma G(u_1) \} \operatorname{tg} \phi \quad 3.3.4$$

The maximum width of the delta at $x = L$ can be expressed in terms of u_1 and known parameters, by combining 3.3.1, 3.3.3 and 3.3.4 rearranging and dividing by L .

$$\frac{y(L,t)}{L \operatorname{tg} \phi} = \frac{1 + \gamma F(u_1)}{\sqrt{\pi} u_1 (1 + \gamma G(u_1))} \quad 3.3.5$$

For the application of Figure 3.3.5 it is essential that $y(L,t)$, e.g. the distance between the baseline and the mouth of the river, is known. In the next example the baseline is unknown and in that case use will be made of a characteristic length of the shape of the shoreline in order to obtain an estimate of $\sqrt{4at}$.

4. Kelantan Minor Port Project

4.1 Introduction

The Kelantan Minor Port will be located in the north-eastern part of Malaysia, along the coast in between the mouths of Kemasin and Pengkalan Datu rivers (see Figure 3). The first part of the study was focussed upon the general morphology followed by an assessment of the

morphological consequences of the projected harbour.

4.2 Description of the morphological system

The proposed harbour is located along the border of the delta of the Kelantan. This delta can be traced back upto 18 km inwards. The sediment yield of the remaining rivers on the delta is small relative to that of the Kelantan. West of the mouth of the Kelantan a spit is growing in N.W. direction, pointing towards a predominantly SE-NW sanddrift. East of the Kelantan, at a distance of about 50 km, an ondulation in the delta can be observed. This ondulation is caused by the presence of the offshore Perhentian islands leading to a kind of tombolo formation on the delta. At some stage of the delta formation, probably around 1700, the Kelantan has shifted its course, cutting off the sediment yield to the delta. Parts of the delta are presently eroding.

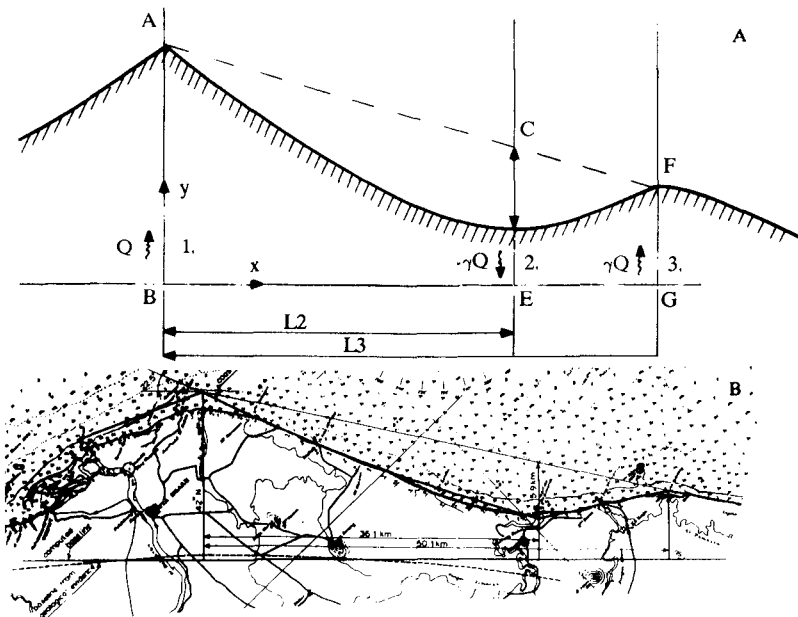


Figure 3: Before (A) and after (B) the change of the Kelantan.

4.3 Mathematical schematisation of the sediment balance

The delta formation has been represented by means of three rivers (Figure 3). The first river is the Kelantan with a sediment yield of $Q \text{ m}^3/\text{yr}$. The second and third river are jointly representing the ondulation of the delta. Due to

the Perhentian islands part of the coast is protected against the incoming wavefield, resulting along the shoreline in a reduced transport capacity of the waves behind the islands. In order to allow for the continuous SE - NW sandtransport, an increased angle between coastline and incoming wave field in the area has resulted. This feature has been represented by two rivers, which together do not affect the overall sediment balance. The second river is located at a distance of $L_2 = 36,1$ km from the Kelantan and acts like a sink with a negative sediment yield of γQ m³/yr, where γ is a constant. The third river is located at $L_3 = 50,1$ km from the Kelantan and has a sediment yield of γQ . In the mathematical formulation superposition of a continuous sanddrift from SE to NW does not change the shape of the delta and has therefore not been included. Loss of sediment in offshore direction, out of sediment balance, is not envisaged.

In the mathematical representation of the formation of the Kelantan delta, each point of the delta experiences the influence of the three rivers. These contributions can be expressed in terms of $y_1(x,t)$, $y_2(x,t)$ and $y_3(x,t)$, where the numbers refer to the numbers of the rivers. In terms of the influence functions of chapter 2 these contributions are:

$$y_1(x,t) = \text{tg } \phi \sqrt{\frac{4at}{\pi}} F(u_1); u_1 = |x|/\sqrt{4at} \quad 4.3.1$$

$$y_2(x,t) = -\gamma \text{tg } \phi \sqrt{\frac{4at}{\pi}} F(u_2); u_2 = |x - L_2|/\sqrt{4at} \quad 4.3.2$$

$$y_3(x,t) = \gamma \text{tg } \phi \sqrt{\frac{4at}{\pi}} F(u_3); u_3 = |x - L_3|/\sqrt{4at} \quad 4.3.3$$

The resulting delta is formed by superposition of these three contributions. For practical reasons use will be made of one parameter for instance u_2 instead of the three parameters u_1 , u_2 and u_3 . This can be achieved by simple algebra. The formation of the delta in dimensionless form follows from superposition of y_1 , y_2 , y_3 , dividing by a length scale, say L_2 , and rearranging:

$$\frac{y(x,t)}{\text{tg } \phi L_2} = \frac{1}{\sqrt{\pi}} \frac{1}{u_{22}} \left\{ F\left(\frac{|x|}{L_2} u_{22}\right) - \gamma F\left(\frac{|x-L_2|}{L_2} u_{22}\right) + \gamma F\left(\frac{|x-L_3|}{L_2} u_{22}\right) \right\}$$

$$\text{where } u_{22} = L_2/\sqrt{4at} \quad 4.3.5$$

In this representation of the Kelantan delta $tg\phi$ is the angle between the baseline and the shoreline near the mouth of the Kelantan in absence of rivers 2 and 3. The combined effects of the three rivers on $tg\phi$ results in $tg\phi_0$, where ϕ_0 can be measured from a map near the mouth of the Kelantan.

$$tg \phi_0 = tg \phi \left\{ 1 - \gamma G(u_{22}) + \gamma G\left(\frac{L3}{L2} u_{22}\right) \right\} \tag{4.3.6}$$

In this formulation the first term between brackets represents the influence of the Kelantan on $tg\phi_0$ (note that $G(0) = 1$), the second term refers to river 2. The third term refers to river 3, but has been expressed in terms of 4.2.2.

Introducing 4.3.6 in 4.3.4 leads to expression 4.3.7.:

$$y(x,t) = \frac{1}{tg_0 \phi L2} \frac{1}{\sqrt{\pi}} \frac{1}{u_{22}} \frac{\left\{ F\left(\frac{|x|}{L2} u_{22}\right) - \gamma F\left(\frac{|x-L2|}{L2} u_{22}\right) + \gamma F\left(\frac{|x-L3|}{L2} u_{22}\right) \right\}}{\left\{ 1 - \gamma G(u_{22}) + \gamma G\left(\frac{L3}{L2} u_{22}\right) \right\}} \tag{4.3.7}$$

representing the shape of the delta in terms of known variables and one parameter u_{22} . In the next paragraph the value of u_{22} or in fact the value of $\sqrt{4at}$ will be determined from a characteristic dimension of the shape of the delta.

4.4 Determination of the value of $\sqrt{4at}$ and γ from the shape of the delta.

As a characteristic dimension of the shape of the delta in Figure 5 the distance CD has been selected. Obviously the width of the delta AB could also have been selected, however at the beginning of the project the position of the baseline was not known and the influence of river 2 and 3 is rather small for a large range values of $\sqrt{4at}$.

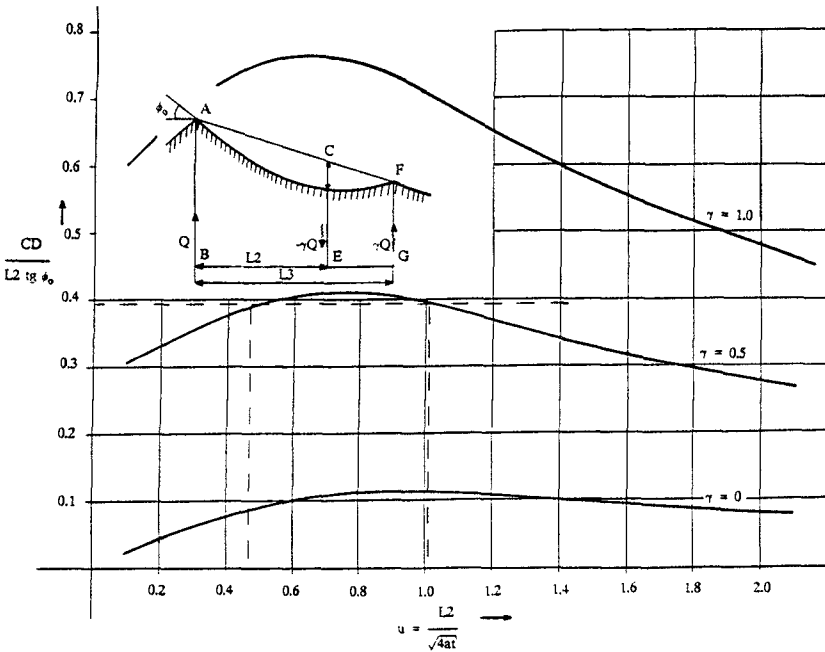


Figure 4: Characteristic dimension CD, expressed in terms of $\sqrt{4at}$.

The distance CD in Figure 4 can be expressed in geometrical dimensions of the delta as follows:

$$CD + DE = AB - (AB - FG) L2/L3 \tag{4.4.1}$$

In terms of x, y and t, equation 4.4.1 can be expressed as:

$$CD + y(L2,t) = y(0,t) - \{ y(0,t) - y(L3,t) \} L2/L3 \tag{4.4.2}$$

Taking the angle near the mouth of the Kelantan as the reference angle, the following expression of CD in terms of u^2 can be obtained:

$$\frac{CD}{L2 \text{ tg } \phi_0} = \frac{1}{L2 \text{ tg } \phi_0} \{ y(0,t) - y(L2,t) - (y(0,t) - y(L3,t)) L2/L3 \} \tag{4.4.3}$$

where the displacement of the delta $y(x,t)$ is described by 4.3.7.

The functional relation between CD, u^2 and γ , as represented by equation 4.4.3, is shown in Figure 4.

The following geometrical parameters have been selected for the Kelantan delta: $CD = 5,900m$, $L_2 = 36,100m$, $L_3 = 50,100m$ and $\phi_0 = 22,5^\circ$. The value of parameter $CD/(L_2 \text{ tg } \phi_0)$ equals $0,395$. According to Figure 4 both $u = 0,47$ and $u = 1,07$ satisfy 4.4.3 for $\gamma = 0,5$. It is interesting to note that there are two values of u ($u_1 = 0,47$ and $u_2 = 1,07$) which satisfy $CD = 5,900m$. This implies that both at time t_1 and t_2 after the start of the build up of the delta, that $CD/(L_2 \text{ tg}_0) = 0,395$. For a constant value of a and L , it follows from the definition of u that:

$$\frac{t_2}{t_1} + \left(\frac{u_1}{u_2} \right)^2 \quad 4.4.4$$

If the present shoreline is the result of a continuous process of $t_1 = 6000$ years, that at $t_2 = 1150$ years after the start of the build up of the delta CD reached also the present value. This is an example of many valuedness in the analysis of shoreline evolution.

In the next paragraph the selected values of γ and $\sqrt{4at}$ will be validated.

4.5 Validation of the values of $\sqrt{4at}$ and γ . The shoreline

A fair reconstruction of the shoreline by means of influence functions is shown in Figure 3. The following values of the parameters have been used: $\sqrt{4at} = 75,790m$, $\gamma = 0,5$, $\phi_0 = 22.5^\circ$.

The base line

On basis of a LANDSAT image of the Kelantan delta the alignment of the various series of beach ridges could be reconstructed. In Figure 3 a tentative line is drawn to indicate the delta growth over the last 6000 years. The distance between baseline and the mouth of the Kelantan is roughly $18,000m$. A theoretical estimate of the position of the baseline, using 3.2.1 and realising that $x = 0$ or $F(u) = 1$ at the origin of the river, than 3.2.1 leads to a value of $y = 17,711m$. The fact that the effect of the rivers 2 and 3 on the width of the delta near the Kelantan is small, is due to the fact that the location of both rivers is of the same order of magnitude as the length scale $\sqrt{4at}$ in the diffusion equation, and that both rivers are of equal magnitude, but of opposite sign.

Sediment yield of the river.

The natural geological rate of erosion in the Kelantan delta is in the order of $100m^3/km^2/yr$ from the totally

undisturbed catchment area. The yearly sediment yield of the Kelantan would be in the order of 1,300,000 m³/yr. In the last century, due to human activities, this figure has increased to 1,700,000 m³/yr. Only the bedload will contribute to the growth of delta. From measurements the bedload appeared to be 50% of the total load, leading to a sediment yield of the Kelantan in the order of 700.000 m³/yr to 800,000 m³/yr.

A numerical estimate of the sediment yield Q_t of the Kelantan can be obtained from the continuity equation. Near the mouth of the river this formula leads to:

$$Q_t = 2St = 2at h \text{tg } \phi \quad 4.5.2$$

Assuming an accretion depth of 4 m. to 5 m., this leads to a total sediment yield of $4,8 * 10^9 \text{ m}^3$ to $5,9 * 10^9 \text{ m}^3$. According to the geological study the present delta formation has continued over the last 6000 years, leading to an annual sediment yield of the Kelantan of 790.000 m³/yr to 991.000m³/yr.

The conclusion is that on all three aspects: the shape of the shoreline, the position of the baseline and the total sediment the theoretical approximation and the selected parameters yield a reasonable approximation.

5. Summary and remarks

The approach presented in this paper has been tested in various coastal morphological projects, where wave drive longshore sediment transport played a dominant role. In the analysis the morphological project is placed within a larger framework, allowing for various disciplines to contribute. The experience is that application of the approach is rather straightforward, highlighting the important aspects and conflicting sources of data and theory for a specific site.

The use of influence functions requires a clear perception of the large scale morphology. The set up of the equations such as shown in paragraph 4.3. and 4.4 is rather straightforward. Personal Computers are particularly suitable for the construction of the dimensionless graphs as shown in Figures 2 and 4. Reconstruction of the present coastline using the obtained values of $\sqrt{4at}$ requires a similar approach as for the construction of the dimensionless graphs. For the verification of the longterm morphology, information can be used from geological and geophysical sources. For calibration of recent developments particularly use is made of the rate of accretion in recent decades.

The framework of analysis allows for highlighting

conflicting data sources and the resulting effects on the large scale morphology if either of the data sources would be true. Equally important however is that influence functions can be used to form a test for the basic hypothesis that the longshore transport process related to ϕ_{br} is the dominant process for the coast under consideration. If this is not the case a different approach than the one-line theory should be devised. An example is the offshore transport term S_y . However the concept of influence functions remains applicable for those beaches where offshore transport can be represented as : $S_y = \text{constant}$ or $S_y = \text{constant}$ fraction of the longshore transport gradient $\partial S/\partial x$. The effect on the shape of this offshore transport on the present shoreline in that case is nil. Obviously the effect can be noted in the large scale delta evolution and in the total volume of longshore transport.

In some morphological projects it appeared that long term trends in beach evolution differed considerably from recent trends in beach evolution. In that case the values of the parameters for the recent evolution were used for prediction of future changes. Within the realm of the projects it was not possible to find the cause for the changing trends on different time scales. It may be that if experience from more sites are combined a coherent picture may emerge, for instance the effects of a rise of mean sea level.

Acknowledgement

The theory of influence functions has been developed by the author in the period 1976 - 1987. In this period the author was employed as an project engineer of Delft Hydraulics. The theoretical development was initiated by the investigations for the Gioia Tauro Port project. The Kelantan Minor Port project, carried out by mr. W. Tilmans led to a further elaboration and illustration of the theory. The author acknowledges the permission of colleagues, Delft Hydraulics and the clients of the Gioia Tauro Port project and the Kelantan Minor Port project to allow publication of the results.

Notation

a	diffusion coefficient
A	constant
C	characteristic dimension of a beach plan
c_0	deep water wave celerity
F	influence function for shoreline displacement
G	influence function for shoreline rotation
h	depth of accretion
H_0	significant deep water wave height
H	influence function for rate of accretion of the shoreline
L, L_2, L_3	distance between two rivers

Q	sediment yield of the river
S	sediment transport rate
t	time
u	$x/\sqrt{4at}$; parameter
u1	idem $L/\sqrt{4at}$
u2	idem $ x - L2 /\sqrt{4at}$
u3	idem $ x - L3 /\sqrt{4at}$
u22	idem $L2/\sqrt{4at}$
x	co-ordinate axis
y	co-ordinate axis
γ	ratio of the sediment yield of two rivers
η	reduction factor of the sediment yield of the river
ϕ_b, ϕ_o	angle between deep water wave crest respectively the breakerline and the positive x-axis
subscripts	
b	breakerline, y
x,y	parallel to x,y-axis
pet., mes.	Petrace, Mesima
1,2,3	referring to river 1,2 or 3
0	deep waterwave characteristics

References

- Bakker, W.T. and Edelman, T. 1964, The Coastline of River-Deltas, Proc. of the 8th Conf. on Coast. Eng., 1964: pp 199-128.
- Broquaire, M., Etienne, M. and Blosset M, 1935, Ontwerp van werken buitengaats van een haven etc. XVI International Shipping Congress, Brussels.
- Grijm, W., 1960, Theoretical forms of shorelines, Proc. of the 7th Conf. on Coast. Eng. 1960: pp 197-203.
- Grijm, W., 1964, Theoretical forms of shorelines, Proc. of the 8th Conf. on Coast. Eng., 1964: pp 219-235.
- Pelnard Considère, R. 1956, Essai de theorie de l'evolution des formes de rivage en plages de sables et de galets, Societé Hydrotechnique de France, IV en Journees de L'Hydraulique (Paris, 1956), Question III, rapport 1, 74-1-10.
- Walton, T.L. and Chui, T.Y., 1979, A review of analytical techniques to solve the sand transport equation and some simplified techniques, Coastal Structures 1979; 809-837.
- DELFT HYDRAULICS, Kemasin-Semerato Integrated Rural Development Project, Impact assessment of seaworks at rivermouths in coastal morphology Report H1051, 1989.
- DELFT HYDRAULICS, Morphological aspects of Gioia Tauro Port, Theoretical analysis of shoreline computations, Report M1857, Volume II, 1982
- DELFT HYDRAULICS, Kelantan Minor Port Project, Part 3 - General Morphology, Report M1997, 1984.

SUBJECT INDEX

Page number refers to first page of paper.

- Accretion, 1975, 2580
Advection, 1186
Alaska, 1687
Algorithms, 136, 255, 478, 516
Analytical techniques, 2682
Anemometers, 450, 489, 557
Arctic regions, 1687
Armor units, 1270, 1306, 1334, 1375, 1403, 1417, 1446, 1460, 1538, 1552, 1578, 1620, 1634, 1716, 1730, 1755, 1805, 1819, 2768, 2782, 2796, 3194
Artificial islands, 2768
Assessments, 41
Asymmetry, 396, 637
Atmospheric pressure, 95, 826
Australia, 2241, 2265
- Backwashing, 2360
Bank erosion, 2385
Barges, 1648
Barrier design, 2950
Barrier islands, 783, 3254
Barriers, 1564
Bars, 959, 2101, 2145, 2265
Bars, riverine, 757, 2964
Bathymetry, 597, 1292, 2279, 2416, 2782
Bays, 2047
Beach cusps, 2101
Beach erosion, 95, 570, 1862, 1975, 2010, 2020, 2073, 2173, 2241, 2304, 2360, 2385, 2457, 2471, 2580, 2644, 2710, 2726, 2740, 2782, 2796, 2810, 3063, 3254
Beach nourishment, 783, 1984, 1998, 2020, 2241, 2304, 2394, 2542, 2796, 3183, 3227, 3254
Beaches, 109, 227, 281, 516, 557, 570, 798, 867, 1292, 1702, 2061, 2117, 2159, 2265, 2291, 2443, 2481, 2552, 2566, 2682
Bed load movement, 2332, 2536, 3037
Bed ripples, 661, 2186, 2200
Bed roughness, 450
Bedforms, 2318
Berms, 1730, 2073, 2101, 2304, 3194, 3207, 3222
Blocks, 1606
Boring, 1019
- Boundaries, 2227
Boundary conditions, 1292, 1948
Boundary element method, 840, 1270, 1389, 3140
Boundary layer, 281, 2360
Boundary layer flow, 450, 544, 661, 853, 993
Boundary shear, 2536
Brazil, 3207
Breaking waves, 32, 68, 123, 136, 150, 164, 218, 306, 330, 516, 716, 895, 923, 973, 1019, 1033, 1060, 1362, 1473, 1827, 2145, 2159, 2173
Breakwaters, 136, 164, 306, 1060, 1200, 1270, 1320, 1348, 1362, 1375, 1403, 1473, 1538, 1592, 1620, 1634, 1675, 1702, 1716, 1730, 1755, 1781, 1805, 1827, 1837, 1851, 2020, 2034, 2416, 2603, 2616, 2740, 3194, 3207, 3222, 3239
Bridge foundations, 3268
Bridges, 3268
Building design, 2908
Bulkheads, 1837
Buried pipes, 2508
- Caissons, 1403, 1675, 1827
Channel stabilization, 2922, 2975
Channels, waterways, 2430, 2936, 2975, 3024, 3088, 3126
Characteristics, 82
China, People's Republic of, 82, 2047
Cnoidal waves, 109, 1144
Coastal engineering, 1, 7, 516, 769, 881, 935, 1005, 1513, 1862, 1984, 1998, 2010, 2975, 3112, 3281
Coastal environment, 177, 867, 959, 1088, 1144, 1172, 2047, 2768, 2894, 2908
Coastal management, 7, 41, 1895, 1909, 2589, 2824
Coastal morphology, 1876, 1888, 1948, 1962, 1975, 2589, 2682, 2922, 2950, 2964, 3050, 3171
Coastal processes, 444, 557, 743, 1074, 1876, 1895, 1909, 1935, 1962, 1975, 2061, 2087, 2101, 2117, 2227, 2265, 2332, 2346, 2402, 2443, 2457, 2481, 2522, 2552, 2566, 2589, 2682, 2710, 2810, 3037, 3154

Volume 1, 1-1116 Volume 2, 1117-2172 Volume 3, 2173-3308

- Coastal structures, 371, 743, 757, 923, 1200, 1306, 1375, 1431, 1446, 1460, 1487, 1499, 1524, 1552, 1578, 1592, 1687, 1795, 2457, 2726
- Cohesive sediment, 2984, 3012, 3037
- Computation, 164, 191, 444, 1019, 1060, 1513, 1909, 2255
- Computerized simulation, 1172
- Concrete, 1687, 2768
- Concrete blocks, 1431
- Concrete construction, 1578, 1634, 1755, 1819
- Conferences, 1, 7
- Construction, 1280, 2020, 2950, 3239
- Construction materials, 1648, 3222
- Construction methods, 1648, 1675, 3207
- Contamination, 2894, 3194, 3222
- Control structures, 1060
- Coral reefs, 330
- Coriolis effect, 95
- Critical load, 2671
- Currents, 95, 205, 241, 316, 384, 444, 450, 489, 853, 993, 1074, 1088, 1186, 2131, 2227, 2443, 2495, 2866, 3171
- Cyclones, 358, 2852
- Cylinders, 973, 1280, 1389, 1795
- Cylindrical shells, 1675
- Dam construction, 3050
- Damage, 743, 1446, 1552, 1851, 2416, 2908, 3074
- Damage estimation, 2796
- Damping, 1592
- Data analysis, 345
- Decision making, 1
- Deep water, 623, 1827
- Deltas, 2984
- Design, 136, 597, 923, 1160, 1254, 1320, 1362, 1403, 1417, 1431, 1487, 1524, 1552, 1819, 1827, 1837, 2020, 3102, 3194, 3207, 3239, 3268
- Design criteria, 1634, 3024, 3074
- Design storms, 2304
- Design waves, 18, 647, 1306
- Diffusion, 1186
- Diffusion coefficient, 2998
- Dikes, 895, 1254, 1431, 1487, 1662, 2010, 2087, 2671, 2880, 2998, 3171, 3183
- Dimensions, 959
- Disposal, 2430
- Distribution functions, 18, 345
- Disturbances, 597
- Dolos, 1417, 1805, 1819
- Drag coefficient, 1716, 1769
- Dredge spoil, 1362, 2430, 2824
- Dredging, 2964, 3024, 3088, 3126
- Drift, 3140
- Dunes, 1922, 1984, 2304, 2471
- Dynamic characteristics, 1837
- Dynamic loads, 1755
- Dynamic models, 2265
- Dynamic stability, 1270, 1730
- Dynamic tests, 1755
- Dynamics, 2227, 2346
- Ecology, 2984
- Economics, 2796
- Embankments, 1662, 2754
- Energy dissipation, 123, 1334, 1499, 1620, 2522
- Energy transfer, 123
- Entrainment, 2200
- Environmental effects, 3171
- Environmental impacts, 3024
- Equations of motion, 881, 1513, 3112
- Equilibrium, 2291, 3050, 3063
- Erosion, 935, 1922, 2087, 2998, 3012
- Erosion control, 1662, 2740
- Estimates, 464
- Estuaries, 1962, 2047, 2542, 2866, 2922, 2936, 2950, 2964, 2984, 2998, 3012, 3050, 3154
- Evolution, development, 1876, 1962
- Experimental data, 1242
- Experimentation, 584, 1592
- Extraction procedures, 1998
- Failures, 1755, 2087, 2671
- Failures, investigations, 3222
- Feasibility studies, 1702
- Fences, 2754
- Field investigations, 82, 867, 2047, 2710
- Field tests, 330, 703, 1074, 1702, 2087, 2471, 2644
- Filters, 1524
- Floating bodies, 3140
- Floating structures, 1320, 2740, 2852
- Flood control, 1254, 1862, 1895
- Flood plain insurance, 41
- Flood plain regulation, 2908
- Flooding, 218
- Flow characteristics, 316
- Flow measurement, 489, 503
- Flow profiles, 1922
- Flow visualization, 1033, 2186
- Fluid-structure interaction, 1564
- Flumes, 255, 489, 544, 661, 993, 1046, 1538, 1730, 2536, 2552, 2630

- Forecasting, 986
Foundation construction, 1648
France, 2936, 3088
Frequency analysis, 293, 1102
Friction factor, 420, 637
- Geography, 2589
Geomorphology, 2984
Geotextiles, 1524, 1687
Granular materials, 1524, 2616
Grasses, 1662
Gravity waves, 55, 557, 611
Great Lakes, 2291
Grid systems, 2255
Groins, structures, 783, 2173, 3227, 3254
Groundwater flow, 2644
Gulfs, 986
- Harbors, 597, 1935, 2481, 2894, 3074, 3102, 3154, 3183, 3239
Histograms, 909
History, 1876
Hurricanes, 358
Hydraulic design, 3102
Hydraulic jump, 2880
Hydraulic loading, 1564
Hydraulic models, 267, 371, 1446, 1460, 1538, 2402, 2950, 3207
Hydraulic performance, 1578
Hydraulics, 1033, 1186, 1228, 2880
Hydrodynamics, 68, 123, 241, 1186, 1769, 2213, 2824, 3154
Hydrographic surveys, 3024
Hydrostatics, 1005
- Ice forces, 2768
Image analysis, 1033
Impact, 1473
Implementation, 2241
In situ tests, 2671
Indonesia, 2385
Inertia, 1716, 1769
Information systems, 2589
Inlets, waterways, 2522
Installation, 2852
Instrumentation, 1634
Interactions, 450, 489, 826, 853, 1088, 1200, 1389, 2443, 2696, 3112, 3140
International treaties, 935
Islands, 826, 2010
Italy, 218
- Japan, 18, 623, 769, 1280, 2726, 2754
Jetties, 410
- Kalman filter, 1769
Kinematics, 503, 935, 1513
- Laboratory tests, 255, 420, 503, 661, 1131, 1662, 2471, 2495, 2552, 2668, 2740, 2975
Lagoons, 330, 2880
Land reclamation, 2964
Landfills, 3227
Lasers, 544
Least squares method, 464
Limit design, 358
Littoral currents, 68, 281, 584, 729, 783, 826, 1005, 1118, 1242, 2061, 2173, 2402, 2603
Littoral drift, 783, 2542, 2710, 2880, 3183
Loads, 1606, 1742, 1769
Long waves, 410, 570, 1131, 1144, 1200, 1228, 1270, 1781, 2073
- Maintenance costs, 2010
Mapping, 2279
Marinas, 3239
Marine terminals, 3074, 3207
Mass transport, 544, 2998
Mat foundations, 1687, 2768
Mathematical models, 218, 597, 1060, 1473, 2131, 3126, 3281
Measurement, 584, 909, 1118, 2332, 2668
Methodology, 1592, 2894
Microcomputers, 2159
Mixing, 2346
Mixtures, 2696
Model studies, 2964, 3194
Model tests, 430, 1348, 1606, 1805, 1837, 2782
Model verification, 109, 191, 530, 1564
Modeling, 109, 123, 973, 1131, 1487, 1975, 2213, 2346, 2443, 2566, 2984, 2998
Models, 55, 150, 241, 316, 410, 584, 716, 769, 923, 959, 986, 1922, 1935, 2061, 2087, 2471, 2603
Monitoring, 1564, 3227
Monsoons, 623, 769
Mooring, 3074
Moorings, 1320
Movable bed models, 420, 2372, 2457, 2536, 2566
Mud, 2936, 2975, 2998, 3037
- National Flood Insurance Program, 2908

- Navigation, 2430, 2936, 2975, 3088, 3126
- Nearshore circulation, 150, 241, 267, 316, 444, 729, 783, 826, 1074, 2061, 2241
- Netherlands, 1, 1160, 1254, 1862, 1876, 1888, 1895, 1909, 1935, 1948, 1962, 1984, 1998, 2010, 2984
- New Jersey, 2020
- Nonlinear analysis, 55
- Nonlinear systems, 396
- Nonuniform flow, 281
- North Sea, 1214, 1888, 1948, 2589, 2824, 2838, 3254
- Numerical calculations, 150, 306
- Numerical models, 68, 136, 191, 205, 384, 623, 853, 1088, 1186, 1306, 1320, 1389, 1742, 1795, 2034, 2173, 2186, 2304, 2372, 2430, 2508, 2668, 2824, 2866, 3012, 3024, 3037, 3112, 3140
- Ocean disposal, 2824
- Ocean engineering, 935
- Ocean waves, 82, 384, 410, 503, 557, 623, 703
- Oceanographic surveys, 986
- Offshore structures, 1280
- Oil pipelines, 3171
- Oscillations, 584
- Oscillatory flow, 661, 2186, 2346, 2372, 2495, 2616
- Overtopping, 177, 1348, 1375, 1487
- Overturning tests, 840
- Paddles, 675
- Parameters, 2922
- Peak values, 647
- Performance, 2020, 2768
- Permeability, 1060, 1499, 2616
- Perturbation theory, 478
- Pipelines, 2508
- Planning, 3102
- Plates, 1046, 1228
- Plunging flow, 895, 973
- Policies, 1862
- Pontoons, 2852
- Pore pressure, 1334, 1499
- Porosity, 2616, 2754
- Porous media, 2616
- Porous media flow, 1046
- Ports, 82, 1675, 2975, 2998
- Potential flow, 923
- Predictions, 55, 241, 345, 358, 371, 530, 623, 853, 959, 1446, 1795, 1922, 1935, 1975, 2034, 2145, 2265, 2508, 2603, 3063, 3281
- Pressure distribution, 1606
- Pressure measurement, 1144
- Pressures, 164, 191, 611
- Probabilistic models, 1160
- Probability density functions, 909
- Probability distribution, 371
- Probes, instruments, 2936
- Profile measurement, 2682, 2710
- Profiles, 2566
- Projects, 1984
- Protective structures, 1160, 2810, 3254, 3268
- Prototype tests, 2630
- Prototypes, 2671
- Public opinion, 2394
- Radar, 703, 2279
- Radioactive tracers, 2710
- Random waves, 41, 68, 255, 478, 647, 689, 798, 1102, 1460, 2117
- Reefs, 743, 1375, 1781, 2852
- Reliability analysis, 1403
- Remote sensing, 703
- Repairing, 2416
- Reports, 935
- Research, 729, 935, 1538, 1975, 2471
- Revetments, 1306, 1431, 1524, 1606, 1662, 1837, 2810
- Rheological properties, 2936, 2975
- Rip currents, 729, 959
- Riprap, 2810
- Rock structures, 1306, 1446, 1460
- Roughness, 41
- Rubble-mound breakwaters, 177, 410, 1334, 1417, 1499, 1552, 1578, 1620, 1648, 1805, 1819
- Safety programs, 1254
- Salinity, 2866
- Salt water intrusion, 2866
- Salt water-freshwater interfaces, 2866
- Sand, 1362, 1998, 2087, 2291, 2416
- Sand transport, 1895, 1909, 1948, 1962, 2173, 2213, 2318, 2360, 2495, 2508, 2580, 2668, 2696, 2754, 3154, 3183, 3227
- Sand waves, 2508, 2668
- Scale effect, 973, 1716
- Scale models, 2394, 2457, 3088
- Scour, 2457, 2782, 2950, 3227, 3268
- Scouring, 1795
- Sea floor, 757, 853, 2279, 2508, 2668
- Sea level, 95, 867, 1160, 1862, 1876, 1948, 1962, 2644, 2838, 3063
- Sea state, 345, 358, 464, 478, 647, 675,

- 895, 1851
Sea walls, 1292, 1742, 2241, 2782,
2810
Sediment, 2894
Sediment concentration, 716, 1922,
2047, 2318, 2360, 2630
Sediment control, 2603
Sediment transport, 68, 123, 281, 293,
420, 637, 783, 959, 1074, 1795,
1922, 1935, 2087, 2101, 2131, 2145,
2159, 2186, 2200, 2227, 2255, 2291,
2318, 2332, 2346, 2372, 2402, 2430,
2443, 2481, 2495, 2508, 2522, 2536,
2552, 2603, 2630, 2668, 2682, 2710,
2726, 2824, 2880, 3012, 3037, 3102,
3171
Sedimentation, 2047, 3239
Sedimentology, 2394
Sensitivity analysis, 675, 798
Sensors, 2227, 2279
Shallow water, 267, 293, 637, 812,
895, 1019, 1088, 1200, 2213, 3126
Shear flow, 584, 2696
Shear stress, 637, 993, 2145, 2536
Shear tests, 2696
Shear waves, 729, 1242
Ship motion, 3074, 3088, 3112, 3126
Shoaling, 55, 109, 267, 396, 430, 530,
1102, 2481
Shore protection, 1160, 1431, 1592,
1687, 1702, 1837, 1862, 1895, 1935,
1984, 1998, 2010, 2265, 2385, 2542,
2589, 2603, 2796, 2810, 3254
Shoreline changes, 1292, 1998, 2020,
2034, 2101, 2522, 2566, 2726, 2740,
3281
Silts, 3088
Simulation, 255, 267, 420, 464, 675,
798, 812, 1033, 1270, 1606, 2318,
2443, 2726, 3102
Slope stabilization, 1687, 2768
Slopes, 293, 306, 371, 544, 570, 1060
Social aspects, 7
Solitary wave, 689, 840, 881, 923,
1019, 1033, 1144, 1200, 1270, 1487
Spain, 826, 3154, 3183
Spatial data, 812
Spectral analysis, 32, 703
Speeches, 1
Stability, 1306, 1362, 1375, 1403,
1446, 1552, 1716, 1805, 2922
Standing waves, 1033, 1742
Static tests, 1755
Statistical analysis, 516, 909, 2838
Statistical models, 371, 1851
Statistics, 18, 358, 812
Steady flow, 2495
Steel construction, 2852
Stochastic models, 516
Stochastic processes, 255
Stones, 1837
Storm surges, 1214, 1564, 1895, 1922,
2304, 2950
Storms, 18, 218, 227, 358, 743, 1118,
1702, 1851, 2073, 2332, 2372, 2457,
2580, 2671, 2908, 3222
Stratification, 1186, 2047
Stratified flow, 3024
Strength, 2671
Stress, 1417, 1578, 1819
Structural design, 1634, 1819
Structural response, 1634
Structural stability, 1578, 1578
Structural strength, 1417
Surf beat, 32, 743, 1102, 1131, 1781
Surf zone, 32, 68, 95, 123, 150, 177,
227, 241, 316, 330, 516, 557, 716,
867, 1118, 1348, 2073, 2145, 2402
Surface waves, 55, 293, 396, 503, 611,
757, 840, 1046, 1228, 3012
Surfing, 516
Suspended sediments, 716, 2117,
2131, 2159, 2200, 2227, 2824
Taiwan, 1675
Testing, 1592
Thailand, 986
Theories, 647, 757
Thermal stresses, 1755
Thickness, 1805
Three-dimensional flow, 2255
Three-dimensional models, 267, 444,
1005, 1186, 2131, 2159, 2255, 2402,
2481, 2782
Tidal currents, 909, 1214, 2430, 2964
Tidal power plants, 3050
Tidal waters, 1948, 2522, 2838, 2922,
3063
Tides, 2644, 3050, 3171
Time dependence, 205, 293
Time series analysis, 2838
Time studies, 1102
Topography, 2101, 2117, 2173, 2213,
2279, 2332, 2481
Transducers, 1280
Transformations, 1102
Transport phenomena, 2998
Tsunamis, 1172
Turbulence, 150, 557, 661, 716, 1019
Turbulent boundary layers, 853
Two phase flow, 2346, 2372
Two-dimensional models, 689

- Typhoons, 623, 769
 Undertow, 123, 150, 227, 783, 2061
 Unsteady flow, 993, 2880
 Urban areas, 2394
 Velocity, 191, 227, 503, 557, 909
 Velocity distribution, 661, 2866
 Velocity profile, 281, 450, 993, 2372
 Vertical cylinders, 840, 1769
 Visual perception, 345
 Vortex shedding, 3171
 Vortices, 661, 1019, 1242, 2186, 2200
 Walls, 164
 Waste site cleanup, 2894
 Water depth, 205, 3268
 Water flow, 3063
 Water level fluctuations, 2291, 2838
 Water levels, 826, 1909
 Water quality, 2394
 Water surface, 227, 993, 1144, 1172, 1742
 Water table, 867, 2644
 Water tunnels, 2318
 Water waves, 164, 503, 689, 881, 935, 1389, 1769, 2213, 3140
 Wave action, 41, 191, 205, 895, 1131, 1306, 1730, 1795, 1805, 1819, 1935, 2061, 2073, 2117, 2385, 2542, 2552, 2580, 2630, 2644, 2768, 2908, 3037, 3112, 3194
 Wave attenuation, 330, 420, 1228
 Wave climatology, 986, 1088, 1292, 1888, 2159, 2416, 2542
 Wave crest, 396, 973
 Wave damping, 743, 1046, 1334
 Wave diffraction, 840
 Wave energy, 267, 530, 611, 1118, 1131, 1228, 1242, 1292, 1334, 1375, 1499, 1620, 2522
 Wave equations, 306
 Wave forces, 95, 164, 241, 840, 935, 1005, 1280, 1320, 1334, 1348, 1362, 1389, 1403, 1446, 1473, 1513, 1538, 1606, 1716, 1742, 1781, 1827, 2131, 3126, 3140
 Wave generation, 384, 430, 478, 675, 689, 769, 1172, 1214
 Wave groups, 32, 82, 177, 371, 729, 743, 812, 1131, 1552, 2117
 Wave height, 18, 177, 205, 293, 330, 345, 358, 464, 530, 675, 812, 881, 986, 993, 1102, 1742, 1851, 1888, 2034, 2117, 2145, 2402, 2630
 Wave measurement, 330, 430, 703, 895
 Wave pressure, 1473, 1564, 1620, 1781
 Wave propagation, 32, 306, 316, 384, 410, 420, 530, 544, 611, 689, 703, 798, 812, 881, 1088, 1172, 1214, 1228, 2186, 2213, 3112
 Wave reflection, 109, 136, 306, 570, 757, 923, 1046, 1172, 1460, 1702
 Wave refraction, 109, 205, 384, 530, 1088
 Wave runup, 41, 68, 191, 371, 557, 570, 867, 895, 1200, 1242, 1270, 1662, 2360, 2471
 Wave spectra, 32, 109, 177, 205, 267, 430, 464, 478, 623, 647, 703, 769, 798, 1102, 1320
 Wave velocity, 396, 853, 2200
 Wavelength, 2034
 Waves, 55, 450, 489, 597, 637, 993, 2318, 2332, 2443, 2495
 Weirs, 1487
 Wetlands, 2542
 Wind direction, 1888
 Wind forces, 95, 218, 444, 1074, 1118, 1888, 2385, 2754
 Wind pressure, 826
 Wind tunnel test, 2754
 Wind velocity, 986
 Wind waves, 32, 218, 611, 1214

AUTHOR INDEX

Page number refers to first page of paper.

- Ahrens, John P., 1837
Alejo, Miguel, 826
Allsop, N. W. H., 1446, 1460
Alonso, Ignacio, 2580
Al-Salem, Abdullah, 2318
Alvarez, Ricardo, 2580
Anastasiou, K., 973
Andrassy, Christopher J., 41
Anglin, C. D., 1634
Anton, Jeffrey P., 757
Araújo, Luiz C., 3171
Asano, Toshiyuki, 2372
- Bailard, James A., 1702
Bakker, K. J., 1524
Bakker, W. T., 1935, 2360
Bakker, Willem T., 2696
Bandeira, Jefferson V., 3171
Basco, David R., 1292
Battjes, J. A., 32, 1975
Bellessort, Bernard, 2394
Bertotti, L., 218
Bezuijen, A., 1431, 1606
Bijker, Romke, 2508
Bjordal, S., 3074
Blázquez, Rafael, 345
Blondeaux, Paolo, 2186
Boczar-Karakiewicz, B., 2213, 2265
Bodge, Kevin R., 2796
Booij, N., 530
Borgman, Leon E., 255
Bosman, D. E., 3239
Bowen, Anthony J., 2061, 2227
Bowers, E. C., 3126
Bradbury, A. P., 1446
Breteler, M. Klein, 1431, 1524
Breteler, Mark Klein, 191
Briand, Marie-Hélène G., 2159
Briggs, Michael J., 267
Brorsen, Michael, 3140
Brossard, C., 3088
Bundgaard, Henrik I., 3140
Burcharth, H. F., 1417
Burcharth, Hans F., 1819
Burger, A. M., 1431
Bürger, W. W., 1578
- Caldas, Felipe, 3194
Canestrelli, P., 218
Cavaleri, L., 218
Chandler, Bruce D., 358
Chang, J. J., 1172
Chapalain, G., 2213
- Charulakana, Supot, 986
Chen, W. J., 637
Chiaia, Giancarlo, 1102
Chian, Chimin, 1270
Collado, F., 316
Cooker, M. J., 164, 1473
Costa, Rui G., 2047
Cox, Daniel T., 1306
Craeymeersch, Johan A., 2984
Crapps, David K., 3268
Crowley, J. B., 293, 1074
- Daemrich, K. F., 430
Dally, William R., 516
Dalrymple, Robert A., 675, 729
Damiani, Leonardo, 1102
Davis, A. B., 3227
de Jong, H., 2922
de Kok, J. M., 2824
De Rouck, J., 1755
de Vriend, H. J., 1005
de Vriend, Huib J., 1962
de Vroeg, J. H., 1935
Dean, Robert G., 2145, 2522
Dean, William L., 3268
Dedeyne, R., 1755
Degrieck, J., 1755
Deguchi, Ichiro, 2603
Deigaard, Rolf, 959
Dekker, J., 530
Delouis, A., 3088
den Adel, H., 1524, 1606
den Adel, J. D., 530
Dette, Hans H., 2566
DeVries, Jack, 1702
Diez, J. J., 3154
Dijkman, M. J., 1935
Dijkzeul, Johan C. M., 2255
do Valle, Antonio B., 3171
Dodd, N., 584
Drapeau, G., 2710
- Edge, B. L., 3268
Ekebjærge, Lars C., 1186
Elgar, Steve, 55
Endo, Taiji, 1403
Escobar, V. A., 3154
Eysink, W. D., 1948
- Farrell, Stewart C., 2020
Fassardi, Claudio, 1552
Feral, Alain, 2936
Fernandes, J. L. M., 689

- Fernández, José, 3183
 Fisher, J. S., 2471
 Fleming, C. A., 2589
 Flick, Reinhard E., 557
 Fournier, Charles P., 3194
 Fowler, Jimmy E., 2457
 Fowler, Rachel E., 729
 Franken, A. F., 530
 Fredsøe, Jørgen, 959
 Freilich, M. H., 55
 Funke, E. R., 464
- Gadd, P. E., 2768
 Gadd, Peter E., 1687
 Galichon, P., 3088
 Galichon, Pascal, 2936
 George, Ronald A., 557
 Gerritsen, F., 2922
 Gerritsen, Franciscus, 1270
 Giménez, Marcos H., 255
 Goda, Yoshimi, 18
 Gómez Pina, Gregorio, 1592, 3183
 González, Angel, 345
 González Madrigal, B., 1348
 Gordon, A. D., 2880
 Götschenberg, A., 430
 Gourlay, M. R., 330
 Granboulan, J., 3088
 Granboulan, Jérôme, 2936
 Grassa, José María, 798
 Green, Malcolm O., 2200
 Greenwood, Brian, 227, 2061, 2227
 Griggs, Gary B., 2810
 Grilli, Stéphan T., 1200
 Grosche, Sven, 895
 Grummitt, Alan Albert Campbell, 2852
 Grüne, Joachim, 895
 Gudmestad, Ove T., 935
 Guifen, Wang, 2430
 Guza, R. T., 55, 410, 611
 Guza, Robert T., 1702
- Haidekker, Mark, 895
 Hall, Kevin R., 1620, 1730, 2616
 Hallermeier, Robert J., 41
 Hallie, Frank P., 1998, 2984
 Hamerlynck, Olivier, 2984
 Hamm, Luc, 2975
 Hansen, Niels-Erik Ottesen, 3024
 Hanson, Hans, 2034, 2173
 Hara, Masanori, 923
 Hardy, T. A., 330
 Harkins, Gordon S., 675
 Harper, Bruce A., 358
 Hatada, Yoshio, 205, 623
- Hattori, Masataro, 396
 Hay, Alex E., 2227
 Hayashi, Katsuyuki, 177
 Hazen, David G., 2061, 2227
 Headland, John R., 1320
 Herbers, T. H. C., 611
 Herbich, John B., 2894
 Hino, Mikio, 743, 1781
 Hirakuchi, Hiromaru, 703
 Hirasawa, Mitsunari, 1280
 Holman, Rob, 1118, 1242
 Houthuijsen, L. H., 384
 Holtzhausen, A. H., 1805
 Hoozemans, Frank M. J., 1888
 Horikawa, Kiyoshi, 661, 2754
 Hotta, Shintaro, 2754
 Hou, Ho-Shong, 1827
 Houston, Samuel H., 2145
 Howd, Peter, 1242
 Howd, Peter A., 1118
 Howell, Gary L., 1417, 1819
 Hudspeth, R. T., 1513
 Hudspeth, Robert T., 255, 1552
 Hughes, Steven A., 2457
 Hunter-Blair, A., 2589
 Hwung, H. H., 544
- Ijima, Takeshi, 1228
 Ikeda, Syunsuke, 661
 Ikeno, Masaaki, 703
 Irie, Isao, 2998
 Isobe, Masahiko, 123, 136, 647, 1060, 2495
 Ito, Kazunori, 812
 Iwata, Koichiro, 2740
 Izumiya, Takashi, 306
- Jackson, L. A., 2241, 2265
 Jasińska, Ewa, 2866
 Jeng, Dong-Sheng, 1742
 Jensen, John, 2671
 Jensen, Jürgen, 2838
 Jensen, Ole Juul, 1538, 3074, 3102, 3222
 Jones, J. Sterling, 3268
 Jongeling, Tom, 1564
 Jonsson, Ivar G., 1131, 1389
 Juhl, Jørgen, 1538
- Kadono, Takashi, 1280
 Kai, Yen, 2964
 Kajima, Ryoichi, 1716
 Kamphuis, J. W., 2710
 Kamphuis, J. William, 2159, 2402
 Kang, Hong-Yoon, 371
 Kao, Joseph S., 1730

- Kapp, J. F., 3239
Kardana, 2385
Katoh, Kazumasa, 95, 2073
Katopodi, Irene, 2131
Katsuragawa, Tetsuyuki, 396
Kawata, Yoshiaki, 281, 2332
Kim, Ga-Ya, 2603
Kirby, James T., 109, 757, 1702
Kitou, N., 1005
Klatter, Leo, 1564, 2950
Klomp, Wim H. G., 2696
Kloos, M., 3239
Klopman, Gert, 478
Kluger, J. W. J., 2416
Kobayashi, Nobuhisa, 1306
Kobune, Koji, 18
Kojima, Haruyuki, 1228
Komaguchi, Tomoaki, 769
Komar, Paul, 1242
Komar, Paul D., 1118
Kondo, Hideo, 3063
Kondo, Kosuke, 2481
Konter, Jan, 1564, 2950
Kraus, Nicholas C., 2034, 2173
Kriebel, David L., 2304
Kubota, Susumu, 570
Kuik, Ton (A) J., 1862
Kunz, H., 3254
Kuo, C. T., 637
Kuo, Shih-Duenn, 1675
Kyriacou, Andreas G., 993
- Langerak, A., 2922
Larson, Magnus, 2173
Latham, J. -P., 1446
Laubscher, W. I., 3227
Laustrup, Chr., 2671
Lean, G. H., 3126
Lee, J. J., 1172
Leendertse, Jan J., 444, 2255
Leidersdorf, C. B., 2768
Leidersdorf, Craig B., 1687
Leitão, J. M., 689
Lemos, M., 316
Lin, C., 544
Lin, D. T., 1046
Lionello, P., 218
Liu, Shiao-Kung, 444
Liu, Shu-xue, 82
Long, B., 2710
Losada, Miguel A., 675
Louisse, Cees (C) J., 1862
Louisse, Cees J., 1998
Louters, Teunis, 2984
Lundgren, J., 3074
- McDougal, W. G., 1417
McDougal, William G., 1687
McLaren, P., 2589
Madsen, H. Toxvig, 2671
Madsen, Ole S., 420
Madsen, Per A., 3112
Manoha, Bruno, 2542
Mansard, E. P. D., 464
Martinez, Javier, 345
Martínez, Jesús, 2580
Mase, Hajime, 177
Mathisen, Paul P., 420
Matsumi, Yoshiharu, 1648
Medina, Josep R., 255, 1552
Mehta, Ashish J., 2047
Melo, Eloi, 410
Migniot, Claude, 2975
Mitsunobu, Norihiko, 2668
Mizuguchi, Masaru, 570
Mizumura, Kazumasa, 1403
Mizuno, Yuzo, 1280, 1362
Møller, Jacob Steen, 3024
Monadier, P., 3088
Moutzouris, C. I., 2552
Mügge, Hans-Eckart, 2838
Mulder, Herman P. J., 3012
Mulder, Jan P. M., 2984
Muñoz, Angel, 3183
Murakami, Kazuo, 2998
Murakami, Noritaka, 2740
Murray, Malcolm, 3207
- Nadaoka, Kazuo, 2346
Nagai, Yutaka, 1280
Nairn, Robert B., 68
Nakamura, Kazuo, 2117
Nakaza, Eizo, 743, 1781
Nelson, R. C., 330
Nicholson, John, 3050
Nielsen, Peter, 867
Niemeyer, H. D., 530, 783, 2360
Nishi, Ryuichiro, 2117
Nishimura, Hitoshi, 1033
Nnadi, Fidelia N., 2536
Nodani, Hitoshi, 2481
Nosek, Kevin B., 41
- Obana, E., 716
Ochi, Michel K., 909
O'Connor, Brian, 3050
Ohnaka, Susumu, 2443
Ohyama, Takumi, 840
Okayasu, Akio, 123
Okuno, Masakazu, 3037
Olivares Prud'Homme, J., 1348
Oltman-Shay, J., 584
Oltman-Shay, Joan, 1118, 1242

- Osborne, Philip D., 227, 2227
 Ostrowski, R., 2101
 Oumeraci, H., 1334, 1578
 Overton, M. F., 2471
 Özhan, Erdal, 1487
- Partensky, H. W., 1334, 1578
 Peregrine, D. H., 164, 1019, 1473
 Petrillo, Antonio, 1102
 Pfaff, W. M., 3227
 Philipse, Leo, 1662
 Pilarczyk, K. W., 1431
 Pilarczyk, Krystian W., 1375
 Pluijm, Marco, 2010
 Postma, Renske, 2984
 Poulsen, L., 2671
 Prins, J. E., 7
 Prüser, H. -H., 1088
 Pruszek, Z., 2101
 Putrevu, Uday, 241
- Raichlen, Fredric, 1144
 Ramsden, Jerald D., 1144
 Rasmussen, Erland B., 1186
 Rayner, Ralph, 3050
 Refaat, Hossam El-din A. A., 281
 Retief, G. de F., 3239
 Rhee, Joon P., 1819
 Ribberink, Jan S., 1998, 2131, 2318
 Ridge, A. B., 3239
 Rivero, F., 316
 Roelse, Piet, 1984
 Roelvink, Dano (J) A., 1962
 Roelvink, J. A., 1909, 1998
 Roelvink, J. A. (Dano), 68
 Rogers, Spencer M., Jr., 2908
 Rojanakamthorn, Somchai, 1060
 Romańczyk, W., 1769
 Rosengaus, M. Michel, 420
 Rouch, Franck, 2394
 Ryu, Cheong-Ro, 371
- Saito, Eiichi, 1795
 Sakai, T., 716
 Sakakiyama, Tsutomu, 1716
 Sánchez-Arcilla, A., 316
 Sánchez-Carratalá, Carlos R., 255
 Sand, Stig E., 3102
 Sato, Michio, 2117, 2644
 Sato, Shinji, 1795, 2668, 3037
 Sawaragi, Toru, 2603
 Sayao, Otavio J., 3194, 3207
 Schäffer, Hemming A., 1131
 Schönfeld, Wolfgang, 2838
 Schoonees, J. S., 2416, 3227
 Scott, Katherine, 2810
- Scott, R. D., 1634
 Seiffert, Jan Willem, 1662
 Shibayama, Tomoya, 1795, 3037
 Shih, Robert W. K., 1499
 Shimizu, Takuzo, 2481
 Shimoda, Naokatsu, 2740
 Shiraishi, Naofumi, 769, 1403
 Silvester, Richard, 2726
 Simons, Richard R., 993
 Skjelbreia, James E., 503
 Skourup, Jesper, 1389
 Sleath, J. F. A., 450
 Smallman, Jane V., 597
 Smith, Gregory M., 2616
 Smith, Jane M., 267
 Sobey, Rodney J., 358
 Sobierajski, E., 1769
 Son, Huynh-Thanh, 853
 Sørensen, Ole R., 3112
 Sørensen, Torben, 3222
 Southgate, Howard N., 68
 Spanhoff, R., 2824
 Sparboom, Uwe, 895
 Spencer, J. M. A., 3126
 Staub, Carsten, 2508
 Steetzel, Henk J., 1922
 Stive, M. J. F., 1909
 Stive, Marcel J. F., 1876, 1962
 Stockberger, M. Todd, 2291
 Stolk, A., 1895
 Stone, A. L., 2471
 Struik, P., 1254
 Suriamihardja, Dadang Ahmad, 150
 Svendsen, Ib A., 241, 1200
 Swan, Christopher, 489
 Swart, D. H., 293, 1074, 3227
 Syamsudin, 2385
- Tada, Y., 716
 Taerwe, L., 1755
 Tait, James F., 2810
 Takewaka, Satoshi, 1033
 Takezawa, Mitsuo, 570
 Tanaka, Mitsuhiro, 881
 Teisson, Charles, 1851, 2542
 Tejedor, Begonia, 826
 Tejedor, Luis, 826
 Teles da Silva, A. F., 1019
 Temperville, André, 853
 Terwindt, J. H. J., 1975
 Thomsen, J., 3074
 Thornton, E. B., 584
 Tokikawa, Kazuo, 1280
 Tolman, H. L., 384
 Tolman, Hendrik L., 1214
 Tomlinson, R. B., 2241

- Tørum, Alf, 503, 935
 Toue, Takao, 2566, 2782
 Toumazis, A. D., 973
 Townend, I. H., 2589
 Tozer, Nigel P., 597
 Tsai, Ching-Piao, 1742
 Tsuchiya, Yoshito, 150, 281, 769,
 2332, 2726
 Tsukayama, S., 743, 1781
 Tsuruya, Hiroichi, 2998
 Tuah, Hang, 255
 Turcke, D. J., 1634
 Twu, S. W., 1046
- Udink, Connie, 3012
 Ukai, Akiyuki, 812
 Uliczka, Klemens, 2630
 Umezawa, Nobutoshi, 1362
- Valdés Fernández de Alarcón, J. M.,
 1592
 Vallianos, Limberios, 1320
 van Alphen, Jos S. L. J., 1998
 Van Beurden, I. J. C. A., 1160
 Van Damme, L., 1755
 van de Graaff, Jan, 2682
 van der Burg, G., 2279
 van der Meer, Jentsje W., 191, 1375
 van Halsema, D., 2279
 van Heuvel, Tj., 2824
 van Kesteren, Walther G. M., 2696
 van Leeuwen, P. J., 32
 Van Leeuwen, Peter Jan, 478
 van Vessem, P., 1895
 Verhagen, H. J., 2087
 Vested, Hans Jacob, 1186
 Viggosson, G., 3074
 Viguier, Jacques, 2936
 Vincent, Christopher E., 2200
 Visser, P. J., 2087
 Vittori, Giovanna, 2186
 Vogel, J. A., 530
 Vogelzang, J., 2279
- von Amsberg, Claus, 1
 Vrijling, J. K., 1160, 2087
 Vrouwenvelder, A. W. C. M., 1254
- Walker, James R., 1144
 Wang, Hsiang, 2566, 2782
 Watanabe, Akira, 123, 136, 1060,
 2443, 2495
 Weesakul, Sutat, 986
 Weggel, J. Richard, 2020
 Wensink, G. J., 2279
 Wiersma, Hans (J.), 1876
 Wilde, P., 1769
 Wilson, Kenneth C., 2536
 Wind, H. G., 3281
 Work, Paul A., 2522
 Wouters, J., 1606
 Wurjanto, Andojo, 1306
- Yagi, Hiroshi, 2346
 Yalçmer, Ahmet Cevdet, 1487
 Yamaguchi, Masataka, 205, 623
 Yamamoto, Masato, 1403
 Yamashita, Takao, 150, 177, 2726
 Yanagishima, Shin-ichi, 95, 2073
 Yanase, Tomoyuki, 1362
 Yano, Kenji, 1362
 Yasuda, Takashi, 812, 923
 Yixin, Yan, 2964
 Yoshida, Akinori, 1228
 Yoshioka, Hiroshi, 2332
 Young, I. R., 330
 Yu, Xiping, 136
 Yu, Yu-xiu, 82
 Yu, Z., 2360
- Zeidler, R. B., 2101
 Zhou, Liu, 1417
 Zielke, W., 1088
 Zitman, Tjerk J., 1876
 Zude, Cao, 2430
 Zwamborn, J. A., 1805, 2416
 Zyserman, Julio, 959